Actinides: Inorganic & Coordination Chemistry

D. Webster Keogh[1,2]

[1] *Applied Marine Technology, Inc., Virginia Beach, VA, USA*
[2] *Glenn T. Seaborg Institute for Transactinium Science, Los Alamos, NM, USA*

Based in part on the article Actinides: Inorganic & Coordination Chemistry by Grigorii L. Soloveichik which appeared in the Encyclopedia of Inorganic Chemistry, First Edition.

1 History 1
2 Uses 3
3 Overview of General Trends 6
4 Structure and Bonding with f Orbitals 7
5 Electrochemical Properties 10
6 Characterization of Actinide Complexes 12
7 Aqueous Coordination Complexes 13
8 Nonaqueous Coordination Complexes 17
9 Solid-state Materials 21
10 Health and Safety Factors 29
11 References 29

1 HISTORY

1.1 Definition

The series of 14 elements from thorium (atomic number 90) through lawrencium (atomic number 103) are commonly referred to as the actinides. In the current periodic table, the f-block elements, actinides (5f) and lanthanides (4f) are separated from the other elements. This modern placement as well as their name is attributed to Prof. Glenn T. Seaborg, who in the 1930s proposed the actinide theory. As a result of this concept, the actinides were removed from their original placement in the Hubbard Periodic Chart of the Elements and joined in a new period with their rare earth analogs, the lanthanides. This arrangement allowed for the transactinide elements ($Z > 103$) to be properly placed within the d-block elements. While other machinations of the periodic table have been derived, for example, three dimensional with the f-block extending behind the main table, there remains one fundamental classification issue. The debate revolves around which element starts and ends the actinides. Traditionally, actinium has been considered a group III element and thorium, the first f-block; however, it has been postulated that lawrencium should occupy the position as the first group III element. This has led to a number of different graphical representations; however, the chemistry tends to be such that all 15 elements, actinium through lawrencium, may be considered and discussed together, as will be the case in this chapter.

1.2 Discovery and Production

The actinides are all radioactive elements. Actinium, thorium, protactinium, and uranium are the only four actinides that have been found in the environment; the others are artificial, being produced through various nuclear reactions. It should be noted that at the creation of the universe some amount of ^{244}Pu could have been formed; however, with an 80 million year half-life, it would have fully decayed during the past 10 billion years.

Uranium was the first actinide element to be identified. In 1789, M. H. Klaproth discovered the presence of a new element in a sample of pitchblende (impure, mineralized form of UO_2). Klaproth named the element uranite after the recently discovered planet Uranus. Nearly 100 years later, Becquerel made the initial discovery of the radioactive behavior of uranium through experiments with uranium minerals and photographic plates.

Thorium was discovered in 1828 by J. J. Berzelius in a Norwegian mineral. As a result of its Norwegian legacy, thorium was named after Thor, a mythological Scandinavian god. In addition to having a natural long-lived isotope, thorium is constantly produced in nature through the decay of ^{235}U and ^{238}U.

The earliest discovery of actinium is attributed to A. Debierne in 1899, with F. Giesel also identifying and isolating the element in 1902. The name actinium is derived from the Greek word for ray, ‘aktinos’, which acknowledges the radioactive behavior of the element.

Protactinium was the last of the naturally occurring actinides to be identified. The original name for the element, brevium (latin for ‘brief’), was suggested by K. Fajans and O. H. Göhring, who first identified the radioactive element in 1913. However, after ^{231}Pa was isolated by groups in Germany (O. Hahn and L. Meitner) and the United Kingdom (F. Soddy and J. Cranston), it was ultimately named after the Greek word ‘protos’, meaning first. It is the rarest and most expensive of the naturally occurring actinide elements.

As previously stated, the remainder of the actinides are artificial, produced either through neutron irradiation or heavy-ion bombardment followed by various nuclear decay paths. Table 1 provides the details of the original synthesis, including date, discovering group, and nuclear process.

1.3 Radioactivity

All of the actinide elements have unstable nuclei and therefore are radioactive. The types of radiation that can be encountered are alpha, beta, neutron, and gamma. This ionizing radiation provides both advantages and disadvantages when studying the chemistry of the actinides.

VISIT…

LANZAROTE
Caliente.COM

Table 1 Identification and synthesis of the actinide elements

Element	Date	Discovering group(s)	Synthesis	Available quantities
Actinium (89) Ac derived from Greek word for ray (*akinos*)	1899	A. Debierne	Naturally occurring	kg
Thorium (90) Th named after Thor, mythological Norse god	1828	J. J. Berzelius	Naturally occurring	kg
Protactinium (91) Pa derived from Greek word for first (*protos*)	1913	K. Fajans, O. Gorhing O. Hanh, L. Meitner F. Soddy, J. Cranston	Naturally occurring	kg
Uranium (92) U named after the planet uranus	1789	M. H. Klaproth	Naturally occurring	kg
Neptunium (93) Np named after the planet neptune	1940	E. M. McMillian, P. H. Abelson	Bombardment of $^{238}_{92}$U with $^{1}_{0}$n	kg
Plutonium (94) Pu named after the planet pluto	1940	G. T. Seaborg, E. M. McMillian, A. C. Wahl, J. Kennedy	Bombardment of $^{238}_{92}$U with $^{2}_{1}$H	kg
Americium (95) Am named after America	1944	G. T. Seaborg, R. A. James, L. O. Morgan	Bombardment of $^{239}_{94}$Pu with $^{1}_{0}$n	kg
Curium (96) Cm named after P. and M. Curie	1944	G. T. Seaborg, R. A. James, L. O. Morgan, A. Ghiorso	Bombardment of $^{239}_{94}$Pu with $^{4}_{2}$He	g
Berkelium (97) Bk named after University of California, Berkeley	1949	S. G. Thompson, A. Ghiorso, G. T. Seaborg	Bombardment of $^{241}_{95}$Am with $^{4}_{2}$He	mg
Californium (98) Cf named after the State and University of California	1950	S. G. Thompson, K. Street, A. Ghiorso, G. T. Seaborg	Bombardment of $^{242}_{96}$Cm with $^{4}_{2}$He	µg
Einsteinium (99) Es named after A. Einstein	1952	Argonne Nat'l Lab, Los Alamos Nat'l Lab, University of California	Multiple neutron capture by $^{235}_{92}$U in a thermonuclear explosion	µg
Fermium (100) Fm named after E. Fermi	1953	Argonne Nat'l Lab, Los Alamos Nat'l Lab, University of California	Multiple neutron capture by $^{235}_{92}$U in a thermonuclear explosion	µg
Mendelevium (101) Md named after D. Mendeleev	1955	A. Ghiorso, B. G. Harvey, G. R. Choppin, S. G. Thompson, G. T. Seaborg.	Bombardment of $^{253}_{99}$Es with $^{4}_{2}$He	atoms
Nobelium (102) No named after A. Nobel	1957–1963	A. Ghiorso, T. Sikkeland, J. R. Walton, G. T. Seaborg	Bombardment of $^{243}_{95}$Am with $^{15}_{7}$He	atoms
Lawrencium (103) Lr named after E. Lawrence	1961–1965	A. Ghiorso, T. Sikkeland, A. E. Larsh, R. M. Latimer	Bombardment of $^{249-252}_{98}$Cf with $^{10}_{5}$B and $^{11}_{5}$B or $^{243}_{95}$Am with $^{18}_{8}$O	atoms

One of the most common topics asked of those who work with the actinides relates to handling procedures. The radioactive nature of these elements does require the use of special facilities, processes, and precautions. However, working with radioactive elements in subcritical quantities is as safe, if not safer, than handling many of the toxic chemicals found in a typical synthetic laboratory. The primary advantage in handling radioactive material is the ease with which these elements can be detected. Unlike other toxic chemicals, for example, lead, thallium, arsenic, and so on, a simple survey (seconds) with a radiation detector will show if containment of the material has been lost, where it is, and approximately how much is present. With appropriate monitoring, virtually no uptake of radioactive material occurs, and if any personnel contamination does occur, it is quickly detected and treated. It is interesting to note that with proper planning and limiting the quantity of material that is handled in an experiment, the overall annual radiation exposure for people working in a synthetic or analytical radiological laboratory is less than that found for aircraft crew. In order to fully mitigate the risks of handling radioactive material and maintain a minimum radiation fields, it is important to have an understanding of the nuclear processes that are typically involved or could occur.

An example of a common situation that leads to greater radiation exposure levels than would be expected occurs with some uranium compounds. Depleted uranium ^{238}U is an α-emitting isotope with an extremely long half-life, 4 billion years. As a result of this long half-life, ^{238}U is generally not considered to present a significant radiation hazard. However, uranium fluorides, a typical synthetic starting material, can undergo an αn reaction in which a neutron is released from the fluorine nucleus upon reaction with the uranium-emitted α-particle.

The interaction of radiation with matter can have profound effects. Whether in solid, solution, or gaseous states, radioactivity can impact the environment and therefore change the molecular speciation of the actinides. To put this into perspective, three examples are discussed below: plutonium metal, americium crystals, and an aqueous solution of plutonium.

The most commonly used isotope of plutonium is ^{239}Pu, which has a half-life of 2.41×10^4 years. When the ^{239}Pu atom decays, an α-particle with an energy of 5 MeV and an ^{235}U atom with an energy of 86 keV are emitted. For Pu metal, this emitted α-particle or He nucleus travels approximately 10 µm, while the heavier α-recoil atom, ^{235}U, travels 12 nm. As these fragments travel through the metallic structure, Pu atoms are displaced off their lattice positions, forming Frenkel Pairs. For each disintegration, approximately 2600 Frenkel Pairs are formed, and over the course of 20 years, every atom in a piece of Pu metal has switched positions. This property becomes critical when trying to predict the long-term behavior of Pu materials.

While metallic structures can do a significant degree of self-annealing, single crystals of molecular complexes can suffer irreversible damage in a relatively short time. The best example of this can be found in crystals of Am compounds. ^{241}Am has a half-life of 432.7 years. When a single crystal containing this highly radioactive material is isolated and analyzed by X-ray analysis, the intensity of the diffraction from the crystal has been observed to decrease with time, presumably as the crystal lattice is damaged. In the extreme, a visible change can occur where an originally clear crystal can become opaque in less than a day. These issues can partially be alleviated by using ^{243}Am, which has a half-life of 7.38×10^3 years. However, the radiation clearly provides a certain level of difficulty in obtaining crystal structures of molecular Am compounds.

In aqueous solutions of ^{239}Pu, the emission of α-particles has an entirely different effect. Scheme 1 shows the reactions that can occur in acidic solutions of Pu. The highly energetic α-particle causes the radiolysis of water, producing H and OH radicals as well as hydrogen peroxide. In acidic conditions, these species reduce Pu^{4+} and $PuO_2{}^{2+}$ ions to give Pu^{3+} and $PuO_2{}^{+}$, respectively. The radiolysis along with the disproportionation and reproportionation reactions shown in Scheme 2 results in oxidation state changes for ^{239}Pu solutions. An example of this instability is represented by an acidic solution of $PuO_2{}^{2+}$, which degrades by being reduced to Pu^{4+} at a rate of approximately 1.5% per day.

The effect of radiation on actinide containing materials and solutions can be altered by careful selection of the isotopes. For uranium, plutonium, americium, and curium, there are a number of different isotopes with varying half-lifes that can be used. In Table 2, the commonly available isotopes of the light actinides are listed along with the production methods and decay mechanisms. In the case of the plutonium example given above, by using the ^{242}Pu isotope, which has a half-life an order of magnitude greater than ^{239}Pu, solutions that show much lower radiation effects, for example longer oxidation state stability, can be made.

$$2Pu^{4+} + 2H_2O \rightleftharpoons Pu^{3+} + PuO_2{}^{+} + H^{+}$$
$$Pu^{4+} + PuO_2{}^{+} \rightleftharpoons Pu^{3+} + PuO_2{}^{2+}$$
$$2PuO_2{}^{+} + H^{+} \rightleftharpoons Pu^{4+} + PuO_2{}^{2+} + 2H_2O$$

Scheme 1

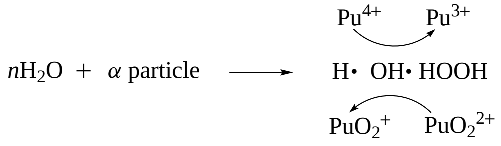

Scheme 2

2 USES

This section is not intended to be an inclusive list of the uses of the actinides. The uses highlighted were selected on the basis of how widespread the use is or where inorganic and/or coordination chemistry of the actinides play a central role.

2.1 Nuclear Fuel Cycle

There are more than 400 operating nuclear reactors throughout the world. These reactors supply nearly 17% of the world's total electricity production capacity. The dependence on nuclear power varies significantly from country to country with some like Lithuania and France, which derive approximately 80% of their electricity from nuclear power to the United States, which while having the largest number of reactors at 104, only pulls 20% of its electricity from nuclear sources.

In order to address the needs for nuclear fuel, many countries have gone to a closed fuel cycle, which entails multiple steps, including mining, conversion, enrichment, fuel fabrication, fuel burning, spent fuel storage, reprocessing, stabilization, and disposal. Owing to the many transformations and separations required during these steps, inorganic coordination chemistry plays vital roles throughout the entire nuclear fuel cycle. As such, the fuel cycle is a prime example of the juncture of fundamental, applied, and environmental actinide chemistry.

Table 2 Half-lifes, mode of production, and decay mechanisms for the most widely used isotopes of the light actinides

Element	Isotope	Half-life (year)	Route of production	Decay
89 Ac	227	21.8	Natural	β
90 Th	232	1.40×10^{10}	Natural	α
91 Pa	231	3.25×10^{4}	Natural	α
92 U	235	7.04×10^{8}	Natural	α
	238	4.47×10^{9}	Natural	α
93 Np	237	2.14×10^{6}	${}^{235}_{92}\mathrm{U} \xrightarrow{{}^{1}_{0}\mathrm{n}} {}^{236}_{92}\mathrm{U} \xrightarrow{{}^{1}_{0}\mathrm{n}} {}^{237}_{92}\mathrm{U} \longrightarrow {}^{237}_{93}\mathrm{Np} + \beta^-$	α
94 Pu	238	86.4	${}^{237}_{93}\mathrm{Np} \xrightarrow{{}^{1}_{0}\mathrm{n}} {}^{238}_{93}\mathrm{Np} \xrightarrow{{}^{1}_{0}\mathrm{n}} {}^{238}_{94}\mathrm{Pu} + \beta^-$	α
	239	2.41×10^{4}	${}^{238}_{92}\mathrm{U} \xrightarrow{{}^{1}_{0}\mathrm{n}} {}^{239}_{92}\mathrm{U} \xrightarrow{{}^{1}_{0}\mathrm{n}} {}^{239}_{93}\mathrm{Np} + \beta^- \longrightarrow {}^{239}_{94}\mathrm{Pu} + \beta^-$	α
	242	3.76×10^{5}	${}^{239}_{94}\mathrm{Pu} \xrightarrow{3{}^{1}_{0}\mathrm{n}} {}^{242}_{94}\mathrm{Pu}$	α
	244	8.26×10^{7}	${}^{242}_{94}\mathrm{Pu} \xrightarrow{2{}^{1}_{0}\mathrm{n}} {}^{244}_{94}\mathrm{Pu}$	α
95 Am	241	432.7	${}^{239}_{94}\mathrm{Pu} \xrightarrow{2{}^{1}_{0}\mathrm{n}} {}^{241}_{94}\mathrm{Pu} \xrightarrow{{}^{1}_{0}\mathrm{n}} {}^{241}_{95}\mathrm{Am} + \beta^-$	α
	243	7.38×10^{3}	${}^{241}_{95}\mathrm{Am} \xrightarrow{2{}^{1}_{0}\mathrm{n}} {}^{243}_{95}\mathrm{Am}$	α
96 Cm	248	3.40×10^{5}		α

Uranium ore is typically mined or leached *in situ*. For the mined ore, the raw material is milled to produce a high surface area slurry, which is then treated with H_2SO_4. The sulfuric acid oxidizes the uranium to the soluble hexavalent state. The addition of base to the solution precipitates an oxide of uranium known as 'yellowcake', U_3O_8. A similar process is used for the in situ leaching of uranium ore except that the initial treatment is performed on bores with a slightly acidic and high oxygenated aqueous solution that is raised to the surface and allowed to go through an extraction process to remove the uranium.

No matter which mining process is used, the final U_3O_8 is converted to UF_6 through a multistep process that takes the uranium through multiple species and oxidation states. In the first step of the conversion process, the uranium is purified by dissolving the yellowcake in nitric acid to produce the soluble uranyl ion, $UO_2{}^{2+}$, and purifying the aqueous stream through a solvent extraction process. The purified uranyl nitrate, $UO_2(NO_3)_2{\cdot}6H_2O$, is heated to produce uranium trioxide, UO_3. The conversion of UO_3 to UF_6 is not an efficient process, so the oxide is reduced at high temperatures by H_2. The resulting UO_2 is treated with HF to give UF_4, commonly known as 'green salt'. A reaction between UF_4 and gaseous F_2 is the final step in the conversion process and yields nearly quantitatively gaseous UF_6.

The purpose of going through the entire conversion process is to obtain a uranium compound that can be run through a separations process to produce a product that is enriched in ^{235}U. Natural uranium is about 0.7% ^{235}U; however, electricity producing light water nuclear reactors require 3 to 5% ^{235}U. The gaseous UF_6 allows for multiple enrichment techniques to be used, including gaseous diffusion, gaseous centrifugation, and laser techniques. The first two techniques rely on the mass differences between ^{235}U and ^{238}U to effect the separation. By far the most commonly used physical method for enrichment is gaseous diffusion.

Once enriched, the UF_6 needs to be reduced to either uranium metal or UO_2 to be formed into fuel pins. A variety of methods can be used to accomplish the conversion to the oxide; however, the predominately used technique involves reduction of the UF_6 to U metal fully, using Ca at high temperatures, followed by burning in oxygen. Once formed, the UO_2 is pressed into pellets, which are then fed into fuel rods.

The burning of the uranium-based nuclear fuel causes a cavalcade of chemical and physical transformations. Nuclear reactions lead to the formation of a variety of actinide elements, for example, Np, Pu, Am, and Cm, as radioactive fission products. As a result of the production of these highly radioactive elements, burnt nuclear fuel must be allowed to 'cool' until the short-lived isotopes decay away and reduce the thermal generation. The cooling typically takes place in either water ponds or engineered dry casks/facilities.

Once 'cooled', the fuel can be manipulated within hot cell facilities for fuel reprocessing. In the United States, the reprocessing of spent nuclear fuel has not been embraced. The primary basis for this decision is the reduction of the threat of nuclear proliferation by avoiding the production of pure streams of plutonium. Some of the other concerns for reprocessing are based in economics. Through the Advanced Fuel Cycle Initiative within the U.S. Department of Energy, the technical feasibility of an economically, politically, and environmentally viable fuel cycle that includes recycling is being investigated. Despite the US efforts, most of countries that have nuclear production capabilities use reprocessing.

The chemistry of reprocessing is quite complex, but it embodies nearly every common aspect of inorganic chemistry: coordination, reduction/oxidation reactions, hard–soft acid–base theory, and so on. The primary purpose of reprocessing is to separate uranium and plutonium from the rest of the actinides and fission products that are present in the spent nuclear fuel. The method of choice to perform these separations is liquid–liquid extraction, for example PUREX process. To effect the primary separation, the spent fuel is dissolved in 7 M HNO_3. The resulting solution contains the uranyl ion, $UO_2{}^{2+}$, and tetravalent plutonium cation, Pu^{4+}. This aqueous solution is contacted with an organic solvent, for example kerosene, which contains tributylphosphate, $OP(OBu_n)_3$ (TBP). The TBP molecule coordinates uranium and plutonium nitrate complexes and makes them soluble in the organic phase. The molecules predominately attributed to this extraction are $UO_2(NO_3)_2(TBP)_2$ and $Pu(NO_3)_4(TBP)_2$; however, research continues to show that these simple formulations may not accurately represent the speciation or the chemical environment during the extraction. In order to separate the uranium and plutonium, a reducing agent, for example $Fe(SO_3NH_2)_2$, in an aqueous phase is contacted with the actinide-laden organic phase. The Pu^{VI} is reduced to Pu^{III}, which does not form a strong complex and therefore selectively partitions to the aqueous phase. The uranium and plutonium can be purified further and the respective oxides produced. The oxides are then combined to produce a new nuclear fuel called *mixed oxide fuel* (*MOX*).

The remaining actinides and fission products must be stabilized for interim storage, long-term storage or final disposal. In order to optimize the storage facilities, some additional separations of the remaining actinides and fission products are required. The European Union has been leading the course in the implementation of advanced separation schemes, including diamide extraction (DIAMEX), selective actinides extraction (SANEX) and SESAME. In DIAMEX, a diamide is used to separate the actinides and the lanthanides from the fission products. In SANEX, a dithiophosphinic acid is proposed to separate the actinides from the lanthanides. The reason this process works is the slightly higher degree of covalency that occurs in the bonding of the actinides versus the lanthanides. In the SESAME process, americium and curium are separated using heteropolyanions, for example phosphotungstate $P_2W_{17}O_{61}{}^{10-}$, that coordinate Am(IV) but not Cm(III).

The stabilization of the nuclear waste products is usually performed by immobilizing the oxides of the radioactive material in glass. This process is known as vitrification. The environmental aspects of storing large quantities of radioactive glass logs are related to the leachability of the elements from the glass structure.[**1,2**]

2.2 Nuclear Weapons

Outside of nuclear energy, the most well-known utilization of the actinides is in nuclear weapons. The fissile nature of ^{235}U and ^{239}Pu has been exploited in the creation of nuclear arsenals throughout the world. Primarily found in the metallic state within the weapons, the isotopic and chemical purifications of these elements require complex separation chemistry and physics that are dependent on inorganic and coordination compounds.

2.3 Depleted Uranium Armor and Projectiles

Another military use of the actinide metals is in tank armor and armor piercing projectiles. Depleted uranium metal is an extremely dense material, for example, density of α-phase U is $\sim$19 g cm^{-3}, and is only mildly radioactive, half-life of ^{238}U is 4.5×10^9 years. When this metal is incorporated into a projectile, the density and metallic properties allow it to penetrate deeply into heavily armored vehicles.

2.4 Heat Sources

The portable generation or storage of power is essential to space exploration. In addition, maintaining working parts in the cold vacuum of space requires constant generation of heat. The electrical and heat requirements for a typical space mission, for example, landing a rover on the surface of Mars, drive the need for extremely dense power sources. One of the densest sources of energy is stored within the nucleus of radioactive materials. In order to tap into this energy source, space agencies have relied on plutonium in the form of the α-emitting ^{238}Pu isotope. The half-life for ^{238}Pu is 87 years, and when the dioxide is formed into pellets, it self-heats, producing an orange glow. The following example can be used to emphasize the energy density of these materials: a 250-g (3 cm in diameter) $^{238}PuO_2$ ball acts as a 100-W heat source. The publicity of using these heat sources peaked in 1997 with the launch of the Cassini–Huygens Mission to Saturn and Titan. The Cassini spacecraft was equipped with more than 200 $^{238}PuO_2$ pellets (150 g each) within three radioisotope thermoelectric generators (RTGs). Each one of these RTGs put out 4400 W of thermal energy at 1200 to 1300 °C. Thermocouples are able to convert this thermal energy into 285 W of electricity. As for pure heat generation, the Cassini spacecraft and the Huygens probe use radioisotope heating units (RHUs). The RHUs are constructed with 2.7-g pellets of $^{238}PuO_2$ and maintain a temperature of 35 to 40 °C.

2.5 Smoke Detectors

Americium plays a vital role in maintaining the safety of homes across the world. The α-emitting ^{241}Am isotope can be found in most smoke detectors in the form of the dioxide, AmO_2. The α-particle emission causes the air to ionize between two electrodes. The ionization of the oxygen and nitrogen allows a steady current to flow between the electrodes. However, when smoke enters the detector, the α-particles are absorbed by the smoke and therefore ionize less of the air, which causes the current to drop and the alarm to signal.

2.6 Lantern Mantles

One of the primary uses of thorium was in the production of lantern mantles. (Note: new materials have replaced Th, but older Th-based lantern mantles can still be found.) The mixture of 99% ThO_2 and 1% CeO_2 particles were impregnated into the mantle fabric. The burning of the ThO_2 produces a fairly bright light. However, the addition of the CeO_2 increases the thermal conductivity and catalyzes the combustion of the gas, allowing the flame to be brighter than would be possible with a thorium-only system.

2.7 Catalysis

Thorium and uranium are used in commercial catalytic systems. Industrially, thorium is used in the catalytic production of hydrocarbons for motor fuel. The direct conversion of synthetic gas to liquid fuel is accomplished by a Ni-ThO_2/Al_2O_3 catalyst that oxidatively cracks hydrocarbons with steam. The primary benefit to the incorporation of thorium is the increased resistance to coke deactivation. Industrially, U_3O_8 also has been shown to be active in the decomposition of organics, including benzene and butanes and as supports for methane steam reforming catalysts. Uranium nitrides have also been used as a catalyst for the cracking of NH_3 at 550 °C, which results in high yields of H_2.

3 OVERVIEW OF GENERAL TRENDS

Discussions of the chemistry and physical properties of the actinide elements are based typically around the nature of the 5f-electrons. Comparisons are routinely made between the actinides and their 4f-bretheren, the lanthanides. For true comparisons, it is convenient to separate the actinides into two distinct groups, the light or early actinides (Ac–Am) and the heavy or late actinides (Cm–Lr). The chemistry of the light actinides is intermediate between that of the transition metals, for example, the ability to access multiple oxidation states and engage covalent bonding, and that of the lanthanides, for example, significant degree of ionic bonding. Conversely, the chemistry of the late actinides is very reminiscent of their lanthanide analogs. The most common and stable oxidation state for the heavy actinides is the trivalent state, and the bonding is almost entirely ionic in nature.

3.1 Oxidation States

The chart of oxidation state and f-electron configuration between the actinides and the lanthanides is provided in Figure 1. The light actinides exhibit significant oxidation state variability with valences from II to VII. The boxes with question marks indicate oxidation states that have been reported in the literature once but are questionable and have not

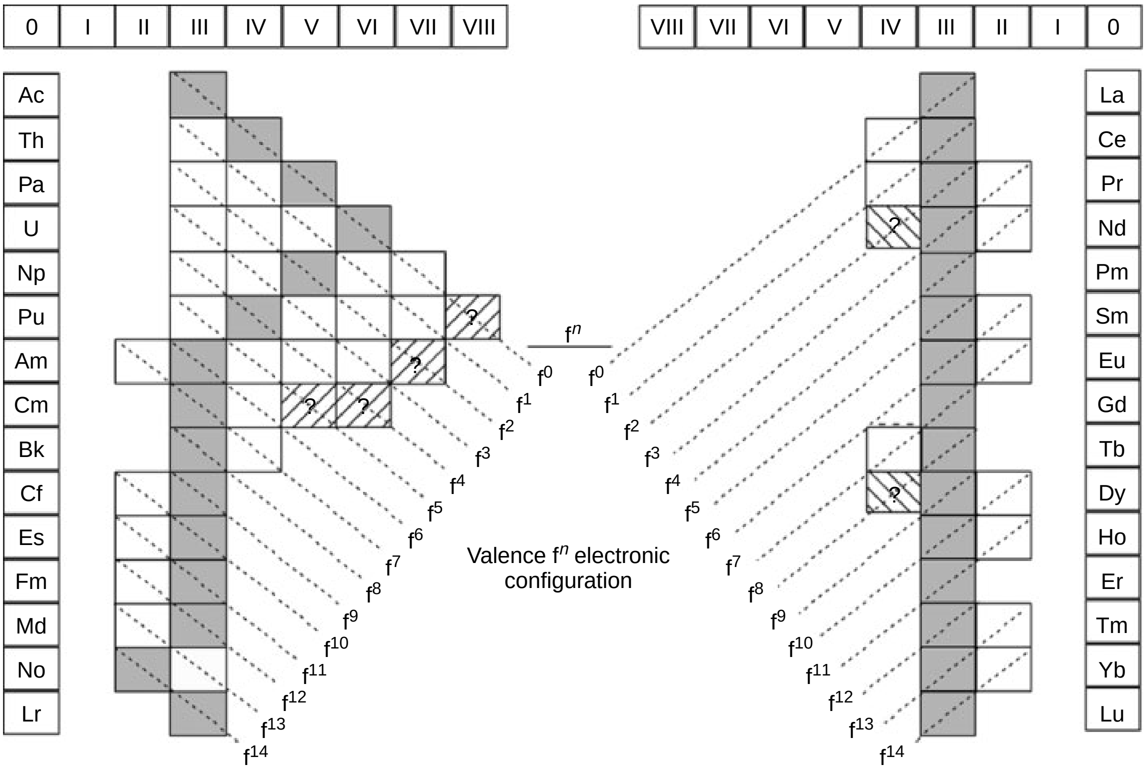

Figure 1 Classification of actinides and lanthanides

been verified by a secondary source. The maximum possible oxidation state can be reached for the elements from Ac through Np. There has been a single report for the synthesis of a Pu^{VIII} complex; however, this result has not been confirmed. In addition to being able to reach the maximum possible oxidation state to get to a f^0 system, the most stable oxidation state increases from Ac to U, Ac^{III}, Th^{IV}, Pa^{V}, and U^{VI}. After U, the most persistent oxidation state declines, for example, Np^{V}, Pu^{IV}, Am^{III}, until Cm, in which the trivalent ion continues to be the stable species. The only exception to this is No, where the divalent state predominates.

3.2 Chemical Characteristics

The majority of the chemistry that has been investigated for the actinide elements has been in aqueous solutions. For the light actinides in acidic solutions, four types of cations persist: trivalent, tetravalent, pentavalent, and hexavalent. The later two ions are always found to have trans oxo ligands, making up a linear dioxo unit. Actinide ions of this type are typically referred to 'yls' and have the names, uranyl (**1**, $UO_2{}^{+/2+}$), neptunyl (**2**, $NpO_2{}^{+/2+}$), plutonyl (**3**, $PuO_2{}^{+/2+}$), (**4**, $AmO_2{}^{+/2+}$) and so on.

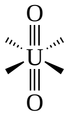

(**1**)

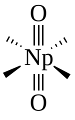

(**2**)

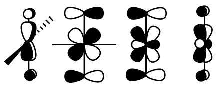

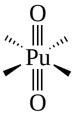

(**3**)

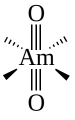

(**4**)

The metal ion affinity to form complexes is dependent on the oxidation state and the actinide element. For the cations stable in acidic solutions, the ligand-binding constants are generally greatest for the tetravalent state, followed by the trivalent and hexavalent states, which tend to be similar, and least for the pentavalent state. It should be noted that the lack of binding affinity of the pentavalent state for the light actinides, for example, Np and Pu, leads to some of the primary issues in the environmental migration of the ions. This general trend can be attributed to changes in the charge to size ratio of the ion as well as the electronic repulsion of the oxo ligands on the penta- and hexavalent ions. The charge to size ratio can also change for a given oxidation state on going across the actinide series. The increase in this ratio across the series is due to the decreasing ionic radii of the actinide ions through a phenomenon called the *actinide contraction*. The actinide contraction is discussed in the next section but is equivalent to the lanthanide contraction that leads to similar ionic radii being observed between second- and third-row transition metals.

The electrochemistry of the light actinides is impacted by the stability of the linear dioxo unit. The redox reactions in which there is no making or breaking of an An=O bond are fast and reversible, for example, reducing the tetravalent to the trivalent. However, when the making or a breaking of the An=O bond is required, for example, oxidizing the tetravalent to the pentavalent, the electrochemistry tends to be slow and irreversible.

The structure and bonding within coordination complexes of the light actinides will be discussed in the following section. However, the general trend between the actinides and the lanthanides is a larger degree of covalency in An–L bonds versus Ln–L bonds. In aqueous solutions, the predominant bonding interaction with ligands is ionic in character, and, therefore, the number and geometry of the ligands is mainly determined by pure steric and electrostatic considerations. For example, a wide range of coordination numbers (6–14) has been found for the actinide ions.

4 STRUCTURE AND BONDING WITH f ORBITALS

As was noted in the previous section, the structure and bonding of the actinides is partly driven by the nature of the 5f orbitals. For the lanthanides, the 4f orbitals are deeply buried and do not penetrate the core. Being almost completely screened by the 5s- and 5p-electrons, 4f orbitals have little to no chemical significance. This is one of the reasons that the trivalent state of the lanthanides are the most stable, formed through the ionization of the two 5s- and one 5p-electrons. Conversely, the 5f orbitals have a greater spatial expansion and also penetrate the core. Owing to the relatively small energy differences between the 5f, 6d, 7s, and 7p orbitals, multiple oxidation states can be obtained and covalent bonding can be engaged.

4.1 Electronic Configuration

The electronic configurations of the gas-phase actinide ions are given in Table 3. In order to determine these configurations, electronic spectra are taken. These spectra tend to be very complicated and, thus, make absolute determination of the configuration difficult. As a result, a number of configurations have question marks appended, indicating that either disagreement or doubt in the assignment exists. Despite these controversies, a general trend in the sequential filling of the f orbitals does exist.

4.2 Coordination Numbers and Stereochemistry

The coordination chemistry of the actinides in aqueous environments can be segregated along two lines, low valency (di-, tri- and tetravalent) and high valency (penta- and hexavalent). For actinide ions with a low valency, the coordination chemistry is dominated by ionic bonding. As a result, the coordination number and geometry of these aqueous complexes is dictated by the steric bulk and electronic

Table 3 Valence level electronic configuration of the actinides in the gas phase

Actinide	Ac	Th	Pa	U	Np	Pu	Am	Cm	Bk	Cf	Es	Fm
Z	89	90	91	92	93	94	95	96	97	98	99	100
M (g)	$6d\,7s^2$	$6d^2\,7s^2$	$5f^2\,6d\,7s^2$	$5f^3\,6d\,7s^2$	$5f^4\,6d\,7s^2$	$5f^6\,7s^2$	$5f^7 7s^2$	$5f^7\,6d\,7s^2$	$5f^9\,7s^2$	$5f^{10}\,7s^2$	$5f^{11} 7s^2$	$5f^{12}\,7s^2$
M^+ (g)	$7s^2$	$6d\,7s^2$	$5f^2\,7s^2$	$5f^3\,7s^2$	$5f^5$ 7s ?	$5f^6$ 7s	$5f^7$ 7s	$5f^7\,7s^2$	$5f^9$ 7s	$5f^{10}$ 7s	$5f^{11}\,7s^2$	$5f^{12}$ 7s
M^{2+} (g)	7s	5f 6d	$5f^2$ 6d	$5f^3$ 6d ?	$5f^5$	$5f^6$	$5f^7$	$5f^8$	$5f^9$	$5f^{10}$	$5f^{11}$	$5f^{12}$
M^{3+} (g)		5f	$5f^2$	$5f^3$	$5f^4$	$5f^5$	$5f^6$	$5f^7$	$5f^8$	$5f^9$	$5f^{10}$	$5f^{11}$
M^{4+} (g)			5f	$5f^2$	$5f^3$	$5f^4$	$5f^5$	$5f^6$	$5f^7$	$5f^8$	$5f^9$	$5f^{10}$

repulsion of the ligands. The actinide ions are relatively large with the ionic radii for the An^{3+} and An^{4+} ions being 1.12 to 0.95 Å and 0.94 to 0.82 Å, respectively. As a result of their size, the actinides are found to have large coordination numbers, 6 to 14. Some examples of the typical coordination geometries for the tri- and tetravalent actinide ions are shown in structures (**5–10**). Structure (**5–8**) are the potential geometries for the aquo ions, $An(H_2O)_{8/9}{}^{3+/4+}$. Structures (**5–7**) are eight-coordinate with a cubic, square antiprism, and a bicapped trigonal prism arrangement of the ligands, respectively. The coordination number in Structure (**8**) is nine with a tricapped trigonal prismatic geometry. The higher coordination numbers are observed with multidentate ligands, for example, $CO_3{}^{2-}$ and $NO_3{}^{-}$. Structure (**9**) represents the $An(CO_3)_5{}^{6-}$ anion that has a coordination number of 10, resulting from five bidentate carbonate ligands in an irregular geometry. The structure can almost be compared with the high-valent linear dioxo compounds with two trans carbonate ligands occupying the axial sites and three nearly planar carbonate ligands occupying a pseudo-equatorial plane. The $An(NO_3)_6{}^{2-}$ anion is extremely important in the purification and processing of actinides, for example plutonium. Structure (**10**) represents the coordination geometry for this anion, which has six bidentate nitrate ligands, giving the ion a coordination number of 12. The symmetry for Structure (**10**) is T_h with three sets of trans nitrato groups, each making a plane in the Cartesian coordinate system.

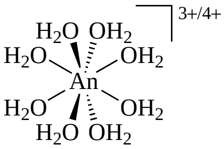

(**5**)

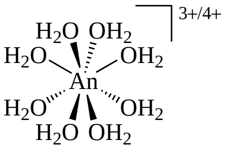

(**6**)

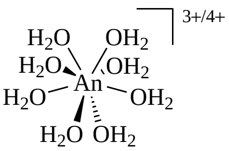

(**7**)

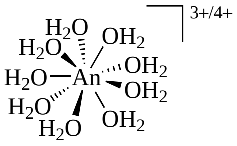

(**8**)

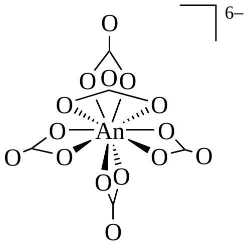

(**9**)

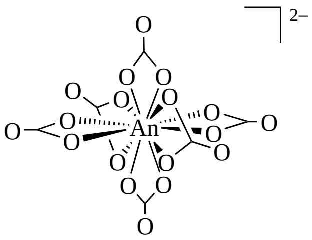

(**10**)

The nonaqueous chemistry of the tri- and tetravalent ions follows similar trends as the aqueous complexes. Coordination numbers are dictated by the steric bulk and electronic properties of the ligands; two structures, $U(MeBH_3)_4$ (**11**) and $[\{U(N(CH_2CH_2NSiMe_3)_3)\}_2(\mu^2\text{-}\eta^2:\eta^2\text{-}N_2)]$ (**12**), are shown. Direct comparisons of the latter species can be made to the behavior of transition metals in both coordination and reactivity.

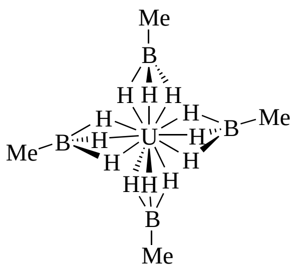

(**11**)

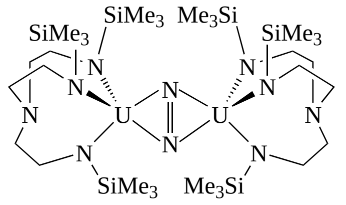

(**12**)

For the high-valent aqueous actinide species, the predominant linear dioxo unit, $AnO_2{}^{+/2+}$, drives all of the coordination variability into the equatorial plane. It is interesting to note that the bonding for these ions have significant covalency with the axial An–O ligands. However, for the majority of the ligands residing in the equatorial plane ('belly-band'), the bonding is primarily ionic. This shows the dual behavior (strong covalency and ionicity) of the trans dioxo ions. As a result of this behavior, the linear dioxo unit is unperturbed (with the exception of bond distance changes) throughout all of the aqueous-based complexes and the coordination numbers are dictated by the equatorial ligands' size and electronic properties. The structures of a variety of aqueous-based coordination complexes have been observed. Compounds with a D_{4h} symmetry are represented by the complexes, $AnO_2Cl_4{}^{2-}$ (**13**) and $NpO_4(OH)_2{}^{3-}$ (**14**). Seven-coordinate structures are also prevalent in actinide chemistry and are the highest coordination numbers achievable with all monodentate ligands. The aquo ion (**15**) and pentafluoro (**16**) complex for the hexavalent actinides are represented below. Coordination complexes under aqueous conditions with eight atoms bound to the actinide are achievable.

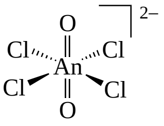

(**13**)

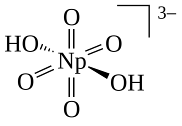

(**14**)

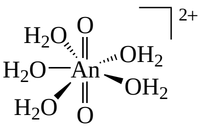

(**15**)

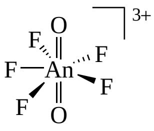

(**16**)

4.3 Ionic Radii and the Actinide Contraction – A Partial Relativistic Effect

The ionic radii of the actinides is shown graphically in Figure 2. The ionic radii for a given oxidation state gradually decreases with increasing atomic number. This phenomenon is known as the actinide contraction. Similar to the lanthanide contraction, the cause of the contraction is an increase in the effective nuclear charge experienced by the valence shell electrons. The increase in the effective nuclear charge is a result of the additional protons and the poor shielding ability of the f-electrons due to their diffuse angular radial function. Relativistic effects also contribute to the lanthanide and actinide contractions. With heavy atoms, the core electrons approach speeds that are close to the speed of light. When these fast rates are obtained, the mass of the electron increases as described by the special theory of relativity. The mass of the electron has an inverse relationship with the Bohr radius, meaning as the mass increases the electron radius decreases. There are two different relativistic effects, direct and indirect. In general, direct relativistic effects are found for the s and p orbitals, which contract owing to an increase in the mass of these electrons. Indirect relativistic effects are predominantly found for the d and f orbitals, which generally have increased radii resulting from the enhanced shielding of the nuclear charge by the contracted s- and p-electrons. Understanding the difference between direct and indirect relativistic effects is actually a function of analyzing the angular wavefunctions of the s, p, d, and f orbitals. The s- and p-electrons have a greater probability of being found at the nucleus (minimal angular nodality) and, thus, greater probability of approaching the speed of light. The diffuse nature of the d and f orbitals reduces the lifetime of the electrons close to the nucleus and, therefore, the probability of being accelerated. Relativistic effects increase as a function of the atomic number, Z^n ($n > 1$), and, therefore, actinides have greater relativistic effects compared to the lanthanides. The effect can be recognized easily by looking at the calculated radial distribution functions of Sm^{3+} and Pu^{3+} with and without relativistic effects. In both ions, the s and p orbitals contract and the d and f orbitals expand; however, the magnitude of the effect is clearly greater in the case of the Pu^{3+} ion.

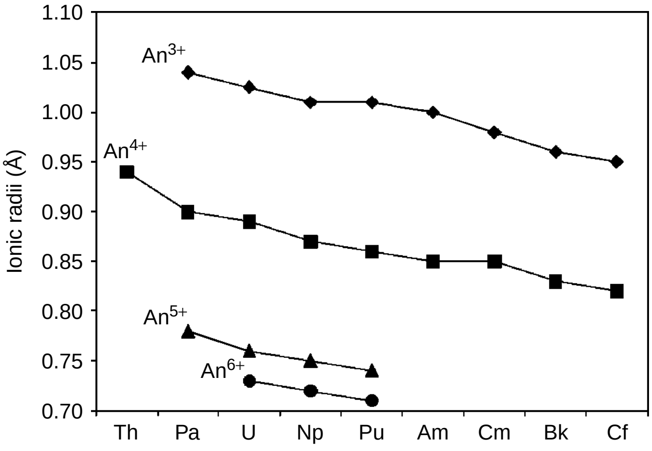

Figure 2 Ionic radii of actinide ions

4.4 Molecular Orbital Descriptions – The Linear Dioxo Diagram

Actinide complexes rarely follow the conventional rules, for example, 18-electron rule, typically found in inorganic and coordination chemistry of the transition metals. A prime example of the difference in actinide chemistry is the pervasiveness of the linear dioxo unit, which is unmatched in transition metal chemistry. For the actinides, the trans dioxo structure is maintained through different metal ions, oxidation states, and valence electron counts, for example, $UO_2^{2+/+}$ (f^0/f^1), $NpO_2^{2+/+}$ (f^1/f^2), $PuO_2^{2+/+}$ (f^2/f^3) and $AmO_2^{2+/+}$ (f^3/f^4). In transition metal dioxo complexes, MO_2L_x, the oxo ligand geometry (cis or trans) is almost entirely dependent on the electron count. For $ReO_2(CH_3)_3$ (d^0 system) (**17**), the oxo ligands are cis in order to maximize the π-bonding, while the oxo ligands in $ReO_2(py)_4$ (d^2 system) (**18**) are found in a trans geometry to minimize electronic repulsions with the unpaired metal-based electrons residing in the equatorial dx^2-y^2 orbital.

As a result of this disparity, many questions on the structure and bonding of the actinides center on the role of the 5f-electrons. The molecular orbital descriptions for the bonding of the actinide elements continue to evolve. One of the first general models used to describe the chemical bonding in d- and f-electron complexes is the ‘FEUDAL’ model. FEUDAL is an acronym for ‘f *orbitals* essentially unaffected **d** orbitals accommodate ligands’. This model is represented in Figure 3, which depicts the molecular orbital

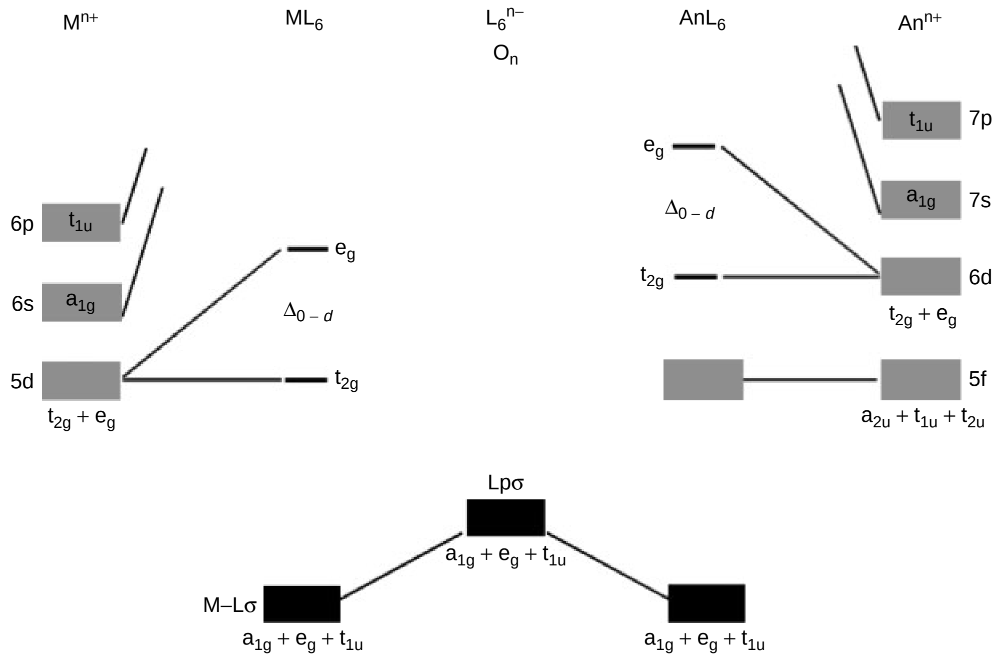

Figure 3 Bonding in actinide complexes

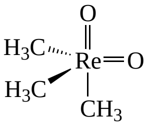

(**17**)

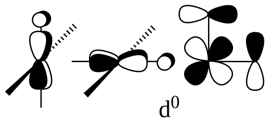

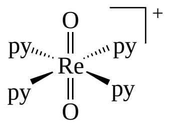

(**18**)

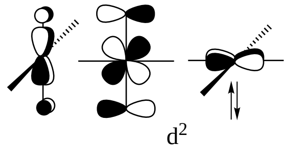

diagram for a transition metal ion (left) and an actinide ion (right) binding to six monodentate ligands in an octahedral geometry.

The transition metal diagram shows the valence shell 5d, 6s, and 6p orbitals being raised in energy due to interactions with the ligand's p-based σ-orbitals. The typical splitting of the d orbitals occurs and the electrons fill these orbitals on the basis of the transition metal being investigated. For the actinide, there is a greater energy mismatch between the ligand's orbitals and the 7s, 7p, and 6d orbitals. This energy difference weakens the covalent bonding. The 5f orbitals are also at energy levels that are below the 6d orbitals and therefore act as a reservoir of the metal-based electrons. As can be seen, the f-electrons have orbitals of the correct symmetry to interact, t_{1u}; however, their spatial expansion is believed to be insufficient to overlap with the ligand's orbitals. This lack of overlap is the reasoning for essentially leaving the f orbitals unaffected.

In general, the FEUDAL model appears to answer many of the fundamental questions regarding the bonding within f-electron systems; however, certain discrepancies exist within the physical data of the actinide systems and the theoretical understanding of the radial distribution functions of the actinides. Evidence that the f orbitals are accessible for covalent bonding continues to be found.

A number of important observations can be made from the calculated radial distribution functions of the f elements, including: the 4f orbital are considerably buried within the core; the 5f orbitals have a great enough spatial extension such that ligands that approach close enough to the metal center (<2 Å) can engage these orbitals for bonding; and the 7s and 7p orbitals are really too diffuse to be useful for chemical bonding.

On the basis of these observations and new quantum calculations[3] using density functional theory, a more accurate molecular orbital diagram for the linear dioxo actinide system has emerged (Figure 4). In this diagram, mixing of the actinide $5fz^3$ orbital with the filled 6pz occurs, which allows for a more significant overlap with the oxygen 2p σ-orbitals. For oxo ligands, the f orbitals can also engage in π-bonding as evidenced by the raising of the π_u 5f orbitals.

5 ELECTROCHEMICAL PROPERTIES

The ability of the light actinides to access multiple oxidation states leads to rich, and, sometimes, complex electrochemistry. The standard reduction potentials at $\mathrm{pH} = 0$ for each of the

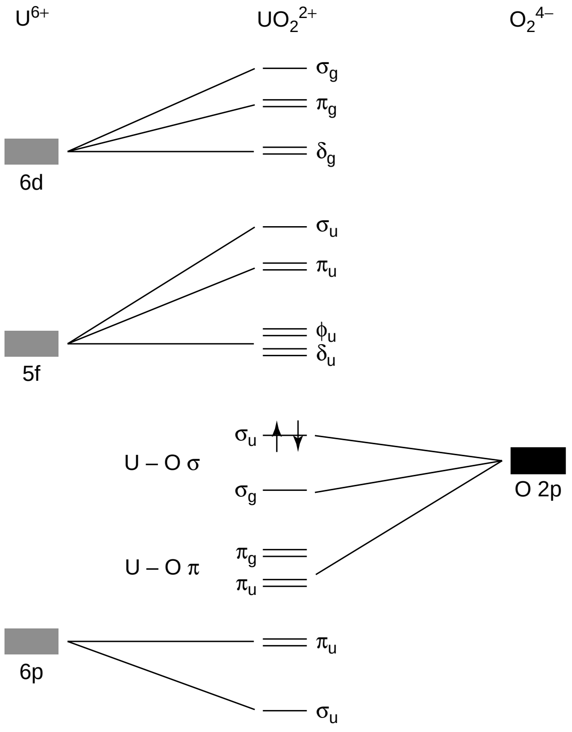

Figure 4 Bonding in uranyl complexes

actinides are given in Table 4. The stability of the oxidation states shown in Figure 1 are supported by these data and some interesting properties of the actinides can be derived. For example, U^{III} is able to reduce H_2O, while U^{IV} and Np^{IV} can be stabilized in anaerobic aqueous solutions. Another example is the unique electrochemical properties of plutonium. The reduction potentials for the four common oxidation states of plutonium under acidic conditions are all close to 1 V. The physical manifestation of having similar reduction potentials is an aqueous solution in which the plutonium can exist in four different oxidation states simultaneously (PuO_2^{2+}, PuO_2^{+}, Pu^{4+} and Pu^{3+}). Equations (1) and (2) dictate the equilibrium of these species. The equilibrium constants for these equations are dependent on the ionic strength and equation (2) has a fourth order dependence on the $[H^+]$, making the equilibria quite complicated. For a one molal solution ($HClO_4$), the equilibrium constants are 12.7 and 6.46×10^{-4}, respectively. With these constants, the speciation of an aqueous Pu solution at pH = 1 can be calculated at ∼60% Pu^{III}, ∼20% Pu^{VI}, and ∼10% each of Pu^{IV} and Pu^{V}.

$$Pu^{4+} + PuO_2^{+} \rightleftharpoons Pu^{3+} + PuO_2^{2+} \tag{1}$$

$$Pu^{4+} + 2H_2O \rightleftharpoons Pu^{3+} + PuO_2^{+} + 4H^{+} \tag{2}$$

The reduction potentials are also dependent on the pH of the solution. Dramatic changes in the redox potentials of Np and Pu have been observed on progressing from acid (1 M) to base (1–10 M). For example, the reduction potential for Np^{VII}/NpO_2^{2+} is reduced by nearly 2 V! Scheme 3 shows the reduction potentials for Np and Pu at either 1 or 10 M NaOH solutions. As can be seen, the potentials are such that the

1 M NaOH

$$Np^{VII} \xrightarrow{+0.59\ V} NpO_2^{2+} \xrightarrow{+0.14\ V} NpO_2^{+} \xrightarrow{-0.95\ V} Np^{4+}$$

$$Pu^{VII} \xrightarrow{+0.26\ V} PuO_2^{2+} \xrightarrow{+0.76\ V} PuO_2^{+} \xrightarrow{-0.95\ V} Pu^{4+}$$

10 M NaOH

$$Np^{VII} \xrightarrow{+0.25\ V} NpO_2^{2+} \xrightarrow{+0.05\ V} NpO_2^{+} \xrightarrow{-1.0\ V} Np^{4+}$$

Scheme 3

Table 4 Standard electrode potentials of the actinides in aqueous solutions at pH = 0

Redox couple	Ac	Th	Pa	U	Np	Pu	Am	Cm
An^{2+}/An^0	−0.7	+0.7	+0.3	−0.1	−0.3	−1.2	−1.95	−1.2
An^{3+}/An^{2+}	−4.9	−4.9	−5.0	−4.7	−4.7	−3.5	−2.3	−3.7
An^{3+}/An^0	−2.13			−1.66	−1.79	−2.00	−2.07	−2.06
An^{4+}/An^0		−1.83	−1.47	−1.38	−1.30	−1.25	−0.90	
An^{4+}/An^{3+}		−3.8	−1.4	−0.52	+0.15	+1.01	+2.62	+3.1
AnO_2/An^0		−2.56						
AnO_2^{+}/An^{4+}			−0.05	+0.38	+0.67	+1.04	+0.82	
AnO_2^{+}/An^{3+}							+1.72	
AnO_2^{2+}/AnO_2^{+}				+0.17	+1.24	+0.94	+1.60	
AnO_2^{2+}/An^{4+}				+0.27	+0.94	+0.99	+1.21	
Redox couple	Bk	Cf	Es	Fm	Md	No	Lr	
An^{VII}/AnO_2^{2+}					+2.04			
An^{2+}/An^0	−1.54	−1.976	−2.2	−2.5	−2.5	−2.6		
An^{3+}/An^{2+}	−2.8	−1.6	−1.55	−1.15	−0.15	+1.45		
An^{3+}/An^0	−1.96	−1.91	−1.98	−2.07	−1.74	1.26	−2.1	
An^{4+}/An^{3+}	+1.67	+3.2	+4.5	+5.2				

higher oxidation states can be stabilized in aqueous solutions, including the heptavalent ions of Np, Pu, and possibly Am. It should be noted that this phenomenon follows the expected trend based on an increase in the electron density on the metal center with changing the speciation from $AnO_2(H_2O)_x{}^{2+}$ in acidic conditions to $AnO_2(OH)_{4/5}{}^{2-/3-}$ in highly alkaline solutions.

The equilibria and variety of species discussed above would seem to make studying the specific oxidation states of actinides difficult. However, through careful control of the conditions, oxidation state pure solutions for all of the actinides can be obtained for synthetic, quantitative and/or qualitative studies.

6 CHARACTERIZATION OF ACTINIDE COMPLEXES

The radioactive nature of the actinides, especially the transuranics, can introduce significant challenges in the characterization of their complexes. In order to prevent contamination, multiple layers of containment are often required, which can limit the types of studies that can be undertaken. However, a suite of spectroscopic tools has been used to study the chemistry and speciation of the actinides. A partial list of these techniques includes absorption, emission and vibrational spectroscopies, X-ray absorption and diffraction, and multinuclear magnetic resonance.

The absorption spectroscopy in the UV-Vis-NIR is especially rich for the actinides, allowing for fairly simple determinations of the metal oxidation state. The primary absorption bands result from $f \rightarrow f$ transitions, $f \rightarrow d$ and ligand-to-metal charge transfers. The $f \rightarrow f$ transitions are typically weak since they are forbidden under the LaPorte selection rules. Distortions in symmetry allow for relaxation in these rules and bands in the visible to near-infrared range result. Complexes that contain an inversion symmetry, for example $PuO_2Cl_4{}^{2-}$, have weaker $f \rightarrow f$ transitions ($\varepsilon < 20\,M^{-1}\,cm^{-1}$). The direct interactions of the 5f orbitals with the ligand set generally make the absorption bands broader than the absorption spectra of comparable lanthanide species. The charge transfer bands in actinide complexes can be intense and lead to the variety of colors observed for the actinides with varying oxidation states or ligands. Vibronic coupling also plays a significant role in the absorption spectra of actinide complexes. The prime example of this vibronic coupling is observed in the visible spectra of $UO_2{}^{2+}$ species. In these complexes, the ν_1 stretching mode ($\sim$800–900 cm^{-1}) resulting from an excited state of the linear dioxo unit couples with the absorption manifold to give the appearance of multiple peaks with approximately the same energetic separation. Absorption techniques have been used extensively in studying the aqueous chemistry of the actinides, especially when linked with potentiometric titrations.

The emission spectroscopy is also used to study the speciation of the actinides. Compounds with isotopes of uranium, americium, and curium fluoresce in the visible range, making detection relatively easy. Neptunium and plutonium fluoresce in the near-infrared region, and recent developments in detectors may allow for more facile measurements. The power of emission spectroscopy is the ability to run at variable temperatures and low concentrations in both solution and solid phases. The luminescence from the actinide complexes is strongly dependent on both energy and lifetime of the speciation products. In a similar fashion as the absorption spectra of $UO_2{}^{2+}$, vibronic coupling occurs. The primary difference between the two is that in the emission spectra the ground-state vibrations of the $AnO_2{}^{2+}$ are probed.

The ubiquitous linear dioxo unit gives an excellent handle to use vibrational spectroscopy in studying the speciation of high-valent aqueous complexes of the actinides. Both IR and Raman spectroscopy have been utilized. For IR, the observation of the stretching frequencies of the dioxo unit are complicated by the relatively small window available for water. Attenuated total reflectance cells have significantly aided the examination of aqueous actinyl complexes by providing the requisite background subtraction. Raman spectroscopy does not have the same issues when measuring actinide complexes in water. For actinyl complexes, the ν_1 stretch is dependent on ligands in the equatorial plane. In general, the ν_1 stretch of the O=An=O weakens with the addition of better σ- or π-donor ligands.

Nuclear magnetic resonance (NMR) techniques have been increasingly used for studying the actinides. Th(IV), U(VI), and Np(VII) complexes are diamagnetic, and a range of multinuclear methods can be used, including ^{13}C, ^{1}H, ^{19}F, and so on. Most complexes with the other actinides and other oxidation states of uranium and neptunium are paramagnetic. The paramagnetism causes a shift and broadening of the NMR signals similar to transition metal species. One of the nuclei that has relatively narrow lines for paramagnetic complexes is the quadropolar ^{17}O. The oxo groups of the actinyl ions can be labeled with ^{17}O by reducing the metals to the tetravalent state and reoxidizing to the penta- or hexavalent state in an ^{17}O-enriched aqueous solution. Unlike the transition metals, the actinide complexes that have the narrowest line-widths are those with either an f^0 or odd f-electron configuration. For example, Np^{VII} (f^0) and $NpO_2{}^{2+}$ (f^1) have visible ^{17}O-NMR peaks, whereas the peaks for $NpO_2{}^{+}$ (f^2) are so broad that they cannot be observed.

Another technique that has been increasingly used for determining actinide speciation is X-ray absorption. These measurements are typically made at synchrotron radiation laboratories where extremely high energy X-rays (15–25 keV) with high fluxes can be generated and used to interrogate a sample. The techniques are element specific, which allows for the ability to probe heterogeneous samples, for example environmental substances. The X-ray absorption near edge spectrum (XANES) is able to give information on the oxidation state of the actinide. For example, a linear relationship between the edge energy and oxidation state of plutonium has been reported. The structure near the absorption edge can also shed light on the structure of the actinide, for example, presence of an actinyl unit. The variability in the ligands can also cause a shift in the edge position; however, this is typically a much smaller effect than the oxidation state. The X-ray absorption fine structure (XAFS) that results after the primary absorption can be used to give structural information. This technique essentially gives the ability to obtain data from any solid or solution similar to that gained from a single-crystal X-ray diffraction study. The primary difference is that no angular information can be determined from XAFS, but the type, number, and bond distances of atoms bound to a metal can be.

7 AQUEOUS COORDINATION COMPLEXES

The most basic coordination complex in aqueous solutions is the aquo ion. For most metals in the periodic table that form ions in aqueous solutions, the coordination number and geometry of the aquo ion is well known. For a majority of the actinides, controversies still exist as to the exact number of H_2O molecules that are bound to the metal centers. The uncertainty in the structures is linked to the limited number of crystal structures that exist for actinide aquo complexes. This lack of data is related to the difficulty in crystallizing materials from aqueous solutions. The most well studied aquo ion of the actinides is $UO_2(H_2O)_5{}^{2+}$. This ion has been crystallized from noncoordinating perchloric acid solutions through either concentration or addition of 18-crown-6. For the latter case, the crown ether interacts with the H_2O molecules bound to the uranium through hydrogen bonds. These same crystallization techniques have been attempted to obtain crystal structures of the hexavalent Np, Pu, and Am ions; however, X-ray quality single crystals of the aquo ions have not been obtained, sometimes due to oxidation state changes or inner-sphere complexation by the crown ether. From EXAFS, structural data on the aquo ions have been obtained for the hexavalent ions, $AnO_2(H_2O)_5{}^{2+}$ (An = U–Am). For calibration purposes, the bond distance for the oxo ligands of the $UO_2{}^{2+}$ species obtained from XAFS and single-crystal analyses show a nearly identical length. The bond An = O distance was found to be 1.76, 1.75, 1.74, and 1.80 Å for An = U, Np, Pu, and Am, respectively. The An–OH_2 distance for the same complexes was found to be 2.42, 2.42, 2.41, and 2.40, respectively.

For those actinides stable in the pentavalent state, ions of the form $AnO_2(H_2O)_x{}^+$ (An = Np, Pu; $x = 4, 5, 6$) have been postulated. Pa^V is not included in this list since it readily hydrolyzes in aqueous solutions to form $Pa_2O_5 \cdot xH_2O$. All of the structural data for these complexes come from XAFS. The bond distances for both An=O (1.83 Å for both Np and Pu) and An–OH_2 (2.51 and 2.5 Å, respectively) expand in the pentavalent ions in line with an increase in the ionic radii with the change in oxidation state.

Tetravalent ions of the actinides can be stabilized in aqueous solutions for Th to Am. Owing to the more intense radiation fields generated by Am, maintaining oxidation state pure samples is difficult (α radiolysis spontaneously promotes the reduction of Am^{IV} to Am^{III}). For those ions that have been studied, complexes of the form $An(H_2O)_x{}^{4+}$ (An = Th, U, Np, Pu; $x = 9–12$) have been proposed. The most widely accepted values for the number of H_2O molecules bound to the metal center are 10 for Th and 9 for U to Pu. The An–OH_2 distances in these ions range from 2.50 to 2.46 Å.

The trivalent plutonium aquo ion, $[Pu(H_2O)_9]^{3+}$, has been crystallized with nine H_2O ligands in a tricapped trigonal prismatic geometry.**[4]**

Salts of oxo anions, such as nitrate, sulfate, perchlorate, iodate, hydroxide, carbonate, phosphate, oxalate, and so on, are important for the separation and reprocessing of technologically important actinides, while hydroxide, carbonate, and phosphate ions are important for the chemical behavior of the actinides in the environment. The general trends of complexes formed in aqueous solutions are as follows:

- for $AnO_2{}^{n+}$ ($n = 1, 2$) complexes: as H_2O is replaced as a ligand by better σ-, π-, or ionic donors, for example, OH^-, F^-, Cl^-, $CO_3{}^{2-}$, the An=O distance increases and the ν_1 decreases;
- on transitioning between $AnO_2{}^+$ to An^{4+}: the lack of the linear dioxo unit in the lower valent complexes results in a slight decrease in the An–L bond distance;
- the determination of end members for a specific ligand in an aqueous-based actinide system will be the easiest to determine because of the ubiquitous presence of multiple equilibria, for example, $UO_2Cl_2(H_2O)_2$, $UO_2Cl_3(H_2O)^-$, and $UO_2Cl_4{}^{2-}$ for the uranyl chloride system.

7.1 Nitrates

Hexavalent. Nitrate complexation with actinide ions is very weak, and the determination of the formation constants for aqueous nitrate solution species is extremely difficult. Under aqueous conditions with high nitric acid concentrations, complexes of the form $AnO_2(NO_3)(H_2O)_x{}^+$, $AnO_2(NO_3)_2(H_2O)_2$, and $AnO_2(NO_3)_3{}^-$ (An = U, Np, Pu) are likely to be present. Solids of the anionic trisnitrato complex have been isolated for U and Np**[5,6]** however, minimal structural data have been obtained. Solid uranyl nitrate, $UO_2(NO_3)_2 \cdot xH_2O$, is obtained as the orthorhombic hexahydrate from dilute nitric acid solutions and as the trihydrate from concentrated acid. The Np analog can be precipitated from a mixed aqueous HNO_3 and MeCN solution by the addition of 18-crown-6. Multiple structural determinations have been made for the hexavalent uranium nitrate complexes, and all show the common formula unit of

$UO_2(NO_3)_2(OH_2)_2$ (**19**) with a local hexagonal bipyramidal coordination about the central uranyl ion. The average $An{=}O$ bond distances for the actinyl dinitrate complex were found to be 1.76 and 1.74 Å for U and Np, respectively, while the $An{-}OH_2$ distances (2.44 Å) and $An{-}O_{nitrate}$ (2.49 Å) distances were identical for the two actinides. The actinyl dinitrato complex is also known to bind other neutral donors to form compounds of the form $AnO_2(NO_3)_2L_2$ (L = TBP, MeCN, DMF, $MeCO_2Et$, etc.). As with all of the other neutral adducts, the technologically important $AnO_2(NO_3)_2(TBP)_2$ (An = U, Np, Pu) (**20**) complex displays trans nitrate ligands with the TBP ligands occupying the same coordination sides as H_2O in (**19**).

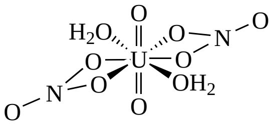

(**19**)

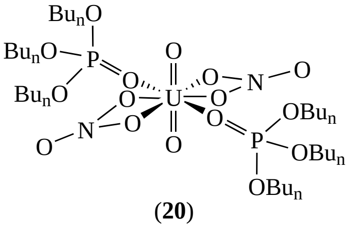

(**20**)

Pentavalent. The complexation of the Pa and Np pentavalent ions by nitrate is known; however, limited thermodynamic and structural data are known. For Pa, mixed hydroxo/nitrato or oxo/nitrato complexes have been proposed. The presumed structure for the Np^V species is $NpO_2(NO_3)(H_2O)_x$.

Tetravalent. Nitrate complexes for tetravalent actinides, for example, Th and Pu, are extremely important in actinide separation and purification processes. The limiting species in the nitrate series is the hexanitrato complex, $An(NO_3)_6{}^{2-}$.[7] There is reasonable evidence for the formation of aqueous U(IV) nitrate complexes of the general formula $U(NO_3)_n{}^{4-n}$, where $n = 1$ to 4. However, owing to the inherent weakness of the complexes, quantitative data on the formation constants is only available for $U(NO_3)^{3+}$ and $U(NO_3)_2{}^{2+}$. No neutral U(IV) nitrates have been obtained from aqueous solutions, but a number of anionic complexes of general formula $M_2[U(NO_3)_6]$, where M = NH_4, Rb, Cs, and $M[U(NO_3)_6]{\cdot}8H_2O$, where M = Mg, Zn, have been isolated and characterized. These solids contain the 12-coordinate anionic U(IV) center. Neutral, U(IV) nitrate complexes of formula $U(NO_3)_4L_2$ (L = $OP(C_6H_5)_3$, $OP(NC_4H_8)_3$) have also been isolated from aqueous solutions and structurally characterized.

7.2 Sulfates

Hexavalent. The aqueous actinyl sulfate systems have been widely studied for uranium and complexes of formula $AnO_2(SO_4)_n{}^{2-2n}$, where $n = 0$, 1, and 2, are likely to be formed in solution. For the transuranics, the neutral compounds $AnO_2(SO_4){\cdot}2.5H_2O$ (An = Np, Pu) have been isolated and characterized by the X-ray analysis, which confirmed comparable structures with the U analog. A number of ternary An(VI) sulfates of the general formula $(M)_k(AnO_2)_m(SO_4)_n{\cdot}xH_2O$, where M = monovalent cation, that is, NH_4 or alkali metals, $M(AnO_2)_m(SO_4)_n{\cdot}xH_2O$, where M = bivalent cation, such as alkaline-earth or transition metals (Mn, Cd, Hg), have been reported. In one of the more simplistic systems, $K_4UO_2(SO_4)_3$, each uranium has a pentagonal bipyramidal geometry with five-coordinated oxygen atoms from four sulfate groups in the equatorial plane. The crystal structure for $Cs_2NpO_2(SO_4)_2$ is composed of anionic layers of $[NpO_2(SO_4)_2]_n{}^{2n-}$ with bridging sulfate groups.

In addition to traditional aqueous chemistry to produce actinide sulfate phases, hydrothermal synthetic methods have been utilized. The novel phases, $[N_2C_5H_{14}]_2[UO_2(SO_4)_3]$, $[N_2C_5H_{14}][UO_2(H_2O)(SO_4)_2]$, $[N_2C_4H_{14}][UO_2(SO_4)_2]$, and $[N_2C_4H_{14}][(UO_2)_2(H_2O)(SO_4)_3]{\cdot}H_2O$ have been synthesized by high-temperature organic-templated reactions.

Pentavalent. Protactinium is known to bind sulfate in solutions of H_2SO_4; however, very limited data are available on the molecular species. Sulfate complexes with the general formula of $NpO_2(SO_4)_n{}^{1-2n}$ ($n = 1$–3) have been reported. In most of these complexes, the Np is found in a seven-coordinate pentagonal bipyramid geometry.

Tetravalent. The An^{IV} (An = Th, U, Np and Pu) sulfate system has also been studied in strongly acidic solutions. $An(SO_4)_2{\cdot}xH_2O$ ($x = 4, 6, 8, 9$) can be precipitated from weak and concentrated sulfuric acid solutions. For $An(SO_4)_2{\cdot}4H_2O$ (An = Th, U, Np, Pu), the actinide atoms are surrounded by a square antiprism of O atoms, with each An bonded to four molecules of water and linked by bidentate bridging sulfate groups to other metal atoms. In these compounds, the bond distances observed for the $An{-}O_{phosphate}$ are significantly shorter than the $An{-}OH_2$, for example, 2.308 Å and 2.361 Å, respectively for the Np compound. Ternary An(IV) sulfates have also been described in the literature. Many of the compounds have layered structures and/or unusual coordination environments. The trisulfate of Np(IV) has been isolated as a Cs salt, $Cs_2Np(SO_4)_3{\cdot}2H_2O$. In this compound, the Np^{IV} cation is coordinated to nine oxygen atoms in an irregular geometry. The structure of $K_4Pu(SO_4)_4{\cdot}2H_2O$ was determined from powder diffraction and consists of dimeric units of $[(\mu^2\text{-}SO_4)_3Pu(\eta^2\text{-}\mu^2\text{-}SO_4)_2Pu(\mu^2\text{-}SO_4)_3]^{8-}$.[8]

Trivalent. The trivalent ions of the actinides have been found to bind sulfate ions. The simple hydrated sulfate salt, $An_2(SO_4)_3{\cdot}xH_2O$ has been proposed for U, Np, Pu, Am, and Cm. A crystal structure of $Am_2(SO_4)_3{\cdot}8H_2O$ showed significant cross-linking of the Am atoms through sulfate ligands and an extensive hydrogen bonding network. The coordinate sphere of the Am atoms is composed of eight oxygen atoms, four from sulfate ions and four from H_2O molecules. The $Am{-}O_{sulfate}$ distances ranged from 2.38 to 2.95 Å while the $Am{-}OH_2$ distances varied from 2.41 to 2.55 Å. Ternary complexes of the trivalent actinides are also known. For example, $MPu(SO_4)_2{\cdot}xH_2O$ has been isolated with a number of alkali metals and ammonium. The Pu in these compounds is nine-coordinate and is analogous to the lanthanide compounds of the same formula. It is interesting to note that the U^{III} sulfates, $U_2(SO_4)_3{\cdot}xH_2O$ ($x = 2, 5, 8$) and $M_2U_2(SO_4)_4$ are essentially the only available salts of trivalent uranium.

7.3 Hydroxides

Hydrolysis dominates the aqueous chemistry of actinide ions under conditions of high pH. The tendency for hydrolysis follows the acidity of the actinide cations, that is $An^{4+} > AnO_2^{2+} > An^{3+} > AnO_2^{+}$. The AnO_2^{2+} would appear to be an anomaly, since a 3+ cation would normally be predicted to be more acidic than a 2+ cation. However, the effective charge on the metal center is the key factor. The oxo groups of the AnO_2^{2+} ion do not completely 'quench' the hexavalent charge, and as a result, the residual effective charge on the metal center is approximately +3.3.

The hydrolysis products of the actinides have a tendency to undergo polymerization reactions, which can hamper the structural investigations of the speciation. One of the most observed plutonium species is the highly insoluble green colloidal Pu^{IV} hydroxide. In general, high concentrations of an actinide ion in near-neutral solution conditions (pH = 2–13) will lead to polymeric materials, while solutions with low actinide concentrations (10^{-5}–10^{-6} M, depending on the actual ion) favor monomeric complexes. Under highly alkaline conditions, some of the hydroxides of the actinides become amphoteric in nature, producing soluble monomeric and polymeric anions.

Tetravalent. The hydrolysis of tetravalent actinide ions can begin to occur in solutions with pH levels < 2. Under dilute conditions, species of the form $An(OH)_n^{4-n}$ ($n = 1$–4) are predicted; however, most hydrolysis studies have only been able to identify the first hydrolysis product, $An(OH)^{3+}$. It should be noted that in all of these compounds the remainder of the coordination sphere is made up of bound H_2O molecules. The end member of the speciation is the neutral $An(OH)_4$ or $AnO_2{\cdot}2H_2O$. This complex has low solubility but has been postulated to exist in solutions from solubility experiments when using the isolated solid as the starting material. Under more concentrated conditions, polymeric materials have been postulated. In modeling the hydrolysis of thorium at concentrations greater than mM, polynuclear species of the form $Th_2(OH)_2^{6+}$, $Th_2(OH)_4^{4+}$, $Th_4(OH)_8^{8+}$, $Th_6(OH)_{14}^{10+}$, and so on, have been included.

Hexavalent. As with most reactions, the hydrolysis of UO_2^{2+} is the best studied of the hexavalent actinides. The hydrolysis of UO_2^{2+} begins at pH ~ 3, while the onset for the hydrolysis of NpO_2^{2+} and PuO_2^{2+} each occur at a higher pH. The monomeric hydrolysis products of the uranyl ion, $UO_2(OH)_n^{2-n}$ ($n = 1, 2$) can be studied in solutions with uranium concentrations less than 10^{-4} M. For solutions with higher uranium concentrations, multinuclear cationic species dominate the speciation, for example, $(UO_2)_2(OH)_2^{2+}$, $(UO_2)_3(OH)_4^{2+}$, and $(UO_2)_3(OH)_5^{+}$. These cations have been crystallized from solutions with the formulas $(UO_2)_2(\mu_2\text{-}OH)_2(OH_2)_6^{2+}$ and $(UO_2)_3(\mu_3\text{-}O)(\mu_2\text{-}OH)_3(OH_2)_6^{+}$ (**21**). For Np and Pu, the dimer of the first hydrolysis product, $(AnO_2)_2(OH)_2^{2+}$ (**22**), has also been identified but not fully structurally characterized.

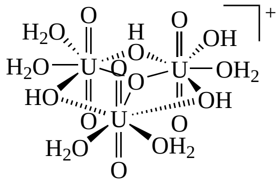

(**21**)

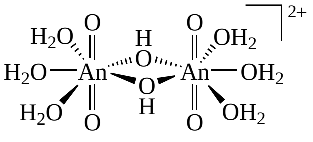

(**22**)

When alkali metal bases are used to raise the solution pH to moderate levels, the uranium will precipitate from the solution in the form of hydrous uranyl hydroxides or uranates, for example, $Na_2U_2O_7$. However, through judicious choice of a base, for example, tetramethylammonium hydroxide, (TMA)OH, or tetramethylammonium trifluoromethansulfonate, the study of the amphoteric behavior of uranyl hydroxides can be undertaken. Polynuclear anions of the form $(UO_2)_3(OH)_7^{-}$, $(UO_2)_3(OH)_8^{2-}$, and $(UO_2)_3(OH)_{10}^{4-}$ are examples of soluble species in solutions where the pH < 14. When the concentration of the (TMA)OH is increased (>0.6 M OH^-), highly soluble (~ 0.1 M) monomers of the form $UO_2(OH)_n^{2-n}$ ($n = 3, 4, 5$) have been reported. These three species are in equilibrium with each other; however, in solutions where the $[OH^-]$ is greater that 1 M, the pentahydroxo complex predominates the speciation.

One of the common theories in actinide chemistry is the analog theory, which implies that the chemistry of the transuranics will mirror that of uranium. The behavior of Np and Pu in highly alkaline solutions offers an excellent example of the limitations of this theory. Unlike U, both Np and Pu are highly soluble (~ 0.1 M) in a variety of bases, for example MOH (M = Li, Na, K; $[OH^-] > 1$ M). Monomeric anions of the form, $AnO_2(OH)_x^{2-}$ ($x = 4, 5$) have been identified to be in equilibrium with each other, and, as for the uranium analog, the neptunyl tetrahydroxide has been crystallographically characterized by addition of $[Co(NH_3)_6]^{3+}$ to alkaline solutions. The bond lengths for the $AnO_2(OH)_4^{2-}$ have been established by both single-crystal X-ray diffraction studies and XAFS. The average An=O distances for U, Np, and Pu are 1.82, 1.80, 1.77 Å, respectively, while the average An–OH distances are 2.26, 2.24, and 2.29 Å respectively.

Heptavalent. In highly alkaline solutions ($[OH^-] = 0.5-18\,M$), the redox potentials for Np and Pu have shifted to the point that the heptavalent state can be stabilized for a limited time in aqueous solutions. The lifetime of the An^{VII} species is dependent on the base concentration; however, in general, Np^{VII} is significantly more stable than Pu^{VII}, for example, weeks versus days, respectively. Over the past few years, a significant interest has evolved in studying the structure of the heptavalent actinide ions. Two forms of Np^{VII} have been crystallographically characterized, $NpO_4(OH)_2{}^{3-}$ and $NpO_4{}^-$. The latter anion was isolated as a salt with Na^+ and K^+ cations. The structure of $KNpO_4$ is layered with the Np atoms bound to two oxo-type ligands (Np=O 1.?? Å) in axial positions and four bridging oxygen atoms (Np–O 2.?? Å) that make up the plane of the layer. The former complex has four shorter bonds (1.88 Å) corresponding to the four Np=O and two longer bonds Np–OH (2.33 Å) (**14**). This planar teraoxo arrangement is unique to heptavalent actinides having no transition metal or f element analogs.

7.4 Carbonates

Actinide carbonate complexes are of interest not only because of their fundamental chemistry and environmental behavior but also because of extensive industrial applications, primarily in uranium recovery from ores and nuclear fuel reprocessing.

Trivalent. The trivalent actinides form simple carbonates of the formula $An_2(CO_3)_3$. When these solids are dissolved in aqueous solutions of alkali metal carbonates, anionic complexes are formed, for example $An(CO_3)_n{}^{3-2n}$ ($n = 2-4$).

Tetravalent. The best-studied tetravalent actinide carbonato complex is $An(CO_3)_5{}^{6-}$ (An = Th, U, Pu). This anion has been isolated using a variety of cations, including Na^+, K^+, Tl^+, $[Co(NH_3)_6]^{3+}$ and $C(NH_2)_3{}^+/NH_4{}^+$. In solution, the pentacarbonato complex is the end member of the series $An(CO_3)_n{}^{4-2n}$ ($n = 1-5$); however, in the mineral tuliokite, $Na_6BaTh(CO_3)_6{\cdot}6H_2O$, thorium exists as a hexacarbonato complex. The analysis of the thermodynamic data for these actinide carbonate systems has led to differences of opinion on the actual speciation. The data appear to support both the stepwise addition of $CO_3{}^{2-}$ and subsequent loss of H_2O molecules within the An^{4+} cation coordination sphere as well as the formation of mixed hydroxo carbonato complexes, for example $Pu(CO_3)_3(OH)^{3-}$.

Pentavalent. The binding of carbonate to pentavalent actinide ions has been studied for most of the light actinides (An = U, Np, Pu, Am). The primary species that have been reported are $AnO_2(CO_3)^-$, $AnO_2(CO_3)_2{}^{3-}$, and $AnO_2(CO_3)_3{}^{5-}$. As with all of the actinyl complexes, the carbonate ligands bind in the equatorial plane and in a bidentate fashion. As a result, the likely coordination geometry for the mono- and biscarbonato complexes in solution is a pentagonal bipyramid, while the triscarbonato complex has a hexagonal bipyramidal geometry. When crystallized, the mono- and biscarbonato complexes condense, allowing the carbonate ligands to bridge multiple actinide centers and typically resulting in a hexagonal bipyramidal geometry.

Hexavalent. The aqueous An(VI) carbonate system has been well studied. A multitude of An(VI) carbonate complexes have been identified, including monomeric, multinuclear, and mixed hydroxo carbonato complexes. The monomeric materials generally have the form $AnO_2(CO_3)_n{}^{2-2n}$ ($n = 1-3$). The end member of the carbonate series, $AnO_2(CO_3)_3{}^{4-}$ (**23**), has a hexagonal bipyramid geometry with the three bidentate carbonates occupying the equatorial plane. The mono- and biscarbonato complexes are typically five coordinate, with bidentate carbonate ligands and either three or one H_2O molecule. Under conditions with high actinide metal concentrations, multinuclear species can predominate, for example $(AnO_2)_3(CO_3)_6{}^{6-}$ (**24**). The U(VI) is the best studied of the hexavalent actinide carbonate complexes. The known uranium(VI) carbonate solids have empirical formulas $UO_2(CO_3)$, $M_2UO_2(CO_3)_2$, and $M_4UO_2(CO_3)_3$ ($M = Na^+$, K^+, Rb^+, Cs^+, $NH_4{}^+$, etc.). The monocarbonato compound, $UO_2(CO_3)$, is a mineral known as rutherfordine, and its structure has been determined from crystals of both the natural mineral and synthetic samples. Rutherfordine is a layered solid in which the local coordination environment of the uranyl ion consists of a hexagonal bipyramidal arrangement of oxygen atoms. Each uranium atom forms six equatorial bonds with the oxygen atoms of four carbonate ligands, two in a bidentate manner and two in a monodentate manner. The biscarbonato complex has been shown to form a trimeric anion of the form $(UO_2)_3(CO_3)_6{}^{6-}$ (**7**). This molecule possesses a D_{3h} planar structure in which all six carbonate ligands and the three uranium atoms lie within the molecular plane. The six uranyl oxygen atoms are perpendicular to the plane, with three above, and three below the plane. The local coordination geometry about each uranium is hexagonal bipyramidal.

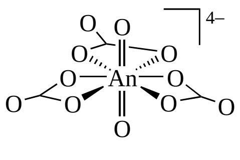

(**23**)

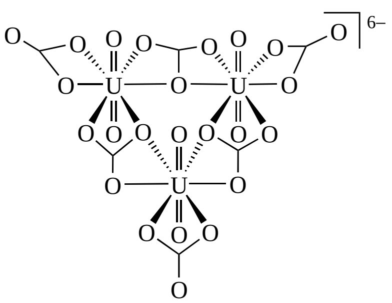

(**24**)

7.5 Phosphates

Inorganic phosphate ligands are important with respect to the behavior of actinides in the environment and as potential waste forms. There have been a number of experimental studies to determine the equilibrium constants in the actinide–phosphoric acid system, but they have been complicated by the formation of relatively insoluble solid phases and the formation of ternary actinide complexes in solution.

The chemistry of the phosphate system is complicated by the number of different ligands that are possible. In acidic solution (hydrogen-ion concentration range 0.25–2.00 M), H_3PO_4 and $H_2PO_4^-$ are potential ligands, whereas in neutral to basic solution, HPO_4^{2-} and PO_4^{3-} ligands are predominant. The phosphate salts are slightly soluble in water and dilute mineral acids. The synthetic methods to obtain solid phases of actinide phosphates include precipitation and high-temperature methods.

The trivalent actinides form simple insoluble phosphate salts of the form, $AnPO_4{\cdot}xH_2O$. Tetravalent actinides form a number of different phases including metaphosphates $An(PO_3)_4$, the pyrophosphate $An(P_2O_7)$, double phosphates $MAn_2(PO_4)_3$ and $M_2An(PO_4)_2$, and orthophosphates, $An(HPO_4)_2{\cdot}xH_2O$. Phosphates of the hexavalent actinyl ions also form complex complexes and solid phases. The predominate compounds include $AnO_2(HPO_4){\cdot}xH_2O$, orthophosphates $M(AnO_2)_n(PO_4)_m{\cdot}xH_2O$, hydrogenphosphates $M(AnO_2)_n(H_kPO_4)_m{\cdot}xH_2O$, pyrophosphates An_mO_n-P_2O_7, metaphosphates $(AnO_2)_n(PO_3)_m{\cdot}xH_2O$, and polyphosphates $(AnO_2)_n(P_aO_b)_m{\cdot}xH_2O$.

7.6 Halides

The best-studied aqueous actinide halide systems are the fluorides and the chlorides. Fluoride and chloride ions are added to the actinyl centers in a stepwise fashion (Scheme 4). The end member in the actinyl fluoride system is the pentafluoride, $AnO_2F_5^{3-}$. For the uranyl analog, the $U=O$ and U–F bond distances were found to be 1.79 and 2.18 Å respectively. The uranium tetrafluoride ion, $UO_2F_4^{2-}$, has been isolated as a dimer with two bridging fluoride ligands. The $U=O$, $U{-}F_{\text{terminal}}$, and $U{-}F_{\text{bridging}}$ distances for this complex were found to be 1.79, 2.15 to 2.20 Å, and 2.30 Å, respectively.

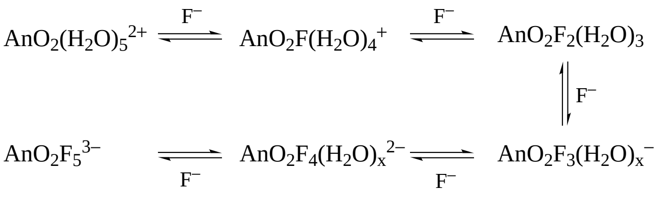

Scheme 4

For the larger chloride ion, the final member in the series is the tetrachloride, $AnO_2Cl_4^{2-}$. The uranium, neptunium, and plutonium tetrachloride dianions have been isolated with a number of different cations, for example, Na^+, NH_4^+, K^+, Cs^+, $K^+{\cdot}$18-crown-6, and so on. The An=O distances were found to be 1.768, 1.751, and 1.737 Å for An = U, Np, and Pu, respectively. The An–Cl distances in these complexes is virtually unchanged: 2.675 Å (U), 2.659 Å (Np), and 2.656 Å (Pu). These structural data suggest that the chloride ligands are bound in essentially a purely ionic manner while the covalent nature of the An=O bond is preserved.

The lower valent actinide ions also bind the halides to form cationic complexes, for example, $AnX_n(H_2O)_m^{z-n}$ ($z = 3$, $n = 1$–6; $z = 4$, $n = 1$–7)**[9]** and $AnO_2X_n(H_2O)_m^{1-n}$ ($n = 1$–4).

7.7 Multidentate Ligands

Polycarboxylic Acids. Carboxylic acids have been found to bind strongly to actinide ions. The primary binding mode for the carboxylic acids is bidentate. The affinity of the low-valent actinides with these ligands increases with the density of the ligand, for example, ethylenediaminetetraacetate (EDTA) > acetate. For An^{4+}, the EDTA ligand is hexadentate with a twist conformation. Diethylenetriaminepentaacetate (DTPA) has an even higher affinity for both An^{3+} and An^{4+} ions.

Crown Ethers. The crown ether macrocycle, for example, 18-crown-6, has been found to coordinate An^{3+} and An^{4+} in both aqueous and nonaqueous conditions via an inner-sphere mechanism. For UO_2^{2+}, multiple compounds that contain crown ether ligands have been isolated. In most of these compounds, the crown ether interacts in an outer-sphere manner, engaging in hydrogen bonding with the ligands on the metal center. Inner-sphere coordination of UO_2^{2+} occurs only under strictly anhydrous conditions. For the Np system, the presence of a crown ether in aqueous solutions causes a reduction of the metal center from Np^{VI} and Np^{V} and a spontaneous inner-sphere coordination of the crown ether to form $NpO_2(18\text{-crown-}6)^+$. The linear dioxo unit in this complex sits perpendicular to the plane created by the six oxygen atoms of the crown ether molecule. The average Np=O distance for this complex is 1.85 Å and the average $Np{-}O_{\text{crown}}$ distance is 2.?? Å.

8 NONAQUEOUS COORDINATION COMPLEXES

The coordination chemistry of the actinides, especially thorium and uranium, continues to be of great interest. Considered ‘hard’ metal ions, An(III to VI) have the greatest affinity for hard donor atoms such as N, O, and the light halides. Tetravalent thorium and tetra- and hexavalent uranium, neptunium, and plutonium coordination complexes are the most common; however, trivalent and pentavalent complexes are being identified with increasing frequency. As with all of the actinides, the ionic radii of the ions are significantly larger compared to a transition metal ion in an identical oxidation state. The result of this increased ionic radius is an expansion of the possible coordination environments (3- to 14-coordinate) and electron counts (up to 24 electrons). The structure and bonding in the nonaqueous complexes of the actinides like that of the aqueous complexes involves a mixture of ionic and covalent bonding. While it is impossible to positively correlate which orbitals are being utilized or if bonding is covalent or ionic, the fact that the 5f elements form complexes with ligands like N_2 and CO suggests that a significant covalent component is present in the complex formation.

8.1 Starting Materials

Choosing, obtaining, or synthesizing the appropriate starting material is critical in order to investigate the coordination chemistry of the actinides in nonaqueous environments. For thorium, the two most common starting materials are $ThCl_4$ and $ThBr_4(THF)_4$. In synthesizing $ThBr_4(THF)_4$, thorium metal is reacted with two equivalents of Br_2 in THF at 0 °C. This reaction can be run on very large scales, 100 to 200 g product. For uranium, neptunium, and plutonium, the three common starting materials for tri-, tetra- and hexavalent complexes are $AnI_3(THF)_4$, $AnCl_4$, and AnO_2Cl_2 (An = U, Np, Pu), respectively. The first material, $AnI_3(THF)_4$, is prepared in THF at 0 °C by adding I_2 to metal chips or turnings.[10] The uranium analog is deep purple, the neptunium is orange, and the plutonium analog is off-white. The synthetic routes to obtain $AnCl_4$ are provided in Section 9. For the green UCl_4, the preferred synthetic method involves the reaction of UO_3 with hexachloropropene. For the hexavalent starting material, AnO_2Cl_2, the most efficient synthetic route is the oxidation of $AnCl_4$ with O_2 at 350 °C.

8.2 Nitrogen Donors

The coordination chemistry of the light actinides with N-donating ligands is one of the better-studied areas. Numerous N-donor ligands have been complexed with the actinides, including neutral mono-, bi-, and polydentate ligands, that is, ammonia, primary, secondary, and tertiary amines, alkyl–aryldiamines (en = ethylenediamine, 1,4-diaminobenzene), N-heterocycles (py = pyridine, bipy = bipyridine, terp = terpyridyl), nitriles (CH_3CN), anionic amides ($[N(C_2H_5)_2]^-$, $[N(Si(CH_3)_3)_2]^-$), thiocyanates, and polypyrazolylborates. A majority of the published work with these ligand sets has been with complexes of Th and U; however, some complexes of Np and Pu have also been reported.

Trivalent. The study of trivalent light actinide coordination complexes with N-donors is complicated by the relative ease of oxidation. Some examples of the isolated materials include $AnX_3(NH_3)_n$ (X = Cl, Br), AnI_3py_4, $AnI_3(tmed)_2$, and $AnCl_3(CH_3CN)$. The homoleptic complexes $[An(CH_3CN)_9]^{3+}$ (An = U, Pu)[11] have been synthesized by dissolution of $UI_3(THF)_4$ and oxidation of plutonium metal in CH_3CN. Both complexes have a nine-coordinate trigonal prismatic geometry. The pyramidal tris-silylamido complexes, $An[N(Si(CH_3)_3)_2]_3$ (An = U, Np, Pu)[10,12] (**25**) have been synthesized and have been shown to be useful starting materials for the synthesis of other trivalent or tetravalent compounds.

Other less bulky trisamido An^{III} complexes, for example, $U[N(R)Ar]_3$ (R = Bu and Ar = 3-5-$Me_2C_6H_3$), have been shown to elicit some interesting chemistry. When the $U(NRAr)_3$ complex is produced *in situ* by reduction of $UI(NRAr)_3$ in the presence of $Mo[NPh(t\text{-}Bu)]_3$ and N_2, an end-on N_2-bridged complex of the form $[(NRAr)_3U(\mu\text{-}N_2)Mo_3^{13}]$.[13] A similar reaction has also been found with cyanoimide where a dinuclear uranium complex was isolated, $(\mu^2;\eta^1,\eta^1\text{-NCN})\{U[N(R)Ar]_3\}_2$ (**26**).[14]

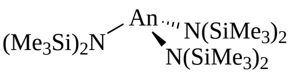

(**25**)

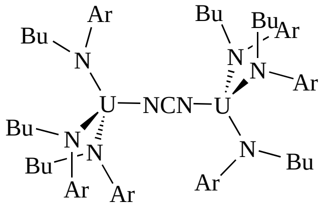

(**26**)

Another ligand that has received considerable attention in actinide chemistry over the past few years is tren- or trisamidoamine, $[N(CH_2CH_2N)SiMe_2Bu_t]^{3-}$ (NN'_3).[15–20] This ligand forms more stable complexes than the trisamido complexes owing to the forced facial coordination and the chelate effect. The purple $U(NN'_3)$ can be synthesized by reduction of the tetravalent $UI(NN'_3)$ complex with K in pentane or by fractional sublimation of $[\{U(NN'_3)\}_2(\mu\text{-Cl})]$. Lewis bases adducts, for example, pyridine, HMPA, of $U(NN'_3)$ have been isolated. The oxidation of $U(NN'_3)$ or its derivatives using trimethylamine N-oxide gives rise to U^{IV} and U^{V} complexes of the form, $[^{18}_{2}(\mu\text{-O})]$ and '$U(NN'_3)O$', respectively. As with the other trisamido complexes, $U(NN'_3)$ reacts reversibly with N_2 to give a side-on bound product, $[^{16}_{2}(\mu^2\text{-}\eta^2{:}\eta^2\text{-}N_2)]$. While the N–N bond distance in this complex is essentially the same as in free dinitrogen, the preference for the side-on over end-on bonding is explained on the basis of covalent interactions where the dinitrogen πp orbital is a better σ-donor than the σp orbital to trivalent uranium.[21]

Polypyrazol-1-yl borates of the form $U(HBpz_3)_mI_{3-m}(THF)_n$ ($m = 1$, $n = 2$; $m = 2$, $n = 0$) and $[PuCl(\mu\text{-}Cl)^{22}\text{-}(Me_2pzH)]_2$[22] have been reported. For the $(UI[HB(Me_2pz)_3])_2$ complex, the pyrazolyl borate ligand binds in an unusual side-on fashion.

Tetravalent. A number of coordination complexes of An^{IV} with N-donor ligands have been characterized. Traditional adducts of AnX_4 (An = Th, U, X = halogen, alkoxide) have been isolated with a variety of neutral N-donor ligands, for example, monodentate (ammonia, primary to tertiary amines, nitriles, isocyanides, N-heterocyclics) and bidentate (diaminoalkanes, diaminoarenes, N-heterocyclics). The coordination numbers for these complexes generally range from 8 to 12. As with transition metals, increasing the steric bulk of the ligands can lead to lower coordination numbers, for example, $An(OR)_4(NH_3)_n$ (R = alkyl, aryl; $n = 1, 2$).

Amido complexes of An^{IV} are highly reactive to insertion reactions and protonation. For example, $[An(NR_2)_4]_n$ (R = alkyl, aryl)[23] undergo insertion reactions with CO_2, COS, CS_2, and CSe_2 to form carbamate complexes and react with alcohols to form alkoxide complexes. The structure of the amido complexes varies with the steric bulk of the ligand. With larger groups, for example, phenyl and pseudo-tetrahedral, monomeric complexes result, while with smaller alkyl groups, dimeric complexes with a trigonal bipyramidal geometry predominate (**27**). Cationic complexes have also been stabilized with amido ligands, for example, the pseudo-octahedral $[U(N(C_2H_5)_2)_3(THF)_3]B(C_6H_5)_4$ (**28**).[24–26]

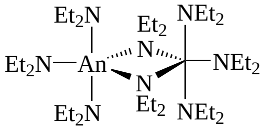

(**27**)

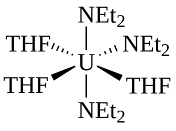

(**28**)

As with the case of the trivalent actinides, the tren, trisamidoamine (NN'_3), ligand has been used to stabilize An^{IV} complexes. The preparation of $[An(NN'_3)Cl]_2$ is accomplished by the reaction of the trilithium salt of NN'_3 with $AnCl_4$ (An = Th, U).[27] The chloride ligand can be exchanged using metathetical reactions to form $An(NN'_3)X$ (X = Br, I, NR_2, OR). Anionic complexes, $An(NN'_3)XX'$ (X = OR, X′ = OR′) can also be formed by addition of alkoxide salts to the neutral species.[28] Complexes of An^{IV} with diamidoamine ligands have also been studied.[29]

Polypyrazol-1-yl borate coordination with An^{IV} also results in stable complexes. The fully characterized complexes are typically of the form, $AnCl_2L_2$ (L = $HBpz_3$, Ph_2Bpz_2, Bpz_4)[30,31] and AnL_4 (L = H_2Bpz_2, $HBpz_3$).

Another unique N-donor ligand is $Fe(CN)_6{}^{3-/2-}$. The ferrocyanide ion has been found to complex with An^{IV} (An = Th, U, Np)[32] to form molecular compounds. In these complexes, the $Fe(CN)_6$ octahedra are maintained with the An ion binding the N atoms of the ferrocyano ligands.

Pentavalent. A limited number of pentavalent actinide complexes have been isolated with N-donor ligands. The primary reason for this is the inability of Th to attain the pentavalent state and the propensity of U^V complexes to disproportionate into U^{IV} and U^{VI} complexes. Some of the typical complexes that have been reported are adducts of $U(OR)_5$ and UX_5 with the ligands described for the tri- and tetravalent actinide complexes.

Homoleptic amido compounds of U^V, $U(NR_2)_5$, have been synthesized by oxidation of anionic tetravalent complexes, $[U(NR_2)_5]^-$. A unique hexakisamido U^V complex has been isolated using 2,3:5,6-dibenzo-7-azabicyclo[2.2.1]hepta-2,5-diene. The $[U(dbabh)]^-$ anion can be oxidized to form a U^{VI} species both of which have a near-perfect octahedral geometry with the six amido ligands.[33]

The oxidation of tetravalent or reduction of hexavalent uranium compounds with the tren ligand present can produce stable U^V complexes. The one-electron oxidation of $[U(NN'_3)(OBu_t)(OPh)Li\text{-}(THF)]$ by either electrolysis or chemical means yields the neutral $[U(NN'_3)(OBu_t)(OPh)]$. The reaction of $UO_2Cl_4{}^{2-}$ with the lithium salt of tren leads to the formation of a U^V/U^{VI} dinuclear trianion, $[UO(\mu^2\text{-}NCH_2CH_2N(CH_2CH_2NSiBu_tMe_2)_2)]_2{}^-$.[34] The formation of this anion is complex due to the activation of both the uranyl unit and the tren ligand. The structure for this complex consists of capped trigonal bipyramid uranium atoms. The tren ligand binds through the amine and two of the amido linkages with the third becoming an imido ligand. The remaining oxygen atoms complete the coordination sphere as a terminal ligand.

Hexavalent. The majority of An(VI) coordination chemistry with N-donors has been explored with the uranyl cation, $UO_2{}^{2+}$. Stable adducts with the ligands discussed in the tri- and tetravalent complexes have been described, for example, $UO_2X_2L_n$ (X = halide, OR, NO_3, RCO_2). The coordination numbers observed for these complexes are typically 6, 7, or 8 with octahedral, pentagonal bipyramidal, or hexagonal bipyramidal geometries, respectively. Neutral and anionic thiocyanates have also been isolated, for example $[UO_2(NCS)_x]^{2-x}\cdot yH_2O$ ($x = 2-5$).

A unique amido complex of $UO_2{}^{2+}$ has recently been reported, $[UO_2(N(SiMe_3)_2)_3]^-$ (**29**).[35] This anion has a uranium center with a rarely observed coordination number of 5 in a trigonal bipyramidal geometry. This complex was synthesized by protonolysis of the dianion, $[UO_2(N(SiMe_3)_2)_4]^{2-}$ (**30**) or through a reaction of $UO_2Cl_2(THF)_2$ with three equivalents of $K[N(SiMe_3)_2]$. The crystal structure of this anion revealed long U=O bonds (1.80 Å) and relatively short U–N bonds (2.31 Å).

Homoleptic U^{VI} amido complexes are also known. $U(NMe_2)_6$ is synthesized by a two-electron oxidation of

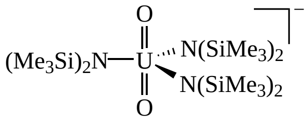

(**29**)

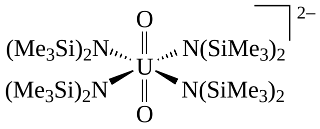

(**30**)

the tetravalent anion $[U(NMe_2)_6]^{2-}$. The complex has an octahedral geometry and slowly decomposes over several hours.

8.3 Phosphorus Donors

The actinides are hard acids and therefore phosphine coordination complexes are rare. Most of the isolated actinide–phosphine complexes contain the chelating ligand 1,2-(bisdimethylphosphine)ethane, (DMPE), for example, $An(BH_4)_3(dmpe)$ and $AnX_4(dmpe)_2$ ($X = Cl$, Br, I, CH_3). For thorium, dmpe complexes are the only ones that have been stabilized; however, uranium complexes with monodentate phosphines, that is, $P(CH_3)_3$, have been reported. Uranium(V) phosphine complexes have also been synthesized using amido ligands with phosphine linkages, for example, $UCl_2[N(CH_2CH_2PPri_2)_2]_3$.

The tetrakis(dialkylphosphido) complexes, $An(PPP)_4$ ($An = Th$, U); $PPP = P(CH_2CH_2P(CH_3)_2)$,**[36]** were prepared by reacting $AnCl_4$ with four equivalents of the lithium or potassium salt of the PPP tetra-anion. The structure of these compounds shows triangulated dodecahedra distorted toward bicapped trigonal prisms. These complexes represent one of the first actinide systems containing exclusively metal–phosphorus bonds. These complexes are known to undergo insertion reactions as seen in actinide amido compounds.**[37]**

A unique complex has been recently reported with uranium bound to elemental phosphorus, $(\mu\text{-}\eta^4,\eta^4\text{-}P_4)[U(NRAr)_3]_2$ ($R = t$-Bu, Ar = 3,5-dimethylphenyl).**[38]** The compound was prepared by reaction of the trivalent $U(NRAr)_3$ with white phosphorus.

8.4 Oxygen Donors

A wide variety of *O*-donors have been used to complex uranium. The predominate oxidation states are IV and VI; however, complexes with An(III) and An(V) are also known. The majority of the complexes have coordination numbers of 6 to 12, depending mostly on the steric bulk of the ancillary ligands. Owing to the prevalence of *O*-donating ligands in natural systems, that is, aquo, hydroxide, carbonate, phosphate, carboxylate, and catecholate, understanding the complexation of the actinides is important to environmental, waste processing and storage, and bioinorganic chemistry. Some of the other *O*-donating ligands that have been studied are crown ethers, Schiff bases, polyglycols, and cryptands. These ligands have been proposed as actinide sequestering agents.

8.5 Oxygen-containing Organics

The actinides have a high degree of specificity for neutral and anionic oxygen-containing organic molecules. The actinide complexes with *O*-donor ligands that are most widely studied include alkoxides, aryloxides amide, carboxylates, and oxalates. Complexes with alcohols, ethers, esters, ketones, aldehydes, ketoenolates, and carbamates have also been reported.

8.5.1 Alkoxides and Aryloxides

Alkoxide and aryloxide ligands are excellent ligands for the actinides. As a result, these ligands have been studied extensively in the coordination chemistry and reactivity**[39]** of tri-, tetra-, penta-, and hexavalent actinides. The alkoxides and aryloxides can be synthesized by a variety of routes; the two most popular routes include: direct reaction of actinide halides with alkali metal salts of the alkoxide or aryloxide of interest and protonolysis of actinide amides by alcohols.

For the tri-, tetra-, and pentavalent light actinides, the structure of the alkoxide and aryloxides are strongly dependent on the steric bulk of the ligand. In order to stabilize monomeric complexes, for example, $An(OR)_n$ or $An(OAr)_n$ ($n = 3, 4, 5$), sterically demanding ligands must be utilized, for example $[O\text{-}2,6\text{-}t\text{-}(C_4H_9)_2C_6H_3]^-$. This ligand has been used to prepare monomers of Np^{III}/Pu^{III} $(An(O\text{-}2,6\text{-}t\text{-}(C_4H_9)_2C_6H_3)_3)$ (**31**), Th^{IV}/U^{IV} $(An(O\text{-}2,6\text{-}t\text{-}(C_4H_9)_2C_6H_3)_4$ ($An = Th$, U)), and so on. As the steric bulk is decreased, dimers $(Th_2(OCH(i\text{-}C_3H_7)_2)_8)$ (**32**), trimers $(U_3O(O\text{-}t\text{-}C_4H_9)_{10})$ (**33**), tetramers $(Th_4(O\text{-}i\text{-}C_3H_7)_{16}(py)_2$, and other oligomers can be formed. In the case of the pentavalent actinide alkoxide complexes, the actinide metal can significantly influence the degree of

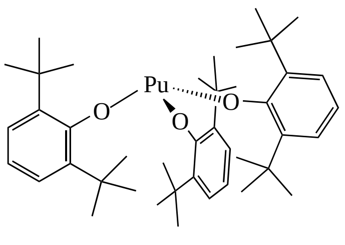

(**31**)

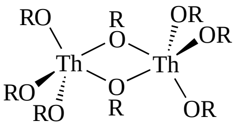

(**32**)

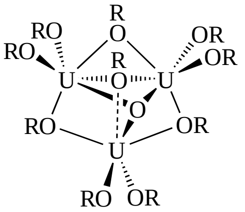

(**33**)

oligomerization. For example, the reaction of $PaCl_5$ with five equivalents of NaOEt results in the formation of $Pa(OEt)_5$, which has been estimated to have a degree of oligomerization of 5.7. However, for U^{V}, a trimer is observed with the less bulky methoxide ligand, $U(OMe)_5$.

A mononuclear trivalent uranium complex has been synthesized with the six-coordinate trisalkoxide ligand, 1,4,7-tris(3,5-di-*tert*-butyl-2-hydroxybenzyl)-1,4,7-triazacyclononane), $((ArO)_3tacn)$.**[40]** The neutral complex $U((ArO)_3tacn)(CH_3CN)$ was found to react with organic azides to form U^{IV} azido or U^{V} imido compounds of the form $[((ArO)_3tacn)U(N_3)]$ and $[((ArO)_3tacn)U(NSiMe_3)]$, respectively.

Homoleptic An^{VI} alkoxides and aryloxides tend to form monomers of the formula $An(OMe)_6$. The octahedral $U(OMe)_6$ is synthesized by oxidation of the tetravalent $[U(OMe)_6]^{2-}$ by Pb^{IV} and sublimes at 87 °C. Other stable An^{VI} alkoxides and aryloxides include the actinyl unit. Using simple metathetical reactions, for example, $AnO_2Cl_2(THF)_2$ (An = U, Np, Pu) reacted with potassium salts of alkoxides and aryloxides, complexes of the form $AnO_2(OR)_n{}^{2-n}$ (R = alkyl, $CHPh_2$, $CH(t\text{-Bu})Ph$, 2,6-$(t Bu_2)C_6H_3$, 2,6-$Ph_2C_6H_3$, 2,6-$Cl_2C_6H_3$, 2,6-$Me_2C_6H_3$, other aryl) can be isolated.**[41,42]** As with the lower valent compounds, the steric bulk of the ligand dictates the nuclearity of the complex. For diphenylmethoxide, a monomer $UO_2(OCHPh_2)_2(THF)_2$ results, while the diisopropylmethoxide analog results in the formation of a tetramer, $[UO_2(OCH(i\text{-Pr})_2)_2]_4$. Both of these compounds have pseudo-octahedral geometries. The coordination sphere of the latter complex has the following ligands: one terminal alkoxo, two bridging alkoxo, and one bridging oxo.

8.6 Macrocyclic Ligands

Porphyrins have been found to bind the tetravalent ions of Th and U in the form of the bisporphyrin complexes, $An(P)_2$ (An = Th, U; P = octaethylporphyrin, tetra-*p*-tolylporphyrin).**[43]** These sandwich-type complexes are useful for studying the electronic structure of porphyrins. For example, Th is electrochemically inactive, which allows the porphyrin-based electrochemistry to be studied exclusively for its role in photosynthesis.

Expanded porphyrins have recently been used to coordinate actinyl ions in an inner-sphere fashion.**[44]** The expanded porphyrins have 4–6 nitrogen-containing rings making very large cavities that can accommodate the actinide ions. The actinyl ions bind to the expanded porphyrins in an inner-sphere manner such that the ring of N atoms takes up the equatorial plane, leaving the oxo ligands above and below the porphyrin ring. The isolated and fully characterized neptunium-expanded porphyrin complex, $[NpO_2(Hexaphyrin(1.0.1.0.0.0))]^-$ (**34**), represented the first all-aza donor ligand to be bound to the neptunyl ion.**[45]**

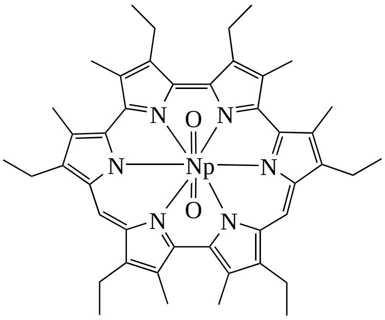

(**34**)

9 SOLID-STATE MATERIALS

9.1 Metals

Actinides display a variety of metallic structures along the series, and many allotropic modifications are seen for Pa, U, Np, and Pu. In Table 5, the physical properties and metallic structures for the various allotropes are provided. Plutonium is probably one of the most interesting metals from a metallurgical standpoint. It has seven different allotropes existing between room temperature and the relatively low melting point of 641 °C. In addition to these phases, some high-pressure phases can also be stabilized. The α-phase of Pu is extremely brittle, with mechanical properties similar to cast iron. The δ-phase is quite ductile, having mechanical properties resembling aluminum, which makes it better suited for machining. The δ-phase can be stabilized at room temperature by alloying with small quantities of other elements, for example, Al, Ce, Ga, Si, and so on. In addition to the different phases of plutonium that can be stabilized by alloying, superconductivity has been discovered in a plutonium intermetallic compound, $PuCoGaa_5$. The T_c for this compound is unusually high at 18.5 K.**[46]**

The variety in metallic structure can be explained by the role of the 5f-electrons with their greater radial distribution. In the beginning of the actinide series, f-electrons interact with each other and with d- and s-electrons to give broad energy bands as in the transition metals. This delocalized character of the 5f-electrons differs greatly from the highly localized 4f-electrons found in the lanthanides beyond Ce. As the 5f level is filled moving across the actinide series, the extent of 5f-electron localization increases and the electron energy decreases below the Fermi band level. In the crossover region (U through Am), there is only a small energy difference between the localized and the delocalized 5f-electrons.

For elements with localized 5f-electrons (Am to Cf), the symmetric dhcp metal structure resembles that of the light lanthanides. However, high pressure relieves the f–f overlap and the americium structure becomes the same as uranium.

Table 5 Physical properties for selected actinide metals

		Thorium	Protactinium	Uranium	Neptunium	Plutonium	Americium	Curium	Californium
Atomic number		90	91	92	93	94	95	96	98
Melting point (°C)		1750	1552	1132	637	641	1176	1340	900
Boiling point (°C)		3800	4277	3930	4082	3352	2340	3192	–
Enthalpy of fusion (kJ mol^{-1})		14	16.7	12.6	5.19	2.82	14.39	14.6	–
Enthalpy of vaporization, 25 °C, (kJ mol^{-1})		598	481	417	464	347	284	387	163
α-phase	Structure	fcc	bct	rhomb	rhomb	monocl.	dhcp	dhcp	dhcp
	Temperature range (°C)	<1360	<1105	<668	<280	<115	<758	<1176	<600
	Density ($\mathrm{g\,cm^{-3}}$)	11.72	15.37	19.07	20.4	19.8	13.7	13.5	9.3
β-phase	Structure	bcc	bcc	tetrag	bct	bc monocl.	fcc	fcc	fcc
	Temperature range	1360–1750	1105–1552	668–775	280–577	115–200	758–1064	1176–1340	600–900
	Density ($\mathrm{g\,cm^{-3}}$)	11.10		18.11	19.4	17.7	–	–	–
γ-phase	Structure			bcc	bcc	fc rhomb	Unknown		
	Temperature range			775–1132	577–640	200–310	1064–1158		
	Density ($\mathrm{g\,cm^{-3}}$)			18.06	18.0	17.1	–		
δ-phase	Structure					Fcc			
	Temperature range					310–452			
	Density ($\mathrm{g\,cm^{-3}}$)					15.9			
δ'-phase	Structure					Bct			
	Temperature range					452–480			
	Density ($\mathrm{g\,cm^{-3}}$)					16			
ε-phase	Structure					Bcc			
	Temperature range					480–641			
	Density ($\mathrm{g\,cm^{-3}}$)					16.5			

The consequent increase in the nuclear charge and reduction of the shielding of the 6d- and 7s-electrons lead to a contraction of the atomic radius, similar to that previously discussed for the ionic radius. In Am and Cm, the 5f-electrons are localized in the core, which causes an expansion of the atomic radius. The differences in localization of f-electrons between light and heavy actinides are also illustrated by their different superconductive and magnetic behavior. The Th, Pa, and Am metals are superconductors (T_c of 1.37, 0.42, and 0.79 K, respectively), whereas the heavier actinide metals are not superconductors but have larger magnetic moments at low temperatures.

The production of the light actinide metals is usually accomplished through the reduction of tri- or tetrafluorides with an electropositive metal, for example, Ca, Zn, or Mg. The heavy actinides are typically made through the direct reduction of oxide phases. An alternative method to access the actinide metals is through pyrochemical methods. In this technique, actinides in high-temperature molten salts, for example, NaCl-KCl or LiCl-KCl eutectics, are electrolyzed to give pure metals at the cathode. Pyrochemistry is currently being investigated as an alternative to the aqueous-based separation methods for nuclear fuel reprocessing since pure streams of Pu can be avoided, thereby reducing proliferation risks. All actinides in elemental form are lustrous silvery dense metals. Only Th has a rather high melting point, and both Th and Np have high boiling points. The other actinides can be purified by volatilization.

The reactivity of the actinide metals is in line with other electropositive highly reactive metals. In air, the actinides are rapidly covered with an oxide film. For Pu, the film has two distinct layers, PuO_2 on the surface and Pu_2O_3 on the subsurface. The relative quantity of each of these layers is dependent on the quantity of oxygen in the atmosphere. The metals also react with metalloids and nonmetals to form a number of solid-state stoichiometric and nonstoichiometric compounds. The following sections detail many of the products from direct interaction of the actinide metals with other elements.

9.2 Oxides

The oxides of the actinides are some of the most prevalent and technologically important binary actinide compounds known. The oxides of thorium, uranium, and plutonium are used throughout the nuclear fuel cycle and, for many of the actinides, are the stable phase in the environment. The oxides can be quite complex, forming nonstoichiometric and polymorphic materials. Anionic oxides of the actinides can also be formed, for example, $AnO_4{}^{2-}$, $An_2O_7{}^{2-}$, $AnO_4{}^{-}$, and so on. The focus of this section will be on the predominant or technologically relevant binary oxide phases. A complete summary of the properties and crystal structure data for actinide oxides can be obtained from *Kirk Othmer Encyclopedia of Chemical Technology*, 4th Edition: Actinides and Transactinides, Wiley-Interscience, NY, 1999.

The thorium oxide system is dominated by ThO_2. The dioxide can be synthesized by burning a number of thorium compounds, including hydroxides, oxalates, carbonates, and so on. The ThO_2 crystallizes in the cubic fluorite structure. ThO_2 is very heat resistant as are all of the actinide oxides and melts at 3390 °C, which is the highest for any known metal oxide.

Protactinium oxides can be stabilized in the tetravalent and pentavalent state. The most stable oxide phase obtained by the burning of metal or protactinium compounds is the white pentoxide, Pa_2O_5. The structure of the pentoxide is related to fluorite and has cubic symmetry. PaO_2 is a black solid that crystallizes in the cubic fluorite structure.

Numerous oxide phases of uranium have been characterized, including uranium oxide, UO, UO_2, U_4O_9, U_3O_7, U_3O_8, UO_3; hydrated species such as $UO_3{\cdot}xH_2O$ and the peroxo complex, $UO_4{\cdot}xH_2O$; and anionic uranates including $[U_2O_7]^{2-}$ and $[U_4O_{13}]^{2-}$. The most important phases for the nuclear fuel cycle are UO_2, U_3O_8, and UO_3. UO_2 is a brown to black solid that has a melting point of 2875 °C. UO_2 may be synthesized through a variety of mechanisms, including (i) oxidation of uranium metal, (ii) reduction of higher valent oxides, (iii) thermal decomposition of uranyl uranates, (iv) oxidation or reduction of uranium halides, (v) decarboxylation of uranium compounds of carbonic acids, (vi) hydrometallurgical preparation, and (vii) electrolysis of uranium halides. As with all of the actinide dioxides, it has a cubic fluorite structure and significantly high density at $10.95\,\mathrm{g\,cm^{-3}}$. U_3O_8 is a mixed valent oxide, containing U^{IV} and U^{VI}. Two modifications of U_3O_8 are known both having a black-green color and crystallizing in an orthorhombic structure. The density of U_3O_8 at 8.16 to $8.41\,\mathrm{g\,cm^{-3}}$ is significantly less than the dioxide. This property is problematic in nuclear fuels. During the 'burning' of UO_2 nuclear fuel, the presence of O_2 within the fuel pins causes the formation of U_3O_8. Owing to the nearly 20% change in the density, any significant buildup of U_3O_8 will cause swelling and eventual cracking of the fuel pellet. UO_3 is the only well-characterized hexavalent actinide oxide. Six different modifications are known for the trioxide with the orange γ-UO_3 being the most important and having a density of $7.80\,\mathrm{g\,cm^{-3}}$. The predominant method for synthesizing UO_3 is by thermal decomposition of U^{VI} compounds in the presence of O_2. While most actinide oxides are thermally stable with high melting points, γ-UO_3 decomposes at 650 °C.

Hyper- and hypostoichiometric, UO_{2+x} and UO_{2-x}, respectively, are also known and have been analyzed by X-ray crystallography. In the case of the UO_{2+x}, extra oxygen atoms occupy central lattice holes in the normal UO_2 structure.

The anhydrous oxide phases for Np consist of the tetravalent NpO_2 and pentavalent Np_2O_5. A hydrated form of a hexavalent neptunium oxide has also been characterized. The neptunium dioxide has an apple green color and can be synthesized by burning the metal in an atmosphere of O_2. The density of NpO_2 is $11.14\,\mathrm{g\,cm^{-3}}$. Np_2O_5 is a dark brown solid that crystallizes in a monoclinic space group. The primary synthetic routes to obtain dineptunium pentaoxide include thermal decomposition of Np^V compounds or high-temperature ignition of the metal. The synthesis of the hexavalent neptunium oxide, $NpO_3{\cdot}xH_2O$, requires strongly oxidizing conditions. The most efficient synthetic route consists of reacting NpO_2 with O_3 in a high-temperature molten salt.

The plutonium oxygen phase diagram is complex. The two most important oxides of plutonium are the dioxide, PuO_2, and the sesquioxide, Pu_2O_3. PuO_2 is used in the nuclear fuel cycle with the fabrication of MOX in either the recycle of spent nuclear fuel or the destruction of plutonium from nuclear weapons. Having a fluorite structure, the yellow–brown to green PuO_2 has a density of $11.46\,\mathrm{g\,cm^{-3}}$ and a melting point of 2400 °C. Pu_2O_3 is a black solid with a hexagonal structure similar to the La_2O_3.

Both of these oxides are present on nearly any piece of plutonium metal that has undergone some corrosion. Under normal conditions, the outside surface of Pu contains PuO_2, while the sesquioxide forms between the PuO_2 layer and the metal. The relative amount of these phases is dictated by the partial pressure of oxygen in the atmosphere.

Obtaining pure and well-ordered PuO_2 is difficult. The presence of hypo- and hyperstoichiometric compounds, PuO_{2-x} and PuO_{2+x}, respectively, pervades nearly any synthetic technique. In recent years, interest in the study of the hyperstoichiometric, PuO_{2+x}, ($x < 0.27$) oxide phases has increased.[47–50] Through the use of a variety of techniques, it has been determined that Pu^V is present in the crystal lattice as the oxygen content increases. This finding was originally thought to have a significant impact on the modeling of nuclear waste repositories due to the increase in solubility of Pu^V species in the environment. However, all of the models were based on solubility studies with PuO_2 that inevitably had hyperstoichiometric oxide phases present. As a result, the published solubility data already represent the bulk solubility of plutonium oxides, including the Pu^V species in PuO_{2+x}.

For the actinide elements heavier than Pu, the predominant phases that have been isolated are An_2O_3 and AnO_2.

9.3 Nitrides

Actinide nitrides are known for Th through Cm. All of the nitrides are high melting compounds with melting points of 2630 °C, 2560 °C, and 2580 °C for Th, Np, and Pu, respectively. The actinide nitrides can decompose to give N_2. Thorium, uranium, and plutonium nitrides are well known and can be used as nuclear fuels. Fuels of this type, especially uranium and mixed uranium–plutonium nitrides, can be used in lead-cooled fast reactors, which have been proposed as a possible next-generation nuclear reactor and for use in deep-sea research vehicles.

Two stoichiometric phases of thorium nitrides have been investigated: ThN and Th_3N_4. ThN is a superconductor with a relatively low T_c. Both of these phases can be made by high-temperature reactions of thorium metal with N_2. An alternative synthetic route to Th_3N_4 involves the reaction of thorium metal with NH_3 to form $Th(NH)_2$, which upon further heating degrades to $Th_2N_2(NH)$ and finally to Th_3N_4.

For uranium, three nitrides of exact stoichiometry are known: UN, U_2N_3, and U_4N_7. As was the case with the oxides, nonstoichiometric complexes can also be synthesized to be of the form, U_2N_{3+x}, where the N/U ratio ranges from 1.64 to 1.84. The brown mononitride, which is the only nitride complex stable above 1300 °C, melts at 2600 °C, and has a density of 14.31 g cm^{-3}. The uranium nitrides can be made by direct interaction of the elements. Some of the other routes to access the nitrides include: uranium metal under static NH_3 at 300 to 350 °C to yield U_2N_3, uranium metal or uranium carbides with NH_3 or N_2 at 600 to 900 °C to produce U_2N_{3+x}, uranium carbide fuels reacted with N_2/H_2 to form UN, and a self-propagating metathetical reaction. The structures of some of the nitrides have been determined with the mononitride having a face-centered cubic NaCl-type structure. The sesquinitride complex has two modifications: the α-phase is found with a body-centered cubic Mn_2O_3-type structure, while the high-temperature β-phase crystallizes in a hexagonal Mn_2O_3-type structure.

The studies on the neptunium nitride system are somewhat limited with the mononitride, NpN, being the predominant phase. PuN is also the only known compound in the plutonium series. The AnN (An = Np, Pu) has been synthesized by reaction of an actinide hydride with NH_3 at high temperatures.

9.4 Carbides

Actinide carbides are also a potential nuclear fuel. The typical reactors that can be fueled by carbides are thermionic, used for space power and propulsion systems, and high-temperature gas-cooled reactors. Three basic carbides have been isolated for the light actinides, AnC, An_2C_3, and AnC_2. Ternary carbides formed from transition metals and the light actinides have also been studied. Uranium carbides are all dark gray solids with a metallic luster. The melting points of UC and U_2C_3 are 2400 and 2417 °C, respectively, and the dicarbide melts at 2475 °C and boils at 4370 °C (760 mm Hg). The densities of the uranium carbide series are 13.60 g cm^{-3} for UC, 12.85 g cm^{-3} for U_2C_3, and 11.69 g cm^{-3} for UC_2. Techniques for the synthesis include the reduction of AnO_2 with CO_2 and the direct interaction of uranium and carbon under highly exothermic conditions. The crystal structure of AnC is a face-centered cubic NaCl-type lattice, identical to that of UN. The sesquicarbides crystallize with a body-centered cubic Pu_2C_3-type structure. Multiple modifications of the AnC_2 are known, for example, α-phase UC_2 has a body-centered tetragonal CaC_2-type structure and the β-phase crystallizes in a face-centered cubic KCN-type lattice. Most of the carbides are sensitive to oxidation by air.

In order to be used as nuclear fuel, carbide microspheres are required. These microspheres have been fabricated by a carbothermic reduction of UO_3 and elemental carbon to form UC. In addition to these uses, the carbides are also precursors for uranium nitride–based fuels.

9.5 Hydrides

Actinide metals react with hydrogen at elevated temperatures to yield a number of hydride phases with compositions resembling AnH_2 and AnH_3. The dihydrides are known for Ac, Th, and Np–Bk and the trihydrides have been isolated for Pa–Bk. Thorium forms a unique hydride phase with the formula Th_4H_{15}. This compound is a superconductor with a T_c between 7.5 and 8 K. It is interesting to note that the superconductivity of thorium metal is destroyed by the primary hydrogenation, for example, formation of ThH_2. This behavior of alternating superconductivity could be attributed to the presence of two types of hydrogen atoms in the Th_4H_{15} structure.

The AnH_2 (An = Ac, Np–Bk) have the fluorite structure. ThH_2 is unique in that it has tetragonal symmetry. In β-UH_3, the metal atoms have a coordination number of 12 and the H atoms occupy tetrahedral intersites. For the other AnH_3 (An = Np–Bk), the crystals have a trigonal structure.

The hydrogenation reaction of the actinides is a reversible process. By heating the hydrides to high temperatures, H_2 gas is driven off, leaving the pure metal. This process has been adopted in the dismantling of plutonium pits from excess nuclear weapons.[51] In this process, the plutonium part is reacted with H_2 gas, which forms a powdered plutonium hydride. The powder is collected and heated past the melting point of plutonium to drive off the dihydrogen gas and leave a Pu ingot.

9.6 Borohydrides

The borohydrides of the tetravalent actinides can be prepared through the reaction of the tetrafluoride with $Al(BH_4)_3$. The products of this reaction are $An(BH_4)_4$ and $AlF_2(BH_4)$.[52] The uranium complex is polymeric in the solid state and is similar to the Zr and Hf analogs. The metal center is bound to 14 hydrogen atoms from two tridentate BH_4^- ligands and four bridging bidentate BH_4^- ligands. These complexes represent the highest coordination number observed for an actinide species.

9.7 Borides

A number of borides of composition AnB_2, AnB_4, AnB_6, and AnB_{12} are known. The AnB_6 and AnB_{12} phases have cubic structures like CsCl and NaCl, respectively. All of the borides are resistant to the action of H_2SO_4, HCl, and HF, but readily dissolve in $HNO_3-H_2O_2$.

Recently, a novel synthesis of UB_4 has been accomplished through a solid-state metathesis reaction.[53] The reaction is performed at $\leq 850\,°C$ by mixing UCl_4 with 2 equivalents of MgB. The resulting UB_4 product can be purified by washing with H_2O.

9.8 Silicides

The silicides of the actinides have not been widely characterized. A uranium silicide of the form U_3Si_2 has received the maximum amount of study owing to its use as a dispersion fuel in research reactors. Another common phase observed for actinide silicides is $AnSi_2$. One of the common synthetic routes to the silicides is the reaction of actinide fluorides, for example, AnF_4, with elemental Si at high temperatures. One of the thermodynamic driving forces for this reaction is the release of SiF_4.

9.9 Pnictides

Five pnictide phases have been identified: An_4X_3, AnX, An_3X_4, An_2X_3, and An_4X_3. The best studied of the pnictides outside of the nitrides are the phosphides. Some interesting properties are observed for the phosphides; for example, Th_3P_4 is a semiconductor. Most of the actinide pnictides are prepared by direct interaction of the elements at high temperatures. Monopnictides have been obtained from U through Cf for Sb. They are produced by the direct interaction of the elements at elevated temperatures.

9.10 Chalcogenides

The interaction of the actinides or of their hydrides with chalcogens or H_2X, respectively, give a number of nonstoichiometric phases with a composition close to AnX, An_2X_3, AnX_2, An_2X_5, or AnX_3. Their thermal stability decreases in the order $S > Se > Te$. The magnetic susceptibility and Mössbauer spectroscopy show that the latter compounds may be formulated as $[An^{3+}]_2(S^{2-})_2(S\text{-}S)^{2-}$, $[An^{4+}]_2(S^{2-})_3(S\text{-}S)^{2-}$, and $[An^{4+}](S^{2-})(S\text{-}S)^{2-}$. These compounds have coordination numbers of 8, 10, and 6, respectively. The oxidation state of the actinides in monochalcogenides has metallic conductivity but U_2S_3 is a semimetal, while the Np and Pu analogs are ionic compounds.

Recently, the first quaternary plutonium metal thiophosphates of the form $KPu(PS_4)_2$ and $MPuP_2S_7$ ($M = K^+$, Rb^+, Cs^+) were prepared using reactive flux methods.[54,55] The structure of $KPu(PS_4)_2$ shows an eight-coordinate bicapped trional prism geometry about the Pu center. The polyhedra are linked through edge-sharing and thiophosphate tetrahedral. The $MPuP_2S_7$ contains $P_2S_7^{4-}$ corner-shared bitetrahedral ligands.

The first polychalcogenide complex, K_4USe_8, was obtained by a solid-state reaction.[56] It has a molecular structure with a distorted dodecahedral anion, $[U(Se_2)_4]^{4-}$, which is isostructural with the known peroxoanions $[M(O_2)_4]^{n-}$, where $M = V$, Nb, Ta, Cr ($n = 3$) or Mo, W ($n = 2$). Recently, two additional uranium selenides have been synthesized, MU_2Se_6 ($M = K^+$, Cs^+), using a reactive flux method. The oxidation state of the uranium in these compounds was found to be tetravalent. The selenium has two distinct oxidation states, Se^{2-} and one similar to a polyselenide network.

New solid-state compounds of phosphoselenates also have been synthesized by reaction of Th and P in a reactive flux of K_2Se_4/Se or Cs_2Se_3/Se at high temperatures.[57,58] For the potassium system, the β-$K_2ThP_3Se_9$ was crystallographically characterized and showed the Th atoms being coordinated to nine Se atoms from phosphoselenate ligands. The coordination geometry is best described as a distorted tricapped trigonal prism. In the Cs system, the compound $Cs_4Th_4P_4Se_{26}$ was isolated.[59,60] The molecule is best described as $[Cs_2Th_2(P_2Se_9)(Se_2)_2]_2$ with the $P_2Se_9^{6-}$ anion having a linear Se–Se–Se backbone.

9.11 Halides

Actinide halide compounds have found extensive utility in the processing of actinide materials as well as for starting materials for synthetic inorganic and coordination chemistry, for example, $AnX_m(THF)_n$ ($m = 3, 4, 5$). The actinide halides can be made in a variety of oxidation states (III–VI) through room-temperature and high-temperature techniques. The trihalides, AnX_3, are stable for all of the actinides except Th and Pa. As a result of the important industrial applications of binary fluorides and chlorides, the majority of the halide discussion focuses on the binary systems. A selected listing of physical constants for the binary uranium halides is provided in Table 6. The bond distances for ThX_4 and UX_4 compounds are given in Table 7.

Some of the general trends among the actinide halides are as follows:

- Stability of the halide is dependent on the redox chemistry of actinides (Pu^{IV} is reduced by Cl^-, Br^-, and I^-).
- Fluoride stabilizes the higher oxidation states of the actinides.

Table 6 Physical constants for selected uranium halides

Compound	Density, g mL^{-1}	Melting point, °C	Boiling point, °C
UF_6	4.68	64.5–64.8	56.2^{765}
UF_4	6.70	960	
UF_3		>1000	
Ucl_5	3.81	>300	
Ucl_4	4.87	590	792^{760}
Ucl_3	5.44	842	
Ubr_4	5.35	516	792^{760}
Ubr_3	6.53	730	Volatile
UI_4	5.6	506	759^{760}

Table 7 Bond distances for thorium and uranium halides, ThX_4 and UX_4

	F	Cl	Br	I
Th-X$_{gas}$ (Å)	2.14	2.58	2.72	
Th-X$_{solid}$ (Å)	2.34	2.88	3.00	3.21
U-X$_{terminal}$ (Å)	2.28	2.71	2.61	2.92
U-X$_{bridging}$ (Å)			2.88	3.10

Table 8 Coordination numbers and geometries for UX_4 and U^n bromides

UX_4	F	Cl	Br	I
CN	8	8	7	6
Geometry	Square antiprism	Dodecahedron	Pentagonal bipyramid	Octahedral
U^n-bromides	V	IV	III	
CN	6	7	9	
Geometry	Octahedral	Pentagaonal bipyramid	Tricapped trigonal prism	

- Coordination numbers decrease with increasing size of the halogen (Table 8).
- Coordination numbers decrease with higher oxidation state (Table 8).
- Reactions with X_2 generally lead to high oxidation state materials (reaction of U with F_2 produces UF_6).
- Reactions with HX lead to stabilization of the lower oxidation states (reaction of PaO_2 with HF/H_2 produces PaF_4).

9.11.1 Fluorides

The fluorides of the actinides, especially uranium, play an important role in the nuclear fuel cycle as well as in the production of actinide metals.

Trivalent. The actinide trifluorides have a structure that is isomorphous with LaF_3, in which each metal has a basic tricapped triganol prismatic geometry with an additional two fluoride ions at a significantly longer distance. The trifluorides tend to be insoluble in H_2O but quite soluble in strong acids, that is, nitric, hot sulfuric, and perchloric. For the actinides with very stable trivalent oxidation states, for example heavy actinides, the synthetic routes to form the AnF_3 are straightforward (equations 3–5). For the light actinides, the isolation of the trifluorides requires the addition of a reducing agent, for example H_2 (equations 6–7).

$$Ac(OH)_3 \xrightarrow[700\,°C]{HF} AcF_3 \tag{3}$$

$$AmO_2 \xrightarrow[\Delta]{HF} AmF_3 \tag{4}$$

$$Cm^{3+}_{(aq)} \xrightarrow{F^-} CmF_3{\cdot}xH_2O \xrightarrow[P_2O_5]{dry} AmF_3 \tag{5}$$

$$MO_2 \xrightarrow[500\,°C]{HF/H_2} MF_3 \quad (M = Np, Pu) \tag{6}$$

$$UF_4 \xrightarrow[900\,°C]{Al\ or\ UH_3\ or\ H_2} UF_3 \tag{7}$$

Tetravalent. The tetrafluorides of the actinides are typically synthesized through the reaction of HF or Freon with the actinide metals, oxides, or hydrides. Since the highest possible oxidation state for Th is the tetravalent state, F_2 can be used to synthesize ThF_4. The solid-state structure of the light actinide tetrafluorides consists of polymers that are created through bridging fluoride ions. The geometry around the metal center is a distorted square antiprism. In general, the tetrafluorides are soluble in strong acids and bases, insoluble in dilute acids and bases, and slightly soluble in cold water. Equations (8–10) provide some examples of potential synthetic routes.

$$U_{metal} \xrightarrow[\Delta]{HF} UF_4 \tag{8}$$

$$NpO_2 \xrightarrow[500\,°C]{HF} NpF_4 \tag{9}$$

$$Pu^{4+}_{(aq)} \xrightarrow{F^-} PuF_4{\cdot}xH_2O \xrightarrow[\Delta]{HF} PuF_4 \tag{10}$$

Pentavalent. The pentafluorides of Pa, U, and Np have been reported. The synthetic routes to obtain the pentafluorides are given in equations (11) and (12). Uranium pentafluoride, UF_5, gives two different modifications that have been structurally characterized, α (grayish white solid) and β (yellowish white). The α-phase, which is produced from the reaction of UF_6 with HBr or mildly heating a mixture of UF_6 and UF_4, has infinite chains of UF_6 units. The β-phase produced by heating a mixture of UF_6 and UF_4 to higher temperatures has eight-coordinate uranium atoms in an irregular geometry.

$$Pa_2O_5 \xrightarrow{HF/H_2} PaF_4 \xrightarrow[700\,^\circ C]{F_2} PaF_5 \tag{11}$$

$$NpF_4 \xrightarrow[500\,^\circ C]{KrF_2/HF} NpF_5 \tag{12}$$

Hexavalent. Uranium hexafluoride, UF_6, is one of the best-studied uranium compounds in existence due to its importance for uranium isotope separation and large-scale production (~70 000 tons per year). All of the actinide hexafluorides are extremely corrosive white (U), orange (Np), or dark brown (Pu) crystalline solids, which sublime with ease at room temperature and atmospheric pressure. The synthetic routes into the hexafluorides are given in equation (13). The volatility of the hexafluorides increases in the order $Pu < Np < U$ in the liquid state and $Pu < U < Np$ in the solid state. UF_6 is soluble in H_2O, CCl_4, and other chlorinated hydrocarbons, is insoluble in CS_2, and decomposes in alcohols and ethers. The oxidative power of the actinide hexafluorides are in line with the transition metal hexafluorides and the order of reactivity is as follows: $PuF_6 > NpF_6 > UF_6 > MoF_6 > WF_6$. The UF_6 molecule can also react with metal fluorides to form $UF_7{}^-$ and $UF_8{}^{2-}$. The same reactivity is not observed for the Np and Pu analogs.

$$An_{metal} \text{ or } AnO_2 \xrightarrow[500\,^\circ C]{F_2} AnF_6 \tag{13}$$

9.11.2 *Chlorides*

Trivalent. The trichlorides, $AnCl_3$, are stable across the series, and two structure types have been observed: nine-coordinate UCl_3 (tricapped trigonal prism) and eight-coordinate $PuBr_3$ (bicapped trigonal prism). The early actinides favor the former structure type, while Bk and Cr are found in the latter. A variety of synthetic routes can be used to access the trihalides, including metathesis, reduction, oxidation, and so on (equations 14–19).

$$Ac(OH)_3 \xrightarrow[250\,^\circ C \text{ or } 500\,^\circ C]{NH_4Cl \text{ or } CCl_4} AcCl_3 \tag{14}$$

$$AmCl_3{\cdot}xH_2O \xrightarrow[250\,^\circ C]{NH_4Cl} AmCl_3 \tag{15}$$

$$M_2O_3 \xrightarrow[400-600\,^\circ C]{HCl} MCl_3 \quad (M = Cm, Es) \tag{16}$$

$$Pu_{metal} \xrightarrow[450\,^\circ C]{Cl_2} PuCl_3 \tag{17}$$

$$UH_3 \xrightarrow[350\,^\circ C]{HCl/H_2} UCl_3 \tag{18}$$

$$NpCl_4 \xrightarrow[600\,^\circ C]{H_2} NpCl_3 \tag{19}$$

Tetravalent. The tetrachlorides $AnCl_4$ are stable for all of the light actinides, Th–Pu. The structure for $AnCl_4$ ($An = Th–Np$) have a dodecahedral geometry of the chlorine atoms about a central actinide metal center. The methods used to synthesize the tetrachlorides are dependent on the actinide of interest. For Th, the direct interaction of the metal with Cl_2 is the most direct method. $PaCl_4$ can be made by reduction of $PaCl_5$ with hydrogen or aluminum at high temperatures. Uranium tetrachloride is a dark green solid that can be prepared in multiple ways. The most efficient synthesis involves the reaction of UO_3 with boiling hexachloropropene. UH_3 can also be treated with Cl_2 to give UCl_4. The red $NpCl_4$ is predominantly made by reacting CCl_4 at high temperatures. The reaction of $PuCl_3$ with Cl_2 results in an equilibrium between the tri- and tetrachloride.

Pentavalent. Actinide pentachlorides are limited to $PaCl_5$ and UCl_5. $PaCl_5$ has a chain-type structure with seven-chloride ions bound to each metal center. UCl_5 consists of an edge-sharing bioctahedral dimer, U_2Cl_{10}. The protactinium pentachloride is most easily accessed through a high-temperature reaction of Pa_2O_5 with a mixture of C, Cl_2, and CCl_4. UCl_5 is a reddish brown solid that can be prepared by reaction of UO_3 under flowing CCl_4. While this procedure can be used to make UCl_4, the reaction can be controlled to stop at U^V by lowering the temperature. The direct oxidation of UCl_4 by Cl_2 can also be used to synthesize the pentachloride. The pentachloride decomposes in H_2O and acid, is soluble in anhydrous alcohols, and insoluble in benzene and ethers.

Hexavalent. The best-studied actinide hexachloride is uranium hexachloride, UCl_6. This compound is prepared by chlorination of UCl_4 with $SbCl_5$. The disproportionation of UCl_5 to form UCl_4 and UCl_6 provides a second route to access the hexachloride. An alternative preparative approach is the disproportionation of UCl_5 to UCl_4 and UCl_6. The hexachloride is isostructural with the hexafluoride, being monomeric with an octahedral arrangement of the chlorine atoms around the uranium center.

9.11.3 *Bromides and Iodides*

Trivalent. Owing to the weakly oxidizing power of bromine and iodine, the majority of the isolated compounds consist of trivalent actinides, for example, AnX_3 ($X = Br, I$). The tribromides $AnBr_3$ have been isolated for $An = Ac–Bk$. The light actinides Ac–Np have the nine-coordinate UCl_3 structure, while Pu, Am, and Cm are found with an eight-coordinate bicapped trigonal prismatic geometry. With the decreasing ionic radius due to the actinide contraction, the Bk analog crystallizes with a six-coordinate structure. The general synthetic methods to synthesize the actinide tribromides are given in equations (20–24).

$$M_2O_3 \xrightarrow[600-800\,^{\circ}C]{HBr} MBr_3 \quad (M = Cm, Cf) \tag{20}$$

$$U_{metal} \xrightarrow[500\,^{\circ}C]{Br_2} UBr_3 \tag{21}$$

$$UH_3 \xrightarrow[\Delta]{HBr} UBr_3 \tag{22}$$

$$NpO_2 \xrightarrow[\Delta]{Al/AlBr_3} NpBr_3 \tag{23}$$

$$PuBr_3 \cdot xH_2O \xrightarrow[70-120\,^{\circ}C]{vac} PuBr_3 \tag{24}$$

As with the other trihalides, the structures of the triiodides vary across the actinide series. AcI_3 is nine-coordinate and AnI_3 (An = Pa–Am) are eight-coordinate. A six-coordinate isomer of AmI_3 with the $FeCl_3$ structure is also accessible at high temperatures. Equations (25–30) detail the synthetic methods used to obtain the actinide triiodides.

$$Ac_2O_3 \xrightarrow[\Delta]{AlI_3} AcI_3 \tag{25}$$

$$MO_2 \xrightarrow[350\,^{\circ}C]{AlI_3} MI_3 \quad (M = Np, Am) \tag{26}$$

$$PaI_5 \xrightarrow[360\,^{\circ}C]{vac} MI_3 \tag{27}$$

$$UH_3 \xrightarrow[300\,^{\circ}C]{HI} UI_3 \tag{28}$$

$$Pu_{metal} \xrightarrow[500\,^{\circ}C]{HgI_2} PuI_3 \tag{29}$$

$$CfCl_3 \xrightarrow[\Delta]{HI} CfI_3 \tag{30}$$

Tetravalent. Actinide tetrabromides, $AnBr_4$, are stable for An = Th, Pa, U, and Np. The tetraiodides, AnI_4, are known for An = Th, Pa, and U. The UI_4 is actually unstable over time, producing UI_3 and I_2. The best synthetic approach to AnX_4 (X = Br, I) is by direct interaction of the elements or AnX_3 with X_2 at elevated temperatures. The tetrabromide is soluble in H_2O and liquid NH_3 but decomposes in alcohols, whereas the tetraiodide is soluble in cold H_2O and acetonitrile and decomposes in hot H_2O.

Pentavalent. The only stable pentabromides and pentaiodides are found for the Pa system, $PaBr_5$ and PaI_5. The primary synthetic method to access $PaBr_5$ and PaI_5 is through the pentavalent oxide Pa_2O_5. The uranium pentabromide, UBr_5, is unstable toward reduction but can be made by reaction of UBr_4 with Br_2 or by bromination of uranium turnings with Br_2 in acetonitrile. The metastable pentabromide is isostructural with the pentachloride, having edge-sharing octahedra U_2Br_{10}.

9.11.4 Oxyhalides

Nearly all of the halides of the actinides can undergo partial oxidation or hydrolysis to form actinide oxyhalide compounds and complexes. Actinide tetrahalides react with dioxygen or other oxygen donors to give $AnOX_2$. Protactinium halides undergo a number of oxidation reactions to form compounds of the form PaO_2F, $PaOBr_3$, PaOI, and PaO_2I. The predominant uranium oxyhalides are of the form UOX_n ($n = 2, 3$) and $[UO_2X_n]^{2-n}$ ($n = 1-4$). Multiple oxidation states of neptunium(III–VI) have been found to form oxyhalides. Compounds of the form $NpOF_3$, NpO_2F_2, $NpOF_4$, NpOCl, and NpOI are examples of the breadth of neptunium oxyhalides. For plutonium, oxyhalides of the form PuOX (X = F, Cl, Br, I), $PuOF_4$, and PuO_2F_2 have all been reported.

9.11.5 Anionic Complexes

A wide variety of anionic actinide halide complexes are well known and typically are isolated with alkali or alkaline-earth metal ions. The tendency and stability of the anionic complexes follow the trend $F \gg Cl > Br \gg I$. The trivalent fluorides and chlorides typically form complexes of the form AnX_4^{-} and AnX_6^{2-}. Plutonium has also been shown to give the following complexes: $PuCl_5^{2-}$, $Pu_2Cl_7^{-}$, and $PuCl_9^{6-}$. The anionic tetravalent actinide fluorides represent a broad class of complexes, for example, M_xAnF_y ($x = 1$, $y = 5$; $x = 2$, $y = 6$; $x = 3$, $y = 7$; $x = 4$, $y = 8$). Tetravalent actinide chloro, bromo and iodo complexes can be isolated from aqueous solutions in the form of octahedral $AnCl_6^{2-}$ ions.

The pentahalides of Pa and U generally add another ligand to form octahedral complexes of the form AnX_6^{-}. The fluorides of Np^{V} and Pu^{V} have been isolated as AnF_6^{-}, AnF_7^{2-} and AnF_8^{3-}. The predominate anionic complexes for the hexavalent actinides are based on UF_6. Uranium hexafluoride will add up to two additional fluoride ions to form UF_7^{-} and UF_8^{2-} using standard techniques. The unique UF_9^{3-} ion is formed from the thermal decomposition of Na_2UF_8.

9.12 Special Topics

Ionic Liquids. Room-temperature ionic liquids are molten salts that are liquid over a broad temperature range.[61] These liquids can be prepared with a variety of cations, for example, *N*-alkyl-pyradinium, asymmetric dialkyl-imidazolium, and so on, and anions, for example, PF_6^{-}, BF_4^{-}, $(CF_3SO_2)_2N^{-}$, and so on. Through judicious choice of the cation/anion pair, ionic liquids can be synthesized that are miscible and immiscible with H_2O. As a solvent, ionic liquids typically are highly solvating and noncoordinating. Being molten salts, the RTILs have high electrical conductivity, and based on the cation/anion combination can have very large electrochemical windows. As a result of these properties, significant research is being performed to study the behavior of the actinides in these novel solvents.[62–67] In addition to being potential 'green' solvents for actinide separations, the large electrochemical windows allow for the use of pyrochemical methods to electroplate actinide metals at room temperature. The current pyroprocessing technologies for reprocessing spent nuclear fuel require the use of high-temperature molten NaCl/KCl eutectics.

Hydrothermal Synthesis. Hydrothermal synthesis**[68,69]** and reactive fluxes have been increasingly used as a method for synthetic actinide chemistry. Unique phases of actinide selenites, tellurites, iodates**[70]** and periodates**[71]** have all been synthesized under hydrothermal reaction conditions. New compounds and phases of oxyfluorides, phosphates, and sulfates using organic templates also have been synthesized with hydrothermal methods.**[72–74]**

10 HEALTH AND SAFETY FACTORS

10.1 Exposure and Health Effects

Actinides are heavy metals that can act as general cellular poisons, which can potentially affect any organ or tissue. The actinides and their compounds can be damaging due to chemical toxicity and by the injury caused by ionizing radiation. The chemical toxicities of actinide compounds depend on their solubility in biological media. Highly soluble, and therefore highly transportable, and toxic compounds include fluorides, chlorides, nitrates, and carbonates; slightly transportable compounds include oxides, hydrides, and carbides.

Most actinides can enter the human body orally, by inhalation, and through the skin and mucous membranes. Actinide compounds, both soluble and insoluble, are absorbed most readily from the lungs. Both uranium and plutonium have been found to be stored in bones, while deposition in soft tissues is almost negligible. Occupational exposure to actinides usually involves inhalation of aerosols carrying particles varying in size and density and containing a mixture of uranium compounds with different solubilities. Insoluble particles are deposited in the lungs, retained there for a long time, and can cause radiation damage of varying degree or silicosis.

Results of extensive studies have demonstrated that the consumption of drinking water containing uranium at elevated levels of 0.04 to 0.05 mg L^- is not detrimental to human health.

10.2 Personnel Protection and Radiation Considerations

The main adverse factor working with actinide materials is airborne dust. Personal protection should include respirators, protective clothing, surgical gloves, suitable footwear, use of wet processes wherever possible, and in operations involving dust formation, face masks, constant ventilation, and glove boxes. Finely divided actinide metals, some alloys, and the hydrides are pyrophoric; therefore, such materials should be handled in an inert atmosphere glove box.

Isotopes that emit fairly strong γ-radiation, should be handled in a hot cell; ^{238}Pu, ^{241}Am, ^{243}Am and similar isotopes should be handled in glove boxes; ^{237}Np, ^{239}Pu, ^{242}Pu, ^{244}Pu, and ^{248}Cm can be handled in a fume hood or glove box; ^{235}U and ^{238}U can be handled on the bench top or in a fume hood because of their lower radiation fields. The laboratory should be equipped as an α-laboratory. In the handling of the actinides, as in the case of all radionuclides, radioactivity due to the progeny, such as Th, Ra, Rn, and so on, should be considered, as should alternative radiation-generating decay paths, for example, α-n reaction from uranium fluorides.

Large quantities of fissile isotopes, ^{233}U and ^{235}U, ^{237}Np, ^{239}Pu, and so on, should be handled and stored appropriately to avoid a critical hazard. Clear and relatively simple precautions, such as dividing quantities so that the minimum critical mass is avoided, following administrative controls, using neutron poisons, and avoiding critical configurations (or shapes), must be followed to prevent an extremely treacherous explosion.

11 REFERENCES

1. L. R. Morss, M. A. Lewis, M. K. Richmann, and D. Lexa, *J. Alloys Compd.*, 2000, **303–304**, 42.
2. V. Pirlet, *J. Nucl. Mater.*, 2001, **298**, 47.
3. N. Kaltsoyannis, *Chem. Soc. Rev.*, 2003, **32**, 9.
4. J. H. Matonic, B. L. Scott, and M. P. Neu, *Inorg. Chem.*, 2001, **40**, 2638.
5. J. Wang, M. Nakada, T. Kitazawa, T. Yamashita, M. Takeda, '^{237}Np Mossbauer Spectra of $M[NpO_2(NO_3)_3](M = K, NH_4$ and Rb) Complexes', Faculty of Science, Toho University, Japan, FIELD URL, 2001.
6. J. Wang, T. Kitazawa, M. Nakada, T. Yamashita, and M. Takeda, *Bull. Chem. Soc. Jpn.*, 2002, **75**, 253.
7. J. H. Matonic, M. P. Neu, A. E. Enriquez, R. T. Paine, and B. L. Scott, *J. Chem. Soc., Dalton Trans.*, 2002, 2328.
8. K. D. S. Mudher and K. Krishnan, *J. Alloys Compd.*, 2000, **313**, 65.
9. J. M. Berg, S. D. Conradson, J. H. Matonic, M. P. Neu, and S. D. Reilly, *AIP Conf. Proc.*, 2003, **673**, 236.
10. B. D. Zwick, A. P. Sattelberger, and L. R. Avens, *Transuranium Elem. Symp.*, 1992, 239.
11. A. E. Enriquez, J. H. Matonic, B. L. Scott, and M. P. Neu, *Chem. Commun.*, 2003, 1892.
12. L. R. Avens, S. G. Bott, D. L. Clark, A. P. Sattelberger, J. G. Watkin, and B. D. Zwick, *Inorg. Chem.*, 1994, **33**, 2248.
13. A. L. Odom, P. L. Arnold, and C. C. Cummins, *J. Am. Chem. Soc.*, 1998, **120**, 5836.

14. D. J. Mindiola, Y.-C. Tsai, R. Hara, Q. Chen, K. Meyer, and C. C. Cummins, *Chem. Commun.*, 2001, 125.
15. P. Roussel, P. B. Hitchcock, N. D. Tinker, and P. Scott, *Inorg. Chem.*, 1997, **36**, 5716.
16. P. Roussel, P. Scott, and N. D. Tinker, *J. Alloys Compd.*, 1998, **271–273**, 150.
17. P. Roussel and P. Scott, *J. Am. Chem. Soc.*, 1998, **120**, 1070.
18. P. Roussel, N. W. Alcock, R. Boaretto, A. J. Kingsley, I. J. Munslow, C. J. Sanders, and P. Scott, *Inorg. Chem.*, 1999, **38**, 3651.
19. P. Roussel, W. Errington, N. Kaltsoyannis, and P. Scott, *J. Organomet. Chem.*, 2001, **635**, 69.
20. P. Roussel, R. Boaretto, A. J. Kingsley, N. W. Alcock, and P. Scott, *J. Chem. Soc., Dalton Trans.*, 2002, 1423.
21. N. Kaltsoyannis and P. Scott, *Chem. Commun.*, 1998, 1665.
22. C. Apostolidis, A. Carvalho, A. Domingos, B. Kanellakopulos, R. Maier, N. Marques, A. P. De Matos, and J. Rebizant, *Polyhedron*, 1998, **18**, 263.
23. M. Ephritikhine, J. C. Berthet, C. Boisson, M. Lance, and M. Nierlich, *J. Alloys Compd.*, 1998, **271–273**, 144.
24. A. K. Dash, J. X. Wang, J. C. Berthet, M. Ephritikhine, and M. S. Eisen, *J. Organomet. Chem.*, 2000, **604**, 83.
25. J. Q. Wang, A. K. Dash, J. C. Berthet, M. Ephritikhine, and M. S. Eisen, *Organometallics*, 1999, **18**, 2407.
26. J. Wang, M. Kapon, J. C. Berthet, M. Ephritikhine, and M. S. Eisen, *Inorg. Chim. Acta*, 2002, **334**, 183.
27. P. Scott and P. B. Hitchcock, *Polyhedron*, 1994, **13**, 1651.
28. P. Scott and P. B. Hitchcock, *J. Chem. Soc., Dalton Trans.: Inorg. Chem.*, 1995, 603.
29. D. J. Wilson, A. Sebastian, F. G. N. Cloke, A. G. Avent, and P. B. Hitchcock, *Inorg. Chim. Acta*, 2003, **345**, 89.
30. M. P. C. Campello, M. J. Calhorda, A. Domingos, A. Galvao, J. P. Leal, A. Pires de Matos, and I. Santos, *J. Organomet. Chem.*, 1997, **538**, 223.
31. M. P. C. Campello, A. Domingos, A. Galva, A. P. de Matos, and I. Santos, *J. Organomet. Chem.*, 1999, **579**, 5.
32. I. Bonhoure, C. Den Auwer, C. C. dit Moulin, P. Moisy, J.-C. Berthet, and C. Madic, *Can. J. Chem.*, 2000, **78**, 1305.
33. K. Meyer, D. J. Mindiola, T. A. Baker, W. M. Davis, and C. C. Cummins, *Angew. Chem., Int. Ed. Engl.*, 2000, **39**, 3063.
34. P. B. Duval, C. J. Burns, W. E. Buschmann, D. L. Clark, D. E. Morris, and B. L. Scott, *Inorg. Chem.*, 2001, **40**, 5491.
35. C. J. Burns, D. L. Clark, R. J. Donohoe, P. B. Duval, B. L. Scott, and C. D. Tait, *Inorg. Chem.*, 2000, **39**, 5464.
36. S. J. Coles, P. G. Edwards, M. B. Hursthouse, and P. W. Read, *Acta Cryst. C.: Cryst. Struct. Commun.*, 1995, **C51**, 1060.
37. P. G. Edwards, J. S. Parry, and P. W. Read, *Organometallics*, 1995, **14**, 3649.
38. F. H. Stephens, P. L. Arnold, P. L. Diaconescu, C. C. Cummins, *Abstr. Pap. – Am. Chem. Soc.* 2000, **220**, INOR-018.
39. B. P. Warner, J. A. D'Alessio, A. N. Morgan III, C. J. Burns, A. R. Schake, J. G. Watkin, *Inorg. Chim. Acta* 2000, **309**, 45.
40. I. Castro-Rodriguez, K. Olsen, P. Gantzel, and K. Meyer, *J. Am. Chem. Soc.*, 2003, **125**, 4565.
41. M. P. Wilkerson, C. J. Burns, H. J. Dewey, J. M. Martin, D. E. Morris, R. T. Paine, and B. L. Scott, *Inorg. Chem.*, 2000, **39**, 5277.
42. D. E. Morris, M. P. Wilkerson, C. J. Burns, B. L. Scott, and R. T. Paine, *AIP Conf. Proc.*, 2000, **532**, 371.
43. A. K. Burrell, G. Hemmi, V. Lynch, and J. L. Sessler, *J. Am. Chem. Soc.*, 1991, **113**, 4690.
44. J. L. Sessler, A. E. V. Gorden, D. Seidel, S. Hannah, V. Lynch, P. L. Gordon, R. J. Donohoe, C. Drew Tait, and D. Webster Keogh, *Inorg. Chim. Acta*, 2002, **341**, 54.
45. J. L. Sessler, D. Seidel, A. E. Vivian, V. Lynch, B. L. Scott, and D. W. Keogh, *Angew. Chem., Int. Ed. Engl.*, 2001, **40**, 591.
46. J. L. Sarrao, L. A. Morales, and J. D. Thompson, *J. Metals*, 2003, **55**, 38.
47. J. M. Haschke, T. H. Allen, and L. A. Morales, *J. Alloys Compd.*, 2001, **314**, 78.
48. J. M. Haschke and T. H. Allen, *J. Alloys Compd.*, 2002, **336**, 124.
49. L. Morales, T. Allen, and J. Haschke, *AIP Conf. Proc.*, 2000, **532**, 114.
50. M. T. Paffett, D. Farr, and D. Kelly, *AIP Conf. Proc.*, 2003, **673**, 193.
51. C. K. Rofer, D. A. Martinez, and V. L. Trujillo, *NATO Sci. Ser. 1: Disarmament Technol.*, 2000, **29**, 131.
52. S. M. Cendrowski-Guillaume, G. Le Gland, M. Lance, M. Nierlich, and M. Ephritikhine, *C. R. Chim.*, 2002, **5**, 73.
53. A. J. Lupinetti, J. L. Fife, E. Garcia, P. K. Dorhout, and K. D. Abney, *Inorg. Chem.*, 2002, **41**, 2316.
54. R. F. Hess, K. D. Abney, J. L. Burris, H. D. Hochheimer, and P. K. Dorhout, *Inorg. Chem.*, 2001, **40**, 2851.
55. R. F. Hess, P. L. Gordon, C. D. Tait, K. D. Abney, and P. K. Dorhout, *J. Am. Chem. Soc.*, 2002, **124**, 1327.
56. B. C. Chan, Z. Hulvey, R. F. Hess, K. D. Abney, P. K. Dorhout, Abstracts of papers, *227th ACS National Meeting*, Anaheim, CA, March 28 – April 1, 2004, INOR-993.
57. P. M. Briggs-Piccoli, K. D. Abney, and P. K. Dorhout, *J. Nucl. Sci. Technol.*, 2002, 611.
58. P. M. B. Piccoli, K. D. Abney, J. R. Schoonover, and P. K. Dorhout, *Inorg. Chem.*, 2000, **39**, 2970.
59. P. M. B. Piccoli, R. F. Hess, P. K. Dorhout, K. D. Abney, and J. R. Schoonover, *AIP Conf. Proc.*, 2000, **532**, 384.
60. P. M. B. Piccoli, K. D. Abney, J. D. Schoonover, and P. K. Dorhout, *Inorg. Chem.*, 2001, **40**, 4871.
61. A. I. Bhatt, I. May, V. A. Volkovich, M. E. Hetherington, B. Lewin, R. C. Thied, and N. Ertok, *J. Chem. Soc., Dalton Trans.*, 2002, 4532.
62. A. Chaumont and G. Wipff, *J. Phys. Chem. B*, 2004, **108**, 3311.

63. A. E. Bradley, J. E. Hatter, M. Nieuwenhuyzen, W. R. Pitner, K. R. Seddon, and R. C. Thied, *Inorg. Chem.*, 2002, **41**, 1692.

64. W. J. Oldham Jr, D. A. Costa, W. H. Smith, *ACS Symp. Ser.* 2002, **818**, 188.

65. A. E. Visser and R. D. Rogers, *Proc. – Electrochem. Soc.*, 2002, **19**, 516.

66. A. E. Visser and R. D. Rogers, *J. Solid State Chem.*, 2003, **171**, 109.

67. A. E. Visser, M. P. Jensen, I. Laszak, K. L. Nash, G. R. Choppin, and R. D. Rogers, *Inorg. Chem.*, 2003, **42**, 2197.

68. A. A. Bessonov, M. S. Grigoriev, A. B. Ioussov, N. A. Budantseva, and A. M. Fedosseev, *Radiochim. Acta*, 2003, **91**, 339.

69. P. M. Almond, R. E. Sykora, S. Skanthakumar, L. Soderholm, and T. E. Albrecht-Schmitt, *Inorg. Chem.*, 2004, **43**, 958.

70. R. E. Sykora, A. C. Bean, B. L. Scott, W. Runde, and T. E. Albrecht-Schmitt, *J. Solid State Chem.*, 2004, **177**, 725.

71. W. Runde, A. C. Bean, and B. L. Scott, *Chem. Commun.*, 2003, 1848.

72. M. B. Doran, A. J. Norquist, and D. O’Hare, *Inorg. Chem.*, 2003, **42**, 6989.

73. M. B. Doran, C. L. Stuart, A. J. Norquist, and D. O’Hare, *Chem. Mater.*, 2004, **16**, 565.

74. J.-Y. Kim, A. J. Norquist, and D. O’Hare, *J. Am. Chem. Soc.*, 2003, **125**, 12688.

Actinides: Organometallic Chemistry

Carol J. Burns, David L. Clark & Alfred P. Sattelberger
Los Alamos National Laboratory, Los Alamos, NM, USA

1 Introduction 1
2 Cyclopentadienyl and Substituted Cyclopentadienyl Complexes 1
3 Cyclooctatetraene Complexes 9
4 Allyl, Pentadienyl, and Related Complexes 11
5 Arene Complexes 12
6 Other Carbocyclic Ligands 13
7 Alkyl Complexes 14
8 Hydride Complexes 18
9 Carbonyl Complexes 18
10 Phosphoylide Complexes 19
11 Organoactinide Surface Chemistry and Catalysis 19
12 Electronic Structure and Bonding 21
13 Related Articles 23
14 References 23

1 INTRODUCTION

The past 50 years have witnessed many important and exciting developments in the chemistry of transition metal complexes containing hydrocarbon-based ligands (often referred to as hydrocarbyl ligands, *see Hydrocarbyl*). Transition metal organometallic chemistry is a vibrant and evolving field, one stimulated by many factors including inorganic and organic chemists' interests in new synthetic, mechanistic, and structural chemistry, materials chemistry, nanoscience and nanotechnology, and homogeneous and heterogeneous catalysis. Despite a few early reports on the synthesis of uranium and thorium cyclopentadienyl complexes (see below), actinide or 5f-element organometallic chemistry is a field of more recent vintage. All known isotopes of these elements are radioactive, with half-lives varying from seconds to billions of years. Radioactive decay, and the attendant high costs of equipping laboratories for working with, monitoring, and disposing of radionuclides, represents an activation barrier (for the transuranic elements, a very significant one) for organoactinide research and there are relatively few academic and national laboratories equipped to explore this area of chemistry. It is the authors' belief that there is much more to be learned about the organometallic chemistry of the early actinides, that is, thorium through plutonium, particularly through systematic studies of related complexes.

The large size of actinide ions permits coordination numbers and attendant polyhedra that are uncommon among the transition elements. For the same set of ligands, a 5f-element ion will be more coordinatively unsaturated than a d-element ion. The availability of 5f valence orbitals also suggests a greater variety of metal–ligand binding possibilities, smaller ligand field stabilization energies, smaller energy barriers to intra- and intermolecular ligand exchange, and a greater degree of ionic character in metal–ligand bonding that leads to more electrophilic metal centers and correspondingly more nucleophilic ligand centers. Modern organoactinide chemistry is now characterized by the existence not only of actinide analogs to many classes of d-transition metal complexes, but increasingly common reports of compounds and types of reactions unique to the actinide series. We will touch on these points throughout this chapter.

The first actinide organometallic complex, red-brown $(C_5H_5)_3UCl$, was prepared and characterized by Reynolds and Wilkinson in 1956[1] or shortly after the discovery of ferrocene (*see Ferrocene*), $(C_5H_5)_2Fe$. However, it was not until the preparation and structural characterization of bis(cyclooctatetraenyl)uranium, $(C_8H_8)_2U$ ('uranocene', *see Uranocene*) in 1968[2] and the isolation and characterization of uranium alkyls (*see Alkyl Complexes*) in 1973[3] that the field developed momentum. The purpose of this chapter is to provide an overview of organoactinide chemistry that reflects historical as well as recent developments and achievements in the field; it is not meant to be an exhaustive review of the primary literature. More detailed discussion, background material, and extensive references to the literature can be found in several excellent reviews.[4–10]

Not every actinide element has known or well-developed organometallic chemistry. By far the most research has been done on thorium and uranium compounds, a consequence of favorable isotope-specific nuclear properties and, at least until recently, the commercial availability of key starting materials such as ^{232}Th metal, anhydrous $^{232}ThCl_4$, U metal, and anhydrous $^{238}UCl_4$.[11] Thorium chemistry is dominated by the $+4$ oxidation state and has some similarities to the chemistry of the heavier group 4 metals. For uranium, one can access oxidation states from $+3$ to $+6$ in organic media. Although there are some similarities to the chemistry of the heavier group 6 elements, for example, tungsten, there are also some remarkable differences made possible by the availability of the 5f valence orbitals.

2 CYCLOPENTADIENYL AND SUBSTITUTED CYCLOPENTADIENYL COMPLEXES

Organoactinide chemistry initially developed around the use of the ubiquitous cyclopentadienyl ligand (*see Cyclopentadienyl*), $Cp = C_5H_5^-$, and subsequently its alkyl- and silyl-substituted derivatives. The tetravalent oxidation state dominates the cyclopentadienyl chemistry of the early actinides, but the number of reports on trivalent actinide cyclopentadienyl systems has grown steadily over the past decade. The literature on protactinium(IV) and tetravalent and trivalent *transuranic* cyclopentadienyl compounds is sparse, and the reaction chemistry of these compounds is not particularly well developed. A remarkable series of uranium(V) and uranium(VI) cyclopentadienyl compounds that have no transition metal analogs are of more recent vintage and will be described in due course.

2.1 Cp_4An Compounds

Tetrakis(cyclopentadienyl) actinide complexes, $(C_5H_5)_4An$, were among the earliest organoactinide complexes synthesized and can be prepared by metathesis (*see Metathesis*) of the anhydrous tetrachlorides ($AnCl_4$) with potassium cyclopentadienide (KCp) in refluxing benzene (equation 1, for An = Th, U, and Np).**[12]** Another member of this series, Cp_4Pa,

$$AnCl_4 + 4KCp \xrightarrow[\Delta]{C_6H_6} AnCp_4 + 4KCl \qquad (1)$$

has been synthesized in a solvent-free reaction between protactinium tetrachloride, $PaCl_4$, and Cp_2Be (equation 2).**[12]** All of the Cp_4An compounds are sparingly soluble in organic

$$PaCl_4 + 2Cp_2Be \xrightarrow{\Delta} Cp_4Pa + 2BeCl_2 \qquad (2)$$

solvents. The thorium and uranium compounds have been structurally characterized.**[13]** IR spectra and X-ray powder diffraction data indicate that the other two members of the series are isostructural. The molecular structure of Cp_4U features a nearly tetrahedral coordination geometry as shown in (**1**), with four η^5-cyclopentadienyl ligands whose average U–C_{ring} distance is 2.81(2) Å.

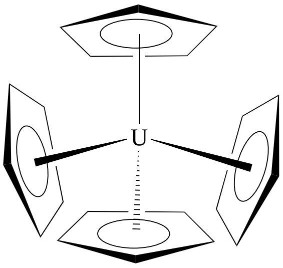

(**1**)

These U–C distances are roughly 0.1 Å longer than typically observed in other U(IV) cyclopentadienyl complexes and likely reflect the pronounced crowding associated with four η^5-C_5H_5 ligands about the metal center. The mean bond dissociation energy in Cp_4U has been estimated from thermochemical combustion data to be 247 kJ mol^{-1}.**[14]** The latter may be compared to the value of 297 kJ mol^{-1} found for Cp_2Fe (ferrocene, *Ferrocene*). Compilations of thorium and uranium metal–ligand bond disruption enthalpies (*see* ***Bonding Energetics of Organometallic Compounds***) are available and are quite useful for interpreting and even predicting the course of organoactinide reactions.**[15]**

Concomitant with the development of synthetic, mechanistic, and structural organoactinide chemistry, there has been an ongoing debate regarding the extent of covalency in actinide–ligand bonds.**[8,10]** It is important to emphasize that the debate is usually about the *degree* of covalency in a particular actinide–ligand bond, rather than whether or not it exists. Most workers in the field agree that covalency contributes to *early* actinide-ligand bonding in compounds where the formal oxidation state of the metal is +3 or greater. There is also general agreement that actinide-ligand interactions are predominantly ionic for late actinide organometallic compounds in which the formal oxidation state of the metal is +3. A discussion of current theoretical views on this topic will be delayed until later, but along the way we will cite experimental data that suggests that actinide–ligand bonds have appreciable covalent character. A comparison of the ^{237}Np Mössbauer spectra of Cp_4Np and $NpCl_4$ is one such example.**[16]** The organometallic compound exhibits an isomer shift that is 1.06 cm s^{-1} higher than that observed for the chloride. This difference has been taken as an indication of substantially greater shielding of the 6s shell in Cp_4Np and enhanced metal–ligand bond covalency.

2.2 Cp_3AnX Compounds

As mentioned in the Introduction, $(C_5H_5)_3UCl$ was the first organoactinide compound reported in the literature. Its preparation from UCl_4 and sodium cyclopentadienide in tetrahydrofuran has been generalized, and most of the early actinide tris(cyclopentadienyl) halides can be prepared by the synthetic methodology outlined in equation (3).**[1,6]** Solvents for this reaction are generally polar organics such as THF or DME.

$$AnX_4 + 3M'Cp \xrightarrow{DME} AnCp_3X + 3M'Cl \qquad (3)$$

The X-ray structure of Cp_3UCl reveals a distorted tetrahedral uranium coordination geometry as shown in (**2**) with three η^5-Cp ligands at 2.74(1) Å from the metal center and the U–Cl bond (2.559(16) Å) coincident with the molecular threefold axis.**[17]** This type of structure is essentially identical for all Cp_3UX derivatives. A more accurate X-ray diffraction study of tris(benzylcyclopentadienyl)uranium(IV) chloride gave an average U–C_{ring} distance of 2.733(1) Å and a U–Cl distance of 2.627(2) Å.**[18]**

In contrast to the reactions of trivalent lanthanide Cp compounds (Cp_3Ln) with iron(II) chloride, Cp_3UCl does

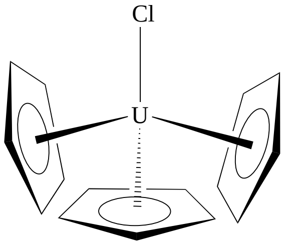

(**2**)

not react with $FeCl_2$ to give ferrocene and it decomposes rather slowly in water. Although the latter results may be taken as an indication of a greater degree of covalency in the uranium(IV)–Cp bond, theoretical considerations suggest that the bonding is more ionic than found in the vast majority of d-block cyclopentadienyl compounds.[8,10] The chloride ligand of Cp_3UCl, on the other hand, is labile and this lability has facilitated the syntheses of a rather large number of other tris(cyclopentadienyl)-uranium(IV) compounds. Thus Cp_3UX compounds with U–P, U–N, U–Si, U–Ge, U–Fe, and U–Ru bonds have been synthesized by metathesis of the chloride ligands in Cp_3UCl.[9] The uranium(IV) diphenylphosphido compound, Cp_3UPPh_2, can also be isolated from the reaction of $Cp_2U(NEt_2)_2$ with $HPPh_2$, during which a redistribution of Cp ligands occurs, presumably after $Cp_2U(NEt_2)(PPh_2)$ is generated.[19] Redistribution reactions (*see Redistribution Reaction*), as we shall see below, are frequently encountered in the chemistry of Cp_2AnX_2 compounds. A reaction scheme illustrating the utility of Cp_3UCl as a synthon in Cp_3UX chemistry is delineated in Scheme 1. Noteworthy in Scheme 1 is the preparation of unbridged metal–metal bonds between uranium and iron or ruthenium.[20] The molecular structures of a number of Cp_3AnX complexes have been determined, as well as the structures of related tris(indenyl)actinide halide compounds (see below). All possess a pseudotetrahedral geometry with the X ligand on an approximate threefold axis of symmetry. The An–C_{ring} and An–X bond lengths are normal for most of the complexes, with Th–C_{ring} and Th–X distances being slightly longer than their counterparts in analogous uranium complexes, consistent with the slightly larger ionic radius of thorium. The average U–C_{ring} and U–X bond lengths are significantly longer in the tris(pentamethylcyclopentadienyl) complexes, $(C_5Me_5)_3UX$ or $Cp^*{}_3UX$ (X = F, Cl), reported by Evans and coworkers.[21] For example, the average U–C_{ring} distance (2.833(9) Å) in $Cp^*{}_3UCl$ is ∼0.1 Å longer and U–Cl bond length (2.90(1) Å) is ∼0.3 Å longer than that found in $(C_5H_5)_3UCl$. The origin of this difference is clearly the steric crowding engendered by the bulky pentamethylcyclopentadienyl ligands.

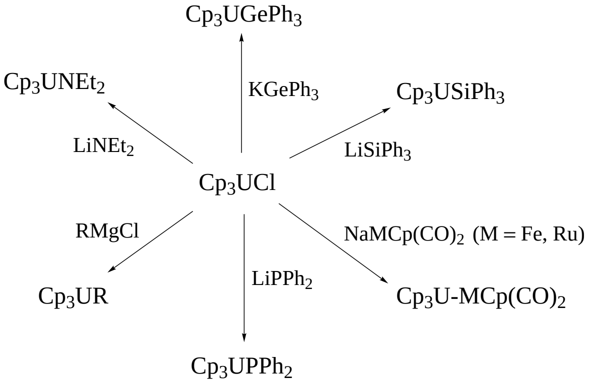

Scheme 1 Some reactions of tris(cyclopentadienyl)uranium(IV) chloride

In addition to metathesis reactions involving Cp_3UCl, it is possible to protonate one Cp ring off of Cp_4U to generate Cp_3UX complexes. A prototypical reaction is shown in equation (4).[22] In addition to neutral Cp_3UX complexes, it is possible, with the appropriate choice of reaction conditions, to prepare anionic $[Cp_3UX_2]^-$ complexes,[23] and cationic species such as $[Cp_3U(THF)]^+$,[24] $[(t\text{-}BuC_5H_4)_3U]^+$,[25] and $[Cp_3U(CH_3CN)_2]^+$.[26]

$$UCp_4 + HCN \xrightarrow{C_6H_6} UCp_3CN + CpH \qquad (4)$$

Many complexes of general formula Cp_3UX (X = NEt_2, PPh_2, $SiPh_3$) are known to react with substituted isocyanides (*see Isocyanide Ligands*) to give insertion products of general formula $Cp_3U[C(X){=}NR]$ in which the resulting carbamoyl ligand is coordinated in an η^2 fashion; the basic structural type is shown in (**3**).[27]

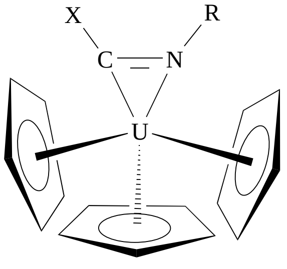

(**3**)

A remarkable, and at the time surprising, addition to the family of Cp_3UX complexes were the organouranium(V) imido complexes (*see Imide Complexes*) of formula $(MeC_5H_4)_3U{=}NR$.[28] These compounds were prepared via the 2-electron oxidation of trivalent $(MeC_5H_4)_3U(THF)$ with the organic azides Me_3SiN_3 and PhN_3 (equation 5). An X-ray structure of the phenylimido complex reveals a very short U–N bond distance of 2.019(6) Å and a nearly linear U–N–C angle of 167.4(6)°, indicative of substantial multiple bond character between uranium and nitrogen.

$$(MeC_5H_4)_3U(THF) + PhN_3 \xrightarrow{Et_2O} (MeC_5H_4)_3U(NPh) + N_2 \qquad (5)$$

2.3 Cp_2AnX_2 Compounds

Complexes of general formula $(C_5H_5)_2AnX_2$ have proven difficult to synthesize and are prone to redistribution reactions. Thus, 'Cp_2UCl_2' prepared in DME via the metathesis of UCl_4 with two equivalents of thallium(I) cyclopentadienide is actually a mixture of Cp_3UCl and $CpUCl_3(DME)$.[29] Cp_2AnCl_2 compounds have, in some instances, been successfully stabilized against ligand redistribution by adding ancillary ligands. The Cp_2ThX_2 unit, for example, can be stabilized by adding the chelating alkyl phosphine $Me_2PCH_2CH_2PMe_2$ (dmpe) to form Cp_2ThX_2(dmpe) for X = Cl, Me (equation 6).[30] Analysis of X-ray diffraction data reveals a pseudo-octahedral coordination environment as shown in (**4**).

$$ThCl_4(dmpe) + 2NaCp \xrightarrow{THF} Cp_2ThCl_2(dmpe) + 2NaCl \qquad (6)$$

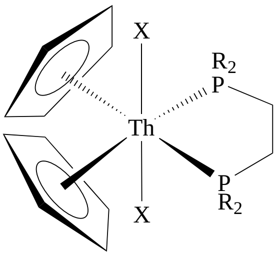

(**4**)

Stabilization against redistribution has also been achieved through the use of sterically demanding X groups (e.g. η^3-BH_4^-), the use of ligands capable of both σ- and π-donation to the actinide metal center (e.g. NEt_2^-), or the use of ring-bridged Cp ligands $[Me_4C_5–X–C_5Me_4]^{2-}$ (X = CH_2, Me_2Si, $CH_2CH_2CH_2$).[31] For example, treatment of $Cp_2U(NEt_2)_2$ with bulky alcohols gives a variety of stable Cp_2UX_2 complexes (X = $OC(t\text{-}Bu)_3$, O-2,6-$Me_2C_6H_3$, etc.)[32] and reaction of thorium or uranium tetrachloride with two equivalents of $(C_5Me_5)MgCl(THF)$ in toluene gives stable $(C_5Me_5)_2AnCl_2$ complexes (equation 7).[33]

$$AnCl_4 + 2(C_5Me_5)MgCl(THF) \xrightarrow[\Delta]{PhCH_3} (C_5Me_5)_2AnCl_2 + 2MgCl_2 \qquad (7)$$

The C_5Me_5 or Cp* ligand has evolved as one of the most widely used ligands in organoactinide chemistry owing to the thermal stability, solubility, and crystallizability it imparts to compounds. The molecular structures of $Cp^*{}_2UCl_2$ and $Cp^*{}_2ThX_2$ (X = Cl, Br, I) have been determined.[34] All of the $Cp^*{}_2AnX_2$ complexes are mononuclear and members of the pseudotetrahedral, 'bent metallocene' (*see Bent Metallocenes*) family. The analogous neptunium complex has been reported from the reaction of $NpCl_4$ with Cp*MgCl·THF.[35]

Other substituted cyclopentadienyls, such as $[1,3\text{-}(Me_3Si)_2C_5H_3]^-$ and $[1,3\text{-}(Me_3C)_2C_5H_3]^-$ (Cp'' and $Cp^‡$ for short), have been used to stabilize tetravalent thorium and uranium ions. The complexes can be synthesized by reaction of the metal tetrachlorides with either lithium or magnesium reagents.[36] Metathetical reactions of Cp''_2UCl_2 or $Cp^‡{}_2UCl_2$ with $XSiMe_3$ (X = Br, I) or $BF_3(Et_2O)$ provide a convenient route to the other halide analogs. The molecular structures of $(1,3\text{-}R_2C_5H_3)_2UX_2$ (R = $SiMe_3$, X = F, Cl, Br; R = CMe_3, X = F, Cl) have been reported, as well as the structure of $[1,3\text{-}(Me_3Si)_2C_5H_3]_2ThCl_2$. With the exception of $[Cp''_2UF(\mu\text{-}F)]_2$, all of the complexes are monomeric in the solid state. In solution, the fluoride dimer is apparently in equilibrium with its mononuclear counterpart. The ^1H NMR chemical shifts and magnetic susceptibility data for the two fluoride complexes indicate that the ligands produce significantly different electronic environments about the uranium(IV) center.[36]

In some cases where bulky cyclopentadienyl ligands are used, it is still possible to isolate Lewis base adducts. Two examples are $Cp^*{}_2UCl_2(pz)$ (pz = pyrazole)[37] and $[1,3\text{-}(Me_3Si)_2C_5H_3]_2ThCl_2(dmpe)$.[38] In compounds of the type $Cp^*{}_2UX_2(L)$, the neutral ligand L occupies the central position in the equatorial wedge.

Metathesis routes have been used to prepare terminal amido, phosphido, and thiolato complexes (equations 8–10) from $Cp^*{}_2AnCl_2$ starting materials.[39] For the bulky bis(trimethylsilyl)phosphido ligand, only mono substitution occurs.

$$Cp^*{}_2AnCl_2 + 2LiNR_2 \xrightarrow{Et_2O} Cp^*{}_2An(NR_2)_2 + 2LiCl \qquad (8)$$

$$Cp^*{}_2ThCl_2 + 2LiPPh_2 \xrightarrow{PhCH_3} Cp^*{}_2Th(PPh_2)_2 + 2LiCl \qquad (9)$$

$$Cp^*{}_2UCl_2 + 2NaSR \xrightarrow{THF} Cp^*{}_2U(SR)_2 + 2NaCl \qquad (10)$$

Toluene solutions of the thorium complex, $Cp^*{}_2Th(PPh_2)_2$ reacts smoothly with $Pt(COD)_2$ in the presence of trimethylphosphine to provide $Cp^*{}_2Th(\mu\text{-}PPh_2)_2Pt(PMe_3)$, a complex with a thorium–platinum bond. The latter can be regarded as a formal donor–acceptor or dative bond from the filled d^{10} shell of Pt into the empty d shell of Th.[40]

The bis-MeC_5H_4 or bis-Cp* framework is a useful template for organoimido and organophosphinidene complexes. Comproportionation of uranium(III) and uranium(V) metallocenes provides a route to dinuclear uranium(IV) imido complexes (equation 11).[41] The molecular structure of $[(MeC_5H_4)_2U(NPh)]_2$ is depicted in (**5**).

$$(C_5H_4Me)_3U(THF) + (C_5H_4Me)_3U(NPh) \xrightarrow{THF} [(C_5H_4Me)_2U]_2(\mu\text{-}NPh)_2 \qquad (11)$$

Terminal organoimido complexes of uranium(IV) are a more recent discovery. An α-elimination reaction (*see α-Elimination*) was designed for the synthesis of $Cp^*{}_2U(=N\text{-}2,4,6\text{-}t\text{-}Bu_3C_6H_2)$ (equation 12). The structure of $Cp^*{}_2U(=N\text{-}2,4,6\text{-}t\text{-}Bu_3C_6H_2)$ reveals a very short U=N distance 1.95(1) Å

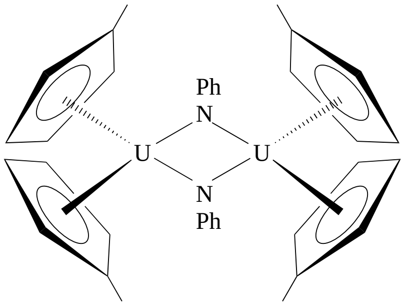

(**5**)

and a large U–N–C_{ipso} angle of 162.3(10)°.[42]

$$Cp^*_2UMe_2 + H_2N\text{-}t\text{-}Bu_3C_6H_2 \xrightarrow{\Delta} Cp^*_2U({=}N\text{-}t\text{-}Bu_3C_6H_2) + 2CH_4 \quad (12)$$

With less bulky aryl groups on nitrogen, it is possible to isolate Lewis base adducts (*see Lewis Acids & Bases*) of the type $Cp^*_2U^{IV}({=}NAr)L$ (Ar = C_6H_5, 2,4,6-$Me_3C_6H_2$, 2,6-*i*-$Pr_2C_6H_3$; L = py, THF, $Me_3P{=}O$). These complexes are precursors to a remarkable series of uranium(VI) bis-imido complexes, for example, $Cp^*_2U({=}NPh)_2$, and mixed imido-oxo compounds, for example, $Cp^*_2U({=}N\text{-}2,4,6\text{-}t\text{-}Bu_3C_6H_2)({=}O)$. Organic azides are used to oxidize the uranium(IV) mono-imido complexes to bis-imido uranium(VI) complexes (equation 13). Either N_2O or pyridine-N-oxide is effective in introducing the oxo functional group (equation 14). The uranium(VI) bis-imido and imido-oxo complexes have no counterparts in the chemistry of the group 6 elements, a reflection of the availability of additional valence orbitals on the 5f metal center that facilitate an unprecedented degree of actinide–ligand multiple bonding.[42] We should also point out that these complexes are isoelectronic with compounds containing the familiar uranyl ion, $[O{=}U{=}O]^{2+}$. The O=U=O angle is always 180° (trans) in such compounds, but the N=U=N angle in, for example, $Cp^*_2U(NPh)_2$ is 98.7(4)° and the U–N distance is 1.952(7) Å. The N=U=N unit may be viewed as the cis equivalent of the uranyl group.

$$Cp^*_2U({=}NPh)(py) + PhN_3 \xrightarrow{Et_2O} Cp^*_2U({=}NPh)_2 + N_2 + py \quad (13)$$

$$Cp^*_2U({=}N\text{-}t\text{-}Bu_3C_6H_2) + N_2O \xrightarrow{PhCH_3} Cp^*_2U({=}N\text{-}t\text{-}Bu_3C_6H_2)({=}O) + N_2 \quad (14)$$

A terminal uranium(IV) phosphinidene complex has been prepared in fashion similar to that used to prepare $Cp^*_2U({=}N\text{-}2,4,6\text{-}t\text{-}Bu_3C_6H_2)$. Reaction of $Cp^*_2U(Me)Cl$ with $K(HP\text{-}2,4,6\text{-}t\text{-}Bu_3C_6H_2)$ in the presence of trimethylphosphine oxide yields the adduct $Cp^*_2U({=}P\text{-}2,4,6\text{-}t\text{-}Bu_3C_6H_2)(O{=}PMe_3)$.[43]

The uranium(IV) imido complex $Cp^*_2U({=}N\text{-}2,4,6\text{-}t\text{-}Bu_3C_6H_2)$ also reacts with diphenyldiazomethane to give the uranium(VI) mixed bis-imido complex $Cp^*_2U({=}N\text{-}2,4,6\text{-}t\text{-}Bu_3C_6H_2)({=}N{-}N{=}CPh_2)$.[44] The latter compound does not lose dinitrogen to give a uranium(VI) alkylidene (*see Alkylidene*) complex. Instead, mild solution thermolysis (toluene, 100 °C, 20 min) provides a novel cyclometalated (*see Cyclometalation*) uranium(IV) bis(amide) complex, a consequence of the addition of a C–H bond from one of the ortho *t*-butyl groups across the N=U=N core (equation 15).[44]

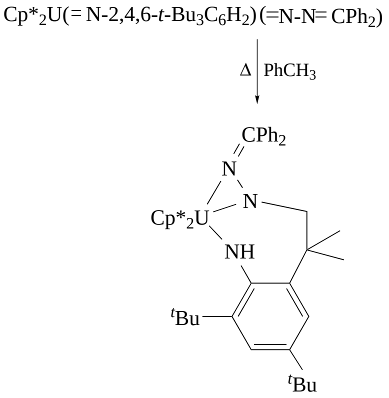

(15)

Another interesting uranium(IV) system is the bis-ketimido complex, $Cp^*_2U({-}N{=}CPh_2)_2$, formed via the reduction of $Cp^*_2UCl_2$ in ether with 2 mol of potassium graphite (KC_8) in the presence of benzophenone azine, $Ph_2C{=}N{-}N{=}CPh_2$. The molecular structure is depicted in (**6**).[45]

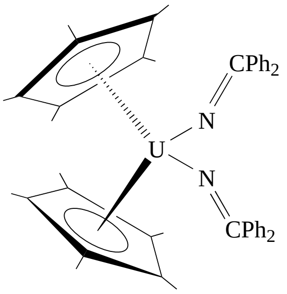

(**6**)

2.4 $CpAnX_3$ Compounds

Compounds of general formula $CpAnX_3L_2$ were first prepared by the metathesis of $AnCl_4$ with a cyclopentadienyl reagent in ethereal solvents (equation 16).[46] Since that time, other Lewis base adducts employing both monodentate and bidentate ligands have been synthesized.

$$AnCl_4 + TlCp \xrightarrow{DME} CpAnX_3(DME) + TlCl \quad (16)$$

The molecular structure of $(MeCp)UCl_3(THF)_2$ has been determined by single-crystal X-ray diffraction and reveals an approximately octahedral coordination environment about U as indicated in (**7**).[29] The average U–Cl distance is 2.620(9) Å, the average U–C_{ring} distance is 2.70(4) Å, and the average U–O distance is 2.44(2) Å. The disposition of the Cl ligands cis and trans to the cyclopentadienyl ring apparently minimizes intramolecular nonbonded repulsions. Other routes to $CpUX_3L_2$ compounds begin with the corresponding UX_4L_2 complexes. Thorium and uranium pentamethylcyclopentadienyl complexes of the type $Cp^*AnCl_3(THF)_2$ can be prepared from $AnCl_4$ and one equivalent of $Cp^*MgCl{\cdot}THF$ in THF.[47] Lithium reagents, for example, $Li[1,2,4\text{-}(Me_3Si)_3C_5H_2]^-$ (Cp‴) can lead to 'ate' complexes (equation 17).[48]

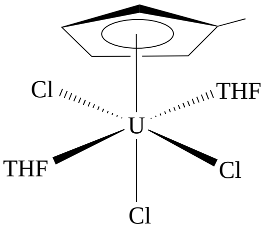

(**7**)

$$UCl_4 + Li[1,2,4\text{-}(Me_3Si)_3C_5H_2] \xrightarrow{THF} Cp'''Cl_2U(\mu\text{-}Cl)_2Li(THF)_2 + LiCl \qquad (17)$$

One study has examined the metathesis reactions of $Cp^*ThBr_3(THF)_2$ where $Cp^*ThBr_2(OAr)(THF)$ and $Cp^*ThBr(OAr)_2$ ($OAr = O\text{-}2,6\text{-}t\text{-}Bu_2C_6H_3$) are produced via reaction with one or two equivalents of KOAr in THF, respectively.[49]

2.5 Cp_3An Complexes

Tris(cyclopentadienyl) actinide complexes are strong Lewis acids and form adducts with a wide variety of Lewis bases. Many routes exist for their preparation, but a fairly general route to the THF adducts is via reduction of Cp_3AnCl (An = Th, U, Np) in THF solution (equation 18). By introducing bulky substituents on the Cp ring, Andersen was able to synthesize monomeric, base-free $(C_5H_4R)_3U$ complexes for R = t-Bu and $SiMe_3$.[50] Methyl-substituted complexes $(MeC_5H_4)_3UL$ were employed for the study of equilibrium constants for the ligand displacement reaction shown in equation (19), and demonstrated that the order for ligand displacement is $PMe_3 > P(OMe)_3 >$ pyridine $>$ THF $>$ quinuclidine $>$ CO.[51]

$$Cp_3AnCl + NaC_{10}H_8 \xrightarrow{THF} Cp_3An(THF) + NaCl + C_{10}H_8 \qquad (18)$$

$$(MeCp)_3UL + L' \overset{PhCH_3}{\rightleftharpoons} (MeCp)_3AnL' + L \qquad (19)$$

The molecular structure of $Cp_3U(THF)$ features a distorted tetrahedral coordination geometry (**8**) with U–C = 2.76–2.82 Å and U–O = 2.55(1) Å,[52] while $(Me_3SiC_5H_4)_3U$ ($Cp^\dagger{}_3U$) is trigonal planar.[53] The trigonal geometry of $Cp^\dagger{}_3U$ is only moderately perturbed by interaction with ethyl isocyanide to form $Cp^\dagger{}_3U(CNEt)$.[54]

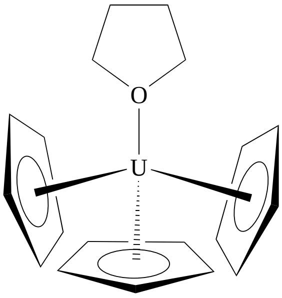

(**8**)

The trivalent thorium complex $(C_5H_5)_3Th$ has been reported from the sodium naphthalide reduction of Cp_3ThCl in THF solution. The violet product can be isolated as a THF adduct; the THF can be removed in vacuo.[55] Cp_3Th was characterized by elemental analysis, IR and UV–V is spectroscopies, and magnetic susceptibility ($\mu_{eff} = 0.403\mu_B$). Cp_3Th is isomorphous (*see Isomorphous*) with other tris(cyclopentadienyl) complexes of the 4f and heavier 5f elements. A dark-green $(C_5H_5)_3Th$ has been prepared from $Cp_3Th(i\text{-}Pr)$ or $Cp_3Th(n\text{-}Bu)$ via UV irradiation. At room temperature, $\mu_{eff} = 0.404\mu_B$. The mechanism of the photochemical process, β-hydride elimination (*see β-Hydride Elimination*), was supported by deuterium labeling studies and other experiments.[56] The relationship of the violet and green forms of Cp_3Th has not been established and neither complex has been crystallographically characterized.

The homoleptic (*see Homoleptic Compound*), dark-blue, paramagnetic organothorium(III) compounds $[1,3\text{-}(Me_2RSi)_2C_5H_3]_3Th$ (R = Me, t-Bu) were obtained in good yield from the appropriate precursors and Na/K in toluene at room temperature with sonication (equation 20). The coordination environment around thorium is trigonal planar in both complexes, with a Th–C_{ring} distance of ca. 2.80(2) Å. The EPR spectra are consistent with $6d^1$ ground states.[57]

$$[1,3\text{-}(Me_2RSi)_2C_5H_3]_3ThCl + Na/K \xrightarrow{PhCH_3} [1,3\text{-}(Me_2RSi)_2C_5H_3]_3Th + MCl \qquad (20)$$

Transneptunium tris(cyclopentadienyl) complexes can be prepared on a microscale from the reaction of molten Cp_2Be with the anhydrous trichlorides (equation 21).[58] The products are isolated by fractional sublimation. X-ray powder diffraction indicates that these Cp_3An complexes are isostructural with their early actinide analogs.**[4]**

$$2AnCl_3 + 3BeCp_2 \xrightarrow{\Delta} 2AnCp_3 + 3BeCl_2 (An = Pu, Am, Cm, Bk, Cf) \qquad (21)$$

A useful development in the synthetic chemistry of trivalent actinide complexes in recent years has been the development of the more soluble iodide starting materials, AnI_3L_4 (An = U, Np, Pu; L = THF, py, DMSO, etc.).**[59]** These species, generated from actinide metals and iodide sources (e.g. HgI_2, I_2, etc.) in coordinating solvents, are readily soluble in organic solvents, and serve as convenient precursors to a variety of trivalent actinide species. Potassium reagents are preferred for reactions in THF as the metathesis by-product KI is quite insoluble in this solvent. Interestingly, a tungsten(III) analog of $UI_3(THF)_4$, viz., octahedral, *mer*-$WCl_3(THF)_3$, has only recently been prepared.**[60]** It illustrates the fact that actinide centers typically accommodate a larger ligand set than their transition metal analogs.

Despite the common use of the pentamethylcyclopentadienyl ligand in actinide and lanthanide chemistry, it is only recently that a tris-complex, Cp^*_3An, has been prepared with this ligand. It was previously thought that the large steric bulk associated with this ligand might preclude incorporation of three Cp* groups in the coordination sphere of an actinide and, in fact, direct metathesis routes are not successful. The complex $(\eta^5\text{-}C_5Me_5)_3U$ was initially prepared by reaction of a trivalent hydride complex with tetramethylfulvene (equation 22).**[61]** Since its discovery, several other routes to Cp^*_3U have been developed.**[61]** The molecular structure is depicted in (**9**). The average U–C_{ring} bond distance in this compound (2.858(3) Å) is longer than in other crystallographically characterized U(III) pentamethylcyclopentadienyl complexes (~2.77 Å), suggesting a significant degree of steric crowding.

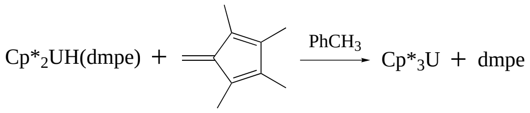

(22)

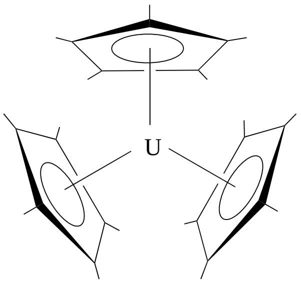

(**9**)

One of the most remarkable reactions of Cp^*_3U is that with dinitrogen at moderate pressure (80 psi) to yield the mononuclear, end-on bonded $Cp^*_3U(\eta^1\text{-}N_2)$. The latter is the first monometallic f-element dinitrogen complex.**[62]**

2.6 Cp_2AnX Complexes

While complexes of general formula Cp_2MX are very common in organolanthanide chemistry, they are relatively rare in organoactinide chemistry. Sodium amalgam or *tert*-butyl lithium reduction of Cp''_2UX_2 and $Cp^‡_2UX_2$ provides dimeric $[Cp''_2UX]_2$ or $[Cp^‡_2UX]_2$ (equation 23).**[63]** The dimers are readily cleaved in THF to give monomeric $Cp''_2UX(THF)$ or $Cp^‡_2UX(THF)$. The related compound $Cp^*_2UI(THF)$ is conveniently prepared by reaction of two equivalents of KCp* with $UI_3(THF)_4$ in THF solution (equation 24).**[64]**

$$\begin{tikzcd} Cp^‡_2UX_2 + t\text{-BuLi} \arrow[r, "C_6H_{14}"] & {[Cp^‡_2UX]_2 + LiCl} \arrow[d, "THF"] \\ & 2Cp^‡_2UX(THF) \end{tikzcd} \qquad (23)$$

$$UI_3(THF)_4 + 2KCp^* \xrightarrow{THF} Cp^*_2UI(THF) + 2KI \qquad (24)$$

The uranium(III) complexes $\{[1,3\text{-}R_2C_5H_3]_2U(\mu\text{-}OH)\}_2$ (R = Me_3Si or Me_3C) have been prepared by reaction of one equivalent of water with Cp''_3U and $Cp^‡_2UH$, respectively. Upon heating, these complexes undergo an unusual 'oxidative elimination' reaction to yield the corresponding μ-oxo uranium(IV) complexes (equation 25).**[65]** The kinetics of this process has been examined, and the reaction is found to be intramolecular, probably involving a stepwise α-elimination process (*see* α-*Elimination*).

$$Cp^‡_4U_2(\mu\text{-}OH)_2 \xrightarrow[\Delta]{PhCH_3} Cp^‡_4U_2(\mu\text{-}O)_2 + H_2 \qquad (25)$$

One of the most thoroughly investigated 'Cp_2AnX' systems is the chloride-bridged, trimeric complex $[Cp^*_2U(\mu\text{-}Cl)]_3$.**[66]** The complex can be prepared by a number of routes, one of which is shown in equation (26). $[Cp^*_2U(\mu\text{-}Cl)]_3$ reacts with a variety of Lewis bases to generate mononuclear adducts, and will undergo metathesis reactions.

$$Cp^*_2UH_2 + Cp^*_2UCl_2 \xrightarrow{PhCH_3} \frac{2}{3}[Cp^*_2U(\mu\text{-}Cl)]_3 + H_2 \qquad (26)$$

A cationic bis(pentamethylcyclopentadienyl)uranium(III) complex has been reported. $[Cp^*_2U(THF)_2][BPh_4]$ is generated by protonation of the complex $Cp^*_2U[N(SiMe_3)_2]$ with $[NH_4][BPh_4]$.**[67]**

2.7 CpAnX_2 Complexes

Mono-ring cyclopentadienyl complexes of trivalent actinides are exceedingly rare. The borohydride ligated anions $CpU(BH_4)_3^-$ and $Cp^*U(BH_4)_3^-$ have been reported through sodium amalgam reduction of the corresponding uranium(IV) precursors.[68] Neutral $Cp^*UI_2(THF)_3$ is readily prepared by treatment of $UI_3(THF)_4$ with one equivalent of KCp* in THF solution. The solid-state structure reveals a pseudo-octahedral coordination geometry with a trans–mer arrangement of iodide and THF ligands, as indicated in (**10**).[59]

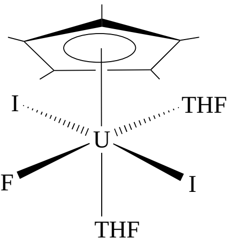

(**10**)

In the presence of excess pyridine, this complex can be converted to the analogous pyridine adduct $Cp^*UI_2(py)_3$. $Cp^*UI_2(THF)_3$ will react further with KCp* to generate the bis-ring product, $Cp^*_2UI(THF)$, or will react with two equivalents of $K[N(SiMe_3)_2]$ to produce $Cp^*U[N(SiMe_3)_2]_2$. The solid-state structure of the bis(trimethylsilyl)amide derivative reveals close contacts between the uranium center and two of the methyl carbons (2.80(2), 2.86(2) Å).[64]

2.8 Indenyl Compounds

Tetrakis(indenyl)thorium(IV), $Th(C_9H_7)_4$, is known and well characterized.[69] As depicted in (**11**), the thorium is bonded to carbons of the five-membered ring of the indenyl ligand, albeit not in an η^5 fashion. The shortest thorium–carbon distances are to the three nonbridging carbons in a tri-hapto or η^3 fashion (Th–C_{ave} = 2.83 Å).[70]

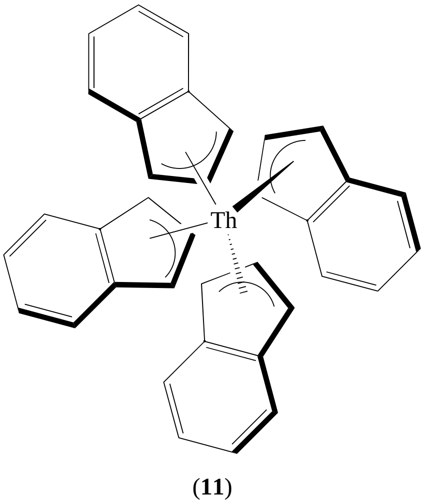

(**11**)

The indenide anion is analogous to the cyclopentadienide anion, but differs significantly in electronic structure and steric requirements. Tris(indenyl)thorium(IV) and uranium(IV) halides, $(C_9H_7)_3AnX$, have been prepared by metathesis of the halide ligands of AnX_4 with 3 equivalents of indenyl potassium in THF solution.[71] Mono(indenyl)thorium, -uranium, and -neptunium compounds of the type $(C_9H_7)AnX_3L$, where L is a Lewis base, can be prepared by modifying the reaction stoichiometry.

The molecular structure of $(C_9H_7)_3UCl$ is indicated in (**12**) and reveals a distorted tetrahedral coordination geometry with η^5-indenyl ligation. The U–Cl distance is 2.593(3) Å, and the average U–C_{ring} distance is 2.78 Å, with a range of 2.67(1)–2.89(1) Å. The $(C_9H_7)_3ThX$ compounds can be converted to alkoxide and tetrahydroborate derivatives by straightforward metathesis.[72] In the case of $(C_9H_7)_3UCl$ plus $NaBH_4$, reduction to trivalent $(C_9H_7)_3U(THF)$ is reported to occur. Complexes similar to $(\eta^5\text{-}C_9H_7)_3MCl$ compounds have also been prepared and characterized with substituted indenyl ligands.

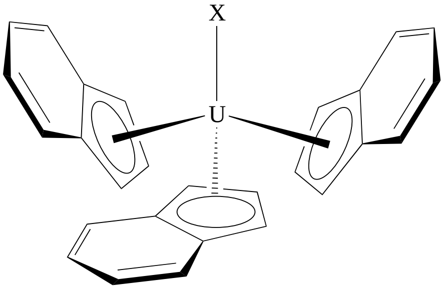

(**12**)

The bis(indenyl) complex $(\eta^5\text{-}C_9H_7)_2U(BH_4)_2$ can be prepared by the reaction of $Na(C_9H_7)$ with $U(BH_4)_4$ and its structure has been reported.[73] Peralkylated indenyl ligands have also been used to produce ‘metallocene’ (*see Metallocene Complexes*) derivatives. Thus, reaction of $ThCl_4$ with $Li(C_9Me_7)$ yields the dichloride complex $(\eta^5\text{-}C_9Me_7)_2ThCl_2$.[74] This species serves as a reagent for the synthesis of a number of derivatives, including $(C_9Me_7)_2Th(NMe_2)_2$ and $(C_9Me_7)_2Th(\eta^3\text{-}H_3BH)_2$. The permethylindenyl ligand binds with a nearly idealized η^5-coordination mode, with the Th–C bonds for the five-membered ring of the indenyl ligands varying by less than 0.05 Å. The indenyl rings are not entirely planar, indicating that there are steric repulsions between the proximal methyl groups of the two $(\eta^5\text{-}C_9Me_7)$ ligands.

Thorium(III) and uranium(III) indenyl compounds, $(C_9H_7)_3An$, are also known and the molecular structure of $U(C_9H_7)_3$ has been reported. The uranium coordination geometry is approximately trigonal, with U–C bond distances ranging from ca. 2.75(2) to 2.81(2) Å.[75]

3 CYCLOOCTATETRAENE COMPLEXES

3.1 (cot)$_2$An Complexes

Streitwieser's synthesis of the bright green uranium(IV) sandwich complex $(C_8H_8)_2U$ (*see Uranocene*) was an important and stimulating discovery in the history of organoactinide chemistry.[2] Bis(cyclooctatetraene)actinide(IV) complexes were subsequently prepared for thorium, protactinium, neptunium, and plutonium.[76] These complexes are generally synthesized by metathesis of the actinide tetrachloride $AnCl_4$ with $K_2(C_8H_8)$ in THF (equation 27). The exception is plutonium, which does not have a stable tetrachloride. Its preparation has, however, been achieved using the pyridinium salt of $PuCl_6{}^{2-}$ (equation 28).

$$AnCl_4 + 2K_2C_8H_8 \xrightarrow{THF} An(C_8H_8)_2 + 4KCl \quad (27)$$

$$(pyH)_2PuCl_6 + 2K_2C_8H_8 \xrightarrow{THF} Pu(C_8H_8)_2 + 4KCl + 2pyHCl \quad (28)$$

The molecular structure of uranocene has been determined by single-crystal X-ray diffraction, and is shown schematically in (**13**).[77] The molecule possesses rigorous D_{8h} symmetry with the eight-membered rings arranged in an eclipsed conformation. The mean U–C bond distance is 2.647(4) Å, and the mean C–C bond distance is 1.392(13) Å. The C_8 rings are planar to within experimental error. The structure of thoracene in the solid state is isomorphous with that of uranocene, with mean Th–C and C–C bond distances of 2.701(4) and 1.386(9) Å, respectively.[78] X-ray powder diffraction data on the Pa, Np, and Pu analogs indicate that these complexes are also isomorphous with uranocene. The neptunium(IV) complex $(C_8H_8)_2Np$ exhibits a ^{237}Np Mössbauer isomer shift (*see Isomer Shift*) of $+1.94\,cm\,s^{-1}$. This may be compared to the shifts of $-0.34\,cm\,s^{-1}$ found for $NpCl_4$ and $+0.72\,cm\,s^{-1}$ found for Cp_4Np and is taken as an indication of appreciable covalency in the Np^{IV}–ring bond.[76]

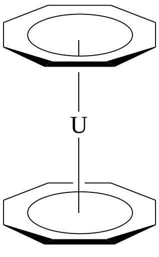

(**13**)

All of the $(C_8H_8)_2An$ complexes are exceedingly sensitive to oxygen. Metal–ring bonding appears to be more 'ionic' in thoracene than uranocene. $(C_8H_8)_2Th$ is rapidly destroyed by protic reagents, whereas uranocene is hydrolyzed only slowly. Mechanistic studies indicate that electron-withdrawing ring substituents accelerate $C_8H_8{}^{2-}$ cleavage, suggesting a rate-limiting ($k_{H_2O}/k_{D_2O} = 11.8$) proton transfer from a uranium-bound water molecule.[79]

A large number of substituted (cyclooctatetraenyl) complexes have also been reported. The addition of substituents has been employed to improve solubility, alter electronic properties, or investigate the dynamics of ring rotation. The largest class are the 1,1′-disubstituted derivatives (equation 29).[80]

$$UCl_4 + 2K_2C_8H_7R \xrightarrow{THF} U(C_8H_7R)_2 + 2KCl \quad (29)$$

A number of uranocene derivatives with higher degrees of substitution have been reported, including several with exocyclic ligands. The tri-silylated derivatives $[1,3,5\text{-}(SiMe_3)_3C_8H_5]_2An$ have been prepared for An = Th, U, and Np.[81] There is also one example of a ring-bridged uranocene, [1,2-bis(cyclooctatetraenyldimethylsilyl)-ethane]uranium (**14**).[82]

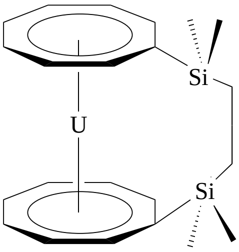

(**14**)

Ring dynamics (rotation and exchange) have been studied by means of variable-temperature NMR spectroscopy for substituted derivatives (*see* ***Stereochemical Nonrigidity of Organometallic Complexes***). Uranocenes undergo rapid ligand exchange with cyclooctatetraene dianions, and the barrier to ring rotation has been estimated at $8.3\,kcal\,mol^{-1}$ for $(1,4\text{-}t\text{-}Bu_2C_8H_6)_2U$.[83]

Actinide(III) complexes of the type [K(solvent)][An(cot)$_2$] are known for U, Np, Pu, and Am.[84] They may be prepared by interaction of $K_2(cot)$ with a trivalent halide or reduction of $(RC_8H_7)_2U$ with KC_8H_{10} in diglyme. The structure of $[K(diglyme)][(MeC_8H_7)_2U]$ has been determined and is shown schematically in (**15**).[85] The U–C distances average 2.707(7) and 2.732(8) Å; the shorter average is associated with the ring remote from the potassium cation. These are both appreciably longer than the U–C distance of 2.647(4) Å found in uranocene, consistent with the larger size of U^{+3}.

The Mössbauer spectrum of the neptunium compound $[(C_8H_8)_2Np]^-$ confirms that the metal is in the trivalent oxidation state, and suggests a lower overall degree of covalency in metal–ligand bonding than in tetravalent derivatives.[84] Most recently, the reduction route has been extended

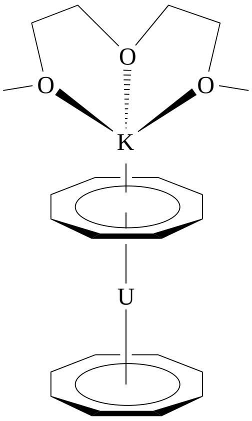

(**15**)

to generate the trivalent actinocenes, $[K(DME)_2]\{[1,4\text{-}(t\text{-}BuMe_2Si)_2C_8H_6]_2An\}$ (An = Th, U).[86] The complexes also display asymmetric An–C_{ring} distances, owing to the 'capping' of one ring by the potassium counterion. The Th(III) compound has a $6d^1$ ground state as shown by the room temperature EPR (*see Electron Paramagnetic Resonance*) spectrum ($g_{ave} = 1.918$).

Intermolecular electron-transfer rates have been studied for uranocene and substituted derivatives of uranium, neptunium, and plutonium by examining the variable-temperature NMR spectra of mixtures of $(C_8H_8)_2An$ and $[(C_8H_8)_2An]^-$.[87] In all cases, electron-transfer rates are rapid. Specific rates could not be derived for uranium and plutonium derivatives owing to the small chemical shift differences between analogous An(IV) and An(III) compounds, but in the case of $(t\text{-}BuC_8H_7)_2Np$, the rate has been estimated to be of the same order of magnitude as comparable lanthanide cyclooctatetraene compounds ($\sim 10^7\ M^{-1}\ s^{-1}$).[87]

3.2 (cot)AnX$_2$ Complexes

The chemistry of actinide complexes containing a single cyclooctatetraenyl ring ('half-sandwich' complexes) began with a report of $(C_8H_8)NpI(THF)_x$, prepared by reaction of $NpI_3(THF)_4$ and one equivalent of $K_2(C_8H_8)$ in THF.[88] Mono-ring Th(IV) complexes, with cyclooctatetraene and substituted cyclooctatetraenes have been prepared by reaction of $ThCl_4$ with one equivalent of $K_2[C_8H_7R]$ (R = alkyl or H) or by redistribution between $(C_8H_7R)_2Th$ and $ThCl_4$ in THF solution (equation 30).[89,90]

$$ThCl_4 + Th(C_8H_7R)_2 \xrightarrow{THF} 2(C_8H_7R)ThCl_2(THF)_2 \qquad (30)$$

The solid-state molecular structure of $(C_8H_8)ThCl_2(THF)_2$ reveals a half-sandwich (*see Half-sandwich Complexes*) structure that is similar to the four-legged piano stool in transition metal systems, and this structural unit is shown in (**16**). The average Th–Cl distance is 2.686(6) Å, the average Th–O distance is 2.57(2) Å, and the average Th–C_{ring} distance is 2.72(2) Å.[91]

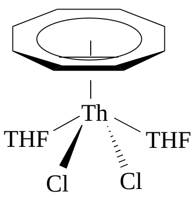

(**16**)

The aforementioned preparative routes are not applicable to mono-cot uranium(IV) complexes. The groups of Cloke,[92] Streitwieser,[93] and Ephritikhine[94,95] have developed several successful routes for the preparation of such complexes; some of these are indicated in equations (31–34). The displacement of a π-coordinated ligand under oxidizing conditions (equation 32) is quite remarkable and otherwise unprecedented in organoactinide chemistry.

$$U(C_8H_8)_2 + U(BH_4)_4 \xrightarrow{PhCH_3} 2U(C_8H_8)(BH_4)_2 \qquad (31)$$

$$U(C_8H_8)_2 + I_2 \xrightarrow{THF} U(C_8H_8)I_2(THF)_2 + C_8H_8 \qquad (32)$$

$$(Et_2N)_2UCl_2 + K_2C_8H_8 \xrightarrow{THF} (C_8H_8)U(NEt_2)_2(THF) + 2KCl \qquad (33)$$

$$U(C_8H_8)_2 + 3LiNEt_2 \xrightarrow{OEt_2} Li[(C_8H_8)U(NEt_2)_3] + Li_2C_8H_8 \qquad (34)$$

The mono-cot complexes are more reactive than their actinocene congeners, and all react with Lewis bases to form adducts, such as $(C_8H_8)UCl_2(PMe_3)$, $(C_8H_8)UCl_2(py)_2$, $(C_8H_8)UI_2(HMPA)_2$, and $(C_8H_8)U(BH_4)_2(THF)$. In addition, considerable effort has been expended on the metathesis of the halide ligands to produce mono(cyclooctatetraenyl) actinide amides and alkyls (equations 35 and 36).[90,95]

$$(C_8H_8)ThCl_2(THF)_2 + 2NaN(SiMe_3)_2 \xrightarrow{THF} (C_8H_8)Th[N(SiMe_3)_2]_2 + 2NaCl \qquad (35)$$

$$(C_8H_8)UI_2(HMPA) + 2LiCH(SiMe_3)_2 \xrightarrow{PhCH_3} (C_8H_8)U[CH(SiMe_3)_2]_2(HMPA) + 2LiCl \qquad (36)$$

Cationic derivatives, for example, $[(C_8H_8)U(BH_4)(THF)_2][BPh_4]$, may be produced by protonation of tetravalent $(C_8H_8)U(BH_4)_2(THF)$ with $[NEt_3H][BPh_4]$.[96] Reaction of $(C_8H_8)U(BH_4)_2(THF)$ with additional ammonium salt in the presence of hexamethylphosphoramide (HMPA) yields the unique dicationic species $[(C_8H_8)U(HMPA)_3][BPh_4]_2$.[96]

An interesting class of pentavalent complexes supported by the cyclooctatetraenyl ligand has been developed. Oxidation of anionic U(IV) mono-ring amide complexes with $TlBPh_4$ or $AgBPh_4$ generates the corresponding pentavalent amide complexes as shown in equations (37) and (38).[97] The molecular structure of $[(C_8H_8)U(NEt_2)_2(THF)][BPh_4]$

$$\mathrm{Li[(C_8H_8)U(NEt_2)_3] + TlBPh_4 \xrightarrow{THF} (C_8H_8)U(NEt_2)_3 + Tl^0 + LiBPh_4} \quad (37)$$

$$\mathrm{(C_8H_8)U(NEt_2)_2(THF) + AgBPh_4 \xrightarrow{THF} [(C_8H_8)U(NEt_2)_2(THF)][BPh_4] + Ag^0} \quad (38)$$

has been determined. The amide ligands are susceptible to protonation by alcohols to yield alkoxide complexes. Pentavalent cyclooctatetraenyluranium compounds have been studied by EPR and X-ray absorption spectroscopy. Analysis of EPR spectra suggest that chemical bonding with the cyclooctatetraenyl ligand occurs principally with the uranium 6d orbitals, except possibly in the case of the tris(isopropoxide) complex $(C_8H_8)U(O\text{-}i\text{-}Pr)_3$.[98]

3.3 Mixed-ring (cot)AnCp Complexes

$(C_8H_8)ThCl_2(THF)_2$ has been employed as a precursor to mixed-ring cot-Cp* complexes via the metathesis reactions indicated in equations (39) and (40).[90] Brown (cot)UCp*(I)(THF) can be prepared from $(cot)UI_2(THF)_2$ and KCp*.[99]

$$\mathrm{(C_8H_8)ThCl_2(THF)_2 + Cp^*MgCl(THF) \xrightarrow{PhCH_3} (C_8H_8)ThCp^*Cl(THF) + MgCl_2} \quad (39)$$

$$\mathrm{(C_8H_8)ThCp^*Cl(THF) + LiCH(SiMe_3)_2 \xrightarrow{PhCH_3} (C_8H_8)ThCp^*[CH(SiMe_3)_2] + LiCl} \quad (40)$$

The only successful preparation of a mixed-ring uranium(III) complex was achieved by reacting $Cp^*UI_2(THF)_3$ with $K_2[C_8H_7R]$ (R = H, alkyl, silyl) to produce $(C_8H_7R)Cp^*U(THF)$ (equation 41).[100] Several Lewis base adducts have been prepared and the solid-state structures of $[(Me_3Si)C_8H_7]Cp^*U(THF)$ and $(C_8H_8)Cp^*U(4,4'\text{-}Me_2\text{-}2,2'\text{-bipy})$ have been determined. A schematic representation of $[(Me_3Si)C_8H_7]UCp^*(THF)$ is shown in (**17**).

$$\mathrm{Cp^*UI_2(THF)_3 + K_2C_8H_8 \xrightarrow{THF} Cp^*U(C_8H_8)(THF) + 2KI} \quad (41)$$

$(C_8H_8)Cp^*U(THF)$ reacts with cyclooctatetraene to form the cot-bridged uranium(IV) compound $[(C_8H_8)Cp^*U]_2(\mu\text{-}C_8H_8)$ in quantitative yield. The same compound can be prepared from the reaction of 2 mol of $Cp^*{}_3U$ and 3 mol of cyclooctatetraene (equation 42).[101]

$$\mathrm{2(C_8H_8)UCp^*(THF) + C_8H_8 \xrightarrow{PhCH_3} [(C_8H_8)Cp^*U]_2(\mu\text{-}C_8H_8)} \quad (42)$$

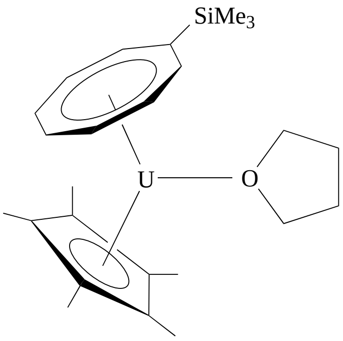

(**17**)

4 ALLYL, PENTADIENYL, AND RELATED COMPLEXES

4.1 Allyl (*see Allyl Complexes*) Complexes

Tetrakis(allyl) complexes of thorium and uranium have been synthesized via the addition of allyl Grignard to the metal tetrachloride (equation 43).[102,103] Alkyl-substituted allyl

$$\mathrm{AnX_4 + 3C_3H_5MgCl \xrightarrow{Et_2O} An(C_3H_5)_4 + 4MgCl_2} \quad (43)$$

complexes can be prepared using a similar approach. The parent $An(\eta^3\text{-allyl})_4$ complexes are unstable above about 0 °C. Low-temperature proton NMR spectroscopy reveals the characteristic A_2B_2X patterns indicative of η^3-allyl ligation. $U(\eta^3\text{-}C_3H_5)_4$ is readily protonated by hydrogen halides or alcohols to remove successive allyl ligands (equations 44 and 45).[104] The molecular structure of the *t*-butoxyallyl dimer is shown schematically in (**18**), and consists of a centrosymmetric, alkoxy-bridged dimer with η^3-allyl ligands (U–C = 2.644(16)–2.736(18) Å).

$$\mathrm{U(C_3H_5)_4 + HX \xrightarrow{Et_2O} U(C_3H_5)_3X + C_3H_6} \quad (44)$$

$$\mathrm{2U(C_3H_5)_4 + 4HOR \xrightarrow{Et_2O} [U(C_3H_5)_2(OR)_2]_2 + 4C_3H_6} \quad (45)$$

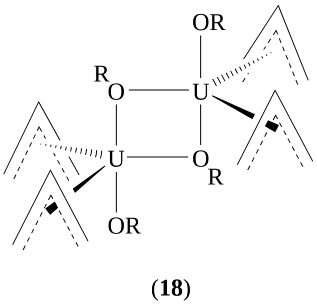

(**18**)

Quite recently, Hanusa and coworkers have isolated the bulky allyl complexes $[(Me_3Si)_nC_3H_{5-n}]_4Th$ (n = 1,2) from the reaction of $ThBr_4(THF)_4$ and four equivalents of $K[(Me_3Si)_nC_3H_{5-n}]$ in THF at $-78\,°C$. The isolated complexes are stable up to 90 °C ($n = 1$) or 124 °C ($n = 2$) and are the first structurally authenticated homoleptic (*see Homoleptic Compound*) Th-allyl complexes. The Th–C distances in $[(Me_3Si)_2C_3H_3]_4Th$ range from 2.617(5) to 2.892(5) Å, a spread (0.275 Å) similar to that of the Th–C bond lengths in the slipped indenyl complex $(C_9H_7)_4Th$ (2.66(3)–2.97(4) Å).**[105]**

4.2 Pentadienyl (*see Pentadienyl Ligand*) and Related Complexes

A more stable 'open' π-system is provided by the pentadienyl ligand. The 2,4-dimethylpentadienyl ligand was first used in the generation of homoleptic $(\eta^5\text{-}2,4\text{-}Me_2C_5H_5)_3U$ (equation 46).**[106]** The mixed-ligand uranium(III) complex [K(18-crown-6)][$(2,4\text{-}Me_2C_5H_5)_2U(BH_4)_2$] has been prepared by reaction of $(2,4\text{-}Me_2C_5H_5)_3U$ with potassium borohydride in the presence of the crown ether.**[107]** The reaction of $(2,4\text{-}Me_2C_5H_5)_3U$ with $[Et_3NH][BPh_4]$ generates the cationic U(III) complex $[(2,4\text{-}Me_2C_5H_5)_2U][BPh_4]$.**[107]** The tetravalent uranium derivatives $(2,4\text{-}Me_2C_5H_5)_2U(BH_4)_2$ and $(2,4\text{-}Me_2C_5H_5)U(BH_4)_3$ have been synthesized by the reactions of $(2,4\text{-}Me_2C_5H_5)_3U$ with $TlBH_4$, or $U(BH_4)_4$ with $K(2,4\text{-}Me_2C_5H_5)$, respectively.**[108]**

$$UCl_3(THF)_x + 3K(2,4\text{-}Me_2C_5H_5) \xrightarrow{THF} (2,4\text{-}Me_2C_5H_5)_3U + 3KCl \qquad (46)$$

Similar reactions have also been carried out with the related 6,6-dimethylcyclohexadienyl ligand. Reaction of $U(BH_4)_4$ with $K(6,6\text{-}Me_2C_6H_5)$ provides the bis(ligand) compound, $(\eta^5\text{-}6,6\text{-}Me_2C_6H_5)_2U(BH_4)_2$ as shown in equation (47).**[108]**

$$U(BH_4)_4 + 2K(6,6\text{-}Me_2C_6H_5) \xrightarrow{THF} (BH_4)_2U(\eta^5\text{-}6,6\text{-}Me_2C_6H_5)_2 \qquad (47)$$

5 ARENE (*See Arene Complexes*) COMPLEXES

The first organoactinide arene complex $(\eta^6\text{-}C_6H_6)U(AlCl_4)_3$ was prepared in 1971 by Cesari and coworkers via the Friedel–Crafts reduction of UCl_4 in benzene (equation 48).**[109]** This reducing Friedel–Crafts methodology was developed further by Cotton *et al.*, who isolated a series of hexamethylbenzene complexes whose stoichiometry was dependent upon the reaction conditions and the quantities of $AlCl_3$ and reducing agent (Zn or Al) used in the synthesis. One of these reactions is shown in equation (49). The molecular structures of all of these complexes have been determined, and those of $(C_6H_6)U(AlCl_4)_3$ and $[(C_6Me_6)_2U_2Cl_7][AlCl_4]$ are shown schematically in (**19**) and (**20**). The arene ligands are all bonded in an η^6 fashion with relatively long average $U\text{–}C_{ring}$ distances in the range of 2.92–2.94 Å.**[110]**

$$UCl_4 + Al + AlCl_3 \xrightarrow{C_6H_6} (C_6H_6)U(AlCl_4)_3 \qquad (48)$$

$$UCl_4 + Zn + xs\ AlCl_3 \xrightarrow{C_6Me_6} [(C_6Me_6)_2U_2Cl_7][AlCl_4] \qquad (49)$$

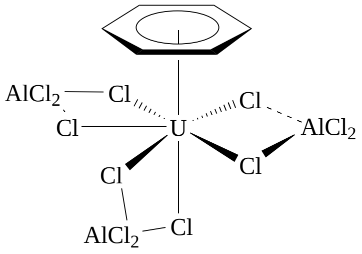

(**19**)

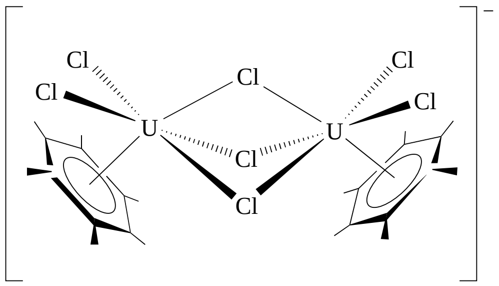

(**20**)

Ephritikhine showed that thermal reduction of $U(BH_4)_4$ in mesitylene produces $(C_6H_3Me_3)U(BH_4)_3$.**[111]** Unlike the tetrachloroaluminate complexes, this complex is soluble in toluene and NMR spectroscopy shows that the arene ligand undergoes reversible dissociation. X-ray diffraction reveals a pseudotetrahedral coordination geometry with an average U–C distance of 2.93 Å.

More recently, Cummins and coworkers have reported that reduction of tetravalent uranium amide complexes provides an interesting series of *bridging* (*see Bridging Ligand*) arene complexes. Reduction of $[N(t\text{-}Bu)Ar]_3UI$ ($Ar = 3,5\text{-}Me_2C_6H_3$) by KC_8 in toluene generates the complex $[N(t\text{-}Bu)Ar]_2U(\mu\text{-}\eta^6,\eta^6\text{-}C_7H_8)U[N(t\text{-}Bu)Ar]_2$. Structural characterization reveals that the complex contains a bridging toluene molecule bound symmetrically to the two metal centers (**21**).**[112]**

The $U\text{–}C_{ring}$ distances are short relative to other η^6-arene complexes, ranging from 2.503(9) to 2.660(8) Å. In addition, there is a slight distortion in the bound toluene ligand; the average C–C distance increases by approximately 0.04 Å compared to that found in free toluene. Density functional calculations carried out on the molecule suggest that four

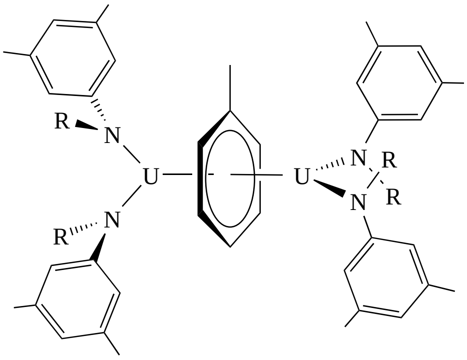

(21)

electrons are engaged in the formation of two δ-symmetry back-bonds (*see Back Bonding*) involving U 6d and 5f orbitals and the LUMO of the bridging arene molecule. $[N(t\text{-Bu})Ar]_2U(\mu\text{-}\eta^6,\eta^6\text{-}C_7H_8)U[N(t\text{-Bu})Ar]_2$ presents something of a dilemma in terms of assigning formal oxidation states. In the limit of complete transfer of electrons from the metal to the arene, uranium would be in the +4 oxidation state and the bridging ligand would be $[\text{arene}]^{4-}$. At the other extreme of negligible electron transfer, uranium would be in the +2 oxidation state and the bridging ligand would be $[\text{arene}]^0$. In between, we obviously have U^{+3} and $[\text{arene}]^{2-}$. The authors prefer the latter interpretation based on the metrical data and the reduction potential of the free ligand. Further experimental studies, for example, using techniques such as X-ray adsoprtion near edge structure spectroscopy (XANES), will be required to sort out the actual degree of oxidation of the uranium centers. We note that a similar oxidation state ambiguity exists in the complex $[Cp^*{}_2U]_2(\mu\text{-}\eta^6,\eta^6\text{-}C_6H_6)$ recently reported by Evans *et al.*[113] On the basis of chemical, structural, and electronic structure analysis, these authors propose that $[Cp^*{}_2U]_2(\mu\text{-}\eta^6,\eta^6\text{-}C_6H_6)$ contains U(III) metal centers complexed to an arene dianion.

6 OTHER CARBOCYCLIC LIGANDS

Complexes of the early actinides with five-, six-, and eight-membered rings have already been described. The series was completed recently with the addition of complexes employing the cycloheptatrienyl ligand. The sandwich complex $[K(18\text{-crown-6})][(\eta^7\text{-}C_7H_7)_2U]$ was prepared according to equation (50) and the structure determined by X-ray crystallography.[114] The molecular structure of the anion $[(C_7H_7)_2U]^-$ is depicted in (**22**).

$$UCl_4 + 4KC_7H_7 \xrightarrow[\text{18-crown-6}]{\text{THF}} [K(18\text{-crown-6})][U(C_7H_7)_2] \qquad (50)$$

The complex has crystallographically imposed C_{2h} symmetry and the cycloheptatrienyl ligands are planar to within 0.02 Å. The uranium–carbon bond distances average 2.53(2) Å, significantly shorter than those found for typical tetravalent uranium cyclopentadienyl and cyclooctatetraenyl complexes. Similar bond shortening has been observed in M–C bonds in early transition metal cycloheptatrienyl complexes and has been explained in terms of electron transfer from the metal to the ligand, with an increase in metal valency.

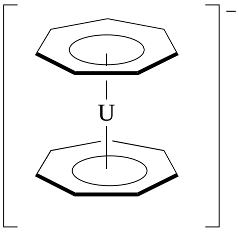

(22)

Treatment of UX_4 ($X = NEt_2$, BH_4) with $K[C_7H_9]$ affords the inverse cycloheptatrienyl sandwich complexes $K[X_3U(\mu\text{-}\eta^7\text{:}\eta^7\text{-}C_7H_7)UX_3]$.[115]

Another C_8 system, the pentalene dianion ($C_8H_6{}^{2-}$), has been far less studied than the cyclooctatetraenyl ligand. This ligand may be considered to be derived from $C_8H_8{}^{2-}$ by removal of two hydrogen atoms with generation of a C–C bond to yield two fused five-membered rings (**23**)

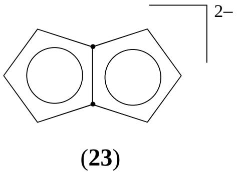

(23)

A substituted derivative of the pentalene ligand, $[1,5\text{-}(i\text{-}Pr_3Si)_2C_8H_4]^{2-}$, has been employed to generate the neutral bis(ligand) uranium and thorium compounds $[1,5\text{-}(i\text{-}Pr_3Si)_2C_8H_4]_2Th$ and $[1,5\text{-}(i\text{-}Pr_3Si)_2C_8H_4]_2U$, which are rare examples of η^8-coordinated pentalene ligands.[116] The molecular structure of the thorium compound revealed it to be a near-equal mixture of staggered and eclipsed sandwich isomers in a disordered structure (**24**). The two isomers are

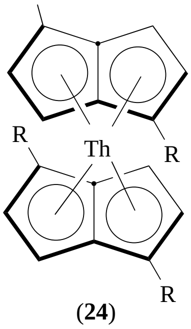

(24)

generated by thorium binding to two different prochiral faces of the ligand. The isomers do not interconvert on the NMR timescale in solution.

The larger actinide ion accommodates a smaller bending, or 'folding' angle about the bridgehead C–C bond (24° compared to 33° in a related tantalum compound). The Th–C_{ring} bond lengths vary from 2.543(10) to 2.908(11) Å. Photoelectron spectroscopy (PES) studies and density functional calculations present a consistent picture of the bonding in these complexes. Metal–ligand bonding takes place chiefly through four molecular orbitals with both 6d and 5f orbital involvement; the uranium accommodates two unpaired electrons in 5f-based orbitals. Both the f-ionization and the highest-lying ligand orbitals have lower ionization energies than uranocene or $(C_5H_5)_4U$, suggesting that the pentalene dianion is a stronger π-donor than these other carbocyclic groups.[117]

Cloke and Hitchcock have also prepared an interesting uranium(III) complex containing the silyl-substituted pentalene ligand.[118] Reaction of anhydrous UI_3 with KCp* in ether, followed by addition of $K_2[1,5\text{-}(i\text{-}Pr_3Si)_2C_8H_4]$ to the isolated Cp^*UI_2 in toluene affords the deep purple complex, $Cp^*(1,5\text{-}(i\text{-}Pr_3Si)_2C_8H_4)U$. The latter complex has been structurally characterized; it is a slightly bent sandwich compound. The most interesting chemistry reported thus far for $Cp^*(1,5\text{-}(i\text{-}Pr_3Si)_2C_8H_4)U$ is the reversible reaction with dinitrogen to form binuclear $[Cp^*(1,5\text{-}(i\text{-}Pr_3Si)_2C_8H_4)U]_2(\mu\text{-}\eta^2{:}\eta^2\text{-}N_2)$ in which the two uranium units are bridged by a sideways-bound dinitrogen molecule. The key structural feature of the latter is the N–N bond length of 1.232(10) Å, consistent with an N–N double bond.[118] DFT calculations on the model compound $[(C_5H_5)(C_8H_6)U]_2(\mu\text{-}\eta^2{:}\eta^2\text{-}N_2)$ support the initial hypothesis that $[Cp^*(1,5\text{-}(i\text{-}Pr_3Si)_2C_8H_4)U]_2(\mu\text{-}\eta^2{:}\eta^2\text{-}N_2)$ consists of two U(IV) centers bridged by an $N_2{}^{2-}$ ligand.[119]

Among the largest of discrete organometallic ligands are the class of molecules called fullerenes (*see* ***Carbon: Fullerenes***), and many metal-encapsulated derivatives, or endometallofullerene complexes, have been synthesized. The first reports of uranium encapsulation suggested that the principal products from laser vaporization experiments using graphite impregnated with UCl_3 in a supersonic cluster beam apparatus included U@C_{60} and a product of the unusually small cage U@C_{28}.[120] X-ray photoelectron spectroscopic (XPS) studies of the bulk product suggested a uranium valence of +4. Most recently, metallofullerenes of uranium, neptunium, and americium have been produced via arc-discharge using a carbon rod containing lanthanum as a carrier with ^{237}U, ^{239}Np, and ^{240}Am as radiotracers.[121] The metallofullerenes were purified by CS_2 extraction and toluene HPLC elution. The dominant products identified for neptunium and americium were An@C_{82}. Two uranium-containing metallofullerenes were identified, U@C_{82} and U_2@C_{80}. Based upon comparison with the optical spectra of lanthanide analogs, it was suggested that the oxidation state in these complexes might best be regarded as +3.

7 ALKYL COMPLEXES

7.1 Homoleptic Alkyls

The synthesis of stable, homoleptic (*see Homoleptic Compound*) actinide alkyl (*see Alkyl Complexes*) complexes has been a goal of inorganic and organometallic chemists since early days of the Manhattan Project. Standard alkylation techniques involving UCl_4 and alkyllithium reagents in diethyl ether or saturated hydrocarbons afford thermally sensitive mixtures. Marks and Seyam demonstrated that the unstable products, assumed to be uranium(IV) tetraalkyl complexes, readily undergo β-hydride elimination (*see β-Hydride Elimination*) for R = n-butyl.[122] Some aspects of this work were subsequently challenged by Evans and coworkers, who concluded that UCl_4 suspended in alkane solvent is reduced to UCl_3 by the first equivalent of added RLi.[123]

Sigurdson and Wilkinson found that the reaction of UCl_4 with a stoichiometric *excess* of alkyllithium reagents in ether gives isolable products of formula $[Li(L)_4]_2UR_6$ (L = Et_2O, THF) through saturation of the metal coordination sphere (equation 51). With TMEDA the $[Li(L)_4]_2UR_6$ complexes produce $Li_2UR_6\cdot 7TMEDA$ derivatives.[124]

$$UCl_4 + \text{xs LiR} \xrightarrow{Et_2O} [Li(Et_2O)_4][UR_6] \qquad (51)$$

Marks and coworkers isolated a heptamethyl complex, stable at room temperature for many hours, from the reaction between $ThCl_4$ and excess methyllithium in the presence of TMEDA in ethereal solvents (equation 52).[125]

$$ThCl_4 + \text{xs LiMe} + \text{TMEDA} \xrightarrow{Et_2O} [Li(TMEDA)]_3ThMe_7\cdot\text{TMEDA} + 4LiCl \qquad (52)$$

The molecular structure has been determined by X-ray diffraction, and the result is illustrated schematically in (**25**). Seven methyl groups surround the thorium atom in a distorted monocapped trigonal prismatic arrangement. Six of the methyl groups [Th–C = 2.667(8)–2.765(9) Å] are coordinated in a pair-wise manner to $Li(TMEDA)^+$ cations, while the seventh [Th–C = 2.571(9) Å] is not.

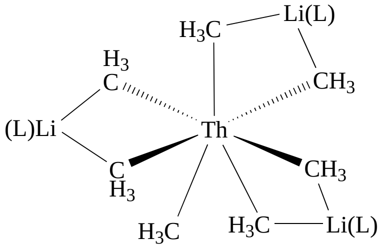

(**25**)

Homoleptic tetrabenzyl complexes are prepared by reaction between $ThCl_4$ and benzyllithium in THF solution at low temperature (equation 53).[126] It is unlikely that these complexes are η^1-alkyls, since the X-ray structure of $Cp^*Th(CH_2Ph)_3$ revealed multihapto coordination of the benzyl ligand.[127]

$$ThCl_4 + 4LiCH_2Ph \xrightarrow[-20\,°C]{THF} Th(CH_2Ph)_4 + 4LiCl \qquad (53)$$

The first example of a neutral homoleptic uranium(III) alkyl complex was prepared by reaction of bis(trimethylsilyl)methyllithium with a monomeric uranium aryloxide, $U(O\text{-}2,6\text{-}t\text{-}Bu_2C_6H_3)_3$, in hydrocarbon solution (equation 54).[128] Attempts to prepare $U[CH(SiMe_3)_2]_3$ by direct combination of $UCl_3(THF)_x$ and the alkyllithium reagent produced a salt of formula $[Li(THF)_3][UCl\{CH(SiMe_3)_2\}_3]$. The X-ray structure of $U[CH(SiMe_3)_2]_3$ revealed a monomeric trigonal pyramidal coordination geometry about the uranium metal center, as illustrated in (**26**). Agostic M–H–C interactions were suggested by the metrical parameters. The royal blue compound decomposes in solution over a period of several hours at room temperature.

$$U(O\text{-}2,6\text{-}t\text{-}Bu_2C_6H_3)_3 + 3LiCH(SiMe_3)_2 \xrightarrow{C_6H_{14}} U[CH(SiMe_3)_2]_3 + 3LiO\text{-}2,6\text{-}t\text{-}Bu_2C_6H_3 \qquad (54)$$

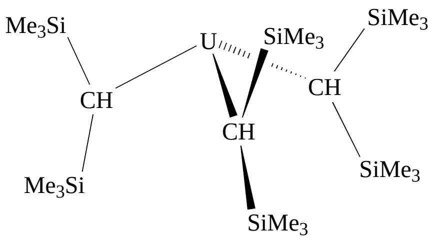

(**26**)

7.2 Phosphine and Amido Stabilized Alkyls

Andersen has found that chelating phosphine ligands greatly enhance the thermal stability of certain actinide alkyls. Methyl, benzyl, and mixed methyl/benzyl derivatives can be prepared according to equation (55) using dmpe.[129] Equation (55) does not provide stable compounds with alkyl groups containing β-hydrogen atoms.

$$AnCl_4(dmpe)_2 + 4LiR \xrightarrow{Et_2O} AnR_4(dmpe)_2 + 4LiCl \qquad (55)$$

Thermally stable thorium(IV) and uranium(IV) methyl compounds of the type $MeAn[N(SiMe_3)_2]_3$ have been prepared from the corresponding chlorides via the routes shown in equations (56) and (57).[130] Thermolysis of the methyl compounds (equation 57) or treatment of $ClAn[N(SiMe_3)_2]_3$ with alkylating agents other than those shown in equations (56) and (57) leads to γ-hydrogen atom abstraction and formation of the corresponding metallacycles (*see Metallacycle*) (equation 58).[131] The metallacycles exhibit a rich chemistry themselves, some of which is outlined in Scheme 2.

$$[(Me_3Si)_2N]_3UCl + LiMe \xrightarrow{Et_2O} [(Me_3Si)_2N]_3UMe + LiCl \qquad (56)$$

$$[(Me_3Si)_2N]_3ThCl + Me_2Mg \xrightarrow{Et_2O} [(Me_3Si)_2N]_3ThMe + MgCl_2 \qquad (57)$$

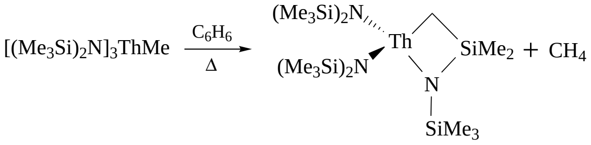

(58)

7.3 Cyclopentadienyl Alkyls

A review of the literature reveals that cyclopentadienyl or substituted cyclopentadienyl ligands play an important role in stabilizing alkyl complexes of the actinides, and there is a great deal of organometallic chemistry associated with these complexes.

7.3.1 *Tris(cyclopentadienyl) Alkyls*

As noted earlier, the chloride ligand in Cp_3AnCl (An = Th, U, Np) is labile and this feature has facilitated the synthesis of a great many tris(cyclopentadienyl)actinide(IV) alkyl derivatives by metathesis with alkyllithium or Grignard reagents. The properties and reactivity of these complexes have been extensively studied and reviewed.[4] They exhibit remarkable thermal stability. As members of the general class of Cp_3AnX complexes, they adopt the ubiquitous pseudotetrahedral coordination geometry that was illustrated earlier in (**2**).

The Cp_3ThR complexes have been used to measure metal–alkyl bond disruption enthalpies for a series of thorium alkyl complexes for both solution and gas phases. The thorium–carbon bonds appear to be relatively strong when compared to other metal–carbon linkages, and solution bond disruption enthalpies range from ca. 75 to 90 $kcal\,mol^{-1}$.[15]

The reactivity of Cp_3AnR complexes has been studied in some detail and is dominated by insertion of CO, CO_2, and CNR ligands to give η^2-acyl, η^2-carboxylate, and η^2-iminoalkyl complexes. The resulting insertion products are illustrated schematically in (**27**), (**28**), and (**29**), respectively.

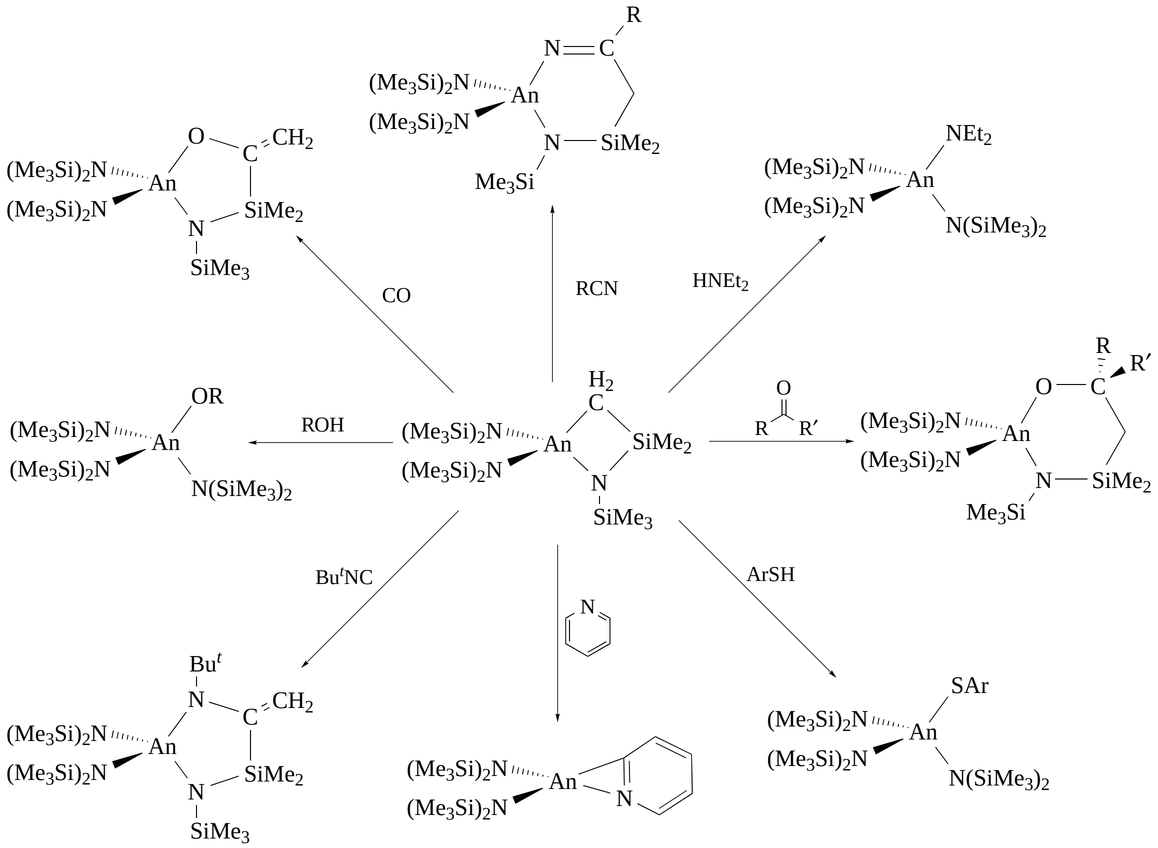
R
N=C
(Me3Si)2N
An
(Me3Si)2N
N—SiMe2
Me3Si
O
C
CH2
(Me3Si)2N
An
(Me3Si)2N
N
SiMe2
SiMe3
NEt2
(Me3Si)2N
An
(Me3Si)2N
N(SiMe3)2
CO
RCN
HNEt2
R
R′
O—C
(Me3Si)2N
An
(Me3Si)2N
N—SiMe2
Me3Si
OR
(Me3Si)2N
An
(Me3Si)2N
N(SiMe3)2
ROH
H2
C
(Me3Si)2N
An
SiMe2
(Me3Si)2N
N
SiMe3
O
R R′
Bu^tNC
N
ArSH
Bu^t
N
C
CH2
(Me3Si)2N
An
(Me3Si)2N
N
SiMe2
SiMe3
(Me3Si)2N
An
(Me3Si)2N
N
SAr
(Me3Si)2N
An
(Me3Si)2N
N(SiMe3)2

Scheme 2 Some reactions of the actinide (IV) metallacycles of the type

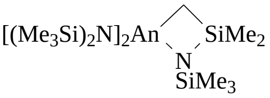
[(Me3Si)2N]2An
SiMe2
N
SiMe3

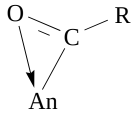

(27)

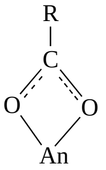

(28)

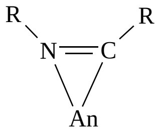

(29)

7.3.2 Bis(peralkylcyclopentadienyl) Actinide Alkyls

Bis(pentamethylcyclopentadienyl)actinide(IV) mono- and dialkyl complexes are readily prepared from $\mathrm{Cp^*{}_2AnCl_2}$.[132] A rather large number of alkyl groups have been employed, and compounds of this class are generally prepared by metathesis (equation 59). In the solid state, complexes of formula $\mathrm{Cp^*{}_2AnR_2}$ adopt a pseudotetrahedral coordination geometry about the actinide metal. A neutron diffraction study of the thorium neopentyl complex $\mathrm{Cp^*{}_2Th(CH_2\text{-}\mathit{t}\text{-}Bu)_2}$ also revealed agostic Th–H–C interactions with the α-CH bonds.[133]

$$\begin{tikzcd}
\mathrm{Cp^*{}_2AnCl_2 + LiR} \arrow[r, "\mathrm{Et_2O}"] & \mathrm{Cp^*{}_2AnClR + LiCl} \arrow[d, "+\mathrm{LiR}"', "-\mathrm{LiCl}"] \\
 & \mathrm{Cp^*{}_2AnMe_2}
\end{tikzcd} \tag{59}$$

The $\mathrm{Cp^*{}_2ThR_2}$ complexes exhibit a rich variety of thermally induced C–H activating cyclometalation processes. Kinetic and labeling studies indicate that the reactions involve rate-limiting intramolecular abstraction of a γ-hydrogen atom. The thermochemical data indicate that these reactions are largely endothermic and are entropically driven ($T\Delta S > \Delta H > 0$). Steric crowding is evident in the structural studies of $\mathrm{Cp^*{}_2Th(CH_2\text{-}\mathit{t}\text{-}Bu)_2}$ and no doubt makes a significant enthalpic contribution to the driving force for cyclometalation.[133]

The reaction chemistry of thoracyclobutanes is rich and can be predicted largely on the basis of thermochemical data.[15] Scheme 3 illustrates some representative transformations.

The $\mathrm{Cp^*{}_2AnR_2}$ compounds also display a rich CO migratory insertion (*see Migratory Insertion*) chemistry. The key products in this chemistry are carbene-like η^2-acyl complexes (**30**).

There is a class of cationic bis(pentamethylcyclopentadienyl)thorium alkyls that deserve special mention. Marks and coworkers have discovered that treatment of $\mathrm{Cp^*{}_2ThMe_2}$ with protolytic reagents, in the form of sterically encumbered ammonium salts, provides an efficient route to $\mathrm{Cp^*{}_2ThMe^+X^-}$ complexes (equation 60).[134] These complexes exhibit characteristic low-field thorium-methyl ^{13}C NMR signals that

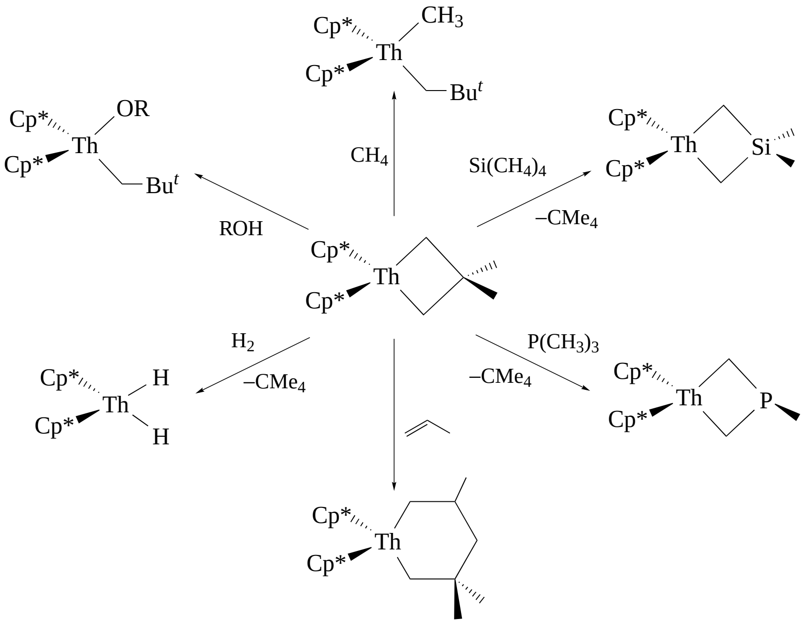

Scheme 3 Some reactions of the thorium(IV) metallacycle, Cp^*_2Th 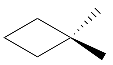

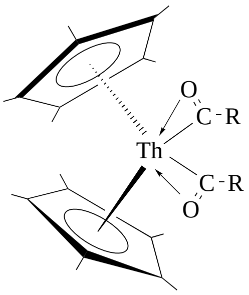

(**30**)

are in good agreement with surface spectroscopic data (see Section 11 below). The catalytic activity of $[Cp^*_2ThMe]^+[B(C_6F_5)_4]^-$ for homogeneous 1-hexene hydrogenation (*see Hydrogenation*) approaches that of $Cp^*_2ThMe_2$ adsorbed on dehydroxylated alumina (DA).

$$Cp^*_2ThMe_2 + R_3NH^+X^- \xrightarrow{C_5H_{12}} [Cp^*_2ThMe]^+X^- + R_3N + CH_4 \qquad (60)$$

Burns and coworkers have discovered a remarkable reaction involving $Cp^*_2U(Me)Cl$. Treatment of the latter with 1-lithio-1,2-diphenylhydrazine in ether solution generates lithium chloride and methane, and provides the uranium(VI) bis-imido compound $Cp^*_2U(NPh)_2$, conceivably via a uranium(IV) hydrazido species $Cp^*_2U(\eta^2\text{-}PhNNPh)$.[42,135] A plausible reaction sequence is laid out in equations (61) and (62). $Cp^*_2U(NPh)_2$ was the first uranium(VI) organometallic complex. In the solid state, $Cp^*_2U(NPh)_2$ adopts the familiar pseudotetrahedral geometry common to all Cp_2MX_2 species; the U–N distance is 1.952(7) Å and the imido groups are essentially linear with U–N–C_{ipso} = 177.8(6)°. The electronic absorption spectrum in toluene, devoid of f–f transitions, is consistent with the U^{VI} assignment.

$$Cp^*_2U(Me)Cl + Li[PhNNPh(H)] \xrightarrow{Et_2O} Cp^*_2U(Me)[N(Ph)N(Ph)(H)] + LiCl \qquad (61)$$

$$\begin{array}{c} Cp^*_2U(Me)[N(Ph)N(Ph)(H)] \longrightarrow Cp^*_2U[\eta^2\text{-}N(Ph)N(Ph)] + CH_4 \\ \downarrow \\ Cp^*_2U({=}NPh)_2 \end{array} \qquad (62)$$

In the case of uranium, it is also possible to prepare a uranium(III) alkyl complex of the type Cp^*_2UR via metathesis of $[Cp^*_2U(\mu\text{-}Cl)]_3$.[66] The only stable compound isolated from such reactions is the bis(trimethylsilyl)methyl compound $Cp^*_2U[CH(SiMe_3)_2]$.

7.3.3 Mono(peralkylcyclopentadienyl) Actinide Alkyls

Considerably less is known about single ring complexes of the type Cp^*AnR_3. According to Marks, thermal stability is a sensitive function of both the metal and the alkyl group. The synthetic approach of equation (63) has yielded only a few isolable compounds despite considerable effort. The X-ray structures of the tris-benzyl compounds $Cp^*Th(CH_2C_6H_5)_3$ and $Cp^*U(CH_2C_6H_5)_3$ revealed multihapto metal–benzyl interactions.[127,136] The latter may explain the stability of these compounds relative to those compounds prepared with simple alkyls such as methyl and neopentyl. In contrast to the literature on $Cp^*{}_2AnR_2$ compounds, very little is known about the chemistry of Cp^*AnR_3 compounds.

$$Cp^*AnCl_3(THF)_2 + 3LiR \xrightarrow{Et_2O} Cp^*AnR_3 + 3LiCl \qquad (63)$$

8 HYDRIDE COMPLEXES

8.1 Peralkylcyclopentadienyl Hydrides

The first organoactinide hydrides (*see **Hydride Complexes of the Transition Metals***) were prepared by hydrogenolysis of the bis(pentamethylcyclopentadienyl)alkyls, $Cp^*{}_2AnR_2$ (equation 64).**[33]** These reactions are thought to take place via σ-bond metathesis, as depicted in Scheme 4. The neutron diffraction structure of $[Cp^*{}_2ThH_2]_2$ has been determined: it adopts the geometry indicated in (**31**).**[137]** The mean Th–H(terminal) and Th–H(bridge) distances are 2.03(1) and 2.29(3) Å, respectively. The H–Th–H angle is 58(1)° and the Th–H–Th angle is 122(4)°. These angles and the Th–Th separation of 4.007(8) Å indicate minimal direct metal–metal interaction.

$$Cp^*{}_2AnR_2 + H_2 \xrightarrow{C_5H_{12}} Cp^*{}_2AnH_2 + 2RH \qquad (64)$$

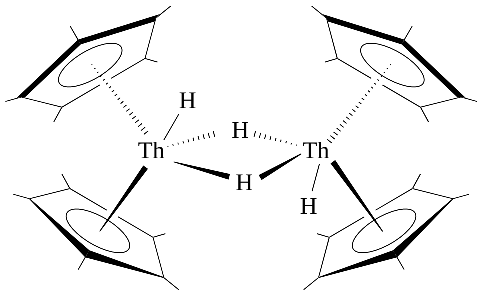

(**31**)

$[Cp^*{}_2UH_2]_2$ is unstable with respect to the uranium(III) hydride $[Cp^*{}_2UH]_x$, which can be trapped with dmpe (equation 65).**[138]** Earlier, Marks and coworkers had observed that the reaction of $Cp^*{}_2U(R)Cl$ with H_2 does not provide the anticipated $Cp^*{}_2U(H)Cl$ but rather a trinuclear uranium(III) chloride compound $[Cp^*{}_2U(\mu\text{-}Cl)]_3$ mentioned earlier.**[66]**

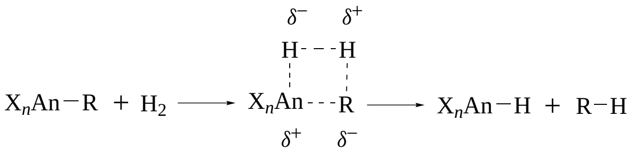

Scheme 4 Sigma bond metathesis of actinide-alkyl bonds

$$Cp^*{}_2UH_2 + dmpe \xrightarrow{C_5H_{12}} Cp^*{}_2U(dmpe)H + 0.5H_2 \qquad (65)$$

One $(C_5H_5)_3UX$ molecule that has proven elusive is Cp_3UH. As noted above, uranium(IV) hydrides can decompose via intermolecular reactions that produce hydrogen and generate uranium(III) products. Surprisingly then, the complexes $[\eta^5\text{-}RC_5H_4]_3UCl$ (R = $SiMe_3$, CMe_3) react with $KBEt_3H$ in THF to yield the thermally stable hydrides $[RC_5H_4]_3UH$.**[139]** Related thorium compounds, $[RC_5H_4]_3ThH$ and $Cp^*{}_3ThH$, can also be prepared.**[140,141]**

Actinide hydrides are rather 'hydridic' and undergo rapid reactions typical of such systems; for example, reactions with ketones and halocarbons provide actinide alkoxides and halides, respectively. Rapid quantitative addition of terminal alkenes (the reverse of β-hydride elimination) is consistent with the known bond disruption enthalpies (equation 66).**[15]**

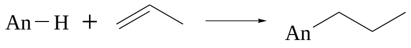

(66)

9 CARBONYL COMPLEXES

Stable homoleptic (*see Homoleptic Compound*) mononuclear and polynuclear complexes (*see **Polynuclear Organometallic Cluster Complexes***) of carbon monoxide are known for most of the transition elements (*see **Carbonyl Complexes of the Transition Metals***). One might ask whether an actinide carbonyl compound, such as $U(CO)_6$, an analog of the well-known group 6 carbonyls $M(CO)_6$ (M = Cr, Mo, W), could also be prepared. Uranium carbonyls, $U(CO)_x$, have in fact been observed in cryogenic matrices. The cocondensation of uranium vapor with CO in an argon matrix at 4 K yields species clearly identifiable as uranium carbonyls $U(CO)_x$ by IR spectroscopy.**[142]** Derived force constants suggest bonding patterns similar to those observed for zerovalent early transition and lanthanide metal carbonyls. Complete decomposition of these uranium carbonyls occurs at temperatures above ca. 30 K. In dilute matrices, the chemistry of uranium atoms and CO is much more complex and initially leads to insertion of uranium into the C≡O bond to form CUO.**[143]**

The first 'stable' actinide complex of carbon monoxide was prepared by reaction of $(Me_3SiC_5H_4)_3U$ ($Cp^\dagger{}_3U$) with CO in solution or in the solid state to produce $Cp^\dagger{}_3U(CO)$, which reversibly dissociates CO.**[144]** $Cp^\dagger{}_3U(CO)$ exhibits a carbonyl stretch in the IR spectrum at 1976 cm^{-1}, or approximately 170 cm^{-1} lower than the υ_{CO} for free carbon monoxide. This is taken as an indication of uranium-to-carbonyl π-back bonding (*see Back Bonding*). Electronic structure calculations on the model complex Cp_3UCO indicated a significant U 5f–CO 2π

back bonding, which results in a stabilization of the uranium 5f atomic orbitals.[145] Other $(R_nC_5H_{5-n})_3U(CO)$ complexes have been prepared and characterized.[144] The molecular structure of $(C_5Me_4H)_3U(CO)$ ($\upsilon_{CO} = 1880\,cm^{-1}$) possesses a short U–$C_{CO}$ bond distance of 2.383(6) Å.[146] Comparison of the ν_{CO} stretching frequencies for a series of compounds with different ring substituents indicates that electron-donating substituents increase the electron density at the metal center and increase metal-to-ligand back donation.[146] $Cp^*{}_3U(CO)$ is a more recent addition to the family of tris-Cp uranium carbonyl complexes.[147] The U–C_{CO} distance in the latter complex is 2.485(9) Å and its C–O stretching mode is located at 1922 cm^{-1}.

10 PHOSPHOYLIDE COMPLEXES

Gilje, Cramer, and their coworkers have studied the synthesis, structure, and reactivity of uranium(IV) phosphoylide complexes prepared according to equation (67).[148] The X-ray

$$Cp_3UCl + Li(CH_2)_2PRR' \xrightarrow{THF} Cp_3UCHPMeRR' + LiCl \quad (R, R' = Me, Ph) \qquad (67)$$

structure of $Cp_3UCHPMe_2Ph$ and the neutron diffraction structure of $Cp_3UCHPMe_3$ revealed the shortest U–C distances yet measured (~2.29 Å) and large U–C–P angles (~143°), indicative of uranium–carbon multiple bond character.[149] The negative charge on the α-carbon in these systems is stabilized by the presence of an electron-withdrawing heteroatom substituent. Reactions of these compounds with weak acids and polar unsaturated molecules are summarized in Scheme 5. Despite repeated efforts, no one has yet developed the requisite synthetic methodology to prepare actinide alkylidenes (*see Alkylidene*), $L_nAn{=}CR_2$. The authors are, however, optimistic that the synthesis of such molecules will be achieved in the next few years.

11 ORGANOACTINIDE SURFACE CHEMISTRY AND CATALYSIS

Studies of organoactinide surface chemistry and catalysis have been carried out by the Marks group under rigorously anhydrous/anaerobic conditions on either partially dehydroxylated alumina (PDA) or DA at surface coverages of ≈0.25–0.50 molecules nm^{-1}.[150] The PDA and DA surfaces are represented schematically in equation (68). Product yields, isotopic labeling, and surface reactivity indicate that the irreversible γ-alumina adsorption chemistry of $Cp^*{}_2AnMe_2$ can be described by three methane-evolving pathways (equations 69–71). Equation (69) dominates on PDA. On DA,

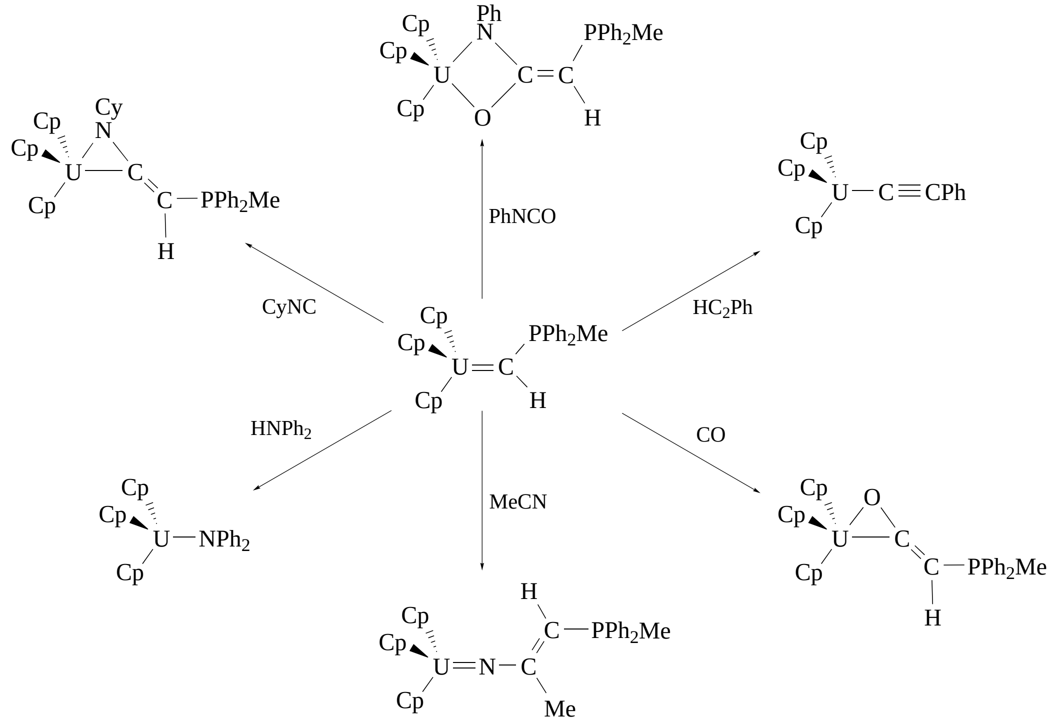

Scheme 5 Some reactions of the uranium(IV) phosphoylide complex, $Cp_3U{=}CHPPh_2Me$

equations (70) and (71) account for ≤16% of all available actinide methyl groups. The majority of methyl groups remain bound to the surface in some way not revealed in the experiments. Chemical probes, such as H_2, reveal that an additional 10–20% of the methyl groups can be liberated by hydrogenolysis. $Cp^*{}_2ThMe_2$ and $Cp^*{}_2UMe_2$ are virtually indistinguishable in these experiments, arguing that changes in metal oxidation state are not an important aspect of the surface adsorption chemistry. In addition, there is no evidence for significant Cp*H liberation.

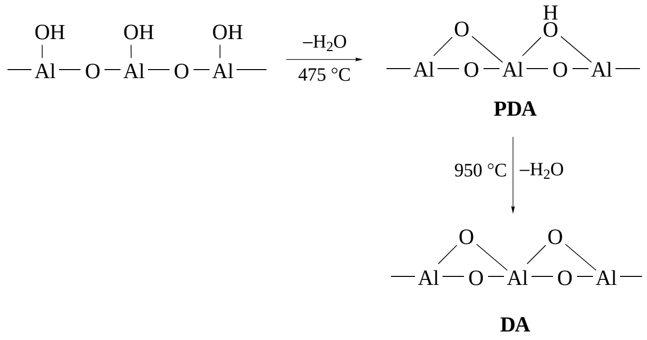

(68)

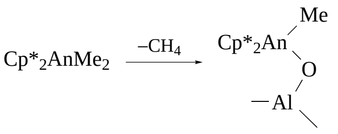

$$Cp^*{}_2AnMe_2 \xrightarrow{-CH_4} Cp^*{}_2An(Me){-}O{-}Al{-} \quad (69)$$

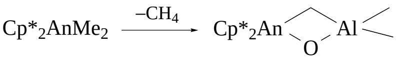

$$Cp^*{}_2AnMe_2 \xrightarrow{-CH_4} Cp^*{}_2An(\mu\text{-}O)Al \quad (70)$$

$$Cp^*{}_2AnMe_2 \xrightarrow{-CH_4} Cp^*(\eta^5, \eta^1\text{-}C_5Me_4CH_2)AnMe \quad (71)$$

Complexes such as $Cp^*{}_2ThMe_2$ are only marginally active for alkene hydrogenation or polymerization in homogeneous solution (*see* ***Oligomerization & Polymerization by Homogeneous Catalysis***). Adsorption on DA effects a dramatic enhancement in catalytic activity. Using propylene hydrogenation as a probe reaction, kinetic experiments revealed catalytic activities comparable to those of heterogeneous platinum metal catalysts. Separate ‘poisoning’ studies indicated that only ≈4% of the actinide sites sustain the bulk of hydrogenation activity. These sites have turnover frequencies for propylene hydrogenation greater than the active sites of Pt/SiO_2 under the same conditions ($N_t \sim 2\,s^{-1}$ vs. $0.05\,s^{-1}$ at $-63\,°C$). Kinetic/mechanistic studies are in accord with the sequence outlined in Scheme 6 but leave unanswered atomic-level questions regarding the exact nature of the organoactinide–surface interaction. This question can, however, be addressed using ^{13}C cross polarization with magic angle spinning (CPMAS) NMR spectroscopy. The spectra of $Cp^*{}_2ThMe_2/DA$ have been completely assigned and lead to the remarkable conclusion that a methide ion is transferred from the actinide center to a Lewis acid site on the surface. This is shown pictorially in (**32**). The CPMAS spectra of $Cp^*{}_2ThMe_2$ on PDA is quite different and indicates structure (**33**).[151]

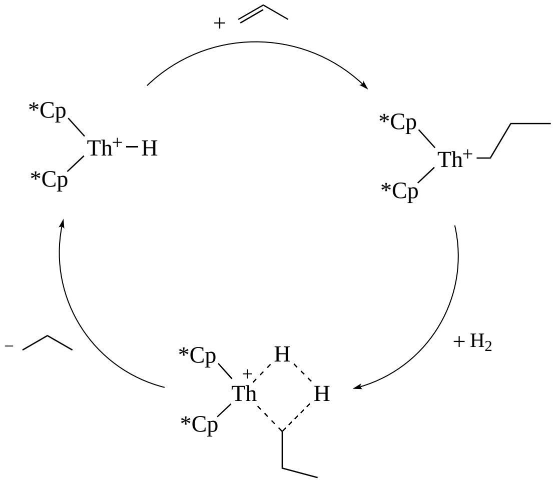

Scheme 6 Proposed catalytic cycle for alkene hydrogenation mediated by supported cationic complexes derived from $Cp^*{}_2ThMe_2$

The tetraallyl complex $Th(\eta^3\text{-}C_3H_5)_4$ supported on dehydroxylated γ-alumina is an outstanding heterogeneous catalyst for arene hydrogenation that rivals the most active platinum metal catalysts in activity. $Th(\eta^3\text{-}C_3H_5)_4/DA$ also catalyzes the rapid and selective deuteration of linear and cyclic alkanes. C–H reactivities fall in the order primary > secondary > tertiary.[152]

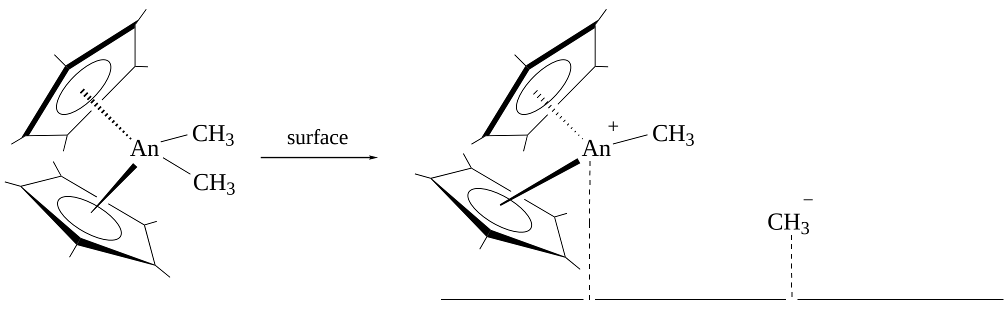

(**32**)

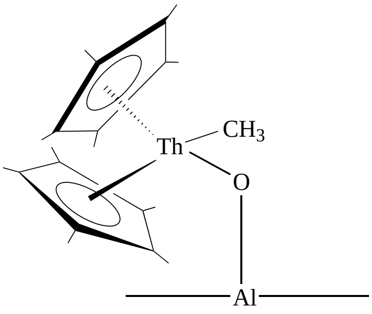

(**33**)

12 ELECTRONIC STRUCTURE AND BONDING

In contrast to the situation with main-group and d-block elements, a detailed understanding of the electronic structure and bonding of the 5f elements has posed a considerable theoretical challenge. There are no simple rules that help rationalize the stoichiometry of organoactinide complexes or that guide the synthesis of new organoactinide compounds (e.g. the effective atomic number or EAN rule in transition metal organometallic chemistry). One of the more passionate issues discussed in the literature concerns the level of involvement of 5f orbitals in the metal–ligand bonding of organoactinide complexes.

12.1 Molecular Orbital Calculations

Moffitt's seminal contribution in 1956,[1] that ligand-based orbitals could span a space of the proper symmetry to interact with either d or f orbitals, or both, preceded a number of detailed theoretical studies of organoactinide bonding. These symmetry considerations were an extension of the bonding theories that were widely accepted and had worked very well in describing 'sandwich' compounds (*see Sandwich Compound*) of the transition elements such as ferrocene (*see Ferrocene*). Since that time, descriptions of organoactinide electronic structure ranging in complexity from 'back-of-the envelope', to extended Hückel, to SCF-Xα, to DV-Xα, to DFT, to ab initio calculations (*see Ab Initio Calculations*) (including spin–orbit coupling, configuration interaction, and relativistic core potentials) have been reported.

One of the most thoroughly investigated organoactinide compounds is the uranium sandwich complex uranocene.[8,10] Simple symmetry considerations predicted its existence, which in turn prompted its synthesis.[2] Early extended Hückel calculations on uranocene produced a bonding scheme that was very attractive. In this model, the $[C_8H_8]^{2-}$ ligand orbitals only interacted with uranium atomic 5f orbitals; the virtual atomic 6d orbitals were considered too high in energy for significant interaction. This overlap of orbitals of e_{2u} symmetry (metal 5f and ligand pπ) seemed a logical extension of the bonding descriptions of d-block sandwich compounds.

When more sophisticated computaional methods were applied to the uranocene system,[153] it became clear that the simple Hückel treatment was misleading. Incorportaion of relativistic effects (*see Relativistic Effects*) has provided a more complete and accurate description of the bonding. Although the various relativistic calculations differ in methodology (relativstically-parameterized extented Hückel. Xα-SW, DV-Xα, DFT, ab initio), they present a consistent picture wherein the primary metal-ligand bonding is derived through a combination of 6d(e_{2g}) and 5f(e_{2u}) atomic orbital interactions with the ligands. Both interactions are between metal-based δ-symmetry orbitals and pπ orbitals of the C_8H_8 rings. All of the calculations indicate that the ligand field generated by the cot ligands lifts the degeneracy of the atomic 5f orbitals, spreads them out in energy, and results in a ground state with two unparied electrons, consistent with the observed paramagnetism (*see Paramagnetism*) of the complex. This general model for the bonding in uranocene is supported by gas phase photoelectron spectroscopy (PES) experiments.[154] Comparison of PES spectra for thorocene and uranocene revealed that the lowest energy ionizaion of uranocene is from valence 5f electrons, and that the next two ionizations occur from the e_{2u}(5f) and e_{2g}(6d) metal-ligand bonding orbitals (see Figure 1). Variable photon energy PES studies reveal a substantial increase in relative intensity of the e_{2u} band demonstrating a significant 5f orbital covalent interaction. The relative stability of the e_{2g} orbital with respect to the e_{2u} orbtial was taken as evidence for strong 6d bonding.[155] These two metal-ligand bonding orbitals are shown qualitatively in (**34**) and (**35**). PES data on substituted uranocenes indicate that overlap with both 6d and 5f orbitals increases with alkylation on the cot ring.[156]

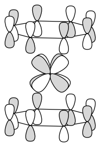

e_{2u}–f_δ

(**34**)

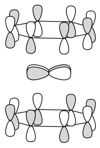

e_{2g}–d_δ

(**35**)

Cyclopentadienyl complexes (*see Cyclopentadienyl*) have also received a considerable amount of attention from theoretical chemists, primarily to gain a better understanding of metal–ligand bonding in organotransition metal versus organoactinide complexes. Here again, a range of computational techniques have been employed that, in general, predict that the uranium 5f manifold is only slightly perturbed by Cp ligand interactions. A comparison of the bonding of UCl_4, Cp_2UCl_2, and Cp_4U revealed a progressive destabilization and splitting of the 5f manifold, which was interpreted as indicating a stronger metal–ligand interaction in metal–Cp than metal–chloride bonds.[8] Concomitantly, a stabilization of the Cp ligand π_2 orbitals was interpreted as

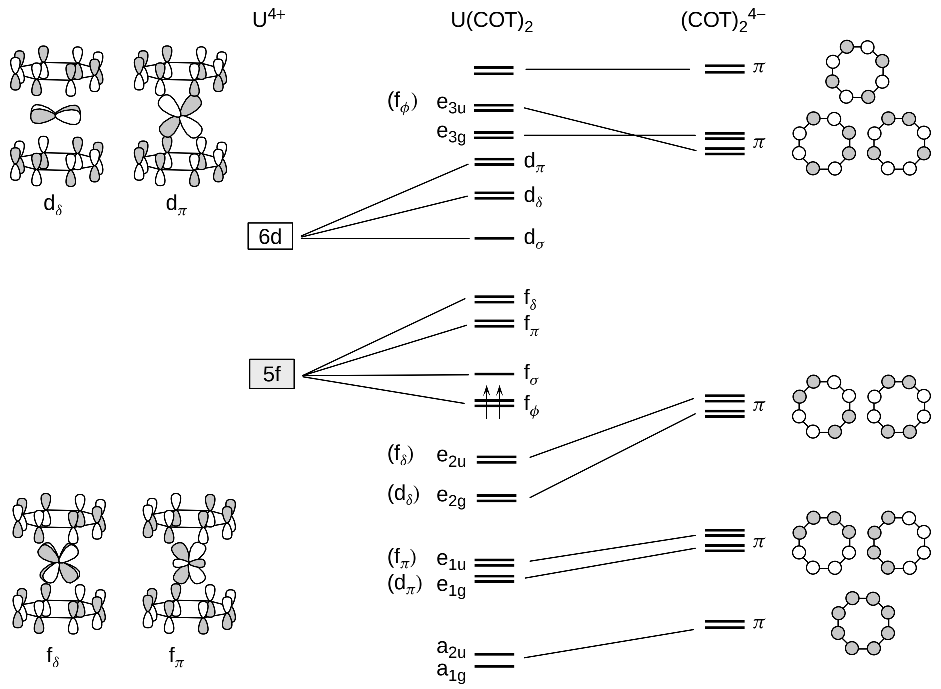

Figure 1 Molecular orbital diagram of uranocene[155]

a stronger metal–ligand d orbital interaction. Computational studies have been reported for a fair number of complexes containing cyclopentadienyl ligands. Collectively, all the calculations on complexes containing cot and Cp ligands indicate that the 6d atomic orbitals of the early actinides dominate the metal–ligand bonding and that the 5f orbitals are relatively unaffected, and serve as a reservoir for the valence electrons. Relativistic corrections tend to increase the contribution of the uranium 6d orbitals and decrease the contribution of the 5f orbitals. This view of bonding has been extended to heterobimetallic complexes (*see* ***Dinuclear Organometallic Cluster Complexes***), which contain a direct actinide–transition metal interaction such as $Cp^*_2Th(\mu\text{-}PPh_2)_2Pt(PMe_3)$ and $(I)Cp^*_2Th\text{–}RuCp(CO)_2$. Calculations on these systems indicate a metal–metal bonding HOMO made up of an occupied transition metal d orbital donating into a vacant actinide 6d acceptor orbital, and is best described as a 'dative' metal–metal bond.[20,40,157]

A density functional theoretical study has examined the question of bonding in the complexes $[(\eta^7\text{-}C_7H_7)_2An]^n$ (Th, Pa, U, Np, Pu, Am).[158] It was found that the 5f δ-symmetry orbitals not only participate in the bonding with e_2'' pπ orbitals of the C_7H_7 rings, but are as important as the symmetry appropriate 6d orbitals in stabilizing the ligand-based fragment orbitals. The 5f percentage in frontier e_2'' molecular orbitals increases across the series, and the contribution of the 6d orbitals gradually decreases across the series. The ground electron configurations, ionization energies, electron affinities, and An–C_7H_7 bond energies are strongly affected by these effects.

Although only one valence electron resides in a 5f-localized orbital on uranium in $[U(C_7H_7)_2]^-$, a formal oxidation state of $+3$ ($5f^3$) was assigned, based on the fact that the HOMO $3e_2''$ molecular orbitals (occupied by four electrons) are nearly 50% 5f in character, and so two of these electrons were assigned to the metal. EPR and electron-nuclear double resonance (ENDOR) studies of $[(C_7H_7)_2U]^-$ suggest that the complex could be treated as $5f^1$, with a ground-state molecular orbital comprised of both $5f_\pi$ and $5f_\sigma$ orbitals.[114]

The role of actinide virtual 6d orbitals and relativistic corrections in describing metal–ligand bonding has been extended to sophisticated calculations on trivalent alkyl complexes $AnMe_3$ (An = U, Np, Pu)[159] and pentavalent uranium imido complexes $(R_2N)_3U{=}NR$.[160] The calculations on $AnMe_3$ (An = U, Np, Pu) were carried out at the complete active space (CAS)-SCF level including relativistic core potentials, and indicate that the experimentally determined pyramidal geometry is more stable than a planar geometry in AnL_3 complexes owing to involvement of 6d character in the An–C bonding orbitals upon bending. The relativistic discrete variational-local density functional (DV-LDF) calculations on $(NR_2)_3U{=}NR$ complexes also point to the importance of 6d orbital participation and indicate the presence of U=NR multiple bonding. These calculations have been used to reassign the gas-phase PES of $[(Me_3Si)_2N]_3U{=}N(SiMe_3)$.[161]

Electronic structure calculations, including relativistic core potentials and the spin-orbit coupling, have been carried out on the C_{28}, Pa@C_{28}, and U@C_{28} species.[162] The ground state of C_{28} is described well by Hartree-Fock (*see Hartree–Fock Theory*) wave functions, and the computed electron affinity and ionization potential are similar to those of C_{60}. Strong metal-cage binding is found for Pa@C_{28} and U@C_{28}, similar to that in $U(C_8H_8)_2$. The ground electronic states depend on the order of the lowest energy cage π^* and metal 5f orbitals, with $(\pi^*)^1$ and $(\pi^*)^1(5f)^1$ found to be the ground electronic configurations for the Pa and U complexes, respectively. The uranium fullerene is calculated to be diamagnetic.

13 RELATED ARTICLES

Bonding Energetics of Organometallic Compounds; Carbon: Fullerenes; Carbonyl Complexes of the Transition Metals; Dinuclear Organometallic Cluster Complexes; Heterogeneous Catalysis by Metals; Hydride Complexes of the Transition Metals; Hydrogenation & Isomerization of Alkenes; Mechanisms of Reaction of Organometallic Complexes; Oligomerization & Polymerization by Homogeneous Catalysis; Polynuclear Organometallic Cluster Complexes; Scandium, Yttrium & the Lanthanides: Inorganic & Coordination Chemistry; Stereochemical Nonrigidity of Organometallic Complexes.

14 REFERENCES

1. L. T. Reynolds and G. Wilkinson, *J. Inorg. Nucl. Chem.*, 1956, **2**, 246.
2. A. Streitwieser and U. Müller-Westerhoff Jr, *J. Am. Chem. Soc.*, 1968, **90**, 7364.
3. T. J. Marks and A. M. Seyam, *J. Am. Chem. Soc.*, 1972, **94**, 6545; A. E. Gabala and M. Tsutsui, *J. Am. Chem. Soc.*, 1973, **95**, 91; T. J. Marks, A. M. Seyam, and J. R. Kolb, *J. Am. Chem. Soc.*, 1973, **95**, 5529; G. Brandi, M. Brunelli, G. Lugli, and A. Mazzei, *Inorg. Chim. Acta*, 1973, **7**, 319.
4. T. J. Marks, *Science*, 1982, **217**, 989; T. J. Marks and R. D. Ernst, in ‘Comprehensive Organometallic Chemistry’, eds. G. Wilkinson, F. G. A. Stone, and E. W. Abel, Pergamon Press, Oxford, 1982, Vol. 3, Chap. 21; F. T. Edelmann, in ‘Comprehensive Organometallic Chemistry II’, eds. G. Wilkinson, F. G. A. Stone, and E. W. Abel, Elsevier Science, New York, 1995, Vol. 4, Chap. 2; T. J. Marks, in ‘Fundamental and Technological Aspects of Organo-f-Element Chemistry’, eds. T. J. Marks and I. Fragala, Reidel, Dordrecht, 1985, p. 115; T. J. Marks, in ‘The Chemistry of the Actinide Elements’, eds. J. J. Katz, G. T. Seaborg, and L. R. Morss, Chapman & Hall, New York, 1986, Chap. 23; T. J. Marks, *Acc. Chem. Res.*, 1992, **25**, 57; T. J. Marks, M. R. Gagne, S. P. Nolan, L. E. Schock, A. M. Seyam, and D. Stern, *Pure. Appl. Chem.*, 1989, **61**, 1665; A. Dormond and D. Barbier-Baudry, *Sci. Synth.*, 2003, **2**, 943.
5. T. J. Marks and A. Streitwieser Jr, in ‘The Chemistry of the Actinide Elements’, eds. J. J. Katz, G. T. Seaborg, and L. R. Morss, Chapman & Hall, New York, 1986, Chap. 22.
6. J. Takats, in ‘Fundamental and Technological Aspects of Organo-f-Element Chemistry’, eds. T. J. Marks and I. Fragala, Reidel, Dordrecht, 1985, p. 159.
7. I. Santos, A. Pires de Matos, and A. G. Maddock, *Adv. Organomet. Chem.*, 1989, **34**, 65.
8. B. E. Bursten and R. J. Strittmatter, *Angew. Chem., Int. Ed. Engl.*, 1991, **30**, 1069; C. J. Burns and B. E. Bursten, *Comments Inorg. Chem.*, 1989, **9**, 61.
9. M. Ephritikhine, *Chem. Rev.*, 1997, **97**, 2193; M. Ephritikhine, *New J. Chem.*, 1992, **16**, 451.
10. N. Kaltsoyannis, *Chem. Soc. Rev.*, 2003, **32**, 9.
11. Uranium metal is available from Oak Ridge National Laboratory. The Oak Ridge isotope catalog is available on line at www.ornl.gov/isotopes/catalog.html.
12. E. O. Fischer and A. Treiber, *Z. Naturforsch.*, 1962, **173**, 276; F. Baumgaertner, E. O. Fischer, B. Kanellakopulos, and P. Laubereau, *Angew. Chem.*, 1969, **81**, 182; E. O. Fischer and Y. Hristidu, *Z. Naturforsch.*, 1962, **173**, 275; D. G. Karraker and J. A. Stone, *Inorg. Chem.*, 1972, **11**, 1742.
13. R. Maier, B. Kanellakopulos, C. Apostolidis, D. Meyer, and J. Rebizant, *J. Alloys Compd.*, 1993, **190**, 269; J. H. Burns, *J. Am. Chem. Soc.*, 1973, **95**, 3815.
14. V. I. Tel’noi, I. B. Rabinovich, M. R. Leonov, G. V. Solov’eva, and N. I. Gramoteeva, *Dokl. Akad. Nauk SSSR (Engl. Trans.)*, 1979, **245**, 1430.
15. J. A. Connor, *Top. Curr. Chem.*, 1977, **71**, 71; J. W. Bruno, T. J. Marks, and L. R. Morss, *J. Am. Chem. Soc.*, 1983, **105**, 6824; C. M. Fendrick and T. J. Marks, *J. Am. Chem. Soc.*, 1984, **106**, 2214; D. C. Sonnenberger, L. R. Morss, and T. J. Marks, *Organometallics*, 1985, **4**, 352; J. W. Bruno, H. A. Stecher, L. R. Morss, D. C. Sonnenberger, and T. J. Marks, *J. Am. Chem. Soc.*, 1986, **108**, 7275; L. E. Schock and T. J. Marks, *J. Am. Chem. Soc.*, 1988, **110**, 7701; T. J. Marks, M. R. Gagne, S. P. Nolan, L. E. Schock, A. M. Seyam, and D. Stern, *Pure Appl. Chem.*, 1989, **61**, 1665; Z. Lin and T. J. Marks, *J. Am. Chem. Soc.*, 1990, **112**, 5515; S. P. Nolan, M. Porchia, and T. J. Marks, *Organometallics*, 1991, **10**, 1450.
16. D. G. Karraker and J. A. Stone, *Inorg. Chem.*, 1972, **8**, 1742.
17. C. Wong, T. Yen, and T. Lee, *Acta Crystallogr.*, 1965, **18**, 340.
18. P. Zanella, G. Rossetto, G. DePaoli, and O. Traverso, *Inorg. Chim. Acta*, 1980, **44**, L155.
19. G. Paolucci, G. Rossetto, P. Zanella, and R. D. Fischer, *J. Organomet. Chem.*, 1985, **284**, 213.
20. R. S. Stern and T. J. Marks, *Organometallics*, 1987, **6**, 2621; S. P. Nolan, M. Portia, and T. J. Marks, *Organometallics*, 1991, **10**, 1450.
21. W. J. Evans, G. W. Nyce, M. A. Johnston, and J. W. Ziller, *J. Am. Chem. Soc.*, 2000, **122**, 12019.

22. B. Kanellakopulos, E. Dornberger, and H. Billich, *J. Organomet. Chem.*, 1974, **76**, C42.
23. K. W. Bagnall, M. J. Plews, D. Brown, R. D. Fischer, E. Klaehne, G. W. Landgraf, and G. R. Sienel, *J. Chem. Soc., Dalton Trans.*, 1982, 1999.
24. J. C. Berthet, C. Boisson, M. Lance, J. Vigner, M. Nierlich, and M. Ephritikhine, *J. Chem. Soc., Dalton Trans.*, 1995, 3027.
25. J. C. Berthet, J. F. LeMarechal, M. Lance, M. Nierlich, J. Vigner, and M. Ephritikhine, *J. Chem. Soc., Dalton Trans.*, 1992, 1573.
26. H. Aslan, K. Yunlu, D. Fischer, G. Bombieri, and F. Benetollo, *J. Organomet. Chem.*, 1988, **354**, 63.
27. M. Porchia, N. Brianese, U. Casellato, F. Ossola, G. Rossetto, P. Zanella, and R. Graziani, *J. Chem. Soc., Dalton Trans.*, 1989, 677; P. Zanella, N. Brianese, U. Casellato, F. Ossola, M. Porchia, G. Rossetto, and R. Graziani, *J. Chem. Soc., Dalton Trans.*, 1987, 2039.
28. J. G. Brennan and R. A. Andersen, *J. Am. Chem. Soc.*, 1985, **107**, 514.
29. R. D. Ernst, W. J. Kennelly, C. S. Day, V. W. Day, and T. J. Marks, *J. Am. Chem. Soc.*, 1979, **101**, 2656.
30. A. Zalkin, J. G. Brennan, and R. A. Andersen, *Acta Crystallogr., Sect. C*, 1987, **C43**, 418.
31. P. Zanella, G. De Paoli, G. Bombieri, G. Zanotti, and R. Rossi, *J. Organomet. Chem.*, 1977, **142**, C21; J. D. Jamerson and J. Takats, *J. Organmomet. Chem.*, 1974, **78**, C23; A. K. Dash, I. Gourevich, J. Q. Wang, M. Kapon, and M. S. Eisen, *Organometallics*, 2001, **20**, 5084.
32. A. Berton, M. Portia, G. Rossetto, and P. Zanella, *J. Organomet. Chem.*, 1986, **302**, 351.
33. P. J. Fagan, J. M. Manriquez, E. A. Maatta, A. M. Seyam, and T. J. Marks, *J. Am. Chem. Soc.*, 1981, **103**, 6650.
34. M. R. Spirlet, J. Rebizant, C. Apostolidis, and B. Kanellakopulos, *Acta Crystallogr., C*, 1992, **C48**, 2135; D. Rabinovich, G. L. Schimek, W. T. Pennington, J. B. Nielson, and K. D. Abney, *Acta Crystallogr., C*, 1997, **C53**, 1794; D. Rabinovich, S. G. Bott, J. B. Nielson, and K. D. Abney, *Inorg. Chim. Acta*, 1998, **274**, 232.
35. D. C. Sonnenberger and J. G. Guadiello, *J. Less-Common Met.*, 1986, **126**, 411; D. C. Sonnenberger and J. G. Guadiello, *Inorg. Chem.*, 1988, **27**, 2747.
36. W. W. Lukens, S. M. Beshouri, L. L. Blosch, A. L. Stuart, and R. A. Andersen, *Organometallics*, 1999, **18**, 1235.
37. C. W. Eigenbrot and K. N. Raymond Jr, *Inorg. Chem.*, 1982, **21**, 2653.
38. M. A. Edelman, P. B. Hitchcock, J. Hu, and M. F. Lappert, *New J. Chem.*, 1995, **19**, 481.
39. P. J. Fagan, J. M. Manriquez, S. H. Vollmer, C. S. Day, V. W. Day, and T. J. Marks, *J. Am. Chem. Soc.*, 1981, **103**, 2206; D. A. Wrobleski, R. R. Ryan, H. J. Wasserman, K. V. Salazar, R. T. Paine, and D. C. Moody, *Organomtallics*, 1986, **5**, 90; S. W. Hall, J. C. Huffman, M. M. Miller, L. R. Avens, C. J. Burns, D. S. Arney, A. F. England, and A. P. Sattelberger, *Organometallics*, 1993, **12**, 752; Z. Lin, C. P. Brock, and T. J. Marks, *Inorg. Chim. Acta*, 1998, **141**, 145; C. Lescop, T. Arliguie, M. Lance, M. Nierlich, and M. Ephritikhine, *J. Organomet. Chem.*, 1999, **580**, 137.
40. P. J. Hay, R. R. Ryan, K. V. Salazar, D. A. Wrobleski, and A. P. Sattelberger, *J. Am. Chem. Soc.*, 1986, **108**, 313.
41. J. G. Brennan, R. A. Andersen, and A. Zalkin, *J. Am. Chem. Soc.*, 1988, **110**, 4554.
42. D. S. J. Arney and C. J. Burns, *J. Am. Chem. Soc.*, 1995, **117**, 9448.
43. D. S. J. Arney, R. C. Schnabel, B. L. Scott, and C. J. Burns, *J. Am. Chem. Soc.*, 1996, **118**, 6780.
44. J. K. Kiplinger, D. M. Morris, B. L. Scott, and C. J. Burns, *Chem. Commun.*, 2002, 30.
45. J. K. Kiplinger, D. M. Morris, B. L. Scott, and C. J. Burns, *Organometallics*, 2002, **21**, 3073.
46. K. W. Bagnall, J. Edwards, and A. C. Tempest, *J. Chem. Soc., Dalton Trans.*, 1978, 295.
47. E. A. Mintz, K. G. Moloy, T. J. Marks, and V. W. Day, *J. Am. Chem. Soc.*, 1982, **104**, 4692.
48. M. A. Edelman, M. F. Lappert, J. L. Atwood, and H. Zhang, *Inorg. Chim. Acta*, 1987, **139**, 185; M. A. Edelman, P. B. Hitchcock, J. Hu, and M. F. Lappert, *New J. Chem.*, 1995, **19**, 481.
49. R. J. Butcher, D. L. Clark, S. K. Grumbine, B. L. Scott, and J. G. Watkin, *Organometallics*, 1996, **15**, 1488.
50. J. G. Brennan, R. A. Andersen, and A. Zalkin, *Inorg. Chem.*, 1986, **25**, 1756; S. D. Stults, R. A. Andersen, and A. Zalkin, *Organometallics*, 1990, **9**, 1623.
51. J. G. Brennan, S. D. Stults, R. A. Andersen, and A. Zalkin, *Organometallics*, 1988, **7**, 1329; J. G. Brennan, Ph.D., Organoactinide Chemistry: Synthesis, Structure and Solution Dynamics, Thesis, University of California, Berkeley, 1985.
52. H. J. Wasserman, A. J. Zozulin, D. C. Moody, R. R. Ryan, and K. V. Salazar, *J. Organomet. Chem.*, 1983, **254**, 305.
53. A. Zalkin, J. G. Brennan, and R. A. Andersen, *Acta Crystallogr.*, 1988, **C44**, 2104.
54. J. G. Brennan, R. A. Andersen, and J. L. Robbins, *J. Am. Chem. Soc.*, 1986, **102**, 335.
55. B. Kanellakopulos, E. Dornberger, and F. Baumgärtner, *Inorg. Nucl. Chem. Lett.*, 1974, **10**, 155.
56. D. G. Kalina, T. J. Marks, and W. A. Wachter, *J. Am. Chem. Soc.*, 1977, **99**, 3877.
57. P. C. Blake, M. F. Lappert, R. G. Taylor, J. L. Atwood, and H. Zhang, *J. Chem. Soc., Chem. Commun.*, 1986, 1148; P. C. Blake, N. M. Edelstein, P. B. Hitchcock, W. K. Kot, M. F. Lappert, G. V. Shalimoff, and S. Tian, *J. Organomet. Chem.*, 2001, **636**, 124.
58. F. Baumgartner, E. O. Fischer, B. Kanellakopulos, and P. Laubereau, *Angew. Chem., Int. Ed. Engl.*, 1966, **5**, 134.

59. D. L. Clark, A. P. Sattelberger, S. G. Bott, and R. N. Vrtis, *Inorg. Chem.*, 1989, **28**, 1771; D. L. Clark and A. P. Sattelberger, *Inorg.Synth.*, 1997, **31**, 307.

60. E. Kim, A. L. Odom, and C. C. Cummins, *Inorg. Chim. Acta*, 1998, **278**, 103.

61. W. J. Evans, K. J. Forrestal, and J. W. Ziller, *Angew. Chem., Int. Ed. Engl.*, 1997, **36**, 774; W. J. Evans, G. W. Nyce, K. J. Forrestal, and J. W. Ziller, *Organometallics*, 2002, **21**, 1050.

62. W. J. Evans, S. A. Kozimor, and J. W. Ziller, *J. Am. Chem. Soc.*, 2003, **125**, 14264.

63. P. C. Blake, M. F. Lappert, R. G. Taylor, J. L. Atwood, and H. Zhang, *Inorg. Chim. Acta*, 1987, **139**, 13; W. W. Lukens, S. M. Beshouri, A. L. Stuart, and R. A. Andersen, *Organometallics*, 1999, **18**, 1247.

64. L. R. Avens, C. J. Burns, R. J. Butcher, D. L. Clark, J. C. Gordon, A. R. Schake, B. L. Scott, and J. G. Watkin, *Organometallics*, 2000, **19**, 451.

65. W. W. Lukens, S. M. Beshouri, L. L. Blosch, and R. A. Andersen, *J. Am. Chem. Soc*, 1996, **118**, 901.

66. J. Manriquez, P. J. Fagan, T. J. Marks, S. H. Vollmer, C. S. Day, and V. W. Day, *J. Am. Chem. Soc.*, 1979, **101**, 5075.

67. C. Boisson, J. C. Berthet, M. Ephritikhine, M. Lance, and M. Nierlich, *J. Organomet. Chem.*, 1997, **533**, 7.

68. J.-F. Le Maréchal, E. Bulot, D. Baudry, M. Ephritikhine, D. Hauchard, and R. Godard, *J. Organomet. Chem.*, 1988, **354**, C17; J.-F. Le Maréchal, C. Villiers, P. Charpin, M. Nierlich, M. Lance, J. Vigner, and M. Ephritikhine, *J. Organomet. Chem.*, 1989, **379**, 259.

69. J. Goffart and S. Bettonville, *J. Organomet. Chem.*, 1989, **361**, 17.

70. J. Rebizant, M. R. Spirlet, B. Kanellakopulos, and E. Dornberger, *J. Less-Common Metals*, 1986, **122**, 211.

71. J. H. Burns and P. G. Laubereau, *Inorg. Chem.*, 1971, **10**, 2789.

72. J. Goffart, G. Michel, B. P. Gilbert, and G. Duyckaerts, *Inorg. Nucl. Chem. Lett.*, 1978, **14**, 393.

73. J. Goffart and S. Bettonville, *J. Organomet. Chem.*, 1988, **356**, 297; J. Rebizant, M. R. Spirlet, S. Bettonville, and J. Goffart, *Acta Crystallogr., C*, 1989, **C45**, 1509.

74. T. M. Trnka, J. B. Bonanno, B. M. Bridgewater, and G. Parkin, *Organometallics*, 2001, **20**, 3255.

75. J. Meunier-Piret, J. P. Declercq, G. German, and M. van Meersche, *Bull. Soc. Chim. Belg.*, 1980, **89**, 121.

76. D. F. Starks and A. Streitwieser Jr, *J. Am. Chem. Soc*, 1973, **95**, 3243; D. F. Starks, T. C. Parsons, A. Streitwieser, and N. Edelstein Jr, *Inorg. Chem.*, 1974, **13**, 1307; D. G. Karraker, J. A. Stone, E. R. Jones, and N. Edelstein, *J. Am. Chem. Soc.*, 1970, **92**, 4841.

77. A. Zalkin and K. N. Raymond, *J. Am. Chem. Soc.*, 1969, **91**, 5667.

78. A. Avdeef, K. N. Raymond, K. O. Hodgson, and A. Zalkin, *Inorg. Chem.*, 1972, **11**, 1083.

79. A. Streitwieser Jr and S. A. Kinsey, in 'Fundamental and Technological Aspects of Organo-f-Element Chemistry', eds. T. J. Marks and I. Fragala, Reidel, Dordrecht, 1985, p. 77.

80. C. A. Harmon and A. Streitwiser Jr, *J. Am. Chem. Soc.*, 1972, **94**, 8926.

81. C. Apostolidis, F. T. Edelmann, B. Kanellakopulos, and U. Reissmann, *Z. Naturforsch. B*, 1999, **54**, 960.

82. A. Streitwieser, M. T. Barros, H. K. Wang, and T. R. Boussie Jr, *Organometallics*, 1993, **12**, 5023.

83. W. D. Luke and A. Streitwieser Jr, *J. Am. Chem. Soc.*, 1981, **103**, 3241.

84. D. G. Karraker and J. A. Stone, *J. Am. Chem. Soc.*, 1974, **96**, 6885; D. G. Karraker, *J. Inorg. Nucl. Chem.*, 1977, **39**, 87; F. Billiau, G. Folcher, H. Marquet-Ellis, P. Rigny, and E. Saito, *J. Am. Chem. Soc.*, 1981, **103**, 5603.

85. T. R. Boussie, D. C. Eisenberg, J. Rigsbee, A. Streitwieser, and A. Zalkin, *Organometallics*, 1991, **10**, 1992.

86. J. Parry, F. G. N. Cloke, S. J. Coles, and M. B. Hursthouse, *J. Am. Chem. Soc.*, 1999, **121**, 6867.

87. D. C. Eisenberg, A. Streitwieser, and W. K. Kot, *Inorg. Chem.*, 1990, **29**, 10.

88. D. G. Karraker and J. A. Stone, *J. Inorg. Nucl. Chem.*, 1977, **39**, 2215.

89. C. LeVanda, J. P. Solar, and A. Streitwieser Jr, *J. Am. Chem. Soc.*, 1980, **102**, 2128.

90. T. M. Gilbert, R. R. Ryan, and A. P. Sattelberger, *Organometallics*, 1988, **7**, 2514; T. M. Gilbert, R. R. Ryan, and A. P. Sattelberger, *Organometallics*, 1989, **8**, 857.

91. A. Zalkin, D. H. Templeton, C. Le Vanda, and A. Streitwieser Jr, *Inorg. Chem.*, 1980, **19**, 2560.

92. N. C. Burton, G. N. Cloke, P. B. Hitchcock, H. C. deLemos, and A. A. Sameth, *Chem. Commun.*, 1989, 1462.

93. T. R. Boussie, R. M. Moore, A. Streitwieser, A. Zalkin, J. G. Brennan, and K. A. Smith Jr, *Organometallics*, 1990, **9**, 2010.

94. D. Baudry, E. Bulot, M. Ephritikhine, M. Nierlich, M. Lance, and J. Vigner, *J. Organomet. Chem.*, 1990, **388**, 279.

95. T. Arliguie, D. Baudry, J. C. Berthet, M. Ephritikhine, and J.-F. Le Maréchal, *New J. Chem.*, 1991, **15**, 569.

96. S. M. Cendrowski-Guillaume, M. Lance, M. Nierlich, and M. Ephritikhine, *Organometallics*, 2000, **19**, 3257.

97. J. C. Berthet and M. Ephritikhine, *Chem. Commun.*, 1993, 1566.

98. J. C. Berthet, J.-F. Le Maréchal, and M. Ephritikhine, *J. Organomet. Chem.*, 1990, **393**, C47.

99. D. Gourier, D. Caurant, J. C. Berthet, C. Boisson, and M. Ephritikhine, *Inorg. Chem.*, 1997, **36**, 5931; C. Boisson, J. C. Berthet, M. Lance, J. Vigner, M. Nierlich, and M. Ephritikhine, *J. Chem. Soc., Dalton Trans.*, 1996, 947.

100. A. R. Schake, L. R. Avens, C. J. Burns, D. L. Clark, A. P. Sattelberger, and W. H. Smith, *Organometallics*, 1993, **12**, 1497.

101. W. J. Evans, G. W. Nyce, and J. W. Ziller, *Angew. Chem., Int. Ed. Engl.*, 2000, **39**, 240.

102. G. Wilke, B. Bogdanovic, P. Hardt, P. Heimbach, W. Keim, M. Kröner, W. Oberkirch, K. Tanaka, E. Streinrücke, D. Walter, and H. Zimmerman, *Angew. Chem., Int. Ed. Engl.*, 1966, **5**, 151.

103. G. Lugli, W. Marconi, A. Mazzei, N. Paladino, and U. Pedretti, *Inorg. Chim. Acta*, 1969, **3**, 253.

104. G. Lugli, A. Mazzei, and S. Poggio, *Makromol. Chem.*, 1974, **175**, 2021.

105. C. N. Carlson, T. P. Hanusa, and W. W. Brennessel, *J. Am. Chem. Soc.*, 2004, **126**, 10550.

106. T. H. Cymbaluk, J. Z. Liu, and R. D. Ernst, *J. Organomet. Chem.*, 1983, **255**, 311.

107. D. Baudry, E. Bulot, and M. Ephritikhine, *Chem. Commun.*, 1989, 1316.

108. D. Baudry, E. Bulot, P. Charpin, and M. Ephritikhine, *J. Organomet. Chem.*, 1989, **371**, 163.

109. M. Cesari, U. Pedretti, G. Lugli, and W. Marconi, *Inorg. Chim. Acta*, 1971, **5**, 439.

110. F. A. Cotton and W. Schwotzer, *Organometallics*, 1985, **4**, 942; G. C. Campbell, F. A. Cotton, J. F. Haw, and W. Schwotzer, *Organometallics*, 1986, **5**, 274; F. A. Cotton, W. Schwotzer, and C. Q. Simpson, *Angew. Chem., Int. Ed. Engl.*, 1986, **25**, 637; F. A. Cotton and W. Schwotzer, *Organometallics*, 1987, **6**, 1275; F. A. Cotton, *Inorg. Chem.*, 2002, **41**, 463.

111. D. Baudry, E. Bulot, P. Charpin, M. Ephritikhine, M. Lance, M. Nierlich, and J. Vigner, *J. Organomet. Chem.*, 1989, **371**, 155.

112. P. I. Diaconescu, P. L. Arnold, T. A. Baker, D. J. Mindiola, and C. C. Cummins, *J. Am. Chem. Soc.*, 2000, **122**, 6108.

113. W. J. Evans, S. A. Kozimor, J. W. Ziller, and N. Kaltsoyannis, *J. Am. Chem. Soc.*, 2004, **126**, 14533 (in press).

114. T. Arliguie, M. Lance, M. Nierlich, J. Vigner, and M. Ephritikhine, *Chem. Commun.*, 1995, 193; D. Gourier, D. Caurant, T. Arliguie, and M. Ephritikhine, *J. Am. Chem. Soc.*, 1998, **120**, 6084.

115. T. Arliguie, M. Lance, M. Nierlich, J. Vigner, and M. Ephritikhine, *Chem. Commun.*, 1994, 847; T. Arliguie, M. Lance, M. Nierlich, and M. Ephritikhine, *J. Chem. Soc., Dalton Trans.*, 1997, 2501.

116. F. G. N. Cloke and P. B. Hitchcock, *J. Am. Chem. Soc.*, 1997, **119**, 7899.

117. F. G. N. Cloke, J. C. Green, and C. N. Jardine, *Organometallics*, 1999, **18**, 1080; F. G. N. Cloke, *Pure Appl. Chem.*, 2001, **73**, 233.

118. F. G. N. Cloke and P. B. Hitchcock, *J. Am. Chem. Soc.*, 2002, **124**, 9352.

119. F. G. N. Cloke, J. C. Green, and N. Kaltsoyannis, *Organometallics*, 2004, **23**, 832.

120. T. Guo, M. D. Diener, Y. Chai, M. J. Alford, R. E. Haufler, S. M. McClure, T. Ohno, J. H. Weaver, G. E. Scuseria, and R. E. Smalley, *Science*, 1992, **257**, 1661; R. E. Haufler, J. Conceicao, L. P. F. Chibante, Y. Chai, N. E. Byrne, S. Flanagan, M. M. Haley, S. C. O'Brian, C. Pan, Z. Xiao, W. E. Billups, M. A. Cuifolini, R. H. Hauge, J. L. Musgrave, L. J. Wilson, R. F. Curl, and R. E. Smalley, *J. Phys. Chem.*, 1990, **94**, 8634.

121. K. Akiyama, Y. Zhao, K. Sueki, K. Tsukada, H. Haba, Y. Nagame, T. Kodama, S. Suzuki, T. Ohtsuki, M. Sakaguchi, K. Kikuchi, M. Katada, and H. Nakahara, *J. Am. Chem. Soc.*, 2001, **123**, 181.

122. T. J. Marks and A. M. Seyam, *J. Organomet. Chem.*, 1974, **67**, 61.

123. W. J. Evans, D. J. Wink, and D. R. Stanley, *Inorg. Chem.*, 1982, **21**, 2565.

124. E. R. Sigurdson and G. Wilkinson, *J. Chem. Soc., Dalton Trans.*, 1977, 815.

125. H. Lauke, P. N. Swepston, and T. J. Marks, *J. Am. Chem. Soc.*, 1984, **106**, 6841.

126. E. Koehler, W. Brueser, and K. H. Thiele, *J. Organomet. Chem.*, 1974, **76**, 235.

127. E. A. Mintz, K. G. Moloy, T. J. Marks, and V. W. Day, *J. Am. Chem. Soc.*, 1982, **104**, 4692.

128. W. G. Van Der Sluys, C. J. Burns, and A. P. Sattelberger, *Organometallics*, 1989, **8**, 855.

129. P. G. Edwards, R. A. Andersen, and A. Zalkin, *Organometallics*, 1984, **3**, 293.

130. H. W. Turner, R. A. Andersen, A. Zalkin, and D. H. Templeton, *Inorg. Chem.*, 1979, **18**, 1221.

131. S. J. Simpson, H. Turner, and R. A. Andersen, *Inorg. Chem.*, 1981, **20**, 2991; S. J. Simpson and R. A. Andersen, *J. Am. Chem. Soc.*, 1981, **103**, 4063.

132. J. Manriquez, P. J. Fagan, and T. J. Marks, *J. Am. Chem. Soc.*, 1978, **100**, 3939.

133. J. W. Bruno, G. M. Smith, K. Fair, A. J. Schultz, T. J. Marks, and J. M. Williams, *J. Am. Chem. Soc.*, 1986, **108**, 40.

134. X. Yang, C. Stern, and T. J. Marks, *Organometallics*, 1991, **10**, 840.

135. D. S. J. Arney, C. J. Burns, and D. C. Smith, *J. Am. Chem. Soc.*, 1992, **114**, 10 068.

136. J. L. Kiplinger, D. E. Morris, B. L. Scott, and C. J. Burns, *Organometallics*, 2002, **21**, 5978.

137. R. Broach, A. J. Schultz, J. M. Williams, G. M. Brown, J. M. Manriquez, P. J. Fagan, and T. J. Marks, *Science*, 1979, **203**, 172.

138. M. R. Duttera, P. J. Fagan, T. J. Marks, and V. W. Day, *J. Am. Chem. Soc.*, 1982, **104**, 865.

139. J. C. Berthet, J.-F. Le Maréchal, and M. Ephritikhine, *Chem. Commun.*, 1991, 360; J. C. Berthet, J.-F. Le Maréchal,

M. Lance, M. Nierlich, J. Vigner, and M. Ephritikhine, *J. Chem. Soc., Dalton Trans.*, 1992, 1573.

140. X. Jamine, J. Goffart, M. Ephritikhine, and J. Fuger, *J. Organomet. Chem.*, 1993, **448**, 95.
141. W. J. Evans, G. W. Nyce, and J. W. Ziller, *Organometallics*, 2001, **20**, 5489.
142. J. Ogden, in ‘Cryochemistry’, eds. M. Moskovitz and G. A. Ozin, Wiley, New York, 1976, Chap. 7.
143. L. Andrews, B. Liang, J. Li, and B. E. Bursten, *New J. Chem.*, 2004, **28**, 289; B. Liang, L. Andrews, J. Li, and B. E. Bursten, *Inorg. Chem.*, 2004, **43**, 882.
144. J. G. Brennan, R. A. Andersen, and J. L. Robbins, *J. Am. Chem. Soc.*, 1986, **108**, 335.
145. B. E. Bursten and R. J. Strittmatter, *J. Am. Chem. Soc.*, 1987, **109**, 6606.
146. J. Parry, E. Carmona, S. Coles, and M. Hursthouse, *J. Am. Chem. Soc.*, 1995, **117**, 2649; M. Del Mar Conejo, J. S. Parry, E. Carmona, M. Schultz, J. G. Brennan, S. Beshouri, R. A. Andersen, R. D. Rogers, S. Coles, and M. Hursthouse, *Chemistry*, 1999, **5**, 3000.
147. W. J. Evans, S. A. Kozimor, G. W. Nyce, and J. W. Ziller, *J. Am. Chem. Soc.*, 2003, **125**, 13831.
148. R. E. Cramer, K. Panchanatheswaran, and J. W. Gilje, *Angew. Chem., Int. Ed. Engl.*, 1984, **23**, 912; R. E. Cramer, K. Panchanatheswaran, and J. W. Gilje, *J. Am. Chem. Soc.*, 1984, **106**, 1853; R. E. Cramer, U. Engelhardt, K. T. Higa, and J. W. Gilje, *Organometallics*, 1987, **6**, 41; R. E. Cramer, J. W. Jeong, and J. W. Gilje, *Organometallics*, 1987, **6**, 2010; R. E. Cramer, M. A. Bruck, F. Edelman, D. Afzal, J. W. Gilje, and H. Schmidbauer, *Chem. Ber.*, 1988, **121**, 417.
149. R. C. Stevens, R. Bau, R. E. Cramer, D. Afzal, J. W. Gilje, and T. F. Koetzle, *Organometallics*, 1990, **9**, 964.
150. M. S. Eisen and T. J. Marks, *J. Am. Chem. Soc.*, 1992, **114**, 10 358.
151. T. J. Marks, *Acc. Chem. Res.*, 1992, **25**, 57.
152. M. S. Eisen and T. J. Marks, *Organometallics*, 1992, **11**, 3939; M. S. Eisen and T. J. Marks, *J. Mol. Catal.*, 1994, **86**, 23.
153. A. H. H. Chang and R. M. Pitzer, *J. Am. Chem. Soc.*, 1989, **111**, 2500. references therein.
154. J. P. Clark and J. C. Green, *J. Chem. Soc., Dalton Trans.*, 1977, 505.
155. J. G. Brennan, J. C. Green, and C. M. Redfern, *J. Am. Chem. Soc.*, 1989, **111**, 2371.
156. J. C. Green, M. P. Payne, and A. Streitwieser Jr, *Organometallics*, 1983, **2**, 1707.
157. B. E. Bursten and K. J. Novo-Gradic, *J. Am. Chem. Soc.*, 1987, **109**, 904.
158. J. Li and B. E. Bursten, *J. Am. Chem. Soc.*, 1997, **119**, 9021.
159. J. V. Ortiz, P. J. Hay, and R. L. Martin, *J. Am. Chem. Soc.*, 1992, **114**, 2736.
160. G. A. Bowmaker, A. Görling, O. Häberlen, N. Rösch, G. L. Goodman, and D. E. Ellis, *Inorg. Chem.*, 1992, **31**, 577.
161. J. G. Brennan, J. C. Green, and C. M. Redfern, *Inorg. Chim. Acta*, 1987, **139**, 331.
162. A. H. H. Chang, K. Zhao, W. C. Ermler, and R. M. Pitzer, *J. Alloys and Compounds*, 1994, **213/214**, 191.

Acknowledgment

The authors are grateful to the Division of Chemical Sciences, Geosciences, and Biosciences, Office of Basic Energy Sciences, U.S. Department of Energy, for their support of actinide organometallic chemistry research at Los Alamos National Laboratory.

Alkali Metals: Inorganic Chemistry

Wing-Por Leung & Queenie Wai-Yan Ip
The Chinese University of Hong Kong, Hong Kong, China

Based in part on the article Alkali Metals: Inorganic Chemistry by Francis S. Mair & Ronald Snaith which appeared in the Encyclopedia of Inorganic Chemistry, First Edition.

1	Introduction	1
2	The Elements	1
3	Compounds	6
4	Coordination Compounds	14
5	Metal-organics	18
6	Related Articles	20
7	References	20

1 INTRODUCTION

The alkali metals lithium (symbol Li), sodium (Na), potassium (K), rubidium (Rb), and cesium (Cs) constitute Group 1 of the Periodic Table, each having an outer electronic configuration s^1. (The sixth member, francium (Fr), has been little investigated (and will not be discussed here) since all of its isotopes are radioactive (the longest-lived, $^{223}_{87}Fr$, has a half-life of only 21 min) and are found only in certain natural decay series and as products of nuclear reactions). The group has been much studied as it best illustrates the effects of increasing atomic size and mass on chemical and physical properties (*see* ***Periodic Table: Trends in the Properties of the Elements***). Thus, all of these elements are metals which show a regular gradation in physical properties as the group is descended. They are the most electropositive metals known, and their chemistry is dominated by the +1 oxidation state, M^+ (*see* ***Coordination & Organometallic Chemistry: Principles***). However, other ionic, atomic, and molecular forms of the elements have been much studied both experimentally and theoretically; notably, alkalide anions M^-, atoms and diatomic gas-phase molecules, and atoms and clustered species (M_n, $M_n{}^{x+}$, $M_n{}^{x-}$) trapped and isolated in materials such as graphite and zeolites (*see* ***Intercalation Chemistry***; ***Zeolites***).

Lithium, sodium, and potassium, and their compounds, are of considerable biochemical and industrial importance.[1–3] Lithium salts can control manic-depressive psychoses,[4,5] the Na^+/K^+ concentration ratio is crucial to nerve impulse transmission, and potassium formulations dominate the plant fertilizer market. Lithium and its salts are used in the production of high-strength and low-density alloys, of lubricating greases, of toughened glass, and in porcelain and ceramics production. Organolithium reagents (e.g. n-butyllithium) are of increasing importance as reagents in synthetic organic chemistry[6] (*see* ***Alkali Metals: Organometallic Chemistry***) and as anionic polymerization initiators to produce, for example, styrene–butadiene copolymers for car tyres (*see* ***Oligomerization & Polymerization by Homogeneous Catalysis***).[7] Sodium chloride is of particular importance, being more used for inorganic chemical manufacture than any other material. In the future, lithium (especially) and sodium are likely to assume even more commercial importance: lithium metal as a source of tritium (from the ^7Li + neutron reaction) for nuclear fusion processes and as a nuclear reactor coolant, and both elements as likely components of energy storage systems for off-peak electricity and of batteries for electric cars.[8]

2 THE ELEMENTS

2.1 History, Abundance, and Production

Although compounds of sodium and potassium were known in ancient times, it was not until Humphrey Davy's famous electrolytic experiments in 1807 on molten caustic soda and potash that the metals themselves were first isolated.[9] Lithium was first recognized as an alkali metal in various silicate and mica minerals in 1817 (by Arfvedson, who thus named it from the Greek word for stone) and first isolated, again by Davy, in 1818. The discovery of cesium (1860) and rubidium (1861) had to await the development of atomic spectroscopy (by Bunsen and Kirchoff); their names reflect the colors of their dominant spectral lines (Latin; caesius, sky blue, and rubidus, deep-red).

The terrestrial (Earth's crust, oceans, atmosphere) and cosmological abundances[10] of the elements fall into two clear sets. Sodium (Earth, $\approx$23 000 ppm by mass; Universe, $\approx$20 ppm) and potassium ($\approx$17 000 ppm; $\approx$3 ppm) are relatively abundant, and indeed they constitute the seventh and eighth most abundant elements in the Earth's crust. The most important sodium-containing minerals are the chloride (rock salt), carbonate, nitrate (saltpetre), and borate (borax); in addition, there are vast supplies of sodium chloride in oceanic waters ($\approx$30 kg m^{-3}). Major sources of potassium are the chloride KCl (sylvite) and the mixed-metal chloride $KCl{\cdot}MgCl_2{\cdot}6H_2O$ (carnallite). In contrast, the other three metals are relatively scarce, abundances on Earth and in the Universe being $\approx$20 and 0.006 ppm respectively for Li, $\approx$70 and 0.01 ppm for Rb, and $\approx$2 and 0.008 ppm for Cs. Lithium occurs mainly in silicates such as spodumene ($LiAlSi_2O_6$).

Commercial production of lithium[1] and sodium is by electrolysis of their fused chlorides. For the former, spodumene is washed with H_2SO_4 at 250 °C and water-leached to give $Li_2SO_4{\cdot}H_2O$; successive treatment with Na_2CO_3 and HCl affords insoluble Li_2CO_3 and LiCl. Alternatively, the ore is heated with CaO to give LiOH which is then converted to the chloride. Fused low-melting eutectics such as LiCl + KCl (450 °C) and NaCl + $CaCl_2$ (505 °C) are used in the electrolysis process, which employs a carbon anode and a steel cathode. The other three metals are also extracted from their chlorides; small quantities of RbCl and CsCl are obtained as by-products of lithium mineral processing. In their cases, however, the molten metal chlorides are treated with the vapor of a reactive metal (Na vapor at 850 °C or Ca vapor at 750 °C) in a countercurrent fractionating tower.

2.2 Uses of the Metals and Their Compounds

Although Rb and Cs, and their compounds, are so far mainly of academic interest, Li, Na (especially), and K, and their compounds, have considerable commercial value. Lithium metal itself[1] is used in the manufacture of alloys with magnesium and aluminum; these combine toughness with low density and so are employed in the construction of armor plate and aircraft/aerospace components (*see* ***Alloys***). Until recently, the major use of sodium was also in alloy manufacture, specifically of the Pb/Na alloy needed for the production of tetraethyllead, the antiknock additive (*see* ***Lead: Organometallic Chemistry***). However, the market here is declining on account of the environmental problems caused by lead emissions. Molten Na (and, to a lesser but increasing extent, molten Li) is employed also as a heat-exchange coolant around nuclear reactors; properties such as a low-melting point and low viscosity but a high heat capacity are valuable in this respect, although there are many technical problems such as melt containment, corrosion, and reactions with the atmosphere and with the reactor walls.[11]

The major bulk-produced lithium salts are the stearate, used to thicken and gel oils to provide lubricating greases; the carbonate, used as a flux in porcelain and enamel production, as an additive to bauxite in aluminum production (where it lowers the fusion temperature of the electrolyte and raises the melt conductivity), and as a source of Li^+ ions to replace larger Na^+ ions in the production of toughened glass; and the hydroxide, which is used to absorb carbon dioxide from enclosed spaces such as submarines. More ‘specialty’ lithium compounds find use in organic syntheses; for example, lithium aluminum hydride as a reducing agent and various organolithium compounds (particularly n-butyllithium) as selective proton abstractor reagents and as anionic polymerization initiators.[1,6,7,12,13] Most industrial-scale compounds are derived from sodium chloride, annual world consumption of which is of the order of 170 million tonnes. Salt itself has major uses in road clearance and in animal feeds, but most of it is converted by large-scale processes to products such as sodium hydroxide, chlorine, and sodium carbonate (which, taken together, constitute the chloralkali industry). The major potassium salt is also the chloride, used to formulate most potassic plant fertilizers. Other less employed, but still important, potassium compounds include the hydroxide, used mainly to produce phosphates for liquid detergents; the carbonate, used in fluorescent lamps and in optical lenses; the bromide, which is the normal source of bromine gas for organic syntheses; and the superoxide (KO_2), which is used in breathing masks in mines and space vehicles since it reacts with traces of moisture in the breath to generate oxygen.

A more unusual use of the alkali metals and their compounds, but one of high industrial importance, is as promoters of various catalysts.[14] For example, addition of Li^+, Na^+, or K^+ to MgO or CaO catalysts for the oxidative coupling of CH_4 to give valuable C_2 products (ethane, ethylene) improves the yields greatly; spectroscopic investigations have implied that $[M^+O^-]$ active sites are produced on the catalyst surface and that these sites abstract H from CH_4 to give $\cdot CH_3$ radicals, which then couple.[15–17] Similarly, catalysts for various transformations of syngas (H_2/CO mixtures) can be promoted by alkali metals, for example, doping of a Cu/ZnO catalyst with Cs doubles methanol yields from H_2/CO mixtures, an effect attributed partly to formation of surface formate (CsCHO)[18,19] (*see* ***Oxide Catalysts in Solid-state Chemistry*** and *see Synthesis Gas*).

Sodium and potassium are among the 25 or so elements now thought to be essential for animal life.[4,20] They perform electrophysiological functions based on the fact that the Na^+:K^+ concentration ratio is different in the fluids inside and outside cells. Because of these concentration gradients across cell membranes, a potential difference is set up and this is responsible for the transmission of nerve impulses. Lithium also is of biochemical importance, but as a drug in the treatment of manic-depressive psychosis; in the United Kingdom, for example, about 1 in every 1500 people take prescribed gram quantities of Li_2CO_3 daily. The inorganic pharmacology of lithium has been reviewed recently[5,21] but it seems likely that its prime role is to affect the mobilization of calcium into and out of cells by inhibiting certain enzymes in inositol phosphate pathways (*see* ***Metal-based Drugs***; ***Metal-based Imaging Agents***).

A future bulk use of lithium and sodium might well be as components of batteries, particularly for off-peak electricity storage and in electric cars. The latter use will be prompted by legislation; for example, in California alone, by the year 2003, 10% of all new cars (over 200 000) must be emission-free.[8] However, development of such batteries will be a major challenge. Those produced to date give limited range (having to be recharged frequently) and poor acceleration, and they are expensive, requiring complicated installation engineering. For example, sodium/sulfur batteries use a liquid sodium anode, a sulfur cathode, and a solid electrolyte of β-alumina (Al_2O_3), but the snag is that they operate at 300 °C.[22] Similarly, Li/FeS_x batteries employ Li and FeS_x electrodes with a molten electrolyte of LiCl/KCl at 400 °C.[23,24] Clearly, it would be preferable to avoid molten/liquid systems which require elevated temperatures and which pose severe containment problems. However, development of solid-only cells has been hampered by the scarcity of low-temperature solid electrolytes with good ion conductivity (*see* ***Ionic Conductors***). Materials of promise in this regard include solid $LiAlCl_4$ (with Li_xTiS_2 and Li_xCoO_2 intercalated electrodes),**[25]** solid solutions based on lithium titanium phosphate,**[26]** and LiI·4MeOH which has the highest conductivity so far observed for Li^+ (due to mobile complexed cations in the solid-state structure, $Li(MeOH)_4{}^+ \cdot I^-$).**[27]**

2.3 Atomic, Physical, and Chemical Properties

Fundamental atomic and physical properties of the alkali metals are given in Tables 1, 2, and 3. The elements are characterized by having electron configurations each with a single s orbital electron outside a noble gas core (see Table 1). Sodium and cesium are mononuclidic so that their relative atomic masses are known extremely accurately; in effect, the same can be written for potassium and rubidium since their isotopes (of which there are three and two, respectively) have extremely long half-lives. Lithium occurs naturally as ^{6}Li (7% abundance) and ^{7}Li (93%); its other three isotopes are radioactive, with very short half-lives. At least one isotope of each element has a nuclear spin (I) and hence, potentially, useful information can be gleaned from NMR studies: ^{6}Li, $I = 1$; ^{7}Li, $I = 3/2$; ^{23}Na, $I = 3/2$; ^{39}K (93%), $I = 3/2$; ^{87}Rb (28%), $I = 3/2$; ^{133}Cs, $I = 7/2$. In practice, ^{7}Li NMR spectroscopy has found most use; for example, in elucidating solution structures and solution equilibria for many lithium compounds and in monitoring concentrations and mobilities of lithium ions in vivo.**[28–32]**

The radii of the metals increase progressively with increasing atomic number, and these elements are the largest in their respective periods. Such features lead to relatively small first ionization energies for the atoms, and the chemistry is dominated by this fact. Thus the elements are highly reactive metals and form M^+ ions in the vast majority of their compounds. The very high second ionization energies prohibit formation of M^{2+} species. However, although the electron affinities (or 'electron attachment energies') are only

Table 1 Atomic and related properties of the alkali metals

Metal	Electronic configuration	Atomic number	Relative atomic mass	Metal radius (Å)	Ionization energies ($kJ\ mol^{-1}$) 1st	Ionization energies ($kJ\ mol^{-1}$) 2nd	Electron affinity ($kJ\ mol^{-1}$)	Electronegativity (Pauling scale)
Li	$[He]2s^1$	3	6.941	1.52	520.1	7296	59.8	0.98
Na	$[Ne]3s^1$	11	22.9898	1.86	495.7	4563	52.9	0.93
K	$[Ar]4s^1$	19	39.0983	2.27	418.7	3069	48.3	0.82
Rb	$[Kr]5s^1$	37	85.4678	2.48	402.9	2640	46.9	0.82
Cs	$[Xe]6s^1$	55	132.9054	2.65	375.6	2260	45.5	0.79

Table 2 Physical and related properties of the alkali metals

Metal	Melting point (°C)	Boiling point (°C)	Density ($g\ cm^{-3}$, 20 °C)	Electrical conductivity ($10^4 \Omega$ cm, 0 °C)	Enthalpy of fusion ($kJ\ mol^{-1}$)	Enthalpy of vaporization ($kJ\ mol^{-1}$)	Covalent radius (Å)	Dissociation enthalpy of M_2 ($kJ\ mol^{-1}$)
Li	180.5	1326	0.534	11.8	2.93	148	1.34	108
Na	97.8	883	0.968	23.0	2.64	99	1.57	73
K	63.7	756	0.856	15.9	2.39	79	2.02	49
Rb	39.0	688	1.532	8.6	2.20	76	2.16	47
Cs	28.5	690	1.90	5.6	2.09	67	2.35	43

Table 3 Properties of alkali metal cations

Metal	Electrode potential $M(s) \rightarrow M^+(aq) + e^-$ (V)	M^+ Ionic radius (Å 6 coord.)	Hydration numbers	Enthalpy of hydration ($kJ\ mol^{-1}$)	Hydrated M^+ radius (Å)	Relative ionic mobilities (∞ dilution, 18 °C)
Li	3.02	0.74	25.3	519	3.40	33.5
Na	2.71	1.02	16.6	406	2.76	43.5
K	2.92	1.38	10.5	322	2.32	64.6
Rb	2.99	1.49	–	293	2.28	67.5
Cs	3.02	1.70	9.9	264	2.28	68.0

mildly exothermic, M^- ions can be produced for all the alkali metals (lithium excepted) under carefully controlled conditions (see Section 2.4).

The bonding in alkali metal compounds is held to be essentially ionic, involving electrostatic attractions between ‘bare’ or solvated M^+ ions and associated anions. This reflects the ease of formation of M^+ ions and the relative weakness of any covalent bonds formed: the valence orbitals available to these atoms are diffuse, leading to poor overlap. This ionic character is predictable also from the low electronegativities of the alkali metals (cf. approximate electronegativity values for typical nonmetals: C 2.5, N 3.0, O 3.5, F 4.0). On this basis, the degree of covalency would be highest for lithium (Li^+ is the smallest, most polarizing cation of the group). However, it is now generally agreed that the bonding even in, say, lithium–carbon bonds is essentially electrostatic in nature.[33,34]

Turning to the properties of the metals themselves (Table 2), all are soft and low-melting materials, Li to Rb being silvery white in color and Cs golden yellow. Their densities are extremely low (Li has the lowest density of any solid at room temperature), although they show very high electrical conductivity. Such properties reflect the fact that, with only one available valence electron per atom, the metallic-binding energy is very low within rather open body-centered cubic lattices. Indeed, such binding energies decrease as the group is descended, and this is apparent in decreasing values for enthalpies of fusion and vaporization. The vapors themselves consist of covalently bonded M_2 diatomic molecules and, mainly, single M atoms. Within the former, the M–M bond energy is expectedly greatest when $M = Li$, since Li has the smallest covalent radius. When vaporized, the elements all have characteristic flame colors: Li crimson, Na yellow, K violet, Rb red–violet, and Cs blue. These arise because of the ready excitation of the single s^1 outer electron and they form the basis of the analytical determination of element concentrations by atomic absorption spectroscopy.

The high reactivities of the alkali metals are reflected in very positive electrode potentials (Table 3, shown as oxidation potentials in aqueous media). The exceptionally high value for lithium appears at first sight anomalous given that, being the smallest atom, it has the highest ionization energy. However, Li^+ is the smallest of the Group 1 cations, and hence is the most heavily and most strongly solvated. Although only four H_2O molecules are bonded directly to each Li^+, over 20 others are affected and form a secondary solvation sphere to give a total solvation number of ca. 25. Hence Li^+ has the most exothermic hydration energy, and the ${Li^+}_{aq}$ ion is the largest and the least mobile of the hydrated alkali metal cations. As related in Section 4, which is concerned with complexes of alkali metal compounds, such features are general ones and pertain to a diversity of polar solvents.

2.4 Solutions of Alkali Metals: Solvated Electrons, Alkalides, and Electrides

In common with certain other metals (e.g. the alkaline earths Ca, Sr, and Ba and the lanthanides Eu and Yb) the alkali metals will dissolve in liquid ammonia and in certain other solvents such as organic ethers, organic amines, and HMPA (*see* ***Ammonia & N-donor Ligands***). However, the solubility is greatest in liquid ammonia and it is dramatic; for example, at −50 °C, 1 mole of Cs (132.9 g) will dissolve in only 2.34 mole of NH_3 (39.8 g). Discovery of this phenomenon is usually attributed to Wehl in 1863, but it now seems likely that these solutions were first prepared by Davy as early as 1808. The solutions have remarkable properties, particularly regarding color, electrical conductivity, and magnetic susceptibility. Dilute solutions are blue owing to an intense absorption at a wavelength of around 1500 nm and tailing into the visible. The position of this absorption, and hence the blue color, is independent of the metal present, so indicating the presence of a species common to all such solutions. At higher concentrations, the color changes to a metallic bronze. The solutions conduct electricity and the current carrier is plainly highly mobile since the conductivity of dilute solutions is considerably higher (7 or 8×) than that of fully ionized salts in water. On concentration, the conductivity first decreases gradually to a minimum at about 0.05 M, but then increases very markedly until, at around 1 M, it is comparable to that of the metal itself. Magnetic susceptibility measurements reveal that dilute solutions are paramagnetic to the extent of one free electron per metal atom. Concentration first leads to a decrease in susceptibility, and indeed solutions of minimal conductivity are also diamagnetic; however, further concentration restores some paramagnetism.

The above findings have been fully reviewed.[35,36] There is a widespread consensus as to their interpretation and it is one which tallies with the low lattice enthalpies of the alkali metals, their low ionization energies, and the high solvation energies of M^+ ions. Thus, in dilute solutions the M atoms ionize to give M^+ cations (which are solvated by NH_3 molecules) and electrons (equation 1). These electrons occupy cavities of around 3.3 Å diameter in the liquid ‘lattice’, such cavities being produced by displacement of 2 or 3 NH_3 molecules which occurs because of repulsion between each electron and the electrons within these solvent molecules. This cavity concept can explain why solutions are of considerably lower density than that of liquid ammonia itself. The blue color of dilute solutions is due to wavefunction transitions undergone by these solvated (yet quasi-free) electrons. The presence of such relatively mobile species explains also the high conductivities and paramagnetism of dilute solutions. At higher concentrations, solvated electrons begin to pair up and they are removed by formation of solvated alkalide anions (equation 2). Both processes lead to reductions in paramagnetism and conductivity.

$$\underset{\text{(dispersed)}}{\mathrm{M(s)}} \rightleftharpoons \mathrm{M(NH_3)} \rightleftharpoons \mathrm{M^+(NH_3)} + \mathrm{e^-(NH_3)} \quad (1)$$

$$\mathrm{M(NH_3)} + \mathrm{e^-(NH_3)} \rightleftharpoons \mathrm{M^-(NH_3)} \quad (2)$$

Liquid ammonia solutions of the alkali metals have found use as strong and selective reducing agents in diverse areas of chemistry. Such solutions are quite stable providing the ammonia is pure and anhydrous, and especially providing that no transition metal ions are present. Such ions catalyze decomposition to metal amide (equation 3). Synthetic uses in inorganic chemistry include the generation of transition metal species in unusually low-oxidation states (see Section 3.5) and of clustered polyanions of main group elements, for example, Sn_9^{4-}, Pb_7^{4-}, As_5^{3-}, and Sb_7^{3-}. A recent use with considerable scope has been the reduction of transition metal salts to give small (2–15 nm diameter) metal particles.[37] However, probably the most widespread application of these alkali metal solutions has been as reducing agents in organic synthesis[6,38] since they will frequently effect reductions that are otherwise impossible. The reagents have been especially valuable in peptide synthesis.[39] Among these alkali metal reagents, sodium naphthalenide is commonly used as a one-electron donor in these organic reduction reactions. However, two-electron transfer via two-step has been proposed in organic reactions involving K^+ (18-crown-6)K^-.[40,41]

$$\mathrm{e^-{\cdot}NH_3} + \mathrm{e^-{\cdot}NH_3} \longrightarrow \mathrm{H_2} + \mathrm{NH_2}^- \quad (3)$$

$$\mathrm{2M(s)} \rightleftharpoons \mathrm{M^+(solv)} + \mathrm{M^-(solv)} \quad (4)$$

As mentioned above, solutions of the alkali metals (except Li) contain solvated M^- anions as well as solvated M^+ cations and solvated electrons;[35] indeed, there is some evidence to suggest that the reducing abilities of such solutions are due largely to the presence of these anions. Alkalide containing Li^- has not been observed in solution or in the solid state, which is due to the strong solvation/complexation of Li^+.[42] Isolation of stable solids containing these alkalide anions has depended on driving the equilibrium shown in equation (4) to the right and then on protecting the anion from the polarizing effects of the cation. Both aims have been realized by using two-dimensional and three-dimensional macrocyclic ethers (crowns and cryptands, respectively; see Section 4.3). The cryptands are particularly effective in encapsulating M^+ cations. For example, addition of Na metal to a solution of $N[(CH_2CH_2O)_2CH_2CH_2]_3N$ (called *2,2,2-crypt*) in $EtNH_2$ allows isolation of golden yellow crystals with a metallic luster, $[Na(2,2,2\text{-crypt})]^+{\cdot}Na^-$. In the crystal, each Na^- ion sits over an open face where the captured Na^+ is visible through the crypt molecule. The anion has an apparent radius of around 2.2 Å, cf. 1.02 Å for six-coordinate Na^+ and 1.54 Å for the covalent radius of Na. Similar crystalline alkalides are preparable for the heavier Group 1 metals, for example, $[Cs(18\text{-crown-}6)]^+{\cdot}Cs^-$, and mixed-metal species are also known, for example, $[Rb(15\text{-crown-}5)]^+{\cdot}Na^-$. Recently, structures of alkalides contain mixed-sandwich complexes of alkali metal cations with 18-crown-6, 15-crown-5, and 12-crown-4 have been determined.[43] An unusual barium azacryptand sodide $Ba^{2+}(H_5Azacryptand[2.2.2]^-)Na^-{\cdot}2MeNH_2$ has been synthesized and structurally characterized by X-ray crystallography and ^{23}Na MAS NMR.[44] Novel dimer of $(Na_2)^{2-}$ has been found in the crystal lattice with internuclear distance of 4.17 Å, 1.3 Å shorter than the average diameter (5.5 Å) of Na^-. Dimers of K^- and Rb^- and chains of Rb^- and Cs^- have also been observed.[45] Solid-state NMR spectra of the homo-metallic systems reveal separate resonances for M^+ and M^-, confirming that they behave as independent entities. Solution NMR spectra also give sharp signals for M^-, indicating that the anion is essentially unsolvated.

It is also possible to prepare crystalline electrides in which a trapped electron acts in effect as the anion. The bulk of the 'excess' electron density in electrides resides in the 'X-ray empty' cavities and in the interconnecting channels. Structures of electrides $[Li(2,1,1\text{-crypt})]^+{\cdot}e^-$ $[K(2,2,2\text{-crypt})]^+{\cdot}e^-$, $[Rb(2,2,2\text{-crypt})]^+{\cdot}e^-$, $[Cs(18\text{-crown-}6)_2]^+{\cdot}e^-$, $[Cs(15\text{-crown-}5)_2]^+{\cdot}e^-$ and mixed-sandwich electride $[Cs(18\text{-crown-}6)(15\text{-crown-}5)^+e^-]_6{\cdot}18\text{-crown-}6$ are known.[46–48] Silica-zeolites with pore diameters of ∼7 Å have been used to prepare silica-based electrides.[49] The potassium species contains weakly bound electron pairs which appear to be delocalized, whereas the cesium species have optical and magnetic properties indicative of electron localization in cavities with little interaction between the electrons or between them and the cation. The structural model of the stable cesium electride synthesized by intercalating cesium in zeolite ITQ-4 has been confirmed by the atomic pair distribution function (PDF) analysis.[50] The synthetic methods, structures, spectroscopic properties, and magnetic behavior of some electrides have been reviewed.[51] Theoretical study on structural and electronic properties of inorganic electrides has also been addressed recently.[52]

2.5 Metal Atoms and Clusters Trapped in Zeolites and Graphite

The section above described how alkali metal species such as solvated M^+ ions and M^- ions can be formed and isolated within the 'lattices' of certain liquid solvents. It is also possible to obtain single alkali metal atoms (M) and clusters (usually cationic ones, $(M)_n{}^{x+}$) in various solid 'hosts' such as zeolites and graphite. There is considerable interest in clustered species since they are especially relevant to the question of what has been called the '*metal/nonmetal transition*', that is, how many atoms need to be gathered together before metallic (rather than molecular, nonmetallic) properties become apparent? The few electron alkali elements lend themselves to state-of-the-art quantum mechanical calculations which probe this question, and this area has been reviewed recently.[53]

Zeolites (e.g. Zeolite A, (**1**)) are a class of aluminosilicates which are built up from corner-sharing SiO_4 and $A1O_4$ tetrahedra arranged in three-dimensional networks and which provide channels and cavities of molecular dimensions (*see* ***Zeolites***). Electroneutrality is maintained by the presence of metal (usually alkali metal) cations. Clustered cationic species such as $Na_3{}^{2+}$, $Na_4{}^{3+}$, $Na_5{}^{4+}$, $Na_6{}^{5+}$, $K_3{}^{2+}$, and $K_4{}^{3+}$, as well as neutral alkali metal particles, $(M)_n$, can be formed within such ‘hosts’ by a variety of methods including high-vacuum deposition of metal atoms,[54] treatment of the zeolite with an alkali metal azide (which decomposes to give the metal),[55] and reduction of the cations already present in zeolites with solutions containing solvated electrons.[56] Species produced (which are frequently paramagnetic) have been studied by ESR spectroscopy and by metal NMR spectroscopy.[57] K^- and Rb^- in metal-loaded zeolites have been prepared and studied by ^{87}Rb NMR.[58]

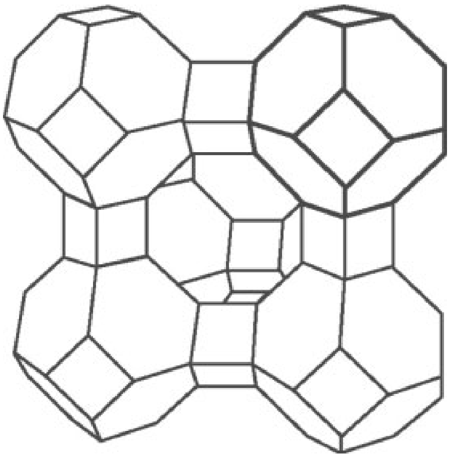

(**1**)

Alkali metals can also be inserted (‘intercalated’) into various forms of elemental carbon, particularly of graphite.[59] This allotrope has a lamellar structure containing flat cojoined hexagons of carbon atoms which form flat layers. Such layers, separated by 3.35 Å, are not superimposed but alternate, usually in an ABAB pattern, and alkali metal atoms can be placed in the gaps simply by treating finely divided graphite with weighed quantities of alkali metals (K, Rb, Cs) in an evacuated vessel. Species produced are commonly of general formula C_xM with $x = 8$, 24, 36, 48, and 60. In C_8K, all the layers (now 5.43 Å apart) are separated by layers of K atoms (see (**2**)), whereas in the other species M atoms are found only in each nth interlamellar spacing. Quite typically, lithium behaves differently, giving intercalates such as C_6Li, $C_{12}Li$, $C_{18}Li$, and others of uncertain and variable composition such as $C_{15-25}Li$ and $C_{19-33}Li$. All such materials are colored (e.g. C_8M bronze, $C_{24}M$ blue) and have high conductivity due to fairly ready exchange of electrons between graphite and the metal. Interest in them centers mainly on this latter property. In this context, it has recently been found[60] that fullerenes such as C_{60} (isolated from soot extracts) can also be doped by alkali metal vaporization to give films such as $C_{60}K_3$ and $C_{60}Rb_3$ which have superconductivity transition temperatures of around 20 K (*see* ***Carbon: Fullerenes***).

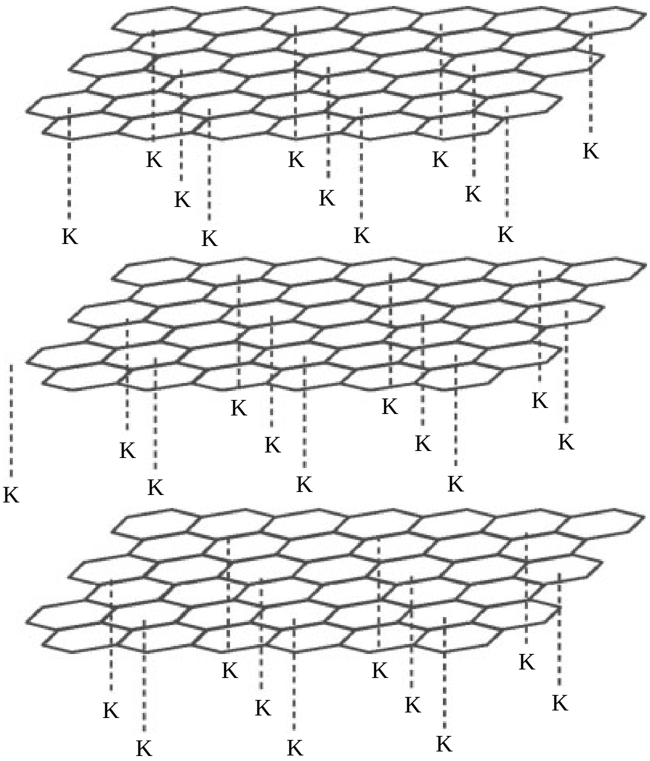

(**2**)

3 COMPOUNDS

3.1 Introduction

It is apparent from the ionization energy and electronegativity data given in Section 2.3 (Table 1) that the chemistry of alkali metal compounds is, with few exceptions, the chemistry of the +1 state. This is, of course, an approximation since total charge separation is unknown, but it is generally believed to be a fairly accurate one in the case of the alkali metals. The matter has been a source of past debate,[33,34,61] especially in the case of lithium where the high-charge density associated with the small lithium cation can lead to appreciable degrees of polarization of anions. The most modern calculations estimate that this effect accounts for ≈10% of bonding at the most, even with the most polarizable, least electronegative anions. In the lithium alkyls, for example, the high volatilities, low-melting points, and alkane and arene solubilities often cited in support of covalent bonding are in fact determined by the strength of bonding between the aggregated molecular units in these compounds. They say nothing of the bonding of the metal within the aggregates. These compounds and their heavier congeners are fully discussed in ***Alkali Metals: Organometallic Chemistry***. Other failings of the ionic bond model will be discussed as they arise. Limits of space preclude a fully comprehensive treatment of alkali metal compounds but all chemical principles and classes of compound to which the identity of the metal is relevant will be covered, with appropriate citations to sources of further information.

3.2 Binary Compounds

3.2.1 Hydrides

The alkali metal hydrides may be formed by direct combination of the elements. All adopt the fcc structure. The hydride anion is small and thus lattice energies are high, especially for LiH with the smallest cation.[62] Evidence for the existence of H^- in these species came from the observation of a large increase in conductivity on melting, and the production of hydrogen at the anode upon electrolysis. All react as strong bases and reducing agents. The reaction of LiH with H_2O has been used as a convenient H_2 source, but reactivity increases down the group such that RbH and CsH ignite spontaneously in dry air. The apparent ionic radius of H^- varies with the cation, since the electron density around the single proton nucleus is easily polarized (r^- in LiH $= 1.37$ Å, in RbH $= 1.54$ Å). The hydrides find most use in the form of complexes such as Li^+ AlH_4^-, useful as selective reducing agents. For further details, *see* ***Hydrogen: Inorganic Chemistry***.

The interstitial hydride $[Li_8(H)\{N(2\text{-pyridyl})Ph\}_6]^+$ $[Li(Me_2Al^tBu_2)_2]^-$ has been reported.[63] Similar hydride compound $[Li_7(H)\{N(2\text{-pyridyl})Ph\}]_6$ has also been obtained by further treatment of the above reaction mixture with THF. Recently, main-group polyhedral clusters with the $Li_8(H)$ moieties has been synthesized by the reaction of a bicyclic 1,3,4,6,7,8-hexahydro-2*H*-pyrimida[1,2-a]pyridimine (hpp) in tandem with $ZnMe_2$ and ^{t}BuLi. The product is an ion-separated compound $[Li_8(H)(hpp)_6]^+$ $[Zn^tBu3]^-$, which has been structurally characterized by X-ray crystallography. It has shown that the hydride is enclosed by an unusual $(Li^+)_8$ cubic cage whose six faces are straddled by the six pyridylamide moieties.[64]

'Inverse Sodium Hydride', a crystalline salt that contains the reverse H^+ and Na^- formed by reversible encapsulation of H^+ in 3^6adamanzane (Adz), has been synthesized and characterized.[65] Theoretical studies of the analogous $Me_3N^-H^+\cdots Na^-$ suggest that the species is indeed metastable with respect to deprotonation in solvents having dielectric constants below $\sim$2.[66]

Table 4 Lattice energies and enthalpies of formation for the alkali metal halides

Compound	Lattice energy (kJ mol^{-1})	ΔH_f° (kJ mol^{-1})
LiF	1036	−147.22
LiCl	853	−97.66
LiBr	807	−83.94
LiI	757	−64.63
NaF	923	−137.10
NaCl	786	−98.27
NaBr	747	−86.30
NaI	704	−68.78
KF	821	−135.58
KCl	715	−104.38
KBr	682	−94.12
KI	649	−78.37
RbF	785	−133.30
RbCl	689	−104.05
RbBr	660	−94.31
RbI	630	−79.78
CsF	740	−132.30
CsCl	659	−105.89
CsBr	631	−94.30
CsI	604	−82.84

3.2.2 Halides

These, the classic 'ionic compounds', provide an oft-used example of periodic trends (*see* ***Periodic Table: Trends in the Properties of the Elements***). All are high melting, colorless crystalline solids. Table 4 shows their enthalpies of formation and lattice energies. There is a steady decrease in lattice energies moving down both Group 1 and Group 17, clearly demonstrating the influence of ion sizes. Size is also important in dictating crystal packing arrangements[67] (*see* ***Halides: Solid-state Chemistry***). The comparable sizes of Cs^+ and Cl^- result in the bcc structure (often termed '*CsCl structure*') which maximizes the coordination number of each ion at 8, whereas a greater size mismatch as in LiCl allows the structure to be determined by closest packing of halide ions in a cubic close-packed lattice with the metal occupying the octahedral holes, so giving a mutual coordination number of 6. From this hard-sphere ionic bond model, limiting values of cation/anion radius ratios may be calculated geometrically. The successes and failures of this model are presented in Table 5. Failures in the hard-sphere ionic bond model have been ascribed to polarization effects, resulting in deformation of the ions. The overpreponderance of the fcc lattice has been attributed to the fact that this geometry maximizes any covalent contributions from p orbitals on the metals. A molecular orbital approach to bonding, treating the lattice as an infinite 'molecule', would seem more appropriate where covalent contributions were thought to be important.

Trends in enthalpies of formation (Table 4) are not as regular as those of lattice energy. For fluorides, lattice energies dominate ΔH_f; therefore the smallest cation gives the most stable fluoride. For the other halides, the ease of production

Table 5 Ion radius ratios and predicted and found coordination numbers for the alkali metal halides

Compound	r^+/r^- (Pauling radii)	Predicted CN	Experimental CN
LiF	0.44	6	6
LiCl	0.33	4	6
LiBr	0.31	4	6
LiI	0.28	4	6
NaF	0.70	6	6
NaCl	0.52	6	6
NaBr	0.49	6	6
NaI	0.44	6	6
KF	0.98	8	6
KCl	0.73	6/8	6
KBr	0.68	6	6
KI	0.62	6	6
RbF	1.09	8	6
RbCl	0.82	8	6
RbBr	0.76	8	6
RbI	0.68	6	6
CsF	1.24	8	6
CsCl	0.93	8	8
CsBr	0.87	8	8
CsI	0.78	8	8

of gaseous cations from the metal becomes the main variant parameter; therefore the easily sublimed (low lattice energy of the metal), least electronegative Cs produces the more stable chlorides, bromides, and iodides. All may be produced by neutralization of aqueous alkali hydroxide or carbonate with the appropriate hydrohalic acid. NaCl (and KCl) are, of course, available directly from rock-salt deposits or by evaporation from sea waters.

Solubilities are hindered by large lattice energies and helped by energy gained in solvent–cation binding. Thus, LiF is only sparingly soluble in water (very high lattice energy) while the other alkali halides become progressively more soluble with increasing size (lower lattice energy) and greater solvation (more room to bind more solvent molecules). In all cases, highly polar, small molecules (like H_2O and NH_3) are most efficient, but LiCl will dissolve in THF, and LiBr and LiI in alcohols, SO_2, and so on. This chemistry is fundamentally the coordination chemistry of the cations, and will be covered more fully later (see Section 4.4.2). Reactions in solution are generally those of the solvent-separated anions, not strongly dependent on alkali cation, and are dealt with as reactions of the halogens (*see **Fluorine: Inorganic Chemistry*** and ***Chlorine, Bromine, Iodine, & Astatine: Inorganic Chemistry***).

Unusual and interesting reactions of alkali halides have been seen in argon matrices by IR spectroscopy. For example, codeposition of CsF with SOF_2 results in the novel $Cs^+[SOF_3]^-$. An interesting new area of research is emerging in the study of 'nanocrystals' such as $Na_{14}Cl_{13}$, a tiny fragment of the rock-salt lattice, whose properties are dominated by surface effects.**[68]**

Solubility and Raman spectroscopic studies of molten mixtures of $ZrCl_4$-CsCl, $ThCl_4$-MCl (M = Li, Na, K or Cs), and ZrF_4-KF has been considered useful in the electrorefining of Zr and Th metal which would be an alternative and less-expensive process than the batch-type metallothermic Kroll process.**[69–71]**

3.2.3 *Chalcogenides*

A variety of oxides of the alkali metals are known, illustrating the varying catenation and oxidation states of oxygen. Also, they provide some of the rare examples of compounds where the metals are not, formally at least, +1 cations. All the metals form stable salts of O^{2-}, the most stable being Li_2O, the major product of burning Li in air. All have the antifluorite structure except Cs_2O which has the layered anti-$CdCl_2$ structure. Peroxide salts M_2O_2 are most readily prepared for Li and Na but careful oxidation of K, Rb, and Cs allows isolation of their ${O_2}^{2-}$ salts. The paramagnetic superoxides $M^+{O_2}^-$ are the major combustion products of K, Rb, and Cs, while being unstable for Li and only accessible with difficulty for Na. This is a good example of the alkali metal affecting the route of a reaction by its size/coordinating ability. Among the more unusual oxides are the poorly characterized sesquioxides 'M_2O_3' and the red 'ozonides' $M^+{O_3}^-$, also stable only with large cations. Interestingly, while the solid lithium ammoniate $[Li(NH_3)_4]^+[O_3]^-$ is isolable, removal of the ammonia causes the coordinative demands of the lithium ion to 'rip apart' ${O_3}^-$, possibly due to the high-charge density on Li^+. Some interesting suboxides exist for the larger metals, originally thought to be impure solid solutions of metal and metal monooxide, but now fully characterized in the cases of Rb_6O, Rb_9O_2, and Cs_7O. For example, Rb_9O_2 consists of two Rb_6 octahedra sharing a common face (**3**), each octahedron having a central O atom. Short Rb–Rb distances imply metal–metal bonding. All these species have excess electrons (e.g. Rb_9O_2 is better represented as $(Rb^+)_9\cdot(O^{2-})_2\cdot 5e^-$) and hence they have metallic properties and also show air, moisture, and temperature

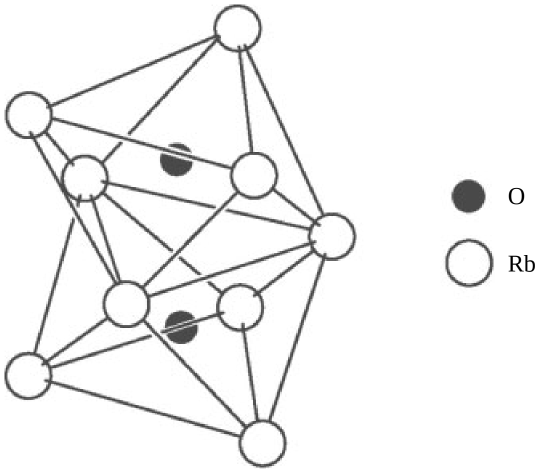

(**3**)

sensitivity.[72] More coverage may be found in ***Oxides: Solid-state Chemistry*** and ***Oxygen: Inorganic Chemistry***.

All alkali sulfides are preparable by reaction of the metal–ammonia solution with sulfur. Exact stoichiometry is important to prevent formation of polysulfides.[73] Sulfur will support combustion of the metals, but products are impure. All the sulfides M_2S adopt the antifluorite structure and are susceptible to hydrolysis, giving them the characteristic odor of H_2S. Hydrolysis is not necessarily complete, however, and alkali sulfide structures containing coordinated water are known. Reaction of the sulfides with further sulfur produces the polysulfides M_2S_x ($x = 2–6$). As in the oxides, higher catenation is favored by larger cations. The polysulfides are low-melting yellow to red solids. The sodium polysulfides Na_2S_x ($x = 2–5$) have significance in their potential use in battery systems.[22] The chemistry and structure of the dianions in these systems will be dealt with in ***Chalcogenides: Solid-state Chemistry*** and ***Sulfur: Inorganic Chemistry***.

The selenides and tellurides are similar to the sulfides, being preparable from ammonia solutions of the alkali metals. They are water-soluble yet partially hydrolyzed like the sulfides, but are more susceptible to oxidation back to the element. Not every member of the class M_xSe_y/Te_y has been fully investigated, but the many that have promise few surprises (*see* ***Selenium: Inorganic Chemistry*** and ***Tellurium: Inorganic Chemistry***). The polonides are similar, and also have their own article (*see* ***Polonium: Inorganic Chemistry***).

3.2.4 Nitrides, Phosphides, Arsenides, Antimonides, and Bismuthides

The most stable of the nitrides, Li_3N, will form spontaneously from the elements at room temperature. The red crystalline solid reacts with water to give LiOH and NH_3, and will combust in air. It is handled in an inert atmosphere. The structure is unique, having two lithiums forming the apices of a hexagonal bipyramid at 1.94 Å and the remaining six in a hexagonal array at 2.11 Å. These hexagons pack in layers bridged by the apical lithiums (**4**). The lithium ions seem to be mobile in the lattice, making Li_3N an ionic conductor.[1] Among the alkali metal nitrides, only Li_3N has been well characterized. The preparation of the heavier alkali metal nitrides has not been successful. However, the preparation of Na_3N has been developed recently.[74] The anti-ReO_3 type structure of Na_3N has also been determined and it has shown that the nitrogen atom is surrounded by six sodium atoms to form an octahedron with a Na-N bond distance of 2.37 Å. The coordination number of the nitrogen atom changes from eight (in Li_3N) to six (in Na_3N) because the sodium atom has a larger radius than the lithium atom.[75] Convincing evidence for other pure alkali nitrides M_3N is absent, but binary compounds of nitrogen are, however, known for all alkali metals in the form of azides $M^+N_3^-$. These hygroscopic, ionic salts are amongst the most stable of the azides, being fusible with minimal decomposition. They may be prepared from aqueous solutions of HN_3 by neutralization with metal hydroxide or carbonate, though direct industrial routes to NaN_3 have been developed (e.g. equation 5). Most azides of other elements are made from NaN_3, some finding use as explosives and detonators.

$$3N_2O + 4Na + NH_3 \longrightarrow NaN_3 + 3NaOH + 2N_2 \qquad (5)$$

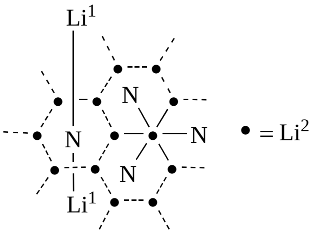

(**4**)

For phosphides, a wide variety of stoichiometries are preparable, from simple K_3P to Rb_2P_5 to Cs_4P_6, NaP_5, Na_3P_{11}, Na_3P_{21}, Li_2P_{16}, Li_3P_{21}, and so on containing complex catenating anions.[76] The alkali metals play little part in the chemistry, so the reader is referred to ***Phosphides: Solid-state Chemistry*** for further information.

For the heavier elements As, Sb, and Bi, further diversity in structure and stoichiometry is found. The ionic bond model becomes less useful as these species may be thought of as intermetallics, possessing metallic luster, and conduction or semiconduction properties. Typical examples include Na_3Bi and NaBi, which becomes superconducting at low temperatures (<2.5 K). Further details will be found in the relevant article for each element, As, Sb, and Bi. Zintl anions of these elements are also known.[77]

3.2.5 Carbides

The alkali metals form only ionic carbides, mostly simple ionic salts of acetylene, M_2C_2, which liberate acetylene on reaction with moisture. There has been much recent interest[78] in permetalated and hypermetalated hydrocarbon species, or 'methanides'. Most studied in this respect has been lithium, presumably because of its volatility and amenability to calculation. Mass spectrometric and calculational evidence has been presented for CLi_6, CLi_3, and C_2Li_4, but real samples of CLi_4, C_3Li_4, and C_5Li_4 are preparable. All are pyrophoric powders. The heavier metals form another class of 'carbide', the graphite intercalation compounds, but as the electron has not been totally freed from the metal, these were considered in the previous section.

3.2.6 Silicides, Germanides, Stannides, and Plumbides

Germanium, tin, and lead give alloy-type binaries of the alkali metals of variable stoichiometry, but when dissolved in ammonia with the alkali metals they produce colored Zintl-type anions (*see* ***Zintl Compounds***) in solution which can be isolated as crystals with appropriate complexants for the alkali metal. Apart from crystallizing from the molecular solvents, several clusters can be isolated from the solid-state reactions in which direct synthesis of the elements is performed.**[79]** Silicon has not yet been shown to share this behavior in solution but several alkali silicide phases are known,**[80]** with widely variable catenation patterns reminiscent of the sulfides and phosphides, for example, Li_7Si_2, NaSi, $Li_{12}Si_7$, and so on. The latter contains $Si_5{}^{6-}$ rings and $Si_4{}^{12-}$ trigonal planar 'stars'.**[81]** Silicon- and alkali-rich alloy-like phases also exist, for example, Na_8Si_{46}, $Li_{22}Si_5$. The rarity of isostructural compounds with different alkali metals underlines the folly of ignoring the alkali cations in compounds of this type.

A series of alkali tetrelides $M_{12}Tt_{17}$ (M = alkali metals; Tt = tetrels = group 14 elements), which contain the anionic clusters of $Tt_4{}^{4-}$ and $Tt_9{}^{4-}$ with the naked cations, have been prepared by direct synthesis from the corresponding elements**[79–84]** in solid state. $Ge_9{}^{4-}$ was the first deltahedral cluster of the tetrels in solid state being isolated and structurally characterized although the $Tt_4{}^{4-}$ has been made few decades ago. Single-crystal X-ray structure determination revealed that the unit cell of $Rb_{12}Si_{17}$ contains isolated clusters of $Si_4{}^{4-}$ and $Si_9{}^{4-}$.**[82]** The Zintl anions $Tt_4{}^{4-}$ and $Tt_9{}^{4-}$ isolated from these alkalide tetrelides adopt tetrahedral and deltahedral geometry, respectively.**[79–84]**

Some other Zintl anions (*see* ***Zintl Compounds***) of $Sn_9{}^{4-}$, $Pb_9{}^{4-}$ such as $[K_4Sn_9(18\text{-crown-}6)_3]\cdot$ethylenediamine, $[Li(NH_3)_4]_4[Pb_9]NH_3$, $[K(18\text{-crown-}6)]_4[Pb_9]\cdot$en.$\cdot$tol, are known.**[85–87]** The interesting linear, trimer, and tetramer of rubidium Ge_9 clusters $[Ge_9{=}Ge_9{=}Ge_9]^{6-}$ and $[Ge_9{=}Ge_9{=}Ge_9{=}Ge_9]^{8-}$ have been synthesized and characterized recently.**[88,89]**

3.2.7 Borides and Others

Best known are the MB_6 borides, for example, NaB_6, comprising an interconnected cubic lattice of B_6 octahedra with the metal atom at the center of each cube in a CsCl-like arrangement. Phases M_3B have also been reported, more saltlike in nature with little covalent B–B bonding. The exact composition of 'NaB_6' was found to be 'NaB_{15}'. Recently, the actual phase composition has been found to be Na_3B_{20},**[90,91]** and its structural framework consists of interconnected boron atom icosahedra and additional interstitial boron atoms.**[92]** So far, the exact compositions and crystal structures of four alkali metal borides Li_2B_6,**[93]** Li_3B_{14}, Na_3B_{20},**[90,91]** and Na_2B_{29}**[92]** have been found. Other alkali metal borides such as potassium, rubidium, or cesium borides have not yet been obtained. Further information is given in ***Borides: Solid-state Chemistry***.

Few distinct points arise from discussion of the chemistry of compounds of the alkali metals with the other metallic elements. Most are alloy- or amalgam-like in nature. Whether they deserve the title 'compounds' has been the subject of debate.**[94]**

The recent advances in the cluster chemistry of triels (particularly Ga, In, and Tl) generally recognize the alkali trielides as traditional Zintl polyanions or nonclassical Zintl clusters in which an extra electron is present. The alkali metals form binary and ternary network compounds with indium and gallium, which are composed of fused clusters or cluster fragments. In contrast, thallium forms individual cluster anions.**[95–97]** The alkali metal cations play a decisive role in the structure by filling up spaces efficiently and keeping the cluster apart.**[98]** Examples of trielide clusters include anions of $Ga_{11}{}^{7-}$, $In_{11}{}^{7-}$, $In_4{}^{8-}$, $Tl_4{}^{8-}$, $Tl_5{}^{7-}$, $Tl_6{}^{6-}$, $Tl_{11}{}^{7-}$, and so on.**[99,100]** These isolated anionic clusters display different structures, such as a pentacapped trigonal prism in Cs_8Ga_{11}, K_8In_{11}, and Rb_8In_{11},**[99]** a three-dimensional indium network built of layers of In_{12} icosahedra and zigzag chains in KNa_3In_9,**[101]** and an arachno 12-vertex polyhedra 'drums' and closo icosahedra in $K_3Na_{26}In_{48}$.**[102]**

3.3 Oxoacid Salts

The vast majority of the chemistry of alkali metal salts of oxoanions shows little dependency on the identity of the cation. Much of the chemistry has been comprehensively covered before,**[73]** and receives further up-to-date coverage in the articles on the relevant element. However, a few important examples and general points are included here.

3.3.1 Borates

Alkali borates occur in a few very large Salt-like deposits. A great many phases exist, which may be formulated in equivalents of metal ion, boron oxide, and H_2O, but this says nothing of structure. The identity of the metal (often an alkali metal) clearly is one of the determining factors in the occurrence of a given phase, but these complex matters have their own article (*see* ***Borates: Solid-state Chemistry***). Most common is borax, $Na_2B_4O_7\cdot 10H_2O$, more informatively written as $Na_2[B_4O_5(OH)_4]\cdot 8H_2O$, which is used as an alkaline buffer, in glass manufacture, and in fire retardants. Its reaction with hydrogen peroxide forms 'sodium perborate', $Na_2[B_2(O_2)_2(OH)_4]\cdot 6H_2O$, used as a bleach in washing powders. This use is declining with lower-washing temperatures and the growing use of liquid detergents.

Mixed-alkali metal polyborates $CsLiB_6O_{10}$ has been found as a promising nonlinear optical material.**[103]**

3.3.2 Carbonates and Silicates

Most alkali carbonates form a wide variety of hydrates, for example, $Na_2CO_3(H_2O)_x$ ($x = 1, 7, 10$). The decahydrate has pairs of sodiums octahedrally surrounded by water ligands, with no metal–anion close contacts. The paired octahedra share an edge to give $[Na_2(H_2O)_{10}]^{2+}[CO_3]^{2-}$. In contrast, the monohydrate has two independent sodiums coordinated to 5 and 4 carbonate oxygens, respectively. Further variety in structure and stoichiometry is found when carbonic acid acts monobasically to give the ‘bicarbonates’, for example, $NaHCO_3$, which also form a variety of hydrates, as well as mixed carbonate/bicarbonate systems, notably the major natural carbonate ‘trona’ $Na_2CO_3{\cdot}NaHCO_3{\cdot}2H_2O$. Similar behavior is found for other alkali metals and indeed mixed-metal phases are common, for example, $K_2CO_3{\cdot}Na_2CO_3{\cdot}6H_2O$, $KLiCO_3$, and so on. Lithium forms no bicarbonates. Its carbonate is rather insoluble in water, and is easily prepared anhydrous. All the carbonates are susceptible to thermolysis (equation 6). The temperature required for this reaction increases with increasing cation size. This periodic trend is shared with other oxoanion salts since the lattice energy of the product oxide is the dominant factor.

$$M_2CO_3 \xrightarrow{\Delta} M_2O + CO_2 \qquad (6)$$

It will be seen in the article ***Zeolites*** that the chemistry of the metal ion is often unimportant in their complex structures. Consequently, there is little to discuss in terms of periodic trends and differences. It should be noted, however, that sodium silicate is important for its use as a builder in washing powders.

3.3.3 Oxoacid Salts of Nitrogen, Phosphorus, Arsenic, Antimony, and Bismuth

All alkali metals form nitrates MNO_3 and nitrites MNO_2. The former decompose to the latter with strong heating in the absence of O_2. This tendency is greatest for the smaller metal ions, following a group trend. All are hygroscopic and crystalline hydrates are common.

The nitrates are prepared by neutralization of nitric acid with the appropriate hydroxide. In some cases, metathesis reactions have been commercially exploited (equation 7). Through manipulation of the differing aqueous solubility/temperature relationships of the various salts in the equilibrium mixture, KNO_3 is isolable.

$$NaNO_3 + KCl \rightleftharpoons KNO_3 + NaCl \qquad (7)$$

The nitrites are preparable thermally as mentioned above, or by reaction of nitrogen oxides with metal hydroxide or carbonate (e.g. equation 8). The nitrites are all water-soluble but with a smaller tendency to hydrate formation than the nitrates. $NaNO_2$ is used as an oxidant and a nitrogen source in the production of azo dyes, and so on. It has also found wide use in curing meats, although recent concern has been expressed over the safety of the products of the reactions of $NO_2{}^-$ with the organic compounds in foods. Salts of other nitrogen oxoacids exist, for example, $Na_4N_2O_4$ and Na_3NO_4, and these receive coverage in ***Nitrogen: Inorganic Chemistry***.

$$Na_2CO_3 + NO + NO_2 \longrightarrow 2NaNO_2 + CO_2 \qquad (8)$$

Phosphorus has an even wider range of oxoacid chemistry, and a commensurately wide range of phosphates, phosphites, polyphosphates, hypophosphites, and so on of the alkali metals are preparable. Sodium and potassium are the most common cations used, largely because of their availability and low cost. The cation often has little effect on the properties and applications, which are covered in ***Phosphates: Solid-state Chemistry***. Most form a variety of crystalline hydrates, which have been well covered in previous treatments[73] and need not be repeated here. True to form, lithium is the exception, forming no stable hydrates with phosphorus oxoanions.

A variety of alkali–arsenic oxides has been isolated, including Na_2HAsO_4, NaH_2AsO_4, RbH_2AsO_4, $LiAsO_3$, $KAsO_3$, $NaAsO_2$, $NaAsO_3$, Na_3AsO_3, and Na_3AsO_4. Some find use as wood preservatives, bacteriocides, and herbicides. Hydrates are common. Many are salts of the poorly characterized arsenious acid $As(OH)_3$,[104] but salts of arsenic acid, H_3AsO_4, are also known. They are good oxidizing agents. Structures are complex, with polymeric anions being common (cf. phosphates). The identity of the metal can affect the catenation mode of the anions, for example, $LiAsO_3$ has a dimeric repeat-unit in its infinite chains of AsO_4 tetrahedra, while $NaAsO_3$ has a tetrameric repeat-unit, and $KAsO_3$ has a cyclic trimeric anion $As_3O_9{}^{3-}$.

There is a greater tendency to salts of Sb^V over Sb^{III}. $NaSb(OH)_6$, $NaSbO_3$, $LiSbO_3$, and Li_3SbO_4 are all known. Polyanion motifs are again common. While $Bi(OH)_3$ forms no anions, being basic, Bi^v oxoanions are rare and very strongly oxidizing. However, $NaBiO_3$, prepared from Bi_2O_3 and Na_2O_2, is sold as a powerful oxidant, and has an ilmenite structure. Hydrates are also known.

3.3.4 Oxoacid Salts of the Chalcogens

The chemistry of polonium may be discounted because of the short half-life and extreme rarity of the element. Tellurates are mostly salts of telluric acid, $Te(OH)_6$, and are not similar to the sulfates. Selenates are more similar, forming compounds such as $Na_2SeO_4(10H_2O)$ exactly like sulfur, but the chemistry is not so extensive as to define the role (if any) of the alkali metal in the compound. The extensive oxo chemistry of sulfur, however, allows such comparisons to be drawn. For example, both $RbHSO_3$ and $CsHSO_3$ are isolable, while the salts of the smaller cations produce the disulfites $M_2S_2O_5$. The full variety is too rich to explore here (*see* ***Sulfur: Inorganic Chemistry***) but the great industrial importance of Na_2SO_4 in the paper and cardboard industry should be noted.

3.3.5 Oxyhalides

Those oxyhalide anions that find use are most often used as alkali metal salts. A particular metal is often chosen to optimize physical properties; for example, $LiClO_4$ is used as an oxidant in rocket propellants because the light metal maximizes energy density, while the larger ion in $KClO_3$ gives the nonhygroscopic properties that are desired for use in safety matches and pyrotechnic displays. The metal has little chemical effect on the anions; indeed, a structure determination on $NaClO_3$ was used to define the precise geometry of the isolated ClO_3^- anion.[105]

Periodic trends are apparent, again due to size effects in crystal packing. The very soluble $LiClO_4$ crystallizes from water as a trihydrate with each lithium surrounded by face-sharing octahedra of water molecules which weakly hydrogen-bond to the poorly coordinating perchlorate ions.[106] In $CsClO_4$, however, the sparingly soluble salt crystallizes anhydrous from aqueous solution in a $BaSO_4$-type structure. Further examples may be found in the relevant chapters on halogen chemistry.

3.4 Some Salts of Other Inorganic Acids

3.4.1 *Hydroxides*

The alkali hydroxides are the strongest bases accessible in aqueous solution, since the alkali metals are the most electropositive elements in the Periodic Table. NaOH and KOH are made and used on a massive scale industrially, as well as being ubiquitous laboratory reagents. They are able to deprotonate even weak carbon acids such as cyclopentadiene when poorly donating anhydrous reaction media are employed (the reaction produces water which can then solvate the excess hydroxide, thereby providing a driving force). All are hygroscopic to varying degrees, and form numerous hydrates. Lithium hydroxide has the lowest tendency to hydrate, since the small hydroxide ion can pack efficiently with the lithium cations (cf. perchlorates). It forms a stable, nondeliquescent monohydrate that can be easily dehydrated by vacuum or heat. It is also the weakest base in the gas phase, where it exists predominantly as ring dimers. Base strength increases down the group, as the hold of the metal on the hydroxide becomes weaker. In aqueous solution, of course, there is little difference between the basicity of the alkali hydroxides due to the effects of solvent leveling.

All the hydroxides absorb CO_2 from the air to form carbonates. Similarly, formates may be prepared by heating solid hydroxides with carbon monoxide (e.g. equation 9).

$$\mathrm{NaOH + CO \xrightarrow{180\,^{\circ}C} HCO_2Na} \tag{9}$$

The hydroxides are formed by electrolysis of aqueous brines as part of the chloralkali process. The metal formed at the cathode immediately reacts with water to produce the hydroxide and hydrogen gas.

3.4.2 *Amides*

The metal–ammonia solutions discussed in Section 2.4 are metastable. Their decomposition, catalyzed by transition metal ions, yields the ionic salts $M^+NH_2^-$. They may also be formed by passing ammonia gas over the heated molten metals. They are only sparingly soluble in ammonia, and decompose on contact with moisture. $NaNH_2$ (sodamide) has historically been widely used as a very strong base in anhydrous media in organic synthesis. It also serves as a source of the NH_2^- nucleophile. Where this second mode of reactivity is undesired, it has largely been superseded by the stronger, more soluble, less nucleophilic dialkylamide bases, such as lithium diisopropylamide (LDA) (see Section 5). The sodium and potassium counterparts of LDA was found to be a better reagent over the metallation of diphenylmethane.[107,108] Structurally, the alkali amides behave as simple ionic salts. All have high-temperature modifications where the anions are freely rotating pseudospheres. NaCl-type lattices are found for high-temperature potassium, rubidium, and cesium amides. The low-temperature forms are distorted close-packed lattices due to the asymmetry of the NH_2^- anions.[109]

By using a combination of gas-phase synthesis and millimeter/submillimeter-wave spectroscopy, $LiNH_2$ was found to be a monomeric unsolvated planar molecule. The lithium amide $\{[H_2NCH_2CH_2N(H)Li]_\infty\}$ has a polymeric ladder structure with two types of $(NLi)_2$ ring which alternate throughout its infinite length.[110]

Superbases react readily with organic substrates to give heavy metal derivatives of the substrate function as exceptional strong proton abstraction reagents in organic synthesis. The lithium amide-alkoxide complex is composed of four LiNLiO units, whereas the bimetallic lithium/heavier alkali metal mixed amide-alkoxide complexes are constructed from $Li_xM_yN_aO_b$ units $(x + y = a + b)$. The trimetallic Li-Na-K amide-alkoxide compounds consist of a twelve-vertex $Li_2Na_2K_2N_4O_2$ cage as in $[\{RN(H)_2(Bu^tO)[LiNaK{\cdot}(TMEDA)_2]_2\}]$ has been reported.[111]

3.4.3 *Alkali Pseudohalides*

The salts of hydrazoic acid, $M^+N_3^-$, have already been discussed in Section 3.2.4, but a variety of other alkali pseudohalides exist. The most important of these are the cyanides M^+CN^-, preparable by neutralization of HCN with the appropriate alkali base. NaCN and KCN reached such industrial importance that alternative bulk syntheses have been developed (e.g. equation 10). This Castner process fed the gold extraction industry and continued to feed the electroplating and nylon synthesis markets until cheaper routes directly to HCN were found. In cases where the alkali cyanides are still required, the simple neutralization route is now most economic.

$$\mathrm{Na + NH_3 \xrightarrow{-1/2H_2} NaNH_2 \xrightarrow[+C\ \ -H_2]{600\,^{\circ}C} \frac{1}{2}Na_2CN_2 \xrightarrow[+C]{800\,^{\circ}C} NaCN} \tag{10}$$

Structurally, the alkali cyanides are truly pseudohalides, all except LiCN adopting either NaCl or CsCl structures at normal temperatures. The required high symmetry is produced by rapid solid-state fluxionality in which the $C{\equiv}N^-$ dumbbell ions rotate to sweep out a sphere of radius intermediate between those of Cl^- and Br^-. Low-temperature phases exist[112] where this fluxionality is not present, for example, CsCN. Once again, lithium is the exception, exhibiting a fully ordered but loosely packed structure related to zinc blende in which each lithium has three N contacts and one C contact. A preference for N coordination is rare among those compounds where it is possible to distinguish between C and N. The highly polarizing cation seems to distort the anion, its $C{\equiv}N$ bond length being 1.15 Å in LiCN but 1.05 Å in NaCN. The variety of possible bonding modes of $C{\equiv}N$ (linear, bent, η^2, η^1, μ^2, etc.) in less aggregated forms of M^+ CN^- has been the subject of calculational[113] and gas-phase and matrix IR investigation, but solid-state data at present are limited to a few crown complexes and complex transition metal cyano anions.

Other alkali pseudohalides may be prepared from the cyanides. Mild oxidation of M^+CN^- in solution with lead oxides produces M^+OCN^-. The heavier chalcogens may be directly combined (e.g. equation 11).

$$KCN + S \xrightarrow{\Delta} KNCS \qquad (11)$$

Potassium thiocyanate, like others in the series, a soluble and hygroscopic ionic salt, finds use in photographic developers. KNCSe may be similarly prepared.[114] The $TeCN^-$ anion is only isolable with very large organic cations, and so no solid alkali tellurocyanate is known. Metastable solutions of M^+TeCN^- may, however, be prepared.

3.5 Salts of Some Important Complex Anions

Aside from the compounds that fall into the well-defined categories above, there are of course a multitude of alkali salts of complex anions of different types, many of which are unknown as the free acids. A selection of the more important and unusual is included here.

Sodium borohydride, prepared as in equation (12), is reaching the status of a bulk inorganic commodity. This industrial preparation was developed to supersede the less economic, but more convenient, direct route (equation 13). Lithium borohydride may be prepared similarly (equation 14). Both sodium and lithium borohydrides have been much used as reducing agents. $NaBH_4$ requires polyethers for efficient dissolution, while $LiBH_4$ is quite soluble in THF. $NaBH_4$ is the more selective reagent, able to reduce ketones to alcohols in the presence of nitriles, nitro groups, alkenes, and so on. This difference in reactivity underlines the fact that as soon as highly ionizing, strongly solvating media (such as H_2O) are excluded, the alkali metal 'salts' are much more associated in solution, and hence the identity of the cation has a much greater effect on the reactivity of the compound. The nature of the structural origins of such differences will be discussed in Section 4. Apart from specialty uses in organic (and inorganic) syntheses, $NaBH_4$ is widely used in the bleaching of wood pulp and in chemical plating of metals such as nickel on to nonmetal surfaces.

$$Na_2B_4O_7 + 7SiO_2 + 16Na + 8H_2 \xrightarrow{500\,^\circ C} 4NaBH_4 + 7Na_2SiO_3 \qquad (12)$$

$$4NaH + BCl_3 \longrightarrow NaBH_4 + 3NaCl \qquad (13)$$

$$4LiH + BF_3{\cdot}OEt_2 \longrightarrow LiBH_4 + 3LiF + Et_2O \qquad (14)$$

The heavier congeners $M^+EX_4{}^-$ (E = Al, Ga, In) are progressively more reactive. The most common, $LiAlH_4$, has been widely used as a reducing agent and hydrogenating agent. It is a more potent reductant than the borohydrides and is more soluble and hence more reactive in ethers. This greater reactivity makes $LiAlH_4$ less selective than borohydrides and makes handling under an inert nitrogen atmosphere advisable. It is much used as a rigorous drying agent in laboratory solvent distillations, especially of ethers. The bonding in $LiAlH_4$ may have appreciable covalent character since the crystal packing is not a simple close-packed arrangement[115] and contains some short Li–H distances [$4Li–H = 1.88–2.00$ Å, $1Li–H = 2.16$ Å, cf. $(Li^+H^-)_\infty = 2.04$ Å].

Complex hydrides are known for transition metals also. Evidence has been presented[115] suggesting substantial covalency in the W–H–Li bonds of $[W(PMe_3)_3H_5Li]_4$ (**5**).

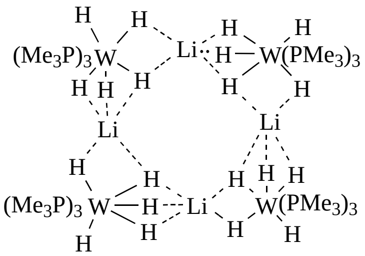

(**5**)

A further interesting class of molecules are the alkali salts of transition metal carbonylates. Reduction of neutral metal carbonyls with alkali metals in liquid ammonia produces materials such as $Na_2Fe(CO)_4$. These form valuable synthons in inorganic chemistry, and hence have received much study in their own right. Reactions and spectroscopic properties are often highly dependent on alkali cation and donor-solvent present.[116] This shows how an alkali metal can be closely involved in directing the chemistry of a 'salt'. Structurally, the metal has an important rôle. The $K_2Fe(CO)_4$ salt is known and crystallographically characterized without external donors. The K sits between carbonyls (see (**6**)) and direct metal–metal interaction cannot be ruled out. The less unusual terminal contacts to O of other units complete the coordination of the cation. The anion is distorted in this arrangement, but when crypt ligands (see Section 4.3) are introduced to shield the anion from the alkali metal a regular tetrahedral form is resumed.[117] HMPA solutions of sodium can reduce these complexes even further, so that formally M^{3-} transition metals are formed. However, in these highly shock-sensitive and pyrophoric materials the electrons are almost certainly spread on to the carbonyl ligands and perhaps on to the alkali metals themselves.[118] The extreme reducing power of HMPA/Na solutions stems from the presence of 'sodide' $Na(HMPA)_x^-$ anions. Typical examples of these 'superreduced' species include $Na_3Re(CO)_4$ and $Na_3V(CO)_5$.

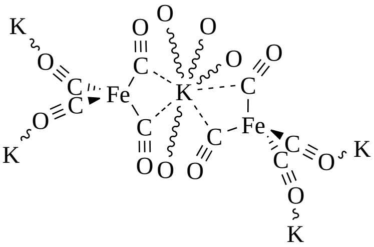

(**6**)

4 COORDINATION COMPOUNDS

4.1 Introduction

All alkali metal-containing materials have close contacts from the metal to another atom, or group of atoms, and to this extent all compounds may be termed '*coordination compounds*'. However, the term is usually reserved for those compounds containing a metal coordinated to a neutral ligand, normally (but not necessarily) one containing organic functions. The coordination chemistry of the alkali metals has in the past been viewed as a rather poor area of research. Their unipositive charge and relatively large size gave the metals a rather poor coordinating ability. Consequently, aqueous coordination chemistry often gave only hydrates, with a few examples of salicylates and diketonates, rendered stable by the chelate effect. However, interest and systematic study has blossomed over the last 20 years, largely because of two phenomena. The first was the Nobel prize-winning discovery of the crown ethers and their development into the field of 'molecular recognition', making use of the 'macrocyclic effect' in overcoming the low charge density of the heavier alkali metals. The second is the increased investigation of nonaqueous alkali metal chemistry, triggered largely by the growing importance of lithium in organic synthesis. Few ligands are superior to water in their ability to coordinate to alkali metals, but by excluding H_2O and limiting the supply of available Lewis base donor molecules, a rich structural chemistry has developed, challenging that of the transition metals in its diversity.

4.2 General Principles

The coordinating ability of the alkali metals generally decreases with charge density in the sequence $Li > Na > K > Rb > Cs$ but 'molecular recognition' arguments may sometimes dictate a different order (see Section 4.3). The predominance of ionic bonding removes the directional constraints often seen in transition metal complexes, and therefore geometries vary widely, depending upon the minimization of interligand repulsions and the maximization of contacts from metal to electronegative center. For the larger metals, extensive polymerization often ensues where it is not hindered by the use of chelating ligands (most notably in the case of crowns and crypts) or very bulky ligands. However, in some cases this tendency to polymerize may be limited by judicious choice of appropriate ligands and synthetic route. The smallness of lithium in comparison to most anions makes this tendency to limited oligomerization most prevalent for that metal (exemplified in the hexameric, molecular nature of $(n\text{BuLi})_6$, cf. $(n\text{BuNa})_\infty$; *see* ***Alkali Metals: Organometallic Chemistry***). Molecular aggregates containing up to 20 lithium cations have been prepared,[119] but dimers are most common, and solid-state monomers are comparatively rare in the absence of highly chelating ligands.[120]

Coordination numbers are so dependent on ligand geometry that the concept of 'preferred' coordination number is of limited use. For example, lithium may be said to prefer 4 coordination, but examples of 1 to 12 coordination are known. Low formal coordination numbers are often accompanied by secondary interactions with other sources of electron density, such as C–H bonds and arene π-systems. There are even examples of C–H activation caused by a low-coordinate sodium cation.[121] Of course, there is a trend towards higher preferred coordination for the heavier group members (6 for Na, K; 8 for Rb, Cs).

4.3 Macrocyclic Complexes

The serendipitous discovery by Pedersen of the 'crown' ether ligands[122] sparked the development of what is now a systematically and intensively investigated, and well-reviewed,[123,124] field. The crowns are cyclic polyether molecules containing a variable number of oxygen atoms (commonly 4, 5, or 6) linked by (normally) ethylene (e.g. 18-crown-6, (**7**)) or 1,2-dibenzo bridges (e.g. dibenzo-14-crown-4, (**8**)). These ligands wrap around the metal, and can displace water ligands due to the entropically dominated 'macrocyclic effect'. The resultant 'organic sheath' around the cation confers solubility in organic solvents which leads to uses in phase transfer catalysis. The coordination of the cation by the crown weakens its interaction with the anion, sometimes to the point of total separation. The substantially increased nucleophilicity of the anion then leads to much more rapid reaction (the 'naked anion effect'). The discovery of the crown ethers also sparked the development of research into ‘molecular recognition’, since the crown ether ‘host’ could ‘recognize’ specific alkali metal (and other) cation ‘guests’ due to the fixed size of the macrocyclic cavity. The different ionic radii of the M$^+$ ions induced the selective complexation effects that form the basis of the use of crowns in cation separation, and recently in ion-specific measurement devices.[125] The crown ethers, tribanzo-21-crown-7 and tetrabenzo-24-crown-8, are found to exhibit modest selectivity for Rb$^+$ and Cs$^+$ over other alkali metal ion, respectively.[126,127]

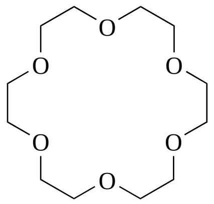

(**7**)

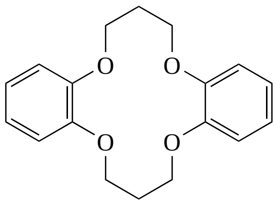

(**8**)

In a crown complex, the metal generally sits slightly above an approximate plane formed by the oxygen donor atoms, with further weak coordinations to water molecules and/or the anion. In some cases a 2:1 crown:metal ratio is preferred, resulting in a sandwich structure. Total encapsulation of the metal was more closely achieved with the synthesis of the cryptands,[128] which are simply bicyclic crowns, rendered so by the introduction of tertiary amine bridgeheads (e.g. 2,2,2-crypt, (**9**)). This leads to a much more strict and inflexible control of macrocyclic cavity size as well as greater encapsulation. Total ion separation is common. Selectivity between K$^+$ and Na$^+$ can be as great as 10^5:1. It is noted that the large-size cryptands such as 3,3,2-crypt and 3,3,3-crypt do not show generally better complexation and selectivity for two large cations, Rb$^+$ and Cs$^+$, than for the other cations of alkali metals. The poor complexation and low selectivity for these cations are mainly due to the large cavity radius and high flexibility of these cryptands.[129]

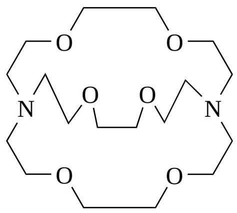

(**9**)

This Na$^+$/K$^+$ selectivity is of paramount importance since many physiological functions depend upon its maintenance. The selective transport of K$^+$ across cell membranes is achieved by the natural antibiotic valinomycin (**10**), which contains a crownlike cycle of ether oxygens, but also a number of amide linkages. The cycle would seem too large to bind K$^+$ as effectively as valinomycin is known to do, but Nature is ingenious: the amide units engage in reversible, intramolecular hydrogen bonding to ‘sew-up’ the cycle in a ‘tennis-ball seam’ arrangement, having the combined effects of making the cavity smaller, making it three-dimensional (cryptand-like) and presenting the hydrophobic isopropyl groups to the outside of the molecule and so allowing good transport through lipids. It is this flexibility which makes valinomycin effective; its avidity and selectivity generated by its three-dimensionality is accompanied by the facile complexation and decomplexation kinetics that are essential for efficient transport. While the cryptands possess the former characteristics, the reliance on inflexible covalent linkages to achieve them make the ion uptake and (especially) release kinetics unsuitable for a transport function. The synthetic answer came with the development of the lariat ethers,[130] which are crown ethers with additional Lewis base donor side-arms that mimic the natural system by giving reversible three-dimensional incarceration of the alkali metal ion upon complexation.

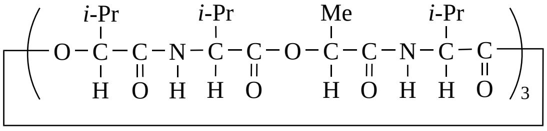

$$\left(-\mathrm{O}-\underset{\mathrm{H}}{\overset{i\text{-Pr}}{\mathrm{C}}}-\underset{\mathrm{O}}{\overset{}{\mathrm{C}}}-\underset{\mathrm{H}}{\mathrm{N}}-\underset{\mathrm{H}}{\overset{i\text{-Pr}}{\mathrm{C}}}-\underset{\mathrm{O}}{\mathrm{C}}-\mathrm{O}-\underset{\mathrm{H}}{\overset{\mathrm{Me}}{\mathrm{C}}}-\underset{\mathrm{O}}{\mathrm{C}}-\underset{\mathrm{H}}{\mathrm{N}}-\underset{\mathrm{H}}{\overset{i\text{-Pr}}{\mathrm{C}}}-\underset{\mathrm{O}}{\mathrm{C}}-\right)_3$$

(**10**)

Another class of macrocyclic molecules for binding with alkali metal cations is calix[n]arene ($n = 4,6,8$) and its derivatives. They are made up of phenol and methylene units which provide a rigid arrangement of various number of oxygen donor atoms for metal complexation. Some of them are proved to display exceptional selectivity for K$^+$ and Cs$^+$.[131] Further details of this developing field will be found in ***Macrocyclic Ligands***.

A new type of macrocyclic complex with the arrangement of Lewis acidic and Lewis basic sites opposite to that encountered in conventional crown ether complexes described above is named inverse crown ethers. They are formed by eight-membered [MNM′N]$_2$ rings (M = Li, Na, K; M′ = Mg, Zn; N = HMDS, TMP) with peroxide or oxide ions occupying the core of the ring. The core atoms are introduced into the cyclic rings by deliberately exposing the reaction mixture to molecular oxygen. Apart from occupying by oxygen atoms or anions, the core atoms can also be placed by other anion species such as arene anions. This type of inverse crowns contains no core oxygen atoms anion.[132]

4.4 Other Complexes

4.4.1 *Introduction*

It was said in the preceding section that highly chelating ligands can exclude water from the coordination sphere of alkali metals. In those cases where highly chelating ligands are not present (i.e. most inorganic cases), hydrates predominate. Inorganic hydrates were dealt with in Section 3, and organic cases will be covered in Section 5, so it remains here to discuss the nonaqueous inorganic coordination chemistry of the alkali metals.

There are broadly two routes to coordination complexes of alkali inorganics. The first is dissolution of the salt in an excess of the coordinating ligand. This is often kinetically unfavorable, since it requires rupture of a very large number of bonds. The second is to form the desired salt in situ in the presence of a stoichiometric amount of donor from a reactive metal source, either a metal hydride, organyl, or the metal itself, for example, equations (15) and (16). The second of these routes has found more general success.**133**

$$C_4H_9Cl + C_4H_9{}^-M^+ + xL \longrightarrow C_8H_{18} + (M^+Cl^-{\cdot}L_x)_y \qquad (15)$$

$$NH_4{}^+NCS^- + M + xL \longrightarrow \frac{1}{2}H_2 + NH_3 + (M^+NCS^-{\cdot}L_x)_y \qquad (16)$$

4.4.2 *Alkali Halide Complexes*

It has not yet proved possible to isolate a solid complex of lithium fluoride, since its lattice energy is too high to make complex formation thermodynamically feasible. There are a considerable number of complexes of lithium chloride, from the fully ion-separated $Li(en)_2{}^+{\cdot}Cl^-$, prepared by dissolution of $(Li^+Cl^-)_\infty$ in a vast excess of the bidentate ligand,**134** through contacted monomeric $(4\text{-}t\text{-Bu-py})_3LiCl$, prepared in a similar manner,**135** to more aggregated species that might be considered as fragments of the LiCl lattice. Interestingly, all of these ‘intercepted lattice’ species were prepared by the in situ generation and complexation route. Examples are $Li_4Cl_4{\cdot}(PMDETA)_3$ and $[Li_6Cl_6{\cdot}(TMEDA)_4]_\infty$. In these cases, multidentate amine donors were employed to limit association. The bulky and very powerfully donating monodentate base HMPA also traps a fragment of the LiCl lattice in the cubanelike complex $(LiCl{\cdot}HMPA)_4$ (**11**).**136**

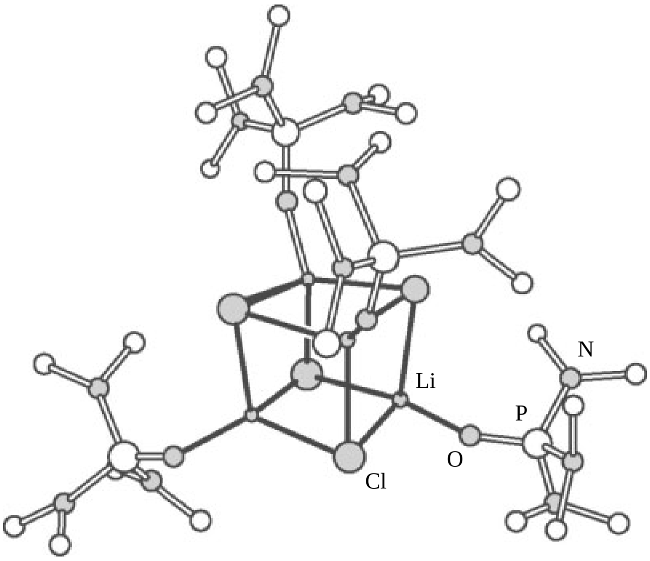

(**11**)

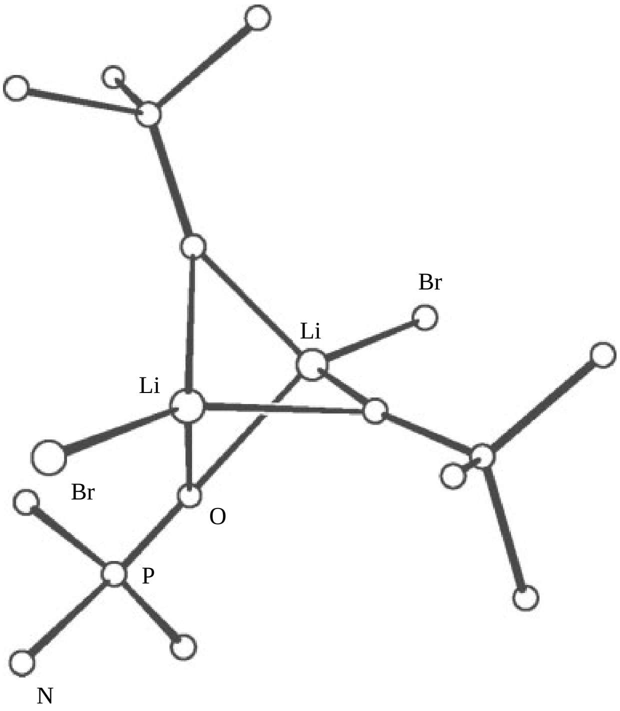

(**12**)

The greater size mismatch between Li^+ and Br^- makes aggregation less pronounced in LiBr complexes. Simple ring dimers, for example, $(LiBr{\cdot}TMEDA)_2$, are common. The complex LiBr·PMDETA is dimeric in the solid state with 5-coordinate lithium, but in benzene solution this rather asymmetric dimer is in equilibrium with a monomeric form.**137** An unusual ‘dimeric’ LiBr complex which may be considered as two monomers of LiBr connected only by bridging HMPA ligands is also known.**138** This complex, $[LiBr{\cdot}(HMPA)_{1.5}]_2$ (**12**), was synthesized by the in situ ‘ammonium salt route’.**133** A LiBr complex with another, rather weaker, monodentate pyridine donor in the same ligand:salt ratio results in a more aggregated structure, $[(2,6\text{-}Me_2C_5H_3N)_6Li_4Br_4]$, and is a product of dissolution in excess donor.**139** A 4-runged ‘step ladder’ arrangement results because the internal lithiums are solvated giving a pseudotetrahedral 4-coordination at each point, in contrast to the near-planar ladders obtained in the case of lithium amides and phosphides (see Section 5).

Iodides show still less propensity to aggregate. Ion-separated species (e.g. $Li^+\ (Ph_3PO)_4I^-{\cdot}Ph_3PO$) are common, and dimers are the highest oligomeric unit found as yet. The dimeric $(LiI{\cdot}TMEDA)_2$ prepared by an in situ route contrasts with the ion-separated $Li^+(TMEDA)_2I^-$ prepared by dissolution.**140**

There are considerably less data for the complexes of the heavier alkali metals. Because the cations are larger, they are better able to make effective contact with a larger number of anions than an equivalent lithium salt. Oligomeric complexes with the lighter halogen anions are therefore rare. With chelating ligands, some ion-separated complexes are known (e.g. $(Ph_2P(O)CH_2P(O)Ph_2)_3Na^+Br^-\cdot 3H_2O$), and for heavier halogens a dimer $(NaI\cdot PMDETA)_2$ and a polymer $(NaI\cdot diglyme)_\infty$, that contains an unusual bridging mode for the diglyme ligand,[141] have been isolated.

These are some examples of simple complexes, but when the alkali halides interact with other systems, further variety results. Reactions often produce alkali halides which become incorporated into the structure of the desired product. For example, it is sometimes difficult to produce halide-free organolithiums from the standard synthesis (equation 17). So-called '*mixed aggregates*' sometimes result,[142] as shown by the crystallographically characterized phenyllithium–lithium bromide aggregate (**13**) crystallized from ether. Since the presence of alkali halide in a reaction medium can affect structure, it can also affect reactivity, as demonstrated in lithium amide chemistry. Stereoselectivity of enolization has been shown to be dramatically affected by added salts.[143] Mixed aggregates such as the LDA–LiCl structure (**14**) may be responsible.[144] A further 'added salt effect' is seen in the interaction of lithium salts with large biomolecules, for example, [(Gly-Gly-Gly)·LiBr]. Addition of the salt disrupts hydrogen-bonding networks and results in much greater solubility in organic solvents.[145]

$$RX + 2Li \longrightarrow RLi + LiX \tag{17}$$

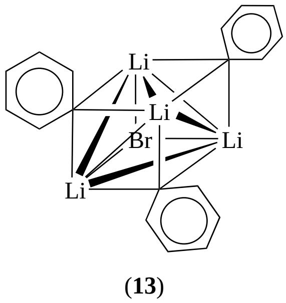

(**13**)

4.4.3 Complexes of Other Inorganic Anions

The largest contiguous group of nonmacrocyclic, molecular complexes is provided by the alkali thiocyanates. The HMPA complex of lithium thiocyanate crystallizes as an unusual asymmetric dimer. The sodium complex of the same stoichiometry exists in a more normal symmetric dimer arrangement, while the potassium thiocyanate complex adopts an unprecedented trimeric arrangement.[146] The thiocyanate prefers a terminal, N-bonding mode in all these complexes, although solution evidence exists for a μ^2 N-bridging mode in the complex LiNCS·TMEDA, dimeric in solution. In

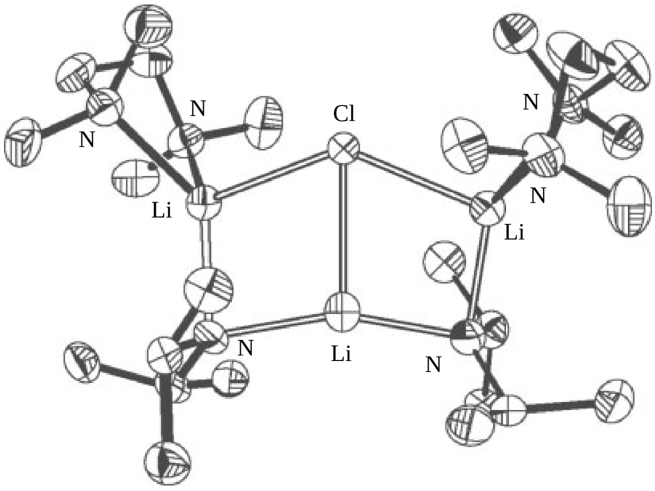

(**14**)

the solid, a polymeric linear structure is obtained, held by weaker Li···S coordinations. A recent paper discussed the first μ^2 N-bridge alkali thiocyanate complex,[147] but even here the bridge is highly asymmetric (see (**15**)) and the compound could be viewed as a loosely held dimer of (TMPDA)LiNCS monomers, where NCS approaches a linear Li···N···C geometry.

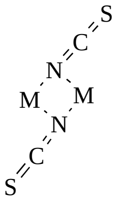

(**15**)

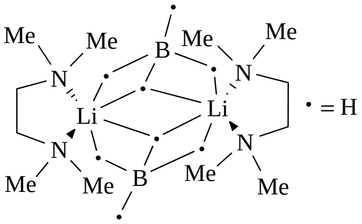

(**16**)

Nonmacrocyclic complexes of other alkali pseudohalides are rare indeed, though many other inorganic anions are found in alkali metal complexes. Oxoanion salts, such as $LiNO_3$, are found to form complexes. The binding mode of the anion in such cases would be expected to be highly dependent on the nature of the base employed, and this is found to be the case. In dissolution syntheses, 2-methyl- and 3,5-dimethylpyridine gave polymeric $LiNO_3\cdot(L)_2$ and monomeric $LiNO_3\cdot(L)_3$ complexes, respectively. In the polymer, links were through bridging *bis* η^1 nitrate oxygens, while the monomer contained only one nitrate–Li contact.[148]

Complex hydrides give a variety of interesting structures. For $LiBH_4$ derivatives, a monomeric example crystallized from THF[149] shows three μ B–H–Li bridges and a very short B–Li distance of 2.19 Å (cf. C–Li, 2.36 Å in the analogous $(\mu\text{-H})_3C$ environment of solid $(MeLi)_\infty$). However, when TMEDA is used as the donor in the parent borohydride, a dimeric complex (**16**) results, containing four μ^2 and two μ^3 B–H–Li contacts.[150] A tetrameric complex with μ^4

B–H(Na)$_3$ bonds was obtained from a diethyl ether solution of NaBHMe$_3$. This could also be considered as a lattice fragment of sodium hydride where each metal is coordinated by one Lewis base (Et$_2$O), and each hydride coordinates one Lewis acid (Me$_3$B).[151]

This list of examples could contain complexes obtained from a very wide variety of alkali metal compounds where lattice energy considerations make complex formation thermodynamically favorable. The in situ preparative routes even make trapping of kinetic, as opposed to thermodynamic, products feasible. Furthermore, complexation can stabilize a compound unknown in the uncomplexed state. (For example, it was stated in Section 3.2.3 that the heavier alkali metals favor higher catenation in sulfides. Consequently, Li$_2$S$_2$ is the most highly catenated parent lithium sulfide known, but the complex Li$_2$S$_6$·(TMEDA)$_2$ is preparable by a number of routes.[152]) While there are many such complexes not covered here, and doubtless many more to be discovered, no further major structural or bonding trends in this section remain to be discussed at this still comparatively early stage in the development of alkali metal coordination chemistry.

5 METAL-ORGANICS

Those compounds with metal–carbon bonds that fit the strict definition of the term ‘organometallic’ deservedly have their own article in this encyclopedia (*see* ***Alkali Metals: Organometallic Chemistry***), but a large and important class of compounds exists that contain organic groups bound to noncarbon central anions that give the compounds a ‘molecular’ character distinct from the latticelike behavior of most of the inorganic salts discussed previously. This class, which for the purist may be described as ‘metal-organics’ rather than organometallics, is briefly discussed here.

5.1 Alkali Metal Organoamides[153,154]

5.1.1 Amidolithiums

The term ‘amidolithium’ is the unambiguous name for the compounds RR′NLi (R, R′ = alkyl, aryl, silyl, etc.) more often termed ‘*lithium amides*’. They derive their importance from the near-ubiquity of their bulkier members lithium diisopropylamide (LDA), lithium tetramethylpiperidide (LTMP), and lithium hexamethyldisilazide (LHMDS) in organic synthesis.[6] Using such powerful but nonnucleophilic bases, many useful reactions may be performed, notably the enolization of ketones and esters, which can proceed both regio- and stereoselectively under kinetic control at low temperatures.[155]

Amidolithiums have the same ionic bonds and tendencies to aggregation as other lithium salts. The primary unit is normally the planar ring dimer (LiNRR′)$_2$. Groups R and R′ project orthogonally from the Li$_2$N$_2$ ring plane (**17**), thus preventing vertical association. However, when the R groups are small and restricted, lateral association (laddering, (**18**)) of rings results.[153,154] Polymerization in this way can lead to amorphous materials, as for piperididolithium, (C$_5$H$_{10}$NLi)$_\infty$, but a soluble, oligomeric precursor (**19**) to infinite laddering has been isolated in this case.[156] Lithiation of the terminal piperidine ligands would result in completion of the ladder structure. A bend is discernible in this ladder structure of (**19**), which in hexamethyleneiminolithium (**20**) has increased so that both ends of the ladder meet in a six-membered cycle.[153] The original Li$_2$N$_2$ dimers may still be discerned as being connected by the shortest Li–N bond lengths.

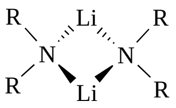

(**17**)

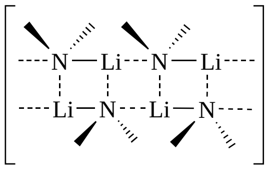

(**18**)

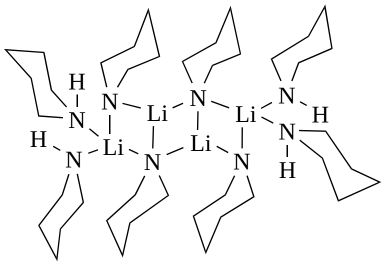

(**19**)

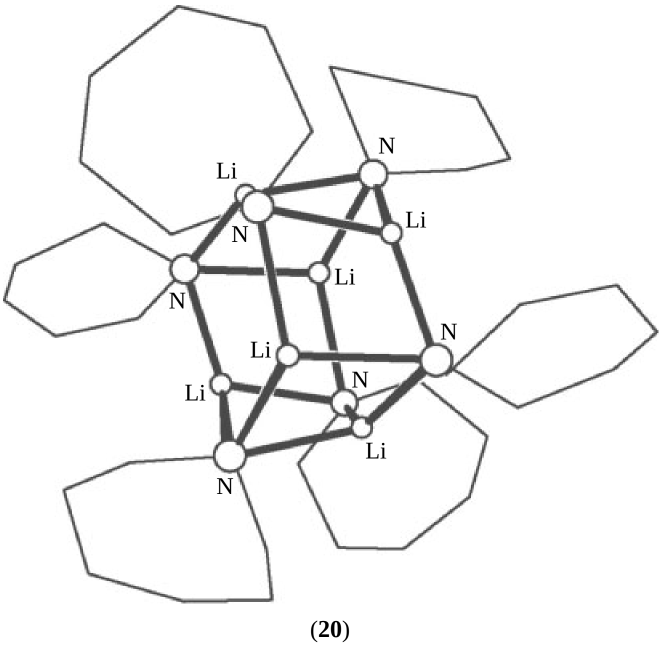

(**20**)

When R and R′ are large and/or floppy, this laddering is less favorable. In the exceptionally bulky case of $[LiN(SiMe_3)(2,6\text{-}i\text{-}Pr_2C_6H_3)]_2$, a simple dimer is most stable,[157] but normally ring size increases in order to distance the N^- centers from each other and symmetrize charge distribution around Li. Thus, LTMP forms a cyclic tetramer, virtually linear at lithium, while LHMDS forms a trimer.[153] LDA exists in nondonating solution as cyclic oligomers and normally precipitates as an amorphous polymer, but crystallizes from hexane/TMEDA as a polymeric helix.[158]

The effect of solvation by Lewis base donor solvents is to reduce this complexity. THF, the most widely used solvent for these bases, forms bis-solvated dimeric complexes with most amidolithiums, since this smallest Li_2N_2 ring provides maximum room for the additional donor molecules. Chelating donors may even produce monomers, but ion separation is found in the solid state only when the anion is stabilized by electron-accepting heteroatoms.[159]

5.1.2 Amides of the Other Alkali Metals

The longer bond lengths of the heavier alkali amides remove the constringent aggregation patterns of lithium chemistry.[154] Variety abounds, and too few data exist to draw convincing generalizations about uncomplexed amide geometries. Above it was noted that LiHMDS was trimeric in the solid state; NaHMDS is an infinite chain polymer, but KHMDS is a dimer.[160] Other ‘rule’ violations include the stacked amide structures of $(Me_2NNa)_{10}\cdot(TMEDA)_4$ and $(Me_2NNa)_{12}\cdot(TMEDA)_4$.[161] However, in these and most other known structures, the M_2N_2 subunit dominates in both complexed and uncomplexed amides.

The heavier alkali amides have yet to find widespread use in synthesis owing to the inferior selectivity imparted by their greater reactivity. However, in situ mixtures of heavy alkali alkoxides and lithium amides are finding increasing use as very strong bases.[6,155] The nature of the reactive species is as yet unclear.

5.2 Alkali Metal Enolates

These form a class of compounds which has received much study because of their part in the important C–C bond-forming aldol reaction.[162] The primary structural units are again rings but here association is vertical (stacking) rather than lateral, since the organic groups can align themselves in the same plane (approximately) as the $(LiO)_x$ rings (see (**21**)). The uncomplexed lithium enolate of pinacolone is a stack of two trimers but shrinks to a stack of two dimers when solvated by THF. The sodium enolate of pinacolone crystallizes with one unenolized ketone per metal; therefore it also forms a four-metal stack of two bis-solvated dimers. In contrast, the THF complex of potassium pinacolonate (**22**) can accommodate donor molecules while maintaining the higher aggregation state due to the longer K–O bonds.[163] Similar aggregated species have been observed in solution.[162]

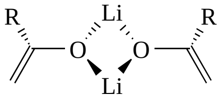

(**21**)

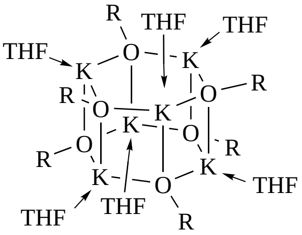

(**22**) R = t-BuC(=CH_2)–

Mixed-metal enolate has also been found. The core of the lithium sodium enolate of pinacolone forms an ‘open stack’ structure in which two edges of the face-sharing cubes are absent.[164]

5.3 Others

Of the vast plethora of alkali-organic structures,[61,165] a few groups deserve special mention, even if they have yet to find the widespread synthetic significance of the above two classes.

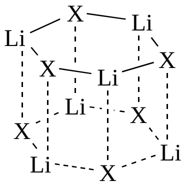

(**23**)

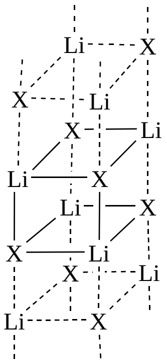

(**24**)

The imidoalkalis, RR′C=NM, are important because it was in the attempt to explain their structures that the widely applicable stacking principle was developed.[153,154] The uncomplexed lithium cases, for example, LiN=C(t-Bu)$_2$, form hexameric structures, that is, double stacks of trimers (**23**). Further stacking is precluded by the bulky R groups. If both of these are flat, for example, Ph, infinite stacking (**24**) results in precipitation of amorphous powders. One such material, $(LiN{=}CPh_2)_\infty$, can be broken down by pyridine to a double stack of solvated dimers (**25**). For bulky donors (e.g. HMPA) and imines, only the simple dimer can form, for example, $(t\text{-}Bu_2C{=}NLi\cdot HMPA)_2$. No uncomplexed heavier imidoalkali has yet been prepared crystalline, except as a constituent of mixed-metal species $Li_4Na_2(N{=}CRR')_6$. These have the same stoichiometry as the double-stacked trimers in which each lithium attains three coordination, but the structure

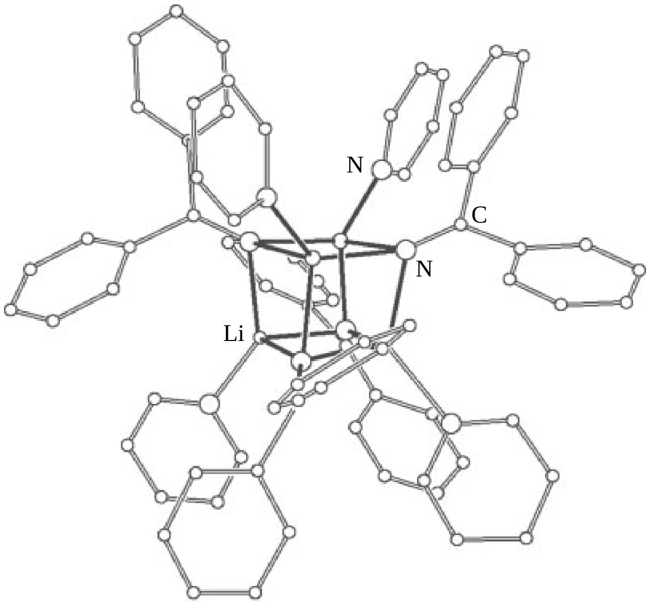

(**25**)

changes to a triple stack of dimers with the introduction of sodium. The smaller ring size gives more room for the ligands to stack, while giving the Na^+ ions the opportunity of four coordination in the center of the triple stack.[154]

Even larger stacks have been observed with the sterically undemanding acetylide ligands in $(t\text{-BuC}\equiv\text{CLi})_{12}\cdot(\text{THF})_4$. These aggregation tendencies are also apparent in simple alkoxides, for example, NaO-*t*-Bu exists as a mixture of nonameric and hexameric aggregates in the solid state.[166] Alkoxides such as this are often used in syntheses of high nuclearity mixed-metal clusters.[167] Lithium alkoxides have a wide range of applications such as precursor materials for chemical vapor deposition, ceramics and sol-gel processes, and as reagents in organic synthesis. The structure of unsolvated lithium *tert*-butoxide has only been confirmed as hexamer in 2002.[168] However, the unusual octameric structure has also been revealed recently. It has sections resembling both a cubane and a cyclic hexamer.[169] It was found that both hexamer and octamer coexist in the solution of lithium tert-butoxide. For the heavier alkali metal alkoxides, they adopt various forms of aggregates such as $\text{Cs}(o\text{-}2,6\text{-}i\text{-PrC}_6\text{H}_3)$ in which the two-dimensional infinite-sheet structure is uncommon.[170] For the heterometallic alkoxides, mixed lithium-heavier alkali metal alkoxides are found to be highly aggregated cage structures, for example, $[(t\text{-BuO})_8\text{Li}_4\text{M}_4]$ contains a sixteen-vertex $\text{O}_8\text{Li}_4\text{M}_4$ cage structure comprising of one $\text{M}^+{}_4$ plane and two $(\text{O}_4\text{Li}_2)^{2-}$ dianions.[171]

Phosphides $\text{RR}'\text{P}^-\text{M}^+$ are found to follow laddering principles in common with the amides,[172] while thiolates RS^-M^+ give more variety, and depart from the behavior of their lighter congeners. Crystalline one-dimensional chains, stepped ladders[173] (a polymeric equivalent of the monosolvated double stack of dimers) and even high nuclearity clusters are found. In $\text{Li}_{14}(\text{SCH}_2\text{Ph})_{12}\text{S(TMEDA)}$, the cluster forms around a central S^{2-} ion.[174]

Bonding to anions centered on the heavier p-block elements tends to give either polymers or highly solvated monomers or dimers. The nature of bonding between organotin- and lead anions and alkali metals has recently come under study. These bonds are found to be both weak and predominantly ionic.[175]

Most of the above relates to anions with one center of charge. Structural and chemical diversity takes on a further dimension with the alkali complexes of multiply centered organic anions such as carboxylates (the lithium salts are important as automotive greases), diketonates, sulfonates, and so on.[61,165] One such complex was recently shown to be the first example of a lithium amide containing water in its coordination sphere.[176] Study of others has shown how the coordination chemistry of the metal can profoundly affect the anion, causing rearrangements and extrusions.[121,177] The breadth and speed of current developments means that events will soon overtake this brief account.

6 RELATED ARTICLES

Alkali Metals: Organometallic Chemistry; Periodic Table: Trends in the Properties of the Elements; Zeolites.

7 REFERENCES

1. R. O. Bach ed., ‘Lithium: Current Applications in Science, Medicine, and Technology’, Wiley, New York, 1985.
2. R. Thompson ed., ‘The Modern Inorganic Chemicals Industry’, The Chemical Society, London, 1977.
3. N. N. Greenwood and A. Earnshaw, ‘Chemistry of the Elements’, Pergamon Press, Oxford, 1984, Chap. 4, p. 77.
4. P. J. Sadler, *Adv. Inorg. Chem.*, 1991, **36**, 1.
5. N. J. Birch and J. D. Phillips, *Adv. Inorg. Chem.*, 1991, **36**, 49.
6. M. Fieser, ‘Reagents for Organic Synthesis’, Wiley, New York, 1990, Vol. 15.
7. M. Morton, ‘Anionic Polymerization: Principles and Practice’, Academic Press, London, 1983.
8. *The Economist*, 1992, 105.
9. J. R. Partington, ‘A Short History of Chemistry’, 3rd edn., Harper & Brothers, New York, 1957, p. 182.
10. W. W. Porterfield, ‘Inorganic Chemistry: A Unified Approach’, Addison-Wesley, Reading, MA, 1984, Chap. 1.
11. C. C. Addison, ‘The Chemistry of the Liquid Alkali Metals’, Wiley, New York, 1984.
12. B. J. Wakefield, ‘Organolithium Methods’, Academic Press, New York, 1988.

13. L. Brandsma and H. D. Verkruijsse, ‘Preparative Polar Organometallic Chemistry’, Springer, Berlin, 1987, Vol. 1.
14. Faraday Symposium 21, R.S.C. Autumn Meeting, Bath, September 1986, reported in *J. Chem. Soc., Faraday Trans. 1*, 1987, **83**, 7.
15. T. Ito, J.-X. Wang, C.-H. Lin, and J. H. Lunsford, *J. Am. Chem. Soc.*, 1985, **107**, 5062.
16. G. J. Hutchings, M. S. Scurrell, and J. R. Woodhouse, *J. Chem. Soc., Chem. Commun.*, 1987, 1388.
17. C.-H. Lin, T. Ito, J.-X. Wang, and J. H. Lunsford, *J. Am. Chem. Soc.*, 1987, **109**, 4808.
18. I. L. C. Freriks, P. C. de Jong-Versloot, A. G. T. G. Kortbeek, and J. P. van den Berg, *J. Chem. Soc., Chem. Commun.*, 1986, 253.
19. J. Nunan, K. Klier, C.-W. Young, P. B. Himelfarb, and R. G. Herman, *J. Chem. Soc., Chem. Commun.*, 1986, 193.
20. R. J. P. Williams, *Proc. R. Soc. London*, 1981, **213**, 361.
21. N. J. Birch ed., ‘Lithium: Inorganic Pharmacology and Psychiatric Use’, IRL Press, Oxford, 1988.
22. J. L. Sudworth and A. R. Tilley, ‘The Sodium–Sulfur Battery’, Chapman & Hall, London, 1985.
23. J. P. Gabano ed., ‘Lithium Batteries’, Academic Press, New York, 1983.
24. H. V. Venkatasetty ed., ‘Lithium Battery Technology’, Wiley, New York, 1984.
25. E. J. Plichta, W. K. Behl, D. Vujic, W. H. S. Chang, and D. M. Schleich, *J. Electrochem. Soc.*, 1992, **139**, 1509.
26. H. Aono, E. Sugimoto, Y. Sadaoka, N. Imanaka, and G.-Y. Adachi, *J. Electrochem. Soc.*, 1989, **136**, 590.
27. W. Weppner, W. Welzel, R. Kniep, and A. Rabenau, *Angew. Chem., Int. Ed. Engl.*, 1986, **25**, 1087.
28. H. Günther, D. Moskau, P. Bast, and D. Schmalz, *Angew. Chem., Int. Ed. Engl.*, 1987, **26**, 1212.
29. L. M. Jackman and L. M. Scarmoutzos, *J. Am. Chem. Soc.*, 1987, **109**, 5348.
30. A. S. Galiano-Roth, E. M. Michaelides, and D. B. Collum, *J. Am. Chem. Soc.*, 1988, **110**, 2658.
31. P. L. Hall, J. H. Gilchrist, A. T. Harrison, D. J. Fuller, and D. B. Collum, *J. Am. Chem. Soc.*, 1991, **113**, 9575.
32. J. J. Dechter, *Prog. Inorg. Chem.*, 1982, **29**, 285.
33. P. v. R. Schleyer, *Pure Appl. Chem.*, 1983, **55**, 355; 1984, **56**, 151.
34. A. Streitwieser, *Acc. Chem. Res.*, 1984, **17**, 353.
35. J. L. Dye, *Prog. Inorg. Chem.*, 1984, **32**, 327.
36. P. P. Edwards, *Adv. Inorg. Chem. Radiochem.*, 1982, **25**, 135.
37. K.-L. Tsai and J. L. Dye, *J. Am. Chem. Soc.*, 1991, **113**, 1650.
38. A. J. Birch and H. Smith, *Q. Rev. Chem. Soc.*, 1958, **12**, 17.
39. I. Schön, *Chem. Rev.*, 1984, **84**, 287.
40. Z. Jedliński, A. Czech, H. Janeczek, and M. Kowalczuk, *J. Am. Chem. Soc.*, 1995, **117**, 8678.
41. C. L. Perrin, J. Wang, and M. Szwarc, *J. Am. Chem. Soc.*, 2000, **122**, 4569.
42. R. H. Huang, S. Z. Huang, and J. L. Dye, *J. Coord. Chem.*, 1998, **46**, 13.
43. R. H. Huang, J. L. Eglin, S. Z. Huang, L. E. H. McMills, and J. L. Dye, *J. Am. Chem. Soc.*, 1993, **115**, 9542.
44. M. Y. Redko, R. H. Huang, J. E. Jackson, J. F. Harrison, and J. L. Dye, *J. Am. Chem. Soc.*, 2003, **125**, 2259.
45. R. H. Huang, D. L. Ward, and J. L. Dye, *J. Am. Chem. Soc.*, 1989, **111**, 5707.
46. S. B. Dawes, J. L. Eglin, K. J. Moeggenborg, J. Kim, and J. L. Dye, *J. Am. Chem. Soc.*, 1991, **113**, 1605.
47. R. H. Huang, M. J. Wagner, D. J. Gilbert, K. A. Reidy-Cedergren, D. L. Ward, M. K. Faber, and J. L. Dye, *J. Am. Chem. Soc.*, 1997, **119**, 3765.
48. Q. Xie, R. H. Huang, A. S. Ichimura, R. C. Phillips, W. P. Pratt Jr, and J. L. Dye, *J. Am. Chem. Soc.*, 2000, **122**, 6971.
49. A. S. Ichimura, J. L. Dye, M. A. Camblor, and L. A. Villaescusa, *J. Am. Chem. Soc.*, 2002, **124**, 1170.
50. J. L. Dye, *Inorg. Chem.*, 1997, **36**, 3816.
51. V. Petkov, S. J. L. Billinge, T. Vogt, A. S. Ichimura, and J. L. Dye, *Phys. Rev. Lett.*, 2002, **89**, 7502.
52. Z. Li, J. Yang, J. G. Hou, and Q. Zhu, *J. Am. Chem. Soc.*, 2003, **125**, 6050.
53. V. Bonačić-Koutecký, P. Fantucci, and J. Koutecký, *Chem. Rev.*, 1991, **91**, 1035.
54. V. I. Srdanov, K. Haug, H. Metiu, and G. D. Stucky, *J. Phys. Chem.*, 1992, **96**, 9039.
55. B. Xu and L. Kevan, *J. Phys. Chem.*, 1992, **96**, 2642.
56. P. A. Anderson, D. Barr, and P. P. Edwards, *Angew. Chem., Int. Ed. Engl.*, 1991, **30**, 1501.
57. P. A. Anderson and P. P. Edwards, *J. Am. Chem. Soc.*, 1992, **114**, 10608.
58. V. V. Terskikh, I. L. Moudrakovski, C. I. Ratcliffe, J. A. Ripmeester, C. J. Reinhold, P. A. Anderson, and P. P. Edwards, *J. Am. Chem. Soc.*, 2001, **123**, 2891.
59. R. Csuk, B. I. Glänzer, and A. Fürstner, *Adv. Organomet. Chem.*, 1988, **28**, 85.
60. S. H. Glarum, S. J. Duclus, and R. C. Haddon, *J. Am. Chem. Soc.*, 1992, **114**, 1996.
61. C. Schade and Pv. R. Schleyer, *Adv. Organomet. Chem.*, 1987, **27**, 169.
62. K. M. MacKay, ‘Hydrogen Compounds of the Metallic Elements’, E. & F. N. Spon, London, 1966, p. 19.
63. D. R. Armstrong, W. Clegg, R. P. Davies, S. T. Liddle, D. J. Linton, P. R. Raithby, R. Snaith, and A. E. H. Wheatley, *Angew. Chem., Int. Ed. Engl.*, 1999, **38**, 3367.
64. S. R. Boss, M. P. Coles, R. Haigh, P. B. Hitchcock, R. Snaith, and A. E. H. Wheatley, *Angew. Chem., Int. Ed. Engl.*, 2003, **42**, 5593.

65. M. Y. Redko, M. Vlassa, J. E. Jackson, A. W. Misiolek, R. H. Huang, and J. L. Dye, *J. Am. Chem. Soc.*, 2002, **124**, 5928.

66. A. Sawicka, P. Skurski, and J. Simons, *J. Am. Chem. Soc.*, 2003, **125**, 3954.

67. A. F. Wells, ‘Structural Inorganic Chemistry’, 4th edn., Clarendon Press, Oxford, 1975, p. 261.

68. R. L. Whetten, *Acc. Chem. Res.*, 1993, **26**, 49.

69. G. M. Photiadis and G. N. Papatheodorou, *J. Chem. Soc., Dalton Trans.*, 1998, 981.

70. G. M. Photiadis and G. N. Papatheodorou, *J. Chem. Soc., Dalton Trans.*, 1999, 3541.

71. V. Dracopoulos, J. Vagelatos, and G. N. Papatheodorou, *J. Chem. Soc., Dalton Trans.*, 2001, 1117.

72. A. Simon, *Struct. Bonding*, 1979, **36**, 81.

73. J. C. Bailar, H. J. Emeléus, R. Nyholm, and A. F. Trotman-Dickenson eds, ‘Comprehensive Inorganic Chemistry’, Pergamon Press, Oxford, 1973, Vol. 1.

74. D. Fischer and M. Jansen, *Angew. Chem., Int. Ed. Engl.*, 2002, **41**, 1755.

75. R. Niewa, *Angew. Chem., Int. Ed. Engl.*, 2002, **41**, 1701.

76. D. E. C. Corbridge, ‘The Structural Chemistry of Phosphorus’, Elsevier, Amsterdam, NY, 1974, Chap. 3, p. 25.

77. H. Schäfer, B. Eisemann, and W. Müller, *Angew. Chem., Int. Ed. Engl.*, 1973, **12**, 694.

78. A. Maercker, *Angew. Chem., Int. Ed. Engl.*, 1992, **31**, 584.

79. V. Quéneau and S. C. Sevov, *Angew. Chem., Int. Ed. Engl.*, 1997, **36**, 1754.

80. B. J. Aylett, in ‘Silicon Chemistry’, eds. E. R. Corey, J. Y. Corey, and P. P. Gaspar, Ellis Horwood, Chichester, 1988, Chap. 33, p. 357.

81. R. Nesper, H. Gv. Schnering, and J. Curda, *Chem. Ber.*, 1986, **119**, 3576.

82. V. Quéneau, E. Todorov, and S. C. Sevov, *J. Am. Chem. Soc.*, 1998, **120**, 3263.

83. V. Quéneau and S. C. Sevov, *Inorg. Chem.*, 1998, **37**, 1358.

84. E. Todorov and S. C. Sevov, *Inorg. Chem.*, 1998, **37**, 3889.

85. T. F. Fässler and R. Hoffmann, *Angew. Chem., Int. Ed. Engl.*, 1999, **38**, 543.

86. N. Korber and A. Fleischmann, *J. Chem. Soc., Dalton Trans.*, 2001, 383.

87. T. F. Fässler and R. Hoffmann, *J. Chem. Soc., Dalton Trans.*, 1999, 3339.

88. A. Ugrinov and S. C. Sevov, *J. Am. Chem. Soc.*, 2002, **124**, 10990.

89. A. Ugrinov and S. C. Sevov, *Inorg. Chem.*, 2003, **42**, 5789.

90. B. Albert, *Angew. Chem.*, 1998, **110**, 1135.

91. B. Albert and K. Hofmann, *Z. Anorg. Allg. Chem.*, 1999, **625**, 709.

92. B. Albert, *Eur. J. Inorg. Chem.*, 2000, 1679.

93. G. Mair, H. G. von Schnering, M. Wörle, and R. Nesper, *Z. Anorg. Allg. Chem.*, 1999, **625**, 1207.

94. H. Schäfer, *Ann. Rev. Mater. Sci.*, 1985, **15**, 1.

95. Z.-C. Dong and J. D. Corbett, *J. Am. Chem. Soc.*, 1994, **116**, 3429.

96. Z.-C. Dong and J. D. Corbett, *Angew. Chem., Int. Ed. Engl.*, 1996, **35**, 1006.

97. Z.-C. Dong and J. D. Corbett, *J. Am. Chem. Soc.*, 1995, **117**, 6447.

98. B. Li and J. D. Corbett, *Inorg. Chem.*, 2003, **42**, 8768.

99. R. W. Henning and J. D. Corbett, *Inorg. Chem.*, 1997, **36**, 6045.

100. Z.-C. Dong and J. D. Corbett, *Inorg. Chem.*, 1996, **35**, 3107.

101. B. Li and J. D. Corbett, *Inorg. Chem.*, 2002, **41**, 3944.

102. S. C. Sevov and J. D. Corbett, *Inorg. Chem.*, 1993, **32**, 1612.

103. J.-M. Tu and D. A. Keszler, *Mater. Res. Bull.*, 1995, **30**, 209.

104. W. S. Sheldrick and H.-J. Häusler, *Z. Anorg. Allg. Chem.*, 1987, **549**, 177.

105. M. E. Burke-Laing and K. N. Trueblood, *Acta Crystallogr., Sect. B*, 1977, **33**, 2698.

106. A. Sequeira, I. Bernal, I. D. Brown, and R. Faggiani, *Acta Crystallogr., Sect. B*, 1975, **31**, 1735.

107. P. C. Andrews, N. D. R. Barnett, R. E. Mulvey, W. Clegg, P. A. O’Neil, D. Barr, L. Cowton, A. J. Dawson, and B. J. Wakefield, *J. Organomet. Chem.*, 1996, **518**, 85.

108. W. Clegg, S. Kleditzsch, R. E. Mulvey, and P. O’Shaughnessy, *J. Organomet. Chem.*, 1998, **558**, 193.

109. R. Juza, H. H. Weber, and K. Opp, *Z. Anorg. Allg. Chem.*, 1956, **284**, 73.

110. D. B. Grotjahn, P. M. Sheridan, I. Al Jihad, and L. M. Ziurys, *J. Am. Chem. Soc.*, 2001, **123**, 5489.

111. F. M. Mackenzie, R. E. Mulvey, W. Clegg, and L. Horsburgh, *J. Am. Chem. Soc.*, 1996, **118**, 4721.

112. K.-D. Ehrhardt, W. Press, and G. Heger, *Acta Crystallogr., Sect. B*, 1983, **39**, 171.

113. C. J. Marsden, *J. Chem. Soc., Dalton Trans.*, 1984, 1279.

114. D. D. Swank and R. D. Willett, *Inorg. Chem.*, 1965, **4**, 499.

115. A. Berry, M. L. H. Green, J. A. Brady, and K. Prout, *J. Chem. Soc., Dalton Trans.*, 1991, 2185.

116. M. Y. Darensbourg, *Prog. Inorg. Chem.*, 1985, **33**, 221.

117. M. Y. Darensbourg and C. E. Ash, *Adv. Organomet. Chem.*, 1987, **27**, 1.

118. J. E. Ellis, *Adv. Organomet. Chem.*, 1990, **31**, 1.

119. D. R. Armstrong, D. Barr, W. Clegg, S. R. Drake, R. J. Singer, R. Snaith, D. Stalke, and D. S. Wright, *Angew. Chem., Int. Ed. Engl.*, 1991, **30**, 1707.

120. N. S. Poonia and A. V. Bajaj, *Chem. Rev.*, 1979, **79**, 389.

121. P. C. Andrews, D. R. Armstrong, R. E. Mulvey, and D. Reed, *J. Am. Chem. Soc.*, 1988, **110**, 5235.

122. C. J. Pedersen, *Angew. Chem., Int. Ed. Engl.*, 1988, **27**, 1021.

123. R. M. Izatt, K. Pawlak, J. S. Bradshaw, and R. L. Bruening, *Chem. Rev.*, 1991, **91**, 1721.
124. D. Parker, *Adv. Inorg. Chem. Radiochem.*, 1983, **27**, 1.
125. S. R. Cooper, 'Crown Compounds–Towards Future Applications', VCH, Cambridge, MA, 1992.
126. J. C. Bryan, R. A. Sachleben, J. M. Lavis, M. C. Davis, J. H. Burns, and B. P. Hay, *Inorg. Chem.*, 1998, **37**, 2749.
127. J. C. Bryan, R. A. Sachleben, and B. P. Hay, *Inorg. Chim. Acta*, 1999, **290**, 86.
128. B. Dietrich, J. M. Lehn, and J. P. Sauvage, *Tetrahedron Lett.*, 1969, **2885**, 2889.
129. X. X. Zhang, R. M. Izatt, J. S. Bradshaw, and K. E. Krakowiak, *Coord. Chem. Rev.*, 1998, **174**, 179.
130. G. W. Gokel, *Chem. Soc. Rev.*, 1992, **21**, 39.
131. S. E. Matthews, P. Schmitt, V. Felix, M. G. B. Drew, and P. D. Beer, *J. Am. Chem. Soc.*, 2002, **124**, 1341.
132. A. R. Kennedy, R. E. Mulvey, and R. B. Rowlings, *Angew. Chem., Int. Ed. Engl.*, 1998, **37**, 3180.
133. D. Barr, R. Snaith, D. S. Wright, R. E. Mulvey, and K. Wade, *J. Am. Chem. Soc.*, 1987, **109**, 7891.
134. F. Durant, P. Piret, and M. Van Meerssche, *Acta Crystallogr.*, 1967, **23**, 780.
135. C. L. Raston, B. W. Skelton, C. R. Whitaker, and A. H. White, *Aust. J. Chem.*, 1988, **41**, 341.
136. D. Barr, W. Clegg, R. E. Mulvey, and R. Snaith, *J. Chem. Soc., Chem. Commun.*, 1984, 79.
137. M. G. Davidson, R. Snaith, D. Stalke, and D. S. Wright, *J. Org. Chem.*, 1993, **58**, 2810.
138. D. Barr, M. J. Doyle, P. R. Raithby, R. Snaith, D. S. Wright, R. E. Mulvey, and D. Reed, *J. Chem. Soc., Chem. Commun.*, 1989, 318.
139. C. L. Raston, C. R. Whitaker, and A. H. White, *Inorg. Chem.*, 1989, **28**, 163.
140. C. L. Raston, B. S. Skelton, C. R. Whitaker, and A. H. White, *Aust. J. Chem.*, 1988, **41**, 1925.
141. D. Barr, W. Clegg, R. E. Mulvey, and R. Snaith, *Polyhedron*, 1986, **5**, 2109.
142. H. Hope and P. P. Power, *J. Am. Chem. Soc.*, 1983, **105**, 5320.
143. P. L. Hall, J. H. Gilchrist, and D. B. Collum, *J. Am. Chem. Soc.*, 1991, **113**, 9571.
144. F. S. Mair, W. Clegg, and P. A. O'Neil, *J. Am. Chem. Soc.*, 1993, **115**, 3388.
145. D. Seebach, *Aldrichimica Acta*, 1992, **25**, 59.
146. D. Barr, M. J. Doyle, S. R. Drake, P. R. Raithby, R. Snaith, D. Stalke, and D. S. Wright, *Inorg. Chem.*, 1989, **28**, 1768.
147. D. R. Armstrong, A. H. Khandelwal, P. R. Raithby, R. Snaith, D. Stalke, and D. S. Wright, *Inorg. Chem.*, 1993, **32**, 2132.
148. C. L. Raston, C. R. Whitaker, and A. H. White, *Aust. J. Chem.*, 1988, **41**, 1917.
149. C. Eaborn, M. N. A. El-Kheli, P. B. Hitchcock, and J. D. Smith, *J. Chem. Soc., Chem. Commun.*, 1984, 1673.
150. D. R. Armstrong, W. Clegg, H. M. Colquhoun, J. A. Daniels, R. E. Mulvey, I. R. Stephenson, and K. Wade, *J. Chem. Soc., Chem. Commun.*, 1987, 630.
151. N. A. Bell, H. M. M. Shearer, and C. B. Spencer, *J. Chem. Soc., Chem. Commun.*, 1980, 711.
152. K. Tatsumi, Y. Inoue, A. Nakamura, R. E. Cramer, W. Van Doorne, and J. W. Gilje, *Angew. Chem., Int. Ed. Engl.*, 1990, **29**, 422.
153. K. Gregory, P. v. R. Schleyer, and R. Snaith, *Adv. Inorg. Chem.*, 1991, **37**, 47.
154. R. E. Mulvey, *Chem. Soc. Rev.*, 1991, **20**, 167.
155. V. Snieckus, 'Advances in Carbanion Chemistry', JAI, Greenwich, CT, 1992, Vol. 1.
156. G. Boche, I. Langlotz, M. Marsch, K. Harms, and N. E. S. Nudelman, *Angew. Chem., Int. Ed. Engl.*, 1992, **31**, 1205.
157. D. K. Kennepohl, S. Brooker, G. M. Sheldrick, and H. W. Roesky, *Chem. Ber.*, 1991, **124**, 2223.
158. N. D. R. Barnett, R. E. Mulvey, W. Clegg, and P. A. O'Neil, *J. Am. Chem. Soc.*, 1991, **113**, 8187.
159. P. P. Power, *Acc. Chem. Res.*, 1988, **21**, 147.
160. K. F. Tesh, T. P. Hanusa, and J. C. Huffman, *Inorg. Chem.*, 1990, **29**, 1584.
161. N. P. Lorenzen, J. Kopf, F. Olbrich, U. Schumann, and E. Weiss, *Angew. Chem., Int. Ed. Engl.*, 1990, **29**, 1441.
162. D. Seebach, *Angew. Chem., Int. Ed. Engl.*, 1988, **27**, 1624.
163. P. G. Williard and G. B. Carpenter, *J. Am. Chem. Soc.*, 1986, **108**, 462.
164. K. W. Henderson, P. G. Williard, and P. R. Bernstein, *Angew. Chem., Int. Ed. Engl.*, 1995, **34**, 1117.
165. W. N. Setzer and P. v. R. Schleyer, *Adv. Organomet. Chem.*, 1985, **24**, 353.
166. T. Greiser and E. Weiss, *Chem. Ber.*, 1977, **110**, 3388.
167. K. G. Caulton and L. G. Hubert-Pfalzgraf, *Chem. Rev.*, 1990, **90**, 969.
168. H. Nekola, F. Olbrich, and U. Behrens, *Z. Anorg. Allg. Chem.*, 2002, **628**, 2067.
169. J. F. Allan, R. Nassar, E. Specht, A. Beatty, N. Calin, and K. W. Henderson, *J. Am. Chem. Soc.*, 2004, **126**, 484.
170. D. L. Clark, D. R. Click, R. V. Hollis, B. L. Scott, and J. G. Watkin, *Inorg. Chem.*, 1998, **37**, 5700.
171. D. R. Armstrong, W. Clegg, A. M. Drummond, S. T. Liddle, and R. E. Mulvey, *J. Am. Chem. Soc.*, 2000, **122**, 11117.
172. E. Hey-Hawkins and E. Sattler, *J. Chem. Soc., Chem. Commun.*, 1992, 775.
173. A. J. Banister, W. Clegg, and W. R. Gill, *J. Chem. Soc., Chem. Commun.*, 1987, 850.

174. A. J. Banister, W. Clegg, and W. R. Gill, *J. Chem. Soc., Chem. Commun.*, 1988, 131.

175. D. R. Armstrong, M. G. Davidson, D. Moncrieff, D. Stalke, and D. S. Wright, *J. Chem. Soc., Chem. Commun.*, 1992, 1413.

176. D. Barr, P. R. Raithby, P. v. R. Schleyer, R. Snaith, and D. S. Wright, *J. Chem. Soc., Chem. Commun.*, 1990, 643.

177. F. A. Banbury, M. G. Davidson, P. R. Raithby, R. Snaith, and D. Stalke, *J. Chem. Soc., Chem. Commun.*, 1992, 1492.

Alkali Metals: Organometallic Chemistry

Melanie J. Harvey
University of Saint Mary, Leavenworth, KS, USA

Based in part on the article Alkali Metals: Organometallic Chemistry by Charles M. Lukehart which appeared in the Encyclopedia of Inorganic Chemistry, First Edition.

1 Introduction 1
2 General Aspects of the Chemistry of Organoalkali Metal Compounds 1
3 Alkyl, Alkenyl, Alkynyl, and Aryl Compounds 3
4 Allyl, Pentadienyl, and Benzyl Compounds 7
5 Cyclopentadienyl and Related Compounds 8
6 Hydrocarbon Radical Anion and Dianion Compounds 9
7 Related Articles 9
8 Further Reading 9
9 References 9

1 INTRODUCTION

Organolithium compounds have been more widely used than compounds of the heavier alkali metals. Smith has published an extensive review that focuses on the organometallic chemistry of sodium, potassium, rubidium, and cesium.**[1]** An important textbook that covers the general aspects of organoalkali metal chemistry was written by Elschenbroich and Salzer.**[2]** These publications, along with this article in the first edition of this encyclopedia,**[3]** were used as foundational sources for this overview of the organometallic chemistry of the alkali metals.

Organolithium complexes, like the organomagnesium Grignard reagents, are important reactants in organic synthesis (*see* ***Beryllium & Magnesium: Organometallic Chemistry***). The similarity in structure, bonding, and reactivity of organolithium and -magnesium compounds exemplifies the common chemistry exhibited by representative elements having a diagonal placement within the periodic table (*see* ***Periodic Table: Historical Aspects*** and ***Periodic Table: Trends in the Properties of the Elements***).

Additional aspects of the chemistry of lithium that have facilitated research are (1) the ability to acquire lithium NMR data, and (2) the possibility of performing high-level theoretical calculations of organolithium compounds (*see* ***Molecular Orbital Theory***). Lithium exists naturally as two isotopes, ^{6}Li (7.4% natural abundance) having a nuclear spin of 1, and ^{7}Li (92.6% natural abundance) having a nuclear spin of 3/2, both of which are NMR active. Organolithium compounds enriched in ^{6}Li have also been prepared and studied by NMR. Lithium NMR data are used to determine structural and bonding information about organolithium compounds, and variable-temperature NMR studies are specifically useful in elucidating dynamic exchange processes that occur with these molecules (*see* ***Stability Constants & their Determination***). Lithium chemical shift values are used to distinguish contact ion paring from solvent-separated ion paring and also the degree of covalency in Li–C bonds (increased covalency shifts lithium resonances to lower field). The magnitude of $J_{\text{Li–C}}$ coupling is used as a more direct measure of the degree of Li–C bond covalency. UV-Visible spectrophotometry also provides important information about ion paring in solutions of organolithium compounds.

Theoretical calculations of organolithium species have received considerable attention. The low atomic number of lithium is suitable for the most sophisticated molecular orbital methods. Although much debate exists over the degree of covalency within lithium – carbon-bonding interactions, the presence of some covalent character in Li–C bonds of alkyllithium compounds is widely accepted.

The bonding interactions within organoalkali metal complexes of the heavier alkali metals are generally considered to be strongly electrostatic or ionic in nature. This is supported by a large collection of evidence, consisting primarily of solution NMR data, single-crystal X-ray analyses, and gas-phase computational studies.

2 GENERAL ASPECTS OF THE CHEMISTRY OF ORGANOALKALI METAL COMPOUNDS

2.1 Synthesis

Organoalkali metal compounds must be synthesized and handled under inert atmosphere conditions because of their high sensitivity to air and moisture. Many of the organolithium compounds are soluble in hydrocarbons, but organometallic compounds of the heavier group 1 metals generally require more polar solvents. In general, a synthetic route is chosen based on the typical yield, expense of reagents, and the relative solubilities of all products formed in the reaction. The following are examples of general methods for synthesizing organoalkali metal compounds.

2.1.1 Direct Synthesis

The direct reaction of an organic halide with an alkali metal is one of the most important methods for synthesizing organolithium compounds. The reaction of two equivalents of the alkali metal with one equivalent of the organohalide produces the organoalkali metal compound and metal halide

(equation 1).

$$2M + RX \longrightarrow RM + MX \quad (1)$$

This route is useful for the synthesis of organolithium compounds, but is often hindered with the more reactive and heavier alkali metals because of the tendency toward Wurtz coupling (equation 2).

$$RM + RX \longrightarrow R\text{–}R + MX \quad (2)$$

The formation of the metal halide as a by-product limits the use of this method for the synthesis of reagents intended for further reactions. The relative solubilities of the organoalkali metal compounds and the metal halides formed in these reactions do not generally allow for easy separations.

The assay of organoalkali metal reagent solutions can be performed using hydrolysis (equation 3), followed by simple acid–base titration (equation 4).

$$RM + H_2O \longrightarrow RH + MOH \quad (3)$$

$$MOH + HCl \longrightarrow MCl + H_2O \quad (4)$$

2.1.2 *Metallation*

There are three general types of metallation reactions (metal–hydrogen exchange) that are commonly used to synthesize organoalkali metal compounds from organic molecules: Direct reaction with an alkali metal, reaction with an alkali metal hydride, or reaction with an organo- or amido-alkali metal. Since these reactions involve acid/base equilibria, they are dependent on both the C–H acidity of the organic molecule and the basicity of the alkali metal source.

The direct reaction of an organic molecule with an alkali metal produces an organoalkali metal compound and hydrogen gas (equation 5).

$$2M + 2RH \longrightarrow 2RM + H_2 \quad (5)$$

This synthetic route can be useful for organic molecules with exceptionally acidic protons, such as acetylenes or cyclopentadienes. These reactions often require the alkali metal to be present as very small particles. Sodium ‘sand’ can be formed by refluxing in THF with minor agitation to break up the sodium into tiny particles. Reactions with potassium may require a ‘mirror’ that can be formed by dissolving potassium metal in liquid ammonia followed by evaporation of the ammonia from the reaction vessel. Ultrasound has also been used to aid in the formation of organolithium compounds from lithium metal.[4–7]

Like the reaction shown in equation (5), the reaction of an alkali metal hydride with an organic molecule also produces an organoalkali metal compound and hydrogen gas (equation 6).

$$2M + 2RH \longrightarrow 2RM + H_2 \quad (6)$$

Relatively acidic organic molecules will react directly with alkali metal hydrides. Crown ethers, strong amines, or ether donors are often used in reactions with the heavier alkali metal hydrides to give more soluble organometallic products. This synthetic route has become increasingly less common due to the generally low solubility of organoalkali metal products and marginal purity of alkali metal hydrides.

The reaction of an organo- or amido-alkali metal reagent with an acidic organic molecule produces an organoalkali metal compound and the amine or organic compound (equation 7).

$$RM + R'H \longrightarrow R'M + RH \quad (7)$$

Methyl lithium and butyl lithium are widely used for the synthesis of other organolithium compounds. For example, lithium cyclopentadienides are generally prepared by the reaction of the cyclopentadiene with butyl lithium. In contrast, the amido-alkali metal compounds are becoming increasingly important in the synthesis of organoalkali metal compounds with the heavier alkali metals. For example, 1,2,4-tris(trimethylsilyl)-1,3-cyclopentadiene reacts with potassium bis(trimethylsilyl)amide to form potassium 1,2,4-tris(trimethylsilyl)cyclopentadienide.[8]

2.1.3 *Transmetallation*

Organoalkali metal compounds can be formed from the reaction of an organometallic compound with an alkali metal (equation 8) or organoalkali metal compound (equation 9). This reaction generally works for transferring an organic ligand from a less electropositive metal to a more electropositive metal. Typically, organometallic compounds of Bi, Cd, Hg, Pb, Sb, Si, Sb, and Zn are used for this type of transfer to an alkali metal. This can be useful for preparing organoalkali metal compounds when working with organic ligands that are highly functionalized. It is also effective when halide contamination of the organoalkali metal compounds would be a problem for subsequent reactions.

$$M + RM' \longrightarrow RM + M' \quad (8)$$

$$RM + R'M' \longrightarrow R'M + RM' \quad (9)$$

By reacting directly with the alkali metal, organomercury compounds are commonly used to synthesize organoalkali metal compounds of the heavier alkali metals. This route has been used to make various alkyl compounds, such as butyl[9] and trimethylsilylmethyl[10] derivatives (equation 10).

$$HgR_2 + 2M \longrightarrow 2MR + Hg \quad (10)$$

Since organolithium compounds are often more readily available, transmetallation can also be useful for preparing an organometallic compound of the heavier group 1 metals from an organolithium compound. In fact, the reaction of a heavier alkali metal alkoxide with an organolithium compound is the most widely used method for preparing organoalkali metal compounds of the heavier alkali metals (equation 11). For example, 1,3-bis(trimethylsilyl)allyl potassium was prepared by the reaction of 1,3-bis(trimethylsilyl)allyl lithium with potassium *t*-butoxide (equation 12).[11] This reaction was effected in hexanes with additional TMEDA. The allyl potassium compound is insoluble and can be isolated by filtration in high yield. In general, these reactions are performed in hydrocarbon solvents with some ether present. The alkoxide is generally chosen for easy separation following the reaction. Organostannanes can be reacted with phenyllithium to give tetraphenyl tin and a different organolithium compound[12] (equations 13 and 14).

$$\mathrm{LiR + MOR'} \longrightarrow \mathrm{MR + LiOR'} \qquad (\mathrm{M = Na, K, Rb, Cs}) \tag{11}$$

$$\mathrm{Li[C_3H_3(SiMe_3)_2] + KOC(CH_3)_3} \longrightarrow \mathrm{K[C_3H_3(SiMe_3)_2] + LiOC(CH_3)_3} \tag{12}$$

$$\mathrm{4PhLi + (H_2C{=}CH)_4Sn} \longrightarrow \mathrm{Ph_4Sn + 4H_2C{=}CHLi} \tag{13}$$

$$\mathrm{Ph_3SnCH_2AsPh_2 + PhLi} \longrightarrow \mathrm{Ph_4SnCH_2AsPh_2 + Ph_2AsCH_2Li} \tag{14}$$

2.1.4 Carbometallation

The electropositive nature of alkali metals allows for insertions into alkali metal–carbon bonds. Thus, the reaction of an organoalkali metal reagent with an unsaturated organic molecule produces a more complex organoalkali metal compound. In particular, organolithium compounds will react in this way with conjugated dienes, even under mild conditions. For example, 1,3-butadiene reacts with *tert*-butyl lithium to give an allyl lithium compound[3] (equation 15).

$$\mathrm{(CH_3)_3CLi + H_2C{=}CH{-}CH{=}CH_2} \longrightarrow (Z\text{ and }E)\text{-}\mathrm{(CH_3)_3C{-}CH_2CH{=}CHCH_2Li} \tag{15}$$

2.1.5 Thermolysis and Thermal Rearrangements

Organolithium compounds can be converted to other organolithium compounds under high temperatures. For example, dilithiomethane is produced from methyl lithium when heated between 223 and 226 °C.[13]

2.2 Structure

The structures of organolithium compounds have been extensively studied, and there are a number of reviews available.[14–16] A recent review of the structures of organoalkali metal compounds of the heavier group 1 metals has also been made available.[1] Specific details of the structures formed by various types of organoalkali metal compounds both in solution and in the solid state will be discussed in following sections.

2.3 Reactivity

In general, the reactivity of the alkali metals and the reactivity of the organometallic compounds of these metals increase as we go down the group or column. Organoalkali metal compounds are similar to, but more reactive than Grignard reagents. For example, the carbanions of organoalkali metal compounds have been widely used as nucleophiles in reactions with various ‘electrophilic’ organic compounds. Organolithium compounds have been particularly useful in this way for the formation of new carbon–carbon bonds. Organoalkali metal compounds are both air- and moisture-sensitive and are sometimes pyrophoric. In addition, organoalkali metal compounds will react as Brønsted bases with protic reagents.

There are a couple of other general features of the reactivity of organoalkali metal compounds worth mentioning. (1) Most organoalkali metal compounds form complexes with crown ethers, provided the ‘crown’ is an appropriate size for the particular alkali metal (*see* ***Alkali Metals: Inorganic Chemistry***). (2) In general, the thermal stability of organoalkali metal compounds decreases as their size and reactivity increases. Both α- and β-eliminations are usual pathways of thermal decomposition for group 1 organometallic compounds.

3 ALKYL, ALKENYL, ALKYNYL, AND ARYL COMPOUNDS

3.1 Alkylalkali Metal Compounds

In recent years, considerable attention has been given to organoalkali metal compounds containing bulky silicon-substituted alkyl groups. The use of these ligands has provided compounds that differ dramatically in structure and reactivity from compounds with smaller alkyl groups. Organometallic compounds with bulky silicon-substituted alkyl groups have been reviewed.[17]

3.1.1 Synthesis

Most alkyllithium compounds are prepared by the direct synthesis method shown in equation (1). For example, lithium metal reacts with bromomethane in ether to form methyl lithium and lithium bromide (equation 16).[2]

$$\mathrm{2Li + CH_3Br} \longrightarrow \mathrm{LiCH_3 + LiBr} \tag{16}$$

The heavier alkylalkali metal compounds can be prepared from a transmetallation reaction with an alkyllithium compound. For example, methyl potassium is formed from the reaction of methyl lithium with potassium *t*-butoxide (equation 17).[18]

$$\mathrm{MeLi} + t\mathrm{BuOK} \longrightarrow \mathrm{MeK} + t\mathrm{BuOLi} \qquad (17)$$

Organoalkali metal compounds of the heavier alkali metals with more highly substituted alkyl groups can be formed from the reaction of an alkane with the appropriate methyl derivative (MMe; M = Na,[19] K,[20] Rb,[21] and Cs[21]) (equation 18).

$$\mathrm{RH} + \mathrm{MMe} \longrightarrow \mathrm{RM} + \mathrm{MeH}(\mathrm{R} = \mathrm{C(SiMe_3)_3}) \qquad (18)$$

Alkylalkali metal compounds are also commonly formed from reactions with organomercury compounds. Solvent-free $\mathrm{LiC(SiMe_3)_3}$ has been prepared by the reaction of an organomercuryhalide with butyl lithium in hexanes (equation 19).[17]

$$2\mathrm{BuLi} + \mathrm{BrHgR} \longrightarrow \mathrm{LiR} + \mathrm{LiBr} + \mathrm{HgBu_2} \qquad (\mathrm{R} = \mathrm{C(SiMe_3)_3}) \ (19)$$

3.1.2 Structures

In solutions, the extent of the oligomerization or the degree of association of alkylalkali metal compounds is dependent on several factors: the size of the metal, the steric bulk of the alkyl substituent, the concentration of the compound, the identity of the solvent, the presence of additional bases, and the temperature of the solution. More information is available on the structures of organolithium compounds than the heavier alkali metal compounds since they are widely used as reagents in organic synthesis and because of the availability of ^{6}Li NMR data.

In the solid state[22,23] and in the gas phase,[24–26] methyl lithium exists as a tetramer. The tetramer of methyllithium in the solid state can be viewed as a distorted cube of carbon and lithium atoms (Li–C, 2.36 Å; Li· · ·Li, 2.68 Å) (**1**).

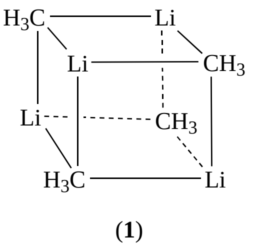

(**1**)

Structurally similar tetramers are maintained in solutions with electronic donors (THF or TMEDA).[27,28] For example, the same core structure exists for the methyllithium TMEDA adduct. Ab initio methods have been used to study the aggregation of various methyl lithium oligomers in the presence of various donor ligands.[29] The heavier alkali metal (M = K, Rb, Cs) methyl compounds have more ionic bonding and crystallize in a nickel arsenide-type lattice.[30] *Tert*-butyllithium also exists as a tetramer in the gas phase[26] and in hexanes or benzene.[31,32] Aggregation energies and conformer preferences have been investigated for *tert*-butyllithium using density functional theory.[33]

The synthesis, structures, and reactions of silicon-substituted alkyl derivatives of metals from groups 1, 2, and 3 have been recently reviewed.[17] A diverse range of structures has been discovered with the alkali metals. More recently, some additional structures and an important discussion of structural trends observed among the silicon-substituted alkyl derivatives of the alkali metals have also been published.[34] Tris(trimethylsilyl)methyl lithium forms a solvent-free dimer, as well as several ‘ate’ complexes in the presence of bases (THF or TMEDA). In the alkyl-bridged dimer of tris(trimethylsilyl)methyl lithium (**2**), there are interactions between the C–H bonds of the silyl ligand and the lithium atoms (**3**) (Li to C distances of 254.1(7) and 246.6(6) pm).[17]

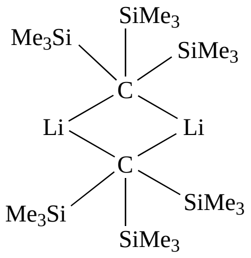

(**2**)

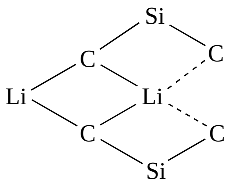

(**3**)

Silicon-substituted alkyl derivatives of the heavier alkali metals are increasingly being used in the synthesis of other organometallic compounds because of their solubility. Perhaps, it is this enhanced solubility that has allowed for the structural characterization of many of these compounds in recent years. Tris(trimethylsilyl)methyl potassium and rubidium both crystallize as solvent-free compounds from ether solution. The potassium derivative consists of infinite, linear chains of alternating potassium cations and alkyl anions (average K–C = 309.7(11) pm).[17,20] There are weak interactions between the chains, potassium to six methyl groups (three on each side), allowing the potassium to be eight-coordinate (K· · ·C range from 318.7 to 331.1 pm).[17,20]

The solvent-free bis(trimethylsilyl)methyl sodium and bis(trimethylsilyl)methyl lithium are isostructural and crystallize as polymeric chains of alternating cations and anions.[35,36] The potassium compound also crystallizes as an infinite polymer chain of alternating cations and anions with one thf molecule on each potassium cation.[37] Bis(trimethylsilyl)methyl cesium crystallizes as a polymeric chain with one TMEDA ligand coordinated to each cesium cation.[38] The PMDTA adduct of the rubidium derivative (**4**) crystallizes as an alkyl-bridged dimer (Rb−C−Rb, 104.7(2); Rb−C, 336.1(10), 348.5(8)) with terminal PMDTA ligands.[37]

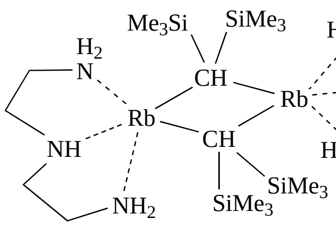

(**4**)

The unusual bis-silyl methyl ligand, $(CH(SiMe_3)(SiMe_2OMe)^-)$, forms a cyclo octamer with lithium (**5**).[39] The bis(trimethylsilyl)dimethylphenylsilylmethyl ligand forms monomeric compounds with lithium and sodium in the presence of additional electron donors (TMEDA, diethyl ether, and THF).[34] In each structure, there are additional interactions between the metal ions and carbons from the phenyl rings. The tris(dimethylphenylsilyl)methyl compounds of sodium, potassium, rubidium, and cesium crystallize in polymeric chains. Each of these compounds also has intra- and intermolecular phenyl-metal cation interactions.[34] The monomeric $[LiC(SiMe_2CH_2PPh_2)_3]$ forms as a base-free compound even in the presence of a large excess of electron donors (such as TMEN) (**6**).[40]

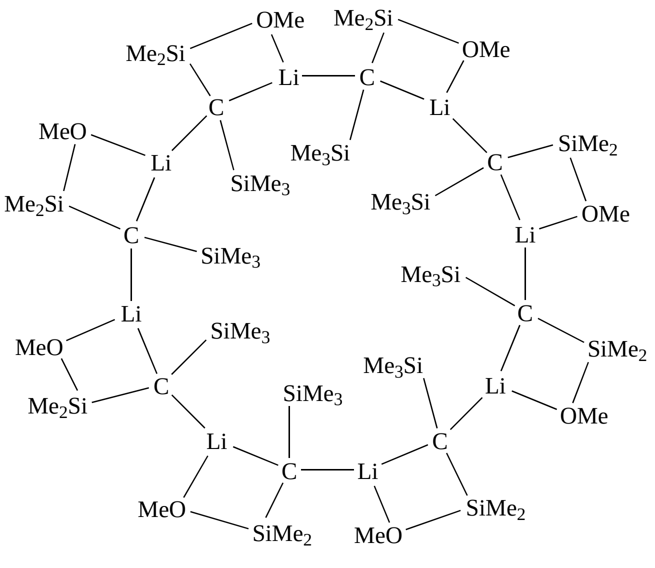

(**5**)

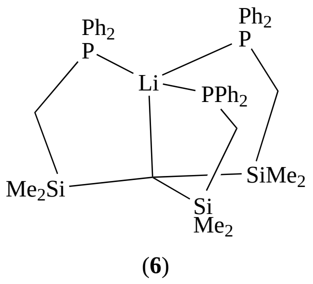

(**6**)

3.1.3 *Reactivity*

Two exchange processes have been elucidated for 2-methylbutyllithium in solution. A slow intra-oligomer exchange gives inversion of configuration at the C_α bonded to lithium. A more rapid inter-oligomer exchange of Li–C bonds is also observed. Menthyllithium is configurationally rigid to at least 50 °C in hydrocarbon solutions, but only to below 0 °C in ether. Chiral cyclopropylmetal compounds of lithium, sodium, or potassium are configurationally stable as prepared. However, the presence of THF leads to rapid racemization as solvent-separated ion pairs are formed. Mixtures of $(MeLi)_4$ and $(EtLi)_4$ give mixed RLi oligomers via inter-oligomer exchange of Li–R bonds. Carbenoids, such as BuCHBrLi, are configurationally stable at −120 °C.[41]

Alkyllithium reagents can be converted to acylsilanes by reaction of RLi with CO and Me_3SiCl (equation 20).[42]

$$\mathrm{RLi + CO + Me_3SiCl \xrightarrow[-110\,^\circ C]{THF/Et_2O/C_5H_{12}} RC(O)SiMe_3} \tag{20}$$

3.2 Alkenylalkali Metal Compounds

3.2.1 *Synthesis*

For synthetic application, the formation of substituted alkenylalkali metal compounds with high regio- and stereoselectivity is desirable. Alkenyl halides react with organolithium reagents by metal-halide exchange to give alkenyllithium compounds. The halides of choice include bromide and iodide; alkenyl chlorides favor α-hydrogen metallation. Low-reaction temperatures permit retention of the stereochemistry of the original alkenyl halide in the alkenyllithium product (equation 21). Vinylsodium and – potassium can be prepared from direct reaction of the metals with vinyl bromide or vinyl chloride respectively.

$$\begin{gathered}(E)\text{-}\mathrm{RHC{=}CHBr} + 2t\text{-}\mathrm{BuLi} \xrightarrow[-120\,^\circ\mathrm{C}]{\mathrm{THF/Et_2O/C_5H_{12}}} \\ (E)\text{-}\mathrm{RHC{=}CHLi} + t\text{-}\mathrm{BuH} + \mathrm{Me_2C{=}CH_2}\end{gathered} \tag{21}$$

Alkenyllithium compounds can also be prepared by metallation of alkenes, particularly when alkenyl hydrogens are rendered acidic by an α-substituent (equation 22). Transmetallation of alkenyl stannanes with organolithium reagents gives alkenyllithium compounds with retention of alkene stereochemistry (equation 23). Tin–lithium transmetallation has been used to prepare 1,4-dilithio-1,3-butadiene.[43] Monosubstituted alkenyllithium compounds RHC=CHLi, can also be prepared from the corresponding diorganotelluride, RHC=CHTeBu, by reaction with butyllithium in

THF.[44]

$$\text{RHC{=}C(SO}_2\text{Ph)H} + \text{MeLi} \longrightarrow \text{RHC{=}C(Li)(SO}_2\text{Ph)} \quad (22)$$

$$(E)\text{-Me}_3\text{SiHC{=}CHSnR}_3 + \text{BuLi} \xrightarrow{\text{low temp.}} (E)\text{-Me}_3\text{SiHC{=}CHLi} \quad (23)$$

3.2.2 *Structures and Reactivity*

Vinyllithium is tetrameric in THF solution. Alkenyllithium compounds containing α-hydrogen or – alkyl substituents do not isomerize readily; however, the presence of donor solvents promotes (Z)-to-(E) isomerization. Those compounds containing α-aryl substituents isomerize readily. The configurational stabilities of HDC=C(Li)X, where X is CN or CO_2Me, and RHC=C(Li)Y, where Y is OR′ or Me_3Si, have been investigated.[45,46]

Lithio-enynes of the type (Z)-RHC=C(Li)C≡CHR′ are configurationally stable at temperatures below −120 °C, and the lithio-diene, (Z,Z)-BuHC=C(Li)CHC=CHBu, is configurationally stable at temperatures below −78 °C.[47] X-ray structural determinations of alkenylalkali metal compounds are particularly sparse.

3.3 Alkali Metal Acetylene Compounds

3.3.1 *Synthesis*

The high acidity of the C–H bonds in acetylene compounds allows for the synthesis of alkali metal acetylene compounds by direct reaction with the metals.

3.3.2 *Structures*

The heavier alkali metal compounds of the formula MC≡C–CH_3 (M = Na, K, Rb, Cs) have been studied by X-ray powder diffraction and are found to be isostructural, crystallizing with a tetragonal unit cells.[48–51] The heavier alkali metals prefer a double π-bridged structure (**7**) rather than a linear σ-bonding structure (**8**). The metal–carbon distances are similar for both carbon atoms in the acetylides, M–C≡C–H and M–C≡C–CH_3. The polymer-sheet structure (**9**) has increasing symmetry in π-bonding between layers with an increase in the size of the metal. Lithium acetylides typically crystallize with more linear structures. For example, the single-crystal X-ray structure of $[(\text{Ph–C≡C–Li})\text{tmpda}]_2$ shows a preference for ‘end-on’ bonding rather than ‘side-on’ bonding (**10**).[52]

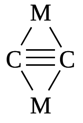

(**7**)

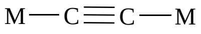

(**8**)

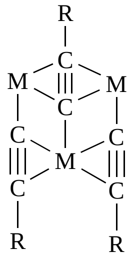

(**9**)

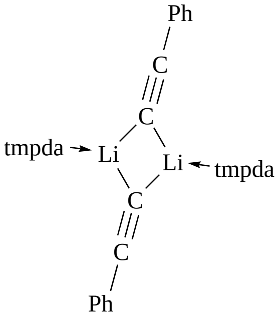

(**10**)

The differences in bonding preferences in lithium acetylides may be confused by the competition from coordinating solvents. In the absence of solvent interactions, as in the crystal structure of Li–C≡C–$SiMe_2$–C_6H_4–OMe, nearly symmetric π-interactions are observed.[53] Computational studies suggest that these interactions are weak in alkali metal acetylide compounds (only 0.73 kcal mol^{-1} for Li–C≡C–R), and the strength apparently decreases with increasing size (0.07 kcal mol^{-1} for Cs).[53]

3.4 Arylalkali Metal Compounds

3.4.1 *Synthesis*

Orthometallation of substituted arenes has been reviewed.[54,55] The ortho-directing ability of substituents in (η^6-arene)$Cr(CO)_3$ complexes decreases as F > CONHR > NHCOR > CH_2NR_2 ≈ OMe ≫ CH_2OMe.[56] Heavier alkali metal arenes can be formed from the reaction of phenyl lithium with sodium or potassium alkoxides.

3.4.2 *Structures and Reactivity*

The degree of oligomerization of various aryllithium compounds in the presence of donor species has been determined by NMR (^{13}C and ^{7}Li).[57,58] X-ray structures of $[\text{PhLi·OEt}_2]_4$ (**11**),[59] $[\text{PhLi·TMEDA}]_2$ (**12**),[60] and PhLi·PMDTA (**13**)[61] illustrate the diversity of structures of aryllithium compounds containing donor ligands. Recently, the utility of aryllithium compounds in aryl–aryl coupling has been demonstrated to produce a range of unusual substituted biaryls.[62]

The solvent-free phenyl derivatives of the heavier alkali metals have not been structurally characterized. Phenyl sodium dimers crystallize in the presence of donors such as, PMDTA and TMEDA.[18] Using the bulky mesityl-substituted derivatives, a solvent-free arylsodium compound has been characterized $[\text{Na(C}_6\text{H}_3\text{Mes}_2\text{-2,6)}]_2$.[63]

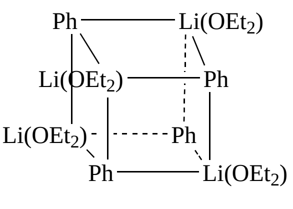

(**11**)

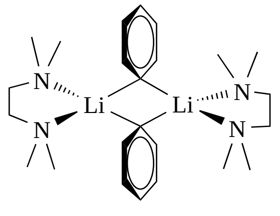

(**12**)

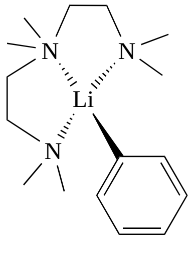

(**13**)

4 ALLYL, PENTADIENYL, AND BENZYL COMPOUNDS

4.1 Allylalkali Metal Compounds

4.1.1 Synthesis

The direct reaction of allyl halides and alkali metals leads to extensive coupling of the allyl fragments, so other synthetic routes must be used for the preparation of allylalkali metal compounds. The metallation of appropriate alkenes is an effective route to allyl compounds. A wide variety of metalating agents have been used, including lithium amides, alkyllithium reagents, Me_3SiCH_2K, and Me_2SiCH_2Cs. Transmetallation of allylstannanes or -mercury compounds gives convenient routes to halide-free allylalkali metal compounds (equations 24–26).**64** The thermal ring-opening of the cyclopropyllithium species can also be used to prepare allyllithium complexes (equation 27).

$$(H_2C{=}CHCH_2)_2Hg + 2M \longrightarrow 2(H_2C{=}CHCH_2)M + Hg \qquad (24)$$

$$M = Li\text{–}Cs$$

$$4(H_2C{=}CHCH_2)Li \xleftarrow[-Sn]{4Li} (H_2C{=}CHCH_2)_4Sn\ 4$$

$$\xrightarrow[-R_4Sn]{4RLi} (H_2C{=}CHCH_2)Li \qquad (25)$$

$$R'_3SnCH_2CR{=}CH_2 \xrightarrow[-R'_3SnR'']{MeLi\ or\ Me_3SiCH_2M} [CH_2CRCH_2, M] \qquad (26)$$

$$M = K\ or\ Cs;\ R'' = Me\ or\ CH_2SiMe_3$$

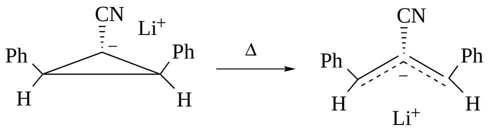

(27)

4.1.2 Structural Studies

The preferred structure of allylalkali metal compounds of lithium through cesium as predicted from ab initio calculations is one having a symmetrical bridging geometry (**14**) with mainly electrostatic bonding between the allyl anion and the metal cation.**65** Allyllithium in ether solution appears to be highly oligomerized, while in THF solution it exists as an unsymmetrical, rapidly equilibrating dimer.**66** However, allylmetal complexes of sodium or potassium have symmetric and presumably monomeric structures in THF solution, like (**14**).**66**

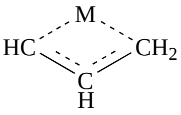

(**14**)

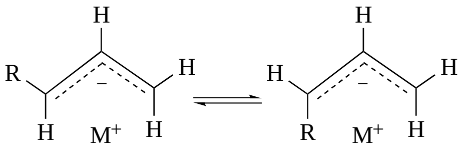

(**15*E***) (**15*Z***)

Allylalkali metal compounds exhibit dynamic isomerizations and bond rotations in solution. In THF solution, allylalkali metal complexes undergo C–C bond rotations with activation energies normally in the range of 45–75 kJ mol^{-1}. 1-Alkylallylalkali metal compounds usually exist as a dynamic mixture of (E) and (Z) isomers (**15**), with a thermodynamic preference for the (Z) configuration. The rates of isomerization of *trans*-neopentylallyl metal complexes in THF solution decreases in the sequence Li > Na > K.**67** Numerous studies of the structures and dynamic properties of allyllithium compounds have been reported.**68–72**

4.2 Pentadienylalkali Metal Compounds

Pentadienyl carbanions are analogous to allyl anions with an extended delocalization of charge. Reaction of 1,3- or 1,4-pentadienes and alkali metals in THF in the presence of a base, such as NMe_3 or TMEDA, affords crystalline pentadienylalkali metal complexes. A contact ion pair structure is predicted for these compounds by theoretical calculations and is consistent with solution structural data obtained by NMR. The pentadienyl anion usually interacts with the cation as an η^3- or η^5-ligand depending on the structural orientation of the backbone carbon atoms of the pentadienyl anion (W-, S-, or U-shaped skeletal structures). A η^3 contact ion pair structure having a 'W-shaped' pentadienyl ligand is shown (**16**). 2,4-Disubstituted pentadienyl complexes favor the η^5 ‘U-shaped’ structure (**17**). This structure has been confirmed by X-ray diffraction for 2,4-dimethylpentadienylpotassium·TMEDA.[73] The potassium ion is coordinated to a chelating TMEDA ligand, and the K–C contact distances to the five pentadienyl skeletal carbon atoms range from 3.152(7) to 3.219(8) Å. In THF solution, 1,3,5-triphenylpentadienyllithium exists in one W-shaped and two S-shaped conformations.

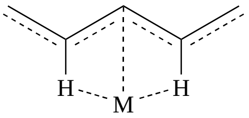

(**16**)

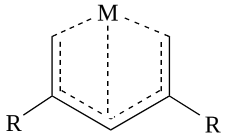

(**17**)

4.3 Benzylalkali Metal Compounds

4.3.1 Synthesis

As with preparing allyl complexes, direct reaction of benzyl halides and alkali metals is not a generally useful route to benzylalkali metal compounds due to R–R coupling. Benzylalkali metal compounds can be prepared by (1) addition of organometallic reagents to arylalkenes, (2) cleavage of benzyl ethers (equation 28), (3) transmetallation (equations 29–31), and (4) metallation of methyl substituted aromatics. α,α-Bis(trimethylsilyl)benzyl potassium can be prepared by metallation with a mixture of butyllithium and potassium 3-methyl-3-pentanolate in THF.[73]

$$\mathrm{PhCR'R''OMe} + 2 \longrightarrow \mathrm{KPhCR'R''^{-}K^{+}} + \mathrm{KOMe} \quad (28)$$

$$\mathrm{ArCH_2SnBu_3} + \mathrm{BuLi}/t\text{-}\mathrm{BuOM} \longrightarrow \mathrm{ArCH_2^{-}M^{+}} + \mathrm{Bu_4Sn} \quad (29)$$

$$\mathrm{(PhCH_2)_2Hg} + 2\mathrm{Li}\ 2 \longrightarrow \mathrm{PhCH_2Li} + \mathrm{Hg} \quad (30)$$

$$\mathrm{PhCH_2Li} + \mathrm{MOR} \longrightarrow \mathrm{PhCH_2M} + \mathrm{LiOR} \quad (31)$$

$$\mathrm{M} = \mathrm{Na–Cs}$$

4.3.2 Structural Studies

Benzylalkali metal compounds exist as aggregate structures in most solutions. NMR and UV-visible spectrophotometry are useful techniques for elucidating these solution-phase structures. Benzyllithium is dimeric in benzene solution; the carbanion charge is probably more delocalized in THF solution. NMR studies of a THF solution of α-(dimethylamino)benzyllithium reveals a dynamic equilibrium between the η^1- and η^3-structures (**18**) and (**19**). The monohapto isomer (**18**) is preferred thermodynamically.[74] The effects of various donor ligands on this type of dynamic behavior in solution is continually being studied.[75,76]

The crystal structure of α,α-Bis(trimethylsilyl)benzyl potassium consists of a linear coordination polymer with alternating benzyl and potassium ions.[73] In this structure, the potassium is primarily η^3-coordinated to the benzyl ligand with interactions to a lesser extent with a neighboring aromatic ring. There are numerous agostic interactions, both between the potassium ions and trimethylsilyl groups and between neighboring chains.

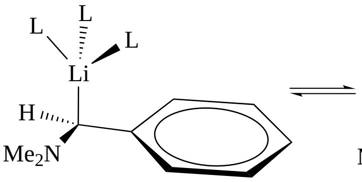

(**18**)

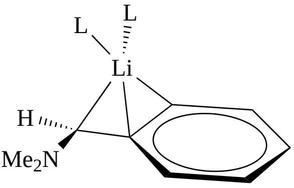

(**19**)

5 CYCLOPENTADIENYL AND RELATED COMPOUNDS

5.1 Synthesis

The relatively strong Brønsted acidity of cyclopentadienes, indenes, and fluorenes, permits the formation of alkali metal compounds of the conjugate bases of these organic molecules by direct reaction with the metal. The effect of substituents on the rate of formation of 9-R-fluorenyllithium compounds in THF solution and on the degree of ion pairing in solutions of these species has been determined.[77–79] Potassium derivatives are commonly prepared by the reaction of the cyclopentadiene with potassium bis(trimethylsilyl)amide.[8] Fluorenyl and indenyl compounds with the heavier alkali metals, Rb and Cs, are also prepared by reaction with the metal bis(trimethylsilyl)amide.[80,81] The cyclopentadienyl ring in alkali metal compounds can also be coordinated to other metals.[82]

5.2 Structural Studies

CpLi exists in ethers as a contact ion pair, in which the lithium ion is located above the cyclopentadienyl ring. The crystal structure of CpLi(12-crown-4) reveals analogous structural features. This complex has a sandwich-type structure in which the lithium ion is coordinated to the four oxygen atoms of the crown ether on one side and to the Cp ring on the other. Several X-ray structures of alkali metal cyclopentadienyl compounds containing silyl substitution of the Cp ligand have been reported.[83,84] The structures of fluorenyl alkali metal complexes (Li–Cs) stabilized by diglyme have also been reported.[85] The crown-ether-stabilized compounds of cyclopentadienyl, indenyl, and fluorenyl with the heavier metals, Rb and Cs, have also been reported.[80] A common structural feature is the η^5 coordination of the Cp ring to the metal ion, although ion pair structures having uncoordinated substituted Cp anions are observed with chelating donors, such as polyethers or crown ethers.

6 HYDROCARBON RADICAL ANION AND DIANION COMPOUNDS

6.1 Synthesis and Reactivity

Many unsaturated hydrocarbons, especially aromatic compounds, react with alkali metals by electron transfer to form paramagnetic radical anions or diamagnetic dianions. Such species are usually highly colored and have sufficient stability to be studied because the added electron density is delocalized in the LUMO of the hydrocarbon. ESR spectroscopy is useful for characterizing these radical anion species.[86–88] Compounds containing these anions are usually soluble in ether solvents, although crown ethers can affect the solubility of these salts in hydrocarbon solvents. Cyclooctatetraene reacts with potassium to give a radical monoanion and eventually reacts further to form the aromatic dianion (abbreviated K_2COT). Silyl substituents appear to facilitate reduction by alkali metals. The hexasubstituted benzene $(Me_3Si)_6C_6$ reacts with lithium in THF to give the dianionic salt $[(Me_3Si)_6C_6][Li(THF)]_2$.[89,90]

The reactivity of hydrocarbon anion or dianion compounds of the alkali metals with respect to alkylation, electron transfer, and protonation has been studied.[91] These species have also been used as reagents in the preparation of organoalkali metal compounds.[92,93]

6.2 Structural Studies

In the solution phase, aromatic radical anions of alkali metals exist as free ions, ion pairs, or as oligomers. Aromatic dianion salts probably form relatively tight ion pairs or oligomers. Solid-state structures of several aromatic radical anion or dianion alkali metal compounds have been determined.[94] In the dianion $Naph_2^-$ $[Li{\cdot}TMEDA]_2^+$, a lithium ion is located over each six-membered ring on opposite sides of a nearly planar naphthalene dianion. The X-ray structure of $(C_8H_8)_2^-$, $2K^+{\cdot}3THF$ reveals a planar dianion bonded on either side as an η^8-ligand to the two potassium ions. The K–C distances range from 2.936 to 2.983 Å.[95] In $[(Me_3Si)_6C_6][Li(THF)]_2$, both lithium ions are located on the same side of the dianion, which has adopted a boat-shaped ring conformation. This structure is maintained in solution. The related salt $[1,2,4,5\text{-}(Me_3Si)_4C_6H_2][Li(DME)]_2$ is structurally different in that the ring of the dianion is essentially planar, and the lithium ions are located on opposite sides of the aromatic ring.[89,90]

7 RELATED ARTICLES

Alkali Metals: Inorganic Chemistry; Alkaline Earth Metals: Organometallic Chemistry; Beryllium & Magnesium: Organometallic Chemistry; Periodic Table: Trends in the Properties of the Elements.

8 FURTHER READING

L. Gong, N. Hu, Z. Jin, and W. Chen, *J. Organomet. Chem.*, 1988, **352**, 67.

9 REFERENCES

1. J. D. Smith, *Adv. Organomet. Chem.*, 1999, **43**, 267.
2. Ch. Elschenbroich and A. Salzer, ‘Organometallics’, 2nd edn., VCH, Weinheim, 1992.
3. C. M. Lukehart, ‘Encyclopedia of Inorganic Chemistry’, 1st edn., John Wiley & Sons, Chichester, 1994, p. 54.
4. J. L. Luche, *Ultrasonics*, 1987, **25**, 40.
5. J. Einhorn and J. L. Luche, *J. Org. Chem.*, 1987, **52**, 4124.
6. P. Boudjouk, *Am. Chem. Soc. Symp. Ser.*, 1987, **333**, 209.
7. P. Boudjouk, R. Sooriyakumaran, and B. H. Han, *J. Org. Chem.*, 1986, **51**, 2818.
8. M. Harvey and T. P. Hanusa, *Organometallics*, 2000, **19**, 1556.
9. C. G. Screttas and B. R. Steele, *J. Organomet. Chem.*, 1993, **453**, 163.
10. A. J. Hart, D. H. O’Brien, and C. R. Russell, *J. Organomet. Chem.*, 1974, **72**, C19.
11. M. Harvey, T. P. Hanusa, and V. G. Young Jr, *Angew. Chem., Int. Ed. Engl.*, 1999, **38**, 217.
12. H. Viebrock, U. Behrens, and E. Weiss, *Chem. Ber.*, 1994, **127**, 1399.
13. J. A. Gurak, J. W. Chinn Jr, and R. J. Lagow, *J. Am. Chem. Soc.*, 1982, **104**, 2637.
14. G. Boche, *Angew. Chem., Int. Ed. Engl.*, 1989, **28**, 277.
15. W. N. Setzer and Pvon. R. Schleyer, *Adv. Organomet. Chem.*, 1985, **24**, 353.
16. Pvon. R. Schleyer, *Pure Appl. Chem.*, 1984, **56**, 151.
17. C. Eaborn, K. Izod, and J. D. Smith, *J. Organomet. Chem.*, 1995, **500**, 89.
18. E. Weiss, *Angew. Chem., Int. Ed. Engl.*, 1993, **32**, 1501.
19. S. S. Al-Juaid, C. Eaborn, P. B. Hitchcock, K. Izod, M. Mallien, and J. D. Smith, *Angew. Chem., Int. Ed. Engl.*, 1994, **33**, 1268.
20. C. Eaborn, P. B. Hitchcock, K. Izod, A. J. Jaggar, and J. D. Smith, *Organometallics*, 1994, **13**, 753.
21. C. Eaborn, P. B. Hitchcock, K. Izod, and J. D. Smith, *Angew. Chem., Int. Ed. Engl.*, 1995, **34**, 687.

22. E. Weiss and G. J. Hencken, *J. Organomet. Chem.*, 1970, **21**, 265.
23. H. Köster, D. Thoennes, and E. Weiss, *J. Organomet. Chem.*, 1978, **160**, 1.
24. F. J. Landro, J. A. Gurak, J. W. Chinn Jr, and R. J. Lagow, *J. Organomet. Chem.*, 1983, **249**, 1.
25. J. W. Chinn Jr and R. J. Lagow, *Organometallics*, 1984, **3**, 75.
26. D. Plavšić, D. Srzić, and L. Klasinc, *J. Phys. Chem.*, 1986, **90**, 2075.
27. M. Schlosser, *Angew. Chem., Int. Ed. Engl.*, 1993, **32**, 580.
28. W. Bauer, W. R. Winchester, and Pv. R. Schleyer, *Organometallics*, 1987, **6**, 2371.
29. E. Kaufmann, K. Raghavachari, A. E. Reed, and Pv. R. Schleyer, *Organometallics*, 1988, **7**, 1597.
30. E. Weiss, T. Lambertsen, B. Schubert, and J. K. Cockcroft, *J. Organomet. Chem.*, 1988, **358**, 1.
31. W. McLean, P. T. Munoy, and R. C. Jarnagin, *J. Chem. Phys.*, 1978, **69**, 2715.
32. W. M. Scowell, B. Y. Kimura, and T. G. Spiro, *J. Coord. Chem.*, 1971, **1**, 107.
33. O. Kwon, F. Sevin, and M. L. McKee, *J. Phys. Chem. A*, 2001, **105**, 913.
34. C. Eaborn, W. Clegg, P. B. Hitchcock, M. Hopman, K. Izod, P. N. O’Shaughnessy, and J. D. Smith, *Organometallics*, 1997, **16**, 4728.
35. P. B. Hitchcock, M. F. Lappert, W.-P. Leung, D.-S. Liu, and T. Shun, *J. Chem. Soc., Chem. Commun.*, 1993, 1386.
36. J. L. Atwood, T. Fjeldberg, M. F. Lappert, N. T. Luong-Thi, R. Shakir, and A. J. Thorne, *J. Chem. Soc., Chem. Commun.*, 1984, 1163.
37. P. B. Hitchcock, A. V. Khvostov, and M. F. Lappert, *J. Organomet. Chem.*, 2002, **663**, 263.
38. W. M. Boesveld, P. B. Hitchcock, M. F. Lappert, D.-S. Liu, and S. Tian, *Organometallics*, 2000, **19**, 4030.
39. F. Antolini, P. B. Hitchcock, M. F. Lappert, and X. H. Wei, *Organometallics*, 2003, **22**, 2505.
40. A. G. Avent, D. Bonafoux, C. Eaborn, M. S. Hill, P. B. Hitchcock, and J. D. Smith, *J. Chem. Soc., Dalton Trans.*, 2000, 2183.
41. R. W. Hoffmann, T. Ruhland, and M. Bewersdorf, *J. Chem. Soc., Chem. Commun.*, 1991, 195.
42. D. Seyferth and R. M. Weinstein, *J. Am. Chem. Soc.*, 1982, **104**, 5534.
43. A. J. Ashe III and S. Mahmoud, *Organometallics*, 1988, **7**, 1878.
44. S. M. Barros, J. V. Comasseto, and J. Berriel, *Tetrahedron Lett.*, 1989, **30**, 7353.
45. B. A. Feit, U. Melamed, H. Speer, and R. R. Schmidt, *J. Chem. Soc., Perkin Trans. 1*, 1984, 775.
46. R. Knorr and T. von Roman, *Angew. Chem., Int. Ed. Engl.*, 1984, **23**, 366.
47. J. A. Miller, W. Leong, and G. Zweifel, *J. Org. Chem.*, 1988, **53**, 1839.
48. E. Weiss, *Angew. Chem., Int. Ed. Engl.*, 1993, **32**, 1501.
49. R. J. Pulham, D. P. Weston, T. A. Salvesen, and J. J. Thatcher, *J. Chem. Res.-S*, 1995, 254.
50. R. J. Pulham and D. P. Weston, *J. Chem. Res. -S*, 1995, 406.
51. E. Weiss and H. Plass, *Chem. Ber.*, 1968, **101**, 2947.
52. B. Schubert and E. Weiss, *Chem. Ber.*, 1983, **116**, 3212.
53. B. Goldfuss, Pv. R. Schleyer, and F. Hampel, *J. Am. Chem. Soc.*, 1997, **119**, 1072.
54. V. Snieckus, *Chem. Rev.*, 1990, **90**, 879.
55. V. Snieckus, *Pure Appl. Chem.*, 1990, **62**, 671.
56. J. P. Gilday, J. T. Negri, and D. A. Widdowson, *Tetrahedron*, 1989, **45**, 4605.
57. E. Wehman, J. T. B. H. Jastrzebski, J.-M. Ernsting, D. M. Grove, and G. von Koten, *J. Organomet. Chem.*, 1988, **353**, 133.
58. E. Wehman, J. T. B. H. Jastrzebski, J.-M. Ernsting, D. M. Grove, and G. von Koten, *J. Organomet. Chem.*, 1988, **353**, 145.
59. H. Hope and P. P. Power, *J. Am. Chem. Soc.*, 1983, **105**, 5320.
60. D. Thoennes and E. Weiss, *Chem. Ber.*, 1978, **111**, 3157.
61. U. Schumann, J. Kopf, and E. Weiss, *Angew. Chem., Int. Ed. Engl.*, 1985, **24**, 215.
62. F. Leroux and M. Schlosser, *Angew. Chem., Int. Ed. Engl.*, 2002, **41**, 4272.
63. M. Niemeyer and P. P. Power, *Organometallics*, 1997, **16**, 3258.
64. O. Desponds and M. Schlosser, *J. Organomet. Chem.*, 1991, **409**, 93.
65. N. J. Rvan. E. Hommes, M. Buhl, Pvon. R. Schleyer, and Y. D. Wu, *J. Organomet. Chem.*, 1991, **409**, 307.
66. W. R. Winchester, W. Bauer, and Pvon. R. Schleyer, *J. Chem. Soc., Chem. Commun.*, 1987, 177.
67. R. T. McDonald and S. Bywater, *Organometallics*, 1986, **5**, 1529.
68. G. Fraenkel and F. Qiu, *J. Am. Chem. Soc.*, 1997, **119**, 3571.
69. G. Fraenkel, A. Chow, and W. R. Winchester, *J. Am. Chem. Soc.*, 1990, **112**, 1382.
70. G. Fraenkel, A. Chow, and W. R. Winchester, *J. Am. Chem. Soc.*, 1990, **112**, 2582.
71. G. Fraenkel and W. R. Winchester, *Organometallics*, 1990, **9**, 1314.
72. G. Fraenkel and W. R. Winchester, *J. Am. Chem. Soc.*, 1989, **111**, 3794.
73. F. Feil and S. Harder, *Organometallics*, 2000, **19**, 5010.
74. H. Ahlbrecht, J. Harbach, T. Hauck, and H. O. Kalinowski, *Chem. Ber.*, 1992, **125**, 1753.
75. G. Fraenkel, J. H. Duncan, K. Martin, and J. Wang, *J. Am. Chem. Soc.*, 1999, **121**, 10538.

76. S. Schade and G. Boche, *J. Organomet. Chem.*, 1998, **550**, 381.
77. M. J. Kaufmann, S. Gronert, and A. Streitwieser Jr, *J. Am. Chem. Soc.*, 1988, **110**, 2829.
78. S. Gronert and A. Streitwieser Jr, *J. Am Chem. Soc.*, 1988, **110**, 2836.
79. S. Gronert and A. Streitwiese Jr, *J. Am Chem. Soc.*, 1988, **110**, 2843.
80. C. Üffing, R. Köppe, and H. Schnöckel, *Organometallics*, 1998, **17**, 3512.
81. S. Neander, U. Behrens, and F. Olbrich, *J. Organomet. Chem.*, 2000, **604**, 59.
82. F. Rebiere, O. Samuel, and H. B. Kagan, *Tetrahedron Lett.*, 1990, **31**, 3121.
83. M. A. Edelman, P. B. Hitchcock, M. F. Lappert, D. S. Liu, and S. Tian, *J. Organomet. Chem.*, 1998, **550**, 397.
84. M. J. Harvey, T. P. Hanusa, and M. Pink, *J. Chem. Soc., Dalton Trans.*, 2001, 1128.
85. S. Neander, J. Körnich, and F. Olbrich, *J. Organomet. Chem.*, 2002, **656**, 89.
86. N. L. Holy, *Chem. Rev.*, 1974, **74**, 243.
87. M. Szwarc, *Acc. Chem. Res.*, 1972, **5**, 169.
88. G. R. Stevenson, M. K. Ballard, and R. C. Reiter, *J. Org. Chem.*, 1991, **56**, 4070.
89. A. Sekiguchi, K. Ebata, C. Kabuto, and H. Sakurai, *J. Am. Chem. Soc.*, 1991, **113**, 1464.
90. A. Sekiguchi, K. Ebata, C. Kabuto, and H. Sakurai, *J. Am. Chem. Soc.*, 1991, **113**, 7081.
91. J. L. Wardell, in ‘Comprehensive Organometallic Chemistry’, eds. G. Wilkinson, F. G. A. Stone, and E. W. Abel, Pergamon Press, Oxford, 1982, Vol. 1, Chap. 2, p. 43.
92. E. Bartmann, *Angew. Chem., Int. Ed. Engl.*, 1986, **25**, 653.
93. J. Barluenga, J. Florez, and M. Yus, *J. Chem. Soc., Perkin Trans. 1*, 1983, 3019.
94. G. D. Stucky, *Adv. Chem. Ser.*, 1974, **130**, 56.
95. N. Hu, L. Gong, Z. Jin, and W. Chen, *J. Organomet. Chem.*, 1988, **352**, 61.

Alkaline Earth Metals: Inorganic Chemistry

William S. Rees, Jr
Georgia Institute of Technology, Atlanta, GA, USA

1 Introduction 1
2 The Elements 2
3 Nuclear Magnetic Resonance 3
4 Biological Roles 4
5 Compounds of Group 2 Elements with Hydrogen 6
6 Compounds of Group 2 Elements with Group 14 Elements 7
7 Compounds of Group 2 Elements with Nitrogen 7
8 Hydroxides, Carbonates, Bicarbonates, Oxides, and Peroxides of Group 2 Elements 8
9 Compounds of Group 2 Elements with Group 17 Elements 10
10 Compounds of Group 2 Elements with Complex Ligands 12
11 Additional Group 2 Element Compounds 17
12 Electronic Materials Containing Group 2 Elements 18
13 Group 2 Element Alkoxides 18
14 Related Articles 19
15 References 20

Abbreviations

:LB = Lewis base; bht = 2,6-di(*t*-butyl)-4-methylphenoxide; bo = 1-metalla-2,6-dioxo-3-aza-4,5-diphenylcyclohex-3-ene; CBD = Chronic beryllium disease; dbp = 2,6-di(*t*-butyl)phenoxide; dfhd = 1,1,1,2,2,3,3,7,7,7-decafluoroheptane-4,6-dionato; dmmhd = 2,6-dimethyl-2-methoxyheptane-3,5-dionato; dmmod = 2,2-dimethyl-8-methoxyoctane-3,5-dionato; fod = 1,1,1,2,2,3,3-heptafluoro-7,7-dimethyloctane-4,6-dionato; Hbht = 2,6-di(*t*-butyl)-4-methylphenol; Hbo = Benzoin α-oxime; Hdbp = 2,6-di(*t*-butyl)phenol; Hdfhd = 1,1,1,2,2,3,3,7,7,7-decafluoroheptane-4,6-dione; Hdmmhd = 2,6-dimethyl-2-methoxyheptane-3,5-dione; Hdmmod = 2,6-dimethyl-8-methoxyoctane-3,5-dione; Hfod = 1,1,1,2,2,3,3-heptafluoro-7,7-dimethyloctane-4,6-dione; Hhfac = 1,1,1,5,5,5-hexafluoropentane-2,4-dione; Hhipa = 2-hydroxyiminopropionic acid; hipa = 2-hydroxyiminopropionate; Htdfnd = 1,1,1,2,2,3,3,7,7,8,8,9,9,9-tetradecafluorononane-4,6-dione; Htfac = 1,1,1-trifluoropentane-2,4-dione; Htmhd = 2,2,6,6-tetramethylheptane-3,5-dione; Htmmhd = 2,6,6-trimethyl-2-methoxyheptane-3,5-dione; J_c = Critical current density of a superconducting material; n.b. = Nonbonding; n^0 = Neutron; RE = Rare earth element; SMO = Superconducting metal oxide; T_c = Temperature of zero electrical resistance; tdfnd = 1,1,1,2,2,3,3,7,7,8,8,9,9,9-tetradecafluorononane-4,6-dionato; tfac = 1,1,1-trifluoropentane-2,4-dionato; tmhd = 2,2,6,6-tetramethylheptane-3,5-dionato; tmmhd = 2,6,6-trimethyl-2-methoxyheptane-3,5-dionato.

Glossary

Curie: that amount of radioactivity which has the identical disintegration rate as 1 g of ^{226}Ra, specifically 3.70×10^{10} s^{-1}
Quasiaromatic: compound with resonance stability incurred by coordination of a metal cation with the bidentate ligand derived from deprotonation of a β-diketone

1 INTRODUCTION

An alkaline earth is an oxide of an element in group 2 of the periodic table. In their pure forms, these elements collectively are referred to as the alkaline earth metals. These metals, like their neighbors the alkali metals (group 1 elements, *see* ***Alkali Metals: Inorganic Chemistry***), are strong reducing agents and are, therefore, not observed uncompounded in Nature. The group 2 elements readily give up their two valence electrons, present in an s atomic orbital subshell, and thus portray a chemistry dominated by dications.

In previous arrangements of the *Periodic Table* (*see* ***Periodic Table: Trends in the Properties of the Elements***), the elements beryllium, magnesium, calcium, strontium, barium, and radium were referred to as members of Group IIa, or 2A. As inclusion of the word ‘metal’ in their title implies, these elements are both malleable and extrudable; however, they are rather brittle. They are electrical conductors. When pure, all except the lightest, beryllium, react with atmospheric O_2 and/or H_2O to form a protective coating of metal oxide, which acts as a surface barrier to inhibit bulk oxidation. In the specific case of calcium, this coating is primarily composed of the nitride.

The inorganic chemistry of the group 2 elements can be categorized succinctly into a rather limited focus. The overwhelming preponderance of the +2 oxidation state rules the chemistry of these elements. This ubiquitous observation, coupled with the severely limited energetic accessibility of other oxidation states, has dictated the development of the area. These elements are comparable in much of their chemistry, diverging most in aspects dependent on atomic size rather than electronic charge. It is in this regard that the greatest diversity is displayed in these congeners. The span encompasses a quite broad range (Be, 111 pm; Ra, 223 pm) and thereby influences some of the observed trends. This effect emerges most noticeably in the realm of coordination chemistry.

All six elements are found in Nature. Radium has no stable isotopes (*see Isotopes & Isotope Labeling*); however, ^{226}Ra has a half-life of 1600 years. Its decay mode is by α (4.780 MeV) and γ emission. As a consequence of this radioactive nature (*see Radioactive Decay*), its chemistry remains relatively unexplored. In several arenas, rather comprehensive studies have examined various properties of all of the lighter group 2 elements. Efforts have been made to extend all given comparisons to radium; however, in some instances this has proven rather difficult.

One significant deviation from the influence of ionic chemistry for the group 2 elements is beryllium. Although the chemistry of this lightest element of the group exhibits indications of the presence of some covalent bonding (*see Covalent Bonds*), it does not overwhelm the dominating trend toward ionic behavior. There are several well-understood reasons for the uniqueness of beryllium. Its comparatively large charge/size ratio, relatively high *Electronegativity* and low z nature combine to produce this observed effect. The first of these items may be adequately explained by proper application of *Fajans' Rules*. The second of these is manifested by the comparatively small resultant electronegativity difference between Be and other atoms entering into a bonding arrangement, thus inhibiting bond polarity and promoting covalency. The final factor is a controlling variable of the number of atomic orbitals potentially available to accommodate bonding electrons (*see* ***Electronic Structure of Main-group Compounds***). One consequence of its location early in the periodic table is the limitation on this number of orbitals to four (one s and three p), and the concomitant delegation to be, in the primary examples, four coordinate. Such restraints are removed for the other group 2 elements and, as we shall discover below, coordination numbers (*see* ***Coordination Numbers & Geometries***) of 6, 8, 10, and, in certain instances, even 12, commonly are observed for these elements.

2 THE ELEMENTS

The date, location, and credited scientist of discovery, comparable information for initial pure isolation, and historical derivation of the name of each of the group 2 elements are summarized in Table 1. The principal ore found in Nature, the industrial preparation and purification, and the principal contemporary uses are outlined in Table 2. Several important properties of each element are listed in Table 3. These properties can be broken down into the categories of general information (name, symbol,

Table 1 Historical information

Element	Discovery Year	Discoverers	1st pure isolation	Isolators	Named after
Beryllium	1797	Vauquelin (Paris)	1828	Wöhler (Berlin) Bussy (Paris)	Beryllos (Greek: beryl)
Magnesium	1755	Black (Edinburgh)	1808	Davy (London)	Magnesia (Greek: Thessaly district)
Calcium	1808	Davy (London)	1808	Davy (London)	Calx (Latin: lime)
Strontium	1790	Crawford (Edinburgh)	1808	Davy (London)	Strontian, Scotland
Barium	1774	Scheele	1808	Davy (London)	Barys (Greek: heavy)
Radium	1898	Curie (Paris)	1910	Curie (Paris)	Radius (Latin: ray)

Table 2 Industrial information

Element	Principle ore	Industrial preparation/purification	Principal uses
Beryllium	Beryl ($Be_3Al_2Si_6O_{18}$)	Electrolysis of fused $BeCl_2$ or reduction of BeF_2 with magnesium	Alloy with copper Highly X-ray permeable Nuclear reflector/moderator
Magnesium	Dolomite ($[Mg,Ca]CO_3$)	Electrolysis of fused $MgCl_2$ (obtained from brines)	Lightweight structures (alloys) Sacrificial electrodes Flares, pyrotechnics, incendiary bombs
Calcium	Limestone ($CaCO_3$)	Electrolysis of fused $CaCl_2/CaF_2$	Reductant in preparation of Zr, Th, U, RE Plaster (as CaO)
Strontium	Celestite ($SrSO_4$)	Reduction of SrO with Al or electrolysis of $SrCl_2/KCl$	Fireworks (red) Glass manufacturing
Barium	Baryte ($BaSO_4$)	Reduction of BaO with Al or electrolysis of $BaCl_2$	Petroleum drilling fluids (as $BaSO_4$) Pesticide (as $BaCO_3$)
Radium	Uraniums	Separation	Luminous paint Cancer therapy } (both decreasing)

Table 3 Properties of the elements

	Beryllium	Magnesium	Calcium	Strontium	Barium	Radium
Symbol	Be	Mg	Ca	Sr	Ba	Ra
Atomic number	4	12	20	38	56	88
Relative atomic mass	9.012182	24.3050	40.078	87.62	137.327	226.0254
Abundance	5×10^{-4}	1.94	3.39	0.01	0.03	10^{-10}
Number of isotopes	1	3	6	4	7	13
Density ($g\,cm^{-3}$, 20 °C)	1.85	1.74	1.54	2.54	3.59	5.50
Melting point (°C)	1278	648.8	839	769	725	700
Boiling point (°C)	2970	1090	1484	1384	1637	1140
Atomic radius (pm)	111.3	159.9	197.4	215.1	217.4	223
Covalent radius (pm)	89	136	174	191	198	–
Electronegativity (Pauling)	1.57	1.31	1.00	0.95	0.89	0.89
1st ionization potential ($kJ\,mol^{-1}$)	900	738	590	549	503	509
2nd ionization potential ($kJ\,mol^{-1}$)	1757	1450	1145	1064	965	975
3rd ionization potential ($kJ\,mol^{-1}$)	14 848	7733	4910	4210	3600	3300
Electron affinity ($kJ\,mol^{-1}$)	−18	−21	−186	−146	−46	–
ΔH_{vap} ($kJ\,mol^{-1}$)	309	128	151	154	151	137
ΔH_f° (gas, $kJ\,mol^{-1}$)	324	148	178	164	180	159
Electrical resistivity ($10^{-8}\,\Omega\,m$)	4.0	4.45	3.43	23.0	50	100
E° ($M^{2+} \rightarrow M^0$; eV)	−1.85	−2.37	−2.87	−2.89	−2.91	−2.92
Thermal conductivity ($W\,m^{-1}\,K^{-1}$ @ 300 K)	200	156	200	35.3	18.4	∼19
Mass magnetic susceptibility ($m^3\,kg^{-1} \times 10^{-9}$)	−13	+6.8	+14	+13	+1.9	–
Coefficient of linear thermal expansion ($K^{-1} \times 10^{-6}$)	11.5	26.1	22	23	19	20.2
Thermal n^0 cross section (barn)	0.0092	0.063	0.43	1.2	1.3	20

atomic number, and relative atomic mass), chemical (radii, electronegativity, and reduction potential), physical (melting point, boiling point, density, ΔH_{vap}, $\Delta H^0{}_{f(gas)}$, electrical resistivity, thermal conductivity, mass magnetic susceptibility, and coefficient of linear thermal expansion), nuclear (number of isotopes, thermal n^0 cross section, and NMR (see below)), environmental (abundance), and electronic (first, second, and third *Ionization Potential*, and *Electron Affinity*). Several excellent compilations of more exhaustive data have been assembled.**[1–12]**

2.1 Radium

The known inorganic chemistry of radium does not differ significantly from that of barium.**[13]** The isotopes of radium are compiled in Table 4. The chloride, bromide, and nitrate salts of Ra are all water soluble. For example, $RaCl_2$ (24.5 g/100 mL H_2O at 25 °C) has a comparable solubility to $BaCl_2$ (30.7 g). This slight difference is the primary mode of separation of Ra from Ba. Barium sulfate frequently plays the role of a carrier for Ra. The solubility of $RaSO_4$ (2.1×10^{-4} g/100 mL H_2O at 25 °C) is perhaps the lowest of any of the group 2 elements. Other aqueous insoluble salts of Ra include $CO_3{}^{2-}$ and $CrO_4{}^{2-}$.

Owing to the difficulty in separating Ba and Ra cleanly, Hahn erroneously attributed Ra radioactivity to Ba and thereby passed over the discovery of nuclear fission (*see Binding Energy of Nuclei*). His sample of $BaSO_4$ was not the pure Ba compound, and the unknown Ra contaminant led to his observation and incorrect conclusion.

Table 4 Isotopes of radium

Mass	Mode of decay	Half-life	Source
213	α	2.7 min	Th + p; Pb + C^{6+}
219	α	$\sim 10^{-3}$ s	Daughter Th^{223}
220	α	∼0.03 s	Daughter Th^{224}
221	α	30 s	Daughter Th^{225}
222	α	38 s	Daughter Th^{226}
223 (AcX)	α	11.435 day	Natural; descendant U^{235}
224 (ThX)	α	3.64 day	Natural; descendant Th^{232}
225	β^-	14.8 day	Daughter Th^{229}
226	α	1622 year	Natural; descendant U^{238}
227	β^-	41.2 min	$Ra^{226}(n, \gamma)$
228 ($MsTh_1$)	β^-	6.7 year	Natural; descendant Th^{232}
229	β^-	∼1 min	Daughter Th^{233}
230	β^-	1 h	Th + d

3 NUCLEAR MAGNETIC RESONANCE

The gaining of widespread acceptance for the great utility of magnetic resonance imaging in the medical community has served to bring the field of NMR out of the research laboratory and into contact with the everyday lives of many citizens. Although the most widely exploited nuclei remain ^1H, ^{13}C, and ^{31}P, the inorganic chemist has available a much wider variety of potential choices. Each of the group 2 elements, except Ra, has an isotope that possesses the requisite properties for NMR observation. These are presented in Table 5, together with

Table 5 Nuclear magnetic resonance

Nuclide	^{9}Be	^{25}Mg	^{43}Ca	^{87}Sr	^{137}Ba	^{13}C
Abundance (%)	100	10.00	0.135	7.00	11.23	1.10
Nuclear spin	3/2	5/2	7/2	9/2	3/2	1/2
Frequency	14.053	6.1195	6.728	4.333	11.113	25.144
Sensitivity ($\times 10^{-3}$)	13.9	2.67	6.40	2.69	0.776	15.9
Receptivity	78.8	1.54	0.0527	1.07	4.41	1.00
Quadrupole moment ($\times 10^{-28}$)	0.052	0.22	0.05	0.36	0.28	0

comparative data for ^{13}C. This will allow the reader to place these rather esoteric nuclei in their proper perspective with respect to a commonly employed organic analytical technique. It is noteworthy that all of the group 2 elements except for ^{43}Ca have a higher receptivity than ^{13}C, several of them significantly (^{137}Ba $> 4\times$) and one of them overwhelmingly (^{9}Be $> 78\times$) larger than the corresponding relative assignment of $^{13}\mathrm{C} \equiv 1.00$. In all probability, the development of techniques based on these nuclei have been hampered, to date, by the high odd-halves ($>1/2$) spin associated with all of the nuclides of interest. This impedance may be diminished, however, by the recent elegant work employing a double rotating solid-state probe for NMR that reduces the quadrupole moment contribution to line-broadening.[14] The applicability of this technique to mineralogy, geology, and catalyst identification should be widespread.

4 BIOLOGICAL ROLES

In a comparable manner to the discrimination found for the group 1 elements ([Na^{+}] is higher outside cells and [K^{+}] is higher inside cells) the observation is that [Mg^{2+}] is higher inside animal cells and [Ca^{2+}] is higher in the body fluids outside the cells.[15] Complexes between ATP and Mg^{2+} are one component of phosphohydrolase and phosphotransferase enzymes (*see Enzyme*) involved in the release of energy from ATP. In animals, the utilization of Mg^{2+} plays a major role in nerve fiber impulse transmission. In animal teeth (enamel (fluoroapatite, $[3\{Ca_3(PO_4)_2\}\cdot CaF_2]$)) and bones (apatite, $Ca_3(PO_4)_2$), the key contribution of Ca^{2+} to the structural formation of biological systems is manifested. Additionally, Ca^{2+} plays a role in the clotting of blood and the mechanism of muscle contraction that maintains a consistent heart rhythm (*see* ***Calcium-binding Proteins***).[16] The composition of green plant *Chlorophyll* is centered around Mg^{2+}. This nitrogen-based macrocyclic ligand-containing molecule is a derivative of the tetrapyrrole porphine, a highly conjugated heterocyclic tetradentate alkaloid. During plant photosynthesis, it is this ligand that participates in one-electron redox reactions, not the metal. The apparent function of the Mg^{2+} is predominantly structural in origin. The two-dimensional rigidity imparted to the ring system reduces thermal vibration energy loss, and thus increases the percent conversion. Additionally, the role of a five-coordinate species formed by the inclusion of hydrogen bonds from water is integral in the stacking of units into the three-dimensional antenna arrays required for absorption of light (680–700 nm).[17] Although, in principle, any nonredox-active metal of the proper ionic radius could fulfill this role, in Nature only Mg^{2+} has been observed to perform this seminal contribution to the biological systems.

The total mass per element in a human of average mass (70 kg), the oral toxic intake, and the daily dietary intake for the group 2 elements are summarized in Table 6. These numbers reflect the total concentrations of the elements in all forms; however, it is primarily as the divalent *Cation* that they are found. In this capacity, they also serve an essential function by their contribution to specific ionic equilibria in living cells. Both calcium and magnesium have been classified as essential bulk elements, falling into the subcategory of macrominerals. Although one report claims that omission of either strontium or barium from the diet of rats and guinea pigs resulted in depressed growth and reduced calcification of bones and teeth, this hint at the essential role of the heavier group 2 elements has neither been confirmed nor rejected in the past four decades.[15] It is relatively well understood that both Sr and Ba show some stimulatory action, are relatively nontoxic (see Table 6 for Ba), and will mimic (spare) Ca in most biological systems. To date, no essential or stimulatory function has been found for Be.[18] The obvious toxicity due to the radioactive nature of Ra is discussed elsewhere.

4.1 Beryllium Biochemistry

There has been much confusion about the toxicity of Be.[19] Numerous reports are based on incomplete research and, in a limited number of instances, have been misquoted at great length in the subsequent scientific literature. For example,

Table 6 Biological concentrations for group 2 elements

	Be	Mg	Ca	Sr	Ba	Ra
Mass in human	0.036 mg	19 g	1.00 kg	320 mg	22 mg	31×10^{-9} mg
Oral toxic intake	Close to zero	Nontoxic	Nontoxic	Nontoxic	200 mg	na
Daily dietary intake (mg)	0.01	250–380	600–1400	0.8–5	0.60–1.7	2×10^{-9}

one authoritative work states ‘It should be noted that not more than 500 g Be total, in *any chemical form*, should be kept in a laboratory; otherwise, in the event of fire, beryllium compounds could be vaporized or blown about to such an extent as to constitute a hazard to the surrounding area’.[7] Yet, in 1948, after a major fire and explosion in a Lorain, Ohio, beryllium manufacturing facility, which included the ignition of some 2.5 tons of Mg in the BeO processing factory, no firefighters, police, naval reserve personnel (activated for crowd control), or spectators reported any evidence of the symptoms of beryllium diseases.[19]

With the data available at this point, it does not appear that ingestion of beryllium compounds presents a significant health hazard. Likewise, there is no evidence to indicate that simple skin contact with elemental beryllium or its compounds will result in dermatoses. The unequivocal establishment of an immunological basis for Chronic beryllium disease (CBD) located this disorder to be a pulmonary granulomatous process. CBD is a localized response to an insoluble and persistent irritant. Acute pulmonary beryllium disease is caused by airborne particulates of soluble beryllium salts, primarily $BeSO_4$ or BeF_2. This disease is generally limited to the upper respiratory tract. Although there were 30–60 new cases per year during the period 1942–1947, there have been less than 10 total confirmed cases within the past 40 years. In almost each instance, it was a single isolated case resulting from accidental exposure during maintenance work at a manufacturing facility. Thus, although perhaps not as benign as its heavier congeners Mg and Ca, the relative risk posed by Be is rather small. When compared with other inorganic compounds, such as AsH_3, the exposure limits of 25 µg m^{-3} per 30 min place this threat in perspective.

Table 7 Ionic radius (pm)

Coordination number	Element[a] Be	Mg	Ca	Sr	Ba	Ra
4	27	57				
6	45	72	100	118	135	
8			112	126	142	148
12						170

[a] All ions have 2+ charge and [group 18] electron shell configuration.

4.2 Coordination Chemistry

The ionic radii (Table 7) of the group 2 elements follow the predicted trends.[6] The coordination numbers of the elements differ, as expected, from 4 (for Be) to 12 (for Ba) (*see* ***Coordination & Organometallic Chemistry: Principles***).[3] On the whole, all observed geometries are standard (*see* ***Coordination Numbers & Geometries***). The absolute solubilities of typical salts have been summarized (Table 8).[7] The gas-phase bond dissociation energies trail the pattern forecast by examination of electronegativity and orbital overlap differences (Table 9).[8] A wide array of typical reactions could be found for the group 2 elements; a minor sampling of this diverse chemistry is presented here (Table 10).[12]

Table 9 Strengths of bonds in diatomic molecules of the alkaline earth metals with halogens (kcal mol^{-1})

	Be	Mg	Ca	Sr	Ba
F	151	123	132	132	138
Cl	110	97	103	112	114
Br	89	81	96	97	102
I	69	63	78	80	86

Table 8 The solubilities of the salts of the alkaline earth metals in water at 25 °C and 100 °C (g/100 g solution)[a]

	Mg		Ca		Sr		Ba		Ra	
Fluoride ($\times 10^{-3}$)	0.013	–	1.8	–	12	–	160	–		
Chloride	35.5	42.3	45.3	61.4	36	50	27.1	37.0	19.6 (20 °C)	–
Bromide	50	56	61	75	52	69	50	58		
Iodide	59	65	68	81	64	79	69	73		
Hydroxide	1×10^{-3}	0.4×10^{-3}	0.12	0.05	2.2	48	4.5	>50		
Carbonate ($\times 10^{-3}$)	1	–	1	4	1	–	1.8	–		
Acetate	40	–	26	23	40	36	43	43		
Oxalate ($\times 10^{-3}$)	30	40	0.6	14	5	–	11	21		
Nitrate	42	>52	58	78	80	>100	9	26	12 (20 °C)	–
Sulfate	27	43	0.21	0.16	13×10^{-3}	11×10^{-3}	0.22×10^{-3}	0.39×10^{-3}	0.21×10^{-3}	–
Chlorate	59	>73	66	79	64	67	27.5	51.2		
Perchlorate	100	–	65	–	66	–	75	85		
Bromate	50	72	–	–	27	41	0.79	5.4		
Iodate	8.5	>14	0.31	0.67	0.17	0.35	0.04	0.2	0.04	

[a] In each column the first figure is the solubility for 25 °C and the second for 100 °C, unless otherwise indicated.

Table 10 Some typical reactions of group 2 elements

Reaction	Comment
$M + 2H_2O \rightarrow M(OH)_2 + H_2$	Be probably reacts with steam; Mg with hot water, and Ca, Sr, and Ba react rapidly with cold water
$M + 2HX \rightarrow MX_2 + H_2$	All the metals react with acids, liberating hydrogen
$Be + NaOH \rightarrow Na_2[Be(OH)_4] + H_2$	Be is amphoteric
$2M + O_2 \rightarrow 2MO$	Normal oxide formed by all group members with excess oxygen
$Ba + O_2 \rightarrow BaO_2$	Ba also forms the peroxide
$M + H_2 \rightarrow MH_2$	Ionic 'saltlike' hydrides formed at high temperatures by Ca, Sr, and Ba
$3M + N_2 \rightarrow M_3N_2$	All the metals form nitrides at high temperatures
$3M + 2P \rightarrow M_3P_2$	All the metals form phosphides at high temperatures
$M + S \rightarrow MS$	All the metals form sulfides
$M + Se \rightarrow MSe$	All the metals form selenides
$M + Te \rightarrow MTe$	All the metals form tellurides
$M + F_2 \rightarrow MF_2$	All the metals form fluorides
$M + Cl_2 \rightarrow MCl_2$	All the metals form chlorides
$M + Br_2 \rightarrow MBr_2$	All the metals form bromides
$M + I_2 \rightarrow MI_2$	All the metals form iodides
$M + 2NH_3 \rightarrow M(NH_2)_2 + H_2$	All the metals form amides at high temperatures

5 COMPOUNDS OF GROUP 2 ELEMENTS WITH HYDROGEN

The group 2 elements Mg, Ca, Sr, and Ba all react with $H_2(g)$ to form *Hydrides* of the formula MH_2 (e.g. equation 1). The dihydride of beryllium is difficult to prepare and less thermodynamically stable than the dihydrides of the heavier group 2 congeners. Impure BeH_2 (contaminated with various amounts of diethyl ether) was made historically by reducing $BeCl_2$ with lithium aluminum hydride ($LiAlH_4$) (equation 2). Pure samples can be obtained by reducing $BeCl_2$ with lithium borohydride ($LiBH_4$) to give BeB_2H_8 (equation 3), then heating BeB_2H_8 in a sealed tube with triphenylphosphine (PPh_3) (equation 4). Alternatively, it may be prepared by a thermal *β-Hydride Elimination* of isobutene from bis(*t*-Bu)beryllium at temperatures of ~100 °C (equation 5).**[20]** Additionally, convenient methods for the preparation of MgH_2 are reduction of Mg(anthracene) (equation 6) and exchange between alkyl magnesium compounds and phenylsilyl hydrides (equation 7).**[21]**

$$Ca(s) + H_2(g) \longrightarrow CaH_2(s) \qquad (1)$$

$$2BeCl_2 + LiAlH_4 \longrightarrow 2BeH_2 + LiCl + AlCl_3 \qquad (2)$$

$$BeCl_2 + 2LiBH_4 \longrightarrow BeB_2H_8 + 2LiCl \qquad (3)$$

$$BeB_2H_8 + 2PPh_3 \xrightarrow{\Delta} BeH_2 + 2Ph_3P{\cdot}BH_3 \qquad (4)$$

$$Be(t\text{-}Bu)_2 \xrightarrow{100\,^{\circ}C} BeH_2 + 2H_2C{=}CMe_2 \qquad (5)$$

$$Mg(anthracene) \xrightarrow{H_2} MgH_2 \qquad (6)$$

$$MgBu_2 + 2Ph_3SiH \longrightarrow MgH_2 + 2Ph_3SiBu \qquad (7)$$

All the metal hydrides are reducing agents and readily are decomposed by water, dilute acids, alcohols, thiols, primary and secondary amines, and other protic compounds, with the evolution of H_2 (equation 8). This specific property has led to wide employment of the compounds as agents for removal of water and other protic impurities from large volumes of organic liquids as one predistillation purification technique.

$$CaH_2 + 2H_2O \longrightarrow Ca(OH)_2 + 2H_2(g) \qquad (8)$$

The heavier group 2 dihydrides (CaH_2, SrH_2, and BaH_2) are ionic (*see Ionic Bonds*, *Ionic Character*), containing the hydride ion (H^-). Beryllium and magnesium dihydrides are covalent and polymeric (*see Polymer*). $(BeH_2)_n$ presents an interesting structural challenge. In the gas phase, it seems probable that several species may be present, comprising polymeric chains and rings. The solid state is polymeric, and the single-crystal X-ray diffraction structure indicates that it consists of chains of beryllium atoms containing hydrogen bridges between them (Figure 1).

Each Be atom is connected to four H atoms, and each H atom is connected to two Be atoms. Since Be has two valence electrons, and H only one, obviously there are insufficient electrons to fulfill the traditional organic two-center, two-electron bonding description. Alternatively, three-center interactions persist, whereby 'banana-shaped' molecular orbitals (a three-center, two-electron bond, *see Three-center Bond*) connect the Be–H–Be atoms, each containing two electrons (see Figure 2 for the molecular orbital scheme (*see Molecular Orbitals*) for this type of *Delocalized*

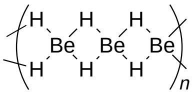

Figure 1 Polymeric structure of BeH_2, containing three-center, two-electron Be–H–Be bridging bonds

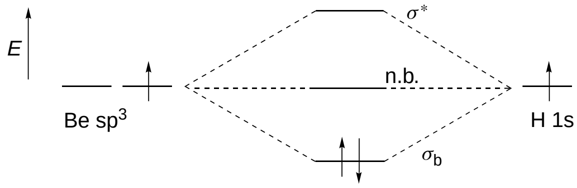

Figure 2 Molecular orbital description of a three-center, two-electron bonding arrangement

Bonding arrangement). This is a primitive example of a *Cluster* compound, where the monomeric molecule BeH_2 (formed with normal bonds) would result in only four electrons in the outer shell of the beryllium atoms.[9] This situation is termed 'electron deficient' (*see Electron Deficient Compound*) and, by entering into a cluster arrangement, each atom shares its electrons with several neighbors and receives a share in their electrons. Clustering is important in the bonding descriptions of metals and the boron hydrides and in the halides of the second and third row transition elements. Typically, when the *Valence Orbitals* are less than one-half full, such clustering interactions may be observed.

6 COMPOUNDS OF GROUP 2 ELEMENTS WITH GROUP 14 ELEMENTS

The broadest representation of this class of compounds is the organomagnesium halides, or *Grignard Reagents*.[22] In detail, the organometallic chemistry of the group 2 elements is covered elsewhere in this Encyclopedia (*see* ***Beryllium & Magnesium: Organometallic Chemistry***). However, there is one important class of *inorganic* compounds formed between the elements of Groups 2 and 14. The carbides of the elements fall within the scope of this section of the work.

Group 2 elements typically form ionic carbides of formula MC_2.[23] When BeO is heated with C at 1900–2000 °C, a brick red colored carbide of formula Be_2C results. This ionic compound adopts the antifluorite structure, that is, like the CaF_2 structure except that the positions of the cations and *Anions* are interchanged. It is unusual because it reacts with water, forming methane, and is thus called a methanide (equation 9).

$$Be_2C\,(s) + 4H_2O\,(l) \longrightarrow 2Be(OH)_2(s) + CH_4(g) \qquad (9)$$

The elements Mg, Ca, Sr, and Ba each form carbides of formula MC_2, either when the metal is heated with carbon in an electric furnace (e.g. equation 10), or when their oxides are heated with carbon (e.g. equation 11). CaC_2 prepared by this manner is a gray colored solid, but is colorless when pure. BeC_2 is made by heating Be with acetylene. On heating, MgC_2 changes into Mg_2C_3. This contains C_3^{4-}, and it reacts with water to form methylacetylene ($CH_3C{\equiv}CH$). The MC_2 carbides all have a distorted sodium chloride type of structure. M^{2+} replaces Na^+ and $C{\equiv}C^{2-}$ replaces Cl^-. The $C_2{}^{2-}$ ions are elongated, not spherical like Cl^-. Thus, the axis along which the $C_2{}^{2-}$ ions lie is lengthened, compared with the other two axes, and this results in a tetragonal distortion. At temperatures above 450 °C, the $C_2{}^{2-}$ ions adopt random positions, rather than being aligned, and the unit cell then becomes cubic instead of tetragonal.

$$Ca + 2C \xrightarrow{1100\,^\circ C} CaC_2 \qquad (10)$$

$$CaO + 3C \xrightarrow{2000\,^\circ C} CaC_2 + CO \qquad (11)$$

Among the carbides of the group 2 elements, calcium carbide is the best known. It reacts with water, liberating acetylene, and thus is called an acetylide (equation 12). At one time, this reaction was the main source of $HC{\equiv}CH$ for oxyacetylene welding. Production of CaC_2 peaked at 7 million tonnes per year in 1960, but declined slightly to 6.2 million tonnes in 1985 because acetylene now is obtained from petrochemical processing.

$$CaC_2(s) + 2H_2O(l) \longrightarrow Ca(OH)_2(s) + C_2H_2(g) \qquad (12)$$

7 COMPOUNDS OF GROUP 2 ELEMENTS WITH NITROGEN

7.1 Liquid Ammonia Solutions of the Elements

The group 2 elements all dissolve in $NH_3(l)$, as do the group 1 elements.[2] Dilute solutions are bright blue in color owing to the spectrum from the solvated electron. These solutions slowly decompose, forming amides and evolving hydrogen; however, the reaction may be accelerated by the presence of transition elements or their compounds (equation 13). Evaporation of the ammonia from solutions of group 1 elements returns the metal, but with group 2 elements, evaporation of the ammonia gives the hexaammoniates of the metals. These slowly decompose to give the bis(amides) (equation 14). Concentrated solutions of the metals in ammonia are bronze colored, owing to the formation of metal clusters.

$$2NH_3 + 2e^- \xrightarrow{[cat]} 2NH_2{}^- + H_2(g) \qquad (13)$$

$$M(NH_3)_6 \longrightarrow M(NH_2)_2 + 4NH_3 + H_2(g) \qquad (14)$$

7.2 Nitrides of the Elements

The group 2 elements all burn in nitrogen and form ionic nitrides of the formula M_3N_2 (e.g. equation 15). Owing to the tremendous stability of the N_2 molecule, a large amount of energy is required to convert one dinitrogen molecule with a triple bond into two N^{3-} (nitride ions). The large amount of energy required comes from the substantial quantity of *Lattice Energy* released upon formation of the crystalline solid. The lattice energy is particularly high as a consequence of the high charges on the ions (M^{2+} and N^{3-}). This prevalence of group 2 elements to form nitrides contrasts with the group 1 elements, where Li_3N is the only nitride reported. The very small size of Li^+, resulting in a high lattice energy, explains this observation. These thermodynamic values may be calculated using a *Born–Haber Cycle*. Be_3N_2 is rather volatile, in accord with the greater tendency of Be to covalency, but the other nitrides are involatile. All the nitrides are crystalline solids that decompose on heating and react with water, liberating ammonia and forming either the metal oxide or hydroxide, (e.g. equation 16).

$$3Ca(s) + N_2(g) \longrightarrow Ca_3N_2(s) \tag{15}$$

$$Ca_3N_2 + 6H_2O \longrightarrow 3Ca(OH)_2 + 2NH_3 \tag{16}$$

7.3 Bis[bis(trimethylsilyl)amides] of the Elements

The primary amides of the group 2 elements, $M(NH_2)_2$, are nonmolecular species.[24] When the NH_2^- ligand is replaced by the bulky bis(trimethylsilyl)amido group, however, molecular complexes are formed. A complete set of structures has been obtained for Be through Ba (Table 11). The barium bis(trimethylsilyl)amides form a progression of compounds that illustrate the important relationship between ligand bulk and metal nuclearity.[25] The base-free compound, $[Ba\{N(SiMe_3)_2\}]_2$, exists as a dimer that can accommodate a single THF ligand at each metal center without gross structural change (i.e. $[Ba\{N(SiMe_3)_2\}_2(THF)]_2$). Addition of a second molecule of neutral THF, however, provides enough steric bulk to ensure that the $Ba\{N(SiMe_3)_2\}_2(THF)_2$ adduct crystallizes as a monomer. Remarkably, isostructural dimers of the form $[M\{N(SiMe_3)_2\}_2]_2$ exist for all the metals Mg to Ba. Even though the metal radii in these compounds vary by more than a factor of two (Table 7), the bis(trimethylsilyl)amido ligands adapt to the range of metal–ligand distances without requiring changes in nuclearity.

8 HYDROXIDES, CARBONATES, BICARBONATES, OXIDES, AND PEROXIDES OF GROUP 2 ELEMENTS

The elementary forms, hydroxides, carbonates, bicarbonates, oxides, and peroxides of the group 2 elements all are highly interrelated (equations 17–24) and hence are discussed together (*see* ***Oxides: Solid-state Chemistry*** and ***Chalcogenides: Solid-state Chemistry***).[12]

$$M + 2H_2O \longrightarrow M(OH)_2 + H_2(g) \tag{17}$$

$$M(OH)_2 + CO_2 \longrightarrow MCO_3 + H_2O \tag{18}$$

$$MCO_3 + H_2O + \text{xs } CO_2 \longrightarrow M(HCO_3)_2 \tag{19}$$

$$MCO_3 \xrightarrow{\Delta} MO + CO_2 \tag{20}$$

$$MO + H_2O \longrightarrow M(OH)_2 \tag{21}$$

$$MO + CO_2 \longrightarrow MCO_3 \tag{22}$$

$$MO + \tfrac{1}{2}O_2 \longrightarrow MO_2 \tag{23}$$

$$MO_2 \xrightarrow{\Delta} MO + \tfrac{1}{2}O_2 \tag{24}$$

Table 11 Structural data for group 2 bis[bis(trimethylsilyl)amides] and their adducts[26]

Compound	Central metal coordination number	Nuclearity	Average M–N distance (Å)	Method[a]
$Be[N(SiMe_3)_2]_2$	2	Monomeric	1.566 (17)	E[27]
$[Mg\{N(SiMe_3)_2\}_2]_2$	3	Dimeric	1.975 (5) t-N 2.151 (6) μ-N	X[28]
$Mg[N(SiMe_3)_2]_2(THF)_2$	4	Monomeric	2.021 (7)	X[29]
$[Ca\{N(SiMe_3)_2\}_2]_2$	3	Dimeric	2.275 (9) t-N 2.47 (1) μ-N	X[30]
$Ca[N(SiMe_3)_2]_2(DME)$	4	Monomeric	2.271 (3)	X[30]
$[Sr\{N(SiMe_3)_2\}_2]_2$	3	Dimeric	2.43 (2) t-N 2.63 (2) μ-N	X[31]
$Sr[N(SiMe_3)_2]_2(DME)_2$	4	Monomeric	2.538 (7)	X[31]
$[Sr\{N(SiMe_3)_2\}_2(dioxane)]_n$	4	1-D polymer	2.449 (7)	X[32]
$[Ba\{N(SiMe_3)_2\}_2]_2$	3	Dimeric	2.576 (3) t-N 2.798 (3), 2.846 (4) μ-N	X[25]
$[Ba\{N(SiMe_3)_2\}_2(THF)]_2$	4	Dimeric	2.602 (9) t-N 2.834 (9), 2.903 (10) μ-N	X[25]
$Ba[N(SiMe_3)_2]_2(THF)_2$	4	Monomeric	2.592 (8)	X[25]

[a] E = gas-phase electron diffraction; X = single-crystal X-ray diffraction; t = terminal; μ = bridging.

$Be(OH)_2$ is amphoteric, but the hydroxides of Mg, Ca, Sr, and Ba are basic. The basicity increases from Mg to Ba, and group 2 elements portray the usual trend that basic properties increase on descending a group. Solutions of $Ca(OH)_2$, called lime water, are used to detect carbon dioxide. When $CO_2(g)$ is bubbled through these solutions, they become opaque (‘milky’), owing to the formation of a suspension of $CaCO_3$. If additional CO_2 is passed through these cloudy solutions, the turbidity dissipates and soluble calcium bicarbonate is formed from the excess CO_2 (equation 25).

$$Ca(OH)_2(aq) + CO_2(g) \longrightarrow CaCO_3(\downarrow) + H_2O(l) \xrightarrow{\text{excess } CO_2} Ca(HCO_3)_2(aq) \quad (25)$$

The bicarbonates of group 2 elements are stable only in solution. An interesting and aesthetically pleasing consequence of this in Nature greets spelunkers (cavers) to sights of ‘cavern columns’. Underground caves, which occur predominately in regions of the planet heavily concentrated with limestone deposits and which are rather somewhat more arid today than in historical times, often have stalactites growing down from the roof, and stalagmites growing up from the floor. Water percolating through the limestone contains some $Ca(HCO_3)_2$ in solution. The soluble bicarbonate slowly decomposes into the insoluble carbonate, thus resulting in the slow growth of the stalactites and stalagmites. The observation of a wide array of colors in these natural structures eminates from trace concentrations of elements of the d-block metals of the periodic table. These transition elements possess electrons that undergo optical transitions between orbitals in the visible region of the electromagnetic spectrum, thereby treating the observer to a ‘wonder of the world’ (Carlsbad Caverns in New Mexico, USA).[33]

The heavier group 2 elements (Ca, Sr, Ba) have oxidation potentials similar to those of the corresponding group 1 metals, and are rather high in the electrochemical series. They react with cold water quite readily, liberating hydrogen and forming metal hydroxides (e.g. equation 26) (Table 10). The reduction potential of beryllium is much less than those for the rest of the group (Table 3). This indicates that beryllium is much less electropositive (less metallic) than the others, and beryllium does not react with water. There is some doubt whether it reacts with steam to form the oxide (BeO), or fails to react at all (Table 10). Magnesium has an intermediate reduction value, and although it does not react with cold water, it decomposes in hot water (equations 27 and 28). Magnesium forms a protective layer of oxide, so, despite its favorable reduction potential, it does not react readily unless the oxide layer is removed by amalgamation with mercury. In the formation of the oxide film, it resembles the group 13 element aluminum.

$$Ca + 2H_2O \longrightarrow Ca(OH)_2 + H_2(g) \quad (26)$$

$$Mg + 2H_2O \longrightarrow Mg(OH)_2 + H_2(g) \quad (27)$$

Table 12 Desirable properties for furnace liners

1. High melting points (>2500 °C)
2. Low vapor pressures
3. High thermal conductivities
4. Low chemical reactivities
5. Low electrical conductivities

$$Mg + H_2O \longrightarrow MgO + H_2(g) \quad (28)$$

All the elements in group 2 burn in $O_2(g)$ to form oxides (MO). Metallic Be is relatively unreactive in the bulk form, and does not combust below 600 °C, but the powder, as a result of the higher surface area, is significantly more reactive and burns brilliantly. The elements also burn in air, forming a mixture of oxide and nitride. Mg burns with dazzling brilliance in air, evolving substantial amounts of heat (equation 29). This is used to start the *Thermite Reaction* between iron oxide and aluminum, and also to provide light in flash photography using light bulbs, not electronics.

$$Mg + \text{air} \longrightarrow MgO + Mg_3N_2 \quad (29)$$

Beryllium oxide usually is prepared by ignition of the metal, but the other metal oxides are predominately obtained by thermal decomposition of the carbonates (MCO_3). Other oxosalts, such as $M(NO_3)_2$ and MSO_4, and also $M(OH)_2$, all decompose to the oxide on heating. The oxosalts are less stable to heat than the corresponding group 1 salts because the metals and their hydroxides are less basic than those of group 2.

Magnesium oxide is not very reactive, especially if it has been ignited at high temperatures, and for this reason it is used as a refractory. BeO also is used as a refractory. They combine a number of properties that make them useful for lining furnaces. These factors are summarized in Table 12. Calcium oxide, SrO, and BaO react exothermically with water, forming hydroxides (e.g. equation 30). Magnesium hydroxide is extremely insoluble in water ($\sim 1 \times 10^{-4}\,g\,L^{-1}$ at 20 °C) but the other hydroxides are soluble and the solubility increases as one progresses down the group: $Ca(OH)_2 \approx 2\,g\,L^{-1}$; $Sr(OH)_2 \approx 8\,g\,L^{-1}$; $Ba(OH)_2 \approx 39\,g\,L^{-1}$. Beryllium hydroxide is soluble in solutions containing an excess of OH^-, and therefore is amphoteric (*see Amphoterism*). Magnesium hydroxide is weakly basic, and is widely used to treat acid indigestion in human stomachs. The other group 2 element hydroxides are strong bases.

$$CaO + H_2O \longrightarrow Ca(OH)_2 \quad (30)$$

Beryllium oxide is covalent and has a zinc blende (wurtzite) structure, but all the others are ionic and have a rock salt structure (Figure 3).[23] Attempts to predict the structures (using the ionic sizes and the radius ratio) only are partly successful.

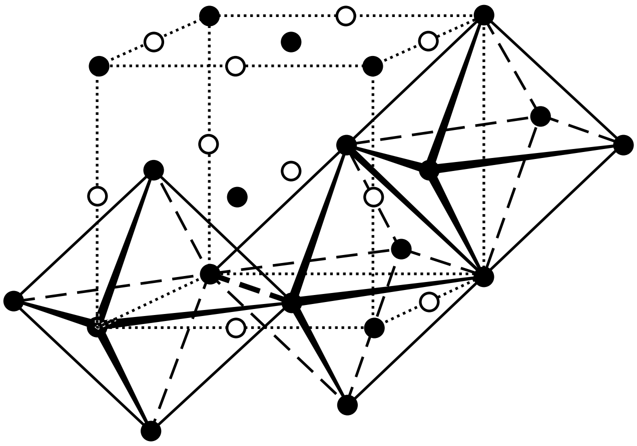

Figure 3 Unit cell of the rock salt structure adopted by MO for the group 2 elements (M $\neq$ Be), depicting edge-sharing of octahedra

The correct structure is predicted for BeO, MgO, and CaO, but for SrO and BaO the predicted coordination number is eight, although the structures found are six coordinate. Crystals adopt the structure that has the most favorable lattice energy, and the failure of the radius ratio concept in this case leads us to examine the assumptions on which it is based. Ionic radii are not known with great accuracy and they change with different coordination numbers (Table 7). Also, ions are not necessarily spherical, or inelastic (*see* ***Structure & Property Maps for Inorganic Solids***).[24]

As the atoms get larger, the ionization energy decreases and the compounds of the elements also become more basic. Beryllium oxide is insoluble in water but dissolves in acids to give salts, and in alkalis to give beryllates, which on standing precipitate as the hydroxide. Therefore, BeO is amphoteric. Magnesium oxide reacts with water, evolving a substantial quantity of heat and forming $Mg(OH)_2$, which is a weak base. Strontium hydroxide and barium hydroxide are stronger bases. The oxides usually are prepared by thermal decomposition of the carbonates, nitrates, or hydroxides. The increase in basic strength is illustrated by the temperatures at which the carbonates decompose (Table 13).[12] The carbonates all are ionic, but $BeCO_3$ is unusual because it contains the hydrated ion $[Be(H_2O)_4]^{2+}$ rather than Be^{2+}.

Calcium carbonate occurs as two different crystalline forms, calcite and aragonite.[23] Both forms occur naturally as minerals (*see Mineralogy*). Calcite is the more stable: each Ca^{2+} is surrounded by six oxygen atoms from $CO_3{}^{2-}$ ions. Aragonite is a metastable form, and its standard enthalpy of formation is about 5 kJ mol^{-1} higher than that of calcite. In principle, aragonite should decompose to calcite, but a high *Activation* energy prevents this from happening. Aragonite can be made in the laboratory by precipitation from a hot solution. Its crystal structure consists of Ca^{2+} ions surrounded by nine oxygen atoms in a display of a rather unusual coordination number.

Table 13 Decomposition temperatures for MCO_3

Compound	$BeCO_3$	$MgCO_3$	$CaCO_3$	$SrCO_3$	$BaCO_3$
Temperature	<100 °C	540 °C	900 °C	1290 °C	1360 °C

Table 14 Large volume uses of lime

1. In steel making: to remove phosphates and silicates as slag
2. By mixing with SiO_2 and alumina or clay to make cement
3. For making glass
4. In the lime-soda process, which is part of the chlor-alkali industry, converting Na_2CO_3 to NaOH or vice versa
5. For 'softening' water
6. To make CaC_2
7. To make slaked lime $[Ca(OH)_2]$ by treatment with water

Calcium oxide (quicklime) is prepared on a large scale (18 million tonnes in 1988) by heating $CaCO_3$ in lime kilns (equation 31).[1] Calcium hydroxide is called slaked lime. Soda lime is a mixture of NaOH and $Ca(OH)_2$ and is made from quicklime (CaO) and aqueous sodium hydroxide. It is much easier to handle than NaOH. Some of the more important, large volume uses of *Lime* are summarized in Table 14. Bleaching powder is made by passing $Cl_2(g)$ into slaked lime, and about 90 000 tonnes a year are produced.[12] Though bleaching powder is often written as $Ca(OCl)_2$, really it is a mixture (equation 32).

$$CaCO_3 \xrightarrow{\Delta} CaO + CO_2 \tag{31}$$

$$3Ca(OH)_2 + 2Cl_2 \longrightarrow Ca(OCl)_2{\cdot}Ca(OH)_2{\cdot}CaCl_2{\cdot}2H_2O \tag{32}$$

Peroxides are formed with increasing ease and increasing stability as the metal ions become larger.[34] Barium peroxide (BaO_2) is formed by passing air over BaO at 500 °C. Strontium peroxide can be formed in a similar way; however, this requires the employment of both high pressure and temperature. Calcium peroxide is not formed in this way, but it can be made as the hydrate by treating $Ca(OH)_2$ with H_2O_2 and then dehydrating the product. Crude MgO_2 has been made using H_2O_2, but no peroxide of beryllium is known. Presumably, this may be attributed to the desire for Be to form covalent bonds. The known peroxides all are white ionic solids that contain the $[O–O]^{2-}$ ion and can be regarded as salts of the very weak acid hydrogen peroxide. Treating peroxides with acid liberates hydrogen peroxide (e.g. equation 33).

$$BaO_2 + 2HCl \longrightarrow BaCl_2 + H_2O_2 \tag{33}$$

9 COMPOUNDS OF GROUP 2 ELEMENTS WITH GROUP 17 ELEMENTS

Dihalides of the group 2 elements, MX_2, can be prepared either by heating the metals with the halogen, or by the action of hydrohalic acid on the metal (*see* ***Halides: Solid-state Chemistry***). The beryllium halides are covalent and hygroscopic and fume in air owing to hydrolysis. They sublime, and do not conduct electricity (Table 9). Anhydrous beryllium halides cannot be obtained from materials made in aqueous solutions because the hydrated ion $[Be(H_2O)_4]^{2+}$ is formed, for example, $[Be(H_2O)_4]Cl_2$ or $[Be(H_2O)_4]F_2$. Attempts to dehydrate these hydrates result in hydrolysis (equation 34).

$$[Be(H_2O)_4]Cl_2 \xrightarrow{\Delta} Be(OH)_2 + 2HCl + 2H_2O \quad (34)$$

The anhydrous halides are prepared best by the reactions shown in equations (35–37) (Table 10). Reaction with CCl_4 is a standard method for making anhydrous chlorides, which cannot be obtained by dehydrating hydrates (equation 37). The anhydrous halides are polymeric in the solid state (Figure 4). Beryllium chloride vapor contains $BeCl_2$ and $(BeCl_2)_2$; however, the solid is a catenated chain. Although, on initial examination, the $(BeCl_2)_n$ polymer structurally is similar to that observed for $(BeH_2)_n$, the bonding is different. Both portray clustering, but the hydride demonstrates three-center, two-electron bonding, whereas the halides exhibit halogen bridges, whereby a halogen atom is σ-bonded to one beryllium atom (classical two-center, two-electron covalent interaction) and uses a lone pair of electrons to form a coordinate bond to another beryllium atom. Thus, the contrast is one of a three-center, two-electron bonding arrangement with a three-center, four-electron configuration (Figure 5).[9]

$$BeO + NH_4F \longrightarrow (NH_4)_2[BeF_4] \xrightarrow{\Delta} BeF_2 + 2NH_4F \quad (35)$$

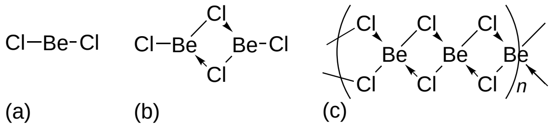

Figure 4 $BeCl_2$ structures: (a) monomer, (b) dimer, and (c) polymer. Solid lines represent covalent bonds and arrowed lines represent coordinate (Lewis base → Lewis acid) bonds. Note that the depicted structure is in resonance with other formal electron placement schemes. Thus, on average, all Be–Cl interactions appear equivalent

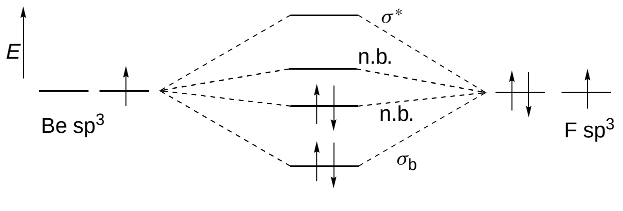

Figure 5 Molecular orbital description of a three-center, four-electron bonding arrangement

$$BeO + C + Cl_2 \xrightarrow{700\,^\circ C} BeCl_2 + CO \quad (36)$$

$$2BeO + CCl_4 \xrightarrow{800\,^\circ C} 2BeCl_2 + CO_2 \quad (37)$$

Beryllium fluoride is quite soluble in water, resulting from the high solvation energy of Be in producing $[Be(H_2O)_4]^{2+}$. Fluorides of the other metals are ionic, have high melting points, and are insoluble in water. Calcium fluoride commands industrial importance as the main source of both F_2 and HF (equations 38 and 39).[12] World production of fluorite (CaF_2) was 5.1 million tonnes in 1988. The main sources are China 22.5%, Mexico and Mongolia each 16%, the former Soviet Union 11%, and South Africa 6%. CaF_2 also is used to make prisms and cell windows for spectrophotometers. The structure of fluorite is one of the more important general solid-state forms (Figure 6) (*see* ***Solids: Characterization by Powder Diffraction*** and ***Fluorides: Solid-state Chemistry***).

$$CaF_2 + H_2SO_4 \longrightarrow 2HF + CaSO_4 \quad (38)$$

$$HF + KF \longrightarrow KHF_2 \xrightarrow{\text{electrolysis}} F_2 \quad (39)$$

The chlorides, bromides, and iodides of Mg, Ca, Sr, and Ba are ionic, have much lower melting points than the fluorides, and are readily soluble in water. The solubility decreases somewhat with increasing atomic number. The halides all form *Hydrates* and they are hygroscopic (absorb water vapor from the air). Several million tonnes of $CaCl_2$ are produced each year. Large amounts are discarded in solution as a waste product from the Solvay process as a consequence of the low market demand and concomitant uneconomical cost position. Calcium chloride is used widely for treating ice on roads, particularly in very cold climates, because a 30% eutectic mixture of $CaCl_2/H_2O$ freezes at $-55\,^\circ C$, compared with $NaCl/H_2O$ at $-18\,^\circ C$. Calcium chloride also is used to make concrete set more quickly and to improve its strength, and as 'brine' in refrigeration plants. A minor use is in laboratories as a desiccant (drying agent). Anhydrous $MgCl_2$ is important in the electrolytic method for extracting magnesium.

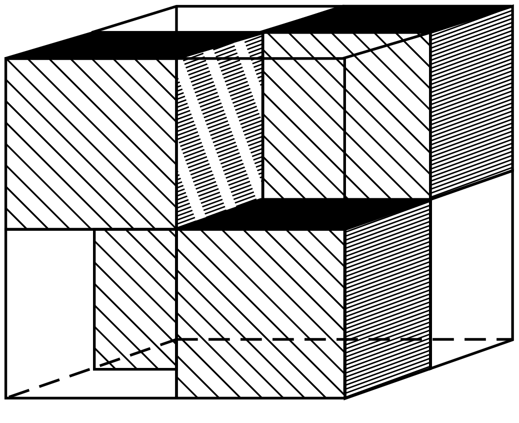

Figure 6 The solid-state structure of fluorite (CaF_2)

Beryllium fluoride (BeF_2) readily coordinates two extra F^- ions, forming the $[BeF_4]^{2-}$ complex. The tetrafluoroberyllates $M_2[BeF_4]$ are well-known complex ions, and resemble the sulfates in properties. In most cases, beryllium is four-coordinate in complexes and the tetrahedral arrangement adopted correlates with the sp^3 hybrid orbitals (*see Hybridization*) available for complex formation. The structural discussion follows from *Valence Shell Electron Pair Repulsion Model* theory. In a similar way, complexes of the type $BeCl_2{\cdot}(LB)_2$ are formed (where: Lewis base (LB) is an ether, aldehyde, or ketone with an oxygen atom that has a lone pair of electrons that can be donated). The complexes, such as $[Be(H_2O)_4]^{2+}$, are tetrahedral. Magnesium also forms halide complexes; however, they are not as prevalent as for beryllium. Complexes such as $[NEt_4]_2[MgCl_4]$ exist, but no comparable examples are reported for the heavier group 2 elements Ca, Sr, or Ba.

10 COMPOUNDS OF GROUP 2 ELEMENTS WITH COMPLEX LIGANDS

Superconductivity was discovered in 1911. For the first 75 years, it was confined to being observed in metallic (or intermetallic) systems. Most present superconducting materials are binary compositions that are widely utilized in the fabrication of magnets for MRI. The specific form of the material demanded for incorporation into an MRI magnet is a wire. Such wires are composed of multifilament woven compositions. Although several methods exist for the preparation of these materials, in general the traditional routes of metallurgy are applicable, owing to the nature of the compositions.

In 1986, the presence of superconductivity was observed in a metal oxide system (*see* ***Electronic Structure of Solids***). This ceramic was brittle, not ductile as for metallic samples. *Chemical Vapor Deposition* is one method for preparing metal oxide compositions. All presently known superconducting metal oxide compositions contain a group 2 element (Figure 7). Owing to the importance of this area to the future development of the inorganic chemistry of the group 2 elements, it is covered in the present context.

The proven utility of *Chemical Vapor Deposition* in other electronic materials systems (semiconductors, conductors, and insulators) has driven several research efforts to investigate its potential for SMO thin-film growth (*see Metal–Organic Chemical Vapor Deposition*). CVD potentially is well suited for the preparation of thin films of SMO on a wide range of substrates, including those of nonplanar geometries (*see* ***Thin Film Synthesis of Solids***). CVD offers the advantages of mild process conditions (i.e. low temperatures), control over microstructure and composition, high deposition rates, and possible large-scale processing. As with any CVD process, however, the critical factor in the deposition process has been the selection of precursors with suitable transport properties (*see Organometallic Chemical Vapor Deposition*).[35]

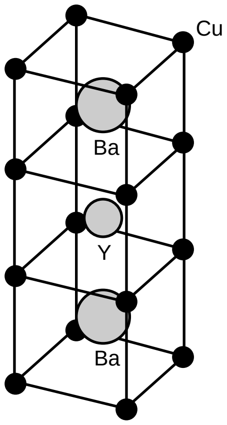

Figure 7 Unit cell depiction of the group 2 element containing superconducting metal oxide $YBa_2Cu_3O_{7-\delta}$

The choice of the β-diketonate compounds (*see Diketones*) was based on the earlier elegant work of Sievers,[36] who demonstrated vapor-phase separation of compounds of the general form $M(L)_n$ where n is the cation charge of the metal M, and L is either the parent pentane-2,4-dionato (i.e. acac), or a terminally alkyl-substituted derivative.[37] These metal coordination compounds, described by Coleman as 'quasiaromatic', all have the common feature of the β-diketonate ligand.[38] This bidentate, monoanionic ligand forms a six-membered MO_2C_3 ring upon resonance stabilization of the alkoxide ene–one configuration (**1**).

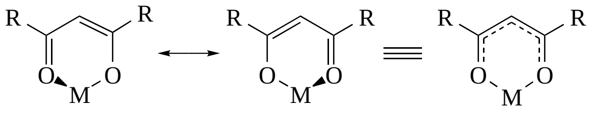

(**1**) R = Me: Macac; R = *t*-Bu: Mtmhd

Although the commercially available copper and yttrium precursors $Cu(tmhd)_2$ and $Y(tmhd)_3(H_2O)$ readily sublime under ambient pressures between 125 and 160 °C,[39] much higher temperatures (>250 °C) are required for the equivalent barium source, '$Ba(tmhd)_2$'. Thus, although progress has been made, currently the future development of CVD for SMO applications is hampered by the lack of suitable group 2 precursors, particularly those of Ba.[40] Precursor development for CVD of group 2 containing materials has focused primarily on substituted acac complexes.[41]

Quite recently, it has been shown that '$Ba(tmhd)_2$' does not exist as written. Supplied commercially as 'anhydrous $Ba(tmhd)_2$' this compound is, in reality, a pentabarium cluster, which was formulated as $Ba_5(tmhd)_9(OH)(H_2O)_3$; however, based upon literature precedent and by full consideration of the ligand geometries, a better formulation

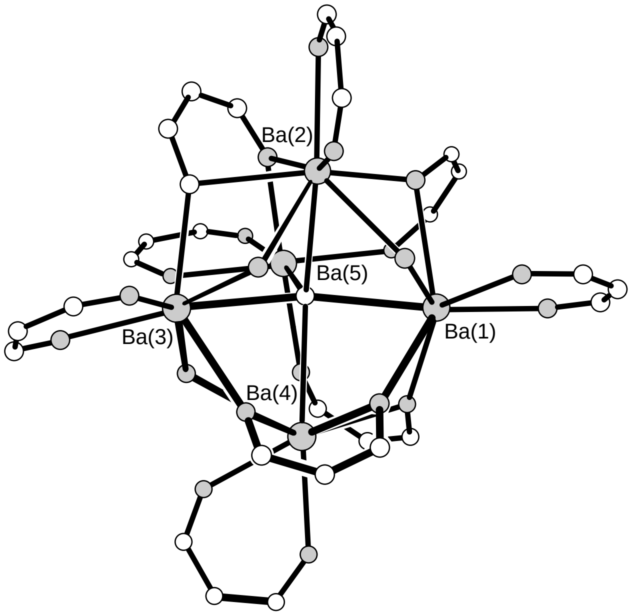

Figure 8 The molecular structure of the pentabarium cluster originally formulated as $Ba_5(tmhd)_9(OH)(H_2O)_3$, but more probably consistent with $Ba_5(tmhd)_5(Htmhd)_4(O)(OH)_3$. The *t*-butyl groups have been omitted for clarity

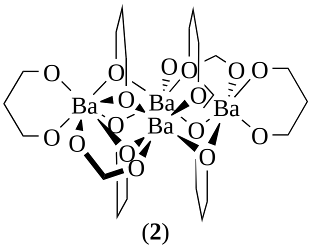

(**2**)

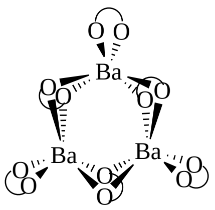

(**3**)

is $Ba_5(tmhd)_5(Htmhd)_4(O)(OH)_3$ (Figure 8).[42] The authentic anhydrous compound is a mixture of the trimer and tetramer, $[Ba(tmhd)_2]_n$ $(n = 3, 4)$.[43] The crystal structure of $[Ba(tmhd)_2]_4$[44] (**2**) has been determined recently. The proposed structure of $[Ba(tmhd)_2]_3$, formulated by analogy with the tetramer, is depicted in (**3**).[43,45] Therefore, the tendency of these species to cluster in an effort to achieve electronically neutral, coordinatively saturated status is rather evident. Upon prolonged heating at temperatures required for sufficient mass transport, decomposition of the pentabarium cluster to nonvolatile products occurs.[46] It is likely that one of these species is $Ba_6(tmhd)_{10}(OH)_2$, since a derivative of this compound, $Ba_6(tmhd)_{10}(O_2SiMe_2)\cdot H_2O$, has been isolated by reaction with $(Me_2SiO)_n$.[47] The most probable next step is elimination of H_2O, followed by the formation of higher molecular weight, lower vapor pressure species. The decomposition of the pentabarium cluster leads to a change in concentration of barium in the vapor over time, and therefore, devastating changes in deposition rate and film composition.[48] This decomposition has been followed in a time/temperature/pressure/humidity study by the technique of TGA–PES.[49] These results are in complete agreement with the hypothesis of hydrolysis of the metal–ligand bond (M–L) to give the protonated ligand (HL) and a metal hydroxide (M–OH). The latter species subsequently dimerizes to yield an oxide (M–O–M) and regenerate water for further reaction.[50] In addition, the high temperatures required to volatilize $[Ba(tmhd)_2]_n$ require that the entire CVD system be maintained above 250 °C to ensure that condensation of the barium source does not occur outside the deposition chamber. It is clear, therefore, that an alternative barium source with a lower evaporation temperature and higher thermal stability is desirable for research purposes and essential if thin films of SMO are to be prepared routinely by CVD.

Although the problems described above for barium precursors also are associated, albeit less severely, with the other two group 2 elements used for obtaining SMO, that is, calcium and strontium, the major research effort in several groups has been focused towards the substantially more difficult volatilization of barium.

Purdy *et al.*[51] reported the synthesis of the calcium, barium, and strontium complexes of hexafluoroacetylacetone (Hhfac) (**4**) and trifluoroacetylacetone (Htfac) (**5**). CVD experiments were performed with the group 2 hfac complexes, and with $Ca(tfac)_2$ to give metal fluoride films, while $Ba(hfac)_2$ has been used to prepare films of $YBa_2Cu_3O_{7-\delta}$.[52] As with the tmhd derivative, the tfac and hfac barium complexes decompose at, or slightly above, their sublimation temperatures, resulting in significant premature thermolysis of the precursors during deposition.

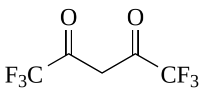

(**4**)

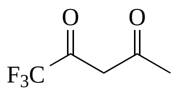

(**5**)

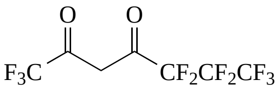

(**6**)

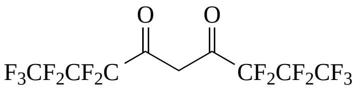

(**7**)

Recent work by Cole-Hamilton and coworkers[53] has demonstrated that stability and volatility are enhanced by the use of long-chain fluorinated β-diketonate ligands, that is those derived from Hdfhd (**6**) and Htdfnd (**7**). The hydrated bis(β-diketonate) complexes $M(dfhd)_2(H_2O)$ and $M(tdfnd)_2(H_2O)$ were prepared for Cu, Ca, Sr, and Ba and were all found to sublime below 200 °C with weight loss ranging from 85 to 98% (see Table 15). In addition, the anhydrous compound $Ba(tdfnd)_2$ was reported to melt at 196 °C and volatilize at 220 °C with essentially no decomposition (residual mass by TGA ca. 1%).

The only commercially available barium compound that possesses both the desired volatility and thermal stability is

Table 15 Selected physical data for barium complexes

Compound	Ambient state[a]	Oxygen sensitivity[b]	Vapor pressure[c]	Stability[d]	
				Solid	Vapor
$Ba(acac)_2$	s	l	?	x	?
$Ba(fod)_2$	s	l	10/150	√	x
$Ba(hfac)_2 \cdot tetraglyme$	s	l	75/150	√	√
$[Ba(tmhd)_2]_{3,4}$	s	l	3/250	x	√
$Ba_5(tmhd)_9(OH)(H_2O)_3$	s	l	5/230	xx	√
$[Ba(tmhd)_2(NH_3)_2]_2$	s	l	5/170	?	√
$Ba(tmhd)_2(MeOH)_2$	s	l	?	xx	?
$Ba(dmmod)_2$	l	1	100/85	√	?
$Ba(dfhd)_2(H_2O)$	s	l	?	√	√
$Ba(tdfnd)_2(H_2O)$	s	l	?	√	√
$Ba(C_5H_5)_2$	s	h	?	x	?
$Ba(C_5Me_5)_2$	s	h	$10^{-4}/200$	?	?
$Ba[C_5H(i\text{-}Pr)_4]_2$	s	h	$10^{-3}/100$	√	√
$Ba(C_5Me_5)_2 \cdot py$	s	h	$10^{-3}/100$	√	√
$Ba(C_5H_4CH_2OMe)_2$	s	h	$10^{-3}/100$	√	x
$Ba(Ome)_2$	s	l	?	x	?
$Ba[OC_2H_4N(C_2H_4OH)_2]_2(EtOH)_2$	s	l	?	xx	?
$Ba(bht)_2(THF)_4$	s	l	?	x	?
$Ba_5(H)(O)(OPh)_9(THF)_8$	s	l	?	x	?
$Ba_6(H)_3(O)(O\text{-}t\text{-}Bu)_{11}(OCEt_2CH_2O)(THF)_3$	s	l	?	x	?
$Ba(H\text{-}dbp)_2(OCH_2CH_2NMe_2)_4$	s	l	?	xx	?
$Ba_3(OSiPh_3)_6(THF)_{1.5}$	s	l	?	x	?
$Ba[O(C_2H_4O)_2Me]_2$	l	1	$10^{-3}/200$	√	x

[a] s = solid, l = liquid; [b] h = high, l = low; [c] in mmHg/°C, ? = unknown; [d] √ = satisfactory, x = unsatisfactory, xx = very unsatisfactory, ? = unknown.

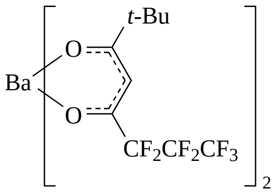

(**8**)

the complex $Ba(fod)_2$ (**8**).[54] Two groups independently, and almost simultaneously, reported the use of $Ba(fod)_2$ in the preparation of $YBa_2Cu_3O_{7-\delta}$ films.[55,56] For deposition to be carried out at ambient pressure, the precursor must be heated to temperatures above 300 °C. Unlike the other precursors discussed above, no decomposition is reported. If a low pressure (5 Torr) CVD system is employed, the sublimation temperature is significantly reduced (190 °C)

Although sufficiently volatile, the fluorinated bis(β-diketonate) compounds are unsuited for preparing high quality SMO since thin films grown using either of the fluorine-containing complexes, $Ba(hfac)_2$ or $Ba(fod)_2$, contain significant quantities of BaF_2. While the formation of BaF_2 may assist in promoting epitaxy, these films require a postdeposition hydrolysis step to remove the fluorine. Although SMO lattices appear to be forgiving enough to permit observation of acceptable T_c and J_c values on BaF_2 contaminated films, goals of electronic device fabrication demand epitaxial material. Thus, obviously postdeposition washes removing contaminating material are to be avoided.

Therefore the most critical chemical issue in the CVD of barium-containing SMO thin films is the need for thermally stable nonfluorine-containing source compounds with enhanced volatility. The desire to eliminate fluorine incorporation in deposited films has prompted the investigation of methods to increase the volatility of the nonfluorinated β-diketonates by the formation of Lewis type acid–base adducts (*see Lewis Acids & Bases*), either in situ or as stable precursor compounds. Prior to the availability of definitive structural data, it had been commonly assumed (and correctly so) that the bis(β-diketonate) complexes of Ba are coordinatively unsaturated, and therefore are prone to oligomerization and/or coordination by solvent molecules, especially water (see above). It has been postulated that neutral oxygen-containing donor molecules can limit oligomerization by making a stable Lewis acid–base complex in which the metal ion is coordinatively saturated (*see Coordinative Saturation & Unsaturation*) and, as a consequence, increase the volatility of the resultant complex.

10.1 Intermolecular Stabilization

Coleman *et al.* have reported that the addition of vapors of the free ligand Htmhd to the carrier gas stabilizes the vaporization rate of ‘$Ba(tmhd)_2$’ so that its vapor pressure remains constant for several hours.[57] This effect was previously observed by Fujinaga *et al.* while trying to separate β-diketonate compounds by gas chromatography.[58–61] Although decomposition of ‘$Ba(tmhd)_2$’ is reduced by the addition of excess neutral β-diketone, high temperatures (280–300 °C) are still required to volatilize the precursor.

The first report of enhanced volatility of a barium source compound was made by Spee, Mackor, and coworkers, who noted that thermally stable complexes can be synthesized using $Ba(hfac)_2$ and a neutral coordinating donor ligand such as a polyether, $MeO(CH_2CH_2O)_nMe$ ($n = 1-4$) (Figure 9).[62–66] These complexes show an increased volatility at reduced pressures relative to their uncomplexed parent compounds. The best results were obtained with $Ba(hfac)_2[MeO(CH_2CH_2O)_4Me]$, which becomes volatile at 150 °C at 0.03 Torr. Despite the increased volatility of the barium source, the films deposited still contain significant quantities of BaF_2, and there has been no report that the nonfluorinated ‘$Ba(tmhd)_2$’ can be volatilized by this method. This approach has been expanded by others.[67,68] Although demonstrative of the desire of barium to achieve coordination numbers of 8–12, this new chemistry has not led, at this point, to a reported volatilization of fluorine-free barium compounds.

Other workers have added THF or H_2O to the carrier gas stream in efforts to affect the requisite vapor pressure increase in $Ba(\beta\text{-diketonate})_2$ compounds.[69–71] The objective of all these experiments was to coordinatively saturate the barium atom in the vapor phase by incorporation of the lone pair electrons on the oxygen atoms of the neutral ligands into the bonding sphere of the metal. At the temperatures demanded for vapor transport, the equilibrium for dissociation of these ligands is rather unfavorable; therefore, any anticipated gain will be minimal.

A more dramatic change in volatility and stability of barium bis(β-diketonate) complexes is seen when a nitrogen-containing base, such as an amine or ammonia, is added to or used as the carrier gas, instead of an oxygen donor.[72] It has been reported that addition of a nitrogen-containing base to the carrier gas causes the barium source to melt between 70 and 100 °C and to become volatile between 130 and 230 °C (1 atm), without any visible decomposition, depending on the amine used. One difference between the nitrogen and oxygen donor ligands is that, while stable, isolable complexes were obtained between the oxygen donor ligands and barium bis(β-diketonate) complexes, no such species were initially reported for amines or ammonia. Nitrogen-free films of barium oxides have been deposited at 500 °C under ambient pressure, with NEt_3 vapor added to the nitrogen/oxygen carrier gas, while for the barium precursor, ‘$Ba(tmhd)_2$’, the temperature was maintained at 130 °C.[73]

Subsequent to the initial report of enhanced vapor transport of $[Ba(tmhd)_2]_x$ by addition of NH_3 to the carrier gas, it was discovered that an isolable compound is formed between these two species (equation 40). The X-ray diffraction crystal structure of $[Ba(tmhd)_2(NH_3)_2]_2$ indicated it to be a highly symmetric dimer (Figure 10). The localized geometry around the eight-coordinate barium atoms is nearly perfectly square-antiprismatic. The coordinated ammonia is not retained upon vapor transport. Thus, in all probability, it is the primary purpose of the added $NH_3(g)$ to break up $[Ba(tmhd)_2]_x$ from the solid and transport it as $[Ba(tmhd)_2(NH_3)_2]_2$, or some other comparably lowered nuclearity species, in the vapor phase.

$$[Ba(tmhd)_2]_n \underset{-NH_3}{\overset{+NH_3}{\rightleftharpoons}} [Ba(tmhd)_2(NH_3)_2]_2 \qquad (40)$$

Several additional examples of intermolecular stabilization have been reported. Pez[74] has prepared $Ba(hfac)_2$(18-crown-6) and Gléizes[75] has obtained the structure of $Ba(tmhd)_2(MeOH)_2$. The isolation of $Ba(tmhd)_2(TMEDA)_2$ (Figure 11) has been achieved as well, although the vapor-phase composition of this species was not determined.[76]

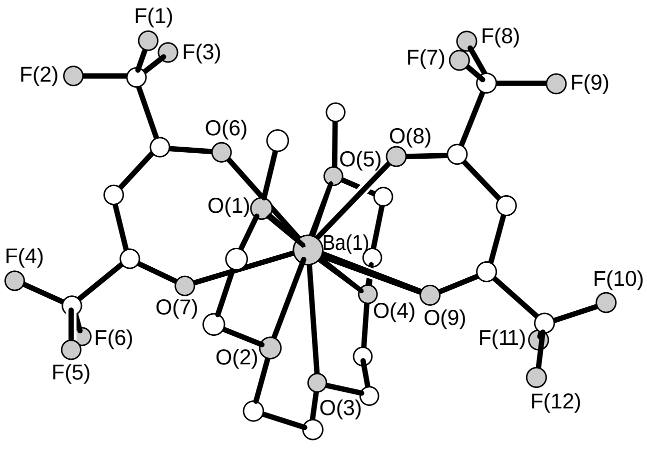

Figure 9 The molecular structure of $Ba(hfac)_2[Me_3O(CH_2CH_2O)_4Me]$

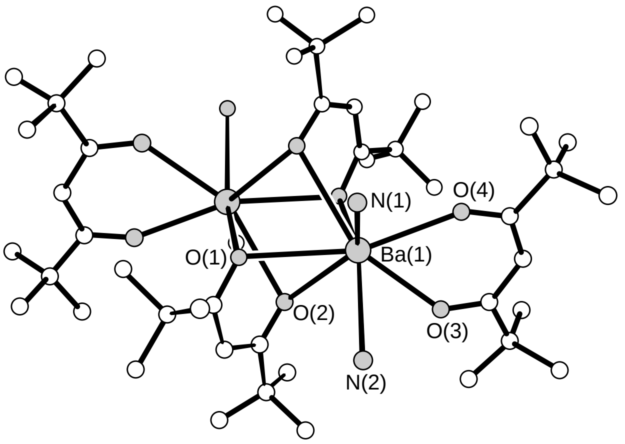

Figure 10 The molecular structure of $[Ba(tmhd)_2(NH_3)_2]_2$

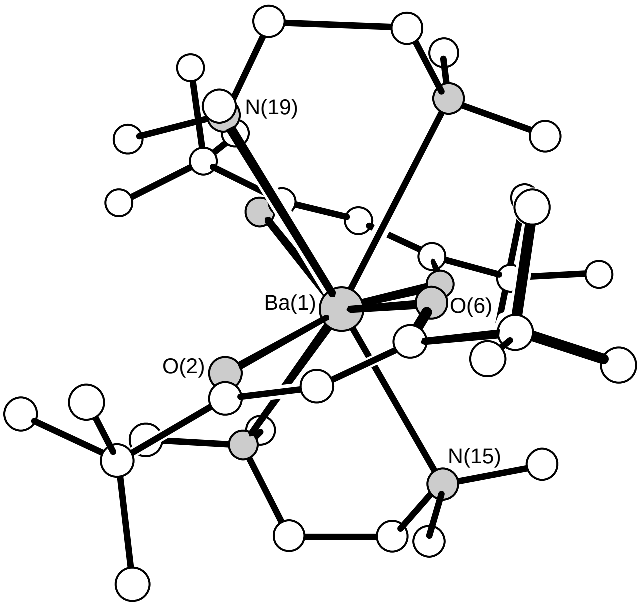

Figure 11 The molecular structure of $Ba(tmhd)_2(tmeda)_2$

Gléizes[77] quite recently has prepared $Ba(tmhd)_2(MeOH)_2(H_2O)_2$ and reports it to be stable to repeated vapor transport without decomposition at 10^{-3} mmHg and 80 °C.

It is important to note that in none of these examples of intermolecularily stabilized barium bis(β-diketonate) complexes was found complete achievement of the criteria for CVD precursors for SMO given at the outset of this section. Therefore, other routes had to be explored in the search for the required higher volatility, higher stability vapor transport vehicles to be employed for the heavy group 2 elements desired for electronic materials applications.

10.2 Intramolecular Stabilization

Whereas each of these above-described new compositions offered significant advantages over existing CVD sources, each also suffered some limitation that prohibited widespread exploration in the preparation of thin films (Table 15). In a radical departure from more traditional routes, the preparation of a new class of ligands, namely the β-diketo ethers, and their utilization in the formation of novel families of both main group and transition element complexes, has been investigated.[78]

Building in parallel upon the discoveries of the lowering of the molecularity of $[Ba(tmhd)_2]_{3,4}$ by intermolecular addition of Lewis bases (see above), and of the isolation of *monomeric* clam-shell oligoether alkoxides (see below),[79,80] the successful incorporation of intramolecular stability, in the form of a 'scorpion-tail', on to the well-known β-diketonate ligand backbone was achieved. The synthesis of the first example of such a ligand, Hdmmod (**9**), is a straightforward Claisen condensation (equation 41). While this procedure currently is unoptimized, it proceeds in sufficient yield (ca. 66%) to permit useful exploration of the properties of $[Hdmmod]^-$ as a potential ligand upon deprotonation at the acidic methylene position between the two carbonyl groups.

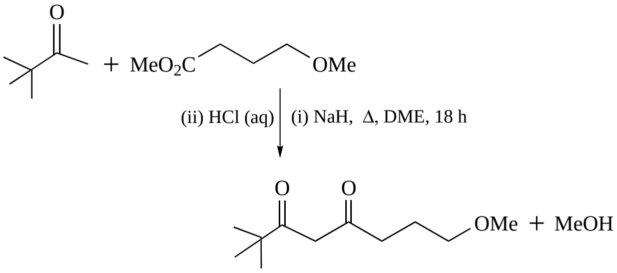

(41)

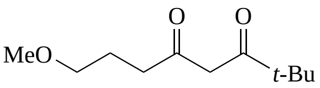

(**9**)

Following the strategy depicted in equation (42), $Cu(dmmod)_2$ was prepared from the deprotonated ligand and a Cu^{II} salt. The molecular structure of the product was determined by X-ray diffraction (Figure 12). The ligands pack over each other in the unit cell and an intermolecular fifth oxygen coordination distance of 2.98 Å is observed. The in-plane Cu–O distances are all 1.97 ± 0.03 Å and the observed geometry is almost perfectly square planar (deviation <0.02 Å). The λ_{max} in the UV (298 nm) does not indicate any significant presence of a five-coordinate square-based pyramid species in solution, when compared with $Cu(acac)_2$ (295 nm),

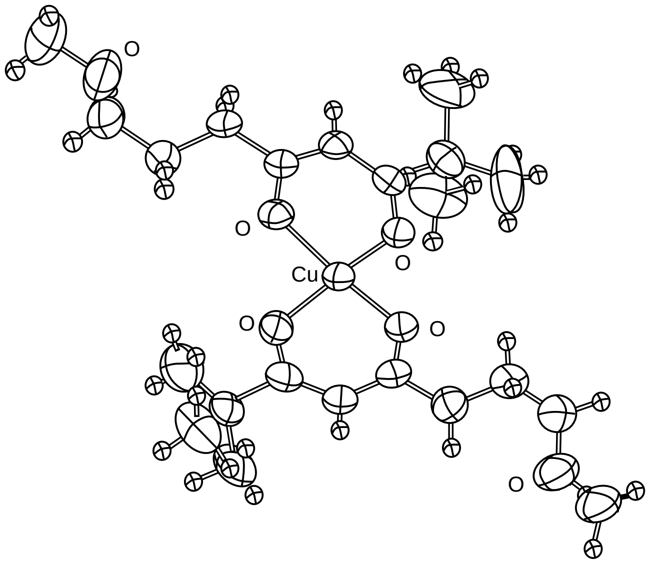

Figure 12 The molecular structure of $Cu(dmmod)_2$

a known four-coordinate square-planar complex.[2] Thus, at this time, the observation of the presence of a rather weak fifth oxygen atom interaction with each copper center in the solid state may be explained as being the consequence of molecular packing, and not strongly dominated by tightly bound intermolecular interactions.

$$2\text{Hdmmod} + \text{Cu(NO}_3)_2 \xrightarrow[\text{EtOH/H}_2\text{O}]{\text{2KOH}} 2\text{KNO}_3 + \text{H}_2\text{O} + \text{Cu(dmmod)}_2 \qquad (42)$$

The barium bis(dmmod) complex is readily prepared by a redox reaction combining elemental barium with Hdmmod (equation 43). Purified by distillation of the excess Hdmmod, $Ba(dmmod)_2$ was identified to be authentic by elemental analysis, and found to be monomeric in benzene solution. Examination of the literature reports currently available indicates that this represents the first observation of an ambient condition liquid barium compound that is based on β-diketonate ligands.[81] Utilizing the data, it would appear that the metal center is six coordinate. Examination of space-filling molecular models lends some credence to this suggestion.

$$\text{Ba} + \text{xs Hdmmod} \longrightarrow \text{Ba(dmmod)}_2 + \text{H}_2 \qquad (43)$$

Although not reported as anhydrous compounds, $Ba(L)_2(H_2O)_n$ have been prepared for HL = Htmmhd (**10**) and Hdmmhd (**11**).

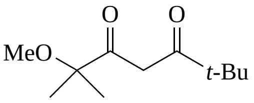

(**10**)

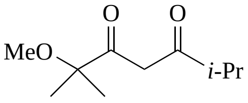

(**11**)

11 ADDITIONAL GROUP 2 ELEMENT COMPOUNDS

While research into SMO film growth has been conducted almost exclusively with the above-described bis(β-diketonate) complexes, an emerging emphasis is being placed on the development of alternative classes of group 2 compounds; some of these new efforts are discussed here.

11.1 Metal Halides

One report at the fall 1988 Materials Research Society Meeting,[82] during the early days of the investigation of the preparation of thin films of the SMO, described the utilization of MI_2 species as CVD sources. This preliminary disclosure does not appear to have been followed up on by subsequent workers. However, it is important to realize that the use of fluorinated β-diketonates (see above) has always been found to result in the primary deposition of BaF_2, and that this material is then subsequently converted in a second reaction step (hydrolysis) to the sought-after metal oxide. BaX_2(18-crown-6) type compounds also have been reported (X = Cl, Br, I, NO_3, OH, SCN) (*see **Macrocyclic Ligands***).[83]

11.2 Metal Amides

This class of compounds was, until recently, almost completely unexplored for the group 2 elements. Lappert's treatise on metal amides gives brief mention to the existence of such species.[84] Although the compounds have not yet been proven as precursors for metal oxides, several examples of compounds employing the bis[bis(trimethylsilyl)] ligand were discussed above in the section on compounds formed between group 2 elements and group 15 elements. Perhaps there will be some additional work here, which is directed towards SMO CVD, that will eventually come out from this same approach.

11.3 Metal Carboxylates

Apblett and Gueorguieva[85] have investigated the synthesis of novel low-temperature metal–organic deposition precursors for BaO, Y_2O_3, and CuO. Substantial improvement in the pyrolysis process over simple carboxylates has been realized via the rational design of the molecular precursors so that the ligands decompose readily into small, volatile fragments. One promising ligand is Hhipa (**12**), the metal complexes of which are readily prepared by reaction of the metal chlorides with the sodium salt of the carboxylate (equation 44). The calcium compound $[Ca(hipa)_2(H_2O)]_\infty$ has been characterized

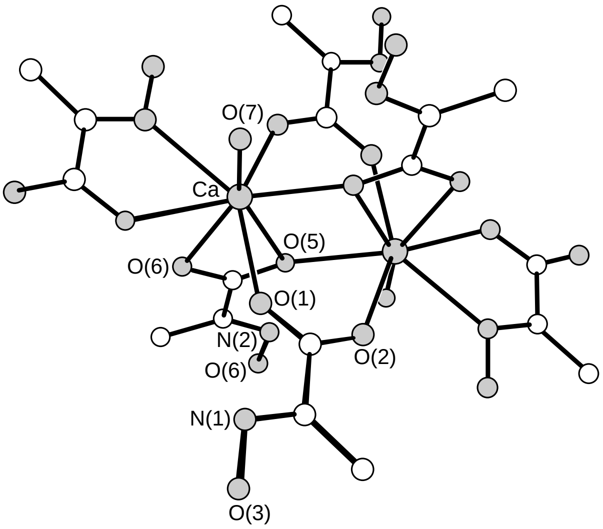

Figure 13 Section of the infinite chain structure of $[Ca(hipa)_2(H_2O)]_\infty$

by X-ray crystallography (Figure 13).

$$MCl_x + x\mathrm{Na(hipa)} \longrightarrow M(\mathrm{hipa})_x + x\ \mathrm{NaCl} \qquad (44)$$

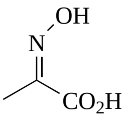

(**12**)

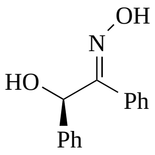

(**13**)

All of these complexes decompose cleanly at low temperature to produce acetonitrile, carbon dioxide, and initially, the metal hydroxide (equation 45). The decomposition temperatures are 144, 176, and 198 °C for Ba, Cu, and Y, respectively. In the case of copper and yttrium, the final product is the metal oxide produced by the dehydration of the hydroxide, while barium hydroxide recombines with carbon dioxide to yield the carbonate. Barium carbonate formation can be avoided, however, by use of a different ligand that avoids carbon dioxide formation. Benzoin α-oxime (Hbo) (**13**) has been found to be a quite suitable diprotic ligand for this purpose. The barium salt is easily prepared by reaction of the oxime with the metal dihydride (equation 46), and it decomposes cleanly to barium oxide by loss of benzaldehyde and benzonitrile at 250 °C (equation 47).

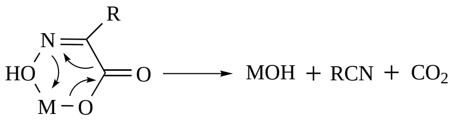

(45)

$$BaH_2 + \mathrm{Hbo} \longrightarrow \mathrm{Ba(bo)} + 2H_2(g) \qquad (46)$$

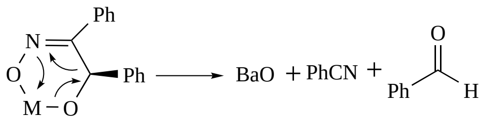

(47)

The crown ether complexes (*see Crown Ethers*) of barium carboxylates, $Ba(O_2CR)_2$(18-crown-6), have been isolated;[86] however, no studies have been reported of their suitability as BaO precursors.

12 ELECTRONIC MATERIALS CONTAINING GROUP 2 ELEMENTS

Several members of the $MM'O_3$ class of ternary metal oxides adopt the perovskite-type ($CaTiO_3$) structure and are sought as worthy target materials possessing ferroelectric properties (*see Ferroelectricity*).[87,88] Among the more widely investigated members of this class are $BaTiO_3$ and $SrTiO_3$. Clearly, use of these materials as potential memory device components demands the presence of a viable processing route to electronically pure material. Traditional ceramic methods (*see Ceramics*) for powder compaction, followed by organic binder burnout, serve unsatisfactorily in this capacity.[89] Bulk single-crystal growth for all necessary compositions is not yet mature enough to provide the quantities of high quality material demanded for evaluation purposes. Thus, investigators have been forced to examine alternate synthetic schemes. Closed space vapor transport is, in general, not well suited to metal oxide growth. It does not appear that any work has been reported in the area of liquid phase epitaxy of these systems. Certainly, this would be a worthy pursuit and should be explored for its potential.

13 GROUP 2 ELEMENT ALKOXIDES

While the earliest work in this area was from Bradley,[90] Chisholm and Caulton, and their group, have recently prepared both cluster alkoxides and siloxides that have some increased solubility properties, for example, $HBa_5(O)(OPh)_9(THF)_8$, $H_3Ba_6(O)(O\text{-}t\text{-}Bu)(OCEt_2CH_2O)(THF)_3$,[91] $H_4Ba_6(\mu_6\text{-}O)(OCH_2CH_2OMe)_{14}$,[92] $Ba_3(OSiPh_3)_6(THF)$,[93] and $Ba(Hdbp)_2(OCH_2CH_2NMe_2)_2(HOCH_2CH_2NMe_2)_2$.[94] However, as cluster aggregates, they both are coordinatively unsaturated and involatile. The former is addressed by parasitic addition of reaction medium, whereas the latter is an intrinsic property and therefore chemically unaddressable (*see* ***Sol–Gel Synthesis of Solids***). Oligomeric species have been prepared by Hubert-Pfalzgraf[95] based on triethanolamine. Buhro[96] has isolated a mega-cluster, $Ca_9(OCH_2CH_2OMe)_{18}(HOCH_2CH_2OMe)_2$, from short-tail base-stabilized alkoxides. This work has recently been extended by Page to include mixtures of Ba, Y, and Cu for sol–gel processing.[97]

The formation of the first monomeric heavy group 2 element alkoxides has been postulated based on oligoether ligands (**14**), the molecularity of which is supported by cryoscopic molecular weight data.[80] This contrasts with the initial publications of $Ba(OR)_2$ preparations.[90] When a saturated hydrocarbon is the parent alcohol, apparently only involatile and insoluble alkoxides are formed. Quite recently, a benzene soluble bis(aryloxide), $Ba(bht)_2(THF)_2$, has been prepared; however, no volatility was reported.[98]

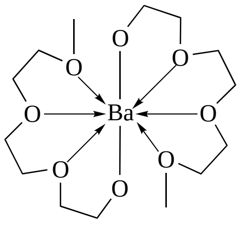

(**14**)

Historically, the first alkoxides of Ca, Sr, and Ba isolated were those containing sterically compact groups (OMe, OEt), which formed $[M(OR)_2]_n$ derivatives that are presumably oligomeric or polymeric.[90] The use of somewhat more sterically bulky groups has led, in recent years, to the isolation of a variety of structurally characterized cluster complexes, such as $Sr_4(OPh)_8(PhOH)_2(THF)_6$,[99] $\{Ba_4(\mu_4\text{-}O)[\mu_2\text{-}OC_6H_2\text{-}2,4,6\text{-}(CH_2NMe_2)_3]_6\}\cdot 3(\text{toluene})$,[100] and $HBa_5(O)(OPh)_9(THF)_8$.

The number of crystallographically characterized monomeric or dimeric group 2 bis(alkoxides) or bis(aryloxides) also has expanded, and includes complexes with a diverse array of ligand geometries. They include the calcium and barium aryloxides $M(bht)_2(THF)_3\cdot(THF)$,[101,102] the related strontium complex $Sr(OC_6H_2\text{-}t\text{-}Bu)_2(THF)_3$,[103] calcium bis(2,4-dinitrophenoxide),[104] barium bis(2,4,6-trinitrophenoxide),[105] hydrogen-bonded $Ba(2,6\text{-}t\text{-}Bu_2C_6H_3O)_2(HOCH_2CH_2NMe_2)_4$,[106] and the alkoxides $Ca(OR)_2(THF)_3\cdot(THF)$, $[Ca(\mu\text{-}OR)(OR)(THF)]_2$ ($OR = OC(C_6H_5)_2\text{-}4\text{-}Cl\text{-}CH_2C_6H_4$),[102] $Ba[OC_2H_4)(HOC_2H_4)_2N]_2\cdot 2EtOH$,[107] $Ba_2(OCPh_3)_4(THF)_3$,[108] and the siloxide $Ba_2(OSi\text{-}t\text{-}Bu_3)_4(THF)$.[108] It is noteworthy that the calcium, strontium, and barium $M(OAr)_2(THF)_3$ complexes are isostructural; just as with the $[M\{N(SiMe_3)_2\}_2]_2$ complexes, the interligand interactions in the bis(aryloxides) (apparently) override the structural differences that might be expected to accompany the ca. 0.35 Å change in metal radius (Table 7).

Despite the interest in group 2 bis(alkoxides) and bis(β-diketonates) as precursors to metal oxides via CVD routes, systematic studies that correlate their structure and volatility still are few. The solid-state structures of many bis(alkoxides) used for CVD work are not known, and the identity of the materials may vary greatly depending on their mode of preparation. As shown above, the widely used bis(β-diketonate) derivative '$Ba(tmhd)_2$' for example, has that formula only if prepared under rigorously anhydrous conditions; in the presence of moisture the pentanuclear cluster $Ba_5(tmhd)_9(H_2O)_3(OH)$ can form. Such uncertainties make the identification of trends in volatilities difficult.

The sublimation temperatures (onset at 10^{-5} Torr) for a series of barium bis(alkoxides) and bis(fluoroalkoxides) are plotted with the corresponding formula weights in Figure 14.[109] The greater bulk (and presumably lower oligomerization) associated with the larger alkoxides appears to counterbalance the increases in molecular weight, so that the sublimation temperatures of $Ba(O\text{-}t\text{-}Bu)_2$ and $Ba[OCH(t\text{-}Bu)_2]_2$, for example, differ by only 10 °C, despite the latter's nearly 50% greater weight. The two fluoroalkoxides are remarkably volatile for their masses; the perfluoro-t-butoxy derivative sublimes 10 °C higher than the parent compound, although the relative molecular weight has risen from 284 to 607. Increases in the volatility of complexes with fluorinated ligands have been observed in bis(β-diketonate) systems as well, and presumably stem from the disruption of intermolecular interactions.[110] Interestingly, the barium tetrahydrofurfuroxide decomposes before subliming; the C_4H_8O ring probably binds to adjacent complexes, increasing the effective molecular weight and suppressing volatility.

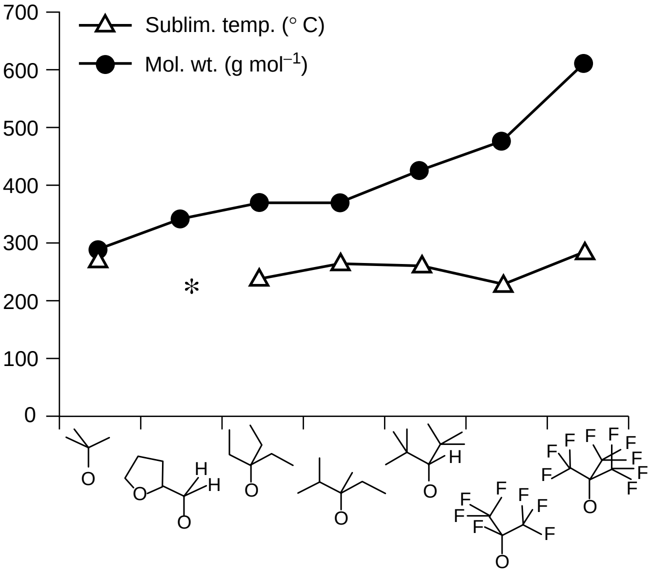

Figure 14 Plot of vapor pressure as a function of molecular weight for a series of barium bis(alkoxides) and bis(fluoroalkoxides)[26]

Comparisons of the volatility of adducts of alkoxides with the relevant unsolvated species are difficult. For example, as discussed above, the volatility of $[Ba(tmhd)_2]_{3,4}$ is increased in the presence of excess free ligand, possibly by suppressing ligand loss in the gas phase through adduct formation.[42,57] No actual adducts of the form '$Ba(tmhd)_2\cdot(Htmhd)_n$' have been isolated from these experiments, however. The presence of ammonia has also been found to increase the volatility of $Ba(tmhd)_2$ under CVD conditions, and the NH_3 adduct $[Ba(tmhd)_2\cdot 2NH_3]_2$ has been independently prepared and structurally characterized.[43] On sublimation the coordinated NH_3 is lost, however, and the volatility of the parent compound and the adduct are nearly the same. Loss of coordinated neutral ligands on sublimation often renders the stoichiometry of gaseous species uncertain, although mass spectroscopic techniques have been used in attempts to identify oligomeric bis(alkoxides) and bis(β-diketonates) in the vapor phase.[42,109,110]

14 RELATED ARTICLES

Alkali Metals: Inorganic Chemistry; Beryllium & Magnesium: Organometallic Chemistry; Calcium-binding Proteins; Chalcogenides: Solid-state Chemistry; Coordination Numbers & Geometries; Coordination & Organometallic Chemistry: Principles; Electronic Structure of Main-group Compounds;

Electronic Structure of Solids; Fluorides: Solid-state Chemistry; Halides: Solid-state Chemistry; Macrocyclic Ligands; Metallic Materials Deposition: Metal-organic Precursors; Oxides: Solid-state Chemistry; Periodic Table: Trends in the Properties of the Elements; Sol–Gel Synthesis of Solids; Solids: Characterization by Powder Diffraction; Structure & Property Maps for Inorganic Solids; Superconductivity; Thin Film Synthesis of Solids.

15 REFERENCES

1. N. N. Greenwood and A. Earnshaw, ‘Chemistry of the Elements’, Pergamon Press, Oxford, 1984, p. 117.
2. F. A. Cotton and G. Wilkinson, ‘Advanced Inorganic Chemistry’, 5th edn., Wiley, New York, 1988, p. 3, 143.
3. J. Emsley, ‘The Elements’, 2nd edn., Clarendon Press, Oxford, 1991, p. 251.
4. (a) E. Fluck and J. Heumann, ‘Periodic Table of the Elements’, VCH, Deerfield Beach, FL, 1986; (b) R. C. Weast ed., ‘CRC Handbook of Chemistry and Physics’, 58th edn., CRC Press, Cleveland, OH, 1977.
5. G. Wilkinson, F. G. A. Stone, and E. W. Abel eds, ‘Comprehensive Organometallic Chemistry’, Pergamon Press, Oxford, 1982, Vol. 1.
6. (a) G. Wilkinson, R. D. Gillard, and J. A. McCleverty eds, ‘Comprehensive Coordination Chemistry’, Pergamon Press, Oxford, 1987, Vol. 2, p. 1179; (b) D. E. Fenton, ‘Comprehensive Coordination Chemistry’, Pergamon Press, Oxford, 1987, Vol. 3, p. 1.
7. (a) P. A. Everest, in ‘Comprehensive Inorganic Chemistry’, eds. J. C. Bailar Jr, H. J. Emeléus, R. Nyholm, and A. F. Trotman-Dickenson, Pergamon Press, Oxford, 1973, Vol. 1, p. 531; (b) R. D. Goodenough and V. A. Stenger, in ‘Comprehensive Inorganic Chemistry’, eds. J. C. Bailar Jr, H. J. Emeléus, R. Nyholm, and A. F. Trotman-Dickenson, Pergamon Press, Oxford, 1973, Vol. 1, p. 591.
8. J. E. Huheey, ‘Inorganic Chemistry: Principles of Structure and Reactivity’, 2nd edn., Harper and Row, New York, 1978, p. 889.
9. K. F. Purcell and J. C. Kotz, ‘Inorganic Chemistry’, Saunders, London, 1977, p. 1116.
10. J. A. Dean, ‘Lange’s Handbook of Chemistry’, 13th edn., McGraw-Hill, New York, 1985.
11. M. Windholz ed., ‘The Merck Index’, 9th edn., Merck, Rahway, NJ, 1976.
12. J. D. Lee, ‘Concise Inorganic Chemistry’, 4th edn., Chapman & Hall, New York, 1991, p. 325.
13. H. W. Kirby and M. L. Salutsky, ‘The Radiochemistry of Radium’, National Institute of Standards and Technology, National Academy of Sciences–National Research Council Subcommittee on Radiochemistry, Springfield, VA, 1964, p. 205.
14. K. T. Mueller, B. Q. Sun, G. C. Chingas, J. W. Zwanziger, T. Terao, and A. Pines, *J. Magn. Res.*, 1990, **86**, 470.
15. E. Frieden, in ‘Biochemistry of the Essential Ultratrace Elements’, ed. E. Frieden, Plenum Press, New York, 1984, p. 1.
16. (a) W. E. C. Wacker, ‘Magnesium and Man’, Harvard University Press, London, 1980; (b) M. N. Hughes, ‘The Inorganic Chemistry of Biological Processes’, Wiley, London, 1972, p. 256; (c) G. L. Eichhorn ed., ‘Inorganic Biochemistry’, Elsevier, Amsterdam, 1973, Vol. 2, p. 1263; (d) B. S. Cooperman, in ‘Metal Ions in Biological Systems’, ed. H. Sigal, Dekker, New York, 1976, Vol. 5, p. 80; (e) K. S. Rajan, R. W. Colburn, and J. M. Davis, in ‘Metal Ions in Biological Systems’, ed. H. Sigal, Dekker, New York, 1976, Vol. 6, p. 292; (f) F. N. Briggs and R. J. Solaro, in ‘Metal Ions in Biological Systems’, ed. H. Sigal, Dekker, New York, 1976, Vol. 6, p. 324.
17. K. Ballschmiter and J. J. Katz, *J. Am. Chem. Soc.*, 1969, **91**, 2661.
18. O. Rygh, *Bull. Soc. Chim. Biol.*, 1949, **31**, 1052.
19. (a) L. B. Tepper, in ‘Beryllium: Biomedical and Environmental Aspects’, eds. M. D. Rossman, O. P. Preuss, and M. B. Powers, Williams and Wilkins, San Francisco, CA, 1991, p. 3; (b) M. B. Powers, in ‘Beryllium: Biomedical and Environmental Aspects’, eds. M. D. Rossman, O. P. Preuss, and M. B. Powers, Williams and Wilkins, San Francisco, CA, 1991, p. 9; (c) A. L. Reeves, in ‘Beryllium: Biomedical and Environmental Aspects’, eds. M. D. Rossman, O. P. Preuss, and M. B. Powers, Williams and Wilkins, San Francisco, CA, 1991, p. 59.
20. C. Elschenbroich and A. Salzer, ‘Organometallics: A Concise Introduction’, 2nd edn., VCH, New York, 1992.
21. M. J. Michalczyk, *Organometallics*, 1992, **11**, 2307.
22. M. S. Kharasch and O. Reinmuth, ‘Grignard Reactions of Non-metallic Substances’, Constable, Prentice-Hall, New York, 1954.
23. A. R. West, ‘Solid State Chemistry and its Applications’, Wiley, New York, 1984, p. 734.
24. A. F. Wells, ‘Structural Inorganic Chemistry’, 5th edn., Clarendon Press, Oxford, 1984.
25. B. A. Vaartstra, J. C. Huffman, W. E. Streib, and K. G. Caulton, *Inorg. Chem.*, 1991, **30**, 121.
26. T. P. Hanusa, *Chem. Rev.*, 1993, **93**, 1023.
27. A. H. Clark and A. Haaland, *Acta Chem. Scand.*, 1970, **24**, 3024.
28. M. Westerhausen and W. Schwarz, *Z. Anorg. Allg. Chem.*, 1992, **606**, 39.
29. D. C. Bradley, M. B. Hursthouse, A. A. Ibrahim, K. M. Abdul-Malik, M. Motevalli, R. Möseler, H. Powell, and A. C. Sullivan, *Polyhedron*, 1990, **9**, 2959.
30. M. Westerhausen and W. Schwarz, *Z. Anorg. Allg. Chem.*, 1991, **604**, 127.

31. M. Westerhausen and W. Schwarz, *Z. Anorg. Allg. Chem.*, 1991, **606**, 177.

32. F. G. N. Cloke, P. B. Hitchcock, M. F. Lappert, G. A. Lawless, and B. J. Royo, *J. Chem. Soc., Chem. Commun.*, 1991, 724.

33. R. S. Phillips ed., ‘Funk and Wagnalls New Encyclopedia’, Donnelley, New York, 1983, Vol. 5, p. 309.

34. W. Hesse, M. Jansen, and W. Schnick, *Prog. Solid State Chem.*, 1989, **19**, 47.

35. G. B. Stringfellow, ‘Organometallic Vapor Phase Epitaxy: Theory and Practice’, Academic Press, New York, 1989, p. 398.

36. R. W. Moshier and R. E. Sievers, ‘Gas Chromatography of Metal Chelates’, Pergamon Press, Oxford, 1965.

37. R. C. Mehrotra, R. Bohra, and D. P. Gaur, ‘Metal β-Diketonates and Allied Derivatives’, Academic Press, New York, 1978, p. 382.

38. J. P. Collman, *Adv. Chem. Ser.*, 1963, **37**, 78.

39. W. W. Rees Jr, H. A. Luten, M. W. Carris, E. J. Doskocil, and V. L. Goedlen, *MRS Symp. Proc.*, 1992, **271**, 141.

40. (a) W. S. Rees Jr, Y. S. Hascicek, and L. R. Testardi, *MRS Symp. Proc.*, 1992, **271**, 925; (b) W. S. Rees Jr, in ‘Proceedings of the 4th Florida Microelectronic Material Conference’, University of South Florida Press, Tampa, FL, 1992, p. 83.

41. (a) W. S. Rees Jr and A. R. Barron, *Mater. Sci. Forum*, 1993, **137–139**, 473; (b) A. R. Barron and W. S. Rees Jr, *Adv. Mater. Opt. Electron.*, 1993, **2**, 271; (c) W. S. Rees Jr, *Ceram. Ind. Int.*, 1993.

42. S. B. Turnipseed, R. M. Barkley, and R. E. Sievers, *Inorg. Chem.*, 1991, **30**, 1164.

43. W. S. Rees Jr, M. W. Carris, and W. Hesse, *Inorg. Chem.*, 1991, **30**, 4479.

44. A. Gleizes, S. Sans-Lenain, and D. Medus, *C. R. Acad. Sci., Paris*, 1991, **313**, 761.

45. W. S. Rees Jr and M. W. Carris, unpublished results.

46. E. W. Berg and N. M. Hewera, *Anal. Chim. Acta*, 1972, **60**, 117.

47. W. S. Rees Jr, M. W. Carris, W. Hesse, and V. L. Goedken, unpublished results.

48. T. Nakamori, H. Abe, T. Kanamori, and S. Shibata, *Jpn. J. Appl. Phys.*, 1988, **27**, L1265.

49. N. Kuzmina, *Russ. J. Coord. Chem.*, 1991, **36**, 2739.

50. W. S. Rees Jr, K. A. Dippel, M. W. Carris, C. R. Caballero, D. A. Moreno, and W. Hesse, in ‘Proceedings of the Materials Research Society Symposium’, 1992, p. p. 127.

51. A. P. Purdy, A. D. Berry, R. T. Holm, M. Fatemi, and K. K. Gaskill, *Inorg. Chem.*, 1989, **28**, 2799.

52. K. Shinohara, F. Munahata, and M. Yamanaha, *Jpn. J. Appl. Phys.*, 1988, **27**, L1683.

53. S. C. Thompson, D. J. Cole-Hamilton, D. D. Gilliland, M. L. Hitchman, and J. C. Barnes, *Adv. Mater. Opt. Electron.*, 1992, **1**, 81.

54. R. Belcher, C. R. Cranley, J. R. Majer, W. I. Stephen, and P. C. Uden, *Anal. Chim. Acta*, 1972, **60**, 109.

55. A. D. Berry, D. K. Gaskill, R. T. Holm, E. J. Cukauskas, R. Kaplan, and R. L. Henny, *Appl. Phys. Lett.*, 1988, **52**, 1743.

56. H. Yamane, H. Kurosawa, and T. Hirai, *Chem. Lett.*, 1988, 939.

57. P. H. Dickinson, T. H. Geballe, A. Sanjurjo, D. Hildenbrand, G. Craig, M. Zisk, J. Collman, S. A. Banning, and R. E. Sievers, *J. Appl. Phys.*, 1989, **66**, 444.

58. T. Fujinaga, T. Kuwamoto, and S. Maurai, *Talanta*, 1971, **18**, 429.

59. T. Fujinaga, T. Kuwamoto, and S. Maurai, *Anal. Chim. Acta*, 1974, **71**, 141.

60. T. Fujinaga, T. Kuwamoto, K. Sugiura, and S. Ichiki, *Talanta*, 1981, **28**, 295.

61. T. Fujinaga, T. Kuwamoto, K. Sugiura, and N. Matsubara, *Anal. Chim. Acta*, 1982, **136**, 175.

62. C. I. M. A. Spee, H. A. Meinema, K. Timmer, E. A. van der Zouwen, and A. Mackor, Materials Research Society Meeting, Boston, 1989.

63. C. I. M. A. Spee, A. Mackor, and P. P. J. Ramaekers, in ‘Advances in Superconductivity: Proceedings of the First International Symposium on Superconductivity’, eds. K. Kitazawa, and T. Ishiguro, Springer, New York, 1988, p. 499.

64. C. I. M. A. Spee and A. Mackor, in ‘Science and Technology of Thin Film Superconductors’, eds. R. D. McConnell, and S. A. Wolf, Plenum Press, New York, 1988, p. 281.

65. H. A. Meinema, K. Timmer, C. I. M. A. Spee, G. deKoning, and A. Mackor, Abstracts of the 27th International Conference on Coordination Chemistry, Australia, 1989, W3.

66. A. L. Spek, P. van der Sluis, K. Timmer, and H. A. Meinema, *Acta Crystallogr., Sect. C*, 1990, **46**, 1741.

67. R. Gardiner, D. W. Brown, P. S. Kirlin, and A. L. Rheingold, *Chem. Mater.*, 1991, **3**, 1053.

68. G. Malandrino, D. S. Richeson, T. J. Marks, D. C. DeGroot, J. L. Schindler, and C. R. Kannewurf, *Appl. Phys. Lett.*, 1991, **58**, 182.

69. S. Matsuno, F. Urchikawa, and K. Yoshizaki, *Jpn. J. Appl. Phys.*, 1990, **29**, L947.

70. J. Zhao, K.-H. Dahmen, H. O. Marcy, L. M. Tonge, T. J. Marks, B. W. Wessels, and C. R. Kannewurf, *Appl. Phys. Lett.*, 1988, **53**, 1750.

71. J. Zhao, H. O. Marcy, L. M. Tonge, B. W. Wessels, T. J. Marks, and C. R. Kannewurf, *Physica C*, 1989, **159**, 710.

72. A. R. Barron, J. M. Buriak, and R. Gordon, *U.S. Pat.*, pending.

73. A. R. Barron, J. M. Buriak, L. Cheatham, and R. Gordon, The Electrochemical Society 177th Meeting, Abstract 943 HTS, Montreal, 1990.

74. J. A. T. Norman and G. P. Pez, *J. Chem. Soc., Chem Commun.*, 1991, 971.

75. A. Gleizes, S. Sans-Lenain, D. Médus, and R. Morancho, *C.R. Acad. Sci., Paris,* 1991, **312 II**, 983.
76. L. G. Hubert-Pfalzgraf, personal communication.
77. A. Gleizes, D. Médus, and S. Sans-Lenain, Materials Research Society, Spring Meeting, San Francisco, CA, 1992, Abstract N4.7/P3.7.
78. W. S. Rees Jr, C. R. Caballero, and W. Hesse, *Angew. Chem., Int. Ed. Engl.*, 1992, **31**, 735.
79. W. S. Rees Jr and D. A. Moreno, *J. Chem. Soc., Chem. Commun.*, 1991, 1759.
80. W. S. Rees Jr and D. A. Moreno, in 'Spectroscopy and Structure of Molecules and Nuclei', eds. N. R. Johnson, W. N. Shelton, and M. A. El-Sayed, World Scientific, London, 1992, p. 367.
81. L. M. Tonge, D. S. Richeson, T. J. Marks, J. Zhao, B. W. Wessels, H. O. Marcy, and C. R. Kannewurf, *Adv. Chem. Ser.*, 1990, **226**, 351.
82. T. Kimura, M. Ihara, H. Yamawaki, K. Ikeda, and M. Ozeki, Materials Research Society Fall Meeting, 1988, Boston, MA, Abstract F9.7.
83. K. Timmer and H. A. Meinema, *Inorg. Chim. Acta*, 1991, **187**, 99.
84. M. F. Lappert, P. P. Power, A. R. Sanger, and R. C. Srivastava, 'Metal and Metalloid Amides: Syntheses, Structures, and Physical and Chemical Properties', Ellis Horwood, Chichester, 1980.
85. A. W. Apblett, personal communication.
86. J. M. Boncella, C. J. Coston, and J. K. Cammack, *Polyhedron*, 1991, **10**, 769.
87. S. S. Flacher, *J. Am. Chem. Soc.*, 1955, **77**, 6194.
88. A. R. West, 'Solid State Chemistry and its Applications', Wiley, New York, 1984, p. 540.
89. W. D. Kingery, H. K. Bowen, and D. R. Uhlmann, 'Introduction to Ceramics', 2nd edn., Wiley, New York, 1976, p. 1032.
90. D. C. Bradley, R. C. Mehrotra, and D. P. Gaur, 'Metal Alkoxides', Academic Press, New York, 1978, p. 411.
91. K. G. Caulton, M. H. Chisholm, S. R. Drake, and K. Folting, *J. Chem. Soc., Chem. Commun.*, 1990, 1349.
92. K. G. Caulton, M. H. Chisholm, S. R. Drake, and J. C. Huffman, *J. Chem. Soc., Chem. Commun.*, 1990, 1498.
93. K. G. Caulton, M. H. Chisholm, S. R. Drake, and W. E. Streib, *Angew. Chem., Int. Ed. Engl.*, 1990, **29**, 1483.
94. K. G. Caulton, M. H. Chisholm, S. R. Drake, and K. Folting, *Inorg. Chem.*, 1991, **30**, 1500.
95. L. G. Hubert-Pfalzgraf, O. Poncelet, C. Sirio, and J. C. Daran, in 'Chemical Processing of Advanced Materials', eds. L. L. Hench and J. K. West, Wiley, New York, 1992, p. 277.
96. S. C. Goel, M. A. Matchett, M. Y. Chiang, and W. E. Buhro, *J. Am. Chem. Soc.*, 1991, **113**, 1844.
97. C. J. Page, C. S. Houk, and G. A. Burgoine, Materials Research Society Spring Meeting, San Francisco, CA, 1992, Abstract N1.4.
98. P. B. Hitchcock, M. F. Lappert, G. A. Lawless, and B. Royo, *J. Chem. Soc., Chem. Commun.*, 1990, 1141.
99. S. R. Drake, W. E. Streib, M. H. Chisholm, and K. G. Caulton, *Inorg. Chem.*, 1990, **29**, 2707.
100. K. F. Tesh and T. P. Hanusa, *J. Chem. Soc., Chem. Commun.*, 1991, 879.
101. P. B. Hitchcock, M. F. Lappert, G. A. Lawless, and B. Royo, *J. Chem. Soc., Chem. Commun.*, 1990, 1141.
102. K. F. Tesh, T. P. Hanusa, J. C. Huffman, and C. Y. Huffman, *Inorg. Chem.*, 1992, **31**, 5572.
103. S. R. Drake, D. J. Otway, M. B. Hursthouse, and K. M. Abdul-Malik, *Polyhedron*, 1992, **11**, 1995.
104. L. B. Cole and E. M. Holt, *J. Chem. Soc., Perkin Trans. 2*, 1986, 1997.
105. D. L. Huges and J. N. Wingfield, *J. Chem. Soc., Chem. Commun.*, 1977, 804.
106. K. G. Caulton, M. H. Chisholm, S. R. Drake, and K. Folting, *Inorg. Chem.*, 1991, **30**, 1500.
107. O. Poncelet, L. G. Hubert-Pfalzgraf, L. Toupet, and J. C. Daran, *Polyhedron*, 1991, **10**, 2045.
108. S. R. Drake, W. E. Streib, K. Folting, M. H. Chisholm, and K. G. Caulton, *Inorg. Chem.*, 1992, **31**, 3205.
109. A. P. Purdy, C. F. George, and J. H. Callahan, *Inorg. Chem.*, 1991, **30**, 2812.
110. A. P. Purdy, A. D. Berry, R. T. Holm, R. T. Fatermi, and D. K. Gaskill, *Inorg. Chem.*, 1989, **28**, 2799.

Alloys

Bill C. Giessen[1] **& Rafael Hidalgo**[2]

[1]*Northeastern University, Boston, MA, USA*
[2]*Springfield Technical Community College, Springfield, MA, USA*

1 Introduction 1
2 Alloy Phases and Phase Diagrams 2
3 Technical Alloys and Their Applications 4
4 Structural Intermetallics 6
5 Selected Application: Specific Alloys 7
6 Preparation and Characterization 12
7 Related Articles 12
8 References 12

1 INTRODUCTION

1.1 Definition of the Topic

In the metallurgical sense, alloys are mixtures of metals with each other or with certain nonmetals, resulting in substances that may be single phase or multiphase. It should be noted that the term alloy, as referring to a macroscopically homogeneous mixture, is also used for nonmetals such as ceramics and semiconductors (e.g. Si–Ge alloys) and polymers (e.g. block copolymers); these alloys, however, are outside the scope of the present article.

The principal areas of science and engineering dealing with metals and alloys are chemical metallurgy and physical metallurgy. Subjects of chemical metallurgy are the extraction and refining of metals, liquid metal treatments, corrosion protection, and surface treatment of metals.[1] The study of metals and alloys with respect to their crystal structures, constitution, microstructure, and properties (especially, mechanical) is the subject of physical metallurgy.[2,3]

Although physical metallurgy had one of its roots in the theory of phase equilibria, which is a part of physical chemistry (the other root of physical metallurgy was metallurgical practice), it is a fact that, until recently, alloy chemistry and the science of alloys have not been major research subjects of inorganic chemists. This has at least two major reasons. First, the languages of bond formation are different for chemists, physicists, and metallurgists:[4] chemists tend to think in terms of Hückel theory based on the overlap of angularly dependent valence orbitals represented in real space and are not very familiar with the physicist's band structure language expressed in reciprocal space; alloy theorists come from physics and calculate cohesive and structural properties by solving local density functional (LDF) Schrödinger equations; metallurgists regard atoms as 'fuzzy balls' interacting via pair potentials. These three approaches, the number of atoms that can be treated by each of them, and the accuracy of the results obtained are shown in Figure 1.[4]

The second and perhaps most important reason is that the central concept of alloy work, namely, the microstructure and its modification by alloying and treatment, is not a chemical concept; there is no equivalent for it in chemistry. Only recently, with the rising interest in solid-state chemistry, has this begun to change; chemists adopt the band language,[5] and, largely through the use of inorganic compounds as precursors for microelectronic materials[6] and the increasing involvement of chemists in ceramics science,[7] materials chemistry[8] has become a branch of inorganic chemistry. One may now anticipate an increasing interest of chemists in the synthesis and properties of metallic alloys, motivating the comprehensive treatment presented here.

1.2 Alloy Constitution

Microstructurally, alloys are composed of alloy constituents that include alloy phases and, in some cases, unalloyed metals. Crystalline alloy phases can be subdivided into intermetallic phases, metal–nonmetal compounds such as borides or carbides (*see* ***Borides: Solid-state Chemistry***; ***Carbides: Transition Metal Solid-state Chemistry***), and terminal or complete solid solutions.

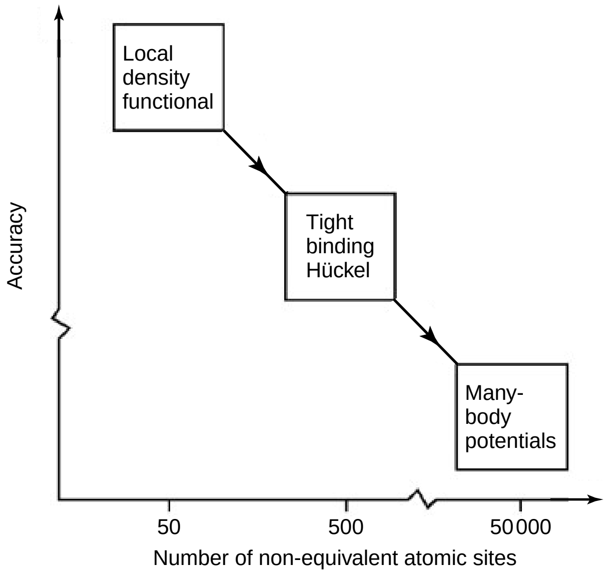

Figure 1 Schematic representation of the decrease in accuracy with increasing number of nonequivalent atomic sites that can be treated computationally by different levels of approximation. (Ref. 4. Reproduced by courtesy of D. Pettifor)

Intermetallics are stoichiometric or nonstoichiometric phases composed of two or more metallic components[9] (with possible admixtures of nonmetals as stabilizers) that crystallize with structures other than those of their metallic components. In the following, reference is often made to intermetallics, but in this article they will not be treated structurally further.

The extent and type of solid solution formation depends on several parameters.[2] If both component elements are isostructural and, in addition, similar in size, valence electron concentration, and electronegativity, a series of complete substitutional solid solutions may form across the diagram, as for V–Cr, Ni–Cu, Cu–Au, and Sb–Bi; otherwise, limited terminal solid solutions form which are substitutional for elements with a solute–solvent size difference less than ±15%, but may be interstitial for element pairs with size ratios of more than ±20%, for example, for Fe(C) or Pb(Au) (here, the bracketed element is the solute).

We also list three other alloy phase types of current interest that are not treated here in detail. Quasicrystals are alloy phases partially or completely lacking translational symmetry (*see* ***Quasicrystals***); they form both equilibrium and nonequilibrium alloy phases. Metallic glasses[10] lack crystalline symmetry entirely; they are always metastable and generally require gas-phase deposition or rapid solidification[11] to be retained, although in some cases their equilibration kinetics are so slow that they can be prepared in bulk from the melt (bulk metallic glasses).[12]

A third alloy state of great current interest is the mixed state containing both crystalline and amorphous metals or alloys, which is seen when the crystallite grain size decreases into the nm range, forming nanometer scale or, in short, 'nanocrystalline' alloys with large proportions of noncrystalline material on the grain boundaries (Figure 2) and new properties. Thus, nanocrystalline materials may exhibit superplasticity,[13] novel electronic properties,[14] or enhanced hydrogen storage capabilities (see the following text).

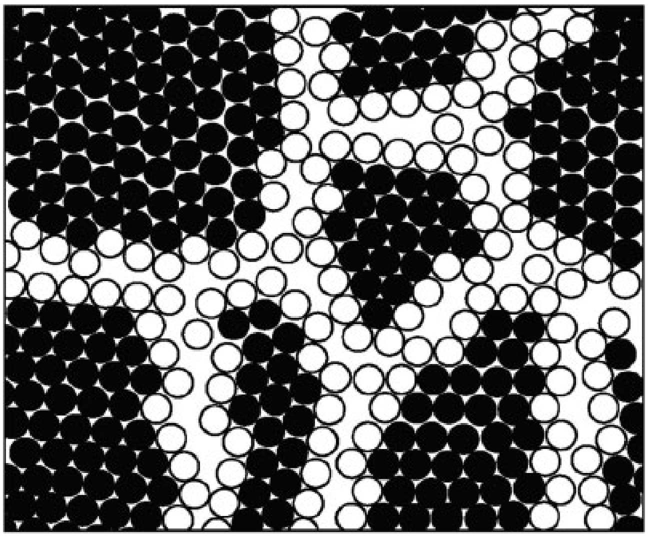

Figure 2 Atomic structure of a two-dimensional nanocrystalline material computed using pair interaction potentials. The atoms in the central portions of the nanocrystals are indicated in black; atoms in the nanograin boundary regions are represented by open circles. (Ref. 13. Reproduced by permission of Springer)

The properties of an alloy are primarily determined by those of its constituent alloy phases; however, as stated, the microstructure, that is, the phases' grain size, perfection, distribution, and so on, which is due to the thermal and mechanical history of the alloy, plays a major, modifying role. It is in this area that modern methods of alloy processing have had their most visible results, as will be seen from the review of specific types of alloys in Sections 3–5.

2 ALLOY PHASES AND PHASE DIAGRAMS

2.1 Alloy Phases

Alloy phases will be described structurally using the following multiple (and somewhat redundant) nomenclature: Name(s); Prototype (Pearson Symbol, Structure Report Symbol). As an example: CuZn (β-Cu–Zn, β-brass); CsCl (cP2, B2) type. (Note: The Pearson symbol already contains the crystal system and Bravais lattice). Alloy phase compilations with structural data are available.[15]

With reference to the classification of alloy phases given above, only a small amount of structural information on alloy phases is required for the alloys treated in this article. Disordered solid solutions are based on the terminal elements and therefore mostly belong to the three most common elemental structure types: Cu (cF4, A1) type, Mg (hP2, A3) type, and W (cI2, A2) type. Following very common usage, these three types are also occasionally referred to in the text as fcc (=face-centered cubic), hcp (=hexagonal close packed), and bcc (=body-centered cubic), respectively, although the rigour of these designations leaves something to be desired. The alloy phases of interest in the following sections on commercial and developmental alloys will be introduced as they are treated.

Next, the current status of the theoretical understanding of alloy phases is reviewed. The techniques available for first-principles calculations for alloys (and alloy phase equilibria) up to the 1990s are listed and reviewed by de Fontaine.[16] Current thinking is reviewed by Pettifor[17] who is also a major contributor to the understanding of alloy properties by fundamental computations.

For perfectly ordered crystals at absolute zero, solutions to the Schrödinger equation can be calculated on fast computers using density functional theory (DFT) based on the self-consistent local density approximation (LDA);[17] simplifying procedures using different basis functions include augmented plane wave (APW), augmented spherical waves (ASW), the Korringa–Kohn–Rostoker (KKR), and the linear muffin-tin orbital (LMTO) methods, as well as further developments originating from these designed to include variable axial ratios. Transition metals can be handled by modern versions of the tight binding (TB) approximation, which is derived from the linear combination of atomic orbital (LCAO) method well familiar to chemists (*see LCAO Approximation*), with semiempirical matrix elements derived from the LMTO method and treated self-consistently.

For disordered systems, the task is harder because translational symmetry is lost. The direct configurational averaging (DCA) method takes all possible local cluster configurations of given stoichiometry into account and averages them; to obtain manageable computation times, this method is used in connection with the relatively simple TB method and hence applies best to transition metals. Alternatively, 'average atoms' are created to restore translational symmetry, leading to the coherent potential approximation (CPA), a mean-field technique that is used in connection with TB, KKR, or LMTO–ASA (ASA = atomic sphere approximation).[16]

Introduction of partial order at finite temperatures adds another level of complexity and difficulty. This situation is handled by the cluster variation method (CVM) free energy functional, which is expressed as a function of multisite correlation functions, whose coefficients are obtained by the generalized perturbation method (GPM) or the embedded cluster method (ECM). All of these methods are highly computationally intensive; at present, this area is probably the principal frontier of alloy phase theory.

To work around the complexities of these calculations (which greatly multiply when multicomponent systems are involved as is the case in superalloys, see Section 3.3) an empirically useful method of alloy phase prediction, PHACOMP, has been developed;[18] its predictions are based on electron concentration rules, especially d-electron shell hole concentrations (see Section 3.3).

An attractive, semiempirical application of physical insight into alloy formation is found in classifications of alloy phase data into structure maps, quantum diagrams, and so on (*see* ***Structure & Property Maps for Inorganic Solids***) where a necessarily limited number of coordinates (one to three) must reflect the physical parameters determining the property of interest. An example is given below in the Pettifor map for Ti–Al intermetallics.[4,19] Further developments in the mapping of intermetallics are due to Ceder.[20]

2.2 Phase Diagrams, Determination, and Computation

Phase diagrams provide the thermodynamic foundation for all alloy work by presenting the equilibrium constitution of alloys. Systematic phase diagram studies were first initiated about 100 years ago, when the thermodynamic foundations of phase diagrams were being established; an additional impulse came with the start of systematic crystal-structure studies following the introduction of X-ray crystallography, beginning in the 1920s.[9] Since then, vast efforts have been spent on the experimental determination of phase diagrams. As a result, for common elements such as Fe, Cu, C, and so on, almost every binary $T-x$ phase diagram is known; in the case of many other elements, constitution diagrams are known at least for their binary systems with some elements representing every group of crystal chemically similar elements, such as the early long period transition metals, noble (platinum group) metals, or the rare earth metals. Work on ternaries has also proceeded well. Binary alloy constitution diagrams have been compiled.[21,22]

From an economic viewpoint, the classical determination of alloy phase diagrams is a laborious process, involving alloy preparation and heat treatment, compositional, structural, and microstructural analysis (and, even then, not yielding reliable phase boundary information at low temperatures due to kinetic limitations). While this investment is justified for alloys of major technical importance, the need for better economics has driven an effort to use alternative methods of phase discovery such as multiple source, gradient vapor deposition or sputter deposition followed by automated analysis; alternatively, multicomponent diffusion 'couples' are used to map binary or ternary alloy systems structurally and by properties (see Section 6). These techniques have been known for decades, but they have been reintroduced more recently as high-efficiency methodologies to create 'compositional libraries' by a combinatorial approach,[23] inspired perhaps by the recent, general introduction of combinatorial methods in chemistry.

Until recently, one might have considered this immense collection of experimental information as one of the major experimentally gathered, but theoretically unexplained, bodies of data in all of the chemical sciences. As shown above, however, in recent years major progress has been made on the theory of alloys and in establishing empirical or semiempirical correlations for alloy phase formation; this, in turn, has benefited phase diagram prediction, which remains an important goal of computational alloy theory. Two principal approaches exist, which are presently in the process of slow convergence.

In the ideal case, one would have ab initio calculations (such as those described above) for all competing crystalline phases and the liquid (or liquids) involved, yielding their free energies as functions of composition and temperature and enabling standard common-tangent constructions to be made. However, since up to now first-principles calculations having the accuracy required to differentiate between competing phases are only possible for crystalline phases, complete phase diagrams (which must include the liquid) cannot yet be handled in this way.[4,16] Nonetheless, it is very valuable to be able at least to calculate the solid-state portion of relevant phase diagrams, thereby obtaining information about metastable phases, phase boundaries, phase decompositions, and ordered phases (superstructures) that are not measurable experimentally because of slow kinetics at low temperatures. While this field of work is just opening up, it can be expected to produce important results.

At present, inclusion of the liquid into such calculations requires use of fitted free energy curves, such as those used in the more empirical approach described below, but as liquid alloy theory advances, this situation will improve. Thus, complete phase diagram calculations based on pseudopotential calculations have been presented by Hafner.[24]

The other approach, which so far has had the greater practical impact, is primarily empirical. The CALPHAD (from CALculated PHAse Diagrams) approach was pioneered by L. Kaufman,[25] a more recent presentation is by Saunders and Miodownik[26] The work of the CALPHAD group focuses on calculations based on thermochemical data such as those compiled by the Scientific Group Thermodata Europe (SGTE),[27] the ASM−NBS Alloy Phase Data Activity, PHACOMP (see above), and CALPHAD itself, but also uses the results of ab initio structural energy calculations for elements and compounds as these become available.

Phase diagrams are calculated from these data using regular solution or other appropriate solution models. Some of the great strengths of the CALPHAD approach are that it provides immediate, approximate diagrams for new systems of interest and that it can be readily extended to ternary and higher order systems that would be prohibitively complex and expensive to study experimentally. A comparison of the observed and calculated Co–V phase diagrams is shown in Figure 3.[25] To construct this diagram, the existence and structures of the intermediate phases Co_3V, σ, and CoV_3 were considered as given; the pair potential (PP) approach mentioned in Section 1.1 as preferred by metallurgists has been used in the energy computation.

Pettifor[17] showed how density functional theory (DFT, see above) may strengthen the CALPHAD conclusions for complex alloy systems by providing information on compositionally 'nearby' metastable alloy phases that may affect alloy properties.

3 TECHNICAL ALLOYS AND THEIR APPLICATIONS

In the following, a survey of the principal types of alloys in current use is provided, with emphasis on those alloys designed for advanced metals technology, as well as the directions of current development. An excellent introductory source on these alloys and on further developments in this area is Smith,[28] from whom much in this section is drawn.

3.1 Steels

Steels of many types constitute 90% of the world's use of metals. Carbon steels are the backbone of the steel industry;

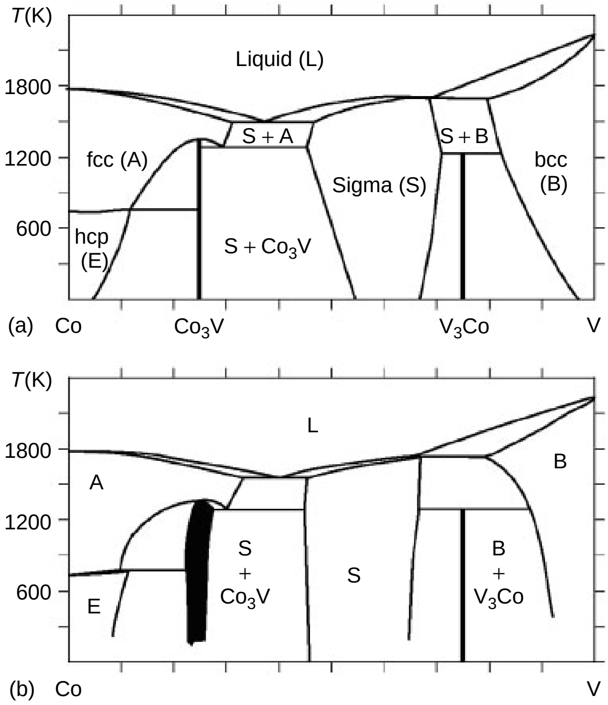

Figure 3 Co–V phase diagram: (a) calculated by CALPHAD methodology, (b) observed. (Ref. 25. Reproduced by kind permission of Springer Science & Business Media)

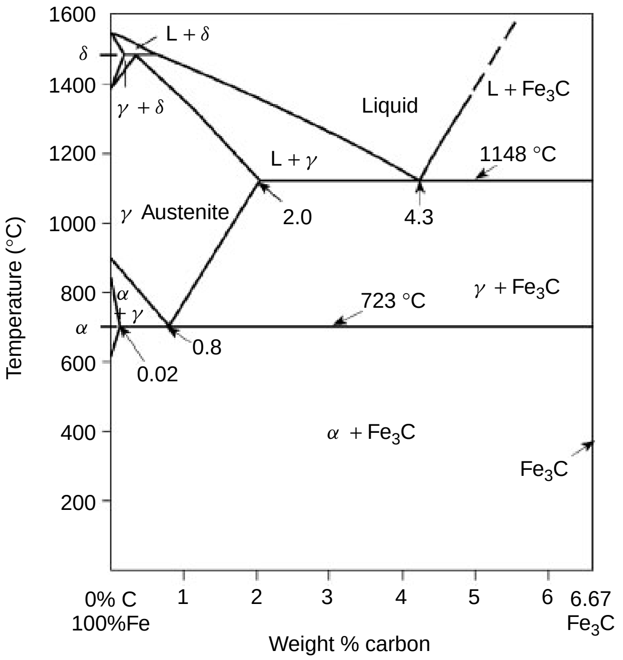

Figure 4 The Fe–Fe_3C metastable system underlying the carbon steel making technology. (Ref. 28. Reproduced by permission of McGraw-Hill)

the underlying Fe–C phase diagram (Figure 4) is therefore without doubt the most important alloy constitution diagram. Its features include the wide phase field of fcc Cu (cF4, A1) type γ-Fe (austenite), which terminates in a eutectoid decomposition of austenite into bcc W (cI2, A2) type β-Fe (ferrite) and the (metastable) compound Fe_3C (oP16, DO_{11}) type (cementite). Much of the art of steelmaking consists of controlling and modifying the formation of this eutectoid, or preventing it altogether by formation of the hard and brittle tetragonal martensite phase (see also Hornbogen[29]).

Alloy steels form the next category; they contain small levels (up to about 3%) of transition metal additives such as Ni, Cr, Mo, Mn, or Si in addition to C; the principal effect of these elements is to increase hardenability and toughness, for example, by influencing martensite formation. Even higher alloying contents, especially of Cr (up to 25%) and Ni (up to 20%) are used to obtain ferritic, martensitic, or austenitic stainless steels (with Cr favoring ferrite and Ni promoting austenite formation); the principal wrought austenitic stainless steel (AISI-304) contains 19% Cr, 9% Ni, and $<0.08\%$ C.

Despite the maturity of the steelmaking field, processing advances continue to be made. Thus, intricate thermal processing paths designated by self-explanatory terms such as ‘austempering’ and ‘marquenching’ have improved the impact resistance of plain-carbon steels. Further, two classes of high-strength, low-alloy (HSLA) steels have been developed in recent years, and such steels now play important technological roles. In one case, microalloying (of plain-carbon steels) with very small amounts of strong carbide formers such as Nb, Ti, and V has given these steels a finer grain structure associated with much greater strength (making use of a general linear correlation between yield strength and the reciprocal square root of the grain size; this is the Hall–Petch relationship).[3] Another new class consists of dual-phase steels containing hard martensite in a soft ferrite matrix, producing high values of tensile strength and total elongation. ‘Maraging’ (from *mar*tensite and *age* hardening) produces ultra-high strength, structural low-C steel with 18% Ni, 10% Co, 4% Mo, and 1% Ti by aging a highly martensitic steel at 500 °C for several hours, thereby forming ultrafine strengthening zones of Ni_3Mo and Ni_3Ti lying along dislocations and martensite lath boundaries. Finally, in the area of stainless steels, ferritic–austenitic duplex structures have also produced an incremental property improvement in yield strength and corrosion resistance.

Combinations of sophisticated alloying and thermal treatment thus continue to advance the science of mankind’s principal structural metal.

3.2 Aluminum Alloys

Wrought heat-treatable Al alloys contain Mg, Zn, and Cu on the level of several percent as precipitation and solid solution hardening ingredients. The precipitation process forms nanometer size Guinier–Preston (GP) zones that are coherent with the matrix and produce the age-hardening effect first observed in 1906 in binary Al–Cu alloys. An alloy constitutional requirement for age hardening is a terminal solid solubility (e.g. of Cu in Al) that sharply decreases with decreasing temperature, allowing nonequilibrium precipitates (GP zones) to form from a supersaturated Al-base solid solution (age hardening). Thus, the solubility of Cu in Al decreases from 5.65% at 548 °C to $<0.2\%$ at 20 °C.

The complex Al alloys mentioned above are the mainstay of the airframe industry; however, the search for ever lighter and stronger Al alloys has recently led to the development of aluminum–lithium alloys (with $\sim$2% Li), which have a 10% higher elastic modulus and an 8% lower density than the current major high-strength aircraft alloy. Although elemental Li has a low density of $0.5\,\mathrm{g\,cm^{-3}}$ and is a soft, low-melting metal, upon introduction into an Al–Cu–Mg alloy it is quite beneficial to the strength-to-weight ratio. Unfortunately, this improvement is also expensive: due to the difficulties of manufacture and the cost of Li, Al–Li alloys have a price several times that of the alloys they replace.[30]

Amorphous Al alloys have been prepared by rapid solidification processing (RSP, see 6.); nanostructural alloys prepared from these glasses[10] have potential applications as high-strength, low-density alloys.[31]

3.3 Superalloys

This is the generic name for a class of Ni-, Co-, or Ni–Fe-based, heat-resistant alloys with high strength at high temperatures (up to 1100 °C). We focus here on Ni-based superalloys. They typically contain 15–20% Cr, 15%–20% Co, 4–10% Mo, 1–5% Al, 2–4% Ti and 0.05–0.20% C, and they derive their strength from the presence of a fine dispersion of refractory metal or Cr carbides of compositions M_6C, $M_{23}C_6$, and MC, an oriented γ' precipitate such as Ni_3(Al, Ti) that is coherent with the Ni solid solution matrix, and the absence of deleterious phases such as cellular carbides and embrittling σ phases. The latter is a complex, tetrahedrally close-packed (or Frank–Kasper) phase.[32] The elimination of the σ phase in modern superalloys was an early example of the use of an electron theoretical (and, with hindsight, somewhat oversimplifying) concept in alloy design: it had been noted that the σ phase occurred at a specific range of the average number of d-electron shell holes; subsequent alloys were designed such as to avoid this hole concentration range and thus to avoid σ phase formation. The PHACOMP method[18] mentioned above was specially designed for use in such applications; semiempirical PHACOMP/CALPHAD calculations have been used in gas turbine component alloy development work involving alloys with up to 9 functional elemental components.[33]

Superalloys are continuously being developed further for use at ever increasing temperatures (Figure 5) in response to the need for running engines at higher temperatures to increase fuel efficiency.[34] Milestones in the advancement of superalloy technology were reached with the development of directional

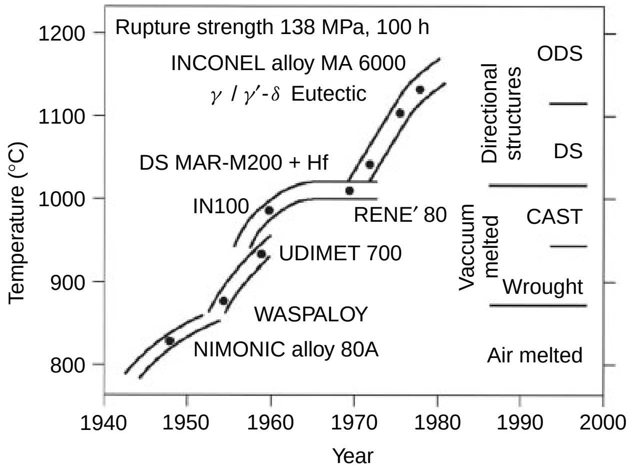

Figure 5 Progress in high-temperature engine component alloy development as a function of date, as measured by use temperature. The figure represents the service temperature at which a rupture life of 100 h would be obtained under a stress of 138 MPa. (Ref. 34. Reproduced by kind permission of Springer Science & Business Media)

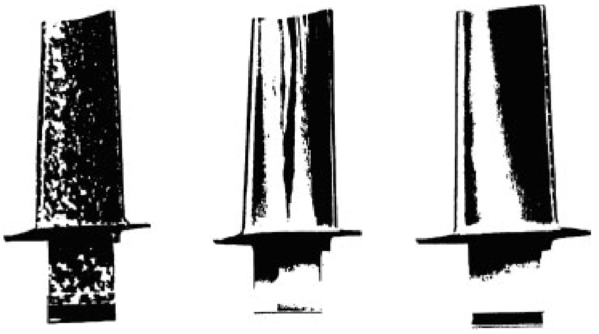

(a) Polycrystal (b) Columnar crystal (c) Single crystal

Figure 6 Advances in turbine airfoil technology from polycrystal to columnar crystal to single-crystal castings. (Ref. 28. Reproduced by permission of McGraw-Hill)[34]

casting technologies, leading from the earlier, polycrystalline turbine blades to directionally solidified, columnar grained, and then to single crystalline blades (Figure 6).[28] The latter are made by an ingenious grain selection process using a spiral solidification channel. In single crystalline material, grain boundary modifying additives are obviously no longer required, and heat treatments to reach optimum strength can be carried out without concern for coarsening grain boundary particulates that might coarsen detrimentally during treatment.

3.4 Titanium Alloys

With density and elastic modulus values between those of aluminum and iron, excellent chemical resistance, a β (bcc) → α (hcp) phase transition enabling strengthening heat treatments to be made, and ready alloyability with other transition metals and Al, Ti alloys have been developed for many uses in aerospace and the chemical industry. The principal currently used alloy is an $\alpha-\beta$ Ti alloy with 6% Al and 4% V; the next most commonly manufactured form is commercially pure, unalloyed Ti, which is also used in surgical implants. Recent developments include multicomponent alloys such as the low-creep rate $\alpha-\beta$ Ti-1100 alloy (with 6% Al, 2.75% Sn, 4.0% Zr, 0.40% Mo, and 0.45% Si) for jet engine compressors and the age-hardened Beta-C alloy (3% Al, 8% V, 6% Cr, 4% Mo, 4% Zr) with high corrosion resistance for high-temperature chloride environments.[35]

3.5 Cemental Carbides

These materials are extremely hard and wear resistant up to high temperatures (800 °C) and are used as high-speed cutting tools. They contain finely dispersed (1–3 µm size) particles of W, Ti, or Ta carbides (primarily WC) in a cobalt binder matrix (70–97.5% carbide). The direction of further development here is to produce and compound increasingly fine particulates, for example, by use of chemical precursor processes.[36]

4 STRUCTURAL INTERMETALLICS

Because of their special place in stimulating modern research on fundamental principles and the application of such principles to alloy design, we treat structural intermetallics in a special section. Due to their ordered structures and the concomitant additional bonding interactions between unlike neighbors, stoichiometric or near-stoichiometric intermetallics tend to be harder than a disordered phase of the same composition, but, at room temperature, much less ductile than such a hypothetical phase. However, some titanium and nickel aluminide intermetallics have such promising high-temperature properties that it became a challenging task for alloy designers to overcome the problem of low room-temperature ductility and absence of fracture toughness. Several causes for these deficiencies were identified, leading to different, specific alloying approaches to their remediation.[37,38]

The candidate materials are M_3Al, MAl, and MAl_3 aluminides, specifically Ti_3Al, TiAl, NiAl, Ni_3Al, and perhaps $TiAl_3$. Their structures are shown in Figure 7. It is seen that they all represent stoichiometric, ordered structures based on the three common metallic element structure types, the fcc, hcp, and bcc types (see above, Section 2.1). Compared to a material with cubic structure, hexagonal or tetragonal materials such as Ti_3Al or TiAl, respectively, have fewer available slip systems and hence, lower ductility; alloying to change their structures to a cubic one has therefore been

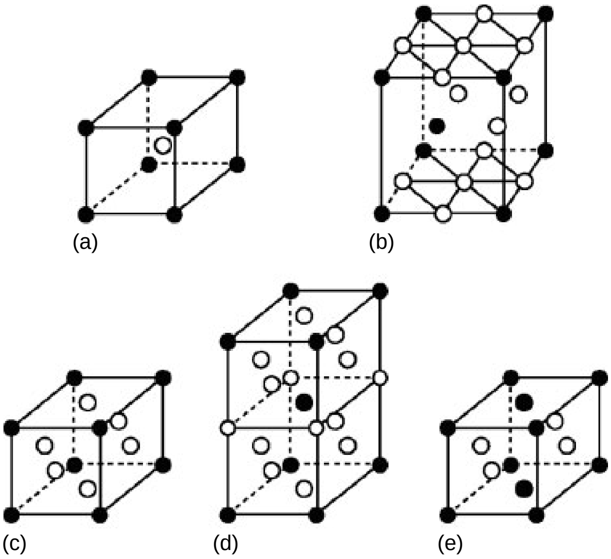

Figure 7 The unit cells of alloy phases of interest as high-temperature structural intermetallics; their structure types are: (a) NiAl: CsCl (cP2, B2) type; (b) Ti_3Al: Ni_3Sn (hP8, DO_{19}) type; (c) Ni_3Al: Cu_3Au (cP4, $L1_2$) type; (d) $TiAl_3$: $TiAl_3$ (tI8, DO_{22}) type; (e) TiAl: AuCu (tP4, $L1_{0)}$) type

considered semiempirically and theoretically and has been attempted experimentally.

One semiempirical theoretical approach has been based on structure maps (*see* ***Structure & Property Maps for Inorganic Solids***) such as the neighborhood map by Pettifor,[19,39] which is presented in a version most relevant to the issue at hand (Figure 8). These M_1–M_2–x maps, shown here for the system Ti–Al, represent selected stoichiometries for the compositions $A_{1-x}B_x$, with $x = 0$, 0.25, 0.33, 0.5, 0.67, 0.75, and 1. The plots are centered on $Ti_{1-x}Al_x$, and have as their planar coordinates the 'Mendeleev numbers' M_A and M_B of the constituents. They show the competing structure types forming in the neighborhood of the reference compound. The 'Mendeleev number' used in these maps expresses a mapping of the two-dimensional periodic table into a one-dimensional space; it characterizes the location of each element along a string run through the periodic table. If desired (i.e. cubic) phases are found in the neighborhood of the central phase, the map gives guidance in which direction along the A, B Mendeleev strings alloying should proceed. In the example chosen, it is seen that cubic phases are not found immediately near TiAl or $TiAl_3$, although for Ti_3Al the nearby (although not adjacent) phase Zr_3Al is seen to have the desired Cu_3Au type and suggests partial substitution of Ti by Zr; there are also potential substitutions with elements such as Fe or Ni that lie outside the range of this map. As mentioned above, the construction and availability of Pettifor maps has been much advanced recently by Ceder and associates.[20]

First-principles quantum mechanical calculations based on the Local Density Functional approximation have been able to obtain correctly the stable form of a given compound and to predict the energy difference between the ground state and the competing, desired Cu_3Au phase.[4] The theoretical alloy chemical approach has been complemented by many experimental studies on the effects of alloying on structure and properties.[37,38]

Another cause of poor room-temperature properties has been the grain boundary brittleness in a polycrystalline intermetallic such as Ni_3Al, which has good room-temperature strength as a single crystal. This problem was overcome when it was discovered[40,41] that minute additions of boron dramatically improve the room-temperature ductility and change the fracture mode of Ni_3Al, as seen in Figure 9.[41] Boron was found to segregate to the grain boundaries, but the mechanism of its dramatic effect is not clear. In one model it increases the cohesive strength of the grain boundaries and thus the bulk ductility (which is an unusual effect, since grain boundary segregation generally produces intergranular brittle fracture in otherwise ductile metals).[42] Another model for the boron-induced ductility effect assumes that the boron in the grain boundaries facilitates the motion of slip (the essential deformation mechanism in these intermetallic compound crystallites) across the grain boundaries, perhaps by inducing local disorder in the latter.

Briefly reviewing the technical structural intermetallic alloys, a commercial alloy based on Ni_3Al with small B, Zr, Hf, and Cr additions is now being commercialized for propulsion applications; TiAl- and Ti_3Al-based alloys are considered especially promising as matrix materials for metal-matrix composites that are given high-temperature strength by SiC or Al_2O_3 fibers.[28]

5 SELECTED APPLICATION: SPECIFIC ALLOYS

5.1 Magnetic Alloys

Magnetic alloys are classified into two categories:[44,45] soft (with low coercive field and small hysteresis loop) for alternating current devices and hard (with high coercive field and large energy product) for permanent magnet uses. Alloys for the former purpose are based on iron (which has the highest room-temperature saturation magnetization of all elements) and is alloyed for power transformer applications with about 3% Si to increase its electrical resistivity (thereby reducing eddy currents) and to reduce the loss-producing magnetic anisotropy. Amorphous Fe–Ni–Co based alloys (metallic glasses) with B and Si as glass formers produced by melt spinning constitute a new class of promising low loss alloys.[46] For higher frequencies, 'Permalloys' with 80% Fe, 20% Ni offer high magnetic permeability.

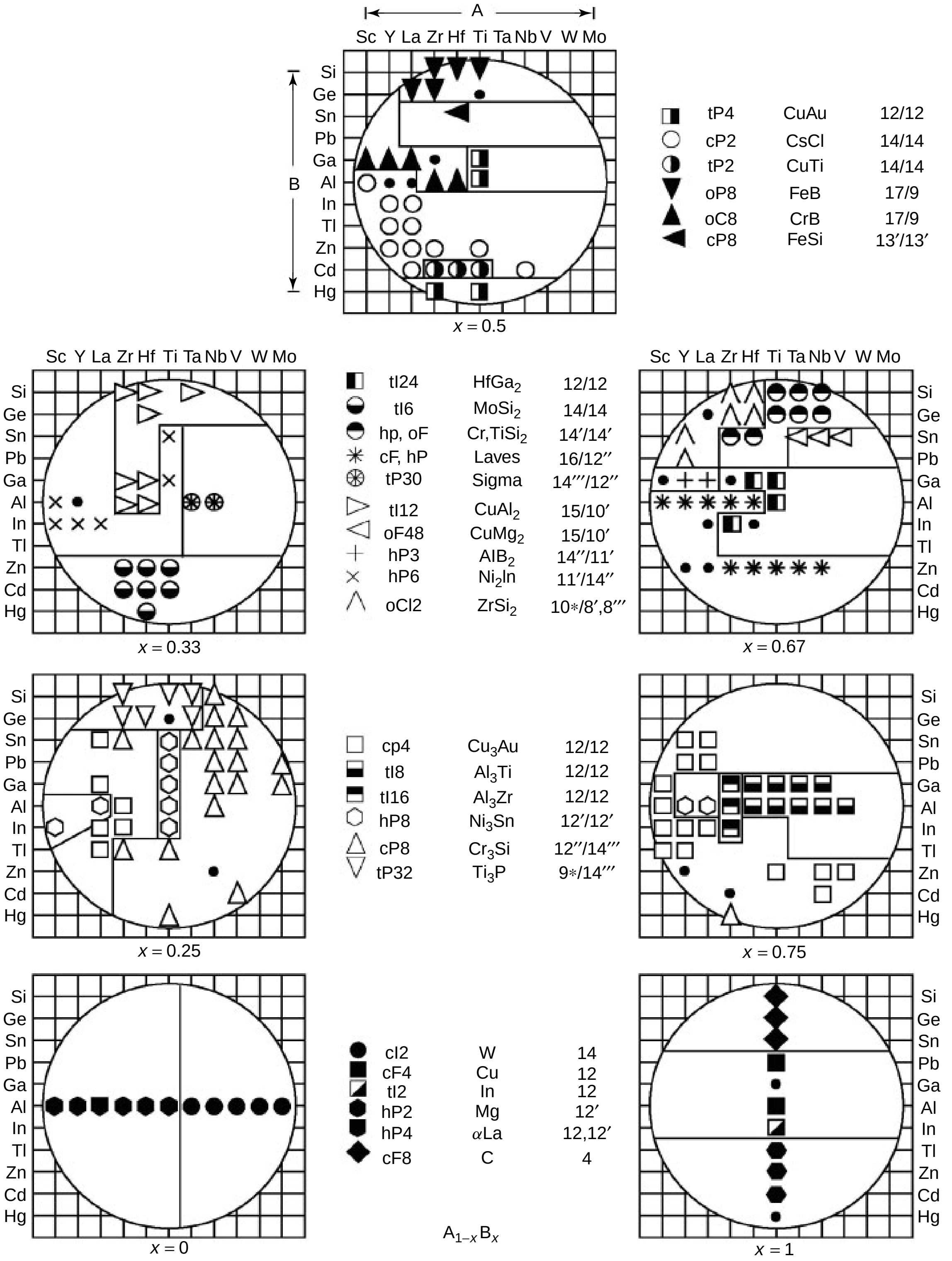
A
Sc Y La Zr Hf Ti Ta Nb V W Mo
B
Si Ge Sn Pb Ga Al In Tl Zn Cd Hg
x = 0.5
tP4 CuAu 12/12
cP2 CsCl 14/14
tP2 CuTi 14/14
oP8 FeB 17/9
oC8 CrB 17/9
cP8 FeSi 13′/13′
x = 0.33
x = 0.67
tI24 HfGa2 12/12
tI6 MoSi2 14/14
hp, oF Cr,TiSi2 14′/14′
cF, hP Laves 16/12″
tP30 Sigma 14‴/12″
tI12 CuAl2 15/10′
oF48 CuMg2 15/10′
hP3 AlB2 14″/11′
hP6 Ni2In 11′/14″
oCl2 ZrSi2 10*/8′,8‴
x = 0.25
x = 0.75
cp4 Cu3Au 12/12
tI8 Al3Ti 12/12
tI16 Al3Zr 12/12
hP8 Ni3Sn 12′/12′
cP8 Cr3Si 12″/14‴
tP32 Ti3P 9*/14‴
x = 0
x = 1
cI2 W 14
cF4 Cu 12
tI2 In 12
hP2 Mg 12′
hP4 αLa 12,12′
cF8 C 4
A1−x Bx

Figure 8 Titanium–aluminum neighborhood maps. (Ref. 4. Reproduced by courtesy of D. Pettifor)

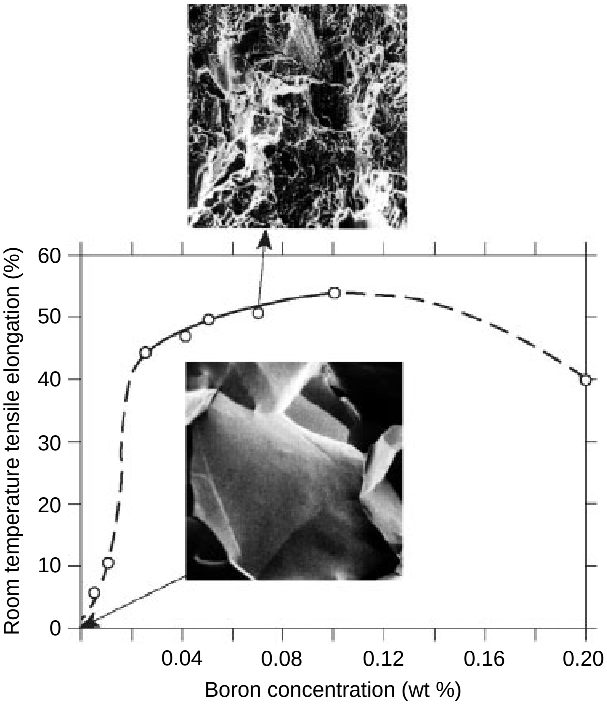

Figure 9 Enhancement of tensile elongation and change of fracture type of Ni_3Al (with 24 at. % Al) by small boron additions. (Ref. 43. Reproduced by kind permission of Springer Science & Business Media)

Hard (permanent) magnet materials have advanced from hardened steel via cast Alnico (iron–aluminum–nickel–cobalt) magnets to modern AB_5 and A_2B_{17} rare earth–cobalt alloy magnets such as $SmCo_5$ and Sm_2Co_{17}, which are made from powder particles compacted in a magnetic field and subsequently sintered to fully bring out their magnetic anisotropy. The $SmCo_5$ magnetic compound has the hexagonal $CaCu_5$ structure discussed and shown for $LaNi_5$ in the section on hydrogen absorbing alloys, below. A further advance in this area was the discovery and development[47] of the compound $Fe_{14}Nd_2B$, which can be made by rapid solidification processing, grinding the melt-quenched ribbons, and hot pressing the powder to final shape. These high-energy-product magnets are now widely available at low cost.

5.2 Superconductor Alloys

Superconductivity is the absence of resistance to dc conduction; this occurs only below a critical temperature T_c, a critical magnetic field H_c (which is a function of T and current density j), and a critical current density j_c, which is a function of T and H.[48] For alloys, T_c does not exceed 23–24 K (by contrast, some of the recently discovered ceramic high-T_c cuprate superconductors, such as $HgBa_2Ca_2Cu_3O_x$, have T_c values as high as 140 K and can have comparable j_c values),[49] Designers of superconducting solenoid magnets for use in laboratory equipment, magnetic resonance imaging devices, and particle accelerators require current densities of 10^5–10^6 A cm^{-2} in fields of 10–15 T (100–150 kG) at liquid He temperature (4.2 K). These properties can only be met by alloys displaying type II superconductivity; in these, the magnetic field (which is completely excluded by a type I superconductor when it is in its superconducting state) may penetrate the superconductor partially, producing a mixed state of normal (nonsuperconducting) regions containing the magnetic flux (flux lattice) and superconducting regions carrying the supercurrent.

Currently used magnet coil alloys are of two kinds: Nb–Ti solid solutions with $T_c < 9.5$ K and $H_c \leq 10$ T and intermetallic compound superconductors with the Cr_3Si (cI8, A15) type structure shown in Figure 10, such as Nb_3Sn with $T_c = 18.3$ K and $H_c \sim 15$ T; even larger H_c values are possible. In Nb–Ti the flux lattice is pinned by defects introduced by a high degree of cold working that occurs in the course of drawing the alloy rods clad in copper into a complex, multistrand wire. For the brittle A15 type materials, drawing in this way would introduce cracks; the compound is therefore formed in situ by a diffusion process combining Nb cores and Sn supplied either by a pool of Sn or a Cu–Sn bronze matrix. An actual wire with a diameter of 1–2 mm made by this process is composed of thousands of filaments formed into bundles.[50]

5.3 Shape Memory Alloys (SMAs) and Magnetostrictive Alloys

Certain intermetallics, among them stoichiometric NiTi and some CuZn-based phases, transform from a high-symmetry elevated temperature phase (CsCl type for NiTi) to

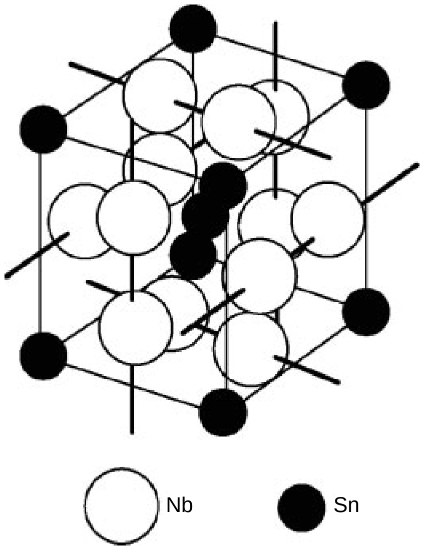

Figure 10 Unit cell of the Cr_3Si (cP8, A15) type superconducting intermetallic Nb_3Sn showing interpenetrating, orthogonal Nb atom chains. (Ref. 48. Reproduced by courtesy of W.L. Johnson)

a lower-symmetry room-temperature form by a diffusionless martensitic shear transformation.[43,51,52] The TiNi alloy is especially prominent under the designation NITINOL.[53]

These martensites have a large plastic deformability such that an SMA wire or sheet can be deformed into an arbitrary shape at ambient temperatures, for example, made into a loop. Upon heating and reversal to the cubic form, the part regains its original shape. In some properly 'trained' SMAs the reversible shape change occurs on cooling and subsequent reheating of the alloy. The martensites responsible for this remarkable effect form in lenticular shapes or laths as seen in Figure 11(a) for an Fe–Ni–Al SMA that exhibits a fractal behavior of self-similar lenses on ever-smaller scales, as shown in Figure 11(b) together with a measurement of the pertinent fractal dimension.[43] SMAs with their complex thermomechanical behavior are perhaps among the first alloy representatives of 'intelligent materials' or 'smart materials' that can sense their environment and adapt their properties to it. SMAs are industrially manufactured for applications as sensors, actuators in safety devices, spacecraft and automotive parts, and medical devices such as vascular implants (stents), blood vessel screens and probes.[54]

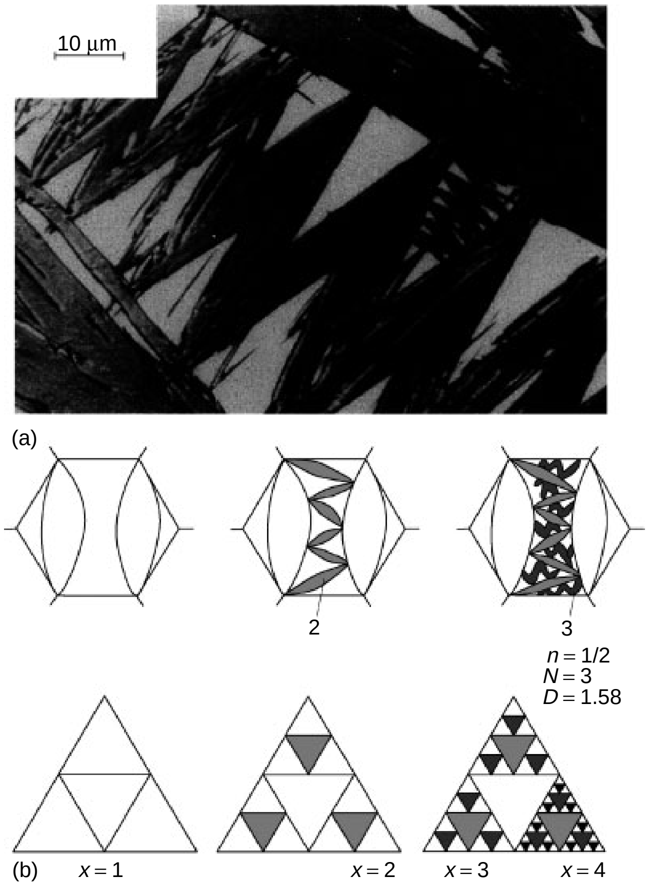

Figure 11 (a) Fractally distributed martensite phase α (dark) and residual, untransformed austenite phase γ (light) in an Fe–Ni–Al shape memory alloy (SMA); (b) (top row) schematic representation of the fractal fragmentation of austenite crystallite by martensite formation, resulting (top right) in the structure shown in (a); (bottom row) a fractal process of dimension $D = 1.58$ (Sierpinski triangle) shown for comparison. (Ref. 43. Reproduced by permission of Springer)

Magnetostrictive alloys form a subset of shape memory alloys; they undergo reversible martensitic transformations upon application and reversal of magnetic fields, resulting in large recoverable strains. Such alloys are useful as sensors and activators; a typical, widely used magnetostrictive sensor alloy is TERFENOL-D ($Tb_{1-x}Dy_xFe_2$) for which the strain is about 0.2%; large values (up to 6% in some experimental alloys such as Ni_2MnGa) are evidence of giant magnetostriction.[55]

5.4 Hydrogen Absorbing Alloys

A number of pure metals and alloys form hydrides with densities of hydrogen atoms per unit volume exceeding that of liquid hydrogen (Table 1),[56] suggesting their use as hydrogen storage media for hydrogen-based energy applications such as automotive systems.[57] Further, the reversible uptake of hydrogen can be used to form the anode (negative terminal) in secondary (storage) batteries as a hydrogen charged (metal hydride) electrode.

To be useful for storage, a candidate alloy should have a room-temperature hydride dissociation pressure in the range of 1–2 atm, with a pressure plateau ranging up to a stoichiometric ratio of hydrogen:metal ~1, with good resistance to degradation of these properties on cycling and with a reasonable materials cost. These conditions are best met by intermetallics such as FeTi, NiTi, Mg_2Ni, and $LaNi_5$, which combine an early group element having a large negative enthalpy of hydride formation with a late transition element having a small positive enthalpy, thus reducing the compound's enthalpy of hydride formation into the range appropriate for the desired dissociation pressure; possibly, the Fe or Ni component also catalyzes the reaction. (Enthalpy of formation is the dominant component-variable term in the Gibbs free energy of hydride formation, the entropy of the process being uniformly large and negative.)

Table 1 Hydrogen content of various media[56]

Medium	Density ($g\,cm^{-3}$)	Wt % of H	Atoms of H/cm^3 (10^{22})
H_2 (liquid)	0.07	100	4.2
H_2 (gas, 150 atm, 20 °C)	0.012	100	0.38
NH_3 (liquid)	0.6	17.7	6.5
MgH_2	1.4	7.6	6.7
TiH_2	3.8	4.0	9.1
VH_2	–	2.08	11.37
Mg_2NiH_4	2.6	3.6	5.6
$FeTiH_{1.74}$–$FeTiH_{0.14}$	–	1.52	5.5
$LaNi_5H_6$	8.25	1.37	6.76

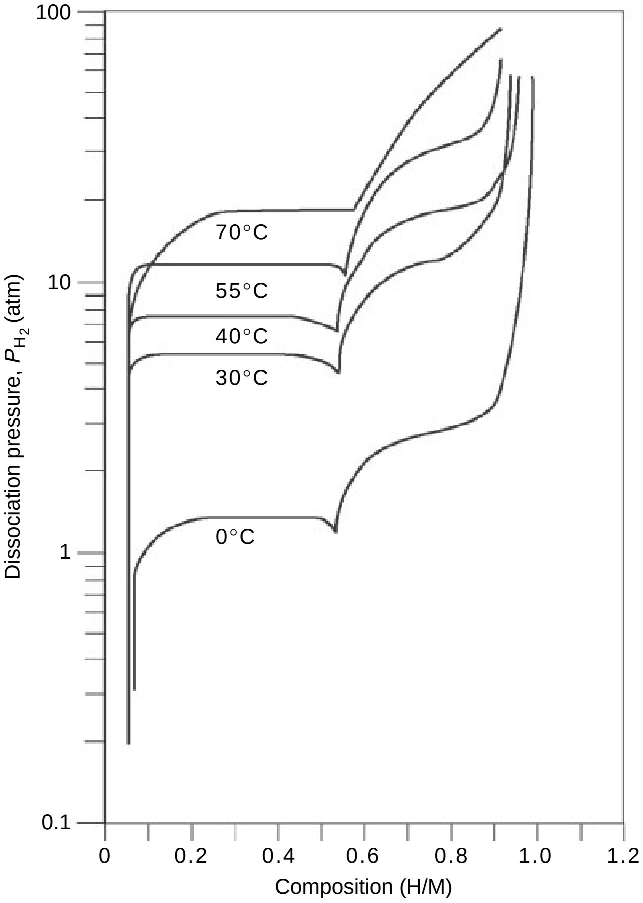

Figure 12 Hydrogen pressure–composition isotherms for the FeTi–hydrogen system.[56] (Reprinted with permission from Ref. 58. © 2003 American Chemical Society)

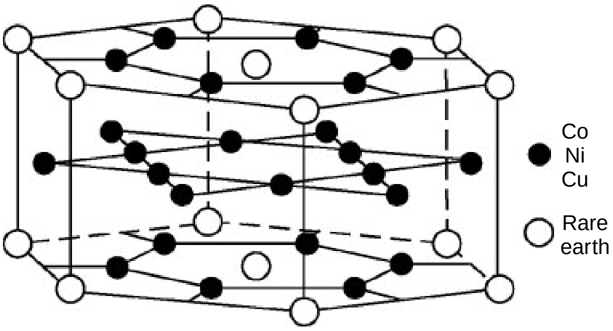

Figure 13 Pictorial representation of three unit cells of the $CaCu_5$ (hP6, $D2_d$) type structure of $LaNi_5$ and $SmCo_5$. (Ref. 32. Reproduced by permission of Kamal Girgis-deceased)

A representative isotherm plot is shown for FeTi in Figure 12.[58]

FeTi and NiTi have the ordered CsCl (cP2, A2) type structure shown in a different context for AlNi in Figure 5. $LaNi_5$ has the hexagonal $CaCu_5$ (hP6, $D2_d$) type structure shown in Figure 13.[32] (This structure type is also adopted by the magnetic compound $SmCo_5$, as mentioned above in Section 5.1.)

FeTi and $LaNi_5$ are currently the preferred ambient temperature storage and battery materials. FeTi and alloys derived from it by substitution are less expensive than $LaNi_5$ (by a factor of 5, based on recent raw materials cost) and therefore preferred for bulk storage applications, but $LaNi_5$ appears to have functional advantages such as lower sensitivity to degradation and deactivation and is currently preferred for secondary batteries. To lower the price of $LaNi_5$, La can be replaced by Mischmetal (M), a less expensive, commercial mixture of unseparated rare earth metals with about 50% Ce, 30% La, and 15% Nd, the rest consisting of the other 10 stable rare earth metals. This replacement, however, raises the plateau pressure and requires additional alloying with Ca (substituting for M) and elements chosen from the group Fe, Co, Mn, Cu, or Al (substituting for Ni) to modify the plateau pressure back to acceptable values.[59] Practical hydrogen absorbing alloy systems thus require complex alloy chemistry. In advanced FeTi type bcc alloys such as Ti-V-Mn and Ti-V-Cr, up to 2 H atoms per metal atom can be reversibly absorbed.[60]

This field receives additional attention as the interest in a hydrogen fuel economy increases; a recent review comparing storage of H in alloys with that in other media is found in Ref. 57.

5.5 Soldering and Brazing Alloys

Solders are relatively low-melting alloys used over a wide range of applications from plumbing to electronic device interconnects. They are generally eutectic alloys (a eutectic, i.e. a 'well-melting' composition in a binary alloy system lies at the intersection of two liquidus (melting) curves and thus is the composition where the melt is in equilibrium with the corresponding two solid phases; it represents the lowest melting temperature in that portion of the phase diagram).

The classical electronics solder alloy (Sn + 37 wt% Pb) contains the inhalation-toxic element lead and is being replaced in electronics for health reasons.[61] A Pb-free solder is Sn-3.5 wt% Ag;[62] indium and bismuth alloys are other eutectic-forming alloying additives to Sn.[21,22] The classical brazing alloy is at the Cu–Ag eutectic (Ag + 28.1 w% Cu) and is well suited for mechanically strong contacts with Cu and its alloys.

5.6 Coatings and Alloy Corrosion

New technologies are advancing the age-old methods for giving alloys high surface hardness for wear resistance and fatigue resistance, while retaining the toughness and strength of the core.[28] Traditional induction thermal methods have now been joined by the capability for laser treatment; the high energy density of the laser beam and the self-quenching aspect of the process, where the workpiece itself acts as an efficient cooling medium, have combined in research arrangements to produce local cooling rates as high as 10^8 °C/s. If alloys are surface-melted under these conditions, metastable phase formation may result.[63]

Glow discharge of plasmas as a means of producing reactive ions for enhanced surface reaction are exploited in the ion nitriding[64,65] and ion carborizing[66] processes. The rather complex surface and near-surface gas-phase chemistry may involve gas reactions with sputtered surface ions and redeposition of the product.[66] Other coating technologies include ion implantation of Ti or N to improve fatigue resistance in steels, physical vapor deposition (PVD) and plasma-assisted PVD to produce hard TiN coatings,[28] and boridation.[67]

Corrosion and corrosion protection of pure metals form a vast field not covered here. For alloys, corrosion may involve de-alloying (preferential loss of one constituent) if they have different electrochemical potentials;[68] such processes have been modeled on the atomic scale by Monte Carlo methods.[69]

More generally, with greater understanding of bulk properties, interest in alloy surface processes and their dynamics has risen.[70]

6 PREPARATION AND CHARACTERIZATION

6.1 Alloy Preparation

Traditional methods comprising the vast field of alloy preparation such as smelting, purification, fabrication are not covered here; however, a few selected methods of current interest are listed with references. These include:

Rapid solidification processing (RSP), for example, by melt spinning onto a cooled copper drum, which is capable of retaining many alloys in a glassy (amorphous) state or in nanocrystalline form;[11]

Deposition by sputtering and laser ablation (vapor-phase transfer from a target bombarded by inert gas ions or laser beam) or ion beam mixing of nanoscale multilayers,[71] all of which similarly can produce nonequilibrium species;

Mechanical alloying, a process in which elemental powders are blended and alloyed by ball milling, can produce ultrafine grain sizes and nonequilibrium phases that store the mechanical energy imported in the process.[72]

6.2 Alloy Characterization

The current detailed knowledge of atomic-scale processes in alloys and the technical products made from them is due to the enormous recent advances in instrumentation, primarily in the area of analytical electron microscopy (AEM). High-resolution transmission electron microscopy (HRTEM)[73] and scanning transmission electron microscopy (STEM) permit resolution into the 0.1 and 0.2 nm range, respectively; corresponding micro-diffraction data for local structure analysis are obtained by convergent beam electron diffraction (CBED). These structural methods are further supported by submicron volume chemical analysis, by electron energy loss spectroscopy (EELS) and atom location by channeling-enhanced microanalysis (ALCHEMI),[74] supplementing the standard method of energy dispersive X-ray emission spectroscopy (EDS).[73] Three-dimensional atom distribution probes (3DAPs), a further development of field ion microscopy (FIM), permits atomic-scale materials analysis.[75]

An overview of methods for surface and interface analysis of metals and alloys is available.[76] Important atomic-scale surface structure information can be gathered by scanning tunneling microscopy (STM) or scanning atomic force microscopy (SAFM), complementing scanning electron microscopy (SEM), field ion microscopy (FIM), and small-angle neutron scattering (SANS).[69]

7 RELATED ARTICLES

Borides: Solid-state Chemistry; Carbides: Transition Metal Solid-state Chemistry; Electronic Structure of Solids; Quasicrystals; Structure & Property Maps for Inorganic Solids; Superconductivity; Zintl Compounds.

8 REFERENCES

1. J. J. Moore, ‘Chemical Metallurgy’, Butterworths, London, 1981.
2. R. W. Cahn and P. Haasen eds, ‘Physical Metallurgy’, 4th edn., North-Holland, Amsterdam, 1996.
3. P. Haasen and B. L. Mordike, ‘Physical Metallurgy’, 3rd edn., Cambridge University Press, Cambridge, 1996.
4. D. G. Pettifor, in ‘Ordered Intermetallics – Physical Metallurgy and Mechanical Behavior’, NATO-ASI Series E, Vol. 213, eds. C. T. Liu, R. W. Cahn, and G. Sauthoff, Kluwer Academic Publishers, Dordrecht, 1992, p. 47.
5. R. Hoffmann, ‘Solids and Surfaces: A Chemist’s View of Bonding in Extended Structures’, Wiley-VCH, New York, 1989.
6. L. H. Dubois, L. V. Interrante, M. E. Gross, and K. F. Jensen eds, ‘Chemical Perspectives of Microelectronic Materials II’, MRS Symposium Proceedings, Vol. 204, Materials Research Society, Pittsburgh, PA, 1991.
7. C. J. Brinker, D. E. Clark, D. R. Ulrich, and B. J. J. Zelinsky eds, ‘Better Ceramics through Chemistry IV’, MRS Symposium

Proceedings, Vol. 180, Materials Research Society, Pittsburgh, PA, 1990.

8. ‘Chemistry of Materials’, A Journal of the American Chemical Society, Washington, DC.
9. J. Westbook, *Met. Trans.*, 1977, **8A**, 1327.
10. A. Inoue, *Prog. Mater. Sci.*, 1998, **43**, 365.
11. H. H. Liebermann eds, ‘Rapidly Solidified Alloys: Processes, Structures, Properties, Applications’, Marcel Dekker, Parsippany, NJ, 1993.
12. W. L. Johnson, *Mater. Res. Soc. Symp. Proc.*, 1999, **554**, 311.
13. H. Gleiter, in ‘Advanced Structural and Functional Materials’, ed. W. G. J. Bunk, Springer, Berlin, 1991, p. 1.
14. L. M. Marzan and D. J. Norris, *Mater. Res. Soc. Bull.* 2001, **26**(12), 981.
15. P. Villars and L. D. Calvert, ‘Pearson’s Handbook of Crystallographic Data for Intermetallic Phases’, ASM International, Materials Park, OH, 1985.
16. D. de Fontaine, in ‘Ordered Intermetallics – Physical Metallurgy and Mechanical Behavior’, NATO-ASI Series E, Vol. 213, eds. C. T. Liu, R. W. Cahn, and G. Sauthoff, Kluwer Academic Publishers, Dordrecht, 1992, p. 37.
17. D. G. Pettifor, *Acta Mater.*, 2003, **51**, 5649.
18. C. T. Sims, in ‘Superalloys 2’, eds C. T. Sims, N. S. Stoloff, and W. C. Hagel, Wiley, New York, 1987, p. 217.
19. D. G. Pettifor and J. Phys, *Cond. Mater.*, 2003, **15**, V13.
20. D. Margan, J. Rodgers, and G. Ceder, *J. Phys.: Condens. Matter.*, 2003, **15**, 4361.
21. M. Hansen, ‘Constitution of Binary Alloys’, McGraw-Hill, New York, 1958; R. P. Elliott, ‘First Supplement’, McGraw-Hill, New York, 1965; F. A. Shunk, ‘Second Supplement’, McGraw-Hill, New York, 1969.
22. T. Massalski ed., ‘Binary Alloy Phase Diagrams’, 2nd edn., ASM International, Materials Park, OH, 1990.
23. J.-C. Zhao, *J. Mater. Res.*, 2001, **16**, 1565.
24. J. Hafner, ‘From Hamiltonians to Phase Diagrams’, Springer-Verlag, Berlin, 1987.
25. L. Kaufman, in ‘Alloy Phase Stability’, NATO-ASI Series E, Vol. 163, eds. G. M. Stocks and A. Gonis, Kluwer Academic Publishers, Dordrecht, 1989, p. 145.
26. N. Saunders and A. P. Miodownik, ‘CALPHAD, a Comprehensive Guide’, Elsevier Science, New York, 1998.
27. I. Ansara and B. Sundman, in ‘Computer Handling and Dissemination of Data’, ed. P. S. Glaeser, Elsevier Science, New York, 1987, p. 154.
28. W. F. Smith, ‘Structure and Properties of Engineering Alloys’, 2nd edn., McGraw-Hill, New York, 1993.
29. E. Hornbogen, in ‘Physical Metallurgy’, 3rd edn., eds. R. W. Cahn and P. Haasen, North-Holland, Amsterdam, 1983, Chap. 16.
30. A. J. W. Martin, *Annu. Rev. Mater. Sci.*, 1988, **18**, 101.
31. A. L. Greer, *Mater. Sci. Eng.*, 2001, **A 304–306**, 68.
32. K. Girgis, in ‘Physical Metallurgy’, 3rd edn., eds. R. W. Cahn and P. Haasen, North-Holland, Amsterdam, 1983, Chap. 5.
33. C. J. Small and N. Saunders, *Mater. Res. Soc. Bull.* 1999, **24**(4), 22.
34. J. K. Tien, G. E. Vignoul, E. P. Barth, and M. W. Kopp, in ‘Structural and Phase Stability of Alloys’, eds J. L. Moran-Lopez, F. Mejia-Lira, and J. M. Sanchez, Plenum Press, New York, 1992, p. 1.
35. C. G. Rhodes and N. E. Paton, *Met. Trans.*, 1977, **8A**, 1749.
36. M. Nowakowski, K. Su, L. Sneddon, and D. Bonnell, in ‘Nanophase and Nanocomposite Materials’, MRS Symposium Proceedings, Vol. 286, eds. S. Komarneni, J. C. Parker, and G. J. Thomas, Materials Research Society, Pittsburgh, PA, 1993, p. 425.
37. S. H. Whang, C. T. Liu, D. P. Pope, and J. O. Stiegler eds, ‘High-Temperature Aluminides and Intermetallics’, TMS, Warrendale, PA, 1990.
38. L. A. Johnson, D. P. Pope, and J. O. Stiegler eds, ‘High-Temperature Ordered Intermetallic Alloys IV’, MRS Symposium Proceedings, Vol. 213, Materials Research Society, Pittsburgh, PA, 1991.
39. D. G. Pettifor, in ‘Intermetallic Compounds, Structure and Mechanical Properties’, ed. O. Izumi, Japanese Institute of Metals, Sendai, 1991, p. 149.
40. K. Aoki and O. Izumi, *J. Jpn. Inst. Met.*, 1979, **43**, 1190.
41. C. T. Liu, in ‘Alloy Phase Stability’, NATO-ASI Series E, Vol. 163, eds. G. M. Stocks and A. Gonis, Kluwer Academic Publishers, Dordrecht, 1989, p. 7.
42. S. P. Chen, A. F. Voter, P. C. Alberts, A. M. Boring, and P. J. Hay, *J. Mater. Res.*, 1990, **5**, 955.
43. E. Hornbogen, in ‘Advanced Structural and Functional Materials’, ed. W. G. J. Bunk, Springer, Berlin, 1991, p. 133.
44. F. E. Luborsky, J. D. Livingston, and G. Y. Chin, in R. W. Cahn and P. Haasen eds, ‘Physical Metallurgy’, 4th edn., North-Holland, Amsterdam, 1996, Chap. 26.
45. C. D. Graham Jr, in ‘Encyclopedia of Physics’, 2nd edn., eds. R. G. Lerner and G. L. Trigg, VCH, New York, 1991, p. 669.
46. F. E. Luborsky ed., ‘Amorphous Metallic Alloys’, Butterworths, London, 1983.
47. J. J. Croat, J. F. Herbst, R. W. Lee, and F. E. Pinkerton, *J. Appl. Phys.*, 1984, **55**, 2078.
48. W. L. Johnson, in ‘Physical Metallurgy’, 3rd edn., eds. R. W. Cahn and P. Haasen, North-Holland, Amsterdam, 1983, Chap. 27.
49. A. Schilling, M. Cantoni, J. D. Guo, and H. R. Ott, *Nature*, 1993, **363**, 56.
50. A. R. Kaufmann and J. J. Pickett, *J. Appl. Phys.*, 1971, **42**, 58.
51. C. T. Liu, H. Kunsmann, K. Otsuka, and M. Wuttig eds, ‘Shape Memory Materials and Phenomena – Fundamental Aspects and Applications’, MRS Symposium Proceedings, Vol. 246, Materials Research Society, Pittsburgh, PA, 1992.
52. K. Otsuka and T. Kakeshita, *Mater. Res. Soc. Bull.* 2002, **27**(2), 91.

53. W. J. Buehler, J. W. Gilfrich, and R. C. Wiley, *J. Appl. Phys.*, 1963, **34**, 1475.
54. T. W. Duerig, *Mater. Res. Soc. Bull.* 2002, **27**(2), 91.
55. T. Kakeshita and K. Ullakko, *Mater. Res. Soc. Bull.* 2002, **27**(2), 105.
56. T. Ohta ed., 'Solar-Hydrogen Energy Systems', Pergamon Press, Oxford, 1979, p. 200.
57. L. Schlapbach, *Mater. Res. Soc. Bull.*, 2002, **27**(9), 675.
58. J. J. Reilly and R. H. Wiswall Jr, *Inorg. Chem.*, 1974, **13**, 218.
59. G. D. Sandrock, in 'Hydrogen Energy System', eds. T. N. Veziroglu and W. Seifritz, Pergamon Press, Oxford, 1979, Vol. 3, p. 1625.
60. E. Akiba and M. Okada, *Mater. Res. Soc. Bull.*, 2002, **27**(9), 699.
61. J. Bath, C. Handwerker, and B. Bradley, *Circuits Assem.*, 2000, **11**, 30.
62. T. Y. Lee, W. J. Choi, K. N. Tu, J. W. Jang, S. M. Kuo, J. K. Lin, D. R. Frear, K. Zeng and J. K. Kivilahti, *J. Mater. Res.*, 2002, **17**, 291.
63. C. J. Lin and F. Spaepen, *Acta Metall.*, 1986, **34**, 1367.
64. E. I. Melitis, V. Singh, and J. C. Jiang, *J. Mater. Sci. Lett.*, 2002, **21**, 1171.
65. K. Marchev, R. Hidalgo, M. Landis, R. Vallerio, C. V. Cooper, and B. C. Giessen, *Surf. Coat. Technol.*, 1999, **112**, 67.
66. J. L. Marchand, D. Ablitzer, H. Michel, and M. Gantois, in 'Ion Nitriding and Ion Carborizing', eds. T. Spalvins, and W. L. Kovacs, ASM International, Materials Park, OH, 1990, p. 67.
67. J. Cataldo, F. Galligani and D. Harraden, *Adv. Mater. & Proc.*, 2000, **157**(4), 35.
68. A. J. Forty and G. Rowlands, *Phil. Mag.*, 1981, **43**, 171.
69. R. C. Newman, S. G. Corcoran, J. Erlebacher, M. J. Aziz, K. Zieradzki, *Mater. Res. Soc. Bull.*, 1999, **24**(7), 24.
70. N. C. Bartelt, *Mater. Res. Soc. Bull.*, 2002, **27**(12), 961.
71. R. F. Zhang and B. X. Liu, *J. Mater. Res.*, 2003, **18**, 1499.
72. S. Lauer, Z. Guan, H. Wolf, and Th. Wichert, *J. Mater. Res.*, 2002, **17**, 2130.
73. P. Buseck, J. Cowley, and Le. Roy. Eyring eds, 'High-Resolution Transmission Electron Microscopy and Associated Techniques', Oxford University Press, New York, 1992.
74. Y. L. Hao, R. Yang, Y. Y. Cui and D. Li, *J. Mater. Res.*, 2000, **15**, 2475.
75. A. Cerezo, D. J. Larson, and G. D. W. Smith, *Mater. Res. Soc. Bull.* 2001, **26**(2), 102.
76. P. H. Holloway and P. N. Vaidyanathan eds, 'Characterization of Metals and Alloys', Butterworth-Heinemann, Boston, MA, 1993.

Aluminum: Inorganic Chemistry

Allen W. Apblett
Oklahoma State University, Stillwater, OK, USA

1 Introduction 1
2 Preparation and Uses of Metallic Aluminum 2
3 Aluminum Hydrides and Related Complexes 4
4 Aluminum Halides 5
5 Aluminum Oxides and Hydroxides 7
6 Ternary and More Complex Oxide Phases 9
7 Aluminum Oxyacid Salts 11
8 The Aqua Ions and Aqueous Chemistry 12
9 Aluminosilicates 13
10 Aluminum Chalcogenides 13
11 Aluminum Pnictides 13
12 Mixed Aluminum Chalcogenide Halides 14
13 Aluminum Carbide and Borides 14
14 Alkoxides 14
15 Aluminum Carboxylates 15
16 Related Articles 15
17 Further Reading 15
18 References 15

Glossary

Astringent: any substance or agent that causes tissues to contract or that inhibits secretion of fluids such as mucus or blood
Friedel–Crafts reaction: an alkylation or acylation of an aromatic using alkyl or acyl chlorides in the presence of a Lewis acid catalyst
Trityl: the Ph_3C^+ cation

1 INTRODUCTION

Aluminum, having an abundance of 8.3% by weight, is the commonest metallic element in the Earth's crust. It occurs widely in igneous minerals such as feldspars and micas. Weathering of these has produced the clay minerals such as vermiculite $[Mg_{1.8}Fe^{2+}_{0.9}Al_{4.3}SiO_{10}(OH)_2(H_2O)_4]$, montmorillonite $[Na_{0.2}Ca_{0.1}Al_2Si_4O_{10}(OH)_2(H_2O)_{10}]$, and kaolinite $[Al_2(OH)_4Si_2O_5]$. The most commercially important mineral source of aluminum is bauxite $[AlO_x(OH)_{3-2x}\ (0 < x < 1)]$, which occurs in tropical and subtropical regions as a result of exhaustive leaching of silica and other metals from aluminosilicates. Aluminum also occurs in numerous well-known but rarer minerals such as spinel $[MgAl_2O_4]$, garnet $[Ca_3Al_2(SiO_4)_3]$, beryl $[Be_3Al_2Si_6O_{18}]$, cryolite $[Na_3AlF_6]$, and turquoise $[CuAl_6(PO_4)_4(OH)_8(H_2O)_4]$. Pure aluminum oxide, Al_2O_3, is known as corundum while many impure forms of Al_2O_3 occur naturally and find application as gemstones. For example, sapphires and rubies are primarily composed of aluminum oxide, but owe their distinctive colors to trace impurities. In the case of rubies, chromium yields a red color while titanium leads to the characteristic blue color of sapphires (the result of charge-transfer transitions involving the aluminum and titanium ions). Different concentrations of various impurities produce a range of colors from quite pale, owing to low concentrations, to quite deep blue. Other colors include: purple and pink, yellow, orange, green, and so on. Chrysoberyl ($BeAl_2O_4$) is both a useful gemstone and an important source for beryllium.

The high abundance of aluminum has resulted in a multitude of applications for the element and its compounds. Aluminum derives its name from alum, the double sulfate $KAl(SO_4)_2{\cdot}12H_2O$, which was used medicinally as an astringent in ancient Greece and Rome. Today, aluminum plays an important role as the pure metal and its alloys while its compounds have extensive applications as structural and medical ceramics, electronic and optical materials, catalysts, ionic conductors, coagulants for water purification, and reagents for preparation of other chemicals.[1–3]

Chemically, aluminum exhibits typical metallic behavior but it shows many similarities to boron. It combines with almost all nonmetallic elements to form compounds with aluminum in the +3 oxidation state. It also forms intermetallic compounds with metallic elements from all groups of the periodic table (*see* ***Alloys***). Aluminum exhibits exceptional affinity for oxygen and is often used as a reducing agent to obtain Cr, Mn, V (*see Thermite Reaction*). Finely powdered aluminum metal explodes upon contact with liquid oxygen but ordinarily the metal is protected from reaction with oxygen, water or dilute acids by an adherent protective oxide film. Complete reaction of aluminum may be accomplished by amalgamation with mercury or contact with solutions of salts of electropositive elements (e.g. $HgCl_2$) that destroy the oxide film. Aluminum dissolves readily in hot, concentrated hydrochloric acid (equation 1) and in aqueous NaOH or KOH at room temperature (equation 2).

$$Al(s) + 3HCl(aq) + 6H_2O \longrightarrow [Al(H_2O)_6]^{3+}(aq) + 3Cl^-(aq) + \frac{3}{2}H_2(g) \qquad (1)$$

$$Al(s) + MOH(aq) + 3H_2O \longrightarrow M^+(aq) + [Al(OH)_4]^-(aq) + \frac{3}{2}H_2(g) \qquad (2)$$

$Al(OH)_3$ is *amphoteric*, behaving both as a Brønsted acid and base. Thus, freshly precipitated hydroxide is readily soluble in both acid (equation 3) and alkali (equation 4).

$$Al(OH)_3(s) + 3H_3O^+(aq) \longrightarrow [Al(H_2O)_6]^{3+} \qquad (3)$$

$$\mathrm{Al_2(SiO_3)_3} \xleftarrow{\mathrm{SiO_2}} \mathrm{Al_2O_3} \xrightarrow{\mathrm{CaO}} \mathrm{Ca_3(AlO_3)_2}$$

Scheme 1 Solid-state amphoteric reaction of alumina

$$\mathrm{Al(OH)_3(s) + OH^-(aq) \longrightarrow [Al(OH)_4]^-(aq)} \tag{4}$$

Amphoteric behavior is also exhibited in the solid-state reactions of aluminum (Scheme 1).

Aluminum compounds of weak acids hydrolyze readily to $Al(OH)_3$ and the protonated acid. For example, aluminum sulfide hydrolyzes with production of H_2S (equation 5). Similar reactions of the selenide and telluride provide the most facile method for synthesis of H_2 Se and H_2Te, respectively.

$$\mathrm{Al_2S_3 + 6H_2O \longrightarrow 2Al(OH)_3 + 3H_2S} \tag{5}$$

Similarly, the nitride, carbide, cyanide, carboxylate, and carbonate salts of aluminum are unstable in aqueous solution. Aluminum salts of strong acids form solutions of the hydrated cation (*see Hydrates*). These solutions are acidic owing to the partial dissociation of one of the coordinated water molecules (equation 6), the pK_a of $[Al(H_2O)_6]^{3+}$ being 4.95 (*see Acidity Constants*). Note that this pK_a is quite similar to that of acetic acid. The second step in the hydrolysis reaction yields a dihydroxide species that undergoes condensation to form polynuclear cations (see Section 8). Antiperspirants often include an ingredient called *aluminum chlorhydrate* that is really a mixture of the chloride salts of the monohydroxide and dihydroxide aluminum cations. The aluminum in these compounds causes pores on the surface of the skin to contract leading to a reduction in perspiration.

$$\mathrm{[Al(H_2O)_6]^{3+} \rightleftharpoons [Al(H_2O)_5(OH)]^{2+} + H^+(aq)} \tag{6}$$

If the pH of the solution is gradually increased, the deprotonation is accompanied by formation of hydroxide bridges to give polynuclear species and then to precipitation of the hydrous oxide. This hydrolysis is particularly useful for water clarification since the hydroxide nucleates on fine suspended particles, precipitating them from solution.

The amphoterism and facile hydrolysis of hydrates of aluminum salts make it impossible to prepare anhydrous salts by dehydration. For example, the strength of the aluminum–oxygen bond in $[Al(H_2O)_6]Cl_3$ precludes the formation of Al–Cl bonds and Al_2O_3 is obtained upon heating (equation 7).

$$\mathrm{2[Al(H_2O)_6]Cl_3 \xrightarrow{\Delta} Al_2O_3 + 6HCl + 9H_2O} \tag{7}$$

Some physical and chemical properties of aluminum are presented in Table 1. As expected for the [Ne] $3s^23p^1$ configuration, the fourth ionization potential is prohibitively high. Therefore, the most common oxidation state of aluminum is three although compounds of aluminum(I) can be prepared. However, the latter species quickly disproportionate to elemental aluminum and aluminum(III) compounds.

Table 1 Atomic and physical properties of aluminum

Property	Value
Atomic number	13
Number of naturally occurring isotopes	1
Atomic weight	26.98154
Electronic configuration	$[Ne]3s^23p^1$
Ionization energy ($kJ\,mol^{-1}$)	
I	577.4
II	1816.1
III	2744.1
IV	11563.0
Mp (°C)	660
Bp (°C)	2327
E^0 for $M^{3+} + 3e^- \rightarrow M(s)$ (V)	-1.66
Metal radius (pm)	143
Ionic radius (pm) (6-coord.) III	53.5

While compounds with three coordination are known, these species are strong Lewis acids and usually achieve four coordination by formation of three-center two-electron bonds, for example, Al_2Cl_6 (**1**) (*see Bridging Ligand*). Aluminum is not restricted to an octet of electrons in its valence shell and compounds with coordination numbers of five and six may be prepared, for example, $Cl_3Al{\cdot}2NMe_3$ (**2**), $[AlF_6]^{3-}$ (**3**).

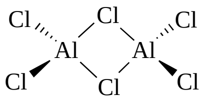

(**1**)

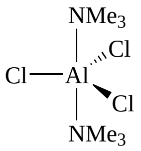

(**2**)

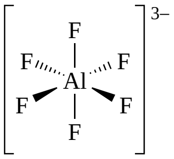

(**3**)

Aluminum-27 NMR is particularly useful for the identification of the coordination number of aluminum, both in solution and the solid state. This nucleus is 100% abundant and fairly easy to observe despite its quadrupolar nature ($I = 5/2$, $Q = 1.49 \times 10^{-29}\,m^2$). Tetrahedrally coordinated aluminum is found in the range $\delta = 40{-}140$ ppm, octahedrally coordinated aluminum between -46 and 40 ppm, and five-coordinate aluminum between 25 and 60 ppm.

2 PREPARATION AND USES OF METALLIC ALUMINUM

While aluminum occurs most commonly in aluminosilicate minerals, its extraction from them is prohibitively difficult. It is therefore prepared from bauxite in a two-step procedure. First, bauxite is purified by the Bayer process; this involves dissolution in aqueous NaOH, separation from insoluble impurities (red mud containing Fe_2O_3), and then precipitation of $Al(OH)_3$ by treatment of the solution with carbon dioxide. Calcining at 1200 °C produces Al_2O_3, which is subsequently electrolyzed to produce aluminum metal. The electrolysis is performed at 950 °C in molten cryolite (Na_3AlF_6); graphite-lined tanks are used as the cathodes and graphite rods as the anodes. The molten aluminum thus produced sinks to the bottom of the cell and is drawn off. The process requires vast amounts of electrical power and aluminum production is therefore usually associated with hydroelectric power generation.

Pure aluminum metal is a hard silvery-white metal with the face-centered cubic close-packed structure (*see Close Packing*). Among its many desirable properties are: it is light, nonmagnetic, nonsparking, and nontoxic, and is capable of taking a high polish. As well, it has high thermal and electrical conductivity, excellent corrosion resistance, and high malleability and ductility.

The use of aluminum as a structural metal appears to contradict the fact that it is a very reactive metal with a high negative standard reduction potential. Metallic aluminum is not found in nature for this reason. The cause of aluminum metal's stability is the formation of a protective oxide layer on the surface of the metal. Any exposed surface of aluminum metal reacts with dioxygen to form an impermeable layer of aluminum oxide, Al_2O_3 that is 1–100 nm thick. This layer protects the underlying aluminum from further chemical reaction with oxygen, water, and many other reactive chemicals. However, any reagent that can disrupt the oxide layer (especially acids, bases, chloride ions, and mercury salts) can result in corrosion or rapid reaction of aluminum. The formation of a strongly adherent, protective oxide layer can be explained by the close similarity between the ionic radius of the oxide anion (124 pm) and the metallic radius of aluminum (143 pm) as well as the extremely small radius of aluminum(III) ions (53.5 pm). As a consequence, the oxygen ions can pack readily on the aluminum surface while the aluminum ions formed by oxidation enter the interstitial octahedral sites of the oxygen lattice as shown in Figure 1.

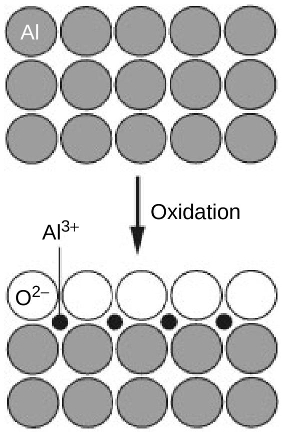

Figure 1 Schematic representation of the formation of the oxide layer on aluminum metal

The protection afforded by the native oxide layer may be enhanced by anoding the metal. This is done by immersing the metal in 15–20% sulfuric acid and connecting it to the positive terminal so that the metal at the surface is oxidized to alumina. Usually, a layer 10–20 µm thick is used and this provides protection between pH 4.5 and 8.7 and makes the metal quite suitable for outdoor use. Thicker oxide layers also provide excellent abrasion resistance. Furthermore, the oxide layer may be colored by incorporating suitable organic or inorganic compounds. Photographic plates can also be prepared by incorporation of photosensitive materials.

Aluminum is now used extensively in the construction industry, for domestic utensils, drink containers, electrical cables (having twice the weight-for-weight conductance of copper) and as alloys in ship, aircraft, and spacecraft construction. In the last respect, the mechanical properties of aluminum can be greatly improved by alloying it with copper, manganese, silicon, magnesium, or zinc. The properties and uses of a number of typical alloys are given in Table 2. One particularly interesting intermetallic compound, Al_4Li_9, is formed by the reaction of lithium with aluminum. It

Table 2 Composition, properties, and applications of aluminum and its alloys

Alloy designation	Alloying metals	Properties and applications
1000 Series	Pure Al (<1% of other elements)	Good properties except for limited mechanical strength. Used in chemical equipment, reflectors, heat exchangers, buildings, and decorative trim.
2000 Series	Copper (~5%)	Excellent strength and machinability, limited corrosion resistance. Used for components requiring high strength/weight ratio, e.g. truck trailer panels, aircraft structure parts.
3000 Series	Manganese (~1.2%)	Moderate strength, high workability. Used for cooking utensils, heat exchangers, storage tanks, awnings, furniture, highway signs, roofing, side panels, etc.
4000 Series	Silicon (≤12%)	Low mp and low coefficient of expansion. Used for castings and as filler material for brazing and welding; readily anodized to attractive gray colors.
5000 Series	Magnesium (0.3–5%)	Good strength and weldability coupled with excellent corrosion resistance in marine atmospheres. Used for ornamental and decorative trim, streetlight standards, ships, boats, cryogenic vessels, gun mounts, and crane parts.
6000 Series	Magnesium/silicon	Good formability and high corrosion resistance. Used in buildings, transportation equipment, bridges, railings, and welded construction.
7000 Series	Zinc (3–8%) and magnesium	When heat treated and aged have a very high strength. Used principally for aircraft structures, mobile equipment, and equipment requiring high strength/weight ratio.

has a structure that contains polymeric zig-zag aluminum chains with lithium atoms between them. Each atom attains coordination number 14 (*see **Alloys***).

3 ALUMINUM HYDRIDES AND RELATED COMPLEXES

Allane, AlH_3, can be detected as a monomer and dimer when aluminum is vaporized in hydrogen but AlH_3 is a colorless involatile solid that is extensively polymerized via Al–H–Al bonds. Several crystalline and amorphous phases of $(AlH_3)_n$ have been reported and the structure of α-AlH_3 has been determined by X-ray and neutron diffraction. Each aluminum is surrounded by six hydrogen atoms that bridge to six other aluminum atoms. All Al–H distances are identical (172 pm), suggesting three-center two-electron bonding. The Al–H–Al angle is 141° and the closest Al–Al distance is 324 pm. The latter is appreciably shorter than that found in aluminum metal (340 pm) but it is believed that there is no metal–metal bonding.**4**

AlH_3 is most conveniently prepared by the reaction of $LiAlH_4$ and $AlCl_3$ in diethyl ether (equation 8).

$$3LiAlH_4 + AlCl_3 \xrightarrow{Et_2O} 4AlH_3(OEt_2)_n + 3LiCl \qquad (8)$$

The LiCl is filtered off and, upon sitting, the filtrate deposits an intractable etherate of variable composition. This can be avoided by working up the solution with an excess of $LiAlH_4$ and some $LiBH_4$ in a large excess of benzene at reflux. This leads to the eventual formation of crystals of α-AlH_3. Variation of the conditions produces other crystalline modifications of AlH_3.

AlH_3 is thermally unstable above 150 °C and is a strong-reducing agent that reacts violently with water and other protic reagents with the liberation of hydrogen. Such reactions may be used to form $Al(NH_2)_3$, $Al(PH_2)_3$, and $Al(N_3)_3$. It readily forms adducts with strong Lewis bases but these are more conveniently prepared from the reaction of the aluminum trichloride adducts with lithium hydride (equation 9).

$$3LiH + L\cdot AlCl_3 \xrightarrow{Et_2O} L\cdot AlH_3 + 3LiCl \qquad (9)$$

The most studied adducts are the trialkylamine alanes. Trimethylamine reacts to give both 1:1 and 2:1 adducts with AlH_3, but the latter is stable only in the presence of an excess of amine. The monoamine has a tetrahedral structure (**4**) and is a white, volatile crystalline solid (mp 75 °C) that is readily hydrolyzed by water. Like the etherate, it slowly decomposes to $(AlH_3)_n$. The bisamine has a trigonal bipyramidal structure with the amines in the axial positions (**5**). This was the first compound in which aluminum was demonstrated to adopt a five-coordinate structure. Tetrahydrofuran also gives 1:1 and 1:2 complexes but diethyl ether only gives the 1:1 complex.

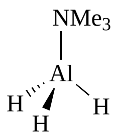
(**4**)

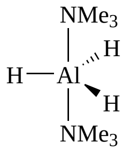
(**5**)

Lithium aluminum hydride, $LiAlH_4$, is a white solid that is stable in dry air but is rapidly decomposed by moisture. It is highly reactive towards all protic reagents and many organic functional groups. It is thermally unstable, decomposing rapidly at 100 °C. It may be synthesized by the reaction of LiH with $AlCl_3$ (equation 10). It is also prepared on the industrial scale by metathesis of $NaAlH_4$ with LiCl in diethyl ether, the sodium salt being prepared by direct high-pressure reaction of the elements (equation 11).

$$4LiH + AlCl_3 \xrightarrow{Et_2O} LiAlH_4 + 3LiCl \qquad (10)$$

$$Na + Al + 2H_2 \xrightarrow[350\ \text{atm}]{140\,^\circ C,\ THF} NaAlH_4 \qquad (11)$$

The structure of $LiAlH_4$, deviates considerably from the simple ionic formulation, $Li^+[AlH_4]^-$. It consists of tetrahedral AlH_4 groups (Al–H 155 pm) that are bridged by Li so that each Li is surrounded by four hydrogen atoms at 188–200 pm (cf. 204 pm in LiH) and a fifth at 216 pm.

$LiAlH_4$ is an outstanding versatile reducing and hydrogenating reagent for both organic and inorganic compounds.**4–6** The reaction of $LiAlH_4$ with inorganic halides produces a variety of products depending on the relative stabilities of the corresponding tetrahydroaluminate and element. The halides of groups 15 and 16 are converted cleanly to the corresponding hydrides (equation 12) while the halides of groups 9 and 10 are converted to unstable hydrido species that decompose to the metals (equation 13). Other transition metals and group 11 metals form complexes with AlH_4 (equation 14). In the latter complexes, aluminum is usually five-coordinate with structural units such as (**6**), (**7**), and (**8**).**7**

$$4MX_n + nLiAlH_4 \longrightarrow 4MH_n + nLiAlX_4 \qquad (12)$$

$$4MX_n + nLiAlH_4 \longrightarrow 4M + 2nH_2 + nLiAlX_4 \qquad (13)$$

$$4MX_n + nLiAlH_4 \longrightarrow M(AlH_4)_n + nLiX_4 \qquad (14)$$

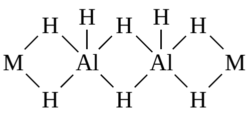
(**6**)

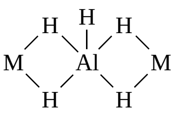
(**7**)

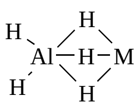
(**8**)

$LiAlH_4$ also reacts readily with inorganic oxides. For example, $COCl_2$ is converted to MeOH, CO_2 to $LiAl(OMe)_4$ or $LiAl(OCH_2O)$, and NO is reduced to hyponitrous acid, HON=NOH.

The most important applications of $LiAlH_4$ are in organic synthesis. It reacts with more than 60 organic functional groups (Table 3). Reactions are usually performed in ether, in which $LiAlH_4$ is highly soluble (22 wt%). For

Table 3 Products of reduction by $LiAlH_4$

Compound	Product
Reactive alkenes	Alkanes
$RCH{=}CH_2$	$[Al(CH_2CH_2R)_4]$
C_2H_2	$[AlH(CH{=}CH_2)_3]$
$RC{\equiv}CH$	$RCH{=}CH_2$
RX	RH (R not aryl)
ROH	$[Al(OR)_4]^-$ or $[AlH(OR)_3]^-$
RCHO	RCH_2OH
R_2CO	R_2CHOH
Quinone	Hydroquinone
RCO_2H, or $(RCO)_2O$, or RCOX	RCH_2OH
RCO_2R	$RCH_2OH + R'OH$
Lactones	Diols
$RCONH_2$	RCH_2CH_2
Epoxides	$RC(OH)CHR_2$
Episulfides	$R_2C(SH)CHR_2$
RSSR	RSH
RCOSR	RCH_2OH
$RCSNH_2$	RCH_2CH_2
RSCN	RSH
R_2SO or R_2SO_2	R_2S
RSO_2X	RSH
$ROSO_2R'$	RH
$ArOSO_2R'$	ArOH
RSO_2H	RSSR + RSH
RNC, RNCO, RNCS	RNHMe
RCN	RCH_2CH_2 or RCHO
$R_2C{=}NOH$	R_2CHNH_2
R_3NO	R_3N
R_2NNO	R_2NNH_2
RNO_2, RNHOH, RN_3	RNH_2
$ArNO_2$	ArN=NAr

many reactions, however, $LiAlH_4$ has been replaced by more selective, less expensive borohydrides or organometallic hydrides.

Lithium and sodium salts of $AlH_6{}^{3-}$ can be prepared by direct interaction of the metals under pressure or by reaction of $NaAlH_4$ with two equivalents of NaH (equation 15).

$$2NaH + NaAlH_4 \longrightarrow Na_3(AlH_6) \tag{15}$$

Another complex hydride, $Al(BH_4)_3$ (**9**), a colorless liquid (mp −64.5 °C, bp 44.6 °C), was the first compound demonstrated to be fluxional (*see Fluxional Molecule*). Its thermal decomposition also led to the first compound to be discovered and structurally characterized by NMR spectroscopy, $Al_2B_4H_{18}$ (**10**). Reaction of $Al(BH_4)_3$ with a variety of boranes produces compounds analogous to boron hydride clusters such as AlB_4H_{11}, $AlB_5H_{11}{}^-$, AlB_5H_{12}, $AlB_6H_{12}{}^-$, and AlB_6H_{13} (*see* ***Boron Hydrides***).[8]

4 ALUMINUM HALIDES

The monohalides of aluminum are produced as short-lived diatomic species in the gas phase by the reaction of the trihalides with aluminum at 1000 °C. The instability of these species is not a result of an unfavorable enthalpy of formation but is due to the facile disproportionation into the more stable AlX_3 species (equation 16, Table 4).

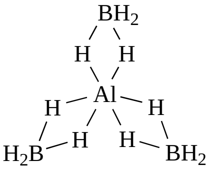

(**9**)

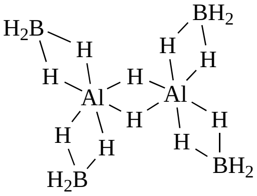

(**10**)

$$3AlX \longrightarrow 2Al + AlX_3 \tag{16}$$

AlF_3 is made by reaction of Al_2O_3 with HF gas at 700 °C (equation 17), while the rest of the trihalides may be prepared by the direct combination of the elements, a highly exothermic process. Of the four aluminum trihalides, AlF_3 is unique in being nonvolatile, insoluble, and in possessing a much higher heat of formation (Table 5).

$$Al_2O_3 + 6HF \longrightarrow 2AlF_3 + 3H_2O \tag{17}$$

These differences may result, in part, from the higher coordination number of aluminum in AlF_3. In it, each aluminum atom is surrounded by a distorted octahedron of six fluorine atoms. Each fluorine is two-coordinate, being corner-shared by pairs of octahedra. Thus, the structure is similar to ReO_3 and has a relatively open lattice. As a result, numerous sites exist for water molecules, leading to the occurrence of a wide range of nonstoichiometric and stoichiometric hydrates ($AlF_3{\cdot}(H_2O)_n$; $n = 1, 3, 9$). Quite curiously, no hexahydrate corresponding to $[Al(H_2O)_6]Cl_3$ is known.

The interaction of AlF_3 with metal fluorides provides an extensive family of structures that all contain octahedral AlF_6 units. AlF_6 octahedral units also occur in Na_3AlF_6 and $Li_3Na_3Al_2F_{12}$, but these do not contain discrete $[AlF_6]^{3-}$ ions since there is significant bonding between the AlF_6 units and the other metals. The Na_3AlF_6 structure is closely related to perovskite (ABO_3) in which one-third of the sodium and all the aluminum atoms occupy the octahedral ‘B’ sites and

Table 4 Properties of AlX

Compound(s)	AlF	AlCl	AlBr	AlI
ΔH_f° (kJ mol^{-1})	−393	−188	−126	−46
$\Delta H_{disprop}^\circ$ (kJ mol^{-1})	−105	−46	−50	−59
d(Al–X)	165.4	213.0	–	–

Table 5 Properties of crystalline AlX_3

Properties	AlF_3	$AlCl_3$	$AlBr_3$	AlI_3
Mp (°C)	1290	192.4	97.8	189.4
Sublimation pt (1 atm/°C)	1272	180	256	382
ΔH_f° (kJ mol^{-1})	1498	707	527	310

the remaining two-thirds of the sodium atoms occupy the 12-coordinate 'A' sites (*see* ***Oxides: Solid-state Chemistry***).

The sharing of two opposite vertices of AlF_6 units, as in Tl_2AlF_5, leads to polymeric chains with 'AlF_5' stoichiometry. In $TlAlF_4$ and $KAlF_4$, AlF_6 units share four equatorial vertices, yielding layers with 'AlF_4' stoichiometry.

More complex patterns of sharing vertices occur in compounds with intermediate stoichiometries. For example, $Na_5Al_3F_{14}$ contains layers of 'Al_3F_{14}' built up by one-third of the AlF_6 octahedra sharing four equatorial vertices and the remainder sharing two opposite vertices. Na_2MgAlF_7 contains both AlF_6 and MgF_6 octahedra that are linked together by sharing four vertices of the AlF_6 units and all those of the MgF_6 units (*see* ***Fluorides: Solid-state Chemistry***).

As indicated earlier, Na_3AlF_6 (cryolite) is the most important aluminum fluoride since it serves as the solvent for the electrolytic preparation of aluminum.

Solid $AlCl_3$ also contains six-coordinate aluminum. The layered lattice exhibits a rapid increase in electrical conductivity as the melting point (192.4 °C) is approached, at which temperature it rapidly falls to zero. This coincides with an 85% increase in volume, which results from a change in coordination of aluminum from six to four. The melt consists of discrete Al_2Cl_6 molecules (**11**). These molecules predominate in the gas phase up to 400 °C, beyond which they dissociate to trigonal planar $AlCl_3$ monomers.

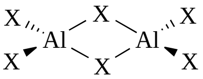

(**11**)

On the other hand, Al_2Br_6 and Al_2I_6 are both dimeric in the solid state as well as in the liquid and gaseous states. They also dissociate to monomers in the gas phase with $\Delta H_{\text{dissoc}} = 59$ and $50\ \text{kJ mol}^{-1}$ for the bromide and iodide, respectively.

In all the dimeric Al_2X_3 species, the terminal M–X distance is 10–20 pm shorter than the bridging M–X distance (Table 6). The external X–M–X angle is in the range 110–125° while the internal one is in the range 70–102° (*see* ***Hard & Soft Acids and Bases***).[9]

The trihalides of aluminum are very strong Lewis acids, and $AlCl_3$ finds extensive use as a Friedel–Crafts catalyst as a result of this. A wide variety of adducts are known and these exhibit an enormous range of stability, modes of bonding, structures, and properties.[10] Aromatic hydrocarbons and alkenes only interact weakly but crystalline adducts may be isolated, for example, the clathrate complex $Al_2Br_6{\cdot}C_6H_6$. Mesitylene and xylenes interact more strongly, forming weak monomeric complexes, $Br_3Al{\cdot}L$. A typical strong complex is formed by Me_3N, which forms both the tetrahedral 1:1 complex (**12**) and the 1:2 trigonal bipyramidal complex (**13**).

Table 6 Bond distances in Al_2X_6 molecules

X	M–X bridge (pm)	M–X terminal (pm)
Cl	2.21	2.06
Br	2.33	2.21
I	2.58	2.53

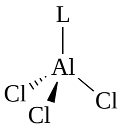

(**12**)

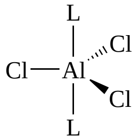

(**13**)

Vibrational spectroscopy indicates that alkyl halides form weak R–X–AlX_3 complexes. On the other hand, halides that are readily ionized (e.g. trityl chloride) show a high degree of charge separation and may be formulated as $R^+[AlCl_4]^-$. Acyl halides, RCOX, may coordinate through the halide atom, the carbonyl oxygen, or form ionic species, $RCO^+AlX_4{}^-$. However, vibrational spectroscopy and X-ray crystallography have not provided conclusive evidence concerning the reactive species present in Friedel–Crafts alkylations in nonaqueous solvents.

Aluminum's tendency to form tetrahedral $AlCl_4{}^-$ anions is exhibited in the formation of many interesting compounds. For example, the compound $Cl_3Al{\cdot}ClICl_2$ may be described as $[ICl_2]^+[AlCl_4]^-$. $POCl_3$ reacts with $AlCl_3$ to form three types of compounds, the ordinary 1:1 and 2:1 complexes (where $AlCl_3$ is O-bonded) and a third ionic species with the unusual formulation$[Al(OPCl_3)_6]^{3+}[AlCl_4]_3{}^-$. Similarly, $AlCl_3$ reacts with THF to form $[AlCl_2(THF)_4]^+[AlCl_4]^-$ while with acetonitrile, $[(MeCN)_5AlCl]^{2+}[AlCl_4]_2{}^-$ is obtained. Crystalline salts of $[AlCl_4]^-$ may also be obtained by reaction of alkali metal chlorides or $[R_4N]Cl$ with $AlCl_3$ in an organic solvent. $[AlBr_4]^-$ and $[AlI_4]^-$ salts may be obtained in a similar manner.

An oxonium salt may be readily prepared from the reaction of $AlCl_3$ with HCl in diethyl ether (equation 18). This is a viscous oil similar to quaternary ammonium salt ionic liquids.

$$AlCl_3 + HCl \xrightarrow{Et_2O} [(EtO)_nH]^+[AlCl_4]^- \tag{18}$$

Aluminum chloride/sodium chloride mixtures have been much used as a molten salt medium (mp 173 °C) for electrolytic and other reactions.[11] The principal equilibria that occur in solution are given in Scheme 2.

Conducting liquids are produced at room temperature by the reaction of 1-methyl-3-ethylimidazolium chloride or *N*-butylpyridinium chloride with $AlCl_3$. These liquids are good

$$2AlCl_4{}^- \rightleftharpoons Al_2Cl_7{}^- + Cl^-$$

$$2Al_2Cl_7{}^- \rightleftharpoons Al_3Cl_{10}{}^- + Cl^-$$

$$2Al_3Cl_{10}{}^- \rightleftharpoons Al_2Cl_6 + 2Cl^-$$

Scheme 2 Equilibria in $AlCl_3$/chloride melts solvents for both organic and inorganic compounds. The principal equilibrium in this case is between $AlCl_4^-$ (**14**) and $Al_2Cl_7^-$ (**15**) (equation 19). The bromide and iodide analogs of (**14**) and (**15**) are obtained from KX/AlX_3 ($X = Br, I$) melts.[11]

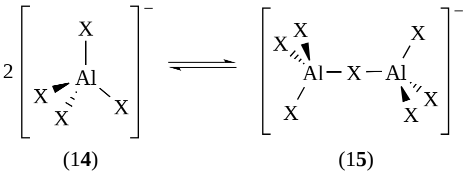

(19)

(**14**) (**15**)

$AlCl_3$ reacts with other metal chlorides such as $CaCl_2$, $NbCl_5$, $NdCl_3$, $CrCl_3$, or UCl_5 to produce mixed halides with halogen bridges, for example, $Cl_4Nb(\mu\text{-}Cl)_2AlCl_2$ (**16**). Many of these complexes are very volatile; for example, the vapor pressure of $NdCl_3$ is increased by a factor of 10^{13} at 600 °C. A related reaction of $AlCl_3$ with $HgCl_2$ and mercury at 200 °C yields the molecular species $Hg_3Cl_2\cdot 2AlCl_3$ (**17**).

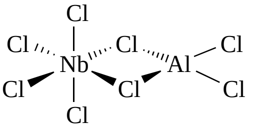

(**16**)

$AlCl_3$— ClHgHgCl—$AlCl_3$

(**17**)

A wide range of aluminum compounds may be conveniently prepared from $AlCl_3$ and alkali metal salts of various anions (equations 20–23).

$$LiY + AlCl_3 \longrightarrow AlCl_2Y + LiCl \quad (20)$$

$$2LiY + AlCl_3 \longrightarrow AlClY_2 + 2LiCl \quad (21)$$

$$3LiY + AlCl_3 \longrightarrow AlY_3 + 3LiCl \quad (22)$$

$$4LiY + AlCl_3 \longrightarrow LiAlY_4 + 3LiCl \quad (23)$$

$$(Y = R, OR, NR_2, N{=}CR_2, H)$$

Also, $AlCl_3$ is a good transhalogenation reagent for the conversion of nonmetal fluorides to the corresponding chloride; for example, BF_3 to BCl_3 (equation 24).

$$BF_3 + AlCl_3 \longrightarrow AlF_3 + BCl_3 \quad (24)$$

5 ALUMINUM OXIDES AND HYDROXIDES

The oxides, hydroxides, and mixed oxyhydroxides of aluminum form an extended family of compounds that have immense technological importance.[12]

Al_2O_3 occurs as the mineral corundum (α-Al_2O_3) and as emery, a granular form of corundum that is contaminated with silica and iron oxide. In α-Al_2O_3, the oxide ions form a hexagonal close-packed array with aluminum ions regularly distributed among the octahedral holes (Figure 2). It is a very hard material (Moh 9) (*see Moh's Hardness*), has a high melting point (2045 °C), and is nonvolatile, inert, and a good electrical insulator. As a result, it finds many applications in abrasives, refractories, and ceramics. Larger crystals when colored with metal ions are prized as gemstones, for example, ruby (Cr^{III}, red), sapphire ($Fe^{II/III}$, Ti^{IV}, blue), oriental emerald (Cr^{III}/V^{III}, green), oriental amethyst (Cr^{III}, Ti^{IV}, violet), and oriental topaz (Fe^{III}, yellow). Many aluminum-oxide based gemstones are synthesized for use as laser materials. Indeed, the first laser was created in 1961 by Theodore Maimanat using a rod of synthetic ruby as the lasing medium. Another example is alexandrite (chromium-doped chrysoberyl), which is both a particularly attractive precious gem and a uniquely versatile solid-state laser material with the distinction of being the first solid-state laser medium capable of tunable operation at room temperature.

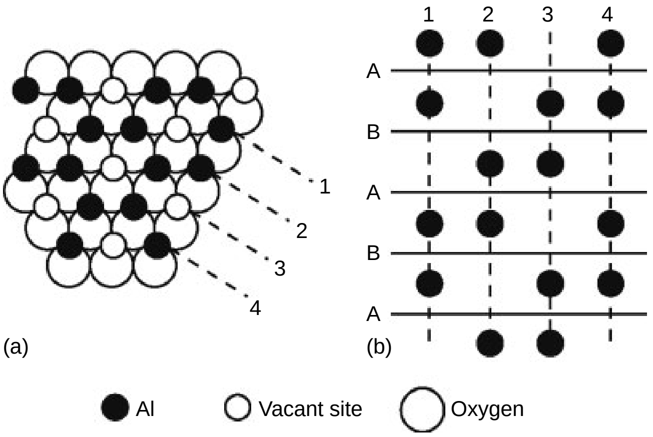

Figure 2 Schematic representation of the structure of α-Al_2O_3. (a) Pattern of occupancy by aluminum of the octahedral sites between the hexagonal close-packed planes of oxide ions and (b) stacking sequences of successive planes of aluminum atoms

Pure α-Al_2O_3 may be prepared by calcination of various Al salts, firing γ-Al_2O_3 or any of the hydrous oxides above 1200 °C, and by the oxidation of aluminum metal. Often single crystals of pure alumina that are prepared industrially are called *sapphires*. Large boules of synthetic sapphire are grown by melting aluminum oxide above 2060 °C and then directionally cooling. The resulting synthetic sapphires are anisotropic, monoaxial crystals that have a variety of technological applications and are also gaining popularity as gemstones known as white sapphires. Synthetic sapphire is one of the hardest and strongest materials, and is rated mechanically only second to diamond; It is one of the hardest materials available that when combined with a high modulus of elasticity and high tensile strength, makes it extremely wear, abrasion and impact resistant. For example, its abrasion stability is eight times higher than that of steel. It is colorless with an optical transmission window that ranges from 190 nm in the ultraviolet to 5 µm in the infrared. It had good dielectric qualities that make it a very good electrical insulator and it is thermally very stable and does not lose any of its mechanical and optical qualities from cryogenic temperatures to over 2000 °C. It has a thermal conductivity greater than most dielectrics, and even better than many metals. It is also very corrosion resistant to a wider range of chemicals than just about any standard hard material available. Because of these unique properties sapphire is used as the material for production of ultraviolet, visible and near-infrared optics for operation under critical conditions such as high temperature, high pressure, or in chemically aggressive or abrasive environments. The high thermal conductivity also makes it an ideal substrate for GaN microelectronics.

γ-Al_2O_3, the second modification of alumina, has a less compact cubic close-packed structure. This is a defect spinel-type structure (see below) that is composed of a face-centered cubic array of 32 oxygen atoms with the aluminum atoms randomly occupying $21\frac{1}{3}$ of 16 octahedral and eight tetrahedral interstices. It is readily prepared by the low-temperature ($<450\,°C$) dehydration of gibbsite, γ-$Al(OH)_3$, or boehmite, γ-AlOOH. Quite unlike α-Al_2O_3, γ-Al_2O_3 or 'activated alumina' readily absorbs water and dissolves in acids. Progressive dehydration of γ-alumina leads to porous materials that have great value as catalysts, catalyst supports, ion-exchangers, and chromatographic media.

Yet another form of Al_2O_3 forms on the surface of aluminum metal. This has a defect sodium chloride structure with aluminum ions occupying two-thirds of the octahedral holes.

In 1974, ICI announced the production of alumina fibers known as '*saffil alumina*'. These microcrystalline fibers are flexible, resilient, and have high tensile strength. They are easily fashioned into rope, yarn, cloth, blankets, paper, boards, and objects of any shape. Numerous small pores (10–20 pm) occur between the microcrystals, providing significant surface area ($100–150\,m^2\,g^{-1}$) that enhances the fiber's performance as insulation, filtration media, and catalyst supports. The fibers are very inert, withstanding temperatures to 1400 °C and attack by hot alkali and acids. The fibers are therefore employed as high-temperature insulation, electric-cable sheathing, and in the filtration of hot corrosive liquids. They have also found significant application in metal/ceramic composites in which they contribute high structural stiffness coupled with low density.

Diaspore, α-AlO(OH), occurs in some types of clay and bauxite and can be synthesized by hydrothermal treatment of boehmite, γ-AlO(OH), in 0.4% aqueous NaOH at 380 °C and 500 atm. Crystalline boehmite is easily obtained upon warming the amorphous, gelatinous precipitate that forms when cold solutions of aluminum salts are treated with ammonia.

Both α-AlO(OH) and γ-AlO(OH) contain double chains of edge-shared AlO_6 octahedra. In γ-AlO(OH), these chains share a further two edges to form puckered sheets, while in α-AlO(OH) the edge-sharing produces a 3-D structure (Figure 3). The latter leads to hexagonal close-packing of the oxygen atoms, accounting for the ready dehydration of diaspore to α-Al_2O_3 at 450 °C. As noted earlier, boehmite dehydrates to γ-alumina.

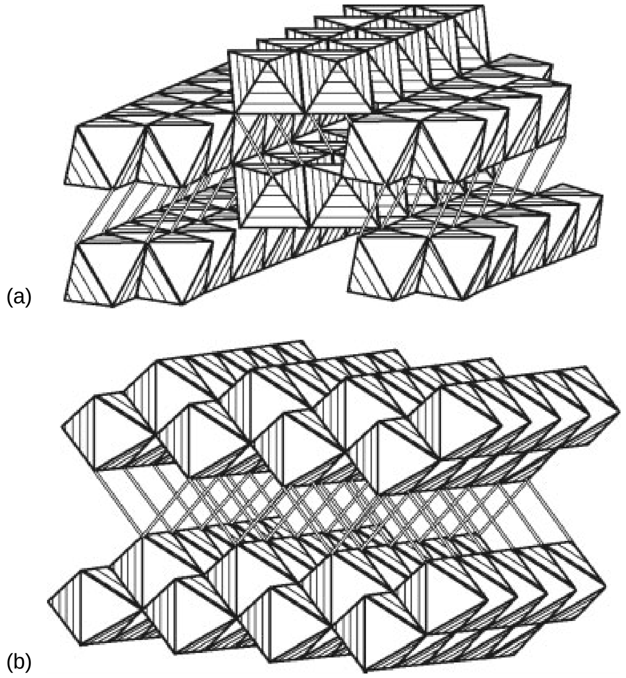

Figure 3 Structure of (a) diaspore and (b) boehmite. The aluminum atoms are octahedrally surrounded by five oxide and one hydroxide anions. The hydrogen bonds are shown as double lines

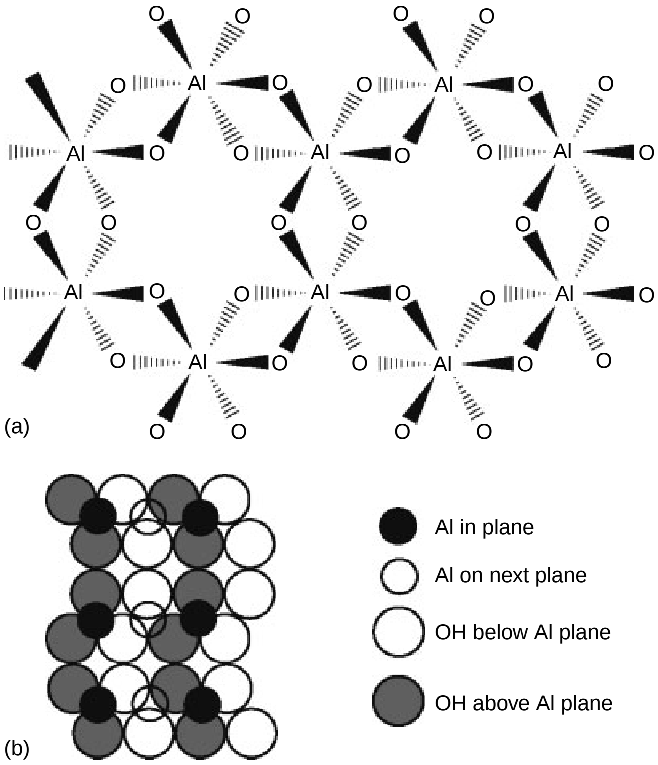

Figure 4 (a) Part of a layer of $Al(OH)_3$. (b) Structure of γ-$Al(OH)_3$ viewed in a direction parallel to the layers

Bayerite, α-Al(OH)$_3$, is not a naturally occurring mineral but it can be made by precipitation from cold, alkaline solutions (equation 25).

$$2[\mathrm{Al(OH)_4}]^-(\mathrm{aq}) + \mathrm{CO_2(g)} \longrightarrow 2\mathrm{Al(OH)_3(s)} + \mathrm{CO_3}^{2-}(\mathrm{aq}) + \mathrm{H_2O} \qquad (25)$$

Gibbsite, γ-Al(OH)$_3$, is a more stable form that is prepared by slow precipitation from warm alkaline solutions or by heating bayerite in aqueous sodium aluminate solution at 80 °C. Both bayerite and gibbsite have layers of composition Al(OH)$_3$ formed by the sharing of Al(OH)$_6$ octahedra in such a way that a pair of close-packed OH$^-$ layers are formed with aluminum atoms in two-thirds of the octahedral holes. The two phases differ in the way the layers are stacked; in α-Al(OH)$_3$, it is approximately hexagonal close-packing but in the γ-form two out of three layers stack together directly on top of each other (Figure 4). It should also be noted that a third form of Al(OH)$_3$, nordstrandite, has an intermediate stacking arrangement between those of the α- and γ-forms. It is prepared by aging the gelatinous hydroxide in the presence of a chelating agent such as ethylene glycol, ethylene diamine, or EDTA. As indicated earlier, gibbsite can be dehydrated to boehmite at 100 °C and to anhydrous γ-Al$_2$O$_3$ at 150 °C. It is also amphoteric, reacting both with bases and acids (equations 26–28). Reaction with acids usually results in formation of the [Al(H$_2$O)$_6$]$^{3+}$ cation while those with base afford a variety of products such as [Al(OH)$_4$]$^-$ (**18**), [Al$_2$(OH)$_{10}$]$^{4-}$ (**19**), and [Al(OH)$_6$]$^{3-}$ (**20**).

$$\mathrm{Al(OH)_3(s)} + 3\mathrm{H_3O^+(aq)} \longrightarrow [\mathrm{Al(H_2O)_6}]^{3+}(\mathrm{aq}) \qquad (26)$$

$$\mathrm{Al(OH)_3(s)} + \mathrm{OH^-(aq)} \longrightarrow [\mathrm{Al(OH)_4}]^-(\mathrm{aq}) \qquad (27)$$

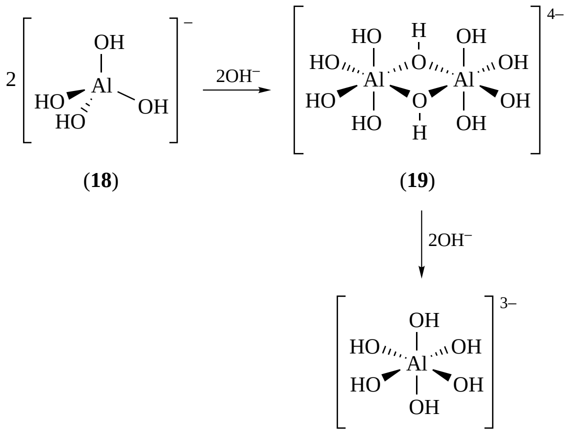

(**18**) (**19**) (28) (**20**)

The Al/O/OH family form an important catalytic system and numerous recipes have been reported for preparing catalysts of differing reactivity and absorptive power. Additionally, the basic character of the surface diminishes and the acidic nature increases in the following series: amorphous Al oxide hydrate $<$ γ-AlO(OH) $<$ α-Al(OH)$_3$ $<$ γ-Al$_2$O$_3$ (pH of isoelectric points: 9.45, 9.45–9.40, 9.20, 8.00, respectively).

6 TERNARY AND MORE COMPLEX OXIDE PHASES

Numerous important mixed oxide phases are formed by the combination of aluminum oxide and one or more other metal oxides. The foremost of these from an industrial viewpoint are spinels, β-aluminas, and tricalcium aluminate, an important constituent of Portland cement.

6.1 Spinels and Related Compounds

Spinels are a large family of compounds that possess the structure of the mineral spinel, MgAl$_2$O$_4$. The general formula is AB$_2$X$_4$ and the unit cell contains eight of these formula units with the 32 oxygen atoms in a nearly perfect cubic close-packed array. In the normal spinel structure, eight ‘A’ metal atoms occupy tetrahedral sites while the 16 ‘B’ atoms occupy octahedral sites. Thus, the unit cell can be thought of as being composed of eight alternating cubic building blocks of Zn–S and Na–Cl type structures surrounded by an additional 14 ‘A’ atoms in a face-centered cubic array (Figure 5).

Many spinel compounds adopt an alternative structure where half the B cations occupy the tetrahedral sites while the remaining B cations and A cations occupy the octahedral sites. These are known as inverse spinels. The occupancy of the latter sites may be random or ordered. The adoption of an inverse spinel versus a spinel structure depends on a variety of factors; the relative size of the A and B cations, the relative lattice energies, ligand-field stabilization, energies of octahedral versus tetrahedral coordination, and polarization or covalency effects. For example, in MgAl$_2$O$_4$ one might expect the small

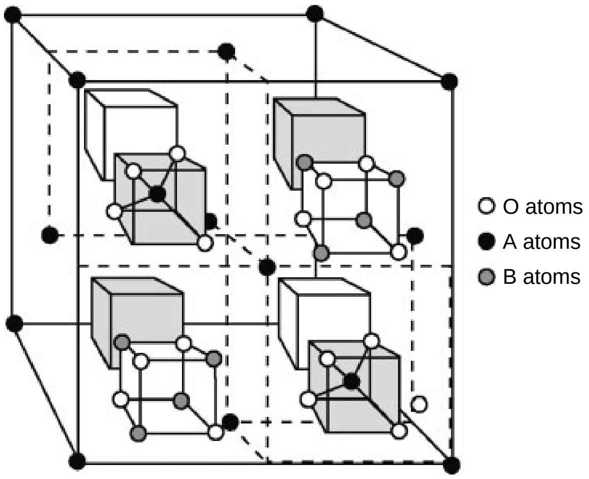

Figure 5 Spinel structure, AB$_2$O$_4$, composed of eight octants of alternating AO$_4$ tetrahedra and B$_2$O$_4$ cubes. The four oxygen atoms have the same orientation in all octants and therefore build up a face-centered cubic lattice of 32 ions. The four ‘A’ octants contain four ‘A’ ions while the four ‘B’ octants contain 16 ‘B’ ions. The unit cell is completed by a surrounding face-centered cubic array of 14 ‘A’ ions. These are shared with adjacent unit cells and comprise the remaining four ‘A’ ions required for the stoichiometry A$_8$B$_{16}$O$_{32}$

Al^{3+} ion to occupy the tetrahedral site but this is outweighed by the greater lattice energy associated with having the cation of higher charge on the octahedral site, that is, $(Mg)_{tet}[Al_2]_{oct}O_4$. On the other hand, in $NiAl_2O_4$ the crystal field stabilization energy of Ni^{II} is greater in octahedral sites leading to a disordered spinel; $[Al_{0.75}Ni_{0.25}]_{tet}[Ni_{0.75}Al_{1.25}]_{oct}O_4$.

Inverse and disordered spinels are called *defect structures* because all the identical crystallographic sites are not occupied by the same cation. A different defect structure is formed when spinels have disordered valencies. For example, the divalent cations in AB_2O_4 may be replaced by equal numbers of M^I and M^{III} ions of appropriate size. As an illustration, the magnesium atoms of spinel may be replaced by lithium and aluminum atoms to give a spinel with formula $LiAl_5O_8$. This has a defect structure in which two-fifths of the aluminum atoms occupy all the tetrahedral sites: $(Al_2)_{tet}[LiAl_3]_{oct}O_8$. Similarly, disordering on the tetrahedral sites occurs in $(MAl)_{tet}[Al_4]_{oct}S_8$ where $M = Ag^+$ or Cu^+. Valency disordering can also occur when all the A^{II} ions are replaced by M^I, necessitating the replacement of the B^{III} ions by M^{IV} to achieve charge balance, for example, $(Li)_{tet}[AlTi]_{oct}O_4$. The possibilities of cation substitution are almost limitless, and cubic spinels such as $LiZn_8Al_5Ge_9O_{36}$ have been prepared.[13,14]

As mentioned earlier, γ-Al_2O_3 has a defect-spinel structure in which not all the cation sites are occupied. This can be thought of as being derived from spinel by replacing magnesium by aluminum and maintaining charge balance by leaving one site vacant for every three magnesium atoms replaced, that is, $Al_{\frac{64}{3}}[\ ]_{\frac{8}{3}}O_{32}$.

The sensitive dependence of electrical and magnetic properties of spinels on temperature, composition, and detailed cation arrangement allows extensive tailoring of their properties for use in the solid-state electronics industry. For example, $CuAl_2O_4$ and $CoAl_2O_4$ are used extensively in negative temperature coefficient resistors. Spinels are also employed in catalysis: $NiAl_2O_4$ for methanation and dehydrogenation, $FeAl_2O_4$ for oxidation of chlorocarbons and ammonia production, $CoAl_2O_4$ for oxidation and desulfurization, and $ZnAl_2O_4$ for oxidations of organics, aromatization, dehydrogenation, and cracking and reforming of hydrocarbons (*see* ***Oxide Catalysts in Solid-state Chemistry***). As well, $ZnAl_2O_4$ and $FeAl_2O_4$ are used in glass ceramics, Co_2AlO_4 is used as a pigment in photography, Fe_2AlO_4 as an absorbent for H_2S, and $ZnAl_2O_4$ is used as an anticorrosion coating, an abrasive, a pigment, in moisture sensors, and as a screen-printable dielectric compound for printed circuits.

When the divalent cation becomes too large for the spinel structure to be adopted (e.g. Ca^{2+}, Ba^{2+}, and Pb^{2+}), a tridymite (SiO_2) structure is obtained that has the divalent cation in the interstices (*see* ***Silicon: Inorganic Chemistry***). These are synthesized by reaction of the oxides at temperatures over 800 °C. The barium and calcium derivatives are used in ceramics and refractories. In particular, $BaAl_2O_4$ is used in nuclear reactors; $BaAl_2O_4$ and $CaAl_2O_4$ are also used as supports for transition and lanthanide metal phosphors.

6.2 β-Aluminas and Related Compounds

Sodium β-alumina has achieved substantial importance as a solid-state electrolyte owing to its extremely high ionic conductivity (*see* ***Ionic Conductors***).[15,16] The compound has the idealized formula of $NaAl_{11}O_{17}$ (i.e. $Na_2O{\cdot}11Al_2O_3$) and only bears the name of β-alumina because earlier studies either did not detect or ignored the presence of sodium. Indeed, it is the latter cations that stabilize the structure. This is closely related to spinel with no fewer than 50 of 58 atoms in the unit cell being arranged exactly as in spinel. The large sodium atoms along with an equal number of oxygen atoms are arranged in loosely packed planes between the spinel blocks. There are several sites in the layer between the spinel blocks that the sodium ions can occupy, permitting rapid 2-D diffusion of sodium in this plane and resulting in a low resistivity of 30 ohm cm. The structure can easily accommodate additional sodium ions and even single crystals often contain 20–30% more sodium than indicated by the idealized formula.

Sodium β-alumina can be prepared by heating Na_2CO_3, $NaNO_3$, or NaOH with any modification of alumina or its hydrates to 1500 °C in a sealed platinum vessel (to prevent loss of Na_2O). The processing temperature may be dropped to 1000 °C by addition of fluoride in the form of NaF or AlF_3. The sodium is easily replaced by other metals (Li, K, Rb, Cu^I, Ag^I, Ga^I, In^I, or Ti^I) by heating sodium β-alumina with an appropriate molten salt. The NO^+, $NH_4{}^+$ and H_3O^+ salts have also been prepared.

The β-aluminas have been extensively used as permeable membranes in sodium–sulfur batteries since they provide the unique properties of allowing sodium transport but neither sulfur nor electron conduction and they are not attacked by molten sodium or sulfur.

Numerous other sodium aluminates are known including a number of alkali-rich aluminates with quite different structures from the β-aluminas. Depending on stoichiometry, the solid-state reaction of α-Al_2O_3 with Na_2O at 700 °C yields colorless crystals of Na_5AlO_4, $Na_7Al_3O_8$, and $Na_{17}Al_5O_{16}$. Na_5AlO_4 and the isoelectronic Li_5AlO_4 contain discrete AlO_4 tetrahedra. $Na_7Al_3O_8$ contains rings of six AlO_4 tetrahedra that are linked together by four oxygen bridges to form an infinite chain. $Na_7Al_{15}O_{10}$ contains discrete chain anions, $[O_3Al(OAlO_2)_3OAlO_3]^{17-}$, formed by linking the corners of five AlO_4 tetrahedra.[17,18] Li_5AlO_4 is an ionic conductor with possible applications in batteries. It is also used as a blanket material in the nuclear power industry. $MAlO_2$ (where M = Li, Na, K) are prepared by reaction of Al_2O_3 with the alkali metal carbonates at elevated temperatures. The latter two compounds have the $NaFeO_2$ structure (*see* ***Iron: Inorganic & Coordination Chemistry***). $NaAlO_2$ is used in water treatment, sizing of paper, and as a raw material for manufacture of zeolites, ceramics, and catalysts in the petroleum industry (*see* ***Zeolites***).

6.3 Calcium Aluminates

The calcium aluminates are an extensive family of compounds that amply demonstrate the diverse structural chemistry of aluminum. They are easily prepared by reaction of CaO and Al_2O_3 in appropriate ratios.

Tricalcium aluminate is one of the components of Portland cement (a mixture of 26% Ca_2SiO_4, 51% Ca_3SiO_5, 11% $Ca_3Al_2O_6$, and 1% $Ca_4Al_2FeO_{10}$). The structure of $Ca_3Al_2O_6$ contains a 12-membered ring composed of six-fused AlO_4 tetrahedra (**21**). This compound is readily hydrolyzed and, depending on the temperature, forms the hexahydrate (above 21 °C) or a mixture of $2CaO{\cdot}Al_2O_3{\cdot}5{-}9H_2O$ and $4CaO{\cdot}Al_2O_3{\cdot}12{-}14H_2O$ (below 21 °C).

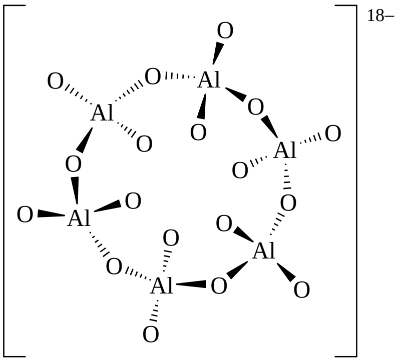

(**21**)

Another important calcium aluminate occurs in high-alumina cement, also known as *ciment fondu*. This is manufactured by fusing limestone, bauxite, and small amounts of SiO_2 and TiO_2 at 1500 °C. The most important components of the cement are $CaAl_2O_4$, $Ca_2Al_2SiO_7$, and $Ca_6Al_8FeSiO_{21}$. High-alumina cement develops very high strength in the very early stages of hydrolysis (within one day). It is not resistant to long exposure to warm moist conditions but it does have superior resistance to corrosion by seawater and acids. Owing to its ability to withstand temperatures to 1500 °C, it has also been used as a refractory cement. As noted earlier, $CaAl_2O_4$ has the tridymite structure.

$CaAl_4O_7$ has a structure that is composed of linked, distorted AlO_4 tetrahedra and seven-coordinate calcium atoms. It is used in laser materials as a host for Nd^{3+}.

$Ca_4Al_6O_{13}$ [better formulated as $Ca_4O(Al_6O_{12})$] has a structure that is related to sodalite (*see* ***Zeolites***). This contains AlO_4 tetrahedra that are linked to form cubooctahedra. These are, in turn, linked to form an infinite framework with OCa_4 tetrahedra in the cavities.

$Ca_5Al_6O_{14}$ has twisted sheets of distorted AlO_4 tetrahedra that are linked by their corners. The calcium atoms are six-coordinate and lie between the Al_6O_{14} sheets.

$CaAl_{12}O_{19}$ occurs as a constituent of cement and is a component of steel-making slags. It is used as a support for rare-earth phosphors and as a refractory material. It has a very complex structure containing four, five, and six-coordinate aluminum.

7 ALUMINUM OXYACID SALTS

The propensity of aluminum salts to form the hexaaqua ion, $[Al(H_2O)_6]^{3+}$, upon exposure to water requires that most aluminum oxyacid salts be prepared by nonaqueous routes. Some of these salts are of particular technological value.

7.1 Aluminum Phosphates

Aluminum reacts readily with hot phosphoric acid to give a variety of products depending on the reaction conditions. Thus $Al(PO_4H_2)_3$ is formed at 25 °C, $Al(PO_4H_2)(PO_4H)$ is formed at 100–120 °C, and $AlPO_4$ is formed at higher temperatures. $Al(PO_4H_2)_3$ is used as a binder for glazes, a metal coating, and in dental cements. $Al(PO_4H)(PO_4H_2)$ is a constituent of many commercial binders and adhesives.[19]

$AlPO_4$ is isoelectronic with silica and, as such, readily forms glasses and SiO_2-like crystalline materials. As well, framework structures similar to zeolites may be prepared by the use of amines as templates. Like zeolites, these are active in catalytic reactions such as methanol conversion to hydrocarbons (*see* ***Zeolites***).[20,21] As a ceramic material, $AlPO_4$ is an infusible material that is insoluble in water but is soluble in alkali hydroxides. It is often used with calcium sulfate and sodium silicate for dental cements. $AlPO_4$ is also used as a white pigment that also acts as a corrosion inhibitor.

Aluminum trimetaphosphate, $Al(PO_3)_3$, is obtained from a melt of Al_2O_3 and HPO_3. The structure is composed of chains of PO_4 tetrahedra that are connected by AlO_6 octahedra. $Al(PO_3)_3$ is a constituent of glasses, coatings, binders, and ceramics as well as a catalyst for esterifications and oxidation of alkenes (*see* ***Phosphates: Solid-state Chemistry***).

There are a number of minerals composed of aluminum phosphate that form geologically as precipitates from circulating phosphate-rich water. These include variscite, $AlPO_4{\cdot}2H_2O$, wavellite, $Al_3(PO_4)_2(OH,F)_3{\cdot}5(H_2O)$, wardite $NaAl_3(PO_4)_2(OH)_4{\cdot}2(H_2O)$, and brazilianite, $NaAl_3(PO_4)_2(OH)_4$ (one of a very few phosphate gemstones). Synthetic sodium aluminum phosphate is used as a leavening agent or acid in baking powders. Unlike other leavening agents; it reacts slowly with sodium bicarbonate in the mixing stage, leading to the majority of carbon dioxide delivery occuring during the oven stage. The result is a baked product that is crunchy and has fine texture. Turquoise, $CuAl_6(PO_4)_4(OH)_8{\cdot}5(H_2O)$, is another important aluminum phosphate that is possibly the most valuable, nontransparent mineral in the jewelry trade. It has been mined for centuries since at least 6000 BC by early Egyptians.

7.2 Aluminum Nitrates

Reaction of $AlBr_3$ with N_2O_5 produces white hygroscopic crystals of the salt $[NO_2]^+[Al(NO_3)_4]^-$. The $[Al(NO_3)_4]^-$ anion (**22**) may also be obtained as the alkali metal or tetraethylammonium salts by the reaction of the appropriate nitrate salt, nitric acid, or N_2O_5 with $AlBr_3$. Use of an excess of metal nitrate affords the $[Al(NO_3)_5]^{2-}$ anion (**23**).

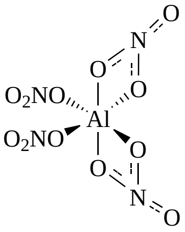

(**22**)

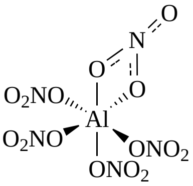

(**23**)

Thermal decomposition of $Al(NO_3)_2N_2O_5$ produces anhydrous $Al(NO_3)_3$. All the nitrates of aluminum are powerful oxidants and may react explosively with organic solvents. They also decompose to oxides rather readily, as low as 65 °C in the case of $Al(NO_3)_3$.

7.3 Aluminum Sulfates and Selenates

$Al_2(SO_4)_3$ occurs in the hydrated form as the mineral alunogen, $Al_2(SO_4)_3 \cdot 18H_2O$, and may also be obtained by treatment of $Al(OH)_3$ with sulfuric acid. $Al_2(SeO_4)_3$ is obtained in a similar manner. Unlike most hydrated aluminum salts, the anhydrous forms are obtained simply upon heating the hydrates to 325 °C. $Al_2(SO_4)_3$ is used in water purification as a flocculent and as sizing for paper. It is also used as a mordant in the dying of cloth, a process by which it fixes the dye to the cloth by rendering the dye insoluble. In one important water-treatment process, aluminum sulfate is used to precipitate phosphate from water as aluminum phosphate. This is important in preventing algal blooms that are detrimental to aquatic life.

The alums, $MAl(SO_4)_2$, are obtained from reaction of $Al(OH)_3$ with M_2SO_4/H_2SO_4 mixtures (equation 29). The structure is composed of alternating layers of six-coordinate aluminum and potassium ions with the sulfate anions between them. The potassium derivative is used as a mordant, paper sizing, deodorant, and coagulation agent for rubber, and for curing furs and water purification. The sodium salt is used as a flame retardant, in tanning and the dying and printing of fibers, in the preparation of inks, lacquers, paper, vegetal gum, cement, porcelain, explosives, ammonia synthesis catalysts, and is a component of baking powder.

$$2Al(OH)_3 + M_2SO_4 + 3H_2SO_4 \longrightarrow 2MAl(SO_4)_2 + 6H_2O \quad (29)$$

(M = any monovalent cation except Li)

7.4 Aluminum Salts of Halogen Oxyacids

Aluminum perchlorate, $Al(ClO_4)_3$, is synthesized by treatment of $AlCl_3$ with $AgClO_4$ in C_6H_6 (equation 30). It is a very strong oxidant that reacts slowly with paraffin hydrocarbons. It decomposes at 150 °C and should be considered a potential explosive. Aluminum periodate may be obtained in the same manner. Aluminum iodate, $Al(IO_3)_3$, is obtained by thermal decomposition of $[Al(OH_2)_6][IO_3][HI_2O_6] \cdot HIO_3$ at 340 °C.

$$3AgClO_4 + AlCl_3 \longrightarrow Al(ClO_4)_3 + 3AgCl \qquad (30)$$

8 THE AQUA IONS AND AQUEOUS CHEMISTRY

Aluminum forms a wide variety of salts including chlorides, nitrates, perchlorates, and so on that contain the hexaaquaaluminum(III) cation, $[Al(H_2O)_6]^{3+}$. These ions exist both in aqueous solution and crystalline solids. The ions are acidic and as salts of weak acids are extensively hydrolyzed (equation 31) by water. The $[Al(H_2O)_5OH]^{2+}$ ion has been observed in dilute solution but there is a very high equilibrium constant for formation of a hydroxide-bridged dimer (**24**). This dimer has been characterized in several crystalline salts. The hydrolysis of $[Al(OH_2)_6]^{3+}$ over a wide range of pH provides a great variety of species including the $[(H_2O)_5Al(OH)]^{2+}$ monomer and dimer listed above, $Al(OH)_3$, $[Al(OH)_4]^-$, $[Al_3(OH)_{11}]^{2-}$, $[Al_6(OH)_{15}]^{3+}$, and $[Al_8(OH)_{22}]^{2+}$. The formation of these hydrolyzed species depends markedly on the exact conditions used.[22] One remarkable species, $[AlO_4 \cdot Al_{12}(OH)_{24}(H_2O)_{12}]^{7+}$, is obtained by hydrolysis of (**24**) with sodium carbonate. This has a Keggin-type structure with a central AlO_4 tetrahedral core surrounded by 12 AlO_6 octahedra.

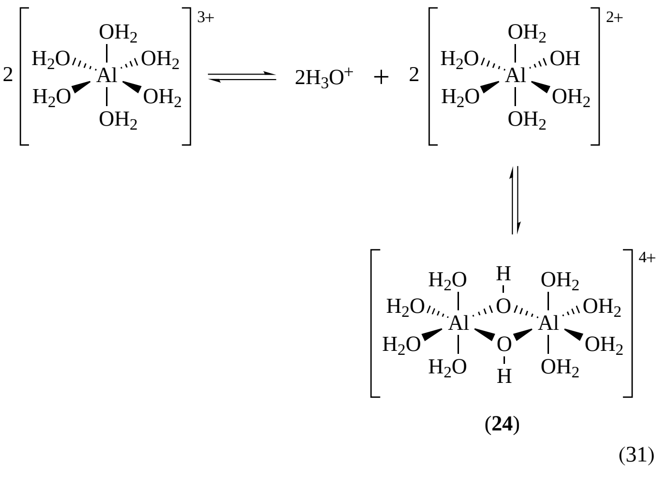

(**24**)

(31)

9 ALUMINOSILICATES

Aluminosilicates form an extensive family of compounds that include layered compounds (such as clays, talc, and micas), 3-D compounds, (e.g. feldspars, such as granite), and microporous solids known as molecular sieves.**[23]** The structural diversity of these materials is contributed to by aluminum's ability to occupy both tetrahedral and octahedral holes as it also does in γ-Al_2O_3. Thus, aluminum substitution for silicon in silicate minerals may lead to replacement of silicon in tetrahedral sites or the aluminum can occupy an octahedral environment external to the silicate lattice. Replacement of Si^{IV} with Al^{III} requires the presence of an additional cation such as H^+, Na^+, or 0.5 Ca^{2+} to balance the charge. These additional cations have a profound effect on the properties of the aluminosilicates. This accounts for the many types of layered and 3-D structures (*see* ***Silicon: Inorganic Chemistry***).

The molecular sieves are aluminosilicates of particular importance. They are crystalline materials that have open structures that contain pores and channels that have molecular dimensions. This family of materials includes the zeolites, which have numerous applications in heterogeneous catalysis, ion-exchange materials, absorption of molecular species, and gas separation. While some zeolites occur naturally, they are usually manufactured from silicon and aluminum oxides mixed with tetraalkylammonium 'templates' in a high-pressure autoclave (*see* ***Zeolites***).

10 ALUMINUM CHALCOGENIDES

Under ordinary conditions, the stable binary chalcogenides (*Chalcogens*) of aluminum are Al_2S_3 (white), Al_2Se_3 (gray), and Al_2Te_3 (dark gray). Their band gaps are 4.1, 3.1, and 2.2 eV, respectively, showing the expected trend to smaller band gap (*see Band Gap*). They are prepared by the direct combination of the elements at 1000 °C and must be protected from moisture owing to rapid hydrolysis to $Al(OH)_3$ and H_2X ($X = S, Se, Te$) (equation 32). The relatively large size of the anions with respect to aluminum leads to tetrahedral coordination of the latter. Therefore, the various polymorphs adopt a wurtzite structure with two-thirds of the available metal sites being occupied by aluminum. If this occupation is ordered, the modification is called α-Al_2X_3; if not, then the phase is called β-Al_2X_3. Al_2S_3 also forms a γ-form similar to γ-alumina (*see* ***Chalcogenides: Solid-state Chemistry***).

$$Al_2Y_3 + 6H_2O \longrightarrow 2Al(OH)_3 + 3H_2Y \qquad (32)$$
$$(Y = S, Se, Te)$$

Al_7Te_{10} may be prepared by fusion of the elements. It is one of the few compounds with an Al–Al bond. The structure consists of Te_4Al_4–Al_4Te_4 units that contain Al_2Te_2 four-membered rings (*see* ***Tellurium: Inorganic Chemistry***).

11 ALUMINUM PNICTIDES

The compounds of group 13 and group 15 have achieved considerable technological importance owing to their application as III–V semiconductors (these compounds are isoelectronic with Si and Ge) (*see Compound Semiconductor*). AlN, AlP, AlAs, and AlSb may all be prepared by direct combination of the elements at elevated pressures (*see Pnictide*). All have the sphlaerite structure with the exception of aluminum nitride, which has the wurtzite structure. The properties of the compounds are given in Table 7 and they show the clear trends towards lower-melting point and smaller band gap with increasing atomic number of the pnictide (*see also* ***Phosphides: Solid-state Chemistry***).

Aluminum nitride was first synthesized in 1877, but it was a relatively unimportant material until mid-1980s when its potential for application in microelectronics was realized. It has very high thermal conductivity for a ceramic material (320 W/m·K) that is second only to beryllium oxide Unlike BeO, AlN is nontoxic so it became the material of choice for substrates for microelectronic circuits that require rapid removal of heat. A high dielectric strength (>20 kV/mm) and high resistivity (10^{10} ohm·cm) also contribute to the performance of AlN in these applications. AlN is generally synthesized by carbothermal reduction of alumina or by direct nitridation of aluminium. AlN can also be prepared by reaction of $AlCl_3$ and NH_3 at 1200 °C (equation 33).**[24]** Fashioning AlN into ceramic bodies and substrates is difficult because it does not have a melting point but dissociates above 2500 °C at atmospheric pressure. The material's strong covalent bonding makes it resistant to sintering without the assistance of liquid forming additives. Such additives include oxides like Y_2O_3 or CaO that allow sintering to be achieved at temperatures between 1600 and 1900 °C. As a powder, aluminum nitride is susceptible to hydrolysis by water or humidity to produce aluminum hydroxide and ammonia. This is not a problem for ceramic monoliths since the reaction is limited to the surface. Items manufactured from AlN are resistant to attack from most molten salts including chlorides and cryolite and most molten metals including aluminium, lithium, and copper. Unfortunately, aluminum nitride is readily attacked

Table 7 Some properties of Al III–V compounds

Property	AlN	AlP	AlAs	AlSb
Color	Pale/yellow	Yellow	Orange	Black
Mp (°C)	>2200 decomp	2000	1740	1060
E_g (eV)	4.26	2.45	2.16	1.50

by acids and alkalis as are most aluminum compounds. Films of AlN can provide useful wear resistance and may be obtained by various chemical vapor deposition methods (*see Metal–Organic Chemical Vapor Deposition*).

$$AlCl_3 + 4NH_3 \longrightarrow AlN + 3NH_4Cl \qquad (33)$$

Aluminum phosphide, like aluminum nitride, reacts with moisture but in this case the gaseous product is phosphine, PH_3, a very toxic gas. For this reason, AlP is used as a fumigant to control insects in stored products such as raw agricultural products, animal feeds, processed foods (for example, flour and sugar), tobacco, wood, paper, leather, hair, and feathers. It is also used for control of rodents such as rats, mice, squirrels, and gophers in and around mills, food processing plants, warehouses and silos, and in rail cars, ships, and shipping containers.

12 MIXED ALUMINUM CHALCOGENIDE HALIDES

The reaction of aluminum halides with a variety of oxides at elevated temperatures yields the aluminum oxyhalides, AlOX (equation 34). These compounds are insoluble, moisture-sensitive compounds that have an interesting layered structure. The aluminum atoms have tetrahedral coordination by three oxygen atoms and one halide atom. The oxygen atoms of the tetrahedra are shared between three aluminum atoms, providing a puckered 'AlO' layer. The halide atoms cap the tetrahedra, half of them above and half of them below the AlO layer in an alternating fashion.[25] The hydrate of AlOCl is used as an antiperspirant.

$$3AlX_3 + M_2O_3 \longrightarrow 3AlOX + 2MX_3 \qquad (34)$$

$$(M = As, Bi, Sb; X = Cl, Br, I)$$

Analogous sulfur, selenium, and tellurium compounds are easily prepared by reaction of the aluminum halides with the appropriate aluminum chalcogenide (equation 35).

$$Al_2Y_3 + AlX_3 \longrightarrow 3AlYX \qquad (35)$$

$$(Y = S, Se, Te; X = Cl, Br, I)$$

Several oxyhalide anions have also been characterized, for example, $[Al_3OCl_8]^-$ and $[Al_4O_2Cl_{10}]^{2-}$.

13 ALUMINUM CARBIDE AND BORIDES

Al_4C_3 is prepared by direct union of the elements at elevated temperatures. It forms pale-yellow crystals (mp 2200 °C) with a very complex structure. This consists of AlC_4 tetrahedra that are linked to form a layered lattice. There are two types of carbon atoms: one that is surrounded by a distorted octahedron of aluminum atoms at 217 pm and one that is surrounded by four aluminum atoms at 190–194 pm and a fifth one at 221 pm. Aluminum carbide hydrolyzes very readily to $Al(OH)_3$ and methane (equation 36) (*see* ***Carbides: Transition Metal Solid-state Chemistry***).

$$Al_4C_3 + 12H_2O \longrightarrow 4Al(OH)_3 + 3CH_4 \qquad (36)$$

There are several aluminum boride phases known.[26] One of the more common, AlB_{12}, is employed in the manufacture of lightweight armor, as a catalyst for organic reactions, and as a economical replacement for diamond abrasive. It has a complex structure composed of B_{12} icosahedra, B_{19} units (twinned icosahedra), and single boron atoms in a 2:1:1 ratio. The aluminum atoms are distributed statistically over all the boron sites. AlB_{12} is synthesized by direct combination of the elements at 1100 °C or by reaction of aluminum with $Na_4B_4O_7$ at 1100 °C.

AlB_2 may be conveniently prepared by reaction of aluminum with H_3BO_3, KBF_4, or B_2O_3/KCl mixtures at temperatures between 800 and 1300 °C. AlB_2 is a metallic conductor (conductivity of $333\,\Omega^{-1}\,m^{-1}$) that slowly reacts with water and aqueous hydrochloric acid. The structure consists of hexagonal nets of boron atoms with each boron atom surrounded by six aluminum atoms at the corners of trigonal prisms.

An aluminum boride that is intermediate between the two extremes above, AlB_4, has a structure consisting of B_6 octahedra that are linked by B_2 units forming tunnel-like cavities in which the aluminum atoms lie (*see* ***Boron: Inorganic Chemistry***).

14 ALKOXIDES

The alkoxides of aluminum have become particularly important owing to their utility in sol–gel processes[18] (*see* ***Sol–Gel Synthesis of Solids***). They are also useful as reducing agents for aldehydes and ketones and other catalytic reactions.[27]

Aluminum alkoxides can be prepared by reaction of alcohols with the metal in the presence of catalytic amounts of $HgCl_2$ or I_2 (equation 37). As mentioned previously, they can also be obtained by treatment of $AlCl_3$ with sodium alkoxides. Furthermore, the alkoxides may be interconverted by a transesterification reaction (equation 38).

$$2Al + 6ROH \longrightarrow 2Al(OR)_3 + 3H_2 \qquad (37)$$

$$Al(OR)_3 + 3MeCO_2R' \longrightarrow Al(OR')_3 + 3MeCO_2R \qquad (38)$$

The alkoxides of aluminum are polymeric with aluminum achieving four or six coordination. The adopted structure depends greatly on the bulkiness of the alkyl groups. For sterically large groups, for example, tertiary butyl, the preferred structure is a dimer (**25**). The isopropoxide, on the other hand, is trimeric (**26**) at elevated temperatures but tetrameric (**27**) at room temperature.[27]

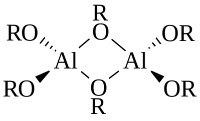

(**25**)

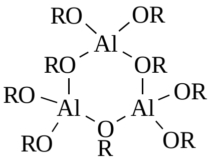

(**26**)

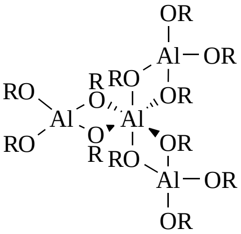

(**27**)

The siloxides of aluminum can be prepared in the same manner as the alkoxides and exhibit similar structural features. Interest in these compounds arose from a desire for sol–gel or polymeric precursors for aluminosilicates. Unfortunately, these compounds extensively hydrolyze, losing most of the silicon as the silanol. However, the investigation of the hydrolysis of $(Et_3SiO)_3Al$ has generated considerable insight into the structure and composition of alkoxy- and siloxy-substituted alumoxane polymers, '$(ROAlO)_n$'.[28] These macromolecules are now believed to have a structure related to that of boehmite.

15 ALUMINUM CARBOXYLATES

Aluminum carboxylates have been extensively investigated because of their applications as textile finishing, gelling, and therapeutic agents. Despite this, the structural aspects of their chemistry are not well established.[29]

Aluminum tricarboxylates may be synthesized by methods analogous to those employed for the alkoxides. However, they are best obtained by the reaction of the alkoxides with carboxylic acids (equation 39). The tricarboxylates have been demonstrated to be monomeric in benzene and octahedral coordination (**28**) of aluminum was proposed.

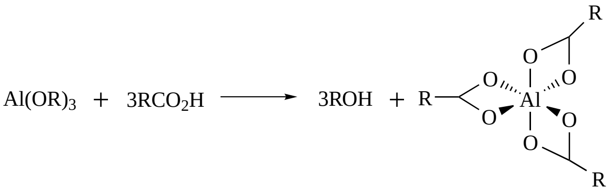

(**28**)

(39)

The tricarboxylates are highly susceptible to hydrolysis, are nonvolatile, and thermally unstable. They lose one equivalent of acid anhydride upon heating to 200 °C to form carboxy-substituted alumoxanes, $(RCO_2AlO)_n$. The latter compounds have been used as precursors for alumina fibers and films and are more conveniently prepared from the mixed aluminum alkoxide monocarboxylate (equation 40).

$$\begin{aligned} &Al(OR)_2(O_2CR') + H_2O \longrightarrow ROH + Al(OR)(OH)(O_2CR') \xrightarrow{\Delta} \\ &\qquad ROH + [OAl(O_2CR')]_n \end{aligned} \qquad (40)$$

16 RELATED ARTICLES

Boron: Inorganic Chemistry; Fluorides: Solid-state Chemistry; Gallium: Inorganic Chemistry; Halides: Solid-state Chemistry; Indium: Inorganic Chemistry; Oxide Catalysts in Solid-state Chemistry; Oxygen: Inorganic Chemistry; Phosphates: Solid-state Chemistry; Phosphides: Solid-state Chemistry; Silicon: Inorganic Chemistry; Sol–Gel Synthesis of Solids; Tellurium: Inorganic Chemistry; Zeolites.

17 FURTHER READING

J. W. Akitt, in 'Multinuclear NMR', ed. J. Mason, Plenum, New York, 1987, Chap. 9, p. 259.

C. J. Brinker and G. W. Scherer, 'Sol–Gel Science', Academic Press, San Diego, CA, 1990.

A. K. Vasudevan and R. D. Doherty, in 'Aluminum Alloys – Contemporary Research and Applications', eds. A. K. Vasudevan and R. D. Doherty, Academic Press, Boston, 1989.

18 REFERENCES

1. D. L. Hart ed., 'Aluminum Chemicals Science and Technology Handbook', American Ceramic Society, Washington, DC, 1990.

2. W. C. Sleppy, 'Kirk–Othmer Encyclopedia of Chemical Technology', 5th edn., Wiley, New York, 2004, Vol. 2.
3. H. L. Hurlburt, in 'Encyclopedia of Chemical Processing and Design', eds. J. J. McKetta and W. A. Cunningham, Marcel Dekker, New York, 1977, Vol. 3.
4. E. Wiberg and E. Anberger, 'Hydrides of the Elements of Main Groups I–IV', Elsevier, Amsterdam, 1971.
5. A. E. Finhold, A. C. Bond, and H. L. Shlesinger, *J. Am. Chem. Soc.*, 1947, **69**, 1199.
6. N. G. Gaylord, 'Reduction with Complex Metal Hydrides', Interscience, New York, 1956.
7. A. R. Barron and G. Wilkinson, *Polyhedron*, 1986, **5**, 1897.
8. F. L. Himpsl and A. C. Bond, *J. Am. Chem. Soc.*, 1981, **103**, 1098.
9. A. F. Wells, 'Structural Inorganic Chemistry', 4th edn., Oxford University Press, Oxford, 1975.
10. N. N. Greenwood and K. Wade, in 'Friedel–Crafts and Related Reactions', ed. G. A. Olah, Interscience, New York, 1963, Vol. 1, Chap. 7, p. 569.
11. C. L. Hussey, *Adv. Molten Salt Chem.*, 1983, **5**, 185.
12. C. Misra, 'Industrial Alumina Chemicals', American Chemical Society, Washington, DC, 1986.
13. N. N. Greenwood, 'Ionic Crystals, Lattice Defects, and Nonstoichiometry', Butterworths, London, 1968.
14. J. K. Burdett, G. D. Price, and S. L. Price, *J. Am. Chem. Soc.*, 1982, **104**, 92.
15. J. T. Kummer, *Prog. Solid State Chem.*, 1972, **7**, 141.
16. J. H. Kennedy, *Top. Appl. Phys.*, 1977, **21**, 105.
17. M. G. Parker, P. G. Gadd, and M. J. Begley, *J. Chem. Soc., Chem. Commun.*, 1981, 379.
18. M. G. Parker, P. G. Gadd, and S. C. Wallwork, *J. Chem. Soc., Chem. Commun.*, 1982, 516.
19. J. H. Morris, P. G. Perkins, A. E. A. Rose, and W. E. Smith, *Chem. Soc. Rev.*, 1977, **6**, 173.
20. J. M. Bennett, W. J. Dytrych, J. J. Pluth, J. W. Richardson, and J. V. Smith, *Zeolites*, 1986, **6**, 349.
21. S. T. Wilson, B. M. Lok, C. A. Messina, T. R. Cannan, and E. M. Flanigan, *J. Am. Chem. Soc.*, 1982, **104**, 1146.
22. C. F. Baes and R. E. Mesmer, 'The Hydrolysis of Cations', Wiley, New York, 1976.
23. F. Liebav, 'Structural Chemistry of the Silicates', Springer-Verlag, New York, 1985.
24. D. D. Marchant and T. E. Nemecek, *Adv. Ceram.*, 1989, **26**, 19.
25. S. S. Batsanov and V. N. Kolomiichuk, *J. Struct. Chem. USSR*, 1968, **9**, 282.
26. N. N. Greenwood, R. V. Parish, and P. Thornton, *Q. Rev. Chem. Soc.*, 1966, **20**, 441.
27. D. C. Bradley, R. C. Mehrotra, and D. P. Gaur, 'Metal Alkoxides', Academic Press, London, 1978.
28. A. Barron and A. Apblett, *Chem. Mater.*, 1992, **69**, 167.
29. R. C. Mehrotra and R. Bohra, 'Metal Carboxylates', Academic Press, London, 1983.

Aluminum: Organometallic Chemistry

Mark R. Mason
University of Toledo, Toledo, OH, USA

Based in part on the article Aluminum: Organometallic Chemistry by Gregory H. Robinson which appeared in the Encyclopedia of Inorganic Chemistry, First Edition.

1 Introduction 1
2 Aluminum(III) Alkyls, Aryls, Hydrides, and Halides 1
3 Low-valent Organoaluminum Compounds 9
4 Organoaluminum Heterocycles and Cage Compounds 11
5 Cationic Organoaluminum Compounds 17
6 Anionic Organoaluminum Compounds 19
7 Applications of Organoaluminum Compounds in Synthesis 20
8 Applications of Organoaluminum Compounds in Industry 20
9 Safety Considerations 22
10 Related Articles 22
11 References 22

Glossary

Aluminum alkyl: compounds of aluminum in which a bond exists between aluminum and a carbon of an alkyl group

1 INTRODUCTION

Aluminum is the most abundant metal and the third most abundant element in the Earth's crust, behind only oxygen and silicon. Its low weight and useful properties make aluminum and its alloys valuable materials for manufacturing and electrical applications. Inorganic compounds of aluminum are plentiful and used as absorbents, catalysts, ionic conductors, ceramics, and electrical materials. Organometallic compounds of aluminum are also of great industrial importance and fundamental discoveries continue to be made regarding the variety of coordination numbers, structures, oxidation states, and reactivity exhibited by aluminum.[1–4]

The preparation of the first organoaluminum compound, $Et_3Al_2I_3$, was reported by Hallwachs and Schafarik in 1859, but the utility of organoaluminum reagents was not realized for nearly a hundred years. This was likely due to the misconception that organoaluminum compounds were less reactive than the better-studied organozinc and organomagnesium reagents. This perception and the status of organoaluminum compounds changed suddenly with the pioneering work of Karl Ziegler in 1949.[5] Ziegler discovered that base-free alkylaluminum compounds could be synthesized on large scale by direct synthesis from aluminum, hydrogen, and alkenes. He also showed that these organoaluminum compounds react with ethylene to give long-chain terminal alkenes and alcohols, products that are still used today for the production of surfactants and detergents. In 1953, Ziegler applied for his first patent on the polymerization of ethylene under mild conditions using a catalyst comprised of a trialkylaluminum compound and an early transition metal such as titanium and zirconium. Karl Ziegler shared the 1963 Nobel Prize in Chemistry with Giulio Natta for his contribution to Ziegler–Natta alkene polymerization catalysis.

During the same period, Edwin Vandenberg and his colleagues at Hercules were independently working on Ziegler-type catalysts for the polymerization of propylene and polar monomers. As part of this effort, the use of an old bottle of wet epichlorohydrin led Vandenberg to serendipitously discover that partially hydrolyzed aluminum alkyls are active catalysts for the ring-opening polymerization of epoxides and oxetanes.[6] Vandenberg catalysts composed of a partially-hydrolzed aluminum alkyl, acetylacetonate, and various proprietary additives led to the commercial production of polyether elastomers that are still of significant industrial importance today. For his contributions to polymerization catalysis using organoaluminum reagents, Ed Vandenberg was awarded the Priestley Medal, the highest honor bestowed by the American Chemical Society, in 2003.

The discoveries of Ziegler, Vandenberg, and many others in the 1950s and 1960s ushered in the modern age of organometallic chemistry of aluminum and a host of applications followed. By 1967, U.S. production capacity for organoaluminum compounds was estimated at 50–60 million lb/year. The importance of aluminum alkyls continues to rise to this day as organoaluminum compounds are used in organic synthesis, catalysis, and the preparation of new materials.

This contribution provides a summary of basic principles of the organometallic chemistry of aluminum and emphasizes new developments since publication of the first edition of the Encyclopedia of Inorganic Chemistry. References are intended to guide readers to detailed reviews covering all aspects of the organometallic chemistry of aluminum. In particular, readers should consult the classic work of Mole and Jeffery[7] and reviews by Eisch[8,9] and Robinson.[10,11]

2 ALUMINUM(III) ALKYLS, ARYLS, HYDRIDES, AND HALIDES

2.1 Preparative Routes

Four methods are used for the industrial production of simple aluminum alkyls: direct synthesis, the displacement reaction, the growth reaction, and reduction of alkylaluminum sesquihalides.[7] In the direct synthesis developed by Ziegler, aluminum alkyls are prepared by reaction of aluminum metal, hydrogen, and a terminal alkene (equation 1). The reaction

$$\mathrm{Al} + \frac{3}{2}\mathrm{H_2} + 3\mathrm{RR'C{=}CH_2} \longrightarrow (\mathrm{RR'CHCH_2})_3\mathrm{Al} \qquad (1)$$

proceeds by formation of a dialkylaluminum hydride followed by insertion of an alkene into the Al–H bond. The insertion of a substituted alkene proceeds in a Markovnikov fashion with the hydride transferred to the most substituted carbon atom of the double bond. For this reason, the use of propene or isobutene yields tri-*n*-propylaluminum or tri-*iso*-butylaluminum, respectively. Tri-*iso*-propylaluminum and tri-*tert*-butylaluminum cannot be prepared by direct synthesis.

In the case of ethylene, additional insertions occur to give mixtures of long-chain trialkylaluminum compounds via the Aufbau, or growth, reaction (equation 2). The resulting

$$\mathrm{R_3Al} + 3n\mathrm{H_2C{=}CH_2} \longrightarrow \{\mathrm{R(CH_2CH_2)}_n\}_3\mathrm{Al} \qquad (2)$$

aluminum alkyls are useful for the commercial production of long-chain terminal alkenes and alcohols, but pure aluminum alkyls are not typically prepared in this manner. This is a convenient route for the preparation of research quantities of trineohexylaluminum and trineopentylaluminum according to equations (3) and (4).

$$^{t}\mathrm{Bu_3Al} + 3\mathrm{H_2C{=}CH_2} \longrightarrow (^{t}\mathrm{BuCH_2CH_2})_3\mathrm{Al} \qquad (3)$$

$$\mathrm{Me_3Al} + 3\mathrm{Me_2C{=}CH_2} \longrightarrow (\mathrm{Me_3CCH_2})_3\mathrm{Al} \qquad (4)$$

In the displacement reaction, reversible β-hydride elimination of an alkene from an aluminum alkyl (equation 5) is followed by insertion of a different alkene into the Al–H bond of the resulting dialkylaluminum hydride (equation 6). Three repetitions of this process yield the new trialkylaluminum compound as in equation (7). Tri-*iso*-butylaluminum obtained from the direct synthesis is a convenient starting aluminum alkyl for this process.

$$^{i}\mathrm{Bu_3Al} \overset{\Delta}{\rightleftharpoons} {}^{i}\mathrm{Bu_2AlH} + \mathrm{Me_2C{=}CH_2} \qquad (5)$$

$$^{i}\mathrm{Bu_2AlH} + \mathrm{RR'C{=}CH_2} \longrightarrow {}^{i}\mathrm{Bu_2AlCH_2CHRR'} \qquad (6)$$

$$^{i}\mathrm{Bu_3Al} + 3\mathrm{RR'C{=}CH_2} \rightleftharpoons (\mathrm{RR'CHCH_2})_3\mathrm{Al} + 3\mathrm{Me_2C{=}CH_2} \qquad (7)$$

Trimethylaluminum cannot be prepared by any of the above processes, which rely on alkene insertion. The industrial preparation of trimethylaluminum is achieved by reaction of ground aluminum with chloromethane to yield the sesquichloride, $\mathrm{Me_3Al_2Cl_3}$, and subsequent reduction with sodium metal (equation 8). This procedure also works for the preparation of $\mathrm{Et_3Al}$, but direct synthesis is preferred because of the expense of the reducing agent. This method has limited utility for higher alkyls owing to competitive Lewis acid-catalyzed elimination of HX from the alkyl halide. It is worth noting that Hallwachs and Schafarik prepared the first organoaluminum compound, $\mathrm{Et_3Al_2I_3}$, by reaction of aluminum with iodoethane.

$$4\mathrm{Al} \xrightarrow{6\mathrm{MeCl}} 2\mathrm{Me_3Al_2Cl_3} \xrightarrow{6\mathrm{Na}} 2\mathrm{Me_3Al} + 2\mathrm{Al} + 6\mathrm{NaCl} \qquad (8)$$

Additional synthetic protocols are available for the preparation of research quantities of aluminum alkyls that are not commercially available by the above routes. Of these, reaction of an organomercury reagent with aluminum metal

$$2\mathrm{Al} + 3\mathrm{R_2Hg} \longrightarrow 2\mathrm{R_3Al} + 3\mathrm{Hg} \qquad (9)$$

(equation 9) is the oldest and of general utility. However, owing to the toxicity of organomercury compounds (*see* ***Mercury: Organometallic Chemistry***) and environmental concerns, the use of organomercury reagents has been widely supplanted by reactions of aluminum halides with organolithium or Grignard reagents according to equations (10) and (11), respectively.

$$\mathrm{AlX_3} + 3\mathrm{RLi} \longrightarrow \mathrm{R_3Al} + 3\mathrm{LiX} \qquad (10)$$

$$\mathrm{AlX_3} + 3\mathrm{RMgX} \longrightarrow \mathrm{R_3Al} + 3\mathrm{MgX_2} \qquad (11)$$

Reaction of anhydrous aluminum trichloride with an organolithium compound is convenient for preparation of base-free aluminum alkyls such as $^{i}\mathrm{Pr_3Al}$,[12] $^{t}\mathrm{Bu_3Al}$,[12] $(^{t}\mathrm{BuCH_2})_3\mathrm{Al}$,[13] and $\{(\mathrm{Me_3Si})_2\mathrm{CH}\}_3\mathrm{Al}$.[14] In contrast, the use of Grignard reagents often results in the isolation of Lewis acid-base complexes $\mathrm{R_3Al{\cdot}L}$ (L = THF, ether) rather than the more Lewis acidic $\mathrm{R_3Al}$. An exception is the synthesis of tri-*tert*-amylaluminum from $\mathrm{AlCl_3}$ and $\mathrm{(Me_2EtC)MgCl}$ in diethyl ether and hexane.[15] The ether adduct $\mathrm{(Me_2EtC)_3Al{\cdot}OEt_2}$ is not isolated, presumably owing to the steric congestion at aluminum based on comparison of the estimated Tolman cone angle[16] for the *tert*-amyl substituent (135–140°) with that for *tert*-butyl (126°) and isopropyl (114°) substituents.

Organoaluminum halides are most conveniently prepared by redistribution reactions. Mixing a trialkylaluminum and an aluminum halide in a 1:1, 2:1, or 1:2 ratio yields bis halide-bridged compounds $\mathrm{R_3Al_2X_3}$, $\mathrm{R_2AlX}$, or $\mathrm{RAlX_2}$, respectively. Alternative routes include reactions of aluminum halides with organolithium or Grignard reagents in the desired stoichiometry and reaction of trialkylaluminum compounds with halogen to give the organoaluminum halide and alkyl halide. Reactions of alkyl halides with aluminum metal can also be used to prepare organoaluminum halides as previously mentioned.

The preparation of organoaluminum fluorides differs somewhat from that of other organoaluminum halides.[17] Redistribution reactions using $\mathrm{AlF_3}$ do not work well, nor do reactions of $\mathrm{AlF_3}$ with Grignards or organolithium reagents. Organoaluminum fluorides are best prepared by salt metathesis upon mixing R_2AlX or $RAlX_2$ with sodium fluoride. Exchange reactions with BF_3 and reactions of a trialkylaluminum with HF also work well as shown in equations (12) and (13).

$$3R_3Al + BF_3 \longrightarrow 3R_2AlF + R_3B \tag{12}$$

$$R_3Al + 2HF \longrightarrow RAlF_2 + 2RH \tag{13}$$

Organoaluminum halides can be used to prepare pseudohalide derivatives, such as azides[18] and cyanides, by salt metathesis. Azides are prepared by trimethylsilylhalide elimination (equation 14) and by reaction of a trialkylaluminum with chloroazide, ClN_3. Organoaluminum cyanides have also been prepared by reactions of a trialkylaluminum with HCN (equation 15).[7]

$$R_2AlX + Me_3SiN_3 \longrightarrow R_2AlN_3 + Me_3SiX \tag{14}$$

$$R_3Al + HCN \longrightarrow R_2AlCN + RH \tag{15}$$

Several methods exist for the preparation of organoaluminum hydrides R_2AlH and $RAlH_2$.[7,19] Organoaluminum hydrides are obtained by alkene elimination upon heating trialkylaluminum compounds that possess a β-hydrogen (equation 5). Hydrogenolysis of Al–C bonds can be used to form hydrides (equation 16), but high temperatures and pressures are required in the absence of a transition metal catalyst. Ligand redistribution reactions and reduction of organoaluminum halides with metal hydrides are also employed.

$$Et_3Al + H_2 \xrightarrow[300\,\text{atm}]{120\,^\circ\text{C}} Et_2AlH + CH_3CH_3 \tag{16}$$

Several of the trialkylaluminum and alkylaluminum halides and hydrides mentioned above are commercially available. Alkynyl, alkenyl, cyclopentadienyl, and aryl derivatives are, in general, not commercially available and must be synthesized for laboratory use. Alkynyl derivatives can be prepared by salt metathesis, as in the reaction of Et_2AlCl with $NaC{\equiv}CEt$ to give $Et_2AlC{\equiv}CEt$.[20] The acidity of terminal alkynes is sufficient for preparation of alkynyl aluminum compounds by alkane or hydrogen elimination upon reaction with a trialkylaluminum or an aluminum hydride (equation 17), respectively.[21] Trialkynyl aluminum compounds are typically isolated as Lewis base adducts to stabilize them against otherwise facile polymerization. Alkenyl compounds of aluminum have similarly been prepared.

$$H_3Al(NMe_3) + 3HCCPh \xrightarrow{-3H_2} (PhCC)_3Al(NMe_3) \tag{17}$$

Cyclopentadienyl compounds of aluminum have been increasing studied over the past decade.[22–25] They are prepared using the same methods used for simple aluminum alkyls. Tris(cyclopentadienyl)aluminum, for example, can be prepared by reaction of Cp_2Hg with aluminum and by reaction of $AlCl_3$ with magnesocene (equation 18). Magnesocene derivatives are very effective for preparing cyclopentadienylaluminum compounds such as $(C_5MeH_4)_3Al$, (1,2,4-$C_5Me_3H_2)_3Al$, and $(C_5Me_4H)_3Al$. Incomplete exchange occurs upon reaction of $(C_5Me_5)_2Mg$ with $AlCl_3$ and Cp^*AlCl_2 is obtained. Cyclopentadienyl aluminum compounds are often prepared by salt metathesis reactions of $AlCl_3$ or an organoaluminum halide with a CpM derivative (M = Li, Na, K, Tl), but again, exchange is not always complete and cyclopentadienylaluminum halides are sometimes obtained. Cyclopentadienylaluminum compounds have also been prepared by trimethylsilylchloride elimination and alkane elimination reactions, but these preparative routes are less common. Redistribution reactions can occur as in the conversion of Cp_2AlMe to Cp_3Al and $CpAlMe_2$.

$$3Cp_2Mg + 2AlCl_3 \longrightarrow 3MgCl_2 + 2Cp_3Al \tag{18}$$

Jordan and coworkers have recently prepared several *ansa*-bis(indenyl) compounds $\{(AlMe_2L)indenyl\}_2SiMe_2$ and 1,2-$\{(AlMe_2L)indenyl\}_2C_2H_4$ (L = THF, Et_2O, 1,4-dioxane) by a salt metathesis route.[26] These were reacted with $M(NMe_2)_4$ (M = Zr, Hf) to eliminate $[Me_2AlNMe_2]_2$ and form *ansa*-metallocene complexes of bis(dimethylamido)zirconium and bis(dimethylamido)hafnium. A simple tris(indenyl)aluminum compound has been prepared by reaction of bis(indenyl)mercury with aluminum metal.[7]

Similar to aluminum alkyls, aluminum aryls are prepared from organomercury, organomagnesium, organolithium, organoborane, or organotin reagents. Triphenylaluminum and substituted derivatives can be prepared by several of these methods. Halide derivatives such as Ph_2AlCl and $PhAlCl_2$ are prepared by ligand redistribution upon reaction of Ph_3Al with $AlCl_3$.

Monomeric trimesitylaluminum is prepared from Mes_2Hg and aluminum,[27] or by removing THF or ether from $Mes_3Al{\cdot}L$ (L = THF, OEt_2) with heating in vacuo.[28] Mesityl derivatives $Mes_2MeAl{\cdot}THF$, $Mes_2EtAl{\cdot}THF$, and $Mes_2ClAl{\cdot}THF$ were prepared by reactions of MesMgBr with $MeAlCl_2$, $EtAlCl_2$, and $AlCl_3$, respectively,[29] and the chloro-bridged dimer $[Mes_2AlCl]_2$ has been prepared by ligand redistribution. Tris(pentamethylphenyl)aluminum is obtained base-free by reaction of $AlCl_3$ with C_6Me_5MgBr in diethyl ether.[30] The isolation of the base-free alane is in contrast to the formation of $Mes_3Al{\cdot}L$ by the Grignard route.

There are fewer preparative methods for *m*-terphenyl derivatives of aluminum.[31] Aluminum bromide reacts with $[2,4,6\text{-}Ph_3C_6H_2Li]_2$ to give $2,4,6\text{-}Ph_3C_6H_2AlBr_2{\cdot}OEt_2$, but analogous procedures do not give the corresponding dichlorides. Alternatively, reaction of $[2,6\text{-}Mes_2C_6H_3Li]_2$ with $AlH_3{\cdot}NMe_3$ in ether, followed by reaction with chlorotrimethylsilane yields $(2,6\text{-}Mes_2C_6H_3)AlH_2{\cdot}OEt_2$. Ether can be removed in vacuo and additional treatment with chlorotrimethylsilane yields the organoaluminum dichloride as the etherate complex. The base-free dichloride can be obtained by refluxing in hexane. Wehmschulte and coworkers reacted (2,6-$Mes_2C_6H_3$)$AlH_2{\cdot}OEt_2$ with [2,6-$Mes_2C_6H_3Li$]$_2$ to give (2,6-$Mes_2C_6H_3$)$_2$AlH, a rare example of a monomeric aluminum hydride.[32]

The synthesis of highly Lewis acidic fluorinated arylaluminum compounds such as $Al(C_6F_5)_3$ has been of interest in recent years,[33] but efforts have been hindered by the proclivity of aluminum to abstract fluoride, often resulting in violent decomposition. The preferred synthesis of $Al(C_6F_5)_3$ is by stirring commercially available $B(C_6F_5)_3$ with Me_3Al at room temperature in toluene and hexanes (equation 19).[34] The reaction does not go to completion but can be driven to do so by precipitation of the desired product as the toluene solvate $(C_6F_5)_3Al{\cdot}0.5$ toluene upon addition of hexanes. Isolation of the toluene solvate is preferred since it has greater thermal and shock stability than the solvate-free material. Aluminum halides react with C_6F_5Li to yield $(C_6F_5)_3Al{\cdot}OEt_2$, but attempts to remove the ether resulted in an explosion.[7] Roesky and coworkers prepared $(C_6F_5)_3Al{\cdot}THF$ by ligand redistribution upon heating $(C_6F_5)AlMe_2$ and distilling off the trimethylaluminum as it formed.[35] The intermediate $(C_6F_5)AlMe_2$ was not, however, purified or characterized. An alkyl derivative of a pentafluorophenyl alane, $(C_6F_5)_xAlR_{3-x}$ (R = alkyl; $x = 1, 2$), has been isolated and structurally characterized, that being the bis methyl-bridged $(C_6F_5)_3Al_2Me_3$ prepared by reaction of $B(C_6F_5)_3$ and Me_3Al.[36] The compounds $(C_6F_5)_2AlMe$ and $(C_6F_5)AlMe_2$ and their ether adducts $(C_6F_5)_2MeAl{\cdot}OEt_2$ and $(C_6F_5)Me_2Al{\cdot}OEt_2$ have been generated in situ and characterized by NMR spectroscopy.[36,37] Spectroscopic data suggest that $(C_6F_5)_2AlMe$ and $(C_6F_5)AlMe_2$ exist as methyl-bridged dimers. The formation of $(C_6F_5)_2AlEt$ was implicated in ethene and propene polymerizations catalyzed with a mixture of $Al(C_6F_5)_3$ and Et_3Al.[38] Pentafluorophenylaluminum halides $(C_6F_5)AlBr_2$ and $(C_6F_5)_2AlBr$ have been prepared from the reaction of $(C_6F_5)HgMe$ and $AlBr_3$.[7] Chen recently prepared $(C_6F_5)_2AlCl$ by reaction of $Al(C_6F_5)_3$ with CH_2Cl_2.[39] Attempts to prepare tris(perfluorobiphenyl)aluminum instead led to the formation of the fluoroaluminate $Li[(C_{12}F_9)_3AlF]$, presumably by a fluoride abstraction reaction.[40]

$$Me_3Al + B(C_6F_5)_3 \xrightarrow{\text{toluene}} Al(C_6F_5)_3 + Me_3B \qquad (19)$$

Tin–aluminum exchange has been used to prepare bidentate aryl aluminum compounds and aluminoles as illustrated in equations (20) and (21).[41]

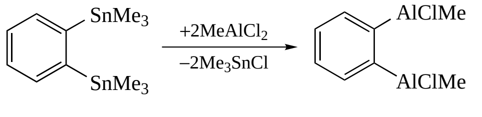

(20)

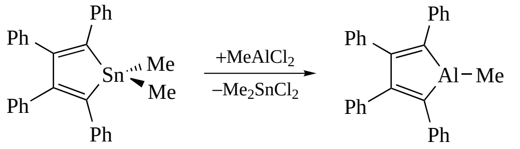

(21)

2.2 Associative Properties and Structures

Aluminum alkyls, alkylaluminum halides, and alkylaluminum hydrides strongly associate in solution and in the solid state.[42] The association of trialkylaluminum compounds is in stark contrast to the monomeric nature of trialkylboron (*see **Boron: Organoboranes***) and trialkylgallium (*see **Gallium: Organometallic Chemistry***) compounds.

Trialkylaluminum and alkylaluminum hydrides associate with alkyl or hydride bridges. Since there are no available lone-pair electrons with which to form bridges by standard two-center two-electron interactions, multicenter bonding is invoked in the same manner as for electron-deficient boranes (*see **Boron Hydrides***), alkyllithium (*see **Alkali Metals: Organometallic Chemistry***), dialkylberyllium and dialkylmagnesium compounds (*see **Beryllium & Magnesium: Organometallic Chemistry***).

Trialkylaluminum compounds exist predominately as dimers with two bridging alkyl groups as for trimethylaluminum (**1**). The bonding in Me_6Al_2 is analogous to that in diborane. The aluminum atoms are sp^3 hybridized and four of the sp^3 hybrid orbitals are utilized for formation of two-center two-electron bonds to the four terminal methyl groups. The bonding interaction for each bridging methyl can be described as overlap of two Al sp^3 hybrid orbitals and an sp^3 hybrid orbital from the methyl carbon as in (**2**). The resulting molecular orbital for each bridge interaction is populated with two electrons to give a three-center two-electron bond.

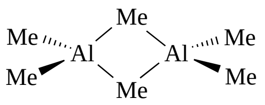

(**1**)

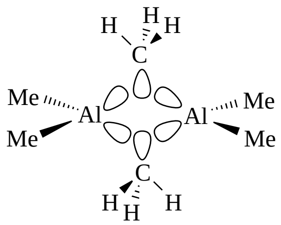

(**2**)

Trialkylaluminum compounds undergo monomer-dimer equilibria (equation 22) in noncoordinating solvents. Cryoscopic molecular weight measurements indicate that trimethylaluminum is predominately a dimer in toluene solutions, and this is confirmed by NMR spectroscopy. The ^1H NMR spectrum of Me_3Al in toluene at −70 °C exhibits two resonances in a 2:1 ratio for the terminal and bridging methyl groups, respectively, of the dimer. Similar ^1H NMR data was obtained in support of dimeric triethylaluminum at −70 °C. Exchange is rapid as evidenced by a single sharp methyl resonance in the room temperature ^1H NMR spectrum of Me_3Al.

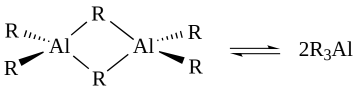

(22)

The position of monomer-dimer equilibria for trialkylaluminum compounds shift to favor monomer formation with increasing length and bulk of the alkyl. The percent dissociation of Me_6Al_2, Et_6Al_2, $^nPr_6Al_2$, $^nBu_6Al_2$, and $^iBu_6Al_2$ at 20 °C in 0.05 mole fraction cyclohexane solutions are 2.9×10^{-4}, 5.01×10^{-3}, 2.53×10^{-2}, 3.76×10^{-2}, and 1.64×10^{-1}, respectively. Monomer concentration also increases with increasing temperature and decreasing concentration of the aluminum alkyl.**[43]**

Redistribution reactions of aluminum alkyls require dissociation into monomers. Enthalpy of dissociation for trimethylaluminum is 19.40 kcal mol^{-1} whereas for $^iBu_6Al_2$ it is 8.1 kcal mol^{-1}. For comparison, enthalpies of dissociation of simple Lewis acid-base adducts $Me_3Al{\cdot}L$ (L = amine, ether, phosphine, phosphine oxide) are generally in the range of 17–32 kcal mol^{-1}, with most being greater than 20 kcal mol^{-1}.**[7]**

In contrast to the dimeric trialkylaluminum compounds, many dialkylaluminum hydrides prefer trimeric structures with bridging hydrides as shown for $^iBu_2AlH$ (**3**). Uhl and coworkers have prepared and structurally characterized the novel tetrameric sesquihydride $[^tBu_3Al_2H_3]_2$ (**4**), which also exhibits bridging hydrides with large Al–H–Al angles of 149(2) and 155(2)°.**[44]**

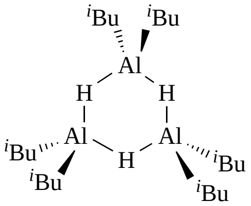

(**3**)

The alkyl groups do not bridge in the organoaluminum hydrides, and this is in keeping with decreasing bridging ability in the order H > Me > Et > ^nBu > ^iBu. Alkyls with branching at the α or β positions are particularly poor bridging groups for aluminum compounds and cryoscopic molecular weight measurements indicate that several aluminum trialkyls are monomeric in solution. These include $^tBu_3Al$,**[12]** $(^tBuCH_2)_3Al$,**[13]** $(Me_2EtC)_3Al$,**[15]** and $\{(Me_3Si)_2CH\}_3Al$.**[14]**

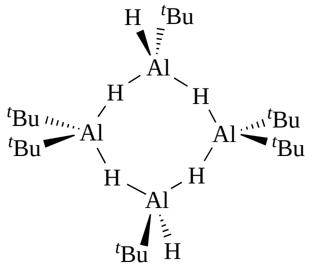

(**4**)

Aluminum alkynyl groups can be either terminal or bridging. In Lewis acid-base complexes where the aluminum centers are four-coordinate, such as in $(PhC{\equiv}C)_3Al{\cdot}NMe_3$, alkynyl substituents are terminal with Al–C–C angles ranging from 160 to 180°. In the absence of a strong σ-donor, however, additional interactions between the alkynyl π system and aluminum may exist. The alkynyl compound $[PhC{\equiv}CAlPh_2]_2$ (**5**) exists as a dimer with bridging alkynyl groups. The bonding is described as σ bonding of the alkynyl C_α to one aluminum and π donation to the second aluminum center.

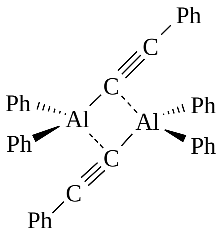

(**5**)

The structures of organoaluminum halides R_nAlX_{3-n} are dominated by dimeric structures with Al_2X_2 four-membered rings for X = Cl, Br, and I. Unlike the aluminum alkyls, these halide bridges are electron-precise and result from intermolecular Lewis acid-base complexation. These dimers do dissociate and readily react with Lewis bases, but the enthalpies of dissociation are higher than those for the aluminum alkyls. In many cases, the strength of the association is sufficient that dimers are observed in the gas phase.

Organoaluminum fluorides differ from the chloride, bromide, and iodide analogs in that bridging structures with large Al–F–Al angles are preferred (*see* ***Fluorides: Solid-state Chemistry***).**[17,45]** Dialkylaluminum fluorides, R_2AlF, exist as tetramers (**6**) with Al_4F_4 eight-membered rings in solution and in the solid state for R = Me, Et, ^iPr, ^tBu, and as trimers with six-membered Al_3F_3 rings for R = ^nPr and ^iBu. This linear bridging ability is also observed upon reaction of organoaluminum fluorides with alkali fluoride to form alanates such as the cubanoidal cage compound $[(Me_3Si)_3CAlF_3M(THF)]_4$ (M = Li, Na) (**7**). Linear fluoride bridges are observed in $K[R_3AlFAlR_3]$ (R = Me, Et).

The structures of cyclopentadienylaluminum(III) compounds are highly fluxional.**[22–25]** In solution, aluminum centers

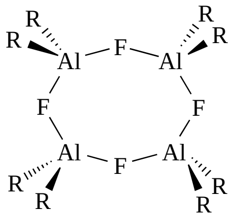

(**6**)

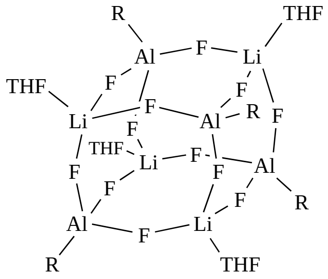

(**7**)

migrate freely around the Cp rings and this migration cannot be frozen out on the NMR timescale even at −90 °C. Simple signal-averaged spectra with sharp Cp resonances are observed. In the solid state, cyclopentadienyl rings adopt a variety of coordination modes including η^1, η^2, η^3, and η^5. Only the η^4 coordination mode has yet to be observed by X-ray crystallography. The η^2 coordination mode is most prevalent and calculations suggest a slight energetic preference for η^2 coordination, but this is obviously dependent on steric and electronic factors. Drew and Haaland originally proposed η^2 coordination for gas-phase $CpAlMe_2$ based on electron diffraction data. Dihapto coordination has since been observed in the solid-state structures of Cp_2AlMe and Cp^*_2AlMe. $CpAlMe_2$ exhibits a polymeric structure with each Cp coordinated η^1 at C_1 to one aluminum atom and η^1 at C_3 to a different aluminum atom. The η^3 coordination mode is observed in the chloride-bridged dimers $[Cp^*AlClR]_2$ (R = Me, Et, ^{i}Bu). Observation of η^5 coordination has been more common in recent years. Examples of η^5-cyclopentadienyl groups include $[Cp^*AlCl_2]_2$, $CpAl(BHT)_2$, $[(BHT)CpAl]_2O$, and $[Cp^*_2Al]^+$. In the molecular structure of $(1,2,4\text{-}Me_3C_5H_2)_3Al$, one of the trimethylcyclopentadienyl groups is coordinated η^5 whereas the other two are coordinated η^1. Pentahapto coordination is also observed in many Cp^* derivatives of aluminum(I).

Cryoscopic molecular weight determinations and X-ray crystallography confirm that triphenylaluminum (**8**) is a dimer in solution and in the solid state. The bridging phenyl group in the molecular structure of Al_2Ph_6 bridges through one carbon. The plane of the bridging phenyls is perpendicular to that of the core Al_2C_2 four-membered ring. Mesityl groups are sufficiently bulky that Mes_3Al is a monomer in solution and in the solid state,**[27]** as is the related triarylaluminum compound $(C_6Me_5)_3Al$ (**9**).**[30]** In each compound, the aluminum center is trigonal planar with the aryl groups propellered to reduce steric interactions. In contrast, $(C_6F_5)_3Al$ crystallizes as solvates $(C_6F_5)_3Al\cdot$toluene (**10**) and $(C_6F_5)_3Al\cdot$benzene, the molecular structures of which reveal an η^1-toluene or η^1-benzene bound to the slightly pyramidalized four-coordinate aluminum.**[46]** The Al–C–C angles for the bound arenes are 99.1 and 96.1°, suggesting that this is a π-arene complex rather than a Wheland intermediate. Arene coordination is attributed to the high Lewis acidity of $(C_6F_5)_3Al$ and is analogous to coordination of toluene to silylium cations as in the structurally characterized $[Et_3Si\cdot\text{toluene}]^+$. The arene-aluminum interactions in $(C_6F_5)_3Al\cdot$toluene and $(C_6F_5)_3Al\cdot$benzene are retained in C_6D_6 solutions.

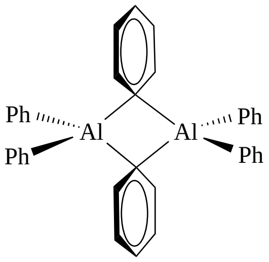

(**8**)

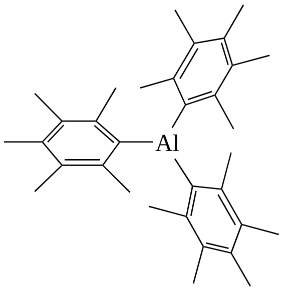

(**9**)

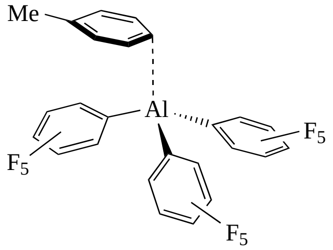

(**10**)

Those new to the subject and wanting more information on the characterization of organoaluminum compounds can consult several good references. Joan Mason has published a text in which she discusses the structural information that can be gleaned from ^{27}Al NMR spectroscopy and the problems associated with the technique.**[47]** The text tabulates ^{27}Al NMR chemical shift and $W_{1/2}$ data. Shapiro has also tabulated ^{27}Al NMR chemical shifts for cyclopentadienylaluminum compounds.**[22]** Holloway and Melnik published a review of structural data for organoaluminum compounds.[48] There is also a compilation of 727 organoaluminum compounds with references to the synthesis and spectroscopic and structural characterization of each compound.[49]

2.3 Reactivity

Neat aluminum trialkyls are highly reactive, colorless liquids that spontaneously ignite in the presence of oxygen, react violently with water, and must be manipulated and stored under an inert atmosphere. Trialkylaluminum compounds react vigorously with halogenated solvents and even react with silicone stopcock grease[50] with cleavage of Si–O and formation of Al–O bonds. Reactivity is greatest for trimethylaluminum (37.4 wt% Al) and decreases with decreasing weight percent of aluminum. Handling aluminum alkyls as dilute solutions in inert hydrocarbons reduces the risk of ignition. Tri-*iso*-butylaluminum is typically available as a 25-wt% solution in toluene. Bulky alkyl and aryl groups moderate the reactivity. Aluminum triaryls are white solids that fume in air, but oxidize more slowly than do aluminum trialkyls.

The reactivity of organoaluminum compounds is attributed to their low thermodynamic stability and high kinetic lability. The mean bond enthalpy for the Al–C bond in Me_3Al is $274\,kJ\,mol^{-1}$ (Table 1).[51] This is less than the E–C bond enthalpies for E = boron, carbon, nitrogen, and silicon and only 55 and 65% of the Al–O and Al–Cl bond enthalpies, respectively. There is clearly a strong thermodynamic driving force for oxidation and hydrolysis. Enthalpies of combustion and hydrolysis for Et_3Al, for example, are 5104 and $527\,kJ\,mol^{-1}$, respectively.[7] Although Al–C bonds may be considered weak based on mean bond enthalpies, they are comparable in strength to P–C bonds, which are considerably less reactive than Al–C bonds in aluminum trialkyls. Thus, the reactivity of organoaluminum compounds is equally related to their kinetic lability. This lability is due to the availability of a low-lying acceptor orbital in three-coordinate monomeric trialkylaluminum compounds and potential participation of empty *d* orbitals. Furthermore, the Al–C bond is highly polarized in the direction $Al^{\delta+}$–$C^{\delta-}$ since the difference in the Pauling electronegativity of aluminum (1.6) and carbon (2.5) is greater than for any other M–C bond of a *p*-block metal besides thallium. Selected Pauling electronegativities are as follows: C (2.5), B (2.0), Si (1.9), Ga (1.8), In (1.8), Al (1.6).

Table 1 Selected mean bond dissociation enthalpies ($kJ\,mol^{-1}$) for *p*-block elements

B–C	365	C–C	358
Al–C	274	Si–C	311
Ga–C	247	Ge–C	249
Al–O	500	N–C	314
Al–Cl	420	P–C	276

Much of the reaction chemistry of aluminum trialkyls can be classified by the following reaction types, some of which are illustrated in Scheme 1: oxidation, alkane elimination in the presence of protic reagents, Al–C bond cleavage via halogenation and hydrogenation, insertion reactions, β-hydrogen elimination (equation 5), and coordination of Lewis bases.

Protic reagents such as water, alcohols, acids, and primary and secondary amines react rapidly with aluminum alkyls resulting in alkane elimination and coordination of the conjugate base of the protic reagent. Reagents must be added slowly to avoid dangerous exothermic reaction and gas evolution, particularly for Me_3Al and Et_3Al. Subsequent reactivity of the Al–C bonds decreases as more alkyl groups are removed, and vigorous conditions are often required to remove the last aluminum alkyl. Reaction of Me_3Al with alcohol rapidly forms Me_2AlOR' followed by formation of $MeAl(OR')_2$, but the last methyl group in $MeAl(OR')_2$ reacts with alcohols reluctantly.

Insertion reactions are commonplace for organoaluminum compounds. Insertion of oxygen into the Al–C bonds of alumium trialkyls proceeds cleanly at low temperatures in hydrocarbon solvents to give aluminum alkoxides. The first insertion is rapid, as usually is the second. The third insertion is considerably slower depending on the steric bulk of the resulting alkoxide complexes. Oxygen insertion is believed to proceed via an alkylperoxy intermediate R_2AlOOR by analogy to the structurally characterized gallium and indium alkylperoxides $[{}^tBu_2MOO{}^tBu]_2$ (M = Ga, In).[52] Lewinski and coworkers have structurally characterized an alkylperoxide complex of aluminum (**11**) isolated after O_2 insertion into the Al–C bonds of ${}^tBu_2Al$(methylsalicylate).[53,54] Complex

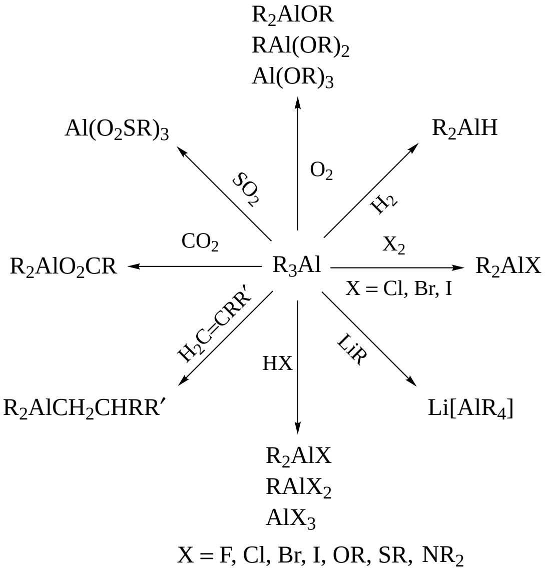

Scheme 1 Representative reactions of trialkylaluminum compounds

(**11**) slowly decomposes in solution at room temperature with conversion of the *tert*-butylperoxy group to a *tert*-butylalkoxide ligand. Analogous to reactions of oxygen with aluminum trialkyls, sulfur, selenium, and tellurium insert into Al–C bonds of R_3Al to give $[R_2Al(\mu\text{-}ER)]_2$ and in some cases $[RAlE]_4$ (E = S, Se, Te).[15,55]

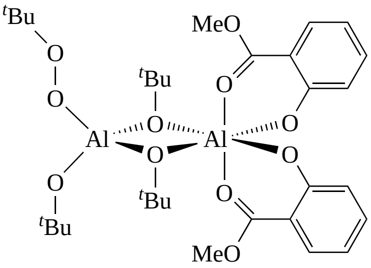

(**11**)

Insertions of carbon dioxide, sulfur dioxide, and sulfur trioxide yield aluminum carboxylates, sulfinates, and sulfonates, respectively. Treatment of the resulting complexes with aqueous acid yields the corresponding alkylcarboxylic, alkylsulphinic, and alkylsulphonic acids. High pressure and temperatures of 220–240 °C are required for multiple insertions of CO_2 to yield more than one equivalent of carboxylic acid per aluminum. Excess aluminum trialkyl must be avoided or the initially formed carboxylate is completely alkylated to a trialkylcarbinol. Reaction of Et_3Al with CO_2, for example, gives a 90% yield of triethylcarbinol.

There are examples of insertion for many other unsaturated molecules including N_2O_4, CS_2, N≡CR, $R_2C{=}O$, CO, and C≡NR. Reaction of N_2O_4 with Et_3Al gives diethylhydroxylamine upon protic workup. For carbon disulfide, C–S bond cleavage is often observed, leading to formal insertion of thiocarbonyl and sulfur. Shapiro recently reported the first example of isocyanide insertion into an Al–C bond.[56] Compound (**12**) was obtained by insertion of two molecules of *tert*-butylisocyanide into an Al–C bond of $(C_5Me_5H)_3Al$. Isocyanide insertion did not occur for less bulky cyclopentadienyl derivatives, prompting the authors to speculate that the reaction was promoted by labilization of the Al–C bond by steric congestion at the aluminum center. The first example of CO insertion into an Al–C bond has also been reported recently. Mason and coworkers found that $^tBu_3Al$ reacts rapidly with CO at room temperature and atmospheric pressure to give the bridging acyl dimer (**13**).[57] As in the isocyanide case, relief of steric congestion may be a factor in promoting this reaction. Insertion of CO was not observed for more common aluminum trialkyls such as Me_3Al, Et_3Al, and $^iBu_3Al$ under a variety of conditions. Nitriles insert more readily into Al–C bonds than do isocyanides and CO to give dialkylaluminum ketimides (**14**). A table of many known examples is provided in the text by Mole.[7]

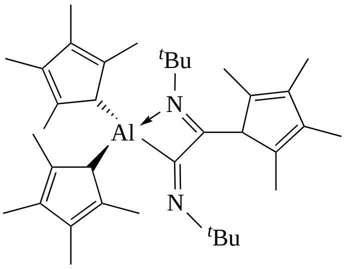

(**12**)

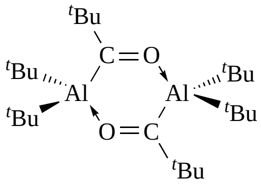

(**13**)

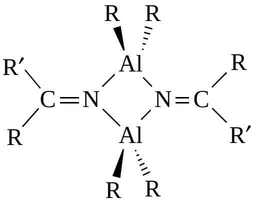

(**14**)

The most prominent insertion reactions are those of alkenes and alkynes into Al–H and Al–C bonds. These hydroalumination and carbalumination reactions are of tremendous importance in the synthesis of aluminum alkyls as already described for the Aufbau reaction and direct synthesis, as well as for the use of aluminum alkyls in organic synthesis. Carbalumination gives *cis*-addition products with the R_2Al fragment bound to the least substituted carbon atom of the alkene and alkynes react faster than alkenes. In hydroalumination, the R_2Al fragment is also bound to the least substituted carbon of the starting alkene. Hydroalumination becomes more difficult with increasing substitution of the alkene in the order

$$H_2C{=}CH_2 > H_2C{=}CHR > H_2C{=}CR_2 > HRC{=}CHR$$

Synthetic applications of double hydroalumination and double carbalumination are discussed in a recent review.[58]

Aluminum alkyls are stronger Lewis acids than the trialkyls of boron and gallium, and complex formation in the presence of Lewis bases is an important aspect of the reaction chemistry of organoaluminum compounds. The Lewis acidity of organoaluminum compounds accounts for the strong association of aluminum alkyls and hydrides by three-center two-electron bonds, as well as association of organoaluminum

Table 2 Bond dissociation enthalpies of selected trimethylaluminum complexes

Lewis base	$\Delta H°$ (kcal mol^{-1})	Solvent
$Me_3P{=}O$	32.0 ± 0.2	benzene
Me_3N	30.0 ± 0.2	hexane
$Me_2S{=}O$	28.6 ± 0.2	hexane/5% benzene
pyridine	27.6 ± 0.2	hexane
Et_3N	26.5 ± 0.2	hexane
2-picoline	26.1 ± 0.2	hexane
THF	22.9 ± 0.2	hexane
Et_3P	22.1 ± 0.3	hexane
Me_3P	21.0 ± 0.2	hexane
Me_2O	20.3 ± 0.2	hexane
2,6-lutidine	19.9 ± 0.2	hexane
Me_2S	16.6 ± 0.2	hexane

halides and pseudohalides by coordinate covalent bonds. The strength of the association of trimethylaluminum with Lewis bases is evident in enthalpies of dissociation, representative examples of which are shown in Table 2.[7] The data also show that trimethylaluminum is a hard acid in the Pearson Hard-Soft Acid-Base (*see* ***Hard & Soft Acids and Bases***) sense as indicated by the high enthalpies of dissociation for the hard donors $Me_3P{=}O$ and $Me_2S{=}O$. For pairs of structurally similar donors, enthalpies of dissociation are greatest for the harder donor, such as $Me_3N > Me_3P$, $Et_3N > Et_3P$, and $Me_2O > Me_2S$. Competition experiments also support the enthalpy data. Trimethylphosphine oxide, for example, will displace diethyl ether from $Me_3Al{\cdot}OEt_2$ to form $Me_3Al{\cdot}O{=}PMe_3$. Enthalpies are also affected by steric interactions, with greater steric bulk of the base leading to lower enthalpies of dissociation. This is seen in decreasing enthalpies of dissociation for complexes of heterocyclic bases in the order pyridine > 2-picoline > 2,6-lutidine.

Organoaluminum compounds are sufficiently Lewis acidic to interact with weak Lewis bases such as alkyl halides, although stable and thoroughly characterized examples are few. Instead, many trialkylaluminum compounds react violently with halogenated solvents. The adduct $Me_3SiF{\cdot}AlEt_3$, with weak F→Al donation, has been characterized by NMR spectroscopy and this adduct is thermally stable to 30 °C. Structurally characterized examples of aryl halides forming dative bonds to aluminum have been reported for cationic organoaluminum complexes as will be discussed later.

In other recent developments, Sanchez, Arrington, and Arrington reported that Me_3Al binds CO to form $OC{\rightarrow}AlMe_3$ (**15**) in an argon matrix at 15–35 K.[59] Robinson reported the first neutral carbene complex (**16**) of an aluminum trialkyl in 1996.[60] Complexes in which there is intramolecular base coordination have been reviewed.[61]

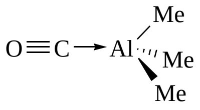

(**15**)

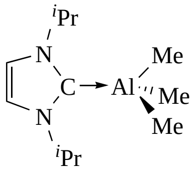

(**16**)

3 LOW-VALENT ORGANOALUMINUM COMPOUNDS

The organometallic chemistry of aluminum is dominated by the chemistry of aluminum(III), but lower oxidation state compounds are now accessible.[10,62] The first examples of this class of compounds are carbonyl complexes such as Al(CO), $Al(CO)_2$, and $Al_3(CO)$, which were generated upon exposure of aluminum atoms to CO in matrix-isolation experiments near 20 K.[63] The number, relative intensities, and frequency of the carbonyl stretches in the IR spectra, along with isotopic labeling and EPR studies were used to verify these compositions. These complexes exhibit ν_{CO} values of 1868, 1985 and 1904, and 1715 cm^{-1}, respectively, indicative of Al→CO π^* backbonding. The carbonyl species are unstable at higher temperatures and no stable carbonyl complex of aluminum, in any oxidation state, has been reported. The monomeric aluminum-alkene adducts $Al(\eta^2\text{-}C_2H_4)$ and $Al(\eta^2\text{-}C_6H_6)$ were similarly identified in inert matrices at low temperature.[10] No room-stable alkene complexes of aluminum have been reported.

Isolable low-valent organoaluminum compounds have recently become accessible based mainly on the works of Uhl[64] and Schnöckel.[65,66] In 1988, Uhl synthesized the first organoaluminum compound to contain an Al–Al bond, $\{(Me_3Si)_2CH\}_2Al\text{–}Al\{CH(SiMe_3)_2\}_2$, by reduction of $\{(Me_3Si)_2CH\}_2AlCl$ with potassium metal (equation 23). Surprisingly, the Al_2C_4 core of $\{(Me_3Si)_2CH\}_2Al\text{–}Al\{CH(SiMe_3)_2\}_2$ is nearly planar. The steric bulk

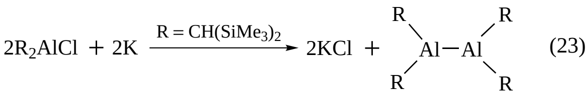

$$2R_2AlCl + 2K \xrightarrow{R\,=\,CH(SiMe_3)_2} 2KCl + R_2Al\text{–}AlR_2 \qquad (23)$$

of the bis(trimethylsilyl)methyl substituents are important in stabilizing the dialane from disproportionation to an aluminum trialkyl and aluminum metal. Bulky silyl and aryl derivatives have since been prepared and these dialanes have been shown to add Lewis bases, insert small molecules, and accept an electron to form Al–Al π-bonding. The dialane reacts, for example, with insertion of sulfur to form $[R_2Al\text{–}S\text{–}AlR_2]$. The dialane also reacts with simple Lewis bases such as LiBr and MeLi to give adducts $[R_2Al\text{–}AlR_2Br]^-$ and $[R_2Al\text{–}AlR_2Me]^-$. A two-electron reduction of the Al–Al bond in $R_2Al\text{–}AlR_2$ compounds would formally yield the aluminum analog of an alkene (*see* ***Main Group: Multiple Bonding***). The dianion, however, remains elusive. A one-electron reduction of $R_2Al–AlR_2$ to form $[R_2Al–AlR_2]^{\bullet -}$ has been successful for both 2,4,6-triisopropylphenyl and bis(trimethylsilyl)methyl substituents.**67** Reduction leads to a planar Al_2C_4 core structure and a decrease in the Al–Al bond distance by 6–7%, from 2.660(1) Å in $\{(Me_3Si)_2CH\}_2Al–Al\{CH(SiMe_3)_2\}_2$ to 2.53(1) Å in $[\{(Me_3Si)_2CH\}_2Al–Al\{CH(SiMe_3)_2\}_2]^{\bullet -}$ and from 2.647(3) Å in $R_2Al–AlR_2$ to 2.470(2) Å in $[R_2Al–AlR_2]^{\bullet -}$ (R = 2,4,6-$^iPr_3C_6H_2$). The decrease in Al–Al distance upon reduction is consistent with increased bond order. Power has similarly attempted to reduce I(R)Al–Al(R)I with two equivalents of potassium to give the dialuminene species RAl=AlR (R = 2,6-$^iPr_2C_6H_3$).**68** The desired compound was not isolated, but its formation was indicated by isolation of a cycloaddition product with toluene.

In 1991, Uhl reported that reduction of $^iBu_2AlCl$ with potassium in hexanes yielded $K_2[Al_{12}{}^iBu_{12}]$ (Figure 1). The Al–Al distances in $[Al_{12}{}^iBu_{12}]^{2-}$ average 2.660 Å, comparable to that in $\{(Me_3Si)_2CH\}_2Al–Al\{CH(SiMe_3)_2\}_2$. Despite the extensive chemistry of icosahedral boranes (*see* ***Boron: Polyhedral Carboranes***), this is the first analog of an icosahedral borane for the heavier group 13 elements. Aluminum has been incorporated into polyhedral boranes and carboranes. Polyhedral carbaalanes have also been prepared and recent developments in this area have been reviewed.**69**

Also in 1991, Schnöckel**65,66** reported that reaction of AlCl with Cp^*_2Mg yielded $[Cp^*Al]_4$ (**17**). This can also be synthesized by reaction of $[Cp^*AlX_2]_2$ with Na/K alloy. Substituted-cyclopentadienyl and silyl derivatives of aluminum(I) have similarly been prepared.**23,24** The Al–Al bonds in $[Cp^*Al]_4$ (average 2.769 Å) are longer than those in the dialanes and may be cleaved thermally to give monomeric Cp*Al in the gas phase. The Al–Al bonds in $[Cp^*Al]_4$ insert selenium and tellurium to give the chalcogenide cubanes $[Cp^*AlE]_4$ (E = Se, Te), react with P_4 to give the cage compound $(Cp^*Al)_6P_4$, and react with $[^tBuAs]_4$ to give $As_2(AlCp^*)_3$ in which arsenic atoms cap the two trigonal faces of the $[AlCp^*]_3$ core. Monomeric Cp*Al retains a lone pair of electrons and may be considered a CO analog with both σ-donor and π-acceptor potential. The Cp*Al moiety functions as a ligand towards main group and transition metals to form complexes such as $Cp^*Al\!\rightarrow\!B(C_6F_5)_3$ (**18**), $Cp^*Al\!\rightarrow\!Al(C_6F_5)_3$, $Cp^*Al\!\rightarrow\!Cr(CO)_5$, and $Cp^*Al\!\rightarrow\!Fe(CO)_4$. The only hexameric organoaluminum(I) cluster containing Al–Al bonds is $[Al_6{}^tBu_6]^{\bullet -}$ (**19**).

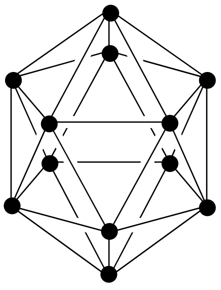

Figure 1 Icosahedral $Al_{12}{}^{2-}$ core of $K_2[Al_{12}{}^iBu_{12}]$. Potassium atoms and organic substituents are omitted for clarity

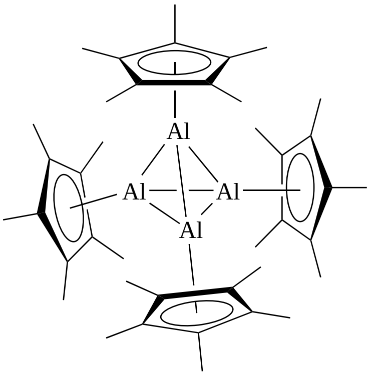

(**17**)

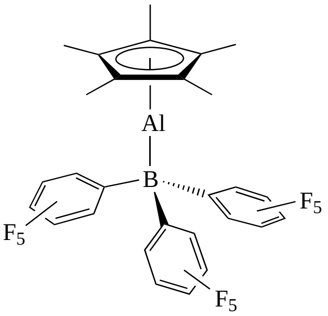

(**18**)

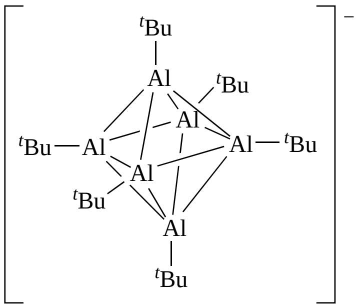

(**19**)

Although aluminum(I) halides are useful for the low-temperature preparation of organoaluminum(I) compounds, aluminum(I) halides disproportionate to AlX_3 and $2Al_{metal}$ as temperature increases from −78 °C to −30 °C. Schnöckel**65,66** has taken advantage of this disproportionation for the preparation of metalloid clusters such as $SiAl_{14}Cp^*_6$, $Al_{50}Cp^*_{12}$, and the amazing inorganic cluster $[Al_{77}\{N(SiMe_3)_2\}_{20}]^{2-}$, all of which have been characterized by X-ray crystallography.**70**

These are referred to as metalloid clusters since they contain metal atoms bound only to other metal atoms and since the cores resemble bulk metal. The structure of $SiAl_{14}Cp^{*}_{12}$ can be described as a body-centered Al_8 cube encapsulating a single silicon atom. Each of the six faces of the Al_8 cube are capped with an AlCp* group. The structure of $Al_{50}Cp^{*}_{12}$ can similarly be described as an Al_8 core surrounded by an icosahedral Al_{30} shell. Each pentagonal face of the Al_{30} shell is capped by an AlCp* moiety. The Al–Al distances in $Al_{50}Cp^{*}_{12}$ average 2.770 Å, but range from 2.578 to 2.877 Å. The average Al–Al distances increase from the Al_8 core (2.664 Å) to the Al_{30} shell (2.765 Å) to those between the Al_{30} shell and the Cp*Al moieties (2.867 Å).

4 ORGANOALUMINUM HETEROCYCLES AND CAGE COMPOUNDS

Organoaluminum compounds form a variety of heterocycles and cage compounds with heteroatoms or polyanions that possess one or more lone pairs of electrons for use in bridge formation. Heterocycles of the type $[R_2Al(\mu_2\text{-}ER'_x)]_n$ ($n = 2, 3$) are extremely common with a diversity of bridging groups (ER'_x = F, Cl, Br, I, O, S, OR, SR, SeR, NR_2, PR_2, AsR_2, SbR_2,[71] BiR_2,[71] OH, SH, SeH, O_2SR, O_2PR, O_2AsR_2). Some of these heterocycles exhibit dimer-trimer equilibria in solution as evidenced by NMR spectroscopy and cryoscopic molecular weight measurements.

An interesting structural motif containing bridging groups is that found in alkylaluminum sesquialkoxides, which are prepared by reaction of a trialkylaluminum with an alcohol in a 2:3 ratio (equation 24) or by ligand redistribution upon reaction of a trialkylaluminum with a homoleptic aluminum alkoxide (equation 25).[72,73] Although the sesquialkoxide compounds can be formulated as $R_3Al_2(OR')_3$, this is an inaccurate reflection on their structure. The formula $[Al\{(R'O)_2AlR_2\}_3]$ is more descriptive. Structural studies confirm that alkylaluminum sesquialkoxides are tetramers comprised of an octahedral Al^{3+} ion connected to three tetrahedral $[R_2Al(OR)_2]^-$ moieties via bridging alkoxides as shown in (**20**). This core structure of approximate D_3 symmetry is the same as that observed for the Meerwein-Ponndorf-Verley reduction reagent, $[(^iPrO)_3Al]_4$. There are relatively few examples of alkylaluminum sesquialkoxides, but their aluminum to oxygen ratio of 2:3 makes these compounds of interest as potential precursors to Al_2O_3 materials.

$$4R_3Al + 6R'OH \xrightarrow{-6RH} [Al\{(R'O)_2AlR_2\}_3] \qquad (24)$$

$$2R_3Al + 2Al(OEt)_3 \longrightarrow [Al\{(EtO)_2AlR_2\}_3] \qquad (25)$$

$$R = Me, Et, {}^tBu$$

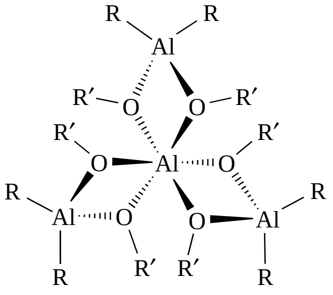

(**20**)

Bridging groups with additional donor atoms or available lone pairs of electrons can bridge three aluminum centers resulting in cage formation of the type $[RAl(\mu_3\text{-}ER)]_n$ (ER = O, S, Se, Te, NR, O_3PR, O_3AsR, O_3POR). Structures of these cage compounds are consistent with those observed for other electron-precise cage compounds of the main group elements as summarized by Veith.[74] Examples include the chalcogenide[15,55] and phosphide[75] tetramers (**21**) and (**22**). Three of the more common classes of organoaluminum heterocycles and cage complexes that have received investigation over the past 15 years are discussed in greater detail in the following three subsections.

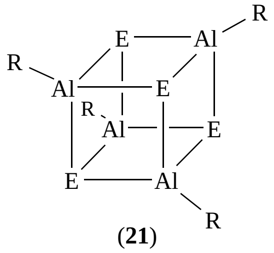

(**21**)

E = S, Se, Te; R = ^tBu, CMe_2Et

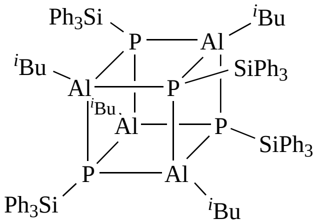

(**22**)

4.1 Organoaminoalanes and Organoiminoalanes

Amines react with organoaluminum compounds to give Lewis acid-base adducts. However, ammonia and primary and secondary amines may coordinate to organoaluminum compounds with subsequent alkane or hydrogen evolution to form heterocyclic aminoalanes, oligomeric iminoalanes, or in the case of ammonia, aluminum nitride.[10,11] A classic example is the reaction of trimethylaluminum with methylamine as shown in equation (26). The reaction initially yields the

$$7Me_3Al + 7MeNH_2 \xrightarrow[-14CH_4]{215\,^\circ C} [MeAlNMe]_7 \qquad (26)$$

complex $Me_3Al{\cdot}NH_2Me$, and heating this complex to 70 °C yields cis and trans isomers of the cyclic aminoalane $[Me_2AlNHMe]_3$. Continued heating to 215 °C results in further methane elimination and formation of the heptameric iminoalane, $[MeAlNMe]_7$, via intermediate $[(Me_2AlNHMe)_2(MeAlNMe)_6]$ (**23**).

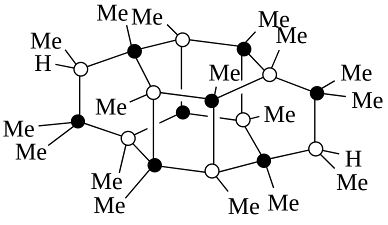

(**23**)

This reaction sequence is quite general. Primary amines react with trialkylaluminum compounds to form Lewis acid-base adducts $R_3Al{\cdot}NH_2R'$, followed by alkane elimination to form cyclic dimers and trimers of the formula $[R_2AlNHR']_n$ ($n = 2$, 3). Further alkane eliminates from the dimers and trimers at higher temperature to afford oligomeric iminoalanes $[RAlNR']_n$. The degree of association for iminoalanes ranges from 3 to 16 and structurally characterized examples exist for a trimer ($n = 3$), tetramers ($n = 4$), hexamers ($n = 6$), heptamers ($n = 7$), and octamers ($n = 8$). Structures of some of the larger oligomers, such as $[HAlN^iPr]_{10}$, $[HAlNEt]_{15}$, and $[HAlNEt]_{16}$ are not known. Each of the known structures (Figure 2) is composed of four- and six-membered rings of alternating aluminum and nitrogen atoms. The tetrahedral aluminum atoms are coordinated by three μ_3-NR′ groups.

Tetramers adopt the familiar cubane structure and hexamers adopt a drum-like structure as found in some main group metal alkoxides. The heptamer may be described as the fusion of two partial cubanes, one of which is missing an aluminum atom and the other which is missing a nitrogen atom. The octamer appears to result from the fusion of two Al_4N_4 cubanes, each opened along an edge prior to their linkage. Structurally characterized examples of cage iminoalanes include the following: $[HAlN^iPr]_4$, $[MeAlN^iPr]_4$, $[MeAlNMes]_4$, $[^tBuAlNSiPh_3]_4$, $[PhAlNPh]_4$, $[HAlN^iPr]_6$, $[HAlN^nPr]_6$, $[MeAlNPh]_6$, $[MeAlNMe]_7$, $[EtAlNMe]_7$ and $[HAlNEt]_8$. In all of these examples, Al–N distances average approximately 1.92 Å, albeit with some minor variations. For example, the Al–N distances in the six-membered rings of $[MeAlNPh]_6$ (1.912(6) Å) are slightly shorter than those between the six-membered rings (1.951(6) Å).

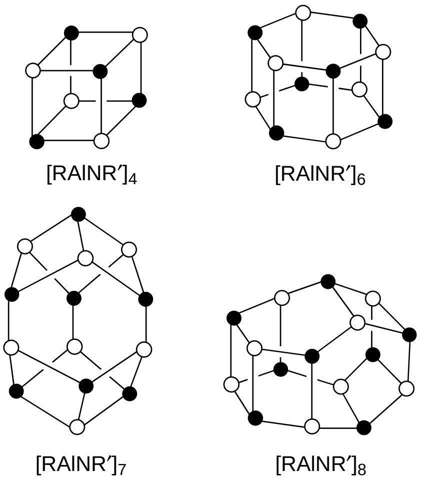

Figure 2 Core structures for organoiminoalanes with nitrogen and aluminum atoms alternating at cage vertices. Organic substituents R and R′ are omitted for clarity

In the absence of crystallographic data, mass spectrometry has been used to verify the extent of oligomerization for several iminoalanes. Cryoscopic molecular weight measurements were less reliable. NMR (^1H, ^{13}C) spectroscopy is also quite useful because the symmetries of these cage compounds differ. Substituents on aluminum will give rise to a single set of resonance in tetramers, hexamers, and octamers of a drum-like structure. In contrast, aluminum substituents in an octamer of the type shown in Figure 2 give rise to two sets of resonances in a 1:1 ratio, and aluminum substituents in a heptamer give rise to three sets of resonances in a 3:3:1 ratio. Of course, the same distinctions hold true for the substituents on nitrogen.

The degree of association of iminoalanes is dependent on reaction conditions as well as on the steric requirements of the substituents on aluminum and nitrogen. Smaller substituents allow the formation of larger cages as in $[MeAlNMe]_8$, whereas sterically demanding substituents favor tetramer formation as observed for $[MeAlNMes]_4$. The steric bulk of the 2,6-diisopropylphenyl substituent on nitrogen results in formation of the trimeric iminoalane $[MeAlN(2,6\text{-}^iPr_2C_6H_3)]_3$ as shown in equation (27).[76] This trimer is unusual in that it contains both three-coordinate aluminum atoms and adjacent three-coordinate nitrogen atoms in a planar Al_3N_3 ring. The Al–N distance of 1.782(4) Å is very short by comparison with other oligomeric iminoalanes (average Al–N of 1.92 Å) and the normal range of Al–N distances (1.85–2.00 Å). This suggests the presence of $N \rightarrow Al$ π-donation and has prompted reference to this trimer as alumazine by analogy to borazine. Although there are six nitrogen lone-pair electrons available for delocalized π-bonding, no ring current suggesting aromaticity was observed by NMR spectroscopy.

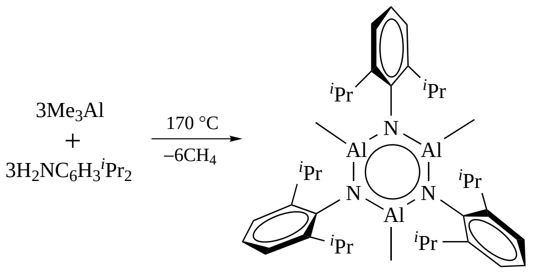

(27)

4.2 Alkylaluminoxanes

Alkylaluminoxanes, or alkylalumoxanes as they are often called, contain at least one oxide bridge between two or more aluminum centers that contain an organic substituent. Alkylaluminoxanes are most commonly obtained by partial hydrolysis of aluminum trialkyls under controlled conditions, but many other preparative routes have been described in the literature and in patents. The structures and compositions of most alkylaluminoxanes are the subject of much debate. Often referred to as black box materials, proposed structures previously focused on cyclic or polymeric structures as described in an excellent review by Pasynkiewicz.[77] New structural models for alkylaluminoxane have emerged over the past 15 years.

The hydrolysis of aluminum alkyls is believed to follow the reaction path depicted in Scheme 2.[78] Although not isolated for aluminum trialkyls, aqua complexes (**24**) have been observed by NMR spectroscopy below – 30 °C and their formation is precedented by the crystallographically characterized aqua complexes $[Al(OSiPh_3)_3(OH_2)]\cdot 2THF$ and $[(C_6F_5)_3Al\cdot OH_2]$.[79] Alkane elimination from the water complexes produces oligomers of dialkylaluminum hydroxides (**25**). Dimeric (**28**) and trimeric (**29**) oligomers of ($R = Et$, $(Me_3Si)_2CH$) have been characterized by NMR and IR spectroscopy. In addition, hydroxyl compounds $[^tBu_2Al(\mu\text{-}OH)]_2$, $[^tBu_2Al(\mu\text{-}OH)]_3$, $[^tBu_2Al(\mu\text{-}OH)]_3\cdot 2THF$, $[^tBu_2Al(\mu\text{-}OH)]_3\cdot 2NCCH_3$, $[Mes_2Al(\mu\text{-}OH)]_2\cdot 2THF$, and $[\{(Me_3Si)_3C\}MeAl(\mu\text{-}OH)]_2\cdot 2THF$ have been isolated and characterized by X-ray crystallography. The hydroxyl protons are acidic and capable of hydrogen bonding to Lewis bases such as acetonitrile and THF. The acidity of the hydroxyl protons also allows further reaction of (**25**) with an additional equivalent of aluminum alkyl to form a tetraalkyldialuminoxane (**26**). Tetraalkyldialuminoxanes were previously proposed to be dimeric or trimeric based on molecular weight measurements. Monomeric tetraalkylaluminoxanes are not anticipated since the presence of two-coordinate oxygen and three-coordinate aluminum centers should lead to rapid oligomerization. However, Uhl isolated and structurally characterized the sterically protected monomeric tetraalkylaluminoxane $[\{(Me_3Si)_2CH\}_2AlOAl\{CH(SiMe_3)_2\}_2]$ (**30**).[64] Compound (**30**) exhibits a planar C_4Al_2O core with a linear Al–O–Al linkage and a very short Al–O distance of 1.687(4) Å. A dimeric structure with two three-coordinate aluminum centers has been substantiated by X-ray crystallography for $[^tBu_2Al(\mu\text{-}OAl^tBu_2)]_2$ (**31**).[80]

$$R_3Al + H_2O \longrightarrow \underset{\mathbf{(24)}}{R_3Al(OH_2)}$$

$$n\,R_3Al(OH_2) \xrightarrow{-n\,RH} \underset{\mathbf{(25)}}{[R_2AlOH]_n}$$

$$[R_2AlOH]_n + n\,R_3Al \xrightarrow{-n\,RH} \underset{\mathbf{(26)}}{[R_2AlOAlR_2]_m}$$

$$[R_2AlOH]_n \xrightarrow[\Delta]{-n\,RH} \underset{\mathbf{(27)}}{[RAlO]_n}$$

Scheme 2 Proposed reaction scheme for hydrolysis of aluminum trialkyls

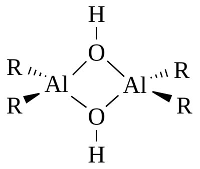

(**28**)

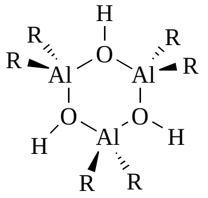

(**29**)

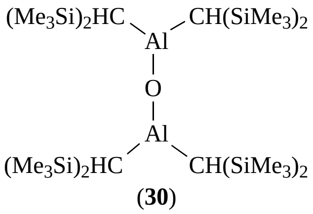

$$\begin{array}{c} (Me_3Si)_2HC \quad CH(SiMe_3)_2 \\ Al \\ | \\ O \\ | \\ Al \\ (Me_3Si)_2HC \quad CH(SiMe_3)_2 \end{array}$$

(**30**)

In the absence of excess trialkylaluminum, the hydroxide oligomers (**25**) undergo further alkane elimination to give oligomers of the formula $[RAlO]_n$ (**27**). Initially believed to be linear or cyclic oligomers comprised of four- and six-membered rings of alternating aluminum and oxygen atoms, isolation of a series of *tert*-butylaluminoxanes $[^tBuAlO]_n$ ($n = 6$ (**32**), 7, 8, 9 (**33**)) and crystallographic characterization demonstrated three-dimensional cage structures.[80–82] The cage

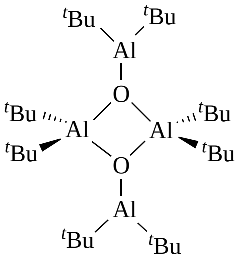

(**31**)

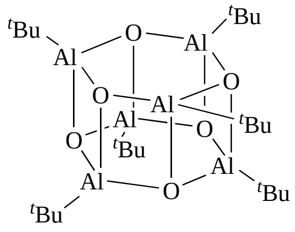

(**32**)

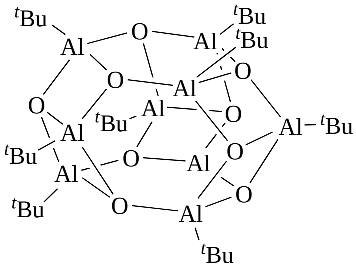

(**33**)

structures are analogous to those adopted by some alkali metal alkoxides, organogallium sulfides, and organoiminoalanes. Barron proposed that aluminoxanes with cage structures are strong Lewis acids despite the aluminum atoms being four-coordinate.[83] The cages possess a latent Lewis acidity, which is defined as proclivity of the cage to dissociate one or more Al–O bonds to form highly Lewis acidic three-coordinate aluminum centers. The driving force is proposed to be the relief of ring-strain in the cage structure. Hessen and coworkers have provided reactivity data for a boraluminoxane in support of the proposed latent Lewis acidity in cage alkylaluminoxanes.[84]

Tetrameric cage compounds with cubane structures have not been isolated. Tetramer formation is observed for $[\mathrm{Mes^*AlO}]_4$ (**34**) in which the aluminum atoms remain three-coordinate and cage formation is precluded by the steric bulk of the Mes* substituents.[85] Compound (**34**) was prepared by reaction of $[\mathrm{Mes^*AlH_2}]_2$ with $[\mathrm{Me_2SiO}]_3$ and was not obtained by hydrolysis.

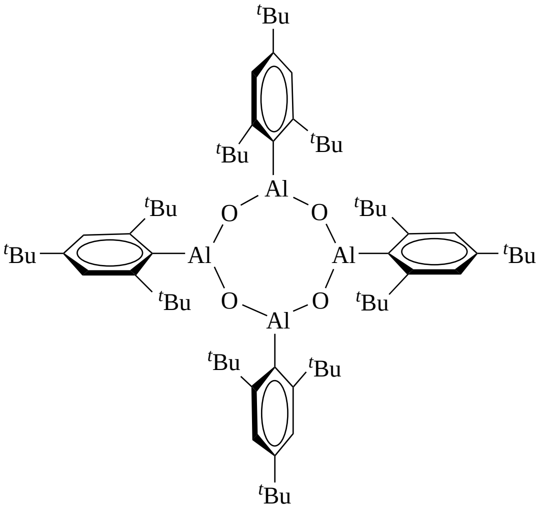

(**34**)

Methylaluminoxane (MAO), sometimes referred to as polymethylaluminoxane (PMAO), currently garners the most industrial interest of all the alkylaluminoxanes owing to its activity as a cocatalyst for metallocene-catalyzed alkene polymerization (*see* ***Oligomerization & Polymerization by Homogeneous Catalysis***).[33,86–88] MAO is synthesized by careful hydrolysis of trimethylaluminum by one of a variety of patented procedures that vary in the mode of water delivery, including the use of water-saturated nitrogen vapor, water emulsions in organic solvents, ice, molecular sieves, and various hydrates such as $\mathrm{Al_2(SO_4)_3{\cdot}18H_2O}$, $\mathrm{MgCl_2{\cdot}6H_2O}$, $\mathrm{CuSO_4{\cdot}5H_2O}$, and $\mathrm{FeSO_4{\cdot}7H_2O}$. Nonhydrolytic routes have also been described. The method of synthesis has a dramatic influence on the catalytic activity of the resulting MAO. Changes in compositions and structures of aluminoxane products as a function of reaction conditions were detailed in studies of the hydrolysis of $^t\mathrm{Bu_3Al}$.

The structure of MAO remains enigmatic. NMR and IR spectroscopy, cryoscopic molecular weight measurements, mass spectrometry, gel-permeation chromatography (GPC), and computational methods have been used to probe the structure of MAO, but compositions and structures of components remains elusive. No neutral methylaluminoxanes have been characterized by X-ray crystallography. Atwood has characterized the anionic aluminoxanes $\mathrm{K[Al_7O_6Me_{16}]}$ (**35**) and $\mathrm{[Me_4As]_2[Me_2AlOAlMe_3]_2}$.[10,11]

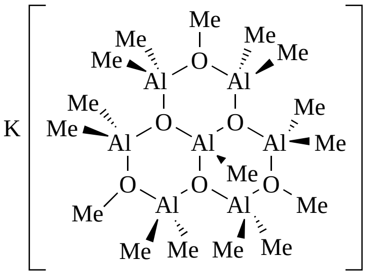

(**35**)

In contrast to investigations of aluminoxanes bearing bulky ^{t}Bu, Mes, Mes*, and $\mathrm{CH(SiMe_3)_2}$ substituents, the study of

MAO is complicated by the proclivity of methyl groups to bridge aluminum centers, as well as by the high rate of methyl exchange. This leads to the presence of multiple equilibria, the positions of which are shifted upon the addition or removal of trimethylaluminum or change in conditions. Thus, MAO is likely a mixture of species rather than a single, well-defined compound. The situation is even more complicated in that the compositions, structures, and catalytic activities of MAO samples vary depending on reaction conditions and the source of water as already mentioned. Although it is appealing to denote MAO as oligomers of the formula $[\mathrm{MeAlO}]_n$ by analogy to the well-defined *tert*-butylaluminoxanes, data suggests that trimethylaluminum accounts for up to 28% of the aluminum present in some commercial samples of MAO. GPC and ^{1}H NMR data also indicate that the methyl to aluminum ratio is closer to 1.5 rather than 1. Recent proposals for structures of MAO center on cage or partially opened cage structures. Sinn has proposed a cage compound of formula $\mathrm{Me}_{24}\mathrm{Al}_{16}\mathrm{O}_{12}$ to be a major component of MAO.[33] Other authors have proposed a $\mathrm{Me}_{18}\mathrm{Al}_{12}\mathrm{O}_9$ cage based on DFT calculations.[89] The latter structure is envisioned as resulting from addition of three $\mathrm{Me}_3\mathrm{Al}$ molecules to a $[\mathrm{MeAlO}]_9$ cage.

Modified MAOs (MMAO) that incorporate ^{i}Bu and other alkyl groups to improve stability and optimize catalytic activity are commercially available. The use of additional modifiers such as boranes, boroxines, and pentafluorophenyl derivatives has been investigated in recent years. MAO has also been supported on silica and other materials for the preparation of heterogeneous alkene polymerization catalysts. These developments are detailed in several reviews.[33,86–88,90]

4.3 Alkylaluminophosphates, -phosphinates, -phosphonates, and -arsonates

Molecular phosphates, phosphinates, phosphonates, and arsonates of aluminum adopt heterocyclic and cage structures[91,92] that are larger than those observed for iminoalanes and aluminoxanes, but topologically similar based on the isolobal relationship of a μ_3-phosphonate to a μ_3-amide and μ_3-oxide.[93] There is also an isoelectronic and structural relationship of the aluminophosphonate compounds and their analogs to the extensively studied organosilsesquioxanes of the formula $[\mathrm{RSiO}_{1.5}]_n$. Furthermore, the molecular phosphates, phosphinates, phosphonates, and arsonates of aluminum have been investigated as soluble models of secondary building units (SBUs; Figure 3) in microporous aluminophosphate (*see* ***Phosphates: Solid-state Chemistry***) molecular sieves and as precursors[94] to new aluminophosphate and aluminoarsenate materials. The majority of these studies have been conducted since 1996.

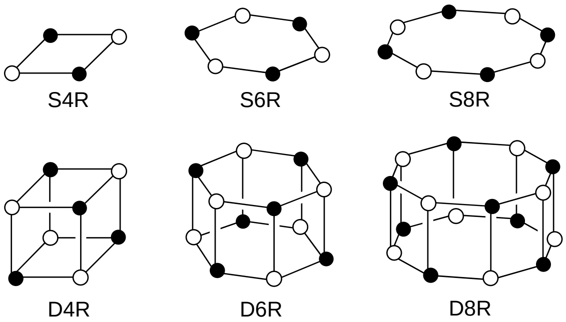

Figure 3 Secondary building units common to aluminophosphate molecular sieves. Phosphorus and aluminum atoms alternate at vertices. Not shown are the μ_2-oxo bridges on each edge

Cyclic alkylaluminophosphinates $[\mathrm{R}_2\mathrm{AlO}_2\mathrm{PR}'_2]_n$ ($n = 2$, 3) were first synthesized in 1964 by Coates and Mukherjee by reaction of a phosphinic acid, $\mathrm{R}'_2\mathrm{P(O)OH}$, with an aluminum alkyl. Cryoscopic molecular weight measurements, IR and Raman spectroscopic data, and selected NMR data confirm the structures to be cyclic dimers ($n = 2$) of C_{2h} symmetry. X-ray crystallography confirmed that the core structure of $[^t\mathrm{Bu}_2\mathrm{AlO}_2\mathrm{PPh}_2]_2$ consists of an eight-membered $\mathrm{Al}_2\mathrm{P}_2\mathrm{O}_4$ ring. These $\mathrm{Al}_2\mathrm{P}_2\mathrm{O}_4$ cores have a structural relationship to four-ring (4R) SBUs common to aluminophosphate and metal-substituted aluminophosphate (MAPO) molecular sieves such as AlPO_4-5, AlPO_4-12, AlPO_4-25, AlPO_4-31, MAPO-36, and MAPO-39. Cyclic trimers were reported for $[\mathrm{Me}_2\mathrm{AlO}_2\mathrm{PX}_2]_3$ ($\mathrm{X} = \mathrm{Cl}$, F, H), but their structures have not been confirmed by X-ray crystallography.

Reactions of phosphonic acids, $\mathrm{R}'\mathrm{P(O)(OH)}_2$, with aluminum alkyls are similarly expected to form cyclic dimers $[\mathrm{R}_2\mathrm{MO}_2\mathrm{P(OH)R}'_2]_2$, but facile alkane elimination to yield oligomers $[\mathrm{RAlO}_3\mathrm{PR}']_n$ hinders the isolation of the intermediate dimers. The cyclic dimer $[^t\mathrm{Bu}_2\mathrm{AlO}_2\mathrm{P(OH)Ph}]_2$ was isolated as a crystalline solid at low temperature with the aid of bulky substituents. The poorly stable dimer was derivatized upon reaction with $\mathrm{Me}_3\mathrm{SiNMe}_2$ and the cyclic structure of the trimethylsilyl derivative $[^t\mathrm{Bu}_2\mathrm{AlO}_2\mathrm{P(OSiMe}_3)\mathrm{Ph}]_2$ was confirmed by X-ray crystallography.

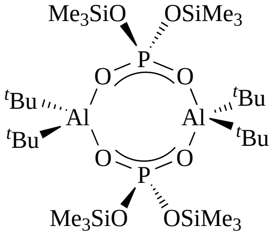

(**36**)

A cyclic alkylaluminophosphate $[^t\mathrm{Bu}_2\mathrm{AlO}_2\mathrm{P(OSiMe}_3)_2]_2$ (**36**) was obtained by $\mathrm{Me}_3\mathrm{SiCl}$ elimination from reaction of $(\mathrm{Me}_3\mathrm{SiO})_3\mathrm{P{=}O}$ with $^t\mathrm{Bu}_2\mathrm{AlCl}$. Analogous heterocycles have also been prepared by dealkylsilylation upon reaction of $\mathrm{R}_3\mathrm{Al}$ with $(\mathrm{Me}_3\mathrm{SiO})_3\mathrm{P{=}O}$ at 200 °C.[95] In both cases, product formation was thermodynamically favored by the strength of the new Al–O bonds. Attempted reactions of

H_3PO_4 with ^{t}Bu$_3$Al to give $[\mathrm{R_2AlO_2P(OH)_2R'}]_2$, followed by derivatization with $\mathrm{Me_3SiNMe_2}$, gave complicated mixtures that contained $[{}^t\mathrm{Bu_2AlO_2P(OSiMe_3)_2}]_2$, but isolated yields are very low.

Equimolar reactions of an aluminum alkyl with a phosphonic acid under room temperature or reflux conditions yields oligomers of the formula $[\mathrm{RAlO_3PR'}]_n$ ($n = 4, 6, 10$) (equation 28).[91,92] Tetrameric ($n = 4$) derivatives (**37**) are the most common and are obtained in high yield. Three hexamers have been isolated and structurally characterized as has the decamer $[{}^t\mathrm{BuAlO_3PMe}]_{10}$,[96] but these were minor components of mixtures that consist mainly of tetramers. The tetramers (**37**) possess a cubanoidal $\mathrm{Al_4P_4O_{12}}$ core structurally analogous to double-four-ring (D4R) SBUs found in aluminophosphate molecular sieves. The drum-like $\mathrm{Al_6P_6O_{18}}$ core of hexameric derivatives resembles double-six-ring (D6R) SBUs common to $\mathrm{AlPO_4}$-18, $\mathrm{AlPO_4}$-52, and MAPOs isotypic to the aluminosilicates chabazite and faujasite. The structure of the decamer can be described as two edge-opened tetramers linked via Al–O–P bridges to an eight-membered $\mathrm{Al_2P_2O_4}$ heterocycle.

$$n\mathrm{R_3Al} + n\mathrm{R'P(O)(OH)_2} \xrightarrow[-2n\mathrm{RH}]{\Delta} [\mathrm{RAlO_3PR'}]_n \qquad (28)$$

$$(n = 4, 6, 10)$$

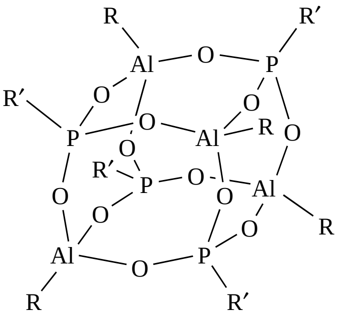

(**37**)

The tetrameric alkylaluminophosphonates (**37**) are thermally quite stable and those with smaller substituents sublime without decomposition. The most volatile of these, $[\mathrm{MeAlO_3PMe}]_4$, sublimes to give crystals at 150 °C/0.1 mm Hg. The tetrameric alkylaluminophosphonates are also moderately stable to air and moisture. In contrast, the alkylaluminophosphate $[{}^t\mathrm{BuAlO_3P(OSiMe_3)}]_4$, which is obtained from $\mathrm{Me_3SiCl}$ elimination upon reaction of $^t\mathrm{BuAlCl_2}$ with $\mathrm{(Me_3SiO)_3P{=}O}$, is readily hydrolyzed.

Cage fragmentation and rearrangements have been observed for some tetrameric alkylaluminophosphonates.[97] Reaction of $[{}^t\mathrm{BuAlO_3PMe}]_4$ with acetylacetone in toluene at 70 °C results in precipitation of the decamer $[{}^t\mathrm{BuAlO_3PMe}]_{10}$. This decamer rearranges to a mixture of tetramer and hexamer in $\mathrm{CDCl_3}$ over several days. In another example, CuCl and $[{}^t\mathrm{BuAlO_3PC_6H_4CN}]_4$ react to give crystals of $[\mathrm{Al}({}^t\mathrm{BuAl})_6(\mathrm{O_3PC_6H_4CN})_8\mathrm{Cu(NCCH_3)_2}]_x$. This is a one-dimensional polymer in which $[\mathrm{Al}({}^t\mathrm{BuAl})_6(\mathrm{O_3PC_6H_4CN})_8]^-$ units are linked to $\mathrm{Cu(NCCH_3)_2}^+$ moieties via two of the cyanophenyl substituents. The core structure of $[\mathrm{Al}({}^t\mathrm{BuAl})_6(\mathrm{O_3PC_6H_4CN})_8]^-$ can be described as two $\mathrm{Al_4P_4O_{12}}$ cubanoids sharing a common vertex occupied by an octahedral aluminum. The formation of this compound is not understood. Structural rearrangements have been better-studied for analogous alkylgallophosphonates.

Fluoride is often used as a mineralizer and structure-directing agent in the formation of aluminophosphate molecular sieves, some of which retain fluoride by encapsulation in $\mathrm{Al_4P_4O_{12}}$ D4R cages.[98] Attempts to encapsulate fluoride in molecular compounds such as (**37**) have not been highly successful. However, Roesky and coworkers were able to prepare the unique fluoride-containing aluminophosphonate $[\mathrm{Cs_3(THF)_3F}({}^i\mathrm{BuAl})_3({}^t\mathrm{BuPO_3})_4]_2[({}^i\mathrm{BuAl})_2(\mu\text{-F})_2({}^t\mathrm{BuPO_3})_4]$.[99] The encapsulated fluoride resides in an $\mathrm{Al_4P_4O_{12}}(\mu\text{-F})_2\mathrm{F_2}$ cage in which two aluminum centers each have an ^{i}Bu substituent and the remaining two aluminum centers have lost their alkyl substituent and have fluoride bridges to two partial tetramers. Roesky and coworkers have also characterized several aluminophosphonate cage compounds that incorporate alkali metal cations and these are described in a recent review.[92]

Aluminum alkyls react with bulky silane triols to give cage aluminosiloxanes that are structurally related to the molecular alkylaluminophosphonates.[100] If these reactions are conducted in a 1:1 molar ratio cyclic dimers or cubanoidal aluminosiloxanes are obtained depending on temperature. The cyclic dimer $[{}^i\mathrm{Bu(THF)AlO_2Si(OH)R}]_2$ ($\mathrm{R} = (2,6\text{-}{}^i\mathrm{Pr_2C_6H_3})\mathrm{N(SiMe_3)}$) is obtained at low temperature. It contains an eight-membered $\mathrm{Al_2Si_2O_4}$ ring similar to that found in the mineral gismondine. If the reaction of $\mathrm{RSi(OH)_3}$ with $\mathrm{Me_3Al}$ or $^i\mathrm{Bu_2AlH}$ is conducted in a 1:1 ratio at 65 °C, compounds $[\mathrm{RSiO_3Al{\cdot}L}]_4$ ($\mathrm{R} = \mathrm{N(Ar)SiMe_3}$, $\mathrm{Co_3(CO)_9C}$; L = THF, 1,4-dioxane) (**38**) are obtained. These contain an inorganic $\mathrm{Al_4Si_4O_{12}}$ core that is isoelectronic to the $\mathrm{Al_4P_4O_{12}}$ core of the aluminophosphonates (**37**) and analogous to the D4R SBUs common to some aluminosilicates (*see* ***Zeolites***). Three oxygen bridges in the $\mathrm{Al_4Si_4O_{12}}$ cage and a neutral donor define the coordination sphere of the approximately tetrahedral aluminum atoms. Organometallic derivatives are obtained upon reaction of the silane triol with $\mathrm{NaAlEt_2H_2}$ or $\mathrm{LiAlH_4}$ to yield $[\mathrm{Li(THF)}]_4[\mathrm{RSiO_3AlH}]_4$ or $[\mathrm{Na(THF)}]_4[\mathrm{RSiO_3AlEt}]_4$, respectively. An aluminosiloxane with a drum-like $\mathrm{Al_4Si_2O_6}$ core is obtained if the reaction of $\mathrm{RSi(OH)_3}$ to $^i\mathrm{Bu_2AlH}$ is conducted with a 1:2 ratio.

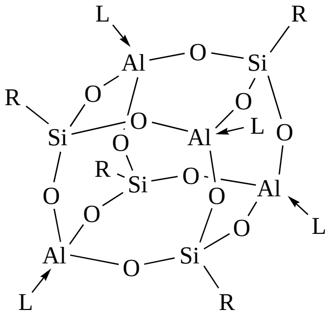

(**38**)

5 CATIONIC ORGANOALUMINUM COMPOUNDS

A strong interest in cationic organoaluminum compounds has developed over the past decade with the anticipation that the increased Lewis acidity of cationic reagents will allow cationic complexes to outperform their neutral analogs in various Lewis acid-catalyzed reactions. Atwood has reviewed the synthesis of group 13 cations and has classified preparative routes to organoaluminum cations into four general types: asymmetric cleavage, halide displacement, ligand redistribution, and abstraction.**[101]** In asymmetric cleavage, a Lewis base cleaves a halide-bridged dimer $[R_2AlX]_2$ into a base-stabilized cation and a dihaloaluminate anion. Reaction of $[Me_2AlCl]_2$ with 15-crown-5, for example, forms the cationic complex $[Me_2Al(15\text{-crown-5})]^+$ $[Me_2AlCl_2]^-$ in which the aluminum atom resides in a pentagonal bipyramidal coordination environment of the five crown ether oxygens and two *trans*-oriented methyl groups (equation 29).

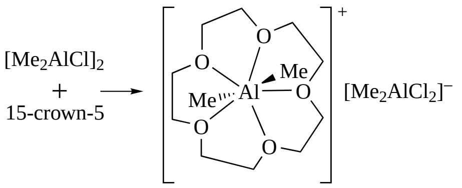

(29)

The Me_2Al^+ fragment is nearly linear with a C–Al–C angle of 178° and an Al–C distance of 2.00(2) Å. Similarly, the reaction of $[^tBu_2AlCl]_2$ with N,N,N',N'-tetramethylethylenediamine (tmeda) gives $[^tBu_2Al(\text{tmeda})]^+$ $[^tBu_2AlCl_2]^-$. Additional tmeda may displace the remaining halide to give the base-stabilized cation with halide counterion, $[^tBu_2Al(\text{tmeda})]^+[Cl]^-$. This is referred to as halide displacement or symmetric cleavage. Cationic complexes can also result from ligand redistribution as in the formation of the first aluminocenium cation $[Cp^*_2Al]^+$ $[Cp^*AlCl_3]^-$ from reaction of Cp^*_3Al and $AlCl_3$ (equation 30).**[22]**

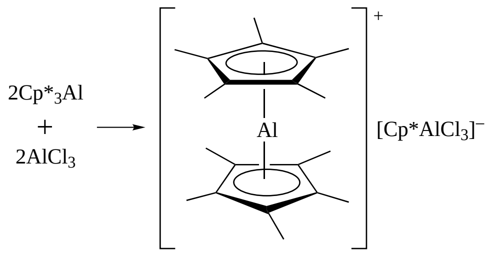

(30)

These synthetic approaches typically yield base-stabilized cations with coordination numbers at aluminum of four or more. Complexation and increased coordination number at aluminum moderates the desired increase in Lewis acidity of the cationic reagent. For this reason, the alkyl, hydride, or halide abstraction route dominates recent attempts to prepare base-free organoaluminum cations with two- or three-coordinate aluminum centers. Strategies parallel those employed for generating cationic metallocene complexes of the early transition metals, with the most common abstracting agents being $B(C_6F_5)_3$ or trityl salts of weakly coordinating $[B(C_6F_5)_4]^-$, $[B\{3,5\text{-}(CF_3)_2C_6H_3\}_4]^-$, or carborane anions. The commercial availability of these reagents and their precursors further favors their use. Abstraction with dimethylanilinium salts or $[(Et_2O)_2H]^+[B\{3,5\text{-}(CF_3)_2C_6H_3\}_4]^-$ is less frequent since these often lead to dimethylaniline or diethyl ether coordination. Reaction of $(R_3SiO)Al_2Me_5$ with $[PhMe_2NH]^+[B(C_6F_5)_4]^-$, for example, yields the aniline-stabilized salt $[Me_2Al(NMe_2Ph)_2]^+[B(C_6F_5)_4]^-$.**[102]** The borane $B(C_6F_5)_3$ is a useful methide abstracting reagent, although methyl transfer is reversible in solution. Nonetheless, $B(C_6F_5)_3$ was used to prepare $[Cp_2Al]^+[MeB(C_6F_5)_3]^-$ and $[R_2Al(OEt_2)_2]^+[RB(C_6F_5)_3]^-$ (R = Me, Et, octyl) by alkide abstraction (equation 31). Klosin and coworkers also used tris(perfluorobiphenyl)borane in the presence of $AlMe_3$ and ether to form the structurally characterized salt $[Me_2Al(OEt_2)_2]^+[MeB(C_{12}F_9)_3]^-$.**[36]**

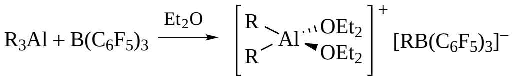

$$R_3Al + B(C_6F_5)_3 \xrightarrow{Et_2O} \left[R_2Al(OEt_2)_2\right]^+ [RB(C_6F_5)_3]^- \qquad (31)$$

Jordan and coworkers have prepared cationic aluminum complexes utilizing amidinate ligands using the alkide abstraction route.**[103]** Reaction of $\{MeC(N^iPr)_2\}AlMe_2$ with $B(C_6F_5)_3$ or $[Ph_3C]^+[B(C_6F_5)_4]^-$ yields the unstable cation $[\{MeC(N^iPr)_2\}AlMe]^+$. The cation can be stabilized by coordination of a Lewis base to give $[\{MeC(N^iPr)_2\}Al(Me)L]^+$ (L = NMe_2Ph, Me_3P) or with one equivalent of the starting amidinate complex to give the methyl-bridged complex $[\{MeC(N^iPr)_2\}Al(Me)(\mu\text{-}Me)Al(Me)\{(^iPrN)_2CMe\}]^+$. Jordan has structurally characterized a related three-coordinate aluminum cation supported by a β-diketiminate ligand (**39**) and a methyl-bridged dimer (**40**) supported by an aminotroponiminate ligand.**[104,105]** The aluminum atom in (**39**) is perturbed slightly from planar to pyramidal by a weak interaction with the anion. The shortest contact between the cation and anion is the Al–F_{meta} interaction at a distance of 2.151(1) Å. In (**40**), the bridging methyl is trigonal bipyramidal with the hydrogen atoms residing in the equatorial plane. Aluminum–carbon distances for the bridging methyl (2.177(3), 2.120(3) Å) are significantly longer than those for the terminal methyls (1.949(3), 1.953(3) Å) as expected owing to the three-center two-electron bonding for the bridging methyl group.

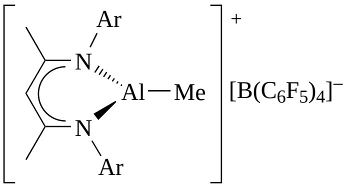

Ar = 2,6-^{i}Pr$_2$C$_6$H$_3$

(**39**)

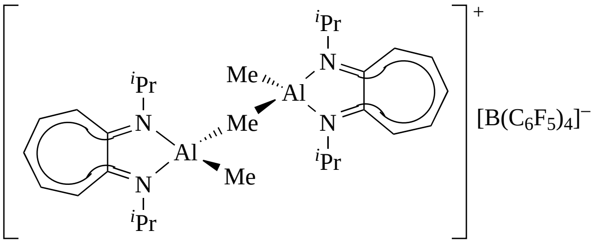

(**40**)

Chlorobenzene has been shown by NMR spectroscopy and X-ray crystallography to coordinate to aluminum in the cationic complex (**41**).**106** The Al–Cl distance of 2.540(3) Å is slightly longer than Al–Cl distances in chloride-bridged aluminum dimers (2.2–2.5 Å) and consistent with a coordinate covalent Cl→Al bond. The orientation of the chlorobenzene ring with respect to the diisopropylaminotroponiminate ligand suggests that π-stacking may help to stabilize the complex. The interaction between the anion and aluminum cation is very weak. The Al–F distance in (**41**) is 3.23 Å, considerably longer than the Al–F distance of 2.151(1) Å found in complex (**39**).

Many attempted syntheses of two- and three-coordinate base-free cations are unsuccessful owing to facile decomposition of the target cationic complex by aryl transfer from the borate anion to the aluminum center. Attempted synthesis of alumenium ions R_2Al^+ from reaction of R_3Al and $[Ph_3C]^+$ $[B(C_6F_5)_4]^-$, for example, results in initial formation of an unstable R_2Al^+ intermediate followed by aryl transfer to give $R_2AlC_6F_5$ and $B(C_6F_5)_3$.**37** Jordan,**103–105** Arnold,**107** and Gibson**108** have reported analogous aryl transfers from borate anions to cationic aluminum complexes supported by β-diketiminate, amidinate, and carbazolyl ligands.

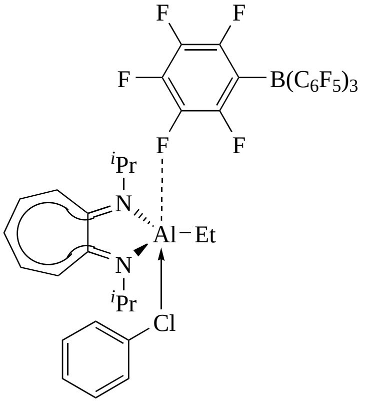

(**41**)

Polyhedral borane and carborane anions are more robust and less coordinating than the perfluoroarylborates and thus may serve to stabilize reactive alumenium species. Reed and coworkers reacted $[Ph_3C]^+[CB_{11}H_6Br_6]^-$ with Et_3Al to give $[Et_2Al][CB_{11}H_6Br_6]$.**109** The molecular structure of $[Et_2Al][CB_{11}H_6Br_6]$ shows an approximately tetrahedral aluminum coordinated by two of the bromine atoms of the carborane anion with distances of 2.581(2) and 2.542(2) Å. The compound is formulated as a tight-ion pair, $[Et_2Al]^{\delta+}$ $[CB_{11}H_6Br_6]^{\delta-}$, and shows alumenium ion-like behavior. It reacts with pyridine to form $[Et_2Al(py)_2]^+[CB_{11}H_6Br_6]^-$, likely coordinates ethylene, and effects alkylation of benzene and formation of butene.

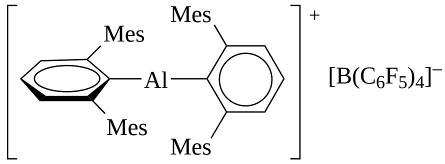

(**42**)

A two-coordinate base-free alumenium ion (**42**) was prepared by Wehmschulte using bulky terphenyl groups to provide steric protection of the aluminum center and protect against aryl transfer.**32** There is no interaction of the anion with the cationic aluminum center in the solid state. The shortest Al–F distance is 5.498 Å. There are, however, contacts between the Lewis acidic aluminum and carbons of the mesityl groups as short as 2.353(1) Å. The C–Al–C angle in (**42**) is 159.17(5)°.

Much of the recent work on cationic organoaluminum complexes was stimulated by Jordan's report that $\{MeC(N^iPr)_2\}AlMe_2$ activated with $B(C_6F_5)_3$ polymerizes ethylene to high molecular weight polymer, although with low activity.**103** Reaction of $\{^tBuC(N^iPr)_2\}AlMe_2$ with $[Ph_3C]^+$ $[B(C_6F_5)_4]^-$ gives an analogous cationic complex but with superior activity for the polymerization of ethylene. Molecular weights of the resulting polymer were as high as 272 200 with low polydispersity. This is consistent with polymerization by a single-site catalyst. Activities are far below what is achieved with single-site transition metal complexes.

The key to using aluminum complexes to polymerize rather than oligomerize ethylene to C_8-C_{14} alkenes as in the Aufbau reaction is steric hindrance that will prevent approach of the growing alkyl chain to the aluminum center. This precludes chain termination by β-hydrogen elimination. Computational studies on the mechanism of this have been reported and some indicate that mechanisms involving two aluminum centers are plausible.[110] Following on this discovery, other nitrogen-donor ligands (*see* ***Ammonia & N-donor Ligands***) have been investigated in search of cationic aluminum complexes for the polymerization of alkenes. Gibson has briefly discussed cationic aluminum complexes for alkene polymerization in a recent review.[111] Cationic organoaluminum complexes may also function as catalysts for the ring-opening polymerization of epoxides, lactones, and lactides, but this area of research is still in its infancy and it is unclear in some cases if the polymerizations occur by a coordination/insertion mechanism or by cationic polymerization.

6 ANIONIC ORGANOALUMINUM COMPOUNDS

Organoaluminum compounds react with anionic Lewis bases to form aluminate complexes, the compositions and structures of which are diverse. Many aluminates exhibit structures in which aluminum and a metal cation are connected by one or more bridging groups, including alkyls, alkoxides, amides, halides, hydrides, and phosphides. Simple reactions of a carbanion with an aluminum trialkyl form complexes $M[R_3AlR']$. These may be monomeric as in $Na[AlR_4]$ ($R = Me$, Et, ^{n}Pr, ^{n}Bu) or polymeric with bridging alkyls as in $[KAlCH_2{}^iPr_4]_n$ and $[LiAlEt_4]_n$. Lithium hydridoaluminates may exhibit linear bridging hydrides as in $Na[Me_3AlHAlMe_3]$, nonlinear hydride bridges as found in many tetramers, and triply-bridging hydrides as in $[LiHAl{}^tBu_3]_2$. More complex structures are observed, such as the 14-atom $Li_4Al_4P_6$ cage found in $[(THF{\cdot}Li)_4(MeAl)_4(CyP)_6]$ (**43**), shown below without the THF molecules. Linton, Schooler, and Wheatley recently reviewed the structural diversity of aluminates.[112]

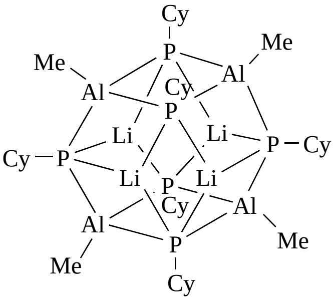

(**43**)

Particularly interesting are reactions of aluminum alkyls with halide or pseudohalide salts in a 2:1 ratio to form complexes $M[Al_2R_6X]$. Although some of these complexes possess linear bridges, as in the previously mentioned $K[Al_2Et_6F]$, many consist of bent structures as determined by X-ray crystallography and spectroscopy. Upon the addition of an aromatic solvent to those with bent structures and gentle heating, liquid clathrates of the formula $M[Al_2R_6X]{\cdot}n$(arene) phase-separate into a dense phase below a phase of pure solvent. Clathrate formation is dependent on the shape of the anion, the size of the cation, the lattice energy of MX, the strength of the anion-cation interaction, and the presence of arene molecules. The liquid clathrates do not form for the linear compounds or the 1:1 compounds $M[AlR_3X]$, nor do they form in the absence of an aromatic solvent. Each clathrate phase $M[Al_2R_6X]{\cdot}n$(arene) has a maximum number of solvent molecules (n) and Atwood has determined how arene to anion ratios vary as a function of cation and anion size. Interactions between the cation and the arene molecules are also important to clathrate formation and several crystal structures of these salts show π interactions between arene molecules and potassium or cesium cations. Some common components of liquid clathrate phases are shown in Table 3. Incorporation of crown ethers allows the preparation of additional liquid clathrates having the formula [M·crown ether]$[Al_2R_6X]$ $\cdot n$(arene). Some 3:1 and 4:1 complexes such as $K_2[SO_4(AlMe_3)_4]$ also form liquid clathrates in the presence of aromatic solvents. There are currently no uses for these air- and water-sensitive liquid clathrates. Further information is available in the chapter by Atwood in the text by Robinson.[10]

Table 3 Components of $M[Al_2R_6X]$ compounds used for liquid clathrate formation

M	R	X
Na^+	Me	F^-
K^+	Et	Cl^-
Rb^+	^{n}Pr	Br^-
Cs^+	^{n}Bu	I^-
$NR'_4{}^+$		H^-
$PR'_4{}^+$		$N_3{}^-$
Ph_2Cr^+		SCN^-
Ph_2Co^+		$SeCN^-$
Me_2Tl^+		$NO_3{}^-$
Ba^{2+}		$NO_2{}^-$
		$HCO_2{}^-$
		$MeCO_2{}^-$
		$O_2{}^-$
		$SO_4{}^{2-}$
		$CO_3{}^{2-}$
		$C_2O_4{}^{2-}$

7 APPLICATIONS OF ORGANOALUMINUM COMPOUNDS IN SYNTHESIS

Organoaluminum compounds are used to effect a variety of organic transformations. They are excellent reducing agents and examples of reductions are shown in Table 4. Organoaluminum reagents serve as Lewis acid catalysts for Diels–Alder reactions, and they are also used to transfer alkyl groups to transition metal complexes for metal-catalyzed coupling reactions as in the coupling of alkynes to dienes. As already mentioned, hydroalumination (*see* ***Hydroboration Catalysis***) and carbalumination of alkenes followed by oxidation can be used to prepare alcohols.

Organoaluminum compounds are heavily used in organic synthesis and the pertinent literature is too extensive to be adequately reviewed here. Readers are directed to excellent articles by Eisch[8,9] for a general overview of the subject and are encouraged to search for specific transformations in the texts published by March[113] and Larock.[114] The text by Ojima cites several examples of enantioselective reactions using chiral complexes of aluminum.[115]

Organoaluminum compounds also have applications in the synthesis of inorganic and organometallic complexes of the transition metals. Since aluminum is more electropositive than most of the transition metals, aluminum alkyls are excellent alkylating agents for transition metal complexes. Alkylation followed by subsequent β-hydrogen and reductive elimination (e.g. equation 32) is a convenient means of reducing transition metals to lower oxidation states. In the presence of additional ligands, this reductive ligation provides a preparative route to low-valent transition metal carbonyl, phosphine, and alkene complexes as shown in equations (33) and (34).

$$\mathrm{Ni(acac)_2 + 2Et_3Al + 2COD \longrightarrow Ni(COD)_2 + 2AlEt_2(acac) + C_2H_4 + C_2H_6} \qquad (32)$$

$$\mathrm{WCl_6 + 3Et_3Al + CO \longrightarrow W(CO)_6} \qquad (33)$$

$$\mathrm{Mn(OAc)_2 + {}^{i}Bu_3Al + CO \longrightarrow Mn_2(CO)_{10}} \qquad (34)$$

Table 4 Organoaluminum compounds as alkylating and reducing agents

Substrate	Aluminum reagent	Product
RX	R'_3Al	R–R′
R_3COH	Me_3Al	R_3CMe
RC(O)R′	Me_3Al	$RR'CMe_2$
RC(O)(OR′)	R''_3Al	RC(O)R″
RC(O)OH	Me_3Al	$RCMe_3$
RC(O)H	Et_3Al	R(Et)(H)COH

8 APPLICATIONS OF ORGANOALUMINUM COMPOUNDS IN INDUSTRY

Organoaluminum compounds are best known and most utilized as cocatalysts in the polymerization of alkenes. In 1953, Karl Ziegler discovered that suspensions of $TiCl_3$, prepared by reduction of $TiCl_4$ with Et_3Al in a hydrocarbon solvent, actively polymerize ethylene and propylene to high molecular weight polymers at low pressure (*see* ***Oligomerization & Polymerization by Homogeneous Catalysis***). This catalyst system and related catalysts comprised of an early transition metal (e.g. Ti, V, Cr) and an aluminum alkyl, some supported on an inorganic support such as $MgCl_2$, became known as Ziegler–Natta alkene polymerization catalysts. Modification of Ziegler–Natta catalysts by the addition of various iodide promoters increased catalytic activity for the polymerization of butadiene to *cis*-1,4-polybutadiene. Alkene polymerizations continue to be of major commercial importance today. Annual production of polyethylene (PE) and polypropylene (PP) in 1993 exceeded 50 million tons and by 1996 worldwide production of PE and PP was 40 million and 20 million tons, respectively.

More recently, metallocene complexes activated by methylaluminoxane (MAO) were found to polymerize ethylene and propylene to high molecular weights with unprecedented control over molecular weight, polydispersity, and stereoregularity of the resulting polymer.[33,86–89] The main role of MAO is proposed to be as a methylating agent and methide abstracting reagent as shown in equation (35), but MAO is also believed to scrub oxygen, water, and other protic impurities from the system and hence protect against catalyst deactivation. Polymerization occurs by a coordination/insertion mechanism at the resulting cationic transition metal complex and the polymer properties and activity of the single-site catalyst are controlled by the steric and electronic properties of the ligands and further influenced by ion-pairing effects. Other activators such as $B(C_6F_5)_3$ and trityl salts of noncoordinating anions better stabilize well-defined cationic complexes for ease of characterization. MAO also has drawbacks including its high cost and the high aluminum content in resulting polymers owing to the use of Al:M ratios up to 1000:1 or higher. Nonetheless, MAO continues to be the activator of choice for commercial applications of both homogeneous and heterogeneous single-site alkene polymerization catalysts. This makes MAO one of the most important organoaluminum compounds currently utilized in industry.

$$\mathrm{Cp_2ZrMe_2 + (MeAlO)_{\mathit{n}} \rightleftharpoons [Cp_2ZrMe][Me(MeAlO)_{\mathit{n}}]} \qquad (35)$$

Aluminum alkyls are used as Lewis acids and activators for several related transition metal-catalyzed reactions.[116] In the Dimersol® process, nickel complexes activated by an aluminum alkyl catalyze alkene dimerization, as in the conversion of butene to isooctene for use in preparing plasticizers and in the dimerization of propylene/butene mixtures to form branched C_6 to C_8 products for use as fuels. Hexadiene is similarly prepared from butadiene and ethylene. Triethylaluminum activates nickel carboxylates and cobalt complexes ligated by acetylacetonate and phosphines for mild catalytic hydrogenation of arenes to cyclohexanes. Aluminum alkyls are also used to prepare molded products from poly(dicyclopentadiene) using reaction injection molding. In a process developed at Hercules, solutions of WCl_4 and $EtAlCl_2$ in dicyclopentadiene are injected into a mold and heated to form the polymer. Aluminum alkyls are also used to alkylate WCl_6 or $WOCl_4$ to form active alkene metathesis catalysts. The role of the aluminum alkyl is as an activator, presumably via alkylation, and the active catalyst is believed to be a tungsten alkylidene complex.

In all of the above processes, the organoaluminum compounds serve as cocatalysts that activate a transition metal for the desired organic transformations. There are several important processes that do not involve transition metals and in which the organoaluminum reagents acts as a catalyst or stoichiometric reagent. The two most important of these are the formation of fatty alcohols and terminal alkenes from ethylene.**[7,116]** These capitalize on the Aufbau reaction for formation of alkyl chains that can reach to C_{200}, but the commercially important alkyls are those from C_{14} to C_{20}. Oxidation of the aluminum alkyl followed by acidic hydrolysis yields predominately C_{14} to C_{20} alcohols and alumina (equation 36). The alcohols are converted to biodegradable sulfates for use in detergents and to esters for use as plasticizers. The alumina coproduct is of high quality and sold separately. In the absence of oxygen, these alkyls are heated to 280–320 °C to facilitate β-hydride elimination and formation of terminal alkenes (equation 37). This regenerates an aluminum hydride capable of further ethylene insertion, making this process catalytic. In the production of alcohols, the aluminum is a stoichiometric reagent.

$$\{Et(CH_2CH_2)_n\}_3Al \xrightarrow[(ii)H_3O^+]{(i)O_2} 3Et(CH_2CH_2)_nOH + Al(OH)_3 \qquad (36)$$

$$\{Et(CH_2CH_2)_n\}_3Al \xrightarrow{280-320\,^\circ C} 3CH_2{=}CH(CH_2CH_2)_nH \qquad (37)$$

Only single insertions into an Al–C bond occur for propene and higher alkenes and this is utilized for catalytic dimerization of propene as illustrated in Scheme 3.**[7,116]** Insertion of propene into an Al–C bond of ^{n}Pr$_3$Al followed by β-hydride elimination yields an aluminum hydride and 2-methylpent-1-ene. Insertion of propene into the Al–H bond regenerates ^{n}Pr$_3$Al. Thermal cracking of 2-methylpent-1-ene gives isoprene, which is subsequently polymerized with a Ziegler–Natta catalyst to form the synthetic rubber, *cis*-1,4-polyisoprene.

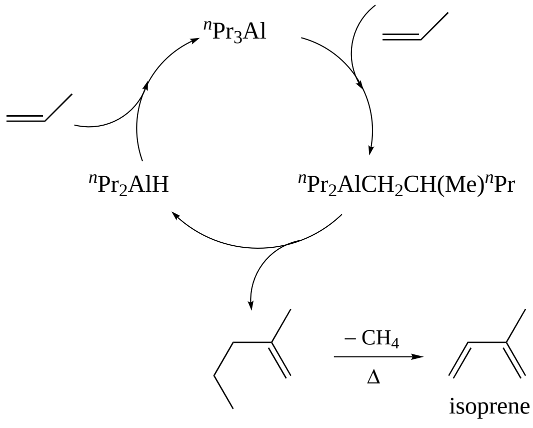

Scheme 3 Aluminum-catalyzed dimerization of propene

In the fine chemicals industry, (+)-citronellol for use in L-menthol synthesis has been prepared by hydroalumination of L-citronellene followed by oxidation of the Al–C bond and hydrolysis (Scheme 4), similar to the procedure used for the preparation of fatty alcohols.**[116]** Note that the hydroalumination is selective for the less-substituted of the two olefinic bonds in the L-citronellene.

In another example in the fine chemicals industry, organoaluminum complexes direct the *ortho*-ethylation of anilines to form intermediates for the manufacture of the herbicides Lasso® and Dual®. In this synthesis, Et_3Al is reacted with aniline to form the active catalyst, $Al(NHPh)_3$, which subsequently reacts with ethylene to give either *ortho*-ethylaniline or 2,6-diethylaniline depending on reaction conditions (equation 38). One author has suggested that this may occur by aluminum migration from nitrogen to an ortho carbon of the arene, followed by ethylene insertion into the Al–C_{arene} bond and liberation of the product upon reaction with aniline to regenerate the aluminum anilide.**[116]**

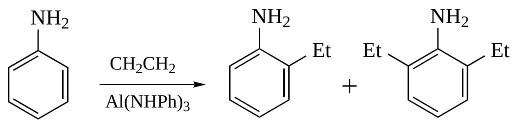

(38)

Another commercial application of organoaluminum compounds is as catalysts for the ring-opening polymerization of epoxides to form homopolymers of epichlorohydrin (ECH) and copolymers and terpolymers of ECH, ethylene oxide, propylene oxide, and allyl glycidyl ether.**[6,117]** The resulting

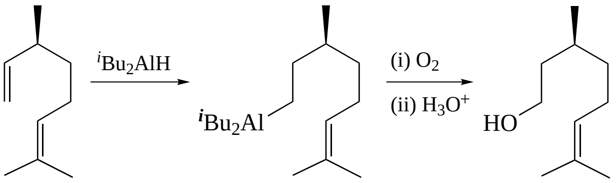

Scheme 4 Formation of (+)-citronellol from L-citronellene

polyether elastomers find use in automotive and industrial applications that require materials with low gas permeability, retention of flexibility at both low and high temperatures, and stability upon extended exposure to heat, hydrocarbons, and ozone. Catalysts are the so-called 'Vandenberg catalysts' prepared by partial hydrolysis of aluminum trialkyls, often with additional components such as acetylacetone. Annual production of polyether elastomers using aluminoxane-based Vandenberg catalysts was estimated at nearly 13 000 tons in 1991. Several research groups are developing organoaluminum catalysts for polymerization of epoxides, lactones, and lactides, as well as for copolymerization of carbon dioxide and epoxides.[118–122] These efforts have not yet resulted in commercial processes.

Organoaluminum compounds are also utilized as precursors for the preparation of aluminum-containing materials. Electronic-grade trimethylaluminum is sold in 99.9999% purity for the production of semiconductors (*see* ***Semiconductors***) and other electronic-grade metal alkyls. Aluminum trialkyls and a variety of organoaluminum alkoxides, halides, amides, azides, and β-diketonate derivatives continue to be studied as single-source precursors to thin films of Al_2O_3, AlN, AlGaAs, and AlGaSb by MOCVD, MOVPE and other pyrolysis methods.[123–126] High-purity films of aluminum can be deposited by thermal decomposition of aluminum alkyls, particularly those that possess a β-hydrogen.

9 SAFETY CONSIDERATIONS

The safe handling of organoaluminum compounds, particularly aluminum trialkyls, requires procedures to minimize the risk of exposure of the organoaluminum reagent to oxygen, water, halogenated solvents, excessive heat, and ignition sources.[7] Exposure to oxygen and water is minimized by handling organoaluminum compounds in dried glassware under an atmosphere of purified nitrogen or argon. This is accomplished using standard inert-atmosphere techniques on a dual-manifold Schlenk or vacuum line, or in an inert-atmosphere glove box. Liquid transfers between septum-capped reagent bottles and reaction vessels are made by double-tipped stainless steel cannula or syringes lubricated with hydrocarbon grease. Silicone greases must be avoided since they react with aluminum alkyls. Volatile compounds can be manipulated via vacuum line transfers. A glove box is essential for convenient weighing and storage of samples as well as for the preparation of samples for NMR and IR spectroscopy and X-ray crystallography. Reactions can be carried out in standard air-free glassware designed for use on Schlenk or vacuum lines, but care must be taken to avoid the use of water-cooled condensers and aqueous heating and cooling baths to avoid severe reactions in the event of glass breakage.

If a spill occurs, vermiculite or sand can be used to absorb the pyrophoric material and to slow the aerial oxidation by suffocation. Slow oxidation will continue to take place until the material is consumed. The absorbent should be disturbed periodically to expose fresh material to air. When all material appears to be oxidized, a mist of water can be used to hydrolyze any remaining organoaluminum compound. Solid waste can then be collected and disposed of in a suitable hazardous waste container.

Sand and vermiculite can also be used to suffocate a fire if the spill ignites. In the case of a fire, standard dry chemical (BC, sodium bicarbonate) extinguishers are used to suffocate the fire and suppress the burning process. Carbon dioxide extinguishers can also be used to suffocate and cool the fire. Obviously, water cannot be used.

Severe burns can occur if exposed skin comes into contact with an aluminum alkyl, either neat or in solution. The severity and depth of the burn will increase with increasing exposure time. In case of an accident, rinse the exposed skin with copious amounts of water to hydrolyze any remaining aluminum alkyl, to dilute the reagent, and to cool the skin. Rubber gloves, goggles, and a lab jacket are required when working with aluminum alkyls. A splash-protective face shield and a separate safety shield are also recommended.

Small quantities of organoaluminum distillation residues and waste solutions may be destroyed by slow addition of a 25% isopropanol solution in a hydrocarbon solvent. Safety procedures for handling large volumes of organoaluminum reagents can be obtained from commercial vendors.

10 RELATED ARTICLES

Alkali Metals: Organometallic Chemistry; Aluminum: Inorganic Chemistry; Beryllium & Magnesium: Organometallic Chemistry; Boron Hydrides; Boron: Organoboranes; Boron: Polyhedral Carboranes; Gallium: Inorganic Chemistry; Gallium: Organometallic Chemistry; Indium: Inorganic Chemistry; Indium: Organometallic Chemistry.

11 REFERENCES

1. D. A. Atwood and B. C. Yearwood, *J. Organomet. Chem.*, 2000, **600**, 186.
2. H. W. Roesky, *Inorg. Chem.*, 2004, **43**, 7284.
3. A. H. Cowley, *J. Organomet. Chem.*, 2004, **689**, 3866.
4. P. J. Shapiro and D. A. Atwood, 'Group 13 Chemistry: From Fundamentals to Applications', ACS Symposium Series 822, American Chemical Society, Washington, DC, 2002.
5. G. Wilke, *Angew. Chem. Int. Ed. Engl.*, 2003, **42**, 5000.
6. E. J. Vandenberg, Catalysis: A Key to Advances in Applied Polymer Chemistry, in 'Catalysis in Polymer Synthesis', ACS Symposium Series 496, eds. E. J. Vandenberg and

J. C. Salamone, American Chemical Society, Washington, DC, 1992, p. 2.

7. T. Mole and E. A. Jeffery, ‘Organoaluminum Compounds’, Elsevier, New York, 1972.
8. J. J. Eisch, in ‘Comprehensive Organometallic Chemistry II’, eds. E. W. Abel, F. G. A. Stone, and G. Wilkinson, Elsevier, New York, 1995, Vol. 1, Chap. 10.
9. J. J. Eisch, in ‘Comprehensive Organometallic Chemistry II’, eds. E. W. Abel, F. G. A. Stone, and G. Wilkinson, Elsevier, New York, 1995, Vol. 11, Chap. 6.
10. G. H. Robinson, ‘Coordination Chemistry of Aluminum’, VCH Publishers, New York, 1993.
11. G. H. Robinson, Aluminum and Gallium, in ‘Comprehensive Coordination Chemistry II’, eds. J. A. McCleverty, T. J. Meyer, and G. F. R. Parkin, Elsevier, Amsterdam, 2004, p. 347.
12. H. Lehmkuhl, O. Olbrysch, and H. Nehl, *Liebigs Ann. Chem.*, 1973, 708.
13. O. T. Beachley Jr and L. Victoriano, *Organometallics*, 1988, **7**, 63.
14. W. Uhl, *Z. Anorg. Allg. Chem.*, 1989, **579**, 75.
15. C. J. Harlan, E. G. Gillan, S. G. Bott, and A. R. Barron, *Organometallics*, 1996, **15**, 5479.
16. C. A. Tolman, *Chem. Rev.*, 1977, **77**, 313.
17. B. Neumüller, *Coord. Chem. Rev.*, 1997, **158**, 69.
18. J. Müller, *Coord. Chem. Rev.*, 2002, **235**, 105.
19. S. Aldridge and A. J. Downs, *Chem. Rev.*, 2001, **101**, 3305.
20. W. Zheng and H. W. Roesky, *J. Chem. Soc., Dalton Trans.*, 2002, 2787.
21. M. Schiefer, N. D. Reddy, H.-J. Ahn, A. Stasch, H. W. Roesky, A. C. Schlicker, H.-G. Schmidt, M. Noltemeyer, and D. Vidovic, *Inorg. Chem.*, 2003, **42**, 4970.
22. P. J. Shapiro, *Coord. Chem. Rev.*, 1999, **189**, 1.
23. P. Jutzi and N. Burford, *Chem. Rev.*, 1999, **99**, 969.
24. L. O. Schebaum and P. Jutzi, Pentamethylcyclopentadienyl Complexes of the Monovalent Group 13 Elements, in ‘Group 13 Chemistry: From Fundamentals to Applications’, ACS Symposium Series 822, eds. P. J. Shapiro and D. A. Atwood, American Chemical Society, Washington, DC, 2002, p. 16.
25. P. J. Shapiro, A Comparison of the Structural and Chemical Properties of Cyclopentadienyl Compounds of B(III), Al(III), Ga(III), In(III), and Tl(III), in ‘Group 13 Chemistry: From Fundamentals to Applications’, ACS Symposium Series 822, eds. P. J. Shapiro and D. A. Atwood, American Chemical Society, Washington, DC, 2002, p. 31.
26. B. Thiyagarajan, R. F. Jordan, and V. G. Young Jr, *Organometallics*, 1999, **18**, 5347.
27. J. J. Jerius, J. M. Hahn, A. F. M. M. Rahman, O. Mols, W. H. Ilsley, and J. P. Oliver, *Organometallics*, 1986, **5**, 1812.
28. V. S. J. De Mel and J. P. Oliver, *Organometallics*, 1989, **8**, 827.
29. M. S. Lalama, J. Kampf, D. G. Dick, and J. P. Oliver, *Organometallics*, 1995, **14**, 495.
30. J. K. Vohs, L. E. Downs, J. Stasalovich, M. Barfield, and G. H. Robinson, *J. Cluster Sci.*, 2002, **13**, 601.
31. J. A. C. Clyburne and N. McMullen, *Coord. Chem. Rev.*, 2000, **210**, 73.
32. J. D. Young, M. A. Khan, and R. J. Wehmschulte, *Organometallics*, 2004, **23**, 1965.
33. E. Y.-X. Chen and T. J. Marks, *Chem. Rev.*, 2000, **100**, 1391.
34. S. Feng, G. R. Roof, and E. Y.-X. Chen, *Organometallics*, 2002, **21**, 832.
35. T. Belgardt, J. Storre, H. W. Roesky, M. Noltemeyer, and H.-G. Schmidt, *Inorg. Chem.*, 1995, **34**, 3821.
36. J. Klosin, G. R. Roof, E. Y.-X. Chen, and K. A. Abboud, *Organometallics*, 2000, **19**, 4684.
37. M. Bochmann and M. J. Sarsfield, *Organometallics*, 1998, **17**, 5908.
38. J. S. Kim, L. M. Wojcinski II, S. Liu, J. C. Sworen, and A. Sen, *J. Am. Chem. Soc.*, 2000, **122**, 5668.
39. D. Chakraborty and E. Y.-X. Chen, *Inorg. Chem. Commun.*, 2002, **5**, 698.
40. Y.-X. Chen, M. V. Metz, L. Li, C. L. Stern, and T. J. Marks, *J. Am. Chem. Soc.*, 1998, **120**, 6287.
41. J. J. Eisch, P. O. Otieno, K. Mackenzie, and B. W. Kotowicz, Electronic and Steric Design of Novel Group 13 Lewis Acids and Their Synthesis via Metal-Tin Exchange Reactions (1): Toward the Ideal Olefin Polymerization Catalyst, in ‘Group 13 Chemistry: From Fundamentals to Applications’, ACS Symposium Series 822, eds. P. J. Shapiro and D. A. Atwood, American Chemical Society, Washington, DC, 2002, p. 88.
42. J. P. Oliver, *Adv. Organomet. Chem.*, 1977, **16**, 111.
43. M. B. Smith, *J. Phys. Chem.*, 1967, **71**, 364.
44. W. Uhl, L. Cuypers, R. Graupner, J. Molter, A. Vester, and B. Neumüller, *Z. Anorg. Allg. Chem.*, 2001, **627**, 607.
45. H. Hatop, M. Schiefer, H. W. Roesky, H.-G. Schmidt, and M. Noltemeyer, *J. Fluorine Chem.*, 2001, **112**, 219.
46. G. S. Hair, A. H. Cowley, R. A. Jones, B. G. McBurnett, and A. Voigt, *J. Am. Chem. Soc.*, 1999, **121**, 4922.
47. J. W. Akitt, Aluminum, Gallium, Indium, and Thallium, in ‘Multinuclear NMR Spectroscopy’, ed. J. Mason, Plenum Press, New York, 1987, p. 259.
48. C. E. Holloway and M. Melnik, *J. Organomet. Chem.*, 1997, **543**, 1.
49. A. McKillop, J. D. Smith, and I. J. Worrall eds, ‘Organometallic Compounds of Aluminum, Gallium, Indium and Thallium’, Chapman and Hall, New York, 1985.
50. I. Haiduc, *Organometallics*, 2004, **23**, 3.
51. Ch. Elschenbroich and A. Salzer, ‘Organometallics, A Concise Introduction’, 2nd edn., VCH, Weinheim, 1992, p. 11.
52. A. R. Barron, *Chem. Soc. Rev.*, 1993, 93.
53. J. Lewinski, J. Zachara, and E. Grabska, *J. Am. Chem. Soc.*, 1996, **118**, 6794.

54. J. Lewinski, J. Zachara, P. Gos, E. Grabska, T. Kopec, I. Madura, W. Marciniak, and I. Prowotorow, *Chem. Eur. J.*, 2000, **6**, 3215.
55. A. R. Barron, *Comments Inorg. Chem.*, 1993, **14**, 123.
56. P. J. Shapiro, A. Vij, G. P. A. Yap, and A. L. Rheingold, *Polyhedron*, 1995, **14**, 203.
57. M. R. Mason, B. Song, and K. Kirschbaum, *J. Am. Chem. Soc.*, 2004, **126**, 11812.
58. I. Marek and J.-F. Normant, *Chem. Rev.*, 1996, **96**, 3241.
59. R. Sanchez, C. Arrington, and C. A. Arrington Jr, *J. Am. Chem. Soc.*, 1989, **111**, 9110.
60. X.-W. Li, J. Su, and G. H. Robinson, *Chem. Commun.*, 1996, 2683.
61. G.-J. M. Gruter, G. P. M. van Klink, O. S. Akkerman, and F. Bickelhaupt, *Chem. Rev.*, 1995, **95**, 2405.
62. M. N. S. Rao, H. W. Roesky, and G. Anantharaman, *J. Organomet. Chem.*, 2002, **646**, 4.
63. A. J. Downs, H.-J. Himmel, and L. Manceron, *Polyhedron*, 2002, **21**, 473.
64. W. Uhl, *Coord. Chem. Rev.*, 1997, **163**, 1.
65. G. Linti and H. Schnöckel, *Coord. Chem. Rev.*, 2000, **206–207**, 285.
66. H. Schnöckel and H. Köhnlein, *Polyhedron*, 2002, **21**, 489.
67. P. P. Power, *Chem. Rev.*, 2003, **103**, 789.
68. R. J. Wright, A. D. Phillips, and P. P. Power, *J. Am. Chem. Soc.*, 2003, **125**, 10784.
69. W. Uhl and F. Breher, *Eur. J. Inorg. Chem.*, 2000, 1.
70. J. Vollet, J. R. Hartig, and H. Schnöckel, *Angew. Chem. Int. Ed. Engl.*, 2004, **43**, 3186.
71. F. Thomas, S. Schulz, H. Mansikkamäki, and M. Nieger, *Angew. Chem. Int. Ed. Engl.*, 2003, **42**, 5641.
72. M.-A. Munoz-Hernandez, P. Wei, S. Liu, and D. A. Atwood, *Coord. Chem. Rev.*, 2000, **210**, 1.
73. B. Neumüller, *Chem. Soc. Rev.*, 2003, **32**, 50.
74. M. Veith, *Chem. Rev.*, 1990, **90**, 3.
75. A. H. Cowley, R. A. Jones, M. A. Mardones, J. L. Atwood, and S. G. Bott, *Angew. Chem. Int. Ed. Engl.*, 1990, **29**, 1409.
76. K. M. Waggoner and P. P. Power, *J. Am. Chem. Soc.*, 1991, **113**, 3385.
77. S. Pasynkiewicz, *Polyhedron*, 1990, **9**, 429.
78. H. W. Roesky, M. G. Walawalkar, and R. Murugavel, *Acc. Chem. Res.*, 2001, **34**, 201.
79. D. Chakraborty and E. Y.-X. Chen, *Organometallics*, 2003, **22**, 207.
80. M. R. Mason, J. M. Smith, S. G. Bott, and A. R. Barron, *J. Am. Chem. Soc.*, 1993, **115**, 4971.
81. C. J. Harlan, M. R. Mason, and A. R. Barron, *Organometallics*, 1994, **13**, 2957.
82. A. R. Barron, Alkylalumoxanes: Synthesis, Structure, and Reactivity, in ‘Metallocene-Based Polyolefins’, eds. J. Scheirs and W. Kaminsky, John Wiley & Sons, Chichester, 2000, Vol. 1, p. 33.
83. C. J. Harlan, S. G. Bott, and A. R. Barron, *J. Am. Chem. Soc.*, 1995, **117**, 6465.
84. B. Richter, A. Meetsma, B. Hessen, and J. H. Teuben, *Angew. Chem. Int. Ed. Engl.*, 2002, **41**, 2166.
85. R. J. Wehmschulte and P. P. Power, *J. Am. Chem. Soc.*, 1997, **119**, 8387.
86. S. S. Reddy and S. Sivaram, *Prog. Polym. Sci.*, 1995, **20**, 309.
87. J.-N. Pedeutour, K. Radhakrishnan, H. Cramail, and A. Deffieux, *Macromol. Rapid Commun.*, 2001, **22**, 1095.
88. H. Sinn and W. Kaminsky, *Adv. Organomet. Chem.*, 1980, **18**, 99.
89. M. Ystenes, J. L. Eilersten, J. Liu, M. Ott, E. Rytter, and J. A. Stovneng, *J. Polym. Sci., Part A: Polym. Chem.*, 2000, **38**, 3106.
90. G. G. Hlatky, *Chem. Rev.*, 2000, **100**, 1347.
91. M. R. Mason, *J. Cluster Sci.*, 1998, **9**, 1.
92. M. G. Walawalkar, H. W. Roesky, and R. Murugavel, *Acc. Chem. Res.*, 1999, **32**, 117.
93. M. R. Mason and A. M. Perkins, *J. Organomet. Chem.*, 2000, **599**, 200.
94. C. G. Lugmair, T. D. Tilley, and A. L. Rheingold, *Chem. Mater.*, 1999, **11**, 1615.
95. J. Pinkas, D. Chakraborty, Y. Yang, R. Murugavel, M. Noltemeyer, and H. W. Roesky, *Organometallics*, 1999, **18**, 523.
96. M. R. Mason, A. M. Perkins, V. V. Ponomarova, and A. Vij, *Organometallics*, 2001, **20**, 4833.
97. M. R. Mason, R. M. Matthews, A. M. Perkins, and V. V. Ponomarova, Molecular Phosphates and Phosphonates of Aluminum and Gallium: Potential Applications in Materials Synthesis, in ‘Group 13 Chemistry: From Fundamentals to Applications’, ACS Symposium Series 822, eds. P. J. Shapiro and D. A. Atwood, American Chemical Society, Washington, DC, 2002, p. 181.
98. R. E. Morris, A. Burton, L. M. Bull, and S. I. Zones, *Chem. Mater.*, 2004, **16**, 2844.
99. Y. Yang, J. Pinkas, M. Schäfer, and H. W. Roesky, *Angew. Chem. Int. Ed. Engl.*, 1998, **37**, 2650.
100. R. Murugavel, A. Voigt, M. G. Walawalkar, and H. W. Roesky, *Chem. Rev.*, 1996, **96**, 2205.
101. D. A. Atwood, *Coord. Chem. Rev.*, 1998, **176**, 407.
102. O. Wrobel, F. Schaper, and H. H. Brintzinger, *Organometallics*, 2004, **23**, 900.
103. M. P. Coles and R. F. Jordan, *J. Am. Chem. Soc.*, 1997, **119**, 8125.
104. C. E. Radzewich, I. A. Guzei, and R. F. Jordan, *J. Am. Chem. Soc.*, 1999, **121**, 8673.
105. E. Ihara, V. G. Young Jr, and R. F. Jordan, *J. Am. Chem. Soc.*, 1998, **120**, 8277.
106. A. V. Korolev, F. Delpech, S. Dagorne, I. A. Guzei, and R. F. Jordan, *Organometallics*, 2001, **20**, 3367.

107. J. A. R. Schmidt and J. Arnold, *Organometallics*, 2002, **21**, 2306.
108. S. K. Spitzmesser and V. C. Gibson, *J. Organomet. Chem.*, 2003, **673**, 95.
109. K.-C. Kim, C. A. Reed, G. S. Long, and A. Sen, *J. Am. Chem. Soc.*, 2002, **124**, 7662.
110. G. Talarico and P. H. M. Budzelaar, *Organometallics*, 2002, **21**, 34.
111. V. C. Gibson and S. K. Spitzmesser, *Chem. Rev.*, 2003, **103**, 283.
112. D. J. Linton, P. Schooler, and A. E. H. Wheatley, *Coord. Chem. Rev.*, 2001, **223**, 53.
113. M. B. Smith and J. March, 'March's Advanced Organic Chemistry', 5th edn., John Wiley & Sons, New York, 2001.
114. R. C. Larock, 'Comprehensive Organic Transformations', 2nd edn., Wiley-VCH, New York, 1999.
115. I. Ojima, 'Catalytic Asymmetric Synthesis', 2nd edn., John Wiley & Sons, New York, 2000.
116. G. W. Parshall and S. D. Ittel, 'Homogeneous Catalysis', 2nd edn., John Wiley & Sons, New York, 1992.
117. K. Owens and V. Kyllingstad, 'Kirk-Othmer Encyclopedia of Chemical Technology', 4th edn., Wiley, New York, 1993, Vol. 8, p. 1079.
118. D. Chakraborty, A. Rodriguez, and E. Y.-X. Chen, *Macromolecules*, 2003, **36**, 5470.
119. T. Sarbu and E. J. Beckman, *Macromolecules*, 1999, **32**, 6904.
120. H.-L. Chen, B.-T. Ko, B.-H. Huang, and C.-C. Lin, *Organometallics*, 2001, **20**, 5076.
121. N. Nomura, R. Ishii, M. Akakura, and K. Aoi, *J. Am. Chem. Soc.*, 2002, **124**, 5938.
122. T. M. Ovitt and G. W. Coates, *J. Am. Chem. Soc.*, 1999, **121**, 4072.
123. J. A. Jegier and W. L. Gladfelter, *Coord. Chem. Rev.*, 2000, **206–207**, 631.
124. A. C. Jones, *Chem. Soc. Rev.*, 1997, 101.
125. R. A. Fischer, A. Miehr, H. Sussek, H. Pritzkow, E. Herdtweck, J. Muller, O. Ambacher, and T. Metzger, *Chem. Commun.*, 1996, 2685.
126. D. A. Neumayer and J. G. Ekerdt, *Chem. Mater.*, 1996, **8**, 9.

Ammonia & N-donor Ligands

Donald A. House
University of Canterbury, Christchurch, and Massey University, Albany, New Zealand

1 Introduction 1
2 Ligands Containing Only One N-atom 4
3 Ligands Containing Two N Atoms 8
4 Catenated N Atoms 13
5 Polyamine Ligands 16
6 Miscellaneous Nitrogen Donor Ligands 21
7 Reactions of Coordinated Nitrogen Ligands 22
8 Supramolecular Assemblies 23
9 Conclusion 24
10 Related Articles 24
11 Further Reading 24
12 References 24

Glossary

Amine complex: complex with amine ligands, other than ammonia
Ammine complex: complex with NH_3 (ammonia) as the only N-donor ligand, for example, *trans*-$PtCl_2(NH_3)_2$
Facultative ligand: multidentate ligands that are capable of arranging their donor atoms around a metal ion in a number of different ways
Homoleptic Complex: complex with only one type of ligand

Abbreviations

Abbreviations used are listed in *Nomenclature of Inorganic Compounds*:**[1]** other abbreviations will be described in the text.

1 INTRODUCTION

The nitrogen atom can adopt oxidation states (*see* ***Coordination & Organometallic Chemistry: Principles*** and *Oxidation Number*) from −III to +V (*see* ***Nitrogen: Inorganic Chemistry***). Consequently, there are many different types of N-donor ligands incorporating different oxidation states and different types of metal−nitrogen bonding (**1**)−(**14**) with a sometimes complicated nomenclature.**[1]**

$M{\equiv}N{:}$

Imino
(nitrido)
(**1**)

$M{\equiv}N{-}H$

Imido
(nitrene)
(**2**)

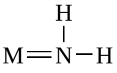

$M{=}\overset{H}{N}{-}H$

Amido
(amino)
(**3**)

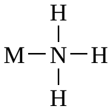

$M{-}\overset{H}{\underset{H}{N}}{-}H$

Ammine
(**4**)

$M{-}N{\equiv}N{:}$

Dinitrogen
(**5**)

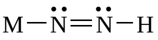

$M{-}\ddot{N}{=}\ddot{N}{-}H$

Diazenido
(**6**)

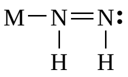

$M{-}\underset{H}{N}{=}\underset{H}{N}{:}$

Diazene
(**7**)

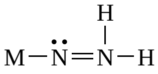

$M{-}\ddot{N}{=}\overset{H}{N}{-}H$

Isodiazene
(**8**)

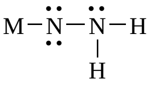

$M{-}\underset{\cdot\cdot}{\ddot{N}}{-}\underset{H}{\ddot{N}}{-}H$

Hydrazido(2-)-N,N
(**9**)

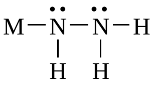

$M{-}\underset{H}{\ddot{N}}{-}\underset{H}{\ddot{N}}{-}H$

(**10**)

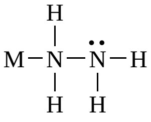

$M{-}\overset{H}{\underset{H}{N}}{-}\underset{H}{\ddot{N}}{-}H$

(**11**)

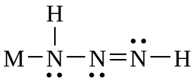

$M{-}\overset{H}{\underset{\cdot\cdot}{N}}{-}\underset{\cdot\cdot}{N}{=}\ddot{N}{-}H$

Triazene
(**12**)

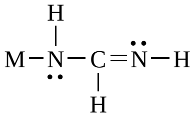

$M{-}\overset{H}{\underset{\cdot\cdot}{N}}{-}\underset{H}{C}{=}\ddot{N}{-}H$

Aminidinate
(**13**)

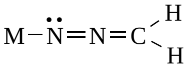

$M{-}\ddot{N}{=}N{=}C\begin{smallmatrix}H\\H\end{smallmatrix}$

(**14**)

Nitrogen forms catenated**[2,3]** (*see Catenation*) ligands such as N_3^-, as well as mixed donor atom ligands such as NCS^-, NCO^-, CN^-, NO, NS, NO_2^-, NH_2OH**[4–6]** (*see* ***Mixed Donor Ligands***). We will restrict the present discussion to those ligands containing only N, C and, H atoms.

The equilibrium

$$R_3N{:} + H_3O^+ \rightleftharpoons R_3NH^+ + H_2O \qquad (1)$$

(protonation) constant (*see* ***Stability Constants & their Determination***) for the reversible protonation of an N-donor ligand (equation 1) is a measure of the basicity.**[7]** Multi-N-containing ligands have a series of such constants that can cover a considerable range (Table 1).

The interaction of an N-donor ligand with a metal ion also covers a wide range, from the very weak chelate or macrocycle-assisted association of an alkali metal cation to the very robust Co^{III} and Ru^{III} metal−nitrogen bonds. In aqueous solution, this interaction (equation 2) is essentially a substitution

$$M\text{–}OH_2{}^{n+} + {:}NR_3 \rightleftharpoons M\text{–}NR_3{}^{n+} + H_2O \qquad (2)$$

Table 1 Representative protonation constants for some N-donor ligands[7]

L	$-\mathrm{p}K_n[\mathrm{H}^+]$	$-\mathrm{p}K_1[\mathrm{Ni(L)}]^{10}$	$-\mathrm{pK}_1$ $[\mathrm{Cu(L)}]^{10}$
en	7.18, 9.98	7.35	10.5
dien(**159**)	4.47, 9.17, 9.96	10.7	15.9
trien(**178**)	3.6, 6.84, 9.22, 9.92	14.4	20.1
tetren(**207**)		17.4	22.8
penten(**223**)		19.1	–

reaction of a coordinated water molecule by the incoming N-ligand, and there may also be competing hydrolytic equilibria (equation 3). Such hydroxo

$$\mathrm{M{-}OH_2}^{n+} \rightleftharpoons \mathrm{M(OH)}^{(n-1)+} + \mathrm{H}^+ \qquad (3)$$

complexes can be much more substitution-inert, and may also result in metal ion hydroxide precipitation. The competition can be overcome to a certain extent by using nonaqueous solvents, for example, DMSO or DMF in $\mathrm{Cr^{III}}$ N-ligand synthesis.[8,9]

For labile systems with reasonably well defined coordination numbers, for example, first-row transition metal divalent cations, chelating and macrocyclic ligands have a greater stability than would be expected from an additive relationship, that is, from equations (4) and (5), $\mathrm{K_{ML}} > \mathrm{K_{ML2}}$. However, there is a simple relationship

$$\mathrm{M}^{2+} + 2\mathrm{NH_2Me} \rightleftharpoons \mathrm{M(NH_2Me)_2}^{2+} \quad \mathrm{K_{ML2}} \qquad (4)$$

$$\mathrm{M}^{2+} + \mathrm{en} \rightleftharpoons \mathrm{M(en)}^{2+} \quad \mathrm{K_{ML}} \qquad (5)$$

between the formation constants for $\mathrm{M(NH_3)}_n{}^{2+}$ and $\mathrm{M(polyamine)}^{2+}$ (polyamine = en, dien(**159**), trien(**178**), tetren(**207**), penten(**223**), i.e. the homologous series of linear polyamines increasing by $\mathrm{CH_2CH_2NH_2}$,

$$\log \mathrm{K_1(polyamine)} = 1.152 \log \mathrm{K}_n(\mathrm{NH_3}) + (n-1)\log 55.5 \qquad (6)$$

equation 6). In this equation, n is the denticity (number of N atoms) of the polyamine, 1.152 is an inductive effect correction [$= \mathrm{p}K_\mathrm{a}(\mathrm{CH_3NH_2})/\mathrm{p}K_\mathrm{a}(\mathrm{NH_3})$], and $(n-1)\log 55.5$ is the entropy contribution.[10]

There are also systematic trends in stability constants when five-membered polyamine rings are replaced by six-membered rings, or when linear polyamine ligands are replaced by macrocyclic ligands of a similar strain (*see Chelate Effect*). These effects can be well accounted for in terms of enthalpy contributions to the formation constant.[11]

Both kinetic and thermodynamic classifications of metal–nitrogen complexes have been proposed. The former gives systems that are either coordinatively inert or labile (*see Coordinatively Inert & Labile Complexes*), with inert being defined as those that allow geometric isomers (*see Isomer, Types of*) or react (via M–N bond rupture) with half-lives (*see Radioactive Decay*) of longer than 1 min. The latter involves the hard-acid, soft-base concept[12] with the amine nitrogen being considered as a hard center (*see* ***Hard & Soft Acids and Bases***), as it binds strongly to protons, and is thus expected to bind strongly to 'hard' metal centers (good lone pair acceptors). In this classification, it is usual to compare the accessibility or stability of M–N complexes with those of analogous M–P donor ligands (a typical 'soft' donor). In both methods of classification, the boundaries are not sharp and the stability of a particular metal amine complex depends to a considerable extent on the nature of the ligand. For example, most open chain Cu^{2+} amine complexes such as $\mathrm{Cu(tetren)}^{2+}$ (**15**) (**207**) are rapidly decomposed in acid solution, but when the Cu^{2+} is encapsulated in an $\mathrm{N_5}$ polyamine cage such as L (**16**), the resulting complex is stable for days in 1 M $\mathrm{HClO_4}$ at 50 °C[13] (*see* ***Macrocyclic Ligands***).

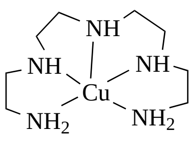

$[\mathrm{Cu(tetren)}]^{2+}$

(**15**)

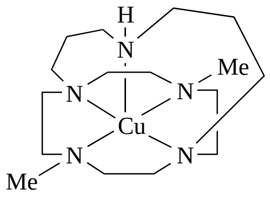

$[\mathrm{CuL}]^{2+}$

(**16**)

Very often, amine complexes are designed to illustrate some subtle mechanistic (*see* ***Mechanisms of Reaction of Organometallic Complexes***) or stereochemical effect in coordination chemistry and much effort has been exercised in the design of specific amine ligands. For example, the reaction shown in equation (7) is very sensitive to steric effects, and the introduction of a pyridine ligand in place of an

$$\mathrm{CoCl(N_5)}^{2+} + \mathrm{OH}^- \longrightarrow \mathrm{Co(OH)(N_5)}^{2+} + \mathrm{Cl}^- \qquad (7)$$

alkylamine results in a modest (45×) rate increase.[14] The incorporation of a 'flat secondary nitrogen donor' (see Section 5) in a coordinated polyamine chain results in a significant rate increase ($\sim 10^3\times$). The combination of both effects, requiring the synthesis of bispicdien (**17**), preparation of the $\mathrm{Co^{III}}$ complex, and characterization of the correct isomer,[15] has quite a remarkable acceleratory effect on reaction (7) (Table 2).

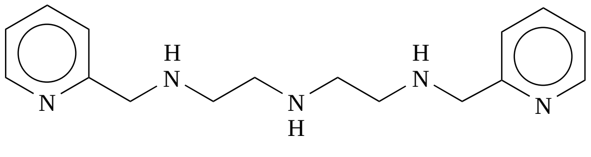

Bispicdien

(**17**)

Table 2 Structural effects on base hydrolysis rates (equation 7)[14–16]

Complex	k_{OH}(25.0 °C)($M^{-1}\ s^{-1}$)
CoCl(en)$_2$(MeNH$_2$)$^{2+}$	7.3
CoCl(en)$_2$(py)$^{2+}$	332
cis-α-CoCl(trien)(NH$_3$)$^{2+}$ (**193**)	10.6
cis-β_2-CoCl(trien)(NH$_3$)$^{2+}$ (**195**)	4.8×10^4
$\alpha\beta$-CoCl(bispicdien)$^{2+}$ (see **218**)	2.0×10^7
t-CoCl(dmptacn)2+ (**18**)	4×10^{-2}
t-CoCl(dmpmetacn)2+ (**19**)	7×10^{-1}

An essential requirement in the SN$_1$CB mechanism for reaction (7) is the presence of an NH proton. There are now several polyamine ligands that have either one (**18**) or zero (**19**) such protons (see also Section 5.3). Despite having zero NH protons, [CoCl(dmpmetacn)]$^{2+}$ reacts with base at a rate proportional to the OH$^-$ concentration and faster than [CoCl(dmptacn)]$^{2+}$ (Table 2). Proton exchange at the CH$_2$ position in the pyridyl arm trans to the leaving group was observed, and amido activation through the pyridine ring is believed to be responsible for the OH$^-$ dependent rate law.[16]

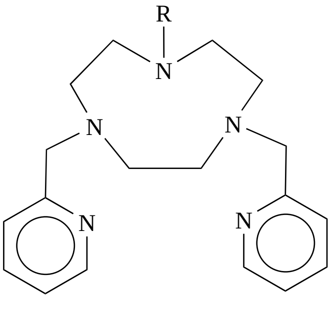

(**18**) Dmptacn (R=H)
(**19**) Dmpmetacn (R=Me)

For aliphatic amines, coordination of the lone pair to a central metal ion completes the tetrahedral stereochemistry about the nitrogen atom (equation 8), and

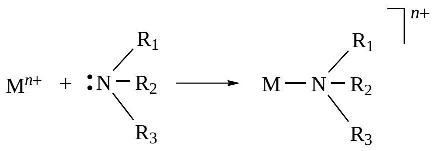

$$M^{n+} + {:}N(R_1)(R_2)(R_3) \longrightarrow \left[M{-}N(R_1)(R_2)(R_3)\right]^{n+} \qquad (8)$$

nitrogen bases with three different substituents now become potentially chiral. Inversion about the nitrogen center is generally rapid for labile complexes, but for inert complexes, both geometric and optical isomers can be isolated.[14,17,18]

Although such isomers have not been resolved for monodentate amines (suitable tertiary amines[19] are not easily coordinated to inert metal centers), the phenomenon is quite widespread with coordinated aliphatic polyamines (**20**), (**21**) and (**22**), (**23**).[20] It should be noted that current nomenclature systems[1] are not sufficient to distinguish between isomers (**22**) and (**23**) (see, however, Reference 21).

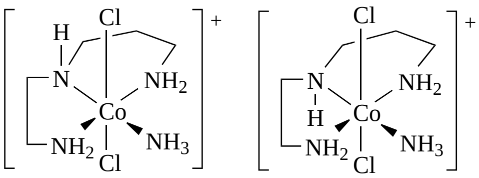

R–(**20**) S–(**21**)

Optical isomers of *trans*-[CoCl$_2$(2,3-tri)NH$_3$]$^+$

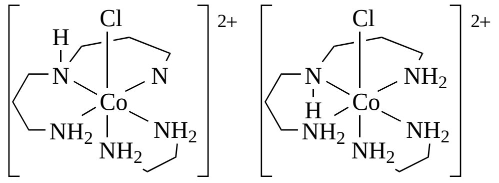

(**22**) (**23**)

Structural isomers of *mer*-[CoCl(3,3-tri)(en)]$^{2+}$

The interchange of the stereochemically significant sec-NH proton in (**20**) $\rightleftharpoons$ (**21**) (inversion) or (**22**) $\rightleftharpoons$ (**23**) (isomerization) is a base-catalyzed process and takes place via a deprotonation–protonation mechanism. This interchange is one of the simplest types of 'reaction of a coordinated ligand', and proton exchange rates have been measured for quite a number of inert transition metal–amine complexes.[22] With suitable central metals (Pt^{IV})[23] or ligands,[24] the deprotonated intermediates can be isolated and characterized. Other reactions of coordinated amine ligands will be considered in Section 7.

Amines containing a *Chiral* carbon center in the aliphatic residue attached to the nitrogen atom, for example, α-methyl benzylamine (**24**), (**25**), are of considerable interest to the coordination chemist as, when coordinated, these ligands induce chirality in the metal–ligand chromophore. Methods for the resolution of more than 1000 racemic nitrogen containing organic compounds have been described.[25]

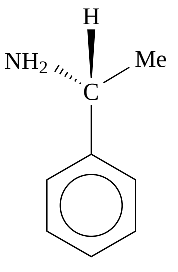

(R)–(+)–α–Methylbenzylamine
(**24**)

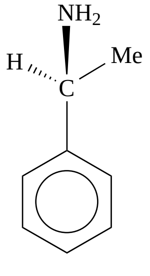

S–(–)–α–Methylbenzylamine
(**25**)

Many of the simple mono- and polyamines are commercially available, but designer specific ligands[26,27] require the use of conventional organic synthetic techniques.[28,29] Methods of amine complex synthesis are usually central-metal specific, but summaries of procedures used for Cr^{III}[8,9] and Co^{III}[30] are available. In the case of the inert metal centers, geometrical isomers are frequently encountered. Fractional crystallization is still widely used for isomer separation procedures,[14] but column chromatography has the potential for separation of both optical and geometric isomers and the advantage that isomers or by-products at the 1% level can be detected and concentrated (see Section 5.2).[31–34]

Molecular Mechanics calculations can be used (1) in the analysis of disordered structures, (2) in the prediction of known structures, (3) in the prediction of isomer ratios, and (4) in the prediction of conformer ratios. The majority of studies have dealt with Co^{III} hexaamine systems,[35] but now[36,37] force fields are available for amine complexes of Co^{II}, Ni^{II},[38] Cu^{II}, Zn^{II}, Cr^{III}, Fe^{III}, and Rh^{III}.

2 LIGANDS CONTAINING ONLY ONE N-ATOM

The deprotonation of ammonia leads successively from NH_3 (Section 2.1) through NH_2^- and NH^{2-} to N^{3-}, and these anions can act as ligands.[39,40] In addition to the binding modes shown in (**1**) to (**3**), bridging and bent structures (**26**–**31**) are possible. Indeed, the amido-bridged complex, $[(NH_3)_5CoNH_2Co(NH_3)_5]^{5+}$ was isolated and characterized by Werner (*see Werner Complexes*). In many cases, the NH protons can be replaced by alkyl or more bulky $Si(Me)_3$ groups and these N donors stabilize unusually low-coordination numbers, for example, $Cr^{III}(NPr^i_2)_3$ or $Fe^{II}\{N(SiMe_3)_2\}_3$. Such alkyl systems are often more stable than their ‘proton only’ analogs, and bent $MNCH_3$ (**28**) species can undergo further reversible deprotonation to give methyleneamido (**31**) ligands (equation 9). These methyleneamido ($-N{=}CH_2$) or substituted ($-N{=}CR_2$) ligands can also adopt linear (**32**) and bridged modes (**33**).[41] In (**33**), there is a striking analogy with alkenes.

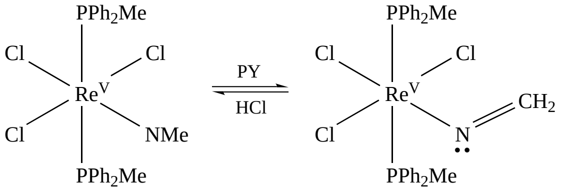

(9)

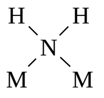

(**26**)

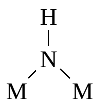

(**27**)

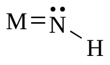

(**28**)

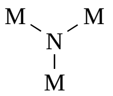

(**29**)

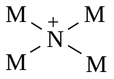

(**30**)

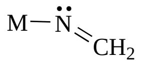

(**31**)

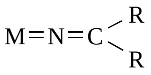

(**32**)

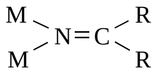

(**33**)

$M-N-M'$

(**34**)

Complete deprotonation gives the exceptionally strong π-donor N^{3-} anion (*see π-Bond*). Complexes such as $Os^{VII}Br_4N$ or $[Os^{VIII}O_3N]^-$ have Os≡N bonds in the 1.6–1.8 Å range, and the N^{3-} ligand has a strong *Trans Influence*. The available *Lone Pair* (**1**), allows such complexes to act as ligands forming bridged nitrido species (**34**). Rearrangement of the bonds leads to triangular planar N-centered systems (**29**), such as $[Ir^{III}_3N(SO_4)_6(H_2O)_3]^{6-}$ and tetrahedral M_4N^+ (**30**) arrangements, such as $[(Ph_3PAu^I)_4N]^+$ (analogous to quaternary ammonium salts). The nitrido ligand is much more prominent in second and third-row transition metal chemistry than in the first-row elements, for example, (**35**).

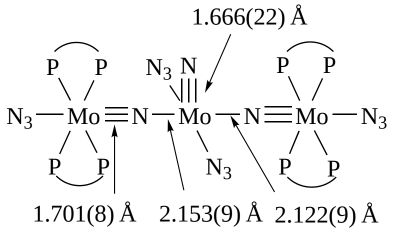

(**35**)

2.1 Ammonia and Ammines[42]

Metal ion complexes with ammonia are called ammines. At room temperature, ammonia is a gas, but liquid ammonia (b.p. −33 °C) is relatively easy to handle[43] and is an excellent solvent and reagent (equation 10)[44]

$$\textit{trans}\text{-}CrCl_2(2,3,2\text{-tet})^+ + NH_3(l) \longrightarrow \textit{trans}\text{-}CrCl(NH_3)(2,3,2\text{-tet})^{2+} + \textit{trans}\text{-}Cr(NH_3)_2(2,3,2\text{-tet})^{3+} \qquad (10)$$

somewhat analogous to water.[45]

$NH_3(g)$ is extremely soluble and the aqueous solution is best described as $NH_3(aq)$ with the equilibrium (pK_b[25] = 4.75) written as equation (11). Thus, $NH_3(aq)$ (1 M) is an important laboratory source of NH_3, NH_4^+, or OH^-.

$$NH_3(aq) + H_2O \rightleftharpoons NH_4^+ + OH^- \qquad (11)$$

Almost all cations show some sort of interaction with the NH_3 molecule.[46] For $M(NR_3)_x{}^{n+}$ systems, the maximum x is often achieved with ammonia.

The ammine chemistry of group 2,[47] group 3,[48] Co^{III},[30,42] Cr^{III},[8,9,49] $Ru^{III/II}$,[47–51] and Os^{II},[49] has been reviewed. Synthetic procedures for many ammine complexes are given by Schlessinger.[52] Table 3 lists some (sometimes exotic) salts of representative ammine complexes, together with the average metal–NH_3 bond distance and an estimate[53] of the average M–NH_3 bond energy.

Transition metal–ammine cations have been used in the isolation of unusual anions.

Co^{III} and Cr^{III} ammines were among the first to be investigated by Reinecke, Jørgensen, Werner (Nobel prize, 1912), and Pfeiffer in the early days of coordination chemistry (*see* ***Coordination Chemistry: History***), and this work continues today (Taube, Nobel Prize, 1984). $[MX(NH_3)_5]^{n+}$ (X = anionic or neutral group) is particularly well-studied[14] and has even been used as a protecting group in peptide synthesis. Variation of M has a considerable influence on the rate of the *Solvolysis* of X (Table 4).

Two possible isomers [*trans*-(**36**), *cis*-(**37**)] for $[MX_2(NH_3)_4]^{n+}$ (M = *inert* transition metal) are usually separable, although in a number of cases only one isomeric form is known and the isolation of the other isomer is still a challenge to the synthetic chemist.

Table 3 Typical ammine complexes[52]

Complex	M–NH_3(av.) distance (Å)	M–NH_3(av.)[53] bond energy (kJ mol^{-1})
$[Mg^{II}(NH_3)_6](ClO_4)_2$		176.8
$(NH_4)_2[V^{III}Cl_5(NH_3)]$	2.138	
$[Cr^{III}(NH_3)_6]ZnCl_4\cdot Cl$	2.071(3)	
Fe^{III}–N	2.00(est)	
Fe^{II}–N	2.15(est)	
$[Ru^{II}(NH_3)_6]I_2$	2.144(4)	
$[Ru^{III}(NH_3)_6](BF_4)_3$	2.104(4)	
$[Co^{II}(NH_3)_6]Cl_2$	2.114(9)	186.4
$[Co^{III}(NH_3)_6](Hg_3Cl_9)$	1.971(7)	389.3
$[Ni^{II}(NH_3)_6]^{2+}$	2.15	197.3
c-$[Pt^{II}Cl_2(NH_3)_2\cdot(HgCl_2)_3]_n$	2.093(17)	
$[Pt^{II}(NH_3)_4][Pt^{IV}Br_2(NH_3)_4](HSO_4)_4$	2.059	
$[Cu^{I}(NH_3)_2][Ag(NCS)_3]$	2.00	128.0
$[Cu^{II}(NH_3)_6]Cl_2$	2.07(7) eq 2.62(11)ax	213.5
$K[Cu^{II}(NH_3)_5](PF_6)_3$	2.00, 2.048 eq 2.193ax	
$[Cu^{II}(NH_3)_4]I_4$	2.025(8)	
$[Ag^{I}(NH_3)_2][Ag^{I}(NO_3)_3]$	2.114	106.6
$[Zn^{II}(NH_3)_6](I_3)_2$	2.05(1)	218.9
$[Cd^{II}(NH_3)_6]I_4$	2.341(8)	191.7

Table 4 Acid hydrolysis rates (k_H) for some $[M(CF_3SO_3)(NH_3)_5]^{n+}$ complexes at 25 °C

M	k_H (s^{-1})
Cr^{III}	0.125
Ru^{III}	0.093
Co^{III}	0.027
Rh^{III}	0.019
Os^{III}	0.0018
Ir^{III}	0.00026
Pt^{IV}	<0.0001

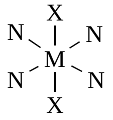

trans-(**36**)

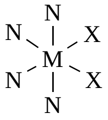

cis-(**37**)

For the triammines, there are two potential isomers [*mer*-(**38**) and *fac*-(**39**)] (these are now to be called OC-6-12 and OC-6-22 respectively, although the ranking order may change with X[1]). $[Co(NO_2)_3(NH_3)_3]$[52] should be a nonelectrolyte using Werner's octahedral coordination ideas, but should be an electrolyte according to Jørgensen's chain theory. Both schools succeeded in preparing compounds with the above stoichiometry with the Werner sample being a conductor and the Jørgensen sample a nonelectrolyte! The situation was finally resolved when it was shown that the Werner sample was heavily contaminated with $[Co(NO_2)_2(NH_3)_4{}^+][Co(NO_2)_4(NH_3)_2{}^-]$[52] and hence was conducting. Even today, it is sometimes difficult to establish the configuration of, say, $[Co(N_3)_3(py)_3]$, without resource to X-ray crystallography.

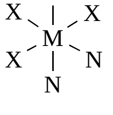

mer-(**38**)

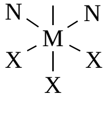

fac-(**39**)

Despite intensive work, few metals give a complete monotonic series $[MX_{6-x}(NH_3)_x]^{(x-3)+}$, $x = 0, 1 \ldots 6$ (X = *Monodentate Ligand*). The missing member is usually the $x = 1$ compound, with the most extensive examples being $M = Cr^{III}$, $X = NCS^-$ ($x \neq 1$) or H_2O[8]; $M = Co^{III}$, $X = NO_2{}^-$ ($x \neq 1$).

Some ammine complexes are metal ion specific, for example, the dinuclear Co^{III} μ-peroxo and μ-superoxo (*see*

Peroxo Complexes) decaammines (**40**),[54] the dinuclear Cr^{III} μ-oxo decaammines (**41**), and the dinuclear, electron-delocalized Ru μ-pyrazine decaammines (**42**).

Both Cr^{III} and Co^{III} form tetranuclear ammine 'hexols' $[M_4(OH)_6(NH_3)_{12}]^{6+}$. There are two isomers of the Cr^{III} complex, one with a tetrahedral M_4 array isomorphous with the Co^{III} analog (**43**), and the other with a planar M_4 array (**44**). There is a variety of $Cr_m(OH)_x(NH_3)_y{}^{n+}$ systems based on the μ-dihydroxodichromium(III) core (**45**–**47**).

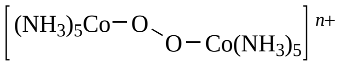
$$\left[(NH_3)_5Co{-}O\diagdown O{-}Co(NH_3)_5\right]^{n+}$$

(**40**)

$n = 4$, brown peroxo bridged
$n = 5$, green superoxo bridged

$$\left[(NH_3)_5Cr-O-Cr(NH_3)_5\right]^{4+}$$

(**41**)

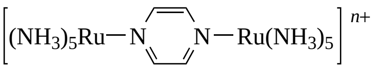

(**42**)
$n = 4, 5, 6$

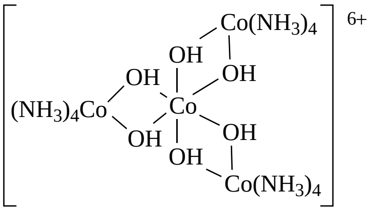

(**43**)

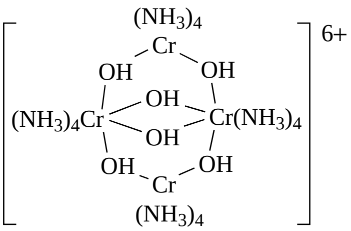

(**44**)

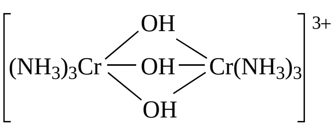

(**45**)

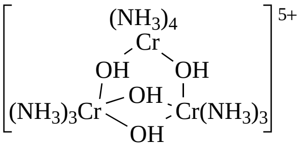

(**46**)

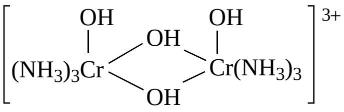

(**47**)

The heavier transition metal elements also form multinuclear ammine complexes, many with mixed oxidation states, for example, $[Ru_3O_2(NH_3)_{14}]^{6+}$ ('ruthenium red') (**48**), $[Ru_2(\mu Cl)_3(NH_3)_6]^{2+}$ (**49**), $[Os_3(\mu N)_2(NH_3)_8(H_2O)_6]^{6+}$ (**50**), $[Ru_2(\mu N)Cl_2(NH_3)_8]^{3+}$ (**51**), and $[Pt_2(NH_3)_8Cl_2]$ $(HSO_4)_4$ (**52**).

$$\left[(NH_3)_5Ru^{III}-O-Ru^{IV}(NH_3)_4-O-Ru^{III}(NH_3)_5\right]^{6+}$$

(**48**)

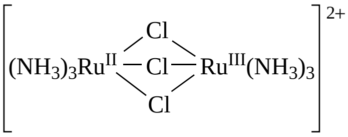

(**49**)

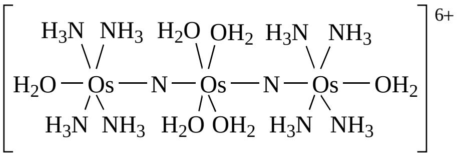

(**50**)

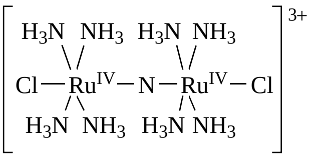

(**51**)

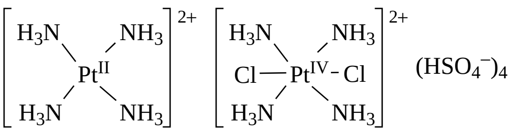

(**52**)

Finally, there are square-planar Pt^{II} antitumor ammine complexes (*see* ***Platinum-based Anticancer Drugs***) with the most well known being *cis*-dichlorodiammineplatinum(II) (*cis*-DDP) *cis*-$PtCl_2(NH_3)_2$. When dissolved in aqueous solution, the chloro ligands can be partially or completely substituted by either H_2O or OH^-, and the pH-dependent kinetics and equilibria have been measured.[55–61]

2.2 Monoamines

Like ammonia, the simple aliphatic monoamines are gases at room temperature, but as the length of the

Table 5 Properties of some simple monodentate amines

Amine	m.p. (°C)	b.p. (°C)	Amine	m.p. (°C)	b.p. (°C)
NH_3[a]	−77.7	-33.35	$MeNH_2$[b]	−93.5	-6.3
$EtNH_2$[c]	−80	16.6	n-NH_2Pr	−83	48
i-$PrNH_2$	−101	33	n-NH_2Bu	−50	78
s-$BuNH_2$[d]	−140	63	t-NH_2Bu	−73	44
$Me\ (CH_2)_4NH_2$	−50	104	$Me\ (CH_2)_5NH_2$	−23	132
$Me(CH_2)_6NH_2$		155	$Me\ (CH_2)_7NH_2$	−5	176
$Me\ (CH_2)_8NH_2$		201	$Me\ (CH_2)_9NH_2$	13	217
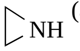 (aziridine)	−74	57	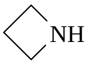 (azetidine)		61
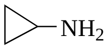		50	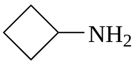		82
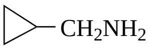		83	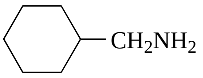		161
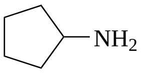		106	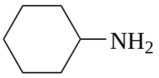		134
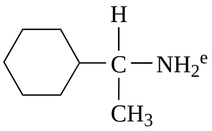		177	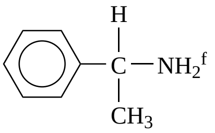		187

[a]Available as the anhydrous liquid or as a 28% aqueous solution ($\rho = 0.880$). [b]Available as the anhydrous liquid, or as a 40% aqueous solution ($\rho = 0.902$). [c]Available as the anhydrous liquid or as a 70% aqueous solution ($\rho = 0.796$). [d](S)–(+): $\alpha_D = +7.8°$. [e](S)–(+): $\alpha_D = +3.8°$. [f](R)–(+): $\alpha_D = +30°$.

hydrocarbon chain increases, the room temperature form is a more or less malodorous, fuming liquid or waxy solid (Table 5). The neat amines strongly absorb CO_2 from the atmosphere and should be kept in well-protected screw-cap bottles.

The replacement of the six NH_3 ligands about the octahedral metal center by six alkylamine groups apparently causes considerable nonbonded interaction, but $[Co(NH_2CH_3)_6]^{3+}$, $[Ru^{II}(NH_2R)_6]^{2+}$, and $[Co(NH_2OH)_6]^{3+}$ are known.[35]

More common are the $[M^{III}X(NH_2R)_5]^{2+}$ systems (M = Co, Cr, Rh),[42] and such complexes have played a significant role in assessing the importance of steric effects on the rates of substitution reactions (*see Steric Effect*). Another extensive series of Co^{III} complexes are those of the *cis*-$[CoX(en)_2(NH_2R)]^{2+}$ type[14] but only those with R = H are known for Cr^{III}. Even in the Co^{III} series, examples of coordinated monoamines with substituents on the α-carbon atom, for example, s-$BuNH_2$ or $PhCH(CH_3)NH_2$, are known, but are rare, and secondary or tertiary amines are even more difficult to coordinate. Aziridine, however, seems to coordinate[62] much more freely than other secondary monoamine ligands and can be synthesized in situ according to equation (12). The larger cyclic *sec*-NH monoamines, for example, (**55**) also coordinate quite well in a series of $[CoCl(en)_2(NH(CH_2)_x)]^{2+}$ complexes.[14]

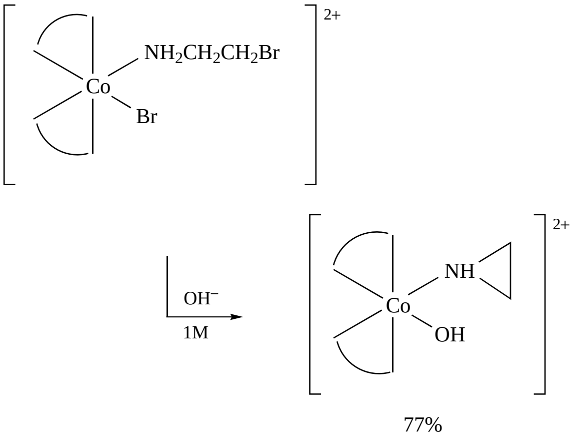

(12)

The above restrictions are not nearly so marked for square-planar Pt(II) or Pd(II) systems, and even the most sterically hindered N-donor ligands have a good chance for coordination.

Once the alkylamine is coordinated, the ‘arms’ can adopt a variety of conformations that appear to be controlled by packing arrangements. Thus, the two modes observed for $[Pt(NH_2Et)_4]^{2+}$ are (**53**) and (**54**).

For aniline (**56**),[63] there are steric differences that can lead to an enhanced reactivity for leaving groups in inert

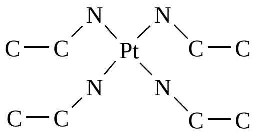

(**53**)

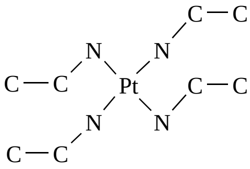

(**54**)

systems (equation 7). For pyridine (**57**), complexes[64] such as *t*-$[RhCl_2(py)_4]^+$ probably represent the maximum number of py ligands that can bind to an inert central metal. Similar stereochemical restrictions probably apply to the four-coordinate Cu^{II} complexes of N-Me-imidazole[65] (see **78**) and 1,2,4-triazoles,[66] but six-coordinate $[M^{II}(LH)_6]^{2+}$ (LH = pyrazole, **77**) are known for all first-row divalent transition metal ions.[67] While the N-bonded chemistry of pyrrole (**58**)[68] is only poorly developed, that of piperidine (**55**) is quite well established.[69]

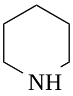

(**55**) Piperidine

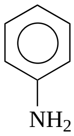

(**56**) Aniline

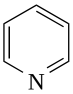

(**57**) Pyridine

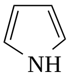

(**58**) Pyrrole

3 LIGANDS CONTAINING TWO N ATOMS

The dinitrogen complex $[Ru^{II}(N_2)(NH_3)_5]^{2+}$ (**60**), described in 1965 by Allen and Senoff, led to much subsequent research related to nitrogen fixation.[70–75] The reduction of coordinated N_2 in simple systems is shown in Figure 1, but the hydrazido(-2) (**9**) system is the only coordinated intermediate characterized in the conversion of N_2 to NH_3. The coordinated dinitrogen (**60**) may also act as a bridging ligand (**59**), (**61**), and (**62**) N_2 forms reasonably stable and well characterized complexes[74,75] with $Ru^{I/II}$, Os^{II}, Mo^0, W^0, Mn^0, $Co^{0/I}$, Ta^0, Ti^0, Ni^0, Zr^0, and Ir^I.

$$\left[(NH_3)_5Ru-N\equiv N-Ru(NH_3)_5\right]^{4+}$$

(**59**)

$$M-N\equiv N\colon$$

(**60**)

$$M-N\equiv N-M$$

(**61**)

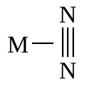

$$M-\overset{N}{\underset{N}{|||}}$$

(**62**)

Complete protonation of dinitrogen results in hydrazine,[76] which can bind through either one (**11**) or both (bridging) N atoms, but high oxidation state metals are readily reduced.[77]

The nomenclature for substituted hydrazines is very confusing (**63**–**67**).[78] Three types of ligands are available with a formal double bond between the two N atoms (1) diazenido (**6**), obtained from diazonium compounds ($ArN_2{}^+$), (2) 1,2-diazines (**7**) (azo compounds, Ar–N=N–Ar), and (3) 1,1-diazines (**8**).

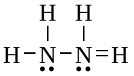

(**63**) Hydrazine

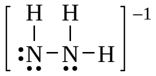

(**64**) Hydrazido(-l)
(diazanido)

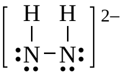

(**65**) Hydrazido(2-)-N,N′)
(diazane-1,2-diido)

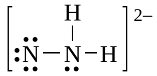

(**66**) Hydrazido(2-)-N,N
(diazane-1,1-diido)

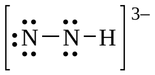

(**67**) Hydrazido(3-)
(diazanetriido)

The diazenido ligand can be regarded as $RN_2{}^+$, $RN_2{}^-$, or RN_2 and when coordinated, there is a considerable range in the observed N=N stretch (2100–1440 cm^{-1}). Obviously, there is a close analogy between NO and RN_2 as ligands.[4,78] Diazines can be formed from diazenido complexes by electrophilic

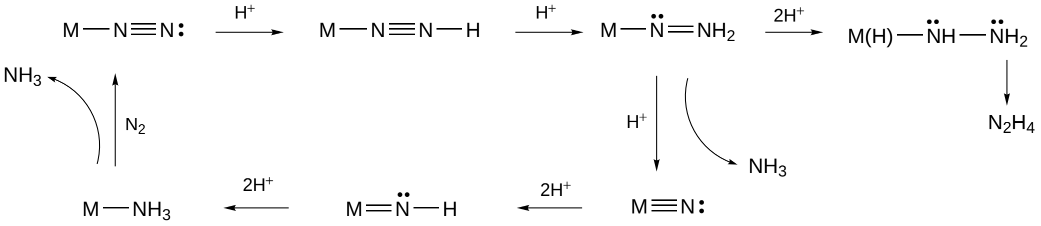

Figure 1 Formation of N_2H_4 and NH_3 from N_2

attacks (especially H^+) (equation 13).

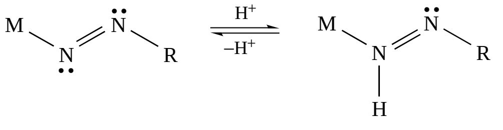

(13)

Diazenido 1,2-Diazene

An important reaction of aryl azo ligands is *Cyclometallation* by activation of the ortho C–H proton and subsequent C–M coordination[79] (equation 14).

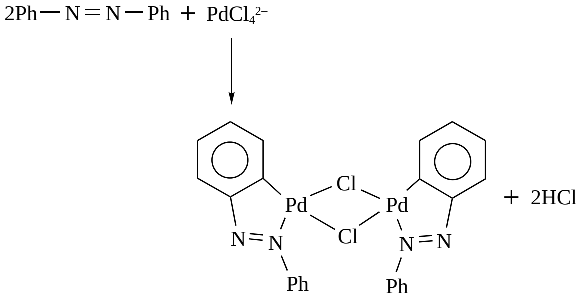

(14)

Finally, diazoalkanes $R_2C{=}N{=}N{:}$(**14**), such as diazomethane, can bind to metals but, more importantly, are a useful route to ***Carbene Complexes*** by the extrusion of N_2 (equation 15).[80]

$$\begin{aligned}&\mathrm{OsCl(NO)(PPh_3)_3 + CH_2N_2}\\ &\longrightarrow \mathrm{H_2C{=}OsCl(NO)(PPh_3)_2 + PPh_3 + N_2}\end{aligned} \qquad (15)$$

3.1 Diamine Ligands

The coordination chemistry of the simplest of these, methanediamine, $NH_2CH_2NH_2$ (a fully hydrogenated form of the aminidinato (**13**) ligand), is very poorly investigated. Of more recent interest are poly(methylene) amines, for example, (**68**) formed by reaction of formaldehyde and amines in the presence of a metal ion.[81] The stability of such ligands in the absence of metal ions has yet to be established.

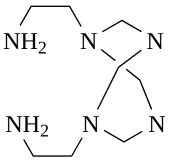

(**68**)

3.1.1 1,2-Diaminoethane and related ligands

The parent ligand has played an important part in the history of coordination chemistry, as the stereochemical arrangement of bidentate bis or tris (en) complexes lead to the concept of optical activity in octahedral coordination. Ethylenediamine is commercially available either as the anhydrous (bp 118°) or monohydrate liquid forms; the vapor can cause asthma on repetitious exposure. It can adopt either the cis (*gauche*) (**69**) or trans (**70**) conformations with an energy difference of about $4\,\mathrm{kJ\,mol^{-1}}$. Consequently, the conformation adopted in the solid state can be temperature and anion dependent.

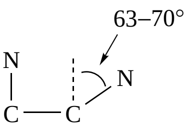

(**69**) cis (*gauche*)

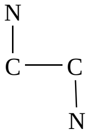

(**70**) trans

The $[\mathrm{enH_2}^{2+}]$ cation in the [(*R,R*)-(+)-tartrate(-2)] salt adopts the trans conformation, while in the [(*R,R*)-(+)-tartrate(-1)]$_2$ salt, the *gauche* form is observed. Similarly, in $[\mathrm{enH_2}^{2+}][\mathrm{Hg_2Cl_6}^{2-}]$ the conformation is trans, while in $[\mathrm{enH_2}^{2+}]_2[\mathrm{HgCl_4}^{2-}][\mathrm{Cl}^-]_2$ the conformation is *gauche* [69.2° in (**69**)].[82]

There are also an increasing number of examples where en (or a longer chain polyamine) is monodentate[83] or bridging[84] (**71**–**72**). Polyamine ligands, in complexes with uncoordinated NH- or NH_2-sites[85] (**71**), have been called hypodentate.[86] Such systems have the potential to produce highly charged inert cations, for example, $[\mathrm{Co(NH_3)_5(trenH_3)}]^{6+}$.

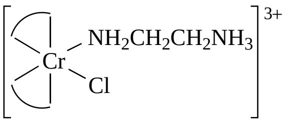

(**71**)

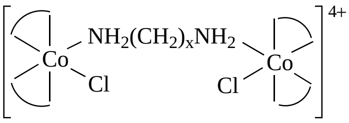

(**72**)

The N–CH_2–CH_2–N group forms a five-membered puckered ring with a twofold axis of symmetry as shown in (**73**) and (**74**). When undistorted, the C–C bond makes a dihedral angle of ±48.8° with respect to the N–M–N plane. The two enantiomeric conformations are labelled δ (**73**) (left-handed helicity) and λ(**74**) (right handed helicity)[87] with an inversion energy barrier of about $20\,\mathrm{kJ\,mol^{-1}}$ that increases with N-alkylation.

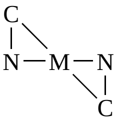

(**73**) δ

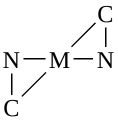

(**74**) λ

Although quite a few chelated mono(ethylenediamine) complexes are known for inert transition metal centers, for example, (**75**–**77**), it is not possible to separate the δ,λ conformational isomers as these exist in equal amounts in the solid state (see also the discussion with respect to structure (**220**)). Introduction of a second chelating ethylenediamine into the coordination sphere gives rise to two geometric isomers, *trans*-(**78**) and *cis*-(**79**), (see also (**36**) and (**37**)). The diamine rings in (**78**) and (**79**) can be either λ,λ; δ,δ or, λ,δ; in (**78**), the λ,λ and δ,δ conformations are enantiomeric and energetically equivalent, and are estimated to be about $4\,\mathrm{kJ\,mol^{-1}}$ more stable than the trans δ,λ form. In the solid state, however, the majority of the square-planar $[M(en)_2]^{2+}$ (M = Ni, Cu) and *trans*-$[CoX_2(en)_2]^+$ complexes adopt the δ,λ conformation.[42] *cis*-Bis(bidentate chelate) complexes like (**79**) lack a plane of symmetry and thus have the potential to be separated into enantiomeric Λ(**80**), Δ(**81**) forms. The separation of $\Delta\Lambda$-*cis*-$[CoBr(en)_2(NH_3)]^{2+}$ into the Δ and Λ forms[88] using the method of racemic modification (Werner, 1911) was perhaps one of the most significant achievements in the development of modern coordination chemistry. Approximately 10% of racemic systems like (**80**), (**81**) form conglomerates[89] on crystallization (spontaneous resolution), and such systems are under active investigation.[90]

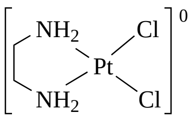

(**75**)

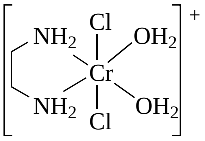

(**76**)

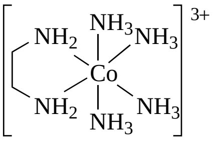

(**77**)

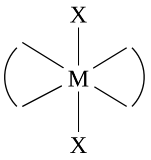

(**78**) trans

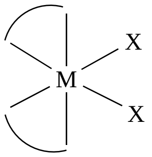

(**79**) cis

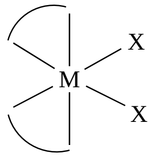

(**80**) Λ-cis

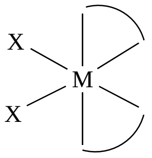

(**81**) Δ-cis

The X ligands in (**80**), (**81**) can be replaced by another chelate ring to give, for example, $[M(en)_3]^{3+}$. Now, four conformers can be constructed for each absolute configuration Λ(**82**), or Δ(**83**) *viz*, $\lambda\lambda\lambda$, $\lambda\lambda\delta$, $\lambda\delta\delta$, and $\delta\delta\delta$ with $\Delta(\lambda\lambda\lambda)$ energetically equivalent to $\Lambda(\delta\delta\delta)$. This classification is useful when separate enantiomers are available, but with the racemate, a chirality invariant nomenclature can be used. Here, the two possible chelate ring conformations are named *lel* or *ob* when the central C–C bond of the diamine ring is (approximately) paral*lel* or *ob*lique with respect to the C_3 symmetry axis of the $[M(en)_3]^{n+}$ complex.[35,87] The four conformers are symbolized as *lel*$_3$, *lel*$_2$*ob*, *lelob*$_2$, and *ob*$_3$, with *lel*$_3$ being equivalent to $\Delta(\lambda\lambda\lambda)$ or $\Lambda(\delta\delta\delta)$. In the solid state, the actual ring conformations adopted in $[M(en)_3]^{n+}$ complexes depend on the anion and are apparently related to the degree of hydrogen bonding.[35,42]

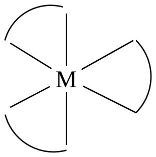

(**82**) Λ-$M(en)_3{}^{n+}$

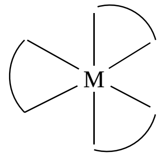

(**83**) Δ-$M(en)_3{}^{n+}$

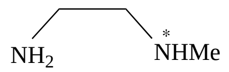

(**84**) (*R* or *S* at * when coordinated)

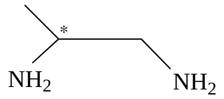

(**85**) (*R* or *S* at *)

Many N and C-substituted ethylenediamine ligands are available.[35,42] A single substituent on the N-atom will give an unsymmetrical prochiral ligand (**84**), and on the C atom the unsymmetrical ligand is racemic (**85**). Symmetrical substitution on both C atoms will give meso (**86**) and racemic ligands (**87**).

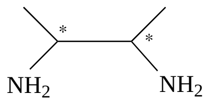

(**86**) *meso* (*R*, *S* at *)

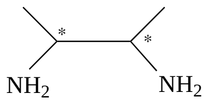

(**87**) racemic (*R*,*R* or *S*,*S* at *)

Resolution of such racemic amine ligands is frequently achieved by crystallization of the (*R*,*R*)-tartrate salt,[25] but the assignment of the absolute configuration to the resolved diamine is much more difficult especially as the sign of rotation at the Na_D lines may be pH dependent. An X-ray study[91] of racemic 1,2-diphenylethylenediamine (*RR*,*SS*-stien) shows the less soluble $(?)_{589}$-$[(?)_{589}$-stien$H_2{}^{2+}][(+)_{589}(RR)$tart$^{2-}]$ salt crystallizing from 96% ethanol to have the (*SS*)-stien absolute configuration. ORD measurements show that this salt gives $(-)_{589}$-(*SS*)-stien.

Considerable isomeric complexity results when ligands with both C and N substituents are used, for example, (**88**), (**89**).[42]

The fully N-alkylated ethylenediamine ligand, for example, 1,1,4,4-Me_4en, is not always carefully distinguished from the

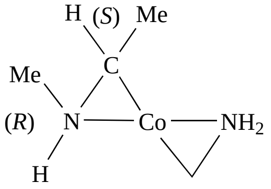

(**88**)

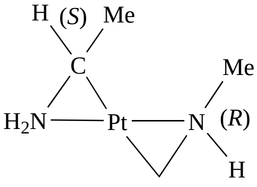

(**89**)

fully C-alkylated isomer 2,2,3,3-Me_4en[35] in the coordination chemistry literature.

If the two amine groups are located in the 1,2- (or 1,3-)[92] positions of a cycloaliphatic ring, there is potential for both geometric and optical isomers. The most widely studied of such ligands is cyclohexane-1,2-diamine (chxn).[35] The commercially available free base is available as a (not always equal) mixture of the cis-(R,S)- and trans-(RR,SS)-isomers, conveniently separated via the Ni^{II} complexes with yellow, diamagnetic [Ni(*cis*-R,S-chxn)$_2$]Cl_2 being insoluble in MeOH. After pH adjustment, and addition of water, the mother liquor deposits crystals of blue, paramagnetic *trans*-[Ni(*trans*-(RR,SS)-chxn)$_2$(H_2O)$_2$]Cl_2. The amines can be recovered (as hydrochloride salts) from the Ni^{II} complexes by decomposition with HCl, and the *trans*-(RR,SS)-chxn can be resolved into the $(-)_{589}$-(R,R) enantiomer with $(+)_{589}$-(R,R)-tartaric acid.[93,94]

3.1.2 *1,3-Diaminopropane and Related α,ω-Aliphatic Diamine Ligands*

Coordination of 1,3-diaminopropane (tn) in the chelating mode results in a six-membered ring, and chair (c), boat (b), or twist (t) conformations. Simple tn complexes prefer chair or twist conformations in the solid state and there are a variety of chair orientations possible in $[M(tn)_3]^{n+}$ systems.[35,42] For labile central atoms (Cu^{2+}, Ni^{2+}, Cd^{2+}), the stability constants for metal–ligand binding are always tn < en due to a more negative enthalpy.[10] Extrapolation of these trends to inert systems might suggest that tn complexes would be less stable than the en analogs. In these cases, however, we are now discussing kinetic stability, and for Cr^{III} at least, the tn complexes are more robust than the en systems.[8,9]

In $[CoCl(N_5)]^{2+}$ systems, the replacement of en by tn almost always results in increased labilization of the coordinated chloro ligand. This effect has been attributed to greater ease of distortion for the tn complex.[14]

Among the more esoteric six-membered ring diamines is α-isospartine (**90**), and a Cu^{II} complex has been characterized.[95]

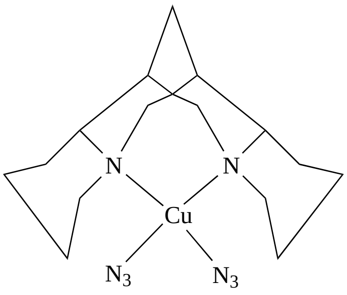

(**90**)

Increasing the ring size even further to α,ω-aliphatic diamines results in an increased propensity for polymerization or hydroxo formation rather than chelation. Seven membered diamine rings are found in $[Cu(bn)_2]^{2+}$ and $[Co(bn)_3]^{3+}$ (bn = 1,4-butanediamine) and with inert metal centers, complexes with several ring sizes, for example, $[Co(en)(tn)(bn)]^{3+}$ can be prepared.[42] We will see later (Section 6) how larger chelate rings can be incorporated into the skeleton of polyamine ligands.

3.1.3 *Heterocyclic Ligands with Two N Atoms.*[96–103]

This section covers the vast field of the coordination chemistry of pyrazole (**91**), imidazole (**92**), pyrazine (**93**), pyrimidine (**94**), pyridazine (**95**), 2,2′-bipyridine (**96**), *o*-phenanthroline (**97**), piperazine (**98**), and dabco (**99**) as ligands.

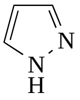

(**91**) Pyrazole

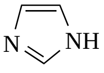

(**92**) Imidazole

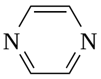

(**93**) Pyrazine

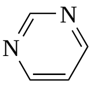

(**94**) Pyrimidine

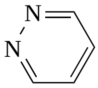

(**95**) Pyridazine

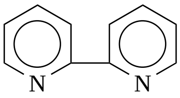

(**96**) 2,2′-bipyridine

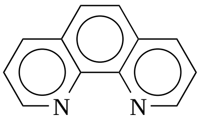

(**97**) 1,10-phenanthroline

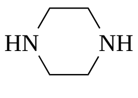

(**98**) Piperazine

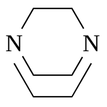

(**99**) Dabco

Many of these can only act as monodentate or bridging ligands (**91**)–(**95**),[100] (**98**), (**99**): in the bridging mode, M···M interactions can be mediated by the bridge. Such interactions are measured by magnetic coupling or electron transfer (*see* ***Electron Transfer in Coordination Compounds***), and the

M$\cdots$M distance can be closely controlled. Note, however, that pyrazole (**91**) and imidazole (**92**) can only bridge after deprotonation (**100**–**102**), and in highly substituted ligands, coordination usually takes place at the least sterically hindered nitrogen atom.

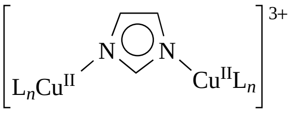

(**100**)

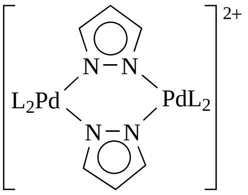

(**101**)

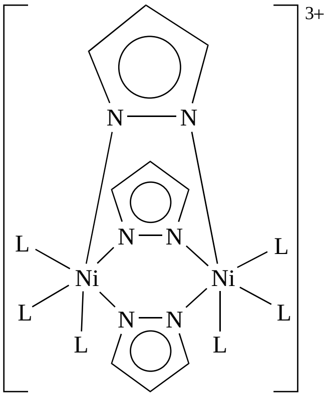

(**102**)

In the six-membered diazine systems, (**93**–**95**), the most widely investigated ligand is pyrazine (**93**)[96,97] in the 'model' pyrazine bridged mixed valence compound (**103**) (*see* ***Mixed Valence Compounds*** and *Creutz–Taube Complex*). The coordination chemistry of the aliphatic analog, piperazine (**98**), is not well developed.

The chelating ligands, 2,2′-bipyridine (bipyridyl) (**96**)[98–100] and *o*-phenanthroline (**97**), have distinctive metal complexes. When compared to say 1,2-diaminoethane, bipy is less basic, more rigid, and larger; when coordinated, the ligand orbitals can participate in an extensive π-overlap with the metal orbitals. Consequently, not only do bipy and related ligands bind to metals that form strong complexes with en, but these ligand systems also form complexes with metal centers such as Fe^{II}/Fe^{III} that have only a poorly developed aliphatic polyamine chemistry.

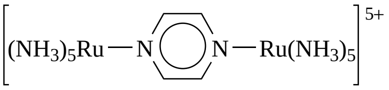

(**103**)

Of significant interest are the Ru(bipy)$_3{}^{n+}$[101] and Cr(bipy)$_3{}^{n+}$[102] complexes. The former, along with derivatives, can be used as sensitizers in photolytic systems such as the photolysis of water, and the Ru^{II}/Ru^{III} couple can be tuned by varying the nature of the bipy ligand. The Cr(bipy)$_3{}^{3+}$ cation is one of the 'standard' substances for probing excited state photochemistry (*see* ***Photochemistry of Transition Metal Complexes***).[102]

Other diimine ligands[103] are shown in (**104**–**106**) with systems containing one pyridine and one other heterocyclic mono-aza ligand, and the C atoms of the py ring can be replaced by one or more N atoms to give, for example, (**107**). Other coupled sets are: pyrazole plus pyrazole (**108**), pyrazole plus imidazole (**109**), and imidazole plus imidazole (**110**) together with coupled pyrazines (**111**), pyrimidines (**112**), (**113**), and pyridazines (**114**).

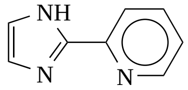

(**104**)

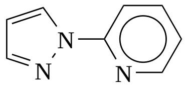

(**105**)

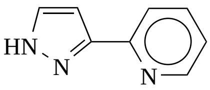

(**106**)

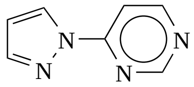

(**107**)

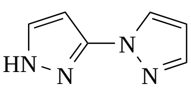

(**108**)

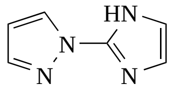

(**109**)

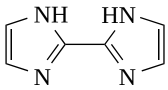

(**110**)

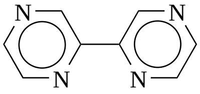

(**111**)

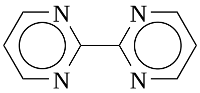

(**112**)

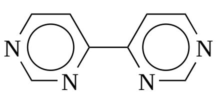

(**113**)

The combinations are limited only by imagination and the coordination chemistry of many of these systems is yet to

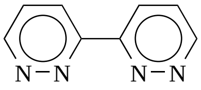
(**114**)

be fully developed.[98] Ligands of this type have potential in homogeneous asymmetric catalysts: (**115**–**117**) illustrate the approach.[104] Structure (**117**) shows that the chelate ring size can be expanded with no marked loss of chelating ability and all the ligands shown in (**104**–**114**) have the potential for this development.

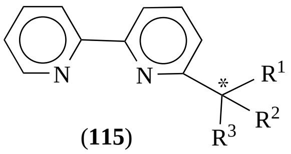
(**115**)

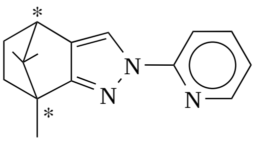
(**116**)

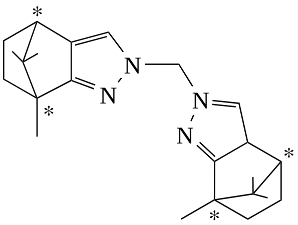
(**117**)

3.1.4 *Miscellaneous Diamine Ligands*

In this section, we include ligands that are heterocyclic based, but with an aliphatic ‘arm’, such as (**118**–**121**). The last two ligands are commercially available and may be useful in enabling a pyridine group to coordinate as part of a chelate system, when the unchelated pyridine ligand fails to bind.

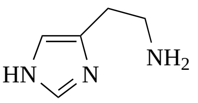
(**118**)

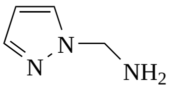
(**119**)

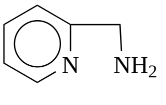
(**120**)

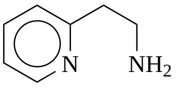
(**121**)

Also included here is 1,2-diaminobenzene (**122**) (*o*-phenylenediamine), kept separate because of its tendency for internal redox reactions (equation 19)[42] and the bidentate pyridine-type ligand (**123**)[96,97] that forms a very small bite angle.

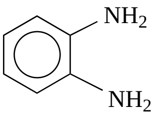
(**122**)

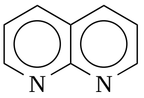
(**123**)

4 CATENATED N ATOMS[2,3,105]

Although the parent triazine (**12**) is very unstable, aryl triazines (**124**) are commercially available, and deprotonation gives anionic ligands that can bind in monodentate (**125**), chelating (**126**), or bridging (**127**) modes. The Ni^{II} complex analogous to (**127**) has an Ni–Ni distance of 2.359 (Å) and the Cu^{II} complex a Cu–Cu distance of 2.441(Å). The Cu^{I} systems, however, form a reversible 2(dimer) (**128**) $\rightleftharpoons$ tetramer (**129**) equilibrium. In the chelating mode (**126**), the triazine ligand forms a four-membered ring with a bite angle of 56–65° (65° in [Co(PhN$_3$Ph)$_3$]).

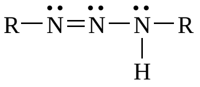
$R{-}\ddot{N}{=}\ddot{N}{-}\underset{H}{\ddot{N}}{-}R$

(**124**) R = Ph

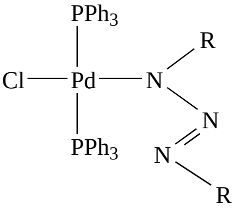
(**125**) R = p-tol

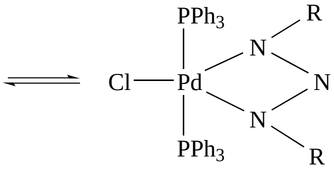
(**126**) R = p-tol

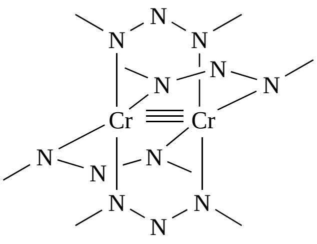
Cr$\equiv$Cr = 1.85 Å
(**127**) $Cr_2(PhN_3Ph)_4$

The central N atom in the triazine system can be replaced by the CH group to give imidines (**13**),[41,105] and complexes with structures similar to (**125**–**127**) are known,

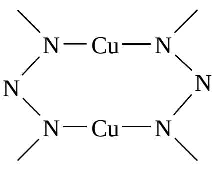

Cu....Cu = 2.451 Å

(**128**) R = Ph

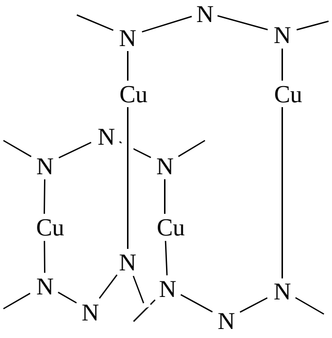

Cu....Cu = 2.66 Å

(**129**) R = Me

for example, [$Mo_2(PhNC(Ph)NPh)_4$]. However, no complexes containing fully saturated triazanes (**130**) or tetraazanes (**131**) appear to have been described. On the other hand, both tetrazines (**132**) and tetrazadienes (**133**) form stable metal complexes,[2,105] despite the fact that the parent tetrazadienes do not exist in the free state.

$$R_2N{-}N(R){-}NR_2$$

(**130**)

$$H_2N{-}NH{-}NH{-}NH_2$$

(**131**)

$$R_2N{-}N{=}N{-}NR_2$$

(**132**) R = Et

$$R{-}N{=}N{-}N{=}N{-}R$$

(**133**)

The N atoms in (**133**) can be replaced by C atoms to give 1,4-diaza-1,3-butadiene systems (**134**)[105] that have a close skeletal relationship to bipyridyl ligands (**96**) (Section 3.1.3).

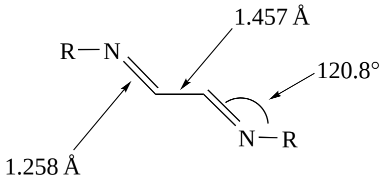

(**134**) R = Cyclohexyl

The bond lengths and bond angles in (**134**) suggest little electron delocalization in the free ligand, and rotation about the C–C bond allows coordination in the planar chelating mode (**135**).

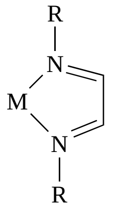

(**135**)

Further catenation of the nitrogen chain leads to pentazadienes (**136**) with bridging structures (**137**) and (**138**) for the Ni^{II} and Cu^{I} complexes, respectively.

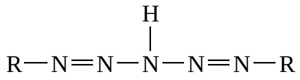

$$R{-}N{=}N{-}\overset{H}{N}{-}N{=}N{-}R$$

(**136**) R = *p*-tol

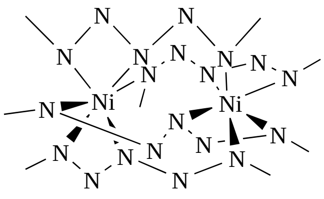

(**137**)
[Ni_2(**136**)$_4$]

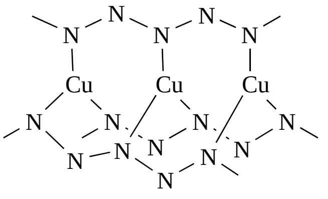

(**138**)
[Cu_3(**136**)$_3$]

4.1 Azides

The azide ion (N_3^-) is a *Pseudohalide*[105,106] because its properties resemble those of the halides. The free ion has a linear N–N–N skeleton with equal N–N distances (1.167 Å), but the anion coordinates terminally (**137A**) with an M–N–N angle of 116–140° and an N–N–N distortion of about 4° from linearity. Other possible modes of coordination are shown in (**137B**)–(**144**). As yet, there are no examples of (**143**).

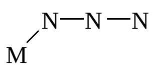

(**137A**)

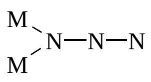

(**137B**)

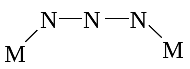

(**139**)

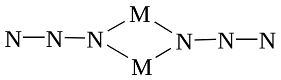

(**140**) μ-(1,1)–

The azido ligand is particularly versatile as a leaving group, as the displacement is acid catalyzed.[107] Coordinated azide ligands also have the potential to react via 1,3-dipolar cycloaddition with organic isonitriles or nitriles to give 1- or

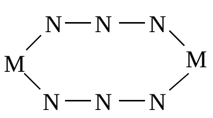
(**141**) μ-(1,3)–

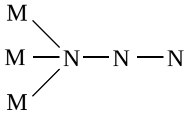
(**142**) μ-(1,1,1)–

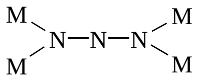
(**143**) μ-(1,1,3,3)–

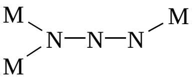
(**144**) μ-(1,1,3)–

5-substituted tetrazolate anions (Section 4.2) respectively (equations 16 and 17). Alternatively, the azide ion can be added to coordinated isonitrile or nitrile ligands to give the same products.[108] The rate of reaction between N_3^- and RCN is considerably enhanced by coordination of the nitrile (Section 7).

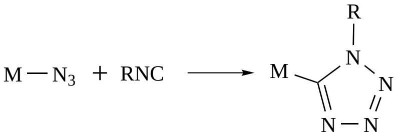
(16)

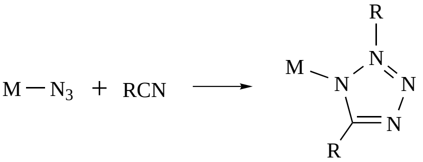
(17)

4.2 Cyclic Catenated N Ligands[3,97]

Three adjacent N-atom carbocyclic systems are found in triazine (**145**) and triazole (**146**) with the coordination chemistry of the former being poorly investigated. There are, however, many derivatives (**147**–**148**) of the weak acid 1,2,3-triazole (pK_a = 9.26) (**146**). Triazoles (**146**) and the conjugate anion generally bind through N(3) for the parent and N(1) for the anion, but all three N atoms can exhibit metal–nitrogen binding (**149**–**154**). The reaction of 8-azaadenine (**148**) and $CuCl_2$ in HCl results in a six-membered ring opening to give (**155**). Extension of the nitrogen chain gives tautomeric tetrazoles (**156**), (**157**) that are quite strong acids (pK_a 4.8) but neutral molecules (**158**) with weaker base strengths can be formed. Monodentate coordination through the N(1), N(2), and N(4) positions has been observed and N(3)–N(4) bridging is the most common. The N(2)-isomer of $[Co(5\text{-CN-tetrazole})(NH_3)_5](ClO_4)_2$ is a commercial explosive.

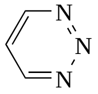
(**145**) Triazine

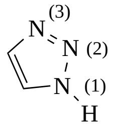
(**146**) Triazole

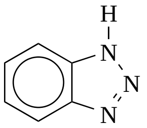
(**147**) Benztriazole

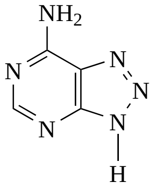
(**148**) 8-Azaadenine

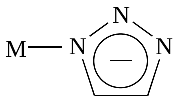
(**149**)

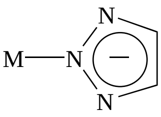
(**150**)

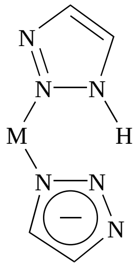
(**151**)

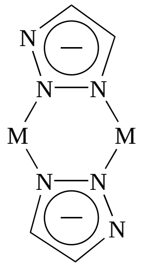
(**152**)

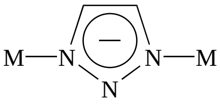
(**153**)

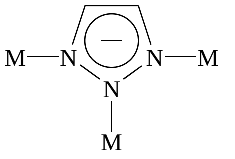
(**154**)

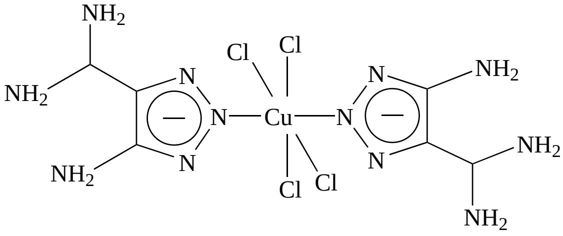
(**155**)

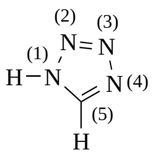

(156)

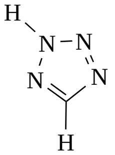

(157)

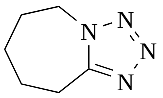

(**158**) 1,5-Pentamethylenetetrazole

5 POLYAMINE LIGANDS

5.1 Triamine Ligands[27,42,96,97]

Structures (**159**–**176**) illustrate representative ligands. Some, such as (**164**–**166**) are restricted to *fac* (**39**) coordination, others (**167**)–(**172**) to *mer* (**38**), and the rest are facultative. For the aliphatic triamine ligands (**159**–**163**), (**168**),[109] there are potentially three geometric isomers in bis(tridentate) octahedral coordination, and when the ligand is unsymmetrical (**160**, **162**, **163**), there is the potential for optical isomers at the coordinated *sec*-NH center (**20**) (**21**). Spermidine (**163**), together with spermine (**182**), are important biologically occurring polyamines[110,111] with the potential to form large ring coordination compounds,[42] but the longer side-arm may not always be chelated.[112]

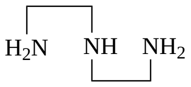

(**159**)

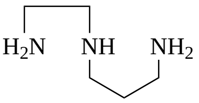

(**160**)

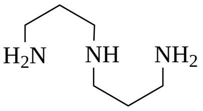

(**161**)

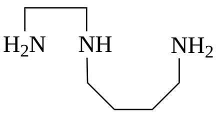

(**162**)

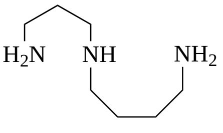

(**163**)

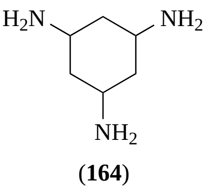

(**164**)

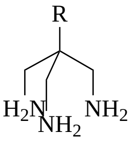

(**165**) tame

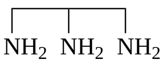

(**166**)

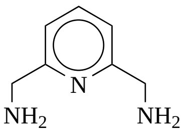

(**167**)

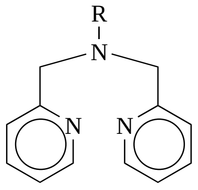

(**168**)

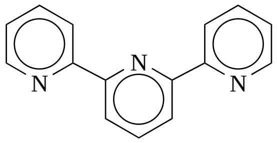

(**169**)

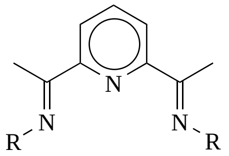

(**170**)

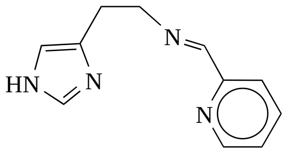

(**171**)

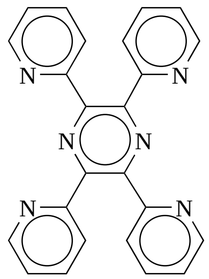

(**172**)

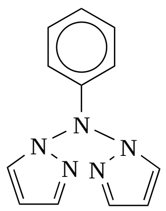

(**173**)

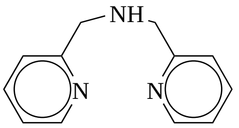

(**174**)

In ligands like (**169**) and (**174**), the pyridine 'arms' can be replaced with N-linked pyrazole (**91**)[113,114] (see **173**, **176**), C-linked imidazole (**29**)[115–117] (see **177**), N-linked 1,2,4-triazole,[118] or C-linked pyrimidine (**94**).[119] Similar 'arm' replacement in (**165**) has been achieved with pyrazole to give (**176**).[120,121] For some formal hexaamines, like (**172**) and (**175**), the rigidity of the ligand restricts the coordination to triamines.[122] A triamine can also be formed by adding an imidazole 'arm' to an N atom in 1,5-diazacyclooctane (**177**).[123]

5.2 Tetraamine Ligands[42,96,97]

Of the potential *Quadridentate Ligands* shown in (**178**–**192**), spermine (**182**) is a naturally occurring polyamine

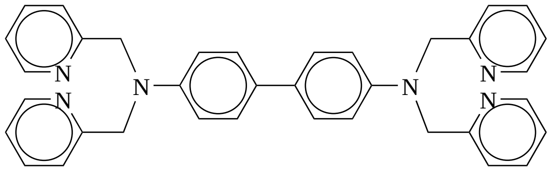

(**175**)

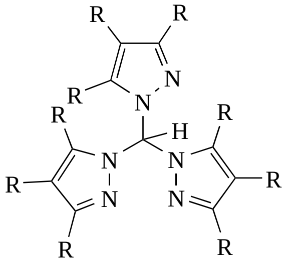

(**176**)

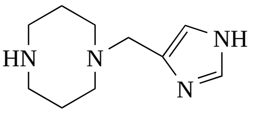

(**177**)

and others like (**178**), (**179**), and (**183**) are commercially available or relatively easily prepared.[42] The unsymmetrical ligands (**181**) and (**182**) are less common. A useful (but nonspecific) polyamine synthesis has been devised where polyalcohol(polybenzenesulfonates) are reacted with neat diamines[124] or $NH_3(l)$[125] at boiling temperature (Figure 2). After distillation of the excess diamine, the crude polyamine product mixture is complexed with Co^{III} or Cu^{II}, and the complexes are separated using cation-exchange resins. The hydrochloride salts of the free ligands can be obtained from the column fractions by treating the Cu^{II} complexes with HCl, or the Co^{III} and Cu^{II} complexes can be characterized directly.[126]

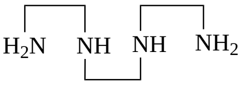

(**178**)

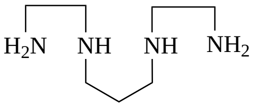

(**179**)

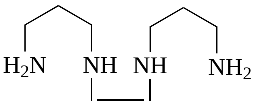

(**180**)

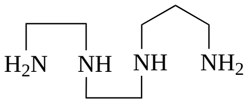

(**181**)

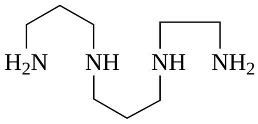

(**182**)

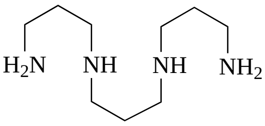

(**183**)

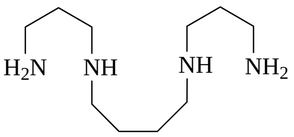

(**184**)

The amine (**186**) in $[CoCl(en)(LH)]^{3+}$ binds as a monoprotonated fac triamine, (**187**) in *trans*-$[CoCl_2(LH_2)]^{3+}$ as a square-planar diprotonated tetraamine, (**188**) in $[(CuCl)_2L]^{2+}$ as a dinuclear tetraamine, and (**189**) in *trans*-$[CoCl_2(L)]ClO_4$ as a square-planar tetraamine that crystallizes as a conglomerate (see Section 3.1.1).

The planar quaterpyridine ligand (**190**)[127,128] can coordinate in a somewhat strained square-planar arrangement with Cu^{II}, Co^{III}, Co^{II}, Ni^{II}, Cr^{III}, and Pd^{II} but with potentially tetrahedral metal centers such as Cu^{I} or Ag^{I}, a subtle interplay of steric factors (metal and ligand) allows the formation of dinuclear dibridged helical structures (see Section 8).[26]

The quadridentate ligand, trien (**178**), played an important role in demonstrating the stereochemical significance of the s-NH proton in octahedral complexes with inert metal centers (Figure 3).

For example, the complete isomeric set of $[Co(trien)(NH_3)_2]^{3+}$ has been isolated, and only the meso–trans isomers (**197–198**) with two different axial ligands, remain to be distinguished. There is also an extensive chemistry of N and C-alkylated derivatives of (**178–180**)[42] as *cis*-$[Co(OH)(trien)(OH_2)]^{2+}$ assists the hydrolysis of amino acid esters, amino acid amides, and peptides to form *cis*-β_1 (**194**) and *cis*-β_2-$[Co(ON)(trien)]^{2+}$ (**195**)(ON = amino acid) complexes. Chiral alkylated trien ligands have the potential for chiral stereospecificity in such reactions.

The quadridentate *Tripodal Ligand*, tren (**191**), is often found as an impurity in commercial samples of trien (**178**) and this has sometimes led to isomeric misinterpretation. Techniques for the separation of these isomers are available when mixtures are suspected.[42] The coordination chemistry of tren and its 'longer arm' analogs has been reviewed.[129]

The crystal structures of $[Cu(\mathbf{183})](ClO_4)_2$ and $[Cu(\mathbf{184})](ClO_4)_2$ show that all N atoms are coordinated and the central ring lies above the plane of the two-chair six-membered rings.[42]

Of the tetraamine ligands (**199–206**), some like (**199**), (**200**), (**202**),[130] and (**205**)[131] require two metal centers to accommodate all the N-donor atoms.

5.3 Pentaamine Ligands

Some pentaamine ligands are shown in (**17**), (**19**), and (**207–215**). Commercially available technical 'tetraethylenepentamine' is a mixture of linear tetren (**207**) and branched chain trenen (**208**), so five-coordinate $[Cu(trenen)]^{2+}$ and octahedral $[CoCl(tetren)]^{2+}$ can be obtained in reasonable yields from the same polyamine mixture.[132] Alternatively, these ligands can be synthesized in situ from Co^{III} complexes of tren (**191**) or trien (**178**), and coordinated amino-acetaldehyde.[42,133]

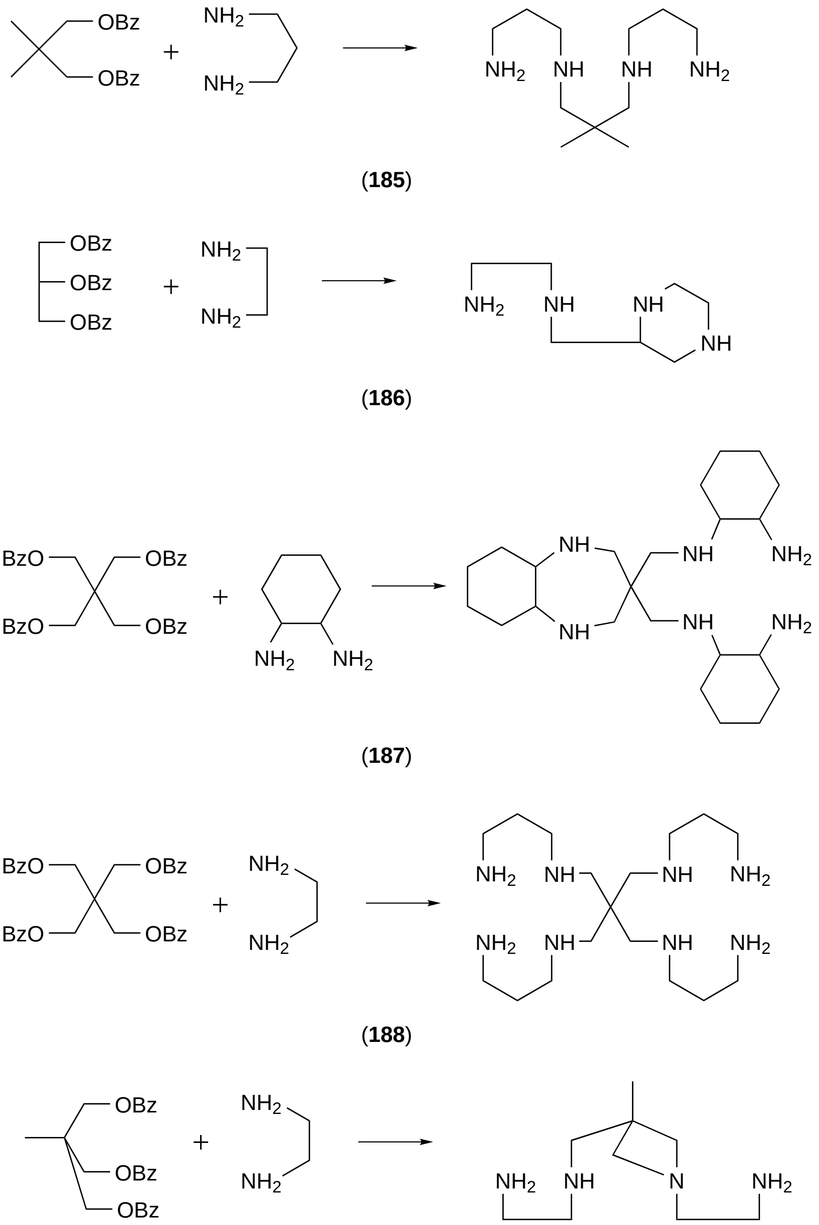
OBz
OBz
NH2
NH2
NH2
NH
NH
NH2
OBz
OBz
OBz
NH2
NH2
NH2
NH
NH
NH
BzO
OBz
BzO
OBz
NH2
NH2
NH
NH
NH
NH2
NH
NH2
BzO
OBz
BzO
OBz
NH2
NH2
NH2
NH
NH
NH2
NH2
NH
NH
NH2
OBz
OBz
OBz
NH2
NH2
NH2
NH
N
NH2

(**185**)

(**186**)

(**187**)

(**188**)

(**189**)

Figure 2 Polyamine synthesis

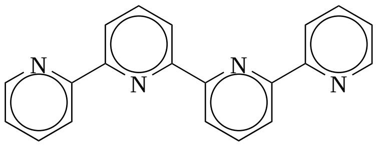

(**190**)

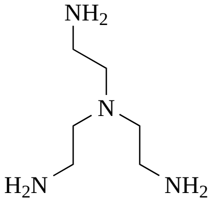
NH2
N
H2N
NH2

(**191**)

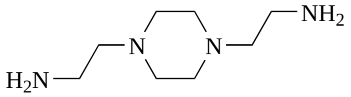

(**192**)

There are seven distinct topological arrangements for tetren (**207**) coordinated to an octahedral metal center, with one unidentate ligand (Figure 4). One of the more interesting tetren complexes is that formed by Fe^{III} *viz*, $[Fe_2(tetren)_2O]^{4+}$ with the well known Fe–O–Fe core. The oligopyridine (**210**)

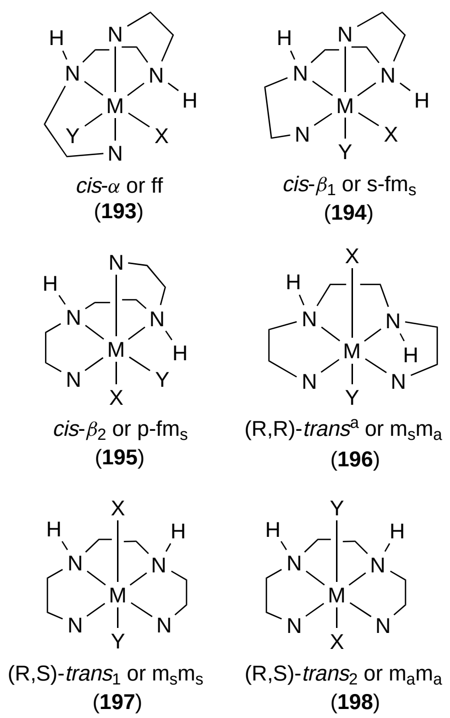

cis-α or ff
(**193**)

cis-β_1 or s-fm$_\mathrm{s}$
(**194**)

cis-β_2 or p-fm$_\mathrm{s}$
(**195**)

(R,R)-*trans*[a] or m$_\mathrm{s}$m$_\mathrm{a}$
(**196**)

(R,S)-*trans*$_1$ or m$_\mathrm{s}$m$_\mathrm{s}$
(**197**)

(R,S)-*trans*$_2$ or m$_\mathrm{a}$m$_\mathrm{a}$
(**198**)

Figure 3 Topological forms possible for ligands (**178**–**184**) in an octahedral complex, $[\mathrm{M^{III}XY(N_4)}]^{n+}$ [a] The R, R-nomenclature is valid for (**178**) and (**180**) but should be assigned for each individual polyamine. The alternative (chirality independent) nomenclature[**21**] is based on X having a higher priority than Y

cannot bend to form octahedral arrangements as shown in Figure 4, but can adopt planar five-coordinate complexes such as [Ag(**210**)] $\mathrm{PF_6}$, coordinate in a square plane with one 'arm' free, or bridge between two metal centers.[**128**] Ligands such as (**214**)[**134**] and (**215**)[**135**] have one and zero NH protons respectively and the base hydrolysis rates of the $[\mathrm{CoClN_5}]^{2+}$ complexes would be of interest. In this regard, $[\mathrm{CoCl}(\mathbf{212})]^{2+}$ has one of the slowest base hydrolysis rates on record.[**136**]

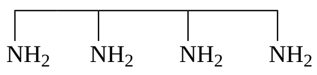

(**199**)

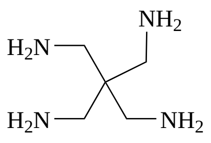

(**200**)

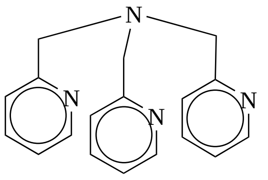

(**201**) tpa

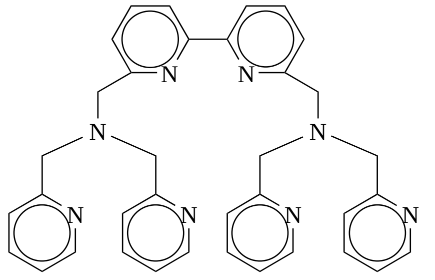

(**202**) bistpa

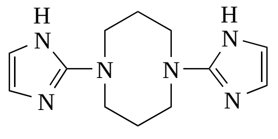

(**203**)

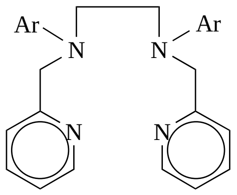

(**204**)

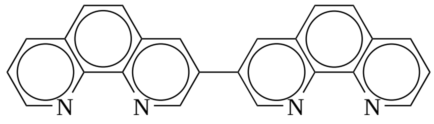

(**205**) Bis(1,10-phenanthroline)

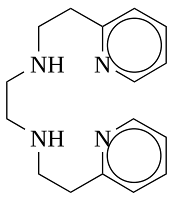

(**206**)

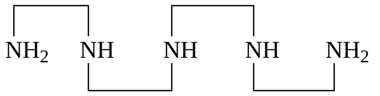

(**207**)

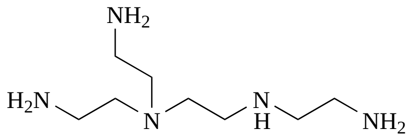

(**208**)

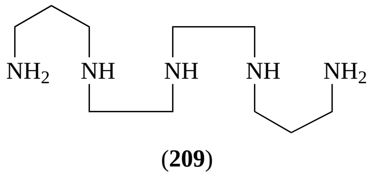

(**209**)

5.4 Hexaamine Ligands (223)–(233)

All eight isomers of $[\mathrm{Co}(\mathbf{223})]^{3+}$ have been separated using chromatographic techniques and the structure of $[\mathrm{Co}(\mathbf{225})]^{3+}$ shows the six N atoms bound in an arrangement similar to that of coordinated EDTA. The structure of

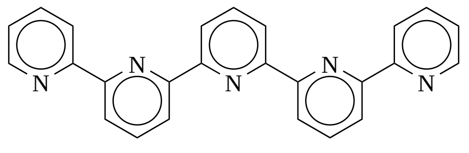

(**210**)

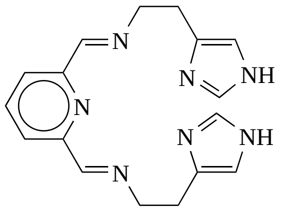

(**211**)

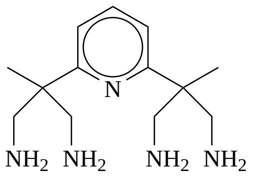

(**212**)

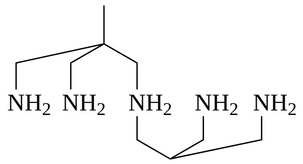

(**213**)

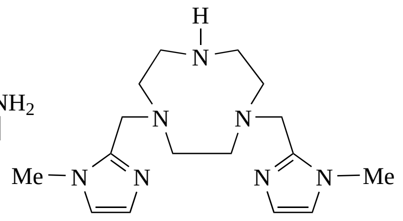

(**214**)

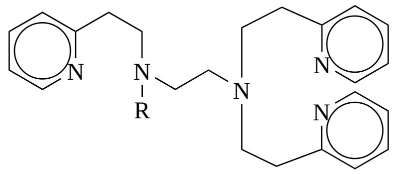

(**215**)

the isolated [Co(bpytrien)]$^{3+}$ isomer(**233**) has the ffm$_a$f configuration.[137,138] Structures (**225**) and (**226**) are also available with different C-atom chain lengths.[42] The violet Ni^{II} complex of (**226**) also has all six N atoms bound but there are two crystallographically distinct cations in the unit cell, differing in conformation of the central N(CH$_2$)$_2$N chelate ring.[139] The sexipyridine ligand (**228**) binds to Mn^{II}, Fe^{II}, Co^{II}, Ni^{II}, Cu^{II}, Zn^{II}, Cd^{II}, and Hg^{II} to form six-coordinate [M$_2$(**228**)$_2$]$^{2+}$ in a symmetrical double helical arrangement[128] (see Section 8) and Zn^{II}, Cd^{II}, and Hg^{II} complexes are known for (**232**).[140]

Ligands (**227**) and (**229**–**231**) are major products from the synthetic strategy shown in Figure 2.[124]

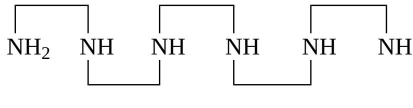

(**223**)

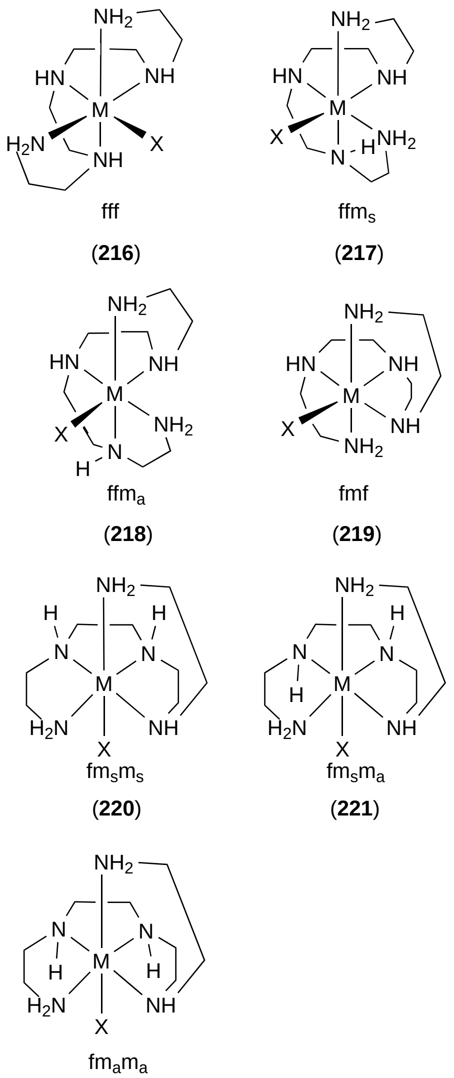

fff (**216**)

ffm$_s$ (**217**)

ffm$_a$ (**218**)

fmf (**219**)

fm$_s$m$_s$ (**220**)

fm$_s$m$_a$ (**221**)

fm$_a$m$_a$ (**222**)

Figure 4 Possible topological arrangements for a linear facultative N$_5$ polyamine in an octahedral complex[14,21]

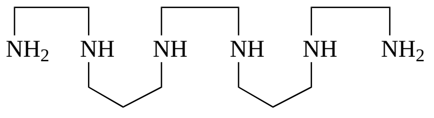

(**224**)

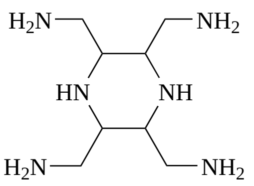

(**225**)

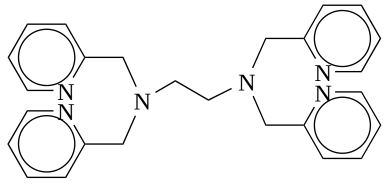

(**226**)

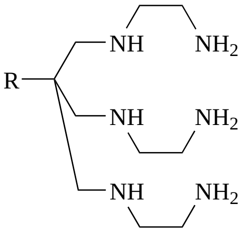

(**227**)

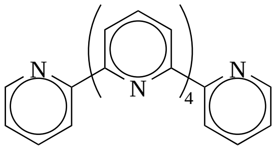

(**228**)

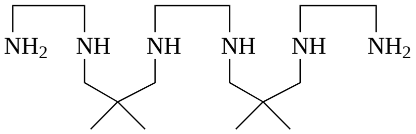

(**229**)

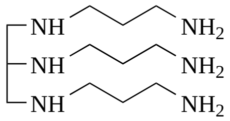

(**230**)

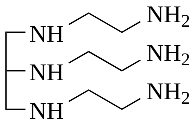

(**231**)

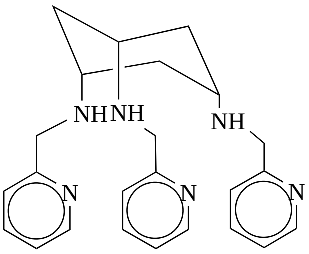

(**232**) Tachpyr

6 MISCELLANEOUS NITROGEN DONOR LIGANDS[141]

This section deals with nonmacrocyclic ligands containing only C, H, and N atoms.

A well-developed coordination chemistry of the chelating biguanide (**234**) (big) ligand has been reviewed,[41,142,143] but the prevalence of hydrates and the acid-base properties of the coordinated ligand has caused confusion in the structural assignment. The two series of salts $[M(big)_3]\cdot xH_2O$ and $[M(bigH)_3]X_3$ ($X = Cl^-$, Br^-, $1/2SO_4{}^{2-}$ etc.) are best represented as (**235**) and (**236**).

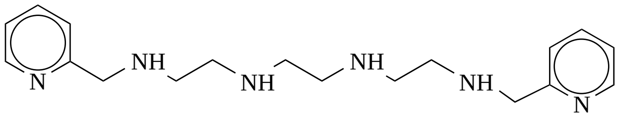

(**233**) Bpytrien

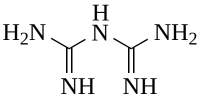

(**234**)

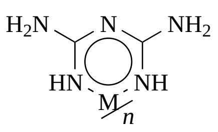

(**235**) $[M(big)_n]$

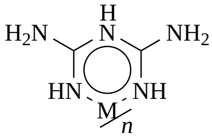

(**236**) $[M(bigH)_n]X_n$

Quadridentate ligands such as (**237**) are prepared by what must be one of the first (1944) uses of metal ion template ligand synthesis (Figure 5).[143]

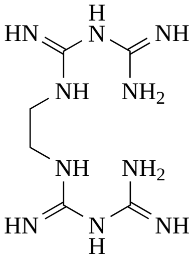

(**237**)

In the biologically relevant, usually monodentate, adenine[144] (**238**) and related ligands (**239**–**241**), it is often difficult in deciding if binding takes place at the N-1 or N-7 sites, and it is possible[144] that the binding position for adenine may be metal ion specific: Ni^{II}, Cu^{II}, Co^{II}, Cd^{II} at N-7; Zn^{II} at both; Hg^{I} and Mn^{II} at N-1 (*see* ***Nucleic Acid–Metal Ion Interactions***).

The incorporation of many-membered chelate rings into the metal ion coordination sphere is possible with ligands that

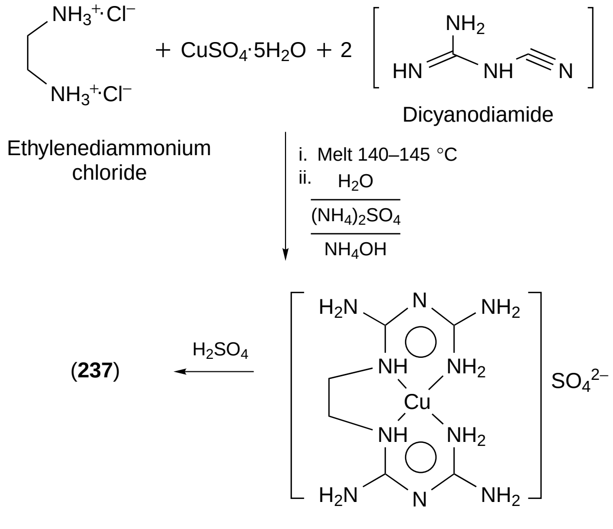
NH3+·Cl−
NH3+·Cl−
+ CuSO4·5H2O + 2
NH2
HN
NH
N
Dicyanodiamide
Ethylenediammonium chloride
i. Melt 140–145 °C
ii. H2O
(NH4)2SO4
NH4OH
(237)
H2SO4
H2N
N
NH2
NH
NH2
Cu
NH
NH2
H2N
N
NH2
SO4 2−

Figure 5 Synthesis of $[Cu\{en(big)_2\}]SO_4$

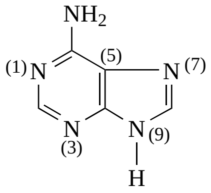
NH2
(1) N
(5)
N (7)
N
(3)
N (9)
H

(**238**) Adenine

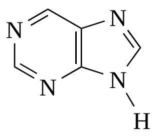

(**239**) Purine

have chelating groups at either end of the long hydrocarbon chain (**242**–**243**). While most work has been done with salicylaldehyde-diimine[145] type systems (**242**), there are also polyamines (**243**) with similar potential.

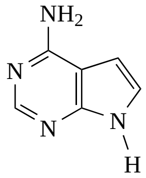

(**240**)

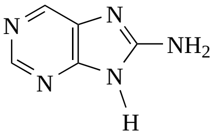

(**241**)

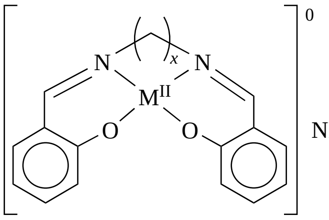

(**242**)

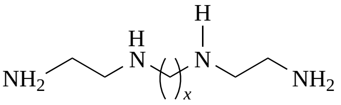
H
H
N
N
NH2
x
NH2

(**243**)

Complexes of aminopolymers[146] such as polyvinylpyridine[14] (PVP) or poly(ethyleneimine) (PEI) are known, for example, *cis*-$[CoCl(en)_2PVP]Cl_2$ has been prepared with up to 108 repeat units and up to 50 Co^{III} atoms, and Ni^{II} complexes of PEI are readily formed in solution.

7 REACTIONS OF COORDINATED NITROGEN LIGANDS

A variety of reactions can take place with coordinated nitrogen ligands. In many instances, the products are controlled by the template effect (*see Templating*). In other cases, coordination can induce a dramatic increase in the reaction rate.

7.1 Coordinated NH_2

7.1.1 *Dehydrogenation*

Oxidation of coordinated diamines (especially for Ru or Fe)

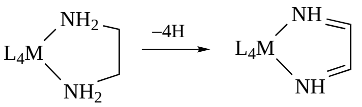
NH2
L4M
NH2
–4H
NH
L4M
NH

(18)

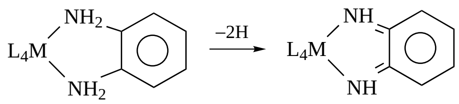
NH2
L4M
NH2
–2H
NH
L4M
NH

(19)

$$L_5M\text{–}NH_2CH_2Me \xrightarrow{-4H} L_5M\text{–}N{\equiv}C\text{–}Me \qquad (20)$$

can yield imines or nitriles (equations 18–20) if the M–N bond is sufficiently inert.

7.1.2 *Condensation*[13,147,148]

More commonly, the coordinated – NH_2 group can undergo condensation reactions with carbonyl compounds to form imines (Figure 6) in both labile and inert metals. Dicarbonyl systems can bridge between two independent NH_2 groups to form linear or macrocyclic ligands (equation 21) (*see* ***Macrocyclic Ligands***). The resulting imines can then be

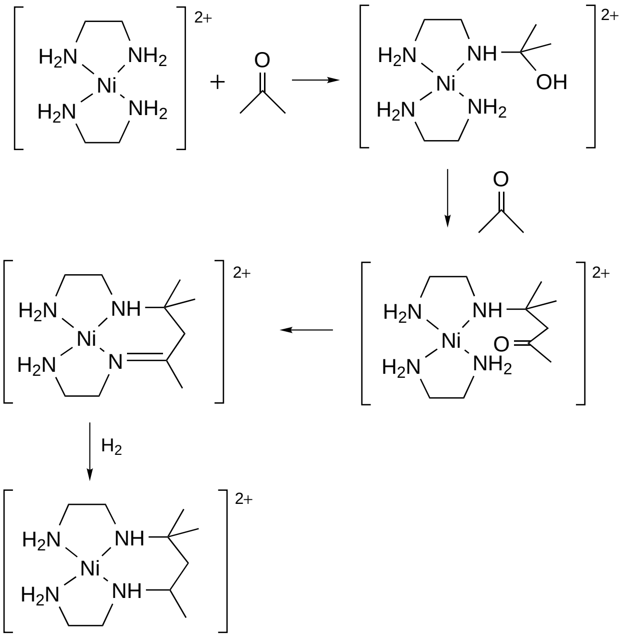
2+
H2N
NH2
Ni
H2N
NH2
+
O
2+
H2N
NH
Ni
OH
H2N
NH2
O
2+
H2N
NH
Ni
H2N
N
2+
H2N
NH
Ni
O
H2N
NH2
H2
2+
H2N
NH
Ni
H2N
NH

Figure 6 Carbonyl condensation

hydrogenated to give saturated amines.

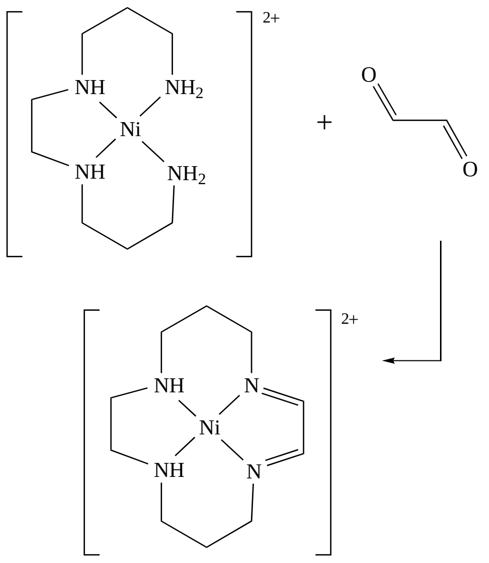

(21)

Oxidative deamination followed by carbonyl condensation is thought to be the pathway by which *mer*-tridentate imine systems are isolated from diamine precursors (Figure 7) using Co as the metal center.[149]

7.1.3 Deprotonation

A number of reactions of inert metal complexes are nicely explained by a preliminary deprotonation of the NH_2 ligand. These include base hydrolysis (equation 7), NH $\rightleftharpoons$ ND exchange,[22] s-NH racemization, and some N−C bond formation reactions (equation 12). In every case, the rate of the reaction is proportional to the OH^- concentration and, as mentioned earlier (see Section 1), in favorable cases the deprotonated species can be isolated and characterized.[23,24]

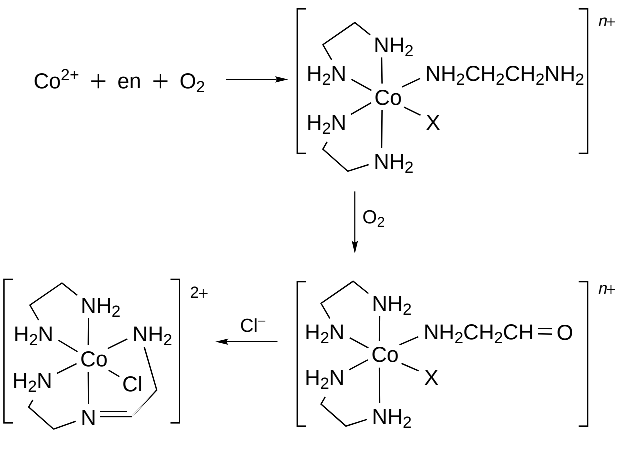

Figure 7 Imine formation

7.2 Other Reactions

Equations (16) and (17) show how coordinated azides can be expanded to give coordinated tetrazoles, and coordinated nitriles can be hydrolyzed to give amides (equation 22).[150,151]

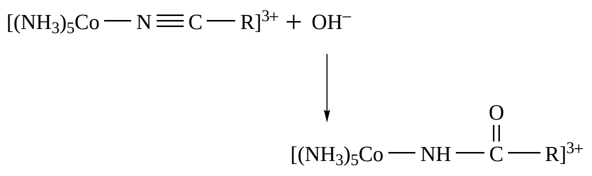

$$[(NH_3)_5Co-N\equiv C-R]^{3+} + OH^- \longrightarrow [(NH_3)_5Co-NH-\overset{\overset{\displaystyle O}{\|}}{C}-R]^{3+} \tag{22}$$

Finally, reactions of coordinated ligands can produce amines. These include oxidation of coordinated thiocyanate (equation 23) and hydrolysis of coordinated cyanate (equation 24).[152]

$$trans\text{-}[Co(NCS)Cl(en)_2]^{2+} \xrightarrow{[O]} trans\text{-}[CoCl(NH_3)(en)_2]^{2+} \tag{23}$$

$$[Cr(NCO)(NH_3)_5]^{2+} \xrightarrow{H+} [Cr(NH_3)_6]^{3+} \tag{24}$$

$$Cr(NO_3)_6 \cdot 9H_2O + \text{urea} \xrightarrow[130\,^\circ C]{\text{melt}} [Cr(NCO)(NH_3)_5]^{2+} \tag{25}$$

8 SUPRAMOLECULAR ASSEMBLIES[153–156]

While much of the earlier work in polyamine chemistry focused on chelate formation, there is now a growing interest in the use of more rigid amine ligands to produce geometric clusters[153–157] (*see* ***Self-assembled Inorganic Architectures***). Such arrangements include triangles,[158] squares,[159] cubes, tetrahedra, boxes, ladders, and helicates.[160,161] The strategy is based, not only on the ligand design, but also on the stereochemistry of the coordinated metal ion.[157] For example, using the ligand (**244**), an M_2L_2 cyclic dimer is formed with Ag^I (linear N_2 geometry) and an M_4L_4 cage with Pd^{II} (square-planar N_4 geometry). With Zn^{II} (tetrahedral) and Co^{II} (octahedral), one-dimensional zigzag chains and infinite one-dimensional polymacrocyclic networks are formed respectively.[162]

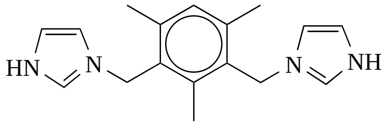

(**244**)

To construct a tetrahedral M_4L_6 cluster, four octahedral metal centers with threefold symmetry and six rigid bis-bidentate ligands of twofold symmetry are needed. (An M_2L_3

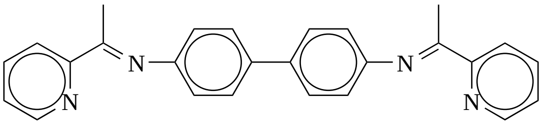

(**245**)

triple helix is an alternative outcome.[159]) The tetrahedral M_4L_6 arrangement has been achieved with (**245**) and Zn^{II}.[163]

9 CONCLUSION

In such an enormous variety of N-donor ligands, we can only cover most of the core systems, but the nature of the ligand can be changed in an almost limitless fashion by the addition of substituents, for example, 6-Me-purine (**239**) or 2-Me-pyrazine(**93**). Such substituents can change the donor properties of the ligand via both electronic and steric factors, and the chemistry of the metal complex may or may not follow that of the unsubstituted parent. Since we are not yet in a position to predict the magnitude of these changes, we are provided with a fascinating field of chemical discovery.

10 RELATED ARTICLES

Cobalt: Inorganic & Coordination Chemistry; Coordination Chemistry: History; Macrocyclic Ligands; Mixed Valence Compounds; Nitrogen: Inorganic Chemistry.

11 FURTHER READING

E. C. Constable, *Adv. Inorg. Chem.*, 1989, **34**, 1.

S. Trofimenko, *Prog. Inorg. Chem.*, 1986, **34**, 116.

12 REFERENCES

1. G. J. Leigh, ‘Nomenclature of Inorganic Chemistry’, Blackwell Scientific (IUPAC), Oxford, 1990, Tables I-10.5, X, p. 160.
2. D. S. Moore and S. D. Robinson, *Adv. Inorg. Chem. Radiochem.*, 1986, **30**, 1.
3. D. S. Moore and S. D. Robinson, *Adv. Inorg. Chem.*, 1988, **32**, 171.
4. F. A. Cotton and G. Wilkinson, ‘Advanced Inorganic Chemistry’, 5th edn., Wiley, New York, 1988.
5. G. Wilkinson ed., ‘Comprehensive Coordination Chemistry’, Pergamon Press, Oxford, 1987, Vol. 2, p. 715.
6. J. L. Burmeister, in ‘The Chemistry and Biochemistry of Thiocyanic Acid’, ed. A. A. Newman, Academic Press, New York, 1975.
7. L. D. Pettit and K. J. Powell, ‘SC-Database: Stability Constant Database: IUPAC’, Academic Software, 2001.
8. C. S. Garner and D. A. House, *Transition Met. Chem. (N. Y.)*, 1970, **6**, 59.
9. J. C. Chang, *J. Indian Chem. Soc.*, 1977, **54**, 88.
10. R. D. Hancock and A. E. Martell, *Comments Inorg. Chem.*, 1988, **6**, 237.
11. R. D. Hancock, *J. Chem. Educ.*, 1992, **68**, 615.
12. R. G. Pearson, *J. Chem. Educ.*, 1968, **45**, 581.
13. M. Micheloni, *Comments Inorg. Chem.*, 1988, **8**, 79.
14. D. A. House, *Coord. Chem. Rev.*, 1977, **23**, 223.
15. E. Ahmed, C. Chatterjee, C. J. Cooksey, M. L. Tobe, G. Williams, and M. Humanes, *J. Chem. Soc., Dalton Trans.*, 1989, 645.
16. J. Dickie, BSc. Hons. Project, School of Chemistry, Australian Defence Force Academy, Canberra, 1995.
17. D. A. House, *Comments Inorg Chem.*, 1977, **19**, 327.
18. G. R. Brubaker, D. P. Schaefer, J. H. Worrell, and J. I. Legg, *Coord. Chem. Rev.*, 1971, **7**, 161.
19. L. Spialter and J. A. Pappalardo, ‘The Acyclic Aliphatic Tertiary Amines’, Macmillan, New York, 1965.
20. D. A. House, *Inorg. Chim. Acta*, 1986, **121**, 167.
21. R. M. Hartshorn and D. A. House, *J. Chem. Soc., Dalton Trans.*, 1998, 2577.
22. D. A. House, *Coord. Chem. Rev.*, 1992, **114**, 249.
23. J. E. Sarneski, A. T. McPhail, K. D. Onan, L. E. Erikson, and C. N. Reilley, *J. Am. Chem. Soc.*, 1977, **99**, 7376.
24. R. J. Geue, T. W. Hambley, J. Mac. B. Harrowfield, A. M. Sargeson, and M. R. Snow, *J. Am. Chem. Soc.*, 1984, **106**, 5478.
25. P. Newman, ‘Optical Resolution Procedures for Chiral Compounds’, Optical Resolution Information Center, Manhattan College, Riverdale, NY, 1978, Vol. 1.
26. C. Piguet, G. Bernardinelli, B. Bocquet, A. Quattropani, and A. F. Williams, *J. Am. Chem. Soc.*, 1992, **114**, 7440.
27. K. Bernauer and F. Gretillat, *Helv. Chim. Acta*, 1989, **72**, 477.
28. D. Ginsberg, ‘Concerning Amines’, Pergamon Press, Oxford, 1967.
29. C. Caldarera, V. Zappia, and U. Bachrach eds, ‘Advances in Polyamine Research’, Raven Press, New York, 1978–1983.
30. P. R. Mitchell, *Method. Chim.*, 1976, **8**, 307.
31. S. Utsuno, Y. Sakai, Y. Yoshikawa, and H. Yamatera, *J. Am. Chem. Soc.*, 1980, **102**, 6903.
32. H. Nakazawa and H. Yoneda, *J. Chromatog.*, 1978, **160**, 89.

33. G. H. Searle, S. F. Lincoln, S. G. Teague, and D. G. Rowe, *Aust. J. Chem.*, 1979, **32**, 519.
34. G. H. Searle, *Aust. J. Chem.*, 1980, **33**, 2159.
35. P. Hendry and A. Ludi, *Adv. Inorg. Chem.*, 1990, **35**, 117.
36. P. V. Bernhardt and P. Comba, *Inorg. Chem.*, 1992, **31**, 2638.
37. P. Comba and T. W. Hambley, 'Molecular Modeling of Inorganic Compounds', VCH, Weinheim, 1995.
38. R. D. Hancock, *Prog. Inorg. Chem.*, 1988, **37**, 187.
39. F. M. Lappert, A. R. Sanger, R. C. Schrivaster, and P. P. Power, 'Metal and Metalloidal Amides', Wiley, New York, 1979.
40. M. H. Chisholm and I. P. Rothwell, in 'Comprehensive Coordination Chemistry', ed. G. Wilkinson, Pergamon Press, Oxford, 1987, Vol. 2, p. 161.
41. R. C. Mehorta, in 'Comprehensive Coordination Chemistry', ed. G. Wilkinson, Pergamon Press, Oxford, 1987, Vol. 2, p. 269.
42. D. A. House, in 'Comprehensive Coordination Chemistry', ed. G. Wilkinson, Pergamon Press, Oxford, 1987, Vol. 2, p. 23.
43. W. L. Jolly, 'Synthetic Inorganic Chemistry', Prentice Hall, New York, 1960.
44. K. Beveridge, G. W. Bushnell, and A. D. Kirk, *Acta Crystallogr., Sect. C*, 1985, **41**, 899.
45. S. Balt and A. Jelsma, *Inorg. Chem.*, 1981, **20**, 733.
46. J. W. Mellor, 'Comprehensive Treatise of Inorganic and Theoretical Chemistry', Longmans, London, 1931.
47. W. S. Glaunsinger, *J. Phys. Chem.*, 1980, **84**, 1163.
48. Y. Pauleau, J. J. Hantzpergue, and J. C. Remy, *Bull. Soc. Chim. Fr.*, 1978, 246.
49. P. C. Ford, *Coord. Chem. Rev.*, 1970, **5**, 75.
50. H. Taube, *Pure Appl. Chem.*, 1979, **51**, 901.
51. D. Waysbort and G. Navon, *Inorg. Chem.*, 1979, **18**, 9.
52. G. G. Schlessinger, 'Inorganic Laboratory Preparations', Chem. Pub. Co., New York, 1962.
53. G. Glidewell, *J. Coord. Chem.*, 1977, **6**, 189.
54. S. Fallab and P. R. Mitchell, *Adv. Inorg. Bioinorg. Mech.*, 1984, **3**, 111.
55. S. E. Miller and D. A. House, *Inorg. Chim. Acta*, 1989, **161**, 131.
56. S. E. Miller and D. A. House, *Inorg. Chim. Acta*, 1989, **166**, 189.
57. S. E. Miller and D. A. House, *Inorg. Chim. Acta*, 1990, **173**, 53.
58. S. E. Miller and D. A. House, *Inorg. Chim. Acta*, 1991, **187**, 125.
59. S. E. Miller, Huo. Wen, D. A. House, and W. T. Robinson, *Inorg. Chim. Acta*, 1991, **184**, 111.
60. S. E. Miller, K. J. Gerard, and D. A. House, *Inorg. Chim. Acta*, 1991, **190**, 135.
61. E. Koubek and D. A. House, *Inorg. Chim. Acta*, 1992, **191**, 103.
62. M. Kojima, A. Sakurai, M. Murata, K. Nakajima, S. Yashino, and nd. Y. Yoshikawa, *J. Coord. Chem.*, 1997, **42**, 95.
63. D. A. Thompson, *J. Coord. Chem.*, 1991, **24**, 261.
64. M. M. Muir and H. M. Torres, *Inorg. Chem.*, 1992, **31**, 4160.
65. J. Castro, P. P. Lourido, A. Sousa-Pedrares, E. Labisbal, M. Carabel, and J. A. Garcia-Vazquez, *Acta. Crystallogr.*, 2002, **58C**, m65.
66. A. M. Mills, K. Flinzner, A. F. Stassen, J. G. Haasnoot, and A. L. Spek, *Acta Crystallogr.*, 2002, **58C**, m243.
67. T. Otieno, J. R. Blanton, M. J. Hatfield, S. L. Asher, and S. Parkin, *Acta Crystallogr.*, 2002, **58C**, m182.
68. R. A., Jones ed., 'Heterocyclic Compounds', Wiley, New York, 1990, Vol. 48, Part 1.
69. S. R. A. Kkan, I. Guzman-Jimenez, K. H. Whitmire, and A. R. Kohkhar, *Polyhedron*, 2000, **19**, 975.
70. J. Chatt, J. R. Dillworth, and R. L. Richards, *Chem. Rev.*, 1978, **78**, 589.
71. R. A. Henderson, G. J. Leigh, and C. J. Pickett, *Adv. Inorg. Chem. Radiochem.*, 1983, **27**, 198.
72. H. M. Colquhoun, *Acc. Chem. Res.*, 1984, **17**, 23.
73. G. J. Leigh, *Transition Met. Chem.*, 1986, **11**, 118.
74. M. Hidai and Y. Mizobe, in 'Reactions of Coordinated Ligands', ed. P. S. Braterman, Plenum Press, New York, 1989, Vol. 2, p. 53.
75. J. E. Fergusson and J. L. Love, *Rev. Pure Appl. Chem.*, 1970, **20**, 33.
76. K. Kohata, T. Fukuyama, and K. Kuchitsu, *J. Phys. Chem.*, 1982, **86**, 602.
77. G. Stedman, *Adv. Inorg. Chem. Radiochem.*, 1979, **22**, 114.
78. B. F. Johnston, B. L. Haymore, and J. R. Dillworth, in 'Comprehensive Coordination Chemistry', ed. G. Wilkinson, Pergamon Press, Oxford, 1987, Vol. 2, p. 99.
79. A. D. Ryabov, *Chem. Rev.*, 1990, **90**, 403.
80. M. P. Doyle, *Acc. Chem. Res.*, 1986, **19**, 348.
81. M. P. Suh, S.-G. Kang, V. L. Goedken, and S.-H. Park, *Inorg. Chem.*, 1991, **30**, 365.
82. Huo. Wen, S. E. Miller, D. A. House, V. McKee, and W. T. Robinson, *Inorg. Chim. Acta*, 1992, **193**, 77.
83. D. A. House, V. McKee, and W. T. Robinson, *Inorg. Chim. Acta*, 1989, **157**, 15.
84. D. A. House and P. J. Steel, *Inorg. Chim. Acta*, 1999, **288/1**, 53.
85. J. Ellermeier, R. Stahler, and W. Bensch, *Acta Crystallogr.*, 2002, **58C**, m70.
86. R. Fanshawe, A. Mobinikhaledi, C. R. Clark, and A. G. Blackburn, *Inorg. Chim. Acta*, 2000, **307**, 26.
87. K. F. Purcell and J. C. Kotz, 'Inorganic Chemistry', W.B. Saunders, 1977, p. 636; G. J. Leigh, 'Nomenclature of

Inorganic Chemistry’, Blackwell Scientific (IUPAC), Oxford, 1990 Tables I-10.5, X, p. 184.

88. G. B. Kauffman and E. V. Lindley, *J. Chem. Educ.*, 1974, **51**, 424.

89. I. Bernal, *J. Chem. Educ.*, 1992, **69**, 468.

90. H. Chun, S. S. Massoud, R. Wen, and I. Bernal, *Polyhedron*, 1999, **18**, 3647.

91. M. Abdou, C. Krathy, and G. Uray, *Monatsh. Chem.*, 1990, **121**, 1039.

92. S. T. Chan, C. I. Dickie, L. T. Ellis, V. P. Monk, B. A. Messerle, and T. W. Hambley, *J. Chem. Soc., Dalton Trans.*, 2001, 2769.

93. R. Saito and Y. Kidani, *Chem. Lett.*, 1976, 123.

94. K. J. Gerard, J. Morgan, P. J. Steel, and D. A. House, *Inorg. Chim. Acta*, 1997, **260**, 27.

95. B.-J. Kim, Y.-M. Lee, E. H. Kim, S. K. Kang, and S.-N. Choi, *Acta Crystallogr.*, 2002, **58C**, 361.

96. J. Reedijk, in ‘Comprehensive Coordination Chemistry’, ed. G. Wilkinson, Pergamon Press, Oxford, 1987, Vol. 2, p. 73.

97. P. J. Steel, *Coord. Chem. Rev.*, 1990, **106**, 227.

98. E. C. Constable and P. J. Steel, *Coord. Chem. Rev.*, 1989, **93**, 205.

99. C. Kaes, A. Katz, and M. W. Hosseini, *Chem. Rev.*, 2000, **100**, 3552.

100. G. Chelucci and R. P. Thummel, *Chem. Rev.*, 2002, **102**, 3129.

101. E. Krause and J. Ferguson, *Prog. Inorg. Chem.*, 1989, **37**, 293.

102. L. E. Foster, *Chem. Rev.*, 1990, **90**, 331.

103. R. Mukherjee, *Coord. Chem. Rev.*, 2000, **203**, 151.

104. D. A. House, P. J. Steel, and A. A. Watson, *Aust. J. Chem.*, 1986, **39**, 1525.

105. K. Vrieze and G. van Koten, in ‘Comprehensive Coordination Chemistry’, ed. G. Wilkinson, Pergamon Press, Oxford, 1987, Vol. 2, p. 189.

106. A. N. Golub, H. Kohler, and V. V. Skopenko eds, ‘Chemistry of the Pseudohalides’, Elsevier, Amsterdam, NY, 1986.

107. G. A. Lawrance, *Adv. Inorg. Chem.*, 1989, **34**, 145.

108. R. W. Hay and F. M. McLaren, *Transition Met. Chem.*, 1999, **24**, 398.

109. A. Hazell, C. J. McKenzie, and L. P. Nielsen, *Polyhedron*, 2000, **19**, 1333.

110. D. R. Morris and L. Marton eds, ‘Polyamines in Biology and Medicine’, Dekker, New York, 1981.

111. C. W. Tabor and H. Tabor, *Ann. Rev. Biochem.*, 1984, **53**, 749.

112. C. Navarro-Ranninger, F. Zamora, J. M. Pérez, I. López-Solera, S. Martinez-Carrera, J. R. Masaguer, and C. Alonso, *J. Inorg. Biochem.*, 1992, **47**, 267.

113. M. Harlerow and C. A. Kilner, *Acta Crystallogr.*, 2002, **58C**, m424.

114. K. H. Kim, *Acta Crystallogr.*, 2000, **56C**, e557.

115. M. Scarplline, *Acta Crystallogr.*, 2001, **57C**, 356.

116. R. Balamurugan, M. Palaniandavar, and R. S. Gopalan, *Inorg. Chem.*, 2001, **40**, 2246.

117. G. Muller, J.-C. G. Bunzli, K. J. Schenk, C. Piguet, and G. Hopfgartner, *Inorg. Chem.*, 2001, **40**, 2642.

118. C. W. Glynn and M. M. Turnbull, *Inorg. Chim. Acta*, 2002, **332**, 92.

119. G. A. van Albade, I. Mutikainen, U. Turpeinen, and J. Reedijk, *Acta Crystallogr.*, 2002, **58C**, m179.

120. D. L. Reger, C. A. Little, M. D. Smith, A. L. Rheingold, L. M. Liable-Sands, G. P. A. Yap, and I. A. Guzie, *Inorg. Chem.*, 2002, **41**, 19.

121. D. Martini, M. Pellei, C. Pettinari, B. W. Skelton, and A. H. White, *Inorg. Chim. Acta*, 2002, **333**, 72.

122. W. Yang, L. Chen, and S. Wang, *Inorg. Chem.*, 2001, **40**, 507.

123. X.-H. Bu, M. Du, L. Zhang, Z.-L. Shang, R.-H. Zangand, and M. Shionoya, *J. Chem. Soc., Dalton Trans.*, 2001, 729.

124. M.-H. Choi, B. J. Kim, I.-C. Kim, S.-H. Kim, Y. Kim, J. M. Harrowfield, M.-K. Lee, M. Mocerino, E. Rukmini, B. W. Skelton, and A. H. White, *J. Chem. Soc., Dalton Trans.*, 2001, 707.

125. B. Fabins, R. J. Geue, R. G. Hazell, W. G. Jackson, F. K. Larsen, C. J. Qin, and A. M. Sargeson, *J. Chem. Soc., Dalton Trans.*, 1999, 3961.

126. J. M. Harrowfield, G. H. Jang, Y. Kim, P. Thuery, and J. Vicens, *J. Chem. Soc., Dalton Trans.*, 2002, 1241.

127. E. C. Constable, *Adv. Inorg. Chem. Radiochem.*, 1986, **30**, 69.

128. E. C. Constable, *Tetrahedron*, 1992, **48**, 10013.

129. S. G. Zipp, A. P. Zipp, and S. K. Madan, *J. Indian Chem. Soc.*, 1977, **54**, 149.

130. A. Dossing, A. Hazell, and H. Toftlund, *Acta Chem. Scand.*, 1996, **50**, 95.

131. F. C. Sanudo, A. A. Grillo, M. J. Knapp, J. C. Bollinger, J. C. Huffman, D. N. Hendrickson, and G. Christou, *Inorg. Chem.*, 2002, **41**, 2441.

132. D. A. Buckingham, W. G. Jackson, P. A. Marzilli, and A. M. Sargeson, *Aust. J. Chem.*, 1999, **52**, 185.

133. J. M. W. Browne, J. Wikaira, and R. M. Hartshorn, *J. Chem. Soc., Dalton Trans.*, 2001, 3513.

134. M. D. Vaira, F. Mani, and P. Stoppioni, *Inorg. Chim. Acta*, 2000, **303**, 61.

135. F. V. Rybak-Akimova, A. Y. Nazarenko, L. Chen, P. W. Krieger, A. M. Herrera, V. V. Tarasov, and P. D. Robinson, *Inorg. Chim. Acta*, 2001, **324**, 1.

136. A. Grohmann and F. Knoch, *Inorg. Chem.*, 1996, **35**, 7932.

137. C. Jubert, A. Mohomadou, E. Guillon, and J.-P. Barbier, *Polyhedron*, 2000, **19**, 1447.

138. S.-D. Kim, J.-W. Kim, and W.-S. Jung, *Polyhedron*, 1998, **17**, 1223.

139. D. da Luz, C. V. Franco, I. Vencato, A. Neves, and Y. P. Mascarenhas, *J. Coord. Chem.*, 1992, **26**, 269.

140. G. Park, N. Ye, R. D. Rogers, M. W. Brechbiel, and R. P. Planalp, *Polyhedron*, 2000, **19**, 1155.

141. T. Mashiko and D. Dolphin, in ‘Comprehensive Coordination Chemistry’, ed. G. Wilkinson, Pergamon Press, Oxford, 1987, Vol. 2, p. 813.

142. P. Ray, *Chem. Rev.*, 1961, **61**, 313.

143. P. Ray, *Inorg. Synth.*, 1960, **6**, 75.

144. H. Sigel, N. A. Corfu, L.-N. Ji, and R. B. Martin, *Comments Inorg. Chem.*, 1992, **13**, 35.

145. A. E. Martell and M. Calvin, ‘Chemistry of the Metal Chelate Compounds’, Prentice-Hall, New York, 1956, p. 140.

146. P. Ferruti and R. Barbucci, *Adv. Polym. Sci.*, 1984, **58**, 155.

147. N. F. Curtis, in ‘Comprehensive Coordination Chemistry’, ed. G. Wilkinson, Pergamon Press, Oxford, 1987, Vol. 2, p. 899.

148. N. F. Curtis and O. P. Gladkikh, *Aust. J. Chem.*, 2000, **53**, 597.

149. A. Riesen, M. Zehnder, and D. A. House, *Inorg. Chim. Acta*, 1986, **113**, 163.

150. B. N. Storhoff and H. C. Lewis, *Coord. Chem. Rev.*, 1972, **23**, 1.

151. H. Endres, in ‘Comprehensive Coordination Chemistry’, ed. G. Wilkinson, Pergamon Press, Oxford, 1987, Vol. 2, p. 261.

152. D. Yang and D. A. House, *Polyhedron*, 1983, **2**, 1267.

153. F. Swiegers and T. J. Malefetse, *Chem. Rev.*, 2000, **100**, 3483; *Coord. Chem. Rev.*, 2002, **225**, 91.

154. S. Leininger, B. Olenyuk, and P. J. Stang, *Chem. Rev.*, 2000, **100**, 853.

155. B. J. Holliday and C. A. Mirkin, *Angew. Chem., Int. Ed. Engl.*, 2001, **40**, 2022.

156. C. V. K. Sharma, *J. Chem. Educ.*, 2001, **78**, 617.

157. P. J. Steel, *Chem. New Zealand*, 2003, **67**, 57.

158. G. Dong, D. Chun-ying, F. Chan-jie, and M. Qing-jin, *J. Chem. Soc., Dalton Trans.*, 2002, 834.

159. A. Kunze, R. Gleiter, F. Rominger, and T. Oeser, *J. Chem. Soc., Dalton Trans.*, 2002, 1217.

160. D. L. Caulder and K. N. Raymond, *J. Chem. Soc., Dalton Trans.*, 1999, 1185.

161. M. Albrecht, *Chem. Rev.*, 2001, **101**, 3457.

162. H.-K. Liu, J. Hu, T.-W. Wang, X.-L. Yu, J. Liu, and B. Kang, *J. Chem. Soc., Dalton Trans.*, 2001, 3534.

163. C. He, L.-Y. Wang, Z.-M. Wang, Y. Liu, C.-S. Liao, and C.-H. Yan, *J. Chem. Soc., Dalton Trans.*, 2002, 134.

Analytical Chemistry of the Transition Elements

Alan T. Hutton
University of Cape Town, Rondebosch, South Africa

Based in part on the article Analytical Chemistry of the Transition Elements by Harry M. N. H. Irving & Alan T. Hutton which appeared in the Encyclopedia of Inorganic Chemistry, First Edition.

1 Introduction 1
2 Historical Perspective 2
3 Pretreatment of the Sample 3
4 Qualitative Analysis 4
5 Gravimetric Analysis 4
6 Titrimetric Analysis 5
7 Spectrophotometric Analysis 6
8 Atomic Emission Spectroscopy 6
9 Atomic Absorption Spectroscopy 7
10 X-ray Methods 8
11 Activation Analysis 9
12 Electrochemical Methods 10
13 Platinum Group Metals (PGMs) 10
14 References 10

1 INTRODUCTION

The analytical chemistry of the transition elements (*see Transition Metals*), that is, those with partly filled shells of d (*see* d^n *Configuration*) or f electrons (*see f-Block Metals*), should include that of the first transition period (Sc, Ti, V, Cr, Mn, Fe, Co, Ni, and Cu) and that of the second transition series (Y, Zr, Nb, Mo, Tc, Ru, Rh, Pd, and Ag). The third transition series embraces Hf, Ta, W, Re, Os, Ir, Pt, and Au, and although it formally begins with lanthanum, for historical reasons this element is usually included with the lanthanoids (rare-earth elements) (*see* ***Scandium, Yttrium & the Lanthanides: Inorganic & Coordination Chemistry***; *Rare Earth Elements*). The actinoid elements (*see* ***Actinides: Inorganic & Coordination Chemistry***) are all radioactive (*see Radioactive Decay*) and those with atomic number (*see Atomic Number*) greater than uranium ($Z = 92$) are artificial; the analytical chemistry of these elements is too specialized to consider here.

Chemical analysis originally sought to determine what elements were present in a particular sample and their concentrations, that is, answers to the questions ‘What’s in it?’ and ‘How much?’ were sought. As time went on the questions became more searching and the analyst had to address considerations of speciation, that is, the form in which the element is present, its oxidation state, or its occurrence as a specific chemical compound. When the element in question is not distributed uniformly throughout the matrix, the question of its location, for example, at a particular site in a solid catalyst (*see Catalysis*) or grain boundary (*see Grain Boundary*) of an alloy (*see* ***Alloys***), becomes of special interest.

Since the analyte is often present in quite a complex matrix comprising other elements or substances that may or may not interfere with any projected method of determination, and may indeed be quite a minor constituent of the whole sample, these considerations will effectively dominate the working details of any analytical procedure. There can therefore be no case for prescribing a single definitive method for (say) nickel that would be universally applicable to its determination in alloys (*see* ***Alloys***), organometallic compounds (*see Organometallic Complexes*), inorganic salts (*see Ionic Bonds*), or coordination compounds (*see Coordination Complexes*), to its presence as a trace constituent (*see Trace Element*) in maize or other plant products, or in natural waters or effluents.

The environmental scientist will often wish to distinguish between the total mercury in a sample of sea-water and the amounts of methylmercury compounds in it (*see* ***Metal Ion Toxicity***). Other factors that influence the choice of an analytical method for a particular element and the details of procedure stem from the actual reasons for carrying out the analysis in the first place. Do we need the highest possible precision and accuracy, as when assessing the purity of gold and silver or a material for use in semiconductors? Are routine analyses to be conducted on large numbers of samples of very similar type? Is the desired level of precision one set by the eventual use of the analytical result purely for quality control? Is the speed of obtaining a result of overriding importance, as when analyzing the molten contents of a furnace? Or the need to limit the cost of each analytical determination? Or the need to use semi-skilled labor? Other factors that affect the choice of analytical method and the details of procedure depend on the amount of sample available and perhaps its unique character. These considerations apply with special force to the elemental analysis of archaeological artifacts[1] and museum specimens.[2]

For the above reasons it seems appropriate to describe the methods available for analyzing, in particular, the transition metals and to do so in rather broad outline; details of procedure have thus been relegated to representative specialist textbooks[3–6] and research publications. Major reference works include the multivolume *Treatise on Analytical Chemistry* series,[7] the ongoing *Wilson and Wilson’s Comprehensive Analytical Chemistry* series (now up to volume 43),[8,9] the *Encyclopedia of Analytical Science* (10 volumes),[10,11] and the recent *Encyclopedia of Analytical Chemistry* (15 volumes).[12] The latter work provides an outstanding source of information on the theory, instrumentation, and applications of modern analytical chemistry.

2 HISTORICAL PERSPECTIVE

2.1 Introduction

As soon as chemical substances of plant or mineral origin became the objects of commerce, the need for what we nowadays think of as ‘quality control’ became evident, for the realities of human nature soon ensured that problems of adulteration, false weights, and even plain deception had to be taken into account. Thus, Pliny (23–79 AD) recorded that the adulteration of copper sulfate by iron sulfate could be detected by testing a solution with a strip of papyrus soaked in gall-nuts, which blackened if iron was present.

In the absence of mineral acids only ‘dry’ methods could be employed to detect fraud or defeat the counterfeiters, who became active from the very early days of jewellery and precious vessels of gold and silver. In the earliest references to fire assay, found in cuneiform tablets, the King of Babylon complained to the Egyptian Pharaoh Amenophis IV (reigned 1375–1350 BC), ‘Your Majesty did not look at the gold which was sent me last time ... after putting them in the furnace this gold was less than its weight.’ The Bible contains many references to fire assaying, for example, ‘As the fining pot for silver, and the furnace for gold; so is a man to his praise’ (Prov. **27**, 21); ‘. . . for he is like a refiner’s fire, . . . and he shall purify the sons of Levi, and purge them as gold and silver’ (Mal. **3**, 2–3); ‘As they gather silver, and brass, and iron, and lead, and tin, into the midst of the furnace, to blow the fire upon it, to melt it . . .’ (Eze. **22**, 20); ‘And I will turn my hand upon thee, and purely purge away thy dross, and take away all thy tin’ (Isa. **1**, 25).[13,14]

The separation of silver from gold was a difficult task, and Pliny refers to an essentially chemical method in which the alloy is roasted with iron sulfate and common salt in the presence of brick dust, which absorbs the silver chloride formed and leaves pure gold. However, some 250 years earlier, Hieron, King of Syracuse (200 BC), had asked Archimedes to examine the composition of a new golden crown that he suspected might have been made from a gold–silver alloy. Since the density of gold (19.3) is nearly twice that of silver (10.5) the composition of the crown was easily determined by a purely physical method, probably the first use of a nondestructive method in analysis.

The process of fire assay is essentially quantitative in the sense that it concerns a change in weight before and after some heat treatment. The essential balance was a familiar piece of equipment employed by generations of traders, as evidenced by the fact that weights used in Babylon in 2600 BC are still in existence.

The process of assaying gold was current from early times and in the thirteenth century it was clearly described in the *Summa perfectionis magisterii* (ascribed to Geber). This also described the preparation of aqua fortis (nitric acid), which was known to dissolve silver but not gold, and aqua regia, prepared from a mixture of nitric acid with ammonium chloride, which even dissolved gold and separated the silver as its insoluble chloride. By the fourteenth century, cupellation had become a statutory method for assaying gold, and Charles I of Hungary decreed in 1342 AD that a special laboratory for this purpose (*domus regalis*) should be set up in every mining town.[13] However, problems arising from unreliable analysis did not go away so easily and even in the nineteenth century astute dealers in France found that they could make a tidy profit by buying silver with a ‘low assay’ from some laboratories and selling it elsewhere where they knew they could receive a ‘high assay’. In 1829 the embarrassed administration sought for a solution by offering a prize for a simple and rapid method of analysis with an error of less than 4 to 5 parts in 10^4 that could be universally accepted. Joseph Gay-Lussac was the successful prizewinner with his method of adding a standard solution of sodium chloride to a solution of the silver in nitric acid until one drop of the dilute standard solution no longer produced further turbidity due to the precipitation of silver chloride. With minor improvements for detecting the endpoint, this simple method is still in use 175 years later.[13]

During the fifteenth century the metals zinc, antimony, bismuth, and probably cobalt were discovered, together with many new reactions now used in quantitative analysis.[13,14] For example, A. Libavius (1540–1616) noted how ammonia in water could be determined by the blue color formed with a copper salt. Robert Boyle (1627–1691) was the first to use a solution of hydrogen sulfide (which he made from flowers of sulfur, potash, and ammonium chloride) as an analytical reagent, and he noted the black precipitate it formed with lead, gold, and mercury.

Chemical analysis came into being to meet the demands of early technology. The need for metals in the eighteenth century led to the shortage of the wood and charcoal needed for smelting iron. Replacing them by coal gave a brittle product and it was not until about 1750 that careful analytical work revealed the reason. More mining exploration led to the discovery of new minerals and produced additional problems for the analysts who had to devise new qualitative and quantitative methods, particularly in those countries with the richest mineral deposits, and notably in Sweden. M. H. Klaproth’s contributions (1743–1817) in Germany were especially noteworthy, for he originated the technique of alkali fusion for opening up minerals and used silver or gold vessels for the purpose. He realized that foreign materials could be introduced into his samples when they were finely ground in a mortar and he made appropriate corrections. He made significant advances in the analysis of mixtures of iron, manganese, aluminum, and chromium in solutions containing phosphates and arsenates.[13]

2.2 Blowpipe Methods

An important technique developed in the mid-eighteenth century was to miniaturize large-scale metallurgical operations by adapting the blowpipe, which had long been used by glassblowers and goldsmiths, to provide an indispensable adjunct for the examination of minerals in the laboratory and especially in the field. In the hands of Gahn and Cronstedt in the eighteenth century it became a simple instrument for directing a fine and concentrated flame into a small portion of the powdered sample in a hollowed-out block of charcoal. With the aid of fluxes such as borax, soda, and sodium ammonium phosphate ('microcosmic salt'), many metal oxides could be reduced and valuable information gained from the color and reactions of the bead that remained. Bergmann was a great exponent of this technique and his book *De tubo feruminatorio* (1779) summarized all the knowledge of his time. J. J. Berzelius disseminated it widely through his book *Abhandlung om Blasrorets awendende i kemien och mineralogien* (1820) and its translations into many European languages. This technique, which was once a stable feature of every course on qualitative analysis, fell into disuse around 1910.[14]

2.3 Titrimetry and Gravimetry

At first, quantitative analysis by titrimetry was confined to such problems as measuring the strength of vinegar and the basic articles of commerce such as sulfuric acid, hydrochloric acid, and solutions of chlorine in water. Thus, the amount of alkali in pearl ash was arrived at by measuring the number of teaspoonfuls of a dilute solution of nitric acid needed before effervescence ceased; detection of the endpoint by a change in the color of litmus was a later improvement by William Lewis (1767). Titrimetry took a step forward when F. A. H. Descroizilles (1757–1825) introduced the first form of 'burette' and a crude 'standard flask' described as a 'small jug ... in the neck of which a mark is made with a diamond indicating the place up to which the vessel contains just 2 dl.'[13–15] In about 1846, F. Margueritte introduced potassium permanganate for the titration of iron and Penny's process (1850) extended this with a standard solution of potassium chromate since permanganate could not be used when the iron was taken into solution with hydrochloric acid.[16] Later developments in titrimetry centered around the use of electrochemical methods, these being especially useful for detecting the endpoint since they could be adapted to recording devices and automatic control.[14] Complexometric titrations (see Section 6.3) for many metals date from G. Schwarzenbach's work in the early 1940s.

Classical analysis by gravimetry (see Section 5) took a new turn when L. H. Tschugaeff reported the novel use of a new organic reagent, dimethylglyoxime, in 1905, but several decades passed before other reagents such as cupferron (*see Cupferron*), 8-hydroxyquinoline, 1-nitroso-2-naphthol, the alkyl- and arylarsonic acids, and so on, became firmly established.[14,15]

2.4 Physical Methods

Physical methods such as spectroscopy (1925), atomic absorption (A. Walsh, 1955) (see Section 9), atomic fluorescence (T. S. West, 1966) and X-ray fluorescence (XRF) (1923) (see Section 10.1), and optical absorption spectrophotometry (ca. 1940) (see Section 7) gained increasing importance as the relevant apparatus became more refined and commercially available.[14] Although radiochemical methods began to be exploited from the early years of the last century, a new and major analytical technique, that of neutron activation analysis (see Section 11.1), had to await the availability of nuclear reactors as neutron sources, following the stimulus of the Second World War. This also provided the stimulus for many analytical procedures based on liquid–liquid extraction (or 'solvent extraction'), although its potential had been realized as early as the beginning of the twentieth century.[14]

3 PRETREATMENT OF THE SAMPLE

When the desired element is present in the sample at quite a low concentration, it may be necessary to take a large amount for analysis and this raises the important question of securing a truly representative sample if the initial material is not homogeneous.[17] An aliquot portion of a solution can be obtained with suitable accuracy, but this does not solve the problem of how to obtain a homogeneous solution of the original specimen without introducing large amounts of reagents that cannot readily be removed and may complicate the subsequent procedures. The rate of dissolution is always increased if the sample to be analyzed is presented in the form of a fine powder and such comminution has been achieved by a variety of techniques contrived to disperse the specimen without contamination by the equipment, vessels, or reagents used.[3,4]

Although fusion with alkaline or acidic fluxes such as KHF_2, $K_2S_2O_5$, or Na_2CO_3 (with or without KNO_3) is usually effective, it may introduce materials that subsequently produce complications. HNO_3 and HF are often used for Zr, Hf, Ta, Nb, Ti, and other metals, refractory oxides (*see* ***Oxides: Solid-state Chemistry***), borides (*see* ***Borides: Solid-state Chemistry***), carbides, and nitrides (*see* ***Nitrides: Transition Metal Solid-state Chemistry***). The removal of unwanted material, especially organic matter, by dry- or wet-ashing demands special care, as unacceptable losses of certain elements may arise from these processes.[18] For voltammetric analyses, where the analyte must be in an ionic form, organic material must be removed completely, as well as interfering substances such as oxygen, hydrogen peroxide, complexing agents, surfactants, and any substances that might be adsorbed on the electrode surfaces.

The modern trend has been to carry out digestions in closed vessels of quartz using suitable mineral acids (HNO_3, HCl, H_2SO_4, or $HClO_4$) or in glassy carbon or Teflon-lined bombs (for HF). The digestions are often carried out under high pressure (up to 30 bar) and high temperature (up to 320 °C). Microwave heating is increasingly used to speed the process and avoid any possible contamination from flames or other heat sources.[19] In a modern UV digestor, samples containing a small volume of pure hydrogen peroxide are arranged in stoppered quartz vessels around a high-pressure mercury-vapor lamp which generates OH radicals that degrade organic matter. A typical digestion of an hour or less at 90 °C is used in the determination of Ni ($\sim 1\,\mu g\,dm^{-3}$) or Cu ($\sim 30\,\mu g\,dm^{-3}$) in lake water or municipal waste water.

4 QUALITATIVE ANALYSIS

The discovery of so many elements up to the beginning of the twentieth century led to innumerable schemes for their qualitative analysis, with special regard to the circumstances that frequently occurred in complex mixtures, so that some degree of separation was mandatory. Contemporary advances in analytical methods have made much of this work of historical or pedagogical interest only.[20]

Immense effort was at one time devoted to devising ‘spot-tests’ to enable a specific element or chemical group to be identified in a minute amount of analyte.[21] With the advent of techniques that permit of the simultaneous identification of the components of a complex mixture, these too are less widely used except in special circumstances.

5 GRAVIMETRIC ANALYSIS

5.1 Classical Gravimetry

In classical methods of gravimetric analysis[22] the desired element was separated completely from the matrix and weighed as such or precipitated from aqueous solution as a sulfide or hydroxide (whence a stoichiometric oxide was obtained by ignition) or as a suitable inorganic or organic salt. The conditions governing the quantitative precipitation of the analyte, its freedom from contamination by adsorption or inclusion, and its drying to constant weight required a meticulous observance of the prescribed experimental details and demanded trained experimental skills and were thus time-consuming and costly. The development of homogeneous precipitation (or ‘precipitation from homogeneous solution’), which ensured a low rate of precipitation by slow generation of the effective precipitant *in situ* (*see In Situ Reaction*), did much to provide experimental conditions whereby precipitates could be produced under the most favorable conditions.[23]

5.2 Organic Reagents for Metals

With the introduction of dimethylglyoxime by Tschugaeff in 1905 and the later development of a variety of new organic reagents, it became feasible to precipitate a desired element as a metal coordination compound (*see Coordination Complexes*) that often had a low solubility and a favorably high equivalent weight.[24] Organic precipitating reagents are generally bidentate (*see Bidentate Ligand*) chelating ligands (*see Chelating Ligands*), with O, N, and S being the most commonly encountered donor atoms (*see Donor Atom*). At first it was hoped that it would be possible to synthesize a reagent *specific* for each element, thus obviating the need for elaborate separation procedures. This now seems to have been an impossible goal and the best that can be achieved is provision of a reagent which, under carefully specified reaction conditions (e.g. control of pH and the presence of certain auxiliary complexing agents), shows a high *selectivity*.

There appears to be no specific and quantitative precipitant for scandium, the first of the transition metals. The principal difficulty is that of separating scandium from the other metals, since it occurs in practically all yttrium and lanthanum minerals, in smaller amounts in tin, tungsten, zirconium, beryllium, titanium, and niobium minerals, and in minute amounts in almost all rocks. Many of the classical gravimetric procedures depend on the precipitation of its hydroxide or oxalate and subsequent ignition to Sc_2O_3, which unfortunately has a high gravimetric factor. If interfering elements are first removed, it gives a precipitate with oxine

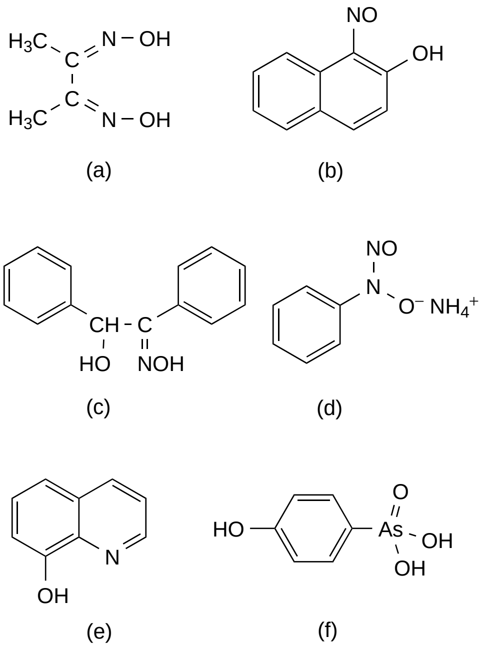

Figure 1 Selection of typical organic precipitating agents (commonly precipitated transition metal ions given in parentheses): (a) dimethylglyoxime (Ni^{2+}, Pd^{2+}), (b) 1-nitroso-2-naphthol (Fe^{3+}, Co^{2+}, Zr^{4+}, Pd^{2+}), (c) α-benzoin oxime (‘cupron’) (Cu^{2+}, $MoO_2{}^{2+}$, $WO_2{}^{2+}$), (d) ammonium N-nitroso-N-phenylhydroxylamine (‘cupferron’) (Ti^{4+}, $VO_2{}^{+}$, Fe^{3+}, Zr^{4+}, Ce^{4+}, U^{4+}), (e) 8-hydroxyquinoline (‘oxine’) (TiO^{2+}, Fe^{3+}, Cu^{2+}, Zr^{4+}, $MoO_2{}^{2+}$, $WO_2{}^{2+}$, Th^{4+}, $UO_2{}^{2+}$), (f) 4-hydroxyphenylarsonic acid (Ti^{4+}, Zr^{4+})

(8-hydroxyquinoline) from a buffered acetate solution at pH 6.5–8.5 of composition $Sc(C_9H_6NO)_3 \cdot C_9H_7NO$ (M_r 622.7) having a low gravimetric factor.[25]

Gravimetric methods for other transition metals are detailed by several authors in reference texts;[3,4,24,26,27] a representative selection of well-known organic reagents and their common analytes is given in Figure 1.

6 TITRIMETRIC ANALYSIS

6.1 Advantages of Titrimetry

Whereas in gravimetric analysis a reagent is added in excess to a solution of the analyte and the resulting precipitate is collected, washed, dried, and weighed, in titrimetry (formerly 'volumetric analysis') a reagent of precisely known concentration is added to the test solution in just sufficient amount as to be stoichiometrically equivalent to the amount of analyte. No excess is used and the endpoint is detected visually (by a change in color or fluorescence (*see Fluorescence*) of a suitable indicator) or instrumentally (e.g. photometrically or by some electrochemical method). Titrimetric methods are intrinsically quicker than gravimetric procedures and demand less operator skill. The whole procedure can be automated, conducted on a small scale (with volumes down to a few microliters), and adapted to work with highly radioactive materials (*see Radioactive Decay*).[3,4,28]

6.2 Individual Determinations

In a back-titration of silver by chloride ions, potassium chromate can be used to indicate the endpoint (Mohr's method) but with potassium thiocyanate as titrant, ammonium iron(III) sulfate ('ferric alum') is preferred. In the direct titration (Gay-Lussac's method) the location of the 'turbidimetric' endpoint has been improved in detail.[3,4]

A number of transition metals can be determined conveniently if their cations undergo a definite change of oxidation state (*see Oxidation Number*) on titration with a standard solution of potassium permanganate, potassium dichromate, cerium(IV) sulfate, or ammonium hexanitratocerate(IV). Several visual indicators have been proposed, including diphenylamine and its derivatives, xylene cyanole FF, and especially *N*-phenylanthranilic acid and tris(1,10-phenanthroline)iron(II) sulfate ('ferroin'). Solutions of Cr^{II} have been used in the determination of iron, copper, titanium, vanadium, molybdenum, tungsten, mercury, gold, silver, and bismuth, and standard solutions of V^{II} and V^{IV}, Sn^{II}, U^{IV}, W^{III} and W^{V}, and Mo^{V} have also been proposed as reductants. In the indirect determination of chromium, $PbCrO_4$ is precipitated and its lead content determined titrimetrically. Molybdenum and tungsten have been determined similarly by measuring the calcium content of precipitated $CaMoO_4$ and $CaWO_4$.[26,28]

6.3 Complexometric Titrations

A titrimetric procedure for the determination of most of the transition metals using a common titrant could obviously be of considerable value. This possibility arose from the pioneering work of G. Schwarzenbach in 1945.[29]

If we consider the determination of a transition metal M by the reaction $M + L \rightarrow ML$ (where L is an organic ligand (*see Ligand*) and the charges on the various species are omitted in the interests of generality), a successful analytical method must meet the following requirements: (i) the reaction must be sufficiently fast; (ii) it should lead stoichiometrically to a single product ML without any intermediate reactions or by-products; (iii) there should be a large increase in free energy (*see Gibbs Energy*), so that the reaction is effectively complete, that is, the stability constant (*see* ***Stability Constants & their Determination***) K_{ML} must be large;[30] (iv) the ligand L must be readily available and give stable standard solutions; and (v) there must be some simple means of monitoring the course of the reaction, that is, for following changes in the concentration [M] or [ML]. These conditions are generally met if L is the conjugate base of an aminopolycarboxylic acid such as ethylenediaminetetraacetic acid (EDTA, H_4Y), which is known to form very stable 1:1 complexes with a large number of metals (Table 1) by coordinating to the central metal atom through its nitrogen and oxygen atoms to give up to five chelate rings (*see Chelating Ligands*) of optimum size (five atoms).[27] The structure of a representative transition metal–EDTA complex is illustrated in Figure 2.

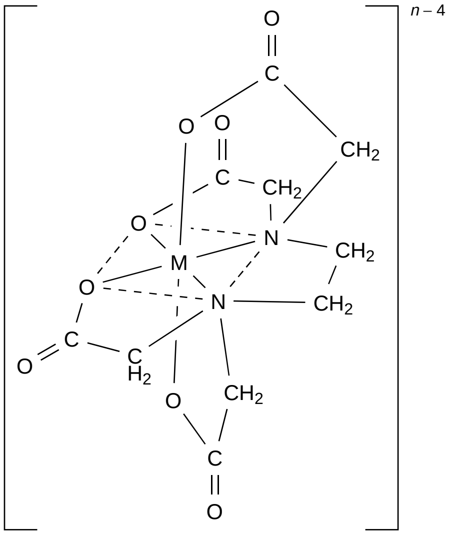

Figure 2 Typical structure of the 1:1 complex formed between a transition metal ion M^{n+} and EDTA (H_4Y)

Table 1 Metal–EDTA complexes: typical values[a] of log K_{ML}

		V^{2+}	Cr^{2+}	Mn^{2+}	Fe^{2+}	Co^{2+}	Ni^{2+}	Cu^{2+}	Zn^{2+}		
		12.7	13.6	13.87	14.32	16.31	18.62	18.80	16.50		
Sc^{3+}	Ti^{3+}	V^{3+}	Cr^{3+}	Mn^{3+}	Fe^{3+}	Co^{3+}				Ga^{3+}	
23.1	21.3	26.0	23.4	25.3	25.1	40.7				20.3	
Y^{3+}	Zr^{4+}	Nb	Mo	Tc	Ru	Rh	Pd^{2+}	Ag^{+}	Cd^{2+}	In^{3+}	Sn^{2+}
18.09	29.5	–	–	–	–	–	18.5	7.32	16.46	25.0	18.3
										Tl^{+}	
										6.54	
La^{3+}	Hf^{4+}	Ta	W	Re	Os	Ir	Pt	Au	Hg^{2+}	Tl^{3+}	Pb^{2+}
15.50	29.5	–	–	–	–	–	–	–	21.7	35.3	18.04
Lanthanoids ($Z = 58–71$)											
Ce^{3+} 15.98; Pr^{3+} 16.40; Nd^{3+} 16.61; Pm^{3+} 17.0; Sm^{3+} 17.14; Eu^{3+} 17.35; Gd^{3+} 17.37; Tb^{3+} 17.93; Dy^{3+} 18.30; Ho^{3+} 18.62; Er^{3+} 18.85; Tm^{3+} 19.32; Yb^{3+} 19.51; Lu^{3+} 19.83											
Actinoids ($Z = 90–103$)											
Th^{4+} 23.2; U^{4+} 25.8; Pu^{3+} 18.1; Am^{3+} 17.8; Cm^{3+} 18.1; Bk^{3+} 18.5; Cf^{3+} 18.7											

[a] Data at 20–25 °C and $I = 0.1–1.0$ M.[30]

The pure salt $Na_2H_2Y{\cdot}2H_2O$ is commercially available; it is readily soluble in water and its high molecular weight (372.16) facilitates the preparation of standard solutions that keep extremely well in hard glass, borosilicate (Pyrex), or polythene containers, although they are aggressive toward soft glass.[29] Complexation proceeds rapidly except in the case of Cr^{III}. A few cations tend to form polynuclear complexes in alkaline solution and react sluggishly with EDTA at room temperature; several problems are overcome by heating with a known excess of EDTA, then adjusting the pH and back-titrating. The endpoint is detected visually with a variety of metallochromic indicators, which change color when [M] decreases to a small value, or electrochemically with, for example, a mercury drop or amalgamated gold foil electrode. Titrimetric methods have been proposed for all the metals listed in Table 1. For example, plutonium can be determined by complexation with excess EDTA at pH 2.5 and the excess back-titrated with Th^{IV} using Alizarin S as indicator. Molybdenum and tungsten are determinable through the calcium content of $CaMoO_4$ and $CaWO_4$, and chromium through the lead content of $PbCrO_4$ or other means. Good methods are available for all the lanthanoids, and although no really satisfactory method has been established for gold and the individual platinum group metals (PGMs), silver is readily obtained in terms of the nickel ion displaced in the reaction $2Ag^+ + K_2[Ni(CN)_4] \rightarrow 2K[Ag(CN)_2] + Ni^{2+}$.[28,29,31]

7 SPECTROPHOTOMETRIC ANALYSIS

The absorption of radiant energy when a beam of light traverses a solution in a cell of length l is given by $A_\lambda = \varepsilon_\lambda lc$, where c is the molar concentration of the solution and ε_λ is the molar absorption coefficient at a specified wavelength λ (Beer's law). This linear relationship between the absorbance (formerly 'optical density') and the concentration forms the basis of innumerable methods for determining the concentration of solutions that absorb in the visible or UV regions (*see UV–Visible Spectroscopy*). Since values of A_λ are additive, procedures are readily found for evaluating the composition of mixtures provided there is no interaction between the molecules.[32–34]

The absorption coefficients of the transition metal cations themselves are seldom large enough to permit a satisfactory spectrophotometric (absorptiometric) determination, but complexation of copper with amines (*see* ***Ammonia & N-donor Ligands***) (blue color) or iron(III) with thiocyanate (red color) has long been exploited. Innumerable organic compounds have been found to give coordination compounds of high ε values and 2,2′-bipyridyl, 1,10-phenanthroline and 2,4,6-tris(2′-pyridyl)-1,3,5-triazine and their derivatives (*see* ***Ammonia & N-donor Ligands***) are of special value in the determination of iron(II). Bathocuproine (2,4-dimethyl-4,7-diphenyl-1,10-phenanthroline) is a very sensitive and selective reagent for determining copper(I) in the presence of considerable amounts of iron since for steric reasons (*see Steric Effect*) it does not coordinate to Fe^{II}.[27]

1,5-Diphenylthiocarbazone ('dithizone') forms intensely colored complexes with, for example, Mn, Fe, Co, Ni, Cu, Zn, Pd, Ag, Cd, Pt, Au, and Hg, which are soluble in CCl_4 and $CHCl_3$, a property which facilitates their separation and individual determination.[35,36] Solutions of most metal dithizonates in organic solvents have the interesting property of being photochromic (*see Photochromism*), and the relatively long half-life of the photoexcited mercury(II) dithizonate complexes ($t_{1/2}$ ca. 1 min) has facilitated their investigation by conventional spectroscopic techniques.[37]

8 ATOMIC EMISSION SPECTROSCOPY

The fact that every element can give rise to characterizing spectra when suitably excited was known early in the nineteenth century,[13,14] but the numerous practical applications for qualitative and quantitative analyses, especially for quality control in industry and for research purposes, developed with the growing demands of analytical chemistry and the availability of more efficient and sophisticated instrumentation. The source of excitation transforms the sample into a plasma of atoms, ions, and molecular radicals that can be excited electronically (*see Excited State*). The decay of these excited species (*see Electronic Transition*) involves radiation of light quanta which can be sorted by wavelength in a suitably designed spectrometer, and this emission spectrum, recorded in the early days photographically, is now digitally captured using photomultiplier tubes or diode arrays.

Excitation by flame is less effective than by electric arc or spark, glow, or plasma discharge, or by lasers which produce a more line-rich spectrum; on the other hand, these advantages can only be exploited by instruments capable of higher resolution.[6]

8.1 Arc and Spark Excitation

One of the most convenient sources of excitation is the low voltage (10–150 V d.c.), high current (1–35 A) discharge between two electrodes. The finely powdered sample is contained in a cup machined from a pure graphite rod (usually the anode) and a pointed graphite rod forms the counter electrode. When the arc is struck, the temperature of the conducting channels between the electrodes ranges between 4000 and 7000 K and although the emission lines for any given element appear simultaneously, the elements in a sample matrix do not vaporize at the same rate and various factors determine their sequential emission. In some techniques the separation of a volatile element from others less volatile is deliberately enhanced (e.g. when determining trace impurities in uranium) by the addition of such substances as silver chloride (‘carrier distillation method’). In other applications the arc temperature is stabilized to promote uniform and simultaneous evaporation by mixing the sample with a spectrochemical buffer such as lithium carbonate, which supplies the arc with a constant supply of ions and electrons. Detection limits for some typical elements range from 0.1 to 1.0% for Nb, Ta, and W, from 0.01 to 0.1% for Bi, Cd, La, Y, Zn, and Zr, from 0.001 to 0.01% for Au, Fe, Ir, Mo, and Sn, and from as little as 0.0001 to 0.001% for Ag, Co, Cr, Cu, Ni, Os, Pd, Pt, Rh, and Ru.[6,38]

With high (1000 V) or medium voltages, events occur very rapidly in spark discharges. The spectra depend not only on the physical conditions of operating but on that part of the spark gap actually viewed by the spectrograph and also on the selected time interval during the discharge. Owing to such factors and purely matrix effects which affect the absolute intensity of lines emitted by elements in a sample, quantitative measurements normally involve a comparison of the spectra of the analytical sample with those of artificial standards containing the desired elements at comparable concentrations in as closely a similar matrix as possible, with sample and standards being excited under precisely the same conditions.[6,38]

8.2 Inductively Coupled Plasma (ICP) Sources

Since 1974, the inductively coupled plasma (ICP) torch has become commercially available and is among the most effective sources for emission spectroscopy in use today. An ICP discharge is produced by the effect of a radio frequency field (typically 27 to 40 MHz), which creates a magnetic field inside a stream of argon which is first made conducting by a pilot electric spark, arc or Tesla discharge. A spectrally intense plasma at a temperature of 9000 to 10 000 K is obtained in the annulus of an ICP discharge operating at 1–2 kW input power. Samples are introduced as powders, gases, or liquids using the type of spray chamber already made available in flame spectroscopy.[6] Because of the inert atmosphere of the ICP discharge, some of the difficulties encountered in flame excitation are avoided: for example, the air–acetylene flame favors the formation of neutral atoms, while the very hot nitrous oxide–acetylene flame contains high concentrations of CN and NH species and produces a strongly reducing atmosphere. Chemical interferences of this kind, leading to the formation of stable compounds in flames, are almost negligible in the ICP discharge and spectra arising from molecular species such as CN are minimized. Simultaneous determination of as many as 35 elements in a single sample can be carried out without modifying the conditions for each element: less than 5 cm^3 of sample solution is generally required. Detection limits are generally in the range 0.02–2 ppb (ppb $= 10^{-7}\%$).[39,40]

9 ATOMIC ABSORPTION SPECTROSCOPY

The Maxwell–Boltzmann distribution law shows that the ratio of the number of atoms N_u in an excited upper state (*see Excited State*) to the number in the ground state N_o increases exponentially with temperature. For example, the ratio $N_\mathrm{u}/N_\mathrm{o}$ for Cs (resonance line at 852.1 nm), Ca (422.7 nm), and Zn (213.8 nm) increases from 4.44×10^{-4}, 1.21×10^{-7}, and 7.29×10^{-15} at 2000 K to 2.98×10^{-2}, 6.04×10^{-4}, and 1.48×10^{-6} at 4000 K. Even so, this means that for many transition metals only a small fraction of the vaporized atoms are in an excited state capable of emitting a line spectrum, even at the temperature of an ICP.

In 1955, A. Walsh[41] recognized this and showed how the absorption from the great preponderance of unexcited molecules could be exploited analytically.[42–44] Thus, in atomic absorption spectroscopy (AAS) the light from a (usually modulated) source emitting the spectrum of the desired analyte element is passed through a sample atomization cell (such as a flame or graphite tube furnace), a monochromator (to isolate the desired source emission line) and finally into a detector to allow measurement of the change in source line intensity due to absorption by sample atoms. The narrow waveband (0.001–0.005 nm) light source is usually a hollow cathode discharge lamp prepared with the desired element, although some multielement lamps are now available. In the sample atomization cell a fraction of light from the essentially monochromatic source is absorbed by atoms from the sample, which is sprayed as a solution into the flame by a pneumatic nebulizer, or vaporized electrothermally from a solid in a graphite furnace. The amount of radiation remaining can then be monitored, the concentration of atoms in the path of the light beam being determined by Beer's law. Calibration is achieved with standard solutions containing known concentrations of the element being determined.

In the case of flame atomization, fuel–oxidant mixtures like acetylene–air are used for most easily atomized elements; for the less easily atomized elements, for example, those that exist mainly as monoxides, the analytical sensitivity can be greatly enhanced by going to a higher-temperature flame, such as acetylene–nitrous oxide, thus shifting the equilibrium $M + O \rightleftharpoons MO$ toward the metal.

The development of nonflame atomization systems, particularly the graphite tube furnaces, resulted in a significant improvement in the analytical sensitivity for many elements.[45] While the flame-based technique is capable of measuring sample concentrations down to $100\,\mathrm{ng\,cm^{-3}}$ (parts per billion), graphite furnace devices offer detection limits of the order of $0.1\,\mathrm{ng\,cm^{-3}}$, a 1000-fold gain. These devices consist of a graphite tube, into which a small amount of sample is placed, which is then heated electrically to a high temperature, vaporizing and atomizing the sample. They are particularly useful when the amount of sample available is limited, since sample volumes are usually in the microliter range. Unfortunately, these devices often suffer from matrix effects and exhibit relatively poor precision because of the small sample size. However, a typical detection limit for many elements using furnace AAS is 10^{-13} g.

In general, as an analytical technique for trace metal (*see Trace Element*) determinations, AAS has important advantages. It has high sensitivity for many elements, with perhaps 60 or so elements measurable with flame atomization in the ppm range ($\sim 0.1–10\,\mu\mathrm{g\,cm^{-3}}$, or $\sim 10^{-7}–10^{-5}$ g on an absolute basis), and more than half of these measurable at significantly lower concentrations with nonflame atomization. In addition it is simple, rapid, and relatively low cost and can be highly specific, exhibiting few interferences.

9.1 Applications of AAS

In considering the applications of AAS,[46] the technique has made the biggest contribution to the determination of nonferrous metals and for the transition elements Cu and Ag, in particular, whose measurement is completely free from interferences due to Zn, Cd, Hg, Sn, Pb, Bi, or Sb. Blood sera and other body fluids are analyzed after deproteination using concentrated HCl, while for the analysis of plants, milk, and wine the samples are commonly mineralized by incineration or by wet-ashing with acids. In metals and alloys these elements are frequently present in somewhat higher concentrations and these materials may, therefore, be analyzed directly after dissolution in appropriate acids.

The ferrous metals, which include Co, Ni, Cr, Mn, and Mo, besides Fe, all have line-rich spectra and with the exception of iron all are used as alloying elements in steels. No specific interference effects have been observed for Fe, Co, or Ni; for Cr and Mn the effects are only slight; for Mo they can be considerable. The tendency to exhibit interference effects corresponds to the tendency to form oxides in the flame and is, therefore, predominantly due to the formation of nonvolatile compounds and may be eliminated by using releasing elements. Thus, for example, the depressive effect of Si on Cr and Mn may be eliminated by the addition of Ca or Sr to the solution sprayed.

The sensitivity of AAS is usually sufficient to allow determination of these elements in steels after simply dissolving the sample. Most often a mixture of hydrochloric and nitric acids is used, but sometimes sulfuric and phosphoric acids with several drops of nitric acid to facilitate oxidation are preferred. In any case, the volumes of acids in all the solutions sprayed must be kept constant, because generally the acids have a depressive effect. For the analysis of organic materials, plants, fertilizers, and so on, the ash is often digested with acids and the undissolved residue filtered off.

A special group of materials analyzed are crude and lubricating oils. Ni, V, and Fe act as poisons on cracking catalysts (*see Catalysis*), and the wear of mechanical parts of engines can be indicated by the content of trace elements (*see Trace Element*) in lubricating oils. Their determination is therefore an important task. To eliminate the tedious mineralization of the samples, they can be analyzed directly after dilution with some nonpolar solvent, usually xylene, or methyl isobutyl ketone (MIBK).

Among the noble metals, Au and Pd are most easily accessible to AAS determinations. Both are easily atomized in the flame and are not subject to any specific interference effects, so that their determination is sensitive and without complications. Pt, Rh, Ru, Ir, and Os may be determined, but with several specific interference effects, especially in low-temperature flames.

10 X-RAY METHODS

The bombardment of a metal target with a beam of high-energy electrons produces X rays with a line spectrum characteristic of each element present. This is virtually independent of chemical combination or physical state and, for example, the K_α lines from molybdenum appear at the same place whether the target is the oxide, sulfide or the element itself; the frequency ν is related to the atomic number Z by Moseley's law, $\nu = k(Z-1)^2$.[6]

By focusing an electron beam of moderate energy (10–50 keV) on a very small area of the sample the X ray characteristic of the local elements are excited (electron probe microanalysis, EPMA), enabling details of surface structure such as inclusions and grain boundaries (*see Grain Boundary*) to be examined.[47] A further development following on from this is scanning electron microscopy (SEM) (*see Electron Microscopy*).[48] On the other hand, if a material is irradiated with X rays it is possible to measure the energy of electrons ejected from the sample, and this leads to a method of analysis known as X-ray photoelectron spectroscopy (XPS) (*see* ***Photoelectron Spectroscopy of Transition Metal Systems***) or electron spectroscopy for chemical analysis (ESCA) (*see Electron Spectroscopy for Chemical Analysis*),[49] particularly suitable for the nondestructive study of the composition of solid surfaces (*see* ***Surfaces***).

10.1 X-ray Fluorescence (XRF) Analysis

When a beam of X rays is absorbed in an element, electronically excited atoms (*see Excited State*) are produced and those with vacant K-shells return to the ground state by a series of electronic transitions (*see Electronic Transition*) manifested by the emission of XRF. Proportional counters may be used to measure the intensity of a fluorescence line and by using a pulse-height analyzer with suitable electronics a form of spectrometer results in which a wavelength solution is obtained without the need for a diffracting crystal.[6] Such XRF spectroscopy is now widely applied to every type of element determination in control and research laboratories.[50] Solids or liquids are generally held in shallow metal or plastic containers covered with a thin Mylar window transparent to X rays. For trace analysis a sample is suitably diluted to reduce matrix effects to negligible proportions. Preconcentration may involve ion-exchange resins or papers (*see Ion Exchange*) or the use of appropriate chelating agents (*see Chelating Ligands*).[27]

The accuracy and precision of XRF methods, which can be applied for constituents ranging from a few ppm to almost 100% by weight, are related to the care taken in preparing the sample and standards, the quality of the apparatus, and the use of the appropriate correction factors. In industrial control analysis a relative analytical accuracy of 1% is not unusual.[50]

11 ACTIVATION ANALYSIS

When a target nucleus ${}^{A}_{Z}\mathrm{X}$ is bombarded with a stream of particles ${}^{a}_{z}\mathrm{x}$, there is a definite probability measured by the capture cross-section σ of producing a new compound nucleus ${}^{A+a}_{Z+z}\mathrm{B}$ which rapidly rearranges to give a new nuclide ${}^{A+a-1}_{Z+z-1}\mathrm{C}$. This process always occurs in less than 10^{-12} s so that the concomitant prompt radiation cannot be measured while the irradiation is still in progress. The product nuclide C is a radioactive species which starts decaying as soon as it is produced, with a characteristic half-life $t_{1/2}$ and the emission of α, β, and γ rays in the usual way.[6,51,52]

11.1 Neutron Activation Analysis

If the irradiation is carried out for t seconds in a stream of neutrons of flux f (neutrons cm^{-2} s^{-1}), the resulting activity due to W g of sample is given by

$$A(\text{disintegrations s}^{-1}) = \frac{f\sigma\theta W N_{\mathrm{A}}[1-\exp(-0.693t/t_{1/2})]}{M}$$

where M is the atomic mass of the isotope of abundance θ, σ is its capture cross-section (cm^2), and N_{A} is the Avogadro constant, 6.023×10^{23}. The values of σ for different nuclei cover a wide range from about 0.07 up to several thousand barns (1 barn $= 10^{-24}$cm^2), and values of $t_{1/2}$ range from seconds to many years (e.g. 1662 years for ^{9}Be).[6,51]

In practice, the sample of analyte and a standard containing about the same mass of the element of interest are irradiated simultaneously in the same neutron flux f and for the same time t before being removed to the counting laboratory. A period of 'cooling' may be allowed to let any high activity from extraneous elements die away. If the resulting sample emits γ-rays, counting is carried out with a scintillation spectrometer which is especially effective when a number of elements are to be determined simultaneously and where a nondestructive analysis is essential.[2,53] If chemical separations are required to obtain a radiochemically pure specimen for β-counting, various carriers may have to be employed but since these will not be radioactive, no blanks are thereby introduced; this is one of the great advantages of the neutron activation procedure.[52] We can estimate the sensitivity of neutron activation analysis by calculating the smallest mass of a given element that can be determined after irradiation of a sample to saturation in a flux of 1.5×10^{12} neutrons cm^{-2} s^{-1}, assuming that 2 hours had elapsed between irradiation and counting and that the limit of detection was 10 counts min^{-1} (Table 2).[51] The value of the method in the case of the less common elements will be obvious.

11.2 Charged Particle and Gamma Photon Activation Analysis

In addition to activation by thermal (~0.04 eV), epithermal (>0.1 eV), or fast neutrons (14 MeV), a variety of charged particles (p, d, α, etc.) and γ-rays have been used when special sources are available.[6,51,52] For example, 1–5 MeV protons from a van de Graaff electrostatic generator produce X rays from the excited intermediate ${}^{A+a}_{Z+z}\mathrm{B}$ in a technique designated by the acronym PIXE (proton-induced X-ray emission),[54]

Table 2 Estimated sensitivity of neutron activation analysis[51]

Sensitivity (g)	Element
1×10^{-12}	Dy, Eu
5×10^{-12}	Au, Ho, Lu
1×10^{-11}	In, Mn, Re, Sn
5×10^{-11}	As, Kr, La, Pr, Sc, Tb, Tu, W, Yb
1×10^{-10}	Sb, Br, Cu, Er, Ga, Pd, Na, Ta, Yt
5×10^{-10}	Al, Cs, Co, Gd, Hf, Nd, Li(n,α), P, Rb
1×10^{-9}	Ba, B(n,α), Cd, Ce, Hg, Os, Pt, K, Ru
5×10^{-9}	Cl, Ge, I, Ag, Te, Th, Sn, U, Xe, Zn
1×10^{-8}	Mo, Ni, Si, Th
5×10^{-8}	Bi, Se
1×10^{-7}	Cr, Fe, Sr, Zr
5×10^{-7}	Ca, S

which gives better discrimination between similar elements and is particularly suited for the simultaneous determination of a large number of elements in many varied specimens. Disadvantages of charged particle methods are the low flux of particles and the small penetration depth.

12 ELECTROCHEMICAL METHODS

There is a whole gamut of electrochemical methods available for the determination of the transition elements.[55] Electrogravimetric methods are available for large numbers of metals (e.g. Cu, Ag, Cd, Co, Ni, Sn, Zn, Pb, and Tl) provided these are available in weighable amounts. Controlled potential electrolysis at a mercury pool electrode is best suited for separations (e.g. Cu, Cd, and Pd from uranium) or removing traces of metallic impurities when preparing very pure electrolytes for use in polarography.[6]

Polarography (discovered by Jaroslav Heyrovský in 1922)[56] is a technique in which the potential between a dropping mercury electrode and a reference electrode is slowly increased at a rate of about 50–200 mV min^{-1} while the resultant current (carried through an auxiliary electrode) is monitored; the reduction of metal ions at the mercury cathode gives a diffusion current proportional to the concentration of the metal ions. The method is especially valuable for the determination of transition metals such as Cr, Mn, Fe, Co, Ni, Cu, Zn, Ti, Mo, W, V, and Pt, and less than 1 cm^3 of analyte solution may be used. The detection limit is usually about 5×10^{-6} M, but with certain modifications in the basic technique, such as pulse polarography, differential pulse polarography, and square-wave voltammetry, lower limits down to 10^{-8} M can be achieved.

Especially for those metals that form amalgams (e.g. Cu, Pb, Cd, In, Bi, and Zn), the sensitivity can be increased 10- to 1000-fold by preconcentrating the analyte electrochemically in a hanging mercury drop (or on a solid electrode surface) and then plotting the current–potential curve of the stripping voltammogram (anodic stripping voltammetry, ASV).[57]

13 PLATINUM GROUP METALS (PGMs)

Owing to great similarities in chemical properties and their association together in Nature, the second and third triads of groups 8–10 of the periodic table (Ru, Rh, Pd and Os, Ir, Pt) present many difficulties for the analyst. Their comparative rarity and intrinsic value demand their recovery from spent catalytic converters in the petroleum and many other chemical industries, from the increasing number of pollution control units in motor vehicles, from scrapped jewellery and the scrap of the electronics industry, as well as material from geochemical exploration, the exploitation from mineral deposits, and ‘sweeps’. The first requirement is to collect a homogeneous alloy (*see **Alloys***).[58,59]

Often a friable alloy can be produced simply by melting with aluminum; this can then be ground into a powder. Collection by fire-assay methods involving the use of tin and iron–nickel–copper alloys has been extensively studied and collection by melting with nickel sulfide, copper sulfide, and copper alone has its advocates. Lead oxide, as used in the fire assay of gold and silver, is less suitable for isolating platinum and palladium and still less so for rhodium, ruthenium, and iridium, while osmium is largely volatile in the cupellation stage. The optimum procedure is naturally highly dependent on the nature of the sample and in many cases some form of acid digestion is preferable.[58,59]

With modern instrumentation it is often possible to make determinations of individual elements without the necessity for any chemical separations, but while mutual interferences for AAS and ICP emission spectrometry are often small the sensitivity, for example, for iridium, may be unacceptably low and chemical separations are required.[60] The separation of rhodium from iridium is one of the most challenging analytical tasks. Ruthenium and osmium are most commonly separated from other PGMs and matrix elements by distillation of their tetroxides.[59]

Separation of PGMs by solvent extraction or using cation exchangers (*see Ion Exchange*) is well documented[58,59] and gravimetric and titrimetric methods are prominent, especially in the older monographs.[61] The most important instrumental techniques include emission spectroscopy, XRF, AAS, and, of course, the use of activation analysis (see Section 11).[58,59]

14 REFERENCES

1. A. M. Pollard and C. Heron, ‘Archaeological Chemistry’, Royal Society of Chemistry, Cambridge, 1996.

2. M. J. Hughes, *Chem. Ind. (London)*, 1992, **23**, 897.
3. I. M. Kolthoff, E. B. Sandell, E. J. Meehan, and S. Bruckenstein, 'Quantitative Chemical Analysis', 4th edn., Macmillan, London, 1969.
4. J. Bassett, R. C. Denney, G. H. Jeffery, and J. Mendham, 'Vogel's Textbook of Quantitative Inorganic Analysis', 4th edn., Longman, London and New York, 1978.
5. D. C. Harris, 'Quantitative Chemical Analysis', 6th edn., W. H. Freeman, New York, 2002.
6. H. H. Willard, L. L. Merritt Jr, J. A. Dean, and F. A. Settle Jr, 'Instrumental Methods of Analysis', 7th edn., Wadsworth Publishing, Belmont, CA, 1988.
7. I. M. Kolthoff, P. J. Elving, and other eds., 'Treatise on Analytical Chemistry', 2nd edn., John Wiley & Sons, New York, 1978–1993.
8. C. L. Wilson and D. W. Wilson eds., 'Comprehensive Analytical Chemistry', Elsevier, Amsterdam, 1959–1975, Vols. I–IID.
9. G. Svehla and other eds., 'Wilson and Wilson's Comprehensive Analytical Chemistry', Elsevier, Amsterdam, 1975–2004, Vols. III–XLIII.
10. A. Townshend, P. J. Worsfold, S. J. Haswell, R. Macrae, H. W. Werner, and I. D. Wilson eds., 'Encyclopedia of Analytical Science', Academic Press, London and San Diego, CA, 1995, 10 Vols.
11. P. J. Worsfold, A. Townshend, and C. Poole eds., 'Encyclopedia of Analytical Science', 2nd edn., Academic Press, London and San Diego, CA, to be published 2005, 10 Vols.
12. R. A. Meyers ed., 'Encyclopedia of Analytical Chemistry: Applications, Theory and Instrumentation', John Wiley & Sons, Chichester, 2000, 15 Vols.
13. H. M. N. H. Irving, 'The Techniques of Analytical Chemistry', HMSO, London, 1974.
14. H. M. N. H. Irving, *Analyst (London)*, 1974, **99**, 787.
15. F. Szabadváry and A. Robinson, The History of Analytical Chemistry, in 'Wilson and Wilson's Comprehensive Analytical Chemistry', ed. G. Svehla, Elsevier, Amsterdam, 1980, Vol. X, Chap. 2, pp. 61–.
16. H. Irving, *Sci. Prog. (Oxford)*, 1951, **39**, 63.
17. J. Pawliszyn, 'Sample Preparation in Field and Laboratory', Elsevier, Amsterdam, 2002.
18. R. Bock, 'A Handbook of Decomposition Methods in Analytical Chemistry', Translated and revised I. L. Marr, International Textbook Company (Blackie Group), Glasgow, 1979.
19. H. M. Kingston and L. B. Jassie eds., 'Introduction to Microwave Sample Preparation: Theory and Practice', American Chemical Society, Washington, DC, 1988.
20. P. W. West, A. O. Parks, and H. Weisz, Inorganic Qualitative Analysis, in 'Comprehensive Analytical Chemistry', eds. C. L. Wilson and D. W. Wilson, Elsevier, Amsterdam, 1959, Vol. IA, p. 328.
21. F. Feigl and V. Anger, 'Spot Tests in Inorganic Analysis', 6th edn., Elsevier, Amsterdam, 1972.
22. C. L. Wilson, F. E. Beamish, W. A. E. McBryde, and L. Gordon, Inorganic Gravimetric Analysis, in 'Comprehensive Analytical Chemistry', eds. C. L. Wilson and D. W. Wilson, Elsevier, Amsterdam, 1959, Vol. IA, p. 430.
23. P. F. S. Cartwright, E. J. Newman, and D. W. Wilson, *Analyst (London)*, 1967, **92**, 663.
24. F. Holmes, Organic Reagents in Inorganic Analysis, in 'Comprehensive Analytical Chemistry', eds. C. L. Wilson and D. W. Wilson, Elsevier, Amsterdam, 1959, Vol. IA, p. 210.
25. M. L. Salutsky, Scandium, in 'Comprehensive Analytical Chemistry', eds. C. L. Wilson and D. W. Wilson, Elsevier, Amsterdam, 1962, Vol. IC, p. 423.
26. Various authors, Transition Elements, in 'Comprehensive Analytical Chemistry', eds. C. L. Wilson and D. W. Wilson, Elsevier, Amsterdam, 1962, Vol. IC, p. 367.
27. H. M. N. H. Irving, Applications in Analysis, in 'Comprehensive Coordination Chemistry', eds. G. Wilkinson, R. D. Gillard, and J. A. McCleverty, Pergamon Press, Oxford, 1987, Vol. 1, Chap. 10, p. 521.
28. Various authors, Inorganic Titrimetric Analysis, in 'Comprehensive Analytical Chemistry', eds. C. L. Wilson and D. W. Wilson, Elsevier, Amsterdam, 1960, Vol. IB, p. 1.
29. G. Schwarzenbach and H. Flaschka, 'Complexometric Titrations', Translated and revised H. M. N. H. Irving, Methuen, London, 1969.
30. A. E. Martell, R. M. Smith, and R. J. Motekaitis, 'NIST Standard Reference Database 46: Critically Selected Stability Constants of Metal Complexes, Version 7', National Institute of Standards and Technologies, Gaithersburg, MD, 2002, http://www.nist.gov/srd/nist46.htm.
31. R. Přibil, 'Applied Complexometry', Translated R. Přibil and M. Štulíková, ed. R. A. Chalmers, Pergamon Press, Oxford, 1982.
32. E. Upor, M. Mohai, and Gy. Novák, Photometric Methods in Inorganic Trace Analysis, in 'Wilson and Wilson's Comprehensive Analytical Chemistry', ed. G. Svehla, Elsevier, Amsterdam, 1985, Vol. XX, p. 1.
33. H. Onishi, 'Photometric Determination of Traces of Metals', 4th edn., John Wiley & Sons, New York, 1989, Vol. 1.
34. Z. Marczenko and M. Balcerzak, 'Separation, Preconcentration and Spectrophotometry in Inorganic Analysis', Translated E. Kloczko, Elsevier, Amsterdam, 2000.
35. G. Iwantscheff, 'Das Dithizon und seine Anwendung in der Mikro- und Spurenanalyse', 2nd edn., Verlag Chemie, Weinheim, 1972.
36. H. M. N. H. Irving, 'Dithizone', Analytical Sciences Monographs No. 5, The Chemical Society, London, 1977.
37. N. L. Cromhout and A. T. Hutton, *Appl. Organomet. Chem.*, 2000, **14**, 66 and refs cited.

38. K. Slickers, ‘Automatic Atomic Emission Spectroscopy’, 2nd edn., Brühlsche Universitätsdruckerei, Giessen, D-35334 Germany, 1993 (ISBN 3-9803333-1-0).
39. A. Montaser and D. W. Golightly, ‘Inductively Coupled Plasmas in Analytical Atomic Spectroscopy’, VCH, Weinheim, 1987.
40. C. B. Boss and K. J. Fredeen, ‘Concept, Instrumentation and Techniques in Inductively Coupled Plasma Optical Emission Spectrometry’, 2nd edn., Perkin-Elmer, Norwalk, CT, 1997.
41. A. Walsh, *Spectrochim. Acta.*, 1955, **7**, 108.
42. A. Walsh, *Anal. Chem.*, 1991, **63**, 933A.
43. S. R. Koirtyohann, *Anal. Chem.*, 1991, **63**, 1024A.
44. W. Slavin, *Anal. Chem.*, 1991, **63**, 1033A.
45. B. V. L’vov, *Anal. Chem.*, 1991, **63**, 924A.
46. B. Welz and M. Sperling, ‘Atomic Absorption Spectrometry’, 3rd edn., Wiley-VCH, Weinheim, 1999.
47. B. K. Agarwal, ‘X-ray Spectroscopy’, 2nd edn., Springer-Verlag, Berlin, 1991.
48. J. I. Goldstein, D. E. Newbury, P. Echlin, and D. C. Joy, ‘Scanning Electron Microscopy and X-Ray Microanalysis: A Text for Biologists, Materials Scientists, and Geologists’, 2nd edn., Plenum Publishing, New York, 1992.
49. T. L. Barr, ‘Modern ESCA: The Principles and Practice of X-ray Photoelectron Spectroscopy’, CRC Press, Boca Raton, FL, 1994.
50. R. E. Van Grieken and A. A. Markowics eds., ‘Handbook of X-ray Spectrometry’, Marcel Dekker, New York, 1993.
51. T. B. Pierce, *Sel. Annu. Rev. Anal. Sci.*, 1971, **1**, 133.
52. Z. B. Alfassi ed., ‘Activation Analysis’, CRC Press, Boca Raton, FL, 1990.
53. S. Amiel ed., ‘Nondestructive Activation Analysis’, Elsevier, Amsterdam, 1981.
54. S. A. E. Johansson, J. L. Campbell, and K. G. Malmqvist eds., ‘Particle-induced X-Ray Emission Spectroscopy (PIXE)’, John Wiley & Sons, Chichester, 1995.
55. A. J. Bard and L. R. Faulkner, ‘Electrochemical Methods: Fundamentals and Applications’, 2nd edn., John Wiley & Sons, New York, 2001.
56. A. M. Bond, ‘Modern Polarographic Methods in Analytical Chemistry’, Marcel Dekker, New York, 1980.
57. P. T. Kissinger and W. R. Heineman eds., ‘Laboratory Techniques in Electroanalytical Chemistry’, 2nd edn., Marcel Dekker, New York, 1996.
58. S. Kallmann, *Anal. Chem.*, 1984, **56**, 1020A.
59. S. Kallmann, *Talanta*, 1987, **34**, 677.
60. H. Jäger, Precious Metals, in ‘Applied Atomic Spectroscopy’, ed. E. L. Grove, Plenum Press, New York and London, 1978, Vol. 2, p. 1.
61. F. E. Beamish and J. C. Van Loon, ‘Recent Advances in the Analytical Chemistry of the Noble Metals’, Pergamon Press, Oxford, 1972.

Acknowledgment

In revising and updating our original article from the first edition of the Encyclopedia of Inorganic Chemistry, I have tried to preserve the clear, inimitable style of the late Harry Irving’s writing, particularly in the historical overview presented, and have attempted to retain his insightful perspectives throughout the article. Ten years after his death, this article is dedicated to his memory.

Antimony: Inorganic Chemistry

Hans Joachim Breunig
University of Bremen, Bremen, Germany

Based in part on the article Antimony: Inorganic Chemistry by R. Bruce King which appeared in the Encyclopedia of Inorganic Chemistry, First Edition.

1 Introduction 1
2 Antimony Hydrides 2
3 Antimonides 2
4 Antimony Group 13 Metal (Al, Ga, In) and Group 15 Metal (Si, Ge, Sn, Pb) Compounds 3
5 Antimony Pnicogen (N, P) Compounds 3
6 Antimony Chalcogen (O, S, Se, Te) Compounds 3
7 Antimony Halides 5
8 Transition-metal Complexes with Sb_n Ligands 6
9 References 7

1 INTRODUCTION

1.1 History, Occurrence, Use, and Isotopes

Antimony compounds were known to the ancients. In Egypt and other ancient oriental cultures, Sb_2S_3 (stibnite) was used as medicine and for cosmetic purposes, for example, as a component of black eye makeup. The names of the element in different languages originate from the Latin words stibium and antimonium. The former was used in 50 BC by Pliny for Sb_2S_3. It is probably of Egyptian origin. For the word antimonium, there are several more or less fantastic etymologies (against the monks, against loneliness etc.). Probably it is a retranslation of the Arabic word for stibium into Medieval Latin.

Antimony is among the less abundant elements in the earth's crust (0.6 ppm). The most important antimony ore is stibnite, which occurs in large quantities in China, South Africa, Bolivia, and other countries. Other antimony sulfide ores are tetrahedrite ($Cu_3Sb_2S_3$), wolfsbergite ($CuSbS_2$), and jamesonite ($FePb_4Sb_6S_{14}$). Weathering of stibnite leads to valentinite (Sb_2O_3).

It is not very difficult to recover stibnite from other minerals because the melting point of this antimony mineral is low (546 °C). Heating in the range of 550 to 600 °C results in selective melting of the stibnite, which can be collected as crude concentrate. Roasting in air produces Sb_2O_3 that can be reduced with coke. Another method is to reduce the Sb_2S_3 concentrate directly with scrap iron to give elemental antimony (equation 1), which can be purified by melting with sodium nitrate and sodium carbonate.[1]

$$Sb_2S_3 + 3Fe \longrightarrow 2Sb + 3FeS \qquad (1)$$

More complex antimony ores can be treated by leaching with alkali hydroxide or sulfide and by electrolysis of the resulting solution of sodium thioantimonate, Na_3SbS_4. Elemental antimony can also be recovered from the flue dust of lead smelters.

The dominant use of antimony is as an alloying element to harden lead, notably for grids in motor car batteries.[1] Pb–Sb alloys have also been used for ammunition or for movable types in printing presses.[1] Antimony is a component of many bearing alloys, like Babitt metal (an alloy of antimony, tin, copper, and other metals), which are useful as bearings because they are soft and slippery. Sb_2O_3 can be applied in chemicals used to impregnate plastics, textiles, rubber, and other materials as a flame retardant. The orange–red form of Sb_2S_3, which is obtained from Sb(III) and H_2S, has been used for pyrotechnical articles and as a pigment in paints, plastics, or rubber. An important medicinal use of antimony compounds is the treatment of tropical diseases caused by parasites like leishmaniasis or bilharziasis.[2,3] Therapies include potassium antimony(III) tartrate, sodium antimony(V) gluconate (Pentostam®) or *N*-methyl-glucamine antimonate(V) (Glucantime®). Proposed structures are shown in Schemes 1 and 3. It is thought that Sb(V) is reduced to Sb(III) *in vivo*. Potassium antimony(III) tartrate (tartar emetic) is an emeticum. It is also used in the therapy of infections in veterinary medicine.

Natural antimony consists of the isotopes ^{121}Sb (57.3%) and ^{123}Sb (42.7%). Important artificial isotopes include ^{122}Sb ($\tau_{1/2} = 2.8$ days), ^{124}Sb ($\tau_{1/2} = 60.4$ days), and ^{125}Sb ($\tau_{1/2} = 2.7$ years).

1.2 Elemental Antimony

The form of elemental antimony that is stable at normal temperatures and pressures is the gray, metallic rhombohedral α-form, mp 630.7 °C, bp 1587 °C, density 6.70 g cm^{-3}. Crystals are lustrous. They have a relatively high electrical resistivity (41.7 μΩ cm at 20 °C). The structure of α-Sb consists of sheets of covalently bonded antimony stacked in layers, which are formed of puckered six-membered rings. Each antimony forms three shorter bonds (2.91 Å) in the same layer as well as three longer bonds (3.36 Å) to antimony atoms in the adjacent layer. In addition to the α-form, other allotropes include a very unstable yellow form and black forms obtained electrolytically or by condensing the vapor on cold surfaces. Two crystalline allotropes are made by high-pressure techniques. At 85 kbar, a modification with a primitive cubic lattice is formed where each antimony atom is in an octahedral environment of six equidistant (2.96 Å) neighbors. Further

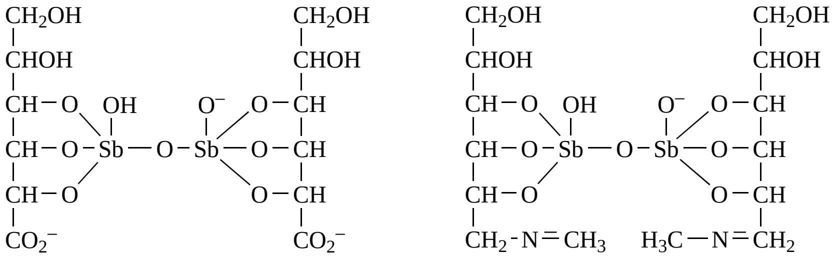

Sodium antimony(v) gluconate
(Pentostam®)

N-methyl-glucamine
(Glucantime®)

Scheme 1

increase in the pressure to 90 kbar gives a hexagonal close-packed form with Sb–Sb distances of 3.28 Å for the 12 nearest neighbors. Thin films of amorphous antimony on surfaces of $AuSb_2$ and MoS_2 contain crystalline structures of Sb_4 tetrahedra.**[4]** Antimony vapor consists of Sb_2 and Sb_4 molecules. The calculated Sb–Sb bond length in Sb_4 tetrahedra is 2.687 Å.

Elemental antimony is stable in air and moisture at room temperature but oxidizes upon heating to give Sb_2O_3, Sb_2O_4, and Sb_2O_5. It reacts with Cl_2 to give $SbCl_5$ and also reacts with the other halogens and with sulfur. Antimony is not soluble in HCl or dilute H_2SO_4. Hot concentrated H_2SO_4 gives $Sb_2(SO_4)_3$ and concentrated HNO_3 gives hydrated Sb_2O_5.

1.3 General Aspects of Antimony Chemistry

The ground state electronic configuration of antimony is [Kr] $4d^{10}5s^25p^3$. Its covalent radius is 1.4 Å and its ionic radii are 0.76 and 0.60 Å for six-coordinate Sb(III) and Sb(V) respectively. Both the +3 and the +5 oxidation states are stable for antimony. Compounds with a formal oxidation state of +4 such as Sb_2O_4 and $SbBr_6^{2-}$ are diamagnetic, containing equal amounts of Sb(III) and Sb(V). Negative oxidation states are found in alkali metal antimonides. The most frequently encountered coordination numbers are 3 (e.g. trigonal pyramidal in SbH_3), 4 (tetrahedral in $Sb(CH_3)_4^+$, ψ-trigonal bipyramidal in $(CH_3)_2SbBr_2^-$), 5 (square pyramidal in SbF_5^{2-}, $SbPh_5$, trigonal bipyramidal in SbF_5), and 6 (octahedral Sb in $SbBr_6^{3-}$, SbF_6^-). Also, coordination numbers 1 ($Sb{\equiv}Sb$) and 2 (stibabenzene, C_6H_5Sb, $RSb{=}SbR$, $RSb{=}CR_2$, Ph_2Sb^-) are known.

2 ANTIMONY HYDRIDES

The most important antimony hydride, stibine, SbH_3 is a malodorous, extremely toxic gas (bp −18 °C, mp −88 °C) formed from soluble antimony compounds and hydrogen in statu nascendi (equation 2), by reaction of Mg_3Sb_2 with dilute hydrochloric acid, or, at best, by reaction of $SbCl_3$ with $NaBH_4$ (equation 3) in hydrochloric acid.

$$Sb(OH)_3 + 6H \longrightarrow SbH_3 + 3H_2O \qquad (2)$$

$$SbCl_3 + 3NaBH_4 \longrightarrow SbH_3 + 3NaCl + 3BH_3 \qquad (3)$$

The structure is pyramidal with a H–Sb–H angle of 91.54°, and an Sb–H bond length of 1.70 Å.**[5]** SbH_3 is an endothermic compound ($\Delta H_f^\circ = 145.1\ \mathrm{kJ\,mol^{-1}}$) decomposing at room temperature to metallic antimony and hydrogen. As a side product of the syntheses of SbH_3, small amounts of distibine Sb_2H_4 were also detected. SbH_3 is used in Metal Organic Chemical Vapor Deposition (MOCVD) processes, but because of its instability, it has to be generated on site.**[1]** SbH_2, H_2SbOH, and $HSbO_2$ are products of the photolysis of SbH_3 and O_3 in an Ar matrix at 12 K.**[5]**

3 ANTIMONIDES

Reduction of antimony by alkali metals or by other methods leads to alkali metal antimonides (Zintl anions) of various types. Known antimonides include isolated Sb^{3-} ions (in Li_3Sb, Na_3Sb), dumbbells Sb_2^{4-} in Cs_4Sb_2, discrete antimony chains, for example, Sb_6^{8-} in $SrSb_3$, infinite spirals $(Sb^-)_x$ (in NaSb, RbSb), planar four-membered rings Sb_4^{2-} in $K(crypt)_3Sb_4$, Sb_7^{3-} cages in Cs_3Sb_7 or $Na_3Sb_7{\cdot}3TMEDA{\cdot}3THF$ (TMEDA = tetramethylethylenediamine, THF = tetrahydrofuran), and net shaped anions Sb_3^{2-} in $BaSb_3$.**[6,7]** Also, transition metals, lanthanides and actinides, form a variety of intermetallic compounds with antimony. Typical transition metal/antimony intermetallics are MSb_2 (M = Ni, Pd, Pt, Au) with Sb_2 units and MSb_3 (M = Co, Rh, Ir) with Sb_4 rings.

4 ANTIMONY GROUP 13 METAL (Al, Ga, In) AND GROUP 15 METAL (Si, Ge, Sn, Pb) COMPOUNDS

Important intermetallics are the III–V semiconductors for infrared detectors AlSb (band gap, 2.2 eV), GaSb (band gap, 0.7 eV), and InSb (band gap, 0.2 eV), which can be used as diodes and Hall effect devices. Precursors of these semiconductors are products obtained by reactions of $Sb(SiR_3)_3$ and alkyl derivatives of group 13 metals, for example, Lewis acid–base adducts $R_3M–Sb(SiR_3)_3$ ($M = Al$, Ga, In; $R =$ alkyl) or heterocycles $[R_2MSb(SiMe_3)_2]_n$ ($n = 2, 3$).[8–11]

Known molecular compounds with bonds between antimony and group 15 metals ($M =$ Si, Ge, Sn, Pb) include organometal stibines $(R_3M)_3Sb$, distibines $(R_3M)_4Sb_2$, or the silyl antimonide $[(DME)LiSb(SiMe_3)_2]$.[9,12–16] The reaction of the latter with $i Pr_3SiCl$ yields the mixed stibine $i Pr_3SiSb(SiMe_3)_2$.[9] Sodium tri(*tert*-butyl)silanide reacts with $SbCl_3$ to form the bicyclic stibine R_6Sb_8 (**1**) (equation 4).[17]

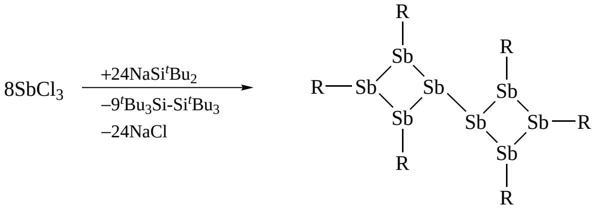

(4)

R = Si^tBu_3

(**1**)

Exchange reactions of $(Me_3Si)_3Sb$ with Me_3MCl give $(Me_3M)_3Sb$ ($M =$ Ge, Sn, Pb). $(Me_3Pb)_3Sb$ decomposes with the formation of $(Me_3Pb)_2$ and $(Me_3Pb)_4Sb_2$.[18] Organosilylstibines $(R_3Si)_3Sb$ generally adopt molecular structures with pyramidal antimony. The distibines $(R_3M)_4Sb_2$ are remarkable for the unusual red color of their crystalline phases where the molecules in the trans conformation are aligned to linear chains through short intermolecular Sb···Sb contacts.[14]

5 ANTIMONY PNICOGEN (N, P) COMPOUNDS

Although antimony–nitrogen bonds are unstable to hydrolysis, many well-characterized compounds where antimony atoms are bonded exclusively to nitrogen atoms are known.[19–24] They include tris-amido species, for example, $Sb(NR_2)_3$, formed by the reaction of $SbCl_3$ with secondary amines (equation 5).

$$SbCl_3 + 6R_2NH \longrightarrow Sb(NR_2)_3 + 3R_2NH_2Cl \qquad (5)$$

Other examples are dinuclear imido–amido compounds $Sb_2(NR_2)_2(\mu\text{-}NR)_2$ and a range of species based on anions, for example, $[Sb(NR)_3]_3^-$, $[Sb_2(NR)_2(\mu\text{-}NR)_2]_2^-$, or $[Sb_3(NR_2)_2(\mu\text{-}NR)_4]$.[23] The reaction between $SbCl_3$ and Li[NHPh] affords the remarkable twenty-four-membered imido antimony metallacycles $Sb_{12}(NPh)_{18}$ (**2**).[23,24]

The reaction of $SbCl_3$ with $[(PNR)_2(NRLi{\cdot}THF)_2]$ leads to a polycyclic cage complex of the formula $[(PNR)_2(NR)_2Sb]Cl$ where antimony is bonded to three nitrogen and one chlorine atom.[25] Antimony in a square planar environment of four nitrogen atoms exists in porphyrins and related macrocycles.[26,27] Sb–N bonds also exist in antimony azides. The mixed chloride diazide $SbCl(N_3)_2$ is formed from NaN_3 and $SbCl_3$ at room temperature.[28]

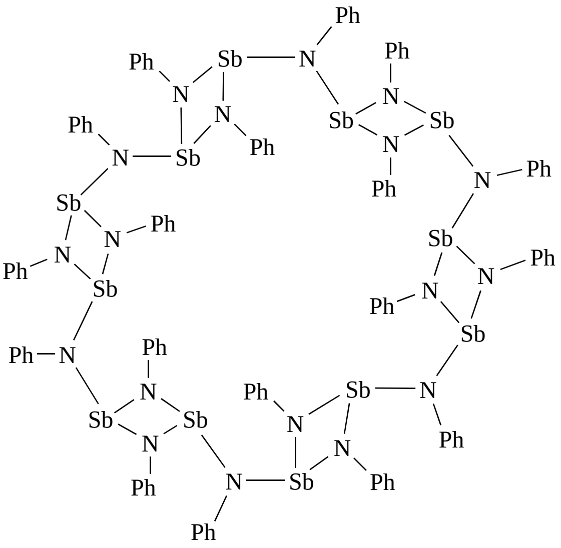

(**2**)

Molecular compounds with Sb–P bonds are very rare. One example is the anion $[cyclo\text{-}(RP)_4Sb]^-$, which is formed by reactions of $Sb(NMe_2)_3$ with primary phosphines.[7,29]

6 ANTIMONY CHALCOGEN (O, S, Se, Te) COMPOUNDS

6.1 Antimony Oxygen Derivatives

Antimony(III) oxide Sb_2O_3 occurs in two forms, cubic senarmontite containing discrete tetrahedral Sb_4O_6 molecules and orthorhombic valentinite (Scheme 2). The vapor phase consists of discrete Sb_4O_6 molecules. Senarmontite contains Sb_4O_6 units with each Sb having three Sb–O intramolecular bridging bonds (1.98 Å) and three intermolecular Sb···O distances (3.8 Å). Upon heating to 606° the cubic form is transformed into the valentinite form, which consists of infinite Sb–O double chains, the opening antimony atoms of which are bridged by oxygen in such a

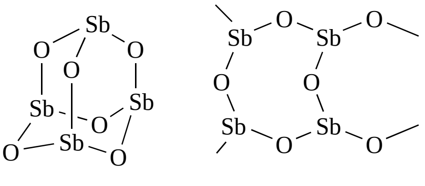

senarmontite valentinite

Scheme 2

way that strongly puckered eight-membered rings are formed.[30]

$Sb_2O_3$is insoluble in water or dilute nitric or sulfuric acids. It is regarded as amphoteric because it is soluble both in strong acids, which form complexes with Sb(III) such as hydrochloric acid, and in bases. In concentrated sulfuric acid, it is dissolved with the formation of $(SbO)_2SO_4$ or $Sb_2(SO_4)_3$. Sb_2O_3 dissolves in base to form antimonates(III), mostly, with polymeric structures. By fusing the oxides of sodium and antimony(III), one obtains Na_3SbO_3, which has a tetrameric structure. An example for antimony(III) incorporated in a polyoxometalate is the anion $(SbW_9O_{33})^{9-}$.[31,32] The presence of Sb_2O_3 and organic acids leads to soluble complexes of Sb(III). The best known example is tartar emetic, dipotassium bis[μ-D-tartratodiantimonate] trihydrate where tartaric acid acts as a tetradentate bimetallic ligand. The environment of antimony is a highly distorted Ψ-trigonal bipyramid. The axial oxygen atoms are from the carboxylate moiety and the equatorial oxygen atoms are hydroxyl derived (Scheme 3).

Antimony(V) oxide can be obtained by reaction of Sb_2O_3 with oxygen at high pressures and temperatures or by hydrolysis of $SbCl_5$ with aqueous ammonia. Sb_2O_5 is polymeric, with octahedrally coordinated antimony atoms. A third antimony oxide, Sb_2O_4 is best described as antimony(III) antimonate(V) $Sb^{III}Sb^{V}O_4$. It consists of layers of SbO_6 octahedra sharing vertices and Sb(III) centers between the layers. A simple oxo anion $SbO_4{}^{3-}$ is not known. Instead, the anion $Sb(OH)_6{}^-$ with six-coordinate octahedral antimony(V) is generated in basic solutions of Sb(V), for example, by treating $SbCl_5$ with aqueous sodium hydroxide. The sodium salt $NaSb(OH)_6$ is the least soluble of the alkali metal salts. The soluble potassium salt $KSb(OH)_6$ is used as a reagent for the precipitation of Na^+ as $NaSb(OH)_6$. Other antimonates(V) include $[Mg(H_2O)_6][Sb(OH)_6]_2$ and $[Cu(NH_3)_3(H_2O)_3][Sb(OH)_6]_2$. Dehydration of these hydrates affords edge-sharing polymeric octahedra $[SbO_6]_n{}^{n-}$.

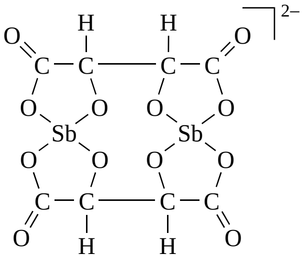

tartar emetic

Scheme 3

Alkoxides of Sb(III) or Sb(V) with known structures are compounds of the types $Sb(OR)_3$ (**3**) and $Sb(OR)_5$ (**4**). They are both dimeric in the solid state, with bridging alkoxy groups and trigonal pyramidal geometry or octahedral coordination about antimony.[33,34]

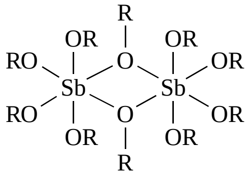

(**3**)

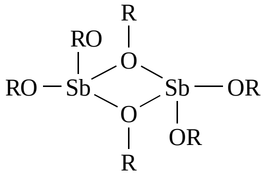

(**4**)

Homoleptic antimony(III) β-diketonates $Sb(thd)_3$ (Hthd = tetramethylheptanedione) and $Sb(fod)_3$ (Hfod = dimethylheptafluoroheptanedione) are obtained from $Sb(OEt)_3$ and three equivalents of the appropriate ligand. The compounds are monomeric in the solid state with ψ-seven coordination at antimony.[35] A polymeric structure is adopted by antimony (III) ethylene glycolate $[Sb_2(OCH_2CH_2O)_3]_n$ (**5**).[36]

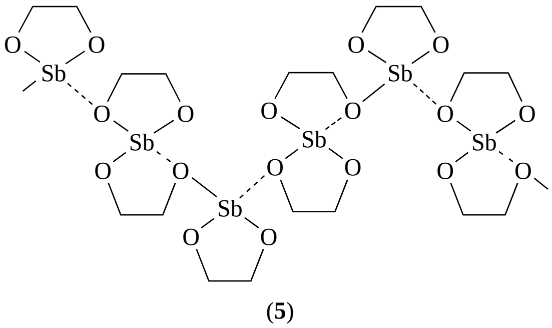

(**5**)

Monomeric Sb(III) dialkylcarbamato complexes $Sb(O_2CNR_2)_3$ form in reactions between trisamidostibines and CO_2 (equation 6).[37]

$$Sb(NR_2)_3 + 3CO_2 \longrightarrow Sb(O_2CNR_2)_3 \qquad (6)$$

6.2 Antimony Sulfides, Selenides, Tellurides

Antimony(III) sulfide is the most important sulfur compound of antimony, which occurs naturally as the mineral stibnite often forming a beautiful array of black crystalline needles. There is also an amorphous red-bronze form. Preparation of Sb_2S_3 in the laboratory by passing H_2S into acidic solutions of Sb(III) or Sb(V) gives the orange–red form of Sb_2S_3, which is also obtained by the combination of Sb and S. Heating the orange form in the absence of air gives the gray-black form. The structure of stibnite consists of indefinite Sb_4S_6 ribbons, which may be described as zigzag chains of face sharing Sb_4S_4 cubes.[30] Antimony(III) selenide is a gray material formed by fusion of the elements. It has a chain structure involving short Sb–Se bonds (2.58–2.77 Å), the chains being held in pairs by weaker bonding (2.9 Å). These pairs are bonded into sheets with Sb–Se interactions of 3.26 Å and the sheets are held by Sb···Se interactions of about 3.46 Å. Antimony telluride is a gray material formed by direct syntheses from the elements at elevated temperatures, and adopts a layer structure. The bond lengths Sb–Te lie between 2.98 and 3.17 Å. With band gaps of 1.7 eV, Sb_2S_3; 1.3 eV, Sb_2Se_3; and 0.3 eV, Sb_2Te_3, these compounds are of importance as semiconductors.

Great structural diversity is displayed by metal derivatives of thio- or seleno-antimonates $[SbS_3]^{3-}$, $[SbSe_3]^{3-}$, $[SbS_4]^{3-}$, $[Sb_4S_8]^{4-}$, $[Sb_6S_{10}]^{2-}$, which can be prepared by various methods.[38–43] In $Cr(en)_2SbS_3$ (en = ethylenediamine), the pyramidal anion $[SbS_3]^{3-}$ is coordinated as a bidentate ligand through two sulfur atoms to the chromium center, whereas $Cr(en)_2SbS_4$ contains isolated SbS_4^{3-} anions.[40] In the structure of $[Ni(C_4H_{13}N_3)_2]_2Sb_4S_8$, there are cyclic $[Sb_4S_8]^{4-}$ anions (**6**), where four pyramidal SbS_3 units share common corners to build an eight-membered ring in a chair conformation.[38]

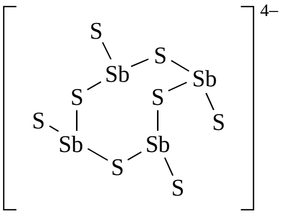

(**6**)

The reaction of $[CpCr(CO)_3]_2$ with Sb_2S_3 under mild reaction conditions gives a tetrachromium complex $[Cp(CO)_3Cr]_2Sb–S–Sb[Cr(CO)_2Cp]_2$.[44] The affinity of antimony(III) to sulfur is also reflected in the great number of complexes with xanthate, dithiocarbamate, dithiophosphinates, and other sulfur ligands.[45] These complexes display a great structural diversity, which ranges from monomeric to polymeric supramolecular assemblies. They are usually prepared by reactions of $SbCl_3$ and the corresponding acids or salts.

7 ANTIMONY HALIDES

7.1 Antimony(III) Halides and Sb_2I_4

Antimony trihalides SbX_3 are well known as stable compounds with X = F, Cl, Br, I.

The trifluoride, SbF_3, is a colorless crystalline solid, which can be prepared by the reaction of Sb_2O_3 with hydrogen fluoride. The structure contains pyramidal SbF_3 molecules (Sb–F 1.92 Å) linked through fluorine bridges (Sb···F 2.61 Å) to give each antimony atom a very distorted octahedral environment. SbF_3 is a useful fluorinating agent for many inorganic and organic compounds, for example, for the preparation of PF_3 from PCl_3. As strong Lewis acid, SbF_3 reacts with alkali metal fluorides with the formation of M_2SbF_5, $MSbF_4$, or other salts. The SbF_5^{2-} ion is a distorted ψ-octahedral with Sb below the basal plane of four F atoms. The SbF_4^- ion is associated through fluorine bridges to dimers $(SbF_4^-)_2$ (**7**) in $NaSbF_4$ or to tetramers $(SbF_4^-)_4$ in $KSbF_4$. More complex anions include $Sb_2F_{11}^-$, $Sb_3F_{16}^-$, $Sb_4F_{17}^-$, and $Sb_4F_{13}^-$.[46]

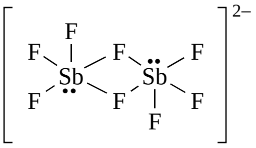

(**7**)

Antimony trichloride, $SbCl_3$, is made by reaction of Sb_2O_3 with hydrochloric acid. The crystals of $SbCl_3$ (mp 73 °C) are hygroscopic. They form a clear solution in water. Dilution results in the formation of insoluble oxy chlorides through the sequence of reactions shown in equation (7).

$$SbCl_3 \xrightarrow[H_2O]{\text{limited}} SbOCl \xrightarrow[H_2O]{\text{more}} Sb_4O_5Cl \xrightarrow{460\,^{\circ}C} Sb_8O_{11}Cl_2 \qquad (7)$$

The structure of SbOCl consists of polymeric sheets of the composition $Sb_6O_6Cl_4^{2+}$ formed by linking Sb atoms through oxygen and chlorine bridges. The positive charge in the SbO_6Cl_4 sheet is balanced by layers of chloride ions. Melts of $SbCl_3$ (bp 223 °C) can be used as nonaqueous solvents, particularly for chloride transfer reactions. However, its self-ionization to give $SbCl_2^+$ and $SbCl_4^-$ is very low (conductivity 1.4 $10^{-6}\,\Omega^{-1}\,cm^{-1}$). $SbCl_3$ has a pyramidal structure in the gas phase. In the solid state, there are strong intermolecular Sb···Cl interactions.[46] $SbCl_3$ is an important antimony reagent. Some reactions are shown in Scheme 4.

$SbCl_3$ is a weak electron pair donor but an excellent acceptor and many complexes of $SbCl_3$ with donor molecules L are known.[47,48] There are complexes of the types $LSbCl_3$ or L_2SbCl_3 with bisphenoidal or tetragonal pyramidal structures respectively. Addition of Cl^- to $SbCl_3$ gives bisphenoidal

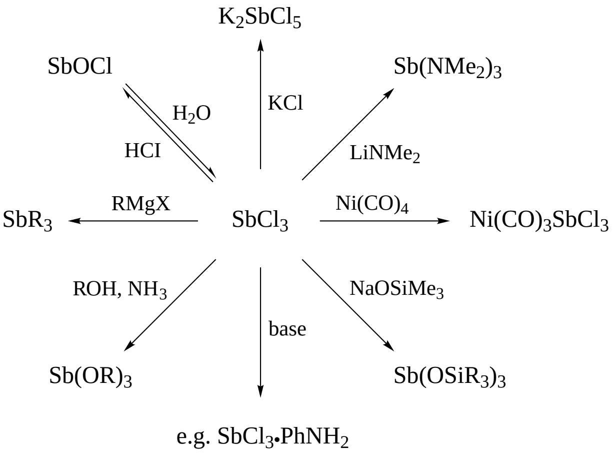

Scheme 4

$SbCl_4^-$, square pyramidal $SbCl_5^{2-}$, and octahedral $SbCl_6^{3-}$. The successive additions of Cl^- are made trans to Cl in pyramidal $SbCl_3$, probably, using the vacant Sb–Cl σ^* orbital as acceptor orbital. The resulting Cl–Sb–Cl units can be treated as 3 center, 4 electron systems. Octahedral coordination is also observed in the bifacial bioctahedral anions $Sb_2Cl_9^{3-}$ (**8**).[46]

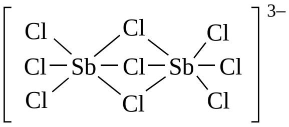

(**8**)

Colorless $SbBr_3$ (mp 96.6 °C, bp 288 °C) and red SbI_3 (mp 171 °C, bp 400 °C) can be made from the elements or by reaction of HX with Sb_2O_3. In SbI_3, the Sb atom occupies octahedral interstices in hexagonal close-packed assemblies of I atoms (3 Sb–I 2.87 Å, 3 Sb$\cdots$I 3.32 Å). Many complex derivatives of SbI_3 are known (e.g. $Sb_2I_9^{3-}$, $Sb_3I_{11}^{2-}$, $Sb_5I_{18}^{3-}$, $[SbI_4^-]_x$, $[Sb_2I_7^-]_x$).[46] A binuclear Sb(III) complex with bridging iodine and sulfur atoms of the type $LSb(\mu\text{-}I)_2(\mu\text{-}S)SbL$ is formed by reacting antimony powder with diiodine and $(SPPh_2NHPPh_2S)$ (HL).[49]

Sb_2I_4 is formed in SbI_3 melt at 230 °C according to equation (8).

$$4SbI_3 + 2Sb \rightleftharpoons 3Sb_2I_4 \qquad (8)$$

7.2 Antimony(V) Halides

Known halides of Sb(V) are SbF_5 and $SbCl_5$. Antimony pentabromide and antimony pentaiodide are unknown because Sb(V) is too strongly oxidizing for these heavier halogens.

Antimony pentafluoride, SbF_5, is a colorless, very viscous liquid (mp 8.3 °C, bp 141 °C) formed by reaction of HF with $SbCl_5$. The viscosity is probably a result of the polymeric chains of cis-bridged SbF_6 octahedra, $[cis\text{-}SbF_4(\mu\text{-}F)]_x$. In the crystalline state, SbF_5 exists as a tetramer $(SbF_5)_4$. Antimony pentafluoride is a very powerful Lewis acid and readily abstracts fluoride ions from metal fluorides (MF) to form $M^+SbF_6^-$ or with additional SbF_5 complexes of the type $[F_5Sb–F–SbF_5]^-$ forms $[F_5Sb–F–SbF_5–FSbF_5]^-$. The low nucleophilicity of these anions is useful for the stabilization of salts like $O_2^+SbF_6^-$, $Me_3C^+SbF_6^-$, $AuXe_4^{2+}[Sb_2F_{11}^-]_2$, $[XeCl][Sb_2F_{11}]$, $[Pt(CO)_4][Sb_2F_{11}]_2$, and $S_4^{2+}(Sb_3F_{11}^-)_2$.[50–52]

SbF_5 is also the key ingredient of the strongest known protonic acids (super acids). Addition of SbF_5 to liquid HF or HSO_3F substantially increases its acidity owing to the formation of $H_2F^+SbF_6^-$, $H_3F_2^+SbF_6^-$, $H_2F^+Sb_2F_{11}^-$, or $H[F_5SbOSO_2F]$. Superacid solutions derived from $SbF_5/HSO_3F/SO_2$ and HF/SbF_5 are useful for the protonation of very weak bases such as formaldehyde to give H_2COH^+ or of carbonic acid to give $C(OH)_3^+$. Crystals of $C(OH)_3^+SbF_6^-$ were obtained by reaction of carbonic acid trimethylsilyl ether with HF/SbF_5 (equation 9).[53]

$$OC(OSiMe_3)_2 \xrightarrow[-\,Me_3SiF]{HF/SbF_5} C(OH)_3^+\ SbF_6^- \qquad (9)$$

Antimony pentachloride, $SbCl_5$, is a liquid (mp 4 °C, bp 140 °C dec.), which can be obtained by reaction of $SbCl_3$ with elemental chlorine. Solid $SbCl_5$ exists in two modifications: above – 54.1 °C, it is trigonal bipyramidal, below this temperature, it changes reversibly into a double chlorine-bridged dimer.[54] $SbCl_5$ decomposes at 140 °C with formation of $SbCl_3$ and Cl_2. It is a Lewis acid with a strong tendency to interact with a ligand (L) to give octahedral complexes $LSbCl_5$.[55] Reactions with chloride ion donors lead to ionic compounds with $SbCl_6^-$ anions and unusual cations. Examples are shown in equations (10) and (11).

$$AlCl_3 + SbCl_5 \longrightarrow AlCl_2^+SbCl_6^- \qquad (10)$$

$$PCl_5 + SbCl_5 \longrightarrow PCl_4^+SbCl_6^- \qquad (11)$$

Methyl sulfonic acid reacts with antimony(V) chloride and water to yield $Cl_3SbO(OH)(O_2S(O)CH_3)SbCl_3$, a binuclear complex with bridging sulfonato groups.[56] Binuclear Sb(V) complexes are also formed from $SbCl_5$ and diphenylphosphoric acid or benzylphosphonic acid alkyl ester in water.[57,58]

8 TRANSITION-METAL COMPLEXES WITH Sb*n* LIGANDS

The coordination of 'naked' antimony atoms Sb_n is achieved in complexes with Sb, Sb_2, *cyclo*-Sb_3, and *cyclo*-Sb_5 ligands.[59] Terminal Sb ligands exist in the anionic

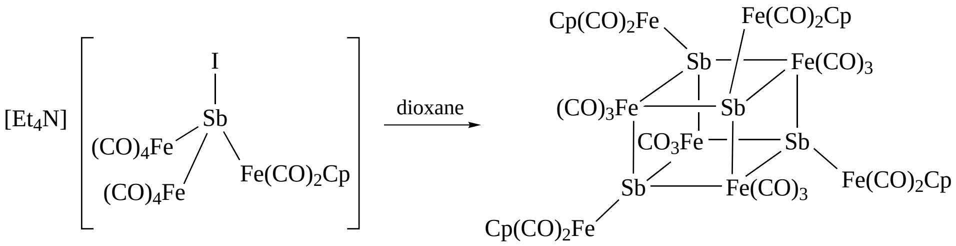

Scheme 5

complexes of the type $(CO)_nM{\equiv}Sb^-$ ($n = 6$, M = Cr, Mo, W; $n = 5$, M = Fe). These unstable species are obtained by reactions of transition-metal carbonyls with the anion Sb_2^- formed by the laser ablation of elemental antimony.[60] $[\{Cp^x(CO)_2Fe\}SbCl_2]$ ($Cp^x = \eta^5\text{-}C_5H_3{}^t Bu$) reacts with Mg to give $[Sb\{Fe(CO)_2Cp^x\}_3]$ or with $Na_2[Fe(CO)_4]$ to give the clusters $[\{SbFe(CO)_2Cp^x\}_3\{Fe(CO)_3\}_4]$ and $[\{Fe_3(CO)_9\}\{SbFe(CO)_2Cp^x\}_2]$.[61,62]

Oxidation of $[NEt_4]_2[Ni_{15}Sb(CO)_{24}]$ with $SbCl_3$ leads to the $[Ni_{31}Sb_4(CO)_{40}]^{6-}$ hexa anion, which displays four semi-interstitial Sb atoms.[63] The $[Fe_2Sb(CO)_5Cp]_4$ ($Cp = C_5H_5$) cluster is formed by thermolysis of $[Et_4N][\{Fe(CO)_4\}_2\{Fe(CO)_2Cp\}SbI]$ (Scheme 5). The cluster contains the cubane $[Fe_4Sb_4]$ core.[64]

The reaction of $SbCl_3$ with $[Ni_6(CO)_{12}]^{2-}$ gives the cluster anions $[Ni_{15}Sb(CO)_{24}]^{2-}$ and $[Ni_{11}Sb_2(CO)_{18}]^{3-}$.[65] Sb_2, *cyclo*-Sb_3, and *cyclo*-Sb_5 units are stabilized as ligands in transition-metal complexes, for example, the tetrahedranes $Sb_2[Mo(CO)_2Cp^*]_2$ and $Sb_3[Mo(CO)_2Cp^*]$, or in the triple-decker $Cp^xMo(Sb_5)MoCp^x$.[66,67]

9 REFERENCES

1. N. C. Norman ed., ‘Chemistry of Arsenic, Antimony and Bismuth’, Blackie Academic and Professional, London, 1998.
2. E. R. T. Tieking, *Crit. Rev. Oncol. Hematol.*, 2002, **42**, 217.
3. S. Yan, K. Ding, L. Zhang, and H. Sun, *Angew. Chem.*, 2000, **112**, 4430; *Angew. Chem., Int. Ed. Engl.*, 2000, **39**, 4260.
4. T. M. Bernhardt, B. Stegemann, B. Kaiser, and K. Rademann, *Angew. Chem.*, 2003, **115**, 209; *Angew. Chem., Int. Ed. Engl.*, 2003, **42**, 199.
5. S. Aldridge and A. J. Downs, *Chem. Rev.*, 2001, **101**, 3305.
6. C. Hirschle and C. Röhr, *Z. Anorg. Allg. Chem.*, 2000, **626**, 1992.
7. A. Bashall, M. A. Beswick, N. Choi, A. D. Hopkins, S. J. Kidd, Y. G. Lawson, M. E. G. Mosquera, M. McPartlin, P. R. Raithby, A. A. E. H. Wheatley, J. A. Wood, and D. S. Wright, *J. Chem. Soc., Dalton Trans.*, 2000, 479.
8. S. Schulz, *Coord. Chem. Rev.*, 2001, **215**, 1.
9. C. von Hänisch, P. Scheer, and B. Rolli, *Eur. J. Solid State Inorg. Chem.*, 2002, 3268.
10. E. E. Foos, R. J. Jouet, R. L. Wells, and P. S. White, *J. Org. Chem.*, 2000, **598**, 182.
11. E. E. Foos, R. J. Jouet, R. L. Wells, A. L. Rheingold, and L. M. Liable-Sands, *J. Org. Chem.*, 1999, **582**, 45.
12. C. J. Carmalt and J. W. Steed, *Polyhedron*, 2000, **19**, 1639.
13. C. von Hänisch, *Z. Anorg. Allg. Chem.*, 2000, **627**, 1414.
14. H. J. Breunig, Thermochromism of organometallic derivatives containing As, Sb, or Bi, in ‘The Chemistry of Organic Arsenic, Antimony and Bismuth Compounds’, ed. S. Patai, John Wiley & Sons, Chichester, UK, 1994, p. 441.
15. H. J. Breunig and R. Rösler, *Coord. Chem. Rev.*, 1997, **163**, 33.
16. H. J. Breunig, M. Jönsson, R. Rösler, and E. Lork, *J. Org. Chem.*, 2000, **608**, 60.
17. M. Westerhausen, S. Weinrich, and P. Mayer, *Z. Anorg. Allg. Chem.*, 2003, **629**, 1153.
18. M. Ates, H. J. Breunig, and M. Denker, *Phosphorus, Sulfur Silicon*, 1995, **102**, 287.
19. A. Bashall, M. A. Beswick, N. Feeder, A. D. Hopkins, S. J. Kidd, M. McPartlin, P. R. Raithby, and D. S. Wright, *J. Chem. Soc., Dalton Trans.*, 2000, 1841.
20. D. C. Haagenson, L. Stahl, and R. J. Staples, *Inorg. Chem.*, 2001, **40**, 4491.
21. F. García, D. J. Linton, M. McPartlin, A. Rothenberger, A. E. H. Wheatley, and D. S. Wright, *J. Chem. Soc., Dalton Trans.*, 2002, 481.
22. L. H. Gade, B. Findeis, O. Gevert, and H. Werner, *Z. Anorg. Allg. Chem.*, 2000, **626**, 1030.
23. R. Bryant, S. C. James, J. C. Jeffery, N. C. Norman, A. G. Orpen, and U. Weckenmann, *J. Chem. Soc., Dalton Trans.*, 2000, 4007.
24. M. A. Beswick, M. K. Davies, M. A. Paver, P. R. Raithby, A. Steiner, and D. S. Wright, *Angew. Chem.*, 1996, **108**, 1660; *Angew. Chem., Int. Ed. Engl.*, 1996, **35**, 1508.
25. D. F. Moser, I. Schranz, M. C. Gerrety, L. Stahl, and R. J. Staples, *J. Chem. Soc., Dalton Trans.*, 1999, 751.
26. K. M. Kadish, C. Erben, Z. Ou, V. A. Adamian, S. Will, and E. Vogel, *Inorg. Chem.*, 2000, **39**, 3312.
27. T. Ogawa, H. Furuta, M. Takahashi, A. Morino, and H. Uno, *J. Org. Chem.*, 2000, **611**, 551.

28. T. M. Klapötke, H. Nöth, T. Schütt, and M. Warchold, *Z. Anorg. Allg. Chem.*, 2001, **672**, 81.
29. M. A. Beswick, N. Choi, A. D. Hopkins, M. McPartlin, M. E. G. Mosquera, R. Raithby, A. Rothenberger, D. Stalke, A. J. Wheatley, and D. S. Wright, *Chem. Commun.*, 1998, 2485.
30. H. J. Breunig, E. Lork, R. Rösler, G. Becker, O. Mundt, and W. Schwarz, *Z. Anorg. Allg. Chem.*, 2000, **626**, 1595.
31. D. Volkmer, B. Bredenkötter, J. Tellenbröker, P. Kögerler, D. G. Kurth, P. Lehmann, H. Schnablegger, D. Schwahn, M. Piepenbrink, and B. Krebs, *J. Am. Chem. Soc.*, 2002, **124**, 10489.
32. U. Kortz, M. G. Savelieff, B. S. Bassil, B. Keita, and L. Nadjo, *Inorg. Chem.*, 2002, **41**, 783.
33. H. Fleischer, H. Bayram, S. Elzner, and N. W. Mitzel, *J. Chem. Soc., Dalton Trans.*, 2001, 373.
34. G. A. Horley, M. F. Mahon, K. C. Molloy, and M. M. Venter, *Inorg. Chem.*, 2002, **41**, 1652.
35. G. A. Horley, M. F. Mahon, M. Mazhar, K. C. Molloy, P. W. Haycock, and C. P. Myers, *J. Chem. Soc., Dalton Trans.*, 2002, 4416.
36. S. M. Biros, B. M. Bridgewater, A. Villeges-Estrada, J. M. Tanski, and G. Parkin, *Inorg. Chem.*, 2002, **41**, 4051.
37. G. A. Horley, M. F. Mahon, K. C. Molloy, P. W. Haycock, and C. P. Myers, *Inorg. Chem.*, 2002, **41**, 5052.
38. W. Bensch, C. Näther, and R. Stähler, *Chem. Commun.*, 2001, 477.
39. R. Stähler, C. Näther, and W. Bensch, *Eur. J. Solid State Inorg. Chem.*, 2001, 1835.
40. M. Schur, H. Rijnberk, C. Näther, and W. Bensch, *Polyhedron*, 1998, **18**, 101.
41. H. Brunner, A. Lange, J. Wachter, and M. Zabel, *J. Org. Chem.*, 2003, **665**, 214.
42. W. Bronger, A. Donike, and D. Schmitz, *Z. Anorg. Allg. Chem.*, 1999, **625**, 435.
43. P. Vaqueiro, A. M. Chippindale, and A. V. Powell, *Polyhedron*, 2003, **22**, 2839.
44. L. Y. Goh, W. Chen, and R. C. S. Wong, *Chem. Commun.*, 1999, 1481.
45. S. S. Garje and V. K. Jain, *Coord. Chem. Rev.*, 2003, **236**, 35.
46. G. A. Fisher and N. C. Norman, *Adv. Inorg. Chem.*, 1994, **41**, 233.
47. A. J. Barton, N. J. Hill, W. Levason, and G. Reid, *J. Chem. Soc., Dalton Trans.*, 2001, 1621.
48. N. C. Norman, *Phosphorus, Sulfur Silicon*, 1994, **87**, 167.
49. M. Arca, A. Garau, F. A. Devillanova, F. Isaia, V. Lippolis, G. Verani, G. L. Abbati, and A. Cornia, *Z. Anorg. Allg. Chem.*, 1999, **625**, 517.
50. H. Willner and F. Aubke, *Chem. – Eur. J.*, 2003, 1669.
51. S. Seidel and K. Seppelt, *Angew. Chem.*, 2001, **113**, 4318; *Angew. Chem., Int. Ed. Engl.*, 2001, **40**, 4225.
52. S. Seidel and K. Seppelt, *Science*, 2000, **290**, 131.
53. R. Minkwitz and S. Schneider, *Angew. Chem.*, 1999, **111**, 749; *Angew. Chem., Int. Ed. Engl.*, 1999, **38**, 714.
54. S. Haupt and K. Seppelt, *Z. Anorg. Allg. Chem.*, 2002, **628**, 729.
55. D. Bellamy, N. C. Brown, N. G. Connelly, and A. G. Orpen, *J. Chem. Soc., Dalton Trans.*, 1999, 3191.
56. G. Lang, K. W. Klinkhammer, T. Schlecht, and A. Schmidt, *Z. Anorg. Allg. Chem.*, 1998, **624**, 2007.
57. A. Burchardt, K. W. Klinkhammer, and A. Schmidt, *Z. Anorg. Allg. Chem.*, 1998, **624**, 35.
58. G. Lang, M. Lauster, K. W. Klinkhammer, and A. Schmidt, *Z. Anorg. Allg. Chem.*, 1999, **625**, 1799.
59. H. J. Breunig and I. Ghesner, *Adv. Org. Chem.*, 2003, **49**, 95.
60. F. P. Arnold, D. P. Ridge, and A. L. Rheingold, *J. Am. Chem. Soc.*, 1995, **117**, 4427.
61. T. Gröer and M. Scheer, *J. Chem. Soc., Dalton Trans.*, 2000, 647.
62. T. Gröer, T. Palm, and M. Scheer, *Eur. J. Solid State Inorg. Chem.*, 2000, 2591.
63. C. Femoni, M. C. Iapalucci, G. Longoni, and P. H. Svensson, *Chem. Commun.*, 2000, 655.
64. S. N. Konchenko, A. V. Virovets, S. A. Apenina, and S. V. Tkachev, *Inorg. Chem. Commun.*, 1999, **2**, 555.
65. V. G. Albano, F. Demartin, C. Femoni, M. C. Iapalucci, G. Longoni, M. Monari, and P. Zanello, *J. Org. Chem.*, 2000, **325**, 593.
66. H. J. Breunig and R. Rösler, *Chem. Soc. Rev.*, 2000, **29**, 403.
67. H. J. Breunig, N. Burford, and R. Rösler, *Angew. Chem.*, 2000, **112**, 4320; *Angew. Chem., Int. Ed. Engl.*, 2000, **39**, 4150.

Antimony: Organometallic Chemistry

Hans Joachim Breunig
University of Bremen, Bremen, Germany

Based in part on the article Antimony: Organometallic Chemistry by Alan Berry which appeared in the Encyclopedia of Inorganic Chemistry, First Edition.

1 Introduction 1
2 Trivalent Antimony 1
3 Compounds with Sb–Sb Single Bonds 4
4 Low-coordination Organoantimony Chemistry 5
5 Pentavalent Organoantimony Compounds 6
6 Transition Metal Complexes with Organoantimony Ligands 7
7 Further Reading 7
8 References 7

1 INTRODUCTION

The first organoantimony compound, triethylstibine, was reported in 1850. Since then, a wide range of compounds with antimony mainly in the +3 and +5 oxidation states was studied. In this article, the focus is mainly on the results published between 1993 and 2003. Several general overviews of the chemistry of organoantimony compounds were presented in this period in books and annual reviews.[1–5]

2 TRIVALENT ANTIMONY

2.1 Tertiary Stibines

A common method for the synthesis of tertiary stibines with alkyl, aryl, or other organic groups is the reaction between Grignard reagents and $SbCl_3$ (equation 1) in diethylether or tetrahydrofuran.

$$3RMgX + SbX_3 \longrightarrow R_3Sb + MgX_2 \qquad (1)$$

However, when trimethylstibine is synthesized in this way, it is difficult to separate the product from the solvent. Pure trimethylstibine can be obtained together with $MeSbBr_2$ by a scrambling reaction (equation 2) of Me_2SbBr in the absence of a solvent.[6]

$$2Me_2SbBr \longrightarrow Me_3Sb + MeSbBr_2 \qquad (2)$$

Me_3Sb is also formed in very low yield by the process of biomethylation of Sb_2O_3 or other antimony compounds by the wood rotting fungus *Phaeolus schweinitzii*.[7]

Other useful organometallic reagents for the preparation of tertiary stibines or related heterocyclic compounds are compounds of lithium, aluminum, tin, copper, zirconium, and other metals.[8–13] In most cases, these metal compounds are reacted with antimony chlorides or bromides. Good yields of tertiary stibines were, however, also obtained by the interaction (equation 3) of trialkylaluminium reagents and tris(dimethylamino)stibine.[11]

$$6R_3Al + 2Sb(NMe_2)_3 \longrightarrow 2R_3Sb + 3[R_2AlNMe_2]_2 \qquad (3)$$

A dilithium reagent is used for the synthesis of a stibaindol (**1**) (equation 4).[13]

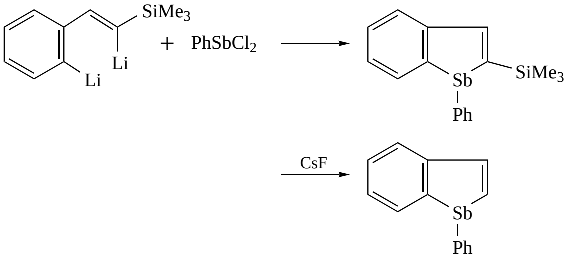

(4)

(**1**)

Tertiary stibines are volatile liquids or solids. The aryl derivatives are air-stable but the trialkyl stibines are air-sensitive compounds, with at least the lower members being spontaneously flammable in air. They are strong reducing agents and can be used for the removal of halogen atoms from many substrates.

Triphenylstibine Ph_3Sb and, less frequently, trialkylstibines or bi- and tridentate stibine ligands, for example, $CH_2(SbPh_2)_2$ and $CH_3C(CH_2SbPh_2)_3$ are used as donor ligands in transition metal complexes.[14,15] $(CF_3)_3Sb$ is exceptional because it does not act as a donor but as an electron pair acceptor in the reaction with a carbene (equation 5).[16]

$$(CF_3)_3Sb + {:}\overline{CN(Mes)C_2(Cl)_2N}Mes \longrightarrow$$
$$(CF_3)_3Sb{-}\overline{CN(Mes)C_2(Cl)_2N}Mes \qquad (5)$$

2.2 Organoantimony(III) Halides and Pseudohalides

Methods to synthesize organoantimony(III) halides include the thermal elimination of organohalides from organoantimony(V) dihalides or trihalides, redistribution reactions, or partial substitution of halogens in antimony trihalides using organometallic reagents.[17,18] The latter method was used in the reaction of tris(trifluoromethyl)phenyl lithium and antimony trichloride, which yields the corresponding chlorostibine (equation 6).[19]

$$2RLi + SbCl_3 \longrightarrow R_2SbCl + 2LiCl \qquad (6)$$
$$R = 2,4,6\text{-}(CF_3)_3C_6H_2$$

A racemic monochloride with a chiral antimony center, $RR'SbCl$ [$R = 2\text{-}(Me_2NCH_2)C_6H_4$, $R' = CH(SiMe_3)_2$], is formed by the reaction of $R'SbCl_2$ with RLi. The compound is stable to inversion up to 160 °C in solution.[20] Alkylantimony(III)chlorides of high purity are formed by reacting alkylphenylstibines with gaseous HCl. This method was used for the synthesis of Me_2SbCl from $PhSbMe_2$. Subsequent halide exchange with NaI gives crystalline Me_2SbI.[21]

Many organoantimony(III) halides are Lewis amphoteric. They have acidic sites on the Sb atoms and they are also basic through the lone pairs of electrons on the halogen atoms. A frequently encountered consequence of this dual nature is the formation of coordination polymers in the solid state. The resulting structures formed through self-assembly of molecules were considered in a book and in a review article.[22,23] The Lewis acidity of organoantimony halides is also reflected in the tendency to form stable adducts with neutral donors or with halide anions. The 1:1 adduct (**2**) is formed by reaction of methylantimony dichloride with 2,2′-bipyridine.[24]

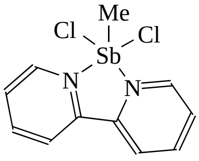

(**2**)

Intramolecular N··Sb interactions exist in $RSbCl_2$ [$R = 6\text{-}Me\text{-}2\text{-}Pyr(Me_3Si)_2C$].[25] The addition of tetramethylstibonium iodide to $PhSbI_2$ leads to the salts $[Me_4Sb]_2[Ph_2Sb_2I_6]$. The dianions $[Ph_2Sb_2I_6]^{2-}$ (**3**) form as cis- and trans-isomers.[26]

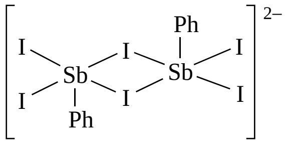

trans-(**3**)

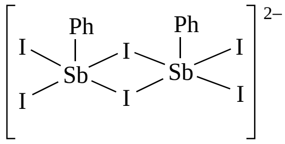

cis-(**3**)

Self-association occurs also in organoantimony pseudohalide derivatives. $K[PhSb(SCN)_3]$ has a polymeric structure in which the S atoms of one SCN are in bridging positions between pairs of Sb atoms.[27]

2.3 Diorganoantimony Cations and Anions

Diorganoantimony cations R_2Sb^+ with six valence electrons at antimony are unstable species. Coordination of donors leads to stable cationic adducts. One example is $[SbPh_2\{OP(NMe_2)_3\}_2]PF_6$, where two hexamethylphosphoric acid triamide molecules are coordinated to the cationic antimony center.[28] Intramolecular coordination of both amine arms of the aryl ligands leads to the stabilization of $[SbR_2][PF_6]$ ($R = 2\text{-}Me_2NCH_2C_6H_4$).[28] Cationic Sb(III) compounds exist also as sandwich complexes in $[Cp'_2Sb][AlCl_4]$($Cp' = C_5Me_5$, $C_5H_2{}^tBu_3$-1,2,4).[29]

Anionic diorganoantimony species, that is, diorganoantimonides R_2Sb^- are formed by cleavage of tertiary stibines with alkali metals or by metalation of primary stibines. Cleavage of a Sb–C bond of triarylstibines with formation of diarylantimonides is easily achieved in solutions of sodium in liquid ammonia (equation 7).[30]

$$R_3Sb + 2Na \longrightarrow R_2SbNa + RNa \qquad (7)$$

Metalation of $RR'SbH$ with BuLi gives the chiral lithium antimonide $RR'SbLi$ [$R = 2\text{-}(Me_2NCH_2C_6H_4$, $R' = CH(SiMe_3)_2$] (**4**) that forms $RR'SbNa$ after transmetalation with ${}^tBuONa$ in the presence of tetramethylethylenediamine.[20] The pendant amine arm of (**4**) is coordinated to the alkali metal center.

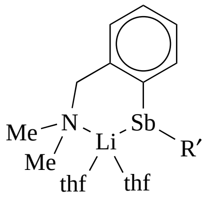

(**4**)

2.4 Organoantimony Hydrides

The chemistry of organoantimony hydrides (primary stibines, $RSbH_2$, or secondary stibines, R_2SbH) has been discussed in a recent review article.[31] Hydrides with smaller organic groups tend to be less stable and result in lower yields, whereas those with bulkier groups are more stable and yields of 50% and above are common. Comparatively stable monomeric species of the type $RSbH_2$ and R_2SbH have been formed with substituents R, which may be either an alkyl group containing no β-hydrogen atoms, for example, Me_3CH_2, Me_3SiCH_2 $(Me_3Si)_2CH$, or bulky aryl groups. The primary stibine $2,6\text{-}Trip_2C_6H_3SbH_2$ (Trip = 2,4,6-triisopropylphenyl) is of extraordinary stability. It is a white crystalline solid that decomposes at 195 °C and is indefinitely stable at room temperature under N_2 in the absence of light.[32] The reaction with BuLi gives $2,6\text{-}Trip_2C_6H_3(Li)SbH$.

The most frequently used synthetic procedure for organoantimony hydrides is the reaction of an organoantimony halide with lithium aluminum hydride at low temperatures in an ether solvent. Isobutylstibine $Me_2CHCH_2SbH_2$ is formed in 59% yield by this method.[33] Not only a primary stibine $RSbH_2$ but also a distibine R(H)Sb–Sb(H)R [R = $(Me_3Si)_2CH$] is formed when bis(trimethylsilyl)methylantimony dichloride is reacted with $LiAlH_4$.[34] The distibine is a yellow crystalline compound that exists in the meso form in the solid state. A racemic chiral stibine RR′SbH R = $(Me_3Si)_2CH$, R′ = CH_3 is formed from $RSbH_2$ and MeI in the presence of a base.[34]

Other methods of organoantimony hydride synthesis are reactions of R_2SbLi with $(Me_3NH)Cl$ or methanolysis of silylstibines $RSb(SiMe_3)_2$ or $R_2SbSiMe_3$. Vinyl stibine $H_2C{=}C(H)\text{-}SbH_2$ is obtained from vinyl tributylstannane on successive reactions (equation 8) with $SbCl_3$ and Bu_3SnH.[35]

$$H_2C{=}C(H){-}SnBu_3 \xrightarrow{SbCl_3} H_2C{=}C(H){-}SbCl_2 \xrightarrow{Bu_3SnH} H_2C{=}C(H){-}SbH_2 \qquad (8)$$

Arylstibines $RSbH_2$, R = Ph, *p*-Tol react with a range of organic substrates, for example, styrene, alkynes, prochiral ketones, with transfer of the hydrogen atoms.[36] $RSbH_2$ (R = Me_3SiCH_2) can be used together with trimethylindium to deposit thin films of InSb at 450 °C.[37]

2.5 Group 13–15 Element Derivatives of Sb(III)

Organoantimony compounds with bonds between Sb and group 13 elements were discussed in a recent review.[38] They are known as Lewis acid–base adducts $R_3Sb\text{-}MR_3$ (M = Al, Ga, In) and as four- or six-membered heterocycles $(R_2Sb\text{-}MR_2)_n$ (n = 2, 4). Pyrolysis of these compounds leads to the semiconducting materials AlSb, GaSb, and InSb.

Organoantimony group 14 element compounds include organometallic stibines of the types R_2SbMR_3 and $RSb(MR_3)_2$ (M = Si, Ge, Sn). They are formed by reactions of R_2SbLi with R_3MCl (M = Si, Ge, Sn), by dehalogenation of $RSbBr_2$ and Me_3MCl with Mg, or by exchange reactions.[39,40] The silyl derivatives R_2SbSiR_3 and $RSb(SiR_3)_2$ are useful reagents for the synthesis of compounds with Sb–H, Sb–Sb, or Sb–metal bonds.[41]

Nitrogen derivatives of organoantimony(III) are known as moisture-sensitive amides R_2SbNR_2, $RSb(NR_2)_2$, and stibino amines $(R_2Sb)_3N$. The amides are obtained from the reactions of organoantimony(III) mono- and dihalides with $LiNR_2$ or R_2NH in the presence of Et_3N.[42,43] Tris(diphenylstibino)amine $(Ph_2Sb)_3N$ is formed by ammonolysis of Ph_2SbCl in liquid NH_3.[44] It contains an almost planar Sb_3N core.

2.6 Chalcogen Derivatives of Sb(III)

The principal organoantimony(III) chalcogen derivatives of Sb(III) are compounds of the types $(RSbE)_n$, $(R_2Sb)_2E$, $[(R_2Sb)_3E]^+$, $RSb(ER)_2$, and R_2SbER, (E = group 16 element).

A four-membered heterocycle *trans*-$(RSbO)_2$ [R = 2,4,6-$(Me_3Si)_2CH)_3C_6H_2$] is formed by reaction of single crystals of RSb=SbR with atmospheric oxygen with retention of crystallinity.[45,46] Hydrolysis of $RSbCl_2$ [R = $(Me_3Si)_2CH$] leads to *cyclo*-$(RSbO)_n$ (n = 3, 4). The core of crystalline *cyclo*-$[(Me_3Si)_2(CHSbO)_4{\cdot}H_2O]$ is a boat-shaped 8-membered Sb_4O_4 ring with the organic substituents in trans positions.[47] Distibine oxides of the type $R_2SbOSbR_2$ are obtained by hydrolysis of diorganoantimony halides or by oxygenation of distibines. $(Me_2Sb)_2O$ is best prepared by reaction of Me_2SbBr with aqueous NaOH. In the solid state, the molecules are arranged as *zigzag* chains through intermolecular Sb–O interactions (Figure 1).[48]

Oxygen in the environment of three antimony atoms exists also in the planar oxonium salt $[(Me_2Sb)_3O]Br$, which is formed by reaction of $(Me_2Sb)_2O$ with Me_2SbBr.[49] Tetraaryldistibine oxides are formed by air oxidation of the corresponding distibines.[50]

The most common method for synthesizing organoantimony(III) mono and di alkoxides is the reaction of R_2SbX or $RSbX_2$ with the appropriate sodium alkoxide. Related organometallic compounds are the group 14 element derivatives $RSb(OMR_3)_2$ (M = Si, Ge, Sn; R = alkyl, aryl).[51] $[R_2GaOSbEt_2]_2$ (**5**), a compound where oxygen is in the environment of two Ga atoms and a Sb center, is formed by reaction of R_3Ga (R = Me_3SiCH_2), Et_4Sb_2, and oxygen.[52]

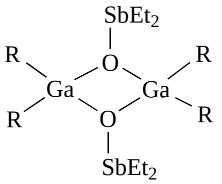

R = (Me_3SiCH_2)

(**5**)

Organoantimony derivatives of the heavier chalcogens of the types $(RSbE)_n$ (E = S, Se, Te) are formed by

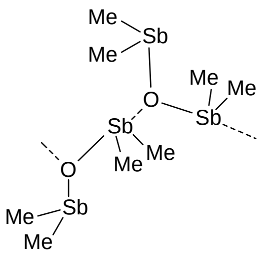

Figure 1 Chains in the crystals of $Me_2SbOSbMe_2$

elimination of salt from $RSbCl_2$ and Na_2E. Reaction of $RSbH_2$ with sulfur provides the cyclic polysulfides $RSbS_n$ ($R = 2,4,6$-$[(Me_3Si)_2CH]_3C_6H_2$, $n = 5$, 7).[53] The binuclear chalcogenides $(R_2Sb)_2E$ are obtained by insertion of elemental chalcogens into the Sb–Sb bonds of distibines or by reaction of R_2SbCl with Na_2E.[54,55] Reaction of distibines with disulfides, diselenides, or ditellurides give monochalcogentate R_2SbER ($E = S$, Se, Te), which undergo redistribution to dichalcogenates and other products like $RSb(ER)_2$.[54,56,57] The affinity of antimony to sulfur is reflected in the stability of organoantimony(III) complexes with bidentate sulfur ligands, for example, dithiocarbamates and phosphinates.[54] The dithiophosphinate $Me_2SbS_2PMe_2$ has a polymeric chain structure with intermolecular Sb···S contacts. It is formed by reaction of $Me_2SbSbMe_2$ with $[Me_2P(S)S]_2$.[58] The reaction of $PhSbCl_2$ with $K[(SPPh_2)_2N]$ gives $PhSb[(SPPh_2)_2N]_2$ (**6**), a complex where the Sb center is in a square pyramidal environment.[59]

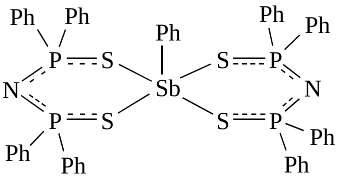

(**6**)

1,3-dioxa, -thia-, -selena-, tellura-ferrocenophanes (**7**) containing antimony in the central bridge position are formed by HCl elimination from $^tBuSbCl_2$ and the corresponding ferrocene derivatives containing EH or ELi bonds.[60]

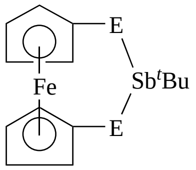

E = O, S, Se, Te

(**7**)

3 COMPOUNDS WITH Sb–Sb SINGLE BONDS

Known neutral organometallic compounds with normal covalent Sb–Sb bonds comprise distibines, R_2SbSbR_2, cyclostibines R_nSb_n ($n = 3$–6), *catena*-stibines $R_2Sb(SbR)_nSbR_2$ ($n = 1,2$), and polycycles R_nSb_m ($m > n$). Dative Sb–Sb bonds exist in the adducts R_3Sb-$Sb(R)X_2$, or in ionic species of the types R_3Sb-SbR_2^+ or $[R_2Sb$-SbR_2-$SbR_2]^+$. Also dicationic and anionic species, $[R_3Sb$-$SbR_3]^{2+}$ and $[R_2Sb$-Sb-$SbR_2]^-$, are known.[54,61–63] Distibines are formed by reaction of R_2SbBr with Mg, by elimination of dihydrogen from R_2SbH, by reactions of R_2SbNa with $BrCH_2CH_2Br$ in liquid NH_3, or by other methods. Distibines like almost all organometallic compounds with Sb–Sb bonds are yellow. However, the distibines R_2Sb-SbR_2 [$R = CH_3$, $R_2 = Me_2C_4H_2$] are exceptional. They form red solid phases that consist of linear chains of molecules with close intermolecular Sb···Sb contacts. Cyclostibines with known crystal structures are trimers (tristibiranes) R_3Sb_3 [$R = (Me_3Si)_2CH$], tetramers (tetrastibetanes) R_4Sb_4 [$R = {}^tBu$, $(Me_3Si)_2CH$, Me_5C_5], pentamers (pentastiboles) R_5Sb_5 ([$R = Me_3CCH_2$), or hexamers (hexastibanes) R_6Sb_6 ($R = Ph$, Tol). *Cyclo*-R_3Sb_3 has been prepared by reaction of $RSbCl_2$ with Li_3Sb or by photochemical ring contraction of the corresponding tetrastibetane. The rings *cyclo*-R_nSb_n ($n = 4$–6) are formed from $RSbBr_2$ and Mg in THF, by air oxidation of $RSb(SiMe_3)_2$, or by elimination of hydrogen from $RSbH_2$. Several *catena*-stibines $R_2Sb(SbR)_nSbR_2$ exist as components of ring-chain equilibria (equation 9).

$$R'_2Sb\text{-}SbR\text{-}SbR'_2 \rightleftharpoons 1/n\ cyclo\text{-}(RSb)_n + R'_4Sb_2$$

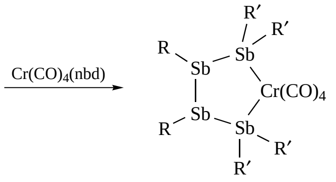

(9)

$R = Me_3SiCH_2$, $R' =$ Me, Ph; nbd = norbornadiene

Structurally established antimony polycycles include the types R_4Sb_8 and R_6Sb_8. R_4Sb_8 ($R = (Me_3Si)_2CH$) is formed by reduction of $RSbCl_2$ with Mg or by reaction of $RSbH_2$ with $SbCl_3$ and pyridine. The photochemical ring contraction of Sb_8R_4 leads to *cyclo*-$(RSb)_3$ (Scheme 1).[61,64]

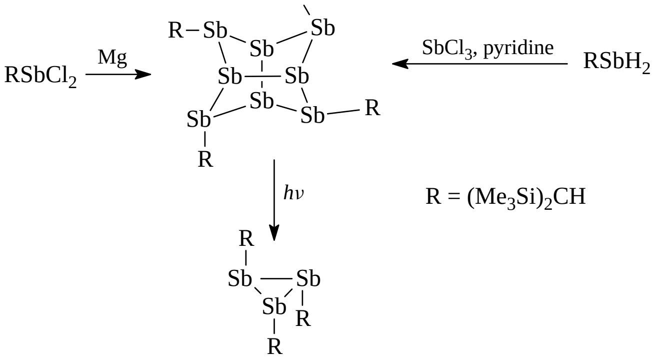

Scheme 1

A pentachloro hexastibane Sb_6R_5Cl is obtained by reaction of $RSbCl_2$ with Na/K (equation 10).[65]

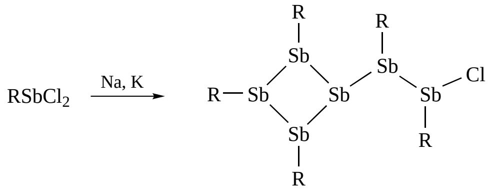

(10)

$^t\mathrm{Bu}_4\mathrm{Sb}_4$ is a source for the syntheses of complexes with Sb_n ligands or four polynuclear antimonides.[63] Reduction of $^t\mathrm{Bu}_4\mathrm{Sb}_4$ with alkali metals (M = Li, Na, K) in the presence of $(\mathrm{Me_2NCH_2CH_2})_2\mathrm{NMe}$ gives the anionic species $^t\mathrm{Bu}_4\mathrm{Sb}_3{}^-$ and $^t\mathrm{Bu}_3\mathrm{Sb}_2{}^-$ (equation 11).[61,63]

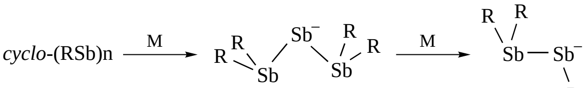

(11)

R = ^{t}Bu, M = alkali metal

Cationic species with Sb–Sb bonds are formed by scrambling reactions or addition of a stibine donor to a Lewis acidic antimony center. Scrambling reactions of Me_2SbBr lead to the ionic complex $(Me_3Sb\text{-}SbMe_2)_2(MeSbBr_2)_2$ containing cations (**8**) that consist of pyramidal Me_3Sb bonded to bent Me_2Sb units through short (2.82 Å) Sb–Sb bonds.[66]

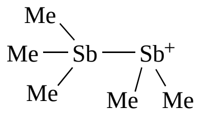

(**8**)

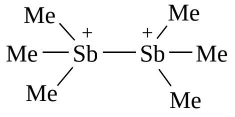

(**9**)

The dicationic species (**9**) in $(Me_3Sb\text{-}SbMe_3)(SbF_6)_2$ is formed from Me_3Sb and HF/SbF_5.[67]

4 LOW-COORDINATION ORGANOANTIMONY CHEMISTRY

Low-coordination organoantimony compounds are species with the coordination numbers 1 or 2 at the antimony centers, for example, stibinidenes R–Sb, distibenes R–Sb=Sb–R, stibaalkenes, R–Sb=CR_2, or cyclic compounds.[45] Stable monomeric stibinidenes or stibaalkenes are not known. Complexes with stibinidene ligands are, however, well established, and trapping of a sterically hindered stibinidene, RSb, R = 2,4,6-$(Me_3Si)_2CH]_3C_6H_2$ is achieved as a cycloadduct with 1,3-butadienes.[68] Stibaalkene monomers have been considered as intermediates in various reactions. Structurally authenticated compounds with Sb=C bonds are stiba dionato complexes, stiba enols, or distibabutadienes formed from $LiSb(SiMe_3)_2$ and RCOCl. (Scheme 2).[45,69,70]

Monomeric distibenes *trans*-RSb=SbR exist with protection of very bulky aryl groups. They are formed by dehalogenation of the corresponding dihalides with Mg or by deselenation of a triselenatristibane (Scheme 3).[45,46,71,72]

With sterical protection also, a compound of the type RBi = SbR featuring a double bond between antimony and bismuth is stabilized.[72]

Known structures where two coordinate Sb centers are incorporated in aromatic ring systems are shown in Figure 2. The chemistry of these heterocycles is well documented in review articles.[45,73]

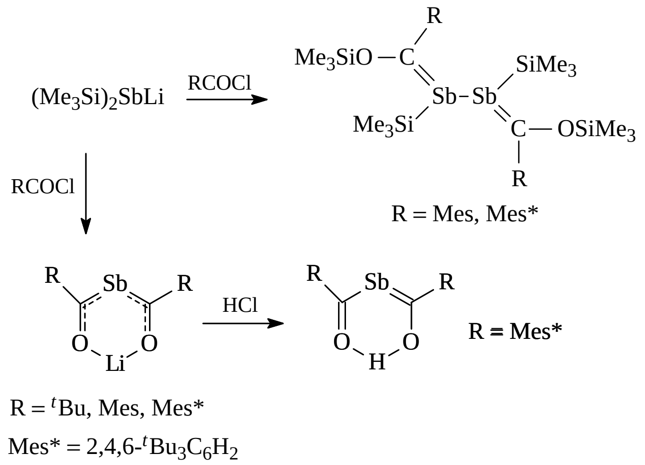

Scheme 2

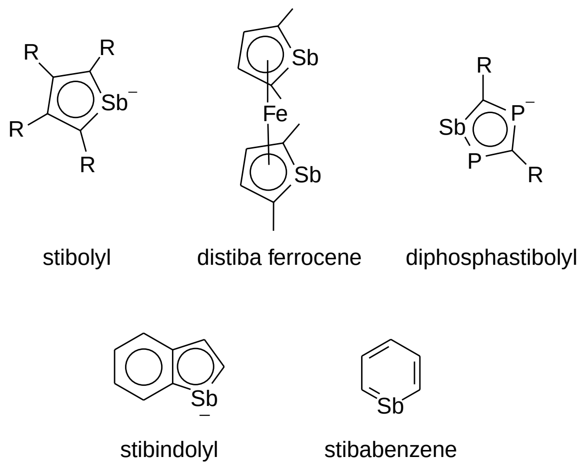

Figure 2 Heterocycles with two coordinate antimony atoms

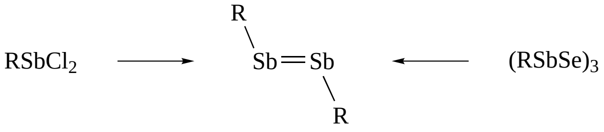

R = 2,6-$Mes_2C_6H_3$, 2,6-$({}^{i}Pr_3C_6H_2)_2C_6H_3$ R = 2,4,6-$(Me_3Si_2)_2CH)_3C_6H_2$

Scheme 3

5 PENTAVALENT ORGANOANTIMONY COMPOUNDS

Antimony forms numerous stable pentavalent organometallic compounds; among these are penta alkyls and aryls, mixed organohalides, and various chalcogen and nitrogen derivatives.

5.1 Penta Alkyls and Aryls

The pentaorgano compounds are thermally stable but air sensitive. They are generally synthesized by the reaction of Grignard or organolithium reagents with triorganoantimony dihalides and have monomeric molecular structures. Me_5Sb and Ph_3Me_2Sb are trigonal bipyramidal molecules.[74] Ph_5Sb is, however, approximately square pyramidal in the solid state.[75] The lithium salt of the octahedral $[Me_6Sb]^-$ ion is obtained from Me_5Sb and MeLi in tetrahydrofuran.[75] Reactions of R_5Sb with protic species including acids, alcohols, and thiols give R_4SbX products.

5.2 Organoantimony(V) Halides and Stibonium Salts

Examples of organoantimony(V) halides exist, ranging from $RSbX_4$ to R_4SbX. The stability decreases according to R_4SbX, R_3SbX_2, $>R_2SbX_3$ $>RSbX_4$. Tetraorganoantimonhalides R_4SbX form by addition of RX to R_3Sb.[76] They usually have ionic structures of stibonium salts, $R_4Sb^+X^-$. Ph_4SbI, however, is a molecular species with distorted trigonal bipyramidal geometry.[77] Triorganoantimony dihalides are formed by addition of X_2 to the corresponding to triorganostibines. They adopt trigonal bipyramidal structures with axial halogen atoms.[78] The reductive elimination of RX from R_3SbX_2 is an important synthetic pathway leading to diorganoantimony halides. Diorganoantimony trihalides are generally less stable than their dihalide counterparts undergoing reductive elimination to RX and $RSbX_2$ easily. They usually are strong Lewis acids and tend to form dimers with bridging halogen atoms in the solid state unless protected by bulky groups. One example for a dimeric structure is Me_2SbCl_3, where the methyl groups are on both sides of the $Cl_2Sb(\mu\text{-}Cl)_2SbCl_2$ plane and the environment of the Sb centers is octahedral. The Lewis acidic character is exemplified by the formation of a 1:1 adduct between Ph_2SbCl_3 and Ph_3SbO.[79] Organoantimony tetrahalides are the least stable in this series. However, adducts with donor ligands or the type $RSbX_4{\cdot}L$ are known.

5.3 Organoantimony(V) Chalcogen and Nitrogen Derivatives

A series of compounds analogous to organoantimony halides exist also for alkoxides and other compounds of the type $R_nSb(OR')_{(5-n)}$. Antimony tetraorganyls R_4SbOR' are formed from R_5Sb and ROH or from R_4SbCl and MOR' (M = Na, Ag).[80] Reactions of R_5Sb with water give tetraorganoantimony hydroxides R_4SbOH.

Compounds of the type $R_3Sb(OR')_2$ are usually obtained by reactions of R_3SbX_2 with $NaOR'$. They adopt trigonal bipyramidal structures with the oxygen atoms in axial positions. Hydrolysis of R_3SbX_2 can lead to dihydroxides $R_3Sb(OH)_2$, hydroxy halides $R_3Sb(X)OH$, or binuclear condensation products $(R_3SbX)_2O$.[81–83] Heating $R_3Sb(OH)_2$ under vacuum gives R_3SbO. A complex with intramolecular coordination of two oxygen atoms to an R_3Sb unit is the complex (**10**) that contains chiral centers at antimony and at two carbon atoms. It exists as a pair of configurationally stable diastereomers. The rates of interconversion between the diastereomers is accelerated in donor solvents and probably procedes through a hexacoordinate transition state.[84]

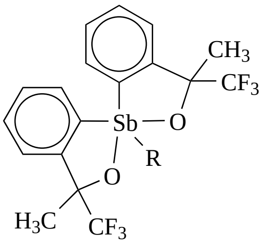

R = *p*-Tol

(**10**)

Alkoxides of the type $R_2Sb(OR)_3$ react with water with the formation of stibinic acids $R_2Sb(O)OH$. Their anhydrides have the formula $(R_2Sb)_4O_6$. They are molecular compounds with bridging oxygen atoms between four Sb atoms in a cage structure (**11**). The anhydrides (**11**) are formed by air oxidation of distibines $R_2Sb\text{-}SbR_2$ or by other methods.

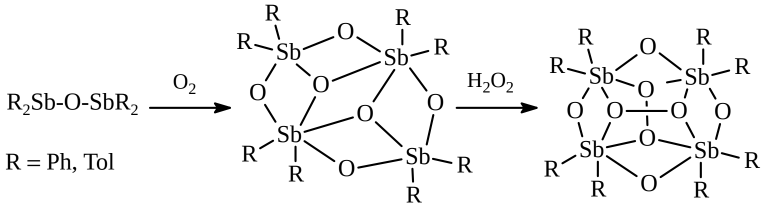

(**11**) (**12**)

Scheme 4

Further oxidation with hydrogen peroxide gives peroxo antimony complexes $(R_2SbO)_4(O_2)_2$ (**12**) with quadruply bridging peroxo groups (Scheme 4).[85]

A mixed anhydride of stibinic and arsinic acid has been synthesized by reaction of $(SbPh_2BrO)_2$ with $Na(O_2AsMe_2)$.[86]

Reaction of sulfur with R_3Sb or other methods give R_3SbS. R_4SbSR' or $R_3Sb(SR')_2$ is obtained from R_5Sb and HSR' or from R_3SbCl_2 and HSR in the presence of Et_3N. R_3SbBr_2 reacts with $NH_4S_2PPh_2$ to form $R_3Sb(S_2PPh_2)_2$.[87] Reaction of Se with R_3Sb leads to R_3SbSe.

Nitrogen derivatives of Sb(V) include imines $(R_3SbCl)_2NH$, diamides $R_3Sb(NR_2)_3$, and diazides $R_3Sb(N_3)_2$, which are formed by reaction of R_3SbCl_2 with NaN_3. A compound with a double-bond character of the Sb−N bond is the monomeric iminostibane $R_3Sb{=}NSO_2CF_3$ (R = 2-MeC_6H_4).[88]

6 TRANSITION METAL COMPLEXES WITH ORGANOANTIMONY LIGANDS

Organoantimony ligands were frequently used in the coordination chemistry of transition metals. Two recent reviews summarize this field.[14,15] The most popular antimony ligand is triphenylstibine, which is not only a good donor but also commercially available and is easy to handle. Trialkylstibines and bidentate antimony ligands like bistibino methane $(R_2Sb)_2CH_2$ are also used. An important approach is also the protection of sensitive organoantimony compounds like distibines R_2SbSbR_2, distibenes RSb=SbR, or stibinidenes RSb, in the coordination sphere of transition metal complexes.

7 FURTHER READING

C. Jones and R. C. Thomas, *J. Organomet. Chem.*, 2001, **622**, 61.

T. Sasamori, N. Takeda, and N. Tokitoh, *Chem. Commun.*, 2000, 1353.

8 REFERENCES

1. S. Patai ed., 'The Chemistry of Organic Arsenic, Antimony and Bismuth Compounds', John Wiley & Sons, Chichester, 1994, p. 207.
2. N. C. Norman ed., 'Chemistry of Arsenic, Antimony and Bismuth', Blackie Academic and Professional, London, 1998.
3. I. Fleming, ed., 'Science of Synthesis, Houben-Weyl Methods of Molecular Transformations Category 1.Organometallics', Vol. 4: Compounds of Group 15 (As, Sb, Bi) and Silicon Compounds, Georg Thieme Verlag, Stuttgart, 2002.
4. L. D. Freedman and G. O. Doak, *J. Organomet. Chem.*, 1995, **496**, 137.
5. C. Jones, *Organomet. Chem.*, 2001, **29**, 153.
6. G. Balazs, L. Balazs, H. J. Breunig, and E. Lork, *Appl. Organomet. Chem.*, 2002, **16**, 155.
7. P. Andrewes, W. R. Cullen, E. Polishuk, and K. J. Reimer, *Appl. Organomet. Chem.*, 2001, **15**, 473.
8. L. Balázs, H. J. Breunig, I. Ghesner, and E. Lork, *J. Organomet. Chem.*, 2002, **648**, 33.
9. S. Sasaki, K. Sutoh, F. Murakami, and M. Yoshifuji, *J. Am. Chem. Soc.*, 2002, **124**, 14830.
10. L. Dupuis, N. Pirio, P. Meunier, A. Igau, B. Donnadieu, and J.-P. Majoral, *Angew. Chem.*, 1997, **109**, 1017; *Angew. Chem., Int. Ed. Engl.*, 1997, **36**, 987.
11. C. J. Thomas, L. K. Krannich, and C. L. Watkins, *Polyhedron*, 1993, **12**, 89.
12. H. Sashida, A. Kuroda, and T. Tsuchiya, *Chem. Commun.*, 1998, 767.
13. J. Kurita, M. Ishii, S. Yasuike, and T. Tsuchiya, *J. Chem. Soc., Chem. Commun.*, 1993, 1309.
14. H. J. Breunig and I. Ghesner, *Adv. Organomet. Chem.*, 2003, **49**, 95.
15. N. R. Champness and W. Levason, *Coord. Chem. Rev.*, 1994, **133**, 115.
16. A. J. Arduengo, III, R. Krafcyk, R. Schmutzler, W. Mahler, and W. J. Marshall, *Z. Anorg. Allg. Chem.*, 1999, **625**, 1813.
17. H. J. Breunig, M. Denker, and K. H. Ebert, *Trends Organomet. Chem.*, 1994, **1**, 323.
18. M. Lahrech, J. Thibonnet, S. Hacini, M. Santelli, and J.-L. Parrain, *Chem. Commun.*, 2002, 644.

19. J.-K. Buijink, M. Noltemeyer, and F. T. Edelmann, *J. Fluorine Chem.*, 1993, **61**, 51.
20. H. J. Breunig, I. Ghesner, M. E. Ghesner, and E. Lork, *Inorg. Chem.*, 2003, **42**, 1751.
21. H. J. Breunig, H. Althaus, R. Rösler, and E. Lork, *Z. Anorg. Allg. Chem.*, 2000, **626**, 1137.
22. G. Balazs and H. J. Breunig, in 'Unusual Stuctures and Physical Properties in Organometallic Chemistry', eds. M. Gielen, R. Willem, and B. Wrackmeyer, John Wiley & Sons, Chichester, 2002, p. 387.
23. I. Haiduc and F. T. Edelmann eds, 'Supramolecular Organometallic Chemistry', Wiley-VCH, Weinheim, 1999.
24. H. Althaus, H. J. Breunig, and E. Lork, *Organometallics*, 2001, **20**, 586.
25. T. R. van den Ancker, P. C. Andrews, S. J. King, J. E. McGrady, C. L. Raston, B. A. Roberts, B. W. Skelton, and A. H. White, *J. Organomet. Chem.*, 2000, **607**, 213.
26. H. J. Breunig, M. Denker, and E. Lork, *Z. Anorg. Allg. Chem.*, 1999, **625**, 117.
27. G. E. Forster, M. J. Begley, and D. B. Sowerby, *J. Chem. Soc., Dalton Trans.*, 1995, 1173.
28. C. J. Carmalt, D. Walsh, A. H. Cowley, and N. C. Norman, *Organometallics*, 1997, **16**, 3597.
29. H. Sitzmann, Y. Ehleiter, G. Wolmershäuser, A. Ecker, C. Uffing, and H. Schnöckel, *J. Organomet. Chem.*, 1997, **527**, 209.
30. H. J. Breunig, T. Krüger, and E. Lork, *J. Organomet. Chem.*, 2002, **648**, 209.
31. S. Aldridge and A. J. Downs, *Chem. Rev.*, 2001, **101**, 3305.
32. B. Twamley, C.-S. Hwang, N. J. Hardman, and P. P. Power, *J. Organomet. Chem.*, 2000, **609**, 152.
33. A. Berry, *Polyhedron*, 1999, **18**, 2609.
34. G. Balázs, H. J. Breunig, E. Lork, and S. Mason, *Organometallics*, 2003, **22**, 576.
35. S. Legoupy, L. Lassalle, J.-C. Guillemin, V. Metail, A. Senio, and G. Pfister-Guillouzo, *Inorg. Chem.*, 1995, **34**, 1466.
36. H. J. Breunig and J. Probst, *J. Organomet. Chem.*, 1998, **571**, 297.
37. D. G. Hendershot and A. D. Berry, *J. Organomet. Chem.*, 1993, **449**, 119.
38. S. Schulz, *Coord. Chem. Rev.*, 2001, **215**, 1.
39. H. J. Breunig, K. H. Ebert, S. Gülec, and J. Probst, *Chem. Ber.*, 1995, **128**, 599.
40. H. J. Breunig and R. Kaller, *Phosphorus, Sulfur Silicon Relat. Elem.*, 1994, **88**, 275.
41. I.-P. Lorenz, R. Schneider, H. Nöth, K. Polborn, and J. Breunig, *Z. Naturforsch.*, 2001, **56b**, 671.
42. S. J. Coles, M. B. Hursthouse, J. S. Joy, and M. A. Paver, *J. Chem. Soc., Dalton Trans.*, 2000, 3239.
43. K. Singhal, *Synth. React. Inorg. Met. -Org. Chem.*, 1993, **23**, 1363.
44. L. Balazs, H. J. Breunig, T. Krüger, and E. Lork, *Z. Naturforsch.*, 2001, **56b**, 1325.
45. C. Jones, *Coord. Chem. Rev.*, 2001, **215**, 151.
46. N. Tokitoh, Y. Arai, T. Sasmori, R. Okazaki, S. Nagase, H. Uekusa, and Y. Ohashi, *J. Am. Chem. Soc.*, 1998, **120**, 433.
47. H. J. Breunig, M. A. Mohammed, and K. H. Ebert, *Z. Naturforsch.*, 1994, **49b**, 877.
48. H. J. Breunig, E. Lork, R. Rösler, G. Becker, O. Mundt, and W. Schwarz, *Z. Anorg. Allg. Chem.*, 2000, **626**, 1595.
49. H. J. Breunig, M. A. Mohammed, and K. H. Ebert, *Polyhedron*, 1994, **13**, 2471.
50. H. J. Breunig, T. Krüger, and E. Lork, *J. Organomet. Chem.*, 2002, **648**, 209.
51. M. Wieber, M. Schroepf, and U. Simonis, *Phosphorus, Sulfur Silicon Relat. Elem.*, 1995, **104**, 215.
52. H. J. Breunig, M. Stanciu, R. Rösler, and E. Lork, *Z. Anorg. Allg. Chem.*, 1998, **624**, 1965.
53. N. Tokitoh, Y. Arai, and R. Okazaki, *Chem. Lett.*, 1995, 959.
54. H. J. Breunig and R. Rösler, *Coord. Chem. Rev.*, 1997, **163**, 33.
55. H. J. Breunig, R. Kaller, and A. Silvestru, *Phosphorus, Sulfur Silicon Relat. Elem.*, 1994, **91**, 165.
56. A. Haaland, H. P. Verne, H. V. Volden, H. J. Breunig, and S. Gülec, *Z. Naturforsch.*, 1993, **48b**, 1065.
57. R. S. Dickson and K. D. Heazle, *J. Organomet. Chem.*, 1995, **493**, 189.
58. K. H. Ebert, H. J. Breunig, C. Silvestru, and I. Haiduc, *Polyhedron*, 1994, **13**, 2531.
59. I. Ghesner, L. Opris, G. Balázs, H. J. Breunig, J. E. Drake, A. Silvestru, and C. Silvestru, *J. Organomet. Chem.*, 2002, **642**, 113.
60. M. Herberhold and H. D. Brendel, *J. Organomet. Chem.*, 1993, **458**, 205.
61. H. J. Breunig and R. Rösler, *Chem. Soc. Rev.*, 2000, **29**, 403.
62. P. Sharma, A. Cabrera, N. K. Jha, N. Rosas, R. Le Lagadec, M. Sharma, and J. L. Arias, *Main Group Met. Chem.*, 1997, **20**, 697.
63. L. Balazs and H. J. Breunig, *Coord. Chem. Rev.*, 2004, **248**, 603.
64. G. Balázs, H. J. Breunig, E. Lork, and S. Mason, *Organometallics*, 2003, **22**, 576.
65. G. Balázs, H. J. Breunig, and E. Lork, *Z. Anorg. Allg. Chem.*, 2003, **629**, 637.
66. H. Althaus, H. J. Breunig, and E. Lork, *J. Chem. Soc., Chem. Commun.*, 1999, 1971.
67. R. Minkwitz and C. Hirsch, *Z. Anorg. Allg. Chem.*, 1999, **625**, 1674.
68. T. Sasmori, Y. Arai, N. Takeda, R. Okazaki, and N. Tokitoh, *Chem. Lett.*, 2001, 42.
69. C. Jones, J. W. Steed, and R. C. Thomas, *J. Chem. Soc.*, 1999, 1541.

70. C. Jones, P. C. Junk, J. W. Steed, R. C. Thomas, and T. C. Williams, *J. Chem. Soc., Dalton. Trans.*, 2001, 3219.
71. B. Twamley, C. D. Sofield, M. M. Olmstead, and P. P. Power, *J. Am. Chem. Soc.*, 1999, **121**, 3357.
72. N. Tokitoh, *J. Organomet. Chem.*, 2000, **611**, 217.
73. A. J. Ashe III and S. Al-Ahmad, *Adv. Organomet. Chem.*, 1996, **39**, 325.
74. A. Haaland, A. Hammel, K. Rypdal, O. Swang, J. Brunvoll, O. Gropen, M. Greune, and J. Weidlein, *Acta Chem. Scand.*, 1993, **47**, 368.
75. S. Wallenhauer and K. Seppelt, *Inorg. Chem.*, 1995, **34**, 116.
76. D. W. Allen, T. Gelbrich, and M. B. Hursthouse, *Inorg. Chim. Acta*, 2001, **318**, 31.
77. P. J. Cox, R. A. Howie, J. N. Low, and J. L. Wardell, *Inorg. Chem. Commun.*, 1998, **1**, 463.
78. H. Barucki, S. J. Coles, J. F. Costello, T. Gelbrich, and M. B. Hursthouse, *J. Chem. Soc. Dalton Trans.*, 2000, 2319.
79. D. Cunningham, E. M. Landers, P. McArdle, and N. Ni Chonchubhair, *J. Organomet. Chem.*, 2000, **612**, 53.
80. K. V. Domasevitch, N. N. Gersimchuk, and A. Mokhir, *Inorg. Chem.*, 2000, **39**, 1227.
81. G. Lang, K. W. Klinkhammer, C. Recker, and A. Schmidt, *Z. Anorg. Allg. Chem.*, 1998, **624**, 689.
82. M. N. Gibbons, A. J. Blake, and D. B. Sowerby, *J. Organomet. Chem.*, 1997, **543**, 217.
83. M. N. Gibbons and D. B. Sowerby, *J. Organomet. Chem.*, 1998, **555**, 271.
84. S. Kojima, Y. Doi, M. Okuda, and K.-Y. Akiba, *Organometallics*, 1995, **14**, 1982.
85. H. J. Breunig, T. Krüger, and E. Lork, *J. Organomet. Chem.*, 2002, **648**, 209.
86. M. G. Gibbons and D. B. Sowerby, *J. Chem. Soc., Dalton Trans.*, 1997, 2785.
87. A. Silvestru, H. J. Breunig, R. Rösler, M. Stanciu, and E. Lork, *J. Organomet. Chem.*, 1999, **588**, 256.
88. Y. Matano, H. Nomura, and H. Suzuki, *Inorg. Chem.*, 2000, **39**, 1340.

Arsenic: Inorganic Chemistry

Miguel-Ángel Muñoz-Hernández
Universidad Autónoma del Estado de Morelos, Centro de Investigaciones Químicas, Morelos, Mexico

Based in part on the article Arsenic: Inorganic Chemistry by Ralph A. Zingaro which appeared in the Encyclopedia of Inorganic Chemistry, First Edition.

1 Introduction 1
2 Preparation 2
3 Intermetallic and Zintl Phases with Arsenic 2
4 Arsenic Hydrides 3
5 Arsenic Halides 5
6 Arsenic Chalcogen Compounds 7
7 Arsenic Compounds Containing Carbon 15
8 Arsenic Pnictogen Compounds and Complexes Based on Ligands with Pnictogen Donor Atoms 15
9 Arsenic in the Environment 18
10 Related Articles 20
11 References 20

Abbreviations

K_a = Acidity constant; cm = Centimeter; en = Ethylendiamine; LD_{50} = 50% of a lethal dose; Et = ethyl; i-Bu = Isobutyl; hcp = Hexagonal close packed; i-Pr = Isopropyl; LED = Light-emitting diode; Me = Methyl; MOCVD = Metalorganic chemical vapor deposition; $E°$ = Normal standard potential; NMR = Nuclear magnetic resonance; n-Bu = n-butyl; n-Pr = n-propyl; OEP = Octaethylporphyrin; t-Bu = Tert-butyl; THF = Tetrahydrofurane; TPP = Tetraphenylporphyrin; V = Volt.

1 INTRODUCTION

Despite the popular association of arsenic to poisons, the element has found several uses. Alloys are made with Pb and to a lesser extent with Cu. The addition of small quantities of As improves the properties of Pb/Sb for storage batteries. Automotive body solder is Pb (92%), Sb (5.0%), Sn (2.5%), and As (0.5%). The III-V semiconductors especially GaAs and InAs are very important in the fabrication of LEDs, tunnel diodes, infrared emitters, laser windows, and Hall-effect devices. It also found use in agriculture as herbicide and pest controls but now is very restricted because of environmental issues. Arsenic acid, $AsO(OH)_3$, is still used in the formulation of wood preservatives but banned recently in the United States. Sodium arsenate is used to control fungi which cause measles on grapes. Sodium arsenite and monomethylarsonate are used as simple bulk weedkillers, and arsenicals such as sodium arsenate and copper acetoarsenite $[Cu(CH_3COO)_2Cu(AsO_2)_2]$ can be found in commercial household insecticides. Arsenic is also a common component of fire retardants.[1]

The toxicity of arsenic has been put into practical use in medicine. Ehrlich in 1909 developed Salvarsan, the trade name for arsphenamine (**1**), which was the first modern chemotherapeutic agent effective in the treatment of syphilis, which was eventually phased out by better organoarsenicals and latter by penicillin. Some specialist arsenical drugs are still the treatment of choice for amoebic infections like glycobiarsol (**2**).[2]

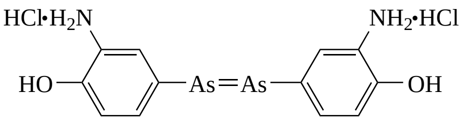

(**1**)

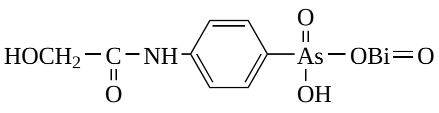

(**2**)

Arsenic has a prominent place in the development of modern inorganic chemistry. Lois-Claude Cadet de Gassicourt in 1757 during his experiments with arsenic-containing cobalt ores, $CoAs_2$ and $CoAsS_2$, prepared by the combination of arsenious oxide, As_2O_3, and potassium acetate, CH_3CO_2K, a red malodorous fuming liquid (Cadet's fuming liquid) that contained the first organometallic or more rigorously stated organometallioid compounds (equation 1). Latter, in the early nineteenth century it was found that the main components of the red liquid are tetramethyldiarsine (**3**) (40%) and tetramethyldiarsine oxide (**4**) (56%).[3]

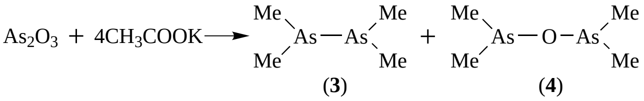

$$As_2O_3 + 4CH_3COOK \longrightarrow \underset{(\mathbf{3})}{Me_2As{-}AsMe_2} + \underset{(\mathbf{4})}{Me_2As{-}O{-}AsMe_2} \qquad (1)$$

This article will focus on the inorganic chemistry of arsenic rather on the species that feature arsenic–carbon bonds, in which the carbon atom is part of an alkyl or aryl group, for example, (**3**) or (**4**) (these organoarsenicals may be found in the article *see* ***Arsenic: Organoarsenic Chemistry***). Only a few organoarsenicals are presented to illustrate applications or important species that were stabilized by means of bulky organic ligands such as the arsines (**9**) and (**10**) in Section 4.1.

2 PREPARATION

The commonly encountered oxidation states of arsenic are +3, as in As_2O_3, and +5, as in As_2O_5. Formally, a −3 oxidation number can be assigned in AsH_3. But the simple ions As^{3-}, As^{3+} and As^{5+} are not known.

Arsenic is produced almost entirely as a by-product formed during the smelting of nonferrous metal ores. It occurs in appreciable amounts in a number of copper, lead, and zinc ores. The ores are treated in a manner which promotes the formation of As_2O_3. This form of arsenic sublimes at 193 °C and this physical property greatly assists in its separation and purification. The volatile arsenic compounds are collected in cooling chambers where the temperatures are gradually lowered from 220 to 100 °C or less. The condensed solids contain 90–95% arsenic trioxide. A product of very high purity can be prepared by resublimation of the solids. About 97% of arsenic produced commercially enters the commercial market as resublimed As_2O_3. Only about 3% is utilized as the metal. The free metal is prepared industrially by smelting loellingite, $FeAs_2$, or arsenopyrite, FeAsS, at 650–700 °C in the absence of air. The element is deposited under these conditions in the gas phase by condensation (equation 2).

$$\mathrm{FeAsS} \xrightarrow{650-700\,^{\circ}\mathrm{C}} \mathrm{FeS} + \mathrm{As(g)} \longrightarrow \mathrm{As(s)} \qquad (2)$$

Table 1 Properties of elemental arsenic[1,4]

Atomic radius (calc.)	1.15 (1.14) Å
Covalent radius	1.19 Å
van der Waals radius	1.85 Å
Crystal structure	Rhombohedral
Melting point (α-As)	816 °C (at 38.6 atm)
Boiling point (α-As)	615 °C (subl.)
Density (α-As)	5.778 g cm^{-3}
Yellow As_4	1.97 g cm^{-3}
$\Delta H_{\mathrm{fusion}}$	369.9 kJ mol^{-1}
ΔH_{vap}	34.76 kJ mol^{-1}
Thermal conductivity	50 W m^{-1} K^{-1}
Electrical resistivity	33.3 µΩ cm (at 20 °C)
Hardness	3.5 Mohs
Electronic configuration	[Ar]$3d^{10}4s^24p^3$
Ionization energies (kJ mol^{-1})	
$M \rightarrow M^+$	947.0
$M^+ \rightarrow M^{2+}$	1798.0
$M^{2+} \rightarrow M^{3+}$	2736.0
$M^{3+} \rightarrow M^{4+}$	4837.0
$M^{4+} \rightarrow M^{5+}$	6043.0
$M^{5+} \rightarrow M^{6+}$	12310.0
Electronegativity χ (Pauling)	2.18
Stable isotopes (mass and natural abundance)	
^{75}As	74.92160 100%

In Table 1 can be found a summary of some of the more important data associated with elemental arsenic and the arsenic atom.

At laboratory scale a useful reagent for the preparation of arsenic derivatives is arsenic (III) chloride, $AsCl_3$. A convenient synthetic method involves the reaction of As_2O_3 with sulfinyl chloride ($SOCl_2$) as shown in equation (3).[5]

$$\mathrm{As_2O_3} + 3\mathrm{SOCl_2} \longrightarrow 2\mathrm{AsCl_3} + 3\mathrm{SO_2} \qquad (3)$$

3 INTERMETALLIC AND ZINTL PHASES WITH ARSENIC

3.1 Intermetallic Phases Containing Arsenic

Many metals form arsenides with interesting structures and valuable physical properties. In most cases these compounds are prepared by direct reaction of the elements in the required proportions.

The group 12 metals form intermetallics with the M_3As_2 composition. The M_3As compounds are formed with metals that are not usually thought to be univalent, for example, Ti, Zr, Hf, V, Nb, Ta, Mn. Many of the M_3As have the structure of Na_3As which is described below in the text.

With actinides one of the possible compositions found is MAs_2 like in $ThAs_2$ in which each Th atom has 9 As neighbors. Three types of structures are important with transition metals and arsenic, $CoAs_3$, NiAs and those related to FeS_2. $CoAs_3$ is a diamagnetic semiconductor that occurs in the mineral skutterudite. It has a cubic structure related to that of ReO_3 but with distortions that result in planar As_4 rings. The NiAs structure is one of the most common MX structural types. In the structure each Ni is 8-coordinate and surrounded by 6 As and by 2 Ni atoms. The As atoms form a hcp lattice in which the interstices are occupied by Ni atoms in a way that each As is surrounded by a trigonal prims of 6 Ni.[1]

Intermetallic compounds of arsenic with group 13 metals comprise the important III–V semiconductors of which GaAs along with GaP remain the most important optoelectronic emitter materials in volume production (*see* ***Semiconductors***). These include arsenides of boron, aluminum, gallium, and indium. Continuous operation at room temperature of semiconducting lasers with an operating wavelength of about 0.8 µm has been achieved with the use of GaAs/AlGaAs double heterostructure with a GaAs light-emitting layer between the AlGaAs layers. These lasers are widely used in displays and compact-disk memory-storage systems. Also InGaAsP/InP lasers with wavelengths from 1.3 to 1.5 µm are used in optical-communication systems. For these applications the detectors are equally as important as the laser sources, and optical response at frequencies greater than 70 GHz has been achieved from a waveguide structure composed of InGaAs and InP. Intermetallic arsenides with group 14 metals form interesting materials. SnAs has a NaCl structure and it is superconductor below 3.5 K and Sn_4As_3 shows a defect NaCl structure and it is also a superconductor below 1.2 K.[6,7]

3.2 Zintl Phases with Arsenic

With arsenic, the alkaline and the alkaline earth metals form intermetallic polar compounds that are described in the literature as Zintl phases. The alkaline metals form phases with the composition M_3As whilst the alkaline earth metals form M_3As_2 phases. These compounds are not very ionic and have many metallic properties. For example, Na_3As has an hexagonal (anti-LaF_3) structure in which equal number of Na and As form hexagonal nets as in boron nitride and the remaining Na atoms are arranged in layers on either side of these nets. Each As has five neighbors at the corners of a trigonal bipyramid and six other Na atoms in a trigonal prismatic arrangement, making the total coordination number for As 11. The Na atoms have two types of environments. The Na in the NaAs net has three As atoms and six Na nearest neighbors. The structure of LiAs consists of parallel infinite spirals of As atoms (As–As distance 2.46 Å), the metallic luster and electrical conductivity indicate rather metallic bonding than ionic in this material.[1]

Ternary Zintl phases that incorporate arsenic are exemplified by Ba_4SiAs_4 (*see **Zintl Compounds***). The material is made of tetrahedral $SiAs_4^{8-}$ units whose charge is compensated for by the Ba cations.

Zintl phases that include transition metals and arsenic are also known. There are those that are isostructural with known main group Zintl phases. For example, Na_8TiAs_4 and Na_5HfAs_3 are isostructural with A_8SnSb_4 ($A = Na$, K) and Na_5SnAs_3, respectively. Other class of Zintl phases include all electronically balanced compounds that contain transition metal ions with d^0 or d^{10} closed-shell configurations. These ions are the early and late transition metals of groups 4, 5, and 6 as d^0 ions and of groups 10, 11, and 12 as d^{10} ions. There are also a couple of phases that incorporate transition metal ions with partially filled d-orbitals in which the compounds are electronically balanced, like $A_{14}MnAs_{11}$ ($A = Ca$, Sr, Ba, Eu). Another variant has been recently introduced with the preparation of the first examples of a mixed-valence, transition metal Zintl phase that incorporate arsenic namely, $K_{38}Nb_7As_{24}$ and $Cs_9Nb_2As_6$. The structure of $K_{38}Nb_7As_{24}$ contains isolated tetrahedra of $NbAs_4$ and two types of dimers of edge-sharing tetrahedra: dimers with only Nb^V, $[Nb_2^VAs_6]^{8-}$, and mixed-valence dimers with both Nb^{IV} and Nb^V, $[Nb^{IV}Nb^VAs_6]^{9-}$. The structure of $Cs_9Nb_2As_6$ contains only the latter dimers.[8]

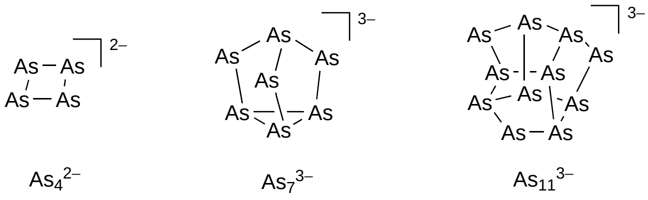

Figure 1 A few of the As_n^{m-} ions structurally characterized

3.3 Zintl Anions with Arsenic

Reaction of group 15 elements like arsenic with alkali or alkaline earth metals forms Zintl anions of the general type As_n^{m-}. Characterization of these species has been accomplished dissolving the solids in liquid NH_3 or ethylenediamine ($H_2NCH_2CH_2NH_2$) and adding the macrocycle, 2,2,2-crypt (**5**) to complex the cations and stabilize the polyatomic anions. The fully characterized Zintl arsenic anions As_4^{2-}, As_7^{3-} and As_{11}^{3-} are shown in Figure 1.[9–12]

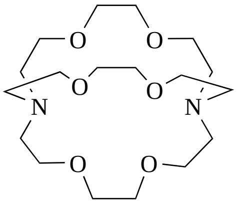

(**5**)

4 ARSENIC HYDRIDES

4.1 Arsine and Other Hydrides of Arsenic

Pentavalent hydrides of arsenic are not known in any form.[13] The simplest hydride of arsenic^{III}, arsine (AsH_3) is a very toxic gas (m.p. −116 °C, b.p. −62 °C) with a characteristic garlic-like odor, which in the presence of air oxidizes to As_4O_6. It is thermally unstable depositing a mirror of As in hot surfaces, a property that is used in the qualitative determination of arsenic (Marsh test).

In the laboratory, convenient synthetic routes to prepare AsH_3 is the reduction of $AsCl_3$ with $LiAlH_4$ in diethylether or THF solutions at low temperature and the reaction between arsenite and KBH_4 in acid solution (equation 4). Arsenides of electropositive metals (Na, Mg, Zn, etc.) upon treatment with acidic solutions also afford AsH_3.[1,9,14]

$$4As(OH)_4^- + 3BH_4^- + 7H^+ \longrightarrow 3H_3BO_3 + 7H_2O + 4AsH_3 \quad (4)$$

Arsine reacts with HBr and HI in the gas phase forming the corresponding onium salts $[AsH_4]Br$ and $[AsH_4]I$ (equation 5). Arsonate formation does not occur with HF and HCl because these acids have stronger H–X bonds than their heavier group 17 congeners.[15]

$$\mathrm{AsH_3 + HX(g) \longrightarrow [AsH_4]X} \tag{5}$$
$$\mathrm{X = Br, I}$$

Diarsines are known but as AsH_3 they are also very unstable. Tetrahydrodiarsine, As_2H_4, has been prepared by the reaction between (Mg/Al) arsenide and cold 20% sulfuric acid. The gases are condensed in a liquid nitrogen trap and fractionally distilled. Small quantities of As_2H_4 are trapped at $-196\,°C$. As_2H_4 undergoes decomposition at $-100\,°C$ into AsH_3 and solid, polymeric, red $(As_2H)_n$. Dihydrodiarsine, As_2H_2 has been characterized as a brown solid. It has been prepared by the reaction between $AsCl_3$ and $SnCl_2$ in HCl solution (equation 6).

$$\mathrm{AsCl_3 + 4SnCl_2 + 2HCl \longrightarrow As_2H_2 + 4SnCl_4} \tag{6}$$

Tetraarsine dihydride, As_4H_2, prepared from AsH_3 and $SnCl_4$ has been characterized as a brown-red amorphous solid. It is stable when stored in a dry atmosphere free from oxidizing agents. In the absence of air it thermally decomposes into arsenic metal and AsH_3.

Stable monomeric arsenic hydride species of the type $RAsH_2$ and R_2AsH have been prepared using substituents R which have no β-hydrogen atoms and are sterically demanding like $(Me_3Si)_2N$-,[16] trisalkylphenyl ligands (**6**), 2,6-bis(trialkylphenyl)phenyl ligands (**7**)[17] and recently triptycene (Trip) (**8**).[18] Figure 2 shows the X-ray structures of two examples of these arsines: $[(Me_3Si)_2N]_2AsH$ (**9**)[16] and the air-stable $TripAsH_2$ (**10**).[18] Interestingly, compound (**9**) shows a monomeric pyramidal structure in the solid state contrary to the phosphine analog $\{[(Me_3Si)_2N]_2PH_2\}_2$ which is planar and features a planar P_2H_2 core.[16] The monomeric nature of (**9**) has been ascribed to the poor overlap of orbitals between As and the H atoms that prevents the formation of H-As-H bridges.

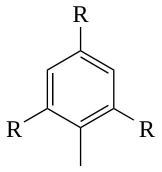

(**6**)

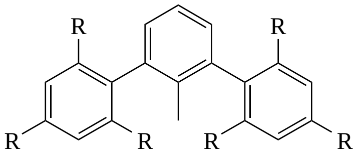

(**7**)

R = Me, *i*-Pr, *t*-Bu

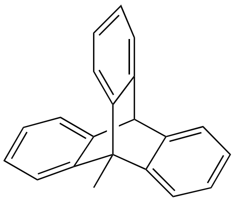

(**8**)

4.2 Arsine as a Ligand

Structurally characterized complexes with AsH_3 as a terminal ligand have yet to be reported.[13] This has been

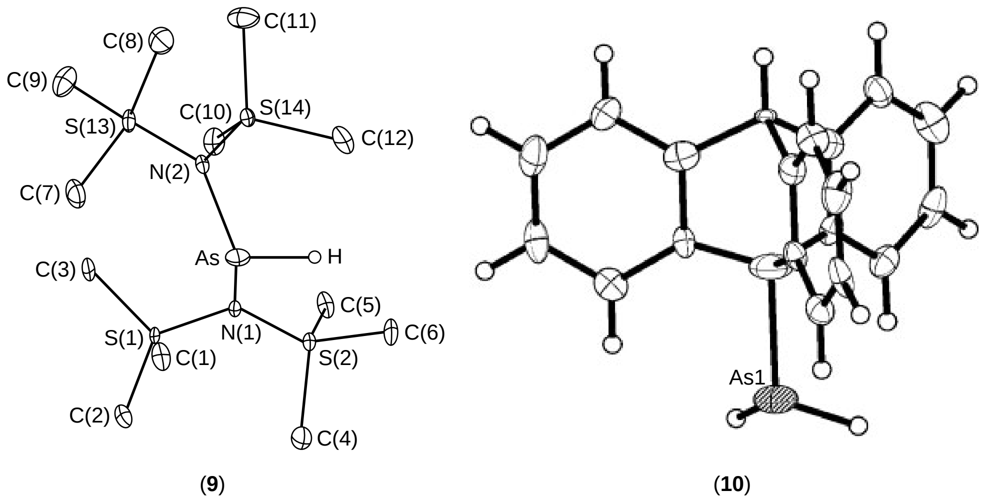

(**9**) (**10**)

Figure 2 X-ray structures of $[(Me_3Si)_2N]_2AsH$ (**9**)[16] and $TripAsH_2$ (**10**)[18]

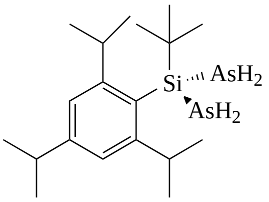

(**11**)

attributed to the weakness of the As–H bond which readily promotes elimination of H_2 to give As–As bonded compounds.[19] However complexes have been isolated that contain the AsH_2 moiety as in the silane ((*i*-Pr)$_3C_6H_2$)(*t*-Bu)Si(AsH_2)$_2$ (**11**)[20] and the iridium^{III} complex *trans*-[Ir(CO)XH(PEt_3)$_2$(AsH_2)] with X = Cl, Br (**12**) prepared by oxidative addition of AsH_3 to the Ir^I precursor (equation 7).[21] Reaction of AsH_3 with group 13 compounds afford oligomeric adduct complexes of the type [R_3M-AsH_3]$_n$ which on heating eliminate alkanes. This is exemplified by the reaction of *t*-Bu_3Ga with AsH_3 which renders the trimer [*t*-Bu_2GaAsH_2]$_3$ (**13**) shown in equation (8).[22] Complex (**13**) was prepared in the context of the search of single-source precursors to GaAs by MOCVD (*see* ***Metallic Materials Deposition: Metal-organic Precursors***).

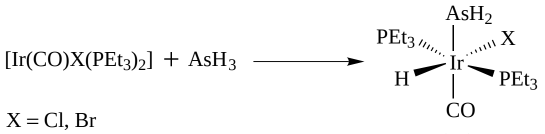

(**12**)

(7)

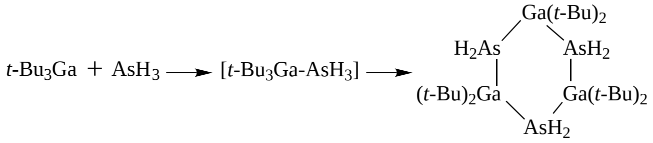

(**13**)

(8)

5 ARSENIC HALIDES

5.1 Trihalides

All the arsenic trihalides are known compounds; this is also true for the rest of the group 15 cognates. Selected physical and molecular parameters for the arsenic halides are given in Table 2.[23]

The four arsenic halides are molecular compounds in the gas phase which have been shown by electron diffraction and microwave spectroscopy to have C_{3v} pyramidal structures.[23,24]

AsF_3 must be prepared in anhydrous conditions to prevent its hydrolysis from a CaF_2/concentrated H_2SO_4 mixture. The H_2O formed during the course of the reaction can be effectively sequestered by the sulfuric acid (equation 9).[23] In common with other pyramidal molecules AsF_3 undergoes inversion around the arsenic atom. Contrary to other pyramidal molecules that invert trough *vertex* inversion via a planar intermediate (D_{3h}), AsF_3 has been shown by theoretical calculations to invert trough *edge* inversion via a T-shaped intermediate (C_{2v}) (Figure 3).[25] Although AsF_3 is a weaker fluorinating agent than SbF_3, it is preferred for the preparation of high boiling point fluorides despite its obvious toxicity since $AsCl_3$ (b.p. 130 °C) can be distilled off, for example, equation (10).[1] AsF_3 with chlorine undergoes an interesting oxidation–reduction reaction to form $[AsCl_4]^+$ $[AsF_6]^-$.

$$As_4O_6 + 12HF \longrightarrow 4AsF_3 + 6H_2O \tag{9}$$

$$[PCl_4]^+[PCl_6]^- + 2AsF_3 \longrightarrow [PCl_4]^+[PF_6]^- + 2AsCl_3 \tag{10}$$

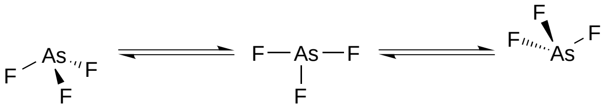

Figure 3 Inversion of AsF_3 trough *edge* inversion via a T-shaped intermediate

Table 2 Selected physical and molecular parameters for the arsenic halides[23]

	AsF_3	$AsCl_3$	$AsBr_3$	AsI_3
Melting point (°C)	−6.0	−16.2	31.1	140.4
Boiling point (°C)	62.8	130.2	221 89 at 11 torr	*c*. 400
Density (g mL^{-1})	2.67 (at 0 °C)	2.205 (at 0 °C)	3.28 (at 50 °C)	4.39
Color and Phase	Colorless liquid	Colorless liquid	Yellow crystals	Red crystals
ΔH_f° (kJ mol^{-1})	−956.5	−305.0	−197.0	−58.2
Bond length (As–X[23]) (Å)	1.708[b]	2.1621[c] 2.17[b]	2.33[c] 2.36[b]	2.55[c] 2.59[b]
Bond angle (X–As–X[a]) (Å)	95.97[b]	98.63[c] 97.7[b]	99.7[c] 97.7[b]	100.2[c] 99.7[b]

[a] X = F, Cl, Br, I respectively. [b] Determined by electron diffraction; gas phase. [c] Determined by X-ray crystallography.

The preparation of $AsCl_3$ at laboratory scale has been described in Section 2 (see equation 3). By comparison to the other elements of group 15, the arsenic–chlorine bond is more resistant to hydrolysis, therefore its preparation from aqueous solutions is possible, for example, using concentrated HCl (equation 11). Other methods for the synthesis of $AsCl_3$ include the direct reaction between the elements, the reaction between As_2O_3 and S_2Cl_2, and the treatment of AsF_3 with PCl_3, PCl_5, $PSCl_3$, $SiCl_4$, or $SOCl_2$. $AsBr_3$ has been prepared by the direct combination of arsenic metal powder with bromine. The direct reaction between As_2O_3, sulfur and bromine has also been described (equation 12). The synthesis of AsI_3 an orange-red crystalline solid can be accomplished in aqueous solution by the reaction between potassium iodide and arsenic trioxide in concentrated HCl (equation 13). The solid-state structure of $AsCl_3$ shows three short molecular As–Cl bonds (Table 2) and three longer intermolecular bonds from the nearest chloride atoms from other $AsCl_3$ molecule affording $AsCl_6$ with a distorted octahedral geometry. The same structure is found for $AsBr_3$ and AsI_3.[23] $AsCl_3$ is not as susceptible to nucleophilic attack as PCl_3 is. Therefore, the reactions of $AsCl_3$ proceed stepwise and it is much easier to stop at a lower level of substitution than with PCl_3. A few examples of reactions that illustrate the reactivity of $AsCl_3$ and the rest of arsenic trihalides are given in Scheme 1. Although the self ionization equilibrium of $AsCl_3$ to give $AsCl_2{}^+$ and $AsCl_4{}^-$ is very low (conductivity 1.4×10^{-6} $(\Omega\,\mathrm{cm})^{-1}$), $AsCl_3$ has been used as a nonaqueous solvent for chloride transfer reactions.

$$As_2O_3 + 6HCl \longrightarrow 2AsCl_3 + 3H_2O \qquad (11)$$

$$2As_2O_3 + 3S + 6Br_2 \longrightarrow 4AsBr_3 + 3SO_2 \qquad (12)$$

$$As_2O_3 + HCl \longrightarrow AsCl_3 + Kl \longrightarrow AsI_3 \qquad (13)$$

5.2 Pentahalides

The only known arsenic pentahalides are AsF_5 and $AsCl_5$ of which the fluoride is the most stable species. The relative instability of the heavier arsenic halides can be ascribed to a tendency towards reduction to give the arsenic trihalides and elemental halogen (equation 14) owing to the shielding properties of the underlying full 3d orbitals of arsenic that reduce the availability of the electrons in the 4s orbital.[23]

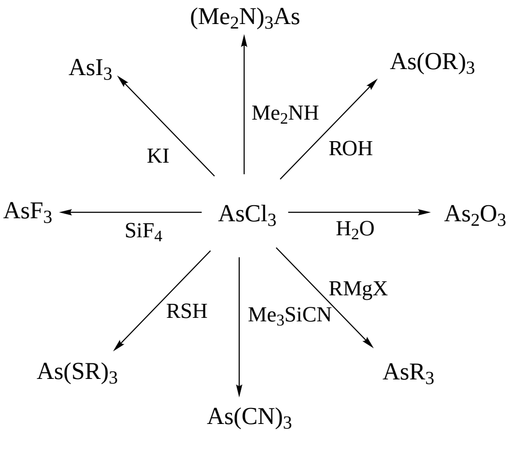

Scheme 1

$$AsX_5 \longrightarrow AsX_3 + X_2 \qquad (14)$$
$$X = Cl, Br, I$$

A simple route to prepare AsF_5, which is a colorless gas, involves the reaction of fluorine with arsenic. In the laboratory it is conveniently prepared by the reaction between AsF_3, SbF_5, and bromine (equation 15). The electron diffraction structure in the gas phase of AsF_5 shows the expected trigonal bipyramidal arrangement around arsenic with axial bond lengths of 1.711 Å and equatorial bond lengths of 1.656 Å.

$$2SbF_5 + Br_2 + AsF_3 \longrightarrow AsF_5 + 2SbBrF_4 \qquad (15)$$

Arsenic pentachloride was an elusive compound until it was finally obtained by the ultraviolet irradiation of an $AsCl_3/Cl_2$ mixture at −105 °C. Above −50 °C, a redox reaction occurs affording $AsCl_3$ and molecular chlorine (see equation 14 above). The identity of $AsCl_5$ was confirmed by elemental analysis and by comparison of its Raman spectrum with those of liquid PCl_5 and $SbCl_5$.[26]

Although not as convenient as PF_5 or SbF_5, AsF_5 has found some use as halide acceptor when a large anion is needed.

5.3 Mixed Arsenic Halides

The mixed arsenic trihalides $AsX_nX'_{3-n}$ and pentahalides $AsX_nX'_{5-3n}$ are essentially unstable compounds. But it has been observed that mixtures of $AsCl_3$ and AsI_3 favor the formation of $AsCl_2I$ according to equation (16). A mixture of AsF_3 and $AlCl_3$ has been shown to form small amounts of AsF_2Cl and $AsFCl_2$ by ^{19}F NMR. In a similar fashion, the combination of $AsCl_3$ and $AsBr_3$ forms $AsCl_2Br$ and $AsBr_2Cl$.

$$2AsCl_3 + AsI_3 \rightleftharpoons 3AsICl_2 \qquad (16)$$

All the series of $AsF_{5-n}Cl_n$ ($n = 0-5$) compounds have all been observed, although some of them in an argon matrix. The structure of these halides is as it would be anticipated trigonal bipyramidal with the fluorine atoms in apical positions and the less electronegative chlorine atoms in equatorial sites.[23]

5.4 Haloarsenate Ions

The formation of the fluroarsenate anion $[As_2F_{11}]^-$ has served to stabilize the arsonium cation $[(CH_3)_3AsH]^+$ (equation 17), the colorless solid is stable for several months at −70 °C under a nitrogen atmosphere, decomposing at 5 °C.[27]

$$AsCH_3 + HF + 2AsF_3 \xrightarrow{HF/-78\,^\circ C} [(CH_3)_3AsH]^+[As_2F_{11}]^- \qquad (17)$$

A number of chloroarsenate ions are known, and salts with the protonated cations of the bases dimethylamine, ethylamine, pyridine, guanidine, and quinoline with the following anions have been prepared: $[AsCl_4]^-$, $[AsCl_5]^{2-}$, $[AsCl_6]^-$, $[As_2Cl_9]^{3-}$, and $[As_3Cl_{11}]^{2-}$. Other identified haloarsenates are: $[As_3Br_{12}]^{3-}$, $[As_6Br_8]^{2-}$, $[As_6I_8]^{2-}$, and $[As_8I_{28}]^{4-}$.[28–30]

6 ARSENIC CHALCOGEN COMPOUNDS

6.1 Oxides of Arsenic

Arsenic^{III} oxide, As_4O_6, commonly referred to arsenic trioxide (As_2O_3) is the most important arsenic compound of commercial value since it is the raw material most widely used for the synthesis of arsenic compounds. As_4O_6 exists in both molecular and polymeric modifications. The cubic modification (arsenolite) contains discrete As_4O_6 (**14**) molecules with T_d symmetry in an adamantine-like structure in the vapor, liquid and solid phases. The structure is extremely stable and it is the main product obtained by burning arsenic in air. The second form of As_4O_6 has a monoclinic crystal system and it is commonly referred as claudetite which exists in two forms, claudetite I and II, each of which has a layered structure of arsenic atoms joined through oxygen atoms. This form of As_4O_6 is 8.7% more dense than the cubic form. Arsenic^{III} oxide is produced as a by-product of the nonferrous metals industry, primarily from the smelting of copper ores. Naturally occurring metal arsenides, realgar, and orpiment also convert to the trivalent oxide when roasted in air. The formation of the trioxide by the roasting of a sulfidic ore is illustrated in equation (18).[23,24]

$$2FeAsS + 5O_2 \longrightarrow Fe_2O_3 + As_2O_3 + 2SO_2 \qquad (18)$$

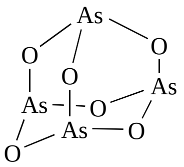

(**14**)

Elemental arsenic undergoes reaction with oxygen to yield the trioxide (equation 19).

$$4As + 3O_2 \longrightarrow 2As_2O_3 \qquad (19)$$

This direct reaction between the elements yields the trioxide almost exclusively. The reaction in air proceeds very slowly, but the rate increases rapidly with increasing temperature, decreasing particle size, and in the presence of moisture. It has also been noted that amorphous arsenic reacts with oxygen at a slower rate than the three recognized crystalline allotropes. Reacting As_4O_6 with water affords solutions of ‘‘arsenious acid’’, which is believed to be $As(OH)_3$. Arsenite ions are formed treating As_4O_6 with bases. These ions are formed by ionization of $As(OH)_3$, namely $[AsO(OH)_2]^-$, $[AsO_2OH]^{2-}$, and $[AsO_3]^{3-}$. The mixed-valence Arsenic^{III,V} oxide or more commonly known as arsenic dioxide, AsO_2 is formed by heating As_4O_6 in an autoclave for fourteen days at 260 °C under dioxygen pressure (5–50 MPa).[31] The structure consists of infinite layers of arsenic atoms coordinated to three or four oxygen atoms. The three coordinated arsenic atom is considered As^{III} and the four coordinated As^{V}. The complete range of possible oxides between $As^{III}_4O_6$ and $As^{V}_4O_{10}$ has been observed by means of matrix-isolation techniques. The structures proposed of these oxides are shown in Figure 4.

Arsenic^{V} oxide, As_4O_{10}, cannot be formed by the direct combination between the elements owing to the greater thermodynamic stability of As_4O_6, which promotes the back dissociation reaction illustrated in equation (20). The most useful preparative method involves the oxidation of elemental arsenic with concentrated nitric acid, followed by careful dehydration of H_3AsO_4 (equation 21).

$$As_4O_6 + 2O_2 \rightleftharpoons As_4O_{10} \qquad (20)$$

$$4H_3AsO_4 \longrightarrow 6H_2O + As_4O_{10} \qquad (21)$$

Hypochlorous, chloric, and perchloric acids also oxidize the metal or As_2O_3 to the pentavalent state. Interestingly, dilute HIO_3 oxidizes elemental arsenic to the pentavalent state more easily than the concentrated acid.

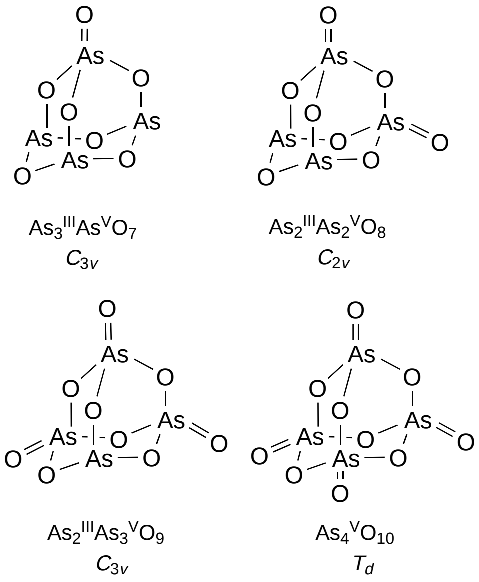

$As_3{}^{III}As^{V}O_7$ C_{3v}

$As_2{}^{III}As_2{}^{V}O_8$ C_{2v}

$As_2{}^{III}As_3{}^{V}O_9$ C_{3v}

$As_4{}^{V}O_{10}$ T_d

Figure 4 Mixed-valence arsenic oxides

6.2 Sulfides of Arsenic

Yellow arsenic^{III} sulfide (orpiment), As_2S_3 is prepared by heating the elements in stoichiometric amounts or by heating As_4O_6 with sulfur. It is also formed by passing H_2S into acidified aqueous solutions containing As^{III} compounds. Electron diffraction in the gas phase reveals a cage structure As_4S_6 similar to As_4O_6. In the solid state, the structure is composed of trigonal pyramidal AsS_3 units,[32] which is quite similar to what it is observed for As_2O_3. One of the principal impurities which accompanies the formation of As_2S_3 is elemental sulfur. This has been removed by extraction with carbon disulfide.

As_2S_3 has found use in the manufacture of glass, especially infrared transmitting glass, in pyrotechnics and, because it is a semiconductor, in photoconducting devices.

Arsenic has a very well-developed mixed-valence chemistry with sulfur in part to the occurrence of several of these species as arsenic minerals. Tetraarsenic trisulfide, As_4S_3, is orange-yellow and occurs as the mineral dimorphite which is found in α and β forms. The solid-state structure of both the α and β forms exhibit C_{3v} symmetry (**15**), differences arise due to crystal packing effects.[23]

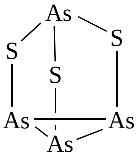

(**15**)

Tetraarsenic tetrasulfide, As_4S_4, occurs as the orange-red to orange-yellow mineral realgar. Heating dimorphite with a carbon disulfide solution of sulfur renders realgar as shown in equation (22). Mild oxidizing agents such as MgO, BiO, HgO, Pb_3O_4, MoO_3, and $CuSO_4$ have been reported to convert As_4S_6 to As_4S_4.

$$As_4S_3 + S \xrightarrow{CS_2} As_4S_4 \qquad (22)$$

On an industrial scale realgar has been prepared by the reaction between sulfur and an excess of elemental arsenic or As_2O_3. Other commercial procedure involves the sublimation of a mixture of pyrites (FeS_2), arsenopyrite (FeAsS), or the heating of arsenical pyrites, but these methods yield an impure product.

In the laboratory, realgar can be accessed by the fusion between stoichiometric quantities of arsenic metal with sulfur.

The reaction between As_4O_6 and sulfur is reported to follow the stoichiometry of equation (23).

$$2As_2O_3 + 7S \longrightarrow As_4S_4 + 3SO_2 \qquad (23)$$

As_4S_4 is normally prepared as an impure material and must be purified by sublimation under an atmosphere of CO_2.

As a result of crystal packing, synthetic As_4S_4 exists as an α and a β forms (**16**). The As_4S_4 units in the solid and in the vapor phases are identical. The α form is stable at ambient temperature and is the same to the mineral realgar, whereas the β form is a high-temperature modification. In the third isomer of realgar γ-As_4S_4 (**17**) there is arsenic with a coordination sphere composed of three, two, and one sulfur neighbors.[33]

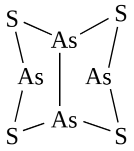

α and β-As_4S_4

(**16**)

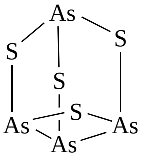

γ-As_4S_4

(**17**)

Pentavalent arsenic sulfides are not well defined. The only accepted compound is As_2S_5 which is prepared from H_2S and a solution of an As^{V} compound (equation 24) or acidification of a thioarsenate salt (equation 25).[34]

$$2H_3AsO_4 + 5H_2S \xrightarrow{H^+} As_2S_5 + 8H_2O \qquad (24)$$

$$2Na_3AsS_4 + 6HCl \longrightarrow As_2S_5 + 6NaCl\ 3H_2S \qquad (25)$$

6.3 Selenides of Arsenic

Arsenic^{III} selenide, As_2Se_3, is isomorphous with As_2S_3. The reaction between As_2Se_3 and liquid ammonia gives a small yield of the unusual salt $[NH_4][AsSe(NH_2)_2]$. The latter loses NH_3 to give NH_2AsSe.

The pentavalent arsenic selenide species has not been yet structurally characterized and it is produced in similar manner to As_2S_5.

Mixed valent arsenic selenide compounds are known, and they are related to the arsenic sulfide species. For example, As_4Se_4 is isomorphous with realgar As_4S_4 and As_4Se_3 is isomorphous with As_4S_3. However, chemical reactivity is different due to the larger size of the selenium atom.[23]

6.4 Tellurides of Arsenic

By the direct fusion of the elements in the appropriate stoichiometric ratios, the following tellurides of arsenic have been prepared: As_2Te_3, As_2Te_2, and As_8Te_3. A weakly acidic solution of $AsCl_3$ deposits a precipitate of As_2Te_3 when saturated with H_2Te. Because hydrogen telluride decomposes at 0 °C, temperature control is important. These compounds have not been the subject of a great deal of investigation.

6.5 Oxoacids of Arsenic

Arsenic trioxide is the anhydride of arsenous acid, H_3AsO_3. The solubility of arsenic trioxide in water at 25 °C is 21.6 g L^{-1}. The rate of dissolution of the trioxide in water is painstakingly slow, sometimes requiring up to 50 h of continuous agitation. The free acid has never been isolated. The solubility of arsenic trioxide increases greatly and occurs much more rapidly in both acid and alkaline media.

Proton NMR studies of aqueous arsenious acid solutions show only a single proton resonance attributable to arsenious acid. This result together with Raman spectroscopy suggest the species having a pyramidal structure which can be formulated as $As(OH)_3$. This is to be contrasted with H_3PO_3, which is $HP(O)(OH)_2$ with four-coordinate phosphorus and which exhibits two distinct proton NMR resonances. Spectroscopic evidence supports the formation of the three anions $[H_2AsO_3]^-$, $[HAsO_3]^{2-}$, and $[AsO_3]^{3-}$ when solutions of $As(OH)_3$ are treated with hydroxide ion. This observation agrees with a three-step acid dissociation. The pK_a for the dissociation of the first proton is 9.2, which means that H_3AsO_3 is a very weak acid.

Dissolution of As_4O_{10} in water the anhydride of arsenic acid, H_3AsO_4, is very soluble in cold water and dissolves to form a solution of arsenic acid. The free acid can be obtained as a hydrate, $H_3AsO_4{\cdot}0.5H_2O$, by the evaporation of a cold aqueous solution. When crystallization is carried out above 100 °C, hydrates of arsenic pentoxide are formed, examples of which are $3As_2O_5{\cdot}5H_2O$ and $As_2O_5{\cdot}4H_2O$.

Industrially, solutions of arsenic acid are prepared by the oxidation of readily available As_2O_3 with nitric acid (equation 26).

$$As_2O_3 + 2NO_3^- + 2H_2O \longrightarrow 2H_2AsO4^- + 2NO + 0.5O_2 \quad (26)$$

Arsenic acid is about as strong an acid as H_3PO_4. The acid dissociation pK_a constants are: pK_{a1}, 2.25; pK_{a2}, 6.77; and pK_{a3}, 11.60. In arsenic acid the oxidation state of arsenic is formally +5.[23] It behaves as a moderately strong oxidizing agent ($E^0 = 0.559$ V) in a number of reactions. The following are some typical examples.[24]

1. Reduction with Sn/HCl yields arsine. This reaction is catalyzed by divalent transition metal ions including Cu^{2+}, Fe^{2+}, and Hg^{2+}. Reduction by $[BH_4]^-$ also converts $AsO_4{}^{3-}$ to AsH_3.
2. In hydrochloric acid, together with a reducing agent such as Cu^+ or SO_2, $AsO_4{}^{3-}$ is converted to $AsCl_3$.
3. In a solution containing a nonoxidizing acid, for example, HCl, H_2S converts $AsO_4{}^{3-}$ to the trivalent sulfide As_2S_3, together with the precipitation of sulfur.
4. Sulfurous acid converts arsenic acid to arsenious acid (equation 27).

$$H_3AsO_4 + SO_2 + H_2O \longrightarrow H_2SO_4 + H_3AsO_3 \quad (27)$$

5. The following compounds are oxidized by H_3AsO_4: $TiCl_3$, $SnCl_2$, $CrCl_2$, $FeCl_2$, and Cu_2Cl_2. In each case the oxidation state of the metal is increased.
6. Hydrazine and hydroxylamine both reduce arsenic acid. Hydrazine is converted to nitrogen and water.

6.6 Oxoanions of Arsenic

Arsenites of the alkali metals are very soluble in water. Successive deprotonation of arsenous acid forms a series of salts: MH_2AsO_3, M_2HAsO_3, and M_3AsO_3. These salts may be stepwise dehydrated to two other series of salts, the pyroarsenites, $[As_2O_5]^{4-}$ and the meta-arsenites, $[AsO_2]^-$. Sodium meta-arsenite, $[NaAsO_2]_n$, consists of pyramidal AsO_3 units (**18**) which are linked together by shared oxygen atoms into linear chains.

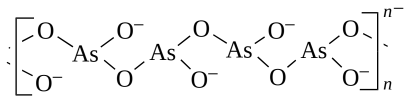

(**18**)

Alkaline earth metal arsenites are less soluble than those of the alkali metals and heavy metal arsenites tend to be insoluble. Orthoarsenites are known, for example, Ag_3AsO_3. Once utilized as a green pigment was the copper arsenite $CuHAsO_3$, and as an insecticide, Paris green, $3Cu(AsO_2)_2{\cdot}Cu(C_2H_3O_2)_2$, which is an acetate arsenite. None of these is in use at the present time.

There are a number of heteropolyanions that contain arsenic and oxygen. An interesting example being the blue As^{III} heteropolyanion, $[H_6As^{III}_{10}Mo^{V}_{8}Mo^{VI}_{16}O_{90}]^{8-}$.[35] The anion is composed of two $As_4Mo_{12}O_{42}$ spherical moieties of C_{3v} symmetry with a central AsO_3 group.

Metal arsenates are easily prepared in solution by simple neutralization of arsenic acid with the appropriate base. For example, stepwise addition of sodium hydroxide to a solution of H_3AsO_4 affords $NaH_2AsO_4{\cdot}H_2O$ and $Na_2HAsO_4{\cdot}12H_2O$. On heating these arsenates easily lose water to ultimately give polyarsenate, $(NaAsO_3)_n$, which is an extended linear polyanion. Its structure parallels that of $(NaPO_3)_n$ (Maddrell's salt), a pair of AsO_4 tetrahedra share a corner oxygen and the resulting As_2O_7 units are joined by sharing two oxygen corners with the edge of a connecting AsO_4 tetrahedron.

A vast number of arsenates with metals of the rest of the *s*-block, and the *p*-, *d*- and *f*-blocks are known. The discussion of these anions is beyond the scope of this article, the interested reader may refer to the works of Godfrey *et al.*[23] and Thilo.[36]

6.7 Anions of Arsenic with Sulfur, Selenium, and Tellurium

Research involving chalcogenidoarsenic anions with heavier group 16 elements has been prompted by the technological potential of solid-state compounds having regularly spaced pores and cavities. The realization of these phases has been accomplished using mild solvothermal regimes (100–600 °C) with strongly polarizing media such as molten salts (T = 200–600 °C) or molecular solvents (100–400 °C). Under these conditions it is possible to assemble anion networks in which characteristic molecular building units such as chains or rings can be identified. The resulting channels or cavities are often found to reflect the geometry and size of structure-directing metal or alkylammonium cations. Thus, the rest of this section will be presented with an emphasis on the possible final structure of the materials and the building blocks that originated them rather than on the methods of synthesis. An exhaustive review of all the known phases will be avoided. For this matter the interested reader may refer to the excellent review of Sheldrick and Wachhold.[37]

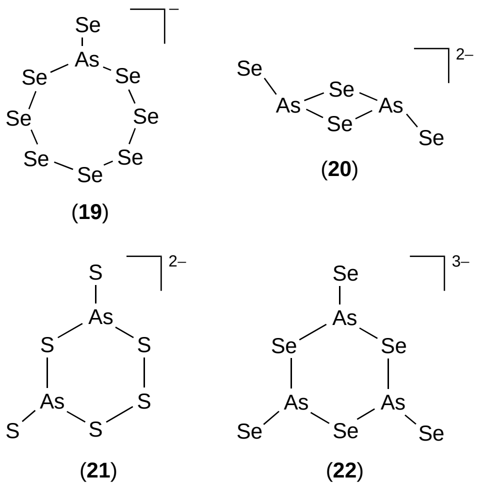

Figure 5 Discrete anions in $(Et_4N)[AsSe_8]$ (**19**), $Ba_2[As_2Se_5]$ (**20**) (anion with a trans configuration), $(Ph_4P)_2[As_2S_6]$ (**21**) and $[Sr(en)_4]_2[As_3Se_6]Cl$ (**22**)[37]

Isolated pyramidal arsenic anions with sulfur and selenium of the type M_3AsE_3 (M = Na, K, Tl; E = S and M = Tl; E = Se) and pseudotetrahedral geometry Ba_2AsE_2 (E = S, Se) are known. The anions within these phases

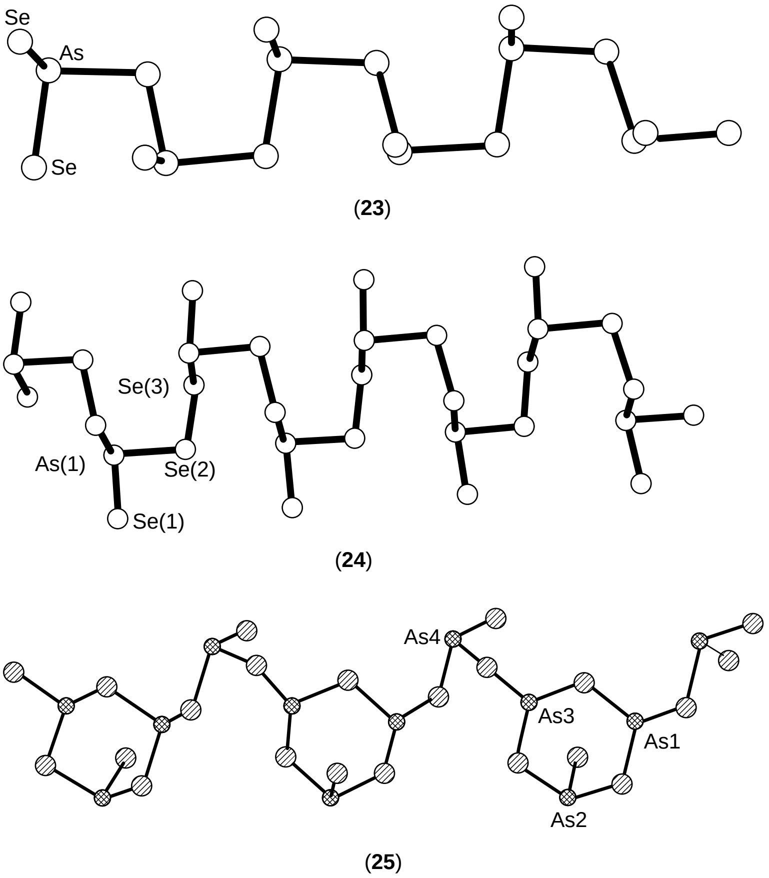

Figure 6 1-D chain-like polymers formed with mononuclear AsE_3 building units in $Na[AsSe_2]$ (**23**) and $K[AsSe_3]\cdot H_2O$ (**24**) or with cyclic molecular building units in $(Me_4N)_2As_4S_7$ (**25**)[37]

arrange in the crystal with discrete molecules. To this class of solid-state materials belong also those arsenic anions that show a cyclic molecular structure with one, two and three arsenic atoms in the ring. Examples are those anions found in $(Et_4N)[AsSe_8]$ (**19**), $Ba_2[As_2Se_5]$ (**20**) (anion with a trans configuration), $(Ph_4P)_2[As_2S_6]$ (**21**) and $[Sr(en)_4]_2[As_3Se_6]Cl$ (**22**) which are depicted in Figure 5. From (**19**–**22**) it is evident that stabilization of these species is accomplished with a large cation.

Polymer chain-like anions with 1-D dimensionality are formed either by assembling mononuclear AsE_3 building units like those in $Na[AsSe_2]$ (**23**) and $K[AsSe_3]\cdot H_2O$ (**24**) or with cyclic molecular building units in $(Me_4N)_2[As_4S_7]$ (**25**) (Figure 6).

A 2-D anionic structure has been achieved with the assembling of individual As_4S_4 rings that are connected to three further eight-membered rings trough As-S-As bridges in $Cs_2[As_8S_{13}]$ (**26**) (Figure 7). The Cs^+ cations function as templates for the construction of this material.

Selenium and tellurium arsenates in low oxidation states with direct As–As bonds can be generated either by controlled oxidation of elemental As or by reduction of a suitable binary As^{III} chalcogenide, for example, As_2Te_3. Rich tellurium phases $Na_4[As_2Te_4]$ and $K_4[As_2Te_4]$ are afforded by the first approach. The dinuclear anion $[As_2Te_4]^{4-}$ have a *gauche* (**27**) conformation in its Na^+ salt but a trans (**28**) conformation in its K^+ or Rb^+ salt (Figure 8). The trans conformation generates a larger cavity that can readily accommodate the voluminous cations K^+ or Rb^+. A derivative of the trans anion (**28**) is found in $Cs_4[As_2Te_6]$ (**29**), which is the product of the solvothermal reaction of Cs_2CO_3 and As_2Te_3 in methanol at 145 °C. The substitution of a terminal Te^{2-} by a $Te_2{}^{2-}$ dumbbell on each of the As atoms may be ascribed to the larger Cs^+ cation (Figure 8). The dinuclear anion $[As_2Se_5]^{4-}$ (**30**) present in the phase $K_5[Ag_2As_3Se_9]$ shows direct As–As bonding between a

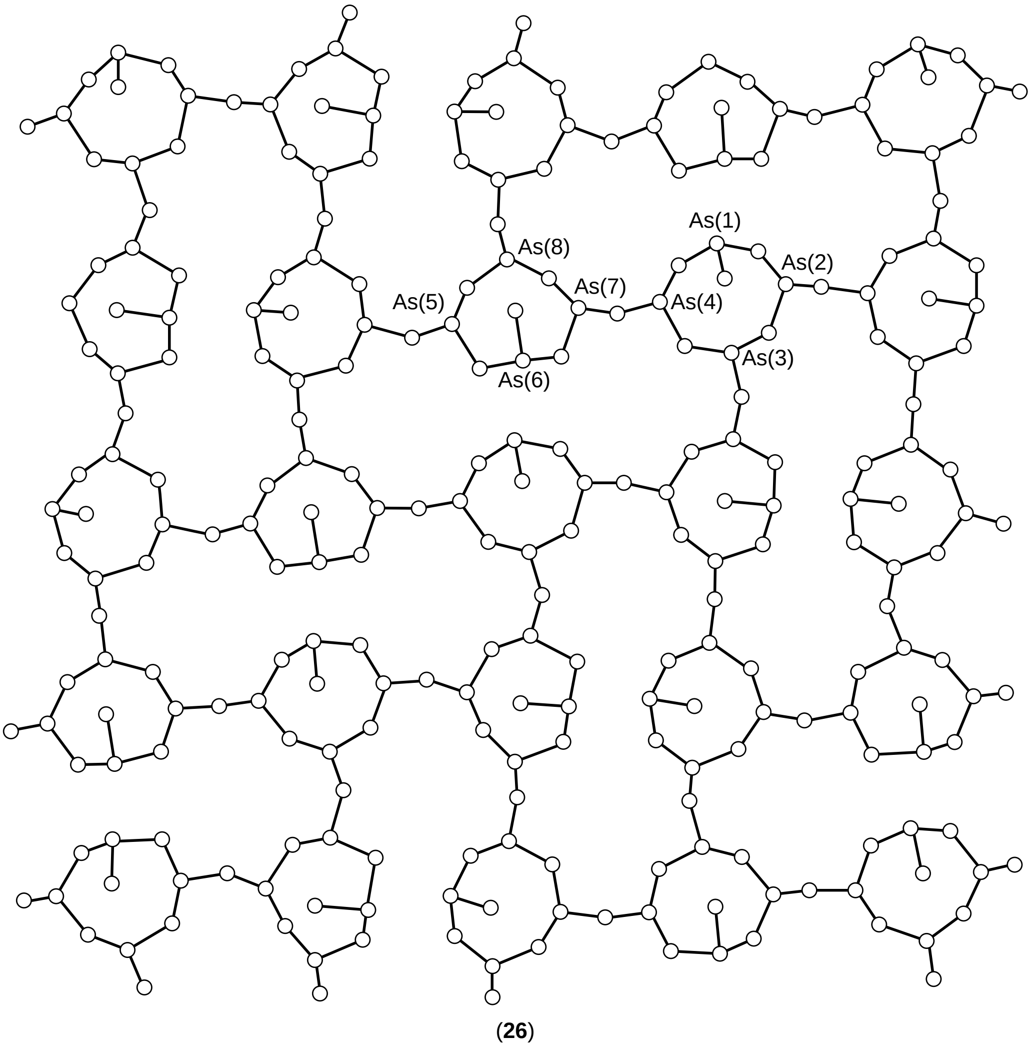

(**26**)

Figure 7 Two-dimensional structure found in $Cs_2[As_8S_{13}]$ (**26**)[37]

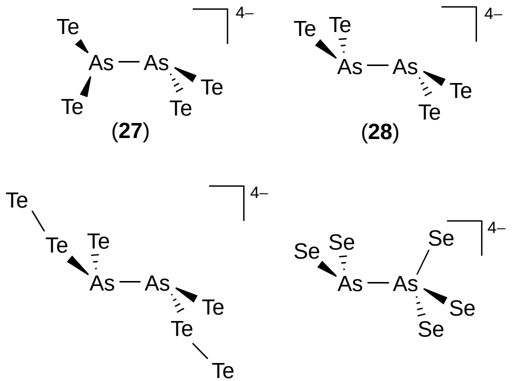

(27) (28) (29) (30)

Figure 8 *gauche*-$[As_2Te_4]^{4-}$ (**27**) in $Na_4[As_2Te_4]$, *trans*-$[As_2Te_4]^{4-}$ (**28**) found in $K_4[As_2Te_4]$ or $Rb_4[As_2Te_4]{\cdot}en$, *trans*-$[As_2Te_6]^{4-}$ with a dumbbell $Te_2{}^{2-}$ on each As atom in $Cs_4[As_2Te_6]$ (**29**), $[As_2Se_5]^{4-}$ (**30**) in $K_5[Ag_2(AsSe_4)(As_2Se_5)]$ the ion fragment displays an As^{II} and As^{III} direct bond[37]

pyramidally coordinated As^{II} and a tetrahedrally coordinated As^{IV} center (Figure 8).

The basic $[As_2E_4]^{4-}$ building block can be related to other low oxidation state phases. In this regard, $[Ba(en)_4]_2[As_4Te_6]$, contains two $[As_2Te_4]^{4-}$ anions linked together in an 'head to head'/'tail to tail' fashion trough two common Te atoms to create a $[As_4Te_6]^{4-}$ six-memebered ring (**31**) (Figure 9). The same olygomeric anion is found in $(Me_4N)_4[As_4Te_6]{\cdot}2en$. On the other hand, linear polymeric anion $[As_2Te_5]^{2-}$ (**32**) is contained in the telluridoarsenate $(Me_4N)_2[As_2Te_5]$ which can be thought to be the result of the condensation product of *trans*-$[As_2Te_4]^{4-}$ fragments and square-planar $[TeTe_4]^{6-}$ anions (Figure 9).

Interestingly, two different conformations of the eight-membered ring As_4Se_4 have been observed for the $[As_4Se_6]^{2-}$ anion (**33**) and (**34**) (Figure 10). When the counteranion is $[PPh_4]^+$, a boat–boat conformation (endo–endo with respect to the remaining selenium atoms) is observed.[38] Exchange of the counteranion for $[K(2,2,2\text{-cryptand})]^+$ renders a boat–chair conformation (endo-exo).[39]

Arsenic chalcogen-poor anions of the type $[As_{10}E_3]^{2-}$ are likely to represent a rather stable cluster variety and are known for the chalcogenides S-Te. They have been prepared by reduction of As_4E_4 (E = S, Se) or As_2Te_3 with

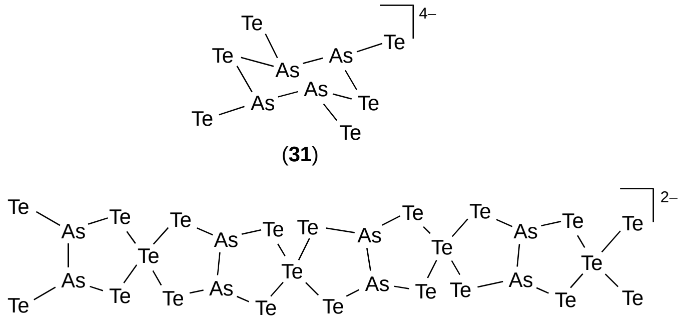

(31)

(32)

Figure 9 Olygomeric $[As_4Te_6]^{4-}$ anion (**31**) in $[Ba(en)_4]_2[As_4Te_6]$ or $(Me_4N)_4[As_4Te_6]{\cdot}2en$ and the polymeric anionic chain $[As_2Te_5]^{2-}$ (**32**) in $(Me_4N)_2[As_2Te_5]$[37]

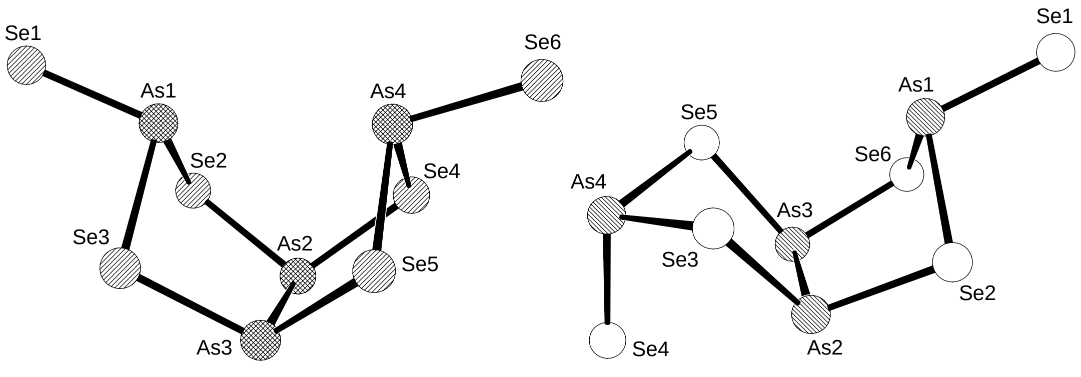

(33) (34)

Figure 10 Boat–boat conformation of $[As_4Se_6]^{2-}$ anion (**33**) in $[PPh_4]_2[As_4Se_6]$ and the boat–chair conformation (**34**) in $[K(2,2,2\text{-cryptand})]$ $[As_4Se_6]$[38,39]

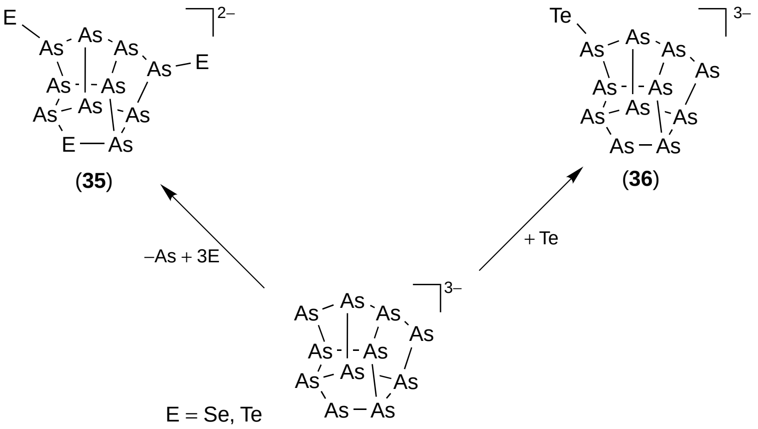

Figure 11 Arsenic-rich chalcogenide anions related to As_{11}^{3-}. $[As_{10}E_3]^{2-}$ ions (**35**) found in $[PPh_4]_2[As_{10}Se_3]$, $[PPh_4]_2[As_{10}Te_3]$, and $[K(2,2,2\text{-cryptand})]_2[As_{10}S_3]$; and the chalcogen-poorest arsenic anion $[As_{11}Te]^{3-}$ (**36**) in $[K(2,2,2\text{-cryptand})]_3[As_{11}Te]\cdot en$[37]

elemental K in NH_3 or ethylenediamine in the presence of $[PPh_4]^+$ or $[K(2,2,2\text{-cryptand})]^+$ as the counterion. The general structure of these anions which are closely related to that of As_{11}^{3-} (see also Figure 1) is represented by (**35**) in Figure 11. The arsenic chalcogen-poorest known anion, $[As_{11}Te]^{3-}$ (**36**) in $[K(2,2,2\text{-cryptand})]_3[As_{11}Te]\cdot en$ has been obtained by ethylenediamine extraction of a nominal alloy $K_8As_8Te_5$ in the presence of the sequestering agent 2,2,2-crypt. The As–As bond distances in the above mentioned As-rich clusters range from 2.388 to 2.479 Å and are significantly shorter than the distances found in elemental gray arsenic (2.517 Å).

6.8 Arsenic Complexes Based on Ligands with Chalcogen Donor Atoms

Inorganic arsenic complexes based on oxygen ligands is scarce. Simple esters of arsenic acid, $As(O)(OR)_3$ (R = Me, Et, *n*-Pr, *n*-Bu, C_6H_{13}) have tetragonal structures.[2] Reaction of the diol ligand 2,4-dimethyl-2,4-pentanediol with $AsCl_3$ affords an arsenic chloride complex in which the As atom is part of a six-membered ring (**37**).[40]

Reaction of $W(CO)_6$ and $[PPh_4]_2[As_2Cl_8]$ and of $Cr(CO)_6$ and $[PPh_4][As_2SBr_5]$ in THF yields the arsenic^V anionic complexes $[PPh_4][AsCl_4(thf)_2]$ (**38**) and $[PPh_4][AsBr_4(thf)_2]$ (**39**) both complexes display an octahedral coordination with a trans configuration (equation 28).[41] The anionic arsenic^V chatecholate complex $[H_7O_3][As(C_6H_4O_2)_3]\cdot$2,4-dioxane (**40**) prepared from $C_6H_4(OH)_2$ and $AsCl_3$ exhibits an octahedral geometry with the anionic arsenic-containing fragment having D_3 symmetry (equation 29).[42]

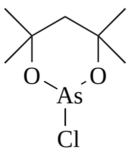

(**37**)

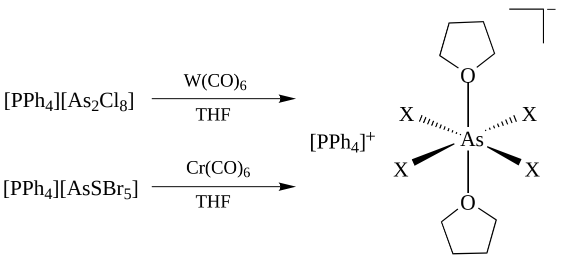

(28)

X = Cl (**38**), Br (**39**)

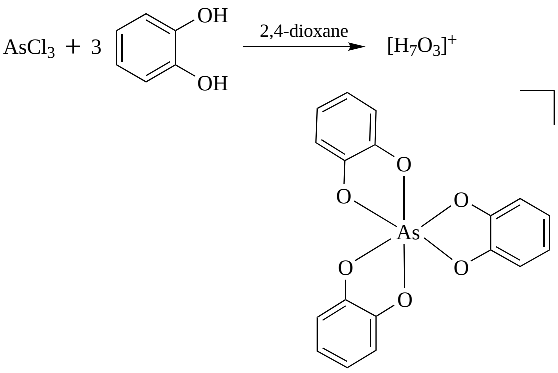

(29)

(**40**)

The chemistry of inorganic arsenic complexes with ligands that bear S donor atoms or S and O is more extensive. The chemistry of arsenic with xanthate (**41**), dithiocarbamate (**42**) and phosphorus based ligands (**43**) (Figure 12) has been reviewed.[43–46]

Homoleptic trisquelate arsenic complexes have been only structurally characterized with ligands (**41**) and (**42**). The complexes show mainly a distorted octahedral geometry, that is, $[As(S_2COMe)_3]$ (**44**), or antiprismatic, that is, $[As\{S_2CN(CH_2CH_2OH)\}_3]$ (**45**) (Figure 13). These

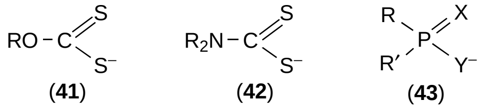
RO−C
S
S⁻
R₂N−C
S
S⁻
R
R′
P
X
Y⁻

(**41**) (**42**) (**43**)

R′ = R or OR; R = alkyl or aryl; X, Y = O, S

Figure 12 General structures of xanthate (**41**), dithiocarbamate (**42**), and phosphorous-based ligands (**43**)

trisquelate complexes are generally synthesized by reaction between arsenic halides and sodium, ammonium, lead or silver. The free acids, particularly the dithiophosphorus, have been also employed.

Mixed ligand arsenic complexes have been reported. The chloro derivatives of general formula $[\mathrm{AsCl}_{3-n}\{\mathrm{S_2P(OR)_2}\}n]$ ($n = 1, 2$; R = Et, *n*-Pr, *i*-Pr, *i*-Bu) and $[\mathrm{AsBr(S_2CNEt_2)_2}]$ have been synthesized. The homoleptic complexes $[\mathrm{As(S_2CNR_2)_3}]$ react with bromine or iodine affording $[\mathrm{AsX(S_2CNR_2)_2}]$ (X = Br, I). Complexes that incorporate dithiolates and ligands (**43**) are also known, for example, reaction of $[\mathrm{Y(CH_2CH_2O)_2AsCl}]$ (Y = O, S) with $[\mathrm{NH_4}][\mathrm{S_2PPh_2}]$ in $\mathrm{CH_2Cl_2}$ affords $[\mathrm{O(CH_2CH_2O)_2As(S_2PPh_2)}]$ (**46**) and $[\mathrm{S(CH_2CH_2O)_2As(S_2PPh_2)}]$ (**47**) respectively. The arsenic atom in (**46**) and (**47**) display a pseudobipyramidal geometry and Y···As transannular bonding. Additionally, one of the sulfur atoms of the phosphorus ligand binds the metal with a long S···As interaction (Figure 14).[47]

An interesting benzothiazarsolium arsenic cation (**49**) has been isolated from the reaction of the chlorobenzothiazarsole (**48**) with $\mathrm{AlCl_3}$ in $\mathrm{CH_2Cl_2}$ (equation 30).[48] The spectroscopic data and the X-ray structure confirm in (**49**) a dicoordinate cationic environment around arsenic. Part of the

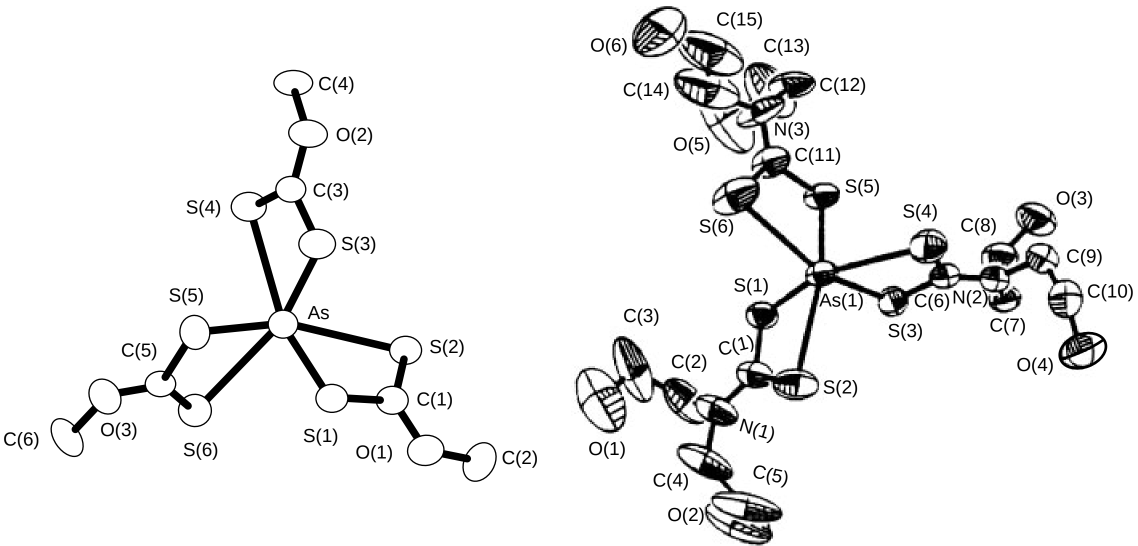
C(4)
O(2)
S(4)
C(3)
S(3)
S(5)
As
C(5)
S(2)
C(1)
C(6)
O(3)
S(6)
S(1)
O(1)
C(2)
C(15)
O(6)
C(13)
C(14)
C(12)
O(5)
N(3)
C(11)
S(5)
S(6)
S(4)
C(8)
O(3)
C(9)
S(1)
As(1)
C(6)
N(2)
C(10)
C(3)
S(3)
C(7)
C(2)
C(1)
O(4)
S(2)
N(1)
O(1)
C(4)
C(5)
O(2)

(**44**) (**45**)

Figure 13 Homoleptic trisquelate arsenic complexes $[\mathrm{As(S_2COMe)_3}]$ (**44**) and $[\mathrm{As\{(S_2CN(CH_2CH_2OH)\}_3}]$ (**45**)[46]

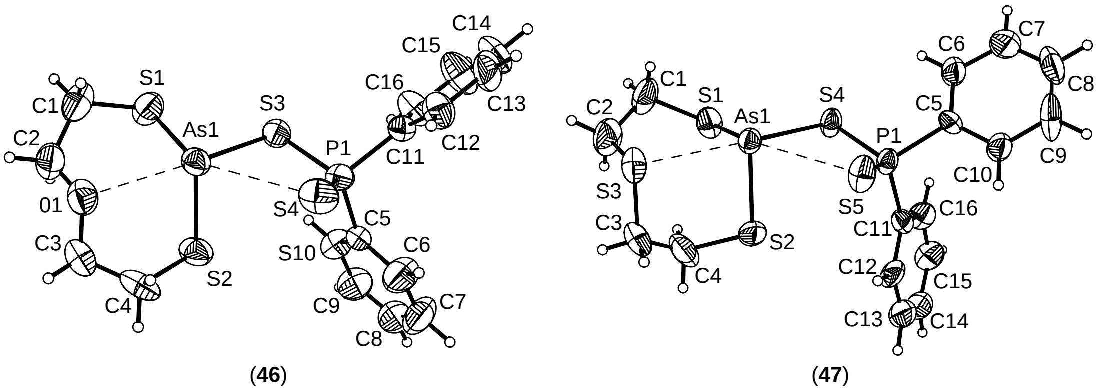
C14
C15
C16
C13
S1
S3
C1
As1
P1
C11
C12
C2
01
S4
C5
C3
S10
C6
S2
C4
C9
C7
C8
C6
C7
C1
C8
C2
S1
As1
S4
C5
P1
C9
C10
S3
S5
C16
C3
C11
S2
C4
C12
C15
C13
C14

(**46**) (**47**)

Figure 14 X-ray structures of $\mathrm{O(CH_2CH_2O)_2As(S_2PPh_2)}$ (**46**) and $\mathrm{S(CH_2CH_2O)_2As(S_2PPh_2)}$ (**47**)[47]

stabilization in (**49**) comes from the delocalized 10π-electron, naphtalenic framework, which necessitates the employment of As–S $4p\pi - 3p\pi$ and As–N $4p\pi - 2p\pi$ bonding. As a consequence of $p\pi$ bonding in this arsenic cation the As–S and As–N distances (2.1536(15) and 1.776(4) Å respectively) are amongst the shortest known for As^{III} species.

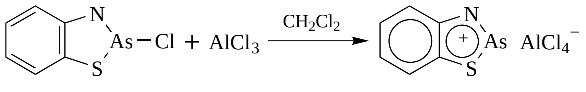

(**48**) (**49**) (30)

Electron deficient coordinatively unsaturated thiaarsolidinium cations (**50**)[49] and (**51**)[50] have also been isolated. These *carbenic* arsenium cations have been prepared by the combination of the appropriate chlorodithiaarsolidine complex and a Lewis acid such as $AlCl_3$ or $GaCl_3$ that function as a halide abstractor. The reaction can be carried out in CH_2Cl_2 as the solvent (Scheme 2).

X-ray crystallography revealed that the arsolidinium cation (**50**) exists as a dimeric dication. The dimmer is formed via intermolecular As···S interactions (2.422(6) Å). Addition of another equivalent of $[(CH_2CH_2S_2)AsCl]$ to (**50**) affords a bicyclic monocation, which can be viewed as the Lewis complex (**52**) of the corresponding chloroarsolidine $[(CH_2CH_2S_2)AsCl]$, and the arsolidine cation (**50**).[49]

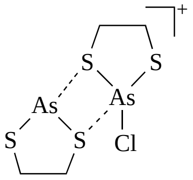

(**52**)

7 ARSENIC COMPOUNDS CONTAINING CARBON

A compound that can be formulated as the carbide As_2C_6 has been obtained in a most unexpected manner: by the reaction between arsenic trichloride and the Grignard reagent prepared by acetylene (equation 31).

$$2AsCl_3 + 3IMgC{\equiv}CMgI \longrightarrow As_2C_6 + 3MgI_2 + 3MgCl_2 \quad (31)$$

The reaction is carried out in ether, out of which it separates as a brown, amorphous solid. It is chemically resistant to both acids and bases. On heating, or by frictional action, the material decomposes violently into the elements. Based on this behavior it has been proposed that the compound is a derivative of acetylene, that is, essentially arsenic acetylide.

The action of CNI on metallic arsenic gives a mixture of AsI_3 and $As(CN)_3$, from which the iodide can be separated by extraction with CS_2. The arsenic tricyanide hydrolyzes to As_2O_3 and HCN on exposure to moisture.

In a benzene solution the reaction between silver isocyanate and $AsCl_3$ forms a precipitate of $AgCl{\cdot}As(ONC)_3$ is obtained upon evaporation of the benzene in the form of a white, crystalline solid which melts at 97.1 °C. The cyanate $Ag(CNO)_3$ is obtained by heating the isocyanate to 230 °C under reflux. At this temperature it isomerizes to the cyanate. $Ag(CNO)_3$ decomposes rapidly in the presence of water or acid.

In a parallel manner, the reaction between $Pb(CNS)_3$ and arsenic trichloride in CS_2, followed by filtration to remove $PbCl_2$ and evaporation of the solvent, gives $As(CNS)_3$. The same product, a colorless, crystalline solid, can be prepared in benzene solution from AgCNS and $AsCl_3$.

8 ARSENIC PNICTOGEN COMPOUNDS AND COMPLEXES BASED ON LIGANDS WITH PNICTOGEN DONOR ATOMS

8.1 Nitrogen Compounds of Arsenic

A normal amide of trivalent arsenic, $As(NH_2)_3$, can be synthesized by the reaction between gaseous ammonia and an arsenic trihalide (except the fluoride) at low temperatures

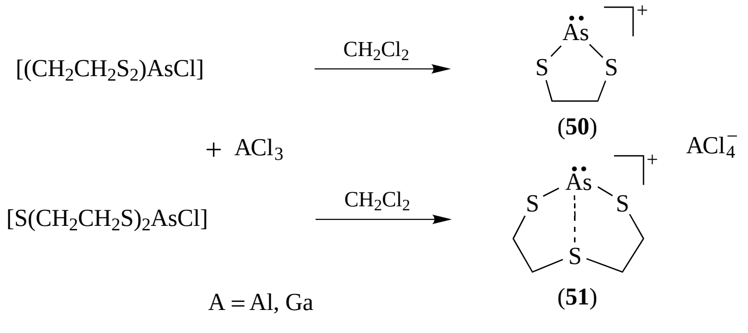

Scheme 2

(−30 to −40 °C). The white, amorphous solid is washed with liquid ammonia in which it does not dissolve. This amide hydrolyzes readily to form arsenite.

The amide begins to decompose at 0 °C into the imide (equation 32). The decomposition is complete at 60 °C.

$$2As(NH_2)_3 \longrightarrow As_2(NH)_3 + 3NH_3 \qquad (32)$$

The imide is a clear yellow solid which is much more resistant to hydrolysis than the amide and which possesses greater thermal stability. At 250 °C it evolves ammonia and converts to the binary nitride (equation 33), which is a red-orange solid that decomposes violently on heating.

$$As_2(NH)_3 \xrightarrow{250\,°C} 2AsN + NH_3 \qquad (33)$$

The above mentioned nitride has also been synthesized by passing a gaseous mixture of 10% nitrogen and 90% argon through an electric arc between two arsenic electrodes.

Alquilaminoarsines can be prepared by stepwise addition of amines to arsenictrihalides in cooled ether solutions. The halogens are replaced successively by the alkylamino groups as shown in Scheme 3.

The As–N bond is labile compared to the As–C, As–O, or As–S bonds and this has been widely exploited in synthetic arsenic chemistry. For example, heating secondary amines with tris(dialkylamino)arsines effects transamination (equation 34).

$$As(NMe_2)_3 + 3HNR_2 \xrightarrow[\text{reflux}]{C_6H_6} As(NR_2)_3 + 3HNMe_2 \qquad (34)$$

$$AsCl_3 + 2Me_2NH \xrightarrow[0\,°C]{Et_2O} [(Me_2N)AsCl_2] + [Me_2NH_2]Cl \quad (a)$$

$$[(Me_2N)AsCl_2] + 2Me_2NH \longrightarrow [(Me_2N)_2AsCl] + [Me_2NH_2]Cl \quad (b)$$

$$[(Me_2N)_2AsCl] + 2Me_2NH \longrightarrow [(Me_2N)_3As] + [Me_2NH_2]Cl \quad (c)$$

Scheme 3

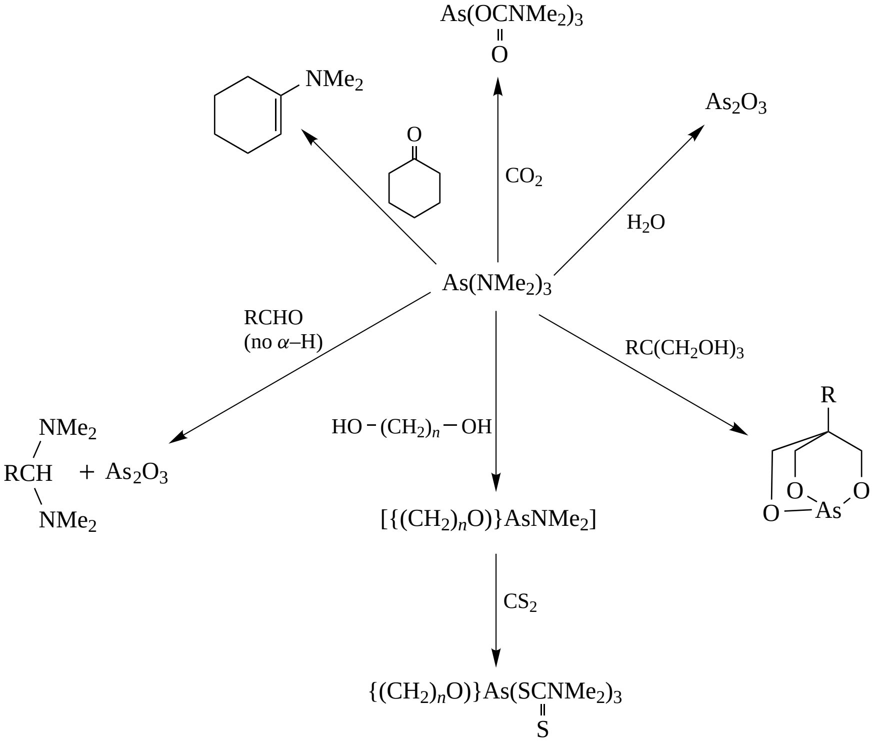

Scheme 4

These tris(dialkylamino)arsines give access to a wide variety of compounds, which is illustrated for $As(NMe_2)_3$ in Scheme 4.[2]

8.2 Arsenic Complexes Based on Ligands with Nitrogen Donor Atoms

In the context of the preparation of novel arsenic hypervalent species and the systematic study of ruffling in porphyrins by the influence of axially coordinated ligands to a central element, complexes with arsenic and porphyrins were isolated and fully characterized. The porphyrins used are octaethylporphyrin, (OEP) and tetraphenylporphirin (TPP). Reaction of $OEPH_2$ or $TPPH_2$ with $AsCl_3$ in the presence of lutidine give [(OEP)AsCl] (**53**) or [(TPP)AsCl] (**54**) according to equation (35).[51]

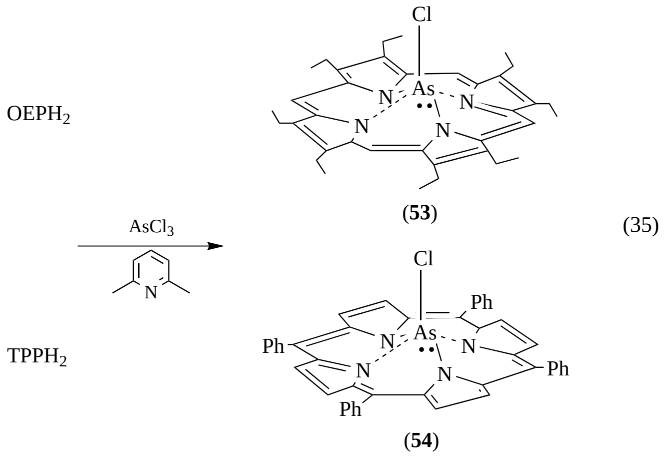

(35)

After bromination and subsequent hydrolysis of (**53**) the cationic arsenic complex (**55**) with arsenic in the 5+ oxidation state is obtained (equation 36).

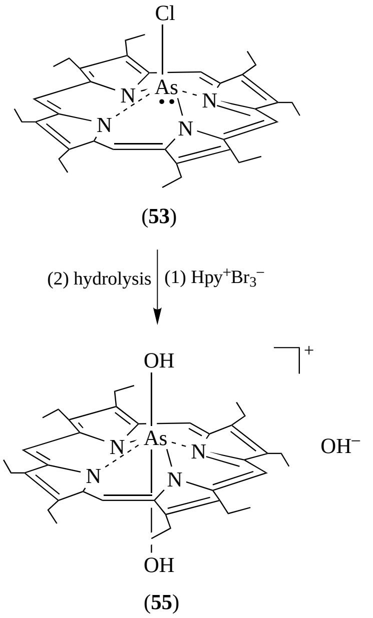

(36)

Interestingly, the X-ray structure of the arsenic^V fluoride porphyrin complex, $[(OEP)AsF_2]^+PF_6^-$ shows an almost planar conformation within the porphyrin core, which contrasts the S4 ruffled conformation found for $[(TPP)AsF_2]^+\ PF_6^-$.

A limited number of dicoordinate arsenium cations with nitrogen based ligands have been isolated. Reaction of the chlorodiazaarsenanes, $[\{(CH_2CH_2)(NMe)_2\}AsCl]$ and $[\{(CH_2CH_2CH_2)(NMe)_2\}AsCl]$ with $AlCl_3$ or $GaCl_3$ in CH_2Cl_2 afford the corresponding arsenium cations (**56**)[48] and (**57**)[52] in good yield (Scheme 5).

X-ray crystallography revealed a dimeric structure for cation (**56**), whereas cation (**57**) is monomeric in the solid state. The dimer in (**56**) is made with intermolecular As···N interactions (2.103(4) Å).

Cations (**56**) and (**57**) react rapidly with 2,3-dimethyl-1,3-butadiene in CH_2Cl_2 to give the bicyclic cationic products (**58**) and (**59**). The quantitive formation of (**58**) and (**59**) imply a concerted process, possibly a Diels–Alder type cycloaddition

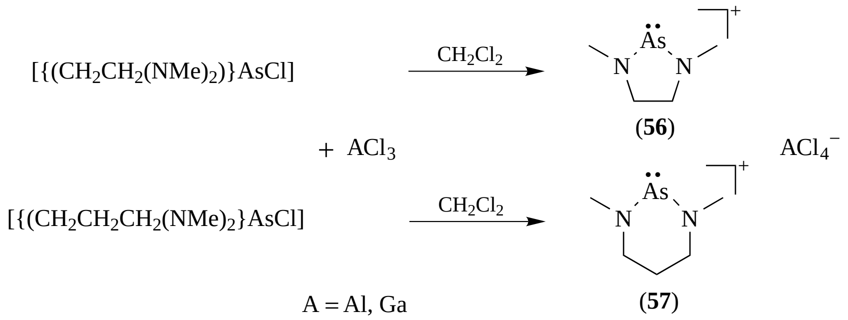

Scheme 5

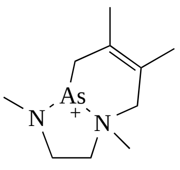

(**58**)

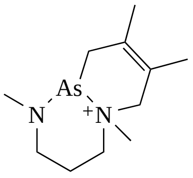

(**59**)

involving the As–N bond of either the monomer or dimmer as the dienophile.**[50,52]**

A monomeric arsenium cation with 6π electrons (**60**) has been isolated by a metal exchange reaction according to equation (37).**[53]**

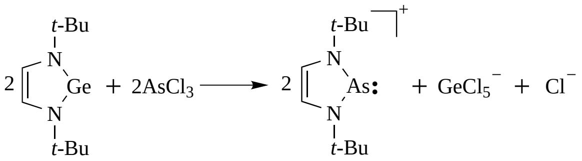

(37)

(**60**)

The reaction depicted in equation (37) proceeds with the oxidation of germanium from the 2+ to the 4+ state. The metrical parameters in (**60**) are in agreement with a localized electron distribution within the five-membered ring, which contrasts the view of aromatic 6π-stabilization that was invoked for the 10π electrons arsenium cation (**49**).

8.3 Phosphorus Compounds of Arsenic

Two binary As–P compounds have been reported. They are As_2P and AsP. Diarsenic phosphide has been prepared by heating a mixture of elemental phosphorus with As_2O_3, As_2O_5, or As in phosphoric acid. It is described as black and lustrous and turning brown on exposure to air. It has not been well characterized.

Arsenic monophosphide, AsP is described as a lustrous, red-brown powder. It has been synthesized by the direct fusion of the elements, by the reaction between AsH_3 and PCl_3, and by the reduction of a solution of As_2O_3 in HCl ($AsCl_3$) by PH_3.

A normal arsenic orthophosphate, $AsPO_4$, has been prepared by heating pyrophosphoric acid ($H_4P_2O_7$) with As_2O_3. The temperature is maintained between 230 and 245 °C and then finally taken to 280 °C. At a stoichiometric ratio of 2 moles of $AsPO_4$ to 3 moles of H_3PO_4, followed by heating to 320 °C, there is formed a compound whose stoichiometry corresponds to $4AsPO_4 \cdot 3H_3PO_4$.

A mixture of As_2S_3 and P_2S_5 yields, upon fusion, the tetrathiophosphate, $AsPS_4$.

9 ARSENIC IN THE ENVIRONMENT

Arsenic is widely distributed on earth in the atmosphere, in the aquatic environment, in soils and sediments, and in organisms. Just in the earth crust arsenic ranks 51st in abundance with a concentration of 1.8 g tonne^{-1}. It is frequently found to occur as a component of sulfidic ores, especially those of the nonferrous metals in which it occurs in the following forms: nickel diarsenide, cobalt diarsenide, nickel arsenide, cobalt arsenide sulfide, copper arsenide sulfide, and iron diarsenide. Arsenates of aluminum, barium, bismuth, calcium, cobalt, copper, iron, lead, magnesium, manganese, uranium, and zinc have also been found to occur naturally. Arsenic trioxide (arsenolite), As_2O_3, which is formed when arsenides are oxidized on exposure to the atmosphere, has also been found to occur naturally. Some naturally occurring arsenic minerals are realgar As_4S_4, orpiment As_2S_3, arsenolite As_2O_3, arsenopyrite FeAsS and Enargite Cu_3AsS_4.**[1,54,55]**

The element is very widely distributed in Nature. It is found in igneous rocks (1–3 ppm), in sedimentary rocks (1–25 ppm, but concentrations as high as 400 ppm have been reported), and in virtually all soils (0.1–40 ppm). In waters, it occurs in rivers, lakes, streams, groundwaters, and in the seas and oceans. Concentrations vary greatly, from 0.1 ppb in Lake Superior to as high as 276, 000 ppb in the Waiotapu Valley rivers of New Zealand.

Arsenic is distributed widely among plant and animal species. In plant tissues, its normal concentration varies from 0.01 to 5 ppm on a dry-weight basis. When plants are grown in soils which have been treated by arsenic compounds, these concentrations can reach 5 ppm on a dry-weight basis. Marine plants have been found to possess much higher arsenic concentrations. Seaweed growing along the British coast has been reported to possess arsenic concentrations as high as 94 ppm. Brown algae also concentrate arsenic in their tissues.

Arsenic is always present in all animals. Human body tissues generally average less than 0.3 ppm of the element. Marine organisms are noteworthy for their ability to concentrate arsenic. Cod, shrimp, oysters, and lobsters have been reported to contain up to 128 ppm of arsenic on a dry-weight basis. Values from 3 to 30 ppm are common among marine organisms. The typical human ingests between 29 and 169 mg of arsenic per day.**[56]**

The main introduction of arsenic into the biosphere is anthropogenic as result of industrial activity and the use of herbicides and biocides that contain the element. Arsenic is mainly released into the atmosphere as a consequence of its isolation, burning of fossil fuels and the smelting of ores (combustion). The oxides generated thermally are particulate in nature, which owing to their small size (in the nanometer scale) are held up in the exhaust gases and are easily vented into the local atmosphere and then distributed by the prevailing air currents. Models for the transport of arsenic predict that currently 285 tonnes are deposited annually on the Artic as a consequence of industrial activity in the northern hemisphere.

The ability of arsenic to incorporate to the food chain and become transformed into a variety of organic forms during its pass through the biological hierarchy is known.

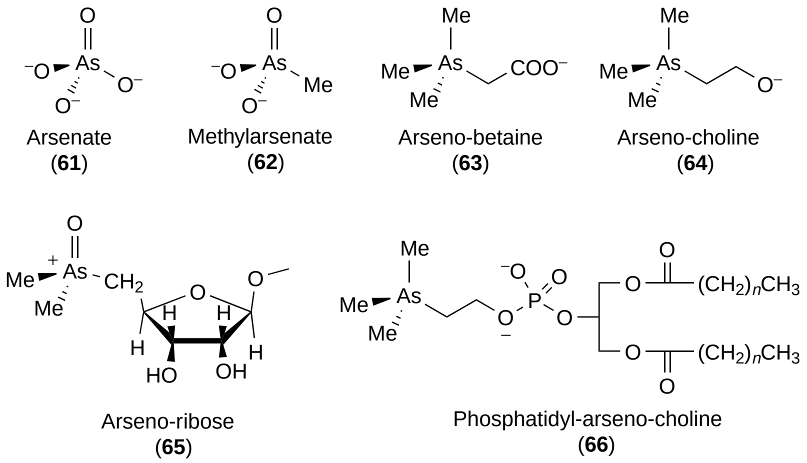
Arsenate (**61**)

Methylarsenate (**62**)

Arseno-betaine (**63**)

Arseno-choline (**64**)

Arseno-ribose (**65**)

Phosphatidyl-arseno-choline (**66**)

Figure 15 The structures of some common arsenic-containing natural products

The simple oxides $[AsO_2]^-$ or $[AsO_4]^{3-}$ (**61**) are slowly organified to produce simple methylarsonic acids (**62**), more complex betaines (**63**), cholines (**64**), sugar derivatives (**65**), and lipids (**66**) (Figure 15).

Biological methylation of arsenic is effected via the transfer of a carbocation, a process known as oxidative methylation. The methyl transfer agent can vary from simple sulphonium salts, for example, *S*-adenosyl-*S*-methionine (**67**) (equation 38) to specific methyltransferase enzymes. The oxidation and methylation of the arsenite ion, $[AsO_3]^{3-}$, at physiological pH with (**67**) is illustrated in equation (38). In solution under these conditions the major species is $[H_2AsO_3]^-$ (**68**). The cycle is completed trough the re-reduction of new methylated arsenical^V by a range of nonspecific reductants (Scheme 6). The organoarsenicals produced during biomethylation can be reduced by bacteria with lipoic acid and by mammals with the ubiquitous thiolate glutathione, as has been reported in *in vitro* studies.[57]

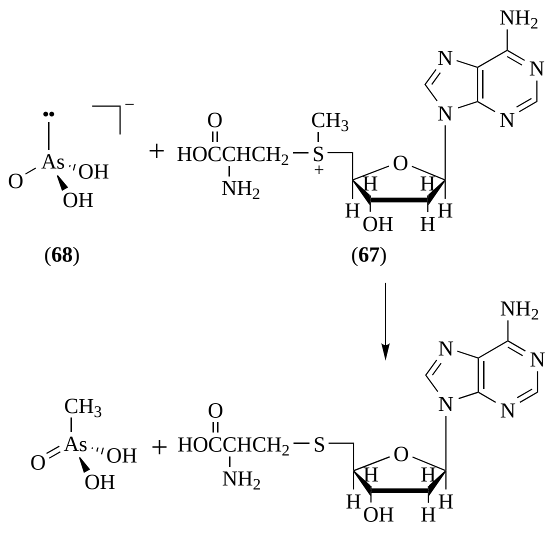
(**68**) (**67**)

(38)

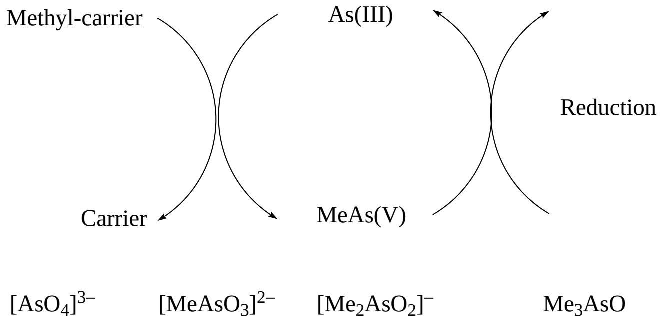

Scheme 6

Studies of microbial systems have shown that the production of trimethylarsine from the various methylarsonates is more rapid than their respective thioarsinites, for example, Me_2AsSR, $MeAs(SR)_2$. However, there is a possible role for the thioarsinite in arsenic methylation. Studies on the binding of arsenic to the methyltransferase enzyme suggest that prior to the transfer of the methyl group the arsine oxide becomes bound to a thiolate at the active site. In this way it is possible to assist the binding of the softer arsenic^{III} substrate prior to methylation and facilitate the release of the harder arsenic^V species.[54,57]

In general the toxicity of arsenic is more pronounced with the lower oxidation states. The nature of the ligands around arsenic has also a profound effect on the overall toxicity of the element. For example, dimethylarsonate, $[Me_2AsO_2]$ has a $LD_{50} = 700\,mg\,kg^{-1}$ while a richer oxygen environment in arsenate, $[AsO_4]^{3-}$ (**61**) makes the element much more toxic with a $LD_{50} = 20\,mg\,kg^{-1}$. Small inorganic species are more toxic than are organoarsenicals. Libile ligands such as Cl^- or NH_2 and the presence of lone pairs would seem to increase toxicity, for example, $[Me_2AsCl]$ with a $LD_{50} = 5\,mg\,kg^{-1}$. Quaternary arsonium salts effectively protect the arsenic center giving relatively nontoxic and almost inert compounds, for example, [Me_3AsCH_2COO].

Compounds that contain arsenic^{V} in general are carcinogenic. This is probably the result of its reduction to arsenic^{III}. The thiophilicity of arsenic^{III} affect key enzymes, such as acetylcholine estereases, lipoic acid, and hemoglobin. Long-term contact with the organometallic forms cause hyperactivity, dizziness, speech, and psychological problems, possibly linked to methylation which in turn facilitates its transport across the blood-brain barrier.[54]

10 RELATED ARTICLES

Antimony: Inorganic Chemistry; Arsenic: Organoarsenic Chemistry; Bismuth: Inorganic Chemistry; Phosphorus: Inorganic Chemistry.

11 REFERENCES

1. N. N. Greenwood and A. Earnshaw, ‘Chemistry of the Elements’, 2nd edn., Pergamon Press, New York, 1998, Chap. 13.
2. C. A. McAuliffe, in ‘Comprehensive Coordination Chemistry – The Synthesis, Reactions, Properties and Applications of Coordination Compounds’, eds. Sir G. Wilkinson, R. D. Guillard, and J. A. McCleverty, Pergamon Press, New York, 1987, Vol. 3, Chap. 28.
3. D. Seyferth, *Organometallics*, 2001, **20**, 1488.
4. W. E. Dasent, ‘Inorganic Energetics’, Cambridge University Press, New York, 1988.
5. S. K. Pandey, A. Steiner, and H. Roesky, *Inorg. Synth.*, 1997, **31**, 148.
6. K. Masumoto and W. A. McGahan, *MRS Bull.*, 1996, **21**, 44.
7. I. R. Grant, in ‘Chemistry of Aluminum, Gallium, Indium and Thalium’, ed. A. J. Downs, Chapman & Hall, London, 1993, Chap. 5.
8. F. Gascoin and S. C. Sevov, *Inorg. Chem.*, 2002, **41**, 5920.
9. F. A. Cotton, G. Wilkinson, C. A. Murillo, and M. Bochmann, ‘Advanced Inorganic Chemistry’, 6th edn., John Wiley & Sons, New York, 1999, Chap. 10.
10. J. D. Corbett, *Chem. Rev.*, 1985, **85**, 383.
11. W. Schemettow and H. G. Schnering, *Angew. Chem.*, 1977, **89**, 895.
12. J. D. Corbett, *Inorg. Chem.*, 1968, **7**, 198.
13. S. Aldridge and A. J. Downs, *Chem. Rev.*, 2001, **101**, 3305.
14. D. M. P. Mingos, ‘Essential Trends in Inorganic Chemistry’, Oxford University Press, Oxford, 1998, Chap. 2.
15. A. G. Massey, ‘Main Group Chemistry’, 2nd edn., John Wiley & Sons, New York, 2000, Chap. 9.
16. M. M. Olmstead, P. P. Power, and G. A. Sigel, *Inorg. Chem.*, 1988, **27**, 2045.
17. B. Twamley, C. S. Hwang, N. J. Hardman, and P. P. Power, *J. Organomet. Chem.*, 2000, **609**, 152.
18. M. Brynda, G. Bernardinelli, C. Dutan, and M. Geoffroy, *Inorg. Chem.*, 2003, **42**, 6586.
19. W. A. Herrmann, B. Koumbouris, T. Zahn, and M. L. Ziegler, *Angew. Chem., Int. Ed. Engl.*, 1984, **23**, 812.
20. M. Driess and H. Pritzkow, *Chem. Ber.*, 1994, **127**, 477.
21. E. A. Ebsworth, R. O. Gould, R. A. Mayo, and M. Walkinshaw, *J. Chem. Soc., Dalton Trans.*, 1987, 2831.
22. A. H. Cowley, P. R. Harris, R. A. Jones, and C. M. Nunn, *Organometallics*, 1991, **10**, 652.
23. S. M. Godfrey, C. A. McAuliffe, A. G. Mackie, R. G. Pritchard, in ‘Chemistry of Arsenic, Antimony and Bismuth’, ed. N. C. Norman, Blackie Academic & Professional, London, 1998, Chaps. 3 and 4.
24. R. B. King, ‘Inorganic Chemistry of the Main Group Elements’, VCH-Weinheim, 1994, Chap. 5.
25. D. A. Dixon and A. J. Arduengo, *J. Am. Chem. Soc.*, 1987, **109**, 338.
26. K. Seppelt, *Z. Anorg. Allg. Chem.*, 1977, **434**, 5.
27. R. Minkwitz, C. Hirshc, and T. Berends, *Eur. J. Inorg. Chem.*, 1999, 2249.
28. W. S. Sheldrick and H. J. Hausler, *Angew. Chem., Int. Ed. Engl.*, 1987, **26**, 123.
29. U. Müller and H. Sinnino, *Angew. Chem., Int. Ed. Engl.*, 1989, **28**, 185.
30. C. A. Ghilardi, S. Mildollini, S. Moneti, and A. Orlandini, *J. Chem. Soc., Chem. Commun.*, 1988, 1241.
31. P. J. Jones, W. Beesk, G. M. Sheldrick, and E. Schawarzmann, *Acta Crystallogr.*, 1980, **B36**, 439.
32. D. L. Hilderbrand, K. H. Kau, and R. D. Brittain, *J. Chem. Phys.*, 1982, **86**, 4429.
33. A. Kutoglu, *Z. Anorg. Allg. Chem.*, 1976, **419**, 176.
34. E. Thilo, K. Hertzog, and A. Winkler, *Z. Anorg. Allg. Chem.*, 1970, **373**, 111.
35. A. Muller, E. Krickmeyer, and M. Penk, *Angew. Chem., Int. Ed. Engl.*, 1999, **29**, 88.
36. E. Thilo, in ‘Advances in Inorganic Chemistry and Radiochemistry’, eds. H. J. Emeléus and A. G. Sharpe, Academic Press, New York, 1962, Vol. 4, p. 59.
37. W. S. Sheldrick and M. Wachhold, *Coord. Chem. Rev.*, 1998, **176**, 211.
38. M. A. Ansari, J. A. Ibers, S. C. O’Neal, W. T. Pennington, and J. W. Kolis, *Polyhedron*, 1992, **11**, 1877.
39. D. M. Smith, C. W. Park, and J. A. Ibers, *Inorg. Chem.*, 1996, **35**, 6682.

40. P. van Nuffle, A. T. H. Lenstra, and H. J. Teise, *Acta Crystallogr., Sect. B*, 1982, **38**, 3089.
41. B. Siewert, U. Muller, *Z. Naturforsch., Teil B*, 1992, **47**, 680.
42. B. A. Borgias, G. G. Hardin, and K. N. Raymond, *Inorg. Chem.*, 1986, **25**, 1057.
43. R. C. Mehrotra, G. Srivastava, and B. P. S. Chauhan, *Coord. Chem. Rev.*, 1984, **55**, 207.
44. C. Silvestru and I. Haiduc, *Coord. Chem. Rev.*, 1996, **147**, 117.
45. H. P. S. Chauhan, *Coord. Chem. Rev.*, 1998, **173**, 1.
46. S. S. Garje and V. K. Jain, *Coord. Chem. Rev.*, 2003, **236**, 35.
47. M. A. Muñoz-Hernández, R. Cea-Olivares, G. E. Pérez, and S. H. Ortega, *J. Chem. Soc., Dalton Trans.*, 1996, 4135.
48. N. Burford and B. W. Royan, *J. Am. Chem. Soc.*, 1989, **111**, 3746.
49. N. Burford, T. M. Parks, B. W. Royan, B. Borecka, T. S. Cameron, J. F. Richardson, E. J. Gabe, and R. Hynes, *J. Am. Chem. Soc.*, 1992, **114**, 8147.
50. N. Burford, T. M. Parks, P. K. Bakshi, and T. S. Cameron, *Angew. Chem., Int. Ed. Engl.*, 1994, **33**, 1267.
51. Y. Yamamoto and K.-Y. Akiba, *J. Organomet. Chem.*, 2000, **611**, 200.
52. N. Burford, C. L. B. Macdonald, T. M. Parks, G. Wu, B. Borecka, W. Kwiatkowski, and T. S. Cameron, *Can. J. Chem.*, 1996, **74**, 2209.
53. C. J. Carmalt, V. Lomeli, B. G. McBurnett, and A. H. Cowley, *J. Chem. Soc., Chem. Commun.*, 1997, 2095.
54. J. Reglinsky, in ‘Chemistry of Arsenic, Antimony and Bismuth’, ed. N. C. Norman, Blackie Academic & Professional, London, 1998, Chap. 8.
55. W. R. Cullen and K. J. Reimer, *Chem. Rev.*, 1989, **89**, 713.
56. R. A. Schraufnagel, in ‘Arsenic: Industrial, Biomedical, Environmental Perspectives’, eds. W. H. Lederer and R. J. Fensterheim, Van Nostrand Reinhold, New York, 1983, Chap. 3.
57. J. S. Thayer, *Appl. Organomet. Chem.*, 2002, **16**, 677.

Arsenic: Organoarsenic Chemistry

Larry K. Krannich & Charles L. Watkins
University of Alabama at Birmingham, Birmingham, AL, USA

1	Introduction	1
2	Fully Substituted Organoarsenic Compounds	2
3	Organoarsines Containing As–H Bonds	4
4	Organoarsenic Compounds Containing As–Halogen Bonds	5
5	Organoarsenic Compounds Containing As–Group 13 Bonds	6
6	Organoarsenic Compounds Containing As–Group 14 Bonds	10
7	Organoarsenic Compounds Containing As–Group 15 Bonds	11
8	Organoarsenic Compounds Containing As–O Bonds	16
9	Related Articles	18
10	References	18

Glossary

Arsinic acid: general formula $R_2As(O)OH$, where R is an alkyl or aryl group
Arsinous acid: general formula R_2AsOH, where R is an alkyl or aryl group
Arsonic acid: general formula $RAsO(OH)_2$, where R is an alkyl or aryl group
Arsonous acid: general formula $RAs(OH)_2$, where R is an alkyl or aryl group
Diarsoxane: arsinous acid anhydride having the formula $(R_2As)_2O$
Diarsene: general formula $RAs{=}AsR'$, where R and R′ are bulky groups
Haloarsorane: general formula R_nAsX_{5-n}, where $n = 1-3$
Phosphaarsene: general formula $RP{=}AsR'$, where R and R′ are bulky groups

1 INTRODUCTION

The organometallic chemistry of arsenic has a long history that dates back to the synthesis and discovery in 1760 of the first organometallic compound, $Me_2AsAsMe_2$, by L. C. Cadet de Gassicourt. During the late-1800s, there was considerable interest in the synthesis of organoarsenic compounds that paralleled the heightened pursuit of synthetic organic chemistry. This led to the development of synthetic pathways to the organohalo, organoamino, and tertiary arsines. A significant upsurge in activity in synthetic organoarsenic chemistry occurred with the discovery by P. Ehrlich in 1910 that 3,3′-diamino-4,4′-dihydroxyarsenobenzene (Salvarsan base) was an effective cure for syphilis. The next 33 years witnessed the synthesis and biological testing of thousands of new organoarsenic compounds and the development of new synthesis strategies to heterocyclic compounds. With the advent of penicillin as a cure for syphilis in the 1940s, a lull occurred in the synthetic chemistry of organoarsenicals. The decreased activity and interest in main group chemistry that occurred from the late-1960s to the mid-1980s brought few developments to the organometallic chemistry of arsenic, but saw their use as ligands in transition-metal chemistry. Beginning with the mid-1980s and the renewed interest in main group synthetic chemistry as it relates to materials chemistry, there has been a resurgence in research activity in organometallic arsenic chemistry. Much of this has occurred in the quest to develop viable single-source precursors for group 13–15 thin-film technologies. Thus, the areas of arsenic–aluminum, arsenic–gallium, arsenic–indium, and multiple bonding in As/As and As/P systems have received significant attention and many new bonding and As– group 13 core systems have been explored. Synergistic, spectroscopic, structural, and materials studies have occurred.

This review surveys the chemistry and reactivity of several major classes of organometallic arsenic compounds that serve as the core of the field and represent those major areas of current research thrusts. General structural and recent spectroscopic data are discussed for each class of organometallic compound. Because of the great diversity of organoarsenic compounds and limited space, not all areas of organoarsenic chemistry can be covered nor can all the synthetic strategies and reactivity be discussed. For example, we have chosen not to cover transition-metal complexes that employ organometallic arsenic compounds as ligands, so we refer the reader to a book that provides a basic overview.[1] Also, the heterocyclic chemistry of arsenic is not presented and the reader is referred to a book that surveys that field.[2] For the same reason, we have not covered the biological and environmental aspects of organoarsenic chemistry. The latter has been reviewed.[3]

In each section, we have referenced several books,[4–14] monographs, and review articles that provide in-depth coverage of the chemistry that is presented and give references to the primary literature for developments in the field that have taken place subsequent to the latest applicable review article. We have focused on reviewing the primary synthetic routes and reactivity that appear in previously published books and monographs and providing the reader with more in-depth coverage of the latest developments.

The physical, structural, and spectroscopic properties of organoarsenic compounds have been summarized in a series of excellent reviews and monographs (1966,[7] 1968,[8,9] 1970,[6] 1972,[10,15] 1975,[5] 1979,[11] and 1985[4]). In addition, annual reviews have provided key access to the literature (see cf. *Journal of Organometallic Chemistry*, *Coordination Chemistry Reviews*, and *Organometallic Chemistry*, Royal Society of Chemistry). The reader is referred to these sources for specific information on given organoarsenic compounds.

2 FULLY SUBSTITUTED ORGANOARSENIC COMPOUNDS

2.1 Tricoordinate Arsenic

Tertiary arsines comprise the most common class of tricoordinate, fully organosubstituted arsenic compounds. Although there are a variety of methods for synthesizing C–As bonds in tertiary arsines,[4–11,16] the most extensively utilized routes involve the reaction of *Grignard Reagents* with arsenic trihalides to give symmetric tertiary arsines (equation 1). The yields of trialkylarsines are generally low to moderate and those of triarylarsines high. This reaction has been used to prepare the trineopentylarsine, $As(CH_2CMe_3)_3$.[17]

$$AsX_3 + 3RMgX \longrightarrow AsR_3 + 3MgX_2 \qquad (1)$$

When the Grignard reagents react with primary and secondary haloarsines, As_2O_3, As_2S_3, trialkyl arsenites, and arsenic thioacid esters, the resulting tertiary arsines are often contaminated with other arsenicals. Lithium alkyls are frequently used when the Grignard is difficult to obtain, but side-products serve as contaminants. Although the reaction times are long and yields depend upon the alkyl group, aluminum alkyls also effectively alkylate As_2O_3 and arsenic trihalides. The Würtz–Fittig reaction is seldom used in synthesizing trialkylarsines, but has been utilized to prepare cyclic arsines (equation 2).

$$\begin{aligned} &C_6H_4(CH_2Br)_2 + MeAsCl_2 + 4Na \longrightarrow \qquad (2)\\ &\quad C_6H_4(CH_2)_2AsMe + 2NaCl + 2NaBr \end{aligned}$$

Zinc and mercury dialkyls have found limited application in alkylating arsenic trihalides. The advantage with the zinc dialkyls is that they give very pure tertiary arsines even though the arsines are obtained in low yields. Numerous other methods that employ redistribution of alkylhaloarsines at elevated temperatures, reduction of arsonium salts, pyrolysis of arsonium salts and arsine oxides, reaction of arsenic halides with diazoalkanes, reaction of SnR_4 and alkyl radicals with elemental arsenic, alkylation of diarsines and aminoarsines with organolithium, or the action of *Penicillium brevicaule* on bread that contains sodium cacodylate have provided unique routes to specific, symmetric tertiary arsines. Probably the most exhaustive coverage with references to the primary literature for known synthetic routes to tertiary arsines is provided by Dub,[9,10] Cullen,[7] Doak and Freedman,[6] and Aylett.[11]

Two practical synthetic methods have been reported for the high-yield preparation of tertiary arsines. The reactions of chlorodioxarsolane, $\overline{OCH_2CH_2OAs}Cl$, with aluminum alkyls, Grignard reagents, organolithium, and dialkylzinc give high yields of the fully substituted organoarsines.[18] Grignard reagents and aluminum alkyls readily react with $As[NMe_2]_3$ to give tertiary arsines.[19] The latter method is an adaptation of the high-yield route to Me_3As[20] that does not require using a complexing agent for the Me_3As (equation 3).

$$2As(NMe_2)_3 + 3[Me_3Al]_2 \longrightarrow 2Me_3As + 3[Me_2AlNMe_2]_2 \qquad (3)$$

Unsymmetric arsines of the type R_2AsR' and $RR'R''As$ are well known.[3–11,16,21,22] The most common synthetic procedure involves alkylating the organomonohalo- or organodihaloarsine with the desired Grignard or organolithium reagent. Di-Grignard reagents have also been used to prepare cyclic arsolanes.[23] Good yields of heteroleptic tertiary arsines are obtained in the reaction of an organohalide with the appropriate metal arsenide. The reaction of an organohalide with a diarsine, R_2AsAsR_2, or a primary arsine, $RAsH_2$, is another route to unsymmetric arsines. The microbial activity of molds acting on arsenicals in anthropogenic and natural sources has also been exploited in producing unsymmetric arsines.[3,24,25] Et_4Pb and n-Bu_3Sb alkylate the haloorganoarsines to give ethyl and butyl derivatives. Bn_2Hg gives a quantitative yield of Me_2AsBn when Me_2AsI is used, but a lesser yield and by-product contamination result when Me_2AsH is alkylated.[26] By capitalizing on the reactivity of Me_2AsNMe_2 toward Grignard reagents and aluminum alkyls, a general protocol has also been developed to the Me_2AsR arsines (equation 4).[27]

$$2Me_2AsNMe_2 + 2Et_3Al \longrightarrow 2Me_2AsEt + [Me_2NAlEt_2]_2 \qquad (4)$$

Dinuclear arsines containing a bridging methylene unit, $R_2AsCH_2AsR_2$, have been prepared from the parent haloarsine using RLi.[28] With $PhC{\equiv}CLi$, cleavage of the $AsCH_2As$ backbone occurs and $As(C{\equiv}CPh)_3$ is isolated.

Tertiary arsines are readily oxidized with common oxidizing agents (H_2O_2, $KMnO_4$) to the arsine oxide. Oxidation of the alkyl derivatives with H_2O_2 or HgO gives the trialkylarsine oxide R_3AsO, but air oxidation produces the dialkylarsinic acids, $R_2As(O)OH$. With sulfur and selenium, the trialkylarsines are oxidized to the corresponding sulfide and selenide. They readily form adducts with diborane, aluminum alkyls, $AlCl_3$, and gallium alkyls.[29] Their reactions with NH_2Cl, MeNHCl, and Me_2NCl produce the respective aminoarsonium chlorides (equation 5).[30,31]

$$Et_3As + Me_2NCl \longrightarrow [Et_3AsNMe_2]Cl \qquad (5)$$

Et_3As reacts with $AsCl_3$ in *n*-pentane to give a quantitative yield of the sublimable dimer $[Et_3As\cdot AsCl_3]_2$,**[32]** which disproportionates above its melting point to a mixture of Et_2AsCl and $EtAsCl_2$. Tertiary arsines react with a stoichiometric amount of halogen to form the R_3AsX_2 species (equation 6). These disproportionate on heating to give the haloarsine and an alkyl halide (equation 7). This can serve as a convenient synthetic route to the dialkylhaloarsines. Although the tertiary arsines have been extensively used as ligands in transition-metal complexes,**[1,9–11]** this chemistry will not be treated here as part of the chemistry of organometallic arsenic compounds.

$$R_3As + X_2 \longrightarrow R_3AsX_2 \qquad (6)$$

$$R_3AsX_2 \longrightarrow R_2AsX + RX \qquad (7)$$

There is a very extensive heterocyclic chemistry of tricoordinate arsenic wherein arsenic is incorporated in four- to ten-membered ring systems.**[2,9,10]** Although the most prevalent synthetic route involves the reaction of a dihaloarsine with a di-Grignard or dilithium reagent, there are many custom syntheses to specific heterocycles. The synthesis and reactivity of the heterocyclic arsenic chemistry will not be reviewed here. Instead, the reader is referred to the comprehensive treatise by Mann and the primary literature that is cited therein.**[2]**

Gas-phase electron diffraction and solid-state *X-ray diffraction* studies on R_3As indicate pyramidal geometry about the arsenic.**[4–7,11]** In Me_3As, the As–C bond distance is 1.968 Å and the C–As–C angle has an average value of 96.1°. Correspondingly, for $(CF_3)_3As$, the As–C bond distance is increased to 2.053 Å and the C–As–C angle opened to 100.1°. X-ray diffraction studies on $As(CH_2CMe_3)_3$**[17]** give an average As–C distance of 1.998 Å and a C–As–C angle equal to 94.6°. For Ph_3As, there are four symmetrically independent molecules in the crystal structure, which are connected in pairs by the elements of symmetry.**[33]** The average As–C bond distance value is 1.957 Å and that of the C–As–C angle is 100.1°. Substitution in the p-position on the aromatic ring does not significantly affect these values, that is, tri-*p*-tolylarsine, 1.964 Å and 99.3°; tri-*p*-chlorophenylarsine, 1.958 Å and 99.8°; tri-*p*-methoxyphenylarsine, 1.963 Å and 98.3°. However, substitution of methyl groups in the 2 and 6 positions of the phenyl rings leads to an increase of the C–As–C angle by approximately 7°. For the perfluoro derivative, $(C_6F_5)_3As$, the average As–C bond distance is 1.959 Å and the average C–As–C angle is 100.5°.**[34]**

Early ^1H NMR data were obtained on trimethyl and dimethylphenyl derivatives of the group 15 elements, Me_3E and Me_2PhE ($E = N, P, As, Sb, Bi$). The methyl group chemical shift changes in each series were attributed to the electronegativity of the central atom.**[6,7]** Subsequently, similar studies were reported by ^{13}C NMR.**[35,36]** Detailed ^1H and ^{13}C NMR data have been reported for two series of tertiary arsines, R_3As**[18]** and Me_2AsR.**[27]**

Barriers to inversion of about 200 kJ mol^{-1} have been determined for tertiary arsines, both by experimental and semiempirical quantum mechanical calculations (*see Semi Empirical Theoretical Methods*).**[5,11]** The inversion barriers in arsines are considered to be the maximum for the group 15 elements, with values being about 60 kJ mol^{-1} higher than for corresponding phosphines.**[11]** For partially and fully substituted silylarsines,**[11,37]** the inversion barrier at arsenic decreases as more silicon atoms are directly attached.

2.2 Dicoordinate Arsenic

Several heterocyclic arsenines, which are derivatives of the unsubstituted arsenine $HC(CH)_4As$, are known and their chemistry has been reviewed.**[38,39]** Arsenine is prepared by the reaction of 1,4-dihydro-1,1-dibutylstannabenzene with $AsCl_3$ (equation 8).**[40]** The reader is referred to two reviews**[38,39]** and the references that are cited therein for information on the chemistry of the arsenines.

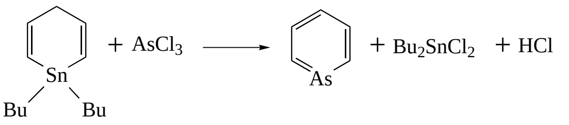

(8)

2.3 Tetracoordinate Arsenic

There are two classes of organoarsenic compounds in which the arsenic is tetracoordinated to only organo moieties, namely the tetraorganoarsonium salts**[4,7,9–11]** and the organoarsenic ylides.**[4,5,9–11]** Alkylation of the tertiary arsines with organohalides is the common mode of preparation of the arsonium salts. The alkyl iodides are more reactive than the alkyl bromides and chlorides. Alkyl halides can be reacted with elemental arsenic to yield the respective arsonium halides. The arylarsonium halides can be obtained from the reaction of the arylarsine oxide and the corresponding Grignard reagent (equation 9).

$$Ph_3AsO + PhMgX \longrightarrow [Ph_4As]X + MgO \qquad (9)$$

X-ray and spectroscopic studies indicate that the arsonium halides are ionic. Me_4AsBr consists of tetrahedral Me_4As^+ units and separate bromide ions.**[11]** X-ray structures have also been obtained on a series of tetraphenylarsonium salts.**[4–7,11,41]** A regular tetrahedral structure is found about the arsenic atom when the counterion is a halide or ion of similar size. However, as the size of the counterion increases, the crystals become more disordered.**[41]** In solution, tetraphenylarsonium salts are almost completely dissociated, but ion pairing can be significant and is dependent primarily on the dielectric constant of the solution.

^{13}C and ^1H NMR data have been reported for several tetraalkylarsonium salts**[36,42]** and the ^{13}C NMR chemical shifts compared with the corresponding tertiary arsines. Similar multinuclear NMR data have been summarized for $Ph_4As^+X^-$.[41,42]

Deprotonation of arsonium salts $[R_3AsCHR_2]X$ with phenyllithium or -sodium in liquid ammonia yields the ylides $R_3As{=}CR_2$ (*see Ylide*). $Me_3As{=}CH_2$ can be synthesized from Me_3As by first quaternizing the arsine with Me_3SiCH_2Cl, then using BuLi to deprotonate the arsonium salt, and finally removing the Me_3Si by the reaction with Me_3SiOH. The first mixed P/As double ylide, $Ph_2(Me)P{=}C{=}As(Me)Ph_2$, was prepared from the reaction of the arsonium salt $[Ph_2(Me)P–CH_2–As(Me)Ph_2](SO_3F)_2$ with $NaNH_2$ in liquid ammonia.[43]

The ^1H NMR chemical shift for the CH_2 group in $Me_3As{=}CH_2$ is to high field, above TMS. This suggests the importance of the canonical form $Me_3As^+–^-CH_2$ in contributing to the structure.[4,5,11,15]

2.4 Pentacoordinate Arsenic

A limited number of pentaorganoarsoranes, AsR_5, are known.[4,5,44,45] Me_5As is prepared in high yield by the reaction of methyllithium with Me_3AsCl_2. On the other hand, Ph_5As is formed by reacting phenyllithium with either Ph_3AsO, $[Ph_4As]Br$, or the tosylimine $Ph_3As{=}NSO_2C_6H_4Me$. A redox reaction occurs when $(Me_3SiCH_2)_3As$ is mixed with $AsCl_3$ to give $(Me_3SiCH_2)_3AsCl_2$ and elemental arsenic.[46] A recent review article[45] provides references on the synthesis and reactivity of several other arsoranes.

A trigonal bipyramidal solution structure (*see Trigonal Bipyramidal*) has been proposed for Me_5As from vibrational and ^1H NMR studies.[11,44,45] ^1H NMR, vibrational, and crystal-structure data indicate that Ph_5As is trigonal bipyramidal in solution and the solid state.[4–7,11,44,45]

3 ORGANOARSINES CONTAINING As–H BONDS

3.1 Primary and Secondary Arsines

Organoarsines containing the As–H bond are limited to the primary and secondary organoarsines.[4,5,7,9–11,47] Both the alkyl and aryl derivatives are usually synthesized by the reduction of the arsinous acid $[R_2AsOH]$, arsonic acid $[RAsO(OH)_2]$, arsinic acid $[R_2As(O)OH]$, or organohaloarsines $[RAsX_2$ or $R_2AsX]$ with powdered zinc or zinc amalgam and hydrochloric acid (equations 10 and 11). Reduction of $(Me_3SiCH_2)_2AsCl$ with Zn/Cu amalgam in a hydrochloric acid/THF solution gives a high yield of the secondary arsine and avoids the formation of the diarsine.[48]

$$RAsO(OH)_2 + 3Zn + 6HCl \longrightarrow RAsH_2 + 3ZnCl_2 + 3H_2O \quad (10)$$

$$R_2AsCl + Zn + HCl \longrightarrow R_2AsH + ZnCl_2 \quad (11)$$

Reduction of the dialkylchloroarsines with $LiAlH_4$ affords an alternative route to the secondary arsines, but gives low yields of primary arsines in the reduction of alkyldichloroarsines. In the latter case, the formation of Al–As bonded species is thought to significantly lower the arsine yields, but with the bulky Me_3SiCH_2 and Me_3CCH_2 groups, both the primary and secondary arsine are readily obtainable through the reduction of the respective haloarsine with $LiAlH_4$.[46,49,50] Similarly, 2,6-$(Me_2NCH_2)_2C_6H_3AsCl_2$ is easily reduced to the primary arsine using $LiAlH_4$.[51] $LiBH_4$ is excellent for reducing $PhAsCl_2$. Although a complex mixture of alkylated arsines and AsH_3 is obtained when $LiAlH_4$ is used to reduce vinylchloroarsines, good yields (ca. 60%) of the respective primary and secondary vinyl arsines are obtained using butylstannane.[52] Benzene reacts with $AsCl_3$ in the presence of $AlCl_3$ to give a mixture of Ph_2AsH and $PhAsH_2$. The alkylarsines are also prepared by the reaction of an alkyl halide with $NaAsH_2$. When potassium diaryl- or arylalkylarsenide is reacted with water, a high yield of the secondary arsine results. MeAsHCl can be synthesized by reacting $MeAsCl_2$ with $EtSbH_2$ (equation 12).[53]

$$2MeAsCl_2 + EtSbH_2 \longrightarrow 2MeAsHCl + EtSbCl_2 \quad (12)$$

Although primary and secondary arsines do not react with water, they are easily oxidized by oxygen.[4–6,9–11,54] For this reason, oxygen must be rigorously excluded in their synthesis. In the presence of oxygen, primary arsines give the cyclopolyarsines (equation 13), but in a stoichiometric excess of oxygen yield the arsonic acids $RAs(O)(OH)_2$ (equation 14). The hydrogens are easily replaced by treatment with sodium, organolithium, or Grignard reagents to give organoarsenides of the type R_2AsM, $RAs(H)M$, and $RAsM_2$ (M = Li, Na, K, MgX), which are useful in the synthesis of tertiary, ditertiary, and tritertiary arsines.

$$10MeAsH_2 + 5O_2 \longrightarrow 2(MeAs)_5 + 10H_2O \quad (13)$$

$$2MeAsH_2 + 3O_2 \longrightarrow 2MeAs(O)(OH)_2 \quad (14)$$

Both the primary and secondary arsines are strong reducing agents and undergo facile oxidization with the halogens, aliphatic and aromatic aldehydes, haloarsines, chloramine and dimethylchloramine, SO_2Cl_2, and Me_3PbOMe to give the corresponding diarsines or cyclopolyarsines.[4–6,9–11,54] In the absence of triethylamine or with higher stoichiometric amounts of the halogen, halogenation of the primary and secondary arsines leads to substitution and formation of the dihalo- and haloarsine (equations 15−18).

$$6PhAsCl_2 + 12Ph_2AsH \longrightarrow (PhAs)_6 + 6(Ph_2As)_2 + 12HCl \quad (15)$$

$$5MeAsH_2 + 5H_2NCl \longrightarrow (MeAs)_5 + 5NH_4Cl \quad (16)$$

$$6PhAsH_2 + 6SO_2Cl_2 \longrightarrow (PhAs)_6 + 12HCl + 6SO_2 \quad (17)$$

$$2Me_2AsH + Cl_2 + 2Et_3N \longrightarrow Me_2AsAsMe_2 + 2Et_3NHCl \quad (18)$$

$MeAsH_2$ reacts with $Me_2AsAsMe_2$ to give $(MeAs)_5$ and Me_2AsH.[55] With Me_2AsNMe_2, the products are $(MeAs)_5$,

Me_2AsH, and Me_2NH.[56] Other primary arsines easily react with $(MeAs)_5$ to generate the respective cyclopolyarsine $(RAs)_n$, where $n = 5$ or 6, and $MeAsH_2$.[57,58] Me_2AsH reacts with Me_2AsNMe_2 (and its BH_3 adduct) to produce $Me_2AsAsMe_2$.[59] Secondary arsines also react with symmetric diarsines to give mixtures of unsymmetric and symmetric diarsines (equation 19).[60] The analogous reaction of Me_2AsH with Et_2PPEt_2 yields a mixture of Et_2PH, $Me_2AsAsMe_2$, and Me_2AsPEt_2.[60] Ph_2AsH will cleave the Sn–N bond in Me_2NSnMe_3 to give $Ph_2AsSn(Me_3)_3$.[61]

$$3R_2AsH + 2R'_2AsAsR'_2 \longrightarrow R_2AsAsR_2 + R_2AsAsR'_2 + 3R'_2AsH \quad (19)$$

The reaction of Me_2AsH with diborane produces $Me_2AsH\cdot BH_3$. When the reaction is carried out at 50 °C, $[Me_2AsBH_2]_3$ and $[Me_2AsBH_2]_4$ are formed. The reaction of Me_2AsH, $(t\text{-Bu})_2AsH$, or Ph_2AsH with aluminum alkyls proceeds through a 1,2-elimination reaction to yield arsinoalanes of the following type: $[Me_2AlAsMe_2]_3$,[62,63] $[Me_2AlAsPh_2]_3$,[64] $[Me_2AlAs(t\text{-Bu})_2]_2$,[65] and $[Et_2AlAs(t\text{-Bu})_2]_2$.[66] Other secondary arsines react in an analogous fashion with organogallanes and organoindanes to give $[Me_2GaAs(i\text{-Pr})_2]_3$,[67] $[Ph_2GaAs(CH_2SiMe_3)_2]_2$,[48] $[Me_2GaAs(CH_2CMe_3)_2]_2$,[50] $[(i\text{-Pr})_2GaAs(i\text{-Pr})_2]_2$,[68,69] $[Me_2InAsMe_2]_3$,[62] $[Me_2InAsPh_2]_2$,[70] and $[Me_2InAs(t\text{-Bu})_2]_2$.[65] With primary arsines, the reactions proceed to give uncharacterized oligomers, except when there are bulky substituents on arsenic or gallium. For example, the reaction of $Me_3CCH_2AsH_2$ with Me_3Ga gives $[Me_2GaAs(H)CH_2CMe_3]_n$[50] and that of $PhAsH_2$ with $[Me_3SiCH_2]_3Ga$ produces the unique gallium–arsenic cluster compound $(PhAsH)\{[Me_3SiCH_2]_2Ga\}(PhAs)_6[Me_3SiCH_2Ga]_4$ (see Section 5).[71]

Vibrational and NMR spectroscopic techniques have been employed to investigate general conformational properties in primary and secondary organoarsines, as well as the determination of As–H bond strength and lability.[6,15,37,72] Molecular orbital calculations (*see* ***Molecular Orbital Theory***) have also been published on a series of $RAsH_2$.[73] There has been considerable interest in the characterization of organoarsines, including ^{13}C NMR data.[49,50,55,56,58,60,74,75] Most of this interest is due to the assessment of their possible use as replacements for AsH_3 in the production of gallium arsenide thin films and in the synthesis of precursors for group 13–15 semiconductors.[76]

4 ORGANOARSENIC COMPOUNDS CONTAINING As–HALOGEN BONDS

4.1 Mono- and Dihaloarsines

The haloarsines are most commonly prepared from the reduction of the arsonic or arsinic acids by sulfur dioxide in the presence of a hydrogen halide and a trace of KI.[4–7,9–11,77] Because haloarsines are in equilibrium with their respective arsonous or arsinous acids in aqueous solution, they can be prepared by the addition of excess hydrohalic acid to the respective acids (equation 20). Highly pure alkyldichloroarsines are obtained by heating the 10-alkyl-5,10-dihydrophenarsazines with hydrogen chloride (equation 21). Cleavage of the As–N bond in aminoarsines with hydrogen halides provides another route to the haloarsines (equation 22).

$$RAs(OH)_2 + 2HX \longrightarrow RAsX_2 + 2H_2O \quad (20)$$

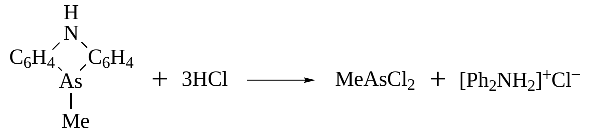

(21)

$$EtAs(NMe_2)_2 + 4HCl \longrightarrow EtAsCl_2 + 2[Me_2NH_2]^+Cl^- \quad (22)$$

Redistribution reactions that involve heating the appropriate stoichiometric mixtures of the tertiary arsines with $AsCl_3$ produce the mono- and dihaloarsines (equations 23 and 24). Disproportionation of a dihaloarsorane at high temperatures serves as a convenient synthetic route to the dialkylhaloarsines (equation 25).

$$2AsR_3 + AsCl_3 \longrightarrow 3R_2AsCl \quad (23)$$

$$AsR_3 + 2AsCl_3 \longrightarrow 3RAsCl_2 \quad (24)$$

$$2RAsX_2 \longrightarrow R_2AsX + AsX_3 \quad (25)$$

Alkylation of AsX_3 using organomercury and tetraalkyllead works well for those haloarsines that are difficult to prepare by the more drastic conditions of the disproportionation and redistribution reactions. Although incomplete alkylation of $AsCl_3$ with aluminum alkyls gives haloarsines, these usually are obtained as mixtures of the mono- and dihaloarsines with the tertiary arsines. Because complete alkylation of $AsCl_3$ does not generally occur with the Grignard reagents, this method is only used in a few special cases. The reaction of organohalides at moderate temperatures with elemental arsenic in the presence of copper yields mixtures of R_2AsX, $RAsX_2$, R_3As, AsX_3, and As_2X_4. The salt elimination reaction has been used in the recent synthesis of $(\eta\text{-}C_5Me_5)_2AsCl$ from $AsCl_3$ and LiC_5Me_5.[78] Vinylhaloarsines have been prepared in high yields by the reaction of $AsCl_3$ with 1:1 and 1:2 mol ratios of vinylstannane.[51] Numerous other methods are employed to prepare specific haloarsines and references to the primary literature for these can be found in reviews.[4–7,9–11,77] In general, the chloro- and bromoarsines are the most easily synthesized and are used in halogen exchange reactions to prepare the fluoro- and iodoarsines (equation 26).

$$Ph_2AsCl + AgF \longrightarrow Ph_2AsF + AgCl \quad (26)$$

The organohaloarsines are very reactive species and are commonly used to prepare heteroleptic tertiary arsines (see Section 2), primary and secondary arsines (see Section 3), and aminoarsines and catenated arsines (see Section 7.3). They easily hydrolyze to their respective arsonous and arsinous acids (equation 27) and are oxidized in air to the corresponding arsonic and arsinic acids (equation 28).

$$\mathrm{RAsX_2 + 2H_2O \longrightarrow RAs(OH)_2 + 2HX} \tag{27}$$

$$\mathrm{2R_2AsX + O_2 + 2H_2O \longrightarrow 2R_2As(O)OH + 2HX} \tag{28}$$

Both the monohalides, R_2AsX, and the dihalides, $RAsX_2$, are pyramidal molecules.[5–7,11,37] Electron diffraction studies on Me_2AsX show a regular variation in the As–X bond length, where As–F = 1.95 Å[79] and As–Cl = 2.18 Å, As–Br = 2.34 Å, and As–I = 2.52 Å.[5,11] The As–F bond length in $MeAsF_2$ is 1.74 Å[5,6] (microwave) while the As–I value in $MeAsI_2$ = 2.54 Å[5–7] (X ray). Ph_2AsX (X = Cl, Br, I) are isomorphous from X-ray data, where the As–X bond lengths[5–7] are Cl, 2.26 Å, Br, 2.40 Å, and I, 2.53 Å. The phenyl rings are rotated about 36° and 80° from their positions in an ideal model, which would allow maximum overlap of the π-orbitals of the aromatic groups with the arsenic lone pair electrons.[7] The structure of $PhAsBr_2$ has been studied by electron diffraction.[80]

4.2 Haloarsoranes

Haloarsoranes of the type $RAsX_4$, R_2AsX_3, and R_3AsX_2 are conveniently prepared by the direct reaction of the halogen with $RAsX_2$, R_2AsX, and R_3As respectively.[4–7,9–11,45,77] Other halogenating agents (SF_4, $TlCl_3$, $PbCl_4$, $HgCl_2$, PCl_5) have been used to halogenate the arsinous acid anhydrides, arsonic and arsinic acids, and tertiary arsines. Generally, the fluoro- and chloroarsoranes are pentacoordinate, while the bromo and iodo compounds of these compositions are ionic arsonium salts when the R substituent is not very sterically demanding. Hydrolysis of $RAsX_4$ and R_2AsX_3 yields the corresponding arsonic or arsinic acids and pyrolysis produces the organohalide and AsX_3 and $RAsX_2$, respectively. R_3AsX_2 hydrolyzes to R_3AsO and gives R_2AsX and RX when heated above the melting point.

A trigonal bipyramidal structure has been postulated for $PhAsCl_4$ where the phenyl group occupies an equatorial site.[45] Similarly, Me_2AsCl_3, Ph_2AsCl_3, and Ph_2AsF_3 are trigonal bipyramidal from spectroscopic data. However, Me_2AsF_3 is associated in solution.[45] The structures of R_3AsX_2 have been studied in much greater detail[4,5,7,11,37,45] and are generally thought to be either trigonal bipyramidal or ionic, $[R_3AsX^+]X^-$, in nature, although certain systems such as Ph_3AsI_2 are complex. The R_3AsX_2 species (R = Me, Et, Ph; X = F, Cl) have a trigonal bipyramidal structure. Me_3AsBr_2, Et_3AsBr_2, and Me_3AsI_2 are ionic with the expected tetrahedral geometry about the arsenic atom.[17] Interestingly, X-ray studies have established that the neopentyl derivative $As(CH_2CMe_3)Br_2$ is trigonal bipyramidal.[17]

5 ORGANOARSENIC COMPOUNDS CONTAINING As–GROUP 13 BONDS

5.1 As–B Bonded Compounds

Relatively few organoarsenic compounds that contain an As–B bond are known.[11,15,81–84] In most cases, these are synthesized by the straightforward reaction of the primary, secondary, and tertiary arsine with diborane or $BH_3{\cdot}THF$ (equation 29). As–B bonding also results when the BH_3 moiety reacts with Sn–As and As–P–As bonded compounds (equations 30 and 31).[81]

$$\mathrm{2Me_2AsH + B_2H_6 \longrightarrow 2Me_2AsH{\cdot}BH_3} \tag{29}$$

$$\mathrm{Me_3SnAsPh_2 + THF{\cdot}BH_3 \longrightarrow Me_3SnAs({\cdot}BH_3)Ph_2 + THF} \tag{30}$$

$$\mathrm{(Me_2As)_2PCF_3 + B_2H_6 \longrightarrow (Me_2As)_2PCF_3{\cdot}2BH_3} \tag{31}$$

BH_3 coordinates at arsenic in Me_2NAsF_2.[85] At low temperatures, As–B bonded adducts are observed in the reaction of $THF{\cdot}BH_3$ with Me_2AsNEt_2, $Me_2AsN(n\text{-}Pr)_2$, and $Me_2AsN(i\text{-}Pr)_2$.[82,84] The ethyl and n-propyl derivatives also exhibit N–B bonded adducts, with the As–B adduct being favored over the N–B adduct with increasing steric bulk of the alkyl substituent on the nitrogen. Arsine–borane adducts that contain As–H, As–As, and As–N bonds decompose at moderate temperatures to cycloarsinoborines, $[Me_2AsBH_2]_{3,4}$ (equation 32).

$$\mathrm{B_2H_6 + 2Me_2AsH \xrightarrow{50\,^{\circ}C} \frac{2}{n}[Me_2AsBH_2]_{\mathit{n}} + 2H_2} \tag{32}$$

Dehalosilylation in the reaction of Ph_2BCl with $Me_2AsSiMe_3$ gives $[Ph_2BAsMe_2]_3$ (equation 33).[86] The reaction of Me_2BBr with $Me_2AsSnMe_3$ produces the corresponding trimer and with $MeBBr_2$ gives $[Me(Br)BAsMe_2]_3$.[87] Using the salt elimination procedure, $[PhAs(BNMe_2)]_2$ has been synthesized from a 1:1 reaction of Li_2AsPh with $B_2(NMe_2)_2Br_2$.[88] This procedure has also been used to prepare $[PhB(Cl)As(t\text{-}Bu)_2]_2$, $PhB[As(t\text{-}Bu)_2]_2$, $Cp^*B(Cl)As(t\text{-}Bu)_2$, $(C_{20}H_{30})BAs(t\text{-}Bu)_2$, and $Mes_2BAs(Ph)SiMe_3$.[89] The reaction of Mes_2BF with Li_2AsPh in THF gives the compound $Li(THF)_3PhAsBMes_2$, which contains a B–As double bond. By adding two equivalents of TMEDA to a solution of this compound in diethyl ether, another B–As double-bonded compound is formed, $[Li(TMEDA)_2][PhAsBMes_2]$.[90] On the other hand, Mes_2BF reacts with $LiAs(i\text{-}Pr)_2$ and $LiAs(t\text{-}Bu)_2$ to give the monomeric arsinoboranes, $Mes_2BAs(i\text{-}Pr)_2$ and $Mes_2BAs(t\text{-}Bu)_2$.[91] The cyclic $(i\text{-}Pr)_2NB(N\text{-}t\text{-}Bu)B(N\text{-}i\text{-}Pr_2)AsPh$[92] and monomeric arsenoborane[83] $Cp^*(Cl)BAs(t\text{-}Bu)_2$ have been reported.

$$3\mathrm{Ph_2BCl} + 3\mathrm{Me_3SiAsMe_2} \longrightarrow [\mathrm{Ph_2BAsMe_2}]_3 + 3\mathrm{Me_3SiCl} \quad (33)$$

The addition compounds formed by the interaction of BX_3 ($X = F$, Cl, Br, I) and B_2H_6 Lewis acids (*see Lewis Acids & Bases*) with arsines have been characterized by several spectroscopic methods.[82,84,93] Multinuclear NMR chemical shift data have been used extensively to explore the comparative donor properties of structurally similar amines, phosphines, and arsines toward boron-containing acceptors. Relative adduct stabilities have been determined for BX_3 and B_2H_6 with several homologous series of compounds containing group 15 elements. From these studies, Lewis acid and base strengths within given series have been proposed. For example, $\mathrm{Me}_n\mathrm{AsH}_{3-n}\cdot\mathrm{BH_3}$ ($n = 1-3$) adduct stability decreases as n decreases[5,11] and $\mathrm{BH_3}\cdot\mathrm{ER_3}$ adduct stability follows the order $E = P > N > As > Sb$.[84]

Arsenoboranes like $[\mathrm{Ph_2BAsMe_2}]_3$ and $[\mathrm{Me_2AsBH_2}]_{3,4}$ have been assumed to be ring structures with head-to-tail As–B arrangements, σ-type bonding, and tetrahedral B and As geometries, although no structural data have been reported. Monomeric arsenoboranes, as discussed above, have been obtained by introduction of bulky groups on boron.[83,90] Strategies have also been developed to create planarity at the arsenic center and enhance As–B multiple bonding.[83] For example, As–B double bonding has been proposed in $\mathrm{Li(THF)_3PhAsBMes_2}$ and $\mathrm{[Li(TMEDA)_2][PhAsBMes_2]}$ from As–B bond distance and other structural and spectroscopic data.[90] X-ray data indicate multiple As–B bonding in $\mathrm{Li(THF)_3PhAsBMes_2}$,[90] and $\mathrm{[Li(TMEDA)_2][PhAsBMes_2]}$[90] with the As–B bond lengths being 1.926 and 1.936 Å respectively. As–B bond lengths of 2.063, (2.200 and 2.184), 2.064, 2.084, 2.031, and 2.085 Å are found in cyclic $(i\text{-Pr})_2\mathrm{NB}(\mathrm{N}\text{-}t\text{-Bu})\mathrm{B}(\mathrm{N}\text{-}i\text{-Pr}_2)\mathrm{AsPh}$,[92] $[\mathrm{PhB(Cl)As}(t\text{-Bu})_2]_2$, $\mathrm{PhB[As}(t\text{-Bu})_2]_2$, $\mathrm{C_{20}H_{30}BAs}(t\text{-Bu})_2$, $\mathrm{Mes_2BAs(Ph)SiMe_3}$, and $\mathrm{Cp^*(Cl)BAs}(t\text{-Bu})_2$[83] respectively. With $[\mathrm{PhAs(BNMe_2)_2}]_2$, the six-membered $\mathrm{As_2B_4}$ ring is in a chair configuration with four As–B bond lengths of 2.082, 2.063, 2.041, and 2.068 Å.[88] These distances are to be compared with As–B values in boron arsenide (2.069 Å) and in the Zintl compound (*see* ***Zintl Compounds***) $\mathrm{K_3BAs_2}$ (1.868 Å),[94] where the boron is dicoordinate.

5.2 As–Al Bonded Compounds

The tertiary arsines easily form adducts with the aluminum alkyls.[29,95] The reaction of $\mathrm{R_2AlCl}$ ($R = \mathrm{Me}$, i-Bu) with $\mathrm{As[SiMe_3]_3}$ does not lead to a dehalosilylation reaction, but yields the adducts $\mathrm{R_2(Cl)Al\cdot As[SiMe_3]_3}$.[96] The other known As–Al bonded compounds are base-stabilized monomeric arsinoalanes and the cycloarsinoalanes. Although a few secondary arsines react with aluminum alkyls to give the cycloarsinoalanes (equations 34 and 35),[65,66,70] this 1,2-elimination route to arsinoalanes becomes impractical as the steric bulk of the substituents increases.[97] $\mathrm{AsH_3}$ reacts with $t\text{-Bu}_3\mathrm{Al}$ to produce the trimeric $[(t\text{-Bu})_2\mathrm{AlAsH_2}]_3$.[98] The salt elimination method, which has been widely used in organometallic synthesis, has been used to synthesize As–Al ring compounds with bulky moieties on the arsenic and aluminum (equation 36).[96,99] Equilibration of an equal molar mixture of $\mathrm{[Et_2AlP(SiMe_3)_2]_2}$ and $\mathrm{[Et_2AlAs(SiMe_3)_2]_2}$ produced a four-membered ring compound, $\mathrm{Et_2AlP(SiMe_3)_2(Et_2Al)As(SiMe_3)_2}$, with P and As atoms bridging the two aluminum centers.[100] The trimeric borazine analogue, $[\mathrm{Mes^*AlAsPh}]_3\cdot\mathrm{Et_2O}$ ($\mathrm{Mes^*} = 2,4,6\text{-}(t\text{-Bu})_3\mathrm{C_6H_2}$), was synthesized by heating a mixture of $\mathrm{Mes^*AlH_2}$ and $\mathrm{H_2AsPh}$ at 160°.[101] The first base-stabilized arsinoalane monomer was prepared using the salt elimination procedure (equation 37).[102] $\mathrm{Me_3N\cdot Al(H_2)As(SiMe_3)_2}$ results from the dehydrosilylation reaction of $\mathrm{H_3Al\cdot NMe_3}$ with $\mathrm{As(SiMe_3)_3}$.[103] Recently, the base-stabilized monomeric species $\mathrm{dmap\cdot R_2AlAs(SiMe_3)_2}$ ($R = \mathrm{Me}$, Et) have been isolated and characterized from the reaction of dmap with $\mathrm{[Me_2AlAs(SiMe_3)_2]_3}$ and $\mathrm{[Et_2AlAs(SiMe_3)_2]_2}$.[104] Table 1 lists the known arsinoalanes and the preparative route to each.

$$2(t\text{-Bu})_2\mathrm{AsH} + 2\mathrm{AlEt_3} \xrightarrow{220\,^\circ\mathrm{C}} [(t\text{-Bu})_2\mathrm{AsAlEt_2}]_2 + 2\mathrm{EtH} \quad (34)$$

$$2(t\text{-Bu})_2\mathrm{AsH} + \mathrm{Al_2Me_6} \xrightarrow{220\,^\circ\mathrm{C}} [(t\text{-Bu})_2\mathrm{AsAlMe_2}]_2 + 2\mathrm{MeH} \quad (35)$$

$$2\mathrm{Et_2AlCl} + 2\mathrm{LiAs(SiMe_3)_2} \longrightarrow [\mathrm{Et_2AlAs(SiMe_3)_2}]_2 + 2\mathrm{LiCl} \quad (36)$$

$$\mathrm{H_2AlCl\cdot NMe_3} + \mathrm{LiAsMes_2} \longrightarrow \mathrm{H_2AlAsMes_2\cdot NMe_3} + \mathrm{LiCl} \quad (37)$$

Computational studies[95] of $\mathrm{R_3Al{-}ER'_3}$ ($E = P$, As, Sb, Bi) Lewis acid–base adducts indicate that Al–E bond length does not directly correlate with adduct stability. Rather, Al–C(H)

Table 1 Known arsinoalanes

Arsinoalane	Preparative method
$\mathrm{Tmp_2AlAsPh_2}$	Salt elimination[105]
$\mathrm{[Me_2AlAsMe_2]_3}$	1,2-elimination;[62] H_2-elimination[63]
$\mathrm{[Me_2AlAsPh_2]_3\cdot(C_7H_8)_2}$	1,2-elimination[64]
$[\mathrm{Me_2AlAs}(t\text{-Bu})_2]_2$	1,2-elimination[65]
$[\mathrm{Et_2AlAs}(t\text{-Bu})_2]_2$	1,2-elimination[66]
$[(t\text{-Bu})_2\mathrm{AlAsH_2}]_3$	1,2-elimination[98]
$\mathrm{[Me_2AlAs(SiMe_3)_2]_2}$	Salt elimination;[96] Dehydrosilylation[104]
$\mathrm{[Et_2AlAs(SiMe_3)_2]_2}$	Salt elimination;[99] Dehydrosilylation[104]
$[(i\text{-Bu})_2\mathrm{AlAs(SiMe_3)_2}]_2$	Salt elimination[96]
$\mathrm{[Me_2AlAs(CH_2SiMe_3)_2Ph]_3}$	1,2-elimination[64]
$\mathrm{[2,6\text{-}Mes_2C_6H_3(H)AlAs(H)Ph]_2}$	H_2-elimination[106]
$\mathrm{H_2AlAsMes_2\cdot NMe_3}$	Salt elimination[102]
$\mathrm{Me_2AlAs(SiMe_3)_2\cdot dmap}$	Ring cleavage[104]
$\mathrm{Et_2AlAs(SiMe_3)_2\cdot dmap}$	Ring cleavage[104]
$\mathrm{H_2AlAs(SiMe_3)_2\cdot NMe_3}$	Dehydrosilylation[103]
$\mathrm{[Mes^*AlAsPh]_3\cdot Et_2O}$	H_2-elimination[101]

bond distances and C(H)–Al–C(H) bond angle parameters are useful in predicting adduct stability. Four cycloarsinoalane dimers have been characterized by single-crystal X-ray analysis. In each case, the $(\text{Al–As})_2$ ring is planar with a distorted tetrahedral geometry about both the Al and As atoms and the endocyclic angle subtended at arsenic is larger than at aluminum. The Al–As bond distances and the Al–As–Al and the As–Al–As angles are as follows: $[\text{Me}_2\text{AlAs(SiMe}_3)_2]_2$[96] (triclinic: 2.536 Å, 91.71°, 88.29°); $[\text{Et}_2\text{AlAs(SiMe}_3)_2]_2$[99] (monoclinic: 2.535 Å, 91.01°, 88.99°); $[(i\text{-Bu})_2\text{AlAs(SiMe}_3)_2]_2$[96] (monoclinic: 2.550 Å, 92.23°, 87.77°); $[\text{Et}_2\text{AlAs}(t\text{-Bu})_2]_2$[66] (monoclinic: 2.567 Å, 94.54°, 85.46°). For the base-stabilized monomeric aminoalanes, the Al–As bond distances are as follows: $\text{Me}_2\text{AlAs(SiMe}_3)_2\cdot\text{dmap}$, 2.470 and 2.472 Å;[104] $\text{Et}_2\text{AlAs(SiMe}_3)_2\cdot\text{dmap}$, 2.473 Å;[104] and $(\text{Me}_3\text{Si})_2\text{AsAlH}_2\cdot\text{NMe}_2$, 2.438 Å.[103] The borazine analogue, $[\text{Mes}^*\text{AlAsPh}]_3$, exhibits a nonplanar boat conformation with little or no arsenic lone pair delocalization and bond lengths consistent with Al–As single bonds.[101]

5.3 As–Ga Bonded Compounds

Prior to 1986, there were very few known and characterized As–Ga compounds.[29,107,108] Since that time, there has been a significant increase in the number of synthesized and fully characterized As–Ga species. Table 2 contains a listing of the organometallic As–Ga bonded compounds that have been synthesized from 1986 to 2003 and indicates their method of synthesis.

These compounds can be classified according to the As–Ga bonding nucleus as simple As–Ga adducts, twist-boat conformation $(\text{As–Ga})_3$ rings, planar or nonplanar $(\text{As–Ga})_2$ rings, nonplanar Ga–As–Ga–X rings (X = halogen), pyramidal Ga_3As gallanoarsines, and planar As_3Ga arsinogallanes. Much of the synthesis activity is a consequence of the search for volatile, single-source, gallium arsenide precursors that will not incorporate As–C bonds into thin films grown from OMCVD processes.[141] There has been a judicious variation of substituents and the application of three general synthesis methodologies, other than direct adduct formation, to give compounds that contain these As–Ga linkages: 1,2-elimination (equation 38), salt elimination (equation 39), and dehalosilylation (equation 40).

$$2(\text{Me}_3\text{SiCH}_2)_2\text{AsH} + 2\text{GaPh}_3 \longrightarrow [(\text{Me}_3\text{SiCH}_2)_2\text{AsGaPh}_2]_2 + 2\text{PhH} \tag{38}$$

$$2(\text{Me}_3\text{Si})_2\text{AsLi} + 2\text{ClGa}(\text{CH}_2\text{SiMe}_3)_2 \longrightarrow [(\text{Me}_3\text{Si})_2\text{AsGa}(\text{CH}_2\text{SiMe}_3)_2]_2 + 2\text{LiCl} \tag{39}$$

$$(\text{Me}_3\text{SiCH}_2)_2\text{AsSiMe}_3 + 2\text{GaBr}_3 \longrightarrow [(\text{Me}_3\text{SiCH}_2)_2\text{AsGaBr}]_2 + 2\text{Me}_3\text{SiBr} \tag{40}$$

Dehydrosilylation occurs in the reaction of $\text{H}_3\text{Ga}\cdot\text{NMe}_3$ with $\text{As(SiMe}_3)_3$ to provide an efficient route to $[(\text{Me}_3\text{Si})_2\text{AsGaH}_2]_3$.[123]

Table 2 As–Ga bonded compounds synthesized after 1985

As–Ga bonded compounds	Method of preparation
$\text{Et}_3\text{As}\cdot\text{GaMe}_n(\text{C}_6\text{F}_5)_{3-n}$	Direct[109]
$[\text{ClMe}_2\text{Ga}\cdot\text{AsEt}_2]_2\text{CH}_2$	Direct[110]
$(t\text{-Bu})_2(\text{H})\text{As}\cdot\text{Ga}(i\text{-Pr})_3$	Direct[69]
$(\text{Me}_3\text{Si})_3\text{As}\cdot\text{GaPh}_3$	Direct[111]
$(\text{Me}_3\text{Si})_3\text{As}\cdot\text{Ga(Cl)(CH}_2\text{CMe}_3)_2$	Direct[112]
$\text{Ph}_3\text{As}\cdot\text{GaI}_3$	Direct[113]
$(p\text{-MeOC}_6\text{H}_4)_3\text{As}\cdot\text{GaI}_3$	–[114]
$(\text{Et}_3\text{As})_2\cdot\text{Ga}_2\text{I}_4$	–[114]
$[(\text{THF})\text{Br}_2\text{Ga}]_3\text{As}$	Dehalosilylation[115]
$\{[2,4,6\text{-}(i\text{-Pr})_2\text{C}_6\text{H}_2]_2\text{Ga}\}_2\text{AsPh}$	Salt elimination[116]
$(\text{Ph}_3\text{Si})[(\text{Me}_3\text{Si})_2\text{CH}]\text{AsGa}(t\text{-Bu})_2$	Salt elimination[117]
$[(\text{Mes})_2\text{As}]_3\text{Ga}$	Salt elimination[97,118]
$(t\text{-Bu}_2\text{As})_3\text{Ga}$	Salt elimination[65,119]
$[(\text{Me}_3\text{Si})_2\text{As}]_3\text{Ga}$	–[120]
$\{[(\text{Me}_3\text{SiCH}_2)_2\text{As}]_3\text{Ga}\}_2$	Salt elimination[121]
$[(\text{Me}_3\text{SiCH}_2)_2\text{AsGaMe}_2]_{2,3}$	Dehalosilylation[122]
$[(\text{Me}_3\text{CCH}_2)_2\text{AsGaMe}_2]_2$	1,2-elimination[50]
$[(\text{Me}_3\text{SiCH}_2)_2\text{AsGaPh}_2]_2$	1,2-elimination[48]
$[\text{Me}_3\text{SiCH}_2(\text{H})\text{AsGaPh}_2]_3$	1,2-elimination[49]
$[(\text{Me}_3\text{Si})_2\text{AsGa(CH}_2\text{CMe}_3)_2]_2$	Salt elimination[112]
$[(\text{Me}_3\text{Si})_2\text{AsGaH}_2]_3$	Dehydrosilylation[123]
$[(\text{Me}_3\text{Si})_2\text{AsGa(CH}_2\text{SiMe}_3)_2]_2$	Salt elimination[124]
$[(\text{Me}_3\text{Si})_2\text{AsGa}(t\text{-Bu})_2]_2$	Salt elimination[125]
$[(\text{Me}_3\text{Si})_2\text{AsGaPh}_2]_2$	Salt elimination[126,127]
$[(\text{Me}_3\text{Si})_2\text{AsGaMe}_2]_2$	Dehalosilylation[128]
$(\text{Me}_3\text{Si})_2\text{AsGa(C}_5\text{Me}_5)_2$	Salt elimination[129]
$[(t\text{-Bu})_2\text{AsGaMe}_2]_2$	Salt and 1,2-elimination[65,119]
$[(t\text{-Bu})_2\text{AsGaEt}_2]_2$	–[130]
$[(t\text{-Bu})_2\text{AsGaBu}_2]_2$	Salt elimination[119]
$[(t\text{-Bu})_2\text{AsGa(allyl)}_2]_2$	Salt elimination[131]
$[(t\text{-Bu})_2\text{AsGa(benzyl)}_2]_2$	Salt elimination[131]
$[(t\text{-Bu})_2\text{AsGa(vinyl)}_2]_2$	Salt elimination[131]
$[(t\text{-Bu})(\text{H})\text{AsGa}(t\text{-Bu})_2]_3$	1,2-elimination[98]
$[(t\text{-Bu})_2\text{AsGa(CH}_2)_4]_2$	Salt elimination[132]
$(t\text{-Bu})_2\text{AsGa}(t\text{-Bu})_2$	Salt elimination[133]
$[\text{H}_2\text{AsGa}(t\text{-Bu})_2]_3$	1,2-elimination[134]
$[(i\text{-Pr})_2\text{AsGaMe}_2]_3$	1,2-elimination[67]
$[(\text{Me}_3\text{SiCH}_2)_2\text{AsGaCl}_2]_3$	Dehalosilylation[97]
$[(\text{Me}_3\text{SiCH}_2)_2\text{AsGaBr}_2]_3$	Dehalosilylation[135,136]
$[(\text{Me}_3\text{SiCH}_2)_2\text{AsGaClMe}]_{2,3}$	Dehalosilylation[135]
$[(\text{Me}_3\text{SiCH}_2)_2\text{AsGaClPh}]_{2,3}$	Dehalosilylation[135]
$[\{(\text{Me}_3\text{SiCH}_2)_2\text{As}\}_2\text{GaCl}]_2$	Dehalosilylation[97]
$[\{(\text{Me}_3\text{SiCH}_2)_2\text{As}\}_2\text{GaBr}]_2$	Dehalosilylation[135]
$[\{(\text{Me}_3\text{SiCH}_2)_2\text{As}\}_2\text{GaPh}]_2$	–[122]
$(t\text{-Bu})_2\overline{\text{GaAs(SiMe}_3)_2\text{Ga}(t\text{-Bu})_2\text{Cl}}$	Direct[125]
$\text{Ph}_2\text{Ga}\overline{\text{As(SiMe}_3)_2\text{Ga(Ph)}_2\text{Cl}}$	Dehalosilylation[126,127]
$\text{Ph}_2\text{Ga}\overline{\text{As(SiMe}_3)_2\text{Ga(Ph)}_2\text{Br}}$	Dehalosilylation[127]
$(\text{Me}_3\text{SiCH}_2)_2\text{GaAs(SiMe}_3)_2\overline{\text{Ga-}}$ $\overline{(\text{CH}_2\text{SiMe}_3)_2\text{Cl}}$	Dehalosilylation[124]
$(\text{Me}_3\text{CCH}_2)_2\text{Ga}\overline{\text{As(SiMe}_3)_2\text{Ga-}}$ $\overline{(\text{CH}_2\text{CMe}_3)_2\text{Cl}}$	Dehalosilylation[112]
$[(t\text{-Bu})_2\text{GaAsC}_6\text{H}_3(\text{CH}_2\text{NMe}_2)\text{-}$ $\text{CH}_2\text{NMe}_2]_2$	Salt elimination[137]
$\text{Ph}_2\overline{\text{GaCl(Ph)}_2\text{Ga(Me}_3\text{Si)As(CH}_2)_3\text{-}}$ $\overline{\text{As(SiMe}_3)\text{Ga(Ph)}_2\text{Cl}}\text{GaPh}_2$	Dehalosilylation[138]
$(\text{PhAsH})[(\text{Me}_3\text{SiCH}_2)_2\text{Ga}](\text{PhAs})_6\text{-}$ $(\text{Me}_3\text{SiCH}_2\text{Ga})_4$	1,2-elimination[71]
$[(\text{C}_4\text{Me}_4\text{As})_4\text{Ga}]\text{Li(THF)}_4$	Salt elimination[139]
$\text{Ga}_2\{\text{As(Si}(i\text{-Pr})_3)\}_4$	Salt elimination[140]

The first example of an arsinogallane that contains the H_2As moiety, $[(t\text{-Bu})_2GaAsH_2]_3$, has been prepared in quantitative yield from the reaction of $t\text{-}Bu_3Ga$ with AsH_3.[134] Although the 1,2-elimination route was first used to prepare $[Me_2AsGaMe_2]_3$[62] and $[Me_2AsGaPh_2]_2$,[70] as the steric bulk of the substituents increases the utility of this approach becomes impractical to prepare arsinogallanes. For example, the reaction of $(t\text{-Bu})_2AsH$ with $Ga(i\text{-Pr})_3$ gives only the simple adduct $(t\text{-Bu})_2AsH{\cdot}Ga(i\text{-Pr})_3$[69] and the reaction of $PhAsH_2$ with $Ga(CH_2SiMe_3)_3$ yields the As–Ga cluster compound $(PhAsH)\{[Me_3SiCH_2]_2Ga\}(PhAs)_6[Me_3SiCH_2Ga]_4$.[71] Salt elimination and dehalosilylation have now become the preferred synthetic routes to the nonadduct systems (see Table 2).[122]

Arsenic–halogen mixed-bridge compounds, $R_2GaAs(SiMe_3)_2Ga(R)_2X$, have been prepared by dehalosilylation that involves $As(SiMe_3)_3$ and R_2GaX ($R = Ph$, $X = Cl$, Br; $R = Me_3SiCH_2$, Me_3CCH_2, $X = Cl$) (equation 41).[112,122,124,126,127] The dimeric arsinogallanes also react with halogallanes to yield the mixed-bridge species (equation 42), which can be reconverted to the respective dimer by reaction with the $LiAs(SiMe_3)_2$.[112] Reaction of the mixed-bridge $Ph_2GaAs(SiMe_3)_2Ga(Ph)Cl$ with $LiP(SiMe_3)_2$ leads to substituent transfer at both Ga and As to yield the adduct $Ph_3Ga{\cdot}As(SiMe_3)_3$, which can also form from the direct reaction of Ph_3Ga and $As(SiMe_3)_3$.[111] An As_2Ga_2 ring that is intramolecularly base-stabilized, $[(t\text{-Bu})GaAsC_6H_3(CH_2NMe_2)(CH_2NMe_2)]_2$, has been prepared by treating $t\text{-}BuGaCl_2$ with $Li_2AsC_6H_3(CH_2NMe_2)_2$.[137]

$$(Me_3Si)_3As + 2Ph_2GaCl \longrightarrow Ph_2GaAs(SiMe_3)_2GaPh_2Cl + Me_3SiCl \tag{41}$$

$$[(Me_3Si)_2AsGa(CH_2CMe_3)_2]_2 + 2(Me_3CCH_2)_2GaCl \longrightarrow 2(Me_3CCH_2)_2GaAs(SiMe_3)_2Ga(CH_2CMe_3)_2Cl \tag{42}$$

The salt elimination reaction has been employed to prepare two volatile monomeric arsinogallanes with bulky substituents on both As and Ga (equations 43 and 44).[129,133] Three sterically hindered trisarsinogallanes, $(Mes_2As)_3Ga$,[118] $\{[(Me_3SiCH_2)_2As]_3Ga\}_2$,[121] and $(t\text{-}Bu_2As)_3Ga$,[65,119] have been synthesized by salt elimination in the reaction of the lithium arsenide and the respective chlorogallane. Dehalosilylation is an alternative route to the mesityl compound.[97] $[(Me_3Si)_2As]_3Ga$ has been isolated as one of the products from the reaction of $LiAs(SiMe_3)_2$ and $[Cl_2GaP(SiMe_3)_2]_2$.[120]

$$(t\text{-Bu})_2AsLi + ClGa(t\text{-Bu})_2 \longrightarrow (t\text{-Bu})_2AsGa(t\text{-Bu})_2 + LiCl \tag{43}$$

$$(Me_3Si)_2AsLi + ClGaCp^*{}_2 \longrightarrow (Me_3Si)_2AsGaCp^*{}_2 + LiCl \tag{44}$$

The first arsinogallate $[(C_4Me_4As)_4Ga]Li(THF)_4$ has been reported.[139] It is synthesized from the lithium salt of the $[C_4Me_4As]^-$ anion, which is a permethylated arsole derivative, and $GaCl_3$. $Li(THF)_2Ga_2\{As[Si(i\text{-Pr})_3]_3\}_4$ is synthesized by an analogous route.[140]

A few studies have been carried out on the arsinogallanes as potential single-source GaAs precursors. Pyrolysis of $(t\text{-Bu})_2GaAs(t\text{-Bu})_2$,[133] $[(t\text{-Bu})_2GaAsH_2]_2$,[134] $[Me_2GaAs(t\text{-Bu})_2]_2$,[130] and $[Et_2GaAs(t\text{-Bu})_2]_2$[130] gives polycrystalline GaAs. GaAs films have been obtained from $[Me_2GaAs(t\text{-Bu})_2]_2$[142,143] and $[Et_2GaAs(t\text{-Bu})_2]_2$[130,143] using these as single sources in a chemical beam epitaxy reactor. $[(t\text{-Bu})_2As]_3Ga$ also produces thin films, which are n-type.[143] The pyrolysis mechanism of $Et_3As{\cdot}GaMe_n(C_6F_5)_{3-n}$[109] and $[ClR_2GaAsEt_2]_2CH_2$[110] ($R = Me$, Et) has been studied using mass spectrometry in GaAs vapor-phase epitaxy.

Mono(arsino)gallanes can occur as monomers, dimers, or trimers (see Table 2). More sterically demanding substituents enhance monomer or dimer formation. In three instances,[122,135] dimer/trimer equilibrium has been detected by NMR spectroscopic techniques. $(Me_3Si)_2AsGa(C_5Me_5)_2$[129] and $(t\text{-Bu})_2AsGa(t\text{-Bu})_2$[133] are monomeric. The following $R_2AsGaR'_2$ arsinogallanes are dimeric: $R = Me_3CCH_2$, $R' = Me$;[50] $R = Me_3SiCH_2$, $R' = Ph$;[48] $R = Me_3Si$, $R' = CH_2CMe_3$,[112] CH_2SiMe_3,[124] Me,[128] t-Bu,[125] or Ph;[126,127] $R = t\text{-Bu}$, $R' = Me$,[65,119] Et,[130] or n-Bu.[119] In each case, available X-ray data indicate planar $(Ga–As)_2$ rings. Trimers have been reported for $Me_3SiCH_2(H)AsGaPh_2$,[49] $(t\text{-Bu})(H)AsGa(t\text{-Bu})_2$,[98] $H_2AsGa(t\text{-Bu})_2$,[134] $(i\text{-Pr})_2AsGaMe_2$,[67] and $(Me_3SiCH_2)_2AsGaX_2$ ($X = Cl$,[97] Br[135,136]). X-ray studies[67,136] have indicated that the $(Ga–As)_3$ ring exists in a distorted or twisted-boat conformation. Trimers of $H_2GaAs(SiMe_3)_2$ exist as flattened $(Ga–As)_3$ rings.[123]

The bis(arsino)gallanes $[(Me_3SiCH_2)_2As]_2GaX$ ($X = Cl$,[97] Br[135]) are dimers with a planar $(Ga–As)_2$ ring and crystallize[135] in the trans configuration. The tris(arsino)gallane $(Mes_2As)_3Ga$ is nearly trigonal planar[97,118] and $[(Me_3Si)_2As]_3Ga$ is trigonal planar,[120] while $(t\text{-}Bu_2As)_3Ga$ has distorted pyramidal geometry.[65,119] However, $[(Me_3SiCH_2)_2As]_3Ga$ is dimeric[121] with a nonplanar $(Ga–As)_2$ ring.

The tris(gallyl)arsines $As[GaBr_2(THF)]_3$ and $Ph_3Si[(Me_3Si)_2CH]AsGa(t\text{-Bu})_2$ have a pyramidal Ga_3As skeleton.[115] From X-ray data, the halogen mixed-bridge species contain a Ga–As–Ga–X ring that may be planar[112,125] or nonplanar,[124,126,127] depending on the steric requirements of the substituents.[122] $Ga_2\{As[Si(i\text{-Pr})_3]_4\}$ has a structure suggesting gallium–arsenic double bonds involving the exocyclic As moieties bound to the Ga atoms in the planar Ga_2As_2 ring.[140] The reader is referred to two excellent reviews on the characterization of these and other gallium–arsenic compounds.[122,141]

5.4 As–In Bonded Compounds

Prior to 1994, very few As–In bonded compounds were known. In the intervening 10 years, salt elimination, 1,2-elimination, and dehalosilylation preparative routes have been extended to As–In chemistry. Table 3 contains a listing of the

Table 3 Known As–In bonded compounds

As–In bonded compounds	Method of preparation
$[Me_2AsInMe_2]_3$	1,2-elimination[62]
$[Ph_2AsInMe_2]_2$	1,2-elimination[70]
$[(t\text{-}Bu)_2AsInMe_2]_2$	1,2-elimination[65]
$[(Me_3Si)_2AsInEt_2]_2$	1,2-elimination[146]
$[EtInAsSi(i\text{-}Pr)_3]_4$	1,2-elimination[147]
$[Ph_2InAs(SiMe_3)_2]_2$	Dehalosilylation[145]
$[(Me_3Si)_2AsIn(CH_2SiMe_3)_2]_2$	Dehalosilylation[144]
$(Me_3SiCH_2)_2InAs(SiMe_3)_2In\text{-}(CH_2SiMe_3)_2Cl$	Dehalosilylation[144]
$[(Me_3Si)_2AsInMe_2]_2$	Dehalosilylation[148]
$(Me_3Si)_3AsIn(Me_3SiCH_2)_3$	Salt elimination;[111] direct[111]
$(MesInCl)_4(InCl)_2[As(t\text{-}Bu)]_4$	Salt elimination[149]
$[Li(THF)_4]_2(MesInCl)_6(InCl)_2\text{-}[(AsBu)t\text{-}Bu]_6$	Salt elimination[149]
$(Me_3Si)_3AsIn(CH_2CMe_3)_3$	Direct[150]
$(Me_3SiCH_2)_2InAs(SiMe_3)_2\text{-}In(CH_2SiMe_3)_2P(SiMe_3)_2$	Equilibration[151]

organometallic As–In bonded compounds and indicates their method of synthesis. $[Me_2AsInMe_2]_3$,[62] $[Ph_2AsInMe_2]_2$,[70] and $[(t\text{-}Bu)_2AsInMe_2]_2$[65] were prepared by reacting the respective secondary arsine with Me_3In. Four-membered arsinoindanes with arsenic and mixed As–Cl bridging have been synthesized by the salt elimination and dehalosilylation methods.[65,128,144,145] Dehalosilylation results in the formation of $[Ph_2InAs(SiMe_3)_2]_2$ from the room-temperature reaction of Ph_2InCl and $As(SiMe_3)_3$ (equation 45).[145]

$$2Ph_2InCl + 2As(SiMe_3)_3 \longrightarrow [Ph_2InAs(SiMe_3)_2]_2 + 2Me_3SiCl \quad (45)$$

When $(Me_3SiCH_3)_2InCl$ and $(Me_3Si)_3As$ are reacted in a 1:1 mol ratio, $[(Me_3Si)_2AsIn(CH_2SiMe_3)_2]_2$ results. With a 2:1 mol ratio, the mixed-bridge species, $(Me_3SiCH_2)_2\overline{In\text{-}As(SiMe_3)_2In(CH_2SiMe_3)_2Cl}$, forms.[144] This mixed-bridge species can also be obtained from the reaction in equation (46), which is preferable to dehalosilylation as a preparative method and gives the mixed-bridge compound in greater yield.

$$2(Me_3SiCH_2)_2InCl + [(Me_3SiCH_2)_2InAs(SiMe_3)_2]_2 \longrightarrow 2(Me_3SiCH_2)_2InAs(SiMe_3)_2In(CH_2SiMe_3)_2Cl \quad (46)$$

Reaction of the mixed-bridge $(Me_3SiCH_2)_2\overline{InP(SiMe_3)_2\text{-}In(CH_2SiMe_3)_2Cl}$ species with $LiAs(SiMe_3)_2$ gives the adduct $(Me_3SiCH_2)_3In{\cdot}As(SiMe_3)_3$.[111] This adduct can also be prepared from the direct reaction of $(Me_3Si)_3As$ and $In(CH_2SiMe_3)_3$.[111] Similarly, $(Me_3CCH_2)_3In{\cdot}As(SiMe_3)_3$ forms from the 1:1 mol ratio reaction of $(Me_3Si)_3As$ and $In(CH_2CMe_3)_3$.[150] When Me_3SiAsH_2 reacts with $Et_3In{\cdot}PR_2$ ($R = Et$, i-Pr), $[Et_2InAs(SiMe_3)_2]_2$ results.[146] $(t\text{-}Bu_2As)_3In$ has been synthesized from the reaction of $(t\text{-}Bu)_2AsLi$ with $InCl_3$ at −78 °C.[65] Equilibration of $[(Me_3SiCH_2)_2InP(SiMe_3)_2]_2$ with $[(Me_3SiCH_2)_2InAs(SiMe_3)_2]_2$ in a 1:1 mol ratio yields $(Me_3SiCH_2)InAs(SiMe_3)_2In(CH_2SiMe_3)_2P(SiMe_{32})_2$, which has a four-membered planar (InAsInP) ring.[151] Et_3In reacts with $H_2AsSi(i\text{-}Pr)_3$ to yield the $[EtInAsSi(i\text{-}Pr)_3]_4$, which exhibits a heterocubane structure.[147] Other In–As cage type compounds have resulted by reacting $MesInCl_2$ and $InCl_3$ with the dilithium arsenide, $(BuAsLi)_2(t\text{-}Bu)$, in a 4:2:4 mol ratio to produce $(MesInCl)_4(InCl)_2[As(t\text{-}Bu)]_4$. Using Me_2InCl and $MeInCl$ with $(BuAsLi)_2(t\text{-}Bu)$ in a 6:2:6 ratio, $[Li(THF)_4]_2[(MesInCl)_6(InCl)_2[(AsBu)(t\text{-}Bu)]_6]$ is isolated.[149]

An X-ray diffraction study indicates that $[Me_2AsInMe_2]_3$ contains two independent molecules per asymmetric unit in the solid state,[152] one with a planar $(AsIn)_3$ ring while the other is puckered. However, a dynamic ^1H NMR study indicates equivalence of the indium methyls and of the arsenic methyls in solution down to −80 °C. $[(t\text{-}Bu)_2AsInMe_2]_2$[65,119] is dimeric by X-ray and mass spectral studies and the $(AsIn)_2$ core is planar.

The $(AsIn)_2$ ring is slightly puckered in $[(Me_3Si)_2AsInPh_2]_2$,[145] whereas the $(PIn)_2$ core in $[(Me_3Si)_2PInPh_2]_2$ is planar in the solid state. Both the $(AsIn)_2$ ring of $[(Me_3Si)_2AsIn(CH_2SiMe_3)_2]_2$ and the In–As–In–Cl ring of $(Me_3SiCH_2)_2\overline{InAs(SiMe_3)_2In(CH_2SiMe_3)_2Cl}$ are planar by single-crystal X-ray diffraction studies.[144]

6 ORGANOARSENIC COMPOUNDS CONTAINING As–GROUP 14 BONDS

6.1 As–Si Bonded Compounds

Several references review the chemistry associated with organoarsines that contain the As–Si bond.[7,9–11,16,122,141,153,154] Silylation of the alkali metal organoarsenide leads to salt elimination and the formation of the silylarsines (equations 47–49).

$$Na_3As + 3Me_3SiCl \longrightarrow (Me_3Si)_3As + 3NaCl \quad (47)$$

$$Me_2SiCl_2 + 2Me_2AsLi \longrightarrow Me_2Si(AsMe_2)_2 + 2LiCl \quad (48)$$

$$Me_2SiCl_2 + 2(Me_3Si)_2AsLi{\bullet}2THF \longrightarrow [(Me_3Si)_2As]_2SiMe_2 + 2LiCl + 4THF \quad (49)$$

The reaction of $LiAs(H)Me$ with Me_3SiCl at low temperature produces the unstable $Me_3SiAs(H)Me$, which decomposes with loss of $MeAsH_2$ to $(Me_3Si)_2AsH$. With Me_2SiCl_2, both $Me_2Si(AsHMe)_2$ and $(Me_2SiAsMe)_4$ form. When $ClSi(Me)_2SiMe_3$ and $ClSiMe(SiMe_3)_2$ react with Na_3As/K_3As in DME, the silicon-rich $As[Si(Me)_2SiMe_3]_3$ and $As[SiMe(SiMe_3)_2]_3$ are obtained respectively.[155]

The silylarsines readily undergo cleavage and insertion reactions and are quite useful in the synthesis of As–B, As–Al, As–Ga, As–Ge, and As–Sn bonded compounds and transition-metal[156] complexes. The reaction of BF_3 with $Me_3SiAsMe_2$ at −50 °C gives a quantitative yield of $(Me_2As)_2BF$ and Me_3SiF. With MeI, cleavage of the Si–As bond occurs with a dehalosilylation reaction that gives alkylation on the arsenic (equation 50). Hydrolysis produces the arsine and silyl ether (equation 51), and $SiCl_4$ cleaves the As–Si bond to give a Cl_3Si derivative (equation 52). $Me_3SiAsMe_2$ has been used for fluorine substitution with an $AsMe_2$ group in polyfluoroarenes and C_5NF_5.[157]

$$Me_3SiAsMe_2 + MeI \longrightarrow Me_3As + Me_3SiI \quad (50)$$

$$2Me_3SiAsMe_2 + H_2O \longrightarrow 2Me_2AsH + (Me_3Si)_2O \quad (51)$$

$$Me_3SiAsMe_2 + SiCl_4 \longrightarrow Me_2AsSiCl_3 + Me_3SiCl \quad (52)$$

The importance of the silylarsines in the synthesis of arsinoalanes and arsinogallanes has been discussed in Section 5. Their use in synthesizing germyl- and stannylarsines is discussed below.

6.2 As–Ge Bonded Compounds

Relatively few germylarsines are known. They are usually prepared from the respective silylarsine by a salt elimination or dehalosilylation reaction (equations 53–55).[11,16,158] Cleavage of the Ge–N bond with a secondary arsine also leads to the formation of germylarsines (equation 56).[158] Oxidation of the germylarsines with oxygen leads to the respective metal arsinates, $R_3Ge–O–As(O)R'_2$.

$$Me_3GeCl + LiAsMe_2 \longrightarrow Me_3GeAsMe_2 + LiCl \quad (53)$$

$$Me_2As(CH_2)_2GeCl + Me_3SiAsMe_2 \longrightarrow Me_2As(CH_2)_2GeAsMe_2 + Me_3SiCl \quad (54)$$

$$Me_3GeCl + (t\text{-}Bu)_2AsSiMe_3 \longrightarrow Me_3GeAs(t\text{-}Bu)_2 + Me_3SiCl \quad (55)$$

$$Me_2NGe(CH{=}CH_2)Me_2 + Me_2AsH \longrightarrow Me_2AsGe(CH{=}CH_2)Me_2 + Me_2NH \quad (56)$$

6.3 As–Sn Bonded Compounds

The substantial number of known stannylarsines has been generally synthesized by the salt elimination or amine elimination reactions (equations 57–59).[11,16,61,159,160,161] Dehydrohalogenation in the presence of triethylamine is a convenient route to the stannylarsines (equation 60), and dehalosilylation has also been used to synthesize $(Me_3Sn)_3As$ (equation 61).

$$Et_2SnCl_2 + 2NaAsPh_2 \longrightarrow Et_2Sn(AsPh_2)_2 + 2NaCl \quad (57)$$

$$Ph_3SnLi + ClAsPh_2 \longrightarrow Ph_3SnAsPh_2 + LiCl \quad (58)$$

$$Me_3SnNMe_2 + Ph_2AsH \longrightarrow Me_3SnAsPh_2 + Me_2NH \quad (59)$$

$$Me_3SnCl + Me_2AsH + Et_3N \longrightarrow Me_3SnAsMe_2 + [Et_3NH]^+Cl^- \quad (60)$$

$$(Me_3Si)_3As + 3Me_3SnCl \longrightarrow (Me_3Sn)_3As + 3Me_3SiCl \quad (61)$$

Pyramidal geometry at arsenic has been inferred in $(Me_3Sn)_3As$ from vibrational data, in comparison with planar geometry at N in $(Me_3Sn)_3N$.[5,11] Because the stannylarsines are not sensitive toward hydrolysis, they can be prepared in aqueous oxygen-free solution. In the presence of oxygen, they are oxidized to the stannylarsinates, $R_3Sn–O–As(O)R'_2$. Methyl iodide cleaves the Sn–As bond and gives the respective tin iodide and arsonium iodide. Phenyl azide reacts with the mono- and bisstannylarsines to give the respective tin-substituted aminoiminoarsines (equation 62).

$$Ph_3SnAsPh_2 + 2PhN_3 \longrightarrow Ph_3Sn(NPh)As({=}NPh)Ph_2 + 2N_2 \quad (62)$$

6.4 As–Pb Bonded Compounds

The few known plumbylarsines have been prepared by the reaction of the organolead halide with the sodium arsenide in liquid ammonia (equation 63).[61]

$$Ph_3PbCl + NaAsPh_2 \longrightarrow Ph_3PbAsPh_2 + NaCl \quad (63)$$

7 ORGANOARSENIC COMPOUNDS CONTAINING As–GROUP 15 BONDS

7.1 As–N Bonded Compounds

7.1.1 Tricoordinate Arsenic

There have been several reviews that provide a comprehensive coverage of the synthesis and reactivity of organoarsenic compounds that contain tricoordinate arsenic with an As–N bond.[4,7,9–14,31,162–164] The acyclic aminoarsines, $R_nAs(NR'_2)_{3-n}$, are routinely synthesized by the aminolysis of a haloarsine or transamination of another aminoarsine (equations 64–68).

$$AsCl_3 + 6HNMe_2 \longrightarrow As(NMe_2)_3 + 3[Me_2NH_2]^+Cl^- \quad (64)$$

$$MeAsI_2 + 4HNPr_2 \longrightarrow MeAs(NPr_2)_2 + 2[Pr_2NH_2]^+I^- \quad (65)$$

$$AsCl_3 + 2HNEt_2 \longrightarrow Et_2NAsCl_2 + [Et_2NH_2]^+Cl^- \quad (66)$$

$$Me_2AsNMe_2 + HNPr_2 \longrightarrow Me_2AsNPr_2 + Me_2NH \quad (67)$$

$$PhAs(NMe_2)_2 + 2HNEt_2 \longrightarrow PhAs(NEt_2)_2 + 2Me_2NH \quad (68)$$

The association of the amine hydrochloride with the aminoarsine complicates the purification of the aminoarsine. When aminolysis of the arsenic trihalide is followed by alkylation of the mono- or bisaminohaloarsine with a Grignard reagent to synthesize the aminoalkyl(or aryl)arsine, the stoichiometry of the reaction must be carefully controlled to avoid cleavage of the As–N bond and formation of the tertiary arsine (see Section 2.1).[27] A recent study has shown that the highest yields are obtained from the transamination reaction when the reactant aminoarsine is mixed neat with the desired secondary amine in the exact mole ratio for complete substitution.[165] Transamination becomes less effective as the steric bulkiness of the amine increases.

Although both aminolysis and salt elimination reactions can be used to give cyclic aminoarsines, aminolysis with a diamine is the best route (equation 69). Transamination of $As(NMe_2)_3$ with a symmetrical hydrazine provides a synthetic route to a caged species (equation 70). Cleavage of the heterocyclic N–P–N bond with $AsCl_3$ yields the cage compound $As[MeNCH_2CH_2NMe]_3As$ (equation 71).

$$2HN(Me)CH_2CH_2N(Me)H + AsCl_3 \longrightarrow (H_2C\text{–}NMe)_2AsCl + [H_2N(Me)CH_2]_2Cl_2 \qquad (69)$$

$$3HN(Me)N(Me)H + 2As(NMe_2)_3 \longrightarrow As[N(Me)N(Me)]_3As + 6Me_2NH \qquad (70)$$

$$3MeNCH_2CH_2N(Me)PMe + 2AsCl_3 \longrightarrow As(MeNCH_2CH_2NMe)_3As + 3MePCl_2 \qquad (71)$$

Although salt elimination is another synthetic route to aminoarsines,[166] it has not found wide use. It has been used to synthesize silicon-substituted aminoarsines (equation 72). Dehalosilylation has been used to prepare a few aminoarsines, including bis- and tris-arsinoamines (equations 73 and 74). AsF_3 reacts with Me_3SnNMe_2 to cleave the Sn–N bond and produce $As(NMe_2)_3$ (equation 75). Perfluoromethyl-substituted aminoarsines have been prepared by the reaction of $(CF_3)_2NX$ ($X = Cl, Br$) and $(CF_3)_2NON(CF_3)_2$ with $(CF_3)_3As$ (equation 76).

$$O(SiMe_2NMeLi)_2 + AsCl_3 \longrightarrow O(SiMe_2NMe)_2AsCl + 2LiCl \qquad (72)$$

$$Et_2NSiMe_3 + AsCl_3 \longrightarrow Et_2NAsCl_2 + Me_3SiCl \qquad (73)$$

$$(Me_3Si)_2NH + 3Me_2AsCl \longrightarrow (Me_2As)_3N + 2Me_3SiCl + HCl \qquad (74)$$

$$3Me_3SnNMe_2 + AsF_3 \longrightarrow As(NMe_2)_3 + 3Me_3SnF \qquad (75)$$

$$(CF_3)_3As + (CF_3)_2NX \longrightarrow (CF_3)_2AsN(CF_3)_2 + CF_3X \qquad (76)$$

Sodium amide cleaves the As–O bond in the arsoxane $Me_2AsOAsMe_2$ to give the trisarsinoamine $(Me_2As)_3N$. The analogous ethyl derivative can be synthesized by the ammonolysis of Et_2AsCl. As the steric bulk of the alkyl group increases, ammonolysis does not lead directly to the trisarsinoamine (equations 77 and 78). Generally, the bisarsinoamines can be prepared by the aminolysis of the dialkylhaloarsine with a primary amine (equation 79).

$$Bu_2AsCl + 2NH_3 \longrightarrow Bu_2AsNH_2 + NH_4Cl \qquad (77)$$

$$2Bu_2AsNH_2 \xrightarrow{\Delta} (Bu_2As)_2NH + NH_3 \qquad (78)$$

$$2Me_2AsCl + 3EtNH_2 \longrightarrow (Me_2As)_2NEt + 2[EtNH_3]^+Cl^- \qquad (79)$$

Both aminolysis and transamination reactions that involve primary amines and AsX_3 ($X =$ halogen) or dihaloarsines lead to the formation of cyclic or cage compounds that contain an As–N bonded core. The bulkiness of the amine substituent and reaction stoichiometry determine the nature of the cyclic or cage As–N core. For example, reaction of $PhNH_2$ with AsI_3 in a 4:1 mol ratio yields $As(HNPh)_2I$, which decomposes with cyclization to an As–N tetrameric core, $[IAs\text{–}NPh]_4$ (equations 80 and 81).

$$4PhNH_2 + AsI_3 \longrightarrow As(HNPh)_2I + 2[PhNH_3]^+I^- \qquad (80)$$

$$4As(HNPh)_2I \longrightarrow [IAs\text{–}NPh]_4 + 4PhNH_2 \qquad (81)$$

When the reaction is carried out in an excess of the amine, the fully aminated adamantane-type compound, $As_4(NPh)_6$, forms. This compound and its alkyl-substituted homologs are easily formed by transaminating $As(NMe_2)_3$ or $As_4(NPh)_6$ with an excess of the respective primary amine (equations 82 and 83).

$$6BuNH_2 + 4As(NMe_2)_3 \longrightarrow As_4(NBu)_6 + 12Me_2NH \qquad (82)$$

$$6BuNH_2 + As_4(NMe)_6 \longrightarrow As_4(NBu)_6 + 6MeNH_2 \qquad (83)$$

When the transamination with $As(NMe_2)_3$ is carried out in a 1:1 mol ratio, the cyclic compound $[Me_2NAs\text{–}NBu]_2$ forms. This compound disproportionates upon heating to give $As_4(NBu)_6$ and $As(NMe_2)_3$. As the bulkiness of the amine substituent increases, the cyclic As–N ring is favored over the adamantane cage structure. For example, with t-$BuNH_2$, aminolysis yields the dimer $[t\text{-}BuN(H)As\text{–}N\text{-}t\text{-}Bu]_2$. The reaction of AsF_3 with $(Me_3Si)_2NLi$ in a 1:2 mol ratio gives $[(Me_3Si)_2N]_2AsF$, which upon heating undergoes dehalosilylation and yields the dimeric $[(Me_3Si)_2As\text{–}NSiMe_3]_2$.

Ammonolysis of methyldichloroarsine provides a route to a cyclic As–N compound that contains a N–H bond (equation 84). On the other hand, ammonolysis of $PhAsCl_2$ yields the bicyclic species $(PhAs)_6N_3(NH)_3$. This involves a trigonal prismatic arrangement of arsenic atoms and a trigonal bipyramidal arrangement of nitrogen atoms.[14] Dehalosilylation has also been used to prepare the cyclic As–N species (equation 85). The reaction of $AsCl_3$ with $Me_3SiN(t\text{-}Bu)Cl$ produces the dimeric $[ClAs\text{–}N\text{-}t\text{-}Bu]_2$. Arsenic-containing disulfonylamine derivatives have been prepared using $MeAsCl_2$, $PhAsCl_2$, and Me_2AsCl in a salt elimination reaction with $AgN(SO_2Me)_2$.[167]

$$18NH_3 + 6MeAsCl_2 \longrightarrow [MeAs\text{–}NH]_6 + 12NH_4Cl \qquad (84)$$

$$3AsCl_3 + 3EtNHSiMe_3 \longrightarrow [ClAs\text{–}NEt]_3 + 3Me_3SiCl + 3HCl \qquad (85)$$

The As–N bond is very reactive toward moisture and air and is easily cleaved by protonic acids, alcohols, thiols, water, ketones, aldehydes, and carboxylic acids (equations 86–89).[13,162,163] The reader is referred to these reviews for details and references to the original literature. Thus, aminoarsines are used as multipurpose precursors to numerous other organoarsenic compounds that are otherwise difficult to prepare (see Section 2).[162,163]

$$\mathrm{MeAs(NMe_2)_2 + 4HCl \longrightarrow MeAsCl_2 + 2[Me_2NH_2]^+Cl^-} \quad (86)$$

$$\mathrm{2Et_2AsNMe_2 + H_2O \longrightarrow (Et_2As)_2O + 2Me_2NH} \quad (87)$$

$$\mathrm{Me_2AsNEt_2 + EtOH \longrightarrow Me_2AsOEt + Et_2NH} \quad (88)$$

$$\mathrm{2As(NMe_2)_3 + 3EtCH_2CHO \longrightarrow As_2O_3 + 3Me_2NH + 3Me_2NCH{=}CHEt} \quad (89)$$

Several studies have been conducted on the reactivity of diborane, $\mathrm{BH_3{\cdot}THF}$, μ-$\mathrm{Me_2NB_2H_5}$, and aluminum alkyls toward aminoarsines.[19,20,63,82,84,168,169] These reactions have been followed using multinuclear NMR to establish bonding site in the adducts and deduce the reaction pathway to the thermodynamic stable products. With the series $\mathrm{Me_2AsNR_2}$ (R = Me, Et, Pr, *i*-Pr), the $\mathrm{BH_3}$ binding site is dependent upon the bulkiness of the R group. Increasing bulkiness favors binding on the arsenic atom. Whereas, at low temperature, exclusive N–B binding occurs when R = Me, both As–B and N–B binding is observed with Et and Pr derivatives, and only As–B binding arises when R = *i*-Pr (equation 90).

$$\mathrm{2Me_2AsNEt_2 + 2BH_3{\bullet}THF \longrightarrow Me_2As({\bullet}BH_3)NEt_2 + Me_2AsN({\bullet}BH_3)Et_2 + 2THF} \quad (90)$$

With increasing temperature the As–B adducts convert to the N–B adduct, except for the *i*-Pr compound, which is stable at room temperature, and decomposition leads to the formation of $\mathrm{Me_2AsAsMe_2}$, $\mathrm{Me_2AsH}$, $\mathrm{[R_2NBH_2]_2}$, and $\mathrm{R_2NH{\cdot}BH_3}$. The results from the aluminum alkyl reactions have been used to develop new syntheses to tertiary arsines (see Section 2).

$\mathrm{Me_{3-\mathit{n}}As(NMe_2)_\mathit{n}}$ reacts with $\mathrm{R_2PPR_2}$ (R = Me, Et, Ph) to give the respective aminophosphine and $\mathrm{Me_2AsPR_2}$, which further reacts to give $\mathrm{Me_2AsAsMe_2}$.[170] With $\mathrm{(MeP)_5}$ the reaction yields $\mathrm{MeP(NMe_2)_2}$, $\mathrm{Me_2AsAsMe_2}$, $\mathrm{(MeAs)_5}$, and elemental arsenic. Aminoarsines also react with diarsines to generate unsymmetric diarsines, which undergo symmetrization.[171] The unsymmetric diarsines are also formed from the reaction of aminoarsines with secondary arsines, $\mathrm{R_2AsH}$,[172] while cyclopolyarsines form in the reactions with primary arsines, $\mathrm{RAsH_2}$.[56]

7.1.2 Tetracoordinate Arsenic

Typical tetracoordinate arsenic compounds that contain an As–N bond are the aminoarsonium salts, the arsazenes, and the arsinimines.[4,7,11,12,31,162] The aminoarsonium chlorides are synthesized by the reaction of tertiary arsines with the following chloramines: $\mathrm{NH_2Cl}$, $\mathrm{MeN(H)Cl}$, and $\mathrm{Me_2NCl}$ (equations 91 and 92).[30,31]

$$\mathrm{Et_3As + NH_2Cl \longrightarrow [Et_3AsNH_2]Cl} \quad (91)$$

$$\mathrm{Pr_3As + Me_2NCl \longrightarrow [Pr_3AsNMe_2]Cl} \quad (92)$$

Heating $\mathrm{Ph_2AsN_3}$, which is synthesized from the reaction of $\mathrm{Ph_2AsCl}$ with lithium azide, leads to the tetrameric arsazene $\mathrm{[Ph_2AsN]_4}$ (equation 93). Pyrolysis of the dialkylarsine azides does not yield an As–N bonded product. The tetrameric $\mathrm{[Ph_2AsN]_4}$ can also be obtained by the reaction of $\mathrm{Ph_2AsCl_3}$ with $\mathrm{NH_4Cl}$ in liquid ammonia (equation 94) or from the conversion of the trimeric $\mathrm{[Ph_2AsN]_3}$ that occurs in hot acetonitrile (equation 95). This trimer forms from the high-pressure, room-temperature ammonolysis of $\mathrm{Ph_2AsCl_3}$ (equation 96), or the chloramination of $\mathrm{Ph_2AsCl}$ in the presence of $\mathrm{NH_3}$ (equation 97). Treating $\mathrm{As(OMe)_5}$ with ammonia in methanol gives $\mathrm{NH_4[As(OMe)_6]}$, which loses methanol in vacuo to give material that is primarily $\mathrm{[AsN(OMe)_2]_3}$, but also contains the tetramer, pentamer, and hexamer.

$$\mathrm{4Ph_2AsN_3 \longrightarrow [Ph_2AsN]_4 + 4N_2} \quad (93)$$

$$\mathrm{4Ph_2AsCl_3 + 4NH_4Cl \longrightarrow [Ph_2AsN]_4 + 16HCl} \quad (94)$$

$$\mathrm{4[Ph_2AsN]_3 \longrightarrow 3[Ph_2AsN]_4} \quad (95)$$

$$\mathrm{3Ph_2AsCl + 6NH_3 \longrightarrow [Ph_2AsN]_3 + 3NH_4Cl + 3H_2} \quad (96)$$

$$\mathrm{3Ph_2AsCl + 6NH_3 + 3NH_2Cl \longrightarrow [Ph_2As(NH_2){=}N{-}As(NH_2)Ph_2]Cl \xrightarrow{\Delta} [Ph_2AsN]_3 + 6NH_4Cl} \quad (97)$$

Dehydrochlorination of the aminoarsonium chloride $\mathrm{[Ph_3AsNH_2]Cl}$ with sodium amide in liquid ammonia produces the triphenylarsinimine $\mathrm{Ph_3As{=}NH}$. $(p\text{-}\mathrm{MeC_6H_4})_3\mathrm{As}$ reacts with $\mathrm{S_4N_4}$ at 50 °C to produce $(p\text{-}\mathrm{MeC_6H_4})_3\mathrm{As{=}NS_3N_3}$.[173] Treating $\mathrm{Ph_3As}$ with the azide $\mathrm{C_6F_5N_3}$ gives, upon heating, the arsinimine $\mathrm{Ph_3As{=}NC_6F_5}$. $\mathrm{Ph_3As{=}NSO_2R}$ species have been prepared from the reaction of $\mathrm{Ph_3As}$ with $\mathrm{PhI{=}NSO_2R}$.[174] Also, triphenylarsine oxide reacts with isocyanates to produce triphenylarsinimines.[175] $(o\text{-tolyl})_3\mathrm{B{=}NCOCCl_3}$ transfers the nitrenoid group to $\mathrm{Ph_3As}$ to yield $\mathrm{Ph_3As{=}NOCCl_3}$.[176] The arsinimines hydrolyze with addition of water across the As=N bond to give $\mathrm{R_3As(OH)N(H)R'}$. Methylation of the nitrogen atom occurs in the reaction with MeI to yield an arsonium salt (equation 98). The reaction between $\mathrm{Ph_3AsCl_2}$ and $\mathrm{(Me_3Si)_3N}$ produces $\mathrm{[Ph_3AsNAsPh_3]^+Cl^-}$ (equation 99),[177] which can also be prepared by heating $\mathrm{[Ph_3AsNH_2]Cl}$. A P–N–As bonded analog, $\mathrm{[Me_3PNAsMe_3]^+I^-}$, is synthesized by methylating the product of the reaction between $\mathrm{Me_3PNLi}$ and $\mathrm{Me_2AsCl}$ (equations 100 and 101).

$$\mathrm{R_3As{=}NSiMe_3 + MeI \longrightarrow [R_3AsN(Me)SiMe_3]I} \quad (98)$$

$$\mathrm{2Ph_3AsCl_2 + (Me_3Si)_3N \longrightarrow [Ph_3AsNAsPh_3]^+Cl^- + 3Me_3SiCl} \quad (99)$$

$$\mathrm{Me_3PNLi + Me_2AsCl \longrightarrow Me_3P{=}NAsMe_2 + LiCl} \quad (100)$$

$$\mathrm{Me_3P{=}NAsMe_2 + MeI \longrightarrow [Me_3PNAsMe_3]^+I^-} \quad (101)$$

An X-ray study of $\mathrm{(Ph_2AsN)_3}$ has shown that the six-membered ring is slightly puckered with all As–N distances equal. The ring in the phosphorus analog $\mathrm{(Ph_2PN)_3}$ is more nearly planar.[11] The corresponding tetramer, $(Ph_2AsN)_4$, has a nonplanar ring and is isostructural with $(Ph_2PN)_4$.[14] The As–N distances, in the trimer (1.758 Å) and the tetramer (1.73 Å), are shorter than the single bond value (1.87 Å). This suggests some degree of π-bonding in the oligomers. Other As–N ring systems have been reviewed.[14] The As–N bond distance in $[Ph_3AsNAsPh_3]^+Cl^-$ has been reported as 1.749 Å.[177]

Variable-temperature NMR has been employed to study barriers of rotation in As–N bonded compounds.[12,37] Both ^{13}C and ^1H NMR spectral data have been published for a homologous series of tertiary arsines, aminoarsines, and arsonium and aminoarsonium salts.[42] In addition, individual ^1H and ^{13}C NMR spectral data are available for individual aminoarsines.[20,30,84,165,169,171]

7.1.3 Pentacoordinate Arsenic

The general synthesis route to pentacoordinate arsenic compounds that contain an As–N bond is the aminolysis of a pentacoordinate oxyarsorane with a primary amine (equation 102).[13,31,45] With $PhNH_2$ in excess, polymeric pentacoordinate arsenic species are obtained. The chlorination of $(CF_3)_2AsN(SiMe_3)_2$ in a 1:1 mol ratio gives $(CF_3)_2As(Cl)_2N(SiMe_3)_2$, while an excess of Cl_2 produces $[(CF_3)_2As(Cl)NSiMe_3]_2$ via a dehalosilylation reaction. Several other pentacoordinate arsenic species have been prepared by specialized routes, which have been reviewed.[31,45]

$$2(MeO)_5As + 4H_2NPr \longrightarrow [(MeO)_2(PrNH)AsNPr]_2 + 6MeOH \qquad (102)$$

7.2 As–P Bonded Compounds

Both As–P and As=P bonded compounds have been prepared.[12,31,178–187] The earliest demonstrated routes to arsinophosphines were the exchange reactions involving $(CF_3P)_4$ and $Me_2AsAsMe_2$ to give $Me_2AsP(CF_3)AsMe_2$ and Me_2AsH and $(CF_3)_2PP(CF_3)_2$ to yield $(CF_3)_2PAsMe_2$. A quantitative yield of $(CF_3)_2PAsMe_2$ also results from the reaction of $(CF_3)_2PP(CF_3)_2$ with $Me_2AsAsMe_2$.[188] An analogous exchange reaction that includes $(CF_3)_2PP(CF_3)_2$ and $(CF_3)_2AsAs(CF_3)_2$ gives an equilibrium statistical distribution of reactants and $(CF_3)_2PAs(CF_3)_2$. An equilibrium distribution of reactants and products, with $K_{eq} = 0.37$ in benzene at 30 °C, occurs when Ph_2PPPh_2 and $Ph_2AsAsPh_2$ are mixed (equation 103).

$$Ph_2PPPh_2 + Ph_2AsAsPh_2 \rightleftharpoons 2Ph_2PAsPh_2 \qquad (103)$$

The reaction of Me_2AsNMe_2 with R_2PPR_2 (R = Me, Et, Ph) gives R_2PNMe_2 and R_2PAsMe_2, and the latter reacts further with Me_2AsNMe_2 to produce $Me_2AsAsMe_2$ and R_2PNMe_2.[170] Silane elimination occurs in the reaction of $Me_3SiAsMe_2$ with $(CF_3)_2PH$ to give $(CF_3)_2PAsMe_2$. Dehalosilylation also provides a pathway to arsinophosphines (equation 104).

$$2H_3SiPH_2 + F_3CAsI_2 \longrightarrow 2H_3SiI + F_3CAs(PH_2)_2 \qquad (104)$$

The direct reaction between a tertiary phosphine and a haloarsine yields an arsinophosphonium salt (equation 105).

$$Me_2AsCl + Et_3P \longrightarrow [Me_2AsPEt_3]Cl \qquad (105)$$

The introduction of sterically demanding substituents on P and As coupled with particular synthetic strategies has blocked oligomerization and permitted the preparation of P=As bond containing species, that is arsaphosphenes.[185] For example, base-promoted (DBU) condensation has provided a synthetic pathway to (2,4,6-t-$Bu_3C_6H_2$)P=AsCH$(SiMe_3)_2$ from (2,4,6-t-$Bu_3C_6H_2$)PH_2 and $(Me_3Si)_2C(H)AsCl_2$.[186] Similarly the analogous (2,4,6-t-$Bu_3C_6H_2$)As=PCH$(SiMe_3)_2$ has been synthesized, in addition to MesP=AsCH$(SiMe_3)_2$, MesAs=PCH$(SiMe_3)_2$, and MesAs=PCp*. MesP=AsC_6H_3-2,6-Trip$_2$ (Trip = 2,4,6-i-Pr_3) forms in the direct reaction of $MesPLi_2$ and 2,6-Trip$_2H_3C_6AsCl_2$.[187] A t-BuLi reductive coupling reaction between $(Me_3Si)_3CAsCl_2$ and $(Me_3Si)_3CPCl_2$ gives $(Me_3Si)_3CAs{=}PC(SiMe_3)_3$. Two pathways have been developed to (2,4,6-t-$Bu_3C_6H_2$)P=AsCp* that use either dehydrochlorination or dehalosilylation (equations 106 and 107).[179]

$$Cp^*AsCl_2 + (2,4,6\text{-}t\text{-}Bu_3C_6H_2)PHLi + DBU \longrightarrow (2,4,6\text{-}t\text{-}Bu_3C_6H_2)P{=}AsCp^* + LiCl + DBU{\cdot}HCl \qquad (106)$$

$$Cp^*AsCl_2 + (2,4,6\text{-}t\text{-}Bu_3C_6H_2)P(SiMe_3)Li \longrightarrow (2,4,6\text{-}t\text{-}Bu_3C_6H_2)P{=}AsCp^* + LiCl + Me_3SiCl \qquad (107)$$

All the P–As and P=As bonded compounds are sensitive to hydrolysis and to oxidation by air. The reaction of Cp*As=PMes with diazomethane adds a CH_2 group across the double bond and yields the three-membered heterocyclic phosphaarsirane Cp*AsCH_2PMes.[184] Sulfur and selenium add across the double bond to form three-membered heterocycles.[186] Dimerization of Cp*As=PCp* produces two isomeric diphosphadiarsetanes, one containing the P–P–As–As and the other the P–As–P–As core. Photolysis of Cp*As=PMes, Cp*P=AsMes, and (2,4,6-t-$Bu_3C_6H_2$)P=AsCp* yields the diarsadiphosphacyclobutanes.[183,186] Metal complexes of several of the P=As compounds have been prepared and characterized.[189]

^{31}P NMR chemical shift data have been used extensively to confirm double bond formation in phosphaarsenes and diphosphenes.[178,186] The ^{31}P chemical shift range for these compounds is typically from +500 to +700 ppm (85% H_3PO_4). The shifts are among the lowest known in ^{31}P NMR. ^{31}P NMR chemical shifts for phosphinoarsines are similar to those for diphosphines and aminophosphines.[170,179,188]

From X-ray crystallographic studies, the observed distances for P=P, P=As, and As=As (see Section 7.3) bonds are 2.0, 2.1, and 2.2 Å respectively.[178,181,186] In general, the compounds adopt a trans configuration and the R–E=E′–R′ skeleton is planar. Normal P–As and As–As single bond distances are assumed to be 2.34 and 2.44 Å respectively. However, the P–As and As–As distances are 2.35 and 2.38 Å in $[2,4,6\text{-}t\text{-Bu}_3C_6H_2PAs]_2$.[183]

7.3 As–As Bonded Compounds

The As–As bonded diarsines and cyclopolyarsines have been extensively reviewed.[4–7,9–12,14,54] The first synthesized organometallic compound was $Me_2AsAsMe_2$, which was prepared by heating As_2O_3 with $KC_2H_3O_2$. This compound and other symmetric or unsymmetric diarsines can be readily obtained by the reduction of the corresponding arsinic acid, RR′As(O)OH, or diarsoxane, RR′AsOAsRR′, with hypophosphorous acid in HCl or HI solution. Reaction of the diarsoxane or a monohaloarsine with a secondary arsine gives the diarsines (equations 108 and 109). When the substituents on the haloarsine and the secondary arsine are dissimilar, two different symmetric diarsines are formed (equation 110). This is a consequence of the exchange reactions that readily occur in mixtures of As–As bonded species.

$$(Ph_2As)_2O + 2Ph_2AsH \longrightarrow 2Ph_2AsAsPh_2 + H_2O \qquad (108)$$

$$Me_2AsCl + Me_2AsH \longrightarrow Me_2AsAsMe_2 + HCl \qquad (109)$$

$$2Ph(CF_3)AsCl + 2(CF_3)_2AsH \longrightarrow Ph(CF_3)AsAs(CF_3)Ph + (CF_3)_2AsAs(CF_2)_2 + 2HCl \qquad (110)$$

The salt elimination reaction has also been used as a route to diarsines. Reductive coupling of a monohaloarsine with Hg or Zn gives diarsines. Oxidation of Me_2AsH and Ph_2AsH with Cl_2, NH_2Cl, or Me_2NCl gives good yields of $Me_2AsAsMe_2$ and $Ph_2AsAsPh_2$ respectively (equation 111). $Ph_2AsAsPh_2$ can also be prepared from the oxidation of $Ph_2AsMgBr$ with I_2, $HgCl_2$, Ph_2CCl_2, and Ph_2CHBr (equation 112). Reductive coupling occurs in the reaction of Ph_2AsCl with Bu_3P (equation 113).

$$2Me_2AsH + NH_2Cl \longrightarrow Me_2AsAsMe_2 + NH_4Cl \qquad (111)$$

$$2Ph_2AsMgBr + HgCl_2 \longrightarrow Ph_2AsAsPh_2 + 2MgClBr + Hg \qquad (112)$$

$$2Ph_2AsCl + Bu_3P \longrightarrow Ph_2AsAsPh_2 + Bu_3PCl_2 \qquad (113)$$

$Mes_2AsAsMes_2$ has been prepared from the reaction of $Fe[N(SiMe_3)_2]_2$ with $HAsMes_2$.[190] $Me_2AsAsMe_2$ can also be obtained from the reaction of Me_2AsH with Me_2AsNMe_2 or $Me_2AsNMe_2{\cdot}BH_3$ (equation 114).[59] The polyarsines $(Ph_2As)_3As$ and $(Ph_2As)_2AsPh$ are obtained by reacting Ph_2AsI with the respective stannylarsine (equation 115).[54]

$$Me_2AsH + Me_2AsNMe_2 \longrightarrow Me_2AsAsMe_2 + Me_2NH \qquad (114)$$

$$(Ph_3Sn)_2AsPh + 2Ph_2AsI \longrightarrow (Ph_2As)_2AsPh + 2Ph_3SnI \qquad (115)$$

Very few asymmetric substituted diarsines are known. $Cp^*(CH_3)AsAs(CH_3)Cp^*$ has been prepared in high yield by reacting MeLi with $Cp^*(Cl)AsAs(Cl)Cp^*$. The latter is obtained in high yield from the reductive coupling of Cp^*AsCl_2 with cobaltocene in hexane.[191]

Most of the synthetic pathways to the cyclopolyarsines $(RAs)_n$, where $n = 3{-}6$, are analogous to those to the diarsines. For example, the reduction of arsonic acids, arsonous acids, and organodihaloarsines with hypophosphorous acids has been widely used. Primary arsines can also be oxidized by aromatic or aliphatic aldehydes, I_2, Cl_2, SO_2Cl_2, NH_2Cl, and Me_2NCl. The salt elimination reaction has been used in the low-temperature (−78 °C) synthesis of $(t\text{-BuAs})_3$, which converts to $(t\text{-BuAs})_4$ at room temperature (equations 116 and 117). The methyl and ethyl pentamer derivatives have been prepared in good yields by the reaction of the primary arsines with dibenzylmercury.

$$t\text{-BuAs(K)As(K)-}t\text{-Bu} + t\text{-BuAsCl}_2 \longrightarrow (t\text{-BuAs})_3 + 2KCl \qquad (116)$$

$$4(t\text{-BuAs})_3 \longrightarrow 3(t\text{-BuAs})_4 \qquad (117)$$

Reductive coupling of dihaloarsines with Na and Hg provides another pathway to several cyclopolyarsines. $(Me_3SiCH_2As)_5$ has been prepared from the reduction of $Me_3SiCH_2AsCl_2$ with Mg turnings.[49] Using Mg, Ca, Zn, Li, or $CoCp_2$ in THF as the reducing agents toward $t\text{-BuAsI}_2$ promotes reductive coupling and gives high yields of $(t\text{-BuAs})_4$. With $CoCp_2$ in a 1:1 mol ratio in n-pentane, the reduced species is $(t\text{-BuAsI})_2$.[192]

When primary arsines are reacted with $(MeAs)_5$, the respective cyclopolyarsine $(RAs)_n$ is prepared in high yield (equation 118).[57,58] Also the reaction of primary arsines with aminoarsines[56] and diarsines[55] generates cyclopolyarsines.

$$n\ RAsH_2 + \frac{n}{5}(MeAs)_5 \longrightarrow n\ MeAsH_2 + (RAs)_n \qquad (118)$$

$(MeAs)_5$ is the yellow form of polymethylarsine, $(MeAs)_n$. An involatile red form and a sublimable purple-black form also exist. The interconversion of these forms on heating is catalyzed by impurities.

The As–As bond in the di- and cyclopolyarsines is easily cleaved using $RAsH_2$, R_2AsH, Me_2AsNR_2, halogens, methyl iodide, alkali metals, oxygen, and unsaturated organic compounds. In some cases, these reactions provide pathways to arsenic-containing heterocycles. Reaction of the diarsines with moist air results in oxidation to the corresponding arsinic acid (equation 119) and with polyarsines to the arsonic acid (equation 120).

$$2Me_2AsAsMe_2 + 3O_2 + 2H_2O \longrightarrow 4Me_2As(O)OH \qquad (119)$$

$$(MeAs)_5 + 5O_2 + 5H_2O \longrightarrow 5MeAs(O)(OH)_2 \qquad (120)$$

With the halogens, As–As bonds are cleaved in the diarsine to produce the monohaloarsine and in the cyclopolyarsine to give the dihaloarsine. Sulfur and selenium react via an insertion reaction (equation 121). The reactions of primary and secondary arsines toward di- and cyclopolyarsines have been discussed in Section 3. Aminoarsines cleave the As–As bond in diarsines to yield unsymmetric diarsines, which undergo symmetrization (equations 122 and 123).[171]

$$15Se_8 + 24(MeAs)_5 \longrightarrow 40(MeAsSe)_3 \quad (121)$$

$$Me_2AsNMe_2 + Et_2AsAsEt_2 \longrightarrow Me_2AsAsEt_2 + Et_2AsNMe_2 \quad (122)$$

$$2Me_2AsAsEt_2 \longrightarrow Me_2AsAsMe_2 + Et_2AsAsEt_2 \quad (123)$$

By analogy with the phosphaarsenes, the bulky $(Me_3Si)_3C$ and Mes moities on arsenic facilitate the isolation of As=As species.[185,193] During the reductive coupling of $(Me_3Si)_3CPCl_2$ and $(Me_3Si)_3CAsCl_2$ with t-BuLi, the diarsene $(Me_3Si)_3CAs{=}AsC(SiMe_3)_3$ is formed.[186] This diarsene is also produced by the reductive coupling of $(Me_3Si)_3CAsCl_2$ with t-BuLi and in the reaction of $(Me_3Si)_3CAsCl_2$ with $Na_2Cr_2(CO)_{10}$. The bulky Mes substituent also prevents oligomerization and permits isolation of MesAs=AsMes (equation 124). The latter is also formed from the reaction of $Cp^*(CO)_2FeP(SiMe_3)_2$ and $MesAsCl_2$. The base-catalyzed condensation reaction yields an unsymmetric diarsene (equation 125).

$$2MesAsCl_2 + 2Mg \longrightarrow MesAs{=}AsMes + 2MgCl_2 \quad (124)$$

$$(Me_3Si)_2CH{-}AsCl_2 + H_2AsMes + 2DBU \longrightarrow (Me_2Si)_2CHAs{=}AsMes + 2HCl{\cdot}DBU \quad (125)$$

$2,6\text{-}(Mes)_2H_3C_6As{=}AsC_6H_32,6\text{-}(Mes)_2$ and $2,4,6\text{-}(i\text{-}Pr)_3H_2C_6As{=}AsC_6H_2\text{-}2,4,6\text{-}(i\text{-}Pr)_3$ were synthesized by reductive coupling with Mg of the corresponding dihaloarsines.[194] A salt elimination reaction involving $2,4,6\text{-}(t\text{-}Bu)_3C_6H_2AsF_2$ and $LiAsC_6H_2\text{-}2,4,6\text{-}(t\text{-}Bu)_3$ gives excellent yields of $2,4,6\text{-}(t\text{-}Bu)_3C_6H_2As{=}AsC_6H_2\text{-}2,4,6\text{-}(t\text{-}Bu)_3$.[195] Sulfur adds across the diarsene double bond to produce the three-membered heterocyclic thiadiarsiranes MesAs(S)AsMes and $(Me_3Si)_3C{-}As(S)AsC(SiMe_3)_3$. Diazomethane reacts with MesAs=AsMes to give the three-membered heterocyclic diarsirane $MesAs(CH_2)AsMes$.

The transition-metal chemistry and nature of the complexes formed with As–As bonded compounds has been reviewed.[196] The reader is referred to this comprehensive review for an overview of the nature of complexes that contain chains of coordinated R–As units, heterocyclic As–chalcogen rings, and unsubstituted arsenic atoms and for references to the primary literature. The limited transition-metal chemistry of the phosphaarsenes and diarsenes is also reviewed.[186]

Few diarsines have been structurally characterized. From X-ray data, crystalline tetramethyldiarsine exists in the trans form. However, Raman spectra of the liquid and electron diffraction and photoelectron spectroscopy data of the vapor indicate both gauche and trans forms present.[79] In the solid state, $Ph_2AsAsPh_2$ has an As–As bond length of 2.458 Å with the phenyl groups in a staggered conformation. $Mes_2AsAsMes_2$ possesses C_2 symmetry with the As–As distance being 2.472 Å.[190] $(C_6F_5)_4As_2$ is rotated 16.5° from a perfect trans conformation, while $(Me_3Si)_4As_2$ deviates significantly (54.3°) from a trans arrangement. In these two diarsines, the As–As bond distances are 2.479 and 2.458 Å, respectively.[34] Dynamic NMR spectroscopy has been used to study inversion processes of diarsines.[15]

Several X-ray diffraction studies of cyclopolyarsines, $(MeAs)_5$,[7,11,15] $(CF_3As)_4$, $(t\text{-}BuAs)_4$, $(Me_3SiCH_2As)_5$,[49] and $(PhAs)_6$, have been reported.[14] $(MeAs)_5$ has a puckered five-membered ring of arsenic atoms with a mean As–As distance of 2.428 Å. In contrast, the purple-black form of $(MeAs)_n$ has an unusual ladder-like structure in which the horizontal As–As distances are typical of single As–As bonds (2.4 Å), but the vertical distances are very long (2.9 Å).[11,197] In $(CF_3As)_4$, the four-membered ring is nonplanar with an As–As bond distance of 2.454 Å. $(Me_3SiCH_2As)_5$ has a solid-state conformation similar to $(MeAs)_5$.[49] In the hexamer $(PhAs)_6$, the ring is puckered (chair) and the average As–As distance is 2.459 Å. The ^1H NMR spectrum of $(MeAs)_5$ consists of three single resonances with relative intensities of 2:2:1.[11] However, in the solid state, all methyl groups are nonequivalent.[15] Variable-temperature NMR studies on this and other cyclopolyarsines have been performed.[14]

From these studies, two motional processes have been postulated, a low-energy pseudorotational motion and a higher-energy arsenic atom inversion process. Detailed equilibrium studies have been conducted involving ring, chain, and oligomeric forms of these species.[11,15,197]

8 ORGANOARSENIC COMPOUNDS CONTAINING As–O BONDS

The synthesis and reactivity of organoarsenic compounds that contain As–O bonds has been extensively reviewed.[4–7,9–11] Because of space limitations, the extensive chemistry associated with As–O bonded systems cannot be covered. Instead, the highlights of the chemistry will be presented here and the reader is referred to the reviews for the vast quantity of more detailed information. These highlights have been grouped according to the more common classes of As–O bonded compounds that serve as precursors to many of the compounds discussed in earlier sections of this review.

8.1 Arsonous Acids, Anhydrides, and Esters

These As–O bonded species are related by the fact that they contain arsenic in the +3 oxidation state and have one organo substituent bonded to the arsenic. The general formulas are as follows: arsonous acids, $RAs(OH)_2$; arsonous acid anhydrides, RAsO; arsonous acid esters, $RAs(OR')_2$.

The arsonous acids or acid anhydrides are obtained in the hydrolysis of dihalo-, dialkoxy-dicyano-, and bisaminoarsines. The nature of R usually determines whether the acid or the anhydride is formed. When R is aliphatic or aromatic, with an unsubstituted ring, the anhydride is the primary product (equation 126).

$$\mathrm{MeAs(NMe_2)_2 + H_2O \longrightarrow \frac{1}{\mathit{n}}(MeAsO)_{\mathit{n}} + 2Me_2NH} \qquad (126)$$

If R is aromatic with electron-withdrawing substituents, the acid is the major product. Because the anhydride is thought to be in equilibrium with the acid in solution, the separation conditions can determine whether the acid or anhydride is obtained. Because many dihaloarsines dissolve in water without appreciable hydrolysis, the addition of base is required to form the acid salt. Reduction of an arsonic acid, $RAsO(OH)_2$, in hydrochloric acid with SO_2 and I^- as a catalyst gives the anhydride (equation 127). The anhydride is also produced during the oxidation of cyclopolyarsines and primary arsines in the absence of water (equation 128).

$$\mathrm{MeAsO(OH)_2 + SO_2 \longrightarrow \frac{1}{\mathit{n}}(MeAsO)_{\mathit{n}} + H_2SO_4} \qquad (127)$$

$$\mathrm{\frac{\mathit{n}}{5}(MeAs)_5 + \frac{\mathit{n}}{2}O_2 \longrightarrow (MeAsO)_{\mathit{n}}} \qquad (128)$$

The arsonous esters are easily synthesized by the reaction of the dihaloarsines with alcohols or alkoxides. With alcohols, $CaCl_2$ must be present because the esters are very sensitive toward hydrolysis, which leads to the reformation of the anhydride (equation 129). The reaction of an alcohol with a bisaminoarsine leads to an arsonous ester (equation 130), as does the alcoholysis of the anhydride. Reaction of diols with bis(dimethylamino)alkylarsines leads to esters of macrocyclic arsinous acid.[198,199]

$$\mathrm{EtAsCl_2 + 2NaOMe \longrightarrow EtAs(OMe)_2 + 2NaCl} \qquad (129)$$

$$\mathrm{MeAs(NMe_2)_2 + 2PhOH \longrightarrow MeAs(OPh)_2 + 2Me_2NH} \qquad (130)$$

8.2 Arsinous Acids, Anhydrides, and Esters

These As–O bonded species are related by the fact that they contain arsenic in the +3 oxidation state and have two organo substituents bonded to the arsenic. The general formulas are as follows: arsinous acids, R_2AsOH; arsinous acid anhydrides or diarsoxanes, $(R_2As)_2O$; arsinous acid esters, R_2AsOR'. The arsinous acids and diarsoxanes can be prepared by the hydrolysis of the monohalo-, amino-, or alkoxyarsines or the base hydrolysis of diarsoxanes (equation 131).

$$\mathrm{(Ph_2As)_2O + H_2O \longrightarrow 2Ph_2AsOH} \qquad (131)$$

The diarsoxanes are formed in the base hydrolysis of aminoarsines and monohaloarsines (equation 132) and in the reaction of aluminum trialkyls or Grignard reagents with As_2O_3 (equation 133). $(Me_2As)_2O$ is also obtained, in addition to other products, upon heating a mixture of As_2O_3 and potassium acetate.

$$\mathrm{2Me_2AsNMe_2 + H_2O \longrightarrow (Me_2As)_2O + 2Me_2NH} \qquad (132)$$

$$\mathrm{(Me_3Al)_2 + As_2O_3 \longrightarrow (Me_2As)_2O + 2MeAlO} \qquad (133)$$

By analogy with the arsonous acid esters, the arsinous acid esters form in the reaction of monohaloarsines with sodium alkoxides (equation 134). The alcoholysis of the diarsoxanes in the presence of copper sulfate also produces arsonous acid esters.

$$\mathrm{Et_2AsCl + NaOPh \longrightarrow Et_2AsOPh + NaCl} \qquad (134)$$

8.3 Arsonic and Arsinic Acids

These As–O bonded species are related by the fact that they contain arsenic in the +5 oxidation state. The arsonic acids, $RAsO(OH)_2$, have one organo substituent bonded to the arsenic, while the arsinic acids, $R_2As(O)OH$, have two. The most common preparative methods involve isolating the sodium or potassium salt.

Historically, the Meyer reaction, which consists of alkylating metal arsenites with alkyl halides, is the most widely used preparative method for alkylarsonic acid salts (equation 135). Subsequent alkylation of the alkylarsonic acid salt gives the alkylarsinic acid salt (equation 136). Excellent yields of alkylarylarsinic acid salts are obtained upon alkylating an arylarsonic acid salt. Aryl halides do not give satisfactory yields of the arylarsonic acid salts.

$$\mathrm{EtI + Na_3AsO_3 \longrightarrow EtAs(O)(ONa)_2 + NaI} \qquad (135)$$

$$\mathrm{EtI + EtAs(O)(ONa)_2 \longrightarrow Et_2As(O)(ONa) + NaI} \qquad (136)$$

The Bart reaction, which consists of reacting Na_3AsO_3 (sodium arsenite) with aromatic diazonium salts in buffered alkaline solution (pH = 8.8–9.2), provides an established route to the arylarsonic acids (equation 137). A useful variation consists of reacting the diazonium fluoroborates with $AsCl_3$ in a nonaqueous solvent and then hydrolyzing the products to produce a mixture of arylarsonic and diarylarsinic acids. Anhydrous conditions favor the arsonic acid, while the presence of water favors the arsinic acid.

$$\mathrm{RN_2{}^+X^- + Na_3AsO_3 \longrightarrow RAsO(ONa)_2 + N_2 + NaX} \qquad (137)$$

H_3AsO_4 arsonates phenyl ethers, phenols, and aromatic amines. The yields are usually low and arsonation occurs in the *para* position (equation 138).

$$\mathrm{C_6H_5OH + H_3AsO_4 \longrightarrow \mathit{p}\text{-}HOC_6H_4AsO(OH)_2 + H_2O} \qquad (138)$$

A useful route to dialkylarsinic acids involves the acid hydrolysis of aminoarsines (equation 139), followed by oxidization with H_2O_2 to give moderate to high yields of the acids (equation 140).

$$Et_2AsNEt_2 + H_2O + HCl \longrightarrow Et_2AsOH + [Et_2NH_2]^+ Cl^- \quad (139)$$

$$Et_2AsOH + H_2O_2 \longrightarrow Et_2As(O)OH + H_2O \quad (140)$$

8.4 Tertiary Arsine Oxides

Tertiary arsine oxides, R_3AsO, are known with alkyl and aryl substituents. The trialkylarsine oxides are prepared by the oxidation of the trialkylarsine using HgO or H_2O_2. For the triarylarsines, $KMnO_4$ and SeO_2 can also be used as oxidizing agents in synthesizing R_3AsO. These oxidizing agents cannot be used for the alkyl derivatives, because As–C bond cleavage occurs.

9 RELATED ARTICLES

Aluminum: Organometallic Chemistry; Bonding Energetics of Organometallic Compounds; Gallium: Organometallic Chemistry; Indium: Organometallic Chemistry; Mechanisms of Reaction of Organometallic Complexes.

10 REFERENCES

1. J. C. Cloyd, Jr and C. A. McAuliffe, in 'Transition Metal Complexes of Phosphorus, Arsenic and Antimony Ligands', ed. C. A. McAuliffe, John Wiley & Sons, New York, 1973, p. 202.
2. F. G. Mann, 'The Heterocyclic Derivatives of Phosphorus, Arsenic, Antimony and Bismuth', 2nd edn., John Wiley & Sons, London, 1970.
3. W. R. Cullen and K. J. Reimer, *Chem. Rev.*, 1989, **89**, 713.
4. I. Haiduc and J. J. Zuckerman, 'Basic Organometallic Chemistry', de Gruyter, Berlin, 1985, Chap. 9, p. 183.
5. J. D. Smith, 'The Chemistry of Arsenic, Antimony and Bismuth', Pergamon Press, Oxford, 1975, p. 622.
6. G. O. Doak and L. D. Freedman, 'Organometallic Compounds of Arsenic, Antimony, and Bismuth', John Wiley & Sons, New York, 1970.
7. W. R. Cullen, in 'Advances in Organometallic Chemistry', eds. F. G. A. Stone and R. West, Academic Press, New York, 1966, Vol. 4, p. 145.
8. G. E. Coates, M. L. H. Green, P. Powell, and K. Wade, 'Principles of Organometallic Chemistry', Methuen, London, 1968, p. 14.
9. M. Dub, 'Organometallic Compounds, Methods of Synthesis, Physical Constants and Chemical Reactions', 2nd edn., Springer-Verlag, New York, 1968, Vol. 3.
10. M. Dub, 'Organometallic Compounds, Methods of Synthesis, Physical Constants and Chemical Reactions', 2nd edn., First Supplement, Springer-Verlag, New York, 1972, Vol. 3.
11. B. J. Aylett, 'Organometallic Compounds. The Main Group Elements', 4th edn., Chapman & Hall, London, 1979, Vol. 1, Part 2, p. 387.
12. R. G. Cavell and A. R. Sanger, in 'MTP International Review of Science, Main Group Elements Groups V and VI', eds. C. C. Addison and D. B. Sowerby, Butterworths, London, 1972, Series 1, Vol. 2, p. 203.
13. L. K. Krannich, 'Compounds Containing As–N Bonds', John Wiley & Sons, New York, 1976.
14. I. Haiduc and D. B. Sowerby, 'The Chemistry of Inorganic Homo- and Heterocycles', Academic Press, London, 1987, Vol. 2, p. 701.
15. J. P. Crow and W. R. Cullen, in 'MTP International Review of Science, Organometallic Derivatives of the Main Group Elements', ed. B. J. Aylett, Butterworths, London, 1972, Series 1, Vol. 4, p. 355.
16. H. J. Breunig, in 'Inorganic Reactions and Methods', ed. J. J. Zuckerman, VCH Publishers, Weinheim, 1988, Vol. 7, p. 71.
17. J. C. Pazik and C. George, *Organometallics*, 1989, **8**, 482.
18. D. K. Srivastava, L. K. Krannich, and C. L. Watkins, *Inorg. Chem.*, 1990, **29**, 3502.
19. C. J. Thomas, L. K. Krannich, and C. L. Watkins, *Polyhedron*, 1993, **12**, 89.
20. L. K. Krannich, C. L. Watkins, and D. K. Srivastava, *Polyhedron*, 1990, **9**, 289.
21. W. Wolfsberger, *Chem.-Ztg.*, 1991, **115**, 7.
22. P. Jutzi, S. Pilotek, B. Neumann, and H. G. Stammler, *J. Organomet. Chem.*, 1998, **552**, 221.
23. J. W. Pasterczyk and A. R. Barron, *Phosphorus, Sulfur Silicon*, 1990, **48**, 157.
24. P. Gugger, A. C. Willis, and S. B. Wild, *J. Chem. Soc., Chem. Commun.*, 1990, 1169.
25. S. B. Wild, *Pure Appl. Chem.*, 1990, **62**, 1139.
26. A. L. Rheingold and P. Choudhury, *J. Organomet. Chem.*, 1977, **128**, 155.
27. C. J. Thomas, L. K. Krannich, and C. L. Watkins, *Synth. React. Inorg. Met.-Org. Chem.*, 1992, **22**, 461.
28. M. A. Paver, J. S. Joy, S. J. Coles, M. B. Hursthouse, and J. E. Davies, *Polyhedron*, 2003, **22**, 211.
29. A. P. Kurbakova, L. A. Leites, and E. N. Zorina, *Sov. J. Coord. Chem.*, 1980, **6**, 503; *Chem. Abstr.*, 1980, **93**, 158184t.
30. L. K. Krannich, R. K. Kanjolia, and C. L. Watkins, *Inorg. Chim. Acta*, 1986, **114**, 159.
31. L. K. Krannich, in 'Inorganic Reactions and Methods', ed. J. J. Zuckerman, VCH Publishers, Weinheim, 1988, Vol. 7, p. 39.
32. G. Baum, A. Greiling, W. Massa, B. C. Hui, and J. Lorberth, *Z. Naturforsch., Teil B*, 1989, **44**, 560.

33. A. N. Sobolev, V. K. Belsky, N. Y. Chernikova, and F. Y. Akhmadulina, *J. Organomet. Chem.*, 1983, **244**, 129.

34. A. L. Rheingold, D. L. Staley, and M. E. Fountain, *J. Organomet. Chem.*, 1989, **365**, 123.

35. G. M. Bodner, C. Gagnon, and D. N. Whittern, *J. Organomet. Chem.*, 1983, **243**, 305.

36. G. Balimann and P. S. Pregosin, *Helv. Chim. Acta*, 1975, **58**, 1913.

37. L. K. Peterson, in 'MTP International Review of Science, Organometallic Derivatives of the Main Group Elements', ed. B. J. Aylett, Butterworths, London, 1975, Series 2, Vol. 4, p. 319.

38. E. N. Dianova and E. Y. Zabotina, *Russ. Chem. Rev.*, 1991, **60**, 162; *Chem. Abstr.*, 1991, **114**, 228983f.

39. A. J. Ashe, *Acc. Chem. Res.*, 1978, **11**, 153.

40. A. J. Ashe, *J. Am. Chem. Soc.*, 1971, **93**, 3293.

41. J. L. Aubagnac, F. H. Cano, R. Claramunt, J. Elguero, R. Faure, C. Foces-Foces, and P. Raj, *Bull. Soc. Chim. Fr.*, 1988, 905.

42. C. L. Watkins, L. K. Krannich, R. K. Kanjolia, and D. K. Srivastava, *Magn. Reson. Chem.*, 1989, **27**, 616.

43. H. Schmidbaur and P. Nussstein, *Chem. Ber.*, 1987, **120**, 1281.

44. D. Hellwinkel, *Top. Curr. Chem.*, 1983, **109**, 1.

45. R. Bohra and H. W. Roesky, in 'Advances in Inorganic Chemistry and Radiochemistry', eds. H. J. Emeléus and A. G. Sharpe, Academic Press, Orlando, 1984, Vol. 28, p. 203.

46. R. L. Wells, A. P. Purdy, and C. G. Pitt, *Phosphorus, Sulfur Silicon*, 1991, **57**, 1.

47. A. D. Norman, in 'Inorganic Reactions and Methods', ed. J. J. Zuckerman, VCH Publishers, Weinheim, 1987, Vol. 2, p. 30.

48. R. L. Wells, A. P. Purdy, A. T. McPhail, and C. G. Pitt, *J. Organomet. Chem.*, 1986, **308**, 281.

49. R. L. Wells, C. Kwag, A. P. Purdy, A. T. McPhail, and C. G. Pitt, *Polyhedron*, 1990, **9**, 319.

50. J. C. Pazik, C. George, and A. Berry, *Inorg. Chim. Acta*, 1991, **187**, 207.

51. D. A. Atwood, A. H. Cowley, and J. Ruiz, *Inorg. Chim. Acta*, 1992, **200**, 271.

52. J. C. Guillemin and L. Lassalle, *Organometallics*, 1994, **13**, 1525.

53. P. Choudhury, M. F. El-Shazly, C. Spring, and A. Rheingold, *Inorg. Chem.*, 1979, **18**, 543.

54. H. H. Sisler, in 'Inorganic Reactions and Methods', ed. J. J. Zuckerman, VCH Publishers, Weinheim, 1988, Vol. 7, p. 29.

55. V. K. Gupta, L. K. Krannich, and C. L. Watkins, *Inorg. Chim. Acta*, 1987, **132**, 163.

56. V. K. Gupta, L. K. Krannich, and C. L. Watkins, *Inorg. Chim. Acta*, 1987, **126**, 173.

57. V. K. Gupta, L. K. Krannich, and C. L. Watkins, *Synth. React. Inorg. Met.-Org. Chem.*, 1987, **17**, 501.

58. V. K. Gupta, L. K. Krannich, and C. L. Watkins, *Inorg. Chem.*, 1987, **26**, 1638.

59. V. K. Gupta, L. K. Krannich, and C. L. Watkins, *Inorg. Chem.*, 1986, **25**, 2553.

60. V. K. Gupta, L. K. Krannich, and C. L. Watkins, *Inorg. Chim. Acta*, 1987, **134**, 197.

61. H. Schumann, *Angew. Chem., Int. Ed. Engl.*, 1969, **8**, 937.

62. O. T. Beachley and G. E. Coates, *J. Chem. Soc.*, 1965, 3241.

63. C. L. Watkins, L. K. Krannich, C. J. Thomas, and D. Srivastava, *Polyhedron*, 1994, **13**, 3299.

64. J. A. Laske, A. P. Purdy, R. L. Wells, and P. S. White, *Organometallics*, 1996, **15**, 84.

65. A. M. Arif, B. L. Benac, A. H. Cowley, R. A. Jones, K. B. Kidd, and C. M. Nunn, *New J. Chem.*, 1988, **12**, 553.

66. D. E. Heaton, R. A. Jones, K. B. Kidd, A. H. Cowley, and C. M. Nunn, *Polyhedron*, 1988, **7**, 1901.

67. A. H. Cowley, R. A. Jones, M. A. Mardones, and C. M. Nunn, *Organometallics*, 1991, **10**, 1635.

68. G. G. Hoffmann and R. Fischer, *Z. Anorg. Allg. Chem.*, 1990, **590**, 181.

69. G. G. Hoffmann, R. Fischer, U. Schubert, and B. Hirle, *J. Organomet. Chem.*, 1992, **441**, 7.

70. G. E. Coates and J. Graham, *J. Chem. Soc.*, 1963, 233.

71. R. L. Wells, A. P. Purdy, A. T. McPhail, and C. G. Pitt, *J. Chem. Soc., Chem. Commun.*, 1986, 487.

72. D. C. McKean, I. Torto, and A. R. Morrisson, *J. Phys. Chem.*, 1982, **86**, 307.

73. Y. Kikuzono and T. Maeda, *Appl. Organomet. Chem.*, 1991, **5**, 331.

74. R. Batchelor and T. Birchall, *J. Am. Chem. Soc.*, 1982, **104**, 674.

75. R. H. Marking, W. L. Gladfelter, and K. F. Jensen, *Chem. Mater.*, 1990, **2**, 499.

76. See, for example, recent volumes of *J. Cryst. Growth*, *J. Electron. Mater.*, and *Chem. Mater*.

77. G.-V. Röschenthaler, M. Fild, and H. J. Breunig, in 'Inorganic Reactions and Methods', ed. J. J. Zuckerman, VCH Publishers, Weinheim, 1989, Vol. 3, p. 194.

78. R. J. Wiacek, J. N. Jones, C. L. B. Macdonald, and A. H. Cowley, *Can. J. Chem.*, 2002, **80**, 1518.

79. A. J. Downs, N. I. Hunt, G. S. McGrady, D. W. H. Rankin, and H. E. Robertson, *J. Mol. Struct.*, 1991, **248**, 393.

80. N. M. Zaripov, R. G. Khusnutdinov, I. A. Litvinov, L. V. Ermolaeva, and V. A. Naumov, *J. Struct. Chem.*, 1989, **30**, 748; *Chem. Abstr.*, 1990, **112**, 139222y.

81. R. Geanangel, in 'Inorganic Reactions and Methods', ed. J. J. Zuckerman, VCH Publishers, Weinheim, 1988, Vol. 7, p. 198.

82. R. K. Kanjolia, L. K. Krannich, and C. L. Watkins, *Inorg. Chem.*, 1985, **24**, 445.

83. P. P. Power, A. Moezzi, D. C. Pestana, M. A. Petrie, S. C. Shoner, and K. M. Waggoner, *Pure Appl. Chem.*, 1991, **63**, 859.

84. R. K. Kanjolia, L. K. Krannich, and C. L. Watkins, *J. Chem. Soc., Dalton Trans.*, 1986, 2345.

85. J. G. Morse and K. W. Morse, *Inorg. Chem.*, 1973, **12**, 2119.

86. E. W. Abel and S. M. Illingworth, *J. Chem. Soc. A*, 1969, 1094.

87. R. Goetze and H. Nöth, *Z. Naturforsch., Teil B*, 1975, **30**, 875.

88. A. Moezzi, M. M. Olmstead, D. C. Pestana, and P. P. Power, *Z. Anorg. Allg. Chem.*, 1995, **621**, 1933.

89. M. A. Petrie, M. M. Olmstead, H. Hope, R. A. Bartlett, and P. P. Power, *J. Am. Chem. Soc.*, 1993, **115**, 3221.

90. M. A. Petrie, S. C. Shoner, H. V. R. Dias, and P. P. Power, *Angew. Chem., Int. Ed. Engl.*, 1990, **29**, 1033.

91. M. A. Mardones, A. H. Cowley, L. Contreras, R. A. Jones, and C. J. Carrano, *J. Organomet. Chem.*, 1993, **455**, C1–C2.

92. K.-H. van Bonn, P. Schreyer, P. Paetzold, and R. Boese, *Chem. Ber.*, 1988, **121**, 1045.

93. J. M. Chehayber and J. E. Drake, *Inorg. Chim. Acta*, 1986, **112**, 209.

94. H.-G. von Schnering, M. Somer, M. Hartweg, and K. Peters, *Angew. Chem., Int. Ed. Engl.*, 1990, **29**, 65.

95. A. Kuczkowski, S. Schulz, M. Nieger, and P. R. Schreiner, *Organometallics*, 2002, **21**, 1408.

96. R. L. Wells, A. T. McPhail, and T. M. Speer, *Eur. J. Solid State Inorg. Chem.*, 1992, **29**, 63.

97. C. G. Pitt, A. P. Purdy, K. T. Higa, and R. L. Wells, *Organometallics*, 1986, **5**, 1266.

98. D. A. Atwood, A. H. Cowley, P. R. Harris, R. A. Jones, S. U. Koschmieder, C. M. Nunn, J. L. Atwood, and S. G. Bott, *Organometallics*, 1993, **12**, 24.

99. R. L. Wells, A. T. McPhail, and T. M. Speer, *Organometallics*, 1992, **11**, 960.

100. J. A. L. Cooke, R. L. Wells, and P. S. White, *Organometallics*, 1995, **14**, 3562.

101. R. J. Wehmschulte and P. P. Power, *J. Am. Chem. Soc.*, 1996, **118**, 791.

102. D. A. Atwood, L. Contreras, A. H. Cowley, R. A. Jones, and M. A. Mardones, *Organometallics*, 1993, **12**, 17.

103. J. F. Janik, R. L. Wells, and P. S. White, *Inorg. Chem.*, 1998, **37**, 3561.

104. F. Thomas, S. Schulz, and M. Nieger, *Eur. J. Inorg. Chem.*, 2001, 161.

105. K. Knabel, I. Krossing, H. Noth, H. Schwenk-Kirchner, M. Schmidt-Amelunxen, and T. Seifert, *Eur. J. Inorg. Chem.*, 1998, 1095.

106. R. J. Wehmschulte and P. P. Power, *New J. Chem.*, 1998, **22**, 1125.

107. D. G. Tuck, in 'Comprehensive Organometallic Chemistry', eds. G. Wilkinson, F. G. A. Stone, and E. W. Abel, Pergamon Press, Oxford, 1982, Vol. 1, p. 694.

108. G. E. Coates, *J. Chem. Soc.*, 1951, 2003.

109. F. Maury and A. El Hammadi, *J. Cryst. Growth*, 1988, **91**, 97.

110. F. Maury and A. El Hammadi, *J. Cryst. Growth*, 1988, **91**, 105.

111. R. L. Wells, A. T. McPhail, L. J. Jones, M. F. Self, and R. J. Butcher, *Organometallics*, 1992, **11**, 2694.

112. R. L. Wells, A. T. McPhail, J. W. Pasterczyk, and A. Alvanipour, *Organometallics*, 1992, **11**, 226.

113. L. J. Baker, C. E. F. Rickard, and M. J. Taylor, *J. Organomet. Chem.*, 1994, **464**, C4–C6.

114. B. Beagley, S. M. Godfrey, K. J. Kelly, S. Kungwankunakorn, C. A. McAuliffe, and R. G. Pritchard, *J. Chem. Soc., Chem. Commun.*, 1996, 2179.

115. R. L. Wells, S. Shafieezad, A. T. McPhail, and C. G. Pitt, *J. Chem. Soc., Chem. Commun.*, 1987, 1823.

116. M. A. Petrie and P. P. Power, *Inorg. Chem.*, 1993, **32**, 1309.

117. M. P. Petrie and P. P. Power, *J. Chem. Soc., Dalton Trans.*, 1993, 1737.

118. C. G. Pitt, K. T. Higa, A. McPhail, and R. L. Wells, *Inorg. Chem.*, 1986, **25**, 2483.

119. A. M. Arif, B. L. Benac, A. H. Cowley, R. Geerts, R. A. Jones, K. B. Kidd, J. M. Power, and S. T. Schwab, *J. Chem. Soc., Chem. Commun.*, 1986, 1543.

120. R. L. Wells, M. F. Self, R. A. Baldwin, and P. S. White, *J. Coord. Chem.*, 1994, **33**, 279.

121. R. L. Wells, A. P. Purdy, K. T. Higa, A. T. McPhail, and C. G. Pitt, *J. Organomet. Chem.*, 1987, **325**, C7–C10.

122. R. L. Wells, *Coord. Chem. Rev.*, 1992, **112**, 273.

123. J. F. Janik, R. L. Wells, V. G. Young, A. L. Rheingold, and I. A. Guzei, *J. Am. Chem. Soc.*, 1998, **120**, 532.

124. R. L. Wells, J. W. Pasterczyk, A. T. McPhail, J. D. Johansen, and A. Alvanipour, *J. Organomet. Chem.*, 1991, **407**, 17.

125. R. L. Wells, A. T. McPhail, and A. Alvanipour, *Polyhedron*, 1992, **11**, 839.

126. R. L. Wells, W. K. Holley, S. Shafieezad, A. T. McPhail, and C. G. Pitt, *Phosphorus, Sulfur Silicon*, 1989, **41**, 15.

127. W. K. Holley, R. L. Wells, S. Shafieezad, A. T. McPhail, and C. G. Pitt, *J. Organomet. Chem.*, 1990, **381**, 15.

128. A. Schaller, H. D. Hausen, W. Schwarz, G. Heckmann, and J. Weidlein, *Z. Anorg. Allg. Chem.*, 2000, **626**, 1047.

129. E. K. Byrne, L. Parkanyi, and K. H. Theopold, *Science*, 1988, **241**, 332.

130. J. E. Miller, M. A. Mardones, J. W. Nail, A. H. Cowley, R. A. Jones, and J. G. Ekerdt, *Chem. Mater.*, 1992, **4**, 447.

131. R. D. Culp, A. H. Cowley, A. Decken, R. A. Jones, M. R. Bond, L. M. Mokry, and C. J. Carrano, *Inorg. Chem.*, 1997, **36**, 5165.

132. A. H. Cowley, S. Corbelin, R. A. Jones, R. J. Lagow, and J. W. Nail, *J. Organomet. Chem.*, 1994, **464**, C1–C3.

133. K. T. Higa and C. George, *Organometallics*, 1990, **9**, 275.

134. A. H. Cowley, P. R. Harris, R. A. Jones, and C. M. Nunn, *Organometallics*, 1991, **10**, 652.

135. A. P. Purdy, R. L. Wells, A. T. McPhail, and C. G. Pitt, *Organometallics*, 1987, **6**, 2099.

136. R. L. Wells, A. P. Purdy, A. T. McPhail, and C. G. Pitt, *J. Organomet. Chem.*, 1988, **354**, 287.

137. D. A. Atwood, A. H. Cowley, R. A. Jones, and M. A. Mardones, *J. Organomet. Chem.*, 1992, **439**, C33–C35.

138. W. K. Holley, J. W. Pasterczyk, C. G. Pitt, and R. L. Wells, *Heteroat. Chem.*, 1990, **1**, 475.

139. S. C. Sendlinger, B. S. Haggerty, A. L. Rheingold, and K. H. Theopold, *Chem. Ber.*, 1991, **124**, 2453.

140. C. von Hanisch and O. Hampe, *Angew. Chem., Int. Ed. Engl.*, 2002, **41**, 2095.

141. A. H. Cowley and R. A. Jones, *Angew. Chem., Int. Ed. Engl.*, 1989, **28**, 1208.

142. J. E. Miller and J. G. Ekerdt, *Chem. Mater.*, 1992, **4**, 7.

143. A. H. Cowley and R. A. Jones, *Polyhedron*, 1994, **13**, 1149.

144. R. L. Wells, L. J. Jones, A. T. McPhail, and A. Alvanipour, *Organometallics*, 1991, **10**, 2345.

145. R. L. Wells, A. T. McPhail, L. J. Jones, and M. F. Self, *Polyhedron*, 1993, **12**, 141.

146. C. von Hanisch, *Z. Anorg. Allg. Chem.*, 2001, **627**, 68.

147. C. von Hanisch and B. Rolli, *Z. Anorg. Allg. Chem.*, 2002, **628**, 2255.

148. F. Thomas, S. Schulz, and M. Nieger, *Z. Anorg. Allg. Chem.*, 2002, **628**, 235.

149. E. Iravani, A. Dashfi-Mommertz, and B. Neumuller, *Z. Anorg. Allg. Chem.*, 2003, **629**, 1136.

150. M. F. Self, A. T. McPhail, L. J. Jones, and R. L. Wells, *Polyhedron*, 1994, **13**, 625.

151. L. J. Jones, A. T. McPhail, and R. L. Wells, *Organometallics*, 1994, **13**, 2504.

152. A. H. Cowley, R. A. Jones, K. B. Kidd, C. M. Nunn, and D. L. Westmoreland, *J. Organomet. Chem.*, 1988, **341**, C1–C5.

153. H. Büger, in 'MTP International Review of Science', ed. B. J. Aylett, Butterworths, London, 1972, Series 1, Vol. 4, p. 229.

154. G. Becker, G. Gutekunst, and H. J. Wessely, *Z. Anorg. Allg. Chem.*, 1980, **462**, 113.

155. K. Hassler and S. Seidl, *J. Organomet. Chem.*, 1990, **384**, 263.

156. M. Börner and H. Vahrenkamp, *Chem. Ber.*, 1981, **114**, 1382.

157. L. I. Goryunov, V. D. Shteingarts, J. Grobe, B. Krebs, and M. U. Triller, *Z. Anorg. Allg. Chem.*, 2002, **628**, 1770.

158. K. Betka and J. Grobe, *J. Organomet. Chem.*, 1981, **210**, 19.

159. M. Bonaterra, S. E. Martin, and R. A. Rossi, *Org. Lett.*, 2003, **5**, 2731.

160. D. Hanssgen, R. Jeske, N. Korber, C. Mohr, and M. Nieger, *Z. Anorg. Allg. Chem.*, 1998, **624**, 1202.

161. J. C. Guillemin and K. Malagu, *Organometallics*, 1999, **18**, 5259.

162. F. Kober, *Chem.-Ztg.*, 1976, **100**, 313.

163. F. Kober, *Synthesis*, 1982, 173.

164. M. F. Lappert, P. P. Power, A. R. Sanger, and R. C. Srivastava, 'Metal and Metalloid Amides', Halsted Press, New York, 1980, Chap. 7.

165. C. J. Thomas, L. K. Krannich, and C. L. Watkins, *Synth. React. Inorg. Met.-Org. Chem.*, 1991, **21**, 427.

166. J. Kiketsu, Y. Shibata, and K. Khashi, *Chubu Kogye Daigaku Kiyo*, 1976, **12A**, 107; *Chem. Abstr.*, 1977, **87**, 84098.

167. A. Weitze, A. Blaschette, and P. G. Jones, *Phosphorus, Sulfur Silicon*, 1993, **85**, 77.

168. D. K. Srivastava, L. K. Krannich, and C. L. Watkins, *Inorg. Chem.*, 1991, **30**, 2441.

169. L. K. Krannich, C. L. Watkins, D. K. Srivastava, and R. K. Kanjolia, *Coord. Chem. Rev.*, 1992, **112**, 117.

170. D. K. Srivastava, L. K. Krannich, and C. L. Watkins, *Polyhedron*, 1988, **7**, 2553.

171. V. K. Gupta, L. K. Krannich, and C. L. Watkins, *Polyhedron*, 1987, **6**, 1229.

172. V. K. Gupta, L. K. Krannich, and C. L. Watkins, *Inorg. Chim. Acta*, 1988, **150**, 51.

173. C. J. Thomas, R. Ceaolivares, G. Espinosaperez, and R. W. Turner, *J. Organomet. Chem.*, 1995, **493**, 101.

174. W. Ou, Z. G. Wang, and Z. C. Chen, *Synth. Commun.*, 1999, **29**, 2301.

175. Y. Matano, H. Nomura, H. Suzuki, M. Shiro, and H. Nakano, *J. Am. Chem. Soc.*, 2001, **123**, 10954.

176. P. Froyen, *Phosphorus, Sulfur Silicon*, 1993, **81**, 37.

177. H. W. Roesky, N. Bertel, F. Edelmann, M. Noltemeyer, and G. M. Sheldrick, *Z. Naturforsch., Teil B*, 1988, **43**, 72.

178. A. H. Cowley and N. C. Norman, in 'Progress in Inorganic Chemistry', ed. S. J. Lippard, John Wiley & Sons, New York, 1986, Vol. 34, p. 18.

179. P. Jutzi and U. Meyer, *J. Organomet. Chem.*, 1987, **326**, C6–C8.

180. J. E. Byrne and C. R. Russ, *J. Inorg. Nucl. Chem.*, 1974, **36**, 35.

181. A. H. Cowley, *J. Organomet. Chem.*, 1990, **400**, 71.

182. A. H. Cowley, J. G. Lasch, N. C. Norman, M. Pakulski, and B. R. Whittlesey, *J. Chem. Soc., Chem. Commun.*, 1983, 881.

183. P. Jutzi, U. Meyer, S. Opiela, M. M. Olmstead, and P. P. Power, *Organometallics*, 1990, **9**, 1459.

184. P. Jutzi and S. Opiela, *Z. Anorg. Allg. Chem.*, 1992, **610**, 75.

185. P. P. Power, *J. Chem. Soc., Dalton Trans.*, 1998, 2939.

186. L. Weber, *Chem. Rev.*, 1992, **92**, 1839.

187. B. Twamley and P. P. Power, *Chem. Commun.*, 1998, 1979.

188. L. R. Avens, L. V. Cribbs, and J. L. Mills, *Inorg. Chem.*, 1989, **28**, 211.

189. P. Jutzi, U. Meyer, S. Opiela, B. Neumann, and H.-G. Stammler, *J. Organomet. Chem.*, 1992, **439**, 279.

190. H. Chen, M. O. Olmstead, D. C. Pestana, and P. P. Power, *Inorg. Chem.*, 1991, **30**, 1783.
191. X.-W. Li, J. Lorberth, and K. Harms, *J. Organomet. Chem.*, 1994, **483**, 229.
192. K. Megges, E. V. Avtomonov, and J. Lorberth, *Z. Naturforsch., Teil. B*, 1997, **52**, 790.
193. A. H. Cowley, J. G. Lasch, N. C. Norman, and M. Pakulski, *J. Am. Chem. Soc.*, 1983, **105**, 5506.
194. B. Twamley, C. D. Sofield, M. M. Olmsted, and P. P. Power, *J. Am. Chem. Soc.*, 1999, **121**, 3357.
195. M. Bouslikhane, H. Gornitzka, J. Escudie, and H. Ranaivonjatovo, *J. Organomet. Chem.*, 2001, **619**, 275.
196. A. J. Dimaio and A. L. Rheingold, *Chem. Rev.*, 1990, **90**, 169.
197. A. L. Rheingold, in ‘Homoatomic Rings, Chains, and Macromolecules of Main-Group Elements’, ed. A. L. Rheingold, Elsevier, Amsterdam, 1977, p. 385.
198. F. Kober and P. Aslanidis, *J. Prakt. Chem./Chem. Ztg.*, 1994, **336**, 421.
199. X. Y. Chen and W. T. Tao, *Chin. J. Org. Chem.*, 2000, **20**, 930.

Asymmetric Synthesis by Homogeneous Catalysis

Patrick J. Walsh
University of Pennsylvania, Philadelphia, PA, USA

Based in part on the article Asymmetric Synthesis by Homogeneous Catalysis by Brice Bosnich which appeared in the Encyclopedia of Inorganic Chemistry, First Edition.

1 Introduction 1
2 The Traditional Method to Screening Asymmetric Catalysts 2
3 Nontraditional Approaches to Asymmetric Catalysis 4
4 Final Perspective 22
5 Related Articles 22
6 References 22

Abbreviations

ee = enantiomeric excess; TOF = turnover frequency; TON = turnover number; HKR = hydrolytic kinetic resolution; BINOL = 1, 1′-bi-2-naphthol; BIPHEP = 2, 2′-bis(diphenylphosphino)-1,1′-biphenyl; DPEN = 1,2-diphenylethylenediamine; Xyl-BINAP = 2,2′-bis(di(3,5-dimethylphenyl)phosphino)-1,1′-binaphthalene; BINAP = 2, 2′-bis-(diphenylphosphino)-1,1′-binaphthalene; DM-DABN = *N*, *N*-dimethyl diaminobinaphthyl; Tol-BINAP = 2, 2′-bis(di(4-methylphenyl)phosphino)-1,1′-binaphthalene; MBP-H_2 = methylene bis(phenol); MBP = methylene bis(phenoxide).

1 INTRODUCTION

The field of asymmetric catalysis has moved to the forefront of organic chemistry, culminating with the award of the 2001 Nobel Prize in Chemistry to Knowles, Noyori, and Sharpless. The goal of this tremendous effort continues to be the efficient generation of enantioenriched organic compounds. It is not surprising, therefore, that the practitioners of this popular field are overwhelmingly organic chemists, despite the fact that asymmetric catalysis is a discipline that is dependent on the synthesis and evaluation of inorganic catalysts. The chemical community has stressed the importance of generating functionalized chiral products of high enantiomeric excess (ee) and less emphasis has been placed on understanding the structure and the function of the catalyst. To some degree this is understandable, because mechanistic investigations are inherently more difficult than catalyst screening. Furthermore, it is often found that reaction mechanisms are more complicated than initially anticipated. Nonetheless, detailed mechanistic studies are of great value and have increased our understanding of catalytic asymmetric reactions. They can also position researchers to develop improved catalysts, and even new reactions.

The past several years have witnessed enormous advances in the number and variety of reactions that can be catalyzed with excellent enantioselectivities (*see Enantioselectivity*). The area has recently been comprehensively reviewed with volumes edited by the team of Jacobsen, Pfaltz, and Yamamoto[1] as well as Ojima.[2] These important treatises are quite detailed and cannot be summarized here. The goal of this section is to present some of the most important new approaches to asymmetric catalysis. The basic concepts necessary to understanding catalytic asymmetric reactions have been succinctly described by Bosnich[3] in the first edition of *Encyclopedia of Inorganic Chemistry* and will not be duplicated here.

While impressive progress has been made in asymmetric catalysis, it must be emphasized that most catalysts do not meet the criteria of exhibiting high turnover (*see Turnover*) frequency (TOF) and turnover number (TON), and being high yielding, highly enantioselective, easy to prepare, and stable to trace impurities such as air and moisture.[4] Given the limitations of most catalysts, there remains significant room for improvement and innovation in this field.

This summary is designed to introduce chemists with a background in inorganic chemistry to the field of asymmetric catalysis. The skills regularly employed by solution phase inorganic chemists are of great value in this area. The ability to synthesize, isolate, and characterize highly air or moisture sensitive compounds are important tools to probe catalyst structure. Experience in performing detailed kinetic and mechanistic studies are essential to understanding reaction mechanisms in asymmetric catalysis. Based on the insight gained through these studies, the likelihood of developing an improved catalyst is greatly increased. It must be borne in mind that although the development of new catalysts is clearly important, it does not always have the lasting impact and value as mechanistic studies. Catalysts like the titanium tartrate-based system for the asymmetric epoxidation of prochiral allylic alcohols developed by Sharpless and Katsuki,[5,6] which has been the catalyst of choice for this transformation for almost 25 years, are extremely rare. Catalysts with greater efficiency, enantioselectivity, substrate scope, and functional group compatibility are constantly being introduced. As a result, today's best catalyst is tomorrow's dog and may soon to be forgotten. In contrast, mechanistic studies serve as guiding principles on which future catalysts will be developed. Despite the large number of catalysts that have been reported, relatively few are understood. Thus, mechanistic investigations of known reactions represent an excellent entry into the field of asymmetric catalysis.

2 THE TRADITIONAL METHOD TO SCREENING ASYMMETRIC CATALYSTS

The traditional approach to asymmetric catalysis employing metal-based complexes is an iterative process, centered around the synthesis of highly enantioenriched organic ligands.[1,2,7] This task is often the rate limiting step, particularly when racemic ligand components must be resolved. After the enantioenriched ligands have been synthesized they are coordinated to the metal to provide the catalysts or catalyst precursors. Generation of these species can also be accomplished in situ, and this is often the method of choice among researchers working in this area. In situ catalyst generation, however, frequently introduces another level of uncertainty into the analysis of the mechanism. Unless the reaction is monitored spectroscopically, it must be assumed that the assembly of the ligands and metal precursors has taken place to afford catalyst or precatalyst with the expected structure.

After the generation of the catalyst or catalyst precursors, they are examined in the reaction of interest to evaluate their enantioselectivities and activities. The findings of these studies are assessed and the next generation of ligands is designed, beginning the second iteration of the catalyst development.

In the process of catalyst development, the key to efficient reaction optimization is frequently rapid access to catalysts with diverse chiral environments. Therefore, it is important to design ligands that can be generated from common intermediates in a few steps. While it is often useful to synthesize elaborate ligands to probe asymmetric induction and reaction mechanisms, few researchers are willing to perform multistep ligand syntheses in the application of catalysts.

An ideal ligand and catalyst system is outlined below to illustrate the utility of the traditional approach to asymmetric catalysis.

2.1 Application of Salen-based Catalysts to Asymmetric Catalysis

One of the most significant discoveries in asymmetric catalysis in the last 15 years was the importance of chiral metal salen catalysts. Chiral salen complexes exhibit high enantioselectivities in several mechanistically distinct reactions. As a result, they have been classified as ‘privileged structures’.[8]

An important benefit of salen ligands and their metal complexes is that they are easily synthesized. Their straightforward synthesis involves mixing a resolved diamine with two equivalents of a salicyl aldehyde derivative, many of which are commercially available (equation 1). This design allows many derivatives to be prepared, allowing great structural diversity and facilitating catalyst optimization.

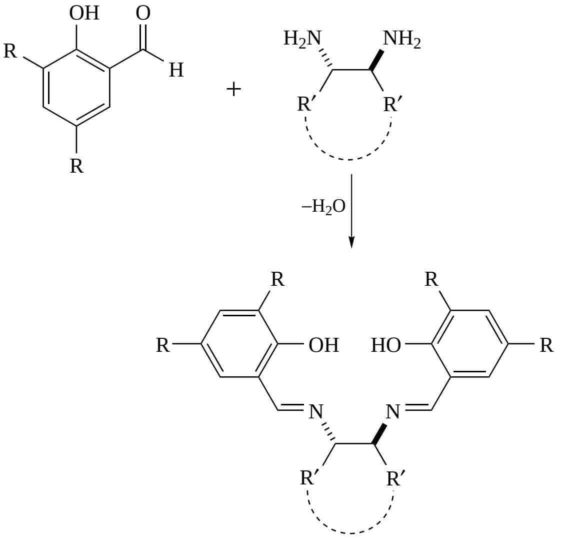

(1)

Initial successes with these ligands came independently from the groups of Jacobsen[9] and Katsuki[10] in the asymmetric epoxidation of unfunctionalized olefins.[9,10] Since these seminal works in 1990, metal salen complexes have become workhorse in asymmetric catalysis, finding applications in a wide variety of reactions. In Figure 1 is illustrated a variety of metal salen complexes. Scheme 1 lists some of the transformations in which they have been used, demonstrating the broad utility of these complexes.

To illustrate the utility of the metal salen complexes, several reactions are outlined in Scheme 1. They include the asymmetric epoxidation of unfunctionalized *cis*-disubstituted and trisubstituted olefins, which are promoted by (salen)Mn complexes.[11,12] In the case of *trans*-disubstituted olefins, the simple (salen)Mn complexes do not exhibit the same levels of enantioselectivity as they do with the *cis*- and trisubstituted derivatives. Promising alternatives include more elaborate (salen)Mn complexes based on the binaphthyl unit,[13] (salen)Cr complexes,[14] and (salen)Ru-based catalysts.[15] Catalysts based on (salen)Co moiety have exhibited amazing levels of selectivity in the hydrolytic kinetic resolution (HKR)[16] of terminal epoxides.[17,18] The HKR allows access to terminal epoxides and diols with very high enantioselectivities.

Terminal epoxides of high enantiopurity are among the most important chiral building blocks in enantioselective synthesis, because they are easily opened through nucleophilic substitution reactions. Furthermore, this procedure can be scaled to industrial levels with low catalyst loading.[19] Chiral metal salen complexes have also been successfully applied to the asymmetric hydroxylation[20,21] of C–H bonds, asymmetric oxidation of sulfides,[22,23] asymmetric aziridination of alkenes,[24] and the asymmetric alkylation of keto esters[25] to name a few.

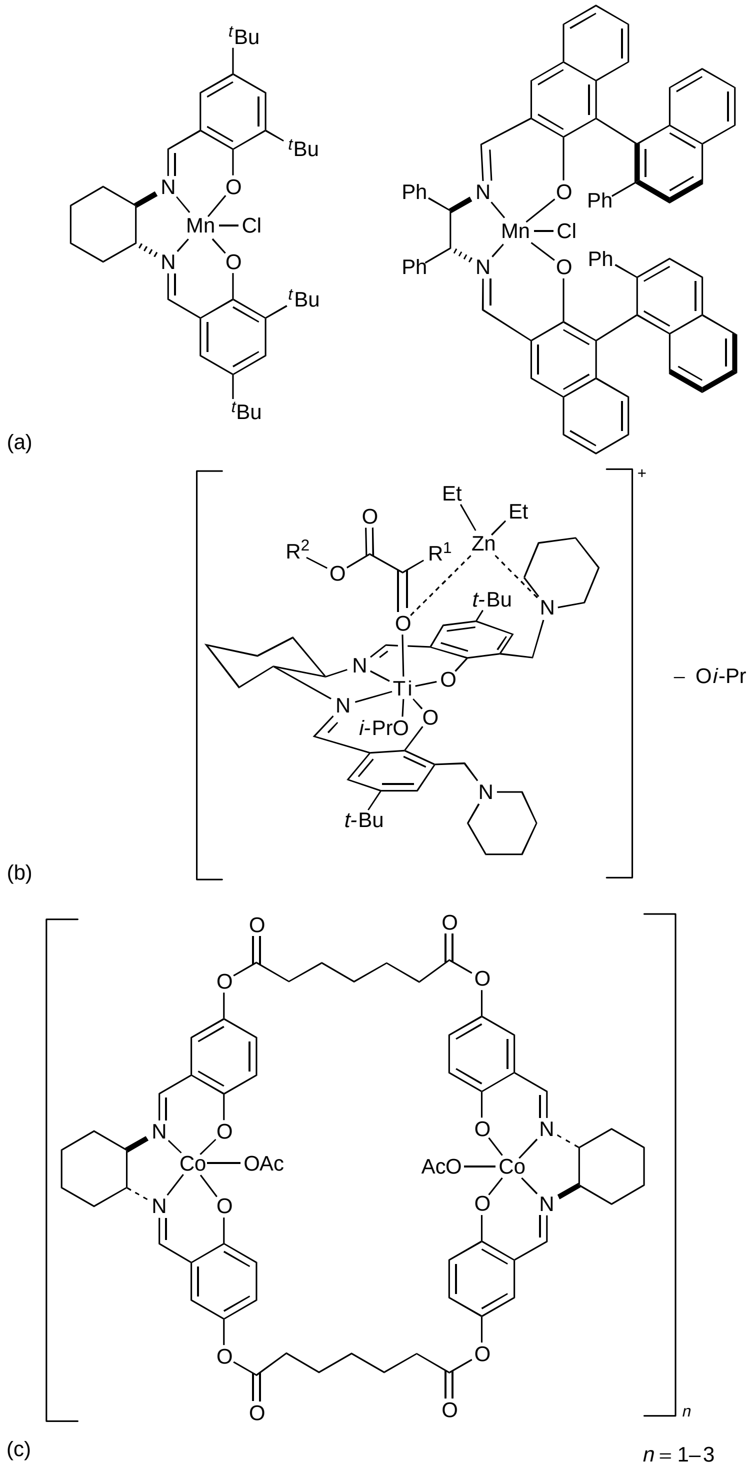

Figure 1 Structures of some metal salen complexes: (a) epoxidation catalysts, (b) proposed structure in the asymmetric addition of alkyl groups to alpha ketoesters with a bifunctional catalyst, and (c) oligomeric bifunctional salen catalyst for the hydrolytic catalytic resolution

These transformations provide an indication of how different salen and metal combinations have been developed to optimize enantioselectivities and efficiency diverse reactions. The modular nature of the salen ligand allows the generation of structurally diverse ligands and complexes. In this regard, there are no ligands systems that are better suited to the traditional approach to asymmetric catalysis.

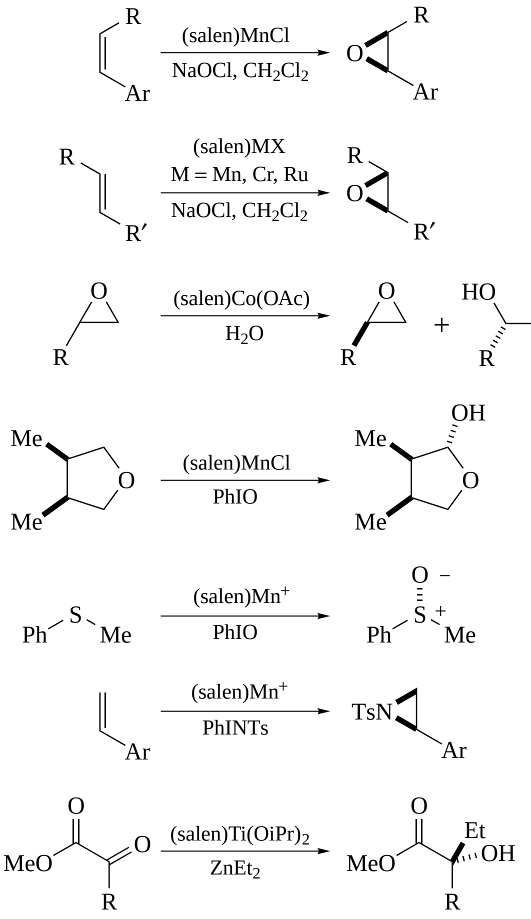

Scheme 1 Selected reactions of chiral salen-based catalysts

3 NONTRADITIONAL APPROACHES TO ASYMMETRIC CATALYSIS

The utility of the traditional approach to asymmetric catalysis, involving synthesis and screening of chiral ligands and complexes in catalytic reactions is a powerful method for the development and optimization of catalytic asymmetric processes. Such an approach, however, can be cumbersome if the ligands are difficult to synthesize and modify. In these cases, alternative strategies to the generation of asymmetric catalysts provide access to a large number of catalysts with minimal effort. The remainder of this section will focus on these methods.

3.1 Screening Mixtures of Chiral Monodentate Ligands

Reactions that result in the formation of C–C bonds are of central importance in the construction of organic molecules. One such reaction is the conjugate addition of organometallic reagents to α,β-unsaturated carbonyl compounds. The asymmetric addition of boronic acids to enones is promoted by rhodium catalysts bearing a bidentate[26] or two monodentate phosphorus-based ligands (equation 2).[27,28]

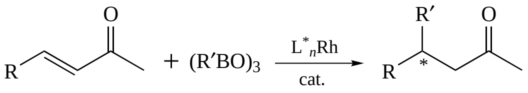

(2)

In the catalyst optimization process, a series of chiral bidentate ligands or chiral monodentate ligands could be screened. An alternative approach that provides access to a greater number of catalysts involves examination of mixtures of two monodentate ligands (L1* and L2*). If these ligands are part of a larger set of monodentate ligands (L1*, L2*, L3*,... Lx*, Ly*), many catalysts with combinations of ligands can be generated. As shown in Figure 2, combining two chiral ligands gives rise to formation of three catalysts, two homochiral complexes, $(Lx^*)_2Rh$ and $(Ly^*)_2Rh$, and a heterochiral complex $(Lx^*)(Ly^*)Rh$.

These catalysts are likely to have different stabilities and be formed in unequal amounts. Both the homochiral complexes $(Lx^*)_2Rh$ and $(Ly^*)_2Rh$ are accessible by combining a chiral ligand with the rhodium precursor. The heterochiral complex, however, is new. If the heterochiral complex exhibits greater activity and enantioselectivity than the homochiral complexes, not only will the resulting combination lead to improved

$$\mathrm{L}x^* + \mathrm{L}y^* + [\mathrm{Rh}] \longrightarrow \begin{array}{l}(\mathrm{L}x^*)_2\mathrm{Rh} + (\mathrm{L}y^*)_2\mathrm{Rh}\\ \quad + (\mathrm{L}x^*)(\mathrm{L}y^*)\mathrm{Rh}\end{array}$$

Figure 2 Combination of two chiral ligands can result in generation of three catalysts, $(Lx^*)_2Rh$, $(Ly^*)_2Rh$, and $(Lx^*)(Ly^*)Rh$

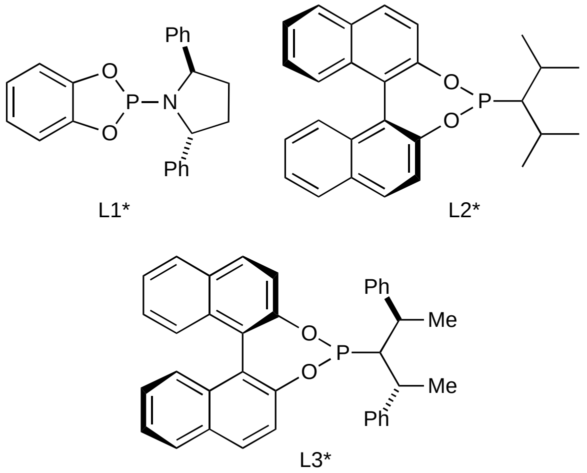

Figure 3 Ligands examined in the asymmetric conjugate addition reaction

Table 1 Ratios of homo- and heterochiral complexes determined by ^{31}P NMR

	$(L1^*)_2Rh$	$(L1^*)(L2^*)$ Rh	$(L2^*)_2Rh$
L1*/L2*	17	78	5
L1*/L3*	5	91	4
L2*/L3*	27	54	19

catalysts, it will indicate that a combinatorial approach to catalyst optimization is possible.

A small collection of ligands was examined to evaluate the potential of this approach (Figure 3).

Initially two equivalents of each ligand were combined with $Rh(acac)(CH_2{=}CH_2)_2$ to determine the ^{31}P NMR chemical shifts of the homochiral complexes. Next, 1:1 mixtures of chiral ligands were combined with an equivalent of the Rh(acac) $(CH_2{=}CH_2)_2$ and the ratio of the resultant complexes determined. As outlined in Table 1, the results of these experiments suggest that when L1*, with the smallest cone angle (*see Cone Angle*), is combined with the sterically bulkier ligands L2* or L3*, the equilibrium lies toward the heterochiral complex. When the sterically demanding ligands L2* and L3* are combined, however, the product ratio is closer to statistical.

These ligand combinations were then applied to the asymmetric addition of aryl boronic acid derivatives to 2-cyclohexenone. The results of this study are illustrated in Figure 4. From this data it can be seen that the heterochiral ligand combination L1*/L2* exhibited the highest conversion during the 3 h evaluation period. Furthermore, the heterochiral complexes L1*/L2* and L1*/L3* are significantly more enantioselectivity than the homochiral combinations.

Despite the small ligand library employed, this study clearly indicates the benefit of combining chiral monodentate ligands in the optimization of catalyst enantioselectivity and efficiency. As illustrated below, larger libraries of bidentate ligands (*see Bidentate Ligand*) can likewise be employed.

3.2 Screening of Heterochiral (L)(L′)Ti Complexes in the Asymmetric Hetero-Diels-Alder Reactions

In a study aimed at the development of a highly enantioselective catalyst for the asymmetric hetero-Diels–Alder reaction, a series of diols and BINOL derivatives was employed (Figure 5, L1–L13). Titanium tetraisopropoxide was chosen as the metal precursor, because it readily undergoes alkoxide exchange reactions with alcohols and phenols. Furthermore, it has been successfully used in many Lewis acid (*see Lewis Acids & Bases*) catalyzed reactions. A beneficial feature of titanium tetraisopropoxide is that chelating alkoxide and aryloxide-based ligands and/or ligands with acidic hydroxyl groups will favor formation of the chiral titanium complex and liberation of isopropanol. By combining all possible combinations of L1–L13, a library of 104 combinations can be generated. Each of the ligand combinations above will likely result in a mixture of compounds that is under thermodynamic control. It is anticipated that the titanium centers will be coordinated to either two of the same ligands giving $(Lm)_2Ti$ and $(Ln)_2Ti$ or two different ligands as in (L*m*)(L*n*)Ti.

Combination of 1 mol% of each ligand and titanium tetraisopropoxide generated the catalyst mixtures that were screened in the asymmetric hetero-Diels–Alder reaction (equation 3). All reactions were conducted in diethyl ether at rt for 24 h and worked up with trifluoroacetic acid. Preliminary screening indicated that combination of ligands with substituents at the 3,3′-positions of the BINOL ligands gave either low yields or enantioselectivities. Combinations involving L4–L7 exhibited high enantioselectivities (77–95%) and good yields (63–100%).

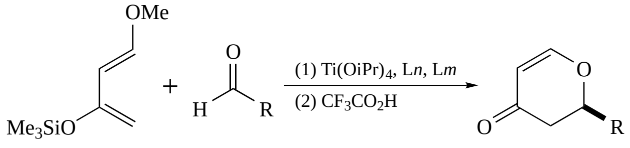

(3)

Further screening identified L5/L5/Ti and L5/L6/Ti combinations as the most enantioselective combinations. Optimization of L5/L5/Ti and L5/L6/Ti combinations allowed

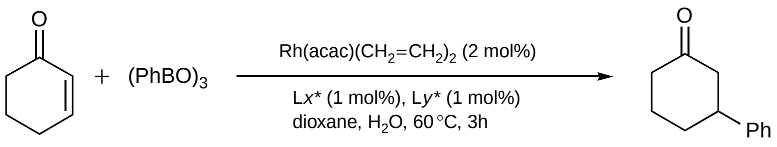

L*x**/L*y**	% conv.	% ee	L*x**/L*y**	% conv.	% ee
L1*/L1*	26	33	L1*/L2*	93	**75**
L2*/L2*	22	–27	L1*/L3*	40	**77**
L3*/L3*	18	–16	L2*/L3*	16	–60

Figure 4 The asymmetric conjugate addition of aryl boronic acids to 2-cyclohexenone with ligand combinations L1*–L3*

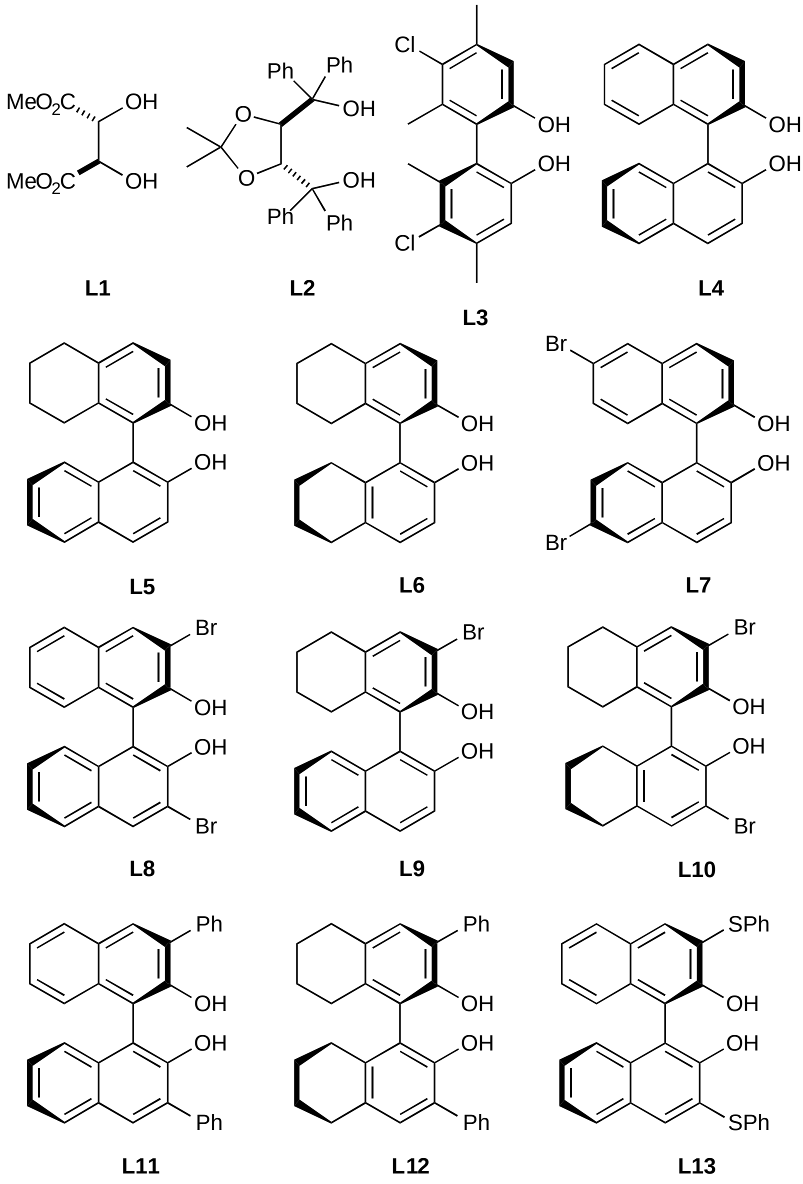
MeO2C
OH
MeO2C
OH
L1
Ph
Ph
O
OH
O
OH
Ph
Ph
L2
Cl
OH
OH
Cl
L3
OH
OH
L4
OH
OH
L5
OH
OH
L6
Br
OH
OH
Br
L7
Br
OH
OH
Br
L8
Br
OH
OH
L9
Br
OH
OH
Br
L10
Ph
OH
OH
Ph
L11
Ph
OH
OH
Ph
L12
SPh
OH
OH
SPh
L13

Figure 5 Ligands L1–L13 for the titanium catalyzed hetero-Diels–Alder reaction

the loading of titanium and the ligands to be dropped to 0.05 mol% under solvent free conditions. In some cases, loadings could be reduced to 0.005 mol%, which is one of the lowest loadings for Lewis acid catalysts known that gave >95% ee.

Selected results employing 0.05 mol% loading of each ligand and titanium tetraisopropoxide are illustrated in Table 2. It is noteworthy that the enantioselectivities obtained with the L5/L6/Ti combination are 0.1–20% higher than the L5/L5/Ti combination. These results indicate that the most enantioselective catalyst contains both ligands.

This series of experiments clearly demonstrates the advantage of screening combinations of ligands. The

Table 2 Comparison of enantioselectivities with L5/L5/Ti and L5/L6/Ti combinations

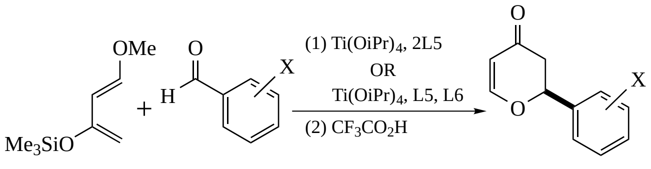
OMe
Me3SiO
+
O
H
X
(1) Ti(OiPr)4, 2L5
OR
Ti(OiPr)4, L5, L6
(2) CF3CO2H
O
O
X

Substrate	ee (%) 2L5/Ti	ee (%) L5/L6/Ti	Δee
X = H	99.3	99.4	0.1
X = 4-OMe	90.8	98.0	7.2
X = 3-OMe	96.6	99.8	3.2
X = 2-OMe	75.1	95.1	20.0

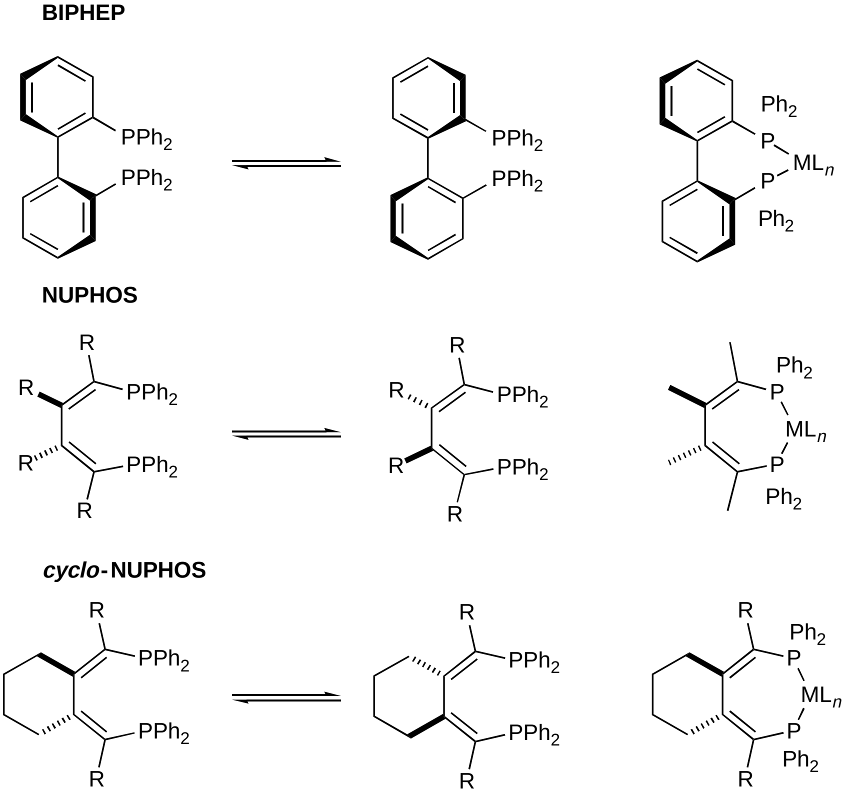

Figure 6 Structures of the normally unresolvable ligands BIPHEN, NUPHOS, and cyclo-NUPHOS and their complexes

disadvantage is that use of mixed ligand combinations can lead to the formation of multiple catalysts under the reaction conditions. In this case, the situation is further complicated by the propensity of titanium complexes to aggregate.[29] Mechanistic studies on a system containing multiple catalysts would be extremely difficult, because the most abundant complex may not be the most active.

3.3 Asymmetric Catalysis with Normally Unresolvable Ligands

Basic coordination chemistry serves as one of the underlying principles in the design, development, and understanding asymmetric catalysts. By taking advantage of strong, kinetically stable metal-ligand bonds, new enantioenriched catalysts have been prepared that contain ligands that cannot be resolved at room temperature. With proper choice of the metal center, however, the barrier to racemization of the metal-ligand assembly is significantly higher than that of the free ligand.

One class of ligands that racemizes readily at room temperature is based on atropisomeric bidentate phosphines such as BIPHEP, NUPHOS, and cyclo-NUPHOS (Figure 6). For example, the barrier to racemization of BIPHEP is 22 kcal mol^{-1},[30] making it very difficult to resolve. The metallocycle formed on binding to a substitutionally inert metal significantly increases the barrier to racemization.

When *rac*-(BIPHEP)PtCl_2 was treated with Na_2[(*S*)-(BINOLate)], a kinetic 1:1 ratio of the (BINOLate)Pt(BIPHEP) diastereomers was isolated. Heating this mixture to 92–122 °C resulted in equilibration of the mixture to form a 95:5 ratio with the (*S*,*S*)-diastereomer being thermodynamically favored (equation 4). Interconversion of the diastereomers likely proceeds by dissociation of a phosphorus from platinum, rotation, and recoordination. The minor (*R*,*S*)-diastereomer was isolated cleanly by fractional precipitation.[31]

Two routes were developed to eliminate the BINOLate ligand from the platinum (Figure 7). Reaction of the [(*R*)-BIPHEP]Pt[(*S*)-BINOLate] with hydrochloric acid gave [(*R*)-BIPHEP]PtCl_2. The dichloride [(*R*)-BIPHEP]PtCl_2 was then subject to two equivalents silver triflate to furnish the Lewis acidic triflate [(*R*)-BIPHEP]Pt$(\text{OTf})_2$. Alternatively, [(*R*)-BIPHEP]Pt[(*S*)-BINOLate] was converted directly to the triflate [(*R*)-BIPHEP]Pt$(\text{OTf})_2$ by exposure to triflic acid.

The stereochemical stability of the resolved (BIPHEP)Pt derivatives was next examined. The possibility of racemization of the [(*R*)-BIPHEP]Pt$(\text{OTf})_2$ was addressed by treatment

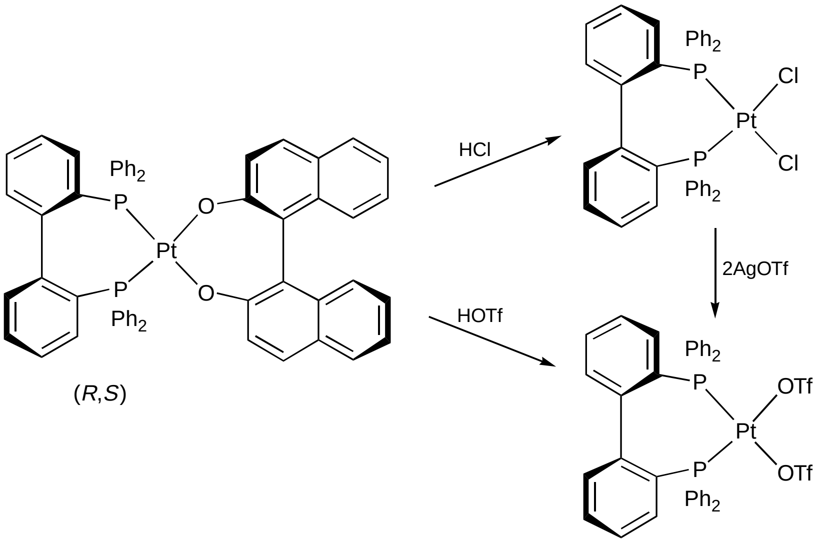

Figure 7 Reaction of [(*R*)-BIPHEP]Pt[(*S*)-BINOLate] with acids gives (*R*)-(BIPHEP)PtX_2 of high enantiopurity

with the resolved diamine (*S*,*S*)-DPEN (equation 5). Examination of the resulting diamine adducts by ^{31}P NMR spectroscopy indicated that the [(*R*)-BIPHEP]Pt$(OTf)_2$ was produced in 98% ee. To determine the stability with respect to racemization of [(*R*)-BIPHEP]Pt$(OTf)_2$, a sample was allowed to stand for 8 h at room temperature then treated with (*S*,*S*)-DPEN. The diastereomeric ratio was determined to by 98:2 indicating that racemization of [(*R*)-BIPHEP]Pt$(OTf)_2$ was slow in solution at room temperature.

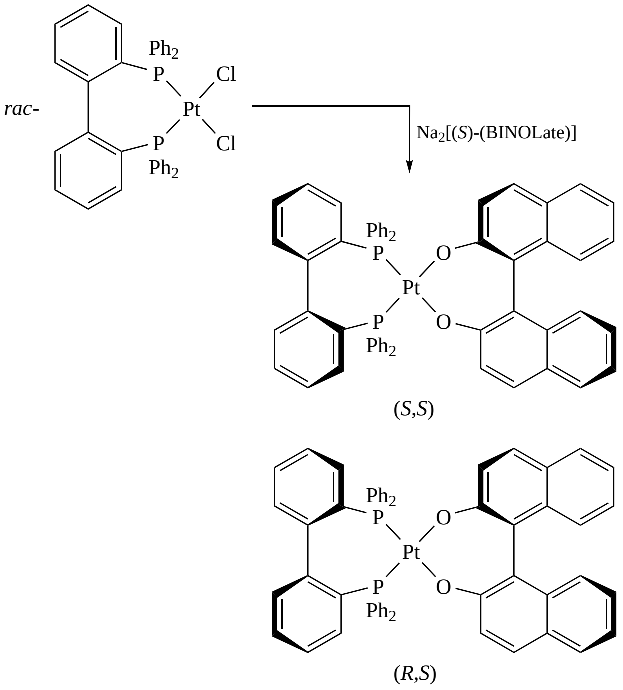

(4)

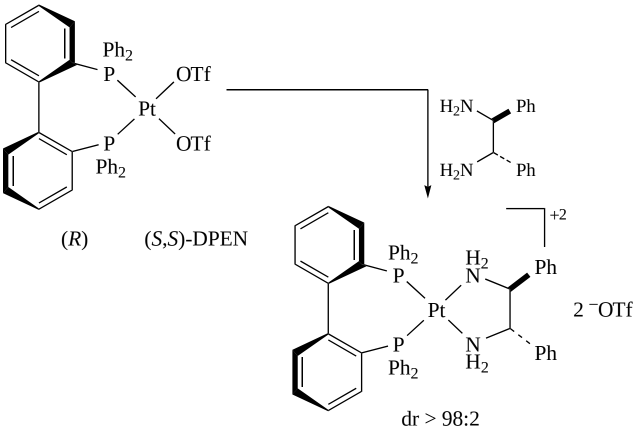

(5)

The stability of (BIPHEP)PtX_2 compounds with respect to racemization over several hours at room temperature suggested that these compounds could be employed as catalysts at room temperature or below. To explore this possibility, [BIPHEP]Pt$(OTf)_2$ was employed in the asymmetric Diels–Alder reaction as illustrated in equation (6). Freshly generated [(*R*)-BIPHEP]Pt$(OTf)_2$ promoted the asymmetric Diels–Alder reaction forming the product in 94:6 endo:exo ratio with the ee of the major diastereomer of 92–94%.**[31]** The enantiomeric excess of the catalyst [(*R*)-BIPHEP]Pt$(OTf)_2$ was not diminished over the course of the reaction, as determined by quenching the reaction at >90% conversion with (*S*,*S*)-DPEN and subsequent ^{31}P NMR analysis of the resulting mixture. The facial selectivity of the asymmetric Diels–Alder reaction catalyzed by [(*R*)-BIPHEP]Pt$(OTf)_2$ was the same as observed with [(*R*)-BINAP]Pt$(OTf)_2$ with the same reagents.[32]

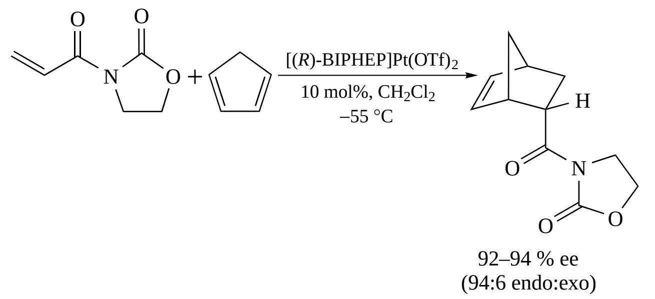

(6)

This, and related systems,[33,34] illustrate that bidentate phosphine ligands that are not resolvable at room temperature can adopt stereochemically robust coordination modes when bound to substitutionally inert metals. The importance of chelating phosphines (*see Chelating Ligands*) in asymmetric catalysis, and the difficulties often encountered in their resolution, should render this nontraditional strategy useful.

Application of N-chirality in Asymmetric Catalysis. Another class of ligands that cannot normally be resolvable is amines. Free amines with three different substituents are not usually considered chiral, because they undergo rapid lone pair inversion at nitrogen with rates on the order of 5×10^5 s^{-1} at rt.[35] Coordination of amines to substitutionally inert metals freeze nitrogen inversion generating N-chiral ligands (Figure 8). Dissociation of the amine ligand from the metal, however, will lead to inversion.

In an effort to synthesize enantioenriched diamine complexes, prochiral diamines were mixed with K_2[(R)-Me_2-BINOLate] and palladium acetate resulting in the formation of the two diastereomers (Figure 9).[36] These diastereomers were both C_2-symmetric and assigned as the (R,R)/(R) and (S,S)/(R) configurations based on NMR and X-ray crystallographic studies. The major diastereomer was separated from the minor by crystallization.

Treatment of the pure (R,R)/(R) diastereomers with HCl allowed isolation of the dichlorides, which were determined to be configurationally stable at nitrogen (equation 7).

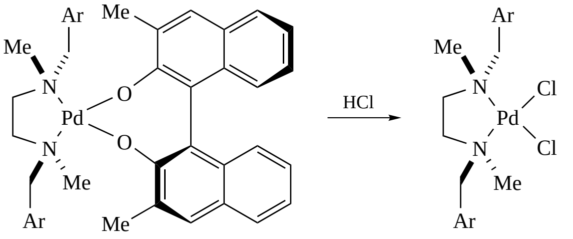

(R,R)/(R) (R,R)-N_2PdCl_2

(7)

These catalyst precursors, abbreviated N_2PdCl_2 in equation (7), were then employed in the asymmetric Diels–Alder reaction of N-acryloyl oxazolidinone with cyclopentadiene (equation 8).

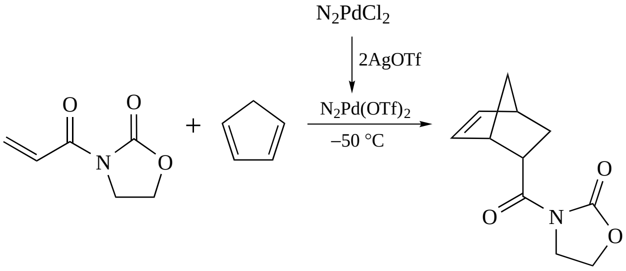

(8)

Although the catalysts typically gave very high endo/exo ratios, the enantioselectivities were low. It was found that the catalyst did not undergo racemization at nitrogen under the reaction conditions, indicating that the poor enantioselectivities reflect the inability of the catalyst to efficiently convey the stereochemical information. This may be due to the similarity in size of the Me and CH_2Ar substituents on the chiral diamine ligand. Nonetheless, this example is illustrates that asymmetric catalysts with only N-chirality are feasible and potentially useful in asymmetric catalysis.

3.4 Chiral Poisoning

It is often found that the resolution of chiral ligands is frequently as difficult as the syntheses of the ligand themselves. To circumvent tedious resolutions, a strategy that involves the use of racemic ligands in asymmetric catalysis has been developed and is termed chiral poisoning.[37,38] The benefit of this approach is that racemic ligands are usually significantly less expensive and easier to access than their enantioenriched counterparts. The chiral poisoning strategy entails generation of a racemic catalyst and selective inhibition of one catalyst enantiomer with a chiral resolved ligand P* (the poison). The binding of the chiral poison to the racemic catalyst would give rise to diastereomeric adducts, which would

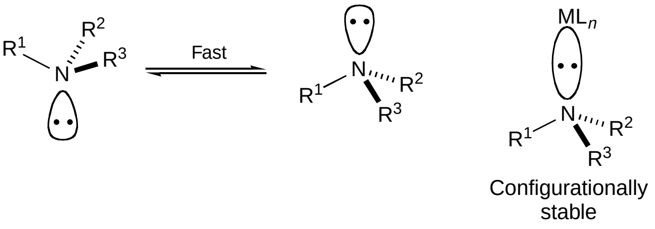

Figure 8 Nitrogen inversion is typically rapid at room temperature. Coordination of the lone pair to a metal center can freeze nitrogen inversion

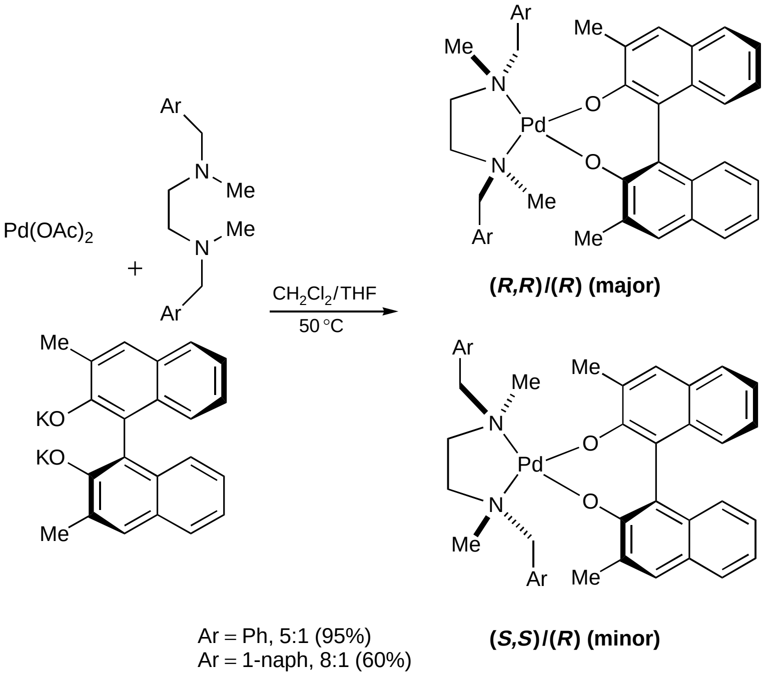

Figure 9 Synthesis of complexes with *N*-chiral diamine ligands

have different association constants. In an ideal scenario the poison binds tightly to one catalyst enantiomer completely disabling it, leaving the other enantiomer free to promote the enantioselective reaction. This situation is illustrated schematically in Figure 10.

An example of how well chiral poisoning strategy can work is illustrated by the asymmetric hydrogenation of β-keto esters. Activation of the enantioenriched (Xyl-BINAP)RuCl$_2$(dmf)$_n$ precatalyst provides a highly enantioselective catalyst for the asymmetric hydrogenation of β-dicarbonyl compounds.[39,40] Application of the chiral poisoning strategy in this system entailed identification of suitable enantioenriched poisons. After screening several potential poisons it was found that 0.5 equivalents the diamine (*S*)-3,3′-dimethyl diaminobinaphthyl, (*S*)-DM-DABN, selectively coordinated to the [(*S*)-Xyl-BINAP]RuCl$_2$ center (Figure 11). Due to an unfavorable steric interaction of the 3,3′-dimethyl substituents on the diamine with the Xyl-groups on the chelating phosphine[41] the [(*R*)-Xyl-BINAP]RuCl$_2$(dmf)$_n$ does not bind the (*S*)-DM-DABN. This steric repulsion is shown in Figure 12.

This system has been applied to the asymmetric hydrogenation (*see Hydrogenation*) of methyl 3-oxobutanoate as illustrated in Table 3. Use of racemic (Xyl-BINAP)Ru complex with (*S*)-DM-DABN gave essentially identical enantioselectivity to the use of enantioenriched (Xyl-BINAP)RuCl$_2$(dmf)$_n$ precatalyst.[41]

These results demonstrate the power of the chiral poisoning strategy under the optimal conditions. Deviations form such ideal behavior can result from incomplete inhibition of one of the enantiomers of the precatalyst. In this case, an excess of the poison may be necessary. It is also possible that the poison inhibits both catalyst enantiomers, but to different degrees. These situations decrease the effectiveness of the chiral poison strategy.

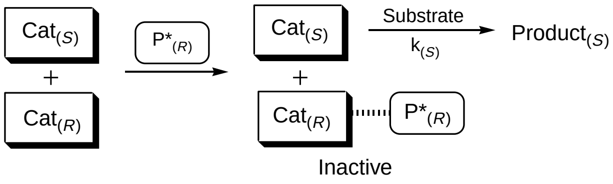

Figure 10 Idealized chiral poisoning involves complete deactivation of one enantiomers of the racemic catalyst, Cat$_{(R)}$ in this example, by the resolved poison $P^*_{(R)}$

Table 3 Comparison of the chiral poisoning strategy to the traditional use of chiral resolved BINAP derivative

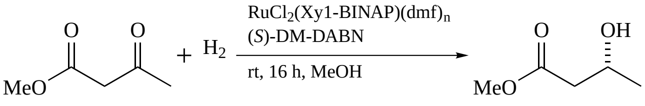

Cat.	(*S*)-DM-DABN	Yield (%)	Product ee (%)
racemic	0.5 equiv.	100%	99.3 (*R*)
(*R*)	none	100%	99.9 (*R*)

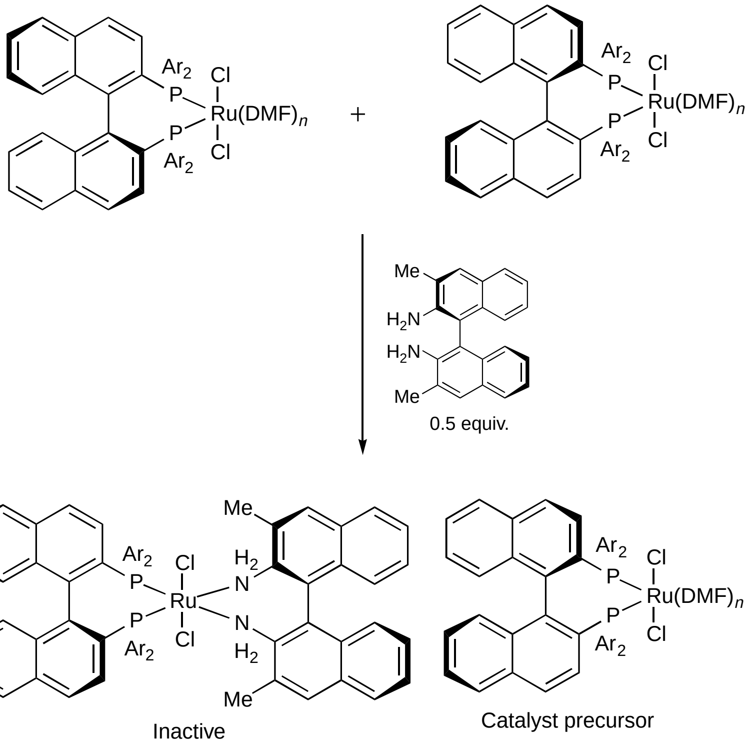
Ar2
P
P
Ar2
Cl
Ru(DMF)n
Cl
+
Ar2
P
P
Ar2
Cl
Ru(DMF)n
Cl
Me
H2N
H2N
Me
0.5 equiv.
Me
Ar2
P
P
Ar2
Cl
Ru
Cl
H2
N
N
H2
Me
Inactive
Ar2
P
P
Ar2
Cl
Ru(DMF)n
Cl
Catalyst precursor

Figure 11 Selective binding of the (*S*)-enantiomer of the precatalyst with the (*S*)-DM-DABN

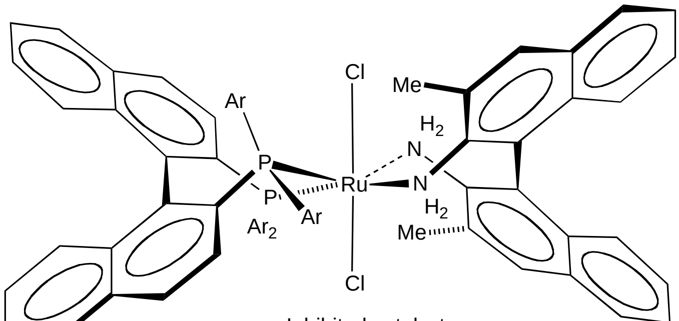
Ar
P
P
Ar2
Ar
Cl
Ru
Cl
Me
H2
N
N
H2
Me

Inhibited catalyst

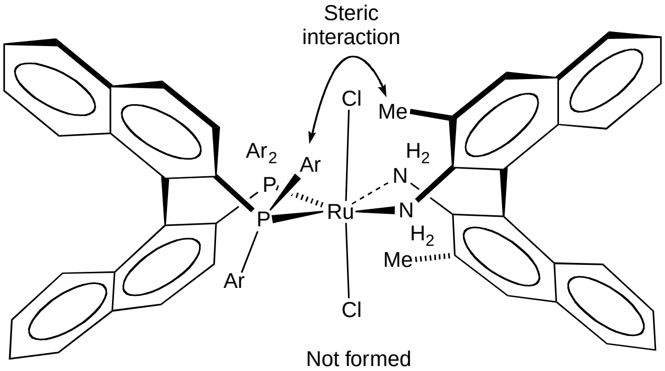
Steric
interaction
Ar2
Ar
P
P
Ar
Cl
Ru
Cl
Me
H2
N
N
H2
Me

Not formed

Figure 12 Three-dimensional drawings of the binding of the (*S*)-enantiomer of the precatalyst with the (*S*)-DM-DABN. The (*R*)-enantiomer of the precatalyst does not bind (*S*)-DM-DABN owing to a repulsive interaction between two aryl groups on the phosphine and the 3,3′-dimethyl groups on the diamine

3.5 Addition of Chiral Additives: Asymmetric Activation

An alternative to the approach chiral poisoning that also involves use of racemic catalysts has been called asymmetric activation.[42,43] In this strategy, a racemic catalyst is reacted with resolved activator that selectively activates one enantiomer of the racemic catalyst precursor. This process involves binding a resolved ligand to a racemic catalyst, resulting in the formation of diastereomeric catalysts. There are several scenarios in which this mixture of diastereomers can give high enantioselectivity. Either both catalysts must give the same enantiomer of the product with high ee, or one of the diastereomeric catalysts must be highly enantioselective *and* significantly more active than the other diastereomer. The advantage of this method over chiral poisoning is that the resultant catalyst system can exhibit greater activity and enantioselectivity than the enantioenriched precatalyst.

3.5.1 Asymmetric Activation of Racemic Hydrogenation Catalysts

Asymmetric hydrogenation of prochiral ketones is an important method for the preparation of chiral secondary alcohols. Until recently, however, such reactions were limited to substrates with pendent metal binding sites, like β-keto esters.[39] Many of the catalysts that efficiently hydrogenate C–C double bonds exhibit little or no reactivity with isolated ketones. This discrepancy may be ascribed to the different binding modes of alkenes and ketones, and the chemoselectivity of catalysts for these groups. While substrates with C–C double bonds can form metal π-complexes, this binding mode is uncommon for ketones. The distinct characteristics of the C–C and C–O π-bonds suggest that catalyst selective for these groups will likely operate by dissimilar mechanisms. This has indeed been found to be the case, and mechanistic investigations indicate that the ketone reduction proceeds by an unexpected pathway that does not involve coordination of the substrate to the metal center.

Ruthenium catalysts bearing diamine and bidentate phosphine ligands, illustrated in equation (9), exhibit high enantioselectivity and efficiency in the reduction of ketones.[39,44–46] Before the application of this catalyst to asymmetric activation can be illustrated, important mechanistic information will be outlined.

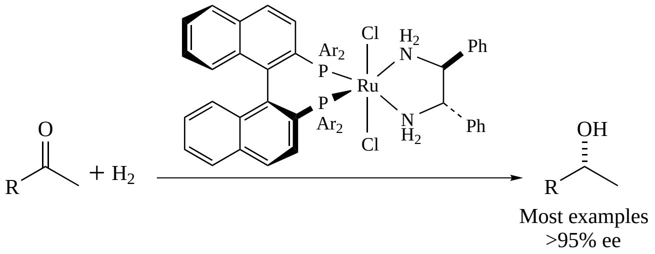

(9)

Detailed experimental and theoretical investigations have provided an accurate picture of the unique mechanism of these remarkable hydrogenation catalysts. The active catalyst is believed to be the dihydride (Figure 13), which is generated by combining the precatalyst in equation (9), alkoxide base, dihydrogen, and the ketone in isopropanol. Analogous compounds have been prepared and characterized crystallographically.[47] The first step in the catalytic cycle is

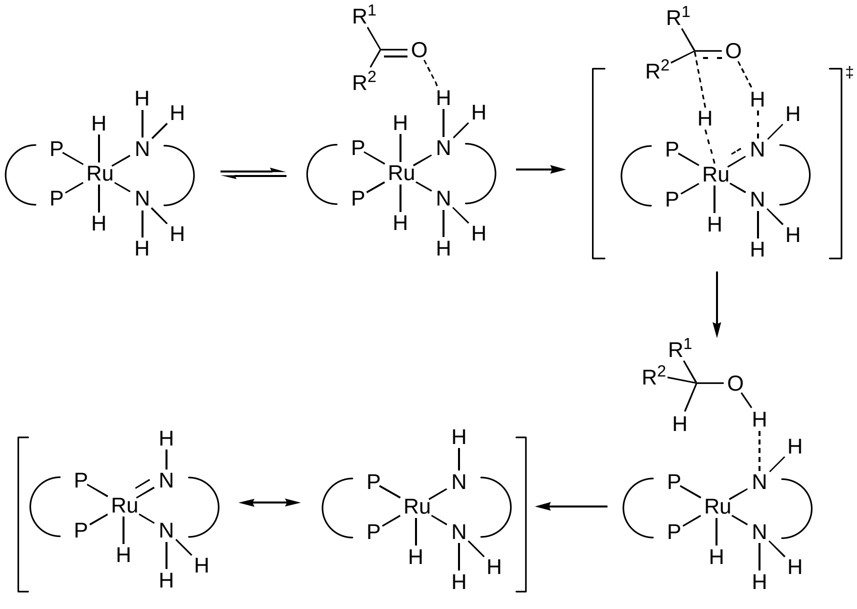

Figure 13 Proposed mechanism for hydrogenation of ketones with (BINAP)RuH$_2$(diamine) derivatives

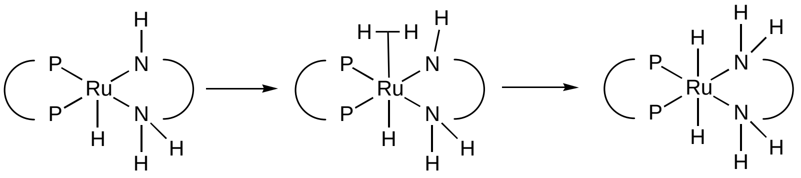

Figure 14 Proposed mechanism of heterolytic cleavage of dihydrogen

believed to be formation of a weak interaction between the ketone substrate and the catalyst, as shown in Figure 13. From this hydrogen-bonded intermediate, facile hydrogenation takes place through a six-membered transition state, resulting in formation of the chiral alcohol and the Ru-amide. Late transition metal amide complexes of this type are very reactive,[48–50] and have been characterized in model systems.[47]

The heterolytic cleavage (*see Heterolytic Cleavage*) of dihydrogen is the turnover-limiting step in the catalytic cycle (Figure 14). It likely occurs via initial formation of a dihydrogen complex (*see* ***Hydrogen Bonding & Dihydrogen Bonding*** followed by proton abstraction by the amide nitrogen to give the dihydride complex. Consistent with this hypothesis, a first-order dependency on the ruthenium catalyst and the dihydrogen is observed. The reaction is zero order in ketone concentration. Additionally, $\Delta S^{\dagger}$ is on the order of $-25\,\mathrm{cal\,molK^{-1}}$, suggesting a highly ordered transition state.

It is interesting to note that these hydrogenation catalysts are 18 electron species and need not open up a coordination site to generate a 16 electron intermediate, as observed with many alkene hydrogenation catalysts. The bifunctional nature of these catalysts allows them to access an unconventional second-coordination sphere hydrogen transfer mechanism. Activation of the ketone through a hydrogen-bond from the ligand eludes to the power of such subtle interaction in enantioselective catalysis.

This system for the asymmetric hydrogenation of ketones has been employed in the asymmetric activation using a racemic BINAP derivative. Combination of $\mathrm{RuCl_2}$[(*S*)-Xyl-BINAP](dmf)$_n$ (Xyl = 3,5-$\mathrm{C_6H_3}$-$\mathrm{Me_2}$) and (*S*,*S*)-DPEN gave the precatalyst $\mathrm{RuCl_2}$[(*S*)-Xyl-BINAP][(*S*,*S*)-DPEN], which exhibited 99% enantioselectivity in the reduction of 1-acetylnaphthone to the (*R*)-alcohol (equation 10).

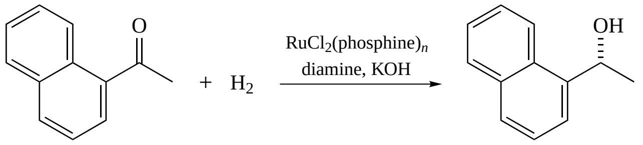

Phosphine	Diamine	% ee
(*S*)-Xyl-BINAP	(*S*,*S*)-DPEN	>99 (*R*)
(*R*)-Xyl-BINAP	(*S*,*S*)-DPEN	56 (*S*)
(*rac*)-Xyl-BINAP	(*S*,*S*)-DPEN	90 (*R*)

(10)

The catalyst composed of the mismatched ligands, (*R*)-Xyl-BINAP and (*S*,*S*)-DPEN, was much slower and furnished the (*S*)-alcohol with 56% ee (equation 10). Employing *racemic* Xyl-BINAP and (*S*,*S*)-DPEN gave a 50:50 mixture of diastereomeric ruthenium complexes that reduced 1′-acetylnaphthone to the (*R*)-alcohol with excellent enantioselectivity (90%).

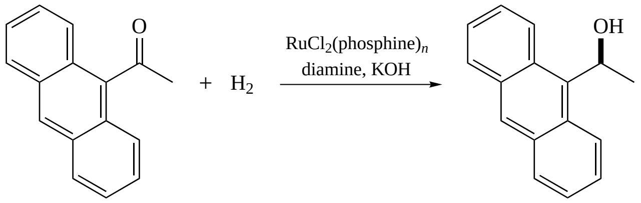

Phosphine	Diamine	% ee
(*S*)-Tol-BINAP	(*S*,*S*)-DPEN	40 (*R*)
(*R*)-Tol-BINAP	(*S*,*S*)-DPEN	81 (*R*)
(*rac*)-Tol-BINAP	(*S*,*S*)-DPEN	80 (*R*)

(11)

Interestingly, when the precatalyst $\mathrm{RuCl_2}$[(*S*)-Tol-BINAP][(*S*,*S*)-DPEN] (Tol = 4-$\mathrm{C_6H_4}$-Me) was employed in the reduction of 9-acetylanthracene the enantioselectivity was only 40% (equation 11). In contrast, use of $\mathrm{RuCl_2}$[(*R*)-Tol-BINAP][(*S*,*S*)-DPEN] resulted in a reduction of the ketone with 81% ee. Employing *racemic* Tol-BINAP and (*S*,*S*)-DPEN gave (*R*)-alcohol with essentially the same enantioselectivity as the enantioenriched (*R*)/(*S*,*S*)-catalyst.

It is noteworthy that in the reduction of 1′-acetylnaphthone the catalyst with the (*S*)/(*S*,*S*)-configuration was the fastest and most enantioselective while in the hydrogenation of 9-acetylanthracene the catalyst with the (*R*)/(*S*,*S*)-configuration gave the highest enantioselectivity, and exhibited a higher turnover frequency.

These high enantioselectivities indicate that the diastereomeric catalysts not only have different enantioselectivities, but must have very different TOFs. Whenever diastereomeric catalysts are applied together in the same reaction, the product ee is governed by the enantioselectivity of each of the diastereomeric catalysts *and* their relative rate.[51–54] This fact complicates reaction optimization. Nonetheless, the results outlined in equation (10) and (11) illustrate how well the chiral activation strategy can work with the correct combination of chiral ligands *and* substrate. It is expected that there will be a great deal of future activity in asymmetric catalysis employing asymmetric activation.

3.6 Asymmetric Activation of Enantioenriched Lewis Acid Catalysts

In the previous example, the asymmetric activation strategy was used to increase the efficiency and enantioselectivity of one catalyst in a diastereomeric mixture of catalysts. This technique can also be applied to resolved asymmetric catalysts. An example of this strategy[42] involves the zinc catalyzed asymmetric addition of alkyl groups to aldehydes.[55,56]

Organozinc catalysts are known to promote the asymmetric addition of alkyl groups to aldehydes with high enantioselectivity.[57] In the case of catalyst generated from (*R*)-3,3-diphenyl BINOL (Ph_2-BINOL) and diethylzinc, however, the asymmetric addition is slow and proceeds in low enantioselectivity (Figure 15). When the catalyst was prepared in the same fashion, followed by addition of enantiopure diimine ligands, new catalysts formed that exhibited increased efficiencies and enantioselectivities. The levels of enantioselectivity of the catalysts were then optimized by screening enantiopure diimine ligands. The best catalyst in this study was derived from (*R*)-Ph_2-BINOL and the (*S*,*S*)-diimine with the stilbene diamine backbone and 2,4,6-trimethylbenzaldehyde (Figure 15). Combination of diimine with Ph_2-BINOL gave a highly enantioselective catalyst that generated 1-phenyl-1-propanol of 90% ee at 0 °C and 99% ee at −78 °C. This catalyst optimization process illustrates the power of asymmetric activation to maximize catalyst efficiency and enantioselectivity.

The asymmetric activation strategy is clearly a useful technique in the optimization of asymmetric catalysis. Racemic catalysts can by selectively activated with enantioenriched activators, resulting in the generation of highly enantioselective catalysts. Resolved catalysts can also be activated with enantioenriched activators, with the potential of increasing their efficiency and enantioselectivity. As illustrated above, this approach can be applied in a combinatorial fashion allowing generation of a large number of catalysts from a small library of ligands.

3.7 Optimization of Enantioselective Catalysts Using Achiral and Meso Ligands

The traditional method for the optimization of asymmetric catalysts involves the synthesis and screening of chiral ligands.[1] As pointed out in previous sections, the resolution of chiral ligands, or their components, can be demanding and time-consuming. In the sections that follow catalyst enantioselectivity and efficiency are maximized by use of achiral and *meso* ligands. The achiral additives can be divided into three classes: (1) achiral ligands with

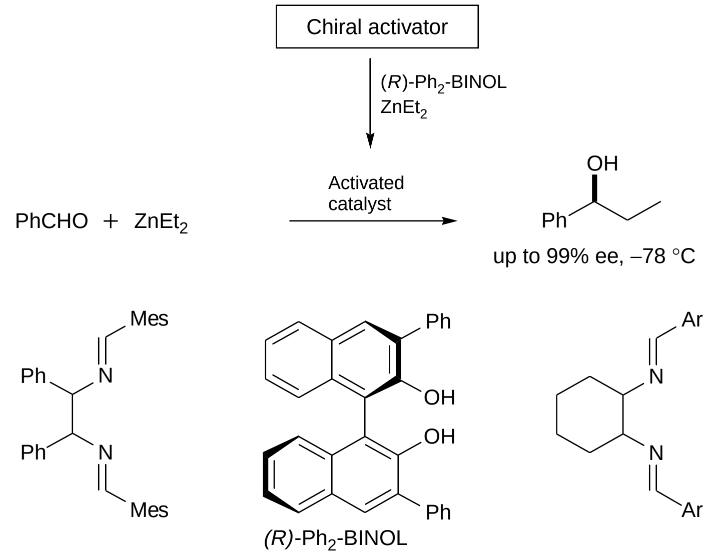

diamine config.	Ar
R,*R*	C_6H_5
R,*R*	2,6-C_6H_3-Cl_2
R,*R*	2,4,6-C_6H_2-Me_3
S,*S*	C_6H_5
S,*S*	2,6-C_6H_3-Cl_2
S*,*S	**2,4,6-C_6H_2-Me_3**

diamine config.	Ar
R,*R*	C_6H_5
R,*R*	2,6-C_6H_3-Cl_2
R,*R*	2,4,6-C_6H_2-Me_3
S,*S*	C_6H_5
S,*S*	2,6-C_6H_3-Cl_2
S,*S*	2,4,6-C_6H_2-Me_3

Figure 15 The asymmetric activation strategy applied to resolved catalysts results in enhanced activity and enantioselectivity

chiral conformations, (2) achiral ligands without chiral conformation, and (3) ligands that become asymmetric in certain metal geometries.

3.7.1 Optimization of the Enantioselective Alkylation of Aldehydes Employing Achiral and Meso Ligands

In the proceeding section on asymmetric activation, (Ph_2-BINOLate)Zn(diimine) complexes containing two resolved ligands were employed in the asymmetric alkylation of aldehydes. In this study, both the Ph_2-BINOL and diimine could be varied to optimize catalyst enantioselectivity (Figure 15).**[55,56]** A different approach to catalyst optimization in this system would involve the use of one resolved ligand and one achiral or *meso* ligand (Figure 16). This strategy could be termed *achiral activation* based on its relation to asymmetric activation. In the study outlined below, the focus was on using achiral or *meso* ligands with *chiral conformations*. These ligands are attached to a metal coordinated to a resolved ligand.**[58,59]** Using this strategy, numerous catalysts can be synthesized from each resolved ligand by combination with an array of achiral and *meso* ligands. One advantage of such an optimization process is that many more achiral and *meso* ligand precursors and ligands are commercially available than enantiopure ligands. The greater variation in ligand components allows generation of catalysts with more diverse chiral environments. This, in turn, increases the likelihood of finding a suitable catalyst. Finally, the cost of achiral and *meso* ligands is less than that of related enantiopure materials.

As proof of principle, and to demonstrate the potential utility of the use of achiral and *meso* ligands in asymmetric catalysis, the catalyst optimization was performed using a single enantioenriched ligand, (*S*)-Ph_2-BINOL. In the asymmetric additions to benzaldehyde with $ZnEt_2$ and 10 mol% (*S*)-Ph_2-BINOL, in the absence of additional ligands, (*S*)-1-phenyl-1-propanol of 44% ee was slowly generated (Table 4, entry 1). After 28 h at 0 °C, conversion to the alcohol was only 83%. Subsequent experiments were performed with achiral or *meso* ligands and Ph_2-BINOL using 10 mol% loading of each of these ligands. Three equivalents of diethylzinc were used relative to benzaldehyde. Although several classes of achiral and *meso* diimines and diamines were employed, with only a few representative examples are listed in Tables 4 and 5. Diimines derived from ethylene diamine were employed and found to lead to enantioselectivities ranging from 52% ee of the (*S*)-enantiomer to 87% ee of the (*R*)-configuration of the alcohol product (Table 4, entries 2–5).

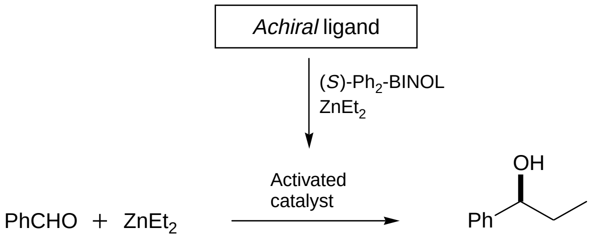

Figure 16 Activation of a chiral catalyst with an achiral or *meso* ligand with chiral conformations can result in an increase in the enantioselectivity of the catalyst

Imine ligands were also prepared based on the 2,2′-diaminobiphenyl backbone. These ligands will bind to zinc and adopt chiral binding modes. The barrier to interconversion of such complexes will be significantly higher than the free ligands, because ring strain will be incurred in the transition state to atropisomerization of the metallocycle. As depicted in Figure 17, the two enantiomeric conformation of the zinc-bound diaminobiphenyl-based ligands are diastereomeric in the presence of the (Ph_2-BINOLate)Zn moiety. If the difference in energy of these diastereomers is large, the equilibrium could lie far to the side of the more stable diastereomer resulting in resolution of the diaminobiphenyl ligand. The chiral conformations of the biphenyl diimine ligands extend the chiral environment of the catalyst (Figure 17). Use of these ligands and (*S*)-Ph_2-BINOL in Figure 16 generated catalysts that exhibited up to 96% enantioselectivity at −45 °C (Table 4, entry 7).

It is interesting to note that catalyst derived from imines of 2,4,6-trimethylbenzaldehyde were found to result in the most enantioselective catalysts with resolved, achiral, and *meso* ligands in the asymmetric addition (Figure 15 and Table 4). This suggests that the placement and orientation of the 2,4,6-trimethylphenyl groups plays a crucial role in the stereoinduction.

In the examination of other nitrogen-based ligands with this catalyst system, it was observed that achiral and *meso* diamines had a marked impact on catalyst enantioselectivities. The simple diamines, TMEDA and *N,N,N′,N′*-tetraethylethylene diamine were found to exhibit the opposite enantiofacial selectivity (Table 5). While TMEDA formed a catalyst that gave the (*S*)-enantiomer of the product in 64% enantioselectivity (0 °C), catalyst based on *N,N,N′,N′*-tetraethylethylene diamine generated the (*R*)-enantiomer in up to 72% ee.

Secondary diamine ligands are particularly interesting because they result in addition of another stereochemical element to the catalyst. Coordination of secondary diamines to zinc stops nitrogen inversion, creating two new stereogenic centers directly attached to the catalyst binding site.**[60,61]** This coordination is likely to be reversible, permitting equilibration of the configuration at nitrogen through a 3-coordinate zinc intermediate. The C_2-symmetric (Ph_2-BINOLate)Zn is expected to bind the diamine in a C_2-symmetric fashion to minimize steric interactions between the diamine and the Ph_2-BINOLate ligand. Positioning of the nitrogen stereocenters in close proximity to the zinc binding site is expected to have a significant impact on the catalyst enantioselectivity in the asymmetric C–C bond forming

Table 4 Results of screening achiral diimines with (*S*)-Ph_2-BINOL in Figure 16

Entry	Ligand	ee at 0 °C (config)	ee at −45 °C (config)
1	No achiral activator	44 (*S*)	–
2	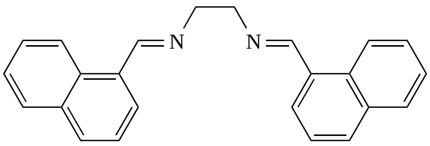	52 (*S*)	–
3	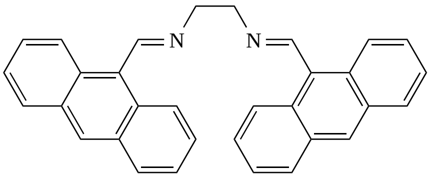	30 (*R*)	–
4	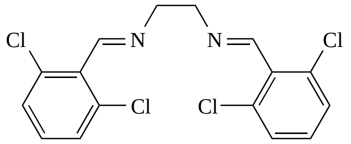	66 (*R*)	74 (*R*)
5	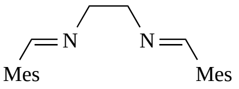	75 (*R*)	87 (*R*)
6	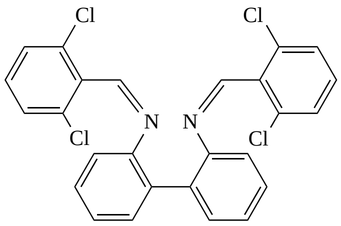	54 (*R*)	–
7	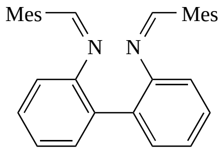	89 (*R*)	96[a] (*R*)

[a] Reactions employed 10 mol% Ph_2-BINOL, 10 mol% diimine ligand, and 300 mol% diethylzinc.

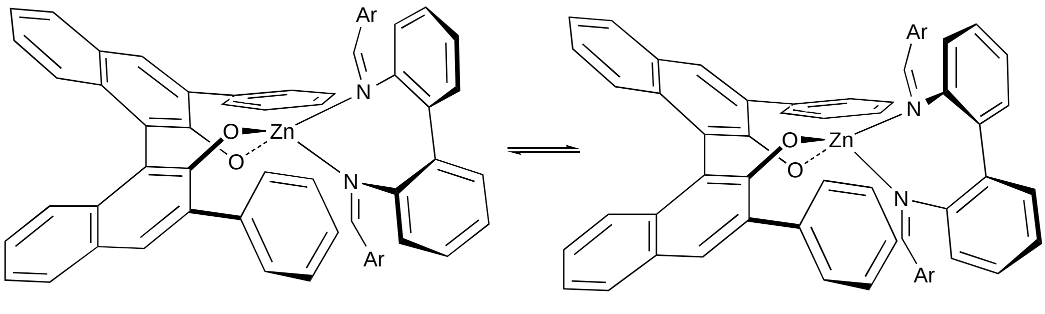

Figure 17 Diastereomeric catalysts derived from different conformations of the diaminobiphenyl ligand

process. Examination of secondary diamines (Table 5, entries 3–5) in Figure 16 resulted in generation of the secondary alcohol with up to 76% enantioselectivity. This is the highest enantioselectivity obtained for the (*S*)-enantiomer in these investigations.

Diamines with pendent biphenyl groups were also employed in the asymmetric addition reaction in Figure 16 (Table 5, entries 6 and 7). It was predicted that atropisomerization of the biphenyl moiety in these ligands would have a low barrier. Interaction of the stereochemically label biphenyl

Table 5 Results of screening achiral diamines with (*S*)-Ph_2-BINOL in Figure 16

Entry	Ligand[a]	ee at 0 °C (config)	ee at −45 °C (config)
1	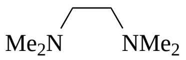	64 (*S*)	–
2	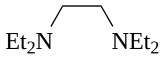	36 (*R*)	72 (*R*)
3	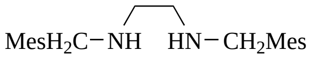	47 (*S*)	–
4	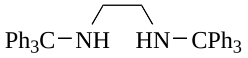	30 (*R*)	–
5	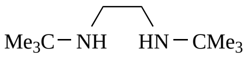	73 (*S*)	76 (*S*)
6	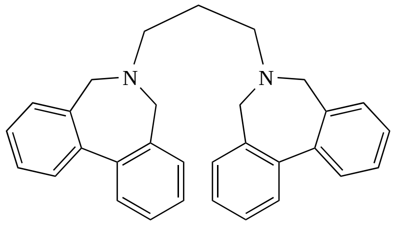	75 (*R*)	87 (*R*)
7	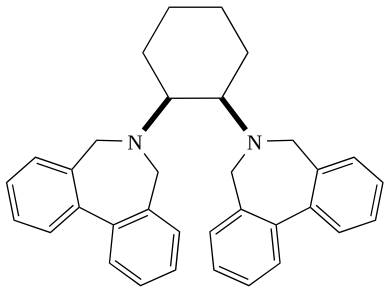	83 (*R*)	92 (*R*)

[a]Reactions employed 10 mol% Ph_2-BINOL, 10 mol% diimine ligand, and 300 mol% diethylzinc.

moiety with the (Ph_2-BINOLate)Zn center is expected to influence the biphenyl stereochemistry and extend the chiral environment of the resulting catalyst.

The catalysts prepared with atropisomeric ligands in entries 6 and 7 gave the product with enantioselectivities as high as 92% at −45 °C. It is interesting to note that catalysts derived from these ligands exhibited greater enantioselectivity than when *N*,*N*,*N*′,*N*′-tetraethylethylene diamine was employed (Table 5, entry 2). Taken together, the results in Tables 4 and 5 clearly indicate the benefit of screening achiral ligands on catalyst enantioselectivity.

The impact of achiral ligands on the TOF of the catalyst in this system was then examined by following reaction conversions with various catalysts. In the absence of both Ph_2-BINOL and diamine ligands, the reaction of diethylzinc with benzaldehyde is very slow, exhibiting about 1% conversion after 8 h at 0 °C. When Ph_2-BINOL was employed in the asymmetric addition to this substrate, the catalyst TOF increased exhibiting 25% conversion after 2 h. To evaluate the TOF of zinc centers bearing diimine derived from ethylene diamine and 2,4,6-trimethylbenzaldehyde (Table 4, entry 5) or the *meso* diamine (Table 5, entry 7), these ligands were combined with diethylzinc and benzaldehyde (no added Ph_2-BINOL). After 2 h it was determined that the reaction with the diimine proceeded to 20% conversion. The reaction with the *meso* diamine was 51% complete in 2 h. Use of Ph_2-BINOL with the diimine or *meso* diamine resulted in a considerable increase in the TOF, with both reactions reaching completion in under 15 min.**[59]** These observations indicate that the achiral ligands have a great impact on the catalyst reactivity as well as the catalyst enantioselectivity.

The catalytically active species in these asymmetric addition reactions are believed to be 4-coordinate (Ph_2-BINOLate)Zn(diimine) and (Ph_2-BINOLate)Zn(diamine) complexes. Support for this hypothesis was gained by synthesis and structure determination of the (Ph_2-BINOLate)Zn(diamine) incorporating the *N*,*N*′-di-*tert*-butyl diamine. The structure of this compound is illustrated in Figure 18. This catalyst likely coordinates the aldehyde substrate generating a 5-coordinate zinc species with an activated aldehyde. Addition of the ethyl group from $ZnEt_2$, possibly by a pathway that involves coordination of the $ZnEt_2$ to a BINOLate oxygen, results in product formation.

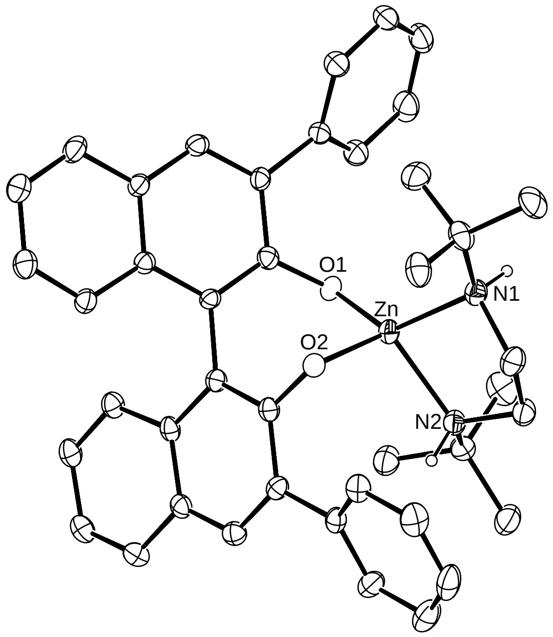

Figure 18 Structure of (Ph$_2$-BINOLate)Zn(diamine). The diamine nitrogens have the expected (*R*,*R*)-configurations

In this study of catalyst optimization with achiral and *meso* ligands, a single chiral ligand, (*S*)-Ph$_2$-BINOL, was employed and led to enantioselectivities between 96% (*R*) and 76% (*S*).[59] This study definitively demonstrates that asymmetric catalysts can be optimized by screening achiral and *meso* ligands. This approach can be adapted to other asymmetric catalysts and holds great promise in asymmetric catalysis.

3.7.2 Use of achiral additives without chiral conformations

The addition of achiral additives lacking chiral conformations to asymmetric catalysts can enhance catalysts enantioselectivity.[62] The exact nature of the interaction between the additive and the chiral catalyst, however, is often not clear. The additives usually contain Lewis basic groups, and can behave as ligands by coordinating to catalysts and changing the metal geometry and/or catalyst aggregation state.

A remarkable example of the impact of achiral ligands on an enantioselective process involved a (BINOLate)Yb-based system.[63,64] In this study, a Lewis acid catalyst was prepared by reacting Yb(OTf)$_3$ with BINOL, followed by addition of two equivalents of *meso*-(1,2,6)-trimethylpiperidine (Figure 19). A speculative structure of the resulting catalyst is illustrated. This complex was found to be an excellent catalyst for the asymmetric Diels–Alder reaction of 3-acyl-1,3-oxazolidin-2-ones with cyclopentadiene (Figure 20).

During this study, the authors noted that aging of the catalyst in the absence of substrate resulted in a decrease in the enantioselectivity in the Diels–Alder reaction. Aging the catalyst in the presence of the substrate, however, provided the most enantioselective catalyst. These results suggested that the substrate stabilized the catalyst. The authors then examined the ability of various substrate-like additives to stabilize the catalyst. It was found that some additives not only stabilized the catalyst, but also impacted the catalyst enantioselectivity. When 3-acetyl-1,3-oxazolidin-2-one was used as additive the endo (2*S*,3*R*)-product was formed with 93% ee. In contrast, acetylacetone derivatives led to a reversal of the facial selectivity. Using the additive 3-phenylacetylacetone as the additive resulted in formation of the (2*R*,3*S*)-product in 81% enantioselectivity. In both instances, the configuration of the chiral ligand was the same: (*R*)-BINOL. A similar reversal of enantioselectivity with these additives was observed when other substrates were employed.

The achiral additives likely bind to the catalyst in a bidentate fashion, and in doing so change the chiral environment around the substrate-binding site. This example illustrates the potential impact that additives can have on catalytic asymmetric reactions.

3.7.3 Metal Geometry-Induced Ligand Asymmetry

Ligand binding modes can play an important role in the enantioselectivity of a catalyst. Some ligands are symmetric in certain metal geometries, but become asymmetric when the metal binds to an additional ligand. This property can be particularly useful in asymmetric catalysis if the achiral ligand adopts an asymmetric binding mode upon coordination of the substrate. Under these circumstances the achiral ligand can impact the chiral environment of the catalyst, changing the

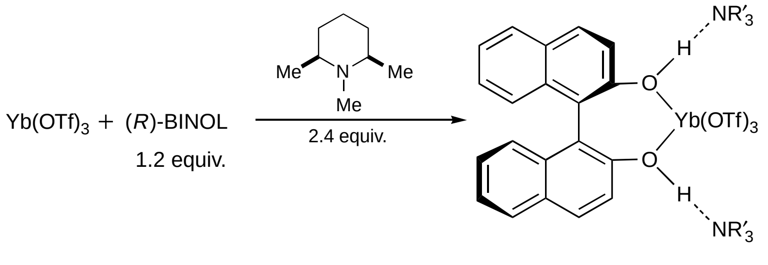

Figure 19 Preparation and proposed structure of chiral Yb(III) triflate Lewis acid

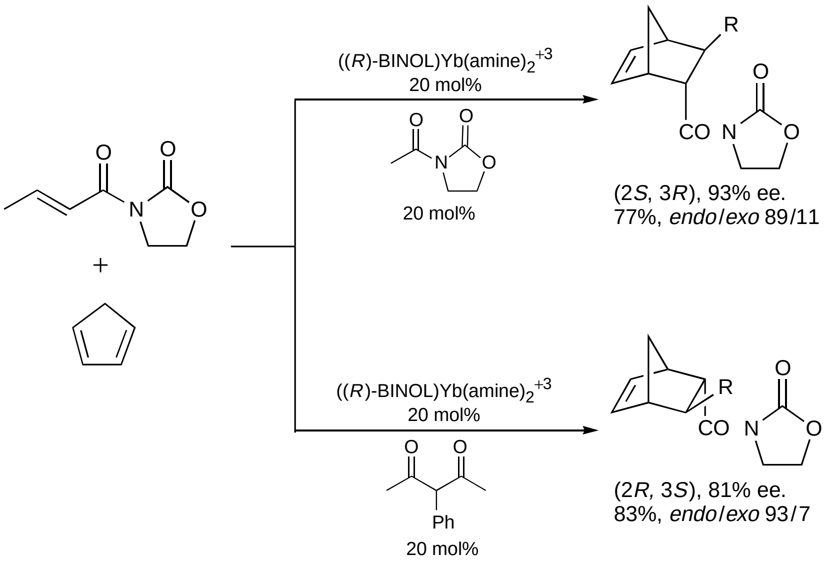

Figure 20 Asymmetric Diels–Alder reaction with achiral additives

enantioselectivity. An example of such a system is illustrated in the following paragraphs.

Compounds of the type (MBP)TiX_2 (MBP = methylene bis(phenoxide) and X = Cl, Figure 21) are achiral, because they possess a plain of symmetry. Upon coordination of a Lewis basic ligand L, however, a 5-coordinate (MBP)TiCl_2 (L) complex is generated. The apical and equatorial oxygens may be inequivalent by virtue of their binding sites (Figure 21). As a result, the (MBP)Ti metallocycle is chiral and (MBP)TiCl_2 (THF) exists as a racemic mixture.[65]

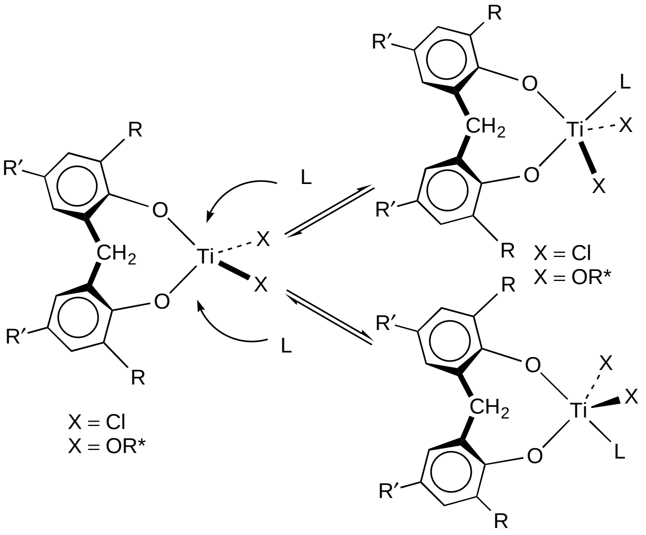

Figure 21 When X = Cl, L = THF two enantiomeric 5-coordinate titanium centers are possible. When X = OR* and L = aldehyde substrate, diastereomeric 5-coordinate titanium complexes may form

The objective of this study was to use the chirality of the (MBP)Ti metallocycle in the trigonal bipyramidal geometry to bias the chiral environment of an enantioselective catalyst. Theoretically, if it were possible to replace the THF in one of the enantiomers of (MBP)TiCl_2(THF) for a substrate, the (MBP)Ti metallocycle would provide a chiral environment for the substrate. Attack on the bound substrate by an achiral reagent would generate a non-racemic product. Substitution of chiral, enantioenriched ligands for the chlorides would cause the configuration of the (MBP)Ti metallocycle to be biased. If the biasing of the enantiomeric forms of the (MBP)Ti metallocycle is efficient, this metallocycle might adopt a single enantiomeric form (Figure 21). In this study, readily available chiral alkoxide ligands were used to introduce asymmetry into the catalyst.

A series of achiral derivatives of MBP-H_2 (20 mol%) were used with Ti(OR*)$_4$ derived from the (*S*)-enantiomer of 1-phenyl-1-propanol in the asymmetric addition to aldehydes (Figure 22). The results of this study are compiled in Table 6. Inspection of the enantioselectivities using various (MBP)Ti-derivatives clearly illustrates that addition of different achiral MBP ligands can have a significant impact on the ee of the product [9% (*R*) to 83% (*S*)]. MBP-H_2 ligands with small R groups were found to be less enantioselective. Nonetheless, when R = H (entries 1 and 2, Table 6), the catalysts exhibited significant differences in enantioselectivity from that of the background reaction in entry 10 [9% ee (*R*) vs. 39% ee (*S*)]. In this example, the background reaction is promoted by the chiral alkoxide complex Ti(OR*)$_4$. Increasing the bulk of the MBP ligand to R = *t*-Bu resulted in an increase in enantioselectivities (entries 6–8). A further increase in ee was observed when R = adamantyl (83% ee, entry 9). Thus, modification of the achiral MBP ligand

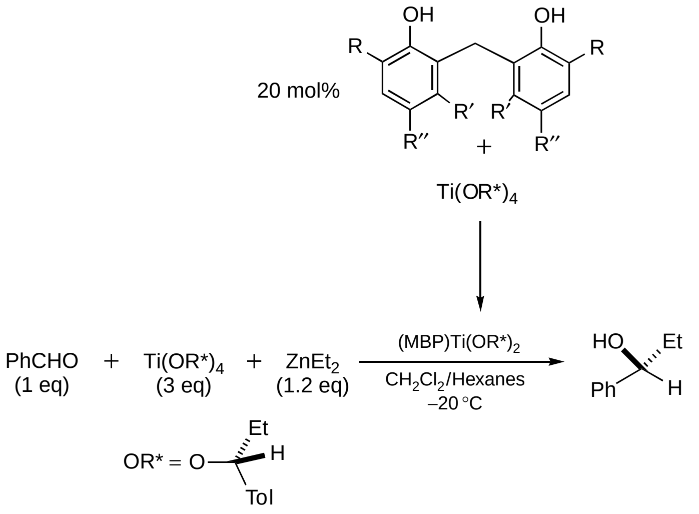

Figure 22 Asymmetric addition of alkyl groups to aldehydes employing (MBP)Ti(OR*)$_2$ catalysts

Table 6 MBP-H$_2$ ligands used in the asymmetric addition of alkyl groups to aldehydes (Figure 22)

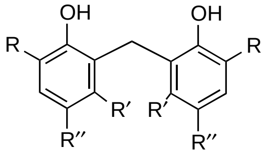

Entry	R	R′	R″	ee %[a] (config)
1	H	H	H	1 (*S*)
2	H	H	Cl	**9 (*R*)**
3	Cl	Cl	Cl	24 (*S*)
4	Me	H	Me	16 (*S*)
5	Ph	H	H	36 (*S*)
6	*t*-Bu	H	*t*-Bu	68 (*S*)
7	*t*-Bu	H	Me	79 (*S*)
8	*t*-Bu	H	H	73 (*S*)
9	Adamantyl	H	Me	**83 (*S*)**
10	NO MBP-H$_2$ Ligand added			39 (*S*)

[a] ee determined after 1 h of reaction.

resulted in a change in ee of over 90% between entries 2 and 9.

As shown in this example, substrate binding may increase the number of stereochemical elements in a catalyst. In these investigations, it is proposed that a change in metal geometry from tetrahedral to trigonal bipyramidal on coordination of a substrate can induce chirality in the (MBP)Ti metallocycle (Figure 21). Once in an asymmetric binding mode, the (MBP)Ti moiety can contribute to, or even dominate, the relay of asymmetry to the substrate. The asymmetry of the bound MBP ligand is illustrated in the ORTEP diagram in Figure 23. An *N*,*N*-dimethylamine plays the role of a substrate analog in this example. The principle of geometry-induced ligand asymmetry can be applied to optimization of other asymmetric catalysts.

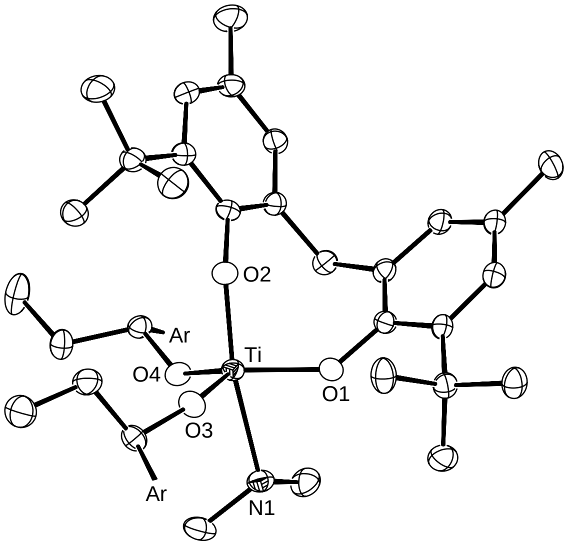

Figure 23 ORTEP drawing of (MBP)Ti(OR*)$_2$ (HNMe$_2$). The aryl groups have been removed for clarity

3.8 Combinatorial Methods for Catalyst Generation

Combinatorial chemistry has been successfully employed in the search for new drug candidates, and has had a significant impact on the pharmaceutical industry. High throughput strategies allow the simultaneous generation of many compounds. The idea of using such methods for the synthesis and screening of chiral ligands and catalysts is an attractive, yet formidable challenge. Three issues to be considered in designing catalyst systems for high throughput screening are (1) sources of diversity, (2) catalyst synthesis, and (3) catalyst screening.[66]

Modular ligands and catalysts are ideal for high throughput screening. They are composed of subunits that can be easily interchanged to generate large numbers of catalysts with a wide range of steric and electronic properties. In metal-based catalyst, the metal can also be varied, providing additional diversity.

One of the requirements of this approach is that catalyst synthesis must be accomplished with clean, high-yielding reactions to avoid time-consuming purification steps. This requirement often limits the classes of ligands and catalysts that are amenable to high throughput methods.

Assaying the enantioselectivity and activity of individual catalyst is often the most difficult and time-consuming aspect of high throughput screening. Most reports involve screening each catalyst individually

Ligands incorporating amino acids fulfill these guidelines and have been used to develop highly enantioselective catalysts for several reactions. A series of peptide-based catalysts for the asymmetric conjugate addition of organozinc reagents to enones has been reported. Closely related ligands derived from dipeptide phophine ligands have been shown to give excellent enantioselectivities for cyclic enones[67] (equation 12) and acyclic enones.[68] However, these ligands were not optimal in the conjugate addition of trisubstituted enones.[69]

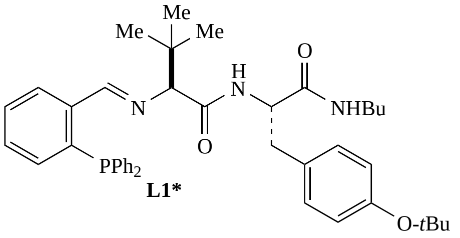

L1*

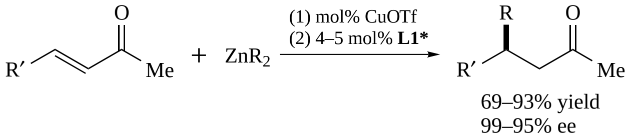

(12)

In developing new ligands for these substrates, the points of diversity are the amino acid residues (AA1 and AA2), the substituents on the phosphine and the metal center (Table 7). Each of these subunits can be varied, leading to a large number of catalysts. Variation of the amino acids was explored, because peptidic systems can be easily prepared in parallel by solid phase protocols. As shown in Table 7, ligand **L1*** which was successfully used with cyclic enones (equation 12) gave 85% ee. Substitution of *tert*-leucine for valine led to a decrease in enantioselectivity and a significant loss in efficiency (**L2***). Surprisingly, substitution of an achiral glycine for the phenylalanine in both **L3*** and **L4*** resulted in an increase in enantioselectivity in each case. Dropping that amino acid residue resulted in the optimal catalyst in this study.

Table 7 Optimization of modular ligands for the asymmetric conjugate addition reaction

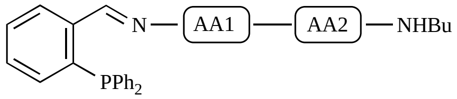

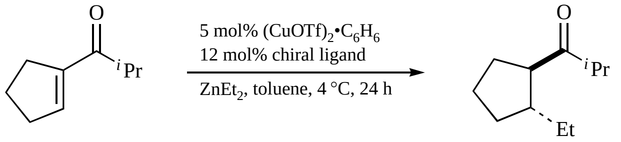

Ligand	AA1	AA2	conv.	ee (%)
L1*	L-*t*-Lue	L-Phe	93	85
L2*	L-Val	L-Phe	32	76
L3*	L-*t*-Lue	Gly	87	93
L4*	L-Val	Gly	92	91
L5*	L-*t*-Lue	–	98	83
L6*	L-Val	–	97	96

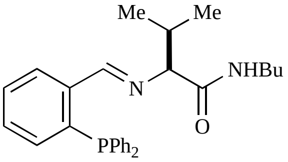

L6*

Table 8 Cu-Catalyzed conjugate addition reaction with ligand **L6*** (6–12 mol%) with ZnR$_2$. Products were obtained with good to excellent diastereoselectivity favoring the anti diastereomer

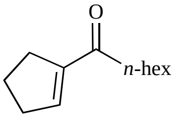	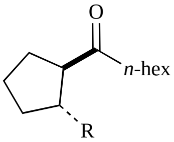	R = Me Et	95 97
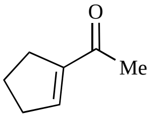	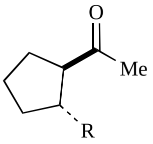	R = Me Et *i*Pr	97 97 98
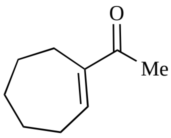	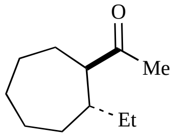		98

As seen in Table 8, the resulting catalyst system gave excellent enantioselectivities with a range of enones and dialkylzinc reagents.

This example illustrates how screening peptide-based ligands can be useful in the development of catalysts. These catalysts could not be rationally designed based on related ligands or understanding of the mechanism. Related nonmetal-based catalysts employing peptide-based ligands have also been optimized using these techniques. These studies employed large libraries of compounds.[70]

4 FINAL PERSPECTIVE

This brief summary of alternative approaches to asymmetric catalysis is not meant to be complete or comprehensive. There are many excellent examples that could have been included in this work and would have served equally as well. Nonetheless, the goal of this section is to expose the reader to concepts in catalyst design and optimization that have not been extensively explored and to inspire those interested in pursuing investigations in this area to take a nontraditional approach.

5 RELATED ARTICLES

Actinides: Inorganic & Coordination Chemistry; Boron: Inorganic Chemistry; Hydrogen Bonding & Dihydrogen Bonding; Palladium: Organometallic Chemistry; Platinum: Organometallic Chemistry; Rhodium: Organometallic Chemistry; Ruthenium: Organometallic Chemistry; Titanium: Organometallic Chemistry; Zinc: Inorganic & Coordination Chemistry; Zinc: Organometallic Chemistry.

6 REFERENCES

1. E. N. Jacobsen, A. Pfaltz, and H. Yamamoto, ‘Comprehensive Asymmetric Catalysis’, Springer, Berlin, 1999, Vol. 1–3.
2. I. Ojima, ed., ‘Catalytic Asymmetric Synthesis’, 2nd ed., Wiley-VCH, New York, 2000.
3. B. Bosnich, in ‘Encyclopedia of Inorganic Chemistry’, ed. R. B. King, John Wiley & Sons, New York, 1994, p. 219.
4. H. I. Blaser and E. Schmidt, in ‘Asymmetric Catalysis on Industrial Scale’, Wiley-VCH, Weinheim, 2004.
5. T. Katsuki and K. B. Sharpless, *J. Am. Chem. Soc.*, 1980, **102**, 5974.
6. T. Katsuki, in ‘Comprehensive Asymmetric Catalysis’, eds. E. N. Jacobsen, A. Pfaltz, and H. Yamamoto, Springer, Berlin, 1999, Vol. 2, p. 621.
7. R. Noyori, ‘Asymmetric Catalysis in Organic Synthesis’, Wiley, New York, 1994.
8. T. P. Yoon and E. N. Jacobsen, *Science*, 2003, **299**, 1691.
9. W. Zhang, J. L. Loebach, S. R. Wilson, and E. N. Jacobsen, *J. Am. Chem. Soc.*, 1990, **112**, 2801.
10. R. Irie, K. Noda, Y. Ito, N. Matsumoto, and T. Katsuki, *Tetrahedron Lett.*, 1990, **31**, 7345.
11. T. Katsuki, in ‘Catalytic Asymmetric Synthesis’, 2nd ed., ed. I. Ojima, Wiley-VCH, New York, 2000, p. 287.
12. E. N. Jacobsen and M. H. Wu, in ‘Comprehensive Asymmetric Catalysis’, eds. E. N. Jacobsen, A. Pfaltz, and H. Yamamoto, Springer, Berlin, 1999, Vol. 2, p. 649.
13. H. Nishikori, C. Ohta, and T. Katsuki, *Synlett*, 2000, 1557.
14. A. M. Daly, M. F. Renehan, and D. G. Gilheany, *Org. Lett.*, 2001, **3**, 663.
15. K. Nakata, T. Takeda, J. Mihara, T. Hamada, R. Irie, and T. Katsuki, *Chem. – Eur. J.*, 2001, **7**, 3776.
16. J. M. Keith, J. F. Larrow, and E. N. Jacobsen, *Adv. Synth. & Catal.*, 2001, **1**, 5.
17. S. E. Schaus, B. D. Brandes, J. F. Larrow, M. Tokunaga, K. B. Hansen, A. E. Gould, M. E. Furrow, and E. N. Jacobsen, *J. Am. Chem. Soc.*, 2002, **124**, 1307.
18. M. Tokunaga, J. F. Larrow, F. Kakuichi, and E. N. Jacobsen, *Science*, 1997, **277**, 936.
19. L. Aouni, K. E. Hemberger, S. Jasmin, H. Kabir, J. F. Larrow, I. Le-Fur, P. Morel, and T. Schlama, in ‘Asymmetric Catalysis on Industrial Scale’, eds. H. I. Blaser and E. Schmidt, Wiley-VCH, Weinheim, 2004, p. 165.
20. J. F. Larrow and E. N. Jacobsen, *J. Am. Chem. Soc.*, 1994, **116**, 12129.
21. T. Hamada, R. Irie, J. Mihara, K. Hamachi, and T. Katsuki, *Tetrahedron*, 1998, **54**, 10017.
22. M. Palucki, P. Hanson, and E. N. Jacobsen, *Tetrahedron Lett.*, 1992, **33**, 7111.
23. K. Noda, N. Hosoya, R. Irie, Y. Yamashita, and T. Katsuki, *Tetrahedron*, 1994, **50**, 9609.
24. H. Nishikori and T. Katsuki, *Tetrahedron Lett.*, 1996, **37**, 9245.
25. E. F. DiMauro and M. C. Kozlowski, *J. Am. Chem. Soc.*, 2002, **124**, 12668.
26. T. Hayashi, M. Takahashi, Y. Takaya, and M. Ogasawara, *J. Am. Chem. Soc.*, 2002, **124**, 5052.
27. M. T. Reetz, D. Moulin, and A. Gosberg, *Org. Lett.*, 2001, **3**, 4083.
28. M. Kuriyama, K. Nagai, K.-i. Yamada, Y. Miwa, T. Taga, and K. Tomioka, *J. Am. Chem. Soc.*, 2002, **124**, 8932.
29. T. J. Davis, J. Balsells, P. J. Carroll, and P. J. Walsh, *Org. Lett.*, 2001, **3**, 699.
30. O. Desponds and M. Schlosser, *Tetrahedron Lett.*, 1996, **37**, 47.
31. J. J. Becker, P. S. White, and M. R. Gagné, *J. Am. Chem. Soc.*, 2001, **123**, 9478.
32. A. K. Ghosh and H. Matsuda, *Org. Lett.*, 1999, **1**, 2157.
33. K. Mikami, K. Aikawa, and Y. Yusa, *Org. Lett.*, 2002, **4**, 95.

34. K. Mikami, K. Aikawa, Y. Yusa, and M. Hatano, *Org. Lett.*, 2002, **4**, 91.
35. M. Saunders and F. Yamada, *J. Am. Chem. Soc.*, 1963, **85**, 1882.
36. K. A. Pelz, P. S. White and M. R. Gagne, *Organometallics*, 2004, **23**, 3210.
37. J. W. Faller and J. Parr, *J. Am. Chem. Soc.*, 1993, **115**, 804.
38. J. W. Faller, A. R. Lavoie, and J. Parr, *Chem. Rev.*, 2003, **102**, 3345.
39. R. Noyori and T. Ohkuma, *Angew. Chem., Int. Ed. Engl.*, 2001, **40**, 40.
40. D. J. Agera and S. A. Lanemana, *Tetrahedron: Asymmetry*, 1997, **8**, 3327.
41. K. Mikami, Y. Yusa, and T. Korenaga, *Org. Lett.*, 2002, **4**, 1643.
42. K. Mikami, M. Terada, T. Korenaga, Y. Matsumoto, M. Ueki, and R. Angelaud, *Angew. Chem., Int. Ed. Engl.*, 2000, **39**, 3532.
43. K. Mikami, M. Terada, T. Korenaga, Y. Matsumoto, and S. Matsukawa, *Acc. Chem. Res.*, 2000, **33**, 391.
44. T. Ohkuma, H. Ooka, S. Hashiguchi, T. Ikariya, and R. Noyori, *J. Am. Chem. Soc.*, 1995, **117**, 2675.
45. R. Noyori, M. Yamakawa, and S. Hashiguchi, *J. Org. Chem.*, 2001, **66**, 7931.
46. J.-H. Xie, L.-X. Wang, Y. Fu, S.-F. Zhu, B.-M. Fan, H.-F. Duan, and Q.-L. Zhou, *J. Am. Chem. Soc.*, 2003, **125**, 4404.
47. K. Abdur-Rashid, S. E. Clapham, A. Hadzovic, J. N. Harvey, A. J. Lough, and R. H. Morris, *J. Am. Chem. Soc.*, 2002, **124**, 15104.
48. J. R. Fulton, M. W. Bouwkamp, and R. G. Bergman, *J. Am. Chem. Soc.*, 2000, **122**, 8799.
49. H. E. Bryndza and W. Tam, *Chem. Rev.*, 1988, **88**, 1163.
50. J. R. Fulton, A. W. Holland, D. J. Fox, and R. G. Bergman, *Acc. Chem. Res.*, 2002, **35**, 44.
51. D. G. Blackmond, T. Rosner, T. Neugebauer, and M. T. Reetz, *Angew. Chem., Int. Ed. Engl.*, 1999, **38**, 2196.
52. C. Bolm, K. Muniz, and J. P. Hildebrand, *Org. Lett.*, 1999, **1**, 491.
53. M. Kitamura, S. Suga, M. Niwa, and R. Noyori, *J. Am. Chem. Soc.*, 1995, **117**, 4832.
54. J. Balsells and P. J. Walsh, *J. Am. Chem. Soc.*, 2000, **122**, 3250.
55. K. Mikami, R. Angelaud, K. L. Ding, A. Ishii, A. Tanaka, N. Sawada, K. Kudo, and M. Senda, *Chem. – Eur. J.*, 2001, **7**, 730.
56. K. Ding, A. Ishii, and K. Mikami, *Angew. Chem., Int. Ed. Engl.*, 1999, **38**, 497.
57. L. Pu and H.-B. Yu, *Chem. Rev.*, 2001, **101**, 757.
58. J. Balsells and P. J. Walsh, *J. Am. Chem. Soc.*, 2000, **122**, 1802.
59. A. M. Costa, C. Jimeno, J. Gavenonis, P. J. Carroll, and P. J. Walsh, *J. Am. Chem. Soc.*, 2002, **124**, 6929.
60. E. L. Eliel and S. H. Wilen, ‘Stereochemistry of Organic Compounds’, Wiley & Sons, New York, 1994.
61. A. von Zelewsky, ‘Stereochemistry of Coordination Compounds’, John Wiley & Sons, Chichester, 1996.
62. E. M. Vogl, H. Groger, and M. Shibasaki, *Angew. Chem., Int. Ed. Engl.*, 1999, **38**, 1570.
63. S. Kobayashi and H. Ishitani, *J. Am. Chem. Soc.*, 1994, **116**, 4083.
64. S. Kobayashi, I. Hachiya, H. Ishitani, and M. Araki, *Tetrahedron Lett.*, 1993, **34**, 4535.
65. J. Okuda, S. Fokken, H.-C. Kang, and W. Massa, *Chem. Ber.*, 1995, **128**, 221.
66. K. D. Shimizu, M. L. Snapper, and A. H. Hoveyda, in ‘Comprehensive Asymmetric Catalysis’, eds. E. N. Jacobsen, A. Pfaltz, and H. Yamamoto, Springer, Berlin, 1999, Vol. 2, p. 1389.
67. S. J. Degrado, H. Mizutani, and A. H. Hoveyda, *J. Am. Chem. Soc.*, 2001, **123**, 755.
68. H. Mizutani, S. J. Degrado, and A. H. Hoveyda, *J. Am. Chem. Soc.*, 2002, **124**, 779.
69. S. J. Degrado, H. Mizutani, and A. H. Hoveyda, *J. Am. Chem. Soc.*, 2002, **124**, 13 362.
70. M. S. Sigman, P. Vachal, and E. N. Jacobsen, *Angew. Chem., Int. Ed. Engl.*, 2000, **39**, 1279.

Beryllium & Magnesium: Organometallic Chemistry

Dovas A. Saulys[1] **& E. Alexander Hill**[2]
[1] *University of Wisconsin, Madison, WI, USA*
[2] *University of Wisconsin, Milwaukee, WI, USA*

Based in part on the article Beryllium & Magnesium: Organometallic Chemistry by E. Alexander Hill which appeared in the Encyclopedia of Inorganic Chemistry, First Edition.

1 Introduction 1
2 Bonding and Structure 1
3 Spectroscopy 6
4 Preparation 7
5 Reactions of Organoberyllium and -Magnesium Compounds 11
6 Special Classes of Compounds 21
7 Related Articles 25
8 References 26

Glossary

Barbier reaction: reaction of an organic halide with a substrate and metal
Grignard reaction: reaction of a preformed organometallic solution
Grignard reagent: in this article, will refer to the solution prepared by reaction of an alkyl halide with magnesium metal, without implication as to molecular species actually present

1 INTRODUCTION

Victor Grignard found in 1900 that solutions of organomagnesium halides may be prepared easily by the reaction of an organic halide with magnesium metal in diethyl ether, and that these solutions undergo useful reactions with many kinds of substrates.[1] This discovery ushered in a new era in organometallic chemistry and provided chemists with a powerful and versatile reagent for synthesis of a wide variety of organic and organometallic compounds. Along with lithium, magnesium remains almost unique among the metals in its ability to react directly and conveniently with a wide variety of organic halogen compounds to produce an organometallic reagent.

The most prominent chemical property of organomagnesium compounds is their ability to deliver an *effectively* ‘anionic’ organic group (alkyl, aryl, vinyl, etc.) with *Nucleophile* or base properties. As nucleophilic alkylating reagents, their important reactions include nucleophilic displacement of less basic leaving groups from saturated carbon atoms or other elements, addition to carbonyl groups and other unsaturated functions, and nucleophilic substitution at the acyl group of carboxylic acid derivatives. They also can transfer an electron as a reductant.

In contrast, organoberyllium compounds are not as easily prepared by direct reaction of beryllium metal with organic substrates. They are less nucleophilic than their magnesium congeners, and have not found a unique niche in organic or organometallic synthesis. The high toxicity of beryllium and its compounds is likely responsible for the latter. There is, however, a substantial body of interesting chemistry, and it is useful to contrast the chemistry of magnesium compounds with their lighter analogs. Indeed, synthetic beryllium research is currently experiencing a revival, after decades of little activity. Important new work on substituted beryllocenes, as well as the advent of beryllium–silicon chemistry are discussed in Sections 6.4 and 6.7, respectively.

The classic monograph of Kharasch and Reinmuth,[2] with its voluminous tables, is still a useful source of information on organomagnesium chemistry. General surveys have appeared in ‘Comprehensive Organometallic Chemistry’,[3–5] in ‘The Chemistry of the Metal–Carbon Bond’,[6] and elsewhere.[7] Especially noteworthy are two recent compilations that cover virtually every aspect of Grignard chemistry.[8,9] The most recent surveys of organoberyllium chemistry are in ‘Comprehensive Organometallic Chemistry II’,[10] and the dedicated volume of the Gmelin series.[11] Details not explicitly referenced may also be found in these general reviews; reviews pertinent to limited aspects are referenced in relevant locations herein. In the case of serial compilations, the latest edition is generally cited.

2 BONDING AND STRUCTURE

Beryllium and magnesium have a formal oxidation state of $+2$ in their compounds (*see Oxidation Number*); other oxidation states appear to exist only as transient reaction intermediates. Therefore, organometallic compounds of general formula R_2M and RMY may exist, in addition to the nonorganometallic MY_2.

Though conceptually simple, monomeric unsolvated R_2M or RMY species are infrequently encountered. The metal center is a Lewis-acidic site with a strong tendency to coordinate basic solvents or ligands (*see Lewis Acids & Bases*). Grignard reagents are most commonly made in ether, and it is frequently impossible to drive off all of the solvent without thermal decomposition. R_2Mg compounds are more easily freed of ether by heating under vacuum, but R_2Be may remain solvated even in the vapor phase. In competition with solvation, the metal centers may also be linked into dimers or higher polymers by bridging ligands ‘Y^-’, or by organic groups which bridge via electron-deficient multicenter bonds (*see Electron Deficient Compound* and *Multicenter Two-electron Bonding*). In any given instance, the actual structure, degree of association, and coordination number of the metal will be a function of the basicity of the solvent, the coordinating/bridging tendencies of the Y^- and organic groups, the acidity of the metal center (as influenced by the electronegativities of the attached groups), and the steric requirements of the various components (*see* ***Coordination Numbers & Geometries***). In general, THF (tetrahydrofuran) is more basic and less bulky than Et_2O, $(i\text{-Pr})_2O$ coordinates less strongly, and *Chelating Ligands* bind strongly. F^- and Cl^- bridge more effectively than the higher halides, and among organic groups, methyl and alkynyl are good bridging groups (Me_2Mg is reported to crystallize solvent-free from diethyl ether).

Recent reviews have surveyed X-ray and electron diffraction structures of organomagnesium compounds[12,13] (*see* ***Diffraction Methods in Inorganic Chemistry***); literature citations for both metals are also included in other reviews.[4,8,9]

2.1 The Metal-to-carbon Bond

The electronegativities of beryllium and magnesium on various scales lie in the vicinity of 1.6 and 1.35, respectively, substantially less electronegative than carbon at about 2.55 (*see Electronegativity*). Simple C–Be and C–Mg bonds should therefore be quite polar, with Pauling 'ionic characters' of about 20 and 30% respectively (*see Ionic Character*). Molecular orbital calculations (*see* ***Molecular Orbital Theory***) also indicate highly polar, perhaps essentially ionic, C–Mg and C–Be bonds, though specific conclusions vary depending on the basis set, type of calculation, and the interpretation.[14–17]

Thermochemical data on organoberyllium and -magnesium compounds are not very extensive. A number of enthalpies of formation for Grignard reagents have been determined via measurement of their heats of hydrolysis,[18,19] and bond dissociation energies have been measured for Np_2Mg.[20] An attempt has also been made using theoretical calculations in combination with experimental data to develop a set of consistent *Bond Energies* for lithium, beryllium, and magnesium compounds.[21]

2.2 Unsolvated Monomers

Several magnesium and beryllium compounds, including Cp_2Mg, $Cp^*{}_2Mg$, Cp(Np)Mg, Np_2Mg, $MgBr_2$, MgI_2, Cp(Me)Be, Me_2Be and $(t\text{-Bu})_2Be$ have been studied in the gas phase. All have the linear geometry predicted for sp *Hybridization* at the metal, as do the extremely hindered (**1**), as well as $(tert\text{-Bu}_3Si)_2Be$ (Section 6.7), in the crystal. C–Mg and C–Be *Bond Lengths* are 211.6–212.6 and 169.8–170.6 pm, respectively. Some [tris(pyrazolyl)hydroborato]metal derivatives (*see Tris(pyrazolyl)borates*) are unsolvated monomers, with approximately tetrahedral geometry about the metal (e.g. (**2**); C–Mg, 212 pm; C–Be, 170.8).[8] Certain β-diketiminateMgR complexes are also monomeric, and exhibit a trigonal planar coordination geometry for magnesium when R is sterically demanding (e.g. R $=$ t-Bu).[22]

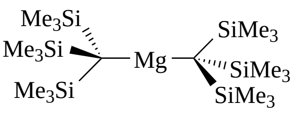

(**1**)

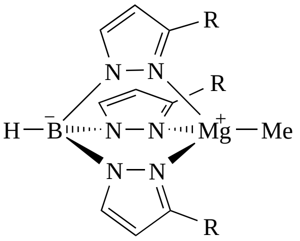

(**2**)

2.3 Solvent-free Aggregates and Polymers

Solid unsolvated Me_2Be, Me_2Mg, and Et_2Mg have polymeric linear chains of metal atoms linked by bridging alkyl groups (**3**) oriented in a distorted tetrahedron around the metal. The bond distances (C–Mg, 224 and 226 pm; C–Be, 193 pm) are longer than in the monomer, since one-electron pair is shared between two bonds in the electron-deficient bridge. The M_2C_2 rings have small angles at the carbon (75°, 72°, and 66°) that maximize overlap of the single carbon orbital with orbitals on the two metal atoms. Higher homologs are usually associated as dimers or small oligomers in noncoordinating solvents, and mass spectra indicate some association of alkylberylliums even in the gas phase. Ph_2Mg also crystallizes in polymeric chains with the phenyl rings perpendicular to the chain direction (C–Mg, 226 pm). Magnesium acetylides containing a cubic $Mg_4(\mu_3\text{-C})_4$ core have recently been prepared; they are the first MgR_2 compounds to exhibit this typically 'organolithium-type' structural motif.[23]

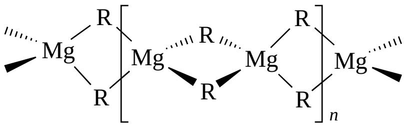

(**3**)

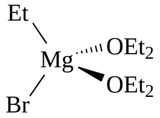

(**4**)

2.4 Solvated or Coordinated R_2M and RMX Monomers

Additional coordination sites in the monomer may be occupied by solvent molecules. Besides solvation by ethers, complexes with a variety of other donors have been studied in solution or isolated, and a number of crystal structures have been reported. Among oxygen ligands, HMPA (hexamethylphosphoramide) is especially basic. In general, nitrogen as a ligating atom is more basic than oxygen, though frequently more hindered, and sulfur is weaker. The chelating diamine TMEDA (tetramethylethylenediamine) is particularly noteworthy for forming stable, monomeric, and often sublimable crystalline complexes. Potential ligands such as water or ammonia, with acidic hydrogens, react to cleave the C–M bond, but there is evidence for the existence of complexes of alkylberyllium compounds with ammonia and amines at low temperatures, and complexes of $(PhC{\equiv}C)_2Be$ with primary amines have been isolated. Comparing metals, the larger size of Mg (1.4 Å) can allow a higher coordination number than for Be (1.12 Å); compare $[Mg(Mesityl)_2(THF)_2]$ with $[Be(Mesityl)_2(Et_2O)]$.

Coordination of two ether or other ligand donors with approximately tetrahedral geometry is most common, and the crystal structure (**4**) probably represents the 'typical' Grignard reagent. Similar coordination of R_2Mg (e.g. $Ph_2Mg(THF)_2$) and R_2Be compounds appears likewise to be the norm. The latter also form less crowded (probably) trigonal 1:1 adducts. Ligand electronegativity determines coordination strength, which decrease as: $MX_2 > RMX > R_2M$. In the four-coordinate complexes, the geometries are distorted from tetrahedral; the C–Mg–C or C–Mg–X angle is usually greater than that expected for tetrahedral geometry, probably reflecting a tendency toward sp hybridization. C–Mg bond distances are mostly in the range 213–219 pm (occasionally up to 234 pm with bulky ligands). Mg–Br and Mg–Cl lengths are 2.44–2.51 and 2.33 pm; Mg–ligand distances are 203–204 pm for oxygen and 215–224 pm for nitrogen

Octahedral tetraetherates and trietherates, respectively, of $MgBr_2$ and MeMgBr with THF have been isolated. $MgI_2(THF)_3$ approximates a trigonal bipyramid, while the cation of $[MgI(THF)_5][I_3]$ assumes a distorted octahedron.[24]

Some unusual coordination numbers and distorted geometries have been found in complexes with *Crown Ethers*, other polyethers, and cryptands (*see Cryptands & Cryptates*), and in organomagnesium compounds with internally coordinating ether or crown ether side-chains. Two examples are (**5**) and (**6**). In crown ether complexes of Et_2Mg and Ph_2Mg, a linear R_2Mg molecule is threaded through the cavity of the crown ether. Other cases of either lower or higher (e.g. (**7**)) coordination numbers are known.

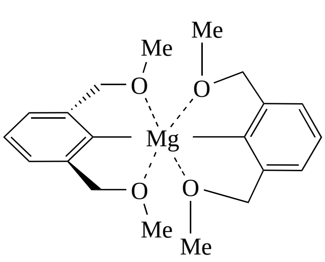

(**5**)

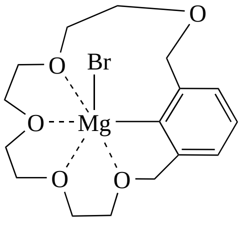

(**6**)

2.5 Species Associated via Solvent or Other Ligands

Colligative property measurements imply that R_2Mg compounds are monomeric up to high concentrations in the more basic THF, partially associated at higher concentrations in diethyl ether, and associated above the dimer stage in diisopropyl ether.[25] Me_2Be in diethyl ether is monomeric, but oligomeric species exist in dimethyl sulfide, and a series of complexes may be formed with dimethyl ether. Association is probably via M–C–M bridges, as in the proposed centrosymmetric dimer structure (**8**) of $[Et_2Mg(OEt_2)]_2$. Crystals of $(p\text{-tol})_2Mg$ from THF contain both monomeric units and dimers similar to (**8**); the dimer structure (**9**) has bridging which is not electron deficient.[10]

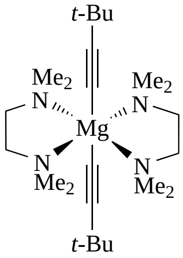

(**7**)

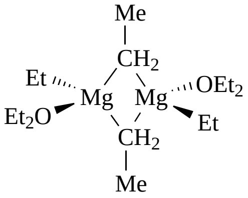

(**8**)

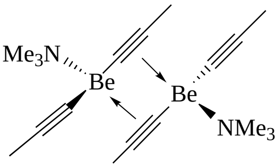

(**9**)

Halide is usually better at bridging than alkyl. RMgCl, RMgBr, and RMgI are monomeric in THF, but the fluoride is a dimer. In Et_2O the fluorides and chlorides are dimeric; bromides and iodides are monomeric in dilute solutions, with apparent association of 2–4 in concentrated solution.[25] (However, an IR/Raman study concluded that EtMgBr is monomeric to high concentrations.[8]) The doubly halide-bridged structure (**10**) for $(EtMgBrL)_2$ ($L = i\text{-}Pr_2O$ or Et_3N) is probably typical for dimers. The Mg_2Br_2 unit is nearly square, with Mg–Br distances slightly longer than in the monomers. The C–Mg bonds (209 and 218 pm) and the bonds to the ligands are similar to the monomers. However, it is likely that a variety of species may be present in any given solution, and a structure which crystallizes may not predominate in solution. For instance, although EtMgBr is probably associated in concentrated ether solution, the crystals consist of monomers. Spectroscopic analysis of an EtMgCl etherate at low temperature indicate both bridging and terminal ethyl groups, and crystals separating from a THF solution have a cluster structure of composition $[EtMg_2Cl_3(THF)_3]_2$ with five- and six-coordinate magnesium.

Other 'Y^-' groups can also be bridging. Numerous RBeOR′ and RBeSR′ compounds have been isolated. Unsolvated

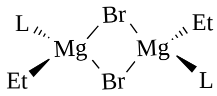

(**10**)

tetramers are common; $(MeBeOSiMe_3)_4$ has the ‘cubane’ structure (**11**), and other Be and Mg tetramers are probably similar. Other degrees of association (dimer, trimer, polymer) are found. Solvated $RMgOR'$ and $RMgSR'$ complexes are often dimeric. Coordinated solvent is lost more easily from $RMgOR'$ than from analogous Grignard reagents. Dialkylamido groups also bridge strongly. Unsolvated compounds $RMNR'_2$ tend to form dimers and trimers (Be), probably with tricoordinate metal as in (**12**). Solvated monomers, dimers, and polymeric aggregates have been demonstrated. An internally coordinated dimer (**13**) is formed in the reaction of R_2M with $MeNHCH_2CH_2NMe_2$.

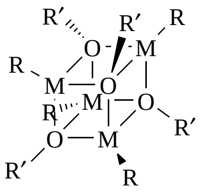

(**11**)

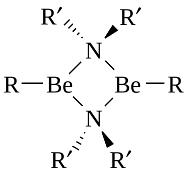

(**12**)

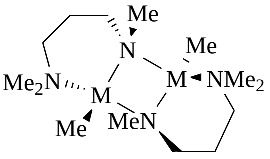

(**13**)

Organomagnesium hydrides (RMgH) with THF solvation are stable. They form dimeric and oligomeric structures associated through bridging hydrides.

2.6 Ate Complexes

Coordination of an anionic ligand to the metal of R_2M or RMY produces a complex with a negative *Formal Charge* on the metal: an ate complex (*see Ate Complexes*). Et_2Be forms a number of complexes with the stoichiometry $M(Et_2Be)_2Y$, where M is an alkali metal or quaternary ammonium ion, and Y is Cl, F, or SCN. The anion Y^- may form a single bridge between two Et_2Be molecules. Other stoichiometries and ligands are also reported.

The reaction of two organometallic compounds may also form an ate complex. For example, PhLi and Ph_2Mg react to form $LiPh_3Mg$ and Li_2Ph_4Mg, while $Li[(t\text{-}Bu)_3Be]$ is formed from $(t\text{-}Bu)_2Be$ and $(t\text{-}Bu)Li$. At high ratios of MeLi, both Me_2Be and Me_2Mg form 3:1 complexes Li_3MMe_5. An operational description is that one reactant (the more ionic compound with the more electropositive metal) transfers alkyl anions to the other. Thus the four methyl groups in Li_2BeMe_4 form a distorted tetrahedron around the beryllium, with longer distances to the lithium ions. However, this description is oversimplified. The low-temperature nuclear magnetic resonance (NMR) spectrum of Li_3MgMe_5 has three different methyl resonances, suggesting structure (**14**), related to the MeLi tetramer. Ate complexes with zinc and aluminum compounds also form. Electron-deficient bridge-bonded structures, exemplified by the X-ray structure of (**15**), are generally proposed. NMR studies show rapid intramolecular and intermolecular exchange processes, and equilibrium with the constituent organometallic compounds. Methyl, ethyl, or phenyl has usually been the organic group; bulkier alkyl groups are less inclined to participate. Compound (**16**) is an unusual internal ate complex.[10,11]

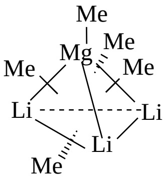

(**14**)

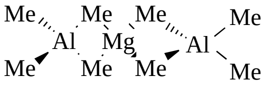

(**15**)

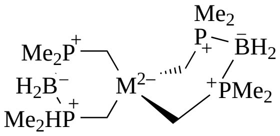

(**16**)

Alkali hydride ate complexes also exist, including MR_2BeH, MR_2MgH, and other compositions, although it appears that KR_2MgH compounds are unstable with respect to KR_3Mg and MgH_2[26] Structural features include hydride bridges and electron-deficient bonding to the alkali metal. In a dimer of $NaEt_2BeH$, the bridging hydrides bind also to the ether-solvated sodium atoms. Ate complexes are also formed in reactions with diborane, $NaBH_4$, AlH_3, and $(Li/Na)AlH_4$.

2.7 Disproportionation/Redistribution (Schlenk) Equilibria

In 1929, Schlenk and Schlenk proposed that Grignard reagents should be represented by the equilibrium of equation (1), rather than simply RMgX. Primary evidence was the precipitation of solvated MgX_2 by addition of dioxane to a Grignard reagent solution, leaving dialkylmagnesium in solution. A 1:1 mixture of MgX_2 and R_2Mg has properties identical to the Grignard reagent. The Schlenk equilibrium was apparently discredited for a period of years by a report that radioactive magnesium did not exchange between $MgBr_2$ and Et_2Mg; the redistribution reaction was then envisaged to yield a $MgX_2{\cdot}R_2M$ complex. Subsequently, exchange was indeed demonstrated, and additional evidence has thoroughly confirmed the reality of the equilibrium.[25,27]

$$MgX_2 + R_2Mg \rightleftharpoons 2RMgX \tag{1}$$

Convincing evidence for the Schlenk equilibrium comes from NMR. Chemical shifts of RMgX and R_2Mg are generally different enough to allow the distinction, provided the equilibration rate is slow. Variable-temperature NMR has allowed determination of the equilibrium constant and thermodynamic and kinetic parameters for the exchange in a number of examples.[9,25,27] Additional evidence has come from calorimetry, IR, polarography, and kinetics of reactions in mixtures of various ratios of MgX_2 and R_2Mg. The issues of association (dimerization), solvation, and redistribution have also been addressed by ab initio MO calculations for MeMgX (X = Cl and Br) with Me_2O; the calculational results corroborate conclusions derived from experiment.[28] A similar equilibrium exists with beryllium compounds.

Several useful generalizations may be made.[25] In diethyl ether, RMgX generally predominates quite strongly ($K \sim 50-1000$ at room temperature; $\Delta H^\circ \sim -10$ to $-20\,\mathrm{kJ\,mol^{-1}}$). In THF, the equilibrium constant is deceptively close to the statistical value of 4; however, it results from a substantially positive ΔH° ($10-25\,\mathrm{kJ\,mol^{-1}}$) and a large positive ΔS° ($40-100\,\mathrm{J\,mol^{-1}\ K^{-1}}$). Of the species in the equilibrium, MgX_2 is the most exothermically solvated, and probably has a larger coordination number in THF. Reaction in the forward direction of equation (1) in THF (compared with diethyl ether) would then be more endothermic, but also would increase entropy by liberating solvent molecules. RMgX also predominates in less basic ethers, as well as in triethylamine and HMPA, and for RMgF dimers. Excess MgX_2, often present from formation of the Grignard reagent, would further drive the equilibrium in that direction.

The rate of the Schlenk exchange is slowed by bulky R groups and stronger solvation. For the methyl Grignard reagent, exchange is fast on the NMR timescale except at very low temperatures, but it is slow even at room temperature in THF for t-butyl or neopentyl reagents. Exchange probably occurs in a bridged intermediate formed by displacement of a solvent molecule from the monomer. The Schlenk-type equilibrium of RBeX compounds also lies well to the right.

The Schlenk equilibrium also influences the nature of materials which are isolated from solutions. MgX_2 may selectively precipitate, and solids of composition RMg_2X_3 have been obtained. Disproportionation of RMgX may also occur on desolvation, and 'Grignard reagents' prepared in noncoordinating hydrocarbon solvents are generally deficient in halogen because of partial precipitation of MgX_2. Other RMY compounds or their coordination complexes may also disproportionate, for example, etherates of some $RMgSR'$ and $RMgNR'_2$ and some N-coordinated RBeY. RMgF and $RMgOR'$ have little tendency to disproportionate, and the exchange between R_2Mg or R_2Be and an alkoxide is often a useful synthesis for $RMOR'$.[4,10]

2.8 Ionization

In simple alkyl or aryl organomagnesium compounds, there is no indication of ionization of the carbon–magnesium bond to a carbanion. Ethereal solutions of Grignard reagents have low but significant conductivities, probably from ionization as in equation (2) (or to more highly associated species). In HMPA, ionization is much more extensive. $MgBr_2$ is completely dissociated and EtMgBr is about 30% dissociated to $EtMg^+$ and Br^- ions. Bromine NQR (nuclear quadrupole resonance) studies in the solid state indicate that Mg–Br bonding is essentially ionic. Conductivities of R_2Mg compounds are low, even in HMPA. However, if the R^- ion is delocalized, bonding to the metal will be more ionic, and dissociation may occur (see Sections 6.4 and 6.5).

$$2RMgX \rightleftharpoons RMgX_2{}^- + RMg^+ \tag{2}$$

Coordination to a crown ether or a cryptand can also induce ionization. For example, an X-ray crystal structure of the complex between Np_2Mg and 2,1,1-cryptand showed it to consist of R_3Mg^- and cryptand-complexed RMg^+ ions.[8]

2.9 Configurational Stability of the C–Mg Bond

When a Grignard reagent is formed by reaction of an alkyl halide with magnesium metal, the stereochemical configuration at the α-carbon is randomized. Radical intermediates in the formation of the Grignard reagent (see Section 4.2) are held responsible. Very rarely, as in the formation of (**17**), is there incomplete racemization.[8]

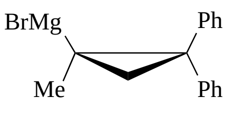

(**17**)

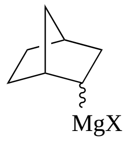

(**18**)

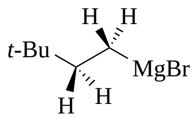

(**19**)

It is also possible for the C–Mg bond to invert configuration after it is formed. If a Grignard reagent can be obtained with one configuration predominant, then conversion to its enantiomer or diastereomer might be observed during a period of standing or heating. The extreme configurational stability of (**17**) (no racemization in 30 min at 120 °C) is attributed to the strain of a planar carbon in the three-membered ring. Interconversion of the diastereomers of (**18**) is also measurably slow.[29] The faster inversion rates of primary C–Mg bonds may be studied by NMR lineshape techniques. The α-hydrogens of (**19**) are magnetically nonequivalent, but are interconverted by inversion of configuration.[8] The rate is second order in monomeric organomagnesium, faster in diethyl ether than in THF, and faster for Cl^- than Br^-. These observations are consistent with a mechanism in which inversion occurs during transfer or exchange of the alkyl group between magnesiums. Inversion is much slower than the total rate of exchange, which occurs predominantly with retention. Recently, stereospecific exchange of the sulfoxide of an enantiomerically pure α-chloroalkylsulfoxide for a magnesium, and subsequent carbenoid homologation (a reaction step that avoids free radical intermediates) has been used to prepare a chiral (93% enantiomeric excess), non- α-heteroatom stabilized Grignard reagent, (**20**) (equation 3). (**20**) is generated as one component of a mixture of Grignard reagents and sulfoxides, and racemizes with a half-life of five hours at $-10\,°C$.[29]

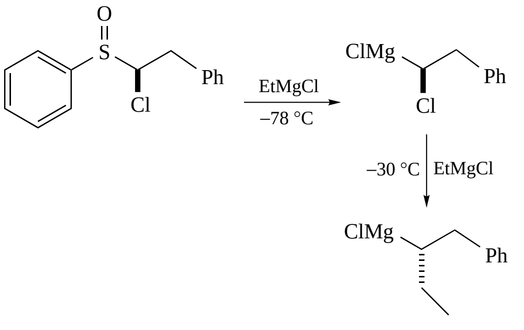

(3)

(**20**)

3 SPECTROSCOPY

A variety of spectroscopic techniques has made invaluable contributions to understanding the structure and reactions of organoberyllium and -magnesium compounds. In this section, general spectroscopic features will be discussed, but their applications will not be detailed.

3.1 Nuclear Magnetic Resonance[4,8,11]

In ^1H NMR (*see Nuclear Magnetic Resonance*), the most characteristic feature of an organomagnesium compound is the high-field position of the protons α to the magnesium. This resonance is at $\delta - 1.5$ or higher for methyl Grignard reagents, and in the vicinity of 0 ppm for secondary ones. R_2Mg resonate at higher field than RMgX, (coordination by base also produces an up-field shift), while R_3Mg^- species resonate at higher field still. The α-hydrogens of alkylberyllium compounds absorb at similarly high fields.

The ^{13}C resonance of the α-carbon of an organomagnesium compound is also shifted to high field, but not so distinctively. A substantial body of data has been tabulated,[30–32] and correlation equations have been given which are reasonably successful at predicting α-, β-, and γ-shifts based on those of the corresponding hydrocarbon.[33,34] In an aryl- or vinylmagnesium compound, the sp^2 α-carbon resonance appears at quite low field (164 ppm for PhMgBr); ortho carbons and the central carbon of the allyl group in allylmagnesium bromide are also deshielded.

Although quite broad, ^{25}Mg resonances of organomagnesium compounds have been reported.[35] The shift is sensitive to solvation and ligand electronegativity, and resonances for the Schlenk equilibrium species have been reported. Beryllium-9 NMR spectra are more informative than those of ^{25}Mg.[36] In addition to a broader chemical shift range, a much smaller quadrupole moment makes for narrower line widths, allowing observation of couplings with other elements (e.g. ^1H, ^{13}C, ^{11}B, ^{19}F, ^{29}Si, ^{31}P).

3.2 Vibrational Spectroscopy[4,8,10]

C–Mg stretching frequencies typically appear in the IR spectrum in the range $360-650\,cm^{-1}$. R_2Mg and RMgX species can be distinguished. Mg–X vibrations in the lower frequency ranges have also been identified. Vibrational assignments have also been made for alkyl- and halogen-bridged associated species. The C–Be stretching frequencies of Me_2Be and $(t\text{-Bu})_2Be$ have been assigned as 1081 and $450\,cm^{-1}$. Bridging and terminal hydrogens in RBeH fall at about 1310–1350 and $1800\,cm^{-1}$, and the Mg–H stretching frequency (probably bridging) is at $1250-1300\,cm^{-1}$. IR studies of matrix-isolated (nonsolvated) MeMgX monomers now include all the halides ($X = F–I$), but peak intensities are weak, and correspondence with calculated spectra remains poor.[14]

3.3 Electronic Spectra[4]

Saturated organomagnesium compounds do not generally have a maximum in the near UV region, although in solutions a tail from shorter wavelength bands extends to 250 nm. Periodic reports of a maximum in some samples could result from charge transfer. Aryl Grignard reagents have an absorption around 250 nm, of greater intensity than the ‘benzenoid’ bands of simple aromatic compounds, and a solvent-dependent shoulder to longer wavelength.

3.4 Mass Spectra[4,10]

Because of the limited volatility of most organomagnesium and -beryllium compounds, there have been fewer mass spectrometric data reported. With Cp_2Mg, positive and negative fragment ions from cleavage of the metal–ring bonds are observed. Mass spectra of Me_2Be vapor show the presence of associated species with up to eight Be atoms, and associated species are also seen in the spectra of Et_2Be and Ph_2Be.

4 PREPARATION

4.1 Direct Reaction of Organic Halogen Compounds with the Metal

The classical method for formation of a Grignard reagent, as originally described by Victor Grignard in 1900, is the reaction of an organic halide in ether solution with magnesium metal (equation 4). Typically, this is an exothermic reaction but, as a heterogeneous process, one which may not start immediately. The Grignard reagent is sensitive to moisture and oxygen.

$$RX + Mg \longrightarrow RMgX \tag{4}$$

In the customary procedure, the magnesium is placed in a dried apparatus under an inert atmosphere of nitrogen or argon. The magnesium may be activated (if necessary), and a small portion of the halide is added to initiate the reaction in concentrated solution. The remainder of the halide in more dilute solution is added at a rate sufficient to maintain the desired temperature (often reflux). Cooling may be needed to moderate the reaction after initiation. Stirring or heating is often continued longer to assure complete reaction, and in the case of less-reactive halides it may be necessary to heat throughout an extended reaction period. Commercial magnesium turnings sold specifically for Grignard reagents are usually satisfactory, and the reaction frequently starts vigorously with gentle warming after a short induction period. Carefully dried solvents improve ease of formation and minimize loss of the reagent by hydrolysis.

The solution so obtained is usually used directly in synthetic applications, frequently without even separation from excess magnesium. Otherwise, the reagent may be transferred by syringe, cannula, or decantation and filtration, or modified by replacement of the solvent or addition of other reactants or catalysts.

The magnesium is critical to the success of a Grignard reagent preparation. An oxide film or other surface blockage may cause an induction period by excluding halide from the underlying magnesium surface. There are numerous recipes for activation, which apparently remove or break through this film. Physical activation may be achieved by crushing or grinding the magnesium turnings or prolonged stirring without solvent.[8,9] Sonication helps remove absorbed water, shortens the induction period, and increases the subsequent rate.[8,9] Variously recommended chemical activation pretreatments[8,9] include heating dry with a small amount of iodine, stirring with a preformed Grignard reagent solution, or reaction with one of a variety of activating reagents, for example, Br_2, $AlBr_3$, $Si(OEt)_4$. The magnesium may then be washed with fresh solvent. Formation of a difficult Grignard reagent may be helped by entrainment: carrying out the reaction in admixture with a reactive halide. 1,2-Dibromoethane is often preferred, as it affords only ethylene and $MgBr_2$. Impurities in the magnesium, amalgamation, or transition metal salts may be activating, but may also decrease the yield or affect subsequent reactions. For mechanism studies, extremely high purity magnesium obtained by sublimation or zone refining may be used.

A number of specially reactive forms of magnesium have been used to reduce induction periods, and also for unreactive halides or low reaction temperatures. They include metal slurries made by reduction of a magnesium salt by potassium or lithium metal (‘Rieke’ magnesium), lithium naphthalene, or potassium-intercalated graphite, and finely divided metal produced by condensation of magnesium vapors in an organic solvent.[8] The anthracene–magnesium complex (see Section 6.3) may be used in stoichiometric amount as a magnesium source or as a catalyst, or pyrolyzed to deposit a reactive magnesium residue.[8,9]

The most common solvents for preparation of Grignard reagents are diethyl ether and THF. The latter is especially useful for making Grignard reagents from aryl and vinyl halides, particularly the relatively unreactive chlorides. A number of other ethers (e.g. butyl, isopentyl, anisole), HMPA, and tertiary amines have also been used. Although a coordinating solvent is generally needed for their facile formation, it is possible to prepare many Grignard reagents in hydrocarbon solvents in the presence of a molar (or less) equivalent of coordinating base: 1M toluene solutions have been prepared.[37] The degree of solvation of a Grignard reagent influences its reactivity, a phenomenon that will be briefly described here. Additions of Grignard reagents to ketones and nitriles, ligand substitution with alkoxysilanes, and oxirane ring openings proceed faster in less-nucleophilic ethers; rates decrease in the order: $t\text{-}Bu_2O > Et_2O > THF$. Partial replacement of ether by toluene accelerates the rate of reaction of Grignard reagents with hydrazones, 1-alkynes, alkylethoxysilanes (but not with alkylchlorosilanes), and increases the ratio of addition to reduction product (Section 5.6.1) with ketones. These effects are attributed to the greater ease of coordination of substrate to Grignard reagent in solvents of lower solvating ability, although the situation for ketones is more complex.[37,38] Additives or cosolvents, typically bases or unsaturated species, are often used to increase yields or enhance selectivity, especially in reactions mediated by transition metals (see Sections 5.4 and 5.5). The relatively (vs. e.g. HMPA) inexpensive and low-toxicity 1-Methyl-2-pyrrolidinone, NMP, is increasingly popular.

Unsolvated ‘Grignard reagents’ have also been formed by cocondensation of magnesium vapor with the organic halide at low temperature, and allowing the resulting matrix to warm.[9] Cluster Grignard reagents, $PhMg_4X$, ($X = F$, Cl, Br), theoretically predicted to be stable, have been similarly prepared, and characterized by MALDI-TOF (matrix-assisted laser desorption/ionization-time of flight) mass spectrometry and elemental analysis. The identities and ratios of hydrolysis/deuterolysis products confirm the presence of Mg–C and Mg–Mg bonds (equation 5). Most recently, room temperature transmetalation reactions in solution have been used to prepare the analogous alkyl derivatives from the phenyl reagents and alkyl halides. This work has implications for the mechanism of Grignard reagent formation (Section 4.2)[39]

$$(C_6H_5)Mg_4X + 7H_2O \longrightarrow C_6H_6 + Mg(OH)X + 3Mg(OH)_2 + 3H_2 \qquad (5)$$

Reactivity in Grignard reagent formation varies in the sequence I > Br > Cl > F. Fluorides are particularly unreactive, but Grignard preparation has been reported with metal vapor[39] and matrix-isolation[14] techniques, Mg anthracene, and most efficiently, with 'Rieke' magnesium. Side reactions with iodides, and to a lesser extent bromides, may lower the yield of the reagent.

The most common side reactions[8] in Grignard reagent formation are coupling and disproportionation of the organic groups (equation 6). These are particularly prominent with benzylic, allylic, and tertiary halides. They may be the consequence of radical intermediates in the formation reaction or may result from reaction between the organometallic and unreacted halide (see Section 5.5). The latter process is promoted by transition metal compounds. A sizeable excess of magnesium, more solvent, and (for allylic and benzylic) use of the chloride at low temperature in THF are often beneficial. Abstraction of hydrogen from the solvent (or other hydrogen donors) also produces R–H solvolysis products and other radical-derived products. The effects of a number of variables on the formation of reagent have been studied.[8]

$$2RX + Mg \longrightarrow \begin{cases} MgX_2 + R\text{–}R \\ \text{or} \\ MgX_2 + R(+H) + R(-H) \end{cases} \qquad (6)$$

Organic halides also react with beryllium metal to form organometallic RBeX products. The reaction does not appear to be as facile as with magnesium, and may require activation with $BeCl_2$ or $HgCl_2$ or extensive heating. Surprisingly, acyl halides also react with beryllium metal to form acylberyllium halides, RCOBeX (see Section 6.6).

4.2 Mechanism of Grignard Reagent Formation[8,9]

There is considerable agreement that the formation of Grignard reagents involves intermediate radicals.[4,8,9] Evidence includes the trapping of intermediates by radical traps, CIDNP (chemically induced dynamic nuclear polarization) observations, and the occurrence of characteristic radical reactions (equation 6) such as disproportionation, solvent attack, coupling, and isomerization, for example, cyclization of the 5-hexenyl radical (**21**) to the cyclopentylmethyl radical (**22**). The rate of reaction is proportional to the concentration of organic halide in solution and to the surface area of the magnesium. With iodides and more reactive alkyl bromides, for example, cyclopentyl, the rate is affected by mass transport, but other bromides and chlorides react at a rate controlled by chemical processes at the surface.[9,40]

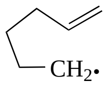

(**21**)

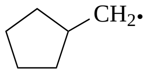

(**22**)

The initial step is heterogeneous electron transfer to the organic halide. In the case of simple alkyl halides, the radical anion so formed decomposes very rapidly into alkyl radical and halide ion. Beyond this point, details of proposed mechanistic schemes vary. Radical pairs [R··MgX] have been proposed, but the multiplet polarization patterns in the CIDNP effect appear to be consistent only with [R··R] pairs,[41] and involvement of radical pairs may only be ancillary to the formation of RMgX. A currently unresolved controversy concerns the nature of the organic radicals. Applying the extensive database on *homogenous* radical chemistry, product distributions for rearranging radicals have been fit to a kinetic model in which the radicals diffuse freely between the magnesium surface and the solution. Reactions leading to by-products compete with reaction of the radicals at the surface to form the Grignard reagent. This 'D-model' ascribes no special properties to radicals on or near the surface. Opposed to this view are a number of observations (comprising the A, for adsorption, model) including the retention of configuration in formation of Grignard reagents (**17**) and (**23**), which seem to require that the radical intermediates behave in a special fashion, presumably because of their association with the surface. The surface-bound radicals are, however, ill-defined. Variations of these models invoke Mg^I intermediates, Mg_n clusters, and radical chain processes as key components of modified mechanisms.[42,43]

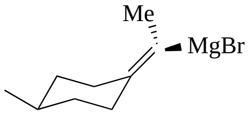

(**23**)

Indications that the mechanism of formation of Grignards from aryl halides differs from that of simple alky halides has prompted recent study. Both dianions, ArX^{2-} (X = halogen), and extremely short-lived aryl radicals are proposed as intermediates or transition states.[42,44]

4.3 Formation by Exchange with Previously Formed Organometallic Compounds

4.3.1 *Alkylation of a Beryllium or Magnesium Salt*

Exchange generally occurs between the organometallic compound of an electropositive metal and the salt of a less electropositive one. This reaction is effectively a nucleophilic substitution by the organometallic 'carbanion' on the electrophilic metal center, resulting in formation of a more 'ionic' salt and a more 'covalent' organometallic compound. In this method, organoalkali starting materials may serve as the alkyl source. Organolithium compounds are most used because of their synthetic accessibility by routes which do not start with the organic halide. Organoberyllium compounds may also be made starting with Grignard reagents. Illustrative examples are shown in equations (7) and (8). Essentially the same process may be used to replace the halogen of RBeX or RMgX, forming R_2Be or R_2Mg.

$$MeO(CH_2)_4MgX \xrightarrow[\text{ether}]{BeCl_2} [MeO(CH_2)_4]_2Be \qquad (7)$$

$$Ph_3\overset{+}{P}-\overset{-}{\ddot{C}}H_2 + MCl_2 \longrightarrow (Ph_3\overset{+}{P}-CH_2)_2M2Cl^- \qquad (8)$$

The Schlenk equilibrium (see Section 2.7) may also be viewed as an example of the same reaction class: one organomagnesium group alkylates the other magnesium. A 'Grignard reagent' may be prepared by mixing R_2Mg and MgX_2 in equimolar proportions; or starting with RMgX, the Schlenk equilibrium serves as a source of R_2Mg compounds. Magnesium halides form complexes with a number of ligands which are considerably less soluble than the other species in the equilibrium, so that nearly quantitative precipitation of the halide occurs, leaving R_2Mg in solution (equation 9). Dioxane was first used for this purpose, but diglyme, pyridine, and other solvents are also useful. The R_2Mg compounds formed in this fashion are likely to contain trace amounts of MgX_2, dioxane or both.

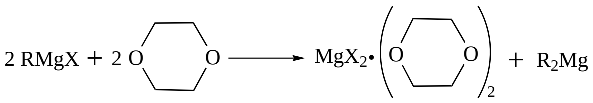

(9)

It should be noted that the same class of reaction, in which the organomagnesium compound serves as the source of the nucleophilic organic group, forms the basis of an important synthetic application in organometallic chemistry (see Section 5.4).

4.3.2 *Redox Exchange of Magnesium or Beryllium Metal with Organometallic Compounds*

An organometallic compound of a less electropositive metal may also serve as the source of the alkyl group by exchange with a more active metal. This reaction is useful for making R_2Mg compounds from mercury or (less commonly) zinc or silicon alkyls. The product is free of the traces of halide or dioxane which may remain when magnesium halide is precipitated from a Grignard reagent, and in hydrocarbon solvents unsolvated R_2Mg is formed. A modification produces RMgX compounds. Beryllium appears to be less reactive, but does behave similarly. Examples are given in equations (10) and (11).

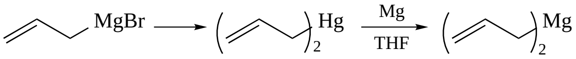

(10)

$$H_2C{=}C{=}CH_2 \xrightarrow[\text{steps}]{\text{several}} RHg(CH_2)_3HgR \xrightarrow[\text{THF}]{Mg/MgBr_2} BrMg(CH_2)_3MgBr \qquad (11)$$

4.3.3 *Metal–Halogen Exchange*

Some examples of this process are given in equations (12) and (13). Unless the organic halide has electronegative substituents, the exchange is relatively slow, may not have a favorable equilibrium, and may suffer from competitive Wurtz-type coupling. Previously, this methodology was constrained by the sensitivity of many organic functional groups to reaction with Grignard reagents (see Section 6.2.) Currently, however, the low-temperature exchange reactions of derivatized aryl (bearing an ester, nitrtile, or imine function), heteroaryl (e.g. halogenated pyridines, pyrimidines, and thiophenes), heterocyclic (e.g. pyrroles, pyrazoles, uracils), cyclopropyl or alkenyl iodides with i-Pr_2Mg or i-PrMgBr yield a wide array of functionalized Grignard reagents.[45] Trialkylmagnesates, R_3MgLi, extend the method to arylbromides, including electron-rich species. Oxidative addition of activated Mg to aryl bromides and heteroaryl halides yields similar results.[46,47]

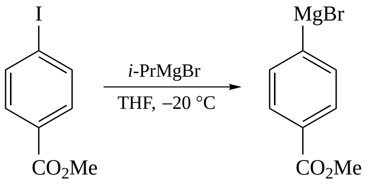

(12)

$$CBr_4 \xrightarrow[-75\,^{\circ}C,\ THF]{i\text{-}PrMgCl} CBr_3MgX \qquad (13)$$

4.3.4 *Metal–Hydrogen Exchange; Metalation*[8]

Organomagnesium compounds are kinetically less-reactive bases toward weakly acidic hydrogens than organolithium compounds. Usually, Metalation using an organomagnesium compound is practically limited to acid hydrogens with pK_a of about 25 or lower. This includes alkynes (equation 14) and derivatives of cyclopentadiene, indene, and fluorene. Even these are not formed quickly in ether solvents, but addition of HMPA markedly increases the reactivity; the less acidic diphenylmethane reacts at 100 °C. Some polyhalogenated compounds are relatively easily metallated, as are aromatic ring positions ortho to O or N substituents (equation 15) and some heteroaromatics. Magnesium amide bases, for example, (**24**) or BuMgN(*i*-Pr)$_2$ effectively magnesiate a variety of substrates, the latter regioselectively.[48] The alkyl amide and *s*-BuMgBu are alkane soluble and commercially available.

$$2\mathrm{PhC{\equiv}CH} \xrightarrow{\text{s-BuMgBu}} (\mathrm{PhC{\equiv}C})_2\mathrm{Mg} \qquad (14)$$

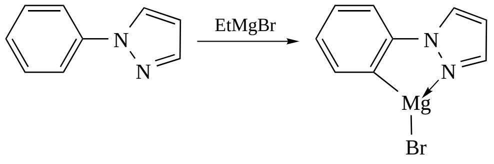

(15)

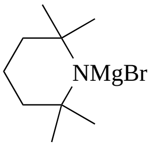

(**24**)

Abstraction of acidic protons α to a carbonyl or nitrile function can occur in competition with desired Grignard addition reactions (see Section 5.6). In HMPA, this is the major reaction, and is useful for preparing magnesium enolates of carbonyl compounds, sulfones, and so on.

4.4 Addition of C–Mg and H–Mg to Carbon–Carbon Multiple Bonds

4.4.1 Carbometalation

Addition of an organomagnesium bond to an alkene, alkyne, or a benzenoid ring generates a new organomagnesium compound. With simple alkenes, addition occurs only under strenuous conditions. This reaction will be discussed later, with appropriate examples, as a reaction of organomagnesium compounds in the Section on Amides and Lactans..

4.4.2 Hydrometalation[8,9]

MgH$_2$ adds to ethylene at high temperatures, and the addition to alkenes in general can be catalyzed by boron, aluminum, and zinc alkyls, and by titanium halides. The latter reagents also catalyze an exchange between Grignard reagents and alkenes (equation 16) which can be synthetically useful. Under like conditions, most internal acetylenes exhibit cis addition of ‘HMgX’ (from RMgX) to the triple bond. The catalyzed reactions involve titanium hydride intermediates.

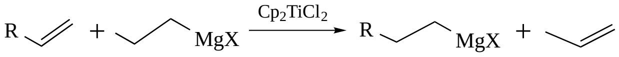

(16)

Terminal alkenes react relatively readily in ether (80 °C) with RBeH, but internal ones are less reactive. The addition is slowed but not completely inhibited by coordination with ether or NMe$_3$. Rearrangement of (*t*-Bu)$_2$Be to the *i*-Bu compound occurs by Be–H elimination and re-addition in the opposite sense.

4.5 Formation of R$_2$Mg

A number of methods discussed in the foregoing sections are specifically useful for forming R$_2$Mg compounds. These include precipitation of magnesium halide from a Grignard reagent, the transition metal-catalyzed reaction of active (prepared with Mg–anthracene) MgH$_2$ with terminal olefins, the reaction of a magnesium halide or Grignard reagent with an organolithium, and exchange of a dialkylmercury compound with magnesium metal. The relative merits of various methods have been discussed.[49] Other methods of narrower applicability include the Metalation of alkynes and other acidic hydrocarbons with R$_2$Mg.

4.6 Other RMY Compounds

The reaction of R$_2$Be or R$_2$Mg compounds with one equivalent of O–H, S–H, N–H, or other acidic hydrogen leads to compounds of the stoichiometry RMY. Variants include the reaction of an alkyl chloride with magnesium and alcohol (or NaOR′) in hydrocarbon solvent. MeBeCN has been prepared from Me$_2$Be and HCN. Redistribution reactions of R$_2$M with M(Y)$_2$ have been used to form the alkoxides, thiolates, and amides. The addition of R$_2$M to one equivalent of an aldehyde, ketone, epoxide, or imine also leads to RMOR′ or RMNR$'_2$ species (equation 17). Dialkylmagnesiums react like Grignard reagents in alkylation and carbonyl addition reactions.

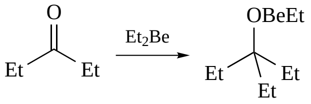

(17)

Hydride compounds (RMH) are formed in a number of ways, but have most often not been isolated and purified. Redistribution of R$_2$Mg with MgH$_2$ has produced pure RMgH and RMg$_2$H$_3$. Mixtures containing organoberyllium or -magnesium hydrides have resulted from exchanges involving borohydrides, aluminohydrides, and some other metal hydrides. They are also formed as intermediates in the thermal decomposition of R$_2$Mg or R$_2$Be compounds, and a number of RBeH complexes have been isolated.

5 REACTIONS OF ORGANOBERYLLIUM AND -MAGNESIUM COMPOUNDS

Most of the chemistry of organoberyllium and -magnesium compounds is associated with the basicity of the organic groups bound to the metal, either in the Brønsted–Lowry or the Lewis (nucleophile) sense. Also associated with their electron-rich character is the potential to function as reducing agents by loss of an electron, and there is increasing evidence that many formally nucleophilic reactions occur, in fact, by a mechanism involving electron transfer (*see* ***Electron Transfer Reactions: Theory***). The metal atom is also an electrophilic or Lewis-acidic site, and electrophilic interaction with the metal doubtless plays a role in many of their nucleophilic reactions.

Shortly before the successful preparation of organomagnesium compounds by Victor Grignard, his mentor, Philippe Barbier, had discovered that reaction of an aldehyde or ketone and an alkyl halide in the presence of magnesium metal led to formation of an alcohol, essentially as in the ‘Grignard reaction’. The use of the older technique, referred to as the Barbier method or as the ‘in situ’ reaction, holds advantages in some cases.**[8]**

As noted previously, much less attention has been directed to synthetic applications of beryllium organometallics.

5.1 Thermal Decomposition

When a β-hydrogen is present, decomposition may occur by *β-Elimination* of an alkene with formation of a M–H bond (equation 18). Tertiary alkyl groups are most easily eliminated. A polar, probably cyclic process is likely, but there is evidence for homolytic cleavage in the decomposition of $(t\text{-Bu})_2\text{Mg}$. Hydrogen is subsequently formed at higher temperature. The decomposition of gaseous $(t\text{-Bu})_2\text{Be}$ is the primary source of unsolvated BeH_2, which is of interest as a high energy propellant and as a fuel source for nuclear fusion reactors. If β-elimination of hydrogen is not possible, thermal stability is greater. Ph_2Mg decomposes at 280 °C to biphenyl and magnesium metal. Me_2Mg and Me_2 both decompose above 200 °C to yield methane and a residue $(\text{CH}_2\text{M})_n$.

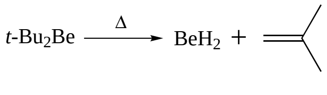

(18)

Appropriately located functional groups also lower the thermal stability. The preparation and stability of a number of these is noted in Section 6.2.

Solutions of Grignard reagents also decompose at temperatures in excess of 100 °C by attack on the solvent.**[50]** From either diethyl ether or THF, ethylene is among the products. In the latter case, the reaction follows two major pathways (equation 19).

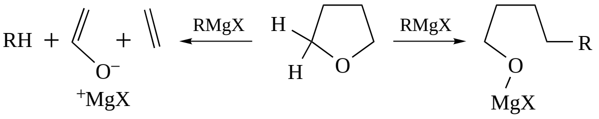

(19)

5.2 Redox Chemistry

In the electrolysis of ethereal Grignard reagent solutions, magnesium species migrate toward both electrodes. At the anode, one-electron oxidation produces organic radicals which combine, disproportionate, react with solvent or other solutes, or attack the electrode (e.g. Pb → PbR_4). Tertiary alkyls are oxidized most easily, and methyl and phenyl least easily. At the cathode, magnesium is deposited, and alkyl radicals appear to be formed also. There are two reduction waves, corresponding to MgX_2 and RMgX.

Organomagnesium and -beryllium compounds are very sensitive to oxidation by air. The reaction appears formally to be a simple addition to the O–O bond. However, it is clearly established that Grignard reagents react by the radical chain process shown in Scheme 1. The subsequent reaction to produce the alkoxide is less clear mechanistically. Sulfur and selenium form analogous products. Grignard and organoberyllium compounds may also be oxidized by other peroxides. Autoxidation of aryl Grignard reagents often is accompanied by chemiluminescence resulting from emission by biaryls.

In the Kharasch reaction (equation 20), Grignard reagents are in effect oxidized by organic halides in the presence of transition metal salts, most commonly cobalt. The Grignard reagent produces mostly disproportionation products (or the biaryl from ArMgX), and products from the organic halide are derived from the corresponding radical. It is likely that the transition metal is alkylated by the Grignard reagent, and that the resulting intermediate decomposes by nonradical pathways to metal species which then abstract a halogen atom from the organic halide.

$$2\text{RMgX} \xrightarrow[\text{CoCl}_2]{\text{R}'\text{X}'} \text{R–R or R}(+\text{H}) + \text{R}(-\text{H}) \qquad (20)$$

$$\begin{aligned}
\text{RMgX} + \text{O}_2 &\longrightarrow \text{R}\bullet + \bullet\text{O}_2\text{MgX}\\
\text{R}\bullet + \text{O}_2 &\longrightarrow \text{ROO}\bullet\\
\text{ROO}\bullet + \text{RMgX} &\longrightarrow \text{ROOMgX} + \text{R}\bullet\\
\text{RMgX} + \text{ROOMgX} &\longrightarrow 2\text{ROMgX}
\end{aligned}$$

Scheme 1

5.3 Reaction as a Brønsted Base: Formation of C–H Bonds[8]

Organometallic compounds of Be and Mg are 'hydrolyzed' by O–H, N–H, S–H, and other hydrogens more acidic than the conjugate acid of the R^- of the organometallic. In practice, this reaction may be quite slow for weak carbon acids which do not coordinate as ligands to the metal. The reaction has been discussed as the metalation reaction (Section 4.3.4) and for the formation of RMY compounds (Section 4.6). It is also used for indirect reduction of organic halides to hydrocarbons via conversion to the Grignard reagent and hydrolysis, and for introducing a deuterium or tritium label.

5.4 Nucleophilic Displacement at Atoms other than Carbon: Alkylation

The organic group of an organometallic compound will alkylate another more electronegative element by displacement of halide or other suitable leaving group (equation 21). The reaction is a nucleophilic displacement which derives its driving force from formation of the more ionic product MXY. Organolithium and -magnesium compounds, because of their ease of formation and the electropositive character of the metal, are most often used for this purpose. Fewer examples have been reported with organoberyllium compounds, although they themselves are often formed in this way (Section 4.3.1).

$$\mathrm{RMgX} + \mathrm{Y{-}Z} \longrightarrow \mathrm{R{-}Z} + \mathrm{MgXY} \qquad (21)$$

Organomagnesium compounds are less reactive as nucleophiles than organolithium compounds, it may be more difficult to separate products from the magnesium salts, and the presence of halide and ether solvent in a Grignard reagent can be disadvantageous. However, one may use the dialkylmagnesium instead of a Grignard reagent, and work with a hydrocarbon suspension rather than an ether solution. The lower reactivity may be an advantage by allowing sequential partial alkylation, and the Grignard reagent has less tendency to form ate complexes (Section 2.6).

Alkylations of a number of metals were among the earliest reported reactions of Grignard reagents, and this reaction remains an important method for the synthesis of organometallic compounds. The alkali metal and higher alkaline earth metal cations are too electropositive to be alkylated by Grignard reagents, but in principle, displacement at any other metal center is feasible. Since this reaction is discussed in other articles as it may apply to the preparation of organometallic compounds of the various metals, only general comments will be made here. A halide ion is the most common leaving group, although OR^-, SR^-, and other anions may be displaced. Reactivity of R_2Mg is greater than that of RMgX, and reactions are usually faster in THF than in diethyl ether. The center to be alkylated decreases in reactivity as electronegative leaving groups are replaced by organic groups, often allowing controlled replacement of leaving groups to produce partially alkylated or mixed polyalkylated products.

As noted, a bimetallic ate complex may be formed instead of a simple alkylation product. For example, addition of Me_2Mg to $ZnCl_2$ in excess of the stoichiometric 1:1 ratio forms the ate complex Me_4ZnMg. A particularly important instance is with Cu^I halides. Complexes of stoichiometry $RCuMgX_2$ or R_2CuMgX, referred to as *Normant Complexes*, are useful reagents in organic synthesis (see Sections 5.5, 5.6.2, and 5.8). There are varied recipes, including other Cu^I salts, and Me_2S or $P(OR)_3$ as additional ligands.[6,8] An active area of study is the catalysis of reactions of Grignard reagents by transition metal salts or complexes. The active reagents in these catalyzed reactions are undoubtedly transition metal species, produced via alkylation by the Grignard reagent.

Many useful synthetic methods involve alkylation of nonmetals by Grignard reagents. Displacement at a halogen leads to an organic halide. This reaction may be useful for replacing one halogen by another, for characterizing the organic group of a Grignard reagent, or when the organomagnesium compound is formed in an indirect fashion. The most obvious reagent for such a displacement is molecular halogen itself, but it can lead to mixtures of products if the halogen is different from that of the Grignard reagent. Organic halogen compounds may serve as alternative halogen sources, for example, 1,2-dibromoethane, hexachloroethane, *N*-chlorosuccinimide, or 1-chloro-2-iodoethane. Perchloryl fluoride and N_2F_2 have been used, but may present explosion hazards.

Oxygen (see Section 5.2) and the other group 16 elements react with organomagnesium compounds. Some other displacements at oxygen and sulfur are shown in equations (22–24).

$$\mathrm{ArMgBr} + (\mathrm{EtO})_2\mathrm{BO{-}O{-}}t\mathrm{{-}Bu} \longrightarrow \mathrm{ArOH} \qquad (22)$$

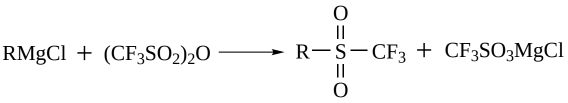

$$\mathrm{RMgCl} + (\mathrm{CF_3SO_2})_2\mathrm{O} \longrightarrow \mathrm{R{-}}\overset{\overset{\displaystyle O}{\|}}{\underset{\underset{\displaystyle O}{\|}}{\mathrm{S}}}\mathrm{{-}CF_3} + \mathrm{CF_3SO_3MgCl} \qquad (23)$$

$$\mathrm{RMgX} + \mathrm{MeSSMe} \longrightarrow \mathrm{RSMe} + \mathrm{MeSMgX} \qquad (24)$$

Primary amines may be made by the reaction of an excess of Grignard reagent with chloramine, methoxyamine, or other O-substituted hydroxylamines (equation 25). Reactions with N-chloroamines and N-substituted hydroxylamines are not as routinely successful, because of competing displacement on the halogen. Displacements at P–X or P–OR bonds are useful for synthesis of trialkylphosphines. Similar displacements also occur with $POCl_3$ and its derivatives. Three organic groups can be introduced in PCl_5.

$$\mathrm{RMgCl} + \mathrm{H_2NOMe} \longrightarrow \mathrm{R{-}NH_2} \qquad (25)$$

Alkylation of group 14 halides is also important synthetically. A number of reactions of R_3SnX compounds with methyl Grignard reagents have been studied kinetically. The reactions occur with low activation enthalpies but large negative entropies of activation. A cyclic four-center mechanism has been proposed to explain the results. Some alkylations, however, probably occur by single-electron transfer (SET) from the Grignard reagent to the substrate, followed by homolytic bond cleavages and recombinations. This mechanism is discussed in the next section in connection with displacement reactions at carbon.

Alkylation of a compound with multiple leaving groups by a di-Grignard reagent can produce a ring. Many important heterocycle and metallacycle syntheses have followed this route. Examples are in equations (26) and (27).

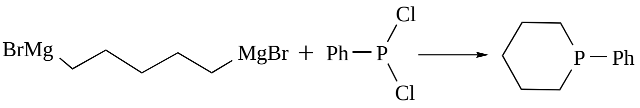

(26)

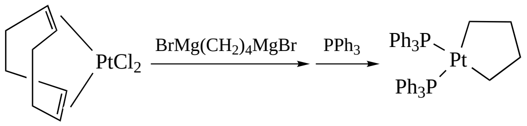

(27)

5.5 Displacements at Carbon: ‘Crossed Coupling’ Reactions

A nucleophilic displacement by an organometallic compound at carbon generates a new C–C bond (Scheme 2). Although a general reaction, its success may be limited because of competing side reactions. These are also outlined in Scheme 2. As a nucleophilic substitution, β-elimination to alkene is an important competitor, becoming progressively more dominant for secondary and tertiary substrates. Metal–halogen exchange, displacement by the halide of the Grignard reagent, and radical processes resulting from SET also occur. Grignard reagents are less reactive than organolithium compounds and give good yields only in the more favorable situations. The partially delocalized allylic or benzylic Grignard reagents are relatively effective.

Of the halide leaving groups, iodide is most easily displaced, but also most reactive in metal halogen exchange; bromide and chloride are successively less reactive. Grignard reagents often couple in quite good yield with methyl iodide and methyl or primary alkyl sulfates or sulfonates (i.e. tosylates). Allylic and benzylic halides and α-haloethers and -sulfides also undergo easy displacement.

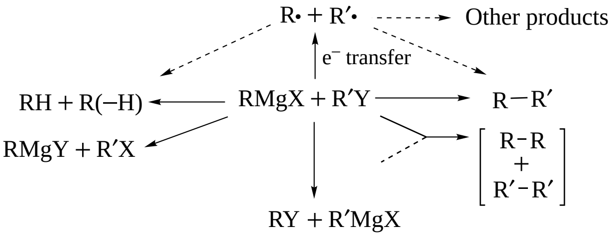

Scheme 2

Alkoxide ions are generally poor leaving groups, but are displaced under special circumstances. Ring opening of the strained oxirane and oxetane rings by addition of a Grignard reagent is such a reaction, and provides a synthetically useful two- or three-carbon chain extension (equation 28). With substituted oxiranes, the Lewis-acidic activity of the magnesium affects the regiochemistry of the addition, and preliminary rearrangement of the oxirane leads to additional products.

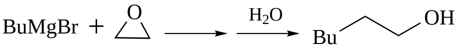

(28)

Alkoxide ions may also be displaced from orthoesters and acetals (e.g. equation 29), including paraformaldehyde. A carbocation generated from any of these structures would be stabilized by conjugation with the adjacent lone pair (i.e. **25**). The substrate may initially form an ion pair assisted by the Lewis-acidic magnesium, or at least react by a transition state with enhanced cationic character. Grignard reagents appear to be more effective than organolithium compounds, and the lithium reagent is also more likely to deprotonate the acetal. Leaving group reactivity is in the sequence $ArO^- > RO^- > RS^- > R_2N^-$. Alkoxy groups may also be displaced from propargyl and allylic ethers (often with attack at the 3-position) and from the homoallylic ether (**26**). Under forcing conditions, aryl alkyl ethers (especially methyl) are cleaved (equation 30). Another generally very poor leaving group, cyanide, is displaced from α-aminonitriles in a useful amine synthesis (equation 31), and biaryls can be prepared by the (Ni-catalyzed) coupling of benzonitrile with aryl Grignard reagents.[51]

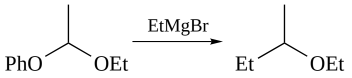

(29)

$$ArOMe + MeMgI \xrightarrow{150\,^\circ C} ArOMgI + Me_2O \qquad (30)$$

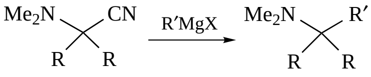

(31)

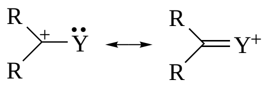

(25)

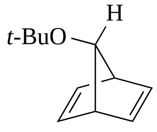

(26)

A variety of mechanisms may participate in the displacement reactions surveyed above. Some displacements, including tosylates and some epoxide ring openings, occur with the high degrees of inversion of configuration expected for an S_N2 reaction. As noted above, electrophilic assistance by the magnesium may be important. In other cases, SET, radical formation, and recombination may be involved, as shown in Scheme 2. A number of reactions which are formally displacements at an unsaturated or aromatic carbon probably occur by a mechanism of addition followed by elimination of a leaving group. As such, they are more closely related to the addition reactions which are covered in Section 5.8.

Addition of a transition metal compound can effectively promote displacement reactions by organomagnesium compounds, often minimizing the side reactions which limit the use of the Grignard reagent itself. Normant reagents or Grignard reagents with catalytic amounts of Cu^I salts are reactive in displacements of halide not only from alkyl halides but also aryl, vinyl, and alkynyl halogen compounds. Complications in additions to oxiranes are often reduced or eliminated. A number of displacements of other leaving groups are also catalyzed by copper salts. These include RO^-, RS^-, OH^-, and OAc^- groups, most commonly from allylic and propargyl substrates. The utility of Ni and Pd catalysts, which are more useful with less-reactive alkenyl and aryl substrates, has been extended to aryl chlorides with the application of bulky, electron-rich (often phosphine-derived) ligands.[52] Inexpensive and nontoxic Fe catalysts are an important recent development, as they enable cross-coupling reactions that are exceptionally fast even at low temperatures, and in the absence of added ligands. Mechanistic studies indicate that in certain cases, 'inorganic Grignard reagents', of monomer composition $Fe(MgCl)_2$, are the active species, likewise able to oxidatively add unactivated aryl chlorides.[53,54] In reactions with Cu catalysts, allylic leaving groups are usually more easily displaced than their saturated analogues, Chiral complexes have been used to achieve asymmetric cross-coupling.[8] These topics are also noted in other articles from the viewpoint of the various transition metals.

5.6 Addition and Substitution at Carbonyl Carbon[8,9]

The addition of organomagnesium reagents to aldehydes and ketones, yielding an alcohol after workup, is their most important organic synthetic reaction, and customarily bears the title 'The Grignard Reaction'. With the derivatives of carboxylic acids the initial adduct may suffer loss of a leaving group, regenerating a new carbonyl compound, which in turn may undergo further addition. Scheme 3 summarizes these processes.

5.6.1 Addition to Aldehydes and Ketones[8,9]

The addition of R_2Mg or RMgX to an aldehyde or ketone is usually very rapid, occurring essentially with mixing. Only with severe steric hindrance, low temperatures, or both, is the reaction noticeably slow. It is generally preferred in competition with displacement of an alkyl halide or addition to most other unsaturated functional groups. Reaction with an acyl halide is usually more rapid, and a Grignard reagent will normally abstract the OH proton ('be hydrolyzed') before adding to the carbonyl of a hydroxyaldehyde or -ketone.

The alkoxide (**27**) is the initial product of addition to the carbonyl group (Scheme 3). Workup with aqueous acid generates alcohol (**28**) and water-soluble magnesium salts. However, with sensitive alcohols this workup may lead to dehydration. Milder workup can be achieved by acidifying with aqueous ammonium chloride, or by hydrolyzing with a minimal amount of water, and attempting to filter or

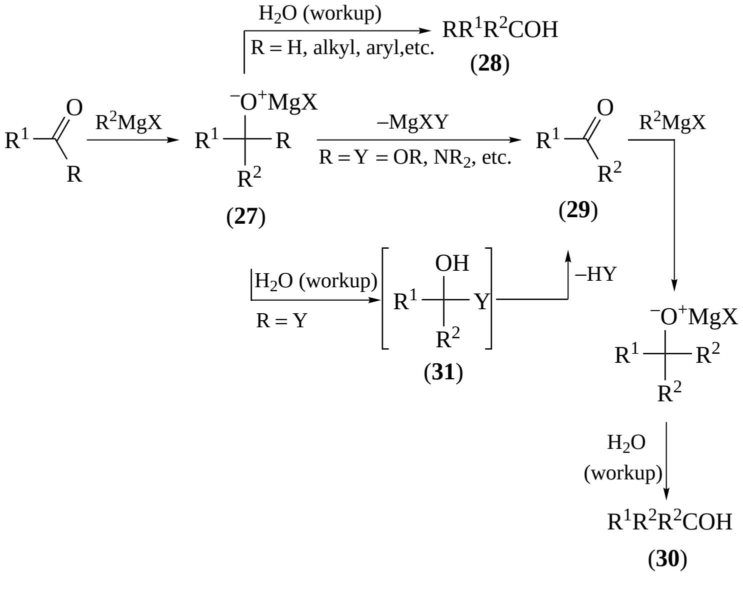

Scheme 3

decant from the frequently gelatinous magnesium salts. The magnesium alkoxide itself may be useful without hydrolysis to the alcohol. It may be acylated by reaction with an acid chloride, undergo elimination to an alkene with a suitable neighboring leaving group (equation 32), or react intramolecularly as a nucleophile.

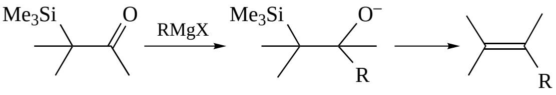

(32)

Despite its apparent simplicity, the addition of a Grignard reagent to an aldehyde or ketone is subject to side reactions which may limit its utility. The transfer of a β-hydrogen from the organomagnesium compound to the carbonyl carbon reduces the ketone to a secondary alcohol rather than producing the expected tertiary alcohol. The alkyl group of the Grignard reagent becomes an alkene. This pathway is more important with sterically hindered ketones and bulky Grignard reagents. Enolization of the carbonyl compound, with the organomagnesium acting as a base, is another side reaction which is more important with substantial steric hindrance. Addition is promoted by lower temperatures, a less-polar medium (Section 4.1), and by the addition of salts. A classic comparison of normal addition, reduction, and enolization is shown in equation (33). When electron transfer occurs between an organometallic and a carbonyl compound, ketyl radicals are formed (see discussion below).

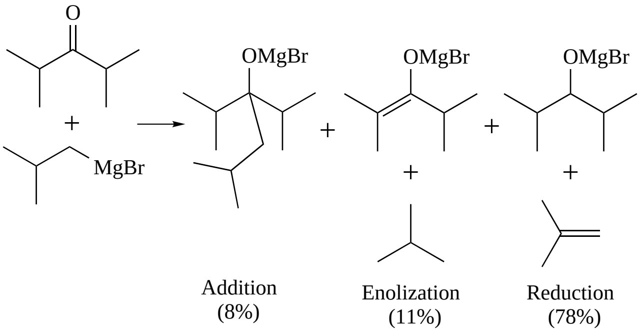

(33)

Organoberyllium compounds react with aldehydes and ketones in a fashion similar to organomagnesium compounds. Reduction competes with addition, and (**32**) is quite effective for asymmetric reductions.[10]

There have been numerous studies of the stereochemistry of the Grignard addition, and attempts to control it. The configuration of a new chiral center generated when a Grignard reagent adds to an aldehyde or ketone is influenced by chiral centers present in the carbonyl compound, in the Grignard reagent, or in chiral solvents or chelating ligands. Examples of structural features designed to control stereochemistry include a carbonyl moiety with an introduced chiral auxiliary (**33**), a chiral organomagnesium amide (**34**),[55] and a chiral ligand additive (**35**).[56] Grignard reagents chiral at the (octahedrally coordinated) metal[57] (**36** depicts Δ-cis-[(p-$CH_3C_6H_4$)MgBr(dimethoxyethane)$_2$]) or the metal-bearing carbon (**20**)[29] are now known. The Y group in RMgY also influences the degree of stereoselectivity.[58]

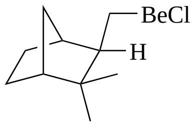

(**32**)

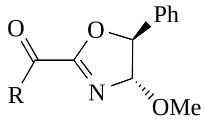

(**33**)

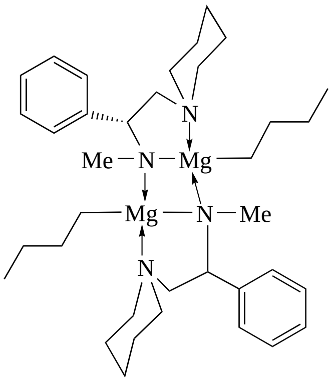

(**34**)

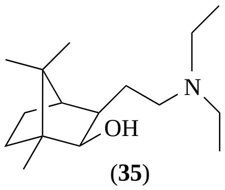

(**35**)

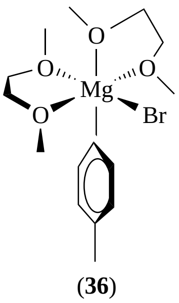

(**36**)

Although the addition of a Grignard reagent to a carbonyl group is readily visualized as a polar nucleophilic addition reaction, evidence has accumulated to suggest that many Grignard additions proceed by an alternative SET mechanism (Scheme 4). The polar process could take place as a cyclic rearrangement of an initially formed coordination complex (**37**). Cyclic transition states (**39**) and (**40**) have also been proposed for reduction and enolization. Alternatively, homolytic cleavage would produce a radical pair (**38**). The

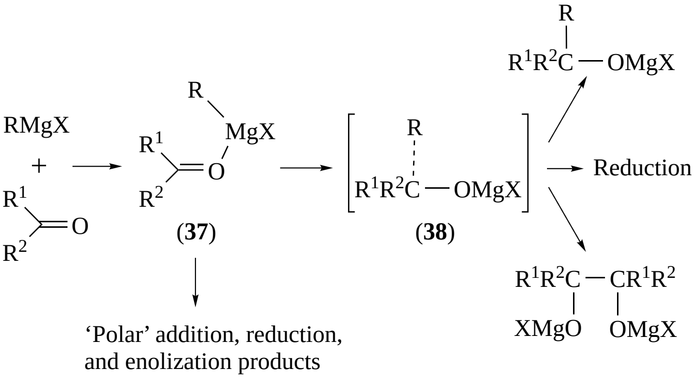

Scheme 4

alkyl and ketyl radicals of this pair can collapse to simple 1,2-addition product, transfer a hydrogen atom to produce reduction product, or diffuse apart. In the latter case the ketyl could either abstract hydrogen from solvent (leading also to reduction product), or dimerize to the pinacol. While early evidence suggested that SET was a side reaction induced by transition metal impurities, subsequent data, including that from radical rearrangement probes, CIDNP enhancements, and isotope effects, implied that many, or possibly all, Grignard additions to aromatic ketones involved SET, and that it may not be limited to aromatic substrates.[8,9,25,59] However, reactions of aldehydes with the chiral (**20**), where the sec-alky radical functions as an ultrafast racemization probe, proceed with retention of configuration, a result consistent with both a polar mechanism and a virtually instantaneous coupling of ketyl and alkyl radicals.[29]

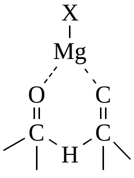
(**39**)

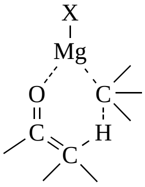
(**40**)

When a carbon–carbon double bond is conjugated to the carbonyl group, simple 1,2-addition to the carbonyl has a competitor in the conjugate or 1,4-addition, resulting in net addition to the carbon–carbon double bond. This situation will be discussed in connection with the addition to carbon–carbon unsaturation (Section 5.8)

5.6.2 Substitution and Addition Reactions with Carboxylic Acid Derivatives

The general picture in Scheme 3, with R = Y, outlines the paths available when an organometallic compound reacts with a carboxylic acid derivative. The eventual product of the reaction depends first upon whether the initial adduct (**27**) survives the reaction conditions, or decomposes to ketone (**29**). If (**29**) is formed before workup, then its reactivity relative to the original acyl compound determines whether it or alcohol (**30**) is the product.

Carboxylic Acids and Carboxylate Ions. Acid–base reaction with a Grignard reagent rapidly converts a carboxylic acid into its anion. The carboxylate ion, either from a carboxylic acid substrate or as a preformed salt, is relatively unreactive, but does undergo either single addition to produce an aldehyde or ketone or double addition to produce an alcohol. Sometimes, as in equation (34), the carbonyl compound may be formed in good yield, but the analogous synthesis with a lithium reagent is more frequently used. More commonly, these products are encountered as side reactions in the carbonation of an organomagnesium compound.

$$2\text{PhMgBr} + \text{HCO}_2\text{H} \longrightarrow \underset{(81\%)}{\text{PhCHO}} \qquad (34)$$

Acyl Halides and Anhydrides. The carbonyl of an acyl halide is at the high end of the reactivity range, and the halide ion is a very good leaving group. Hence, the reaction rapidly forms the ketone. With one equivalent of organometallic at low temperature, especially with some steric hindrance, the less-reactive carbonyl of the ketone may survive unreacted. Otherwise, it is converted to the tertiary alcohol in high yield. More commonly, if a ketone synthesis is sought the Grignard reagent is converted to another organometallic with attenuated reactivity. Historically, organocadmium compounds served this purpose, but the currently popular choice is a Normant reagent (a magnesium organocuprate). Manganese, zinc, and iron salts have also been used. Another helpful ploy is to use HMPA as solvent; in this medium the ketone is rapidly deprotonated to the unreactive enolate. With aromatic acid halides in particular, electron transfer may form the acyl radical, which dimerizes to produce an α-diketone.

Chloroformates, chlorocarbamates, and phosgene are similarly reactive toward organomagnesium compounds. The first two provide useful syntheses of esters and amides, respectively, but phosgene usually leads to the tertiary alcohol.

Carboxylic anhydrides are similar to the halides, producing ketones by reaction with one equivalent of organometallic, but easily reacting with an excess of the reagent. Cyclic anhydrides produce lactones as final products with two equivalents of organometallic (equation 35).

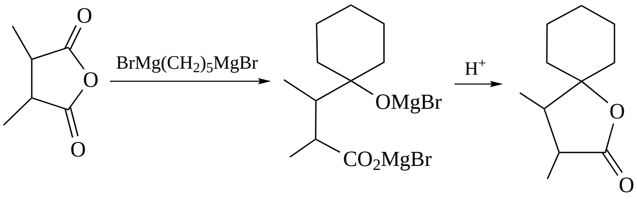

(35)

Esters, Lactones, and their Sulfur Analogs. The ester carbonyl is inherently less reactive than a ketone, so that alcohols are the normal products of addition of a Grignard reagent to an ester. The reaction is useful for forming tertiary alcohols (or secondary from formates) with two 'R' groups identical. Cyclic alcohols may be made using di-Grignard reagents. If the organic groups are somewhat bulky, addition may be stopped at the ketone stage. With some lactones, reaction with one equivalent of reagent is also favored (Scheme 5). Ring strain may enhance the reactivity of the ester group, while the cyclic hemiketal anion (**41**) would partially protect the carbonyl group of the product.

Similar considerations apply to thioesters and -lactones, although they are less studied. Generally, the thioester carbonyl is more reactive toward nucleophiles.

Amides and Lactams. The amide carbonyl group is less reactive than that of aldehydes or ketones, but the intermediate formed on addition of one equivalent of organomagnesium compound is relatively stable to elimination of a magnesium dialkylamide, and so protects against the second addition. Aldehydes, in particular, can be synthesized usefully (equation 36). Under forcing conditions a second addition occurs.

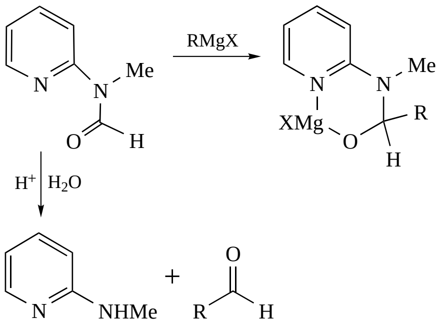

(36)

Carbon Dioxide, Isocyanates, Ketenes, etc. The carboxylation (or carbonation) of organomagnesium compounds is of major importance, both as a synthesis of carboxylic acids and as a means of characterizing the organometallic compound. Customarily, the organomagnesium solution is added to 'dry ice'. Under these conditions the temperature is kept low and the concentration of CO$_2$ high, minimizing further reaction of the organometallic with the initially formed magnesium carboxylate. If dry CO$_2$ is bubbled through a Grignard reagent or passed over the solution, multiple addition is more probable (equation 37).

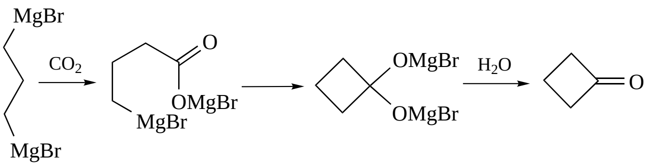

(37)

The cumulated double bonds of ketenes, isocyanates, and carbon suboxide are also very reactive. Disubstituted ketenes yield enolate ions (equation 38), which may be protonated to ketones or used in situ. The very high reactivity

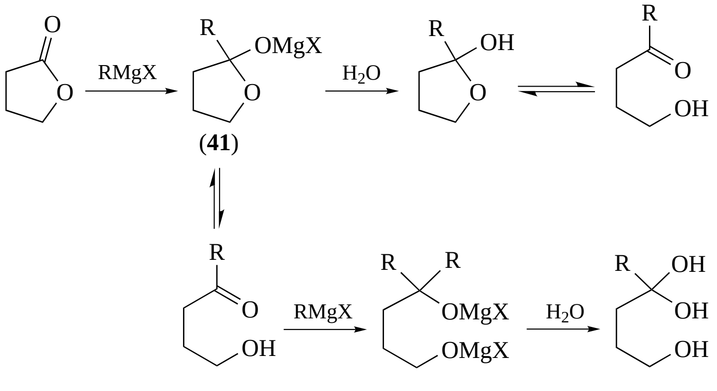

Scheme 5

of an isocyanate is illustrated in equation (39). In simpler examples an N-substituted amide is formed after hydrolysis; the reaction is useful as an amide synthesis, and to characterize the organometallic.

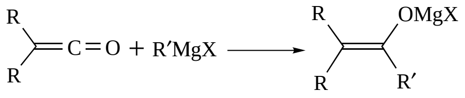

(38)

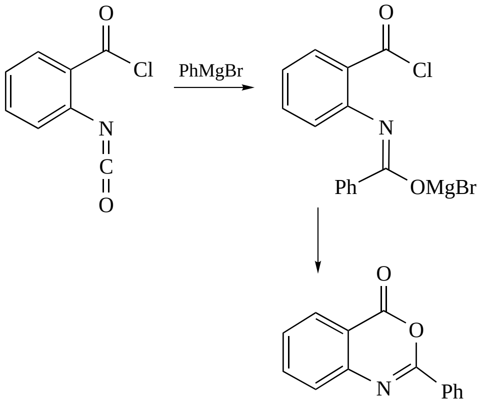

(39)

5.7 Addition and Substitution at C-Nitrogen and C-Phosphorus Unsaturation

5.7.1 Addition and Substitution to Carbon–Nitrogen Unsaturation

Addition to the C=N of an imine forms the magnesium amide, which is hydrolyzed to an amine. Isolated C=N double bonds of simple imines are relatively unreactive toward organomagnesium compounds, and may instead be deprotonated at the α-position. Oximes and other N-substituted imines may react better, although an alternative sequence can produce aziridines. Imminium ions, because of their positive charge, are more reactive, and are useful in making tertiary amines. N-Silylimines yield primary amines after hydrolysis. Grignard reagents also add to one C=N of carbodiimides to produce amidines, and to nitrones to produce hydroxylamines. Some varied examples are shown in Scheme 6.

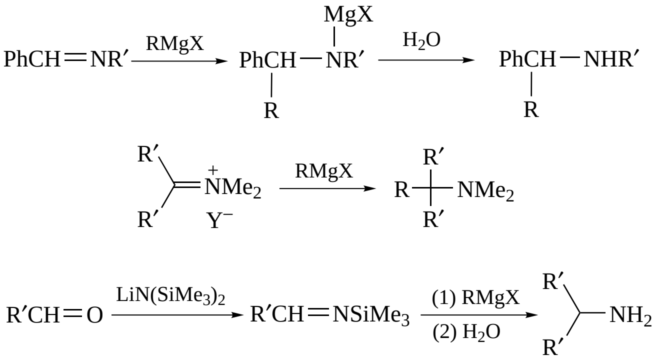

Scheme 6

Addition of organomagnesium compounds to the triple bond of a nitrile, followed by hydrolysis of the resulting imine, is an important synthesis of ketones (Scheme 7). The imine salt has also been alkylated, acylated, or silylated. An important side reaction is abstraction of an α-proton (the equivalent of enolization). A second equivalent of organometallic can add to the remaining double bond of the first adduct, leading after hydrolysis to a t-carbinylamine. With excess nitrile, a complex series of condensations may occur. A useful synthesis of nitriles is a displacement reaction on the cyano group of a cyanate (equation 40).

$$R'\text{–OCN} \xrightarrow{\text{RMgX}} R'\text{OMgX} + \text{RCN} \qquad (40)$$

Addition can also occur to the formal ring double bonds of a nitrogen heteroaromatic compound. The usual preference is for addition adjacent to the nitrogen (equation 41), but this may be modified by substitution, cryptand complexation, quaternization, or copper salt catalysis. Pyridine N-oxides may yield deoxygenated product.

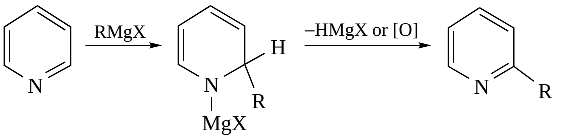

(41)

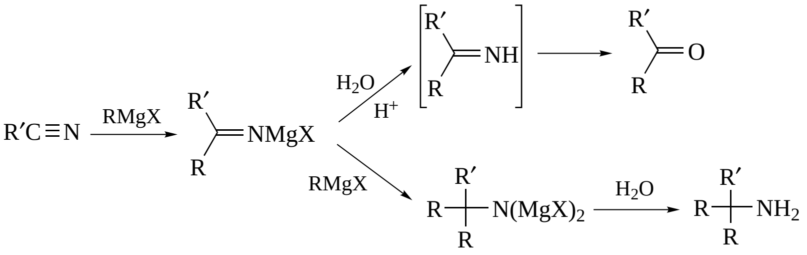

Scheme 7

5.7.2 Addition and Substitution to Carbon–Phosphorus Unsaturation

1,3,5-triphosphabenzene initially undergoes 1,4 addition with Grignard reagents (the R group of the Grignard adds to phosphorus) to ultimately yield unusual diorganomagnesium salts containing a $Mg(THF)_6$ dication, and $C_3(t\text{-Bu})_3P_2P$ anions bearing a partially delocalized charge (equation 42).[60] The phosphaalkyne PC(t-Bu) adds 'RMgCl' to yield the phosphavinyl Grignard reagent RP=C(t-Bu)MgCl, which crystallizes as the chloride-bridged dimer.[61] The polarity of addition (MgX bound to carbon) is opposite to that observed for nitriles.

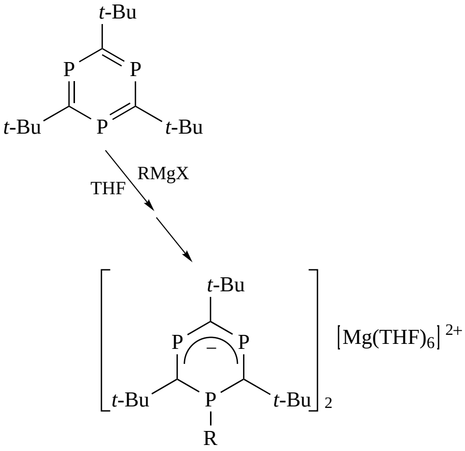

(42)

5.8 Addition to Carbon–Carbon Unsaturation

Carbon–carbon multiple bonds are usually much less reactive to addition of organomagnesium compounds than carbonyl groups. While the coordination of the magnesium to the negatively polarized carbonyl oxygen helps bring together the reacting entities in a 'Grignard reaction', a carbon–carbon multiple bond does not complex strongly enough to magnesium to displace ether solvation. Nevertheless, reactions do occur, and are sometimes quite useful synthetically. Since the product of the addition is itself an organometallic compound, this reaction has been briefly noted earlier in Section 4.4.1. Addition of Grignard reagents to simple unactivated alkenes or alkynes occurs only under relatively strenuous conditions, and then usually with secondary, tertiary, benzylic, and allylic Grignard reagents. Under forcing conditions the ethyl Grignard reagent will add to ethylene. In additions to terminal alkenes, the orientation in equation (43) predominates.[8] The addition of allylic Grignard reagents is most facile, although it still is not competitive with the more common 'Grignard reactions'. Most of the reaction occurs with 'inversion' of the allyl group; a cyclic mechanism is proposed, and the process has been dubbed the 'magnesium-ene' reaction (e.g. equation 44). As shown, rearrangements may follow the initial addition (see also below). In its intramolecular form it is a powerful ring synthesis method.

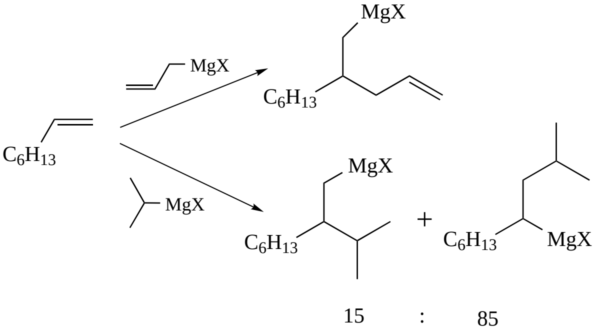

(43)

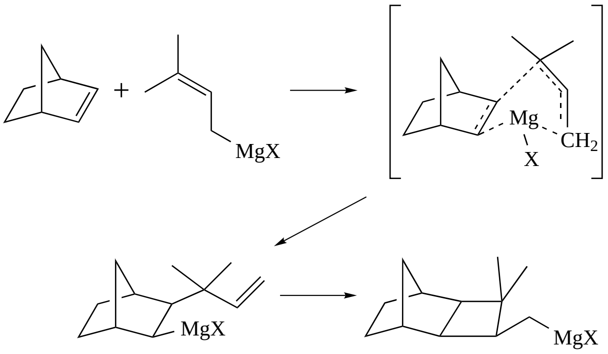

(44)

Additions occur more easily if a 'carbanion' with resonance or inductive stabilization is formed in the addition. Thus, fulvenes are very reactive, vinylsilanes and highly fluorinated alkenes somewhat less so. Styrene, 1,3-dienes, and enynes are more reactive than isolated alkenes, and Grignard reagents may be used to initiate anionic polymerization of styrenes, dienes, and acrylic monomers. Strained alkenes such as norbornenes and cyclopropenes are also more reactive. Examples of additions facilitated by resonance or substitution are shown in Scheme 8.

An extreme of activation is found when the double bond is conjugated to a strongly electron-withdrawing substituent, most importantly, carbonyl or cyano. The competition between '1,2-addition' to the C=O or C≡N and 'conjugate' or '1,4-addition' to the C=C is important synthetically (Scheme 9). Generally, lithium reagents give mostly 1,2-, Grignard reagents more 1,4-, and complete 1,4-addition can be approached using cuprates or Cu^I catalysis. Steric factors affect the product distribution: α,β-unsaturated aldehydes give mostly 1,2-addition even with Grignard reagents. An electron transfer mechanism[62] gives predominantly 1,4-addition. This is favored by HMPA in the solvent, with tertiary alkyl Grignard reagents, and Cu catalysis. The product of the 1,4-addition is an enolate ion, which is usually inert to further addition. On hydrolysis a saturated carbonyl compound is obtained, corresponding effectively to 3,4-addition to the C=C. As in the case with 1,2-addition, stereocontrol of the new C–C bond may be achieved.[63] Reactions with quinones can be quite complicated, with 1,2-addition to one or both carbonyl groups, 1,4-additions to the ring double bonds,

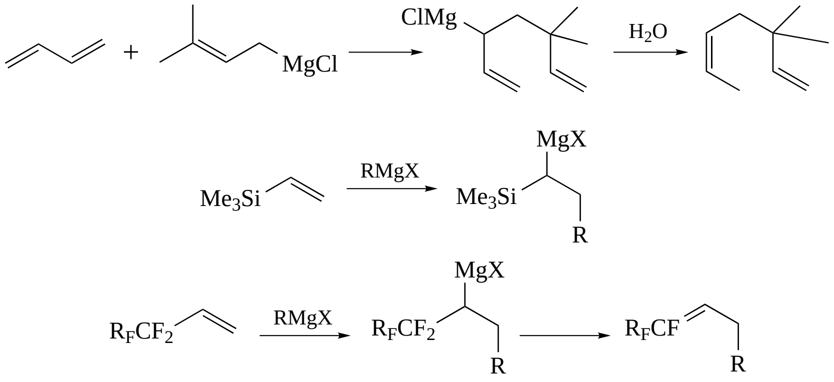
+
MgCl
ClMg
H2O
MgX
RMgX
Me3Si
Me3Si
R
MgX
RFCF2
RMgX
RFCF2
R
RFCF
R

Scheme 8

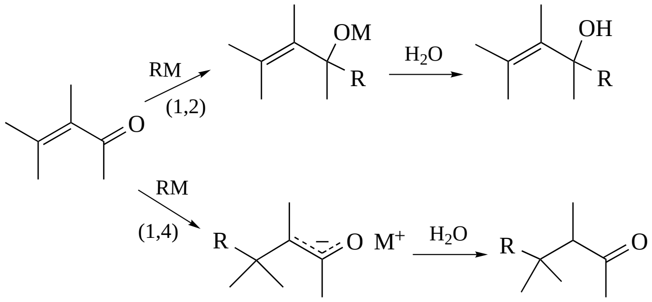
RM
(1,2)
OM
R
H2O
OH
R
O
RM
(1,4)
R
O M+
H2O
R
O

Scheme 9

and additional pathways (including reductions) resulting from electron transfer.

Organomagnesium compounds add to polycyclic aromatic hydrocarbons under forcing conditions, but with electron-withdrawing substituents the addition occurs more easily. Alkyl Grignard reagents add 1,4 and/or 1,6 to nitroaromatics, and the nitronate intermediate may be converted to a number of useful products (equation 45). Aryl Grignards yield hydroxylamines (by means of a 1,2 process), which can be reduced to diarylamines.[64]

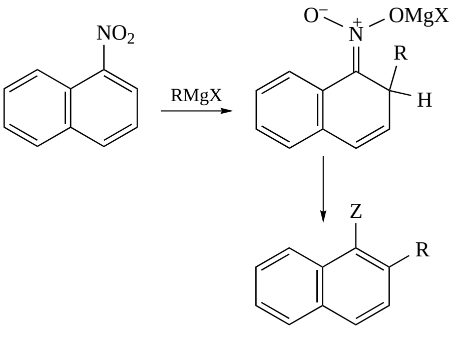
NO2
RMgX
O−
N+
OMgX
R
H
Z
R

Z = NO_2, NO, NH_2, Cl

(45)

Intramolecular additions are also facilitated. Many organomagnesium rearrangements have been reported which consist of either intramolecular additions to a carbon−carbon double or triple bond, the reverse ring-cleavage, or a sequence of such processes (equations 44, 46−48). Mechanistic studies suggest that the intramolecular processes, and by implication organomagnesium additions to C=C in general, are concerted processes occurring via a four-centered transition state.[65]

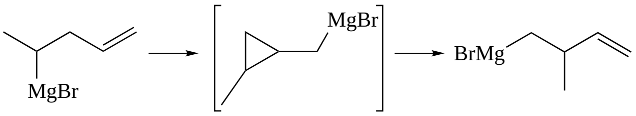
MgBr
MgBr
BrMg

(46)

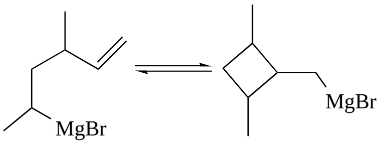

(47)

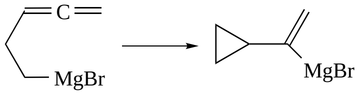

(48)

A Lewis-basic substituent in the alkene can also promote addition of a Grignard reagent to a double or triple bond.[8] Allyl, benzyl, and *t*-butyl Grignard reagents add readily to allylic and homoallylic alcohols and alkynols (equation 49). A magnesium alkoxide, formed initially, apparently assists intramolecularly in the addition. There appear to be multiple mechanistic pathways, with different stereochemistries. OR and NR_2 groups also activate addition.

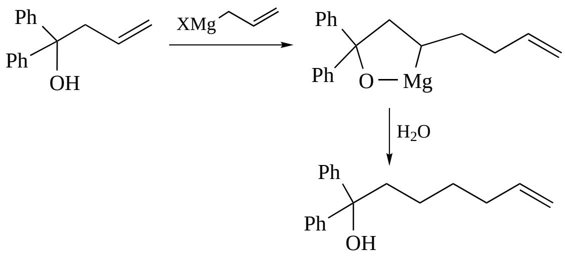
Ph
Ph
OH
XMg
Ph
Ph
O
Mg
H2O
Ph
Ph
OH

(49)

Transition metal salts promote additions, particularly to alkynes, both catalytically and in stoichiometric amounts. Normant reagents or Cu^I catalysis of Grignard reagents are the most explored.[8] Stereochemistry and orientation depend upon substitution, but a syn addition is most common. New chiral zirconocene catalysts have enabled the regio- and stereoselective addition of Grignard reagents (primarily ethyl) to the double bond of allylic alcohols, ethers, and amines.[7,66] A method more general than any previous involves the regioselective addition of alkyl radicals (generated from alkyl halides by electron transfer from a titanate complex) to the terminal carbon of an alkene or diene, followed by transmetalation of a Ti intermediate to the Grignard reagent (equation 50).[67] Alkyl (hindered primary; secondary, and tertiary), vinyl, and aryl halides have been used, and benzyl, α-silylalkyl, and allylmagnesium halides have been formed.

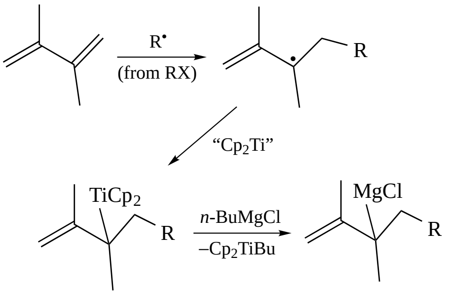

(50)

5.9 Other Reactions

A number of reactions which did not to fit neatly into the foregoing categories are shown in Scheme 10.

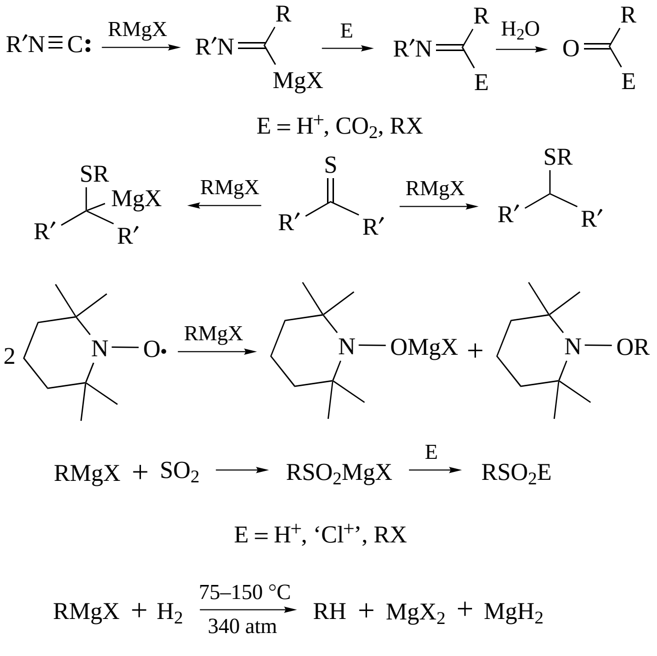

Scheme 10

6 SPECIAL CLASSES OF COMPOUNDS

Several categories of compounds have special features that warrant some consideration as a group.

6.1 Organo-di- and Polymagnesium Compounds[8,9]

Many di-Grignard reagents can be prepared routinely from the corresponding halo compounds, provided the halogens are sufficiently separated, for example, (**42**), $X(CH_2)_4X$, or *m*- and *p*-dihalo aromatics. Precautions such as dilution, low temperature, and active magnesium (particularly Mg anthracene) may be important for a good yield, particularly where the halide is easily displaced, for example benzylic.

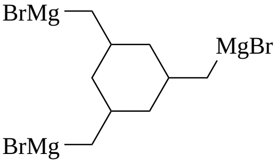

(**42**)

With 1,3-dihalides, elimination to produce a cyclopropane can be a problem. Elimination predominates strongly when the halogens are on adjacent carbons. Aromatic *ortho* di-Grignard reagents and that from 1,2-dibromocyclopropane may be formed because the competing elimination yields a more strained system. $BrMgCH_2CH_2MgBr$ has been made from $LiCH_2CH_2Li$ and $MgBr_2$.

A number of 1,1-di-Grignard reagents have been reported, including $CH_2(MgX)_2$ ($X = Br$, I, from the dihalide and Mg/Hg), and (**43**). Pyrolyzes of Me_2Mg and Me_2Be produce polymeric (MCH_2).

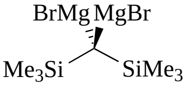

(**43**)

Difunctional Grignard reagents are of interest, because they offer the possibility of ring formation upon reaction with appropriate substrates. Applications include carbocyclic (especially cyclalkanol), heterocyclic and metallacyclic syntheses. Examples are shown in equations (26), (27), (35), (37), and (51). 1,1-di-Grignard reagents also olefinate aldehydes and ketones in a Witting-type manner, although (**43**) is generally of low reactivity.

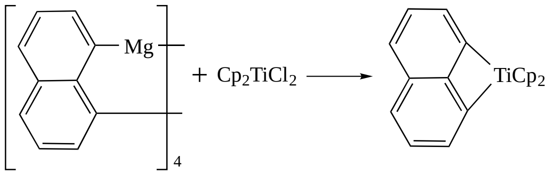

(51)

The structures of dimagnesium compounds are also of interest. With an α,ω-di-Grignard reagent the R_2Mg species in the Schlenk equilibrium can be a magnesiacycle. The cyclic dimer structure in equation (52) has been confirmed by X-ray crystallography. Halide-free organomagnesium compounds from 1,2-dihalobenzene, 1,8-dihalonaphthalene, and 1,2-dihalo-1,2-diphenylethylene have unique tetrameric cluster structures with η^3 bridging organic ligands and a tetrahedral arrangement of magnesiums.**9**

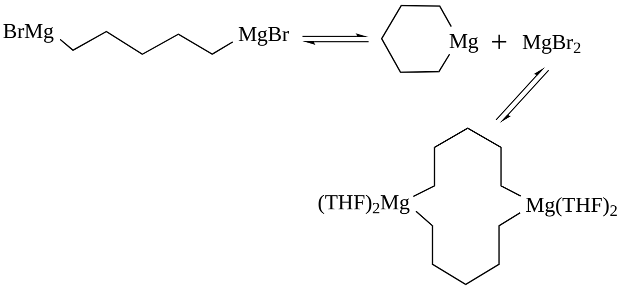

(52)

Aromatic groups containing more than two Mg groups are rare. 1,3,5-$C_6H_3(MgBr)_3$ has recently been prepared from the trilithio analogue and $MgBr_2$, while transmetalation of the permercurated ruthenocene yields the decamagnesiated species (**44**). The latter is thought to be oligomeric.**68**

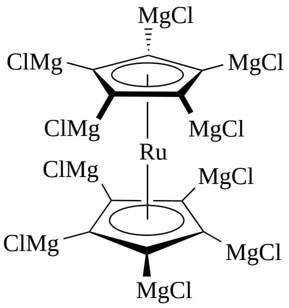

(**44**)

6.2 Functionally Substituted Organic Groups: Protecting Groups

An organomagnesium compound can tolerate a number of additional functional groups on its organic portion. In remote positions, ether, thioether, and tertiary amino groups are quite compatible with the organometallic function and, as noted in Section 2.4, can provide intramolecular 'solvation' of the metal. A halogen substituent is subject to internal displacement ('elimination'), but in many cases a dihalide is converted to a halosubstituted Grignard reagent (if the halogens differ in reactivity), or further to the di-Grignard reagent (see Section 6.1). γ-Substituents are sometimes eliminated, forming a cyclopropane. A β-substituent (equation 53) ($Y =$ halogen, OR, NR_2, etc.), is generally eliminated so readily that no Grignard reagent can be detected. However, Grignard reagents with β-amino groups have been obtained at low temperature, and perfluoroalkyl Grignard reagents have limited stability. *o*-Haloaryl Grignard reagents can also be formed, but these compounds decompose to generate benzyne. Some organomagnesium compounds with α-halogen can be formed at low temperature (equation 13), but decompose on warming, either via free carbenes or to 'carbene-derived' products. Grignard reagents $ROCH_2MgX$ decompose above −15 °C to ethylene and ROMgX. R_3Si and R_3Sn may be in α, β, or more distant positions.

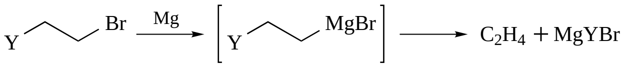

(53)

Functional groups normally reactive to Grignard reagents must be protected either by temporary replacement with an inert moiety or an adjustment (attenuation) of reaction conditions Hydroxyl groups may be protected as *t*-butyl, Me_3Si, or tetrahydropyranyl ethers, or the OH group of a haloalcohol may be converted to an alkoxide before reacting with magnesium metal. Aldehydes and ketones are protected by formation of acetals; (**45**) has protected primary amino groups. The carboxylate group in (**46**) is apparently unreactive enough to be compatible.

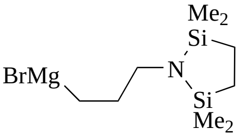

(**45**)

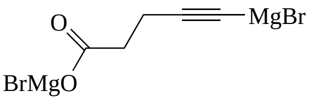

(**46**)

As discussed in Section 4.3.3, the development of extremely mild (−20 to −50 °C) halide–magnesium exchange processes for preparing (unsaturated) Grignard reagents has lessened the importance of protective group strategies.**45** Similarly, Fe catalysts allow alkyl Grignards and aryl electrophiles to cross couple at room temperature or below, conditions compatible with many functional groups (Section 5.5).**53**

6.3 Magnesium–Arene and Magnesium–Diene 'Addition Compounds'

Magnesium reacts with naphthalene and higher polycyclic aromatics in liquid ammonia or HMPA to form the radical ion. Adducts with anthracene and substituted anthracenes form in THF.**9** Depending upon substitution and conditions, they have a variety of structures.**8,9,12** The 1,10-bis(trimethylsilyl) compound had structure (**47**) in the crystal, with magnesium bridging the 1,10-positions (C–Mg =

221–223 pm; C–Mg–C = 78–79°). With anthracene and 1,10-dimethylanthracene the magnesium was coordinated to three THF molecules and was further (232 pm) from the carbons, suggesting a more ionic interaction. Magnesium anthracene compounds serve as active carriers for magnesium atoms, and decompose to deposit a very active finely divided magnesium. Silica and polymer supported Mg anthracene complexes offer certain advantages over Mg (anthracene)(THF)$_3$ in the preparation of Grignard reagents.

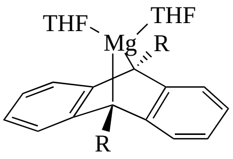

(**47**)

Conjugated dienes also react with magnesium in THF[8] (usually with some activation). With 1,3-butadiene the initial product is THF-solvated [C_4H_6Mg], which can add more butadiene molecules. The 1:1 and 1:2 adducts are reasonably formulated as allylic organomagnesium compounds (**48**) or (**49**). These complexes are diamagnetic, hydrolyze to alkenes with incorporation of two D atoms from D_2O, and undergo reactions typical of Grignard reagents. Net 1,2- or 2,1-addition can be effected, depending on the nature of the electrophiles. Electrophiles with two electrophilic centers can lead to carbocyles, including spiro compounds.[8,9]

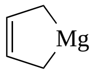

(**48**)

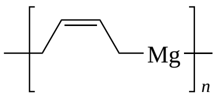

(**49**)

6.4 Cyclopentadienyl Compounds[69]

Crystalline dicyclopentadienylmagnesium[3,12] has a monomeric sandwich structure, with the rings staggered. Its long ring–metal distance, along with vibrational and photoelectron spectroscopic data, imply ionic character, but other experimental (e.g. ^{25}Mg NMR) as well as theoretical studies suggest significant covalent binding.[35,69] Addition of HMPA to an ether solution leads to solvent-separated ions. Mg(C_5H_5)$_2$ forms adducts with many Lewis bases, and is a useful reagent for the transfer of C_5H_5 groups. Mono π-(C_5H_5)Mg complexes, that is, CpMgX, are generally isolable only as base adducts. The TMEDA adduct of CpMgBr and the dimer [CpMgMe(Et$_2$O)]$_2$ have the ring bonded nearly symmetrically to the metal and distorted tetrahedral metal geometry; the latter has bridging methyls. In selected ion flow tube studies, the reactivity of Mg$^+$, CpMg$^+$, and Cp$_2$Mg$^+$ ions with small inorganic molecules and straight chain hydrocarbons has been probed. CpMg$^+$ was the most reactive of the three ions.[70] Magnesocenes with substituted cyclopentadienyl ligands, including rings bearing methyl, trimethylsilyl, *tert*-butyl, and methoxy substituents are known. The recently determined solid-state structure of Mg(C_5Me_5)$_2$ reveals the presence of both staggered and completely disordered conformers.[71] The substituted-ring species form stable adducts with N-heterocyclic carbenes.[72]

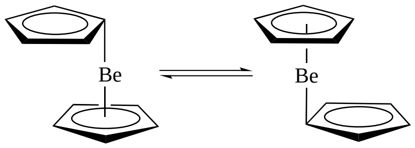

(54)

Dicyclopentadienylberyllium[10] has a substantial dipole moment, indicating an unsymmetrical structure. A variety of structures have been proposed, based on different experimental data. The molecule adopts a ‘slip-sandwich’ structure in the solid and vapor, with the Be atom disordered equally over two sites, and the two rings η^5 and η^1 bonded. Equation (54) depicts the Be atom disorder in the solid-state structure. The metal–ligand bonding is relatively weak: a sharp singlet is observed in the ^{1}H NMR down to $-135\,°$C, indicating rapid averaging of the environments of the two rings. Molecular dynamics calculations credit two ultrafast (activation energies of less than 10 kJ mol^{-1}) processes, a 1,5 sigmatropic shift of the Be(η^5-C_5H_5) unit around the periphery of the η^1- ring (depicted in Scheme 11 for Be(C_5Me_4H)$_2$), and a ring/molecular inversion that interchanges the η^5 and η^1 rings (Scheme 12), for the isomerization.[73] BeCpX complexes (X = H, Cl, Br, Me, CCH, C_5Me_5, BH_4, B_3H_8, B_5H_{10}, and SiMe$_3$ (Section 6.7)) appear to be monomeric in all phases, with C_5H_5–(centroid)–Be distances, where determined, similar to that of the η^5-bonded ring in Be(C_5H_5)$_2$ (147 pm). X-ray diffraction reveals that while the octa- and nonamethylberyllocene derivatives (C_5Me_4H)$_2$Be and (C_5Me_4H)Be(C_5Me_5) exhibit slip-sandwich η^5/η^1 structures (where the η^1 ring bonds Be via the secondary, i.e C–H carbon), the deca methyl derivative Be(C_5Me_5)$_2$ adopts a ferrocene-type η^5/η^5 structure with parallel rings.[74] Insertion of an isocyanide into the Be–η^1(C_5Me_4H) σ bond of (C_5Me_4H)Be(C_5Me_5) yields two different iminoacyl isomers (Scheme 13). As these isomers correspond to those depicted in Structure 11, they constitute chemical evidence for the proposed isomerization mechanism. Half-sandwich compounds (C_5Me_5)BeX, where X = Cl, Br, P(t-Bu$_2$), As(t-Bu$_2$), Me, t-Bu, CH$_2$CMe$_3$, and CH$_2$Ph have been prepared.[75]

6.5 Allylic and Benzylic Organomagnesium Compounds

Allylmagnesium compounds appear to undergo a rapid allylic shift of the magnesium between the two methylene

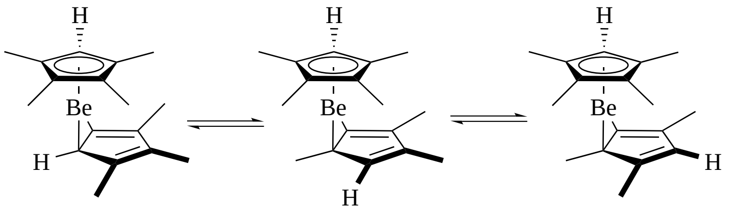

Scheme 11

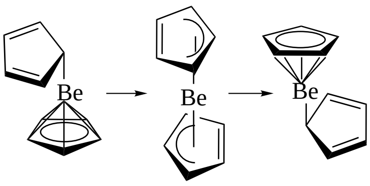

Scheme 12

termini of the allyl group (equation 55). An alternative description is an allyl group symmetrically bonded to the magnesium, either covalently bridging η^3 as depicted in (**50**) or as an ion pair. Early NMR and IR data could not distinguish between these alternatives. More recent, higher field ^{1}H and ^{13}C NMR spectra are likewise ambiguous, in that low-temperature spectra exhibit extreme broadening as opposed to separate methylene resonances. IR spectra of 1,1- or 3,3-dideuterated allymagnesium bromide solutions reveal, however, a pair of bands due to the C=C bond stretch, consistent with the rapid equilibration of unsymmetrical allylic isomers.[76]

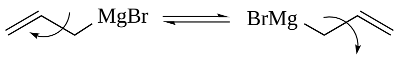

(55)

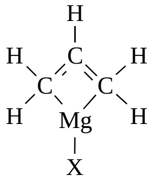

(**50**)

Alkyl substitution (equation 56) destabilizes the allylic isomer (**51**) with the more highly substituted α-carbon, so that it is not detected directly in the equilibrium mixture. However, cis–trans isomerization, rapid on the NMR timescale even at low temperature, likely occurs via rotation about the single bond in the low equilibrium concentration of (**51**). The position of equilibrium has been deduced from ^{1}H NMR coupling constants; with R = Me, the (Z)-isomer is favored

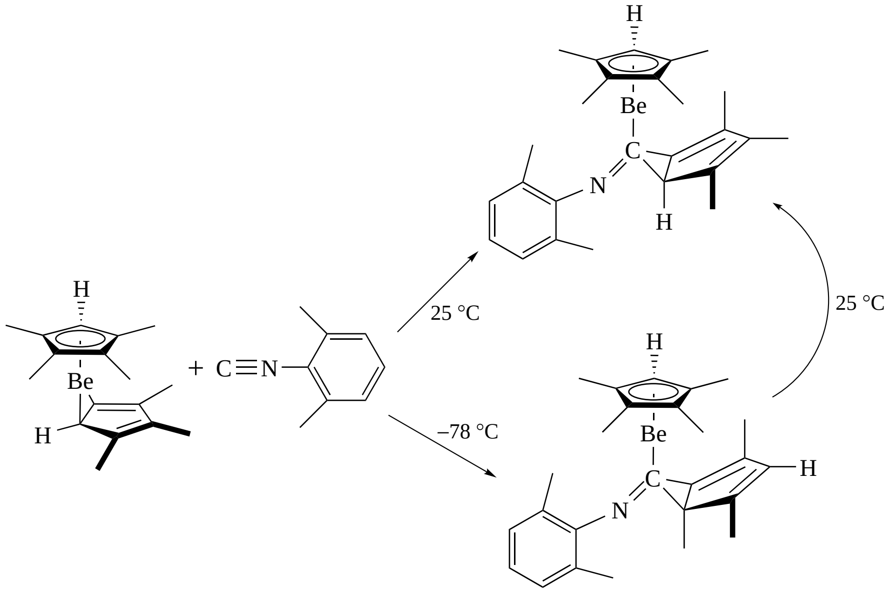

Scheme 13

by about 60:40, but steric hindrance with larger groups shifts the equilibrium toward the (E)-isomer.[77]

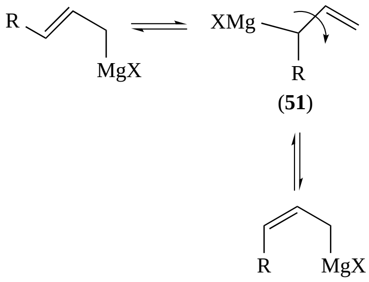

(56)

Both allylic and benzylic organomagnesium compounds appear to be more reactive than typical primary compounds. They also both show some tendency to react with rearrangement. In the equilibrium of equation (56), the primary structures dominate heavily, yet addition to carbonyl groups occurs almost exclusively at the secondary allylic position. It appears that this results from reaction of the primary isomers with rearrangement, rather than reaction of a very small equilibrium concentration of (**51**) without rearrangement. With hindered ketones the addition is slightly reversible, and at longer reaction times the less hindered product of addition at the primary allylic carbon appears.[78] A six-center cyclic transition state for addition with rearrangement has been proposed. In other reactions, for example, with Me_3SiCl, mixtures of allylic isomers are frequently formed. Benzylic Grignard reagents react partially at the ortho position.[79]

6.6 Acylmetal Compounds

Although beryllium metal is rather sluggishly reactive toward most organic halides, it reacts surprisingly easily with acyl halides in ethyl acetate to form acylberyllium halides. These react normally with ketones by addition, producing hydroxy ketones. With aromatic ketones, electron transfer appears to dominate, as the principal product from the ketone is the pinacol.

Carbon monoxide reacts with Grignard reagents, though more slowly than carbon dioxide. The initial reaction is a 1,1-addition to the carbon, resulting in an acylmagnesium halide. Despite potential applications of such species, the reaction usually leads to mixtures of products, and has not been developed synthetically.[80]

6.7 Bonds to Silicon[81]

Mg–Si bonds have long been inferred in reactions that generate hexaorganodisilanes from halo(triorgano)silanes and either a Grignard reagent or Mg metal (‘Silico-Barbier’ reaction). Similarly, the electrochemical reduction of chloro(triorgano)silanes with sacrificial Mg electrodes yields polysilanes in high yield.[82] Silyl ‘Grignard’ reagents are prepared from magnesium halides and alkali metal silyls. Unlike the symmetrically Br-bridged alkyl Grignards (compare Structure 10), the tetramethylethylenediamine adduct of $(Me_3Si)MgBr$, while not strictly monomeric, exhibits pentacoordinate Mg, and Mg–Br bonds of significantly different lengths.[83] (*tert*-Bu_3Si)MgBr(THF), however, features tetracoordinate Mg with symmetrically bridging bromines.[84] Schlenk equilibria yield the bis(silyl) species, also accessible by metathesis reactions. A number of base adducts of $(R_3Si)_2Mg$, where R = Me, *tert*-Bu, or (Me_3Si),[85] have been characterized by X-ray diffraction. The Mg atoms adopt distorted tetrahedral configurations, with Si–Mg–Si angles between 115° and 133°, and Mg–Si bond lengths of 263 to 268 pm (278 pm for R = *tert*-Bu).

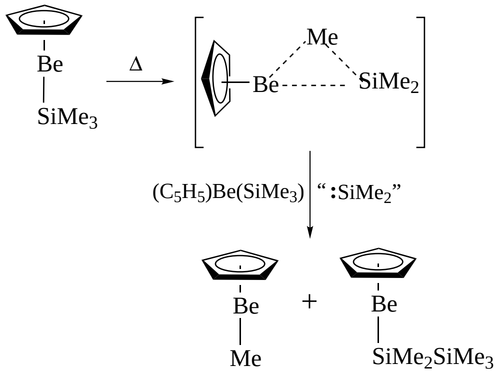

Scheme 14

Beryllium–silicon bonds are a recent development. They are likewise prepared by the reaction of the metal halide with alkali metal silyls, but unlike the Mg analogues, both of the well-characterized Be examples are base-free. While $[(tert\text{-}Bu_3Si)BeCl]_n$ is oligomeric, the molecular structure of $(tert\text{-}Bu_3Si)_2Be$ features a perfectly linear Si–Be–Si unit.[84] $CpBe(SiMe_3)$, prepared from CpBeCl and trimethylsilyllithium in pentane, exhibits an intriguing thermal chemistry. The identity of the primary thermolysis products, Scheme 14, implies the participation of silylene intermediates, a contention supported by DFT/NBO (density functional theory/natural bond order) analysis.[86]

7 RELATED ARTICLES

Alkali Metals: Organometallic ChemistryAlkaline Earth Metals: Inorganic Chemistry;Aluminum: Organometallic Chemistry; Asymmetric Synthesis by Homogeneous Catalysis; Copper: Organometallic Chemistry; Electronic Structure of Main-group Compounds; Nickel: Organometallic Chemistry; Palladium: Organometallic Chemistry; Zinc: Organometallic Chemistry.

8 REFERENCES

1. D. Hodson, *Chem. Br.*, 1987, **23**, 141.
2. M. S. Kharasch and O. Reinmuth, ‘Grignard Reactions of Nonmetallic Substances’, Prentice Hall, New York, 1954.
3. W. E. Lindsell, in ‘Comprehensive Organometallic Chemistry’, eds. G. Wilkinson, F. G. A. Stone, and E. W. Abel, Pergamon Press, Oxford, 1982, Vol. 1, Chap. 4, p. 155.
4. W. E. Lindsell, in ‘Comprehensive Organometallic Chemistry II’, eds. E. W. Abel, F. G. A. Stone, and G. Wilkinson, Pergamon/Elsevier, Oxford, 1995, Vol 1, p. 57.
5. B. J. Wakefield, in ‘Comprehensive Organometallic Chemistry’, eds. G. Wilkinson, F. G. A. Stone, and E. W. Abel, Pergamon Press, Oxford, 1982, Vol. 7, Chap. 44, p. 1.
6. C. L. Raston and G. Salem, in ‘Chemistry of the Metal–Carbon Bond’, ed. F. R. Hartley, Wiley, New York, 1987, Vol. 4, Chap. 2, p. 159.
7. B. Wakefield, ‘Organomagnesium Methods in Organic Synthesis’, Academic Press, London, 1995.
8. G. S. Silverman and P. E. Rakita eds, ‘Handbook of Grignard Reagents’, Marcel Dekker, New York, 1996.
9. H. G. Richey Jr, ed., ‘Grignard Reagents: New Developments’, John Wiley & Sons, New York, 2000.
10. N. A. Bell, in ‘Comprehensive Organometallic Chemistry II’, eds. E. W. Abel, F. G. A. Stone, and G. Wilkinson, Pergamon Press, Oxford, 1994, Vol. 1, Chap. 2, p. 35.
11. H. Schmidbaur, Organoberyllium Compounds, Part 1, System No. 26, in ‘Gmelin Handbook of Inorganic Chemistry’, 8th edn., eds. A. Kubny and M. Mirbach, Springer-Verlag, Berlin, 1987.
12. P. R. Markies, O. S. Akkerman, F. Bickelhaupt, W. J. J. Smeets, and A. L. Spek, *Adv. Organomet. Chem.*, 1991, **32**, 147.
13. C. E. Holloway and M. Melnik, *Coord. Chem. Rev.*, 1994, **135–136**, 287.
14. W. D. Bare and L. Andrews, *J. Am. Chem. Soc.*, 1998, **120**, 7293.
15. K. Hashimoto, Y. Osamura, and S. Iwata, *THEOCHEM*, 1987, **152**, 101.
16. K. B. Wiberg and C. M. Breneman, *J. Am. Chem. Soc.*, 1990, **112**, 8765.
17. S. R. Davis, *J. Am. Chem. Soc.*, 1991, **113**, 4145.
18. T. Holm, *J. Chem. Soc., Perkin Trans.*, 1981, **2**, 464.
19. T. Holm, *Acta Chem. Scand.*, 1983, **B37**, 797.
20. O. S. Akkerman, G. Schat, E. A. I. M. Evers, and F. Bickelhaupt, *Recl. Trav. Chim. Pays-Bas*, 1983, **102**, 109.
21. J. W. Ochterski, G. A. Petersson, and K. B. Wiberg, *J. Am. Chem. Soc.*, 1995, **117**, 11299.
22. V. C. Gibson, J. A. Segal, A. J. P. White, and D. J. Williams, *J. Am. Chem. Soc.*, 2000, **122**, 7120.
23. A. Xia, M. J. Heeg, and C. H. Winter, *Organometallics*, 2003, **22**, 1793.
24. R. J. Wehmschultze, B. Twamley, and M. A. Khan, *Inorg. Chem.*, 2001, **40**, 6004.
25. E. C. Ashby, *Pure Appl. Chem.*, 1980, **52**, 545.
26. E. M. Hanawalt, J. Farkas Jr, and H. G. Richey Jr, *Organometallics*, 2004, **23**, 416.
27. B. J. Wakefield, *Organomet. Chem. Rev.*, 1966, **5**, 477.
28. J. Axten, J. Troy, P. Jiang, M. Trachtman, and C. W. Bock, *Struct. Chem.*, 1994, **5**, 99.
29. R. W. Hoffmann, *Chem. Soc. Rev.*, 2003, **32**, 225.
30. B. E. Mann, *Adv. Organomet. Chem.*, 1974, **12**, 135.
31. L. M. Khalilov, A. A. Panasenko, R. R. Muslukhov, A. G. Ibragimov, G. A. Tolstikova, and U. M. Dzhemilev, *Bull. Acad. Sci. USSR, Div. Chem. Sci.* (Engl. Transl.), 1988, **37**, 458.
32. R. R. Muslukhov, L. M. Khalilov, A. G. Ibragimov, U. M. Dzhemilev, and A. A. Panasenko, *Metalloorg. Khim.*, 1988, **1**, 680; *Chem. Abstr.*, 1989, **110**, 95.
33. R. E. Wasylishen, K. Chum, and J. Bukata, *Org. Magn. Reson.*, 1977, **9**, 473.
34. D. Leibfritz, B. O. Wagner, and J. D. Roberts, *Liebigs Ann. Chem.*, 1972, **763**, 173.
35. R. Benn, H. Lehmkuhl, K. Mehler, and A. Rufinska, *Angew. Chem., Int. Ed. Engl.*, 1984, **23**, 534.
36. D. F. Gaines, K. M. Coleson, and D. F. Hillenbrand, *J. Mag. Res.*, 1981, **44**, 84.
37. M. Sassian and A. Tuulmets, *Helv. Chim. Acta*, 2003, **86**, 82.
38. A. Tuulmets, B. T. Nguyen, D. Panov, M. Sassian, and J. Jarv, *J. Org. Chem.*, 2003, **68**, 9933.
39. L. A. Tjurina, V. V. Smirnov, D. A. Potapov, S. A. Nikolaev, S. E. Esipov, and I. P. Beletskaya, *Organometallics*, 2004, **23**, 1349.
40. E. A. Vogler, R. L. Stein, and J. M. Hayes, *J. Am. Chem. Soc.*, 1978, **100**, 3163.
41. B. J. Schaart, C. Blomberg, O. S. Akkerman, and F. Bickelhaupt, *Can. J. Chem.*, 1980, **58**, 932.
42. J. F. Garst, J. R. Boone, L. Webb, K. E. Lawrence, J. T. Baxter, and F. Ungvary, *Inorg. Chim. Acta*, 1999, **296**, 52.
43. E. Peralez, J. C. Negrel, A. Goursot, and M. Chanon, *Main Group Met. Chem.*, 1999, **22**, 185.
44. N. Bodineau, J. M. Mattalia, V. Thimokhin, K. Handoo, J. C. Negrel, and M. Chanon, *Org. Lett.*, 2000, **2**, 2303.
45. P. Knochel, W. Dohle, N. Gommermann, F. F. Kneisel, F. Kopp, T. Korn, I. Sapountzis, and V. A. Vu, *Angew. Chem., Int. Ed. Engl.*, 2003, **42**, 4302.
46. J. Lee, R. Velarde-Ortiz, A. Guijarro, J. R. Wurst, and R. D. Rieke, *J. Org. Chem.*, 2000, **65**, 5428.
47. O. Sugimoto, S. Yamada, and K. Tanji, *J. Org. Chem.*, 2003, **68**, 2054.
48. P. E. Eaton, M. Zhang, N. Komiya, C. Yang, I. Steele, and R. Gilardi, *Synlett*, 2003, **9**, 1275.
49. E. C. Ashby and R. C. Arnott, *J. Organomet. Chem.*, 1968, **14**, 1.

50. B. A. Trofimov and S. E. Korostova, *Russ. Chem. Rev. (Engl. Transl.)*, 1975, **44**, 41.
51. J. A. Miller, J. W. Dankwardt, and J. M. Penney, *Synthesis*, 2003, **11**, 1643.
52. G. Y. Li and W. J. Marshall, *Organometallics*, 2002, **21**, 590.
53. A. Furstner, A. Leitner, M. Mendez, and H. Krause, *J. Am. Chem. Soc.*, 2002, **124**, 13856.
54. B. Bogdanovic and M. Schwickardi, *Angew. Chem., Int. Ed. Engl.*, 2000, **39**, 4610.
55. K. H. Yong, N. J. Taylor, and J. M. Chong, *Org Lett.*, 2002, **4**, 3553.
56. M. Knollmuller, M. Ferencic, and P. Gartner, *Tetrahedron: Asymmetry*, 1999, **10**, 3969.
57. M. Vestergren, J. Eriksson, and M. Hakansson, *Chem. – Eur. J.*, 2003, **9**, 4678.
58. M. Reetz, N. Harmat, and R. Mahrwald, *Angew. Chem., Int. Ed. Engl.*, 1992, **31**, 342.
59. H. Yamataka, T. Matsuyama, and T. Hanafusa, *J. Am. Chem. Soc.*, 1989, **111**, 4912.
60. J. Renner, U. BergstraBer, P. Binger, and M. Regitz, *Angew. Chem., Int. Ed. Engl.*, 2003, **42**, 1863.
61. D. E. Hibbs, C. Jones, and A. F. Richards, *J. Chem. Soc., Dalton Trans.*, 1999, 3531.
62. T. Holm, *Acta Chem. Scand.*, 1991, **B45**, 925.
63. K. Soai, H. Machida, and N. Yokota, *J. Chem. Soc., Perkin Trans. 1*, 1987, 1909.
64. A. Ricci and M. Fochi, *Angew. Chem., Int. Ed. Engl.*, 2003, **42**, 1444.
65. E. A. Hill, *Adv. Organomet. Chem.*, 1977, **16**, 131.
66. L. Bell, D. C. Brookings, G. J. Dawson, R. J. Whitby, R. V. H. Jones, and M. C. H. Standen, *Tetrahedron*, 1998, **54**, 14617.
67. S. Nii, J. Terao, and N. Kambe, *J. Org. Chem.*, 2004, **69**, 573.
68. K. N. Seneviratne, A. Bretschneider-Hurley, and C. H. Winter, *J. Am. Chem. Soc.*, 1996, **118**, 5506.
69. P. Jutzi and N. Burford, *Chem. Rev.*, 1999, **99**, 969.
70. R. K. Milburn, M. V. Frash, A. C. Hopkinson, and D. K. Bohme, *J. Phys. Chem. A*, 2000, **104**, 3926.
71. J. Vollet, E. Baum, and H. Schnockel, *Organometallics*, 2003, **22**, 2525.
72. H. Schumann, J. Gottfriedsen, M. Glanz, S. Dechert, and J. Demtschuk, *J. Organomet. Chem.*, 2001, **617–618**, 588.
73. P. Margl, K. Schwarz, and P. E. Blochl, *J. Chem. Phys.*, 1995, **103**, 683.
74. M. del Mar Conejo, R. Fernandez, D. del Rio, E. Carmona, A. Monge, C. Ruiz, A. M. Marquez, and J. F. Sanz, *Chem. – Eur. J.*, 2003, **9**, 4452.
75. M. del Mar Conejo, R. Fernandez, E. Carmona, R. A. Andersen, E. Gutierrez-Puebla, and M. A. Monge, *Chem. – Eur. J.*, 2003, **9**, 4462.
76. E. A. Hill, W. A. Boyd, H. Desai, A. Darki, and L. Bivens, *J. Organomet. Chem.*, 1996, **514**, 1.
77. D. A. Hutchison, K. R. Beck, R. A. Benkeser, and J. B. Grutzner, *J. Am. Chem. Soc.*, 1973, **95**, 7075.
78. R. A. Benkeser, M. P. Siklosi, and E. C. Mozdzen, *J. Am. Chem. Soc.*, 1978, **100**, 2134.
79. R. A. Benkeser and D. C. Snyder, *J. Org. Chem.*, 1982, **47**, 1243.
80. P. Sobota and M. Nowak, *J. Organomet. Chem.*, 1988, **340**, 1.
81. P. D. Lickiss and C. M. Smith, *Coord. Chem. Rev.*, 1995, **145**, 75.
82. S. Kashimura, M. Ishifune, N. Yamashita, H. B. Bu, M. Takebayashi, S. Kitajima, D. Yoshiwara, Y. Kataoka, R. Nishida, S. Kawasaki, H. Murase, and T. Shono, *J. Org. Chem.*, 1999, **64**, 6615.
83. R. Goddard, C. Kruger, N. A. Ramadan, and A. Ritter, *Angew. Chem., Int. Ed. Engl.*, 1995, **34**, 1030.
84. H. W. Lerner, S. Scholz, M. Bolte, N. Wiberg, H. Noth, and I. Krossing, *Eur. J. Inorg. Chem.*, 2003, 666.
85. J. D. Farwell, M. F. Lappert, C. Marschner, C. Strissel, and T. D. Tilley, *J. Organomet. Chem.*, 2000, **603**, 185.
86. D. A. Saulys and D. R. Powell, *Organometallics*, 2003, **22**, 407.

Biomineralization

Yannicke Dauphin
Université Paris Sud, Orsay, France

Based in part on the article Biomineralization by Richard B. Frankel which appeared in the Encyclopedia of Inorganic Chemistry, First Edition.

1 Introduction 1
2 Biominerals: Structure and Composition 1
3 Modes of Biomineralization 9
4 Applications 11
5 Related Articles 12
6 Further Reading 12
7 References 13

Glossary

Aragonite – calcite: polymorph calcium carbonate minerals. Aragonite is orthorhombic, calcite is trigonal (=rhomboedric)
Collagen: the main protein of connective tissue (tendons, skin, muscle, etc.). It contains a lot of glycine, proline, hydroxyproline, and hydroxylysine. Another rare feature of collagen is its regular arrangement of amino acids (triple helix structure)
Corals: animals of the Cnidaria phylum (formerly Coelenterata), with a calcareous skeleton. Sea anemones and jellyfishes are Cnidaria without skeletons
Dentine: also called *ivory*; the inner hard tissue of the tooth. The bulk of a tooth is made up of dentine
Enamel: the outer layer covering the tooth
Frustule: the siliceous 'shell' or exoskeleton of a diatom. It is composed of two valves (epitheca and hypotheca), one overlapping the other, like a pill box and its cover
Mollusks: invertebrates having a soft unsegmented body usually enclosed in a shell. Mollusca mainly includes Bivalvia, Gastropoda, and Cephalopoda
Nacre: nacreous layer or mother-of-pearl; the inner shell layer in some mollusks
Odontoblasts: more or less columnar cells on the outer surface of the pulp of a tooth; specialized cells that contribute to many aspects of tooth structure and function. They give rise to the dentine matrix that underlies the enamel of a tooth
Otoliths: earstones, are small calcareous structures found in the head of all bony fishes (other than sharks, rays, and lampreys)

Abbreviations

ACC = Amorphous calcium carbonate; RNA = Ribonucleic Acid; TEM = Transmission Electron Microscope; XANES = X-ray Absorption Near Edge Structure.

1 INTRODUCTION

Biomineralization is widespread in the biosphere (more than 60 different minerals are produced by 55 phyla, from bacteria to humans) (Figure 1), and refers to the process by which living organisms form minerals.[1] Biominerals have morphological, chemical, and physical properties that are very different from the crystal habits produced inorganically. The main role of these 'biominerals' is mechanical reinforcement of tissues and organs, but the resulting materials have biological functions as diverse as lenses, grinding or cutting appendices, gravity sensors, and guidance systems. One paradox is that these 'minerals' are not composed of only minerals. Organic matrices can be extracted from within these minerals (bone, coral skeletons, mollusk shells, etc.), which are hierarchically organized biocomposites. These specialized macromolecules are involved in biomineralization processes: they enable nucleation and growth of carbonates, phosphates, and other inorganic materials.

2 BIOMINERALS: STRUCTURE AND COMPOSITION

Among all the minerals used by organisms, three categories are widely dominant: silica, calcium phosphates, and calcium carbonates. Calcium phosphate minerals are usually associated with 'vertebrates', where they form bone and the dentine and enamel of teeth. However, phosphate minerals are present in some 'invertebrate' shells, such as Brachiopods, whereas vertebrates used calcium carbonate minerals in eggshells and otoliths. Calcium minerals represent about 50% of all biogenic minerals.

2.1 Silica

The hydrated amorphous mineral silica (opal) is widely used by many plants and animals for structural purposes. Most skeletons are formed by unicellular organisms (diatoms Figure 2(a), radiolarians Figure 2(b)), but silica is also present within multicellular organisms (sponge spicules, plant

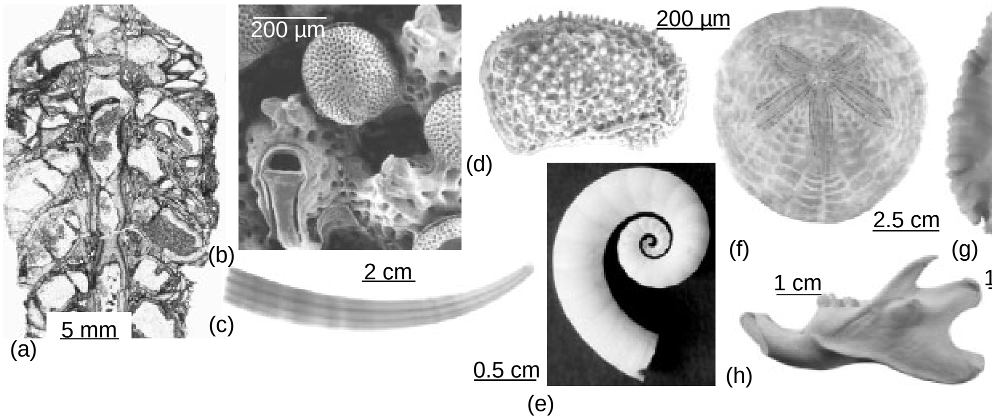

Figure 1 Some examples of mineralized skeletons: (a) Longitudinal section in a mineralizing sponge. (b) Zooids in Bryozoa. (c) Shell of a scaphopod (Mollusks). (d) Ornate shell of an Ostracod (Arthropoda). (e) The coiled shell of *Spirula* (Mollusks, Cephalopods). (f) Apical view of a sea urchin. (g) Fish otolith. (h) Teeth and bone of a small Mammal

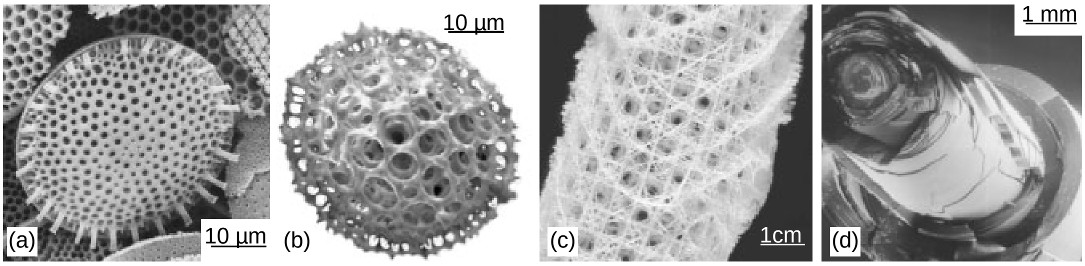

Figure 2 Scanning electron micrographs of biosilica. (a) Ornate morphology of a frustule of a diatom. (b) Ornate test of a radiolaria. (c) A siliceous sponge (*Euplectella*) showing the highly organized spicule framework. (d) Transverse section of a giant spicule showing a concentric growing pattern (*Monoraphis*)

phytoliths). Diatom exoskeletons (=frustules) are composed of globular particles and consist of colloidal aggregates.**[2]** Sponges use specialized cells called *sclerocytes* to synthesize silica spicules, and the shape and arrangement of the spicules depend on the species (Figure 2(c)). The process of extrusion of the spicules is yet poorly understood, but the presence of an axial filament containing proteins suggests they are involved in the formation of the mineral (Figure 2(d)). The transverse section of a spicule shows regular growth lines and an annular organization of nanoparticles of about 70 nm in diameter.**[3]**

In diatoms (unicellular algae), silica is a composite material containing glycoproteins. The walls are almost pure hydrated silica with small amounts of Al and Fe.

2.2 Phosphates

The main part of the calcium phosphate minerals produced by organisms is crystalline and described as apatite. Nevertheless, this common name conceals a large variety of structures and compositions.

2.2.1 Bone

Bone is a true biological tissue, since it contains cells, and is continuously forming and reforming. Different levels of organization have been described, following the progress of microscopes. Adult bone is of two basic architectural, macroscopic types: compact or cortical, and cancellous or spongy, but there is no sharp boundary between them. In compact bone, most of the individual lamellae form concentric lamellae around longitudinal canals (50 μm in diameter) within the bone tissue. These canals typically run parallel to the surface and along the long axis of the bone. The canals and the surrounding lamellae are called a *Haversian system* or an osteon (Figure 3(a)). The cortical and trabecular bones have a hierarchical structure with three or four lower levels. Various models of the plywood structure have been described (Figure 3(b), (c)).**[4–6]** The basic level of organization is the

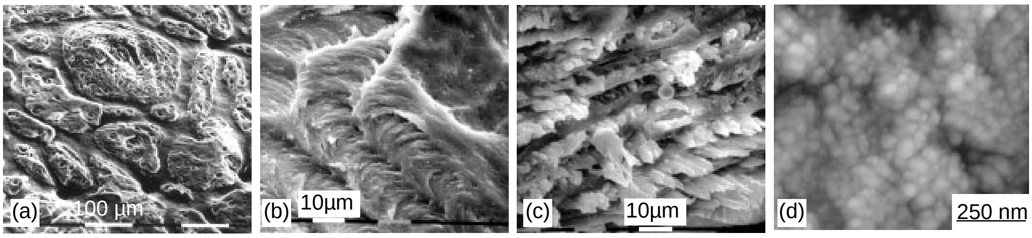

Figure 3 Structures of mammal bone: (a) Haversian systems and osteons. (b) Plywood-like structure with 'twisted' lamella. (c) Lamellar bone showing the different orientations of fibers in successive lamella. (d) Mineralized collagen fibers

relationship between the small crystallites and the organic matrix, mainly composed of collagen fibers. Crystal bones are probably the smallest biocrystals with average dimensions of $50 \times 25 \times 5$ nm.

The mineral fraction of bone is usually called '*hydroxylapatite*', 'carbonated hydroxylapatite', or dahllite. However, bone apatite contains carbonate ions but lacks hydroxyl ions. Polarized light and X-ray diffraction studies have shown that the bone crystal c axes are aligned with the collagen fiber axis. The organo-mineral composition of the bone is clearly shown by infrared spectra (Figure 4). The average chemical composition of mammal bone is illustrated in Figure 5. Na and Mg are mostly associated to the mineral fraction, but S is probably mainly associated with sulfated polysaccharides of the organic matrix. In modern mammals, it has been shown that some elements are sensitive to diet or pregnancy (Sr). The major organic component of bone is type I collagen, and the noncollagenous proteins or NCP contain more than 200 proteins. Four main groups of NCPs are found: proteoglycans, γ-carboxylated (gla)-proteins, glycoproteins, and 'others'. Chondroitin sulfate, heparan sulfate, and keratan-sulfate are present in the side chains of proteoglycans. Almost the entire mineral is found within the collagen fibers. The banding pattern of the collagen is about 70 nm. The alignment of small plates, the thickness of which is about 65 or 140 nm may reflect the collagen matrix (Figure 3(d)).

2.2.2 Dentine (=Ivory)

Dentine structure and chemistry vary between different species. For example, the rodent incisor is an ever growing tooth, and thus differs in the basis of dentine formation from that of the human tooth.

In reptile teeth, under the external thin enamel layer, the dentine shows numerous regular growth lines (Figure 6(a)). Dentine has a highly organized structure, and in reptile and mammal teeth has an array of parallel pores or tubules extending from the central pulp cavity to the dentine–enamel boundary. It is called *orthodentine* (Figure 6(b)–(d)). The average diameter of tubules is about 2 µm. Many other varieties have been described in the fish scales and dermal armors of fossil vertebrates.[7] In some taxa, the dentine may be divided into intertubular and peritubular dentine. The peritubular dentine forms a hypermineralized sheath around the dentinal tubule. The plate-like structures of the apatite crystals of the intertubular dentine have their c-axes parallel to the long axes of the collagen fibrils.

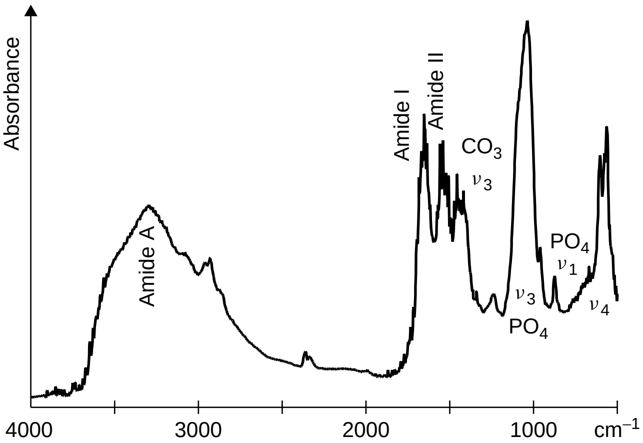

Figure 4 Infrared spectra showing the dual composition of bone with organic (amide) and mineral bands

In human teeth, the mineral fraction constitutes about 70% of the dentine by weight, and about 50% by volume. The average chemical composition is similar to that of bone (Figures 5, 7); however, due to the high Mg contents of ever-growing teeth in mammals (i.e. incisors in rodents and lagomorphs), the profiles are not identical. Sr contents are also different (Figures 5, 7). Ca/P ratio (by weight) is lower than that of bone. As in bone, the fibrous collagen I constitutes about 90% of the organic matrix. The intertubular dentine composition is very similar to that of bones, and consists of a fibrous network of collagen with deposited mineral crystals. The reported maximum differences in the mineral content between peritubular and intertubular dentines vary from 9% to 40%.[8] The peritubular dentine has high P, Ca, and Mg contents, but contradictory results are reported about the presence of collagen. In horse teeth, the peritubular organic matrix is less abundant than the intertubular matrix, both being mainly composed of collagen.[9] In human teeth, the organization of the crystals of peritubular dentine is very similar to that of the adjacent intertubular

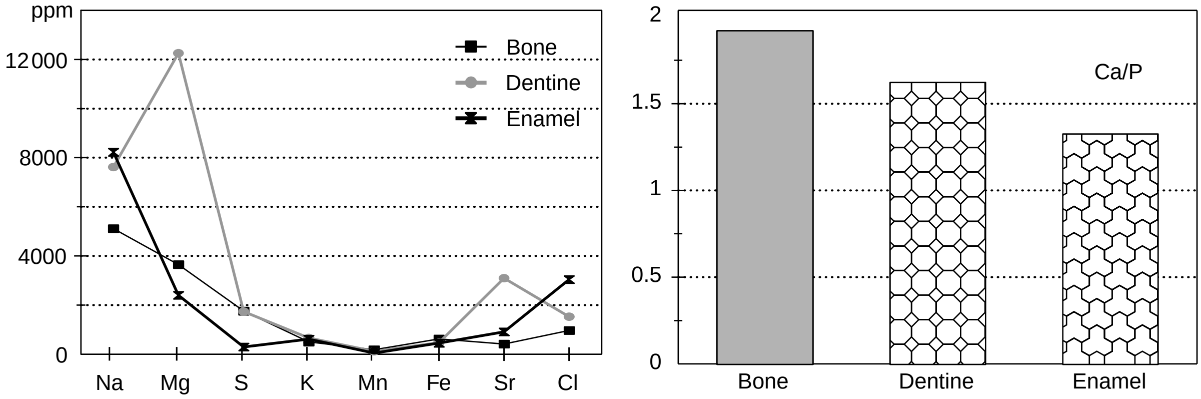

Figure 5 Chemical composition of mammal bone, dentine and enamel, and Ca/P weight ratios

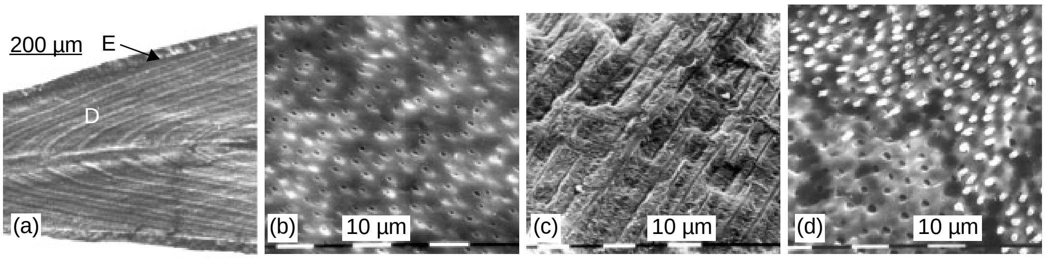

Figure 6 Structure of dentine: (a) Polished and etched longitudinal section of a crocodilian tooth, showing the thin outer enamel layer (E) and the growth lines in the inner dentine (D). (b) Oblique section of orthodentine showing the tubules. (c) Oblique section of the orthodentine of a small mammal incisor showing the tubules. (d) Transverse section of the orthodentine of a small mammal tooth showing empty and filled tubules

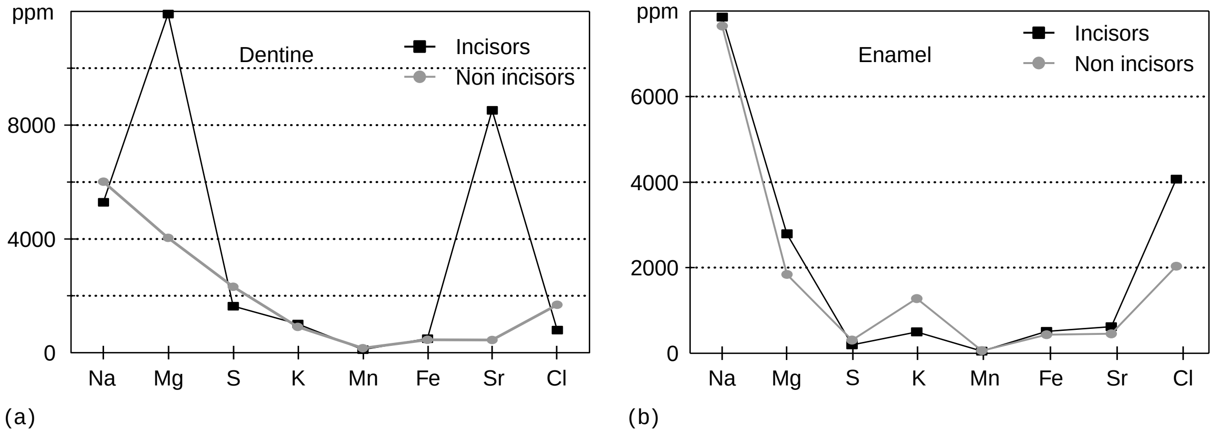

Figure 7 Chemical composition of rodent teeth: (a) Dentine, showing the difference in Mg contents between the ever-growing incisors and the other teeth. (b) Enamel, with no Mg difference between the ever-growing incisors and the brachyodont teeth

dentine. In human intertubular dentine, the apatite crystals are closely associated with the collagen matrix. The main protein in peritubular dentine has a higher molecular weight and a different aminoacid composition than the phosphophoryns of the intertubular dentine. Both dentines are in structural continuity.

2.2.3 Enameloid – Enamel

Enameloid and enamel compose the outer layer of teeth, and both are usually described as hypermineralized tissues, despite the fact that they differ in their structure, composition, and

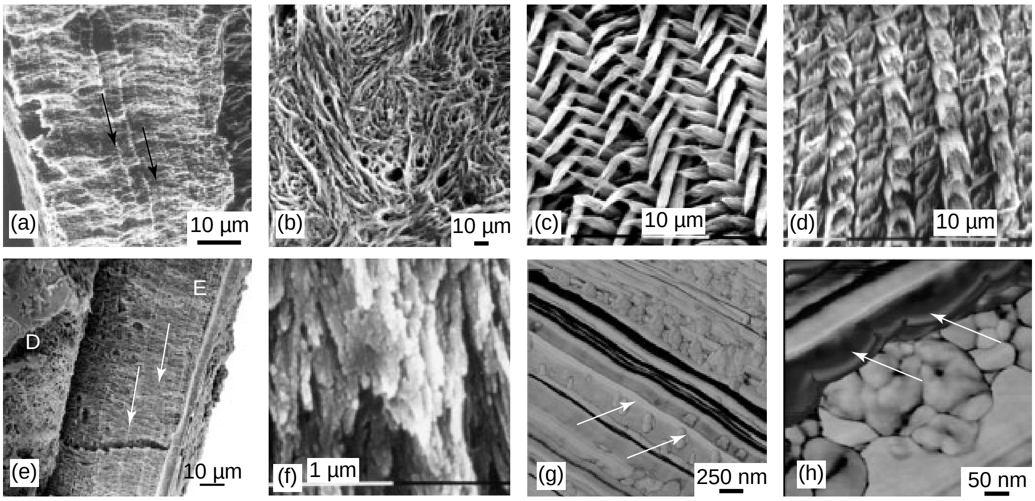

Figure 8 Structure of enameloid and enamel: (a) Ganoine, with incremental lines (arrows) in a fossil fish tooth. (b) Acrodin, with a complex structure, in a fossil fish tooth. (c) Complex and regular pattern of the prismatic enamel in a rodent incisor. (d) Another prismatic pattern in a rodent incisor. (e) Nonprismatic enamel in a polished and etched crocodilian tooth showing growth lines (arrows). D: dentine; E: enamel. (f) Alligator mississippiensis: elongated and parallel enamel rods. (g) Polished and etched section of a tooth of *Crocodylus niloticus*, showing parallel long rods with aggregates and layers of organic material (arrows). Atomic Force Microscopy (AFM) Phase image. (h) Detail of the same; arrows: layers of organic material

formation. Enameloid is the ‘enamel’ of fishes (Figure 8(a)), but there is a confusing variety of names (enamel, enameloid, collar ganoine, etc.), all of which lack adequate chemical or structural definitions. Another structure type present in fish teeth has been described: acrodin is composed of interwoven fibers (Figure 8(b)).[10] The main part of the enamel of mammal teeth is organized in ‘prisms’ or ‘rods’. A prism is composed of parallel acicular crystals of enamel, and the arrangements of the prisms are variable (Figure 8(c), (d)). The tooth enamel has the most unusual morphology of the apatite biocrystals: mature enamel contains crystals that are tens of microns long with an aspect ratio (length/width) of at least 1000. The reptilian enamel is usually without prisms (Figure 8(e)), and is composed of parallel acicular crystals (Figure 8(f), (g)). In recent crocodile teeth, waves of an organic matrix are present between the crystals (Figure 8(g), (h)). Their shape and location are similar to the small droplets and the rows of nanospheres of amelogenins observed in mammal enamel.[11]

The tooth enamel has the most unusual morphology of the carbonate-apatite (dahllite) crystals. In mature enamel, the mineral part may reach 98% by weight (=90% by volume). Mammal enamel has a low Mg and S content compared with the bone and dentine (Figure 5). There is no difference in Mg contents of ever growing and brachyodont teeth (Figures 5, 7). The low S content is probably related to the low organic contents of the tissue. Unlike bone, the enamel organic matrix does not contain collagen. Enameloid is usually rich in F. There are distinct differences in the composition and distribution of sulfated glycoconjugates in enameloid and enamel. The fish enameloid contains chondroitin sulfate associated with collagen fibrils. The reptile aprismatic enamel has no sulfated glycoconjugates, whereas in the mammal prismatic enamel sulfated glycoconjugates are detected preferentially in the surface layer.[12]

2.3 Carbonates

2.3.1 Structure

Calcium carbonate minerals ($CaCO_3$) are ubiquitous in biomineralizing systems, since they are in the skeletons of organisms ranging from bacteria and algae to humans, most commonly as calcite (rhomboedral) or aragonite (orthorhombic). Thus, their structures and compositions are highly diversified. Here, only some examples are discussed.

The most studied taxa is the Mollusks, since the pioneering work of Boggild on the microstructure and mineralogy of modern and fossil shells.[13] Mollusk shells are composed of calcite and/or aragonite, usually separated in different layers. Boggild has classified the structures, has shown that the mollusk shell is layered, and that the spatial distribution of the shell layers is characteristic of the taxa at the genus-species level. Moreover, these structures are characteristic of Mollusks and are not found in other taxa. Of these layers, the best known, but not the most common, is the nacreous layer (Figure 9). The wall of bricks where bricks are ‘mineral tablets’, and mortar is interlamellar and intercrystalline organic membranes, is a common feature of the nacre (Figure 9(a)). However, the shapes and vertical arrangements of the nacreous tablets are different in the Cephalopoda and Gastropoda on one hand (Figure 9(b)), and the Bivalvia on the other

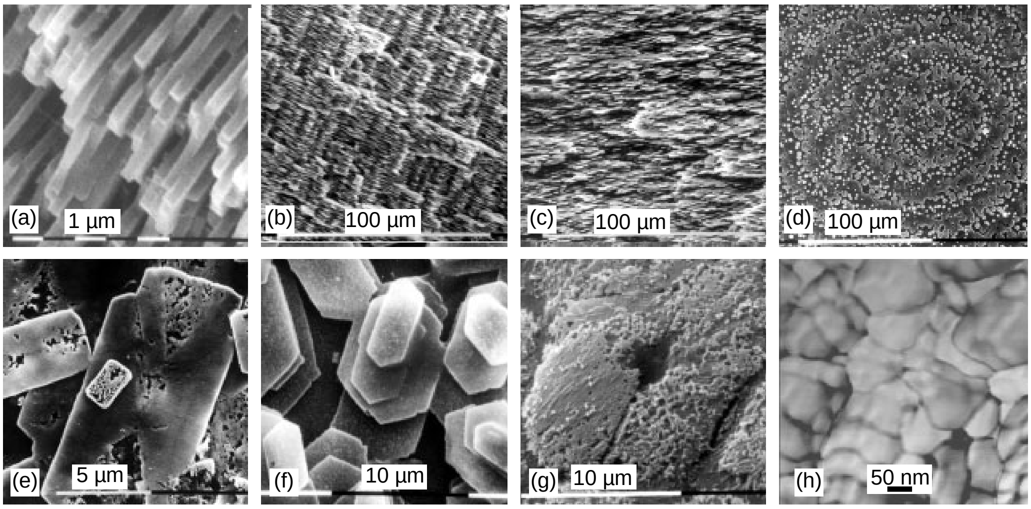

Figure 9 Structure of the aragonitic nacreous layer (mother-of-pearl) in mollusc shells: (a) Typical tablets in *Nautilus* shell (Cephalopod). (b) Vertical section showing the pseudoprismatic pattern of the nacreous layer in Cephalopods and Gastropods.(c) Vertical section showing the lenticular pattern in Bivalves.(d) Tangential section showing the nonsuperposition of the successive tablets in Bivalves and the resulting spiral pattern.(e) Detail of the structure of a tablet of *Pinna* (Bivalve) showing the twin and symmetrical more or less soluble sectors after an enzymatic etching. (f) Tangential section showing the superposition and the hexagonal shape of the successive tablets in a cephalopod shell. (g) Etched tablet of a cephalopod shell showing the 'central hole' and the radial sectors. (h) Rounded granules in a tablet of *Nautilus*. Each granule is surrounded with a thin layer, probably composed of organic materials

hand (Figure 9(c), (d)).[14] This taxonomic dependence and the different growth modes in the two sets were confirmed.[15] Using elaborate preparative processes, Mutvei has shown that the inner structures (= ultrastructures) of the tablets are different in the three main classes of Mollusks: Bivalvia (Figure 9(e)), Gastropoda, and Cephalopoda (Figure 9(f), (g)).[16] Again, the ultrastructures in the two sister groups (Gastropoda and Cephalopoda) are more similar than that of the Bivalvia. The ultrastructures, now called *nanostructures*, are not yet well known and only some samples have been studied. However, the acicular crystallites of the nacreous tablets of cephalopod shells are composed of granules (diameter about 40–50 nm), surrounded with a thin organic envelope (Figure 9(h)). The arrangement of the granules seems dependent on the taxa. Thus, from this example, it appears that the structures, the spatial distribution, and the ultrastructures are strongly dependant on the taxonomy of the organisms, that is, the organisms fully control the minerals they produce.

Another example is given by the calcitic prismatic layer of Pteriomorphid bivalves (Figure 10). The remarkable form and size of these crystals have been recognized for many years.[17] According to Taylor *et al.*, the prisms of *Pinna* and *Pinctada* are similar and called '*simple prisms*': simple prisms are aragonitic or calcitic, their crystallographic *c* axes normal to the layer surfaces, with each prism separated by a thick conchiolin wall.[18] Calcitic prisms have transverse striations, whereas aragonitic prisms have longitudinal and fewer developed transverse striations. The thickness of the organic wall varies from 1 to 8 µm. Nevertheless, repeated observations have shown some differences between the two shells. In *Pinctada*, thin sections observed in polarized light show that each prism extinguishes in several smaller blocks, whereas the individual prism of *Pinna* exhibits a monocrystalline extinction.[13,19,20] Untreated fractures of *Pinna* show long straight parallel prisms with a more or less smooth surface (Figure 10(a)). Occasionally, the surface shows a transverse lineation (Figure 10(b)). Etched transverse sections show the thick organic interprismatic walls and the polygonal shape of the prisms (diameter 70 µm) (Figure 10(c)). These prisms are composite units: on longitudinal sections, transverse synchronous growth lines cross the adjacent prisms (Figure 10(d)). They are composed of aligned oblique and elongated crystallites, the width of which varies from 150 to 180 nm (Figure 10(e), (f)). These crystallites are subdivided into smaller rounded units with distinct boundaries, suggesting that they are surrounded by organic envelopes. The etched longitudinal sections of *Pinctada* also show transverse growth lines (Figure 10(g)). Nevertheless, in transverse sections, enzymatic hydrolyzes reveal intraprismatic sinuous lacunae that are the remains of intraprismatic organic membranes (Figure 10(h)). The orientations of crystallites on both sides of these intraprismatic membranes within a prism are not similar.

Despite their monocrystalline habit, the nacreous tablets and the prismatic units of Mollusks shells are composite structures. We do note that these complex structures are rarely visible on simple fractures of the shells, but enzymatic hydrolyzes or/and acidic etchings are effective from this point of view.

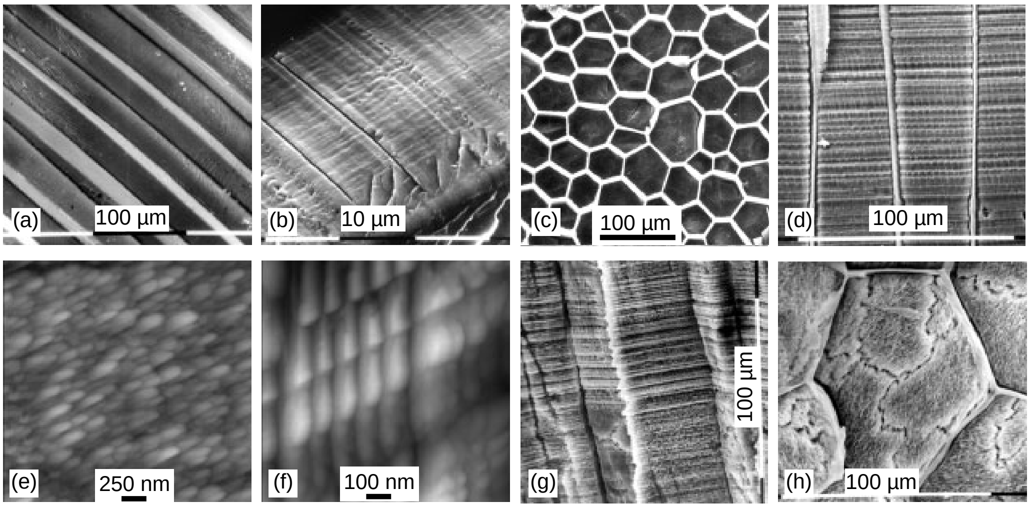

Figure 10 Structure of the outer calcitic prismatic layers of two Bivalve shells: (a) Fracture showing the parallel and straight prisms in *Pinna*. (b) Detail of the same, showing fragments of the interprismatic organic wall and a transverse growth striation in *Pinna*. (c) Etched transverse section showing the hexagonal shape of the prisms and the thick interprismatic organic wall. *Pinna*. (d) Polished and etched section showing the synchronous transverse growth lines. *Pinna*. (e) Fixed and etched polished transverse section of a prism of *Pinna*, showing the regular alignment of crystallites. (f) Fixed and etched prism of *Pinna*, showing the regular arrangement of the longitudinal face. (g) Enzymatic hydrolysis of a fracture of the prisms of *Pinctada*, showing the thin transverse growth lines. (h) Transverse section of the same sample, showing the preserved organic interprismatic wall and the inner prismatic membranes destroyed by the enzymatic hydrolysis

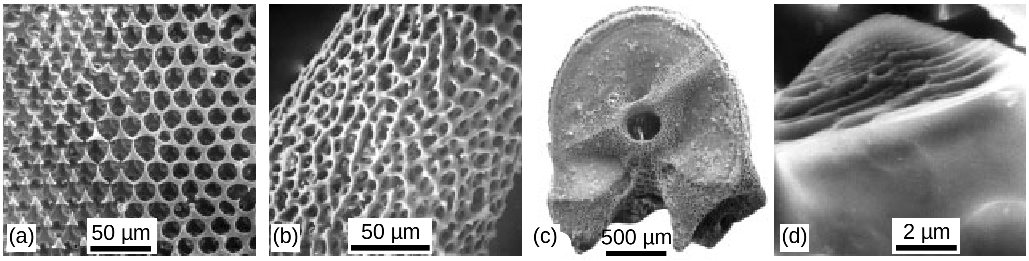

Figure 11 Spongy stereom of Echinoderms: (a) Sea urchin plate showing the various stages of the spongy stereom. (b) Starfish: in this article, the stereom is less regular. (c) Ophiurid vertebrae. The whole structure is a single crystal of calcite. (d) Conchoidal fracture of a sea urchin spine

Opposite to the mineralogical and structural varieties of the mollusk shells are the echinoderm skeletons. All of them show the same microstructural pattern: a calcitic spongy stereom (Figure 11(a)–(c)). Urchin spines and plates are composed of one single crystal of calcite, according to polarized light and X-ray diffraction. However, the fracture surfaces are conchoidal and do not show the cleavage planes of inorganic calcite (Figure 11(d)).

2.3.2 *Composition*

The organisms strongly control not only the shapes of the biominerals, but also their chemical compositions. Within an uniform ‘mineralogy’ (calcite or aragonite), the contents in minor and trace elements are strongly dependent on the taxa. Many skeletons are composed of Mg calcite, with Mg contents greater than 10 mol% (the maximum content of thermodynamically stable magnesium calcite) and some as high as 40 mol%.[21] Echinoderm tests are composed of high Mg calcite, whereas mollusk shells have low Mg calcite shells; brachiopod shell Mg contents are between them.[22,23] Chemical contents of aragonitic sponge, coral, and mollusk skeletons are also easily recognized with their Mg, Sr, and S contents (Figure 12(a)). The Sr/Mg substitution ratio or L coefficient is discriminant for the sedimentary aragonite, sponges, and corals and mollusk shells (Figure 12(b)).[24] Within a single taxa, within a single mineralogy, some chemical element contents differ. The coral skeleton is aragonitic, and composed of two parts: the centers of calcification and the fibers

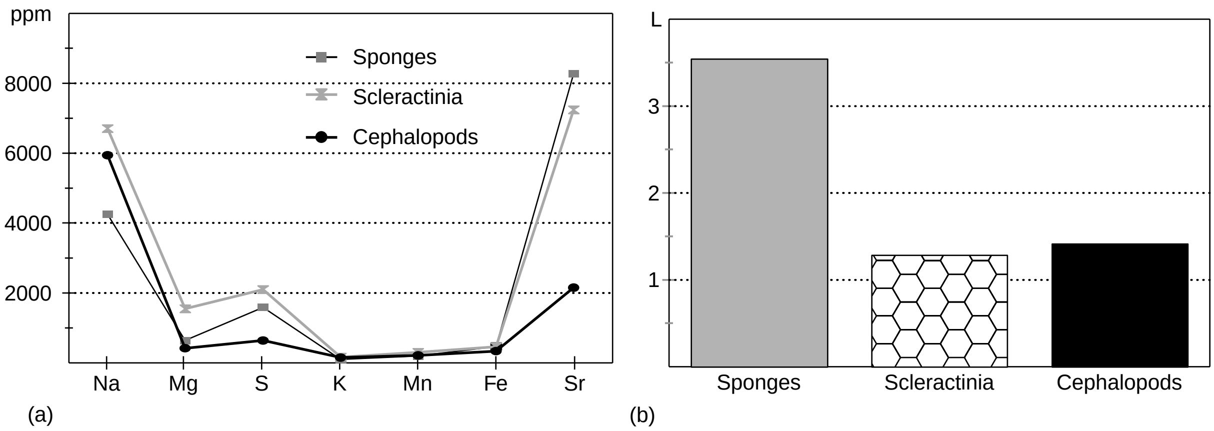

Figure 12 Chemical composition of biogenic aragonites: (a) Chemical composition of the biogenic aragonite of three taxa, showing the strong differences in Sr, Mg, and S contents. (b) Sr/Mg substitution ratio or L coefficient in the three taxa

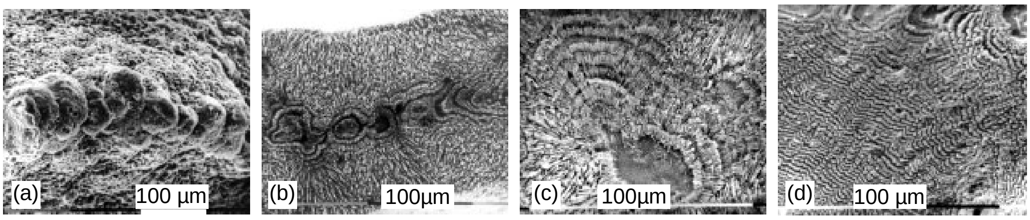

Figure 13 Structure of the Scleractinia skeletons: (a) Septal growing zone showing the ‘centers of calcification’. *Diploastrea.* (b) Polished and etched section showing the median line of centers of calcification and the outer fibrous layer. *Diploastrea.* (c) Detail of centers of calcification with their granular structure, and the growth lines in the fibers. Polished and etched section. *Lobophyllia.* (d) Polished and etched section showing the regular growth lines. *Platygyra*

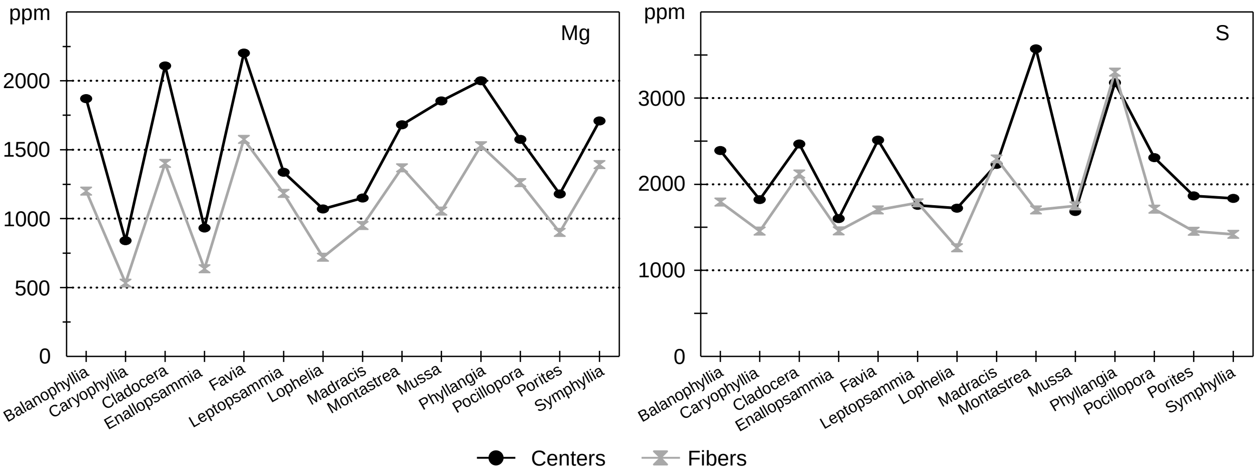

Figure 14 Chemical composition of the centers and fibers in various Scleractinia species

(Figure 13). It has been shown that the ‘centers of calcification’ are the first zones to mineralize in the septa.[25] According to the species, Mg, Sr, and S contents are significantly different in the centers and fibers (Figure 14).[26] Raman and XANES spectra have shown the absence of $CaSO_4$ in these samples, whereas XANES spectra and electrophoretic data have shown that S is associated with acidic sulfated sugars.[27] Similar results have been obtained in some Mollusk shells, in which the main component of S is related to organic sulfates.[28]

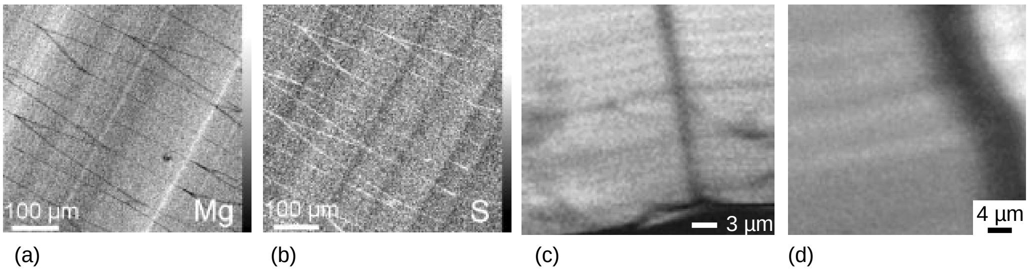

Figure 15 Qualitative chemical maps of the calcitic prisms of *Pinna* (1–3) and *Pinctada* (4): (a), (b) Electron probe maps showing the difference in the zonation in Mg and S, and the high S content of the organic interprismatic walls (C.T. Williams, Department of mineralogy, NHM, London); *Pinna*: average S content 5600 ppm, average Mg content 4600 ppm. *Pinctada*: average S content 3100 ppm, average Mg content 5800 ppm. (d) Organic sulfate map showing the low content of the interprismatic wall and the high content of the intraprismatic matrix. A growth zonation is also visible (M. Salomé, ID21, ESRF, Grenoble)

A growth zonation is usually observed in mineralized skeletons. Different chemical mappings show that this zonation is also compositional. Electron probe maps of Mg and S of longitudinal sections of the calcitic prismatic layer of *Pinna* clearly show the organic composition of the thick walls, lacking Mg and rich in S (Figure 15(a), (b)). It must be noted that the inner part of the prisms show in both maps a different growth zonation. SO_4 maps of the prisms show that the interprismatic wall has a low sulfate content (Figure 15(c)), whereas the inner part has a high sulfate content. Moreover, there is a sulfate growth zonation. Similar results were obtained on *Pinctada* prisms (Figure 15(d)). As for Scleractinia, sulfate is associated with the sugars of the organic matrix.[28,29]

Most shells or exoskeletons are made of crystalline minerals, but amorphous calcium carbonate (ACC) is also present. These biological ACC contain significant amounts of Mg, P and rich glutamic acid proteins.[30]

Mollusk shells are much tougher than inorganic calcium carbonate minerals, and it is still unclear exactly how the growth of these structures is controlled. It is known that the organic macromolecules released by the dissolution of biocrystals are key participants in the control processes of shape and structure in mineralized tissues. But chemical elements also regulate the biomineral properties and formation rates, and provide critical information on crystal growth history. The influences of biological processes on the elemental composition of biominerals, called '*vital effects*', seriously impede efforts to unambiguously interpret biogenic mineral compositions in terms of environmental reconstruction.

3 MODES OF BIOMINERALIZATION

Biomineralization involves the formation of minerals by organisms, and two different modes are summarized by Lowenstam and Weiner.[1] In the *biologically induced mineralization*, an organism modifies its local microenvironment to create conditions suitable for the chemical precipitation of extracellular mineral phases. It is the dominant process in fungi and bacteria.

The second mode is called *biologically controlled* or *organic-matrix-mediated biomineralization*, in which inorganic particles are grown within or on some organic matrix produced by the organism. It is the process in sponges, corals, echinoderms, and so on, in which the mineral units are aligned in a preferred direction. The unique structure and orientation of crystals, the morphology, and composition of these biominerals are clear indications that the processes of crystal nucleation and growth are highly controlled by the organisms. Organisms use macromolecules such as proteins and glycoproteins to control these molecular processes.

3.1 Silica

Biosilicate formation occurs at ambient temperature. Biosilicates grow in closed spaces, and the organic components influence the size and the shape of skeletal parts. In diatoms, the valve formation occurs within the cell. However, the mature mineralized wall is outside the cell. During the first stages of the cell wall development, small vesicles fuse to form the deposition silica vesicle, delimited by a membrane (silicalemna). This membrane is probably integrated in the diatom wall in the adult diatom. The mature diatom wall is composed of amorphous silica, but different forms of silica have been observed at different stages of growth: fibrils, spheres, hexagonal columns.[30] The transport form of intracellular Si is still very poorly understood. Silaffins (polycationic peptides), silicateins and frustulins have been identified as constituents of biosilica. In sponges, a protein (silicatein) is probably implied in the mineralizing process.[31] Silaffins are strongly basic low-molecular weight polypeptides. *In vitro*, silica formation at a $\mathrm{pH} > 7$ is a very slow process. However, in diatoms the same process takes less than one hour.

3.2 Phosphates

The three main structural tissues of vertebrates, bone, dentine, and enamel, have different origin and behavior during the growth of the animal. Most teeth do not change once they are erupted, whereas the bone is continuously modified.

From a biological point of view, bone is a true tissue because it contains cells. Specialized cells are responsible for the replacement of preexisting bone, or remodeling, that takes place both in compact and trabecular bone. Bone remodeling involves the dual processes of bone resorption and redeposition. From TEM observations, it appears that the first step of formation is an ionic adsorption on a substrate, leading to nanoparticle nucleation. The size and orientation of the nanoparticles depend on the substrate.

Dentine is the first calcified tissue to be deposited during tooth embryogenesis by the odontoblasts lining the inner pulp chamber. Odontoblasts lay down the dentinal organic matrix, and the dentine formation proceeds inwards. The mineralization begins when an organic layer of about 10–20 μm thick was deposited, and only cells process encased in the dentinal tubules are present in dentine.

Enameloid and enamel have different structures and compositions, and differ in their genesis: enameloid is produced by both odontoblasts and inner dental epithelial cells; it is deposited before true dentine is formed, and usually includes collagen, epithelial derived proteins, and chondroitin sulfate; enamel is produced by ameloblasts after dentine was deposited; it grows centrifugally, and contains ectoderm-derived proteins (amelogenins and enamelins) but no collagen proteins. These components are almost fully removed throughout the maturation stage. Amelogenins, secreted by the ameloblasts, are believed to function as the scaffold for the initiation and growth of apatite crystals. Amelogenin molecules self assemble to generate nanosphere structures of 1–20 nm in diameter.[11]

In mammals, the eruption of the tooth occurs after the crown is formed, but the tooth gradually moves toward the surface during its development. Nevertheless, all the teeth are not similar and three categories can be recognized. Mammals that feed on abrasive substances have especially high-crowned teeth. These teeth are called *hypsodont*. The teeth of cows and deer are hypsodont. In some species, hypsodont teeth continue to grow throughout an animal's life (e.g. mouse, rabbit). The opposite condition, with a low-crowned tooth, is termed *brachyodont*. These teeth have closed roots and grow to a fixed length and stop erupting (e.g. human teeth).

3.3 Carbonates

From a biological point of view, calcareous shells and tests are not tissues: they do not contain cells, and are not directly produced by cells. For example, neither the calcitic prismatic unit of the *Pinna* shell nor the aragonitic nacreous tablet is the result of the secretion of a mantle cell. Crystals are generally formed in predefined closed spaces, delimited by extracellular macromolecular matrices. Again, the nacreous layer of the mollusk shell is the structure from which some models have been elaborated.

Transmission electron microscope studies have shown that the organic interlamellar membranes have a lamellar structure (Figure 16(a), (b)).[32,33] This structure varies according to the taxa. Some fenestrations or holes have been described, and they have been considered to favor the passage of fluid substances needed for the mineralizing process. The decalcification process of the nacreous layer, and later all the mollusc layers and 'invertebrate' tests, has shown

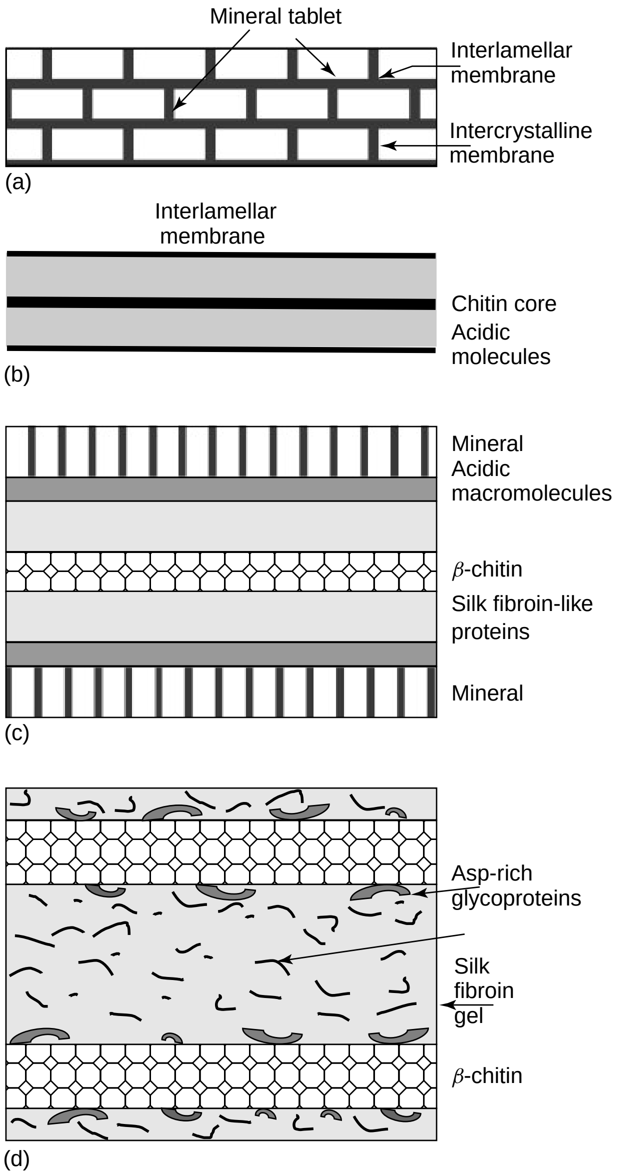

Figure 16 Successive models of the nacreous layer of mollusk shells

that soluble and insoluble organic matrices are present. From the composition of these matrices, and from the ultrastructures, Weiner and Traub have proposed a model (Figure 16(c)).[34] More recently, this model was improved, based on the study of a bivalve shell (Figure 16(d)).[35] Thanks to a fixative-decalcification process, the holes in the interlamellar membranes were not observed. However, the relationships between crystal morphology and surface interactions with the reactive groups of the organic molecules are unclear.

Besides organic growth modifiers, Mg and Sr play a primary role: the incorporation of Mg^{2+} has been shown to modify the morphology, solubility, and polymorphic expression of $CaCO_3$ biominerals. Furthermore, Mg is the principal inhibitor of calcite growth in natural waters. However, the fundamental mechanistic interactions of Mg with the calcite surface remain controversial. *In vitro* experiments show that Mg contents of ACC depend on the Mg/Ca ratio solution, and that Mg stabilizes ACC.[36]

3.4 Magnetite and Ferritin

Among other biominerals, magnetite crystals have a peculiar status. Magnetite biomineralization is a genetically controlled biochemical process having evolved about 2 billion years ago in the magnetotactic bacteria. Magnetite crystals (between 20 and 100 nm) have been extracted from bacteria and some mollusks (chitons).[1] They are arranged in a chain with gaps between the crystals. All the magnetite crystals that have been examined to date are single magnetic domains, and it has been suggested that hydrated iron oxide in ferritin (the major iron storage protein in living organisms) would be the precursor of biological magnetite.[37,38]

4 APPLICATIONS

Studies of biominerals and biomineralization have various applications, from biology to biomimetics.

4.1 Biology

The strict control of the organism on its skeletal units and their arrangement allows us to use the microstructure and composition as taxonomical and phylogenetical criteria. The example of the nacreous layer of the mollusk shells has been described, and reflects the phylogenetic data: similarities of structures (columnar pattern and radial sectors) between the two sister groups, cephalopods and gastropods, differences with the bivalves (noncolumnar pattern, four twinned sectors). Another example is found in scleractinia corals. There is a strong relationship between the spatial arrangement of the septal centers of calcification and the 28 S rRNA phylogeny.[39]

Minor element contents and isotopic ratios are used for physiological purposes. Sr/Ca ratios in bone and teeth are said to reflect the diet of the animal (herbivores versus carnivores). Stable isotope analysis of teeth and bones provides direct information on the lifetime diets: the nitrogen isotopes reflect the trophic level of the protein that has been consumed. Within an ecosystem, they can identify herbivores and carnivores, while the carbon isotopes tell mainly about the amount of protein in the diets from terrestrial *versus* marine ecosystems.

Another unexpected role of some skeletal pieces has been described.[40] Ophiuroids are a large group of Echinoderms that includes the brittlestars. They have five arms, superficially resembling true starfishes (Asteroidea), and can catch fast motile prey. Aizenberg and coworkers have found that calcite crystals in their skeletons act as optical receptors or lenses. However, it is not known whether the system of lenses and nerves is actually an ‘eye’. However, these structures are absent in closely related but not light sensitive species of brittlestars.

Growth lines are a general feature of fossil and modern mineralized tissues: they are present in the enamel of a dinosaur tooth (Figure 17(a)), the calcitic dinosaur eggshell (Figure 17(b)), or the aragonitic fish otolith (Figure 17(c)). Otolith growth rings record daily age and growth patterns.[41] But the growth of all the calcified skeletons is not so easy to decipher (Figure 17(d)).

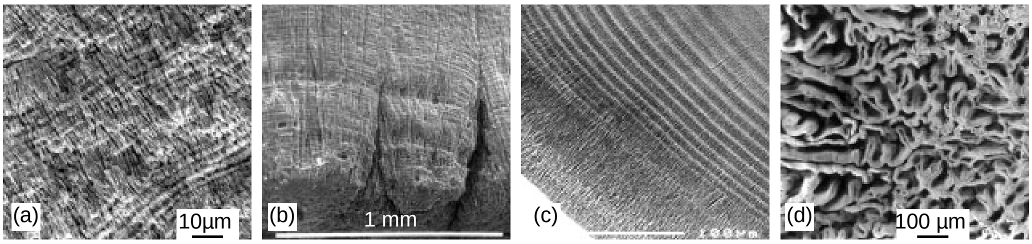

Figure 17 Growth lines: (a) Enamel of a dinosaur tooth. (b) Vertical section in a Dinosaur eggshell. (c) Polished and etched section of a fish otolith. (d) Complex structure of a fossil cephalopod shell (*Belopterina*)

4.2 Geology

Biominerals are strongly dependent on the taxonomy of the organisms, and they are also dependent on the environment. So, modern skeletons can be used as ‘proxies’ because they record the environmental conditions. Still, the biominerals have another advantage: they have a geological history. Carbonate and phosphate skeletons are known from 540 my, and they can be used as ‘paleoproxies’.

Urey *et al*. have shown that the $^{18}O/^{16}O$ ratios in marine carbonates depend on the temperature and on the $^{18}O/^{16}O$ ratios in seawater.**[42]** Subsequently, they established an isotopic temperature scale based on marine biogenic carbonates. This first ‘stable oxygen isotope’ study shows the climatic changes during the Cretaceous from belemnitid rostra (Mollusks, Cephalopoda). However, Urey and coworkers were already aware of the physiological factor, so that the $^{18}O/^{16}O$ ratios in biogenic carbonates are not fully dependent on the temperature. This disequilibrium phenomenon was called ‘vital effect’. The importance of the ‘vital effect’ differs according to the taxa. The aragonite deposited by corals is usually depleted in ^{18}O relative to values of isotopic equilibrium with ambient seawater.**[43]** Moreover, the amplitude of the disequilibrium is different in each coral genus. Recently, the study of *Lophelia*, a deep-sea coral, has shown that the $\delta^{18}O$ in the centers of calcification and in the surrounding fibers are clearly different.**[44]** Moreover, there is a strong contrast between the homogenous $\delta^{18}O$ values of the centers of calcification and the variable $\delta^{18}O$ values in the fibers. Explaining several per mil variations in a few microns between the centers of calcification and the adjacent fibers is difficult, as both grow from the same fluid simultaneously. In the same species, XANES mapping has shown an exact correspondence between concentration of sulfated polysaccharides and centers of calcification.**[27]** This result suggests that heterogeneity in isotopic fractionation could be due to the influence of specifically secreted organic mineralizing matrices known to control both crystallization patterns and minor element concentrations.

The presence of the organic matrices included in biominerals must be taken into account in another phenomenon: fossilization. This is well evidenced in bone: as soon as the animal is dead, bone cells release proteases that hydrolyze the organic matrices. DeNiro and Weiner have shown that the $\delta^{13}C$ of fossil and archaeological bones greatly varies according to the preservation of the organic matrices.**[45]** The diagenetic changes induced in nitrogen isotopic ratios, used for paleophysiology reconstruction (diets) are not yet known. Thus, the usual control of the mineralogy performed on carbonates, bones, and teeth is not sufficient to assert the absence of diagenetic changes. The loss of the organic matrix is not correlative of mineralogical or minor element content changes.

The chemical element compositions of biogenic carbonates reflect the environments in which they formed, resulting in their use as paleoclimate indicators. In aragonite, the Sr contents and the temperature have a negative correlation, and *in vitro* experiments have shown that in calcite, Mg and Sr contents and temperatures have a positive correlation.**[46,47]** Thus, the Mg/Ca and Sr/Ca ratios have emerged as temperature proxies due to their reduced susceptibility to changes in salinity. But, again, fossil carbonates are altered by diagenetic processes, even if the mineralogy and structure do not seem modified.

4.3 Aquaculture

Otoliths (‘earstones’) are small calcified structures found in the head of bony fishes. They are an important tool for understanding the life of fish populations. The growth lines and isotopic ratios of otoliths are used to know the migrations of marine fishes, because they are sensitive to salinity and temperature. Then, the obtained results are helpful to control these parameters in cultivated fishes. In mollusk shells, diseases are usually early diagnosed thanks to shell abnormalities and malformations. These data are then used for fossils and paleoenvironmental reconstructions.

4.4 Medical Uses

For hundreds of years, natural and synthetic materials have been used as substitutes for damaged bones and teeth. Among these materials, some corals have been successfully used to replaced pieces of bones. The porous microstructure of these corals, and the abundance of the acidic sulfated sugars in the organic matrices of their skeletons is probably the main favorable factor. The coral micropores favor the settlement of bone cells which produce bone (osteoblasts), and cells which resorb bone (osteoclasts). Thus the coral skeleton is progressively resorbed and replaced by the bone, according to the usual bone remodeling process. Depending on the size of the coral graft, in some months or some years, all the coral is removed and replaced by the new bone. Now, powder or liquid composites containing coral skeletons are used. At last, there is a demand for low-temperature processing techniques with environmentally friendly materials.

5 RELATED ARTICLES

Calcium-binding Proteins; Iron Proteins for Storage & Transport & their Synthetic Analogs.

6 FURTHER READING

K. Shimizu, J. Cha, G. D. Stucky, and D. E. Morse, *Proc. Natl. Acad. Sci.*, 1998, **95**, 6234.

7 REFERENCES

1. H. A. Lowenstam and S. Weiner, ‘On Biomineralization’, Oxford University Press, 1989.
2. R. Wetherbee, S. Crawford, and P. Mulvaney, The Nanostructure and Development of Diatom Biosilica, in ‘Biomineralization, from Biology to Biotechnology and Medical Application’, ed. E. Baeuerlein, Wiley-VCH, Weinheim, 2000, p. 189.
3. J. Weaver, L. I. Pietrasanta, N. Hedin, B. F. Chmelka, P. K. Hansma, and D. E. Morse, *J. Struct. Biol.*, 2003, **144**, 271.
4. M. M. Giraud-Guille, *Calcif. Tissue Int.*, 1988, **42**, 167.
5. G. Mariotti and M. A. Muglia, *Arch. Ital. Anat. Embriol.*, 1988, **93**, 163.
6. R. B. Martin, D. B. Burr, and N. Sharkey, ‘Skeletal Tissue Mechanics’, Springer Verlag, New York, 1998.
7. B. Peyer, ‘Comparative Odontology’, Chicago University Press, Chicago, 1968.
8. S. Weiner, A. Veis, E. Beniash, T. Arad, J. W. Dillon, B. Sabsay, and F. Siddiqui, *J. Struct. Biol.*, 1999, **126**, 27.
9. D. Magne, J. Guicheux, P. Weiss, P. Gilet, and G. Daculsi, *Calcif. Tissue Int.*, 2002, **7**, 179.
10. T. Ørvig, Phylogeny of Tooth Tissue: Evolution of some Calcified Tissues in Early Vertebrates, in ‘Structural and Chemical Organization of Teeth’, ed. A. E. W. Miles, Academic Press, New York, 1967, p. 45.
11. H. B. Wen, A. G. Fincham, and J. Moradian-Oldak, *Matrix Biol.*, 2001, **20**, 387.
12. Y. Kogaya, *Prog. Histochem. Cytochem.*, 1994, **29**, 1.
13. O. B. Boggild, *D. Kgl. Danske Vidensk. Selsk. Skr., Nat. Mat. Afd.*, 1930, **9**(2) II, 230.
14. S. W. Wise Jr, *Eclogae Geol. Helv.*, 1970, **63**, 775.
15. H. K. Erben, *Biomineralization*, 1972, **4**, 16.
16. H. Mutvei, The Nacreous Layer in Molluscan Shells, in ‘The Mechanisms of Biomineralization in Animals and Plants’, eds. M. Omori and N. Watabe, Tokai University Press, Tokyo, 1980, p. 49.
17. J. S. Bowerbank, *Trans. Microsc. Soc. London*, 1844, **1**, 123.
18. J. D. Taylor, W. J. Kennedy, and A. Hall, *Bull. Brit. Mus. (Nat. Hist.) Zool.*, 1969, (Suppl. 3), 125.
19. K. Wada, *Bull. Natl. Pearl Res. Lab.*, 1961, **7**, 703.
20. Y. Dauphin, J. P. Cuif, J. Doucet, M. Salomé, J. Susini, and C. T. Williams, *J. Struct. Biol.*, 2003, **142**, 272.
21. S. Raz, S. Weiner, and L. Addadi, *Adv. Mat.*, 2000, **12**, 38.
22. J. D. Milliman, ‘Recent Sedimentary Carbonates. Part 1: Marine Carbonates’, Springer-Verlag, Berlin, 1974.
23. Y. Dauphin, *Appl. Spectr.*, 1999, **53**, 184.
24. J. P. Loreau, *Mém. Mus. Natn. Hist. Nat.*, 1982, N.S., sér. C, géologie, **47**, 312.
25. J. P. Cuif and Y. Dauphin, Les étapes de la découverte des rapports entre la Terre et la Vie, ‘Une introduction à la paléontologie’, Éditions Scientifiques GB, Paris, 2003.
26. A. L. Cohen, K. E. Owens, G. D. Layne, and N. Shimizu, *Science*, 2002, **296**, 331.
27. J. P. Cuif, Y. Dauphin, J. Doucet, M. Salomé, and J. Susini, *Geochim. Cosmochim. Acta.*, 2003, **67**, 75.
28. Y. Dauphin, *Int. J. Biol. Macromol.*, 2001, **8**, 293.
29. Y. Dauphin, *J. Biol. Chem.*, 2003, **278**, 15168.
30. S. Weiner, Y. Levi-Kalisman, S. Raz, and L. Addadi, *Conn. Tis. Res.*, 2003, **44**,(Suppl. 1), 214.
31. C. W. Li and B. Volcani, *Phil. Trans. R. Soc. Lond.*, 1984, **B 304**, 519.
32. C. Grégoire, *J. Biophys. Biochem. Cytol.*, 1957, **3**, 797.
33. H. Nakahara, Calcification in Gastropod Nacre, in ‘Biomineralization and Biological Metal Accumulation’, eds. P. Westbroek and E. W. de Jong, Reidel Publishing Company, Dordrecht, 1983, p. 225.
34. S. Weiner and W. Traub, *Phil. Trans. R. Soc. Lond*, 1984, **B 304**, 425.
35. Y. Levi-Kalisman, G. Falini, L. Addadi, and S. Weiner, *J. Struct. Biol.*, 2001, **135**, 8.
36. E. Loste, R. M. Wilson, R. Seshadri, and F. C. Meldrum, *J. Cryst. Growth*, 2003, **254**, 206.
37. D. Schüler, Characterization of the Magnetosome Membrane in *Magnetospirillum gryphiswaldense*, in ‘Biomineralization, from Biology to Biotechnology and Medical Application’, ed. E. Baeuerlein, Wiley-VCH, Weinheim, 2000, p. 109.
38. S. C. Andrews, A. K. Robinson, and F. Rodriguez-Quinones, *FEMS Microbiol. Rev.*, 2003, **27**, 215.
39. J. P. Cuif, G. Lecointre, C. Perrin, A. Tillier, and S. Tillier, *Zool. Scripta*, 2003, **32**, 459.
40. J. Aizenberg, A. Tkachensko, S. Weiner, L. Addadi, and G. Hendler, *Nature*, 2001, **412**, 819.
41. G. Pannella, *Science*, 1971, **173**, 1124.
42. H. C. Urey, H. A. Lowenstam, S. Epstein, and C. R. McKinney, *Geol. Soc. Amer. Bull.*, 1951, **62**, 399.
43. J. N. Weber and P. M. Woodhead, *J. Geophys. Res.*, 1972, **77**, 463.
44. C. Rollion-Bard, D. Blamart, J. P. Cuif, and A. Juillet-Leclerc, *Coral Reefs*, 2003, **22**, 405.
45. M. J. DeNiro and S. Weiner, *Geochim. Cosmochim. Acta*, 1988, **52**, 2197.
46. D. J. J. Kinsman and H. D. Holland, *Geochim. Cosmochim. Acta*, 1969, **33**, 1.
47. H. Fuchtbauer and L. A. Hardie, *Geol. Soc. Am. Abstr.*, 1976, **8**, 877.

Acknowledgments

The author is grateful to Prof. J. P. Cuif (Earth Sciences, UPS) for supplying some pictures, and Dr. A. Denis (Earth Sciences, UPS) for his help in SEM.

Bismuth: Inorganic Chemistry

Kenton H. Whitmire
Rice University, Houston, TX, USA

1	Introduction	1
2	Compounds of Bismuth	1
3	Related Articles	16
4	References	16

Glossary

Cubane: a common geometry adopted by many inorganic cluster complexes of formula A_4B_4 where A and B represent two atom types which occupy alternating vertices of a cube. These atoms may have ligands or other functionalities attached

Stereochemcially active lone pair of electrons: a complex whose observed structure includes a coordination site which is occupied by a lone pair of electrons. Conversely, a complex which contains a stereochemically inactive lone pair of electrons is one in which the geometry does not show a specific vacant site where the electron pair should reside

Abbreviations

Me = Methyl; Et = Ethyl; Ph = Phenyl; hmpa = Hexamethylphosphoramide [$OP(NMe_2)_3$]; THF = tetrahydrofuran; DME = dimethoxyethane.

1 INTRODUCTION

Bismuth, element 83, is a soft gray naturally occurring metal. It is most commonly found as bismite (Bi_2O_3), bismutite ($(BiO)_2CO_3$), or bismuthinite (Bi_2S_3). Bismuth is produced as a by-product of copper and lead smelting. It is the heaviest member of group 15 and the heaviest stable element. While there are many isotopes known, it is found naturally only as ${}^{209}_{83}Bi$ with a nuclear spin of 9/2. A number of physical properties are summarized in Table 1. Because of its low-melting point, high boiling point, and low neutron absorption cross section, it has found application as a coolant in nuclear reactors. Among metals bismuth is unique: it is the most diamagnetic, has the lowest thermal conductivity, and exhibits the highest Hall effect. The element expands upon solidifying, a property that has been used in the printing industry to produce type with clear well-defined edges.

Bismuth crystallizes as rhombohedral crystals with lattice constants $a = 4.5495$ Å and $c = 11.86225$ Å for space group $R3m$ (hexagonal setting). The density of the metal is $9.747\,g{\cdot}cm^{-3}$. When crystallized from molten salt fluxes, elemental bismuth forms highly intricate crystals clearly showing step dislocations (an attractive collector's item often found at commercial gem and mineral shows). The surface of the element is usually tarnished by air oxidation, giving it an appealing multicolored sheen. The chemistry of bismuth may be compared to that of phosphorus, arsenic, and antimony, the lighter members of group 15 (*see* ***Phosphorus: Inorganic Chemistry***; ***Arsenic: Inorganic Chemistry***; ***Antimony: Inorganic Chemistry***). While there are numerous similarities, there are also important differences, many of which arise due to the increasing diffuseness of the s^2 electrons. This means that the $+5$ oxidation state is found less often and is less stable for bismuth than for phosphorus, arsenic, and antimony. Very few inorganic complexes are known in which bismuth is in the $+5$ oxidation state. Exceptions include $NaBiO_3$, BiF_5, and salts of the complex ion $BiF_6{}^-$. An extensive series of organobismuth(V) compounds based on the formula $BiAr_3X_2$ (Ar = aryl) are known (discussed in *Bismuth: Organometallic Chemistry*). Bismuth is, on the other hand, easily oxidized to Bi^{III}, which is its most common oxidation state. The element reacts with dilute nitric acid, hot sulfuric acid, and concentrated hydrochloric acid, giving bismuth(III) salts. Bi^+ has been observed in solid-state phases and molten salts, but is rare. This formal oxidation state is also found in the unstable R_2Bi^- generated as intermediates in the reduction of R_2BiX. Other formal oxidation states which have been reported include Bi^{2+} in tetraorganodibismuthines and Bi^{3-} in BiH_3 and in the alkali metal phases M_3Bi (M–Li, Na, K, Rb, Cs). As will be detailed below compounds of bismuth are important for their biological activity, as high T_C superconductors, and as oxidation catalysts. Bismuth chemistry has been compiled in the Gmelin series[1] and in *Comprehensive Inorganic Chemistry*.[2] Some aspects of the structural chemistry of bismuth are also treated in *Structural Inorganic Chemistry*.[3]

2 COMPOUNDS OF BISMUTH

2.1 Intermetallic Compounds

2.1.1 Antimony Compounds

Not surprisingly, bismuth forms solid solutions with antimony. Recent work has shown that $Bi_{1-x}Sb_x$ nanowires and films can be deposited electrochemically.[4]

Table 1 Physical properties of elemental Bi

Atomic weight	208.98 amu
Melting point	271 °C
Boiling point	1560 °C
ΔH fusion	10.48 kJ mol^{-1}
ΔH vaporization	179.1 kJ mol^{-1}
Density	9.747 g cm^{-3}
$S°$ (298.15 K)	56.74 J K^{-1} mol^{-1}
C_p	25.22 J K^{-1}mol^{-1}
Electrical resistivity	106.8 × 10^{-8} Ωm (273 K)
Thermal conductivity	7.87 W m^{-1} K^{-1}
Mass magnetic susceptibility	-1.684×10^{-8} kg^{-1} m^3 (s)
Coefficient of linear thermal expansion	13.4 × 10^{-6} K^{-1}
Electronegativity	2.02 (Pauling) 1.67 (Allred)
Radii: ionic Bi^{5+}	0.74 Å
Bi^{3+}	0.96 Å
atomic	1.55 Å
covalent	1.52 Å
van der Waals	2.40 Å
Ionization potentials:	
1st	703 kJ mol^{-1}
2nd	1609 kJ mol^{-1}
3rd	2466 kJ mol^{-1}
4th	4370 kJ mol^{-1}
5th	5403 kJ mol^{-1}

2.1.2 *Alkali Metal and Alkaline-earth Metal Compounds*

Bismuth with a formal oxidation state of −3 is found in solid-state phases M_3Bi (M = alkali metal) and M'_3Bi_2 (M′ = alkaline-earth metal). The compound Na_3Bi is metallic. Less reduced intermetallic phases with the alkali metals and alkaline-earth metals are also known. Examples include MBi (M = Li, Na), MBi_2 (M = K, Rb, Cs), and $M'Bi_3$ (M = Mg, Ca, Sr, Ba). The compounds $M'Bi_3$ (M′ = Ca, Sr, or Ba) superconduct at low temperatures. Some of these intermetallic phases have been extracted with amine solvents to yield anionic bismuth clusters in solution (see Section 2.8.2).

2.1.3 *Transition Metal–Bismuth Intermetallic Compounds*

A number of bismuth–transition metal phases have been tabulated.[2] Bi_2Ag, BiCu, BiCo (high-temperature, high-pressure phase), Bi_2Ir, Bi_4Mg to Bi_9Mg, Bi_3Mo, $BiRe_2$, BiRu, Bi_3Sn, Bi_3Te, Bi_3Zn, and $BiZr_3$ are reported to be superconducting at low temperatures.[5] The near stoichiometric BiMn compound known as Bismanol is a very strong permanent magnet material.[6] Bismuth does not form stable binary compounds with iron, chromium, or cobalt under ordinary conditions. The adsorption of Bi on to Au electrodes has been noted to activate the surface to electrocatalytic activity.[7] Ternary phases have also been examined. Direct fusion of alkali metals, indium, and bismuth leads to several alkali metal–indium–bismuth phases showing In-centered tetrahedra of bismuth that are corner- and/or edge-shared. These include $Na_3In_2Bi_3$, Na_3InBi_2, $K_7In_4Bi_6$, $K_{11}In_6Bi_9$, and $Rb_7In_4Bi_6$.[8]

2.1.3 *Posttransition Metal Compounds of Bismuth*

Bismuth is not miscible with cadmium. It is miscible with mercury but does not form any discrete compound. A simple eutectic system is observed with bismuth and zinc. A number of low-melting alloys are known such as Wood's metal (50% Bi, 25% Pb, 12.5% Cd, 12.5% Sn; mp 70 °C).[1,2] These alloys are often used as heating bath materials, in automatic sprinkler systems, fire detection devices, safety plugs in compressed gas cylinders, and so on. Alloys which contain more than 55% Bi expand on freezing and are used in the production of castings, type metal, and accurate dies. Bismuth and antimony are completely miscible and alloys with a small percentage of antimony show large galvanothermomagnetic effects. Bismuth forms compounds of formula MBi with M = In or Tl. In addition, In also forms the compounds In_5Bi_3 and In_2Bi, which are superconducting at low temperature.[9] Bismuth phosphide has been prepared by reaction of $BiCl_3$ and $P(SiMe_3)_3$.[10]

2.2 Bismuth Hydride

Bismuthine, BiH_3, a thermally unstable compound which decomposes above −45 °C, was first prepared in 1961.[11,12] More recently, the compound has been reexamined in order to confirm its existence and physical properties, both experimentally and computationally.[12,13] It is best prepared at −45 °C by the disproportionation of $MeBiH_2$ or Me_2BiH, which are formed from the reaction of the appropriate organobismuth halides with reducing agents such as $NaBH_4$ or $LiAlH_4$. It may also be prepared by the reaction of a Mg/Bi alloy with HCl or of $BiCl_3$ with $LiAlH_4$ at low temperature. The boiling point has been estimated to be 16.8 °C and the heat of formation 277 kJ mol^{-1}. The compound $(2,6\text{-}C_6H_2(CH_3)_2H_3C_6)_2BiH$ was recently been isolated as the first example of a stable bismuth hydride.[14] It derives its stability from the bulky organic protecting groups. Bismuthine has been used in the manufacture of silicon and germanium semiconductors. Because of its instability the chemistry of BiH_3 has not been extensively investigated.

2.3 Bismuth Halides, Pseudohalides, and Complex Halo Ions

Reaction of elemental bismuth with the halogens at elevated temperatures leads to the production of BiX_3. Properties of the trihalides are summarized in Table 2. Bismuth is first oxidized by $F_2(g)$ to BiF_3, with conversion to BiF_5 occuring above 600 °C. The latter is the only known homoleptic bismuth(V) halide, although organic derivatives of the form

Table 2 Physical properties of bismuth halides

	Mp (°C)	Bp (°C)	ΔG°_f (298 K, kJ mol^{-1})	Density (g cm^{-3})	$d_{Bi–X}$ (Å)	$\nu_{Bi–X}$ (a_1) (cm^{-1})
BiF_3	725					
$BiCl_3$	233	441	−314.6	4.750	2.50	280
$BiBr_3$	219	462	−247.7	5.720	2.63	196
BiI_3	409	542	−148.7	5.640	3.07	145

Ar_3BiX_2 (Ar = aryl; X = F, Cl, Br) are well known. BiF_5 is a very powerful oxidizing and fluorinating agent.

The bismuth(III) halides are moisture sensitive and are readily converted into the oxyhalides BiOX (equation 1). Addition of acid to aqueous suspensions of the oxyhalides will regenerate BiX_3, which exist as complex halo anions in solution. Addition of ammonium hydroxide to such solutions results in the formation of insoluble $Bi(OH)_3$, which is easily dehydrated to the oxide.

$$BiX_3 + H_2O \longrightarrow BiOX + 2HX \tag{1}$$

$BiCl_3$ is very easily hydrated and commercial samples may need to be dried or sublimed if anhydrous material for use in sensitive reactions (e.g. with Grignard reactions) is required. Refluxing a thionyl chloride suspension of $BiCl_3$ is an effective method for dehydrating the solid. Anhydrous $BiCl_3$ is soluble in aromatic hydrocarbons and donor solvents such as ethers where complexes are formed. Bismuth(III) halides are useful starting compounds for the production of many other bismuth(III) compounds.[1,2] (*see also* ***Bismuth: Organometallic Chemistry***).

A feature commonly found among bismuth(III) complexes is their ability to function as Lewis acids and expand the octet of the bismuth atom (*see* ***Hypervalent Compounds***). This leads to a number of adducts between the bismuth halides and common donor molecules such as ethers, amines, phosphines, and organosulfur compounds.[15,16] Simple bismuth–arene complexes (*see Arene Complexes*) in which the aromatic ring is π-bonded to the bismuth atom have been structurally characterized.[17] A similar bonding mode has been found when $AlCl_3$ is added to $BiCl_3$ in arene solvents.[18] Bismuth–arene complexation is also observed for the bismuth alkoxides such as $[Bi(OC_6F_5)_3(toluene)]_2$ and $Bi_4(\mu_4\text{-}O)(\mu\text{-}OC_6F_5)_6\{\mu_3\text{-}OBi(\mu\text{-}OC_6F_5)_3\}\cdot 2(C_6H_5CH_3)$.[19–21] The ability to form complexes with arenes is probably dependent on the electronegativity of the groups attached to bismuth.

Ether–bismuth halide adducts also exist. Structural work on bismuth chloride–diethyl ether or THF complexes show that, at low temperature, polymeric chains of BiX_3 linked by halide bridges exist and that the bismuth atoms may be coordinated by one or two ether molecules.[22,23] Bismuth(III) bromide coordinates three THF molecules.[23] These solvent molecules are readily removed under vacuum. The polyethers diglyme and diethylcarbitol give dimeric adducts with $BiCl_3$.[21] In the presence of cyclic polyethers, simple coordination, or formation of polyether-coordinated bismuth cations occurs. Examples include $[BiCl_2(15\text{-crown-}5)(MeCN)]SbCl_6$, $[BiCl(18\text{-crown-}6)(MeCN)_2][SbCl_6]_2$,[24] $BiCl_3(12\text{-crown-}4)$, and $[BiCl_2(18\text{-crown-}6)]_2[Bi_2Cl_8]$.[25] Hexamethylphosphoramide (hmpa, $OP(NMe_2)_3$) also binds to bismuth halides yielding complex halo-hmpa bismuth cations: $[Bi_2I_6(hmpa)_2]$, $[BiI_2(hmpa)_4][I_3]$, and $[BiI_2(hmpa)_4][I_5]$.[26]

Halide ions form adducts with Bi^V or Bi^{III} halides, leading to complex ions. $[BiF_6]^-$ is formed upon reaction of NiF_2 with BiF_5 in anhydrous HF.[27] The resultant $Ni[BiF_6]_2$ compound dissolves readily in MeCN giving $[Ni(NCMe)_6][BiF_6]_2$. The alkali metal/$BiF_6{}^-$ complexes have been prepared by the reaction of elemental fluorine with various salts.[28] For example, $LiBiO_2$, $NaBiO_2$, and $NaBiS_2$ are converted into the corresponding $MBiF_6$ at 450–500 °C. The K^+ compound was prepared from either $KBiS_2$ or a mixture of KCl and Bi_2O_3 at 360–450 °C, while the Rb^+ and Cs^+ salts arose from fluorination of mixtures of the alkali metal carbonates and Bi_2O_3 at 400–450 °C. XeF_4 reacts with BiF_5 in anhydrous liquid HF to give $[XeF_3{}^+][BiF_6{}^-]$, in which there is a tight association between one of the F atoms on the bismuth and the Xe. The Bi–F bond distance is substantially lengthened by this interaction (2.1 Å as against ca. 1.9 Å).[29]

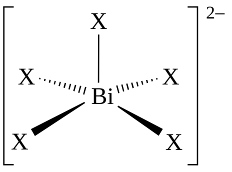

(**1**)

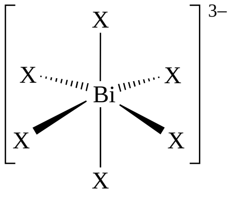

(**2**)

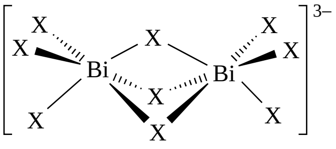

(**3**)

For Bi^{III} halides and pseudohalides, a wide range of complex anion structures has been observed, including $[BiX_5]^{2-}$ (**1**), $[BiX_6]^{3-}$ (**2**), $[Bi_2X_9]^{3-}$ (**3**), $[Bi_2X_8]^{2-}$ (**4**), $[Bi_3I_{12}]^{3-}$, $[Bi_4X_{16}]^{4-}$ (**5**), $[Bi_2Cl_{10}]^{4-}$, $[Bi_4Cl_{20}]^{8-}$ and $[Bi_8X_{28}]^{4-}$.[30–32] In addition to discrete ions such as (**1**)–(**5**), polymeric species may result. Thus $[BiX_4]_n{}^{n-}$ adopt edge-sharing (**6**) and $[BiX_5]_n{}^{2n-}$ vertex-sharing (**7**) octahedral

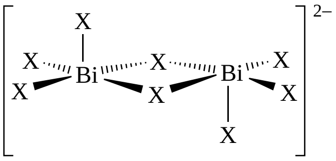

(**4**)

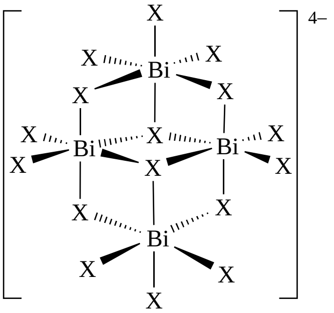

(**5**)

BiX_6 configurations. The polymeric anion $\{Bi_2I_7{}^-\}_n$ is also known.[31] HCl reacts with $BiCl_3$ in ether solution to produce the acid $H[BiCl_4]\cdot(solvent)_x$, in which a complex anion (**5**) exists. As seen in the structures, the bismuth atoms which are hypervalent may or may not show stereochemically active lone pairs of electrons.

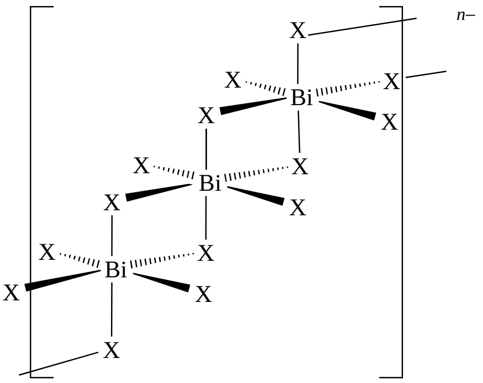

(**6**)

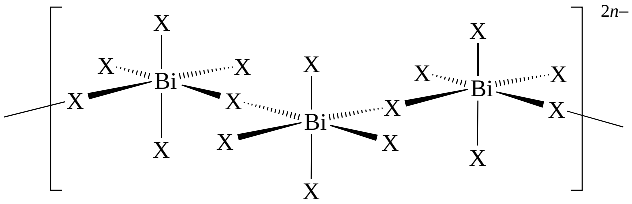

(7)

Related complexes with halide ligands and other donors such as THF, pyridine, picoline, or phosphines have been reported. These include the netural molecules $BiCl_3(pyridine)_4$ and $BiI_3(pyridine)_3$ and the anions $[BiBr_5(picoline)]^{2-}$, $[BiCl_5(pyridine)]^{2-}$, and $[Bi_2Cl_8(THF)_2]^{2-}$.[33,34] Phosphine adducts include $Bi_2Br_6(PME_3)_4$, $Bi_2Br_6(dmpe)_2$ [dmpe = 1, 2-bis(dimethylphinoethane)], $Bi_4Br_{12}(PEt_3)_4$, and $[BiI_4(PMe_2Ph)_2]^-$.[16,35,36] Some mixed halide-aryloxide complexes are also known.[37] Formulations include $Bi_2Cl_4(THF)_2(\mu\text{-}OR)_2$ (R = $OC_6H_3Me_2$-2,6, $OC_6H_2Me_3$-2,4,6), $[Bi_2(OC_6H_2Me_3\text{-}2,4,6)_6(\mu\text{-}Cl)_2]^{2-}$, $[BiBr_3(OC_6H_2Me_3\text{-}2,4,6)_2]^{2-}$.

2.4 Bismuth Compounds with Oxygen-based Ligands

2.4.1 *Alkoxides*

Because of the interest in a variety of heterometallic oxides with potentially valuable applications such as high T_C superconductivity, oxide ion conductivity, piezoelectric properties, and ferroelectric properties, bismuth alkoxides have been prepared for use as sol–gel and vapor deposition precursor compounds.[38] Mehrotra and coworkers found that $Bi(OR)_3$ (R = Me, Et, Pr) were insoluble and probably polymeric.[39] No structural information is available for these simple compounds. The *t*-butoxide complex is soluble, as is the compound for which R = 2,6-$Me_2C_6H_3$.[40] These are monomeric as determined by electron or X-ray diffraction. For the case where R = $CH(CF_3)_2$, the compound is a centrosymmetric dimer which also has coordinated THF.[21] These compounds were prepared by the reaction of $BiCl_3$ and an appropriate alkali metal alkoxide. The mixed halide–methoxide $BiCl(OMe)_2$ has also been prepared by this method or by pyrolysis of $BiCl(O_2COMe)_2$.[41] $Bi(OSiPh_3)_3$ is prepared by this salt metathesis method and has low solubility, except as the THF adduct $Bi(OSiPh_3)_3(THF)_3$ (**8**), which is monomeric and very soluble.[42] $\{BiOSi(O^tBu)_2Ph\}_3$ has also been prepared.[43] The related complex $Bi(OCPh_3)_3$ does not show the solvent coordination but the electron demand at the bismuth center is satisfied by π-interactions between the bismuth and one phenyl ring of each alkoxide ligand.[44] Dimeric monoalkoxide complexes of the type $[Bi(NO_3)_2(triethylene\ glycolate)]_2$ have been synthesized by Rogers and coworkers.[45] Higher order oligomerization is hindered by the chelation by the triethylene glycolate ligand. $Bi(OH)_3$ reacts with triethanolamine to give $Bi(OCH_2CH_2)_3N$.[46] The compound is composed of chains of alkoxo-bridged bismuth units.[47] The chains are aligned in pairs with weak Bi–O interactions between them. Structural features are similar to those found in many of the bismuth complexes with naturally occurring multidentate carboxylate and alkoxide ligands.

Another synthetic method to produce alkoxide complexes of bismuth employs the solvolysis of $\{BiN(SiMe_3)_2\}_3$[48] by alcohols. $Bi(OCH_2CH_2OMe)_3$ has been prepared in this fashion and is dimeric in the solid state.[42,48] The similar complex with $OCMe_2CH_2OMe$ is also known.[49] These complexes are volatile and may be used for chemical

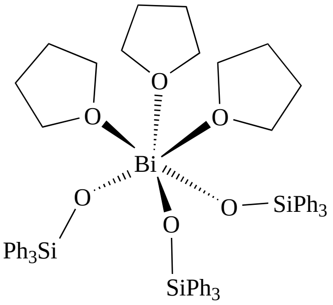

(**8**)

vapor deposition methods. Solvolysis of organobismuth compounds may also be accomplished using acidic alcohols. $BiPh_3$ has also been shown to react with C_6F_5OH to give $[Bi(OC_6F_5)_3(toluene)]_2$ (**9**).[21] The toluene ligands of (**9**) are labile and are replaced with two THF ligands when dissolved in that solvent.

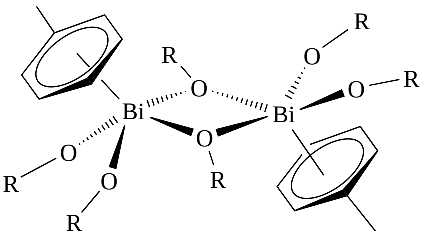

(**9**)

Organobismuth alkoxides have been prepared: Et_2BiOEt and $MeBi(OEt)_2$ are formed from the reaction of Et_2BiBr[50] or $MeBiBr_2$[51] with NaOEt. Siloxy derivatives are also known.[52] $BiEt_3$ undergoes partial solvolysis by phenol or C_6F_5OH, producing $[BiEt_2(OAr)]_\infty$ which is a chain polymer with the alkoxide function bridging between bismuth atoms.[53]

Bismuth alkoxide complexes are easily hydrolyzed and complex bismuth oxo-alkoxide compounds may result as intermediates to full hydrolysis. A number of examples of these are known for the pentafluorophenoxide system and include $Bi_4(\mu_4\text{-}O)(\mu\text{-}OC_6F_5)_6\{\mu_3\text{-}OBi(\mu\text{-}OC_6F_5)_3\}_2\cdot 2(C_6H_5CH_3)$, $Bi_8(\mu_4\text{-}O)_2(\mu_3\text{-}O)_2(\mu\text{-}OC_6F_5)_{16}$, $Bi_6(\mu_3\text{-}O)_4(\mu_3\text{-}OC_6F_5)\{\mu_3\text{-}OBi(OC_6F_5)_4\}_3$, $NaBi_4(\mu_3\text{-}O)_2(OC_6F_5)_9(THF)_2$, $Na_2Bi_4(\mu_3\text{-}O)_2(OC_6F_5)_{10}(THF)_2$, $[NaBi(OC_6F_5)_4(THF)]_\infty$, and $Na_4Bi_2(\mu_6\text{-}O)(OC_6F_5)_8(THF)_4$.[20,54] A hexanuclear compound $Bi_6(\mu_3\text{-}O)_3(\mu\text{-}OR)_7(OR)_5$ has also been observed where $R = C_6H_3Cl_2$-2,6.[55] The formation of oxide ligands can arise not only from hydrolysis but also from condensation of two phenoxide ligands to produce bis(pentafluorophenyl)ether. For example, careful addition of one equivalent of $NaOC_6F_5$ to $[Bi(OC_6F_5)_3(toluene)]_2$ yields first the adduct $[NaBi(OC_6F_5)_4(THF)]_\infty$ as an infinite chain polymer in which there are alternating Bi^{3+} and Na^+ ions with two phenoxides bridging between each metal, but if more phenoxide is added, the ether is eliminated and $Na_4Bi_2(\mu_6\text{-}O)(OC_6F_5)_8(THF)_4$ results.[54] This molecule has an oxide ion sitting in the center of the six metal ions. In addition to the sodium salts, other heterometallic alkoxides have also been prepared. These include $Bi\{Al(O^iPr)_4\}_3$, $Bi\{Al(O^iPr)_4\}_2(O^iPr)$, $CpMo(\mu\text{-}OEt)_2Bi(OEt)_2Cl$, $\{MeC(CH_2)_2\}Mo(CO)_2(\mu_3\text{-}OEt)_3Bi(\mu_3\text{-}OEt)_2Bi((\mu_3\text{-}OEt)_3Mo(CO)_2\{MeC(CH_2)_2\}$, $\{MeC(CH_2)_2\}Mo(CO)_2(OCH_2CH_2OMe)_2(\mu\text{-}Cl)BiCl$, and $[\{MeC(CH_2)_2\}Mo(CO)_2(OCH_2CH_2OMe)_2(\mu\text{-}Cl)Bi(THF)][BF_4]$.[56]

2.4.2 *Carboxylate Complexes*

Bismuth readily forms complexes with organic carboxylates. These compounds are easily prepared from bismuth(III) halides and the alkali metal or silver carboxylates or by reaction of bismuth oxides or bismuth oxycarbonate $(BiO)_2CO_3$ with carboxylic acids or the acid anhydrides. Bismuth acetate is commercially available and has been used to effect addition of acetate to organic substrates. For example, cyclohexenes react with bismuth acetate in the presence of I_2 giving the 1,2-diacetatocyclohexanes. If the reaction is conducted in the absence of water, *trans*-1,2-diacetates are obtained, but if water is present, cis compounds result.[57] Carboxylate linkages from naturally occuring organic acids form the basis for many biologically active bismuth compounds (discussed in the next section). In addition to $Bi(OAc)_3$, bismuth formate[58] and bismuth trifluoroacetate[59] have been studied. Bismuth trifluoroacetate crystallizes with coordinated trifluoroacetic acid when prepared from reaction of Bi_2O_3 with a mixture of trifluoroacetic acid and trifluoracetic anhydride.[60] The adduct $NaBi(O_2CCF_3)_4$ is formed when $NaBiO_3$ is treated with trifluoroacetic acid.[59] Pyrolysis of the formate leads first to $BiO(O_2CH)$ and ultimately to $(BiO)_2CO_3$.

The bismuth(II) compound $[Bi_2(O_2CCF_3)_4]\cdot C_6Me_6$ compound has been prepared in low yield by the pyrolysis of bismuth(III) trifluoroacetate in hexamethylbenzene. It possesses a Bi–Bi bond that is bridged by four bridging carboxylate ligands in a fashion similar to the tetracarboxylate complexes of the metal–metal bonded transition metal dimers.[61] Salicylic acid, $o\text{-}HOC_6H_4CO_2H$, has proven useful for linking bismuth to other metals such as Ti, Ta, or Nb owing to the presence of both the phenol and carboxylic acid functions.[62] The salicylate ligand can be found in either the monodeprotonated form $o\text{-}HOC_6H_4CO_2^-$ and in the dideprotonated version $o\text{-}OC_6H_4CO_2^{2-}$ giving flexibility in both charge and coordination mode. These complexes serve as useful precursors to heterometallic oxides.

2.4.3 *Biologically Active Bismuth(III) Complexes*

Bismuth compounds have long been known for their biological function,[63–65] primarily for treating gastrointestinal disorders.[64,66] Generally bismuth compounds are not very toxic owing to low solubility of bismuth salts in solution and have potential for a variety of medicinal applications.[63,67] Bismuth chloride reacts rapidly with water to form the insoluble subhalide BiOCl and other salts behave similarly. However, bismuth oxalate is reported to be poisonous. Bismuth aluminate, bismuth phosphate, bismuth subgallate, and bismuth subnitrate have antacid properties. Several compounds have been used as antisyphilitics, including bismuth butylthiolaurate, bismuth oxychloride, bismuth tris(ethyl camphorate), bismuth potassium tartrate, bismuth sodium iodide (Na_2BiI_5), and bismuth sodium tartrate. Bismuth oxide, bismuth subgallate, and bismuth tannate have found uses as astringents, and bismuth subnitrate has been used in cosmetics. Gastritis and duodenal ulcers may be treated with bismuth subcitrate, while bismuth iodide oxide, bismuth iodosubgallate, and bismuth tribromophenate find uses as anti-infective agents. Bismuth sodium triglycollamate and bismuth subsalicylate function as suppressants of *lupus erythematosus*.

Complexes of bismuth(III) with naturally occurring organic acids have been synthesized and studied for potential biological activity.[68–71] Citric acid complexes have long been known to have biological activity and a number have been recently synthesized and characterized in solid state and solution.[71,72] Synthetic methods to these compounds are straightforward, as exemplified by the reaction of bismuth nitrate with L-(−)-malic acid and L-(+)-tartaric acid to give bismuth(III) malate monohydrate and tartrate trihydrate,[69] or reaction of $Bi(OH)_3$ with (*S*)-lactic acid to produce bismuth(III) lactate.[70] Bismuth salicylate is conveniently prepared by the reaction of $BiPh_3$ with salicylic acid in refluxing toluene. From this preparation, the structures the bipyridine and phenanthroline adducts of bismuth salicylate have been reported.[73] While the bipyridine simply adds to $Bi(HOC_6H_4CO_2)_3$, the addition of phenanthroline results in the elimination of salicylic acid and the deprotonation of one of the other salicylate ligands. In both cases, the high Lewis acidity of the bismuth center gives rise to dimer formation: $[Bi(HOC_6H_4CO_2)_3(\text{bipyridine})]_2$ and $[Bi(HOC_6H_4CO_2)(HOC_6H_4CO_2)(\text{phenanthroline})]_2$.

While the mechanism of the interaction of these carboxylate complexes with the biological molecules that leads to their activity is not well understood, there is some evidence that the molecules can bind to N-donor and S-donor molecules in proteins. Bismuth(III) has been shown to bind most strongly to the thiolates in glutathione.[74] There is some evidence that Bi(III) can replace metals such as Fe(III) in lactoferrin and transferrin or Zn(II) in metallothionein.[75]

2.4.4 Bismuth Oxides

The common oxide of bismuth is Bi_2O_3, which is found in nature as the mineral bismite, has a variety of uses including the making of enamels for cast iron, in the manufacture of glass and ceramic products, in disinfectants, magnets, catalysts, and rubber vulcanization. It readily dissolves in acidic solution yielding complex halide species. High purity material may be prepared by igniting bismuth nitrate. Four crystalline modifications α, β, γ, and δ are known, which are monoclinic (pseudoorthorhombic), tetragonal, body-centered cubic, and cubic, respectively. The thermodynamically stable α phase converts to the δ phase at 729 °C. Upon cooling to 650 °C the β phase is produced and at 629 °C the γ phase is obtained. Bismuth oxide has been reported to be an oxygen ion conductor at high temperatures and this conductivity varies with the phase in the order $\alpha < \beta < \gamma \ll \delta$.[76] The δ phase is highly disordered and reportedly has about 75% of the disorder of the molten compound. The oxide is very easily contaminated, forming compounds which have the same crystal system and similar lattice parameters to the body-centered cubic γ form. These compounds are based upon a formulation of $[Bi_{24}O_{40}]^{8-}$ in which contaminant cations complete the charge balance. Simple compounds with the formula $EBi_{12}O_{20}$ ($E = Si$, Ge) are examples. Silicon can be incorporated by leaching of that element from porcelain crucibles during high-temperature reactions.

The pentavalent oxide Bi_2O_5 is reportedly prepared by oxidation of Bi_2O_3 in solution or by fusion of Bi_2O_3 with $KClO_3$.[77] The compound is very unstable and has not been isolated in pure form.

Bismuth oxide forms a number of complex mixed-metal phases with the divalent metal oxides of calcium, strontium, barium, lead, and cadmium, and these show a wide variety in composition. With transition metal oxides, mixed-metal oxide phases have been observed which are based upon a Perovskite-type lattice (**10**) containing layers of Bi_2O_2.[78] It is notable that the high T_c superconducting materials which include bismuth[40] also have this Perovskite-type of lattice with layers of copper oxide interleaved with bismuth oxide layers.

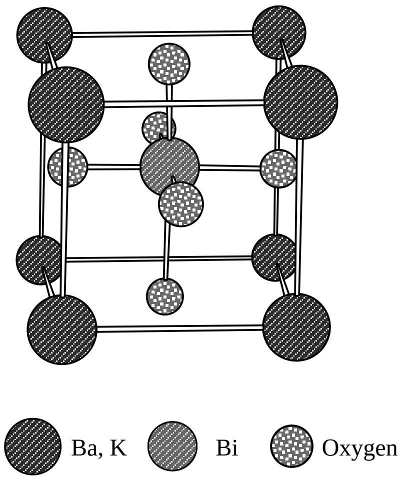

(**10**)

The alkali metal oxides $MBiO_2$ (M = Na, K, Rb, Cs) have been prepared and structurally characterized.[79] The bismuth has a +5 oxidation state in sodium bismuthate ($NaBiO_3$), a well-known but ill-defined substance which has been used as an analytical reagent capable of oxidizing Mn^{2+} to Mn^{7+}. The solid has the ilmenite structure ($FeTiO_3$). It dissolves in strong acid solutions to give an as yet uncharacterized bismuth(V) complex which is stable for a few days in solution. Other phases containing Bi^V have recently been reported.[80] These include $LiSr_3BiO_6$, $NaSr_3BiO_6$, $NaBa_3BiO_6$, Li_6KBiO_6, Li_6RbBiO_6, and $Li_2Ba_5Bi_2O_{11}$ produced in molten salt reactions.

The importance of bismuth oxide species in oxidation of organic molecules is illustrated in Scheme 1, which shows a proposed mechanism for the SOHIO process for the oxidation and ammoxidation of propene using a molybdenum bismuthate catalyst.[81] The intermediates proposed in Scheme 1 have not been observed in discrete molecular systems. Indeed, no molecular molybdenum–bismuth oxide species is known. The reaction of $BiPh_3Cl_2$ with $[Bu_4N]_2[MoO_4]$ has been examined[82] and the products identified as $(BiPh_3MoO_4)_x$ and $[BiPh_3(MoO_4)_2]^{2-}$, but these compounds may be more appropriately considered organobismuth derivatives than bismuth oxide models.

Saturated hydrocarbons may also be oxidized by bismuth oxide catalysts. For example, methane is converted to CO_2 and a mixture of higher hydrocarbons over bismuth oxide catalysts that also contain sodium, calcium, cesium, and/or halide

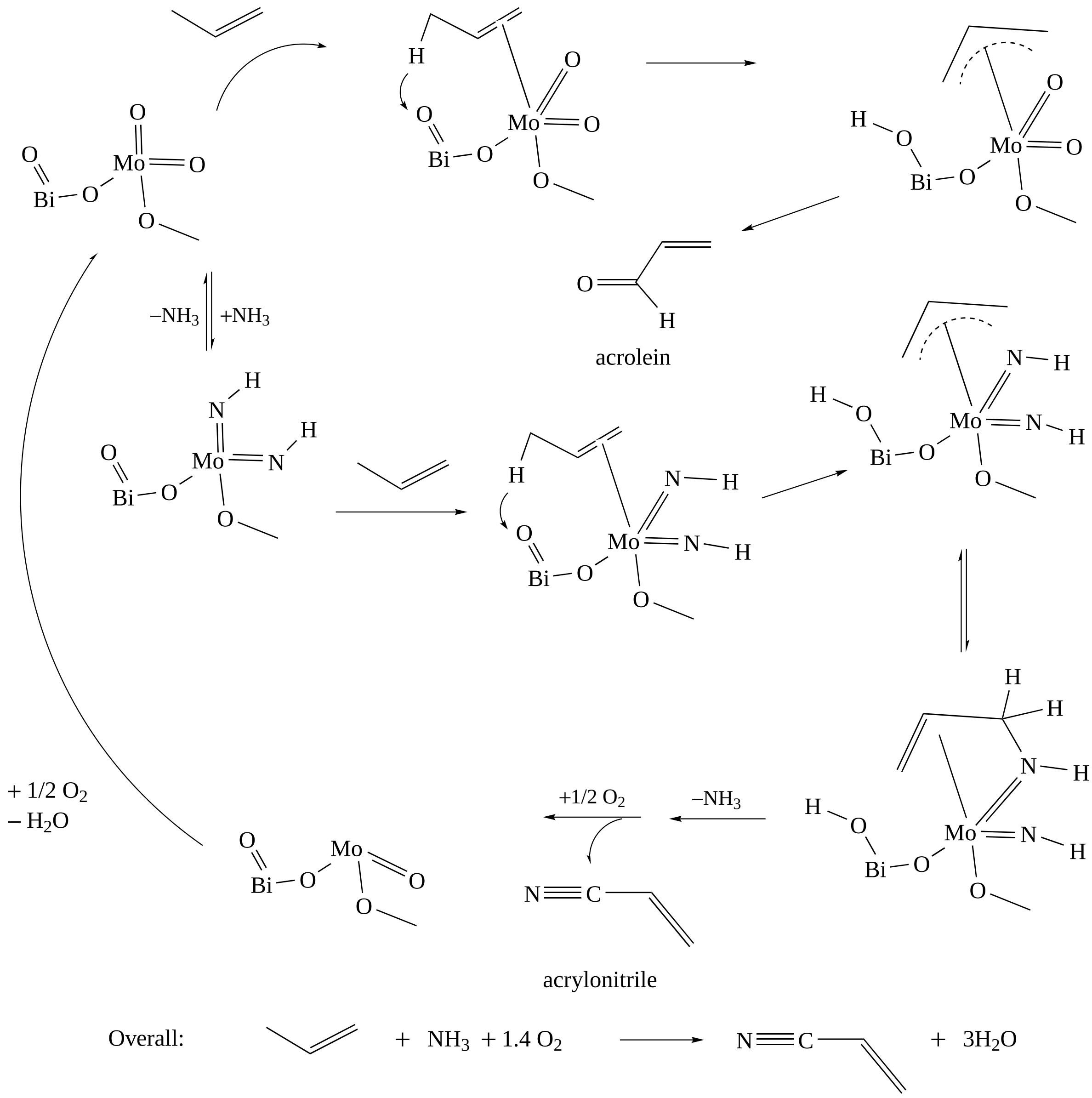

Scheme 1

ions.[83] Propane has been oxidized to acrolein over a silver-doped bismuth–vanadomolybdate catalyst.[84] Heterometallic bismuth oxides containing vanadium, titanium, niobium, or tantalum have also been shown to serve as photocatalysts for a variety of reactions including the splitting of water.[85]

2.4.5 Bismuth Oxo Cluster Complexes and Related Compounds

In very acidic solutions, bismuth(III) exists in the form of the nonaaquo ion $[Bi(H_2O)_9]^{3+}$, which is similar to the aquo complexes of the lanthanide ions,[86] but partial hydrolysis of bismuth(III) salts leads to the formation of bismuth oxo clusters. The core structure of these complexes is often based upon a Bi_6 octahedral core with oxide, hydroxide, or alkoxide functions bridging the edges and/or faces of the octahedron. The $[Bi_6(OH)_{12}]^{6+}$ ion (**11**) has been studied spectroscopically.[87] In oxo clusters, the octahedron is face-bridged by eight oxo or alkoxide functions (**12**). Such core structures have been found in the hydrolysis of bismuth nitrate or perchlorate.[88]

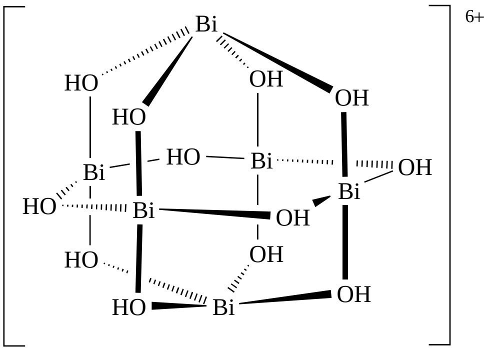

(**11**)

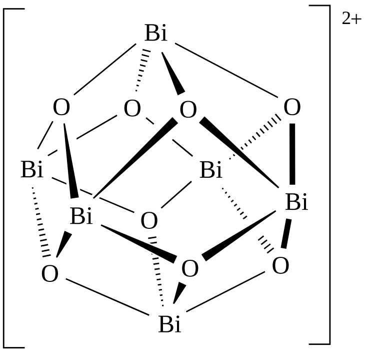

(**12**)

A number of bismuth alkoxo-oxo cluster complexes have been observed in the C_6F_5OH system.[19–21,54,89] These compounds include $NaBi_3(\mu_3\text{-}O)(OR)_8(THF)$, $NaBi_4(\mu_3\text{-}O)_2(OR)_9(THF)_2$, $Na_2Bi_4(\mu_3\text{-}O)_2(OR)_{10}$, and $Bi_6(\mu_3\text{-}OR)(\mu_3\text{-}O)_4[\mu_3\text{-}OBi(OR)_4]_3$, which have been obtained from the reaction of $BiCl_3$ and $NaOC_6F_5$. The reaction of $[Bi(OC_6F_5)_3(toluene)]_2$ with $NaOC_6F_5$ led to the production of $Bi_6(\mu_3\text{-}O)_2(\mu_4\text{-}O)(OR)_{12}$ and $NaBi_3(\mu_3\text{-}O)(OR)_8(THF)_3$. Reaction of $BiPh_3$ with HOC_6F_5 in THF led to the formation of $Bi_6(\mu_3\text{-}OR)(\mu_3\text{-}O)_4[\mu_3\text{-}OBi(OR)_4]_3(THF)_2$. $Bi_6(\mu_3\text{-}OR)(\mu_3\text{-}O)_4[\mu_3\text{-}OBi(OR)_4]_3$ and $Bi_6(\mu_3\text{-}OR)(\mu_3\text{-}O)_4[\mu_3\text{-}OBi(OR)_4]_3(THF)_2$ possess the core geometry in (**12**).[54]

2.5 Bismuth Chalcogenide-based Ligands

2.5.1 Compounds with Organochalcogenide Ligands

Bismuth very readily forms complexes with sulfide and sulfur-containing ligands, and this ability may be important in understanding the biological activity of colloidal bismuth carboxylate complexes. The crown thioether compounds $[9]aneS_3$, $[12]aneS_4$, $[15]aneS_5$, $[18]aneS_6$ and $[24]aneS_8$ add to $BiCl_3$.[90] The bismuth is bonded to each sulfur and the Bi–Cl bonds are retained, as has been established for the $[12]aneS_4$ and $[15]aneS_5$ complexes, (**13**) and (**14**). The Bi–Cl distances are on the order of 2.57 Å and the Bi–S distances range from 2.98 to 3.25 Å. The compound $[SMe_3]_2[Bi_2I_8(SMe_2)_2]$ has dimethylsulfide bonded to bismuth,[91] and the tridentate $MeSi(CH_2SMe)_3$ reacts with BiX_3 (X = Cl, Br) to displace the halide ions forming $[Bi(MeSCH_2)_3SiMe)]X_3$ which is polymeric in the solid state.[92]

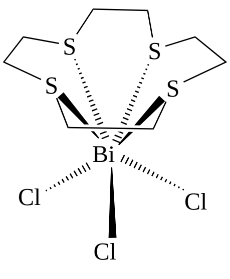

(**13**)

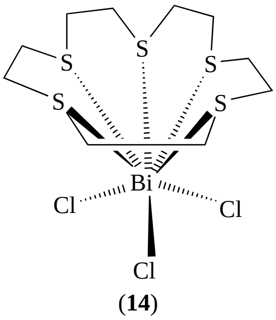

(**14**)

$BiEt_3$ reacts with thiols and the likely product is $Bi(SR)_3$, which has not yet been fully characterized;[93] however, such complexes have been synthesized via other methods.[94] The organic thiolates RS^- examined include those with $R = C_6F_5$, $4\text{-}MeC_6H_4$, $2,6\text{-}Me_2C_6H_3$ or $3,5\text{-}Me_2C_6H_3$. The structure of $BiSC_6H_2\text{-}2,4,6\text{-}\{(CMe_3)_3\}_3$ from the reaction of $BiCl_3$ with the lithium salt of the thiolate has been reported.[95] Bismuth nitrate reacts with 3 equivalents of (3-trimethylsilyl)pyridine-2-thiol to yield the tris{(3-trimethylsilyl)pyridine-2-thiolato}Bi complex[96] which, by comparison with the antimony analog, should have the three ligands chelating the bismuth atom bonded through both the S and N atoms. Cyclic complexes of the formula $BiCl\{(SCH_2CH_2)_2E\}$ (E = O, S) are obtained from the reaction of $BiCl_3$ with the appropriate thiol.[97] While the structures of these compounds have not been reported, that of the compound $PhBi\{(SCH_2CH_2)_2O\}$, prepared from $PhBi(OEt)_2$ and the thiol, is known. The ether oxygen is coordinated to the bismuth atom and one may expect a similar situation in the halide complexes.[98] Similarly, BiX_3 ($X = Cl^-$, Br^-, NO_3^-) form complexes with thiolates that also have amine, alcohol, and ester functions.[99,100] Electrospray mass spectrometry has proven useful for identifying species in solution that are otherwise difficult to characterize.[100,101]

Dithiocarbamate, a popular ligand for bismuth(III), is formed easily in the reaction of an amine, CS_2, and $BiCl_3$. A number of complexes have been reported in which the bidentate ligand is chelating.[102] The coordination geometry about bismuth is similar to that found in the complex halide ions described above. Selenocarbamates of bismuth have been prepared by the same route.[103] Ligands such as hexamethylphosphoramide, Ph_3PO, Ph_3PS, N,N'-dimethylthiourea, and N,N'-dimethylpropyleneurea have been shown to complex to $Bi(SC_6F_5)_3$ giving 1:2 adducts,[104] while addition of excess $C_6F_5S^-$ leads to the formation of $[Bi(SC_6F_5)_5]^{2-}$ and SCN^- to $[Bi(SC_6F_5)_4(SCN)]^-$.[104,105]

2.5.2 Compounds with Inorganic Chalcogenide Ligands

In addition to the chalcogenides of the general formula Bi_2E_3, BiS_2 (high-pressure phase), BiSe, and Bi_3Se_4 are known. The sulfur complex crystallizes in an orthorhombic lattice isostructural to that found for Sb_2S_3. This structure is based upon double chains with two unique types of Bi atoms. One of the chain units is shown in (**15**). In the selenide, telluride, Bi_2Te_2S, and Bi_3Se_4 compounds the anions form close-packed layers with bismuth atoms occupying octahedral holes. The close-packed layer structure in these phases is complex, having regions of ABA and ABC anion alternations. Both the selenide and telluride are semiconductors. The compound $NaBiS_2$ has the rock salt structure. BiEX (E = S, Se; X = Cl, Br, I) are all known and all are isostructural, except BiSeCl. The predominant structure is made up of bromide ions lying between pleated chains of $(BiE)_n{}^{n+}$ (**16**). Bismuth chalcogenides have received attention owing to their thermoelectric properties. Nanowires and thin films of Bi_2Te_3 can be prepared and show enhanced thermoelectric properties.[106]

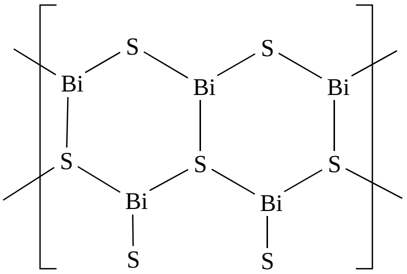

(**15**)

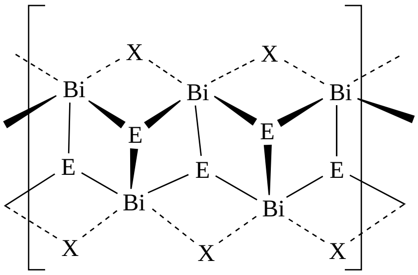

(**16**)

2.6 Bismuth Complexes with Group 15-based Ligands

Simple amine adducts of the bismuth halides have been prepared, although many have not been structurally characterized.[107] Adducts between amines and organobismuth complexes have been better defined (*see* ***Bismuth: Organometallic Chemistry***). Amido complexes of bismuth are conveniently synthesized by the reaction of $BiCl_3$ with the appropriate lithium dialkyl amide, $LiNR_2$ (R = Me, Ph, $SiMe_3$).[108] The R = Me and Ph compounds have been structurally characterized. For R = Me the bismuth atom is pyramidal (sum of angles about bismuth = 292.8°) with Bi–N bond distances averaging 2.184 Å and unique N–Bi–N bond angles on the order of 98.3 and 96.2°. The structure of the R = Ph compound shows it to be slightly more planar (sum of angles about bismuth = 296°) with Bi–N distances ranging from 2.12 to 2.18 Å. The compound $Bi(NMe_2)_3$ is light sensitive and volatile, making it potentially useful for chemical vapor deposition of bismuth for production of thin films. If the amide Li[NHR] ($R = C_6H_3Me_2$-2,6) is employed, the trinuclear complex $Bi_3(\mu\text{-NR})_4(NHR)$ results.[55] Coordination of a cyclic bismuth diamide, $Cp(OC)_3\,W[BiN_2(t\text{-Bu})_2SiMe_2]$, has been confirmed by X-ray diffraction.[109] The compound $Bi(N_3)_3$ has been prepared and examined by Hartree-Fock ab initio calculations.[110]

The chemistry of bismuth with macrocyclic N-donor ligands is not extensive but some reports have appeared. Bismuth octaethylporphyrin nitrate,[111] bismuth tetratolylporphyrin nitrate[112] and $[bismuth(cyclen)(H_2O)](ClO_4)_3$ (cyclen = 1, 4,7,10-tetrazacyclododecane)[113] have been prepared, as has the tetrakis(cumylphenoxy)phthalocyaninebismuth.[114] Reaction of 1,2-dicyanobenzene with bismuth and I_2 at 200 °C yielded mixed valent $[Bi(phthalocyanine)_2]I_{1.5}$ in which there are columnar stacks of $[Bi(phthalocyanine)_2]$ and linear chains of iodine atoms. A similar reaction between Bi_2Se_3 and 1,2-dicyanobenzene yielded the triple-decker $Bi_2(phthalocyanine)_3$.[115]

Triphenylbismuth undergoes complete ammonolysis with KNH_2 in liquid ammonia to yield the binary bismuth nitride BiN, which is explosive.[116] $Bi(NH_2)_3$ is believed to be an intermediate, though it was not detected in this reaction.

Similar to a number of other main group element complexes,[16] phosphines can complex to bismuth halides to form simple adducts such as $Bi_2Br_6(PMe_3)_4$, $Bi_2Br_6(dmpe)_2$, $Bi_4Br_{12}(PEt_3)_4$, and $Bi_2Br_6(PMe_2Ph)_2(OPMe_2Ph)_2$.[35,36,117] In the presence of added halide ions, complex anions such as $[PPh_4][BiI_4(PMe_2Ph)_2]$ containing an octahedral Bi center bonded to four iodide ions and two cis phosphine ligands can be obtained.[36]

2.7 Bismuth Complexes with Si, Ge, and Sn Based Ligands

$Bi(SiMe_3)_3$, a highly air and moisture sensitive colorless liquid, is prepared via the reaction of Me_3SiCl with M_3Bi ($M = $ alkali metal) in DME.[118] The Me_3Sn and Me_3Ge analogs have also been prepared.[119] Bismuth atoms react with SiF_3 radicals generated from Si_2F_6 to yield the volatile and unstable $Bi(SiF_3)_3$ in low yield.[120]

The silyl compound $Bi(SiMe_3)_3$ is cleaved to give $LiBi(SiMe_3)_2 \cdot DME$ upon reaction with lithium alkyls and subsequent reaction with 1,2-dibromoethane yields the tetrakis(trimethylsilyl)dibismuthine, $(Me_3Si)_2Bi–Bi(SiMe_3)_2$. Both $LiBi(SiMe_3)_2 \cdot DME$ and $(Me_3Si)_2Bi–Bi(SiMe_3)_2$ have been structurally characterized.[121] The chemistry of these compounds is related to that of a number of organobismuthine complexes. The structure of $LiBi(SiMe_3)_2 \cdot DME$ is composed of $-(-Bi–Li–)_n-$chains with a Li–Bi distance of 2.92(3) Å. The bismuth–silicon distance is 2.633(14) Å in $LiBi(SiMe_3)_2 \cdot DME$ and 2.683(av) Å in the dibismuthine. The Bi–Bi distance in the dibismuthine is 3.035(3) Å, in agreement with distances found for tetraphenyldibismuthine.

Triethylbismuthine reacts with $(C_6F_5)_3GeH$ and $(C_6F_5)_2GeH_2$ to give compounds containing Bi–Ge bonds.[122] These include $(C_6F_5)_3GeBiEt_2$, $[(C_6F_5)_3Ge]_2BiEt$, and the triply bridged compound $Bi_2\{\mu\text{-}Ge(C_6F_5)_2\}_3$ (**17**). The last compound reacts with $Pt(PPh_3)_3$, undergoing a platinum insertion into a Bi–Ge bond to give (**18**). The Bi–Ge bond distances in these compounds are on the order of 2.73 Å.

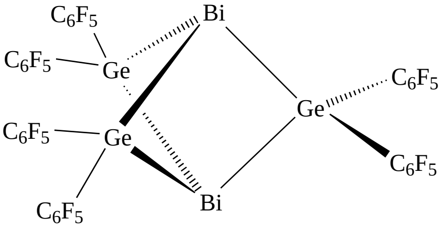

(**17**)

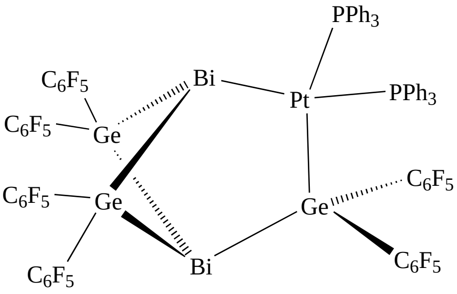

(**18**)

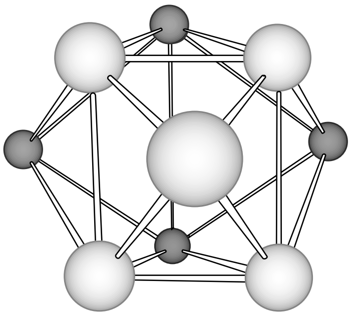

(**19**)

2.8 Bismuth Compounds with Metal–Metal Bonds

2.8.1 *Cationic ‘Naked’ Clusters of Bismuth: Reduced Bismuth Halide Phases*

Bismuth chloride reacts with elemental bismuth at elevated temperatures to give a subhalide phase which contains clusters of Bi atoms linked by halide bridges. The overall stoichiometry of this phase is $Bi_{24}Cl_{28}$ with a complicated structure best described as $[Bi_9{}^{5+}]_2[BiCl_5{}^{2-}]_4[Bi_2Cl_8{}^{2-}]$.[123] The $Bi_9{}^{5+}$ cluster has a tricapped trigonal prismatic geometry (**19**). The Bi–Bi distance within the triangular faces is 3.241(3) Å, while the distances from these atoms to the capping Bi atoms are shorter at 3.086(3) and 3.103(3) Å. The Bi–Bi distances between the two triangular faces is quite long at 3.737(4) Å and probably does not represent a direct bonding interaction. The $Bi_9{}^{5+}$ cluster has also been found, along with a rare example of Bi^+ ions, in $(Bi^+)\,(Bi_9{}^{5+})\,(HfCl_6{}^{2-})_3$.[124] These phases are generated by the reaction of Bi with $BiCl_3$ in the presence of Lewis acids such as $HfCl_4$.[125] Reactions involving $AlCl_3$ give $Bi_5[AlCl_4]_3$ with a trigonal bipyramidal cluster (**20**), or $Bi_8[AlCl_4]_2$ in which a square antiprismatic $Bi_8{}^{2+}$ has been found (**21**).[126] The average Bi–Bi distance in (**21**) is 3.100 Å. Reaction of Bi with AsF_5 in SO_2 also produces the $Bi_8{}^{2+}$ and $Bi_5{}^{3+}$ clusters with $AsF_6{}^-$ as the counterion.[127]

2.8.2 *Anionic ‘Naked’ Clusters of Bismuth: Zintl Ions*

Zintl reported early in this century that reactions of the heavier main group elements with Na or K in liquid ammonia

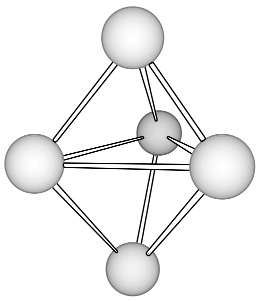

(**20**)

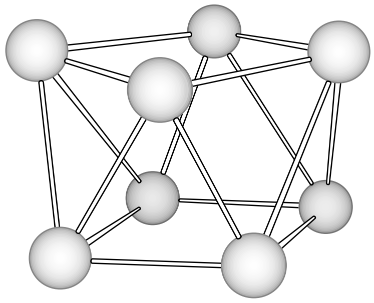

(**21**)

result in highly colored solutions of complex cluster ions (*see* ***Zintl Compounds***).[128] This reaction is general for many main group elements and the naked clusters which result have come to be known as Zintl ions. For bismuth, Zintl's work proposed clusters with compositions $[Bi_3]^{3-}$, $[Bi_5]^{3-}$, and $[Bi_9]^{3-}$, but these have not been structurally confirmed. Often these clusters revert to alloy phases when the solvent is removed, but, in an elegant series of experiments, Corbett has shown that in higher boiling amine solvents such as ethylenediamine the reversion to the alloy phase can be inhibited by the addition of an appropriate encapsulating ligand.[128] The ligand sequesters the alkali metal cation, preventing reversion to the alloy phase. Using this strategy, the planar, six π-electron cluster anion $[Bi_4]^{2-}$ (**22**) was crystallized.[129] The bismuth distances of 2.936(2) and 2.941(2) Å, which are shorter than other Bi–Bi distances, support the contention that there is significant Bi–Bi multiple bonding. The complicated alloy phase $Ca_{11}Bi_{10}$ also contains the $[Bi_4]^{2-}$ unit,[130] while the phases A_5Pn_4 ($A = K$, Rb or Cs; $Pn = As$, Sb, Bi) are reported to have isolated and flat zig-zag chains of the $Pn_4{}^{4-}$ ions with delocalized π-electrons.[131] The $Bi_2{}^{2-}$ ion exhibits a Bi–Bi bond distance of 2.8377(7) Å, consistent with a Bi–Bi double bond.[132] The $Bi_3{}^{3-}$ unit has been stabilized by metal-carbonyl fragments in the trigonal bipyramidal anions $[Bi_3M_2(CO)_6]^{3-}M = Cr$ or Mo (2).[133] The intermetallic ions $[Bi_2Sn_2]^{2-}$ (**23**), $[In_4Bi_5]^{3-}$, $[InBi_3]^{2-}$, and $[GaBi_3]^{2-}$ are also known.[134]

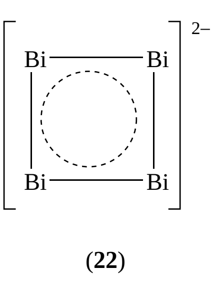

(**22**)

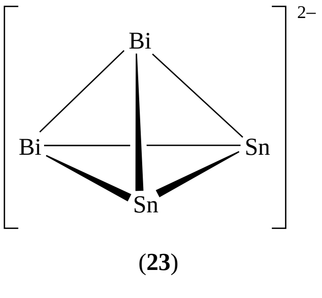

(**23**)

2.8.3 *Transition Metal–Bismuth Clusters*

Several reviews have appeared describing metal-carbonyl complexes incorporating bismuth and the other heavy main group elements (*see* ***Cluster Compounds: Inorganometallic Compounds Containing Transition Metal & Main Group Elements***).[135,136] Transition metal complexes which incorporate organobismuth functions are also described in (*see* ***Bismuth: Organometallic Chemistry***).

Bismuth readily forms bonds to many metals. The most direct route to transition metal–bismuth complexes is the reaction of metal-carbonyl anions with bismuth halides. The complexes $Bi\{Mn(CO)_5\}_3$, $Bi\{CpMo(CO)_3\}_3$, $Bi\{Fe(CO)_2Cp\}_3$, $Bi\{Co(CO)_4\}_3$, $Bi\{Ru(CO)_2Cp\}_3$, and $Bi\{Ni(CO)C_5Me_5\}_3$ (Scheme 2, (**24**)) are obtained by this method.[137–142] A heterometallic compound, $Bi\{Co(CO)_4\}_2\{Fe(CO)_2Cp\}$, is known.[34] Derivatives with one or two metal fragments, for example, $X_2Bi\{ML_n\}$ and $XBi\{ML_n\}_2$ [$X = Cl^-$, $NO_3{}^-$, SCN^-, $SeCN^-$; $ML_n = CpMo(CO)_3$, $CpW(CO)_3$, $(C_5H_4Me)Fe(CO)_2$, $CpRu(CO)_2$, $CpMn(CO)_2$, $(C_5Me_5)Ni(CO)$] have been prepared.[32,34,137,140,142,143] The Mo and W compounds are discrete but the Fe and Mn complexes are oligomeric, being based upon rings of alternating Bi and Cl atoms. The Fe compound is a cyclic trimer, while the Mn compound exists as a dimer. There appear to be similar Bi···X interactions in the solid state for $BrBi\{CpMo(CO)_3\}_2$ and $IBi\{CpMo(CO)_3\}_2$.[144] $ClBi\{MnCp(CO)_2\}_2$ is also interesting in that the Bi is formally in the +1 oxidation state and Mn–Bi multiple bonding is proposed.[145] This is supported by the very short Bi–Mn distances (2.469 Å av). $Bi\{C_5H_4MeM(CO)_3\}_3$ ($M = Mo$, W) convert to tetrahedral clusters $Bi_2M_2(CO)_4(C_5H_4Me)_2$ upon thermolysis in solution.[146] One compound with a bismuth–copper bond is known: $(Me_3Si)_2Bi–Cu(PMe_3)_3$.[147] Its formation is driven by removal of ${}^tBuOSiMe_3$ upon reaction of CuO^tBu with $Bi(SiMe_3)_3$.

Compounds with open framework structures may be induced to lose CO and form metal–metal bonds (**25**). At one time it was believed that the heavy main group elements would not allow the formation of closo configurations in combination with the first-row transition metals because of steric strain imposed by the size of the main group atom. This does not appear to be the case and a number of *closo* species have now been reported. $BiIr_3(CO)_9$ is prepared by addition of $[Ir(CO)_4]^-$ to $BiCl_3$, but the open dodecacarbonyl compound is not observed as an intermediate.[148] The structure is similar to that found for $BiCo_3(CO)_9$ except that it has no bridging CO ligands.[149,150] Compound (**25**) readily adds ligands such as phosphines, arsines, and stibines to give open $Bi\{Co(CO)_3L\}_3$ compounds.[139] $BiNi_3(CO)_3(C_5Me_5)_3$ has also been reported[142] In some cases, closed, tetrahedral compounds are obtained directly as in the reaction of $NaBiO_3$ with $Mo(CO)_6$ to give $[Et_4N]_2[BiMo_4(CO)_{12}(\mu_3\text{-}OMe)_3]$.[151] This interesting compound shows a bismuth atom capping a triangle of Mo atoms with an additional $Mo(CO)_3(OMe)_3{}^{3-}$ fragment bonded to the tetrahedral $BiMo_3{}^+$ unit. It is part of a family of complexes that may also have As or Sb in place of Bi.[152]

Metallated bismuth atoms function as Lewis acids, as exemplified by the addition of $[Co(CO)_4]^-$ to $Bi\{Co(CO)_4\}_3$ to form the hypervalent complex $[Bi\{Co(CO)_4\}_4]^-$ (**28**)

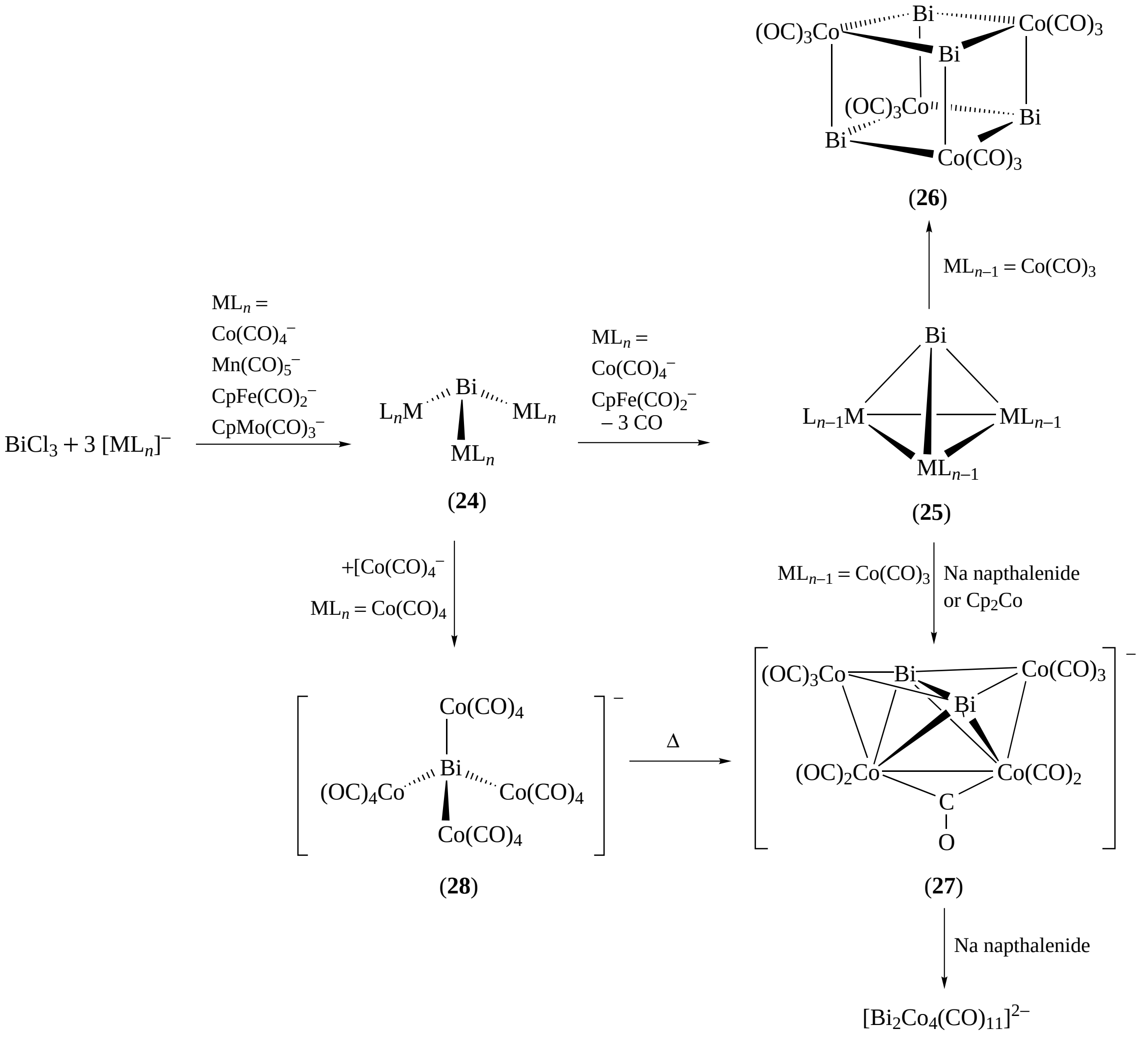

BiCl3 + 3 [MLn]−
MLn = Co(CO)4− Mn(CO)5− CpFe(CO)2− CpMo(CO)3−
LnM Bi MLn MLn
(24)
MLn = Co(CO)4− CpFe(CO)2− − 3 CO
Bi Ln−1M MLn−1 MLn−1
(25)
MLn−1 = Co(CO)3
(OC)3Co Bi Co(CO)3 Bi (OC)3Co Bi Bi Co(CO)3
(26)
+[Co(CO)4−
MLn = Co(CO)4
Co(CO)4 (OC)4Co Bi Co(CO)4 Co(CO)4
(28)
Δ
MLn−1 = Co(CO)3
Na napthalenide or Cp2Co
(OC)3Co Bi Co(CO)3 Bi (OC)2Co Co(CO)2 C O
(27)
Na napthalenide
[Bi2Co4(CO)11]2−

Scheme 2

(*see* ***Hypervalent Compounds***).[153] The Bi–Co distances in this molecule are very long (ca. 2.9 Å) and the lone pair is stereochemically inactive. The ability of the bismuth atom to act as an acceptor may be key in reactions of clusters with nucleophiles. The bismuth centers in these molecules can also act as Lewis acids toward halide ions or other donor ligands as exemplified by the formation of $[Cl_2Bi\{Fe(CO)_2Cp\}_2]^-$, $\{[OP(NMe_2)_3\}_2Bi\{Fe(CO)_2Cp\}_2]^+$, $[Fe(CO)_4Bi_2Cl_4(\mu\text{-}Cl)_2]^{2-}$, $[Bi_3Cl_4(\mu\text{-}Cl)_4\{Fe(CO)_3\}]^{3-}$, and $[(\mu\text{-}H)Fe_2(CO)_6Bi_2\{(\mu\text{-}Cl)_2\}^-\,]_n$.[154,155]

The cubane cluster $Bi_4Co_4(CO)_{12}$ (**26**) is a thermodynamic sink in a number of reactions of the other Bi–Co carbonyl compounds.[149] It does not appear to be stable to substitution or to reduction, but detailed chemistry of this compound has not been reported.

Electrochemical reduction of $BiCo_3(CO)_9$ (**25**) or pyrolysis of (**28**) produces the unusual cluster compound $[Bi_2Co_4(CO)_{11}]^-$ (**27**) (Scheme 2).[156] This compound is reduced to a dianion that is believed to have essentially the same structure as (**27**) based upon the structures of $[Sb_2Co_4(CO)_{11}]^{n-}$ ($n = 1$ or 2) which have both been reported.[157] For that redox pair the major change upon reduction is lengthening of the CO-bridged Co–Co bond by about 0.135 Å. The bismuth compounds are more sensitive to oxidation and fragmentation than are the antimony analogs.

$NaBiO_3$ may also be used to introduce Bi atoms into metal clusters, as has been demonstrated in the case of iron (Scheme 3), osmium, ruthenium, chromium, and molybdenum carbonyls. This reaction works best for $Fe(CO)_5$ in methanolic KOH, where $[Bi\{Fe(CO)_4\}_4]^{3-}$ (**29**) is produced cleanly and in high yield.[158] Similarly, reaction of $Cr(CO)_6$ with $NaBiO_3$ at room temperature in methanol leads to $[Bi\{Cr(CO)_5\}_4]^{3-}$ or to $[MeBi\{Cr(CO)_5\}_3]^{2-}$ at 80 °C.[159] If the $NaBiO_3/Fe(CO)_5$ reaction is carried out with heating in the absence of KOH, the cluster product is $[BiFe_3(CO)_{10}]^-$ (**35**).[160] Alkylation of (**35**) occurs at the μ_3-CO rather than at Bi, giving (**36**), illustrating the low basicity of the main group atom.[161] Compound (**31**) is the starting point for a wide number

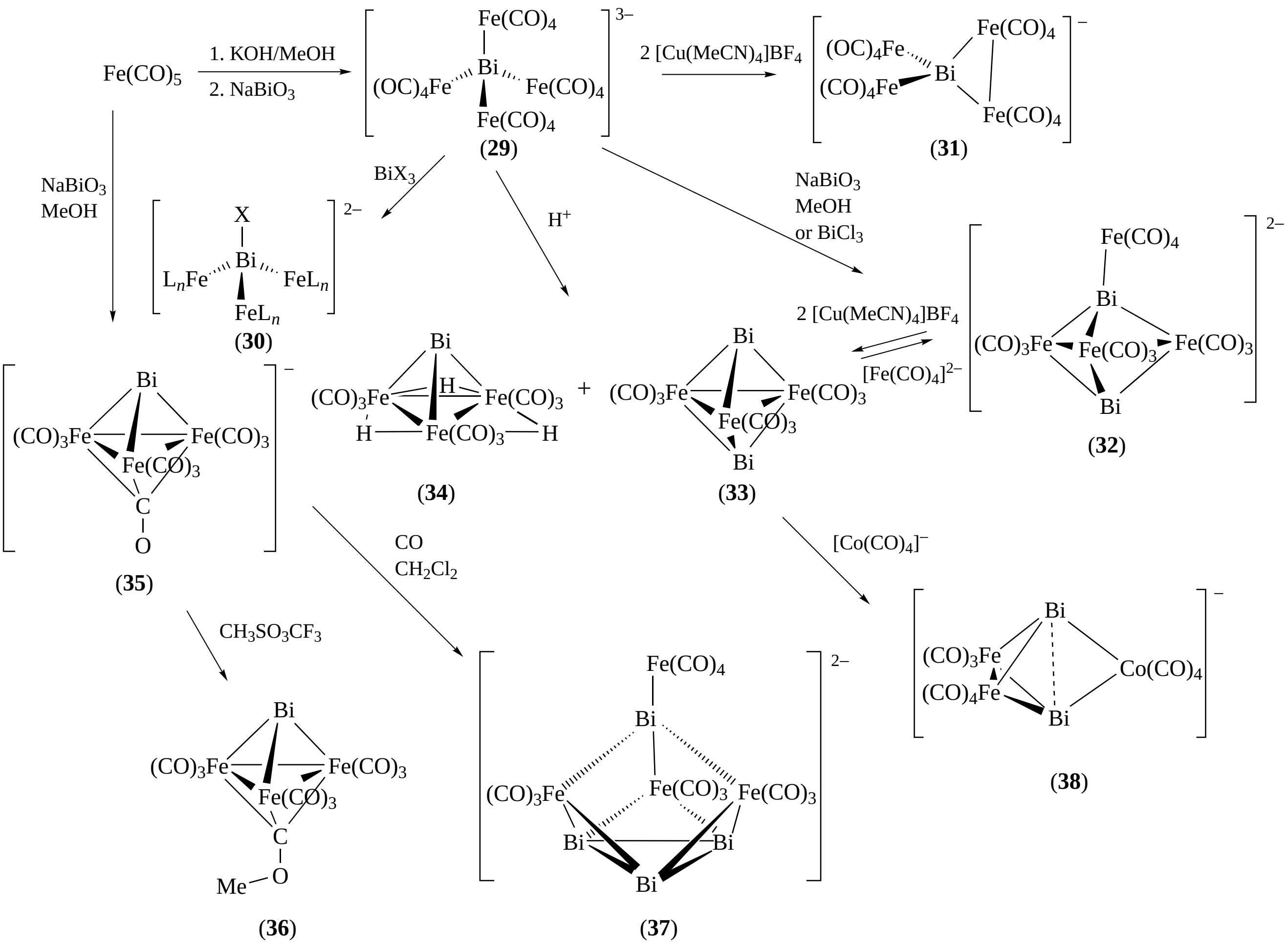

Scheme 3

of Bi–Fe carbonyl complexes. Addition of $BiCl_3$ to (**31**) results in the formation of $[XBi\{Fe(CO)_4\}_3]^{2-}$ (**30**), which appears to be a simple substitution of X^- for $[Fe(CO)_4]^{2-}$, but this exchange does not occur with $[Et_4N]X$ and probably is initiated by initial oxidation of (**31**). The structurally related $[RBi\{Fe(CO)_4\}_3]^{2-}$ ($R = Bu$, $PhCH_2$) are obtained when $[Bi\{Fe(CO)_4\}_4]^{3-}$ is treated with the organic halides, although cyclic $[RBiFe(CO)_4]_2$ compounds may also be obtained.[162] The latter complexes show Bi_2Fe_2 ring structures, but the $R = $ butyl compound has also been crystallized in a polymeric form.[163] Reaction of (**32**) generated in situ with $Cr(CO)_5(THF)$ produces the mixed-metal compound $[Bi\{Fe_2(CO)_8\}\{Fe(CO)_4\}\{Cr(CO)_5\}]^-$. Compound (**31**) is protonated to yield a mixture of $Bi_2Fe_3(CO)_9$ (**35**) and $H_3BiFe_3(CO)_9$ (**34**). The first can be viewed as arising via an oxidation of (**31**), while the second as a protonation reaction with subsequent loss of CO and a metal fragment. Compound (**29**) is also oxidized by $[Cu(NCMe)_4]BF_4$ to give a monoanion with an Fe–Fe bond (**31**). This compound is unstable and decomposes to $[Bi_4Fe_4(CO)_{13}]^{2-}$ (**37**) upon standing in solution.[164,165] This product is a very interesting compound based upon a tetrahedral array of Bi atoms with $Fe(CO)_3$ groups capping three of the triangular faces (it is discussed further below). Compound (**29**) will react further with $NaBiO_3$ to form $[Bi_2Fe_4(CO)_{13}]^{2-}$ (**32**),[166] which is based upon a square pyramidal Bi_2Fe_3 arrangement of metal atoms. Compound (**32**) also arises when $[Fe(CO)_4]^{2-}$ adds to (**33**). This can be viewed as formally adding two electrons to the Bi_2Fe_3 cluster core, giving rise to Fe–Fe bond cleavage as predicted from simply electron counting considerations. Oxidation of (**32**) regenerates (**33**). A series of compounds of the general form $[\{Fe_3(CO)_9EML_n\}_2]$ have been examined and the structural parameters associated with the main group atom can be interpreted in terms of the hybridization at that atom.[167] The compound $Fe_3(CO)_9[BiFe(CO)_2\{Fe(CO)_2C_5H_3{}^tBu_2\}_2]$, another square pyramidal cluster, is obtained when $\{(CO)_2C_5H_3{}^tBu_2\}(CO)_2FeBiCl_2$ is treated with $[Fe(CO)_4]^{2-}$,[34] and the isoelectronic asymmetric species $Fe_3(CO)_9\{SeBiFe(CO)_2C_5H_4{}^tBu\}$ is formed when $[Fe_3(CO)_9Se_2]^{2-}$ is treated with $(C_5H_4{}^tBu)Fe(CO)_2BiCl_2$.[168] Addition of $[Co(CO)_4]^-$ to (**33**) leads instead to vertex replacement and the formation of $[Fe_2(CO)_6Bi_2(\mu\text{-}Co(CO))_4]^-$ (**38**).[169]

This molecule as well as the $[(\mu\text{-H})Fe_2(CO)_6Bi_2\{\mu\text{-Fe(CO)}_4\}]^-$ and $[Fe_2(CO)_6\{BiMo(CO)_3(C_5H_3{}^tBu_2)\}_2\{\mu\text{-Fe(CO)}_4\}]^-$ have tetrahedral Bi_2Fe_2 cores with the Bi–Bi vector bridged by the third transition metal fragment.[155] There appears to be a substantial bonding interaction between the bismuth atoms even though none would be predicted by normal electron counting formalisms. Main group element-main group element bonding of this sort is a hallmark of clusters molecules in this class.[170] Interestingly, when $[W_2(CO)_{10}]^{2-}$ is treated with $(C_5H_4{}^tBu)Fe(CO)_2BiCl_2$ another edge-bridged tetrahedral cluster is obtained. It has the formula $Bi_2W_2(CO)_8\{\mu\text{-BiFe(CO)}_2(C_5H_4{}^tBu)\}$. It is also based upon a M_2Bi_2 tetrahedron, but in this case it is the M–M bond that is bridged.[34]

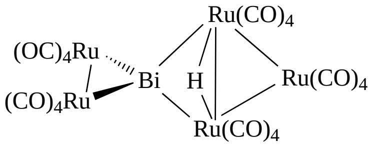

(**39**)

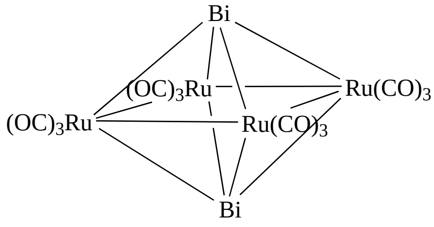

(**40**)

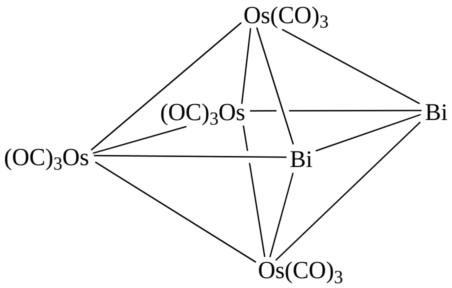

(**41**)

Some analogous ruthenium- and osmium-bismuth clusters have been found.[171] Examples include $Bi_2M_3(CO)_9$ and $H_3BiM_3(CO)_9$ (M = Ru, Os). The structures of the hydride compounds have both been determined and they are isostructural with the iron complexes as is $Bi_2Ru_3(CO)_9$ with $Bi_2Fe_3(CO)_9$. The structure of $Bi_2Os_3(CO)_9$, on the other hand, has not been determined and its IR spectrum indicates that it probably has a different structure. A spirocyclic cluster $[Ru_2(CO)_8(\mu_4\text{-Bi})Ru_3(CO)_{10}(\mu\text{-H})]$ (**39**) has been reported.

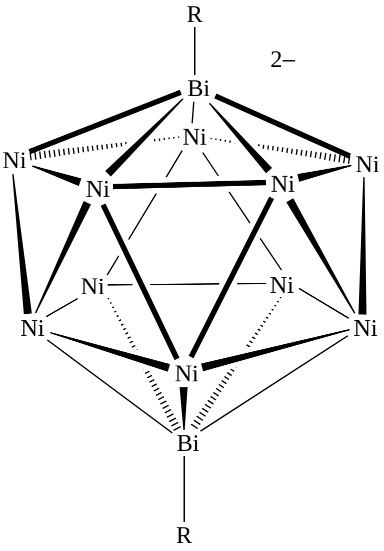

(**42**)

Of particular interest is the observation of different isomers for $Bi_2Ru_4(CO)_{12}$ (**40**) and $Bi_2Os_4(CO)_{12}$ (**41**).

Antimony–iron carbonyl clusters show similarities to the bismuth–iron compounds as well.[172] A key difference between the antimony- and bismuth-containing complexes is that the bismuth atom is generally less basic and more Lewis acidic than the antimony atoms in corresponding compounds. Reaction of $[Ni_6(CO)_{12}]^{2-}$ (1) with $RBiCl_2$ gave icosahedral $[Ni_{10}(CO)_{18}(BiR)_2]^{2-}$ (R = Me, Et; (**42**)) as the major product. These molecules possess noncentered 1,12-$Ni_{10}Bi_2$ icosahedral cages as do the other members of the homologous series $[Ni_{10}(CO)_{18}(EMe)_2]^{2-}$ (E = P, As, Sb).[173] Metal-centered versions of these cluster geometries are also known from the reaction of $BiCl_3$ with $[Ni_6(CO)_{12}]^{2-}$ (equation 2, (**43**)).[174]

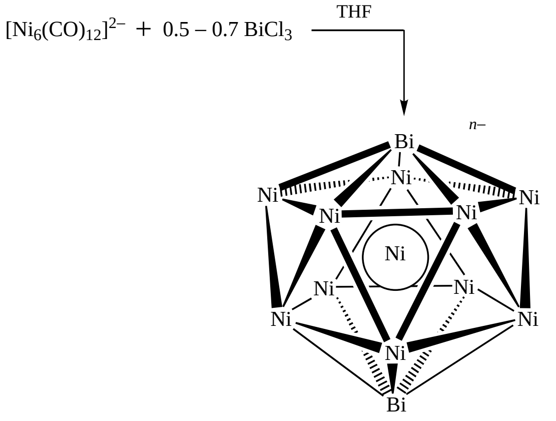

(**43**)

Cluster core structure of $[Bi_2Ni_{10}(\mu_{12}\text{-Ni})(CO)_{18}]^{n-}$

(2)

The reaction of $[W_2(CO)_{10}]^{2-}$ with $BiCl_3$ gives rise to a neutral compound $Bi_2\{\mu\text{-W(CO)}_5\}_3$ (**44**), in which the Bi–Bi

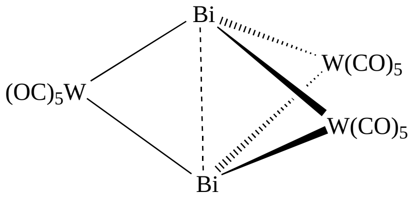

(**44**)

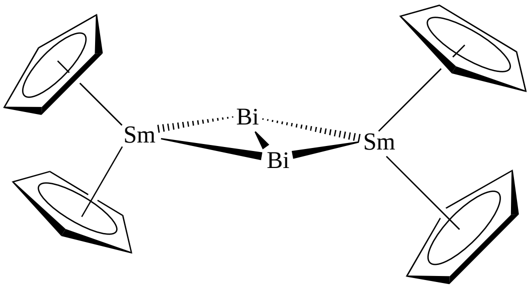

(**45**)

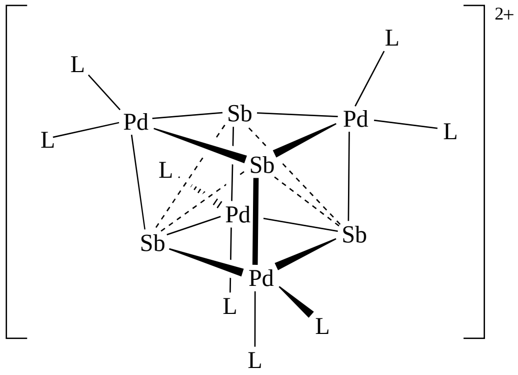

(**46**)

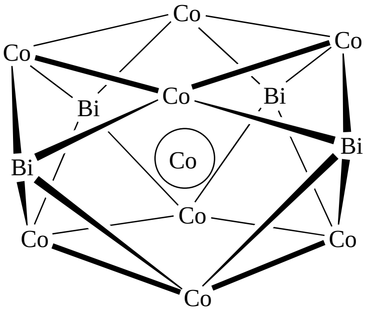

Cluster core structure of $[Bi_4Co_9(CO)_{16}]^{2-}$

(**47**)

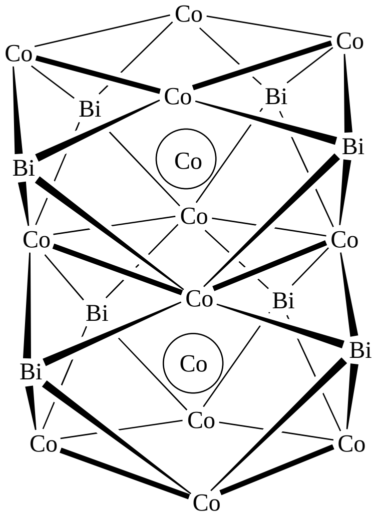

Cluster core structure of $[Bi_8Co_{14}(CO)_{20}]^2$

(**48**)

distance is very short (2.8183(3) Å).[136,175] The molecule is proposed to be based on a Bi–Bi triple-bonded fragment. Reaction of $Me_3SiCH_2BiCl_2$ with $[W(CO)_5]^{2-}$ yields this compound as well as $[Bi_2W_2(CO)_8(\mu\text{-}BiMeW(CO)_5)]$.[176]

Only one early transition metal complex has been reported. That compound is $[(Me_5C_5)_2SmBi_2Sm(C_5Me_5)_2]$ (**45**), which arises from the reaction of $Sm(C_5Me_5)_2$ with $BiPh_3$. The compound is unique in that it contains a planar Sm_2Bi_2 core in which there is a Bi–Bi bond of 2.851(1) Å, a value substantially shorter than most observed Bi–Bi single bonds.[177] Similarly the late transition metal complex PdL_4 ($L = Ph_2Me$), which is known to lose phosphine ligands readily, reacts with Ph_2BiBr to give the cationic cluster $[Bi_4Pd_4L_8]^{2+}$ (**46**) with $Ph_2BiBr_2{}^-$ as the counterion.[178] That reaction proceeds presumably by initial oxidative addition of the Bi–Br bond to the Pd^0 center.

Electron counting rules have been developed to explain the observed geometries of many cluster compounds (*see* ***Electronic Structure of Clusters***). Interesting, heavy main group element-transition metal complexes tend to violate these rules. In simple cluster compounds the bismuth atom will function as a three-electron donor to the skeletal electron count. The bismuth atom retains a lone pair of electrons which, except in the more negatively charged compounds, is not used for further bonding. This is in contrast to antimony-containing cluster compounds where the lone pair is usually donated to some appended metal fragment. But higher nuclearity compounds begin to exhibit unusual electron counts. Bismuth–transition metal clusters which do not obey the simple electron counting rules include $[Bi_4Fe_4(CO)_{13}]^{2-}$ (**37**) (Scheme 3), $[Bi_4\{Fe(CO)_3\}_3\{Fe(CO)_2(C_5H_3{}^tBu_2)\}_2]^{2-}$, and $[Bi_2Co_4(CO)_{11}]^{x-}$ ($x = 1$ or 2) (**27**) (Scheme 2).[34,157,164] These clusters are formally electron-rich and molecular orbital calculations show that the interaction of the bismuth atoms and the transition metals gives rise to additional nonbonding orbitals which can accommodate extra electrons. Both of these compounds show direct Bi–Bi bonding. These compounds can be viewed as Zintl ions being stabilized by coordinated metal fragments, and so direct reaction of Zintl ions with metal fragments would be expected to lead to interesting products. Thus, when the Zintl phase K_5Bi_4 is treated with 4,7,13,16,21,24-hexaoxa-1,10-diazabicylco[8.8.8]hexacosane (crypt) and $Cr(CO)_3$(mesitylene) or $Mo(CO)_3$(cycloheptatriene), the trigonal bipyramidal $[Bi_3M_2(CO)_6]^{3-}$ (M = Cr, Mo) complexes are formed.[133] The two transition metal atoms are located in equatorial positions, leading to the analysis of the bismuth fragment as a bent $Bi_3{}^{3-}$, which is isoelectronic and isostructural with ozone. Further exceptions to the cluster-electron counting rules are $[Bi_4Co_9(CO)_{16}]^{2-}$ (**47**) and $[Bi_8Co_{14}(CO)_{20}]^{2-}$ (**48**), which arise upon oxidation of the reaction product of $[Bi_2Co_4(CO)_{11}]^{-}$ and $Mo(CO)_3$(toluene). These compounds are based upon close-packing of metal atoms and do not have closed-shell electronic configurations.[179]

3 RELATED ARTICLES

Antimony: Inorganic Chemistry; Arsenic: Inorganic Chemistry; Bismuth: Organometallic Chemistry; Cluster Compounds: Inorganometallic Compounds Containing Transition Metal & Main Group Elements; Indium: Inorganic Chemistry; Phosphorus: Inorganic Chemistry; Zintl Compounds.

4 REFERENCES

1. R. J. Meyer and E. H. E. Pietsch, ‘‘‘Bismuth,’’ Gmelins Handbuch der Anorganischen Chemie, A. Kotowski’, Verlag Chemie, Weinheim, 1964.
2. J. D. Smith, Arsenic, Antimony and Bismuth, in ‘Comprehensive Inorganic Chemistry’, eds. J. C. J. Bailar, H. J. Emeleus, R. Nyholm, and A. F. Trotman-Dickenson, Pergamon Press, Oxford, 1973, p. 547.
3. A. F. Wells, ‘Structural Inorganic Chemistry’, Clarendon, Oxford, 1984.
4. (a) A. L. Prieto, M. Martin-Gonzalez, J. Keyani, R. Gronsky, T. Sands, and A. M. Stacy, *J. Am. Chem. Soc.*, 2003, **125**, 2388; (b) M. Martin-Gonzalez, A. L. Prieto, M. S. Knox, R. Gronsky, T. Sands, and A. M. Stacy, *Chem. Mater.*, 2003, **15**, 1676.
5. B. T. Matthias, A. Jayaraman, T. H. Geballe, K. Andres, and E. Corenzwit, *Phys. Rev. Lett.*, 1966, **17**, 640.
6. (a) K. Yoshida, T. Yamada, and Y. Taniguchi, *Acta Crystallogr.*, 1989, **B45**, 40; (b) J. B. Yang, W. B. Yelon, W. J. James, Q. Cai, M. Kornecki, S. Roy, N. Ali, and P. L’Heritier, *J. Phys.: Condens. Matter*, 2002, **14**, 6509; (c) J. B. Yang, K. Kamaraju, W. B. Yelon, W. J. James, Q. Cai, and A. Bollero, *Appl. Phys. Lett.*, 2001, **79**, 1846.
7. (a) C. H. Chen and A. A. Gewirth, *J. Am. Chem. Soc.*, 1992, **114**, 5439; (b) C. H. Chen, K. D. Kepler, A. A. Gewirth, B. M. Ocko, and J. Wang, *J. Phys. Chem.*, 1993, **97**, 7290; (c) X. Li and A. A. Gewirth, *J. Am. Chem. Soc.*, 2003, **125**, 7086; (d) B. K. Niece and A. A. Gewirth, *Langmuir*, 1996, **12**, 4909; (e) I. Oh, M. E. Biggin, and A. A. Gewirth, *Langmuir*, 2000, **16**, 1397.
8. S. Bobev and S. C. Sevov, *J. Sol. St. Chem.*, 2002, **163**, 436.
9. R. Kubiak, *Z. Anorg. Allg. Chem.*, 1977, **431**, 261.
10. (a) C. J. Carmalt, A. H. Cowley, A. L. Hector, N. C. Norman, and I. P. Parkin, *J. Chem. Soc., Chem. Commun.*, 1994, 1987; (b) G. C. Allen, C. J. Carmalt, A. H. Cowley, A. L. Hector, S. Kamepalli, Y. G. Lawson, N. C. Norman, I. P. Parkin, and L. K. Pickard, *Chem. Mater.*, 1997, **9**, 1385.
11. E. Amberger, *Chem. Ber.*, 1961, **94**, 1447.
12. W. Jerzembeck, H. Burger, L. Constantin, L. Margules, J. Demaison, J. Breidung, and W. Thiel, *Angew. Chem., Int. Ed. Engl.*, 2002, **41**, 2550.
13. (a) R. W. Zoellner, *Chemtracts*, 2002, **15**, 637; (b) E. J. Baran, *Z. Naturforsch.*, 2003, **58A**, 126; (c) X. Wang, P. F. Souter, and L. Andrews, *J. Phys. Chem. (A)*, 2003, **107**, 4244; (d) S. S. Gomez, R. H. Romero, and G. A. Aucar, *J. Chem. Phys.*, 2002, **117**, 7942; (e) W. W. Schoeller and R. Schneider, *Chem. Ber.*, 1997, **130**, 1013; (f) J. Breidung and W. Thiel, *J. Mol. Spectrosc.*, 1995, **169**, 166.
14. N. J. Hardman, B. Twamley, and P. P. Power, *Angew. Chem., Int. Ed. Engl.*, 2000, **39**, 2771.
15. (a) G. G. Briand and N. Burford, *Adv. Inorg. Chem.*, 2000, **50**, 285; (b) N. C. Norman, *Phosphorus, Sulfur Silicon Relat. Elem.*, 1994, **87**, 167.
16. N. C. Norman and N. L. Pickett, *Coord. Chem. Rev.*, 1995, **145**, 27.
17. (a) T. Probst, O. Steigelmann, J. Riede, and H. Schmidbaur, *Chem. Ber.*, 1991, **124**, 1089; (b) A. Schier, J. M. Wallis, G. Moeller, and H. Schmidbaur, *Angew. Chem.*, 1986, **98**, 742; (c) H. Schmidbaur, J. M. Wallis, R. Nowak, B. Huber, and G. Mueller, *Chem. Ber.*, 1987, **120**, 1837; (d) H. Schmidbaur, R. Nowak, A. Schier, J. M. Wallis, B. Huber, and G. Mueller, *Chem. Ber.*, 1987, **120**, 1829.
18. W. Frank, J. Weber, and E. Fuchs, *Angew. Chem.*, 1987, **99**, 68.
19. C. M. Jones, M. D. Burkart, R. E. Bachman, D. L. Serra, S. J. Hwu, and K. H. Whitmire, *Inorg. Chem.*, 1993, **32**, 5136.
20. K. H. Whitmire, S. Hoppe, O. Sydora, J. L. Jolas, and C. M. Jones, *Inorg. Chem.*, 2000, **39**, 85.
21. C. M. Jones, M. D. Burkart, and K. H. Whitmire, *Angew. Chem., Int. Ed. Engl.*, 1992, **31**(4), 451.
22. J. R. Eveland and K. H. Whitmire, *Inorg. Chim. Acta*, 1996, **249**, 41.
23. C. J. Carmalt, W. Clegg, M. R. J. Elsegood, R. J. Errington, J. Havelock, P. Lightfoot, N. C. Norman, and A. J. Scott, *Inorg. Chem.*, 1996, **35**, 3709.
24. M. Schaefer, G. Frenzen, B. Neumueller, and K. Dehnicke, *Angew. Chem.*, 1992, **104**, 354; (See also *Angew. Chem., Int. Ed. Engl.*, 1992, **31**(3), 334).

25. (a) N. W. Alcock, M. Ravindran, and G. R. Willey, *J. Chem. Soc., Chem. Commun.*, 1989, 1063; (b) N. W. Alcock, M. Ravindran, and G. R. Willey, *Acta Crystallogr.*, 1993, **B49**, 507; (c) R. Garbe, B. Vollmer, B. Neumueller, J. Pebler, and K. Dehnicke, *Z. Anorg. Allg. Chem.*, 1993, **619**, 271.

26. (a) W. Clegg, L. J. Farrugia, A. McCamley, N. C. Norman, A. G. Orpen, N. L. Pickett, and S. E. Stratford, *J. Chem. Soc., Dalton Trans.*, 1993, 2579; (b) L. J. Farrugia, N. C. Norman, and N. L. Pickett, *Acta Crystallogr.*, 1998, **C54**, 476.

27. R. Bougon, P. Charpin, K. O. Christe, J. Isabey, M. Lance, M. Nierlich, J. Vigner, and W. W. Wilson, *Inorg. Chem.*, 1988, **27**, 1389.

28. (a) C. Hebecker, *Z. Anorg. Allg. Chem.*, 1970, **376**, 236; (b) C. Hebecker, *Z. Anorg. Allg. Chem.*, 1971, **384**, 12.

29. R. J. Gillespie, D. Martin, G. J. Schrobilgen, and D. R. Slim, *J. Chem. Soc., Dalton Trans.*, 1977, 2234.

30. (a) A. L. Rheingold, A. D. Uhler, and A. G. Landers, *Inorg. Chem.*, 1983, **22**, 3255; (b) A. G. Landers, M. W. Lynch, S. B. Raaberg, A. L. Rheingold, J. E. Lewis, N. J. Mammano, and A. Zalkin, *J. Chem. Soc., Chem. Commun.*, 1976, 931; (c) W. G. McPherson and E. A. Meyers, *J. Phys. Chem.*, 1968, **72**, 3117; (d) B. K. Robertson, W. G. McPherson, and E. A. Meyers, *J. Phys. Chem.*, 1967, **71**, 3531; (e) W. G. McPherson and E. A. Meyers, *J. Phys. Chem.*, 1968, **72**, 532; (f) C. J. Carmalt, L. J. Farrugia, and N. C. Norman, *Z. Anorg. Allg. Chem.*, 1995, **621**, 47; (g) F. Benetollo, G. Bombieri, G. Alonzo, N. Bertazzi, and G. A. Casella, *J. Chem. Crystallogr.*, 1998, **28**, 791; (h) L. J. Farrugia, C. J. Carmalt, and N. C. Norman, *Inorg. Chim. Acta*, 1996, **248**, 263; (i) G. Alonzo, F. Benetollo, N. Bertazzi, and G. Bombieri, *J. Chem. Crystallogr.*, 1999, **29**, 913; (j) R. N. Singh and D. K. Padma, *J. Fluorine Chem.*, 1995, **73**, 147.

31. C. J. Carmalt, L. J. Farrugia, and N. C. Norman, *Z. Naturforsch.*, 1995, **50B**, 1591.

32. A. Crispini, R. J. Errington, G. A. Fisher, F. J. Funke, N. C. Norman, A. G. Orpen, S. E. Stratford, and O. Struve, *J. Chem. Soc., Dalton Trans.*, 1994, 1327.

33. (a) S. C. James, N. C. Norman, and A. G. Orpen, *J. Chem. Soc., Dalton Trans.*, 1999, 2837; (b) S. C. James, Y. G. Lawson, N. C. Norman, A. G. Orpen, and M. J. Quayle, *Acta Crystallogr.*, 2000, **C56**, 427; (c) H. J. Breunig, M. Denker, R. E. Schulz, and E. Lork, *Z. Anorg. Allg. Chem.*, 1998, **624**, 81.

34. T. Gröer and M. Scheer, *Organometallics*, 2000, **19**, 3683.

35. W. Clegg, M. R. J. Elsegood, V. Graham, N. C. Norman, N. L. Pickett, and K. Tavakkoli, *J. Chem. Soc., Dalton Trans.*, 1994, 1743.

36. W. Clegg, M. R. J. Elsegood, N. C. Norman, and N. L. Pickett, *J. Chem. Soc., Dalton Trans.*, 1994, 1753.

37. P. Hodge, S. C. James, N. C. Norman, and A. G. Orpen, *J. Chem. Soc., Dalton Trans.*, 1998, 4049.

38. (a) D. L. Nelson, M. S. Whittingham and T. F. George eds, 'Chemistry of High Temperature Superconductors', ACS Symposium Series, American Chemical Society, Washington, DC, 1987; (b) D. L. Nelson and T. F. George, 'Chemistry of High Temperature Superconductors II', ACS Symposium Series, American Chemical Society, Washington, DC, 1988; (c) J. Lynn, eds, ''High Temperature Superconductivity'', Springer Verlag, New York, 1990; (d) K. Matsumura, H. Nobumasa, K. Shimizu, T. Arima, Y. Kitano, M. Tanaka, and K. Sushida, *Jap. J. Appl. Phys. Part 2*, 1989, **28**, L1797; (e) T. Nonaka, K. Kaneko, T. Hasegawa, K. Kishio, Y. Takahashi, K. Kobayashi, K. Kitazawa, and K. Fueki, *Jap. J. Appl. Phys. Part 2*, 1988, **27**, L867; (f) N. Tohge, M. Tatsumisago, and T. Minami, *J. Non-Cryst. Solids*, 1990, **121**, 443; (g) H. Yamane, H. Kurosawa, and T. Hirai, *Chem. Lett.*, 1988, 1515; (h) S. Hirano, T. Hayashi, M. Miura, and H. Tomonaga, *Bull. Chem. Soc. Jpn.*, 1989, **62**, 888; (i) T. Nonaka, M. Green, K. Kishio, T. Hasegawa, K. Kitazawa, K. Kaneko, and K. Kobayashi, *Physica C*, 1989, **160**, 517; (j) K. H. Whitmire, *Chemtracts, Inorg. Chem.*, 1995, **7**, 167; (k) K. G. Caulton and L. G. Hubert-Pfalzgraf, *Chem. Rev.*, 1990, **90**, 969; (l) R. Mehrotra, *Proc. Natl. Acad. Sci. India, Sect. (A)*, 1995, **61**, 253; (m) L. G. Hubert-Pfalzgraf, *Inorg. Chem. Commun.*, 2003, **6**, 102; (n) L. G. Hubert-Pfalzgraf, *Phosphorus, Sulfur Silicon Relat. Elem.*, 2001, **168–169**, 69.

39. R. C. Mehrotra and A. K. Rai, *Ind. J. Chem.*, 1966, **4**, 537.

40. (a) W. J. Evans, J. H. Hain Jr, and J. W. Ziller, *Chem. Commun.*, 1989, 1628; (b) A. Haaland, H. P. Verne, H. V. Volden, R. Papiernik, and L. G. Hubert-Pfalzgraf, *Acta. Chem. Scand.*, 1993, **47**, 1043.

41. G. Gattow and R. Lingenfelder, *Z. Anorg. Allg. Chem.*, 1979, **448**, 115.

42. (a) M. C. Massiani, R. Papiernik, L. G. Hubert-Pfalzgraf, and J. C. Daran, *Polyhedron*, 1991, **10**, 437; (b) M. C. Massiani, R. Papiernik, L. G. Hubert-Pfalzgraf, and J. C. Daran, *J. Chem. Soc., Chem. Commun.*, 1990, 301.

43. K. W. Terry, K. Su, T. D. Tilley, and A. L. Rheingold, *Polyhedron*, 1998, **17**, 891.

44. T. A. Hanna, G. Keitany, C. Ibarra, R. D. Sommer, and A. L. Rheingold, *Polyhedron*, 2001, **20**, 2451.

45. R. D. Rogers, A. H. Bond, and S. Aguinaga, *J. Am. Chem. Soc.*, 1992, **114**, 2960.

46. W. T. Miller, *J. Am. Chem. Soc.*, 1940, **62**, 2707.

47. R. E. Bachman, K. H. Whitmire, J. H. Thurston, A. Gulea, O. Stavila, and V. Stavila, *Inorg. Chim. Acta*, 2003, **346**, 249.

48. M. A. Matchett, M. Y. Chiang, and W. E. Buhro, *Inorg. Chem.*, 1990, **29**, 358.

49. W. A. Herrmann, N. W. Huber, R. Anwander, and T. Priermeier, *Chem. Ber.*, 1993, **126**, 1127.

50. G. Calingaert, H. Soroos, and V. Hnizda, *J. Am. Chem. Soc.*, 1942, **64**, 392.

51. M. Wieber and U. Baudis, *Z. Anorg. Allg. Chem.*, 1978, **439**, 139.

52. H. Schmidbaur and M. Bergfeld, *Z. Anorg. Allg. Chem.*, 1968, **363**, 84.
53. K. H. Whitmire, J. C. Hutchison, A. L. McKnight, and C. M. Jones, *J. Chem. Soc., Chem. Commun.*, 1992, 1021.
54. J. L. Jolas, S. Hoppe, and K. H. Whitmire, *Inorg. Chem.*, 1997, **36**, 3335.
55. S. C. James, N. C. Norman, A. G. Orpen, M. J. Quayle, and U. Weckenmann, *J. Chem. Soc., Dalton Trans.*, 1996, 4159.
56. (a) M. K. Sharma, M. Sharma, A. Singh, and R. C. Mehrotra, *Ind. J. Chem.*, 2001, **40A**, 1226; (b) M. Hunger, C. Limberg, and P. Kircher, *Angew. Chem. Int. Ed. Engl.*, 1999, **38**, 1105; (c) M. Hunger, C. Limberg, and P. Kircher, *Organometallics*, 2000, **19**, 1044.
57. E. M. Campi, G. B. Deacon, G. L. Edwards, M. D. Fitzroy, N. Giunta, W. R. Jackson, and R. Trainor, *J. Chem. Soc., Chem. Commun.*, 1989, 407.
58. G. Gattow and K. Sarter, *Z. Anorg. Allg. Chem.*, 1980, **463**, 163.
59. P. V. Radheshwar, R. Dev, and G. H. Cady, *J. Inorg. Nucl. Chem.*, 1972, **34**, 3913.
60. G. J. Reiss, W. Frank, and J. Schneider, *Main Group Met. Chem.*, 1995, **18**, 287.
61. W. Frank, V. Reiland, and G. J. Reiss, *Angew. Chem., Int. Ed. Engl.*, 1998, **37**, 2984.
62. (a) J. H. Thurston and K. H. Whitmire, *Inorg. Chem.*, 2002, **41**, 4194; (b) J. H. Thurston and K. H. Whitmire, *Inorg. Chem.*, 2003, **42**, 2014.
63. P. J. Sadler and Z. Guo, *Pure Appl. Chem.*, 1998, **70**, 863.
64. (a) H. Sun, H. Li, and P. J. Sadler, *Chem. Ber.*, 1997, **130**, 669; (b) Z. Guo and P. J. Sadler, *Adv. Inorg. Chem.*, 2000, **49**, 183.
65. (a) P. J. Sadler, Congreso Iberoamericano de Quimica Inorganica, 6th, Puebla, April 20–25, 1997, 487; (b) S. J. Berners-Price and P. J. Sadler, *Coord. Chem. Rev.*, 1996, **151**, 1.
66. (a) H. Sun and P. J. Sadler, *Top. Biol. Inorg. Chem.*, 1999, **2**, 159; (b) G. G. Briand and N. Burford, *Chem. Rev.*, 1999, **99**, 2601; (c) P. J. Sadler, H. Li, and H. Sun, *Coord. Chem. Rev.*, 1999, **185–186**, 689; (d) G. S. Sandha, R. LeBlanc, S. J. O. V. Van Zanten, T. D. Sitland, L. Agocs, N. Burford, L. Best, D. Mahoney, P. Hoffman, and D. J. Leddin, *Dig. Dis. Sci.*, 1998, **43**, 2727.
67. Z. Guo and P. J. Sadler, *Angew. Chem., Int. Ed. Engl.*, 1999, **38**, 1512.
68. (a) W. A. Herrmann, E. Herdtweck, and L. Pajdla, *Chem. Ber.*, 1993, **126**, 895; (b) P. J. Sadler and H. Sun, *J. Chem. Soc., Dalton Trans.*, 1995, 1395; (c) M. W. Brechbiel, O. A. Gansow, C. G. Pippin, R. D. Rogers, and R. P. Planalp, *Inorg. Chem.*, 1996, **35**, 6343.
69. W. A. Herrmann, E. Herdtweck, W. Scherer, P. Kiprof, and L. Pajdla, *Chem. Ber.*, 1993, **126**, 51.
70. P. Kiprof, W. Scherer, L. Pajdla, E. Herdtweck, and W. A. Herrmann, *Chem. Ber.*, 1992, **125**, 43.
71. (a) E. Asato, C. M. Hol, F. B. Hulsbergen, N. T. M. Klooster, and J. Reedijk, *Inorg. Chim. Acta*, 1993, **214**, 159; (b) E. Asato, W. L. Driessen, R. A. G. De Graaff, F. B. Hulsbergen, and J. Reedijk, *Inorg. Chem.*, 1991, **30**, 4210.
72. (a) W. A. Herrmann, E. Herdtweck, and L. Pajdla, *Inorg. Chem.*, 1991, **30**, 2579; (b) P. J. Barrie, M. I. Djuran, M. A. Mazid, M. McPartlin, P. J. Sadler, I. J. Scowen, and H. Sun, *J. Chem. Soc., Dalton Trans.*, 1996, 2417.
73. J. H. Thurston, E. M. Marlier, and K. H. Whitmire, *J. Chem. Soc., Chem. Commun.*, 2002, 2834.
74. P. J. Sadler, H. Sun, and H. Li, *Chem. Eur. J.*, 1996, **2**, 701.
75. (a) L. Zhang, K. Y. Szeto, W. B. Wong, T. T. Loh, P. J. Sadler, and H. Sun, *Biochemistry*, 2001, **40**, 13281; (b) H. Sun, H. Li, A. B. Mason, R. C. Woodworth, and P. J. Sadler, *J. Biol. Chem.*, 2001, **276**, 8829; (c) H. Sun, H. Li, A. B. Mason, R. C. Woodworth, and P. J. Sadler, *Biochem. J.*, 1999, **337**, 105; (d) H. Sun, H. Li, I. Harvey, and P. J. Sadler, *J. Biol. Chem.*, 1999, **274**, 29094; (e) H. Sun, M. C. Cox, H. Li, A. B. Mason, R. C. Woodworth, and P. J. Sadler, *FEBS Lett.*, 1998, **422**, 315; (f) H. Li, P. J. Sadler, and H. Sun, *J. Biol. Chem.*, 1996, **271**, 9483.
76. A. Laarif and F. Theobald, *Sol. St. Ionics*, 1986, **21**, 183.
77. (a) A. Gutbier and H. Micheler, *Z. Anorg. Chem.*, 1908, **59**, 143; (b) G. Gattow and W. Klippel, *Z. Anorg. Allg. Chem.*, 1980, **470**, 25.
78. C. N. R. Rao, L. Ganapathi, A. K. Ganguli, R. A. Moha Ram, R. Vijayaraghavan, A. M. Umarji, G. N. Sabbana, and P. Somassundarum, ‘Chemistry of Oxide Superconductors’, Blackwell Scientific Publications (for IUPAC), Boston, 1988, p. 183ff.
79. (a) R. Hoppe and B. Schwedes, *Rev. Chim. Miner.*, 1971, **8**, 583; (b) B. Schwedes and R. Hoppe, *Z. Anorg. Allg. Chem.*, 1972, **391**, 313; (c) B. Schwedes and R. Hoppe, *Z. Anorg. Allg. Chem.*, 1972, **392**, 97.
80. (a) V. A. Carlson and A. M. Stacy, *Proc. Electrochem. Soc.*, 1992, **16**, 104; (b) V. A. Carlson and A. M. Stacy, *J. Sol. St. Chem.*, 1992, **96**, 332.
81. (a) R. K. Grasselli, J. D. Burrington, D. J. Buttrey, P. De Santo Jr, C. G. Lugmair, A. F. Volpe Jr, and T. Weingand, *Top. Catal.*, 2003, **23**, 5; (b) R. K. Grasselli and J. D. Burrington, *Adv. Catal.*, 1981, **30**, 133.
82. W. G. Klemperer and R. S. Liu, *Inorg. Chem.*, 1980, **19**, 3863.
83. (a) W. Ueda and J. M. Thomas, *J. Chem. Soc., Chem. Commun.*, 1988, 1148; (b) J. M. Thomas, W. Ueda, J. Williams, and K. D. M. Harris, *Far. Discuss.*, 1989, **87**, 33.
84. Y. C. Kim, W. Ueda, and Y. Morooka, *J. Chem. Soc., Chem. Commun.*, 1989, 652.
85. (a) C.-H. He and O. B. Yang, *Ind. Eng. Chem. Res.*, 2003, **42**, 419; (b) A. Kudo, *J. Ceram. Soc. Jpn.*, 2001, **109**, S81; (c) X. H. Xu, M. Wang, Y. Hou, W. F. Yao, D. Wang, and H. Wang, *J. Mater. Sci. Lett.*, 2002, **21**, 1655; (d) Z. Zou, J. Ye, K. Sayama, and H. Arakawa, *Chem. Phys. Lett.*, 2001,

343, 303; (e) Z. Zou, J. Ye, and H. Arakawa, *Chem. Phys. Lett.*, 2001, **333**, 57; (f) Z. Zou, J. Ye, and H. Arakawa, *J. Mater. Res.*, 2001, **16**, 35; (g) Z. Zou, J. Ye, and H. Arakawa, *Mater. Sci. Eng., B*, 2001, **B79**, 83; (h) Z. Zou, H. Arakawa, and J. Ye, *J. Mater. Res.*, 2002, **17**, 1446; (i) Z. Zou, J. Ye, and H. Arakawa, *J. Phys. Chem. (B)*, 2002, **106**, 517; (j) Z. Zou, J. Ye, and H. Arakawa, *Int. J. Hydrogen Energy*, 2003, **28**, 663; (k) Z. Zou, J. Ye, and H. Arakawa, *Top. Catal.*, 2003, **22**, 107.

86. W. Frank, G. J. Reiss, and J. Schneider, *Angew. Chem., Int. Ed. Engl.*, 1995, **34**, 2416.
87. (a) V. A. Maroni and T. G. Spiro, *J. Am. Chem. Soc.*, 1966, **88**, 1410; (b) V. A. Maroni and T. G. Spiro, *Inorg. Chem.*, 1968, **7**, 183.
88. (a) F. Lazarini, *Acta Crystallogr.*, 1978, **B34**, 3169; (b) F. Lazarini, *Cryst. Struct. Commun.*, 1979, **8**, 69; (c) F. Lazarini, *Acta Crystallogr.*, 1979, **B35**, 448; (d) B. Sundvall, *Inorg. Chem.*, 1983, **22**, 1906; (e) B. Sundvall, *Acta. Chem. Scand. (A)*, 1974, **A28**, 1036; (f) B. Sundvall, *Acta Chem. Scand. (A)*, 1979, **A33**, 219; (g) B. Sundvall, *Acta Chem. Scand. (A)*, 1980, **A34**, 93.
89. (a) K. H. Whitmire, C. M. Jones, M. D. Burkart, J. C. Hutchison, and A. McKnight, *Mater. Res. Soc. Symp. Proc.*, 1992, **271**, 149; (b) C. M. Jones, M. D. Burkart, and K. H. Whitmire, *J. Chem. Soc., Chem. Commun.*, 1992, 1638.
90. (a) G. R. Willey, M. T. Lakin, and N. W. Alcock, *J. Chem. Soc., Dalton Trans.*, 1992, 591; (b) G. R. Willey, M. T. Lakin, M. Ravindran, and N. W. Alcock, *J. Chem. Soc., Chem. Commun.*, 1991, 271; (c) G. R. Willey, M. T. Lakin, and N. W. Alcock, *J. Chem. Soc., Dalton Trans.*, 1992, 1339; (d) A. J. Blake, D. Fenske, W.-S. Li, V. Lippolis, and M. Schroder, *J. Chem. Soc., Dalton Trans.*, 1998, 3961.
91. W. Clegg, N. C. Norman, and N. L. Pickett, *Polyhedron*, 1993, **12**, 1251.
92. H. W. Yim, K.-C. Lam, A. L. Rheingold, and D. Rabinovich, *Polyhedron*, 2000, **19**, 849.
93. H. Gilman and J. F. Nelson, *J. Am. Chem. Soc.*, 1937, **59**, 935.
94. W. Clegg, M. R. J. Elsegood, L. J. Farrugia, F. J. Lawlor, N. C. Norman, and A. J. Scott, *J. Chem. Soc., Dalton Trans.*, 1995, 2129.
95. D. A. Atwood, A. H. Cowley, R. D. Hernandez, R. A. Jones, L. L. Rand, S. G. Bott, and J. L. Atwood, *Inorg. Chem.*, 1993, **32**, 2972.
96. E. Block, G. Ofori-Okai, H. Kang, J. Wu, and J. Zubieta, *Inorg. Chem.*, 1991, **30**, 4784.
97. (a) R. Engler, *Z. Anorg. Allg. Chem.*, 1974, **407**, 35; (b) R. Engler, *Z. Anorg. Allg. Chem.*, 1974, **406**, 74.
98. M. Draeger and B. M. Schmidt, *J. Organomet. Chem.*, 1985, **290**, 133.
99. (a) G. G. Briand, N. Burford, and T. S. Cameron, *J. Chem. Soc., Chem. Commun.*, 2000, 13; (b) G. G. Briand, N. Burford, and T. S. Cameron, *J. Chem. Soc., Chem. Commun.*, 1997, 2365; (c) G. G. Briand, N. Burford, M. D. Eelman, T. S. Cameron, and K. N. Robertson, *Inorg. Chem.*, 2003, **42**, 3136; (d) G. G. Briand, N. Burford, T. S. Cameron, and W. Kwiatkowski, *J. Am. Chem. Soc.*, 1998, **120**, 11374.
100. N. Burford, D. Eelman Melanie, E. Mahony David, and M. Morash, *J. Chem. Soc., Chem. Commun.*, 2003, 146.
101. N. Burford, M. D. Eelman, and T. S. Cameron, *J. Chem. Soc., Chem. Commun.*, 2002, 1402.
102. (a) C. L. Raston and A. H. White, *J. Chem. Soc., Dalton Trans.*, 1976, 791; (b) C. L. Raston, G. L. Rowbottom, and A. H. White, *J. Chem. Soc., Dalton Trans.*, 1981, 1383; (c) C. L. Raston, G. L. Rowbottom, and A. H. White, *J. Chem. Soc., Dalton Trans.*, 1981, 1379; (d) C. L. Raston, G. L. Rowbottom, and A. H. White, *J. Chem. Soc., Dalton Trans.*, 1981, 1369; (e) C. L. Raston, G. L. Rowbottom, and A. H. White, *J. Chem. Soc., Dalton Trans.*, 1981, 1352; (f) C. L. Raston, G. L. Rowbottom, and A. H. White, *J. Chem. Soc., Dalton Trans.*, 1981, 1389; (g) C. L. Raston, G. L. Rowbottom, and A. H. White, *J. Chem. Soc., Dalton Trans.*, 1981, 1372; (h) C. L. Raston, G. L. Rowbottom, and A. H. White, *J. Chem. Soc., Dalton Trans.*, 1981, 1366.
103. (a) G. E. Manoussakis, C. A. Tsipis, and A. G. Christophides, *Inorg. Chem.*, 1973, **12**, 3015; (b) G. E. Manoussakis, C. A. Tsipis, and A. G. Christophides, *Z. Anorg. Allg. Chem.*, 1975, **417**, 235.
104. L. J. Farrugia, F. J. Lawlor, and N. C. Norman, *J. Chem. Soc., Dalton Trans.*, 1995, 1163.
105. L. J. Farrugia, F. J. Lawlor, and N. C. Norman, *Polyhedron*, 1995, **14**, 311.
106. (a) M. S. Sander, A. L. Prieto, R. Gronsky, T. Sands, and A. M. Stacy, *Adv. Mater.*, 2002, **14**, 665; (b) M. S. Sander, A. L. Prieto, R. Gronsky, T. Sands, and A. M. Stacy, *Mater. Res. Soc. Symp. Proc.*, 2002, **676**, Y8; (c) M. S. Sander, A. L. Prieto, Y. M. Lin, R. Gronsky, A. M. Stacy, T. D. Sands, and M. S. Dresselhaus, *Mater. Res. Soc. Symp. Proc.*, 2001, **635**, C4; (d) A. L. Prieto, M. S. Sander, M. S. Martin-Gonzalez, R. Gronsky, T. Sands, and A. M. Stacy, *J. Am. Chem. Soc.*, 2001, **123**, 7160; (e) A. L. Prieto, M. S. Sander, A. M. Stacy, R. Gronsky, and T. Sands, *Mater. Res. Soc. Symp. Proc.*, 2001, **626**, Z14; (f) M. S. Martin-Gonzalez, A. L. Prieto, R. Gronsky, T. Sands, and A. M. Stacy, *J. Electrochem. Soc.*, 2002, **149**, C546.
107. (a) G. Alonzo, M. Consiglio, N. Bertazzi, and C. Preti, *Inorg. Chim. Acta*, 1985, **105**, 51; (b) A. K. Biswas, J. R. Hall, and D. P. Schweinsberg, *Inorg. Nucl. Chem. Lett.*, 1978, **14**, 275; (c) A. K. Biswas, J. R. Hall, and D. P. Schweinsberg, *Inorg. Chim. Acta*, 1983, **75**, 57.
108. (a) W. Clegg, N. A. Compton, R. J. Errington, N. C. Norman, and N. Wishart, *Polyhedron*, 1989, **8**, 1579; (b) W. Clegg, N. A. Compton, R. J. Errington, G. A. Fisher, M. E. Green, D. C. R. Hockless, and N. C. Norman, *Inorg. Chem.*, 1991, **30**, 4680; (c) M. J. S. Gynane, A. Hudson, M. F. Lappert, P. P. Power, and H. Goldwhite, *J. Chem. Soc., Dalton Trans.*, 1980, 2428; (d) C. J. Carmalt, N. A. Compton, R. J. Errington, G. A. Fisher, I. Moenandar, and N. C. Norman, *Inorg. Synth.*, 1997, **31**, 98.

109. A. M. Caminade, M. Veith, V. Huch, and W. Malisch, *Organometallics*, 1990, **9**, 1798.

110. T. M. Klapötke and A. Schulz, *Main Group Met. Chem.*, 1997, **20**, 325.

111. P. Sayer, M. Gouterman, and C. R. Connell, *Acc. Chem. Res.*, 1982, **15**, 73.

112. T. Barbour, W. J. Belcher, P. J. Brothers, C. E. F. Rickard, and D. C. Ware, *Inorg. Chem.*, 1992, **31**, 746.

113. R. Luckay, I. Cukrowski, J. Mashishi, J. H. Reibenspies, A. H. Bond, R. D. Rogers, and R. D. Hancock, *J. Chem. Soc., Dalton Trans.*, 1997, 901.

114. A. W. Snow and N. L. Jarvis, *J. Am. Chem. Soc.*, 1984, **106**, 4706.

115. J. Janczak, R. Kubiak, J. Richter, and H. Fuess, *Polyhedron*, 1999, **18**, 2775.

116. O. Schmitz-DuMont and B. Ross, *Z. Anorg. Allg. Chem.*, 1967, **349**, 328.

117. W. Clegg, R. J. Errington, R. J. Flynn, M. E. Green, D. C. R. Hockless, N. C. Norman, V. C. Gibson, and K. Tavakkoli, *J. Chem. Soc., Dalton Trans.*, 1992, 1753.

118. G. Becker, H. Freudenblum, O. Mundt, M. Reti, and M. Sachs, *Synth. Meth. Organomet. Inorg. Chem.*, 1996, **3**, 193.

119. H. Schumann and H. J. Breunig, *J. Organomet. Chem.*, 1975, **87**, 83.

120. T. R. Bierschenk, M. A. Guerra, T. J. Juhlke, S. B. Larson, and R. J. Lagow, *J. Am. Chem. Soc.*, 1987, **109**, 4855.

121. O. Mundt, G. Becker, M. Roessler, and C. Witthauer, *Z. Anorg. Allg. Chem.*, 1983, **506**, 42.

122. (a) M. N. Bochkarev, N. I. Gur'ev, and G. A. Razuvaev, *J. Organomet. Chem.*, 1978, **162**, 289; (b) M. N. Bochkarev, G. A. Razuvaev, L. N. Zakharov, and Y. T. Struchkov, *J. Organomet. Chem.*, 1980, **199**, 205.

123. J. Beck, C. J. Brendel, L. Bengtsson-Kloo, B. Krebs, M. Mummert, A. Stankowski, and S. Ulvenlund, *Chem. Ber.*, 1996, **129**, 1219.

124. J. D. Corbett and R. M. Friedman, *J. Chem. Soc., Chem. Commun.*, 1971, 422.

125. R. M. Friedman and J. D. Corbett, *Inorg. Chem.*, 1973, **12**, 1134.

126. (a) B. Krebs, M. Hucke, and C. J. Brendel, *Angew. Chem.*, 1982, **94**, 453; (b) J. D. Corbett, *Inorg. Chem.*, 1968, **7**, 198.

127. R. C. Burns, R. J. Gillespie, and W.-C. Luk, *Inorg. Chem.*, 1978, **17**, 3596.

128. J. D. Corbett, *Chem. Rev.*, 1985, **85**, 383.

129. A. Cisar and J. D. Corbett, *Inorg. Chem.*, 1977, **16**, 2482.

130. K. Deller and B. Eisenmann, *Z. Naturforsch.*, 1976, **31B**, 29.

131. F. Gascoin and S. C. Sevov, *Inorg. Chem.*, 2001, **40**, 5177.

132. (a) F. Gascoin and S. C. Sevov, *J. Am. Chem. Soc.*, 2000, **122**, 10251; (b) L. Xu, S. Bobev, J. El-Bahraoui, and S. C. Sevov, *J. Am. Chem. Soc.*, 2000, **122**, 1838.

133. L. Xu, A. Ugrinov, and S. C. Sevov, *J. Am. Chem. Soc.*, 2001, **123**, 4091.

134. (a) S. C. Critchlow and J. D. Corbett, *Inorg. Chem.*, 1982, **21**, 3286; (b) L. Xu and S. C. Sevov, *Inorg. Chem.*, 2000, **39**, 5383.

135. (a) M. Scheer and E. Herrmann, *Z. Chem.*, 1990, **30**, 41; (b) O. J. Scherer, *Angew. Chem.*, 1985, **97**, 905; (c) T. P. Fehlner, *Comment. Inorg. Chem.*, 1988, **7**, 307; (d) J. N. Nicholls, *Polyhedron*, 1984, **3**, 1307; (e) W. A. Herrmann, *Angew. Chem.*, 1986, **98**, 57; (f) D. Fenske, J. Ohmer, J. Hachgenei, and K. Merzweiler, *Angew. Chem.*, 1988, **100**, 1300; (g) K. H. Whitmire, *J. Coord. Chem.*, 1988, **17**, 95; (h) O. J. Scherer, *Angew. Chem.*, 1990, **102**, 1137; (i) N. C. Norman, *Chem. Soc. Rev.*, 1988, **17**, 269; (j) K. H. Whitmire, in 'Rings, Clusters and Polymers of Main Group and Transition Elements', ed. H. W. Roesky, Elsevier, Amsterdam, NY, 1989, p. 503; (k) N. A. Compton, R. J. Errington and N. C. Norman, *Adv. Organomet. Chem.*, 1990, **31**, 91; (l) K. H. Whitmire, Organotransition Metal Compounds with Element to Transition Metal Bonds, in 'The Chemistry of Arsenic, Antimony and Bismuth', ed. N. C. and Norman, Blackie Academic and Professional Books, Glasgow, 1998, p. 345.

136. G. Huttner, *Pure Appl. Chem.*, 1986, **58**, 585.

137. J. M. Wallis, G. Mueller, and H. Schmidbaur, *J. Organomet. Chem.*, 1987, **325**, 159.

138. (a) J. M. Wallis, G. Mueller, and H. Schmidbaur, *Inorg. Chem.*, 1987, **26**, 458; (b) J. M. Wallis, G. Mueller, J. Riede, and H. Schmidbaur, *J. Organomet. Chem.*, 1989, **369**, 165.

139. G. Etzrodt, R. Boese, and G. Schmid, *Chem. Ber.*, 1979, **112**, 2574.

140. W. Clegg, N. A. Compton, R. J. Errington, N. C. Norman, A. J. Tucker, and M. J. Winter, *J. Chem. Soc., Dalton Trans.*, 1988, 2941.

141. W. Clegg, N. A. Compton, R. J. Errington, and N. C. Norman, *J. Chem. Soc., Dalton Trans.*, 1988, 1671.

142. N. C. Norman, N. L. Pickett, W. D. Storr, N. M. Boag, and A. J. Goodby, *Polyhedron*, 1994, **13**, 2525.

143. (a) W. Clegg, N. A. Compton, R. J. Errington, and N. C. Norman, *Polyhedron*, 1987, **6**, 2031; (b) W. Clegg, N. A. Compton, R. J. Errington, D. C. R. Hockless, N. C. Norman, M. Ramshaw, and P. M. Webster, *J. Chem. Soc., Dalton Trans.*, 1990, 2375; (c) R. J. Errington, L. J. Farrugia, G. A. Fisher, A. Niklaus, and N. C. Norman, *J. Chem. Soc., Dalton Trans.*, 1993, 1201; (d) T. Groer and M. Scheer, *Dalton Trans.*, 2000, 647.

144. (a) W. Clegg, N. A. Compton, R. J. Errington, G. A. Fisher, D. C. R. Hockless, N. C. Norman, N. A. L. Williams, S. E. Stratford, and S. J. Nichols, *J. Chem. Soc., Dalton Trans.*, 1992, 193.

145. J. Von Seyerl and G. Huttner, *J. Organomet. Chem.*, 1980, **195**, 207.

146. W. Clegg, N. A. Compton, R. J. Errington, G. A. Fisher, N. C. Norman, and T. B. Marder, *J. Chem. Soc., Dalton Trans.*, 1991, 2887.

147. D. Fenske, A. Rothenberger, and S. Wieber, *Z. Anorg. Allg. Chem.*, 2003, **629**, 929.

148. W. Kruppa, D. Blaeser, R. Boese, and G. Schmid, *Z. Naturforsch.*, 1982, **37B**, 209.

149. G. Ciani, M. Moret, A. Fumagalli, and S. Martinengo, *J. Organomet. Chem.*, 1989, **362**, 291.

150. K. H. Whitmire, J. S. Leigh, and M. E. Gross, *J. Chem. Soc., Chem. Commun.*, 1987, 926.

151. M. Shieh, F. D. Mia, S. M. Peng, and G. H. Lee, *Inorg. Chem.*, 1993, **32**, 2785.

152. (a) J. W. van Hal, K. H. Whitmire, B. Zouchoune, J.-F. Halet, and J.-Y. Saillard, *Inorg. Chem.*, 1995, **34**, 5455; (b) L. Xu and K. H. Whitmire, *Organometallics*, 2002, **21**, 2581.

153. (b) J. S. Leigh and K. H. Whitmire, *Angew. Chem.*, 1988, **100**, 399; (b) S. Martinengo, A. Fumagalli, G. Ciani, and M. Moret, *J. Organomet. Chem.*, 1988, **347**, 413; (c) C. J. Carmalt, L. J. Farrugia, N. C. Norman, and S. Sunley, *Inorg. Chim. Acta*, 1995, **234**, 189.

154. (a) C. J. Carmalt, L. J. Farrugia, and N. C. Norman, *J. Chem. Soc., Dalton Trans.*, 1996, 455; (b) J. R. Eveland, K. H. Whitmire, and J.-Y. Saillard, *Inorg. Chem.*, 1996, **35**, 4400.

155. J. R. Eveland, J.-Y. Saillard, and K. H. Whitmire, *Inorg. Chem.*, 1997, **36**, 4387.

156. S. Martinengo and G. Ciani, *J. Chem. Soc., Chem. Commun.*, 1987, 1589.

157. T. A. Albright, K. A. Yee, J. Y. Saillard, S. Kahlal, J. F. Halet, J. S. Leigh, and K. H. Whitmire, *Inorg. Chem.*, 1991, **30**, 1179.

158. M. R. Churchill, J. C. Fettinger, K. H. Whitmire, and C. B. Lagrone, *J. Organomet. Chem.*, 1986, **303**, 99.

159. M. Shieh, J.-J. Cherng, Y.-W. Lai, C.-H. Ueng, S.-M. Peng, and Y.-H. Liu, *Chem. Eur. J.*, 2002, **8**, 4522.

160. K. H. Whitmire, C. B. Lagrone, M. R. Churchill, J. C. Fettinger, and L. V. Biondi, *Inorg. Chem.*, 1984, **23**, 4227.

161. K. H. Whitmire, C. B. Lagrone, and A. L. Rheingold, *Inorg. Chem.*, 1986, **25**, 2472.

162. M. Shieh, Y. Liou, and B. W. Jeng, *Organometallics*, 1993, **12**, 4926.

163. M. Shieh, Y. Liou, M.-H. Hsu, R.-T. Chen, S.-J. Yeh, S.-M. Peng, and G.-H. Lee, *Angew. Chem. Int. Ed. Engl.*, 2002, **41**, 2384.

164. K. H. Whitmire, T. A. Albright, S. K. Kang, M. R. Churchill, and J. C. Fettinger, *Inorg. Chem.*, 1986, **25**, 2799.

165. K. H. Whitmire, M. R. Churchill, and J. C. Fettinger, *J. Am. Chem. Soc.*, 1985, **107**, 1056.

166. K. H. Whitmire, M. Shieh, C. B. Lagrone, B. H. Robinson, M. R. Churchill, J. C. Fettinger, and R. F. See, *Inorg. Chem.*, 1987, **26**, 2798.

167. J. R. Eveland, J.-Y. Saillard, and K. H. Whitmire, *Inorg. Chem.*, 1997, **36**, 330.

168. S. N. Konchenko, N. A. Pushkarevsky, A. V. Virovets, and M. Scheer, *J. Chem. Soc., Dalton Trans.*, 2003, 581.

169. K. H. Whitmire, K. S. Raghuveer, M. R. Churchill, J. C. Fettinger, and R. F. See, *J. Am. Chem. Soc.*, 1986, **108**, 2778.

170. S. Kahlal, J.-F. Halet, J.-Y. Saillard, and K. H. Whitmire, *J. Organomet. Chem.*, 1994, **478**, 1.

171. (a) H. G. Ang, C. M. Hay, B. F. G. Johnson, J. Lewis, P. R. Raithby, and A. J. Whitton, *J. Organomet. Chem.*, 1987, **330**, C5; (b) C. M. Hay, B. F. G. Johnson, J. Lewis, P. R. Raithby, and A. J. Whitton, *J. Chem. Soc., Dalton Trans.*, 1988, 2091; (c) B. F. G. Johnson, J. Lewis, P. R. Raithby, and A. J. Whitton, *J. Chem. Soc., Chem. Commun.*, 1988, 401; (d) B. F. G. Johnson, J. Lewis, and A. J. Whitton, *J. Chem. Soc., Dalton Trans.*, 1990, 3129.

172. K. H. Whitmire, *J. Cluster Sci.*, 1991, **2**, 231.

173. P. D. Mlynek and L. F. Dahl, *Organometallics*, 1997, **16**, 1655.

174. V. G. Albano, F. Demartin, M. C. Iapalucci, G. Longoni, M. Monari, and P. Zanello, *J. Chem. Soc., Dalton Trans.*, 1992, 497.

175. G. Huttner, U. Weber, and L. Zsolnai, *Z. Naturforsch.*, 1982, **37B**, 707.

176. A. M. Arif, A. H. Cowley, N. C. Norman, and M. Pakulski, *Inorg. Chem.*, 1986, **25**, 4836.

177. W. J. Evans, S. L. Gonzales, and J. W. Ziller, *J. Am. Chem. Soc.*, 1991, **113**, 9880.

178. J. L. Stark, B. Harms, I. Guzman-Jimenez, K. H. Whitmire, R. Gautier, J.-F. Halet, and J.-Y. Saillard, *J. Am. Chem. Soc.*, 1999, **121**, 4409.

179. (a) K. H. Whitmire and J. R. Eveland, *J. Chem. Soc., Chem. Commun.*, 1994, 1335; (b) B. Zouchoune, F. Ogliaro, J.-F. Halet, J.-Y. Saillard, J. R. Eveland, and K. H. Whitmire, *Inorg. Chem.*, 1998, **37**, 865.

Bismuth: Organometallic Chemistry

Kenton H. Whitmire
Rice University, Houston, TX, USA

1	Introduction	1
2	Trivalent Organobismuth Compounds	1
3	Pentavalent Organobismuth Compounds	9
4	Related Articles	11
5	References	12

Abbreviations

Me = methyl; Et = ethyl; Ph = phenyl; dtc = dithiocarbamate; $^{-}S_2C{=}NR$; BTMG = N-t-butyl-N',N''-tetramethylguanidine; Mes = mesityl (2,4,6-$Me_3C_6H_2$); DMSO = dimethyl sulfoxide.

1 INTRODUCTION

Triethylbismuth, the first known organobismuth compound, was prepared in 1850 by Löwig and Schweizer[1] from iodoethane and a potassium–bismuth alloy. As with most trialkylbismuth compounds, $BiEt_3$ has an extremely pungent and unpleasant odor, and is spontaneously oxidized in air. The development of organobismuth chemistry was, therefore, delayed until better techniques for the handling of air sensitive materials were developed in 20th century. The chemistry of these complexes first began to receive significant attention when Grignard reagents and organolithium compounds became available. These reagents greatly expanded the synthetic capabilities for preparing organobismuth compounds. An excellent book[2] and several detailed reviews of organobismuth chemistry have appeared.[3–6] In addition, the *Journal of Organometallic Chemistry* has published periodic reviews of organobismuth chemistry.[7] Part of the current interest in organobismuth compounds can be attributed to their biological activity/pharmaceutical applications and to their application as precursor compounds to important electronic and/or magnetic materials such as the high T_c superconductors.

2 TRIVALENT ORGANOBISMUTH COMPOUNDS

2.1 Syntheses of Homoleptic Organobismuth Compounds

The most general and widely used methodology for the synthesis of homoleptic trialkyl- and triarylbismuth complexes (**1**) is the reaction of a bismuth trihalide with organolithium or magnesium reagents (equation 1). Besides alkyl and aryl groups, alkynyl, alkenyl, and allyl functions have also been introduced into organobismuth molecules by this method. Fluorinated aryl groups have also been introduced using organolithium reagents.[8] This is a particularly important methodology for creating asymmetric bismuth compounds, as described below. Organomercury compounds also may be used. Perfluoroalkylbismuth compounds have been prepared from an appropriate organo-cadmium or -zinc reagent and BiX_3.[9–12] The reaction of K_3Bi with organic halides (equation 2) was, as mentioned above, the first method used to prepare triorganobismuth compounds. This method is generally more difficult, not as clean, and produces a lower yield. In some cases, however, such as the synthesis of $(Me_3Si)_3Bi$, it is the only available method.[13] Other more esoteric methods have been used to produce trivalent organobismuth compounds, such as the reaction of bismuth atoms from a metal atom reactor with in situ generated organic radicals, but these have limited synthetic utility.[14] Direct reaction of bismuth metal usually produces mixed halo/organobismuth complexes and not homoleptic compounds.

$BiCl_3 + 3LiR \longrightarrow$

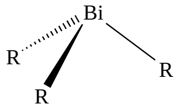

$+\ 3LiCl$ (1)

(**1**)

$$K_3Bi + 3RX \longrightarrow BiR_3 + 3KX \qquad (2)$$

A novel variation on the synthesis of triarylbismuth compounds is the formation of complexes containing two bismuth atoms as shown in (**2**)[15] and (**3**).[16] The triptycene compound (**2**) was prepared via the reaction of 1,2-diiodotetrafluorobenzene with bismuth powder in a sealed tube. The related compound (**3**) was prepared via the reaction of 2,5-dichloro-3,4-dilithiothiophene with $BiCl_3$. Difunctional alkyl reagents such as $X(CH_2)_nX$ are also observed to react with R_2BiNa. Long-chain compounds form the expected dibismuth compounds, but for $n = 4$ or 5, dismutation occurs to give the heterocyclic compounds *cyclo*-$MeBi(CH_2)_n$ and $BiMe_3$.[17] Both cyclic compounds were obtainable directly via the reaction of the Grignard reagents $BrMg(CH_2)_nMgBr$ with Me_2BiBr. Phenylene bridges have been used to connect organic bismuth functions with the goal of creating bismuth-containing polymers and dendrimers.[18]

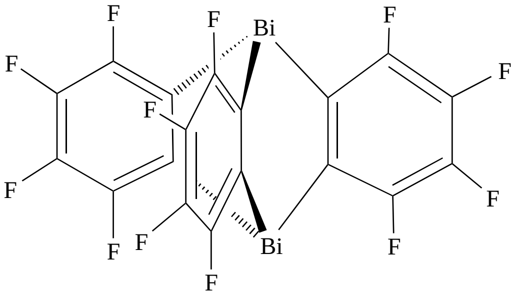

(**2**)

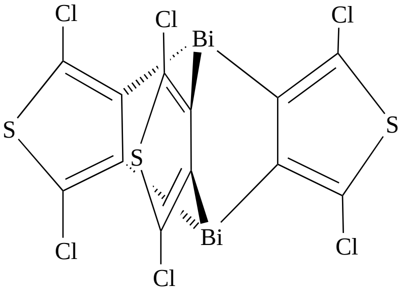

(**3**)

2.2 Syntheses of Asymmetric Organobismuth Complexes

Asymmetric organobismuth compounds are those in which there is more than one type of organic group attached to the bismuth atom. The syntheses of these compounds proceed naturally and most conveniently from the organobismuth halides $RBiX_2$ and R_2BiX. In this fashion, a wide variety of organic functions have been introduced, usually via reaction with an organolithium or organomagnesium reagent. The nature of the end product may be controlled by redistribution reactions, however, as discussed by Gilman and Yale.[4] An alternate route to asymmetric organobismuth complexes is addition of organic halides to R_2BiM. The latter is prepared by reduction of R_2BiX in anhydrous liquid ammonia with active metals such as sodium or potassium. Complexes with three different groups attached are chiral and some examples have been prepared, but they undergo inversion when heated in solution.[19] So far, there are no reports of resolution of organobismuth enantiomers.

2.3 Properties and Structure

Physical properties of a number of organobismuth complexes have been compiled.[3,4] The trialkylbismuth compounds are generally very oxygen sensitive, though stable to moisture. Many triarylbismuth compounds are air stable as well as stable to moisture. The trialkyls with small R groups are colorless liquids, which may be distilled under vacuum. Triphenylbismuth is a commercially available, air stable, white crystalline solid.

The compound $R_2Bi–O–BiR_2$ has been found as an intermediate in the oxidation of trialkylbismuth compounds.[20] Unlike $BiPh_3$, the compound $Bi(R_f)_3$ [$R_f = 2,4,6\text{-}(CF_3)_3C_6H_2$] is air sensitive and slowly evolves R_fOR_f and R_fOH upon standing in air.[21] These findings are consistent with the intermediacy of an $O{=}Bi(R_f)_3$ complex followed by the insertion of O into a Bi−C bond. Reductive elimination from such an intermediate would generate the ether, while hydrolysis would produce the phenol.

Simple trialkyl- and triarylbismuth compounds are pyramidal molecules as expected from simple Valence Shell Electron Pair Repulsion Model (VSEPR) considerations. The degree of pyramidality has been shown to correlate with the charge on the bismuth atom, with barriers to inversion calculated to be in the range of 30−70 kcal mol^{-1}.[22] Structures of several BiR_3 (R = Ph, 4-tolyl, CH_2SiMe_3, $C_6H_2Me_3$, 2,4,6-$C_6H_2(CF_3)_3$) compounds are known from single-crystal X-ray diffraction data[21,23,24] and bond parameters for Me_3Bi are available from electron diffraction.[25] Bismuth−carbon bond distances range from 2.24 Å for small R groups to 2.38 Å where the organic group is sterically demanding. Values for Bi–C bond strengths range from 33−44 kcal mol^{-1} for $BiMe_3$, and from 42−47 kcal mol^{-1} for Ph_3Bi. In spite of the fact that these numbers cover quite a range of values and that it is difficult to compare quantitatively the relative Bi–C bond strengths, it appears that bonds to aryl functions are generally stronger than those to alkyl groups. BiR_3 compounds are much less basic and the lone pair is much more diffuse than the lighter group V analogs.

Bismuth, the heaviest member of group 15, has a strong tendency to form hypervalent complexes. A common structural feature in alkyl- and arylbismuth compounds is the interaction of the bismuth atom with the appended donor functionality (e.g. NH_2, carbonyl, etc.) present in the organic fragment. Specific examples will be seen in subsequent discussions.

The pyramidal bismuth atom may undergo inversion and this has been studied for several chelating ligands, as in (**4**). The findings were consistent with an edge inversion mechanism rather than a vertex inversion process.[26] The edge inversion mechanism proceeds through a T-shaped transition state. This mechanism predicts that the inversion barrier will decrease with an increasing atomic number, and that σ-acceptors will stabilize the transition state as will coordination of nucleophiles to an empty p orbital that appears in the transition state.[27] The chiral bismuth complexes $BiBr(4\text{-tolyl})(C_6H_4CH_2NMe_2)$ and $BiBr(4\text{-tolyl})(C_6H_4CH_2OMe)$ have been prepared and studied by NMR.[28] On the NMR timescale, the diastereotopic methylene protons for the NMe_2 compound can be resolved, but in strongly donating solvents, such as DMSO, inversion occurs readily.

Cyclopentadienylbismuth compounds have been prepared and Cp_3Bi exists in two crystalline forms: a

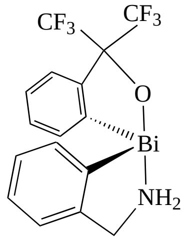

(**4**)

red and a black modification.[29] This has been commonly found for cyclopentadienyl derivatives of bismuth: tris(pentamethylcyclopentadienyl)bismuth and $CpBiCl_2$ also exhibit red/black isomerism. The Cp rings are π-bound in $CpBiCl_2$,[30,31] but the π-interaction is asymmetric and involves η^2- and η^3-coordination to the bismuth atom. $CpBiCl_2$ is polymeric, being held together by intermolecular Cl–Bi bridges (**5**), which further illustrates the ability of the bismuth atom to function as a Lewis acid. π-Bonding may be involved in the tris(allyl) complex, but its structure is not yet known.

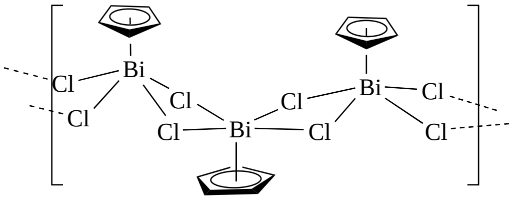

(**5**)

Simple arene solvates of bismuth(III) halides and pseudohalides have been structurally characterized, as have adducts prepared in the presence of $AlCl_3$.[32–34] The solid-state structures of these compounds show π-coordination of the arenes to the bismuth centers, as well as intermolecular $Bi\cdots X$ bonding that produces dimers or polymeric structures. Arene complexes that have been structurally characterized include those of benzene, *o*-, *m*- and *p*-xylene, mesitylene, and hexamethylbenzene.[32] π-Coordination of arenes has also been seen in $[Bi(OC_6F_5)_3(\text{toluene})]_2$ and $Bi_4(\mu_4\text{-}O)(\mu\text{-}OC_6F_5)_6\{\mu_3\text{-}OBi(\mu\text{-}OC_6F_5)_3\}\cdot 2(C_6H_5CH_3)$.[34,35]

2.4 Trialkyl- and Triarylbismuth Compounds as Donors to Transition Metals

R_3Bi compounds possess lone pairs of electrons but, compared to phosphines, very few metal complexes with R_3Bi ligands are known. Exceptions are $M(CO)_5BiPh_3$ (M = Cr, Mo, W),[36] $[CpFe(CO)_2BiPh_3]BF_4$,[37] and $[Ir(BiPh_3)(PPh_3)_2(CO)]ClO_4$.[38] Trialkylbismuth compounds are more basic than the triaryl compounds, as may be expected, and should form more stable donor adducts with transition metals. Trialkylbismuth complexes, which have been reported, include $Ni(CO)_3BiR_3$, $M(CO)_5BiR_3$ (R = Et, *t*-Bu), $[Et_4N][CpV(CO)_5BiEt_3]$, $CpV(CO)_3BiEt_3$, and $CpV(CO)_2(BiEt_3)_2$.[38,39] The complex $Fe(CO)_4(BiPh_3)_2$ was reported a number of years ago[40] but attempts to repeat that preparation have not been successful. Instead, the cluster complex $Bi_2Fe_3(CO)_9$ is obtained, pointing up a complication in the formation of triorganobismuth-metal complexes: the weakness of the Bi–C bond. This property results in facile redistribution reactions or the loss of organic functions from bismuth with the building of higher nuclearity metal complexes. Thus, reactions between $BiPh_3$ and metal halides often give Ph_2BiX and not Ph_3Bi–metal complexes. In contrast to these findings, $BiPh_3$ reportedly forms 1:2 adducts with UCl_5, and 1:1 and 1:2 adducts with $NbCl_5$.[41] These formulations have not, however, been confirmed by X-ray diffraction and in light of the other reports may be questioned.

2.5 Uses of BiR_3 Compounds

BiR_3 compounds have a number of uses. They are effective cocatalysts for the polymerization of substituted acetylenes by $MoCl_5$ or WCl_6.[42] $BiPh_3$ can act as a radiopacifying additive for polymeric materials such as polystyrene, poly(vinyl chloride), polyacrylates, and polyethylenes, with which it forms homogeneous mixtures. Leaching from the polymer can be prevented by using styryldiphenylbismuth, which copolymerizes. BiR_3 compounds have been used for preparing thin films of bismuth or bismuth oxide, and for incorporating bismuth into thin films of high T_c superconductors.

Organobismuth derivatives may undergo solvolysis with compounds that have acidic protons to replace one or more of the organic functions. The production of bismuth alkoxides and biologically relevant bismuth complexes has been accomplished in this way (*see* ***Bismuth: Inorganic Chemistry***). $BiPh_3$ reacts with HOC_6F_5 in toluene to give the dimeric alkoxide complex $[Bi(OC_6F_5)_2(\mu\text{-}OC_6F_5)(\text{toluene})]_2$ (**6**),[34] while $BiEt_3$ reacts with HOPh or HOC_6F_5 to give the polymeric $[Et_2BiOAr]_\infty$ (**7**).[43] Two phenyl groups are displaced when $BiPh_3$ is treated with maleic acid to give $PhBi(O_2CCH{=}CHCO_2H)_2$. The maleic acid functions are themselves displaced when the complex is treated with Na[dtc].[44]

2.6 Organobismuth Halides

Redistribution reactions (equation 3) are a facile method of synthesizing organobismuth halides.[11,45] As an example, when stoichiometric amounts of $BiCl_3$ and $BiPh_3$ (each dissolved in Et_2O) are mixed, an essentially quantitative precipitation of Ph_2BiCl is achieved. Stoichiometric reactions of the appropriate organolithium, -magnesium, or -mercury compounds with bismuth halides may also be used. For example, 2-(2′-pyridyl)phenylmercury chloride reacts with $BiBr_3$ to give dibromo-2-(2′-pyridyl)phenylbismuth.[31] This

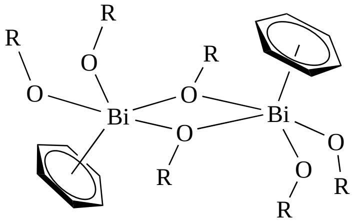

(6)

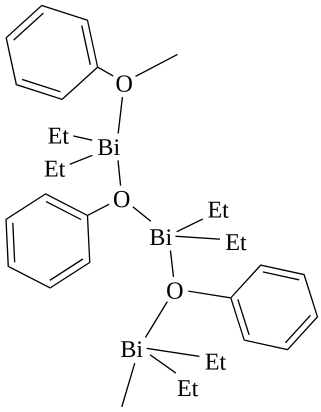

(7)

method has been used for preparing other alkylbismuth halides.

$$BiCl_3 + 2BiPh_3 \longrightarrow 3BiPh_2Cl \qquad (3)$$

Organobismuth(III) halides may be prepared by elimination of aryl halide from triarylbismuth(V) dichlorides or dibromides upon heating (equation 4). Presumably, a bismuth(V) compound is the intermediate when triarylbismuth compounds are treated with iodine or when trialkylbismuth complexes are treated with chlorine, bromine, or iodine, but the intermediates have not been isolated and organobismuth halides are obtained directly (equation 5). The tris(trifluoromethyl)bismuth behaves like the trialkyl compounds without the observation of a bismuth(V) intermediate.[9]

$$BiAr_3X_2 \xrightarrow{\Delta} BiAr_2X + ArX \qquad (4)$$

$$BiAr_3 + I_2 \longrightarrow Ar_2BiI + ArI \qquad (5)$$

Aryl groups appear to be preferentially cleaved with acids, so that addition of HX (X = Cl, Br) to Ph_2BiMe leads to $MeBiX_2$.[46]

Cyclopentadienyl halide complexes have been prepared from the reaction of NaCp or LiC_5Me_5 and $BiCl_3$.[47] As described earlier, $CpBiCl_2$, in its red crystal morphology, has been structurally characterized (**5**) and shows a chain polymeric structure containing both η^2- and η^3-coordination of the Cp ring to bismuth. In $(C_5Me_5)_2BiCl$, the cyclopentadienyl rings are pentahapto.[30] The pentamethylcyclopentadienyl complex $(C_5Me_5)BiBr_2$ was prepared via the reaction of bismuth powder with 5-bromopentamethyl-1,3-cyclopentadiene.[48]

For decades, it has been known that reaction of organobismuth halides with hydride reducing agents often results in intractable products presumably via the intermediacy of highly reactive bismuth hydrides. The use of the bulky organic function 2,4,6-$C_6H_2(^tBu)_3$ allows the isolation of the stable R_2BiH species.[49] When R = $(Me_3Si)_2CH$, the hydride intermediate can be detected but decomposes at room temperature to give the dibismuthine R_2BiBiR_2.[50]

2.7 Lewis Acidity of Organobismuth Compounds

Just as bismuth complexes with inorganic substituents are Lewis acids, so are their organobismuth analogs (*see* ***Bismuth: Inorganic Chemistry***). Lewis acidity is enhanced by the presence of the electronegative ligands, which tend to make the bismuth centers more electropositive. This feature can reduce the solubility of the aryl bismuth halides through intermolecular halide bridges as observed for Ph_2BiCl, $PhBiBr_2$, and $MeBiCl_2$.[51] Not surprisingly then, $RBiX_2$ (R = Me, Ph) can be isolated as THF, bipyridine, or phenanthroline adducts in which there are also Bi···X intermolecular contacts.[46,52] In some cases, weak π interactions are seen between the bismuth atom and the aryl rings of an adjacent molecule. In addition to solvent adducts, organobismuth halides also form complexes with added halide ions. Structurally characterized examples include $[Et_4N][Ph_2BiI_2]$ (**8**) and $[Et_4N]_2[Ph_2Bi_2Br_6]$ (**9**).[33] In the iodide complex, the bismuth has a distorted square-pyramidal geometry in which one phenyl group is in the axial position. The square base is defined by the second phenyl group, two iodide ligands at 3.0517(8) and 3.1415(8) Å, and a close contact to an iodide ligand in an adjacent molecule at 4.0850(11) Å, giving the compound an asymmetric, dimeric nature. In (**9**), the phenyl group in the square base has been

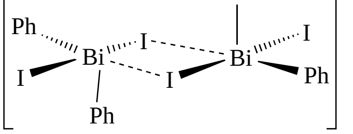

(8)

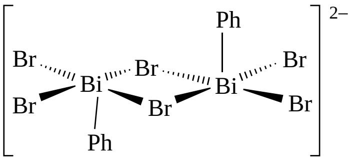

(9)

replaced by a Br^- ion and is similarly dimeric, although more symmetrical. The terminal Bi–Br distances are 2.7417(14) and 2.7559(14) Å, while the bridge distances are significantly longer at 3.0072(14) and 3.0545(14) Å. These complex halo aryl bismuth anions can also be found coordinated by other neutral ligands such as triphenylphosphine oxide and *N*,*N*′-dimethylpropylene urea.[53] Observed structures include those of $Bi_2Ph_2Br_4L_2$ ($L = OPPh_3$ and *N*,*N*′-dimethyl urea), $PhBi_2X(4\text{-}RC_6H_4N)_2$ (X = Cl, Br, I; R = H, Me, ^{t}Bu) and $(Mes)_2Bi(L)Br$ (L = hexamethylphosphoramide or $OSPh_2$). Dibromo-2-(2′-pyridyl)phenylbismuth forms 1:1 adducts with $[Et_4N]I$ and $Na[O_2CEt]$, but reacts with Na[dtc] to displace both of the Br^- ions giving bis(dithiocarbamato){2-(2′-pyridyl)phenyl}bismuth.[44] It is possible to promote displacement of the halides in R_2BiX with halide-abstracting reagents such as $TlPF_6$.[54] In this way, $[BiPh_2L_2][PF_6]$ ($L = OP(NMe_2)_3$ or pyridine) and $[BiPh\{OP(NMe_2)_3\}_4][PF_6]_2$ have been produced. In addition to coordination by external ligands, organic groups that contain donor functionality can form Lewis acid-base adducts intramolecularly as in the case of $[(2\text{-}Me_2NCH_2C_6H_4)_2Bi]^+$, where the amine functions coordinate to bismuth.[55] The bismuth biphenylene complex $[Bi(2,2'\text{-biphenylene})Cl_2]^-$ is another example of a 10-electron organobismuth center.[56]

A very interesting species is $[Bi(CF_3)_4]^-$, which is formed by reaction of $Bi(CF_3)_3$ with Me_3SiCF_3 in the presence of $[NMe_4]F$.[57] Presumably, the fluoride ion displaces $CF_3{}^-$ from the silyl reagent making it available for reaction with $Bi(CF_3)_3$.

2.8 Organobismuth Compounds with E and ER_x Ligands ($E = O, S, Se, Te, x = 1$; As, Sb, $x = 2$; Si, Ge, Sn, $x = 3$)

Organobismuth complexes that contain other heteroatom ligands are known and generally are prepared by (1) anion metathesis reactions or (2) reaction of HER_x with the organobismuth compound BiR'_3 upon the elimination of HR′. A third route involves the use of dibismuthines, as described in Section 2.11. A few examples of a variety of $RBi(ER_x)_2$ and R_2BiER_x complexes produced by methods (1) or (2) are given in equations (6–9). Alkoxide complexes from method (2) have been described above. Similarly, OH^- reacts with R_2BiX to give R_2BiOH, and with $RBiX_2$ to produce RBiO. Neither of these compound types have been particularly well characterized, but they present some interesting possibilities for future work. The mixed alkyl/alkoxide complexes have been implicated as intermediates in the oxidation of alkylbismuth complexes. $RBi(SR)_2$ complexes have been demonstrated to have antitumor activity.[58]

$$MeBiBr_2 + 2LiSMe \longrightarrow MeBi(SMe)_2 + 2LiBr \qquad (6)$$

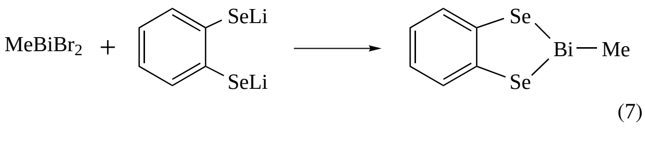

(7)

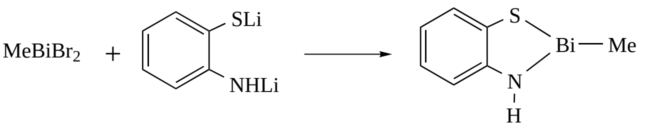

(8)

$$BiEt_3 + HGeEt_3 \qquad Et_2BiGeEt_3 + EtH \qquad (9)$$

2.9 Metallated Organobismuth Fragments

Metallated derivatives of organobismuth fragments may also be prepared. These compounds have synthetic and structural relationships to compounds without organic functionalities attached. These compounds may be prepared via the reaction of the organobismuth mono- and dihalides with a wide variety of metal carbonyl anions in straightforward anion metathesis reactions. For example, Ph_2BiML_n or $PhBi\{ML_n\}_2$ ($ML_n = Mn(CO)_5$, $Re(CO)_5$, $Fe(CO)_4{}^-$, $CpMo(CO)_3$), and $\{Ph_2Bi\}_2Fe(CO)_4$ (**10**) arise from the reaction of Ph_2BiCl and the appropriate metal carbonyl anion (equation 10 and Scheme 1).[59] The mixed species $BiBrPh\{Mo(CO)_3Cp\}$ will act as a Lewis acid toward bromide ions giving $[Br_2Bi(Ph)\{Mo(CO)_3Cp\}]^-$.[60] The latter complex rearranges to give $[Br_2Bi\{Mo(CO)_3Cp\}_2]^-$. Reactions between $[M_2(CO)_{10}]^{2-}$ (M = Cr, Mo, or W) and Ph_2BiCl lead to the production of the dimetallated complex ions $[Ph_2Bi\{M(CO)_5\}_2]^-$ (equation 11). In the case of M = Cr, the monometallated species $[Ph_2BiCr(CO)_5]^-$ has also been obtained. In the iron system, the products may also be accessed via the reaction of in situ generated Ph_2Bi^- with $Fe(CO)_5$.[61]

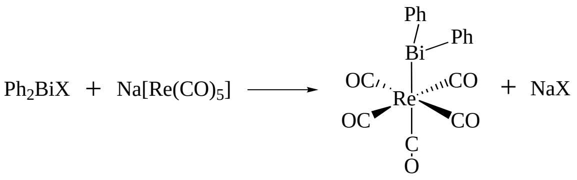

(10)

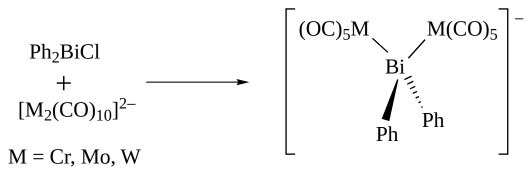

(11)

Organobismuth dihalides ($RBiX_2$) are useful starting materials, as has been demonstrated in the reactions of $PhBiBr_2$ with $Na[CpMo(CO)_3]$ and $Na[Co(CO)_3PPh_3]$ to give the corresponding $PhBi[ML_n]_2$ compounds.[62] The compound $EtBi[CpMo(CO)_3]_2$ can be prepared from the reaction of $ClBi[CoMo(CO)_3]_2$ with $K[HBEt_3]$ (equation 12), and $ClBi[CpFe(CO)_2]_2$ similarly reacts with $AlMe_3$ to give $MeBi[CpFe(CO)_2]_2$.[62] In a number of cases, metallated compounds readily lose one or more organic groups from the bismuth atom or undergo redistribution reactions. An example is the reaction of $BiBrMe_2$ with $[CpM(CO)_x]^-$ (M = Cr,

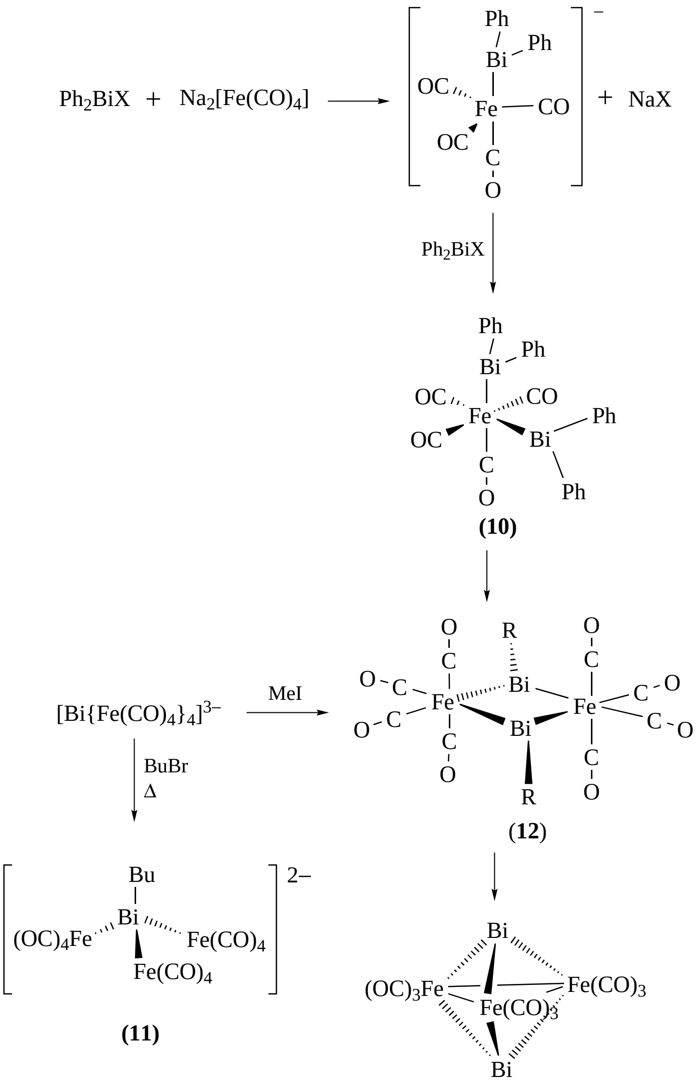

Scheme 1

Mo, W $x = 3$; M = Fe, $x = 2$), giving MeBi[CpM(CO)$_x$]$_2$ instead of the expected Me$_2$Bi[CpM(CO)$_x$].[63] Reaction of [Bi{Fe(CO)$_4$}$_4$]$^{3-}$ with alkyl halides leads to [RBi{Fe(CO)$_4$}$_3$]$^{2-}$ (**11**) or [RBiFe(CO)$_4$]$_2$ (**12**).[64] For R = Bu, two forms are observed. One is the usual cyclic Bi$_2$Fe$_2$ core, while the other shows a polymeric chain of BiFe units.[65]

$$\mathrm{ClBi[CpMo(CO)_3]_2 + K[HBEt_3] \longrightarrow EtBi[CpMo(CO)_3]_2} \qquad (12)$$

Tetraorganodibismuthines and cyclic bismuthines are useful for the preparation of metallated diorganobismuth complexes, as described in Section 2.11.

2.10 Organic Transformations Involving Bi$^{\mathrm{III}}$ Complexes

Bismuth salts are known for promoting a variety of organic reactions, and may have considerable advantages in replacing other metals that are toxic. For example, bismuth metal catalyzes the addition of allyl halides to ketones in the absence of a solvent, and presumably proceeds via Bi(III) intermediates.[66] Bismuth triflate has proven particularly useful and has been widely examined recently.[67–69] Reactions catalyzed by this salt include Diels–Alder reactions, acylations, allylations, and Michael additions among many others. Bismuth chloride has also been used for these same catalytic organic transformations,[68,70,71] but it is sensitive to hydrolysis, producing the insoluble BiOCl. Bismuth triflate, on the other hand, has been used successfully in the presence of water.[69]

Organobismuth(III) complexes may mediate a number of reactions involving allylic compounds and aldehydes. In these reactions, an allyl halide is treated with a bismuth(III) salt such as BiCl$_3$ and a reducing agent (Zn, Fe, or Al) in the presence of an aldehyde (equation 13).[71,72] A likely reaction mechanism involves the reduction of the bismuth halide to an activated metal powder, which can then oxidatively add the organic halide. In cases reported to date, these intermediates have not been isolated or characterized. Some substantiation for this comes from the fact that aldehydes can be allylated in the presence of bismuth powder.

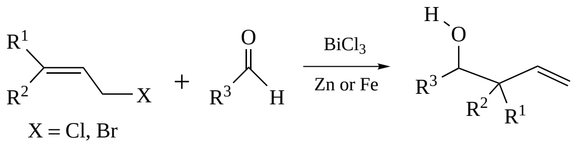

(13)

Bismuth(III) acetate reacts with cyclohexene to produce 1,2-diacetatocyclohexane. If conditions exclude water, a trans configuration arrangement of the two acetate groups is obtained, while the configuration is cis if water is included in the reaction (equations 14 and 15).[73]

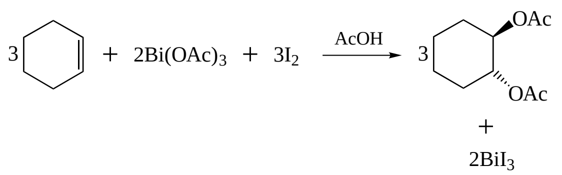

(14)

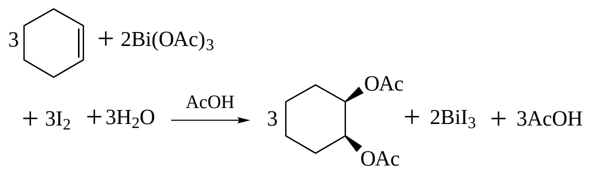

(15)

Copper acetate catalyzes the transfer of CF_3 groups from $Bi(CF_3)_3$ as shown in equations (16) and (17).[12] It is known that $Cu(O_2CCH_3)_2$ and $Bi(CF_3)_3$ undergo redistribution reactions to produce $Bi(CF_3)_2(O_2CCH_3)$ and $Bi(CF_3)(O_2CCH_3)_2$. The bismuth compound is also capable of transferring a methyl group to other metals: with $AgNO_3$ it gives $Ag[Ag(CF_3)_4]$, and with $TeCl_4$ the product is $Te(CF_3)_2Cl_2$.

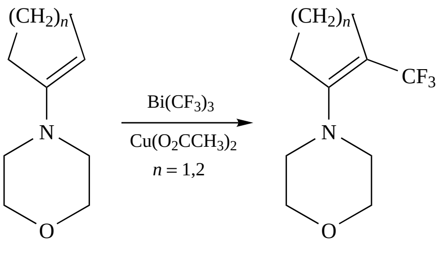

(16)

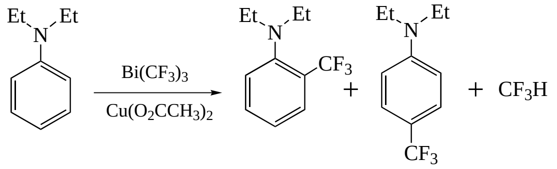

(17)

A number of bismuth/metal oxides are used in the catalytic oxidation of hydrocarbons, and in the oxidation and ammoxidation of alkenes. These transformations are described briefly in ***Bismuth: Inorganic Chemistry***.

2.11 Molecules with Bi–Bi Bonds: Dibismuthines, Dibismuthenes, and Cyclobismuth

Reactions of R_2BiX (X = halide or R) with two equivalents of sodium in liquid ammonia followed by treatment with a dihaloethane results in the formation of the dibismuthines R_2BiBiR_2 (**13**, R = Ph, Me, Et, Pr, *i*-Pr, Bu, Mes; equation 18).[74–76] The heterocyclic derivative 2,2′,5,5′-tetramethylbibismole (**14**) has been similarly prepared from 1-phenyl-2,5-dimethylbismole (see Section 2.12).[77] Presumably $Na^+R_2Bi^-$ is an intermediate, but it has not been isolated. The related $LiBi(SiMe_3)_2 \cdot DME$ complex has, however, been structurally characterized and is converted to the tetrakis(trimethylsilyl)dibismuthine upon reaction with 1,2-dihaloethane.[78] Reduction of Ph_2BiI using Cp_2Co produces $Ph_2BiBiPh_2$, with the advantage that the Cp_2CoI can be recycled (equation 19). Some dibismuthines are thermochromic, as are similar diantimonides.[6,79]

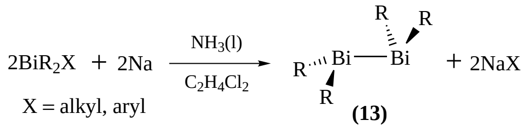

(18)

$$2BiPh_2I + 2Cp_2Co \xrightarrow{THF} R_2Bi{-}BiR_2 + 2Cp_2CoI \qquad (19)$$

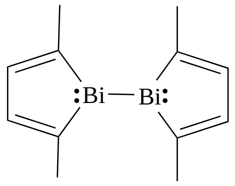

(14)

The dibismuthines with R = phenyl[75,80] and trimethylsilyl[78] have been structurally characterized. Bi–Bi distances are on the order of 3.0 Å. The Bi–Bi bond is reactive and is readily cleaved by a variety of reagents. Chalcogens insert into the Bi–Bi bonds (equation 20).[76] When treated with diarsines, distibines, ditellurides, or diselenides, scrambling of the organo/main group fragments occurs (equation 21), producing $R_2Bi{-}E{-}BiR_2$, which can also be prepared by direct reaction of R_2BiX with Na_2E.[20,81] A similar scrambling occurs with a variety of transition metal carbonyl dimers such as $Co_2(CO)_8$ (equation 22).[82]

$$Ph_2Bi{-}BiPh_2 + E \xrightarrow{E\,=\,O,\,S,\,Se,\,Te} Ph_2Bi{-}E{-}BiPh_2$$
$$\xrightarrow{E\,=\,O} Bi_2O_3 + BiPh_3 \qquad (20)$$

$$Ph_2Bi\text{–}BiPh_2 + R_XE\text{–}EiR_X \longrightarrow 2Ph_2Bi\text{–}E\text{–}R_X \qquad (21)$$

$$E = Sb, X = 2; E = Te, Se, X = 1$$

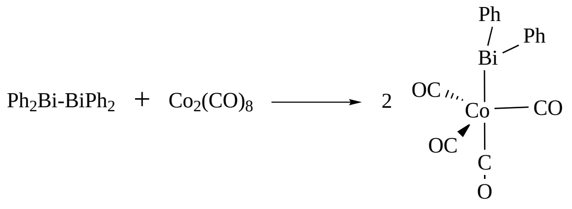

(22)

When extremely bulky aryl groups are attached to bismuth, it has proven possible to isolate dibismuthenes from the reduction of $ArBiX_2$.[83] The aryl groups employed included 2,6-$Mes_2C_6H_3$ and 2,6-$TripC_6H_3$ (Trip = 2,4,6-$^iPr_3C_6H_2$). Analogous complexes of P, As, and Sb were also prepared. Density functional theory calculations on PhBi=BiPh showed good agreement with the experimental X-ray structure and confirmed the presence of a σ and a π bond, both of which are composed almost completely of p orbitals, the s orbitals being used primarily for the nonbonding electron pair.[84]

Cyclic organobismuth compounds of the form $(RBi)_x$ ($x = 3, 4$) result from the reduction of $RBiCl_2$ with Mg [R = $(Me_3Si)_2CH$], $LiAlH_4$ (R = Me_3CCH_2, 2-$Me_2NCH_2C_6H_4$), or $Na/NH_3(l)$ (R = 2-$Me_2NCH_2C_6H_4$).[85,86] These compounds are unstable with respect to disproportionation into BiR_3 and Bi. Metal fragments can be appended to the cyclobismuthines, but the cyclobismuthine structure may not be retained.[50,86,87] For example, reaction of $W(CO)_5(THF)$ with $(RBi)_n$ (R = Me_3CH_2, $n = 3$ or 5) produces $Bi_2R_2\{W(CO)_5\}_2$ (**15**), in which the two tungsten atoms bridge the Bi–Bi bond, and the R groups are cis to each other. Thermal decomposition of $Bi_2R_2\{W(CO)_5\}_2$ (**16**, R = Me_3SiCH_2) results in the elimination of one tungsten carbonyl group, and the R groups end up in a trans configuration.

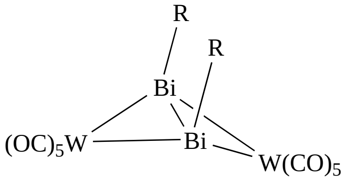

(**15**)

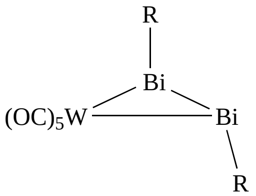

(**16**)

2.12 Heterocyclic Complexes

Inclusion of bismuth atoms in heterocyclic ring complexes has been actively investigated for a number of years. Complexes of the type (**17**), for example, 1-phenyl-2,5-dimethylbismole, have been sought for comparison with pyrrole derivatives and for information about the degree of aromaticity in its heavier analogs. Compound (**17**) is prepared via the addition of 2(*Z*),5(*Z*)-dilithio-3,4-dimethylhexa-2,4-diene to $PhBiI_2$ in 28% yield.[77] This heterocycle is converted to the dibismuthine in the standard fashion: treatment of (**17**) with Na in liquid NH_3 followed by addition of 1,2-dichloroethane.

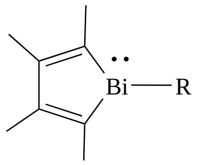

(**17**)

Another method that has been used to prepare bismuth-containing heterocycles is the ligand exchange reaction between $RBiCl_2$ and $Cp_2Zr(C_4Me_4)$ (equation 23).[88] The product where R = Ph can be isolated in 70% yield, but the R = Cl derivative is thermally unstable. Heterocyclobutadienes with one or two bismuth atoms have been studied theoretically.[89]

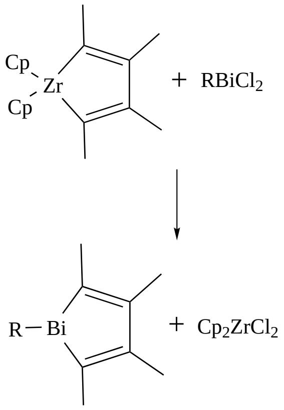

(23)

Bismabenzene (**18**) has been prepared according to Scheme 2.[90] The complex is not stable and will add 1,1,1,4,4,4-hexafluorobutyne to give (**19**). In solution at low temperature, the complex appears to exist as the Diels–Alder dimer (**20**), but raising the temperature gives an NMR spectrum consistent with (**18**).

The heterocyclic complexes incorporating other main group element atoms have been prepared via the reaction of $RBiBr_2$ with an appropriate difunctional salt or chelating ligand (see equations 7 and 8). The compound (**21**) is reported to have anticoccidial and insecticidal properties, as do other $RBi(SR)_2$ compounds.

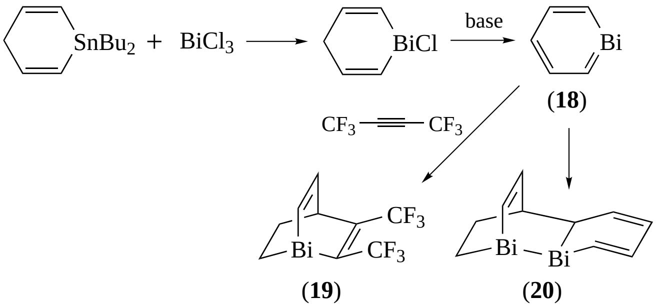

Scheme 2

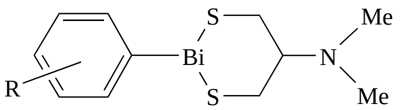

(**21**)

3 PENTAVALENT ORGANOBISMUTH COMPOUNDS

3.1 Syntheses and Structures

Triarylorganobismuth complexes are easily oxidized to bismuth(V) complexes by treatment with chlorine or bromine, giving Ar_3BiX_2 (X = Cl, Br). Reactions with iodine result in elimination to give trivalent $Ar_{3-x}BiI_x$, while reactions with fluorine are too vigorous. Xenon difluoride can be used to prepare Ar_3BiF_2 (Ar = C_6F_5, 2,6-$F_2C_6H_3$).[9,91] Fluoride derivatives are more often prepared by anion metathesis with NaF or $NaBF_4$, but the reaction can be reversed as in the reaction of $(C_6F_5)_3BiF_2$ with Me_3SiCl to form $(C_6F_5)_3BiCl_2$.[92] Substitution of chloride or bromide from Ar_3BiX_2 occurs readily, and has been used to prepare a wide variety of derivatives including the carbonate, the oxide, sulfonates, and carboxylates.[93] Aryloxide complexes of the type $Ph_3Bi(OAr)_2$ may also be prepared by metathesis, while the Ph_4BiOAr complexes are obtained upon alcoholysis of Ph_5Bi.[94] Careful, stoichiometric addition of LiOAr to Ph_3BiX_2 leads to $Ph_3BiX(OAr)$, which undergoes redistribution reactions in solution, presumably through halide- or aryloxide-bridged intermediates.[94] The structure of $(C_6F_5)_3BiF_2$ was shown to have the typical trigonal bipyramidal arrangement with axial fluorine ligands ($d_{\text{Bi–F}} = 2.088(8)$ Å). Each of these fluorine atoms also interacts weakly with the bismuth atoms of the $Bi(C_6F_5)_3$ molecules ($d_{\text{Bi}\cdots\text{F}} = 2.759(8)$ Å) that cocrystallized with the difluoride.[9] Trimethylbismuthine has been chlorinated with thionyl chloride at low temperatures to give unstable Me_3BiCl_2, which was converted into $BiMe_5$ and $[BiMe_6]^-$.[95,96] $BiMe_3$ reacts with $MeSO_3CF_3$ to give $BiMe_4^+$ salts.

3.2 Reactions of Pentavalent Organobismuth Compounds

Heating of Ar_3BiX_2 (**22**, X = Br, Cl) eliminates ArX with the production of Ar_2BiX. Reactions with I_2 do not yield tractable Bi^V complexes, but lead directly to Ar_2BiI and/or $ArBiI_2$ at room temperature, presumably through a similar Bi^V intermediate. For the trialkyl species, bismuth(V) compounds are not observed and halogenation leads directly to the formation of either R_2BiX or $RBiX_2$. The formation of Ar_3BiX_2 is the starting point for the production of a wide range of triarylbismuth(V) complexes (Scheme 3). Cl^- and Br^- have been replaced by such anions as F^-, CO_3^{2-}, SO_4^{2-}, ClO_4^-, ReO_4^-, MoO_4^{2-}, and so on. The oxide Ph_3BiO, prepared by treating Ph_3BiCl_2 with moist Ag_2O, is reported to be soluble in acetonitrile, but may be polymeric in the solid state. Alkaline hydrolysis of Ph_3BiCl_2 (**22**) gives $[ClPh_3Bi]_2O$ (**23**), whereas with an aqueous solution of $AgClO_4$, this product is $[\{(H_2O)Ph_3Bi\}O][ClO_4]_2$. The water is lost under vacuum and anhydrous material is obtained. The nitrate is prepared similarly using $AgNO_3$.

Structural work on Ph_3BiCl_2, $ClBiPh_3OC_9H_6N$, and $O[BiPh_3OClO_3]_2$ confirms the trigonal bipyramidal coordination geometry about the bismuth atom.[97,98] The hydroxyquinolinate complex $Ph_3BiCl(OC_9H_6N)$ shows a weak Bi–N interaction. The displacement of the halides may also occur intramolecularly, as seen for the ligand $OC(CF_3)_2C_6H_4$ in (**24**)–(**26**).[99] Compound (**24**) can be converted into BiL(4-tolyl)$_3$ (L = $OC(CF_3)_2C_6H_4$). This complex reacts with MeLi to give the anionic, octahedral anion $[BiL(4\text{-tolyl})_3Me]^-$, which subsequently reacts with water to give BiL(4-tolyl)$_2$Me.

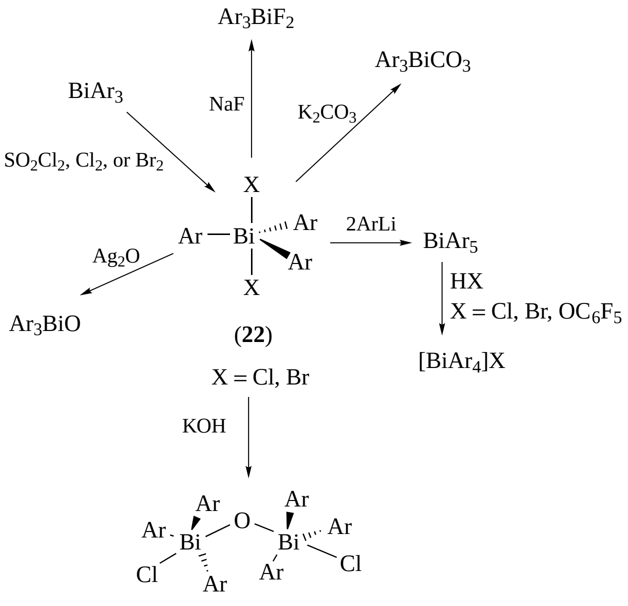

Scheme 3

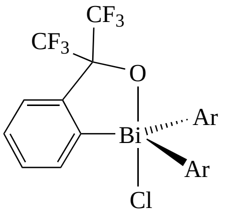
CF3
CF3
O
Bi
Ar
Ar
Cl

(**24**)

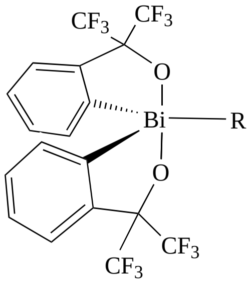
CF3
CF3
O
Bi
R
O
CF3
CF3

(**25**)

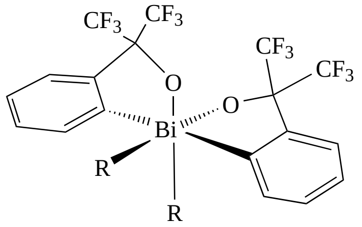
CF3
CF3
O
CF3
CF3
O
Bi
R
R

(**26**)

These two molecules are rare examples of bismuth(V) alkyl complexes.

Reactions of Ar_3BiX_2 with organolithium reagents are common for producing Ar_5Bi complexes. Unstable, purple Ph_5Bi was the first of these to be synthesized.[100] Interesting variations in the structure and color of these complexes as a function of Ar have been reported.[101] The color of $BiPh_5$ has been attributed to relativistic effects.[102] A series of $BiAr_5$ complexes have been structurally characterized. The nature of the aryl ligands is important in determining whether the structure of those complexes is trigonal bipyramidal or square planar, which is also related to their color.[103]

In addition to exchange reactions, a halide ion can be abstracted from the bismuth of Ar_3BiX_2 complexes to give $[Ar_3BiX]^+$ ions. As mentioned before, Ar_3BiI_2 has not been isolated as it apparently undergoes immediate elimination, but at low temperatures, in the presence of $AgAsF_6$ the complex, $[Ar_3BiI][AsF_6]$ has been isolated.[104] This complex has been reported to be a better bactericide than Ph_3Bi. The complex $[Ph_4Bi][MeC_6H_4SO_3]$ is similar, but the tosylate anion is weakly bound to the bismuth atom ($d_{Bi–O} = 2.77$ Å), giving it a distorted trigonal bipyramidal geometry.[98] There is a similar interaction between $[Ph_4Bi]^+$ and an oxygen atom of an acetate ligand in $[Ph_4Bi][Ph_2Bi(O_2CCF_3)_2]$. Pentaphenyl bismuth is Lewis acidic and will react with pyridine to give the adduct $BiPh_5$·pyridine or with LiPh in diethyl ether or THF to produce unstable $Li[BiPh_6]$.[105]

Organobismuth(V) reagents are useful for a wide variety of organic transformations including transfer reactions, oxidation of primary, secondary, benzylic, and allylic alcohols (equations 24–33). Copper or copper salts promote, and may be required for, the transfer reactions.[106,107] These reagents also cleave glycols (equations 27 and 28), and under the appropriate conditions function as aryl group transfer reagents (equations 29–33). These examples are only a small representation of the work that has been done in this area.[108] Reactions of *cis*-cyclohexane-1,2-diol, *meso*-butane-2,3-diol, and *meso*-cyclopentane-1,2-diol with $Ph_3Bi(OAc)_2$ in the presence of catalytic amounts of $Cu(OAc)_2$ have been studied.[109] In the case of the cyclopentanediol, phenylation occurred giving a racemic mixture of the phenoxycyclopentanol. Optical selection was obtained when the reaction was carried out in the presence of one of the enantiomers of chiral 2-pyridyloxazolines. Alkoxide complexes are implicated as intermediates in some of these reactions, and for one case such a complex, $(3,5\text{-}(t\text{-}Bu)_2C_6H_3OBiPh_3Cl)$, has been isolated. The aryl group transfer reaction is thought to proceed via a nonionic, nonradical concerted mechanism.

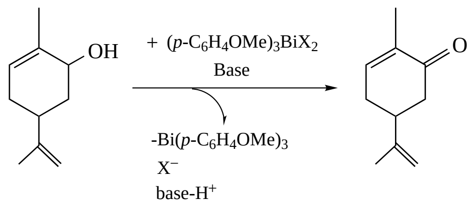
OH
+ (p-C6H4OMe)3BiX2
Base
-Bi(p-C6H4OMe)3
X−
base-H+
O

(24)

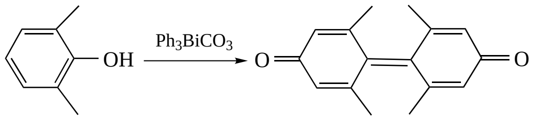
OH
Ph3BiCO3
O
O

(25)

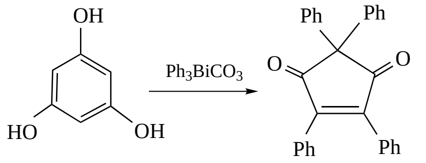
OH
HO
OH
Ph3BiCO3
Ph
Ph
O
O
Ph
Ph

(26)

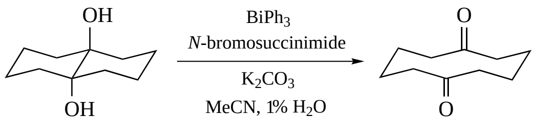
OH
OH
BiPh3
N-bromosuccinimide
K2CO3
MeCN, 1% H2O
O
O

(27)

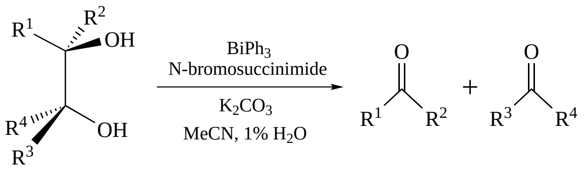
R1
R2
OH
R4
R3
OH
BiPh3
N-bromosuccinimide
K2CO3
MeCN, 1% H2O
O
R1
R2
+
O
R3
R4

(28)

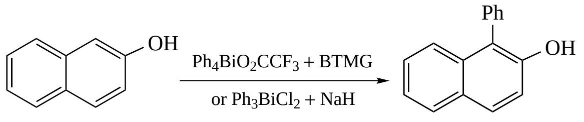
OH
Ph4BiO2CCF3 + BTMG
or Ph3BiCl2 + NaH
Ph
OH

(29)

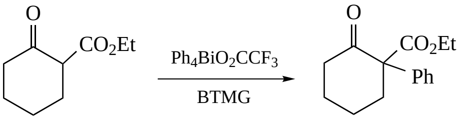
O
CO2Et
Ph4BiO2CCF3
BTMG
O
CO2Et
Ph

(30)

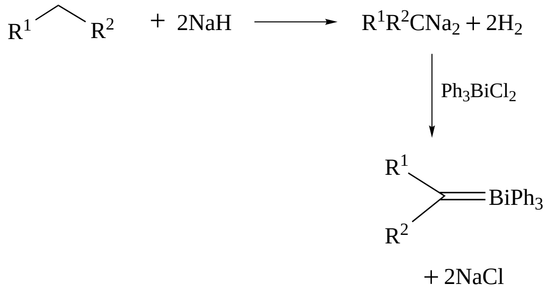

$R^1 = R^2 = MeCO, PhSO_2; R^1 = MeCO, R^2 = PhCO; R^1 = MeCO, R^2 = MeOCO$

Scheme 4

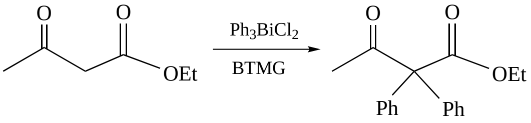

(31)

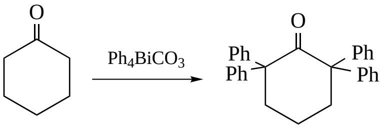

(32)

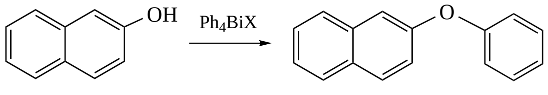

(33)

The compound $Ar_2Bi(O)OMe$, which was prepared via the reaction of Ar_3Bi and $4\text{-}MeC_6H_4SO_2NClNa$, has been reported to acylate amides, thioamides, ureas, and thioureas. The first step of the process is believed to be reaction of the $Ar_2Bi(O)OMe$ compound with acetic acid to replace the methoxide with acetate.[110]

3.3 Bismuth Ylides

Bismuth ylide chemistry is not nearly so well developed compared to the extensive chemistry of phosphorus ylides ($R_3P{=}CR_2$). This is in large part due to the inaccessibility of bismuth alkyl cations R_4Bi^+ for deprotonation to ylides, as is frequently the strategy employed for phosphorus. A theoretical investigation of the group 15 ylides predicted that the formation of $MeBiH_3^+$ from MeCl and BiH_3 is endothermic.[111] Quaternization of bismuth is difficult, but MeO_3SCF_3 will react with $BiMe_3$ to give $BiMe_4^+$.[95] Alternative routes that involve the reaction of sodium salts of methylene compounds with Ph_3BiCl_2 or Ph_3BiO (Schemes 4 and 5) have been developed.[107,112] In many cases, the bismuthonium ylides have not been isolated from solution. Compound (**26**), where R = Me, has yielded to X-ray structural characterization.[113] The $Bi–C_{ylide}$ distance is 2.16 Å, only slightly shorter than the $Bi–C_{phenyl}$ distances, suggesting that there is considerable ionic character in the Bi−ylide bond.

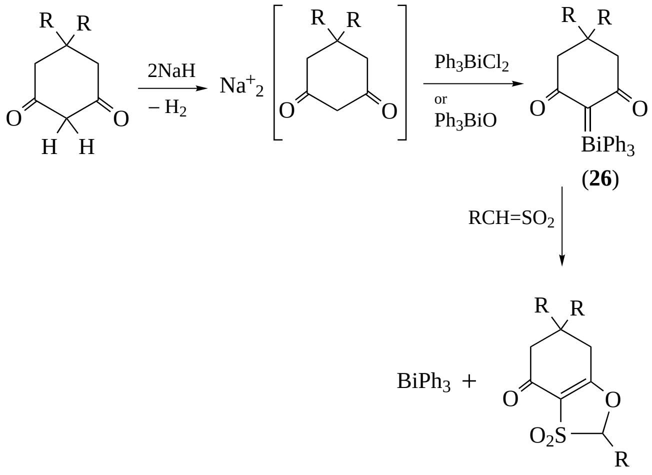

Scheme 5

The ylide function is exchanged upon addition of dimethyl sulfide in the presence of CuCl to give $R^1R^2CSMe_2$ and $BiPh_3$ (Scheme 5). Exchange could also be accomplished to PPh_3 and $AsPh_3$ but not $SbPh_3$. The sodium salt of acetylacetone reacts with Ph_3BiCl_2 to generate an ylide complex that could not be isolated. Attempts at chromatography led to the isolation of the *C*-phenylated acetylacetone instead. This ylide complex, however, reacts with H_2CSO_2 generated in situ to give 1,3-oxathiole-3,3-dioxide.

In related chemistry, $BiPh_3$ is oxidized by anhydrous chloramine-T (RSO_2NClNa, $R = p\text{-}MeC_6H_4$) or with $R_fSO_2NH_2$ ($R = CF_3, 4\text{-}FC_6H_4, CF_2CF_2CF_2CF_3$) in the presence of NaOMe to give $Ph_3Bi{=}NSO_2R$.[114] This may be compared to the same reaction carried out in the presence of wet methanol, which gives the $Ar_2Bi(O)OMe$ complexes described above.

4 RELATED ARTICLES

Antimony: Organometallic Chemistry; Arsenic: Organoarsenic Chemistry; Bismuth: Inorganic Chemistry.

5 REFERENCES

1. C. Löwig and E. Schweizer, *Annalen*, 1850, **75**, 355.
2. H. Suzuki and Y. Matano, 'Organobismuth Chemistry', Elsevier, New York, 2001.
3. (a) M. Wieber, 'Gmelin Handbuch der Anorganischen Chemie', R. J. Meyer ed., Springer Verlag, Berlin, 1977, p. 1; (b) L. D. Freedman and G. O. Doak, *Chem. Rev.*, 1982, **82**, 15; (c) C. Silvestru, H. J. Breunig, and H. Althaus, *Chem. Rev.*, 1999, **99**, 3277.
4. H. Gilman and H. L. Yale, *Chem. Rev.*, 1942, **30**, 281.
5. (a) L. D. Freedman and G. O. Doak, *Organomet. Chem. Rev. (B)*, 1970, **6**, 656; (b) L. D. Freedman and G. O. Doak, *Chem. Met.-Carbon Bond*, 1989, **5**, 397; (c) K.-Y. Akiba and Y. Yamamoto, *Chem. Org. Arsenic, Antimony Bismuth Compd.*, 1994, 761; (d) N. R. Champness and W. Levason, *Coord. Chem. Rev.*, 1994, **133**, 115; (e) N. C., Norman ed., 'The Chemistry of Arsenic, Antimony and Bismuth', Blackie Academic and Professional Books, Glasgow, 1998, p. 483; (f) R. W. Read, *Compr. Org. Funct. Group Transform.*, 1995, **2**, 871; (g) M.-X. Wang, *Compr. Org. Funct. Group Transform.*, 1995, **2**, 479; (h) H. J. Breunig and R. Rosler, *Chem. Soc. Rev.*, 2000, **29**, 403; (i) G. Balazs and H. J. Breunig, *Phys. Organomet. Chem.*, 2002, **3**, 387; (j) J.-P. Majoral and A.-M. Caminade, *Chem. Rev.*, 1999, **99**, 845.
6. H. J. Breunig, *Chem. Org. Arsenic, Antimony Bismuth Compd.*, 1994, 441.
7. (a) G. O. Doak and L. D. Freedman, *Organomet. Chem. Rev. (B)*, 1968, **4**, 426; (b) L. D. Freedman and G. O. Doak, *Organomet. Chem. Rev. (B)*, 1969, **5**, 186; (c) L. D. Freedman and G. O. Doak, *Organomet. Chem. Rev. (B)*, 1971, **8**, 247; (d) L. D. Freedman and G. O. Doak, *J. Organomet. Chem.*, 1973, **48**, 292; (e) L. D. Freedman and G. O. Doak, *J. Organomet. Chem. Rev. (B)*, 1974, **68**, 411; (f) L. D. Freedman and G. O. Doak, *J. Organomet. Chem. Rev. (B)*, 1975, **89**, 183; (g) L. D. Freedman and G. O. Doak, *J. Organomet. Chem. Rev. (B)*, 1976, **106**, 255; (h) L. D. Freedman and G. O. Doak, *J. Organomet. Chem. Rev. (B)*, 1977, **130**, 405; (i) L. D. Freedman and G. O. Doak, *J. Organomet. Chem. Rev. (B)*, 1978, **163**, 141; (j) L. D. Freedman and G. O. Doak, *J. Organomet. Chem. Rev. (B)*, 1978, **147**, 233; (k) L. D. Freedman and G. O. Doak, *J. Organomet. Chem. Rev. (B)*, 1979, **180**, 143; (l) L. D. Freedman and G. O. Doak, *J. Organomet. Chem. Rev. (B)*, 1980, **203**, 359; (m) L. D. Freedman and G. O. Doak, *J. Organomet. Chem. Rev. (B)*, 1982, **237**, 51; (n) L. D. Freedman and G. O. Doak, *J. Organomet. Chem. Rev. (B)*, 1983, **245**, 65; (o) L. D. Freedman and G. O. Doak, *J. Organomet. Chem. Rev. (B)*, 1984, **261**, 59; (p) L. D. Freedman and G. O. Doak, *J. Organomet. Chem. Rev. (B)*, 1985, **17**, 353; (q) L. D. Freedman and G. O. Doak, *J. Organomet. Chem. Rev. (B)*, 1986, **298**, 67; (r) L. D. Freedman and G. O. Doak, *J. Organomet. Chem. Rev. (B)*, 1987, **324**, 39; (s) L. D. Freedman and G. O. Doak, *J. Organomet. Chem. Rev. (B)*, 1988, **351**, 63; (t) L. D. Freedman and G. O. Doak, *J. Organomet. Chem. Rev. (B)*, 1989, **360**, 297; (u) L. D. Freedman and G. O. Doak, *J. Organomet. Chem. Rev. (B)*, 1990, **380**, 35; (v) L. D. Freedman and G. O. Doak, *J. Organomet. Chem. Rev. (B)*, 1991, **404**, 87; (w) L. D. Freedman and G. O. Doak, *J. Organomet. Chem. Rev. (B)*, 1992, **442**, 61; (x) L. D. Freedman and G. O. Doak, *J. Organomet. Chem. Rev. (B)*, 1994, **477**, 31; (y) L. D. Freedman and G. O. Doak, *J. Organomet. Chem. Rev. (B)*, 1995, **496**, 1; (z) L. D. Freedman and G. O. Doak, *J. Organomet. Chem. Rev. (B)*, 1995, **485**, 1.
8. T. Lewe, D. Naumann, G. Nowicki, H. Schneider, W. Tyrra, T. Gilles, and K. F. Tebbe, *Z. Anorg. Allg. Chem.*, 1996, **622**, 2009.
9. (a) D. Naumann and W. Tyrra, *J. Organomet. Chem.*, 1987, **334**, 323; (b) W. Tyrra and D. Naumann, *Can. J. Chem.*, 1989, **67**, 1949.
10. (a) D. Naumann, R. Schlengermann, and W. Tyrra, *J. Fluorine Chem.*, 1994, **66**, 79; (b) N. V. Kirij, S. V. Pasenok, Y. L. Yagupolskii, D. Naumann, and W. Turra, *Russ. J. Org. Chem.*, 2001, **37**, 207; (c) N. V. Kirij, S. V. Pasenok, Y. L. Yagupolskii, A. Fitzner, W. Tyrra, and D. Naumann, *J. Fluorine Chem.*, 1999, **94**, 207.
11. N. V. Kirij, S. V. Pasenok, Y. L. Yagupolskii, D. Naumann, and W. Tyrra, *J. Fluorine Chem.*, 1994, **69**, 219.
12. N. V. Kirij, S. V. Pasenok, Y. L. Yagupolskii, W. Tyrra, and D. Naumann, *J. Fluorine Chem.*, 2000, **106**, 217.
13. G. Becker, H. Freudenblum, O. Mundt, M. Reti, and M. Sachs, *Synth. Meth. Organomet. Inorg. Chem.*, 1996, **3**, 193.
14. J. A. Morrison and R. J. Lagow, *Inorg. Chem.*, 1977, **16**, 1832.
15. N. A. A. Al-Jabar, J. B. Jones, D. S. Brown, A. H. Colligan, A. G. Massey, J. M. Miller, and J. W. Nye, *Appl. Organomet. Chem.*, 1989, **3**, 459.
16. A. R. Al-Soudani and A. G. Massey, *Appl. Organomet. Chem.*, 1988, **2**, 553.
17. M. Wieber and K. Rudolph, *Z. Naturforsch.*, 1988, **B43**, 739.
18. Y. Matano, H. Kurata, T. Murafuji, N. Azuma, and H. Suzuki, *Organometallics*, 1998, **17**, 4049.
19. (a) H. J. Breunig, I. Ghesner, M. E. Ghesner, and E. Lork, *Inorg. Chem.*, 2003, **42**, 1751; (b) H. Suzuki, T. Murafuji, Y. Matano, and N. Azuma, *J. Chem. Soc., Perkin Trans.*, 1993, 2969; (c) H. Suzuki, T. Murafuji, and N. Azuma, *J. Chem. Soc., Perkin Trans.*, 1993, 1169; (d) T. Murafuji, N. Azuma, and H. Suzuki, *Organometallics*, 1995, **14**, 1542.
20. H. J. Breunig and D. Mueller, *Z. Naturforsch.*, 1986, **41B**, 1129.
21. K. H. Whitmire, D. Labahn, H. W. Roesky, M. Noltemeyer, and G. M. Sheldrick, *J. Organomet. Chem.*, 1991, **402**, 55.
22. R. Fossheim, *Inorg. Chim. Acta*, 1999, **284**, 167.
23. D. M. Hawley, G. Ferguson, and G. S. Harris, *Chem. Commun.*, 1966, **4**, 111.
24. (a) E. N. Gur'yanova, A. N. Sobolev, I. P. Romm, and V. K. Bel'skii, *Khim. Svyaz Str. Mol.*, 1984, 97; (b) A. N. Sobolev, I. P. Romm, V. K. Bel'skii, and E. N.

Gur'yanova, *Koordinats Khim+*, 1980, **6**, 945; (c) A. N. Sobolev, V. K. Bel'skii, and I. P. Romm, *Koordinats Khim+*, 1983, **9**, 262; (d) B. Murray, J. Hvoslef, H. Hope, and P. P. Power, *Inorg. Chem.*, 1983, **22**, 3421.

25. B. Beagley and A. R. Medwid, *J. Mol. Struct.*, 1977, **38**, 229.
26. Y. Yamamoto, X. Chen, and K. Akiba, *J. Am. Chem. Soc.*, 1992, **114**, 7906.
27. D. A. Dixon and A. J. Arduengo, III *J. Am. Chem. Soc.*, 1987, **109**, 338.
28. P. Bras, H. Herwijer, and J. Wolters, *J. Organomet. Chem.*, 1981, **212**, C7.
29. E. O. Fischer and S. Schreiner, *Chem. Ber.*, 1960, **93**, 1417.
30. W. Frank, *J. Organomet. Chem.*, 1990, **386**, 177.
31. P. Jutzi, *J. Organomet. Chem.*, 1990, **400**, 1.
32. (a) A. Schier, J. M. Wallis, G. Moeller, and H. Schmidbaur, *Angew. Chem.*, 1986, **98**, 742; (b) H. Schmidbaur, J. M. Wallis, R. Nowak, B. Huber, and G. Mueller, *Chem. Ber.*, 1987, **120**, 1837; (c) H. Schmidbaur, R. Nowak, A. Schier, J. M. Wallis, B. Huber, and G. Mueller, *Chem. Ber.*, 1987, **120**, 1829; (d) W. Frank, J. Schneider, and S. Mueller-Becker, *Chem. Commun.*, 1993, 799.
33. (a) W. Frank, J. Weber, and E. Fuchs, *Angew. Chem.*, 1987, **99**, 68; (b) S. Mueller-Becker, W. Frank, and J. Schneider, *Z. Anorg. Allg. Chem.*, 1993, **619**, 1073; (c) W. Frank and V. Reiland, *Acta Cryst.*, 1998, **C54**, 1626.
34. C. M. Jones, M. D. Burkart, R. E. Bachman, D. L. Serra, S. J. Hwu, and K. H. Whitmire, *Inorg. Chem.*, 1993, **32**, 5136.
35. K. H. Whitmire, S. Hoppe, O. Sydora, J. L. Jolas, and C. M. Jones, *Inorg. Chem.*, 2000, **39**, 85.
36. (a) A. J. Carty, N. J. Taylor, A. W. Coleman, and M. F. Lappert, *Chem. Commun.*, 1979, 639; (b) E. O. Fischer and K. Richter, *Chem. Ber.*, 1976, **109**, 1140.
37. H. Schumann and L. Eguren, *J. Organomet. Chem.*, 1991, **403**, 183.
38. L. Vaska and J. Peone, Jr *Suom Kemistil B*, 1971, **44**, 317.
39. (a) D. Benlian and M. Bigorgne, *Bull. Soc. Chim. Fr.*, 1963, 1583; (b) R. Talay and D. Rehder, *Z. Naturforsch.*, 1981, **B36**, 451; (c) H. Schumann and H. J. Breunig, *J. Organomet. Chem.*, 1975, **87**, 83.
40. F. Hein and H. Pobloth, *Z. Anorg. Allg. Chem.*, 1941, **248**, 84.
41. (a) J. Selbin, N. Ahmad, and M. J. Pribble, *J. Inorg. Nucl. Chem.*, 1970, **32**, 3249; (b) J. Desnoyers and R. Rivest, *Can. J. Chem.*, 1965, **43**, 1879.
42. (a) T. Masuda, T. Hamano, K. Tsuchihara, and T. Higashimura, *Macromolecules*, 1990, **23**, 1374; (b) T. Masuda, T. Matsumoto, T. Yoshimura, and T. Higashimura, *Macromolecules*, 1990, **23**, 4902.
43. K. H. Whitmire, J. C. Hutchison, A. L. McKnight, and C. M. Jones, *Chem. Commun.*, 1992, 1021.
44. M. Ali, W. R. McWhinnie, A. A. West, and T. A. Hamor, *J. Chem. Soc., Dalton Trans.*, 1990, 899.
45. (a) G. Becker, J. Egner, O. Mundt, and H. Stadelmann, *Synth. Meth. Organomet. Inorg. Chem.*, 1996, **3**, 210; (b) G. Becker, J. Egner, M. Meiser, O. Mundt, and J. Weidlein, *Z. Anorg. Allg. Chem.*, 1997, **623**, 941; (c) K. H. Ebert, R. E. Schulz, H. J. Breunig, C. Silvestru, and I. Haiduc, *J. Organomet. Chem.*, 1994, **470**, 93.
46. H. Althaus, H. J. Breunig, and E. Lork, *Organometallics*, 2001, **20**, 586.
47. R. J. Wiacek, J. N. Jones, C. L. B. MacDonald, and A. H. Cowley, *Can. J. Chem.*, 2002, **80**, 1518.
48. P. Jutzi and K. H. Schwartzen, *Chem. Ber.*, 1989, **122**, 287.
49. N. J. Hardman, B. Twamley, and P. P. Power, *Angew. Chem., Int. Ed. Eng.*, 2000, **39**, 2771.
50. G. Balazs, H. J. Breunig, and E. Lork, *Organometallics*, 2002, **21**, 2584.
51. (a) R. Hillwig, F. Kunkel, K. Harms, B. Neumueller, and K. Dehnicke, *Z. Naturforsch. (B)*, 1997, **52**, 149; (b) W. Clegg, M. R. J. Elsegood, R. J. Errington, G. A. Fisher, and N. C. Norman, *J. Math. Chem.*, 1994, **4**, 891; (c) H. J. Breunig and H. Althaus, *Phosphorus Sulfur*, 2001, **168–169**, 123.
52. (a) W. Clegg, R. J. Errington, G. A. Fisher, R. J. Flynn, and N. C. Norman, *J. Chem. Soc., Dalton Trans.*, 1993, 637; (b) S. C. James, N. C. Norman, A. G. Orpen, and J. Starbuck, *Cryst. Eng. Comm.*, 2000, **10**; (c) S. Faleschini, P. Zanella, L. Doretti, and G. Faraglia, *J. Organomet. Chem.*, 1972, **44**, 317.
53. (a) C. J. Carmalt, A. H. Cowley, A. Decken, and N. C. Norman, *J. Organomet. Chem.*, 1995, **496**, 59; (b) S. C. James, N. C. Norman, and A. G. Orpen, *J. Chem. Soc., Dalton Trans.*, 1999, 2837.
54. (a) C. J. Carmalt, L. J. Farrugia, and N. C. Norman, *J. Chem. Soc., Dalton Trans.*, 1996, 443; (b) C. J. Carmalt, N. C. Norman, A. G. Orpen, and S. E. Stratford, *J. Organomet. Chem.*, 1993, **460**, C22.
55. (a) C. J. Carmalt, A. H. Cowley, R. D. Culp, R. A. Jones, S. Kamepalli, and N. C. Norman, *Inorg. Chem.*, 1997, **36**, 2770; (b) C. J. Carmalt, D. Walsh, A. H. Cowley, and N. C. Norman, *Organometallics*, 1997, **16**, 3597.
56. C. J. Carmalt, A. H. Cowley, A. Decken, Y. G. Lawson, and N. C. Norman, *Organometallics*, 1996, **15**, 887.
57. W. Tyrra, D. Naumann, N. V. Kirij, A. A. Kolomeitsev, and Y. L. Yagupolskii, *Dalton Trans.*, 1999, 657.
58. P. Köpf-Maier and T. Klapötke, *Inorg. Chim. Acta*, 1988, **152**, 49.
59. (a) J. M. Cassidy and K. H. Whitmire, *Inorg. Chem.*, 1991, **30**, 2788; (b) A. N. Nesmeyanov, K. N. Anisimov, N. E. Kolobova, and V. N. Khandozhko, *Dok. Akad. Nauk SSSR*, 1964, **156**, 383.
60. R. J. Errington, G. A. Fisher, N. C. Norman, A. G. Orpen, and S. E. Stratford, *Z. Anorg. Allg. Chem.*, 1994, **620**, 457.
61. R. E. Bachman and K. H. Whitmire, *Inorg. Chem.*, 1995, **34**, 1542.

62. W. Clegg, N. A. Compton, R. J. Errington, G. A. Fisher, N. C. Norman, and N. Wishart, *J. Organomet. Chem.*, 1990, **399**, C21.

63. (a) H. A. Kaul, D. Greissinger, M. Luksza, and W. Malisch, *J. Organomet. Chem.*, 1982, **228**, C29; (b) P. Panster and W. Malisch, *J. Organomet. Chem.*, 1977, **134**, C32.

64. M. Shieh, Y. Liou, and B. W. Jeng, *Organometallics*, 1993, **12**, 4926.

65. M. Shieh, Y. Liou, M.-H. Hsu, R.-T. Chen, S.-J. Yeh, S.-M. Peng, and G.-H. Lee, *Angew. Chem. Int. Ed. Eng.*, 2002, **41**, 2384.

66. P. C. Andrews, A. C. Peatt, and C. L. Raston, *Green Chem.*, 2001, **3**, 313.

67. (a) R. Varala, M. M. Alam, and S. R. Adapa, *Synlett*, 2003, 67; (b) A. Oussaid, B. Garrigues, B. Oussaid, and F. Benyaquad, *Phosphorus Sulfur*, 2002, **177**, 2315; (c) B. M. Choudary, S. Chidara, and C. V. R. Sekhar, *Synlett*, 2002, 1694; (d) R. S. Mohan, P. L. Butler, and J. R. Stephens (2002), Abstracts of Papers, *224th ACS National Meeting*, Boston, MA, *August 18–22*, ORGN-719; (e) R. S. Mohan, D. A. Freiberg, N. M. Leonard, B. A. Nattier, M. C. Oswald, and R. C. Smith (2002), Abstracts of Papers, *224th ACS National Meeting*, Boston, MA, *August 18–22*, ORGN-718; (f) R. S. Mohan, L. C. Wieland, and H. M. Zerth (2002), Abstracts of Papers, *224th ACS National Meeting*, Boston, MA, *August 18–22*, ORGN-717; (g) A. Oussaid and B. Garrigues, *Phosphorus Sulfur*, 2002, **177**, 825; (h) N. M. Leonard, M. C. Oswald, D. A. Freiberg, B. A. Nattier, R. C. Smith, and R. S. Mohan, *J. Org. Chem.*, 2002, **67**, 5202; (i) L. C. Wieland, H. M. Zerth, and R. S. Mohan, *Tetrahedron Lett.*, 2002, **43**, 4597; (j) M. D. Carrigan, D. Sarapa, R. C. Smith, L. C. Wieland, and R. S. Mohan, *J. Org. Chem.*, 2002, **67**, 1027; (k) A. Orita, C. Tanahashi, A. Kakuda, and J. Otera, *J. Org. Chem.*, 2001, **66**, 8926; (l) B. Leroy and I. E. Marko, *Tetrahedron Lett.*, 2001, **42**, 8685; (m) M. D. Carrigan, D. A. Freiberg, R. C. Smith, H. M. Zerth, and R. S. Mohan, *Synthesis*, 2001, 2091; (n) M. D. Carrigan, K. J. Eash, M. C. Oswald, and R. S. Mohan, *Tetrahedron Lett.*, 2001, **42**, 8133; (o) K. A. Bhatia, K. J. Eash, N. M. Leonard, M. C. Oswald, and R. S. Mohan, *Tetrahedron Lett.*, 2001, **42**, 8129; (p) R. S. Mohan, N. M. Leonard, K. A. Bhatia and K. J. Eash, *Abstracts of Papers, 222nd ACS National Meeting, Chicago, IL, United States, August 26–30, 2001*, 2001, ORGN-332; (q) R. Mohan, H. M. Zerth and D. A. Freiberg, *Abstracts of Papers, 222nd ACS National Meeting, Chicago, IL, United States, August 26–30, 2001*, 2001, CHED-247; (r) Y. Torisawa, T. Nishi, and J.-i. Minamikawa, *Org. Process Res. Dev.*, 2001, **5**, 84; (s) S. Repichet, C. Le Roux, P. Hernandez, J. Dubac, and J.-R. Desmurs, *J. Org. Chem.*, 1999, **64**, 6479; (t) S. Repichet, C. Le Roux, J. Dubac, and J.-R. Desmurs, *Eur. J. Org. Chem.*, 1998, 2743; (u) M. Leonard Nicholas, C. Oswald Matthew, A. Freiberg Derek, A. Nattier Bryce, C. Smith Russell, and S. Mohan Ram, *J. Org. Chem.*, 2002, **67**, 5202; (v) D. Carrigan Marc, D. Sarapa, C. Smith Russell, C. Wieland Laura, and S. Mohan Ram, *J. Org. Chem.*, 2002, **67**, 1027; (w) J. S. Yadav, B. V. S. Reddy, and T. Swamy, *Tetrahedron Lett.*, 2003, **44**, 9121; (x) S. V. Reddy, R. J. Rao, U. S. Kumar, and J. M. Rao, *Chem. Lett.*, 2003, **32**, 1038; (y) T. Ollevier and T. Ba, *Tetrahedron Lett.*, 2003, **44**, 9003; (z) J. R. Stephens, P. L. Butler, C. H. Clow, M. C. Oswald, R. C. Smith and R. S. Mohan, *Eur. J. Org. Chem.*, 2003, 3827; (aa) K. E. Peterson, R. C. Smith, and R. S. Mohan, *Tetrahedron Lett.*, 2003, **44**, 7723; (ab) M. M. Alam, R. Varala, and S. R. Adapa, *Synth. Commun.*, 2003, **33**, 3035; (ac) J. S. Yadav, B. V. S. Reddy, and G. Satheesh, *Tetrahedron Lett.*, 2003, **44**, 6501; (ad) A. V. Reddy, K. Ravinder, T. V. Goud, P. Krishnaiah, T. V. Raju, and Y. Venkateswarlu, *Tetrahedron Lett.*, 2003, **44**, 6257; (ae) J. S. Yadav, B. V. S. Reddy, P. N. Reddy, and M. S. Rao, *Synthesis*, 2003, 1387; (af) A. Oussaid, F. Benyaquad, B. Oussaid, and B. Garrigues, *Phosphorus Sulfur*, 2003, **178**, 1605; (ag) K. Ikeda, Y. Torisawa, T. Nishi, J. Minamikawa, K. Tanaka, and M. Sato, *Bioorgan. Med. Chem.*, 2003, **11**, 3073; (ah) M. M. Alam, R. Varala, and S. R. Adapa, *Tetrahedron Lett.*, 2003, **44**, 5115; (ai) J. S. Yadav, B. V. S. Reddy, and T. Swamy, *Tetrahedron Lett.*, 2003, **44**, 4861; (aj) S. Gmouh, H. Yang, and M. Vaultier, *Org. Lett.*, 2003, **5**, 2219; (ak) R. Varala, M. M. Alam, and S. R. Adapa, *Synlett*, 2003, 720; (al) A. Kamal, P. S. M. M. Reddy, and D. Rajasekhar Reddy, *Tetrahedron Lett.*, 2003, **44**, 2857; (am) I. Mohammadpoor-Baltork and A. R. Khosropour, *Molecules [online computer file]*, 2001, **6**, 996.

68. (a) C. Le Roux and J. Dubac, *Synlett*, 2002, 181; (b) H. Laurent-Robert, B. Garrigues, and J. Dubac, *Synlett*, 2001, 564; (c) H. Laurent-Robert, B. Garrigues, and J. Dubac, *Synlett*, 2000, 1160; (d) B. Garrigues and A. Oussaid, *J. Organomet. Chem.*, 1999, **585**, 253.

69. (a) A. Orita, C. Tanahashi, A. Kakuda, and J. Otera, *Angew. Chem. Int. Ed. Eng.*, 2000, **39**, 2877; (b) C. Le Roux, L. Ciliberti, H. Laurent-Robert, A. Laporterie, and J. Dubac, *Synlett*, 1998, 1249; (c) H. Laurent-Robert, C. Le Roux, and J. Dubac, *Synlett*, 1998, 1138; (d) J. R. Desmurs, M. Labrouillere, C. Le Roux, H. Gaspard, A. Laporterie, and J. Dubac, *Tetrahedron Lett.*, 1997, **38**, 8871; (e) B. Garrigues, F. Gonzaga, H. Robert, and J. Dubac, *J. Org. Chem.*, 1997, **62**, 4880.

70. I. Mohammadpoor-Baltork and A. R. Khosropour, *Synthetic Commun.*, 2002, **32**, 2433.

71. H. Ohki, M. Wada, and K. Akiba, *Tetrahedron Lett.*, 1988, **29**, 4719.

72. (a) M. Wada, H. Ohki, and K. Akiba, *Bull. Chem. Soc. Japan*, 1990, **63**, 1738; (b) M. Wada, H. Ohki, and K. Akiba, *Chem. Commun.*, 1987, 708; (c) M. Wada, H. Ohki, and K. Akiba, *Tetrahedron Lett.*, 1986, **27**, 4771; (d) M. Wada and K. Akiba, *Tetrahedron Lett.*, 1985, **26**, 4211.

73. E. M. Campi, G. B. Deacon, G. L. Edwards, M. D. Fitzroy, N. Giunta, W. R. Jackson, and R. Trainor, *Chem. Commun.*, 1989, 407.

74. (a) A. J. Ashe, III and E. G. Ludwig, Jr, *Organometallics*, 1982, **1**, 1408; (b) H. J. Breunig and D. Müller, *Angew. Chem.*, 1982, **94**, 448; (c) H. J. Breunig and D. Müller, *Z.*

Naturforsch., 1983, **38B**, 125; (d) F. Calderazzo, R. Poli, and G. Pelizzi, *J. Chem. Soc., Dalton Trans.*, 1984, 2365.

75. F. Calderazzo, A. Morvillo, G. Pelizzi, and R. Poli, *J. Chem. Soc., Chem. Comm.*, 1983, 507.
76. H. J. Breunig, K. H. Ebert, R. E. Schulz, M. Wieber, and I. Sauer, *Z. Naturforsch.*, 1995, **50B**, 735.
77. A. J. Ashe and F. J. Drone, III *Organometallics*, 1984, **3**, 495.
78. O. Mundt, G. Becker, M. Roessler, and C. Witthauer, *Z. Anorg. Allg. Chem.*, 1983, **506**, 42.
79. (a) A. J. Ashe, III *Adv. Organomet. Chem.*, 1990, **30**, 77; (b) H. J. Breunig, *Phosphorus Sulfur*, 1988, **38**, 97; (c) L. L. Lohr and A. J. Ashe, III *Organometallics*, 1993, **12**, 343.
80. K. H. Whitmire and J. M. Cassidy, *Acta Cryst.*, 1992, **C48**, 917.
81. (a) F. Calderazzo, A. Morvillo, G. Pelizzi, R. Poli, and F. Ungari, *Inorg. Chem.*, 1988, **27**, 3730; (b) A. J. Ashe, III and E. G. Ludwig, Jr, *J. Organomet. Chem.*, 1986, **303**, 197; (c) H. J. Breunig, I. Ghesner, and E. Lork, *J. Organomet. Chem.*, 2002, **664**, 130.
82. (a) F. Calderazzo, A. Juris, R. Poli, and F. Ungari, *Inorg. Chem.*, 1991, **30**, 1274; (b) F. Calderazzo, R. Poli, and G. Pelizzi, *J. Chem. Soc., Dalton Trans.*, 1984, 2535.
83. B. Twamley, C. D. Sofield, M. M. Olmstead, and P. P. Power, *J. Am. Chem. Soc.*, 1999, **121**, 3357.
84. F. A. Cotton, A. H. Cowley, and X. Feng, *J. Am. Chem. Soc.*, 1998, **120**, 1795.
85. H. J. Breunig, R. Rosler, and E. Lork, *Angew. Chem.*, *Int. Ed. Eng.*, 1998, **37**, 3175.
86. G. Balazs, L. Balazs, H. J. Breunig, and E. Lork, *Organometallics*, 2003, **22**, 2919.
87. (a) L. Balazs, H. J. Breunig, and E. Lork, *Angew. Chem.*, *Int. Ed. Eng.*, 2002, **41**, 2309; (b) L. Balazs, H. J. Breunig, E. Lork, and C. Silvestru, *Eur. J. Inorg. Chem.*, 2003, 1361.
88. P. J. Fagan and W. A. Nugent, *J. Am. Chem. Soc.*, 1988, **110**, 2310.
89. (a) R. K. Mishra and B. K. Mishra, *Chem. Phys. Lett.*, 1988, **151**, 44; (b) B. K. Mishra, S. C. Varghese, R. Roy, and R. K. Mishra, *Indian J. Chem.*, 1990, **29A**, 370.
90. A. J. Ashe, III, *Tetrahedron Lett.*, 1976, 415.
91. T. Lewe, D. Naumann, G. Nowicki, H. Schneider, and W. Tyrra, *Z. Anorg. Allg. Chem.*, 1997, **623**, 122.
92. D. Naumann, W. Tyrra, and T. Lewe, *J. Fluorine Chem.*, 1997, **84**, 69.
93. T. Arnauld, D. H. R. Barton, and E. Doris, *Tetrahedron Lett.*, 1997, **38**, 365.
94. S. Hoppe and K. H. Whitmire, *Organometallics*, 1998, **17**, 1347.
95. S. Wallenhauer and K. Seppelt, *Angew. Chem.*, 1994, **106**, 1044 (See also *Angew. Chem., Int. Ed. Engl.*, 1994, **33**, 976).
96. (a) S. Wallenhauer and K. Seppelt, *Inorg. Chem.*, 1995, **34**, 116; (b) B. Neumueller and K. Dehnicke, *Angew. Chem.*, 1994, **106**, 1803; (See also *Angew. Chem., Int. Ed. Engl.*, 1994, **33**(17), 1726).
97. (a) D. M. Hawley and G. Ferguson, *J. Chem. Soc. A*, 1968, 2539; (b) F. C. March and G. Ferguson, *J. Chem. Soc., Dalton Trans.*, 1975, 1291.
98. D. H. R. Barton, B. Charpiot, E. Trans Huu Dau, W. B. Motherwell, C. Pascard, and C. Pichon, *Helv. Chim. Acta*, 1984, **67**, 586.
99. K. Akiba, K. Ohdoi, and Y. Yamamoto, *Tetrahedron Lett.*, 1989, **30**, 953.
100. G. Wittig and K. Clauss, *Ann.*, 1952, **578**, 136.
101. (a) A. Schmuck, J. Buschmann, J. Fuchs, and K. Seppelt, *Angew. Chem.*, 1987, **99**, 1206; (b) A. Schmuck and K. Seppelt, *Chem. Ber.*, 1989, **122**, 803; (c) A. Schmuck, D. Leopold, S. Wallenhauer, and K. Seppelt, *Chem. Ber.*, 1990, **123**, 761; (d) A. Schmuck, P. Pyykko, and K. Seppelt, *Angew. Chem.*, 1990, **102**, 211.
102. B. D. El-Issa, P. Pyykko, and H. M. Zanati, *Inorg. Chem.*, 1991, **30**, 2781.
103. K. Seppelt, *Adv. Organomet. Chem.*, 1992, **34**, 207.
104. I. Tornieporth-Oetting and T. Klapötke, *J. Organomet. Chem.*, 1989, **379**, 251.
105. S. Wallenhauer, D. Leopold, and K. Seppelt, *Inorg. Chem.*, 1993, **32**, 3948.
106. (a) D. H. R. Barton, J. P. Finet, and J. Khamsi, *Tetrahedron Lett.*, 1987, **28**, 887; (b) D. H. R. Barton, J. P. Finet, and J. Khamsi, *Tetrahedron Lett.*, 1986, **27**, 3615; (c) D. H. R. Barton, J. P. Finet, J. Khamsi, and C. Pichon, *Tetrahedron Lett.*, 1986, **27**, 3619; (d) D. H. R. Barton, J. P. Finet, and J. Khamsi, *Tetrahedron Lett.*, 1988, **29**, 1115; (e) H. Suzuki, C. Nakaya, Y. Matano, and T. Ogawa, *Chem. Lett.*, 1991, 105; (f) T. Ogawa, T. Murafuji, K. Iwata, and H. Suzuki, *Chem. Lett.*, 1989, 325.
107. H. Suzuki and T. Murafuji, *Bull. Chem. Soc. Japan*, 1990, **63**, 950.
108. (a) D. H. R. Barton and J. P. Finet, *Pure Appl. Chem.*, 1987, **59**, 937; (b) J. P. Finet, *Chem. Rev.*, 1989, **89**, 1487.
109. (a) H. Brunner, U. Obermann, and P. Wimmer, *J. Organomet. Chem.*, 1986, **316**, C1; (b) H. Brunner, U. Obermann, and P. Wimmer, *Organometallics*, 1989, **8**, 821; (c) H. Brunner and T. Chuard, *Monatsh. Chem.*, 1994, **125**, 1293.
110. T. Ogawa, K. Miyazaki, and H. Suzuki, *Chem. Lett.*, 1990, 1651.
111. T. Naito, S. Nagase, and H. Yamataka, *J. Am. Chem. Soc.*, 1994, **116**, 10080.
112. (a) T. Ogawa, T. Murafuji, and H. Suzuki, *J. Chem. Soc., Chem. Comm.*, 1989, 1749; (b) H. Suzuki, T. Murafuji, and T. Ogawa, *Chem. Lett.*, 1988, 847.

113. M. Yasui, T. Kikuchi, F. Iwasaki, H. Suzuki, T. Murafuji, and T. Ogawa, *J. Chem. Soc., Perkin Trans.*, 1990, 3367.

114. (a) G. Wittig and D. Hellwinkel, *Ber.*, 1964, **97**, 789; (b) D. K. Padma, R. A. Shaw, A. R. V. Murthy, and M. Woods, *Phosphorus Relat. Group V Elem.*, 1974, **4**, 25; (c) S. V. Pasenok, N. V. Kirij, Y. L. Yagupolskii, D. Naumann, and W. Tyrra, *J. Fluorine Chem.*, 1993, **63**, 179.

Bonding Energetics of Organometallic Compounds

Reto Dorta & Steven P. Nolan
University of New Orleans, New Orleans, LA, USA

1	Introduction	1
2	Case Studies	1
3	Closing Remarks	17
4	Related Articles	18
5	References	18

1 INTRODUCTION

During the last 10 years, significant advances have been made in the area of organometallic bonding energetics. Most data were obtained from solution calorimetric studies. In the present chapter, a compilation of thermochemical data on organometallic systems is presented. This account represents a survey and is by no means exhaustive yet we have endeavored to provide the reader with as much data as possible in an effort to complement the contribution found in the first edition.

2 CASE STUDIES

The case studies below will provide selected examples of calorimetric studies carried out on metal–ligand exchange reactions of phosphorous-based ligands (such as phosphines, phosphite, *N*-pyrrolyl-phosphines) and *N*-heterocyclic carbene ligands (NHCs) as well as addition reactions relevant to catalytic transformations, involving metals such as ruthenium,[1–15] rhodium,[16–23] platinum,[24,25] and molybdenum.[26,27]

2.1 Binding of Monodentate Phosphine Ligands to Cp-ruthenium Systems

Ligand substitution reactions (*see Ligand Substitution*) are at the heart of many catalytic transformations, since creation of vacant coordination sites oftentimes requires liberation of one or more ligands from the coordination sphere of the metal. Important and/or industrially relevant processes using organoruthenium catalysts include the enantioselective reduction of olefins and ketones developed by Noyori *et al.* (*see* ***Asymmetric Synthesis by Homogeneous Catalysis***),[28,29] the ring-opening and closing metatheses of olefins reported by Grubbs *et al.* (*see* ***Organic Synthesis Using Metal-mediated Metathesis Reactions***),[30–32] or the recently developed ruthenium-catalyzed synthesis of formic acid and formamides in supercritical CO_2.[33,34]

In order to gain insight into the thermodynamics of phosphine binding to ruthenium systems, the tetrameric complex $(Cp^*RuCl)_4$ was chosen as the starting material (*see* ***Polynuclear Organometallic Cluster Complexes***). Complexes of the type $Cp^*Ru(diene)Cl$ are formed from the tetrameric $(Cp^*RuCl)_4$ compound according to equation (1)[35,36] and provide a thermodynamic entryway into the solution calorimetric studies of ligand substitution in these systems. Table 1 gives an overview of the enthalpies of substitution for the reaction in equation (1) and shows that for subsequent ligand substitution chemistry involving phosphines and arsines, the relatively labile nature of the COD ligand in $Cp^*Ru(COD)Cl$ is ideal.

$$(Cp^*RuCl)_{4(s)} + 4diene_{(soln)} \xrightarrow[30\,°C]{THF} 4Cp^*Ru(diene)Cl_{(soln)} \qquad (1)$$

Indeed, reacting this complex with monodentate arsine/phosphine/phosphite ligands provides access into the thermochemistry of the ligand substitution of equation (2). Table 2 gives the respective enthalpies of ligand substitution found by calorimetry for the series of monodentate phosphine ligands.

$$Cp^*Ru(COD)Cl_{(soln)} + 2L_{(soln)} \xrightarrow[30\,°C]{THF} Cp^*Ru(L)_2Cl_{(soln)} + COD_{(soln)} \qquad (2)$$

The enthalpy trend can be examined in terms of electronic and steric contributions to the enthalpy of reaction, the relative importance of which can be quantified in terms of the respective A_1/A_2 ratios obtained in a treatment first proposed by Tolman,[37] where enthalpies of reaction are correlated with steric (θ, cone angle, *see Tolman's Cone Angle*) and electronic (ν, carbonyl stretching frequency in $Ni(CO)_3L$, L = tertiary phosphine) factors. A correlation factor of 0.95 is obtained when enthalpic data are fitted to equation (3) and a value of 2.32 is calculated for the A_1/A_2 and quantitatively denotes the overwhelming influence of steric factors. Since the steric factors have such a profound influence on the enthalpy of reaction, a direct relationship between the enthalpy of reaction and the phosphine cone angle can be established as shown in Figure 1.

$$-\Delta H^o = A_o + A_1\theta + A_2\nu \qquad (3)$$

These results are not unexpected in view of the cis arrangement of the phosphine ligands and the steric bulk of the Cp^* ligand in these complexes. Therefore, the enthalpies of reaction of $CpRu(COD)Cl$ ($Cp = C_5H_5$) with a series of

Table 1 Enthalpies of substitution (kcal mol^{-1}) for equation (1)

Diene	Complex	$-\Delta H_{\mathrm{rxn\ Cp^*}}$^{a}
2,3-dimethyl-1,3-butadiene	Cp′Ru(Me$_2$butadiene)Cl	39.0 (0.2)
1,3-cyclohexadiene	Cp′Ru(CHD)Cl	39.3 (0.5)
cyclooctadiene	Cp′Ru(COD)Cl	39.8 (0.4)
trans,trans-2,4-hexadiene	Cp′Ru(*t*,*t*-hexadiene)Cl	44.2 (0.5)
1,3-pentadiene	Cp′Ru(1,3-pd)Cl	46.1 (0.2)
norbornadiene	Cp′Ru(NBD)Cl	52.1 (0.2)

^{a}Enthalpy values are reported with 95% confidence limits.

Table 2 Enthalpies of substitution (kcal mol^{-1}) for equation (2)

L	Complex	$-\Delta H_{\mathrm{rxn\ Cp^*}}$^{a}
AsEt$_3$	Cp*Ru[AsEt$_3$]$_2$Cl	15.0 (0.2)
PPh$_3$	Cp*Ru[PPh$_3$]$_2$Cl	18.1 (0.2)
P^{n}Bu$_3$	Cp*Ru[P^{n}Bu$_3$]$_2$Cl	26.0 (0.2)
PEt$_3$	Cp*Ru[PEt$_3$]$_2$Cl	27.2 (0.2)
PPh$_2$Me	Cp*Ru[PPh$_2$Me]$_2$Cl	29.4 (0.2)
P(OPh)$_3$	Cp*Ru[P(OPh)$_3$]$_2$Cl	31.2 (0.2)
PPhMe$_2$	Cp*Ru[PPhMe$_2$]$_2$Cl	31.8 (0.3)
PMe$_3$	Cp*Ru[PMe$_3$]$_2$Cl	32.2 (0.4)
P(OMe)$_3$	Cp*Ru[P(OMe)$_3$]$_2$Cl	37.5 (0.4)

^{a}Enthalpy values are reported with 95% confidence limits.

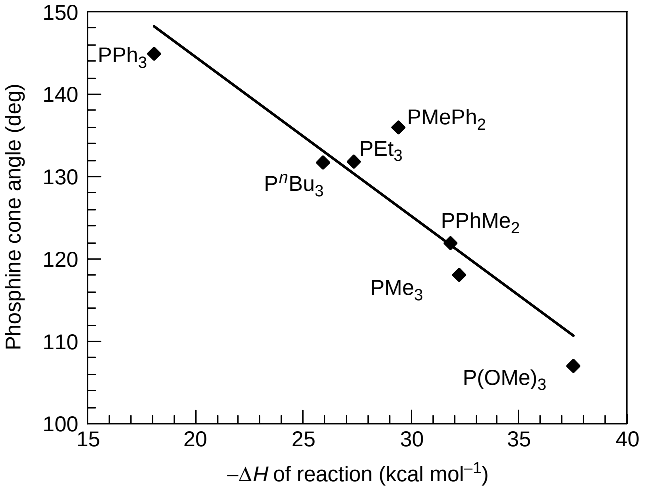

Figure 1 Enthalpy of reaction vs phosphine cone angle for a series of tertiary phosphine ligands in the Cp*Ru(PR$_3$)$_2$Cl system (*slope* $= -1.94$; $R = 0.93$)

Table 3 Enthalpies of substitution (kcal mol^{-1}) in the reaction:

$$\mathrm{CpRu(COD)Cl_{(soln)}} + 2\mathrm{L_{(soln)}} \xrightarrow[30\,^{\circ}\mathrm{C}]{\mathrm{THF}} \mathrm{CpRu(L)_2Cl_{(soln)}} + \mathrm{COD_{(soln)}}$$

L	Complex	$-\Delta H_{\mathrm{rxn\ Cp}}$^{a}
AsEt$_3$	CpRu[AsEt$_3$]$_2$Cl	19.4 (0.2)
PPh$_3$	CpRu[PPh$_3$]$_2$Cl	22.9 (0.4)
PPh$_2$Me	CpRu[P^{n}Bu$_3$]$_2$Cl	32.8 (0.2)
P(OPh)$_3$	CpRu[PEt$_3$]$_2$Cl	34.1 (0.4)
PEt$_3$	CpRu[PPh$_2$Me]$_2$Cl	34.5 (0.2)
P^{n}Bu$_3$	CpRu[P(OPh)$_3$]$_2$Cl	35.4 (0.2)
PPhMe$_2$	CpRu[PPhMe$_2$]$_2$Cl	35.9 (0.2)
PMe$_3$	CpRu[PMe$_3$]$_2$Cl	38.4 (0.4)
P(OMe)$_3$	CpRu[P(OMe)$_3$]$_2$Cl	41.8 (0.2)

^{a}Enthalpy values are reported with 95% confidence limits.

monodentate phosphine and arsenic ligands have also been measured in order to examine how the overall steric and electronic variations accompanying this change in ancillary ligation (Cp* versus Cp) influence the thermodynamic stability of Cp′Ru(PR$_3$)$_2$Cl (with Cp′ = Cp or Cp*). Again, the reactions of CpRu(COD)Cl with a series of phosphines have been found to be quantitative and rapid under the experimental calorimetric conditions. Several trends are observed when looking at the results in Table 3: (1) The arsenic ligand displays enthalpies 15.1 kcal mol^{-1} less exothermic than that of its phosphine relative. (2) Phosphine sterics are the predominant factor influencing the magnitude of the enthalpy of reaction and a direct relationship can be established (Figure 2). (3) The ruthenium complex shows a relatively high affinity for phosphates, which can possibly be explained in terms of back donation (*see Back Bonding*) from the metal into orbitals on the phosphite ligand (phosphorous–oxygen σ^* orbitals).

A comparison between the two Cp′Ru(COD)Cl systems shows the importance of ancillary ligands (*see Ancillary Ligand*). Since Cp is less electron donating than Cp*, the Cp system is able to accommodate greater electron density from the incoming two-electron donor (higher electrophilicity), therefore leading to more exothermic enthalpies of ligand

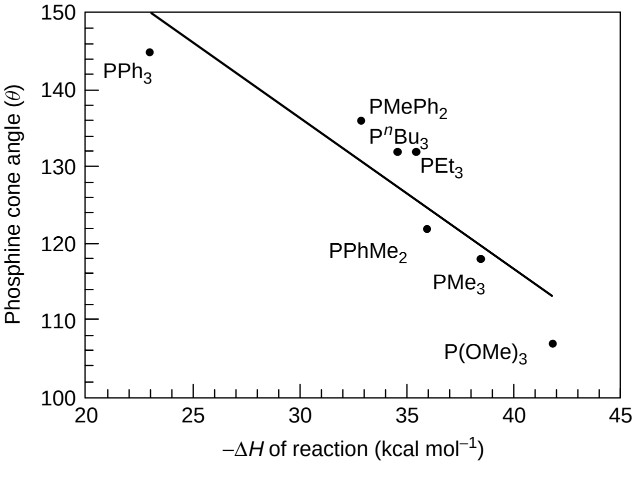

Figure 2 Enthalpy of reaction vs phosphine cone angle for a series of tertiary phosphine ligands in the CpRu(PR$_3$)$_2$Cl system (*slope* $= -1.95$; $R = 0.91$)

Table 4 Enthalpies of substitution (kcal mol^{-1}) in the reaction:

$$\text{Cp}'\text{Ru(COD)Cl}_{(\text{soln})} + 2\text{L}_{(\text{soln})} \xrightarrow[30\,^\circ\text{C}]{\text{THF}} \text{Cp}'\text{Ru(L)}_2\text{Cl}_{(\text{soln})} + \text{COD}_{(\text{soln})}\text{Cp}' = \text{Cp and Cp}^*$$

L	Complex	$-\Delta H_{\text{rxn Cp}^*}{}^a$	$-\Delta H_{\text{rxn Cp}}{}^a$
$(C_6H_5)_3P$	$Cp'Ru[P(C_6H_5)_3]_2Cl$	18.1 (0.2)	22.9 (0.3)
$(p\text{-}CH_3C_6H_4)_3P$	$Cp'vRu[P(p\text{-}CH_3C_6H_4)_3]_2Cl$	–	23.7 (0.3)
$(p\text{-}CF_3C_6H_4)_3P$	$Cp'Ru[P(p\text{-}CF_3C_6H_4)_3]_2Cl$	20.7 (0.3)	24.4 (0.2)
$(p\text{-}CH_3OC_6H_4)_3P$	$Cp'Ru[P(p\text{-}CH_3OC_6H_4)_3]_2Cl$	21.8 (0.4)	24.6 (0.3)
$(p\text{-}ClC_6H_4)_3P$	$Cp'Ru[P(p\text{-}ClC_6H_4)_3]_2Cl$	21.7 (0.4)	24.0 (0.2)
$(p\text{-}FC_6H_4)_3P$	$Cp'Ru[P(p\text{-}FC_6H_4)_3]_2Cl$	22.0 (0.5)	24.2 (0.2)

[a] Enthalpy values are reported with 95% confidence limits.

substitution. One of the best ways to experimentally assess the lack of phosphine electronic factors playing a role in these two systems is to determine the bond dissociation enthalpies of a series of isosteric, para-substituted triphenylphosphine ligands. The enthalpies of reaction of Cp′Ru(COD)Cl (where Cp′ = Cp and Cp*) with several para-substituted monodentate phosphines are listed in Table 4. This study clearly indicates an important lack of sensitivity associated with the enthalpies of ligand substitution reactions as a function of electronic variation and can only be explained in terms of overwhelming steric contribution to the enthalpy of reaction.

Besides the class of traditional phosphines ligands, the related class of phosphite ligands has been utilized as ancillary ligation in various industrially relevant processes such as the hydrocyanation (*see Hydrocyanation*) of dienes or hydroformylation (*see Hydroformylation*) or the copolymerization of CO and olefins.[38,39] The thermochemistry of ligand substitution of a variety of phosphite ligands has therefore been determined by measuring the enthalpies of reaction of Cp′Ru(COD)Cl (where Cp′ = Cp and Cp*) with a series of monodentate phosphite ligands, leading to the formation of $Cp'Ru(P(OR)_3)_2Cl$ complexes. A compilation of phosphine/phosphite ligands with their respective enthalpies of reaction, in solution, is presented in Tables 5 and 6. Not unlike in the case of phosphines discussed above, the tables suggest that the different phosphite reaction enthalpies are overwhelmingly sterically controlled, and a graphical representation of this is shown in Figures 3 and 4 respectively. The increased exothermicity displayed by the $CpRu(PR_3)_2Cl$ system over its Cp* parent can again be taken as a gauge of the increased metal basicity on going from Cp to Cp*.

Another very interesting family of phosphorous ligands is the recently synthesized class of *N*-pyrrolyl phosphine compounds.[40] The pyrrazolyl moiety is known for its π-involvement (back donation from metal to ligand) and should greatly affect the binding ability of the phosphine,

Table 5 Enthalpies of Substitution (kcal mol^{-1}) in the reaction:

$$\text{CpRu(COD)Cl}_{(\text{soln})} + 2\text{L}_{(\text{soln})} \xrightarrow[30\,^\circ\text{C}]{\text{THF}} \text{CpRu(L)}_2\text{Cl}_{(\text{soln})} + \text{COD}_{(\text{soln})}$$

L	Complex	$-\Delta H_{\text{rxn Cp}}{}^a$
$AsEt_3$	$CpRu[AsEt_3]_2Cl$	19.4 (0.2)
PPh_3	$CpRu[PPh_3]_2Cl$	22.9 (0.4)
$P(p\text{-}CH_3C_6H_4)_3$	$CpRu[P(p\text{-}CH_3C_6H_4)_3]_2Cl$	23.7 (0.3)
$P(p\text{-}ClC_6H_4)_3$	$CpRu[P(p\text{-}ClC_6H_4)_3]_2Cl$	24.0 (0.2)
$P(p\text{-}FC_6H_4)_3$	$CpRu[P(p\text{-}FC_6H_4)_3]_2Cl$	24.2 (0.2)
$P(p\text{-}CF_3C_6H_4)_3$	$CpRu[P(p\text{-}CF_3C_6H_4)_3]_2Cl$	24.4 (0.2)
$P(p\text{-}CH_3OC_6H_4)_3$	$CpRu[P(p\text{-}CH_3OC_6H_4)_3]_2Cl$	24.6 (0.3)
PPh_2Me	$CpRu[PPh_2Me]_2Cl$	32.8 (0.2)
$P(O\text{-}o\text{-}MeC_6H_4)_3$	$CpRu[P(O\text{-}o\text{-}MeC_6H_4)_3]_2Cl$	33.2 (0.2)
$P(OPh)_3$	$CpRu[P(OPh)_3]_2Cl$	34.1 (0.4)
PEt_3	$CpRu[PEt_3]_2Cl$	34.5 (0.2)
P^nBu_3	$CpRu[P^nBu_3]_2Cl$	35.4 (0.2)
$P(O^iPr)_3$	$CpRu[P(O^iPr)_3]_2Cl$	35.9 (0.3)
$P(PCH_2)_3CEt$	$CpRu[P(PCH_2)_3CEt]_2Cl$	35.9 (0.4)
$PPhMe_2$	$CpRu[PPhMe_2]_2Cl$	35.9 (0.2)
PMe_3	$CpRu[PMe_3]_2Cl$	38.4 (0.4)
$P(OMe)_3$	$CpRu[P(OMe)_3]_2Cl$	41.8 (0.2)

[a] Enthalpy values are reported with 95% confidence limits.

Table 6 Enthalpies of substitution (kcal mol^{-1}) in the reaction:

$$\text{Cp}^*\text{Ru(COD)Cl}_{(\text{soln})} + 2\text{L}_{(\text{soln})} \xrightarrow[30\,^\circ\text{C}]{\text{THF}} \text{Cp}^*\text{Ru(L)}_2\text{Cl}_{(\text{soln})} + \text{COD}_{(\text{soln})}$$

L	Complex	$-\Delta H_{\text{rxn Cp}}{}^a$
$AsEt_3$	$Cp^*Ru[AsEt_3]_2Cl$	15.0 (0.2)
PPh_3	$Cp^*Ru[PPh_3]_2Cl$	18.1 (0.2)
$P(p\text{-}CF_3C_6H_4)_3$	$Cp^*Ru[P(p\text{-}CF_3C_6H_4)_3]_2Cl$	20.7 (0.2)
$P(p\text{-}ClC_6H_4)_3$	$Cp^*Ru[P(p\text{-}ClC_6H_4)_3]_2Cl$	21.7 (0.4)
$P(p\text{-}CH_3OC_6H_4)_3$	$Cp^*Ru[P(p\text{-}CH_3OC_6H_4)_3]_2Cl$	21.8 (0.4)
$P(p\text{-}FC_6H_4)_3$	$Cp^*Ru[P(p\text{-}FC_6H_4)_3]_2Cl$	22.0 (0.5)
P^nBu_3	$Cp^*Ru[P^nBu_3]_2Cl$	26.0 (0.2)
$P(O\text{-}o\text{-}MeC_6H_4)_3$	$Cp^*Ru[P(O\text{-}o\text{-}MeC_6H_4)_3]_2Cl$	26.0 (0.2)
PEt_3	$Cp^*Ru[PEt_3]_2Cl$	27.2 (0.2)
PPh_2Me	$Cp^*Ru[PPh_2Me]_2Cl$	29.4 (0.2)
$P(OPh)_3$	$Cp^*Ru[P(OPh)_3]_2Cl$	31.2 (0.2)
$P(OCH_2)_3CEt$	$Cp^*Ru[P(OCH_2)_3CEt]_2Cl$	31.6 (0.2)
$PPhMe_2$	$Cp^*Ru[PPhMe_2]_2Cl$	31.8 (0.3)
PMe_3	$Cp^*Ru[PMe_3]_2Cl$	32.2 (0.4)
$P(O^iPr)_3$	$Cp^*Ru[P(O^iPr)_3]_2Cl$	32.7 (0.3)
$P(OMe)_3$	$Cp^*Ru[P(OMe)_3]_2Cl$	37.5 (0.4)

[a] Enthalpy values are reported with 95% confidence limits.

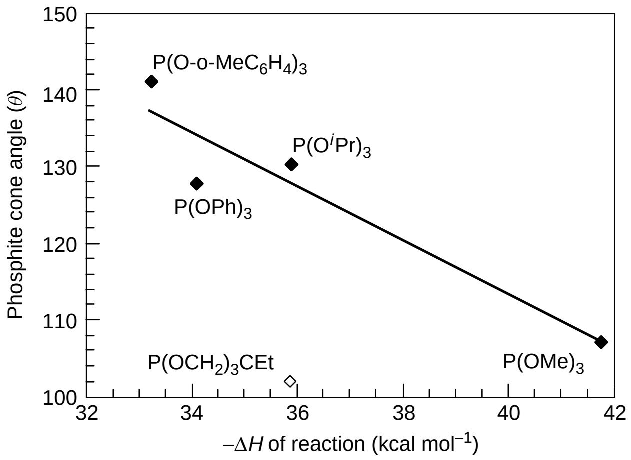

Figure 3 Enthalpy of reaction vs phosphite cone angle for a series of tertiary phosphite ligands in the Cp*Ru(PR$_3$)$_2$Cl system (*slope* $= -3.50$; $R = 0.95$)

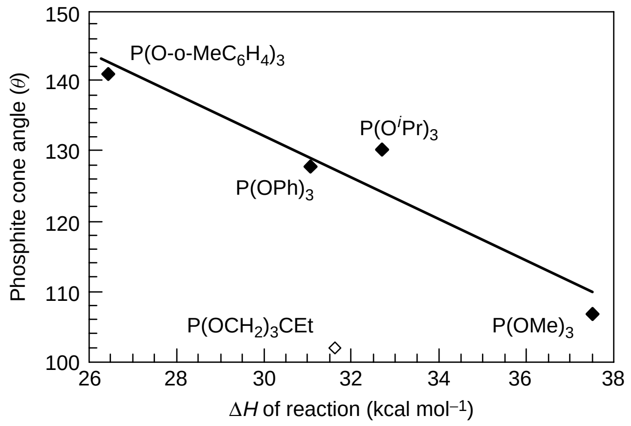

Figure 4 Enthalpy of reaction vs phosphite cone angle for a series of tertiary phosphite ligands in the CpRu(PR$_3$)$_2$Cl system (*slope* $= -2.95$; $R = 0.96$)

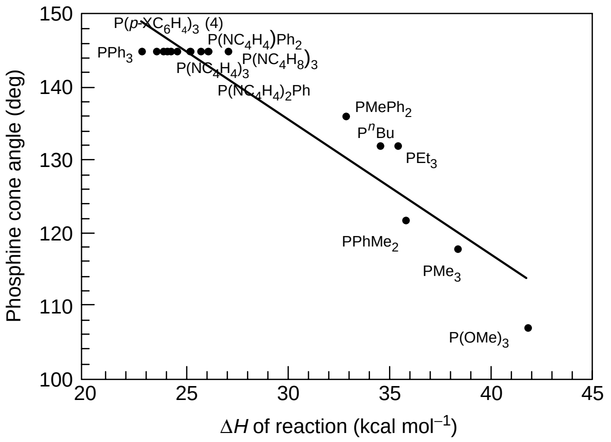

Figure 5 Enthalpies of reaction (kcal mol)$^{-1}$ for the CpRu(PR$_3$)$_2$Cl system vs phosphine cone angle (deg) (*slope* $= -1.85$; $R = 0.95$)

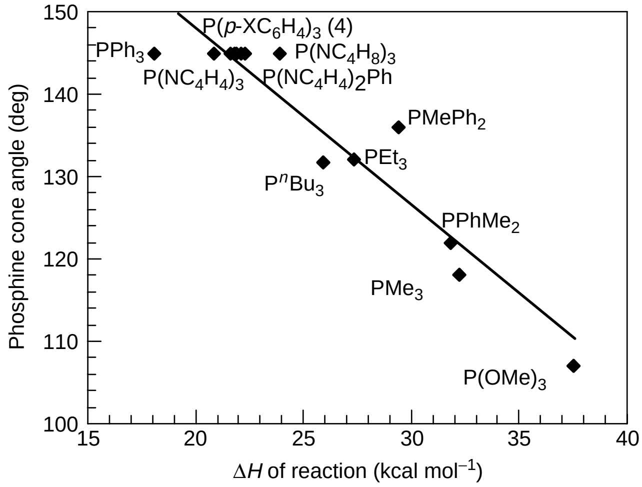

Figure 6 Enthalpies of reaction (kcal mol^{-1}) for the Cp*Ru(PR$_3$)$_2$Cl system vs phosphine cone angle (deg) (*slope* $= -2.15$; $R = 0.95$)

at least if electronic factors play a major role in the system studied. The enthalpies of reaction of Cp′Ru(COD)Cl (Cp′ $=$ C$_5$H$_5$ and C$_5$Me$_5$) with a series of *N*-pyrrazolyl-substituted tertiary phosphine ligands, leading to the formation of Cp′Ru(PR$_3$)$_2$Cl complexes, as well as a comparison with previously investigated phosphines, are given in Table 7. Once again, the observed enthalpies underline the validity of previous results insofar as in these ruthenium systems, steric factors seem to be the principal contributor to the magnitude of the reaction enthalpy. This overwhelming steric contribution accounts for the relatively weaker than expected donor ability of the *N*-pyrrolyl ligand family and can be correlated for both Cp- and Cp*-Ru systems as shown in Figures 5 and 6.

From the thermochemical studies on these Cp′Ru(L)$_2$Cl systems, it was found that the trends can be analyzed in terms of a predominant contribution from the Tolman cone angle (*see Tolman's Cone Angle*) of the incoming ligand. An interesting question would therefore be whether the same trends are present in the metrical parameters obtained from single-crystal X-ray diffraction analysis of the compounds formed (of the general formula CpRu(PR$_3$)$_2$Cl) in the prior investigations. With five X-ray structures of complexes of the type CpRu(ER$_3$)$_2$Cl at hand, a closer examination of the Ru–P bond lengths of the ligands indeed shows that a quantitative relationship between structural and thermodynamic parameters can be established. In fact, there appears to exist a direct correlation between Ru–E bond lengths and the magnitude of the enthalpies of substitution. As shown in Figure 8, an even higher degree of correlation exists between the reaction enthalpies and the Ru–P bond distances in the related Cp*Ru(ER$_3$)$_2$Cl system. The reaction

Table 7 Enthalpies of substitution (kcal mol^{-1}) in the reaction:

$$\mathrm{Cp'Ru(COD)Cl_{(soln)}} + \mathrm{2L_{(soln)}} \xrightarrow[30\,^{\circ}\mathrm{C}]{\mathrm{THF}} \mathrm{Cp'Ru(L)_2Cl_{(soln)}} + \mathrm{COD_{(soln)}}$$

L	Complex	$-\Delta H_{\mathrm{rxn\ Cp^*}}$[a]	$-\Delta H_{\mathrm{rxn\ Cp}}$[a]
$AsEt_3$	$Cp^*Ru[AsEt_3]_2Cl$	15.0 (0.2)	19.4 (0.2)
PPh_3	$Cp^*Ru[PPh_3]_2Cl$	18.1 (0.2)	22.9 (0.4)
$P(NC_4H_4)Ph_2$	$Cp^*Ru[P(NC_4H_4)Ph_2]_2Cl$	20.7 (0.2)	26.2 (0.3)
$P(NC_4H_4)_3$	$Cp^*Ru[P(NC_4H_4)_3]_2Cl$	21.7 (0.4)	25.8 (0.3)
$P(NC_4H_4)_2Ph$	$Cp^*Ru[P(P(NC_4H_4)_2Ph)]_2Cl$	21.8 (0.4)	25.3 (0.1)
$P(NC_4H_8)_3$	$Cp^*Ru[P(NC_4H_8)_3]_2Cl$	22.0 (0.5)	27.2 (0.3)
P^nBu_3	$Cp^*Ru[P^nBu_3]_2Cl$	26.0 (0.2)	35.4 (0.2)
$PPhMe_2$	$Cp^*Ru[PPhMe_2]_2Cl$	31.8 (0.3)	35.9 (0.2)
PMe_3	$Cp^*Ru[PMe_3]_2Cl$	32.2 (0.4)	38.4 (0.4)
$P(OMe)_3$	$Cp^*Ru[P(OMe)_3]_2Cl$	37.5 (0.4)	41.8 (0.2)

[a] Enthalpy values are reported with 95% confidence limits.

enthalpies involved in this correlation are directly related to Ru–P bond dissociation enthalpies, Figure 7 is in fact a bond length-relative bond dissociation enthalpy correlation. The correlation between crystalline Ru–P distances and solution thermochemical measurements suggests that longer bonds are associated with less exothermic reactions (dmpm $>$ PMe_3 $>$ $PPhMe_2$ $>$ PPh_2Me $>$ PEt_3 $>$ P^nBu_3 $>$ PPh_3).

As mentioned above, the ancillary Cp (*see Cyclopentadienyl*) ligands (Cp versus Cp*) can influence the enthalpies of reaction of Cp′RuCl systems with phosphorous ligands. The availability of $[Cp^*Ru(OCH_2CF_3)]_2$,[41,42] permits therefore a direct comparison of alkoxide vs chloride ancillary ligands in this system. The enthalpies of reaction of $[Cp^*Ru(OCH_2CF_3)]_2$ with PR_3 ($PR_3 = PCy_3$, P^iPr_3) have been measured by solution calorimetry giving complexes $[Cp^*Ru(PR_3)(OCH_2CF_3)]$ and in order to test the internal consistency of the approach, a thermochemical cycle, shown in Scheme 1, was constructed leading to the formation of $Cp^*Ru(PR_3)_2(OCH_2CF_3)$. This reactivity is analogous to the one involving chloride ligation and a comparison of the results is shown in Table 8.

Important comparisons can be made between the Cp*RuCl and the $Cp^*Ru(OCH_2CF_3)$ systems and show that enthalpies of reaction involving similar phosphine ligands are more exothermic for the Cp*RuCl moiety. This trend is understood to reflect the increased electron donation residing on the

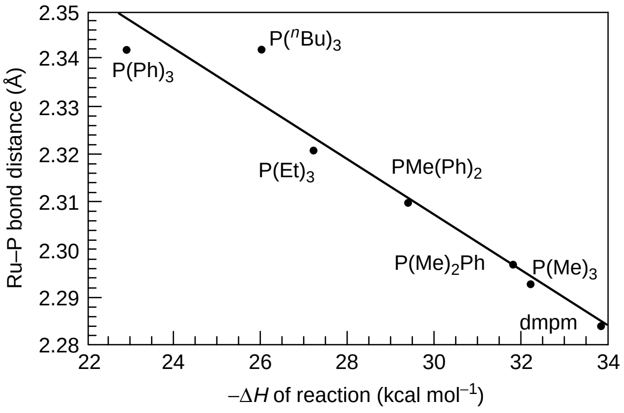

Figure 7 Plot of the Ru–P bond distance (Å) vs the enthalpies of reaction (kcal mol^{-1}) for the $Cp^*Ru(L)_2Cl$ complexes (*slope* $= -2.48$; $R = 0.97$)

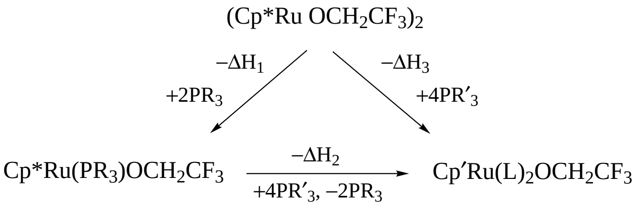

PR_3	PR'_3	$-\Delta H_1$	$-\Delta H_2$	$-\Delta H_3$
PCy_3	PEt_3	18.9 (0.3)	41.6 (0.6)	60.1 (0.5)
PCy_3	$P(OMe)_3$	18.9 (0.3)	65.8 (0.8)	83.8 (0.8)
P^iPr_3	PEt_3	18.6 (0.2)	43.6 (0.8)	60.1 (0.5)
P^iPr_3	$P(OMe)_3$	18.6 (0.2)	67.2 (0.8)	83.8 (0.8)

Enthalpy values are reported with 95% confidence limits.

Scheme 1

Table 8 Relative average Ru–PR_3 bond disruption enthalpies (kcal mol^{-1}) in the reaction:

$$\mathrm{Cp^*RuX} + n\mathrm{L} \longrightarrow \mathrm{Cp^*Ru(L)}_n\mathrm{X} \quad n = 1,2$$

L	Complex	X = OR_f[a]	X = Cl[a]
P^iPr_3	$Cp^*Ru[P^iPr_3]X$	6.5 (0.3)	9.4 (0.3)
PCy_3	$Cp^*Ru[PCy_3]X$	6.7 (0.3)	10.5 (0.2)
PEt_3	$Cp^*Ru[PEt_3]_2X$	14.3 (0.5)	18.4 (0.6)
$P(OMe)_3$	$Cp^*Ru[P(OMe)_3]_2X$	20.2 (0.8)	23.8 (0.4)

[a] Enthalpy values are reported with 95% confidence limits.

metal when the ancillary ligand X is (OCH_2CF_3), leading to a tendency of the $Cp^*Ru(OCH_2CF_3)$ moiety to be able to accept less electron density from the incoming donor ligands, resulting in a lower exothermic value for the enthalpy of reaction.

2.2 Binding of Chelating Diphosphine Ligands to Cp-ruthenium Systems

Chelating diphosphine ligands (*see Chelating Ligands*) have been widely used in organometallic chemistry and are especially indispensable ligand systems in enantioselective catalytic transformations (*see* ***Asymmetric Synthesis by Homogeneous Catalysis***).**28** With the complex $Cp'Ru(COD)Cl$ ($Cp' = Cp$ and Cp^*) at hand, solution thermochemical investigations of ligand substitution involving chelating diphosphines can be carried out, giving complexes of the type $Cp'Ru(PP)Cl$. It might be predicted that a major factor influencing the metal–diphosphine complex reactivity and stability must involve the metal–ligand enthalpy term. This bond disruption enthalpy (BDE) value can be viewed as a sum of the stabilizing metal–phosphorous interaction and the destabilizing strain energy caused by steric and torsional forces present in the metallacyclic fragment.

The enthalpies of ligand substitution for these chelating ligands are presented in Table 9.

Several trends are worth noting: (1) reactions of alkyl-substituted phosphines prove to be more exothermic; (2) ring strain is present in the four- and seven-membered ring systems. For this latter trend, a relative comparison of all the data of these chelating diphosphines with the corresponding monophosphines shows that the strain energy for the seven-membered metallacycle is smaller than for the four-membered analogue; (3) similar to the trend seen for monophosphines, the Cp ligand system shows an increased exothermicity in enthalpies of reaction.

Analogous to the studies with monodentate phosphorous ligands, a thermochemical study of ligand substitution involving diphosphine compounds with weak σ-donor and strong π-acceptor character involving the recently reported ligands $Ph_2PNMeNMePPh_2$, $(PhO)_2PNMeNMeP(OPh)_2$, $(C_4H_4N)_2PCH_2CH_2P(NC_4H_4)_2$, and $((EtO_2C)_2C_4H_2N)_2PCH_2CH_2P[NC_4H_2(CO_2Et)_2]_2$ was undertaken.**43** The results in Table 10 (for Cp and Cp*) clearly suggest that steric factors

Table 9 Enthalpies of substitution (kcal mol^{-1}) in the reaction:

$$Cp'Ru(COD)Cl_{(soln)} + \overset{\frown}{P\;\;P}_{(soln)} \xrightarrow[30\,°C]{THF} Cp'Ru(\overset{\frown}{P\;\;P})Cl_{(soln)} + COD_{(soln)}$$

$$Cp' = C_5Me_5 \text{ and } C_5H_5$$

	$\overset{\frown}{P\;\;P}$	$-\Delta H_{rxn}{}^a$	$-\Delta H_{rxn}{}^b$
dppm	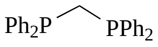 Ph_2P PPh_2	19.4 (0.2)	19.4 (0.2)
dmpm	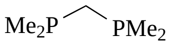 Me_2P PMe_2	23.8 (0.3)	26.2 (0.2)
dppb	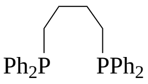 Ph_2P PPh_2	24.7 (0.3)	30.1 (0.3)
dppe	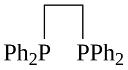 Ph_2P PPh_2	29.8 (0.2)	30.5 (0.2)
dppp	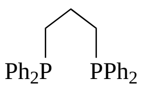 Ph_2P PPh_2	30.7 (0.2)	32.4 (0.2)
dppv	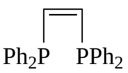 Ph_2P PPh_2	31.3 (0.2)	32.7 (0.2)
depe	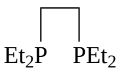 Et_2P PEt_2	35.6 (0.3)	39.4 (0.3)
dmpe	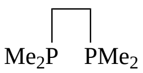 Me_2P PMe_2	34.8 (0.2)	39.7 (0.3)

[a]Enthalpies of reaction for the Cp*-based system which are reported with 95% confidence limits. [b]Enthalpies of reaction for the Cp-based system also reported with 95% confider limits.

Table 10 Enthalpies of substitution ($\mathrm{kcal\,mol^{-1}}$) in the reaction:

$$\mathrm{Cp'Ru(COD)Cl_{(soln)}} + \mathrm{PP_{(soln)}} \xrightarrow[30\,^\circ\mathrm{C}]{\mathrm{THF}} \mathrm{Cp'Ru(PP)Cl_{(soln)}} + \mathrm{COD_{(soln)}}$$

PP	$-\Delta H_{\mathrm{rxn\ Cp}}{}^{a}$	$-\Delta H_{\mathrm{rxn\ Cp^*}}{}^{a}$
$\mathrm{[(EtO_2C)_2C_4H_2N]_2PCH_2CH_2P[NC_4H_2(CO_2Et)_2]_2}$	24.0 (0.4)	19.4 (0.2)
$\mathrm{(C_4H_4N)_2PCH_2CH_2P(NC_4H_4)_2}$	29.1 (0.1)	23.2 (0.4)
$\mathrm{Ph_2PNMeNMe\ PPh_2}$	29.7 (0.4)	22.6 (0.2)
$\mathrm{Ph_2PCH_2CH_2PPh_2}$	30.5 (0.2)	29.8 (0.2)
$\mathrm{(PhO)_2PNMeNMe\ P(OPh_2)}$	32.4 (0.3)	26.4 (0.2)
$\mathrm{Ph_2PCHCHPPh_2}$	32.7 (0.2)	31.3 (0.2)
$\mathrm{Et_2PCH_2CH_2PEt_2}$	26.0 (0.2)	35.6 (0.3)
$\mathrm{Me_2PCH_2CH_2PMe_2}$	39.7 (0.3)	34.8 (0.2)

[a] Enthalpy values are reported with 95% confidence limits.

predominate in all these cases, but at least some electronic effects must be present in minor extend, with reaction enthalpies markedly lower than for basic diphosphines.

2.3 Binding of Sterically Demanding Phosphine Ligands to Cp-ruthenium Systems

Sterically demanding phosphine ligands play an important role in organometallic chemistry in helping to stabilize very reactive species and play crucial roles in several catalytic systems such as the very successful ruthenium-alkylidene catalysts reported by Grubbs *et al.* (*see* ***Organic Synthesis Using Metal-mediated Metathesis Reactions***).[30,31] Direct solution calorimetric measurement of the relative donating properties of large cone-angle phosphines would therefore be highly desirable and have not been reported. The reaction of $\mathrm{(Cp^*RuCl)_4}$ with sterically demanding monodentate tertiary phosphine ligands leads to rapid and clean formation of the unsaturated $\mathrm{Cp^*Ru(PR_3)Cl}$ (where $\mathrm{PR_3 = P^iPr_3}$ or $\mathrm{PCy_3}$),[44] and is therefore amenable to such an investigation (equation 4). Furthermore, the very reactive nature of these unsaturated complexes can be exploited in order to thermodynamically link the $\mathrm{Cp^*Ru(PR_3)Cl}$ to the $\mathrm{Cp^*Ru(PR_3)_2Cl}$ systems discussed earlier according to equation (5). The results show that these two sterically demanding phosphines exhibit the weakest Ru–$\mathrm{PR_3}$ bond yet investigated and relative bond disruption enthalpies were established and are shown in Table 11. As observed for smaller phosphines, the steric factors have a profound influence on the enthalpy of reaction and a direct relationship between the two can be established.

$$\mathrm{(Cp^*RuCl)_{4(s)}} + 4\mathrm{PR_{3(soln)}} \xrightarrow[30\,^\circ\mathrm{C}]{\mathrm{THF}} 4\mathrm{Cp^*Ru(PR_3)Cl_{(soln)}} \tag{4}$$

$$\mathrm{PR_3 = PCy_3};\ \Delta H_{\mathrm{rxn}} = -41.9 \pm 0.2\,\mathrm{kcal/mol}$$

$$\mathrm{PR_3 = P^iPr_3};\ \Delta H_{\mathrm{rxn}} = -37.4 \pm 0.3\,\mathrm{kcal/mol}$$

$$\mathrm{Cp^*Ru(PR_3)Cl_{(soln)}} + 2\mathrm{PR'_{3(soln)}} \xrightarrow[30\,^\circ\mathrm{C}]{\mathrm{THF}} 4\mathrm{Cp^*Ru(PR'_3)_2Cl_{(soln)}} + \mathrm{PR_3}$$

$$\mathrm{PR_3 = PCy_3,\ P^iPr_3};$$

$$\mathrm{PR'_3} = \text{phosphines with smaller } \theta \tag{5}$$

Table 11 Relative bond disruption enthalpies ($\mathrm{kcal\,mol^{-1}}$) in the following reaction

$$\mathrm{(Cp^*RuCl)_{4(soln)}} + n\mathrm{L_{(soln)}} \xrightarrow[30\,^\circ\mathrm{C}]{\mathrm{THF}} 4\mathrm{Cp^*Ru(L)_{\mathit{n}/4}Cl_{(soln)}}$$

L	Complex	n	Relative BDE[a]
$\mathrm{P^iPr_3}$	$\mathrm{Cp^*Ru(P^iPr_3)Cl}$	4	9.4 (0.3)
$\mathrm{PCy_3}$	$\mathrm{Cp^*Ru(PCy_3)Cl}$	4	10.5 (0.2)
$\mathrm{P^nBu_3}$	$\mathrm{Cp^*Ru(P^nBu_3)_2Cl}$	8	18.1 (0.4)
$\mathrm{PEt_3}$	$\mathrm{Cp^*Ru(P\ Et_3)_2Cl}$	8	18.4 (0.6)
$\mathrm{P(OMe)_3}$	$\mathrm{Cp^*Ru(P(OMe)_3)_2Cl}$	8	23.8 (0.4)

[a] Relative BDE values were derived by dividing the enthalpy value by the number of Ru–$\mathrm{PR_3}$ formed during the reaction of interest.

2.4 Phosphine Exchange in a Ruthenium-Alkylidene System

The utilization of neutral 16-electron ruthenium-alkylidene complexes as olefin metathesis catalysts (*see* ***Organic Synthesis Using Metal-mediated Metathesis Reactions***) has had a tremendous impact in both organic and polymer chemistry.[45,46] These complexes of type $\mathrm{(PR_3)_2Cl_2Ru{=}CR'_2}$ (Where $\mathrm{PR_3}$ = sterically demanding phosphine) have been thoroughly investigated, especially with regard to the role played by the phosphine ligands.[47] Yet, this understanding is based principally on kinetic studies and thermochemical investigations are highly desirable. In fact, complex $\mathrm{(PPh_3)_2Cl_2Ru({=}C{-}C{=}CPh_2)}$[30] constitutes an ideal entryway into the thermochemistry of these ruthenium-carbene species insofar as $\mathrm{PPh_3}$ replacement by a series of sterically demanding tertiary phosphine ligands can be investigated by batch calorimetry. This transformation and a list of all reaction enthalpies is provided in Table 12. With these data at hand, the interpretation of these enthalpies of ligand substitution in terms of phosphine steric and electronic parameters according to equation (3) (see above) shows that an excellent correlation

Table 12 Enthalpies of substitution (kcal mol^{-1}) for the reaction:

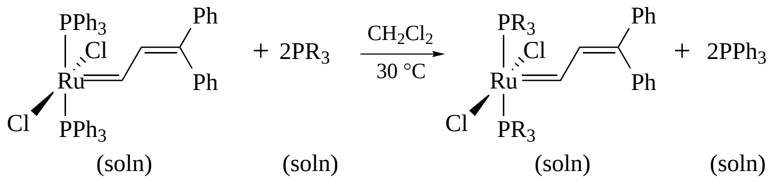

PR_3	θ	χ	$-\Delta H_{rxn}$[a]
PPh_3	145	13.45	0
PBz_3	165	10.3	1.3 (0.2)
$PCyPh_2$	153	9.4	1.8 (0.2)
PCy_2Ph	162	5.35	3.8 (0.2)
P^iBu_3	143	5.7	3.8 (0.2)
P^iPr_3	160	3.45	5.2 (0.1)
PCy_3	170	1.4	6.5 (0.3)

[a] Enthalpy values are reported with 95% confidence limits.

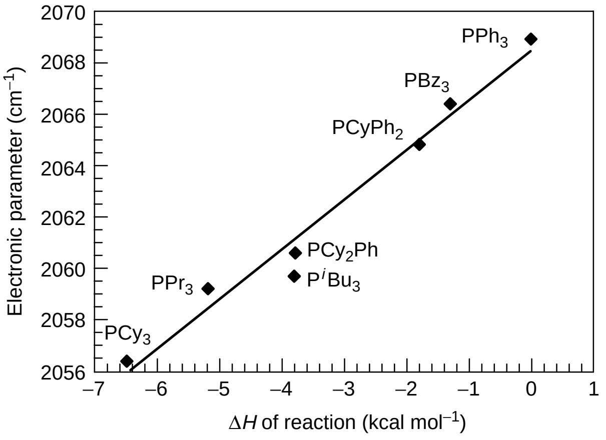

Figure 8 Enthalpy of phosphine exchange reaction (kcal mol^{-1}) vs Tolman electronic parameter (cm^{-1}) for *trans*-$(PR_3)_2Cl_2Ru{=}CH{-}CH{=}CPh_2$ complexes (*slope* = 1.93; *R* = 0.98)

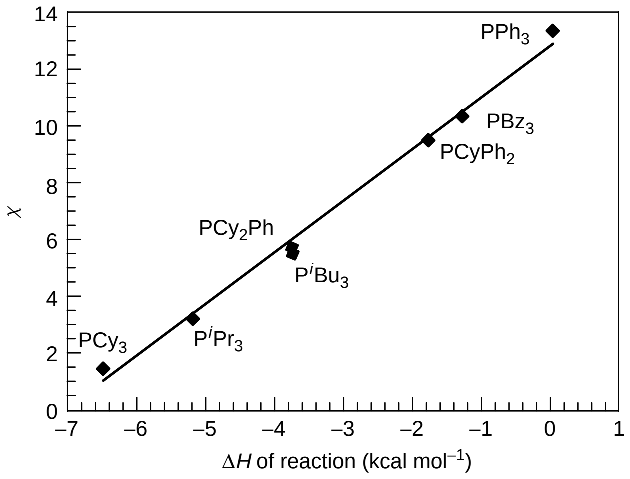

Figure 9 Enthalpy of phosphine exchange reaction (kcal mol^{-1}) vs χ for *trans*-$(PR_3)_2Cl_2Ru{=}CH{-}CH{=}CPh_2$ complexes (*slope* = 1.813; *R* = 0.997)

is found to exist between the enthalpies of phosphine exchange and the Tolman electronic parameter (Figure 8).

Another model from which to extract steric and electronic ligand characteristics is the quantitative analysis of ligand effects (QALE) developed by Giering and coworkers.[48,49] From the excellent correlation between χ and ΔH, the electronic parameter (χ) can be taken as the origin of any variations in measured enthalpies of reaction (Figure 9). In assessing the donor properties of the phosphine ligands, even a simple pK_a model can describe fairly well the overwhelming influence of phosphine electronics in the present system, as shown by the linear relationship found in Figure 10.

2.5 N-heterocyclic Carbene (NHC) Binding to Ruthenium Systems

The description of stereoelectronic factors characterizing tertiary phosphine ligands has greatly assisted synthetic and catalytic efforts. Nucleophilic N-heterocyclic carbenes (NHC) are increasingly attractive alternatives to phosphine ligands in organometallic catalytic systems.[50–52] Especially successful applications of this new ligand class include their use as ligands in ruthenium metathesis catalysts.[53,54] The subtle steric and electronic differences within the NHC class of ligands remain relatively unquantified. The tetrameric $[Cp^*RuCl]_4$ reacts with sterically demanding phosphines to afford coordinatively unsaturated complexes of the general formula $Cp^*Ru(PR_3)Cl$ and reacts rapidly with nucleophilic carbene ligands (L) to give the new NHC-complexes of general formula $Cp^*Ru(L)Cl$. Solution calorimetric investigations provide the enthalpies of ligand substitution shown in Table 13.

Several interesting trends are observed. First, comparing complexes bearing the isosteric (*see Isosteric Groups*) pair of IMes and IMes·Cl, it is clear from the enthalpy data that

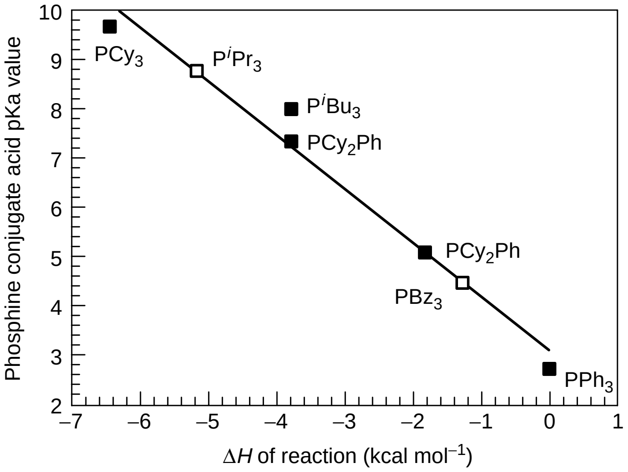

Figure 10 Enthalpy of phosphine exchange reaction (kcal mol^{-1}) vs pK_a of HPR_3^+ for *trans*-$(PR_3)_2Cl_2Ru{=}CH{-}CH{=}CPh_2$ complexes. (*slope* $= -1.092$; $R = 0.983$). Solid: literature value.[16] Hollow: predicted value

Table 13 Enthalpies of substitution (kcal mol^{-1}) and relative Ru–NHC bond disruption enthalpies (kcal mol^{-1}) in the reaction:

$$(Cp^*RuCl)_{4(s)} + 4L_{(soln)} \xrightarrow[30\,°C]{THF} 4Cp^*Ru(L)Cl_{(soln)}$$

L	$-\Delta H^a_{exp}$	Relative BDE^b
SIMes	67.1 (0.3)	16.8
IMes	62.6 (0.2)	15.6
SIPr	48.5 (0.4)	12.1
IPr	44.5 (0.4)	11.1
ITol	75.3 (0.4)	18.8
ICy	85.0 (0.2)	21.2
IpCl	74.3 (0.3)	18.6
IAd	27.4 (0.4)	6.8
IMesCl	48.5 (0.4)	12.1
PCy_3	41.9 (0.2)	10.5
P^iPr_3	37.4 (0.3)	9.4

[a]Enthalpy values are reported with 95% confidence limits. [b]Relative BDE values were derived by dividing the enthalpy value by the numb Ru–NHC formed during the reaction of interest.

the chlorides in the backbone act as electron-withdrawing groups when compared to H in IMes. ITol is a slightly better donor than IpCl, a trend that is again in line with electron-donating/withdrawing abilities of arene substituents.[55] Substituting an aryl group for an alkyl increases the donor ability of the carbene ligand. The case in point is the ICy, which is some 5.6 kcal mol^{-1} more exothermic than IMes. Finally, IAd is the least exothermic ligand examined and steric effects are at the origin of this low enthalpy of ligand substitution.

With the crystallographic data of complexes Cp*Ru(IMes) Cl, Cp*Ru(SIMes)Cl, Cp*Ru(IPr)Cl, Cp*Ru(SIPr)Cl, Cp*Ru (ITol)Cl, and Cp*Ru(IAd)Cl at hand, and knowing the importance of steric factors in the related phosphine systems, it would thus be of use to quantify the steric factors characterizing this class of ligands. They cannot be viewed in the same light as phosphine ligands since a cone angle (as defined by Tolman[37]) cannot be defined in the present system. As a first model to describe the steric parameters of NHCs and of phosphines, the amount of volume of a sphere centered on the metal, buried by overlap with atoms of various NHC ligands, $\%V_{Bur}$, was measured.[15] The volume of this sphere would represent the space around the metal atom that must be shared by the different ligands upon coordination. Of course, the bulkier the specific ligand, the larger the amount of that sphere will be occupied by the ligand, that is, greater $\%V_{Bur}$. A graphical representation of this geometrical analysis is reported in Figure 11 and a compilation of $\%V_{Bur}$ values is presented in Table 14. When the experimental BDEs are plotted versus $\%V_{Bur}$, a linear relationship is found to exist, not unlike the linear relationships found for BDEs versus phosphine cone angle in the corresponding $Cp^*Ru(PR_3)Cl$ and $Cp^*Ru(PR_3)_2Cl$ (Figure 12). This simple model is only a starting point to understand the steric requirements of ligand classes other than

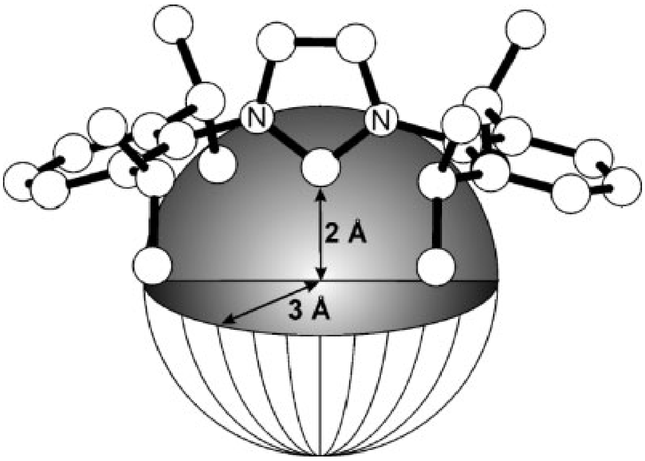

Figure 11 Sphere dimensions for steric parameter determination ($\%V_{Bur}$) of NHC ligands

Table 14 Steric parameters associated with selected NHC and sterically demanding PR_3 ligands

Ligand	$\%V_{Bur}$
ITol	23
IMes	26
SIMes	27
IPr	28
SIPr	29
P^iPr_3	32
PCy_3	32
IAd	37

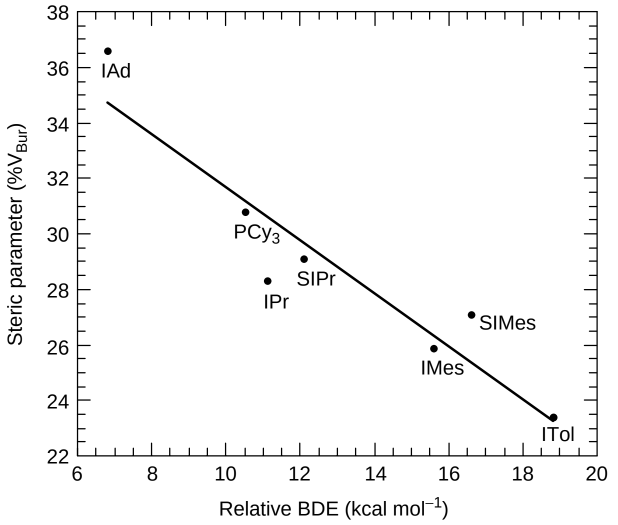

Figure 12 Relative bond disruption enthalpy (kcal mol^{-1}) vs steric parameter (%V_{Bur}) in the Cp*Ru(L)Cl system (*slope* $= -1.01$; $R = 0.94$)

phosphines, but might ultimately lead to a unified treatment of different ligand classes.

2.6 Binding of Phosphines to Rhodium Systems

The utilization of rhodium-phosphine complexes in homogeneous catalysis is widespread and encompasses industrially important processes, hydroformylation (*see Hydroformylation*) being one of the most widely known rhodium-mediated conversions (*see* ***Rhodium: Organometallic Chemistry*** and ***Carbonylation Processes by Homogeneous Catalysis***).[56,57] It was therefore of interest to perform thermochemical studies on a fundamentally important organorhodium–phosphine system, $RhCl(CO)(PR_3)_2$. Direct entry into the thermochemistry of $RhCl(CO)(PR_3)_2$ complexes is made possible by the rapid and quantitative reaction of $[Rh(CO)_2Cl]_2$ with stoechiometric amounts of phosphine ligands and a compilation of phosphine ligands with their respective enthalpies of reaction is presented in Table 15. In this rhodium system, a linear relationship is present between the enthalpy of reaction and corresponding Hammett σ_p parameters, a result that is indicative of the major role played by phosphine electronic effects.

Therefore, simple one-parameter relationships can be established with either the carbonyl stretching frequency (ν_{CO}, Figure 13) or Tolman's electronic parameter (χ, Figure 14),

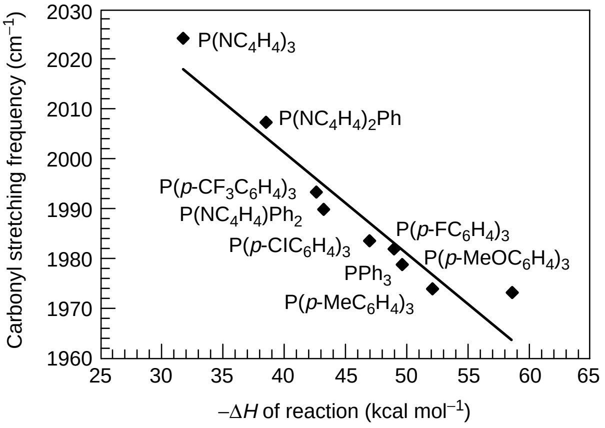

Figure 13 Carbonyl stretching frequency (cm^{-1}) vs enthalpies of reaction (kcal mol^{-1}) for the $RhCl(CO)(PR_3)_2$ system (*slope* $= -2.00$; $R = 0.96$)

Table 15 Enthalpies of substitution (kcal mol^{-1}) in the reaction:

$$[RH(CO)_2Cl]_{2(soln)} + 4PR_{3(soln)} \xrightarrow[30\,^\circ C]{CH_2Cl_2} 2Rh(CO)Cl[PR_3]_{2(soln)} + 2CO$$

L	Complex	v_{CO} (cm^{-1})	$-\Delta H_{rxn}{}^a$
$P(NC_4H_4)_3$	$Rh(CO)(Cl)[P(NC_4H_4)_3]_2$	2024	34.4 (0.2)
$P(NC_4H_4)_2Ph$	$Rh(CO)(Cl)[P(NC_4H_4)_2Ph]_2$	2007	35.3 (0.2)
$P(OPh)_3$	$Rh(CO)(Cl)[P(OPh)_3]_2$	2016	42.6 (0.2)
$P(p\text{-}CF_3C_6H_5)_3$	$Rh(CO)(Cl)[P(p\text{-}CF_3C_6H_5)_3]_2$	1990	43.8 (0.2)
$P(NC_4H_4)Ph_2$	$Rh(CO)(Cl)[P(NC_4H_4)Ph_2]_2$	1993	44.8 (0.2)
$P(p\text{-}ClC_6H_5)_3$	$Rh(CO)(Cl)[P(p\text{-}ClC_6H_5)_3]_2$	1984	47.8 (0.3)
$AsEt_3$	$Rh(CO)(Cl)[AsEt_3]_2$	1952	49.2 (0.3)
$P(p\text{-}FC_6H_5)_3$	$Rh(CO)(Cl)[P(p\text{-}FC_6H_5)_3]_2$	1982	50.1 (0.3)
PPh_3	$Rh(CO)(Cl)[PPh_3]_2$	1978	51.7 (0.3)
$P(p\text{-}CH_3C_6H_5)_3$	$Rh(CO)(Cl)[P(p\text{-}CH_3C_6H_5)_3]_2$	1975	56.1 (0.2)
$P(p\text{-}CH_3OC_6H_5)_3$	$Rh(CO)(Cl)[P(p\text{-}CH_3OC_6H_5)_3]_2$	1973	58.7 (0.3)
PPh_2Me	$Rh(CO)(Cl)[PPh_2Me]_2$	1974	61.7 (0.3)
$P(OMe)_3$	$Rh(CO)(Cl)[P(OMe)_3]_2$	2006	63.7 (0.2)
$PPhMe_2$	$Rh(CO)(Cl)[PPhMe_2]_2$	1968	71.4 (0.3)
PEt_3	$Rh(CO)(Cl)[PEt_3]_2$	1956	77.2 (0.3)

[a] Enthalpy values are reported with 95% confidence limits.

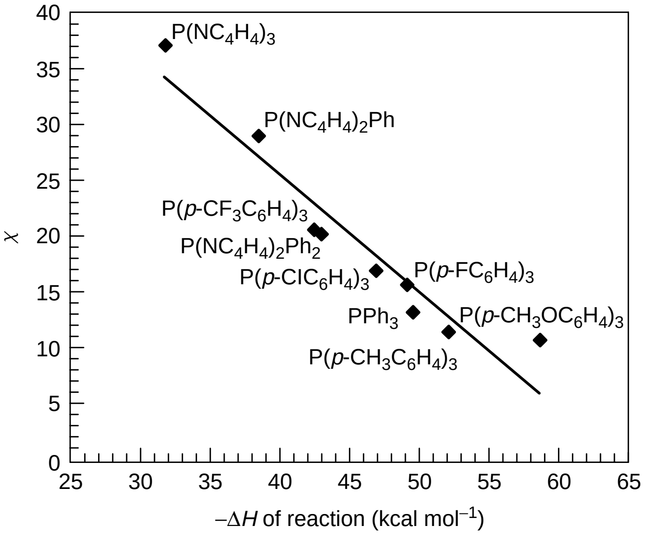

Figure 14 Electronic parameter (χ) vs enthalpies of reaction (kcal mol^{-1}) for the RhCl(CO)(PR$_3$)$_2$ system (*slope* $= -1.05$; $R = 0.96$)

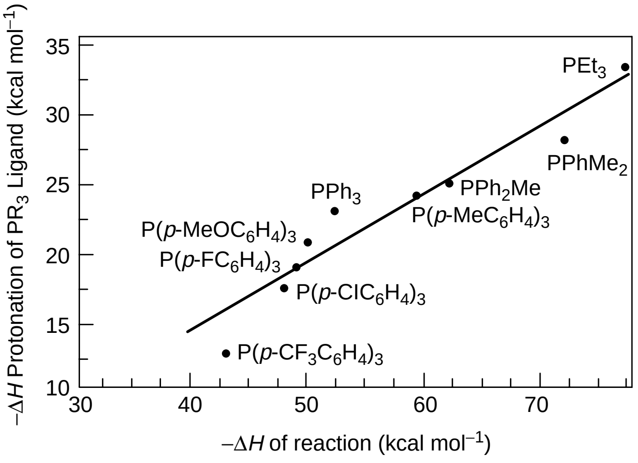

Figure 15 Enthalpies of protonation (kcal mol^{-1}) of phosphine ligands vs enthalpies of reaction (kcal mol^{-1}) for the RhCl(CO)(PR$_3$)$_2$ system (*slope* $= 0.49$; $R = 0.96$)

both exhibiting a very good correlation. The overwhelming influence of phosphine electronics that was found to exist in the ruthenium–carbene systems is also operating for the present rhodium system and a good correlation is provided with a simple relationship linking the measured enthalpies of reaction to the enthalpies of protonation of the free phosphine ligands as shown in Figure 15.

As shown above, the range in stabilities can be quite significant and the calorimetry data show that the enthalpy for the equilibrium shown in equation (6) favors products by 25.9 kcal mol^{-1}, when $PZ'_3 = P(p\text{-}CH_3OC_6H_4)_3$ and $PZ_3 = $ Ppyrl$'_3$.

$$trans\text{-}RhCl(CO)(PZ_3)_2 + 2PZ'_3 \rightleftharpoons trans\text{-}RhCl(CO)(PZ'_3)_2 + 2PZ_3 \quad (6)$$

The data indicate that the exchange reaction is slowed down with phosphines that are good π-acceptors/weak σ-donors, which is the case in all the systems discussed so far. It would therefore be of interest to compare this system with a rhodium system where the observed trend is reversed, that is, where substitution is favored in the case of good π-acceptors/weak σ-donors. Such a system was found in the case of the chelating tridentate bis(phosphino)-amido ligands RPNP (Fryzuk's ligand).[58,59] Substitution of cyclooctene in [RPNP]Rh(COE) with phosphines (or CO) was investigated by solution calorimetry and shows conclusively and convincingly that better acceptor ligands give the more stable complexes in the [RPNP]RhL system (Table 16). An analysis for the reactions of both complexes supports the notion that the observed trends, although opposite, are electronic in nature (all the phosphine ligands being isosteric) and a good correlation was found for the reaction enthalpy versus Tolman's electronic parameter (χ) (Figure 16).

These results thus illustrate the importance of reorganization energies in thermodynamic analyses of metal–ligand bonding, especially in the presence of synergistic bonding involving σ-donor, π-donor, and π-acceptor ligands. The interactions of the whole ligand set of metal complexes through shared metal orbitals (electron push–pull) underscore the caution that must be employed when attempting to interpret experimental chemical results and bond dissociation enthalpies as intrinsic, transferable properties of individual bonds. In fact, even the concept of individual bond strength becomes somewhat ambiguous.

Table 16 Enthalpies of substitution for the reaction

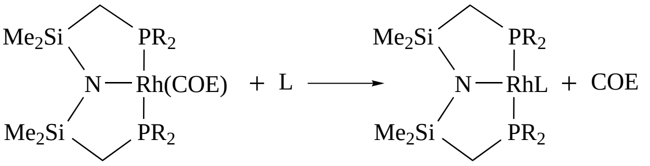

R	L	$-\Delta H_{rxn}$ (kcal mol^{-1})[a]	χ[b]
Ph	PPh$_3$	7.2 (3)	13.25
Ph	PPh$_2$pyrl	11.1 (2)	21
Ph	PPhpyrl$_2$	13.0 (2)	29
Ph	Ppyrl$_3$	13.8 (1)	37
Ph	Ppyrl$'_3$	14.9 (2)	48
Ph	CO	48.9 (3)	
Ipr	PPh$_3$	10.9 (3)	13.25
Ipr	PPh$_2$pyrl	13.0 (4)	21
Ipr	PPhpyrl$_2$	15.4 (3)	29
Ipr	Ppyrl$_3$	18.9 (2)	37
Ipr	Ppyrl$'_3$	20.2 (3)	48
Ipr	CO	53.3 (4)	

[a] Enthalpy values are provided with 95% confidence limits. [b] χ is Tolman's electronic parameter.

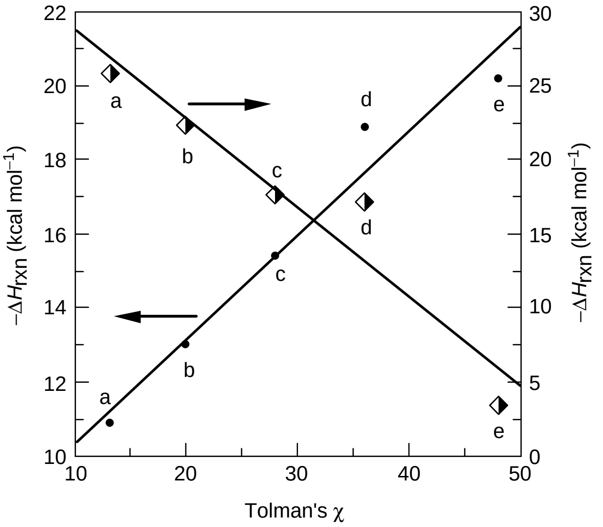

Figure 16 Reaction enthalpy vs Tolman's electronic parameter (χ) for rhodium systems: circles = [^{i}PrPNP]RhL; diamonds = *trans*-RhCl(CO)L$_2$. Letters correspond to the ligands L = PPh$_3$(a), PPh$_2$pyrl (b), PPhpyrl$_2$ (c), Ppyrl$_3$ (d), and Ppyrl$'_3$ (e)

2.7 Addition Reactions to a Rhodium-phosphine System

Very few thermodynamic studies of addition reactions to metal fragments have been reported, and this situation stems in part from the fact that substitution reactions of such complexes generally proceed via facile associative mechanisms (*see Associative Substitution* and ***Mechanisms of Reaction of Organometallic Complexes***), precluding an estimation of BDEs based on rates of ligand dissociation. Goldman, Nolan *et al.* examined the thermodynamics of CO, H$_2$, Bu^{t}NC, aldehyde, and acyl chloride addition to the three-coordinate fragment Rh(PR$_3$)$_2$Cl, to give either square-planar (*see Square Planar*) complexes Rh(PR$_3$)$_2$Cl(CO) and Rh(PR$_3$)$_2$Cl(CNBu^t), or to give the corresponding d^6 five-coordinate adduct Rh(PR$_3$)$_2$Cl(X)(Y).[16–18] The three-coordinate fragment Rh(PR$_3$)$_2$Cl is generated from the dimer [Rh(PR$_3$)$_2$Cl]$_2$ by splitting of the chloride bridges, but is not isolable. This means that the calorimetric determinations of the enthalpies of reaction afford relative enthalpies of addition to the fragment Rh(P^{i}Pr$_3$)$_2$Cl, but not absolute values. On the basis of the observation that no measurable concentration of the monomer exists in solution, a lower limit for the bridge strength of the dimer [Rh(PR$_3$)$_2$Cl]$_2$ was calculated.

2.7.1 Thermodynamics of CO Addition

In order to avoid problems associated with calorimetric measurements with a gas-phase reactant, the following reactions (equation 7) were exploited to determine the enthalpy of equation (8). The enthalpy of equation (8) is subsequently determined using the available thermodynamic data for the components of equation (7).

$$\Delta H\,(\mathrm{kcal\,mol^{-1}})$$

$$(\mathrm{P}^i\mathrm{Pr}_3)_2\mathrm{RhCl}_{(\mathrm{soln})} + \mathrm{C_8H_{16}O}_{(\mathrm{soln})} \longrightarrow (\mathrm{P}^i\mathrm{Pr}_3)_2\mathrm{Rh(CO)(Cl)}_{(\mathrm{soln})} + \mathrm{C_7H_{16}}_{(\mathrm{soln})} \quad -36.0 \pm 0.5 \quad (7)$$

$$\mathrm{C_7H_{16}}_{(\mathrm{g})} + \mathrm{CO}_{(\mathrm{g})} \longrightarrow \mathrm{C_8H_{16}O}_{(\mathrm{g})} \quad -3.3 \pm 0.5$$

$$(\mathrm{P}^i\mathrm{Pr}_3)_2\mathrm{RhCl}_{(\mathrm{soln})} + \mathrm{CO}_{(\mathrm{g})} \longrightarrow (\mathrm{P}^i\mathrm{Pr}_3)_2\mathrm{Rh(CO)(Cl)}_{(\mathrm{soln})} \quad -39.3 \pm 0.7 \quad (8)$$

2.7.2 Thermodynamics of H$_2$ and t-BuNC Addition

In this case, the gas-phase reactants were avoided by measuring two separate enthalpies of reaction (equations 9 and 10), and equation (11) is therefore calculated from equation (10) plus the reverse of equation (9).

$$(\mathrm{P}^i\mathrm{Pr}_3)_2\mathrm{RhClH_2}_{\,(\mathrm{soln})} + \mathrm{Bu}^t\mathrm{NC}_{(\mathrm{soln})} \longrightarrow (\mathrm{P}^i\mathrm{Pr}_3)_2\mathrm{Rh(CNBu}^t)\mathrm{(Cl)}_{(\mathrm{soln})} + \mathrm{H_2} \quad \Delta H = -9.9 \pm 0.4\,\mathrm{kcal\,mol^{-1}} \quad (9)$$

$$0.5[(\mathrm{P}^i\mathrm{Pr}_3)_2\mathrm{RhCl}]_2\,_{(\mathrm{soln})} + \mathrm{Bu}^t\mathrm{NC}_{(\mathrm{soln})} \longrightarrow (\mathrm{P}^i\mathrm{Pr}_3)_2\mathrm{Rh(CNBu}^t)\mathrm{(Cl)}_{(\mathrm{soln})} \quad \Delta H = -33.5 \pm 0.5\,\mathrm{kcal\,mol^{-1}} \quad (10)$$

$$0.5\,[(\mathrm{P}^i\mathrm{Pr}_3)_2\mathrm{RhCl}]_2\,_{(\mathrm{soln})} + \mathrm{H}_{2(\mathrm{g})} \longrightarrow (\mathrm{P}^i\mathrm{Pr}_3)_2\mathrm{RhClH}_{2(\mathrm{soln})} \quad \Delta H = -23.6 \pm 0.6\,\mathrm{kcal\,mol^{-1}} \quad (11)$$

2.7.3 Thermodynamic Studies of the Addition of N$_2$, C$_2$H$_4$, and Alkynes

[Rh(P^{i}Pr$_3$)$_2$Cl]$_2$ reacts in solution with N$_2$, C$_2$H$_4$ and diphenylacetylene, respectively, to give the corresponding adducts Rh(P^{i}Pr$_3$)$_2$ClL (L = N$_2$, C$_2$H$_4$, PhCCPh). The reactions of [Rh(P^{i}Pr$_3$)$_2$Cl]$_2$ with N$_2$ and C$_2$H$_4$ were measured calorimetrically, exploiting the method reported for the determination of the enthalpy of addition of H$_2$, according to equations (12) and (13). Equation (14) shows the enthalpies found for these addition reactions (ΔH_3). In the case of L = PhCCPh, the addendum is not volatile and the addition reaction was measured directly (equation 15).

$$(\mathrm{P}^i\mathrm{Pr}_3)_2\mathrm{RhClL}_{(\mathrm{soln})} + \mathrm{Bu}^t\mathrm{NC}_{(\mathrm{soln})} \longrightarrow (\mathrm{P}^i\mathrm{Pr}_3)_2\mathrm{RhCl(CNBu}^t)_{(\mathrm{soln})} + \mathrm{L} \quad (12)$$

L	$-\Delta H_1$
N$_2$	25.9 (0.5)
C$_2$H$_4$	17.6 (0.3)
PhCCPh	19.9 (0.5)

$$0.5\,[(\mathrm{P}^i\mathrm{Pr}_3)_2\mathrm{RhCl}]_{2(\mathrm{soln})} + {}^t\mathrm{BuNC}_{(\mathrm{soln})} \longrightarrow (\mathrm{P}^i\mathrm{Pr}_3)_2\mathrm{RhCl}({}^t\mathrm{BuNC})_{(\mathrm{soln})} \quad \Delta H_2 = -33.5\ (0.5)\,\mathrm{kcal\,mol^{-1}} \quad (13)$$

$$0.5\,[(\mathrm{P}^i\mathrm{Pr}_3)_2\mathrm{RhCl}]_{2(\mathrm{soln})} + \mathrm{L}_{(\mathrm{soln})} \longrightarrow (\mathrm{P}^i\mathrm{Pr}_3)_2\mathrm{RhCl(L)}_{(\mathrm{soln})} \quad (14)$$

$$\Delta H_3 = \Delta H_2 - \Delta H_1$$

L	$-\Delta H_3$ (kcal mol^{-1})
N$_2$	7.6 (0.7)
C$_2$H$_4$	15.9 (0.6)
PhCCPh	13.6 (0.7)

$$0.5[(P^iPr_3)_2RhCl]_{2(soln)} + PhCCPh_{(soln)} \longrightarrow (P^iPr_3)_2RhCl(PhCCPh)_{(soln)} \quad \Delta H = -14.2\ (0.4)\ \text{kcal mol}^{-1} \qquad (15)$$

2.7.4 Thermodynamics of the Addition of Aldehydes and acyl Chlorides

Thermodynamic studies of the enthalpy of addition of aldehydes and acyl chlorides to $[Rh(P^iPr_3)_2Cl]_2$ and the hypothetical monomer $Rh(P^iPr_3)_2Cl$ gave unsaturated five-coordinate Rh(III) compounds according to equations (16) and (17) and afforded the values shown in Table 17.

$$0.5\,[(P^iPr_3)_2RhCl]_{2(soln)} + RCHO_{(soln)} \longrightarrow (P^iPr_3)_2RhClH[C(O)R]_{(soln)} \qquad (16)$$

$$0.5\,[(P^iPr_3)_2RhCl]_{2(soln)} + RC(O)Cl_{(soln)} \longrightarrow (P^iPr_3)_2RhCl_2[C(O)R]_{(soln)} \qquad (17)$$

Different interesting observations can be made when analyzing the enthalpy data for the addition of molecules to $[Rh(P^iPr_3)_2Cl]_2$. For the addition leading to square-planar rhodium(I) compounds, it can be seen that the better π-acceptors bind more strongly to the $Rh(P^iPr_3)_2Cl$ fragment with the minimum Rh–L BDE increasing from 16.5 kcal mol^{-1} (for N_2) to 48.2 kcal mol^{-1} (for CO). The enthalpies of the oxidative addition (*see Oxidative Addition*) reactions of aldehydes and H_2 are more exothermic than would be expected on the basis of thermodynamic data for related late–transition metal complexes and are more exothermic in comparison with the enthalpy of addition of acyl chlorides. All of the data, though, are quite high compared with previously reported values for second-row transition metals and are consistent with and help explain the remarkable catalytic activity of the $Rh(P^iPr_3)_2Cl$ fragment.

2.8 Binding of Fluorinated Phosphine Ligands

Recent developments in phosphine synthesis have allowed for catalysis to be carried out in nontraditional media, such as aqueous and fluorous solvents, as well as in supercritical carbon dioxide. Horváth and Gladysz have developed and utilized a fluorinated ligand that allows for biphasic segregation of a catalyst from the organic reactants and products.[60–62] The synthesis of this ponytail ligand, $P[CH_2CH_2(CF_3)_5CF_3]_3$, and the synthetic strategies employed for obtaining a series of fluorinated phosphine ligands with more tunable stereoelectronic properties are shown in equations (18–20).

Table 17 Enthalpy of addition of XY to $[(P^iPr_3)_2RhCl]_2$ ($-\Delta H_{rxn}$) and the hypothetical monomer $(P^iPr_3)_2RhCl$ ($-\Delta H_{min}$) in solution (kcal mol^{-1})

XY	$-\Delta H_{rxn}$	$-\Delta H_{min}$
H_2	23.6 (0.6)	32.5
$C_8H_{17}CHO$	15.2 (0.3)	24.1
PhCHO	10.8 (0.4)	19.7
(*p*-Tol)CHO	10.5 (0.4)	19.4
$(p\text{-}CF_3C_6H_4)CHO$	12.7 (0.4)	21.6
$(p\text{-}MeOC_6H_4)CHO$	10.5 (0.3)	19.4
$C_8H_{17}C(O)Cl$	24.6 (0.3)	33.5
PhC(O)Cl	21.7 (0.3)	30.6

$$PH_3 + 3CH_2CH(CF_2)_5CF_3 \xrightarrow{\text{AIBN}} P(CH_2CH_2(CF_2)_5CF_3)_3 \qquad (18)$$

$$R_2PCl + R_fOH \xrightarrow[\text{NEt}_3]{\text{THF}} R_2POR_f + HNEt_3Cl \qquad (19)$$

$$R = R_fO,\ {}^iPr,\ Ph,\ Cy;\ R_f = CH_2CH_2(CF_2)_5CF_3$$

$$R_2PCl + R_fMgI \xrightarrow{\text{Et}_2\text{O}} R_2PR_f + MgICl \qquad (20)$$

$$R = Cy,\ {}^iPr;\ R_f = CH_2CH_2(CF_2)_5CF_3$$

The stereoelectronic properties of these new ligands were then investigated by solution calorimetry involving the rhodium complex $[Rh(CO)_2Cl]_2$ and infrared spectroscopy of the resulting complexes (ν_{CO} stretching) by using the ligand substitution reaction shown in equation (21). Table 18 gives an overview of the data obtained and compares them to previous studies involving nonfluorinated phosphorous ligands. In view of the mutually trans arrangement of the phosphine ligands in these complexes, of general formula $Rh(CO)Cl(PR_3)_2$, the predominant factor dictating the magnitude of the enthalpy of ligand substitution is associated with the electronic factor of the phosphine and a linear relationship exists between the enthalpy of reaction and the experimentally recorded carbonyl stretching frequency, as illustrated in Figure 17.

$$[Rh(CO)_2Cl]_{2(soln)} + 4PR_{3(soln)} \xrightarrow[30\,^\circ C]{CH_2Cl_2} 2Rh(CO)(Cl)(PR_3)_{2(soln)} + 2CO \qquad (21)$$

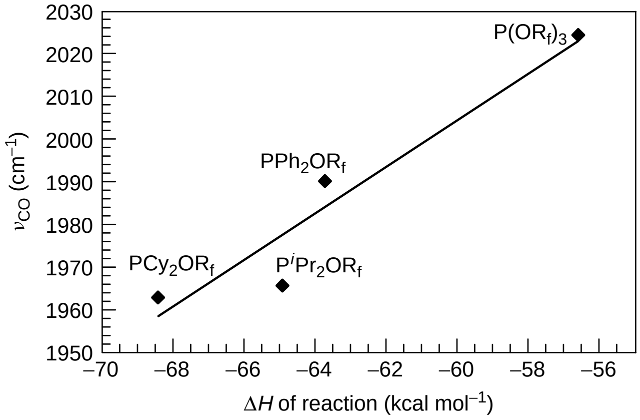

Figure 17 Carbonyl stretching frequency (cm^{-1}) vs enthalpies of reaction (kcal mol^{-1}) for the $RhCl(CO)(PR_3)_2$ system (*slope* = 5.47; $R = 0.96$)

Table 18 Enthalpies of substitution (kcal mol^{-1}) for equation (21)

$\mathrm{PR_3}$	Complex	ν_{CO} (cm^{-1})	$-\Delta H_{(\mathrm{rxn})}$[a]
$\mathrm{P(NC_4H_4)_3}$	$\mathrm{Rh(CO)(Cl)(P[NC_4H_4]_3)_2}$	2024	34.4 (0.2)
$\mathrm{P(NC_4H_4)_2(C_6H_5)}$	$\mathrm{Rh(CO)(Cl)(P[NC_4H_4]_2[C_6H_5])_2}$	2007	35.3 (0.2)
$\mathrm{P(OPh)_3}$	$\mathrm{Rh(CO)(Cl)(P[OPh]_3)_2}$	2016	42.6 (0.2)
$\mathrm{P(\mathit{p}\text{-}CF_3C_6H_5)_3}$	$\mathrm{Rh(CO)(Cl)(P[\mathit{p}\text{-}CF_3C_6H_4]_3)_2}$	1990	43.8 (0.2)
$\mathrm{P(NC_4H_4)(C_6H_5)_2}$	$\mathrm{Rh(CO)(Cl)(P[NC_4H_4][C_6H_5]_2)_2}$	1993	44.8 (0.2)
$\mathrm{P(\mathit{p}\text{-}ClC_6H_5)_3}$	$\mathrm{Rh(CO)(Cl)(P[\mathit{p}\text{-}ClC_6H_4]_3)_2}$	1984	47.8 (0.3)
$\mathrm{AsEt_3}$	$\mathrm{Rh(CO)(Cl)(AsEt_3)_2}$	1952	49.2 (0.3)
$\mathrm{P(\mathit{p}\text{-}FC_6H_5)_3}$	$\mathrm{Rh(CO)(Cl)(P[\mathit{p}\text{-}FC_6H_4]_3)_2}$	1982	50.1 (0.3)
$\mathrm{PPh_3}$	$\mathrm{Rh(CO)(Cl)(PPh_3)_2}$	1978	51.7 (0.3)
$\mathrm{P(\mathit{p}\text{-}CH_3C_6H_5)_3}$	$\mathrm{Rh(CO)(Cl)(P[\mathit{p}\text{-}CH_3C_6H_4]_3)_2}$	1975	56.1 (0.2)
$\mathrm{P(OR_f)_3}$	$\mathrm{Rh(CO)(Cl)(P(OR_f)_3)_2}$	2024	56.6 (0.5)[b]
$\mathrm{P(\mathit{p}\text{-}C\ H_3OC_6H_5)_3}$	$\mathrm{Rh(CO)(Cl)(P[\mathit{p}\text{-}CH_3OC_6H_4]_3)_2}$	1973	58.7 (0.3)
$\mathrm{PPh_2Me}$	$\mathrm{Rh(CO)(Cl)(PPh_2Me)_2}$	1974	61.7 (0.3)
$\mathrm{P(OMe)_3}$	$\mathrm{Rh(CO)(Cl)[P(OMe)_3]_2}$	2006	63.7 (0.2)
$\mathrm{PPh_2(OR_f)}$	$\mathrm{Rh(CO)(Cl)(PPh_2(OR_f))_2}$	1990	63.7 (0.4)
$\mathrm{P^{\mathit{i}}Pr_2(OR_f)}$	$\mathrm{Rh(CO)(Cl)(P^{\mathit{i}}Pr_2(OR_f))_2}$	1966	64.9 (0.5)
$\mathrm{PCy_2(OR_f)}$	$\mathrm{Rh(CO)(Cl)(PCy_2(OR_f))_2}$	1963	68.4 (0.3)
$\mathrm{PR_{f3}}$	$\mathrm{Rh(CO)(Cl)(PR_{f3})_2}$	1977	68.5 (0.2)[b]
$\mathrm{PPhMe_2}$	$\mathrm{Rh(CO)(Cl)(PPhMe_2)_2}$	1968	71.4 (0.3)
$\mathrm{PEt_3}$	$\mathrm{Rh(CO)(Cl)(Pet_3)_2}$	1956	77.2 (0.3)

[a] Enthalpy values are reported with 95% confidence limits. [b] Work performed in THF.

A measure of the steric parameter associated with the widely used fluorous tertiary phosphine ligand $\mathrm{P[CH_2CH_2(CF_2)_5CF_3]_3}$ was obtained by measuring the reaction enthalpies for ligand substitution of this ligand and $\mathrm{Cp'Ru(COD)Cl}$ ($\mathrm{Cp'} = \mathrm{Cp^*}$ and Cp). As discussed earlier, these two systems exhibit a marked dependence on steric parameters and by simple interpolation of the enthalpy reaction value of the phosphorous ligand (equation 22), they can be inserted into the linear relationship existing between the cone angle and the enthalpy of reaction. Respective values of 134° (from Cp* data) and 127° (from Cp data) and an average value of 130 ± 4° were obtained for the Tolman steric parameter θ of $\mathrm{P[CH_2CH_2(CF_2)_5CF_3]_3}$.

$$\underset{\text{soln}}{\mathrm{Cp'Ru(COD)Cl}} + \underset{\text{soln}}{\mathrm{2PR_{f3}}} \xrightarrow[30\,^{\circ}\mathrm{C}]{\mathrm{THF}} \underset{\text{soln}}{\mathrm{Cp'Ru(PR_{f3})_2Cl}} + \underset{\text{soln}}{\mathrm{COD}} \tag{22}$$

$$\Delta H = -34.7\ (0.3)\,\mathrm{kcal\,mol^{-1}},\ \mathrm{Cp'} = \mathrm{Cp}$$

$$\Delta H = -26.1\ (0.3)\,\mathrm{kcal\,mol^{-1}},\ \mathrm{Cp'} = \mathrm{Cp^*}$$

2.9 Reactivity of a Molybdenum System

The trigonal-planar molybdenum(III) compound (**1**) $\mathrm{Mo(N[R]Ar)_3}$ (**[Mo]**, $\mathrm{R = C(CD_3)_2CH_3}$, $\mathrm{Ar = 3{,}5\text{-}C_6H_3Me_2}$), synthesized by Cummins *et al.*,[63,64] shows surprising reactivity toward dinitrogen and white phosphorous to give respectively $\mathrm{Mo(N)(N[R]Ar)_3}$ and $\mathrm{Mo(P)(N[R]Ar)_3}$ via reductive cleavage reactions. Furthermore, a dramatic selectivity for nitrogen over oxygen was observed in the reaction of $\mathrm{Mo(N[R]Ar)_3}$ with nitrous oxide, a reaction found to proceed according to equation (23). Such selectivity is exceedingly unusual for reactions involving nitrous oxide, in that $\mathrm{N_2O}$ typically donates an oxygen atom to reducing agents, thereby liberating dinitrogen. One might therefore have predicted the reaction between $\mathrm{Mo(N[R]Ar)_3}$ and nitrous oxide to occur according to equation (24).

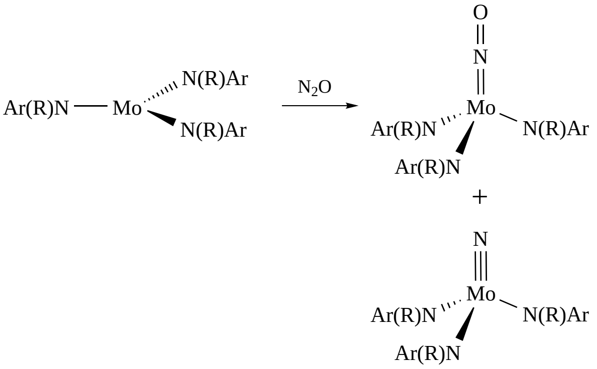

(23)

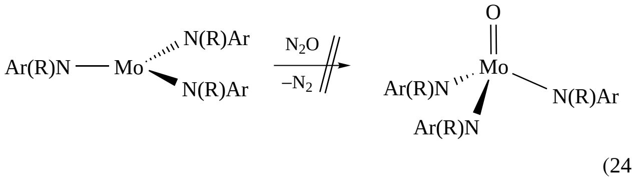

(24)

To explore the unusual display of reactivity of $\mathrm{Mo(N[R]Ar)_3}$ (**[Mo]**), the oxo complex $\mathrm{Mo(O)(N[R]Ar)_3}$ was synthesized by an independent route according to equation (25) and the nitrosyl compound $\mathrm{Mo(NO)(N[R]Ar)_3}$ is obtained according to equation (26). The reaction chemistry of equations (23), (25), and (26) were studied in detail to get kinetic data for these transformations and solution calorimetry studies were carried out in order to assess enthalpic factors relevant to the selective splitting of the nitrous oxide N–N bond by complex **[Mo]**. N_2O splitting reaction as well as the NO and O binding reactions were particularly amenable to analysis by solution calorimetry because of their rapid and essentially quantitative nature.

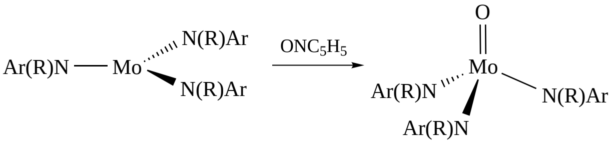

(25)

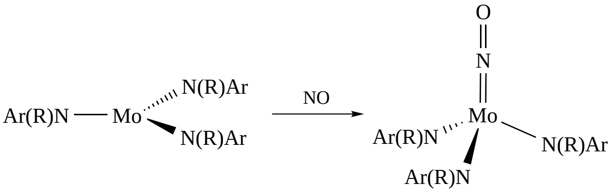

(26)

The enthalpies of these reactions were measured and the results are shown in Figure 18. NO binding to **[Mo]** gives C, the enthalpy of which is found to be $-82.5 \pm 2.5\,\mathrm{kcal\,mol^{-1}}$, while the N_2O splitting reaction is indicated as D, the corresponding enthalpy change being $-123.8 \pm 0.8\,\mathrm{kcal\,mol^{-1}}$. As an aside, the latter two values in combination with A, the $114\,\mathrm{kcal\,mol^{-1}}$ literature value for the N–NO bond dissociation enthalpy,[65] yield the value B for the Mo≡N BDE of $155.3 \pm 3.3\,\mathrm{kcal\,mol^{-1}}$. It appears that the calorimetrically determined Mo≡N BDE for nitride **[Mo]-N** is the first such value to be so obtained, and it is of interest further in that it indicates that the splitting of N_2 by 2 equiv of complex (**1**), giving 2 equiv of **[Mo]-N**, is favored enthalpically by ca. $86\,\mathrm{kcal\,mol^{-1}}$ and serves as a driving force for N_2 cleavage by complex (**1**). The **[Mo]-O** BDE was also determined and was found to be $155.6 \pm 1.6\,\mathrm{kcal\,mol^{-1}}$, a value equal to $F/2$ in Figure 18. This fact, taken in conjunction with the knowledge that the NN-O BDE value is $40\,\mathrm{kcal\,mol^{-1}}$, permits the conclusion that the conversion of 2 equiv of complex **[Mo]** to 2 equiv of **[Mo]-O** (if effected by 2 equiv of N_2O) would be downhill by a quantity equal to G, that is $231.2 \pm 3.2\,\mathrm{kcal\,mol^{-1}}$. Since the latter value is in excess of the value of D by $107.4 \pm 4.0\,\mathrm{kcal\,mol^{-1}}$, one sees that oxidation of complex **[Mo]** by nitrous oxide giving $Mo(O)(N[R]Ar)_3$ would have been vastly preferable to N–N bond splitting, the pathway that prevails evidently for reasons that are entirely kinetic in origin.

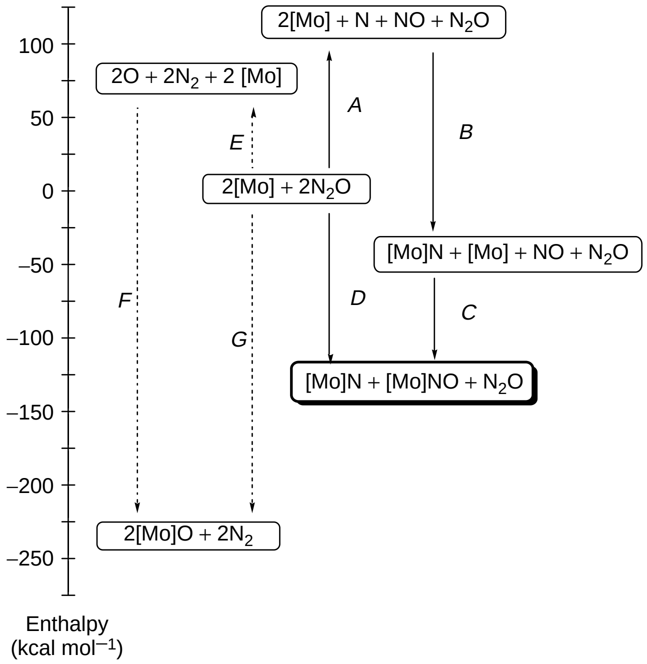

Figure 18 Thermodynamic parameters for the reaction between complex $Mo(N[{}^{\prime}Bu]Ar)_3$, here represented as [Mo], and N_2O

2.10 Binding of Phosphines to a Platinum System

Platinum(II) complexes of the type (COD)PtRX (COD = η^4-1,5-cyclooctadiene; R, X = alkyl, aryl, halide) are known for many combinations of R and X, and their reaction chemistry is well developed (*see* ***Platinum: Organometallic Chemistry***).[66] The lability of the COD–Pt interaction renders these compounds convenient sources of organoplatinum fragments for coordination to Lewis bases such as phosphines, according to equation (27). In an effort to better understand the factors that influence the stability of bis(phosphine)platinum(II) species, a thermodynamical study of the reaction in equation (27) was undertaken for a series of monodentate and bidentate phosphine ligands of varying steric and electronic character.

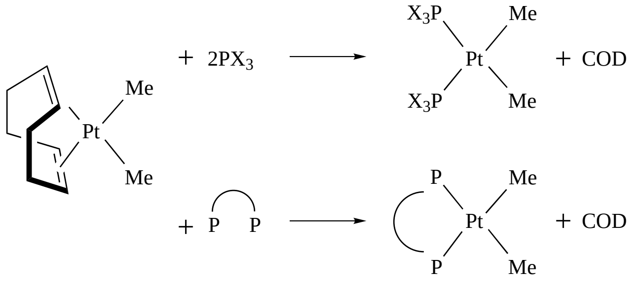

(27)

2.10.1 Monodentate Phosphine Ligands

Table 19 gives the measured enthalpies of reaction that span a range of $15\,\mathrm{kcal\,mol^{-1}}$ and clearly establish that small-θ phosphines give the most stable complexes in the P_2PtMe_2 system, an observation intuitively satisfying, given that phosphine substitution occurs at mutually cis positions on platinum (see also results on $Cp'Ru(L)_2Cl$ systems).

Table 19 Enthalpies of substitution (kcal mol^{-1}) for the reaction:

$$\mathrm{Pt(Me)_2(COD) + 2PX_3 \longrightarrow PtMe_2(PX_3)_2 + COD}$$

Complex	(P∼ P) Ligand	$-\Delta H_{\mathrm{rnx}}{}^{a}$ (kcal mol^{-1})
$PtMe_2(PMe_3)_2$	PMe_3	34.3(2)
$PtMe_2(PEt_3)_2$	PEt_3	32.9(3)
$PtMe_2(PMe_2Ph)_2$	PMe_2Ph	32.0(3)
$PtMe_2(PMePh_2)_2$	$PMePh_2$	29.0(2)
$PtMe_2(P^iBu_3)_2$	P^iBu_3	25.4(3)
$PtMe_2(P(p\text{-}MeC_6H_4)_3)_2$	$P(p\text{-}MeC_6H_4)_3$	24.3(2)
$PtMe_2(P(p\text{-}MeOC_6H_4)_3)_2$	$P(p\text{-}MeOC_6H_4)_3$	23.4(2)
$PtMe_2(P(p\text{-}ClC_6H_4)_3)_2$	$P(p\text{-}ClC_6H_4)_3$	23.2(1)
$PtMe_2(P(p\text{-}FC_6H_4)_3)_2$	$P(p\text{-}FC_6H_4)_3$	23.0(2)
$PtMe_2(PPh_2(pyrl))_2$	$PPh_2(pyrl)$	22.6(3)
$PtMe_2(PPh_3)_2$	PPh_3	22.6(2)
$PtMe_2(P(p\text{-}CF_3C_6H_4)_3)_2$	$P(p\text{-}CF_3C_6H_4)_3$	21.5(3)
$PtMe_2(P^iPr_3)_2$	P^iPr_3	20.7(2)
$PtMe_2(P(pyrl)_3)_2$	$P(pyrl)_3$	20.4(2)
$PtMe_2(PPh(pyrl)_2)_2$	$PPh(pyrl)_2$	20.1(2)
$PtMe_2(PCy_3)_2$	PCy_3	19.2 (3)

[a] Enthalpy values are provided with 95% confidence limit.

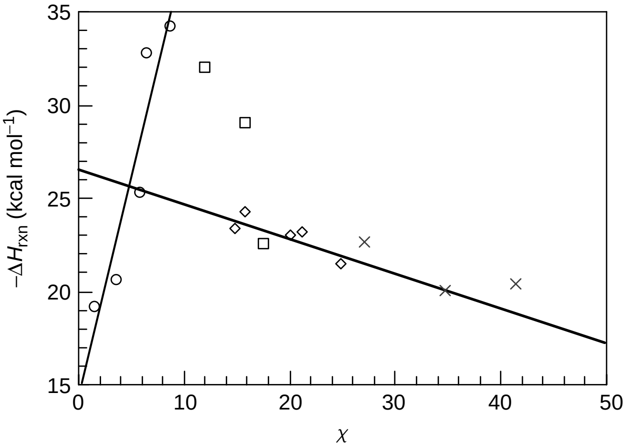

Figure 19 Enthalpy of reaction vs phosphine electronic parameter for (COD)PtMe$_2$ + 2PX$_3$: (circles) P(alkyl)$_3$ (*slope* = 2.34; $R = 0.932$); (squares) $PMe_{3-x}Ph_x$; (diamonds) $P(p\text{-}XC_6H_4)_3$ (*slope* = −0.189; $R = 0.769$); (crosses) $PPh_{3-x}(pyrl)_x$. Carbonyl stretching frequency (cm^{-1}) vs enthalpies of reaction (kcal mol^{-1}) for the RhCl(CO)(PR$_3$)$_2$ system (*slope* = 5.47; $R = 0.96$)

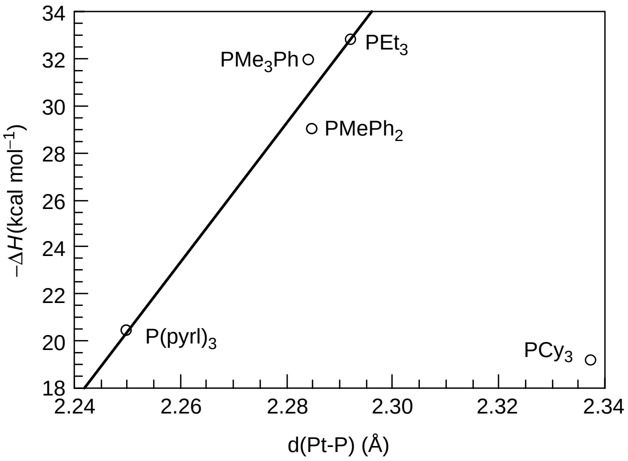

Figure 20 Enthalpy of reaction as a function of Pt–P bond length in (PX$_3$)$_2$PtMe$_2$ (*slope* = 2.95; $R = 0.975$)

Less obvious is the fact that a small but significant χ effect is evidenced by the nonzero slope of the line for $P(p\text{-}XC_6H_4)_3$ and PPh_{3-x}-(pyrl)$_x$ in Figure 19. Without going into detail here, similar electronic effects can be seen when correlating ^{31}P NMR data (chemical shift and platinum–phosphorous coupling) to χ. In an effort to clarify the observed relationships, X-ray diffraction analysis of the complexes with $(PEt_3)_2PtMe_2$, $(PMe_2Ph)_2PtMe_2$, $(P(pyrl)_3)_2PtMe_2$, and $(PCy_3)_2PtMe_2$ were performed and analyzed. The most remarkable relationship between structural and thermodynamic data is that reaction enthalpies are smallest in the complexes with the shortest Pt–P bond lengths, as apparent in Figure 20 (except for the sterically too demanding PCy$_3$ adduct). This counterintuitive result shows that thermochemical measurements such as described here can only determine the total energy difference between states. Energy terms due to distortions in the Pt coordination environment and internal ligand structure, that is reorganization energies (see discussion above), may induce a net destabilizing effect regardless of the intrinsic M–P bond strength.

2.10.2 Bidentate Phosphine Ligands

In light of the results obtained on monodentate ligands and the importance of chelating phosphorus ligands in coordination/organometallic chemistry and catalysis, a thermochemical study on the related bis(phosphine)PtMe$_2$ complexes was undertaken and 13 different chelating ligands were examined for the reaction in equation (27), forming the following complexes: PtMe$_2$(dpype), PtMe$_2$(dppf), PtMe$_2$((+)-diop), PtMe$_2$(dppb), PtMe$_2$(dppe), PtMe$_2$(dppp), PtMe$_2$(dppv), PtMe$_2$(dpmcb), PtMe$_2$(depe), PtMe$_2$(dmpe), PtMe$_2$(dcpe) (*see* ***Platinum: Organometallic Chemistry***).

As shown in Table 20, the overall order of stability is as follows: dpype < dppf < (+)-diop < dppb < dppe < dppp < dppv < dpmcb < depe < dmpe < dcpe. As the Tolman electronic scale predicts, the relative stability of the resulting complexes is strongly influenced by the electronic donor properties of the bidentate phosphine ligand if no larger steric factors are present. For example, better σ donors (*see σ-Donor*), such as, dmpe, depe, and dcpe, give more thermodynamically stable complexes while the isosteric (*see Isosteric Groups*) ligand dpype, which also

Table 20 Enthalpies of substitution in THF at 30 °C for:

$$\mathrm{Pt(Me)_2(COD) + P \sim P \longrightarrow Pt(Me)_2(P \sim P) + COD}$$

Complex	(P~ P) Ligand	$\Delta H_{\mathrm{rnx}}{}^{a}$(kcal mol^{-1})
$PtMe_2$(dpype)	dpype	−21.7(1)
$PtMe_2$(dppf)	dppf	−24.3(2)
$PtMe_2$((+)-diop)	(+)-diop	−25.7(1)
$PtMe_2$(dppb),	dppb	−26.4(3)
$PtMe_2$(dppe)	dppe	−29.9(1)
$PtMe_2$(dppp)	dppp	−30.5(4)
$PtMe_2$(dppv)	dppv	−30.7(3)
$PtMe_2$(dpmcb)	dpmcb	−31.4(3)
$PtMe_2$(depe)	depe	−35.6(3)
$PtMe_2$(dmpe)	dmpe	−36.4(2)
$PtMe_2$(dcpe)	dcpe	−37.2(2)

[a] Enthalpy values are provided with 95% confidence limit.

possesses a five-membered ring, gives the lowest enthalpy of the series because of its weak donor properties. A similar enthalpic trend was observed for the related $PtMe_2(PR_3)_2$ complexes with monodentate phosphine ligands. The present enthalpy data allow for comparison to thermochemical studies for reactions of common chelating bis(phosphine) ligand in the Cp′Ru(PP)Cl (Cp′ = Cp* = η^5-C_5Me_5 or Cp = η^5-C_5H_5). The relative order of stability of the resulting complexes in the Cp*Ru(PP)Cl and CpRu(PP)Cl systems follow a similar trend as the $PtMe_2$(PP) system. A good correlation ($R = 0.96$) is found for the plot of ΔH_{rxn} versus ΔH_{rxn} for a series of common PP ligand substitution reactions in the CpRu(PP)Cl and $PtMe_2$(PP) systems (Figure 21) or the Cp*(PP)RuCl and $PtMe_2$(PP) systems (Figure 22). The thermochemical comparisons between these organoplatinum and organoruthenium systems thus illustrate that common electronic and steric factors of the bis(phosphine) ligands affect the thermodynamic stability of metallacyclic complexes (*see Metallacycle*).

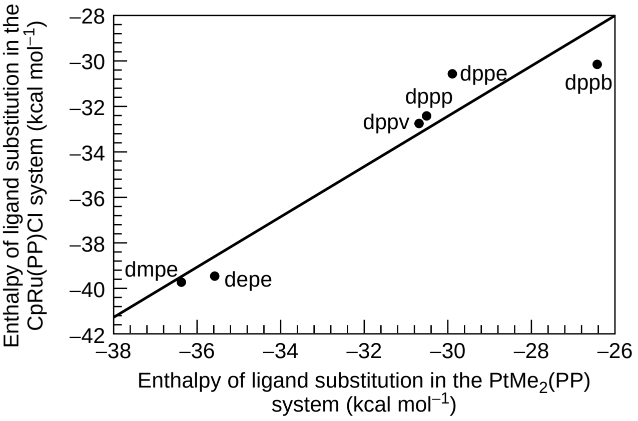

Figure 21 Enthalpy of ligand substitution in the CpRu(PP)Cl system and $PtMe_2$(PP) systems (*slope* = 1.1; $R = 0.96$)

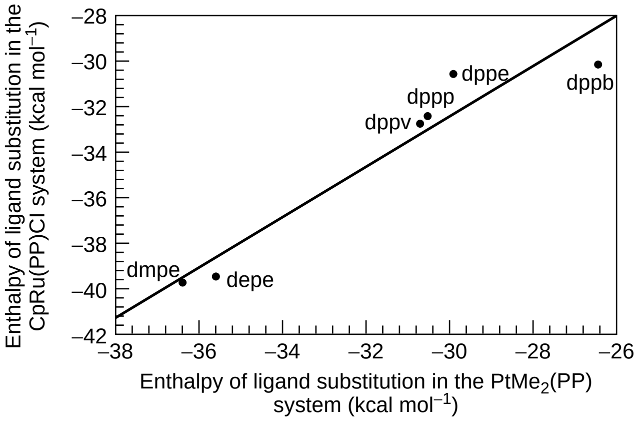

Figure 22 Enthalpy of ligand substitution in the Cp*Ru(PP)Cl system and $PtMe_2$(PP) systems. (*slope* = 1.0; $R = 0.97$)

2.11 Other Examples

Several other examples of calorimetric investigations have appeared in the last decade. For example, phosphine addition to the dimer [(*p*-cymene)$RuCl_2$]$_2$ leads to rapid formation of compounds of the general formula (*p*-cymene)$RuCl_2(PR_3)$.[67] The enthalpies of reaction suggest a more even steric and electronic contributions in this system compared to the Cp′Ru-systems (Sections 3.1–3.3). Thermodynamic influences of ancillary ligand variations on the Ru–X BDE as well as calorimetric investigations on the oxidative additions (*see Oxidative Addition*) of substrates to a Ru(0) complex have also been reported.[68,69] A series of articles has appeared dealing with the thermochemistry of phosphine addition to the complex (BDA)$Fe(CO)_3$.[70–72] Finally, important new results have been obtained through calorimetry on the stability of amido and alkoxy ligands for late−transition metal systems.[73] The thermodynamics of addition of small molecules to iridium complexes of the type $Ir(PR_3)_2Cl$ have also appeared.[74]

3 CLOSING REMARKS

As can be seen above, a significant portion of the recent advances in the area of organometallic thermodynamics has been achieved using solution calorimetric methods. This is not to say that other techniques have not been successfully used to obtain data on such systems. Other methods include experimentally determined bond energy terms by mass spectrometry,[75,76] and a large number of DFT calculations[77–80] have been reported.

Ligand substitution, oxidative addition reaction, and absolute bond enthalpies afford insight into thermodynamic driving forces behind important processes. One of the most striking among the examples given above is the markedly increased donor ability of NHC versus trialkylphosphines, experimentally determined by solution calorimetry and the stability/reactivity consequences that follow in ruthenium-based olefin metathesis (*see Alkene Metathesis*). There remains a great deal of work to be performed in the area of organometallic thermodynamics. The importance of metal–ligand bond energetics cannot be overstated, yet the physical organometallic chemist has so far played a catch-up role to rapidly moving areas of organometallic chemistry and catalysis. The predictive powers of such data are beginning to be realized, yet more data are needed in order to guide synthetic and catalytic chemistries.

4 RELATED ARTICLES

Asymmetric Synthesis by Homogeneous Catalysis; Carbonylation Processes by Homogeneous Catalysis; Hydrocyanation by Homogeneous Catalysis; Iridium: Organometallic Chemistry; Mechanisms of Reaction of Organometallic Complexes; Multi-Heme Cytochromes & Enzymes; Organic Synthesis Using Metal-mediated Metathesis Reactions; Platinum: Organometallic Chemistry; Polynuclear Organometallic Cluster Complexes; Rhodium: Organometallic Chemistry; Ruthenium: Organometallic Chemistry.

5 REFERENCES

1. L. Luo, S. P. Nolan., and P. J. Fagan, *Organometallics*, 1993, **12**, 4305.
2. L. Luo, N. Zhu, N. J. Zhu, E. D. Stevens, and S. P. Nolan, *Organometallics*, 1994, **13**, 669.
3. C. Li, M. E. Cucullu, R. A. McIntyre, E. D. Stevens, and S. P. Nolan, *Organometallics*, 1994, **13**, 3621.
4. L. Luo and S. P. Nolan, *Organometallics*, 1994, **13**, 4781.
5. M. E. Cucullu, L. Luo, S. P. Nolan, P. J. Fagan, N. L. Jones, and J. C. Calabrese, *Organometallics*, 1995, **14**, 289.
6. S. A. Serron and S. P. Nolan, *Organometallics*, 1995, **14**, 4611.
7. S. A. Serron, L. Luo, C. Li, M. E. Cucullu, E. D. Stevens, and S. P. Nolan, *Organometallics*, 1995, **14**, 5290.
8. C. Li, L. Luo, S. P. Nolan, W. Marshall, and P. J. Fagan, *Organometallics*, 1996, **15**, 3456.
9. C. Li, S. A. Serron, S. P. Nolan, and J. L. Peterson, *Organometallics*, 1996, **15**, 4020.
10. S. A. Serron, L. Luo, E. D. Stevens, S. P. Nolan, L. N. Jones, and P. J. Fagan, *Organometallics*, 1996, **15**, 5209.
11. J. Shen, E. D. Stevens, and S. P. Nolan, *Organometallics*, 1998, **17**, 3000.
12. M. E. Cucullu, C. Li, S. P. Nolan, S. T. Nguyen, and R. H. Grubbs, *Organometallics*, 1998, **15**, 5565.
13. D. C. Smith, C. M. Haar, L. Luo, C. Li, M. E. Cucullu, C. H. Mahler, S. P. Nolan, W. J. Marshall, L. N. Jones, and P. J. Fagan, *Organometallics*, 1999, **18**, 2357.
14. J. Huang, H. J. Schanz, E. D. Stevens, and S. P. Nolan, *Organometallics*, 1999, **18**, 2370.
15. A. C. Hillier, W. J. Sommer, B. S. Yong, J. L. Peterson, L. Cavallo, and S. P. Nolan, *Organometallics*, 2003, **22**, 4322.
16. K. Wang, A. S. Goldman, C. Li, and S. P. Nolan, *Organometallics*, 1995, **14**, 4010.
17. K. Wang, T. J. Emge, A. S. Goldman, C. Li, and S. P. Nolan, *Organometallics*, 1995, **14**, 4929.
18. K. Wang, G. P. Rosini, S. P. Nolan, and A. S. Goldman, *J. Am. Chem. Soc.*, 1995, **117**, 5082.
19. S. A. Serron, S. P. Nolan, and K. G. Moloy, *Organometallics*, 1996, **15**, 4301.
20. C. Li, S. P. Nolan, and I. T. Horváth, *Organometallics*, 1998, **17**, 452.
21. C. M. Haar, J. Huang, S. P. Nolan, and J. L. Peterson, *Organometallics*, 1998, **17**, 5018.
22. J. Huang, C. M. Haar, S. P. Nolan, W. J. Marshall, and K. G. Moloy, *J. Am. Chem. Soc.*, 1998, **120**, 7806.
23. D. C. Smith, E. D. Stevens, and S. P. Nolan, *Inorg. Chem.*, 1999, **38**, 5277.
24. D. C. Smith, E. D. Stevens, S. P. Nolan, W. J. Marshall, K. G. Moloy, A. Prock, and W. P. Giering, *Organometallics*, 1999, **18**, 474.
25. D. C. Smith, C. M. Haar, E. D. Stevens, S. P. Nolan, W. J. Marshall, and. Moloy, *Organometallics*, 2000, **19**, 1427.
26. A. R. Johnson, W. M. Davis, C. C. Cummins, S. Serron, S. P. Nolan, D. G. Musaev, and K. Morokuma, *J. Am. Chem. Soc.*, 1998, **120**, 2071.
27. J. P. F. Cherry, A. R. Johnson, L. M. Baraldo, Y. C. Tsai, C. C. Cummins, S. V. Kryatov, E. V. Rybak-Akimova, K. B. Capps, C. D. Hoff, C. M. Haar, and S. P. Nolan, *J. Am. Chem. Soc.*, 2001, **123**, 7271.
28. I. Ojima ed., ‘Catalytic Asymmetric Synthesis’, 2nd edn., Wiley-VCH, New York, 2001.
29. R. Noyori and T. Ohkuma, *Angew. Chem., Int. Ed. Engl.*, 2001, **40**, 40.
30. S. T. Nguyen, L. K. Johnson, R. H. Grubbs, and J. W. Ziller, *J. Am. Chem. Soc.*, 1992, **114**, 3974.
31. S. T. Nguyen, R. H. Grubbs, and J. W. Ziller, *J. Am. Chem. Soc.*, 1993, **115**, 9858.
32. R. H. Grubbs, S. J. Miller, and G. C. Fu, *Acc. Chem. Res.*, 1995, **28**, 446.
33. P. G. Jessop, T. Ikariya, and R. Noyori, *Chem. Rev.*, 1995, **95**, 259.

34. P. G. Jessop, T. Ikariya, and R. Noyori, *Chem. Rev.*, 1999, **99**, 475.

35. P. J. Fagan, M. D. Ward, J. V. Caspar, J. C. Calabrese, and P. J. Krusic, *J. Am. Chem. Soc.*, 1988, **110**, 2981.

36. P. J. Fagan, M. D. Ward, and J. C. Calabrese, *J. Am. Chem. Soc.*, 1989, **111**, 1698.

37. C. A. Tolman, *Chem. Rev.*, 1977, **77**, 313.

38. G. W. Parshall and S. D. Ittel, 'Homogeneous Catalysis', Wiley Interscience, New York, 1992.

39. K. Nozaki, N. Sato, Y. Tonomura, M. Yasutomi, H. Takaya, T. Hiyama, T. Matsubara, and N. Koga, *J. Am. Chem. Soc.*, 1997, **119**, 12779.

40. K. G. Moloy and J. L. Peterson, *J. Am. Chem. Soc.*, 1995, **117**, 7696.

41. T. J. Johnson, K. Folting, W. E. Strieb, J. D. Martin, J. C. Huffman, S. A. Jackson, O. Eisenstein, and K. G. Caulton, *Inorg. Chem.*, 1995, **34**, 488.

42. T. J. Johnson, J. C. Huffman, and K. G. Caulton, *J. Am. Chem. Soc.*, 1992, **114**, 2725.

43. K. V. Katti, V. S. Reddy, and P. R. Singh, *Chem. Soc. Rev.*, 1995, **95**, 655.

44. B. K. Campion, R. H. Heyn, and T. D. Tilley, *J. Chem. Soc., Chem. Commun.*, 1988, 278.

45. K. J. Ivin and J. C. Mol, 'Olefin Metathesis and Metathesis Polymerization', Academic Press, New York, 1997.

46. A. Fürstner, *Angew. Chem., Int. Ed. Engl.*, 2000, **39**, 3012.

47. E. L. Diaz, S. T. Nguyen, and R. H. Grubbs, *J. Am. Chem. Soc.*, 1997, **119**, 3887.

48. A. L. Fernandez, A. Prock, and W. P. Giering, *Organometallics*, 1994, **13**, 2767.

49. H.-Y. Liu, K. Eriks, A. Prock, and W. P. Giering, *Organometallics*, 1990, **9**, 1758.

50. W. A. Herrmann, *Angew. Chem., Int. Ed. Engl.*, 2002, **41**, 1290.

51. D. Bourissou, O. Guerret, F. P. Gabbai, and G. Bertrand, *Chem. Rev.*, 2000, **100**, 39.

52. A. J. Arduengo III, R. L. Harlow, and M. Kline, *J. Am. Chem. Soc.*, 1991, **113**, 361.

53. L. Jafarpour and S. P. Nolan, *Adv. Organomet. Chem.*, 2001, **46**, 181.

54. T. M. Trnka and R. H. Grubbs, *Acc. Chem. Res.*, 2001, **34**, 18.

55. J. March, 'Advanced Organic Chemistry', Wiley-Interscience, New York, 1985, p. 242.

56. J. Falbe, 'Carbon Monoxide inorganic Synthesis', Springer-Verlag, Berlin, 1980.

57. A. van Rooy, J. N. H. de Bruijn, K. F. Roobek, P. C. J. Kamer, and P. W. N. M. Van Leeuwen, *J. Organomet. Chem.*, 1996, **507**, 68.

58. M. D. Fryzuk, P. A. MacNeil, and S. J. Rettig, *Organometallics*, 1986, **5**, 2469.

59. M. D. Fryzuk, P. A. MacNeil, S. J. Rettig, A. S. Secco, and J. Trotter, *Organometallics*, 1982, **1**, 918.

60. I. T. Horváth and J. Rábai, *Science*, 1994, **266**, 72.

61. I. T. Horváth and J. A. Gladysz, *Angew. Chem., Int. Ed. Engl.*, 1997, **36**, 1610.

62. M.-A. Guillevic, A. M. Arif, I. T. Horváth, and J. A. Gladysz, *Angew. Chem., Int. Ed. Engl.*, 1997, **36**, 1612.

63. C. E. Laplaza, A. L. Odom, W. M. Davis, C. C. Cummins, and J. D. Protasiewicz, *J. Am. Chem. Soc.*, 1995, **117**, 4999.

64. C. E. Laplaza, M. J. A. Johnson, J. C. Peters, A. L. Odom, E. Kim, C. C. Cummins, G. N. George, and I. J. Pickering, *J. Am. Chem. Soc.*, 1996, **118**, 8623.

65. P. A. Hintz, M. B. Sowa, S. A. Ruatta, and S. L. Anderson, *J. Chem. Phys.*, 1991, **94**, 6446.

66. See for example: G. K. Anderson, in 'Comprehensive Organometallic Chemistry II', eds. E. W. Abel, F. G. A. Stone, and G. Wilkinson, Pergamon, Oxford, U.K., 1995, Vol. 9, p. 431.

67. S. Serron and S. P. Nolan, *Organometallics*, 1995, **14**, 4611.

68. L. Luo, C. Li, M. E. Cucullu, and S. P. Nolan, *Organometallics*, 1995, **14**, 1333.

69. J. Huang, C. Li, S. P. Nolan, and J. L. Petersen, *Organometallics*, 1998, **17**, 3516.

70. L. Luo and S. P. Nolan, *Organometallics*, 1992, **11**, 3483.

71. L. Luo and S. P. Nolan, *Inorg. Chem.*, 1993, **32**, 2410.

72. C. Li and S. P. Nolan, *Organometallics*, 1995, **14**, 1327.

73. P. L. Holland, R. A. Anderson, R. G. Bergman, J. Huang, and S. P. Nolan, *J. Am. Chem. Soc.*, 1997, **119**, 12800.

74. G. P. Rosini, F. Liu, K. Krogh-Jespersen, A. S. Goldman, C. Li, and S. P. Nolan, *J. Am. Chem. Soc.*, 1998, **120**, 9256.

75. P. B. Armentrout, *J. Mass. Spectrom.*, 1999, **34**, 74.

76. P. B. Armentrout, *Int. J. Mass. Spectrom.*, 2003, **227**, 289.

77. P. Margl, L. Deng, and T. Ziegler, *J. Am. Chem. Soc.*, 1999, **121**, 154.

78. M. H. Baik, T. Ziegler, and C. K. Schauer, *J. Am. Chem. Soc.*, 2000, **122**, 9143.

79. A. Michalak and T. Ziegler, *J. Am. Chem. Soc.*, 2001, **123**, 12266.

80. S. Tobisch and T. Ziegler, *J. Am. Chem. Soc.*, 2002, **124**, 13290.

Borates: Solid-state Chemistry

Douglas A. Keszler
Oregon State University, Corvallis, OR, USA

1 Introduction 1
2 Electronic Structure 1
3 Crystal Structure 2
4 Synthesis 6
5 Optical Properties 7
6 Individual Borates 9
7 Related Articles 9
8 References 9

Abbreviations

BBO $= \beta$-BaB_2O_4; LBO $= LiB_3O_5$.

1 INTRODUCTION

Borates are unique among the oxoanion compounds of the second-row elements in forming anhydrous substances that are both chemically and thermally stable. These characteristics provide a ready accessibility to a large number of synthetic examples that have widespread use. While the borate minerals, precursors to synthetic borates, comprise only a small percentage of the Earth's crust (*see* ***Boron: Inorganic Chemistry***), concentrated deposits in the United States, Turkey, Russia, Argentina, and China have provided an economical source of materials for exploitation. The overall demand for borates in the US for 1993, as measured by B_2O_3 content, is anticipated to be near 400 000 t.[1] More than 50% of this total is used for manufacturing glass, and approximately 25% is used for fiber glass insulation. In other applications, alkali metal borates are active as herbicides, insecticides, fertilizers, and detergents, and high quality borax ($Na_2B_4O_7{\cdot}10H_2O$) is employed in electrolytic capacitors and by the nuclear industry. Selected materials find use in powder and single-crystal form as high-end optical components.

Crystalline metal borates, like silicates, have a rich structural chemistry that extends from the simple orthoanions to their condensation into complex rings, chains, networks, and frameworks. Unlike the fixed coordination number of four for the Si atom in silicates, however, the coordination number of the B atom in borates can be either three or four. This unique feature leads to a variety of unusual structural arrangements that are not found with any other homonuclear polyoxoanion. These arrangements appear extensively, both in anhydrous and hydrated crystals. In fact, many of the large-scale applications of metal borates involve use of hydrated forms. Because the chemistry and technology of these materials have recently been reviewed,[2,3] they will not be considered here. Instead, only those characteristics that are unique to anhydrous borates will be discussed.

2 ELECTRONIC STRUCTURE

2.1 Triangular and Tetrahedral Units

A wide range of borate structures contain the isolated triangular $BO_3{}^{3-}$ group (**1**), while a fewer number contain the isolated tetrahedral $BO_4{}^{5-}$ group (**2**). The triangular group tends to be quite symmetrical with O–B–O angles near 120° and a B–O distance near 1.375 Å[4] that varies as the sum of the B and appropriate O crystal radii. The tetrahedral group exhibits individual O–B–O angles in the range 95.7–119.4° (mean value $=$ 109.4°) and individual B–O distances from 1.373 to 1.699 Å (mean value $=$ 1.47 Å); exaggerated distortions from the triangular and tetrahedral geometries have been compiled.[5]

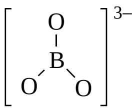

(**1**)

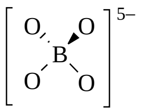

(**2**)

The occurrence of triangular versus tetrahedral coordination in a particular compound may be addressed by considering the information available on the electronic structures of each group. The atomic charge distributions in these groups have commonly been approximated with one of two extreme formalisms: the purely covalent *Formal Charge* model or the purely ionic *Oxidation Number* model. In the triangular unit the formal charge of each O atom is -1 and that of the B atom is 0; these values sum to the overall oxoanionic charge of -3. In the tetrahedral unit the formal charge of each O atom remains -1, but that of the B atom is reduced to -1; again these values sum to the overall charge, now -5. The oxidation numbers in both borate groups are -2 for the O atoms and $+3$ for the B atom, and appropriate overall charges for each group are produced. The charges assigned with the formal-charge model emphasize the strong polarizing power of the B^{3+} ion and the covalent interactions that result from overlap of B and O orbitals having the same principal quantum number ($n = 2$). This model, however, fails to portray the considerable polarity of the B–O bond that results from the significant *Electronegativity* difference ($\Delta\chi = 1.5$) between the B and O atoms. This particular aspect is emphasized in the oxidation-number model. Considering the B–O interaction in the context of a composite model, a small positive charge should be associated with the B atoms in both the triangular and tetrahedral units and a small negative charge with the O atoms; orbital overlap then produces a polar covalent bond. Such a description is consistent with the electron population analysis of the X-ray diffraction data from the mineral Kernite[6] ($Na_2B_4O_6(OH)_2\cdot 3H_2O$) and the results of molecular orbital calculations (*see* ***Molecular Orbital Theory***).[7]

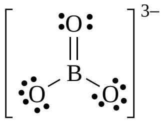

(**3**)

Lewis diagram (**3**) presents an alternative electron structure where the octet rule is satisfied for the B atom. This diagram represents one form of the resonance hybrid associated with delocalization of electron density through the π system of the unit. The relatively short B–O distances of the triangle in comparison to the longer distances of the tetrahedron have been attributed to these $p_\pi - p_\pi$ interactions. The significance of these interactions to the stability of the triangular group, however, remains unclear. The percentage difference between the average B–O distances of the triangle and tetrahedron are smaller than those observed for N- and C-centered oxoanions.[8] The out-of-plane bending force constant for the $BO_3{}^{3-}$ group has been reported to be approximately 65% of the equivalent values found for $CO_3{}^{2-}$ and $NO_3{}^{-}$.[9] These results indicate that π bonding is less significant in borates in comparison with similar interactions in carbonates and nitrates. This is to be anticipated from the large electronegativity difference between the B and O atoms which limits orbital mixing. Additional information on the distribution of charge in B–O interactions may be obtained from NQR data.[10]

The extensive base of structural data on borates also lends little support to the view that the π interaction produces a significant stabilizing energy for the triangle in a particular crystal structure. The adoption of a triangular or tetrahedral coordination by a B atom is largely dictated by the electronic characteristics of the other metal atoms in the matrix. It is well known from studies of aqueous solutions that the central atom of an oxoanion can satisfy its requirements for bonding electron density by adopting a smaller coordination number in a basic solution where the available charge density on the O atoms is greater. Higher coordination numbers are observed in acidic solutions where the central metal atoms must compete with H^+ for the available O electron density. A similar trend is observed for the structures of solid metal borates. Borates rich in metal atoms that form binary basic oxides contain a high or exclusive proportion of BO_3 groups, while those rich in metal atoms that form binary acidic oxides contain a higher concentration of BO_4 groups. These trends are demonstrated with examples in Section 3. In terms of *Crystal Field Theory*, the higher charge of the BO_3 groups also generates stronger crystal fields at the associated metal sites; examples of this effect are given in Section 5.

3 CRYSTAL STRUCTURE

The known structural chemistry of anhydrous borates through 1985 has been summarized,[11] and those borate minerals containing fused octahedra and triangles have been classified according to selected fundamental building blocks.[12]

3.1 Structures with Isolated Triangular Groups

A common packing of planar triangular groups results in the formation of layers, as illustrated by the calcite-type structures of $AlBO_3$, $GaBO_3$, $FeBO_3$, $RhBO_3$, and $ScBO_3$ (Figure 1). In this structure, the BO_3 layers are interleaved by metal atoms occupying distorted octahedral environments. The octahedra are linked by sharing vertices, and each O atom binds one B and two metal atoms. A closely related structure is adopted by the large family of materials having the formula $LnM_3(BO_3)_4$ (Ln = lanthanide; M = Al, Ga, Fe, or Sc). These compounds form in a similar layered structure (Figure 2), except the orientations of the BO_3 groups within the layers are altered to produce a trigonal prismatic O environment about the Ln atom. These materials commonly crystallize in

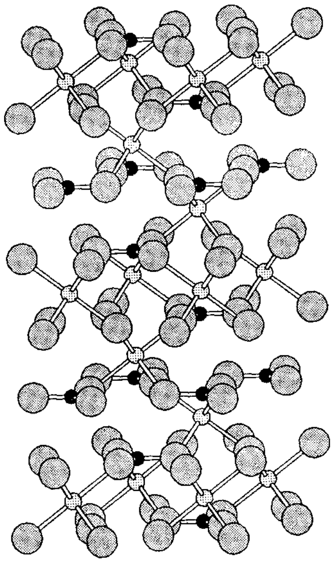

Figure 1 Calcite structure of MBO_3. Small filled circles represent B atoms, large shaded circles represent O atoms, and stippled circles represent M atoms, here, and in Figures 2, 3, and 8

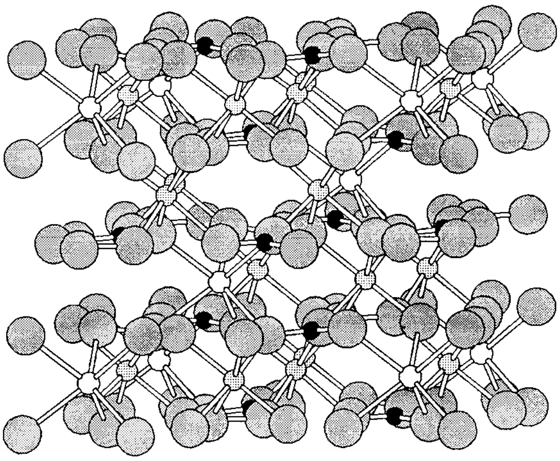

Figure 2 Huntite structure of $LnM_3(BO_3)_4$. Open circles represent Ln atoms

the noncentrosymmetric trigonal form of the mineral Huntite, $CaMg_3(CO_3)_4$, but other forms are known where the packing of the BO_3 groups within the planes is again modified to afford centrosymmetric structures having lower symmetry. Derivatives containing each of the lanthanides have been reported for the Al and Ga compounds, but only those Sc compounds containing the lanthanides La, Ce, Pr, Nd, Sm, Eu, and Gd exist. Apparently, the large size of the Sc atom produces a Sc–borate matrix with a trigonal prismatic site that is too large to be stabilized by the smaller lanthanides.

On the basis of the coordination environments of the metal atoms in this structure type, it is difficult to rationalize the existence of the family. The six-fold coordination at the Ln site is small for a lanthanide atom (*see* ***Coordination Numbers & Geometries*** and ***Scandium, Yttrium & the Lanthanides: Inorganic & Coordination Chemistry***). It might be anticipated that the stoichiometric combination $LaSc_3(BO_3)_4$ would be more thermodynamically stable as a mixture of the separate phases $3ScBO_3 + LaBO_3$ where the coordination number of the La atom in $LaBO_3$ is nine. The stability of the Huntites must then be associated with a higher coordination number for the O atoms. As noted above, the coordination number of the O atoms in the calcite structure of $ScBO_3$ is three, but in the Huntite structure this number is four. The higher number and the attendant increased metal–O interactions provide the stability for the existence of the family. The compound $LaSc_3(BO_3)_4$ does undergo the peritectic reaction $LaSc_3(BO_3)_4 \rightarrow LaBO_3 + 3ScBO_3$ above 1550 °C.

The STACK family**[13]** of compounds provides an example of a simple orthoborate structure type where the BO_3 groups do not pack in such readily perceived planes. These compounds are characterized by the formula $A_6MM'(BO_3)_6$ where A = Sr or Ba, and M and M' = any cation of formal charge +2, +3, or +4 that occupies an octahedral site. With more than 125 known derivatives, these compounds form one of the larger structural families of solid-state oxides.

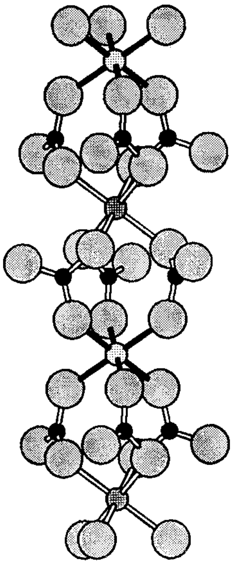

Figure 3 Chain structure of STACK compounds $A_6\,MM'(BO_3)_6$. M atoms are indicated with open bonds and M' atoms with filled bonds

Example formulations are $Sr_6HoFe(BO_3)_6$ (A = Sr, M = Ho, M' = Fe), $Ba_6GdSc(BO_3)_6$ (A = Ba, M = Gd, M' = Sc), and $Sr_3Sc(BO_3)_3$ (A = Sr, M = Sc, M' = Sc).

The structure is characterized by chains formed from a series of M- and M'-centered distorted octahedra that are stacked one atop the other and separated by BO_3 groups (Figure 3). By virtue of their connectivity to the A atoms, the octahedra are crystallographically and chemically dissimilar; the M-centered octahedron is larger than the M'-centered site. As a result, larger cations preferentially occupy the M site and smaller cations the M' site. These octahedra are bridged by intervening A atoms in nine-coordinate AO_9 sites. Although the structure may be portrayed with this chain description, the rich A concentration and high density of AO_9 interconnections actually produce a fully three-dimensional arrangement of the atoms.

3.2 Oligomeric and Polymeric Condensation of Triangular Groups

Like M–O–M linkages in complex oxoanions of the heavier congeners of Groups 14 and 15 (*see* ***Phosphates: Solid-state Chemistry***), B–O–B couplings result in the formation of higher order polyanions. The simplest condensation of BO_3 units affords the pyroborate group (**4**). In this group the terminal B–O distances tend to be somewhat longer than the bridging B–O distances, and a wide variation (111.8–180°) in the bridging B–O–B angle is observed. Although illustrated here as a planar group, a considerable range of interplanar angles between the terminal BO_2 groups has been reported; the angle varies from 0° in the compound $Sr_2Sc_2B_4O_{11}$**[14]** to the nearly orthogonal angle of 84° in the compound $Ba_5(B_2O_5)_2F_2$.**[15]**

This angular variation is not unexpected in view of the isoelectronic relationship between the pyroborate group, the molecule N_2O_5 (**5**), and the malonate anion, where considerable rotations about the N–O and C–O bonds are also observed.

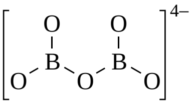

(**4**)

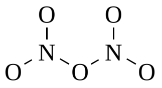

(**5**)

Condensation of three BO_3 groups is known to yield the cyclic metaborate ring B_3O_6 (**6**), but not a linear trimer. Examples of anhydrous materials containing this ring are ABO_2 (A = Na, K, Rb, Cs) and BaB_2O_4 ($\equiv Ba_3(B_3O_6)_2$). Condensation to other oligomeric species of higher order is unknown, except for full condensation to the linear metaborate chain $(BO_2)_n{}^{n-}$ (**7**) in the compounds $LiBO_2$-Type I, CaB_2O_4-Type I, and $La(MoO_4)BO_2$.

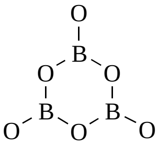

(**6**)

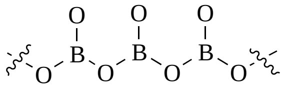

(**7**)

3.3 Structures with Tetrahedral Groups

Compounds containing isolated BO_4 groups are uncommon; examples include $MgAlBO_4$, $MgGaBO_4$, $SrAlBO_4$, $LiGeBO_4$, $NbBO_4$, and $Lu_3O_2BO_4$. Fusion of two or three BO_4 tetrahedra (in the absence of connectivity to BO_3 triangles) to form low-order oligomers is currently unknown in anhydrous systems. Full condensation to form three-dimensional frameworks through vertex-shared BO_4 units occurs in the mineral Johachidolite, $CaAlB_3O_7$, the sodalite analogs typified by $Zn_4O(BO_2)_3$, and the compound SrB_4O_7.

3.4 Structures with Admixture of Triangular and Tetrahedral Groups

Borates containing both BO_3 and BO_4 groups exist as polyborates where the two types of groups fuse by sharing O vertices. A description of these complex anions as the condensation of smaller B–O cyclic systems has been given.[4] For example, the polyborate structure of LiB_3O_5 (Figure 4) is characterized as the condensation of B_3O_7 rings where each ring (**8**) contains two BO_3 units (a pyroborate group) fused to a BO_4 unit. The rings fuse by sharing each terminal O atom to give the polyborate formula $(B_3O_3O_{4/2})^- \equiv (B_3O_5)^-$.

Because several types of small rings exist and their modes of condensation vary depending on the nature of the associated metal atoms, a large number of polyborate structures exist. The compounds LiB_3O_5, CsB_3O_5, and $SrLi(B_3O_5)_3$[16] (Figure 5) all contain a B_3O_5 polyborate framework resulting from the condensation of B_3O_7 rings (**8**), but the details of joining

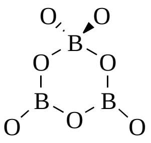

(**8**)

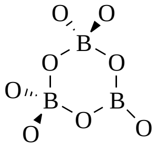

(**9**)

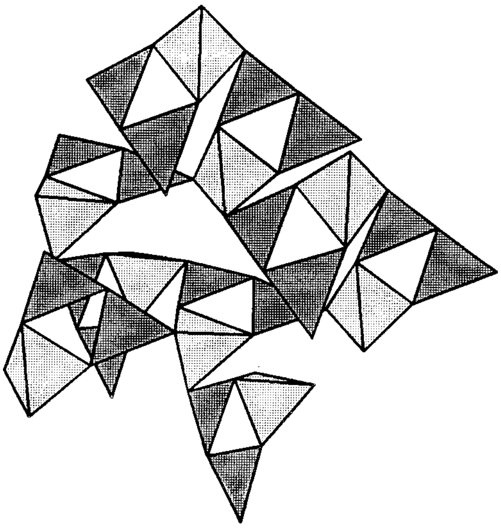

Figure 4 Polyhedral representation of the polyborate anion in the compound LiB_3O_5. BO_4 tetrahedra are lightly shaded, and BO_3 triangles are deeply shaded, here, and in Figures 5–7

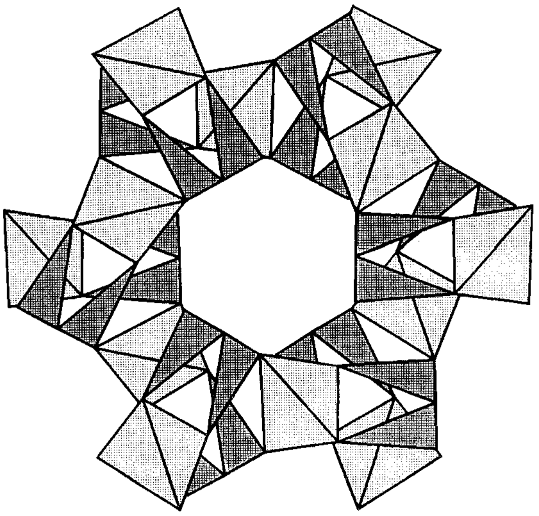

Figure 5 Polyhedral representation of the polyborate anion in the compound $SrLi(B_3O_5)_3$

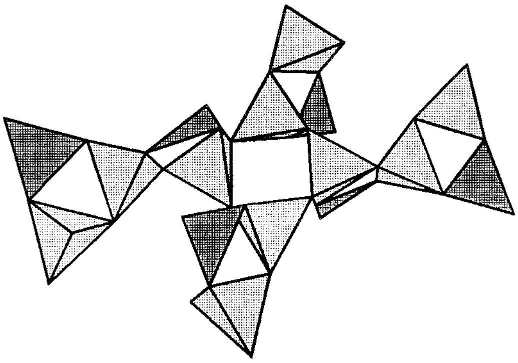

Figure 6 Polyhedral representation of the polyborate anion in the compound $LaMgB_5O_{10}$

the rings differ for each material. To satisfy the bonding requirements of the associated metal atoms (Li, Cs, Sr) the condensed B_3O_7 groups must be rotated, one relative to the other, about selected B–O bonds.

Two additional examples of polyborate anions are illustrated by the arrangements in the compounds $LaMgB_5O_{10}$ and $SrNaB_5O_9$.[17] The La compound contains B_3O_8 rings (**9**) that fuse by sharing a common BO_4 group (Figure 6). The structure of the polyanion in the compound $SrNaB_5O_9$ contains an admixture of this ring and the B_3O_7 ring (Figure 7).

3.5 Glass Structure

Because of the importance of borates in the production of specialty glasses such as Pyrex and Vycor, among others, the structures of vitreous alkali-metal borates have been of considerable interest. Like SiO_2, boron oxide, B_2O_3, is a natural glass-forming substance; alkali metal oxides fuse with H_3BO_3 or B_2O_3 to form clear melts. If these liquids have a significant boron oxide content they become viscous on cooling and form glasses[18] (*see* ***Noncrystalline Solids***).

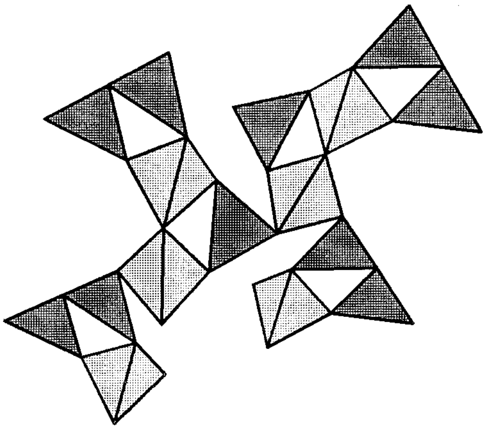

Figure 7 Polyhedral representation of the polyborate anion in the compound $SrNaB_5O_9$

Much of the interest in alkali-metal borate glasses has centered on reports indicating anomalous behavior in physical properties such as viscosity and thermal expansion coefficient as a function of metal oxide content.[19] Each of these properties has been correlated to changes in the molecular structure of the glass. X-Ray[20] and neutron[21] diffraction, NMR[22], Raman,[23] and NQR[10] studies indicate that 75–85% of the B atoms in vitreous B_2O_3 are contained in condensed B_3O_6 boroxin rings; these rings are spatially identical to those of the cyclic metaborate unit (**6**). On addition of A_2O (A = alkali metal) to B_2O_3, the fraction of boroxin groups decreases and the fraction of four-coordinate B atoms increases. Near a mole fraction of 0.20 A_2O, Krogh–Moe complex[24] (**10**) exhibits its maximum concentration, and near a mole fraction of 0.35 A_2O, complex (**11**) appears at its maximum concentration. Beyond a mole fraction of 0.40 the concentration of BO_4 groups diminishes, and the proportion of O atoms that do not bridge B atoms increases. These nonbridging O atoms are associated with orthoborate, pyroborate, and cyclic metaborate groups.

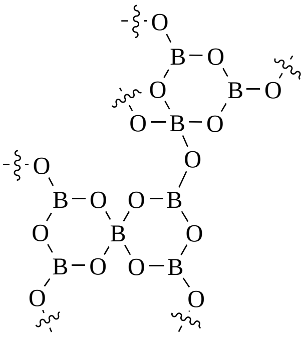

(**10**)

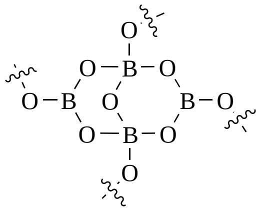

(**11**)

The system $Na_2O–B_2O_3–SiO_2$ contains many technologically important glass compositions. At low Na concentrations (Na/B < 0.5), structures are dominated by fused six-membered rings containing one or two BO_4 groups.[25] This B–O framework is separated from a matrix of condensed SiO_4 tetrahedra similar to that found in SiO_2. At intermediate concentrations of Na (Na/B > 0.5), ring metaborate, pyroborate, and orthoborate units form in conjunction with isolated SiO_4 units. At higher concentrations (Na/B = 1), metaborate ring numbers are observed to increase with SiO_2 content. Again, BO_4 groups are not incorporated into the framework of condensed SiO_4 units, unlike the mixed frameworks of aluminum silicates (*see* ***Zeolites***). Like the binary alkali-metal borate glasses, some loose BO_3 and BO_4 groupings persist in these structures.

4 SYNTHESIS

4.1 Crystalline Solids

Anhydrous metal borates are conveniently prepared by heating hydrated salts or by direct fusion or firing of one or more metal oxides with H_3BO_3 or B_2O_3. Because the melting points of most borates fall well below 1500 °C, heating suitable reagents for only a few hours near 1000 °C generally produces homogeneous microcrystalline powders. Careful consideration should be given to the selection of a crucible when fusing a borate as the melts wet most metals and react with most oxide ceramics.

Crystalline anhydrous metal borates have also been synthesized by hydrothermal methods.[26] To limit the formation of hydrates, many materials have been prepared from highly concentrated aqueous solutions of H_3BO_3. The high B_2O_3 content of these fluids favors the formation of polyborates, e.g. $Ca_2B_6O_{11}$, in many phase systems.

4.2 Crystal Growth

Because of the technological importance of the compounds β-BaB_2O_4 (BBO) and LiB_3O_5 (LBO) as optical frequency converters, considerable effort has been expended on their crystal growth. BBO exists in two modifications, a low-temperature β phase and a high temperature α phase. The phase transition occurs near 925 °C, and the α phase melts at 1095 °C. The low-temperature β phase is noncentrosymmetric and exhibits the desired optical properties. As a result, much of the work on BBO has centered on the development of an efficient top-seeded flux method. From studies on a variety of melt additives, pure Na_2O has emerged as the solvent of choice,[27] although high growth rates have been reported with NaCl.[28] The viscosity of the melt is minimized by achieving saturation as close as possible to the phase transition temperature through incorporation of 20–22 mol% Na_2O. The melt is then generally cooled at 0.5–2 °C day^{-1} to yield a growth rate of 1.5–2.0 g °C^{-1} from a 1 kg melt. This growth method, however, still suffers from a high melt viscosity that contributes to inclusion of solvent in the crystal. With appropriate temperature gradients at the melt–growth interface, it has been found that the low-temperature β phase can be crystallized directly from the stoichiometric melt near 1100 °C.[29] In this way, Czochralski and Bridgman methods may be used to grow the crystals; incorporation of solvent is eliminated and the higher growth temperature reduces the viscosity and contributes to a faster growth rate (4 mm h^{-1}).

LBO also undergoes a peritectic decomposition (834 °C) and must be grown by a flux method. The original phase diagram for the system Li_2O–B_2O_3 indicated that LBO decomposed into $Li_2B_4O_7$ and $Li_2B_8O_{13}$ below 595 °C, but this was subsequently disproved. A stable melt can be produced below 834 °C by adding excess B_2O_3.[30] While pulling crystals from this melt limits the incorporation of impurities, the high viscosity hinders mass transfer and results in the formation of inclusive crystal defects. Addition of LiF to the melt has been found to decrease the viscosity and improve the growth characteristics. Under suitable conditions, crystals of high optical quality can be grown, but at the very slow rate of 1 mm day^{-1}.

The defect chemistry of BBO and LBO crystals appears to be extrinsically controlled by the incorporation of impurities.[31] The total impurity content of selected BBO crystals has been estimated from spark source mass spectrography to be 150 ppm by mass. Carrier concentrations of 0.1–10 ppm (atomic) from conductivity data are consistent with this impurity level. Considering the presence of strong polar covalent interactions in the metaborate rings, it is likely that a greater proportion of the defects are to be found in the Ba sublattice. The intrinsic UV absorption edge for BBO is 190 nm at room temperature. To use the material with high efficiency for frequency doubling near 200 nm the transmittance should be as high as possible. At lower temperatures, additional absorption features at wavelengths longer than that associated with the absorption edge have been observed; the transmittance of a 1-cm thick crystal at 222 nm can fall to 22% at 0 °C. These absorption features have been attributed to unspecified impurities, indicating that the foreign atoms contribute to both the defect structure and the optical transparency.

Impurity concentrations for LBO have been determined to be 500 ppm by mass. Carrier concentrations of several hundred ppm (atomic) from conductivity measurements are consistent with the lithium vacancy concentration determined from the type and amount of impurity atoms. This result again indicates that the defect structure of a borate is dominated by impurities. The extrinsic control and limited defect chemistry in these materials is not surprising, because the small size of the B atom and its strong interaction with the O atoms should limit substitution of other atoms on the B sites.

4.3 Sol–Gel Synthesis

Most of the work on the synthesis of borates by sol–gel processes has centered on the preparation of glasses and glass fibers.[32–34] Precursors to these glasses have included alkoxides and basic aluminum oxides, e.g. $Al(OH)_2(OOCCH_3)\cdot 1/3H_3BO_3$. Detailed studies on the successive hydrolysis and condensation reactions of B alkoxide compounds have been reported. ^{11}B NMR studies of borate gels prepared from $LiOCH_3$ and tri-n-butylborate in the system $x\mathrm{Li_2O}\cdot 1 - x\mathrm{B_2O_3}$ have revealed that the fraction of tetrahedrally coordinated boron atoms $\langle N_4\rangle$ increases linearly with x according to the equation $\langle N_4\rangle = 0.43x + 0.104$. The reaction between lithium methoxide and the boron alkoxide is believed to produce the four-coordinate B atom (equation 1).

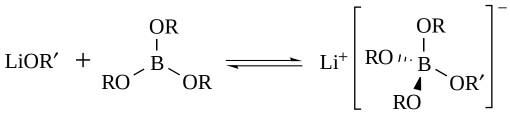

$$\mathrm{LiOR'} + \mathrm{B(OR)_3} \rightleftharpoons \mathrm{Li^+}[\mathrm{B(OR)_3OR'}]^- \quad (1)$$

To form gels in this mixed alcohol solvent system, a critical value of $\langle N_4 \rangle$ must be exceeded. This observation has been rationalized on the basis of the kinetic stability of B–O–B bonds toward hydrolysis or alcoholysis. Because tetrahedrally coordinated borate groups are coordinatively saturated (*see Coordinative Saturation & Unsaturation*), this group is unable to participate in dissociative reactions of the triangular group that hinder polymerization and the formation of gels (equation 2).

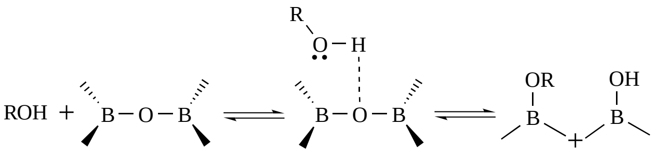

(2)

A sufficient $\langle N_4 \rangle$ is required to give at least one tetrahedrally coordinated B atom as a connection between the oligomeric structural units. Comparison of FTIR spectra of gels with those of molecular and crystalline alkali-metal borates indicates that the initial polyborate species to emerge during hydrolysis are units composed of six-membered rings. Additional hydrolysis is associated with condensation reactions between these rings. Since $\langle N_4 \rangle$ must be >0.23 for formation of stable gels, a network of BO_3 and BO_4 groups has been proposed for the lithium borate polymers near the gel point.

5 OPTICAL PROPERTIES

5.1 Laser Materials

Broad-band laser emission has been observed from Cr^{3+}-doped $ScBO_3$.**35** The luminescence band extends from 700 to 1000 nm, with a peak at 810 nm. This emission is a vibrationally assisted transition from the excited $^4T_2$ level to the ground ^4A level of the Cr^{3+} ion (*see* ***Ligand Field Theory & Spectra***). The centrosymmetric symmetry of the dopant site affords a relatively long fluorescence lifetime of 115 μs. The laser tuning range is 787–892 nm, and the laser pumped output efficiency is near 29%. This value may be compared to the high efficiencies of 51% for Cr^{3+}:$BeAl_2O_3$ and 52% for Cr^{3+}:$LiCaAlF_6$.

Cr^{3+} laser emission has been obtained from a variety of crystals in two very different ways, depending on the strength of the crystal field at the dopant site and whether the emission arises from the excited ^2E or $^4T_2$ state. With its sharp line emission, ruby (Cr^{3+}:Al_2O_3) is an example of a Cr^{3+} laser operating on the basis of ^2E emission. Because this emission occurs primarily in the zero-phonon lines, the ruby laser operates as a three-level system with a rather high threshold for oscillation.

In the late 1970s, Cr^{3+}-doped alexandrite ($BeAl_2O_4$) was found to lase on the vibrational sideband of the $^4T_2 \rightarrow {}^4A$ transition. Because this transition terminates on vibrationally excited states of the ground level, the laser operates as a four-level system with a much lower threshold. Several similar Cr^{3+} lasers were subsequently developed.**36** A limitation in all these systems, however, arises from the $^4T_2 \rightarrow {}^4T_1$ a excited state absorption which overlaps to some extent the $^4T_2 \rightarrow {}^4A_2$ emission. Materials exhibiting higher excited state absorption cross sections and greater overlap with the emission band are found to be less efficient lasers. Examples of Cr^{3+} laser crystal systems with low excited state absorption losses (and therefore high laser efficiency) are emerald, and the aforementioned hosts $BeAl_2O_4$ and $LiCaAlF_6$.

Because excited state absorption losses are generally higher for those materials that emit at longer wavelengths, the compound $Sr_3Sc(BO_3)_3$ was synthesized as a host for shorter wavelength emission.**37** This compound contains BO_3 triangles and a high concentration of the basic oxide SrO that in combination produce a relatively strong crystal field at the Cr^{3+} dopant site. Luminescence from the doped host at room temperature is centered in a broad band at 750 nm (cf. 810 nm in Cr^{3+}:$ScBO_3$), representing a considerable blue shift that could lead to an increased lasing efficiency. As a host, the material is similar to alexandrite in that transitions from both ^2E and $^4T_2$ levels are observed at room temperature.

The huntite Nd:$YAl_3(BO_3)_4$ has also been lased.**38** This crystal has generated interest because, as noted in Section 3, it is noncentrosymmetric and can also function as an optical frequency converter. This host can then self-double the 1064-nm emission line of the Nd^{3+} ion directly to 532 nm, eliminating the need for separate laser and frequency conversion crystals. With diode pumping, the crystal provides a compact source of green light. Because the Nd^{3+} ion absorbs near the doubled frequency, the dopant concentration must be near 4% to achieve an efficient production of green light.

5.2 Nonlinear Optical Materials

Crystals of BBO**39** and LBO**40** are extensively used for generating visible and UV light from high-power pulsed lasers. The general utility of the materials derives from their high optical damage thresholds and transparency ranges that extend to 190 nm for BBO and 170 nm for LBO.

The second-order susceptibility of LBO ($d_{\mathrm{eff}} = 0.7\,\mathrm{pm\,V^{-1}}$) for doubling 1064-nm light from a Nd:YAG laser is approximately 40% of that of BBO ($d_{\mathrm{eff}} = 2.0\,\mathrm{pm\,V^{-1}}$). These susceptibilities have been modeled by summing the second-order polarizabilities of the individual borate rings according to their orientations in the crystals.[39] Although the susceptibility for BBO is larger, LBO generally exhibits the greater efficiency for doubling 1064-nm light because of its favorable linear optical properties. As light travels through a crystal, energy will be efficiently transferred from the fundamental to the second harmonic only if the fundamental and second harmonic have the same phase velocity. This velocity (v) is inversely proportional to the refractive index ($v = c/n$), so efficient second-harmonic generation will occur if $n(\omega) = n(2\omega)$. This condition can be satisfied though the process of angular phase matching with a birefringent crystal.

BBO is an example of a material having a high birefringence. The birefringence is a direct result of the packing of the cyclic metaborate rings into discrete layers (Figure 8). Light polarized parallel to the layers will interact strongly with the rings by moving electron density through the B–O bonds. This interaction will retard the phase velocity of light as indicated by the value of $n_o = 1.6551$ at $\lambda = 1064$ nm. Light polarized orthogonal to the layers will induce less polarization as electron density can not be redistributed through B–O bonds. As a result the phase velocity will be faster and the refractive index smaller, $n_e = 1.5425$ at $\lambda = 1064$ nm. The difference between n_o and n_e ($\Delta n = 0.11$) represents the magnitude of the birefringence. The phase velocity of light having a polarization direction intermediate to these two extremes will be dictated by a value of n between n_o and n_e.

By combining birefringence and the dispersion of the refractive indices with wavelength, the phasematching condition $n(\omega) = n(2\omega)$ can be satisfied. The dispersion curves for BBO are given in Figure 9. Points are indicated where the refractive indices are equivalent for a fundamental wavelength at 1064 nm and its second harmonic at 532 nm. From the diagram, it is seen that the index $n(2\omega)$ occurs at an angle of 22.7° with respect to the n_o (optic) axis. For light traveling at this angle, energy can be efficiently transferred from the fundamental to the second harmonic.

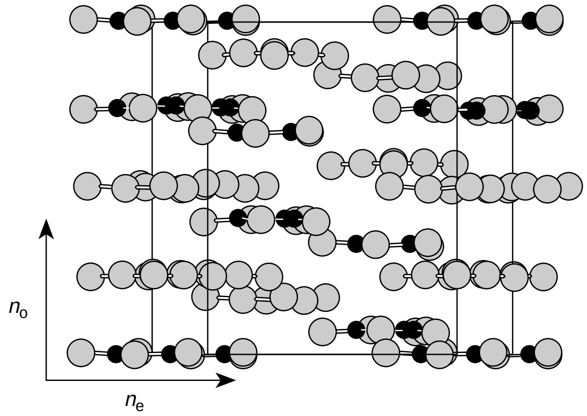

Figure 8 Packing of the cyclic metaborate rings in the structure of β-BaB_2O_4

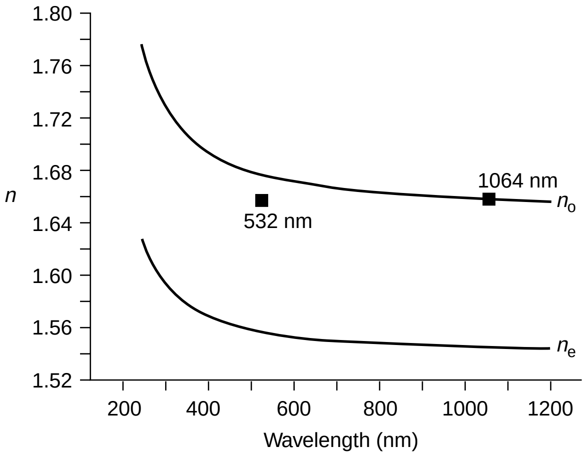

Figure 9 Refractive index dispersion curves for β-BaB_2O_4

The birefringence of BBO is much greater than that of LBO ($\Delta n = 0.025$). Because the flat portions of the B_3O_7 rings are skewed from coplanarity in the condensed framework (Figure 4) of LBO, a smaller Δn is produced. Two important features arise from these differing values. Since Δn is large in BBO, a higher angular sensitivity to phase matching is observed. This sensitivity arises from the variation of n with changes in polarization angle. For intermediate angles between the axes n_o and n_e, n varies rapidly with angle changes, and this variation is amplified by the large Δn of BBO. If a slightly divergent laser beam is directed into a BBO crystal at the phase matching angle, it will sample a range of refractive indices and the condition $n(\omega) = n(2\omega)$ will not be strictly satisfied for the entire beam. The net result is a reduction in conversion efficiency. For LBO, Δn and the variation in n with angle are smaller. The phase matching condition is much less sensitive to angular variations and higher conversion efficiencies obtain.

The magnitudes of the birefringence in each of these materials also governs the method for obtaining UV light. For example, in BBO the birefringence is sufficiently large to allow generation of 266-nm radiation directly from a 532-nm fundamental beam. This is not the case for LBO, where the birefringence is not large enough to provide a value of $n(2\omega)$ that is sufficiently small to achieve phase matching. As a result, LBO is not useful for direct conversion to short wavelengths. Generation of UV light with LBO must be accomplished through other sum frequency-mixing techniques.

5.3 Phosphors

The doped compounds Ce^{3+},Tb^{3+}:$GdMgB_5O_{10}$, and Ce^{3+},Mn^{2+}:$GdMgB_5O_{10}$ are used as phosphors[41] in efficient fluorescent lamps having a high color rendition index (*see* ***Luminescence***). The host is isostructural to the compound

$LaMgB_5O_{10}$ which was described in Section 3. In this structure the Mg-centered distorted octahedra share vertices with the Gd-centered sites, and the Gd-centered environments fuse by sharing edges. The high efficiencies of these materials derive from the efficient transfer of energy from one ion to the next.[42] The Ce^{3+} dopant effectively absorbs the 254-nm light of the Hg emission in the fluorescent lamp. The emission band of this ion is at a sufficiently high energy to provide for the complete transfer of excitation energy to the Gd^{3+} ions. In the Tb^{3+}-doped material the energy migrates through the Gd^{3+} sublattice until it encounters a Tb^{3+} center, where energy transfer ($Gd^{3+} \rightarrow Tb^{3+}$) results in the production of green light at 545 nm. In the Mn^{2+} compound the ion substitutes on the Mg^{2+} site. Similar energy-transfer steps lead to the production of red light characterized by a broad-band emission centered at 620 nm.

Two important characteristics, one electronic and one structural, contribute to the success of these materials. The weak crystal field produced by the polyborate at the Ce^{3+} ion leads to a high-energy emission and a significant overlap between the Ce^{3+} relaxed excited state and Gd^{3+} absorption bands, allowing efficient energy transfer from Ce^{3+} to Gd^{3+}. Also, the linkage of the metal–atom coordination environments provides a pathway for energy migration through the Gd sublattice to the luminescent ions.

The phosphor Tb^{3+}:$InBO_3$ has been promoted as a green phosphor in cathode-ray tubes and as a possible scintillator.[43] It exhibits a quantum efficiency under cathode-ray excitation of 8%, and it is stable to intense electron beams. The emission lifetime of 7.5 ms, however, is likely to be too long for some applications.

6 INDIVIDUAL BORATES

6.1 Borate halides

Although several borate halides exist in Nature, few synthetic examples have been described. Because their stoichiometries mimic that of the fluoride apatite, $Ca_5(PO_4)_3F$, the borates $AE_5(BO_3)_3X$ ($A = Ca, Sr$; $X = F, Cl, Br$)[44,45] have generated some interest. The structures of these materials are substantially different from that of apatite, and they vary depending on the identity of the A and X atoms. Interestingly, in the compound $Ca_5(BO_3)_3F$, one of the Ca atoms and the F atom may be replaced by a Ln = lanthanide atom and an O atom, respectively, to give materials of the type $Ca_4Ln(BO_3)O$.[46]

The compound $Ba_5(B_2O_5)_2F_2$ represents the first established example of a pyroborate halide. The pyroborate group in this compound exhibits the largest deviation from planarity of any such unit.[15]

6.2 $BaLnB_9O_{16}$ (Ln = lanthanide)[47]

The host $BaGdB_9O_{16}$ exhibits a quantum efficiency = 0.65 when doped with the ion Eu^{3+}. Eu^{2+} emission from the same host is characterized by a broad band peaking in the blue at 460 nm. Structural data for these compounds have not been reported.

6.3 $LiBGeO_4$ and $LiSiGeO_4$[48]

These mixed oxides have been considered as nonlinear optical materials (*see Nonlinear Optical Materials*).[49] They crystallize as ordered derivatives of the cristobalite structure. As early X-ray structural studies were performed on twinned crystals grown from congruent melts, their true symmetry was not firmly established. Untwinned single crystals have been produced by hydrothermal methods, and the space group has been convincingly established as $I\bar{4}$.

7 RELATED ARTICLES

Oxides: Solid-state Chemistry; Sol–Gel Synthesis of Solids.

8 REFERENCES

1. R. Will, Y. Sakuma, and R. Willhalm, ‘Chemical Economics Handbook’, SRI International, Menlo Park, CA, 1990, p. 717.1000A.
2. R. A. Smith and R. B. McBroom, ‘Kirk-Othmer Encyclopedia of Chemical Technology’, Wiley, New York, 1993, Vol. 4, p. 365.
3. J. B. Farmer, ‘Advances in Inorganic and Radiochemistry’, Academic Press, New York, 1982, Vol. 25, p. 187.
4. A. F. Wells, ‘Structural Inorganic Chemistry’, Clarendon Press, Oxford, 1984, p. 1065.
5. E. Zobetz, *Z. Kristallogr.*, 1990, **191**, 45.
6. W. F. Cooper, F. K. Larsen, P. Coppens, and R. F. Giese, *Am. Mineral.*, 1973, **58**, 21.
7. D. J. Vaughan and J. A. Tossell, *Am. Mineral.*, 1973, **58**, 765.
8. A. G. Massey, ‘Main Group Chemistry’, Ellis Horwood, Chichester, 1990, p. 190.
9. W. C. Steele and J. C. Decius, *J. Chem. Phys.*, 1956, **25**, 1184.
10. S. J. Gravina, P. J. Bray, and G. L. Petersen, *J. Non-Cryst. Solids*, 1990, **123**, 165.
11. G. Heller, in ‘Topics in Current Chemistry’, ed. F. L. Boschke, Springer-Verlag, Berlin, 1986, Vol. 131, p. 31.
12. F. C. Hawthorne, *Can. Mineral.*, 1986, **24**, 625.
13. K. I. Schaffers, T. Alekel, P. D. Thompson, J. R. Cox, and D. A. Keszler, *J. Am. Chem. Soc.*, 1990, **112**, 7068.

14. P. D. Thompson, J. Huang, R. W. Smith, and D. A. Keszler, *J. Solid State Chem.*, 1991, **95**, 126.
15. T. A. Alekel and D. A. Keszler, *J. Solid State Chem.*, 1993, **106**, 310.
16. K. I. Schaffers, Ph.D. dissertation, Oregon State University, 1992.
17. J. Tu and D. A. Keszler, unpublished results.
18. L. D. Pye, V. D. Frechette, and N. J. Kreidl eds, 'Borate Glasses: Structure, Properties, and Application', Plenum Press, New York, Materials Science Research, 1979, Vol. 12.
19. H. Doweidar, *J. Mater. Sci.*, 1990, **25**, 253.
20. R. L. Mozzi and B. E. Warren, *J. Appl. Crystallogr.*, 1970, **3**, 251.
21. P. A. V. Johnson, A. C. Wright, and R. N. Sinclair, *J. Non-Cryst. Solids*, 1982, **50**, 281.
22. C. Rhee and P. J. Bray, *Phys. Chem. Glasses*, 1971, **12**, 165.
23. W. Konijnendijk and J. M. Stevels, *J. Non-Cryst. Solids*, 1975, **18**, 307.
24. J. Krogh-Moe, *J. Non-Cryst. Solids*, 1969, **1**, 269.
25. W. J. Dell, P. J. Bray, and S. Z. Xiao, *J. Non-Cryst. Solids*, 1983, **58**, 1.
26. L. N. Dem'yanets, *Prog. Cryst. Growth Charact. Mater.*, 1991, **21**, 299.
27. V. Nikolov and P. Peshev, *J. Solid State Chem.*, 1992, **96**, 48.
28. B. H. T. Chai, M. Gualtieri, and M. H. Randles, *Proc. SPIE–Int. Soc. Opt. Eng.*, 1988, **968**, 69.
29. H. Kouta, Y. Kuwano, K. Ito, and F. Marumo, *J. Cryst. Growth*, 1991, **114**, 676.
30. Z. Shuqing, H. Chaoen, and Z. Hongwu, *J. Cryst. Growth*, 1990, **99**, 805.
31. P. A. Morris, in 'Materials for Nonlinear Optics, Chemical Perspectives', ACS Symposium Series, eds. S. R. Marder, J. E. Sohn, and G. D. Stucky, American Chemical Society, Washington, DC, 1991, Vol. 455, p. 380.
32. C. J. Brinker, in 'Glass Science and Technology', eds. D. R. Uhlmann and N. J. Kreidl, Academic Press, Boston, MA, 1991, Vol. 4A, p. 169.
33. N. Venkatasubramanian, B. Wade, P. Desai, A. S. Abhiraman, and L. T. Gelbaum, *J. Non-Cryst. Solids*, 1991, **130**, 144.
34. H. G. Sowman, in 'Sol-Gel Technology for Thin Films, Fibers, Preforms, Electronics, and Specialty Shapes', ed. L. Klein, Noyes, Park Ridge, NJ, 1988, p. 162.
35. S. A. Payne and J. A. Caird, in 'CRC Handbook of Laser Science and Technology, Supplement 1: Lasers', ed. M. J. Weber, CRC Press, Boca Raton, FL, 1990.
36. B. Lu, J. Wang, H. Pan, and M. Jiang, *J. Appl. Phys.*, 1989, **66**, 6052.
37. P. D. Thompson and D. A. Keszler, *Chem. Mater.*, 1989, **1**, 292.
38. D. Eimerl, L. Davis, S. Velsko, E. K. Graham, and A. Zalkin, *J. Appl. Phys.*, 1987, **62**, 1968.
39. S. P. Velsko, M. Webb, L. Davis, and D. Huang, *IEEE J. Quant. Electron.*, 1991, **27**, 2182.
40. C. Chen, Y. Wu, and R. Li, *J. Cryst. Growth*, 1990, **99**, 790.
41. T. Welker, *J. Lumin.*, 1991, **48 & 49**, 49.
42. G. Blasse, *Phys. Stat. Sol. (A)*, 1982, **73**, 205.
43. J. P. Chaminade, A. Garcia, M. Pouchard, C. Fouassier, B. Jacquier, D. Perret-Gallix, and L. Gonzalez-Mestres, *J. Cryst. Growth*, 1990, **99**, 799.
44. L. Shirong, H. Qingzhen, Z. Yifan, J. Aidong, and C. Chen, *Acta Crystallogr., Sect. C*, 1989, **45**, 1989.
45. T. Alekel and D. A. Keszler, *Inorg. Chem.*, 1993, **32**, 101.
46. R. Norrestam, M. Nygren, and J.-O. Bovin, *Chem. Mater.*, 1992, **4**, 737.
47. F. Wen-Tian, C. Fouassier, and P. Hagenmuller, *Mater. Res. Bull.*, 1987, **22**, 899.
48. J. B. Parise and T. E. Gier, *Chem. Mater.*, 1992, **4**, 1065.
49. A. Rulmont, P. Tarte, and J. Winand, *J. Mater. Sci. Lett.*, 1987, **6**, 659.

Borides: Solid-state Chemistry

Torsten Lundström
Uppsala University, Uppsala, Sweden

1 Introduction 1
2 Occurrence and Crystal Chemistry of Borides 1
3 Synthesis 7
4 Band Structure and Bonding 9
5 Properties and Applications 9
6 Related Articles 11
7 References 11

1 INTRODUCTION

The borides are characterized by a great number of unique properties. Most of them are refractory with melting points well above 2000 K and have a high hardness, excellent wear resistance, and very good chemical inertness, for example, toward reactive liquid metals, and a relatively good oxidation resistance. Many properties vary with the nature of the metal component and with composition. As an example, some of the borides display Pauli paramagnetism, some are strong ferromagnets, but some of them are also diamagnets. The electrical properties of the borides include metallic conductivity (five times larger than that of the component metal in TiB_2), high-temperature semiconductivity, which occurs, in particular, in boron-rich borides, and superconductivity. Among the borides several heavy Fermion systems have been discovered and studied in detail. In particular the boron-rich borides display a high stability toward neutron and other types of radiation. Some boride phases have attracted interest for their use as thermionic emitters and as high-temperature thermoelectrics.

In comparison with the related carbides and nitrides, borides are characterized by a great structural complexity, a statement that is valid for both metal-rich and, in particular, for boron-rich compositions. Presently, a total of more than 950 binary and ternary borides have been prepared and characterized. They crystallize in well above 130 different structure types. Some of these have large unit cell volumes in the range 2000–3000 Å^3. The range of composition is extremely large, the metal/boron ratio varies with more than three orders of magnitude in binary and ternary borides. In a systematic approach to the crystal chemistry of borides, it is convenient to consider packing and relative size of the atoms, space filling, the electron deficiency of boron, and the strong tendency toward the formation of boron–boron bonds as the boron/metal ratio increases. The electron deficiency of boron is also of major importance in the theories of bonding and band structure of the borides.

Binary borides are formed with transition and inner transition elements, with alkali and alkaline-earth elements, and with the *p* elements, aluminum, and silicon. In addition, a group of more electronegative elements (C, O, P, S, As, Se) form compounds with boron, which display properties and structures closely related to those of some borides. This group of compounds is also briefly described in the present article as well as the polymorphs of elemental boron.

2 OCCURRENCE AND CRYSTAL CHEMISTRY OF BORIDES

2.1 Occurrence of Borides

Preparation and phase characterization of a great number of binary borides were carried out in the period 1950 to 1980,[1–4] while interest was focused on ternary borides in the time that followed.[5–10] Recently published reviews on phase diagrams RE–T–B[6,8] and surveys on the formation of borides[7–10] contain more details on borides than what is available in general phase diagram compilations.[11] Of particular interest in this connection are the proceedings from a series of 13 international symposia on boron, borides, and related compounds, held after the first symposium on boron in Asbury Park, N.J., USA, 1959. The topics covered in these symposia are synthesis, phase diagrams, chemical bonding, physical properties, and applications. Most of the proceedings from symposia held later than 1972 are available as special issues of international journals. The most recent ones of these are included in the list of references.[12–16]

Improved phase diagrams can be obtained by computer coupling of phase diagrams and thermochemical data. Such modeling has been performed for several boride systems, for instance, V–B, Cr–B, Mn–B, Co–B, Ni–B, Fe–B, and Cu–B.[17]

The occurrence of the binary borides of the alkaline, alkaline earth, aluminum, and transition elements has been collected in Table 1, together with boron compounds of the right main group elements (carbides, etc.). Only relatively well-established phases have been included. Noncorroborated and/or badly characterized borides lacking precise composition and structure data are not included. The reader is referred to other sources for references.[8–11] There are no binary borides among the Cu, Zn, Ga, and Ge group elements with the exception of a noncorroborated early report on diborides in the Ag–B and Au–B systems. Two silicon borides have been established, namely, SiB_{3-4} and SiB_6.

Table 1 Occurrence of binary borides and boron-containing compounds

a. Transition Elements							
ScB_2 ScB_{12} ScB_{19}	TiB Ti_3B_4 TiB_2	V_3B_2 VB V_5B_6 V_3B_4 V_2B_3 VB_2	o-,t-Cr_2B[a] Cr_5B_3 h,l-CrB Cr_3B_4 Cr_2B_3 CrB_2 CrB_4	o-,t-Mn_2B h,l-MnB Mn_3B_4 h-MnB_2 MnB_4	$Fe_{23}B_6$-meta Fe_3B-meta Fe_2B FeB	Co_3B Co_2B CoB	Ni_3B Ni_2B o-Ni_4B_3 m-Ni_4B_3 NiB
YB_2 YB_4 YB_6 YB_{12} YB_{25} YB_{50} YB_{66}	ZrB_2 ZrB_{12}	Nb_3B_2 NbB Nb_5B_6 Nb_3B_4 Nb_2B_3 NbB_2	Mo_2B h,l-MoB MoB_2 $MoB_{2.3}$ $Mo_{1-x}B_3$	Tc_3B Tc_7B_3 TcB_2	Ru_7B_3 $Ru_{11}B_8$ RuB Ru_2B_3 RuB_2	Rh_7B_3 Rh_5B_4 RhB	$Pd_{\sim 5}B$ Pd_3B Pd_5B_2 Pd_2B
LaB_4 $La_{1-x}B_6$	HfB HfB_2 hp-HfB_{12}	Ta_2B Ta_3B_2 TaB Ta_5B_6 Ta_3B_4 TaB_2	W_2B h,l-WB WB_2 W_2B_{5-x} $W_{1-x}B_3$	Re_3B Re_7B_3 ReB_2	OsB Os_2B_3 OsB_2	$IrB_{0.9}$ $IrB_{1.1}$ $IrB_{1.35}$	Pt_4B Pt_2B $PtB_{0.7}$
b. Main Group Elements							
B_2H_6[b]							
LiB Li_3B_{14}	Be_4B Be_2B η-Be_2B_3 BeB_2 BeB_3 BeB_6 BeB_{9-12}	B	B_4C (homogeneity range $B_{4.3}C$-$B_{\sim 9}C$)		$B_{12}N_2$ BN	$B_{12}O_2$ hp-B_2O BO B_2O_2 B_2O_3 BO_2 BO_3	BF_3
Na_3B_{20} Na_2B_{29} NaB_{15}	MgB_2 MgB_4 Mg_2B_{14}	AlB_2 α-AlB_{12} γ-AlB_{12}	$SiB_{2.8}$ SiB_6		$B_{12}P_2$ BP	$B_{12}S_2$ BS B_2S_2 B_2S_3 BS_2	B_2Cl_4 BCl_3
KB_6	CaB_6				$B_{12}As_2$ BAs	$B_{12}Se_2$ BSe B_2Se_3 BSe_2	BBr_3
	SrB_6						BI_3
	BaB_6						

[a]Notations: o = orthorhombic, t = tetragonal, h,l = high, low temperature, meta = metastable, hp = high pressure. [b]and higher boranes.

In addition to the phases of Table 1, there are a large number of lanthanide and actinide borides crystallizing in the structure types of AlB_2, Sm_2B_5, ThB_4, CaB_6, ScB_{19}, UB_{12}, YB_{25}, YB_{50}, and YB_{66}. A total of more than 200 binary borides have been reported until now. More or less complete binary phase diagrams of most of the systems of Table 1 are available[11] with the exception of those of the alkali metals.

A total of more than 700 ternary borides have been prepared and characterized.[3,5,6,8] Most of these phases occur in the RE–T–B systems. A maximum of 12 ternary phases has, for instance, been found in each of the Sm–Co–B and Ce–Co–B systems[6] (see Figure 1). There are also ternary systems without any ternary phase at all, for instance, the system La–Cu–B.

It is very often difficult to establish the existence and composition of borides owing to one or more of the following reasons. The great reactivity of boron toward, for instance, the crucible material leads to the occurrence of impurities in the products. The impurities are often said to ‘stabilize’ a structure type, while in reality a ternary compound has been formed although unintentionally. It is also difficult to analyze chemically or by microprobe the boron content owing to low accuracy of the methods. Indeed, in many cases a single–crystal-structure determination is, together with complementary structural information obtained by other

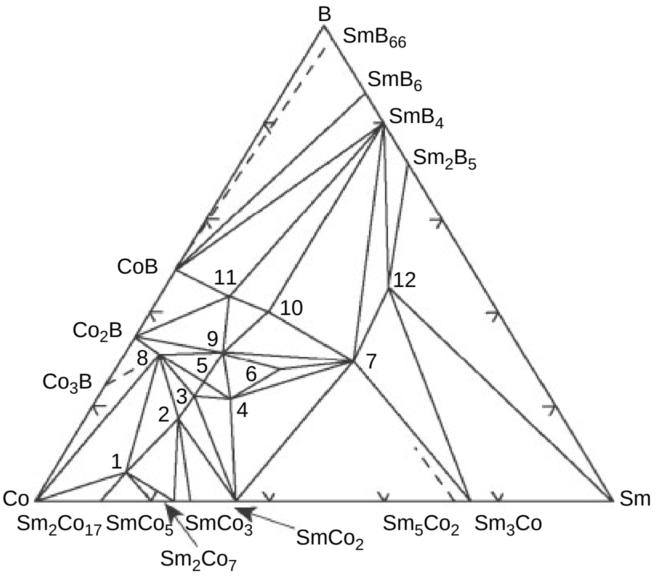

Figure 1 The ternary section Co–Sm–B. 0–33 atom% Sm at 900 K and 33–100 atom% Sm at 700 K. Phases: 1, $Sm_2Co_{14}B$; 2, $SmCo_4B$; 3, $Sm_3Co_{11}B_4$; 4, $Sm_2Co_5B_2$; 5, $Sm_2Co_7B_3$; 6, $\approx Sm_5Co_8B_5$; 7, $\approx Sm_4Co_3B_3$; 8, $SmCo_{12}B_6$; 9, $SmCo_3B_2$; 10, $SmCo_2B_2$; 11, $SmCo_4B_4$; 12, $Sm_{5-x}Co_{2+x}B_6$[6]

methods, the most profitable procedure to determine the composition of a boride. Such studies are, however, often hampered by the nonavailability of single crystals, which means that only powder diffraction methods can be used (*see* ***Solids: Characterization by Powder Diffraction***). This fact may not, however, involve too many restrictions presently, since high-intensity X-ray sources and improved computer capacity and programs are available. Problems are also connected with neutron diffraction studies (*see* ***Diffraction Methods in Inorganic Chemistry***), since B-11 enriched boron is required in the borides owing to the high neutron absorption of the B-10 isotope.

Sluggish reactions are often met with in boride systems even at high temperatures, especially at boron-rich compositions. This often hinders phase equilibria to be established and phase transformations under equilibrium conditions to be investigated.

2.2 Crystal Chemistry

Owing to the great number of structure types represented among the binary and ternary borides, it is not possible to present in this article even a simple description of all known structure types. The following presentation deals mainly with binary boride structures. Ternary boride structures show many similarities with those of binary boride phases but cannot be treated in any detail in the present paper because of space limitations. Binary and ternary boride structures are treated in more detail elsewhere.[3,6,8] It is convenient to describe here some structural principles using coordination polyhedra and cluster formation and to supplement this by selected examples.

The boron atoms of metal-rich borides are usually surrounded by metal atoms, situated at the corners of trigonal prisms (Figure 2a). Outside the rectangular faces of the prism there are three further metal atoms, of which one, two, or all three can be replaced by boron atoms (a tricapped trigonal prism or a tetrakaidecahedron). The coordination polyhedron of a boron atom occasionally consists of an octahedron or an Archimedian antiprism (Figure 2b), consisting of six and eight metal atoms, respectively. The packing of these atomic units in the structure is such that a good space filling is obtained. Furthermore, the linking of the polyhedra is such that with increasing boron content the number of boron–boron contacts increases. In this manner, boron–boron pairs, fragments of boron chains, single chains, double chains, triple chains, branched chains, and hexagonal networks are formed, as illustrated in Figure 3. This tendency toward forming B–B bonds is in contrast to the situation in carbides and nitrides, where contacts between the nonmetal atoms are formed at much higher nonmetal contents than in borides. It is natural that compounds with higher boron–metal ratios display more boron–boron contacts, for instance, monoborides (CrB, MoB, FeB) are characterized by zig–zag boron chains, while V_2B_3-type structures contain triple chains of boron atoms (see Figure 3).

There are no sharp metal–boron ratios for which the transition from isolated boron atoms to boron pairs to boron chains and so on occurs. For example, isolated boron atoms solely occur in borides, crystallizing in the relatively metal-poor $REFe_2B_2$ ($ThCr_2Si_2$)-type structure (M/B = 1.5), while

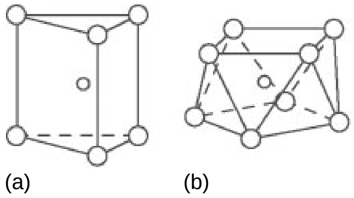

Figure 2 Trigonal prismatic and Archimedian prismatic coordination of boron (small circles)

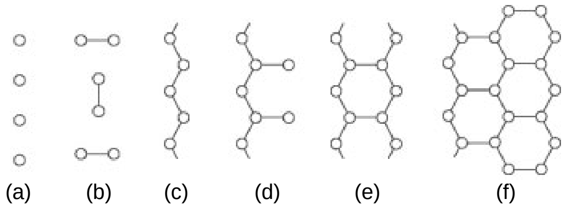

Figure 3 Boron–boron contacts in some metal-rich borides: (a) isolated boron atom ($Nb_2Fe_{14}B$); (b) boron pair (Cr_5B_3); (c) zig–zag chain (FeB); (d) branched chain ($Ru_{11}B_8$); (e) double chain (Ta_3B_4); (f) triple chain (V_2B_3)

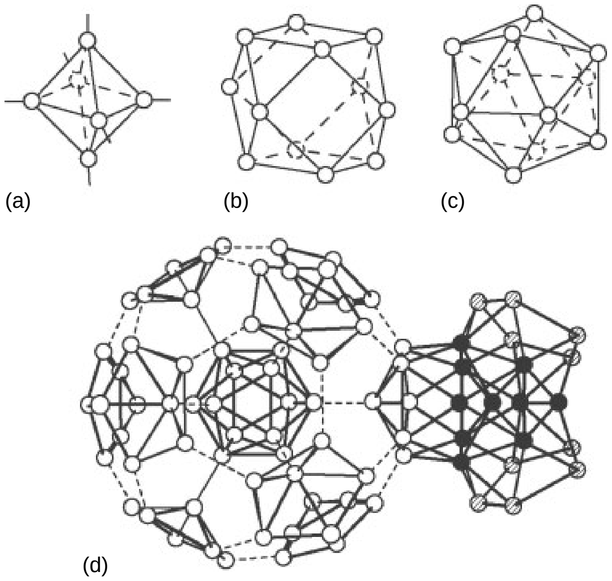

Figure 4 Boron clusters occurring in boron-rich borides and elementary boron; (a) octahedron; (b) cubooctahedron; (c) icosahedron; (d) the main part of a B_{84} unit (β-rh. boron) and an attached B_{10} unit (black circles) with two half-icosahedra (hatched circles)

boron pairs along with isolated boron atoms are found in the relatively metal-rich $Sc_4Ni_{29}B_{10}$-type structure ($M/B = 3.3$).

In boron-rich compounds the structure can often be described as being built up of a three-dimensional network of boron clusters, for instance, octahedra, icosahedra, and cubo-octahedra (see Figure 4), which are linked to each other directly or via noncluster atoms. The metal atoms are accommodated in cages between the octahedra or icosahedra, thereby providing external bonding electrons to the electron deficient boron network. The structures of the boron modifications are also built up of icosahedral boron units.

2.2.1 Modifications of Elementary Boron

The existence of three crystalline and one amorphous modification of boron has been established (Table 2). Reports on further modifications are unreliable and refer to uncharacterized and/or impurity stabilized material. α-tetr. boron, also denoted tetr. I boron (a = 8.75 Å, c = 5.06 Å), was earlier believed to be a boron modification, but has been shown to be a phase of composition $B_{50}(C_{1-x}N_x)_2{}^3$.

Table 2 Crystallographic data for the boron modifications

		Unit cell dimensions	
Modification	Space Group	a(Å)	c(Å)
α-rh. boron[21]	$R\bar{3}m$	4.927(3)	12.564(7)
β-rh. boron[22]	$R\bar{3}m$	10.930(1)	23.815(3)
β-tetr. boron[18]	$P4_1$ or $P4_3$	10.14(1)	14.17(1)

Owing to sluggish phase transformations, the temperature regions of stability for the different modifications are not known with certainty. The β-rh. modification is, however, stable from the melting point of boron, 2573 K, down to 1473 to 1673 K. The β-tetr. modification (also denoted tetr. II boron) is stable in the intermediate range down to approximately 1300 K. α-rh. boron is a low-temperature modification, stable up to approximately 1300 K.

The structures of the boron modifications all display boron icosahedra as structural subunits. In α-rh. boron, which has the simplest structure, the icosahedra form a rigid three-dimensional boron network by direct covalent boron–boron contacts and, in addition, by three-center bonds between boron atoms situated in three different icosahedra.[21] The crystal structure of β-rh. boron can be described as containing B_{84} units (Figure 4d), which consist of a central icosahedron and 12 half-icosahedra. The B_{84} units are linked together via B_{10} units (black atoms in Figure 4d) and via the formation of new icosahedra from two half-icosahedra from different B_{84} units.[22] In addition there are also nonicosahedral boron atoms in the structure. The crystal structure of β-rh boron is highly defective. Of the 20 different symmetry equivalent atomic positions required to describe the structure as many as six positions are only partially occupied. The occupancies of these positions range from 3.7(4)% to 75.5(6)%. Elementary β-rh. boron is a highly defective solid (*see* ***Defects in Solids***), containing numerous twin boundaries in addition to the vacancies mentioned. The structure of tetr. II boron is closely related to that of α-AlB_{12}.[18] It is basically a three-dimensional network structure built up of B_{12} icosahedra and B_{21} units, consisting of completely twinned icosahedra with a common triangular face. In this boron skeleton, some interstitial positions are partially or completely filled with boron atoms.

2.2.2 Solid Solutions of Transition Elements in β-rh. Boron

The boron modifications are semiconductors. β-rh. boron is a high-temperature semiconductor with a band gap of ~1.5 eV. The transition elements and some p elements (C, Si) form solid solutions in β-rh. boron.[10] In this manner, the electrical characteristics are changed (doping). The maximum solid solubility varies with solute and can be as high as 4 to 5 atomic percent. The well-known difficulties to prepare ultra-pure β-rh. boron is partially due to the solid solutions that most of the elements form with boron.

The structure of the solid solutions is very complex. Investigations have shown that partial (and only partial) occupancies of up to five interstitial atomic positions occur. These atomic positions are situated between the icosahedra of the structure. In a few cases a substitutional mechanism for the solid solubility has been demonstrated, similar to the silicon substitution for boron in the structure of $B_{2.89}Si$, which has the ideal composition B_6Si.[23]

2.2.3 *Borides with Isolated Boron Atoms*

Following Rogl,[8] we distinguish three subgroups among the borides with isolated boron atoms, namely, metal framework structures, substitutional metal borides, and proper metal boride structures. The metal framework structures include elemental or binary compound types, which are stabilized by boron atoms filling the voids of the metal host lattice. Examples of such structures are the κ-borides (Hf_9Mo_4B), the τ-borides (mostly ternary $M_{21}M'_2B_6$ phases), and the Cu_3Au-type phases ($Ni_3InB_{0.15}$), with prismatic, antiprismatic, and octahedral coordination of the metal atoms around the boron atoms, respectively.

In substituted metal borides, the boron atoms replace partially or completely, in an ordered or disordered manner, metal atoms in the structure. Structure types belonging to this subgroup are, for instance, two structural series based on the substitution of boron for small metal atoms in the intermetallic structure types $CaCu_5$ and $MgZn_2$, respectively. The structural relationship is nicely demonstrated in the series $CaCu_5 \rightarrow CeCo_3B_2 \rightarrow ErIr_3B_2 \rightarrow ErRh_3B_2$. Another very important structure type belonging to this subgroup is that of $Nd_2Fe_{14}B$, a compound which displays excellent permanent magnetic properties. In the structure of the $Nd_2Fe_{14}B$, the boron atom has a trigonal prismatic environment of metal atoms. In addition, there is a close correspondence between the metal arrangement of $Nd_2Fe_{14}B$ and the intermetallic σ-phase. Thus this structure is also closely related to the metal framework structures already discussed. The substitutional metal borides include approximately 30 structure types.

The proper metal boride structures with isolated boron atoms include approximately 20 structure types with many ternary representatives. The boron coordination is trigonal prismatic (in the Fe_3C, Ti_3P, Re_3B Th_7Fe_3 structure types), octahedral (in Rh_5B_4), or Archimedian prismatic (in the $CuAl_2$-type structure with many M_2B representatives).

2.2.4 *Borides with Chains and Fragments of Chains*

In o-Mn_2B (earlier denoted Mn_4B) and t-Mn_2B ($CuAl_2$ type), a tendency toward chain formation is observed, although the B–B distance in the structures is relatively large, namely, 2.1 Å, as compared 1.8 Å (±0.1 Å) in normal chains. In these structures, the metal surrounding of the boron atom consists of an Archimedian or a distorted Archimedian antiprism. A closer contact between the boron atoms of about 1.8 Å is, however, brought about when trigonal prismatic coordination polyhedra of the boron atoms share rectangular faces. Chain fragments consisting of boron pairs occur in Cr_5B_3 and in V_3B_2 (U_3Si_2-type structure). Chain fragments consisting of three or four boron atoms occur in the structure types of W_3CoB_2 and Mo_2IrB_2, respectively. Distorted prisms are common among ternary compounds containing large and small metal atoms. Chain fragments can also occur as a consequence of boron defects.

Infinite boron zig–zag chains with B–B distances 1.65 to 1.90 Å and bond angles of ~115° are found in the structure types of FeB, CrB, and MoB. The boron coordination is trigonally prismatic with two boron atoms and one metal atom situated outside the rectangular faces. There are a large number of binary and ternary representatives of these and other related structure types. Double and triple chains characterize the structure types Ta_3B_4 and V_2B_3, respectively. Single and double chains occur in the structure type of V_5B_6. In the ternary structures of Cr_2AlB_2 and Cr_3AlB_4, single and double boron chains, respectively, occur together with CsCl-type units. Branched boron chains are found in the $Ru_{11}B_8$ structure and also in the UBC structure with carbon atoms branching off the zig–zag boron chain. Chains or fragments of chains also occur in borocarbides of many structure types, for instance, Sc_2BC_2.[19]

Studies of borides with the composition RT_4B_4 are very rewarding to clarify the interplay between superconductivity and magnetism. A large number of RT_4B_4 compounds have been reported with T = Fe, Co, Ru, Rh, Os, and Ir and with RE comprising nearly all rare-earth metals. The compounds crystallize in at least six structure types, namely, $CeCo_4B_4$, $LuRh_4B_4$, $LuRu_4B_4$, $NdCo_4B_4$, YOs_4B_4, and $Ce_{1+x}Fe_4O_4$ of tetragonal or orthorhombic symmetry. Another group of boron-containing materials of interest for superconductivity and magnetic studies are quaternary borocarbides of composition RE–T–B–C, for instance, $LuNi_2B_2C$, LuNiBC, and Lu_2NiBC_2. A review was published in 2000.[20]

2.2.5 *Borides with Two-dimensional Boron Networks*

Many borides in the composition range B/Me 1.5 to 2.5 crystallize with various stacking sequences of metal layers and boron layers.[8] Ordered or disordered defects often occur in the layers. Most of the structures belonging to the AlB_2 structure family[24] can be described by the stacking sequence of planar or puckered boron and metal layers as shown in Figure 5. The common, simple hexagonal AlB_2 structure is, for instance, described by the sequence AHAH. . . and the structure of W_2B_{5-x} by AHAK‘BHBH’. . ., where the K′ boron layers are slightly puckered. Orthorhombic stacking variants, for instance, RuB_2 and $IrB_{1.35}$, also belong to this structure family. $Mo_{1-x}B_3$ (x small) is a relatively boron-rich compound built up of defective metal layers (every third atom is lacking) and H type layers occurring in AlB_2. It is noticeable that MgB_2, belonging to the simple AlB_2-type structure, is a superconductor with T_c as high as 39 K.[25] The superconducting properties of MgB_2 were not discovered until 2001 although the compound was synthesized already in the 1950s.

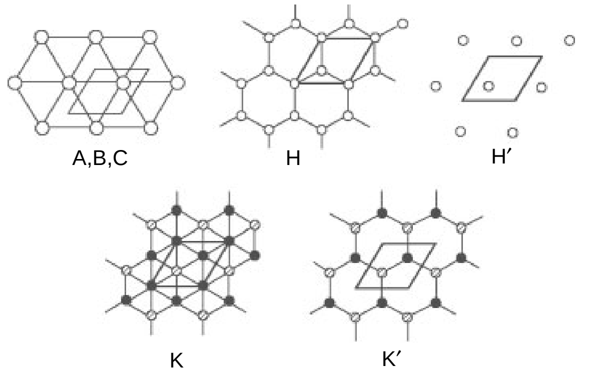

Figure 5 Layers of metal atoms (A, B, C), planar boron layers (H, H′), and puckered boron layers (K, K′), occurring in the AlB_2 and related type structures

There are a large number of ternary compounds crystallizing in $YCrB_4$ and Y_2ReB_6 type structures. These structures are also described as a simple stacking of metal layers and boron layers. The axis perpendicular to the layers is short (3.2–3.6 Å) and comparable to the c axis of the AlB_2-type structure. The boron layers, however, contain 5-atom and 7-atom rings and no 6-atom rings as in the AlB_2-type structure, see Figure 6. In borocarbides of the ScB_2C_2-type, there is boron carbon ordering within the layers. Also planar nets of 8-atom rings linked by a boron pair exist in $ErNiB_4$. Puckered nonmetal layers in ternary structures were reported, for instance, in Er_4NiB_{13} (7- and 4-atom rings).

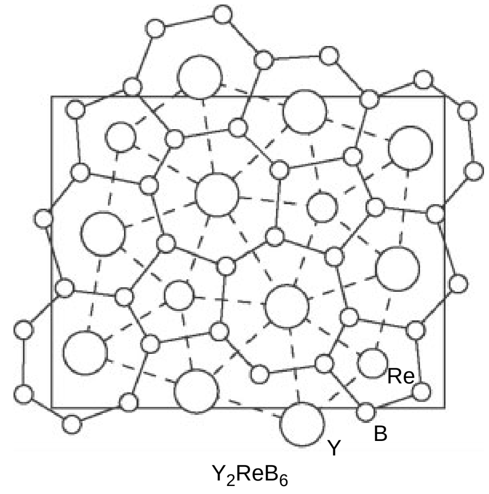

Figure 6 Projection of Y_2ReB_6 along the short axis. The metal atoms are connected with fully drawn lines while the boron atoms are connected with dashed lines within their planes, respectively

2.2.6 *Borides with Three-dimensional Boron Networks*

A presentation of binary and ternary boride structure types, which are built up of a rigid three-dimensional boron network, is given in Table 3. Many ternary boride phases also crystallize in the structure types collected in Table 3. It is noticeable that the B/M ratio ranges as much as from 2.5 to 66.

The structures of Sm_2B_5, Pr_2B_5, and ThB_4 are built up of boron octahedra. In ThB_4, the octahedra are interconnected

Table 3 Structure types of some binary boron-rich compounds

Phase	Symmetry	a(Å)	b(Å)	c(Å)	β(°)	Structural characteristics
Sm_2B_5	Monoclinic	7.183	7.191	7.216	102.03	Octahedra, B pairs[9]
BeB_3	hexagonal	9.800		9.532		Icosahedra, B_{15}[26]
MgB_4	Orthorhombic	5.464	7.472	4.428		Half-icosahedra, chains[9]
CrB_4	Orthorhombic	4.744	5.477	2.866		B-squares in three dimensions[9]
MnB_4	Monoclinic	5.503	5.367	2.949	122.71	B-squares in three dimensions[9]
ThB_4	Tetragonal	7.526		4.113		Octahedra, B pairs[9]
B_4C	Hexagonal	5.599		12.074		Icosahedra, C–B–C chains[23]
B_6P	Hexagonal	6.000		11.857		Icosahedra, B pairs[23]
$B_6O_{0.76}$	Hexagonal	5.367		12.328		Icosahedra, O isolated[23]
CaB_6	Cubic	4.1522				Octahedra[9]
SiB_6	Orthorhombic	14.397	18.318	9.911		Icosahedra, icosihexaedra[27]
Na_3B_{20}	Orthorhombic	18.695	5.701	4.1506		Pentag. bipyramids, icosahedra[28]
Mg_2B_{14}[a]	Orthorhombic	5.970	8.125	10.480		Icosahedra[9]
α-AlB_{12}	Tetragonal	10.158		14.270		Icosahedra, B_{19} units[29]
γ-AlB_{12}	Orthorhombic	16.573	17.510	10.144		Icosahedra, B_{19} units[29]
UB_{12}	Cubic	7.473				Cubo-octahedra[9]
Na_2B_{29}[b]	Monoclinic	5.874	10.403	8.359	90.17	Icosahedra, interstitial B[30]
ScB_{19}	Tetragonal	10.292	14.2463			Icosahedra, related to α-AlB_{12}[31]
YB_{25}	Monoclinic	8.2842	10.3203	5.8570	90.402	Icosahedra, related to $YAlB_{12}$[32]
YB_{50}	Orthorhombic	16.625	17.620	9.4797		Closely related[33] to $YB_{41}Si_{1.2}$[34]
YB_{66}	Cubic	23.446				Icosahedra, Y tunnels[9]

[a] Isostructural to $MgAlB_{14}$. [b] Earlier denoted NaB_{15}.

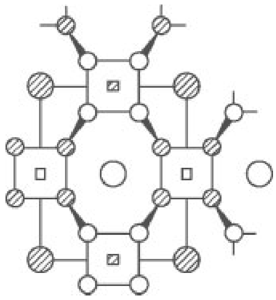

Figure 7 The crystal structure of CrB_4 as seen along the short c axis. Boron atoms (small circles), chromium atoms (large circles) are at $z = 0$ (hatched) or at $z = 1/2$ (open). Squares denote cages

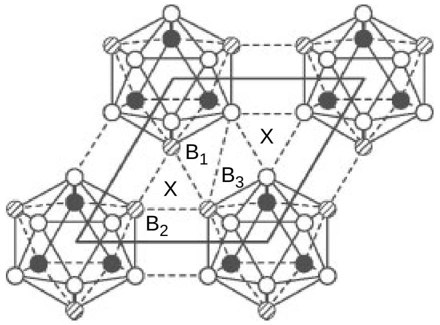

Figure 8 Projection of the B_4C-type structure along the trigonal axis. The end-on view of the three-atom chain (C–B–C or C–B–B) is denoted X. For α-rh. boron, X denotes the three-center bond

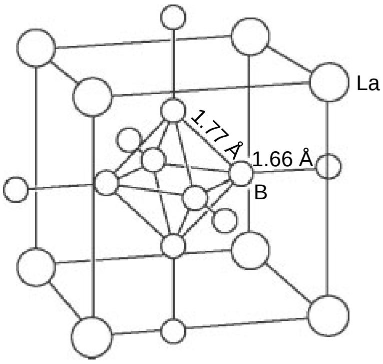

Figure 9 The crystal structure of LaB_6. The boron atoms (small circles) form a three-dimensional rigid network with $\approx$0.1 Å shorter bonds between the octahedra than within the octahedra

by direct bonds in the c direction and via boron pairs in the ab plane. In Sm_2B_5, the octahedra are interconnected via boron pairs in the c direction as well. In the unique structure of CrB_4 (Figure 7), squares of B_4 units are linked to other squares in the third direction so that all boron atoms are four-coordinated by other boron atoms. MnB_4 is a monoclinic distortion of CrB_4.

The structures of B_4C, B_6P, and B_6O are closely related to that of α-rh. boron. The structure of boron carbide is shown in Figure 8, projected in the c direction. In the Figure are seen icosahedra centered at (0,0,0). In the three-dimensional structure, icosahedra are also centered at (1/3, 2/3, 1/3) and (2/3, 1/3, 2/3). An elongated cage, denoted x in Figure 8, is formed in this manner. In α-rh. boron, the atoms B(1), B(2), and B(3) are linked by a three-center bond. In the carbide, phosphide, and oxide, the end atoms of a three- or two-atom chain are linked to these three boron atoms. In the carbide, the chain can consist of a C–B–C or C–B–B sequence depending on composition, while in the phosphide a phosphorus pair (the P atoms are at bonding distance) bonds to two different B(1)-B(2)-B(3) triangles. A study of boron-carbide-like structures has shown that B_6As, $B_{12}S$, and the new $B_{12}Se$ phase display chains of two atoms as B_6P.[23] In the oxide, however, two isolated oxygen atoms are situated more than 3 Å from each other. Each oxygen atom bonds to a triangle of boron atoms, of which each boron belongs to three different boron icosahedra.

Borides, crystallizing in the CaB_6-type structure, are formed by potassium, alkaline earths, and the larger rare-earth elements. The octahedra form a rigid boron network by direct B–B bonds and the metal atoms are accommodated in cages, surrounded by 24 boron atoms (Figure 9). The UB_{12}-type borides can be described on the basis of B_{12}-cubooctahedra, which form a three-dimensional boron skeleton containing B_{24}-cubooctahedral cages. These cages accommodate metal atoms, including Zr, Hf, most of the rare earths, and some actinides.

The remaining icosahedral structures are very complex and contain, in addition to icosahedra, icosihexaedral B_{15} units (SiB_6 and BeB_3) and condensed icosahedra as B_{19} units (α-AlB_{12}), sharing one trigonal face. In SiB_6, some boron atoms in the B_{15} unit are replaced by silicon,[27] while in BeB_3 there are three beryllium atoms and 12 boron atoms in the B_{15} unit.[26] Several new boron-rich phases of the rare-earth elements have been reported recently, of which the binary phases ScB_{19},[31] YB_{25},[32] and YB_{50}[33] are included in Table 3. These structure types also occur as ternary compounds with C, N, or Si as the third component. A total of more than 60 binary or ternary representatives, crystallizing in the structure types mentioned, are known to exist presently. The structure of ScB_{19} is closely related to that of α-AlB_{12}.[31] Furthermore, the structure of $YB_{41}Si_{1.2}$[34] is closely related to that of YB_{50} as apparent from the similarity of the unit cell dimensions.

3 SYNTHESIS

The synthesis of borides often requires high temperatures, involving difficulties in obtaining pure products while simultaneously using simple methods. Direct synthesis from the elements is of particular interest in fundamental research since high-purity products can be obtained. Other processes are suitable for industrial production. The methods for preparation of borides may be classified as follows.

3.1 Direct Combination of the Elements

Direct reaction of the elements is carried out under vacuum or inert gas by melting or by reaction sintering at a temperature below the melting point. The melting procedure is often associated with the crucible problem, which is pronounced at high temperature.[24] The metal–boron melt invariably attacks oxide ceramics, in particular, boron-rich compositions, and to avoid impurities or stabilization effects from such attacks, levitation melting or cold crucible techniques (for instance, arc melting) are preferable, in particular for the highest temperatures. Boron nitride is an excellent crucible material for boron-rich compositions at not too high temperatures. Synthesis can be difficult owing to high volatility of the metals and/or their reactivity toward oxygen (alkali, alkali-earth, and rare-earth metals), which requires a sealed crucible technique and high vacuum or inert gas atmosphere.

3.2 Reduction of a Metal Oxide and Boron Halide with Hydrogen

A mixture of, for instance, metal and boron halides is reduced at temperatures of 1300 to 1600 K. Borides of Ti, Zr, and Hf have been prepared according to:

$$\mathrm{MCl_4(g) + 2BCl_3(g) + 5H_2(g) \longrightarrow MB_2(s) + 10HCl(g)} \qquad (1)$$

Adherent coatings of diborides can also be obtained by thermal decomposition of boron halides.

3.3 Reduction of a Metal Oxide or Other Metal Compound Using B, C or Boron Carbide

The borothermic process for diborides proceeds in vacuo at high temperature (>1300 K) according to the equation:

$$\mathrm{M_nO_m(s) + (2n + m)\cdot B(s) \longrightarrow n\cdot MB_2(s) + 1/2m\cdot B_2O_2(g)} \qquad (2)$$

It can be used for hexaborides as well. Reduction with boron carbide can also be used for diborides as well as hexaborides, although in that case alkaline-earth and rare-earth hexaborides will dissolve some carbon forming $RB_{6-x}C_x$ borocarbides.

3.4 Reduction of Boron Oxide or Boron Halides by Metals

Electropositive metals, for example, Al, Mg, or an alkali metal, are used as reduction agents. The following reaction illustrates the process:

$$\mathrm{CaO + 3B_2O_3 + 10Mg \longrightarrow CaB_6 + 10MgO} \qquad (3)$$

The process is used in industrial production.

3.5 Fused-salt Electrolysis

Electrolysis is carried out at 1000 to 1300 K of a mixture of alkali halide, metal oxide, and a borate. This is a process of industrial interest. However, high-purity and single-phase products are not easily obtained.

3.6 Preparation of Coatings by Chemical Vapor Deposition (CVD)

In Chemical Vapor Deposition (CVD), the gaseous reactants are carried over a heated substrate, where the chemical reactions or thermal decomposition occur.[35] If the process parameters are correctly selected an adherent solid coating is obtained with attractive mechanical or electrical properties. Overall reactions can be of the type already mentioned in Section 3.2.

3.7 Crystal Growth

Crystal growth of boride phases can be carried out by most of the methods known. However, the high melting points and the great reactivity of, in particular, boron-rich compounds limits the techniques applicable and calls for special equipment. The low-temperature, gas-phase methods (1300–1600 K), including CVD and chemical vapor transport, have been used for crystal growth of diborides, especially TiB_2, ZrB_2, and TaB_2 with melting points around 3300 K. Liquid phase methods (crystal pulling, floating zone melting, and flame fusion) are used to produce diboride, hexaboride, and REB_{66} single crystals.[35,36]

An attractive method to produce single crystals (in the dimension range from µm to several mm) is the high-temperature solution (flux) method, because of its simplicity and the low temperature required.[37] The elements are dissolved in the solvent metal (often Al) and subsequently the solution is slowly cooled to room temperature. A prerequisite is, of course, that the solubility of the used solvent in the desired boride is insignificant. The solubility of Al in most boron-rich binary borides has been found to be extremely small. Crystals prepared in this manner are suitable for measurement of physical properties, for instance, microhardness, electrical resistivity, and so on.

3.8 Other Methods

Precipitation from aqueous solution has been reported in a few cases. Amorphous Ni_2B was, for instance, obtained from nickel acetate and a solution of tetrahydroborate at room temperature.

Many borides can be synthesized by novel synthetic methods, including shock-induced chemical reactions, mechanical alloying by ball milling, and self-propagating high-temperature synthesis. In these methods, intimately mixed elemental powders are brought to react by a rapid pressure increase, mechanical deformation including local temperature increase and triggered self-sustaining reaction (exothermic), respectively.

4 BAND STRUCTURE AND BONDING

The nature of the chemical bonding in borides was in early work described by simplified models emphasizing the role of M–M, M–B, and B–B bonding. The question of magnitude and direction of charge transfer has been much debated. There is complete agreement that the bonding in borides involves simultaneous contributions of metallic, covalent, and ionic bonding to the cohesive energy. The proportions, however, depend on the nature of the metallic component and the boron/metal ratio. In recent years, the growth of more powerful experimental methods and greatly improved calculation facilities have contributed immensely to our knowledge of band structure and bonding in borides.

Several band structure calculations (*see* ***Electronic Structure of Solids***) for diborides have been carried out.[38,39] The density of state versus energy for ZrB_2 from a self-consistent calculation is shown in Figure 10. The Figure demonstrates a Fermi level (E_F) at the minimum of the DOS curve between bonding states (left) and antibonding states (right). It is difficult to draw conclusions from the corresponding band structure (not reproduced here), although the authors suggest covalent bonds within the boron layers and some covalency (perhaps also metallic bonding) along the Zr–B directions. At the Fermi level the states are nearly completely of Zr-4*d* character. These calculations are in qualitative, and in some cases in very good quantitative, agreement with experimental data for ZrB_2 from X-ray photoemission spectroscopy, measurements of optical properties, Hall effect, dc resistivity, and specific heat. Experimental and theoretical studies indicate a relatively small transfer of electrons from metal to boron.[40] Band structure calculations of the new medium-T_c superconductor MgB_2 (T_c 39 K) and related diborides have been published.[41] It was early suggested to use a ‘rigid band’ model for the electronic structure of the diborides and only one DOS curve, which was then filled up with the number of electrons available in the boride. This method has often proved to be a very crude approximation.

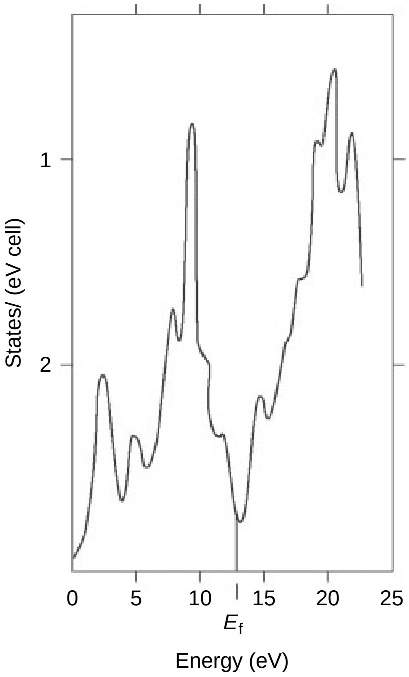

Figure 10 Calculated density of states for ZrB_2 (zero energy at the bottom of the conduction band)[38]

In early studies of hexaborides, the conclusion was reached that there is a finite energy gap between the conduction and valence bands and that the valence band contains 20 electrons. The six boron atoms provide 18 electrons and, if the metal is divalent (Ca, Br, Ba), the hexaboride is anticipated to be insulating (semiconducting), while a higher valence, occurring among the rare-earth elements, is anticipated to lead to metallic conductivity. This is in agreement with experiments. The simple picture involves a charge transfer to the boron network and thus a significant ionicity in the bond. A self-consistent symmetrized APW calculation of the energy band structure of LaB_6[42] has revealed many more details. The calculated density of states for the valence bands agrees well with X-ray photoelectron measurements. The La–B bonding originates in the strong hybridization of La-d states and d-like B-sp states of the six octahedral boron atoms.

A simple treatment of the stability requirements of a boron icosahedron in a solid was presented early.[1] An icosahedral boron cluster was shown to require two external electrons. The icosahedron is linked to its neighbors via normal covalent bonds. This description leads to a simple understanding of the stability of the B_6O and B_6P structures.

The electronic structure of quaternary borides of the type RETBC was presented and discussed recently in a review-type paper.[43] Theoretical calculations, predictions, and syntheses of were also presented for BN analogues of fullerenes (fulborenes) and BN nanotubes.[44]

5 PROPERTIES AND APPLICATIONS

Characteristic properties of borides are high chemical inertness, high thermal stability, and great hardness. Magnetic and electrical properties vary strongly within the boride group of compounds. This is apparent from the compilation of Samsonov and Vinitskii,[45] which contains a large number of values for chemical reactivity of borides (toward acids and bases), thermodynamic and thermal properties, as well as electrical, magnetic, and optical properties. In addition the handbook contains values of mechanical and refractory properties. More recent fundamental data can be found in the proceedings from the boron symposia,[12–16] and specialized textbooks.[46] Values for some physical properties of a few borides are collected in Table 4.

Table 4 displays a broad range of resistivities beginning with the insulator h-BN, continuing with the semiconductors CaB_6, B_4C, and YB_{66}, and ending with the metallic phases Fe_2B, TiB_2, and LaB_6. The resistivity of TiB_2 is remarkably low, being only one-fifth of that for metallic titanium. The band gap of the three semiconductors mentioned are 0.20, 1.6, and 1.36 eV, respectively (*see* ***Semiconductors***).

Superconductors of the RET_4B_4 system are interesting for the study of the interplay between superconducting and magnetic order (*see* ***Superconductivity***). The RET_4B_4 compounds represent a great variety of correlated electron phenomena, consisting of ferromagnetism, antiferromagnetism, superconductivity, valence fluctuation, or Kondo lattice anomalies, and effects which arise from their interplay in the structure.[47] Another very interesting group of superconducting, boron-containing materials are borocarbides of the composition RET_2B_2C (T = Ni, Pd, Pt). The compounds of this group show a relatively high T_c if the rare-earth ions are large, that is, (La, Pr).[43] It was discovered recently (2001), that MgB_2 (known since the 1950s) is a superconductor at as high a temperature as 39 K. This surprising discovery initiated a large number of investigations of *iso*-structural binary and ternary compounds to reveal its basic properties and to search for other related compounds with even higher T_c:s.[48]

The excellent permanent magnetic properties of materials based on $Nd_2Fe_{14}B$ were discovered in 1983.[49] Very soon afterwards strong, small permanent magnets were available commercially with a Curie temperature of 850 K and a very high energy product $(BH)_{max}$. This quantity for $Nd_2Fe_{14}B$ is ~64 MGOe, which is more than twice than that of the very strong $SmCo_5$ magnets.

Most borides are chemically inert in bulk form, which has led to industrial applications as engineering materials, principally at high temperature. The transition metal borides display a considerable resistance to oxidation in air. A few examples of applications are given here. Titanium and zirconium diborides, alone or in admixture with chromium diboride, can endure temperatures of 1500 to 1700 K without extensive attack. In this case, a surface layer of the parent oxides is formed at a relatively low temperature, which prevents further oxidation up to temperatures where the volatility of boron oxide becomes appreciable. In other cases the oxidation is retarded by the formation of some other type of protective layer, for instance, a chromium borate. This behavior is favorable and in contrast to that of the refractory carbides and nitrides, which form gaseous products (carbon oxides and nitrogen) in air at high temperatures. Boron carbide is less resistant to oxidation than the metallic borides.

Borides, especially those of group IV transition metals, exhibit a high resistance to attack by molten metals and nonbasic slags and salts. These properties make them attractive as materials for vaporization boats (TiB_2, hex. BN), for crucibles and containers for liquid metals, for example, Al, and for protective tubes of thermocouples.[50] Composites of TiB_2 and BN are frequently also used as boats for vacuum metallizing of capacitor foils and car mirrors. Titanium diboride is also utilized for collector bars in the aluminum reduction process owing to its low resistivity and great inertness toward liquid aluminum.[50] A major part of the boride production is used for chemical and metallurgical applications. Calcium hexaboride is, for instance, used as a deoxidation agent in copper production, which results in higher conductivity than conventionally phosphorus-deoxidized copper owing to the low solubility of

Table 4 Typical properties of some borides

Phase	Melting temperature (K)	Microhardness (GPa)	ΔH_f (kJ·mole^{-1})	Resistivity (ohm·m·10^8)	T_c (K)
MgB_2	1100^a	11	−92	16	39
TiB_2	3500	33	−280	7–15	
ZrB_2	3450	29.4	−305	7–10	5.5
CrB	2400	12–13		45	
CrB_2	2500	21	−130	21–56	
Fe_2B	1660^a	13.5		38	
FeB	1925	19	−38	80	
CaB_6	2770	27	−120	>200	
LaB_6	3000	27.7	−400	7–15	0.12
CeB_6	2825	−30	>−350	29	
α-AlB_{12}	1725^a	37		10^5	
YB_{66}	~2300	38		$360 \cdot 10^6$	
h-BN		2.3	−255	Insulator	
c-BN	~2700	60–70		Insulator	
B_4C	2725	45	−242	10^5–10^7	

^{a}Decomposes.

boron in copper. Large amounts of Al–Ti–B alloys, containing TiB_2, are used as grain refiners in the aluminum industry.

The most attractive properties of boron-containing materials, in particular diborides and boron carbide, are the high melting point, the high hardness (see Table 4), the excellent wear resistance, and the favorable chemical inertness. However, they are brittle, so special precautions must be taken in their exploitation. They can be used as coatings, either as thick films obtained by packboronizing of structural parts in B_4C powder at high temperature, or as thin films obtained by chemical vapor deposition or physical vapor deposition (*see Chemical Vapor Deposition*) techniques. Hexaboride coatings are even attractive to be used as decorative coatings on consumer products.[51] In these cases advantage is derived from the combination of a ductile core and a wear-resistant adhesive coating. Another solution to the brittleness problem is to produce a composite with a ductile binder, that is, a boride cermet or a 'cemented boride', in analogy to the cemented carbides. This has led to the presently active research interest in cemented borides utilizing TiB_2 as hard substance and iron, iron-based or nickel-based binders. The results indicate that dense sintered parts with good chemical stability and attractive mechanical properties can be obtained.[52] Promising results have also been obtained from studies of the cermet Mo_2FeB_2 with an iron-based binder phase.[53]

The utilization of the outstanding mechanical and wear properties of cubic BN and related superhard materials has been demonstrated, although further process improvements are necessary before a more general use can be expected. Superhard cubic BN exhibits superb inertness to hot steel surfaces under conditions in which diamond would be severely attacked. Other tetrahedral structures, for instance, BCN and B_2O, are anticipated to display similar attractive properties. The high-pressure phase B_2O is a semiconductor with a band gap of $\sim$0.25 eV and a hardness between that of boron carbide and diamond.

Boron carbide is a relatively inexpensive hard material, which is used for its mechanical properties of strength and extreme hardness in armor-plates for body protection, in sandblast nozzles, and as an abrasive for grinding and cutoff wheels.[54] In nuclear plants, boron carbide is used as the neutron absorbing material of the control rods.

Intense research has in recent years been devoted to noncrystalline materials. It was discovered also that the majority of semiconducting boron-rich borides display several properties that resemble those of the noncrystalline solids.[55] Among the 'amorphous' properties are the temperature and field dependencies of electrical conductivity at low temperature, the temperature dependence of thermal conductivity at high temperatures, and the temperature dependence of the magnetic susceptibility. In addition, the boron-rich semiconductors display 'crystalline' properties, for example, the temperature dependence of the thermal conductivity at low temperatures, the lattice absorption spectra and the possibility to change the properties by doping. The boron-rich borides, which display charge carriers with extremely low mobility, are thus intermediate between crystalline and noncrystalline solids as regards certain properties, which probably can be ascribed to their complex and defect-rich structures. Optical studies of boron and boron-rich borides have led to invaluable information on the electronic and vibrational structure of the compounds.[56]

Recently, semiconducting refractory boron compounds have been suggested for high-temperature thermoelectric energy conversion.[57] For such an application, the corresponding figure of merit requires high values of the Seebeck coefficient and the electric conductivity, and a low value of the heat conductivity of the material even at high temperatures. The thermoelectric properties, high melting points, and chemical inertness of boron carbide and related boron compounds make them of special interest in such a context. Another recent application, where the electrical properties are decisive, is the use of LaB_6 and CeB_6 as thermionic emitter materials in applications where very high brightness is required.[58] The materials mentioned are used in electron microscopes and electron beam lithography systems. The borides are preferred to the conventional tungsten emitters owing to their higher brightness and longer service life, although they are more expensive.

The structurally complex semiconducting boride, YB_{66}, with a cubic unit cell axis of 23.44 Å, has been found to be an excellent monochromating material for synchrotron radiation.[36] In this application the attractive properties are high vacuum and thermal stability, good mechanical strength, and radiation-damage resistance and low thermal expansion coefficient. It is also essential that large, high-quality single crystals can be grown, which has been demonstrated successfully.

6 RELATED ARTICLES

Boron: Inorganic Chemistry; Carbides: Transition Metal Solid-state Chemistry; Nitrides: Transition Metal Solid-state Chemistry.

7 REFERENCES

1. J. L. Hoard and R. E. Hughes, Elemental Boron and Compounds of High Boron Content: Structure, Properties and Polymorphism, in 'The Chemistry of Boron and Its Compounds', ed. E. L. Muetterties, Wiley, New York, 1967, p. 25.
2. B. Aronsson, T. Lundström, and S. Rundqvist, 'Borides, Silicides and Phosphides', Methuen, London, 1965, p. 1.
3. V. I. Matkovich ed., 'Boron and Refractory Borides', Springer-Verlag, Berlin, 1977, p. 1.

4. Yu. B. Kuz’ma, ‘Crystal Chemistry of Borides’, Vyshcha Shkola Publishers, Lvov, 1983, p. 1; *Chem. Abstr.*, **100**, 219550, In Russian.
5. Yu. B. Kuz’ma and N. F. Chaban, ‘Binary and Ternary Systems Containing Boron’, Metallurgiya Publisher, Moscow, 1990, p. 1. Russian.
6. P. Rogl, Phase Equilibria in Ternary and Higher Order Systems with Rare Earth Elements and Boron, in ‘Handbook on the Physics and Chemistry of Rare Earths’, eds. K. A. Gschneider, Jr, and L. Eyring, Elsevier, Amsterdam, NY, 1984, Vol. 6, p. 335.
7. D. Emin, T. Aselage, C. L. Beckel, I. A. Howard, and C. Wood eds, ‘Boron-rich Solids, Am. Inst. Phys. Conf. Proc. No. 140’, American Institute Physics, New York, 1986, p. 1.
8. P. Rogl, Existence and Crystal Chemistry of Borides, in ‘Inorganic Reactions and Methods’, eds. J. J. Zuckerman and A. P. Hagen, VCH Publishers, New York, 1991, Vol. 13, p. 85.
9. J. Etourneau, Borides with Three-Dimensional Boron Networks, in ‘Inorganic Reactions and Methods’, eds. J. J. Zuckerman and A. P. Hagen, VCH Publishers, New York, 1991, Vol. 13, p. 167.
10. T. Lundström, Solid Solution of Transition and Inner Transition Metals in Boron, in ‘Inorganic Reactions and Methods’, eds. J. J. Zuckerman and A. P. Hagen, VCH Publishers, New York, Vol. 13, 1991, p. 196.
11. P. Villars, A. Prince, and H. Okamoto, ‘Handbook of Ternary Alloy Phase Diagrams’, ASM International, Materials Park, IH, 1995, Vol. 1–10.
12. D. Emin, T. L. Aselage, A. C. Switendick, B. Morosin and C. L. Beckel, eds., ‘Boron-Rich Solids’, AIP Conference Proc. No 231, American Institute Physics, New York 1991, p. 1.
13. R. Uno and I. Higashi, eds, Proceedings of the 11th International Symposium on Boron, Borides and Related Compounds, *Jap. J. Appl. Physics*, Series No. 10, Tokyo, 1994, 1.
14. P. Rogl, guest ed., Proceedings of the 12th International Symposium on Boron, Borides and Related Compounds, San Diego, CA, USA, Special issue; *J. Solid State Chem.*, 1997, **133**(1), 1.
15. J. Bauer and J.-F. Halet, guest eds, Proceedings of the 13th International Symposium on Boron, Borides and Related Compounds, San Diego, CA, USA, Special issue; *J. Solid State Chem*. 2000, **154**(1), 1.
16. V. N. Gurin and M. M. Korsukova guest eds, Proceedings of the 14th International Symposium on Boron, Borides, and Related Compounds, San Diego, CA, USA, Special issue; *J. Solid State Chem.*, 2004, **177**, No. 2, 381.
17. L. Kaufman, B. Uhrenius, D. Birnie, and K. Taylor, *CALPHAD*, 1984, **8**, 25.
18. M. Vlasse, R. Naslain, J. S. Kasper, and K. Ploog, *J. Solid State Chem.*, 1979, **28**, 289.
19. J. Bauer, G. Boucekkine, G. Frapper, J.-F. Halet, J.-Y. Saillard, and B. Zouchoune, *J. Solid State Chem.*, 1997, **133**, 190.
20. E. Tominez, E. Alleno, P. Berger, M. Bohn, C. Mazumbar, and C. Godard, *J. Solid State Chem.*, 2000, **154**, 114.
21. B. Morosin, A. W. Mullendore, D. Emin, and G. A. Slack, Rhombohedral Crystal Structure of Compounds Containing Boron-Rich Icosahedra, in ‘Boron-rich Solids’, *Am. Inst. Phys. Conf. Proc.* No. 140, eds. D. Emin, T. Aselage, C. L. Beckel, I. A. Howard, and C. Wood, American Institute Physics, New York, 1985, p. 70.
22. G. A. Slack, C. I. Hejna, M. F. Garbauskas, and J. S. Kasper, *J. Solid State Chem.*, 1988, **76**, 52.
23. T. Lundström, and H. Bolmgren, On Refractory Boron Compounds Crystallizing in B_4C-type Structures, in Proceeding of the 11th International Symposium on Boron, Borides and Related Compounds *Jap. J. Appl. Physics*, Series No. 10, eds. R. Uno and I. Higashi, Tokyo, 1994, 1.
24. T. Lundström, *Arkiv Kemi.*, 1969, **31**, 227.
25. J. Nagamatsu, N. Nakagawa, T. Muranaka, Y. Zenitani, and J. Akimitsu, *Nature*, 2001, **410**, 63.
26. R. Mattes, K.-F. Tebbe, H. Neidhard, and H. Rethfeld, *Z. Anorg. Allgem. Chem.*, 1975, **413**, 1.
27. M. Vlasse, G. A. Slack, M. Garbauskas, J. S. Kasper, and J. C. Viala, *J. Solid State Chem.*, 1986, **63**, 31.
28. B. Albert and K. Hofmann, *Z. Anorg. Allgem Chem.*, 1999, **625**, 709.
29. I. Higashi, *J. Solid State Chem.*, 2000, **154**, 168.
30. B. Albert, K. Hofmann, C. Fild, H. Eckert, M. Schleifer, and R. Gruehn, *Chem. Eur. J.*, 2000, **6**, 2531.
31. T. Tanaka, S. Okada, and V. N. Gurin, *J. Alloys Compd.*, 1998, **267**, 211.
32. T. Tanaka, S. Okada, Y. Yu, and Y. Ishizawa, *J. Solid State Chem.*, 1997, **133**, 122.
33. T. Tanaka, S. Okada, and Y. Ishizawa, *J. Alloys Compd.*, 1994, **205**, 281.
34. I. Higashi, T. Tanaka, K. Kobayashi, Y. Ishizawa, and M. Takami, *J. Solid State Chem.*, 1997, **133**, 11.
35. J. Etourneau, P. Peshev, and H. Pastor, Preparation of Borides, in ‘Inorganic Reactions and Methods’, eds. J. J. Zuckerman, and A. P. Hagen, VCH Publishers, New York, 1991, Vol. 13, p. 202.
36. T. Tanaka, Y. Ishizawa, J. Wong, Z. U. Rek, M. Rowen, F. Schäfers, and B. R. Muller, Development of a YB_{66} Soft X-ray Monochromator for Synchrotron Radiation, in Proceeding of the 11th International Symposium on Boron, Borides and Related Compounds, *Jap. J. Appl. Physics*, Series No. 10, eds. R. Uno and I. Higashi, Tokyo, 1994, 110.
37. T. Lundström, *J. Less-common Met.*, 1984, **100**, 215.
38. D. L. Johnson, B. N. Harmon, and S. H. Liu, *J. Chem. Phys.*, 1980, **73**, 1898.
39. A. F. Guillermet and G. Grimvall, *J. Less-Common Met.*, 1991, **169**, 257.
40. A. C. Switendick, Electronic Structure and Charge Density of Zirconium Diboride, in ‘Boron-rich Solids’, eds. D. Emin,

T. L. Aselage, A. C. Switendick, B. Morosin, and C. L. Beckel, American Institute Physics, New York, 1991, p. 54. AIP Conference Proc. **No 231**, pp.

41. N. I. Medvedeva, A. L. Ivanovskij, J. E. Medvedeva, and A. J. Freeman, *Phys. Rev.*, 2001, **B64**, 020202(5 pages).
42. A. Hasegawa and A. Yanase, *J. Phys. F: Metal Phys.*, 1977, **7**, 1245.
43. S.-L. Drechsler, H. Rosner, S. V. Shulga, and H. Eschrig, Superconducting Transition Metal Borocarbides, in 'Proc. NATO Adv. Study Inst. on High-T_c Superconductors and Related Materials', ed. S.-L. Drechsler, T. Mishonov, Kluwer, Holland, 2001, p. 167.
44. V. V. Pokropivny, V. V. Skorokhod, G. S. Oleinik, A. V. Kurdyumov, T. S. Bartnitskaya, A. V. Pokropivny, A. G. Sisonyuk, and D. M. Sheichenko, *J. Solid State Chem.*, 2000, **154**, 214.
45. G. V. Samsonov and I. M. Vinitskii, 'Handbook of Refractory Compounds', IFI/Plenum, New York, 1980, p. 1.
46. H. Werheit, Boron and Boron-Rich Compounds, in 'Electric Refractory Materials', ed. Y. Kumashiro, Marcel Dekker, New York, 2000, p. 589.
47. M. B. Maple, in 'Boron-rich Solids', AIP Conference Proc. No 231, eds. D. Emin, T. L. Aselage, A. C. Switendick, B. Morosin, and C. L. Beckel, American Institute Physics, New York, 1991, p. 165.
48. P. Ravindran, P. Vajeeston, R. Vidya, A. Kjekshus, and H. Fjellvåg, *Phys. Rev.*, 2001, **B64**, 224509 (15 pages).
49. J. F. Herbst, R. W. Lee, and F. E. Pinkerton, *Annu. Rev. Mater. Sci.*, 1986, **16**, 467.
50. K. A. Schwetz, B_4C, BN and Metal Borides, in 'Ullmann's Encyclopedia of Industrial Chemistry', 6th edn., Wiley-VCH, 2003, Vol. 5, p. 497.
51. C. Mitterer, *J. Solid State Chem.*, 1997, **133**, 279.
52. Th. Jüngling, L. S. Sigl, R. Oberacker, F. Thümmler, and K. A. Schwetz, *Int. J. Refractory Met. Hard Mater*, 1993–94, **12**, 71.
53. K.-I. Takagi and Y. Yamasaki, *J. Solid State Chem.*, 2000, **154**, 263.
54. F. Thevenot, *J. Eur. Ceram. Soc.*, 1990, **6**, 205.
55. O. A. Golikova, *Phys. Stat. Sol.*, 1987, **101a**, 277.
56. H. Werheit, *Prog. Cryst. Growth Charact.*, 1988, **16**, 179.
57. H. Werheit, *Mater. Sci. Eng.*, 1995, **B29**, 228.
58. M. M. Korsukova and V. N. Gurin, Single Crystals of Lanthanum Hexaboride: Their Preparation, Properties and Prospective Uses, in 'Current Topics in Materials Science', ed. E. Kaldis, Elsevier Science, New York, 1984, Vol. 11, p. 389.

Boron Hydrides

Narayan S. Hosmane[1] **& John A. Maguire**[2]

[1]*Northern Illinois University, Dekalb, IL, USA*
[2]*Southern Methodist University, Dallas, TX, USA*

Based in part on the article Boron Hydrides by James T. Spencer which appeared in the Encyclopedia of Inorganic Chemistry, First Edition.

1 Introduction 1
2 Nomenclature 3
3 Syntheses 3
4 Reactions 4
5 Related Articles 4
6 References 5

1 INTRODUCTION

Boranes are mixed hydrides of boron and hydrogen.[1] The unusual properties of these compounds arise from the fact that in forming compounds, boron can furnish four orbitals (s, p_x, p_y, p_z) but only three electrons for bonding. Since the number of orbitals exceeds the number of electrons, the boranes are sometimes referred to as 'electron-deficient' compounds. The consequence of this imbalance can be seen in comparing the two simple hydrides of carbon and boron, that is, ethane (C_2H_6) and diborane (B_2H_6), using valence bond formalism. Their Lewis diagrams are shown in Figure 1. The structure of ethane can be understood in terms of seven two-electron-two-center bonds (*2e–2c*) formed between adjacent atoms. However, such a description is not possible for diborane, since there are not enough electrons. The bonding description that is depicted in Figure 1 shows the molecule as consisting of two BH_2 units, in which the two hydrogens (the terminal hydrogens) are attached by *2e–2c* bonds, with the BH_2 units joined by two B–H–B *3c–2e* bridged bonds. Although the bonding can better be understood using molecular orbital theory, the above description does introduce some common descriptive terms, that is, multicentered bonds and bridged and terminal hydrogens. Figure 2 shows the structures of diborane and some higher boranes.

The structures are drawn as polyhedra composed of fused triangular faces (deltahedra), in which boron atoms, bonded to at least one terminal hydrogen, occupy the vertices; bridge hydrogens are shown for the *nido*-complexes.[1] For example, B_5H_9 (pentaborane(9)) has five boron atoms at the vertices of a square pyramidal cage, each one of which is bonded to an *exo*-polyhedral hydrogen (a terminal hydrogen). In addition, there are four hydrogens bridging adjacent borons on the rectangular open face. Note that the lines drawn in the structures show connectivity and do not necessarily indicate *2c–2e* bonds.

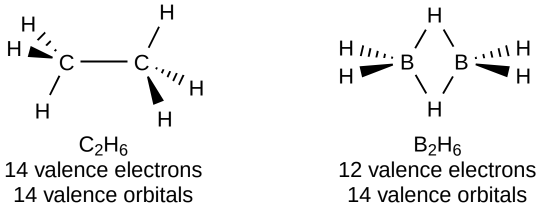

Figure 1 Comparison of ethane and diborane

A useful molecular orbital description can be developed by considering each boron atom to be *sp* hybridized with one *sp* hybrid pointed toward the center of the cage (radially oriented) and the other pointed directly toward its terminal hydrogen, with the two p orbitals oriented tangentially to the cage.[2,3] The outwardly oriented orbital could overlap with a hydrogen s orbital to form a *2c–2e* bond, using one electron from the boron and one from the hydrogen. The radially directed and the two tangentially directed orbitals on each boron can be combined to give the cage molecular orbitals. These molecular orbitals (MO) will be filled by the two electrons left on each boron, those from charges, plus one additional electron from each bridging hydrogen. For example $[B_6H_6]^{2-}$, which has a closed (*closo-*) octahedral structure, will have 18 boron based orbitals (AO) for cage bonding and 14 ($2 \times 6 + 2$) cage electrons. The 18 AOs will yield 18 MOs, 7 of which are bonding and 11 antibonding. The 14-cage electrons are enough to fill the bonding MOs for a stable structure. In general, a closed polyhedral cage, composed of fused deltahedra, with n vertices will have $3n$ AOs for cage bonding that give rise to $n + 1$ bonding MOs and $2n - 1$ antibonding MOs.[2–4] Therefore, such structures should be stabilized by $2n + 2$ cage electrons. Inspection of Figure 2 shows this to be the case. Analysis also shows that the addition of two electrons to *closo*-$[B_6H_6]^{2-}$ causes the cage to open, giving the pentagonal pyramidal *nido*-$[B_6H_6]^{4-}$ cage (which can pick up four bridge hydrogens). Considering only the fate of the cages, the $[B_6H_6]^{4-}$ has 16 cage electrons that fill 8 ($n + 2$) bonding MOs. Note that one could obtain this pentagonal pyramidal cage by removing a single vertex from a seven vertex *closo*-cage (the *closo*-$[B_7H_7]^{2-}$ shown in Figure 2). This brings up a very important relationship: removal of one or more vertices from a *closo*-cage does not change the number of bonding MOs.[4] This forms the basis of the polyhedral electron-counting rules (Wades rules). Table 1 summarizes these rules and Figure 3 shows the progression of several important structural types from *closo* (closed) to *nido* (nest-like) to *arachno* (spiderweb-type).[5] Further removal would lead to more open structures (*hypo, fisco, reticulo*).

Other hybridization schemes could be used; as long as they result in one radially directed and two tangential orbitals

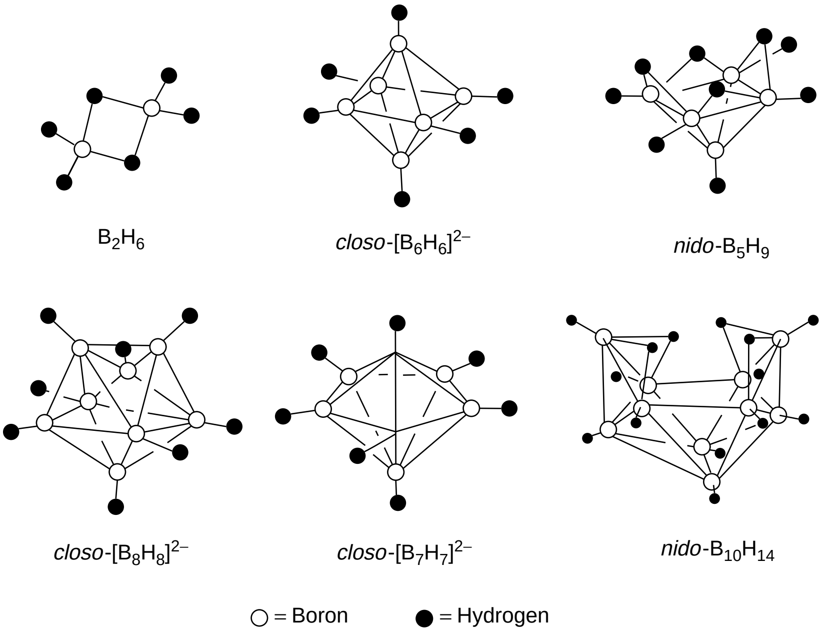

Figure 2 Borane structures

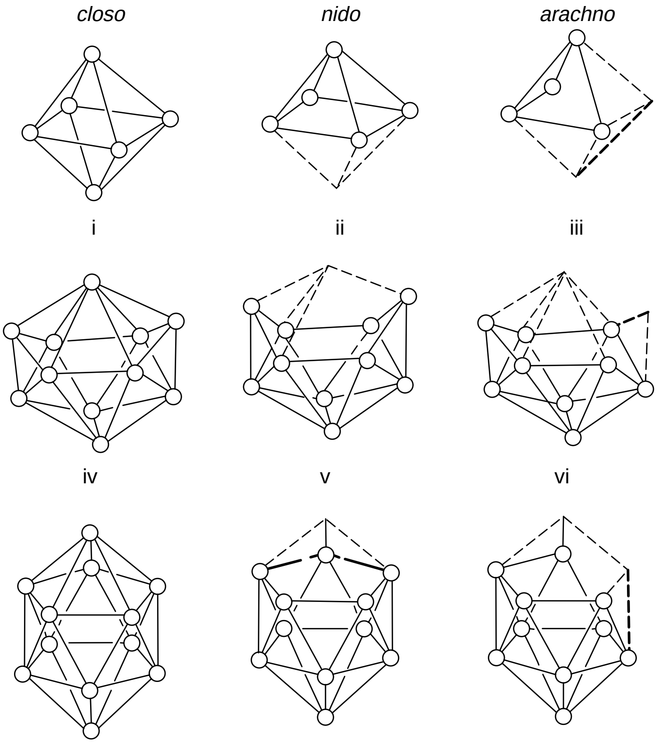

Figure 3 Cage structures

for cage bonding, they would give the same result. The utility of these rules can be extended by noting that the terminal hydrogens could be replaced by any atom or group that forms a single bond (halogen, CH_3, NH_2, etc.) without changing any structural particulars. Also, the replacement of a BH vertex by any group that can furnish a radially directed and two tangentially directed orbitals for cage bonding (i.e. is isolobal with BH), and contribute two electrons, should not substantially change cage geometry. The same would be true when a BH^- is replaced by a three-orbital, three electron group. This leads to a series of mixed atom cages, called *heteroboranes*.[2] When the hetero-atom is a metal, the term metallaborane is used. One of the most important such heteroboranes are those in which two CH groups replace BH^- vertices in a *closo*-$[B_nH_n]^{2-}$ cage to give a neutral *closo*-$[C_2B_{n-2}H_n]$ cage. Since the neutral dicarbaboranes (carboranes) are more stable and easier to work with than are their borane analogues, more studies have been conducted on carboranes than on the parent boranes.[6,7] In general, all the main group elements, with the appropriate substituents, can be thought of as being isolobal with boron. Therefore, the electron-counting rules can be applied to other main group elements by using a formalism in which the particular cage element, X, brings to cage bonding its valence electrons (v), plus those from other ligands attached to it (x), less the two associated with *exo*-polyhedral interactions or $(v + x - 2)$ electrons, as listed in Table 2. A number of heteroboranes, and carboranes incorporating other main group elements have been characterized.[7] Electron-counting rules can be extended to transition metal substitution by assuming that the metal group will have 12 of its $v + x$ electrons not involved in cage bonding; Table 3 gives the electron contributions for the groups 6 through 10 metals.[8,9] Using these numbers and the rules from Table 1, the

Table 1 Wade's rules

	Structural type					
	Closo	Nido	arachno	hypo	fisco	reticulo
Occupied vertices	N	n	N	n	n	n
Skeletal electron pairs	$n+1$	$n+2$	$n+3$	$n+4$	$n+5$	$n+6$

Table 2 Skeletal electron contributions of main group cluster units $(v + x - 2)^a$

		Cluster unit		
Group number	Element	M ($x = 0$)	MR ($x = 1$)	MR_2 or M–L ($x = 2$)
1	Li, Na	–	0	1
2	Be, Mg, Zn, Cd	0	1	2
13	B, Al, Ga, In, Tl	1	2	3
14	C, Si, Ge, Sn, Pb	2	3	4
15	N, P, As, Sb, Bi	3	4	–
16	O, S, Se, Te	4	5	–

[a] v = No. valence electrons on M; x = No. electrons from ligands on M; R = one-electron ligand or H; L = two-electron ligand.

structures of a number of different heteroboranes can be rationalized. Examples of some heteroboranes are given in Figure 4.

2 NOMENCLATURE

The IUPAC nomenclature of the heteroboranes takes the name of the unsubstituted borane as the parent, with the number of hydrogens given in parentheses, that is, B_5H_9 is pentaborane(9).**[10]** The cage geometry is specified using the prefixes *closo* for a closed polyhedron, *nido* when one vertex is missing, *arachno*- when two vertices are removed, and so on, and the prefix *conjuncto*- when two cages are joined by one or more B–B bonds. The cage numbering begins with the apex atom of the polyhedron as '1' and the successive belts of atoms are numbered in a clockwise fashion.**[10,11]** When possible, preference is given to the nonboron atoms by assigning them the lowest numbers. When there is no unique apical atom, the atom with the lowest coordination number is assigned the position '1'. This numbering system, along with the standard replacement nomenclature rules taken from organic chemistry, are used in naming the heteroboranes. This can lead to names that are as impressive as the formulas. For example, in Figure 4, *closo*-2,3-(CH_3)-1,2,3-$SnC_2B_9H_9$ is 2,3-dimethyl-1-stanna-2,3-dicarba-*closo*-dodecaborane(12), *closo*-1-(CH_3)-1,2,3-$GaC_2B_4H_6$ is 1-methyl-1-galla-2,3-dicarba-*closo*-heptaborane(7), while *arachno*-$[B_9H_{13}]^{2-}$ is tridecahydro-*arachno*-nonaborate(2−). More times than not, formal names are avoided in preference to formulas.

3 SYNTHESES

The heteroboranes are derived ultimately from boranes, which, in turn, can be built up from lower molecular weight boron hydrides, the simplest of which is diborane, B_2H_6. There are a number of industrial processes described for the synthesis of diborane, most involving the reduction of boron trihalides with metal hydrides, as shown in equation (1). Other methods involve the reduction of trihaloboranes with group 1

$$2BF_3(g) + 6NaH(s) \xrightarrow{180^\circ} B_2H_6(g) + 6NaCl(s) \qquad (1)$$

hydroborates or the reduction of alkylborate esters with alkali metal hydrides.**[12]** Small amounts of diborane can be obtained by the reaction of alkali metal borohydrides with I_2 (equation 2) or an

$$2NaBH_4 + I_2 \xrightarrow{\text{diglyme}} B_2H_6 + 2NaI + H_2 \qquad (2)$$

Table 3 Skeletal electron contributions of d-block metal groups $(v + x - 12)$

			Metal group		
Group number v	Metals (M)	$ML_2{}^a$ ($x = 4$)	$M(\eta^5\text{-}C_5R_5)$ ($x = 5$)	ML_3 ($x = 6$)	ML_4 ($x = 8$)
6	Cr, Mo, W	–	−1	0	2
7	Mn, Tc, Re	−1	0	1	3
8	Fe, Ru, Os	0	1	2	4
9	Co, Rh, Ir	1	2	3	5
10	Ni, Pd, Pt	2	3	4	–

[a] L = a two-electron donor ligand.

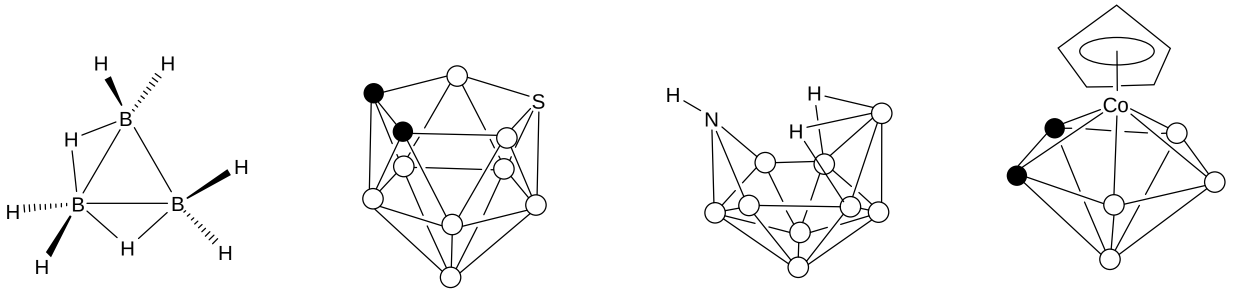

arachno-$[B_3H_8]^-$
6 skeletal pairs
n + 3

nido-7,9,10-$SC_2B_8H_{10}$
13 skeletal pairs
n + 2

nido-6-NB_9H_{12}
12 skeletal pairs
n + 2

closo-1-(η^5-C_5H_5)-1,2,3-$CoC_2B_4H_4$
8 skeletal electron pairs
n + 1

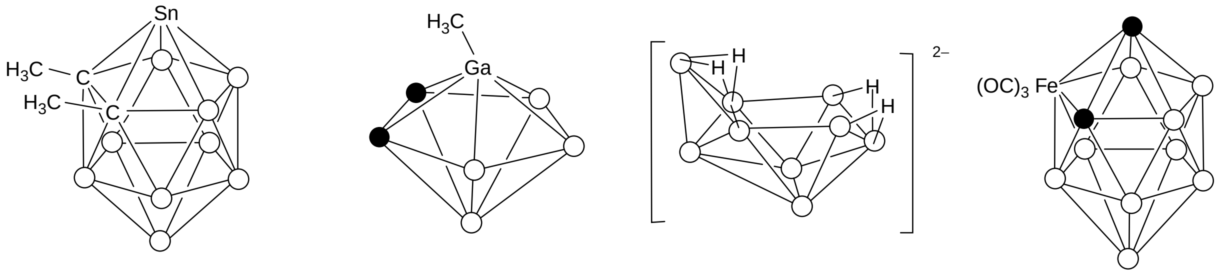

closo-2,3-$(CH_3)_2$-1,2,3-$SnC_2B_9H_9$
13 skeletal pairs
n + 1

closo-1-(CH_3)-1,2,3-$GaC_2B_4H_6$
8 skeletal pairs
n + 1

arachno-$[B_9H_{13}]^{2-}$
12 skeletal pairs
n + 3

closo-1,1,1-$(CO)_3$-1,2,3-$C_2B_9H_{11}$
13 skeletal pairs
n + 1

● = CH ○ = BH

Figure 4 Some boranes and heteroboranes

$$2KBH_4(s) + 2H_3PO_4(l) \longrightarrow B_2H_6(g) + 2NaH_2PO_4(s) + 2H_2(g) \tag{3}$$

$$2M[BH_4] + 2BX_3 \longrightarrow B_2H_6 + 2M[HBX_3] \tag{4}$$

anhydrous acid (equation 3).[13] Hydride abstraction from $[BH_4]^-$ by BX_3 (equation (4)) has also been described. It should be stressed that diborane is an extremely toxic, flammable, and explosively reactive gas that should be handled with extreme care. The controlled pyrolysis of B_2H_6 yields higher boranes plus H_2, culminating in decaborane(14) ($B_{10}H_{14}$), which is quite stable. Hydride ion abstraction reactions of lower molecular mass hydroborates by BX_3 has also produced a number of neutral boranes in good yields.[14] Other methods that target specific boranes, such as B_5H_9 and $B_{10}H_{14}$, have also been described.[15]

4 REACTIONS

The syntheses of the heteroboranes often involves the addition of heteromolecules to *nido*-boranes, in so called cage expansion reactions.[7,16,17] Two of the most used borane precursors are pentaborane(9) (*nido*-B_5H_9) and decaborane(14) (*nido*-$B_{10}H_{14}$); both of which are shown in Figure 2. These boranes react with acetylenes ($RC{\equiv}CR'$) to give, respectively, *nido*-2-R-3-R′-2,3-$C_2B_4H_6$ and *closo*-1-R-2-R′-1,2-$C_2B_{10}H_{10}$.[18] The *closo*-C_2B_{10} carboranes can be degraded to give *nido*-7-R-8-R′-7,8-$C_2B_9H_{11}$ cages or reduced directly to give the corresponding *nido*-7-R-8-R′-7,8-$C_2B_{10}H_{12}$. These *nido*-carboranes have two bridged hydrogens that can be removed to give the more reactive dianions that undergo metallation reactions and are used as ligands that closely resemble cyclopentadienide ($[C_5H_5]^-$) in their bonding interactions. A number of main group,[7,17] transition metal[6] and rare earth[19] metallacarboranes of these and other carboranes have been reported and studied.

In the last 50 years, there has been a wealth of fascinating chemistry published on the boranes and heteroboranes.[1] Their unique structures have forced us to rethink our ideas on bonding and they have proven to be invaluable reagents in other areas of chemistry.[20]

5 RELATED ARTICLES

Boron: Inorganic Chemistry; Boron: Metallacarbaboranes; Boron–Nitrogen Compounds; Boron: Organoboranes; Boron: Polyhedral Carboranes.

6 REFERENCES

1. (a) G. Wilkerson and F. G. A. Stone eds, ‘Comprehensive Organometallic Chemistry’, Pergamon Press, Oxford, 1982, Vol. 1; (b) E. W. Abel, F. G. A. Stone, and G. Wilkerson eds, ‘Comprehensive Organometallic Chemistry’, Pergamon Press, Oxford, 1995, Vol. 1.
2. M. E. O’Neill and K. Wade, in ‘Comprehensive Organometallic Chemistry’, eds. G. Wilsinson and F. G. A. Stone, Pergamon Press, Oxford, 1982, Vol. 1, Chap. 1.
3. G. A. Olah, K. Wade, and R. E., Williams eds, ‘Electron-Deficient Boron and Carbon Clusters’, Wiley, New York, 1991, Chaps. 1–3, and references therein.
4. T. P. Fehlner and C. E. Huosecroft, in ‘Molecular Structure and Energetics’, eds. J. F. Liebman and A. Greenberg, VCH Publishers Deerfield, Florida, FL, 1986, Vol. 1, Chap. 6.
5. R. W. Rudolph, *Acc. Chem. Res.*, 1976, **9**, 446.
6. R. N. Grimes, in ‘Comprehensive Organometallic Chemistry (II)’, eds. E. W. Abel, F. G. A. Stone, and G. Wilkerson, Pergamon Press, Oxford, 1995, Vol. 1, Chap. 5.
7. A. K. Saxena, J. A. Maguire, and N. S. Hosmane, *Chem. Rev.*, 1997, **97**, 2421.
8. D. M. P. Mingos and D. J. Wales, ‘Introduction to Cluster Chemistry’, Prentice Hall, Englewood Cliffs, NJ, 1990.
9. D. M. P. Mingos, in ‘Inorganometallic Chemistry’, ed. T. P. Fehlner, Plenum, New York, 1992, Chap. 4.
10. R. N. Adams, *Pure Appl. Chem.*, 1972, **30**, 683.
11. (a) J. B. Casey, W. J. Evans, and W. H. Powell, *Inorg. Chem.*, 1981, **20**, 1333; (b) J. B. Casey, W. J. Evans, and W. H. Powell, *Inorg. Chem.*, 1981, **20**, 3556.
12. R. L. Hughes, I. C. Smith, and E. W. Lawless, ‘Production of the Boranes and Related Research’, Academic Press, New York, 1967, Chap. III.
13. N. N. Greenwood and A. Earnshaw, ‘Chemistry of the Elements’, Pergamon Press, London, 1984, Chap. 6.
14. M. A. Toft, J. B. Leach, F. L. Himpsl, and S. G. Shore, *Inorg. Chem.*, 1982, **21**, 1952.
15. L. A. Adams, N. S. Hosmane, J. E. Eklund, J. Wang, and N. S. Hosmane, *J. Am. Chem. Soc.*, 2002, **124**, 7292.
16. (a) T. Onak, in ‘Comprehensive Organometallic Chemistry’, eds. G. Wilkerson and F. G. A. Stone, Pergamon Press, Oxford, 1982, Vol. 1, Chap. 5.4; (b) Onak, T. in ‘Comprehensive Organometallic Chemistry’, eds. E. W. Abel, F. G. A. Stone, and G. Wilkerson, Pergamon Press, Oxford, 1995, Vol. 1, Chap. 6.
17. (a) K. Vyakaranam, J. A. Maguire, and N. S. Hosmane, *J. Organomet. Chem.*, 2002, **646**, 21; (b) G. Rana, J. A. Maguire, S. N. Hosmane, and N. S. Hosmane, *Main Group Met. Chem.*, 2000, **23**, 529.
18. R. N. Grimes, ‘Carboranes’, Academic Press, New York, 1970.
19. Z. Xie, *Coord. Chem. Rev.*, 2002, **231**, 23.
20. H. C. Brown, ‘Organic Synthesis via Boranes’, Wiley, New York, 1975; (b) H. C. Brown and P. V. Ramachandran, in ‘Advances in Boron Chemistry’, ed. W. Seibert, Royal Society of Chemistry, Cambridge, 1997, p. 151.

Acknowledgments

We thank the National Science Foundation and the Robert A. Welch Foundation for their continuous support of authors’ research in the area of Boranes and Carboranes.

Boron: Inorganic Chemistry

David M. Schubert & Robert J. Brotherton
U.S. Borax Inc., Valencia, CA, USA

1 Introduction 1
2 Elemental Boron and Refractory Boron Compounds 2
3 Boric Oxides, Boric Acids, and Metal Borates 6
4 Metal Borates 10
5 Nonmetal Borates 15
6 Boric Acid Esters 16
7 Boron–Sulfur Compounds 19
8 Boron–Phosphorus Compounds 20
9 Boron-halogen Compounds 21
10 Related Articles 23
11 Further Reading 23
12 References 23

1 INTRODUCTION

The fifth element in the periodic table, boron, is usually grouped with the nonmetallic elements but has some metallic properties and is sometimes labeled a metalloid. Unlike the other group 13 elements, it is a semiconductor rather than a metallic conductor. Boron is unique among the elements and is notable for exhibiting unusual chemistry in all of its compounds. Although distinctive, the chemistry of boron is more similar to that of silicon and carbon than to the metallic group 13 elements. The electronic structure of boron, $1s^2 2s^2 2p^1$, suggests that it should form univalent compounds, but this is rarely the case and such compounds are difficult to prepare and isolate. Rather, boron utilizes all three of its valence electrons to form compounds having sp^2 hybridized boron of the type BR_3, where R can be halogen, alkyl, alkoxy, and so on, or compounds containing electron deficient multicenter bonds, as found in the boron hydrides. The formation of three covalent bonds provides more than enough energy to offset the cost of converting to the sp^2 hybrid state. Compounds of the BR_3 type are trigonal planar six electron molecules having an empty or partially occupied $2p_z$ orbital. Thus, they exhibit a tendency to react with electron donor species to form tetrahedral complexes complying with the octet rule. For this reason, boron is often called electron deficient.

The Lewis acid character of many boron compounds and the ability of boron to participate in multicenter bonds lead to a vast and complex chemistry. Boron exclusively forms covalent bonds in an immense variety of compounds, often participating in rings, cages, clusters, and networks. It forms strong covalent bonds with electronegative elements, most notably with oxygen; only fluorine forms a stronger bond to boron. Much of boron chemistry can be considered to be iono-covalent in that boron is found covalently bound in many complex anions that in turn form salts with cationic species.

Naturally occurring boron is widely distributed in the environment. With the exception of a few rare boron fluoride minerals, only boron–oxygen compounds are found in nature. Boron has also been identified in space and in the sun and other stars. At a concentration of only 0.001% of the earth's crust, boron is a relatively uncommon element. However, in the form of borate minerals, the element is found universally in rocks and soils, and also occurs at measurable levels in nearly all natural waters. Boron is typically found in rocks and soils at levels of a few $\mu g\, g^{-1}$, although concentrations vary widely. Ocean waters contain approximately $4.6\, \mu g\, g^{-1}$; freshwater lakes and rivers usually have much lower concentration, near $0.1\, \mu g\, g^{-1}$, but can contain significantly higher levels in regions of higher boron geologies.[1] Although boron is widely distributed in the earth's crust, borate ore deposits of sufficient concentration for profitable mining are relatively rare. These deposits are mainly found in arid regions of the world having a history of volcanism and hydrothermal activity.[2]

Boron has been recognized as an essential element for plants since the 1920s.[3] All plants contain measurable levels of boron, and boron deficiency is considered to be one of the most prevalent agricultural micronutrient deficiency problems in the world.[4] In areas of low soil concentrations of boron, it is standard agricultural practice to correct this deficiency by adding boron to the soil, typically using borates mixed with other required fertilizers. Considerable progress has been made in recent years in understanding the biological role of boron in plants. In particular, boron was shown to play an essential role in plant cell wall functions through ester crosslinking with complex carbohydrates (see Section 6.4).[5] Boron concentrations in plants and plant-derived foodstuff typically fall in the $0.1–64\, \mu g\, g^{-1}$ range.[6,7] There is now considerable evidence indicating that boron is also essential to animals and humans.[8,9] Consumption of plants by herbivorous animals introduces boron into the overall food chain, and animals and humans inevitably contain low concentrations of boron. For example, human blood contains boron concentrations of approximately $0.01–0.17\, \mu g\, mL^{-1}$ and urine contains $0.15–2.98\, \mu g\, mL^{-1}$.[7] Body tissues have boron concentrations comparable to those in blood, and bone may contain somewhat higher levels. Essentially, all boron ingested is excreted in the urine within about 24 h. It has been estimated that an adult in the United States consumes approximately 1 mg boron per day. Boron consumption by healthy populations in other parts of the world may be considerably higher depending on regional diets.[10]

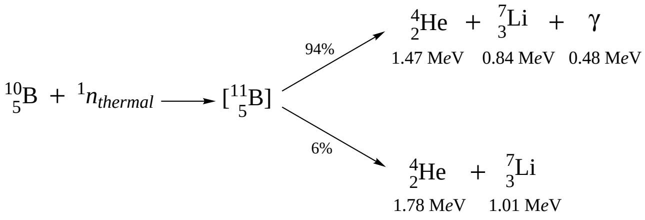

$^{10}_{5}\text{B} + {}^{1}n_{thermal} \longrightarrow [^{11}_{5}\text{B}]$
94%
$^{4}_{2}\text{He} + {}^{7}_{3}\text{Li} + \gamma$
1.47 M*e*V 0.84 M*e*V 0.48 M*e*V
6%
$^{4}_{2}\text{He} + {}^{7}_{3}\text{Li}$
1.78 M*e*V 1.01 M*e*V

Scheme 1

Boron has an atomic weight of 10.81, representing a mixture of about 20% of the ^{10}B isotope and 80% of the ^{11}B isotope. The observed isotope ratio, and thus the average atomic weight, varies slightly from these values depending on the geographical source of the boron. Data on this subject are summarized.**[11]** Other boron isotopes such as ^{8}B, ^{12}B, and ^{13}B are unstable with half-lives of less than a second. The ^{10}B isotope is unique among the light nuclides in having an unusually high-capture cross-section for low-energy thermal neutrons ($3.8 \times 10^{-25}\,\text{m}^2$, 0.02–0.05 *e*V neutron). This reaction yields recoiling α particles and ^{7}Li nuclei with a total energy release of 2.28 M*e*V, as shown in Scheme 1. The primary reaction pathway also yields a 0.48 M*e*V γ-ray, which is exploited in the analytical method for boron determination known as prompt gamma activation analysis. The nuclear chemistry of ^{10}B provides the basis for the experimental treatment for cancers and other diseases known as boron neutron capture therapy, or BNCT.**[12]** This method involves localizing ^{10}B-enriched compounds at tumor cells followed by irradiation with a relatively nondestructive thermal neutron beam. The resulting α particles and ^{7}Li nuclei travel only about one cell diameter but have a high lethality for cells they enter. The BNCT concept has led to extensive research on the design of chemistries for the selective delivery of ^{10}B-containing compounds to tumor and other diseased cells.**[12]** By far, the largest application for the boron neutron capture reaction involves the use by the nuclear industry of unenriched boron compounds, typically boric acid, in neutron radiation shielding.

This article covers only a part of the chemistry of boron. Boron–carbon compounds are covered in other articles in this volume (*see* ***Boron: Organoboranes***; ***Boron: Metallacarbaboranes***, and ***Boron: Polyhedral Carboranes***). The main subject of the latter two articles, and the separate one on ***Boron Hydrides*** is the extensive chemistry of the multicenter bonded boron-hydride systems. This area has been a major focus of boron research for the past 60 years. There is some direct overlap between the two articles ***Borides: Solid-state Chemistry*** and ***Borates: Solid-state Chemistry***, and this more general one covering the inorganic chemistry of boron. ***Boron–Nitrogen Compounds*** are also covered separately. These articles should be consulted for more detailed discussions of the structure, bonding, and properties of borides, solid-state borates, and boron–nitrogen compounds. Several general reference volumes cover, in differing amounts of detail, most of the subjects included in this article.**[13–21]** Each section contains additional, more specific references.

2 ELEMENTAL BORON AND REFRACTORY BORON COMPOUNDS

2.1 Introduction

Elemental boron is a refractory material that is usually isolated either as a shiny black crystalline solid or a softer, browner, more impure amorphous solid. Reduction of readily available boron compounds containing boron–oxygen bonds to elemental boron is energy intensive and costly. This has limited the extent of commercial use of this material. Many related refractory boron compounds have been prepared and characterized including metal borides, boron carbides, boron nitrides, and various boron–metal alloys. These refractory materials and elemental boron are also discussed in some detail in the article ***Borides: Solid-state Chemistry***. Other general references are available on elemental boron and other refractory boron compounds.**[21–24]**

2.2 Elemental Boron

A preliminary description of the preparation of impure elemental boron was presented by Humphrey Davy, who stated in an address to the Royal Society in the fall of 1807 that reduction of moist boric acid with an electric current produced a ‘dark colored combustible matter.’**[25]** Further accounts of the isolation of impure elemental boron, by both electrolysis and reduction with potassium, were made the following year by Guy-Lussac and Thénard and also independently by Davy. A convenient preparation of higher purity boron was not described until 1892, when Moissan reported the preparation of 90–95% amorphous boron by reaction of magnesium with boric oxide. This process is still used in the commercial production of moderate quantities of the amorphous boron. Boron purer than 99% was subsequently obtained by remelting and recrystallizing amorphous boron and by thermal decomposition of boron trichloride in a hydrogen atmosphere. A crystalline product of approximately 95% purity can also be obtained by heating 90% amorphous boron with mixed fluorides at 950–1000 °C followed by heating in a vacuum to near-fusion temperatures. Further upgrading to 99.7–99.9% can be accomplished by recrystallization under vacuum. Thermal decomposition of boron hydrides can produce high-purity crystalline boron.

The principal commercial methods in use for production of elemental boron are the Moissan reduction of boric oxide with magnesium for 90% amorphous boron and thermal decomposition of boron trichloride in hydrogen for crystalline boron filaments. There are numerous small to moderate volume uses for elemental boron. Perhaps the most prominent is the use of boron filaments deposited on tungsten wire as reinforcements in plastics, such as epoxy resins, and metal composites, such as aluminum and titanium. These boron fiber-reinforced composites have an exceptional compressive strength and are used in aerospace applications and in sporting goods, including golf club shafts, tennis racket frames, and fishing rods. Elemental boron has also been used as a fuse to initiate release of nitrogen gas in automobile air bags by its rapid reaction with sodium azide.

Many forms of elemental boron have been reported in the literature. The presence of trace impurities can have major effects on the structure and properties of boron, in some cases leading to false identification of unique forms. Crystalline boron exists in at least three allotropic forms depending on the preparative method used. The structures of the α-rhombohedral, β-rhombohedral, and β-tetragonal allotropes have been defined by X-ray diffraction studies and shown to each incorporate B_{12} icosahedra in their structures. Similar icosahedral structures exist in boron carbide, boron phosphide, $B_{12}P_2$, and boron arsenide, $B_{12}As_2$, discussed below. Details of the structures of these allotropes can be found in ***Borides: Solid-state Chemistry***. The β-tetragonal allotrope, originally thought to consist of B_{12} icosahedra linked by B_2 units, now appears to be an impure boron phase with B_{12} icosahedra linked by C_2 or N_2 units.

Amorphous boron (>90%) melts at 2300 °C, sublimes at approximately 2550 °C, and has a density of $2.35\,\mathrm{g\,mL^{-1}}$. Crystalline α-rhombohedral boron melts at temperatures in the range 2180–2190 °C, sublimes at 3650–3660 °C, and has a density of $2.45\,\mathrm{g\,mL^{-1}}$. The crystalline forms are hard refractory materials with Moh's hardnesses in the range of 9–11, compared to 15 for diamond.

In general, both crystalline and amorphous boron are relatively inert materials with the amorphous form tending to react more readily with chemical reagents. Finely divided micron-sized amorphous boron can react violently with hydrogen, oxygen, and chlorine at elevated temperatures and with water above 100 °C. Crystalline boron can be dissolved in a hot 2:1 mixture of sulfuric and nitric acids, but is nearly inert toward oxygen, water, nitric acid, and sodium hydroxide.

2.3 Metal Borides

A large number of binary metal borides have been prepared and characterized. Their stoichiometries vary from M_5B to MB_{100}, but the most common are M_2B, MB, MB_2, MB_4, MB_6, and MB_{12}. The structures of metal borides vary from isolated boron atoms in borides from M_4B to M_2B, to chains of boron atoms in MB and M_3B_4, to two-dimensional networks of boron atoms in MB_2 and M_2B_5, to complex three-dimensional arrays of boron atoms in MB_4, MB_6, and MB_{12}. In general, metal borides exhibit characteristics of typical metals, for example, high electrical and thermal conductivity. Most of them have high melting points, high hardnesses, and good resistance to chemical attacks. The boron-rich metal borides, having compositions ranging from MB_6 to MB_{60} or greater, are among the hardest known substances.

Most borides are inert toward nonoxidizing acids, although Be_2B and MgB_2 react with aqueous acids to form boron hydrides. Oxidizing acids such as nitric or hot sulfuric dissolve most borides. Hot alkaline salt melts and fused alkali peroxides also dissolve borides to form the more stable borates. Borides are generally resistant to oxidation in dry air due to the formation of a protective oxide layer. Many borides do not oxidize in air below 1000–1400 °C.

More than one boride phase can be formed with most metals, and in many cases a continuous series of solid solutions may be formed. Several methods have been used for the relatively large-scale preparation of metal borides. One that is commonly used is carbon reduction of boric oxide and the appropriate metal oxide at temperatures up to 2000 °C. Fused salt electrolysis of borax or boric oxide and a metal oxide at 700–1000 °C have also been used. Small-scale methods available include direct reaction of the elements at temperatures above 1000 °C and the reaction of elemental boron with metal oxides at temperatures approaching 2000 °C. One commercial use of borides is in titanium boride–aluminum nitride crucibles or boats for evaporation of aluminum by resistance heating in the aluminizing process, and for rare earth hexaborides as electronic cathodes. Borides have also been used in sliding electrical contacts and as cathodes in Hall cells for aluminum processing.

The discovery that magnesium diboride, MgB_2, is a superconductor with a transition temperature of 39 K was first announced in 2001.**[26]** Although 39 K does not qualify magnesium diboride for the status of a high-temperature superconductor, it is a record high transition temperature for a relatively simple and inexpensive material. Magnesium diboride was well known for decades prior to this discovery, but prevailing theories of superconductivity did not predict this high transition temperature. Thus, this discovery resulted in a resurgence of interest in superconductivity and the possibility of developing a new class of low-cost high-performance superconductor materials.**[27]**

Magnesium diboride is a metallic compound having a structure in which boron atoms form hexagonal layers with magnesium atoms located between the layers above and below the centers of the boron hexagons. The unusual properties of this material are thought to result from strong interactions between lattice vibrations (phonons) and the electronic structure of the boron layers. It is proposed that the anomalous superconducting properties of magnesium diboride can be explained by the presence of two, rather than the usual one, superconducting energy gaps in this material.**[28]** These gaps correspond to transition temperatures of 15 K and 45 K, and combine to give an overall transition temperature of 39 K.

The tertiary alloy of composition $AlMgB_{14}$, referred to as 'BAM', has a hardness similar to industrial diamond. Since its discovery was reported in 1999, BAM has been the subject of intense research interest.[29] It is reported to be an excellent material for use in cutting tools. One unique property of this ultrahard substance is its ability to cut hot materials without becoming hot itself. It is also less reactive with steel than diamond is, and so can be used to cut both masonry and steel. Although still produced on a laboratory scale, current efforts are focused on developing methods for its manufacture on industrial scale. This has required development of improved methods for the preparation of high-purity low-oxygen content elemental boron, since oxygen impurity lowers the hardness of BAM by forming spinel, Al_2MgO_4. The use of BAM may eventually reduce energy consumption and other wear-related costs in industrial cutting and grinding operations.[30]

Another important application of metal borides is in permanent magnets. Metal–boron alloys such as neodymium iron boron, having a base composition of $Nd_2Fe_{14}B$, exhibit the highest energy product of any readily available magnetic material. Produced commercially since the early 1980s, rare earth magnets are used extensively in the manufacture of hard disc drives, high-performance electric motors, speakers, and instruments. These magnets are typically manufactured using a metallurgical process in which a powder of the appropriate alloy composition is first produced and then sintered into the desired shape for a given application.[31] A coating of protective material, such as nickel, is often applied to Nd–Fe–B magnets because they tend to be susceptible to oxidation.

2.4 Boron Carbide

Boron carbide is usually obtained in a form written empirically as B_4C to indicate the ratio of boron to carbon atoms. However, the actual stoichiometry can vary from this ratio of 20 atom % carbon in B_4C to $B_{10.4}C$ with only 8.8 atom % carbon. Boron carbide belongs to a family of solid solution compounds, including B_4Si, $B_{12}P_2$, $B_{12}As_2$, $B_{12}O_2$, $B_{12}S$, based on α-rhombohedral boron-containing various interstitial elements.[21–24] Boron carbide with B_4C stoichiometry was originally thought to exist as a rhombohedral structure consisting of B_{12} icosahedra joined by C_3 chains. Therefore, $B_{12}C_3$ would be a more descriptive formula. In this structure, which is similar to the rhombohedral crystalline forms of elemental boron, each polyhedral boron atom is bonded to five others in the same icosahedron, and to either a boron atom in an adjacent icosahedron, or to a carbon atom in one of the chains. However, studies indicate that this relatively simple structure is incorrect, and that the three chain positions and some of the icosahedral positions can be filled by boron or carbon atoms. X-ray, Raman, and electrical and thermal transport studies support a disordered structure for $B_{12}C_3$. These data indicate that boron carbides exist as single-phase materials from approximately 9–20 atom % carbon. At 20 atom % carbon, or $B_{12}C_3$, the structure is composed of $B_{11}C$ icosahedra linked by C–B–C chains. With decreasing carbon content from 20 to 13%, the C–B–C chains are progressively replaced by C–B–B chains, and below 13%, the $B_{11}C$ icosahedra are replaced by B_{12} icosahedra.

The properties of boron carbide are similar to elemental boron. It has a theoretical density of $2.52\,\mathrm{g\,mL^{-1}}$ and a melting point of approximately 2400 °C. Boron carbide has a high compressive strength, but its tensile strength is limited. Boron carbide is prepared commercially by the reduction of boric oxide with carbon in a hydrogen atmosphere in an electric furnace at 1400–2300 °C (equation 1). In a related reaction, magnesium is added to boric oxide in the presence of carbon black at 1400–1800 °C (equation 2), and magnesium-containing by-products are removed by acid treatment. Usually, boron carbide is converted to a granular form that can be molded or bonded into useful shapes. In order to achieve high strengths and high densities, boron carbide is hot pressed at 1800–2400 °C in graphite molds. Although it is brittle and sensitive to thermal shock, the exceptional hardness of boron carbide, with a Moh's hardness of approximately 10 compared to 15 for diamond, has resulted in moderate commercial usage in its hot-pressed form in ceramic armor plates, sandblasting nozzles, wear parts, and in dressing grinding wheels. Because of its radiation stability, chemical inertness, and the ability of boron to capture neutrons, boron carbide has also found use in radiation shielding and control devices in nuclear reactors.

$$2B_2O_3 + 7C \longrightarrow B_4C + 6CO \tag{1}$$

$$2B_2O_3 + 6Mg + C \longrightarrow B_4C + 6MgO \tag{2}$$

2.5 Boron Nitride

A review of boron nitride chemistry is available.[32] Boron nitride, BN, is a so-called III–V compound. It is isoelectronic with the carbon allotropes, diamond and graphite, and has several forms that, like these two forms of carbon, display very different properties. Hexagonal boron nitride (h-BN) has a graphite-like structure consisting of layers of fused six-membered $(BN)_3$ planar rings. Alternate sheets are located such that boron atoms are directly over nitrogen atoms. This structure results in planes that readily slide relative to each other, similar to those in graphite. As a result, hexagonal boron nitride, sometimes called 'white graphite,' has good lubricant properties. The rhombohedral form is similar to the hexagonal form, except with sheets stacked in groups of three rather than two. Two dense forms have also been described. The one usually referred to as 'cubic' boron nitride (c-BN) has a zinc blende lattice and the other has a wurtzite lattice. Both forms are unstable at atmospheric pressure, but transfer rates to hexagonal boron nitride are so slow as to be inconsequential for practical purposes.

Hexagonal boron nitride melts at approximately 3000 °C under nitrogen pressure and sublimes at 2500 °C at atmospheric pressure. Its theoretical density is 2.27 g mL^{-1}. In contrast to graphite, hexagonal boron nitride is a good electrical insulator. Cubic boron nitride has a theoretical density of 3.49 g mL^{-1}, a structure resembling diamond, and a Moh's hardness near the maximum of 15 for diamond. Cubic boron nitride is widely regarded as the second hardest substance known after diamond.

Hexagonal boron nitride can be prepared by a variety of reactions starting with boric oxide, boric acid, or borate salts. These include heating boric oxide or boric acid with ammonia, and heating boric oxide, boric acid, or borate salts with ammonium chloride, alkali metal cyanides, or calcium cyanamide. High-purity hexagonal boron nitride can be prepared by reaction of ammonia with boron trichloride or boron trifluoride. The rhombohedral form of boron nitride is prepared by rapid heating of a mixture of sodium borohydride and ammonium chloride to 750–1000 °C in the presence of added sodium chloride. Both hexagonal and rhombohedral boron nitride can be converted to the cubic zinc blende form by heating at 1400–1700 °C and 4–6 GPa pressure. This conversion is accelerated by the presence of additives including lithium and alkaline earth nitrides and amides. The wurtzite form is obtained in the absence of additives at higher pressures.

The various forms of boron nitride are all relatively inert to chemical attack under normal conditions. For example, hexagonal boron nitride does not react with oxygen, chlorine, or steam up to 700 °C. Reaction with steam begins at 900 °C. Rapid reactions are observed with hot alkali or fused alkali carbonate, but reactions are slow with most acids and alcohols, and boron nitride is not wetted by most molten metals and glasses. The cubic forms have similar reactivity but rates are slower because of their dense structures.

Both hexagonal and cubic boron nitride are important commercial products, and consumption of both forms has gradually increased in recent years. Hexagonal boron nitride is used as a lubricant and release agent in engineering polymer and molten metal extruding and forming operations. Hexagonal boron nitride is a good electrical insulator and a thermal conductor, a combination of properties that leads to applications in the electronics industry. In this application, h-BN is blended into elastomeric or thermoplastic parts used to transfer heat away from electronic components while maintaining electrical insulation. Hexagonal boron nitride powder is often hot-pressed at temperatures up to 2000 °C and pressures up to 14 Mpa to form articles of various shapes, such as high-temperature vessels. Its low coefficient of thermal expansion, excellent thermal shock resistance, and resistance to chemical attack makes such vessels useful for many high-temperature processes. Hexagonal boron nitride is often combined with other nonoxide ceramic materials and intermetallic composites to improve their physical properties. Hexagonal boron nitride is sold as powders and hot-pressed articles, as well as paste and liquid dispersions in water or organic solvents for use as coatings and aerosol sprays.

Another commercial form is known as pyrolytic boron nitride, p-BN. This form is a variation of standard h-BN and is manufactured by pyrolyzing boron trihalides in the presence of ammonia at about 2000 °C and allowing the pyrolysis products to deposit on a graphite substrate. This process results in boron nitride having a high degree of crystal orientation, with hexagonal layers running parallel to the substrate surface. This gives anisotropic characteristics valuable in the fabrication of articles, such as high-temperature crucibles. Pyrolytic boron nitride has exceptional thermal properties, high tensile strength that increases with temperature, and the highest dielectric properties of any readily available material. It is also extremely resistant to attack by most chemical reagents even at high temperatures.

Crystalline cubic boron nitride is mainly used as an extremely hard abrasive, similar to how industrial diamond is used. As 1–500 µm particles, it is sold as an abrasive material with trade names including Borazon and Amborite. This material is used in cutting tools and as grit for grinding and polishing wheels. Cubic boron nitride is bonded into cutting tools used to shape hard ferrous- and nickel-based alloys, which tend to react with diamond cutting tools, and also to cut masonry and glass.

Subsequent to the much acclaimed discovery of carbon nanotubes, techniques were developed to prepare boron nitride nanotubes.**[33]** These bear a similar isostructural relationship to carbon nanotubes as diamond and cubic boron nitride, and can be prepared as multiwall tubes.**[34]** Boron nitride nanotubes have been prepared by electric arc-discharge in the gas phase and by depositing boron and nitrogen ions on a hot, electrically biased tungsten surface. Boron nitride nanotubes have some potential advantages over carbon nanotubes in being more resistant to oxidation and thus suited for high-temperature applications. In addition, BN nanotubes are expected to be semiconducting with conductivities less dependent on the specific nanotube geometry.

2.6 Boron Phosphides

Two boron phosphides have been isolated, BP and $B_{12}P_2$. Heating elemental boron and red phosphorus at 900–1100 °C yields BP as refractory brown crystals having a cubic zinc blende structure similar to cubic boron nitride. This material can also be prepared by a number of other methods including the pyrolysis of $Cl_3P{\cdot}BCl_3$, reaction of boron or boron trichloride with zinc phosphide or phosphine, and hydrogen reduction of $Cl_3P{\cdot}BC1_3$.

Cubic boron phosphide is a III–V semiconductor with a large band gap. It is stable to 2500 °C at high pressure but decomposes at 1100 °C under vacuum with elimination of volatile white phosphorus, and formation of gray $B_{12}P_2$, which can be recrystallized from molten iron or aluminum to give black crystals. X-ray studies indicate that this material contains B_{12} icosahedra linked by P_2 moieties. The related boron arsenide, $B_{12}As_2$, has a similar structure with the icosahedra joined by As_2 moieties.

3 BORIC OXIDES, BORIC ACIDS, AND METAL BORATES

3.1 Introduction

Boric oxides, boric acids, and metal borates are of primary importance in any discussion of boron chemistry since these include essentially all boron minerals and the vast majority of boron compounds produced and used worldwide on a weight basis. Reviews of this chemistry and the commercial aspects of this general subject are available.[2,18]

3.2 Boric Oxides

Reviews of boron oxide chemistry are available.[13,35] The fundamental material B_2O_3 is referred to in the literature as boric oxide, boron trioxide, and diboron trioxide. In the commercial context it is called boric oxide, anhydrous boric acid, boric anhydride, and boric acid anhydride. This material, the only significant commercial form of boric oxide, is usually isolated as a vitreous solid at room temperature. It is prepared in large quantities by fusing refined boric acid in a furnace. The resulting molten glass is drawn out of the furnace, cooled on chill rolls, crushed, and screened. Two crystalline forms of B_2O_3 have been prepared in laboratory quantities. The α form, or B_2O_3-I, is prepared as hexagonal crystals by seeding with this form or with boron phosphate at 250 °C. The more exotic β form has only been obtained by heating vitreous boric oxide at 400 °C and 22 000 atmospheres. Some physical properties of the vitreous and crystalline forms are shown in Table 1.

Structural features of vitreous and molten boric oxide have been subject to debate. It appears that only trigonal boron is present in the solid glass, in a branched network containing $(BO)_3$ boroxin rings. The percentage of boron in B_2O_3 glass participating in boroxin rings has been controversial. Spectroscopic data indicate that 60–70 mol percent of boron in this material is present in boroxin ring structures; however theoretical calculations have predicted only 15–20%.[36] As the glass melts, boroxin ring structures break down, and above 800 °C, the strong boroxin line in the Raman spectrum disappears. Above 800 °C, the melt apparently consists of strongly associated discrete small molecules. The large discrepancy between spectroscopic observations and calculations may be related to the inability of computations to accurately simulate realistic cooling rates. Structures of the crystalline forms of B_2O_3 have been determined. The B_2O_3-I crystalline phase is hexagonal with trigonal boron-geometry. The crystal lattice of monoclinic B_2O_3-II consists of a compact network of BO_4^- tetrahedra with the four apical oxygens that are shared by two or three boron atoms. The Lewis acid character usually associated with trigonal BO_3 groups is absent in this crystalline form, and reactions with water and fluoride ion, as examples, are sluggish. Reaction of vitreous boric oxide with water is exothermic and gives boric acid (equation 3). Vitreous boric oxide is mildly hygroscopic at room temperature, and commercial samples usually contain approximately 1% water as a surface layer of boric acid. Molten boric oxide reacts readily with water above 1000 °C to form metaboric acid vapor (equation 4).

Table 1 Some physical properties of boric oxides

Property	Vitreous form	Crystalline forms	
		B_2O_3-I	B_2O_3-II
Mp (°C)	Softens 300–325	455–475	510
Bp (°C)	2316 (extrap.)	–	–
Density (g mL^{-1})	1.84	2.46	2.95
B-O geometry	trigonal	trigonal	tetrahedral

$$B_2O_3 + 3H_2O \longrightarrow 2B(OH)_3 \qquad (3)$$

$$B_2O_3(\text{molten}) + H_2O(g) \longrightarrow 2HBO_2(g) \qquad (4)$$

Values for the physical properties of boric oxide are somewhat confused in the literature due to the tendency of this substance to react readily with water. Many physical properties of boric oxide are sensitive to water content, and the water content of samples used for measurements was not always carefully controlled. For example, at 0.28% water, the density of vitreous boric oxide is 1.853 g mL^{-1} and the softening point 240–275 °C. Reducing the water concentration to 20 µg g^{-1} reduced the density to 1.829 g mL^{-1} and raised the softening point to 300–325 °C.[37] Other properties, such as thermal expansion, viscosity, and refractive index, are also significantly affected by moisture content. Water concentrations can be reduced to as low as 10 µg g^{-1} by prolonged heating in vacuum.

In addition to its reactivity toward water, the Lewis acidity of boric oxide leads to coordination with even relatively weak bases to form tetrahedral boron species. Molten boric oxide dissolves most metal oxides at high temperatures ($>$1000 °C), and is therefore corrosive to metals in the presence of oxygen. Boric oxide reacts readily with alcohols to form boric acid esters and boroxins, and with P_2O_5 to give boron phosphate. Because of its fluxing action, boric oxide is used as a solvent for metal reductions, for growing crystals at high temperatures, and in the preparation of metal salts such as lead titanate and calcium zirconate from the oxides. The general fluxing action of boric oxide is important in preparing many types of glasses, glazes, frits, ceramic coatings, and porcelain enamels, and this property is also utilized in soldering and welding fluxes. Boric oxide is a chemical intermediate in the production of a variety of other boron compounds, including esters, carbides, nitrides, and metal borides.

3.3 Boron Suboxides

Boron suboxides have boron:oxygen mole ratios equal to or greater than one. These compounds range from molecular species to refractory solid-state materials. Monomeric vapor-phase BO and B_2O_2 have been studied by spectroscopic techniques. In addition to these rather unstable high-temperature species, several forms of solid noncrystalline boron suboxides have been reported. A water-soluble low-temperature form is obtained by the vacuum dehydration of tetrahydroxydiborane at 220 °C (equation 5). At 500 °C, this form converts to a light brown modification that has also been obtained by reactions of boric oxide with elemental boron, boron carbide, or carbon at high temperatures ($>1250\,°C$).

$$nB_2(OH)_4 \longrightarrow (BO)_{2n} + 2nH_2O \qquad (5)$$

Refractory suboxides with boron:oxygen ratios significantly greater than one have been isolated as by-products from elemental boron production or by reactions of boron with boric oxide at high temperatures. These are related materials represented as B_6O, B_7O, and $B_{13}O_2$. The suboxide B_6O was prepared by reaction of elemental boron with zinc oxide at 1350 °C in argon, and has a structure based on an α-rhombohedral boron with interstitial oxygen atoms. This structure is similar to an α-rhombohedral boron carbide with each B_{12} icosahedron connected through oxygen atoms to adjacent icosahedra. Single crystals of boron suboxide prepared by dissolving elemental boron in molten B_2O_3 at $>2000\,°C$ and >5000 Mpa were recently reported to be close in hardness to cubic boron nitride (see Section 2.5) and to have greater fracture toughness.[37] In theory, boron suboxide can be prepared at lower pressures than c-BN, making this an attractive material for larger-scale industrial use.

A special case of molecular boron suboxides is found in the hydroxylated polyhedral boranes (*see* ***Boron Hydrides***). For example, the icosahedral anion *closo*-$[B_{12}H_{12}]^{2-}$ and related compounds can be completely hydroxylated to form discrete molecular boron suboxides, including *closo*-$[B_{12}(OH)_{12}]^{2-}$.[38] These can be regarded as members of a class of formally hydrated suboxides related to compounds such as tetrahydroxydiborane, $B_2(HO)_4$ ($BO{\cdot}H_2O$). The terminal hydroxyl groups of these compounds can be functionalized as esters or ethers to produce a variety of large molecule derivatives.

3.4 Boric Acids

3.4.1 Introduction

Boric acid, $B(OH)_3$, or H_3BO_3, is the only boric acid of commercial significance. It is also referred to as orthoboric acid, but usually only when context requires specifying this particular form. It can also be written as $B_2O_3{\cdot}3H_2O$, emphasizing the relationship with its acid anhydride B_2O_3. The formula $B(OH)_3$ denotes the correct structure (**1**) and is preferred to H_3BO_3, which gives the misleading impression that boric acid is a tribasic Brønsted acid such as H_3PO_4. Boric acid occurs as the relatively rare mineral sassolite that at one time was extracted commercially from hot springs in Italy. Metaboric acid, HBO_2 or $B_2O_3{\cdot}H_2O$, has been isolated in three crystalline modifications (see Section 3.4.3), including the boroxin or orthorhombic form (**2**). Summaries of boric acid chemistry are available.[13,39,40]

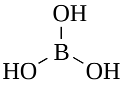

(**1**)

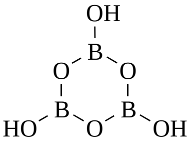

(**2**)

Properties. Boric acid is a white solid that crystallizes from aqueous solutions as triclinic waxy plates. The crystal structure of boric acid consists of planar sheets of planar trigonal $B(OH)_3$ molecules (**1**) linked by hydrogen bonds. This produces a graphite-like structure, accounting for the slippery feel of boric acid and the ease with which crystals cleave into flakes. This tribological property, or lubricity, has led to uses of boric acid as a lubricant.[41]

Preparation and Uses. Boric acid can be prepared in the laboratory by acid hydrolysis of a variety of boron compounds, including halides, esters, salts, and hydrides. It is produced commercially by reactions of sulfuric acid with sodium borates in the United States, and with sodium and calcium borates in Turkey. In South America, boric acid is produced by reaction of sulfuric acid with ulexite, a mixed sodium-calcium borate. Boric acid is also produced in Russia from the borosilicate mineral datolite.

Boric acid has many uses. Several hundred thousand tons are consumed annually in the manufacture of industrial and consumer products. Its most significant use is as a source of B_2O_3 in glasses and other vitreous products, including textile fiberglass, heat-resistant borosilicate glasses, ceramic glazes, porcelain enamels, and sealing and optical glasses. Boric acid is a versatile synthetic reagent and serves as a starting material in the production of many other commercial boron chemicals and reagents. In addition to potassium, ammonium, and zinc borates, boric acid is used in the manufacture of borate esters, boron hydrides, fluoroborates, refractory boron compounds, such as boron carbide and boron nitride, and amorphous metals and metal alloys, including ferroboron and permanent magnets. Other applications include preservatives for natural products such as wood and natural fibers. Boric acid acts as a mild antiseptic in a wide variety of consumer products and is frequently used in eye wash formulations. It is effective in the control of cockroaches and wood-boring insects. Boric acid is used to reduce the flammability and smoke production of cellulosic materials such as wood, cellulose insulation, and cotton batting for mattresses and furniture. Boric acid is also used in nuclear reactors because of the high neutron-absorbing cross section of the ^{10}B isotope. It is also used as an additive in the air oxidation of hydrocarbons, and related reactions, where its presence hinders unwanted oxidation side reactions.

Although the melting point of boric acid is given as 170.9 °C, some water loss occurs at temperatures as low as 100 °C when boric acid is heated slowly. Below 160 °C, the vapor phase includes water and gaseous boric acid. Boric acid is volatile in steam, and loss of boric acid from boiling aqueous solutions can be a problem in some industrial operations. At higher temperatures (600–1000 °C), gaseous metaboric acid is the principal compound formed by equilibration of water vapor and molten boric oxide.**42**

3.4.2 *Metaboric Acid*

Metaboric acid, HBO_2, has been offered commercially in the past, but no significant market has developed. Three crystalline forms can be prepared by the controlled dehydration of boric acid. Some of their physical properties are included in Table 2. The α form, or HBO_2-III, forms as orthorhombic crystals at approximately 130 °C when boric acid is heated slowly. This compound, of structural formula $(HOBO)_3$ (**2**), has a layered structure having B_3O_3 rings joined by hydrogen bonding between the hydroxyl groups on boron. On further heating, the α form gradually converts to the monoclinic β form or HBO_2-II. The boron atoms in this form are in BO_4 tetrahedra as well as in chains of trigonal B_2O_5 groups. Above 150 °C, dehydration continues beyond the metaborate composition. The third modification, the χ-form or HBO_2-I, is the most stable crystalline form and is prepared as cubic crystals by melting a mixture of boric acid and HBO_2-III in a vacuum at 180 °C for several weeks. Some physical properties of the boric acids are given in Table 2.

3.4.3 *Aqueous Chemistry of Boric Acid and its Salts: Polyborates and pH Effects*

Boric acid is moderately soluble in water and has a large negative heat of solution. The aqueous solubility of boric acid therefore increases greatly with increasing temperature (Table 3). In dilute aqueous solution, boric acid exists almost exclusively as the undissociated monomers $B(OH)_3$ and $B(OH)_4^-$. It is a weak monobasic acid primarily due to its Lewis acid or base acceptor character. Brønsted acidity, or the tendency to donate protons, plays little or no role in the aqueous chemistry of boric acid. The calculated equilibrium constant for the reaction shown in equation (6) is 5.80×10^{-10} at 25 °C.

Table 2 Some properties of boric acids

Property	H_3BO_3	HBO_2-III	HBO_2-II	HBO_2-I
Mp (°C)	170.9	176	200.9	236
Density (g mL^{-1})	1.517	1.784	2.045	2.49

Table 3 Solubility of boric acid

Temp. (°C)	$B(OH)_3$ dissolved (wt%)
0	2.52
20	4.72
40	8.08
50	10.27
60	12.97
80	19.10
100	27.53

$$B(OH)_3 + H_2O \longrightarrow B(OH)_4^- + H^+ \tag{6}$$

Boric acid is a relatively weak acid compared to other common acids, as illustrated by the acid equilibrium constants given in Table 4. Boric acid has a similar acid strength to silicic acid. Calculated pH values based on the boric acid equilibrium constant are significantly higher than those observed experimentally. This anomaly has been attributed to secondary equilibria between $B(OH)_3$, $B(OH)_4^-$, and polyborate species. Interestingly, the aqueous solubility of boric acid can be increased by the addition of salts such as potassium chloride and sodium sulfate, but decreased by the addition of others salts, such as the chlorides of lithium and sodium. Basic anions and other nucleophiles such as fluorides and borates significantly increase boric acid solubility.

Although $B(OH)_3$ and $B(OH)_4^-$ are monomeric in dilute solutions, at concentrations above about 0.1 mol L^{-1}, condensed borate species that are often referred to as polyborates form. Titration of a boric acid solution with one molar equivalent of a strong base leads to formation of the tetrahydroxyborate anion, $B(OH)_4^-$, as the principal species in solution. Mixtures of boric acid and its conjugate base, the tetrahydroxyborate anion, form what appears to be a classical buffer system where the pH is determined primarily by the acid:salt ratio with $[H^+] = K[B(OH)_3]/[B(OH)_4^-]$. This relationship is approximately correct for sodium and potassium borates with a sodium:boron ratio of 1:2. Here the $B(OH)_3$:$B(OH)_4^-$ ratio equals one, and the solution pH remains near 9 over a wide range. However, for borate solutions with pH values significantly above or below 9,

Table 4 Acid equilibrium constants of some common acids

Acid	Equilibrium constant (mol L^{-1})
Phosphoric	7.5×10^{-3}
Acetic	1.75×10^{-5}
Boric	5.80×10^{-10}
Silicic	2×10^{-10}

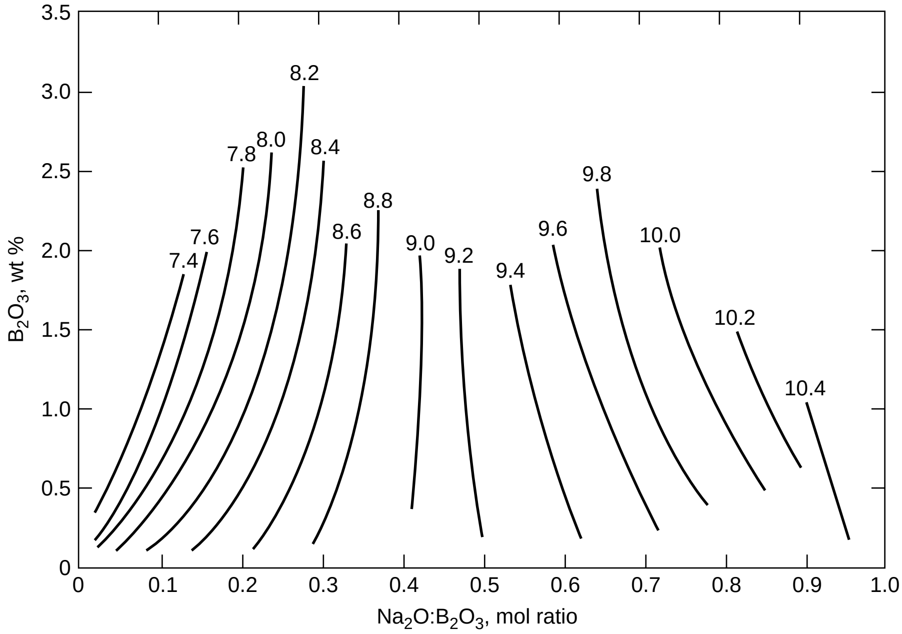

Figure 1 pH values of the Na_2O-B_2O_3-H_2O system at 25 °C

the solution pH becomes sensitive to concentration change, as shown in Figure 1.[43] This anomalous behavior results from the formation of the polyborate anions (**3–6**), which dissociate into the monomeric species $B(OH)_3$ and $B(OH)_4^-$ when the solutions are diluted. Below pH 9, the pH increases on dilution. Above 9, the pH decreases with dilution. This is probably due to shifts in the equilibria between monomeric and polymeric species and their relative acidities. At a sodium:boron molar ratio of 0.41, the pH of 8.91 is independent of concentration. This ratio and the pH attained have been referred to as the isohydric point. The isohydric point for potassium solutions is slightly different from sodium solutions: pH 9.0 at a potassium:boron ratio of 0.405.

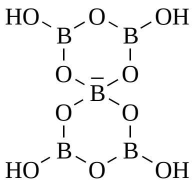
(**3**)

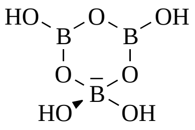
(**4**)

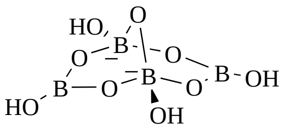
(**5**)

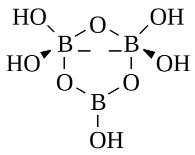
(**6**)

The addition of metal salts, particularly alkaline earth cations and/or halides, can result in significant shifts in the monoborate-polyborate equilibria. Equilibrium constants have been calculated for the equilibria between $B(OH)_3$ and $B(OH)_4^-$ and several polyborates: the pentaborate monoanion (**3**), the triborate monoanion (**4**), the tetraborate dianion (**5**), and triborate dianion (**6**).[44] Figure 2 illustrates the relative populations of borate species as a function of pH for a B_2O_3 concentration of 13.93 g L^{-1}. The formation of polyanions is particularly significant in the intermediate pH range. These polyborate anions form successively in the order (**3**) to (**6**) with increasing pH and have been identified in solution by their colligative properties and by Raman and ^{11}B NMR spectroscopy. These anions are also found in crystalline, synthetic, and minerals borates. Alkali metal borate glasses probably contain similar structures.[45]

In addition to pH effects resulting from formation of polyanions in solution, significant enhancements in the solubilities of boric acid and alkali metal borates are also observed at certain mole ratios. For example, soluble borate salts can be dissolved in saturated boric acid solutions to produce solutions having significantly higher B_2O_3 concentrations. The formation of polyborate anions decreases the concentrations of $B(OH)_3$ and $B(OH)_4^-$ in equilibrium with undissolved borate salts, thereby permitting more borate salts to dissolve. In the case of alkali metal borates, maximum solubility is achieved at a metal:boron ratio of approximately 1:4. This provides the basis for the commercial product $Na_2B_8O_{13}4H_2O$ (see Section 4.4), which dissolves readily in water with little temperature change to form concentrated borate solutions.

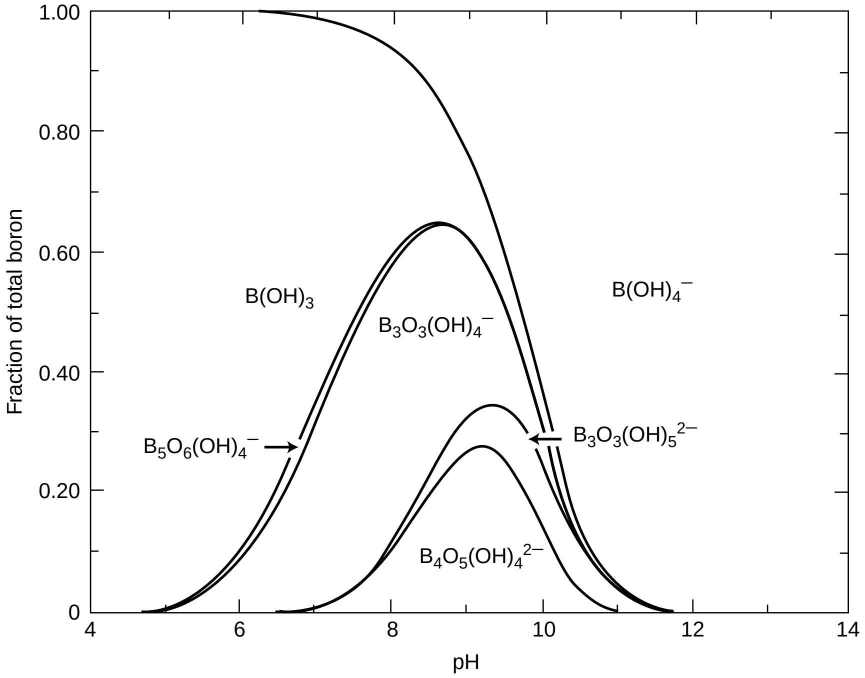

Figure 2 Estimated population distribution of borate species in aqueous solution as a function of pH

It is important to note that the presence of polyborate anions, as shown in Figure 2, is only significant in relatively concentrated solutions. This is relevant to the environmental and biological aspects of boron chemistry, since boron is present in both natural waters and biological systems at low concentrations. Under these conditions, only $B(OH)_3$ and $B(OH)_4{}^-$ are significant species; and at near neutral pH, the concentration of the $B(OH)_4{}^-$ anion is minor. Ocean waters contain an average boron concentration of about $4.6\,g\,\mu g\,g^{-1}$, which is almost entirely present in the form of naturally occurring boric acid. Boron in plants and animals is also present mainly as boric acid, even if the dietary source of boron is a borate salt.

4 METAL BORATES

4.1 Introduction

Metal borates can be divided into two broad classes: hydrated and anhydrous. So-called hydrated borates, which have the general formula $aM_xO{\cdot}bB_2O_3{\cdot}CH_2O$, contain B-OH groups, sometimes interstitial OH^-, and may also contain interstitial water. Anhydrous borates do not contain water, OH^-, or B-OH groups, and have the general formula $aM_xO{\cdot}bB_2O_3$. As crystalline compounds, hydrated borates typically crystallize from aqueous solutions under relatively mild conditions. Anhydrous borates nearly always form at high temperatures, often crystallizing from molten inorganic systems. It is unusual to obtain anhydrous borates from aqueous solutions except occasionally under hydrothermal conditions. In terms of tonnage, the vast majority of synthetic industrial borates are hydrated, and most mineral borates also fall into this category. However, crystalline anhydrous borates have received considerable attention in the scientific literature because of their potential for use in smaller-scale advanced technology applications, such as optoelectronic devices. The structural chemistry of anhydrous metal borates has been reviewed.[46]

Metal borates have been prepared in hydrated or anhydrous forms from most metals in the periodic table and have many small to medium scale applications. The general method used to prepare hydrated metal borates involves mixing an aqueous solution of boric acid or an alkali metal borate with aqueous solutions or suspensions of metal oxides, halides, or sulfates. The resulting precipitates of metal borates may be either crystalline or amorphous solids of slight to moderate solubility. Most metals can produce several different crystalline borates. In the case of crystalline hydrated borates, the specific crystalline form obtained generally depends on the relative concentrations of starting materials and the temperature. Salts of metals that produce highly insoluble hydroxides frequently produce complex hydroxide gels upon reaction with soluble borate salts rather than metal borate compounds. These gels, which may contain significant amounts of adsorbed borate, have often been incorrectly described as true metal borate compounds, particularly in the older literature. Anhydrous metal borates are either prepared by dehydration of the appropriate hydrate at 300–1000 °C, or by direct fusion of metal oxides with boric acid or boric oxide, with the crystalline form produced governed by temperature and reactant ratios.

Both hydrated and anhydrous metal borates have numerous industrial uses. Some of the major uses of hydrated metal borates are the manufacture of glasses, ceramics, and industrial fluids, and as micronutrient fertilizers, fire retardants, and biostats. Anhydrous borates find use as heterogeneous catalysts, scintillation hosts, and in the fabrication of optoelectronic devices. Anhydrous aluminum borates are used as additives in oxide ceramics to promote the formation of desirable phases. Also, aluminum borate whiskers are used as reinforcing additives in composite materials. Specific uses of sodium, calcium, zinc, and barium borates are discussed in sections below.

Two fundamental problems are encountered when discussing metal borates. One is nomenclature, and the other is the chemical formulation or notation of chemical structures. To illustrate this dilemma, consider the common mineral and commercial product, borax. It is usually referred to as sodium tetraborate decahydrate and written as $Na_2B_4O_7 \cdot 10H_2O$. Alternatively, it is often written in the oxide formula, $Na_2O \cdot 2B_2O_3 \cdot 10H_2O$ and named sodium(1:2)borate decahydrate. Finally, the structural formula $Na_2[B_4O_5(OH)_4] \cdot 8H_2O$, or sodium tetraborate octahydrate, is used on the basis of the actual structure of this compound, which contains the tetraborate anion (**5**).

The sodium tetraborate decahydrate system is used almost exclusively in commerce, the oxide system in classical mineralogy, and the more correct structural designation in chemical discussions. The *Chemical Abstract Service* (CAS) has devised another more computer-compatible system for inorganic borates based on hypothetical acid salts. The CAS system is not used except in indexing by that reference source. The metal salt names are used commonly for refined products, for example, sodium tetraborate decahydrate for borax. The problem with this nomenclature is that it is based on the fictitious $[B_4O_7]^{2-}$ ion, gives an incorrect count for waters of hydration, and does not recognize the presence of hydroxyl groups. This is also true of the oxide formulas, which are often used for mineral and glass compositions. The structural designation $Na_2[B_4O_5(OH)_4] \cdot 8H_2O$ correctly identifies the tetraborate ion (**5**) in the crystalline compound and correctly defines the hydroxyl groups and waters of hydration.

4.2 Borate Minerals

Most boron-containing minerals are alkali metal and alkaline earth borate salts. These compounds are the subject of earlier reviews.[2,15,47,48] More than 230 naturally occurring borate minerals have been identified.[2] The most abundant of these is the tourmaline group of aluminoborosilicate minerals, $(Na,Ca)(Mg,Li,Al,Fe^{2+})_3Al_6B_3Si_6(OH)_4$, which may contain roughly 10% boron by weight but have not been found in sufficient grades for economic mining. Concentrated, commercially exploitable borate deposits are found mainly in arid parts of the world. By far, the most extensive deposits have been located in Turkey and western United States. Other important deposits are located in Russia, China, Chile, and Argentina. Table 5 identifies the principal minerals that serve as sources of industrial borates. Over 80% of the world's borate production is divided between Turkey and the United States. In some cases, minerals, particularly colemanite and ulexite, are sold directly as commercial products after minimal refining steps that might include crushing, grinding, and blending. Major uses for these beneficiated minerals are in the manufacture of fiberglass and ceramics, and as raw materials for the production of boric acid and other boron-containing products. Table 6 lists the quantities of the principal minerals being mined worldwide.[49]

4.3 Sodium Tetraborates

Four sodium tetraborates are important as boron minerals and/or large tonnage items of commerce. Borax, or sodium tetraborate decahydrate, is extracted from large open-pit mines in Turkey and the United States. Turkish beneficiated native borax, also referred to by the mineral name tincal, is used directly in glass making and other applications. Refined borax is used widely in consumer products and as

Table 5 Commercially significant borate minerals

Mineral	Oxide formula	Structural formula	B_2O_3 (wt%)
Ascharite (szaibelyite)	$2MgO \cdot B_2O_3 \cdot H_2O$	$Mg_2(OH)[B_2O_4(OH)]$	41.4
Colemanite	$2CaO \cdot 3B_2O_3 \cdot 5H_2O$	$Ca[B_3O_4(OH)_3] \cdot H_2O$	50.8
Datolite	$2CaO \cdot B_2O_3 \cdot 2SiO_2 \cdot H_2O$	$Ca_4[B_4(SiO_4)_4(OH)_4]$	21.8
Howlite	$4CaO \cdot 5B_2O_3 \cdot 2SiO_2 \cdot 5H_2O$	$Ca_2[B_3O_4(OH)_2SiB_2O_5(OH)_3]$	44.4
Hydroboracite	$CaO \cdot MgO \cdot 3B_2O_3 \cdot 6H_2O$	$CaMg[B_3O_4(OH)_3]_2 \cdot 3H_2O$	50.5
Inderite	$2MgO \cdot 3B_2O_3 \cdot 15H_2O$	$Mg[B_3O_3(OH)_5] \cdot 5H_2O$	37.3
Kernite	$Na_2O \cdot 2B_2O_3 \cdot 4H_2O$	$Na_2[B_4O_6(OH)_2] \cdot 3H_2O$	50.9
Meyerhofferite	$2CaO \cdot 3B_2O_3 \cdot 7H_2O$	$Ca[B_3O_3(OH)_5] \cdot H_2O$	46.7
Tincal (borax)	$Na_2O \cdot 2B_2O_3 \cdot 10H_2O$	$Na_2[B_4O_5(OH)_4] \cdot 8H_2O$	36.5
Ulexite	$Na_2O \cdot 2CaO \cdot 5B_2O_3 \cdot 16H_2O$	$NaCaB_5SiO_6(OH)_6 \cdot 5H_2O$	43.0

Table 6 Worldwide production of boron minerals in 2002[49]

Country	Metric tons (×1000)	Minerals
Turkey	1500	tincal, colemanite, ulexite
United States	1200	tincal, kernite, borate brines
Russia	1000	ascharite, datolite, inderite, hydroboracite
Argentina	500	tincal, ulexite, colemanite, hydroboracite
Chile	330	ulexite
China	150	ascharite, tincal, meyerhofferite, kernite
Bolivia	35	ulexite
Peru	30	ulexite

a starting material for the manufacture of other chemicals. Sodium tetraborate pentahydrate, also known as the mineral tincalconite, is produced by recrystallization of borax above approximately 60.8 °C, and is the boron compound sold in the largest quantities worldwide. Sometimes referred to as borax pentahydrate, this is the borate product produced in the largest tonnage worldwide. Its largest use is in the manufacture of insulation fiberglass. The crystal structures of sodium tetraborate pentahydrate and decahydrates are both based on the tetraborate ion (**5**), with three and eight molecules of water of hydration respectively. A single-crystal X-ray analysis shows that the pentahydrate contains only 4.67 equivalent waters of hydration because two of the three hydration sites in its structure are only partially occupied.[50] The structural formula of the 'pentahydrate' is therefore $Na_2[B_4O_5(OH)_4]\cdot 2.67H_2O$, and the common and the oxide formulas are $Na_2B_4O_7\cdot 4.67H_2O$ and $Na_2O\cdot 2B_2O_3\cdot 4.67H_2O$ respectively.

The oxide formula of the mineral kernite, $Na_2B_4O_7\cdot 4H_2O$, gives the impression that it contains the same tetraborate structure as sodium tetraborate penta- and decahydrates, but its actual structure is quite different. Kernite has the structural formula $Na_2[B_4O_6(OH)_2]\cdot 3H_2O$ and contains an anionic borate structural unit consisting of infinite parallel chains of composition $[B_4O_6(OH)_2]_n^{2n-}$ (**7**), made up of triborate rings linked through shared tetrahedral boron atoms.[51] The relatively slow dissolving and crystallization rates of kernite are consistent with this polymeric structure. Kernite is mined in the United States and converted to boric acid. Kernite can also be hydrated to borax decahydrate and refined into borax pentahydrate.

Anhydrous sodium tetraborate can exist in several crystal forms but it most commonly occurs as a glassy amorphous product that is used in fused glasses and related products. The commercial compound is prepared by fusing sodium tetraborate hydrates in a furnace. The resulting melt is pressed between chilled rollers to produce sheets of glassy product that is ground, screened to appropriate sized granules, and packaged for sale.

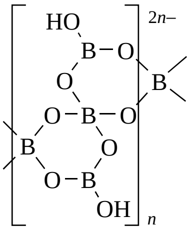

(**7**)

Aqueous solubilities of these sodium borates, as well as other borate salts of commercial interest, are listed in Table 7. Kernite, because of its polymeric structure, is the least soluble of the sodium borates.

4.4 Other Sodium Borates

Four additional sodium borates are produced commercially in smaller quantities. So-called 'disodium octaborate tetrahydrate' is a commercial product having the hypothetical formula $Na_2B_8O_{13}\cdot 4H_2O$. This is not a discrete crystalline compound but rather an amorphous spray-dried material having an approximate composition in agreement with this chemical formula. It has a little crystalline character and dissolves rapidly in water without the temperature decrease that normally occurs when crystalline sodium borates are dissolved. It also readily forms supersaturated solutions in hot water. The ratio of sodium to boron in this material is such that maximum solubility is achieved. Table 8 illustrates the increased solubility of disodium octaborate tetrahydrate compared to borax or sodium borate decahydrate and the magnitude of the supersaturation observed. Disodium octaborate tetrahydrate is marketed under various trade names depending on intended use. Major uses of this product are as a boron source in agriculture, a diffusible wood preservative, a flame retardant for cellulosic materials, and for the control of insect pests.

Table 7 Aqueous solubilities of some alkali metal and ammonium borates

Compound	0 °C	20 °C	40 °C	60 °C	100 °C
$Na_2O\cdot 5B_2O_3\cdot 10H_2O$	5.77	10.55	17.50	26.88	51.0
$Na_2O\cdot 2B_2O_3\cdot 10H_2O$	1.18	2.58	6.00	15.90	–
$Na_2O\cdot 2B_2O_3\cdot 4.67H_2O$[a]	–	–	–	16.40	34.63
$Na_2O\cdot 2B_2O_3\cdot 4H_2O$[b]	–	–	–	14.82	28.22
$Na_2O\cdot B_2O_3\cdot 8H_2O$[c]	14.5	20.0	27.9	–	–
$Na_2O\cdot B_2O_3\cdot 4H_2O$	–	–	–	38.3	52.4
$K_2O\cdot 5B_2O_3\cdot 8H_2O$	1.56	2.82	5.12	9.05	22.3
$K_2O\cdot 2B_2O_3\cdot 4H_2O$	–	12.1	19.4	28.4	48.4
$Li_2O\cdot 2B_2O_3\cdot 4H_2O$	2.2	2.81	3.26	3.76	5.17
$(NH_4)_2O\cdot 2B_2O_3\cdot 4H_2O$	3.75	7.63	15.8	27.2	–
$(NH_4)_2O\cdot 5B_2O_3\cdot 8H_2O$	4.00	7.07	11.4	18.2	–

[a] Commonly known as the pentahydrate, transition point to decahydrate at 60.7 °C, 16.6 wt% $Na_2B_4O_7$. [b] Transition point to decahydrate at 58.2 °C, 14.55 wt% $Na_2B_4O_7$. [c] Transition point to tetrahydrate at 53.6 °C, 36.9 wt% $Na_2B_4O_7$.

Table 8 Aqueous solubilities of disodium octaborate tetrahydrate and borax decahydrate

	Disodium octaborate tetrahydrate (wt% B_2O_3)		Borax decahydrate (wt% B_2O_3)
Temp. (°C)	Supersaturated	Saturated	Saturated
0	2.4	1.6	0.7
20	9.5	6.3	1.7
50	32.0	21.2	6.5
94	45.3	30.0	21.0

A sodium pentaborate having the oxide formula $Na_2O{\cdot}5B_2O_3{\cdot}10H_2O$ is a minor commercial product. It exists in nature as the relatively rare mineral sborgite, and can be prepared synthetically by crystallization from a solution having a Na_2O to B_2O_3 molar ratio of 0.2. It is sometimes referred to in the literature as sodium pentaborate pentahydrate based on the formula written as $NaB_5O_8{\cdot}5H_2O$. Its structural formula is $Na[B_5O_6(OH)_4]{\cdot}3H_2O$, containing the pentaborate anion (**3**). This borate occurs as monoclinic crystals with a specific gravity of 1.713. It melts at 54 °C and is stable in air to approximately 75 °C. Above 75 °C, the interstitial water begins to be released.

There are two sodium metaborates of commercial significance. These have oxide formulas $Na_2O{\cdot}B_2O_3{\cdot}4H_2O$ and $Na_2O{\cdot}B_2O_3{\cdot}8H_2O$. Here again, there is considerable confusion in the nomenclature applied to these borates. As articles of commerce, these are referred to as 'sodium metaborate 4 Mol' and 'sodium metaborate 8 Mol', according to the oxide formulas. However, these are often referred to in the literature as sodium metaborate dihydrate and sodium metaborate tetrahydrate based on their formulas written as $NaBO_2{\cdot}2H_2O$ and $NaBO_2{\cdot}4H_2O$. These compounds have the structural formulas $Na[B(OH)_4]$ and $Na[B(OH)_4]{\cdot}2H_2O$, respectively, and contain the tetrahedral $B(OH)_4{}^-$ anion with either no or one interstitial water molecule. The $Na[B(OH)_4]{\cdot}2H_2O$ compound is obtained as monoclinic crystals, sp gr 1.743, by cooling a borax solution containing slightly more than the theoretical amount of sodium hydroxide. This is the stable phase in contact with its saturated solution at 11.5–53.6 °C. Above 53.6 °C, $Na[B(OH)_4]$ becomes the stable solid in contact with its solution. This compound is obtained as triclinic crystals, sp gr 1.909, by heating a slurry of the tetrahydrate above 53.6 °C, by crystallization from metaborate solution at 53.6–80 °C, or by vacuum dehydration of the tetrahydrate. The higher hydrate loses water slowly on standing at room temperature and melts at 90–95 °C. The metaborates are currently produced in relatively small quantities for use in industrial applications, such as photographic solutions. It can be seen from Table 7 that the sodium metaborates are among the most soluble of the sodium borates. They dissolve in water to give solutions having a pH of about 11 and can be considered as the endpoint products of the titration of boric acid with strong base.

4.5 Sodium Perborates

Perborates, or peroxoborates, are usually written as if the perborate anion were $BO_3{}^-$. The three known sodium perborates are therefore commonly referred to as the mono-, tri-, and tetrahydrates, $NaBO_3{\cdot}nH_2O$, where $n = 1$, 3, and 4. However, these actually contain the cyclic dianion (**8**). On the basis of this structure, these compounds are more correctly referred to as anhydrous, tetrahydrate, and hexahydrate.

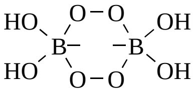

(**8**)

Using the established nomenclature, the so-called mono- and tetrahydrates, which are also referred to as PBS-1 and PBS-4 respectively, are important commercial products. Both have been used extensively as bleaching agents in home laundry detergent formulations. These are crystalline powders that decompose in water with formation of peroxoborate species, including $(HO)_2BOOH$, $[(HO)_3BOOH]^-$, and $[(HO)_2B(OOH)_2]^-$, and ultimately liberate hydrogen peroxide. Thus, they provide a convenient means of handling latent hydrogen peroxide in a dry powder form. There is considerable evidence that peroxoborates provide greater selectivity in oxidation reactions than H_2O_2 alone. The tetrahydrate is manufactured in large tonnages by reaction of hydrogen peroxide with a metaborate solution prepared from sodium hydroxide and sodium tetraborate pentahydrate. The monohydrate is produced by the reversible dehydration of the tetrahydrate. The tetrahydrate contains 10.4 wt% active oxygen, and its decomposition in water is accelerated by metal and transition metal catalysts and temperature. Unless a stabilizer is added, solutions will slowly lose active oxygen at room temperature. It melts in its own water of hydration at 63 °C. On heating to 250 °C, it decomposes rapidly to oxygen and sodium metaborate. Water solubilities of the tetrahydrate are 2.5 wt% at 20 °C and 3.6 wt% at 29 °C. Sodium perborate monohydrate, $NaBO_3{\cdot}H_2O$, has a higher active oxygen content of 16.0% and is prepared commercially by dehydration of the tetrahydrate. The monohydrate also exhibits a much faster rate of solubility in water than the tetrahydrate. Sodium perborate trihydrate, $NaBO_3{\cdot}3H_2O$, is not a commercial product but can be prepared as a triclinic solid containing 11.8 wt% active oxygen by the controlled dehydration of the tetrahydrate, or by seeding a hydrogen peroxide-sodium metaborate solution. Sodium perborates can be used as convenient and versatile oxidizing agents for organic syntheses.[52] Perborates salts of other metals are also know, for example, magnesium perborate.

4.6 Other Alkali Metal Borates

Although potassium and lithium borates are produced commercially, their usage is small compared to sodium and calcium borates. Potassium tetraborate, $K_2[B_4O_5(OH)_4]\cdot 2H_2O$ ($K_2B_4O_7\cdot 4H_2O$), and pentaborate, $K[B_5O_6(OH)_4]\cdot 4H_2O$ ($KB_5O_8\cdot 4H_2O$), have the same borate anions as found in the corresponding crystalline sodium borates (**5** and **3**, respectively). When the tetraborate is heated, reversible water loss begins between 85 and 111 °C. Thermogravimetric analysis shows that two moles of water are lost by 140 °C, one more at 200–230 °C, and the last one at 250–290 °C. Potassium pentaborate tetrahydrate is stable in a vacuum to 105 °C and up to 170 °C in an atmosphere saturated with water at 90 °C. Lithium tetraborate, $Li_2[B_4O_5(OH)_4\cdot H_2O]$ ($Li_2B_4O_7\cdot 3H_2O$), and lithium metaborate, $Li[B(OH)_4]$ ($LiBO_2\cdot 2H_2O$), are manufactured in relatively small quantities.

Single crystals of anhydrous lithium borates are grown from high-temperature molten salt for use in optoelectronic devices. Crystalline anhydrous lithium triborate, LiB_3O_5, is used commercially as a nonlinear optical material to convert light from high-powered lasers from higher to lower frequencies. Its attributes in this application include a wide transparency range and high-damage threshold. Crystalline anhydrous lithium tetraborate, $Li_2B_4O_7$, is used as a piezoelectric material in mobile communications devices such as cellular phones and pagers.

4.7 Calcium Borates

A number of crystalline calcium borates are known that occur as either minerals or synthetic compounds. The most important calcium borate mineral is colemanite, $2CaO\cdot 3B_2O_3\cdot 5H_2O$. This mineral exists in nature as monoclinic crystals having a specific gravity of 2.42. Colemanite contains polymeric chains of the triborate anion $[B_3O_4(OH)_3]_n^{2n-}$.[53] At 480 °C, colemanite decrepitates violently, losing all of its water and forming a low-bulk density powder. The water solubility of colemanite is relatively low for a borate, 0.1 wt% at 25 °C and 0.38 wt% at 100 °C.

A second important calcium borate is the mineral ulexite, $NaCaB_5O_9\cdot 8H_2O$ or $Na_2O\cdot 2CaO\cdot 5B_2O_3\cdot 16H_2O$. It can also be prepared synthetically by seeding an aqueous solution of calcium metaborate, boric acid, borax, and probertite, $NaCaB_5O_9\cdot 5H_2O$. Ulexite crystals are triclinic with a specific gravity of 1.95. When ulexite is heated, four moles of water are lost at 80–100 °C, 8.5 more at 175 °C, and the remaining 3.5 moles at 450 °C. Ulexite has the structural formula $NaCa[B_5O_6(OH)_6]\cdot 5H_2O$ and contains the pentaborate trianion.[54] This anion is similar to (**3**) with two additional hydroxyl groups bound to two of the trigonal borons making them tetrahedral. An unusual property of some ulexite crystals is their ability to behave as fiber optic material and project images through the crystals in one direction. Ulexite has a relatively low water solubility, 0.5 wt% as NaB_5O_9 at 25 °C. The related mineral probertite, $NaCaB_5O_9\cdot 5H_2O$ or $Na_2O\cdot 2CaO\cdot 5B_2O_3\cdot 10H_2O$, is less common than ulexite. Its crystals are monoclinic and have a specific gravity of 2.1. It has the structural formula, $NaCa[B_5O_6(OH)_4]\cdot 3H_2O$ based on a polymeric pentaborate anionic structural unit.[55] Both colemanite and ulexite are mined in large tonnages in Turkey and sold as impure concentrates for use worldwide in the manufacture of textile and insulation fiberglass. Colemanite is also used in the manufacture of ceramic glazes. Ulexite ores are also produced in South America and used as a raw material for the production of boric acid.

4.8 Zinc Borates

The industrial importance of the zinc borates has increased in recent years. Several unique crystalline hydrated zinc borates are known, exhibiting a range of structure types illustrative of the diversity of borate chemistry. Well substantiated crystalline zinc borates have the compositions $4ZnO\cdot B_2O_3\cdot H_2O$,[56–59] $ZnO\cdot B_2O_3\cdot 1.12H_2O$,[60] $ZnO\cdot B_2O_3\cdot 2H_2O$ (or $2ZnO\cdot 2B_2O_3\cdot 3H_2O$), $6ZnO\cdot 5B_2O_3\cdot 3H_2O$,[61] $2ZnO\cdot 3B_2O_3\cdot 7H_2O$,[62] $2ZnO\cdot 3B_2O_3\cdot 3H_2O$,[57] $2ZnO\cdot 3B_2O_3\cdot 9H_2O$ (or $3ZnO\cdot 5B_2O_3\cdot 14H_2O$), and $ZnO\cdot 5B_2O_3\cdot 4.5H_2O$,[61] spanning a range of B_2O_3:ZnO mole ratios from 0.25 to 5. Each of these compounds can be prepared selectively by aqueous reactions of zinc oxide with boric acid, or by reactions of zinc and borate salts, with the specific compound obtained determined by reactant concentrations and temperature. Only $4ZnO\cdot B_2O_3\cdot H_2O$, $ZnO\cdot B_2O_3\cdot 1.12H_2O$, $2ZnO\cdot 3B_2O_3\cdot 7H_2O$, and $2ZnO\cdot 3B_2O_3\cdot 3H_2O$ have been structurally characterized, and compositions of the remaining four should be considered approximate until their structures are elucidated. The compound $4ZnO\cdot B_2O_3\cdot H_2O$ has the structural formula $Zn_2(BO_3)OH$ and consists of corrugated sheets of oxygen-sharing ZnO_3OH tetrahedra interconnected by BO_3 triangles into an infinite network.[58,59] This structure is noncentrosymmetric as first shown some years after this compound had become a commercial product, by the structure determination of the closely related OH/F disordered compound $Zn_2(BO_3)(OH)_{0.75}F_{0.25}$, which gives essentially the same X-ray pattern.[59] The compound $ZnO\cdot B_2O_3\cdot 1.12H_2O$ consists of a complex extended network of unusual, large $B_{12}O_{24}^{12-}$ polycyclic borate units interconnected by cationic Zn_3O_3 clusters into an infinite network.[60] This results in an open framework solid containing one water molecule coordinated to each zinc atom as well as some additional interstitial water. The compound $2ZnO\cdot 3B_2O_3\cdot 7H_2O$ has the structural formula $Zn[B_3O_3(OH)_5]\cdot H_2O$, and contains isolated $[B_3O_3(OH)_5]^{2-}$ anions.[62] The compound $2ZnO\cdot 3B_2O_3\cdot 3H_2O$ has the structural formula $Zn[B_3O_3(OH)_5]\cdot H_2O$, and contains infinite chains of triborate rings similar to those found in the calcium borate mineral colemanite, interconnected by coordination with zinc (**9**).[57]

A few zinc borates are currently manufactured in significant tonnages. Most of the zinc borates listed above have

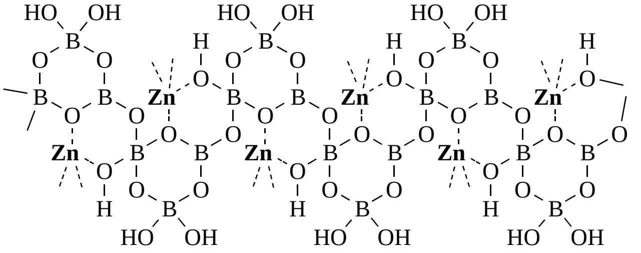

(**9**)

limited usefulness because of their low dehydration on-set temperatures, ruling out uses requiring processing at elevated temperatures. The most important commercial zinc borate in use today is $2ZnO{\cdot}3B_2O_3{\cdot}3H_2O$, which has worldwide annual production greater than 10 000 metric tons. This zinc borate is mainly used as a polymer additive and as a preservative for wood composites and other engineered wood products. As a polymer additive, it serves as a fire retardant synergist, char promoter, antidrip agent, smoke and afterglow suppressant, and modifier of electrical and optical properties.[63] It has also been used as an adhesion promoter in steel-belted tires. Addition to ceramic bodies can also improve green strength and reduce firing times and temperatures. Added to coatings, it functions as a corrosion inhibitor, fire retardant, preservative, mildewstat, and tannin stain blocker.[64] Important properties of $2ZnO{\cdot}3B_2O_3{\cdot}3H_2O$ include a relatively low water solubility of about 0.28 wt% and a relatively high dehydration on-set temperature, >290 °C. The latter property permits processing in a wide range of polymer systems and construction products. Also, its low refractive index (1.58) permits the manufacture of transparent or translucent articles. As an article of commerce, $2ZnO{\cdot}3B_2O_3{\cdot}3H_2O$ is generally referred to as $2ZnO{\cdot}3B_2O_3{\cdot}3.5H_2O$ or $4ZnO{\cdot}6B_2O_3{\cdot}7H_2O$. These slightly incorrect formulas result from an original error in characterization.[57]

In addition to $2ZnO{\cdot}3B_2O_3{\cdot}3H_2O$, the zinc borates $2ZnO{\cdot}3B_2O_3{\cdot}7H_2O$, $2ZnO{\cdot}3B_2O_3{\cdot}9H_2O$, $ZnO{\cdot}B_2O_3{\cdot}2H_2O$, and $4ZnO{\cdot}B_2O_3{\cdot}H_2O$ have all been produced commercially on multiton scale. The first two exhibit low thermal stability, limiting their commercial applicability, and $ZnO{\cdot}B_2O_3{\cdot}2H_2O$ is stable to about 200 °C. The compound $4ZnO{\cdot}B_2O_3{\cdot}H_2O$ or $Zn_2(BO_3)OH$ has the highest thermal stability of the commercially manufactured hydrated zinc borates, with a dehydration on-set temperature of 410–415 °C.[56] This high dehydration temperature allows the use of this zinc borate in engineering thermoplastics processed at high temperatures. More than a decade after this compound was in commercial production on a multiton scale, it was rediscovered by the materials science community and reported to have interesting photoluminescent and photovoltaic properties.[58]

4.9 Barium Borates

Both hydrated and anhydrous barium borates find significant commercial use. Barium metaborate monohydrate, $BaO{\cdot}B_2O_3{\cdot}H_2O$, is used as a corrosion inhibitor in industrial paints and primers, a biocide in paints and plastics, and to a lesser extent as a fire retardant additive. It is generally manufactured by reacting barium sulfate with a sodium tetraborate hydrate in water. Several other crystalline hydrated barium borates are also known but have less industrial importance.

Crystalline anhydrous beta barium borate, β-$BaO{\cdot}B_2O_3$ or β-BaB_2O_4, has technological importance as a nonlinear optical material. Its attributes in this application include transparency over a wide range of frequencies and phase matching ranges, a large nonlinear coefficient, high-damage threshold, and good optical homogeneity well in the UV region.[65]

5 NONMETAL BORATES

5.1 Introduction

Ammonia, alkylamines, and other proton acceptor species can react with boric acid in aqueous or alcoholic solutions to form a wide range of crystalline nonmetal borate salts.[66] Borate salts of aprotic nonmetal cations, such as quaternary ammonium cations, have also been characterized.[67,68] The ammonium borates are significant commercial products, and the recognition that both protic and aprotic nonmetal cations can stabilize unusual borate anions has led to increased interest in the study of this area.

5.2 Ammonium Borates

The ammonium cation represents one of the simplest examples of a nonmetal cation. This cation is only slightly less acidic than boric acid itself and cannot form salts with borate anions more basic than tetraborate (**5**), and even this salt has marginal stability. Thus, the hypothetical ammonium metaborate, NH_4^+ $[B(OH)_4]^-$, does not exist as a stable solid. Of the nonmetal borates, only ammonium pentaborate, $NH_4[B_5O_6(OH)_4]{\cdot}2H_2O$ or $(NH_4)_2O{\cdot}5B_2O_3{\cdot}8H_2O$, and ammonium tetraborate, $NH_4[B_4O_7(OH)_4]{\cdot}4H_2O$ or $(NH_4)_2O{\cdot}2B_2O_3{\cdot}4H_2O$, are manufactured in significant commercial quantities. Ammonium pentaborate is more stable than the tetraborate, which exhibits a significant vapor pressure of ammonia under atmospheric conditions. When the pentaborate is heated from 100 to 230 °C, it loses 75% of its water content but less than 1% of its ammonia. The pentaborate crystallizes in two forms, orthorhombic and monoclinic. The orthorhombic form crystallizes as the kinetic product, which is sold commercially. Solubilities of ammonium borates are given in Table 7.

Prolonged reflux of an aqueous slurry of ammonium pentaborate results in quantitative conversion to $[NH_4]_3[B_{15}O_{20}(OH)_8]{\cdot}4H_2O$, also known as the mineral ammonioborite. This compound contains the unusual 15-boron anion, $[B_{15}O_{20}(OH)_8]^{3-}$ (**10**), produced by the formal condensation of three pentaborate anions (**3**). Another ammonium borate mineral, larderellite, $[NH_4][B_5O_7(OH)_2]\cdot H_2O$, contains an anionic structural unit composed of an infinite chain of condensed pentaborate anions (**11**). Both the isolated trianion (**10**) in ammonioborite and the chain polyanions (**11**) in larderellite are so far known to occur only with the ammonium cation.

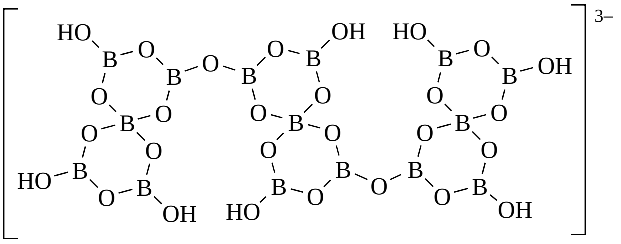

(**10**)

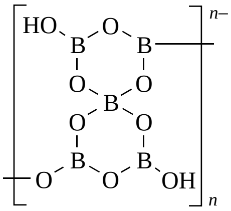

(**11**)

5.3 Other Nonmetal Borates

Most nonmetal borates reported in the literature are ammonium and substituted ammonium salts. In general, boric acid forms salts with alkyl- or aryl-amines that are roughly as or more basic than pyridine. Depending on the reaction conditions, a number of different crystalline borates might be isolated from a given amine. However, the chemistry of substituted amine borates is dominated by the occurrence of pentaborates, and relatively few compounds in this class have been reported containing more basic borates anions.

Nonmetal cations can stabilize other unusual borate structures. For example, the tetraethylammonium cation can be used to crystallize the compound $[NEt_4]_2[BO(OH)_2]_2\cdot B(OH)_3\cdot 5H_2O$, which contains a rare example in a crystal structure of the Arrhenius conjugate base of boric acid, the $[BO(OH)_2]^-$ anion.[67] This anion is also found in the related urea inclusion compound $[NMe_4]_2[BO(OH)_2]\cdot 2(NH_2)_2CO\cdot H_2O$, containing the tetramethylammonium cation.[68] Another unusual borate species found only with nonmetal cations is the nona-borate trianion, $[B_9O_{12}(OH)_6]^{3-}$. This isolated anion is found in the imidazolium and guanidinium borates, $[C_3H_5N_2]_3[B_9O_{12}(OH)_6]$ and $[C(NH_2)_3]_3[B_9O_{12}(OH)_6]$, which form readily upon reaction of boric acid with imidazole or guanidinium carbonate, respectively, in hot water.[69]

6 BORIC ACID ESTERS

6.1 Introduction

Ebelman and Bouquet prepared the first examples of boric acid esters in 1846 from boron trichloride and alcohols.[70] Literature reviews of this subject are available.[71,72] The general class of boric acid esters includes the more common orthoboric acid based trialkoxy- and triaryloxyboranes, $B(OR)_3$ (**1**), and also the cyclic boroxins, $(ROBO)_3$, which are based on metaboric acid (**2**). The boranes can be simple trialkoxyboranes, cyclic diol derivatives, or more complex trigonal and tetrahedral derivatives of polyhydric alcohols. Nomenclature is confusing in boric acid ester chemistry. Many trialkoxy- and triaryloxyboranes such as methyl, ethyl, and phenyl are commonly referred to simply as methyl, ethyl, and phenyl borates. The IUPAC boron nomenclature committee has recommended the use of trialkoxy- and triaryloxyboranes for these compounds, but they are referred to in the literature as boric acid esters, trialkoxy and triaryloxy borates, trialkyl and triaryl borates or orthoborates, and boron alkoxides and aryloxides. The IUPAC nomenclature will be used in this review except for relatively common compounds such as methyl borate. Boroxins are also referred to as metaborates and more commonly as boroxines. Boroxin is preferred by the IUPAC nomenclature committee and will be used in this review.

6.2 Trialkoxy- and Triaryloxyboranes

6.2.1 Properties

Trialkoxy- and triaryloxyboranes are more systematic names for $B(OR)_3$ and $B(OAr)_3$ compounds. These are more commonly referred to simply as alkyl and aryl borates, for example, methyl borate for $B(OCH_3)_3$ and phenyl borate for $B(OC_6H_5)_3$. This class contains compounds ranging from low-boiling liquids to high-melting solids. Some physical properties of selected members of this class are included in Table 9. These compounds contain sp^2 hybridized trigonal planar boron atoms. As with other trivalent boron compounds, the vacant $2p_z$ orbital imparts a Lewis acid character, and many of their reactions involve a tendency to accept unshared electrons from donor species. Trialkoxy- and triaryloxyboranes are generally monomeric and soluble in most organic solvents. They also dissolve in water with reactions as discussed below.

6.2.2 Preparation and Uses

Trialkoxy- and triaryloxyboranes can be prepared by a variety of methods. The original procedure from boron trichloride and alcohols (equation 7) is not practical on a commercial scale but can be used to prepare laboratory

Table 9 Some properties of boric acid esters

Compound	Formula	Mp (°C)	Bp (°C)	d_4^t
Methyl borate	$B(OMe)_3$	−29	68.0–68.5	0.920
Methyl borate azeotrope	$B(OMe)_3 \cdot MeOH$	–	54.3	0.880
Ethyl borate	$B(OEt)_3$	−84.8	117–119	0.859
Ethyl borate azeotrope	$B(OEt)_3 \cdot 7.75EtOH$	–	76.6	–
n-Propyl borate	$B(O\text{-}n\text{-}Pr)_3$	–	176–179	0.856
Isopropyl borate	$B(O\text{-}i\text{-}Pr)_3$	–	139–140	0.815
n-Butyl borate	$B(O\text{-}n\text{-}Bu)_3$	–	227	0.856
2,2′-Oxybis(4,4,6-trimethyl-1,3,2-dioxaborinane) (**12**)	$C_{12}H_{24}B_2O_5$	–	114–115 at 0.27 kPa	1.013
2,2′-[(l-Methyl-1,3-propanediyl)-bis(oxy)1-bis(4-methyl-1,3,2-dioxaborinane)] (**13**)	$C_{12}H_{24}B_2O_6$	–	207–213	1.071
Phenyl borate	$B(OPh)_3$	80–90	360–370	–
Triethanolamine borate (**15**)	$B(OCH_2CH_2)_3N$	–	235–237	–
Methylboroxin	$(OBOMe)_3$	–	dec.	1.2286
n-Propylboroxin	$(OBO\text{-}n\text{-}Pr)_3$	52–54	235–239 dec.	–

quantities of esters. For larger quantities, boric acid or boric oxide is generally reacted with alcohols or phenols (equations 8 and 9). The equilibria in these reactions, which lie far to the left, must be shifted to the right by removal of product water. This is usually accomplished by isotropic distillation with excess alcohol or phenol or by adding a suitable azeotroping solvent. The preparations of methyl and ethyl borates are further complicated because these borates form azeotropes with their respective alcohols. In these cases, the azeotrope must be isolated and the pure ester separated in a second step. Improved yields of trialkoxy- and triaryloxyboranes and boroxins can be achieved by removing product water with anhydrous calcium hydride.[73] Derivatives of slow reacting, sterically hindered alcohols can be successfully prepared by this method.

$$BX_3 + 3ROH \longrightarrow B(OR)_3 + 3HX \qquad (7)$$

$$B(OH)_3 + 3ROH \longrightarrow B(OR)_3 + 3H_2O \qquad (8)$$

$$B_2O_3 + 6ROH \longrightarrow 2B(OR)_3 + 3H_2O \qquad (9)$$

The largest volume uses of boric acid esters are in the captive production of methyl borate as an intermediate in the production of sodium borohydride and isopropylborate as an intermediate in the production of triphenylboron for use as a cocatalyst in polyamide production. Also significant, are uses of boric acid esters as fuel additives, wood preservatives, and as components in many different kinds of industrial fluids, including lubricants, hydraulic fluids, metal cutting fluids, and so forth. A mixture of the two dioxaborinanes (**12**) and (**13**) is sold as the microbiocide that is used as an additive for control of slime and sediment-producing microorganisms in hydrocarbon jet and diesel fuels. Methyl borate azeotrope is used as a gaseous flux in welding and brazing. Borate esters may also be used as polymer additives and epoxy resin curing agents.

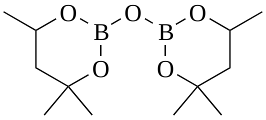

(**12**)

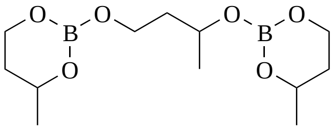

(**13**)

Another convenient method, for the preparation of higher-boiling trialkoxy- and triaryloxyboranes, in particular, is the transesterification of lower-boiling boranes (equation 10). The lower boiling alcohol is removed continuously by distillation.

$$B(OR)_3 + 3R'OH \longrightarrow B(OR')_3 + 3ROH \qquad (10)$$

The conversion of boron compounds to trialkoxyboranes is the basis for a widely used historic prospecting procedure for identification of borate minerals. By adding a mineral acid and methanol to a ground mineral sample and then igniting the mixture, one can observe whether it burns with the green flame of volatile methyl borate.

6.2.3 *Reactions*

Most trialkoxy- and triaryloxyboranes react readily with water, hydrolyzing to boric acid and alcohol (reverse of equation 8). This susceptibility to hydrolysis, even with atmospheric moisture, has limited their usefulness in commercial applications. Partially hydrolyzed intermediates such as $(RO)_2BOH$, are usually isolated only with compounds containing large substituent groups, but hydrolysis usually proceeds completely to boric acid. Hydrolysis rates observed with esters derived from short-chain primary aliphatic alcohols and unhindered phenols are very fast, but significant rate decreases are observed as the substituent groups become large and bulky. This probably results from the demanding steric requirements of the sp^3 hybridized transition state formed when the boron center undergoes a nucleophilic attack by water. Compounds that have internal coordination to boron, for example, the transannular bond from the electron pair on nitrogen to boron in compounds such as tripropanolamine borate (**14**) and triethanolamine borane (**15**), exhibit good hydrolytic stability. Owing to lower ring strain, tripropanolamine borate is more resistant to hydrolysis than triethanolamine borate. Some comparative hydrolysis rates in homogeneous water-dioxane are shown in Table 10.[74] Reactions were run either at 21 °C in 60% dioxane or at 55 °C in 91% dioxane, and the relative rates adjusted to comparable values are shown in the table.

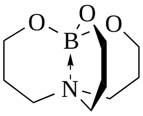
(**14**)

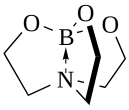
(**15**)

Transesterification with other alcohols and phenols (equation 10), particularly if they are high boiling, is another typical reaction of trialkoxy- and triaryloxyboranes. Similar reactions with amines proceed very slowly, and preparation of triaminoboranes by displacement of alcohols from trialkoxyboranes is not a practical synthetic route.

6.3 Boroxin

Boroxins have properties and reactivities similar to orthoborate esters. The six-membered boroxin ring structure (**2**) is approximately planar, generally exhibiting a small out-of-plane envelope deformation. The trigonal boron atoms in trialkoxyboroxins generally exhibit a stronger Lewis acid character than comparable borons in trialkoxyboranes because there is only one electron-donating alkoxy group per boron. Preparative methods are essentially the same as those noted for trialkoxyboranes except that the stoichiometry is changed. The calcium hydride method is particularly efficient for preparation of boroxins, which are difficult to prepare using azeotropic distillation. Although some boroxins have been offered commercially, no significant applications for them have been developed.

Table 10 Relative hydrolysis rates of boric acid esters in aqueous dioxane

R in $B(OR)_3$	Relative rates
Methyl, ethyl, propyl, isopropyl, *n*-butyl, isobutyl, phenyl, *o*-cresyl, *o*-phenylphenyl, *o*-cyclohexylphenyl	$>5.87 \times 10^5$
n-Pentyl	5.87×10^5
n-Hexyl	2.02×10^5
sec-Butyl	1.68×10^5
n-Octyl	3.67×10^4
Oleyl	3.53×10^4
n-Dodecyl	2.77×10^4
Stearyl	2.71×10^4
2-Octyl	4.33×10^3
2-Ethylhexyl	2.77×10^3
tert-Butyl	1.37×10^3
tert-Pentyl	4.49×10^2
3-Heptyl	4.15×10^2
Diisobutylmethyl	5.9
2-Cyclohexylcyclohexyl	3.7
Dicyclohexylmethyl	1

6.4 Esters of Polyhydroxy Compounds

Boric acid esters are generally hydrolytically unstable and decompose to boric acid and alcohol rapidly when exposed to moisture. However, reaction of boric acid with 1,2- and 1,3-diols having the appropriate configurations results in the formation of five- and six-membered cyclic esters (equation 11).[75] Although still hydrolytically labile, these cyclic esters have sufficiently enhanced kinetic stability to shift the reaction equilibrium significantly to the right in aqueous media. Since this reaction produces a proton, reaction of boric acid with appropriate polyols can result in strongly acidic complexes. This reaction is commonly used in procedures for determination of boric acid and other boron compounds. In this method, a sugar, such as mannitol or sorbitol, is added to boric acid and the resulting strong acid is titrated with base, where a distinct endpoint characteristic of strong acids is observed.

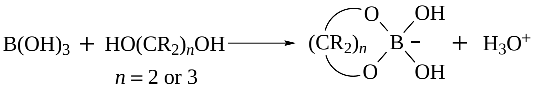
$$\mathrm{B(OH)_3 + HO(CR_2)_nOH \longrightarrow (CR_2)_n(O)_2B^-(OH)_2 + H_3O^+} \quad (11)$$

$n = 2$ or 3

Boric acid reacts with two equivalents of diol to form spiro ester complexes as shown in equation (12). In the case where the diol is part of a polymer chain, this reaction leads to crosslinking. Addition of borates to aqueous solutions of appropriate polyhydroxylated polymers, for example, polyvinyl alcohols, guar gums, and starches, can have a dramatic effect on rheology, often resulting in gel formation. Borate crosslinking of polymers is utilized commercially in the manufacture of starch adhesives for corrugated boxes and in the formation of polyvinyl alcohol gel films to protect metal surfaces and for other applications. Reactions of this type are also exploited in boron-specific exchange resins and adsorbents to remove borates from aqueous solutions.

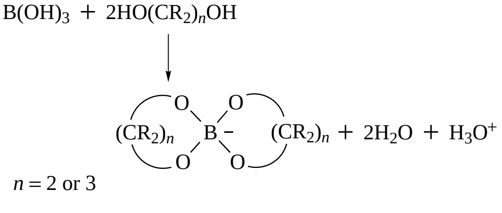
$$\mathrm{B(OH)_3 + 2HO(CR_2)_nOH \longrightarrow (CR_2)_n(O)_2B^-(O)_2(CR_2)_n + 2H_2O + H_3O^+} \quad (12)$$

$n = 2$ or 3

The interaction of borates with carbohydrates and other polyhydroxy compounds, including perhaps proteins and glycoproteins, provides a basis for the biological role of boron. It has been shown that at least one essential role of boron in plants involves ester crosslinking of the complex carbohydrate rhamnogalacturonan II (RG II) as part of an intricate control mechanism vital to the maintenance of proper plant cell wall function.[7]

Once thought rare, boron-containing natural products are now known to be widespread. Traditional methods for the isolation of organic natural product compounds involve procedures that typically result in the hydrolytic loss of boron. Thus, only in recent years have significant numbers of boron-containing natural products become recognized. Among the first boron-containing natural products characterized were macrolide antibiotics, including boromycin (**16**),[76] aplasmomycin,[77] and tartrolon B,[78] derived from streptomycetes, myxobacteria, and cyanobacteria. Studies of the metabolic roles of boron in higher plants have now revealed numerous other boron-containing natural products. For example, plants utilize borate ester of sugars to transport boron.[79] A protein specifically responsible for the active transport of boron has been identified in plants.[80]

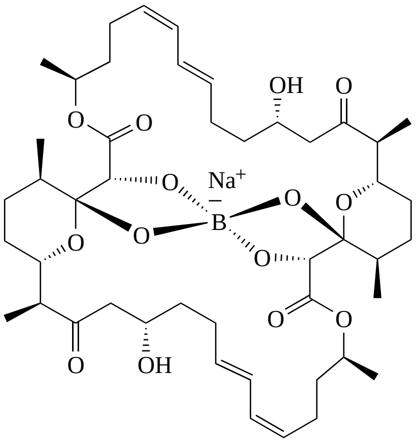
Tartrolon B
(**16**)

The presence of adequate supplies of boron has been shown to be essential for the proper development of frogs and fish, and considerable evidence indicates that boron plays a vital role in other animals and humans.[4] Although precise biochemical mechanisms are yet to be revealed for animals, it appears likely that boron interacts through reversible ester formation in significant and necessary ways with membrane components and enzymes in animal cells.

7 BORON–SULFUR COMPOUNDS

7.1 Introduction

The detailed chemistry of boron–sulfur and related boron–selenium compounds has emerged only slowly because of a lack of suitable experimental techniques to handle these highly reactive compounds until recently. The B–S bond energy has been estimated at 100 kcal mol^{-1} in B_2S_3 compared to 164 kcal mol^{-1} for the average B–O bond in B_2O_3, and this difference is reflected in the relative reactivities of the two classes of compounds. Only in the past decade and a half have sufficient advances been made in preparative methods to allow the isolation and characterization of many compounds in this class, revealing a number of unusual compounds. Although some parallel features are shared with the more common boron–oxygen derivatives, boron exhibits a considerably different structural chemistry when combined with the heavier chalcogenides. Boron–oxygen structural chemistry is dominated by the B_3O_3 boroxin ring, whereas in boron-sulfur chemistry we see many compounds containing four- and five-membered boron–sulfur rings, leading to even greater complexity. The chemistry of boron–sulfur and boron–selenium compounds has been the subject of a review.[81] To date there are no significant commercial uses of these compounds.

7.2 Binary Boron–sulfur Compounds

A number of binary boron–sulfur compounds has been reported. Of these, B_2S_3, $(BS_2)_n$, and B_8S_{16} are probably best characterized. Diboron trisulfide, B_2S_3, can be prepared by the high-temperature reactions of elemental boron, boron hydrides, or metal borides with sulfur or other sulfur-containing compounds. It is generally obtained as a white amorphous sublimate that reacts with water and atmospheric moisture. It has been described as pale yellow, probably because of the presence of impurities. It softens at approximately 320 °C. Its reactivity leads to its use as a starting material for the preparation of a variety of organoboron compounds. Reactions with alcohols lead to borate esters, $B(OR)_3$, and with amines to triaminoboranes, $(R_2N)_3B$.

Crystalline B_2S_3 has a layered structure with sheets of interconnected six-membered B_3S_3 and four-membered B_2S_2 rings, linked by shared sulfur atoms, extending throughout the crystal. Boron disulfide, $(BS_2)_n$, has a layered structure consisting of five-membered 1,2,4-trithia-3,5-diborolane rings connected into zigzag chains by shared sulfur atoms. These chains run parallel within planes and run antiparallel to chains in adjacent layers. An analogous $(BSe_2)_n$ has been characterized. The compound B_8S_{16} contains the same trithiadiborolane rings as found in $(BS_2)_n$ except, instead of forming infinite chains, sets of four rings are linked by shared sulfur atoms into planar porphin-like macrocycles. These tetramers stack to form parallel columns.

Other reported binary boron sulfides include subvalent $B_{12}S$, a black crystalline material prepared by a high-temperature reaction of amorphous boron with elemental sulfur, and BS, which has been studied spectroscopically in an electric discharge. A vapor-phase dimer, $(BS)_2$, was identified, and a refractory condensed form of BS was reported from the reaction of elemental boron with sulfur at 1850 °C and a pressure of 94 500 atmospheres. Boron disulfide, BS_2, has been identified in the gas phase and appears to be the primary compound present in the vapor phase over diboron trisulfide or elemental boron and sulfur.

7.3 Ternary Thioborates

A few dozen metal thioborate compounds have been structurally characterized. These include $TlBS_2$, M_3BS_3 (M = Li, Tl), $Cs_2B_2S_4$, $K_2B_2S_7$, $M_3B_3S_6$ (M = Na, K, Rb), $Tl_3B_3S_{10}$, $M_6B_{10}S_{18}$ (M = Li, Ag), $Li_5B_7S_{13}$, $Li_9B_{19}S_{33}$, MB_2S_4 (M = Ba, Sr), $M_3[BS_3]_2$ (M = Ba, Sr), $Sr_3[B_3S_6]_2$, among others. These contain thioborate anions such as the trigonal planar $[BS_3]^{3-}$ and the four-, five-, and six-membered cyclic anions, $[B_3S_6]^{3-}$, $[B_2S_4]^{2-}$, and $[B_2S_5]^{2-}$, all having terminal B–S groups. A few related selenoborates have also been characterized, including Tl_3BSe_3, and the unusual selenoborate $Cs_8[B_{12}(BSe_3)_6]$, which contains a central B_{12} icosahedron, in which each boron atom is bound to a selenium atom of a bichelating BSe_3 moiety to form the $[B_{12}(BSe_3)_6]^{8-}$ anion, which has six terminal B–Se group projecting radially. The central B_{12} polyhedron possesses $2n + 2$ skeletal electrons (for n vertices), in agreement with Wade's rules, with six excess negative charges located on the terminal selenium atoms. Considerable interest has been focused on lithium and silver thioborates containing rigid anionic frameworks, since these are good candidates for superionic conducting materials.

7.4 Trialkyl- and Triarylthioboranes

Many compounds with B-S-R groups have been synthesized, including thioborates or trialkyl- and tiaryl-thioborates, $B(SR)_3$, the sulfur analogs of trialkoxy- and triaryloxyboranes, and trialkyl- and triarylborathiins, $(SBR)_3$, the sulfur analogs of boroxins. Simple thioborates are usually prepared by reactions of boron halides with thiols (equation 13).

$$BX_3 + 3RSH \longrightarrow B(SR)_3 + 3HX_3 \qquad (13)$$

These reactions usually proceed more slowly than the reactions of the corresponding alcohols or phenols with boron halides. In some cases, where direct reaction is too slow, the lead or mercury derivatives of thiols are used. Attempts to use the reactions of thiols with diboron trisulfide to prepare trialkylthioboranes have usually been unsuccessful, although analogous reactions with oxygen compounds are commonly used to prepare trialkoxyboranes. Formation of B–S bonds is more difficult than the corresponding B–O bonds, and nucleophilic displacement of RS groups proceeds more readily than with RO groups upon attack by nucleophiles such as water, alcohols, and amines. Exchange reactions with thiols also proceed readily, and these reactions can be used to prepare thioborates of higher boiling thiols (equation 14). Although a sulfur analog of boric acid has not been reported, the cyclic metaboric acid (**1**) analog, $(HSBS)_3$, has been characterized. The dimer $(HSBS)_2$ was also isolated and shown to readily convert to the trimer on heating.

$$B(SR)_3 + 3HSR' \longrightarrow B(SR')_3 + 3RSH \qquad (14)$$

8 BORON–PHOSPHORUS COMPOUNDS

The chemistry of boron–phosphorus compounds has been reviewed.[82,83] Numerous boron–phosphorus derivatives have been reported, but relatively few boron–arsenic or boron–antimony compounds have been described. Boron-phosphorus compounds are similar in many ways to boron–nitrogen derivatives, but the tendency to share bonding electrons in covalent tetrahedral compounds is much more evident with phosphorus than with nitrogen. In fact, most boron–phosphorus chemistry involves tetrahedral boron. They are typically either phosphine–borane complexes, such as $R_3P{\cdot}BR'_3$, or phosphinoboranes $(R_2PBR'_2)_n$, cyclic or polymeric derivatives of the hypothetical $H_3P{\cdot}BH_3$. The chemistry of these compounds and that of boron phosphate and thiophosphate is described below. Boron phosphides are discussed in Section 2.6.

Many phosphine-borane complexes $Y_3P{\cdot}BZ_3$ have been characterized. They include compounds where Y = alkoxy, alkyl, amino, halide, and hydride groups, and Z = alkyl, halide, and hydride. The stabilities of these complexes vary widely depending on the Lewis acidity and basicity of the boron and phosphorus moieties, respectively. The relative stabilities of Lewis acid-base complexes with BH_3 are $R_3P > R_3N > R_3As > R_3Sb$, but with BF_3 the order is $R_3N > R_3P > R_3As > R_3Sb$. The stabilities of the boron halide complexes of phosphines follow the same order as the amine complexes: $BI_3 > BBr_3 > BCl_3 > BF_3$.

The pyrolysis of phosphine-borane complexes was reported in the 1950s to give a series of cyclic and polymeric products.[84] A relatively stable monomer, H_2PBMe_2, which slowly polymerized, was isolated from the reaction of phosphine with $BrBMe_2$ in the presence of triethylamine. Pyrolysis of $Me_2PH{\cdot}BH_3$, however, yielded not the monomeric phosphinoborane but a trimer, $(Me_2PBH_2)_3$, a tetramer, $(Me_2PBH_2)_4$, and a polymeric residue with the approximate composition $(Me_2PBH_2)_n$. Since these early studies were made, a large number of phosphinoboranes has been prepared. Most of them are cyclic trimers plus a few tetramers and dimers. Although most monomers tend to cyclize or polymerize, some stable derivatives of the type $R_2PBR'_2$, where R and R′ are bulky groups, have been isolated. The six-membered rings in phosphinoborane trimers and eight-membered rings in tetramers consist of alternating boron and phosphorus atoms with some out-of-plane puckering of the rings. These cyclic compounds are colorless crystalline solids having thermal stability. The P-hexamethyl trimer, for example, is stable to 250 °C in vacuum. However, decomposition is rapid in the presence of air. The boron–hydrogen bonds in these compounds are unexpectedly resistant to hydrolysis. The hypothetical compound $(HPBH)_3$, the phosphorus analog of the common boron–nitrogen trimer borazine, has not been isolated. However, derivatives of this compound containing the six-membered $(PB)_3$ moiety can be stabilized using bulky substituents on the boron and phosphorus atoms, as in (2,4,6-$Me_3C_6H_2BPC_6H_{11})_3$.[85]

Boron phosphate, BPO_4, is prepared by the dehydration of a mixture of boric acid and phosphoric acid at temperatures of 1000–1200 °C. Although BPO_4 begins to form in these mixtures at much lower temperatures, complete dehydration requires temperatures above 1000 °C. Boron phosphate is a white infusible solid that slowly vaporizes above 1450 °C without decomposition. The structure of boron phosphate prepared under atmospheric conditions consists of tetragonal bipyramids analogous to the high cristobalite forms of silica. Both boron and phosphorous atoms are tetrahedrally coordinated by oxygen. Heating the common form of boron phosphate to 500 °C at 5 GPa (50 000 atm) yields a quartz-like form. A number of hydrates of boron phosphate have been prepared: $BPO_4 \cdot nH_2O$ where $n = 3, 4, 5,$ or 6. All the hydrates decompose in water to give the parent acids; anhydrous boron phosphate hydrolyzes similarly. The anhydride is used as a heterogeneous catalyst. The related compound, boron thiophosphate, BPS, is prepared by reaction of the elements or from diboron trisulfide, phosphorus, and sulfur.

9 BORON-HALOGEN COMPOUNDS

9.1 Introduction

Boron-halogen compounds, or boron halides, can be divided into three major categories that are defined by the ratios of halogens to borons. The boron trihalides (halogen:boron ratio = 3) were discovered and characterized first and represent the most common and thoroughly investigated boron halide category. Haloborates, with a halogen:boron ratio of 4, are important because of the relatively widespread commercial usage of fluoroborates. The third category, boron subhalides, with halogen:boron ratios <3, represents a theoretically interesting class of compounds that have been prepared only in relatively small quantities.

9.2 Boron Trihalides

9.2.1 Properties

A chronology of the discovery and characterization of the four boron trihalides is interesting since the scientists involved were some of the most prominent chemists of the 19th century:

1809	boron trifluoride	Davy, Gay-Lussac, Thénard
1824	boron trichloride	Berzelius
1846	boron tribromide	Poggiale
1891	boron triiodide	Moissan

Boron trihalides were studied extensively in subsequent years, and their chemistry has been summarized in several reviews.[86–88] They are also referred to as trihaloboranes, but boron trihalide is used more frequently. Boron trihalides are trigonal molecules with bond angles of the expected 120°. This sp^2 hybridized state leaves a vacant $2p_z$ orbital on boron, a characteristic that, as with other boron compounds, provides the basis for much of the chemistry of boron halides. The measured bond lengths in boron trihalides are shorter than calculated, and their Lewis acidities ($BI_3 > BBr_3 > BC1_3 > BF_3$) are reversed from the order expected from a consideration of the relative electronegativities of the halogens. For example, boron trifluoride is the weakest acceptor with electron donors such as amines even though fluorine is the most electronegative of the halogen substituents. These observations are usually rationalized by assuming back-bonding in which nonbonding halogen electrons interact with the vacant p orbital on boron. If this does occur to a significant extent, fluoride would be the most effective back-bonding halogen and iodide the least, thereby rationalizing the observed order of Lewis acidity and the unexpectedly short bond lengths observed in all the trihalides. This presumed bonding order was confirmed experimentally in investigations of gas-phase photolysis spectra of boron trihalides.[89]

Table 11 outlines some physical properties of the trihalides including bond lengths and bond energies. Each property tends to vary continuously from gaseous boron trifluoride to the relatively high-boiling boron triiodide. All of the pure compounds are colorless, although the bromide and iodide become colored when exposed to light, apparently as the result of photolytic liberation of the free halogens.

Table 11 Physical properties of boron trihalides

Property	BF_3	BCl_3	BBr_3	BI_3
Mp (°C)	−127.1	−107	−46	−49.9
Bp (°C)	−99.9	12.5	91.3	210
B-X Bond length, Å	1.30	1.75	1.87	2.10
B-X Bond Energy, kJ mol^{-1}	646	444	368	267

Note: X = halogen.

9.2.2 Preparation and Uses

Boron Trifluoride. Boron trifluoride is prepared commercially by the reaction of fluorosulfonic acid (HSO_3F) with boric acid in sulfuric acid followed by purification using fractional distillation. It can also be prepared by the reaction of fluorspar (CaF_2) with boric acid or its equivalent, borax ($Na_2B_4O_7 \cdot 10H_2O$) and sulfuric acid, or by the two-step reaction of borax with hydrofluoric acid and sulfuric acid. Various other methods have been reported for laboratory-scale synthesis or preparation of high-purity boron trifluoride. One example of a procedure for preparation of high-purity material is thermal decomposition of benzenediazonium fluoroborate. Boron trifluoride is used in significant quantities as a Lewis acid catalyst in the large-scale production of organic compounds, particularly in Friedel-Craft reactions, and as an epoxy resin curing agent. In this application, boron trifluoride is either used directly, as one of its coordination compounds, or mixed with a promoter. Distillation of the dimethyl etherate of boron trifluoride is used commercially for the separation of ^{10}B and ^{11}B isotopes and the subsequent production of isotopically enriched boron compounds.

Boron Trichloride. Boron trichloride is prepared commercially by the chlorination of boron carbide (equation 15). Direct chlorination of boric acid or a sodium borate in the presence of carbon is an alternative method. Most of the boron trichloride produced is converted to filaments of elemental boron by chemical vapor deposition (CVD) on tungsten wire in a hydrogen atmosphere. Numerous laboratory preparations of boron trichloride have been reported. One of the most convenient is the halogen exchange reaction of aluminum chloride with boron trifluoride or a metal fluoroborate.

$$B_4C + 6Cl_2 \qquad 4BCl_3 + C \tag{15}$$

Boron Tribromide and Boron Triiodide. Boron tribromide is prepared commercially in relatively small quantities by the bromination of boron carbide, and its commercial use is limited. No commercial use for boron triiodide has been reported. Laboratory quantities of boron tribromide can be prepared by the reaction of aluminum bromide with boron trifluoride or a metal fluoroborate. Boron triiodide can be prepared in small quantities by the reaction of boron or a metal tetrahydroborate with iodine.

9.2.3 Reactions

The four boron trihalides are quite reactive and undergo similar reactions with a variety of other chemicals. Most of these reactions are based on the strong Lewis acidity of the halides. The boron trihalides form complexes with ethers (equation 16) and other Lewis bases based on N, S, P, and As atoms.

$$BX_3 + OR_2 \longrightarrow R_2O \cdot BX_3 \tag{16}$$

If the donor molecule contains reactive hydrogen, as H_2O, NH_3, PH_3, AsH_3, R_2NH, RNH_2, and lower alcohols, hydrogen halides are produced (equations 17–19). In these reactions the initial adducts formed with boron trifluoride are much more stable to protonolysis than with the other trihalides, and these reactions proceed slowly or not at all.

$$BX_3 + H_2O \longrightarrow B(OH)_3 + 3HX \tag{17}$$

$$BX_3 + R_2NH \longrightarrow (R_2N)_3B + 3HX \tag{18}$$

$$BX_3 + 3ROH \longrightarrow (RO)_3B + 3HX \tag{19}$$

Some of these reactions, particularly with the strongest Lewis acids, are rapid or even violent at room temperature. In general, boron trifluoride is significantly less reactive than the other halides. For example, it forms two distinct hydrates that are stable to 20 °C. This resistance to hydrolysis and strong Lewis acid character has led to the relatively wide use of boron trifluoride as a reaction catalyst in a number of organic reactions.

Exchange reactions are common between boron halides and alkyl or aryl substituents, other halides, alkoxy and aryloxy groups, and diborane. Some examples are shown in Scheme 2.

Reduction of boron trihalides to elemental boron can be accomplished by heating with alkali metals, alkaline earth metals, or hydrogen. Under the proper conditions, reductions of this type can also yield diborane and, under selected conditions, boron subhalides (see below). Metal hydrides also react with boron trihalides to give diborane. Boron nitride and boron carbide have been prepared by the high-temperature reductions of boron trihalides with ammonia and methane, respectively, and deposited on metal substrates by CVD.

9.3 Fluoroborates

These compounds are also referred to as tetrafluoroborates, but the tetra-prefix is usually dropped. Fluoroborates and fluoroboric acid have been studied extensively because of their commercial uses as fluxes and in metal-plating baths.**[90]** Fluoroboric acid, HBF_4, does not exist as such but can be stabilized as a solvated ion pair in aqueous solution. Commercially available solutions contain approximately 48% HBF_4 as $H_3O^+ \, BF_4^- \cdot 4H_2O$. Other names used less frequently for this reagent are hydrofluoroboric acid, hydroborofluoric acid, and tetrafluoroboric acid. The boron atom in fluoroboric acid is nearly tetrahedral, with almost equidistant B–F bonds,

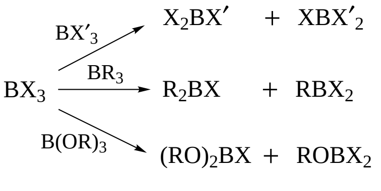

Scheme 2

and F–B–F angles close to the theoretical 109°. It is a strong acid in water with a pK of -4.9 compared to -4.3 for nitric acid.

Fluoroboric acid is produced commercially by the reaction of 70% hydrofluoric acid with boric acid. Fluoroborate solutions must be treated like hydrofluoric acid and handled in corrosion resistant equipment consisting of polyethylene, polypropylene, or neoprene-type rubber. The major use of fluoroboric acid is as an intermediate in the preparation of fluoroborate salts. It is also used in electroplating aluminum and in metal cleaning operations.

Metal fluoroborates are produced either from fluoroboric acid and metal salts or by reactions of boric acid and hydrofluoric acid with metal salts. Fluoroborates of alkali metals and ammonium ions tend to crystallize as hydrates and are water soluble except for those of potassium, rubidium, and cesium. The major use for these compounds is as a high-temperature flux. Transition metal and other heavy metal fluoroborates are not as well known and well characterized. They are usually prepared from fluoroboric acid and an appropriate salt and are sold as 40–50% water solutions. Some fluoroborates from metals such as tin, lead, copper, and nickel are prepared by electrolysis of fluoroboric acid. The transition and other heavy metal fluoroborate solutions are used primarily as plating solutions and catalysts.

9.4 Boron Subhalides

A review of the boron subhalides (halogen:boron ratios <3) is available.[91] The simplest monohalides such as BCl, BBr, and BI are unstable and highly reactive. Unstable boron dihalide radicals (BX_2) have been studied spectroscopically. Diboron tetrahalides B_2X_4 are known for fluorine, chloride, bromine, and iodine. Research on these compounds has been limited by difficulties in preparing suitable quantities for investigations. The fluoride and bromide derivatives are usually prepared from the tetrachloride, which is obtained in the laboratory by passing BCl_3 through an electric discharge, or more efficiently, by using a radio frequency discharge in the presence of mercury. Methods have been devised to convert B_2Cl_2 into B_2F_4 or B_2Br_4. The corresponding iodide has been prepared by the radio frequency discharge reaction of BI_3. Diboron tetrachloride, a yellow solid having a melting point of 94 °C, has been studied in the greatest detail.

Diboron tetrachlorides undergo a variety of reactions, including facile additions to alkenes similar to hydroboration (equation 20). The reactions of boron subhalides, particularly B_2Cl_4, with organic and organometallic compounds, have been studied in some detail.

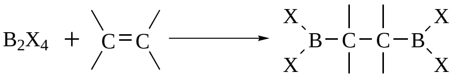

$$B_2X_4 + \ce{>C=C<} \longrightarrow X_2B-\overset{|}{\underset{|}{C}}-\overset{|}{\underset{|}{C}}-BX_2 \qquad (20)$$

Diboron tetrahalides undergo complex pyrolysis reactions resulting in interesting higher molecular weight subhalides with boron:halogen ratios of 1. These compounds are structurally analogous to the polyhedral boranes (*see* ***Boron Hydrides***), but exhibit significant differences in reactivity and other properties. The polyhedral boron hydrides are colorless liquids or white solids, whereas many polyhedral perhaloboranes are intensely colored, ranging from yellow to purple and black. The simplest polyhedral derivative is tetraboron tetrachloride, B_4Cl_4, which has tetrahedral geometry. This yellow solid is also prepared using radio frequency discharge syntheses. The bromide and the mixed chlorobromo derivatives can be prepared by the exchange reaction of diboron tetrachloride with boron tribromide. Larger polyhedral perhaloboranes, including B_nCl_n ($n = 8-12$) and B_nBr_n ($n = 7-10$) have been described. Although structures have yet to be determined for all of the B_nX_n clusters, it is clear that most of them do not conform to the electron counting rules to which the polyhedral boron hydrides and many other inorganic cluster systems generally adhere. For example, the structure of B_8Cl_8 is that of a regular closed 8-vertex polyhedron, yet this compound has only $2n$ framework electrons (for n vertices), rather than $2n + 2$ framework electrons stipulated by electron counting formalisms. The structures of several boron subfluorides, including B_8F_{12} and $B_{10}F_{12}$, were recently determined revealing unusual open structures.[92] The chemistry of boron subhalide compounds remains an area of academic research interest.

10 RELATED ARTICLES

Borates: Solid-state Chemistry; Borides: Solid-state Chemistry; Boron Hydrides; Boron: Metallacarbaboranes; Boron–Nitrogen Compounds; Boron: Organoboranes; Boron: Polyhedral Carboranes.

11 FURTHER READING

W. Poch, *Glastech Ber.*, 1964, **37**, 533.

12 REFERENCES

1. P. Argust, *Biol. Trace Elem. Res.*, 1998, **66**, 131.
2. G. L. Smith and M. D. Medrano, in ‘Boron Mineralogy, Petrology and Geochemistry’, eds. E. S. Grew and L. M. Anovitz, *Reviews in Mineralogy*, Vol. 33, Mineralogical Society of America, Washington, DC, 1996, Chap. 6, p. 263.
3. K. Warington, *Ann. Bot.*, 1923, **37**, 629.
4. D. G. Blevins and K. M. Lakaszewski, *Annu. Rev. Plant Physiol. Mol. Biol.*, 1998, **49**, 481.

5. M. A. O'Neill, S. Eberhard, P. Albersheim, and A. G. Darvill, *Science*, 2001, **294**, 846.
6. D. L. Anderson, W. C. Cunningham, and T. R. Lindstrom, *J. Food Comp. Anal.*, 1994, **7**, 59.
7. P. R. Abou-Shakra, J. M. Havercroft, and N. I. Ward, *Trace Elem. Med.*, 1989, **6**, 141.
8. F. H. Nielsen, *Nutrition*, 2000, **16**, 512.
9. H. E. Goldbach, P. H. Brown, B. Rerkasem, M. Thellier, M. A. Wimmer, R. W. Bell eds, 'Boron in Plant and Animal Nutrition', Kluwer Academic/Plenum Publishers, New York, 2002.
10. C. Rainey and L. Nyquist, *Biol. Trace. Elem. Res.*, 1998, **66**, 79.
11. M. R. Palmer and G. H. Swihart, in 'Boron Mineralogy, Petrology and Geochemistry', eds. E. S. Grew and L. M. Anovitz, *Reviews in Mineralogy*, Vol. 33, Mineralogical Society of America, Washington, DC, 1996, Chap. 13, p. 709.
12. A. H. Soloway, W. Tjarks, B. A. Barnum, F. G. Rong, R. F. Barth, I. M. Codogni, and J. G. Wilson, *Chem. Rev.*, 1998, **98**, 1515.
13. R. A. Smith and R. B. McBroom, 'Kirk-Othmer Encyclopedia of Chemical Technology', 4th edn., John Wiley & Sons, New York, 1992, Vol. 4, p. 365.
14. R. Thompson and A. J. E. Welsh, eds. 'Supplement to Mellor's Comprehensive Treatise on Inorganic and Theoretical Chemistry', Vol. 5, *Boron*, Part A, *Boron-oxygen Compounds*, Longman, London, 1980.
15. N. N. Greenwood, 'Chemistry of the Elements', Pergamon Press Ltd., Oxford, 1984, Chap. 6, p. 155.
16. *Boron: Group IIIA(13)*, in 'Advanced Inorganic Chemistry', eds. F. A. Cotton and G. Wilkinson, 5th edn., John Wiley & Sons, New York, 1988, Chap. 6, p. 162.
17. D. M. Schubert, Borates in Industrial Use, 'Structure and Bonding', Springer-Verlag, Berlin, 2003, p. 1.
18. D. L. Garret, 'Borates, Handbook of Deposits, Processing, Properties, and Use', Academic Press, San Diego, CA, 1998.
19. E. L. Muetterties ed., 'The Chemistry of Boron and Its Compound', John Wiley & Sons, New York, 1967.
20. A. E. Newkirk, in 'Boron, Metallo-boron Compounds and Boranes', ed. R. M. Adams, Interscience Publications, New York, 1964, Chap. 4, p. 233.
21. V. I. Matkovich ed., 'Boron and Refractory Borides', Springer-Verlag, Berlin, 1977, p. 57.
22. J. L. Hoard and R. E. Hughes, in 'Boron, Metallo-boron Compounds and Boranes', ed. R. M. Adams, Interscience Publications, New York, 1964, Chap. 2, p. 25.
23. R. Uno and I. Higashi eds, *Proceedings of the 11*th *International Symposium on Boron, Borides, and Related Compounds*, Tsukuba, 1993; *Jpn. J. Appl. Phys.*,1 1994.
24. D. Emin, T. L. Aselage, A. C. Switdick, B. Morosin, and C. L. Beckel eds, 'AIP Proceedings No. 231 – Boron Rich Solids', American Physical Society, New York 1991.
25. H. Davy, *Philos. Trans. R. Soc. London*, 1808, **98**, 35.
26. J. Nagamatsu, N. Nakagawa, T. Muranaka, Y. Zenitani, and J. Akimitsu, *Nature*, 2001, **410**, 63.
27. S. Mollah, H. D. Yang, and B. K. Chaudhuri, *Indian J. Phys. A*, 2003, **77A**(1), 9.
28. H. J. Choi, D. Roundy, H. Sun, M. L. Cohen, and S. G. Louie, *Nature*, 2002, **418**, 758.
29. B. A. Cook, J. L. Harringa, T. L. Lewis, and A. M. Russell, *Scripta Mater.*, 2000, **42**, 597.
30. B. A. Cook, J. L. Harringa, and A. M., Russell, U.S. Patent No. 6,099,605 2000.
31. K. H. J. Buschow, F. H. Feijen, and K. de Kort, *J. Magn. Magn. Mater.*, 1995, **140**, 9 http://WWW.Sciencedirect.com.
32. R. T. Paine and C. K. Narula, *Chem. Rev.*, 1990, **90**, 73.
33. E. Bengu and L. D. Marks, *Phys. Rev. Lett.*, 2001, **86**, 2385.
34. N. G. Chopra, R. J. Luyken, K. Cherrey, V. H. Crespi, M. L. Cohen, S. G. Louie, and A. Zettl, *Science*, 1995, **269**, 966.
35. J. Dulat, 'Supplement to Mellor's Comprehensive Treatise on Inorganic and Theoretical Chemistry', Vol. 5, *Boron*, Part A, *Boron-oxygen Compounds*, Longman, London, 1980, Sect. A4, p. 170.
36. S. Kroeker and J. F. Stebins, *Inorg. Chem.*, 2001, **40**, 6239.
37. D. He, Y. Zhao, L. Daeman, J. Qian, T. D. Shen, and T. W. Zerda, *Appl. Phys. Lett.*, 2002, **81**, 643.
38. T. Peymann, C. B. Knobler, S. I. Khan, and M. F. Hawthorne, *J. Am. Chem. Soc.*, 2001, **123**, 2182.
39. R. W. Sprague, 'Supplement to Mellor's Comprehensive Treatise on Inorganic and Theoretical Chemistry', Vol. 5, *Boron*, Part A, *Boron-oxygen Compounds*, Longman, London, 1980, Sect. A6, p. 224.
40. R. P. Bell, J. O. Edwards, and R. B. Jones, in 'The Chemistry of Boron and Its Compounds', ed. E. L. Muetterties, John Wiley & Sons, New York, 1967, Chap. 4, p. 209.
41. A. Erdemir, G. R. Fenske, R. A. Erck, F. A. Nichols, and D. E. Busch, *Lubr. Eng.*, 1991, **47**, 179.
42. D. White, D. E. Mann, P. N. Walsh, and A. Somer, *J. Chem. Phys.*, 1960, **32**, 488.
43. N. Ingri, *Sven. Kem. Tidskr.*, 1963, **75**, 199.
44. M. Attina, E. Cacace, G. Occhiucci, and A. Ricci, *Inorg. Chem.*, 1992, **31**, 3114.
45. P. J. Bray, in 'Borate Glasses, Crystals & Melts', eds. A. C. Wright, S. A. Feller, and A. C. Hannon, Society of Glass Technology, Sheffield, 1997, p. 1.
46. P. Becker, *Z. Kristallogr.*, 2001, **216**, 523.
47. C. Erd, 'Supplement to Mellor's Comprehensive Treatise on Inorganic and Theoretical Chemistry', Vol. 5, *Boron*, Part A, *Boron-oxygen Compounds*, Longman, London, 1980, Sect. A1, p. 7.
48. J. D. Grice, P. C. Burns, and F. C. Hawthorne, *Can. Mineral.*, 1999, **37**, 731.
49. P. A. Lyday, Boron, 'U.S. Geological Survey, Mineral Commodity Summaries', U.S. Government printing office, Washington, January 2003, p. 34.

50. D. R. Powell, D. F. Gaines, P. J. Zerella, and R. A. Smith, *Acta Crystallogr.*, 1991, **C47**, 2279.

51. W. F. Cooper, F. K. Larsen, P. Coppens, and R. F. Giese, *Am. Mineral.*, 1973, **58**, 21.

52. A. McKillop and W. R. Sanderson, *Tetrahedron*, 1995, **51**, 6145.

53. P. C. Burns and F. C. Hawthorne, *Can. Mineral.*, 1993, **31**, 297.

54. S. Ghose, C. Wan, and J. R. Clark, *Am. Mineral.*, 1978, **63**, 160.

55. S. Menchetti, C. Sabelli, and R. Trosti-Ferroni, *Acta Crystallogr.*, 1982, **B38**, 3072.

56. D. M. Schubert, U. S. Patent Nos. 5,342,553 1994, and 5,472,644 1995.

57. D. M. Schubert, F. Alam, M. Z. Visi, and C. B. Knobler, *Chem. Mater.*, 2003, **15**, 866.

58. G. Corbel, E. Suard, J. Emery, and M. Leblanc, *J. Alloys Compd.*, 2000, **305**, 49.

59. Z.-T. Yu, J.-J. Xu, Y.-S. Jiang, Z. Shi, Y. Guo, D.-J. Wang, and J.-S. Chen, *J. Mater. Chem.*, 2003, **13**, 2227.

60. A. Choudhury, S. Neeraj, S. Natarajan, and C. N. R. Rao, *J. Chem. Soc., Dalton Trans.*, 2002, 1535.

61. H.-A. Lehmann, K. Sperschneider, and G. Kessler, *Z. Anorg. Allg. Chem.*, 1967, **354**, 37.

62. Y. K. Ozols, I. V. Tetere, and A. F. Ievins, *Akad. Nauk. Latv. SSR, Ser. Kim.*, 1973, **1**, 3.

63. K. K. Shen, in ‘Acs Symposium Series’, eds. G. L. Nelson and C. A. Wilkie, American Chemical Society, Norwalk, Connecticut, 2001, Vol. 797, p. 228.

64. D. M. Schubert, *Mod. Paint Coat.*, August,1992, 42.

65. D. N. Nikogosyan, *Appl. Phys. A*, 1991, **52**, 359.

66. D. M. Schubert, R. A. Smith, and M. Z. Visi, *Glass Technol.*, 2003, **44**, 63.

67. C. C. Freyhardt and M. Wiebcke, *J. Chem. Soc., Chem. Commun.*, 1994, 1675.

68. D. M. Schubert, M. Z. Visi, and C. B. Knobler, *Inorg. Chem.*, 2000, **39**, 2250.

69. Q. Li, F. Xue, and T. C. W. Mak, *Inorg. Chem.*, 1999, **38**, 4142.

70. J. J. Ebelman and M. Bouquet, *Ann. Chim. Phys.*, 1846, **17**, 54.

71. E. L. Docks, ‘Kirk-Othmer Encyclopedia of Chemical Technology’, 4th edn., John Wiley & Sons, New York, 1992, Vol. 4, p. 413.

72. D. B. Green, ‘Supplement to Mellor’s Comprehensive Treatise on Inorganic and Theoretical Chemistry’, Vol. 5, *Boron*, Part A, *Boron-oxygen Compounds*, Longman, London, 1980, Sect. A17, p. 703.

73. T. E. Cole, R. Quintanilla, and S. Rodewald, *Synth. React. Inorg. Met.-Org. Chem.*, 1990, **20**, 55.

74. H. Steinberg and D. L. Hunter, *Ind. Eng. Chem.*, 1957, **49**, 174.

75. T. E. Acree, *Adv. Chem. Ser.*, 1973, **117**, 208.

76. V. Prelog in, ‘Frontiers in Bioorganic Chemistry and Molecular Biology’, eds. Yu. A. Ovchinnikov and M. N. Kolosov, M. M. Sheriakin, Elsevier/North Holland Biomedical Press, Amsterdam, 1979, p. 87.

77. H. Nakamura, Y. Iitaka, T. Kitahara, T. Okazaki, and Y. Okami, *J. Antibiot.*, 1977, **30**, 714.

78. T. Hemsheidt, M. P. Puglisi, L. K. Larsen, G. M. I. Paterson, R. E. Moore, J. I. Rois, and J. Clardy, *J. Org. Chem.*, 1994, **59**, 3467.

79. P. H. Brown, N. Bellaloui, M. A. Wimmer, E. S. Bassil, J. Ruiz, H. Hu, H. Pfeffer, F. Dannel, and V. Römheld, *Plant Biol.*, 2002, **4**, 205.

80. J. Takano, K. Noguchi, M. Yasumori, M. Kobayashi, Z. Gajdos, K. Miwa, H. Hayashi, T. Yoneyama, and T. Fujiwara, *Nature*, 2002, **420**, 337.

81. O. Conrad, C. Jansen, and B. Krebs, *Angew. Chem., Int. Ed. Engl.*, 1998, **37**, 3208.

82. G. W. Parshall, in ‘The Chemistry of Boron and Its Compounds’, ed. E. L. Muetterties, John Wiley & Sons, New York, 1967, Chap. 9, p. 617.

83. H. Steinberg and R. J. Brotherton, ‘Organoboron Chemistry’, Interscience Publishers, New York, 1964, Vol. 2, p. 479.

84. A. B. Burg and R. I. Wagner, *J. Am. Chem. Soc.*, 1953, **75**, 3872.

85. H. V. R. Dias and P. P. Power, *Angew. Chem., Int. Ed. Engl.*, 1987, **26**, 1270.

86. F. Alam, ‘Kirk-Othmer Encyclopedia of Chemical Technology’, 4th edn., John Wiley & Sons, New York, 1992, Vol. 4, p. 430.

87. F. Evans, ‘Kirk-Othmer Encyclopedia of Chemical Technology’, 4th edn., John Wiley & Sons, New York, 1994, Vol. 10, p. 300.

88. G. Urry, in ‘The Chemistry of Boron and Its Compounds’, ed. E. L. Muetterties, John Wiley & Sons, New York, 1967, Chap. 6, p. 325.

89. D. B. Beach and W. L. Jolly, *J. Phys. Chem.*, 1984, **88**, 4647.

90. J. R. Papcun, ‘Kirk-Othmer Encyclopedia of Chemical Technology’, 4th edn., John Wiley & Sons, New York, 1994, Vol. 10, p. 309.

91. J. A. Morrison, *Chem. Rev.*, 1991, **91**, 35.

92. J. A. J. Purdoe, N. C. Norman, P. L. Timms, S. Parsons, I. Mackie, C. R. Pulham, and D. W. H. Rankin, *Angew. Chem., Int. Ed. Engl.*, 2003, **42**, 571.

Boron: Metallacarbaboranes

Catherine E. Housecroft
University of Basel, Basel, Switzerland

1 Introduction 1
2 Classes of Compound and Geometrical Aspects 2
3 Bonding 8
4 Synthesis 9
5 Skeletal Isomerism 13
6 Electrochemistry 15
7 Reactivity 15
8 Applications 17
9 Future Ways Forward 19
10 Related Articles 20
11 References 20

Abbreviations

H_2OEP = Octaethylporphyrin; PPN = Bis(triphenylphosphino)iminium(1+); PSEPT = Polyhedral skeletal electron pair theory; TMEDA = N,N,N',N'-Tetramethylethylenediamine; nbd = Norbornadiene; *cod* = 1,5-Cyclooctadiene.

Glossary

Metallacarbaborane (also called metallacarborane): an *electron-deficient compound,* usually a polyhedral *cluster* comprising an array of boron–hydride (BH), carbon–hydride (CH), and metal (ML_x, where L = ligand) fragments; the inclusion of a substituted carbon fragment CR (R = alkyl, aryl, or trimethylsilyl) in place of a CH unit is common

1 INTRODUCTION

Metallacarbaboranes (or metallacarboranes) are compounds that contain cluster polyhedra comprising carbon, boron, and metal atoms in various combinations. The first metallacarbaborane clusters were prepared by Hawthorne in 1965,[1] and were derived from the icosahedral *closo*-carbaborane 1,2-$C_2B_{10}H_{12}$ (*see **Boron: Polyhedral Carboranes***) by the replacement of one BH vertex with a metal center. Compounds such as $[Fe(C_2B_9H_{11})_2]^{n-}$ ($n = 1$ or 2) can be represented as the *commo*-metallacarbaborane (**1**) or as the *sandwich compound* (**2**). Structure (**1**) emphasizes that the iron atom is an integral part of $[Fe(C_2B_9H_{11})_2]^{n-}$, while (**2**) shows that $[Fe(C_2B_9H_{11})_2]^{n-}$ can be considered as consisting of two *nido*-carbaborane clusters, each of which behaves as an η^5 ligand to the Fe(II) or Fe(III) center. The $[C_2B_9H_{11}]^{2-}$ (dicarbollide) ligand (**3a**) behaves in a similar fashion to a Cp^- ligand (**3b**)[2] and, therefore, a parallel can be drawn between the iron(II) metallacarbaborane $[Fe(C_2B_9H_{11})_2]^{2-}$ and the organometallic π-complex $FeCp_2$ (*ferrocene*). Despite the apparent analogy between $[C_2B_9H_{11}]^{2-}$ and Cp^-, experimental observations indicate that metallacarbaboranes are often more stable than their metallocene analogs. The carbaborane units are typically robust, and metallacarbaborane chemistry is generally more extensive than metallocene chemistry.

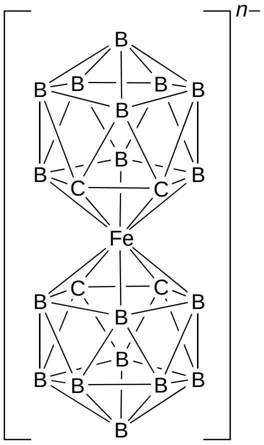

B = BH, C = CH, n = 1, 2

(**1**)

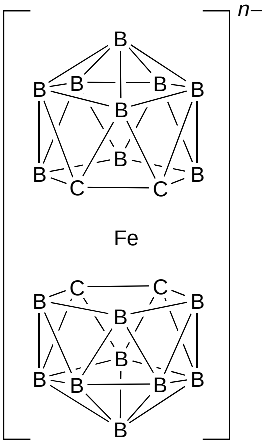

B = BH, C = CH, n = 1, 2

(**2**)

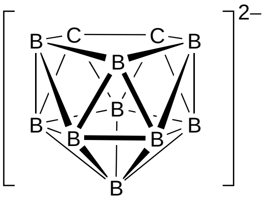

B = BH, C = CH

(**3a**)

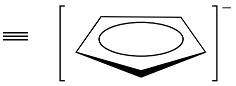

(**3b**)

Early studies of metallacarbaboranes centered on the icosahedral framework.[3] The precursor 1,2-$C_2B_{10}H_{12}$ was readily prepared from $B_{10}H_{14}$ (*see **Boron Hydrides***), and the 1,7- and 1,12-isomers of $C_2B_{10}H_{12}$ were obtained by thermolysis of 1,2-$C_2B_{10}H_{12}$ (see equation 24). Studies pertaining to the chemistry of smaller metallacarbaboranes followed in later years, and a recent advance has been the isolation of clusters with more than 12 vertices (see Section 4.10). Two frameworks have received particular attention: metallacarbaboranes containing MC_2B_4 cores and those with $M(C_2B_3)_2$ sandwich units.[4–8] Metallacarbaborane chemistry

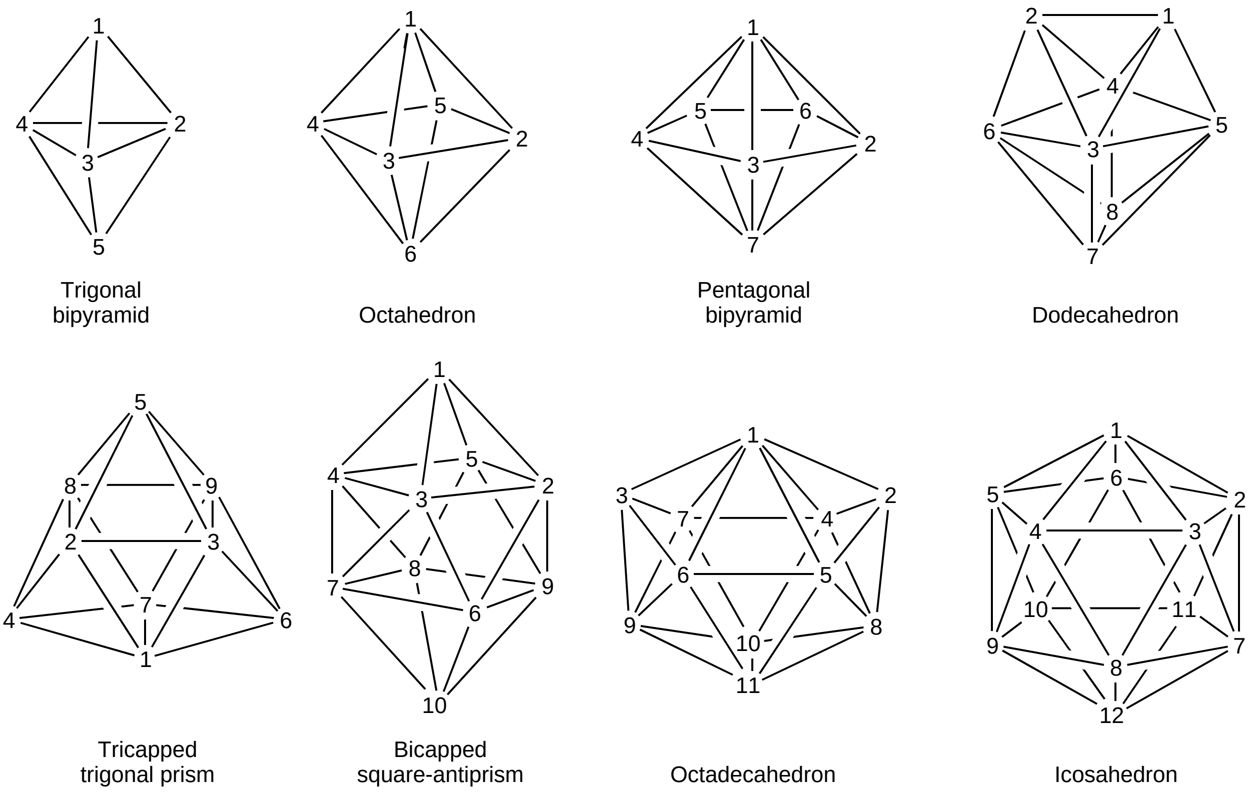
Trigonal bipyramid

Octahedron

Pentagonal bipyramid

Dodecahedron

Tricapped trigonal prism

Bicapped square-antiprism

Octadecahedron

Icosahedron

Figure 1 Closed deltahedra (polyhedra with triangular faces) with 5–12 vertices and the IUPAC numbering system for each cage. The structures of most metallacarbaboranes are based on or derived from these eight deltahedra

is especially well developed for icosahedral and pentagonal bipyramidal cages (see Figure 1), and it has progressed from the inclusion of d-block metal atoms to main group[9,10] and f-block[6,11,12] metal atoms.

Three general reference works cover metallacarbaborane chemistry in a systematic manner up to around 2005,[4–6] and several books include articles covering topical developments.[13–16] Annual reports[17] have surveyed advances in the subject since 1971, and continue to do so.

Details of the preliminary IUPAC nomenclature for metallacarbaborane clusters are described in the 1990 recommendations.[18] However, care is needed in interpreting compound names in the literature. Over the years, there has been some variation with respect to the order in which boron, carbon, and metal atoms are numbered in a given cluster. An example is (**4**), which is described as 3-Cp-3-Fe-1,2-$C_2B_{10}H_{12}$ by the IUPAC 1990 recommendations, but is also found in the literature as 3-(CpFe)-1,2-$C_2B_{10}H_{12}$, 1-Cp-1-Fe-2,3-$C_2B_{10}H_{12}$, or 1-(CpFe)-2,3-$C_2B_{10}H_{12}$.

Most of the structures of metallacarbaborane clusters derive from triangular-faced polyhedra. Figure 1 shows regular deltahedra up to the icosahedron with the corresponding IUPAC vertex numbering schemes. General cluster classes are *closo* (a complete deltahedral structure), *nido* (a deltahedron with one vertex vacant), *arachno* (a deltahedron with two vertices removed), and *commo* (a structure derived from the fusion of, for example, two deltahedra sharing a common vertex).

2 CLASSES OF COMPOUND AND GEOMETRICAL ASPECTS

2.1 Single Cages

In a single-cage metallacarbaborane, the cluster skeleton consists of one complete polyhedron or one polyhedral fragment. Examples of *closo*-metallacarbaboranes in which one metal fragment has replaced a BH unit in the carbaborane 1,2-$C_2B_{10}H_{12}$ are $CpFeC_2B_9H_{11}$ (**4**), $CpCoC_2B_9H_{11}$, $(OC)_3RhC_2B_9H_{11}$, and $[(OC)_3MoC_2B_9H_{11}]^{2-}$. Each of these compounds adopts an icosahedral framework. Many metallacarbaborane clusters with closed-cage structures smaller than the icosahedron are known, for example, the 11-vertex *closo*-1-(η^6-MeC_6H_4-4-*i*-Pr)-2,3-Me_2-1-Ru-2,3-$C_2B_8H_8$ (**5**). A large group of metallacarbaboranes adopts the *closo*-C_2B_4M core and each possesses a pentagonal bipyramidal structure, for example, 1-Cp*Co-2,3-$C_2B_4H_6$ (**6**), 1-Ge-2,3-$(SiMe_3)_2$-2,3-$C_2B_4H_4$ (**7**), and 1-$Fe(CO)_3$-2,4-$C_2B_4H_6$ (**8**).

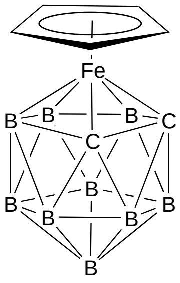

B = BH, C = CH

(**4**)

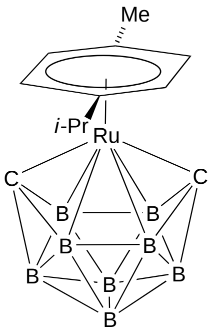

B = BH, C = CH

(**5**)

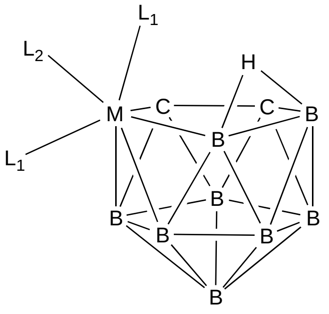

(**9**) B = BH, C = CH, M = Pt, $L_1 = PEt_3$, L_2 = H

(**10**) B = BH, C = CH, M = Rh, $L_1 = L_2 = PMe_3$

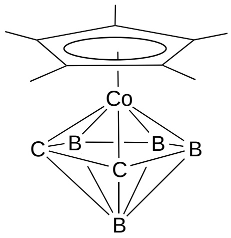

B = BH, C = CH

(**6**)

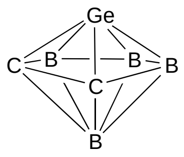

B = BH, C = C$(SiMe_3)$

(**7**)

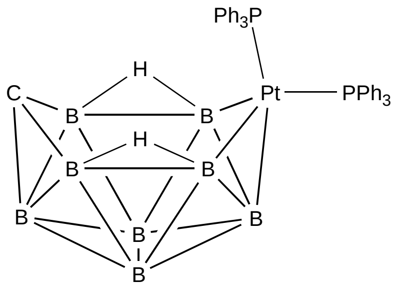

B = BH, C = CH_2

(**11**)

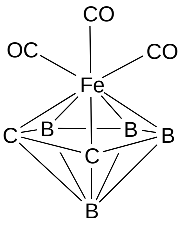

B = BH, C = CH

(**8**)

The number of metallaboranes and metallacarbaboranes in which the metal is from the s block has grown over the past two decades,[19–21] but is still not large when compared to metallacarbaboranes incorporating d-block metal centers. Single-cage metallacarbaboranes include *closo*-1,1,1,1-$(MeCN)_4$-1,2,4-$CaC_2B_{10}H_{12}$,[22] (*closo*-1,1,1-$(MeCN)_3$-1,2,4-$SrC_2B_{10}H_{12})_n$,[23] and *closo*-1-Mg(TMEDA)-2,3-$(SiMe_3)_2$-2,3-$C_2B_4H_4$.[24] Group 1 metal ions are often associated through interactions to the outside of the cage rather than being part of the skeleton of the cluster. An example, in which M^+ participates in both the roles, is [*exo*-Cs(TMEDA)-1-Cs-$(SiMe_3)_4C_4B_8H_8]_n$.[25] Metallacarbaborane clusters incorporating f-block metal atoms are actively being developed, and the last 15 years have seen a significant growth in this area.[11,12]

Large numbers of metallacarbaboranes in which the metal atom effectively closes an otherwise open carbaborane cluster are known. However, there are also many compounds in which the metal fragment occupies a site in an open (*nido* or *arachno*) polyhedral cage, for example, *nido* clusters (**9**–**11**).

2.2 Sandwich Complexes

The open face of *nido*-$[C_2B_9H_{11}]^{2-}$ may behave in a similar manner to a cyclopentadienyl ring (see Section 1) and coordinate to M^{n+} to give sandwich complexes such as *commo*-$[Fe(C_2B_9H_{11})_2]^{n-}$ ($n = 1$ or 2), (**1**) and (**2**). Related clusters are the chromium(III) complex *commo*-$[Cr(C_2B_9H_{11})_2]^-$ and the nickel(IV) complex $Ni(C_2B_9H_{11})_2$. In f-block metal complexes, the higher coordination numbers of the metal center lead to the addition of halide or solvent ligands and a concomitant tilting of the carboranyl ligands, for example, in $[(C_2B_9H_{11})_2MX_2]^{2-}$ (M = U, Th; X = halide) (see below).[26,27] Mixed metallacarbaborane/π-organometallic complexes such as (**4**) may also be recognized as sandwich molecules. Similarly, the zirconium(IV) metalloporphyrin–carbaborane compound $(OEP)Zr(C_2B_9H_{11})$ (**12**) can be classed as a sandwich complex.[28]

Like *nido*-$[C_2B_9H_{11}]^{2-}$, the dianion *nido*-$[C_2R_2B_4H_4]^{2-}$ (R = H, Me, $SiMe_3$) exhibits an open pentagonal face, and the frontier orbitals of the two *nido*-carbaborane anions are similar. Thus, it is not surprising to find complexes of the type *commo*-Ge{2,3-$(SiMe_3)_2$-2,3-$C_2B_4H_4\}_2$ (**13**) and *commo*-FeH_2(2,3-Me_2-2,3-$C_2B_4H_4)_2$ (**14**) in which the pentagonal faces of the two *nido*-carbaborane ligands are parallel to one another. The tin(IV) complex *commo*-Sn{2-$(SiMe_3)$-3-Me-2,3-$C_2B_4H_4\}_2$ (**15**) adopts a bent-sandwich structure, with the two C_2B_3 rings subtending an angle of 142.5° at the metal center. This observation is of interest in view of the bent geometries observed for the stannocenes Cp_2Sn and $Cp^*{}_2Sn$.

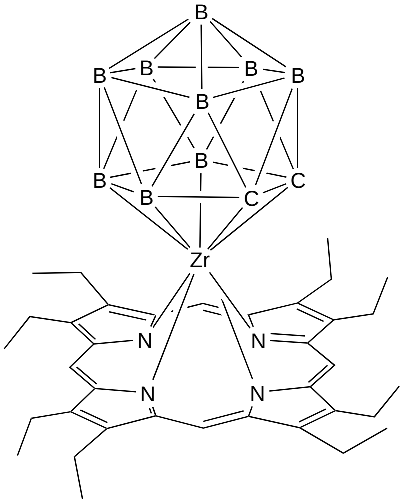

B = BH, C = CH

(**12**)

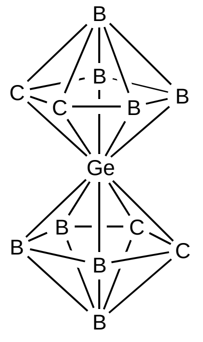

B = BH, C = C(SiMe$_3$)
(**13**)

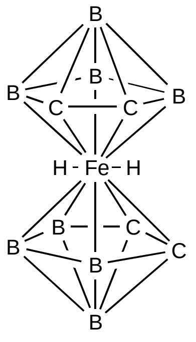

B = BH, C = CMe
(**14**)

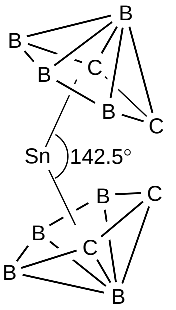

B = BH, C = C(SiMe$_3$)
(**15**)

The first actinoid metal-containing metallacarbaborane, $[U(C_2B_9H_{11})_2Cl_2]^{2-}$, was reported in 1976; the $[C_2B_9H_{11}]^{2-}$ ligands are in a bent-sandwich geometry.[29,30] The same feature is observed in $[(THF)_2Sm(C_2B_9H_{11})_2]^-$ (**16**), one of the first *closo*-lanthanacarbaboranes to be reported[31]; in anion (**16**), the open faces of the $[C_2B_9H_{11}]^{2-}$ ligands subtend an angle of 131.9(5)° at the Sm atom. The bent geometry is a general feature of f-block bis(dicarbollide) complexes because donor or solvent molecules also tend to coordinate the lanthanoid metal ion. In $[(THF)_2Eu(C_2B_{10}H_{12})_2]^{2-}$ (**17**), the *nido*-$[C_2B_{10}H_{12}]^{2-}$ coordinates through its six-membered open face.[32] Larger molecular architectures can result from the involvement of B–H–M bridges from one cage on one sandwich unit to the metal center of another, for example, in $[(\eta^7\text{-}C_2B_{10}H_{12})_2(\eta^6\text{-}C_2B_{10}H_{12})_2U_2]^{4-}$.[33]

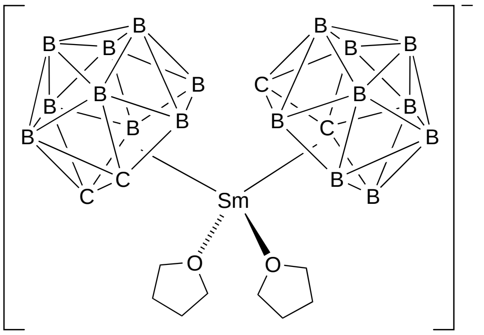

B = BH, C = CH

(**16**)

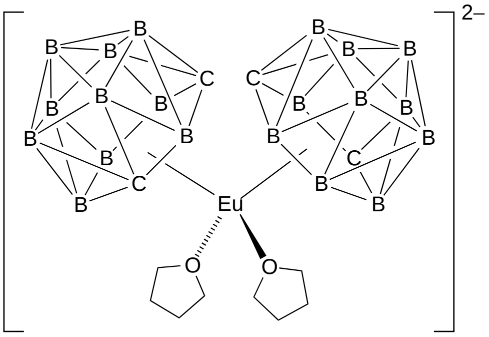

B = BH, C = CH

(**17**)

Advances in the substitution chemistry of $[C_2B_9H_{11}]^{2-}$ have allowed linked dicarbollide *nido* clusters to be prepared. Ligands with the built-in capacity to form sandwich complexes can therefore be accessed to give the so-called Venus flytrap clusters (VFCs)[34,35] (see also Section 8). The length of the chain linking the two carbaborane clusters must be short enough to allow the approach of the linked dicarbollide ligands to the metal ion that is being bound into the sandwich. The interligand gap is controlled by both the nature of the bridging group and the mutual twisting of the two metal-bonding faces. The first such metallacarbaborane was the zwitter-ionic cobalt(III) compound (**18**). In (**19**), the small pyrazole bridging unit restricts the two C_2B_9 cages to an eclipsed conformation.[34] (The description ‘‘eclipsed’’ is used to refer to the relative positions of the two five-membered rings rather than the relative positions of the C and B atoms in the two rings.) In both (**18**) and (**19**), the carbaborane cages are B-substituted. Examples of C-substituted VFCs were reported in 1992.[35] Ether-bridged VFCs have been prepared as model compounds for the development of radiotransition metal carriers.[36]

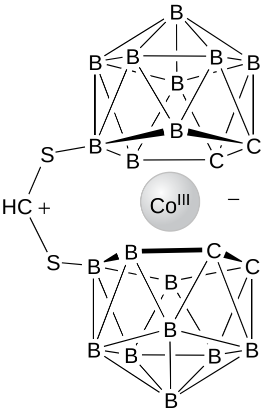

B = BH, C = CH

(**18**)

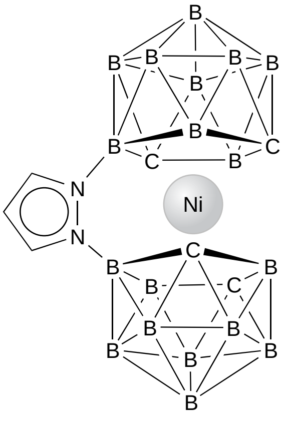

B = BH, C = CH

(**19**)

2.3 Stacked Complexes

Extended stacks containing small boron–carbon rings acting as spacers between metal centers are well established.[37–39] *nido*-Carbaborane ligands such as $[C_2B_4H_6]^{2-}$ can terminate a stack that has a central π-organometallic sandwich unit. Combined with a variety of organic π ligands, metallacarbaborane units can be incorporated into linked stacks. In the simplest type of stack, a carbaborane unit sandwiches together two organometallic fragments, as in $CpCo(C_2Me_2B_3H_3)CoCp$ (**20**). This is called a *triple-decker sandwich* because it contains two metal atoms and three π ligands. Similarly, a tetradecker sandwich is constructed from three metal atoms and four π ligands. By choosing suitable polyarene bridging ligands, linked stacks such as (**21**) can be prepared. The structural variation within the class of stacked complexes can be controlled by careful choice of molecular precursors. One significant development in this area has been to combine the CpM(carboranyl) units into nanoscale assemblies, the properties of which are of active research interest.[40–44] For example, the electrochemical behavior of the planar macrocycle (**22**) is consistent with significant intramolecular electronic communication.[42]

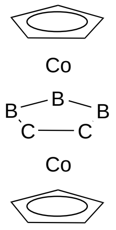

B = BH, C = CMe

(**20**)

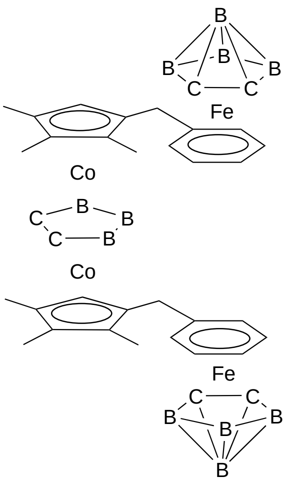

B = BH, C = CEt

(**21**)

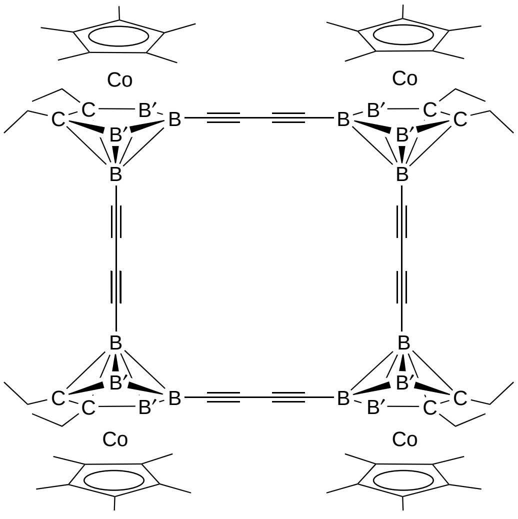

B′ = BH

(**22**)

2.4 Slip Distortion

In a sandwich complex, one might expect the two π ligands on either side of a metal atom to lie directly over one another, and to be mutually eclipsed or staggered. However, the occurrence of *commo*-metallacarbaboranes with slipped geometries (a so-called slip distortion) is quite common, notably in cases where a d-block metal ion has a near-complete d-electron configuration, e.g., Ni^{II}, Cu^{II}, or Au^{III}. Thus, in $[Au(C_2B_9H_{11})_2]^-$ (**23**), the gold(III) center interacts more strongly with the boron than the carbon atoms in the open faces of the two ligands. Rather than being similar to a metal–cyclopentadienyl complex, a slipped-sandwich complex starts to resemble a metal–allyl complex (*see* ***Cadmium: Inorganic & Coordination Chemistry***). This structural phenomenon is also observed in many main group *commo*-metallacarbaboranes.[20,45] In the chromium(IV) complex *commo*-$Cr(2,3\text{-}(SiMe_3)_2\text{-}2,3\text{-}C_2B_4H_4)_2$, slip distortion in the opposite sense is observed; the M–C bond lengths are

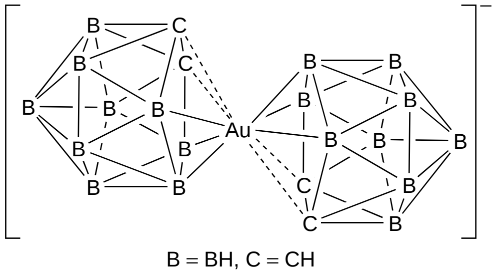

B = BH, C = CH

(**23**)

shorter than the M–B distances (Cr–B_{av} = 232.1 pm and Cr–C_{av} = 217.9 pm).

In single-cage *closo*-metallacarbaboranes containing a main group metal atom, the slippage of the heteroatom with respect to the open face of a *nido*-$[C_2B_9H_{11}]^{2-}$ or *nido*-$[C_2B_4H_6]^{2-}$ ligand, or C-substituted analogs of these ligands, is commonly observed.[20] In general, interaction with the three boron atoms is greater than that with the two carbon atoms. The p-block atom may or may not carry a terminal substituent. In cases where a bare metal atom is incorporated into the metallacarbaborane cluster, it may function as a Lewis acid. In 1-Sn-2,3-$(SiMe_3)_2$-2,3-$C_2B_4H_4$ (**24**), distances from Sn to the adjacent B and C atoms are Sn–B_{av} = 242.8 pm and Sn–C_{av} = 249.8 pm. In the adduct 1-(bipy)-1-Sn-2,3-$(SiMe_3)_2$-2,3-$C_2B_4H_4$ (**25**), not only is the slip distortion more pronounced than in (**24**) (Sn–B_{av} = 248 pm and Sn–C_{av} = 273 pm) but the plane of the donor 2,2′-bipyridine (bipy) molecule is acutely tilted with respect to the metallacarbaborane cluster core. Tilting of terminal substituents or donor molecules is observed in many related metallacarbaboranes, e.g., 1-Me-1-Ga-2,3-$C_2B_4H_6$ (**26**), 1-Me-1-In-2,3-$C_2B_4H_6$, 1-bipy-1-Sn-2,3-Me_2-2,3-$C_2B_9H_9$, 1-THF-1-Sn-2,3-Me_2-2,3-$C_2B_9H_9$. For the donor–acceptor complexes, the trend is for an increase in the slip distortion and a decrease in the tilting of the donor ligand as the Lewis acid–base interaction becomes stronger. A number of theoretical studies have addressed the origins of slip distortion.[9]

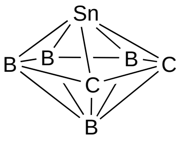

B = BH, C = C(SiMe$_3$)
(**24**)

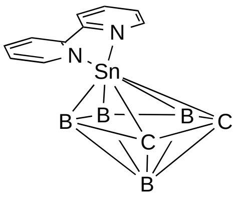

B = BH, C = C(SiMe$_3$)
(**25**)

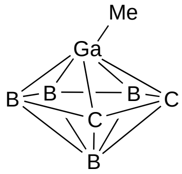

B = BH, C = CH
(**26**)

2.5 Ion Pairing

In most metallacarbaboranes, the interaction between the metal atom and carbaborane cage is considered to be essentially covalent, and this is supported by the experimentally determined M–B and M–C distances. However, in [3-Tl-1,2-$C_2B_9H_{11}]^-$, the distances from the thallium(I) center to the C and B atoms in the open face of the C_2B_9 cage are particularly long, suggesting Tl^+ $[1,2\text{-}C_2B_9H_{11}]^{2-}$ ion pairing. Consistent with this is the fact that the Tl(I) center is readily displaced by other metal ions. In the solid state, variation in the structure of $[3\text{-Tl-}1,2\text{-}R_2\text{-}C_2B_9H_9]^-$ (R = H or Me) is observed as a function of the counterion; slip distortion is observed in all cases and is extreme in Tl[3-Tl-1,2-$C_2B_9H_{11}$]. Table 1 lists selected structural data for the $[3\text{-Tl-}1,2\text{-}R_2\text{-}1,2\text{-}C_2B_9H_9]^-$ anion in several salts. In [PPN][3-Tl-1,2-$C_2B_9H_{11}$], dimer formation for the anion (**27**) is observed in the solid state with an internuclear separation between the symmetry-related thallium atoms of 424.1 pm; the dimeric structure is stabilized by B–H–Tl bridges.[46] A novel case of ion pairing is exemplified in {[*closo*-1-Nd(μ-H)$_6$-2,4-$(SiMe_3)_2$-2,4-$C_2B_4H_4]^+$ [1,1′-$(THF)_2$-2,2′,4,4′-$(SiMe_3)_4$-5,5′,6,6′-(μ-H)$_4$-1,1′-*commo*-Nd(η^5-2,4-$C_2B_4H_4$)]$^-$}$_2$. This complex consists of a half-sandwich cationic neodymacarbaborane coordinated to an anionic, fully sandwiched neodymacarbaborane.[47]

Table 1 Structural data to illustrate the interaction of Tl(I) with the C_2B_3 open face of the $[1,2\text{-}R_2\text{-}1,2\text{-}C_2B_9H_9]^-$ ligand in [X][1,2-R_2-3-Tl-1,2-$C_2B_9H_9$]$^{(a)}$

X	R	Tl–B (pm)	Tl–C (pm)
Tl	Me	273.9(82), 268.2(72), 296.9(73)	317.3(73), 327.8(25)
PPN	H	266.4(7), 274.4(8), 274.1(7)	291.5(6), 292.3(6)
$Ph_3MeP^{(b)}$	H	274.3(6), 274.1(6), 265.9(6)	292.1(5), 291.0(5)

$^{(a)}$Distances should be compared with the sums of appropriate covalent radii: r_{cov} for B = 82, C = 77, Tl = 155 pm. $^{(b)}$The structure of the anion is dimeric in the solid state; see (**27**).

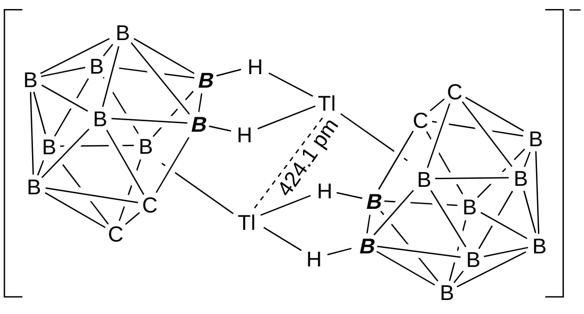

B = BH, ***B*** = B, C = CH
(**27**)

2.6 σ-Bonded and Edge-bridging Metal Fragments

In the extreme, the slip distortion described above leads to the C_2B_3 face of a dicarbollide ligand interacting with a metal atom through only three B atoms. The similarity to an organometallic allyl complex results in the term *borallyl* being used for this type of bonding mode. Examples where the metal binds to only one or two B atoms are also known, that is, M replaces H in a terminal (B–H) or bridging (B–H–B) unit. In anion (**28**), the $AuPPh_3$ unit interacts strongly with one boron atom (Au–B = 222.2(9) pm) and weakly with the two other boron atoms (Au···B = 248.6(9) and 252.8(9) pm). A similar situation is observed for the $Ph_3PHg(II)$ unit in 10-(Ph_3PHg)-7,8-$C_2B_9H_{11}$. Such metallacarbaboranes show a tendency toward the metal fragment being bonded externally to the polyhedral cage via a direct two-center two-electron M–B σ bond. An example involving a p-block metal is [10-(Ph_3Sn)-10-μ-H-7,8-$C_2B_9H_{10}$]$^-$, which is structurally similar to (**28**) but with the Sn atom bonded to only one B atom; the Sn–B interaction is supported by a bridging hydrogen atom.

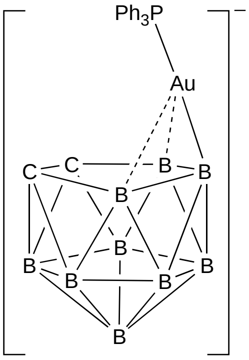

B = BH, C = CH

(**28**)

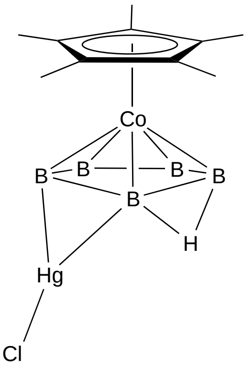

B = BH, C = CH

(**29**)

Copper(I), silver(I), gold(I), and mercury(II) fragments exhibit a tendency to bridge the edges of polyhedral clusters of various types. In metallacarbaborane clusters, one example is (μ-$AuPPh_3$)-9-SMe_2-7,8-$C_2B_9H_{10}$; the structure is related to that of (**28**) except that the gold(I) unit bridges one B–B edge asymmetrically. The preference is for the metal atom to bridge a B–B rather than a B–C or a C–C edge, and this reflects the observed preferences for bridging H atoms in borane and carbaborane clusters (*see* ***Boron: Polyhedral Carboranes***). An example of an edge-bridging mercury(II) unit is shown in (**29**). In the above examples, the metal atom associates with the carbaborane polyhedral cage via a boron–metal bond. Association through a carbon–metal σ bond is also well established. Important precursors to C-substituted derivatives (not necessarily metallated derivatives) of $C_2B_{10}H_{12}$ are the lithiacarbaborane 1,2-Li_2-1,2-$C_2B_{10}H_{10}$ and its 1,7- and 1,12-isomers (see later). The presence of an M–C bond means that members of this class of metallacarbaboranes can be considered as organometallic complexes. Some of the examples are the organomercury complexes $Hg_4(C_2B_{10}H_{10})_4$ (**30**)**[48]** and (9,12-$Me_2C_2B_{10}H_8Hg)_3$; the latter reacts with LiI to give the unusual sandwich complex (**31**).**[49]** In contrast to the usual linear coordination environment observed at Hg(II), that in $Hg_4(C_2B_{10}H_{10})_4\cdot(THF)_4\cdot 2H_2O$ is nonlinear (C–Hg–C = 167.7(8)°).

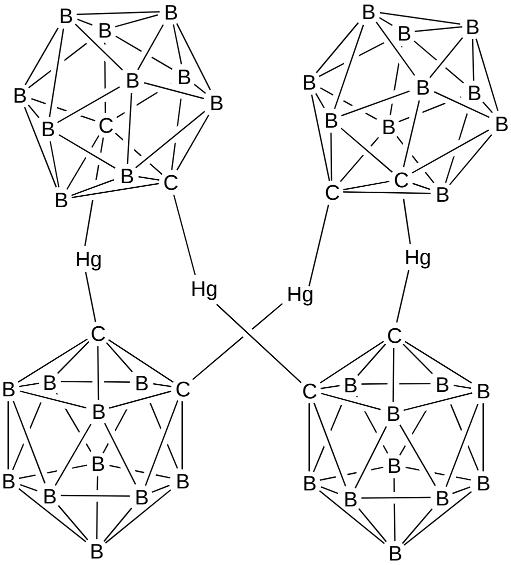

B = BH

(**30**)

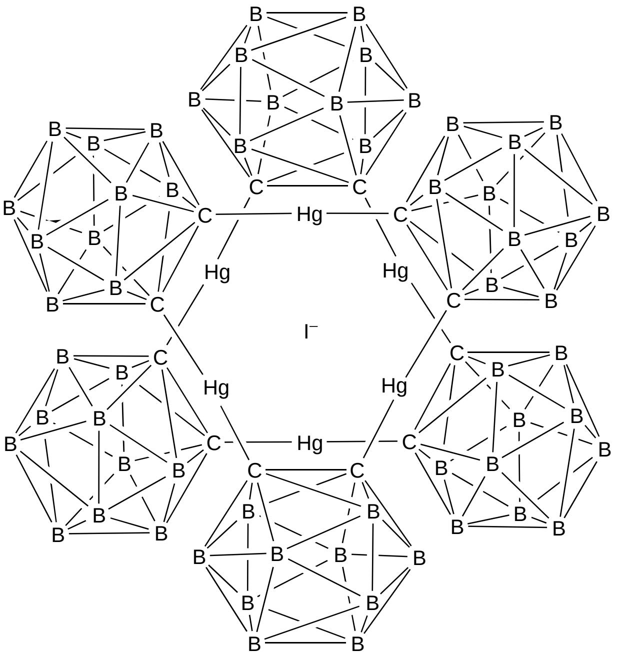

Me groups omitted

(**31**)

2.7 Exo-metallated Clusters

In some metallacarbaborane clusters, a metal fragment is supported on the outside of the carbaborane skeleton, typically by B–H–M interactions, for example, complex (**27**) involves exo interactions between the Tl(I) atom of one cage and two terminal boron–hydrogen bonds of a second cage. The exo descriptor illustrates the relationship of the metal fragment to the carbaborane and the *nido* descriptor classifies the carbaborane cage.

2.8 Metal-rich Clusters

In almost all metallacarbaboranes, the total number of B and C atoms in the polyhedral cluster exceeds the number of metal atoms. A rare example of a metal-rich metallacarbaborane is *closo*-$Fe_3(CO)_9BHCHCMe$ (**32**); the complex has also been described in terms of an η^3-borirene ligand coordinating to an Fe_3 unit.[50]

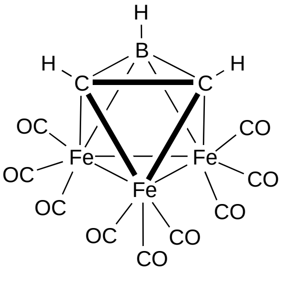

(**32**)

3 BONDING

The polyhedral structures adopted by most metallacarbaborane compounds can usually be rationalized using polyhedral skeletal electron pair theory (PSEPT) (*see* ***Electronic Structure of Clusters***). This approach is summarized as follows:

- A *closo* cluster has a closed deltahedral (triangular-faced) structure with n vertices and has $(n + 1)$ pairs of cluster-bonding electrons.
- A *nido* cluster possesses a cage based on an n vertex deltahedron with one vertex vacant and has $(n + 1)$ pairs of cluster-bonding electrons.
- An *arachno* cluster has a cage based on an n vertex deltahedron with two vertices vacant and has $(n + 1)$ pairs of cluster-bonding electrons.

Figure 2 shows the *closo, nido,* and *arachno* skeletons for an eight-electron pair ($n = 7$) cluster based on a pentagonal bipyramid. A BH or BR unit (where R is a one-electron substituent such as an alkyl or aryl group) provides two electrons, and a CH or CR unit provides three electrons for cluster bonding. A transition metal fragment ML_y provides x electrons where x is defined in equation (1) and a main group metal fragment EL_y provides x electrons where x is defined in equation (2). When a main group metal atom is incorporated into a cluster as a naked metal atom, it retains a lone pair of electrons localized outside the cluster and contributes the remaining valence electrons to cluster bonding.

Fortransitionmetalfragment : $x = v + l - 12$ (1)

For main group metal fragment: $x = v + l - 2$ (2)

(v = number of valence electrons of metal atom;

l = number of electrons provided by ligans, L)

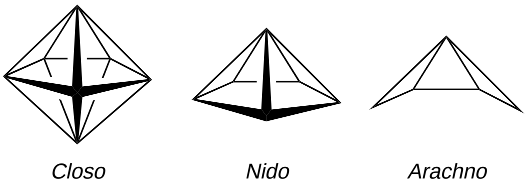

Closo *Nido* *Arachno*

Figure 2 The *closo, nido,* and *arachno* skeletons for an eight-electron pair ($n = 7$) cluster based on a pentagonal bipyramid (seven vertices)

Examples are as follows; in each case, PSEPT predicts the skeletal geometry but not the particular isomer(s) that is (are) adopted in practice.

1. In $(CpCo)C_2B_9H_{11}$, the CpCo fragment provides two electrons, each BH unit is a source of two electrons, and each CH unit gives three electrons. The metallacarbaborane has 13 pairs of electrons with which to bind the 12 cluster units. This means that $CpCoC_2B_9H_{11}$ is a *closo*-metallacarbaborane with an icosahedral skeleton (Figure 1).
2. In $Ge(CSiMe_3)_2B_4H_4$, the Ge atom contributes two electrons, each $CSiMe_3$ unit gives three electrons, and each BH unit gives two electrons. $Ge(CSiMe_3)_2B_4H_4$ has eight pairs of bonding electrons for seven cluster units. Thus, $Ge(CSiMe_3)_2B_4H_4$ has a *closo* structure with a pentagonal bipyramidal structure; in practice, the isomer shown in (**7**) is observed.
3. In $PtH(PEt_3)_2C_2B_8H_{11}$, the $PtH(PEt_3)_2$ unit provides three electrons, each CH unit gives three electrons, each BH unit provides two electrons, and the extra H atom provides one electron. The metallacarbaborane has 13 pairs of electrons for cluster bonding over 11 cluster centers, and $PtH(PEt_3)_2C_2B_8H_{11}$ has a *nido* structure based upon an icosahedron with one vertex left vacant. The observed isomer is (**9**). The extra H atom adopts a B−H−B bridging position on one edge of the open face of the *arachno* cage (*see* ***Boron Hydrides***).

Compounds like $[Fe(C_2B_9H_{11})_2]^{n-}$ can be represented either as *commo*-metallacarbaboranes comprising two vertex-fused icosahedra (**1**) or as organometallic-type sandwich complexes (**2**) (see Section 1). Similarly, two approaches can be taken when considering the bonding in such compounds: they may be described in terms of the two separate polyhedra by using PSEPT or in terms of the 18-electron rule (*see Effective Atomic Number Rule*). With regard to bonding, complexes with icosahedral cluster units give rise to some exceptional cases (see below). A better general example is *commo*-$FeH_2(2,3\text{-}Me_2\text{-}2,3\text{-}C_2B_4H_4)_2$ (**14**). This structure comprises two pentagonal bipyramidal cages fused via a common FeH_2 unit. Each $(CMe)_2B_4H_4$ unit possesses $[(2 \times 3) + (4 \times 2)]$ electrons for cluster bonding. An Fe atom has an s^2d^6 configuration; of these eight electrons, six occupy nonbonding orbitals. The FeH_2 unit therefore has four electrons available for cluster bonding, two for each half of the *commo* cluster. This gives a total of 16 electrons (eight pairs) per half-cluster and so each half-cluster has a *closo* structure. Alternatively, if $FeH_2(2,3\text{-}Me_2\text{-}2,3\text{-}C_2B_4H_4)_2$ is similar to a π-organometallic complex, then the 18-electron rule can be applied to the Fe atom. Each $[(CMe)_2B_4H_4]^{2-}$ ligand is a 6π-electron donor to the Fe(II) center (d^6 configuration); in this model, the H atoms are counted as protons and provide no electrons. A neutral-atom model can also be adopted in which each neutral $(CMe)_2B_4H_4$ unit is a 4π-electron donor to the Fe(0) center (s^2d^6 configuration). In this model, each H atom provides one electron to the Fe(0) atom. Either way, the 18-electron rule is satisfied.

Bonding within multiple stacks such as (**20**) and (**21**) is best dealt with in terms of the organometallic model, extended to give electron counts for the stack as a whole. Triple-decker stacks (three ligands and two metal atoms) usually require 30 electrons overall to give a stable diamagnetic complex, although there is flexibility and between 26 and 34 electrons can be accommodated. For an extra unit of the stack, 12 more electrons should be added; thus, a tetradecker stack (four ligands and three metals) is stable with 42 electrons. Units within the stacks are often derivatized Cp^- or $[C_2B_3H_5]^{2-}$ ligands; both are sources of 6π electrons.

We now return to clusters with icosahedral cages. By PSEPT, the 12-vertex *closo* icosahedral cluster requires 26 bonding electrons. However, there are numerous examples in which the number of electrons observed deviates from 26. In $CpFeC_2B_9H_{11}$, the total electron count for cluster bonding is 25. In $[Fe(C_2B_9H_{11})_2]^-$, it is not possible to allocate 26 electrons to each half-cluster. For clusters with 24–26 electrons, an icosahedral cage is usually adopted despite the apparent violation of PSEPT. An increased number of electrons provides an explanation for the origin of the slip distortion described earlier, for example, in $[Au(C_2B_9H_{11})_2]^-$ (**23**), each half-cluster has 27 electrons (for each half-cluster, 2 CH = 6 electrons, 9 BH = 18 electrons, Au^- contributes three electrons per cluster after six electrons have been accommodated in nonbonding orbitals).

4 SYNTHESIS

Although, in this section, an attempt has been made to systematize some synthetic routes to metallacarbaboranes,[4–6,51] many other syntheses have been reported, which lack the strategic quality that is desirable for efficient preparative chemistry.

If a metallacarbaborane is represented as {MCB}, then obvious methods of synthesis would be based on the following combinations: (i) {M} + {CB}, (ii) {MB} + {C}, (iii) {MC} + {B}, or (iv) aggregation of {M}, {C}, and {B}. The nonspecific nature of particle aggregation makes (iv) unattractive in most instances.

4.1 Carbaborane Anion with Metal Halide

The most general synthetic strategy in the preparation of metallacarbaborane clusters is the addition of a metal fragment to an anionic carbaborane cluster, that is, {M} + {CB}. Many methods involve the metallic capping of a *nido*-carbaborane to generate a *closo*-metallacarbaborane. The examples given in equations (3–6) illustrate cases in which the electron count for the cluster remains unaltered during the reaction and hence the polyhedral skeleton of the *closo* product is related to that of the *nido* precursor. In each case, the metal fragment being added provides two electrons to cluster bonding. In equations (3) and (4), the two electrons from the metal fragment replace those originally provided by the 2− charge. In equation (5), the monoanionic precursor loses H^+ during the reaction.

$$\textit{nido}\text{-}[C_2B_9H_{11}]^{2-} + SmI_2(THF)_x \longrightarrow \textit{closo}\text{-}Sm(THF)_4C_2B_9H_{11} + 2I^- \quad (3)$$

$$\textit{nido}\text{-}[C_2Me_2B_9]^{2-} + SnCl_2 \longrightarrow \textit{nido}\text{-}SnC_2Me_2B_9H_9 + 2Cl^- \quad (4)$$

$$\begin{array}{l} \textit{nido}\text{-}[C_2(SiMe_3)_2B_4H_5]^- + SnCl_2 \\ \quad \Big\downarrow \text{THF} \\ \textit{closo}\text{-}Sn(THF)_2C_2(SiMe_3)B_4H_4 \\ \quad \Big\downarrow 100\,^{\circ}C \\ \textit{closo}\text{-}SnC_2(SiMe_3)_2B_4H_4 \end{array} \quad (5)$$

$$\begin{array}{l} \textit{nido}\text{-}[C_2Me_2B_9H_9]^{2-} + W(CR)Br(CO)_4 \quad R = 4\text{-}MeC_6H_4 \\ \quad \Big\downarrow \\ \textit{closo}\text{-}[W(CR)(CO)_2(C_2Me_2B_9H_9)]^- \end{array} \quad (6)$$

The addition of a metal fragment to a *nido*-carbaborane anion may result in an increase in the number of cluster-bonding electrons. For example, in equation (7), the reaction of *nido*-$[C_2B_8H_{11}]^-$ with $RhCl(PMe_3)_3$ leads to the displacement of Cl^- and the combination of the carbaborane anion and $[Rh(PMe_3)_3]^+$ fragments. The latter is a source of three electrons (see equation 1) and hence the total cluster-electron count increases by two during the reaction. Such an increase will generate a change in skeletal geometry (see Section 3). Both $[C_2B_8H_{11}]^-$ and $(PMe_3)_3RhC_2B_8H_{11}$ are *nido* clusters, but each is based on a different deltahedral framework. An alternative pathway might have been for $(PMe_3)_3RhC_2B_8H_{11}$ to extrude H_2 or a PMe_3 ligand, thus effectively reducing the electron count by two.

$$\textit{nido}\text{-}[C_2B_8H_{11}]^- + RhCl(PMe_3)_3 \longrightarrow \textit{nido}\text{-}(PMe_3)_3RhC_2B_8H_{11} + Cl^- \quad (7)$$

The reaction of *nido*-carbaborane anions with metal halides is also a method of preparing *commo*-metallacarbaboranes (equations 8–10). In equation (8), there is competition between the formation of the *closo*- and *commo*-germacarbaboranes.

$$nido\text{-}[C_2(SiMe_3)_2B_4H_4]^{2-} + GeCl_4 \xrightarrow{\text{THF, } 0\,^\circ\text{C}} closo\text{-}GeC_2(SiMe_3)_2B_4H_4 + commo\text{-}Ge\{C_2(SiMe_3)_2B_4H_4\}_2 \quad (8)$$

$$2nido\text{-}[C_2B_9H_{11}]^{2-} + SiCl_4 \xrightarrow{\text{Reflux in } C_6H_6} commo\text{-}Si(C_2B_9H_{11})_2 \quad (9)$$

$$2nido\text{-}[C_2B_9H_{11}]^{2-} + EuI_4(THF)_2 \xrightarrow{\text{THF}} [1,1\text{-}(THF)_2\text{-}commo\text{-}Eu(C_2B_9H_{11})_2]^{2-} \quad (10)$$

4.2 Use of Thallium(I)-containing Carbaboranes

In Section 2.5, the special nature of $[TlC_2B_9H_{11}]^-$ was described. The Tl(I) center can be replaced by a variety of p-, d-, and f-block metal atoms, e.g., equations (11–16). The use of Tl(I)-containing carbaboranes for the synthesis of other metallacarbaboranes is of general reaction type {M} + {TlCB}. Reactions of $[X][TlC_2B_9H_{11}]$ (e.g., X = Tl or PPN) with metal halides proceed with loss of thallium(I) halide. Equation (11) shows a designed route to a *commo*-samaracarbaborane by the displacement of two THF ligands from *closo*-$Sm(THF)_4C_2B_9H_{11}$ by a dicarbollide ligand. The reaction also involves a redox change: Tl(I) to Tl(0) and Sm(II) to Sm(III). The product of the reaction of $[TlC_2B_9H_{11}]^-$ with CuCl and PPh_3 depends on the reaction stoichiometry. For a cluster anion : copper(I) ratio of 1:1, the reaction proceeds according to equation (13). With a 1:2 ratio, a second Cu atom is introduced as an exo-polyhedral unit (**33**), with two of the cluster B–H hydrogen atoms stabilizing the structure by forming B–H–Cu_{exo} bridging interactions.

$$[PPN][TlC_2B_9H_{11}] + closo\text{-}Sm(THF)_4C_2B_9H_{11} \longrightarrow [PPN][(THF)_2\text{-}commo\text{-}Sm(C_2B_9H_{11})_2] + Tl + 2THF \quad (11)$$

$$Tl[TlC_2Me_2B_9H_9] + GeCl_2 \longrightarrow closo\text{-}GeC_2Me_2B_9H_9 + 2TlCl \quad (12)$$

$$[TlC_2B_9H_{11}]^- + CuCl + PPh_3 \longrightarrow closo\text{-}[(PPh_3)CuC_2B_9H_{11}]^- + TlCl \quad (13)$$

$$Tl[TlC_2B_9H_{11}] + PdCl_2(TMEDA) \longrightarrow closo\text{-}Pd(TMEDA)C_2B_9H_{11} + 2TlCl \quad (14)$$

$$2[TlC_2B_9H_{11}]^- + CoCl_2 \longrightarrow commo\text{-}[Co(C_2B_9H_{11})_2]^{2-} \xrightarrow{\text{Oxidation}} commo\text{-}[Co(C_2B_9H_{11})_2]^- \quad (15)$$

$$[TlC_2B_9H_{11}]^- + Ph_3PAuCl \longrightarrow [(Ph_3P)AuC_2B_9H_{11}]^- + TlCl \quad (16)$$

4.3 Neutral Carbaborane with a Metal Fragment

Syntheses of metallacarbaboranes from neutral carbaborane precursors, that is reaction type {M} + {CB}, are exemplified in equations (17–20). Reaction conditions often involve thermolysis or photolysis. Capping a *nido* cluster to form a skeletally related *closo* cluster proceeds with the extrusion of ligands if the cluster-electron count is to remain constant. In equation (17), the structure of *nido*-$C_2B_4H_8$ is derived from an eight-electron pair pentagonal bipyramidal cluster (Figure 2). Reaction of *nido*-$C_2B_4H_8$ with $Fe(CO)_5$ results in the addition of an $Fe(CO)_3$ unit to the open face of the *nido* cluster. The $Fe(CO)_3$ unit provides two electrons to cluster bonding; in order to retain the pentagonal bipyramidal skeleton, the carbaborane responds to the addition of the metal fragment by eliminating H_2.

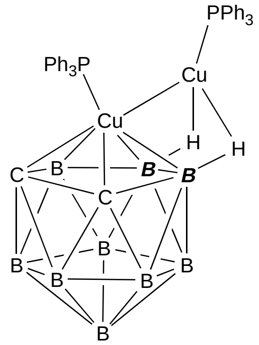

B = BH, C = CH, ***B*** = B

(**33**)

Metal fragment addition with *nido* to *closo* cluster change:

$$nido\text{-}C_2B_4H_8 + Fe(CO)_5 \xrightarrow{\Delta} closo\text{-}Fe(CO)_3C_2B_4H_6 + H_2 + 2CO \quad (17)$$

Metal fragment insertion into a *closo* cluster:

$$nido\text{-}C_2B_4H_6 + Fe(CO)_5 \xrightarrow{\Delta} closo\text{-}Fe(CO)_3C_2B_4H_6 + 2CO \quad (18)$$

Metal fragment-for-BH unit substitution in a *closo* cluster:

$$closo\text{-}C_2B_{10}H_{12} + CpCo(CO)_2 \longrightarrow closo\text{-}CpCoC_2B_9H_{11} + 2CO \quad (19)$$

Metal fragment insertion into a *nido*-cluster:

$$nido\text{-}C_2B_8H_{12} + Cp_2Ni \longrightarrow nido\text{-}CpNiC_2B_8H_{11} + C_5H_6 \quad (20)$$

The insertion of a two-electron cluster fragment into a *closo*-carbaborane cluster can result in the expansion of the cluster framework. Thus, in equation (18), the insertion of an $Fe(CO)_3$ fragment into the octahedral cluster *closo*-$C_2B_4H_6$ yields a pentagonal bipyramidal metallacarbaborane. On the other hand, fragment substitution may be preferred to fragment insertion. This is particularly true for the icosahedral skeleton. Reaction 19 shows the substitution of a CpCo for an isolobal BH unit. This type of fragment replacement is called *subrogation*. Finally, equation (20) illustrates the insertion of a metal fragment into a *nido* cluster; the CpNi unit is a source of three electrons and one H atom is lost from the precursor in order to retain an even electron count for the cluster.

4.4 Metallaborane with an Alkyne

An important method for the synthesis of carbaboranes is the reaction of a borane cluster with an alkyne. However, an analogous reaction of a metallaborane cluster with an alkyne is not commonly used to prepare metallacarbaborane clusters. Equation (21) illustrates one example.

$$nido\text{-}2\text{-}(\mathrm{CpCo})\mathrm{B_4H_8} + \mathrm{C_2H_2} \longrightarrow nido\text{-}2\text{-}(\mathrm{CpCo})\mathrm{C_2B_3H_7} \qquad (21)$$

Reactions between a metallaborane and alkyne are not always predictable. For example, *nido*-1,2-$(Cp^*Rh)_2B_3H_7$ catalyzes the cyclotrimerization of alkynes rather than undergoing insertion of the alkyne into the cluster cage.[52]

4.5 Aggregation of Metal Atoms, Borane, and Alkynes

Metal-atom vapor synthesis techniques have been successfully applied to the preparation of metallacarbaboranes, that is, reaction type {M} + {C} + {B}. A disadvantage is that product distribution tends to be nonspecific, for example, when Co metal is vaporized by electrical heating and cocondensed at −196 °C with cyclopentadiene, B_5H_9, and the alkyne MeC≡CMe, 1-(CpCo)-2,3-Me_2-2,3-$C_2B_4H_4$, 1,7-$(CpCo)_2$-2,3-Me_2-2,3-$C_2B_3H_3$, and 1,7-$(CpCo)_2$-2,5-Me_2-2,5-$C_2B_5H_5$ are formed in low yield. If B_6H_{10} is used instead of B_5H_9 as the borane precursor, the products are 3-(CpCo)-1,2-Me_2-1,2-$C_2B_5H_5$, 2,5-$(CpCo)_2$-6,7-Me_2-6,7-$C_2B_6H_8$, and 2,4-$(CpCo)_2$-6,7-Me_2-2,4–6,7-$C_2B_6H_6$.

4.6 Borane with an Organometallic Complex

The method of metallacarbaborane synthesis that involves the combination of {MC} + {B} fragments is not commonly used. However, the designed synthesis shown in Scheme 1 works well. The reagent BH_3·THF is a source of boron for the metallacarbaborane product, and is also able to abstract phosphine from the organometallic precursor. Monoborane (BH_3) is a Lewis acid and forms adducts with Lewis bases; PPh_3 displaces THF from BH_3·THF and is transferred from $(PPh_3)CpCoC_4Ph_4$ to form PPh_3·BH_3, leaving an active {$CpCoC_4Ph_4$} fragment, which can interact with a second mole of borane.

4.7 Construction of Stacked Complexes

Work directed at preparing and characterizing stacked complexes has been developed since the late 1980s, and the syntheses are carefully controlled.[39,51] The principles of the approach are outlined below, but may be summarized as an example of the method. The archetypal sandwich compound is ferrocene, in which two coparallel C_5H_5 rings sit on either side of Fe. Both the Cp^- and $[C_2B_3H_5]^{2-}$ ligands are sources of 6π electrons and both have similar frontier orbitals. Similarly, the *nido* cluster $[2,3\text{-}C_2B_4H_6]^{2-}$ can present an open C_2B_3 pentagonal face to a metal center. Organometallic sandwich complexes utilize organometallic π ligands other than Cp^-, for example, benzene can act as a 6π-electron ligand. These and other chemical building blocks can be used to assemble stacks with alternating metal and organic or carbaborane units. Extension of these principles could lead to three-dimensional networks.[43]

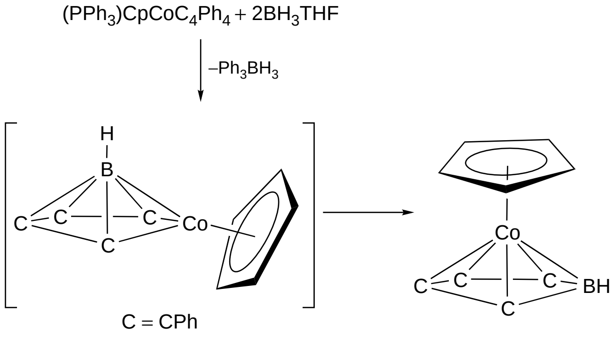

Scheme 1

In the simplest type of reaction, a double-decker sandwich is prepared as shown in equation (22). The next step in the assembly of a stack might be the removal of the BH apex from a $(\eta^n\text{-}C_nH_n)M(2,3\text{-}R_2\text{-}2,3\text{-}C_2B_4H_4)$ complex, where typically $n = 5$ and M = Co, Ni, or $n = 6$ and M = Ru, Fe (first step in Scheme 2). The decapping of $(\eta^6\text{-}C_6H_6)Ru(2,3\text{-}(SiMe_3)_2\text{-}2,3\text{-}C_2B_4H_4)$ is accompanied by double protonation of the newly

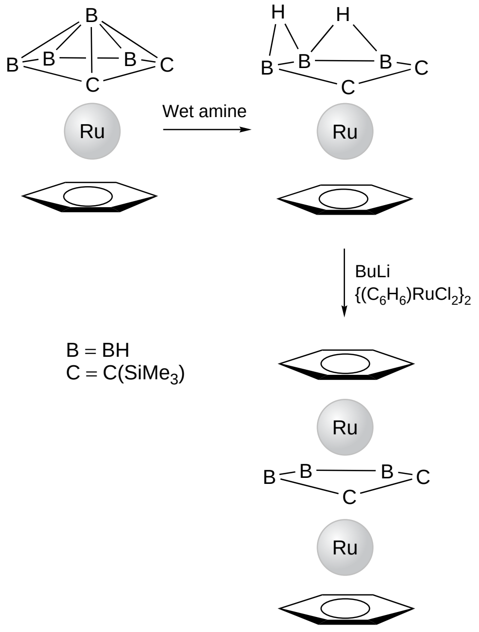

Scheme 2

exposed C_2B_3 face. The two protons (present as B–H–B bridges) can be removed by treatment with a base such as *n*-BuLi; the dianion so formed reacts with an organometallic metal halide, adding a new metal-containing unit to the stack, and yielding a triple-decker sandwich complex. This general strategy can be adapted to generate a variety of multiple stacks.

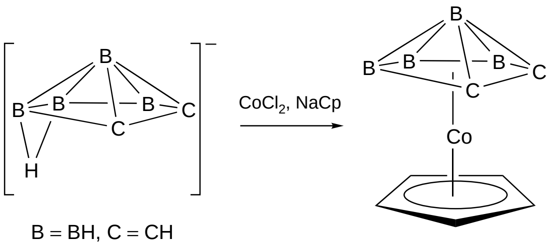

(22)

B = BH, C = CH

Linking stacks together can be achieved by incorporating ligands with pendant arms into the first stack, which are themselves potential ligands, for example (**34**). One of the results of this strategy is the formation of (**21**).

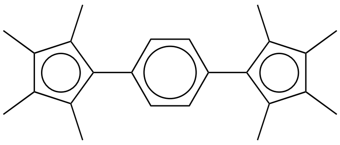

(**34**)

4.8 Use of Lithiated Carbaboranes

The carbon-bound hydrogen atoms in *closo*-1,2-$C_2B_{10}H_{12}$ (**35**) are acidic, and lithiation occurs readily (equation 23). The monolithiated cluster disproportionates to a mixture of 1,2-$C_2B_{10}H_{12}$ and 1,2-Li_2-1,2-$C_2B_{10}H_{10}$. Protection of one C site can be achieved by using a *t*-$BuMe_2Si$ group; the cluster can be deprotected with $[n\text{-}Bu_4N]F$. Lithiated derivatives are used to prepare a range of C-substituted derivatives.[53]

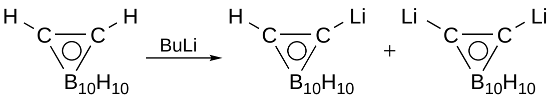

(23)

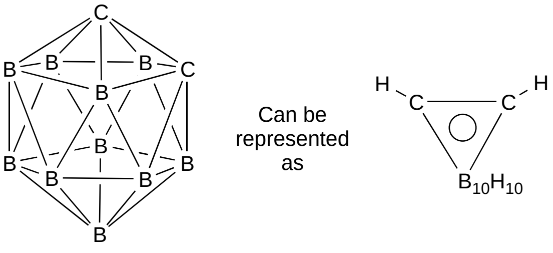

Can be represented as

B = BH, C = CH

(**35**)

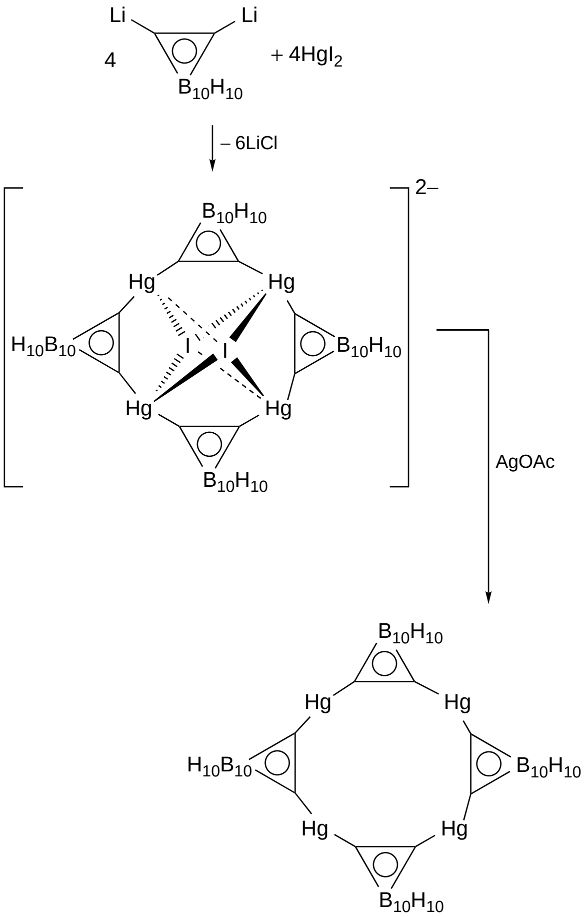

(**30**)

Scheme 3

The reaction of lithiated derivatives of 1,2-$C_2B_{10}H_{12}$ with mercury(II) halides is a route to organomercury complexes with Hg–$C_{\text{carbaborane}}$ bonds.[54] An interesting example is shown in Scheme 3; 1,2-Li_2-1,2-$C_2B_{10}H_{10}$ reacts with HgI_2 to give $Li_2[Hg_4(C_2B_{10}H_{10})I_2]$. When LiI is removed, a cyclic tetrameric complex, which is described as a macrocyclic Lewis acid, is produced.

4.9 *commo*-Clusters

commo-Metallacarbaborane clusters in which the two dicarbollide ligands are connected by a bridging unit can be prepared by introducing the bridge after the *commo* cluster has been synthesized. For example, (**18**) is prepared by the reaction of $K[Co(C_2B_9H_{11})_2]$ with CS_2 and HCl in the presence of aluminum chloride. Alternatively, VFC (see Section 2.2), are prepared by first assembling a ligand consisting of two carboranyl ligands that are strapped together. The strap can either be a B $\cdots$ B or C $\cdots$ C link, where B or C is a B- or C-substituted site on one carboranyl unit.

The protected monosubstituted derivative 1-(t-BuMe$_2$Si)-1,2-$C_2B_{10}H_{11}$ is the starting point for the synthesis of ligands of type $[H_2L]^{2-}$ shown in Scheme 4. The length of the strap is critical if $[H_2L]^{2-}$ is to be a precursor to *commo*-metallacarbaboranes of type $[ML]^-$. Scheme 4 illustrates a sequence used to link together two dicarbollide ligands via a C $\cdots$ C link. Ligand $[H_2L]^{2-}$ interacts with a variety of first-row transition metal(III) ions (M^{3+}), for example, Co^{3+}, Cr^{3+}, with concomitant deprotonation of the two *nido* cages to give $[ML]^-$. The pyrazole-containing ligand present in complex (**19**) is synthesized from *closo*-$C_2B_9H_{11}$ and $[C_3H_3N_2]^-$.

The development of preparative routes to ligands such as $[H_2L]^{2-}$ in Scheme 4 has been a breakthrough in the controlled synthesis of the VFC group of *commo* complexes, which have potential biological uses (see Section 8).

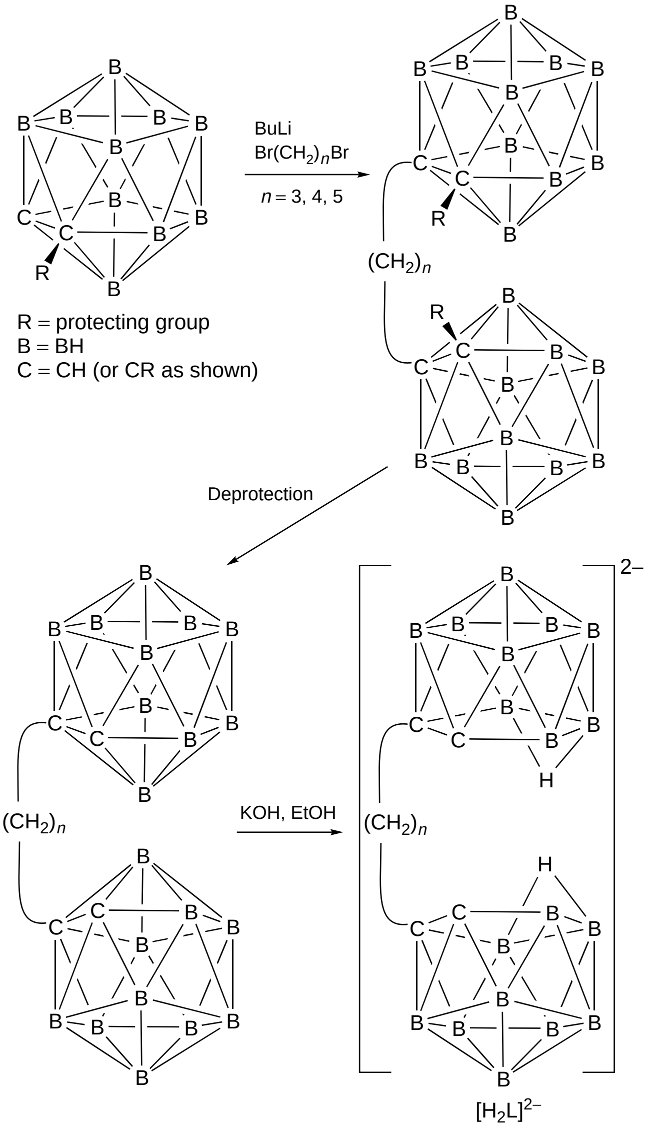

Scheme 4

4.10 Clusters with More than 12 Vertices

Although the chemistry of metallacarbaborane clusters with $\leq$12 vertices is extremely well established, that of larger, single-cage compounds is a more recent development. Preparative routes to dicarbon metallacarbaboranes of the platinum group metals having 11, 12, or 13 vertices have been reviewed.[55] Metal capping of *nido*-[7,9-$R_2C_2B_{10}H_{10}]^{2-}$ is a general route to 13-vertex metallacarbaboranes. The *nido* precursor is produced by reduction of *closo*-1,2,-$R_2C_2B_{10}H_{10}$, but this step always results in a separation of the carbon atoms in the cluster cage (the ''carbons-apart'' product). Tethering the C_2 unit to a C,C′-bridging substituent allows the ''carbons adjacent'' product to be isolated (Scheme 5). The ''carbons-apart'' and ''carbons-adjacent'' species exhibit different redox properties, with the dianion in Scheme 5 being further reduced by Li metal to the corresponding tetraanionic *arachno* cluster. By altering the length and flexibility of the organic bridge, it is possible to gain control over the final positions of the two carbon atoms in the reduced product.[56] A significant achievement has been the use of the carbon-tethered *nido* or *arachno* clusters in reactions with $RBCl_2$ to prepare the first examples of 13- or 14-vertex carbaboranes, respectively.[57,58] Advances in the syntheses of metallacarbaboranes with 13 vertices (MC_2B_{10}, MC_4B_8, $M_2C_2B_9$, $M_2C_3B_8$, $M_3C_3B_7$) or 14 vertices (MC_2B_{11}, $M_2C_2B_{10}$, $M_2C_4B_8$) have been reviewed.[56,59] Most recently, reduction of the carbon-tethered 1,2-μ-$(CH_2)_3$-1,2-*closo*-$C_2B_{11}H_{11}$ by Na and subsequent reaction of the reduced, open cage with $[(p\text{-cymene})RuCl_2]_2$ has given rise to the isomeric, 15-vertex clusters (**36**) and (**37**).[60]

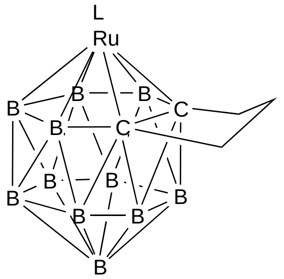

(**36**)

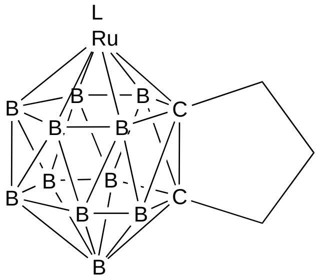

(**37**)

5 SKELETAL ISOMERISM

Of the polyhedra in Figure 1, only the octahedron and icosahedron possess equivalent vertices. *closo*-$[B_{12}H_{12}]^{2-}$ contains only one B environment and the introduction of one C atom in place of B generates $[CB_{11}H_{12}]^-$ for which there is only one structure. Introduction of two C atoms to

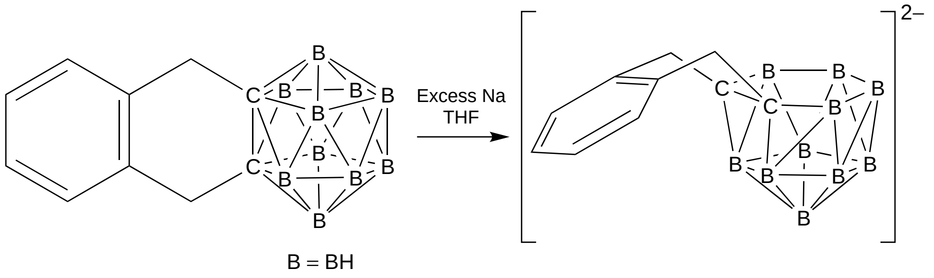

Scheme 5

give $C_2B_{10}H_{12}$ leads to three possible isomers: 1,2-, 1,7-, and 1,12-$C_2B_{10}H_{12}$ (equation 24).

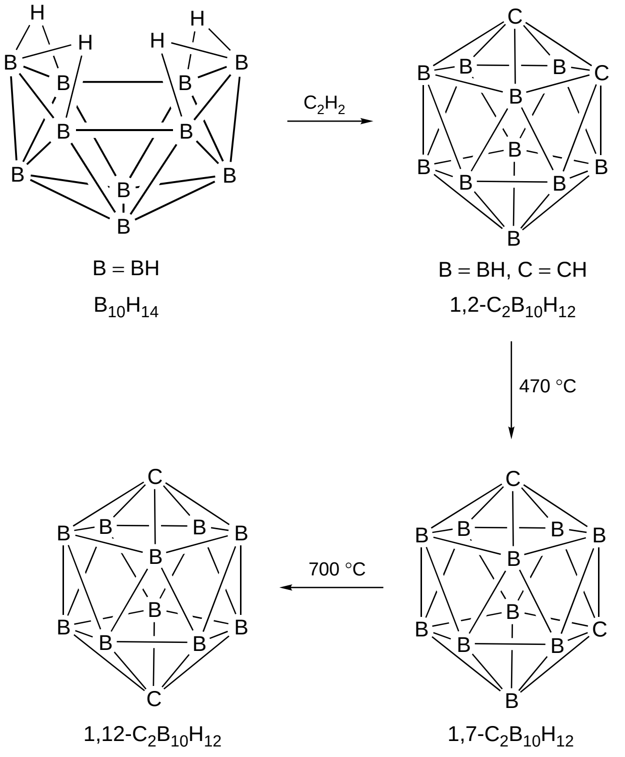

(24)

Introducing a metal atom into the carbaborane framework increases the number of possible isomers. In the synthesis of a metallacarbaborane, the kinetic product may not necessarily be the thermodynamically preferred isomer, for example, in the synthesis of $CpCoC_4Ph_4BH$, the first isomer to be formed rearranges spontaneously to the thermodynamically favored one (Scheme 1). An understanding of the mechanisms for polyhedral rearrangements among metallacarbaboranes remains relatively undeveloped, but proposals usually involve nondissociative processes. General preferences follow the guidelines that (i) carbon atoms prefer sites of low *connectivity*, (ii) carbon atoms tend to be apart from one another (but see Section 4.10), (iii) metal atoms show a tendency for sites of relatively high connectivity, and (iv) a metallacarbaborane cluster tends to exhibit some degree of symmetry. However, these are guidelines, not rules. In (**5**), for example, all four guidelines are met: the Ru atom occupies the unique site of the octadecahedron with connectivity six, while the two C atoms are mutually apart (a ‘‘carbons-apart’’ isomer) and are in sites of connectivity four.

Examples of thermal skeletal isomerization are as follows. The 11-electron pair cluster *closo*-$Cp_2CoNiCB_7H_8$ (Scheme 6) has a structure based upon a bicapped square antiprism (Figure 1). This polyhedron has two distinct types of vertex: (i) two apical sites each of which has a connectivity of four within the cage and (ii) eight equatorial or square antiprism sites each of which has a connectivity of five within

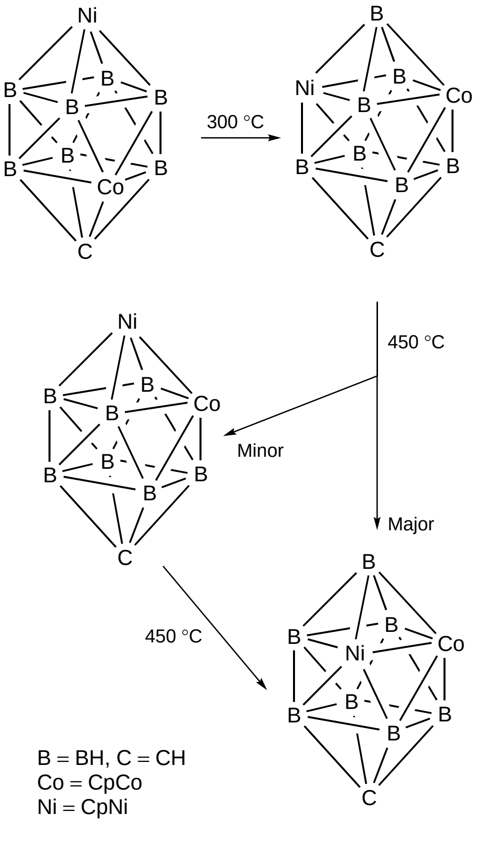

Scheme 6

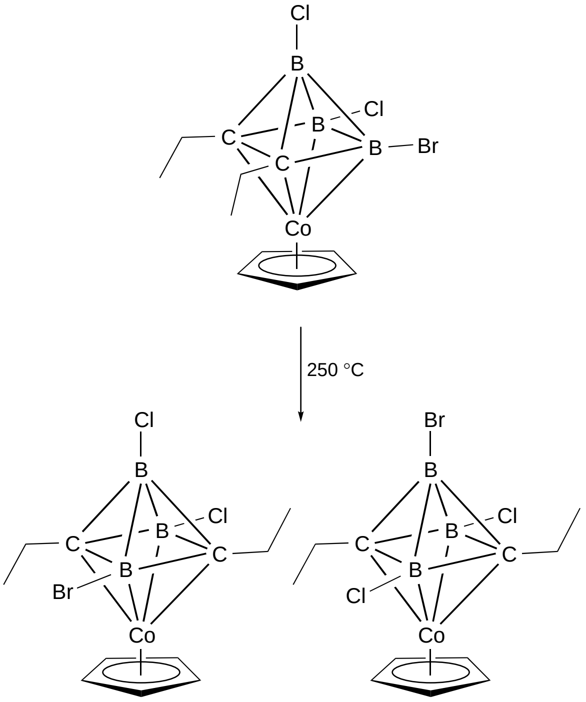

Scheme 7

the cage. After thermolysis, the metal atoms end up in the sites of higher connectivity and the carbon atom remains in a site of low connectivity.[61]

When 1-(CpCo)-2,3,-$C_2B_9H_{11}$ is heated between 400 and 700 °C, six isomers are obtained in which the carbon atoms have migrated around the cage positions.[62] Thermal rearrangements of $(CpCo)_2C_2B_nH_{n+2}$ ($n = 6$–8) lead to isomeric products,[63] and an *exo*–*nido* → *closo* skeletal rearrangement is observed when *exo*–*nido*-5,6,10-$(Cl(PPh_3)_2Ru)$-5,6,10-$(\mu\text{-}H)_3$-10-H-7,8-$C_2B_9H_8$ is heated in benzene under reflux conditions.[64,65] In the rearrangement of icosahedral $[3,1,2\text{-}(CO)_2(C_3H_5)Mo(PhC_2B_9H_{11})]^-$ to the carbons-apart isomer $[3,1,9\text{-}(CO)_2(C_3H_5)Mo(PhC_2B_9H_{11})]^-$, a nonicosahedral intermediate has been isolated; the rearrangement is facile, occurring at room temperature, apparently to relieve steric crowding.[66] A final example involves the little-studied six-membered *closo*-MC_2B_3 cage. When heated to 250 °C, *closo*-1,2,3-Cp*Co($Et_2C_2B_3$-4,6-Cl_2-5-Br) rearranges as shown in Scheme 7, while heating *closo*-1,2,3-Cp*Co($Et_2C_2B_3Br_3$) leads to a single ‘‘carbons-apart’’ isomer.[67]

6 ELECTROCHEMISTRY

The discussion of the electrochemical properties of metallacarbaboranes involves the compounds that are best subdivided into clusters and stacked complexes.

$$[\text{Co–Co}]^{2+} \leftarrow [\text{Co–Co}]^{+} \rightleftharpoons [\text{Co–Co}] \rightleftharpoons [\text{Co–Co}]^{-} \rightleftharpoons [\text{Co–Co}]^{2-}$$

Scheme 8

Electrochemical data for a wide range of metallacarbaborane clusters have been collected together in several reviews.[68–70] For metallacarbaboranes containing transition metal atoms, the measured redox couple is usually assigned to the process $M^{n+} + e^- \rightarrow M^{(n-1)+}$. However, this may be a formal designation since the bonding in a metallacarbaborane cluster is delocalized. Some general conclusions[68] are as follows: (i) if the carbon atoms are adjacent to the transition metal atom, the reduction process for the cluster occurs more easily than when the carbon atoms are more remote from the metal atom; (ii) metallacarbaborane clusters containing an $MC_2B_{10}H_{12}$ core exhibit lower reduction potentials than clusters with an $MC_2B_9H_{11}$ core for a common metal, M; and (iii) when more than one metal is present in a metallacarbaborane cluster core, the metals influence one another.

Electrochemical studies of sandwich complexes have also included multiple stacked systems.[5,7,68] In triple-decker complexes such as (**20**), a series of diffusion-controlled reversible one-electron redox processes is observed. Thus, for (**20**) (CMe replaced by CEt), the processes are summarized in Scheme 8 in which [Co–Co] represents the core of the triple-decker sandwich complex. It is the metal atoms (not the sandwich layers) that are the centers for the redox changes; however, the reduced or oxidized species are stabilized by the ability of the multiple-sandwich structure to delocalize electronic charge. Detailed studies of $(4\text{-}MeC_6H_4CHMe_2)Ru(Et_2C_2B_3H_3)Ru(4\text{-}MeC_6H_4CHMe_2)$ (Ru–Ru) and $CpCo(Et_2C_2B_3H_3)Ru(4\text{-}MeC_6H_4CHMe_2)$ (Co–Ru) by voltammetric, coulometric, electron paramagnetic resonance (EPR) spectroscopic, and optical spectroelectrochemical methods have been used to illustrate that there is complete delocalization of charge in the cations $(Ru\text{–}Ru)^+$ and $(Co\text{–}Ru)^+$. This is encouraging for the application of the stacked complexes in the construction of electroactive polymers.[71] A redox series involving a linked stack with iron centers is shown in Scheme 9. Related studies with Co- and Fe-containing systems have been reported.[72,73] The alkyne-coupled clusters in (**22**) exhibit double one-electron reductions followed by a single two-electron reduction. These results are interpreted in terms of significant electronic communication between the four metal centers.[42]

7 REACTIVITY

It is extremely difficult to generalize about the reactivity patterns of metallacarbaborane clusters. Some properties are

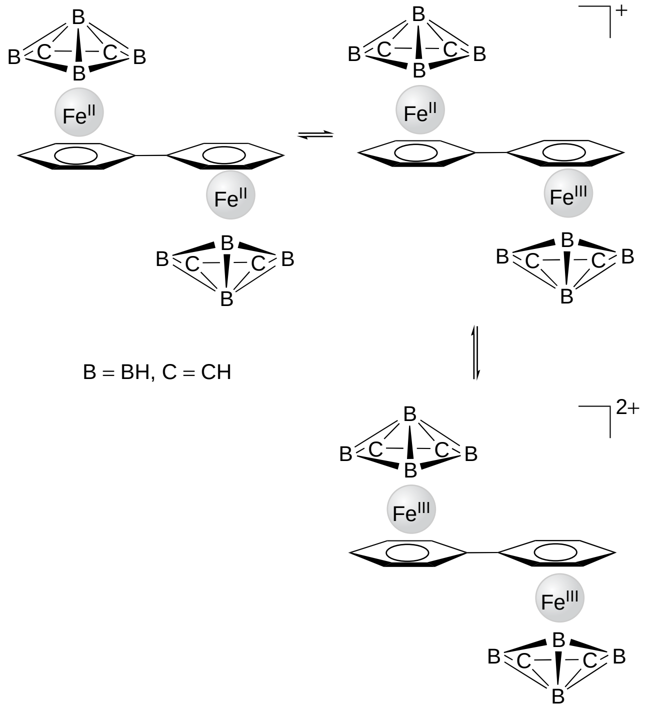

Scheme 9

outlined below, but the reader is directed to the literature for details of the reactions of specific compounds.**[4–6,12–17]**

7.1 Metal Exchange Reactions

The use of thallium(I) metallacarbaboranes in the synthesis of a range of other metal-containing clusters (equations 11–16) is well documented. The exchange of lithium in 1,2-Li_2-1,2-$C_2B_{10}H_{10}$ and 1-Li-$C_2B_{10}H_{11}$ for selected metals (Section 4.8) provides routes to metal derivatives in which the metal atom is bonded externally to the carbaborane cage via a C–M σ bond. The exchange of other metal atoms is less general. One example is shown in equation (25), but the Co-for-Sn exchange competes with the insertion of Co into the cluster.

$$\begin{aligned} &closo\text{-1-Sn-2,3-}C_2Me_2B_4H_4 + CpCo(CO)_2 \xrightarrow{\text{Gas phase}} \\ &closo\text{-}CpCoC_2Me_2B_4H_4 + closo\text{-}CpCoSnC_2Me_2B_4H_4 \end{aligned} \qquad (25)$$

7.2 Ligand Substitution at the Metal Atom

For transition metal–containing metallacarbaboranes, reactions at the metal center with no concomitant change to the cluster core are possible. The simplest type of reaction is ligand substitution. In equation (26), the three carbonyl ligands (each a two-electron donor) are replaced by a π-bonded benzene ring (a six-electron donor). When the net electron count for the cluster remains unchanged, there is no change in the skeletal geometry of the cluster.

$$closo\text{-Fe}(CO)_3C_2B_9H_{11} \xrightarrow{h\nu,C_6H_6} closo\text{-Fe}(\eta^6\text{-}C_6H_6)C_2B_9H_{11} \qquad (26)$$

As an example of simple ligand replacement, the THF ligands in $(THF)_4YbC_2B_9H_{11}$ (**38**) can be displaced by MeCN or DMF. Metallacarbaboranes containing naked p-block metal atoms can function as Lewis acids forming adducts with Lewis bases, for example, the reaction of 1-Sn-2,3-$(SiMe_3)_2$-2,3-$C_2B_4H_4$ with 2,2′-bipyridine gives complex (**25**). When a dinucleating ligand such as 2,2′-bipyrimidine is used, the metallacarbaborane clusters may be linked together as in (μ-L){1-Sn-2,3-$(SiMe_3)_2$-2,3-$C_2B_4H_4$}$_2$ (**39**).

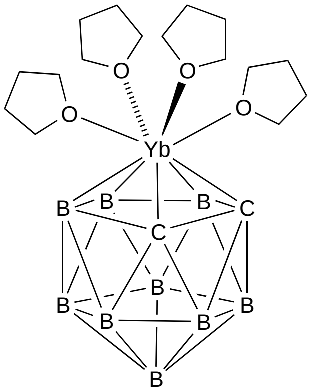

B = BH, C = CH

(**38**)

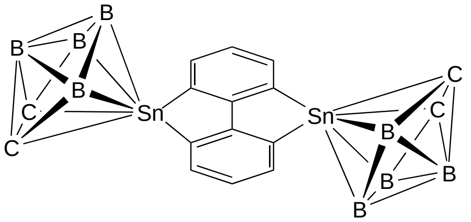

B = BH, C = C($SiMe_3$)

(**39**)

7.3 C and B Derivatization

For C-derivatized metallacarbaborane clusters, the substituents attached to the cage carbon atoms are usually introduced into the carbaborane precursor. Examples have been given earlier in equations (4), (5), (8), and (12), and Scheme 4.

Electrophilic substitution reactions are used to introduce B substituents into metallacarbaboranes. For example, the electrophilic bromination of 1-(CpCo)-2,3-$C_2B_8H_{10}$ gives a mixture of 10-Br-1-(CpCo)-2,3-$C_2B_8H_9$ and 4-Br-1-(CpCo)-2,3-$C_2B_8H_9$. In the presence of $AlCl_3$ and at higher temperatures, 4,5,6,10,11-Br_5-1-(CpCo)-2,3-$C_2B_8H_5$ is produced. Similarly, the bromination of 1-(CpFe)-2,3-$C_2B_9H_{11}$ occurs at room temperature to give the 8-bromo derivative; with an $AlCl_3$ catalyst, the 8,9-dibromo and 8,9,12-tribromo derivatives are formed. This substitution pattern is consistent with the electron distribution in the polyhedral cage. Friedel–Crafts acetylation of 1-(CpCo)-2,3-$C_2B_9H_{11}$ occurs at the 8-position; other organic substituents can be introduced in an analogous manner. The introduction of multiple B-Me groups is illustrated in the formation of (**40**) by reaction of the parent anion with ICl followed by MeMgBr.[74]

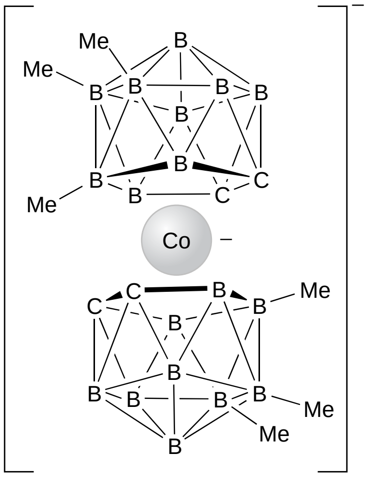

B = BH (or BMe as shown), C = CH

(**40**)

Cycloboronation (similar to an *orthometalation* reaction in organometallic chemistry) occurs in a range of iridaborane, platinaborane, iridacarbaborane and platinacarbaborane. The reaction involves the activation of an ortho C–H bond in a phenyl substituent of a triphenylphosphine ligand attached by the metal (equation 27).[75] The result is the elimination of H_2 and the formation of a B–C bond within a five-membered MPC_2B ring. Other examples include the formation of [10-(PPh_3)-2,6:2,9-(μ-S_2CH)$_2$-2-(*o*-$Ph_2PC_6H_4$)-*closo*-2-IrB_9H_5-1][76] and the cycloboronation of thiobenzoates, resulting in five-membered Ni–S–C–O–B rings.[77]

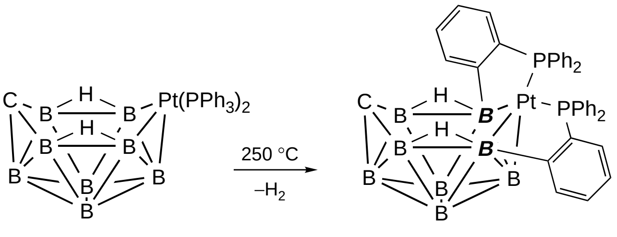

(27)

B = BH, ***B*** = B, C = CH_2

An unusual example of migration of an Me_3N substituent from a cluster-C atom to an adjacent B atom is observed when Li_2[7-NMe_3-*nido*-7-$CB_{10}H_{10}$] reacts with [$Mo(CO)_3(NCMe)_3$] to give a molybdenacarbaborane intermediate which, following oxidation and addition of [$(PPh_3)_2N$]Cl, gives [$N(PPh_3)_2$][2,2,2-$(CO)_3$-2-X-3-NMe_3-*closo*-2,1-$MoCB_{10}H_{10}$] (X = Br or I).[78]

7.4 Alkylidyne Derivatives and Those with Bridging Carbene or Carbyne Ligands

Metallacarbaborane clusters incorporating an M(≡CR) unit (e.g., M = W, Mo) have been studied in depth by Stone and coworkers.[79–81] The $[C_2R_2B_9H_9]^{2-}$ ligand can replace a Cp^- (or $C_5R_5{}^-$) ligand in, for example, CpW(≡CR)$(CO)_2$. In the presence of H^+ (e.g., $HBF_4 \cdot OEt_2$), cluster coupling via CR bridge formation has led to a number of dimetallic derivatives. Grimes and coworkers[82] have reported the linkage of [Cp*Co($Et_2C_2B_3H_5$)] sandwich units by alkynyl and diethynylphenylene connectors; the linking groups are attached to the Cp* ligands and to the C_2B_3 rings. For example, *nido*-[{(C_5Me_4(C≡CH))}Co($Et_2C_2B_3H_5$)] can be converted to 1,4-[*nido*-($Et_2C_2B_3H_5$)Co{(C_5Me_4(C≡C))}]$_2C_6H_4$.

Reactions between small metallacarbaboranes and organic substrates, more generally, have been reviewed.[43]

8 APPLICATIONS

The potential applications of metallacarbaboranes discussed below are selective; Grimes' recent look at metallacarbaboranes in the new millennium includes a range of potential applications.[43] Of particular significance is the development of biological/medicinal applications.

A number of metallacarbaborane clusters are effective catalysts. The Rh(III) cluster 3,3-$(PPh_3)_2$-3-H-3-Rh-1,2-$C_2B_9H_{11}$ was the first example of this type of cluster to exhibit high reactivity as a homogeneous catalyst.[83] It catalyzes the hydrosilylation of PhCOR (R = Me, Et, Me_2CH) with Me_2PhSiH, and the isomerization of unsaturated alcohols to aldehydes and ketones; 3,3-$(PPh_3)_2$-3-H-3-Rh-1-Ph-1,2-$C_2B_9H_{10}$ behaves similarly. The complexes 3,3-$(PPh_3)_2$-4-py-3-Rh-1,2-$C_2B_9H_{10}$ and 3-PPh_3-3-CO-4-py-3-Rh-1,2-$C_2B_9H_{10}$ are hydroformylation catalysts and the former catalyzes the hydrosilylation of alkenes (e.g., styrene) and alkynes (e.g., PhC≡CH). 3,3-$(PPh_3)_2$-3-H-3-Rh-1,2-$C_2B_9H_{11}$ and related clusters exist as a mixture of isomers that are in equilibrium in solution (equation 28). In the *closo* form, the Rh(III) center is coordinatively saturated. In the *exo–nido* form, Rh(I) is coordinatively unsaturated (*see Coordinative Saturation & Unsaturation*); it is this form of the cluster that is catalytically active.

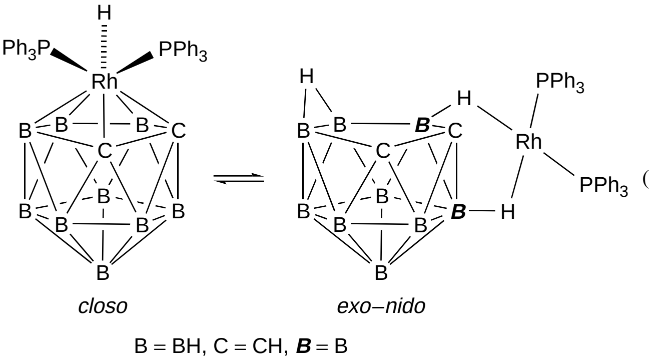

(28)

The *exo–nido* and *closo* cage ruthenium clusters $RuCl(PPh_3)_2(C_2R_2B_9H_{10})$ (R = H or Me) (**41**) and (**42**), respectively, exhibit a high activity as cyclopropanation catalysts, for example, in the reaction between ethyl diazoacetate and alkenes (equation 29). During cyclopropanation, an *exo–nido* → *closo* rearrangement should occur. $[(7\text{-}PPh_2\text{-}8\text{-}R\text{-}7,8\text{-}C_2B_9H_{10})Rh(PPh_3)_2]$ (R = H, Me) and $[(7\text{-}PPh_2\text{-}8\text{-}Me\text{-}7,8\text{-}C_2B_9H_{10})Rh(cod)]$ are also active in the cyclopropanation of alkenes with diazoacetates.[84]

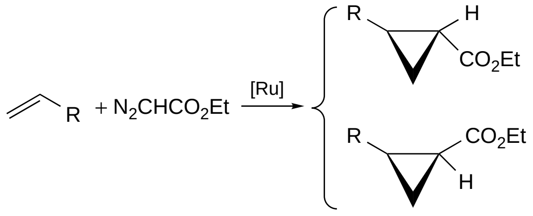

(29)

Silver phosphines in association with $[1\text{-}closo\text{-}CB_{11}H_{12}]^-$ and $[1\text{-}closo\text{-}CB_{11}H_6Br_6]^-$ are highly active Lewis acid catalysts for some hetero-Diels–Alder reactions. Very low catalyst loadings are required (0.1 mol%) and turnover frequencies of 4000 h^{-1} are observed.[85] The complexes $[(PPh_3)_2Rh(nbd)][closo\text{-}CB_{11}H_{12}]$ and $[(PPh_3)_2Rh(nbd)][closo\text{-}CB_{11}H_6Br_6]$ have been tested using cyclohexene, 1-methylcyclohexene, and 2,3-dimethylbut-2-ene for their catalytic activity (under ambient conditions) in internal alkene hydrogenation.[86] Further examples of metallacarbaborane catalytic activity have been reviewed by Grimes.[43] The complex $(Ph_3P)_2Ir(H)_2(closo\text{-}CB_{11}H_6Br_6)$ catalyzes the hydrogenation of cyclohexane and can be recycled up to five times without decomposition; related results for ethene are summarized in Scheme 10.[87] The effects of the halogen substituent and of the steric demands of the phosphine have been detailed.[88]

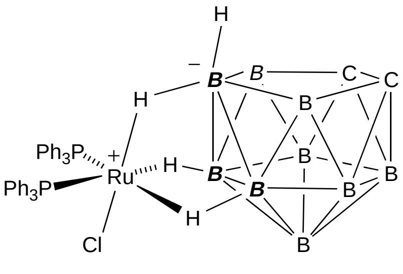

B = BH, C = CH, ***B*** = B

(**41**)

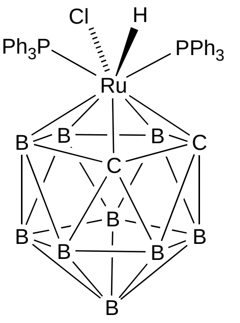

B = BH, C = CH

(**42**)

Group 4 metallocenes with constrained geometries are highly active catalysts. The replacement of one or two $[C_5R_5]^-$ ligands by *nido*-$[C_2B_9H_{11}]^{2-}$ ligands (see (**3**)) gives a means of modifying metallocene catalysts.[89,90] Examples include (**43**), which is proposed as the active catalytic species in the hydrogenation of internal alkynes to (*Z*)-alkenes.[91] Complex (**44**) incorporates a *nido*-C_2B_4 cage and this complex catalyzes the polymerization of ethene to high molecular weight polymers under ambient conditions.[92] The catalytic activity of single-walled carbon nanotube-supported nickellacarbaboranes has also been explored.[93]

The application of metallacarbaborane clusters as radiometal carriers for radioimmunodiagnosis and radioimmunotherapy has been explored, with ''VFCs'' (see Sections

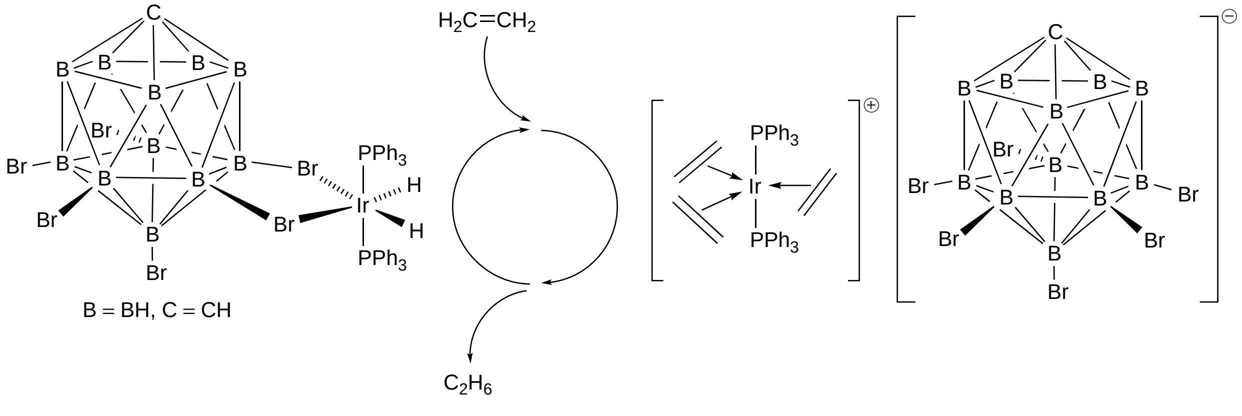

Scheme 10

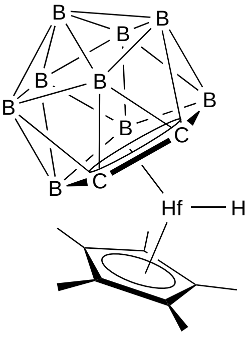

(**43**)

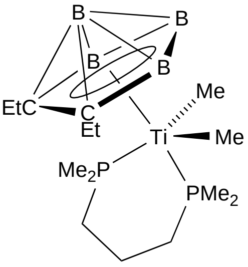

(**44**)

2.2 and 4.9) being central to these studies.[36,94,95] It is necessary to provide a radiometal-containing system (the metallacarbaborane) that is suitably functionalized to enable conjugation to monoclonal antibodies. The dicarbollide ligand present in complex (**19**) can encapsulate a radiometal atom (e.g., ^{57}Co) to form a particularly stable metallacarbaborane *commo* cluster. The first examples of direct labelling of proteins with ^{121}At using a *nido*-carbaborane, a ''VFC'', or *closo*-decaborate(2-) clusters were reported in 2007.[96] Salts of $[1\text{-CpFe-2-Me-2,3,4-}C_3B_7H_9]^+$ and the complex $1\text{-CpFe-2-Me-2,3,4-}C_3B_7H_9$ have been found to be effective cytotoxic agents against human and murine tumor cell lines; the agents act by inhibiting the *de novo* purine synthesis of L-1210 cells, thus reducing DNA and RNA syntheses.[97] $1\text{-Cp-1-Br-2-Ph-1,2,3,4-}VC_3B_7H_9$ and *commo*-$\text{Nb-1-Cl-(4-Me-1,2,3,4-}NbC_3B_7H_9)_2$ are also cytotoxic agents; the vanadium-containing complex exhibits significant activity against the growth of cultured human solid tumors.[98] The tantalum and niobium-containing species $CpTaCl_2(Et_2C_2B_4H_4)$, $CpNbCl_2(Et_2C_2B_4H_4)$, $Cp^*TaCl_2(Et_2C_2B_4H_4)$, $CpTaCl_2\{(Me_3Si)_2C_2B_4H_4\}$, and $CpTaCl_2(Me_2C_2B_4H_4)$ are active against suspended tumors, and result in cell death in a number of tissue culture lines including murine L1210 lymphoid leukemia.[99] Metallacarbaborane-containing nucleoside conjugates with thymidine, 2′-*O*-deoxyadenosine, 2′-*O*-deoxyguanine, or 2′-*O*-deoxycytidine[100,101] provide building blocks for the synthesis of, for example, iron(III) and cobalt(III)-containing dinucleotides (**45**). The synthetic pathway to (**45**) generates a series of synthons for the preparation of bioinorganic DNA/metallacarbaborane conjugates.[102] Related mononucleotide conjugates may function as electrochemical tags, and are proposed as labels for electrochemical coding of DNA.[103]

Technetium and rhenium coordination chemistry associated with the introduction of ^{99m}Tc into radiotherapy and radioimaging agents is of active current interest, and the application of *nido*-carbaborane ligands has recently been explored. Microwave heating assists the formation of rhenium η^5-carbaborane complexes in aqueous solution, and similar conditions are effective at the tracer level for the preparation of ^{99m}Tc complexes.[104]

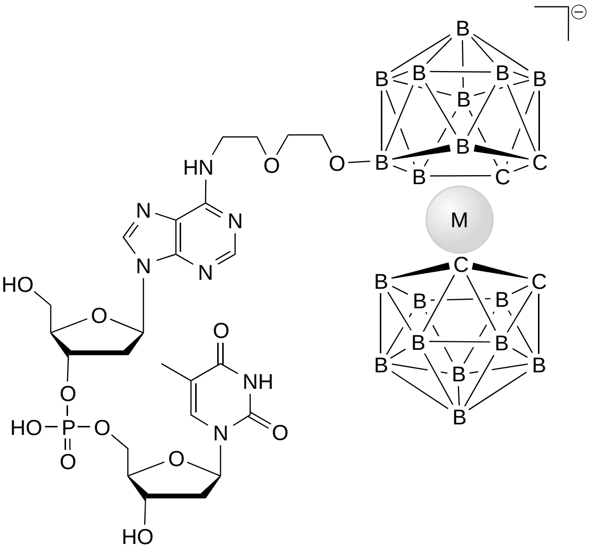

(**45**)

The ability of $[3,3'\text{-M}(1,2\text{-}C_2B_9H_{11})_2]^-$ ($M^{3+} = Co^{3+}$, Fe^{3+}, Ni^{3+}) to act as Cs^+ sensors in ion selective electrodes has been assessed. The related complexes $[3,3'\text{-Co}(1\text{-Me-}2\text{-}(CH_2)_nOR\text{-}1,2\text{-}C_2B_9H_9)_2]^-$ ($n = 3$, R = Et; $n = 3$, R = $(CH_2)_2OMe$; $n = 3$, R = $(CH_2)_3Me$; $n = 6$, R = $(CH_2)_3Me$) and $[3,3'\text{-Co}(1\text{-Ph-}1,2\text{-}C_2B_9H_{10})_2]^-$ and $[3,3'\text{-Co}(1,7\text{-}Ph_2\text{-}1,7\text{-}C_2B_9H_9)_2]^-$ act efficiently in ^{137}Cs, ^{90}Sr, and ^{152}Eu extraction.[105,106]

One challenge within the area of conducting electroactive polymers such as polypyrrole (PPy) is increasing the stability of the materials. By doping PPy with $[Co(C_2B_9H_{11})_2]^-$, the material becomes more resistant to overoxidation by 300–500 mV.[107]

9 FUTURE WAYS FORWARD

In addition to the areas already discussed in this article and, in particular, development of applications in biological, medicinal, and materials chemistry, several aspects are of current research interest. Section 4.10 introduced the steadily expanding area of single-cage metallacarbaborane clusters with more than 12 vertices. The role of carbaboranes and metallacarbaboranes within supramolecular chemistry[108] has been actively investigated in the last decade. One of the best-explored areas is that of multicluster mercuracarbaboranes, which act as macrocyclic Lewis acidic hosts for electron-rich (anionic or neutral) guests.[54]

Finally, small metallacarbaboranes containing the C_2B_4 unit have been the subject of much study in the last few decades. However, Hosmane has made a pertinent point: the area has depended on supplies of B_5H_9 from government surplus, which are no longer available.[109]

10 RELATED ARTICLES

Boron Hydrides; Boron: Polyhedral Carboranes; Electronic Structure of Clusters.

11 REFERENCES

1. M. F. Hawthorne, D. C. Young, and P. A. Wegner, *J. Am. Chem. Soc.*, 1965, **87**, 1818.
2. P. Jutzi, *Pure Appl. Chem.*, 1990, **62**, 1035.
3. M. F. Hawthorne, *J. Organomet. Chem.*, 1975, **100**, 97.
4. R. N. Grimes, in 'Comprehensive Organometallic Chemistry', eds. G. Wilkinson, F. G. A. Stone, and E. W. Abel, Pergamon Press, Oxford, 1982, Vol. 1, p. 459.
5. R. N. Grimes, in 'Comprehensive Organometallic Chemistry II', eds. E. W. Abel, F. G. A. Stone, and G. Wilkinson, Pergamon Press, Oxford, 1995, Vol. 1, p. 373.
6. N. S. Hosmane and J. A. Maguire, in 'Comprehensive Organometallic Chemistry III', eds. R. H. Crabtree, and D. M. P. Mingos, Elsevier, Oxford, 2007, Vol. 3, p. 175.
7. R. N. Grimes, *Chem. Rev.*, 1992, **92**, 251.
8. N. S. Hosmane and J. A. Maguire, *Comment Inorg. Chem.*, 2005, **26**, 183.
9. N. S. Hosmane and J. A. Maguire, *Adv. Organomet. Chem.*, 1990, **30**, 99.
10. N. S. Hosmane, *Pure Appl. Chem.*, 1991, **63**, 375.
11. Z. Xie, *Coord. Chem. Rev.*, 2002, **231**, 23.
12. F. T. Edelmann, in 'Comprehensive Organometallic Chemistry III', eds. R. H. Crabtree, and D. M. P. Mingos, Elsevier, Oxford, 2007, Vol. 4, p. 110.
13. J. F. Liebman, A. Greenberg, and R. E. Williams eds, 'Advances in Boron and the Boranes', VCH Publishers, New York, 1988.
14. G. A. Olah, K. Wade, and R. E. Williams eds, 'Electron Deficient Boron and Carbon Clusters', John Wiley & Sons, New York, 1991.
15. W. W. Siebert, ed., 'Advances in Boron Chemistry', Royal Society of Chemistry, Cambridge, 1997.
16. M. G. Davidson, A. K. Hughes, T. B. Marder, and K. Wade eds, 'Contemporary Boron Chemistry', Royal Society of Chemistry, Cambridge, 2000.
17. P. A. Jelliss, in 'Specialist Periodical Reports: Organometallic Chemistry', ed. M. Green, Royal Society of Chemistry, London, 2007, Vol. 33, p. 81.
18. IUPAC, 'Nomenclature of Inorganic Chemistry: Recommendations 1990', ed. G. J. Leigh, Blackwell, Oxford, 1990, Chap. 1–11, p. 207.
19. G. Rana, J. A. Maguire, S. N. Hosmane, and N. S. Hosmane, *Main Group Met. Chem.*, 2000, **23**, 529.
20. A. K. Saxena, J. A. Maguire, and N. S. Hosmane, *Chem. Rev.*, 1997, **97**, 2421.
21. L. Wesemann, in 'Comprehensive Organometallic Chemistry III', eds. R. H. Crabtree, and D. M. P. Mingos, Elsevier, Oxford, 2007, Vol. 3, p. 113.
22. R. Khattar, C. B. Knobler, and M. F. Hawthorne, *J. Am. Chem. Soc.*, 1990, **112**, 4962.
23. R. Khattar, C. B. Knobler, and M. F. Hawthorne, *Inorg. Chem.*, 1990, **29**, 2191.
24. N. S. Hosmane, D. Zhu, J. E. McDonald, H. Zhang, J. A. Maguire, T. G. Gray, and S. C. Helfert, *Organometallics*, 1998, **17**, 1426.
25. N. S. Hosmane, H. Zhang, J. A. Maguire, Y. Wang, T. Demissie, T. J. Colacot, M. B. Ezhova, K.-J. Lu, D. Zhu, T. G. Gray, S. C. Helfert, S. N. Hosmane, J. D. Collins, F. Baumann, W. Kaim, and W. N. Lipscomb, *Organometallics*, 2000, **19**, 497.
26. D. Rabinovich, C. M. Haswell, B. L. Scott, R. L. Miller, J. B. Nielsen, and K. D. Abney, *Inorg. Chem.*, 1996, **35**, 1425.
27. D. Rabinovich, R. M. Chamberlin, B. L. Scott, J. B. Nielsen, and K. D. Abney, *Inorg. Chem.*, 1997, **36**, 4216.
28. J. Arnold, S. E. Johnson, C. B. Knobler, and M. F. Hawthorne, *J. Am. Chem. Soc.*, 1992, **114**, 3996.
29. F. R. Fronczek, G. W. Halstead, and K. N. Raymond, *J. Chem. Soc., Chem. Commun.*, 1976, **279**, 279.
30. F. R. Fronczek, G. W. Halstead, and K. N. Raymond, *J. Am. Chem. Soc.*, 1977, **99**, 1769.
31. M. J. Manning, C. B. Knobler, and M. F. Hawthorne, *J. Am. Chem. Soc.*, 1988, **110**, 4458.
32. R. Khattar, M. J. Manning, C. B. Knobler, S. E. Johnson, and M. F. Hawthorne, *Inorg. Chem.*, 1992, **31**, 268.
33. Z. Xie, C. Yan, Q. Tang, and T. C. W. Mak, *Angew. Chem. Int. Ed. Engl.*, 1999, **38**, 1761.
34. A. Varadarajan, S. E. Johnson, F. A. Gomez, S. Chakrabarti, C. B. Knobler, and M. F. Hawthorne, *J. Am. Chem. Soc.*, 1992, **114**, 9003.
35. F. A. Gomez, S. E. Johnson, C. B. Knobler, and M. F. Hawthorne, *Inorg. Chem.*, 1992, **31**, 3558.
36. J. M. Nabakka, D. E. Harwell, C. B. Knobler, and M. F. Hawthorne, *J. Organomet. Chem.*, 1998, **550**, 423.
37. G. E. Herberich, in 'Comprehensive Organometallic Chemistry', eds. G. Wilkinson, F. G. A. Stone, and E. W. Abel, Pergamon Press, Oxford, 1982, Vol. 1, p. 381.
38. G. E. Herberich, in 'Comprehensive Organometallic Chemistry II', eds. E. W. Abel, F. G. A. Stone, and G. Wilkinson, Pergamon Press, Oxford, 1995, Vol. 1, p. 197.
39. R. N. Grimes, in 'Comprehensive Organometallic Chemistry III', eds. R. H. Crabtree, and D. M. P. Mingos, Elsevier, Oxford, 2007, Vol. 3, p. 1.
40. R. N. Grimes, *Mol. Cryst. Liq. Cryst A*, 2000, **342**, 7.
41. H. Yao, M. Sabat, and R. N. Grimes, *Organometallics*, 2002, **21**, 2833.

42. H. Yao, M. Sabat, R. N. Grimes, F. Fabrizi de Biani, and P. Zanello, *Angew. Chem. Int. Ed. Engl.*, 2003, **42**, 1002.

43. R. N. Grimes, *Coord. Chem. Rev.*, 2000, **200**, 773.

44. F. Fabrizi de Biani, M. Corsini, P. Zanello, H. Yao, M. E. Bluhm, and R. N. Grimes, *J. Am. Chem. Soc.*, 2004, **126**, 11360.

45. N. S. Hosmane, J. Yang, K.-J. Lu, H. Zhang, U. Siriwardane, M. S. Islam, J. L. C. Thomas, and J. A. Maguire, *Organometallics*, 1998, **17**, 2784.

46. M. J. Manning, C. B. Knobler, M. F. Hawthorne, and Y. Do, *Inorg. Chem.*, 1991, **30**, 3589.

47. J. Wang, S. Li, C. Zheng, J. A. Maguire, and N. S. Hosmane, *Inorg. Chem. Commun.*, 2003, **6**, 549.

48. X. G. Yang, S. E. Johnson, S. I. Khan, and M. F. Hawthorne, *Angew. Chem. Int. Ed. Engl.*, 1992, **31**, 893.

49. H. Lee, M. Diaz, C. B. Knobler, and M. F. Hawthorne, *Angew. Chem. Int. Ed. Engl.*, 2000, **39**, 776.

50. X. Meng, T. P. Fehlner, and A. L. Rheingold, *Organometallics*, 1990, **9**, 534.

51. R. N. Grimes, *Coord. Chem. Rev.*, 1995, **143**, 71.

52. T. P. Fehlner, *Pure Appl. Chem.*, 2006, **78**, 1323.

53. V. I. Bregadze, *Chem. Rev.*, 1992, **92**, 209.

54. T. J. Wedge and M. F. Hawthorne, *Coord. Chem. Rev.*, 2003, **240**, 111.

55. I. T. Chizhevsky, *Coord. Chem. Rev.*, 2007, **251**, 1590.

56. L. Deng and Z. Xie, *Organometallics*, 2007, **26**, 1832.

57. A. Burke, D. Ellis, B. T. Giles, B. E. Hodson, S. A. MacGregor, G. M. Rosair, and A. J. Welch, *Angew. Chem. Int. Ed.*, 2003, **42**, 225.

58. L. Deng, H.-S. Chan, and Z. Xie, *Angew. Chem. Int. Ed.*, 2005, **44**, 2128.

59. L. Deng and Z. Xie, *Coord. Chem. Rev.*, 2007, **251**, 2452.

60. R. D. McIntosh, D. Ellis, G. M. Rosair, and A. J. Welch, *Angew. Chem. Int. Ed.*, 2006, **45**, 4313.

61. C. G. Salentine and M. F. Hawthorne, *J. Am. Chem. Soc.*, 1975, **97**, 6382.

62. M. K. Kaloustian, R. J. Wiersema, and M. F. Hawthorne, *J. Am. Chem. Soc.*, 1972, **94**, 6679.

63. W. J. Evans, C. J. Jones, B. Stibr, R. A. Grey, and M. F. Hawthorne, *J. Am. Chem. Soc.*, 1974, **96**, 7405.

64. I. T. Chizhevskii, I. A. Lobanova, V. I. Bregadze, P. V. Petrovskii, A. V. Polyakov, A. I. Yanovskii, and Yu. T. Struchkov, *Metalloorg. Khim.*, 1991, **4**, 957.

65. I. T. Chizhevskii, I. A. Lobanova, V. I. Bregadze, P. V. Petrovskii, V. A. Antonvich, A. V. Polyakov, A. I. Yanovskii, and Yu. T. Struchkov, *Mendeleev Commun.*, 1991, 47.

66. S. Dunn, G. M. Rosair, R. L. Thomas, A. S. Weller, and A. J. Welch, *Angew. Chem., Int. Ed. Engl.*, 1997, **36**, 645.

67. H.-J. Schanz, M. Sabat, and R. N. Grimes, *Angew. Chem., Int. Ed. Engl.*, 2001, **40**, 2705.

68. J. H. Morris, H. J. Gysling, and D. Reed, *Chem. Rev.*, 1985, **85**, 51.

69. W. E. Geiger Jr, in ‘Metal Interactions with Boron Clusters’, ed. R. N. Grimes, Plenum Press, New York, 1982, Chap. 6.

70. M. Corsini, F. Fabrizi de Biani, and P. Zanello, *Coord. Chem. Rev.*, 2006, **250**, 1351.

71. J. W. Merkert, J. H. Davis, W. E. Geiger, and R. N. Grimes, *J. Am. Chem. Soc.*, 1992, **114**, 9846.

72. M. Stephan, J. Hauss, U. Zenneck, W. Siebert, and R. N. Grimes, *Inorg. Chem.*, 1994, **33**, 4211.

73. F. Fabrizi de Biani, M. Fontani, E. Ruiz, P. Zanello, J. M. Russell, and R. N. Grimes, *Organometallics*, 2002, **21**, 4129.

74. M. D. Mortimer, C. B. Knobler, and M. F. Hawthorne, *Inorg. Chem.*, 1996, **35**, 5750.

75. G. A. Kukina, V. S. Sergienko, and M. A. Porai-Koshits, *Koord. Khim.*, 1985, **11**, 400.

76. R. S. Coldicott, J. D. Kennedy, and M. Thornton-Pett, *J. Chem. Soc., Dalton Trans.*, 1996, 3819.

77. C.-H. Hu, J.-M. Dou, H.-J. Yao, W. Li, R.-S. Jin, and P.-J. Zheng, *Acta Crystallogr. C*, 1997, **53**, 695.

78. S. Du, J. A. Kautz, T. D. McGrath, and F. G. A. Stone, *Inorg. Chem.*, 2002, **41**, 3202.

79. F. G. A. Stone, *Adv. Organomet. Chem.*, 1990, **31**, 53.

80. F. G. A. Stone, *Pure Appl. Chem.*, 1986, **58**, 529.

81. S. A. Brew and F. G. A. Stone, *Adv. Organomet. Chem.*, 1993, **35**, 135.

82. D. Malaba, M. Sabat, and R. N. Grimes, *Eur. J. Inorg. Chem.*, 2001, 2557.

83. M. F. Hawthorne, in ‘Advances in Boron and the Boranes’, eds. J. F. Liebman, A. Greenberg, and R. E. Williams, VCH Publishers, New York, 1988, Chap. 10, p. 225.

84. F. Teixidor, R. Nunez, M. A. Flores, A. Demonceau, and C. Viñas, *J. Organomet. Chem.*, 2000, **614–615**, 48.

85. N. J. Patmore, C. Hague, J. H. Cotgreave, M. F. Mahon, C. G. Frost, and A. S. Weller, *Chem. Eur. J.*, 2002, **8**, 2088.

86. A. Rifat, N. J. Patmore, M. F. Mahon, and A. S. Weller, *Organometallics*, 2002, **21**, 2856.

87. A. Rifat, G. Kociok-Köhn, J. W. Steed, and A. S. Weller, *Organometallics*, 2004, **23**, 428.

88. G. L. Moxham, T. M. Douglas, S. K. Brayshaw, G. Kociok-Köhns, J. P. Lowe, and A. S. Weller, *Dalton Trans.*, 2006, **46**, 5492.

89. Z. Xie, *Coord. Chem. Rev.*, 2006, **250**, 259.

90. T. J. Colacot and N. S. Hosmane, *Z. Anorg. Allg. Chem.*, 2005, **631**, 2659.

91. M. Yoshida, D. J. Crowther, and R. F. Jordan, *Organometallics*, 1997, **16**, 1349.

92. T. Dodge, M. A. Curtis, J. M. Russell, M. Sabat, M. G. Finn, and R. N. Grimes, *J. Am. Chem. Soc.*, 2000, **122**, 10573.

93. Z. Yinghuai, S. L. P. Sia, K. Carpenter, F. Kooli, and R. A. Kemp, *J. Phys. Chem. Solids*, 2006, **67**, 1218.

94. M. F. Hawthorne, *Pure Appl. Chem.*, 1991, **63**, 327.

95. D. E. Harwell, J. Nabakka, C. B. Knobler, and M. F. Hawthorne, *Can. J. Chem.*, 1995, **73**, 1044.

96. D. S. Wilbur, M.-K. Chyan, D. K. Hamlin, R. L. Vessella, T. J. Wedge, and M. F. Hawthorne, *Bioconjugate Chem.*, 2007, **18**, 1226.

97. I. H. Hall, A. E. Warren, C. C. Lee, M. D. Wasczcak, and L. G. Sneddon, *Anticancer Res.*, 1998, **18**, 951.

98. I. H. Hall, R. W. Durham, M. Tram, S. Mueller, B. M. Ramachandran, and L. G. Sneddon, *J. Inorg. Biochem.*, 2003, **93**, 125.

99. I. H. Hall, C. E. Tolmie, B. J. Barnes, M. A. Curtis, J. M. Russell, M. G. Finn, and R. N. Grimes, *Appl. Organomet. Chem.*, 2000, **14**, 108.

100. Z. J. Lesnikowski, E. Paradowska, A. B. Olejniczak, M. Studzinska, P. Seekammp, U. Schüßler, D. Gabel, R. F. Schinazi, and J. Plešek, *Bioorg. Med. Chem.*, 2005, **13**, 4168.

101. A. B. Olejniczak, J. Plešek, and Z. J. Lesnikowski, *Chem. Eur. J.*, 2007, **13**, 311.

102. A. B. Olejniczak, P. Mucha, B. Grüner, and Z. J. Lesnikowski, *Organometallics*, 2007, **26**, 3272.

103. A. B. Olejniczak, M. Corsini, S. Fedi, P. Zanello, and Z. J. Leonikowski, *Electrochem. Commun.*, 2007, **9**, 1007.

104. A. E. C. Green, P. W. Causey, A. S. Louie, A. F. Armstrong, L. E. Harrington, and J. F. Valliant, *Inorg. Chem.*, 2006, **45**, 5727.

105. C. Viñas, S. Gomez, J. Bertran, J. Barron, F. Teixidor, J.-F. Dozol, H. Rouquette, R. Kivekä, and R. Sillanpää, *J. Organomet. Chem.*, 1999, **581**, 188.

106. C. Viñas, J. Bertran, S. Gomez, F. Teixidor, J.-F. Dozol, H. Rouquette, R. Kivekä, and R. Sillanpää, *J. Chem. Soc., Dalton Trans.*, 1998, 2849.

107. E. Crespo, S. Gentil, C. Viñas, and F. Teixidor, *J. Phys. Chem. C*, 2007, **111**, 18381.

108. J.-M. Lehn, J. L. Atwood, J. E. D. Davies, D. D. MacNicol, and F. Vögtle eds, ‘Comprehensive Supramolecular Chemistry’, Pergamon, Oxford, 1996.

109. N. S. Hosmane and J. A. Maguire, *J. Organomet. Chem.*, 2000, **614**, 10.

Boron–Nitrogen Compounds

Ronald C. Bakus II & David A. Atwood
University of Kentucky, Lexington, KY, USA

Based in part on the article Boron–Nitrogen Compounds by Robert T. Paine which appeared in the Encyclopedia of Inorganic Chemistry, First Edition.

---

1 Introduction 1
2 Amine-boranes 1
3 Aminoboranes 3
4 Iminoboranes 7
5 Other Low-coordinate Conditions 9
6 Pseudohaloboranes 9
7 Cationic Species 10
8 Borazines 11
9 Pyrazaboles 11
10 Polypyrazolylborate Coordination Chemistry 12
11 Additional Ring Systems 12
12 Boron Nitride 13
13 Related Articles 14
14 References 14

---

1 INTRODUCTION

The chemistry of boron–nitrogen compounds is extremely rich and varied, and much of the evolution of this field derives from attempts to obtain compounds both electronically and structurally comparable with well-known organic molecules.[1,2] In addition, a great deal of effort has been devoted to establishing reactivity parallels between the isoelectronic/isostructural organic and inorganic compounds. Some known isoelectronic/isostructural compound pairs are summarized in Figure 1.

Boron–nitrogen chemistry has been regularly reviewed as part of the Gmelin series.[3] In addition, regular coverage of B–N chemistry is found in annual or semiannual contributions to Coordination Chemistry Reviews (elements of group 3).[4] Summaries of new organoborane compounds containing B–N bonds also are found in the Journal of Organometallic Chemistry (article on the group 3 element chapter).[5] As a result, most of the illustrative chemistry summarized in this article appears in the original literature after 1984. The classes of B–N compounds described parallels the classification used in the Gmelin series. Where practical, parallels with isoelectronic organic chemistry are drawn. It is pointed out that the literature coverage in this article is not complete. Only a selection of work that illustrates recent advances in each subfield has been presented. However, recent reviews were sought for each of the sections listed in the table of contents.

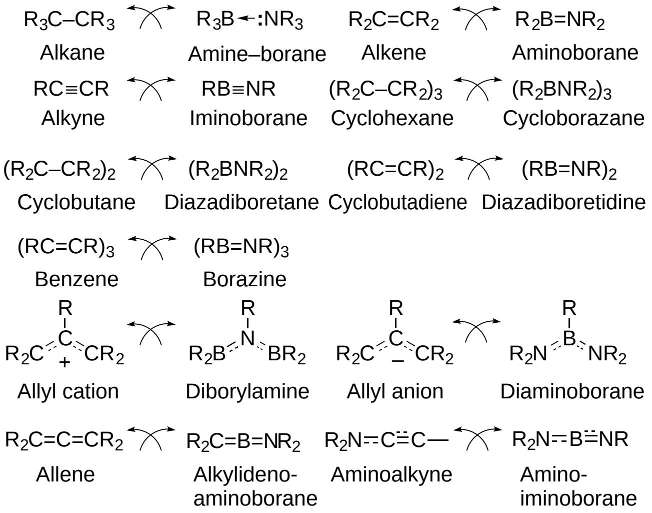
$R_3C–CR_3$
Alkane
$R_3B←:NR_3$
Amine–borane
$R_2C=CR_2$
Alkene
$R_2B=NR_2$
Aminoborane
RC≡CR
Alkyne
RB≡NR
Iminoborane
$(R_2C–CR_2)_3$
Cyclohexane
$(R_2BNR_2)_3$
Cycloborazane
$(R_2C–CR_2)_2$
Cyclobutane
$(R_2BNR_2)_2$
Diazadiboretane
$(RC=CR)_2$
Cyclobutadiene
$(RB=NR)_2$
Diazadiboretidine
$(RC=CR)_3$
Benzene
$(RB=NR)_3$
Borazine
Allyl cation
Diborylamine
Allyl anion
Diaminoborane
$R_2C=C=CR_2$
Allene
$R_2C=B=NR_2$
Alkylideno-aminoborane
$R_2N=C≡C—$
Aminoalkyne
$R_2N=B≡NR$
Amino-iminoborane

Figure 1 Some known isoelectrical/isostructural compound pairs

2 AMINE-BORANES

Amine-boranes are coordination complexes formed by combination of an amine Lewis base with a tricoordinate Lewis acid borane fragment (equation 1), and as noted in Figure 1, they are analogs of alkanes.

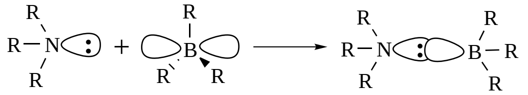
(1)

Their reactions have been studied extensively,[6] and a great deal is known about the factors that control the stability of the complexes in the gas phase and in solution. Nonetheless, studies of these compounds are popular, and new features are continuously revealed. For example, the structure of the simplest complex, H_3BNH_3, has been redetermined in the solid state, and the B–N bond distance confirmed to be relatively short at 1.564(6) Å.[7] This distance contrasts with the B–N distance of 1.672 Å found for the gaseous molecule by using microwave spectroscopy. These results and subsequent ab initio MO calculations for the molecule at several levels suggest that the molecular geometry is strongly dependent on environment. The MO calculations reveal a relatively flat potential surface in the bond distance range r_0(BN) approximately 1.55 to 1.70 Å, a figure mirrored by experimental studies that have shown common B–N bond distances of 1.55 to 1.75 Å.[6] Furthermore, it is found that, starting from the gas-phase value, the B–N bond distance decreases with increasing solvent polarity (1.62 Å in hexane and 1.57 Å in water). This suggests that the short B–N distance found in the solid-state structure may arise from 'crystal medium effects'. Calculations of ^{11}B NMR shifts (IGLO) also suggest that variations in ^{11}B delta data with solvent may be less a result of solvent effects on nuclear shielding and more a result of structural changes induced in the molecule by the medium.

The thermal decomposition of H_3BNH_3 has been studied by ^{11}B NMR in aprotic solvents at temperatures above 80 °C.[8] Three reaction types were found. In etheral solvents, decomposition occurred by hydrogen loss with formation of cycloborazanes and eventually borazine, $(HBNH)_3$. In pyridine solution, base displacement took place with generation of pyridine·BH_3; in acetonitrile solution, hydrogen loss and solvent hydrogenation or hydroboration occurred. These results suggest that it may not be possible to study the reaction chemistry of the monomeric aminoborane H_2BNH_2 in solution prior to its undergoing condensation reactions. A triarylborane with orthohydrogen bonding groups was shown to strangely bind ammonia through all four of its atoms.[9] This was a rare example of a host-guest system[10] able to recognize ammonia.

The reactivity of BX_3 fragments toward bifunctional Lewis bases (e.g. $R_2ENR'_2$, $RE(NR'_2)_2$, and $E(NR'_2)_3$; E=P, As) are also of fundamental interest.[11] It is clear that a combination of substituent inductive effects, $E \overset{\cdots}{-} N$ p_π–d_π electronic effects, as well as steric influences are responsible for the BX_3 coordination site selectivity and selected bond-breaking chemistry found in these complexes. The mechanism for hydrolytic decomposition of amine-borane complexes also continues to be of interest. A comparison of the hydrolysis of benzylamine-borane with the hydrolysis of various arylamine-boranes has been reported,[12] and the results are important for the selection of borane adducts as practical hydridic reagents in aqueous phase reductions.

Although tertiary amine-borane and aromatic amine-borane complexes are common, azo-boranes (**1**) and (**2**) were unknown until recently. Borane complexes (**3**) and (**4**) of 2,3-diazabicyclo[2.2.1]hept-2-ene and 2,3-diazabicyclo[2.2.2]oct-2-ene have now been isolated,[13,14] and in most other cases the azo-borane complex is stable in the presence of alkenic unsaturation. The Lewis acidity of methylene boranes has been recognized for some time, and satisfaction of the electron deficiency in these species has been considered to occur by nonclassical (**5**) and classical (**6**) intramolecular interactions. It has now been reported that intermolecular Lewis acid-base complexes (**7**) of these unique species can also be formed.[15] The strong Lewis acid $(CF_3)_3B$ can only be isolated with a base such as ammonia. While the B–N bonds are extremely strong, the N–H groups undergo a wide range of interesting reactions. For example, $(CF_3)_3B–NH_3$ forms $Cs[(CF_3)_3B–NX_2]$ (X=Cl, Br), when combined with the appropriate cesium hypohalite.[16]

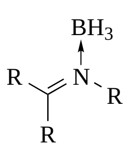

(**1**)

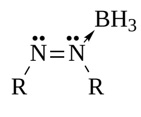

(**2**)

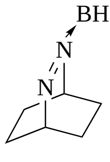

(**3**)

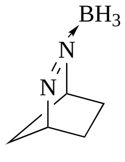

(**4**)

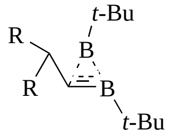

(**5**)

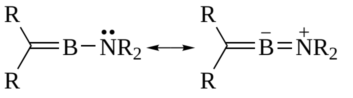

(**6**)

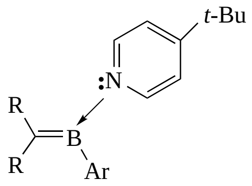

(**7**)

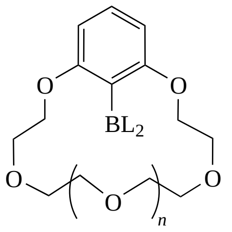

(**8**)

amine•BH_2X

(**9**)

X = CONHR, CO_2H, CO_2R,C(OR)=NR′

Several amine-borane complexes have recently been reported that have potential applications. For example, borylated crown ethers (**8**) provide a host-guest environment for molecular recognition of primary amines.[17] There is also interest in the synthesis and study of pharmacological properties of boron analogs of isoelectronic/isosteric biologically important molecules. These include selected amino acid analogs (**9**)–(**11**) and boronated nucleosides and nucleotides (**12**) and (**13**).[18–23] Studies have shown that amine carboxyboranes (amine·BH_2X) may be useful as treatments for cancer, osteoporosis, and inflammation.[24] A technique to break strong amine-borane bonds involves methanolysis catalyzed by palladium or Rainey nickel.[25]

amine•B(H)(R)X
(**10**)
X = C(O)NHR,
C(OR)=NR′

$(RO)_2P(O)CH_2N(H)Me•BH_2X$
(**11**)
X = CON(H)R, CO_2R,
C(OR)=NR′

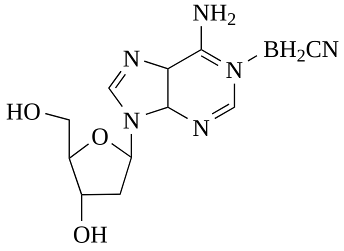

(**12**)

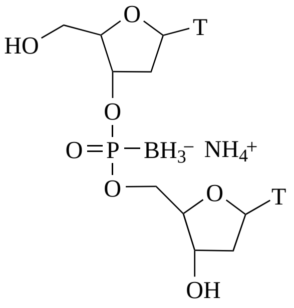

(**13**)

3 AMINOBORANES

Aminoboranes have the general formula $R_2B\text{⩦}NR'_2$, and they are the isoelectronic analog of alkenes. The boron and nitrogen atoms are formally three-coordinate, and the electron deficient and coordinatively unsaturated boron atom in monomeric molecules is stabilized by sterically bulky groups and by electron donation from the amido group. When these steric and electronic influences do not provide sufficient stabilization for the boron atom, the fragment typically forms cyclic aminoboranes, for example, $(R_2BNR_2)_2$ and $(R_2BNR_2)_3$. The factors influencing this chemistry have been systematically studied. Extensive reviews of aminoborane chemistry appeared in 1970,[26] 1980,[27] and in 1991 Noth briefly summarized some recent work from his group.[28] Recent emphasis on these molecules has centered on the development of precursors for formation of low-coordinate fragments, for example, amino-iminoboranes, $R_2N–B{=}NR$, and amino-phosphanylidene boranes, $R_2N\text{⩦}B{=}PR$. The subfield of amino-iminoboranes will be discussed in Section 4, while selected advances in other aspects of aminoborane chemistry are discussed here.

Historically, aminoboranes have typically been prepared by XY elimination reactions between borane BX_3 and amine NY_3 reagents (equation 2) and by salt elimination reactions (equation 3). Dehydrocoupling catalyzed by rhodium has recently been discovered as a convenient, clean route to aminoboranes.[29–31] Many seemingly straightforward elimination reactions of haloboranes with NH_3 and primary and secondary amines have been examined.[27] In many cases, oligomeric products are obtained, and in some cases the desired aminoborane products are difficult to separate from organoammonium salt by-products. In other cases, the expected amino substitutions could not be achieved in good yields owing to sluggish elimination reaction kinetics. As a result, a significant effort has been given to the development of silane and stannane elimination pathways by utilizing silylamine and stannylamine reagents.[28] For example, stannazane cleavage of $Cl_{3-n}Me_nSiN(SnMe_3)_2$ with excess BCl_3 gives bis(dichloroboryl)silylamines (equation 4), while reactions of equimolar amounts of $RN(SnMe_3)_2$ and $Me_3SiN(SnMe_3)_2$ with various boron halides give monoborylated amines (equations 5 and 6). These reagents are very useful for subsequent elimination reactions involving further N–Sn or B–X bond breaking. This includes the formation of borazine derivatives (equation 7).

$$X_3B + NY_3 \xrightarrow{-XY} X_2B{=}NY_2 \tag{2}$$

$$X_3B + LiNY_2 \xrightarrow{-LiX} X_2B{=}NY_2 \tag{3}$$

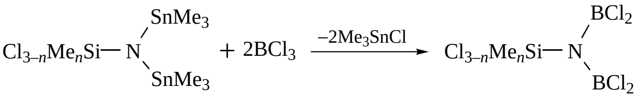

$$Cl_{3-n}Me_nSi{-}N(SnMe_3)_2 + 2BCl_3 \xrightarrow{-2Me_3SnCl} Cl_{3-n}Me_nSi{-}N(BCl_2)_2 \tag{4}$$

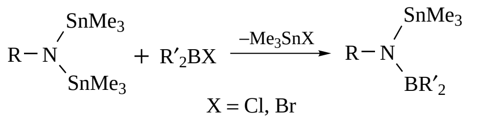

$$R{-}N(SnMe_3)_2 + R'_2BX \xrightarrow{-Me_3SnX} R{-}N(SnMe_3)(BR'_2) \qquad X = Cl, Br \tag{5}$$

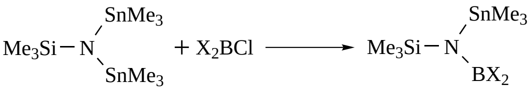

$$Me_3Si{-}N(SnMe_3)_2 + X_2BCl \longrightarrow Me_3Si{-}N(SnMe_3)(BX_2) \tag{6}$$

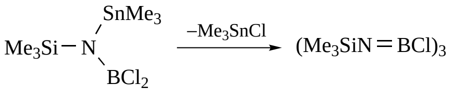

$$Me_3Si{-}N(SnMe_3)(BCl_2) \xrightarrow{-Me_3SnCl} (Me_3SiN{=}BCl)_3 \tag{7}$$

The related reaction chemistry of the B-silylaminoborazine $[(Me_3Si)_2NBNH]_3$ with HCl has been examined as a means to produce condensed polyborazine materials.[32] The reaction of BCl_3 and $(Me_3Si)_3N$ at 23 °C gives the expected aminochloroborane (equation 8), but in surprisingly low yield; at higher temperatures, methylation of the boron center occurs (equation 9). This result points out the potential limitations of this chemistry. In related studies directed at developing boron nitride precursors, Paciorek[33] examined routes to several silylaminoborane open-chain compounds through Me_3SiCl elimination reactions (equations 10 and 11).

$$(Me_3Si)_3N + BCl_3 \longrightarrow (Me_3Si)_2N–BCl_2 \tag{8}$$

$$(Me_3Si)_3N + BCl_3 \xrightarrow{\Delta} MeBCl_2 + N(SiMe_2Cl)_x(SiMe_3)_{3-x} \tag{9}$$

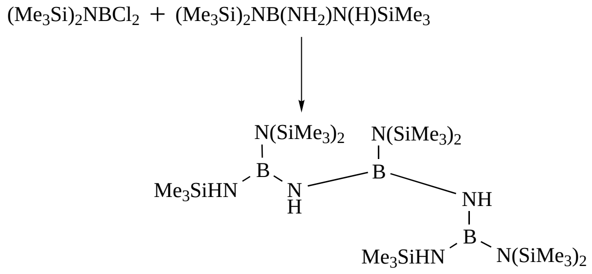

(10)

$$3(Me_3Si)_2NB(NH_2)NH(SiMe_3) + BCl_3 \cdot NEt_3 \longrightarrow B[N(H)B[N(SiMe_3)_2][N(H)SiMe_3]] \tag{11}$$

Several novel, new aminoboranes with electronically or sterically demanding substituents have been reported.

For example, trifluoromethyl aminoboranes $(CF_3)(Cl)BNEt_2$, $(CF_3)(Br)BNEt_2$, $(CF_3)_2BNEt_2$, and $(CF_3)_2BN(i\text{-Pr})_2$ have been obtained from the reactions of Cl_2BNEt_2, Br_2BNEt_2, and $Br_2N(i\text{-Pr})_2$ with a mixture of CF_3Br and $P(NEt_2)_3$ in CH_2Cl_2.[34] The trifluoromethyl groups should provide a highly electron-deficient B atom, which in turn should enhance B=N π bonding. Consistent with this reasoning, a crystal-structure determination for $(CF_3)_2BN(i\text{-Pr})_2$ (**14**) reveals a short B–N bond distance of 1.37(1) Å.

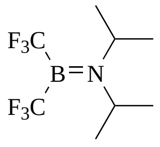

(**14**) B–N = 1.37Å

The tris(trimethylsilyl)methyl, $(Me_3Si)_3C$, substituent is a sterically bulky group, and can be used in the formation of low-coordination number environments at boron. Eaborn[35] has reported the synthesis of the diaminoborane (**15**) from aminolysis of $(Me_3Si)_3CBCl_2$. This compound is unusual since most other bis(amino)boranes without organic groups on nitrogen readily undergo decomposition with loss of ammonia and ring or oligomer formation. Compounds of comparable stability include $HB(NH_2)_2$, which is stable in the gas phase or in liquid NH_3 but decomposes with NH_3 loss in the liquid state, and $B(NHAr^*)(NH_2)_2$, which is thermally stable. Compound (**15**) can be sublimed in vacuo at 80 °C, but sublimation is accompanied by formation of (**16**) (equation 12). This compound is the first example of a bis(aminoboryl)amine without N-organyl substituents. Known analogs with N-alkyl or -aryl substituents typically decompose with formation of cyclic products.[36]

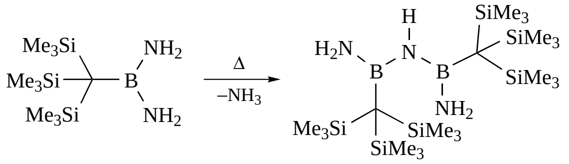

(12)

(**15**) (**16**)

The fluorenyl fragment should also provide considerable steric protection, and to this end, bis(fluorenyl)aminoboranes (**17**) have been prepared by reaction of R_2NBCl_2 with fluorene deprotonated by potassium or by combination of R_2NBCl_2 (R=Et, *i*-Pr, *i*-Bu, *s*-Bu) with $LiC_{13}H_9$.[37] This result contrasts in its outcome in an important way with related reductions involving R_2NBCl_2. For example, it has been observed that reduction of $(Me_2N)_2BCl$ with Na/K alloy leads to a series of acyclic $Bn(NMe_2)_{n+2}$ ($n = 2–5$) compounds containing B–B bonds. Noth[28] and Baudler[38] further observed the formation of several cyclic and cage subvalent B^I compounds including $B_6(NMe_2)_6$ (**18**). Paetzold[39] has subsequently discussed the occurrence of subvalent group 13 species, and it is clear that transient carbenoid R_2NB species should have considerable reactivity toward various unsaturated organic fragments. Meller[40] has exploited this theme to prepare several subvalent boron species, and much of that work has been briefly reviewed.[40] For example, the tetrahydroborolo[3.2-b] borane (**19**) and triborabicyclo[3.3.1]nona-3,6-diene (**20**) were obtained in reaction with benzene. That care must be exercised over the generality of these systems is illustrated by the fact that Na/K reduction of $F_2BN(Me)(i\text{-}Pr_2C_6H_3)$ in DME gave a complex mixture of products including some that contained methoxylated borane fragments. Finally, in a related system, the combination of $PbCl_4$ with $Li_2PhB(N\text{-}t\text{-}Bu)_2$ gave a 1,3-diaza-2-plumba-4-boracyclobutane (**21**).

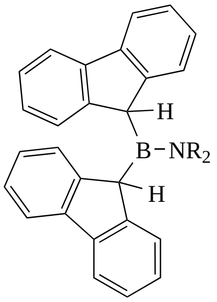

(**17**)

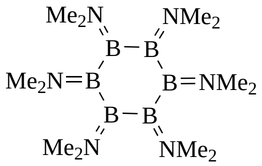

(**18**)

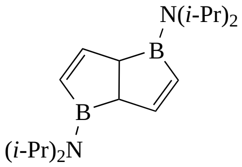

(**19**)

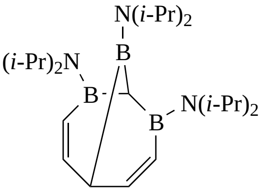

(**20**)

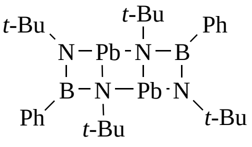

(**21**)

It was noted that the bis(fluorenyl)aminoboranes (**17**) are relatively stable compounds. The corresponding monofluorenyl aminohaloboranes (**22**) can also be prepared, and they serve as a source of the alkylidenylaminoborane (**23**).[41,42] The compound (**23**) was the first of a family of alkylideno aminoboranes, $R_2N{=}B{=}CR'_2$ that can be considered to be allene or aminoalkyne analogs. These compounds, containing two-coordinate boron, are kinetically stabilized by sterically

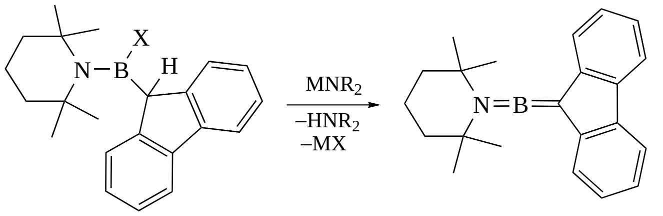
X
N–B
H
MNR$_2$
–HNR$_2$
–MX
N=B=

(**22**) X = Cl, Br (**23**)

demanding substituents R and R′ and by π electron donation from the amino group to the coordinatively unsaturated boron center. The tmp (t-Bu)$_2$N, and (t-Bu)(Me$_3$Si)N groups serve well in this role; however, the (Me$_3$Si)$_2$N group does not. In the last case, the incipient (Me$_3$Si)$_2$N=B=fluorenyl compound spontaneously dimerizes. Despite kinetic stabilization, the B=C bond in the fluorenyl aminoboranes is highly reactive (Scheme 1) toward polar addition reactions as well as [2 + 2] and [2 + 3] cycloadditions.**[41–43]** In addition, transition metal reagents $TiCl_4$, $Fe_2(CO)_9$, $Fe(CO)_5$, $CpCo(CO)_2$, $CpMn(CO)_3$, and $(C_6\ H_6)Cr(CO)_3$ have been observed to react with (**23**) (Scheme 2).**[44–46]**

The reactivity of two related alkylideno aminoboranes, i-Pr$_2$N=B=C(SiMe$_3$)$_2$**[47,48]** and tmp=B=C(SiMe$_3$)$_2$,**[48]** has been extensively studied. The chemistry displayed is similar to that depicted in Scheme 1, and additional reaction patterns are summarized in Scheme 3.

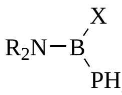

(**24**)

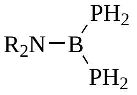
PH$_2$
R$_2$N–B
PH$_2$

(**25**)

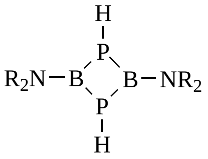
H
P
R$_2$N–B
B–NR$_2$
P
H

(**26**)

Aminoborane fragments R$_2$NB have recently been reported to stabilize a variety of phosphanyl species where the phosphorus atom carries H, SiMe$_3$, or organyl fragments.**[49]** This includes the formation of boryl phosphanes (**24**), boryl bis(phosphanes) (**25**), diazadiphosphetidines (**26**), cage species,**[50]** and the first stabilized phosphanylidene borane fragment (**27**) having a formal P=B double bond.**[51]** Some of the reaction chemistry of one phosphanylborane is summarized in Scheme 4.

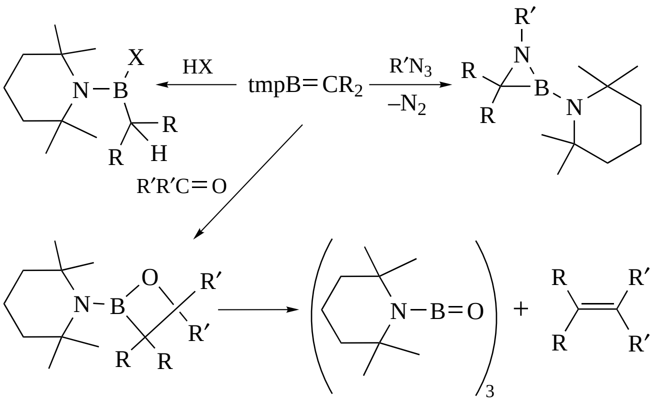
X
N–B
HX
tmpB=CR$_2$
R′N$_3$
–N$_2$
R′
N
R
B
N
R
R
R H
R′R′C=O
O
R′
N–B
R′
R R
N–B=O
3
+
R R′
R R′

Scheme 1

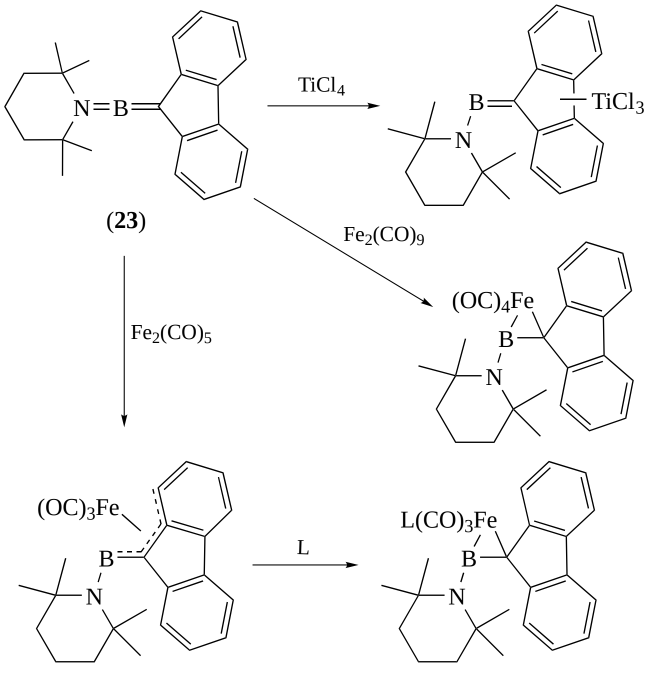
N=B=
TiCl$_4$
B=
TiCl$_3$
N
(23)
Fe$_2$(CO)$_9$
(OC)$_4$Fe
B
N
Fe$_2$(CO)$_5$
(OC)$_3$Fe
B
N
L
L(CO)$_3$Fe
B
N

Scheme 2

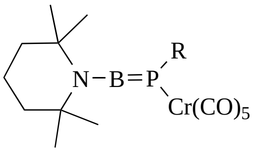

(**27**)

Finally, several years ago, Richman**[52]** reported the formation of a boron inclusion compound (**28**) that alternatively could be considered to be a tris(amino)borane. Practical applications have been found for several aminoboranes. For example, an aminoborane reagent (**29**) has been reported to be useful in enantioselective addition of allyl to aldehydes.**[53]**

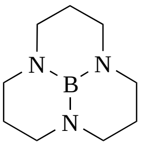

(**28**)

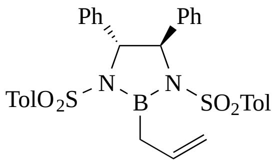
Ph
Ph
TolO$_2$S
N
B
N
SO$_2$Tol

(**29**)

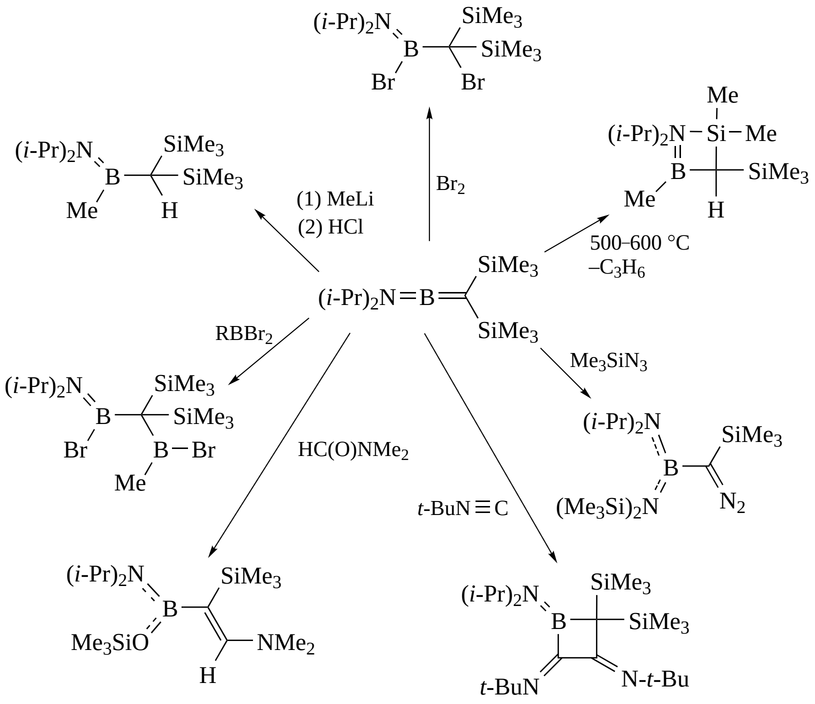
(i-Pr)2N=B=C(SiMe3)2
Br2
(1) MeLi
(2) HCl
500–600 °C
–C3H6
RBBr2
HC(O)NMe2
t-BuN≡C
Me3SiN3
(i-Pr)2N
SiMe3
B
Br
Me
H
Si
(Me3Si)2N
N2
Me3SiO
NMe2
t-BuN
N-t-Bu

Scheme 3

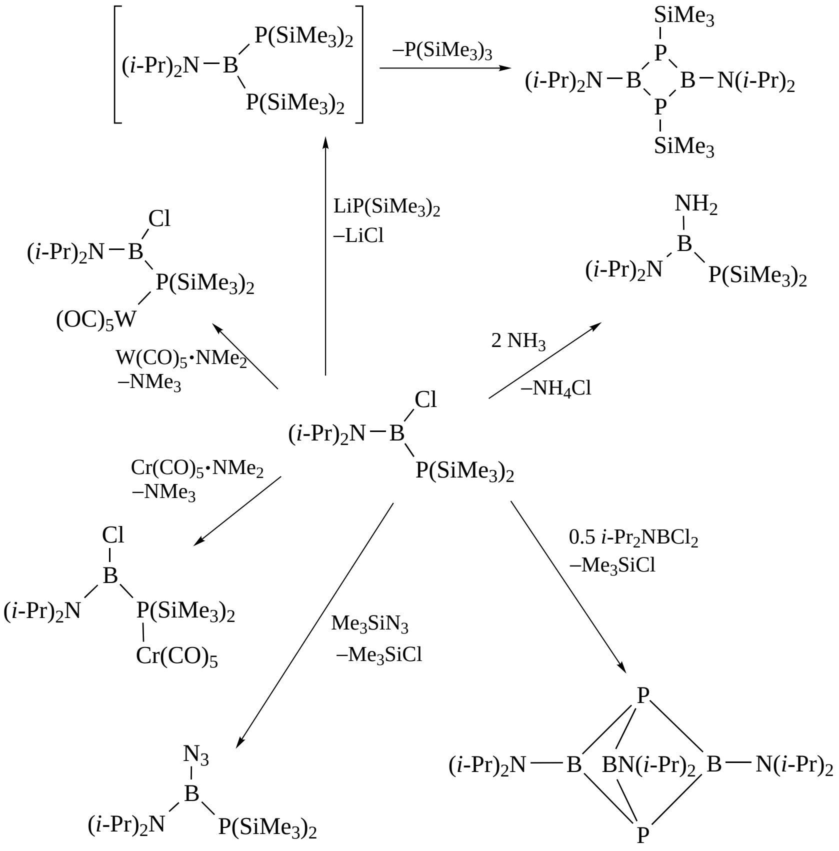
(i-Pr)2N–B(Cl)P(SiMe3)2
–P(SiMe3)3
LiP(SiMe3)2
–LiCl
W(CO)5·NMe3
–NMe3
2 NH3
–NH4Cl
Cr(CO)5·NMe3
–NMe3
Me3SiN3
–Me3SiCl
0.5 i-Pr2NBCl2
–Me3SiCl
(OC)5W
Cr(CO)5
NH2
N3
P
BN(i-Pr)2
B–N(i-Pr)2
SiMe3

Scheme 4

4 IMINOBORANES

Unlike aminoboranes, which have had a lengthy development history, the acetylene analogs diorgano-iminoboranes (R–B≡N–R) and amino-iminoboranes ($R_2N\overset{..}{-}B\overset{..}{=}NR'$) were first reported in 1979 and 1983, respectively. The boron atom is two-coordinate, electron deficient, and coordinatively unsaturated. Consequently, it is expected that, in order to isolate these species, some amount of kinetic stabilization will be required through steric and/or electronic effects. Without stabilization it would be expected, and is observed, that these fragments cyclodimerize or cyclotrimerize. Despite their late arrival in the development of boron–nitrogen chemistry, the synthesis, structure, and reaction chemistry of –B≡N–species has been pursued and consequently reviewed.[1,2,54,55] A good description of the π bonding[56] and aromaticity[57] in these and related systems is available.

Iminoboranes have typically been prepared from appropriate organo aminoboranes, R(X)BN(Y)R′, that are designed to undergo (1) chemically induced elimination of XY, (2) thermally induced elimination of XY, or (3) thermally induced rearrangement (or from an aminoborane oligomer by thermally induced ring opening). Examples for each of these general methods have been described.[1,55] It has been noted that the bond distances, stretching frequencies, and force constants for alkynes and iminoboranes are closely comparable, and the dipole moments for various –B≡N–species are less than 1.0 D. These experimental data, as well as theoretical analyses of several –B≡N–species, are consistent with a relatively nonpolar electronic structure with a slight $\delta+$ charge on the B atom and $\delta-$ on the N atom.

Most nonpolar alkynes are relatively stable at 23 °C and are not highly reactive. Polar alkynes, on the other hand, are often unstable at 23 °C, and they participate in a host of chemical reactions. Although their polarity is generally small, iminoboranes tend to be reactive unless they are very sterically constrained. The general reaction types found include (1) lone pair donation from the imino nitrogen atom; (2) cyclodimerization giving diazadiboretidines (cyclobutadiene analogs), cyclotrimerization giving borazines (benzene analogs), or cyclotetramerization giving cyclooctatetraene analogs; (3) 1,2-addition of HY and XY with the more electronegative fragment Y bonded to the B atom; (4) insertion reactions; and (5) various cycloaddition reactions. A few general results are summarized in Scheme 5, and ample additional examples are provided in the recent review literature.[1,2,54,55]

It should be stressed that in some cases, for example, chloroboranations, alkylideno-iminoboranes give different product types when compared to amino-iminoboranes. Some additional reactivity studies are summarized for *t*-BuB≡N-*t*-Bu (**30**) and tmpB≡N-*t*-Bu (**31**) in Schemes 6 and 7. Note that the outcome of silylene cycloaddition to (**30**) is dependent on the size of the organic fragment on the silylene,[58] and the addition of the cyclostannylene occurs

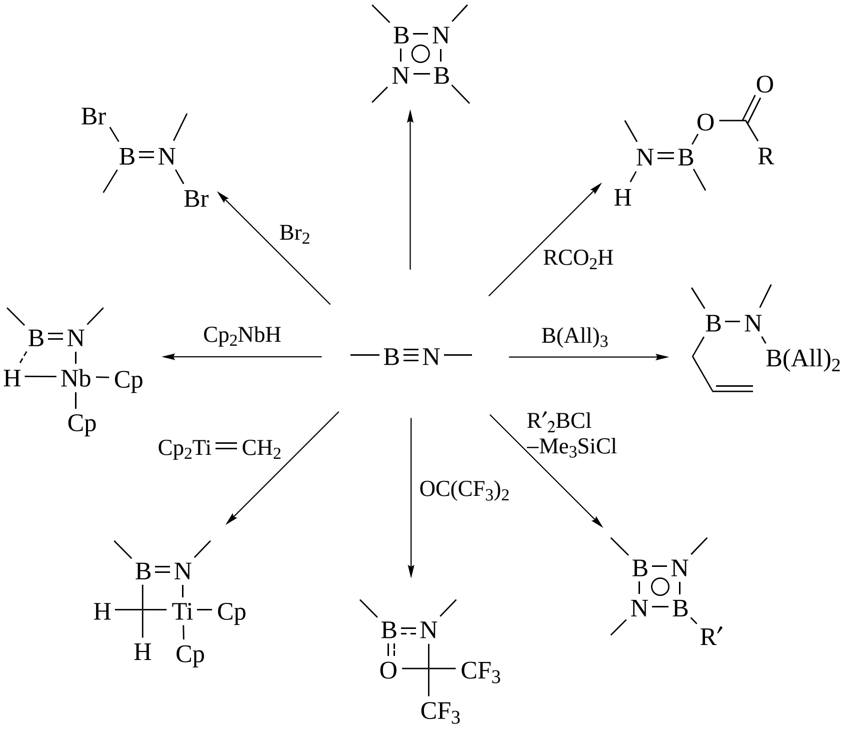

Scheme 5

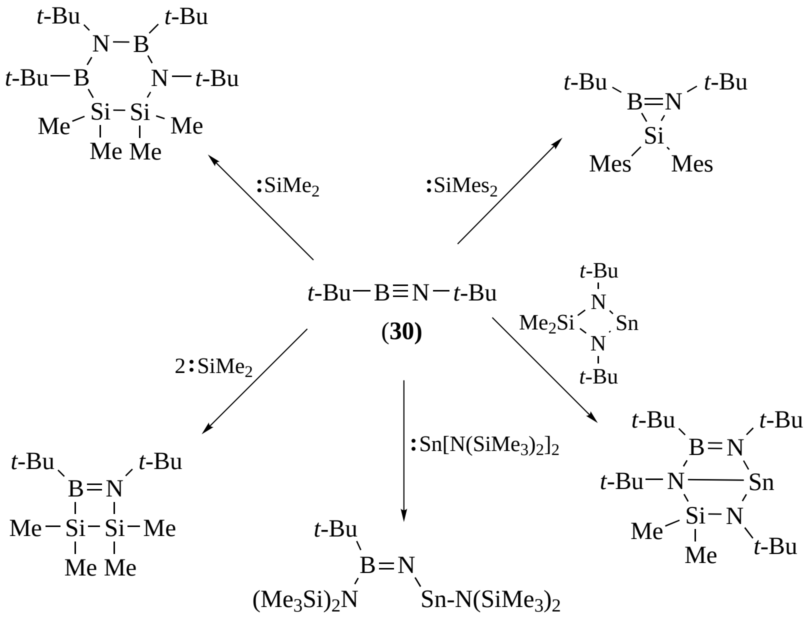
t-Bu–B≡N–t-Bu
(30)
:SiMe2
:SiMes2
2:SiMe2
:Sn[N(SiMe3)2]2
Me2Si
Sn
t-Bu
Me
Mes
B=N
Sn-N(SiMe3)2
(Me3Si)2N

Scheme 6

at the boron atom across a Sn–N bond.[59] The reaction of acetamide with (**31**) gives an O,N-diborylated acetimidic acid, while N-methylacetamide leads to N-borylated N-methylacetamide.[60] Pyrrolidone reacts with (**30**) to form a borylated lactam,[61] and phosphonic and phosphinic acids produce O-borylated phosphonates and phosphinates.[62] These reactions may in fact find some use in organic synthesis. Finally, Noth and coworkers[63] have explored the reactions

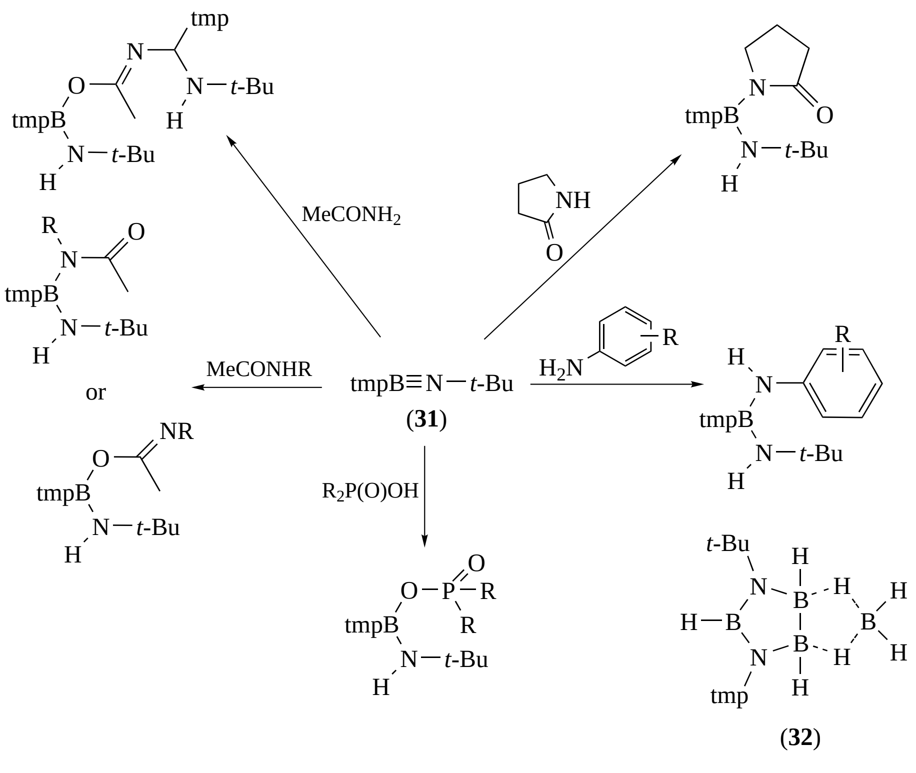
tmpB≡N–t-Bu
(31)
MeCONH2
MeCONHR
H2N
R2P(O)OH
or
tmp
tmpB
N–t-Bu
NH
O
NR
R
H
(32)

Scheme 7

of (**31**) with B_5H_9, $B_3H_7{\cdot}THF$, and $B_{10}H_{14}$. Pentaborane(**9**) is unreactive, but $B_3H_7{\cdot}THF$ hydroborates the $B{\equiv}N$ bond, giving (**32**). More recently, it was shown that (**31**) combines with ECl_3 (E=Ga, In) to yield tmp=B=N(ECl_3)*t*-Bu.[64] Combination of *t*-BuB≡N-*t*-Bu amd $Cp_2M(H)Cl$ (M=Zr, Hf) leads to the compounds {*t*-BuB(H)=N(*t*-Bu)}MCp_2Cl where the iminoborane appears to be bound side-on in a manner analogous to alkynes.[65]

5 OTHER LOW-COORDINATE CONDITIONS

Compounds with $\mathrm{B}\overset{\cdots}{-}\mathrm{N}$ units in open-chain molecules, are known and summarized here. Power[66–68] has reported the synthesis of sterically hindered aminoboranes $R(H)N{=}BMes_2$ (R=Ph, Mes) and their lithium salts. Structure determinations for the aminoboranes and lithium salts reveal that the B and N atoms are planar, and the twist angle between the planes is small. As a result, it is expected that the anions $R\ddot{N}{=}BR_2^{-}$ should display weak sigma-bridging characteristics, and they should stabilize low-coordinate monomeric structures with relatively low-valent metal ions. This is indeed found to be the case as each of the complexes $Li[Co(Cl)(L)_2]$, MnL_2, CrL_2, FeL_2, and NiL_2 is monomeric, confirming that the 'free' lone pair on nitrogen is strongly associated with B–N π bonding. In several cases, there appears to be a degree of interaction between the metal and the ipso carbon atom of the Mes substituent on boron. Power[68] has also reported formation of a diboryl amine $(Mes_2B)_2NH$, and its lithium amido salt, which is related to allene and borinium cations $[R_2NBNR_2]^{+}$. Schmid[69] has reported the formation of several interesting amino vinylboranes, $Me_2N(R)B{-}CH{=}CH_2$ (**33**), and these ligands form (alkene)$Fe(CO)_4$ complexes as well as (butadiene)$Fe(CO)_3$ analog complexes, as summarized in Scheme 8.

Extending this 1,3-butadiene analogy to an all BN backbone composition, Power[70] reports the synthesis of diboron species $R(R'_2N)BB(NR'_2)R$. A structure determination for a compound with R=Ph, R′=Me shows that the π interaction is localized between the $\mathrm{B}\overset{\cdots}{-}\mathrm{NMe_2}$ groups, the $\mathrm{B}\overset{\cdots}{-}\mathrm{B}$ bond is long, and the N-B-B planes are twisted out of coplanarity by approximately 60 degrees. Subsequent reduction of this species produces a dianion $[Ph(Me_2N)\mathrm{B}\overset{\cdots}{-}\mathrm{B}(NMe_2)Ph]^{2-}$. Its structure shows that the B_2N_2 array is planar and the B–B bond is shortened, but this occurs at the expense of B=N π overlap, as evidenced by elongation of the B–N bond distances. This is consistent with the valence bond representation shown in equation (13).

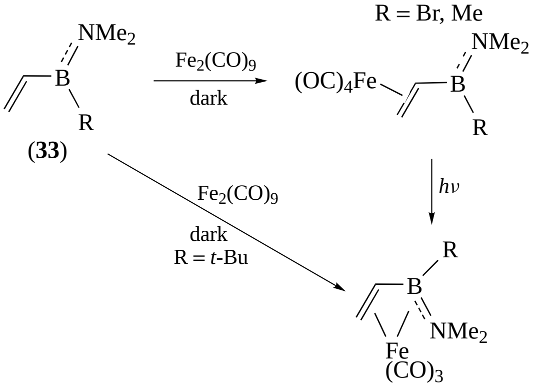

Scheme 8

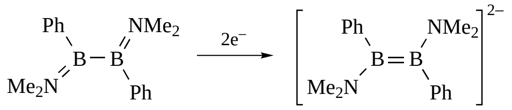

(13)

Siebert[71] has recently reported the syntheses of two related diborolanes (**34**) and (**35**), as well as two diborylamines (**36**) and (**37**). Reaction of (**34**) with $CpCo(C_2H_4)_2$ leads to formation of (**38**). The open-chain ligand can be considered as a B-heterobutadiene.

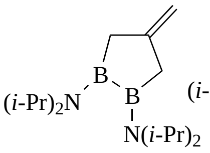

(34)

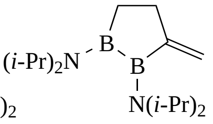

(35)

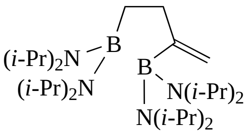

(36)

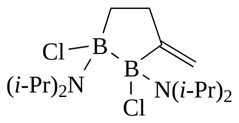

(37)

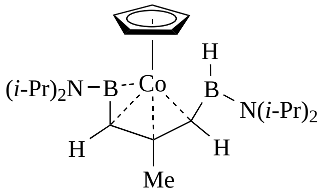

(38)

6 PSEUDOHALOBORANES

As described by Paetzold,[1,72] azidoboranes have played an important role in the synthesis of iminoboranes and various boron–nitrogen heterocycles discussed elsewhere in this article. As a result, there is continuing interest in these reactive reagents. Neilson[73] has reported the synthesis of the stable azidoborane $(Me_3Si)_2N(t\text{-}Bu)BN_3$ by treatment of a chloroborane precursor with Me_3SiN_3. This reagent was then used to oxidize (silylamino)phosphines by the Staudinger reaction (equation 14) to (borylimino)phosphoranes (**39**). Similar chemistry is found for three-coordinate aminophosphines (equation 15). It is interesting to note that the two-coordinate methylene- and iminophosphines also undergo oxidation to give three-coordinate P^{V} centers (see (**40**); equation 16).

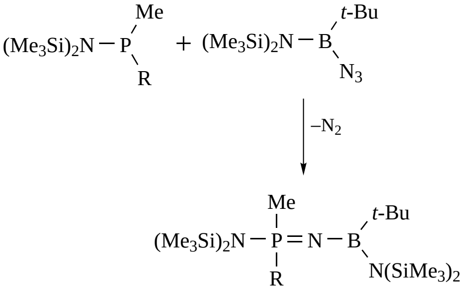

(14)

(**39**)

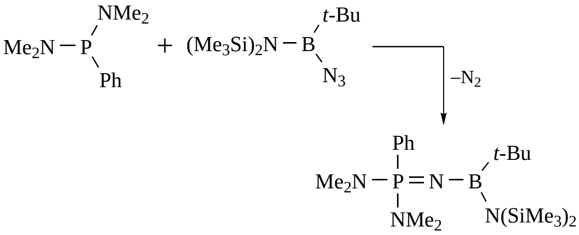

(15)

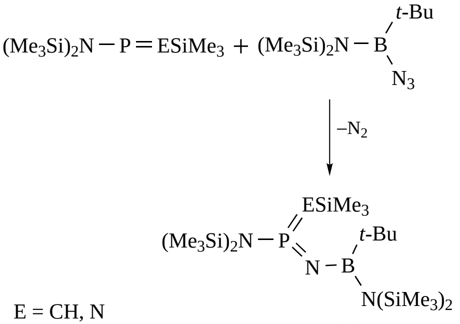

(16)

E = CH, N

(**40**)

The reaction of i-Pr$_2$NB(Cl)P(SiMe$_3$)$_2$ with Me$_3$SiN$_3$ gives a stable azido borane i–Pr$_2$NB(N$_3$)P(SiMe$_3$)$_2$,[49] which when heated in vacuo at 80 °C produces nitrogen. The incipient nitrene dimerizes accompanied by silyl group migration from phosphorus to nitrogen (equation 17). The (P–B–N)$_3$ ring has a boat conformation, and the decomposition pathway resembles that reported for R$_2$BN$_3$ species that produce borazines (RBNR)$_3$.[1] In contrast, use of the C$_6$F$_5$ group in a similar reaction allows for the structurally characterized diamer [(Ar)$_2$B(N$_3$)]$_2$. X-ray diffraction studies have shown a B–N bond length of approximately 1.59 Å.[74] The bis-azido compound, C$_6$F$_5$B(N$_3$)$_2$, is readily prepared through a TMSCl elimination reaction. It can be isolated as the pyridine adduct, but in the absence of base, will trimerize in the solid state.[75] In a recent breakthrough for this chemistry, crystal structures of [B(N$_3$)$_3$]$_x$·L (L = quinoline, X = 1 and L = pyrazine, X = 2) and [B(N$_3$)$_4$]$^-$ (isolated as the 2,2,6,6-tetramethylpiperidinium salt) were reported. B-N$_{\mathrm{quin}}$ was found to be 1.619(2) Å and B–N$_\alpha$ was found to be approximately 1.52 Å in the quinoline derivative. [B(N$_3$)$_4$]$^-$ demonstrated variable B–N distances, depending on whether the γ-nitrogen was involved in hydrogen bonding (B–N of 1.529(7)–1.549(6) Å for the nonhydrogen-bonded groups and 1.509(8)–1.535(8) Å for the hydrogen-bonded groups). The dissociation enthalpy for a pyridine complex of [B(N$_3$)$_3$] was calculated to be 10 kcal·mol^{-1}.[76]

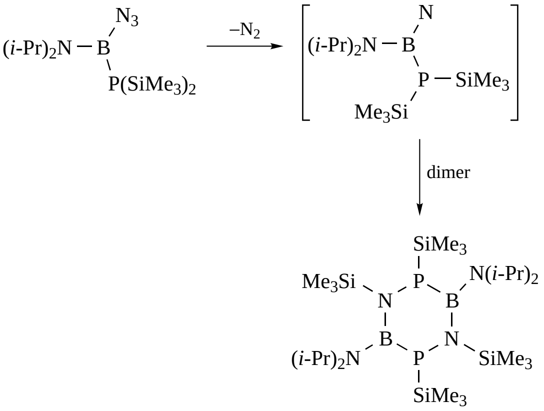

(17)

The gas-phase molecular structures of Me$_2$BN$_3$ and Me$_2$BNCO have been determined by electron diffraction.[77] The BN$_3$ and BNCO units are planar and bent. MO calculations for the B-azido compound reproduce the observed bent structure, but they predict a linear structure for the B-isocyanato analog.

7 CATIONIC SPECIES

Examples of tetra-coordinate boronium ions (**41**) have been known for many years.[78] The quest for low-coordinate, neutral borane compounds also stimulated interest in the formation of three-coordinate borenium ions (**42**) and two-coordinate borinium ions (**43**).[78–80]

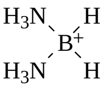

(**41**)

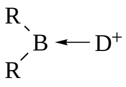

(**42**)

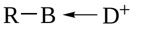

(**43**)

The cations are typically prepared by (1) boron-halogen bond heterolysis (for example, by displacement of Br$^-$ by pyridine to form [BF$_2$(py)$_2$]$^+$),[81] (2) electrophilic attack on BN bonds, (3) nucleophilic displacement, or (4) metathesis (for example, by silanol elimination from the chelate B(OSiPh$_3$) with trific acid to acid to form [LB(thf)]$^+$OTP$^-$).[82] The cationic B center is stabilized by amino substituents, which π donate to boron, and by bulky substituents. The formation of cations with electrophilic reagents in fact suggests that some previously studied reactions of boranes may proceed through cationic intermediates as opposed to neutral coordination complexes. For example, Ph$_2$B(ClO$_4$) catalyzes aldehyde condensations.[83] Although it has a polar covalent B–O bond in nitromethane (having a ^{11}B NMR shift of 46 ppm),[84] it is likely to be cationic in the presence of the aldehyde. Borenium salts are obtained from n-$Bu_2B(O_3SCF_3)$ and 9-$BBN(O_3SCF_3)$ when combined with sterically demanding bases, while neutral acid-base complexes are obtained with less demanding bases. Neutral complexes are also obtained with n-Bu_2BCl and 9-BBNCl. Several adducts of $R_2BCl{\cdot}L$ produce borenium ions when combined with $AlCl_3$ or $GaCl_3$. Similarly, $SbCl_5$ abstracts Cl^- from Ph_2BCl in CD_3NO_2 to form a transient cation having a ^{11}B NMR shift of 20 ppm.**[85]**

8 BORAZINES

Borazines, $(RBNR)_3$, can be considered to be cyclotrimers of parent iminoboranes, RB≡NR.**[86–88]** In general the compounds are relatively stable, and as a result they can be obtained through many routes. In fact, they are often undesired side-products or decomposition products. The simplest borazine, $(HBNH)_3$, is often referred to as inorganic benzene, a correspondence that is probably overemphasized. The compound displays D_3h symmetry with equivalent, relatively short B–N bond distances of 1.44 Å. The ^1H NMR data for substituted borazines suggest some degree of transannular electronic conjugation. However, reactivity patterns of borazine differ markedly from benzene. For example, borazine takes part in little electrophilic substitution chemistry, but does undergo many addition reactions. These observations suggest that borazine reaction chemistry is more dictated by B–N bond polarity than the π HOMO/LUMO character of the molecule. Needless to say, these divergent pictures have led to a number of experimental and theoretical studies of the electronic structure of borazine.**[89,90]** The current view appears to favor a picture in which the π system is highly polarized, but significantly resonance stabilized.

Borazine is often prepared by reaction of NH_4Cl and $LiBH_4$ or $NaBH_4$, or by thermal decomposition of $H_3B{\cdot}NH_3$. Trichloroborazine, $(ClBNH)_3$, is prepared by combination of BCl_3 and NH_4Cl. Both compounds undergo a variety of substitution reactions at boron. It is often straightforward to obtain complete substitution, for example, $(XBNH)_3$, but difficult to obtain mono- or disubstitution products, $(XB)\ (HB)_2(NH)_3$ and $(XB)_2(HB)\ (NH)_3$, in pure form. Many N-substituted borazines are obtained by using substituted amines or ammonium halides. Again, complete symmetrical substitutions, for example, $(HBNR)_3$ or $(ClBNR)_3$, are usually straightforward; however, incomplete or asymmetrical substitutions are difficult. The majority of available substitution possibilities have been summarized.**[87]**

The recent interest in boron–nitrogen-containing polymers has spurred some renewed interest in borazine preparations since these compounds are potential monomers. The direct reaction between $(ClBNH)_3$ and NH_3 produces an organic solvent insoluble polymer. In an attempt to control ammonolysis chemistry, the reactions of $(Me_2NBNH)_3$ with NH_3 have been examined,**[91,92]** and Kimura**[92]** has succeeded in isolating $(H_2NBNH)_3$ (**44**), which rapidly polymerizes with loss of NH_3.

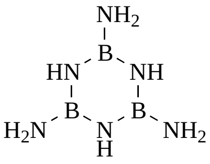

(**44**)

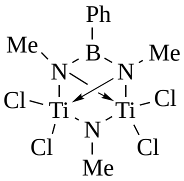

(**45**)

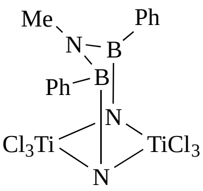

(**46**)

In a parallel area, and as part of the effort to develop polymers suitable for formation of ceramics and ceramic composites, Roesky**[93]** has reported formation of several metalloborazines. For example, reactions of $MeN[PhBN(Me)SiMe_3]_2$ with $TiCl_4$ produce nonplanar bicyclic rings such as (**45**) and (**46**).

9 PYRAZABOLES

Pyrazaboles of the general types represented by (**47**) and (**48**) have been under study for a number of years, and the syntheses of numerous derivatives have been reviewed.**[87,94,95]** The compounds are relatively stable, and a significant body of C-atom organic substitution chemistry has been developed. In addition, the anionic character of (**47**) has made these species particularly attractive ligands for both metal and nonmetal cations. That topic is summarized in Section 10 of this article.

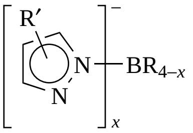

(**47**)

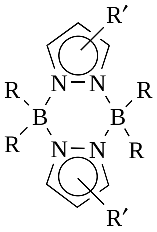

(**48**)

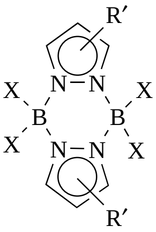

(**49**)

Niedenzu initiated studies of B-substituted analogs of (**47**) and (**48**) and various X = chloro, fluoro, alkyl, aryl, alkoxy, and amido derivatives of (**49**).**[96]** These compounds should be very useful for further synthetic transformations. Koster and coworkers**[97,98]** have examined the reactions of sterically congested pyrazoles with $(9H\text{-}9\text{-}BBN)_2$ and unique neutral, monomeric products with tricoordinate boron centers (**50**) are obtained. The compounds are stable toward dimerization. When bulky pyrazoles are allowed to react with activated trialkylboranes, for example, BEt_3 at 170 °C, a monomeric pyrazoleborane (**51**) is obtained. At 220 °C the *t*-Bu group is likely to undergo beta-hydride elimination, and the alkene intermediate may undergo hydroboration with resultant formation of a C-borylated pyrazoleborane dimer (**52**).

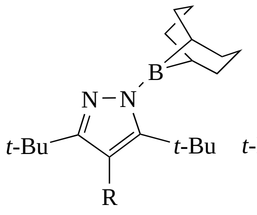

(**50**)

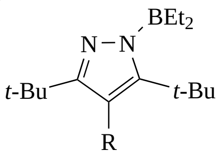

(**51**)

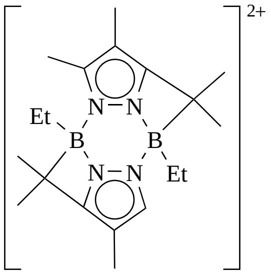

(**52**)

An IGLO NMR study and MO calculations have been used to show that the ground-state structures of compounds like (**50**) and (**51**) in solution as well as the solid state are as shown and not of the symmetrical bridging type (**53**). Nevertheless, the structure represented by (**53**) is likely to be involved in degenerate, fluxional isomerization processes.[99] Koster[100] has also prepared a series of compounds illustrated by (**54**) where X=O, S, Se. There has also recently been some success at preparation of new triazaboles.[101]

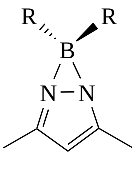

(**53**)

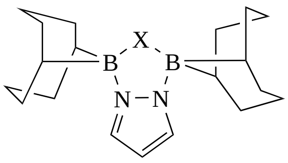

(**54**)

10 POLYPYRAZOLYLBORATE COORDINATION CHEMISTRY

Ligands of the type (**48**) display a very large number of interesting coordination complexes with main group elements, transition metal cations, and *f*-element cations. This extensive chemistry has been thoroughly reviewed,[102–104] and only a few recent advances are summarized here for illustrative purposes. The HB(pz*)$_3$K ligand, in combination with PCl_3, gives rise to [HB(pz*)$_3$]PCl_2 in which the ligand is likely to be bonded in a *trihapto* fashion to the P atom. Subsequent reaction with $Na_2Fe(CO)_4$ gives [HB(pz*)$_3$]PFe(CO)$_4$, a complex containing a novel terminal phosphinidene ligand.[105] Parkin[106,107] has reported the use of other C-alkylated HB(pz*)$_3$K and H_2(pz*)$_2$K salts to form a new set of complexes with Al, Mg, and Be. Niedenzu[108] and Reger[109] have reported tin(II) complexes while using $H_2B(pz)^-$, $H_2B(pz^*)_2{}^-$, $B(pz)_4{}^-$, and $B(pz^*)_4{}^-$.

Many new transition metal complexes of these ligands continue to be prepared. The most interesting aspects of this chemistry are not so much the evolution of specific new ML, ML_2, and ML_3 compositions, but the purposes that the ligands serve or are suggested to serve. For example, poly(pyrazolyl)borate anions have been used to stabilize a 17-electron radical fragment, a seven-coordinate W^{II} complex, half-sandwich HB(pz*)MCl compounds, and to mimic a variety of natural bioinorganic coordination conditions.[110–112]

11 ADDITIONAL RING SYSTEMS

A variety of B–N ring systems have been prepared that do not easily fall into the general classes described previously. Some of these rings include other heteroatoms, some include carbon, and they range in size from three-membered to eight-membered. Some examples of cubane cages are also known. Examples of these systems have appeared in previous reviews.[3,86,87] Some representative new contributions in this area are summarized in this section.

Borole dianions should be 6π-electron systems analogous to Cp^-, and one example (**55**) of this ring has been prepared with *exo* amino groups NR_2 (R=Me, Et, or *i*-Pr).[113] Metal complexes of the dianion have also been reported.

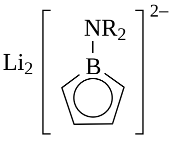

(**55**)

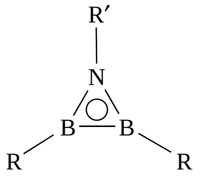

(**56**)

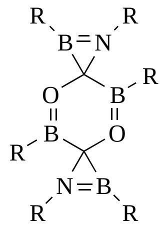

(**57**)

Several examples of azadiboridines (**56**) have been prepared,[114,115] and this ring with R=*t*-Bu reacts with CO to give (**57**) and with BuN_3 to give (**58**). The reductive reaction of *t*-BuB(Cl)-N(*t*-Bu)-B(Cl)*t*-Bu with Na/K that gives (**56**) with R=*t*-Bu also produces a novel diaza-*nido*-hexaborane (**59**).[116]

The reaction of several examples of (**56**) with $H_3B{\cdot}THF$ produces a novel four-membered bicycle represented by (**60**).[117]

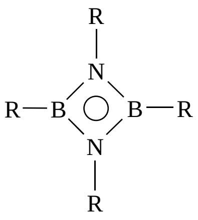
(**58**)

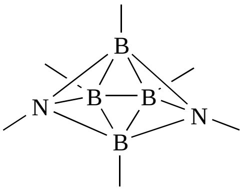
(**59**)

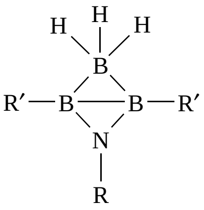
(**60**)

The substitution of B–N for a C=C unit in pyrrole gives a class of diazaboroles (**61**). Some of the most recent advances involving this ring, including π-complexes with the $Cr(CO)_3$ fragment and a potassium salt, have appeared.[118] The reactivity of four-membered diazadiboretene rings continues to be of interest, and a recent paper summarizes the variety of larger rings that can be prepared via insertion reactions on $(t\text{-BuNBR})_2$.[119] Koster and coworkers[120] explored in some detail the reactions of Et_3B, $i\text{-}Pr_3B$, and $t\text{-}Bu_3B$ with a family of alkyl cyanides at 200 °C. A variety of heterocycles, including (**62**), (**63**), and (**64**), was produced, and the specific products obtained depended on the alkyl groups on the borane, the cyanide, and the reaction conditions. In another study, reactions of $(Me_2N)_2BR$ with dimethylurea were found to give bicyclic species of the general type represented by (**65**).[121]

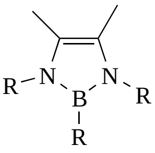
(**61**)

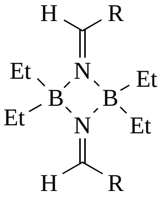
(**62**)

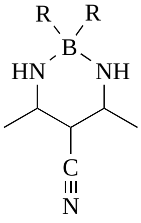
(**63**)

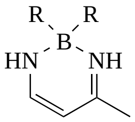
(**64**)

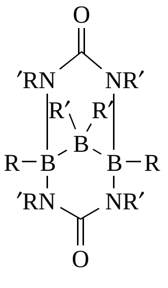
(**65**)

Finally, it is noted that some utility is being found for some of these apparently esoteric ring compounds. Oxozaborolidines and dioxaborolidines serve as enantioselective catalysts for ketone reductions, asymmetric allylations, Diels–Alder reactions, and aldol condensations.[122]

12 BORON NITRIDE

Extending the B–N/C–C analogies employed throughout this article, it is found that the allotropes of BN have a close correspondence with those of carbon. For example, the hexagonal form of BN forms a layered structure related to graphite, and the cubic form of BN closely resembles diamond. A number of properties for the two materials are similar but, interestingly enough, some properties are quite different. These differences include color, electrical properties, and optical properties. Practical interests in various forms of BN have spurred significant growth in boron–nitrogen monomer and polymer chemistry. A thorough review of BN appeared in 1990,[123] and aspects of the synthesis of BN from preceramic polymers were updated in brief reviews appearing in 1991[124] and 1992.[125] The present growth in this area should continue as new applications for the material are made possible by the availability of processible precursors and new synthetic techniques.

Within this section, it is appropriate to point out that there is interest in preparing isoelectronic B–N analogs of the newest form of carbon, C_{60},[126,127] and this offers a challenge to molecular chemists interested in this area of inorganic chemistry.

Boron nitride can be prepared by many routes such as CVD (NH_3 + organoborane),[128] pyrolysis of preceramic polymers derived from borazine,[129] and solid-state metathesis ($NaBF_4 + 3NaN_3$, for example).[130,131] The type of BN formed in these reactions parallels the materials that can be obtained from carbon. Thin films and coatings of BN have been studied extensively.[132] BN nanotubes can be prepared by CVD at 1100 °C using borazine (see Section 8) and catalytic NiB_2.[133] The tube formation is proposed to occur through a root-growth mechanism where growth occurs at the tube-catalyst interface. A low-temperature route (450–600 °C) to BN nanotubes using NH_4BF_4, KBH_4, and NaN_3 has recently been reported.[134] They have a diameter range of 60 to 350 nm. Hexagonal BN 'onions' and other structures can be prepared by combining BBr_3 with $NaNH_2$ and NH_4Cl at approximately 400 °C.[135] The materials were characterized by XRD, FT-IR, XPS, and EDXA spectra. Using activated carbon as a template, activated BN was synthesized with a specific surface area of $168\,m^2\,g^{-1}$, a total pore volume of $0.27\,cm^3\,g^{-1}$ and an average pore radius of 32.2 Å.[136] Spherical particles of 50 to 400 nm in diameter have been prepared through thermolysis of trimethoxyborane under an ammonia atmosphere.[137] BN fibers[138] and nanowires[139] are also known.

BN materials have many potential applications beyond use in ceramics. For example, the vacuum pyrolysis of poly(4,6-borazinylamine) produces highly microporous BN with surface areas of 53 to 696 $m^2\,g^{-1}$ and pore volumes of 0.036 to 0.39 $cm^3\,g^{-1}$. Since BN has an inherently polar surface, porous BN should be an ideal gas adsorbent.[140] Indeed, BN nanotubes are capable of storing H_2 at ambient temperature.[141] Hexagonal BN can serve as a template for diamond synthesis.[142]

13 RELATED ARTICLES

Boron Hydrides; Boron: Inorganic Chemistry; Boron: Organoboranes; Boron: Polyhedral Carboranes; Cluster Compounds: Inorganometallic Compounds Containing Transition Metal & Main Group Elements; Electronic Structure of Main-group Compounds.

14 REFERENCES

1. P. Paetzold, *Adv. Inorg. Chem.*, 1987, **31**, 123.
2. R. B. King ed., ‘Boron Chemistry at the Millenium’, Elsevier Science, New York, 1999.
3. A. Meller, in ‘Gmelin Handbook of Inorganic Chemistry’, 8th edn., eds. K. C. Buschbeck and K. Niedenzu, Springer-Verlag, Berlin, 1988, Boron Compounds, 3rd Suppl., Vol. 3.
4. G. Davidson, *Coord. Chem. Rev.*, 1990, **102**, 146.
5. G. W. Kabalka, *J. Organomet. Chem.*, 1991, **404**, 1.
6. B. Carboni and L. Monnier, *Tetrahedron*, 1999, **55**, 1197.
7. M. Buhl, T. Steinke, and P. v. R. Schleyer, *Angew. Chem., Int. Ed. Engl.*, 1991, **30**, 1160.
8. J. S. Wang and R. A. Geanangle, *Inorg. Chim. Acta*, 1988, **148**, 185.
9. C. C. Hughes, D. Scharn, J. Mulzer, and D. Trauner, *Org. Lett.*, 2002, **4**, 4109.
10. J. W. Steed and J. L. Atwood, ‘Supermolecular Chemistry’, Wiley, Chichester, 2000.
11. L. K. Krannich, C. L. Watkins, D. K. Srivastava, and R. K. Kanjolia, *Coord. Chem. Rev.*, 1992, **112**, 117.
12. K. E. Bell and H. C. Kelly, *Inorg. Chem.*, 1992, **31**, 2665.
13. S. Hunig and P. Kraft, *Chem. Ber.*, 1990, **123**, 895.
14. U. Brand, S. Hunig, K. Peters, and H. G. v. Schnering, *Chem. Ber.*, 1991, **124**, 1187.
15. H. Lukasch, G. Schmidt-Lukasch, U. Lippold, and A. Berndt, *Angew. Chem., Int. Ed. Engl.*, 1988, **27**, 960.
16. D. J. Brauer, H. Berger, Y. Chebude, and G. Pawelke, *Inorg. Chem.*, 1999, **38**, 3972.
17. M. T. Reetz, C. M. Niemeyer, M. Hermes, and R. Goddard, *Angew. Chem., Int. Ed. Engl.*, 1992, **31**, 1017.
18. V. M. Norwood III and K. W. Morse, *Inorg. Chem.*, 1988, **27**, 302.
19. M. Mittakanti and K. W. Morse, *Inorg. Chem.*, 1991, **30**, 2434.
20. M. R. M. D. Charandabi, D. A. Feakes, M. L. Ettel, and K. W. Morse, *Inorg. Chem.*, 1991, **30**, 2433.
21. W. J. Mills, C. H. Sutton, M. W. Baize, and L. J. Todd, *Inorg. Chem.*, 1991, **30**, 1046.
22. C. H. Sutton, M. W. Baize, W. J. Mills, and L. T. Todd, *Inorg. Chem.*, 1992, **31**, 4911.
23. B. F. Spielvogel, A. Sood, B. R. Shaw, and I. H. Hall, *Pure Appl. Chem.*, 1991, **63**, 415.
24. B. Györi, Z. Berente, and Z. Kovács, *Inorg. Chem.*, 1998, **37**, 5131.
25. M. Couturier, J. Tucker, B. Andresen, P. Dubé, and J. Negri, *Org. Lett.*, 2001, **3**, 465.
26. H. Noth, in ‘Progress in Boron Chemistry’, ed. R. J. Brotherton, Pergamon Press, New York, 1970, Vol. 3, p. 211.
27. M. F. Lappert, P. P. Power, A. R. Sanger, and R. C. Srivastava, ‘Metal and Metalloid Amides’, Wiley, New York, 1980, Chap. 4.
28. H. Noth, *Pure Appl. Chem.*, 1991, **63**, 351.
29. C. Jaska, K. Temple, A. Lough, and I. Manners, *J. Am. Chem. Soc.*, 2003, **125**, 9424.
30. C. Jaska and I. Manners, *J. Am. Chem. Soc. Commun.*, 2004, **126**, 1334.
31. C. Jaska and I. Manners, *J. Am. Chem. Soc. Commun.*, 2004, **126**, 2698.
32. K. J. L. Paciorek, R. H. Kratzer, J. H. Nakahara, and W. Krone-Schmidt, *Inorg. Chem.*, 1989, **28**, 2896.
33. K. J. L. Paciorek, S. R. Masuda, L. A. Hoferkamp, J. H. Nakahara, and R. H. Kratzer, *Inorg. Chem.*, 1991, **30**, 577.
34. D. J. Brauer, H. Burger, F. Dorrenbach, G. Pawelke, and W. Weuter, *J. Organomet. Chem.*, 1989, **378**, 125.
35. S. S. Al-Juaid, C. Eaborn, P. B. Hitchcock, K. Kalipada Kundu, M. Elias Molla, and J. D. Smith, *J. Organomet. Chem.*, 1990, **385**, 13.
36. H. Noth, P. Otto, and W. Storch, *Chem. Ber.*, 1986, **119**, 2517.
37. W. Maringgele, M. Noltemeyer, and A. Meller, *J. Organomet. Chem.*, 1989, **365**, 187.
38. M. Baudler, K. Rockstein, and W. Oehlert, *Chem. Ber.*, 1991, **124**, 1149.
39. P. Paetzold, *Angew. Chem., Int. Ed. Engl.*, 1991, **30**, 544.
40. A. Meller, *Pure Appl. Chem.*, 1991, **63**, 395.
41. B. Glaser and H. Noth, *Angew. Chem., Int. Ed. Engl.*, 1985, **24**, 416.
42. B. Glaser, E. Hanecker, H. Noth, and H. Wagner, *Chem. Ber.*, 1987, **120**, 659.
43. S. W. Helm and H. Noth, *Angew. Chem., Int. Ed. Engl.*, 1988, **27**, 1331.

44. S. Channareddy, G. Linti, and H. Noth, *Angew. Chem., Int. Ed. Engl.*, 1990, **29**, 199.
45. S. W. Helm, G. Linti, H. Noth, S. Channareddy, and P. Hoffman, *Chem. Ber.*, 1992, **125**, 73.
46. B. Glaser and H. Noth, *Chem. Ber.*, 1986, **119**, 3856.
47. A. Tapper, T. Schmitz, and P. Paetzold, *Chem. Ber.*, 1989, **122**, 595.
48. R. Boese, P. Paetzold, and A. Tapper, *Chem. Ber.*, 1987, **120**, 1069.
49. D. Dou, M. Westerhausen, G. L. Wood, G. Linti, E. N. Duesler, H. Noth, and R. T. Paine, *Chem. Ber.*, 1993, **126**, 379.
50. D. Dou, G. L. Wood, E. N. Duesler, R. T. Paine, and H. Noth, *Inorg. Chem.*, 1992, **31**, 3756.
51. G. Linti, H. Noth, K. Polborn, and R. T. Paine, *Angew. Chem., Int. Ed. Engl.*, 1990, **29**, 682.
52. J. E. Richman, N. C. Yang, and L. L. Anderson, *J. Am. Chem. Soc.*, 1980, **102**, 5790.
53. E. J. Cory, C. M. Yu, and S. S. Kim, *J. Am. Chem. Soc.*, 1989, **111**, 5495.
54. P. Paetzold, *Pure Appl. Chem.*, 1991, **63**, 345.
55. H. Noth, *Angew. Chem., Int. Ed. Engl.*, 1988, **27**, 1603.
56. P. P. Power, *Chem. Rev.*, 1999, **99**, 3463.
57. A. T. Balaban, D. C. Oniciu, and A. R. Katritzky, *Chem. Rev.*, 2004, **104**, 2777.
58. P. Paetzold, D. Hahnfeld, U. Englert, W. Wojnowski, B. Dreczewski, Z. Pawelec, and L. Walz, *Chem. Ber.*, 1992, **125**, 1073.
59. P. Paetzold, D. Hahnfeld, and U. Englert, *Chem. Ber.*, 1992, **125**, 1079.
60. A. Brandl, G. Geisberger, and H. Noth, *Chem. Ber.*, 1990, **123**, 63.
61. G. Geisberger, K. Neukirchinger, and H. Noth, *Chem. Ber.*, 1990, **123**, 455.
62. H. Noth and J. Schubel, *Chem. Ber.*, 1991, **124**, 1687.
63. G. Geisberger, G. Linti, and H. Noth, *Chem. Ber.*, 1992, **125**, 2691.
64. B. Bock, U. Braun, T. Habereder, P. Mayer, and H. Noth, *Z. Naturforsch.*, 2004, **59**, 681.
65. E. Bulak and P. Paetzold, *Z. Anorg. Chem.*, 2000, **626**, 1277.
66. R. A. Bartlett, X. Feng, M. M. Olmstead, P. P. Power, and K. J. Weese, *J. Am. Chem. Soc.*, 1987, **109**, 4851.
67. H. Chen, R. A. Bartlett, M. M. Olmstead, P. P. Power, and S. C. Shoner, *J. Am. Chem. Soc.*, 1990, **112**, 1048.
68. R. A. Bartlett, H. Chen, H. V. Rasika-Dias, M. M. Olmstead, and P. P. Power, *J. Am. Chem. Soc.*, 1988, **110**, 446.
69. G. Schmid, F. Alraun, and R. Boese, *Chem. Ber.*, 1991, **124**, 2255.
70. A. Moezzi, R. A. Bartlett, and P. P. Power, *Angew. Chem., Int. Ed. Engl.*, 1992, **31**, 1082.
71. G. Gabbert, W. Weinmann, H. Pritzkow, and W. Siebert, *Angew. Chem., Int. Ed. Engl.*, 1992, **31**, 1603.
72. P. Paetzold, *Fortschr. Chem. Forsch.*, 1967, **8**, 437.
73. B. L. Li, P. Mukherjie, and R. H. Neilson, *Inorg. Chem.*, 1989, **28**, 605.
74. W. Fraenk, T. M. Klapötke, B. Krumm, and P. Mayer, *Chem. Commun.*, 2000, 667.
75. W. Fraenk, T. M. Klapötke, B. Krumm, H. Nöth, M. Suter, and M. Warchhold, *J. Chem. Soc. Dalton Trans.*, 2000, 4635.
76. W. Fraenk, T. Habereder, A. Hammerl, T. M. Klapötke, B. Krumm, P. Mayer, H. Nöth, and M. Warchhold, *Inorg. Chem.*, 2001, **40**, 1334.
77. R. Hausser-Wallis, H. Oberhammer, W. Einholz, and P. Paetzold, *Inorg. Chem.*, 1990, **29**, 3286.
78. H. Noth, S. Weber, B. Rasthofer, C. K. Narula, and A. Kanstantinov, *Pure Appl. Chem.*, 1983, **55**, 1453.
79. P. Kolle and H. Noth, *Chem. Rev.*, 1985, **85**, 399.
80. W. F. Schneider, C. K. Narula, H. Nöth, and B. E. Bursten, *Inorg. Chem.*, 1991, **30**, 3919.
81. M. J. Farquharson and J. S. Hartman, *Can. J. Chem.*, 1996, **74**, 1309.
82. P. R. Wei and D. A. Atwood, *Inorg. Chem.*, 1998, **37**, 4934.
83. S. Kiyooka, H. Fujimoto, M. Mishima, S. Kobayashi, K. M. Uddin, and M. Fujio, *Tetrahedron Lett.*, 2003, **44**, 927.
84. S. Kiyooka, R. Fujiyama, T. Kawai, H. Fujimoto, and K. Goh, *Tetrahedron Lett.*, 2001, **42**, 4151.
85. M. K. Uddin, R. Fujiyama, S. Kiyooka, M. Fujio, and Y. Tsuno, *Tetrahedron Lett.*, 2004, **45**, 3913.
86. H. Steinberg and R. J. Brotherton, ‘Organoboron Chemistry’, Wiley, New York, 1966, Vol. II.
87. W. Maringgele, ‘The Chemistry of Inorganic Homo- and Heterocycles’, Academic Press, New York, 1987, Vol. I, Chap. 2.
88. A. Meller, *Fortschr. Chem. Forsch.*, 1970, **15**, 146.
89. J. T. Nelson and W. J. Pietro, *Inorg. Chem.*, 1989, **28**, 544.
90. J. A. Tossell, J. H. Moore, K. McMillan, C. K. Subramanian, and M. A. Coplan, *J. Am. Chem. Soc.*, 1992, **114**, 1114.
91. C. K. Narula, R. Schaeffer, A. K. Datye, and R. T. Paine, *Inorg. Chem.*, 1989, **28**, 4053.
92. Y. Kimura, Y. Kubo, and N. Hayashi, *J. Organomet. Inorg. Polym.*, 1992, **2**, 196.
93. H. J. Koch, H. W. Roesky, R. Bohra, M. Noltemeyer, and H. G. Schmidt, *Angew. Chem., Int. Ed. Engl.*, 1992, **31**, 598.
94. K. Niedenzu and S. Trofimenko, *Top. Curr. Chem.*, 1986, **131**, 1.
95. S. Trofimenko, *Prog. Inorg. Chem.*, 1986, **34**, 115.
96. L. Komorowski, W. Maringgele, A. Meller, K. Niedenzu, and J. Serwatowski, *Inorg. Chem.*, 1990, **29**, 3845.
97. M. Yalpani, R. Koster, R. Boese, and W. A. Brett, *Angew. Chem., Int. Ed. Engl.*, 1990, **29**, 302.
98. M. Yalpani, R. Koster, and R. Boese, *Chem. Ber.*, 1991, **124**, 1699.

99. P. v. R. Schleyer and M. Buhl, *Angew. Chem., Int. Ed. Engl.*, 1990, **29**, 304.
100. M. Yalpani, R. Boese, and R. Koster, *Chem. Ber.*, 1989, **122**, 19.
101. J. Bai and K. Niedenzu, *Inorg. Chem.*, 1990, **29**, 4693.
102. S. Trofimenko, *Acc. Chem. Res.*, 1971, **4**, 17.
103. S. Trofimenko, *Chem. Rev.*, 1972, **72**, 497.
104. P. K. Byers, A. J. Canty, and R. T. Honeyman, *Prog. Inorg. Chem.*, 1992, **34**, 1.
105. A. H. Cowley, R. L. Geerts, and C. M. Nunn, *J. Am. Chem. Soc.*, 1987, **109**, 6523.
106. R. Han and G. Parkin, *J. Am. Chem. Soc.*, 1992, **114**, 748.
107. R. Han and G. Parkin, *Inorg. Chem.*, 1992, **31**, 983.
108. M. N. Hansen, K. Niedenzu, J. Serwatowska, and J. Serwatowski, *Inorg. Chem.*, 1991, **30**, 866.
109. D. L. Reger, S. J. Knox, M. F. Huff, A. L. Rheingold, and B. S. Haggerty, *Inorg. Chem.*, 1991, **30**, 1754.
110. M. Mohan, S. M. Holmes, R. J. Butcher, J. P. Jasinski, and C. J. Carrano, *Inorg. Chem.*, 1992, **31**, 2029.
111. H. Fukui, M. Ito, Y. Moro-oka, and N. Kitajima, *Inorg. Chem.*, 1990, **29**, 2868.
112. S. H. Cho, D. Whang, K. N. Han, and K. Kim, *Inorg. Chem.*, 1992, **31**, 519.
113. G. Herberich, M. Hostalek, R. Laven, and R. Boese, *Angew. Chem., Int. Ed. Engl.*, 1990, **29**, 317.
114. K. H. v. Bonn, P. Schreyer, P. Paetzold, and R. Boese, *Chem. Ber.*, 1988, **121**, 1045.
115. P. Paetzold, B. Redenz-Stormanns, and R. Boese, *Angew. Chem., Int. Ed. Engl.*, 1990, **29**, 900.
116. R. Boese, B. Krockert, and P. Paetzold, *Chem. Ber.*, 1987, **120**, 1913.
117. P. Paetzold, B. Redenz-Stormanns, R. Boese, M. Buhl, and P. v. R. Schleyer, *Angew. Chem., Int. Ed. Engl.*, 1990, **29**, 1059.
118. G. Schmid, J. Lehr, M. Polk, and R. Boese, *Angew. Chem., Int. Ed. Engl.*, 1991, **30**, 1015.
119. B. Thiele, P. Schreyer, U. Englert, P. Paetzold, R. Boese, and B. Wrackmeyer, *Chem. Ber.*, 1991, **124**, 2209.
120. M. Yalpani, R. Koster, and R. Boese, *Chem. Ber.*, 1992, **125**, 15.
121. L. Komorowski and K. Niedenzu, *Inorg. Chem.*, 1989, **28**, 804.
122. B. B. Lohray and V. Bhushan, *Angew. Chem., Int. Ed. Engl.*, 1992, **31**, 729.
123. R. T. Paine and C. K. Narula, *Chem. Rev.*, 1990, **90**, 73.
124. L. G. Sneddon, M. G. L. Mirabelli, A. T. Lynch, P. J. Fazen, K. Su, and J. S. Beck, *Pure Appl. Chem.*, 1991, **63**, 407.
125. R. T. Paine, *J. Organomet. Inorg. Polym.*, 1992, **2**, 183.
126. X. Xia, D. A. Jelski, J. R. Bower, and T. F. George, *J. Am. Chem. Soc.*, 1992, **114**, 6493.
127. J. R. Bowser, D. A. Jelski, and T. F. George, *Inorg. Chem.*, 1992, **31**, 156.
128. J. J. Pouch and S. A. Alterovitz, ‘Synthesis and Properties of Boron Nitride’, Trans Tech Publications, Zürich, 1990; *Mater. Sci. Forum*, **54 and 55**.
129. U. Schulent and N. Hasing, ‘Synthesis of Inorganic Materials’, Wiley-VCH, Weinheim, p. 308.
130. U. Schulent and N. Hasing, ‘Synthesis of Inorganic Materials’, Wiley-VCH, Weinheim, p. 30.
131. L. Rao and R. Kaner, *Inorg. Chem.*, 1994, **33**, 3210.
132. B. Bonnetot, F. Guilhon, J. C. Viala, and H. Mongeot, *Chem. Mater.*, 1995, **7**, 299.
133. O. R. Lourie, C. R. Jones, B. M. Bartlett, P. C. Gibbons, R. S. Ruoff, and W. E. Buhro, *Chem. Mater.*, 2000, **12**, 1808.
134. L. Xu, Y. Peng, Z. Meng, W. Yu, S. Zhang, X. Liu, and Y. Qian, *Chem. Mater.*, 2003, **15**, 2675.
135. F. Xu, Y. Xie, X. Zhang, S. Zhang, X. Liu, and X. Tian, *Inorg. Chem.*, 2004, **43**, 822.
136. W. Han, R. Brutchey, T. D. Tilley, and A. Zettl, *Nano Lett.*, 2004, **4**, 173.
137. C. C. Tang, Y. Bando, and D. Golberg, *Chem. Commun.*, 2002, 2826.
138. B. Toury and P. Miele, *J. Chem. Mater.*, 2004, **14**, 2619.
139. K. F. Huo, Z. Hu, F. Chen, J. J. Fu, Y. Chen, B. H. Liu, J. Ding, Z. L. Dong, and T. White, *Appl. Phys. Lett.*, 2002, **80**, 3611.
140. T. T. Borek, W. Ackerman, D. W. Hua, R. T. Paine, and D. M. Smith, *Langmuir*, 1991, **7**, 2844.
141. R. Ma, Y. Bando, H. Zhu, T. Sato, C. Xu, and D. Wu, *J. Am. Chem. Soc.*, 2002, **124**, 7672.
142. E. Johansson, K. Larsson, and J. O. Carlsson, *J. Phys. Chem.*, 1995, **99**, 12781.

Boron: Organoboranes

Frieder Jäkle
Rutgers University, Newark, NJ, USA

1 Introduction 1
2 General Synthetic Methods 1
3 Alkylboranes 6
4 Alkynylboranes and Vinylboranes 9
5 Boron Attached to Unsaturated Organic Rings 10
6 Boron as Part of Unsaturated Organic Rings 18
7 Selected Applications of Organoboranes 22
8 Related Articles 32
9 References 32

Abbreviations

9-BBN = 9-borabicyclo[3.3.1]nonyl; cat = Catecholato; cod = 1,5-cyclooctadiene; coe = Cyclooctene; Dur = Duryl = 2,3,5,6-tetramethylphenyl; Fc = 1-ferrocenyl; fc = 1,1′-ferrocenediyl; Ipc = Isopinocampheyl (derived from (+)-α-pinene); Mes = Mesityl = 2,4,6-trimethylphenyl; Np = 2-naphthyl; OLED = Organic light-emitting diode; Pf = Pentafluorophenyl; pin = Pinacolato; SCE = Standard calomel electrode; thexyl = 2,3-dimethyl-2-butyl; TMP = 2,2,6,6-tetramethylpiperidide; tripyl = 2,4,6-tri-*iso*-propylphenyl.

1 INTRODUCTION

The beginning of the chemistry of organoboron compounds dates back to 1859 when Frankland discovered triethylborane, Et_3B. While the subsequent availability of Grignard reagents provided facile access to organoboranes, a major breakthrough was the discovery of the hydroboration of alkenes as a convenient entry point to organoboron chemistry by Brown in 1956. Over the past decade the chemistry of organoboron compounds has developed from an area primarily of interest with regard to organic synthesis applications, where organoboranes play a pivotal role both as reagents and as catalysts, into a highly interdisciplinary research field.

Of particular significance in the chemistry of organoboranes is their behavior as Lewis acids, which is a result of the empty p-orbital of tricoordinate boron. Much recent effort has been devoted to the synthesis and development of highly Lewis-acidic organoboron compounds through introduction of fluorinated organic substituents. Boron can reach the desired octet configuration either through π-overlap with a substituent X or through formation of neutral or ionic Lewis acid Lewis base complexes (Figure 1). These interactions have been exploited in many of the applications of organoboron compounds. For example, overlap of the empty p-orbital on boron with organic π-systems leads to interesting luminescent and nonlinear optical properties. In addition, the selective coordination of nucleophiles D has opened a new avenue to sensor materials. Indeed it is this donor−acceptor interaction that allows organoboron compounds to act as efficient catalysts and cocatalysts in organic synthesis. Moreover, intramolecular donor−acceptor interactions are ubiquitous in the design of new heterocycles, and intermolecular interactions permit the (reversible) assembly of macrocycles and coordination polymers. Finally, organoborates, BR_4^-, have been studied extensively as weakly coordinating anions and are useful, for example, as battery components and cocatalysts in olefin polymerization.

This chapter reviews these new developments and strives to provide an overview of the current state of the highly interdisciplinary field of organoboron chemistry. The focus will be on the synthesis, structural aspects, properties, and applications of new organoboron compounds. Although reference to a few specific and particularly important applications in organic synthesis will be made, the broad applications of organoboranes as reagents in organic synthesis cannot be covered in the context of this review. However, there are ample recent reviews and texts that the interested reader is referred to (general;[1–4] organoboron reagents,[5–13] organoboron catalysts,[14–19] coupling reactions[20–23]). A separate chapter specifically devoted to boron−nitrogen compounds (*see* ***Boron–Nitrogen Compounds***) gives information on the important classes of amino-substituted organoboranes and organoborane amine adducts.

2 GENERAL SYNTHETIC METHODS

A brief overview of some of the most important synthetic routes to organoboranes, that is, (1) transmetallation reactions, (2) the boration of unsaturated compounds, and (3) C–H activation will be given. General aspects of these methodologies will be covered and illustrated with selected recent literature examples. While a large number of transformations are known that convert one boron compound to another, the diversity of these methods does not allow for full treatment in this context. Detailed information is given in several excellent comprehensive reviews that have been published.[1–3]

2.1 Organometallic Precursors

Transmetallation reactions represent an important method for the synthesis of organoboranes.[1–3] Organometallic

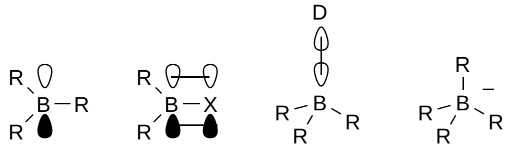

Figure 1 Schematic representation of common organoborane structures

precursors are especially useful but not restricted to the synthesis of methyl, allyl, benzyl, alkynyl, and arylboranes, which cannot be made through hydroboration reactions. In general, an organometallic compound such as an organolithium species is treated with a borane BX_3 to yield the desired organoborane and a metal salt (equation 1).

$$3R_nM + nBX_3 \longrightarrow nBR_3 + 3MX_n \qquad (1)$$

A large variety of organometallic reagents (M = Li, Na, K, Mg, Al, Si, Sn, Pb, Cu, Zn, Hg, Zr) are available for transfer of the organic substituent to boron, but organolithium (*see* ***Alkali Metals: Organometallic Chemistry***) and Grignard (*see* ***Alkaline Earth Metals: Organometallic Chemistry***) reagents are the most important and most readily available precursors. With organolithium reagents, the substitution occurs as a two-step process involving initial formation of a borate intermediate, from which the organoborane is typically liberated with an acid HX as shown in equation (2).

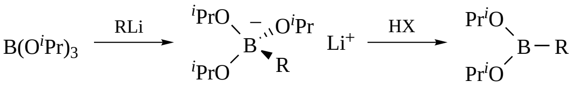

(2)

This procedure is the method of choice for the synthesis of boronic acids. Especially good selectivity is observed with $B(O^iPr)_3$ and $XB(NR_2)_2$ (X = Cl, Br) as the boron source. The method may also be applied to the synthesis of many diorgano- and triorganoboranes. Some recent examples of the formation of organoboranes from organolithium and organopotassium reagents, respectively, are shown in equations (3–6).[24–27]

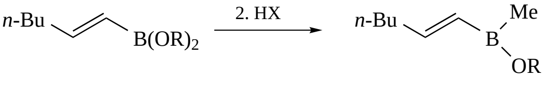

(3)

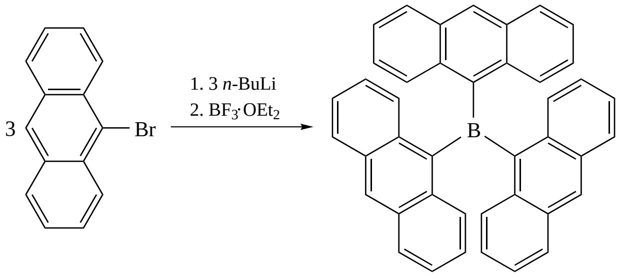

(4)

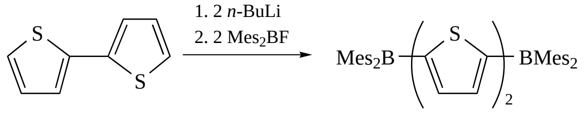

(5)

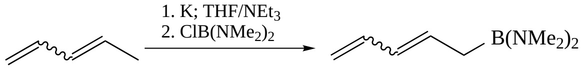

(6)

One drawback is that organolithium and Grignard reagents in certain cases are too reactive to produce the desired organoboranes with high selectivity. Indeed, depending on the type of boron derivative BX_3 used (X = F, Cl, Br, I, OR, NR_2, SR, H), a mixture of organoboron species RBX_2, R_2BX, R_3B, and borates $[R_4B]M$ may form. Another potential problem arises with the more reactive boron halides, BCl_3 and BBr_3, which tend to react with ethers that are typically employed as solvents for the formation of organolithium and Grignard reagents. Other less reactive reagents that are suitable for use in hydrocarbon or chlorinated solvents such as organosilicon (*see* ***Silicon: Organosilicon Chemistry***), organotin (*see* ***Tin: Organometallic Chemistry***), organozinc (*see* ***Zinc: Organometallic Chemistry***), organomercury (*see* ***Mercury: Organometallic Chemistry***), and organocopper (*see* ***Copper: Organometallic Chemistry***) species have therefore been developed and are widely applied.[1,2] These reagents are readily isolable, and can be purified and stored prior to use; importantly, in most cases they show very high selectivity. Some recently reported syntheses involving these organometallic precursors are shown in equations (7–18). For example, the high selectivity of silicon–boron exchange reactions (*ipso* borodesilylation) with aromatic compounds first reported by Haubold and Kaufmann has been exploited for the room temperature synthesis of fully functionalized dibromoboryl-substituted polystyrene (equation 7).[28] Tin–boron exchange reactions occur even more readily, as is nicely demonstrated in the synthesis of a boracycle from a stannacycle in the presence of a vinylic trimethylsilyl group (equation 8).[29] Remarkably high reactivity and good selectivity has been observed when the silicon or tin atom is incorporated into a strained cycle as shown for the ring-opening borylation of a strained ferrocenophane in equation (9).[30] It is interesting to note that cyclic organoboranes and organoborates themselves may serve as precursors to new bifunctional boranes via ring-opening reactions as illustrated in equation (10).[31]

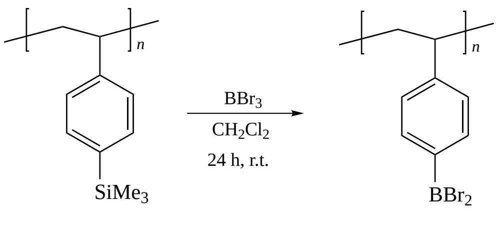

(7)

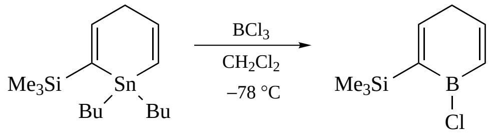
(8)

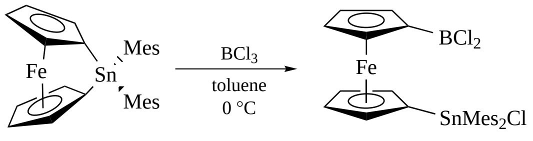
(9)

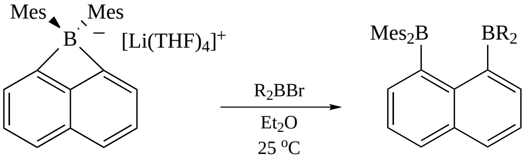
R = Me, Ph

(10)

One of the limitations of silicon – and tin – boron exchange reactions for the synthesis of arylboranes is that preferred transfer of the alkyl substituents in $ArSiMe_3$ or $ArSnMe_3$ over the desired reaction of the silicon–aryl bond may occur in certain cases. Typically $E{-}C(sp^2)$ ($E = Si, Ge, Sn$) and $E{-}C(sp)$ bonds are more reactive in borylation reactions than $E{-}C(sp^3)$ bonds.[32] However, it is well known that tin alkyls are reactive toward haloboranes, and it also has been shown that tetramethylsilane readily reacts with BBr_3 to produce Me_3SiBr and $MeBBr_2$.[33] Thus cleavage of methyl groups from species $ArEMe_3$ ($E = Si, Sn$) has, for example, been observed in the case of electron-deficient groups ($Ar = C_6F_5$) and with silylated and stannylated zirconocenes (equations 11 and 12).[34–36] This problem can generally be avoided if the homoleptic compound Ar_4Sn is readily available and is reactive toward boron halides. In other instances it has been shown that harsh reaction conditions and the use of excess borane can promote tin–boron exchange even in the presence of fluorinated aryl substituents in Ar^FSnMe_3 or $Ar^F{}_2SnMe_2$ (equation 13).[37]

$$C_6F_5SiMe_3 \xrightarrow{BCl_3} C_6F_5SiMe_2Cl + Cl_2BMe \qquad (11)$$

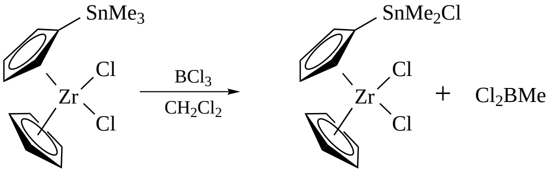
(12)

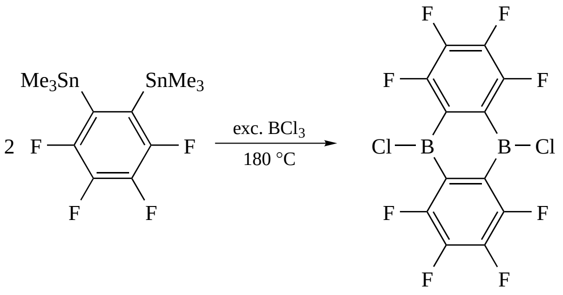
(13)

Organomercury, organozinc, and organocopper reagents have been successfully employed in many cases, in which other more readily accessible reagents did not give satisfactory results. Some examples are illustrated in equations (14–16).[38,39] Reactions involving aluminum and zirconium–boron exchange (organozirconium chemistry: *see* ***Zirconium & Hafnium: Organometallic Chemistry***) have also been reported, and representative transformations are shown in equations (17) and (18). In particular, the commercially available trimethylaluminum is frequently used as a convenient methyl group transfer reagent.[40] Alkyl and vinylzirconium species, which are conveniently obtained via hydrozirconation or zirconocene coupling reactions, react smoothly with boron halides under zirconium–boron exchange.[41,42]

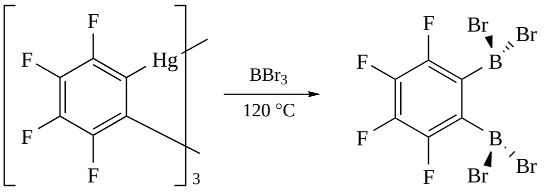
(14)

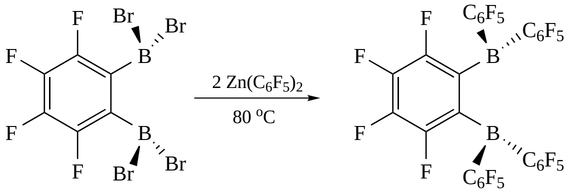
(15)

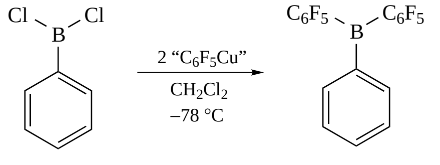
(16)

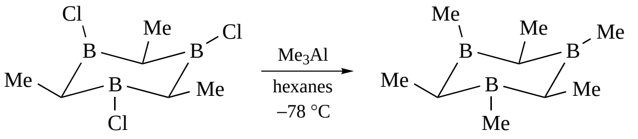
(17)

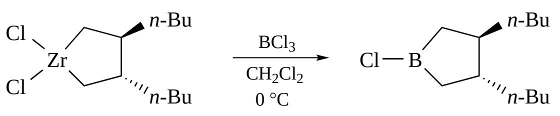
(18)

2.2 Hydroboration, Haloboration, Organoboration, Diboration

The discovery of hydroboration reactions by Brown has greatly advanced the field of organoboron chemistry, and this reaction remains one of the most important and versatile synthetic routes to organoboron compounds. Many excellent reviews and book chapters on this topic have appeared in the literature.[3–7] Thus, only a brief general introduction and some representative recent examples of this chemistry will be provided here.

The hydroboration of olefins and alkynes is shown schematically in equations (19) and (20). In hydroboration reactions *cis*-addition of the borane X_2BH occurs across a double bond or a triple bond. Importantly, in almost all cases the boron atom preferentially goes to the sterically less hindered site. However, in the presence of strongly electron-withdrawing substituents such as fluorinated groups, Markovnikov addition products may be observed in considerable amounts.[43] The mechanism of hydroboration has been thoroughly studied and extensively reviewed.[1–3] For organoboranes such as 9-BBN-H (**4**) the first step is believed to involve dissociation of the dimeric borane $(R_2BH)_2$ into a monomeric species R_2BH, which then adds to the carbon–carbon double bond via a three-center π-complex that precedes the formation of a four-center transition state with no or little activation energy.[2]

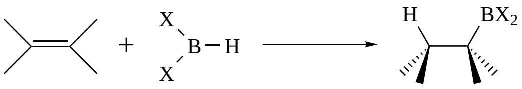

(19)

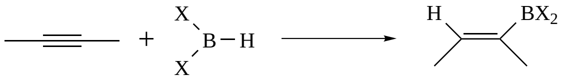

(20)

A large number of hydroboration reagents are available ranging from borane adducts $BH_3{\cdot}D$ (D = Me_2S, THF, NR_3, PR_3) to in situ generated haloboranes X_2BH. Organoboranes RBH_2 and R_2BH are also frequently used and often give higher selectivity in hydroboration reactions. Moreover, the use of chiral substituents on boron provides an opportunity for enantioselective catalysis.[5–7] Some of the most commonly used organoborane reagents are shown (**1–12**) and recent developments will be outlined in the following.

$MeBH_2$

(**1**)

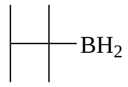

(**2**)

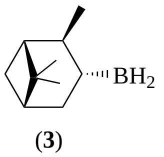

(**3**)

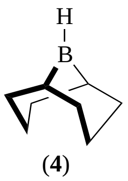

(**4**)

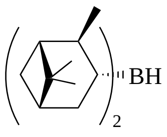

(**5**)

Chiral alkylhaloboranes RBHX that are even more efficient than typical organoboranes RBH_2 and R_2BH were developed by Brown. For instance, isopinocampheylhaloboranes (**6**; IpcBHX, X=Cl, Br) and related 2-organylapopinene

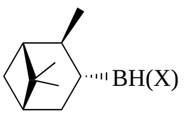

X = H, Cl, Br

(**6**)

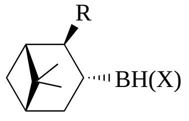

X = H, Cl, Br
R = Et, Pr, *i*-Pr, *i*-Bu, Ph

(**7**)

derivatives (**7**; RapBHX) show not only enhanced reactivity relative to $IpcBH_2$ (**3**), but also excellent selectivities in enantioselective hydroboration reactions.[44] A ring-expanded chiral bicyclic borane (**8**) was described by Soderquist.[45] Compound (**8**) was obtained in high yield through insertion of the diazomethane derivative Me_3SiCHN_2 into the boron–carbon bond of *B*-MeO-9-BBN (equation 21). The borane formed as a racemate, but was readily resolved through its pseudoephedrine complex. The enantiomerically pure boranes (**8**) showed very high stereoselectivity in various hydroboration reactions.[45]

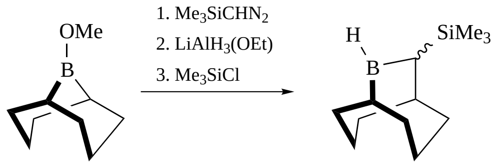

(21)

(**8**)

Arylboranes, $ArBH_2$ and Ar_2BH, have been studied as an alternative to alkylboranes in order to avoid potential problems related to retrohydroboration reactions. Moreover, further stabilization may be readily achieved by 2,6-disubstitution on the phenyl ring. Smith and Pelter reported the synthesis and properties of mesitylborane (**9**) and tripylborane (**10**).[46] Mesitylborane (**9**), which is obtained from Mes_2BH (**11**) and $BH_3{\cdot}THF$, shows not only better stability in solution compared to thexylborane (**2**), but also exhibits very high regio- and chemoselectivity in hydroboration reactions. Polymer-supported versions of these arylboranes have been developed.[47]

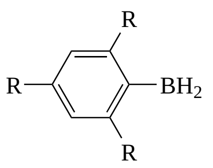

R = Me (**9**)
R = *i*-Pr (**10**)

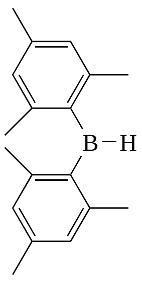

(**11**)

The fluorinated diarylborane $(C_6F_5)_2BH$ (**12**) and its hydroboration activity were studied by Piers.[48,49] This

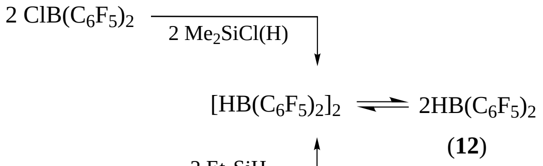

Scheme 1

highly electrophilic borane can be synthesized through two different routes. While $ClB(C_6F_5)_2$ is readily converted to the desired borane (**12**) with $Me_2SiCl(H)$ as the hydrogen source, the chloroborane precursor itself is not readily available (Scheme 1). Thus, an alternative route to (**12**) from commercially available $B(C_6F_5)_3$ was developed. Borane (**12**) shows a dimeric structure in the solid state as confirmed by X-ray crystallography, but partial dissociation to the monomeric borane is observed in solution. Most interesting is the unusually high activity of (**12**) in hydroboration reactions, which provides a means to functionalize sterically hindered substrates that are not attacked by other more commonly used organoborane reagents. The higher reactivity of (**12**) was attributed to the highly electron-deficient nature of the boron center and partial dissociation into the monomeric borane in solution. A similar monomer–dimer equilibrium was also observed for Mes_2BH (**11**).[50] However, this sterically hindered reagent shows low reactivity toward alkenes and is therefore most favorably used in selective alkyne hydroborations.

Haloboration Reactions. The haloboration of carbon–carbon triple bonds provides another entry point for the synthesis of organoboranes.[2,13,51] A wide variety of haloboranes including BBr_3, 9-BBN-Br, and 9-BBN-I has been found to react with terminal alkynes to produce (Z)-2-halo-1-alkenylboranes.[13] The reaction occurs in a stereo-, regio-, and chemoselective fashion specifically with terminal alkynes and has been used to synthesize numerous substituted olefins and related compounds. Diboration reactions of alkynes with B_2Cl_4 are also well known. However, more convenient transition-metal-catalyzed procedures with the less reactive alkoxy substituted diboranes $B_2(OR)_4$ have recently been developed.

1,1-Organoboration Reactions. Alkynyl derivatives R''_3MCCR' of the group 14 elements (M=Si, Ge, Sn, Pb) react with organoboranes R_3B via 1,1-organoboration to give boron-substituted alkenes (Scheme 2).[52] In most cases, high yields and good selectivity are observed for products with the R_2B group and the group 14 element in *cis*-position at the carbon–carbon double bond.

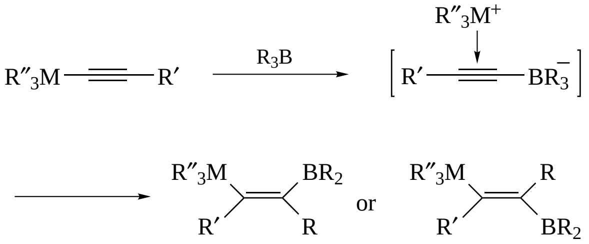

Scheme 2 1,1-Organoboration of alkynes

Organoboranes typically used in these reactions are Et_3B, *i*-Pr_3B, and alkylated 9-BBN derivatives. Interestingly, multiple organoboration steps may take place with di-, tri-, and tetra-1-alkynyl element compounds. Intermediates such as the donor-stabilized zwitterion (**13**) have been identified and fully characterized (equation 22).[52]

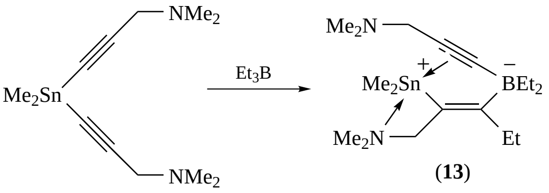

(22)

A large number of intriguing new organoboron compounds including many unusual organoboron heterocycles have been synthesized through organoboration reactions.[52] As an example, the 1,1-organoboration of a silylalkyne is shown in equation (23). The vinylborane (**14**) thus produced shows the first Si–H–B bridge, which was confirmed by multinuclear NMR studies.[53]

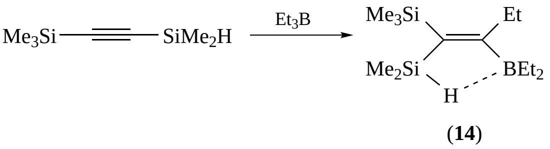

(23)

Catalyzed Boration Reactions. Since the initial report by Männig and Nöth on the rhodium catalyzed room temperature addition of HBcat to alkenes much effort has been devoted to the search for new catalytic hydroboration processes and other boration reactions (*see* ***Hydroboration Catalysis***).[7,54,55] The most intriguing aspect of transition-metal catalysis in boration reactions is that (1) chemoselectivity, (2) regioselectivity, and (3) stereoselectivity may be altered compared to uncatalyzed reactions. New methods for the catalytic addition of diboranes $R_2B–BR_2$,[56,57] B–S,[58] B–Si,[59] and B–Sn[60] moieties have greatly enhanced the scope and utility of catalytic boration chemistry. Moreover, cross-coupling of B–B and B–H compounds with organic halides and triflates provides a convenient one-step procedure for the synthesis of organoboron compounds from organic electrophiles.[55–57] For many of these catalytic processes, boryl–metal species have been identified as key intermediates.

The transition-metal-catalyzed diboration of alkynes can be directed to give highly selective *cis*-addition yielding 1,2-diborylated olefins (equation 24). Depending on the catalyst, tetraborylated alkanes may also be observed. However, in the catalyzed diboration of alkenes not only 1,2-diborylated products, but also various other mono-, di-, and triborylated alkanes are often obtained depending on the specific conditions.[56] This behavior was traced back to competing β-hydroelimination pathways and has been exploited for the selective synthesis of 1,1-diborylated olefins.[61]

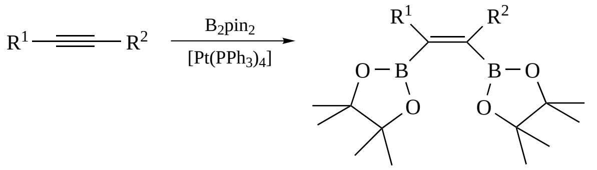

(24)

2.3 C–H Activation

A new direct access to organoboranes via stoichiometric and catalytic C–H activation (*see* ***Alkane Carbon–Hydrogen Bond Activation***) has been developed over the past few years.[62] It is especially interesting that this methodology provides an opportunity to functionalize unreactive C–H bonds of hydrocarbons in a single preparative step thus combining economy, efficiency, elegance, and environmental benignity.[62] Most studies have been performed with diboranes such as $B_2(OR)_4$, but boranes $HB(OR)_2$ may also serve as a precursor.

Initial reports on the borylation of alkanes using isolated transition-metal–boryl complexes date back to 1995, when Hartwig showed that $Cp^*Re(CO)_2(Bpin)_2$ converts pentane to 1-borylpentane with high regioselectivity.[63,64] The catalytic C–H borylation of alkanes with $Cp^*Re(CO)_3$ using photochemical activation was demonstrated soon thereafter (equation 25).[65] Also, an efficient thermal process that involves the use of rhodium catalysts has since been developed (equation 26).[66] It is interesting to note that this methodology is not restricted to small molecules, but has recently been exploited for the direct side-chain functionalization of polyolefins.[67]

$$\mathrm{pin_2B_2 + H{-}R \xrightarrow[h\nu/\mathrm{CO}]{Cp^*Re(CO)_3} pinB{-}R + pinBH} \tag{25}$$

$$\mathrm{pin_2B_2 + 2H{-}R \xrightarrow[150\,^{\circ}C]{Cp^*Rh(\eta^4\text{-}C_6Me_6)} 2pinB{-}R + H_2} \tag{26}$$

Highly electron-rich aromatic compounds are known to undergo direct electrophilic borylation reactions with the strong electrophiles BI_3, BBr_3, BCl_3, or $HB(C_6F_5)_2$ under thermal conditions.[68,69] As an example, the dibromoborylation of ferrocene in refluxing hexanes is shown in equation (27). Facile intramolecular borylation reactions have also been reported.[70,71]

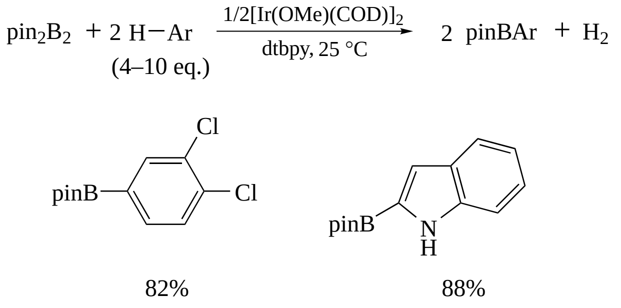

Scheme 3 Borylation of arenes via C–H activation

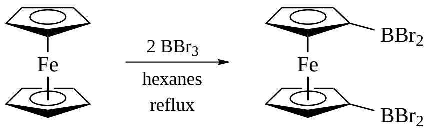

(27)

On the other hand, transition-metal catalysis provides an opportunity to regioselectively borylate even electron-poor aromatic compounds under mild conditions and in the presence of functional groups. The first example of transition metal–catalyzed aromatic C–H borylation was reported in 1993, when Marder found borylation of the solvent toluene during the preparation of the iridium–boryl complex $Ir(\eta^6\text{-}MeC_6H_5)(Bcat)_3$ from $Ir(\eta^5\text{-}C_9H_7)(cod)$ with catecholborane (catBH).[72] The first catalytic process has been reported by Smith, who used iridium complexes containing phosphine ligands.[73,74] Various rhenium and rhodium complexes have since been shown to catalyze the aromatic borylation with B_2pin_2 and HBpin, respectively. More recently, Miyaura and Hartwig have demonstrated the room temperature conversion of arenes to arylboranes with B_2pin_2 in the presence of the iridium complex $[Ir(OMe)(cod)]_2$ and the ligand di-*t*-butylbipyridine (dtbpy) as shown in Scheme 3.[57,75,76]

Marder reported that the alkyl C–H bonds in benzylic compounds are selectively borylated with a rhodium catalyst.[77] Aromatic borylation products were only observed as minor by-products. Similar results were obtained by Miyaura with Pd/C (equation 28).[78]

$$\mathrm{pin_2B_2 + 2PhCH_3 \xrightarrow[100\,^{\circ}C/16\,h]{Pd/C\ 3{-}6\,mol\%} \underset{74\%}{2pinBCH_2Ph} + H_2} \tag{28}$$

3 ALKYLBORANES

Trialkylboranes were the first organoboranes to be discovered by Frankland. Nevertheless, the crystal structure of trimethylborane, which is a gas at ambient temperature and has a melting point of 112 K, has been determined only very recently.[79] In contrast to its heavier group 13 analogues, it consists of layers containing only extremely weakly interacting BMe_3 molecules. The shortest intermolecular B···H contact is 3.04 Å, which is well beyond the sum of the van der Waals radii of B and H (2.83 Å). Numerous higher alkylboranes have been prepared and are commonly encountered as intermediates in synthetic organic chemistry.[1,2,5,7,8,10,12,20,22]

Perfluorinated analogs of trialkylboranes, tris(trifluoromethyl)borane ($B(CF_3)_3$; **15**) and its higher homologs, are still unknown although they have been the subject of a considerable research effort.[80] Many complexes of (**15**) on the other hand have been isolated.[81] Indeed, the B–N bond in amine adducts is extraordinarily stable and withstands even hydrochloric acid and concentrated solutions of KOH. However, the donor-free compound (**15**) could not be liberated. This is believed to be due to facile decomposition under elimination of difluorocarbene and formation of BF_3. The unusual organoboron carbonyl complex $(CF_3)_3B{\bullet}CO$ (**16**) has been prepared very recently.[82] This complex was obtained in high yield through solvolysis of the borate salt $K[B(CF_3)_4]$[83] in concentrated sulphuric acid and was found to be exceptionally stable. In contrast, $(C_6F_5)_3B{\bullet}CO$ needs to be generated in a CO matrix and is only stable at very low temperature. A rich chemistry has been developed with the aminoborane $(CF_3)_2BNMe_2$, which serves as a precursor to other trifluoromethylborane complexes $(CF_3)_2BR{\bullet}D$ (R=H, alkyl, aryl) and numerous heterocyclic compounds.[80]

Diborylated organoboranes with a BCB backbone such as (**17**) are usually prepared by double hydroboration of terminal alkynes (equation 29).[84] The treatment of the diborane B_2pin_2 with diazomethane derivatives provides an interesting alternative that allows for the synthesis of species pinB–CR_2–Bpin (**18**, R=H, Ph; equation 30), which are not accessible via hydroboration reactions.[85]

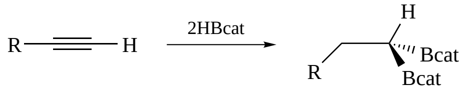

(**17**)

(29)

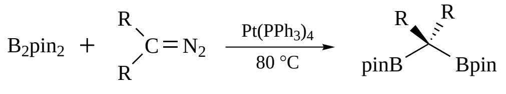

(30)

(**18**)

Compounds containing three or even four boryl groups attached to a single carbon atom are accessible through treatment of $RCCl_3$ with $ClB(OR)_2$ and lithium metal, a synthetic route that has been thoroughly studied by Matteson in the 1970s. Moreover, 1,1,2,2-tetraborylethanes are obtained in good yields from acetylene and B_2Cl_4. More recently, transition-metal-catalyzed hydrogenation, hydroboration and diboration reactions have been used to prepare triborylalkane, tetraborylethane, and hexaborylethane derivatives (Scheme 4, (**19–23**)).[86,87] Interestingly, depending on the catalyst, the diboration of vinylboranes with B_2cat_2 leads via sequential diboration and dehydroboration steps either to 1,1,1-triborylalkanes (**20**) or to 1,1,2-triborylalkanes (**21**).[88] 1,1,1-Triborylalkanes, 1,1,2,2-, and 1,1,1,2-tetraborylethane species have been proposed as intermediates in the reaction of borylated alkynes with excess Et_2BH (''hydride bath'') that eventually leads to the formation of small carboranes.[89–91] Indeed, isolated triborylmethane species with alkyl or halide substituents on boron have recently been shown to rearrange to small carboranes upon thermal treatment.[87]

Tetraborylmethane derivatives continue to attract interest as potential candidates for the stabilization of planar tetracoordinate carbon.[92] Species $C(B(OR)_2)_4$ containing alkoxy substituents on boron adopt classical structures. However, a planar tetracoordinate carbon environment has been suggested based on DFT calculations for compounds $C(BR_2)_4$ (R = alkyl), in which the CB_4 group is incorporated into a cage system thus leading to both 'electronic' and 'mechanical' stabilization.[93,94] The electronic structures of penta- and hexaborylated compounds containing planar pentacoordinate and hexacoordinate carbon have also been studied using theoretical calculations.[95,96]

Numerous cyclic organoboranes are known and only selected recent studies will be highlighted. 1-Boraadamantane (**24**), which is isoelectronic with the 1-adamantyl cation, is a peculiar trialkylborane since the three-coordinate boron atom normally prefers a trigonal planar environment, but

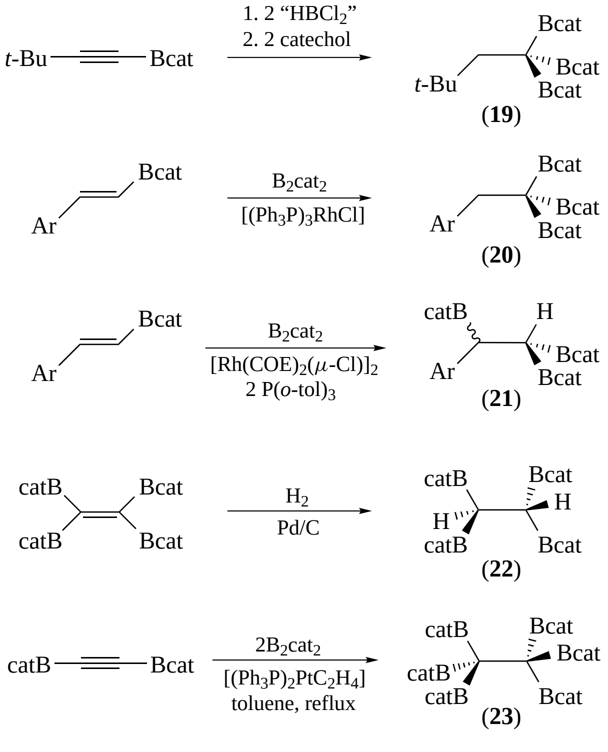

Scheme 4

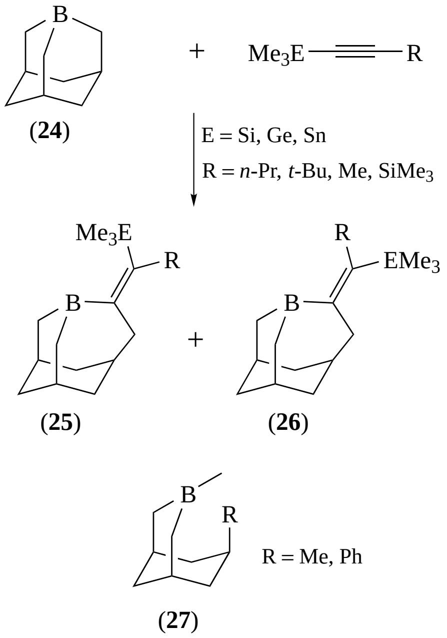
B
(24)
+
Me3E—≡—R
E = Si, Ge, Sn
R = n-Pr, t-Bu, Me, SiMe3
Me3E
R
B
+
R
EMe3
B
(25)
(26)
B
R
R = Me, Ph
(27)

Scheme 5

occupies a bridgehead position with a tetrahedral geometry in (**24**). Consequently, (**24**) exhibits a markedly increased Lewis acidity when compared with other trialkylboranes. Several new ring-enlarged systems and multicyclic organoboron species have recently been obtained via 1,1-organoboration reactions.[97–99] For example, reaction of 1-boraadamantane with *n*-propyltrimethylsilylacetylene yields two isomeric ring-enlarged 4-methylene-3-borahomoadamantane species (**25** and **26**; Scheme 5).

In a different study, a series of substituted 3-borabicyclo[3.3.1]nonanes (**27**) have been prepared and investigated by X-ray crystallography. Intramolecular interactions between the empty *p*-orbital on boron and the substituent R were shown to play an important role in the stabilization of the chair-like conformation in these species.[100]

Cyclic organoboranes containing multiple boron atoms within the ring structure have been extensively studied as precursors to (multidecker) transition-metal complexes and to nonclassical organoboranes (*see* ***Boron: Metallacarbaboranes*** and ***Boron: Polyhedral Carboranes***). Earlier efforts have been thoroughly reviewed.[101–103] Recently, a series of triboracyclopentane derivatives were reported by Berndt and Schleyer (Scheme 6).[104] Reduction of these boracycles gave the nonclassical bishomoaromatic anions (**28**) and homoaromatic dianions (**29**). Related trishomoaromatic dianions obtained via reduction of 1,3,5-triboracyclohexane derivatives with lithium were studied by Siebert and Schleyer.[105,106]

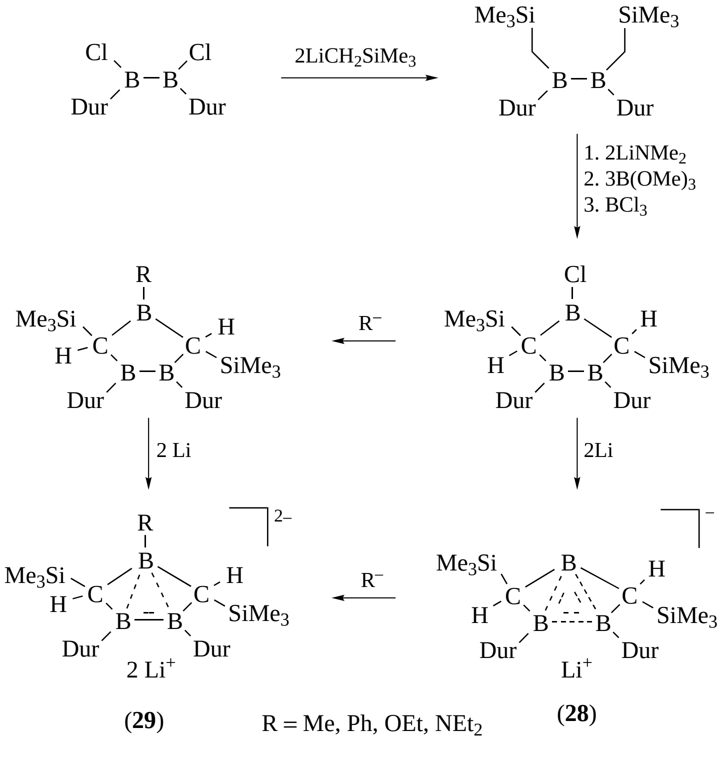
Cl
Cl
B−B
Dur
Dur
2LiCH2SiMe3
Me3Si
SiMe3
B−B
Dur
Dur
1. 2LiNMe2
2. 3B(OMe)3
3. BCl3
Cl
B
Me3Si
C
H
H
C
SiMe3
B−B
Dur
Dur
R⁻
R
B
Me3Si
C
H
H
C
SiMe3
B−B
Dur
Dur
2 Li
2Li
2−
−
Li+
2 Li+
R⁻
(29)
R = Me, Ph, OEt, NEt2
(28)

Scheme 6

4 ALKYNYLBORANES AND VINYLBORANES

Borylated alkynes that are stabilized through Lewis base coordination or π-donation from electron-donating amino and alkoxy substituents on boron are well studied. Their synthesis typically involves either the reaction of a bis(dialkylamino)haloborane with an acetylide to form a diaminoborylacetylene (equation 31), or the treatment of stannylated alkynes with boron halides.[107–109] However, while alkynylboranes are readily available, in the absence of steric protection or electronic stabilization they tend to decompose thermally.

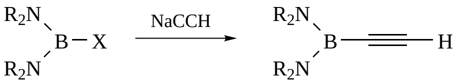

$$(R_2N)_2B{-}X \xrightarrow{NaCCH} (R_2N)_2B{-}C{\equiv}C{-}H \qquad (31)$$

For instance, attempts at isolating donor-free alkynylboranes have been hampered by spontaneous polymerization. The first donor-free tris(alkynyl)borane, tris(3,3-dimethyl-1-butynyl)borane (**30**), has only recently been obtained by reaction of deprotonated 3,3-dimethyl-1-butyne with boron trichloride at −78 °C in pentane (equation 32).[110] The alkynylborane (**30**) was fully characterized by multinuclear NMR spectroscopy, mass spectrometry, and X-ray crystallography. The ^{11}B NMR signal of (**30**) shows a remarkable shift of $\delta = 48$, which is upfield from typical shifts of alkyl- and alkenylboranes. The crystal structure of (**30**) shows similar C–C bond lengths, but significantly shorter B–C bonds in comparison to those observed for the donor-stabilized complexes (**30**) D indicative of a small degree of $p_\pi - p_\pi$ interactions between the sp^2-boron atom and the sp-hybridized carbon. Weak π-overlap was further confirmed by *ab initio* calculations.[109] It is this π-interaction that has been exploited for the development of nonlinear optical (NLO) materials based on alkynylboranes as described in Section 7.1.[111]

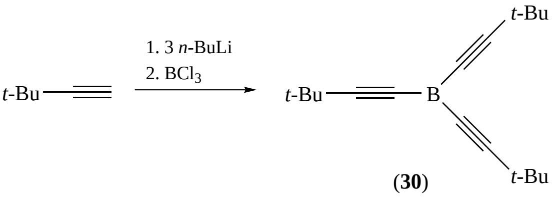

(32)

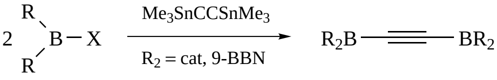

$$2\,R_2B{-}X \xrightarrow[R_2\,=\,\text{cat, 9-BBN}]{Me_3SnCCSnMe_3} R_2B{-}C{\equiv}C{-}BR_2 \qquad (33)$$

Tin–boron exchange reactions provide a convenient route to diborylated acetylene (equation 33).[107] Diborylalkynes show an enhanced Lewis acidity in comparison to diborylalkanes as demonstrated by the coordination of THF in (**31**), but a lack of binding to the related alkyldiborane (**32**). This effect has been attributed to the stronger inductive electron-withdrawing effect of sp-hybridized relative to sp^3-hybridized carbons.[32]

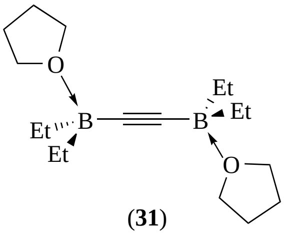

(31)

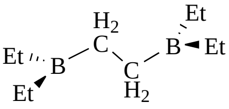

(32)

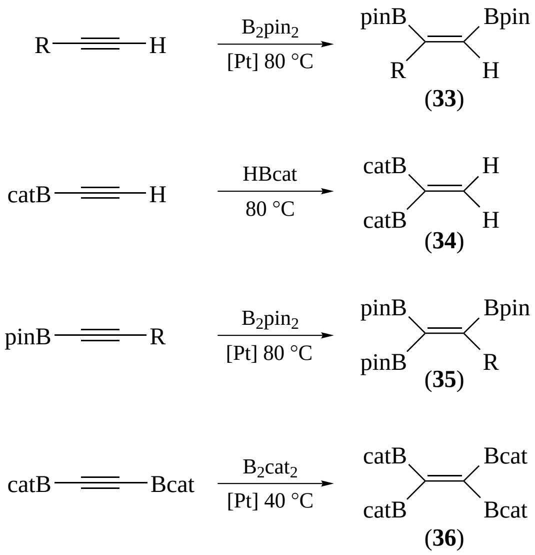

Scheme 7

Many different routes are available for the synthesis of vinylboranes and several of them are shown in Scheme 7. Hydroboration and diboration reactions of alkynes and borylated alkynes provide access to the full series of mono-, di-, tri-, and tetraborylated olefins.[56,57] 1,2-Diborylated olefins (**33**) are obtained via diboration of alkynes and 1,1-diborylated olefins (**34**) are accessible through hydroboration of borylalkynes. An alternative route to 1,1-disubstituted products involves the diboration of carbenoids formed in situ from vinylhalides and butyl lithium.[84] In certain cases, metal-catalyzed dehydrogenative borylation of olefins may be used.[61] Borylalkynes serve as precursors to triborylated (**35**) and tetraborylated (**36**) olefins. Thus, the sparingly soluble tetraborylethylene derivative (**36**) forms in good yield through platinum-catalyzed diboration of diborylacetylene in toluene at 40 °C if the base-free catalyst [Pt(cod)$_2$] is used.[112] If the reaction, however, is performed at higher temperature, further diboration of (**36**) leads directly to the hexaborylated ethane (**23**) shown above. Intramolecular B–O interactions were postulated for (**36**) based on HF-SCF calculations.[112]

Organometallic routes are frequently applied to the synthesis of vinylboranes.[84] Vinyltin and vinylzirconium reagents, for instance, serve as precursors for the preparation of vinylboranes, in which the boron centers are not electronically stabilized by oxygen or nitrogen substituents. Moreover,

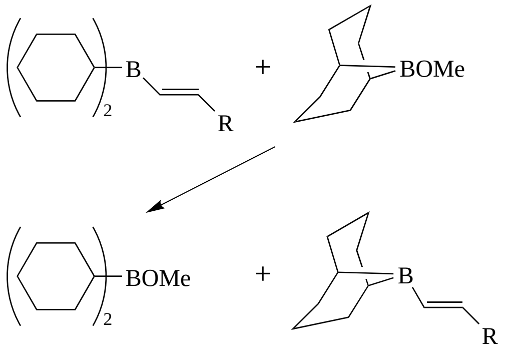

Scheme 8

organoboration of silyl and stannylalkynes provides access to multiply functionalized olefins (see Scheme 2).[52,113,114] Vinylboranes may also be prepared via alkenyl transfer from boron to boron. This reaction, shown in Scheme 8, is particularly useful if the desired alkenylborane is not selectively formed in the hydroboration of alkynes.[115] Haloboration reactions and uncatalyzed diboration of alkynes with B_2Cl_4 allow for preparation of vinyldihaloboranes. The latter typically yields 1,2-diborylated products, but in the presence of silyl and germyl substituents 1,1-diborylated species are formed. In some cases, hydrozirconation of alkynylboranes and zirconocene coupling reactions also provide access to 1,1-diborylated olefins.[116]

The most important applications of borylated olefins and alkynes are certainly in the field of organic synthesis, where they play, for example, major roles as reagents in coupling reactions[20–22] and as dienophiles for Diels–Alder reactions.[117] Vinylboranes and alkynylboranes with bulky mesityl groups on boron have been investigated as nonlinear optical materials (see Section 7.1).[111] Moreover, 1,1- and 1,2-diborylated olefins containing electron-deficient boron centers have been extensively studied as bidentate hosts for the coordination of nucleophiles (see Section 7.2) and also serve as convenient precursors to various diboraheterocycles.[84] Finally, 1,1-diborylated olefins containing electron-withdrawing C_6F_5 groups on boron have been studied as bidentate Lewis acid activators for olefin polymerization and are further described in Section 7.3.3.[84,118]

5 BORON ATTACHED TO UNSATURATED ORGANIC RINGS

5.1 Phenylboranes

Although direct borylation of arenes in specific cases is possible and metal-catalyzed C–H and C–X activation reactions provide new possibilities, most arylboranes are prepared from organometallic precursors. In particular, monoborylated arenes are conveniently obtained through reaction of organolithium or Grignard reagents with boranes BX_3 and have been well studied, and their importance in Suzuki cross-coupling reactions can hardly be overestimated.[20,22]

Triarylboranes Ar_3B continue to attract interest with regard to their stereodynamic behavior that is related to the propeller shape adopted by many triarylboranes containing bulky aryl groups. For instance, the *ortho*-substituted triphenylborane $(2\text{-}CF_3C_6H_4)_3B$, prepared from the corresponding organolithium compound and BCl_3, was studied by spectroscopic methods and MO calculations.[119] The X-ray crystal-structure analysis revealed a propeller-shaped structure of nearly C_3 symmetry, in which the three CF_3 groups are on the same side of the boron sp^2 plane. Two enantiomers crystallized separately and both enantiomers were found to be CD active in the solid state. However, in solution interconversion between the two isomers was observed by variable-temperature ^{19}F NMR spectroscopy. Related to the conformational flexibility of arylboranes is the question whether significant π-bonding occurs between the empty π-orbital on boron and the aromatic substituents. Based on crystallographic and NMR spectroscopic data, boron–carbon π-bonding is thought to be weak in the ground state of triarylboranes.[120] However, a greater π-contribution is evident in the excited state of triarylboranes and in the respective radical anions $[Ar_3B]^{-}$.[120] This effect has been exploited for the design of new photonic and electronic materials based on arylboranes, which are further discussed in Section 7.1.

Various derivatives of bis(boryl)benzene isomers (**37**), (**38**), and (**39**) are readily obtained through metathesis reaction of boron halides with the respective Grignard, trimethylsilyl, or trimethylstannyl reagents.[32,121] Especially the 1,2-disubstituted derivatives (**37**) have been studied extensively in molecular recognition and as activators in olefin polymerization (Sections 7.2 and 7.3.3), whereas species (**38**) and (**39**) have primarily been used for the design of new electronic materials (Section 7.1).

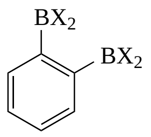

(**37**)

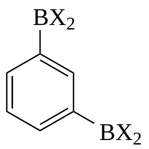

(**38**)

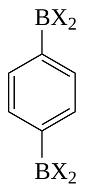

(**39**)

Thermolysis of 1,2-diborylated benzene species (**37**) (X=Cl, Me, Et) leads to cyclization with extrusion of BX_3 (Scheme 9).[32,122] The resulting diboraanthracenes (**40**) formally contain an antiaromatic central 6-membered ring.[32] Piers and Marks have independently developed perfluorinated analogs of diboraanthracene (**40**). Interestingly, borylation of $1,2\text{-}C_6F_4(SnMe_3)_2$ with BCl_3 leads directly to the perfluorinated diboraanthracene derivative (**42**) (Scheme 9).[37,123] Although the monosubstituted species

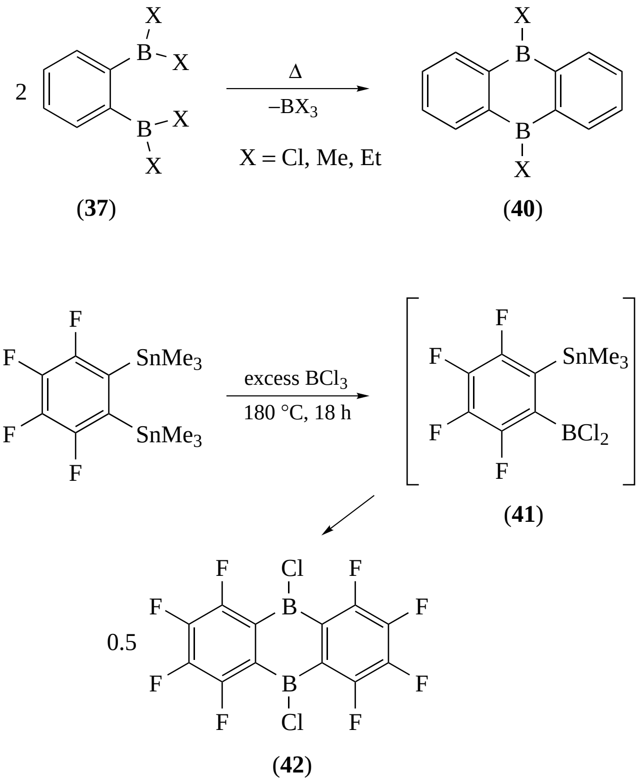

Scheme 9

$1,2\text{-}C_6F_4(SnMe_3)(BCl_2)$ (**41**) was detected initially, the expected diborylated intermediate $1,2\text{-}C_6F_4(BCl_2)_2$ was not observed at any time during the reaction. It was suggested that the decreased nucleophilicity of the perfluoroaryl compounds disfavors the second electrophilic aromatic substitution step relative to coupling. The diborylated species $C_6F_4(BBr_2)_2$ can on the other hand be prepared from the mercurated precursor $(1,2\text{-}C_6F_4Hg)_3$ as shown in equation (14).[38] Perfluorinated arylboranes are further discussed in the context of their use as olefin polymerization activators in Section 7.3.3. Moreover, diboraanthracenes (**40**) and related diboracycles (**43**), (**44**) and (**45**) (X = Cl, Me, NMe_2), which are readily available through tin–boron exchange reactions, have been extensively studied as ligands for transition-metal complexes.[101]

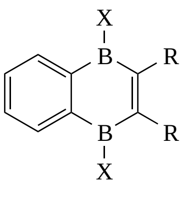

(**43**)

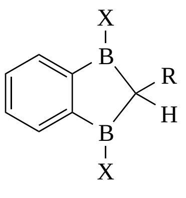

(**44**)

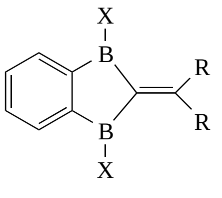

(**45**)

Only a few examples of higher borylated benzene derivatives (**46–50**) have been described. Okada used a Grignard methodology to prepare 1,3,5-tris(dimesitylboryl)benzene (**46**, X = Mes) in low yield and studied its conformational properties by variable-temperature NMR spectroscopy.[124] Silicon-boron exchange between $1,3,5\text{-}C_6H_3(SiMe_3)_3$ and BI_3 provided $1,3,5\text{-}C_6H_3(BI_2)_3$ (**46**, X = I) in somewhat higher yield of ca. 30%.[125] An alternative route to multiborylated benzene species was reported by Siebert, who applied the well-known cobalt-catalyzed cyclotrimerization of alkynes to dialkoxyborylacetylene derivatives $(RO)_2B\text{-}CC\text{-}H$.[109] A mixture of the 1,3,5- and 1,2,4-triborylated benzene derivatives (**46,47**) was obtained in yields of >50%. Subsequent treatment of the isomeric mixture with mesityl lithium and chromatographic workup gave compound (**46**) (X = Mes) in 49% yield.

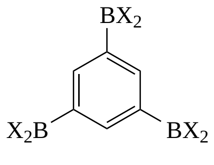

(**46**)

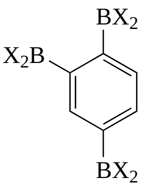

(**47**)

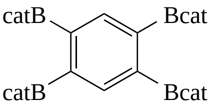

(**48**)

Siebert also used the cobalt-mediated cyclization of alkynes to synthesize the first tetraborylated and hexaborylated benzene compounds (**48–50**; Scheme 10). The boronate ester (**49**) which formed initially was converted into the intriguing base-free hexafunctional triorganoborane (**50**) with trimethylaluminum.[112,121]

The starting point for the synthesis of *peri*-borylated naphthalenes is 1,8-dilithionaphthalene, which may also be transformed into other useful reagents such as 1,8-distannylated and 1,8-dimercuriated naphthalenes.[31] Since the initial report of Katz on the unusual properties of 1,8-bis(dimethylboryl)naphthalene (**51**) as a 'hydride-sponge' new

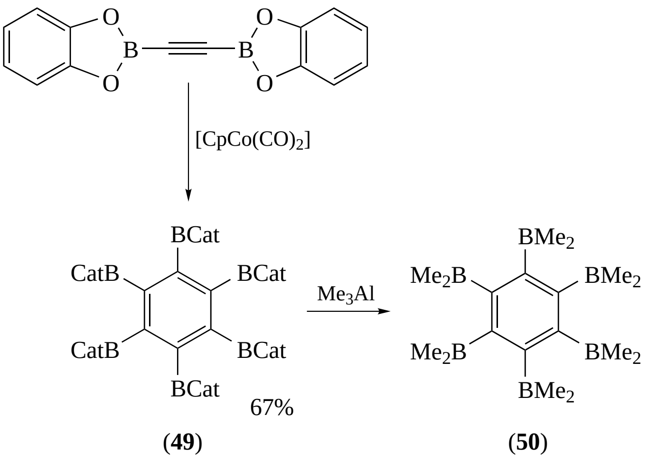

Scheme 10

research has been devoted to the exploration of this class of bidentate Lewis acids (see also Section 7.2).[31] New derivatives such as the phenyl-substituted (**52**) and the amino-substituted species (**53**) have been synthesized (equation 34).[31] The latter form B_2N_2 four-membered rings when small substituents are attached to the amino groups.[126]

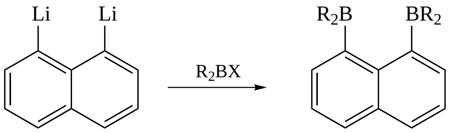

(34)

(**51**) R = Me
(**52**) R = Ph
(**53**) $R = NR'_2$

It is interesting to note that the reaction of 1,8-dilithionaphthalene with diorganoboron halides does not always lead to diborylated naphthalene species. The antiaromatic cyclic 16-π-electron system (**54**) and the strained four-membered ring (**55**) formed upon reaction of dilithionaphthalene with $(C_6F_5)_2BF{\cdot}OEt_2$ and Mes_2BF in diethyl ether, respectively (Scheme 11).[31,127] The boracycle (**55**) serves as a precursor to other 1,8-disubstituted naphthalenes through ring-opening reaction with electrophiles such as Ph_2BBr or Me_3SnCl (see equation 10).[128,129] Other extended π systems that have been borylated include biphenylene and anthracene.[25,130] The borylated derivatives are typically obtained from lithiated species via treatment with Mes_2BF.

The aromatic moiety in phenylboranes and phenylborates may serve as a 6-electron π donor ligand to transition-metal complexes. Half-sandwich complexes of chromium, $Mes_2[B(\eta^6\text{-Mes})Cr(CO)_3]$ (**56**), $MesB[\eta^6\text{-}MesCr(CO)_3]_2$ (**57**), and $B[\eta^6\text{-}MesCr(CO)_3]_3$ (**58**), containing trimesitylborane as a ligand have been prepared and structurally characterized.[131] The $Cr(CO)_3$ moieties interact weakly in the multinuclear systems (**57**) and (**58**) as shown by electrochemical studies. A more extensive exchange interaction was observed between vanadium centers in related trovacenylboranes $Mes_{3-n}B[(\eta^7\text{-}C_7H_7)V(\eta^5\text{-}C_5H_4)]_n$ (**59**).[132] Finally, tetraarylborates have been used for the generation of zwitterionic transition-metal complexes and of borato-bridged complexes, in which one or two aryl groups of the Ar_4B^- moiety bind to the metal.[133,134]

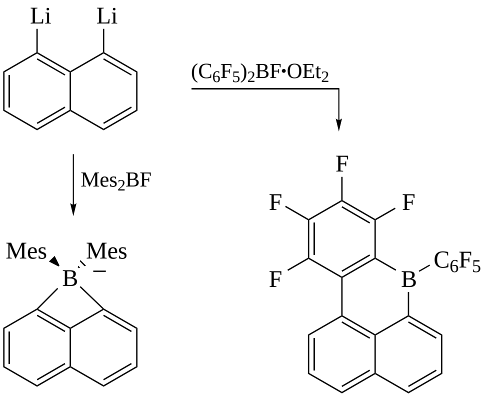

(**55**)

(**54**)

Scheme 11

It is interesting to note in this context that arylboron transition-metal complexes with metal−boron bonds have recently been structurally confirmed. Transition-metal−boryl complexes have been of intense research interest, partly because of their involvement in the hydro- and diboration of carbon−carbon multiple bonds, but also owing to their importance in the stoichiometric and catalytic functionalization of alkanes and arenes under thermal and photolytic conditions *(see* ***Alkane Carbon–Hydrogen Bond Activation****)*.[135–138] While various borane and borylene complexes that feature amino substituents are known, only a few structurally confirmed arylborane complexes have recently been described.[138] Reaction of $[CpFe(CO)_2]Na$ with $BrB(C_6H_5)_2$ and $ClB(C_6F_5)_2$, respectively, led to attachment of diphenylboryl and bis(pentafluorophenyl)boryl groups to the $CpFe(CO)_2$ fragment in complexes (**60**) and (**61**).[139,140] The Fe–B distance in the perfluorinated derivative (**61**) (two independent molecules: 1.965(5) and 1.964(4) Å) is significantly shorter than that in the phenyl species (**60**) (2.034(3) Å). This effect has been attributed to the higher Lewis acidity of the boron center, which in turn results in increased π-overlap between boron and iron. The synthesis of the first terminal and bridging arylborylene complexes (**62**) and (**63**) has also recently been reported (Scheme 12).[141,142]

5.2 Cyclopentadienylboranes

The attachment of boryl groups to cyclopentadiene, indene, and fluorene has attracted much interest over the past decade owing to their utility as precursors to borylated transition-metal complexes, most notably those of group 4. The preparation of cyclopentadienylboranes from organolithium, Grignard, or organotin precursors with boron halides is well established. Cyclopentadienylboranes exist as three constitutional isomers, which can interconvert through sigmatropic rearrangements. Upon preparation at low temperature, the allylic isomer (**64**) is obtained initially. This isomer is fluxional as a result of fast sigmatropic migration of the BR_2 group if alkyl substituents are attached to boron. Upon warming to room temperature a mixture of the thermodynamically favored vinylic boranes (**65**) and (**66**) is formed via a [1,5] sigmatropic hydrogen shift.[143] The deprotonation of cyclopentadienylboranes was studied with the aim of developing convenient precursors for transition-metal complexes. Intriguingly, Herberich found that not only derivatives that are stabilized with amino groups on boron, but also those containing alkyl substituents are readily deprotonated if bulky amides such as LiTMP or cyclopentadienides MCp (M = Li, Na) are used as the

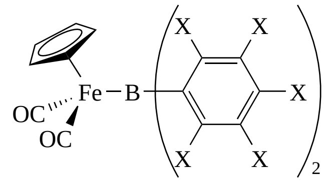

(60) X = H
(61) X = F

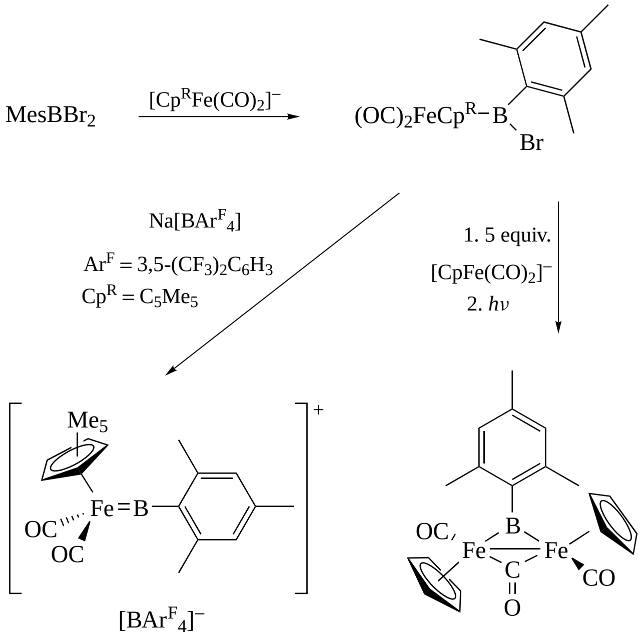

(**62**) (**63**)

Scheme 12

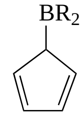

(**64**)

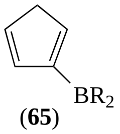

(**65**)

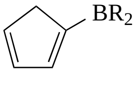

(**66**)

base.[143] The formation of the borylcyclopentadienides (**67**) was confirmed by X-ray crystallography. The crystal structures reveal a strong π-interaction between the Cp ring and the boron atom if alkyl groups are attached to boron. Borylindenides and borylfluorenides were prepared through similar routes.[144,145]

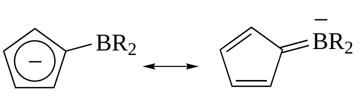

(**67**)

In many cases, deprotonation of the cyclopentadienylboranes is not necessary in order to form transition-metal complexes. For example, a large variety of bis(cyclopentadienyl)aminoboranes Cp$_2$B(NRR$'$) (**68**) and related compounds containing indenyl and fluorenyl groups were reacted directly with group 4 amides to give group 4 *ansa*-metallocene complexes.[146] Moreover, silylated and stannylated cyclopentadienylboranes (**69**) serve as efficient reagents in reactions with transition-metal halides.[147–149]

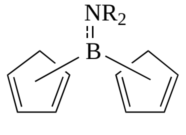

(**68**)

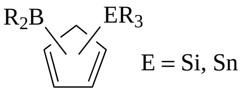

(**69**)

It is interesting to note that boron may also be π-bonded to cyclopentadienyl groups. The decamethylborocenium cation [Cp$^*{}_2$B]$^+$ [AlCl$_4$]$^-$ (**70**) was studied by X-ray crystallography.[150] Compound (**70**) features one η^5-bonded and one η^1-bonded Cp* ring, both of which are essentially planar within the experimental error. The latter is localized and shows a strong bond alternation with average C$_\alpha$–C$_\beta$ and C$_\beta$–C$_\beta$ bond distances of 1.339(5) Å and 1.476(6) Å, respectively. The different geometry in comparison to the ferrocene-like structure of the isovalent decamethylaluminocenium cation (Cp$^*{}_2$Al$^+$) was attributed to the higher electronegativity of boron and a stronger and more covalent B–C versus the Al–C σ-bond. A related η^5-bonded organoboron transition-metal complex (**71**) was obtained from reaction of C$_5$Me$_5$BCl$_2$ with K$_2$[Fe(CO)$_4$].[151]

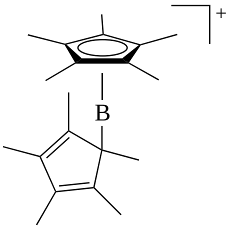

(**70**)

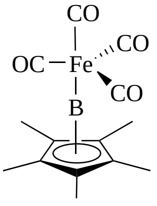

(**71**)

Transition-Metal Complexes of Cyclopentadienylboranes. The rich coordination chemistry of boryl and borate substituted cyclopentadienyl ligands has very recently been reviewed.[69] Group 4 and group 8 complexes have over the years been studied most thoroughly and selected examples of their chemistry and applications will be shown. The interested reader is referred to the review by Aldridge for a more detailed coverage that also includes various complexes of groups 5–7 and group 9.[69]

1. **Group 4 Complexes**. Borylated group 4 complexes have been primarily investigated with regard to their utility as single component olefin polymerization catalysts. The attachment of pendant boryl functionalities was envisioned to obviate the need for external Lewis acid activation (see Section 7.3.3).[152] There are only a few cases of direct borylation of group 4

metallocenes; one example is the reaction of B(C_6F_5)$_3$ with the zirconacycle (**72**) that led to attachment of the boryl group to the Cp ring under formation of a betaine complex (**73**; equation 35).[153] While many other betaines have been reported to form through similar reaction routes, in most cases the borate moiety is not directly attached to the Cp ring.[154–156]

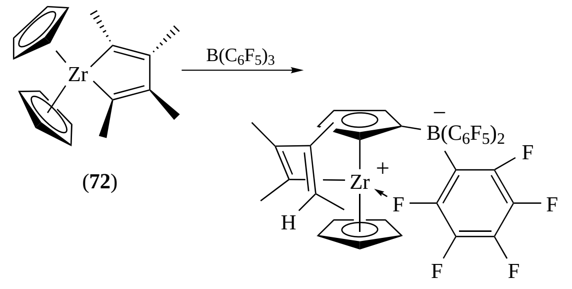

(**72**)

(**73**)

(35)

A more common method for the synthesis of ring-borylated cyclopentadienyl complexes takes advantage of the availability of cyclopentadienylboranes and related ligand precursors described above. This route has been pioneered by Jutzi and Seuferth, who prepared a series of half-sandwich complexes ($C_5H_3RBX_2$)$TiCl_3$ by dehalosilylation of ($C_5H_3RBX_2$)$SiMe_3$ (R=H, Me; X=Cl, Br, OEt, Me). Through similar methods, a number of cyclopentadienyl, indenyl, and fluorenyl complexes containing highly Lewis-acidic B(C_6F_5)$_2$ groups (**74**) as well as compounds with borate moieties (**75**) have been synthesized and studied as 'self-activating' single component olefin polymerization catalysts.[157] Several mono- and diborylated zirconocenes ($R_2BC_5H_4$)(C_5H_5)$ZrCl_2$ and ($R_2BC_5H_4$)$_2ZrCl_2$ (R=Me, Et, OEt, C_6F_5) have also been reported.[158]

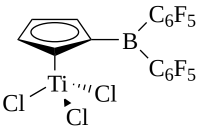

(**74**)

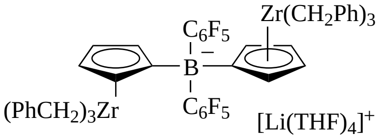

(**75**)

A structurally intriguing alternative design involves the incorporation of the boron center into the bridge of *ansa*-metallocenes.[146,159] First efforts toward this end have been reported independently by Rufanov and Shapiro (Scheme 13).[149,160] Both groups took advantage of the high selectivity of silicon–and tin–zirconium exchange reactions, thus avoiding the need to deprotonate the highly reactive bis(cyclopentadienyl)borane intermediate. Related boron-bridged indenyl complexes have been prepared through similar routes.[148,161] The boron-bridged zirconocene (**76**) has been characterized by NMR spectroscopy, and formation of the Lewis base complex (**77**) that contains a tetracoordinate boron center in the bridge has been confirmed by X-ray crystallography. The donor Me_2S is readily replaced by other ligands such as PMe_3. Moreover, (**77**) may be converted into borato-bridged compounds through treatment with organolithium or organoaluminum reagents.[162,163]

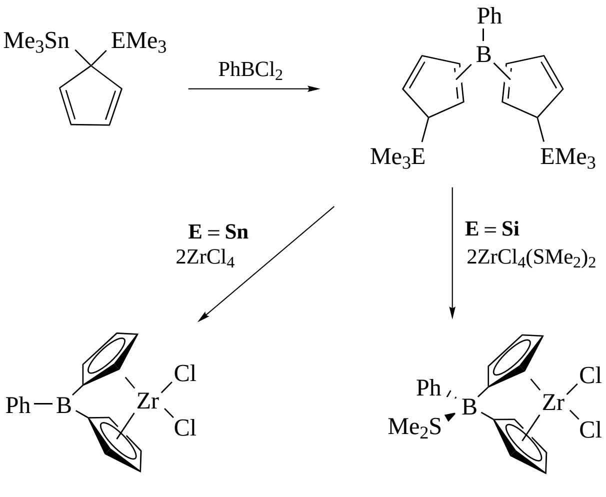

(**76**)

(**77**)

Scheme 13

Boron-bridged titanocene and zirconocene complexes such as (**78**), in which an amino group stabilizes the boron center via boron–nitrogen π bonding are conveniently prepared through a one pot procedure starting from aminodihaloboranes.[146] Intriguingly, this approach also provides facile access to boron-bridged constrained geometry complexes (**79**).[146,164] Finally, the *ansa*-zirconocene (**80**), which operates based on the reversibility of donor–acceptor interactions, adopts a rigid structure in the bridged form, but is flexible in the open-chain form.[165] This type of conformational switch is of much interest for the development of 'smart' Ziegler Natta-type catalysts that produce polyolefins of well-defined architecture.

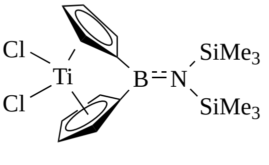

(**78**)

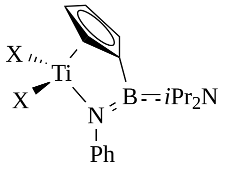

(**79**)

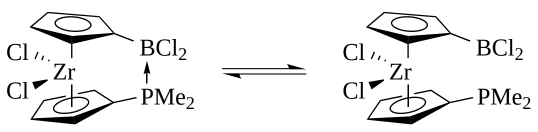

(**80**)

2. **Group 8 Complexes**. Ferrocenylboranes (**81–85**; M=Fe; X=F, Cl, Br, I, Me, Ph, C_6F_5, Mes, Fc, OR, NR_2) are the most thoroughly studied borylated metallocenes. Their synthesis via direct borylation of ferrocene has been extensively investigated since the original discovery by Siebert.[166–169] Depending on the reaction conditions mono-, di-, tri-, and tetraborylated ferrocenes form. The ferrocenyboranes (**81**), (**83**), and (**85**) were readily isolated, while species (**82**) and (**84**) were only spectroscopically confirmed as minor components in the product mixture. Multiborylated ruthenocenes and osmocenes were synthesized through direct borylation, and their structural features were compared with those of ferrocenylboranes.[167,169]

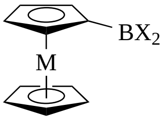

(**81**)

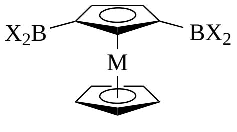

(**82**)

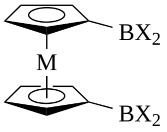

(**83**)

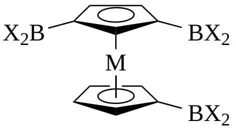

(**84**)

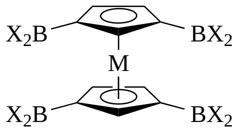

(**85**)

M = Fe
M = Ru
M = Os

Metalated ferrocenes also serve as convenient precursors to ferrocenylboranes. Lithiated ferrocenes have been utilized for the preparation of ferrocenylboronates $FcB(OR)_2$ and 1,1′-$fc(B(OR)_2)_2$ and are especially suitable in the presence of *ortho*-directing donor-substituents.[69] The borylation of disilylated ferrocenes with excess BCl_3 on the other hand was reported to yield varying amounts of 1,3-diborylated product (**82**; M = Fe, X = Cl) in addition to the 1,1′-diborylated species (**83**; M = Fe, X = Cl).[170] In contrast, when 1,1′-distannylated ferrocenes were treated with equimolar amounts of boron halides, 1-stannyl-2-borylferrocenes (**86**) were formed as the major product rather than the expected 1-stannyl-1′-borylferrocenes (Scheme 14).[171] The 1-stannyl-2-borylferrocenes thus obtained underwent further thermal rearrangement to give heteronuclear bidentate Lewis acids (**87**). Interestingly, the boron-bound chloride substituent in (**87**) forms a bridge to the tin center, which consequently adopts an pseudotrigonal bipyramidal geometry as confirmed by X-ray crystallography and multinuclear NMR spectroscopy.

While only trace amounts of 1,1′-disubstituted products were observed in reactions of boron halides with 1,1′-distannylferrocenes, ring-opening addition reactions of boron halides with strained silicon- and tin-bridged [1]ferrocenophanes yielded 1-silyl-1′-boryl- and 1-stannyl-1′-borylferrocenes, respectively, in very high yield and under mild conditions.[30] This ring-opening reaction was exploited for the preparation of diferrocenylboranes (**88**; equation 36) and related multinuclear ferrocenyl assemblies as well as for the incorporation of ferrocenylborane units into polymer structures.

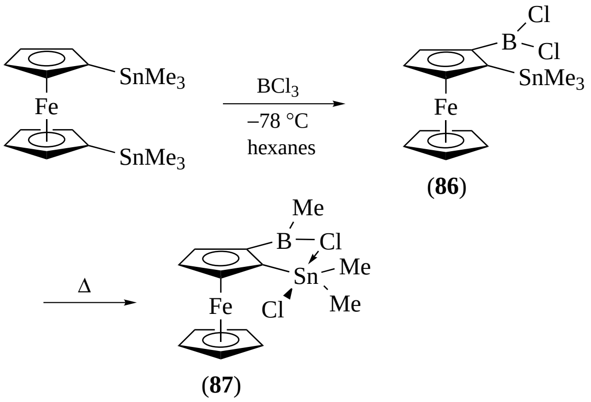

Scheme 14

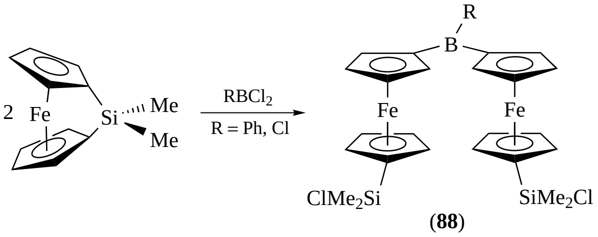

(36)

The structural features and spectroscopic properties of ferrocenylboranes are highly intriguing, especially the interaction of the electron-rich iron atom with strongly Lewis-acidic boron-substituents, which is evident from a tilting of the BX_2 group out of the Cp plane toward the iron center (Figure 2). The bending of the individual boryl groups has been

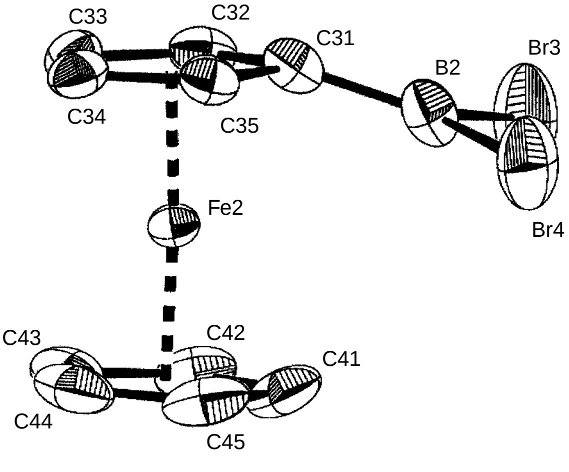

Figure 2 X-ray structure of $FcBBr_2$. (Reprinted with permission from Ref. 172. © 1996 American Chemical Society)

shown by X-ray crystallography to decrease with increasing number of boryl groups.[167,169] Thus, the degree of iron–boron interaction correlates with the number of Lewis-acidic boryl groups attached to the Cp rings; this conclusion was further supported by DFT calculations.[172] The interactions between the metal center and the boryl group increase in the order Fe < Ru < Os.

Piers investigated ferrocenylboranes containing pentafluorophenyl substituents as potential cocatalysts in Ziegler–Natta polymerization.[173,174] The bifunctional borane (**83**) (M = Fe, X = C_6F_5) was found to effect methide abstraction from Cp_2ZrMe_2 under mild conditions. However, significantly reduced polymerization activity was observed with the monoborylated species (**81**) (M = Fe, X = C_6F_5). This effect was rationalized by a stronger degree of interaction with the electron-rich iron center, which lowers the Lewis acidity of the boron center.

Borylated ferrocenes have been exploited by Wagner as building blocks for the assembly of macrocycles and coordination polymers (Scheme 15).[175] Treatment of the diborylated ferrocene 1,1′-fc$(BMe_2)_2$ with the bifunctional aromatic amines pyrazine and 4,4′-bipyridine, respectively, led to spontaneous and reversible formation of (**89**) and related ferrocenylborane polymers.[176,177] The polymeric nature of these materials in the solid state has been confirmed in some cases by single-crystal X-ray crystallography and in others by powder diffraction studies.[178] However, in solution, equilibration and partial dissociation occurs at elevated temperature. Intriguingly, the polymers are intensely colored as a result of charge transfer interactions between the electron-rich iron center and the electron-poor borylated heterocycles.[178] A number of related macrocycles such as (**90**) have been reported.

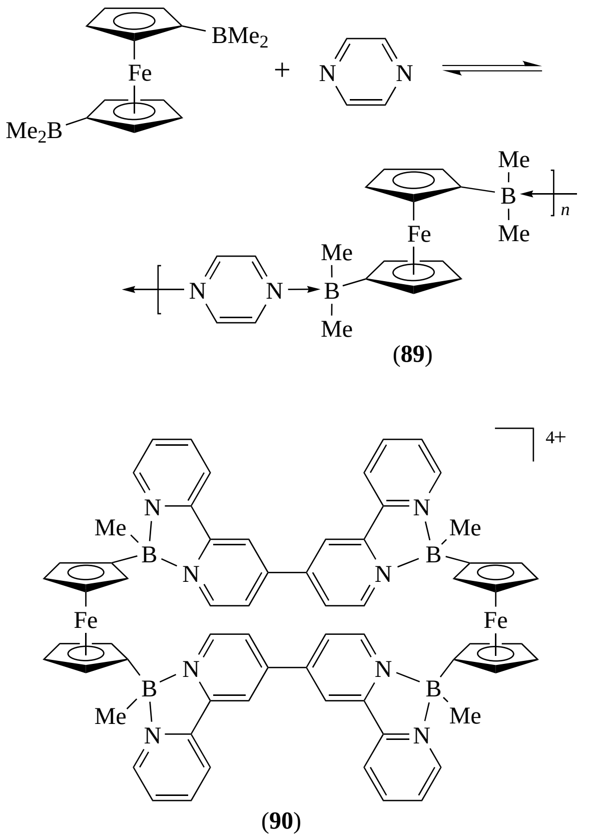

(**89**)

(**90**)

Scheme 15 Coordination polymers and macrocycles from ferrocenylboranes

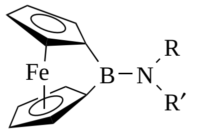

(**91**)

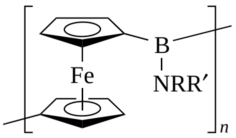

(**92**)

The first boron-bridged [1]ferrocenophane (**91**) was discovered by Manners and Braunschweig.[179,180] This highly strained organoborane shows a tilt-angle between the two Cp rings of 35.2°, the largest reported thus far for a [1]ferrocenophane. As a result of the strain energy, the boracycle (**91**) readily underwent ring-opening reactions, and low–molecular weight polymer accompanied by cyclic oligomers (**92**) ($n = 2{,}3$) formed upon thermolysis at 180–200 °C. The related diborata[1.1]ferrocenophane (**93**) was obtained by Wagner through a different route involving treatment of dilithioferrocene with the diborylated ferrocene 1,1′-$(fcBMe_2)_2$ in the presence of 12-crown-4.[181] The diborate (**93**) tightly binds one lithium counterion in the ferrocenophane cavity. Electrochemical studies suggest that the lithium ion is only released after oxidation of the ferrocenophane.

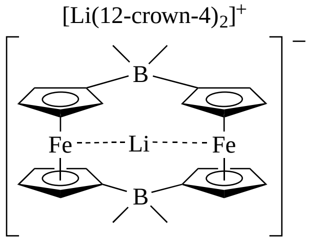

(**93**)

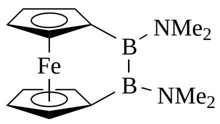

(**94**)

The first dibora[2]ferrocenophane (**94**) was prepared from 1,1′-dilithioferrocene and 1,2-dichlorobis(dimethylamino)diborane. A dynamic process due to motion of the cyclopentadienyl rings between staggered and eclipsed conformations was revealed by low-temperature NMR spectroscopy.[182] A number of 1,3-dibora[3]ferrocenophanes with B–E–B bridges (**95**; E=O, S, Se, Te, NR) were reported.[183] Moreover, Wagner used diborylated ferrocenes for the synthesis of doubly bridged switchable *ansa*-metallocenes (**96**) and (**97**), in which the bridges are created and

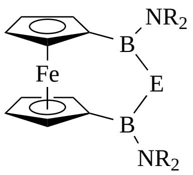

(95)

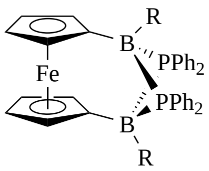

(96)

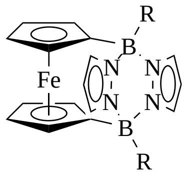

(97)

reopened via reversible formation of donor–acceptor bonds.[184–187]

5.3 Boron Attached to Other Unsaturated Cyclic Compounds

Boron substituents have been attached to a variety of other unsaturated rings; some selected examples are summarized herein. Cyclopropenyliumborates (**99**) and related zwitterionic species were prepared by Erker (Scheme 16).[188] These compounds are believed to form through initial abstraction of an alkynyl ligand from $Cp_2Zr(alkynyl)_2$ followed by insertion of the borate moiety of (**98**) into the remaining Zr–C(alkynyl) bond. Subsequent rearrangement leads to a three-membered ring species that is trapped by nitriles or isonitriles yielding (**99**).

Borylated derivatives of the larger cycles cycloheptatriene, cyclooctatetraene, and cyclononatetraene have been studied with regard to their interesting fluxional behavior and tendency to rearrange to a variety of other cyclic species.[189,190] For instance, cyclononatetraenylborane (**100**) was obtained through reaction of cyclononatetraenyl lithium with Pr_2BCl at −35 °C.[191] A combination of dynamic NMR techniques and *ab initio* calculations showed that [1,3]-dialkylboryl shifts are facile and slightly favored over [1,2]-shifts for (**100**).[190] At 0 °C a number of rearrangement reactions take place leading to various other ring systems (Scheme 17).

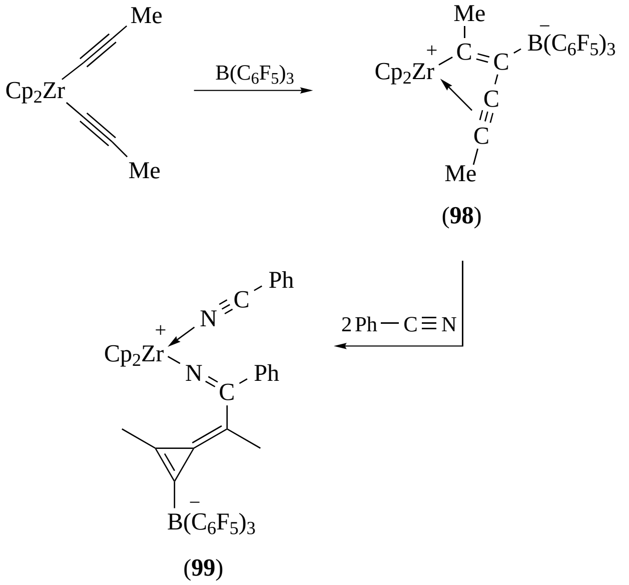

Scheme 16

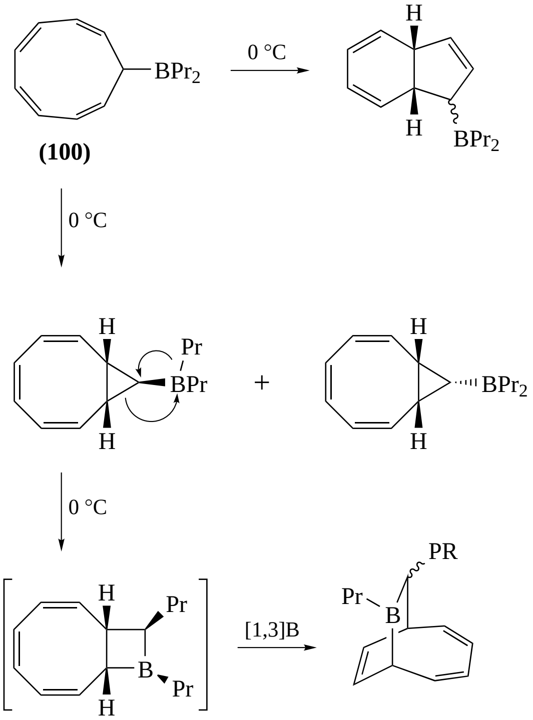

Scheme 17

5.4 Boron Attached to Heterocyclic Arenes

The formation of borylated heterocyclic compounds has attracted much interest with regard to their use as starting materials for cross-coupling reactions, the possible formation of interesting macrocyclic species, and their applications in optoelectronic materials. Several synthetic routes are available for the borylation of the five-membered heterocycles thiophene, furan, pyrrole, and related compounds (**101–103**;

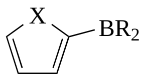

(101)

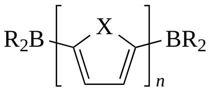

(102)

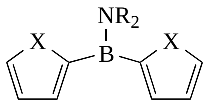

(103)

X = S, O, NR). Lithium–, silicon–, or tin–boron exchange provide facile access to the desired borylated species. On the other hand siloles and stannoles (X = Si, Sn) with organoboron substituents in the 3-position are conveniently prepared via organoboration reactions.[52] Another new approach involves aromatic C–H activation as described in Section 2.3.

If the heterocycle contains a strongly basic site and a Lewis-acidic boryl group is attached, dimerization or oligomerization through donor–acceptor bonding occurs (see also the formation of ferrocene macrocycles described in Section 5.2). Thus, 2-diethylborylpyridine exists as a dimer (**104**), whereas 3-diethylpyridine adopts a tetrameric structure (**105**).[192,193] An isomeric species (**106**), which formally contains a borate anion and a boronium cation center was also reported.[194] Similar isomeric structures were discovered in the case of imidazaboles (**107**) and (**108**).[195,196] Diborylated bipyridine derivatives (**109**; R = NMe_2, 2-thienyl) were also studied. While amino substituents stabilize a monomeric structure through π bonding to boron, the thienyl derivative (**109**; R=Th) is believed to adopt an oligomeric structure.[197]

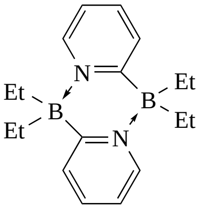

(**104**)

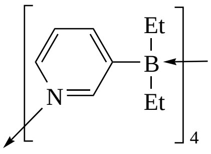

(**105**)

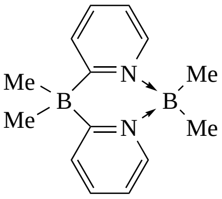

(**106**)

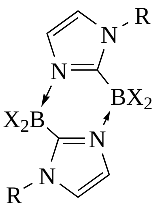

X = H,F,Cl,Me,Et

(**107**)

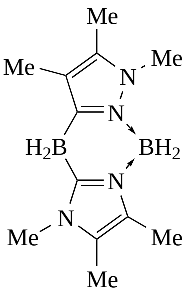

(**108**)

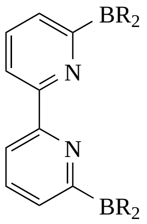

R = NMe_2, Th

(**109**)

Corriu, Douglas, and Siebert reported the synthesis and structure of the tetraboratetrathiaporphyrinogens (**110**)[198,199] and of a number of related diboraporphyrinogens.[200] The macrocycles were obtained in good yield by treatment of dilithiated dithienylboranes with haloboranes Cl_2BNR_2 (Scheme 18). Signs of ring delocalization were not observed for (**110**) since the boron atoms are stabilized by π interaction with the amino groups. The macrocycle is thus colorless and the ring system is nonplanar as shown by X-ray crystallography. A number of other macrocycles in which the boron–carbon bonds are not an integral part of the cyclic structure were reported.[201]

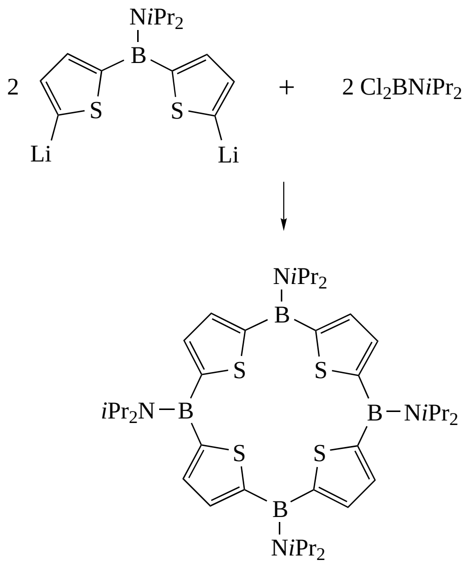

(**110**)

Scheme 18

6 BORON AS PART OF UNSATURATED ORGANIC RINGS

The incorporation of boron into unsaturated rings has attracted much attention. Five-membered boroles (**114**) and six-membered boratabenzenes (**115**) are among the most prominent and most thoroughly studied systems containing one boron atom as part of the ring.[102,103] Related benzannulated systems such as borafluorene and boraanthracene have also been thoroughly investigated. Other fairly common organoboron rings of smaller and larger ring sizes are the borirenes (**111**), the boracyclobutenes (**112**), the boracyclopentenes (**113**), and the seven-membered borepin rings (**116**). Especially intriguing is the question of whether significant interactions exist between boron and the organic π-systems. The presence of such π-overlap in turn has implications on the aromatic or antiaromatic nature of these species.[120]

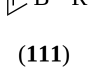

(**111**)

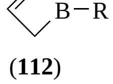

(**112**)

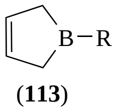

(**113**)

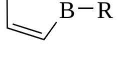

(**114**)

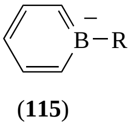

(**115**)

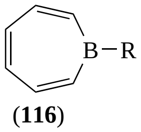

(**116**)

Among organoboron rings with multiple boron centers the five-membered (**117**) and six-membered diboracycles (**118** and **119**) and related benzannulated compounds are commonly studied systems, and a variety of other di- and triboracycles have also been developed.[102] These unsaturated rings have been investigated extensively as ligands to transition metals, which has led for example to the development of various multidecker sandwich complexes.[101,103] Many other cyclic organoboranes containing additional heteroatoms other than boron and carbon (i.e. N, O, S, etc.) and systems with B−B bonds are also known, but will not be covered here. In the following sections some recent developments in the chemistry and applications of borole (**114**), boratabenzene (**115**), and borepin (**116**) species will be highlighted.

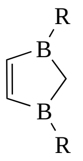

(**117**)

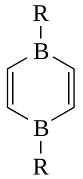

(**118**)

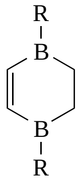

(**119**)

6.1 Boroles and Related Five-membered Boracycles

While the chemistry of borole complexes is well established, free 1*H*-boroles are highly reactive 4-π-electron systems and only a few sterically protected and benzannulated derivatives have been isolated.[102,103,120] The perphenylated species C_4Ph_4BPh is conveniently prepared from the stannacycle $C_4Ph_4SnMe_2$ and $PhBCl_2$. Preparation of the borole C_4Me_4BPh with the smaller methyl substituents attached to the ring was attempted through reaction of the zirconacycle $C_4Me_4ZrCp_2$ with $PhBCl_2$. However, the Diels−Alder dimer (**121**) rather than the borole (**120**) was obtained.[120] Diels−Alder reactions of boroles with olefins and acetylenes are very common. The high reactivity for Diels−Alder chemistry is attributed to a relatively high-energy HOMO and low-energy LUMO for the borole ring. Borole-amine adducts are more stable and may even be obtained through degradation of certain borole transition-metal complexes.[103] The unusual electronic structure of boroles has been studied theoretically.[202]

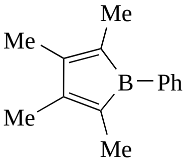

(**120**)

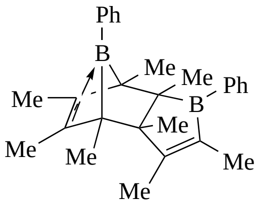

(**121**)

Although 9-borafluorenes may be regarded as benzannulated borole derivatives, their chemistry and physical properties are quite different from those of C_4Ph_4BPh. A convenient route to 9-borafluorenes involves reaction of 2,2′-dimercurated biphenyl with boron halides.[102] The sterically encumbered 9-borafluorene (**122**; Ar = 4-*t*-BuC_6H_4) was recently synthesized by reaction of 2,6-(4-*t*-$BuC_6H_4)_2C_6H_3Li$ with the borane source $H_2BCl(Me_2S)$.[203,204] This borafluorene shows bright yellow luminescence, but addition of pyridine leads to quenching of the fluorescence.[203] In contrast, the tetraphenylborole is blue-colored with $\lambda_{max} = 570$ nm and forms a light yellow pyridine complex.[120] The pyridine complex of (**122**) was studied by single-crystal X-ray crystallography. A long boron−nitrogen distance of 1.638(4) Å in comparison to other organoboron−pyridine complexes suggests formation of a weak adduct. Indeed, the colorless complex partially dissociates in hydrocarbon solvents to give bright yellow fluorescent solutions. Yamaguchi and Tamao exploited the luminescent behavior of 9-borafluorenes for the design of a fluorescent fluoride sensor.[205] A perfluorinated analog has been studied as an activator for olefin polymerization.[206]

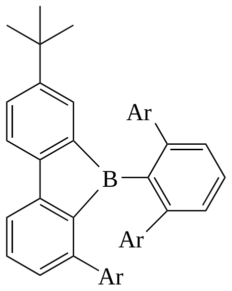

(**122**)

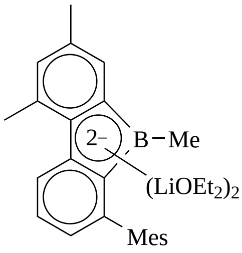

(**123**)

The 9-Borafluorenide dianion (**123**) was obtained upon reduction of the bulky borane 2,6-$Mes_2C_6H_3BX_2$.[207] Formation of the borole ring is believed to occur via initial formation of a monovalent boranediyl species 2,6-$Mes_2C_6H_3B$ that subsequently undergoes an intramolecular insertion into one of the C–C bonds in *ortho*-position of the phenyl group. A similar 9-boratafluorene was generated by reduction of (**122**) with lithium powder.[203,204]

2,5-Dihydro-1*H*-boroles (3-borolenes) serve commonly as precursors to borole complexes.[103,208] The 2,5-dihydro-1*H*-boroles either display a classical structure with a planar ring (**124**) or adopt a nonclassical structure with a folded ring skeleton and an interaction between the empty p_z orbital at boron and the π orbital of the olefinic double bond (**125**). Theoretical calculations on the parent compound C_4H_6BH show that the two structures are very close in energy with a difference of less than 1 kcal mol^{-1}.[209] Generally π-donor substituents such as amino and phenyl groups on boron stabilize the classical structure.[210] 2-Boraindans (**126**) and a number of other bicyclic systems have been reported.[211]

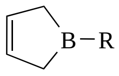

(124)

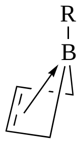

(125)

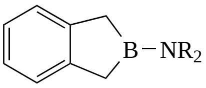

(126)

Treatment of 3-borolenes or 2-boraindans with bulky lithium amides yields the dilithiated aromatic borolide dianions, which are applicable as ligand precursors for transition-metal complexes. Many borole complexes including a number of unusual multidecker sandwich complexes and mixed-metal clusters have been described.[102,103,212] An unexpected new entry into the synthesis of borole complexes has been recently discovered. Bochmann found that attack of $B(C_6F_5)_3$ at a zirconium bound diene leads to a pentafluorophenylborole complex through successive C–H activation steps.[213]

6.2 Borabenzene and Boratabenzene Complexes

Boratabenzenes represent a second important class of unsaturated boracycles.[214] While the dicoordinate borabenzene itself has not yet been reported, many Lewis base adducts, boratabenzene salts, and metal complexes are known. Boratabenzenes are six π-electron aromatic anions that resemble cyclopentadienides. For example, N,N-diisopropyl-1-amino-boracyclohexadiene shows an acidity in DMSO which is similar to that of cyclopentadiene.[215] The chemistry of boratabenzene ligands dates back to work by Herberich and Ashe in the early 1970s, which has been reviewed.[102,103] However, many new achievements have been reported over the last decade and will be discussed in the following sections.

Fu recently developed a convenient general access to borabenzene adducts and boratabenzene ligands that is based on a combination of earlier work by Ashe and Paetzold (Scheme 19).[216,217] Hydrostannation of the commercially available 1-trimethylsilyl-1,4-pentadiyne followed by treatment of stannacycle (**127**) with BCl_3 selectively gives (**128**). This silylated boracycle reacts with any of a variety of Lewis bases L to produce neutral borabenzene-ligand adducts (**129**). Amines, phosphines, isonitriles, and even stable carbenes such as 1,2,3,5-tetramethylimidazol-2-ylidene readily form adducts with borabenzene derivatives.[218] The trimethylphosphine complex (**129**; $L = PMe_3$) serves as a convenient storage form. Subsequent nucleophilic displacement of the Lewis base PMe_3 provides access to a variety of boratabenzene species (**130**) including the parent compound 1-H-boratabenzene (**130**; $R = H$), which is isoelectronic to benzene.[216]

New convenient routes to aminoboratabenzenes from 1,3-pentadienes were developed by Herberich. Ring-closure of [bis(dialkylaminoboryl)]pentadienes (**131**) was accomplished with lithium amides, thereby generating the aminoboratabenzene (**132**) (Scheme 19).[27] Another route from dipotassium salts was also reported.[219] Thus a large number of borabenzene adducts and boratabenzene complexes including annulated boratanaphthalenes and borataanthracenes are readily available now.[214]

The borabenzene adducts themselves have attracted attention as heterocyclic conjugated π-systems that are isoelectronic to organic systems with extended delocalization. The first compound of this type, the borabenzene–pyridine complex (**133**), has already been reported in the 1980s. More recently, the terphenyl analog (**134**) and several other interesting adducts have been prepared.[220,221] Moreover, the intriguing diborabiphenyl complexes (**135**) and (**136**), which are isoelectronic to triphenylene and dibenzo[g,p]chrysene, have been studied by Piers.[222,223] Adducts (**135**) and (**136**) are intensely colored as a result of strong charge transfer bands and show two reversible reduction events according to cyclic voltammetry studies.

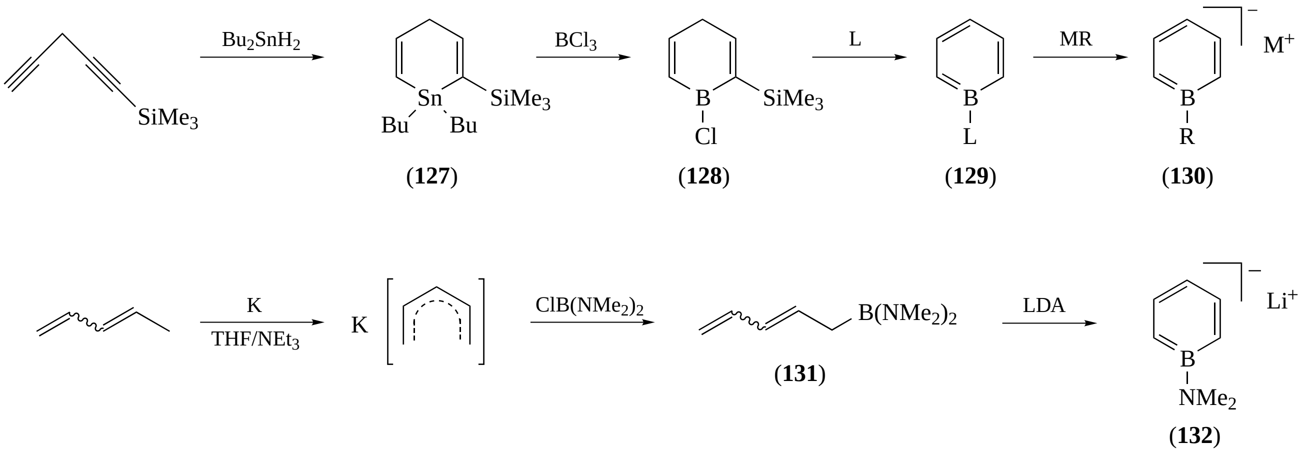

Scheme 19

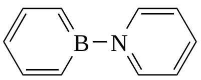

(133)

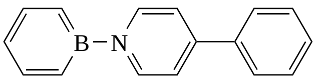

(134)

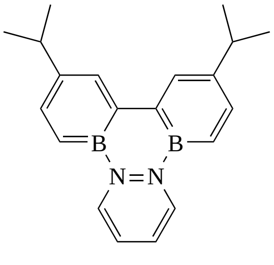

(135)

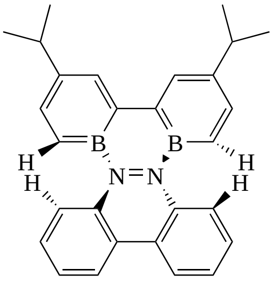

(136)

First examples of chiral boratabenzene complexes, which are of interest owing to potential applications as enantioselective catalysts, have recently been reported. The planar chiral chromium tricarbonyl complex (**137**) was obtained by adduct formation between borabenzene and an (S)-valinol-derived oxazoline ligand.[224] The $Cr(CO)_3$ fragment stereoselectively complexes with this borabenzene adduct. A different approach has been chosen by Herberich, who developed the chiral boratabenzene ligand (**138**), which is derived from α-pinene.[225,226]

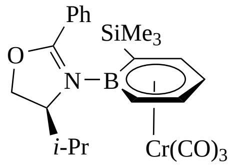

(137)

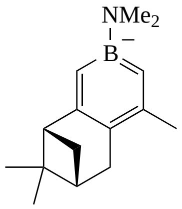

(138)

Several main group derivatives of boratabenzene have been synthesized through reaction of boratabenzene salts with the appropriate metal halides.[214] For example, treatment of $[C_5H_5BMe]Li$ with group 14 electrophiles Me_3EX (E = Si, Ge, Sn, Pb) led to η^1-bonded compounds (**139**) that are fluxional in solution. In contrast, reaction with divalent group 14 halides ECl_2 led to bent-sandwich structures such as the η^6-bonded complex (**140**).[227]

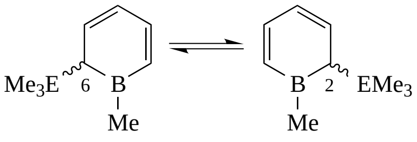

E = Si, Ge, Sn, Pb

(139)

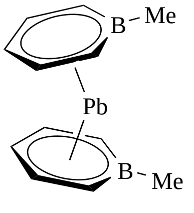

(140)

A large number of boratabenzene transition-metal complexes have been described. For instance, the multinuclear complex (**141**) has been obtained through the original Herberich route from cobaltocene with $FcBBr_2$ (equation 37).[228] Notably, a rhodium complex has recently been reported to be useful in C–H activation catalysis.[229]

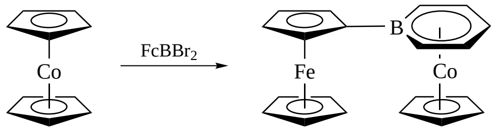

(37)

(141)

Strong interest in potential applications in olefin polymerization has led to a vigorous research effort aimed at the development of group 4 boratabenzene complexes.[214,230] The synthesis of the first group 4 complex, the bis(diisopropylaminoboratabenzene)zirconium dichloride (**142**; R = N*i*Pr_2), was reported by Bazan.[231] Complex (**142**) (R = NMe_2) was activated with methylaluminoxane (MAO) to produce ethylene polymerization catalysts with activities similar to those of Group 4 metallocenes. Interestingly, under similar conditions (**142**) (R = Ph) yielded predominantly 2-alkyl-1-alkenes,[232] while (**142**) (R = OEt) gave exclusively 1-alkenes.[233] The different behavior was related to a difference in the coordination chemistry of the ligands. Indeed, in the presence of amino groups η^5-coordination was observed by X-ray crystallography, while a η^6-bonding mode was found with boron substituents that do not act as π-donors to boron. The electronic nature of the boratabenzene ligand and the interaction of boron and zirconium thus critically influence the catalytic properties of these complexes.

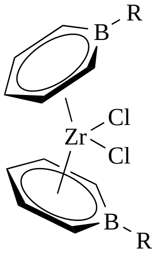

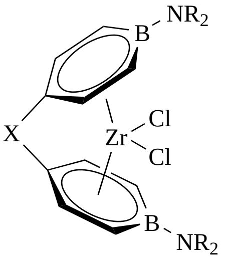

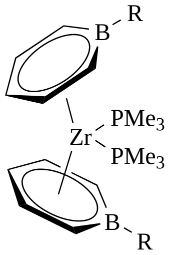

X = $-SiMe_2-$, $-CH_2CH_2-$

(142) **(143)** **(144)**

A variety of *ansa*-bridged complexes such as (**143**) resembling those of *ansa*-zirconocenes have also been reported.[234] Moreover, reduction of the zirconium complexes with *n*-BuLi in the presence of PMe_3 provides an entry point to Zr(II) complexes (**144**); their reactivity toward alkynes has been studied in detail.[235]

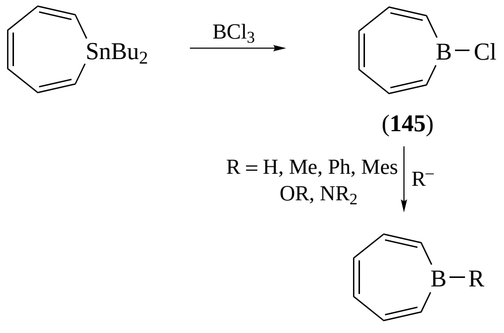

Scheme 20

6.3 Borepins

Although ring-annulated and highly substituted borepins have been known for some time, simple 1-substituted borepins have only been thoroughly studied over the past decade. The discovery of a facile synthetic route to 1-substituted borepins through tin−boron exchange has much opened up the chemistry of these 7-membered boracycles.[236] The chloro-substituted borepin (**145**) serves as a highly useful precursor to many other borepin derivatives via substitution reactions with nucleophiles (Scheme 20). In addition, several transition metal complexes of 1-borepins have been reported.[237]

Of particular interest is the degree of aromatic delocalization within these ring systems. It has been shown that significant delocalization occurs in the presence of halide and alkyl substituents on boron. Consequently, the 1-chloroborepin derivative (**145**) is perfectly planar as shown by X-ray crystallography. However, theoretical calculations demonstrate borepin to be much less aromatic than the isoelectronic tropylium ion.[238] Moreover, amino groups effectively compete with the 6p electron delocalization within the ring by forming a partial BN double bond. The barrier to rotation about the B–N bond of 1-(N-benzyl-N-methylamino)borepin was determined by NMR spectroscopy to be 18 kcal mol^{-1}.[239] DFT calculations suggest that steric hindrance in substituted borepins and attenuated aromatic character result in significant nonplanarity of the seven-membered ring.[240]

7 SELECTED APPLICATIONS OF ORGANOBORANES

7.1 Organoboranes as Optical, Electronic and Device Materials

With its vacant p_z orbital, three-coordinate boron is inherently electron-deficient and acts as a strong π-acceptor.[241] In contrast to other strong π-acceptors such as the nitro group, however, three-coordinate boron is not generally inductively electron withdrawing. Importantly, it is the interaction between the vacant p_z orbital on boron and organic π systems that gives rise to conjugation and a certain degree of delocalization,[120] resulting in interesting linear and nonlinear optical properties of organoboranes (*see* ***Luminescence***).[111,241,242] The electro-optical properties and the rich (and in many cases reversible) reduction chemistry of organoboranes are exploited in applications as emission and electron conduction layers in devices such as organic light-emitting diodes (OLEDs).

The reduction of Ph_3B is known to result in a radical anion $Ph_3B\cdot$ that is in equilibrium with the dimeric species $[Ph_3B{-}BPh_3]^{2-}$. However, if bulky substituents as in Mes_3B are present and thus prevent attack of nucleophiles or dimerization, a blue-colored stable radical anion can readily be identified. While arylboranes are also known to form purple-colored dianions, the second reduction of simple triarylboranes is typically irreversible. In a recent study, Okada and Oda reported the formation of purple-colored solutions of dimesitylphenylborane dianions $[Mes_2BAr]^{2-}$ (**146**; Ar = Ph, 4-$Me_3SiC_6H_4$, biphenyl) upon extended reaction of Mes_2BAr with Na–K alloy in THF (Scheme 21). Formation of dianions was confirmed by multinuclear NMR spectroscopy.[243] While the bulky mesityl groups provide chemical stability to the dianions and thus prevent further chemical reactions, the presence of the unsubstituted phenyl group is believed to allow for effective π-interactions with the p-orbital on boron.

Norton recently showed that the perfluorinated analog $B(C_6F_5)_3$ is rapidly reduced with an equimolar amount of $Cp^*{}_2Co$ in THF solution at −50 °C to give a dark blue solution attributed to the radical anion $B(C_6F_5)_3{}^{\bullet-}$ ($\lambda_{max} = 603$ nm).[244] The radical anion has been detected by EPR spectroscopy, but decomposes at room temperature with a half-life of only about 10 min. The borate salt $[Cp^*{}_2Co]^+$ $[B(C_6F_5)_4]^-$ was identified as one of the decomposition products.

A family of amorphous molecular materials with divergently extended π-conjugation (**147**) was reported by Yamaguchi and Tamao.[25,245] Compounds (**147**) form stable amorphous glasses with high glass-transition temperatures, and are characterized by reversible cathodic reduction and relatively large HOMO−LUMO energy gaps. High-performance blue- and blue-violet-emitting organic electroluminescent

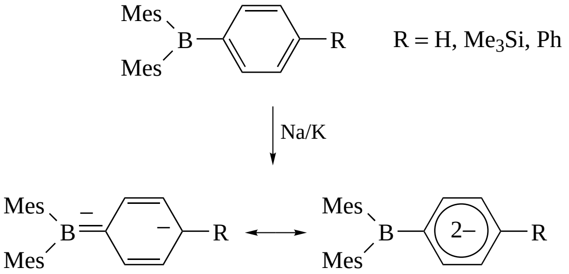

Scheme 21

devices were developed using the boranes as hole blockers and various arylamines as emitters.[246]

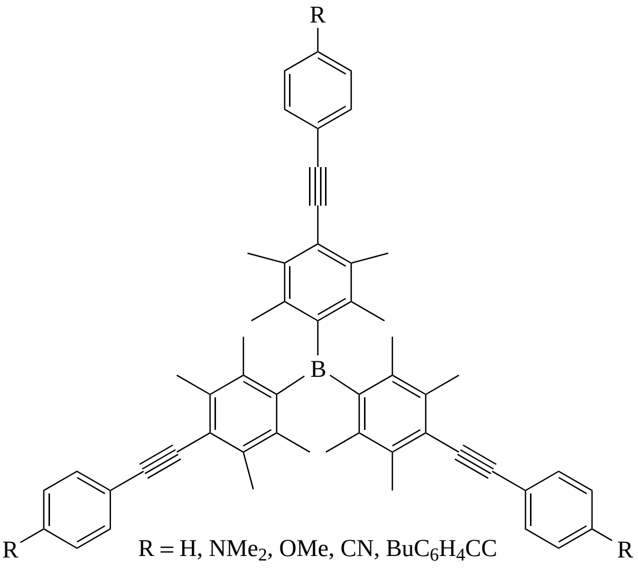

R = H, NMe_2, OMe, CN, BuC_6H_4CC

(**147**)

Kaim reported on the UV/vis/near-IR spectroelectrochemistry of radical anions and dianions formed from bisborylated benzene (**148**) and biphenyl (**149**) (Scheme 22).[130] The negatively charged species exhibit intense long-wavelength absorptions in the visible or near-infrared region resembling the spectral features of the analogous isoelectronic triarylamine radical cations. The quinoidal resonance structures play an important role in the reduced species as confirmed by *ab initio* calculations.

Okada and Oda studied the electrochemical properties of the *meta*-substituted derivative 1,3-bis(dimesitylboryl)benzene (**150**) and the trifunctional species 1,3,5-tris(dimesitylboryl)benzene ($1,3,5\text{-}C_6H_3(BMes_2)_3$; (**151**)).[124] Interestingly, cyclic voltammetry in DMF (*N*,*N*-dimethylformamide) revealed a significantly more anodic reduction potential for (**150**) ($E_1 = -1.95$ V vs. SCE) and (**151**) ($E_1 = -1.98$ V vs. standard calomel electrode (SCE)) relative to that reported by Kaim for the reduction of the *para*-substituted isomer (**148**) with $E_1 = -1.55$ V and $E_2 = -2.25$ V versus SCE. Rajca further studied the electrochemical and preparative reduction of (**150**) (equation 38).[247] Cyclic voltammetry in THF indicated two reversible reduction waves at peak potentials $E_p = -2.02$ V and $E_p = -2.64$ V. By comparison with monofunctional arylboranes, the more anodic peak was attributed to formation of dianionic species. Preparative reduction with sodium metal in THF/2-MeTHF yielded the triplet diradical species (**152**) according to ESR spectroscopy results.

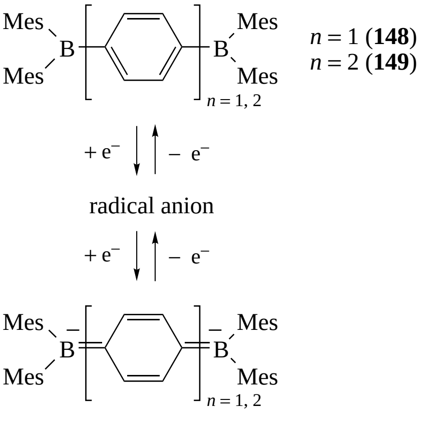

Scheme 22

Reduction of the diborylated naphthalene derivative (**52**) was studied by Gabbaï, who found a reversible reduction wave at −1.81 V (vs. SCE) by cyclic voltammetry. Moreover, treatment of (**52**) with potassium in THF in the presence of 18-crown-6 led to formation of a dark purple EPR-active solution, the spectrum of which suggested coupling of the electron spin of the free radical with two boron centers (equation 39). The presence of an intramolecular one-electron σ-bond in (**153**) leads to a significant shortening of the boron–boron distance as suggested by DFT calculations.[248]

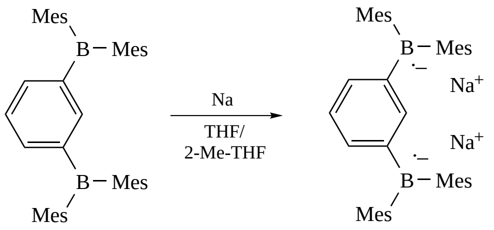

(38)

(**150**) (**152**)

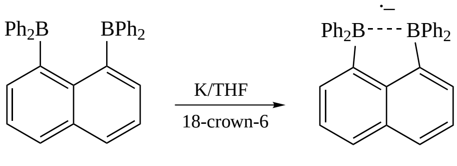

(39)

(**52**) (**153**)

If oligothiophenes are used as the bridge between two $BMes_2$ units, amorphous luminescent materials (**154**) ($n = 2$) and (**155**) ($n = 3$) with relatively high glass-transition temperatures are obtained. Both compounds undergo two sequential reversible cathodic reductions, generating the radical anion and dianion species. The oligothiophene derivatives function not only as excellent electron-transporting materials but also as efficient blue emitters with the most intense fluorescence band at 440 and 488 nm for (**154**) and (**155**), respectively.[26,242] The bithiophene derivative (**154**) has been successfully incorporated as a blue emitter into an organic light-emitting device.[249]

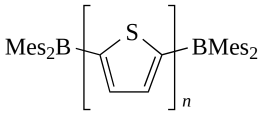

$n = 2$ (**154**)
$n = 3$ (**155**)

Bazan reported the synthesis, structure, and photophysical behavior of a number of boratastilbene derivatives, which are highly emissive in the presence of donor solvents or when crown ethers are added.[250] Extended conjugation in the bifunctional species (**156**) results in an absorption maximum at 396 nm, which is red-shifted by 55 nm relative to that of the monofunctional boratastilbene. The change in the absorption and emission spectra upon addition of dibenzo-18-crown-6 suggests a distinct effect of the counterions and of aggregation phenomena on the photophysical properties of these species.

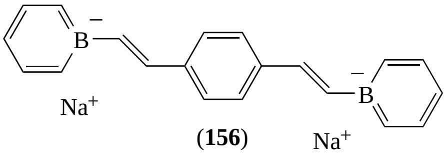

(**156**)

A series of multifunctional anthrylboranes with up to six boron centers and divergently extended π-conjugation have been reported. Trianthrylborane itself is bright orange, whereas the extended system (**157**) is dark red colored.[25] This bathochromic shift was attributed to the more extended delocalization in the starbust oligomer (**157**). Two reversible reduction waves were found for the two different boron environments in (**157**). The anthrylboranes have also been studied as fluorescent fluoride sensors (see Section 7.2.1).

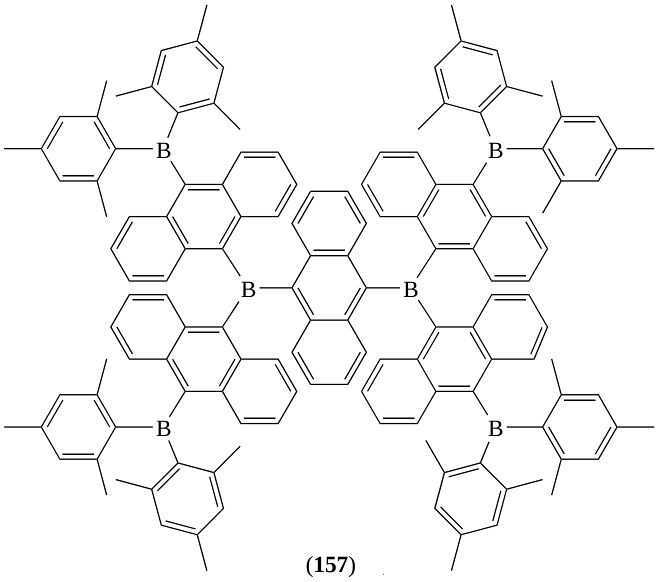

(**157**)

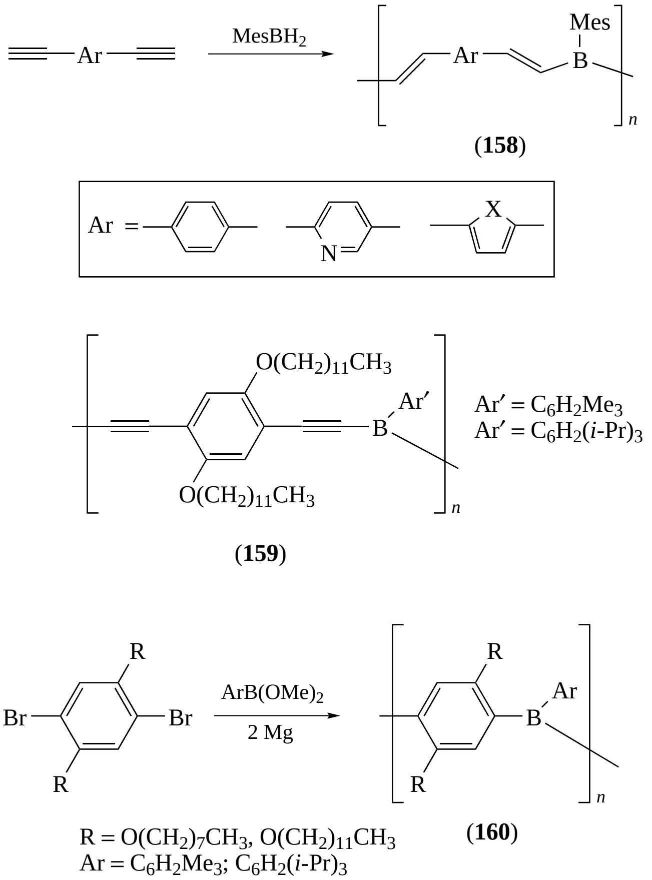

Scheme 23

In an elegant synthetic approach, Chujo used the hydroboration of bifunctional alkynes with boranes RBH_2 ($R = 2,4,6$-trimethylphenyl, Mes) for the synthesis of conjugated organoboron polymers (**158**), that are related to poly-p-phenylene vinylene (PPV) (Scheme 23).[251] Bulky mesityl or tripyl groups on boron prevent attack of nucleophiles on boron and thus provide good stability of these polymers. Interest in the incorporation of boron into the main chain of conjugated organic polymers is based on the expectation that extended delocalization may be observed in a polymer consisting of electron-deficient boron centers alternating with an organic π-system. Despite having relatively low molecular weight, the polymers are highly luminescent with especially large Stokes shifts for heteroaromatic polymers. An unusually large third-order nonlinear optical susceptibility was also observed. Moreover, recent electrical conductivity measurements on polymers with tripyl groups attached to boron and phenylene (or fluorenylene) bridges showed an increase in conductivity upon doping with triethylamine or iodine from less than 10^{-10} to ca. $10^{-8} - 10^{-6}\,\mathrm{S\,cm^{-1}}$.[252] Many other vinyl, alkynyl, and arylborane polymers, all of which show strong fluorescence, have been synthesized. For example, the polycondensation of lithiated diacetylenes with aryldimethoxyboranes was used to produce poly(ethynylene-phenylene-ethynylene-borane)s (**159**).[253] The fluorescent poly(p-phenyleneborane) polymers (**160**) were obtained via polycondensation of aryldimethoxyboranes with a difunctional Grignard reagent that was prepared in situ.[254] Polymers (**160**) with molecular weights M_n of ca. 2000 to 3000 were obtained in high yields. The polymers show absorption maxima in the range of 359 to 367 nm and emit blue–green light upon excitation at 350 nm.

A computational study (DFT, modified B3P86 hybrid functional) on the electronic structure of polyborole (**161**) in comparison to polycyclopentadiene and related polymers containing N, O, Si, S, Se, Te, and P has been performed by Lagowski.[255] Polymer (**161**) was found to differ significantly from the other polymers in that it adopts a quinoid structure and shows a large electron affinity. Intriguingly, (**161**) was predicted to have a very small or no energy band gap, and thus exhibit metallic properties. Similar electronic properties were also predicted for poly(p-2,6-diboraphenylene).[256]

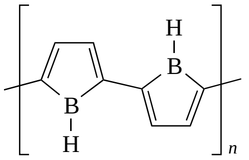

$n = 1,2,3$

(**161**)

Donor-bridge-acceptor systems (also called *push–pull* systems), in which a dimesitylboryl group acts as the acceptor that is separated from a donor group such as an amine, a phosphine, a ferrocene moiety, or other electron-rich groups through a π-conjugated bridge were studied with regard to their linear and nonlinear optical properties.[111] Some recent examples are shown in Figure 3. The fluorescence quantum yield in the *push–pull* systems (**162**) generally increases with increasing donating power of the group D. While typically only small shifts in the absorption spectra of (**162**) are observed as a function of solvent polarity (solvatochromism), a large dependence of the emission wavelength on the solvent polarity was found and attributed to a highly polar excited state. Highly efficient two-photon excited fluorescence (TPEF) was reported recently for the stilbene and styrylthiophene derivatives (**163**) and (**164**).[257]

The nonlinear optical properties of *push–pull* systems were shown to strongly depend on the nature of the bridge and the type of donor group. The first molecular hyperpolarizabilities (β) typically increase with increasing donor strength of D and increasing length of the bridge.[111] The hyperpolarizabilities were found to be significantly larger for the dithienyl-bridged species (**166**) than for related biphenyl systems (**165**).[258] This effect was attributed to stronger conjugation through the bithiophene bridge as a result of the greater planarity of the less sterically hindered conjugated system.

The thienylenephenylene-bridged species (**167**) was found to act as a bipolar radical formant that (1) allows formation of both stable cation and anion radicals, (2) shows intense fluorescent characteristics, and (3) has the capability to form stable amorphous glasses with high glass-transition temperature (T_g) and uniform thin films by vacuum deposition.[259] Compounds (**167**) were shown to function as excellent emitting materials for OLEDs. A related triarylamine with three dimesitylboryl groups was studied as a component of a photovoltaic cell.[260]

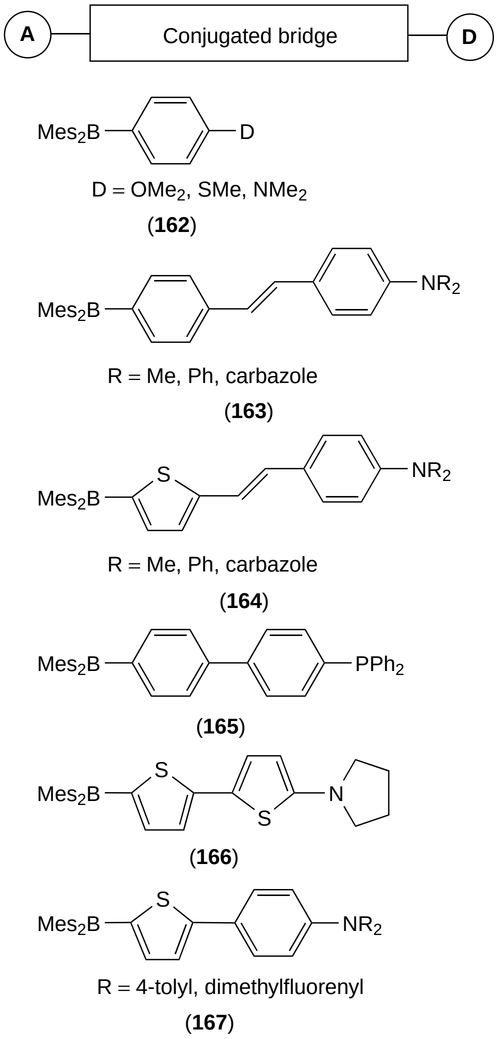

Figure 3 Selected recent examples of organoboron *push–pull* systems

Tetracoordinate Boron. A number of tetracoordinate organoboron species that are photo- and electroluminescent, and thus of interest for device applications have been developed.[261,262] Characteristic of complexes (**168–170**) is the presence of chelating nitrogen ligands such as 8-hydroxyquinoline in (**168**). The quinolate complexes (**168**) were reported to show superior stability over more commonly used aluminum complexes.[261] Moreover, their photophysical properties were shown to be tunable through ligand variation.[263]

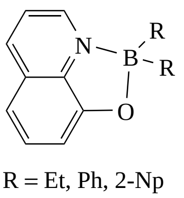

(168)

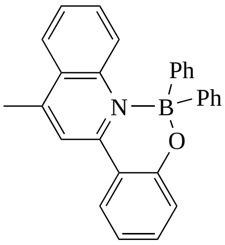

(169)

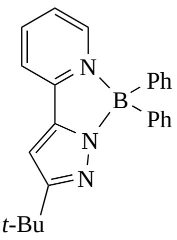

(170)

7.2 Organoboranes in Molecular Recognition

Boronic acids $RB(OH)_2$, boronic esters $RB(OR)_2$, and triorganoboranes R_3B have been studied extensively for the selective recognition of anions.[264–266] Moreover, arylboronic acids have proven highly useful for sensing of saccharides based on the facile formation of esters with diols,[267,268] thus providing an excellent alternative to more commonly employed synthetic molecular receptors based on hydrogen-bonding interactions.[267,268] Absorption and fluorescence spectroscopy, circular dichroism, and cyclic voltammetry have all been successfully used as detection methods for organoboron sensors.

7.2.1 Anion Binding

Boronic Acids and Boronate Esters. Ferrocenylboronic acid (**171**) has been studied as an electrochemical sensor for the recognition of anions. The compound shows excellent selectivity for fluoride over other anions with binding constants that are ca. 1000 times higher than for chloride and bromide.[269] Coordination of fluoride to the boron center results in an increase in electron density on ferrocene thereby facilitating oxidation of the iron center. Oxidation of ferrocene in turn leads to stabilization of the fluoride complex due to a decrease in electron density on the Lewis-acidic boron center. Coupling of this redox process with a dye allows for visual sensing of fluoride ions.[270] A similar effect has been reported for the related ferrocenyldiboronic ester (**172**), which in the presence of air is readily oxidized to a greenish colored ferrocenium species upon binding of fluoride. Thus, a direct optical method for fluoride detection based on the ferrocene/ferrocenium redox couple has been developed.[271] Simple aromatic boronic acids such as (**173**) on the other hand may serve as fluorescent PET (photoinduced electron transfer) sensors; the degree of fluorescence quenching in aqueous solution at pH 5.5 was shown to correspond to the amount of fluoride present.[272]

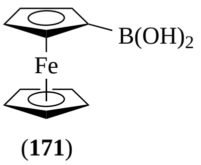

(171)

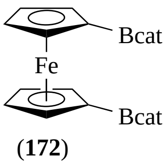

(172)

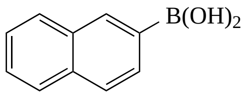

(173)

Using a different approach, the research groups of Fabre and Freund have synthesized boronate-functionalized conjugated polymers, which serve as electrochemical sensors. For example, a conjugated redox-active film of polypyrrole (**174**) was electrodeposited onto a platinum electrode from acetonitrile solution.[273] Addition of fluoride anions led to a new redox system that showed an anodic shift relative to polypyrrole itself, which was attributed to fluoride binding to the boronate group. A related poly(aniline boronic acid) (**175**) was also reported and studied for saccharide detection.[274]

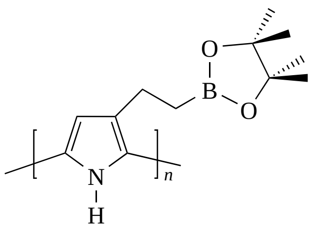

(174)

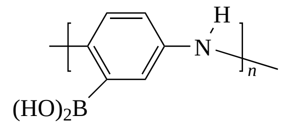

(175)

Triorganoboranes. As outlined above, overlap between the empty p-orbital on boron and an extended organic π-system can be exploited for the design and synthesis of photoluminescent organoboron materials. Interestingly, the coordination of a nucleophile to the boron center in such a system would be expected to lead to either quenching of the luminescence or a change in the fluorescence wavelength if the organic π-system is fluorescent itself.[242] This strategy is illustrated schematically in Figure 4 and has been extensively used by Yamaguchi and Tamao for the design of new fluorescent fluoride sensors based on triarylboranes such as anthrylboranes and 9-borafluorenes (**176**).[25,275]

An interesting example of an organoboron fluorescent sensor with metal binding sites has recently been reported by Wang.[276] The blue luminescent compounds (**177**) consist of three bipyridyl binding sites that are connected to one central three-coordinate arylborane via oligophenylene spacers. Binding of Zn(II) ions to these air-stable polypyridyl assemblies results in a slight red-shift of the emission maximum.

The suitability of conjugated main chain organoboron polymers for fluoride recognition was also investigated. Treatment of the organoboron polymer (**158**) (Ar = phenylene; Scheme 23) with a fluoride source was shown to lead to distinct changes in the emission spectra rendering this polymer a good candidate for fluoride sensing applications.[277]

An intriguing question is whether the use of bidentate Lewis acids may be advantageous for the selective recognition of anions. Early studies by Shriver, Katz, Koester, and Wrackmeyer show that a bidentate organoboron Lewis acid may coordinate a nucleophile in a bridging fashion as illustrated for Katz's hydride-sponge in Scheme 24. The relatively short distance of ca. 3 Å between the boron centers of 1,8-diborylated naphthalenes allows for effective coordination of nucleophiles in a reverse chelate fashion. Many other

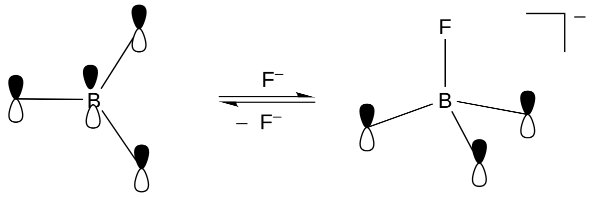

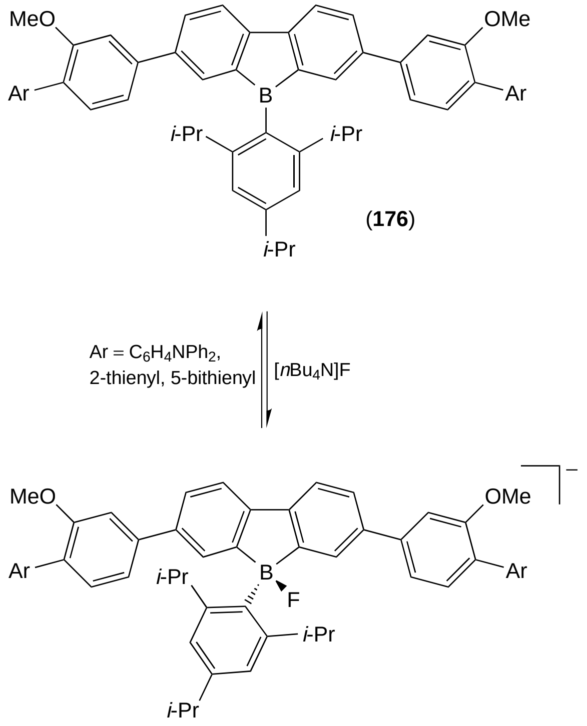
MeO
OMe
Ar
Ar
B
i-Pr
i-Pr
i-Pr
Ar = C6H4NPh2, 2-thienyl, 5-bithienyl
[nBu4N]F
MeO
OMe
Ar
Ar
i-Pr
B
F
i-Pr
i-Pr
−

(**176**)

Figure 4 Fluoride sensing with luminescent triarylboranes

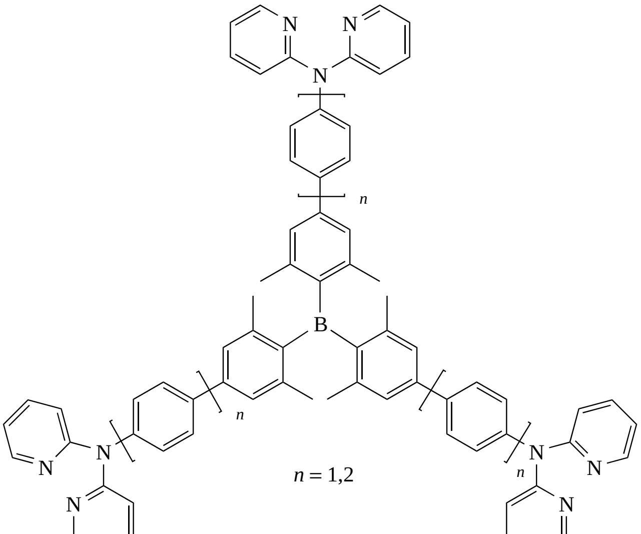
N
N
N
n
B
n
N
N
N
n
N
N
n = 1,2

(**177**)

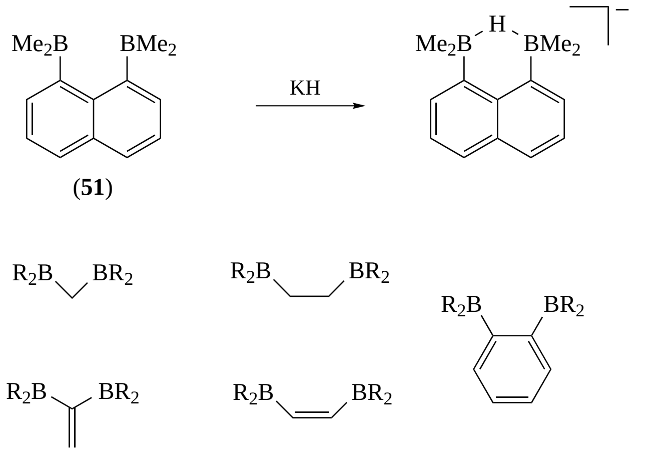
Me2B
BMe2
KH
H
Me2B
BMe2
−
R2B
BR2
R2B
BR2
R2B
BR2
R2B
BR2
R2B
BR2
R2B
BR2

(**51**)

Scheme 24 Schematic representation of selected bidentate hosts for anion binding

systems with aliphatic, olefinic, and aromatic backbones have been developed and their chemistry has been reviewed.[31,84,266]

The diborylated cobaltocenium species $[(CpBR_2)_2Co]^+$ (R = *i*-Pr) is an interesting example that illustrates the different binding modes encountered for bifunctional Lewis acids.[278,279] With hydroxy counterions, an oxygen-bridged complex (**178**), which represents an inverse chelate structure, was confirmed in the solid state and in solution (R = *i*-Pr, F). Salt-like structures on the other hand were observed with PF_6^- as the counterion and a zwitterionic 1:1 complex (**179**) formed upon reaction of the diborylated cobaltocene with hexachloroethane. Low-temperature NMR studies show that the chloride rapidly exchanges position between the two Lewis-acidic boron centers.

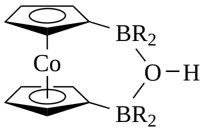
BR2
Co
O−H
BR2

(**178**)

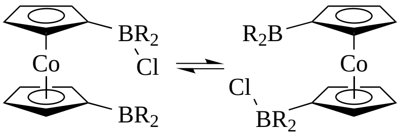
BR2
Co
Cl
BR2
R2B
Co
Cl
BR2

(**179**)

Organoboron rings containing three or more boron centers may be viewed as inverse crown ethers. DFT calculations suggest that triboramacrocycle (**180**), in which the boron centers are connected via ethylene bridges, effectively coordinates halide, hydride and methide ions (equation 40).[280,281] Good selectivity for fluoride over other halides was predicted. Moreover, the binding energy was shown to further increase upon perfluorination of the backbone for all anions studied.

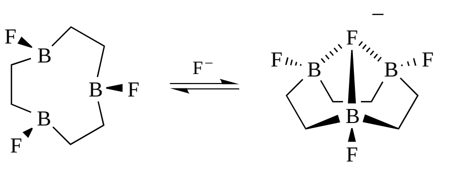

(180)

(40)

Finally, several perfluorinated bidentate organoboron Lewis acids have been developed very recently in a research effort fueled by potential applications in Ziegler–Natta olefin polymerization; they will be discussed in this context in Section 7.3.3.[282]

7.2.2 *Binding of Amines and Ketones to Bifunctional Lewis Acids*

The complexation of pyranone to 1,8-bis(dichloroboryl)-naphthalene has been investigated by Reilly and Oh.[283] NMR and IR spectroscopy suggest that pyranone simultaneously coordinates to both Lewis-acidic centers in solution to form complex (**181**). In the presence of excess pyranone, a 2:1 complex with one pyranone molecule attached to each boron center is formed (Scheme 25).

Nozaki and Takaya studied the binding of amines to bifunctional boranes. Interestingly, benzylamine binds strongly to the bifunctional Lewis acid (**182**) under exclusive formation of a 2:1 complex (**183**) as demonstrated by titration experiments. The failure to observe a 1:1 complex was explained by allosteric effects rendering the binding constant for the second amine K_2 much larger than K_1 for the initial binding process.[284] Similarly, the chiral bifunctional Lewis acid (**184**), prepared from phenylboronic acid and L-tartaric acid, selectively binds 1,6-diaminohexanes over 1,2-diaminoethane by using two boron centers and two carbonyl oxygen atoms, which play an essential role as Lewis basic site.[285]

7.2.3 *Saccharide Binding*

Organoboranes have proven highly useful for selective saccharide binding, which is based on the formation of boronic esters from arylboronic acids in the presence of diols. For example, a number of arylboronic acids containing a ferrocene unit for electrochemical readout have been recently reported.[286] The amino group in (**185**) plays an essential role as it is believed to participate in the sensing process through formation of an intramolecular B–N bond as shown in Scheme 26. Consequently, the phenylboronic acid (**185**) binds saccharides at neutral pH under formation of boronic ester (**186**), while the parent ferrocenylboronic acid requires strongly basic conditions.

Related optical and fluorescent sensor systems have been widely used. For instance, the fluorescence of the pyrene unit in species (**187**) is quenched upon saccharide binding to the boron center.[287] Boronic acid groups were also attached to dendrimers and polymers.[287,288] The benefit of systems containing at least two boronic acid centers, as shown for the luminescent saccharide sensor (**187**), is that two-point binding can more effectively control saccharide binding. Similar

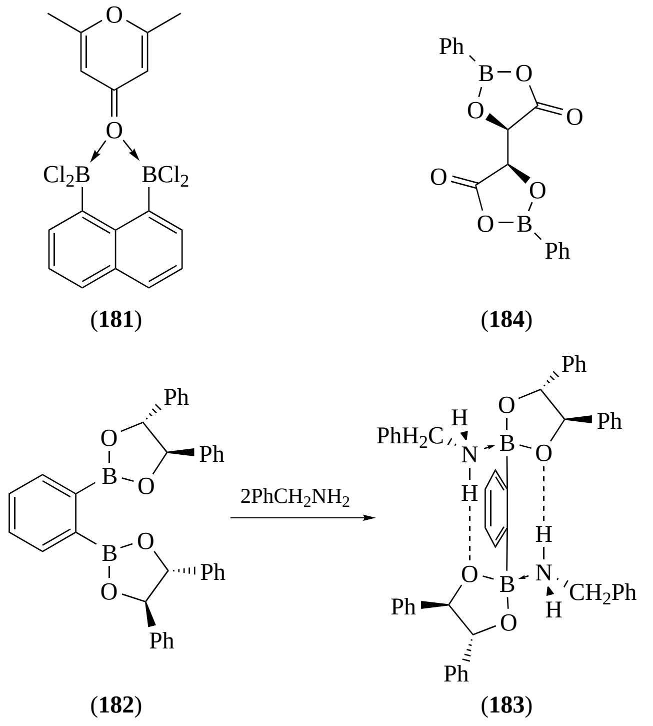

(181) **(184)** **(182)** **(183)**

Scheme 25

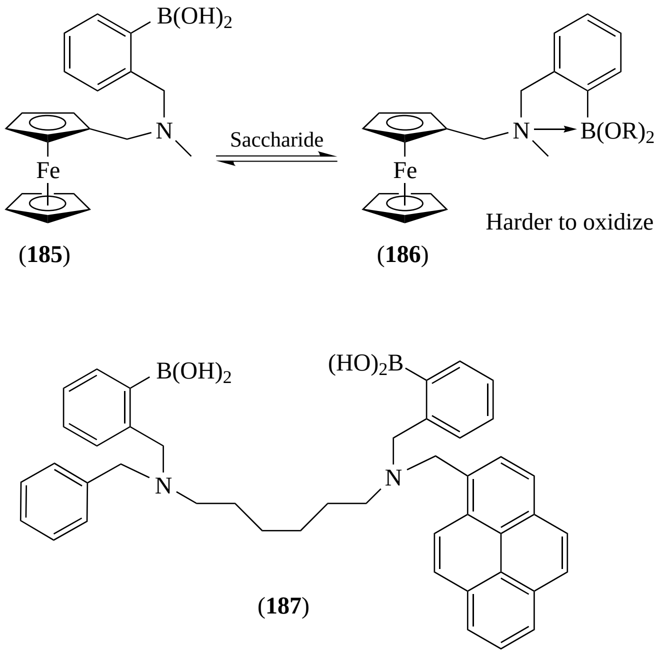

(185) **(186)** **(187)**

Scheme 26

modular electrochemical detection systems with multiple boronic acid groups were developed.[289]

7.3 Organoboranes as Lewis Acid Catalysts in Organic Synthesis

7.3.1 Achiral Organoboron Lewis Acids

The ability of Lewis-acidic boranes to complex with and thus to activate functional groups of organic substrates has been exploited for numerous applications in organic synthesis. Among achiral reagents and catalysts, simple boron halides, BX_3, are most commonly used. However, they suffer from inherently high sensitivity to air and moisture. Therefore, a new class of fluorinated arylboranes has recently been developed and found to be useful for a large variety of organic and organometallic transformations.[16–18,290] Tris(pentafluorophenylborane) ($B(C_6F_5)_3$, (**188**)) behaves as a very strong Lewis acid as a result of the electron-withdrawing fluorine atoms attached to the aromatic rings. The Lewis acid strength has been shown through binding studies with crotonaldehyde and other nucleophiles to be similar to that of BF_3, and thus much higher than that of $B(C_6H_5)_3$.[290] Moreover, $B(C_6F_5)_3$ is remarkably stable both thermally and toward air and moisture. Indeed, the structures and Brønsted acid properties of stable water adducts of $B(C_6F_5)_3$ have been reported.[291–293] $B(C_6F_5)_3$ acts as an efficient catalyst, for example, in various aldol-type reactions, conjugate additions, Diels–Alder reactions, and in hydrosilylations and hydrostannations of alkynes and olefins.

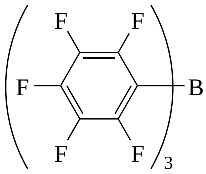

(**188**)

Diarylborinic acids $(C_6F_5)_2BOH$ (**189**) and (3,5-$(CF_3)_2C_6H_3)_2BOH$ (**190**) were also studied as Lewis acid catalysts. The borinic acid (**189**) adopts a trimeric structure in the solid state, but is monomeric in solution.[294] These borinic acids are for example effective catalysts for Mukaiyama aldol condensations and Oppenauer oxidations, and the catalytic activities are typically much higher than those of the corresponding arylboronic acids.[16] Nonetheless, 3,4,5-trifluorophenylboronic acid (**191**) and 3,5-bis(trifluoromethyl)phenylboronic acid (**192**) were found to act as highly active amidation catalysts.[295]

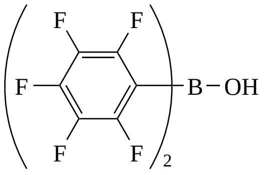

(**189**)

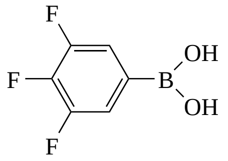

(**191**)

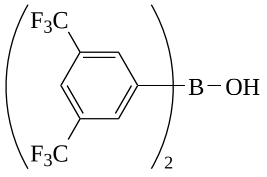

(**190**)

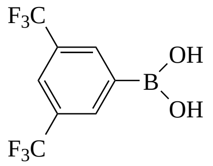

(**192**)

First attempts at developing supported versions of perfluorinated arylboranes have recently been reported.[28,296] Dendrimers containing a carbosilane core with up to 12 tris(perfluorophenylboryl) groups in the periphery have been assembled by Piers (Scheme 27). The borane groups were attached in an elegant self-catalyzed reaction, that involves Lewis acid catalyzed silylation of the arylether derivative (**193**).[296] The organoborane decorated dendrimer (**194**) shows only slightly inferior activities in comparison to $B(C_6F_5)_3$ in the hydrosilylation of acetophenone.

The first polymer containing fluorinated arylborane substituents has recently been reported.[28] The highly functionalized soluble polymer (**195**) was obtained in good yield by treatment of poly(4-dibromoborylstyrene) with equimolar amounts of pentafluorophenylcopper at low temperature. Polymer (**195**) shows a slightly lower Lewis acidity than the perfluorinated borane $B(C_6F_5)_3$ as determined by complexation with crotonaldehyde (equation 41). However, in this

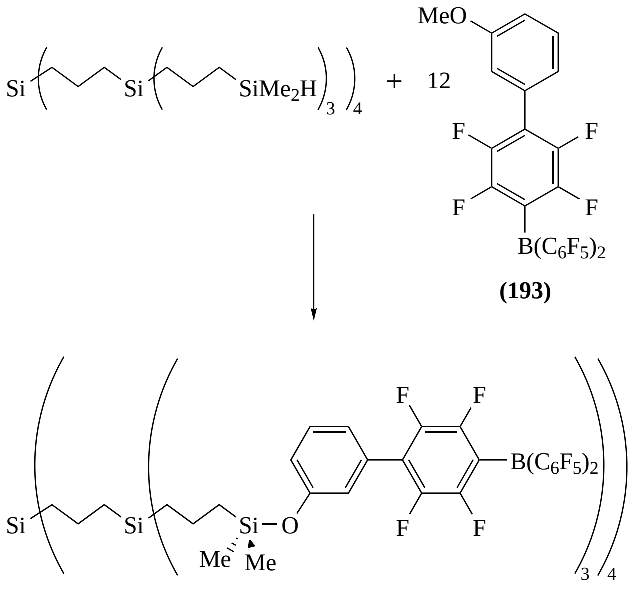

(**193**)

(**194**)

Scheme 27

context it is important to mention that Lewis acid strength does not necessarily correlate with catalyst activity. An intriguing recent study by Piers clearly shows that the weaker Lewis acid $PhB(C_6F_5)_2$ is a much more active catalysts in allylstannation reactions than $B(C_6F_5)_3$.[297]

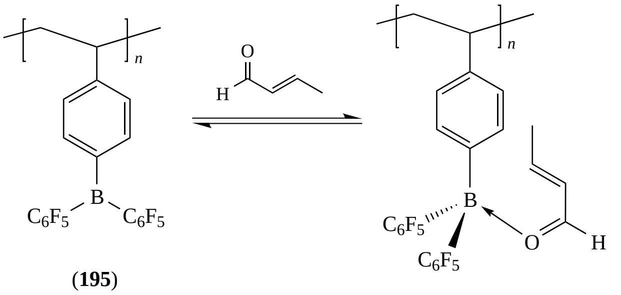

(195)

(41)

7.3.2 *Chiral Organoboron Lewis Acids*

Most chiral organoboron Lewis acids reported to date are based on an organoborane that is attached to a chiral organic moiety such as a diol, aminoalcohol, or other readily available chiral substrates.[14,17,19] Organoboron derivatives recently used as catalysts in enantioselective Diels–Alder reactions include the family of chiral acyloxyboranes (CAB) with (**196**) and (**197**) as representative examples and various cyclic boronic esters such as (**198**) and (**199**). An interesting system that combines the favorable Lewis acid properties of fluorinated arylboranes with a chiral Brønsted acid has been developed by Ishihara and Yamamoto.[298,299] The Brønsted acid-assisted chiral Lewis acids (BLA) (**200**) was found to be highly effective in enantioselective cycloadditions of α,β-enals with various dienes. The presence of the Brønsted acid functionality leads to significant acceleration of the reaction.

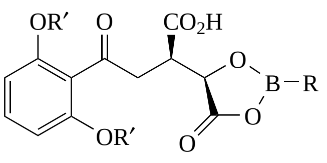

R = alkyl

(196)

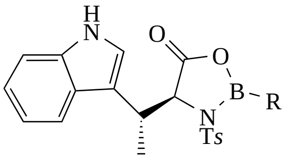

R = alkyl

(197)

In contrast to the examples shown above, the organic group itself is chiral in the alkylborane (**201**) and the binaphthyldichloroboranes (**202**). The naphthyl-functionalized alkyldichloroborane (**201**) serves as an excellent catalyst in enantioselective Diels–Alder reactions.[300] The high selectivity was ascribed to a two-point binding process that involves an interaction of the substrate with the naphthyl group. While chiral alkyldihaloboranes are among the most powerful chiral Lewis acids, in general they decompose relatively easily to alkanes or alkenes as a result of protonolysis or β-hydride elimination.[17,19] It is thus difficult to recover them quantitatively as alkylboronic acids. The chiral aryldichloroboranes (**202**) are relatively more stable and can be reused as the corresponding boronic acid.[301–304] A bifunctional derivative has recently also been synthesized from distannylated binaphthyl through highly selective tin–boron exchange.[301] The binaphthylboranes (**202**) have been studied as catalysts for enantioselective Diels–Alder reactions involving cyclopentadiene as the substrate.

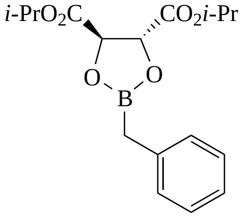

(198)

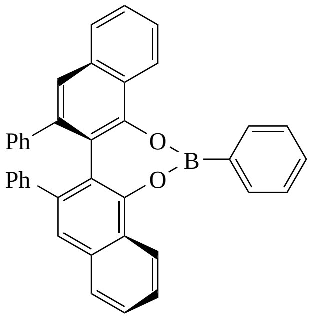

(199)

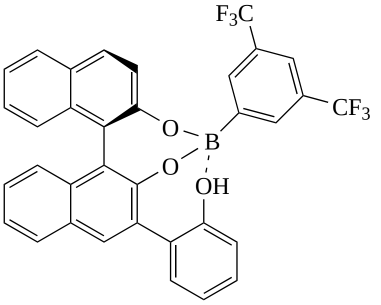

(200)

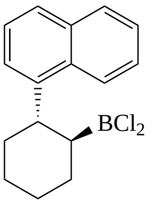

(201)

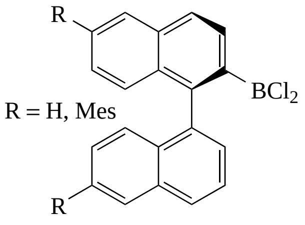

(202)

Although several bifunctional chiral Lewis acids have been described in the literature and binding studies have been performed as outlined in Section 7.2, relatively little is known about their use as Lewis acid catalysts. Most notably, 1,8-bis(dichloroboryl)naphthalene was treated with various chiral organic amines, alcohols, and acids. The resulting products were found to be efficient catalysts for asymmetric Diels–Alder reactions.[305,306] The simultaneous coordination of the substrate by both Lewis acid centers is believed to play a significant role (see also Scheme 25).

7.3.3 *Fluorinated Arylboranes as Cocatalysts for Olefin Polymerization*

Another exciting property of highly Lewis-acidic organoboranes is their ability to abstract ligands from transition-metal complexes, thereby generating highly reactive coordinatively unsaturated species. A tremendous research effort has been sparked by the independent discovery by Marks and Ewen in the early 1990s that tris(pentafluorophenyl)borane ($B(C_6F_5)_3$, (**188**)) may serve as a well-defined and highly effective activator in Ziegler–Natta olefin polymerization (*see* ***Oligomerization & Polymerization by Homogeneous Catalysis***).[152,307] The Lewis-acidic borane is believed to (partially) abstract a methyl group from complexes such as Cp_2ZrMe_2 thus yielding a highly active cationic zirconium species that catalyzes polymerization of olefins (equation 42). Many other examples of the generation of highly active catalysts through abstraction of substituents from transition-metal complexes have been discovered.[152] Experimental and theoretical studies clearly show that the ion pair formation and dissociation critically influences the activity of the transition-metal complexes.[152] One of the challenges in this chemistry has been to further enhance the Lewis acidity of the borane activator and in turn to stabilize the borate anion formed. Toward this end a wealth of highly sophisticated fluorinated organoboranes have been recently reported.[152,282,290,308]

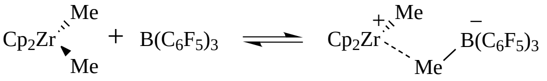

$$Cp_2ZrMe_2 + B(C_6F_5)_3 \rightleftharpoons Cp_2Zr^{+}(Me)\cdots Me{-}B^{-}(C_6F_5)_3 \qquad (42)$$

In an attempt at increasing the Lewis acidity of the borane through use of more highly fluorinated aryl groups, Marks prepared a series of perfluorinated biphenyl compounds.[152] While tris(2,2′,2″-perfluorobiphenylyl)borane (**203**) is highly Lewis-acidic and generally generates cationic species more readily than $B(C_6F_5)_3$, steric effects hinder efficient activation of group 4 metallocene dimethyl compounds.[309] In order to improve the catalytic activity, a related mixed-substituted borane, bis(pentafluorophenyl)(2-perfluorobiphenylyl)borane (**204**) was developed.[310] Moreover, a highly Lewis-acidic perfluorinated naphthylborane derivative, tris(β-perfluoronaphthyl)borane (**205**), was prepared from β-bromoheptafluoronaphthalene.[311] An alternative method to increase the Lewis acidity of the organoborane is to incorporate the electron-deficient boron center into an antiaromatic ring and thus to stabilize the Lewis base adduct relative to the free Lewis acid.[32] The Lewis acidity of (**206**) was found to surpass that of the noncyclic species $B(C_6F_5)_3$, an effect that was attributed to the antiaromaticity of the central 4-π-electron ring. Indeed, a competition experiment showed that (**206**) binds acetonitrile more effectively than $B(C_6F_5)_3$. Thus the incorporation of boron into the antiaromatic ring more than compensates for the loss of two fluorine atoms.

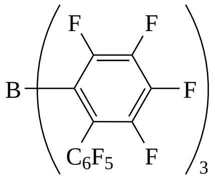

(**203**)

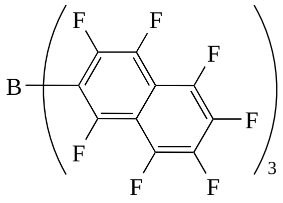

(**205**)

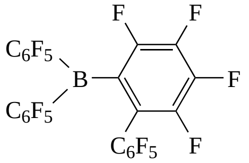

(**204**)

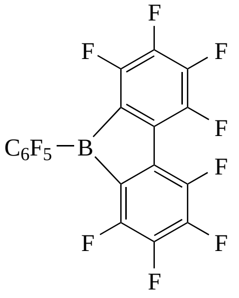

(**206**)

Marks first suggested that the use of bifunctional activators in olefin polymerization might be advantageous. They were expected to show enhanced Lewis acidity since counterions formed from diboranes are potentially less coordinating than $[RB(Ar^F)_3]^-$.[282,312] The bifunctional Lewis acid (**207**) was obtained by double hydroboration of t-butylacetylene followed by treatment of the intermediate bis(dichloroborane) with pentafluorophenyl lithium. In an effort to obtain a more stable analog of (**207**), the bifunctional borane (**208**) was prepared via tin–boron exchange and subsequent hydroboration reaction. Retrohydroboration reactions are not a concern for (**208**), because the two Lewis-acidic centers are connected by an sp^2-carbon atom. However, the stability under catalysis conditions was also found to be moderate in the case of (**208**). More recent efforts have therefore focused on bifunctional boranes that are bridged by fluorinated aromatic groups. Toward this end, Piers recently reported the synthesis of the fully fluorinated bidentate Lewis acid (**209**) (see equations 14 and 15).[38,313] The use of a perfluorinated backbone, while synthetically challenging, has been found to be an essential feature for good proteolytic stability and high Lewis acidity. Thus, the bifunctional Lewis acid shows superior properties in comparison to the more readily accessible protonated analog 1,2-$C_6H_4(B(C_6F_5)_2)_2$. The $B\cdots B$ separation of 3.1328(2) Å is large enough to incorporate first-row element anions comfortably. Indeed, bridging complexes (**210**) are readily formed with a variety of anions ($X = F$, OH, OMe, OC_6F_5, N_3, NMe_2) from either alkali metal salts or trityl derivatives Ph_3CX.[313] Methide abstraction from Cp_2ZrMe_2 on the other hand leads to a borate, in which the methyl group is not bridging. Even in the presence of excess of Cp_2ZrMe_2, only one methyl group is transferred to the bifunctional Lewis acid (**209**). However, complexes (**210**) ($X{=}OR$) themselves serve as highly efficient noncoordinating anions in olefin polymerization catalyst systems.[313]

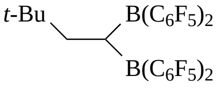
(207)

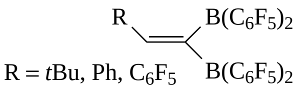
(208)

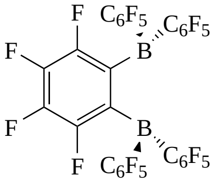
(209)

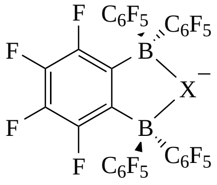
(210)

The perfluorinated diboraanthracene (**211**) shows an unusually high Lewis acidity as a result of the antiaromatic nature of the central six-membered ring as described above for the monofunctional borane (**206**).[37,123] The exocyclic pentafluorophenyl groups are nearly perpendicular to the diboracycle thus preventing any significant π-electron density from being transferred to the boron centers. The bifunctional species (**211**) is capable of coordinating a methyl group to each Lewis acid center and shows very good catalytic activity in combination with a number of transition-metal complexes. Finally, a fluorinated 1,4-diborylbenzene derivative (**212**), was studied as a nonchelating bifunctional activator in olefin polymerization. Use of (**212**) has been shown to result in unusual polymer microstructures and has proven particularly beneficial in copolymerizations.[152]

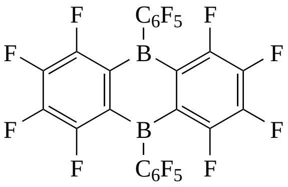
(211)

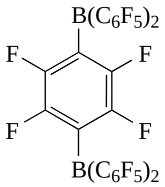
(212)

It is important to note that a large number of perfluorinated tetraorganoborates that are for the most part directly related to the tricoordinate species shown above have been prepared and proven highly useful as activators in olefin polymerization. Usually either trityl, ammonium, or oxonium borates are reacted with a suitable transition-metal complex as shown in Scheme 28.[152] Borate salts may serve as highly active cocatalysts since counterions $\mathrm{BAr}_4^{\mathrm{F}-}$ such as $\mathrm{B(C_6F_5)_4}^-$ typically show a very low tendency for ion pairing with the cation $\mathrm{Cp_2ZrR^+}$.

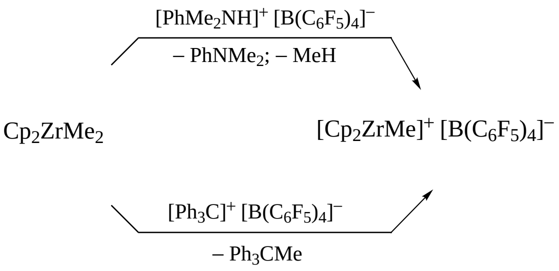
[PhMe$_2$NH]$^+$ [B(C$_6$F$_5$)$_4$]$^-$
– PhNMe$_2$; – MeH
Cp$_2$ZrMe$_2$
[Cp$_2$ZrMe]$^+$ [B(C$_6$F$_5$)$_4$]$^-$
[Ph$_3$C]$^+$ [B(C$_6$F$_5$)$_4$]$^-$
– Ph$_3$CMe

Scheme 28

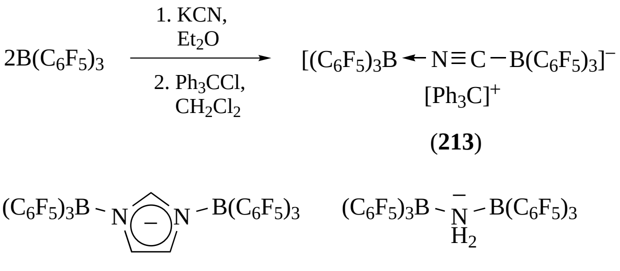

(213)

(214) **(215)**

Scheme 29

Several weakly coordinating anions, in which the anion is bound to more than one borane moiety, and thus the negative charge is more effectively dissipated have been reported. Treatment of $\mathrm{B(C_6F_5)_3}$ with KCN yields the weakly nucleophilic anion (**213**) in a simple one pot procedure (Scheme 29).[314,315] Related imidazolyl and amido-bridged bis(borane)s (**214** and **215**) have also been reported.[316,317] Moreover, borane complexes of transition-metal cyanides such as $[\mathrm{Ni(CN)_4}]^{2-}$ provide access to anions with even more extensive delocalization.[317] Anion complexes of the bidentate Lewis acids 1,2-$\mathrm{C_6F_4(B(C_6F_5)_2)_2}$ (**210**) function on the same principle.[313] All these counterions have been found to be highly effective in olefin polymerization. Finally, borane or borate functionalities may also be directly attached to transition-metal complexes as shown in Section 5.2, thus giving access to 'self-activating' catalyst systems.[146,154–156,159]

8 RELATED ARTICLES

Boron Hydrides; Boron: Inorganic Chemistry; Boron: Metallacarbaboranes; Boron–Nitrogen Compounds; Boron: Polyhedral Carboranes.; Hydroboration Catalysis.

9 REFERENCES

1. A. Pelter, K. Smith, and H. C. Brown, 'Borane Reagents', Academic Press, London, San Diego, CA, New York, Boston, MA, Sydney, Tokyo, Toronto, 1988.
2. M. Vaultier and B. Carboni, Boron, in 'Main-Group Metal Organometallics in Organic Synthesis', ed. A. McKillop, Pergamon Press, Oxford, 1995, Vol. 11, p. 191.

3. D. S. Matteson, 'Stereodirected Synthesis with Organoboranes', Springer, Berlin, Heidelberg, New York, 1995.
4. P. V. Ramachandran and H. C. Brown eds, 'Organoboranes for Syntheses', ACS Symposium Series 783, American Chemical Society, Washington, DC, 2001.
5. H. C. Brown and P. V. Ramachandran, *J. Organomet. Chem.*, 1995, **500**, 1.
6. H. C. Brown and P. V. Ramachandran, Asymmetric Syntheses via Chiral Organoboranes Based on α-Pinene, in 'Advances in Asymmetric Synthesis', ed. A. Hassner, JAI Press, Greenwich, CT and London, England, 1995, Vol. 1, p. 147.
7. K. Burgess and W. A. van der Donk, *Asymmetric Hydroboration*, in 'Advanced Asymmetric Synthesis', ed. G. R. Stephenson, Chapman & Hall, London, Weinheim, New York, Tokyo, Melbourne, Madras, 1996, p. 181.
8. M. Wills, *Contemp. Org. Synth.*, 1996, **3**, 201.
9. A. Boudier, L. O. Bromm, M. Lotz, and P. Knochel, *Angew. Chem., Int. Ed.*, 2000, **39**, 4414.
10. K. J. Shea, *Chem. Eur. J.*, 2000, **6**, 1113.
11. A. Pelter, R. T. Pardasani, and P. Pardasani, *Tetrahedron*, 2000, **56**, 7339.
12. C. Ollivier and P. Renaud, *Chem. Rev.*, 2001, **101**, 3415.
13. G. W. Kabalka, Z. Wu, and Y. Ju, *J. Organomet. Chem.*, 2003, **680**, 12.
14. L. Deloux and M. Srebnik, *Chem. Rev.*, 1993, **93**, 763.
15. E. J. Corey and C. J. Helal, *Angew. Chem., Int. Ed.*, 1998, **37**, 1986.
16. K. Ishihara and H. Yamamoto, *Eur. J. Org. Chem.*, 1999, 527.
17. K. Ishihara, Boron Reagents, in 'Lewis Acid Reagents', ed. H. Yamamoto, Oxford University Press, Oxford, 1999, p. 31.
18. K. Ishihara, Achiral B(III) Lewis Acids, in 'Lewis Acids in Organic Synthesis', ed. H. Yamamoto, Wiley VCH, Weinheim, New York, Chichester, Brisbane, Singapore, Toronto, 2000, Vol. 1, p. 89.
19. K. Ishihara, Chiral B(III) Lewis Acids, in 'Lewis Acids in Organic Synthesis', ed. H. Yamamoto, Wiley VCH, Weinheim, New York, Chichester, Brisbane, Singapore, Toronto, 2000, Vol. 1, p. 135.
20. N. Miyaura and A. Suzuki, *Chem. Rev.*, 1995, **95**, 2457.
21. A. Suzuki, Cross-coupling Reactions of Organoboron Compounds with Organic Halides, in 'Metal-Catalyzed Cross-Coupling Reactions', eds. F. Diederich and P. J. Stang, Wiley-VCH, New York, 1998, p. 49.
22. A. Suzuki, *J. Organomet. Chem.*, 2002, **653**, 83.
23. N. Miyaura, *Top. Curr. Chem.*, 2002, **219**, 11.
24. H. C. Brown, N. Vasumathi, and N. N. Joshi, *Organometallics*, 1993, **12**, 1058.
25. S. Yamaguchi, S. Akiyama, and K. Tamao, *J. Am. Chem. Soc.*, 2000, **122**, 6335.
26. T. Noda and Y. Shirota, *J. Am. Chem. Soc.*, 1998, **120**, 9714.
27. G. E. Herberich, B. Schmidt, and U. Englert, *Organometallics*, 1995, **14**, 471.
28. Y. Qin, G. Cheng, A. Sundararaman, and F. Jäkle, *J. Am. Chem. Soc.*, 2002, **124**, 12672.
29. D. A. Hoic, J. R. Wolf, W. M. Davis, and G. C. Fu, *Organometallics*, 1996, **15**, 1315.
30. F. Jäkle, A. Berenbaum, A. J. Lough, and I. Manners, *Chem. Eur. J.*, 2000, **6**, 2762.
31. J. D. Hoefelmeyer, M. Schulte, M. Tschinkl, and F. P. Gabbaï, *Coord. Chem. Rev.*, 2002, **235**, 93.
32. J. J. Eisch and B. W. Kotowicz, *Eur. J. Inorg. Chem.*, 1998, 761.
33. J. Lewkowski and M. Vaultier, *Main Group Met. Chem.*, 2001, **24**, 13.
34. H.-J. Frohn, A. Lewin, and V. V. Bardin, *J. Organomet. Chem.*, 1998, **570**, 255.
35. X. Cheng, C. Slebodnick, P. A. Deck, D. R. Billodeaux, and F. R. Fronczek, *Inorg. Chem.*, 2000, **39**, 4921.
36. V. V. Bardin and H.-J. Frohn, *Main Group Met. Chem.*, 2002, **25**, 589.
37. M. V. Metz, D. J. Schwartz, C. L. Stern, P. N. Nickias, and T. J. Marks, *Angew. Chem., Int. Ed.*, 2000, **39**, 1312.
38. V. C. Williams, W. E. Piers, W. Clegg, M. R. J. Elsegood, S. Collins, and T. B. Marder, *J. Am. Chem. Soc.*, 1999, **121**, 3244.
39. A. Sundararaman and F. Jäkle, *J. Organomet. Chem.*, 2003, **681**, 134.
40. T. Deforth, M. Kaschke, H. Stock, H. Pritzkow, and W. Siebert, *Z. Naturforsch., B: Chem. Sci.*, 1997, **52**, 823.
41. R. Quintanilla and T. E. Cole, *Tetrahedron*, 1995, **51**, 4297.
42. P. J. Fagan, W. A. Nugent, and J. C. Calabrese, *J. Am. Chem. Soc.*, 1994, **116**, 1880.
43. P. V. Ramachandran and H. C. Brown, Asymmetric Syntheses of Fluoroorganic Compounds via Chiral Organoboranes, in 'Asymmetric Fluoroorganic Chemistry', ACS Symposium Series 746, eds. P. V. Ramachandran, and H. C. Brown, American Chemical Society, Washington, DC, 2000, p. 22.
44. U. P. Dhokte and H. C. Brown, *Organometallics*, 1998, **17**, 2891.
45. J. A. Soderquist, K. Matos, C. H. Burgos, C. Lai, J. Vaquer, J. R. Medina, and S. D. Huang, Novel Silyl-Mediated 10-TMS-9-BBD Organoborane Reagents for Asymmetric Synthesis, in 'Organoboranes for Syntheses', ACS Symposium Series 783, eds. P. V. Ramachandran and H. C. Brown, American Chemical Society, Washington, DC, 2001, p. 176.
46. K. Smith, A. Pelter, and Z. Jin, *Angew. Chem., Int. Ed.*, 1994, **33**, 851.
47. K. Smith, G. A. El-Hiti, D. Hou, and G. A. DeBoos, *J. Chem. Soc., Perkin Trans. 1*, 1999, 2807.
48. D. J. Parks, R. Spence, and W. E. Piers, *Angew. Chem., Int. Ed.*, 1995, **34**, 809.
49. D. J. Parks, W. E. Piers, and G. P. A. Yap, *Organometallics*, 1998, **17**, 5492.

50. C. D. Entwistle, T. B. Marder, P. S. Smith, J. A. K. Howard, M. A. Fox, and S. A. Mason, *J. Organomet. Chem.*, 2003, **680**, 165.
51. A. Suzuki, *Rev. Heteroatom Chem.*, 1997, **17**, 271.
52. B. Wrackmeyer, *Coord. Chem. Rev.*, 1995, **145**, 125.
53. B. Wrackmeyer, O. L. Tok, and Y. N. Bubnov, *Angew. Chem., Int. Ed.*, 1999, **38**, 124.
54. I. Beletskaya and A. Pelter, *Tetrahedron*, 1997, **53**, 4957.
55. N. Miyaura, in 'Catalytic Heterofunctionalization', eds. A. Togni and H. Grützmacher, Wiley-VCH, Chichester, 2001, Chap. 1.
56. T. B. Marder and N. C. Norman, *Top. Catal.*, 1998, **5**, 63.
57. T. Ishiyama and N. Miyaura, *J. Organomet. Chem.*, 2000, **611**, 392.
58. T. Ishiyama, K.-I. Nishijima, N. Miyaura, and A. Suzuki, *J. Am. Chem. Soc.*, 1993, **115**, 7219.
59. M. Suginome and Y. Ito, *Chem. Rev.*, 2000, **100**, 3221.
60. L.-B. Han and M. Tanaka, *Chem. Commun.*, 1999, 395.
61. R. B. Coapes, F. E. S. Souza, R. L. Thomas, J. J. Hall, and T. B. Marder, *Chem. Commun.*, 2003, 614.
62. T. Ishiyama and N. Miyaura, *J. Organomet. Chem.*, 2003, **680**, 3.
63. K. M. Waltz, X. He, C. Muhoro, and J. F. Hartwig, *J. Am. Chem. Soc.*, 1995, **117**, 11357.
64. K. M. Waltz and J. F. Hartwig, *Science*, 1997, **277**, 211.
65. H. Chen and J. F. Hartwig, *Angew. Chem., Int. Ed.*, 1999, **38**, 3391.
66. H. Chen, S. Schlecht, T. C. Semple, and J. F. Hartwig, *Science*, 2000, **287**, 1995.
67. Y. Kondo, D. Garcia-Cuadrado, J. F. Hartwig, N. K. Boaen, N. L. Wagner, and M. A. Hillmyer, *J. Am. Chem. Soc.*, 2002, **124**, 1164.
68. B. Goldfuß, P. Knochel, L. O. Bromm, and K. Knapp, *Angew. Chem., Int. Ed.*, 2000, **39**, 4136.
69. S. Aldridge and C. Bresner, *Coord. Chem. Rev.*, 2003, **244**, 71.
70. H. Laaziri, L. O. Bromm, F. Lhermitte, R. M. Gschwind, and P. Knochel, *J. Am. Chem. Soc.*, 1999, **121**, 6940.
71. A. M. Genaev, S. M. Nagy, G. E. Salnikov, and V. G. Shubin, *Chem. Commun.*, 2000, 1587.
72. P. Nguyen, H. P. Blom, S. A. Westcott, N. J. Taylor, and T. B. Marder, *J. Am. Chem. Soc.*, 1993, **115**, 9329.
73. C. N. Iverson and M. R. Smith III, *J. Am. Chem. Soc.*, 1999, **121**, 7696.
74. J.-Y. Cho, M. K. Tse, D. Holmes, R. E. Maleczka Jr and M. R. Smith III, *Science*, 2002, **295**, 305.
75. T. Ishiyama, J. Takagi, K. Ishida, N. Miyaura, N. R. Anastasi, and J. F. Hartwig, *J. Am. Chem. Soc.*, 2002, **124**, 390.
76. T. Ishiyama, J. Takagi, J. F. Hartwig, and N. Miyaura, *Angew. Chem., Int. Ed.*, 2002, **41**, 3056.
77. S. Shimada, A. S. Batsanov, J. A. K. Howard, and T. B. Marder, *Angew. Chem., Int. Ed.*, 2001, **40**, 2168.
78. T. Ishiyama, K. Ishida, J. Takagi, and N. Miyaura, *Chem. Lett.*, 2001, 1082.
79. R. Boese, A. J. Downs, T. M. Greene, A. W. Hall, C. A. Morrison, and S. Parsons, *Organometallics*, 2003, **22**, 2450.
80. G. Pawelke and H. Bürger, *Appl. Organomet. Chem.*, 1996, **10**, 147.
81. G. Pawelke and H. Bürger, *Coord. Chem. Rev.*, 2001, **215**, 243.
82. M. Finze, E. Bernhardt, A. Terheiden, M. Berkei, H. Willner, D. Christen, H. Oberhammer, and F. Aubke, *J. Am. Chem. Soc.*, 2002, **124**, 15385.
83. E. Bernhardt, G. Henkel, H. Willner, G. Pawelke, and H. Bürger, *Chem. Eur. J.*, 2001, **7**, 4696.
84. V. M. Dembitsky, H. Abu Ali, and M. Srebnik, *Appl. Organomet. Chem.*, 2003, **17**, 327.
85. H. Abu Ali, I. Goldberg, D. Kaufmann, C. Burmeister, and M. Srebnik, *Organometallics*, 2002, **21**, 1870.
86. M. Bluhm, A. Maderna, H. Pritzkow, S. Bethke, R. Gleiter, and W. Siebert, *Eur. J. Inorg. Chem.*, 1999, 1693.
87. M. J. Bayer, H. Pritzkow, and W. Siebert, *Eur. J. Inorg. Chem.*, 2002, 1293.
88. P. Nguyen, R. B. Coapes, A. D. Woodward, N. J. Taylor, J. M. Burke, J. A. K. Howard, and T. B. Marder, *J. Organomet. Chem.*, 2002, **652**, 77.
89. R. Köster, G. Seidel, and B. Wrackmeyer, *Angew. Chem., Int. Ed.*, 1994, **33**, 2294.
90. R. Köster, R. Boese, B. Wrackmeyer, and H. J. Schanz, *J. Chem. Soc., Chem. Commun.*, 1995, 1691.
91. B. Wrackmeyer, H. J. Schanz, and W. Milius, *Angew. Chem., Int. Ed.*, 1997, **36**, 1117.
92. W. Siebert and A. Gunale, *Chem. Soc. Rev.*, 1999, **28**, 367.
93. Z.-X. Wang and P. v. Ragué Schleyer, *J. Am. Chem. Soc.*, 2001, **123**, 994.
94. Z.-X. Wang and P. v. Ragué Schleyer, *J. Am. Chem. Soc.*, 2002, **124**, 11979.
95. Z.-X. Wang and P. v. Ragué Schleyer, *Science*, 2001, **292**, 2465.
96. R. W. A. Havenith, P. W. Fowler, and E. Steiner, *Chem. Eur. J.*, 2002, **8**, 1068.
97. B. Wrackmeyer, E. V. Klimkina, and Y. N. Bubnov, *J. Organomet. Chem.*, 2001, **620**, 51.
98. B. Wrackmeyer, W. Milius, E. V. Klimkina, and Y. N. Bubnov, *Chem. Eur. J.*, 2001, **7**, 775.
99. B. Wrackmeyer, W. Milius, O. L. Tok, and Y. N. Bubnov, *Chem. Eur. J.*, 2002, **8**, 1537.
100. M. E. Gurskii, A. V. Gueiderikh, Y. N. Bubnov, M. Y. Antipin, K. A. Lyssenko, I. D. Gridnev, R. Boese, and D. Blaeser, *J. Organomet. Chem.*, 2001, **636**, 3.
101. W. Siebert, *Adv. Organomet. Chem.*, 1993, **35**, 187.

102. C. E. Housecroft, Compounds with Three- or Four-Coordinate Boron, Emphasizing Cyclic Systems, in 'Comprehensive Organometallic Chemistry', eds. E. W. Abel, F. G. A. Stone, and G. Wilkinson, Pergamon Press, Oxford, 1995, Vol. 1, p. 129.

103. G. E. Herberich, Boron Rings Ligated to Metals, in 'Comprehensive Organometallic Chemistry', eds. E. W. Abel, F. G. A. Stone, and G. Wilkinson, Pergamon Press, Oxford, 1995, Vol. 1, p. 197.

104. D. Scheschkewitz, A. Ghaffari, P. Amseis, M. Unverzagt, G. Subramanian, M. Hofmann, P. v. Ragué Schleyer, H. F. Schaefer, G. Geiseler, W. Massa, and A. Berndt III, *Angew. Chem., Int. Ed.*, 2000, **39**, 1272.

105. W. Lößlein, H. Pritzkow, P. v. Ragué Schleyer, L. R. Schmitz, and W. Siebert, *Angew. Chem., Int. Ed.*, 2000, **39**, 1276.

106. W. Lößlein, H. Pritzkow, P. v. Ragué Schleyer, L. R. Schmitz, and W. Siebert, *Eur. J. Inorg. Chem.*, 2001, 1949.

107. H. Schulz, G. Gabbert, H. Pritzkow, and W. Siebert, *Chem. Ber.*, 1993, **126**, 1593.

108. C. Blanchard, E. Framery, and M. Vaultier, *Synthesis*, 1996, 45.

109. Y. Gu, H. Pritzkow, and W. Siebert, *Eur. J. Inorg. Chem.*, 2001, 373.

110. M. J. Bayer, H. Pritzkow, and W. Siebert, *Eur. J. Inorg. Chem.*, 2002, 2069.

111. Z. Yuan, J. C. Collings, N. J. Taylor, T. B. Marder, C. Jardin, and J.-F. Halet, *J. Solid State Chem.*, 2000, **154**, 5.

112. A. Maderna, H. Pritzkow, and W. Siebert, *Angew. Chem., Int. Ed.*, 1996, **35**, 1501.

113. B. Wrackmeyer, H. Maisel, W. Milius, A. Badshah, E. Molla, and A. Mottalib, *J. Organomet. Chem.*, 2000, **602**, 45.

114. B. Wrackmeyer, G. Kehr, and S. Willbold, *J. Organomet. Chem.*, 1999, **590**, 93.

115. M. Hoshi, K. Shirakawa, and A. Arase, *Chem. Commun.*, 1998, 1225.

116. N. Metzler, H. Nöth, and M. Thomann, *Organometallics*, 1993, **12**, 2423.

117. M. Zaidlewicz, J. R. Binkul, and W. Sokól, *J. Organomet. Chem.*, 1999, **580**, 354.

118. K. Köhler, W. E. Piers, A. P. Jarvis, S. Xin, Y. Feng, A. M. Bravakis, S. Collins, W. Clegg, G. P. A. Yap, and T. B. Marder, *Organometallics*, 1998, **17**, 3557.

119. S. Toyota, M. Asakura, M. Oki, and F. Toda, *Bull. Chem. Soc. Jpn.*, 2000, **73**, 2357.

120. J. J. Eisch, *Adv. Organomet. Chem.*, 1995, **39**, 355.

121. C. Ester, A. Maderna, H. Pritzkow, and W. Siebert, *Eur. J. Inorg. Chem.*, 2000, 1177.

122. P. Müller, S. Huck, H. Köppel, H. Pritzkow, and W. Siebert, *Z. Naturforsch., B: Chem. Sci.*, 1995, **50**, 1476.

123. M. V. Metz, D. J. Schwartz, C. L. Stern, T. J. Marks, and P. N. Nickias, *Organometallics*, 2002, **21**, 4159.

124. K. Okada, T. Sugawa, and M. Oda, *J. Chem. Soc., Chem. Commun.*, 1992, 74.

125. M. Bluhm, H. Pritzkow, W. Siebert, and R. N. Grimes, *Angew. Chem., Int. Ed.*, 2000, **39**, 4562.

126. A. Hergel, H. Pritzkow, and W. Siebert, *Angew. Chem., Int. Ed.*, 1994, **33**, 1247.

127. M. Schulte and F. P. Gabbaï, *J. Organomet. Chem.*, 2002, **643**, 164.

128. J. D. Hoefelmeyer and F. P. Gabbaï, *Organometallics*, 2002, **21**, 982.

129. M. Schulte and F. P. Gabbaï, *Chem. Eur. J.*, 2002, **8**, 3802.

130. J. Fiedler, S. Zalis, A. Klein, F. Hornung, and W. Kaim, *Inorg. Chem.*, 1996, **35**, 3039.

131. C. Elschenbroich, P. Kuhlkamp, A. Behrendt, and K. Harms, *Chem. Ber.*, 1996, **129**, 859.

132. C. Elschenbroich, M. Wolf, O. Burghaus, K. Harms, and J. Pebler, *Eur. J. Inorg. Chem.*, 1999, 2173.

133. Z. Zhou, G. Facey, B. R. James, and H. Alper, *Organometallics*, 1996, **15**, 2496.

134. R. Chauvin, *Eur. J. Inorg. Chem.*, 2000, 577.

135. H. Wadepohl, *Angew. Chem., Int. Ed.*, 1997, **36**, 2441.

136. B. Wrackmeyer, *Angew. Chem., Int. Ed.*, 1999, **38**, 771.

137. H. Braunschweig and M. Colling, *Coord. Chem. Rev.*, 2001, **223**, 1.

138. H. Braunschweig and M. Colling, *Eur. J. Inorg. Chem.*, 2003, 393.

139. J. F. Hartwig and S. Huber, *J. Am. Chem. Soc.*, 1993, **115**, 4908.

140. S. Aldridge, A. Al-Fawaz, R. J. Calder, A. A. Dickinson, D. J. Willock, M. E. Light, and M. B. Hursthouse, *Chem. Commun.*, 2001, 1846.

141. S. Aldridge, D. L. Coombs, and C. Jones, *Chem. Commun.*, 2002, 856.

142. D. L. Coombs, S. Aldridge, C. Jones, and D. J. Willock, *J. Am. Chem. Soc.*, 2003, **125**, 6356.

143. G. E. Herberich and A. Fischer, *Organometallics*, 1996, **15**, 58.

144. E. Barday, B. Frange, B. Hanquet, and G. E. Herberich, *J. Organomet. Chem.*, 1999, **572**, 225.

145. R. Littger, H. Nöth, and M. Suter, *Eur. J. Inorg. Chem.*, 2000, 1571.

146. H. Braunschweig, F. M. Breitling, E. Gullo, and M. Kraft, *J. Organomet. Chem.*, 2003, **680**, 31.

147. R. Duchateau, S. J. Lancaster, M. Thornton-Pett, and M. Bochmann, *Organometallics*, 1997, **16**, 4995.

148. K. Rufanov, E. Avtomonov, N. Kazennova, V. Kotov, A. Khvorost, D. Lemenovskii, and J. Lorberth, *J. Organomet. Chem.*, 1997, **536**, 361.

149. D. S. Stelck, P. J. Shapiro, N. Basickes, and A. L. Rheingold, *Organometallics*, 1997, **16**, 4546.

150. A. Voigt, S. Filipponi, C. L. B. Macdonald, J. D. Gorden, and A. H. Cowley, *Chem. Commun.*, 2000, 911.
151. A. H. Cowley, V. Lomeli, and A. Voigt, *J. Am. Chem. Soc.*, 1998, **120**, 6401.
152. E. Y.-X. Chen and T. J. Marks, *Chem. Rev.*, 2000, **100**, 1391.
153. J. Ruwwe, G. Erker, and R. Fröhlich, *Angew. Chem., Int. Ed.*, 1996, **35**, 80.
154. W. E. Piers, *Chem. Eur. J.*, 1998, **4**, 13.
155. G. Erker, *Acc. Chem Res*, 2001, **34**, 309.
156. M. Bochmann, *Top. Catal.*, 1999, **7**, 9.
157. S. J. Lancaster, S. Al-Benna, M. Thornton-Pett, and M. Bochmann, *Organometallics*, 2000, **19**, 1599.
158. M. T. Reetz, H. Brümmer, M. Kessler, and J. Kuhnigk, *Chimia*, 1995, **49**, 501.
159. P. J. Shapiro, *Eur. J. Inorg. Chem.*, 2001, 321.
160. K. A. Rufanov, V. V. Kotov, N. B. Kazennova, D. A. Lemenovskii, E. V. Avtomonov, and J. Lorberth, *J. Organomet. Chem.*, 1996, **525**, 287.
161. M. T. Reetz, M. Willuhn, C. Psiorz, and R. Goddard, *Chem. Commun.*, 1999, 1105.
162. C. T. Burns, D. S. Stelck, P. J. Shapiro, A. Vij, K. Kunz, G. Kehr, T. Concolino, and A. L. Rheingold, *Organometallics*, 1999, **18**, 5432.
163. S. J. Lancaster and M. Bochmann, *Organometallics*, 2001, **20**, 2093.
164. H. Braunschweig, C. v. Koblinski, and U. Englert, *Chem. Commun.*, 2000, 1049.
165. K. A. O. Starzewski, W. M. Kelly, A. Stumpf, and D. Freitag, *Angew. Chem., Int. Ed.*, 1999, **38**, 2439.
166. B. Wrackmeyer, U. Dörfler, and M. Herberhold, *Z. Naturforsch., B: Chem. Sci.*, 1993, **48**, 121.
167. B. Wrackmeyer, U. Dörfler, W. Milius, and M. Herberhold, *Polyhedron*, 1995, **14**, 1425.
168. B. Wrackmeyer, U. Dörfler, W. Milius, and M. Herberhold, *Z. Naturforsch., B: Chem. Sci.*, 1996, **51**, 851.
169. A. Appel, H. Nöth, and M. Schmidt, *Chem. Ber.*, 1995, **128**, 621.
170. P. A. Deck, T. S. Fisher, and J. S. Downey, *Organometallics*, 1997, **16**, 1193.
171. J. A. Gamboa, A. Sundararaman, L. Kakalis, A. J. Lough, and F. Jäkle, *Organometallics*, 2002, **21**, 4169.
172. A. Appel, F. Jäkle, T. Priermeier, R. Schmid, and M. Wagner, *Organometallics*, 1996, **15**, 1188.
173. B. E. Carpenter, W. E. Piers, M. Parvez, G. P. A. Yap, and S. J. Rettig, *Can. J. Chem. – Rev. Can. Chim.*, 2001, **79**, 857.
174. B. E. Carpenter, W. E. Piers, and R. McDonald, *Can. J. Chem. – Rev. Can. Chim.*, 2001, **79**, 291.
175. K. Ma, M. Scheibitz, S. Scholz, and M. Wagner, *J. Organomet. Chem.*, 2002, **652**, 11.
176. M. Fontani, F. Peters, W. Scherer, W. Wachter, M. Wagner, and P. Zanello, *Eur. J. Inorg. Chem.*, 1998, 1453.
177. M. Grosche, E. Herdtweck, F. Peters, and M. Wagner, *Organometallics*, 1999, **18**, 4669.
178. K. Ma, M. Scheibitz, S. Scholz, and M. Wagner, *J. Organomet. Chem.*, 2002, **652**, 11.
179. H. Braunschweig, R. Dirk, M. Müller, P. Nguyen, R. Resendes, D. P. Gates, and I. Manners, *Angew. Chem., Int. Ed.*, 1997, **36**, 2338.
180. A. Berenbaum, H. Braunschweig, R. Dirk, U. Englert, J. C. Green, F. Jäkle, A. J. Lough, and I. Manners, *J. Am. Chem. Soc.*, 2000, **122**, 5765.
181. M. Scheibitz, R. F. Winter, M. Bolte, H.-W. Lerner, and M. Wagner, *Angew. Chem., Int. Ed.*, 2003, **42**, 924.
182. M. Herberhold, U. Dörfler, and B. Wrackmeyer, *J. Organomet. Chem.*, 1997, **530**, 117.
183. M. Herberhold, U. Dörfler, W. Milius, and B. Wrackmeyer, *J. Organomet. Chem.*, 1995, **492**, 59.
184. F. Jäkle, M. Mattner, T. Priermeier, and M. Wagner, *J. Organomet. Chem.*, 1995, **502**, 123.
185. F. Jäkle, T. Priermeier, and M. Wagner, *J. Chem. Soc., Chem. Commun.*, 1995, 1765.
186. F. Jäkle, T. Priermeier, and M. Wagner, *Organometallics*, 1996, **15**, 2033.
187. E. Herdtweck, F. Jäkle, and M. Wagner, *Organometallics*, 1997, **16**, 4737.
188. S. Venne-Dunker, W. Ahlers, G. Erker, and R. Fröhlich, *Eur. J. Inorg. Chem.*, 2000, 1671.
189. I. D. Gridnev, O. L. Tok, N. A. Gridneva, Y. N. Bubnov, and P. R. Schreiner, *J. Am. Chem. Soc.*, 1998, **120**, 1034.
190. I. D. Gridnev, P. R. Schreiner, M. E. Gurskii, Y. N. Bubnov, A. O. Krasavin, and V. I. Mstislavski, *Chem. Commun.*, 1998, 2507.
191. M. E. Gurskii, I. D. Gridnev, A. V. Buevich, and Y. N. Bubnov, *Organometallics*, 1994, **13**, 4658.
192. Y. Sugihara, R. Miyatake, K. Takakura, and S. Yano, *J. Chem. Soc., Chem. Commun.*, 1994, 1925.
193. M. Ishikura, M. Kamada, and M. Terashima, *Synthesis*, 1994, 936.
194. T. G. Hodgkins and D. R. Powell, *Inorg. Chem.*, 1996, **35**, 2140.
195. I. I. Padilla-Martinez, F. J. Martinez-Martinez, A. Lopez-Sandoval, K. I. Giron-Castillo, M. A. Brito, and R. Contreras, *Eur. J. Inorg. Chem.*, 1998, 1547.
196. A. Wacker, H. Pritzkow, and W. Siebert, *Eur. J. Inorg. Chem.*, 1999, 789.
197. N. Weis, H. Pritzkow, and W. Siebert, *Eur. J. Inorg. Chem.*, 1999, 393.
198. F. H. Carre, R. J. P. Corriu, T. Deforth, W. E. Douglas, W. S. Siebert, and W. Weinmann, *Angew. Chem., Int. Ed.*, 1998, **37**, 652.
199. T. Köhler, H. Pritzkow, and W. Siebert, *Z. Naturforsch., B: Chem. Sci.*, 2002, **57**, 1101.

200. A. Eckert, H. Pritzkow, and W. Siebert, *Eur. J. Inorg. Chem.*, 2002, 2064.

201. N. Farfán, H. Höpfl, V. Barba, M. E. Ochoa, R. Santillan, E. Gómez, and A. Gutiérrez, *J. Organomet. Chem.*, 1999, **581**, 70.

202. P. v. Ragué Schleyer, P. K. Freeman, H. J. Jiao, and B. Goldfuss, *Angew. Chem., Int. Ed.*, 1995, **34**, 337.

203. R. J. Wehmschulte, M. A. Khan, B. Twamley, and B. Schiemenz, *Organometallics*, 2001, **20**, 844.

204. R. J. Wehmschulte, A. A. Diaz, and M. A. Khan, *Organometallics*, 2003, **22**, 83.

205. S. Yamaguchi, T. Shirasaka, S. Akiyama, and K. Tamao, *J. Am. Chem. Soc.*, 2002, **124**, 8816.

206. P. A. Chase, W. E. Piers, and B. O. Patrick, *J. Am. Chem. Soc.*, 2000, **122**, 12911.

207. W. J. Grigsby and P. P. Power, *J. Am. Chem. Soc.*, 1996, **118**, 7981.

208. G. E. Herberich, T. Wagner, and H.-W. Marx, *J. Organomet. Chem.*, 1995, **502**, 67.

209. J. M. Schulman, R. L. Disch, P. v. Ragué Schleyer, M. Bühl, M. Brehmer, and W. Koch, *J. Am. Chem. Soc.*, 1992, **114**, 7897.

210. G. E. Herberich, H.-W. Marx, and T. Wagner, *Chem. Ber.*, 1994, **127**, 2135.

211. G. E. Herberich, U. Eigendorf, and U. Englert, *Chem. Ber.*, 1993, **126**, 1397.

212. P. Braunstein, U. Englert, G. E. Herberich, and M. Neuschutz, *Angew. Chem., Int. Ed.*, 1995, **34**, 1010.

213. G. J. Pindado, S. J. Lancaster, M. Thornton-Pett, and M. Bochmann, *J. Am. Chem. Soc.*, 1998, **120**, 6816.

214. G. C. Fu, *Adv. Organomet. Chem.*, 2001, **47**, 101.

215. A. J. Ashe, J. W. Kampf, C. Müller, and M. Schneider III, *Organometallics*, 1996, **15**, 387.

216. D. A. Hoic, W. M. Davis, and G. C. Fu, *J. Am. Chem. Soc.*, 1995, **117**, 8480.

217. S. Qiao, D. A. Hoic, and G. C. Fu, *J. Am. Chem. Soc.*, 1996, **118**, 6329.

218. X. L. Zheng and G. E. Herberich, *Organometallics*, 2000, **19**, 3751.

219. G. E. Herberich, U. Englert, M. U. Schmidt, and R. Standt, *Organometallics*, 1996, **15**, 2707.

220. D. A. Hoic, W. M. Davis, and G. C. Fu, *J. Am. Chem. Soc.*, 1996, **118**, 8176.

221. S. Qiao, D. A. Hoic, and G. C. Fu, *Organometallics*, 1997, **16**, 1501.

222. D. J. H. Emslie, W. E. Piers, and M. Parvez, *Angew. Chem., Int. Ed.*, 2003, **42**, 1251.

223. F. P. Gabbaï, *Angew. Chem., Int. Ed.*, 2003, **42**, 2218.

224. J. Tweddell, D. A. Hoic, and G. C. Fu, *J. Org. Chem.*, 1997, **62**, 8286.

225. G. E. Herberich, B. Ganter, and M. Pons, *Organometallics*, 1998, **17**, 1254.

226. G. E. Herberich, U. Englert, B. Ganter, and M. Pons, *Eur. J. Inorg. Chem.*, 2000, 979.

227. X. Zheng and G. E. Herberich, *Eur. J. Inorg. Chem.*, 2001, 3013.

228. U. Hagenau, J. Heck, E. Hendrickx, A. Persoons, T. Schuld, and H. Wong, *Inorg. Chem.*, 1996, **35**, 7863.

229. D. H. Woodmansee, X. Bu, and G. C. Bazan, *Chem. Commun.*, 2001, 619.

230. A. J. Ashe, S. Al-Ahmad, and X. Fang III, *J. Organomet. Chem.*, 1999, **581**, 92.

231. G. C. Bazan, G. Rodriguez, A. J. Ashe III, S. Al-Ahmad, and C. Müller, *J. Am. Chem. Soc.*, 1996, **118**, 2291.

232. G. C. Bazan, G. Rodriguez, A. J. Ashe III, S. Al-Ahmad, and J. W. Kampf, *Organometallics*, 1997, **16**, 2492.

233. J. S. Rogers, G. C. Bazan, and C. K. Sperry, *J. Am. Chem. Soc.*, 1997, **119**, 9305.

234. A. J. Ashe III, S. Al-Ahmad, X. Fang, and J. W. Kampf, *Organometallics*, 1998, **17**, 3883.

235. A. J. Ashe III, S. Al-Ahmad, J. W. Kampf, and V. G. Young, *Angew. Chem., Int. Ed.*, 1997, **36**, 2014.

236. A. J. Ashe III, W. Klein, and R. Rousseau, *Organometallics*, 1993, **12**, 3225.

237. A. J. Ashe III, S. M. Al-Taweel, C. Drescher, J. W. Kampf, and W. Klein, *Organometallics*, 1997, **16**, 1884.

238. G. Subramanian, P. v. Ragué Schleyer, and H. J. Jiao, *Organometallics*, 1997, **16**, 2362.

239. A. J. Ashe III, W. Klein, and R. Rousseau, *J. Organomet. Chem.*, 1994, **468**, 21.

240. J. M. Schulman and R. L. Disch, *Organometallics*, 2000, **19**, 2932.

241. C. D. Entwistle and T. B. Marder, *Angew. Chem., Int. Ed.*, 2002, **41**, 2927.

242. Y. Shirota, *J. Mater. Chem.*, 2000, **10**, 1.

243. K. Okada, T. Kawata, and M. Oda, *J. Chem. Soc., Chem. Commun.*, 1995, 233.

244. R. J. Kwaan, C. J. Harlan, and J. R. Norton, *Organometallics*, 2001, **20**, 3818.

245. S. Yamaguchi, T. Shirasaki, and K. Tamao, *Org. Lett.*, 2000, **2**, 4129.

246. M. Kinoshita, H. Kita, and Y. Shirota, *Adv. Funct. Mater.*, 2002, **12**, 780.

247. A. Rajca, S. Rajca, and S. R. Desai, *J. Chem. Soc., Chem. Commun.*, 1995, 1957.

248. J. D. Hoefelmeyer and F. P. Gabbaï, *J. Am. Chem. Soc.*, 2000, **122**, 9054.

249. T. Noda, H. Ogawa, and Y. Shirota, *Adv. Mater.*, 1999, **11**, 283.

250. B. Y. Lee, S. Wang, M. Putzer, G. P. Bartholomew, X. Bu, and G. C. Bazan, *J. Am. Chem. Soc.*, 2000, **122**, 3969.

251. N. Matsumi, N. Kensuke, and Y. Chujo, *J. Am. Chem. Soc.*, 1998, **120**, 5112.

252. H. Kobayashi, N. Sato, Y. Ichikawa, M. Miyata, Y. Chujo, and T. Matsuyama, *Synth. Met.*, 2003, **135–136**, 393.

253. N. Matsumi, T. Umeyama, and Y. Chujo, *Polym. Bull.*, 2000, **44**, 431.

254. N. Matsumi, K. Naka, and Y. Chujo, *J. Am. Chem. Soc.*, 1998, **120**, 10776.

255. U. Salzner, J. B. Lagowski, P. G. Pickup, and R. A. Poirier, *Synth. Met.*, 1998, **96**, 177.

256. Y. Shozo, T. Inoue, T. Aoyagi, and T. Komatsu, *Synth. Met.*, 1992, **46**, 221.

257. Z.-Q. Liu, Q. Fang, D. Wang, G. Xue, W.-T. Yu, Z.-S. Shao, and M.-H. Jiang, *Chem. Commun.*, 2002, 2900.

258. C. Branger, M. Lequan, R. M. Lequan, M. Barzoukas, and A. Fort, *J. Mater. Chem.*, 1996, **6**, 555.

259. Y. Shirota, M. Kinoshita, T. Noda, K. Okumoto, and T. Ohara, *J. Am. Chem. Soc.*, 2000, **122**, 11021.

260. K. Okumoto, T. Ohara, T. Noda, and Y. Shirota, *Synth. Met.*, 2001, **121**, 1655.

261. Q. Wu, M. Esteghamatian, N.-X. Hu, Z. Popovic, G. Enright, Y. Tao, M. D'Iorio, and S. Wang, *Chem. Mater.*, 2000, **12**, 79.

262. S. Wang, *Coord. Chem. Rev.*, 2001, **215**, 79.

263. S. Anderson, M. S. Weaver, and A. J. Hudson, *Synth. Met.*, 2000, **111–112**, 459.

264. D. E. Kaufmann and A. Otten, *Angew. Chem.*, 1994, **106**, 1917.

265. M. M. G. Antonisse and D. N. Reinhoudt, *Chem. Commun.*, 1998, 443.

266. P. D. Beer and P. A. Gale, *Angew. Chem., Int. Ed.*, 2001, **40**, 487.

267. T. D. James, K. R. A. S. Sandanayake, and S. Shinkai, *Angew. Chem., Int. Ed.*, 1996, **35**, 1911.

268. T. D. James and S. Shinkai, *Top. Curr. Chem.*, 2002, **218**, 159.

269. C. Dusemund, K. R. A. S. Sandanayake, and S. Shinkai, *Chem. Commun.*, 1995, 333.

270. H. Yamamoto, A. Ori, K. Ueda, C. Dusemund, and S. Shinkai, *Chem. Commun.*, 1996, 407.

271. S. Aldridge, C. Bresner, I. A. Fallis, S. J. Coles, and M. B. Hursthouse, *Chem. Commun.*, 2002, 740.

272. C. R. Cooper, N. Spencer, and T. D. James, *Chem. Commun.*, 1998, 1365.

273. M. Nicolas, B. Fabre, and J. Simonet, *Chem. Commun.*, 1999, 1881.

274. E. Shoji and M. S. Freund, *J. Am. Chem. Soc.*, 2002, **124**, 12486.

275. S. Yamaguchi, S. Akiyama, and K. Tamao, *J. Am. Chem. Soc.*, 2001, **123**, 11372.

276. W.-L. Jia, D. Song, and S. Wang, *J. Org. Chem.*, 2003, **68**, 701.

277. M. Miyata and Y. Chujo, *Polym. J.*, 2002, **34**, 967.

278. G. E. Herberich, A. Fischer, and D. Wiebelhaus, *Organometallics*, 1996, **15**, 3106.

279. G. E. Herberich, U. Englert, A. Fischer, and D. Wiebelhaus, *Organometallics*, 1998, **17**, 4769.

280. S. Jacobson and R. Pizer, *J. Am. Chem. Soc.*, 1993, **115**, 11216.

281. S. Aldridge, I. A. Fallis, and S. T. Howard, *Chem. Commun.*, 2001, 231.

282. W. E. Piers, G. J. Irvine, and V. C. Williams, *Eur. J. Inorg. Chem.*, 2000, 2131.

283. M. Reilly and T. Oh, *Tetrahedron Lett.*, 1995, **36**, 217.

284. K. Nozaki, M. Yoshida, and H. Takaya, *Bull. Chem. Soc. Jpn.*, 1996, **69**, 2043.

285. K. Nozaki, T. Tsutsumi, and H. Takaya, *J. Org. Chem.*, 1995, **60**, 6668.

286. J. C. Norrild and I. Søtofte, *J. Chem. Soc., Perkin Trans. 2*, 2002, 303.

287. S. Arimori, M. L. Bell, C. S. Oh, K. A. Frimat, and T. D. James, *Chem. Commun.*, 2001, 1836.

288. T. D. James, H. Shinmori, M. Takeuchi, and S. Shinkai, *Chem. Commun.*, 1996, 705.

289. S. Arimori, S. Ushiroda, L. M. Peter, A. T. A. Jenkins, and T. D. James, *Chem. Commun.*, 2002, 2368.

290. W. E. Piers and T. Chivers, *Chem. Soc. Rev.*, 1997, **26**, 345.

291. A. A. Danopoulos, J. R. Galsworthy, M. L. H. Green, S. Cafferkey, L. H. Doerrer, and M. B. Hursthouse, *Chem. Commun.*, 1998, 2529.

292. C. Bergquist, B. M. Bridgewater, C. J. Harlan, J. R. Norton, R. A. Friesner, and G. Parkin, *J. Am. Chem. Soc.*, 2000, **122**, 10581.

293. T. Beringhelli, D. Maggioni, and G. D'Alfonso, *Organometallics*, 2001, **20**, 4927.

294. T. Beringhelli, G. D'Alfonso, D. Donghi, D. Maggioni, P. Mercandelli, and A. Sironi, *Organometallics*, 2003, **22**, 1588.

295. K. Ishihara, S. Ohara, and H. Yamamoto, *J. Org. Chem.*, 1996, **61**, 4196.

296. R. Roesler, B. J. N. Har, and W. E. Piers, *Organometallics*, 2002, **21**, 4300.

297. D. J. Morrison and W. E. Piers, *Org. Lett.*, 2003, **5**, 2857.

298. K. Ishihara, S. Nakamura, M. Kaneeda, and H. Yamamoto, *J. Am. Chem. Soc.*, 1996, **118**, 12854.

299. K. Ishihara, H. Kurihara, M. Matsumoto, and H. Yamamoto, *J. Am. Chem. Soc.*, 1998, **120**, 6920.

300. J. M. Hawkins, S. Loren, and M. Nambu, *J. Am. Chem. Soc.*, 1994, **116**, 1657.

301. B. Schilling, V. Kaiser, and D. E. Kaufmann, *Chem. Ber.*, 1997, **130**, 923.

302. B. Schilling and D. E. Kaufmann, *Eur. J. Org. Chem.*, 1998, 701.

303. K. Ishihara, K. Inanaga, S. Kondo, M. Funahashi, and H. Yamamoto, *Synlett*, 1998, 1053.

304. S. Thormeier, B. Carboni, and D. E. Kaufmann, *J. Organomet. Chem.*, 2002, **657**, 136.

305. M. Reilly and T. Oh, *Tetrahedron Lett.*, 1994, **35**, 7209.

306. M. Reilly and T. Oh, *Tetrahedron Lett.*, 1995, **36**, 221.

307. X. Yang, C. L. Stern, and T. J. Marks, *J. Am. Chem. Soc.*, 1994, **116**, 10015.

308. J.-N. Pedeutour, K. Radhakrishnan, H. Cramail, and A. Deffieux, *Macromol. Rapid Commun.*, 2001, **22**, 1095.

309. Y.-X. Chen, C. L. Stern, S. T. Yang, and T. Marks, *J. Am. Chem. Soc.*, 1996, **118**, 12451.

310. L. Li, C. L. Stern, and T. J. Marks, *Organometallics*, 2000, **19**, 3332.

311. L. Li and T. J. Marks, *Organometallics*, 1998, **17**, 3996.

312. L. Jia, X. Yang, C. Stern, and T. J. Marks, *Organometallics*, 1994, **13**, 3755.

313. V. C. Williams, G. J. Irvine, W. E. Piers, Z. Li, S. Collins, W. Clegg, M. R. J. Elsegood, and T. B. Marder, *Organometallics*, 2000, **19**, 1619.

314. S. J. Lancaster, D. A. Walker, M. Thornton-Pett, and M. Bochmann, *Chem. Commun.*, 1999, 1533.

315. J. M. Zhou, S. J. Lancaster, D. A. Walker, S. Beck, M. Thornton-Pett, and M. Bochmann, *J. Am. Chem. Soc.*, 2001, **123**, 223.

316. R. E. LaPointe, G. R. Roof, K. A. Abboud, and J. Klosin, *J. Am. Chem. Soc.*, 2000, **122**, 9560.

317. S. J. Lancaster, A. Rodriguez, A. Lara-Sanchez, M. D. Hannant, D. A. Walker, D. H. Hughes, and M. Bochmann, *Organometallics*, 2002, **21**, 451.

Acknowledgments

I am grateful to Ramez Boshra, Kshitij Parab, Yang Qin, and Anand Sundararaman for their help with references.

Boron: Polyhedral Carboranes

Narayan S. Hosmane[1] **& John A. Maguire**[2]
[1] *Northern Illinois University, DeKalb, IL, USA*
[2] *Southern Methodist University, Dallas, TX, USA*

Based in part on the article Boron: Polyhedral Carboranes by Robert E. Williams which appeared in the Encyclopedia of Inorganic Chemistry, First Edition.

1 Discovery and Background 1
2 Related Articles 3
3 References 3

1 DISCOVERY AND BACKGROUND

Carbaboranes, commonly known as ‘carboranes’, can formally be considered as arising from the substitution of one or more $\{BH\}^-$ vertices in an electron-deficient polyhedral borane framework by isolobal {CR} (where R = H or a cage carbon substituent) units without altering the gross geometry of the cage molecules.[1] The first carboranes reported in the literature were obtained in low yields (1–2%) from the reaction of pentaborane (B_5H_9) and acetylene (C_2H_2) in an electric glow discharge.[2,3] This reaction is shown in equation (1).

$$B_5H_9 + C_2H_2 \longrightarrow 1{,}5\text{-}C_2B_3H_5 + 1{,}6\text{-}C_2B_4H_6 + 2{,}4\text{-}C_2B_5H_7 \quad (1)$$

Closed polyhedral cage structures were suggested for these carboranes on the basis of spectroscopic characterization. In a series of papers appearing in the 1963 *Inorganic Chemistry*, the preparation of icosahedral carborane, $(CR)_2B_{10}H_{10}$, was reported from the reaction of acetylenes (R_2C_2) with $B_{10}H_{14}$ in the presence of base.[4] In 1974, the first four carbon-containing open-icosahedral carborane, $(C\text{–}Me)_4B_8H_8$, was synthesized in Grimes’s laboratory by oxidative fusion of two $[(C\text{–}Me)_2B_4H_4]^{2-}$ ligands.[5] In recent years, a number of systematic methods were developed for the preparation of a wide variety of carboranes containing one, two, three, four, five, and six carbon atoms as integral parts of the cage framework.[1,6]

1.1 Structures, Properties, and Multicenter Bonding

The electron-deficiency in carboranes arises because of the fact that the number of valence atomic orbitals used in bonding within the molecule is greater than the number of valence electrons available. This can be clearly illustrated by making a comparison between the boron hydrides (boranes) and the carbon hydrides (alkanes), as shown in Figure 1.

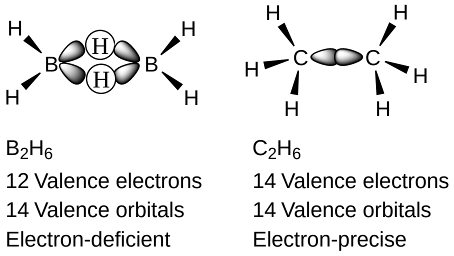

Figure 1 Structures of diborane and ethane

Thus, in carboranes, there are fewer electrons than would be required for a classical Lewis structure in which the bonding can be described in terms of two-electron two-center bonds. Therefore, some type of multicenter bonding, such as shown in Figure 1, for diborane is required.

Almost all of the known carborane cage structures are either closed polyhedra (all faces triangular) or fragments thereof, as shown in Figure 2.[6] According to the general rules of electron counting in clusters, the cage structure would be expected to become progressively more open as the carbon content increased. Thus, carboranes are classified into three geometric categories: (1) closo, (2) nido, and (3) arachno. In the closed (closo) structure (Figure 2), the skeletal atoms occupy all corners of a polyhedron, while in the open (nido) structure (Figure 2) one corner of the polyhedron is vacant. When a heteroatom is introduced into the system, the open face becomes conducive for the location of attachment to the heteroatom. In some cases, two vertices can be removed from the corresponding closo structure to yield an arachno geometry (Figure 2). In general, the structures of carboranes can be predicted from electron-counting rules commonly known as ‘Wade’s rules’.[7] The application of ‘Wade’s rules’ to these compounds provides a relatively simple relationship between the number of skeletal bonding electron pairs and the geometry of a carborane molecule. For a carborane-containing x skeletal atoms with formula $(CH)_a(BH)_{x-a}H_b{}^{c-}$, where a, $x-a$, and b are the number of CH, BH, and bridged H’s, respectively, and c^- is the overall charge on the anionic species, the number of electron pairs (z) involved in cage bonding is $x + 1/2$ $(a + b + c)$. Each CH unit provides three electrons, each BH units furnishes two electrons, and each bridge hydrogen contributes one electron. The electrons are contained in $x + 1$ bonding molecular orbitals (MOs). These bonding MOs are formed by the interaction of three orbitals from each of the framework atoms (C’s and B’s). The orbitals are the radially oriented p or sp hybrid and the tangentially oriented two p orbitals. Generalizing the rules, a closo structure is preferred if $z = x + 1$, nido if $z = x + 2$, arachno if $z = x + 3$, hypo if $z = x + 4$, fisco if $z = x + 5$, and a reticulo structure is preferred if $z = x + 6$ (see Table 1).

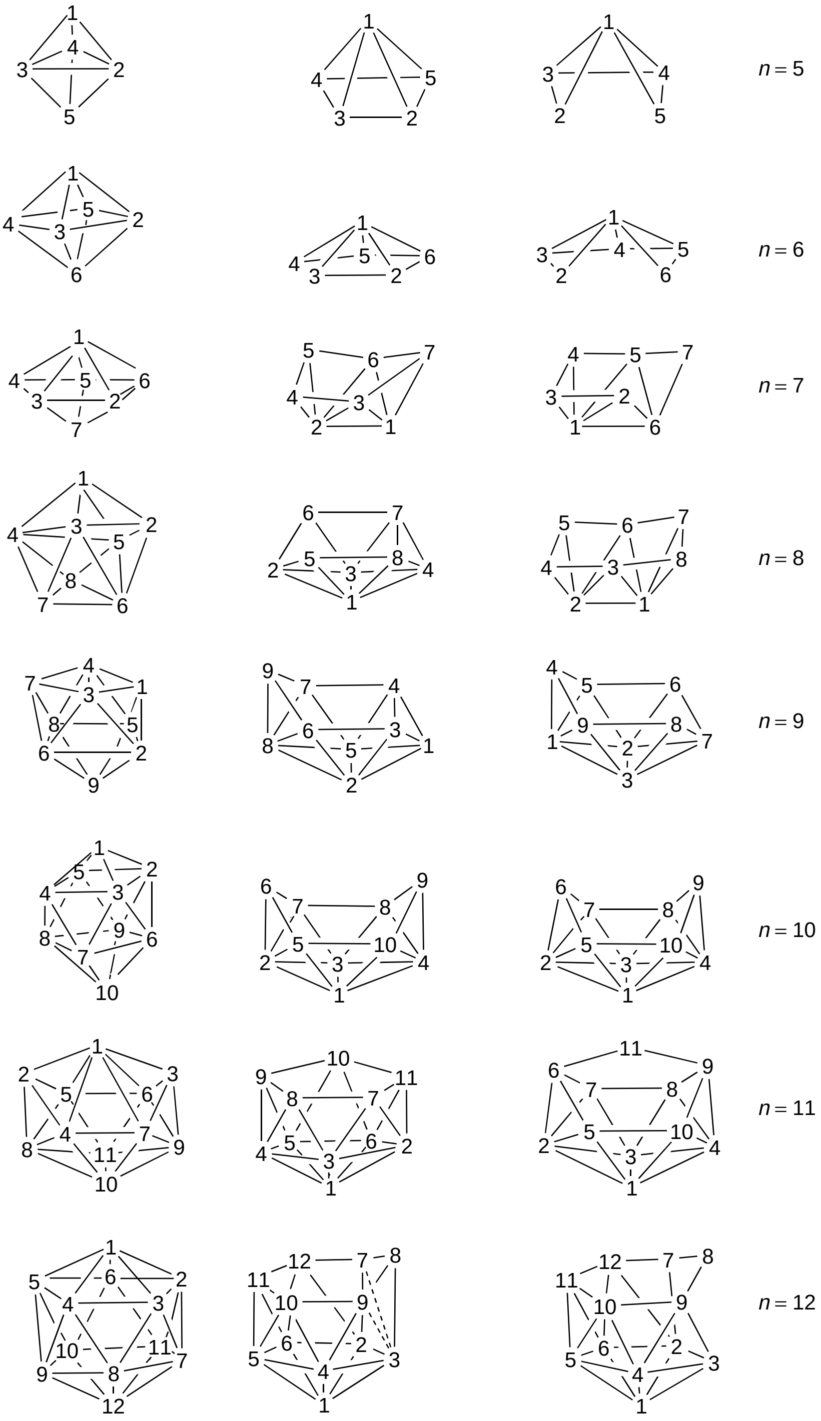

Figure 2 Polyhedral atomic frameworks of idealized (a) *closo*, (b) *nido*, and (c) *arachno* carboranes showing conventional numbering schemes. The lines drawn between cage atoms merely illustrate cluster connectivity, and should not necessarily be taken as bonds[6]

The structures of these compounds seem to dictate their methods of preparation as well as their properties. The closo carboranes are more thermally stable and less air sensitive than the corresponding nido and arachno carboranes. This is due to the fact that the nido and arachno carboranes lack a closed polyhedral structure. The closo carboranes, such as $C_2B_4H_6$, $C_2B_8H_{10}$, $C_2B_{10}H_{12}$, and their $C_{(cage)}$-substituted derivatives, are also fairly stable to 250 °C and above, and they often undergo thermally induced rearrangements that results in greater separation of the relatively negative carbon atoms

Table 1 Summary of electron-counting rules and structure relationship

	Structure types					
	Reticulo	Fisco	Hypo	Arachno	Nido	Closo
Occupied vertices	x	x	x	x	x	x
Skeletal electron pairs	$z = x + 6$	$z = x + 5$	$z = x + 4$	$z = x + 3$	$z = x + 2$	$z = x + 1$

via several diamond-square-diamond (DSD) processes.[8] The nido and arachno compounds, however, seem to generate the corresponding closo carboranes at higher temperatures indicating their thermal instability. Clearly, the structures of these carboranes seem to dictate their properties.

1.2 Practical Applications

The rapid development of carborane chemistry is mainly due to their practical applications. For instance, the potential utility of carborane polymers as gaskets, O-rings, and electrical connector inserts has been reported.[1a] Their functionality for solvent extraction of radionuclides as well as the potential medicinal value of the isoelectronic and isostructural boron analogues of biologically important molecules has been the subject of many review articles.[1,9,10] For example, a number of boron compounds have been found to possess anti-inflammatory and antiarthritic activity in animal model studies. Boron compounds have also been implicated in studies designed to probe the importance of the so-called anionic subsite of acetylcholine esterase and Ach receptors. But, by far the most interesting practical applications of carboranes are in areas of boron neutron capture therapy (BNCT) and supramolecular assembly.

Carboranes in Boron Neutron Capture Therapy of Cancer (BNCT):[9,10] The stable isotope of boron, ^{10}B (19.8% natural abundance), is very effective as a neutron capture agent with the effective nuclear cross section of 3837 barns, while the ^{11}B nucleus is incapable of undergoing a BNC reaction. Therefore, the ^{10}B-enriched carborane and borane-substituted biomolecules and drugs are selectively delivered to the cancer cells in the human body and then the tumor-localized ^{10}B nucleii are bombarded with either thermal or epithermal neutrons that results in a fission reaction producing the high energy alpha (α) particles as shown in equation (2).

$$^{10}{}_{5}\mathrm{B} + {}^{1}{}_{0}\mathrm{n} \longrightarrow {}^{7}{}_{3}\mathrm{Li} + {}^{4}{}_{2}\mathrm{He} + 2.7\,\mathrm{MeV} \qquad (2)$$

Since the α particles travel only 10 µm or less distance, the ^{10}B nucleii-localized cancer cells are destroyed selectively. However, the estimated amount of ^{10}B nucleii needed for tumor destruction is approximately 10^{18} atoms or 10–30 µg ^{10}B/g tumor. Therefore, the polyhedral borane and carborane-containing biomolecules are found to be ideal for use in BNCT as they have a high probability of preferentially localizing in tumor cells rather than normal tissues and are rapidly cleared from normal tissues and blood, while being retained in tumor tissues. This results in high tumor to normal tissue ratios and high tumor to blood ratios. The research to date has shown that BNCT has significantly prolonged the lifespan of patients with deadly brain tumors. A number of carborane compounds such as boronated organic species and boronated monoclonal antibodies have been employed for this purpose.

Molecular Assemblies:[11,12] Because of their rigid, thermally and chemically stable three-dimensional structure, the three icosahedral carborane isomers, commonly known as *o*-, *m*-, and *p*-carborane (or 1,2-, 1,7-, and 1,12-$C_2B_{10}H_{12}$, respectively), are being used as subunits for the assembly of larger arrays. The examples of such molecular assemblies include linear rigid rod-like molecules obtained by direct coupling of the carbon vertices of *p*-carborane, hybrid linear rods by joining opposite boron vertices of *p*-carborane through acetylene or diacetylene linkages, nonlinear oligomers of both *o*- and *m*-carboranes, cycles of *o*- or *m*-carborane connected *via* their carbon or boron vertices through mercury atoms to form novel mercuracarboranes, and carboracycles, which are cyclic compounds composed of *o*- and *m*-carboranes joined through carbon vertices by a series of bifunctional organic linking groups of varying complexity. Thus, the development of the systematic synthetic routes toward nanometer-scale, structurally well-defined and rigid molecules has become a rapidly growing area of chemistry.

2 RELATED ARTICLES

Boron Hydrides; Boron: Inorganic Chemistry; Boron: Metallacarbaboranes; Boron–Nitrogen Compounds; Boron: Organoboranes.

3 REFERENCES

1. (a) R. N. Grimes, ‘Carboranes’, Academic Press, New York, 1970; (b) R. N. Grimes, ‘Comprehensive Organometallic Chemistry (II)’, eds. E. W. Abel, F. G. A. Stone, and G. Wilkerson, Pergamon Press, Oxford, 1995, Vol 1, Chap. 5;

(c) A. K. Saxena, J. A. Maguire, and N. S. Hosmane, *Chem. Rev.*, 1997, **97**, 2421; (d) V. I. Bregadze, *Chem. Rev.*, 1992, **92**, 209; (e) R. N. Grimes, *J. Chem. Educ.*, 2004, **81**, 658; (f) J. Plesek, *Chem. Rev.*, 1992, **92**, 269.

2. I. Shapiro, C. D. Good, and R. E. Williams, *J. Am. Chem. Soc.*, 1962, **84**, 3837.
3. I. Shapiro, B. Keilin, R. E. Williams, and C. D. Good, *J. Am. Chem. Soc.*, 1963, **85**, 3167.
4. (a) T. L. Heying, J. W. Ager Jr, S. L. Clark, D. J. Mangold, H. L. Goldstein, M. Hillman, R. J. Polak, and J. W. Szymanski, *Inorg. Chem.*, 1963, **2**, 1089; (b) M. M. Fein, D. Grafstein, J. E. Paustian, J. Bobinski, B. E. Lichstein, N. Mayes, N. N. Schwartz, and M. S. Cohen, *Inorg. Chem.*, 1963, **2**, 1115; (c) M. M. Fein, J. Bobinski, B. E. Lichstein, N. Mayes, N. N. Schwartz, and M. S. Cohen, *Inorg. Chem.*, 1963, **2**, 1111.
5. (a) W. M. Maxwell, V. R. Miller, and R. N. Grimes, *J. Am. Chem. Soc.*, 1974, **96**, 7116; (b) J. R. Pipal and R. N. Grimes, *Inorg. Chem.*, 1979, **18**, 263; (c) R. B. Maynard and R. N. Grimes, *J. Am. Chem. Soc.*, 1982, **104**, 5983, and references therein.
6. B. Stibr, *Chem. Rev.*, 1992, **92**, 225.
7. (a) K. Wade, *Adv. Inorg. Chem. Radiochem.*, 1976, **18**, 1; (b) R. E. Williams, *Adv. Inorg. Chem. Radiochem.*, 1976, **18**, 67; (c) T. P. Fehlner, C. E. Housecroft, in ‘Molecular Structure and Energetics’, eds. J. F. Liebman and A. Greenberg, VCH, Deerfield Fla, 1986, Vol. 1, Chap. 6, p. 149; (d) R. W. Rudolph, *Acct. Chem. Res.*, 1976, **9**, 446; (e) M. E. O’Neil, K. Wade, in ‘Comprehensive Organometallic Chemistry I’, eds. E. W. Abel, F. G. A. Stone, and G. Wilkinson, Pergamon Press, Oxford, 1982, Vol. 1, Chap. 1.
8. (a) W. N. Lipscomb and D. J. Britton, *Chem. Phys.*, 1960, **33**, 275; (b) W. N. Lipscomb, *Science*, 1966, **153**, 373.
9. G. Rana, K. Vyakaranam, J. A. Maguire, and N. S. Hosmane, in ‘Metallotherapeutic Drugs and Metal-Based Diagnostic Agents: The Use of Metals in Medicine’, eds. M. Gielen, E. Tiekink, John Wiley & Sons, 2004, Chap. 2.
10. (a) M. F. Hawthorne, *Angew. Chem., Int. Ed. Engl.*, 1993, **32**, 950; (b) A. H. Soloway, W. Tjarks, B. A. Barnum, F.-G. Rong, R. F. Barth, I. M. Codogni, and J. G. Wilson, *Chem. Rev.*, 1998, **98**, 1515; (c) R. L. Rawls, *Chem. Eng. News*, 1999, 26.
11. X. Yang, C. B. Knobler, Z. Zheng, and M. F. Hawthorne, *J. Am. Chem. Soc.*, 1994, **116**, 7142, references therein.
12. W. Jiang, I. T. Chizhevsky, M. D. Mortimer, W. Chen, C. B. Knobler, S. E. Johnson, F. A. Gomez, and M. F. Hawthorne, *Inorg. Chem.*, 1996, **35**, 5417, references therein.

Acknowledgments

We thank the National Science Foundation and the Robert A. Welch Foundation for their continuous support of authors’ research in the area of carboranes and metallacarboranes.

Cadmium: Inorganic & Coordination Chemistry

Marco Borsari
University of Modena, Modena, Italy

1	Introduction	1
2	Discovery	1
3	General Remarks	1
4	Occurrence	2
5	Production	3
6	Uses	3
7	Isotopes	4
8	Toxicological and Ecological Information	4
9	Spectroscopy	4
10	Electrochemistry	5
11	Chemical Properties	6
12	Analytical Methods	6
13	Stereochemistry	6
14	Compounds	7
15	Cd^{II} Coordination Chemistry	10
16	Related Articles	16
17	References	16

Glossary

Cottrel's trap: an electrostatic precipitator for removing dust from a gas stream
Cross section: states the probability that an interaction will occur between a projectile particle (e.g. a neutron) and a target particle, which could be a nucleus in a piece of metal
Dendritic form: branching figure, whose form resembles that of a tree or shrub
Zone refining: a method of purifying metals. An ingot of metal passes through an induction heater, and in this way impurities are accumulated in the melted portion of the ingot

Abbreviations

Asn = asparagine; $CitH_2$ = citric acid; tu = thiourea (*see Thiourea*); Ettu = ethylenethiourea; Glu = glutamic acid; Met = methionine; tren = tris(2-aminoethyl)amine; Me_6 tren = tris(2-dimethylaminoethyl)amine, en = ethane-1,2-diamine; pn = propane-1,2-diamine.

1 INTRODUCTION

Cadmium was discovered in Germany in 1817. The first industrial applications were developed in the late 19th century, even if the use of CdS based pigments dates from about 1850. The most remarkable properties of cadmium are great resistance to corrosion, excellent electric conductivity, and low-melting point. For these reasons, cadmium is employed in many important industrial applications, even though its release in the environment can cause ecological and health effects. Its chemistry is similar to that of zinc and shows versatile coordination abilities, giving Cd^{2+} structures ranging from simple complexes to 1D, 2D, and 3D polymeric architectures. Interesting physical properties are exhibited by these polymers. Moreover, Cd^{2+} is able to substitute Zn^{2+} in the active site of Zn-enzymes (*see Enzyme*) and to interfere with the metabolism of Ca^{2+}. This is why several investigations in the last decade have been devoted to the coordination chemistry of cadmium and to development of new kind of compounds of applied interest.

2 DISCOVERY

Cadmium was discovered almost simultaneously in 1817 by F. Stromeyer, professor of metallurgy at the Gottingen University, K.S.L. Hermann, chemical manufacturer, and J.C.H. Roloff, pharmacy inspector, in samples of zinc oxide obtained by roasting zinc carbonate from Salzgitter (Germany).[1] The name cadmium is derived from the Latin *cadmia* (*fornacum* or *fornacea*), used in the ancient times to indicate the most important zinc ore, the zinc carbonate. The Greek *καδμεια* (or *καδμεια γη*) means cadmean earth and in antiquity this mineral was first mined near Thebes, a town founded by king Cadmo (Lat. *Cadmus*, Gr. Κ*αδμος*).

3 GENERAL REMARKS

Cadmium (Cd) is a silvery grey, shining but tarnishable metal, similar to Zn and Sn (*see* ***Zinc: Inorganic & Coordination Chemistry*** and ***Tin: Inorganic Chemistry***).[1] The structure of the form stable at room temperature (γ form) is hexagonal (space group: P63/mmc; cell parameters: $a = 297.94\,\text{pm}$, $b = 297.94\,\text{pm}$, $c = 561.86\,\text{pm}$, $\alpha = 90.00°$, $\beta = 90.00°$, $\gamma = 120.00°$). It deviates from perfect hexagonal close packing (*see Close Packing*) by elongation along the six-fold axis: each atom is regularly surrounded by six near neighbors in the close-packed plane and by three more distant neighbors in each adjacent plane. A stable α form is observed at high temperature. Cd is isostructural with Zn, Be, and

Table 1 Physical properties of cadmium

Electronic configuration	{Kr}$4d^{10}5s^2$
Atomic number	48
Atomic weight	112.411
Ionization potential (eV)	
I	8.99
II	16.90
III	44.5
IV	55
V	73
VI	94
Electronegativity	1.69 (Pauling) 1.46 (Allred-Rochow) 1.4 (Mulliken)
Atomic radius (Å)	1.55
Covalent radius (Å)	1.48
van der Waals radius (Å)	1.58
Density (Kg m^{-3})	(c) 8642 (298 K) (l) 8010 (603 K) (l) 7930 (673 K) (l) 7560 (973 K)
Viscosity (mPa s)	1.44 (622 K), 1.18 (779 K), 1.10 (876 K)
Specific heat (J g^{-1} K^{-1})	0.231 (298 K)
Hardness (Moh's)	2
Young's modulus (GPa)	50
Sound velocity (m s^{-1})	2310
Ohmic resistance (Ω m)	6.83×10^{-8} (293 K), 34.12×10^{-8} (773K)
Thermal conductivity (W cm^{-1} K^{-1})	0.975 (273 K) polycrystalline 0.969 (298 K) polycrystalline 0.953 (373 K) polycrystalline
Melting point (K)	593.9
ΔH_{fusion} (kJ mol^{-1})	6.067
ΔS_{fusion} (J K^{-1} mol^{-1})	10.29
Boiling point (K)	1038
ΔH_{vap} (kJ mol^{-1})	99.87
ΔS_{vap} (J K^{-1} mol^{-1})	95.98
Vapour pressure equation	$\log(P/\text{mm Hg}) = -0.05223a/T + b$ liquid (773–1113 K) $a = 99.90$, $b = 7.897$ solid (423–593 K) $a = 109.00$, $b = 8.564$
C° (J K^{-1} mol^{-1})	25.98 (c, γ), 20.79 (g)
S° (J K^{-1} mol^{-1})	51.76 (c)
$\Delta H°_f$ (kJ mol^{-1})	-0.59 (c, α), 0 (c, γ), 112.01 (g)
$\Delta G°_f$ (kJ mol^{-1})	-0.59 (c, α), 77.45 (g)

Table 2 Physical properties of Cd^{2+}

Cd^{+} ionic radius (Å)	1.14 (Pauling)
Cd^{2+} ionic radius (Å)	0.97 (Pauling) 1.03 (Goldschmidt)
Cd^{2+} hydration energy (kJ mol^{-1})	-1828
$\Delta H_f°$ (kJ mol^{-1})	
Cd^{+}(g)	986.1
Cd^{2+}(g)	2623.5
Cd^{2+}(aq., 1 M)	-75.90
$\Delta G_f°$ (kJ mol^{-1})	
Cd^{2+}(aq., 1 M)	-77.57
S° (J K^{-1} mol^{-1})	
Cd^{2+} (aq., 1 M)	-73.22

Mg. In vapour phase, unstable Cd_2 molecules have been detected[1] (bond energy about 7.4 KJ mol^{-1}). Cd exhibits a certain stability when exposed to dry air, but in the presence of moisture it is slowly covered with an oxide layer. It is softer and more malleable than Zn and can be easily laminated, extruded, drawn, and processed. A characteristic sound (a sort of scream) is generated on bending a bar of the metal. Cd shows a great resistance to corrosion, a low-melting point, and excellent electrical conduction. Unlike zinc, Cd has no amphoteric properties and, although cadmiate anions are known, Cd does not dissolve in bases. With Zn and Hg (*see* ***Zinc: Inorganic & Coordination Chemistry*** and ***Mercury: Inorganic & Coordination Chemistry***), Cd forms Group 12 and has two s electrons outside filled d shells. Its usual oxidation state is +2, but also Cd^{I} species are known. Zn and Cd prove to be considerably more electropositive than their neighbors in the transition groups and no carbonyl, nitrosyl, alkene, and so on complexes of the type given by transition metal are known. However, their ability to form coordination compounds with ammonia, amines, cyanide (*see Cyanides*), and halide ions resembles that found for the d-group elements. Even though Cd chemistry closely resembles that of Zn, in some cases differences are still observed.[2] Physical properties of metal cadmium and Cd^{2+} ion are reported in Tables 1 and 2, respectively.

4 OCCURRENCE

The presence of Cd in the Earth's crust is estimated to range between 0.15 and 0.11 μg g^{-1} (67th element in order of abundance), with a Zn/Cd molar ratio about 450:1 (strongly dependent on the nature of the rocks).[3] Cd^{2+} ionic radius (0.97 Å) is similar to that of Ca^{2+} (0.99 Å) and Na^{+} (0.98 Å), therefore Cd^{2+} is expected to be found substituting for Ca^{2+} and Na^{+} in their minerals. Moreover, Cd^{2+} shows high affinity for calcite[4] and iron oxyhydroxides surfaces. It reveals a chalcophile nature and forms few minerals: the most important are two sulfides, greenockite and hawleyite (hexagonal and cubic form of CdS, respectively), a carbonate (otavite) and an oxide (monteponite). Greenockite, in particular, is formed as a yellow coating on weathering sphalerite (ZnS). Cd^{2+} gives isomorphous replacement in several Zn minerals, which can contain up to 0.5% of Cd. For this reason, sphalerite is the main industrial source of Cd. Under natural conditions, Cd can be found in the atmosphere (0.1 to 5 ng m^{-3}) as a result of volcanic emission and release from vegetation.[3]

5 PRODUCTION

Almost all the metal Cd is obtained as a by-product of the metallurgy of Zn but it may be produced also using flue dusts gathered from lead and copper smelters.**[1,5,6]** Cd can be recovered from Zn minerals as CdO fume (pyrometallurgical process), owing to the higher volatility of CdO over ZnO, or as precipitate from the Zn solutions used in electrolytic production of Zn (hydrometallurgical process). In the first case, during the pyrometallurgical extraction of Zn, a considerable volatilization of Cd compounds (most of all CdO) occurs. In this way a 90–99% recovery of Cd can be obtained. Cd not removed can be recovered in the residual high-boiling fraction from Zn purifying process by fractional distillation. The concentration of Cd in dust is too low to proceed to a direct reduction: therefore the dust, separated by an electrostatic Cottrel's trap, is leached with H_2SO_4. The solution, after elimination of Pb as $PbSO_4$, is treated with Zn dust. After precipitation and filtration, Cd is exposed to reductive distillation and fusion in the presence of NaOH to eliminate Zn and other impurities. A further distillation can be used to obtain higher purity. In the hydrometallurgic process, the roasted zinc mineral is dissolved in H_2SO_4. After elimination of As and Cu, Cd is precipitated with Zn dust and leached again with H_2SO_4. The solution is then electrolyzed (*see* ***Electrochemistry: Applications in Inorganic Chemistry***) using insoluble anodes of Pb (with 1% Ag), coated with MnO_2 to avoid acidic corrosion, and cathodes of Al. Cd is deposited on cathodes, but often in dendritic form. A more compact deposition is obtained using rotating or oscillating cathodes. The applied potential is about $-2.75\,\mathrm{V}$ with a current density of about $100-200\,\mathrm{A\,m^{-2}}$. Thus produced, Cd undergoes double fusion with NaOH to eliminate residual Zn. Ultrapure Cd can be produced using zone refining.**[7]** This last process requires oxygen exclusion. Single crystals of desired orientation can be obtained using the Bridgman technique.

6 USES

Cd and its compounds find applications in several industrial materials: electrode materials in Ni–Cd batteries (about 70% of total produced Cd), pigments in ceramics, glasses, paper, plastics, artists colors (13%), stabilizers for polyvinyl chloride and related polymers (7%), coatings on steel, aluminium, and other nonferrous metals (8%), and specialized alloys**[1,5]** (*see* ***Alloys***) and others (2%).

Ni–Cd batteries are extensively utilized in cordless power tools (cellular telephones, portable computers, toys, and so on), in electric vehicles, and for emergency and starting power. They have excellent performance both at low and high temperature and high cycle life. CdS is an important yellow pigment, with other compounds (CdSe in particular) it gives rise to different colors. Cd pigments show a remarkable ability to withstand high temperature and pressure without fading; they are, therefore, suitable for industrial processes involving severe conditions. Cd stabilizers for polyvinyl chloride (PVC) are usually organic carboxylate Cd salts (such as stearate or laurate), which are included in the polymeric structure before processing and retard degradation processes due to exposure of PVC to ultraviolet light and heat. They are used in mixture with barium and lead organic salts and constitute about 0.5–2.5% of the final polymeric material. Cd plating is used to provide the best combination of corrosion resistance and low friction coefficient on metal component involved in mechanical stress. A thin film of Cd may be applied by electroplating or, less commonly, by dipping in fused Cd, spraying or vacuum deposition. This protection is better than that obtained using Zn and the Cd film reveals a higher resistance to alkali, seawater and salinity. It is highly ductile and easily soldered. Cd surface, unlike Zn, retains a high lustre for a long period, even in a moist environment. In general, Cd electroplating is carried out using sodium cadmiocyanide solutions and anodes of Cd (99.95%). Due to its great cross section towards neutrons (2500 barns), Cd (especially ^{113}Cd) possesses high neutron-absorbing ability and is used for control rods and shielding in nuclear reactors. Copper with 1% of Cd shows a maximum tensile stress, 50% higher than that of electrolytic copper, without appreciable lowering of electrical conductivity. This alloy is used in telephone and trolleybus cables. Also Pb with 1% of Cd proves to be more resistant against repeated mechanical stresses. Small amounts of Cd in Al–Cu alloy delay the natural aging after solution hardening. Cd is a component of special alloys melting at low temperatures: the Wood's alloy (50% Bi, 25% Pb, 12.5 Cd, 12.5 Sn) melts at 70 °C and is used in fuses for telephone installation and fire-prevention systems. Special antifriction bearings can be produced using Cd–Ag or Cd–Ag–Cu alloys. Cd is used as a deoxidizer in melting Ag or Ag alloys and to prepare soft solders. Brazing alloys based on Ag–Cu–Cd–Zn are employed in the mechanical and electrical industry. Some Ag–Cd and Au–Cd alloys display shape memory properties.**[8]** CdS, CdSe, and CdTe are semiconductors (*see* ***Semiconductor Interfaces***) and used in solar cells and a variety of electronic devices. CdS shows photoconductive and electroluminescent properties and can be employed in X-ray fluorescent screens and in scintillation counters. $CdCO_3$ and $CdCl_2$ have fungicides properties, $CdCl_2$ is also used in photography, in dyeing and printing of textiles, in galvanoplasty, in mirror manufacture, and in the preparation of Cd yellows and reds. $CdBr_2$ finds application in photography, process engraving, and lithography. CdO is used in ceramic glazes, in silver-zinc batteries, and in plastics to improve high-temperature properties. $Cd(CH_3COO)_2$ creates iridescent effects in potteries and porcelains. $CdSO_4$ also has applications in industry: electrodeposition of Cd, manufacture of Cd salts, fungicides, production of vacuum tubes, electrolyte in standard cells, as a chemical accelerator in cement formation.

Table 3 Main cadmium isotopes

	Natural abundance (%)	Emitter type	Half-life
97	–	β^+	3 s
98	–	β^+	8 s
99	–	β^+,γ	16 s
100	–	β^+,γ	1.1 min
101	–	β^+,γ	1.2 min
102	–	β^+,γ	6 min
103	–	β^+,γ	7.5 min
104	–	γ	58 min
105	–	β^+,γ	55.5 min
106	1.22	–	stable
107	–	β^+,γ	6.53 h
108	0.88	–	stable
109	–	γ	462 d
110	12.39	–	stable
111	12.75	–	stable
112	24.07	–	stable
113	12.26	–	stable
114	28.86	–	stable
115	–	β^-,γ	59 h
116	7.58	–	stable
117	–	β^-,γ	170 min
118	–	β^-	50.3 min
119	–	β^-,γ	2.96 min
120	–	β^-	50.8 s
121	–	β^-,γ	13.5 s
122	–	β^-	5.3 s
123	–	β^-	2.09 s
124	–	β^-,γ	1.24 s

7 ISOTOPES

Several isotopes (*see Isotopes & Isotope Labeling*) of Cd are known,[8] and 8 are stable (Table 3). For ^{111}Cd and ^{113}Cd, the nuclear spin is 1/2 and they are used for NMR studies of Cd compounds and in biological fields (*see* ***Cadmium: Organometallic Chemistry***). ^{113}Cd is used in the nuclear industry because of its high neutron cross section. Unstable isotopes are prepared from nuclear reactions.[9] Cd stable isotope composition in geological and meteorite samples has been investigated using multiple collector inductively coupled plasma mass spectrometry.[10]

8 TOXICOLOGICAL AND ECOLOGICAL INFORMATION

Extraction and manufacture of Zn, Pb, and Cu ores can give pollution of the environment with Cd derivatives. Cd is present also in industrial sludge and waste water. A source of Cd release is the burning of fossil fuels and the incineration of rubbish. Fertilizers can contain variable amount of Cd. Toxicological characteristics and environmental fate[3,11] of Cd resemble those of Pb and Hg (*see* ***Metal Ion Toxicity***). In aqueous environment Cd^{2+} shows a relative mobility: it depends on pH, presence of organic molecules, and water hardness. Cd concentration in soil can reach high levels,[12] but high acidity increases the release of Cd^{2+} and, consequently, its uptake by plants and bioaccumulation.[3,11] In aquatic environment, invertebrates (most of all molluscs and crustaceans) accumulate Cd rapidly, followed by fish and aquatic plants;[13] as a matter of fact, sea organisms are more resistant to Cd poisoning than those living in freshwater environment. Bioaccumulation in terrestrial plants results in higher Cd level in animals involved in alimentary cycle of the plants; in some cases the presence of Cd in soil inhibits the growth of some plants.[3,11] Workers in Cd, Zn, and Pb processing plants may be exposed to direct poisoning by Cd, but human uptake of Cd occurs mainly through food.[3] Uncontaminated foodstuffs and cigarette smoke contain low amount of Cd (*see* ***Nutritional Aspects of Metals & Trace Elements***) and drinking water normally does not show significant metal content. Ingestion of Cd from contaminated foodstuffs gives rise to several diseases: in the case of that named itai-itai, Cd in the rice was found the etiological agent. Cd is particularly absorbed by the respiratory tract: cigarette smokers may absorb 10–40% of inhaled Cd. Cd fume is an intense irritant and so pulmonary edema develops rapidly. In the case of acute poisoning, the gastrointestinal tract absorbs only a small amount of Cd even though salivation, choking, nausea, vomiting, convulsion, and collapse may occur. Cd tends to accumulate in the liver and kidneys (about 50% of total body Cd). Metalothioneins (*see* ***Metallothioneins***) found in these two organs show high affinity for Cd^{2+}.[14] These metal-binding proteins act as sequestering agents, lowering Cd^{2+} concentration in critical tissue sites. The presence of Cd^{2+} seems to induce the synthesis of the protein in the liver and kidneys. The half-life of Cd in the body is 10–30 years. Cd compounds show high oral toxicity, even though the emetic and irritant action is so violent that only a little Cd is absorbed so that fatal poisoning is rather uncommon.[15] Cd compounds cause damage to kidney and to the central nervous system and are carcinogenic for connective tissue, lungs and liver and, perhaps, teratogenic.[15,16] Direct relationship between Cd poisoning and thyroid dysfunction has been established.

9 SPECTROSCOPY

9.1 NMR Spectroscopy

^{111}Cd and ^{113}Cd NMR spectroscopy has been used to study several complexes, both in solid state and in solution, and to investigate the binding site of the metal ion in different metalloproteins.[17] These isotopes have a spin 1/2 and, therefore, the broadening of the NMR signals due to the quadrupolar contribution to NMR relaxation is avoided. The natural abundance is 12.75 and 12.26% for ^{111}Cd and ^{113}Cd, respectively, but due to the lower receptivity of ^{111}Cd respect to ^{113}Cd, NMR investigations have mainly been performed with the latter isotope. ^{113}Cd chemical shift varies nearly linearly with concentration for cadmium perchlorate, sulphate, and nitrate, while the halide salts show a large nonlinear relationship owing to the formation of mono- and polyhalogeno complexes. Studies on a variety of organic and inorganic ligands bearing different donor atoms (*see Donor Atom*) revealed linear dependence on concentration and that: (i) ligands binding through the oxygen atom (sulphate, nitrate, nitrite, carboxylic acids, etc.) cause increased shielding of the Cd nucleus; (ii) those binding through nitrogen (ammonia, pyridine, azide, ethylenediamine, etc.) induce a marked deshielding; and (iii) ligands binding through the sulphur atom (thiourea (*see Thiourea*), thiocyanate, etc.) cause a remarkable deshielding.**17** Several Cd complexes with N-ligands (*see* ***Ammonia & N-donor Ligands***) show a line broadening, probably due to their slow dissociation rate in solution. In many cases, binding constants of Cd complexes can be calculated by the chemical shift or broadening. Extensive investigations have been performed on Cd^{2+}-halide systems, in aqueous and nonaqueous media, and the equilibria have been characterized.**17** A somewhat surprising effect of halide ions on ^{113}Cd NMR spectra in the presence of ATP as a function of pH can be observed: the $Cd(ClO_4)_2$–ATP system shows a downfield shift on increasing pH; the $CdCl_2$–ATP system, however, shows an upfield shift. In the former case, the downfield shift may be due to the displacement of bound H_2O, whilst in the latter the upfield shift is due to the displacement of coordinated Cl^-. Cd-substituted porphyrins, in particular tetraphenylporphyrin (TPP), have been studied using ^{111}Cd NMR and the ^{111}Cd–^{15}N coupling constants determined.**17** Cd–TPP adducts have been investigated by ^{111}Cd and ^{113}Cd NMR.**17** The ^{113}Cd chemical shift observed for aqueous Cd-EDTA is independent of pH between 4 and 11, but at $pH > 13.8$ gives evidence for the formation of mixed hydroxo complexes. A large group of Cd compounds containing N-donor ligands have been investigated as a function of counterion, chelate ring size, and basicity: in the case of trisdiamine species, the deshielding effect decreases in the order $4 \rightarrow 5 \rightarrow 6 \rightarrow 7$-membered chelate ring. The deshielding effect of anionic N-donors is much greater than for neutral N-donors. ^{113}Cd–^{113}Cd and ^{113}Cd–^{111}Cd coupling constants have been determined for a number of compounds containing multiple Cd centers.**17** The trinuclear anion $(Na[Cd(SOPh)_3]_2)^-$ has been studied through ^{111}Cd NMR spectra in Me_2CO and MeCN. In both the cases retention of bonding between Cd and S,O has been observed. Complexes with simple and N-protected amino acids have been investigated at different pH values. The results are consistent with the presence of Cd complexes in which the ligand is bidentate, acting through N and O atoms. ^{113}Cd NMR chemical shifts strongly depend on substituent effects in alkylcadmium compounds (*see* ***Cadmium: Organometallic Chemistry***). Results have also been obtained by application of magic angle spinning techniques to the ^{113}Cd NMR study of solid compounds, as powders, or as single crystals.**2,17** Cd complexes with glycine, alanine, and cysteine have been investigate using solid-state ^{113}Cd NMR spectroscopy and the principal components of the ^{113}Cd shielding tensor determined. Cross polarization/magic angle spinning NMR experiments have been used to calculate the principal elements of the ^{113}Cd shielding tensor for a collection of N-donor ligands. Composition and structure of a unusually highly charged $[ClCd_8\{SCH(CH_2CH_2)_2NHMe\}_{16}]^{15+}$ cation have been determined by X-ray, XPS, and ^{113}Cd NMR measurements on microcrystalline powder.**18** Solid-state ^{113}Cd NMR spectroscopy has been used to characterize a number of Cd thiocyanate complexes of varying stoichiometry.**19** Several reviews have been published on metalloprotein studies.**17,20** ^{113}Cd NMR spectroscopy has been successfully applied to environmental studies.**21**

9.2 Photoelectron and Vibrational Spectroscopy

Photoelectron spectra of Cd compounds have been reported (*see* ***Photoelectron Spectroscopy of Transition Metal Systems***), but discrepancies have been noted.**2** X-ray photoelectron spectroscopy has been used in surface studies.**22** Simmetry, bond length, and equilibrium constants (*see Equilibrium Constant*) of Cd complexes have been determined through IR and Raman spectroscopy. Resonance Raman spectroscopy and Photoluminescence allow investigation of the optical properties of ultrathin CdS films.**23** Electron diffraction studies have been reported.**24**

10 ELECTROCHEMISTRY

$E°$ and $E_{1/2}$ values of Cd^{2+}/Cd couple and Cd complexes in aqueous solution have been measured through potentiometric and voltammetric methods (Table 4).**25** Few data are available

Table 4 Electrochemical data for Cd^{2+} in aqueous solvents

Standard potentials		
Electrode		$E°$(V) vs. NHE
$Cd^{2+} + 2e^- = Cd$		−0.4025
$Cd^{2+} + 2e^- + Hg = Cd(Hg)$		−0.3515
$Cd(OH)_2 + 2e^- = Cd + 2OH^-$		−0.824
$[Cd(CN)_4]^{2-} + 2e^- = Cd + 4CN^-$		−1.028
$[Cd(NH_3)_4]^{2+} + 2e^- = Cd + 4\,NH_3(aq)$		−0.613
Half-wave Potentials (Hg electrode)		
Species	Conditions	$E_{1/2}$ (V) vs. SCE
Cd^{2+}	$NaClO_4$, 0.1 M	−0.59
Cd^{2+}	KNO_3, 0.1 M	−0.58
$[CdCl_x]^{2-x}$	KCl, 0.1 M	−0.60
$[CdI_4]^{2-}$	KI, 0.1 M	−0.65
$[Cd(NH_3)_4]^{2+}$	NH_4Cl, 1 M; NH_3, 1 M	−0.81
$[Cd(CN)_4]^{2-}$	KNO_3, 0.1 M; KCN, 1 M	−1.16
$[Cd(SCN)_x]^{2-x}$	KSCN, 2 M	−0.664

Table 5 Electrochemical data for Cd^{2+} in nonaqueous solvents

Species	Solvent	Conditions	$E_{1/2}$(V)
$Cd(ClO_4)_2 \cdot 6H_2O$	MeCN	0.1 M, $NaClO_4$	−0.27 vs. SCE
$Cd(ClO_4)_2$	PhCN	0.1 M, TEAP	−0.17 vs. SCE
$Cd(ClO_4)_2$	DMF	0.1 M, TEAP	−0.17 vs. Ag/AgCl$_s$
$Cd(ClO_4)_2 \cdot 2H_2O$	$MeCO_2H$	1 M, $LiClO_4$	−0.295 vs. SCE
$Cd(NO_3)_2$	ethylenediamine	0.1 M, $NaNO_3$	−0.50 vs. NCE
$Cd(ClO_4)_2$	ethylenediamine	0.1 M, $NaNO_3$	−0.70 vs. NCE
$CdCl_2$	ethylenediamine	0.1 M, $NaNO_3$	−0.64 vs. NCE
$CdCl_2$	MeOH	0.2 M, LiCl	−0.595 vs. Ag/AgCl$_s$
$CdCl_2$	$HCONH_2$	0.2 M, LiCl	−0.672 vs. Ag/AgCl$_s$

in nonaqueous media. The potential-pH diagram for Cd^{2+}/Cd system has been determined and discussed in connection with corrosion, immunity, and passivation.[26] Cd can be corroded at acidic and very alkaline pH values, but the corrosion rate is fast only in the presence of oxidizing and complexing agents due to the high hydrogen overpotential. In aqueous solution, Cd^{2+} gives a well-defined voltammetric wave on Hg electrode, corresponding to a reversible, two-electron reduction.[25] In the presence of complexing agents (*see* ***Electrochemistry: Applications in Inorganic Chemistry***), the $E_{1/2}$ value shifts towards more negative values (Table 4): type and stability of the complex(es) can be often determined using DeFord-Hume or Shaap-McMasters methods. In organic solvents, Cd^{2+} undergoes a single step bielectronic reduction; on Hg electrode it is in most the cases reversible or quasi-reversible (Table 5). Cd^{2+} dodecyl sulphate micelles have been characterized using voltammetric methods.[27] CdS thin films can be electrochemically obtained and pulsed sonoelectrochemical synthesis of CdSe nanoparticles has been realized.[28] Cd^{2+} sensitive electrodes are known.

11 CHEMICAL PROPERTIES

Cd dissolves in acids, but more slowly than Zn; warm H_2SO_4 rapidly corrodes the metal. Cd reacts with NH_3 and SO_2 in presence of moisture and with concentrated NH_4NO_3 solutions. Cd is slowly oxidized by moist air, rapidly by steam and by air at very high temperature, giving a brown oxide CdO. Unlike Zn, Cd is insoluble in alkali. NaOH precipitates Cd^{2+} as white hydroxide $Cd(OH)_2$. This is insoluble in excess of NaOH (unlike $Zn(OH)_2$), but dissolves in ammonia solution, giving $[Cd(NH_3)_4]^{2+}$. H_2S precipitates Cd^{2+} as a canary-yellow sulfide, which is insoluble in $(NH_4)_2S$ or $(NH_4)_2CN$, but dissolves in oxidizing acids. White $Cd(CN)_2$ is soluble in CN^- excess, giving $[Cd(CN)_4]^{2-}$. Cd^{2+} precipitates as $CdCO_3$ with $(NH_4)_2CO_3$ and as $CdCrO_4$ with concentrated K_2CrO_4. NH_4SCN and Cd^{2+} form colorless soluble $[Cd(SCN)_n]^{(2-n)}$ ($n = 1-4$), but in presence of pyridine a white precipitate of $[Cd(py)_2(SCN)_2]$ is observed.

12 ANALYTICAL METHODS

Cd^{2+} can be detected by the insolubility of its yellow sulfide (*see* ***Analytical Chemistry of the Transition Elements***). Several reaction and spot tests allow the identification of Cd^{2+}. Quantitative determinations are based on gravimetric (CdS or β-naphthylquinoline complex) or titrimetric (EDTA) methods. Several physical techniques can be used in quantitative and qualitative analysis: polarography (or related techniques, even in the presence of Zn, Cu, Bi and Pb), electrodeposition, colorimetric methods, flamephotometric methods, neutron activation, atomic absorption, and ICP spectrometry and ion selective electrodes.

13 STEREOCHEMISTRY

The stereochemistry of Cd^{2+} is summarized in Table 6. The main coordination numbers (*see* ***Coordination Numbers & Geometries***) are 4, 5, and 6.[29] Due to the larger size, Cd^{2+} assumes coordination number 6 more easily than Zn^{2+}: in the case of $[M(DHA)_2(DMSO)_2]$ (DHA = 3-acetyl-6-methyl-2H-pyran-2, 4(3H)-dione, $M = Cd^{2+}$ or Zn^{2+}), both the crystal structures (*see Crystal Structures*) show a distorted octahedral geometry, but in solid-state significant differences in the coordination sphere of the two complexes are observed.[30] In $CdMe_2$ and dihalides in gas phase, Cd^{2+} is coordinated to only two ligands with $D_{\infty h}$ symmetry. In solid and solution phase, the coordination number is higher than 2. Coordination number 3 characterizes CdX_3^- (D_{3h} symmetry) in organic media, but in aqueous solution $CdBr_3^-$ is pyramidal due to the binding of one or more water molecule. Coordination numbers higher than 3 are observed in solid $MCdX_3$. In aqueous solution, CdX_4^{2-} anions ($X = Cl^-$, I^-, CN^-) are four-coordinated while tetrahedral (*see Tetrahedral*) $CdCl_4^{2-}$ is observed only as diquinolinium salt, less bulky

Table 6 Coordination chemistry of Cadmium

Coordination number	Compound {coordination core}
2	$CdMe_2$, CdX_2(gas phase, $X = F, Cl, Br, I$)
3	CdX_3^- (nonaqueous solvents, $X = F, Cl, Br, I$)
4	$CdS_2\{CdS_4\}$, $CdCl_2$(biuret)$_2\{CdCl_2O_2\}$, $CdCl_2tu_2\{CdCl_2S_2\}$, $CdCl_2py_2\{CdCl_2N_2\}$, $CdCl_2(Ph_3P)_2\{CdCl_2P_2\}$, $Cd(HCO_2)_2tu_2\{CdO_2S_2\}$
5	$[Co(NH_3)_6][CdCl_5]$ $\{CdCl_5\}$, $Cd(S_2CNEt_2)_2\{CdS_5\}$, $CdSO_4tu_3\{CdS_4O\}$, Cd(thioglycollate)$_2\{CdS_4O\}$, CdI_2(py N-oxide) CdI_3O_2
6	CdO $\{CdO_6\}$, $[Cd(H_2O)_6]$ $\{CdO_6\}$, Cd(acac)$_2\{CdO_6\}$, [Cd(imidazole)$_6$]$(NO_3)_2\{CdO_6\}$, $[Cd(en)_3]S_2O_3\{CdN_6\}$, $NH_4CdCl_3\{CdCl_6\}$, $RbCdBr_3\{CdBr_6\}$, $CdCl_2$(urea)$_2\{CdCl_4O_2\}$, $CdCl_2$(imidazole) $\{CdCl_5N\}$, $CdBr_2py_2\{CdBr_4N_2\}$, $Cd(NCS)_2\{CdN_2S_4\}$, Cd(glycinate)$_2\cdot H_2O$ $\{CdO_4N_2\}$, Cd(L-methioninate)$_2\{CdO_4N_2\}$, Cd(histidinate)$_2\{CdO_2N_4\}$
7	$Cd(MeCO_2)_2\cdot 2H_2O$ $\{CdO_7\}$, Cd(salicylate)$_2\cdot 2H_2O$ $\{CdO_7\}$, $Cd(NO_3)_2py_2\{CdO_4N_2\}$, $Cd(NO_2)_2$en $\{CdO_4N_3\}$
8	$CdF_2\{CdF_8\}$, $Cd(NO_3)_2\cdot 4H_2O$ $\{CdO_8\}$, Cd(maleate)$\cdot 2H_2O$ $\{CdO_8\}$, Cd(1,8-naphthpyridine)$_4(ClO_4)_2\{CdN_8\}$

cations give Cd^{2+} coordinated by six chlorides. Cd^{2+} is found tetracoordinated in $RbCdI_3\cdot H_2O$ or in tetralkylammonium salts in which dinuclear (*see Dinuclear*) $[X_2CdX_2CdX_2]^{2-}$ anions are present. $Cd(CN)_2$ and CdS_2 have CdC_2N_2 and CdS_4 cores, respectively. Most CdX_2L_2 complexes show a coordination number higher than 4, but a distorted tetrahedral geometry is found in CdX_2L_2 ($X = I^-$, Cl^-) when L is a P- or S-donor.**[29]** Cd^{2+} is five coordinated in the monomeric $[Cd(NCS)_2L]$ (L = bis(2-dimethylaminoethyl)methylamine), in $CdCl_5^{3-}$ (D_{3h} symmetry) and in [Cd(*o*-ethylxantato)$_3$]$^-$ (CdS_5 core). A very large number of Cd compounds are six coordinated, for example, $[Cd(H_2O)_6]^{2+}$, [Cd(acac)$_2$], and [Cd(acac)$_3$]$^-$ have a CdO_6 core. Six-coordinated CdN_6 ions are formed with mono- and bidentate ligands such as imidazole, en, and thiocarbohydrazide. In the solid state, CdX_2 ($X = Cl^-$, Br^-, I^-) compounds are six coordinated. Halide adducts of the type CdX_4L_2 are common; halogen bridging leads to an approximately octahedral Cd^{2+} for Cl^- and Br^-, but I^- gives either four and five-coordinated Cd^{2+}. A few seven-coordinated compounds are known, but none is mononuclear or involves monodentate ligands (*see Monodentate Ligand*). In the solid state, each Cd^{2+} ion in $[Cd(H_2O)(CH_3OC_6H_4COO)_2]_n$ is seven coordinated in a distorted pentagonal bipyramidal (*see Pentagonal Bipyramid*) geometry. In [Cd(tea)$_2$](sac)$_2$ (tea = triethanolamine, sac = saccharinate anion), the cation [Cd(tea)$_2$]$^{2+}$ adopts a monocapped trigonal prism (*see Trigonal Prism*) geometry and the seven coordination is achieved acting the former tea ligand as tetradentate (*see Tetradentate Ligand*) and the latter as tridentate (*see Tridentate Ligand*). A monocapped trigonal prism (*see Trigonal Prism*) geometry is found also in $[Cd_4(TCPM)_2(DMF)_4]\cdot 4DMF\cdot 4H_2O$ (TCPM = tetrakis(4-carboxyphenyl)methane) that contains a tetranuclear Cd-carboxylate cluster (*see Cluster*).**[31]** Eight coordination is rare. CdF_2 contains a CdF_8 core in a fluorite structure. In $Cd(NO)_3\cdot 4H_2O$, the four water molecules are square planar (*see Square Planar*) and bidentate NO_3^- anions lie above and below this plane. The structure of Cd(tea)$_2$$(NO_3)_2$ (tea = triethanolamine) reveals eight-coordinated Cd^{2+} in a distorted hexagonal bipyramidal geometry.

14 COMPOUNDS

14.1 Cd^I Compounds

Few compounds of Cd^I have been prepared and identified. In melts of LiCl/KCl or $NaAlCl_4$, Cd and $CdCl_2$ react to give Cd_2^{2+}. Solid $Cd_2(AlCl_4)_2$ has been isolated from molten $NaAlCl_4$ by reduction of $Cd(AlCl_4)_2$ with Cd. Spectroscopic and X-ray studies (*see* ***Diffraction Methods in Inorganic Chemistry***) indicate the presence of Cd_2^{2+} ($d_{Cd–Cd} = 2.576$ Å) and $AlCl_4^-$ units: three Cl atoms of each $AlCl_4^-$ unit weakly bridge each Cd atom, which reveals a distorted tetrahedral (*see Tetrahedral*) coordination.**[32]** A complex containing a Cd–Cd bond can be synthesized by reaction between $CdCl_2$ and $LiBHEt_3$ in the presence of Tl[HB(3,5-Me$_2$pz)$_3$] (pz = pyrazolyl ring). No X-ray structure is available but NMR studies indicate a strong bond between Cd atoms. Cd_2^{2+} ion was obtained in aqueous solution (O_2 free) by reaction of $Cd(ClO_4)_2$ or $Cd(O_3SCF_3)_2$ with Cd powder and the redox properties evaluated: $E°$ for Cd(II,I) $= -0.45$ V and $E°$ for Cd(I,0) $= -0.35$ V.**[33]** Cd^+ and Cd_2^{2+} ions have been observed in fully Cd^{2+}-exchanged zeolite A (*see* ***Zeolites***) after exposure to Cd vapour. Cd^+ can be generated in water *via* pulse radiolysis (*see Pulse Radiolysis*).**[34]** Cd^{2+} is rapidly reduced by $[e_{aq}]^-$ or $[CO_2^{\bullet}]^-$ to give Cd^+, which rapidly dimerizes to Cd_2^{2+}. This species is unstable and decomposes in Cd and Cd^{2+}. Cd^+ is oxidized to Cd^{2+} by alkyl and $OH^{\bullet}$ radicals. $[CdL]^+$ (L = [14]ane-1,4,8,11-N_4) was prepared by pulse radiolysis (*see Pulse Radiolysis*).**[2]** Cd^+ and Cd_2^{2+} species have been identified using ^{113}Cd NMR relaxation measurements by adding Cd to CdI_2.**[2]**

14.2 Cd^{II} Compounds

14.2.1 Hydrides

Cd does not dissolve hydrogen in any significant quantities (*see* ***Hydride Complexes of the Transition Metals***).**[35]** CdH_2 is quite unstable at room temperature, but its decomposition is slow below 253 K (*see* ***Hydrides: Solid State Transition Metal Complexes***). It can be obtained in organic solvents as shown in equation (1) and (2):

$$\mathrm{LiAlH_4 + 2CdR_2 \longrightarrow 2CdH_2 + LiAlR_4} \tag{1}$$

$$\mathrm{2LiAlH_4 + CdI_2 \longrightarrow CdH_2 + 2AlH_3 + 2LiI} \tag{2}$$

Gaseous CdH, CdD, CdH^+, and CdD^+ are known, but not gaseous CdH_2.[35] The Cd hydride complex Cs_3CdH_5 has been isolated and characterized.[36] It can be synthesized by reaction of CsH_2 with metal Cd at high temperature and pressure. A tetragonal Cs_3CoCl_5-type structure containing tetrahedral (*see Tetrahedral*) $CdH_4{}^{2-}$ units has been proposed with a Cd–D bond distance of 1.82 Å. In several complexes, Cd–H bond has been observed.[37]

14.2.2 Halides

All four halides (*see* ***Halides: Solid-state Chemistry***) are known (Table 7).[1] CdF_2 has a fluorite structure and is more ionic than the other halides, which have a substantially covalent nature (*see Covalent Bonds*) and a layer structure.[38] In fact, CdF_2 shows higher melting and boiling points and lower solubility. $CdCl_2$, $CdBr_2$, and the α form of CdI_2 consist of cubic close-packed halides with Cd^{2+} in octahedral sites between alternate pairs of layers. In the β form of CdI_2, however, the stacking of iodine layers follows the pattern ABACAB.[38] Unlike the other halides, CdF_2 is not soluble in ethanol, ether, and anhydrous ammonia. CdF_2 and CdI_2 do not form hydrate (*see Hydrates*) while $CdCl_2$ and $CdBr_2$ can crystallize with 4, 2.5, or 1 and 4 or 1 water molecules, respectively. On heating, these hydrate species (*see Hydrates*) generally change into basic halides. CdF_2 may be prepared by reaction between aqueous HF and $CdCO_3$. Several methods are known to obtain $CdCl_2$:[1] (i) reaction between $Cd(OH)_2$ and thionyl chloride; (ii) reaction between $Cd(CH_3COO)_2$ and acetyl chloride in glacial acetic acid; (iii) reaction between metal Cd and gaseous HCl at 450 °C; (iv) reaction between $Cd(NO_3)_2{\cdot}4H_2O$ and concentrated HCl. $CdBr_2$ and CdI_2 may be prepared by direct reaction of the elements.[1] $CdBr_2$ may also be obtained by reaction between $Cd(CH_3COO)_2$ and acetyl bromide in glacial acetic acid. Oriented CdI_2 crystals have been prepared by reaction of gaseous HI with an Langmuir-Blodgett film of cadmium arachidate. Doped cadmium halide crystals have been grown and characterized.[39] $CdCl_2$, $CdBr_2$, and CdI_2 form auto-complexes in aqueous solution.

14.2.3 Pseudohalides

White $Cd(CN)_2$ is sparingly soluble in water, except in the presence of CN^- ions, owing to the formation of soluble anionic complexes.[1] On heating it darkens and decomposes at about 200 °C. $Cd(CN)_2$, like $Zn(CN)_2$, has a cubic anti-cuprite structure. Colorless cadmium thiocyanate is sparingly soluble in water, ethanol, and liquid ammonia. In the solid, Cd^{2+} is surrounded by an N_2S_4 octahedron. Cadmium thiocyanate polymers exhibit highly anisotropic physical properties.[40] Yellow $Cd(N_3)_2$ is prepared by mixing solutions of $Cd(NO_3)_2$ and NaN_3. The crystals are orthorhombic and decompose with detonation when heated. Cadmium pseudohalides (*see Pseudohalide*) may be prepared by metathesis (equation 3).

$$\mathrm{CdSO_4 + Ba(SCN)_2 \longrightarrow BaSO_4 + Cd(SCN)_2} \tag{3}$$

14.2.4 Oxides

CdO is obtained by burning the metal in air or by pyrolysis of nitrates, carbonates, formate, or oxalate;[1] the last two, in

Table 7 Physical properties of cadmium halides

	CdF_2	$CdCl_2$	$CdBr_2$	CdI_2
Crystal structure	Cubic	Rhomb.	Rhomb.	Hexag.
Distance Cd–X (c) (Å)	2.33	2.74	2.82	2.99
Density (298 K) ($\mathrm{Kg\,m^{-3}}$)	6330	4047	5192	5670
Solubility (g/100 g water)	4.35 (25 °C)	140 (20 °C)	95 (18 °C)	86 (25 °C)
Melting point (K)	1383	841	841	660
ΔH_{fusion} ($\mathrm{kJ\,mol^{-1}}$)	22.6	22.2	20.9	33.5
ΔS_{fusion} ($\mathrm{J\,K^{-1}\,mol^{-1}}$)	16.3	26.4	25.1	50.2
Boiling point (K)	2020	1253	1409	1063
ΔH_{vap} ($\mathrm{kJ\,mol^{-1}}$)	234.3	123.0	–	–
ΔS_{vap} ($\mathrm{J\,K^{-1}\,mol^{-1}}$)	115.9	98.3	–	–
$\Delta H^\circ{}_f$ ($\mathrm{kJ\,mol^{-1}}$) (c)	−700.4	−391.5	−316.2	203.3
$\Delta H^\circ{}_f$ ($\mathrm{kJ\,mol^{-1}}$) (aq, 1 M)	−720.2	−410.2	−319.0	186.3
$\Delta G^\circ{}_f$ ($\mathrm{kJ\,mol^{-1}}$) (c)	−647.7	−344.0	−296.3	201.4
$\Delta G^\circ{}_f$ ($\mathrm{kJ\,mol^{-1}}$) (aq, 1 M)	−635.2	−340.1	−285.5	180.7
S° ($\mathrm{J\,K^{-1}\,mol^{-1}}$) (c)	77.4	115.3	137.2	161.1
S° ($\mathrm{J\,K^{-1}\,mol^{-1}}$) (aq, 1 M)	−100.8	39.7	91.6	149.4
C° ($\mathrm{J\,K^{-1}\,mol^{-1}}$)	–	74.68	76.65	79.96

Table 8 Physical properties of cadmium oxide, peroxide and hydroxide

	CdO	CdO_2	$Cd(OH)_2$
Crystal structure	Cubic	Cubic	Hexag.
Distance Cd–O (c) (Å)	2.35	2.29	2.39
Density (298) ($Kg\,m^{-3}$)	8150	–	4790
Solubility (g/100 g water)	Insol.	Insol.	2.6×10^{-4} (25 °C)
$\Delta H°_f$ ($kJ\,mol^{-1}$) (c)	−258.2	–	−560.7
$\Delta G°_f$ ($kJ\,mol^{-1}$) (c)	−228.4	–	−473.6
S° ($J\,K^{-1}\,mol^{-1}$) (c)	54.8	–	96.2

Table 9 Physical properties of cadmium sulfide, selenide and telluride

	CdS	CdSe	CdTe
Crystal structure	Hexag.(α) Cubic(β)	Hexag. Cubic	Cubic Hexag.
Distance Cd–X (c) (Å)	2.52(α)	2.63(hexag.)	2.78(cubic)
Density (298) ($Kg\,m^{-3}$)	4920(α) 4500(β)	5820(hexag.)	6200(cubic)
Solubility (g/100 g water)	1.3×10^{-4} (α, 18 °C)	Insol.	Insol.
$\Delta H°_f$ ($kJ\,mol^{-1}$) (c)	−161.9	–	−92.5
$\Delta G°_f$ ($kJ\,mol^{-1}$) (c)	−156.5	–	−92.0
S° ($J\,K^{-1}\,mol^{-1}$) (c)	64.9	–	100.4

particular, give rise to a particularly finely divided form (*see* ***Oxides: Solid-state Chemistry***). Oxide smoke are formed by combustion of cadmium alkyls. Large single crystals may be prepared hydrothermally. Heat treatment of the oxide produces dramatic changes in electrical properties. CdO color depends on the preparation method and varies from green-yellow to brown or nearly black. It does not melt but sublimes without decomposition at very high temperature (the sublimation pressure is 1 atm at 1559 °C). The crystals are cubic of NaCl type ($a = 4.695$). CdO acts a catalyst in gas reactions and as an intrinsic n-type semiconductor (*see* ***Semiconductor Interfaces***) (Band Gap (*see Band Gap*) energy 222 $kJ\,mol^{-1}$). Large third-order nonlinear optical properties are shown by cadmium oxide thin films. CdO is insoluble in water and alkali solutions but dissolves in acids and aqueous NH_3. Several mixed cadmium oxides are isostructural with their zinc analogs. The peroxide CdO_2 shows a cubic structure of pyrite type ($a = 5.27$), with Cd^{2+} coordinated by six oxygens. Physical properties of CdO and CdO_2 are reported in Table 8.

14.2.5 Hydroxides

$Cd(OH)_2$ is precipitated from aqueous Cd^{2+} by addition of bases.[1] It is colorless and soluble in acids and aqueous NH_4Cl, but only slightly in NaOH solutions. $Cd(OH)_2$ is a base stronger than $Zn(OH)_2$; its solubility product is $10^{-4.4}$ and log K for the equilibrium $Cd^{2+} + OH^- = CdOH^+$ is 6.38. $Cd(OH)_2$ begins to undergo thermal decomposition at about 150 °C (at 200 °C it is complete). Several basic salts are known and may be prepared from alkaline Cd^{2+} solutions or by heating CdO with solutions of Cd^{2+} salts at 200 °C. Hydroxide halides have been carefully investigated both in solution and in solid state.[41] Physical properties of $Cd(OH)_2$ are reported in Table 8.

14.2.6 Sulfide, Selenide and Telluride

CdS may exhibit different structures and its color varies from yellow to orange-brown.[1,42] The stable α-form (greenockite) has a wurtzite type structure. The β-form, however, shows a cubic zinc blende structure. At 20 kbar, CdS adopts a rocksalt form. By doping with other metals or organic molecules it may become luminescent (*see* ***Luminescence***). Crystalline CdS is obtained by reactions of Cd vapour in presence of H_2S at 800 °C. Due to the good lattice match between cubic CdS and Au, low Miller-index planes of Au have been used to template the growth of CdS monolayers. CdS nanoparticles have been formed both in Langmuir-Blodgett films and on graphite surface. CdS nanorods have been synthesized by reaction between CS_2 and $CdCl_2$ in ethylenediamine aqueous solution.[43] The disulfide CdS_2 prepared at high pressure has a pyrite structure. Amorphous polysulfides are also known.[42] Mixed sulfides are obtained by partially replacing of Cd^{2+} with M^{3+} or M^{4+} ions. $CdCr_2S_4$ and $CdIn_2S_4$ exhibit a normal spinel structure, while $CdGa_2S_4$ adopts the so-called thiogallate structure. CdSe is a brown or green solid obtained by direct reaction between Cd and Se vapour;[1] two different forms are known: hexagonal with wurtzite type structure or cubic with zinc blende type structure. CdSe nanoparticles have been formed using different methods; also a synthesis based on pulsed sonoelectrochemical technique is known.[28] CdTe is black and may be prepared by reduction of cadmium tellurate with hydrogen or by treating $Cd(CH_3COO)_2$ with Na_2Te in CH_3COOH. CdTe thin films have been obtained by direct reaction of a CdS film with tellurium vapor. The structure of CdTe is cubic of zinc blende type, but at high temperature a hexagonal, wurtzite type form is stable. Both CdSe and CdTe are intrinsic semiconductors. A variety of mixed selenides and tellurides are known.[38] Physical properties of CdS, CdSe, and CdTe are reported in Table 9.

14.2.7 Oxyacid Salts

$CdSO_4$ is soluble in water, but not in ethanol. It may be prepared as $CdSO_4{\cdot}8/3H_2O$ by dissolving CdO, CdS, or $CdCO_3$ in H_2SO_4. Metal Cd directly reacts with H_2SO_4 to give the sulfate; n water molecules ($n = 1$, 8/3, 4, 7) may be present and the monohydrate species is obtained by heating. Mixed sulfates $M_2Cd_2(SO_4)_3$ (M = K, NH_4, Rb, Tl) show a cubic structure, but $M_2Cd(SO_4)_2{\cdot}6H_2O$ (M = K, NH_4) is monocline.[4] $Cd(NO_3)_2$ is soluble in water, ethanol, and acetone, but insoluble in concentrated HNO_3. $Cd(NO_2)_2$ decomposes at 150–230 °C and is obtained by reaction between $Ba(NO_2)_2$ and $CdSO_4$ in aqueous solution. Mixed species $MCd(NO_2)_3$ ($M = K$, NH_4, Cs, Rb, Tl) have a perovskite type structure.[2] $Cd(PO_4)_2$ is prepared by reaction between $Cd(NO_3)_2$ and KH_2PO_4 in the presence of NaOH. $CdCO_3$ separates in crystalline form on heating a solution containing $CdCl_2$ and $(NH_4)_2CO_3$ in the presence of ammonia. It decomposes at about 332–355 °C, is insoluble in water but dissolves in acids, cyanide (*see Cyanides*) and ammonium solutions. $Cd(ClO_4)_2{\cdot}6H_2O$ may be obtained by reaction between CdO and $HClO_4$. It is soluble in water and ethanol. $Cd(HCO_2)_2{\cdot}2H_2O$ forms monoclinic crystals and decomposes on heating without melting. $Cd(CH_3COO)_2$ is obtained in anhydrous form by heating $Cd(NO_3)_2$ with acetic anhydride. It may crystallize with 1, 2, or 3 water molecules; the hydrate forms become anhydrous at about 130 °C. Cd_2SiO_4 is obtained by fusion or hydrothermal synthesis of CdO and SiO_2. It is a white solid insoluble in water and becomes phosphorescent after activation with manganese. $CdSiO_3$ forms rhombohedral white crystals insoluble in water.

14.2.8 Nitride, Amide, Phosphide, Arsenide, and Antimonide

Cd_3N_2 is a black solid, oxidizable in air and characterized by a cubic, anti-Tl_2O_3 type structure (*see* ***Nitrides: Transition Metal Solid-state Chemistry***). It is prepared by heating $Cd(NH_2)_2$ at 180 °C.[1] $Cd(NH_2)_2$ is an amorphous, slightly yellow, air-sensitive solid obtained by reaction of $Cd(SCN)_2$ and KNH_2 in liquid ammonia.[1] Three distinct cadmium phosphides are known (*see* ***Phosphides: Solid-state Chemistry***).[1] Cd_3P_2 forms grey, lustrous needles or leaflets with a distorted anti-Tl_2O_3 type structure. It is soluble in HCl with an evolution of PH_3 and gives an explosive reaction with HNO_3. Cd_3P_2 is obtained by heating Cd and P in a 3:2 molar ratio at 400–600 °C. Crystalline nanoclusters (*see Cluster*) have been synthesized using a sol-gel like route. CdP_2 forms orange or red tetragonal needles. It is prepared by fusion of Cd and P in a 1:2 molar ratio. CdP_4 forms black, highly reflective, monoclinic crystals. It decomposes into the elements on heating in vacuum and dissolves in boiling aqua regia. It is prepared by heating a Cd/Pd alloy with white phosphorous. Two arsenides of cadmium are known,[38] Cd_3As_2 and $CdAs_2$. Cd_3As_2 is obtained by heating the metal in a stream of hydrogen and arsenic vapour. It is a grey solid, isostructural with Cd_3P_2. It is a semiconductors which exhibits n-type intrinsic conductivity. $CdAs_2$ is prepared in the same way as CdP_2; it is a grey-black solid, harder than Cd_3As_2. Cadmium arsenide chlorides are known. In particular, Cd_8As_7Cl exhibits a peculiar type of crystal structure (*see Crystal Structures*).[44] Two antimonides, Cd_3Sb_2 and CdSb, have also been synthesized.[38] A deformed diamond-like structure characterizes CdSb.[38]

14.2.9 Cadmium-metal Compounds

Volatile $Cd(SiEt_3)_2$ and $Cd(GeEt_3)_2$ contain Cd-Si and Cd-Ge bonds, respectively.[45] Cd is linked to Sn in $[(Me_3SiCH_2)Sn]_2Cd$ and in $[(Ph_3Sn)_2CdL_2]$ (L = bipyridyl, dimethoxyethane or tetramethylenediamine). In several Cd-transition metal derivatives of the type $LCd[ML_n]$ or $Cd[ML_n]_2$, Cd^{2+} forms one or two covalent bonds (*see Covalent Bonds*) to a transition metal ion that bears ligands (*see Ligand*).[45] L may be carbon oxide, halide, pseudohalide (*see Pseudohalide*), or an organic group; M is generally chromium, manganese, iron, cobalt or nickel. Examples are $Cd[Mn(CO)_5]_2$, $Cd[Co(CO)_4]_2$, $Cd[Fe(CO)_2(\pi\text{-}C_5H_5)]_2$ and $Cd[Cr(CO)(\pi\text{-}C_5H_5)]_2$. A Cd_4Fe_4 ring characterizes the structure of $[CdFe(CO)_4]_4{\cdot}(Me_2CO)_2$. Dative $Pt(II)\rightarrow Cd(II)$ bonds have been observed in $[\{Pt(phpy)_2\}\{Cd(cyclen)\}](ClO_4)_2$, $[\{Pt(CH_3)_2(bipy)_2\}\{Cd(cyclen)\}](ClO_4)_2$, and $[\{Pt(thpy)_2\}\{Cd(cyclen)\}](ClO_4)_2$ where Hphpy = 2-phenylpyridine, cyclen = 1,4,7,10-tetraazacyclododecane, bipy = 2,2′-bipyridine, Hthpy = 2-(2-thienyl)pyridine. An unusual decanuclear cluster (*see Cluster*) containing Pt-Cd interactions has been synthesized by reaction between $Cd(ClO_4)_2{\cdot}6H_2O$ and $(NBu_4)_2[Pt(C{\equiv}CPh)_4]$.[46] Intermetallic compounds (*see Intermetallics*) are known: examples are $K_{0.4}Cd_2$, $Na_{26}Cd_{141}$, $Na_8K_{23}Cd_{12}In_{48}$.

14.2.10 Cadmium Glasses

Cd may be present in glasses as Cd, CdO, CdS, and CdF_2.[47] Metallic Cd is formed by reduction in the absence of an excess of sulfur in sulfocadmium glasses. This fact gives a gray or black opacity, similar to that caused by Pd (color firing). A certain electrical conductivity is shown by lithium–cadmium–phosphate glasses.

15 Cd^{II} COORDINATION CHEMISTRY

15.1 Halides and Pseudohalides

In solution, CdX_2 (X = Cl, Br, I) gives complex equilibria involving species of the type $CdX_n^{(2-n)}$.[2] The nature of the solvent medium strongly affects the species distribution. In fact, in aqueous solution, $[Cd(H_2O)_6]^{2+}$, $[Cd(H_2O)I]^+$, $[CdI_3]^-$ and $[CdI_4]^{2-}$ are formed but in DMSO, the main species are $[Cd(DMSO)_6]^{2+}$, $[Cd(DMSO)_nI]^+$, $[CdI_3]^-$, and $[CdI_4]^{2-}$. In both the solvents, $[CdI_3]^-$ and $[CdI_4]^{2-}$ maintain the trigonal and tetrahedral (*see Tetrahedral*) geometry and no evidence for additional solvent coordination is observed. In DMSO, the distance Cd–I in $[CdI_4]^{2-}$, $[CdI_3]^-$, and $[Cd(DMSO)_nI]^+$ is 2.790, 2.773, and 2.75 Å, respectively. Similar equilibria are found in the case of $CdCl_2$ and $CdBr_2$, but also the species $[CdCl_5]^{3-}$ has been observed. In aqueous solution, the role of the hydration sphere in the equilibria involving $CdX_2 (X = Cl$ or Br) has been investigated through experimental and theoretical methods: the results are consistent and suggest that CdX^+ and CdX_2 are strongly hydrated to form a pseudooctahedral (*see Octahedral*) structure around Cd^{2+}, CdX_3^- is weakly hydrated, and CdX_4^{2-} is almost fully unhydrated. In water, DMF, acetone, and ROH solvents, the anion donor strength follows the order $I^- > Br^- > Cl^-$.**[2]** Stability constants of halide complexes in several solvents have been determined.**[48]** A trigonally distorted $CdBr_6$ octahedral (*see Octahedral*) structure characterizes $Cs[CdBr_3]$ in solid phase. Complexes of the type $[CdX_2(C_5H_4NCOOR)_n]$ ($n = 1$, 2) may be obtained by reaction between esters of 2-pyridinecarboxylic acid and CdX_2 ($X = Cl$, Br, I). In the case of $[CdI_2(C_5H_4NCOOR)_2]$, Cd^{2+} shows a distorted octahedral (*see Octahedral*) structure with $CdI_2N_2O_2$ coordination *core*. In aqueous Cd^{2+}–CN^- system, the species $[Cd(CN)_n]^{(2-n)}$ ($n = 1-4$) have been observed with no evidence for the presence of species with $n > 4$. Stepwise complexation pattern in liquid ammonia have been established by IR and Raman spectroscopy. $Cd(CN)_2 \cdot 2/3H_2O \cdot t$-BuOH with 3D honeycomb-like $[Cd(CN)_2]_n$ structure is obtained by recrystallization of cadmium cyanide (*see Cyanides*) in aqueous *ter*-buthyl alcohol. On exposure to chloroform vapour, the $[Cd(CN)_2]_n$ framework undergoes a large-scale reorganization and gives a diamond-like structure with $CHCl_3$ in the interstices. In water, the complexes $[Cd(SCN)_n(H_2O)_x]^{(2-n)}$ ($n = 1-4$) have been detected but no polynuclear species. The solvent plays a certain role in the binding ability of SCN^-: in $[Cd(SCN)_2]$ and $[Cd(SCN)_3]^-$, the anion coordinates the metal ion through nitrogen in water and through sulfur in DMSO.**[2]** $[Cd_2(pn)_2(SCN)_2]$ is polymeric with bridging SCN^-. In $[Cd(en)_2(SCN)_2]$ and $[Cd(en)_2(SCN)Cl]$, SCN^- ion is monodentate via nitrogen, but the complexes have *trans* and *cis* octahedral (*see Octahedral*) structure, respectively. High-resolution ^{113}Cd MAS NMR spectroscopy has been successfully used to investigate the structure of a variety of cadmium thiocyanate coordination compounds in the solid state. The results indicate a correlation between Cd–N distances and values of the Cd–N indirect spin-spin coupling constants.**[19]** Unusual structures have been observed in hybrid crystalline materials based on the anionic $[Cd(SCN)_3^-]_\infty$ polymeric complex and a cationic host-guest complex such as a Cd^{2+}–crown ether (*see Crown Ethers*) system.**[49]** Stability constants of selected Cd^{2+}–halide and –pseudohalide (*see Pseudohalide*) complexes are given in Table 10.

Table 10 Stability constants for Cd^{2+}-halide (or pseudohalide) systems in water

Ligand	$\log K_1$	$\log K_2$	$\log K_3$	$\log K_4$
F^-	1.15	0.41	0.98	–
Cl^-	1.77	0.80	0.64	−0.2
Br^-	1.77	0.56	1.00	0.76
I^-	1.96	1.33	1.15	1.44
CN^-	5.62	5.18	4.90	3.50
SCN^-	1.16	0.33	0.14	0.02

15.2 Oxygen Donor Ligands

Stability constants for Cd^{2+}–oxygen ligand (*see Ligand*) systems are reported in Table 11. Cd^{2+} in aqueous and solid $Cd(ClO_4)_2 \cdot 6H_2O$ is coordinated by six water molecules (d = 2.31 Å).**[2]** The Cd^{2+} ion is easily hydrolyzed in water to give the equilibria shown in equations (4) and (5): the former prevails when $[Cd^{2+}] < 0.1$ M, the latter at higher concentration.

$$Cd^{2+} + H_2O \longrightarrow CdOH^+ + H^+ \quad (4)$$

$$2Cd^{2+} + H_2O \longrightarrow Cd_2OH^{3+} + H^+ \quad (5)$$

NMR and IR studies indicate that in water and methanol the covalency of the metal-oxygen bond varies in the order Hg < Cd < Zn. Several mixed Cd^{2+}–hydroxide complexes are known. Multinuclear species containing Cd–(μ-OH)–M (M = Cd, Co or Cr) units have been structurally characterized. In the case of $[(bmnpaCd)_2(\mu\text{-}OH)_2](ClO_4)_2 \cdot CH_3CN$ (bmnpa = *N,N*-bis-2-(methylthio)ethyl-*N*-((6-neopenthyl-amino-2-pyridyl)methyl)amine), the reaction with CO_2 gives a mixed carbonate complex: $[(bmnpaCd)_2(\mu\text{-}CO_3)_2](ClO_4)_2 \cdot CH_3CN$. $Cd(MeSO_3)_2 \cdot 2H_2O$ may be prepared by reaction of $CdCl_2$ and $MeSO_3H$ in water. In $Cd_2SO_4(OH)_2$, Cd^{2+} lies in a highly distorted CdO_6 environment, while a CdO_7 *core* is found in $Cd(BrO_3)_2 \cdot 2H_2O$. Complexes of the type $[Cd(H_2O)_{(6-n)}(SO_4)_n]^{(2-2n)}$ are observed in concentrated aqueous solution of cadmium sulfate. In the crystalline structure (*see Crystal Structures*) of $CdSO_4$, a very distorted CdO_4 tetrahedron is found while solid $Cd_2(NH_4)_2(SO_4)_3$ is characterized by two nonequivalent Cd^{2+} octahedral (*see Octahedral*) sites. Templated linear and layered Cd^{2+}–sulfate complexes have been obtained by reaction between cadmium salts and H_2SO_4 in the presence of organic amines. In $M[Cd(S_2O_3)_2]$ ($M = NH_4$ or Rb), the ligands (*see Ligand*) behave as bidentate (*see Bidentate Ligand*) through O and S. Cd^{2+} interacts with nitrite in aqueous solution to give

Table 11 Stability constants for Cd^{2+}-O-donor ligand in water

Ligand	$\log K_1$	$\log K_2$	$\log K_3$	$\log K_4$
SO_4^{2-}	0.71	0.13	0.48	−0.02
$S_2O_3^{2-}$	2.08	1.74	1.66	–
NO_2^-	1.82	–	–	–
NO_3^-	0.04	−0.05	−0.9	−1.3
HCO_2^-	1.04	0.19	0.52	–
$MeCO_2^-$	1.08	0.61	0.40	–
Malonate	1.63	0.73	1.04	–
Maleate	1.74	0.92	–	–

$[Cd(NO_2)_n]^{(2-n)}$ ($n = 1$–4). For $n = 1$ or 2, nitrite acts as an O-bidentate ligand but for $n = 3$ or 4, monodentate nitrite is also found. In aqueous solutions of $Cd(NO_3)_2$ spectroscopic measurements suggest the presence of $[Cd(H_2O)_5(NO_3)]^+$ ion.[2] Solid trihydrate species contains an eight-coordinate Cd^{2+}. Cd^{2+}–nitrate coordination polymers of different dimensionality have been synthesized: $[Cd(NO_3)_2$(1,2-bis(4-pyridyl)ethine)$_{1.5}]_n$ has an infinite one-dimensional structure in which Cd^{2+} lies in a heptacoordinate environment, $[Cd(NO_3)_2$(1,4-bis(4-pyridoxy)benzene)$_{1.5}]_n$, however, is characterized by a two-dimensional network in which Cd^{2+} has a pentagonal bipyramidal (*see Pentagonal Bipyramid*) geometry. In $Cd(PO_3)_2$ and $CdBa(PO_3)_4$, Cd^{2+} is octahedral (*see Octahedral*). In $Cd_3(P_3O_9)_2\cdot 14H_2O$ the anion consists of discrete cyclic trimetaphosphate units; in each, Cd^{2+} is octahedrally surrounded by four phosphate oxygen and two water molecules. Layered cadmium-phosphonates have been obtained and their structure solved: in $Cd(O_3PR)\cdot H_2O$ and $Cd(O_3PC_2H_4NH_2)$ the layer arrangement is similar, the only difference being the replacement of the coordinated water molecule with the nitrogen atom of $O_3PC_2H_4NH_2{}^{2-}$. Formate anion acts as a bridging ligand (*see Bridging Ligand*) in $Cd(HCO_2)_2$ and $Cd(HCO_2)_2\cdot 2H_2O$; in the former, Cd^{2+} is seven-coordinate, but in the latter it is octahedral (*see Octahedral*). Systems of the type $Cd(HCO_2)_2\cdot M(HCO_2)_x$ are well known.[2] In $Cd(MeCO_2)_2\cdot 2H_2O$, the acetate ions act as bridging ligands (*see Bridging Ligand*).[50] The structure of $[Cd(MeCO_2)_2(tu)]$ indicates Cd^{2+} six-coordinate by one bidentate and two bridging bidentate acetate groups and by two bridging sulfur atoms of two thiourea (*see Thiourea*) groups.[50] A Cd^{2+}–oxalate polymeric species $Cd(C_2O_4)\cdot 3H_2O$ is obtained by slow decomposition of ascorbic acid in presence of Cd^{2+}. The metal ion is found in a $\{CdO_7\}$ distorted pentagonal bipyramidal (*see Pentagonal Bipyramid*) geometry due to five oxalate and two water oxygens. In cadmium cyanoacetate, Cd^{2+} lies in a NO_5 octahedron.[4] $[CdL_2(H_2O)_n]_m$ (HL = phenylthioacetic acid) has a polymeric structure with Cd^{2+} in an O_5S octahedron. A polymeric structure with bridging oxalate groups has also been observed in $[Cd(C_2O_4)L_2]$ (L = substituted pyridines or 4-toluidine). Cd^{2+} is found in seven-coordinate pentagonal bipyramidal (*see Pentagonal Bipyramid*) O_7 and O_4N_3 environments in $[Cd(SalH)_2(H_2O)_2]_2$ and $[Cd(SalH)_2(py)_3]$, respectively.[50] Other examples of seven-coordinate Cd^{2+} are known.[2,51] Cadmium maleate dihydrate contains both six and eight-coordinate Cd^{2+}. Cd^{2+}–succinate complexes of different dimensionalities may be obtained employing organic amines.[52] The Cd^{2+}–citrate system in aqueous solution includes the species $[Cd(CitH_2)]^+$, $[Cd(CitH)]$, $[Cd(Cit)]^-$, and $[Cd(Cit)_2]^{4-}$.[50] $[Cd(CitH)(H_2O)]_n$ crystallizes in the orthorhombic space group and Cd^{2+} is octahedrally coordinated to citrate molecules and one water molecule. Citrate acts as a tridentate ligand (*see Tridentate Ligand*) through the central and one terminal carboxylate group and the alcoholic oxygen. The complex $[CdLCl_2]$ (L = pyridoxine) consists of infinite chains of chloro-bridged Cd^{2+} in a $CdCl_3O_3$ environment. Each pyridoxine acts as a bidentate ligand through two oxygen donors and a third oxygen of the ligand bridges another Cd^{2+}. $[CdI_2L]$ (L = pyridine N-oxide) has a trigonal bipyramidal (*see Trigonal Bipyramidal*) structure characterized by infinite chains of [CdI] units alternately bridged through two I atoms and two O atoms. In CdL_3Cl_2(L = $OP(NH_2)_3$), Cd^{2+} is hexacoordinate and L acts as a N,O chelate. $[Cd(O_2SR)_2L]$ (L = bipy or phen) and $[Cd(O_2SR)_2L_2]$ (L = bipy or en) are pseudooctahedral; sulfinate acts as bidentate in the former and monodentate in the latter. $[Cd(NCS)_2(urea)_2]$ shows Cd^{2+} in a distorted octahedral configuration forming chains bridged by thiocyanate ions.[2] Bidentate acetate and six-coordinate Cd^{2+} ions have been observed in $[Cd(MeCO_2)_2(urea)_2]$. Synthesis and structure of $[Cd(3,3'\text{-AZDB})_2](H_2Nme_2)(NH_4)$, a complex characterized by interpenetrating diamond networks, have been reported.[53] Cd^{2+} lies in a height-coordinate environment with a tetragonal antiprismatic geometry. In $[Cd(acac)_2(bipy)]$, all the ligands are bidentate, while in $[Cd(acac)(bipy)(H_2O)]$ water is also coordinated to Cd^{2+} and acac acts as a monodentate. Both the compounds show a distorted octahedral (*see Octahedral*) structure, more marked for the bipy adduct.[2] Discrete $[Cd(acac)_3]^-$ units have been identified in $KCd(acac)_3\cdot H_2O$, in which Cd^{2+} is trigonal prismatic (*see Trigonal Prism*). A number of dimethylphosphine oxide complexes of cadmium with halides have been obtained.[50] The complex $[CdL_2(THF)_2]$ (HL = 2,6-*t*-$Bu_2C_6H_3OH$) shows an unusual square-planar Cd^{2+} structure, in which the metal ion is coordinated to four oxygen atoms. This compound was isolated from THF (equation 6).

$$\begin{aligned} Cd[N(SiMe_3)_2]_2 + 2HL + 2THF &\longrightarrow [CdL_2(THF)_2] \\ &\quad + 2HN(SiMe_3)_2 \end{aligned} \tag{6}$$

Cd^{2+} reacts with 3,5-di-*t*-buthyl-1,2-*o*-benzoquinine to form a biradical compound which can add a neutral N-donor ligand (py or bipy) to give 1:1 and 1:2 adducts.

15.3 Sulfur Donor Ligands

Selected stability constants for Cd^{2+}–sulfur ligand systems are reported in Table 12. Heterometallic ion $[Mo_3CdS_4(H_2O)_{12}]^{4+}$ may be obtained by reaction of $[Mo_3S_4(H_2O)_9]^{4+}$ with Cd^{2+} in the presence of a reductant

Table 12 Stability constants for Cd^{2+}-S-donor ligand in water

Ligand	$\log K_1$	$\log K_2$	$\log K_3$	$\log K_4$
2-Thiourail	4.02	3.49	–	–
Thiourea	1.43	0.80	0.52	0.65
N-Ethylthiourea	1.46	0.72	1.32	0.90
Dithiocarbaminoacetate	5.4	3.9	4.4	–
Thiosemicarbazide	2.7	1.7	1.6	–
Ethyl thioacetate	1.27	0.85	0.39	0.21

or with metal Cd in *p*-toluenesulfonic acid aqueous solution. Polymeric compounds of the type $[Cd(RS)_2]_n$ are obtained from electrochemical oxidation of Cd anodes in CH_3CN containing RSH or RSSR.[2] In the polymeric cadmium thiolate of the type $Cd(SC_6H_4R)_2$, nature, and position of the substituent R determine the dimensionality of the structure. In the case of aliphatic thiolates, one, two, and three-dimensional structures have been observed. In *catena*-bis[μ-(N-methylpiperidinium-4-thiolate)] cadmium perchlorate dihydrate, each Cd^{2+} is found in a CdS_4 environment, the structure is characterized by infinite chains of Cd^{2+} ions bridged by sulfur atoms.[2] Polynuclear complexes (*see Polynuclear Complexes*) are observed in a solution of Cd^{2+} and 3-(dimethylamino)-1-propanethiol (HL). In the pH range 3–11, the predominant species are $[Cd(HL)_4]^{2+}$, $[Cd_3(HL)_6]^{6+}$, $[Cd_3(HL)_8]^{6+}$, $[Cd_4(HL)_9]^{8+}$, and $[Cd_4(HL)_{10}]^{8+}$. Both mononuclear and polynuclear species can be formed by ligand deprotonation. Clusters (*see Cluster*) of the type $[ECd_8(E'Ph)_{16}]^{2-}$ (E, E$'$ = S, Se, Te) have been identified using ^{113}Cd NMR. $[ClCd_8\{SCH(CH_2CH_2)_2N(H)Me\}_{16}](CLO_4)_{15}\cdot 16H_2O$ exhibit an unusually high cationic charge and a peculiar structure.[18] The thioacetate complex $[Ph_4P][Cd(SC\{O\}CH_3)_3]$ has been synthesized and the structure determined. Cd^{2+} is strongly bound to the sulfur atoms of three thioacetate anions and weakly to the corresponding oxygen atoms of the carbonyl groups. Thiocarboxylate complexes with 4,4$'$-bipyridine have a polymeric structure.[54] The complexes $[Cd(HL)_2X_2]$ (X = Cl, Br, I), $[Cd(HL)_3](ClO_4)_2\cdot 2H_2O$ and $[CdL_2]$ (HL = 4,6-dimethyl-2(1H)-pyrimidinethione) have been synthesized.[2] A polymeric structure with a bridged halogen characterizes $[Cd(HL)_2X_2]$. In $(Et_4N)[CdL_3]$ (HL = benzothiazole-2(3*H*)-thione) the ligand L is bidentate through N and S. 1,4,6-trimethylpyrimidine-2-thione (L) and 1-methylpyrimidine-2-thione (L$'$) form halogenated complexes with Cd^{2+}.[51] In $[CdL_2X_2]$ (X = Cl, Br) and $[CdL'_2X_2]$ (X = Br, I), the ligands act as bidentate through N,S atoms. $[CdL_2Cl_2]$ (L = 2-thiouracil) shows a pseudotetrahedral structure. In most of the cases, a stronger binding ability of aromatic versus aliphatic sulfur donor has been observed.[51] Cd^{2+} in $[Cd(thiooxinate)_2]$ is found in a distorted tetrahedral CdN_2S_2 environment. Pseudooctahedral Cd^{2+} is observed in $[Cd(ethylxantate)_2(phen)]$, in which the ethylxantate is bidentate. In cadmium thiodiacetate hydrate the ligand is an O_2S donor and the metal ion lies in a distorted octahedral geometry. In $Cd(NH_3)_3S_2O_3$ and $3Rb_2S_2O_3\cdot CdS_2O_3\cdot H_2O$, the thiosulfate acts as a monodentate S-donor, but in $Rb_2Cd(S_2O_3)_2$ it is bidentate. In $[Cd(CS_3)_2]^{2-}$, the ligand binds as bidentate to give a four-membered chelate ring.[2] In $[Cd(tu)_n](ClO_4)_2$ ($n = 4$ or 6), Cd^{2+} is bound through the S atom of the ligand. $[Cd(tu)_2Cl_2]$ is monomeric with the metal ion in a tetrahedral $CdCl_2S_2$ environment. In $[Cd(tu)_2(HCO_3)_2]$ and $[Cd(Ettu)_2(NCS)_2]$, Cd^{2+} is six coordinated with infinite chains bridged by sulfur ligands for the former and by the NCS^- ions for the latter. In the monomeric $[CdL_2Cl_2]$, L (= pyridyl-2-thiourea) binds through the pyridine nitrogen and thione sulfur atoms. $[Cd(tu)_2(MeCO_2)_2]$ exhibits a CdS_2O_4 arrangement. *N,N*-diehtyl- and *N,N*-dimethylthiourea form 1:1 and 2:1 complexes. The 1:1 complex reveals a polymeric, halogen-bridged structure with tetrahedral Cd^{2+}. Two types of 2:1 complexes have been isolated: one is monomeric with tetrahedral metal center; the other is polymeric, halogen-bridged with octahedral (*see Octahedral*) geometry. Cd^{2+} reacts with *N,N*-dimethyl- and *N,N*-dicyclohexyldithiooxamide (L) to give $CdLX_2$ when X = Cl, Br, I or CdL_2X_2 and CdL_3X_2 when X = ClO_4; the former are nonelectrolytes, while the latter are electrolytes; in all the cases the ligand L is bidentate through S and N atoms and in $CdLX_2$ the metal ion is octahedral with bridged halides.[2] Cadmium bis(*N,N*-diethyl-monothiocarbamato) complex $[Cd(OSCNEt_2)_2]_n$ is polymeric and crystallizes in monoclinic group; Cd^{2+} lies in a distorted trigonal-prismatic geometry and interacts with two S,O-bidentate and two O-monodentate ligands (*see Monodentate Ligand*). A structure intermediate between octahedral (*see Octahedral*) and trigonal prismatic (*see Trigonal Prism*) has been found for $(Bu_4N)[CdL_3]$ (HL = Et_2NCS_2H), where each dithiocarbamate (*see Dithiocarbamate*) chelates Cd^{2+} through two nonequivalent S atoms. Using an appropriate tetralkylammonium salt, complexes of the type $(NR_4)[Cd(S_2CNEt_2)_2X]$ (R = Et, X = Cl, Br, SCN; R = *n*-Bu, X = I) have been prepared in acetone by interaction between cadmium bis(dithiocarbamate) and halides or pseudoahalides. In $(Et_4N)[Cd(S_2CNEt_2)_2(SCN)]$, Cd^{2+} shows a distorted trigonal-pyramidal geometry. Bis(thiosemicarbazide)cadmium sulfate is polymeric with a sulfate-bridged structure in which the bidentate N,S-chelating thiosemicarbazide binds an octahedral Cd^{2+}. [Cd(thiazolidine-2-thione)$_2$] exhibits a polymeric structure in which the ligand is bidentate through N,S atoms. In $[CdL_2L'_2]$ (HL = $(EtO)_2PS_2H$, L$'$ = hexamethylenetetramine), Cd^{2+} has a distorted octahedral geometry, but in $(Me_4N)[CdL_3]$ (HL = $(i\text{-PrO})_2PS_2H$) a coordination intermediate between octahedral and trigonal prismatic (*see Trigonal Prism*) is found. Some Cd^{2+} complexes with crown thioethers (*see Crown Ethers*) are known; in $[(CdI_2)_2([24]aneS_8)]$ two CdI_2 units interact with the macrocycle (*see Macrocycle*). Each Cd^{2+} lies in a distorted trigonal bipyramidal environment and is bound to three consecutive S atoms of the macrocycle (*see Macrocycle*) and two I^- ions. In metallothioneins, sequences of the type Cys–Y–Cys are the primary binding sites for Cd^{2+}; the structure and properties of this kind of protein have been extensively investigated.[55,56]

15.4 Nitrogen Donor Ligands

Selected stability constants for Cd-nitrogen ligand systems are reported in Table 13. $[Cd(NH_3)_2X_2]$ (X = Cl, Br) is polymeric with Cd^{2+} octahedrally surrounded by two NH_3 and four bridged halogens. In $[Cd(NH_3)_6]X_2$, however, $[Cd(NH_3)_6]^{2+}$ octahedrons ($d_{Cd–N} = 2.37$ Å) characterize the structure.[2] The

Table 13 Stability constants for Cd^{2+}-N-donor ligand in water

Ligand	$\log K_1$	$\log K_2$	$\log K_3$	$\log K_4$	$\log K_5$
NH_3	2.617	2.179	1.435	0.742	−0.02
py	1.36	0.50	0.04	–	–
bipy	4.22	3.58	2.60	–	–
phen	5.8	4.8	4.0	–	–
en	5.45	4.53	1.76	–	–
dien	8.4	5.4	–	–	–
trien	10.75	–	–	–	–
Gly	4.14	3.46	2.14	–	–
α-Ala	4.02	3.38	–	–	–
β-Ala	2.88	2.65	–	–	–
His	5.39	4.27	–	–	–
Imidazole	2.70	2.40	1.60	0.95	0.60

cation $[Cd(NH_3)_6]^{2+}$ is found to be the prevailing species in aqueous solution of $CdCl_2$ when the molar ratio NH_3/Cd^{2+} is higher than 10. IR and Raman studies on $[Cd(NH_3)_4]^{2+}$ and $[Cd(NH_3)_6]^{2+}$ indicate that the binding strength increases with decreasing the coordination number. The crystal structure (*see Crystal Structures*) of $[Cd(NH_3)_2][Ni(CN)_4]$ shows two-dimensional polymeric sheets of $[Ni(CN)_4]^{2-}$ anions bridged by coordinating $[Cd(NH_3)_2]^{2+}$ ions. This unusual structural arrangement allows clathration of small aromatic molecules such as furan, pyrrole, pyridine, or thiophene, which interact via hydrogen bonds (*see Hydrogen Bonding*) with host lattice ammonias. Similar clathration ability is shown by $[Cd(py)_2][Ni(CN)_4]$. $[Cd(H_2N(CH_2)_8NH_2)][Ni(CN)_4]\cdot PhMe$ has a monoclinic structure in which toluene is found orientationally disordered within a rigid host cage. Cd^{2+} is found to be coordinated through the oxygen atom of $HONH_2$ in $[Cd(HONH_2)_2X_2]$ (X = Cl or Br) but through the N atom of $MeONH_2$ in $[Cd(MeONH_2)_2X_2]$ (X = Cl, Br, I). In aqueous solution, $[Cd(N_3)_n]^{(2-n)}$ ($n = 1-5$) and the mixed species $[Cd(NO_3)(N_3)_n]^{(1-n)}$ ($n = 1-4$) have been observed and the stability constants calculated.[2] Hydrazine in aqueous solution (80%) reacts with CdF_2 to give $(N_2H_5)_2(CdOF_2)$ but in anhydrous hydrazine $CdF_2\cdot 2N_2H_4$ and $CdF_2\cdot 3N_2H_4$ are formed in which the presence of double and triple hydrazine bridges has been suggested. $Cd(C_2O_4)(N_2H_4)\cdot 0.5H_2O$ and $Cd(C_2O_4)(N_2H_4)_2$ may be obtained by reaction between CdC_2O_4 and N_2H_4. In both the compounds hydrazine acts as a bridging ligand (*see Bridging Ligand*), but oxalate is ionic in the former case and bidentate in the latter. N-acylhydrazine derivatives act as N,O-chelate ligands (*see Chelating Ligands*) in complexes of the type $[CdX_2L]$ (X = NCS, NO_2, NCO, $1/2SO_4$; L = formyl-, benzoyl-, or nitrobenzoylhydrazine). $[Cd(PhNH_2)X_2]$ (X = Cl or Br) shows an octahedral Cd^{2+} environment, while in $[Cd_3(PhNH_2)_4Cl_6]$ two types of octahedral sites have been observed: $\{CdCl_6\}$ and $\{CdCl_4N_2\}$.[2] In $[CdCl_2(Ph_3P=NH)]_2$, $[CdI_2(Ph_3P=NH)_2]_2\cdot 2(CHCl_3)$ and $[Cd_2Br_4(Ph_3P=NH)_3]$ IR spectra indicate that $Ph_3P=NH$ acts as a N-donor. In the dimeric complexes the units are linked by *trans*-halogen bridges, while $[Cd_2Br_4(Ph_3P=NH)_3]$ is polymeric with halogen atoms bridging $[CdBr_2(Ph_3P=NH)_2]$ and $[CdBr_2(Ph_3P=NH)]$ structural units. In the aqueous Cd-en system, the prevailing species are $[Cd(en)_2]^{2+}$ and $[Cd(en)_3]^{2+}$ with tetrahedral and octahedral geometry, respectively. Complexes such as $[Cd(en)][Pd(CN)_4]$ and $[Cd(NH_3)_2][Pd(CN)_4]$ are able to form clathrate (*see Clathrate*) compounds and may accept two guest molecules of phenol, thiophene or benzene.[2] $[Cd(en)(NO_2)_2]$ is polymeric with a seven-coordinate Cd^{2+} in pentagonal prismatic geometry. Ethylenediamine and cadmium halides yield polymeric complexes with bidentate bridging en; with $Cd(CN)_2$, however, en gives 1:1 and 1:2 monomeric complexes, binding the metal ion as a bidentate chelating ligand. The polymeric $[Cd(en)(NO_3)_2(4,4'\text{-bipy})]_n$ has a zigzag chain structure bridged by bipyridine molecules. Cd^{2+} exhibits a distorted N_4O_2 octahedral geometry, being coordinated to one μ_2-en, two 4,4′-bipy, and two NO_3^- ions. The observed three-dimensional network is due to two kinds of N–H···O hydrogen bonds (*see Hydrogen Bonding*). A square pyramidal (*see Square Pyramidal*) five-coordinate Cd^{2+} has been found in [bis(2-dimethylaminoethyl)-methylamine] cadmium thiocyanate: the amines and one of the thiocyanate ligand occupy the basal positions while the second thiocyanate is apical. 1:1 complexes are formed by interaction of Cd^{2+} with $MeNH(CH_2)_3NH_2$, dien, $H_2N(CH_2)_2NH(CH_2)_3NH_2$ and $H_2N(CH_2)_3NH(CH_2)_3\ NH_2$. Unusual compounds are formed with tripod-like tetramines: the crystal structure (*see Crystal Structures*) of $Cd_2(Me_6tren)I_4$ reveals the presence of a five-coordinate cation $[CdI(Me_6tren)]^+$ with a slightly distorted trigonal bipyramidal (*see Trigonal Bipyramidal*) structure and of a dinuclear (*see Dinuclear*) anion $[Cd_2I_6]^{2-}$, formed from edge sharing between pairs of CdI_4 tetrahedra.[2] In $[Cd(Me_6tren)X_2]$ (X = Cl, Br), Me_6tren acts as a terdentate ligand and Cd^{2+} is five-coordinate. In $[Cd(tren)Br]Br$, however, tren is tetradentate (*see Tetradentate Ligand*). A five-coordinate Cd^{2+} and tetradentate (*see Tetradentate Ligand*) amines are found in $[Cd(H_2O)L](ClO_4)_2$ (L = Me_6tren or tren). In the corresponding anhydrous complex, a perchlorate ion substitutes the water molecule in the coordination sphere: $[Cd(ClO_4)L](ClO_4)$. Analogously, in the complex $[Cd(NO_3)L](NO_3)$, a nitrate ion binds Cd^{2+}. The coordinative properties of amino acids towards Cd^{2+} have been extensively investigated.[2] Type and stability of the complexes strongly depend on the structure of the amino acid. In absence of interacting side chain, the amino acid acts as a chelate ligand (*see Chelating Ligands*) through the amine nitrogen and the carboxylate oxygen. In $[Cd(L\text{–}Asn)_2]$, Cd^{2+} is octahedrally coordinated in an O_4N_2 environment and the amide of the side chain results unbound. No evidence for any interaction between the metal ion and the thioether group is found in Cd^{2+}–Met system. Two different structures have been found to correspond to the formula $Cd(Glu)\cdot H_2O$. In the former case, Cd^{2+} has a distorted octahedral (*see Octahedral*) geometry and is coordinated by N(amino) and O(α-carboxylate) of one glutamate, by both the oxygen atoms side chain carboxylate of a second glutamate, by an α-carboxylate oxygen of a third glutamate, and by a water molecule. The latter case is better represented by the formula $Cd(Glu)(H_2O){\cdot}Cd(Glu)(H_2O)_2{\cdot}H_2O$; the glutamate binds three Cd^{2+} ions and two different geometries for Cd^{2+} occur: one is a distorted pentagonal bipyramidal (*see Pentagonal Bipyramid*), the other is a distorted square-based trigonal-capped polyhedron. ^{13}C and ^{113}Cd NMR studies indicate Cd^{2+} unable to promote peptide nitrogen deprotonation (*see* ***Peptide–Metal Interactions***). Surprisingly, Cd^{2+} substitutes for nitrogen-bound hydrogen on RSO_2N-protected amino acids, especially in the presence of bipyridyl. In $[CdX_2(acetamide)_2]$ ($X = Cl$, Br, I or SCN), acetamide is an N,O donor and halogens act as bridging ligands (*see Bridging Ligand*).[2] In $[CdCl_2(malonamide)_2]{\cdot}MeOH$, Cd^{2+} is octahedral (*see Octahedral*) and coordinated to bidentate malonamides through N atoms. Complexes of the type $[CdX_2L_2]$, formed by N-(2-pyridyl)acetamide (*see Amide (Amido) Complexes*), are octahedral and the amide binds through the carbonyl oxygen and the heterocyciclic nitrogen. In $[CdL_2(SCN)_2]$ and $[CdL_2](NO_3)_2$ ($L = RCONHNH_2$; $R = Et$, n-Pr, n-C_5H_{11}, n-C_7H_{15}) L behaves as an N,O bidentate ligand, but in $[CdL_nCl_2]$ ($L = i$-$PrCH_2CONHNH_2$, $n = 1$ or 2) L binds only through an N atom. Cd^{2+} is found in a distorted octahedral coordination in $[CdL_2(SCN)_2]$ ($L = PhCONHNH_2$) in which the hydrazide ligand acts as an N,O bidentate ligand and one thiocyanate ion binds through an S atom, but the other through an N atom.[2] In Schiff base complexes obtained from 2-benzoylpyridine and benzoylhydrazine or salicylhydrazine, Cd^{2+} is coordinated by two N and one O atoms. The quinquedentate ligand 2,6-bis(2-methyl-2-benzothiazolinyl)pyridine reacts in basic conditions as deprotonated ligand to give a five-coordinated complex of unusual structure.[2] In tris(ethylenediamine)cadmium dibenzohydroxamate, the metal ion lies in an octahedral (*see Octahedral*) N_6 environment. A number of tetraacetate ligands bind Cd^{2+}. Structural aspects control the stability of such complexes: the formation constant value for the 1:1 complex of ethylene-bis(N,N'-(2,6-dicarboxy)piperidine) is lower than that for EDTA due to the steric hindrance of the piperidine ring. Dinuclear (*see Dinuclear*) species of the type $[Cd_2L]$ have been observed when H_4L is ethylenedinitrilotetraacetic acid or 1,2-trans-cyclohexylenedinitrilotetraacetic acid. $[CdCl_2(imidazole)]$ has a polymeric structure in which octahedrally coordinated Cd^{2+} ions are bridged by two chloride ions.[2] $[Cd(imidazole)_3](SO_4){\cdot}H_2O$ is also polymeric: the metal ion shows an octahedral (*see Octahedral*) geometry due to three imidazole nitrogens, a water molecule, and two oxygens from sulfate. A number of species are observed in Cd^{2+}–imidazole aqueous system: $[CdL]^{2+}$, $[CdL_2]^{2+}$, $[CdL_3]^{2+}$ and $[CdL(OH)]^{+}$. Monomeric tetrahedral (*see Tetrahedral*) species $[Cd(N\text{-alkylimidazole})_2X_2]$ ($X = Cl$, Br, I) or dimeric species have been synthesized. CdL_2F_2 ($L = 3,5$-dimethylpyrazole) is obtained by reaction between $Cd(BF_4)_2$ and L: the octahedrally coordinated Cd^{2+} ions are bridged by F^- ions to form a linear chain. 5-methylpyrazole (L'), however, gives a tetrameric species $[Cd_4F_4L'_{12}](BF_4)_4$ containing a Cd_4F_4 cluster (*see Cluster*). $[Cd(py)X_2]$ ($X = Cl$, Br) reveals a polymeric halogen-bridged structure in which Cd^{2+} is coordinated by one pyridine, two bicoordinated, and three tricoordinated halogens.[51] Cadmium halides react with cyanopyridine to give 1:2 complexes; $CdCl_2$, alone, forms a 1:1 complex with 2-cyanopyridine. The cyano-group does not bind the metal ion. Cd^{2+} is octahedral (*see Octahedral*) with halogen bridges in a 1:2 complex but tetrahedral in a 1:1 species. A polymeric structure containing Cd–SCN–Cd units is observed when 2- and 3-cyanopyridines react with $Cd(SCN)_2$ to give a 1:2 compound.[2] Even in this case, Cd^{2+} is octahedral. In $[Cd(HCO_2)_2L_2(H_2O)_2]$ ($L =$ nicotinamide) and $[Cd(MeCO_2)_2L'_2(H_2O)_2]$ ($L =$ N,N-diethylnicotinamide), the metal ion lies in an octahedral environment and is bound to the amide through the N atom. In the monomeric compounds $[CdL_2I_2][CdLX_2]$ ($X = Cl$, Br; $L =$ bis(2-pyridyl)ketone), L acts as a bidentate N_2 donor. $[CdL(NO_3)_2(H_2O)]_2(NO_3)_2$ ($L =$ adenine) is dimeric, Cd^{2+} lies in a N_2O_6 environment and is bridged by two water and two adenine molecules. In $Na_2Cd_3(ATP)_2{\cdot}6H_2O$, ATP binds through the nitrogen of the base and phosphate oxygens. Aqueous $Cd(ATP)^{2-}$ is proposed to be in dimeric form. Interactions between Cd^{2+} and guanosine occur. Depending on pH, 1:1 complexes of the type $[CdL]^{+}$ and $[Cd(HL)]^{2+}$ have been detected. The structure of $[CdL(H_2O)_5]{\cdot}3H_2O$ ($L =$ guanosine 5′-phosphate) shows Cd^{2+} octahedrally coordinated by five water molecules and the N-7 of the purine ring. 4,6-dimethylpyrimidine-2(1H)-thione (HL) forms the complexes $[Cd(HL)_2X_2]$ ($X = Cl$, Br, I), $[Cd(HL)_3](ClO_4)_2{\cdot}2H_2O$, $[Cd(HL)_2(CF_3CO_2)_2]$, and CdL_2. The ligand binds via S and N; in the chloride and bromide, the ligand seems to coordinate only through the N atom and bridging halides. In $[CdL_2(H_2O)_4]$ ($L = 8$-azohypoxanthinate), Cd^{2+} is octahedrally bound to four water molecules and two N-7of the purine anions. Flavoquinones acts as a chelate via N and O atoms to give complexes of the type $[CdL_3]^{2+}$. In $[Cd(bipy)_2(NO_3)_2]{\cdot}1/2H_2O$, Cd^{2+} is found in two distinct N_4O_2 octahedral environments, being the oxygen donors and two nitrate ions in one case and one nitrate ion and one water molecule in the other. In $[Cd(bipy)_2(SCN)_2]$, Cd^{2+} has a N_6 octahedral geometry. Studies have been performed on the interaction of Cd^{2+} with bipy in water and DMF.[57]

Bipyridyl-based molecules are used as bridging ligands (*see Bridging Ligand*) to obtain a variety of network topologies and structural motifs starting from $Cd(NO_3)_2$.[58] $\{[Cd(4,4'\text{-bipy})_2](NO_3)_2\}_\infty$ gives a clathrate (*see Clathrate*) complex by interaction with o-dibromobenzene and shows catalytic properties towards cyanosilylation of aldehydes. $[Cd(2,4'\text{-bipy})_2(NO_3)_2(H_2O)_2]$ shows a distorted pentagonal bipyramidal (*see Pentagonal Bipyramid*) geometry, being Cd^{2+} coordinated by one monodentate and one bidentate $NO_3{}^-$, two water molecules and two 2,4′-bipy (both through 4-pyridyl N atom).[58] In $[Cd_2(4,4'\text{-bipy})_2(H_2O)_3(SO_4)_2]{\cdot}3H_2O$, the Cd^{2+} ions lies in two nonequivalent octahedral environments and are connected by 4,4′-bipy molecules to form one-dimensional chains. Heptacoordinate Cd^{2+} is found in $[Cd_2(SO_4)_2$(1,3-bis(4-pyridyl)propane$)_3(H_2O)_{2.7}]\cdot 4.5H_2O$ and $[Cd_2(NO_3)_4$(1,5-bis(4-pyridyl)pentane$)_3(H_2O)]$.[58] Triazole ligands such as 3,5-dialkyl-4-amino-1,2,4-triazole give complexes with dimensionality from zero to three.[59] In the phosphoraniminato complexes $[CdX(NPEt_3)]_4$ (X = Cl, Br, I), a $[Cd_4N_4]$ heterocubane core is found. The Cd^{2+} ions are bridged by N atoms of the phosphoranimidate ligands. Interactions between Cd^{2+} and macrocyclic ligands (*see* ***Macrocyclic Ligands***) bearing N and/or O donor atoms (*see Donor Atom*) (cyclic amines, ethers, porphyrin derivatives, etc.) have been extensively investigated:[2,50,51,60] Interesting spectroscopic and photochemical properties are shown by several of these complexes. Generally, Cd^{2+} macrocycles (*see Macrocycle*) undergo metal exchange more easily than the corresponding Zn^{2+} compounds. Some cryptands (*see Cryptands & Cryptates*), however, reveal a remarkable selectivity for Cd^{2+} respect to Zn^{2+} and Ca^{2+} and thus could be used in chelation therapy (*see Chelation Therapy*).[2] The octaazacryptand $L = N(CH_2CH_2NHCH_2CH_2NHCH_2CH_2)_3N$ shows a particularly high affinity for Cd^{2+}. In the cation $[CdL]^{2+}$, the metal ion is eight-coordinated in a bicapped octahedral geometry.

15.5 Phosphorus and Arsenic Donor Ligands

Cadmium halides react with phosphines to give complexes of the type $[CdX_2(R_3P)]_2$ and $[CdX_2(R_3P)_2]$.[61] The former are halogen-bridged dimers, the latter are tetrahedral (*see Tetrahedral*). In $[CdBr_2(Et_3P)]_2$, Cd^{2+} lies in a Br_3P environment with two bridged Br^- ions. In several solvents a monomer/dimer equilibrium occurs. $[CdLI_2]$ ($L = P(CH_2SiMe_3)_3$) is monomeric in $CHCl_3$ and the metal ion seems to be three-coordinated. Complexes with a CdX_2/R_3P molar ratio of 2:3 are rare and of uncertain structure and, as a matter of fact, they are not a mixture of 1:1 and 1:2 compounds. $[Cd(R_3P)(SCN)_2]$ has a polymeric trigonal bipyramidal (*see Trigonal Bipyramidal*) structure, but $[Cd(Ph_3P)(CF_3CO_2)_2]_2$ is dimeric with two Cd^{2+} ions bridged by four carboxylate ligands. Complexes of the type $[(\text{phenoxide})_2CdL_n]$ (L = monotricyclohexylphosphine, $n = 1$, $L = Me_3P$ or n-Bu_3P, $n = 1$ and 2) are obtained by reaction between $Cd[N(SiMe_3)_2]_2$ and the phenol in the presence of the phosphine.[62] [(2,6-di-*ter*-butylphenoxide$)_2$Cd(monotricyclohexylphosphine)] has Cd^{2+} in a near trigonal planar geometry and a Cd-P bond length of 2.5247 Å. In the bis(phosphine) complex [(2,6-di-*ter*-butylphenoxide$)_2Cd(Pme_3)_2]$, however, Cd^{2+} lies in a distorted tetrahedral environment and the (average) Cd-P bond length is 2.737 Å. Adamantanoid cationic complexes of the type $[(\mu\text{-ER})_6(CdPPh_3)_n(Cd)_{4-n}]^{2+}$ ($ER = S{-}Pr^i$, $S{-}c{-}C_6H_{11}$, SPh, SePh, SPr^n, $S{-}n{-}C_5H_{11}$; $n = 2{-}4$) have been synthesized. Cd^{2+} forms $[Cd(diars)X_2]$ (X = Cl, Br, I) and $[Cd(diars)_2](ClO_4)_2$ (*see Arsine & As-donor Ligands*). $[Cd(diars)Cl_2]$ is believed to have a polymeric octahedral structure.[61]

15.6 Multinuclear Complexes

The anions $[CoCdCl_6]^{2-}$ and $[Co_2CdCl_8]^{2-}$ show an unusual structure: in the former, both the metal ions are tetrahedral and a Co–Cd bond is present;[2] in the latter, the tetrahedral (*see Tetrahedral*) Cd^{2+} is connected by four bridging chlorides to two tetrahedral Co^{2+} ions. The polynuclear complex (*see Polynuclear Complexes*) $[I_2Cd\{(\mu\text{-NC})MnL_x\}_2]$ ($L_x = cis$ or *trans*-$(CO)_2\{P(OR)_3\}$(dppm); R = Ph or Et, dppm = $Ph_2PCH_2Ph_2$) is obtained by reaction between CdI_2 and *cis*- or *trans*-$[Mn(CN)(CO)_2\{P(OR)_3\}$(dppm)], Cd^{2+} is tetrahedrally coordinated to two I^- ions and two N atoms of bridged CN^- ions. Complexes of the type $[CoCd(SCN)_4L_n]$ have a structure determined by the nature of the ligand L: when L = py or bipy, the compound is better formulated as $[CoL_n][Cd(SCN)_4]$ ($n = 3$ or 6), when L = phen, as $[Co(phen)_3][Cd(SCN)_4(phen)]$. $[NiCd(SCN)_4(THF)_n]$ ($n = 2$ or 4) shows octahedral Cd^{2+} and Ni^{2+} for $n = 4$, but only octahedral Ni^{2+} with bridging thiocyanate for $n = 2$. In $[CoCd(SCN)_4(en)_3]$, Co^{2+} is square planar (*see Square Planar*). $Cd[Mn(CO)_5]_2$ forms a terpyridyl adduct with a very distorted trigonal bipyramidal (*see Trigonal Bipyramidal*) structure. $CdM(SCN)_4$ (M = Ni, Fe, Zn, Cu, or Co) reacts with a variety of N-donor ligands. Three type of complexes can be obtained: $[Cd(SCN)_4][ML_6]$, polymeric $CdM(SCN)_4\cdot 2L$ or $CdM(SCN)_4\cdot 4L$, and monomeric $CdM(SCN)_4\cdot 2L$ or $CdM(SCN)_4\cdot 4L$. Tetranuclear $[Cd_2Cu_2I_4L_4(DMSO)_2]$, pentanuclear $[Cd_2Cu_3Br_6L_4(DMSO)_2]$, and hexanuclear $[Cd_4Cu_2Cl_6L_6(H_2O)]$ (HL = 2-dimethylaminoethanol) have been prepared and the unusual structures determined.[63] Clathrates (*see Clathrate*) containing octahedral Cd^{2+} and tetracyanonichelate (II) units have been synthesized and structurally characterized.[64]

16 RELATED ARTICLES

Alloys; Analytical Chemistry of the Transition Elements; Cadmium: Organometallic Chemistry; Mercury: Inorganic & Coordination Chemistry; Tin: Inorganic Chemistry; Zinc: Inorganic & Coordination Chemistry.

17 REFERENCES

1. ‘Gmelin’s Handbuch der Anorganischen Chemie: Cadmium’, Verlag Chemie, Weinheim, 1925, and 1959 Vol. 33.

2. R. H. Prince, in 'Comprehensive Coordination Chemistry', eds. G. Wilkinson, R. D. Gillard, and J. A. McCleverty, Pergamon Press, Oxford, 1987, Vol. 5, p. 925.
3. H. Mislin and O. Ravera, 'Cadmium in the Environment', Birkhauser, Basel, 1986.
4. A. Martin-Garin, P. van Cappellen, and L. Charlet, *Geochim. Cosmochim. Acta*, 2003, **67**, 2763.
5. 'Cadmium and Cadmium Alloys', Kirk-Othmer Encyclopedia of Chemical Technology, Wiley, New York, 1993, Vol. 4.
6. H. Fathi, ed., 'Handbook of Extractive Metallurgy', Wiley-VCH, Weinheim, 1997.
7. P. Haasen, 'Physical Metallurgy', Cambridge University Press, Cambridge, 1996.
8. K. Otsuka and C. M. Wayman, eds, 'Shape Memory Materials', Cambridge University Press, Cambridge, 1999.
9. J. R. De Voe, 'Radiochemistry of Cadmium', US Atomic Energy Commission, Washington, 1960.
10. F. Wombacher, M. Rehkämper, K. Mezger, and C. Münker, *Geochim. Cosmochim. Acta*, 2003, **67**, 4639.
11. J. O. Nriagu and J. B. Sprague, eds, 'Cadmium in the Aquatic Environment', Wiley, New York, 1987.
12. Z. Prokop, P. Cupr, V. Zlevorova-Zlamalikova, J. Komarek, L. Dusek, and I. Holoubek, *Environ. Res.*, 2003, **91**, 119.
13. S. Klimmek, H. I. Stan, A. Wilke, G. Bunke, and R. Buchholz, *Environ. Sci. Technol.*, 2001, **35**, 4283.
14. M. J. Stillman, C. F. Shaw III, and K. T. Suzuki, eds, 'Metallothioneins: Synthesis, Structure and Properties of Metallothioneins, Phytochelatins and Metalthiolate Ccomplexes', Wiley, New York, 1992.
15. P. Patnaik, 'A Comprehensive Guide to the Hazardous Properties of Chemical Substance', Wiley, New York, 1999.
16. National Library of Medicine, National Toxicology Information Program, 2003, Hazardous Substance Data Bank.
17. F. M. Summers, *Coord. Chem. Rev.*, 1988, **86**, 43.
18. P. Gonzàlez-Duarte, W. Clegg, I. Casals, J. Sola, and J. Rius, *J. Am. Chem. Soc.*, 1998, **120**, 1260.
19. K. Eichele and R. E. Wasylishen, *Inorg. Chem.*, 1994, **33**, 2766.
20. J. Dechter, *Prog. Inorg. Chem.*, 1985, **33**, 393.
21. W. H. Otto, S. D. Burton, W. R. Carper, and C. K. Larive, *Environ. Sci. Technol.*, 2001, **35**, 4900.
22. J. E. Bowen Katari, V. L. Colvin, and A. P. Alivisatos, *J. Phys. Chem.*, 1994, **98**, 4109.
23. B. E. Boone and C. Shannon, *J. Phys. Chem.*, 1996, **100**, 9480.
24. V. A. Gnatyuk, T. Aoki, Y. Nakanishi, and Y. Hatanaka, *Surf. Sci.*, 2003, **542**, 142.
25. R. J. Latham and N. A. Hampson, in 'Encyclopedia of Electrochemistry of the Elements', ed. A. J. Bard, Dekker, New York, 1973, p. 155.
26. E. Deltombe, M. Pourbaix, and N. de Zoubov, in 'Atlas of Electrochemical Equilibrium in Aqueous Solution', ed. M. Pourbaix, Pergamon Press, Oxford, 1966, p. 414.
27. R. Andriamanampisoa and R. A. Mackay, *Langmuir*, 1994, **10**, 4339.
28. Y. Mastai, R. Polsky, Yu. Koltypin, A. Gedanken, and G. Hodes, *J. Am. Chem. Soc.*, 1999, **121**, 10047.
29. D. G. Tuck, *Rev. Inorg. Chem.*, 1979, **1**, 209.
30. M. Zucolotto-Chalaca, J. D. Figueroa-Villar, J. A. Ellena, and E. E. Castellano, *Inorg. Chim. Acta*, 2002, **328**, 45.
31. H. Chun, D. Kim, D. N. Dybtsev, and K. Kim, *Angew. Chem., Int. Ed.*, 2004, **43**, 971.
32. R. Faggiani, R. J. Gillespie, and J. E. Vekris, *J. Chem. Soc., Chem. Commun.*, 1986, 517.
33. O. A. Babich and E. S. Gould, *Chem. Commun.*, 2001, 998.
34. M. Z. Hoffman, in 'Inorganic Reactions and Methods', ed. J. J. Zuckerman, VCH, Deerfield, 1986, p. 294.
35. B. Siegel and G. G. Libowitz, in 'Metal Hydrides', eds. W. M. Mueller, J. P. Blackledge, and G. G. Libowitz, Academic Press, New York, 1968, p. 550.
36. M. Bortz, M. Gutmann, and K. Yvon, *J. Alloys Compd*, 1999, **285**, L19.
37. A. Albinati and L. M. Venanzi, *Coord. Chem. Rev.*, 2000, **200–202**, 687.
38. B. J. Aylett, in 'Comprehensive Inorganic Chemistry', eds. J. C. Bailar, H. J. Emeleus, R. Nyholm, and A. F. Trotman-Dickerson, Pergamon Press, Oxford, 1973, Vol. 3, p. 254.
39. M. Terakami, H. Nakagawa, K. Fukui, H. Okamura, T. Hirono, Y. Ikemoto, T. Moriwaki, and H. Kimura, *J. Lumin.*, 2004, **108**, 75.
40. H. Zhang, X. Wang, K. Zhang, and B. K. Teo, *Coord. Chem. Rev.*, 1999, **183**, 157.
41. S. Kister, H.-L. Keller, and W. Kockelmann, *Phys. B: Condens Matter*, 2000, **276–278**, 262.
42. F. Jellinek, in 'Inorganic Sulphur Chemistry', ed. G. Nickless, Elsevier, Amsterdam, 1968, p. 692.
43. Y.-T. Chen, J.-B. Ding, Y. Guo, L.-B. Kong, and H.-L. Li, *Mater. Chem. Phys.*, 2003, **77**, 734.
44. A. V. Shevelkov, L. N. Reshetova, and B. A. Popovkin, *J. Solid State Chem.*, 1997, **134**, 282.
45. M. J. Taylor, 'Metal-to-Metal Bonded States', Academic Press, London, 1975, p. 42.
46. J. Fornies, J. Gomez, E. Lalinde, and M. T. Moreno, *Inorg. Chem.*, 2001, **40**, 5415.
47. M. B. Volf, 'Chemical Approach to Glass', Elsevier, Amsterdam, 1984, p. 426.
48. E. Hogfeldt, 'Stability Constants of Metal Ion Complexes. Part A: Inorganic Ligands', Pergamon Press, Oxford, 1982.
49. H. Zhang, X. Wang, H. Zhu, W. Xiao, K. Zhang, and B. K. Teo, *Inorg. Chem.*, 1999, **38**, 886.
50. D. Dakternieks, *Coord. Chem. Rev.*, 1987, **78**, 125.
51. M. N. Huges, *Coord. Chem. Rev.*, 1981, **37**, 297.
52. R. Vaidhyanathan, S. Natarajan, and C. N. R. Rao, *Inorg. Chem.*, 2002, **41**, 5226.

53. Z.-F. Chen, R.-G. Xiong, B. F. Abrahams, X.-Z. You, and C.-M. Che, *J. Chem. Soc., Dalton Trans.*, 2001, 2453.
54. J. J. Vittal, J. T. Sampanthar, and Z. Lu, *Inorg. Chim. Acta*, 2003, **343**, 224.
55. J. Chan, Z. Huang, M. E. Merrifield, M. T. Salgado, and M. Stillman, *Coord. Chem. Rev.*, 2002, **233–234**, 319.
56. G. Henkel and B. Krebs, *Chem. Rev.*, 2004, **104**, 801.
57. S. Ishiguro, K. Ozutsumi, M. Miyauchi, and H. Ohtaki, *Inorg. Chem.*, 1989, **28**, 3258.
58. S. A. Barnett and N. R. Champness, *Coord. Chem. Rev.*, 2003, **246**, 145.
59. L. Yi, B. Ding, P. Cheng, D.-Z. Liao, S.-P. Yan, and Z.-H. Jiang, *Inorg. Chem.*, 2004, **43**, 33.
60. G. W. Franklin, D. P. Riley, and W. L. Neumann, *Coord. Chem. Rev.*, 1998, **174**, 133.
61. C. A. McAuliffe and W. Levason, 'Phosphine, Arsine, Stibine Complexes of Transition Elements', Elsevier, Amsterdam, 1979.
62. D. J. Darensbourg, P. Raney, D. L. Larkins, and J. H. Reibenspies, *Inorg. Chem.*, 2000, **39**, 473.
63. E. A. Vinogradova, O. Yu. Vassilyeva, V. N. Kokozay, B. W. Skeleton, J. K. Bjernemose, and P. R. Raithby, *J. Chem. Soc., Dalton Trans.*, 2002, 4248.
64. H. Yuge, Y. Noda, and T. Iwamoto, *Inorg. Chem.*, 1996, **35**, 1842.

Cadmium: Organometallic Chemistry

Niladri Narayan Gupta & David A. Atwood
University of Kentucky, Lexington, KY, USA

Based in part on the article Cadmium: Organometallic Chemistry by Gerard Parkin which appeared in the Encyclopedia of Inorganic Chemistry, First Edition.

1 Introduction 1
2 R_2Cd: Dihydrocarbylcadmium Compounds 1
3 RCdX: Monoalkylcadmium Compounds 4
4 Organocadmium Anions and Cations 6
5 Organocadmium Compounds in Organic and Organometallic Synthesis 6
6 Related Articles 8
7 References 8

1 INTRODUCTION

The chemistry of organocadmium compounds is closely analogous to that of their zinc analogs, but is noticeably less well developed.**[1]** Organocadmium reagents are in general mild and regioselective.**[2]** Their principal importance is in the preparation of ketones from RCOCl and $(RCO)_2O$. Organocadmium compounds have also been used for the regioselective alkylation of quinones,**[3]** although more recently organocadmium compounds have found use in MOCVD processes (*see Metal–Organic Chemical Vapor Deposition*). Organometallic cadmium compounds, as with cadmium compounds in general, are highly toxic.**[4]** Specifically, mammals accumulate cadmium in the liver and kidneys. A number of review articles on organocadmium compounds and their uses are available.**[1,5–8]**

2 R_2Cd: DIHYDROCARBYLCADMIUM COMPOUNDS

2.1 General Properties

Dialkyl- and diarylcadmium derivatives are colorless compounds that are either liquids or low-melting solids. The compounds are noticeably more stable to air than the corresponding zinc derivatives. For example, whereas Me_2Zn is pyrophoric, Me_2Cd only fumes in air. However, although the cadmium derivatives are more air stable, they are substantially less thermally stable and more light sensitive than the zinc derivatives. As such, R_2Cd compounds should be stored cold and in the absence of light. A notable exception is $[(Me_3Si)_3C]_2Cd$, which decomposes at ca. 300 °C, and is also stable to both air and water (as is the zinc analog).**[9]**

The lower thermal stability of R_2Cd compounds compared with R_2Zn is undoubtedly a consequence of weaker Cd–C bonds. The mean Cd–C bond dissociation energies (D) have been determined for some R_2Cd compounds, and are intermediate between those of the Zn and Hg analogs, as summarized in Table 1**[10]** (*see Bond Energies* and ***Bonding Energetics of Organometallic Compounds***). The individual first and second bond dissociation energies have been calculated for Me_2Cd, demonstrating that the second bond dissociation energy is substantially smaller than the first [$D_1 = 234 \pm 6\,\mathrm{kJ\,mol^{-1}}$; $D_2 = 64 \pm 10\,\mathrm{kJ\,mol^{-1}}$].

R_2Cd compounds have been studied by ^{113}Cd (12.3% abundance) NMR spectroscopy,**[11–13]** which indicates that the ^{113}Cd shielding increases irregularly in the order $Me_2Cd < i\text{-}Bu_2Cd < n\text{-}Bu_2Cd < n\text{-}Pr_2Cd < Et_2Cd < i\text{-}Pr_2Cd$. Organocadmium derivatives are also characterized by the observation of ^{113}Cd-^1H coupling as satellites in the ^1H NMR spectrum (Table 2).

2.2 Synthesis of R_2Cd Compounds

R_2Cd compounds were first obtained by the direct reaction of cadmium metal with alkyl halides. Unfortunately, this method is limited and typically does not readily yield pure products. However, the direct method is facilitated by the use of highly activated cadmium slurries.**[14–16]**

The most general method of preparation of organocadmium derivatives involves the reactions of RLi, RMgX, or R_3Al with cadmium salts.**[17]** For example, Me_2Cd is readily prepared by the reaction of Me_3Al with $Cd(OAc)_2$ (equation 1),

Table 1 Mean bond dissociation energies for some R_2M (M = Zn, Cd, Hg) compounds

	D(M–R) ($\mathrm{kJ\,mol^{-1}}$)		
	Zn	Cd	Hg
Me_2M	183 ± 7	147 ± 4	124 ± 4
Et_2M	133 ± 10	111 ± 8	100 ± 8

Table 2 ^{113}Cd NMR data for some R_2Cd compounds

	$\delta^{113}Cd$ (ppm)	$^2J_{Cd–H}$ (Hz)	$^3J_{Cd–H}$ (Hz)
Me_2Cd	0	52	–
Et_2Cd	−94	53	60
i-Pr_2Cd	−207	–	56
n-Pr_2Cd	−46	50	55
n-Bu_2Cd	−44	52	–
i-Bu_2Cd	−22	50	70

and $(Me_3SiCH_2)_2Cd$ is obtained by (i) the reaction of Me_3SiCH_2Li with $CdCl_2$ (equation 2),[18] and (ii) the reaction of Me_3SiCH_2MgCl with CdI_2 (equation 3).[19] An analogous method has also been used to synthesize the silyl derivative $(Me_3Si)_2Cd$ (equation 4).[20] $(Me_3Si)_2Cd$ is very unstable and decomposes over 2 days at $-20\,°C$.

$$2Me_3Al + 3Cd(OAc)_2 \longrightarrow 3Me_2Cd + 2Al(OAc)_3 \qquad (1)$$

$$2Me_3SiCH_2Li + CdCl_2 \longrightarrow (Me_3SiCH_2)_2Cd + 2LiCl \qquad (2)$$

$$2Me_3SiCH_2MgCl + CdI_2 \longrightarrow (Me_3SiCH_2)_2Cd + 2MgClI \qquad (3)$$

$$CdCl_2 \xrightarrow{LiAl(SiMe_3)_4} (Me_3Si)_2Cd \qquad (4)$$

It is also noteworthy that, in contrast to the synthesis of R_2Zn compounds, R_2Cd derivatives are not readily accessible by transmetalation (*see Transmetalation*) between R_2Hg and Cd metal, presumably since the electropositivity of Cd and Hg is so similar that equilibrium mixtures are obtained.

Cp_2Cd is obtained by reaction of $Cd[N(SiMe_3)_2]_2$ with CpH (equation 5).[21] The orange–red, light-sensitive pentamethylcyclopentadienyl analog $Cp^*{}_2Cd$ has also been prepared by the reaction between $Cd(acac)_2$ and $LiCp^*$ (equation 6).[22] It is worth noting that, in contrast, the analogous reaction between $CdCl_2$ and $LiCp^*$ gives only colloidal cadmium and the organic dimer $Cp^*{}_2$.[23]

$$Cd[N(SiMe_3)_2]_2 + 2CpH \longrightarrow Cp_2Cd + 2HN(SiMe_3)_2 \qquad (5)$$

$$Cd(acac)_2 + 2LiCp^* \longrightarrow Cp^*{}_2Cd + 2Li(acac) \qquad (6)$$

Perfluoroalkyl cadmium compounds are also known. Bis(trifluoromethyl)cadmium has been prepared at $-78\,°C$ by cocondensing Cd atoms with $\cdot CF_3$ radicals generated in a hexafluoroethane plasma (*see* ***Metal Vapor Synthesis of Transition Metal Compounds***),[24,25] and also by the unusual reaction of activated cadmium powder with difluorodihalomethanes, for example, CF_2Cl_2, CF_2Br_2, or CF_2BrCl, in DMF (equation 7).[26]

$$\begin{aligned} 2Cd + 2CF_2X_2 + Me_2NCHO &\longrightarrow CF_3CdX[\text{or } 0.5(CF_3)_2Cd \\ &+ 0.5\, CdX_2] + CdX_2 + CO + [Me_2N{=}CFH]^+X^- \end{aligned} \qquad (7)$$

The related trifluorosilyl derivative bis(trifluorosilyl)cadmium has been obtained by an analogous procedure to $(CF_3)_2Cd$ involving the cocondensation of Cd atoms with $\cdot SiF_3$ radicals (generated in a Si_2F_6 glow discharge).[24,25] $(SiF_3)_2Cd$ is marginally stable with a half-life of approximately 1 day at room temperature, but the adduct $(SiF_3)_2Cd(glyme)$ (*see Addition Compound*) is stable indefinitely in an inert atmosphere.

Although R_2Cd compounds cannot be prepared by transmetalation with R_2Hg, bis(perfluorophenyl)cadmium has been obtained by transmetalation with the thallium derivative $(C_6F_5)_2TlBr$ (equation 8).[27] $(C_6F_5)_2Cd$ can also be prepared by (i) the reaction of $CdCl_2$ with C_6F_5Li (equation 9) and (ii) the decarboxylation of $(C_6F_5CO_2)_2Cd$ (equation 10).[28]

$$(C_6F_5)_2TlBr \xrightarrow{Cd} (C_6F_5)_2Cd \qquad (8)$$

$$CdCl_2 + 2C_6F_5Li \longrightarrow (C_6F_5)_2Cd + 2LiCl \qquad (9)$$

$$(C_6F_5CO_2)_2Cd \longrightarrow (C_6F_5)_2Cd + 2CO_2 \qquad (10)$$

A general synthesis of perfluoroalkyl derivatives $(R_f)_2Cd$ ($R_f = CF_3$, C_2F_5, n-C_3F_7, i-C_3F_7, n-C_4F_9, C_6F_5) that occurs in quantitative yield involves the reaction of perfluoroorganoiodides R_fI with a dialkylcadmium reagent R_2Cd (R = Me, Et) in the presence of a Lewis base (*see Lewis Acids & Bases*), for example, glyme, diglyme, TMEDA, pyridine, or MeCN (equation 11).[29] However, since the perfluoroalkylcadmium derivatives are strong Lewis acids (*see Lewis Acids & Bases*), they are actually isolated as adducts, for example, $(R_f)_2Cd(py)_2$.

$$2R_fI + R_2Cd + 2L \longrightarrow (R_f)_2CdL_2 + 2RI \qquad (11)$$

$$L_2 = \text{glyme, diglyme, } (MeCN)_2,\ (py)_2$$

2.3 Structures of R_2Cd Compounds

Structural studies on simple R_2Cd compounds are rare. However, Me_2Cd is known to be linear with $d(Cd–C) = 2.112(4)$ Å in the gas phase on the basis of Raman studies,[30] and $[(CH_2 = CHMe_2Si)(Me_3Si)_2C]_2Cd$ is linear in the solid state [Cd–C = 2.172(3) Å] on the basis of X-ray diffraction (*see* ***Diffraction Methods in Inorganic Chemistry***) as shown in (**1**).[31] The structure of $Cp^*{}_2Cd$ is not known, but an η^1, η^5-arrangement (*see Hapticity*) of Cp^* ligands (**2**) has been proposed by analogy with that observed for $Cp^*{}_2Zn$. Similarly, on the basis of comparison with the zinc system, Cp_2Cd has been proposed to be polymeric.[32]

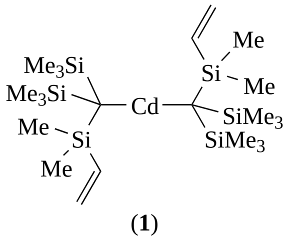

(**1**)

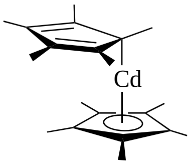

(**2**)

2.4 Reactivity of R_2Cd Compounds

R_2Cd compounds are generally much less reactive than their zinc analogs, although the overall reactions may be similar. A summary of the reactivity of R_2Cd compounds is provided in Scheme 1, and further details concerning these reactions will be found in Sections 2.4–5.

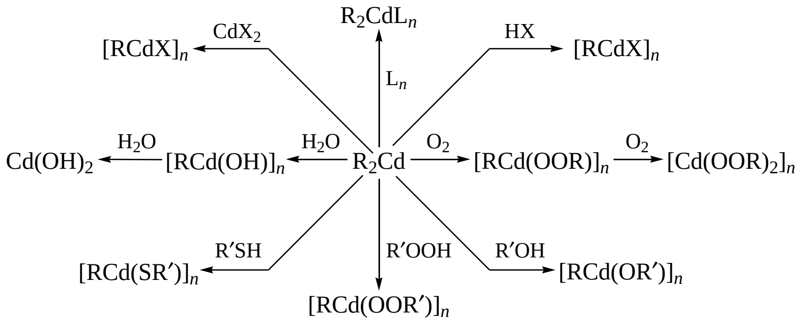

Scheme 1 Summary of the reactivity or R_2Cd derivatives

2.4.1 Adduct Formation

Intermolecular Adduct Formation. The metal center in R_2Cd compounds is noticeably less Lewis acidic than in the corresponding zinc compounds. Hence, R_2Cd compounds form weaker, and fewer, adducts than do the R_2Zn analogs. However, the Lewis acidity of the Cd center may be increased by incorporation of electron-withdrawing substituents.

$[2,4,6\text{-}(CF_3)_3C_6H_2]_2Cd(MeCN)$ (**3**) is an example of a structurally characterized three-coordinate diaryl cadmium compound.[33] The molecule is ‘T’-shaped with Cd–C distances of 2.184(3) and 2.181(3) Å, and a C–Cd–C bond angle of 165.7(1)°.

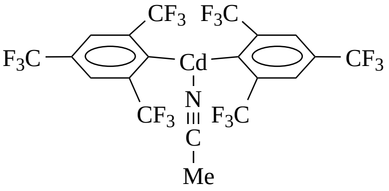

(**3**)

The four-coordinate 2,2′-bipyridyl and triazine adducts $Me_2Cd(bipy)$,[34] $(Me_3SiCH_2)_2Cd(bipy)$,[35] and $Me_2Cd[(CH_2NMe)_3]_2$[36] have been isolated, and the bipyridyl derivatives (**4a**) have been structurally characterized by X-ray diffraction. Notably, the coordination environments about the cadmium centers in both compounds deviate substantially from tetrahedral, with large C–Cd–C bond angles (Table 3).

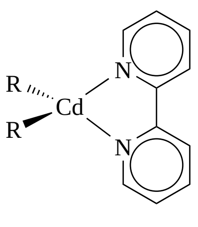

(**4a**)

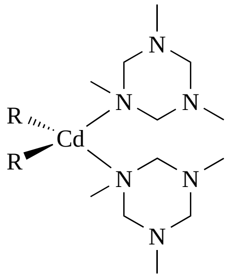

(**4b**)

Table 3 Cd coordination environment in bipyridyl adducts[37]

	$Me_2Cd(bipy)$	$(Me_3SiCH_2)_2Cd(bipy)$
Cd–C	2.17(3) Å	2.19(6) Å
	2.15(2) Å	2.09(5) Å
Cd–N	2.50(1) Å	2.53(3) Å
	2.54(1) Å	2.52(4) Å
C–Cd–C	148.4(8)°	156(2)°
N–Cd–N	64.0(5)°	65(1)

In contrast to the triazine adduct $Me_2Cd[(CH_2NMe)_3]_2$ (**4b**), in which each triazine ligand coordinates to one Cd center, the 1,4-dioxane adduct $[Me_2Cd(1,4\text{-dioxane})]_n$ (**5**) is polymeric, with 1,4-dioxane molecules bridging Cd centers.[38] As with the bipyridyl compounds described above, the coordination environment [d(Cd–C) = 2.09(2) Å; C–Cd–C = 173.0(8)°] also deviates substantially from tetrahedral, and the near linearity of the C–Cd–C bond angle suggests that the Cd–C interactions involve sp hybrids, so that the oxygen lone pairs donate into orbitals on Cd that are mainly p in character.

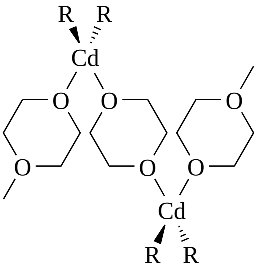

(**5**)

The pyridine adduct of the cyclopentadienyl derivative, $Cp_2Cd(NC_5H_5)_2$, also exhibits a distorted tetrahedral structure (**6**) in which both cyclopentadienyl ligands are coordinated in monohapto fashion [d(Cd–C) = 2.353(5), 2.307(5) Å, d(Cd–N) = 2.309(3), 2.360(3) Å; C–Cd–C = 129.1(2)°].[32,39] The pentamethylcyclopentadienyl complex Cp^*_2Cd also forms a yellow adduct with glyme, $Cp^*_2Cd(glyme)$.[22] The

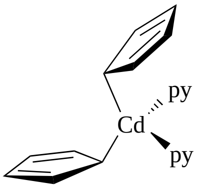

(**6**)

adduct formation is reversible and dissolving $Cp^*{}_2Cd(glyme)$ in toluene regenerates $Cp^*{}_2Cd$.

Perfluoroalkyl derivatives are strong Lewis acids owing to the electron-withdrawing effects of the fluorine substituents, and readily form stable adducts, for example, $(CF_3)_2Cd(glyme)$, that have been characterized by ^{19}F NMR spectroscopy.[29,40,41]

Interest in adducts of R_2Cd compounds derives from their potential as a source for pure R_2Cd for use in metal organic chemical vapor deposition (*see Metal–Organic Chemical Vapor Deposition*).[42]

Intramolecular Adduct Formation. By analogy with zinc compounds, the incorporation of donor atoms in the alkyl groups of R_2Cd derivatives may result in the formation of intramolecular adducts. For example, the pyridyl group in the complex $[(NC_5H_4)(SiMe_3)_2C]_2Cd$ (**7**) coordinates to the Cd center [d(Cd–C) = 2.27 Å; d(Cd–N) = 2.49 Å; C–Cd–C = 174.3°; N–Cd–N = 108.9°].[43]

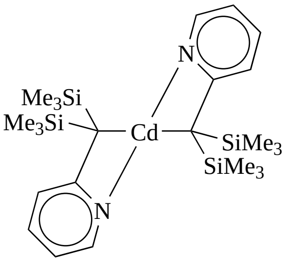

(**7**)

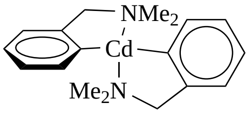

(**8**)

The coordination environment about cadmium in $[2\text{-}(Me_2NCH_2)C_6H_4]_2Cd$ (**8**) is also far removed from tetrahedral, with the best description being a trigonal bipyramid with a vacant equatorial site.[44,45] The Cd–C bond length is 2.154(8) Å, and the C–Cd–C bond angle close to linear [174.1(1)°]. The molecules pack in the crystal lattice in a manner such that there are weak Cd···Cd interactions between adjacent molecules through the vacant coordination sites on cadmium. The Cd···Cd separation of 3.176 Å is close to twice the van der Waals radius of Cd (3.20 Å) (*see van der Waals Forces*).

Some other examples of intramolecular adducts include $(Me_2NCH_2CH_2CH_2)_2Cd$ (**9a**)[46] and $(SPMe_2BH_2PMe_2CH_2)_2Cd$ (**9b**).[47]

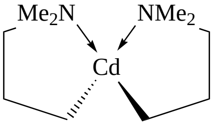

(**9a**)

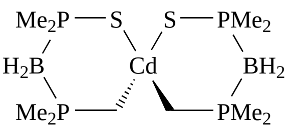

(**9b**)

3 RCdX: MONOALKYLCADMIUM COMPOUNDS

Although there exists a series of monoalkyl cadmium compounds of the type $[RCdX]_n$, such compounds are not as extensive as the zinc analogs. For example, alkylcadmium hydride compounds are unknown. Furthermore, the $[RCdX]_n$ compounds that have been isolated are often not as well characterized as their zinc analogs.

3.1 RCdX (X = Cl, Br, I)

Alkylcadmium halide derivatives are typically obtained by ligand redistribution between R_2Cd and CdX_2 (equation 12).[1] Relatively little is known about their detailed structures, although it is likely that they are either oligomeric or polymeric by comparison with the zinc analogs.

$$R_2Cd + CdX_2 \rightleftharpoons 2RCdX \qquad (12)$$

3.2 RCd(OH)

The pentafluorophenyl derivative $(C_6F_5)_2Cd$ is hydrolyzed by water to give the tetrameric cadmium hydroxide complex $[(C_6F_5)Cd(\mu\text{-}OH)]_4$ (equation 13).[28] The molecular structure (**10**) of $[(C_6F_5)Cd(\mu\text{-}OH)]_4$ is based on a cube with the cadmium and oxygen atoms occupying the vertices. The hydroxy derivative is characterized by observation of a ν(OH) band at 3640 cm^{-1}.

$$4(C_6F_5)_2Cd + 4H_2O \longrightarrow [(C_6F_5)Cd(\mu\text{-}OH)]_4 + 4C_6F_5H \qquad (13)$$

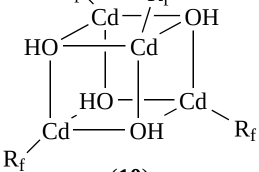

(**10**)

3.3 RCd(OR′)

Alkylcadmium alkoxides may be prepared by the reaction of R_2Cd with one equivalent of R′OH (equation 14).[48,49] The mechanisms of the reactions of Et_2Cd with R′OH have been investigated, confirming that the formation of EtCd(OR′) is more rapid than that for the bis(alkoxide) $Cd(OR')_2$.[50]

$$R_2Cd + R'OH \longrightarrow RCd(OR') + RH \tag{14}$$

The alkoxides $[MeCd(OR)]_4$ (R = Me, Et, *i*-Pr, Ph) are tetrameric and are assumed to have cubic structures (**11**) by analogy with the related zinc compounds. In contrast, the *t*-butoxy derivative $[MeCd(O\text{-}t\text{-}Bu)]_2$ (**12**) has been reported to be dimeric in benzene with the proposed structure shown, whereas the zinc analog is tetrameric. However, methylcadmium alkoxides have also been studied by ^{113}Cd NMR spectroscopy, which has suggested that the *t*-butoxy derivative may in fact also be tetrameric.[51]

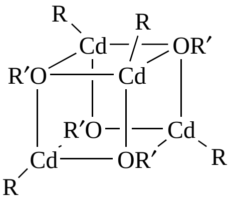

(**11**)

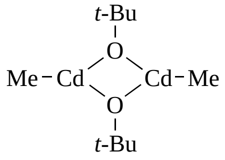

(**12**)

3.4 RCd(OOR′)

R_2Cd compounds react sequentially with O_2 to give alkylperoxo compounds, RCdOOR and $Cd(OOR)_2$ (equation 15).[52–56] Little is known about the detailed structures of the alkylperoxo compounds, but the complex $[MeCd(OOMe)]_4$ is proposed to be tetrameric in solution.

$$R_2Cd \xrightarrow{O_2} RCd(OOR) \xrightarrow{O_2} Cd(OOR)_2 \tag{15}$$

The mechanism of the reaction between Me_2Cd and O_2 has been investigated and a radical chain process has been proposed (see Scheme 2). The initiation step is believed to involve an ill-defined bimolecular reaction between two Me_2Cd molecules. The rate of initiation is inversely related to O_2 concentration, so it has been suggested that O_2 can also react competitively with the dimer. The reaction between Et_2Cd and O_2 has also been studied and it has been claimed that an unusual adduct of composition $Et_2Cd{\cdot}2O_2$ is formed *reversibly* prior to formation of the alkylperoxo complex.[57]

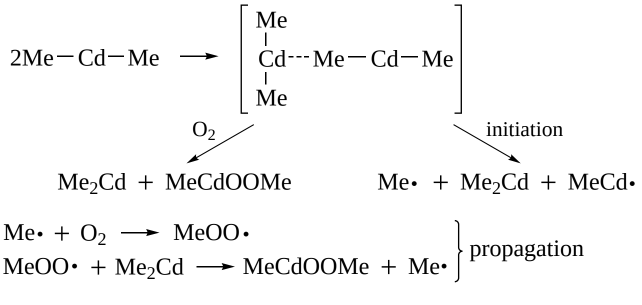

Scheme 2 Possible mechanism for the reactions of R_2Cd with O_2

Mixed alkylperoxide derivatives of the type MeCd(OO-*t*-Bu) may be obtained by the reaction of Me_2Cd with *t*-BuOOH (equation 16). Thermal decomposition of MeCd(OO-*t*-Bu) gives an ill-defined product of composition [MeCdOC(O)H·CdO].

$$Me_2Cd + t\text{-}BuOOH \longrightarrow MeCd(OO\text{-}t\text{-}Bu) + CH_4 \tag{16}$$

Me_2Cd reacts with H_2O_2 to give a complex that is proposed to be the peroxy-bridged derivative MeCdOOCdMe, but was not isolated (equation 17)

$$2Me_2Cd + H_2O_2 \longrightarrow MeCdOOCdMe + 2CH_4 \tag{17}$$

3.5 RCd(SR′)

Alkylcadmium thiolates may be prepared by the reaction of R_2Cd with R′SH (equation 18).[48] As with the alkoxy derivatives, the degree of oligomerization of RCd(SR′) depends upon the R and R′ substituents. For example, the compounds $[MeCd(SMe)]_n$ and $[MeCd(SPh)]_n$ are insoluble and presumably polymeric, whereas $[MeCd(S\text{-}i\text{-}Pr)]_6$ (**13a**) is hexameric and $[MeCd(S\text{-}t\text{-}Bu)]_4$ (**13b**) is tetrameric, with the possible structures shown.

$$R_2Cd + R'SH \longrightarrow RCd(SR') + RH \tag{18}$$

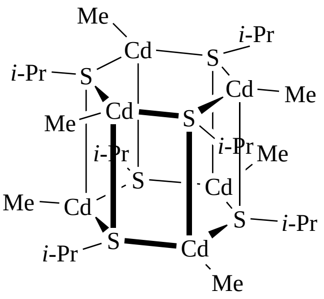

(**13a**)

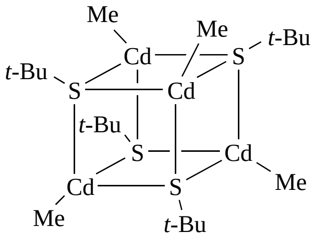

(**13b**)

Dialkylcadmium compounds are also reactive towards H_2S. For example, $(Me_3SiCH_2)_2Cd$ reacts immediately with H_2S to give CdS (equation 19).[37] Other organocadmium compounds with Cd–S bonds include the thiocyanate derivatives RCdSCN that are obtained by the reaction of R_2Cd with $(SCN)_2$ (equation 20).[58]

$$(Me_3SiCH_2)_2Cd + H_2S \longrightarrow CdS + Me_4Si \tag{19}$$

$$R_2Cd + (SCN)_2 \longrightarrow RCd(SCN) + RSCN \tag{20}$$

3.6 $\mathrm{RCd(NR'_2)}$

Alkylcadmium amide derivatives are rare. However, $\mathrm{Cp^*{}_2Cd}$ reacts with $\mathrm{Cd[N(SiMe_3)_2]_2}$ to give the amide bridged dimer $\mathrm{\{Cp^*Cd[\mu\text{-}N(SiMe_3)_2]\}_2}$ (equation 21).**22** The $\mathrm{Cp^*}$ ligands are bonded in an η^1 arrangement as illustrated in (**14**).

$$\mathrm{Cp^*{}_2Cd + Cd[N(SiMe_3)_2]_2 \longrightarrow [Cp^*Cd\{\mu\text{-}N(SiMe_3)_2\}]_2} \qquad (21)$$

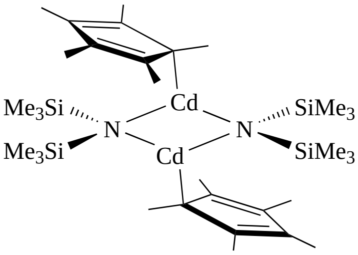

(**14**)

Other alkylcadmium compounds containing Cd–N bonds include the azide derivatives $\mathrm{RCdN_3}$, which are obtained by the reaction of $\mathrm{R_2Cd}$ with $\mathrm{ClN_3}$ (equation 22).**59**

$$\mathrm{R_2Cd + ClN_3 \longrightarrow RCdN_3 + RCl} \qquad (22)$$

3.7 $\mathrm{RCd(PR'_2)}$

$\mathrm{Me_2Cd}$ reacts with $\mathrm{Ga(P\text{-}\mathit{t}\text{-}Bu_2)_3}$ to give the phosphido derivative $\mathrm{[MeCd(\mu\text{-}P\text{-}\mathit{t}\text{-}Bu_2)]_3}$ (equation 23).**60** The phosphido derivative is trimeric (**15**) and contains planar three-coordinate cadmium centers.

$$\begin{aligned}&\mathrm{12Me_2Cd + 6Ga[P(\mathit{t}\text{-}Bu)_2]_3 \longrightarrow 4[MeCd\{\mu\text{-}P(\mathit{t}\text{-}Bu)_2\}]_3}\\ &\quad \mathrm{+\ 3[Me_2Ga\{P(\mathit{t}\text{-}Bu)_2\}]_2}\end{aligned} \qquad (23)$$

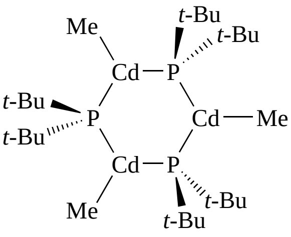

(**15**)

4 ORGANOCADMIUM ANIONS AND CATIONS

4.1 Organocadmium Anions

As described in Section 2.4.1, $\mathrm{R_2Cd}$ derivatives are substantially less Lewis acidic than their zinc analogs. As such, anionic compounds of the types $\mathrm{[R_3Cd]^-}$ and $\mathrm{[R_4Cd]^{2-}}$ are typically not stable. However, incorporation of electronegative substituents may stabilize such species. For example, $\mathrm{(CF_3)_2Cd}$ reacts with alkali metal halides (MX) in polar solvents to give trifluoromethyl cadmate derivatives, for example, $\mathrm{[(CF_3)_2CdX(DMSO)]^-}$ (equation 24).**41** Over a period of days, the samples are converted to the species $\mathrm{[(CF_3)_3Cd(L)]^-}$ (L = DMSO, glyme, MeCN, py) and $\mathrm{[(CF_3)_4Cd]^{2-}}$, on the basis of ^{113}Cd and ^{19}F NMR spectroscopy. For example, the ^{113}Cd NMR resonance of the species $\mathrm{[(CF_3)_3Cd(glyme)]^-}$ is a dectet $[^2J(^{113}\mathrm{Cd}\text{–}^{19}\mathrm{F}) = 281\ \mathrm{Hz}]$ owing to coupling to three $\mathrm{CF_3}$ groups.

$$\begin{aligned}&\mathrm{(CF_3)_2Cd(DMSO)_2 + MX \longrightarrow [M][Cd(CF_3)_2X(DMSO)]}\\ &\qquad\qquad\qquad\qquad \mathrm{+\ DMSO}\end{aligned} \qquad (24)$$

Organocadmate derivatives of the type $\mathrm{[RCdX_2]^-}$ (R = Me, Et, Bu, $\mathrm{CF_3}$, Ph, $\mathrm{C_6F_5}$; X = Cl, Br, I) have been obtained by the direct electrochemical oxidation of cadmium metal in the presence of RX and $\mathrm{[Pr_4N][X]}$ (equation 25).**61** Other organocadmate derivatives, for example, $\mathrm{[(CF_3)CdI_2]^-}$ and $\mathrm{[(C_6F_5)CdBr_2]^-}$, are also known.

$$\mathrm{RX + Cd + [Pr_4N][X] \xrightarrow{Cd\ anode} [Pr_4N][RCdX_2]} \qquad (25)$$

4.2 Organocadmium Cations

Brightly colored (yellow to red) π-arene compounds (*see Arene Complexes*) of cadmium $\mathrm{[(arene)Cd]^{2+}}$ (e.g. arene = $\mathrm{C_6H_6}$, $\mathrm{C_6Me_6}$) have been obtained by the reactions of $\mathrm{Cd(AsF_6)_2}$ or $\mathrm{Cd(SbF_6)_2}$ with the arene in $\mathrm{SO_2}$ (equation 26).**62** The structures of the compounds $\mathrm{[(arene)Cd]^{2+}}$ are not known with certainty.

$$\mathrm{Cd(EF_6)_2 + arene \longrightarrow [(arene)Cd][EF_6]_2} \qquad (26)$$

$$\mathrm{2Ph_3P{=}CH_2 + CdCl_2 \longrightarrow [Ph_3PCH_2CdCH_2PPh_3][Cl]_2} \qquad (27)$$

Other cationic compounds that have been isolated include ylide derivatives of the type $\mathrm{[Ph_3PCH_2CdCH_2PPh_3]^{2+}}$ (equation 27).**63**

5 ORGANOCADMIUM COMPOUNDS IN ORGANIC AND ORGANOMETALLIC SYNTHESIS

As with organozinc reagents, one of the main uses of organometallic cadmium compounds in organic synthesis derives from their relatively low reactivity (compared with their magnesium, lithium, and aluminum analogs), which thereby often allows them to be more selective reagents.**17,64**

The principal synthetic use of organocadmium reagents in organic chemistry is the preparation of ketones from RCOCl and $(RCO)_2O$ (equations 28 and 29).

$$\text{RCOCl} \xrightarrow{R'_2\text{Cd}} \text{RCOR}' \qquad (28)$$

$$(\text{RCO})_2\text{O} \xrightarrow{R'_2\text{Cd}} \text{RCOR}' \qquad (29)$$

A common misconception concerned with the synthetic applications of organocadmium derivatives is that they are unreactive towards aldehydes and ketones.[17] This misconception has arisen because the reactivity of an organocadmium reagent depends markedly upon its method of preparation. Thus, in situ reagents, obtained by addition of RMgX or RLi to a cadmium salt without further purification, are reactive towards carbonyl derivatives (equation 30), whereas isolated pure R_2Cd compounds are inert. The difference in reactivity between the pure and the in situ reagents may be traced to the presence of certain metal halides, for example, MgI_2, which facilitate addition to the carbonyl group.[65,66] Two possibilities for the function of the metal halide include (i) activation of R_2Cd by forming a complex such as $[R_2CdX_2Mg]$, or (ii) activation of the carbonyl group to nucleophilic attack by coordination to the oxygen atom $[R_2C{=}O\cdots MgX_2]$.

$$\text{ArCHO} \xrightarrow[2.\text{H}_2\text{O}]{1.\text{R}_2\text{Cd/MgX}_2} \text{ArC(H)(OH)R} \qquad (30)$$

In contrast to dialkylcadmium compounds, allylcadmium derivatives react readily with aldehydes and ketones in the absence of metal salts (equation 31).[17,64] Substituted allylic derivatives undergo rearrangement upon addition (equation 32).

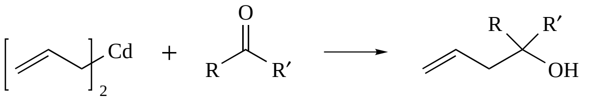

(31)

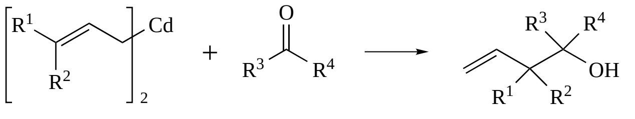

(32)

In a modification of the above procedure, the direct reaction of cadmium powder with an allylic halide in the presence of an organic carbonyl gives homoallylic alcohols in good yield (equation 33).[67]

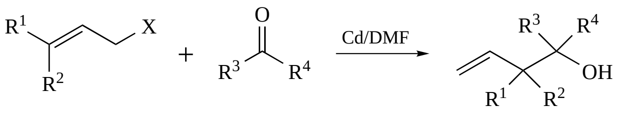

(33)

Dialkylcadmium derivatives readily partake in exchange reactions with other metal compounds. NMR studies on the degenerate alkyl exchange reactions between Me_2Cd and itself, and also between Me_2Cd and Me_nM ($Me_nM = Me_2Zn$, Me_3Ga, or Me_3In), demonstrate that the exchange reactions occur via rapid bimolecular processes.[68,69]

In some cases, alkylation may be accompanied by oxidation of the metal center (equations 34 and 35).[70,71]

$$\text{Me}_2\text{Cd} + 2\text{Cp}^*{}_2\text{TiX} \longrightarrow 2\text{Cp}^*{}_2\text{Ti(Me)X} + \text{Cd} \qquad (34)$$

$$\text{R}_2\text{Cd} + \text{Cp}_2\text{V} \longrightarrow \text{Cp}_2\text{VMe}_2 + \text{Cd} \qquad (35)$$

$(CF_3)_2Cd$ has been used as a reagent to prepare other trifluoromethyl compounds, for example, $(CF_3)_3Ga(DMF)$, $(CF_3)_3In(MeCN)_2$, and $(CF_3)_3Tl(DMF)_2$ (equations 36–38).[72]

$$\text{GaCl}_3 \xrightarrow[\text{DMF}]{(\text{CF}_3)_2\text{Cd}} (\text{CF}_3)_3\text{Ga(DMF)} \qquad (36)$$

$$\text{InCl}_3 \xrightarrow[\text{MeCN}]{(\text{CF}_3)_2\text{Cd}} (\text{CF}_3)_3\text{In(MeCN)}_2 \qquad (37)$$

$$\text{TlCl}_3 \xrightarrow[\text{DMF}]{(\text{CF}_3)_2\text{Cd}} (\text{CF}_3)_3\text{Tl(DMF)}_2 \qquad (38)$$

^1H and ^{19}F NMR studies of the reaction between $(CF_3)_2Cd$ and Me_2Zn have also demonstrated that ligand exchange occurs to give $MeZn(CF_3)$ and $(CF_3)_2Zn$.[73] A summary of trifluoromethyl compounds that have been prepared from $(CF_3)_2Cd$ is provided in Table 4.[74]

Fluorinated alkyl vinyl and aryl cadmium reagents can be prepared in excellent yields just by stirring the fluorinated halides with activated cadmium metal.[75] These reagents can then be used to prepare the corresponding fluorinated stannanes, which are versatile synthetic intermediate, by reacting them with tri-*n*-butyltin chloride at room temperature.[76] Similar methods have been used to synthesize fluorinated copper reagents.[77]

Heterocyclic derivatives of cadmium compounds can be easily prepared by reacting the corresponding Grignard reagent

Table 4 Trifluoromethyl compounds prepared from $(CF_3)_2Cd$[74]

Product	Starting material
$P(CF_3)_xI_{3-x}$	PI_3
$Sn(CF_3)_xBr_{4-x}$	$SnBr_4$
$Ge(CF_3)_xI_{4-x}$	GeI_4
Me_3SnCF_3	$Me_3SnO_2CCF_3$
Me_3PbCF_3	$Me_3PbO_2CCF_3$
$Te(CF_3)_4$	$Te(CF_3)_2Cl_2$
$Sb(CF_3)_3$	$SbCl_3$, $SbBr_3$, SbI_3
$Bi(CF_3)_3$	$BiCl_3$, $BiBr_3$
$Ag[Ag(CF_3)_4]$	$AgNO_3$
$(CF_3)_2Fe(CO)_4$	$Fe(CO)_4X_2$ (X = Cl, Br, I)
$CpCo(CO)(CF_3)_2$	$CpCo(CO)I_2$
$[Cu(CF_3)]$	CuCl
$(CF_3)_2M(PR_3)_2$ (M = Ni, Pd, Pt)	$MX_2(PR_3)_2$ (X = Br, I)

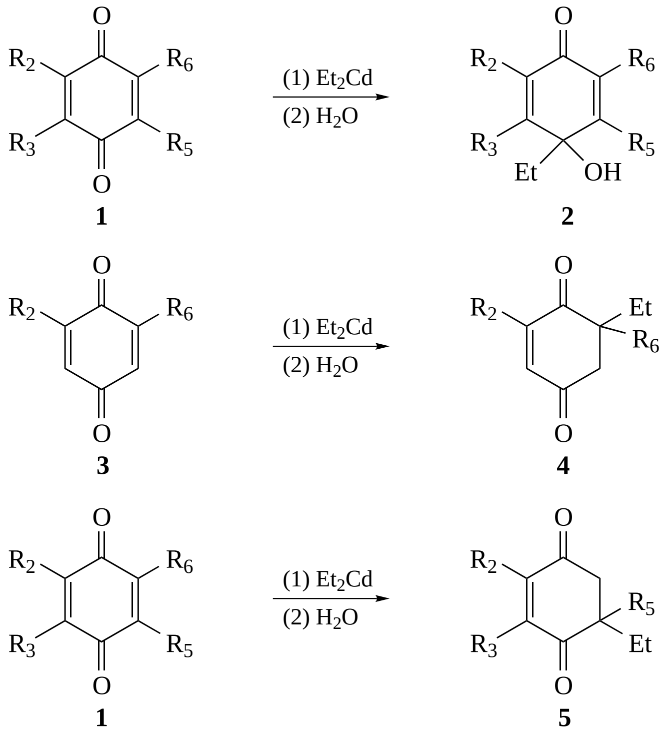

Substrate		Product	
1a	R_2=R_5=Me R_3=R_6=H	**2a**	R_2=R_5=Me R_3=R_6=H (83%)
1b	R_2=R_3=Me R_5=R_6=H	**2b**	R_2=R_3=Me R_5=R_6=H (78%)
3	R_2=R_6=Me	**4**	R_2=R_6=Me (82%)
1c	R_2=R_3=R_5=Me R_6=H	**5a**	R_2=R_3=R_5=Me (80%)
1d	R_2=R_3=OMe R_5=Me R_6=H	**5b**	R_2=R_3=OMe R_5=Me (86%)

Scheme 3

with cadmium(II) chloride. Cadmium derivatives of heteroaryls such as thiophene, benzothiophene, N-methylindole and pyridine have been successfully used to attach these heterocycles to riboses with good stereoselectivity.[78,79]

Naturally occurring quinones and hydroquinones have been reported to have antitumoral, HIV transcriptase inhibiting, and immunomodulating properties.[80] Alkylation of quinones is one of the important routes to prepare biologically active substituted quinones. A series of substituted quinones was alkylated using diethyl cadmium (Scheme 3). The regiochemistry of the addition shifted from quinol formation to conjugate addition as a function of the steric and electronic effects of the substituents.[3,80]

6 RELATED ARTICLES

Beryllium & Magnesium: Organometallic Chemistry; Cadmium: Inorganic & Coordination Chemistry; Mercury: Organometallic Chemistry; Zinc: Organometallic Chemistry.

7 REFERENCES

1. J. Boersma, in ‘Zinc and Cadmium’, eds. G. Wilkinson, F. G. A. Stone, and E. W. Abel, Pergamon Press, 1982.
2. D. A. Shirley, ‘Organic Reactions’, Wiley, 1954.
3. A. Aponick, J. McKinley, and C. T. Wigal, *J. Org. Chem.*, 1998, **63**, 2676.
4. M. Nordberg and G. F. Nordberg, in ‘Heavy Metals in the Environment’, ed. B. Sarkar, Marcell Dekker, 2002.
5. J. L. Warden ed., ‘Organometallic Compounds of Zinc, Cadmium and Mercury’, Chapmann & Hall, 1985.
6. G. E. Coates, M. L. H. Green, and K. Wade, ‘Organometallic Compounds’, Methuen, 1967.
7. C. Elschenbroich and A. Salzer, ‘Organometallics: A Concise Introduction’, VCH, 1992.
8. P. O’’Brien and M. A. Malik, *Sci. Synth.*, 2004, **3**, 91.
9. C. Eaborn, N. Retta, and J. D. Smith, *J. Organomet. Chem.*, 1980, **190**, 101.

10. W. V. Steele, ‘Annual Report on the Progress of Chemistry’, The Chemical Society, 1974.
11. C. J. Turner and R. F. M. White, *J. Magn. Reson.*, 1977, **26**, 1.
12. S. Kidambi and A. Ramamoorthy, *J. Phys. Chem. A*, 2002, **106**, 10363.
13. R. Eujen, B. Hoge, and D. Brauer, *J. Organomet. Chem.*, 1996, **519**, 7.
14. T. O. Murdock and K. J. Klabunde, *J. Org. Chem.*, 1976, **41**, 1076.
15. K. J. Klabunde and T. O. Murdock, *J. Org. Chem.*, 1979, **44**, 3901.
16. E. R. Burkhardt and R. D. Reike, *J. Org. Chem.*, 1985, **50**, 416.
17. P. R. Jones and P. J. Desio, *Chem. Rev.*, 1978, **78**, 491.
18. S. Al-Hashimi and J. D. Smith, *J. Organomet. Chem.*, 1978, **153**, 253.
19. D. M. Heinekey and S. R. Stobart, *Inorg. Chem.*, 1978, **17**, 1463.
20. L. Rosch and G. Altnau, *Angew. Chem., Int. Ed. Engl.*, 1979, **18**, 60.
21. J. Lorberth, *J. Organomet. Chem.*, 1969, **19**, 189.
22. C. C. Cummins, R. R. Schrock, and W. M. Davis, *Organometallics*, 1991, **10**, 3781.
23. R. Blom, *Acta Chem. Scand.*, 1988, **A42**, 445.
24. M. A. Guerra, T. R. Bierschenk, and R. J. Lagow, *J. Am. Chem. Soc.*, 1986, **108**, 4103.
25. T. R. Bierschenk, M. A. Guerra, T. J. Juhike, S. B. Larson, and R. J. Lagow, *J. Am. Chem. Soc.*, 1987, **109**, 4855.
26. D. J. Burton and D. M. Weimers, *J. Am. Chem. Soc.*, 1985, **107**, 5014.
27. G. B. Deacon and J. C. Parrott, *J. Organomet. Chem.*, 1970, **22**, 287.
28. M. Weidenbruch, M. Herrndorf, A. Schafer, S. Pohl, and W. Saak, *J. Organomet. Chem.*, 1989, **361**, 139.
29. H. Lange and D. Naumann, *J. Fluorine Chem.*, 1984, **26**, 1.
30. K. S. Rao, B. P. Stoicheff, and R. Turner, *Can. J. Phys.*, 1960, **38**, 1516.
31. G. A. Aoyoko, N. H. Buttrus, C. Eaborn, P. B. Hitchcock, and J. D. Smith, *J. Organomet. Chem.*, 1987, **320**, 137.
32. B. Fischer, G. P. M. V. Mier, J. Boersma, W. J. Smeets, and A. L. Spek, *J. Organomet. Chem.*, 1987, **322**, C37.
33. S. Brooker, N. Bertel, D. Stalke, M. Noltemeyer, H. W. Roesky, G. M. Sheldrick, and F. T. Edelmann, *Organometallics*, 1992, **11**, 192.
34. M. J. Almond, M. P. Beer, M. G. B. Drew, and D. A. Rice, *Organometallics*, 1991, **10**, 2072.
35. G. W. Bushnell and S. R. Stobart, *Can. J. Chem.*, 1980, **58**, 574.
36. M. B. Hursthouse, M. Motevalli, P. O’Brien, J. R. Walsh, and A. C. Jones, *Organometallics*, 1991, **10**, 3196.
37. C. G. Bauch and C. E. Johnson, *Inorg. Chim. Acta*, 1989, **164**, 165.
38. M. J. Almond, M. P. Beer, M. G. B. Drew, and D. A. Rice, *J. Organomet. Chem.*, 1991, **421**, 129.
39. W. J. J. Smeets, A. L. Spek, B. Fischer, G. P. M. v. Mier, and J. Boersma, *Acta Crystallogr.*, 1987, **C43**, 893.
40. C. D. Ontiveros and J. A. Morrison, *Organometallics*, 1986, **5**, 1446.
41. D. Naumann and W. Tyrra, *J. Organomet. Chem.*, 1989, **368**, 131.
42. G. N. Pain, G. I. Christiansz, R. S. Dickson, G. B. Deacon, B. O. West, K. McGregor, and R. S. Rowe, *Polyhedron*, 1990, **9**, 921.
43. M. J. Henderson, R. I. Papasergio, C. L. Raston, A. H. White, and M. F. Lappert, *J. Chem. Soc., Chem. Commun.*, 1986, **9**, 672.
44. O. F. Z. Khan, D. M. Frigo, P. O’Brien, A. Howes, and M. B. Hursthouse, *J. Organomet. Chem.*, 1987, **334**, C27.
45. J. L. Atwood, D. E. Berry, S. R. Stobart, and M. J. Zaworotko, *Inorg. Chem.*, 1983, **530**, 69.
46. E. Langguth and K.-H. Thiele, *Z. Anorg. Allg. Chem.*, 1985, **530**, 69.
47. H. Schmidbaur, E. Weiss, and W. Graf, *Organometallics*, 1985, **4**, 1233.
48. G. E. Coates and A. Lauder, *J. Chem. Soc. (A)*, 1966, **3**, 264.
49. E. A. Jeffrey and T. Mole, *Aust. J. Chem.*, 1968, **21**, 1187.
50. G. Emptoz and F. Huet, *J. Organomet. Chem.*, 1974, **82**, 139.
51. J. D. Kennedy and W. McFarlane, *J. Chem. Soc., Perkin Trans. 2*, 1977, **9**, 1187.
52. A. G. Davies and J. E. Packer, *J. Chem. Soc. Abstr.*, 1959, 3164.
53. Y. A. Alexandrov, S. A. Lebedev, and R. V. Kuznetsova, *J. Organomet. Chem.*, 1980, **201**, 21.
54. Y. A. Alexandrov, S. A. Lebedev, N. V. Kuznetsova, and G. A. Razuvaev, *J. Organomet. Chem.*, 1979, **177**, 91.
55. G. Sosnovsky and J. H. Brown, *Chem. Rev.*, 1966, **66**, 529.
56. Y. A. Alexandrov and V. P. Masslennikov, *J. Organomet. Chem. Libr.*, 1977, **3**, 75.
57. Y. A. Alexandrov, G. N. Figurova, and G. A. Razuvaev, *J. Organomet. Chem.*, 1973, **57**, 71.
58. T. Wizemann, H. Muller, D. Seybold, and K. Dehnicke, *J. Organomet. Chem.*, 1969, **20**, 211.
59. K. Dehnicke, J. Strahle, D. Seybold, and J. Muller, *J. Organomet. Chem.*, 1966, **6**, 298.
60. B. L. Benac, A. H. Cowley, R. A. Jones, C. M. Nunn, and T. C. Wright, *J. Am. Chem. Soc.*, 1989, **111**, 4986.
61. A. Osman and D. G. Tuck, *J. Organomet. Chem.*, 1979, **169**, 255.
62. L. C. Damude and P. A. W. Dean, *J. Organomet. Chem.*, 1979, **168**, 123.
63. Y. Yamamoto and H. Sugimoto, *Bull. Chem. Soc. Jpn.*, 1980, **53**, 3176.

64. L. Miginiac, in ‘The Chemistry of the Metal–Carbon Bond’, eds. F. R. Hartley and S. Patai, Wiley, 1985.
65. J. Kollonitsch, *J. Chem. Soc. (A)*, 1966, 453.
66. J. Kollonitsch, *J. Chem. Soc. (A)*, 1966, 456.
67. S. Araki, H. Ito, and Y. Butsugan, *J. Organomet. Chem.*, 1988, **347**, 5.
68. K. Henold, J. Soulati, and J. P. Oliver, *J. Am. Chem. Soc.*, 1969, **91**, 3171.
69. J. Soulati, K. L. Henold, and J. P. Oliver, *J. Am. Chem. Soc.*, 1971, **93**, 5694.
70. G. A. Luinstra and J. H. Teuben, *J. Organomet. Chem.*, 1991, **420**, 337.
71. G. A. Razuvaev, V. N. Latyaeva, L. I. Vishinskaya, V. K. Cherkasov, S. P. Korneva, and N. N. Spiridonova, *J. Organomet. Chem.*, 1977, **129**, 169.
72. D. Naumann and W. Tyrra, *J. Organomet. Chem.*, 1991, **407**, 1.
73. E. K. S. Liu and L. B. Asprey, *J. Organomet. Chem.*, 1979, **169**, 249.
74. D. Naumann and W. Tyrra, *J. Organomet. Chem.*, 1987, **334**, 323.
75. P. Heinze and D. Burton, *J. Fluorine Chem.*, 1985, **29**, 359.
76. D. J. Burton and V. Jairaj, *J. Fluorine Chem.*, 2004, **125**, 673.
77. Z. Yang and D. Burton, *J. Fluorine Chem.*, 2000, **102**, 89.
78. R. Chinchilla, C. Najera, and M. Yus, *Chem. Rev.*, 2004, **104**, 2667.
79. M. Yokomaya, H. Toyoshima, M. Shimizu, and H. Togo, *J. Chem. Soc., Perkin Trans. 1*, 1997, **29**.
80. A. Aponick, R. S. Buzdygon, R. J. Tomko, A. N. Fazal, E. L. Shughart, D. M. McMaster, M. C. Myers, and C. T. Wigal, *J. Org. Chem.*, 2002, **67**, 242.

Calcium-binding Proteins

Jenny J. Yang & Wei Yang
Georgia State University, Atlanta, GA, USA

Based in part on the article Calcium-binding Proteins by Natalie C. J. Strynadka & Michael N. G. James which appeared in the Encyclopedia of Inorganic Chemistry, First Edition.

1	Introduction	1
2	General Properties of Calcium-binding Proteins	2
3	EF-hand Calcium-binding Proteins	4
4	Extracellular Calcium-binding Proteins	16
5	Calcium Pumps and Channels	23
6	Membrane Calcium-binding Proteins: Annexins and C_2 Domain	25
7	Calcium-binding Proteins in Endoplasmic Reticulum and Sarcoplasmic Reticulum	28
8	α-Lactalbumin and Lysozyme	30
9	Related Articles	31
10	References	32

Abbreviations

α-LA = α-lactalbumin; ALG-2 = Apoptosis-linked gene 2 product; CaM = Calmodulin; CaMK = CaM-dependent kinase; CaMKK = CaM-dependent kinase kinase; CBD = Calbindin$_{\mathrm{D9k}}$; CaR = Extracellular calcium-sensing receptor; cPLA2 = Cytosolic phospholipase A2; CRD = Carbohydrate recognition domain; CSQ = Calsequestrin; CTLD = C-type lectin-like domain; DREAM = Downstream regulatory element antagonist modulator; EC1 = Extracellular domain 1; eEF-2K = Elongation factor-2 kinase; EGF = Epidermal growth factor; ER/SR = Endoplasmic/sarcoplasmic reticulum; FRET = Fluorescent resonance energy transfer; GAP = GTPase activating proteins; GBP = Galactose-binding protein; K_{d} = Dissociate constant; IF = Intermediate filament; IP3 = Inositol trisphosphate; IP3R = IP3 receptor; MBL/MBP = Mannose binding lectin/protein; MLCK = Myosin light chain kinase; NF = Nuclear factor; NMR = Nuclear magnetic resonance; NK = Natural killer; NOS = Nitric oxide synthase; Parv = Parvalbumin; PKA = Protein kinase A; PKC = Protein kinase C; PLC = Phospholipase C; PMCA = Plasma membrane Ca^{2+}-ATPase; RyR = Ryanodine receptor; SERCA = Sarcoplasmic reticulum Ca^{2+}-ATPase; TMS = Transmembrane segment; TnC = Troponin C.

1 INTRODUCTION

Ca^{2+} is an important second messenger in the regulation of cell life cycle in addition to being an essential component in biomineralization (*see* ***Biomineralization***).**[1–3]** For eukaryotic systems, different intracellular compartments exhibit different ionized Ca^{2+} concentrations that vary from millimolar concentrations in the endoplasmic reticulum (ER) to submicromolar concentrations in the cell cytoplasm. As shown in Figure 1, for eukaryotic cells, Ca^{2+} signaling is affected by a change in cytoplasmic ionized intracellular Ca^{2+} concentration ($[Ca^{2+}]_c$) that is mediated by the entry of Ca^{2+} across the cell membrane from the extracellular space or the release of Ca^{2+} from the major internal store, the ER. This is mediated via second messengers, including IP_3. The Ca^{2+} concentration in the cytoplasm is maintained by membrane-bound ATP-dependent Ca^{2+} pumps. Ca^{2+} mediates its action in regulation by binding to Ca^{2+} receptors/proteins that in turn regulate signal transduction, enzymatic activity, and protein stability. Ca^{2+}-binding proteins are divided into several major classes: trigger/sensors or regulators, buffer proteins, and stabilizing proteins with Ca^{2+} affinities that vary by 10^6-fold or more. The increase of cytosolic free $[Ca^{2+}]_c$ leads Ca^{2+} sensing (trigger) proteins, such as calmodulin (CaM), to bind Ca^{2+} and undergo a conformational change, which, in turn, regulates numerous cellular events and processes.**[4–7]** Ca^{2+} also directly regulates enzyme activities (e.g. proteinase calpain). Buffer proteins (e.g. calbindin$_{\mathrm{D9k}}$ (CBD) and parvalbumin) act as intracellular Ca^{2+} buffers, modulating the free cytosolic Ca^{2+} levels, which are thought to prevent cells from Ca^{2+} overload and apoptosis.**[8]** Ca^{2+} also contributes to the folding and stability of proteins (e.g. thermitase and thermolysin).**[9]** A number of transmembrane spanning Ca^{2+} binding proteins (e.g. cadherins and integrins) support the structural integrity of cells and tissues and contribute to the transduction of signals.**[10,11]**

Although bacterial cells do not have complex subcompartments or organelles, there is strong evidence that Ca^{2+} plays an essential role in bacterial signaling, communication, and stability similar to the role it plays in eukaryotic cells. Bacteria cells also have a well-regulated cytosolic free Ca^{2+} concentration (approximately $0.1–2\,\mu M$) that remains significantly below that in the extracellular medium (mM) owing to Ca^{2+} transporters and channels.**[12–14]** While voltage-gated Ca^{2+} channels have been characterized in eukaryotic cells, their counterparts in bacteria remain to be elucidated. Recent developments have led to the hypothesis of nonproteinaceous Ca^{2+} channels in the cytoplasmic membrane.**[15]** While the function of these putative Ca^{2+} channels remains to be solved, a Ca^{2+} transporter of *S. pneumoniae* is involved in Ca^{2+}-DNA uptake, lysis, and competence.**[16,17]** Uptake of Ca^{2+} and other divalent cations can also accompany uptake of phosphate by the phosphate transport system of *E. coli*. Similar to the eukaryotic systems, P-type ATPase Ca^{2+} efflux pumps have been characterized from *Synechococcus* and *Flavobacterium*. The ChaA Ca^{2+}-proton antiporter from *E. coli* has been characterized for

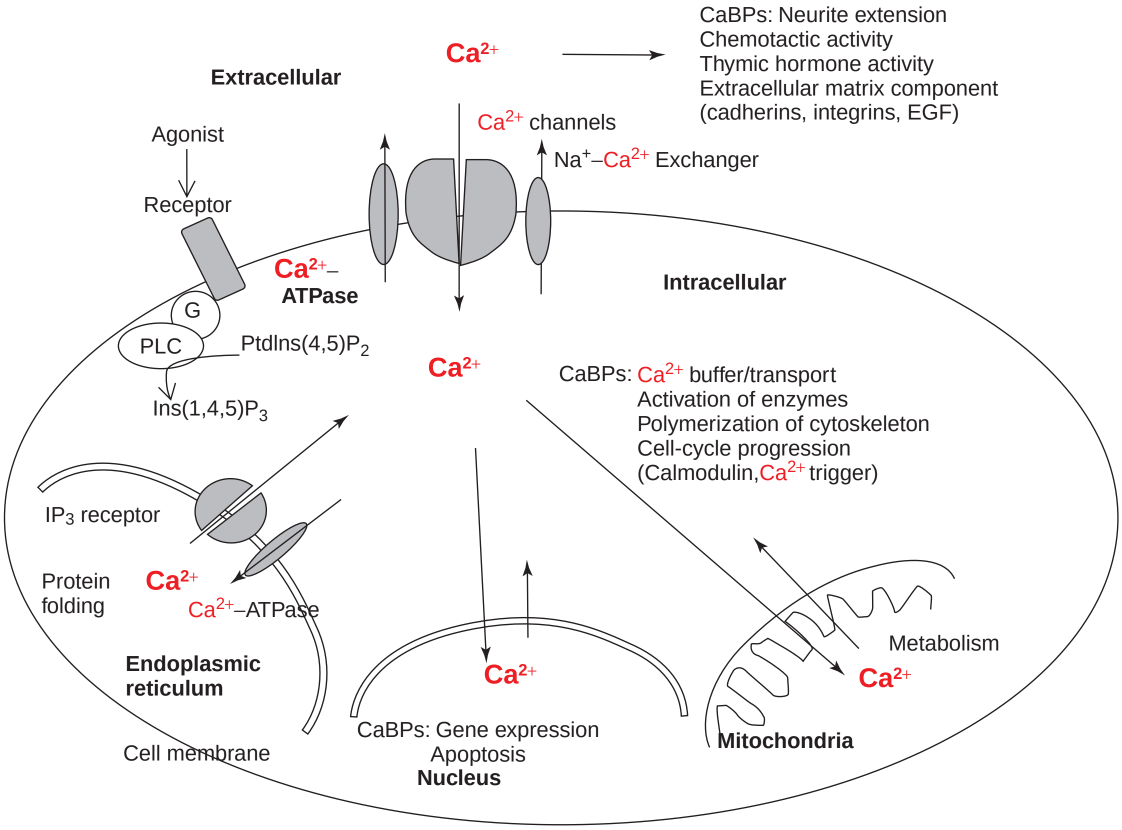
Ca2+
CaBPs: Neurite extension
Chemotactic activity
Thymic hormone activity
Extracellular matrix component
(cadherins, integrins, EGF)
Extracellular
Agonist
Receptor
Ca2+ channels
Na+–Ca2+ Exchanger
Ca2+–ATPase
Intracellular
G
PLC
PtdIns(4,5)P2
Ins(1,4,5)P3
Ca2+
CaBPs: Ca2+ buffer/transport
Activation of enzymes
Polymerization of cytoskeleton
Cell-cycle progression
(Calmodulin,Ca2+ trigger)
IP3 receptor
Protein folding
Ca2+
Ca2+–ATPase
Endoplasmic reticulum
Ca2+
Metabolism
Ca2+
Cell membrane
CaBPs: Gene expression
Apoptosis
Nucleus
Mitochondria

Figure 1 Ca^{2+} signaling and Ca^{2+} binding proteins in a eukaryotic cell. (Reprinted from B.W. Schafer and C.W. Heizmann, *Trends Biochem. Sci.*, 1996, **21**, 134. [© 1996, with permission from Elsevier])

Ca^{2+} circulation at alkaline pH and possession of a sequence domain similar to the eukaryotic Ca^{2+}-binding proteins, such as calsequestrin (CSQ). ChaA homologues and proteins similar to the eukaryotic Na^+/Ca^{2+} antiporter are widely present in the bacterial world. Further, it has been reported that bacteria contain Ca^{2+}-binding proteins are essential for cell adhesion, communication, and differentiation.[18–21] Some of the highly conserved ABC transporters are regulated by Ca^{2+} with Ca^{2+} binding proteins/domains and Ca^{2+}-dependent proteinase. Additionally, previous investigations described CaM-like proteins, such as calerythrin, with EF-hand Ca^{2+}-binding motifs of helix-loop-helix in many bacteria.[22–24] Reddy *et al.* recently reported that a calcium-binding protein CAMLP (calmodulin-like protein) was identified in *Mycobacterium smegmatis*.[25]

Calcium-binding proteins have also been reported for archaea. A calmodulin-like protein with a molecular mass of 24 kD was first found in an archaeon, *Halobacterium salinarium*. This protein is able to stimulate cyclic nucleotide phosphodiesterase in a calcium-dependent manner and can be suppressed by calmodulin inhibitors.[26] In addition, the extremely heat-stable pullulanase from *Pyrococcus wosee*i binds two Ca^{2+} ions. Calcium plays essential roles in activation and stabilization of this protein against thermal and guanidinium chloride-induced unfolding.[27] NMR structural studies of the elongation factor, aEF-1β, from *Methanobacterium thermoautotrophicum* reveal that this protein binds calcium in the groove between helix $\alpha 2$ and strand $\beta 4$. Calcium may play either a structural role for protein stability or a functional role in archaeal protein translation.[28]

During the past few years, owing to the rapid progress in genomic information and structural biological studies, our understanding of calcium-binding proteins has been greatly expanded. Since 1991, the structures of calcium-binding proteins have been extended to more than 500 today and they are found in every cellular compartment. In this article, we will first summarize the current knowledge about the common properties of calcium-binding proteins. We then will highlight recent developments in structural biology and biological functions of several classes of calcium-binding proteins.

2 GENERAL PROPERTIES OF CALCIUM-BINDING PROTEINS

Calcium-binding sites are generally classified into three types.[29–31] Class I includes proteins whose Ca^{2+} binding pockets are formed by a stretch of amino acids in the primary sequence (e.g. EF-hand proteins or α-lactalbumin). EF-hand proteins have a conserved motif of a Ca^{2+}-binding loop flanked by two helices. All of the Ca^{2+} ligand residues of α-lactalbumin are composed of a 10-residue loop flanked by two helices, C and D, plus two water molecules. This type of Ca^{2+} binding site does not belong to the EF-hand family owing to different ligand arrangements and the packing of flanking helices (Figure 2). Class II sites have one ligand supplied by a part of the amino acid sequence far removed from the main binding sequence. D-galactose binding protein (GBP) belongs to this family. Several ligand residues in a short loop with a Glu 63-residue apart form a calcium-binding pocket with the geometry very similar to that of EF-hand proteins (Figure 2). Class III sites are created by amino acids remote from one another in the sequence. Proteins in this group, such as cadherins, C_2 domains, Site I of thermitase, and Phospholipase A_2, have a Ca^{2+} binding site formed by the ligand residues located remotely from one another in the protein sequence.

Detailed analysis for the coordination properties of calcium versus magnesium in proteins and small molecules have been carried out by Einspahr and Bugg,[31] MacPhalen,[29] Glusker,[9] and Natalie *et al.*[36] in the past. An average coordination of 7 for calcium-binding sites in proteins has been identified for several databases containing the structures of calcium-binding proteins. Recently, Pidcock and Moore have carried out surveys of X-ray structures of Ca^{2+}- and Ln^{3+}-containing proteins and coordination complexes.[30] To avoid biasing general conclusions concerning the coordination chemistry of protein-bound calcium, they selected a data set that contained only 44 structures and 60 Ca^{2+} binding sites with a total of 323 ligands from a total of 515 structures of Ca^{2+}-containing proteins. There was only one EF-hand site in this data set. Pidcock and colleagues have found that the average coordination number for Ca^{2+} was 6.0.[30] Calcium-binding sites of EF-hand proteins have a coordination number of 7, which is consistent with previous findings.[36–40] The calcium-binding sites in different classes of proteins can be identified using the structural parameters by a computational program, which is also further used for de novo design of calcium-binding proteins.[41] Among 162 calcium sites surveyed within the Cambridge Structural Database, an average of coordination number of 6.9 was found for small calcium chelators.[30] A polydentate ligand with 3–6 oxygen atoms is able to form calcium complexes with higher coordination numbers. The constraints of the backbone of proteins may be responsible for the relatively low coordination number.

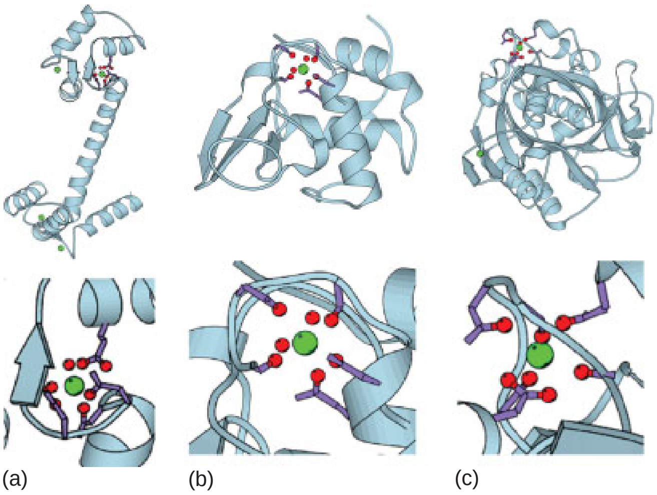

Figure 2 Calcium-binding sites of (a) calmodulin, (b) α-lactalbumin, and (c) thermitase are shown (top) and the pentagonal bipyrimal geometry of calcium-binding sites in each protein is enlarged (bottom). There are one, two, and zero water molecules in the enlarged binding geometries, respectively.[32–34] The structure figures in this article are prepared using the program MOLSCRIPT[35]

A turn or loop structure was found to provide the bulk of the ligands to Ca^{2+}, but helix and sheet secondary structures are slightly better providers of bidentate carboxylate ligation than turn or loop structures. In the database analyzed by Pidcock and Moore, the relative populations of all protein-derived calcium ligand residues are 72.5, 13.4, and 13.5% for turn/loop, helix, and sheet, respectively.[30]

Table 1 shows the relative population of amino acids used in the coordination for calcium binding. Asp has the highest calcium-binding preference as revealed in the all CBP database by Pidcock and Moore[30] and the EF-hand database by Falke *et al.*[42] The relative calcium ligand population is acidic residues > water > mainchain carbonyl > Asn > Ser > Thr > Gln > Tyr. Carboxylate ligand residues of Asp and Glu form the major class of calcium ligands from the protein frame. It is interesting to note that Glu is a preferred bidentate ligand for EF-hand proteins while Asp is commonly used for non-EF-hand proteins.

To understand metal selectivity of proteins, Dudev *et al.* have analyzed the first-second shell interactions in metal binding sites in proteins.[43] As shown in Figure 3, both calcium and magnesium sites prefer carboxylates Asp and Glu as metal ligand residues. On the other hand, magnesium strongly prefers water in the first-shell coordination compared to calcium sites in proteins. Peptide backbone groups were found to be the most common second-shell ligand for calcium-binding sites. The relative orders follow Asp/Glu > Lys/Arg > Asn/Gln > Ser/Thr sidechains.[43] Nayal and Di Cera have found that the bond-strength contribution of each ligating oxygen atom in the inner shell can be evaluated by using an empirical expression successfully applied in the analysis of crystals of metal oxides. The sum of such contributions closely approximates the valence of the bound cation.[44]

A detailed survey of 276 sequences of EF-hand proteins has shown that 64% of the calcium-binding loops have four acidic residues and 27% of the loops have three acidic residues at the ligand positions.[45] Four acidic residues were

Table 1 Amino acids observed as calcium-binding ligands in 567 EF-hand sequences. (Reproduced from J.J. Falke, S.K. Drake, A.L. Hazard, O.B. Peersen, Molecular tuning of ion binding to calcium signalling proteins. *Q, Rev. Biophys.* **27**(3): 219–90 by permission of Cambridge University Press)

Amino acid	Preferences for calcium all type (%)	Preferences for calcium side chain (%)	Preference as bidentate (%)
Asp	45	65	8
Glu	18	21	92
Asn	9.2	14	0
Ser	8.2	11	0
Thr	6.4	3.9	0
Phe	2.6	0	0
Lys	2.1	0	0
Gln	1.9	0.4	0
Gly	1.9	0	0
Tyr	1.5	0	0
Arg	0.79	0	0
Cys	0.50	0.2	0
Leu	0.32	0	0
Ile	0.32	0	0
Val	0.32	0	0
Ala	0.24	0	0
His	0.18	0	0
Met	0.15	0	0

Modified after Falke *et al.*, 1994. Asp has the strongest calcium-binding preference among all residue types. Glu is predominantly used as a bidentate ligand.

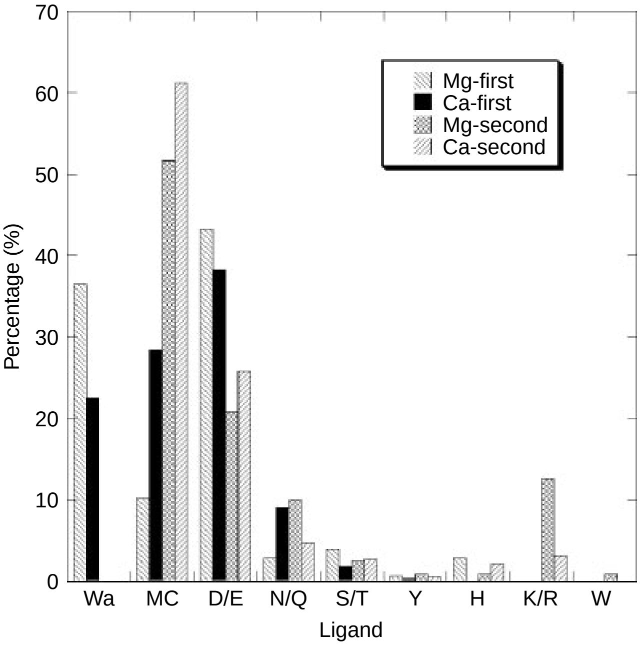

Figure 3 Percentage frequency distribution of the first-shell and the second-shell ligands observed in the 3D structures of proteins bound to Mg^{2+}- and Ca^{2+}-binding proteins. (Adapted with permission from Ref. 43. © 2003 American Chemical Society)

postulated to provide the most stable arrangement of anionic charges.[46] Reducing or increasing the number of acid residues at chelating positions will decrease the stability of the calcium-binding complex.[42,46] Electrostatic distribution outside of the coordination shell of the metal binding site has also been shown to have a strong contribution to calcium binding. Charged side chains that are present on the surface of the proteins can exhibit strong influences on metal binding affinity even if they are not directly involved as ligands.[47,48] As shown in Figure 4, the protein surface of calcium-binding protein α-lactalbumin is mostly negatively charged. In contrast, the non-calcium-binding protein lysozyme has a highly positively charged surface. The X-ray structure of bovine calbindin$_{D9k}$ reveals a cluster of negatively charged amino acid sidechains on the protein surface around the calcium sites. Linse and Forsen and their coworkers have shown that removal of three negative surface charges Glu, Asp, and Glu at positions 17, 19, and 26 in the vicinity of the calcium-binding sites of CBD (6.2, 6.4, and 11.1 Å) leads to a 45-fold decrease in average affinity (per site) at low ionic strength and a five-fold reduction at 0.15 M KCl.[49] The shifts in binding constants due to the reduction in affinity by the substitution of Asp with Asn and Glu with Gln in seven surface charge mutations have been accurately reproduced by Monte Carlo simulation.[50–53] Several other global factors, such as hydrophobic properties and hydrogen-bonding networks have been reported to contribute to calcium affinity.[44,54,55] These factors have less defined roles compared to the electrostatic interaction. They are likely to contribute to the dielectric environment that serves to shape the local electrostatic field.[42,44,47,54,55] Unfortunately, the estimation of the charge contribution to calcium affinity and selectivity in natural calcium-binding proteins is complicated by the interference of cooperative binding, calcium-dependent conformational change, and electrostatic interaction between multiple calcium ions.[9,38–40]

3 EF-HAND CALCIUM-BINDING PROTEINS

3.1 EF-hand Calcium-binding Proteins: Overview

An EF-hand motif with a conserved continuous calcium-binding loop flanked by two helices (helix-loop-helix)[29,37,42] was first described by Dr. Robert Kretsinger, who also described the continuous calcium-binding loop in parvalbumin (Parv).[59] EF-hand calcium-binding proteins are found in prokaryotes to eukaryotes throughout the entire plant (Fungi included) and animal kingdoms. Rapid progress in genome research demonstrates that the EF-hand motif is one of the

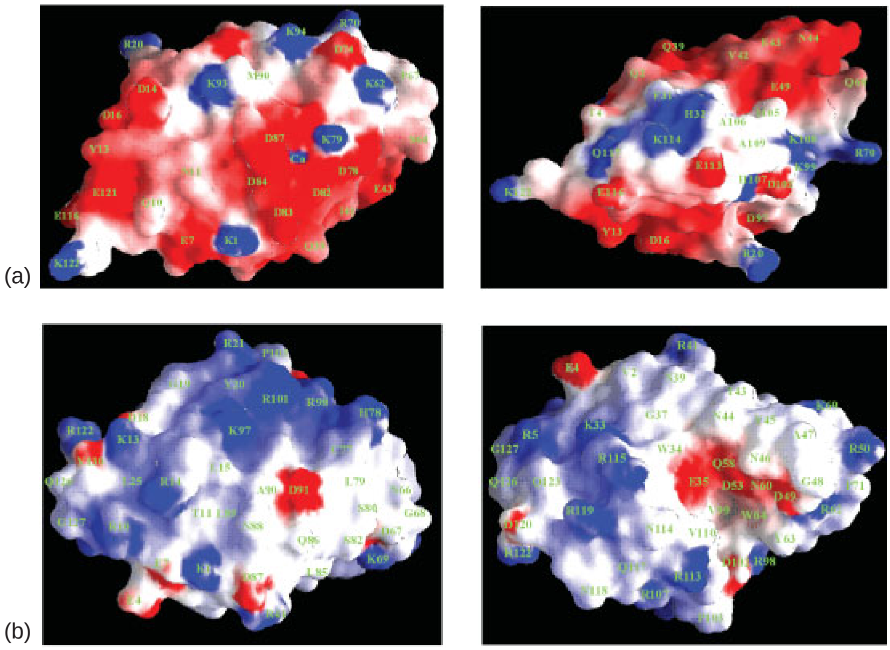

Figure 4 The electrostatic distributions of α-lactalbumin (1ALC)[56] (a) and chicken egg-white lysozyme (1LZ1)[57] (b) calculated by Delphi and presented by Grasp.[58] Both surfaces of calcium-binding protein α-lactalbumin are mostly negatively charged (a) (in red) while the surfaces of noncalcium binding protein lysozyme (b) are mostly positively charged (in blue)

five most common protein motifs in human. Up to 600 entries in animal cells have been identified in all eukaryotes.[59,60] Day *et al*. have identified a maximum of 250 putative EF-hand proteins in the plant Arabidopsis.[61] According to the sequence similarity, EF-hand proteins are classified into 77 distinct subfamilies that contain two to twelve copies of the EF-hand. These include CaM, Parv, troponin C (TnC), sarcoplasmic calcium-binding protein, the essential and regulatory light chains of myosin, CBD, and the S100 and visinin or recoverin (VIS) subfamilies.[62] One of the 77 EF-hand subfamilies is found in viruses and five are found in bacteria.[62]

Transient change of intracellular calcium concentration is sensed primarily by EF-hand calcium-binding proteins such as calmodulin (CaM) and TnC located in the intracellular environment.[63] In addition to EF-hand proteins in the cytoplasm, this highly conserved EF-hand motif was also found in other subcellular compartments and associates with membranes.[64–66] S100, a multigenic family of nonubiquitous calcium-modulated proteins of the EF-hand type expressed in vertebrates exclusively, has been implicated in intracellular and extracellular regulatory activities.[67] Although more analysis of other genomes such as Archaea and virus is needed, given the important function of calcium signaling in cell development and proliferation, it will not be surprising that EF-hand proteins are found in all kingdoms and in every cellular environment.

There are several major functional classes of EF-hand proteins. In the first class, trigger proteins like CaM and TnC bind calcium with a large change in protein conformation, which allows them to regulate target proteins. The second manifests direct calcium-dependent enzymatic activities. Examples include aequorin, calcium-dependent protein kinase, calcineurin, calpain, and CaM domain protein kinase.[68,69] The third type of proteins do not interact with other proteins but act as intracellular calcium buffers modulating the free cytosolic calcium levels and preventing cells from calcium overload and apoptosis.[70] Buffer proteins like CBD and Parv bind calcium without a significant change in the protein conformation. The calcium affinities for EF-hand proteins vary by 10^6-fold or more according to their biological roles. Trigger proteins have affinities with K_d of 10^{-6} M. Parv has the highest affinity of K_d (about 10^{-9} M). Calpain, on the other hand, has a K_d of mM.

As shown in Figure 5, EF-hand motifs can be divided into several major classes: canonical (classical), pseudo-EF-hand motifs, essential light chain (ELC), and BM40.[37,62] The canonical EF-hand consists of α-helix E (helix I, residues -9 to -1), 12-residue calcium-binding EF-loop (1–12) and α-helix F (or Helix II, 10–20).[62] The loop sequence positions 1 (x-axis), 3(y), 5(z), 7($-y$), 9($-x$), 12($-z$) coordinate the calcium ion in a pentagonal bipyramidal geometry. The statistic data shows that the side chain of Asp almost always (99%) serves as the ligand at position 1, and the glutamate side chain at position 12 ($-z$ axis) binds in a bidentate mode to calcium (92%).[47] The $-x$-axis (position 9) is filled by a bridged water molecule connecting the side chain of aspartic acid, serine, or asparagine. The pseudo EF-hand motif has two additional residues with mainchain carbonyl oxygen at positions 1, 4, 6,

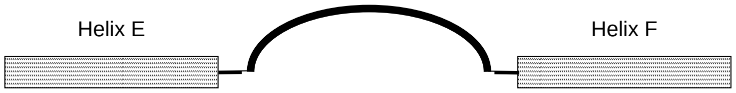

```
Canonic     E n * * n n * * n x * y * z G -y I -x * * -z n * * n n * *
                                            =O   wa     bi
                                                 E/Q

Pseudo    * n * * n n * * n x * * y G z * * -y L -x K * -z n * * n n * *
                            =O    =O  =O    =O   wa     bi
                                                 E/Q

ELC       # n * * V F # L F D F W D G R D G * V D A n K n G D n n R C L
                            x     -x    -y
          D/E         E/D   y     z         -z
                            =O    =O        =O

BM40       P n * W * n * * L x * H p * z * -y L -x * * -z n * P n * * P n
                             D     y   D   =o   wa     bi
                                                E/Q
```

n: hydrophobic residue
wa: bridged water
bi: bidentate ligand

=O: backbone carbonyl
x y z: axis position
Capital letter: one-letter code for residues

Figure 5 The sequence patterns of four different types of EF-hand motifs. (Ref. 62. Reproduced by permission of Springer Verlag)

and 9 and bidentate carboxyl side chain Glu at position 14. All proteins from the S100 family including CBD have the pseudo EF-hand motif in Site I. Position 6 has a conserved Gly for flexibility and hydrophobic residues such as I, V, L and M are found at loop position 8 and flanking helices −9, −5, −4 for Helix I and 13, 16, 17 and 20 for Helix II. Molluscan ELC and BM40 families have several additional insertions of the loop.[62] Slt35, a soluble fragment of the outer membrane-bound lytic transglycosylase B (MltB) from *E. coli*,[71] contains a 15–16 residue Ca^{2+} binding loop flanked by two helices.

The published structural studies show that nearly all the EF-hand proteins contain at least two interactive calcium-binding sites with average metal–metal distances of about 11–12 Å within a domain with strong cooperativity for calcium binding.[72,73] For example, trigger proteins CaM and TnC have four EF-hand motifs in two tightly packed domains (Figures 6 and 7).[74,75] A few exceptions contain an odd number of EF-hand motifs in which the hydrophobic residues of the flanking helices either are buried by another helix as seen in Parv with three EF-hand motifs or form an

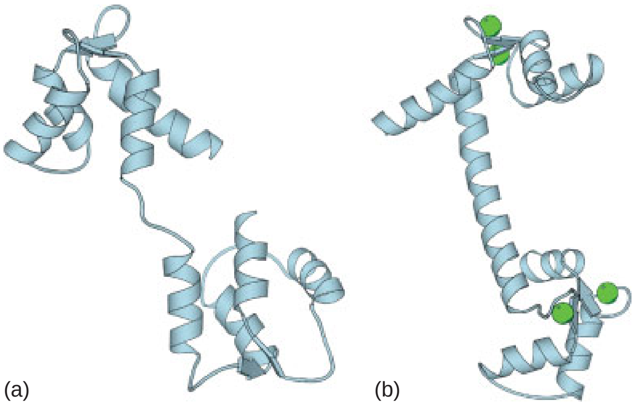
(a) (b)

Figure 6 The structures of calcium free (a, 1CFD) and loaded (b, 3CLN) forms of calmodulin[33,78]

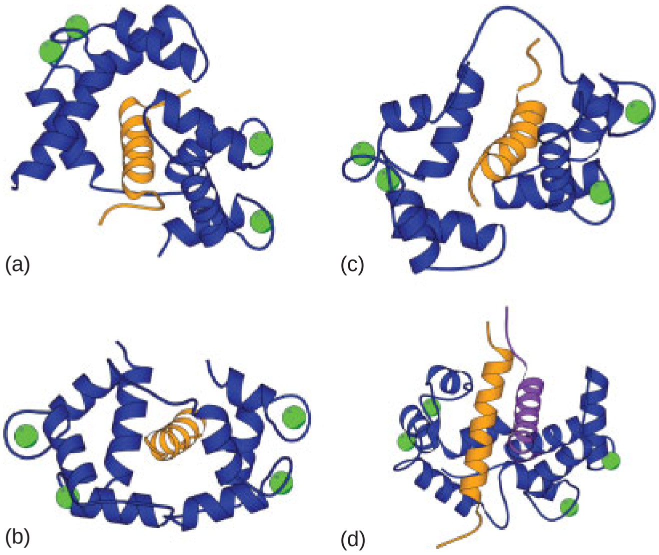
(a) (c) (b) (d)

Figure 7 Structures of calmodulin (blue) complexed to a peptide (yellow) from (a) CaMKK (1IQ5),[79] (b) CaMKII (1CM1),[80] (c) rabbit skeletal myosin light chain kinase (SLMK) (2BBM),[74] and (d) glutamate decarboxylase (1NWD)[81]

intermolecular dimer with five mutated EF-hand motifs as seen in calpain.[76] Almost all the members of S100 proteins such as S100B, calcyclin, psoriasin, p11, as well as calpain and neurocalcin form homodimer or heterodimers. It is clear that dimerization is one of the essential mechanisms that enable EF-hand proteins to effectively regulate multiple target proteins. In the past few years, significant progresses have been achieved in structural analysis of EF-hand proteins both in apo- and holo-forms.[76,77]

3.2 Calmodulin

Calmodulin (CaM) is a ubiquitous intracellular protein that mediates more than 100 different biological systems in both calcium-free and -loaded forms. CaM has 148 amino acids and its primary sequence is highly conserved in all cell types. It shares strong sequence and structure homology to TnC, which is involved solely in the Calcium-dependent regulation of skeletal and heart muscle contraction. Yeast (yCaM) is ∼60% identical in sequence to vertebrate CaMs and contains only three functional sites. Several labs have shown that the prokaryotes have several CaM-like proteins containing two or more authentic EF-hand motifs.[21,82]

As the major calcium-signaling molecule, calmodulin relays initial calcium signals to a large number of functional proteins in various physiological activities. This signal mediation is carried out by calmodulin-target protein interactions. Calmodulin binds to different target molecules at different calcium concentrations and results in different effects.[83] Some proteins, such as phosphorylase kinase, bind to CaM all the time but are only activated in the presence of calcium. Similar to phosphorylase kinase, myosin light chain kinase (MLCK), or calcineurin bind to CaM at both high and low calcium concentrations. This binding process is reversible possibly owing to its relatively weaker affinity to CaM. The binding of CaM either inhibits the protein functions, such as in some of the G-protein-receptor kinases and type-I IP3 receptors, or activates the protein function, as in protein kinases I and II. In protein kinases I and IV, the binding of CaM to two proteins (CaMK and CaMKK) simultaneously is required for the activation. Some proteins, as neuromodulin and neurogranin, bind to calcium-free CaM instead of the calcium-loaded form.[83,84] In the past few years, significant progress has been achieved in understanding calcium-dependent conformational changes and the several different interaction modes of calmodulin-target protein have been reviewed. The calmodulin-target protein interaction is studied mostly by CaM-peptide complex. The peptides for CaM binding share no primary sequence homology. However, some features are observed in many but not all cases, such as the potential to fold into a basic, amphiphilic α-helix, and the large hydrophobic residues at positions 1−5−10 or 1−8−14.[84] Here, we will first briefly discuss calcium-dependent conformational changes of calmodulin. We will then discuss some of the proteins involved in important activities including recent advances in structural information.

3.2.1 Calcium-induced Conformational Change of Calmodulin

High-resolution methods, especially the newly developed residual dipolar coupling (RDC) NMR in a dilute liquid crystalline phase (lipids or phage) have been shown to be a powerful method for monitoring the structural properties of calmodulin upon calcium binding.[74,77,78,85–87] As shown in Figure 6, in the apo-state, CaM is in a closed form and the two flanking helices are in an antiparallel position. Calcium binding to the EF-loop results in the movement of bidentate Glu at position 12 to form a better-defined calcium-binding pocket. Concurrently, this move of Glu 12 pulls residues of the attached helices closer together. Residues on the opposite end of the attached helices move away to each helix with a greater difference in the orientation of Helix I (26°) and IV (22°) in the N-terminal than in that of helices V and VIII in the C-terminal (for 15 and 10°) suggesting that the N-terminal is more open than the C-terminal. This movement of helices results in the exposure of the hydrophobic residues required for the binding of the target molecule (in the open conformation) and the helices become more perpendicular.[74,78,85] A harmonic oscillation of the central helix is observed across an arc with ±20°. Residues 77−81 are located in the middle of this central helix and act as a flexible tether, allowing conformational changes and cooperativity between the two domains in both the calcium-bound form[88] and the calcium-free form.[78,85] Significant backbone plasticity also was revealed by high-resolution 1.0 Å X-ray structure of the calcium-loaded form of CaM from *paramecium tetraurelia*.[89] Finally, Fallon and Quiocho reported that the 1.7 Å X-ray structure of a new native calcium-CaM is in a compact ellipsoidal conformation and shows a sharp bend in the linker helix and a more contracted N-terminal domain.[90]

3.2.2 Calmodulin-dependent Proteins

Calmodulin-dependent Kinases. Calmodulin-dependent kinases further relay and amplify the calcium signal from calmodulin to their target proteins. In animals, the identified calmodulin-dependent kinases include CaM-dependent kinase kinase (CaMKK), CaM kinase I-IV (CaMKI-IV), in which CaMKII is also known as elongation factor-2 kinase (eEF-2K), MLCKs and so on.[84] CaMKK, CaMKI, CaMKII, and CaMKIV have multiple targets that involve them in multiple activities, while eEF-2K and MLCK have much more restricted targets. CaMKK is at the upstream of the CaMKI and CaMKIV kinase cascade. CaMKK activates CaMKI and CaMKIV through the phosphorylation of these two kinases. The other substrate for CaMKK is protein kinase B (PKB). The activity of CaMKK itself is inhibited by protein kinase A (PKA) that phosphorylates two sites in CaMKK.[84] Figure 7(a) shows a 26-residue peptide from CaMKK that binds to calmodulin (1IQ5).[79] This peptide forms an α-helix at the N-terminus and a β-hairpin at the C-terminus. The peptide is engulfed between the two lobes of CaM and its C-terminus interacts with the C-terminal lobe of CaM. Two major CaM-peptide contacts are located at Trp-444 in the α-helix and Phe-459 in the β-hairpin of the peptide, which has a 14-residue gap, longer than the normal 8- or 12-residue space. This binding mode is different from other peptides from CaMKII (Figure 7b) and MLCK (Figure 7c), which bind the C-terminal lobe of CaM with the N-terminus of peptide.

CaMKI is located in cytoplasm and nuclei and is likely to participate in regulation of gene transcription. In vitro CaMKI phosphorylates substrates such as synapsin and the cystic fibrosis transmembrane regulator although its in vivo substrates are yet to be identified. CaMKI is activated by phosphorylation by CaMKK when both kinases are calcium and CaM bound. The 25-residue CaM-binding peptide of CaMKI forms an α-helical structure. Two hydrophobic residues are located at positions 1 and 14 (Trp-303 and Met-316). The peptide induces the bending of the central helix with the interaction of both the N- and C-domains of CaM (pdb 1MXE).[84,91]

The CaMKII family phosphorylates numerous substrates including NR1, NR2A, NR2B, F-actin, α-actinin, densin-180, synGAPb, and cdk5.[92] CaMKII is not a substrate of other kinases. However, with the binding of calcium/CaM, it rapidly undergoes autophosphorylation at Thr-286 to activate itself. Once phosphorylated, the kinase activity is partially retained even after the calcium/CaM dissociates from the protein. Figure 7(b) shows that the binding of CaMKII peptide to CaM unwinds the central helix of CaM (Figure 6). The C- and N-lobes of CaM are bent by 100° and rotate by 120° relative to the substrate-free calcium-bound CaM. Thus, the N- and C-lobes of CaM close together to form a hydrophobic pore that holds the peptide. The binding is mainly driven by the hydrophobic forces where the methionine residues in CaM play a critical role. MLCK has as substrate the regulatory light chain of myosin II. A 25-residue peptide interacts with CaM in a manner similar to that of the other kinase peptides. It bends the central helix of CaM to enable interaction with both lobes of CaM. The peptide forms α-helical structure and the Trp-4 and Phe-17 (positions 1 and 14) of the peptide anchor the peptide to the C- and N-terminus of CaM, respectively (Figure 7c).[80,84]

CaMKIV is responsible for calcium-dependent gene transcription through the phosphorylation of transcription factors cAMP response element-binding protein (CREB), serum response factor (SRF), and myocyte enhancer factor-2 (MEF2). Oncoprotein 18 in the cytoplasm is also a substrate of CaMKIV. The activity of CaMKIV is activated by CaMKK and autophosphorylation. The elongation factor-2 is the only known substrate of CaMKIII (eEF-2K) at present. The phosphorylation of elongation factor-2 inhibits its functions. eEF-2K can be regulated by autophosphorylation and PKA. Other kinases regulated by calmodulin include phosphorylase kinase, phosphatidylinositol 3-kinase, and a series of plant kinases such as cabin1, MCKs, CCaMKs, and CBKs, and so forth.[83,84,93–95]

Calmodulin-regulated Ion Channels. Calmodulin regulates different ion channels including calcium channels. Here we briefly discuss the CaM-regulated potassium channel and sodium channel. All calcium channels and calcium pumps will be discussed in Section 5 in this article. The voltage-gated sodium channel has been shown to be regulated by the CaM-dependent pathway.[96] The calcium-activated potassium channel transports potassium from the cytoplasm to the extracellular environment with a high selectivity for potassium over sodium. Its function is dependent on the cytoplasmic calcium concentration instead of the membrane potential. Calcium increases the frequency of channel opening rather than the duration time of each opening. The potassium channel functions as a homo-tetramer. Each monomer contains six transmembrane segments (TMS) and a pore between TMS-5 and TMS-6. Both the N- and C-termini are located on the cytosolic side. CaM binds to the C-terminus of the protein.[95,97]

Figure 8 shows the structure of the CaM complex with a 96-residue fragment of the C-terminal cytosolic region of the channel with a different protein–protein interaction compared to the CaM-peptide structures.[98] This complex forms a dimer over two extended CaM molecules. The potassium channel

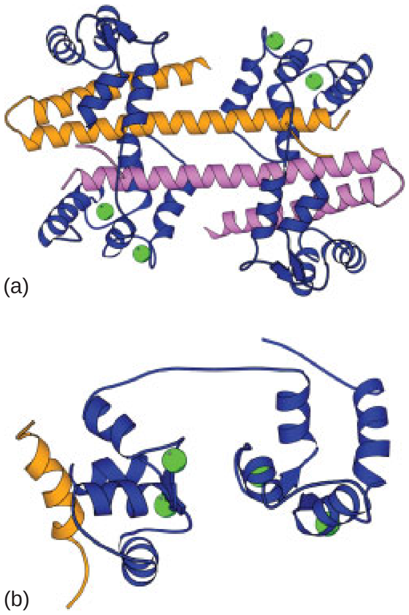

Figure 8 The structures of CaM complex with the peptides from (a) a 96-residue fragment of the C-terminal cytosolic region of the potassium channel (1G4Y) (yellow and pink)[98] and (b) calcium pump (yellow, 1CFF)[99]

fragment forms two antiparallel α-helices with the shorter one binding to the C-terminal lobe of CaM only. On the other hand, the N-terminus of the longer α-helix binds to the C-terminal lobe of CaM and the C-terminus of this helix protrudes to bind to the N-terminal lobe of another CaM. In this structure, CaM is half saturated. Two calcium ions are bound at the N-terminus of CaM. Surprisingly, the C-terminal lobe with a higher calcium affinity is free.[95,98]

Nucleotide Cyclases. Calmodulin regulates the activity of different nucleotide cyclases such as adenylyl cyclase that catalyzes the formation of cAMP from ATP. cAMP is another important molecule in the cell functioning as a second-messenger like calcium. The calmodulin-adenylyl cyclase interaction links these two second messengers together.[83,95]

Edema factor of anthrax is one of the three exotoxins produced by the bacteria. The primary sequence is only slightly homologous to other adenylyl cyclases. When it enters the host cells, edema factor acts as an adenylyl cyclase and transforms ATP to cAMP efficiently. The structure of CaM-edema factor of anthrax complex has been obtained (Figure 9).[100] In the CaM-edema factor complex, only the C-terminal lobe binds two calcium ions while the N-terminal lobe is empty. CaM remains extended and is deeply inserted between the catalytic and the α-helical domains of this exotoxin with a large number of residues of CaM involved in the interaction. CaM binding results in a large domain reorientation of edema factor. The helical domain of edema factor undergoes a 15 Å translation and a 30° rotation. The CaM inserted site is far from the catalytic site and the catalytic site alone has no obvious difference between the CaM-free and – loaded forms. Nevertheless, CaM binding enhances the activity of edema factor 1000-fold.[100] Further, an α-helical peptide of exotoxin contains a typical CaM-binding hydrophobic pattern at positions 1-5-10. The NMR and Fluorescent resonance energy transfer (FRET) studies demonstrated that upon binding to this peptide, CaM is bent with both the N- and C-lobes moving close together in a manner similar to that of CaM-dependent kinases (Figure 7). It is possible that CaM binds to the short peptide and the full-length protein in different topologies.[95,100]

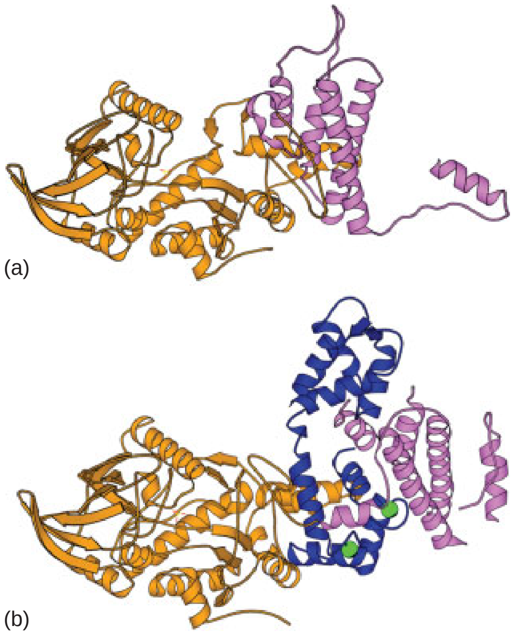

Figure 9 The structures of (a) calmodulin-free (1K8T) and (b) calmodulin-bound (1K93) forms of Edema factor[100]

Other Enzymes and Proteins. In addition to the kinases, cyclases, and ion channels, CaM interacts with and regulates a large, growing number of target proteins from almost every physiologic event of life. These target proteins include enzymes such as phosphodiesterases or phosphatase and other proteins such as gap junction protein connexins or β-2-glycoprotein.[83,95] Recently, the structures of CaM-peptide complexes from two enzymes have been solved, one is glutamate decarboxylase and the other is Nitric oxide synthase (NOS). NOS catalyzes the synthesis of NO, an important physiological messenger and cytotoxin. The 20-residue peptide from NOS binds to CaM to form a structure similar to that of CaMK peptide. The NOS peptide is α-helical and contains a classical pattern with hydrophobic residues at positions 1–5–8–14. Phe-496, Ala-500, Val-503, and Leu-509 in this pattern form critical interactions with CaM. In addition, Ile-505 interacts with several CaM residues such as Met-76, Phe-12, and Ala-15. The central helix of CaM is bent to wrap the peptide inside the pore.[101]

Glutamate decarboxylase in plants is a necessary enzyme for plant growth. It regulates glutamate metabolism and converts the glutamate into CO_2 and γ-aminobutyrate (GABA). The 26-residue peptide from glutamate decarboxylase is predominately unstructured in the absence of CaM. It becomes α-helical upon binding CaM (Figure 7d). Instead of a 1:1 binding, glutamate decarboxyase peptide binds to CaM in a 2:1 ratio. The N-terminal and C-terminal domains of CaM each bind one peptide. The two peptides are antiparallel forming an X-shape with an angle of about 60°. Trp-485 and Ile-482 are the two anchor residues and are critical for peptide-CaM interaction. CaM also bends and the two lobes move close together in this structure with a domain orientation different from that of CaMK peptide-CaM complex. For example, the interhelical angle between CaM helices 4 and 5 is from 114.2° to 123.2° in CaMK peptide complex while in glutamate decarboxylase peptide complex it is 17.2°.[81]

3.3 Troponin C

Tropinin C is a trigger protein that responds to the intracellular calcium concentration in striated muscle cells. An increase in calcium concentration up to 10^{-5} M results in calcium binding to TnC. The binding of calcium to TnC allows

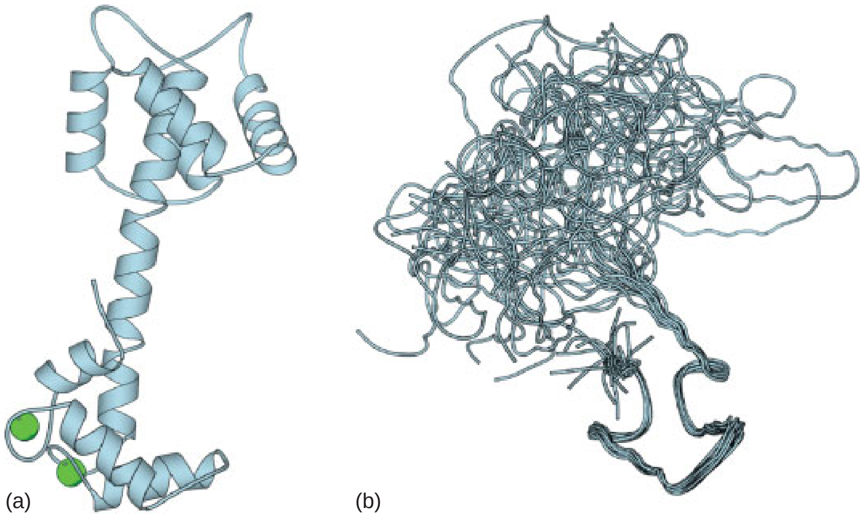

Figure 10 (a) The structures of sTnC with two calcium ions bound.[103] (b) The NMR structures of four-calcium-bound cTnC with the C-terminal of the protein superimposed[104]

it be recognized by the thin filament proteins to regulate muscle contraction. The thin filaments contain tropomysin, actin, and troponin. Troponin is a complex of TnC, troponin I (TnI), and TnT. The thick filaments are composed of myosin and a large ATP binding multi-subunit. Calcium binding to the low affinity of the N-terminal domain of TnC results in a conformational change, which, in turn, causes an alteration in the TnC/TnI/TnT interaction. The signal is then transmitted to other members of the thin filament. The interaction between the thin and the thick filaments are modified and muscle contraction is initiated.[102]

TnC has two isoforms of sTnC in fast striate muscle and cTnC in slow skeletal-cardiac muscle. Both isoforms contain four EF-hand calcium-binding sites. Site I of cTnC is inactive for calcium binding. Like calmodulin, EF-hand motifs I and II are paired in the N-terminal domain and III and IV are paired in the C-terminal domain. The 3D structures of sTnC from both chicken and turkey were first solved in 1985 and refined in 1988. As shown in Figure 10, the calcium-binding sites in the C-terminal domain are occupied while two calcium sites in the N-terminal domain are empty. The apo-N-terminal has different interhelical angles. Based on these observations and molecular modeling, Herzberg *et al*. proposed the HMJ model for the conformational change that occurs in the N-domain of TnC upon calcium binding. In the model, calcium binding leads TnC to change from a closed form to an open structure. The B/C pair of the helices is moved away from the A/D pair, which, in turn, exposes a hydrophobic patch. Since then, many structures of TnC with zero, two and four calcium ions bound have been solved. There are several surprises. First, the NMR structures of the calcium-loaded form of sTnC have a large flexibility in the interdomain linker. Hence the relative orientation of both domains is not fixed (Figure 10b). Second, both the N-terminal domain in isolation and the intact protein of cTnC remain in a predominantly closed conformation upon calcium binding.[102]

3.4 Calcium-buffer Proteins: Parvalbumin and Calbindin$_{\mathrm{D9K}}$

Different from trigger proteins, parvalbumin and calbindin$_{\mathrm{D9k}}$ function as calcium-buffer proteins. Calcium binding to both proteins does not lead to conformational change with an exposed hydrophobic surface. The structure of a carp parvalbumin was the first structure in the EF-hand protein family.[59] It has two isoforms (α and β) with very similar structures. Oncomodulin is the mammalian beta linkage parvalbumin. The structure of parvalbumin comprises three helix-loop-helix motifs, called AB, CD, and EF initially (Figure 11). The calcium-binding loop in the first

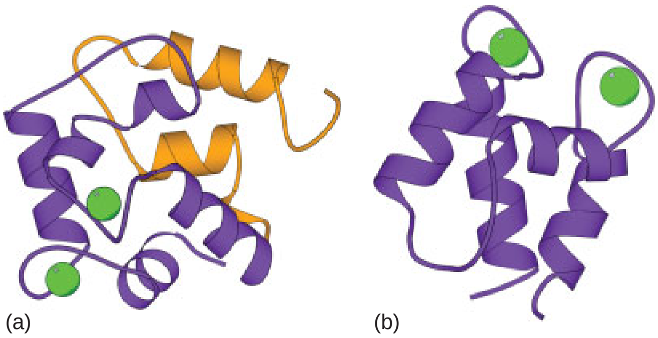

Figure 11 Structures of (a) parvalbumin and (b) CBD. Parvalbumin contains three EF-hand motifs, two of them bind to calcium (purple) and one loses the calcium-binding ability (orange).[105] CBD is monomer while the other S100 proteins are dimer[106]

calcium-binding site has a deletion of two residues. Hence this protein binds two calcium ions in the tightly coupled CD and EF calcium-binding sites. Although the AB site does not bind calcium, it is not 'nonfunctional' since it stabilizes the calcium-loaded form by covering its hydrophobic surfaces and the calcium-binding affinity is dramatically reduced once the AB site is deleted. The role of parvalbumin is proposed to relax muscle after calcium-simulated contraction. Recently parvalbumin has also been shown to play a role in neuron cells.

CBD is the smallest EF-hand protein with two EF-hand motifs. As a member of the S100 protein family, CBD contains one canonical and one pseudo-EF-hand motif at the C-terminus and N-terminus of the protein, respectively (Figure 11). Unlike other S100 proteins, CBD remains monomeric in solution. Chazin and Forsen's groups have carried out extensive structural studies of CBD at different conditions. Like parvalbumin, no significant structure changes have been observed upon calcium binding.[77,107]

3.5 S100 Proteins

The S100 (initially named after soluble in 100% ammonium sulfate) proteins are a group of low molecular weight, soluble calcium-binding proteins.[108] Currently there are more than 20 members in this family. Members of the S100 family often have more than one name. Genes encoding S100A1–14 are clustered together at the human chromosome region 1q21. All S100 members form dimers or oligomers except CBD. The tendency of dimerization is very strong with a K_d in the nanomolar range. This dimerization or oligomerization is critical for S100 proteins to interact with target proteins. It is interesting to note that CBD is the only monomeric S100 member that does not mediate any protein–protein interactions; instead it functions as a calcium-buffer protein. Most of the S100 members are observed in homodimers while S100A8 and S100A9 prefer to interact specifically with each other to form a heterodimer. The S100 family was first identified as intracellular functional proteins expressed in specific cells; for example, S100A8/A9 are mainly expressed in myeloid cells. Some S100 proteins have been shown to function extracellularly.[67,108–111]

The intracellular functions of S100 proteins can be summarized as follows: First, the interactions between S100 proteins and their target proteins result in either stimulating or inhibiting enzyme activities. The enzyme stimulation effects have been observed in cases of S100A1 and S100B binding to fructose-1,6-bisphosphate aldolase, phosphoglucomutase, twitchin kinase, and membrane-bound guanylate cyclase and S100B binding to Ndr. The enzyme inhibition effects have been observed in the process of S100A11 binding to actomyosin ATPase, S100A10 binding to phospholipase A2, S100A8/S100A9 complex binding to casein kinase I and II, and S100A1 binding to phosphoglucomutase and glycogen phosphorylase. Second, S100 binding inhibits protein phosphorylation by blocking the access of kinases to the phosphorylation positions. For example, S100 members regulate the annexin-membrane association by preventing annexin phosphorylation. The inhibition of p53 protein phosphorylation by S100A4 and S100B affects cell growth and tumor occurrence. The phosphorylations of myristoylated alanine-rich C kinase substrate (MARCKS), myosins, caldesmons, and τ protein are also regulated by their S100 partners. Third, S100 proteins control cell morphology, motility, and the dynamics of certain cytoskeleton elements. The components of the cytoskeleton system are a target for many S100 members. For example, microtubules interact with S100A1/S100B. Type-III intermediate filaments (IFs) interact with both the S100A1/S100B and S100A8/S100A9 complex. Caldesmon interacts with S100B and S100A6. Myosin interacts with S100A4. Tropomyosin interacts with S100A4 and S100A2. Microfilaments interact with S100A4 and S100A1. CapZa interacts with S100A1. F-actin interacts with S100A11. Keratin IFs interact with the S100A8/S100A9 complex and three other S100 members, profilaggrin, trychohyalin, and repetin.[67,109,111] Fourth, S100A1 has also been suggested to have chaperone activity as Hsp70/Hsp90.[112] Fifth, monomeric CBD buffers cellular calcium concentrations (Section 3.4).[67,109]

Many S100 proteins function extracellularly although the secretion mechanism is not quite clear. S100B stimulates neurite extension at nM concentration but inhibits it at μM concentration. S100B also induces neuronal apoptosis, IL-6 secretion, and NO secretion, modulates synaptic plasticity, and inhibits myogenesis. The S100A8/S100A9 complex plays a role in the immune system. It has cytostatic and antimicrobial activities. At the same time, it inhibits the activity of macrophage and the synthesis of immunoglobulin. S100A8/S100A9 complex also stimulates CD11b expression and inflammation response. S100A12 stimulates neurite growth at μM concentration and causes monocyte migration at nM concentration. The other extracellular S100 functions include S100A10 inhibiting the extrinsic pathway of blood coagulation, S100A2 inhibiting tumor cell motility, S100A4 stimulating neurite extension, and S100A2 and S100A4 mediating chemotactic processes.[67,109,113]

S100 proteins contain two calcium-binding sites, one canonic EF-hand site at the C-terminus (helix III-loop-helix IV) and one pseudo-EF-hand site at the N-terminus (helix I-loop-helix II) (Figure 5). Calcium binds to these two sites cooperatively.[62,109,111] The majority of the S100 functions are calcium-dependent, but calcium-independent S100-target protein interactions have also been observed.[111] The apo-, holo-, and target-binding-S100 triggers have been studied by NMR and X-ray crystallography. Figures 12 and 13 illustrate the calcium-induced conformational change of S100A6 and S100B.[114–117] The interaction surface of the dimeric structure has small changes. The relative orientations of helices I, IV, I', and IV' are almost the same before and after calcium binding.[67,111]

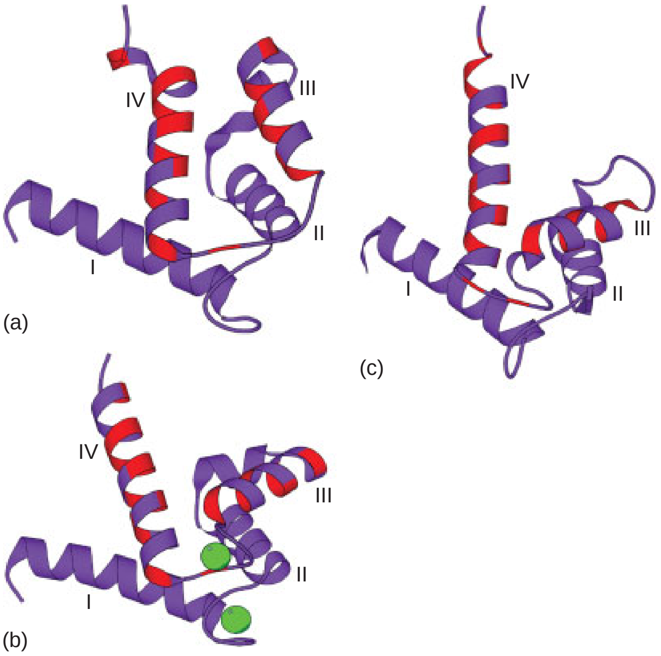

Figure 12 The conformational changes of S100A6 induced by calcium binding. Upon calcium binding (b, 1K96) helix III reorients from that of the calcium-free form (a, 1K9P) and the hydrophobic residues at the second helix-loop-helix motif (red) are exposed.[114] The structure of non-calcium-binding S100 member S100A10 (c, 1A4P) is similar to the calcium-loaded S100A6[118]

The major calcium-induced conformational change occurs in each S100 monomer. In this process, helix III (E-helix in the EF-hand motif II) undergoes reorientation and the hinge region between helix II and helix III reorients as a consequence. This process is different from that of calmodulin and TnC in which the F-helix (corresponding to helix IV here) in the EF-hand motif undergoes the largest reorientation upon calcium binding. Calcium binding exposes the buried hydrophobic residues at helices III and IV of S100 proteins. These exposed hydrophobic residues, together with the residues at helix II and the residues at helix I of the other monomer in the dimeric structure provide the binding surface for the target proteins. As shown in S100B structures (Figure 13), the target peptide binds to the cleft formed by helices III, IV, and the end of I', and the hinge loop between helices II and III. The binding of the target peptide slightly alters the orientation of helix IV, which makes the apparent calcium-binding affinity increase.[67,111,114–117]

In addition to calcium, several S100 proteins bind zinc ion with a K_d at micromolar or submicromolar level. Some S100 proteins, for example, S100B, have zinc-dependent target protein interactions. The zinc-binding and calcium-binding sites in S100 are not clustered together. The zinc-binding site in S100A7 is located between two monomers. It uses two histidines (His-86 and His-90) from one polypeptide chain and one histidine (His-17) and one aspartate (Asp-24) in another polypeptide chain as the ligands. These residues are conserved in other S100 members including S100A8, S100A9, S100A12, and S100B. Copper binding is also observed in S100A12.[67,108,111]

S100A10 is the only S100 member that does not bind calcium. Both calcium-binding sites in S100A10 are missing and the function of S100A10 is calcium-independent. The structure of S100A10 (Figure 12) is closer to the structure of calcium-loaded S100 proteins than the calcium-free proteins. For example, the interhelical angles between helices III and IV of S100A10 is about 120°, close to that of calcium-loaded S100B (105°) and S100A6 (135°) but far from that of calcium-free S100B (−166°) and S100A6 (150°).[111,118]

3.6 Penta-EF-hand Proteins

Most of the naturally existing EF-hand proteins contain an even number of EF-hand motifs although the group of proteins containing an odd number of EF-hand motifs is growing. Currently identified proteins belonging to this group include calpain, sorcin, grancalcin, ALG-2 (apoptosis-linked gene 2 product), peflin, and yeast protein YG25. Among these, calpain is the first penta-EF-hand protein revealed.[119,120]

3.6.1 Calpain

Calpain is a calcium-dependent cysteine protease that regulates many different functions in the cell through cleaving substrate proteins (>100 reported by in vitro test). These substrate proteins mainly belong to four groups: cytoskeletal proteins, kinases and phosphatases, membrane-associated proteins, and transcription factors. For example, calpain regulates the cytoskeletal-membrane attachment by the cleavage of cytoskeletal proteins. The cleavage of kinases and phosphatase such as protein kinase C (PKC) affects the signal transduction pathways in the cell. Calpain also is involved in cell cycle regulation, gene expression, apoptosis, and the long-term potentiation of synaptic transmissions. As a protease, calpain is quickly autolyzed in the presence of calcium, which hampers the study of calcium-binding properties of this protein.[119,120]

There are two types of calpains, μ-calpain and m-calpain, which require an in vitro calcium concentration at µM and mM level, respectively. This calcium-binding affinity is too low to bind calcium at cytoplasmic calcium concentration. However, an in vivo target molecule or other factors that enhance the calcium binding of calpains have not been identified. It is interesting to note that m-calpain is able to function at calcium concentrations less than 10 µM in the presence of excess high concentration of isovalerylcarnitine (a ratio of 20 000 mol isovalerylcarnitine to 1 mol calpain).[120]

Both μ- and m-calpain comprise two chains, one light chain (domain VI) and a heavy chain (domain I-IV). Sequence analysis has revealed a possible EF-hand motif located

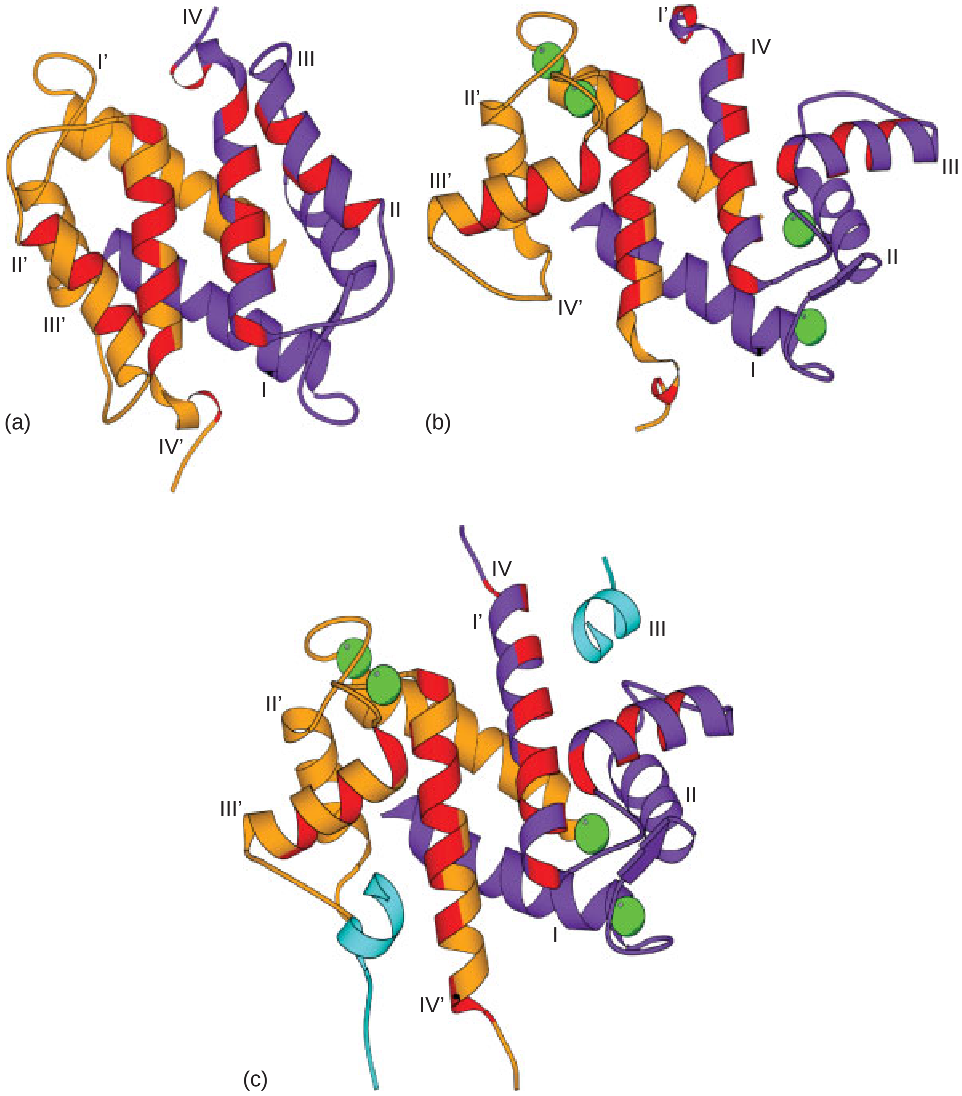

Figure 13 The structures of the calcium-free (a, 1SYM)[115] and the calcium-bound (b, 1QLK)[116] of S100B dimer (c). The structure of S100 dimer complexed to the target peptide (cyan in bottom figure, 1MWN)[117] at the cleft of helices III, IV, I', and the helices II-III hinge

between domain II and domain III. However, the X-ray structure of *m*-calpain indicates this EF-hand motif is not formed and does not bind to calcium. Instead, other loops coordinate two calcium ions. Both domain VI (light chain) and IV (heavy chain) contain five EF-hand helix-loop-helix motifs with mutations. For example, EF-1 (termed from N- to C-terminal) in both domains IV and VI has only 11 residues. The first two side chain ligands in typical EF-hand are missing and a mainchain carbonyl from Ala is used as a ligand. EF-5 is two residues longer than the normal EF-loop. The EF-5 of domain VI lacks the bidentate Glu at the C-terminal.

As shown in Figure 14, domain VI of calpain (1ALV) has eight α-helices forming five helix-loop-helix motifs.[121] Of the eight helices, helix-4 is shared by EF-2 and EF-3 and helix-7 is shared by EF-4 and EF-5. Under the crystal experimental conditions, three calcium ions (green ball) bind to EF-1, EF-2, and EF-3. The other calcium (orange ball) located in EF-4 is not chelated by the typical EF-hand residues. Instead, it uses bidentate Asp-225 and Asp-223 together with Asn-226 and Asp-135. Additional studies suggest that calcium may bind to different loops dependent on protein species and conditions. For example, a mutagenesis study has suggested that the EF-2 and EF-5 of domain VI bind calcium ions. A truncated calpain domain VI structure (removal of EF-5, 1NP8) shows all four remaining EF-hand motifs are occupied by cadmium ions. The removal of the EF-5 of calpain domain VI abolishes the hetero-dimerization ability with the intact calpain domain IV suggesting that EF-5 is responsible for the dimerization. On the other hand, the truncated protein forms homodimer through different contact surfaces.[120,122]

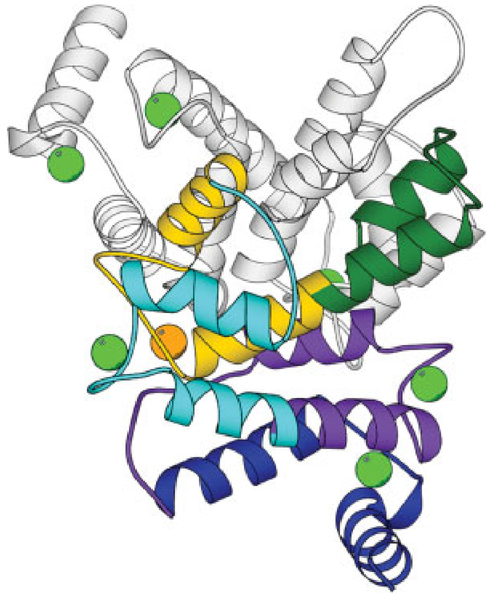

Figure 14 The structure of calpain domain VI dimer (1ALV)[121] with one chain in light gray and the other in color. Each EF-hand motif is in a separate color. From EF-1 to EF-5 they are in blue, purple, cyan, orange, and dark green. Helices 4 and 7 are shared by two EF-hand motifs. The calcium bound to the EF-loop is represented by green balls and that bound to other positions is represented by orange ball

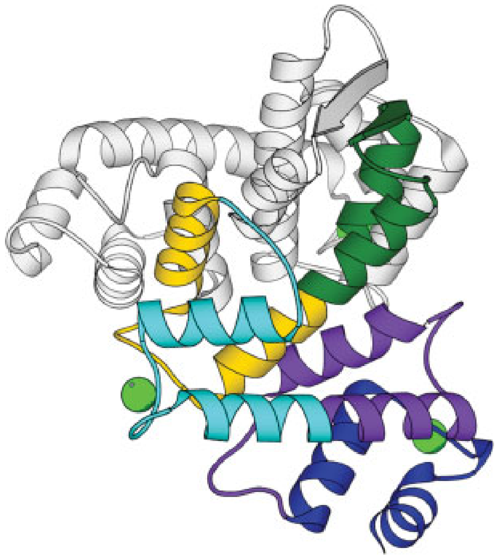

Figure 15 One chain in the dimeric structure of grancalcin (1K94)[125] is shown in light gray and the other in color. Each EF-hand motif is in a separate color, that is, from EF1–5 in blue, purple, cyan, orange, and dark green, respectively. Helices-4 and 7 are shared by two EF-hand motifs. The calcium (green ball) binds to the EF-1 and EF-3 in the colored chain and to the EF-3 in the gray chain

3.6.2 *Grancalcin and Sorcin*

Sorcin is a 22-kDa small protein modulating the sarcoplasmic reticulum (SR) calcium channel ryanodine receptor (RyR). It also interacts with annexin A7. Grancalcin is a 28-kDa protein with unknown functions. It displays a calcium-dependent translocation to the granules and plasma membrane of neutrophils. Both proteins are reported to form homodimers.[119] However, recent studies indicate that sorcin and grancalcin can also form heterodimers and can be coimmunoprecipitated, suggesting that they may function together.[123]

Sorcin and grancalcin contain five EF-hand motifs in each protein. Like calpain, some EF-hand motifs in sorcin and grancalcin are not intact. EF-1 of both proteins comprises only 11 residues, missing the first two Asp/Asn residues. Similar to calpain EF-1 the Ala carbonyl at the beginning of the EF-loop is used as the ligand. EF-2 of grancalcin lacks the bidentate Glu at the end of the loop. EF-4 of both proteins loses two to three side chain ligands at the beginning of the loop and the bidentate Glu is replaced by an Asp. Furthermore, EF-5 also loses the bidentate Glu and side chain ligand at loop position-3. Therefore, it is understood that the calcium-binding affinities of these EF-hand motifs are very low because of the broken patterns.[119,124]

X-ray structures of grancalcin and sorcin show that the overall structure of the proteins is similar to that of calpain domain IV and VI, which contains eight α-helices to form five helix-loop-helix motifs (Figure 15). EF-5 is responsible for the dimerization. When the intact protein is crystallized with 5 mM calcium only one calcium ion is bound to the grancalcin dimer located at one of the two EF-3 motifs. When the calcium concentration is increased to 100 mM three calcium ions are observed in the dimeric structure, two are located at the EF-3 motifs and one is found at one of the EF-1 motifs of the N-terminal truncated grancalcin.[124–126]

3.6.3 *ALG-2 and Peflin*

ALG-2 and peflin are another pair of penta-EF-hand proteins that can form heterodimers and function together.[127] ALG-2 plays a role in cell death. The biological function of peflin currently is not clear. Similar to calpain, sorcin, and grancalcin, the EF-hand motifs in ALG-2 and peflin are also incomplete. This time the EF-1 and EF-3 in both proteins are intact while all the other EF-hand motifs lack one or more calcium ligand residues.[119,124] The structure of ALG-2 (1HQV) shows that two calcium ions bind to two proposed high affinity calcium-binding sites EF-1 and EF-3. The third calcium binds to the EF-5 with the canonic EF-hand ligand residues at Asp-169, Asp-171, Asp-173, and the main chain of Trp-175 without the bidentate Glu. The homodimer shown in the same structure forms a V-shape geometry that is clearly different from that of the calpains and grancalcin. The dimerization surface is again located at the EF-5 region similar to calpain, sorcin, and grancalcin.[128] Unlike the typical

EF-hand proteins, each EF-hand motif of the penta-EF-hand proteins functions separately without cooperativity. Even if even-numbered calcium ions are bound, it is not necessary that they are paired. For example, in grancalcin and ALG-2, two calcium ions bind to EF-1 and EF-3 while the paired partners EF-2 and EF-4 are empty.[121,124,125,128]

3.7 Calcineurin and DREAM

Calcineurin and Downstream regulatory element antagonist modulator (DREAM) are two proteins that are involved in calcium-regulated transcription control pathways. There are several such pathways. One is through calmodulin-dependent kinase, such as CaM kinase I, CaM-kinase IV, or CaM kinase kinase. The other is through S100B that interacts with the tumor suppressor p53 to regulate its transcriptional activity.[93] Both the CaM kinases and S100B have been discussed earlier. Here we will focus on calcineurin and DREAM.

3.7.1 Calcineurin

Calcineurin is a serine/threonine phosphatase (also called protein phosphatase 2B, PP2B) with two subunits calcineurin A and calcineurin B. The catalytic site of calcineurin is located at subunit A, where a Zn–Fe binding site mediates the dephosphorylation reaction. Calcineurin A directly binds to the cytoplasmic subunit of NF-AT (NF-ATc) (nuclear factor of activated T-cell) to dephosphorylate serines in the serine-proline repeats. Only the dephosphorylated NF-ATc can be translocated into the nucleus to form the intact NF-AT complex, which binds to DNA to regulate transcription. The other transcription factors including NF-κ B, Ets1, and MEF2 are regulated by calcineurin.[93,129] The activity of calcineurin is regulated or inhibited by several molecules including FK506 binding protein (FKBP) and FK506, cyclophilin and cyclosporin A, cabin1 (cain), A238L, AKAP79, Csp1, and the calcipressins family. The activity of calcineurin A requires the binding of CaM to calcineurin B.[93,129] Calcineurin B is an EF-hand protein with a structure similar to calmodulin. Four canonic EF-hand motifs are located at residues 30–41, 62–73, 99–110, and 140–151, respectively. The structures of free calcineurin (1AUI) and calcineurin complexed with the inhibitors cyclosporin A/cyclophilin (1MF8) in Figure 16 have revealed that the calcineurin A-calcineurin B interaction is different from the typical known calmodulin-target interactions.[130,131] Calcineurin B uses both domains to interact with the same helix from calcineurin A while calmodulin interacts with its central helix between EF-2 and EF-3 or one of the domains at the N- or C-terminal. Cyclosporin A, as the inhibitor, binds to the interaction surface of calcineurin A-calcineurin B. As shown in Figure 16, the attached cyclophilin blocks the access of protein substrates to the catalytic site of calcineurin.[130,131] The structure of calcineurin complexed with another inhibitor, FK506/FKBP12, reveals a very similar inhibition mechanism (pdb 1TCO).[132]

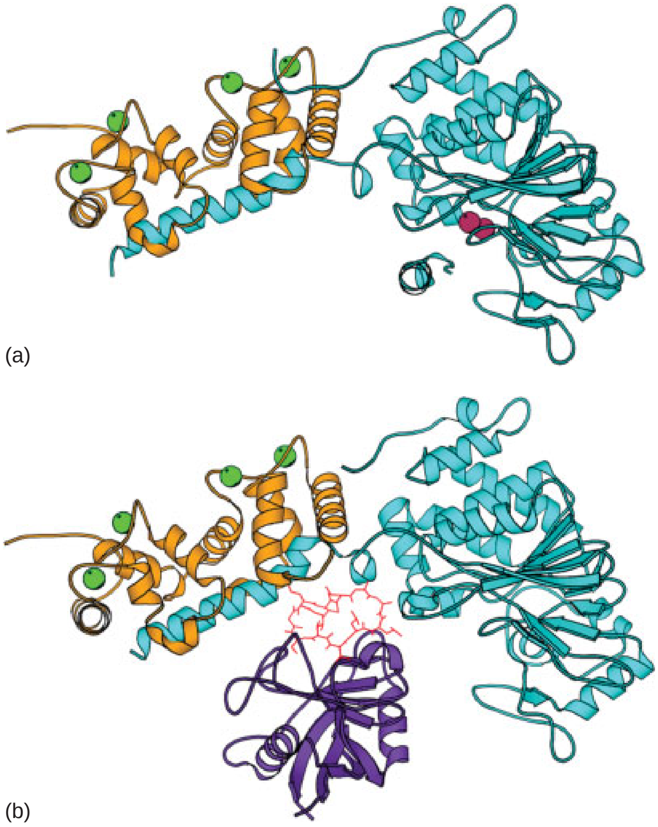

Figure 16 (a) The structure of calcineurin with subunit A in cyan. The catalytic site containing a Zn–Fe binding site is in dark red. Subunit B in orange contains four calcium (green) ions bound to the EF-hand motifs. Both N- and C-terminal domains of calcineurin B interact to the same extended α-helix of calcineurin A.[130] (b) The inhibitor complex cyclosporin A (red) and cyclophilin (violet) interacts with both calcineurin subunits and blocks the catalytic site of calcineurin[131]

3.7.2 DREAM

DREAM (calsenilin, KChIP3) has multiple functions including interacting with presenilin to regulate calcium signals and modulate the activity of A-type voltage-gated potassium channels. In transcription control, calcium-free DREAM directly binds to the downstream regulatory element to block gene expression. DREAM is also essential in sensing pains. DREAM knockout mice display a reduced response to pain.[93]

DREAM is a calcium-binding protein that belongs to the recoverin EF-hand subfamily. One feature of the recoverin subfamily is the CPXG sequence at the beginning of the EF-1 motif. This sequence abolishes the calcium-binding ability of EF-1. As a result, DREAM binds three calcium ions, two at EF-3 and EF-4 with higher affinities (~5 µM) and one at EF-2 with lower affinity (~50 µM). Compared to the other recoverins, DREAM has a long N-terminal sequence but loses the N-terminal myristoylation.[93] No X-ray or NMR structure is available for DREAM at present, but the structural information is available for other recoverin members, such as recoverin (e.g. 1REC, 1OMR, 1IKU, and 1JSA), neurocalcin (1BJF), and frequenin (1FPW and 1G8I).[133–137]

DREAM dimerizes and tetramerizes through a calcium-dependent mechanism. The calcium-free DREAM forms tetramer at protein concentrations higher than 20 μM. The calcium-bound DREAM forms dimer at low protein concentrations and tetramer when protein concentration is higher than 200 μM. There are other recoverin-like proteins with calcium-dependent dimerization with different responses. For example, calcium-free neurocalcin is a monomer while the calcium-loaded one forms a dimer. Conversely, guanylyl cyclase activating protein 2 (GCAP-2) forms a dimer in the calcium-free state and becomes a monomer in the calcium-bound state.[93]

To repress transcription, the calcium-free DREAM tetramer binds to DNA. Upon calcium binding, DREAM becomes a dimer and leaves the DNA to allow the RNA polymerase to perform transcription.[93] URE3-BP is another EF-hand protein that directly interacts with DNA at the upstream regulatory element-3 of the lectin heavy subunit gene. This protein has two EF-hand motifs.[138]

4 EXTRACELLULAR CALCIUM-BINDING PROTEINS

There are several types of extracellular calcium-binding proteins. The majority of these proteins such as cadherins, integrins and growth factors, are from eukaryotic systems. Below we will present how different extracellular calcium proteins carry out their unique biological functions.

4.1 Cadherins

Cadherin family refers to a group of calcium-dependent homophilic cell–cell adhesive molecules (Figures 17–18). Typical cadherins are named based on their expression locations, such as E-cadherin (epithelial), M-cadherin (muscle), and N-cadherin (neuron). Atypical cadherins include T-cadherin (truncated) and protocadherins.[11,139,140] Cadherins are the major constituent of the cell–cell adhesive junctions, functioning together with numerous other proteins such as catenins.[11,139–141] The property of homophilic recognition of cadherins and the formation of adhesive junctions play a key role in morphogenesis. For example, selective expression of different cadherins controls selective cell aggregation, which refers to the suspended cell re-aggregation with only homotypic cells.[140] This process is important in tissue and organ development. Cell condensing, another process in morphogenesis, also requires cadherins. Central nervous system development represents one of the most striking examples of cadherin-regulated morphogenesis. More than 20 different cadherins, involving all key events of neuron formation from the beginning stage of cell aggregation to the formation of synapses, are expressed at different stages and structural layers. Neurite outgrowth is also activated and regulated by cadherin expression. The formation and regulation of junctions between two neurons or neuron-muscle

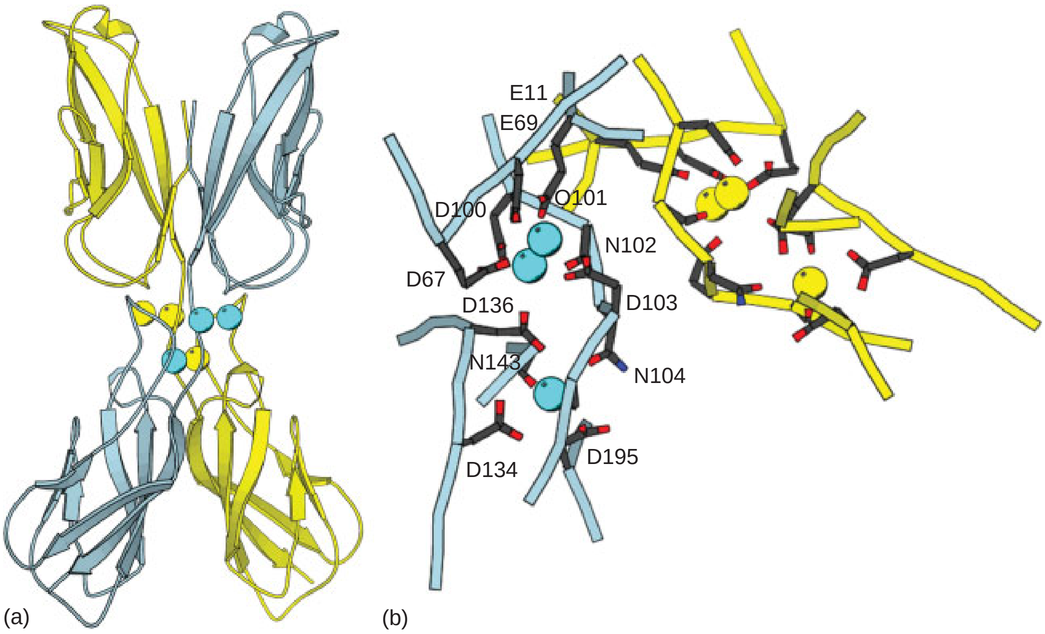

Figure 17 The dimeric structure of E-cadherin EC1–2 (1EDH) (a).[142] Two polypeptide chains and their bound calcium are shown in different colors. (b) A close-up view of the calcium-binding sites. The calcium ligand residues on chain A are labeled. Several ligands are shared by different calcium ions. All calcium binding in cadherin belongs to the discontinuous site class

are also cadherin-dependent. The role of cadherins, especially that of E-cadherins, in cancer growth and tumor invasion, has been investigated. Abnormal expression or abnormal distribution of E-cadherins has been observed in several cancers.[140]

Classical cadherins comprise three different parts, an intracellular C-terminal tail, a transmembrane segment that spans through the cell membrane once, and a long extracellular N-terminal chain.[139,140] The extracellular chain contains five domains termed EC1–5 (Figure 18). Each domain is ~110 residues. The extracellular five domains are highly homologous to each other. The first domain at the N-terminus (EC1) is directly involved in cell–cell interaction. Domain exchange experiments have shown that the homophilic adhesive properties are encoded in the EC1 domain. Substitution of E-cadherin EC1 domain with P-cadherin (placental) EC1 domain leads the protein to bind selectively with P-cadherin. The four repeated domains EC2–5 are required for the maintenance of normal cadherin function. On the other hand, atypical cadherins of T-cadherin (truncated) and protocadherin subfamily have different structural properties.[140,144] T-cadherin (truncated) expressed in the neuronal system does not have the transmembrane and intracellular parts. It is anchored on the cell membrane via glycosylphosphatidylinositol (GPI). The extracellular part still contains five domains but without the conserved HAV sequence in EC1. The protocadherin subfamily has six or more extracellular domains. The sequences of EC3 and EC5 domains are also different from those of classical cadherin. Furthermore, they have different intracellular tails that do not interact with catenin.[140,144]

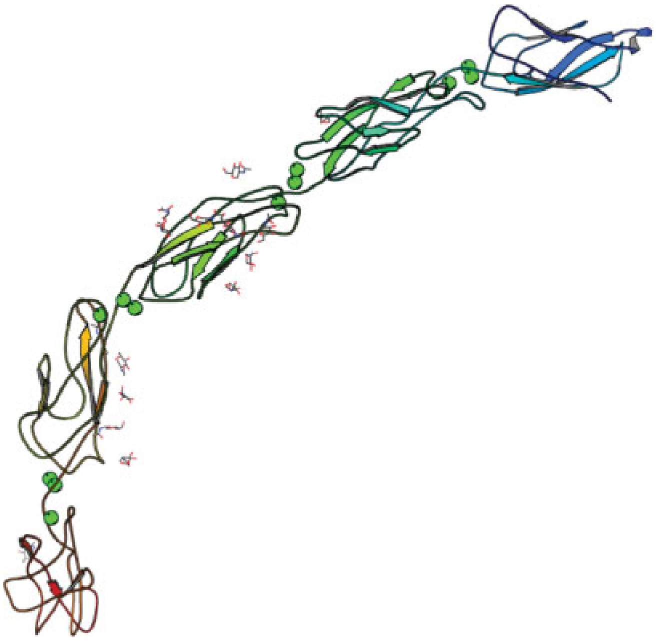

Figure 18 The structure of the extracellular region of Ep-cadherin (1L3W).[143] Calcium ions bind to the loops between each two adjacent domains and the whole protein in the structure forms a curvature. N-acetyl-D-glucosamine molecules attached to the cadherin surface are in gray

The intracellular tail of classic cadherin interacts with β-catenin or γ-catenin directly.[139,140] α-Catenin interacts with the cadherin tail through the mediation of β-catenin. Catenins then interact with the cytoskeleton protein actin. Through this cadherin-catenin-actin complex, cell–cell adhesion is linked with the cytosolic signal pathway. The cadherin-catenin complex regulates the outside cell–cell interaction. The expression level of cadherin also affects the expression of catenins. Another group of cadherin tail binding molecules is the p120 subfamily, which has a structure similar to catenins.[139] Extracellular cell adhesion is regulated by modifying the intracellular cadherin tail and its target. Stimulated by different signals, such as epidermal growth factor (EGF), transforming growth factor β, platelet-derived growth factor, hepatocyte growth factor, hormones, signals from gap junctions, and cholinergic receptor agonists, catenins or p120 will be phosphorylated directly or indirectly. Phosphorylation and dephosphorylation states of catenins or p120 alter the cadherin-target complex and further control the extracellular function of cadherin. This process is controlled by PKC, several signal receptor tyrosine kinases, Src tyrosine kinase, and several protein tyrosine phosphatases.[139,141]

The 15 solved structures of cadherins are mainly E- and N-cadherin. The X-ray structure shows seven β-strands in the EC1 domain. As shown in Figure 17, the EC1–2 domains of E-cadherin form lateral dimers in a calcium-dependent manner. There are three calcium ions bound between EC1-EC2 domains in each monomer in the crystal structure of E-cadherin EC1–2 dimer (1EDH).[142] Some ligands are shared by different calcium ions (Figure 17). The residue ligands for Ca1 are from the side chain of Glu-11, Asp-68, Glu-70, and Asp-103. The side chain carboxyl oxygen atoms of Glu-11, Glu-70, and Asp-103 are used as the ligands for Ca2. Ca2 also shares ligand Asp-136 with Ca3. The additional residue ligands for Ca2 are the side chain of Asp-100 and the mainchain of Gln-101. In addition to Asp-136, the ligands of Ca3 include bidentate Asp-134, the side chain of Asn-102, Asp-195, and the mainchain of Asn-104 and Asn-143.[142] Boggon *et al.* recently reported the structure of full-length ectodomain of the C-cadherin (EC1–5) (Figure 18).[143] Twelve calcium ions bind to the linkage region between neighboring domains, three in each of the four regions to sequentially organize the protein. The HAV tripeptide sequence in EC1 domain has been shown to be important for homophilic recognition.[143] The binding of calcium induces the conformational change of cadherin, including the important process of the Trp-2 in EC1 docking into the HAV sequence, which is believed to be important in exposing the homophilic recognition region. Trp-2 is observed both in cis dimerization and trans orientation (Figure 17). The structure of the five domains has a gentle bend without applied forces. This orientation corresponds to the distance of adhesion junctions revealed by EM. Cadherin monomers on opposed cell membranes forming lateral or cis dimers are likely to mediate cell adhesion by forming trans adhesive interactions with cis dimers on the opposed membrane. The trans binding is proposed to be involved in interactions between the outmost domains or interactions between completely interdigitated proteins from both membranes.[143]

4.2 Integrins

Integrins are transmembrane proteins that mediate divalent cation-dependent cell–cell and cell matrix adhesion through tightly regulated interactions with ligands.[145,146] Integrins are involved in the formation of extracellular matrix by fibronectin binding and translocation and plays very important roles in various cell functions and processes such as secretion, phagocytosis, and migration. The extracellular proteins laminin and collagen also interact with integrin. Integrin mediated signals control the cell cycle by suppressing cyclin-dependent kinase inhibitors and integrins regulate the cell polarity and migration through the Rho-family GTPase pathway.[146,147] Several proteins are colocalized with integrin to function together. For example, secreted matrix metalloproteinases (MMPs) degrade the extracellular matrix via binding to integrin. Membrane growth factor receptors, including insulin receptor, EGF receptor, platelet-derived growth factor (PDGF) receptor, form supramolecular complexes for cooperative functioning. Other proteins associated with integrin include CD16, CD14, CD47, TM4, and P2Y. The biological functions of integrin are also regulated by other factors and proteins, such as intracellular calcium concentration, calpains, TM4, syndecans, and focal adhesion kinase.[146,147]

Integrins are $\alpha\beta$ heterodimers. Each type of integrin is defined by its components, for example, $\alpha 2\beta 1$ or $\alpha v\beta 3$. Currently 18 α-subunits and eight β-subunits have been identified in mammals. Integrin α-subunit contains a transmembrane domain and a short intracellular tail at the C-terminus.[148,149] As shown in Figures 19 and 20, the extracellular region of the α-subunit contains four domains: a β-propeller structure with seven homologous repeats (blades), one C2-like 'thigh' domain, and two β-sandwich like domains (calf-1 and calf-2).[150,151] Some α-subunits contain an approximate 200-residue length A-domain (von Willebrand factor A domain) inserted into the N-terminal β-propeller domain. This inserted A-domain (αA, also named αI as inserted) forms a separated domain without disrupting the β-propeller structure.[148] Integrin β-subunit also contains a short intracellular tail and a transmembrane domain. The extracellular region comprises eight domains: an A-domain (βA), an Ig-like hybrid domain, a PSI domain (plexins, semaphorins, and integrins), four EGF domains (EGF1–4), and a β-tail domain (βTD).[148,149]

At micromolar concentration range, calcium enhances the integrin functions while calcium inhibits integrin function in the mM concentration range. Magnesium and manganese facilitate the association of integrin with its ligands at a broad range of concentrations.[145] The integrin-recognition sequence with exposed acidic residues also contributes to integrin-ligand binding. Integrins that contain αA-domain recognize glutamate-based sequences while integrins without the αA-domain recognize aspartate-based sequences.[149] Integrin $\alpha v\beta 3$ recognizes the RGD sequence in the target molecules.[150]

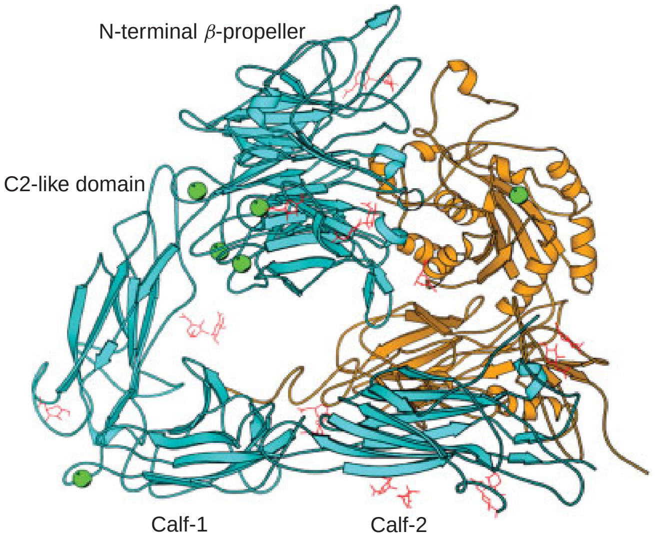

Figure 19 The structure of extracellular regions of integrin $\alpha 3\beta v$ (1JV2).[151] The α-chain is in cyan, β-chain is in orange, and calcium ions are in green. Four domains of the α-chain are labeled

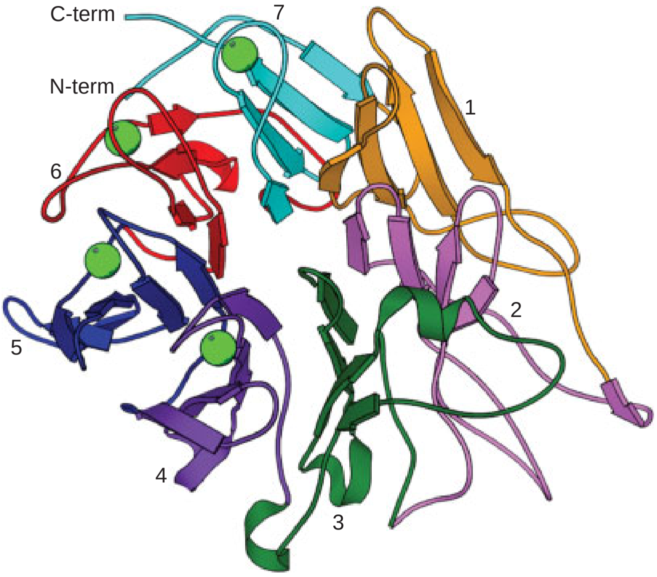

Figure 20 The N-terminal β-propeller domain of α-chain in integrin $\alpha 3\beta v$ (1JV2)[151] contains seven repeated blades. Each blade (shown in one color) comprises four aligned β-strands. Four calcium ions bound in this domain are located at blades 4–7

Before 2000, only structural information of the A-domain was available. Several X-ray and NMR structures of the extracellular integrins have been obtained after 2001 and they revealed detailed metal ion and peptide binding information.[145,150,151] These structures include the $\alpha v\beta 3$ with (1L5G)[150] and without (1M1X and 1JV2)[150,151] RGD sequence, the NMR structures of the N-terminal domain of αIIbβ3 (1KUP and 1KUZ),[152] and the NMR structure of β2 subunit EGF-like domain (1L3Y).[153] The overall structure of the extracellular segments of integrin is like a head with two legs. The head consists of a β-propeller domain, including αA domain also in some types, of the α-subunit and the βA hybrid domains of the β-subunit. These two legs can be bent or extended depended upon different ligand and metal ion binding. The transition positions of these two conformations (bent and extended) are located between the ‘thigh’ and calf-1 domain in the α-subunit and PSI, EGF1, and EGF2 region in the β-subunit. The crystal structure 1M1X (3.3 Å, Mn-loaded) and 1JV2 (3.1 Å, Ca-loaded) revealed six divalent ion-binding positions.[150,151] As shown in Figure 20, four calcium-binding sites are found at the repeated blades 4–7 of the β-propeller structure at the N-terminal of α-subunit. They are exposed to the solvent with a continuous calcium-binding loop similar to the EF-loop of glactose-binding proteins, where a conserved nine-residue segment of D-h-D/N-x-D/N-G-h-x-D contains all the calcium-binding ligands at the side chain of positions 1, 3, 5, and 9 and the mainchain of position 7. The h here refers to hydrophobic residue and x refers to any residue. Another calcium ion binds to α-subunit between the bottom of the ‘thigh’ domain and the top of the calf-1 domain. βA-domain holds calcium at the ADMIDAS (adjacent to metal-ion-dependent adhesion site (MIDAS)) region, which coordinates the calcium by the mainchain carbonyl of Ser-123 and Met-335 and the side chain carboxyl of Asp-126 and Asp-127. When the protein is exposed to the manganese buffer, all six calcium-binding sites can be occupied by manganese.[150,151]

A MIDAS has been proposed in the αA-domain in the αA-containing integrin, as also in the βA-domain, which is the recognition location for the ligand molecules. The MIDAS motif of αA binds magnesium or manganese with high affinity and binds calcium with low affinity.[145,150,151] The RGD peptide binds to the βA and β-propeller structure of $\alpha v\beta 3$ resulting in the disruption of a hydrogen bond between Asp-119 and Glu-220 to allow the Glu-220 function as a ligand for the additional metal binding at the MIDAS motif.[150,151] This metal ion is coordinated with the carboxyl of Asp-119, Asp-251, and Glu-220, and the hydroxyl of Ser-121 and Ser-123. The binding of the short peptide RGD resulted in the binding of a second metal ion. This second metal ion is also located around the MIDAS motif with the ligand oxygen atoms from the side chain of Glu-220, Asp-158, Asn-215, and Asp-217, and the mainchain of Asp-217 and Pro-219. Glu-220 provides its two side chain carboxyl oxygen atoms to both metal ions. Although these two sites are revealed in the manganese bound structure, all the ligands are popular in calcium binding.[150,151]

4.3 Calcium-dependent Epidermal Growth Factor (EGF)

A large protein family that contains extracellular domains homologous to EGF is called the EGF-domain proteins. EGF-like domains or modules are often found in many extracellular and membrane proteins (>70). They are involved in blood coagulation, fibrinolysis and the complement systems, matrix proteins, cell surface receptors, the low-density lipoprotein receptor and the developmentally important receptor, Notch. EGF-like domains may exist as multiple copies within proteins such as in the Drosophila protein Notch with 36 copies or as a single copy as in EGF itself. It can also be found in conjunction with other modules.

EGF-like domains usually contain 40–50 amino acids with 6 conserved cysteine residues that form three disulfide bonds pairing in the pattern of 1–3, 2–4 and 5–6. These three disulfide bonds stabilize their common structure of two regions of double-stranded antiparallel beta sheets (Figure 21). More than 25% of EGF modules bind calcium. They are called calcium-binding EGF (cbEGF) and form one of the most popular extracellular calcium-binding sites. cbEGF is usually phlogenetically related and clusters together in a dendrogram. Fibulins, a newly recognized family of extracellular matrix proteins, have tandem arrays of EGF-like domains.[154]

The coagulation and anticoagulation proteases, factors VII, IX, and X, and protein C, have a common domain structure with an N-terminal gamma-carboxyglutamic acid (Gla)-containing domain that is followed by two EGF-like modules, whereas the C-terminal half of each protein is occupied by a trypsin-like serine protease domain. Prothrombin also has an N-terminal Gla domain and a C-terminal serine protease

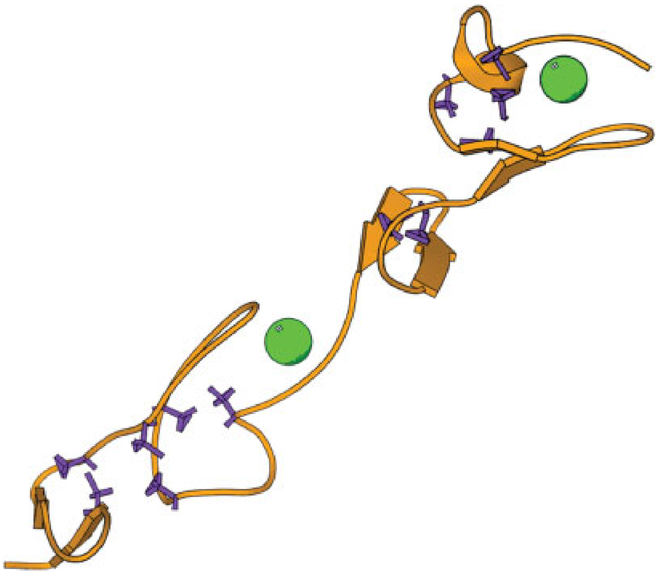

Figure 21 The structure of two EGF-like domains in human low-density lipoprotein receptor is shown with the Cys (violet) highlighted[155]

domain, but they are separated by two so-called kringle domains rather than EGF-like domains.

A protein S, the cofactor of activated protein C, has four EGF-like modules in tandem. The structure of N-terminal EGF modules is very similar to that of non-calcium-binding modules. Calcium binding only results in a limited local conformational change. The N-terminal loop is better defined and moves toward the major β-sheet. The N-terminal non-catalytic Gla and EGF-like domains provide coagulation serine proteases with different calcium affinities for certain biological membranes, and also mediate protein–protein interactions.[156,157]

Fibrillin-1 is composed of 43 cbEGF-like domains.[158] Calcium binding of fibrillins stabilizes interdomain cbEGF interactions and has been shown to be responsible for the formation of a rod-like linear arrangement. In addition, calcium binding significantly protects full length or recombinant fragments of fibrillin-1 from proteolysis by trypsin, elastase, endoproteinase Glu-C, plasmin and matrix metalloproteinase. cbEGF contains more than 60% of the identified mutations of the connective tissue disease Marfan syndrome and related disorders. Mutations at calcium-binding consensus residues on cbEGF such as N2144S in cbEGF32 significantly reduce calcium affinity. Recently NMR studies of the solution structure and dynamic properties of the cbEGF pairs such as cbEGF12–13 reveal a correlation between calcium-binding affinity and backbone dynamics. Calcium plays a key role in stabilizing the rigidity of the domain pair on the pico-to-millisecond timescale.[159,160]

The calcium-binding site in EGF domain is characterized by a consensus D/N-x-D/N-E/Q-x_m-D/N-*-x_n-Y/F (where m and n are variable and $*$ represents beta-hydroxyaspartic acid (Hya) or erythro-beta-hydroxyasparagine (Hyn). Hydroxylation is carried out by Asp/Asn-beta-hydroxylase. Factors IX and X and protein C all have one Hya in the N-terminal EGF module. There are two types of calcium-binding sites. Calcium sites largely locate between domains involved in conserved acidic residues in one EGF-like module and a single calcium ligand from a neighboring repeat. In Class I of repeat pairs, one ligand is donated by the N-terminal adjacent EGF-like domain[161] while for Class II, this ligand is from a repeat on an adjacent molecule.[10] Calcium-binding sites are usually pentagonal bipyrimidal. Usually isolated domain modules have low calcium affinity (~1–6 mM). The calcium affinity of the module pair was shown to be increased by 10–20-fold (K_d is about 0.1 mM).[162] N-terminal neighbor usually influences the calcium affinity of cbEGF modules.[163]

4.4 C-type Lectins

Lectins refer to all of the proteins that have carbohydrate-binding abilities.[164,165] Carbohydrate recognition domain (CRD) is the functional part in lectins for sugar binding. Based on the structural diversity of CRD, lectins are classified as L-, P-, I-, R-, C-type lectins, and galectins, in which C-type lectins are calcium-dependent lectins. C-type lectins are composed of several different subfamilies, including collectins, selectins, the mannose receptor, and NK receptors and so on. They are normally multiple domain proteins that comprise calcium-dependent CRD domain(s) and other domains performing diverse functions. The CRD domain in C-type lectins adopts a mixed α/β structure.[166,167] This section will briefly discuss the major C-type lectins of collectins, mannose receptor, selectins (CD62), asialoglycoprotein receptor (ASGPR) and GBPs. Calnexin and calreticulin will be discussed in the ER/SR calcium-binding protein section.

4.4.1 Collectins

Collectins are the soluble extracellular members of the lectin family. Collectins are secreted to the extracellular matrix and function as sugar pattern recognition molecules that selectively interact with certain microbial surfaces. It is important for immune responses. Mannose binding lectin (MBL) (mannose binding protein (MBP)), surfactant protein A (SP-A), SP-D, conglutinin, collectin-43, and collectin liver-1 belong to the collectin subfamily.[167–169] The collectins comprise four segments: a Cys-containing N-terminal segment that provides inter- and intrachain disulfide bridges, a collagen-like $(\text{-Gly-X-Y})_n$ repeating sequence, a short linkage between the collagen-like segment to the CRD domain, and the calcium-dependent CRD domain at the C-terminal.[169] As shown in Figure 22, the collectins form trimers in which collagen-like segments wind together and their CRD domains are clustered at the top of the collagen helices. The isolated CRD with linkage segment maintains trimeric structure and the CRD without the linkage segment forms a dimer. Both sugar-selective and calcium-binding properties are encoded in the CRD domain; for example, Glu-185 and Asn-187 in MBP-A are specific for mannose recognition, but when they are mutated to Gln-185 and Asp-187, the protein changes its preference to galactoside.[169]

Calcium binding is required not only for function but also for structure stabilization. Here we use rat MBL–A (1RTM)[170] as an example to illustrate the calcium binding in collectins (Figure 22). Each monomer contains three calcium ions. Each CRD binds two calcium ions specifically (Ca1 and Ca2) and one nonspecifically. As shown in Figure 22(b), Ca1 is coordinated by the sidechains of Asp-161 (bidentate), Asp-188, Asp-194, Glu-165, and the mainchain carbonyl of Glu-193. Glu-193 provides the ligands for both specifically bound calcium ions. Ca2 is coordinated by the protein ligands of sidechains of Glu-193, Glu-185, Asn-187, Asn-205, Asp-206, and also the mainchain carbonyl of Asp-206. The bound sugar provides two hydroxyl oxygen atoms as additional ligands for Ca2. Meanwhile, this bound sugar interacts with Glu-185/Asn-187 pair, Asn-205, and Glu-193 of the protein. Thus, Ca2 directly mediates the sugar binding.[169,170]

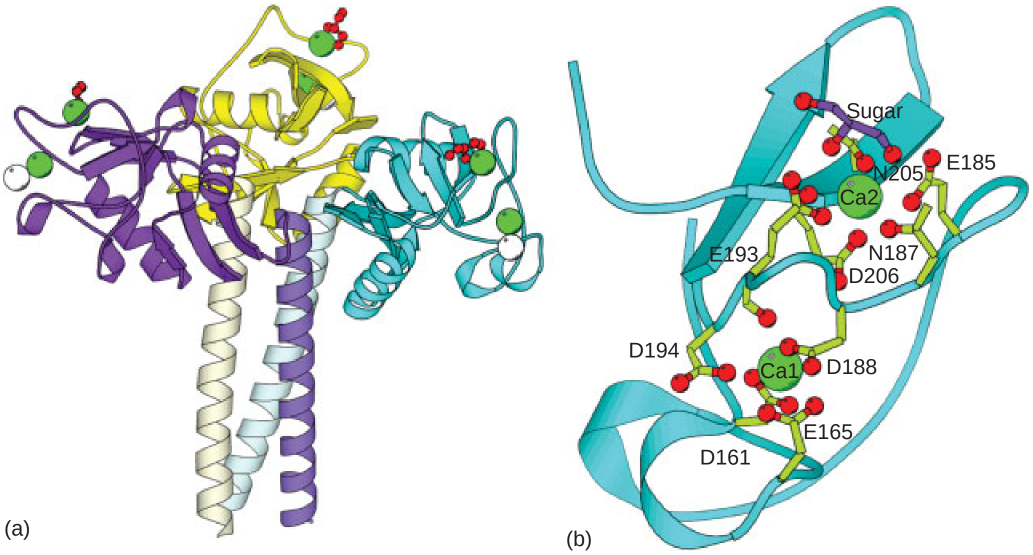

Figure 22 (a) The trimeric structure of MBL-A (1RTM)[170] with each monomer labeled with a different color. The CRDs and the glycan-like domains are labeled in dark and light colors, respectively. Each monomer contains three calcium ions. Two calcium ions (Ca1 and Ca2) that are specifically bound to the CRD are in green. The nonspecific calcium is in the lighter color. The calcium-mediated bound sugars are labeled in red. (b) The local view of the calcium-binding sites of Ca1 and Ca2 of MBL-A with ligand residues highlighted. Several ligands for both calcium ions are highly clustered in the loop from residue 185194, while Glu-193 is shared by two calcium ions. Glycerol is shown in violet

The X-ray structure shows that human SP-D (1PW9),[171] another collectin member, shares the same calcium-binding pattern as rat MBL-A, in which Ca2 binding ligands are encoded in a 22-residue loop E-x-N-5x-E-11x-N-D (Figure 23). The last Asp residue provides both mainchain and side chain ligands. Ca1 binding ligands are encoded in a longer loop D-3x-E-22x-D-4x-E-D, in which the first Asp is bidentate and the second Glu is shared with Ca2. Sequence alignment reveals that similar sequence characteristic properties for calcium binding are also conserved in other collectin members. For example, the Ca1 and Ca2 sharing Glu-residue, the N-D pattern at the end of the Ca2 binding loop, and the Glu-residue at the start of the Ca2 binding loop are conserved in many of the collectin members. Either acidic residue Asp or Glu is used as a bidentate ligand for Ca1.

4.4.2 *Mannose Receptor*

The mannose receptor subfamily is a group of membrane-attached C-type lectins with multiple CRDs. Since most of these domains maintain neither calcium-binding nor sugar-binding properties, the term C-type lectin-like domain (CTLD) is more frequently used lately instead of the term CRD. The mannose receptor subfamily comprises four members including the mannose receptor, the M-type phospholipase A2

	185 187 193 205 206	
Collectin (rat MBL-A)	**E**-x-**N**-x-4x-**E**-11x-**N**-**D**	
	725 727 728 733 445 746	
Mannose receptor (human CTLD4)	**E**-x-**N**-**N**-4x-E-11x-**N**-**D**	
	80 82 88 105 106	
Selectin (human E-selection)	**E**-x-**N**-x-4x-E-16x-**N**-**D**	
	239 241 252 264 265	
ASGPR (human H1)	**Q**-x-**D**-x-9x-**E**-11x-**N**-**D**	

Figure 23 Summary of the amino acid sequence patterns that are involved in calcium binding of the subfamilies of C-type lectins. One example in each subfamily is shown and the ligand position is marked black. The last Asp uses both oxygen atoms from the mainchain carbonyl and side chain carboxyl as the calcium ligand atoms

receptor (PLA2R), Endo180/uPARAP, and DEC-205/gp200-MR6/CD205. The first three contain eight CTLDs and the last one contains ten.[172]

The mannose receptor subfamily members contain an N-terminal Cys-rich domain that provides an additional sugar-binding site, a fibronectin type-II domain that binds to collagen, the repeated CTLDs, a transmembrane segment, and an intracellular tail that interacts with the cytoplasmic proteins. The CTLD4 and 5 instead of the CTLD at the end of the mannose receptor are the most critical domains for calcium binding and sugar binding. Endo180 has also been demonstrated to bind monosaccharides. However, CTLD5 within M-type phospholipase A2 receptor mediates protein–protein interactions instead of protein-sugar interactions.[172]

Figure 24(a) shows the structure of mannose receptor CTLD4 (1EGG),[173] which shares a mechanism of calcium-mediated sugar binding that is similar to that in MBL-A. The same sequence pattern for Ca2 binding in MBL-A is conserved in the mannose receptor CTLD4. As shown in Figure 23, mannose receptor CTLD4 has all of the five conserved ligand residues for calcium binding except Glu-733. Glu-733, corresponding to Glu-193 in MBL-A, is replaced by the side chain carbonyl of Asn-728. This Asn is not conserved in CTLD-5; instead it contains a conserved Glu-residue corresponding to Glu-733. The bound sugar provides an additional two oxygen atoms for Ca2. The Ca1 binding site is clearly different from the mannose receptor and MBL-A. In the mannose receptor CTLD4, Asn-728, Asn-731, Glu-737, and Asn-750 coordinate to Ca1.[173] Both CTLD1 and CTLD2 of Endo180 have the conserved calcium-binding pattern as observed in MBL-A. However, the M-type phospholipase A2 receptor and DEC-205 do not have this conserved calcium-binding pattern and their interaction with carbohydrates is independent of calcium binding.[172]

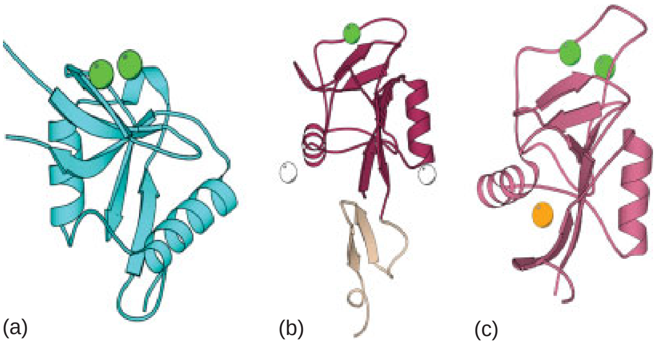

Figure 24 (a) The structure of CTLD4 of mannose receptor (CTLD4, 1EGG)[173] with two bound calcium ions. (b) The structure of CRD (dark red) and EGF-like domain (light colored) of E-selectin with the functional calcium (green) (1ESL).[174] The two nonspecific bound calcium ions are shown in lighter color. (c) The structure of the CRD on H1 subunit of ASGPR with the two calcium ions (green) as in normal C-type lectin (1DV8).[175] The third calcium ion unique to this protein is in orange

4.4.3 *Selectins (CD62)*

Selectins are cell-adhesion molecules that mediate leukocyte recruitment in immune reactions and signal transduction. Selectins comprise three members termed E-, P-, and L-selectin. The CRD is located at the N-terminus, followed by an EGF-like domain. There are various numbers of consensus repeat sequences following the EGF-like domain. P-selectin, L-selectin and E-selectin contain nine, six, and two repeats, respectively. A transmembrane segment and a cytoplasmic tail are located at the C-terminal. The key domains for target recognition and sugar binding are the N-terminal CRD and EGF-like domain.[167,176]

The CRD of selectins is similar to that of MBL, or MBP. As shown in Figure 24(b), selectins do not have the Ca1 binding site of MBL-A. However, crystal structures of E-selectin (1ESL)[174] and P-selectin (1G1Q, 1G1R, 1G1S, and 1G1T)[177] have revealed that the principal calcium-binding site mediating sugar binding (Ca2) is conserved. Similar to the mannose receptor, selectins contain the five conserved residues of the Ca2 binding pattern of MBL-A but only four of them bind to calcium. Glu-88, corresponding to Glu-193 in MBL-A, is not used for calcium binding. The bound sugar provides additional ligands for this calcium.[174,177]

4.4.4 *Asialoglycoprotein Receptor*

The hepatic ASGPR is involved in receptor-mediated endocytosis via coated pits. It is a hetero-oligomeric protein with two subunits of H1 and H2. ASGPR contains multiple CRDs and specifically binds to oligosaccharides in glycans.[178]

The structure of the CRD of H1 subunit (1DV8)[175] is shown in Figure 24(c). There are three bound calcium ions, two of which are similar to the Ca1 and Ca2 in MBL-A. As shown in Figure 23, the calcium-binding pattern of Ca2 in MBL-A is almost conserved in ASGPR CRD, including the E-11x-N-D sequence and the shared Glu ligand with Ca1. The differences include the change of E-x-N sequence at the N-terminus of the loop to Q-x-D, which is critical for galactose selectivity in ASGPR. Further, the distance between this calcium binding sequence to the shared Glu increases to 10 residues. The protein ligands for Ca2 are Gln-239, Asp-241, Glu-252, Asn-264, and Asp-265 (main chain and side chain). Ca1 in ASGPR contains four of the five Ca1 ligands of MBL-A. It is coordinated by Asp-215 (bidentate), Asp-242, Glu-252 (bidentate), and Asp-253. ASGPR has a Pro at the corresponding position of Glu-165 in MBL-A. The third calcium ion is unique to this protein. It is coordinated mainly by two glutamate residues, Glu-196 and Glu-227, both of which provide their two carboxyl oxygen atoms as bidentate ligands. The additional ligands come from the mainchain carbonyl of Val-190 and water.[175]

4.4.5 *NK Receptor and Other C-type Lectins*

Natural killer (NK) receptors are a group of proteins expressed at the surface of NK cells.[167,179] They share some common features including the transmembrane domains, intracellular tails, the formation of homodimers, and the C-terminal CTLD. There are many members, such as Ly49, CD69, and NKG2, in the family of NK receptors. These proteins have reserved the hydrophobic pattern of the C-type lectins such as MBL but lack the conserved calcium-binding residues. Many of them have been shown to function calcium-independently.[167,179] More and more C-type lectins have been discovered as a result of the fast progress in the field. For example, tetranectin and type-II antifreeze proteins are found to be C-type lectins that partially share the calcium-binding geometry and calcium-binding pattern of MBL.

4.4.6 *Galactose-binding Protein*

Galactose-binding proteins contain a unique calcium-binding site that differs from the general C-type lectins. GBPs are not classified as C-type lectins because calcium binding is not required for their biological function. Figure 25 shows the three-dimensional structure of the galactose-binding protein.[180] The calcium-binding geometry of the GBP is very similar to that of EF-hand motif although it is not completely formed by a continuous calcium-binding loop flanked with both helices. The first four ligands of GBPs are the same as EF-hand proteins with the calcium-binding pattern D-x-N/D-x-D/N-x-Mainchain-x. A water-mediated ligand of Glu/Gln is also located at loop position 9. The bidentate Glu (E203) of the GBP is located 63 residues away from the primary sequence (Figure 25).[180]

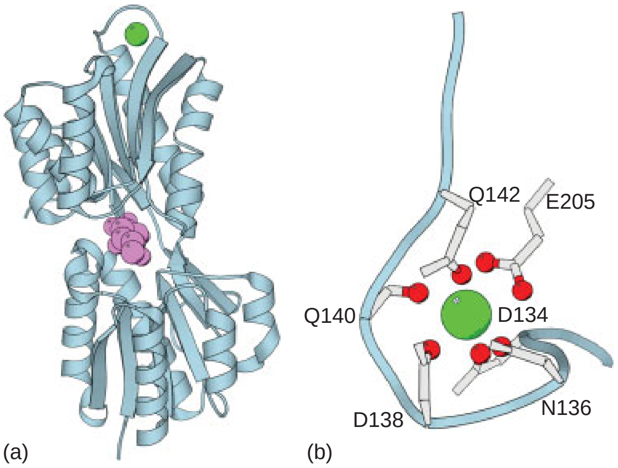

Figure 25 (a) The structure of GBP (1GLG)[180] with the calcium-binding in green and the sugar-binding site in pink. (b) The local view of the calcium-binding site of galactose-binding protein with ligand residues labeled. The calcium-binding geometry of galactose-binding protein is very similar to that of EF-hand motif

4.5 The Extracellular Calcium-sensing Receptor

The extracellular calcium-sensing receptor (CaR) is a detector for the concentration of extracellular calcium in blood and extracellular fluid.[181–184] It is responsible for calcium homeostasis. In this case, calcium functions as a first messenger to activate CaR outside cells. This activation of CaR has several major signal transducing effects. First, it activates phospholipase C (PLC) to generate the second messengers of diacylglycerol (DAG) and inositol triphosphate. Second, it inhibits adenylate cyclase to reduce intracellular cyclic AMP concentration. It can also regulate nuclear function by activating the mitogen-activated protein kinase pathway. Hofer *et al.* have shown that the CaR mediates intercellular communication that allows cells to be informed of the calcium-signaling status of their neighbors.[183]

The CaR is expressed in many cells such as parathyroid cells and C cells in the thyroid gland. It is also expressed in the kidneys, osteoblasts, in the gastrointestinal mucosa, and hematopoietic cells in bone marrow. It has been found that CaR is expressed in different amounts on the cell face of many cell types and in diverse species. CaR is a member of the G protein-coupled receptor family with seven hydrophobic transmembrane helices in the plasma membrane. It has a large N-terminal domain with about 600 amino acids located in the extracellular environment and is essential for sensing extracellular calcium concentration. CaR has a large cytosolic C-terminal domain with about 200 amino acids that is subjected to phosphorylation. A dimeric structure has been proposed based on the known crystal structure of the metabotropic glutamate receptor type 1.

5 CALCIUM PUMPS AND CHANNELS

Calcium pumps, also termed Ca^{2+}-ATPase, are calcium channels that transport calcium from the low concentration cytoplasm to the high concentration extracellular space or ER/SR lumenal side using the energy of ATP hydrolysis. Based on their locations, calcium pumps are classified into two groups, plasma membrane Ca^{2+}-ATPase (PMCA) and sarcoplasmic reticulum Ca^{2+}-ATPase (SERCA).[185–187] Four basic isoforms of PMCA (PMCA1–4) have been identified and the other PMCA isoforms are the alternative splicing products of the basic isoforms. PMCA1 and 4 are ubiquitously expressed in different tissues and PMCA2 and 3 are expressed in nerve cells. Three basic isoforms of SERCA pump and several splicing variants have also been identified.[185]

Both PMCA and SERCA have ten TMS. Several loops are exposed to the extracellular space or the inner

SR/ER lumen. The major parts of the proteins exist in the cytoplasmic solutions to form functional units.[185–187] The PMCA cytoplasmic part comprises four units: the N-terminal unit, the acidic phospholipids binding unit, the ATP-binding unit that contains the catalytic aspartate that is phosphorylated during the ‘pumping’ process, the nucleotide-binding domain containing the ATP-binding motif and a fluorescein isothyocyanate (FITC) binding site, and the C-terminal regulation unit that contains the sites for PKA, PKC, calmodulin, and calcium binding. The calmodulin binding inhibits the protein function. SERCA comprises the first three units similar to PMCA but lacks the long C-terminal sequence. Each ATP is used to pump one calcium ion out of the cytoplasm by PMCA and two calcium ions into SR/ER lumen by SERCA. Two protons are exchanged from SR/ER lumen to cytoplasm at the same time by SERCA.[185–187]

Before 2000, structural information, especially the topology of the pumps was mainly from electron microscopy, structural modeling and low resolution X-ray crystallography.[188] Upon the binding of calcium, a large rearrangement of the cytoplasmic units has been observed. A simple model has been proposed for this observation. The model postulates the existence of two conformations E1 and E2. While in the E1 state the protein has high affinity calcium-binding sites and upon phosphorylation the conformation changes to E2 that has low affinity sites.[185,189] The first high-resolution structure of a P-type ATPase, that of the Ca^{2+}-ATPase of skeletal muscle sarcoplasmic reticulum, was published in 2000.[190] A clearer picture comes from the X-ray structure of SERCA1 protein at the E1 state (1EUL) (Figure 26).[190] Ten TMSs are almost entirely helical with four of them extended into the cytoplasm to form the stalk. Calcium-binding sites are located in these transmembrane domains. The first calcium ion is coordinated by Asn-768 and Glu-771 on TMS-5, Thr-799 and Asp-800 on TMS-6, and Glu-908 on TMS-8. The second calcium ion binds with the side chain of Glu-309 at TMS-4, Asn-796 and Asp-800 at TMS-6 and the mainchain carbonyl of Val-304, Ala-305, and Ile-307 at TMS-4. The phosphorylation position that triggers the calcium transportation is located at Asp-351 in a very conserved sequence of DKTGT, about 40 Å away from the calcium-binding sites.[190] A series of conformational changes are required to mediate these two separated calcium binding and phosphorylation effects and to make them function together.

The structure of the E2 state (1IWO) has also recently been solved by stabilizing the conformation in the calcium-free form using thapsigargin (TG).[191] Consistent with the EM results, a large conformational change has been observed compared to the E1 state. Although the individual cytoplasmic units do not exhibit significant structural change, the overall arrangement of these units is altered. The N-terminal unit rotates about 110° and the phosphorylation domain rotates about 30° with respect to the membrane plane. The nucleotide binding unit rotates 50° further with respect to the phosphorylation unit. This reorientation results in a relatively compact structure in contrast to the relatively open structure in the E1 state.[191] This conformational change also causes the rearrangement of the calcium-binding ligands, such that those at TMS-6 rotate 90° and TMS-4 shifts down 5 Å.[190,191] Unlike the previous postulation that in the E2 state the calcium-binding sites face the SR lumen, the calcium sites in this model face the cytoplasm in both states. The detailed pathway

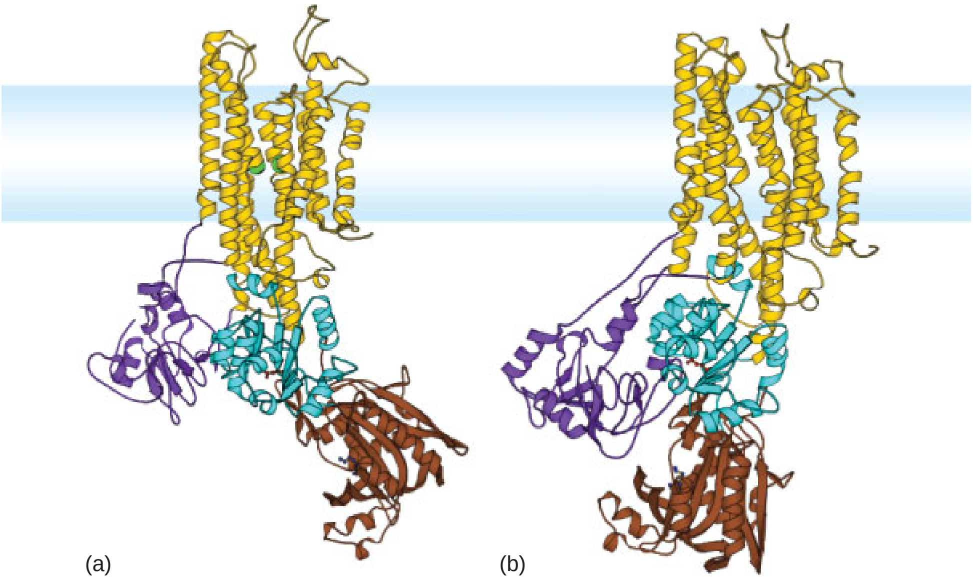

Figure 26 The structures of SERCA at the E1 state (a, 1EUL)[190] and E2 state (b, 1KJU)[191] are shown. The light blue lines represent the phospholipid bilayer membrane. The phosphorylated domain and the ATP-binding domain are labeled as cyan and brown, respectively. Calcium is represented as green ball

of calcium transportation has yet to be identified though some important residue locations (e.g. Glu-309) have been proposed.[186,190,191]

In contrast to SERCA, the Ca^{2+} release channel of the SR (RyR) transports calcium from SR to cytoplasm following the calcium gradient with no specific energy required. RyR has three isoforms. They are activated by low concentration of calcium, adenine nucleotide, and cADP and are inhibited by a high concentration of calcium. Other factors include calmodulin, which is involved in the regulation of RyRs. The protein forms a tetrameric structure and looks like a square prism with several pores.[192] IP_3R (inositol 1,4,5-trisphosphate receptor) is another calcium release channel that transports calcium from ER/SR into cytoplasm. IP_3R is regulated directly by IP3 together with the cytoplasmic calcium concentration and CaM binding.[193]

The other calcium channels that regulate cytoplasmic calcium concentrations include Na^+/Ca^{2+} exchanger and H^+/Ca^{2+} exchanger. Instead of using the energy from ATP hydrolysis, the sodium or proton gradient across the membrane is used to transport calcium. Nine TMS segments and one large cytoplasmic sequence between TMS-5 and TMS-6 are predicted in classical Na^+/Ca^{2+} exchanger. There is no detailed structural information about these families of proteins. The calcium-binding sites are proposed to be located in the cytoplasmic sequence.[187,194]

Voltage-gated calcium-channel and receptor-gated calcium channel are two channels that have the reverse effects of PMCA. They transport the calcium influx following the calcium gradients regulated directly by the electric potential between the two sides of plasma membrane or receptor binding, respectively.[193]

6 MEMBRANE CALCIUM-BINDING PROTEINS: ANNEXINS AND C_2 DOMAIN

6.1 Annexin

Annexin is a family of calcium-binding proteins that bind phospholipid. More than 160 members of this family have been identified. Based on their sources, annexins are classified into five groups. Group A is typically thought to be in vertebrate animals, but studies after 1990 show some of the Group A annexins appear in invertebrates. It is one of the most frequently studied groups of annexins. To date, 13 subfamilies in Group A with different N-terminal tails have been identified. Group B is represented in nonvertebrate metazoans. Groups C, D, and E are annexins in Mycetozoa and fungi, plants, and protists, respectively. Annexin overall is an intracellular protein, but it has also been found in the extracellular matrix (e.g. annexin A1).[195–198]

Annexins play important roles in many cellular processes by binding negatively charged phospholipids in a calcium-dependent manner. As a molecule that binds and aggregates phospholipid vesicles, it frequently accompanies vesicle or membrane fusion. Annexins were shown to be important in membrane organization, membrane transportation, exocytosis (annexin A1, A2, A3, A6, A7, A11, A13, and B7), endocytosis (annexin A1, A2, and A6), and phagocytosis (annexin A1–5, A7, and A11). Annexins A7 and A5 and annexins A2 and A4 regulate calcium and chloride channel activities, respectively.[198] In addition to calcium and phospholipids, several proteins, such as EF-hand proteins S100A6, S100A10, S100A11, and sorcin, and cytoskeletal protein actin, have been identified as interacting with annexins. S100 EF-hand family members S100A6, S100A10 and S100A11 specifically bind to annexins A11, A2, and A1, respectively. Sorcin binds to the GYP-rich N-terminal tail of annexin A7. Several annexins, such as A1, A2, A5, and A6, interact with actin. Other proteins associated with annexin include phospholipase A2, p120 Ras GTPase activating protein (GAP), protein kinase Fyn and Pyk2, and so on, suggesting annexins are involved in many more biological activities that have yet to be explored.[198]

The number of X-ray and NMR structures of annexins exceeds 40, including 23 of annexin A5. Recently, calcium-independent phospholipid binding of annexin has been revealed. Instead of binding calcium, lowering the pH also causes annexin A5 and B12 to interact with the lipid membrane.

All annexins are composed of two principal domains, the conserved C-terminal core and the N-terminal tail unique to their subfamily. The length of the N-terminal tail is shorter than 40 residues in most of the annexins with the exception of the A7 and A11 subfamilies, which have up to 160 and 195 residues, respectively. The current known protein–protein interaction with annexin occurs at the N-terminal tail. The diversity of this small N-terminal tail contributes at least partially to the diversity of annexin functions.[195,198]

Almost all annexins contain a core domain with four subdomains, each with about 70 residues, with the exception of A6 that has eight repeats (Figures 27 and 28).[195,196,198–200] Calcium and lipid binding sites are located at the core domains. As shown in Figure 27, the core domains of A5 are composed of four repeated subdomains. X-ray crystallography has shown that the repeated subdomain contains five α-helices. Two calcium-binding helix-loop-helix motifs (A/B and D/E) are arranged as a four-helix bundle. Helix C crosses over the bundle to hold the two helix-loop-helix structures in the bundle together. The four repeat segments of the annexin core form a planar cyclic structure, in which subdomain 1 interacts with subdomain 4 and all the bundles are lined up in the same orientation, resulting in a hydrophilic pore similar to the ion channels. However, the monomeric annexins are not proposed to be ion channels because of the hydrophilic surface of the helices and the relatively shorter length of the α-helices for spanning through the bilayer membrane.[198,199] The X-ray

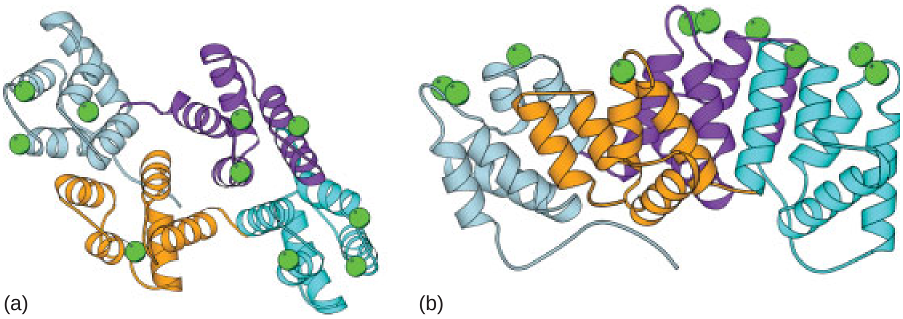

Figure 27 (a) A pore is formed by the four repeated domains of annexin A5 (1A8A)[199] in which the domain I (light blue) interacts with domain IV (orange) directly. (b) The structure of annexin A5 with four domains in which all calcium is bound to the top of the protein

structure of A6 shown in Figure 28 contains eight repeated subdomains that form two regions, each with four domains as in other annexins.[200]

Most of the crystallized structures of annexin contain different numbers of calcium or lanthanide ions. The calcium binds at the AB loop and/or the DE loop in each repeated segment. For example, in annexin A5, the AB-loop calcium-binding site comprises three mainchain carbonyl ligands at the AB-loop and two side chain carboxyl ligands from one bidentate Asp or Glu-residue at the DE-loop. Two solvent molecules are used to obtain the pentagonal bipyramidal geometry. The calcium-binding site at the DE-loop comprises two mainchain ligands at the DE-loop and two ligands from one bidentate acidic residue at E-helix. Up to three solvent molecules are used in this site.[198,199]

The conformational change induced by calcium binding in annexin is relatively small. The largest change that has been detected is the repacking of the repeated segment III D-helix in annexin A1. The X-ray structure shows that without the calcium binding the N-terminal tail of A1 forms an α-helix and replaces the position of the D-helix of segment III, while the D-helix is unwound and partially points out. With the calcium binding, the tail may have to be out of the core domain and the D-helix may have to be switched to a conformation similar to those in the other segments.[198,201]

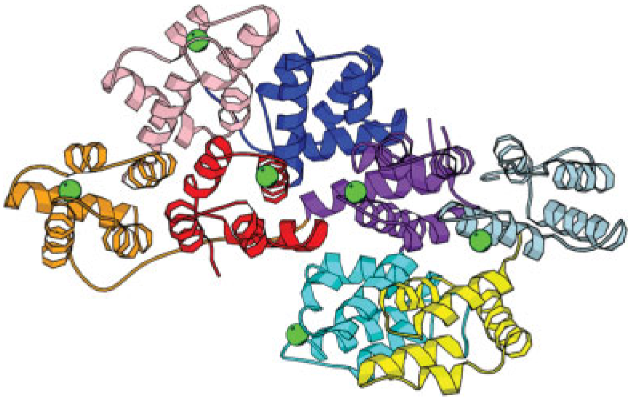

Figure 28 The structure of Annexin A6 (1AVC)[200] with eight repeated domains in different colors

As a protein located at the cytosolic side of the membrane, the calcium-binding affinity of annexin is weak. In vitro measured apparent dissociation constants of calcium are from micromolar to millimolar. Annexins appears to be apo-form at the submicromolar intracellular calcium concentration. Given the fact that the function of annexin is calcium-required in vitro, it is plausible to propose that annexin acts differently in vivo. Either the in vivo function of annexin is calcium independent (less likely), or, more likely, in vivo, by interacting with membrane or target protein ligand, the calcium-binding affinity of annexin increases owing to the environment change. In addition, the calcium concentration near the membrane region may be higher than the average level in the cytosol.[198]

6.2 C2 Domains

The C2 domain was first identified in calcium-dependent PKC isoforms, and refers to the conserved domain 2 in PKC with about 80–160 residues. To date, more than 100 proteins have been identified as containing C2 domains. It is one of the most widely used modules of intracellular calcium-binding proteins. Some proteins contain two or more repeats of the C2 domain in a single peptide chain, such as synaptotagmin, double C2 protein (DOC2), and Munc13.[202,203]

The structural information of C2 domain is primarily from the studies on PLC, PKC, cPLA2 (cytoplasmic phospholipase A2), factors, and synaptotagmin (Figure 29). Synaptotagmin I contains two C2 domains, C2A and C2B, of which C2A is the first C2 domain with a solved structure. Currently, more than twenty structures of C2-domain-containing proteins have been obtained by X-ray and NMR. The C2 domain contains eight β-strands that form a compact β-sandwich structure composed of two layers with four strands in each layer.[202,203] Based on the topology of these β-strands, they are classified as type I and type II C2 domains. In type I C2 domains, such as synaptotagmin and DOC2, β-strands 1, 2, 5, and 8 are in the same layer and β-strands 3, 4, 6,

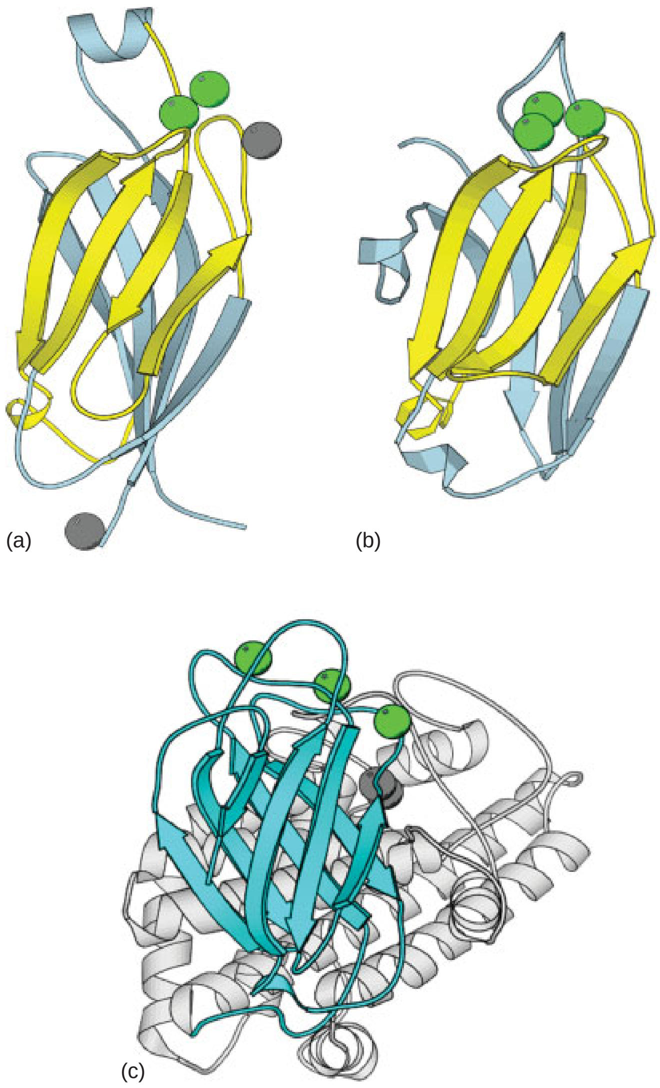

Figure 29 (a) The C2 domain in cPLA2 (1RLW)[205] has type II topology, in which the β-strands 7, 8, 1, and 4 (light blue, left to right) form one layer while the β-strands 6, 5, 2, and 3 (yellow, left to right) form another layer in the β-sandwich structure. (b) The C2 domain in PKCβ (1A25)[206] has type I topology, in which the β-strands 8, 1, 2, and 5 (light blue, left to right) form one layer and the β-strands 7, 6, 3 and 4 form another layer. (c) The C2 domain (blue) in the α-toxin (1QMD)[207] is shown. The calcium ions in all three figures are labeled green and the other metal ions (Zn in α-toxin and Cd in PKCβ) are labeled gray

and 7 are in the other layer. In type II C2 domain, such as cPLA2 and PLC, the β-strands 1, 4, 7, and 8, and 2, 3, 5, and 6 are in two layers, respectively.[202,203] Loops connecting the β-strands are located at the two ends (top and bottom) of the protein. Two or three calcium ions bind to the loop regions located at the top of the protein. The ligand residues of the calcium-binding sites in C2 domain are widely separated in the primary sequence.[202,203] In the X-ray structure of synaptotagmin I C2A domain, three calcium ions (termed Ca1–3) are bound to five Asp, one Ser, and three mainchain carbonyls located at loop 1 and loop 3. Of these ligands, Asp-172 and Asp-230 are shared by Ca1 and Ca2, Asp-238 is shared by Ca2 and Ca3, and Asp-232 is shared by all three calcium ions. The mainchain carbonyl from Leu-171 binds only to Ca2, an Asp-178 side chain and Phe-61 mainchain bind to Ca1, and Ser-235 side chain and Lys-236 bind to Ca3. The substrate phospholipids have been proposed to provide additional ligand atoms to the pentagonal bipyramidal geometry of the calcium-binding sites. In the absence of phospholipids, the calcium dissociation constants of synaptotagmin I C2A domain are low (0.06 mM to >1 mM), a value too weak to bind calcium at the intracellular environment.[203–205]

The calcium binding in PLCδ1 C2 domain revealed by x-ray crystallography has two similar and one distinct site compared to synaptotagmin I. The locations for Ca1 and Ca2 are almost the same, while the ligands for these two calcium ions, Asp-653, Asp-706, Tyr-707, Asp-708, and Asp-714 correspond to Asp-178, Asp-230, Phe-231, Asp-232, and Asp-238 in synaptotagmin I, respectively. The ligands corresponding to Leu-171 and Asp-172 are missing. The ligands corresponding to those for Ca3 are retained and have similar orientation in PLCδ1 but no calcium occupies the pocket. The third calcium in PLCδ1 shares one ligand residue with Ca1 (Asp-653, bidentate in this site) and uses the other three ligands from loop 1 and loop 2 (Asn-677, Ser-650, and Ile-651). Like synaptotagmin I, the additional ligands for pentagonal bipyramidal geometry may come from the target molecule phospholipid.

C2 domain represents a large family of proteins with different functions.[204,208] Most of them bind calcium and phospholipids. Most members of the C2 domain protein family are involved in signal transduction, such as PKC and PLC (phosphoinositide-specific phospholipase C), or membrane traffic, such as synaptotagmin and rabphilin-3.[202,203] To date, several important subfamilies have been extensively studied and their functions are relatively clear. First, the classical PKCs (isoforms α, β, and γ) contains type I C2 domain, and some of the non-classical PKCs (δ, ε, θ, and η) and yeast PKCs contain type II C2 domains. In classical PKCs the C2 follows the C1 domain while for the nonclassical PKC, the C2 domain is before the conserved C1 domain. This family of protein kinases plays important roles in the cell signal transduction pathway by mediating protein phosphorylation. The biological functions of these C2-containing PKCs with a proper calcium-binding pocket are calcium-dependent. Calcium-independent C2-containing PKC does not contain conserved calcium-binding ligand residues.[203,206,209–211] Second, cytosolic phospholipase A2 (cPLA2) cleaves arachidonic acid from glycerophospholipids using the C-terminal catalytic domain. The C2 domain at the N-terminus interacts with neutral phospholipid vesicles containing phosphotidylcholine or phosphotidylethanolamine through a calcium-dependent mode to localize the cPLA2 to its target membrane substrate. The C2 domain in cPLA2 is of type II topology. Four of the five aspartate ligands in synaptotagmin I are retained in cPLA2 and the fifth is mutated to asparigine.[203,205,212] Third, phosphoinositide-specific phospholipase C (PLC) liberates inositol trisphosphate (IP3) and DAG when activated. Both IP3 and DAG are directly involved in the regulation of intracellular functions (e.g. IP3 regulates several calcium channels and DAG regulates several PKC isoforms). The C2 domain in PLC is of type II topology. It facilitates the catalytic domain's interaction with the substrate. PLC also contains an EF-hand calcium-binding domain and a pleckstrin homology(PH) phospholipid binding domain.[203,208,213] Fourth, α-toxin is a eukaryotic phospholipase C, which is capable of binding to mammalian cell membrane and cleaving membrane-bound phosphatidylcholine (or sphingomyelin) to produce phosphocholine and DAG (or ceramide). X-ray crystallography has revealed three calcium ions in the C2 domain of alpha toxin. Unlike the synaptotagmin or PLC, the three calcium ions are clustered but only share one ligand (Asp-298) that interacts with Ca2 with the side chain carboxyl group and with Ca3 with a main chain carbonyl group. The ligands for Ca2 are located continuously (Asp-293, Asn-294 main chain, Gly-296 main chain, and Asp-298) while the ligands for Ca1 (Asp-269 main chain, Gly-271 main chain, Asp-336, Ala-337 main chain, and Glu-32) and Ca3 (Thr-272 main chain, Asp-273, Asn-297, Asp-298 main chain) are discontinuous.[207,214] Fifth, phosphatidylcholine-specific phospholipase D (PLD) catalyzes the cleavage of phospholipid to produce phosphatidic acid and a free head group such as choline. The putative calcium-binding ligands in the C2 domain of PLD are diverse in different isoforms. The apparent calcium-binding affinity without substrate of PLDα, β, γ and δ varies more than two orders of magnitude.[215] Sixth, phosphatidylinositol 3-kinase (PI3K) and PTEN catalyze reverse reactions on phosphorylation and dephosphorylation of phosphoinositides. The isoforms PI3K α, β, and VPS34P have a type II C2 domain while isoform PI3K 68D has a type I C2 domain. The calcium-binding ligands in PI3K C2 domain are not complete. The functions of PI3K and PTEN as a tumor suppressor are not dependent on calcium.[203,216,217] Seventh, synaptotagmin is a family of transmembrane proteins with two type I C2 domains in the cytosol. It is involved in vesicle fusion and exocytosis events in the cell.[218] Synaptotagmin I–V, X, and XI are expressed in the neuron system and the others (VI–IX) are expressed in other tissues. The C2A domain binds with calcium and triggers calcium-regulated exocytosis and secretion. The C2B domain of synaptotagmin I and II binds inositol high polyphosphates and inhibits the exocytosis and secretion by this binding. Synaptotagmin I is also known to be crucial for neurite outgrowth. Synaptotagmins are involved in constitutive vesicular trafficking in addition to regulated exocytosis. The C2B domain of synaptotagmin III, V, VI, and X lacks the inositol high polyphosphate,for example, IP4, binding ability resulting in the deficiency of IP4 inhibition. C2 domains in synaptotagmins also mediate protein–protein interactions through a calcium-dependent or – independent manner. Some known synaptotagmin target proteins include clathrin-AP2, syntaxin, and PKC and so on. The oligomerization of synaptotagmin is also calcium dependent.[203,205,219] Eighth, double C2 (DOC2) protein plays a role in regulating calcium-dependent exocytosis, particularly in vesicle cycling in response to stimuli or phorbol esters (PE). It comprises two type I topology C2 domains and a Munc13 interacting domain (MID). DOC2 is localized to a pre-synaptic vesicular terminal. It interacts with other exocytotic proteins including the presynaptic PE receptor Munc13-1, syntaxin-interacted protein Munc18, and dynein component Tctex-1. The DOC2-Munc13 complex is required for vesicle maturation in certain glutamatergic synapses.[220] Munc13 comprises two type II C2 domains, one type I C2 domain, and one C1 domain. It is expressed in neuronal cells and functions cooperatively together with DOC2 in regulating exocytosis and neurotransmitter release process.[203,220] Ninth, rabphilin-3A is identified as a protein that interacts with Rab3A, a small ras-related membrane-bound GTPase playing a role in neurotransmitter release and exocytosis, in the GTP-bound form. Other partner proteins such as Rab27 have also been observed for rabphilin. The Rab3A-binding domain is at the N-terminal and two type I topology C2 domains are at the C-terminal of rabphilin-3A. The C2 domains of rabphilin-3A interact with phosphatidylserine in the presence of calcium. The C-terminal C2 domain is critical for secretion functions of rabphilin-3A. Mutations in this domain will impair calcium-dependent vesicle binding.[221,222] Tenth, several GAP have been identified as having a C2 domain, including p120-rasGAP, GAP1m, R-Ras-GAP, BCR, ABR, and BUD2. The C2 domain of p120-rasGAP binds phosphotidylserine and phosphotidylinositol in the presence of calcium. Functionally, p120-rasGAP down-regulates the mitogen-activated protein kinase pathway after epidermal growth factor stimulation and also regulates cell proliferation.[223] Eleventh, human coagulation factors are essential for blood clotting through a thrombin-mediated mechanism. Factor V and VIII share a similar sequence and topology. They are each represented by the domain structure A1-A2-B-A3-C1-C2 and share 40% sequence homology in the A and C domains. After cleavage by thrombin or factor X, the domains A3, C1, and C2 form the light chain. The C2 domain in factors V and VIII is critical for mediating the membrane binding of proteins.[224–226] With the increasing number of C2-containing proteins, the C2 domain has become one of the most popular domains in nature. In addition, the currently known C2 domain members also include perforin, phosphatidylserine decarboxylase, SCH9 kinase, RSP5, Ege A, and so on.

7 CALCIUM-BINDING PROTEINS IN ENDOPLASMIC RETICULUM AND SARCOPLASMIC RETICULUM

ER and SR are the major calcium stores in the cell (Figure 1). They play a vital role in regulating cell functions.

With the proper stimuli, calcium in the ER/SR is released to the cytoplasm activating calcium-signal proteins. To restore the rest state of the cell, calcium is pumped out of the cytoplasm by PMCA, SERCA, and Na^+/Ca^{2+} exchanger. Most of the calcium ion in ER is buffered by many lumenal calcium-binding proteins such as CSQ, calreticulin and calnexin. There are other calcium-binding chaperone molecules in the ER such as grp94, PDI family, and BiP. These proteins are more likely to chaperone the non-glycoproteins. One member of the protein disulfide isomerase (PDI) family, ERp57, cooperates with calreticulin and calnexin.[227–229]

7.1 Calsequestrin (CSQ)

CSQ is the major buffer protein in the lumen of the SR of muscle cells, especially those bound at the calcium release channel, the ryanodine receptor, and through junction and triadin. CSQ was shown to determine the functional size and stability of cardiac intracellular calcium stores.[230] As shown in Figure 30, more than 1/3 of the total residues of CSQ are glutamate or aspartate (a total of 110 carboxylate groups) residues.[231] One CSQ molecule is capable of absorbing 40–50 calcium ions with an average calcium-binding affinity of about 0.6–1 mM. All calcium or metal binding ability is mainly determined by the charge–charge interaction without a defined calcium-binding pocket. The calcium binding of CSQ has both high on-rate ($\sim 10^9\ M^{-1}s^{-1}$) and off-rate ($\sim 10^6\ s^{-1}$), which allows this protein to release and bind large quantities of calcium rapidly. Owing to the highly negatively charged surface, calcium or monovalent cation ions are required for the folding of the CSQ. The calcium-loaded CSQ is dimerized and then polymerized to form a long chain, which further allows even more calcium to be bound intermolecularly. The lined CSQ cooperates with the calcium release channel of SR/ER in regulating the cytoplasmic calcium concentration.[227]

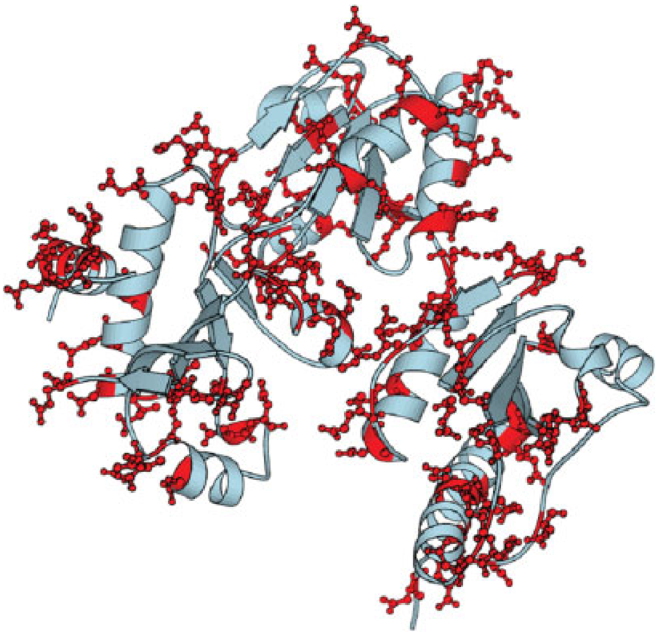

Figure 30 The structure of CSQ (1A8Y)[231] with acidic residues highlighted in red

After more than 10 years of attempting to crystallize CSQ, it was finally accomplished with 0.3 M K^+ in the absence of Ca^{2+} (1A8Y).[231] The solved x-ray structure of CSQ contains three structurally similar domains of a thioredoxin fold although there is no significant repeat sequence in the primary structure (Figure 30). Each thioredoxin-like domain comprises a core that is formed by five β-strands and four surrounding α-helices. The interior of the core is mainly composed of hydrophobic residues. The bulky content of acidic residues is located at the α-helices and the connecting loops. Ca^{2+} ions bind to the protein surface and the spaces between domains (Figure 30).[231] CSQ monomer can associate in ‘front to front’ and ‘back to back’ chains to create additional calcium-binding sites in clefts between the individual molecules. These two distinct dimerization contacts in CSQ crystals suggested a mechanism for Ca^{2+} regulation resulting from the occurrence of coupled Ca^{2+} binding and protein polymerization.[232]

7.2 Calreticulin and Calnexin

Calreticulin functions as a chaperone protein for the folding of newly synthesized proteins and glycoproteins.[229,233] It is also a major calcium-buffer protein residing in the lumen of the ER. Calnexin exhibits a high degree of similarity to calreticulin in primary sequence and structure. It also has functions similar to calreticulin such as calcium binding and recognition of misfolded proteins. The major difference between these two proteins is that calreticulin is able to move in the lumen of the ER while calnexin is an integral membrane protein of the ER, interacting transiently with its protein folding intermediates at the stationary phase. Both proteins bind to the monoglucosylated carbohydrate of the glycoproteins. Misfolded non-glycoproteins may also bind to calreticulin and calnexin.[229,234,235]

Both calreticulin and calnexin comprise three domains: a globular N-domain, an extended proline-rich P-domain, and a transmembrane helix in calnexin or an acidic calcium-binding C-domain in calreticulin.[229,236] The structures of the soluble part of calnexin and the P-domain of calreticulin have been reported. The crystal structure of calnexin (1JHN) shows an unusual structure in that the P-domain extends far away from the N-domain like an arm (Figure 31). The glycoproteins interact with the N-domain surface facing the arm. A calcium ion binds to the N-domain using the ligands from the carbonyl of Ser-75 and the carboxyl of Asp-118 and Asp-437 (bidentate).[236] The P-domain (residue 189–288) NMR structure of calreticulin (1HHN, 1K91 and 1K9C) is very similar to that of calnexin.[237,238] This structure shows an extended hairpin topology, with three short antiparallel beta-sheets, three small hydrophobic clusters, and one helical turn

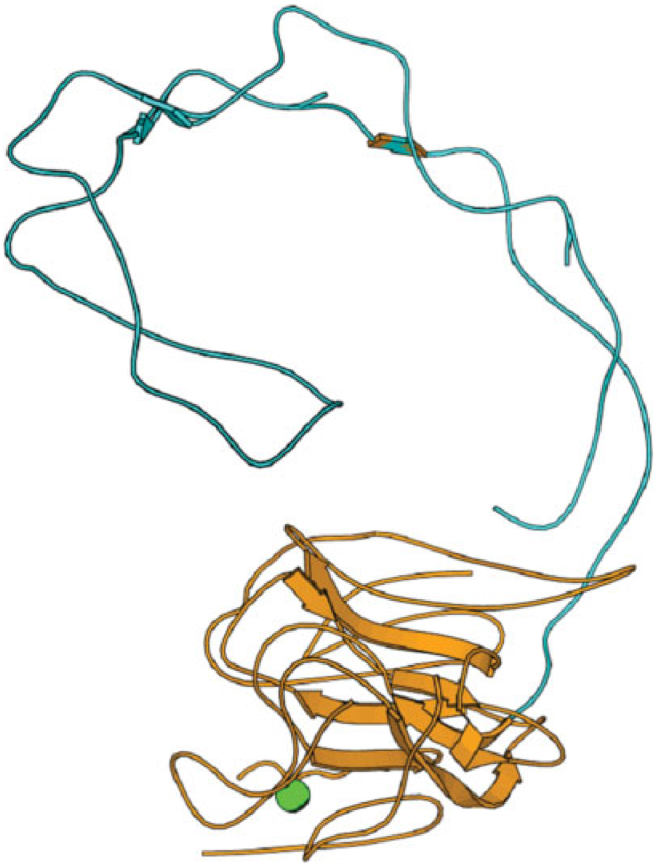

Figure 31 The structure of calnexin (1JHN)[236] with a calcium-binding (green ball) compact domain and a long extended arm. The space between is proposed for the binding of chaperoned proteins at the top of the hairpin.[236–238]

Both calreticulin and calnexin cooperate with an associated co-chaperone, the thiol-disulfide oxidoreductase ERp57, which catalyzes the formation of disulfide bonds in bound glycoprotein substrates.[229,235] Frickel *et al*. demonstrated that the residues 225–251 at the top of the CRT P-domain are involved in direct contacts with ERp57.[239] The CRT P-domain fragment CRT (221–256) constitutes an autonomous folding unit, and has a structure highly similar to that of the corresponding region in CRT (189–288).[234] So far, no structural information is available about the calcium-binding C-domain and N-domain of calreticulin.

8 α-LACTALBUMIN AND LYSOZYME

α-Lactalbumin (α-LA)[240] is a component of mammalian milk. It complexes with β-galactosyl transferase to form lactose synthetase that catalyzes the synthesis of lactose. Unlike most of the other known calcium-binding proteins that have clusters of calcium ions or cooperative calcium binding, only one calcium-binding site with very high calcium-binding affinity ($K_d \sim 10^{-9}$ M) is in this small protein; thus, it has been used as a model protein to study calcium binding. Although recent X-ray studies have revealed an additional calcium-binding site in α-LA, its binding affinity is not comparable to that of the stronger one.[240,241] The following description only refers to the strong calcium-binding site in α-LA.

As shown in Figure 32,[32] the 3D structure of α-LA contains α and β domains. α-Domain is composed of four helices and β-domain is composed mainly of loops and three β-strands. There are four disulfide bridges in α-LA (6–120, 28–111, 61–77, and 73–91), which are shown to be important for the structure and folding of the protein. The disulfide bridge 73–91 links the two subdomains. The ligand residues for the calcium ion are from a continuous loop with residues 79–88 in α-LA. The side chain carboxyl groups from Asp-82, Asp-87, Asp-88, the mainchain carbonyl groups from Lys-79 and Asp-84, and two water molecules form a calcium-binding site with a pentagonal bipyramidal geometry (Figure 2). Removing either residue Asp-87 or Asp-88 eliminates the calcium-binding ability and alters the structure of α-LA.[56,242] Mutation of Lys-79 to Ala destabilizes the protein without significantly reducing the calcium-binding affinity. Mutation Asp-84 to Ala lowers the calcium-binding affinity and destabilizes the protein. The single mutation of Asp-82 to Ala has no obvious effect on the protein structure and calcium binding. Peptide studies show that without the formation of the disulfide bond 73–91, the calcium-binding affinity of the loop decreases several fold. Without the formation of flanking helices after the loop (residue 86–99), the calcium-binding ability is very weak.[243]

The calcium ion in α-LA plays a structural role in stabilizing the protein. The thermal stability of the calcium-bound form of α-LA increases more than 40 °C compared to that of the apo-form. At low pH (e.g. pH 2), α-LA releases the calcium ion and becomes partially unfolded (molten globule state). This partially unfolded protein loses its tertiary structure but retains its secondary structure. Other metals, such as manganese or magnesium, are able to compete with calcium at the same site with a similar stabilizing effect. However, the binding of zinc, which is proposed to bind at different locations, decreases α-LA stability.[240]

Lysozyme is evolutionarily related to α-LA with a divergent function of binding oligosaccharides and cleaving the glycosidic bond. Chicken-type (c-type) lysozymes have a 35–40% primary sequence homology with α-LA. The secondary and tertiary structure are also similar, including overall topology, the two subdomains, and the disulfide bonds (Figure 32).[57,244] Unlike α-LA that has a strong calcium-binding site, most of the members in the lysozyme family do not have any calcium-binding ability despite the high similarity in sequence and structure.[244–247] To date, four lysozymes have been identified as having the calcium-binding site of α-LA. They are canine, equine, pigeon, and echidna. The Asp residues at the ligand positions of α-LA are retained in these lysozymes, while the other members have lost these

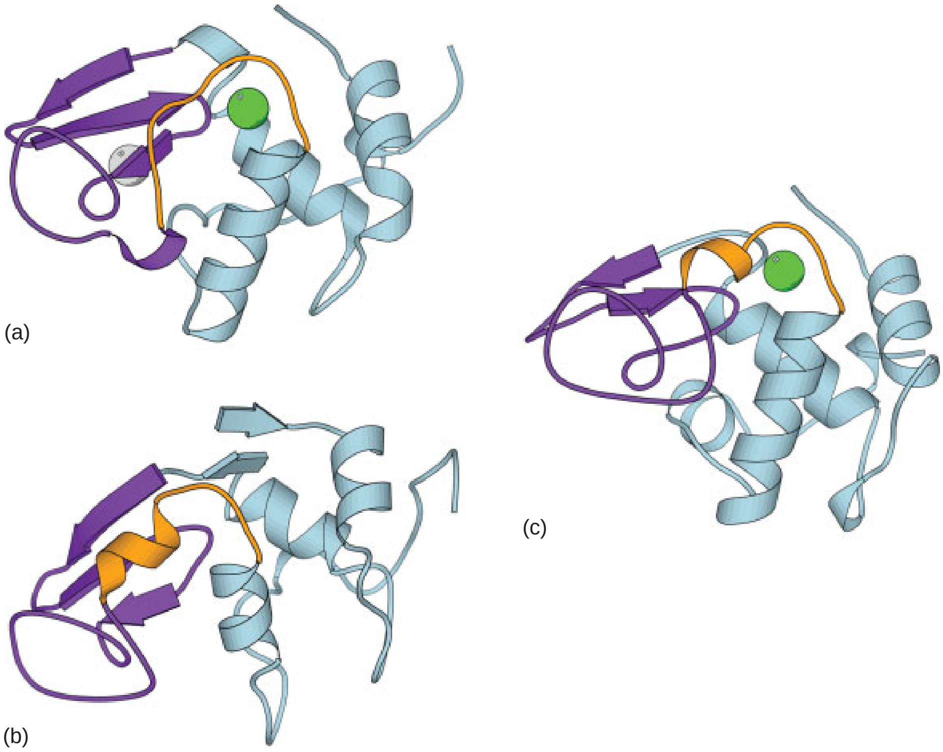

Figure 32 (a) The structure of α-lactalbumin with calcium (green ball) and an additional Zn (gray ball) binding (1HML).[32] (b) The structure of classical lysozyme (1LZ1) without the calcium-binding ability.[57] (c) The structure of calcium-binding echidna lysozyme (1JUG)[244] with calcium binding. All these proteins have similar structures with a flanking loop (orange) located between the α-domain (light blue) and the β-domain (purple)

ligand residues (Figure 32). In addition, the charge and surface electric potential of α-LA and most of the lysozymes are different. α-LA is an overall acidic molecule and lysozyme is basic. As shown in Figure 4, bovine α-LA has a strong negatively charged surface while noncalcium binding protein human lysozyme has a strong positively charged surface. Typical lysozymes also do not have a molten globule state during the unfolding process.[245–249]

To understand the difference between α-LA and typical lysozymes, tremendous work has been done, including peptide analogues, mutagenesis studies, and computational simulations. The calcium-binding loop and the following helix of α-LA have been transported into lysozyme individually or simultaneously. By introducing the Asp residues at the key positions without the following helix, lysozyme gains the calcium-binding ability with a K_d at 10^{-5} M range but not the ability to have a molten globule state. By introducing the helix without the calcium-binding loop, lysozyme can also form the molten globule state without the calcium-binding ability. By introducing both, lysozyme gains both the structural properties of α-LA.[248]

As one of the extensively investigated protein families, hundreds of lysozyme structures are deposited in the Protein Data Bank, including wild type from different sources and numerous mutants. Also available are the structures of antibody binding or substrate binding complexes. The available calcium-binding lysozyme includes X-ray structures of canine lysozymes 1EL1 (holo-form) and 1QQY (apo-form), NMR solution structure of canine lysozyme 1I56, X-ray structures of equine lysozyme (2EQL, apo-form) and echidna lysozyme (1JUG, holo-form).

X-ray structures of apo (1F6R, bovine) and calcium-loaded (1F6S, 1HFY, bovine; 1A4V, 1B9O, human; 1ALC, baboon; 1HFZ, 1FKQ, 1FKV, 1HMK, goat; 1HFX, guinea pig) α-LA are available. The structures of zinc and manganese loaded α-LA are also solved (1HML for zinc and 1PZY for manganese). There are also solution NMR structures (1CB3, human) and complexes with substrate or galactosyltransferase (1NF5, 1NKH, 1NMM, 1NQI, 1NWG, and 1PZY) in the Protein Data Bank.

9 RELATED ARTICLES

Alkaline Earth Metals: Inorganic Chemistry; Biomineralization; Cation-activated Enzymes; Coordination Numbers & Geometries; Metal-related Diseases of Genetic Origin.

10 REFERENCES

1. M. J. Berridge, M. D. Bootman, and P. Lipp, *Nature*, 1998, **395**, 645.
2. E. Carafoli, *Proc. Natl. Acad. Sci. U.S.A.*, 2002, **99**, 1115.
3. D. E. Clapham, *Cell*, 1995, **80**, 259.
4. G. Ermak, T. E. Morgan, and K. J. Davies, *J. Biol. Chem.*, 2001, **276**, 38787.
5. C. B. Klee and T. C. Vanaman, *Adv. Protein Chem.*, 1982, **35**, 213.
6. X. Lin, R. A. Sikkink, F. Rusnak, and D. L. Barber, *J. Biol. Chem.*, 1999, **274**, 36125.
7. X. Zhang and S. K. Joseph, *Biochem. J.*, 2001, **360**, 395.
8. D. R. Dowd, *Adv. Second Messenger Phosphoprotein Res.*, 1995, **30**, 255.
9. J. P. Glusker, *Adv. Protein Chem.*, 1991, **42**, 1.
10. A. K. Downing, V. Knott, J. M. Werner, C. M. Cardy, I. D. Campbell, and P. A. Handford, *Cell*, 1996, **85**, 597.
11. P. Maurer, E. Hohenester, and J. Engel, *Curr. Opin. Cell Biol.*, 1996, **8**, 609.
12. P. Gangola and B. P. Rosen, *J. Biol. Chem.*, 1987, **262**, 12570.
13. H. Tsujibo and B. P. Rosen, *J. Bacteriol.*, 1983, **154**, 854.
14. N. J. Watkins, M. R. Knight, A. J. Trewavas, and A. K. Campbell, *Biochem. J.*, 1995, **306**(Pt 3), 865.
15. R. N. Reusch, R. Huang, and L. L. Bramble, *Biophys. J.*, 1995, **69**, 754.
16. M. C. Trombe, *J. Gen. Microbiol.*, 1993, **139**(Pt 3), 433.
17. M. C. Trombe, V. Rieux, and F. Baille, *J. Bacteriol.*, 1994, **176**, 1992.
18. S. H. Cheng, M. R. Willmann, H. C. Chen, and J. Sheen, *Plant Physiol.*, 2002, **129**, 469.
19. C. R. Hauck, *Med. Microbiol. Immunol. (Berl.)*, 2002, **191**, 55.
20. V. Norris, J. A. Ayala, K. Begg, J. P. Bouche, P. Bouloc, E. Boye, J. Canvin, S. Casaregola, A. J. Cozzone, E. Crooke, *J. Theor. Biol.*, 1994, **168**, 227.
21. D. J. Rigden, M. J. Jedrzejas, and M. Y. Galperin, *FEMS Microbiol. Lett.*, 2003, **221**, 103.
22. N. Bylsma, T. Drakenberg, I. Andersson, P. F. Leadlay, and S. Forsen, *FEBS Lett.*, 1992, **299**, 44.
23. M. L. Herbaud, A. Guiseppi, F. Denizot, J. Haiech, and M. C. Kilhoffer, *Biochim. Biophys. Acta*, 1998, **1448**, 212.
24. D. Laoudj, C. L. Andersen, A. Bras, M. Goldberg, A. Jacq, and I. B. Holland, *Mol. Microbiol.*, 1994, **13**, 445.
25. P. T. Reddy, C. R. Prasad, P. H. Reddy, D. Reeder, K. McKenney, H. Jaffe, M. N. Dimitrova, A. Ginsburg, A. Peterkofsky, and P. S. Murthy, *J. Bacteriol.*, 2003, **185**, 5263.
26. T. Rotharmel and G. Wagner, *J. Bacteriol.*, 1995, **177**, 864.
27. R. M. Schwerdtfeger, R. Chiaraluce, V. Consalvi, R. Scandurra, and G. Antranikian, *Eur. J. Biochem.*, 1999, **264**, 479.
28. G. Kozlov, I. Ekiel, N. Beglova, A. Yee, A. Dharamsi, A. Engel, N. Siddiqui, A. Nong, and K. Gehring, *J. Biomol. NMR*, 2000, **17**, 187.
29. C. A. McPhalen, N. C. Strynadka, and M. N. James, *Adv. Protein Chem.*, 1991, **42**, 77.
30. E. Pidcock and G. R. Moore, *J. Biol. Inorg. Chem.*, 2001, **6**, 479.
31. H. Einspahr, W. J. Cook, and C. E. Bugg, *Biochemistry*, 1981, **20**, 5788.
32. J. Ren, D. I. Stuart, and K. R. Acharya, *J. Biol. Chem.*, 1993, **268**, 19292.
33. Y. S. Babu, C. E. Bugg, and W. J. Cook, *J. Mol. Biol.*, 1988, **204**, 191.
34. P. Gros, M. Fujinaga, B. W. Dijkstra, K. H. Kalk, and W. G. Hol, *Acta Crystallogr. B*, 1989, **45**(Pt 5), 488.
35. P. J. Kraulis, *J. Appl. Cryst.*, 1991, **24**, 946.
36. N. C. Strynadka and M. N. G. James, in ‘Encyclopedia of Inorganic Chemistry’, 1st ed., ed. R. B. King, John Wiley & Sons, New York, 1993, Vol. 1, p. 477.
37. H. Kawasaki, S. Nakayama, and R. H. Kretsinger, *Biometals*, 1998, **11**, 277.
38. K. Julenius, J. Robblee, E. Thulin, B. E. Finn, R. Fairman, and S. Linse, *Proteins*, 2002, **47**, 323.
39. T. Kesvatera, B. Jonsson, A. Telling, V. Tougu, H. Vija, E. Thulin, and S. Linse, *Biochemistry*, 2001, **40**, 15334.
40. J. Fast, M. Hakansson, A. Muranyi, G. P. Gippert, E. Thulin, J. Evenas, L. A. Svensson, and S. Linse, *Biochemistry*, 2001, **40**, 9887.
41. W. Yang, H. W. Lee, H. Hellinga, and J. J. Yang, *Proteins*, 2002, **47**, 344.
42. J. J. Falke, S. K. Drake, A. L. Hazard, and O. B. Peersen, *Q. Rev. Biophys.*, 1994, **27**, 219.
43. T. Dudev, Y. L. Lin, M. Dudev, and C. Lim, *J. Am. Chem. Soc.*, 2003, **125**, 3168.
44. M. Nayal and E. Di Cera, *Proc. Natl. Acad. Sci. U.S.A.*, 1994, **91**, 817.
45. B. J. Marsden, G. S. Shaw, and B. D. Sykes, *Biochem. Cell Biol.*, 1990, **68**, 587.
46. R. E. Reid and R. S. Hodges, *J. Theor. Biol.*, 1980, **84**, 401.
47. S. Linse and S. Forsen, *Adv. Second Messenger Phosphoprotein Res.*, 1995, **30**, 89.
48. R. B. Yelle, N. S. Park, and T. Ichiye, *Proteins*, 1995, **22**, 154.
49. S. Linse, C. Johansson, P. Brodin, T. Grundstrom, T. Drakenberg, and S. Forsen, *Biochemistry*, 1991, **30**, 154.
50. M. Akke and S. Forsen, *Proteins*, 1990, **8**, 23.
51. J. A. Cox, A. Malnoe, and E. A. Stein, *J. Biol. Chem.*, 1981, **256**, 3218.
52. T. H. Crouch and C. B. Klee, *Biochemistry*, 1980, **19**, 3692.
53. M. Fushiki, B. Svensson, B. Jonsson, and C. E. Woodward, *Biopolymers*, 1991, **31**, 1149.

54. Y. C. Sekharudu and M. Sundaralingam, *Protein Eng.*, 1988, **2**, 139.
55. M. M. Yamashita, L. Wesson, G. Eisenman, and D. Eisenberg, *Proc. Natl. Acad. Sci. U.S.A.*, 1990, **87**, 5648.
56. K. R. Acharya, D. I. Stuart, N. P. Walker, M. Lewis, and D. C. Phillips, *J. Mol. Biol.*, 1989, **208**, 99.
57. P. J. Artymiuk and C. C. Blake, *J. Mol. Biol.*, 1981, **152**, 737.
58. A. Nicholls and B. Honig, *J. Comput. Chem.*, 1991, **12**, 435.
59. R. H. Kretsinger and C. E. Nockolds, *J. Biol. Chem.*, 1973, **248**, 3313.
60. S. Henikoff, E. A. Greene, S. Pietrokovski, P. Bork, T. K. Attwood, and L. Hood, *Science*, 1997, **278**, 609.
61. I. S. Day, V. S. Reddy, G. Shad Ali, and A. S. Reddy, *Genome Biol.*, 2002, **3**, RESEARCH 0056.
62. S. Nakayama, H. Kawasaki, and R. H. Kretsinger, in 'Calcium Homeostasis', ed. J. Krebs, Springer, New York, 2000, Vol. 3, p. 30.
63. L. J. van Eldik and D. M. Watterson, 'Calmodulin and Signal Transduction', Academic Press, New York, 1998.
64. N. Mesaeli, K. Nakamura, E. Zvaritch, P. Dickie, E. Dziak, K. H. Krause, M. Opas, D. H. MacLennan, and M. Michalak, *J. Cell Biol.*, 1999, **144**, 857.
65. M. Michalak, P. Mariani, and M. Opas, *Biochem. Cell Biol.*, 1998, **76**, 779.
66. C. Vannahme, S. Gosling, M. Paulsson, P. Maurer, and U. Hartmann, *Biochem. J.*, 2003, **373**, 805.
67. R. Donato, *Microsc. Res. Tech.*, 2003, **60**, 540.
68. Y. C. Liu and D. R. Storm, *J. Biol. Chem.*, 1989, **264**, 12800.
69. J. Jain, P. G. McCaffrey, Z. Miner, T. K. Kerppola, J. N. Lambert, G. L. Verdine, T. Curran, and A. Rao, *Nature*, 1993, **365**, 352.
70. D. R. Dowd, P. N. MacDonald, B. S. Komm, M. R. Haussler, and R. L. Miesfeld, *Mol. Endocrinol.*, 1992, **6**, 1843.
71. E. J. van Asselt and B. W. Dijkstra, *FEBS Lett.*, 1999, **458**, 429.
72. M. T. Henzl, R. C. Hapak, and J. J. Likos, *Biochemistry*, 1998, **37**, 9101.
73. B. R. Sorensen, L. A. Faga, R. Hultman, and M. A. Shea, *Biochemistry*, 2002, **41**, 15.
74. M. Ikura, G. Barbato, C. B. Klee, and A. Bax, *Cell Calcium*, 1992, **13**, 391.
75. S. M. Gagne, S. Tsuda, M. X. Li, L. B. Smillie, and B. D. Sykes, *Nat. Struct. Biol.*, 1995, **2**, 784.
76. K. L. Yap, J. B. Ames, M. B. Swindells, and M. Ikura, *Proteins*, 1999, **37**, 499.
77. M. R. Nelson and W. J. Chazin, *Biometals*, 1998, **11**, 297.
78. H. Kuboniwa, N. Tjandra, S. Grzesiek, H. Ren, C. B. Klee, and A. Bax, *Nat. Struct. Biol.*, 1995, **2**, 768.
79. H. Kurokawa, M. Osawa, H. Kurihara, N. Katayama, H. Tokumitsu, M. B. Swindells, M. Kainosho, and M. Ikura, *J. Mol. Biol.*, 2001, **312**, 59.
80. M. E. Wall, J. B. Clarage, and G. N. Phillips, *Structure*, 1997, **5**, 1599.
81. K. L. Yap, T. Yuan, T. K. Mal, H. J. Vogel, and M. Ikura, *J. Mol. Biol.*, 2003, **328**, 193.
82. J. Michiels, C. Xi, J. Verhaert, and J. Vanderleyden, *Trends Microbiol.*, 2002, **10**, 87.
83. D. Chin and A. R. Means, *Trends Cell Biol.*, 2000, **10**, 322.
84. T. R. Soderling and J. T. Stull, *Chem. Rev.*, 2001, **101**, 2341.
85. M. Zhang, T. Tanaka, and M. Ikura, *Nat. Struct. Biol.*, 1995, **2**, 758.
86. J. J. Chou, S. Li, C. B. Klee, and A. Bax, *Nat. Struct. Biol.*, 2001, **8**, 990.
87. B. E. Finn, J. Evenas, T. Drakenberg, J. P. Waltho, E. Thulin, and S. Forsen, *Nat. Struct. Biol.*, 1995, **2**, 777.
88. G. Barbato, M. Ikura, L. E. Kay, R. W. Pastor, and A. Bax, *Biochemistry*, 1992, **31**, 5269.
89. M. A. Wilson and A. T. Brunger, *J. Mol. Biol.*, 2000, **301**, 1237.
90. J. L. Fallon and F. A. Quiocho, *Structure (Camb.)*, 2003, **11**, 1303.
91. J. A. Clapperton, S. R. Martin, S. J. Smerdon, S. J. Gamblin, and P. M. Bayley, *Biochemistry*, 2002, **41**, 14669.
92. R. J. Colbran, *Biochem. J.*, 2004, **378**, 1.
93. M. Ikura, M. Osawa, and J. B. Ames, *Bioessays*, 2002, **24**, 625.
94. L. Zhang and Y. T. Lu, *Trends Plant Sci.*, 2003, **8**, 123.
95. S. W. Vetter and E. Leclerc, *Eur. J. Biochem.*, 2003, **270**, 404.
96. H. Kobayashi, S. Shiraishi, T. Yanagita, H. Yokoo, R. Yamamoto, S. Minami, T. Saitoh, and A. Wada, *Ann. N. Y. Acad. Sci.*2002, **971**, 127.
97. A. D. Maher and P. W. Kuchel, *Int. J. Biochem. Cell Biol.*, 2003, **35**, 1182.
98. M. A. Schumacher, A. F. Rivard, H. P. Bachinger, and J. P. Adelman, *Nature*, 2001, **410**, 1120.
99. B. Elshorst, M. Hennig, H. Forsterling, A. Diener, M. Maurer, P. Schulte, H. Schwalbe, C. Griesinger, J. Krebs, H. Schmid, T. Vorherr, and E. Carafoli, *Biochemistry*, 1999, **38**, 12320.
100. C. L. Drum, S. Z. Yan, J. Bard, Y. Q. Shen, D. Lu, S. Soelaiman, Z. Grabarek, A. Bohm, and W. J. Tang, *Nature*, 2002, **415**, 396.
101. M. Aoyagi, A. S. Arvai, J. A. Tainer, and E. D. Getzoff, *EMBO J.*, 2003, **22**, 766.
102. S. M. Gagne, M. X. Li, R. T. McKay, and B. D. Sykes, *Biochem. Cell Biol.*, 1998, **76**, 302.
103. O. Herzberg and M. N. James, *J. Mol. Biol.*, 1988, **203**, 761.
104. L. Spyracopoulos, M. X. Li, S. K. Sia, S. M. Gagne, M. Chandra, R. J. Solaro, and B. D. Sykes, *Biochemistry*, 1997, **36**, 12138.
105. S. P. Revett, G. King, J. Shabanowitz, D. F. Hunt, K. L. Hartman, T. M. Laue, and D. J. Nelson, *Protein Sci.*, 1997, **6**, 2397.

106. J. Kordel, D. A. Pearlman, and W. J. Chazin, *J. Biomol. NMR*, 1997, **10**, 231.

107. S. Nakayama, H. Kabayama, and R. H. Kretsinger, *Top. Biol. Inorg. Chem.*, 2000, **3**, 29.

108. C. W. Heizmann and J. A. Cox, *Biometals*, 1998, **11**, 383.

109. R. Donato, *Biochim. Biophys. Acta*, 1999, **1450**, 191.

110. J. C. Deloulme, B. J. Gentil, and J. Baudier, *Microsc. Res. Tech.*, 2003, **60**, 560.

111. D. B. Zimmer, P. Wright Sadosky, and D. J. Weber, *Microsc. Res. Tech.*, 2003, **60**, 552.

112. M. Okada, T. Hatakeyama, H. Itoh, N. Tokuta, H. Tokumitsu, and R. Kobayashi, *J. Biol. Chem.*, 2004, **279**, 4221.

113. W. Nacken, J. Roth, C. Sorg, and C. Kerkhoff, *Microsc. Res. Tech.*, 2003, **60**, 569.

114. L. R. Otterbein, J. Kordowska, C. Witte-Hoffmann, C. L. Wang, and R. Dominguez, *Structure (camb.)*, 2002, **10**, 557.

115. A. C. Drohat, J. C. Amburgey, F. Abildgaard, M. R. Starich, D. Baldisseri, and D. J. Weber, *Biochemistry*, 1996, **35**, 11577.

116. A. C. Drohat, D. M. Baldisseri, R. R. Rustandi, and D. J. Weber, *Biochemistry*, 1998, **37**, 2729.

117. K. G. Inman, R. Yang, R. R. Rustandi, K. E. Miller, D. M. Baldisseri, and D. J. Weber, *J. Mol. Biol.*, 2002, **324**, 1003.

118. S. Rety, J. Sopkova, M. Renouard, D. Osterloh, V. Gerke, S. Tabaries, F. Russo-Marie, and A. Lewit-Bentley, *Nat. Struct. Biol.*, 1999, **6**, 89.

119. M. Maki, Y. Kitaura, H. Satoh, S. Ohkouchi, and H. Shibata, *Biochim. Biophys. Acta*, 2002, **1600**, 51.

120. D. E. Goll, V. F. Thompson, H. Li, W. Wei, and J. Cong, *Physiol. Rev.*, 2003, **83**, 731.

121. G. D. Lin, D. Chattopadhyay, M. Maki, K. K. Wang, M. Carson, L. Jin, P. W. Yuen, E. Takano, M. Hatanaka, L. J. DeLucas, and S. V. Narayana, *Nat. Struct. Biol.*, 1997, **4**, 539.

122. E. K. Leinala, J. S. Arthur, P. Grochulski, P. L. Davies, J. S. Elce, and Z. Jia, *Proteins*, 2003, **53**, 649.

123. C. Hansen, S. Tarabykina, J. M. la Cour, K. Lollike, and M. W. Berchtold, *FEBS Lett.*, 2003, **545**, 151.

124. A. Ilari, K. A. Johnson, V. Nastopoulos, D. Verzili, C. Zamparelli, G. Colotti, D. Tsernoglou, and E. Chiancone, *J. Mol. Biol.*, 2002, **317**, 447.

125. J. Jia, N. Borregaard, K. Lollike, and M. Cygler, *Acta Crystallogr. D Biol. Crystallogr.*, 2001, **57**, 1843.

126. J. Jia, Q. Han, N. Borregaard, K. Lollike, and M. Cygler, *J. Mol. Biol.*, 2000, **300**, 1271.

127. Y. Kitaura, S. Matsumoto, H. Satoh, K. Hitomi, and M. Maki, *J. Biol. Chem.*, 2001, **276**, 14053.

128. J. Jia, S. Tarabykina, C. Hansen, M. Berchtold, and M. Cygler, *Structure (camb.)*, 2001, **9**, 267.

129. S. Feske, H. Okamura, P. G. Hogan, and A. Rao, *Biochem. Biophys. Res. Commun.*, 2003, **311**, 1117.

130. C. R. Kissinger, H. E. Parge, D. R. Knighton, C. T. Lewis, L. A. Pelletier, A. Tempczyk, V. J. Kalish, K. D. Tucker, R. E. Showalter, E. W. Moomaw, L. N. Gastinel, N. Habuka, X. H. Chen, F. Maldonado, J. E. Barker, R. Bacquet, and J. E. Villafranca, *Nature*, 1995, **378**, 641.

131. L. Jin and S. C. Harrison, *Proc. Natl. Acad. Sci. U.S.A.*, 2002, **99**, 13522.

132. J. P. Griffith, J. L. Kim, E. E. Kim, M. D. Sintchak, J. A. Thomson, M. J. Fitzgibbon, M. A. Fleming, P. R. Caron, K. Hsiao, and M. A. Navia, *Cell*, 1995, **82**, 507.

133. K. M. Flaherty, S. Zozulya, L. Stryer, and D. B. McKay, *Cell*, 1993, **75**, 709.

134. Y. Bourne, J. Dannenberg, V. Pollmann, P. Marchot, and O. Pongs, *J. Biol. Chem.*, 2001, **276**, 11949.

135. I. I. Senin, S. A. Vaganova, O. H. Weiergraber, N. S. Ergorov, P. P. Philippov, and K. W. Koch, *J. Mol. Biol.*, 2003, **330**, 409.

136. T. Tanaka, J. B. Ames, T. S. Harvey, L. Stryer, and M. Ikura, *Nature*, 1995, **376**, 444.

137. S. Vijay-Kumar and V. D. Kumar, *Nat. Struct. Biol.*, 1999, **6**, 80.

138. C. A. Gilchrist, C. F. Holm, M. A. Hughes, J. M. Schaenman, B. J. Mann, and W. A. Petri, Jr, *J. Biol. Chem.*, 2001, **276**, 11838.

139. M. S. Steinberg and P. M. McNutt, *Curr. Opin. Cell Biol.*, 1999, **11**, 554.

140. D. B. Ivanov, M. P. Philippova, and V. A. Tkachuk, *Biochemistry (Mosc.)*, 2001, **66**, 1174.

141. V. M. Braga, *Curr. Opin. Cell Biol.*, 2002, **14**, 546.

142. B. Nagar, M. Overduin, M. Ikura, and J. M. Rini, *Nature*, 1996, **380**, 360.

143. T. J. Boggon, J. Murray, S. Chappuis-Flament, E. Wong, B. M. Gumbiner, and L. Shapiro, *Science*, 2002, **296**, 1308.

144. Q. Wu and T. Maniatis, *Proc. Natl. Acad. Sci. U.S.A.*, 2000, **97**, 3124.

145. B. Leitinger, A. McDowall, P. Stanley, and N. Hogg, *Biochim. Biophys. Acta*, 2000, **1498**, 91.

146. C. H. Damsky and D. Ilic, *Curr. Opin. Cell Biol.*, 2002, **14**, 594.

147. K. M. Yamada, R. Pankov, and E. Cukierman, *Braz. J. Med. Biol. Res.*, 2003, **36**, 959.

148. A. P. Mould, E. J. Symonds, P. A. Buckley, J. G. Grossmann, P. A. McEwan, S. J. Barton, J. A. Askari, S. E. Craig, J. Bella, and M. J. Humphries, *J. Biol. Chem.*, 2003, **278**, 39993.

149. M. A. Arnaout, S. L. Goodman, and J. P. Xiong, *Curr. Opin. Cell Biol.*, 2002, **14**, 641.

150. J. P. Xiong, T. Stehle, R. Zhang, A. Joachimiak, M. Frech, S. L. Goodman, and M. A. Arnaout, *Science*, 2002, **296**, 151.

151. J. P. Xiong, T. Stehle, B. Diefenbach, R. Zhang, R. Dunker, D. L. Scott, A. Joachimiak, S. L. Goodman, and M. A. Arnaout, *Science*, 2001, **294**, 339.

152. A. M. Weljie, P. M. Hwang, and H. J. Vogel, *Proc. Natl. Acad. Sci. U.S.A.*, 2002, **99**, 5878.

153. N. Beglova, S. C. Blacklow, J. Takagi, and T. A. Springer, *Nat. Struct. Biol.*, 2002, **9**, 282.

154. R. Timpl, T. Sasaki, G. Kostka, and M. L. Chu, *Nat. Rev. Mol. Cell Biol.*2003, **4**, 479.

155. N. D. Kurniawan, K. Aliabadizadeh, I. M. Brereton, P. A. Kroon, and R. Smith, *J. Mol. Biol.*, 2001, **311**, 341.

156. J. Stenflo, *Crit. Rev. Eukaryot. Gene. Expr.*, 1999, **9**, 59.

157. Y. Stenberg, T. Drakenberg, B. Dahlback, and J. Stenflo, *Eur. J. Biochem.*, 1998, **251**, 558.

158. P. A. Handford, *Biochim. Biophys. Acta*, 2000, **1498**, 84.

159. R. S. Smallridge, P. Whiteman, J. M. Werner, I. D. Campbell, P. A. Handford, and A. K. Downing, *J. Biol. Chem.*, 2003, **278**, 12199.

160. J. M. Werner, V. Knott, P. A. Handford, I. D. Campbell, and A. K. Downing, *J. Mol. Biol.*, 2000, **296**, 1065.

161. Z. Rao, P. Handford, M. Mayhew, V. Knott, G. G. Brownlee, and D. Stuart, *Cell*, 1995, **82**, 131.

162. C. Valcarce, M. Selander-Sunnerhagen, A. M. Tamlitz, T. Drakenberg, I. Bjork, and J. Stenflo, *J. Biol. Chem.*, 1993, **268**, 26673.

163. J. Stenflo, Y. Stenberg, and A. Muranyi, *Biochim. Biophys. Acta*, 2000, **1477**, 51.

164. D. C. Kilpatrick, *Biochim. Biophys. Acta*, 2002, **1572**, 187.

165. H. J. Gabius, S. Andre, H. Kaltner, and H. C. Siebert, *Biochim. Biophys. Acta*, 2002, **1572**, 165.

166. R. Loris, *Biochim. Biophys. Acta*, 2002, **1572**, 198.

167. H. Kogelberg and T. Feizi, *Curr. Opin. Struct. Biol.*, 2001, **11**, 635.

168. U. Holmskov, S. Thiel, and J. C. Jensenius, *Annu. Rev. Immunol.*, 2003, **21**, 547.

169. J. Lu, C. Teh, U. Kishore, and K. B. Reid, *Biochim. Biophys. Acta*, 2002, **1572**, 387.

170. W. I. Weis and K. Drickamer, *Structure*, 1994, **2**, 1227.

171. A. K. Shrive, H. A. Tharia, P. Strong, U. Kishore, I. Burns, P. J. Rizkallah, K. B. Reid, and T. J. Greenhough, *J. Mol. Biol.*, 2003, **331**, 509.

172. L. East and C. M. Isacke, *Biochim. Biophys. Acta*, 2002, **1572**, 364.

173. H. Feinberg, S. Park-Snyder, A. R. Kolatkar, C. T. Heise, M. E. Taylor, and W. I. Weis, *J. Biol. Chem.*, 2000, **275**, 21539.

174. B. J. Graves, R. L. Crowther, C. Chandran, J. M. Rumberger, S. Li, K. S. Huang, D. H. Presky, P. C. Familletti, B. A. Wolitzky, and D. K. Burns, *Nature*, 1994, **367**, 532.

175. M. Meier, M. D. Bider, V. N. Malashkevich, M. Spiess, and P. Burkhard, *J. Mol. Biol.*, 2000, **300**, 857.

176. K. D. Patel, S. L. Cuvelier, and S. Wiehler, *Semin. Immunol.*, 2002, **14**, 73.

177. W. S. Somers, J. Tang, G. D. Shaw, and R. T. Camphausen, *Cell*, 2000, **103**, 467.

178. P. H. Weigel and J. H. Yik, *Biochim. Biophys. Acta*, 2002, **1572**, 341.

179. S. Radaev and P. D. Sun, *Annu. Rev. Biophys. Biomol. Struct.*, 2003, **32**, 93.

180. M. N. Vyas, N. K. Vyas, and F. A. Quiocho, *Biochemistry*, 1994, **33**, 4762.

181. A. M. Hofer and E. M. Brown, *Nat. Rev. Mol. Cell Biol.*, 2003, **4**, 530.

182. S. C. Hebert and E. M. Brown, *Curr. Opin. Cell Biol.*, 1995, **7**, 484.

183. A. M. Hofer, S. Curci, M. A. Doble, E. M. Brown, and D. I. Soybel, *Nat. Cell Biol.*, 2000, **2**, 392.

184. E. M. Brown and R. J. MacLeod, *Physiol. Rev.*, 2001, **81**, 239.

185. E. Carafoli and M. Brini, *Curr. Opin. Chem. Biol.*, 2000, **4**, 152.

186. D. L. Stokes and N. M. Green, *Annu. Rev. Biophys. Biomol. Struct.*, 2003, **32**, 445.

187. D. Guerini, *Biometals*, 1998, **11**, 319.

188. P. Zhang, C. Toyoshima, K. Yonekura, N. M. Green, and D. L. Stokes, *Nature*, 1998, **392**, 835.

189. C. Xu, W. J. Rice, W. He, and D. L. Stokes, *J. Mol. Biol.*, 2002, **316**, 201.

190. C. Toyoshima, M. Nakasako, H. Nomura, and H. Ogawa, *Nature*, 2000, **405**, 647.

191. C. Toyoshima and H. Nomura, *Nature*, 2002, **418**, 605.

192. M. Fill and J. A. Copello, *Physiol. Rev.*, 2002, **82**, 893.

193. J. Marin, A. Encabo, A. Briones, E. C. Garcia-Cohen, and M. J. Alonso, *Life Sci.*, 1999, **64**, 279.

194. K. D. Philipson, D. A. Nicoll, M. Ottolia, B. D. Quednau, H. Reuter, S. John, and Z. Qiu, *Ann. N. Y. Acad. Sci.*, 2002, **976**, 1.

195. M. A. Swairjo and B. A. Seaton, *Annu. Rev. Biophys. Biomol. Struct.*, 1994, **23**, 193.

196. P. Raynal and H. B. Pollard, *Biochim. Biophys. Acta*, 1994, **1197**, 63.

197. V. Gerke and S. E. Moss, *Biochim. Biophys. Acta*, 1997, **1357**, 129.

198. V. Gerke and S. E. Moss, *Physiol. Rev.*, 2002, **82**, 331.

199. M. A. Swairjo, N. O. Concha, M. A. Kaetzel, J. R. Dedman, and B. A. Seaton, *Nat. Struct. Biol.*, 1995, **2**, 968.

200. A. J. Avila-Sakar, C. E. Creutz, and R. H. Kretsinger, *Biochim. Biophys. Acta*, 1998, **1387**, 103.

201. A. Rosengarth, V. Gerke, and H. Luecke, *J. Mol. Biol.*, 2001, **306**, 489.

202. J. Rizo and T. C. Sudhof, *J. Biol. Chem.*, 1998, **273**, 15879.

203. E. A. Nalefski and J. J. Falke, *Protein Sci.*, 1996, **5**, 2375.

204. R. B. Sutton, B. A. Davletov, A. M. Berghuis, T. C. Sudhof, and S. R. Sprang, *Cell*, 1995, **80**, 929.

205. O. Perisic, S. Fong, D. E. Lynch, M. Bycroft, and R. L. Williams, *J. Biol. Chem.*, 1998, **273**, 1596.

206. R. B. Sutton and S. R. Sprang, *Structure*, 1998, **6**, 1395.

207. C. E. Naylor, M. Jepson, D. T. Crane, R. W. Titball, J. Miller, A. K. Basak, and B. Bolgiano, *J. Mol. Biol.*, 1999, **294**, 757.

208. L. O. Essen, O. Perisic, D. E. Lynch, M. Katan, and R. L. Williams, *Biochemistry*, 1997, **36**, 2753.

209. H. Pappa, J. Murray-Rust, L. V. Dekker, P. J. Parker, and N. Q. McDonald, *Structure*, 1998, **6**, 885.

210. N. Verdaguer, S. Corbalan-Garcia, W. F. Ochoa, I. Fita, and J. C. Gomez-Fernandez, *EMBO J.*, 1999, **18**, 6329.

211. W. F. Ochoa, J. Garcia-Garcia, I. Fita, S. Corbalan-Garcia, N. Verdaguer, and J. C. Gomez-Fernandez, *J. Mol. Biol.*, 2001, **311**, 837.

212. G. Y. Xu, T. McDonagh, H. A. Yu, E. A. Nalefski, J. D. Clark, and D. A. Cumming, *J. Mol. Biol.*, 1998, **280**, 485.

213. J. A. Grobler, L. O. Essen, R. L. Williams, and J. H. Hurley, *Nat. Struct. Biol.*, 1996, **3**, 788.

214. C. E. Naylor, J. T. Eaton, A. Howells, N. Justin, D. S. Moss, R. W. Titball, and A. K. Basak, *Nat. Struct. Biol.*, 1998, **5**, 738.

215. X. Wang, *Curr. Opin. Plant Biol.*, 2002, **5**, 408.

216. N. R. Leslie, D. Bennett, Y. E. Lindsay, H. Stewart, A. Gray, and C. P. Downes, *EMBO J.*, 2003, **22**, 5501.

217. N. R. Leslie and C. P. Downes, *Cell Signal.*, 2002, **14**, 285.

218. K. Mikoshiba, M. Fukuda, K. Ibata, H. Kabayama, and A. Mizutani, *Chem. Phys. Lipids*, 1999, **98**, 59.

219. M. Fukuda, E. Katayama, and K. Mikoshiba, *J. Biol. Chem.*, 2002, **277**, 29315.

220. R. R. Duncan, M. J. Shipston, and R. H. Chow, *Biochimie*, 2000, **82**, 421.

221. M. Fukuda, *J. Biol. Chem.*, 2003, **278**, 15373.

222. S. H. Chung, W. J. Song, K. Kim, J. J. Bednarski, J. Chen, G. D. Prestwich, and R. W. Holz, *J. Biol. Chem.*, 1998, **273**, 10240.

223. J. A. Koehler and M. F. Moran, *Cell Growth Differ.*, 2001, **12**, 551.

224. S. W. Kim, M. A. Quinn-Allen, J. T. Camp, S. Macedo-Ribeiro, P. Fuentes-Prior, W. Bode, and W. H. Kane, *Biochemistry*, 2000, **39**, 1951.

225. G. E. Gilbert and J. D. Baleja, *Biochemistry*, 1995, **34**, 3022.

226. S. Macedo-Ribeiro, W. Bode, R. Huber, M. A. Quinn-Allen, S. W. Kim, T. L. Ortel, G. P. Bourenkov, H. D. Bartunik, M. T. Stubbs, W. H. Kane, and P. Fuentes-Prior, *Nature*, 1999, **402**, 434.

227. D. H. MacLennan, M. Abu-Abed, and C. Kang, *J. Mol. Cell Cardiol.*, 2002, **34**, 897.

228. D. H. MacLennan, *Eur. J. Biochem.*, 2000, **267**, 5291.

229. M. Michalak, J. M. Robert Parker, and M. Opas, *Cell Calcium*, 2002, **32**, 269.

230. D. Terentyev, S. Viatchenko-Karpinski, I. Gyorke, P. Volpe, S. C. Williams, and S. Gyorke, *Proc. Natl. Acad. Sci. U.S.A.*, 2003, **100**, 11759.

231. S. Wang, W. R. Trumble, H. Liao, C. R. Wesson, A. K. Dunker, and C. H. Kang, *Nat. Struct. Biol.*, 1998, **5**, 476.

232. H. Park, S. Wu, A. K. Dunker, and C. Kang, *J. Biol. Chem.*, 2003, **278**, 16176.

233. K. H. Krause and M. Michalak, *Cell*, 1997, **88**, 439.

234. L. Ellgaard and A. Helenius, *Nat. Rev. Mol. Cell Biol.*, 2003, **4**, 181.

235. D. N. Hebert, J. F. Simons, J. R. Peterson, and A. Helenius, *Cold Spring Harb. Symp. Quant. Biol.*, 1995, **60**, 405.

236. J. D. Schrag, J. J. Bergeron, Y. Li, S. Borisova, M. Hahn, D. Y. Thomas, and M. Cygler, *Mol. Cell*, 2001, **8**, 633.

237. L. Ellgaard, R. Riek, T. Herrmann, P. Guntert, D. Braun, A. Helenius, and K. Wuthrich, *Proc. Natl. Acad. Sci. U.S.A.*, 2001, **98**, 3133.

238. L. Ellgaard, P. Bettendorff, D. Braun, T. Herrmann, F. Fiorito, I. Jelesarov, P. Guntert, A. Helenius, and K. Wuthrich, *J. Mol. Biol.*, 2002, **322**, 773.

239. E.-M. Frickel, R. Riek, I. Jelesarov, A. Helenius, K. Wuthrich, and L. Ellgaard, *Proc. Natl. Acad. Sci. U.S.A.*, 2002, **99**, 1954.

240. E. A. Permyakov and L. J. Berliner, *FEBS Lett.*, 2000, **473**, 269.

241. N. Chandra, K. Brew, and K. R. Acharya, *Biochemistry*, 1998, **37**, 4767.

242. P. J. Anderson, C. L. Brooks, and L. J. Berliner, *Biochemistry*, 1997, **36**, 11648.

243. B. Kuhlman, J. A. Boice, W. J. Wu, R. Fairman, and D. P. Raleigh, *Biochemistry*, 1997, **36**, 4607.

244. P. K. Qasba and S. Kumar, *Crit. Rev. Biochem. Mol. Biol.*, 1997, **32**, 255.

245. M. Joniau, P. Haezebrouck, K. Noyelle, and H. Van Dael, *Proteins*, 2001, **44**, 1.

246. E. Pardon, P. Haezebrouck, A. De Baetselier, S. D. Hooke, K. T. Fancourt, J. Desmet, C. M. Dobson, H. Van Dael, and M. Joniau, *J. Biol. Chem.*, 1995, **270**, 10514.

247. R. Kuroki and K. Yutani, *J. Biol. Chem.*, 1998, **273**, 34310.

248. M. Tada, Y. Kobashigawa, M. Mizuguchi, K. Miura, T. Kouno, Y. Kumaki, M. Demura, K. Nitta, and K. Kawano, *Biochemistry*, 2002, **41**, 13807.

249. K. Nitta, *Methods Mol. Biol.*, 2002, **172**, 211.

Carbides: Transition Metal Solid-state Chemistry

Walter Lengauer & Alexander Eder
Vienna University of Technology, Vienna, Austria

Based in part on the article Carbides: Transition Metal Solid State Chemistry by Peter Ettmayer & Walter Lengauer which appeared in the Encyclopedia of Inorganic Chemistry, First Edition.

1	Introduction	1
2	Structure and Bonding	1
3	Preparation	2
4	Characterization	3
5	Thermodynamics	4
6	Ternary Transition Metal Carbides	6
7	Transition Metal Carbonitrides	7
8	Properties of Transition Metal Carbides	8
9	Uses	12
10	References	15

1 INTRODUCTION

Transition metal carbides[1–4] show a unique combination of solid-state properties such as very high hardness, excellent electrical and thermal conductivities, and very high melting points. TaC and HfC have the highest melting points of all known materials. Against nonoxidizing acids, except hydrofluoric acid, they are chemically very inert but are oxidized in air at moderate temperatures. Table 1 gives a brief survey of solid-state properties of the technologically most important transition metal carbides.

Moissan was the first to synthesize many of the transition metal carbides and to realize their outstanding properties. In the wake of his basic research, some transition metal carbides were used as molded ingots but with little success. Schröter (German Patents 420 689 (1923) and 434 527 (1925)) succeeded in making composite materials by liquid phase sintering of carbides with iron group metals, thereby achieving a singularly successful combination of hardness with toughness; carbides such as WC, TiC, and TaC are the main components in hardmetals.

Many binary transition metal carbides, especially the δ-phases of group 4 elements, exist over a broad range of composition with an upper limit of the carbon to metal ratio near 1. Practically all solid-state properties show a gradual change with the [C]/[T] ratio (T = transition metal). Only some carbides such as tungsten monocarbide, WC, and the chromium carbides have a very narrow homogeneity region.

2 STRUCTURE AND BONDING

The structure of transition metal carbides are closely related to those of the transition metal nitrides. However, transition metal carbides feature generally simpler structure elements as compared to the nitrides. In carbides, the metal atoms are arranged in such a way that they form close-packed arrangements of metal layers with a hexagonal (h) or cubic (c) stacking sequence or with a mixture of these (*see* ***Nitrides: Transition Metal Solid-state Chemistry***). The carbon atoms in these phases occupy the octahedral interstitial sites. A crystallochemical rule[5,6] claims that the phases of pure h type can have a maximum carbon content of $[C]/[T] = 1/2$ and the c type phases a maximum carbon content of $[C]/[T] = 1$; hence in structures with layer sequences comprising h and c structure elements the maximum nonmetal content follows suit.

The phenomenon of vacancy ordering is often observed in the transition metal carbides.[6–8] While in the group 4 carbides the tendency towards carbon ordering is weak and can be observed only by extended annealing of δ-TC_{1-x} samples at comparably low temperatures (<800 °C), the tendency becomes more pronounced in the group 5 and 6 carbides. By the ordering of vacancies at low temperatures, even the metal atom positions are affected. In some cases, however, such ordered structures probably cannot be regarded as equilibrium phases nor can an impurity influence on the stability of the structures be ruled out.

An extensive compilation of the crystal structures of transition metal carbides is found in Pearson's Handbook.[9] Ward[10] has discussed the structures of carbides extensively. Epicier[7,11] and de Novion[8] have summarized the results of investigations on ordering in transition metal carbides. Lengauer[12] recently reviewed the knowledge on transition metal carbides and carbonitrides. For a comparison of close-packed transition metal carbides with close-packed transition nitrides, *see* ***Nitrides: Transition Metal Solid-state Chemistry***.

The bonding in transition metal carbides can be described as a mixture of metallic, covalent, and ionic bonding. Energy band calculations performed for a variety of transition metal carbides, nitrides, and oxides[13] have shown a minimum in the density of states (DOS) for a valence electron concentration (VEC) of 8, which in fact is the VEC for the stoichiometric carbides TiC, ZrC, and HfC. At higher VEC, the electrons already have to occupy antibonding states leading to successively pronounced destabilization. Transition metal carbides have a lower DOS at the Fermi Level than the corresponding nitrides; hence the transport properties such as electrical and thermal conductivities and the superconducting transition temperature T_c are lower than those of the corresponding nitrides.

The decomposed DOS resulting from energy band calculations can be used to describe the bonding mechanism in terms of the molecular orbital (MO) scheme for covalent

Table 1 Properties of some important Transition Metal Carbides[a]

Phase	Structure	Lattice parameter (room temperature) (nm)	Density ($g\,cm^{-3}$)	Young's modulus (GPa)	Micro-hardness (100 g load) (GPa)	Heat conductivity (room temperature) ($W\,m^{-1}\,K^{-1}$)	Coefficient of thermal expansion ($10^{-6}\,K^{-1}$)	Electrical resistivity (room temperature) ($\mu\Omega$ cm)
TiC	fcc	0.4328	4.93	450	29	15.5	8.5	100
ZrC	fcc	0.4692	6.46	350	23	17	7.1	75
HfC	fcc	0.4638	12.3	420	25	19	6.1	67
$VC_{0.88}$	fcc	0.4164	5.36	430	26–31[b]	39	7.2	69
NbC	fcc	0.4470	7.78	340	18	14	6.6	20
TaC	fcc	0.4455	14.48	290	16	22	6.3	15
Cr_3C_2	orthorhombic	1.14719 (a) 0.55329 (b) 0.28290 (c)	6.68	380	27	19	10.3	75
Mo_2C	cph	0.30233 (a) 0.47344 (c)	9.18	530	17	22	7.8	57
WC	hexagonal	0.29058 (a) 0.28365 (c)	15.72	707	23	197	3.9	17

[a] Stoichiometry implied by the given formula. Most values are for room temperature. For details see Section 8. [b] For ordered $VC_{0.91}$.[44]

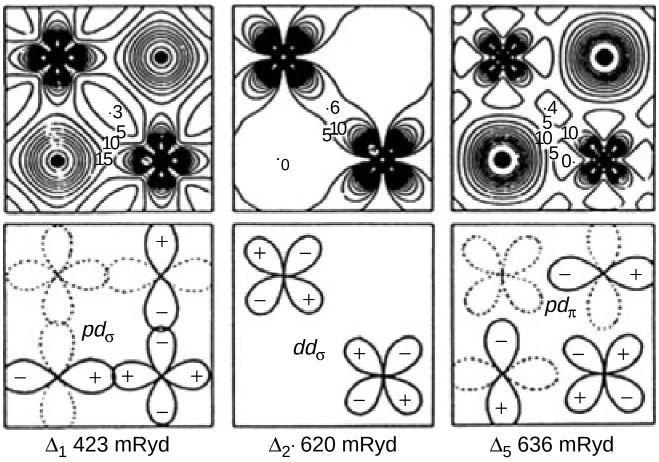

Figure 1 MO bonding scheme for TiC. (Ref. 14. Reproduced by permission of Wiley, Inc.)

bonding. Figure 1 shows these MO schemes for bonding in TiC, which were obtained by calculating the electron densities in the (100) plane just below the Fermi energy.[14] The lower part of the figure gives the schematic bond type indicating pd_σ (left), dd_σ (middle), and pd_π (right) bonds. The ionic contribution to the binding mechanism in transition metal carbides originates from a net charge transfer from the metal to the carbon atom.

3 PREPARATION

Transition metal carbides can be prepared by direct combination of the elements, preferably as powder mixtures, at elevated temperatures. If the heat generated by the reaction such as with Ti and C (equation 1) is exothermic enough to keep up the reaction temperature, the process can be carried out in the form of a self-sustaining high-temperature synthesis (SHS).

$$Ti + C \longrightarrow TiC \qquad (1)$$

Likewise, carbon-containing gases such as methane or benzene can be utilized as well (equation 2).

$$Ti + CH_4 \longrightarrow TiC + 2H_2 \qquad (2)$$

The preparation of TiC, VC, NbC, TaC, Mo_2C, WC, and the chromium carbides are important technical processes for the production of carbide powders for hardmetals. Generally, the carbides are prepared by the reduction of oxides with carbon; only Mo_2C and WC are manufactured by reaction of the metal powders with graphite or carbon black.

Solid solutions of transition metal carbides and carbonitrides, which also play an important role in the hardmetal industry, can be advantageously manufactured by the simultaneous reduction of oxide or oxide-carbide mixtures in the presence of carbon (equation 3).

$$TiO_2 + WC + 3C \longrightarrow (Ti,W)C + 2CO \qquad (3)$$

The chlorides of the transition metals can also be employed to obtain transition metal carbides (equation 4). This reaction proceeds in the gas phase at temperatures above approximately 600 °C. Because transition metal halogenides are rather volatile, this reaction is usually used for chemical vapor deposition of carbide layers on solid substrates or to produce carbide powders with very fine (submicron) grain sizes ('nanopowders'). In the latter case, the nucleation of the carbide particles must proceed in the homogeneous gas phase.

$$ZrCl_4 + CH_4 \longrightarrow ZrC + 4HCl \quad (4)$$

The oxides of the transition metals can be reduced by carbon according to the following overall reaction (equation 5).

$$TiO_2 + 3C \longrightarrow TiC + 2CO \quad (5)$$

Investigations of this reaction have revealed that there are usually several intermediate steps involving lower oxides and carboxides of the transition metals until the final product is reached. Another process to produce coarse carbide powders from oxidic prematerials makes use of calcium carbide and aluminum as the reducing agent. The heat generated by the exothermic process must be sufficient to reach the reaction temperature, which should be high enough to obtain physical separation of the molten slag and the reaction product. This principle has been used to manufacture coarse WC powders from wolframite, a naturally occurring tungsten ore, according to the following overall reaction (equation 6). In order to obtain conditions under which the reaction becomes self-sustaining, aluminum chips and iron oxides are added to the mixture.

$$FeWO_4 + CaC_2 + 2Al \longrightarrow WC + Fe + CaO + Al_2O_3 + C \quad (6)$$

WC and Fe form a regulus from which WC can be separated by an acid leach process (Macro process[15]).

Coarse chromium carbide powders have been produced by reducing Cr_2O_3 with aluminum powder in the presence of carbon (equation 7).

$$3Cr_2O_3 + 6Al + 4C \longrightarrow 3Al_2O_3 + 2Cr_3C_2 \quad (7)$$

Large single crystals of transition metal carbides can be prepared either by the floating zone technique[16] or by the auxiliary metal bath technique.[17] The first process uses an RF induction heating equipment to form a melted zone in a presintered carbide powder rod of typically 1 cm diameter, which is slowly moved along the rod. The samples so−obtained are typically 10 cm long rods containing single crystals up to the size of ca. 1 cm. The auxiliary metal process takes advantage of the fact that the carbides can be dissolved at high temperature in liquid iron group metals (Fe, Ni, and Co) and are reprecipitated upon cooling in the form of large faceted crystals, which can be separated from the metal bath by an acid leach process.

4 CHARACTERIZATION

4.1 Chemical Analysis of Carbon

Carbon analysis of transition metal carbides is nearly exclusively performed by combustion of the carbide in oxygen and measurement of the volatile combustion products CO_2 or CO. There are several methods whereby this analysis can be carried out:

- volumetrically by absorption of CO_2 in alkaline solutions;
- by measurement of the change in electrical conductivity of an alkaline solution resulting from the CO_2 absorption;
- by amperometric titration of a $Ba(OH)_2$–$BaCl_2$ solution after absorption of the CO_2 content;
- by gas chromatographic analysis of the CO_2 (and N_2) content of the carrier gas.

4.2 Physical Analysis of Carbon

Since carbides are extensively used in spatially restricted sizes (thin films, powder particles in cemented carbides), microanalytical techniques of local carbon analysis are of special interest for sample characterization. Electron probe microanalysis (EPMA) is the most successful method for the quantitative analysis of carbon when the lateral resolution needs not to be better than about 2 µm.

The highest accuracy is obtained by the use of external or internal standards and a wavelength-dispersive spectrometer. Problems arise when the carbon atoms in the standard and sample material are differently bonded. This leads to slightly different peak positions and peak shapes. Errors arising from these effects can be either avoided by using the same type of carbide in standard and sample or by measuring the peak area rather than the peak height. Bastin and Heijligers[18] worked out the area-peak-factor procedure, where the ratio peak area to peak height, in XRD the so-called intregral intensity, is determined for a given compound. After this function has been obtained for a specific carbide and a specific microprobe set up (since the peak area and peak height are a function of the spectrometer) relative to the standard, a simple peak height intensity determination of standard and sample is sufficient for quantitative carbon analyses.

In the preparation of standards, diffusional techniques are of special importance. Using such techniques diffusion layers are formed. With a special modification by use of wedge-type samples, these layers are broadened[19,20] and are thus better accessible for the microprobe.[21–23] The samples consist of several diffusion bands because of the various phases in the respective carbide system. Usually, however, the samples should be single phase and homogeneous in order to make chemical gross compositional analysis applicable. Only with a comparison of different techniques a real standardization is possible. Such transition metal carbide standards have been made from the phases VC, NbC, TaC[22] and Cr_3C_2.[23]

In addition, contamination of the analyzed surface by hydrocarbons may coincide in the measurement. Therefore, anticontamination techniques such as using a cold-trap or an oxygen jet should be applied.

Relief effects owing to insufficient or inapplicable polishing routines can be avoided by lapping of the specimens.[21]

5 THERMODYNAMICS

5.1 Free Energy of Formation

The free energy of formation of transition metal carbides does not change significantly with temperature. Hoch[24] has derived interaction parameters between carbon and the metal atoms in group 4 and 5 transition metal carbides from metal and carbon vapor pressure measurements at high temperatures, which quantitatively describe the partial free energy of carbon within the homogeneity region of the monocarbides. From these values it was concluded that with the heavier elements of group 4 and 5, the stoichiometric composition can more easily be attained than with the carbides of the metals of the first long period. Indeed, vanadium carbide shows a maximum carbon content of $VC_{0.92}$. The thermochemical stability of the carbides decreases with increasing group number. While the monocarbides of groups 4 and 5 can be melted congruently, the carbides of group 6 metals decompose peritectically before their melting points are reached. The monocarbide MoC decomposes in a peritectoid reaction at 1170 °C into $Mo_2C + C$.

5.2 Phase Equilibria

5.2.1 Group 4 Transition Metal–Carbon Systems

Figure 2 shows the group 4 transition metal–carbon systems,[25] which are very similar to each other concerning the carbide phases: the monocarbides δ-TiC_{1-x}, δ-ZrC_{1-x} and δ-HfC_{1-x} show extensive homogeneity ranges and have high congruent melting temperatures. These phases are of the NaCl type and are closely related in structure as well as in properties with the transition metal nitrides.

Carbon does not stabilize the hcp low-temperature modifications of these metals (in contrast to nitrogen) and the solubility of C in the α-phases is much smaller as compared to the group 4 transition metal nitride systems.

Several superstructures have been observed at substoichiometric compositions formed by long-range ordering of carbon atoms in fcc δ-TiC_{1-x}.[8]

5.2.2 Group 5 Transition Metal–Carbon Systems

The group 5 transition metal–carbon systems (Figure 3 shows reinvestigated portions of their phase diagrams by means of diffusion couples, information at high temperature including the liquid phase can be obtained from the ASM Handbook[25]) are again very similar to each other and contain structurally identical subcarbide phases β-T_2C and ζ-T_4C_{3-x} as well as the fcc monocarbide phases δ-TC_{1-x}. All carbides of the composition T_2C have high- and low-temperature modifications that differ only by the arrangement of the carbon atoms[5] on the interstitial positions. Furthermore, a large variety of ordered hemicarbides T_2C have been identified by electron microscopy and/or diffraction[7,11] but have not been included in the phase diagrams because of their dubious phase character. Possibly these structures are affected by impurities.

In these systems, the ζ-phases ζ-V_4C_{3-x}, ζ-Nb_4C_{3-x} and ζ-Ta_4C_{3-x} are observed. These phases have a close-packed metal atom stacking sequence of 12 layers per unit cell (ABABCACABCBC...) and a random occupancy of carbon atoms in the octahedral interstices. Their actual compositions deviate from the ideal crystallochemical C/T ratio of 3/4 (see Section 2), a deviation that is largest for ζ-V_4C_{3-x} where the carbon content is below 40 at%. The stabilities and the homogeneity ranges of these phases were investigated by diffusion couples.[22] Peritectoid decomposition/formation of these ζ-T_4C_{3-x} phases occur in which also the β-T_2C and δ-TC_{1-x} phases are involved. Several ordered compounds have been observed in group 5 carbides[8] even at high carbon contents such as V_6C_5, V_8C_7 and Nb_6C_5. The effect of ordering on the hardness has been investigated for δ-VC_{1-x} (see Section 8.5).

5.2.3 Group 6 Transition Metal–Carbon Systems

The crystal structures of the phases in these systems are characterized by the destabilization of the T_6C octahedral

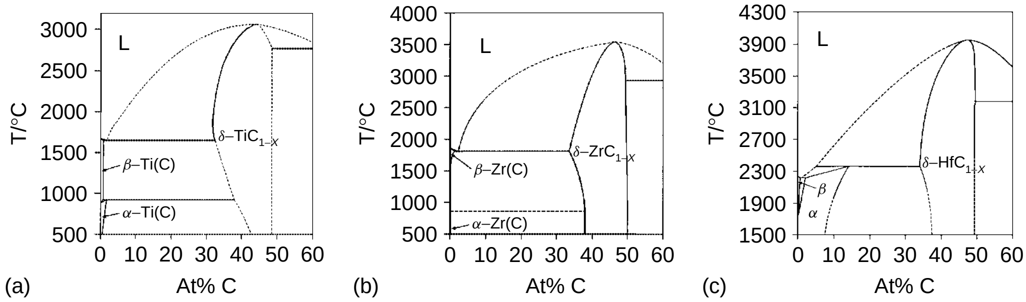

Figure 2 Phase diagrams of the group 4 transition metal–carbon systems. (a) titanium-carbon; (b) zirconium-carbon; (c) hafnium-carbon. (Ref. 25. Reproduced by permission of Materials Information Society/ASM International)

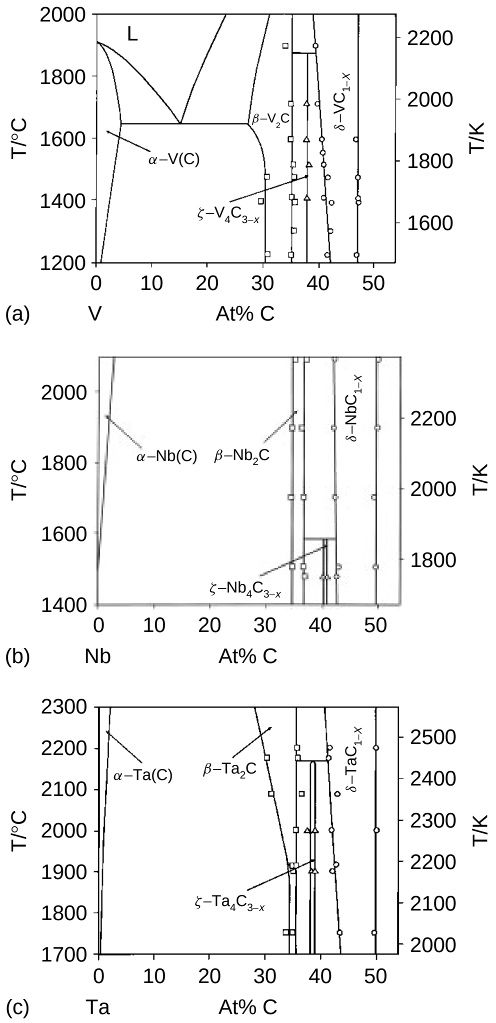

Figure 3 Section of phase diagrams[22] of the group 5 transition metal–carbon systems. (a) vanadium-carbon; (b) niobium-carbon; (c) tantalum-carbon. (Reprinted from Ref. 22. © 1998, with permission from Elsevier)

structure elements, which are replaced by T_6C trigonal prismatic structural elements. Cubic monocarbides MC_{1-x} in the Mo–C and W–C systems (Figure 4) exist only at high temperatures and with substoichiometric compositions. The stoichiometric monocarbides WC and MoC are hexagonal with trigonal prismatic structural elements. An additional phase, γ'-Mo_3C_2, has been observed in the Mo–C system with a layer sequence ABAB... and hence is structurally related to some ternary transition metal nitride phases. The carbides Mo_2C and W_2C undergo a phase transition $\beta \rightarrow \beta'$. In the β'-T_2C phase the cell symmetry with respect to carbon is lower than in the β-phase. In Mo_2C a hexagonal to orthorhombic first-order phase transition occurs. Especially in the W-C system, a large variety of possible ordered structures have been found by electron diffraction in the W_2C phase. Whether they are to be considered as stable phases is not yet clear.[7]

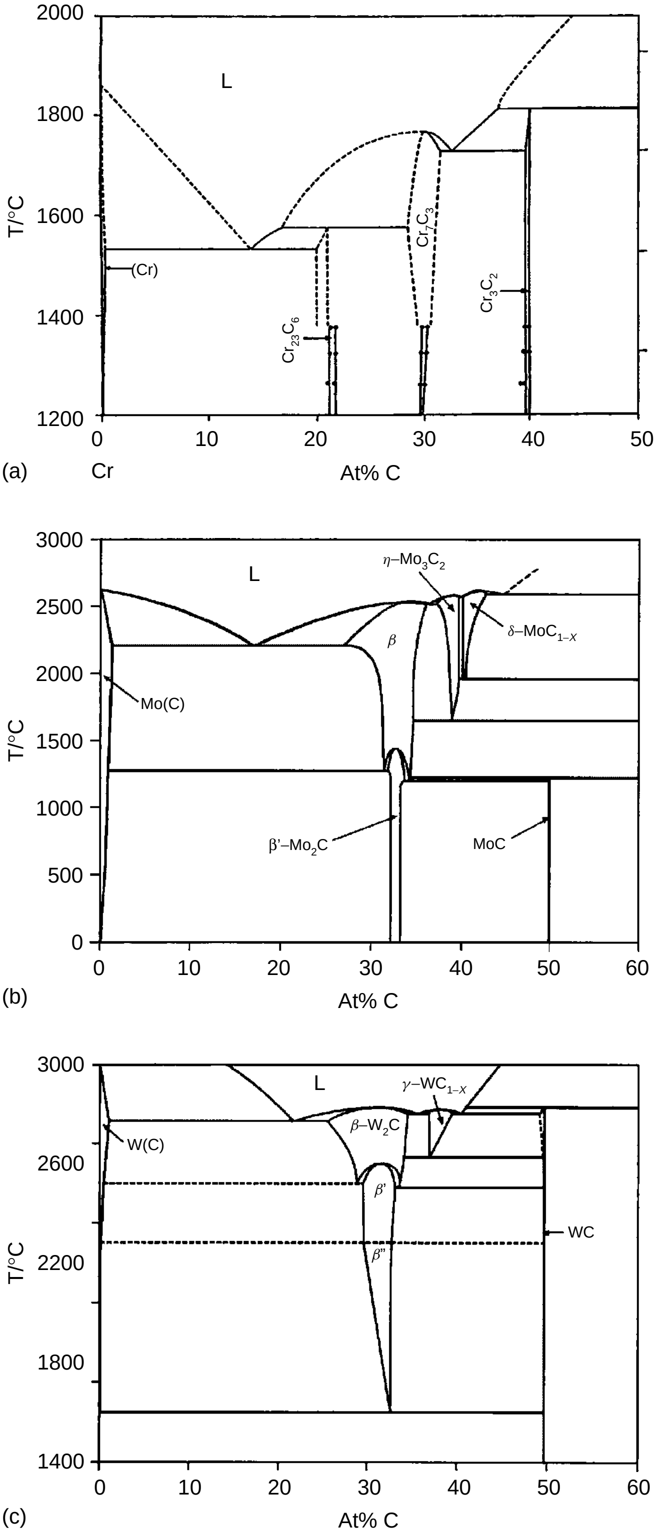

Figure 4 Phase diagrams of the group 6 transition metal–carbon systems. (a) chromium-carbon; (b) molybdenum-carbon; (c) tungstencarbon. (Figure 4(a): Reproduced from Ref. 25 by permission of Materials Information Society/ASM International. Figure 4(b): Reproduced from Ref. 23 by permission of Materials Information Society/ASM International)

The Cr–C system (Figure 4) has been reinvestigated by diffusion couples in which the three chromium carbides form distinct diffusion bands.[23] The system is characterized by the absence of a monocarbide phase. There are three carbide phases ($Cr_{23}C_6$, Cr_7C_3 and Cr_3C_2) with crystal structures that deviate from the simple concept of a densely packed metal atom host lattice with interstitial carbon atoms. Cr_3C_2 has trigonal prismatic structural elements in an orthorhombic lattice. A further orthorhombic chromium carbide phase with the composition Cr_3C is metastable and isotypic to cementite, Fe_3C. The phase Cr_7C_3 has an orthorhombic arrangement of metal atoms and is structurally closely related to the hexagonal T_2C phases. While the hexagonal T_2C do not contain other structural elements than T_2C octahedra, slightly distorted T_6C trigonal prismatic structure groups can be observed in Cr_7C_3. In ternary systems with hexagonal T_2X phases in the boundary system, the solid solubility of Cr_7C_3 in the hexagonal phases is considerable. In $Cr_{23}C_6$, each carbon atom has 8 metal neighbors in the form of a quadratic antiprism. In that respect the structure differs basically from all other transition metal carbides.

5.2.4 The Mn–C and Fe–C Systems

The Mn–C system (Figure 5) has similarities with both the Fe–C and the Cr–C systems with respect to occurring phases. The phase Mn_3C is isotypic with Fe_3C and is a stable phase at high temperatures as opposed to the Fe–C and Cr–C systems. The phases $Mn_{23}C_6$ and Mn_7C_3 are isotypic with the chromium carbide phases of the same compositions. The phase Mn_5C_2 has a monoclinic structure with 28 atoms in the unit cell. As opposed to the above-mentioned manganese carbides, which are line compounds, the ε-Mn_4C has a broad homogeneity region and is a high-temperature compound.

Although in the Fe–C system (Figure 5) no stable carbide phase exists, this system is, nevertheless, the most important system in materials science because on this system the physical metallurgy of steels is based. Cementite (Fe_3C) and several other iron carbides have been reported to be formed in heat treated, quenched, and annealed steels. The broken lines in this figure relate to the metastable Fe–Fe_3C phase diagram. Cementite is metastable but in solid alloys it can persist for very long times even at temperatures up to 700 °C. The decomposition is extremely slow and can be avoided by addition of other carbide forming metals such as Cr and Mn.

5.2.5 The Co–C and Ni–C Systems

In the systems Co–C and Ni–C and in the other transition metal–carbon systems not mentioned so far, no stable carbide phases are observed. The carbon solubilities in the metals are of importance for the fabrication and properties of hardmetals (see Section 9.1.1). The phase diagrams are of the eutectic type. Metastable carbide phases have been reported in rapidly quenched Co–C and Ni–C alloys.

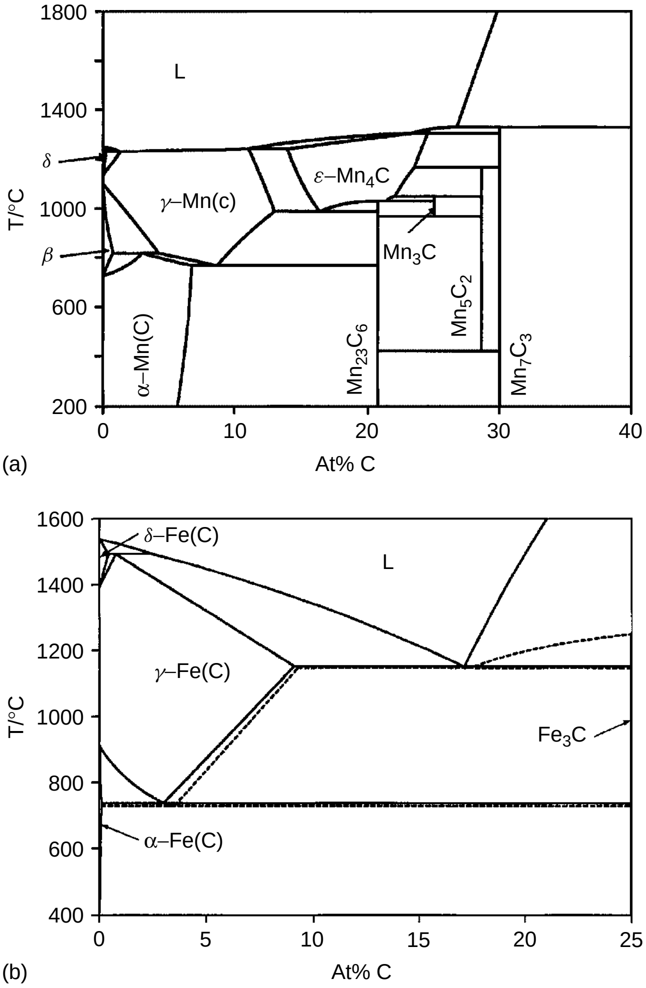

Figure 5 Phase diagrams of the Mn–C (a) and Fe–C (b) systems. (Ref. 25. Reproduced by permission of Materials Information Society/ASM International)

6 TERNARY TRANSITION METAL CARBIDES

Fcc transition metal carbides often form complete solid solutions with each other, particularly at high temperatures and if their lattice parameters do not differ by more than 8–10%. Miscibility gaps have been observed[26] in the quasibinary systems TiC–ZrC, TiC–HfC, VC–NbC and VC–TaC. The solid solubility of 'MoC' and WC in the fcc carbides of Groups 4 and 5 is appreciable, while hexagonal WC does not dissolve any of the fcc carbides except at very high temperatures.

There are several families of ternary carbide phases with transition metals and main group elements. Several of them are of structural interest such as the H-phases, the filled β-manganese type carbides and the κ-carbides. The η-phases are formed in carbon–deficient hardmetals and cause embrittlement.

The H-phases are a large family of ternary interstitial compounds. They have the general formula T_2MX, where T is a transition metal, M is a group 2 or 6 element and X is C or N. The structure can be described as alternating hexagonal layers of octahedra consisting of carbon and main group element atoms (Figure 6). The structure of the H-phases is related to the structures of γ'-Mo_3C_2, η-NbN and η-TaN (*see* ***Nitrides: Transition Metal Solid-state Chemistry***).

The η-phases have the general formula $T1_4T2_2C_x$ or $T1_3T2_3C_x$, where T1 and T2 are transition metals. There are carbides, nitrides, and oxides with the η-carbide structure. Ward[10] has summarized the structure of these phases, which are characterized by T_6C octahedra connected by common faces.

A further group of ternary carbides, T_3MC_2, where T is a transition metal and M is a main group element such as Si or Ge, features a close-packed stacking sequence of Si/Ge and T layers with the sequence $(hhhc)_2$ and where the second h layer in this sequence is the Si/Ge layer. Barsoum *et al.*[27] conducted an intensive investigation of the phase Ti_3SiC_2 in the past years. These phases (also nitride and carbonitride phases belong to this family) show an unusual set of properties (Table 2) owing to the layered structure of the unit cell. They are relatively soft but elastically stiff. Of highest importance is the fact that these compounds can be easily machined by regular tools despite their good high-temperature mechanical properties. They represent a new class of solids that can be identified as thermodynamically stable nanolaminates. A comprehensive treatment of structural aspects in complex carbides has been given by Nowotny and Benesovsky.[28]

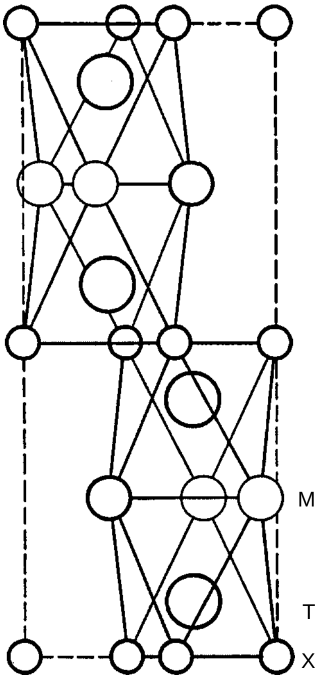

Figure 6 The structure of H-phases. T: transition metal; M: main group element; X: carbon or nitrogen

Table 2 Bulk properties of the H-phase related compound Ti_3SiC_2[27]

Physical and electrical properties		
Density	($g\,cm^{-3}$)	4.5
Electrical Conductivity at RT	10^{-6} ($\Omega^{-1}\,m^{-1}$)	4.5
CTE	10^{-6} (°C^{-1})	9
Thermal Properties		
Thermal Conductivity at RT	($W\,m^{-1}\,K^{-1}$)	37
Thermal Conductivity at 1200 °C	($W\,m^{-1}\,K^{-1}$)	32
Service Temperature, Air	(°C)	1200
Service Temperature, Inert, or Vacuum	(°C)	2000
Mechanical Properties		
Elastic Modulus	(GPa)	300
Hardness Vickers	(GPa)	4
Tensile Strength at RT	(MPa)(brittle)	200
Tensile Strength at 1200 °C	(MPa)(ductile)	40
Flexure Strength at RT	(MPa)(brittle)	400
Flexure Strength at 1200 °C	(MPa)(ductile)	100
Compressive Strength at RT	(MPa)(brittle)	1100
Compressive Strength at 1200 °C	(MPa)(ductile)	500
Fracture Toughness K_{IC}	($MPa\sqrt{m}$)	8
Thermal ShockΔT_c (100 µm grain size)	°C	1400
Thermal ShockΔT_c (5 µm grain size)	°C	700

7 TRANSITION METAL CARBONITRIDES

Because of the evident structural similarities between transition metal carbides and transition metal nitrides the carbon atoms in group 4 and 5 carbides can be replaced completely by nitrogen without changing the structure of the binary phases. So far only one distinct ternary phase $Cr_2(C,N)_2$ has been reported.[29] Intersolubility between the binary nitrides and carbides in the group 6 carbonitride systems Cr–C–N and Mo–C–N is not complete because of the differences in the crystal structures of the carbide and nitride phases.

Carbonitrides of the type (T1,T2)(C,N) also show complete solid solubility if the lattice parameters of the boundary systems are favorable. In the systems Ti–Mo–C–N and Ti–W–C–N complete miscibility between TiC–TiN, MoC–WC and MoN–WN at high temperatures has been predicted[30] (the fcc MoN and WN corners are experimentally not accessible). At lower temperatures, the homogenous fcc phase is claimed to undergo a spinodal decomposition into a (Ti,Mo)C or (Ti,W)C phase with low N contents and a Ti(C,N) phase with low Mo or W contents. The spinodally decomposed fcc phases have very similar lattice parameters. The driving force for the decomposition is based on the fact that in the 'reciprocal salt pair' $TiC + MoN \rightarrow TiN + MoC$ the Gibbs free energy of reaction is negative. This fact has been claimed to be of consequence for the sintering behavior and performance of carbonitride hardmetals (see Section 9.1).

8 PROPERTIES OF TRANSITION METAL CARBIDES

8.1 Melting Points

The transition metal carbides are some of the highest melting known materials. δ-$TaC_{0.89}$ melts congruently at 3985 °C and δ-$HfC_{0.94}$ congruently at 3950 °C. The melting temperatures can be read from the phase diagrams presented in Section 5.2.

8.2 Thermal and Electrical Properties

The thermal conductivities of transition metal carbides increase with increasing temperature, an unexpected phenomenon that has been investigated extensively on titanium, zirconium, hafnium and carbides and carbonitrides.[31,32] Previous studies have reported a linear increase of the thermal conductivity with temperature, but more recent investigations have revealed a nonlinear relationship.[32] Carbon deficiency increases the low-temperature thermal conductivity of δ-TiC_{1-x} but decreases the high-temperature thermal conductivity.

Transition metal carbides have generally a significantly lower thermal conductivity than isotypic transition metal nitrides. Some values are given in Table 1 and a comparison between these two groups is given in the article on (*see* ***Nitrides: Transition Metal Solid-state Chemistry***) as a function of temperature.

The thermal conductivity of WC[33] is much higher than that of the fcc transition metal carbides. The lower thermal conductivity of fcc carbides has been attributed to their generally nonstoichiometric composition and hence the higher concentration of phonon scattering defects in the lattices, but can probably be explained by the stronger covalent bonding in WC and hence the higher efficiency of the heat transport by phonons.

The parallelism in properties between fcc transition metal carbides and nitrides is also valid for room-temperature electrical resistivity, which decreases with increasing carbon content and increases with increasing temperature. Generally the transition metal carbides have higher electrical resistivities than the transition metal nitrides. Figure 7 gives the electrical resistivities of Groups 4 and 5 transition metal carbides as a function of carbon content, as compiled by Storms,[2] compare also Ref. 32. For the electrical resistivity of δ-HfC, values

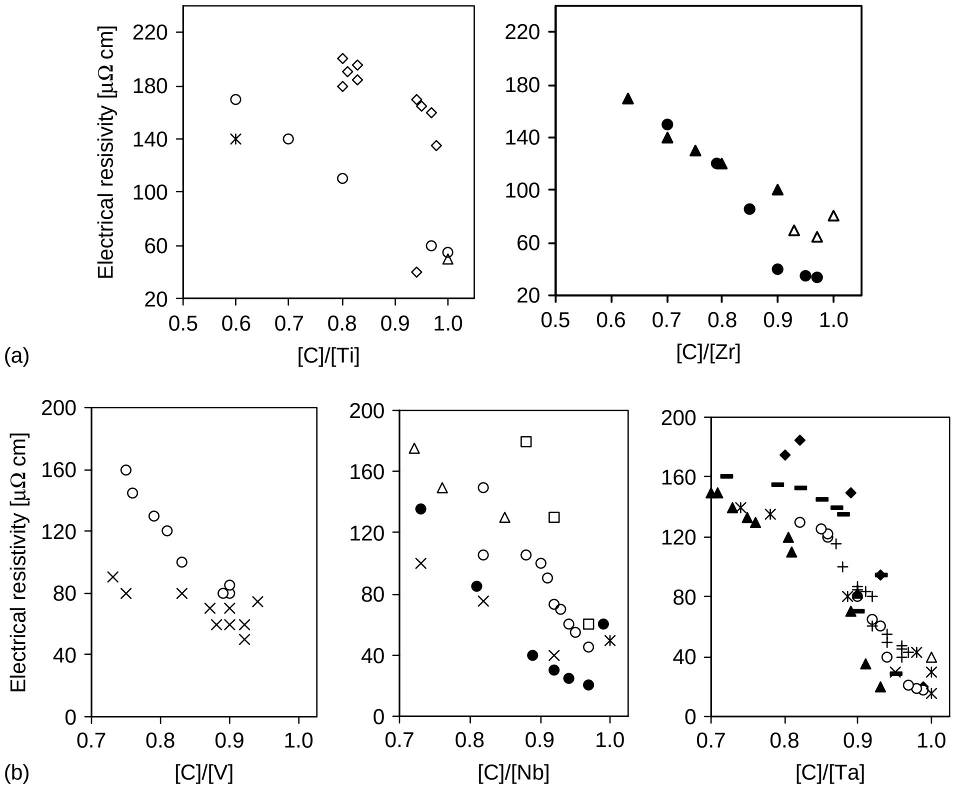

Figure 7 Electrical resistivity versus [C]/[T] ratio for δ-TiC_{1-x}, δ-ZrC_{1-x} (a), and fcc group 5 transition metal carbides (b), from Storms. (Reprinted from Ref. 2. © 1972, with permission from Elsevier)

between 27–51 μΩ cm have been reported, which is probably valid for compositions close to [C]/[Hf] = 1, and where the lower value is most probably due to the purer sample.

Some transition metal carbides are superconducting. The highest T_c values have been reported for δ-NbC (11.1 K), δ-TaC (10.3 K) and hexagonal WC (10.0 K), δ-TiC, δ-ZrC, δ-HfC and δ-VC_{1-x} are not superconducting above 1 K.

8.3 Thermal Expansion

Thermal expansion is an important property of transition metal carbides.[34] They are practically never used in pure form but mostly in composite materials with matrices of other materials (metals). Upon thermal load, the difference in the thermal expansion coefficients of the carbide phase and the matrix may cause degradation of the composite. Generally, the thermal expansion of transition metal carbides is higher than that of the pure metal component. Table 1 gives average thermal expansion coefficients of various carbides. For WC, the thermal expansion has even been measured at various pressures.[33]

The thermal expansion of the group 4 carbonitrides was measured by high-temperature X-ray diffraction[34] and can be expressed as a function of the [C]/([C] + [N]) ratio:

$$\begin{aligned}
&\delta-\mathrm{Ti}(\mathrm{C}_x\mathrm{N}_{1-x}): \quad \alpha_{\mathrm{av}} = \{9.9 - 1.4^*[\mathrm{C}]/([\mathrm{C}]+[\mathrm{N}])\}^*10^{-6}\,\mathrm{K}^{-1}\\
&\delta-\mathrm{Zr}(\mathrm{C}_x\mathrm{N}_{1-x}): \quad \alpha_{\mathrm{av}} = \{7.8 - 0.3^*[\mathrm{C}]/([\mathrm{C}]+[\mathrm{N}])\}^*10^{-6}\,\mathrm{K}^{-1}\\
&\delta-\mathrm{Hf}(\mathrm{C}_x\mathrm{N}_{1-x}): \quad \alpha_{\mathrm{av}} = \{8.5 - 2.4^*[\mathrm{C}]/([\mathrm{C}]+[\mathrm{N}])\}^*10^{-6}\,\mathrm{K}^{-1}
\end{aligned} \tag{8}$$

8.4 Diffusivities

The diffusion of carbon in transition metal carbides proceeds via a vacancy mechanism and thus the diffusivity increases with increasing vacancy concentration in the nonmetal sublattice.[35,36] However, carbon diffusivities versus composition were measured only for very few types of carbides. Diffusivity data are summarized in Figure 8 and Table 3, for which data of Matzke[37] and Lengauer[12] were used. The metal diffusion is even slower and has a higher activation energy. Actual values were obtained for δ-TiC_{1-x} and δ-NbC_{1-x}. A detailed study of concentration-dependent diffusivities was conducted for δ-TiC_{1-x} and δ-ZrC_{1-x} by means of carbon profile measurements in diffusion couples.[38]

Table 3 Diffusivity data for nonmetal diffusivity of transition metal carbides,[12] for compounds with a = 0 no significant concentration dependency is present

Compound	D_0 ($cm^2\,s^{-1}$)	E (eV)	a ($cm^3\,mol^{-1}$)
δ-TiC_{1-x}	0.058	3.12	112
δ-ZrC_{1-x}	0.167	3.59	144
δ-NbC_{1-x}	0.065	3.53	98
δ-TaC_{1-x}	0.023–0.14	3.6	105
β-Nb_2C	2.9	3.95	–
β-Ta_2C	ca. $\approx 10^{-5}$	6.5	–
ζ-Ta_4C_{3-x}	20	5	–
$Cr_{23}C_6$	1.28	3.2	–
Cr_7C_3	0.718	2.9	–
Cr_3C_2	0.0121	2.5	–

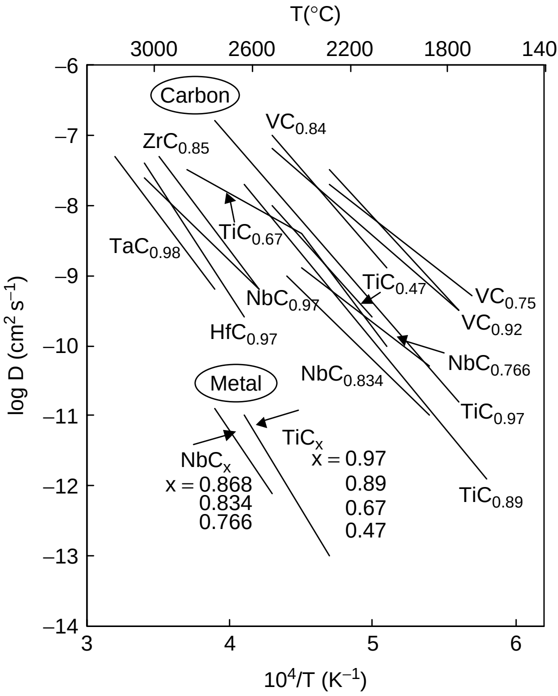

Figure 8 Diffusivity of carbon and metal atoms in some transition metal carbides. (Ref. 38. Reproduced by permission of Springer Verlag)

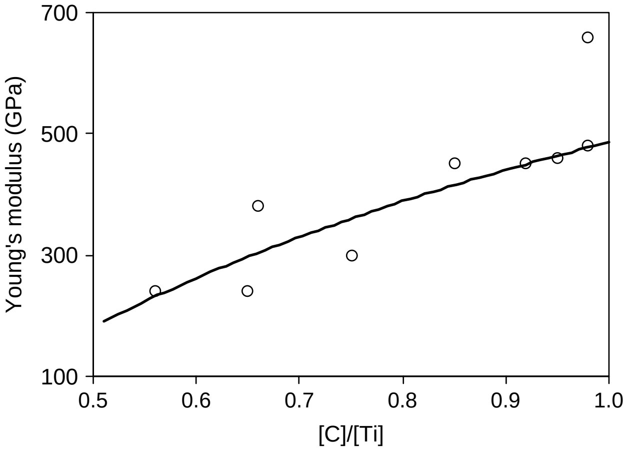

Figure 9 Young's modulus of δ-TiC_{1-x} as a function of carbon/metal ratio, from Török *et al.* (Reprinted from Ref. 39. © 1987, with permission from Elsevier)

8.5 Microhardness and Elastic Properties

The Young's moduli E of group 4 transition metal carbides are on the order of about several hundred GPa (Table 1) and appear to depend on the carbon/metal ratio. This is at least true for δ-TiC_{1-x}, where E increases with increasing [C]/[Ti] approximately linearly from 200 GPa at Ti$C_{0.50}$ to 460 GPa at Ti$C_{0.98}$ (Figure 9). Values for δ-ZrC_{1-x} and δ-HfC_{1-x} are 370–480 and 420–460 GPa, respectively, for unspecified but probably near-stoichiometric compositions.[39,40] The highest Young's modulus is that of WC (Table 1) and has been measured for temperatures of up to 2200 K.[33] It drops almost linearly from about 710 GPa at room temperature to 557 GPa at 2200 K.

For Ti, Zr, and Hf carbonitrides, including also binary carbides and nitrides, the Young's, shear, and bulk modulus as well as the Poisson number have been measured by ultrasonic measurements as a function of the C/N ratio.[41] The data are given in Figure 10.

Many of the transition metal carbides such as TiC are very hard compounds. In δ-TiC_{1-x} the microhardness increases with increasing carbon content, a phenomenon that is probably closely related to the VEC, with the maximum stability at VEC $= 8$ at the composition TiC. Figure 11 shows this behavior for δ-TiC_{1-x},[42] other data are contained in Table 1. Both microhardness and nanohardness were recently measured for Ti, Zr, and Hf carbonitrides as a function of the C/N ratio.[41] The data are

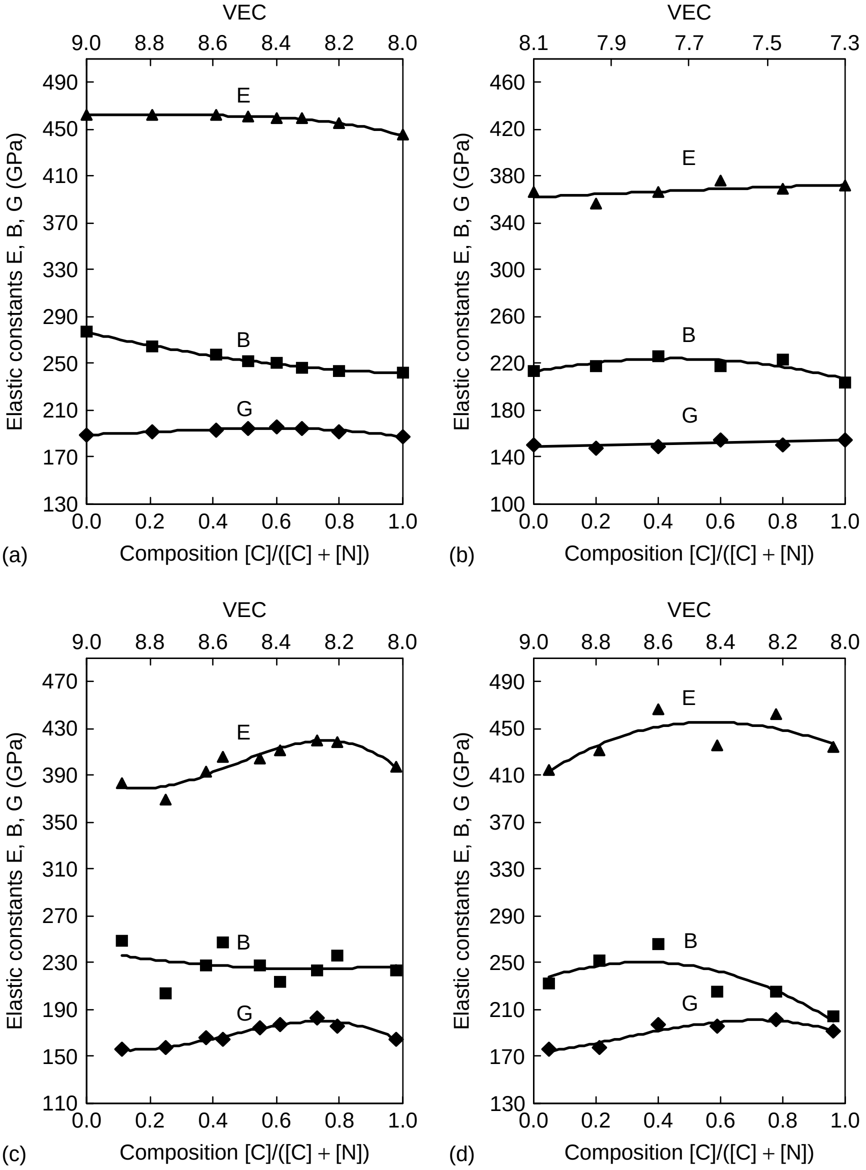

Figure 10 Young's (E), shear (G), and bulk modulus (B) of (a) Ti(C_xN_{1-x}), (b) Ti(C_xN_{1-x})$_{0.81}$, (c) Zr(C_xN_{1-x}) and (d) Hf(C_xN_{1-x}), as a function of the C/N ratio as well as of the VEC. (Reprinted from Ref. 41. © 2000, with permission from Elsevier)

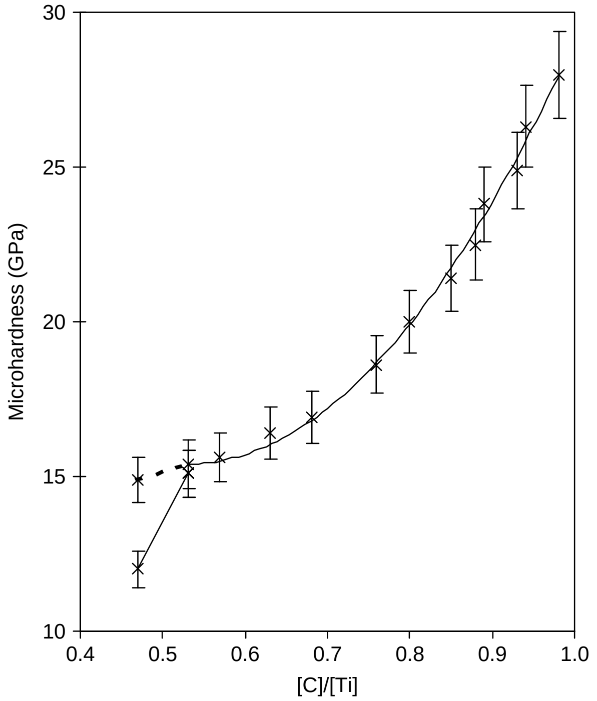

Figure 11 Microhardness of δ-TiC_{1-x} as a function of the carbon/metal ratio, from Chermant *et al.* (Reprinted from Ref. 42. © 1970, with permission from Elsevier)

given in Figure 12 and show a higher nanohardness than microhardness.

Interestingly, as-grown δ-$VC_{0.91}$ has the highest hardness among these compounds ($HK_{0.1} = 30.8$ GPa). This value corresponds to the ordered state, whereas that of the disordered is 26 GPa, depending on the composition.[43] δ-TiC has the highest hardness for annealed single crystals ($HK_{0.1} = 30.4$ GPa). Both values correspond to the (100) plane, which has the highest hardness. Generally, the hardness values of annealed crystals (Table 1) are lower than that of as-grown crystals owing to their lower dislocation density. Polycrystalline material has 1–2 GPa higher hardness values than single crystals owing to the grain boundary influence on hardness (Hall–Petch relation).

On single crystals of transition metal carbides it has been shown for hexagonal WC and also for fcc NbC_{1-x} that the microhardness is dependent of orientation.[44,45]

Single-crystal and polycrystalline transition metal carbides have been investigated with respect to creep, microhardness, plasticity, and slip systems. The fcc carbides show slip upon mechanical load within the (111) plane in the {110} direction.[45,46] The ductile-to-brittle transformation temperature of TiC is about 800 °C and is dependent on the grain size. The yield stress of TiC obeys a Hall–Petch type relation, that is, the yield stress is inversely proportional to the square root of the grain size.[47] TiC and ZrC show plastic deformation at surprisingly low temperatures around 1000 °C.

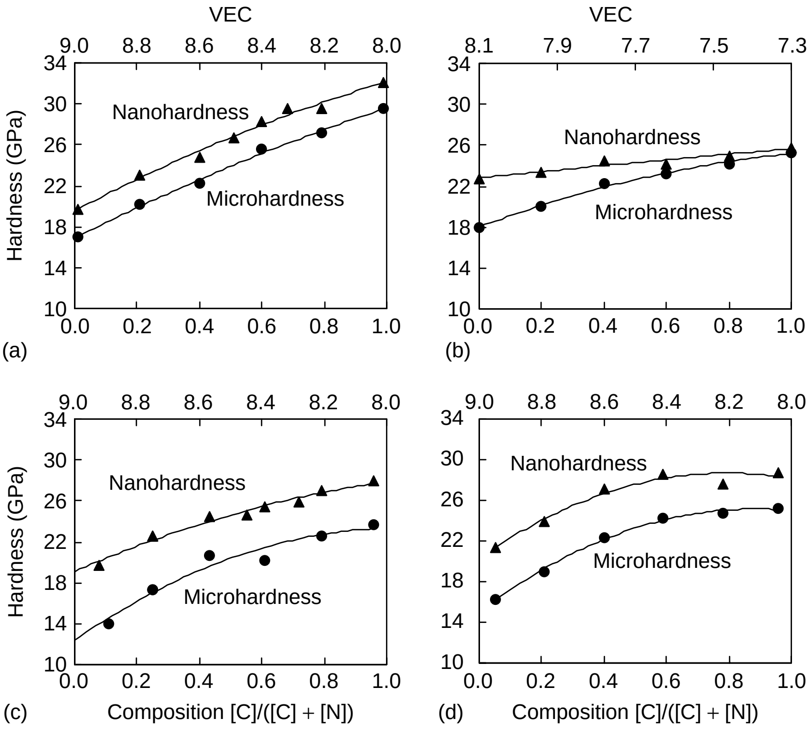

Figure 12 Nanohardness (▲) and microhardness (●) for (a) $Ti(C_xN_{1-x})$, (b) $Ti(C_xN_{1-x})_{0.81}$, (c) $Zr(C_xN_{1-x})$ and (d) $Hf(C_xN_{1-x})$ as a function of the [C]/([C] + [N]) ratio as well as of the VEC. For stoichiometric carbonitrides the two functions are practically parallel, from Yang *et al.* (Reprinted from Ref. 41. © 2000, with permission from Elsevier)

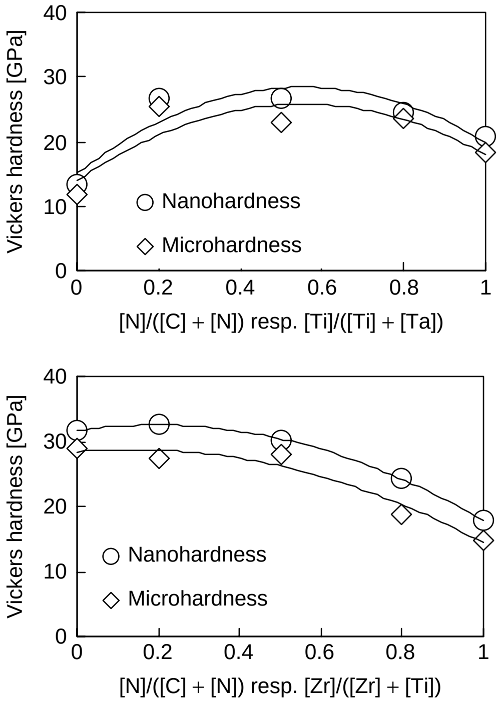

Figure 13 Micro- and Nanohardness of quaternary phases (Ti,Zr)(C,N) and (Ti,Ta)(C,N)

Upon additional alloying ternary carbonitrides quaternary carbonitrides are obtained. The group 4 and 5 transition metal carbides and nitrides are completely miscible except TiN-VC and ZrN-VC. Thus, modified material properties can be obtained (see also Section 9.2). Information on the properties of these carbides are still scarce,[48] a few data are given in Figure 13 and Table 4.

9 USES

9.1 Cemented Carbides (Hardmetals)

9.1.1 Metallurgy of Hardmetals and Cermets

The most widely used transition metal carbide is tungsten carbide, hexagonal WC, which is employed as the hard constituent in WC–Co hardmetals. These hardmetals are sintered composite materials with 80–90% of hard particles such as WC embedded in a ductile binder phase such as Co and/or Ni. For these applications, WC combines a number of favorable properties such as high hardness and wear resistance, exceptional high modulus of elasticity, good electrical and heat conductivities and is readily wetted by the binder metals Co and Ni. The ternary system W–C–Co is shown in Figure 14 for 1350 °C.[49] WC coexists with the Co phase and forms a pseudobinary lower melting eutectic between WC and Co. This eutectic facilitates full densification during liquid phase sintering. The carbon content must be kept close to the theoretical value because a decrease in total carbon content will lead to the formation of η-carbides $(W,Co)_6C$, which are brittle and harmful to the performance of these materials. Modern hardmetals, particularly for metal cutting applications, contain other carbides such as TaC, NbC, and TiC, which are admixed to increase the high-temperature performance and wear resistance. Figure 15 shows a microstructure of a WC–Co hardmetal.

Shortly after the invention of WC–Co hardmetals, TiC–based hardmetals were proposed as cutting tools but have not found extended use because of their comparative brittleness. Only in the last two decades, TiC-based hardmetals have found wider use when titanium nitride, δ-TiN, was

Table 4 Properties of some important Transition Metal Carbides, Nitrides, and Quarternary Carbonitrides

Phase	Structure	Lattice parameter (room temperature) (Å)	Density (g cm^{-3})	Nano-hardness (GPa)	Micro-hardness (100 g load) (GPa)	Young's modulus (from nanohardness) (GPa)	Young's modulus (Ultrasonic) (GPa)
TiC	fcc	4.3261	4.80	31.6	28.9	435	424
$(Ti_{0,8}Zr_{0,2})(C_{0,8}N_{0,2})$	fcc	4.3849	5.42	32.7	27.3	463	447
$(Ti_{0,5}Zr_{0,5})(C_{0,5}N_{0,5})$	fcc	4.4801	6.11	30.2	28.0	448	408[a]
$(Ti_{0,2}Zr_{0,8})(C_{0,2}N_{0,8})$	fcc	4.5469	6.62	24.3	18.8	421	374
ZrN	fcc	4.5771	6.94	17.7	14.9	365	375
TaC	fcc	4.4528	12.88	13.2	11.8	342	–
$(Ta_{0,8}Ti_{0,2})(C_{0,8}N_{0,2})$	fcc	4.4197	12.65	26.6	25.4	477	–
$(Ta_{0,5}Ti_{0,5})(C_{0,5}N_{0,5})$	fcc	4.3602	10.12	26.8	22.8	577	–
$(Ta_{0,2}Ti_{0,8})(C_{0,2}N_{0,8})$	fcc	4.2938	9.25	24.5	23.5	425	–
TiN	fcc	4.2405	5.29	20.9	18.4	437	–
$(Ti_{0,5}Nb_{0,5})(C_{0,5}N_{0,5})$	fcc	4.3630	6.65	26.0	21.9	461	435
$(Ti_{0,5}Hf_{0,5})(C_{0,5}N_{0,5})$	fcc	4.4604	9.50	29.3	25.3	460	429[a]
$(Ti_{0,5}V_{0,5})(C_{0,5}N_{0,5})$	fcc	4.2258	5.52	26.4	24.3	467	413[a]
$(Zr_{0,5}Ta_{0,5})(C_{0,5}N_{0,5})$	fcc	4.5162	10.42	–	23.5	–	425

[a] Correction due to porosity is not considered in the calculation.

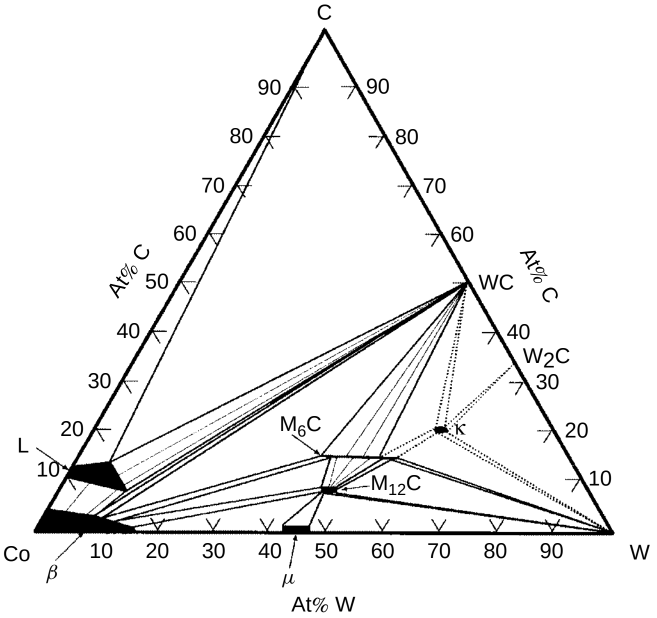

Figure 14 Phase diagram of the W–C–Co system at 1350 °C

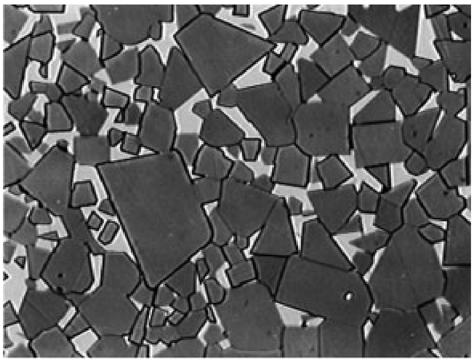

Figure 15 Microstructure of a coarse WC–Co hardmetal with gray WC particles embedded in a Co matrix, the size of the largest grains is about 20 µm

introduced as a further constituent. Generally, these titanium carbonitride hardmetals, often called cermets (an artificial word coined from the words ceramic and metal because of the combination of a brittle 'ceramic' component, which, however, has metallic transport properties as shown above, and a binder metal), are comparable with respect to properties and microstructure to WC-based hardmetals.

The compacted powder mixtures of these materials are usually liquid phase sintered with Ni or Ni–Co binder metal alloys. The microstructure features a core-and-rim structure of the hard phase with a molybdenum- and carbon-rich (Ti,Mo)C rim and a titanium- and nitrogen-rich Ti(C,N) core. This microstructure can be made visible in the SEM (Figure 16). The metallurgy of the phase reactions is not yet fully understood,[50] because of the complexity of the multicomponent system. The theoretical background of the phase reactions within the system Ti–Mo–C–N was developed by Rudy,[30] who claimed that the quaternary compound (Ti,Mo)(C,N) with a random distribution of the metals Ti and Mo on the metal sites and the nonmetals C and N on the nonmetal sites should undergo a decomposition with the formation of two isotypic fcc phases but with a preferential arrangement of N around the Ti atoms and Mo around the C atoms. This decomposition is of a spinodal type, which is a decomposition induced by local composition fluctuations without any activation energy rather than a classical nucleation and growth process. The question whether the spinodal decomposition is a necessary prerequisite for the core-and-rim formation of the hard component is still the topic of discussions because core-and-rim structures may develop via reactions of the hard constituents with the liquid binder metals as well.

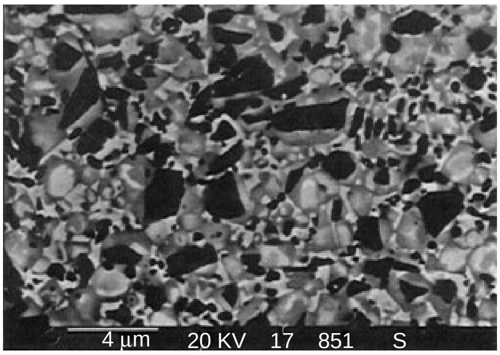

Figure 16 Microstructure of a titanium carbonitride hardmetal (cermet) showing the core-and-rim type structure of hard particles

The core-and-rim type structure has been claimed to have a favorable influence on the mechanical properties because the molybdenum-containing rim is much better wetted by the binder alloy than the nitrogen-containing core. Modern Ti(C,N) hardmetals have been successfully applied for finishing operations of high-strength steel grades and ductile cast irons at high cutting speeds but with moderate cross section of the chips. The main advantages of Ti(C,N) hardmetals over conventional hardmetals are the high chemical resistance and the low frictional welding tendency, resulting in longer life of the cutting edge and a good workpiece surface. For some applications, Ti(C,N) cermets do outperform even coated WC hardmetals.

9.1.2 Cemented Carbide Grades

The cemented carbides are used for a variety of different applications ranging from metal cutting, drilling, and milling (steel and nonferrous alloys) over wood cutting to drilling of circuit boards for electronic devices as well as for structural parts such as dies and cutters for the paper industry. Examples for the tools are given in Figure 17 and 18. Table 5 gives a summary of the various grades in use. One of the most important developments in recent years is the application of submicrometer sized WC powders used for WC–Co hardmetals such as for micro-drilling and wood cutting. Such ultra-fine grained cemented carbides have very high hardness and bending strength. They are doped with VC and/or Cr_3C_2, which serve as a grain-growth inhibitor.

9.2 Wear-resistant Layers

Wear-resistant layers of transition metal carbides that have been deposited by CVD (*see Chemical Vapor Deposition*) and PVD processes on the surface of WC–Co hardmetals further reduce the wear in cutting applications. About 80% of all tool tips for metal cutting are coated. Modern multilayer coating feature a combination of different layers, where TiN is often the base layer adjacent to the substrate, Ti(C,N) is an intermediate layer and TiN is the top layer. This should provide a smooth variation of properties across the layer, from good adherence to the hardmetal to the high chemical inertness and low tool-workpiece frictional welding tendency of TiN. Such layers are usually made by CVD processes where a volatile component such as titanium tetrachloride is reacted with a

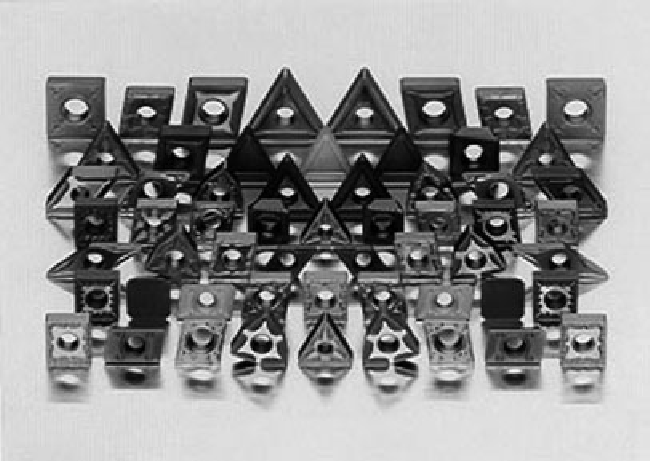

Figure 17 Examples of different cutting inserts used in cutting industry (Kennametal-Widia GmbH)

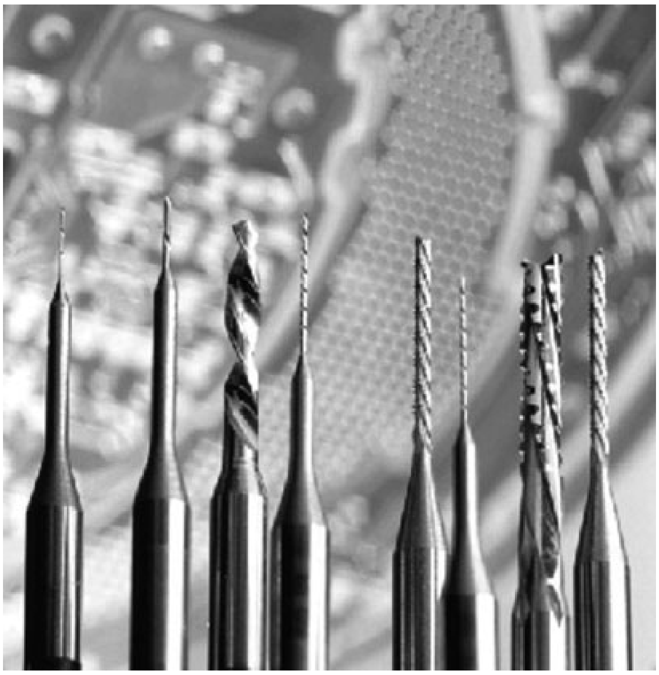

Figure 18 Microdrills used in electronic industry made of ultra-fine WC

Table 5 Characteristics of hardmetal and cermet grades and their applications

Composition	Grain Size μm	Amount of binder metal wt%	Applications
WC–Co	ultra fine	2–4	wood cutting tools, wear parts
	0.2–0.5	6–9	microdrills for PCBs, cutting inserts
		10–16	rotating tools, paper knifes
WC–Co	submicron 0.5–0.8	4–16	cutting inserts, rotating tools
WC–Co	fine 0.8–1.3	4–25	cutting inserts, wear parts noncutting shaping tools
WC–Co	midsize 1.3–2.5	4–25	cutting inserts for heavy cutting noncutting shaping tools
WC–Co	coarse 2.5–6.0	4–25	rock cutting tools
WC–Co	extra coarse >6.0	4–25	forming tools
WC–Ni(Cr)(Co)	0.5–2	4–20	chemical apparatus engineering corrosion resistant and nonmagnetic parts
WC-(Ti,Ta,Nb)C–Co	0.5–2	4–15	cutting tools for steel chipping
Cermets	0.5–3	5–20	cutting tools for steel chipping

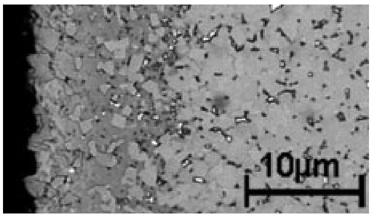

Figure 19 Microstructure of a functionally graded hardmetal

gas, the composition of which is gradually changed from methane-rich to nitrogen/ammonia-rich. The gas pressures are on the order of 100 mbar and temperatures are about 1000 °C. The thicknesses of the coatings are about 1–10 μm. A microstructure of a TiN/TiCN/Al_2O_3/TiN coating is given in the article (*see* ***Nitrides: Transition Metal Solid-state Chemistry***).

Recent developments in the field of CVD and PVD layers are multilayer coatings that consist of carbonitrides, carbides, nitrides, and oxides, whereas the trend goes into the use of ternary and quaternary carbonitrides[51] such as Zr(C,N) and (Ti,Hf)(C,N) as well as mixed oxides such as Al_2O_3/TiO_2, $Al_2O_3/TiO_2/HfO_2$.

PVD (physical vapor deposition) methods can be applied whenever the substrate temperature has to be kept lower than 600 °C (e.g. for quenched-hardened steel items); they make use of a variety of techniques ranging from sputtering to ion beam deposition.

Another recent development on the field of wear-resistant layers is the formation of graded zones in functionally graded hardmetals FGHMs (cemented carbides).[52] These near-surface zones are formed by diffusion of mainly nitrogen into a Ti-containing hardmetal so as to create a Ti(C,N)-enriched surface. Some of these FGHMs show a smooth increase of the nitride phases towards the surface and thus a absence of a macroscopic interface. An example of an microstructure is given in Figure 19. The lifetime of such graded hardmetals is more than tenfold of that of untreated grades. Such FGHMs can be used as a substrate for nitride and carbonitride as well as diamond coatings and outperform hardmetals without graded substrate.

9.3 Diffusion Barriers

Transition metal carbides can be used as diffusion barriers like transition metal nitrides in multilayer metallization schemes for integrated circuits.[53] Layers on the order of 100 nm are applied and are produced by sputtering methods. The high chemical stability of these transition metal carbides, especially those of group 4, are exploited to prevent interaction of metal or component layers such as silicon, aluminum, and silicides upon thermal load in production processes. This load would cause electrical or even structural deterioration of the multilayer packages.

10 REFERENCES

1. P. Schwarzkopf and R. Kieffer, ‘Refractory Hard Metals’, Macmillan, 1953.
2. E. K. Storms, in ‘MTP International Review of Science, Inorganic Chemistry Series One’, ed. L. E. J. Roberts, Butterworths, London, 1972, Vol. 10.
3. L. E. Toth, ‘Transition Metal Carbides and Nitrides’, Academic Press, New York-London, 1971.
4. H. J. Goldschmidt, ‘Interstitial Alloys’, Butterworths, London, 1967.
5. E. Parthé and K. Yvon, *Acta Crystallogr. B*, 1970, **26**, 153.
6. K. Yvon and E. Parthé, *Acta Crystallogr. B*, 1970, **26**, 149.
7. T. Epicier, in ‘The Physics and Chemistry of Carbides, Nitrides and Borides’, ed. R. Freer, Kluwer Academic Publishers, Dordrecht, 1990, p. 215.
8. C. H. de Novion, B. Beuneu, T. Priem, N. Lorenzelli, and A. Finel, in ‘The Physics and Chemistry of Carbides, Nitrides and Borides’, ed. R. Freer, Kluwer Academic Publishers, Dordrecht, 1990, p. 329.
9. P. Villars and L. D. Calvert eds, ‘Pearson’s Handbook of Crystallographic Data for Intermetallic Phases’, 2nd edn., ASM, Metals Park, OH.
10. R. Ward, in ‘MTP International Review of Science’, Inorganic Chemistry Series One, ed. D. W. A. Sharp, Butterworths, London, 1972, Vol. 5.
11. T. Epicier, in ‘The Physics and Chemistry of Carbides, Nitrides and Borides’, ed. R. Freer, Kluwer Academic Publishers, Dordrecht, 1990, p. 297.
12. W. Lengauer, in ‘Handbook of Ceramic Hard Materials’, ed. R. Riedel, Wiley-VCH, Weinheim, 2000, Vol. I, p. 202.
13. A. Neckel, in ‘’The Physics and Chemistry of Carbides, Nitrides and Borides’, ed. R. Freer, Kluwer Academic Publishers, Dordrecht, 1990, p. 458.
14. P. Blaha and K. Schwarz, *Int. J. Quantum Chem.*, 1983, **23**, 1535.
15. P. McKenna, US Patent 3 379 503 1968; *Chem. Abstr.*, 1968, **68**, 116 088.
16. J. Billingham, P. S. Bell, and M. H. Lewis, *J. Cryst. Growth*, 1972, **13/14**, 693.
17. P. McKenna, *Met. Prog.*, 1939, **36**, 152.
18. G. F. Bastin and H. J. M. Heijligers, *J. Microsc. Spectrosc. Electron.*, 1986, **11**, 215.
19. W. Lengauer, D. Rafaja, R. Täubler, C. Kral, and P. Ettmayer, *Acta Metall. Mater.*, 1993, **41**(12), 3505.
20. W. Lengauer, D. Rafaja, G. Zehetner, and P. Ettmayer, *Acta Mater.*, 1996, **44**(8), 3331.
21. W. Lengauer, J. Bauer, M. Bohn, H. Wiesenberger, and P. Ettmayer, *Mikrochim. Acta*, 1997, **126**, 279.
22. H. Wiesenberger, W. Lengauer, and P. Ettmayer, *Acta Mater.*, 1998, **46**(2), 651.

23. W. Mayr, W. Lengauer, D. Rafaja, J. Bauer, and M. Bohn, *J. Phase Equilib.*, 1999, **20**, 35.
24. M. Hoch, in ‘Phase Stability in Metals and Alloys’, eds. P. S. Rudman, J. Stringer, and R. I. Jaffee, McGraw-Hill, New-York, 1967, p. 419.
25. T. B. Massalski ed. ‘Binary Alloys Phase Diagrams’, 2nd edn., ASM International, Metals Park, OH, 1991.
26. R. Kieffer, H. Nowotny, A. Neckel, P. Ettmayer, and L. Usner, *Monatsh. Chem.*, 1968, **99**, 1020.
27. M. W. Barsoum, T. El-Raghy, and M. Radovic, *Interceram*, 2000, **49**(4), 226.
28. H. Nowotny and F. Benesovsky, in ‘Phase Stability in Metals and Alloys’, eds. P. S. Rudman, J. Stringer, and R. I. Jaffee, McGraw-Hill, New-York, 1967, p. 419.
29. P. Ettmayer, G. Vinek, and H. Rassaerts, *Monatsh. Chem.*, 1967, **98**, 1883.
30. E. Rudy, *J. Less-Common Met.*, 1973, **33**, 43.
31. W. S. Williams, in ‘The Physics and Chemistry of Carbides, Nitrides and Borides’, ed. R. Freer, Kluwer Academic Publishers, Dordrecht, 1990, p. 625.
32. W. Lengauer, S. Binder, K. Aigner, P. Ettmayer, A. Guillou, J. Debuigne, and G. Groboth, *J. Alloys Compd.*, 1995, **217**, 137.
33. R. R. Reeber and K. Wang, *J. Am. Ceram. Soc.*, 1999, **82**, 129.
34. K. Aigner, W. Lengauer, D. Rafaja, and P. Ettmayer, *J. Alloys Compd.*, 1994, **215**, 121.
35. D. Rafaja, H. Wiesenberger, W. Lengauer, and M. Joguet, *Metall. Mater. Trans. A*, 1998, **29A**, 439.
36. D. Rafaja, W. Lengauer, and H. Wiesenberger, *Acta Mater.*, 1998, **46**(1), 3477.
37. H. Matzke, in ‘The Physics and Chemistry of Carbides, Nitrides and Borides’, ed. R. Freer, Kluwer Academic Publishers, Dordrecht, 1990, p. 357.
38. F. J. J. van Loo and G. F. Bastin, *Metallurg. Trans. A*, 1989, **20**, 403.
39. E. Török, A. J. Perry, L. Chollet, and W. D. Sproul, *Thin Solid Films*, 1987, **153**, 37.
40. C. Kral, W. Lengauer, D. Rafaja, and P. Ettmayer, *J. Alloys Compd.*, 1998, **265**(1–2), 215.
41. Q. Yang, W. Lengauer, T. Koch, M. Scheerer, and I. Smid, *J. Alloys Compd.*, 2000, **309**, L5.
42. J.-L. Chermant, Delavignette, A. Deschanvres, *J. Less-Common Met.*, 1970, **21**, 89.
43. V. N. Lipatnikov, W. Lengauer, P. Ettmayer, E. Keil, G. Groboth, and E. Kny, *J. Alloys Compd.*, 1997, **261**, 192.
44. Y. Kumashiro, E. Sakuma, Y. Kimura, H. Ihara, and S. Misawa, *J. Cryst. Growth*, 1981, **52**, 597.
45. F. W. Vahldiek and S. A. Mersol, *J. Less-Common Met.*, 1977, **55**, 265.
46. D. W. Lee and J. S. Haggerty, *J. Am. Ceram. Soc.*, 1969, **52**, 641.
47. G. Das, K. S. Mazdiyasni, and H. A. Lipsitt, *J. Am. Ceram. Soc.*, 1982, **65**, 104.
48. R. Könighsofer, A. Liersch, W. Lengauer, T. Koch, M. Scheerer, W. Hohenauer ‘Proceedings of PM2004 World Conference on Powder Metallurgy’, Vienna, EPMA, Shrewsbury, UK, ISBN 1899072 15 2 Vol. 3, p. 593.
49. L. Åkesson, Dissertation, Kungliga Tekniska Högskolan, Stockholm, 1982.
50. P. Ettmayer, *Annu. Rev. Mater. Sci.*, 1989, **19**, 145.
51. H. Westphal, V. Sottke, Patent PCT Int. Appl., WO 2002077312 A2, 2002.
52. W. Lengauer and K. Dreyer, *J. Alloys Compd.*, 2002, **338**(1–2), 194.
53. S. P. Murarka, *Defect Diffus. Forum*, 1988, **59**, 99.

Carbon: Fullerenes

Jonathan D. Crane & Harold W. Kroto
University of Sussex, Brighton, UK

1	Introduction	1
2	Structure and Bonding	1
3	Synthesis and Purification	7
4	Beam Studies	8
5	Physical and Spectroscopic Properties	9
6	Chemistry	12
7	Related Articles	20
8	References	20

Glossary

Fullerene: closed hollow-cage molecule consisting solely of carbon atoms which are arranged as pentagonal and hexagonal rings
IPR Fullerene: fullerene which satisfies the isolated pentagon rule, i.e. there are no edge-sharing pentagonal rings

Abbreviations

IPR = Isolated pentagon rule; Fc/Fc$^+$ = Ferrocene/ferricinium couple (redox potential reference).

1 INTRODUCTION

The fullerene family represents a new *Allotrope* of carbon, which now stands alongside the two more familiar forms: black graphite, with its lubricating properties, and the sparkling gemstone diamond, one of the hardest materials known. The fullerenes are fundamentally different from both these forms of carbon as they are an infinite family of discrete cage-like molecules, of which buckminsterfullerene is the archetype (named after the architect Richard Buckminster Fuller, designer of the geodesic dome). The idealized infinite structures of graphite and diamond are shown in Figure 1, and the 'dangling bonds' at the boundaries of these repeating patterns are usually terminated by another element or group (typically hydrogen and/or oxygen). In contrast, the fullerenes are closed molecules with no edges, and as such they represent a truely 'pure' form of carbon.

1.1 History

The properties of hypothetical closed carbon cages have been the subject of discussion for many years, and the highly symmetric truncated icosahedral (soccer ball) geometry of the archetypal species buckminsterfullerene (C_{60}) had particular appeal. It was suggested that C_{60} would be stable and possibly 'superaromatic',[1] but the deliberate synthesis of such a complex molecule remained too daunting a challenge.[2]

The first major breakthrough in fullerene chemistry occurred in 1985, during an experiment designed to simulate the aggregation of carbon atoms in cool red giant stars. A carbon plasma generated by laser vaporization of graphite spontaneously formed large carbon clusters upon cooling, and mass spectrometric analysis of the products showed that the cluster ions $C_{60}{}^+$ and $C_{70}{}^+$ were particularly stable (Figure 2).[3] Hollow cage structures were proposed, and subsequent experiments showing that other elements could be encapsulated inside these cages were consistent with these proposals.

The second major breakthrough came in 1990, when the presence of macroscopic quantities of C_{60} in the soot generated by arc vaporization of graphite was established.[4] A mixture of C_{60}, C_{70}, and other larger fullerenes was extracted from this soot and shown to be a new crystalline form of carbon (Figure 3). Chromatographic separation of this mixture gave pure C_{60} and C_{70}, and their proposed molecular cage structures were confirmed by ^{13}C NMR spectroscopy (Section 5.3).[5]

2 STRUCTURE AND BONDING

2.1 General Definitions

Fullerenes are closed hollow cages consisting solely of carbon atoms. Each carbon atom is bonded to three neighbors and is sp^2 hybridized, as in the hypothetical structure of graphite (*see Hybridization*). A 'perfect' graphite sheet, however, is an infinite flat array of hexagonal rings and cannot be closed to a cage structure without the incorporation of defects (disclinations). Euler's equation (equation 1) relates the number of vertices (V), edges (E), and faces (F) of a simple polyhedron, and satisfaction of the condition that each vertex is linked to exactly three neighbors gives equation (2), where n_i is the number of i-sided polygons in the polyhedron. In general, the term fullerene refers to cages comprised solely of pentagonal and hexagonal rings, and although other defects may be envisaged (e.g. smaller or larger rings), these are expected to result in strained structures. Thus it can be seen from equation (2) that incorporation of exactly 12 pentagonal rings is sufficient to effect cage closure, and that the general molecular formula for all fullerenes is C_{20+2n} for integral

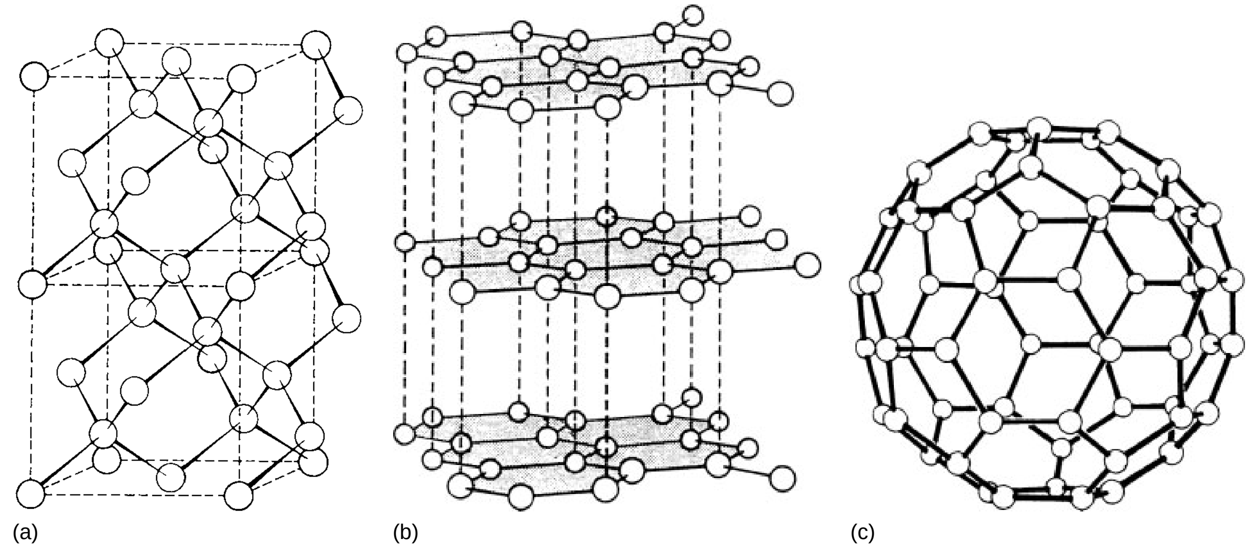

Figure 1 Structures of the three main forms of carbon: (a) diamond; (b) α-graphite; and (c) buckminsterfullerene (I_h-C_{60}), the archetype of the fullerene family

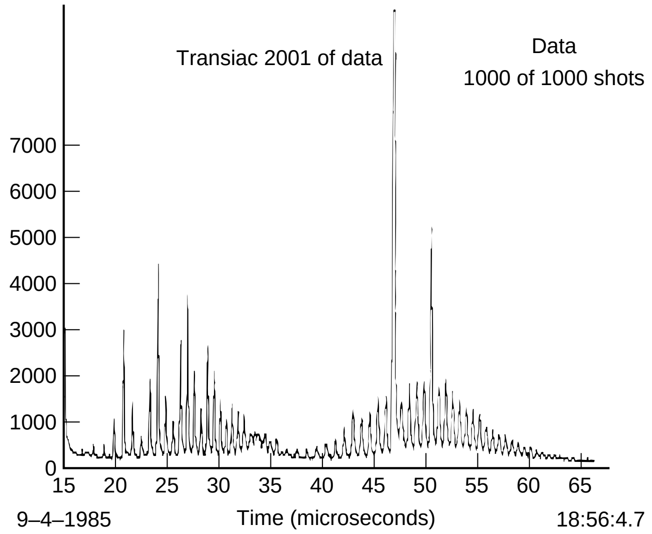

Figure 2 Time-of-flight mass spectrum of carbon clusters produced by laser vaporization of graphite (September 4, 1985) under conditions which first exhibited the dominance of the C_{60} cluster and led to the recognition that 60 might be a magic number. (Reprinted with permission from Ref. 2a. © 1991 American Chemical Society)

values of n ($n \neq 1$; C_{22} cannot be constructed with only hexagonal and pentagonal rings). Fullerenes therefore contain an even number of carbon atoms arranged as a combination of 12 pentagonal rings and any number n ($n \neq 1$) of hexagonal rings, e.g. the archetypal fullerene, buckminsterfullerene (I_h-C_{60}), consists of 12 (isolated) pentagons and 20 hexagons (Figure 1(c)). Buckminsterfullerene is the only fullerene to have acquired an accepted trivial name, albeit a slightly long one. In general the simpler fullerenes are referred to by their symmetry and size, e.g. I_h-fullerene-60, although for convenience and brevity the fullerene cage structure is often assumed and the molecular formula used, e.g. I_h-C_{60}, D_2-C_{76}, or simply by the molecular formula alone if only one cage symmetry is known, e.g. C_{60}, C_{70}.

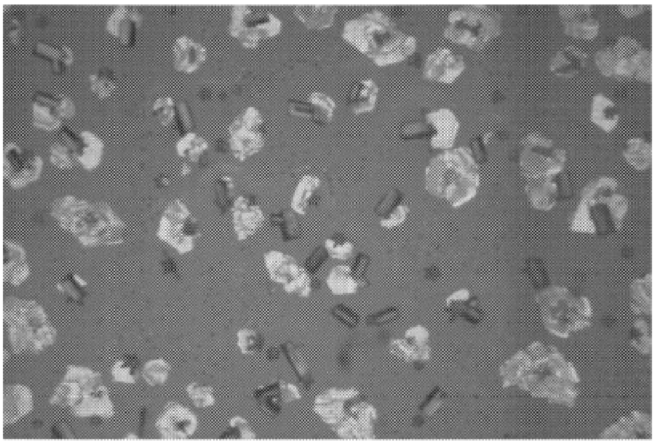

Figure 3 Photograph (by transmitted light) of the fullerene crystals formed by gentle evaporation of the red/brown benzene extract from ‘soot’ produced by the arc vaporization of graphite. (Reprinted with permission of Macmillan from W. Krätschmer *et al.*[4])

$$V - E + F = 2 \qquad (1)$$

$$3n_3 + 2n_4 + n_5 - n_7 - 2n_8 - 3n_9 - \cdots = 12 \qquad (2)$$

Heterofullerenes are derivatives of fullerenes in which one or more carbon atoms have been replaced by a different element without disruption of the basic cage structure, e.g. $C_{59}B$.

Endohedral fullerenes are molecules in which an atom or group of atoms is encapsulated within the cage. In the case of metal encapsulation the compounds are commonly referred to as endohedral metallofullerenes. The accepted symbol to indicate encapsulation is @, e.g. $U@C_{28}$, $La@C_{82}$.

2.2 Fullerene Structure

As the general formula for a fullerene is C_{20+2n} $(n \neq 1)$, the three simplest fullerenes are I_h-C_{20}, D_{6d}-C_{24}, and D_{3h}-C_{26} (Figure 4), and there is only one isomer for each of these. For the larger fullerenes more structures are possible, the number of which increases rapidly with cage size and can be calculated using the Ring Spiral Algorithm.[6] For fullerenes up to C_{380} this algorithm generates all isomers and reduces each to a unique sequence of numbers and therefore provides an unambiguous (although incomprehensible) naming scheme.[7]

The ring spiral algorithm shows that the C_{60} molecule has 1812 different possible isomeric structures; however, experimentally only the I_h-C_{60} isomer is observed. The observation that unsaturated organic molecules containing edge-sharing pentagons tend to be unstable is the basis of the Isolated Pentagonal Rule (IPR) for fullerene stability.[2,8,9] This rule is elegantly confirmed by I_h-C_{60} being the only isomer of C_{60} for which all the pentagonal rings are indeed isolated from one another. Using this principle the fullerene D_{5h}-C_{50} is (correctly) predicted to display enhanced stability since it is the smallest system to exclude triplets of edge-sharing pentagons, although stability is also dependent on several other factors, including electronic structure and molecular strain (Section 2.3). The lowest energy structures of all the smaller fullerenes (C_n, $20 \leq n \leq 70$) have been calculated, and this study confirms that those isomers with the fewest edge-sharing pentagons are indeed the most stable.[10] Under the appropriate experimental conditions (single photon ionization), the enhanced stability of the smaller fullerene cations $C_{28}{}^{+}$, $C_{32}{}^{+}$, and $C_{50}{}^{+}$ is apparent (Figure 5).[11]

To date, all isolable nonderivatized fullerenes satisfy the IPR, although this rule does not necessarily predict that a fullerene will be stable or isolable (Section 2.3). After I_h-C_{60} the next possible IPR fullerene structure is D_{5h}-C_{70}, and historically the observation that C_{60} and C_{70} displayed special stability provided strong evidence for both the cage structures of these molecules and the IPR.[2] Other fullerenes which have been characterized to date are D_2-C_{76}, C_{2v}-C_{78}, C'_{2v}-C_{78}, D_3-C_{78}, C_2-C_{82} (maybe more than one isomer), C_{2v}-C_{82}, C_{3v}-C_{82}, D_2-C_{84}, and D_{2d}-C_{84} (Section 5.3).[12–15] D_2-C_{76} has the interesting feature of being the smallest, chiral fullerene so far isolated (Figure 6). For C_{78} and the larger fullerenes there are many possible IPR isomers, although only a few have been isolated to date. Mixtures containing fullerenes larger than

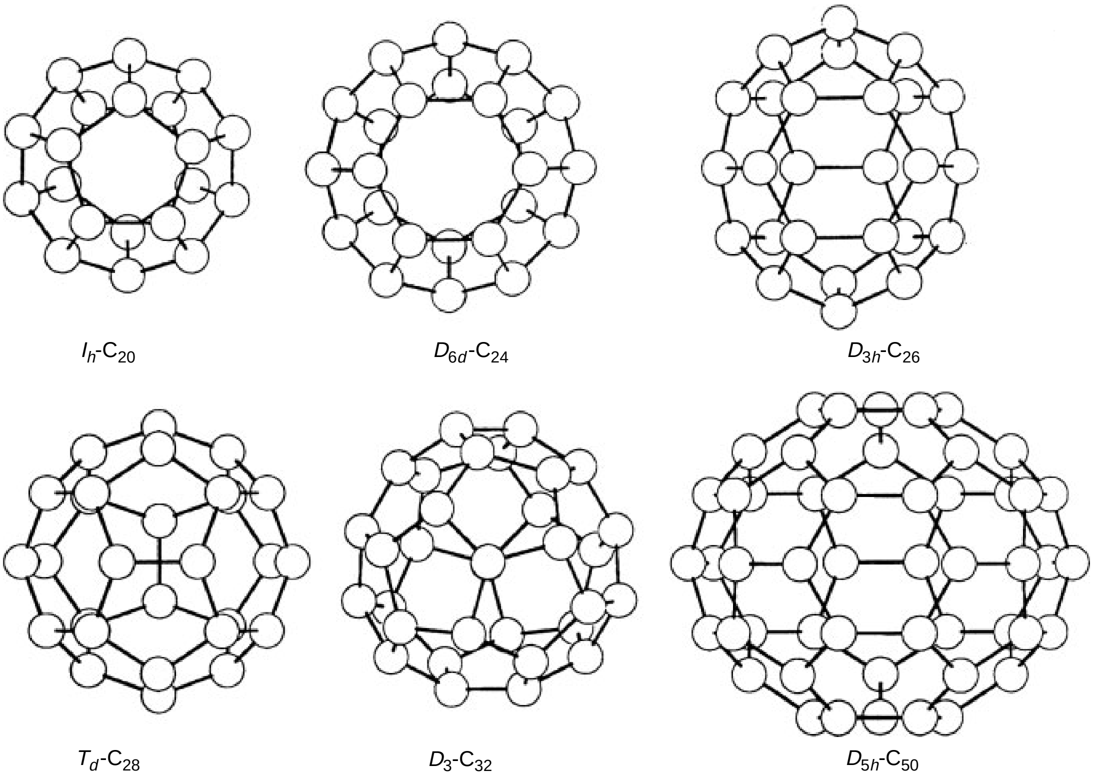
I_h-C_{20} D_{6d}-C_{24} D_{3h}-C_{26}

T_d-C_{28} D_3-C_{32} D_{5h}-C_{50}

Figure 4 Possible cage structures and idealized symmetries of some of the smaller fullerenes

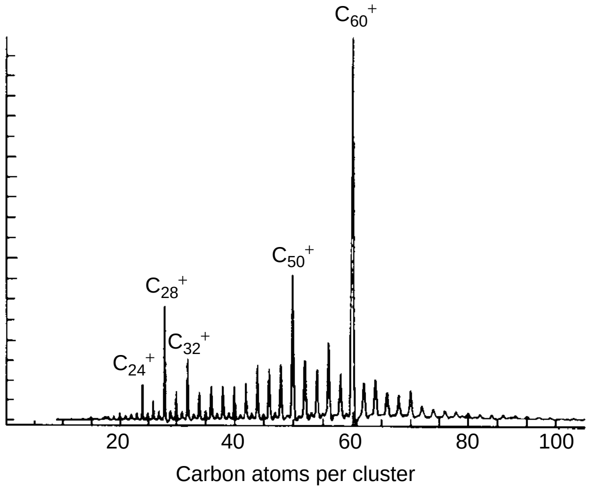

Figure 5 Time-of-flight mass spectrum of carbon clusters with single photon ionization (F_2, 7.87 eV at 0.050 mJ/pulse) showing the relatively high abundance of the smaller fullerene ions $C_{24}{}^+$, $C_{28}{}^+$, $C_{32}{}^+$, and $C_{50}{}^+$. (Reprinted with permission from D.M. Cox, K.C. Reichmann, and A. Kaldor, *J. Chem. Phys.*, 1988, **88**, 1588. © 1988, American Institute of Physics)

C_{84} are known, but their structures and isomeric compositions have yet to be determined.[16]

The isolable fullerenes C_{60} and C_{70} have been chemically functionalized and an unambiguous atom numbering scheme is required for the systematic naming of their derivatives. Although no generally applicable numbering scheme for all fullerenes has been developed, the accepted procedure for the C_{60} cage is to start with a pentagonal ring and spiral clockwise round the molecule (Figure 7), e.g. 1,6,9,12,15,18-hexabromofullerene-60 (Section 6.2.2, Figure 24(b)). Unfortunately this method is not readily adaptable to C_{70} and the other fullerenes.

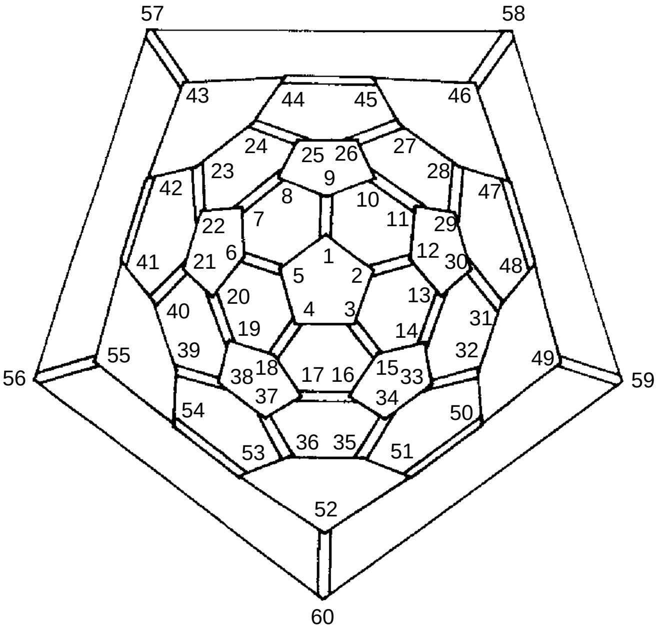

Figure 7 Schlegel diagram of C_{60} showing the accepted carbon atom numbering scheme

Very large (giant) fullerenes can be envisaged. In the family of fullerenes having the same symmetry as I_h-C_{60}, the next two members are C_{240} and C_{540} (Figure 8).[2] In addition, there is a second I_h family based on I_h-C_{80}, and many other fullerenes of lower I symmetry.[17] With increasing size these ideal structures become more icosahedral rather than spherical, although the 20 triangular faces actually form a single, smoothly curved 'graphitic' surface with strain largely localized around the pentagonal defects. Such molecules can be nested inside one another to produce idealized onion-like structures. For the C_{60}/C_{240}/C_{540} family the distance between

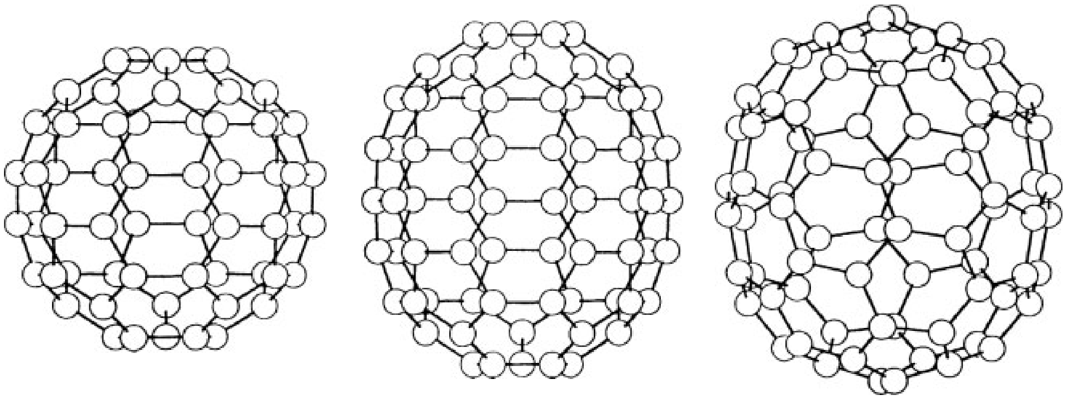

I_h-C_{60} D_{5h}-C_{70} D_2-C_{76}

Figure 6 The spectroscopically confirmed cage structures of the first three fullerenes to be isolated in macroscopic amounts; I_h-C_{60}, D_{5h}-C_{70}, and the chiral fullerene D_2-C_{76}

concentric shells is always ~3.5 Å, which corresponds well to the *inter*-plane distance reported for graphite. Real, albeit imperfect, structures of this type, comprising up to 70 shells, have been observed in transmission electron micrographs of carbon soot that had been annealed by strong electron beam irradiation (Figure 9(a)).**18**

Nanofiber structures, which appear to grow spontaneously from carbon vapor under the appropriate experimental conditions, have also been identified (Figure 9(b)).**19** They consist of concentric cylinders which are closed at the ends by capping groups similar in structure to one half of the onion structures described previously. Under specific experimental conditions (O_2/molten Pb) some endcaps appear to open, and the lead atoms flow inside the tubes.**20**

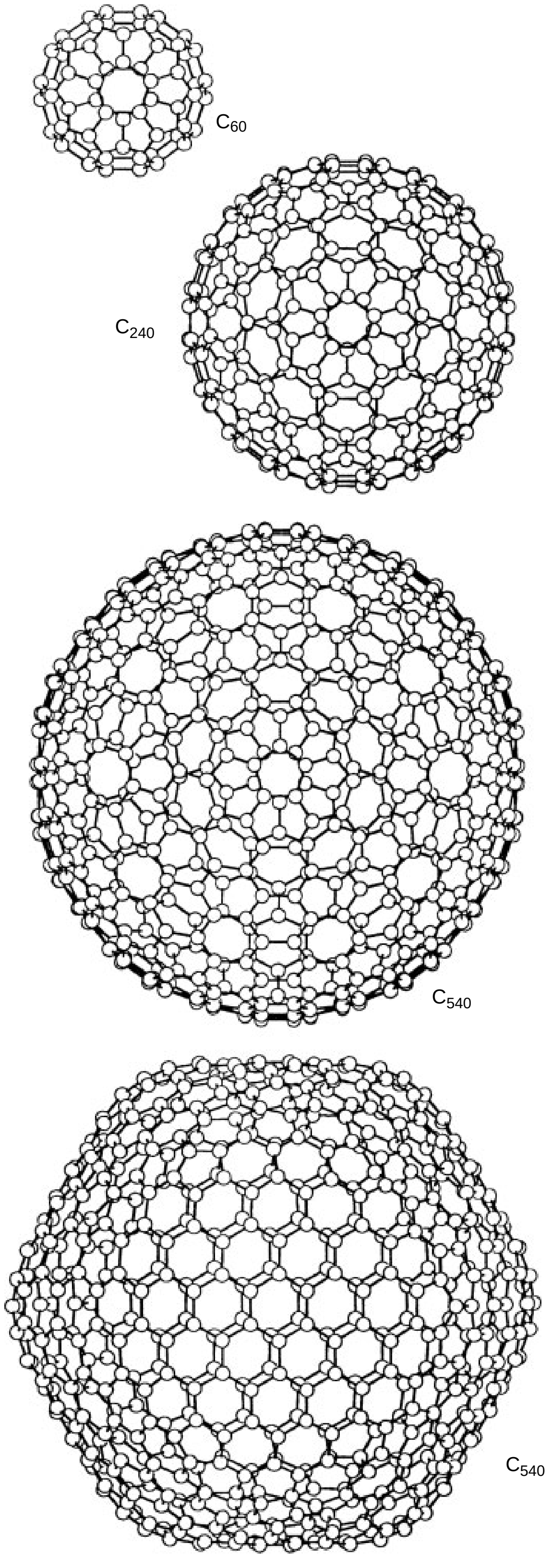

Figure 8 Computer-generated cage structures of the I_h-fullerenes C_{60}, C_{240}, and C_{540} (viewed along C_5-axes). The icosahedral shape of C_{540} is emphasized by viewing along a C_3-axis

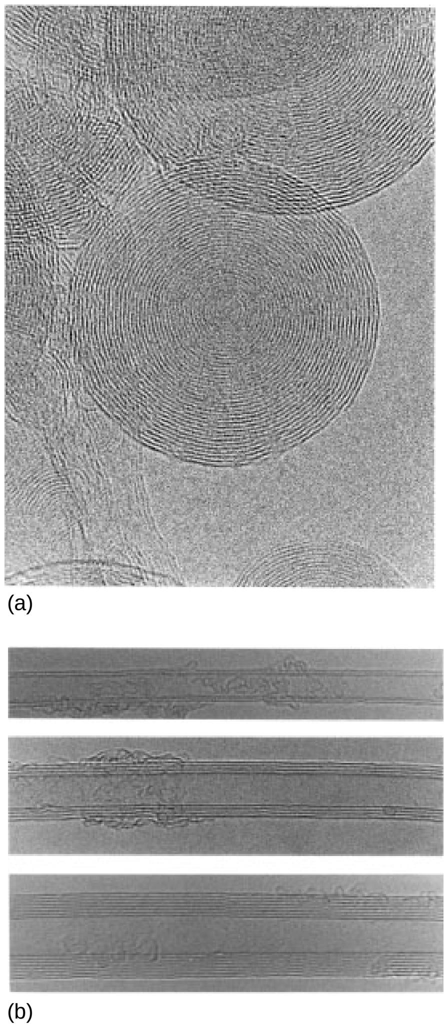

Figure 9 Transmission electron micrographs of nonplanar, carbon structures in which the *inter*-layer distances correspond to graphitic spacing (~3.4 Å). (a) Multishell carbon onions. (Reprinted with permission of Macmillan from D. Ugarte.**18**) (b) Carbon nanotubes. (Reprinted with permission of Macmillan from T.W. Ebbesen and P.M. Ajayan.**19**)

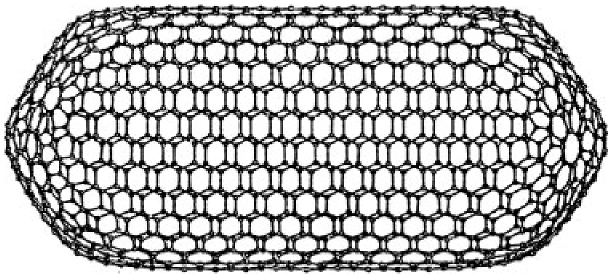

Figure 10 Computer-generated structure of a closed cylindrical fullerene cage (zeppelene). (Reprinted with permission from Ref. 21. © 1992 American Chemical Society)

The term zeppelene (Figure 10) has been coined to describe the discrete molecules formed by closing single cylinders at both ends (or alternatively by elongating a fullerene).[21] The nonplanar nature of all these materials has opened a debate on the relative stabilities of carbon structures on the microscopic and macroscopic scale, and has consequences for the generally accepted planar 2D description of graphite.[22]

In the transmission electron micrographs of these carbon structures, the carbon sheets are sometimes found to have regions of negative curvature. This is only possible with the incorporation of heptagonal or larger ring defects; positive curvature is defined by pentagonal defects and results in closure (fullerenes), whereas negative curvature produces open structures.[23] From equation (2) the theoretical possibility arises that a graphitic sheet can be deformed to enclose a macroscopic volume of any shape or size simply by the incorporation of $12 + n$ pentagonal and n heptagonal defects.

2.3 Stability and Electronic Structure

Stability within the IPR fullerene family is dependent on a balance of electronic and molecular strain factors. The carbon atoms in the fullerenes are approximately sp^2 hybridized (although curvature of the cage causes a small admixture of sp^3), with the remaining p-orbitals (mixed with a small s-orbital contribution) on each carbon forming a π-system which covers both the outside (*exo*) and inside (*endo*) surfaces of the cage. The electronic structure of these extended π-systems are readily modeled with basic Hückel molecular orbital theory (*see Hückel Theory*). These simple calculations show that C_{60} is a closed-shell molecule with a large *HOMO–LUMO Gap* (Figure 11),[24] and is a rare example of an organic molecule with a threefold degenerate t_{1u} LUMO, not to mention a fivefold degenerate h_u HOMO.[2] Theoretical calculations also show that of all the possible resonance (Kekulé) structures for C_{60}, the one in which the 30 six–six ring fusions correspond to the double bonds is the dominant contribution to the π-electronic structure (Figure 7). Thus the π-bonding in C_{60} is best described as localized rather than 'superaromatic', and this localized polyalkene description is in good agreement with the observed chemical reactivity of C_{60} to date (Section 6.2).

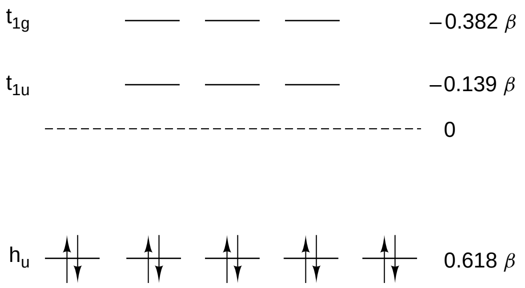

Figure 11 Energy level diagram for the HOMO and first two LUMOs of the 60π-electron system of C_{60}, calculated by simple Hückel molecular orbital theory

The only closed-shell fullerenes predicted by simple Hückel theory fall into two types; the leapfrog fullerenes C_{60+6n} ($n \neq 1$), and the cylinders C_{70+30m} and C_{84+36m} ($m \geq 0$) formed by stretching D_{5h}-C_{70} and D_{6h}-C_{84} along their respective C_5 and C_6 axes.[25] The simplicity of the theory unfortunately prevents these rules having any general utility. Neither of the two IPR-isomers of C_{76} is predicted to be stable but D_2-C_{76} has been isolated, whereas the expected fullerene D_{6d}-C_{72} has not, although its apparent low stability may be

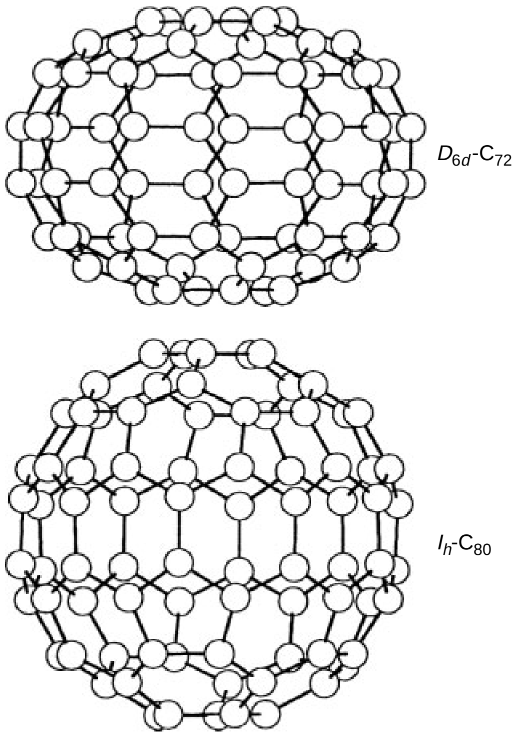

Figure 12 Computer-generated cage structures of the nonisolable IPR fullerenes D_{6d}-C_{72} and I_h-C_{80}. The experimentally elusive nature of these molecules is believed to be due to molecular strain and electronic factors, respectively

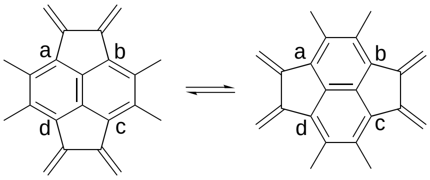

Figure 13 The interconversion of pairs of pentagonal and hexagonal rings through the thermally forbidden Stone–Wales transformation

due to its flattened shape and the consequent concentration of strain around its waist. Hückel theory, however, does predict the high instability of all isomers of C_{80}. In particular, I_h-C_{80} is a spherical molecule which has less strain per carbon atom than C_{60} but has not been isolated as the free fullerene (Figure 12). However, metal encapsulation appears to be able to stabilize formally open-shell fullerenes by the transfer of electrons from the metal to the cage, e.g. $C_{80}{}^{n-}$ in the endohedral fullerenes $M@C_{80}$ (Section 6.3).

The Stone–Wales (pyracyclene) transformation has been proposed as a mechanism for the interconversion of fullerene isomers through the interchange of pairs of pentagons and hexagons (Figure 13).[26] The rearrangement is a high-energy process which is thermally forbidden but photochemically allowed, and may therefore occur within the vicinity of a carbon arc.[27]

Restricted Stone–Wales isomerization (i.e. between IPR structures only) has been invoked to explain why relatively few isomers of the higher IPR fullerenes have been found:[13] three of the possible five for C_{78} have been reported, at least three out of nine for C_{82}, and two out of 24 for C_{84}. It is postulated that near the carbon arc those isomers which are interconvertable are annealed to the thermodynamically most stable one. At first sight the experimental facts appear to contradict this proposal since all nine of the C_{82} isomers can interconvert, yet at least three isomers have been shown to coexist.[28] It is possible, however, that if these three isomers are of similar energy then a statistical distribution of products would be expected, and this distribution would naturally be dependent upon the temperature at which the Stone–Wales interconversion ceases. As a consequence, whenever a particular fullerene is isolated the isomer distribution should be reproducible. Results consistent with this idea have indeed been reported for mixtures of the two Stone–Wales interconvertable C_{84} isomers prepared in different laboratories.[29]

3 SYNTHESIS AND PURIFICATION

Since the synthesis of macroscopic amounts of C_{60} was achieved in late 1990, several strategies for each stage of fullerene synthesis and purification have been developed.

3.1 Soot Generation

Fullerene-containing 'soot' can be prepared either directly from graphite (resistive heating/carbon arc, inductive heating, laser vaporization) or from hydrocarbons by controlled incomplete combustion. The latter two techniques are unsuitable for the bulk generation of soot: laser vaporization results in high fullerene yields but is not easily scaled up, whilst combustion methods are inefficient and the soot produced is contaminated with organic byproducts. The most widespread technique employed is graphite vaporization by resistive heating in an arc, and the yield of extractable fullerenes is typically 3–11%, though up to 44% has been reported.[30] This method produces 'pure' soot that contains C_{60} and C_{70} in the approximate ratio 85:15 along with traces (<1%) of the higher fullerenes, although optimization of the conditions for C_{70} production yields a ratio close to 50:50.[31] Vaporization by inductive heating (2700 °C) gives soot containing 8–12% extractable fullerenes and is reported to give slightly greater yields of the higher fullerenes.[32]

Soot containing small quantities of the endohedral metallofullerenes can be simply prepared by vaporizing graphite doped with a source of the appropriate metal, typically the metal oxide. The characterization of these materials is discussed in Section 6.3.

3.2 Fullerene Extraction and Purification

Soxhlet extraction of the soot with a suitable solvent yields crude fullerene mixtures. The nature of the solvent influences the rate of extraction and the efficiency with which the less soluble, higher fullerenes are extracted. For C_{60} and C_{70} the commonly used solvents are hexane, CH_2Cl_2, and $CHCl_3$, whereas for the larger fullerenes, CS_2, toluene, pyridine, and quinoline are used.[30]

Simple recrystallization of the crude fullerene extract can yield C_{60} of greater than 98% purity.[33] In order to remove all detectable traces of C_{70}, however, chromatographic techniques must be used and several efficient methods for the preparation of pure C_{60} and C_{70} have been published.[34–36] Small amounts of the higher fullerenes (C_{76}, C_{78}, C_{82}, C_{84}, C_{90}, etc.) must be separated and purified by time-consuming preparative HPLC.[12–15] Chromatographically purified fullerenes always contain traces of solvent impurities, although very high purity, solvent-free C_{60} and C_{70} can be obtained by repeated sublimation under high vacuum.

Although the fullerenes are very stable molecules in isolation, over time some degradation is observed both in the solid state and in solution. It is probable that light, combined with the presence of air, moisture, or trace impurities, is responsible (Section 6.2.3).

3.3 Toxicity

The short and long term toxicities of the fullerenes and related materials are unknown, and they should therefore be handled with all suitable precautions. The soot generated from graphite vaporization is very light and fluffy, and contains varying amounts of nanofiber structures. Such materials should not be inhaled because fine particulates are known to be responsible for the crippling and ultimately fatal conditions of asbestosis, silicosis, and emphysema. Although no studies on the toxicity of C_{60} have been reported, it is known to be a potent sensitizer for singlet oxygen and should therefore be handled with caution.[37]

4 BEAM STUDIES

4.1 Fullerene Formation and Fragmentation

The fullerenes were first observed by mass spectrometric techniques: a carbon plasma produced by laser vaporization of graphite aggregating to large carbon clusters C_n upon cooling.[2] The relative gas phase mobilities of these carbon clusters have been rationalized in terms of their structure; the smaller clusters are believed to have chain or ring structures, whereas the larger clusters adopt the closed fullerene structure.[38] This latter assignment is consistent with previous observations that for the larger clusters ($n > 30$) only those with an even number of carbon atoms (a requirement of the closed fullerene structure) are long lived, of which C_{60} and C_{70} exhibit particular stability (Figure 2).[2] Under similar conditions, endohedral fullerenes are formed by the vaporization of graphite doped with a source of the chosen element.

Mass spectrometric study of the gas phase oligomerization of the polyalkyne cyclocarbons (annulynes or cyclocumulenes) C_{18}, C_{24}, and C_{30} shows the preferential formation of the fullerene ions ${C_{60}}^+$ and ${C_{70}}^+$; in particular, C_{30} dimerizes almost exclusively to produce ${C_{60}}^+$.[2] Interestingly, inspection of the C_{60} cage reveals that this dimerization can be achieved by multiple cycloadditions without the need for any C–C bond breaking in the original C_{30} rings.

Multiphoton fragmentation of the fullerenes proceeds with elimination of even carbon fragments C_n ($n = 2, 4, 6$, etc.).[2] ${C_{60}}^+$ and ${C_{70}}^+$ are the preferred fragmentation products of the larger fullerenes C_{2n} ($2n > 70$), which further indicates the special stability of these clusters. For the ${C_{32}}^+$ ion, fragmentation results in the formation of a range of smaller species and the cage structure is lost. The corresponding fragmentation of the endohedral fullerenes (Section 6.3) also proceeds by multiples of C_2 elimination, but now the radius of the encapsulated element sets a lower limit on the size of the cage, e.g. $[K@C_{44}]^+$ and $[Cs@C_{48}]^+$ are the smallest endohedral fullerene ions observed for these elements. This sudden cut-off in stability at a particular cage size correlates well with the size of the encapsulated element, and provides strong evidence for the endohedral structure of these species.

Fullerene coalescence has been observed in the hot dense vapors produced by laser desorption of a fullerene sample into an inert carrier gas.[39] A broad distribution of products is seen, with distinct maxima corresponding to multiples of the starting fullerene: ${C_{118}}^+$ and ${C_{178}}^+$ for pure C_{60}, and ${C_{138}}^+$ for pure C_{70}. Coalescence is not observed in the absence of the carrier gas, indicating that the hot vapor must be constrained in order for reaction to take place. Under these conditions, not only do the initially formed ${C_{120}}^+$ and ${C_{180}}^+$ molecules fragment by loss of multiples of C_2, but aggregation to ${C_{120+2n}}^+$ and ${C_{180+2n}}^+$ also occurs.

4.2 Beam Reactions

C_{60} reacts with electrophiles E^+ (E = H, Me, Et, *t*-Bu) in the gas phase to give $[C_{60}E]^+$.[37] Proton transfer experiments have shown that the proton affinity of the C_{60} molecule lies in the range 204–207 kcal mol^{-1}, and the relatively high stability of the $[C_{60}H]^+$ species is demonstrated by the observation that in single collision experiments of the *t*-Bu$^+$ adduct $[C_{60}\cdots H\cdots C_4H_8]^+$ with Xe, fragmentation predominantly gives $[C_{60}H]^+$ and C_4H_8. Collision of C_{60} with C^+ ions in the gas phase over the energy range 2–78 eV results in the formation of ${C_{61}}^+$, which decays to ${C_{60}}^+$ and carbon atoms.[40] Reaction with $^{13}C^+$ produces ^{13}C enrichment of the ${C_{60}}^+$, clearly demonstrating that atom scrambling occurs in $[^{12}C_{60}{}^{13}C]^+$. Fragmentation to ${C_{58}}^+$, ${C_{56}}^+$, etc. is only observed for collision energies greater than 20 eV.

Adduct formation has been observed for the reaction of the fullerene dications ${C_{60}}^{2+}$ and ${C_{70}}^{2+}$ with neutral unsaturated hydrocarbons and amines, e.g. C_2H_2 and NH_3 produce $[C_{60}{\cdot}C_2H_2]^{2+}$ and $[C_{60}{\cdot}NH_3]^{2+}$ respectively, although for many systems charge transfer is a significant competing reaction.[41] Under different conditions the reaction of ${C_{60}}^{2+}$ with NH_3 is reported to give the adduct $[C_{60}NH_2]^+$,[42] in which the NH_2 fragment is thought to have added across a six–six ring fusion, giving the protonated aziridine analog of the C_{60} epoxide $C_{60}O$ (Section 6.2.3). Depending upon the NH_3 pressure, different amounts of the adducts $[C_{60}NH_2(NH_3)_n]^+$ ($n = 1$–3) are also observed. The NH_3 moieties are more weakly associated than the NH_2 group and are believed to be bound to the NH_2 group through hydrogen bonding.

Exohedral metal complexes $[C_{60}M]^+$ are formed by the reaction of C_{60} with naked M^+ ions (M = Fe, Co, Ni, Cu, Rh, La).[37] For Ni^+ the bis-fullerene complex $[(C_{60})_2Ni]^+$ was also observed. In contrast to the endohedral fullerenes, excitation of these complexes results in facile metal elimination with no associated cage fragmentation.

Collision-induced fragmentation of ${C_{60}}^{n+}$ ($n = 1$–3) with the noble gases helium and neon at high energy (typically 6 keV) results in the formation of encapsulated products, e.g. $[He@C_{60}]^{n+}$.[37,43] The retention of the gas atoms in the fragmentation products $[He@C_{2m}]^{n+}$ ($2m = 58, 56, 54$, etc.) is consistent with endohedral complex formulation. Furthermore, $[He@C_{60}]^+$ has been neutralized in the gas phase to produce $He@C_{60}$ (lifetime $>90\,\mu s$), which was then successfully re-ionized. The observed stability of neutral He@C_{60} is compelling evidence for its proposed endohedral structure.

5 PHYSICAL AND SPECTROSCOPIC PROPERTIES

The fullerenes have been extensively studied by mass spectrometric techniques (Sections 2 and 4) and stable peaks for the cluster ions C_{2n}^+ ($2n \geq 32$), as well as evidence for species down to C_{20}^+, have been observed. Those fullerenes which are sufficiently stable and/or abundant to be isolated in macroscopic amounts have been investigated further using a range of physical and spectroscopic techniques.

5.1 General Properties

As C_{60} is the most readily produced fullerene, it has been the most intensively investigated. It is an approximately spherical molecule with a center-to-carbon distance of ~3.5 Å and a van der Waals radius of ~5.0 Å.[44,45] The cage contains two types of C–C bond: 30 short six–six ring fusions (~1.39 Å) and 60 long five–six ring fusions (~1.45 Å), and this bond length alternation is consistent with the localized polyalkene description of C_{60} (Section 2.3). The structure of the C_{70} molecule is more complex with eight different bond types, ranging in length from 1.37 to 1.48 Å.[46] Some general physical properties of C_{60} are listed in Table 1.

5.2 X-ray and Neutron Diffraction

Diffraction studies (*see* ***Diffraction Methods in Inorganic Chemistry***) show pure, sublimed C_{60} to be crystalline with the near spherical molecules arranged in a face-centered cubic (fcc) array, with a center-to-center *inter*-C_{60} distance of 10.02 Å.[47,49] The presence of traces of solvent impurities appears to stabilize an hexagonal close-packed (hcp) arrangement (*see Close Packing*). In the fcc phase at room temperature, each C_{60} molecule rotates essentially isotropically and has a very short rotational correlation time ($\tau \approx 9$ ps), faster even than in tetrachloroethane solution ($\tau \approx 15$ ps). A phase transition from fcc ($Fm\bar{3}m$) to a simple cubic structure ($Pa\bar{3}$) occurs at 260 K. Neutron diffraction and ^{13}C NMR studies of this phase reveal that the C_{60} molecules appear to be jumping between symmetry-equivalent orientations. Below 90 K this motion is frozen, yielding a partly disordered structure in which the main *inter*-C_{60} interaction is between a relatively electron rich six–six ring fusion (double bond) of one molecule and an electron deficient five-membered ring of an adjacent one (Figure 14).[50]

Table 1 General physical properties of C_{60}

Density[47]	1.65 g cm^{-3}
Bulk modulus[47]	18 GPa
Refractive index[47]	2.2 (630 nm)
Heat of combustion (crystalline C_{60})[37]	545 kcal mol^{-1}
Electron affinity[47]	2.6–2.8 eV
First ionization energy[47]	7.6 eV
Band gap[47]	1.9 eV
Solubility (303 K)[48]	
CS_2	5.16 g L^{-1}
Toluene	2.15 g L^{-1}
Benzene	1.44 g L^{-1}
CCl_4	0.45 g L^{-1}
Hexane	0.04 g L^{-1}

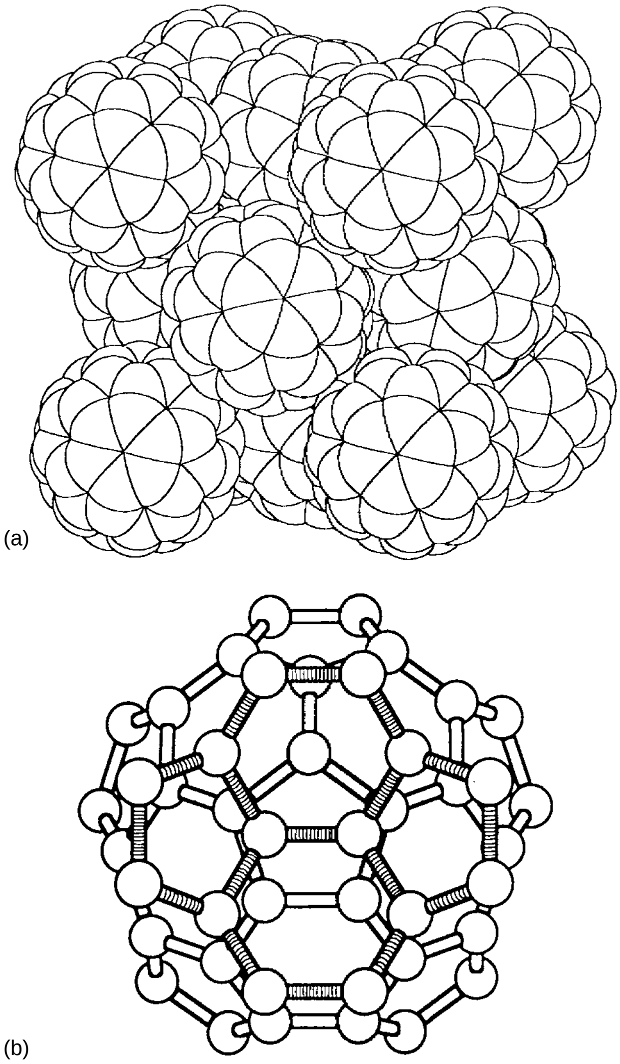

Figure 14 Face-centered cubic (fcc) packing of crystalline C_{60}. (a) At room temperature the C_{60} molecules rotate essentially isotropically, but below 260 K a phase transition occurs from fcc to simple cubic, in which the C_{60} molecules jump between symmetry equivalent positions. (b) At 5 K all rotation is frozen and the resulting *inter*-C_{60} contact is between a six–six ring fusion and a pentagonal face. (Reprinted with permission of Macmillan from W.I.F. David *et al.*[50])

Localized fcc packing is also found in the insoluble C_{60} films formed on a water surface by controlled evaporation of C_{60} solutions.[51,52] These films consist of rigid close-packed layers of fullerene molecules with a reported thickness of 4–8 molecules.

For pure C_{70} a fcc phase and two different hcp phases have been identified and upon annealing at 300 °C in vacuo the two hcp phases are progressively transformed to the pure fcc phase.[53]

5.3 ^{13}C NMR Spectroscopy

For each of the first two isolable fullerenes (C_{60} and C_{70}), only one IPR isomer is possible; however, the next fullerene (C_{76}) has two possible IPR structures, but only one has been observed. For C_{78} and higher fullerenes, several isomers are found to coexist. In the cases where sufficient material has been isolated, the composition of these isomer mixtures and the molecular symmetries of their components have been investigated by ^{13}C NMR spectroscopy.

The study of the fullerenes by ^{13}C NMR spectroscopy is not straightforward. ^{13}C has a low natural isotopic abundance (1.11%) and a low relative receptivity. In addition, the carbon atoms in fullerenes have relatively long relaxation times and spectra for the higher, less symmetric fullerenes can only be obtained within a reasonable time by using paramagnetic relaxation reagents, typically $Cr(acac)_3$.

The carbon atoms in C_{60} are equivalent, and as expected only a single line is observed: δ142.7 ppm (C_6D_6). C_{70} has D_{5h} symmetry and as there are five distinct carbon atom environments, a five-line spectrum is observed: δ150.1, 147.5, 146.8, 144.8, and 130.3 ppm (C_6D_6) of intensity ratio 10:20:10:20:10 (Figure 15).[5] The initial assignments based on chemical intuition have been subsequently confirmed by 2D ^{13}C NMR.[2] The upfield line (δ130.9 ppm) corresponds to the 10 'graphitic' atoms around the waist (type e), that lie at the intersection of three six-membered rings.

A similar atom type partition is found for C_{76}.[12] This molecule has D_2 symmetry and the expected 19-line spectrum is observed. The four upfield lines ($\delta < 137.1$ ppm) are assigned to the 16 (4 × 4 atoms) 'graphitic' carbons, whereas the remaining 60 carbons (15 × 4 atoms, $\delta > 141.3$ ppm) make up the 12 five-membered rings. Some other higher fullerenes have been successfully characterized as mixtures of isomers. Thus for C_{78}, five isomers are possible, but only three have been characterized by ^{13}C NMR: C_{2v} (21 lines), C'_{2v} (21 lines), and D_3 (13 lines). For C_{82}, nine isomers are possible and three (possibly with traces of a fourth) have been seen, at least one C_2 (41 lines), C_{2v} (17 lines), and C_{3v} (12 lines). For C_{84}, 24 isomers are possible, but only two have been seen, D_2 (21 lines) and D_{2d} (10 lines).[13–15]

5.4 Vibrational Spectroscopy

For pure C_{60} all four allowed IR transitions are observed as characteristic, sharp bands: 1429, 1183, 577, and 528 cm^{-1} (Figure 16).[54] Four similar IR bands are also observed in an emission spectrum from hot C_{60} vapor.[2] Furthermore, all 10 allowed bands are seen in the Raman spectrum: 1573, 1467, 1422, 1250, 1099, 772, 711, 495, 429, and 272 cm^{-1}. Pure $^{13}C_{60}$ has also been prepared and the IR bands are shifted by the predicted amount to 1375, 1138, 554, and 506 cm^{-1}.[55]

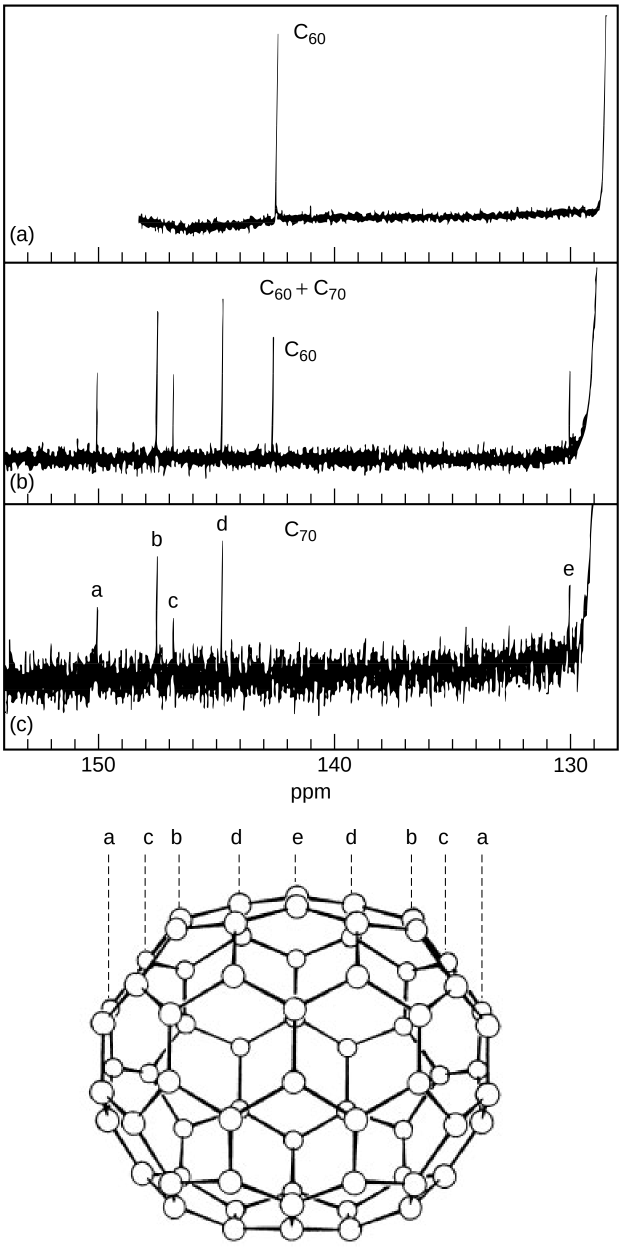

Figure 15 ^{13}C NMR spectra and assignments of C_{60} and C_{70}. (Ref. 5. Reproduced by permission of The Royal Society of Chemistry)

The IR (Figure 16) and Raman spectra of pure C_{70},[2,54] and the 1450–500 cm^{-1} region of the solution IR spectrum (CS_2) of C_{76} have also been reported.[12] They are more

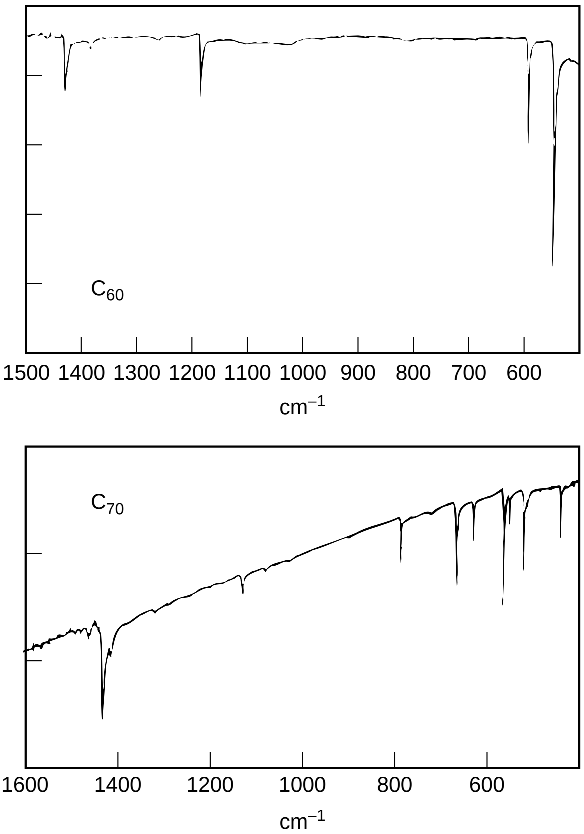

Figure 16 IR spectra (KBr disc) of C_{60} and C_{70}. (Ref. 54. Reproduced by permission of The Royal Society of Chemistry)

complex than the C_{60} spectra due to the lower symmetry of these molecules.

5.5 UV/Visible Spectroscopy and Photophysical Properties

A characteristic feature of the fullerenes is that they form highly colored solutions: C_{60} (magenta), C_{70} (red), C_{76} (yellow/green), C_{2v}-C_{78} (chestnut brown), and D_3-C_{78} (golden yellow). The optical spectra in solution are complex (Figure 17),[56] and the higher fullerenes give spectra that are particularly rich in structure, with many overlapping bands between 400 and 1000 nm.[12,13]

The photophysical properties of C_{60} and C_{70} have been reported.[57] C_{60} does not display any detectable fluorescence or phosphorescence, but is an efficient producer of singlet oxygen ($^1O_2$) with a quantum yield of unity (532 nm). The properties of C_{70} are similar, except that a weak fluorescence is now apparent and the quantum yield of $^1O_2$ is slightly less than unity. These differences are explained by the lower symmetry of the C_{70} molecule relaxing the forbidden nature of some of the absorption and emission processes. In addition, the fluorescence, phosphorescence, and nonlinear optical properties of C_{60} and C_{70} solutions containing the charge-transfer donor *N*,*N*-diethylaniline have been reported.[58,59]

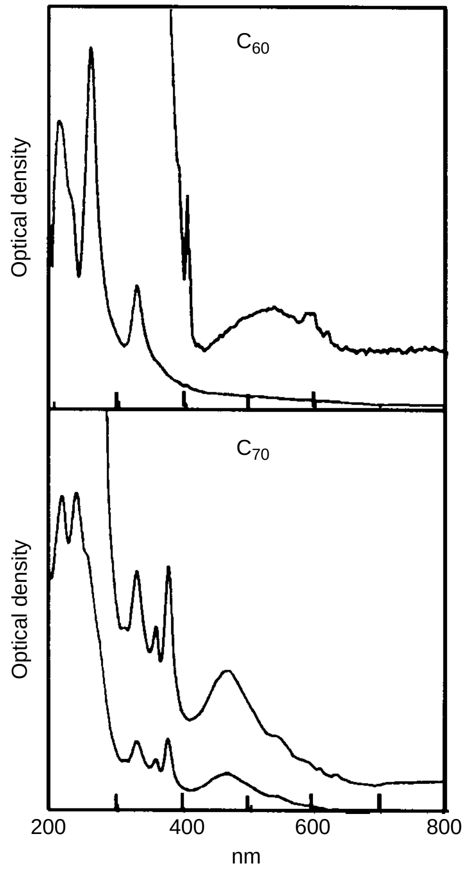

Figure 17 UV/Vis spectra (hexane) of C_{60} and C_{70}. (Reprinted from Ref. 56. © 1991, with permission from Elsevier)

Solutions of C_{60} and C_{70} display optical limiting properties of comparable efficiency with materials used at present.[60] For pulsed light (532 nm) of low intensity these solutions obey Beer's law, but as the intensity increases the transmitted fluence becomes fixed at a maximum value. This behavior is a consequence of the long lifetimes (~40 µs) and greater absorption cross-sections of the photoexcited triplet states of C_{60} and C_{70}.

Table 2 Values for the redox potentials (V) of the fullerenes C_{60}, C_{70}, C_{76}, and C_{84} in solution

	+1/0	0/−1	−1/−2	−2/−3	−3/−4	−4/−5	−5/−6
$C_{60}{}^{a,b}$	–	−0.98	−1.37	−1.87	−2.35	−2.85	−3.26
$C_{70}{}^{a,b}$	–	−0.97	−1.34	−1.78	−2.21	−2.70	−3.07
$C_{76}{}^{a,c}$	−0.67	−1.18	−1.78	−2.23	−2.73	–	–
$C_{84}{}^{a,d}$	–	−0.63	−0.95	−1.28	−1.58	–	–

[a] $E_{1/2}$ values relative to Fc/Fc$^+$. [b] MeCN/PhMe (−10 °C), 0.1 M [n-Bu_4N][PF_6].[61] [c] THF, 0.1 M [n-Bu_4N][BF_4].[63] [d] PhCN, 0.1 M [n-Bu_4N][PF_6].[64]

5.6 Electrochemistry

The electrochemical properties of C_{60}, C_{70}, C_{76}, and C_{84} in solution have been studied (Table 2), and all show some dependence on the nature of the solvent (*see* ***Electrochemistry: Applications in Inorganic Chemistry*** and *Redox Properties & Processes*). C_{60} and C_{70} display very similar behavior: to date, six separate, reversible, one-electron reductions to $C_{60}{}^{6-}$ and $C_{70}{}^{6-}$ respectively have been observed (Figure 18), whereas oxidation is irreversible.[61,62] For both molecules the first reduction occurs at only ~ -1.0 V (versus Fc/Fc^+), highlighting their electron-accepting nature. C_{76} is especially interesting as it displays both donor and acceptor behavior; in THF a single reversible oxidation is observed at -0.57 V (versus Fc/Fc^+) along with four reversible reduction waves.[63] C_{84} has been studied as a mixture of isomers and at least four reversible one-electron reductions, but no oxidations, are observed.[64]

The UV/visible/NIR spectra of the electrochemically generated anions $C_{60}{}^-$, $C_{60}{}^{2-}$, and $C_{60}{}^{3-}$ have been reported and the transitions assigned on the basis of theoretical calculations.[65] The ESR spectra of these ions (frozen solution) suggest singlet, triplet, and singlet magnetic ground states, respectively. There was no evidence for the quartet ($S = 3/2$) state of $C_{60}{}^{3-}$.[66] Pure C_{60} and C_{60}/C_{70} mixtures have also been chemically reduced by lithium metal in THF to yield red/brown diamagnetic solutions, postulated to contain predominantly $C_{60}{}^{6-}$ and $C_{70}{}^{6-}$.[37] The ^{13}C NMR spectra (approximate shifts relative to the neutral molecules in parentheses) consist of a single line at $\delta 156.7$ (+14.0) ppm for $C_{60}{}^{6-}$, and five lines at $\delta 158.3$ (+8.2), 152.3 (+4.8), 149.6 (+2.8), 137.9 (−6.9), and 133.7 (+3.4) ppm for $C_{70}{}^{6-}$. The strong deshielding of the carbon atoms in $C_{60}{}^{6-}$ is remarkable, as carbanions generally exhibit shielding relative to the neutral molecule. This phenomenon is explained by the particular balance of the diamagnetic and paramagnetic contributions to the ^{13}C chemical shifts found in fullerenes and their anions. A small overall deshielding effect is also found for $C_{70}{}^{6-}$; however, one of the carbon atom environments is strongly shielded (type d, Figure 15).

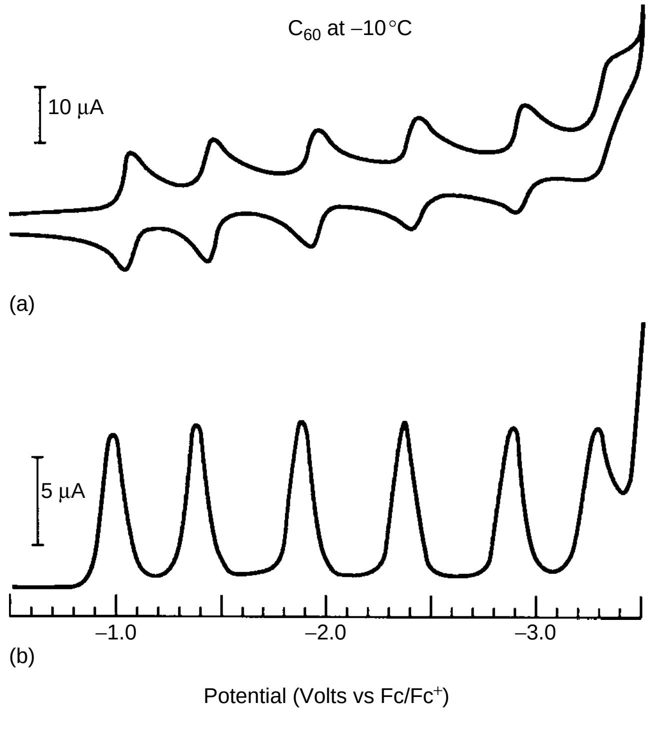

Figure 18 Under the appropriate experimental conditions (PhMe/MeCN, −10 °C), C_{60} undergoes six reversible one-electron reductions: (a) cyclic voltammetry, (b) differential pulse voltammetry. C_{70} displays similar properties. (Reprinted with permission from Ref. 61. © 1992 American Chemical Society)

6 CHEMISTRY

Although macroscopic quantities of the fullerenes have only been available since late 1990, huge advances have been made in their chemistry. Fullerene chemistry may be constructively divided into three broad areas: materials containing discrete fullerene molecules, chemical functionalization of the fullerene cage, and endohedral fullerenes.

6.1 Fullerene Materials

6.1.1 Charge Transfer Salts

Due to its electron acceptor properties (Section 5.6), C_{60} reacts with strong reducing agents (D) to yield salts of general formula $[D]_n{}^+[C_{60}]^{n-}$.[67] With the alkali metals (Group 1), a broad range of compounds has been reported, e.g. $Li_{12}C_{60}$, $Na_{11}C_{60}$, A_6C_{60} (A = K, Rb, Cs), K_4C_{60}, and A_3C_{60} ($A_3 = K_3$, Rb_3, $RbCs_2$).

The compound $Li_{12}C_{60}$ is prepared by the electrochemical intercalation of lithium into solid C_{60} (*see* ***Intercalation Chemistry***).[68] Both the t_{1u} and t_{1g} levels of the C_{60} molecule are completely filled (Figure 11) and theoretical studies indicate that this anion would be stable in the solid state with one Li^+ ion located above each pentagonal face.[69] During the course of its preparation the discrete phases Li_nC_{60} ($n = 0.5$, 2, 3, 4) are also apparent, although their structures are unknown. Intercalation of sodium atoms into C_{60} gives the range of compounds Na_nC_{60} ($2 \le n \le 11$), for which the fcc structure of pure C_{60} is maintained throughout.[70] The highest doping level is proposed to correspond to $Na_{11}C_{60}$, in which each tetrahedral interstice contains a single Na^+ ion and each octahedral interstice contains a body-centered cluster of nine Na^+ ions.

With the heavier alkali metals (K, Rb, and Cs), direct intercalation stops at A_6C_{60} in which only the t_{1u} level is filled.[47,71] The structure of K_6C_{60} at room temperature has been shown to be body-centered cubic (bcc) with the $C_{60}{}^{6-}$ molecules frozen in one orientation and the K^+ ions filling distorted tetrahedral interstices. The A_3C_{60} compounds are especially interesting as they become superconducting at low temperature, with transition temperatures (T_c) of 19 K for K_3C_{60}, 28 K for Rb_3C_{60}, and 33 K for $RbCs_2C_{60}$. The fcc structure of C_{60} is retained (Figure 14), with the A^+ ions filling all the tetrahedral and octahedral interstices.[72] These compounds belong to the third of the three known groups of superconductors (metal alloys, metal oxides/cuprates, ‘organic’ superconductors). They have by far the highest T_c values reported for ‘organic’ superconductors to date, and are only surpassed overall by the cuprate systems (*see* ***Superconductivity***). For the heavier alkali metals the compounds A_nC_{60} with lower doping levels ($n < 3$) have not been observed, and are believed to disproportionate to C_{60} and A_3C_{60}.

C_{60} has also been doped with the alkaline earth metals calcium, strontium, and barium (Group 2).[73] Two discrete phases have been characterized: Ca_5C_{60} is simple cubic with the same cell parameters as pure C_{60}, and Ba_6C_{60} is bcc. These compounds are reported to have superconducting transition temperatures (T_c) of 8.4 and 7 K, respectively.[74,75]

Salts of $C_{60}{}^{n-}$ with large cations have also been prepared.[37] Electroreduction of C_{60} in the presence of $[Ph_4P^+][Cl^-]$ produces crystals of the mixed salt $[Ph_4P^+]_3[C_{60}{}^-][Cl^-]_2$.[76] Direct reaction of C_{60} with the neutral, one-electron reductants (**1**), (**2**), and (**3**) yields the salts $[(\mathbf{1})^+][C_{60}{}^-][THF]_3$, $[(\mathbf{2})]_n[C_{60}]$ ($n \approx 0.87$), and $[(\mathbf{3})^+]_n[C_{60}{}^{n-}]$ ($n = 1$–3).[37,77] In the first compound the electron transfer is reversible in solution and depends upon the solvent used: toluene favors the neutral molecules, whereas in THF the oxidized chromium(III) porphyrin is stabilized through solvation and the compound is ionic.

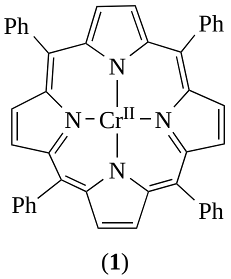

(**1**)

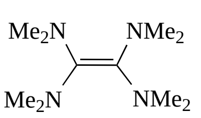

(**2**)

$(\eta^5\text{-}C_5H_5)Fe^I((\eta^6\text{-}C_6H_6)$

(**3**)

6.1.2 *Fullerene Complexation*

C_{60} forms complexes with a variety of molecules. In the solid state the intermolecular interactions in these materials stabilize lattice structures which, because they are novel, are of potentially great interest. This is particularly the case if the resulting systems exhibit the properties associated with partial or complete electron transfer (Section 6.1.1).

Classical charge transfer complexes are formed with weak electron donors. In these cases an electron is not formally transferred from the donor to the C_{60}; however, a charge transfer band is often observed in the solid state UV/visible spectrum. Several compounds with the sulfur- or tellurium-based organic donors (**4**), (**5**), and (**6**) have been prepared.[44,78,79] In $[C_{60}][(\mathbf{4})]_2$ the normally planar molecule (**4**) has curled around the C_{60} molecule to maximize the intermolecular interaction (Figure 20) and a charge transfer band is observed at ~750 nm (KBr pellet). The C_{60} molecules are arranged in parallel double-columnar stacks (Figure 19(b)) separated from one another by the molecules of (**4**), and the center–center *inter*-C_{60} distances in these stacks are 9.92 Å. In $[C_{60}]$[ferrocene]$_2$ the C_{60} molecules are arranged in close-packed layers (Figure 19(c)) separated by layers of *Ferrocene* (**7**) molecules (Figure 21).[45] The three different, in-plane, center–center, *inter*-C_{60} distances are 9.90, 10.37, and 10.39 Å, with a closest *inter*-C_{60} distance between parallel layers of 11.34 Å. The 1D structure of $[C_{60}][(\mathbf{4})]_2$ and the 2D sandwich structure of $[C_{60}]$[ferrocene]$_2$ may confer interesting anisotropic properties on these and related materials, e.g. electrical conduction and/or photophysical properties.

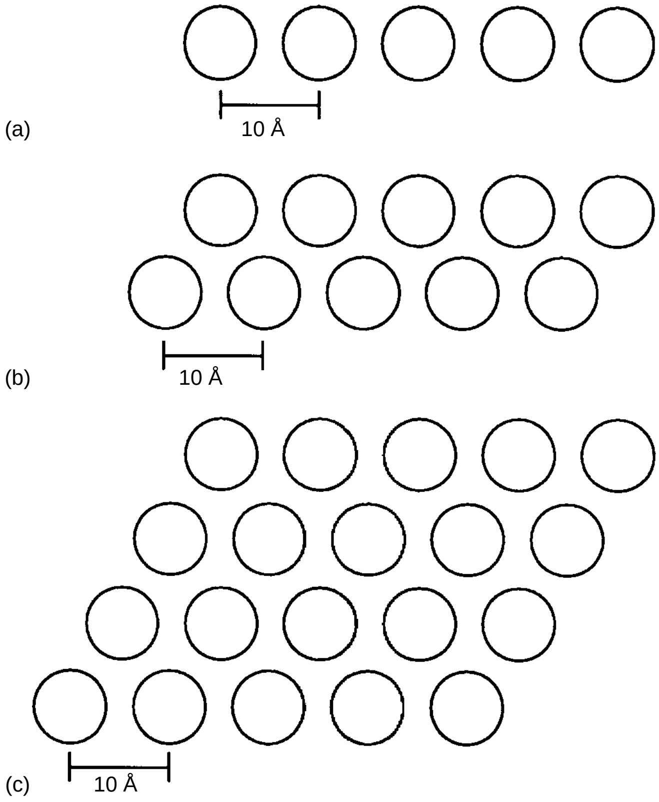

Figure 19 Packing arrangements of C_{60} molecules in composite materials in which the *inter*-C_{60} contacts are restricted to 1- or 2-dimensions: (a) single columnar stacks, (b) double columnar stacks, (c) close-packed layers

In $[C_{60}]$[1,4-dihydroquinone]$_3$ the C_{60} molecules are trapped in a hydrogen-bonded super-polonium network of 1,4-dihydroquinone molecules.[37] Unlike the (**4**) and

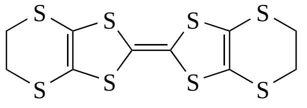

(**4**)

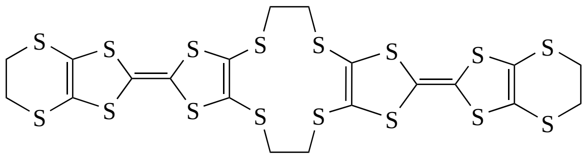

(**5**)

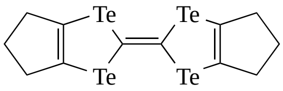

(**6**)

$(\eta^5\text{-}C_5H_5)_2Fe^{II}$

(**7**)

ferrocene complexes, the C_{60} molecules in this material are orientationally disordered. Each C_{60} has six nearest neighbors at 10.44 Å and these *inter*-C_{60} contacts form a 3D network. The solvated C_{60} compounds $[C_{60}][C_6H_6]_4$ and $[C_{60}][CH_2I_2][C_6H_6]$,[80–82] and the intercalate $[C_{60}][I_2]_2$, have also been structurally characterized.[83]

The structure of one C_{70}-containing material has been determined. In $[C_{70}][S_8]_6$ the orientationally ordered C_{70} molecules are arranged in close-packed layers separated by the S_8 molecules.[46]

C_{60} complexes with γ-cyclodextrin to form the encapsulated water soluble system $[C_{60}][\gamma\text{-cyclodextrin}]_2$ (*see Cyclodextrins*).[37] In this compound the C_{60} is weakly bound and readily extracted by shaking the complex with a good solvent for C_{60}, e.g. toluene. C_{70} does not form an analogous compound, presumably because it is larger and nonspherical.

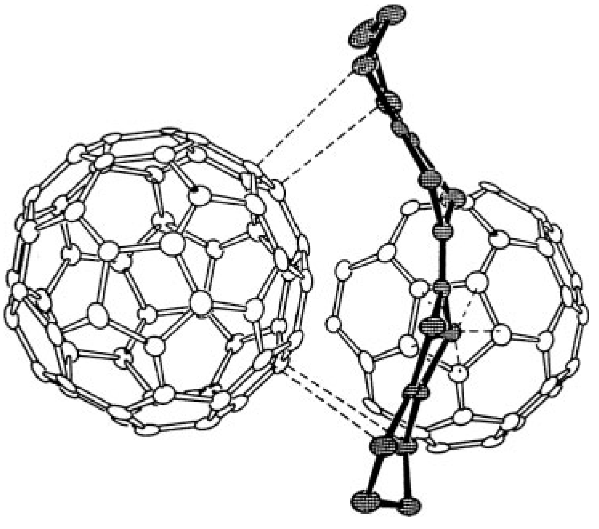

Figure 20 Molecular structure of $C_{60}[(\mathbf{4})]_2$. The dashed lines represent the close $C[C_{60}]-S[(\mathbf{4})]$ interactions. (Reprinted from Ref. 44 by permission of The Royal Society of Chemistry)

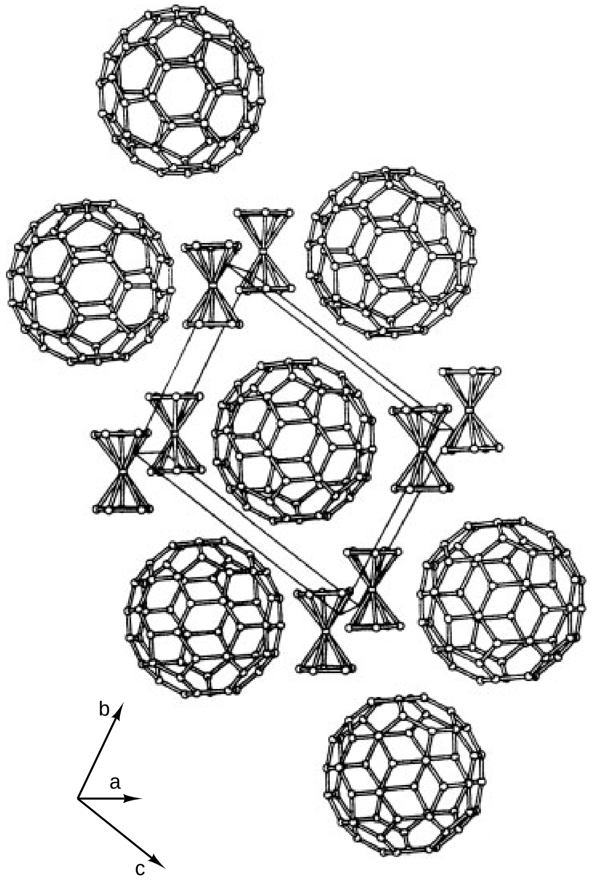

Figure 21 Molecular structure of $C_{60}(\text{ferrocene})_2$. (Reprinted from Ref. 45. Reproduced by permission of The Royal Society of Chemistry)

6.2 Fullerene Derivatives

Although the IPR fullerenes are really quite stable molecules, they are reactive and display a rich chemistry, and research in this field is proving to be an endeavor with many inherent challenges.[37,67] To date only C_{60}, and to a lesser extent C_{70}, can be prepared in sufficient quantities for their chemistry to be thoroughly studied. Since the fullerenes are closed unsaturated cages there are no functional groups which can be substituted by others, and therefore the chemistry is limited to addition to the cage by the removal of unsaturation (perhaps followed by subsequent substitution), and/or to the breaking of bonds within the cage. With formally 30 double bonds and 60 carbon atoms available for addition, C_{60} may potentially yield a huge number of products of different composition and/or structure upon reaction with any particular reagent, e.g. $C_{60}X_2$ has 23 possible isomers! It is therefore of great importance to understand the principles through which the synthesis of fullerene derivatives may be controlled in order to maximize the probability of forming a single major product. A less favorable alternative is the development of techniques for the efficient separation of these complex product mixtures.

Several general features of C_{60} chemistry have emerged. Firstly, the cage is susceptible to nucleophilic attack, with the degree of addition often difficult to control. Secondly, reactivity tends to be associated with the six–six ring fusions (formal double bonds). Both observations are consistent with the accepted description of C_{60} as a localized, electron-deficient polyalkene (Section 2.3). Furthermore, it is generally observed that addition at only one or two carbon atoms of the C_{60} cage does not greatly perturb its redox and spectroscopic (IR, UV/vis) properties. With multiple additions, however, these characteristic spectroscopic fingerprints are rapidly lost.

6.2.1 *Hydrogenation*

The smallest perhydrogenated fullerene known is dodecahedrane ($C_{20}H_{20}$), formally derived from the smallest possible (but unknown) fullerene C_{20} (Figure 4), which comprises just 12 pentagonal faces. The $C_{20}H_{20}$ molecule was first prepared in 1983 by an elegant multistep synthesis and has an interesting organic chemistry, but will not be discussed further here.

The Birch reduction (Li metal, liquid NH_3) of C_{60} yields a material that appears to contain hydrogenated C_{60} (perhaps mixed with aminated derivatives).[37] Chemical oxidation results in reconversion into C_{60}, indicating that the cage structure had remained intact. The mass spectrum shows signals for $C_{60}H_{18}$ and $C_{60}H_{36}$, although it is not known whether these species are present in the reaction mixture or are formed during mass spectrometric sampling. The quenching of $C_{60}{}^{6-}$ solutions with water yields hydrogenated products of unknown composition which are sensitive to reoxidation, and in this case regenerated C_{60} is the sole product observed by mass spectrometric techniques.[37] The reaction of C_{60} with $Li[BHEt_3]$ is reported to give the weak base $[HC_{60}]^-$, isolated as the solvated salt $Li[HC_{60}][H_2O]_{6-9}$.[84]

The relative stabilities of selected isomers of $C_{60}H_n$ ($n = 2$, 36, 60) have been calculated; in particular, the hypothetical molecule $C_{60}H_{60}$, in which all the hydrogen atoms are *exo* to the cage, is expected to be highly strained.[37,85]

6.2.2 *Halogenation*

The preferred pattern for addition of X_2 ($X = H$, F, Cl, Br, I) to C_{60} has been calculated to be 1,9- for small groups and 1,7- for bulky groups (Figure 22).[85] Fluorine atoms are small enough for 1,9-addition to be favored and C_{60} does indeed yield highly fluorinated derivatives upon careful reaction with F_2 gas.[86] Exhaustive fluorination of C_{60} yields a product which exhibits a single ^{19}F NMR line.[87] This result indicates the production of a highly fluorinated species in which all the fluorines appear equivalent. $C_{60}F_{60}$ is a possible structure for this species but is expected to be highly strained, and the formation of another symmetric, less highly substituted (or fluxional) derivative is also consistent with the experimental observations. The potential use of highly fluorinated fullerenes as lubricants is unfortunately prevented because, although they are thermally very stable molecules, they are reactive towards even weakly nucleophilic reagents.[88]

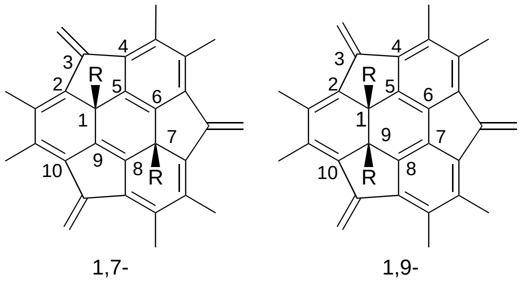

1,7-	1,9-

Figure 22 Of the 23 possible isomers of $C_{60}R_2$, the 1,7- and 1,9-addition products are calculated to be of lowest energy. Usually only one of these isomers is observed experimentally, depending upon the size of R

C_{60} reacts with Cl_2 gas at 250 °C to yield a material of average composition $C_{60}Cl_{24}$, although only C_{60} can be detected by mass spectrometry.[37] However, the chlorinated product can be converted into $C_{60}(OMe)_n$ by refluxing with methanol/KOH, and this material gives mass peaks corresponding to the more robust polymethoxylated species ($n \leq 26$). C_{60} also reacts with liquid Cl_2 at its boiling point (−35 °C) to yield a compound of average composition $C_{60}Cl_{12}$.[89] C_{60} can be recovered in >50% yield from this material by dechlorination with PPh_3 at room temperature. Alternatively, any of the chlorinated derivatives can be reconverted into C_{60} upon heating to 300–400 °C in vacuo.

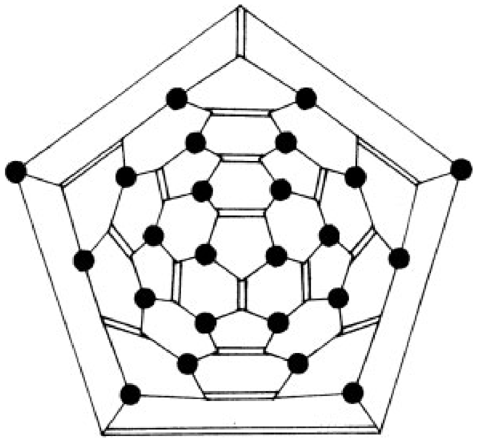

Figure 23 Schlegel diagram of the bromine (filled circles) addition pattern for $C_{60}Br_{24}$

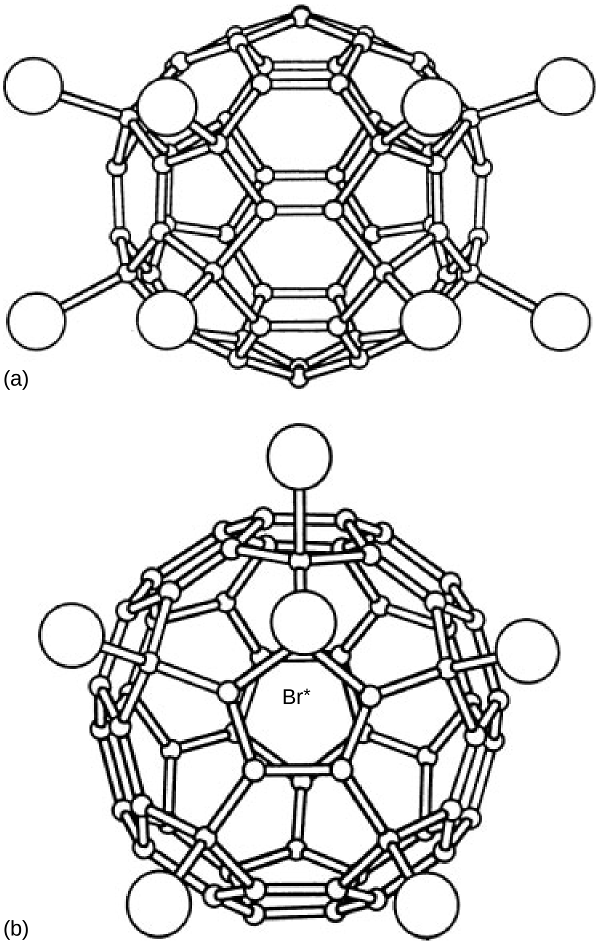

Figure 24 Molecular structures of partly brominated C_{60} derivatives: (a) $C_{60}Br_8$ and (b) $C_{60}Br_6$. (Reprinted with permission of Macmillan from P.R. Birkett *et al.*[91])

C_{60} reacts with liquid Br_2 to yield $C_{60}Br_{24}$ (Figure 23), in which all 24 bromine atoms are equivalent.[90] It is noteworthy that 24 is the maximum number of groups that can be arranged on C_{60} without resorting to the sterically unfavored 1,9-addition (Figure 22). The use of a cosolvent for the bromination results in the formation of partly brominated products: $C_{60}Br_8$ from CS_2, and $C_{60}Br_6$ from C_6H_6 or CCl_4 (Figure 24).[91] In both cases the bromine atoms are gregarious, forming localized aggregates on the cage, rather than being dispersed. In $C_{60}Br_8$ the structure corresponds to a portion of the $C_{60}Br_{24}$ molecule, whereas $C_{60}Br_6$ contains one unfavorable eclipsing interaction. This latter structure may arise by successive 1,7-additions to form the stable cyclopentadienyl radical $[C_{60}Br_5]^\bullet$, which is trapped by addition of the central bromine atom (Br*). All the brominated derivatives may be reconverted into C_{60} by heating to 100–150 °C in vacuo.

The trend to weaker C_{60}–halogen bonds continues with I_2, and indeed no derivative of C_{60} with iodine atoms covalently bound to the cage has been reported to date. The only characterized iodine-containing compounds are the intercalates $[C_{60}][CH_2I_2][C_6H_6]$ and $[C_{60}][I_2]_2$ (Section 6.1.2).

6.2.3 Heteroatom Derivatives

The fullerene oxides $C_{60}O$ and $C_{70}O$ are observed as minor components in fullerene-containing soot, although it is reported that $C_{60}O$ decomposes to C_{60} during the separation process.[92] Other higher oxides $C_{60}O_n$ ($n = 2$–5) and $C_{70}O_2$ have been prepared by electrochemical or photolytic oxidation and characterized by mass spectrometry. The reaction of thin C_{60} films with singlet oxygen ($^1O_2$) to yield $C_{60}O_2$ and $C_{60}O_4$ has been studied by IR spectroscopy.[93] The observation of bands assignable to ketonic C=O groups indicates that some C–C bond cleavage (cage opening) has occurred in these species. Of these fullerene oxides, only $C_{60}O$ has been isolated as a pure compound in macroscopic amounts. It can be prepared from C_{60} either by photooxygenation, or by reaction with dimethyldioxirane (**8**).[92,94] In the latter reaction, unreacted C_{60} is the major product but the dioxolane derivative (**9**), in which (**8**) has added across a six–six ring fusion, is a significant byproduct and has been shown not to be an intermediate in the formation of $C_{60}O$. The spectroscopic properties of $C_{60}O$ indicate that the oxygen atom has added at a six–six ring junction to give the epoxide structure (**10**), and not the isomeric opened 1,9-oxido[10]annulene structure (**11**).

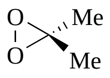

(**8**)

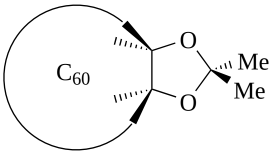

(**9**)

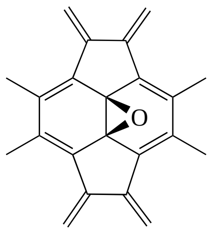

(**10**)

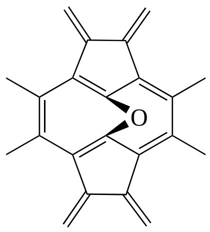

(**11**)

Osmylation of C_{60} with OsO_4, in the presence of 4-*t*-butylpyridine (L), yields the osmyl ester $C_{60}[OsO_4L_2]$ (**12**), the first structurally characterized C_{60} derivative.[67,95] The OsO_4 adds across a six–six ring junction, in a similar manner to the dioxolane derivative (**9**), and the two sp^3 hybridized carbon atoms are moved away from the center of the cage: center-to-C(sp^3) distances, 3.80 Å; average center-to-C(sp^2) distance, 3.55 Å. The bis-osmyl ester $C_{60}[OsO_4L_2]_2$ has been prepared as a mixture of five isomers and probable structures for all five compounds have been deduced from ^1H and ^{13}C NMR studies of the separated components.[96]

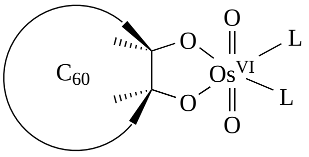

(**12**)

Reaction of C_{60} with $[NO][BF_4]$ in the presence of aryl carboxylic acids ($ArCO_2H$) in H_2O yields a mixture of $C_{60}(O_2CAr)_x(OH)_y$ isomers,[97] which were warmed with aqueous NaOH to yield the water-soluble polyhydroxylated derivatives $C_{60}(OH)_n$ ($n \leq 20$). Similar products ($n \leq 15$) have been prepared by the direct reaction of C_{60} with a mixture of concentrated nitric and sulfuric acids.[98] The polymethoxylated derivatives $C_{60}(OMe)_n$ ($n \leq 26$) have been prepared from polychlorinated C_{60} (Section 6.2.2).

C_{60} is attacked by primary and secondary amines to yield derivatives with the general formula $C_{60}H_n(NR^1R^2)_n$ where n depends on the nature of the amine, e.g. $n \leq 12$ for *n*-propylamine and $n \leq 6$ for morpholine.[37,84] ESR spectroscopy shows that the reaction proceeds by single-electron transfer (SET), followed by covalent bond formation and hydrogen transfer. The hydrogens have been shown to exchange rapidly with a source of D^+ (MeOD) and comparison of the IR spectra of the deuterated and nondeuterated secondary amine derivatives indicates that the hydrogens are bound to carbon atoms of the C_{60} cage rather than to the amine nitrogens.

6.2.4 Alkyl and Aryl Derivatives

Functionalization of C_{60} through C–C bond formation has been achieved by a variety of methods: nucleophilic addition of carbanions, quenching of C_{60} anions with alkyl halides, Friedel–Crafts arylation, radical addition, and cycloadditions.

C_{60} reacts with an excess of Grignard (RMgBr) (*see Grignard Reagents*) or organolithium (RLi) reagents to produce solutions thought to contain anions of general formula $[C_{60}R_n]^{m-}$.[84] These anions may be quenched with an excess of MeI to yield product mixtures of average composition $C_{60}R_nMe_m$, where n and m depend upon the nature of R and the conditions used. The mass spectrum of $C_{60}Me_n$, prepared by quenching $C_{60}{}^{6-}$ with MeI, indicates the presence of species up to $C_{60}Me_{24}$ with the dominant products corresponding to $C_{60}Me_6$ and $C_{60}Me_8$,[37] an interesting observation in the light of the known stability of $C_{60}Br_6$ and $C_{60}Br_8$ (Section 6.2.2). The mechanism for the formation of such highly alkylated derivatives is not known, but may indicate rapid electron transfer from unreacted $C_{60}{}^{6-}$ to partially methylated C_{60}. All these derivatives appear to be mixtures of isomers of unknown structure; however, reaction of C_{60} with one equivalent of *t*-BuLi or EtMgBr followed by quenching with water yields the 1,9-disubstituted products $C_{60}RH$ (**13**) (R = *t*-Bu, Et) in up to 50% yield.[99] The intermediate mono-substituted anion $[C_{60}\text{-}t\text{-Bu}]^-$ (**14**) has been isolated as the green microcrystalline salt $[Li(THF)_4][C_{60}\text{-}t\text{-Bu}]$,[100] and is a very weak base (cf. $[C_{60}H]^-$, Section 6.2.1). Protonation yields $C_{60}(t\text{-Bu})H$ ($pK_a \approx 5.7$, *see Acids & Acidity*) as either the 1,7- or 1,9-isomer (Figure 22), depending the source of H^+. The 1,7-isomer is a kinetic product and slowly converts into the thermodynamically more stable 1,9-isomer.

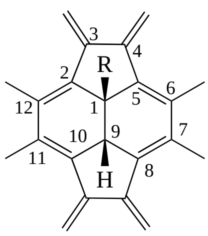

(**13**)

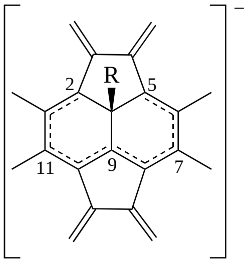

(**14**)

Friedel–Crafts arylation of C_{60} with ArH (PhH and PhMe) catalyzed by $AlCl_3$ yields materials of composition $C_{60}H_nAr_n$.[37] Mass spectra show strong peaks for species up to $C_{60}H_{12}Ar_{12}$, and some evidence for $C_{60}H_{16}Ar_{16}$. Reaction of $C_{60}Cl_n$ ($n \approx 24$) with PhH under similar conditions gives the simple phenylated derivatives $C_{60}Ph_n$ ($n \leq 22$). Arylation with $PhH/FeCl_3/Br_2$ yields $C_{60}Ph_{5-12}$, with relative mass spectral intensities of 2:11:2:11:1:3:1:2, and again the predominant species appear to be the hexa- and octafunctionalized species.[101] The repeated appearance of these two 'magic numbers' for addition to C_{60} is a strong indication of the stability of these species; however, it does not necessarily follow that they are the favored products of the chemical reaction under investigation. It may be that the particular mass spectrometric sampling methods used are either biased towards these species, or in some way anneal the product mixtures to these islands of stability.

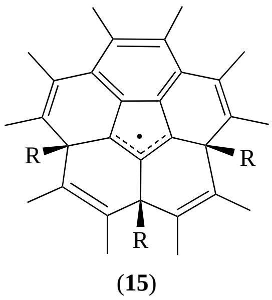

(**15**)

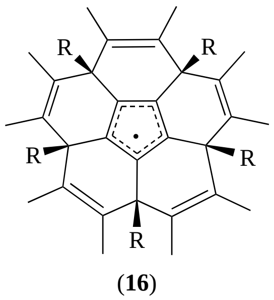

(**16**)

C_{60} reacts with benzyl radicals to give addition products $C_{60}(CH_2Ph)_n$ ($n \leq 15$), as determined by mass spectrometry.**[102]** The formation of allyl (**15**) and cyclopentadienyl (**16**) radical sites on the cage has been revealed by ESR spectroscopy and these sites are thought to arise from multiple 1,7-additions (cf. $[C_{60}Br_5]\bullet$, Section 6.2.2). The corresponding reaction of C_{60} with the *p*-xylylene diradical (**17**) gives an interesting polymeric material.**[103]**

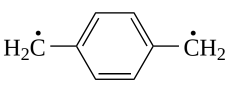

(**17**)

Under appropriate conditions the addition of a single radical (R•) to C_{60} is observed. In $[C_{60}R]\bullet$ the radical is not delocalized over the cage but spin density is almost exclusively restricted to the 2, 5, 7, 9, and 11 positions (see **14**). Variable temperature ESR studies of the bulky group derivatives (R = *t*-Bu, CCl_3, CBr_3) indicate that the radical is in equilibrium with its dimer, which is believed to be linked through the 7 or 11 positions as these are the most sterically accessible.**[104,105]** For the addition of a single radical to C_{70}, the formation of three of the five possible different isomers has been established by ESR.**[106]**

The reaction of C_{60} with benzyne yields the adducts $C_{60}(C_6H_4)_{1-4}$, of which the monoadduct has been isolated and characterized by ^1H and ^{13}C NMR.**[107]** The benzyne adds across a six–six ring fusion with the formation of a four-membered ring. C_{60} also forms Diels–Alder adducts with dienes, although the products are difficult to characterize and the reaction is often reversible.**[84]** The diene (**18**), however, cycloadds at a six–six ring fusion of C_{60}, and subsequent loss of CO ensures the irreversible formation of the stable product (**19**), which has been structurally characterized.**[108]**

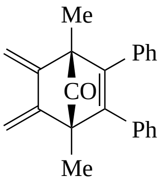

(**18**)

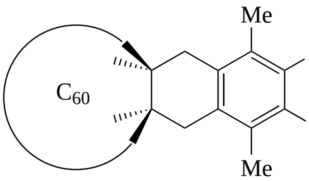

(**19**)

C_{60} undergoes cycloadditions with diaryldiazomethanes (**20**) to form pyrazolines (**21**) which spontaneously lose N_2 to yield diarylhomofullerenes (**22**), in which the 60π electronic structure of the cage is largely preserved (cf. **11**).**[67]** Addition occurs across a six–six ring fusion and species up to $C_{60}(CAr_2)_6$ have been observed, though the monoadducts are the most readily prepared. This strategy has been extended to the preparation of protected *C*-glycoside derivatives of C_{60}.**[109]** Polymers have also been prepared from functionalized diarylhomofullerenes,**[110]** and bis-diazo reagents have been used to prepare soluble bis-homofullerenes as models for the corresponding polymer systems.**[111]** The electrochemical and spectroscopic properties of the bis- and polyhomofullerenes are not significantly perturbed compared to the monomers.

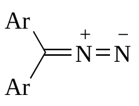

(**20**)

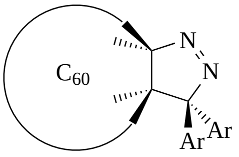

(**21**)

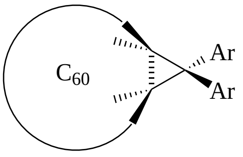

(**22**)

The parent dihydrohomofullerene $C_{60}(CH_2)$ (**23**) is prepared by reaction of C_{60} with CH_2N_2. In this case the intermediate pyrazoline is isolable at room temperature, but loses N_2 upon heating (110 °C).**[112]** Interestingly ^1H and ^{13}C NMR studies show that the CH_2N_2 molecule has added across a six–six ring fusion in the pyrazoline, whereas upon loss of N_2 the CH_2 group migrates to a five–six ring fusion. The two previously equivalent protons are now in distinct chemical environments: ^1H NMR, $\delta 2.87$ (H_a) and 6.35 (H_b) ppm, and $J_{ab} = 9.7$ Hz.

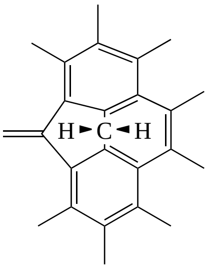

(**23**)

6.2.5 Organometallic Derivatives

The organometallic chemistry of C_{60} is dictated by its spherical geometry and localized polyalkene π-electronic structure. All the derivatives reported to date are η^2 complexes (*see Hapticity*) in which the metal coordinates at a six–six ring fusion (formal double bond); no analogous η^4-diene or η^6-triene complexes have been prepared to date (*see Alkene Complexes*). The instability of these polyene complexes is postulated to be due to the curvature of the C_{60} molecule and the corresponding divergence of the surface p-orbitals, which results in poor overlap with the metal orbitals.**[113]**

The representative complex $C_{60}Pt(PPh_3)_2$ (**24**) displays the salient features of all the η^2 compounds.**[67,113]** The coordinated ‘alkene’ carbon atoms are distorted towards a tetrahedral geometry and the corresponding relief of strain in the cage probably makes a significant contribution to the stability of these complexes. The reaction with excess organometallic reagent yields the hexaadducts $C_{60}[M(PEt_3)_2]_6$ (M = Ni, Pd,

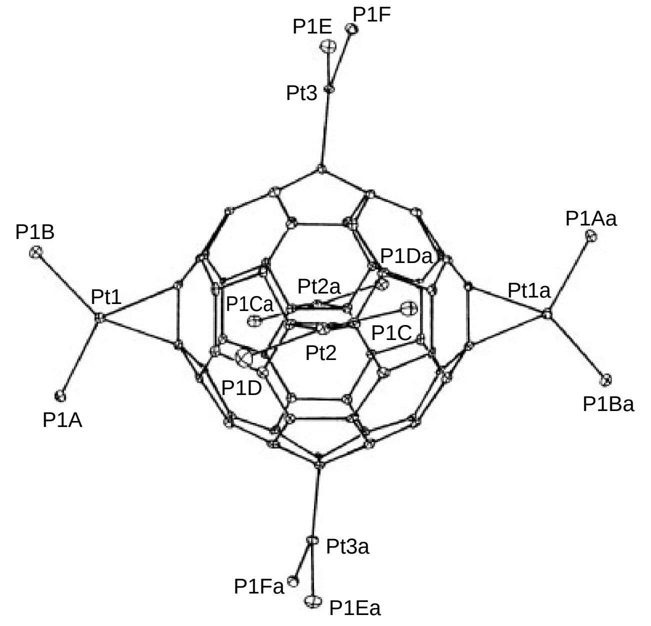

Figure 25 Molecular structure of $C_{60}[Pt(PEt_3)_2]_6$. The phosphine ethyl groups have been omitted for clarity. (Reprinted with permission of the American Chemical Society from P.J. Fagan *et al.*[114])

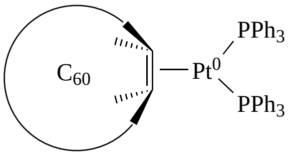

(**24**)

Pt) in which the metals lie at the vertices of an octahedron (Figure 25).[114]

The π*-Back Bonding* from the metal to the C_{60} molecule in these complexes is responsible for band shifts in the C_{60} Raman spectra,[115] and for rendering the cage more resistant to electrochemical reduction;[67] the mono- and hexaadducts being respectively ~0.34 V and >2.7 V harder to reduce than C_{60}.[116] Similar observations have been made for the mono- and bis-iridium complexes $C_{60}Ir(\eta^5\text{-}C_9H_7)(CO)$,[117] $C_{60}Ir(CO)Cl(PPh_3)_2$,[118] and $C_{60}[Ir(CO)Cl(PMe_2Ph)_2]_2$ (*see Vaska's Complex*).[119] The position of the ν_{CO} band for these complexes show that C_{60} is a relatively poor π-acceptor ligand compared to other electron-deficient alkenes, e.g. $F_2C{=}CF_2$ and $(NC)_2C{=}C(CN)_2$. The structures of mono- and bis-iridium complexes of C_{70}, $C_{70}Ir(CO)Cl(PPh_3)_2$ and $C_{70}[Ir(CO)Cl(PPhMe_2)_2]_2$, have also been reported.[37,120]

Reaction of C_{60} with $Pd_2(dba)_3$ yields the organometallic polymer $C_{60}Pd_n$.[121] Material of varying composition may be prepared, but those with $n > 3$ are active for the catalytic hydrogenation of alkenes and alkynes.[122] This material is proposed to consist of catalytically active palladium atoms distributed on an inert 3D polymer $C_{60}Pd_3$.

6.3 Endohedral Fullerenes

The formation and study of endohedral fullerenes in molecular beams has been discussed in Section 4. These molecules are expected to have interesting and potentially very useful bulk properties as well as a fascinating chemistry. Therefore their synthesis in macroscopic amounts is an important goal in fullerene chemistry. Mixtures of normal and endohedral fullerenes can be isolated from the soot generated by vaporizing a mixture of graphite and a source of the desired element (Section 3.1). Present methods allow only very small amounts of the endohedral materials to be synthesized, and their characterization is generally restricted to highly sensitive techniques, e.g. mass spectrometry and ESR.[37]

To date, all the confirmed isolable endohedral fullerenes contain metals; either scandium, yttrium, or one of the f-block elements may be encapsulated, and compounds containing up to three metals have been reported.[123] The proportions of the endohedral fullerenes observed depends upon the manner by which they are extracted from the soot.[124] For lanthanum, predominantly $La@C_{82}$ and $La_2@C_{80}$ are isolated by solvent extraction techniques, whereas direct sublimation from the soot yields $La@C_{60}$, $La@C_{70}$, $La@C_{74}$, and $La@C_{82}$. An explanation for this behavior is that most of the endohedral fullerenes are present as insoluble salts, e.g. $[La@C_{60}]^+[C_{60}]^-$, and only $La@C_{82}$ and $La_2@C_{80}$ are sufficiently redox stable to be extracted as the neutral molecules.

The monometallic endohedral fullerenes are typified by $M@C_{82}$ (M = Sc, Y, La), and ESR studies of these molecules indicate that they are best described as the charge-separated species $M^{3+}@C_{82}{}^{3-}$.[125] For all three species, two distinct signals are seen, indicating the presence of two isomers of $M@C_{82}$, although it is not known whether these correspond to any of the observed isomers of the parent fullerene C_{82}. EXAFS studies of $Y@C_{82}$ indicate that each yttrium atom has seven nearest neighbor carbon atoms at 2.35 Å as well as another yttrium atom at 4.05 Å.[126] These data are not consistent with a simple endohedral structure and further studies are required to clarify this apparent contradiction.

The endohedral fullerenes $U@C_{28}$ and $U@C_{60}$ have been reported to be sufficiently stable to allow chemical isolation.[127] Endohedral complexes of the smaller fullerenes (C_{2n}, $2n < 60$) are commonly observed in molecular beam experiments (Section 4.1), but this stabilization of C_{28} by uranium atom encapsulation is remarkable. A theoretical study of $[T_d\text{-}C_{28}]^{4-}$ and $T_d\text{-}C_{28}H_4$ (**25**) indicate that they are stable molecules, and that the laboratory preparation of their derivatives may be viable.[9,128]

The formation of multimetallic endohedral fullerenes is strongly dependent on the metal to carbon ratio of the vaporized graphite. For the lanthanides the dimetallic fullerenes $M_2@C_{80}$ and/or $M_2@C_{82}$ are often the most abundant, but small amounts of higher species are also seen. In addition, the existence of the mixed metal system $YLa@C_{80}$ has been reported.[124] No ESR spectra have been observed

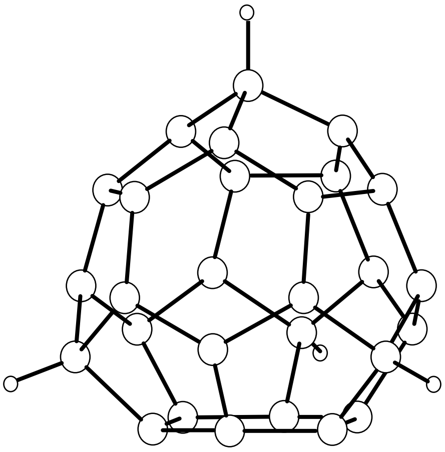

(**25**)

for any of these dimetallic compounds to date, indicating that they may not be paramagnetic. However, the existence of the trimetallic species $Sc_3@C_{82}$ has been demonstrated by its mass spectrum peak and its characteristic ESR signal.[129,130] The scandium atoms are thought to be encapsulated as the triply charged, equilateral triangle cluster Sc_3^{3+}.

7 RELATED ARTICLES

Carbon: Inorganic Chemistry; Diffraction Methods in Inorganic Chemistry; Intercalation Chemistry; Superconductivity.

8 REFERENCES

1. E. Osawa, *Kagaku (Kyoto)*, 1970, **25**, 854; *Chem. Abstr.*, 1971, **74**, 75 698v.
2. (a) H. W. Kroto, A. W. Allaf, and S. P. Balm, *Chem. Rev.*, 1991, **91**, 1213; (b) H. W. Kroto, *Angew. Chem., Int. Ed. Engl.*, 1992, **31**, 111.
3. H. W. Kroto, J. R. Heath, S. C. O'Brien, R. F. Curl, and R. E. Smalley, *Nature (London)*, 1985, **318**, 162.
4. W. Krätschmer, L. D. Lamb, K. Fostiropoulos, and D. R. Huffman, *Nature (London)*, 1990, **347**, 354.
5. R. Taylor, J. P. Hare, A. K. Abdul-Sada, and H. W. Kroto, *J. Chem. Soc., Chem. Commun.*, 1990, 1423.
6. D. E. Manolopoulos, J. C. May, and S. E. Down, *Chem. Phys. Lett.*, 1991, **181**, 105.
7. P. W. Fowler and D. Manolopoulos, 'Atlas of Fullerenes', Oxford University Press, Oxford, 1994.
8. H. W. Kroto, *Nature (London)*, 1987, **329**, 529.
9. T. G. Schmalz, W. A. Seitz, D. J. Klein, and G. E. Hite, *J. Am. Chem. Soc.*, 1988, **110**, 1113.
10. B. L. Zhang, C. Z. Wang, K. M. Ho, C. H. Xu, and C. T. Chan, *J. Chem. Phys.*, 1992, **97**, 5007.
11. D. M. Cox, K. C. Reichmann, and A. Kaldor, *J. Chem. Phys.*, 1988, **88**, 1588.
12. R. Ettl, I. Chao, F. Diederich, and R. L. Whetten, *Nature (London)*, 1991, **353**, 149.
13. F. Diederich, R. L. Whetten, C. Thilgen, R. Ettl, I. Chao, and M. M. Alvarez, *Science*, 1991, **254**, 1768.
14. K. Kikuchi, N. Nakahara, T. Wakabayashi, S. Suzuki, H. Shiromaru, Y. Miyake, K. Saito, I. Ikemoto, M. Kainosho, and Y. Achiba, *Nature (London)*, 1992, **357**, 142.
15. R. Taylor, G. J. Langley, T. J. S. Dennis, H. W. Kroto, and D. R. M. Walton, *J. Chem. Soc., Chem. Commun.*, 1992, 1043.
16. K. Kikuchi, N. Nakahara, T. Wakabayashi, M. Honda, H. Matsumiya, T. Moriwaki, S. Suzuki, H. Shiromaru, K. Saito, K. Yamauchi, I. Ikemoto, and Y. Achiba, *Chem. Phys. Lett.*, 1992, **188**, 177.
17. D. Bakowies and W. Thiel, *J. Am. Chem. Soc.*, 1991, **113**, 3704.
18. D. Ugarte, *Nature (London)*, 1992, **359**, 707.
19. T. W. Ebbesen and P. M. Ajayan, *Nature (London)*, 1992, **358**, 220.
20. P. M. Ajayan and S. Iijima, *Nature (London)*, 1993, **361**, 333.
21. M. Endo and H. W. Kroto, *J. Phys. Chem.*, 1992, **96**, 6941.
22. H. W. Kroto, *J. Chem. Soc., Dalton Trans.*, 1992, 2141.
23. T. Lenosky, X. Gonze, M. Teter, and V. Elser, *Nature (London)*, 1992, **355**, 333.
24. D. A. Bochvar and E. G. Gal'pern, *Dokl. Akad. Nauk. SSSR*, 1973, **209**, 610. (Engl. Transl., p. 239).
25. P. W. Fowler and V. Morvan, *J. Chem. Soc., Faraday Trans.*, 1992, **88**, 2631.
26. A. J. Stone and D. J. Wales, *Chem. Phys. Lett.*, 1986, **128**, 501.
27. P. W. Fowler and J. Baker, *J. Chem. Soc., Perkin Trans. 2*, 1992, 1665.
28. D. E. Manolopoulos, P. W. Fowler, and R. P. Ryan, *J. Chem. Soc., Faraday Trans.*, 1992, **88**, 1225.
29. D. E. Manolopoulos, P. W. Fowler, R. Taylor, H. W. Kroto, and D. R. M. Walton, *J. Chem. Soc., Faraday Trans.*, 1992, **88**, 3117.
30. D. Holmes Parker, P. Wurz, K. Chatterjee, K. R. Lykke, J. E. Hunt, M. J. Pellin, J. C. Hemminger, D. M. Gruen, and L. M. Stock, *J. Am. Chem. Soc.*, 1991, **113**, 7499.
31. A. Mittelbach, W. Hönle, H. G. von Schnering, J. Carlsen, R. Janiak, and H. Quast, *Angew. Chem., Int. Ed. Engl.*, 1992, **31**, 1640.
32. G. Peters and M. Jansen, *Angew. Chem., Int. Ed. Engl.*, 1992, **31**, 223.
33. N. Coustel, P. Bernier, R. Aznar, A. Zahab, J. M. Lambert, and P. Lyard, *J. Chem. Soc., Chem. Commun.*, 1992, 1402.

34. K. C. Khemani, M. Prato, and F. Wudl, *J. Org. Chem.*, 1992, **57**, 3254.

35. A. Gügel, M. Becker, D. Hammel, L. Mindach, J. Räder, T. Simon, M. Wagner, and K. Müllen, *Angew. Chem., Int. Ed. Engl.*, 1992, **31**, 644.

36. W. A. Scrivens, P. V. Bedworth, and J. M. Tour, *J. Am. Chem. Soc.*, 1992, **114**, 7917.

37. H. Schwarz, *Angew. Chem., Int. Ed. Engl.*, 1992, **31**, 293.

38. G. von Helden, M.-T. Hsu, P. R. Kemper, and M. T. Bowers, *J. Chem. Phys.*, 1991, **95**, 3835.

39. C. Yeretzian, K. Hansen, F. Diederich, and R. L. Whetten, *Nature (London)*, 1992, **359**, 44.

40. J. F. Christian, Z. Wan, and S. L. Anderson, *J. Phys. Chem.*, 1992, **96**, 3574.

41. S. Petrie, G. Javahery, J. Wang, and D. K. Bohme, *J. Am. Chem. Soc.*, 1992, **114**, 9177.

42. J. J. Stry, M. T. Coolbaugh, E. Turos, and J. F. Garvey, *J. Am. Chem. Soc.*, 1992, **114**, 7914.

43. K. A. Caldwell, D. E. Giblin, and M. L. Gross, *J. Am. Chem. Soc.*, 1992, **114**, 3743.

44. A. Izuoka, T. Tachikawa, T. Sugawara, Y. Suzuki, M. Konno, Y. Saito, and H. Shinohara, *J. Chem. Soc., Chem. Commun.*, 1992, 1472.

45. J. D. Crane, P. B. Hitchcock, H. W. Kroto, R. Taylor, and D. R. M. Walton, *J. Chem. Soc., Chem. Commun.*, 1992, 1764.

46. G. Roth and P. Adelman, *J. Phys. I (France)*, 1992, **2**, 1541.

47. K. Prassides and H. W. Kroto, *Phys. World*, 1992, **5**(4), 44.

48. N. Sivaraman, R. Dhamodaran, I. Kaliappan, T. G. Srinivasan, P. R. Vasudeva Rao, and C. K. Mathews, *J. Org. Chem.*, 1992, **97**, 6077.

49. H.-B. Bürgi, E. Blanc, D. Schwarzenbach, S. Liu, Y. Lu, M. M. Kappes, and J. A. Ibers, *Angew. Chem., Int. Ed. Engl.*, 1992, **31**, 640.

50. W. I. F. David, R. M. Ibberson, J. C. Matthewman, K. Prassides, T. J. S. Dennis, J. P. Hare, H. W. Kroto, R. Taylor, and D. R. M. Walton, *Nature (London)*, 1991, **353**, 156.

51. R. Back and R. B. Lennox, *J. Phys. Chem.*, 1992, **96**, 8149.

52. P. Wang, M. Shamsuzzoha, X.-L. Wu, W.-J. Lee, and R. M. Metzger, *J. Phys. Chem.*, 1992, **96**, 9025.

53. M. A. Green, M. Kurmoo, P. Day, and K. Kikuchi, *J. Chem. Soc., Chem. Commun.*, 1992, 1676.

54. J. P. Hare, T. J. Dennis, H. W. Kroto, R. Taylor, A. W. Allaf, S. Balm, and D. R. M. Walton, *J. Chem. Soc., Chem. Commun.*, 1991, 412.

55. C.-C. Chen and C. M. Lieber, *J. Am. Chem. Soc.*, 1992, **114**, 3141.

56. J. P. Hare, H. W. Kroto, and R. Taylor, *Chem. Phys. Lett.*, 1991, **177**, 394.

57. J. W. Arbogast and C. S. Foote, *J. Am. Chem. Soc.*, 1991, **113**, 8886.

58. Y. Wang, *J. Phys. Chem.*, 1992, **96**, 764.

59. Y. Wang and L.-T. Cheng, *J. Phys. Chem.*, 1992, **96**, 1530.

60. L. W. Tutt and A. Kost, *Nature (London)*, 1992, **356**, 225.

61. Q. Xie, E. Pérez-Cordero, and L. Echegoyen, *J. Am. Chem. Soc.*, 1992, **114**, 3978.

62. Y. Ohsawa and T. Saji, *J. Chem. Soc., Chem. Commun.*, 1992, 781.

63. Q. Li, F. Wudl, C. Thilgen, R. L. Whetten, and F. Diederich, *J. Am. Chem. Soc.*, 1992, **114**, 3994.

64. M. S. Meier, T. F. Guarr, J. P. Selegue, and V. K. Vance, *J. Chem. Soc., Chem. Commun.*, 1993, 63.

65. G. A. Heath, J. E. McGrady, and R. L. Martin, *J. Chem. Soc., Chem. Commun.*, 1992, 1272.

66. D. Dubois, M. T. Jones, and K. M. Kadish, *J. Am. Chem. Soc.*, 1992, **114**, 6446.

67. Special Issue on Buckminsterfullerenes, *Acc. Chem. Res.*, 1992, **25**(3).

68. Y. Chabre, D. Djurabo, M. Armand, W. R. Romanow, N. Coustel, J. P. McCauley Jr, J. E. Fischer, and A. B. Smith III, *J. Am. Chem. Soc.*, 1992, **114**, 764.

69. J. Kohanoff, W. Andreoni, and M. Parrinello, *Chem. Phys. Lett.*, 1992, **198**, 472.

70. T. Yildirim, O. Zhou, J. E. Fischer, N. Bykovetz, R. A. Strongin, M. A. Cichy, A. B. Smith III, C. L. Lin, and R. Jelinek, *Nature (London)*, 1992, **360**, 568.

71. O. Zhou, J. E. Fischer, N. Coustel, S. Kycia, Q. Zhu, A. R. McGhie, W. J. Romanow, J. P. McCauley, Jr, A. B. Smith III, and D. E. Cox, *Nature (London)*, 1991, **351**, 462.

72. P. W. Stephens, L. Mihaly, P. L. Lee, R. L. Whetten, S.-M. Huang, R. Kaner, F. Diederich, and K. Holczer, *Nature (London)*, 1991, **351**, 632.

73. R. C. Haddon, G. P. Kochanski, A. F. Hebard, A. T. Fiory, and R. C. Morris, *Science*, 1992, **258**, 1636.

74. A. R. Kortan, N. Kopylov, S. Glarum, E. M. Gyorgy, A. P. Ramirez, R. M. Fleming, F. A. Thiel, and R. C. Haddon, *Nature (London)*, 1992, **355**, 529.

75. A. R. Kortan, N. Kopylov, S. Glarum, E. M. Gyorgy, A. R. Ramirez, R. M. Fleming, O. Zhou, F. A. Thiel, P. L. Trevor, and R. C. Haddon, *Nature (London)*, 1992, **360**, 566.

76. P.-M. Allemand, G. Srdanov, A. Koch, K. Khemani, F. Wudl, Y. Rubin, F. Diederich, M. M. Alvarez, S. J. Anz, and R. L. Whetten, *J. Am. Chem. Soc.*, 1991, **113**, 2780.

77. C. Bossard, S. Rigaut, D. Astruc, M.-H. Delville, G. Félix, A. Février-Bouvier, J. Amiell, S. Flandrois, and P. Delhaès, *J. Chem. Soc., Chem. Commun.*, 1993, 333.

78. A. Izuoka, T. Tachikawa, T. Sugawara, Y. Saito, and H. Shinohara, *Chem. Lett.*, 1992, 1049.

79. T. Pradeep, K. K. Singh, A. P. B. Sinha, and D. E. Morris, *J. Chem. Soc., Chem. Commun.*, 1992, 1747.
80. M. F. Meidine, P. B. Hitchcock, H. W. Kroto, R. Taylor, and D. R. M. Walton, *J. Chem. Soc., Chem. Commun.*, 1992, 1534.
81. A. L. Balch, J. W. Lee, B. C. Noll, and M. M. Olmstead, *J. Chem. Soc., Chem. Commun.*, 1993, 56.
82. U. Geiser, S. K. Kumar, B. M. Savall, S. S. Harried, K. D. Carlson, P. R. Mobley, H. H. Wang, J. M. Williams, and R. E. Botto, *Chem. Mater.*, 1992, **4**, 1077.
83. Q. Zhu, D. E. Cox, J. E. Fischer, K. Kniaz, A. R. McGhie, and O. Zhou, *Nature (London)*, 1992, **355**, 712.
84. G. S. Hammond and V. J. Kuck eds, ‘Fullerenes’, ACS Symposium Series 481, American Chemical Society, Washington, DC, 1992.
85. D. A. Dixon, N. Matsuzawa, T. Fukunaga, and F. N. Tebbe, *J. Phys. Chem.*, 1992, **96**, 6107.
86. A. A. Tuinman, P. Mukherjee, J. L. Adcock, R. L. Hettich, and R. N. Compton, *J. Phys. Chem.*, 1992, **96**, 7584.
87. J. H. Holloway, E. G. Hope, R. Taylor, G. J. Langley, A. G. Avent, T. J. Dennis, J. P. Hare, H. W. Kroto, and D. R. M. Walton, *J. Chem. Soc., Chem. Commun.*, 1991, 966.
88. R. Taylor, J. H. Holloway, E. G. Hope, A. G. Avent, G. J. Langley, T. J. Dennis, J. P. Hare, H. W. Kroto, and D. R. M. Walton, *J. Chem. Soc., Chem. Commun.*, 1992, 665.
89. F. N. Tebbe, J. Y. Becker, D. B. Chase, L. E. Firment, E. R. Holler, B. S. Malone, P. J. Krusic, and E. Wasserman, *J. Am. Chem. Soc.*, 1991, **113**, 9900.
90. F. N. Tebbe, R. L. Harlow, D. B. Chase, D. L. Thorn, G. C. Campbell Jr, J. C. Calabrese, N. Herron, R. J. Young Jr, and E. Wasserman, *Science*, 1992, **256**, 822.
91. P. R. Birkett, P. B. Hitchcock, H. W. Kroto, R. Taylor, and D. R. M. Walton, *Nature (London)*, 1992, **357**, 479.
92. K. M. Creegan, J. L. Robbins, W. K. Robbins, J. M. Millar, R. D. Sherwood, P. J. Tindall, D. M. Cox, A. B. Smith, III, J. P. McCauley Jr, D. R. Jones, and R. T. Gallagher, *J. Am. Chem. Soc.*, 1992, **114**, 1103.
93. C. Taliani, G. Ruani, R. Zamboni, R. Danieli, S. Rossini, V. N. Denisov, V. M. Burlakov, F. Negri, G. Orlandi, and F. Zerbetto, *J. Chem. Soc., Chem. Commun.*, 1993, 220.
94. Y. Elemes, S. K. Silverman, C. Sheu, M. Kao, C. S. Foote, M. M. Alvarez, and R. L. Whetten, *Angew. Chem., Int. Ed. Engl.*, 1992, **31**, 351.
95. J. M. Hawkins, A. Meyer, T. A. Lewis, S. Loren, and F. J. Hollander, *Science*, 1991, **252**, 312.
96. J. M. Hawkins, A. Meyer, T. A. Lewis, U. Bunz, R. Nunlist, G. E. Ball, T. W. Ebbesen, and K. Tanigaki, *J. Am. Chem. Soc.*, 1992, **114**, 7954.
97. L. Y. Chiang, R. B. Upasani, and J. W. Swirczewski, *J. Am. Chem. Soc.*, 1992, **114**, 10 154.
98. L. Y. Chiang, J. W. Swirczewski, C. S. Hsu, S. K. Chowdhury, S. Cameron, and K. Creegan, *J. Chem. Soc., Chem. Commun.*, 1992, 1791.
99. A. Hirsch, A. Soi, and H. R. Karfunkel, *Angew. Chem., Int. Ed. Engl.*, 1992, **31**, 766.
100. P. J. Fagan, P. J. Krusic, D. H. Evans, S. A. Lerke, and E. Johnston, *J. Am. Chem. Soc.*, 1992, **114**, 9697.
101. R. Taylor, G. J. Langley, M. F. Meidine, J. P. Parsons, A. K. Abdul-Sada, T. J. Dennis, J. P. Hare, H. W. Kroto, and D. R. M. Walton, *J. Chem. Soc., Chem. Commun.*, 1992, 667.
102. P. J. Krusic, E. Wasserman, P. N. Keizer, J. R. Morton, and K. F. Preston, *Science*, 1991, **254**, 1183.
103. D. A. Loy and R. A. Assink, *J. Am. Chem. Soc.*, 1992, **114**, 3977.
104. J. R. Morton, K. F. Preston, P. J. Krusic, S. A. Hill, and E. Wasserman, *J. Am. Chem. Soc.*, 1992, **114**, 5454.
105. P. J. Krusic, E. Wasserman, B. A. Parkinson, B. Malone, E. R. Holler Jr, P. N. Keizer, J. R. Morton, and K. F. Preston, *J. Am. Chem. Soc.*, 1991, **113**, 6274.
106. P. N. Keizer, J. R. Morton, and K. F. Preston, *J. Chem. Soc., Chem. Commun.*, 1992, 1259.
107. S. H. Hoke II, J. Molstad, D. Dilettato, M. J. Jay, D. Carlson, B. Kahr, and R. G. Cooks, *J. Org. Chem.*, 1992, **57**, 5069.
108. Y. Rubin, S. Khan, D. I. Freedberg, and C. Yeretzian, *J. Am. Chem. Soc.*, 1993, **115**, 344.
109. A. Vasella, P. Uhlmann, C. A. A. Waldraff, F. Diederich, and C. Thilgen, *Angew. Chem., Int. Ed. Engl.*, 1992, **31**, 1388.
110. S. Shi, K. C. Khemani, Q. Li, and F. Wudl, *J. Am. Chem. Soc.*, 1992, **114**, 10 656.
111. T. Suzuki, Q. Li, K. C. Khemani, F. Wudl, and Ö. Almarsson, *J. Am. Chem. Soc.*, 1992, **114**, 7300.
112. T. Suzuki, Q. Li, K. C. Khemani, and F. Wudl, *J. Am. Chem. Soc.*, 1992, **114**, 7301.
113. P. J. Fagan, J. C. Calabrese, and B. Malone, *Science*, 1991, **252**, 1160.
114. P. J. Fagan, J. C. Calabrese, and B. Malone, *J. Am. Chem. Soc.*, 1991, **113**, 9408.
115. B. Chase and P. J. Fagan, *J. Am. Chem. Soc.*, 1992, **114**, 2252.
116. S. A. Lerke, B. A. Parkinson, D. H. Evans, and P. J. Fagan, *J. Am. Chem. Soc.*, 1992, **114**, 7807.
117. R. S. Koefod, C. Xu, W. Lu, J. R. Shapley, M. G. Hill, and K. R. Mann, *J. Phys. Chem.*, 1992, **96**, 2928.
118. A. L. Balch, V. J. Catalano, and J. W. Lee, *Inorg. Chem.*, 1991, **30**, 3980.
119. A. L. Balch, J. W. Lee, B. C. Noll, and M. M. Olmstead, *J. Am. Chem. Soc.*, 1992, **114**, 10 984.
120. A. L. Balch, J. W. Lee, and M. M. Olmstead, *Angew. Chem., Int. Ed. Engl.*, 1992, **31**, 1356.
121. H. Nagashima, A. Nakaoka, Y. Saito, M. Kato, T. Kawanishi, and K. Itoh, *J. Chem. Soc., Chem. Commun.*, 1992, 377.

122. H. Nagashima, A. Nakaoka, S. Tajima, Y. Saito, and K. Itoh, *Chem. Lett.*, 1992, 1361.

123. E. G. Gillan, C. Yeretzian, K. S. Min, M. M. Alvarez, R. L. Whetten, and R. B. Kaner, *J. Phys. Chem.*, 1992, **96**, 6869.

124. M. M. Ross, H. H. Nelson, J. H. Calahan, and S. W. McElvany, *J. Phys. Chem.*, 1992, **96**, 5231.

125. S. Suzuki, S. Kawata, H. Shiromaru, K. Yamauchi, K. Kikuchi, T. Kato, and Y. Achiba, *J. Phys. Chem.*, 1992, **96**, 7159.

126. L. Soderholm, P. Wurz, K. R. Lykke, D. H. Parker, and F. W. Lytle, *J. Phys. Chem.*, 1992, **96**, 7153.

127. T. Guo, M. D. Diener, Y. Chai, M. J. Alford, R. E. Haufler, S. M. McClure, T. Ohno, J. H. Weaver, G. E. Scuseria, and R. E. Smalley, *Science*, 1992, **257**, 1661.

128. B. I. Dunlap, O. D. Häberlen, and N. Rösch, *J. Phys. Chem.*, 1992, **96**, 9095.

129. H. Shinohara, H. Sato, M. Ohkohchi, Y. Ando, T. Kodama, T. Shida, T. Kato, and Y. Saito, *Nature (London)*, 1992, **357**, 52.

130. C. S. Yannoni, M. Hoinkis, M. S. de Vries, D. S. Bethune, J. R. Salem, M. S. Crowder, and R. D. Johnson, *Science*, 1992, **256**, 1191.

Carbon: Inorganic Chemistry

Tomislav Friščić & Leonard R. MacGillivray
University of Iowa, Iowa City, IA, USA

Based in part on the article Carbon: Inorganic Chemistry by R. Bruce King which appeared in the Encyclopedia of Inorganic Chemistry, First Edition.

1 Introduction 1
2 Carbon Isotopes and Elemental Carbon 1
3 Carbon Halides 2
4 Carbon Oxides 3
5 Carbon Oxyacids and Oxyanions 4
6 Carbon−Sulfur Derivatives 5
7 Cyanides and Related Compounds 6
8 Carbon-based Molecular Ladders 9
9 Related Articles 12
10 Further Reading 12
11 References 12

1 INTRODUCTION

Carbon is the basis of organic chemistry; there are more compounds of carbon than of any other element except hydrogen and possibly fluorine. However, most of the chemistry of carbon is the province of organic chemistry and thus not covered in this encyclopedia. The 'inorganic' chemistry of carbon discussed in this article, which is an update of an excellent article written previously by professor R. Bruce King (University of Georgia, Athens), includes the allotropic forms of elemental carbon, simple molecular carbon halides and oxides, carbon oxyacids and oxyanions, carbon−sulfur derivatives, simple cyano derivatives, and carbon-based molecular ladders.

Carbon chemistry has the following features:

1. Carbon normally forms a total of four bonds including both σ- and π-bonds. The coordination number of a carbon atom forming four bonds can be two ($\equiv$C–, as in alkynes, or $=$C$=$, as in allene), three ($=$C$<$, as in alkenes), or four (as in alkanes) with linear, planar triangular, and tetrahedral geometries, respectively. The carbon atoms in carbon monoxide ($:\overset{-}{C}\equiv\overset{+}{O}:$) and the isocyanide carbon atom in isocyanides ($:C\equiv\overset{+}{N}–R:$) have coordination numbers of only one. Stable trivalent carbon 'free radicals,' $R_3C\cdot$, can be isolated if R is an aryl group; tris(pentachlorophenyl)methyl, $(C_6Cl_5)_3C\cdot$, is particularly stable.[1]
2. Exceptional examples of carbon atoms with apparent coordination numbers greater than four include five-coordinate carbon atoms in bridging alkyl groups in metal alkyls (e.g. $Al_2(CH_3)_6$), five- and six-coordinate carbon atoms in deltahedral carboranes of the general formula $C_2B_{n-2}H_n$ $(6 \le n \le 12)$, and five-, six-, and eight-coordinate carbon atoms in transition metal carbide clusters such as a five-coordinate carbon in the center of an Fe_5 square pyramid in $Fe_5(CO)_{15}C$, a six-coordinate carbon in the center of an Ru_6 octahedron in $Ru_6(CO)_{17}C$, and an eight-coordinate carbon in the center of a Co_8 square antiprism in the anion $Co_8C(CO)_{18}{}^{2-}$.
3. The high carbon−carbon bond strength leads to the unusual stability of catenated carbon compounds: the basis of organic chemistry. Thus the C–C bond strength of $\approx$356 kJ mol^{-1} is comparable to the C–O bond strength of $\approx$336 kJ mol^{-1}. This contrasts with the heavier congener of carbon, silicon, as well as with sulfur: Si–O bonds ($\approx$368 kJ mol^{-1}) and S–O bonds ($\approx$330 kJ mol^{-1}) are much stronger than Si–Si bonds ($\approx$226 kJ mol^{-1}) and S–S bonds ($\approx$226 kJ mol^{-1}).

2 CARBON ISOTOPES AND ELEMENTAL CARBON

2.1 Isotopes of Carbon

Table 1 summarizes some of the important properties of the carbon isotopes. Note that only the rare ($\approx$1%), naturally occurring, stable carbon isotope, namely, ^{13}C, has a nuclear spin and is observable by NMR.[2] The organic chemist is fortunate that $\approx$99% of natural carbon is the isotope ^{12}C with no nuclear spin, so that proton and carbon-13 NMR spectra of organic compounds are not complicated by spin−spin splitting arising from adjacent carbon atoms. The radioisotope[3] ^{14}C is made by thermal neutron irradiation of lithium or aluminum nitride (equation 1). It decays back to stable $^{14}_{7}$N by β^- emission, with a half-life of 5570 years (equation 2). Cosmic rays generate thermal neutrons, which leads to the formation of $^{14}CO_2$ in the atmosphere (equation 1). Metabolism of

Table 1 Properties of the Carbon Isotopes

Isotope	Natural abundance (%)	Half-life	Spin	NMR sensitivity^a
^{12}C	98.89	Stable	0	0
^{13}C	1.11	Stable	1/2	0.0159
^{14}C	1.2×10^{-10}	5570 years, β^-	0	0

^{a}Relative to the proton for equal numbers of nuclei.

this $^{14}CO_2$ by living organisms is the basis of radiocarbon dating.

$$^{14}_{7}N + ^{1}_{0}n \longrightarrow ^{14}_{6}C + ^{1}_{1}H \qquad (1)$$

$$^{14}_{6}C \longrightarrow ^{14}_{7}N + \beta^- \qquad (2)$$

2.2 Allotropes of Carbon

Carbon forms three types of allotropes: diamond, graphite, and the recently discovered fullerenes. The properties of these allotropes are compared in Table 2.

2.2.1 Diamond[4]

Diamonds are found naturally in Kimberly, South Africa, in ancient volcanic pipes embedded in a relatively soft, dark colored basic rock in low concentrations ($\approx$1 part per 1.5×10^7). The structure of diamond consists of an infinite three-dimensional lattice of sp^3 carbon atoms in which there are interlocking six-membered C_6 rings, similar to those in cyclohexane or adamantane, and C–C distances of 1.514 Å. Diamond is normally found in the cubic form, but a hexagonal form (lonsdaleite) is found in certain meteorites and is available synthetically. Diamond is the hardest solid known and has the highest melting point ($\approx$4000 °C) and thermal conductivity, as well as the lowest molar entropy ($2.4\ \mathrm{J\,mol^{-1}\,K^{-1}}$) of any element. Diamond is an insulator. The density of diamond ($3.51\ \mathrm{g\,cm^{-3}}$) is much greater than that of graphite ($2.22\ \mathrm{g\,cm^{-3}}$) so that high pressures (e.g. $>$125 kbar) can be used to convert graphite to diamond even though graphite is thermodynamically more stable than diamond by $2.9\ \mathrm{kJ\,mol^{-1}}$. In order to attain useful rates for the high-pressure conversion of graphite to diamond, a transition metal catalyst such as Cr, Fe, or Pt is used. Diamond burns in air at elevated temperatures (600–800 °C).

2.2.2 Graphite[5,6]

Graphite consists of planar layers of hexagons of sp^2 hybridized carbon atoms with a separation of 3.35 Å between layers. The relatively slight forces between graphite layers are consistent with its softness and lubricity. The infinite delocalization of π-electrons in the graphite structure leads to electrical conductivity. The average C–C bond order in graphite is 1.33, corresponding to a C–C distance of 1.415 Å. By contrast, the average C–C bond order in benzene is 1.5, corresponding to the expected shorter C–C distance of 1.39 Å. The most stable and common form of graphite is hexagonal α-graphite with an ABABAB... stacking of the graphite layers. However, rhombohedral β-graphite with an ABCABC... stacking of the layers is also known. Strong oriented graphite fibers can be obtained by pyrolysis of fibers of organic polymers such as poly(acrylonitrile). Amorphous carbons (carbon black, soot, charcoal, etc.) are microcrystalline forms of graphite; their physical properties depend upon their surface area and the nature of their surface (e.g. the presence and type of oxygenated groups).

Table 2 Properties of the carbon allotropes

Allotrope	C Hybridization	Structure
Diamond	sp^3	Infinite 3D-lattice
Graphite	sp^2	Infinite 2D-planar layers of hexagons
Fullerenes	sp^2	Finite C_n cages with 12 pentagons and $n - 12$ hexagons

Molecules and ions can penetrate between the layers of graphite to form interstitial or lamellar compounds. These so-called intercalation compounds are of two types, namely, nonconducting compounds, in which the planarity of the graphite layers is destroyed, and conducting compounds, in which the planarity of the graphite layers is preserved (*see* ***Intercalation Chemistry***).[7,8]

2.2.3 Fullerenes[9,10]

Fullerenes are large molecular carbon cages that are isolated by extraction of specially prepared soot with organic solvents such as benzene. A rich source of fullerene is soot made by arcing graphite rods in a helium atmosphere at 200 Torr pressure.[11] The most common fullerene is C_{60}, which has a truncated icosahedral 'soccer ball' structure with icosahedral (I_h) symmetry. Less symmetrical fullerenes with larger numbers of carbon atoms are known. C_{70} is the next most abundant after C_{60}; C_{76} and C_{84} are also known (*see* ***Carbon: Fullerenes***).

3 CARBON HALIDES

Carbon tetrafluoride, CF_4, mp −185 °C, bp −128 °C, which is the end product of the fluorination of carbon compounds, is a very stable gas. It can also be made by the fluorination of silicon carbide (equation 3). The SiF_4 is removed from the CF_4 by passing the product gases through 20% aqueous NaOH, which removes the SiF_4 as soluble sodium silicate but leaves the CF_4 unaffected. This major difference in hydrolytic reactivity of CF_4 and SiF_4 is a consequence of accessible d orbitals on silicon but not on carbon.

$$SiC + 4F_2 \longrightarrow SiF_4 + CF_4 \qquad (3)$$

Organic compounds containing only carbon and fluorine are called fluorocarbons; the chemistry of fluorocarbons is a vast area far beyond the scope of this encyclopedia.[12–15]

General routes to saturated fluorocarbons include the fluorination of hydrocarbons with higher valent fluorides such as CoF_3 or the fluorination of chlorocarbons with SbF_3, often in the presence of catalytic amounts of Sb^V. Since such fluorination procedures usually add fluorine to all carbon–carbon double and triple bonds giving products with exclusively carbon–carbon single bonds, unsaturated fluorocarbons normally require indirect methods of synthesis, generally using dehalogenation reactions by metals such as zinc or dehydrohalogenation reactions with bases. Fluorocarbons have diverse chemical and physiological properties. Thus poly(tetrafluoroethylene), $(\text{–}CF_2CF_2\text{–})_n$, commonly known as 'Teflon,' is very chemically inert and has a low coefficient of friction. Octafluoroisobutene, $(CF_3)_2C{=}CF_2$, is highly toxic, but other fluorocarbons, such as perfluorodecahydronaphthalene, $C_{10}F_{18}$, are so physiologically inactive that they are the active components of blood substitute, because of the relatively high solubility of oxygen in fluorocarbons.[16]

Carbon tetrachloride, a liquid with mp −23 °C and bp 76 °C, is a common solvent and is useful for converting metal oxides to metal chlorides at elevated temperatures (300–500 °C). It is thermodynamically unstable with respect to hydrolysis, but is kinetically very inert to hydrolysis because of the absence of empty acceptor orbitals (e.g. d orbitals) for nucleophilic attack. However, heating carbon tetrachloride with free alkali metals or other strong reducing agents can lead to dangerous explosions.

Organic compounds containing only carbon and chlorine are called chlorocarbons. The presence of relatively large chlorine atoms on a carbon network makes the properties of chlorocarbons very different than those of corresponding hydrocarbons. In general, chlorocarbons with trigonal sp^2 carbon atoms are more stable than chlorocarbons with tetrahedral sp^3 carbon atoms. As a result, certain chlorocarbons having only sp^2 carbon atoms, for example, perchlorofulvene and perchlorofulvalene, are very stable under normal conditions, whereas their hydrocarbon analogs polymerize rapidly. Chlorocarbon free radicals[1] with trivalent carbon atoms are among the most stable carbon free radicals. For example, the trivalent carbon atom in $(C_6Cl_5)_3C\bullet$ is stable not only to air but even to permanganate oxidation.

Carbon tetrabromide is a pale yellow water-insoluble solid, mp 90.1 °C, bp 189.5 °C. Carbon tetraiodide is a bright red solid which decomposes readily to I_2 and $I_2C{=}CI_2$, again indicating the stability of sp^2 carbon atoms relative to sp^3 carbon atoms in halocarbons (other than fluorocarbons). Carbon tetraiodide is made by an electrophilic halogen exchange reaction (equation 4).[17] The increasing instability of the carbon tetrahalides with increasing atomic weight of the halogen relates to the steady decrease in C–X bond energies from 485 kJ mol^{-1} for the C–F bond to 213 kJ mol^{-1} for the C–I bond.

$$\mathrm{CCl_4 + 4EtI \xrightarrow{AlCl_3} CI_4 + 4EtCl} \qquad (4)$$

Carbonyl halides, $O{=}CX_2$ (X = F, Cl, Br, I), are all known, although the existence of COI_2 has recently been questioned.[18] The fluoride and chloride are made by reaction of carbon monoxide with the corresponding halogen; the bromide is made by the partial hydrolysis of CBr_4 with concentrated sulfuric acid. Carbonyl chloride, $O{=}CCl_2$, bp +7.6 °C, also known as phosgene (from $\phi\omega\zeta$ = *phōs* for *light* and -$\gamma\varepsilon\nu\eta\zeta$ = -*genēs* for *form*, relating to its formation from $CO + Cl_2$ in sunlight), is a toxic gas smelling like 'new-mown hay,' which was used as a war gas in World War I. Thiocarbonyl chloride or 'thiophosgene,' $S{=}CCl_2$, is an evil-smelling orange toxic liquid, bp 73 °C.[19]

4 CARBON OXIDES

The oxides of carbon include the very stable and abundant CO and CO_2, the unstable but isolable C_3O_2, and more complicated carbon oxides derived from organic backbones by removal of all hydrogen, for example, $C_{12}O_9$, from the complete dehydration of mellitic acid (benzenehexacarboxylic acid). Oxocarbon anions, $C_nO_n{}^{2-}$, with apparent 'aromatic' properties are also known.[20,21] The properties of these carbon–oxygen compounds are summarized below.

4.1 Carbon Monoxide

Carbon monoxide, mp −205 °C, bp −190 °C, $:\overset{-}{C}{\equiv}\overset{+}{O}:$, is a colorless, odorless, but very toxic gas that is sparingly soluble in water. Carbon monoxide is formed by burning carbon in a deficiency of oxygen. It therefore is a dangerous product of many combustion processes. Carbon monoxide is also made by the 'water gas reaction' from steam and coal as 'synthesis gas,' a 1:1 CO/H_2 mixture arising from equation (5) at elevated temperatures. On the laboratory scale, pure carbon monoxide may be generated by the acid dehydration of formic acid, HCO_2H, using concentrated sulfuric acid. Transition metals combine with carbon monoxide to form metal carbonyls, which play a key role in vast areas of organometallic and coordination chemistry (*see Metal Carbonyls*; ***Carbonyl Complexes of the Transition Metals***, and ***Carbonylation Processes by Homogeneous Catalysis***). The toxicity of carbon monoxide is a consequence of its binding to the iron in blood hemoglobin, thereby inhibiting the essential function of hemoglobin as an oxygen carrier. Carbon monoxide can bond to transition metals as a terminal or a bridging ligand (Figure 1). Simple, neutral binary-metal carbonyls are volatile covalent compounds, which readily decompose on heating to carbon monoxide and the free metal, and thus are often useful sources of finely divided and/or pure metals such as chromium, molybdenum, iron, and nickel. Carbon monoxide reacts with alkali metals to give the so-called alkali metal carbonyls, which contain salts of the acetylenediolate ion, $^{-}O\text{–}C{\equiv}C\text{–}O^{-}$; on

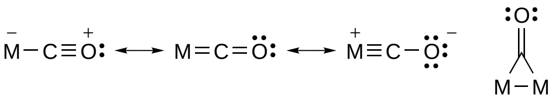

Figure 1 The bonding of CO to transition metals in metal carbonyls as terminal and bridging ligands

hydrolysis, these can give hexahydroxybenzene derivatives.

$$\mathrm{C + H_2O \xrightarrow{\Delta} CO + H_2} \quad (5)$$

4.2 Carbon Dioxide

Carbon dioxide, $:\ddot{O}=C=\ddot{O}:$, mp −57 °C (5.2 atm), bp −79 °C (sublimes), is obtained from the combustion of carbon and hydrocarbons in excess air or oxygen or by the pyrolysis ('calcination') of $CaCO_3$ (limestone). The photosynthesis in plants reduces CO_2 to organic matter, but the similar reduction of CO_2 in a nonliving system ('in vitro') appears to be very difficult. However, CO_2 can be reduced electrochemically to methanol, formate, oxalate, methane, and/or CO depending upon the conditions. Numerous transition metal complexes of CO_2 are known,**[22–28]** which exhibit the modes of metal–CO_2 bonding depicted in Figure 2.

4.3 Carbon Suboxide

Carbon suboxide, C_3O_2, $:\ddot{O}=C=C=C=\ddot{O}:$, also called 1,2-propadiene-1,3-dione, is an evil-smelling unstable gas, bp +6.8 °C, which is obtained by the dehydration of malonic acid with P_4O_{10} in vacuum at 140–150 °C (equation 6). Carbon suboxide polymerizes readily at room temperature to a yellow solid, and above 100 °C to a ruby-red water-soluble solid. Photolysis of C_3O_2 gives C_2O ($:C=C=\ddot{O}:$) as a reactive intermediate, which reacts with alkenes by carbon atom insertion (equation 7).

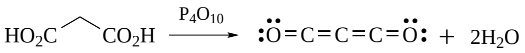

(6)

$$\mathrm{H_2C{=}CH_2 + :C{=}C{=}\ddot{O}: \xrightarrow{h\nu} H_2C{=}C{=}CH_2 + CO} \quad (7)$$

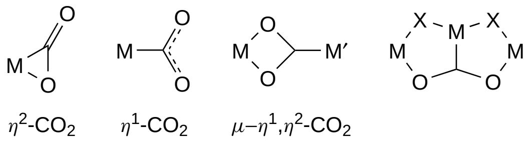

Figure 2 Some bonding modes of carbon dioxide to one or two transition metals (M and M′), illustrating the η^n method for indicating number of attachment points

4.4 More Complicated Carbon Oxides

Some more complicated carbon oxides are known with carbon backbones familiar in organic chemistry. An example is benzenehexacarboxylic acid (mellitic acid) trianhydride, $C_{12}O_9 = C_6[(CO)_2O]_3$ (**1**), a white sublimable solid obtained by dehydration of the corresponding acid with acetyl chloride in a sealed tube at 160 °C.

5 CARBON OXYACIDS AND OXYANIONS

5.1 Carbonic Acid

Carbon dioxide is the anhydride of carbonic acid but hydrolyzes only slowly at pH 7 to H_2CO_3. In aqueous solution, CO_2 is physically dissolved and only loosely solvated so that only ≈0.2% is present as $H_2CO_3/HCO_3^-/CO_3^{2-}$. This relates to the stability of the $:\ddot{O}=C=\ddot{O}:$ structure for CO_2 and the reluctance of water to add to one of the C=O double bonds of CO_2. Carbonic acid is a weak acid with the true dissociation constants $K_1 = 1.6 \times 10^{-4}$ and $K_2 = 4.7 \times 10^{-11}$; determination of K_1 without allowing for the fact that ≈99.8% of an aqueous solution of CO_2 is undissociated CO_2 gives the fictitious dissociation constant of 4.16×10^{-7} for 'K_1' of H_2CO_3. Pure carbonic acid, H_2CO_3, cannot be isolated because of its ready dehydration to CO_2. However, colorless crystals of a white crystalline etherate $H_2CO_3{\cdot}Me_2O$, mp −47 °C, can be isolated by treatment of Na_2CO_3 at −35 °C with hydrogen chloride in dimethyl ether; this etherate decomposes above −26 °C into CO_2, H_2O, and Me_2O.

5.2 Oxocarbon Anions[21,29]

Oxocarbon anions, $C_nO_n^{2-}$ ($3 \le n \le 6$), are derived from the cyclic dihydroxy compounds depicted in Figure 3. Deltic and squaric acids are made by hydrolysis of suitable cyclopropene and cyclobutene derivatives (Figure 4). Much milder conditions (e.g. n-butanol in diethyl ether) are

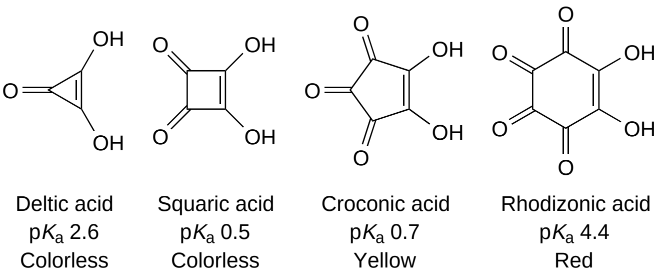

Figure 3 The acids giving the oxocarbon anions $C_nO_n^{2-}$ ($3 \le n \le 6$)

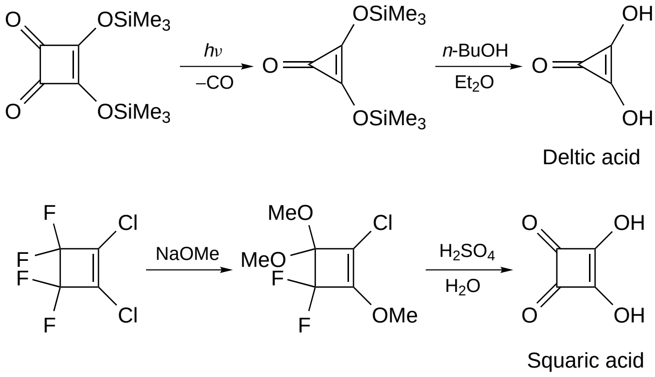

Figure 4 Syntheses of squaric acid and deltic acid

used for the preparation of deltic acid than for squaric acid, in order to avoid cleavage of the three-membered ring in deltic acid. Squaric acid can also be made by the electrolytic reduction of carbon monoxide in DMF at 18 °C/230 atmospheres with tetrabutylammonium bromide as the supporting electrolyte, using the stainless steel pressure vessel as the cathode and an aluminum anode. Rhodizonic acid is obtained from the microbiological oxidation of myoinositol or by the chemical oxidation (HNO_3 followed by O_2/Me_3CO_2K) of hexahydroxycyclohexane. Alternatively, carbon monoxide can be reduced with potassium metal under mild conditions to give potassium ethynediolate, $K_2C_2O_2$, which under heating undergoes cyclotrimerization to the potassium derivative of hexahydroxybenzene, $K_6C_6O_6$, which in turn can be oxidized to potassium rhodizonate, $K_2C_6O_6$. Further oxidation of rhodizonate in basic solution results in ring contraction to give potassium croconate. The preparation of rhodizonic and croconic acids from elemental carbon was already known in the early nineteenth century, long before their structures were known; therefore, the trivial names of these acids are based on the characteristic colors of their salts, that is, *ρωδιζειν* (*rhōdizein*) = rose red and *κρωκσ* (*krōkos*) = yellow. Rhodizonates are used as spot test reagents for alkaline earth and other divalent ions such as Pb^{2+}.

6 CARBON–SULFUR DERIVATIVES

6.1 Carbon Disulfide, Thiocarbonates, and Thiocarbamates

The raw material for much of carbon–sulfur chemistry is carbon disulfide, CS_2 ($:\ddot{S}=C=\ddot{S}:$), a very flammable and reactive liquid, mp −109 °C, bp +46 °C, which can be synthesized from elemental carbon or methane and sulfur at high temperatures.[30] Chlorination of carbon disulfide (equation 8) provides a source of carbon tetrachloride on an industrial scale. The carbon in carbon disulfide is susceptible toward nucleophilic attack by HS^-, RO^-, RNH_2, R_2 NH, and so on. Nucleophilic attack of carbon disulfide with SH^- in basic solution gives the yellow trithiocarbonate ion, $CS_3{}^{2-}$. Further reaction of the trithiocarbonate ion with elemental sulfur gives the ion $CS_4{}^{2-}$, shown to have the disulfide structure $[S_2C–S–S]^{2-}$. The free acids H_2CS_3 and H_2CS_4 can be obtained from these anions as red liquids, stable only at low temperatures. Reaction of carbon disulfide with secondary amines in basic solution leads to dithiocarbamates (equation 9; R = methyl, ethyl, etc.).[31]

$$CS_2 + 3Cl_2 \longrightarrow CCl_4 + S_2Cl_2 \qquad (8)$$

$$CS_2 + R_2NH + NaOH \longrightarrow R_2NCS_2{}^-Na^+ + H_2O \qquad (9)$$

Zinc, manganese, and iron dithiocarbamates are extensively used as agricultural fungicides and zinc dithiocarbamates are used as accelerators in rubber vulcanization. Oxidation of aqueous dimethyldithiocarbamate with Cl_2, H_2O_2, or $S_2O_8{}^{2-}$ gives tetramethylthiuram disulfide, $Me_2NC(=S)–S–S–C(=S)NMe_2$. The lability of its sulfur–sulfur bond makes tetramethylthiuram disulfide a useful free radical source for polymerization initiators and vulcanization accelerators. Tetraethylthiuram disulfide, $Et_2NC(=S)–S–S–C(=S)NEt_2$, is the drug ‘Antabuse’, which is used to treat alcoholism by making the body react to ethanol. Carbon disulfide is a very versatile ligand toward transition metals, forming various types of metal complexes including complex types analogous to those found for carbon dioxide (Figure 2).

6.2 Carbon Monosulfide

Carbon monosulfide, CS, unlike carbon monoxide, is not stable (dec. > -160 °C). However, numerous transition metal complexes of carbon monosulfide are known;[32–34] such complexes are generally called metal thiocarbonyls, by analogy to metal carbonyls. Selenocarbonyls containing the CSe group are also known. The inaccessibility of free CS restricts the variety of metal thiocarbonyls that can be prepared, and relatively few complexes with more than one CS ligand are known. For example, $M(CS)_6$ (M = Cr, Mo, W) and $Fe(CS)_5$, analogous to $M(CO)_6$ and $Fe(CO)_5$ respectively, remain unknown. Sources of CS ligands in metal complexes include CS_2 and $CSCl_2$ (equations 10 and 11).

$$(Ph_3P)_3RhCl + CS_2 \longrightarrow (Ph_3P)_2Rh(CS)Cl + Ph_3PS \qquad (10)$$

$$Na_2W(CO)_5 + S=CCl_2 \longrightarrow W(CO)_5CS + 2NaCl \qquad (11)$$

A problem with equation (11) is the separation of $W(CO)_5CS$ from $W(CO)_6$ formed in side reactions, since these compounds have very similar properties. Coordinated CS is reactive toward an electrophilic attack at sulfur and a nucleophilic attack at carbon (equations 12 and 13). The greater reactivity of metal thiocarbonyl derivatives relative to corresponding metal-carbonyl derivatives provides the best method for separating $W(CO)_5CS$ from $W(CO)_6$. Thus, $W(CO)_5CS$ reacts with iodide ion to give ionic *trans*-$W(CO)_4(CS)I^-$ under conditions where $W(CO)_6$ is unaffected; this reaction coupled with regeneration of $W(CO)_5CS$ from *trans*-$W(CO)_4(CS)I^-$ by treatment with $AgSO_3CF_3$ in a CO atmosphere provides a useful method for separating $W(CO)_6/W(CO)_5CS$ mixtures.

$$L_nM(CS) + RI \longrightarrow [L_nM(CSR)]^+I^- \qquad (12)$$

$$R = Me, etc.$$

$$L_nM(CS) + R_2N^- \longrightarrow [L_nM\text{–}C(=S)MR_2]^- \qquad (13)$$

6.3 More Complicated Carbon Sulfides

Besides carbon sulfides CS and CS_2, described in previous sections, some other binary compounds of sulfur and carbon have been known for a long time, such as C_3S_2 and the two isomers of C_4S_6 and C_9S_9. In the latter, extensive delocalization leads to the formation of disulfide bonds within linear three-sulfur sequences, and the molecule is sometimes considered to be a carbon–sulfur analogue of coronene (Figure 5).[35]

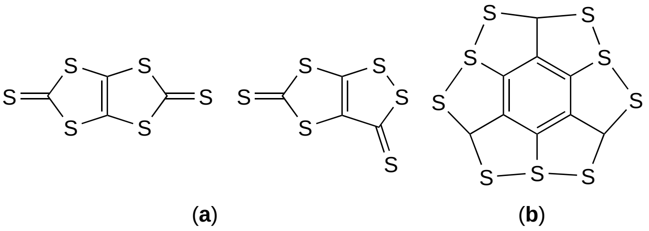
(a) (b)

Figure 5 Schematic representation of (a) two isomers of C_4S_6, and (b) C_9S_9

In addition, potential application of materials containing carbon–sulfur bonds in electronic industries has recently provided an impetus for the synthesis of further binary carbon sulfides, leading to the discovery and characterization of C_3S_7, C_3S_8, C_5S_7, C_6S_8, C_6S_{10}, and C_6S_{12}.[36] The syntheses of the sulfides involve the dithiolate complex of a transition metal ion as a precursor and are based on the oxidative coupling and electrophilic sulfiding (e.g. via S_2Cl_2) of either the α- or β-$C_3S_5{}^{2-}$ anion (Figure 6) and, consequently, molecular structures of such compounds are based on either the α- or β-C_3S_5 subunit, respectively (Figure 6). Specifically, C_3S_7, C_3S_8, C_6S_{10}, and C_6S_{12} are based on the α-C_3S_5 subunit, while C_5S_7 contains the β-C_3S_5 subunit. In case of C_6S_8, two isomers have been obtained, one of which is based on the β-C_3S_5 subunit.

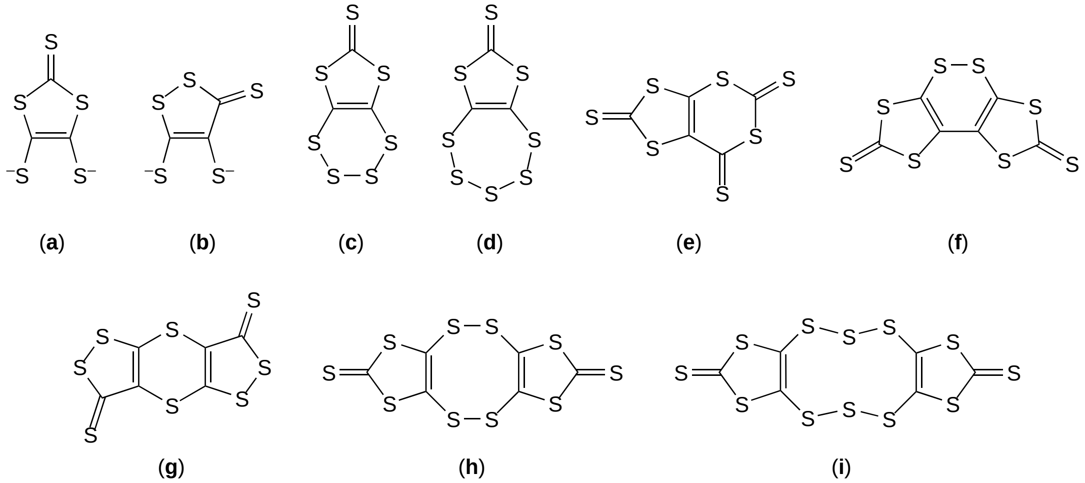
(a) (b) (c) (d) (e) (f)

(g) (h) (i)

Figure 6 Schematic representation of (a) α-C_3S_5 anion, (b) β-C_3S_5 anion, (c) C_3S_7, (d) C_3S_8, (e) C_5S_7, (f) one of two isomers of C_6S_8, (g) the isomer of C_6S_8 based on the β-C_3S_5 unit, (h) C_6S_{10}, and (i) C_6S_{12}

7 CYANIDES AND RELATED COMPOUNDS

7.1 Cyanogen

Cyanogen, $:N{\equiv}C\text{–}C{\equiv}N:$, is a flammable and toxic gas, mp −28 °C, bp −21 °C, which is kinetically stable but endothermic (297 kJ mol^{-1}). It has a linear structure with a sufficiently weak C–C bond to allow dissociation into •CN radicals. Cyanogen can be prepared by various oxidation reactions of cyano derivatives. Thus, cyanogen is obtained from the oxidation of hydrogen cyanide (see below) with oxygen over a silver catalyst, with chlorine over activated carbon or silica, or with nitrogen dioxide over CaO/glass. Cyanogen is also obtained by oxidation of an aqueous

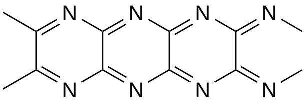

Paracyanogen

Figure 7 Structure of paracyanogen

cyanide ion with copper(II) or persulfate ($S_2O_8{}^{2-}$) in acid solution or by a solid-state reaction between $Hg(CN)_2$ and $HgCl_2$ (equation 14). Cyanogen disproportionates in basic solution (equation 15). Because of its endothermic nature, cyanogen burns in a stoichiometric amount of pure oxygen with one of the hottest known flames from a chemical reaction (5050 K). Cyanogen polymerizes readily on heating to give paracyanogen (Figure 7) as an infinite chain polymer.

$$Hg(CN)_2 + HgCl_2 \longrightarrow Hg_2Cl_2 + {:}N\equiv C{-}C\equiv N{:} \quad (14)$$

$$:N\equiv C{-}C\equiv N{:} + 2OH^- \longrightarrow CN^- + OCN^- + H_2O \quad (15)$$

7.2 Hydrogen Cyanide

Hydrogen cyanide, $H{-}C\equiv N{:}$, is a colorless, extremely toxic, volatile liquid, mp −13.4 °C, bp +25.6 °C, with a high dielectric constant (107 at 25 °C). It functions as a weak acid ($K_a = 4.9 \times 10^{-10}$). It is made by acidifying aqueous solutions of cyanides or industrially by the exothermic reaction of methane with ammonia in a fast flow/rapid quench system (equation 16). Hydrogen cyanide polymerizes readily under a variety of conditions; hydrogen cyanide oligomers include the trimer aminomalononitrile and the tetramer diaminomaleonitrile (Figure 8).

$$CH_4 + NH_3 \xrightarrow[1200\,^\circ C]{\text{Pt catalyst}} HCN + 3H_2 \quad (16)$$
$$\Delta H = -247\,\text{kJ mol}^{-1}$$

7.3 Cyanide Ion

Cyanide ion, ${:}\bar{C}\equiv N{:}$, is made by treatment of hydrogen cyanide with base (e.g. NaOH or Na_2CO_3 for the preparation of sodium cyanide) or from sodium, ammonia, and carbon (equation 17).

$$2Na + 2NH_3 \longrightarrow H_2 + NaNH_2 \quad (17a)$$

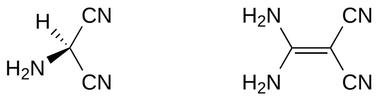

HCN trimer (aminomalonitrile)

HCN tetramer (diaminomaleonitrile; 'DAMN')

Figure 8 Some oligomers of hydrogen cyanide

$$2NaNH_2 + C \longrightarrow 2H_2 + Na_2NCN \quad (17b)$$

Sodium amide or 'sodamide'; Disodium cyanamide

$$Na_2NCN + C \longrightarrow 2NaCN \quad (17c)$$

The cyanide ion in crystalline alkali metal cyanides is rotationally disordered and thus is effectively spherical with a radius of 1.92 Å. Cyanide ion forms strong complexes (e.g. $Fe(CN)_6{}^{4-}$: hexacyanoferrate(II) or ferrocyanide) in aqueous solution with transition metals;[35] the transition metal always bonds to the carbon atom of the cyano group in these complexes (*see* ***Cyanide Complexes of the Transition Metals***). The cyanide ion occupies a high position in the spectrochemical series, giving rise to a large nephelauxetic effect and producing a large trans effect. A unidentate cyanide ion always bonds to the metal through its carbon atom but M–C≡N–M links are present in many solid cyanides, such as AuCN, $Zn(CN)_2$, and the Prussian blues, which are highly colored mixed oxidation state $Fe^{II/III}$ derivatives. Anhydrous acids corresponding to the more stable complex transition metal cyanides can be isolated, for example, $H_3Rh(CN)_6$ and $H_4Fe(CN)_6$; such acids have hydrogen-bonded $M{-}C\equiv N{-}H\cdots N\equiv C{-}M$ units. Related species are the hydrogen isocyanide complexes, such as $HNCW(CO)_5$, obtained by protonation of the coordinated cyano group in $W(CO)_5CN^-$; such protonation reactions indicate the basicity of the nitrogen atoms in coordinated cyano groups. Sodium cyanide is used in the extraction of gold and silver from their ores since it forms very stable linear cyano complexes $[{:}N\equiv C{-}M{-}C\equiv N{:}]^-$ (M = Ag, Au) with these metals. Organic isocyanides, $R{-}\overset{+}{N}\equiv\overset{-}{C}{:}$ (R = alkyl or aryl group), also form an extensive series of transition metal complexes, including zerovalent derivatives such as $(PhNC)_6Cr$; as in the case of metal cyano complexes, the transition metal always bonds to the carbon rather than the nitrogen atom of isocyanides.[37]

7.4 Cyanamide

Cyanamide, $H_2\ddot{N}{-}C\equiv N{:}$, is a crystalline solid, mp 45 °C, prepared by hydrolysis of its calcium salt, CaNCN, under mild conditions (e.g. aqueous CO_2) in order to avoid further hydrolysis of cyanamide. Calcium cyanamide is made on a large industrial scale by a high-temperature reaction of calcium carbide with molecular nitrogen (equation 18). The cyanamide dianion in CaNCN, namely, $CN_2{}^{2-} = {:}\ddot{N}^- = C = \ddot{N}^-{:}$, is isoelectronic and isostructural with carbon dioxide ($CO_2 = {:}\ddot{O}{=}C{=}\ddot{O}{:}$). Cyanamide dimerizes in an aqueous alkaline solution at 80 °C to form dicyandiamide, $(H_2N)_2C{=}NCN$, mp 209 °C (dec.), which undergoes further conversion to a trimer, 1,3,5-triamino-1,3,5-triazine, or melamine, by heating in ammonia (Figure 9). Melamine, which is a useful ingredient in polymers and plastics, can also be made by heating urea under

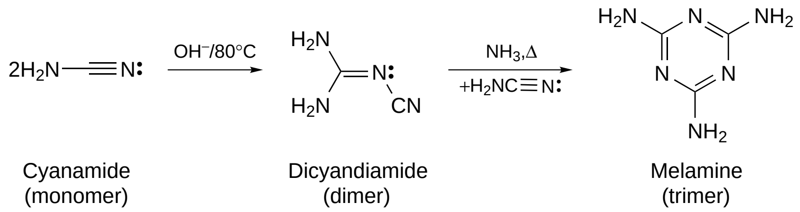

Figure 9 Oligomerization of cyanamide to give dicyandiamide and melamine

pressure (equation 19). The NH_3 and CO_2 produced in this reaction can be recycled to make more urea starting material.

$$CaC_2 + N_2 \xrightarrow{\sim 1000\,^\circ C} CaNCN + C \qquad \Delta H = -297\,kJ\,mol^{-1} \tag{18}$$

$$6H_2NC(=O)NH_2 \xrightarrow[100\,atm]{300\,^\circ C} 6NH_3 + 3CO_2 + C_3N_3(NH_2)_3 \tag{19}$$

7.5 Cyanogen Halides

Cyanogen chloride, $Cl{-}C{\equiv}N\colon$, a toxic gas, bp +13 °C, is obtained by reaction of HCN with Cl_2 or by electrolysis of an aqueous solution containing HCN and NH_4Cl. It readily undergoes trimerization to give cyanuric chloride, $C_3N_3Cl_3$, which has a similar 1,3,5-triazine structure to melamine (Figure 9). The chlorine atoms in cyanuric chloride are reactive toward nucleophilic substitution. Fluorination of cyanuric chloride gives cyanuric fluoride, $C_3N_3F_3$, which can be cracked thermally to give cyanogen fluoride, $F{-}C{\equiv}N\colon$, bp −46 °C, which polymerizes at room temperature. Cyanogen bromide, mp 52 °C, bp 61.4 °C, and cyanogen iodide, mp 147 °C, are volatile solids that can be made by treatment of cyanide ion with the free halogen in aqueous solution. Cyanogen iodide can also be obtained from $Hg(CN)_2$ and I_2.

7.6 Cyanic Acid and Cyanates

The cyanate ion, $\colon\ddot{O}{=}C{=}\ddot{N}^{-}$, like the cyanamide dianion, is isoelectronic and isostructural with carbon dioxide, and is made by the mild oxidation of aqueous cyanide ion (equation 20). Sodium cyanate can also be made by heating sodium carbonate with urea in the absence of a solvent (equation 21). Unstable free cyanic acid (HOCN, bp 23.5 °C, $K_a = 1.2 \times 10^{-4}$) can be obtained by hydrolysis of cyanuric chloride (see above) to 'cyanuric acid,' 1,3,5-trihydroxy-1,3,5-triazine, $C_3N_3(OH)_3$, followed by pyrolysis. Cyanic acid undergoes facile hydrolysis in aqueous solution to give carbon dioxide and ammonia (equation 22). In covalent derivatives or metal complexes, cyanate can bond either through oxygen (cyanates) or nitrogen (isocyanates), thereby providing examples of linkage isomerism.**[38]** The facile isomerization of ammonium cyanate ($NH_4^+\ OCN^-$) to urea ($O{=}C(NH_2)_2$), which was first found in the early nineteenth century, is regarded as the first link between inorganic and organic chemistry.

$$KCN\,(aq) + PbO\,(aq) \longrightarrow Pb\,(s) + KOCN\,(aq) \tag{20}$$

$$Na_2CO_3 + 2O{=}C(NH_2)_2 \xrightarrow[dry]{heat} 2NaOCN + CO_2 + 2NH_3 + H_2O \tag{21}$$

$$HOCN + H_2O \longrightarrow NH_3 + CO_2 \tag{22}$$

7.7 Thiocyanates and Selenocyanates

The thiocyanate ion,**[36]** $\colon\ddot{S}{=}C{=}\ddot{N}^{-}\colon$, also called the 'rhodanid' ion in the early German literature because of the intense red color of its Fe^{III} derivative, is obtained by the fusion of alkali metal cyanides with sulfur. It is also the product of the detoxification of the cyanide ion in living systems. Most thiocyanate salts are very soluble in both water and liquid ammonia and are useful soluble sources of metal ions in liquid ammonia. Thiocyanogen, $\colon N{\equiv}C{-}S{-}S{-}C{\equiv}N\colon$, is the prototypical example of a pseudohalogen, that is, a group of atoms that behaves like a halogen, X_2 (X = Cl, Br, I). Thiocyanogen is made by bromination of a metal thiocyanate in an inert (nonprotonic) solvent (equation 23). Thiocyanogen is rapidly hydrolyzed by water and rapidly and irreversibly polymerized in the pure state. However, it can be handled in solutions in inert solvents including glacial acetic acid, as well as carbon tetrachloride or carbon disulfide.

$$2AgSCN + Br_2 \longrightarrow 2AgBr + \colon N{\equiv}C{-}S{-}S{-}C{\equiv}N\colon \tag{23}$$

Selenocyanates are also known; they are analogous to thiocyanates but are less stable.

7.8 Fulminic Acid

Fulminic acid, $\colon\overset{-}{C}{\equiv}\overset{+}{N}{-}OH \longleftrightarrow \colon C{=}\ddot{N}{-}OH$, is a 'divalent' carbon derivative like carbon monoxide; it is formally an 'oxime' of carbon monoxide. Free fulminic acid is unstable, but the explosive mercury salt, which is used as a detonator, is obtained by treatment of elemental mercury with a mixture of ethanol and nitric acid. The fulminate ion, $\colon\overset{-}{C}{\equiv}\overset{+}{N}{-}\overset{-}{O}$, like carbon monoxide and cyanide ion, functions as a strong-field ligand toward transition metals to form complexes such as $Fe(CNO)_6^{4-}$ analogous to the ferrocyanide ion, $Fe(CN)_6^{4-}$. However, fulminato metal complexes, like mercury fulminate, are frequently explosive. The likewise explosive silver fulminate (AgCNO) and silver cyanate (AgOCN) are of historical interest in being the first pair of isomers discovered, and they led to the first proposal of the concept of isomerism (Liebig, 1823).[39]

8 CARBON-BASED MOLECULAR LADDERS

Structures resembling a ladder are encountered in the chemistry (e.g. Zintl phases) of many elements, but among group IV elements are found only in the case of carbon.[40] The molecular ladders of carbon chemistry are [n]-ladderanes,[41] small molecules built up of n edge-fused four-membered rings, with $n \geq 1$ (Figure 10). The four-membered rings in [n]-ladderanes generally contain only carbon atoms, although derivatives involving nitrogen are known.[42]

8.1 Strain and Isomerism

The simplest member of the class is the [1]-ladderane, a small and familiar strained molecule known as cyclobutane. The strain in a [n]-ladderane increases with the number of fused rings and the introduction of multiple bonds.[43] The [2]-ladderane derivative, Dewar benzene, is highly unstable and converts readily to the conjugation-stabilized counterpart, benzene. Depending on the stereochemistry of bridgehead atoms in the fused-ring system, [n]ladderanes with $n \geq 2$ can exist as different isomers. Specifically, the cis- or trans- positioning of substituents on bridgehead carbon atoms leads to two structurally distinct molecular types, the more strained being the one with substituents in trans-positions. Further possibilities of isomerism in [3]-ladderane and higher members of the family arise from the possibility of a nonterminal cyclobutane ring adopting either the anti or syn configuration (Figure 11).

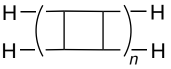

Figure 10 Schematic representation of a [n]-ladderane

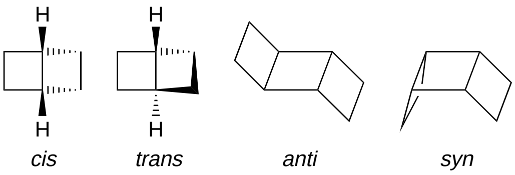

Figure 11 Different types of ladderane isomers

8.2 Significance

The [n]-ladderane framework has gained additional theoretical interest. The framework has been discovered in biology and has been recognized as a potentially useful building block in materials science. These developments have provided an impetus for synthetic methods to construct [n]-ladderanes to be advanced.

8.3 Theoretical

Most recent quantum chemical calculations involving [n]-ladderanes suggest a defect in the ladderane framework, in the form of an olefin pair, can result in fluxional molecules named sigmatropic shiftamers.[44,45] The fluxional nature would stem from the ability of the olefin pair to travel across the defective ladderane framework via a series of Cope rearrangements (Figure 12). Calculations predict the fluxionality of the molecules depends on the size of the framework. Specifically, [n]-ladderanes with $n > 7$ are expected to be fluxional at and above room temperature.

8.4 Biochemistry and Materials Science

Biomolecules containing [3]- and [5]-ladderanes have been discovered within intracellular lipid membranes of *anammox* bacteria[46] that recycle atmospheric nitrogen. The ladderane lipids are found in the membrane surrounding a unique cytoplasmic organelle, the *anammoxosome*, within which the anaerobic oxidation of ammonia into molecular nitrogen occurs. The oxidation, known as the *anammox* process, follows the reaction (equation 24):

$$NH_4^+ + NO_2^- \longrightarrow N_2 + 2H_2O \qquad (24)$$

The ladderane moieties are thought to rigidify and thereby decrease the permeability of the anammoxosome membrane,

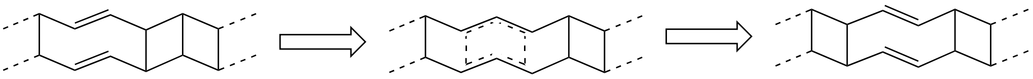

Figure 12 Interconversion of sigmatropic shiftamers via a Cope rearrangement

enabling the containment of small energetic molecules (e.g. hydrazine) within the organelle, making the denitrification process energetically feasible for the bacterium. The ability of [n]-ladderanes to increase the rigidity of the lipid bilayer is supported by experiments involving ladderane-enriched membranes, as well as molecular dynamics simulations. The simulations illustrated the ladderane-containing membrane to have a significantly higher density (up to $1.5\,\mathrm{kg\,m^{-3}}$) than typically encountered in membrane systems (less than $1.2\,\mathrm{kg\,m^{-3}}$). Since approximately up to 50% of Earth's atmospheric nitrogen is believed to be recycled through the bacterial *anammox* process, [n]-ladderanes should be regarded as an important class of biomolecules, rather than just an evolutionary curiosity.[46]

The rigidity of the fused cyclobutane rings system has led to the recognition of [n]-ladderanes as potential architectural components in molecular electronics.[47] Along with poly(norbornanes) as bent rigid constituents, [n]-ladderanes of nanometer length ($n > 7$) have been suggested as molecular beams and rods in nanoscale devices.[48] Fullerene derivatives of [n]-ladderanes have been synthesized, as well as ladderane frameworks carrying chromophore groups.[49] Notably, the square-like structure of the [1]-ladderane ring has been used in the construction of supramolecular ladder-like structures in molecular crystals.[50]

8.5 Synthesis

The two most successful strategies to construct molecular ladders are based upon the [2 + 2] cycloaddition of olefins. The first, involving the polymerization of cyclobutadiene derivatives, has served to produce the highest known member of the family, the [13]-ladderane.[51] The second, relying on the dimerization of conjugated polyenes, has provided [n]-ladderanes in the highest yields and stereoselectivities. Schematically, the first method corresponds to a rung-by-rung construction of a ladder, while the second strategy is similar to assembling a ladder by welding the two sidepieces together (Figure 13).

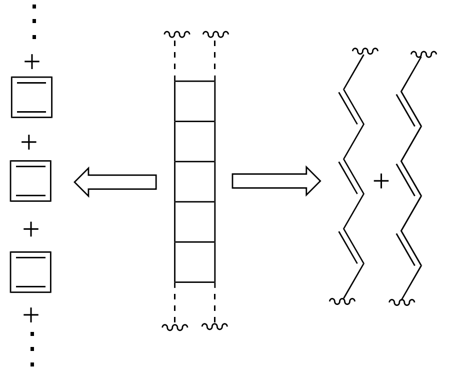

Figure 13 Two retrosynthetic routes to the [n]-ladderane framework

8.5.1 Cyclobutadiene Oligomerization

The Ce(IV)-oxidation of a tricarbonyliron(0)-cyclobutadiene complex releases the cyclobutadiene (**1a–c**) that subsequently oligomerizes to yield a mixture of [n]-ladderanes (Figure 14).[52]

While cyclobutadiene itself yields only a dimer ([3]-ladderane) in such process, some derivatives, such as (**2b**) or (**2c**), provide higher members of the series. The difference in reactivities stems from a difference in the HOMO–LUMO energy gap of the reactants. The energy gap is readily calculated, providing a way to select the most suitable cyclobutadiene derivative to undergo oligomerization to a ladder.[53]

8.5.2 Dimerization of Conjugated Polyenes

The construction of molecular ladders from two conjugated polyenes employs UV-induced [2 + 2] photodimerizations. The task is complicated by a requirement to position the sidepieces, in the form of polyenes, in the orientation for the reaction. Such control of positioning may be accomplished using two distinct approaches. The first one is intramolecular, involving a [2 + 2] cycloaddition of

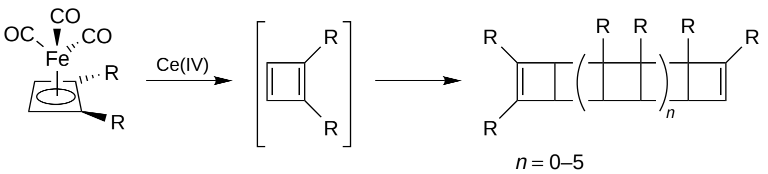

(1a–c)

(2a–c)

(a) R = H
(b) R = COOH
(c) R = $COOCH_3$

Figure 14 Synthesis of [n]-ladderanes through cyclobutadiene oligomerization

conjugated polyenes in the same molecule, while the second one is intermolecular, relying on the reaction between two molecules. The second approach requires the reactants to be highly organized and, so far, has been applied only in the solid state.

The first approach has been pioneered by Hopf and coworkers by covalently attaching polyene chains onto a rigid molecular fragment, a [2.2]-paracyclophane.[54] The paracyclophane scaffold serves as a template to hold the two polyenes in the vicinity for a sequential $[2+2]$ photodimerization. The covalent attachment of the polyene chains onto the cyclophane effectively makes the dimerization an intramolecular process (Figure 15). Upon UV-irradiation in solution, single isomers of the [3]- and the [5]-ladderane are obtained in excellent yields (100% and 80%, respectively).[55]

Using the second approach, [3]-ladderane has been synthesized using arene-perfluoroarene interactions to bring reactant polyenes together in the crystal (Figure 16). The reaction yields are low (20–25%) and limited by the breakdown of the crystal as the reaction proceeds.[56]

Most recently, the methods of template-directed solid-state synthesis[57] were employed to construct the [3]- and the [5]-ladderane. The construction involved a resorcinol derivative (5-methoxyresorcinol) as a linear template to organize pyridine-substituted polyenes for the reaction within discrete molecular assemblies in solids. The assemblies are

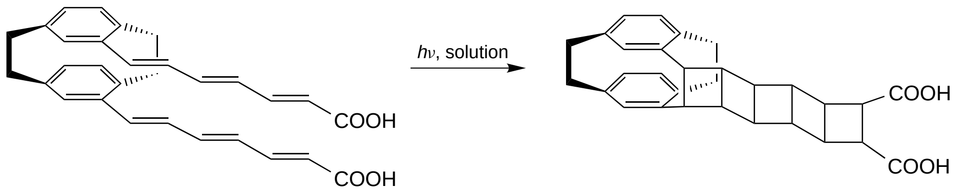

Figure 15 Synthesis of a [5]-ladderane using the paracyclophane scaffolding as a template

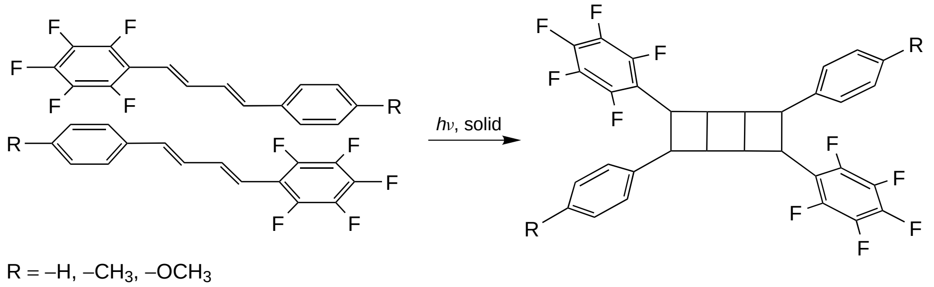

Figure 16 Synthesis of a [3]-ladderane in the solid state

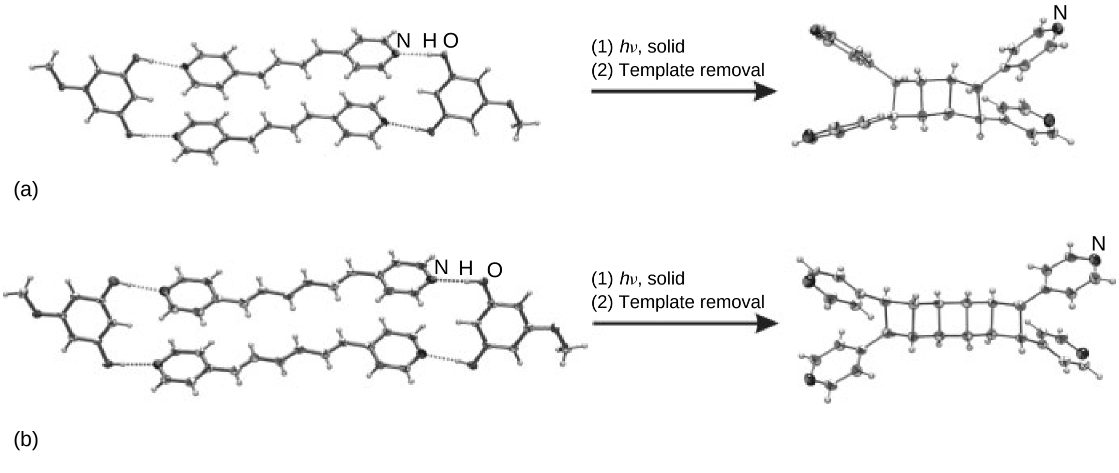

Figure 17 Template-directed solid-state synthesis of the [3]- (a) and the [5]-ladderane (b)

held together via O–H· · ·N hydrogen bonds between hydroxyl groups of the template and pyridine nitrogen atoms of the reactant (Figure 17). While the liaison between the template and the reactant is based on a noncovalent interaction, the intermolecular nature of the photodimerization is retained. Upon UV-irradiation of each assembly in the solid, single isomers of the [3]- and the [5]-ladderane were obtained in 100% yield.**[58]**

9 RELATED ARTICLES

Carbides: Transition Metal Solid-state Chemistry; Carbon: Fullerenes; Carbonyl Complexes of the Transition Metals; Carbonylation Processes by Homogeneous Catalysis; Cyanide Complexes of the Transition Metals; Intercalation Chemistry.

10 FURTHER READING

A. A. Newman ed., ‘Chemistry and Biochemistry of Thiocyanic Acid and its Derivatives’, Academic Press, London, 1975.

A. G. Sharpe, ‘The Chemistry of Cyano Complexes of the *Transition Metals*’, Academic Press, London, 1976.

11 REFERENCES

1. M. Ballester, *Acc. Chem. Res.*, 1985, **18**, 380.
2. E. Breitmaier and W. Voelter, ‘^{13}C NMR Spectroscopy’, Verlag Chemie, Weinheim, 1978.
3. V. F. Raaen, G. A. Ropp, and H. Raaen, ‘Carbon-14’, McGraw-Hill, New York, 1968.
4. E. Bruton, ‘Diamonds’, NAG Press, London, 1970.
5. C. L. Mantell, ‘Carbon and Graphite Handbook’, Interscience, New York, 1968.
6. W. N. Reynolds, ‘Physical Properties of Graphite’, Elsevier, Amsterdam, 1968.
7. L. B. Ebert, *Ann. Rev. Mater. Sci.*, 1976, **6**, 181.
8. H. Selig and L. B. Ebert, *Adv. Inorg. Chem. Radiochem.*, 1980, **23**, 281.
9. H. W. Kroto, A. W. Allaf, and S. P. Balm, *Chem. Rev.*, 1991, **91**, 1213.
10. ‘Fullerenes’, eds. G. S. Hammond and V. Kuck, American Chemical Society, Washington, DC, 1992, ACS Symposium Series 481; ‘Fullerenes, Chemistry, Physics, and Technology’, eds. K. M. Kadish and R. S. Ruoff, John Wiley & Sons, Inc., New York, 2000.
11. D. H. Parker, P. Wurz, K. Chatterjee, K. R. Lykke, J. E. Hunt, M. J. Pellin, J. C. Hemminger, D. M. Gruen, and L. M. Stock, *J. Am. Chem. Soc.*, 1991, **113**, 7499.
12. W. A. Sheppard and C. M. Sharts, ‘Organic Fluorine Chemistry’, Benjamin, New York, 1969.
13. M. Hudlický, ‘Organic Fluorine Chemistry’, Plenum Press, New York, 1971.
14. M. Hudlický, ‘Chemistry of Organic Fluorine Compounds’, Ellis Horwood, Chichester, 1976.
15. R. E. Banks, ‘Preparation, Properties, and Industrial Applications of Organofluorine Compounds’, Ellis Horwood, Chichester, 1982.
16. J. G. Riess and M. Le Blanc, *Pure Appl. Chem.*, 1982, **54**, 2383.
17. M. Hargittai, G. Schultz, P. Schwerdtfeger, and M. Seth, *Struct. Chem*, 2001, **12**, 377.
18. M. J. Parkington, T. A. Ryan, and K. R. Seddon, *J. Chem. Soc., Dalton Trans.*, 1997, 251.
19. T. A. Ryan, C. Ryan, E. A. Seddon, and K. R. Seddon, in ‘Phosgene and Related Carbonyl Compounds, Topics in Inorganic and General Chemistry, Monograph 24’, ed. R. J. H. Clark, Elsevier Science B. V., Amsterdam, 1996.
20. R. West, ed., ‘Oxocarbons’, Academic Press, New York, 1980.
21. D. Braga, L. Maini, and F. Grepioni, *Chemistry – A European Journal*, 2002, **8**, 1804.
22. M. E. Vol’pin and I. S. Kolomnikov, *Organometal. React.*, 1975, **5**, 313.
23. R. Eisenberg and D. E. Hendriksen, *Adv. Catal.*, 1979, **28**, 79.
24. J. A. Ibers, *Chem. Soc. Rev.*, 1982, **11**, 57.
25. D. J. Darensbourg and R. A. Kudaroski, *Adv. Organometal. Chem.*, 1983, **22**, 129.
26. D. A. Palmer and R. van Eldik, *Chem. Rev.*, 1983, **83**, 651.
27. W. M. Ayers ed., ‘Catalytic Activation of Carbon Dioxide’, American Chemical Society, Washington, DC, ACS Symposium Series 363, 1988.
28. A. Behr, ‘Carbon Dioxide Activation by Metal Complexes’, VCH, Weinheim, 1988.
29. R. West and J. Niu, in ‘The Chemistry of the Carbonyl Group’, ed. J. Zabicky, Interscience, London, 1970, Vol. 2, (p. 241).
30. G. Gattow and W. Behrendt, ‘Carbon Sulfides and their Inorganic and Complex Chemistry’, Thieme, Stuttgart, 1977.
31. G. D. Thorne and L. A. Ludwig, ‘The Dithiocarbamates and Related Compounds’, Elsevier, Amsterdam, 1962.
32. I. S. Butler, *Acc. Chem. Res.*, 1977, **10**, 359.
33. P. V. Yaneff, *Coord. Chem. Rev.*, 1977, **23**, 183.
34. P. V. Broadhurst, *Polyhedron*, 1985, **4**, 1801.
35. L. K. Hansen and A. Hordvik, *Chem. Commun.*, 1974, 800.
36. C. P. Galloway, D. D. Doxsee, D. Fienske, T. B. Rauchfuss, S. R. Wilson, and X. Yang, *Inorg. Chem.*, 1994, **33**, 4537.
37. L. Malatesta and F. Bonati, ‘Isocyanide Complexes of Metals’, Wiley, London, 1969.
38. A. H. Norbury, *Adv. Inorg. Chem. Radiochem.*, 1975, **17**, 231.

39. W. Bock, *Eur. J. Inorg. Chem.*, 2003, 4275.
40. G. Nuspl, K. Polborn, J. Evers, G. A. Landrum, and R. Hoffmann, *Inorg. Chem.*, 1996, **35**, 6922.
41. M. A. Miller and J. M. Schulman, *J. Mol. Struc. (Theochem)*, 1988, **163**, 133.
42. R. P. Dave, R. Duddu, J. Li, R. Surapaneni, and R. Gilardi, *Tetrahedron Lett.*, 1998, **39**, 5481.
43. H. Hopf, *Angew. Chem. Int. Ed.*, 2003, **42**, 2822.
44. J. C. Santos and P. Fuentealba, *Chem. Phys. Lett.*, 2003, **377**, 449.
45. D. J. Tantillo and R. Hoffmann, *Angew. Chem. Int. Ed.*, 2002, **41**, 1033.
46. M. M. M. Kuypers, A. O. Sliekers, G. Lavik, M. Schmid, B. B. Jørgensen, J. G. Kuenen, J. S. S. Damsté, M. Strous, and M. S. M. Jetten, *Nature*, 2003, **422**, 608.
47. R. N. Warrener, G. Abbenante, R. G. Solomon, and R. A. Russell, *Tetrahedron Lett.*, 1994, **35**, 7639.
48. R. N. Warrener, G. Abbenante, and C. H. L. Kennard, *J. Am. Chem. Soc.*, 1994, **116**, 3645.
49. W. Li and M. A. Fox, *J. Am. Chem. Soc.*, 1996, **118**, 11752.
50. G. Mehta and R. Uma, *Ind. J. Chem.*, 1999, **38B**, 1154.
51. G. Mehta, M. B. Viswanath, and A. C. Kunwar, *J. Org. Chem.*, 1994, **59**, 6131.
52. M. J. Marsella, S. Estassi, L.-S. Wang, and K. Yoon, *Synlett*, 2004, 192.
53. G. Mehta, M. B. Viswanath, G. N. Sastry, E. D. Jemmis, D. S. K. Reddy, and A. C. Kunwar, *Angew. Chem. Int. Ed. Engl.*, 1992, **31**, 1488.
54. H. Greiving, H. Hopf, P. G. Jones, J.-P. Desvergne, and H. Bouas-Laurent, *Chem. Commun.*, 1995, 1075.
55. H. Hopf, H. Greiving, P. G. Jones, and P. Bubenitschek, *Angew. Chem. Int. Ed.*, 1995, **34**, 685.
56. K. Vishnumurthy, T. N. Guru Row, and K. Venkatesan, *Photochem. Photobiol. Sci.*, 2002, **1**, 427.
57. L. R. MacGillivray, *Cryst. Eng. Commun.*, 2002, **4**, 37.
58. X. Gao, T. Friščić, and L. R. MacGillivray, *Angew. Chem. Int. Ed. Engl.*, 2004, **43**, 232.

Carbonyl Complexes of the Transition Metals

Fausto Calderazzo
Università di Pisa, Pisa, Italy

1	Introduction	1
2	Synthesis	1
3	Molecular Structures	6
4	Reactions of Groups 6–10	8
5	Bonding and Spectral Data	11
6	Metal Carbonyls of the Early Transition Elements	11
7	Metal Carbonyls of the Late Transition Elements	13
8	Metal–CO Bond Dissociation Enthalpy (BDE)	14
9	Reaction Mechanisms	14
10	Related Articles	16
11	References	16

1 INTRODUCTION

Metal carbonyls are compounds containing one or more M–CO bonds, where M is a transition metal, that is, an element possessing an incomplete d shell, of electronic configuration d^n $(0 < n < 10)$. However, there are some examples of compounds of this class containing metals with a completely filled (d^{10}) or an empty (d^0) shell.[1–5] A few carbonyl derivatives are also known for lanthanide[6] and actinide[7] cations, of 4f and 5f electronic configuration, respectively. Outside the d and f transition series, carbonyl derivatives have been reported, the best described examples being those of boron(III), which have been crystallographically established, with ν_{CO}'s at 2176 cm^{-1} for $B(BCl_2)_3(CO)$[8] and at 2251 cm^{-1} for $B(CF_3)_3(CO)$.[9] Moreover, unstable combinations with CO, such as $Be(CO)_n$[10] and $B_4(CO)_2$[11] are known for main group elements, as prepared by the metal vaporization technique, that is, by contacting carbon monoxide with the metal vapor quenched in a solid matrix around 20 K or lower.[10,11]

Carbon monoxide is the product of partial combustion of carbon, the ΔH_f^0 being $-110.4\,\mathrm{kJ\,mol^{-1}}$. Its enthalpy of dissociation ($1073\,\mathrm{kJ\,mol^{-1}}$) is the highest known for a diatomic molecule. In agreement with the oxidation state +II for carbon, CO can be prepared by a *syn*-proportionation reaction ($\Delta G^0 = +120.1\,\mathrm{kJ\,mol^{-1}}$), favored at high temperature (equation 1).

$$C(s) + CO_2(g) \rightleftharpoons 2CO(g) \qquad (1)$$

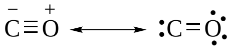

$$\overset{-}{C}\equiv\overset{+}{O} \longleftrightarrow :C=\ddot{\underset{\cdot\cdot}{O}}:$$

(**1**)

The electronic structure of CO, in valence bond terms, can be visualized as (**1**).

Carbon monoxide can undergo base-catalyzed reactions with, for example, alcohols or secondary amines, yielding formates HCO_2R or formamides $HCONR_2$. Also, acid-catalyzed reactions of CO are known, such as the carbonyl insertion in toluene to give *p*-toluylaldehyde (equation 2) in the presence of HF/BF_3.

$$Me–C_6H_5 + CO \xrightarrow{HF/BF_3} p\text{-}Me–C_6H_4CHO \qquad (2)$$

The formyl cation HCO^+ (ν_{CO} at 2110 cm^{-1}) is generated from CO under pressure in the presence of HF/SbF_5.[12] Concentrated sulfuric acid or the HCl/CuCl system, activates carbon monoxide toward the electrophilic attack on aromatic hydrocarbons to form aromatic aldehydes (Gatterman–Koch reaction). Branched carboxylic acids are obtained from alkenes and CO in the presence of concentrated sulfuric acid (Koch process) (equation 3).[13]

$$Me_2C{=}CH_2 + CO + H_2O \longrightarrow Me_3C–CO_2H \qquad (3)$$

Carbon monoxide forms binary combinations with transition metals. Well-established examples are the metal carbonyls of the 3d series: $V(CO)_6$, $Cr(CO)_6$, $Mn_2(CO)_{10}$, $Fe(CO)_5$, $Co_2(CO)_8$, $Ni(CO)_4$.

When carbon monoxide is bonded to a transition element, in a positively charged or even uncharged compound, the electrophilic capacity of carbon increases compared with the isolated molecule. Examples of nucleophilic attack are in equations (4) and (5). The reaction of methyl–lithium with $W(CO)_6$ giving the anionic acyl complex of equation (4a) is followed by alkylation to the carbene derivative of equation (4b). The formation of a carbamoyl complex with *cis*-$PtCl_2(CO)_2$ is shown in equation (5).

$$W(CO)_6 + LiMe \longrightarrow Li[W(CO)_5C(O)Me] \qquad (4a)$$

$$Li[W(CO)_5C(O)Me] \xrightarrow{Me_3O^+} W(CO)_5C(OMe)Me \qquad (4b)$$

$$cis\text{-}PtCl_2(CO)_2 + 2R_2NH \longrightarrow NH_2R_2[cis\text{-}PtCl_2(CO)C(O)NR_2] \qquad (5)$$

2 SYNTHESIS

2.1 Generalities

Binary metal carbonyls span a wide range of oxidation states from positive,[14] for example, +III in $[Ir(CO)_6]^{3+}$, to

Table 1 Binary metal carbonyls stable at room temperature[a]

Compound	d^n Electronic configuration	Color and properties
$[Ti(CO)_6]^{2-}$	$3d^6$	Dark violet[b]
$[Zr(CO)_6]^{2-}$	$4d^6$	Dark purple[b]
$[Hf(CO)_6]^{2-}$	$5d^6$	Deep red[b]
$[V(CO)_6]^-$	$3d^6$	Yellow[c]
$[Nb(CO)_6]^-$	$4d^6$	Yellow[c]
$[Ta(CO)_6]^-$	$5d^6$	Yellow[c]
$V(CO)_6$	$3d^5$	Black–green, slightly soluble in hydrocarbons, paramag., dec. 70 °C
$[Cr(CO)_5]^{2-}$	$3d^8$	Yellow[c]
$[Mo(CO)_5]^{2-}$	$4d^8$	Yellow[c]
$[W(CO)_5]^{2-}$	$5d^8$	Yellow[c]
$Cr(CO)_6$	$3d^6$	Colorless, slightly soluble in hydrocarbons, dec. 130 °C
$Mo(CO)_6$	$4d^6$	Colorless, slightly soluble in hydrocarbons
$W(CO)_6$	$5d^6$	Colorless, slightly soluble in hydrocarbons
$Mn_2(CO)_{10}$	$3d^7$	Golden yellow, moderately soluble in hydrocarbons, mp 154–155 °C
$Tc_2(CO)_{10}$	$4d^7$	Colorless, moderately soluble in hydrocarbons, mp 159–160 °C
$Re_2(CO)_{10}$	$5d^7$	Colorless, moderately soluble in hydrocarbons, mp 177–178 °C
$[Mn(CO)_6]^+$	$3d^6$	Colorless[d]
$Fe(CO)_5$	$3d^8$	Yellow, miscible with hydrocarbons, mp −20.5 °C, bp 103–104 °C (extrap.)
$Fe_2(CO)_9$	$3d^8$	Orange, almost insoluble in inert organic solvents, dec. ca. 100 °C
$Fe_3(CO)_{12}$	$3d^8$	Black–green, moderately soluble in hydrocarbons, dec. ca. 140 °C
$Co_2(CO)_8$	$3d^9$	Orange, soluble in hydrocarbons, dec. 51–52 °C
$Co_4(CO)_{12}$	$3d^9$	Black, slightly soluble in hydrocarbons
$Co_6(CO)_{16}$	$3d^9$	Black, dec. ca. 100 °C
$Rh_4(CO)_{12}$	$4d^9$	Dark red, dec. ca. 150 °C
$Rh_6(CO)_{16}$	$4d^9$	Black, dec. ca. 220 °C
$Ir_4(CO)_{12}$	$5d^9$	Canary yellow, dec. ca. 210 °C
$Ni(CO)_4$	$3d^{10}$	Colorless, miscible with hydrocarbons, mp −19.3 °C, bp −42.1 °C

[a] For the mononuclear and dinuclear compounds, except $V(CO)_6$, the number of valence electrons per metal atom is 18. The EAN (effective atomic number) of the metal is the number of electrons of the d^n configuration added to twice the number of CO groups, one electron being further added in the case of metal–metal bonded dinuclear systems. For trinuclear, tetranuclear, and hexanuclear compounds (metal–carbonyl clusters), the cluster valence electron counting is 48, 60, and 86, respectively. [b] As the $[K(cryptand\ 2.2.2)]^+$ derivative. [c] As the tetraalkylammonium derivative. [d] As the tetrachloroaluminate.

negative,[15,16] for example, −IV in $[M(CO)_4]^{4-}$ (M = Cr, Mo, W). Interesting cases of intermediate oxidation states are the hexacarbonyl metalates(−II)[17–19] of the group 4 metals (Ti, Zr, Hf) of formula $[M(CO)_6]^{2-}$. Some relevant examples of anionic, neutral, and cationic binary metal carbonyls are listed in Table 1.

In practice, nickel is the only metal which, when activated and finely divided, can be converted into the corresponding carbonyl $Ni(CO)_4$ under mild conditions of temperature and pressure (equation 6). This compound, discovered[20] by Mond and coworkers, has played an important role in both the development of nickel-catalyzed organic syntheses[13] and in the technical manufacture of nickel.

$$Ni(s) + 4CO(g) \longrightarrow Ni(CO)_4(g) \qquad (6)$$

Important aspects of the synthesis of metal carbonyls by reductive ligation (*see Reductive Ligation*) are (a) the reducing agent; (b) the reaction medium; and (c) the pressure of CO and the temperature.

2.1.1 *The Reducing Agent*

Reduction of a readily available inorganic compound is usually required to prepare the corresponding carbonyl derivative. The choice of the reducing agent is usually the most critical point in the synthesis. Sometimes, no additional reducing agent is necessary, when CO plays this role. The oxidation products are CO_2 ($\Delta G_f^0 = -394\,kJ\,mol^{-1}$) or $COCl_2$ ($\Delta G_f^0 = -206\,kJ\,mol^{-1}$), if the starting material is a metal oxide or a metal chloride, respectively. The reductive carbonylation is mostly used with metal oxides and metal chlorides of a covalent nature, that is, in relatively high oxidation states. Decacarbonylditechnetium(0) and decacarbonyldirhenium(0) can be prepared by heating $NH_4[MO_4]$, M = Tc, Re, with carbon monoxide under pressure at high temperature, the reducing agent being CO, with the possible participation by the ammonium cation, vide infra.

Molecular hydrogen can be used as a reducing agent in the presence of CO; the equimolar CO/H_2 synthesis gas mixture is employed to reduce metal carboxylates (equation 7). Metal alkyls or aryls, such as Grignard reagents (*see Grignard Reagents*), lithium alkyls or aryls, and aluminum alkyls, have been used for the preparation of metal–carbonyl derivatives. With a metal chloride as the starting material, ligand exchange occurs, followed by reduction due to homolytic cleavage of the metal–carbyl (alkyl or aryl) bond.

$$M(O_2CR)_n + mCO + \frac{n}{2}H_2 \longrightarrow nRCO_2H + M(CO)_m \qquad (7)$$

Electropositive metals characterized by low standard reduction potentials (alkali metals, Mg, Zn) have been frequently used for the reduction of transition metal halides in the presence of carbon monoxide. The finely divided reducing metal is previously activated by one of the conventional methods. Ethers are frequently used as reaction media.

The reduction may be accompanied by secondary reactions with formation of carbon–carbon bonds (see equation 8). The products with $n = 2$ contain the acetylenediolate anion $[C_2O_2]^{2-}$, the sodium, potassium, rubidium, and cesium derivatives being isotypical; the reaction of CO with a potassium melt leads to the product with $n = 6$, containing the anion of hexahydroxybenzene, $[C_6O_6]^{6-}$.[21]

$$nCO + ne^- \longrightarrow [(CO)_n]^{n-} \qquad (8)$$

2.1.2 The Reaction Medium

In dry methods, no solvent is used. In wet methods, an anhydrous organic solvent is employed, normally hydrocarbons or ethers. Exceptionally, in the case of the carbonyl derivatives of palladium(II), platinum(II), and gold(I), thionyl chloride is used as solvent, as it provides the rigorously anhydrous conditions for the survival of the reaction product. In certain cases, water can also be used as the reaction medium with or without the addition of a specific reducing agent. In the latter case, CO is the reducing agent and carbonate is the corresponding oxidation product. Reducing agents such as $Na_2S_2O_4$ or formamidinesulfinic acid have also been used.

2.1.3 Temperature and Pressure of CO

The preparative procedures reported in the literature usually require high temperature (50–200 °C) and pressure (50–300 atm). On a laboratory scale, attention has been paid to design new preparative methods operating at ambient or slightly higher temperature and atmospheric pressure for safety reasons and for avoiding the use of expensive stainless steel autoclaves. The solubility of CO in the reaction medium increases with pressure; in organic solvents, the concentration of CO in solution is about 7×10^{-3} M at atmospheric pressure. The rate of reduction of the metal species must match the rate of transfer of CO from the gas phase to the solution, and efficient stirring is therefore essential. Methods of preparation that use mild reaction conditions will be specifically noted in the following subsections.

Reviews have appeared on preparative and structural aspects of metal carbonyls.[22–25]

2.2 Group 6

The neutral mononuclear carbonyls of this group have the formula $M(CO)_6$ (M = Cr, Mo, W) (see Table 1). Hexacarbonylchromium(0) can be prepared by treating anhydrous $CrCl_3$ with the phenyl Grignard reagent PhMgBr in THF with CO under pressure at temperatures between −4 and +10 °C. The intermediacy of the chromium(III) derivative $CrPh_3(THF)_3$ in this process has been claimed. A hydrolytic step is required to obtain $Cr(CO)_6$, which suggests that chromium under the reaction conditions is possibly converted to $MgPh^+[Cr(CO)_5C(O)Ph]^-$. Another preparation of $Cr(CO)_6$ involves the reductive carbonylation of several chromium(III) salts under CO pressure (100–300 atm) at 130–180 °C in pyridine as the medium; both magnesium and zinc are used as reductants. Pyridine is essential for this reaction, and zinc and magnesium have a synergic effect; presumably, the formation of the pyridine radical anion is important for the reduction.[23]

The hexacarbonyls of chromium, molybdenum, and tungsten can be prepared by reacting a metal salt with AlR_3 in the presence of CO; yields as high as 92% (Cr), 76% (Mo), and 92% (W) are obtained. Anhydrous $CrCl_3$ can be reduced by $Al/AlCl_3$ in benzene at 140–150 °C under a CO pressure. The intermediacy of the $[Cr(C_6H_6)_2]^+$ cation, which is the primary product of the reaction in the $CrCl_3/Al/AlCl_3$/benzene system in the absence of CO, has been suggested in the carbonylation process.[23]

2.3 Group 7

Decacarbonyldimanganese(0), $Mn_2(CO)_{10}$, was originally prepared from MnI_2, Mg, Cu, and CuI in Et_2O under CO pressure (200 atm) at room temperature. The best method available for the preparation of $Mn_2(CO)_{10}$ is the alkylation of anhydrous manganese(II) acetate with AlR_3 in i-Pr_2O under CO pressure at 60–140 °C. A synthesis operating at atmospheric pressure of CO uses the methylcyclopentadienyl derivative of manganese(I), $Mn(MeC_5H_4)(CO)_3$, which is reduced by sodium in diglyme (16–20% yield).[23]

Decacarbonylditechnetium, $Tc_2(CO)_{10}$, requires some special precautions since technetium is a β-emitter. $Tc_2(CO)_{10}$ has been proposed as the starting material for the preparation of technetium compounds with potential radiopharmaceutical properties.[26] The original method of preparing $Tc_2(CO)_{10}$ consists of treating the heptoxide, Tc_2O_7, with CO under pressure (250–350 atm) at 220–275 °C (equation 9; M = Tc).[23]

$$M_2O_7 + 17CO \longrightarrow 7CO_2 + M_2(CO)_{10} \qquad (9)$$

$$M = Tc, Re$$

The rhenium analog, $Re_2(CO)_{10}$, can be prepared similarly. The heptoxides of technetium(VII) and rhenium(VII) are difficult to handle. The primary products of technetium and rhenium manufacturing are the tetraoxo anions $[MO_4]^-$. Some synthetic procedures for preparing $M_2(CO)_{10}$ from the potassium or ammonium tetraoxometalates(VII) have been reported.[23] $K[ReO_4]$ can be reductively carbonylated to form $Re_2(CO)_{10}$ under CO pressure (300 atm) at 300 °C with copper as reducing agent. The carbonylation of $NH_4[ReO_4]$ under CO pressure (100 atm) at about 190 °C is reported to give a 69% yield of $Re_2(CO)_{10}$ with the reduction being carried out by CO. Evidence exists that the ammonium cation also participates in the reduction process: a by-product of the reaction is the cyano derivative $Re_3(CN)_3(CO)_{12}$, whose molecular structure has been established crystallographically to consist of a triangular arrangement of $Re(CO)_4$ units connected by CN bridges (*see* ***Cyanide Complexes of the Transition Metals***).[27] Application of this method to $NH_4[TcO_4]$ gave a 90% yield of $Tc_2(CO)_{10}$ under less drastic conditions than those required for $NH_4[ReO_4]$. The use of $Al(i\text{-}Bu)_2H$ as a reducing agent allows the carbonylation of $NH_4[ReO_4]$ to be carried out at atmospheric pressure of CO at 70–80 °C, the yield of $Re_2(CO)_{10}$ being about 60%.[28]

2.4 Group 8

Pentacarbonyliron(0) is obtained by carbonylation of anhydrous FeI_2 under drastic conditions (200 °C, 200 atm of CO pressure) in the presence of copper as halogen acceptor.[23] This is consistent with the observation that iodo-carbonyls of group 11 metals (Cu, Ag, Au) are unstable with respect to the corresponding metal iodides, and no contamination from other carbonyl products can occur from the use of copper. The yields of $Fe(CO)_5$ are essentially quantitative; considerably lower yields are obtained with $FeCl_2$ (1%) or $FeBr_2$ (20%). Pentacarbonyliron(0) can also be obtained from finely divided iron at 200 °C under pressure (200 atm) of CO, especially in the presence of chalcogens (sulfur or selenium) as promoters. In the presence of sulfur (0.3 at.%), an excellent yield of $Fe(CO)_5$ (94%) is obtained; selenium (0.3 at.%; 93% yield) and tellurium (1 at.%; 89% yield) are equally good under comparable conditions. Probably iron-carbonyl chalcogenides are formed as intermediates.[23] Some compounds of this type have been reported by independent syntheses and have also been structurally characterized.[29–31]

Enneacarbonyldiiron(0), $Fe_2(CO)_9$, is best prepared[23] by visible-light irradiation of solutions of $Fe(CO)_5$ in glacial acetic acid at 10–15 °C (equation 10). The pentacarbonyl is completely miscible in $MeCO_2H$, and the substantially insoluble enneacarbonyl is recovered by filtration. With the quantum yield being 2, this reaction probably occurs by the mechanism shown in equations (11a) and (11b), through the intermediate tetracarbonyl species. Irradiation of $Fe(CO)_5$ in $CF_3COOH/(CF_3CO)_2$ under exclusion of air yields $Fe(CF_3COO)_2$ as the main product, no $Fe_2(CO)_9$ being observed.[32]

$$2Fe(CO)_5 \xrightarrow{h\nu} Fe_2(CO)_9 + CO \tag{10}$$

$$Fe(CO)_5 \xrightarrow{h\nu} {}^*Fe(CO)_4 + CO \tag{11a}$$

$$^*Fe(CO)_4 + Fe(CO)_5 \longrightarrow Fe_2(CO)_9 \tag{11b}$$

The trinuclear $Fe_3(CO)_{12}$ is best prepared in aqueous solution by oxidation of $[FeH(CO)_4]^-$, the latter being obtained from $Fe(CO)_5$ in alkaline solution (see equations 12 and 13). As the oxidizing agent for $[FeH(CO)_4]^-$, dioxygen, copper(II), or MnO_2 can be used.[23]

$$Fe(CO)_5 + 2NaOH \longrightarrow Na[FeH(CO)_4] + NaHCO_3 \tag{12}$$

$$3[FeH(CO)_4]^- \longrightarrow Fe_3(CO)_{12} + 6e^- + 3H^+ \tag{13}$$

Pentacarbonylruthenium(0), $Ru(CO)_5$, a colorless liquid decomposed by light to $Ru_3(CO)_{12}$, can be prepared by reacting RuI_3 with CO (450 atm) at 170 °C in the presence of a large excess of silver as iodine acceptor. The volatile pentacarbonyl is recovered by gas-phase transfer into a cold trap under CO and then converted into $Ru_3(CO)_{12}$ at room temperature by reducing the partial pressure of CO.[23] The vapor pressure of $Ru(CO)_5$, a colorless liquid at room temperature, is 112 mbar at 19.3 °C with the equation $\ln p = -5072/(T + 21.95)$ being obeyed between 258 and 323 K, with a ΔH_{ev}[33] of $(42.2 \pm 0.6)\,\text{kJ mol}^{-1}$. Trisacetylacetonatoruthenium(III) is converted to $Ru(CO)_5$ or $Ru_3(CO)_{12}$ by CO and H_2 under pressure at high temperature in methanol or heptane as solvent. Bis(acetylacetonato)dicarbonylruthenium(II), *cis*-$Ru(acac)_2(CO)_2$, is probably an intermediate in this reaction.[34] Preparations of $Ru_3(CO)_{12}$ at atmospheric pressure of CO have been reported using the hydrated ruthenium(III) chloride $RuCl_3{\cdot}xH_2O$ or $[Ru_3O(MeCO_2)_6(H_2O)_3]MeCO_2$ in 2-ethoxyethanol or *iso*-propanol, respectively.

Pentacarbonylosmium(0) can be prepared by reacting OsO_4 with CO at high temperature and pressure in a hydrocarbon solvent.[35] Precautions should however be taken to avoid the spontaneous decarbonylation of the pentacarbonyl to the trinuclear cluster (see equations 14 and 15). If CO/H_2 mixtures are used, the product of the carbonylation under these conditions is the dihydrido compound *cis*-$OsH_2(CO)_4$ (see equation 16), spectroscopically established.

$$OsO_4 + 9CO \longrightarrow 4CO_2 + Os(CO)_5 \tag{14}$$

$$3Os(CO)_5 \longrightarrow Os_3(CO)_{12} + 3CO \tag{15}$$

$$OsO_4 + 8CO + H_2 \longrightarrow 4CO + cis\text{-}OsH_2(CO)_4 \tag{16}$$

2.5 Group 9

Octacarbonyldicobalt(0), $Co_2(CO)_8$, is usually prepared by carbonylation of cobalt(II) salts of organic or inorganic acids with syngas (1:1, CO/H_2) at high temperature and pressure in a hydrocarbon solvent (see equation 17 for the carboxylate). When a Lewis base is used as solvent and preformed $Co_2(CO)_8$ is introduced, excellent yields of $Co_2(CO)_8$ are obtained at 30 °C and 180 atm of H_2 (100 atm) and CO (80 atm).[23]

In the synthesis of octacarbonyldicobalt(0), an important by-product is the hydride $CoH(CO)_4$, which is promptly decomposed to $Co_2(CO)_8$ by adventitious oxygen or spontaneously (equation 18) (*see* ***Hydride Complexes of the Transition Metals***).

$$Co(O_2CR)_2 + 8CO + 2H_2 \longrightarrow Co_2(CO)_8 + 4RCO_2H \qquad (17)$$

$$2CoH(CO)_4 \rightleftharpoons H_2 + Co_2(CO)_8 \qquad (18)$$

The reverse of equilibrium (equation 18), that is, the formation of $CoH(CO)_4$ from $Co_2(CO)_8$ and dihydrogen has been the subject of several investigations:[36] the hydrido species is formed in an endothermic process, higher concentrations of the product being therefore present at higher temperatures.

The tetracarbonylcobaltate(−I) anion, $[Co(CO)_4]^-$, from which $Co_2(CO)_8$ can be obtained by controlled oxidation, is prepared by carbonylation of an aqueous alkaline solution of cobalt(II) (equation 19). Carbon monoxide is the reducing agent, and the reaction is carried out at atmospheric pressure at room temperature.[23]

$$2Co^{2+} + 12OH^- + 11CO \longrightarrow 2[Co(CO)_4]^- + 3CO_3{}^{2-} + 6H_2O \qquad (19)$$

Finely divided cobalt, as obtained from anydrous cobalt halides with Li/naphthalene in glyme, is converted to $Co_2(CO)_8$ in good yields at 100 °C and 95 atm of pressure.

Dodecacarbonyltetracobalt(0), $Co_4(CO)_{12}$, is the product of thermal decarbonylation of $Co_2(CO)_8$ (equation 20). This equilibrium was the first metal–cluster forming reaction to be studied from a thermodynamic viewpoint, as a function of temperature, in 1954.[37] The thermodynamic parameters were estimated: $\Delta H^0 = (123.3 \pm 2)\,\mathrm{kJ\,mol^{-1}}$, $\Delta S^0 = (564.3 \pm 12.5)\,\mathrm{J\,mol^{-1}\,K^{-1}}$.[38]

$$2Co_2(CO)_8 \rightleftharpoons Co_4(CO)_{12} + 4CO \qquad (20)$$

Dodecacarbonyltetracobalt(0) can be directly prepared by reducing cobalt(II) salts (2-ethylhexanoate or acetylacetonate) with dihydrogen in the presence of the stoichiometric amount of $Co_2(CO)_8$ (equation 21). Yields are 90% or better.[23]

$$3Co_2(CO)_8 + 2Co(O_2CR)_2 + 2H_2 \longrightarrow 2Co_4(CO)_{12} + 4RCO_2H \qquad (21)$$

Dodecacarbonyltetrarhodium(0), $Rh_4(CO)_{12}$, is prepared from $RhCl_3$ and CO at 200 atm in the presence of a halogen acceptor, such as copper, silver, cadmium, or zinc. The nature of the products depends on the temperature: at 50–80 °C the tetranuclear compound is mainly formed, whereas at 80–230 °C the product is $Rh_6(CO)_{16}$. This is consistent with an endothermic equilibrium from the tetramer to the hexamer (equation 22). A two-step synthesis of $Rh_4(CO)_{12}$ at room temperature and atmospheric pressure involves the reduction of the $[RhCl_6]^{3-}$ anion to $[RhCl_2(CO)_2]^-$ with copper, followed by reduction with water and CO in the presence of a sodium citrate buffer. The yields are nearly quantitative.[23]

$$\frac{3}{2}Rh_4(CO)_{12} \rightleftharpoons Rh_6(CO)_{16} + 2CO \qquad (22)$$

Dodecacarbonyltetrarhodium (0) and $Rh_2(CO)_8$ are related by a temperature-dependent equilibrium (see equation 23), similar to the equilibrium (equation 20) involving the corresponding cobalt species. On the other hand, $Rh_2(CO)_8$, characterized by carbonyl stretching vibrations at 2084, 2060, 1862, and 1847 cm^{-1} (hexane) can only be observed at relatively low temperatures (between 19.5 and −15.2 °C) and at elevated pressure of CO (198 atm).[39] The thermodynamic parameters for the formation of the tetranuclear species from $Rh_2(CO)_8$ are: $\Delta H^0 = (58.6 \pm 10)\,\mathrm{kJ\,mol^{-1}}$; $\Delta S^0 = (305 \pm 25)\,\mathrm{J\,mol^{-1}\,K^{-1}}$.

$$2Rh_2(CO)_8 \rightleftharpoons Rh_4(CO)_{12} + 4CO \qquad (23)$$

The $Rh_4(CO)_{12}/H_2/CO$ system was studied[40] under pressure by IR spectroscopy and shown to produce $RhH(CO)_4$ with carbonyl stretching bands at 2124, 2072, and 2042 cm^{-1}. The formation of the hydride from the tetranuclear species was associated with a $\Delta H_r = -(82.4 \pm 16.2)\,\mathrm{kJ\,mol^{-1}}$ and $\Delta S_r = -(0.44 \pm 0.06)\,\mathrm{kJ\,mol^{-1}\,K^{-1}}$.

Decacarbonyltetrairidium(0), $Ir_4(CO)_{12}$, is prepared normally by carbonylation of iridium halides in the presence of a halogen acceptor (copper or silver), usually at high temperature and pressure. A method of preparation operating at atmospheric pressure requires the carbonylation of $Na_2[IrCl_6]$ or $Na_3[IrCl_6]$ in the presence of NaI in methanol, followed by treatment with a base (74–78% yield). A nearly quantitative yield of $Ir_4(CO)_{12}$ is reported by treating $IrCl_3{\cdot}3H_2O$ or $(NH_4)_2[IrCl_6]$ with 98% HCO_2H, which acts as both the reagent and the reaction medium (see equation 24) at 100 °C in a sealed vessel.[23]

$$4IrCl_3 + 18HCO_2H \longrightarrow Ir_4(CO)_{12} + 12H_2O + 6CO_2 + 12HCl \qquad (24)$$

2.6 Group 10

In a systematic study of the carbonylation of nickel halides, NiX_2, in the presence of copper or silver as halogen acceptors (10 h, 250 °C, 200 atm of CO pressure), conversion to $Ni(CO)_4$ decreases from X = I (quantitative) to Br (1%) and Cl (2%). Carbonylation at atmospheric pressure of an aqueous solution of a nickel(II) salt in the presence of a reducing agent such as $[S_2O_4]^{2-}$ gives $Ni(CO)_4$.[23]

Table 2 Carbonyl stretching vibrations of the tetracarbonyls of group 10

Compound	$\tilde{\nu}_{CO}$(cm^{-1})	k_{CO}(mdyn Å^{-1})
$Ni(CO)_4$	2052	17.23
$Pd(CO)_4$[a]	2070	17.55
$Pt(CO)_4$[a]	2053	17.28

[a] Prepared from the metal vapor in a CO matrix at about 20 K.

At variance with the easy accessibility of $Ni(CO)_4$, the corresponding tetracarbonyls of palladium(0) and platinum(0), $Pd(CO)_4$ and $Pt(CO)_4$, have been identified only spectroscopically (IR) at low temperature, both being prepared by vaporization of the metal followed by reaction with CO in a solid matrix at about 20 K. These compounds decompose at higher temperature. Table 2 shows the IR spectroscopic properties of the tetracarbonyls of nickel, palladium, and platinum, as obtained by vaporization of the corresponding metal, measured under the same experimental conditions. The compounds show one carbonyl stretching vibration, as expected for the tetrahedral geometry. The values of $\tilde{\nu}_{CO}$ and the C–O force constant of $Pd(CO)_4$ are higher than those of both $Ni(CO)_4$ and $Pt(CO)_4$ (see Section 7).**[41–43]** Attempts have been made**[44]** to isolate the tetracarbonyl of platinum(0) by carbonylation of some olefin complexes of platinum(0), in particular, the norbornene derivative $Pt(C_7H_{10})_3$. The reaction, carried out in toluene as solvent and at room temperature or lower, was monitored gasvolumetrically and shown to lead to an amorphous, insoluble, and unstable carbonyl derivative of platinum with a CO:Pt molar ratio of 2 under the best conditions. By using catalytic amounts of CO, the starting olefin complex of platinum is converted to platinum metal at room temperature. These experiments show conclusively that platinum(0)-carbonyl derivatives of low nuclearity are not stable even under the mild conditions used for the carbonylation experiments.

3 MOLECULAR STRUCTURES

Uncharged mononuclear and polynuclear metal carbonyls are known for the group 5 to group 10 metals. The EAN rule (*see Effective Atomic Number Rule*) is normally obeyed, so elements with an even atomic number form mononuclear compounds, for example, $Cr(CO)_6$, $Fe(CO)_5$, and $Ni(CO)_4$, while elements with an odd atomic number form dinuclear compounds, for example, $Mn_2(CO)_{10}$ and $Co_2(CO)_8$, containing metal–metal bonds.

Especially with 4d and 5d elements, polynuclear compounds with metal–metal bonds (metal–carbonyl clusters;**[45–49]** *see Cluster*) are formed under reduced carbon monoxide pressure and/or high temperature. Heteronuclear metal–carbonyl clusters are also known (*see* ***Polynuclear Organometallic Cluster Complexes***).**[50]**

The principal bonding arrangements of carbon monoxide are (a) terminal (**2**); (b) doubly bridging (**3**), and (c) triply bridging (**4**) (*see Bridging Ligand*). In polynuclear metal–carbonyl clusters where the metal atoms define a polyhedron, doubly bridging carbonyl groups are also called *edge-bridging*, whereas face-bridging is synonymous with triply bridging ligands. The terminal M–CO bond is nearly linear. Table 3 contains the structural features of some relevant metal carbonyls.

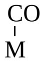

(**2**)

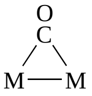

(**3**) μ_2-CO

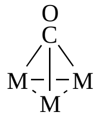

(**4**) μ_3-CO

3.1 Group 6

The hexacarbonyls of chromium, molybdenum, and tungsten are mononuclear; the internal bonding parameters are presented in Table 3. The coordination geometry is that of a regular octahedron of idealized O_h symmetry. The crystal packing is due to weak van der Waals interactions (*see van der Waals Forces*), which explains the volatility of these compounds (the vapor pressures of $Cr(CO)_6$, $Mo(CO)_6$, and $W(CO)_6$ at 30 °C are 0.28, 0.27, and 0.06 mmHg, respectively), and their solubility in organic solvents.**[23]**

3.2 Group 7

The decacarbonyls of manganese, technetium, and rhenium, of formula $M_2(CO)_{10}$, have terminal carbonyl groups and a metal–metal bond. The molecular symmetry is D_{4d} with the two $M(CO)_5$ fragments in a staggered conformation. The heterodinuclear decacarbonyl $MnRe(CO)_{10}$ is also known as obtained by the redox reaction of a rhenium pentacarbonyl halide with the pentacarbonylmanganate(−I) anion at room temperature (at 160 °C or higher, the heterodinuclear carbonyl tends to form the homodinuclear compounds with an equilibrium constant close to the statistical value**[51]**). The X-ray diffraction study of $MnRe(CO)_{10}$ has shown the Mn–Re distance of 2.909 Å to be shorter than the sum of the covalent radii obtained from the homodinuclear compounds (Table 3).

3.3 Group 8

The molecular structure of $Fe(CO)_5$, determined on the solid compound below its freezing point (−20.5 °C) by X-ray diffraction, is trigonal bipyramidal (D_{3h} symmetry). An

Table 3 Crystal and molecular structure of some metal carbonyls of groups 6–10

Compound	Method[a]	Space group	M–CO$_t$[b] (Å)	M–CO$_b$[c] (Å)	M–M (Å)
$Cr(CO)_6$	XR	*Pnma*	1.909(3)[d]	–	–
$Mn_2(CO)_{10}$	XR	$I2/a$	ax. 1.811(3) eq. 1.856(7)	–	2.9038(6)
$Tc_2(CO)_{10}$	XR	$I2/a$	ax. 1.90 eq. 2.00	–	3.036(6)
$Re_2(CO)_{10}$	XR	$I2/a$	ax. 1.929(7) eq. 1.987(15)	–	3.0413(11)
$MnRe(CO)_{10}$	XR	$I2/a$	ax. 1.909(9) eq. 1.92(1)	–	2.909(1)
$Fe(CO)_5$	XR	*Cc*	1.79–1.84	–	–
	ED		ax. 1.797(15) eq. 1.842(15)	–	–
$Fe_2(CO)_9$	XR	$P6_3/m$	1.838(3)	2.016(3)	2.523(1)
$Fe_3(CO)_{12}$	XR	$P2_1/n$	1.82	unsymm. bridge	2.677(2) 2.683(1) 2.558(1)
$Ru_3(CO)_{12}$	XR	$P2_1/n$	ax. 1.942(4) eq. 1.921(5)	–	2.8518(4) 2.8595(4) 2.8512(4)
$Os_3(CO)_{12}$	XR	$P2_1/n$	ax. 1.946(6) eq. 1.912(7)	– –	2.8824(5) 2.8752(5) 2.8737(5)
$Co_2(CO)_8$	XR	$P2_1/m$	ax. 1.815(1) eq. 1.832(4)	–	2.5301(8) 2.5278(8)
$Co_4(CO)_{12}$[d]	XR	*Pccn*	–	–	2.494(12), 2.441(14) 2.508(16), 2.527(10) 2.480(14), 2.486(13)
$Rh_4(CO)_{12}$[d]	XR	$P2_1/c$	–	–	2.706(8), 2.734(7) 2.739(7), 2.716(6) 2.701(8), 2.796(8)
$Ir_4(CO)_{12}$[d]	XR	$P3$	1.87	–	2.693

[a] XR = X-ray diffraction; ED = electron diffraction. [b] CO_t = terminal CO. [c] CO_b = bridging CO. Number in parentheses refers to the estimated standard deviation in the least significant digit. [d] Disordered structure.

electron-diffraction study showed a significant difference in the Fe–CO bond distance between the axial and the equatorial carbonyl groups (see Table 3).

$Fe_2(CO)_9$ is a sparingly soluble molecule in most organic inert solvents; the molecule contains three bridging carbonyl groups connecting the two $Fe(CO)_3$ units, and it can be described as $(OC)_3Fe(\mu_2\text{-}CO)_3Fe(CO)_3$. The iron–iron distance is 2.523 Å, according to an X-ray diffraction study.[24]

$Fe_3(CO)_{12}$ is a trinuclear compound that contains two sets of nonequivalent iron atoms: one iron atom is hexacoordinated to four terminal carbonyl groups and to the other two iron atoms, the rest of the molecule being $(OC)_3Fe(\mu_2\text{-}CO)_2Fe(CO)_3$ with terminal and bridging carbonyl groups. The carbonyl bridges are not symmetrical.

The pentacarbonyls of ruthenium(0) and osmium(0), $M(CO)_5$ (M = Ru, Os), show two carbonyl stretching vibrations in the IR spectrum (heptane) at 2035s, 1999vs (Ru) and 2034s, 1991vs (Os) cm^{-1}. On the basis of the number of IR-active bands observed, a trigonal bipyramidal structure of D_{3h} symmetry is suggested.

The isomorphous $Ru_3(CO)_{12}$ and $Os_3(CO)_{12}$ have a highly symmetrical structure of D_{3h} symmetry with equivalent metal atoms at a bond distance of 2.848 Å (Ru) or 2.88 Å (Os). All carbonyl groups are terminal.

3.4 Group 9

The dinuclear $Co_2(CO)_8$[52,53] has a solid-state structure with two doubly bridging carbonyl groups; each cobalt atom is hexacoordinated to three terminal carbonyl groups, to the other cobalt atom, and to two bridging carbon atoms, that is, $(OC)_3Co(\mu_2\text{-}CO)_2Co(CO)_3$. The cobalt–cobalt distance is 2.530 Å (or 2.528 Å in the independent molecule). Within the terminal carbonyl groups, the M–CO bond distances differ significantly between axial and equatorial groups, as for an X-ray diffraction study at low temperature. A cobalt–cobalt interaction through the bridging carbonyl groups has been suggested on the basis of a charge-density study.[53] In solution, this molecule has been suggested to be in equilibrium with a form not containing bridging carbonyl groups (see equation 25), and further with a third isomer. The ΔG^0 of the reaction is about zero at room temperature, the equilibrium constant being about 1.[54]

$$(OC)_3Co(\mu^2\text{-}CO)_2Co(CO)_3 \rightleftharpoons (OC)_4Co\text{–}Co(CO)_4 \qquad (25)$$

This group of elements forms numerous cluster systems.[48,49] Dodecacarbonyltetracobalt, $Co_4(CO)_{12}$, has a tetrahedral arrangement of the four cobalt atoms. An apical $Co(CO)_3$ group is symmetrically coordinated by Co–Co bonds to a basal $Co_3(CO)_9$ fragment consisting of three $Co(CO)_2$ groups joined by doubly bridging carbonyl groups and by a cobalt–cobalt bond, that is, $Co_4(CO)_9(\mu_2\text{-}CO)_3$.

In hexadecacarbonylhexacobalt(0), $Co_6(CO)_{16}$, the six cobalt atoms define an octahedron. The compound is isomorphous with $Rh_6(CO)_{16}$, whose structure is described below.

Dodecacarbonyltetrarhodium(0), $Rh_4(CO)_{12}$, has essentially the same structure as $Co_4(CO)_{12}$, that is, its structure can be described as $Rh_4(CO)_9(\mu_2\text{-}CO)_3$.

In hexadecacarbonylhexarhodium(0), $Rh_6(CO)_{16}$, the six rhodium atoms form an octahedron. Each rhodium atom binds two terminal carbonyl groups, the remaining four carbonyl groups being triply (face) bridging on four triangular faces of the octahedron, that is, $Rh_6(CO)_{12}(\mu_3\text{-}CO)_4$.

At variance with the corresponding cobalt and rhodium analogs, dodecacarbonyltetrairidium(0), $Ir_4(CO)_{12}$, consists of a tetrahedron of four iridium atoms, each being bonded to three terminal carbonyl groups, no bridging carbonyl groups being present.

Two isomeric forms of hexadecacarbonylhexairidium(0), $Ir_6(CO)_{16}$, are known: a red isomer, isostructural with $Rh_6(CO)_{16}$, and a black isomer that has four *edge-bridging* carbonyl groups rather than face-bridging. The structure of the black isomer is described as $Ir_6(CO)_{12}(\mu_2\text{-}CO)_4$.

3.5 Group 10

An electron-diffraction experiment in the gas phase and an X-ray diffraction study at low temperature on solid $Ni(CO)_4$ have shown the compound to have a regular tetrahedral geometry. An accurate refinement of the structural data has established the carbonyl ligands to be *C*-bonded to nickel.[23]

4 REACTIONS OF GROUPS 6–10

Metal carbonyls can undergo three main types of reaction: (a) substitution of the carbonyl groups, (b) oxidation, or (c) reduction. No change of the oxidation state of the metal occurs for (a), while an increase or decrease of the oxidation state occurs for (b) and (c), respectively.

A special case of redox reaction commonly encountered with metal carbonyls is disproportionation in the presence of Lewis bases, as exemplified for $Co_2(CO)_8$ (see equation 26). A similar reaction (see equation 27) has been reported for hexacarbonylvanadium(0).[55] By these reactions, the tetracarbonylcobaltate(−I) and the hexacarbonylvanadate(−I) anions are generated. The crystal and molecular structure of the product of the disproportionation reaction of $V(CO)_6$ with tetrahydrofuran of formula $[V(THF)_4][V(CO)_6]_2$ has been shown[56] to consist of vanadium(II) octahedrally surrounded by four thf's in the equatorial positions and by two axial carbonyl oxygens from two hexacarbonylvanadate anions resulting in a linear V–O–C–V sequence (*see Isocarbonyl Complexes*).

$$3Co_2(CO)_8 + 12L \longrightarrow 2CoL_6[Co(CO)_4]_2 + 8CO \qquad (26)$$

$$3V(CO)_6 + 6L \longrightarrow VL_6[V(CO)_6]_2 + 6CO \qquad (27)$$

$$L = \text{Lewis base}$$

4.1 Substitutions

Substitution reactions may be carried out thermally, photochemically, and chemically. In a thermal substitution, heat is used to both increase the kinetics of the process and shift the equilibrium, especially when gaseous carbon monoxide is produced, the ΔS^0 of the reaction being normally positive.

One of the more extensively studied substitution reactions of the hexacarbonyls of group 6 is the formation of the tricarbonylarenemetal(0) complexes (equations 28a), satisfactory conversions being obtained by removing the CO. The tricarbonyl derivatives are converted into the hexacarbonyls with CO at room temperature. For $Mo(CO)_3(\eta^6\text{-arene})$, the carbonylation to $Mo(CO)_6$ is accelerated by catalytic amounts of iodine. This effect is explained by the formation of molybdenum(II) carbonyl complexes (some of which have been isolated and crystallographically established) containing terminal iodide ligands that may act as catalysts in the substitution reaction.[57]

$$M(CO)_6 + \text{arene} \rightleftharpoons M(CO)_3(\eta^6\text{-arene}) + 3CO \qquad (28a)$$

$$M = Cr, Mo, W$$

The tricarbonyl-η^6-arene metal complexes of chromium, molybdenum, and tungsten have a pseudooctahedral geometry with the arene occupying the triangular face of the octahedron, the opposite triangular face being defined by the three carbonyl groups, usually in a staggered conformation (**5**).

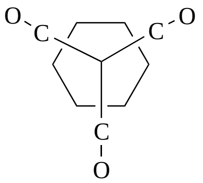

(**5**)

Carbonyl substitution in the hexacarbonyls $M(CO)_6$ (M = Cr, Mo, W) by the cyclopentadienyl anion gives the tricarbonyl Cp derivatives (equation 28b)

$$\mathrm{M(CO)_6 + C_5H_5^- \longrightarrow [M(CO)_3(\eta^5\text{-}C_5H_5)]^- + 3CO} \tag{28b}$$

Photochemical substitution of a carbonyl ligand of $M(CO)_6$ in THF as solvent gives the pentacarbonyl derivatives (equation 29). The substitutionally labile THF ligand can be displaced by other ligands; this method has been used extensively to produce pentacarbonyl derivatives of these metals. Photolysis of $Cr(CO)_6$ with UV light in heptane under dihydrogen pressure (100 atm) gives the dihydrogen complex $Cr(CO)_5(H_2)$, a surprisingly stable compound with a $\tau_{1/2}$ of about 25 s at room temperature.[58]

$$\mathrm{M(CO)_6 + THF \xrightarrow{h\nu} M(CO)_5THF + CO} \tag{29}$$

Pentacarbonyliron(0) with butadiene gives the tricarbonyl derivative $Fe(CO)_3(C_4H_6)$. Cyclobutadienetricarbonyliron(0), $Fe(CO)_3(C_4H_4)$, is prepared by dehalogenation of *cis*-3,4-dichlorobutene in the presence of $Fe_2(CO)_9$. This was the first cyclobutadiene complex to be reported in the literature (see equation 30).[59]

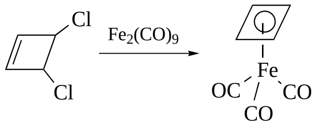

(30)

Several alkene complexes of iron(0) have been reported, of general formula $Fe(CO)_4$(alkene), where the alkene can be ethylene, acrylonitrile, maleic anhydride, or methyl methacrylate. In these complexes, the original trigonal bipyramidal structure of the pentacarbonyl is retained with one of the equatorial positions now being occupied by the alkene ligand. The tetracarbonyliron(0) complex of fumaric acid has idealized C_2 symmetry and has been resolved into its two enantiomers.[60]

Isocyanides displace carbon monoxide from $Fe(CO)_5$, yielding the tetracarbonyl and the tricarbonyl derivatives, $Fe(CO)_4(RNC)$ and $Fe(CO)_3(RNC)_2$, respectively.

Octacarbonyldicobalt gives substitution reactions with some difficulty because this metal carbonyl frequently undergoes facile disproportionation (*see Disproportionation*) (see equation 26), reduction, or oxidation reactions. With diphenylacetylene, $Co_2(CO)_8$ gives the substitution product $Co_2(CO)_6(C_2Ph_2)$. The molecular structure is directly derived from that of the precursor, with the acetylenic ligand being almost perpendicular to the cobalt–cobalt vector, thereby replacing the two bridging carbonyl groups.[23]

Tetracarbonylnickel(0) is quite reactive and several substitution products are known. For example, with tertiary phosphines and similar pnicogen-containing derivatives, many complexes of formula $Ni(CO)_{4-n}(ER_3)_n$ are known (see equation 31). The tertiary phosphine complexes of nickel(0) are important catalytic precursors, as in the trimerization of substituted acetylenes or in the dimerization of butadiene to *cyclo*-octa-1,5-diene.

$$\mathrm{Ni(CO)_4 + \mathit{n}ER_3 \longrightarrow Ni(CO)_{4-\mathit{n}}(ER_3)_\mathit{n} + \mathit{n}CO} \tag{31}$$

$$\mathrm{E = P, As, Sb, Bi}$$

An example of a chemically induced substitution reaction is represented by the halide removal in $MnCl(CO)_5$ by $AlCl_3$ leading to the hexacarbonylmanganese(I) cation. The driving force of this reaction, carried out at room temperature, is represented by the high affinity of aluminum for chloride. Similarly, the corresponding rhenium(I) derivative $[Re(CO)_6]AlCl_4$ can be prepared. This complex has considerable stability in that it can be dissolved in water without prompt decomposition (equation 32).

$$\mathrm{MX(CO)_5 + AlX_3 + CO \longrightarrow [M(CO)_6]AlX_4} \tag{32}$$

$$\mathrm{M = Mn, Re; X = halide}$$

4.2 Oxidations

Neutral metal carbonyls frequently undergo oxidation by air, and most of these compounds must be handled under an inert atmosphere. The derivatives of groups 6 and 7 are sufficiently inert, and the corresponding solid products can be handled in air for short periods of time. In solution, metal carbonyls may be oxidized by halogens, may be converted by dihydrogen to the corresponding hydrido complexes, may react with alkyl halides and with substances containing active protons. Frequently, oxidation of the central metal atom is followed by partial or complete loss of the carbonyl ligands, since the stability of the M–CO bond generally decreases as the oxidation state of the metal increases. Carbonyl derivatives of metals in oxidation state II or higher are known primarily for the 4d and 5d metals of groups 6–10.

Hexacarbonylchromium(0) is readily attacked by chlorine giving $CrCl_3$, CO, and $COCl_2$. Bromine and iodine do not attack $Cr(CO)_6$ to any substantial extent at room temperature. The chromium tricarbonyl arene complexes, $Cr(CO)_3(\eta^6$-arene), are readily oxidized at room temperature by I_2 to give CrI_3; this is a convenient preparative method for the anhydrous iodide. Although the oxidation of the tricarbonyl arene derivatives of chromium with I_2 does not show evidence of intermediate carbonyl complexes in oxidation states >0, the corresponding molybdenum(0) compounds give a series of carbonyl iodides of molybdenum(II),[57] for example, the ionic $[Mo(CO)_3(\eta^6$-arene)]I.

Hexacarbonylmolybdenum and β-diketones yield the molybdenum(III) chelate complexes as shown in equation (33) for acetylacetone.

$$\mathrm{Mo(CO)_6 + 3C_5H_8O_2 \longrightarrow 6CO + Mo(C_5H_7O_2)_3 + \{3H\}} \tag{33}$$

Oxidation of the decacarbonyldimetal(0) compounds of manganese, technetium, and rhenium by halogens gives the corresponding halopentacarbonylmetal(I) complexes (see equation 34).

$$\mathrm{M_2(CO)_{10} + X_2 \longrightarrow 2MX(CO)_5} \quad (34)$$
$$\mathrm{M = Mn, Tc, Re}$$

Carbonyl derivatives of iron(II) exist. Pentacarbonyliron(0) is oxidized by halogens to give carbonyl halide complexes (equation 35). The stability of these compounds with respect to thermal decomposition and hydrolysis increases in the sequence Cl $<$ Br $<$ I.

$$\mathrm{Fe(CO)_5 + X_2 \longrightarrow \mathit{cis}\text{-}FeX_2(CO)_4 + CO} \quad (35)$$

Ruthenium(II) and osmium(II) form two series of halo carbonyls, $[\mathrm{MX_2(CO)_2}]_n$ and $\mathrm{MX_2(CO)_4}$ (M = Ru, Os).

The carbonyls of cobalt(0), $\mathrm{Co_2(CO)_8}$ and $\mathrm{Co_4(CO)_{12}}$, are readily oxidized by air, and halogens normally decompose them to cobalt(II) halides with quantitative evolution of CO.

The rhodium(I) derivative $\mathrm{Rh_2Cl_2(CO)_4}$ is a chloride-bridged dimer with terminal carbonyl groups around the square-planar rhodium(I); each dinuclear unit is connected to similar units in the crystal by rhodium–rhodium contacts of 3.31 Å.

Tetracarbonylnickel(0) is readily decomposed by halogens and by several organic halides yielding nickel(II) halides under exhaustive decarbonylation. From a structural viewpoint, all dinuclear halo carbonyls, for example, $\mathrm{Mn_2X_2(CO)_8}$ and *trans*-$\mathrm{Pt_2X_4(CO)_2}$, have bridging halides and terminal carbonyl groups. An exception to this rule is $[\mathrm{Pd_2Cl_4(CO)_2}]^{2-}$, a derivative of d^9 palladium(I), which has bridging carbonyl groups and terminal halides.[61,62]

4.3 Reductions

Neutral metal carbonyls usually undergo one- or two-electron reductions by several reducing agents. The reduced species normally obey the next inert gas rule and the formulas can be easily predicted accordingly. Dinuclear metal carbonyls on reduction give mononuclear anionic species; mononuclear metal carbonyls may become doubly charged with loss of CO or undergo a one-electron reduction with formation of dinuclear anions (equations 36–38).

$$\mathrm{M_2(CO)}_n + 2e^- \longrightarrow 2[\mathrm{M(CO)}_{n/2}]^- \quad (36)$$
$$\mathrm{M(CO)}_n + 2e^- \longrightarrow [\mathrm{M(CO)}_{n-1}]^{2-} + \mathrm{CO} \quad (37)$$
$$2\mathrm{M(CO)}_n + 2e^- \longrightarrow [\mathrm{M_2(CO)}_{n-2}]^{2-} + 2\mathrm{CO} \quad (38)$$

Reductions are usually carried out in nonaqueous solvents using metals with low standard reduction potentials as electron suppliers. By addition of naphthalene, the system becomes homogeneous due to the formation of the naphthalene radical anion $\mathrm{C_{10}H_8}^-$. Soluble reducing agents in hydrocarbons include $\mathrm{CoCp^*}_2$, or the corresponding vanadium(II) species.

In basic aqueous solution, coordinated carbon monoxide can act as a reducing agent with carbonate being the oxidation product for the case of a mononuclear compound undergoing a two-electron reduction (equation 39).

$$\mathrm{M(CO)}_n + 4\mathrm{OH}^- \longrightarrow \mathrm{CO_3}^{2-} + [\mathrm{M(CO)}_{n-1}]^{2-} + 2\mathrm{H_2O} \quad (39)$$

Carbonyl metalates of alkali metals have been studied in solution by IR spectroscopy (see Section 5). Considerable ion pairing occurs with consequent lowering of the anion symmetry, as evidenced by the appearance of more bands than expected in the 1900–1700 $\mathrm{cm^{-1}}$ region. The alkali metal cation is assumed to establish an ion–dipole interaction with the carbonyl oxygens.

The hexacarbonyls of chromium, molybdenum, and tungsten are reduced by alkali metals giving the pentacarbonylmetalate(–II) anions. Reduction by $\mathrm{NaBH_4}$ gives the dinuclear decacarbonyldimetalates(–I), $[\mathrm{M_2(CO)_{10}}]^{2-}$, in liquid ammonia (equation 40).

$$\mathrm{2M(CO)_6 + 2NaBH_4 + 6NH_3 \longrightarrow Na_2[M_2(CO)_{10}] + 2CO}$$
$$\mathrm{+\, 2B(NH_2)_3 + 7H_2} \quad (40)$$

The dinuclear carbonyls of group 7 are reduced by alkali metals in THF (equation 41). The pentacarbonylmetalate(–I) anions are appropriate entries into the hydrido- or alkyl (aryl) pentacarbonyl derivatives (see equations 42 and 43). These compounds have pseudooctahedral structures of C_{4v} symmetry with the hydrido or alkyl (aryl) ligand occupying one of the positions within the coordination polyhedron.

$$\mathrm{M_2(CO)_{10} + 2Na \longrightarrow 2Na[M(CO)_5]} \quad (41)$$
$$\mathrm{M = Mn, Tc, Re}$$
$$[\mathrm{M(CO)_5}]^- + \mathrm{H}^+ \longrightarrow \mathrm{MH(CO)_5} \quad (42)$$
$$[\mathrm{M(CO)_5}]^- + \mathrm{R}^+ \longrightarrow \mathrm{MR(CO)_5} \quad (43)$$
$$\mathrm{M = Mn, Tc, Re}$$

Iron carbonyls are reduced by sodium metal to the tetracarbonylferrate(–II) anion (see equation 44). The X-ray crystal structure of the sodium derivative, $\mathrm{Na_2(dioxane)_{3/2}[Fe(CO)_4]}$, has shown a number of interactions between the sodium cation and the carbonyl oxygens; one of the sodium cations is hexacoordinated to four $\mathrm{Fe(CO)_4}$ units with Na···OC distances of 2.32 Å and to two oxygen atoms of the dioxane groups. In oxygenated solvents, such as THF or dialkyl ethers, the sodium is partially solvated. In the presence of a specific complexing agent for the metal cation (e.g. a crown ether, *see Crown Ethers*), the carbonylmetalate anion has its expected idealized geometry {D_{3h} for the pentacarbonyl $[\mathrm{Mn(CO)_5}]^-$, trigonal bipyramid; T_d for $[Fe(CO)_4]^{-2}$, tetrahedron}.**[63]** By forcing the reducing conditions, the tetracarbonylmanganato(−III) and the tetracarbonylchromato(−IV) anions have also been obtained,**[15,16]** thus expanding the isoelectronic series of the tetracarbonyl compounds: $Ni(CO)_4$, $[Co(CO)_4]^-$, $[Fe(CO)_4]^{2-}$, $[Mn(CO)_4]^{3-}$, $[Cr(CO)_4]^{4-}$.

$$Fe(CO)_5 + 2Na \longrightarrow Na_2[Fe(CO)_4] + CO \qquad (44)$$

The metal carbonyls of group 9 undergo reduction to the tetracarbonylmetalates(−I) (see equation 45 for $Co_2(CO)_8$). Acidification of an aqueous solution of $Na[Co(CO)_4]$ followed by extraction into an organic solvent produces the hydride $CoH(CO)_4$ (see equation 46), which is a sufficiently strong acid to be converted to the trialkylammonium derivative by tertiary amines R_3N (R = Me, Et) (equation 47). The C_{3v} symmetry of $CoH(CO)_4$ in the gas phase is maintained in the trialkylammonium derivatives as shown by X-ray**[64]** and neutron-diffraction studies.**[65,66]**

$$Co_2(CO)_8 + 2Na \longrightarrow 2Na[Co(CO)_4] \qquad (45)$$

$$[Co(CO)_4]^- + H^+ \longrightarrow CoH(CO)_4 \qquad (46)$$

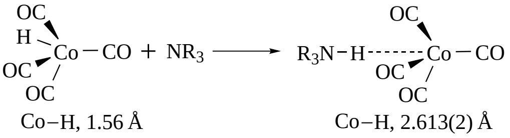

(47)

5 BONDING AND SPECTRAL DATA

Metal carbonyls have been studied by a number of techniques, vibrational spectroscopy in the IR region and ^{13}C NMR spectrometry being those most frequently used.

Metal carbonyls are characterized by IR-active vibrations associated with the carbonyl groups. Especially studied are the carbonyl stretching vibrations around 2000 cm^{-1}. The vibrational spectra give important information about (a) the electronic distribution within the M−CO bond in terminally bonded carbonyl groups; (b) the molecular structure associated with the number of bands observed; and (c) the type of bonding in dinuclear and polynuclear compounds.

The M–CO bond is usually regarded as a σ-bond from the lone pair on carbon to an empty orbital on the metal, reinforced by π back bonding (*see Back Bonding*) from a metal orbital of appropriate symmetry to an antibonding orbital of CO. The σ and π contributions are viewed as synergic, the result being a mutual reinforcement of the bond. As the π back-bonding contribution increases, the carbonyl stretching vibration is likely to be observed at lower frequencies, in agreement with the resonance hybrid description (**6**). The values of the carbonyl stretching vibrations also depend on the total charge on the complex. This is shown by the IR data for the following compounds with the $\tilde{\nu}_{CO}$ of the main carbonyl stretching vibration being reported in parenthesis (cm^{-1}): $[Fe(CO)_6]^{2+}$ (2204), $[Mn(CO)_6]^+$ (2090), $Cr(CO)_6$ (2000), $[V(CO)_6]^-$ (1859), and $[Ti(CO)_6]^{2-}$ (1748) for the isoelectronic series of the hexacarbonyls; $Ni(CO)_4$ (2058), $[Co(CO)_4]^-$ (1883), $[Fe(CO)_4]^{2-}$ (1730), $[Mn(CO)_4]^{3-}$ (1670), and $[Cr(CO)_4]^{4-}$ (1462) for the isoelectronic series of the tetracarbonyl derivatives.

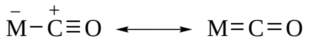

$$\overset{-}{M}-\overset{+}{C}\equiv O \longleftrightarrow M=C=O$$

(**6**)

The number of carbonyl bands increases as the overall symmetry of the molecule decreases. Only one IR-active carbonyl stretching vibration is normally observed for species of high symmetry, such as octahedral (O_h) or tetrahedral (T_d) complexes (see the examples given above; the data for the negatively charged species refer to media with a strong solvating power for the cation).

In polynuclear metal carbonyls, the bonding modes (a), (b), and (c) (see Section 3) are characterized by a decrease of the carbonyl stretching frequency, in agreement with the reduction of C–O bond order from (a) to (c). For neutral compounds, ν_{CO} values for bonding modes (a)−(c) follow the trend: (a) 2200−1850, (b) 1850−1750, (c) 1750−1620 cm^{-1}.

^{13}C NMR spectra have been extensively used**[67]** for analytical and structural purposes in metal−carbonyl chemistry.

6 METAL CARBONYLS OF THE EARLY TRANSITION ELEMENTS

Early transition elements of groups 4 and 5 have a small number of d electrons in their gas-phase configuration and this valence shell electronic configuration influences the properties of their compounds. For neutral carbonyls of group 5, the central metal atom has a d^5 electronic configuration; the next inert gas electronic configuration can be attained by dimer formation (as in the unstable $M_2(CO)_{12}$ complexes observed at low temperature only) or by one-electron reduction to the stable hexacarbonylmetalate(−I) anions, $[M(CO)_6]^-$. For the elements of group 4 in the zerovalent species, the metal has a d^4 electronic configuration and can be stabilized by seven carbonyl groups [giving the hypothetical heptacarbonyl $M(CO)_7$] or by undergoing a two-electron reduction to the dianions $[M(CO)_6]^{2-}$. Although heptacarbonyltitanium(0), $Ti(CO)_7$, is unknown, the substituted derivatives $Ti(CO)_{7-n}L_n$ have been reported.**[68,69]**

The known binary carbonyls of groups 4 and 5 are listed in Table 4. The dinuclear $V_2(CO)_{12}$ is stable at low temperature only as it is prepared from metal vapor and CO at about 20 K. The stable carbonyl compound of

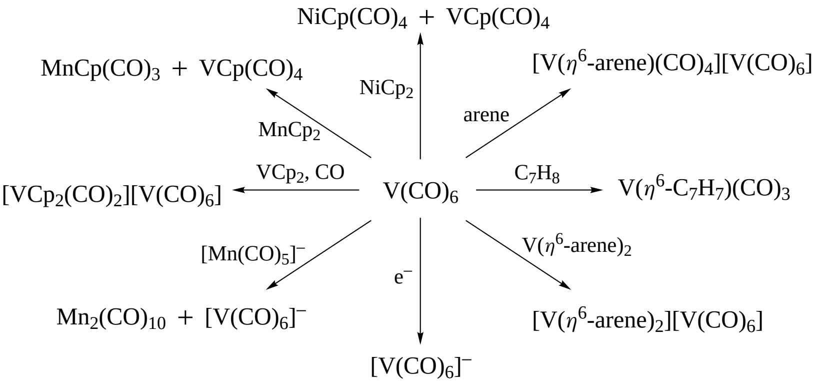

Scheme 1 Redox chemistry of hexacarbonylvanadium(0)

Table 4 Binary metal carbonyls of groups 4 and 5; crystal structures

Compound	Space group	M–CO$_t$(Å)
Group 4		
$[Ti(CO)_6]^{2-a}$	$P2_1/n$	2.038(3)
$[Zr(CO)_6]^{2-a}$	$P2_1/n$	2.210(4)
$[Hf(CO)_6]^{2-a}$	$P2_1/n$	2.178(3)
Group 5		
$V(CO)_6$	*Pnma*	ax. 1.993(2) eq. 2.005(2)
$[V(CO)_6]^{-b}$	$R\bar{3}$	1.931(9)
$[Nb(CO)_6]^{-b}$	$R\bar{3}$	2.089(5)
$[Ta(CO)_6]^{-b}$	$R\bar{3}$	2.083(6)

[a]As the $[K(cryptand\ 2.2.2)]^+$ derivative. [b]As the bis(triphenylphosphine)nitrogen(+), PPN^+, derivative.

vanadium(0), a low-spin d^5 complex of formula $V(CO)_6$, is best prepared by the sequence shown in reaction (48) and in equation (49). Hexacarbonylvanadium(0) has been found to have a regular octahedral structure, and to be isostructural with the hexacarbonyls of group 6.

$$VCl_3 \xrightarrow[\text{[cot]}]{\text{red./CO}} [V(CO)_6]^- \tag{48}$$

$$[V(CO)_6]^- + H^+ \longrightarrow \tfrac{1}{2}H_2 + V(CO)_6 \tag{49}$$

The hexacarbonylvanadate(−I) anion is prepared at room temperature and atmospheric pressure by reducing VCl_3 with sodium in THF in the presence of catalytic amounts of cyclooctatetraene (cot); the actual reducing agent is presumably the cot^{2-} di-anion.[70] The reaction of equation (49) is carried out with dry HCl in a hydrocarbon solvent. Hexacarbonylvanadium(0) is black−green in the solid state and shows the expected magnetic behavior for a d^5, low-spin complex from room temperature to 66 K, in which the $^2T_{2g}$ electronic ground state is coupled to vibrational modes. Below 66 K down to liquid helium temperature, the magnetic moment reduces considerably, and the compound becomes substantially diamagnetic at the lowest temperature.[71,72] An X-ray diffraction study at 245 K[73] shows the compound to be isomorphous with the corresponding chromium analog (see Tables 3 and 4), thus confirming some earlier results.[74,75] The coordination geometry around vanadium is octahedral with a marginally significant tetragonal distortion.

Hexacarbonylvanadium(0) undergoes reduction to $[V(CO)_6]^-$, oxidation to vanadium(I) complexes, or disproportionation to vanadium(II) and vanadium(−I) or to vanadium(I) and vanadium(−I) in the presence of Lewis bases or aromatic hydrocarbons, respectively. The chemistry of $V(CO)_6$ is shown in Scheme 1. Thus, hexacarbonylvanadium behaves as an oxidizing agent toward a number of organometallic compounds, the driving force being the formation of the 18-electron species $[V(CO)_6]^-$. Reductions of biscyclopentadienyl derivatives, such as $NiCp_2$ and $MnCp_2$, by $V(CO)_6$ are also known. A chemical interaction was found between $VCp^*{}_2$, $Cp^* = \eta^5\text{-}C_5Me_5$, and $V(CO)_6$ forming the μ-isocarbonyl compound $VCp^*{}_2(\mu\text{-}OC)V(CO)_5$ containing the linear V–O–C–V arrangement.[76]

The hexacarbonylniobate(−I) and hexacarbonyltantalate(−I) anions are well established. The $[Nb(CO)_6]^-$ anion can be prepared at atmospheric pressure of CO from $NbCl_5$ by using a prereduction step with alkali metal/naphthalene at low temperature, followed by carbonylation of the intermediate at low temperature in DME as solvent.[77] Another method of preparation,[78] also operating at atmospheric pressure of CO, uses the reduction of $NbCl_5$ with Mg/Zn/pyridine at room temperature and gives yields as high as 48% of recrystallized $Na(THF)[Nb(CO)_6]$. The alkali metal derivatives of $[M(CO)_6]^-$, M = Nb, Ta, are rapidly oxidized by air; the PPN derivatives are stable in air for short periods of time. $PPN[Nb(CO)_6]$ and $PPN[Ta(CO)_6]$ are isostructural; the hexacarbonyl anions possess an almost exact octahedral geometry with the following M–C bond distances: Nb–CO, 2.089 Å; Ta–CO, 2.083 Å.

The oxidation of $[Nb(CO)_6]^-$ and $[Ta(CO)_6]^-$ by several halide-containing oxidants (HX, CuX, CuX_2, AgX, FeX_3)

results in a two-electron transfer (see equation 50) leading to the halide-bridged dimers of niobium(I) or tantalum(I). With silver(I) salts containing the poorly coordinating anions NO_2^- or BF_4^-, formation of the tertiary phosphine substituted neutral hexanuclear clusters (equation 51) is observed.[79] Bonding considerations on some of these systems have been presented.[80,81]

$$2[M(CO)_6]^- + 3X^- \longrightarrow [M_2X_3(CO)_8]^- + 4e^- \qquad (50)$$

$$M = Nb, Ta; X = Cl, Br, I$$

$$3NR_4[M(CO)_4(dmpe)] + 3AgX \longrightarrow Ag_3M_3(CO)_{12}(dmpe)_3 + 3NR_4X \qquad (51)$$

$$M = Nb, Ta; X = NO_2, BF_4$$

The hexacarbonylmetalates(−II) of group 4 can be synthesized by reducing the tetrachlorides with potassium in the presence of a cryptand. In the case of hafnium, the starting material is a tertiary-phosphine-carbonyl complex of the zerovalent metal (see equations 52 and 53). The cryptand/(metal cation) system, characterized by a large mass and a low charge density, presumably has a stabilizing effect on the carbonyl anion. Reactions of equations (52) and (53) are carried out with CO at atmospheric pressure.[16]

$$MCl_4(ether)_n \xrightarrow[\text{15-crown-5}]{K/C_{10}H_8/CO} [K(\text{15-crown-5})]_2[M(CO)_6] \qquad (52)$$

$$M = Ti, Zr; ether = THF, n = 2; ether = DME, n = 1$$

$$M(CO)_4(trmpe) \xrightarrow[\text{cryptand 2.2.2}]{K/C_{10}H_8/CO} [K(cryptand)]_2[M(CO)_6] \qquad (53)$$

$$M = Ti, Zr, Hf$$

7 METAL CARBONYLS OF THE LATE TRANSITION ELEMENTS

The only neutral binary metal carbonyl of groups 10–12 is $Ni(CO)_4$. Some cationic-carbonyl derivatives of copper(I) and silver(I) have been detected in small equilibrium concentrations in strongly acidic aqueous solution. The formulas of these species, deduced from spectroscopic data,[82–85] are $M(CO)_n^+$ (M = Cu, Ag). The instability of $Pd(CO)_4$ and $Pt(CO)_4$ with respect to their decomposition to the metal (see equation 54) suggests that the strength of the M–CO bond is not sufficiently high to counterbalance the negative enthalpy change corresponding to the formation of the metal from $M(CO)_4$ and the positive entropy change due to CO evolution. The enthalpy change for the vaporization of nickel (430 kJ mol^{-1}) is higher than that of palladium (381 kJ mol^{-1}),[86–88] thus suggesting that Pd–CO bonds are particularly weak.

$$M(CO)_4 \longrightarrow M + 4CO \qquad M = Pd, Pt \qquad (54)$$

Studies on carbonyl derivatives of palladium(II), platinum(II), silver(I), and gold(I) have established the following points:

1. The halocarbonyl derivatives $Pd_2X_4(CO)_2$, $Pt_2X_4(CO)_2$, $PtX_2(CO)_2$, and AuX(CO) are characterized by carbonyl stretching vibrations at high frequencies, sometimes higher than CO itself ($\tilde{\nu}_{CO} = 2143\,cm^{-1}$) (see Table 5) with values of $\tilde{\nu}_{CO}$ usually decreasing in the sequence $Cl > Br > I$.
2. The tendency to form the halocarbonyls as a function of the halide decreases in the sequence $Cl > Br > I$. The carbonyl bromides of palladium(II), $Pd_2Br_4(CO)_2$, and gold, AuBr(CO), tend to decarbonylate in the solid state even under CO at atmospheric pressure, and the corresponding carbonyl iodides are unknown.
3. The values of the carbon–platinum coupling constants J_{Pt-C} decrease along the sequence $Cl > Br > I$, which may be explained by a corresponding decrease of the Pt–CO σ-bond strength in the same sequence.

The available data suggest a small π-contribution to the M–CO bond in these systems.

The Pd^{II}–CO bond strength has been estimated to be 100 kJ mol^{-1}, which is consistent with the values expected for a 4d element in the +II oxidation state on the basis of known thermochemical data for binary carbonyls of metals belonging to Groups 6–10 (see Section 8). In the absence of a significant π back-bonding contribution, the strength of the M–CO bond would not increase by decreasing the oxidation state. This prediction would therefore justify the observation that $Pd(CO)_4$ and $Pt(CO)_4$ have not been observed as stable species.

A predominant σ-contribution in M–CO bonds can generate a charge polarization within the M–CO bond such that the carbonyl carbon can become a site of nucleophilic attack. It has been pointed out[89] that metal carbonyls with force constants higher than 17.2 mdyn Å^{-1}, as estimated from the IR-active carbonyl stretching vibrations, should react with amines to give carbamoyl derivatives. Accordingly,

Table 5 Carbonyl stretching vibrations (IR) of halocarbonyls of palladium, platinum, and gold[2,84]

Compound	$\tilde{\nu}_{CO}$(cm^{-1})	Solvent
cis-$Pd_2Cl_4(CO)_2$[a]	2160	Toluene
trans-$Pd_2Br_4(CO)_2$	2148	Toluene
trans-$Pt_2Cl_4(CO)_2$[a]	2119	Toluene
	2122	Heptane
cis-$PtCl_2(CO)_2$	2167, 2120	Heptane
cis-$PtBr_2(CO)_2$	2156, 2115	Heptane
trans-$PtBr_2(CO)_2$	2136	Heptane
trans-$PtI_2(CO)_2$	2122	Heptane
AuCl(CO)	2163	$SOCl_2$
AuBr(CO)	2153	*sym*-$C_2H_4Br_2$

[a] Geometry established by X-ray diffractometry.[84]

cis-$PtCl_2(CO)_2$, with CO force constants of 19.01 and 18.3 mdyn Å^{-1}, reacts with secondary amines to give the carbamoyl derivatives shown in equation (5).

Although the formation of Ag–CO bonds in solution had been established in several systems,[82–85] isolation and structural determination of products containing Ag–CO bonds are recent acquisitions.[3,90,91] The carbonyl derivatives of silver, $Ag(CO)(OTeF_5)_2B(OTeF_5)_2$, and $[Ag(CO)_2][B(OTeF_5)_4]$ have been crystallographically established. In the former compound,[90] silver is coordinated to carbon monoxide and to two oxygen atoms of the boron-containing ligand; the $[Ag(CO)_2]^+$ cation is constituted[91] by two-coordinated linear silver(I), whose unique IR carbonyl stretching vibration is observed at 2198 cm^{-1}. The $[Pt(CO)_4]^{2+}$ cation, isolated as the $[Pt(SO_3F)_6]^{2-}$ derivative,[92] has an IR–carbonyl stretching band at 2235 cm^{-1}.

8 METAL–CO BOND DISSOCIATION ENTHALPY (BDE)

The thermodynamic stability of metal carbonyls has attracted the interest of scientists for several decades.[93] The understanding of the nature of the M–CO bond should account for important observations, such as the isolation of stable metal carbonyls for metals in a wide range of oxidation states, +IV to −IV, the latter being encountered in the highly reduced carbonyl metalates. Reliable M–CO bond energies are essential in order to understand the behavior of these compounds, including their reactivity. For simplicity, mainly binary neutral metal carbonyls will be considered here, but the general considerations on this problem usually apply to substituted metal carbonyls as well and to compounds in oxidation states higher or lower than zero. For a neutral binary metal carbonyl and its formation from the corresponding metal, vaporization of the metal and its reaction with CO to form the final product (equations 55a and 55b) are the relevant steps to be considered. The enthalpy and entropy contributions to the free-energy change of the process can be evaluated.

$$\mathrm{M(s)} \longrightarrow \mathrm{M(g)} \qquad (55a)$$

$$\mathrm{M(g)} + n\mathrm{CO(g)} \longrightarrow \mathrm{M(CO)(g)} \qquad (55b)$$

As far as equation (55a) is concerned, the enthalpy term is accurately known for most metals,[86,87] corresponding to the transfer of the solid metal to its state of a monoatomic gas in its high-spin ground-state configuration. Equation (55b) contains the negative value of the bond enthalpy, which, divided by the number of M–CO bonds in the molecule, gives the mean bond dissociation enthalpy. $M(CO)_n(g)$ differs from $M(CO)_n(s)$ or $M(CO)_n(l)$ by the heats of sublimation or vaporization, respectively.

Several experimental techniques, including thermochemistry and some spectroscopic methods, have been used to obtain these data or related ones, and pertinent review articles on the subject have appeared (*see* ***Bonding Energetics of Organometallic Compounds***).[94–97] A different approach to this problem is the evaluation of enthalpy terms according to second-law methods, by measuring equilibrium constants as a function of temperature. This method has been particularly useful for estimating thermodynamic parameters in metal–carbonyl cluster chemistry (see Section 2.5).

Table 6 Mean bond dissociation enthalpies (BDE) and calculated first ligand dissociation energies (FDE) of some binary metal carbonyls

Compound	BDE (kJ mol^{-1})[94,95]	FDE (kJ mol^{-1})[97]
$Cr(CO)_6$	107 ± 1	147
$Mn(CO)_6{}^+$	–	92
$V(CO)_6{}^-$	–	171
$Mo(CO)_6$	152 ± 1	119
$W(CO)_6$	178 ± 1	142
$Fe(CO)_5$	118 ± 2	–
$Ni(CO)_4$	147	106
$Pd(CO)_4$	–	27
$Pt(CO)_4$	–	38

Heats of atomization of metals have well-known trends within *typical* groups of transition elements (groups 6–9),[86,87] that is, they increase down a group from the lighter to the heavier element. By using a combination of several experimental techniques, two main conclusions concerning neutral metal carbonyls have been reached: (a) the M–CO bond enthalpy contribution increases[95] as the heat of atomization increases down a group (typical sequences: Cr–Mo–W; Fe–Ru–Os; Co–Rh–Ir); (b) the M–CO bond enthalpy is normally greater than the metal–metal bond enthalpy estimated from the heat of atomization. Table 6 reports the M–CO_t (CO_t, terminal CO) mean bond enthalpies for some of the common binary metal carbonyls and the calculated[97] first ligand dissociation energies. Within the neutral compounds with the same electronic configuration, the 4d compound generally has the lowest dissociation energy.

Point (b) is particularly relevant for systems such as $Co_2(CO)_8$, which exists in solution in an almost 1:1 ratio between the carbonyl-bridged form and the nonbridged form (see equation 25), and $Mn_2(CO)_{10}$, which is stable only in the nonbridged form both in solution and in the solid state. Single metal–metal bonds are not particularly strong for 3d systems; this may explain the experimental observation that $V(CO)_6$ is mononuclear, since intraligand repulsion in the dinuclear species would not be compensated by a sufficiently strong vanadium–vanadium bond.

9 REACTION MECHANISMS

In metal–carbonyl chemistry, two types of reactions have been studied from a mechanistic viewpoint: (a) substitution reactions, where no change of oxidation state is involved, and (b) redox reactions (*see* ***Mechanisms of Reaction of Organometallic Complexes***). Substitutions (see equation 56) have been extensively studied, while a relatively smaller number of papers have appeared on electron-transfer reactions.

$$\mathrm{M(CO)}_n + \mathrm{L} \longrightarrow \mathrm{M(CO)}_{n-1}\mathrm{L} + \mathrm{CO} \tag{56}$$

For polynuclear metal carbonyls, similar processes have been studied to a great extent, especially for the decacarbonyls of group 7, $M_2(CO)_{10}$ ($M = Mn$, Re). A simple case of substitution is the isotopic exchange reaction, for which the enthalpy is substantially zero. The specific rate constants (or half-lives)[98] for such exchange reactions, under exclusion of light, of some selected metal carbonyls are in Table 7. Slowly reacting species [$Fe(CO)_5$, d^8 configuration; $Cr(CO)_6$, $Mo(CO)_6$, $W(CO)_6$, d^6 low-spin], moderately reactive [$V(CO)_6$, low-spin d^5, possibly subject to Jahn–Teller (*see Jahn–Teller Effect*) distortion], and fast reacting species [$Ni(CO)_4$, d^{10} configuration] can be recognized. The low reactivity of the hexacarbonyls of group 6 is consistent with the well-established observation that d^6, low-spin systems are substitutionally inert, independent of oxidation state. Substitution reactions frequently occur by a dissociative mechanism with a coordinatively unsaturated species being formally present in the rate-determining step (see equation 57).

$$\mathrm{M(CO)}_n \underset{k_{-1}}{\overset{k_1}{\rightleftharpoons}} \mathrm{M(CO)}_{n-1} + \mathrm{CO} \tag{57}$$

Within compounds containing metals belonging to the same vertical sequence, that is, normally isostructural compounds with the same number of valence electrons for the central metal atom (for example, the hexacarbonyls of group 6), the order of reactivity is often $3d < 4d > 5d$,[99] with the exception of the cyclopentadienyl derivatives of group 5, $MCp(CO)_4$ ($M = V$, Nb, Ta), for which the order of reactivity is $V > Nb > Ta$.[100] Relevant to these findings are the data provided in Table 6 showing that the calculated[97] first CO dissociation energy for the hexacarbonyls and the tetracarbonyls is lowest for the 4d term. Thus, at least for dissociative mechanisms, the order of reactivity usually observed has theoretical support. This result is important for catalysis.

Table 7 Rate of CO exchange with some binary metal carbonyls[98]

Compound	t (°C)	Rate	
		k (s^{-1})	$\tau_{1/2}$
$Ni(CO)_4$	0	7.8×10^{-4}	–
$Fe(CO)_5$	25	–	4 y
$Cr(CO)_6$	117	2.0×10^{-5}	–
$Mo(CO)_6$	116	7.5×10^{-5}	–
$W(CO)_6$	142	2.6×10^{-6}	–
$V(CO)_6$	10	–	7 h

A special case of substitution reaction is the migratory insertion (*see Migratory Insertion*) reaction of alkyl or aryl metal carbonyls (see equation 58), by which an alkyl or aryl metal carbonyl is converted into an acyl or aroyl metal carbonyl by the action of a Lewis base. This reaction has been studied extensively, and in the case of $Mn(Me)(CO)_5$ is found to proceed through a coordinatively unsaturated tetracarbonyl resulting from methyl migration on to one of the terminal CO groups in a *cis* position, (see equation 59).[101]

$$\mathrm{MR(CO)}_n + \mathrm{L} \longrightarrow \mathrm{M(COR)(CO)}_{n-1}\mathrm{L} \tag{58}$$

L = Lewis base

$$\mathrm{MnMe(CO)}_5 \underset{k_{-1}}{\overset{k_1}{\rightleftharpoons}} \mathrm{Mn(COMe)(CO)}_4 \underset{-\mathrm{CO},\, k_{-2}}{\overset{+\mathrm{CO},\, k_2}{\rightleftharpoons}} \mathrm{Mn(COMe)(CO)}_5 \tag{59}$$

In the migratory insertion reaction, the central metal atom does not alter its oxidation state, and a new carbon–carbon bond is formed. As such, this reaction is believed to constitute a fundamental step in several carbon–carbon forming catalytic processes (hydroformylation (*see Hydroformylation*), homologation (*see Homologation Reactions*), carbonylation of methanol to acetic acid, alkene polymerization). Migratory insertions can be catalyzed by oxidizing agents[102] or Lewis acids under homogeneous or heterogenous conditions. In both cases, the electrophilic character of the carbonyl carbon is further enhanced, thus making this an even more favorable site of intramolecular attack by the alkyl group, as shown in (**7**).

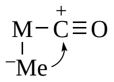

(**7**)

For metal carbonyls, redox reactions (*see Redox Properties & Processes*) have been studied in a smaller number of cases, relative to substitution reactions. The simplicity of binary metal carbonyls and the possibility for these compounds to undergo electron transfers make them excellent substrates for studying redox processes in nonaqueous media. Convenient organometallic one-electron oxidants or reductants (number of valence electrons in parenthesis) are[103,104] $V(CO)_6$ (17)/$[V(CO)_6]^-$ (18); $[FeCp_2]^+$ (17)/$FeCp_2$ (18); $V(\eta^6\text{-arene})_2$ (17)/$[V(\eta^6\text{-arene})_2]^+$ (16); VCp_2 (15)/$[VCp_2L_2]^+$ (18); $CoCp_2$ (19)/$[CoCp_2]^+$ (18). These systems have the advantage that the uncharged species is soluble in organic solvents, including aromatic or aliphatic hydrocarbons. Most common binary metal carbonyls, with the exception of $V(CO)_6$, have redox couples complicated by the formation of metal–metal bonded dimers in the oxidized form (see equations 60–63).

$$[Mn(CO)_5]^- \longrightarrow \tfrac{1}{2}Mn_2(CO)_{10} + e^- \qquad (60)$$

$$[Re(CO)_5]^- \longrightarrow \tfrac{1}{2}Re_2(CO)_{10} + e^- \qquad (61)$$

$$[Co(CO)_4]^- \longrightarrow \tfrac{1}{2}Co_2(CO)_8 + e^- \qquad (62)$$

$$[V(CO)_6]^- \longrightarrow V(CO)_6 + e^- \qquad (63)$$

Evidence for a single-event, two-electron transfer process has been gathered in the reaction between the two d^6 systems, $[Re(CO)_5]^-$ and $[Mn(CO)_6]^+$ (see equation 64), followed by redistribution (equation 65).[105]

$$[Re(CO)_5]^- + [Mn(CO)_6]^+ \longrightarrow [Re(CO)_6]^+ + [Mn(CO)_5]^- \qquad (64)$$

$$[Re(CO)_6]^+ + [Mn(CO)_5]^- \longrightarrow Re_2(CO)_{10} + Mn_2(CO)_{10} + MnRe(CO)_{10} \qquad (65)$$

10 RELATED ARTICLES

Bonding Energetics of Organometallic Compounds; Cobalt: Organometallic Chemistry; Electron Transfer Reactions: Theory; Electronic Structure of Organometallic Compounds; Hydride Complexes of the Transition Metals; Iridium: Organometallic Chemistry; Iron: Organometallic Chemistry; Manganese: Organometallic Chemistry; Mechanisms of Reaction of Organometallic Complexes; Palladium: Organometallic Chemistry; Periodic Table: Trends in the Properties of the Elements; Transition Metal Carbonyls: Infrared Spectra; Vanadium: Organometallic Chemistry.

11 REFERENCES

1. F. Calderazzo and D. Belli Dell' Amico, *Pure Appl. Chem.*, 1986, **58**, 561.
2. F. Calderazzo, *J. Organomet. Chem.*, 1990, **400**, 303.
3. A. J. Lupinetti, S. H. Strauss, and G. Frenking, *Prog. Inorg. Chem.*, 2001, **49**, 1.
4. P. Selg, H. H. Brintzinger, R. A. Andersen, and I. I. Horváth, *Angew. Chem., Int. Ed. Engl.*, 1995, **34**, 791.
5. F. Calderazzo, G. Pampaloni, and G. Tripepi, *Organometallics*, 1997, **16**, 4943.
6. M. Schultz, C. J. Burns, D. J. Schwartz, and R. A. Andersen, *Organometallics*, 2001, **20**, 5690.
7. M. del Mar Conejo, J. S. Parry, E. Carmona, M. Schultz, J. G. Brennann, S. M. Beshouri, R. A. Andersen, R. D. Rogers, S. Coles, and M. Hursthouse, *Chem. Eur. J.*, 1999, **5**, 3000.
8. J. C. Jeffery, N. C. Norman, J. A. J. Pardoe, and P. L. Timms, *Chem. Commun.*, 2000, 2367.
9. M. Finze, E. Bernhardt, A. Terheiden, M. Berkei, H. Willner, D. Christen, H. Oberhammer, and F. Aubke, *J. Am. Chem. Soc.*, 2002, **124**, 15385.
10. L. Andrews, T. J. Tague, G. P. Kushto, and R. D. Davy, *Inorg. Chem.*, 1995, **34**, 2952.
11. M. Zhou, Q. Xu, Z.-X. Wang, and P. von Ragué Schleyer, *J. Am. Chem. Soc.*, 2002, **124**, 14854, references therein.
12. P. J. F. de Rege, J. A. Gladysz, and I. T. Horváth, *Science*, 1997, **276**, 776.
13. K. Weissermel and H. J. Arpe, 'Industrial Organic Chemistry', Verlag Chemie, Weinheim, 1978.
14. For positive oxidation states, see: H. Willner and F. Aubke, *Organometallics*, 2003, **22**, 3612.
15. J. E. Ellis, *Adv. Organomet. Chem.*, 1990, **31**, 1.
16. J. E. Ellis, *Organometallics*, 2003, **22**, 3322.
17. K. M. Chi, S. R. Frerichs, S. B. Philson, and J. E. Ellis, *Angew. Chem., Int. Ed. Engl.*, 1987, **26**, 1190.
18. K. M. Chi, S. R. Frerichs, S. B. Philson, and J. E. Ellis, *J. Am. Chem. Soc.*, 1988, **110**, 303.
19. J. E. Ellis and K. M. Chi, *J. Am. Chem. Soc.*, 1990, **112**, 6022.
20. L. Mond, C. Langer, and F. Quincke, *J. Chem. Soc. (London)*, 1890, **57**, 749.
21. E. Weiss, *Angew. Chem., Int. Ed. Engl.*, 1993, **32**, 1501.
22. F. A. Cotton, *Helv. Chim. Acta*, Alfred Werner Commemoration Volume, Verlag Helvetica Chimica Acta, 1967, 117.
23. F. Calderazzo, R. Ercoli, and G. Natta, in 'Organic Syntheses via Metal Carbonyls', eds. I. Wender, and P. Pino, John Wiley & Sons, New York, 1968, and references therein.
24. F. A. Cotton, *Prog. Inorg. Chem.*, 1976, **21**, 1.
25. G. Brauer, 'Handbuch der Präparativen Anorganischen Chemie', Dritter Band, Enke Verlag, Stuttgart, 1981; W. Hieber, *Adv. Organomet. Chem.*, **8**, 1970, 1.
26. M. Nicolini, G. Bandoli, and U. Mazzi, eds, 'Technetium in Chemistry and Nuclear Medicine', Cortina International, Verona, 1986, Vol. 2.
27. F. Calderazzo, U. Mazzi, G. Pampaloni, R. Poli, F. Tisato, and P. F. Zanazzi, *Gazz. Chim. Ital.*, 1989, **119**, 241.
28. S. Top, P. Morel, M. Pankowski, and G. Jaouen, *J. Chem. Soc., Dalton Trans.*, 1996, 3611.
29. C. H. Wei and L. F. Dahl, *J. Am. Chem. Soc.*, 1968, **90**, 3977.
30. D. L. Stevenson, C. H. Wei, and L. F. Dahl, *J. Am. Chem. Soc.*, 1971, **93**, 6027.
31. C. E. Strouse and L. F. Dahl, *J. Am. Chem. Soc.*, 1971, **93**, 6032.
32. F. Calderazzo, U. Englert, G. Pampaloni, V. Passarelli, G. Serni, and R. Wang, *Can. J. Chem.*, 2001, **79**, 495.
33. R. Koelliker and G. Bor, *Inorg. Chem.*, 1991, **30**, 2236.
34. F. Calderazzo, C. Floriani, R. Henzi, and F. L'Eplattenier, *J. Chem. Soc. A*, 1969, 1378.

35. F. Calderazzo and F. L' Eplattenier, *Inorg. Chem.*, 1967, **6**, 1220.
36. R. Tannenbaum, U. K. Dietler, G. Bor, and F. Ungváry, *J. Organomet. Chem.*, 1998, **570**, 39, and references therein.
37. R. Ercoli and F. Barbieri-Hermitte, *Atti Accad. Naz. Lincei, Cl. Sci. Fis. Mat. Nat., Rend.*, 1954, **16**, 249; (*Chem. Abstr.*, 1954, **48**, 10 408i).
38. G. Bor and U. K. Dietler, *J. Organomet. Chem.*, 1980, **191**, 295.
39. F. Oldani and G. Bor, *J. Organomet. Chem.*, 1983, **246**, 309; *J. Organomet. Chem.*, 1985, **279**, 459.
40. C. Li, E. Widjaja, W. Chew, and M. Garland, *Angew. Chem. Int. Ed.*, 2002, **41**, 3786.
41. H. Huber, P. Kündig, M. Moskovits, and G. A. Ozin, *Nature (London)*, 1972, **235**, 98.
42. J. H. Darling and J. S. Ogden, *Inorg. Chem.*, 1972, **11**, 666.
43. E. P. Kündig, D. McIntosh, M. Moskovits, and G. A. Ozin, *J. Am. Chem. Soc.*, 1975, **95**, 7234.
44. D. Belli Dell' Amico, F. Calderazzo, M. Dittmann, L. Labella, F. Marchetti, E. Schweda, and J. Strähle, *J. Organomet. Chem.*, 1999, **583**, 162.
45. P. Chini, G. Longoni, and V. G. Albano, *Adv. Organomet. Chem.*, 1976, **14**, 285.
46. M. D. Vargas and J. N. Nicholls, *Adv. Inorg. Chem. Radiochem.*, 1986, **30**, 123.
47. J. D. Roth, G. J. Lewis, L. K. Safford, X. Jiang, L. F. Dahl, and M. J. Weaver, *J. Am. Chem. Soc.*, 1992, **114**, 6159.
48. A. Ceriotti, R. Della Pergola, and L. Garlaschelli, High-Nuclearity Carbonyl Metal Clusters, ed. L. J. de Jongh, 'Physics and Chemistry of Metal Cluster Compounds', Kluwer Academic Publishers, Boston, p. 41, 1994.
49. A. K. Hughes and K. Wade, *Coord. Chem. Rev.*, 2000, **197**, 191.
50. L. J. Farrugia, *Adv. Organomet. Chem.*, 1990, **31**, 301.
51. F. Calderazzo, A. Juris, R. Poli, and F. Ungari, *Inorg. Chem.*, 1991, **30**, 1274.
52. G. G. Sumner, H. P. Klug, and L. E. Alexander, *Acta Crystallogr.*, 1964, **17**, 732.
53. P. C. Leung and P. Coppens, *Acta Crystallogr.*, 1983, **B39**, 535.
54. G. Bor and K. Noack, *J. Organomet. Chem.*, 1974, **64**, 367.
55. R. Ercoli, F. Calderazzo, and A. Alberola, *J. Am. Chem. Soc.*, 1960, **82**, 2965.
56. M. Schneider and E. Weiss, *J. Organomet. Chem.*, 1976, **121**, 355.
57. A. Barbati, F. Calderazzo, and R. Poli, *Gazz. Chim. Ital.*, 1988, **118**, 589.
58. R. K. Upmacis, G. E. Gadd, M. Poliakoff, M. B. Simpson, J. J. Turner, R. Whyman, and A. F. Simpson, *J. Chem. Soc., Chem. Commun.*, 1985, 27.
59. G. F. Emerson, L. Watts, and R. Pettit, *J. Am. Chem. Soc.*, 1965, **87**, 131.
60. G. Paiaro, R. Palumbo, A. Musco, and A. Panunzi, *Tetrahedron Lett.*, 1965, 1067.
61. P. L. Goggin, R. J. Goodfellow, I. R. Herbert, and A. G. Orpen, *J. Chem. Soc., Chem. Commun.*, 1981, 1077.
62. N. M. Kostic and R. F. Fenske, *Inorg. Chem.*, 1983, **22**, 666.
63. C. P. Horwitz and D. F. Shriver, *Adv. Organomet. Chem.*, 1984, **23**, 219.
64. F. Calderazzo, G. Fachinetti, F. Marchetti, and P. F. Zanazzi, *J. Chem. Soc., Chem. Commun.*, 1981, 181.
65. L. Brammer, M. C. McCann, R. M. Bullock, R. K. McMullan, and P. Sherwood, *Organometallics*, 1992, **11**, 2339.
66. L. Brammer, *J. Chem. Soc., Dalton Trans.*, 2003, 3145.
67. B. E. Mann and B. F. Taylor, '^{13}C NMR Data for Organometallic Compounds', Academic Press, London, 1981.
68. J. E. Ellis, A. J. DiMaio, A. L. Rheingold, and B. S. Haggerty, *J. Am. Chem. Soc.*, 1992, **114**, 10676.
69. K. M. Chi, S. R. Frerichs, B. K. Stein, D. W. Blackburn, and J. E. Ellis, *J. Am. Chem. Soc.*, 1988, **110**, 163.
70. F. Calderazzo and G. Pampaloni, *J. Organomet. Chem.*, 1992, **423**, 307.
71. H. J. Keller, P. Laubereau, and D. Nöthe, *Z. Naturforsch.*, 1969, **B24**, 257.
72. J. C. Bernier and O. Kahn, *Chem. Phys. Lett.*, 1973, **19**, 414.
73. S. Bellard, K. A. Rubinson, and G. M. Sheldrick, *Acta Crystallogr.*, 1979, **B35**, 271.
74. G. Natta, R. Ercoli, F. Calderazzo, A. Alberola, P. Corradini, and G. Allegra *Rend. Accad. Naz. Lincei*, 1959, **27**, 107; *Chem. Abstr.*, 1960, **54**, 85469.
75. F. Calderazzo, G. Pampaloni, and D. Vitali, *Gazz. Chim. Ital.*, 1981, **111**, 455.
76. J. H. Osborne, A. L. Rheingold, and W. C. Trogler, *J. Am. Chem. Soc.*, 1985, **107**, 6292.
77. C. G. Dewey, J. E. Ellis, K. L. Fjare, K. M. Pfahl, and G. F. P. Warnock, *Organometallics*, 1983, **2**, 388.
78. F. Calderazzo, U. Englert, G. Pampaloni, G. Pelizzi, and R. Zamboni, *Inorg. Chem.*, 1983, **22**, 1865.
79. F. Calderazzo, G. Pampaloni, U. Englert, and J. Strähle, *Angew. Chem., Int. Ed. Engl.*, 1989, **28**, 471.
80. T. W. Bitner and J. I. Zink, *J. Am. Chem. Soc.*, 2000, **122**, 10631.
81. A. Diefenbach, F. M. Bickelhaupt, and G. Frenking, *J. Am. Chem. Soc.*, 2000, **122**, 6449.
82. Y. Souma, I. Iyoda, and H. Sano, *Inorg. Chem.*, 1976, **15**, 968.
83. Y. Souma and H. Sano, *Chem. Lett.*, 1973, 1059.
84. W. Backen and E. Ericsson, *Acta Chem. Scand.*, 1981, **A35**, 1.
85. D. Belli Dell' Amico, F. Calderazzo, L. Labella, F. Lorenzini, and F. Marchetti, *Z. Anorg. Allg. Chem.*, 2002, **628**, 1868.
86. W. E. Dasent, 'Nonexistent Compounds', Dekker, New York, 1965.

87. D. R. Lide, ed., ‘Handbook of Chemistry and Physics’, 82nd edn., CRC Press, 2001–2002, p. 9.
88. F. Bagnoli, D. Belli Dell’ Amico, F. Calderazzo, U. Englert, F. Marchetti, A. Merigo, and S. Ramello, *J. Organomet. Chem.*, 2001, **622**, 180, and references therein.
89. R. J. Angelici, *Acc. Chem. Res.*, 1972, **5**, 335.
90. P. K. Hurlburt, O. P. Anderson, and S. H. Strauss, *J. Am. Chem. Soc.*, 1991, **113**, 6277.
91. P. K. Hurlburt, J. J. Rack, S. F. Dec, O. P. Anderson, and S. H. Strauss, *Inorg. Chem.*, 1993, **32**, 373.
92. G. Hwang, M. Bodenbinder, H. Willner, and F. Aubke, *Inorg. Chem.*, 1993, **32**, 4667.
93. L. Pauling, ‘The Nature of the Chemical Bond’, 3rd edn., Cornell University Press, Ithaca, NewYork, 1960, p. 331.
94. H. A. Skinner, *Adv. Organomet. Chem.*, 1964, **2**, 49.
95. J. A. Connor, *Top. Curr. Chem.*, 1977, **71**, 71.
96. J. A. Martinho Simões and J. L. Beauchamp, *Chem. Rev.*, 1990, **90**, 629.
97. T. Ziegler, V. Tschinke, and C. Ursenbach, *J. Am. Chem. Soc.*, 1987, **109**, 4825.
98. F. Basolo and R. G. Pearson, ‘Mechanisms of Inorganic Reactions’, John Wiley & Sons, New York, 1967, p. 541.
99. F. Basolo, *Polyhedron*, 1990, **9**, 1503.
100. J. W. Freeman and F. Basolo, *Organometallics*, 1991, **10**, 256.
101. F. Calderazzo, *Angew. Chem., Int. Ed. Engl.*, 1977, **16**, 299.
102. J. P. Collman, L. S. Hegedus, J. R. Norton, and R. G. Finke, ‘Principles and Applications of Organotransition Metal Chemistry’, University Science Books, Mill Valley, CA, 1987.
103. M. C. Baird, *Chem. Rev.*, 1988, **88**, 1217.
104. D. Astruc, *Chem. Rev.*, 1988, **88**, 1189.
105. Y. Zhen and J. D. Atwood, *J. Am. Chem. Soc.*, 1989, **111**, 1506.

Carbonylation Processes by Homogeneous Catalysis

M. L. Parr
Trinity College, Hartford, CT, USA

Based in part on the article Carbonylation Processes by Homogeneous Catalysis by George G. Stanley which appeared in the Encyclopedia of Inorganic Chemistry, First Edition.

1 Introduction 1
2 Aldehydes and Alcohols–Hydroformylation 2
3 Carboxylic Acids, Esters, and Acyl Halides 19
4 Ketones 27
5 Lactones and Lactams 28
6 Related Articles 31
7 References 31

Abbreviations

bar $= 1 \times 10^5$ Pa ~ 1 atmosphere of pressure; psig $=$ pounds/square inch gauge pressure (14.70 psig $= 1$ bar).

1 INTRODUCTION

Homogeneous carbonylation catalysis involves the transition metal assisted addition of carbon monoxide (CO) to organic compounds to produce higher molecular weight carbonyl-containing products. Carbonylation chemistry was pioneered by Roelen (Ruhrchemie) and Reppe (IG Farben/Badische Anilin und Soda Fabrik (BASF)) in the late 1930s. Since then, it has developed into the highest volume and most important of the industrial homogeneous catalytic processes. The first 27 years of carbonylation catalysis involved the use of simple metal–carbonyl catalysts, high-reaction temperatures and pressures, and low-product selectivities.

The situation changed in the mid-1960s with Wilkinson and Heck's independent discoveries that organophosphine-substituted rhodium and palladium complexes, respectively, were active catalysts for carbonylation reactions under milder reaction conditions. Since then, significant advances in catalyst design have led to dramatic enhancements in both the rate and regioselectivity of carbonylation catalysts. A number of these improvements have had significant industrial applications, while many more of them have made carbonylation catalysis a very viable laboratory method for organic functionalizations.

Carbonylation catalysis encompasses a large and important area of chemistry. Unlike many other catalytic reactions, most of carbonylation chemistry is homogeneous, principally because homogeneous catalysts generally give higher rates and selectivities than heterogeneous systems (*see* ***Supported Organotransition Metal Compounds***). Numerous reviews and books have appeared on this subject, particularly with respect to the industrially important area of *Hydroformylation* catalysis. Some of the major books and reviews used in preparing this chapter are listed here. Falbe's book on 'New Syntheses with Carbon Monoxide' contains the most extensive compilation of references (almost 2000) on hydroformylation and several other important CO catalysis reactions up through 1978–79.[1] A comprehensive 15-year review of hydroformylation and carbonylation was published by Cornils *et al.* in 1995.[2] The material presented in this excellent review will not be explicitly discussed here. A thorough review of both academic and industrial developments in hydroformylation appears in *Rhodium Catalyzed Hydroformylation*, edited by van Leeuwen and Claver, published in 2000.[3] Asymmetric carbonylation reactions are discussed by Nozaki and Ojima in the second edition of *Catalytic Asymmetric Synthesis*, published in 2000.[4] The second edition of *Applied Homogeneous Catalysis with Organometallic Compounds*, edited by Cornils and Herrmann, was published in 2002.[5] Chapter 2 deals specifically with carbonylation and hydroformylation reactions and the reader is referred to this comprehensive survey for a summary of important advances in these areas. For the past several years, Ungváry has written an annual survey covering advances in the field of hydroformylation. The most recent of these reviews (2004) is cited here.[6]

Most of the palladium chemistry mentioned was found in Heck's[7] classic work 'Palladium Reagents in Organic Synthesis'. Industrial perspectives came from interviews with industrial chemists and the 'Encyclopedia of Chemical Processing and Design', specifically the sections on 'Oxo Process Alcohols' and 'Butyraldehydes and Butyl Alcohols'.[8] If a reaction or result in this review is not referenced it came from one of the books mentioned here.[1,3,7,8]

There was no possibility of even briefly mentioning all the known catalytic-carbonylation reactions in this chapter – it is that huge an area of catalysis. Instead, an industrial orientation has been taken with topics covered more or less in order of their commercial, then academic, significance. About half of this review covers hydroformylation catalysis, which is the largest homogeneous process carried out in industry today. An attempt has been made to present a balanced mixture of the older classic work, new work, and some interpretations based on current knowledge. This review will not cover stoichiometric carbonylation reactions (*see* ***Organic Synthesis using Transition Metal Carbonyl Complexes***).

The most significant advances in carbonylation catalysis in the next several years[9] will undoubtedly occur in the area of novel ligand systems, new solvents, and asymmetric induction, which will be briefly covered here (*see* ***Asymmetric Synthesis by Homogeneous Catalysis***).

2 ALDEHYDES AND ALCOHOLS–HYDROFORMYLATION

Hydroformylation, also known as the oxo reaction, is the largest homogeneous industrial process in the world, with over 8 billion kg of aldehydes and alcohols produced each year. Hydroformylation involves the reaction of alkenes with H_2 and CO to produce aldehyde products (equation 1). Hydroformylation was discovered by Otto Roelen in 1938 during an investigation of the origin of oxygenated products occurring in the cobalt-catalyzed *Fischer–Tropsch Process*. Roelen's observation that ethylene, H_2, and CO were converted into propanal and, at higher pressures, diethyl ketone marked the beginning of hydroformylation catalysis.

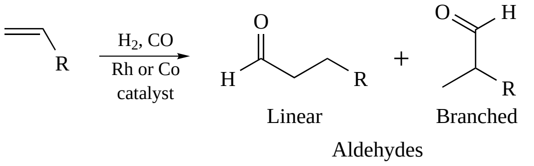

(1)

Cobalt catalysts completely dominated industrial hydroformylation until the early 1970s, when rhodium catalysts were commercialized. Most aldehydes produced are hydrogenated to alcohols or oxidized to carboxylic acids. Esterification of the alcohols with phthalic anhydride produces dialkyl phthalate plasticizers that are primarily used for polyvinyl chloride plastics – the largest single end-use. Detergents and surfactants make up the next largest category, followed by solvents, lubricants, and chemical intermediates.

2.1 $HCo(CO)_4$ Catalyst

Roelen's original research into hydroformylation involved the use of cobalt salts that, under H_2/CO pressure, produced $HCo(CO)_4$ as the active catalytic species (*see* ***Cobalt: Organometallic Chemistry***). In 1960 and 1961, Heck and Breslow[10,11] proposed what is now accepted as the general mechanism for cobalt-catalyzed hydroformylation (Scheme 1). Dissociation of CO from $HCo(CO)_4$ produces the 16e coordinatively unsaturated (*see* ***Coordination & Organometallic Chemistry: Principles*** and ***Electronic Structure of Organometallic Compounds***) complex $HCo(CO)_3$ to which alkene can bind. Alkene *Insertion* into the Co–H bond (*see* ***Mechanisms of Reaction of Organometallic Complexes***) produces either the linear or branched alkyl species (linear alkyl is shown in Scheme 1). Coordination of CO and subsequent alkyl migration produces the acyl intermediate. Loss of CO, followed by oxidative addition of H_2 to the cobalt center produces the dihydride species (*see* ***Hydride Complexes of the Transition Metals***). *Reductive Elimination* of aldehyde and coordination of CO regenerates the starting $HCo(CO)_4$ catalyst. This same general sequence of steps is the foundation for the proposed mechanisms of most other hydroformylation catalysts.

An alternate bimetallic pathway was also suggested, but not favored, by Heck and Breslow (also shown in Scheme 1). The acyl intermediate could react with $HCo(CO)_4$ to undergo intermolecular hydride transfer, followed by reductive elimination of aldehyde to produce the Co–Co bonded dimer $Co_2(CO)_8$. A common starting material for $HCo(CO)_4$-catalyzed hydroformylation, $Co_2(CO)_8$ is well-known to react with H_2 under catalysis reaction conditions to form two equivalents of $HCo(CO)_4$. The bimetallic hydride transfer mechanism is operational for stoichiometric hydroformylation with $HCo(CO)_4$ and has been proposed to be a possibility for slower catalytic hydroformylation reactions with internal alkenes.[12] The monometallic pathway involving reaction of the acyl intermediate with H_2, however, has been

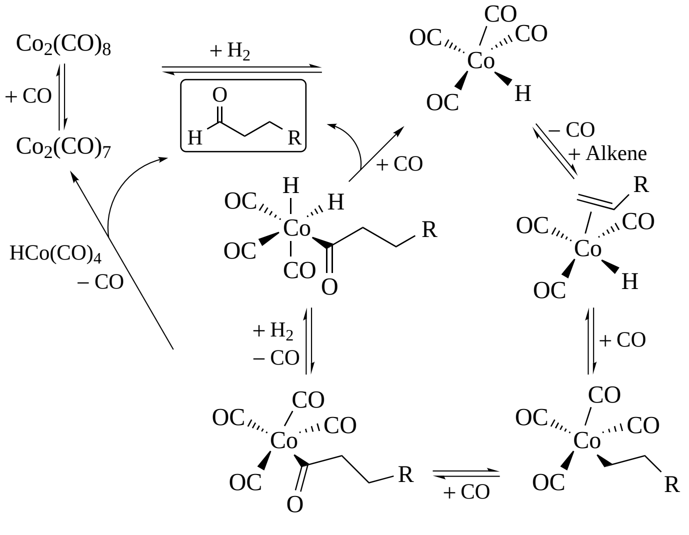

Scheme 1

repeatedly shown to be the dominant mechanism for 1-alkenes and cyclohexene.[13,14]

Kinetic studies (*see Kinetic Methods*) support the mechanism with a general rate expression given in equation (2). The inverse dependence on CO pressure is consistent with the mechanistic requirement for CO dissociation from the various saturated 18e species to open up a coordination site for alkene or H_2 binding. When using a 1:1 ratio of H_2/CO, the reaction rate is essentially independent of pressure owing to the opposing orders of H_2 and CO. Increasing the H_2/CO ratio is of limited use for increasing the overall reaction rate, because $HCo(CO)_4$ is only stable under certain minimum CO partial pressures at a given reaction temperature.

$$\frac{\mathrm{d(aldehyde)}}{\mathrm{d}t} = k[\mathrm{alkene}][\mathrm{Co}][\mathrm{H_2}][\mathrm{CO}]^{-1} \qquad (2)$$

Indeed, the reaction conditions for $HCo(CO)_4$-catalyzed hydroformylation are largely governed by the thermal instability of $HCo(CO)_4$, which produces metallic cobalt if the CO partial pressure is not kept high enough. As the reaction temperature is increased, the CO partial pressure required to maintain stability of $HCo(CO)_4$ increases in a logarithmic fashion (see Figure 1). Thus, the usual reaction temperatures needed to obtain a reasonable reaction rate (110–180 °C) require rather high CO partial, and hence, total H_2/CO pressures (200–300 bar).

Increasing the CO partial pressure decreases the hydroformylation reaction rate and the amount of alkene isomerization side reactions (*see* ***Hydrogenation & Isomerization of Alkenes***), while increasing the aldehyde linear to branched product ratio. Pino proposed that the apparent marked difference between $HCo(CO)_4$-catalyzed hydroformylation at low and high CO partial pressures was due to the existence of two active catalyst species, $HCo(CO)_4$ and $HCo(CO)_3$, formed from the CO association/dissociation equilibrium shown in equation (3).

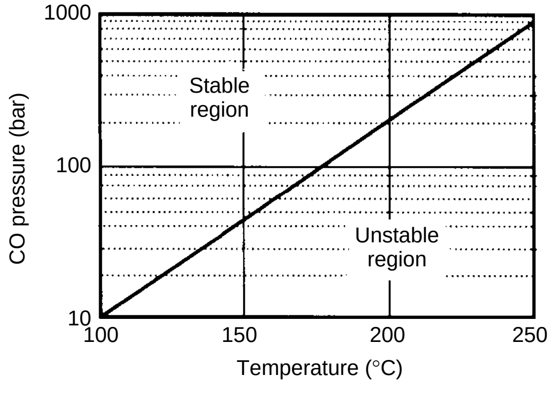

Figure 1 Stability of $HCo(CO)_4/Co_2(CO)_8$ species with respect to precipitation of cobalt metal (cobalt concentration is 0.4 wt%)

$$HCo(CO)_3 + CO \rightleftharpoons HCo(CO)_4 \qquad (3)$$

Pino suggested that $HCo(CO)_4$, favored under high CO partial pressures, could directly react with 1-alkenes to form the cobalt–alkyl species $RCo(CO)_4$.[15] The direct reaction of the 18e saturated $HCo(CO)_4$ with an alkene is somewhat unusual, but not unprecedented. A four-center interaction of the alkene double bond with the Co–H bond leading to direct alkene insertion to the alkyl species was suggested (equation 4).

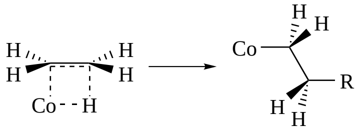

(4)

The extra steric bulk of $HCo(CO)_4$ (compared to $HCo(CO)_3$) should favor addition of the alkene to give linear alkyls. The lower probability of alkene reaction with the saturated $HCo(CO)_4$ catalyst is consistent with the reduced activity at higher CO partial pressures. One can also explain all these features with the 16e $HCo(CO)_3$ catalyst by proposing that alkene isomerization is more facile with the resulting 16e $RCo(CO)_3$ species that results after reaction with alkene (Scheme 2).

Under lower CO partial pressures a 16e $RCo(CO)_3$ species will have a long enough lifetime to allow reverse *β-Hydride Elimination* (*see* ***Mechanisms of Reaction of Organometallic Complexes***) and increase the possibility for alkene reinsertion to the branched alkyl species, which is slightly more favored thermodynamically. At this point, CO addition and insertion will yield a branched aldehyde, or another β-hydride elimination can give alkene isomerization. This second mechanistic explanation is in line with more recent results from Rh/PPh_3-catalyzed hydroformylation studies (see Section 2.4).

The regioselectivity of $HCo(CO)_4$ (or $HCo(CO)_3$) for producing the more valuable linear aldehydes varies with reaction conditions and alkene substrates used. With 1-alkenes one can typically get linear to branched aldehyde ratios of 3–4 to 1. There is a trade-off between rate and regioselectivity. High CO partial pressure slows the rate of catalysis, but increases the linear to branched aldehyde product ratio. Higher CO partial pressures also lower alkene isomerization side reactions. Higher temperatures increase the reaction rate, but lower the linear aldehyde product regioselectivity and increase various undesirable side reactions. Some aldehyde *Hydrogenation* to alcohols is usually observed (5–12%), although alkene hydrogenation is usually quite low ($\approx$1%), particularly under higher CO partial pressures. Aldehyde hydrogenation is not generally considered to be a negative side reaction, since the aldehyde products are usually hydrogenated to alcohols in a subsequent reaction step.

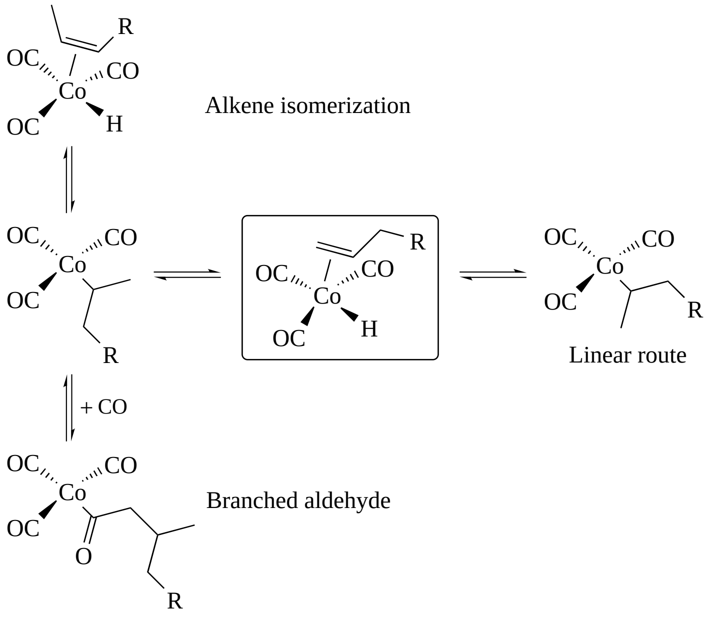

Scheme 2

The aldehyde hydrogenation, however, consumes additional H_2, so H_2/CO ratios greater than 1:1 are used (1–1.5:1 is common).

Very high product regioselectivity is not, however, the major concern for most $HCo(CO)_4$-catalyzed industrial hydroformylations. Exxon Chemical Co. built the first hydroformylation plant located in the United States in 1948 in Baton Rouge, LA, based on high-pressure $HCo(CO)_4$ technology. Exxon uses propylene dimerization/oligomerization to produce a C_7 to C_{12} mixture of branched internal alkenes. This branched internal alkene mixture is then hydroformylated and hydrogenated to a C_8 to C_{13} alcohol mixture. The alkene isomerization ability of $HCo(CO)_4$ turns out to be quite important in this situation (*see* ***Hydrogenation & Isomerization of Alkenes***). $HCo(CO)_4$ is rather good at isomerizing double bonds to essentially all possible locations. This result can be clearly seen from the data shown in Scheme 3, which shows the percentage of aldehyde formed at each site for the $HCo(CO)_4$-catalyzed hydroformylation of 1-octene and 4-octene (150 °C/200 bar, 1:1 H_2/CO).[16]

Under these conditions, the linear to branched aldehyde ratio for the hydroformylation of 1-octene was 1.9:1. Starting with 4-octene one still gets a 1.2:1 linear to branched ratio. Thus, one can start with a considerably less-expensive mixture of terminal and internal alkenes and get a product distribution favoring the linear aldehyde. The product distribution in Scheme 3 can be nicely explained by invoking facile alkene isomerization, with the fastest hydroformylation occurring for double bonds in the 1-position. Labeling studies have shown that alkene isomerization generally occurs without dissociation of the alkene from the cobalt catalyst.[17]

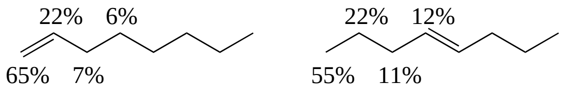

Scheme 3

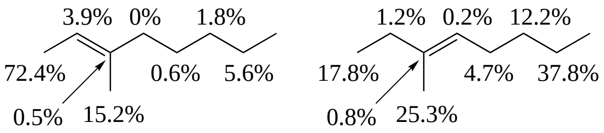

Scheme 4

Alkene branching has a considerable effect on the cobalt-catalyzed alkene isomerization and subsequent hydroformylation. In a study of various methylheptenes, Haymore and coworkers found that there was very little hydroformylation at the carbon center with the branch, even if it was part of the double bond. Scheme 4 shows data for the hydroformylation of two methylheptenes and percentage of aldehyde formed at each site.[18] Note that isomerization past the branching carbon is not a dominant reaction. Once again, terminal aldehydes are the favored products.

Side reactions of the product aldehydes to form heavier products generally occur, particularly at higher-reaction temperatures, and usually account for ≈9% of the product distribution. Aldol condensations, aldols, trimerizations, and Guerbet dimerizations of product alcohols are some of the more common ways to form heavy by-products. These side reactions are common to varying extents for all long-term commercial hydroformylation reactions. Although industrial reactors are usually started with high-boiling solvents, after a while these heavy ends become the main solvent system for the reaction.

One of the major problems in any large-scale industrial homogeneous process, such as hydroformylation, is separation of the product from the catalyst at the end of the reaction. One advantage of $HCo(CO)_4$ technology is that catalyst separation and recycling is well established. The two major methods of separating catalyst from product involve oxidation of $HCo(CO)_4$ to water-soluble Co^{II} salts that are extracted from the product stream, and flash evaporation of volatile $HCo(CO)_4$ from the high-boiling products.

2.2 Cobalt Phosphine-modified Catalysts

The first and only major variation on $HCo(CO)_4$ hydroformylation catalysis involved research at Shell by Slaugh and Mullineaux, in which the addition of trialkylphosphine ligands (*see* ***Cobalt: Organometallic Chemistry*** and ***Phosphorus: Organophosphorus Chemistry***) caused a dramatic change in the rate and regioselectivity.**[19]** The electronic effect of substituting an electron-donating alkylated phosphine for one of the carbonyl ligands, to produce $HCo(CO)_3(PR_3)$, results in stronger Co–CO bonding. This causes a dramatic reduction in the CO partial pressures required to stabilize the catalyst. Instead of 200–300 bar of H_2/CO pressure needed for $HCo(CO)_4$, the monophosphine-substituted catalyst $HCo(CO)_3(PR_3)$ only needed 50–100 bar pressure, and could be run at higher temperatures without any decomposition of catalyst to cobalt metal.

Another electronic effect is that the electron-donating phosphine increases the hydridic nature of the hydride ligand ($HCo(CO)_4$ is quite acidic) and dramatically increases the hydrogenation capabilities of the $HCo(CO)_3(PR_3)$ catalyst. This effect means that aldehydes produced from the initial hydroformylation are subsequently hydrogenated by $HCo(CO)_3(PR_3)$ to produce alcohols as the final product. Less electron-rich phosphines, such as PPh_3, give less hydrogenation to the alcohol product, and lower linear regioselectivities. The increased hydrogenation ability, however, also results in increased alkene hydrogenation that can range from 10–20% of the product distribution, depending on the phosphine ligand used and the exact reaction conditions. Because of the aldehyde hydrogenation step, additional H_2 is needed, so H_2/CO ratios of 2:1 (or slightly higher) are used. The proposed hydroformylation and hydrogenation mechanisms are both shown in Scheme 5.

The final electronic effect of phosphine substitution is that the higher stability of the $HCo(CO)_3(PR_3)$ catalyst, due to

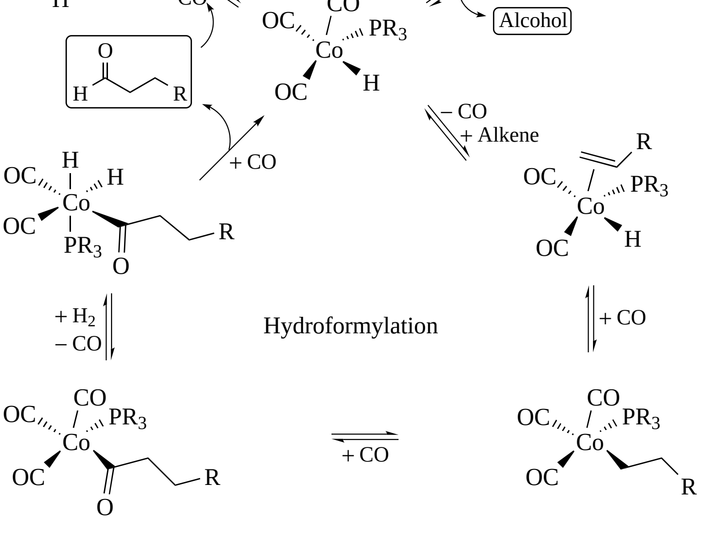

Scheme 5

stronger Co–CO bonding, means that this catalyst is less active than $HCo(CO)_4$ (about 5–10 times slower). Just as with the unmodified cobalt catalyst, CO dissociation from the saturated 18e species is needed to open up an empty coordination site on the cobalt to allow coordination of alkene and H_2. Higher-reaction temperatures, therefore, are used in conjunction with longer-reaction times and larger reactor volumes.

From a steric viewpoint, the considerably bulkier trialkylphosphine ligand should, and does, favor formation of linear products. While linear to branched ratios of only 2–3:1 are typically found for $HCo(CO)_4$, higher regioselectivities of 7–8:1 occur for $HCo(CO)_3(PR_3)$. There is a phosphine *Cone Angle* cutoff at about 132°, after which the steric effects of the phosphine ligand do not increase the product linear regioselectivity any further.

Phosphine-modified cobalt hydroformylation is only used commercially by Shell. It is tightly coupled to Shell's Higher Olefins Process (SHOP, *see* ***Metathesis Polymerization Processes by Homogeneous Catalysis***) that produces a C_4 through C_{20} mixture of linear, internal alkenes for hydroformylation to detergent-grade alcohols.

2.3 $HRh(CO)_4$ Catalyst

In 1952, it was discovered by Schiller that rhodium salts generated highly active hydroformylation catalysts. It was from these early studies that rhodium was estimated to be 1000 to 10 000 times more active than cobalt. Rhodium was also found to be very selective to aldehydes, with little hydrogenation to alcohols observed under normal catalysis conditions. It was suggested early on that $HRh(CO)_4$ was the active catalyst species, analogous to $HCo(CO)_4$, and the same monometallic mechanism was proposed (Scheme 6).

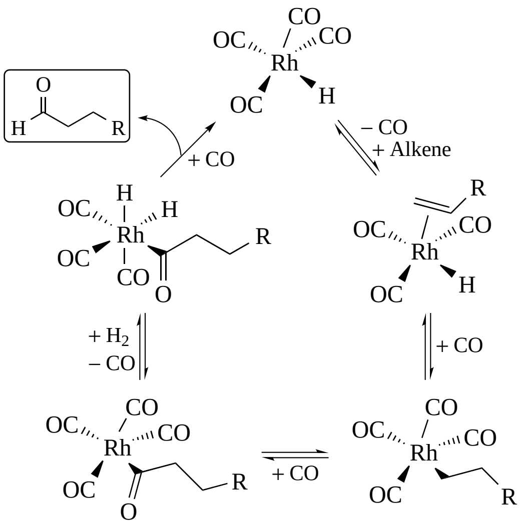

Scheme 6

Table 1 Hydroformylation of 2-pentene as a function of metal and partial CO pressure[a]

P_{CO} (bar)	$Co_2(CO)_8$	$Rh_4(CO)_{12}$
4–5	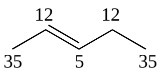	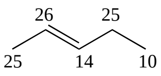
100	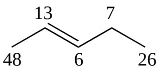	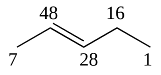

[a] The percentage of aldehyde product formed at each site is indicated.

Perhaps not too unexpectedly, the linear to branched aldehyde regioselectivity of $HRh(CO)_4$ is lower than that found for $HCo(CO)_4$, consistent with the larger size of a rhodium atom relative to cobalt. This results in less steric crowding about the rhodium center, leading to less steric differentiation for the alkene insertion step into the M–H bond to form a linear or branched alkyl group. With 1-pentene, $HCo(CO)_4$ gives a linear to branched aldehyde ratio of 4:1 under optimum conditions, while $HRh(CO)_4$ can only reach a 1.6:1 ratio. As with $HCo(CO)_4$, $HRh(CO)_4$ is an active isomerization catalyst, but its lower regioselectivity leads to more extensive distributions of the aldehyde products. The isomerization ability is related to the partial CO pressure, with considerably more isomerization occurring at lower partial CO pressures. (Table 1 illustrates this for the hydroformylation of 2-pentene from the work of Pino and coworkers.) As with $HCo(CO)_4$, this is explained by the formation of higher amounts of the 16e unsaturated $HRh(CO)_3$ and its longer lifetime under low CO partial pressures.

$HRh(CO)_4$ is used by Ruhrchemie in the hydroformylation of certain branched alkenes that can only give a single product due to the location of the branch that restricts both alkene isomerization and product regioselectivity. In this special case, the high activity of $HRh(CO)_4$ is not off-set by poor aldehyde regioselectivity.

Another similarity between $HCo(CO)_4$ and $HRh(CO)_4$ is that they are only stable under certain reaction conditions. Unlike $HCo(CO)_4$, $HRh(CO)_4$ does not usually precipitate out as metallic rhodium, but rather forms stable rhodium carbonyl clusters such as $Rh_4(CO)_{12}$ and $Rh_6(CO)_{16}$. Indeed, just as $Co_2(CO)_8$ is a common catalyst precursor for cobalt hydroformylation, $Rh_4(CO)_{12}$ is often used as a starting species for rhodium hydroformylation.

Unlike $HCo(CO)_4$ and $(acyl)Co(CO)_4$ species, which are readily observed via FT-IR spectroscopy, the rhodium monometallic analogs are more difficult to observe because of their higher reactivity.**[20]** The ready formation of easily observable and isolable rhodium carbonyl clusters has led to some conflicting reports on whether $HRh(CO)_4$ is the true catalyst.

Garland has reported a detailed kinetic and mechanistic study of the unmodified rhodium catalyst system using in situ FT-IR techniques and has concluded that the active catalyst is indeed $HRh(CO)_4$, or more precisely, $HRh(CO)_3$.[21] The rate-determining step in the catalytic cycle is hydrogenolysis of the $(acyl)Rh(CO)_4$ species, although the concentration of $HRh(CO)_4$ is dependent on cluster fragmentation/reformation equilibrium. In particular, Garland's kinetic data support cluster fragmentation equilibria in the presence of alkenes (equation 5).

$$Rh_4(CO)_{12} + 2CO \rightleftharpoons \{Rh_4(CO)_{14}\} + H_2 \rightleftharpoons 4(acyl)Rh(CO)_4 \qquad (5)$$

2.4 Rhodium Phosphine Catalysts

In 1965, Osborn, Young, and Wilkinson reported that Rh^I–PPh_3 complexes were active and highly regioselective hydroformylation catalysts for 1-alkenes, even at ambient conditions. Although Slaugh and Mullineaux had filed a patent in 1961 that mentioned Rh/phosphine combinations for hydroformylation catalysis, it was Wilkinson's work that really ignited serious interest in rhodium phosphine hydroformylation catalysts. The initial catalyst system was derived from *Wilkinson's Catalyst*, $RhCl(PPh_3)_3$, but it was rapidly discovered that halides were inhibitors for hydroformylation. It is best, therefore, to start with rhodium precursor complexes that do not contain halides. $HRh(CO)(PPh_3)_3$ and $Rh(acac)(CO)_2$ are two commonly used starting materials for hydroformylation. The currently accepted core catalytic mechanism for Rh/PPh_3 hydroformylation is shown in Scheme 7, and is essentially a hybrid of Wilkinson's original associative and dissociative mechanisms. The various steps are directly analogous to Heck's mechanism for $HCo(CO)_4$ (see Scheme 1).

Wilkinson noted that $HRh(CO)(PPh_3)_2$ was very selective for the formation of aldehyde products (no alcohol formation, no alkene hydrogenation or isomerization) and that very high linear to branched aldehyde selectivities of 20:1 for a variety of 1-alkenes could be obtained under ambient conditions (25 °C, 1 bar, 1:1 H_2/CO). At higher temperatures the rate increased, but the regioselectivity dropped (9:1 at 50 °C). Running under 80–100 bar of H_2/CO decreased the linear to branched aldehyde selectivity to only 3:1.

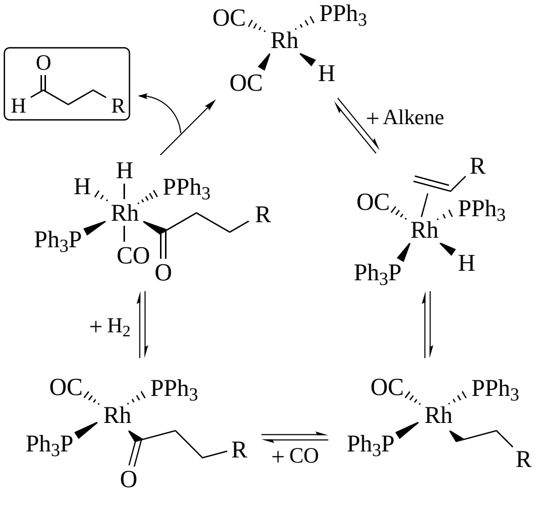

Scheme 7

Table 2 Rate constants and regioselectivities for the hydroformylation of 1-hexene using $Rh(acac)(CO)_2$ with different PPh_3 concentrations[a]

[Rh] (mM)	$[PPh_3]$ (M)	PPh_3/Rh ratio	k_{obs} (min^{-1} mM Rh^{-1})	Linear:branched ratio
0.5	0.41	820	0.032	11
1	0.82	820	0.016	17

[a]Reaction conditions: 90 psig, 1:1 H_2/CO, 90 °C.

Pruett (at Union Carbide) quickly provided the next critical discovery that, along with the work of Booth and coworkers at Union Oil, allowed commercialization of the $HRh(CO)(PPh_3)_2$ technology. They found that the use of rhodium with excess phosphine ligand created an active, selective, and stable catalyst system at 80–100 psig and 90 °C.[22] Union Carbide, in conjunction with Davy Powergas and Johnson Matthey, subsequently developed the first commercial hydroformylation process using rhodium and excess PPh_3. The need for excess phosphine arises from the facile Rh–PPh_3 dissociation equilibrium shown in Scheme 8. Loss of PPh_3 from $HRh(CO)(PPh_3)_2$ generates considerably more active, but less regioselective, hydroformylation catalysts. The addition of excess phosphine ligand shifts the phosphine dissociation equilibrium back towards the more selective $HRh(CO)(PPh_3)_2$ catalyst. This explains why higher CO partial pressures lower the product regioselectivity, in marked contrast to the observation made in the case of $HCo(CO)_4$-catalyzed hydroformylation.

There has been considerable discussion on the exact nature of the rhodium species that yields high product selectivity. Wilkinson originally proposed that high regioselectivities resulted from alkene coordination to the bisphosphine species $HRh(CO)_2(PPh_3)_2$ to generate a 20e six-coordinate complex. Alkene insertion into the Rh–H bond would then produce the 18e $Rh(alkyl)(CO)_2(PPh_3)_2$ complex. This mechanism is commonly referred to as Wilkinson's associative pathway. Since 20e species are generally not favored as intermediates in organometallic mechanisms, the 16e species $HRh(CO)(PPh_3)_2$ has become the generally accepted selective catalyst (see Scheme 7).

The regioselectivity of $HRh(CO)(PPh_3)_2$ is strongly related to the concentration of PPh_3 in solution (up to a certain point) and the H_2/CO ratio used. Commercial hydroformylation reactions are run using solutions that have PPh_3 concentrations of 0.3 M or higher. This corresponds to PPh_3 weight percentages of 8–50% of the total solution in commercial reactors. The effect of PPh_3 concentration on the rate and selectivity for the hydroformylation of 1-hexene can be seen in Table 2.

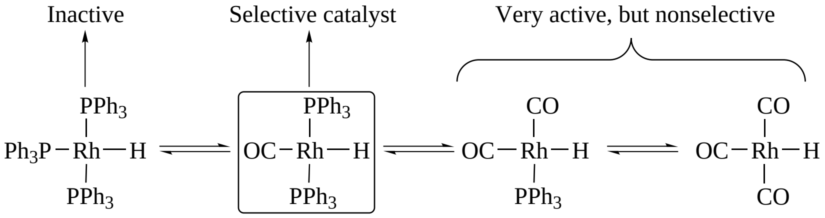

Scheme 8

Note that doubling the PPh_3 concentration cuts the rate constant in half, even though the rhodium concentration was also doubled! The selectivity, on the other hand, increases to 17:1 for the C_7 aldehyde linear to branched ratio. The ‘ultimate’ experiment of running $HRh(CO)(PPh_3)_2$ in molten PPh_3 has been done with propylene, giving a 16:1 linear to branched aldehyde ratio. Commercially, propylene is run with PPh_3 concentrations around 0.4 M, which gives a linear to branched selectivity of $\approx 8-9:1$. Lower CO partial pressures also would be expected to favor higher regioselectivities, and this is indeed the case. Rh/PPh_3 reactions are often run with an excess of hydrogen (2:1 H_2/CO ratios are common). Too high a hydrogen partial pressure, or too low a CO partial pressure, however, will increase the alkene hydrogenation and isomerization side reactions to an unacceptable level.

It was assumed early on, in analogy to the $HCo(CO)_4$ catalyst system, that the rate-determining step was H_2 addition to the Rh^I–acyl species. This assumption has been disputed by several authors. Kastrup and coworkers concluded from ^{31}P NMR studies that the rate-determining step could be the initial coordination of alkene to the $HRh(CO)(PPh_3)_2$ catalyst species.**[23]** Moser and coworkers, in a similar vein, proposed that the rate-determining step is CO dissociation from $HRh(CO)_2(PPh_3)_2$ to once again generate the 16e species $HRh(CO)(PPh_3)_2$.**[24]** Combining both of these proposals, Unruh concluded that several of the fundamental steps in Rh/PPh_3 hydroformylation appear to have similar rate constants, making it difficult to specify one overall rate-determining step, as they may probably vary with the exact reaction conditions. The complexity of the phosphine/CO ligand dissociation/association processes and the many catalytically active rhodium complexes present was most clearly pointed out by Tolman and Faller, who presented a three-dimensional mechanistic scheme for the hydroformylation of alkenes by Rh/PPh_3 complexes.**[25]** Scheme 7, in contrast, only indicates the core catalytic cycle that is believed to give the highest product aldehyde regioselectivity.

The other important reason for adding excess phosphine ligand is to minimize ligand fragmentation reactions that lead to catalyst deactivation. If a 14e highly unsaturated species such as $HRh(CO)(PPh_3)$ is formed, the very electrophilic metal center can attack the PPh_3 ligand (either intra- or intermolecularly) (*see Electrophilic Reaction*). This leads to cleavage of the P–Ph bond and formation of either alkyldiphenylphosphines or, in the worst case, phosphide-bridged dimers which are inactive for hydroformylation (Scheme 9).

This fragmentation process has been studied and proceeds by oxidative addition of the P–Ph bond to an unsaturated Rh center.**[26,27]** A separate PPh_3-activation process involving *Orthometalation* of the phenyl group can also occur. Triarylphosphine ligands and phosphite ligands are particularly susceptible to this fragmentation because of the availability of π- or lone-pair electron density on the ligands that can interact with an empty Rh orbital. The fact that they are moderate to poor electron-donating ligands also enhances the electrophilicity of the rhodium center.**[28]** Trialkylphosphine ligands should be relatively inert to these types of Rh-induced fragmentations due to the lack of any π-electron density on the ligand. The considerably stronger σ-donation ability of alkylated phosphines also works to decrease the electrophilicity of the rhodium center. Unfortunately, trialkylphosphine ligands generally lower both the rate and selectivity of rhodium hydroformylation catalysts.

The electronic and steric properties of the phosphine ligand(s) can have dramatic effects on the rate and selectivity of the rhodium catalysts. As mentioned above, electron-rich alkylated phosphines generally have a negative effect on the rate and regioselectivity, while more electron deficient phosphines such as PPh_3 and phosphites (*see Electron Deficient Compound*) generate more active and regioselective catalysts (Table 3).

Some of the values in Table 3 are deceptive. The very low activity of $P(O\text{-}p\text{-}MeOC_6H_4)_3$ may well be caused by ligand

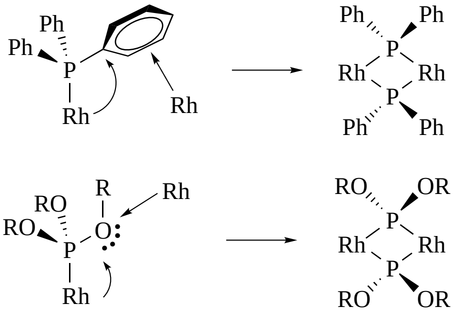

Scheme 9

Table 3 Relative rates and regioselectivities for the hydroformylation of 1-octene using $HRh(CO)(PR_3)_2$ catalysts with different phosphine ligands[a]

Phosphine	Cone angle (°)	Rel. rate	Linear:branched ratio
PPh_3	145	7.7	4.6
$P(OPh)_3$	128	5.4	6.1
$P(O\text{-}o\text{-}MeC_6H_4)_3$	141	5.2	3.6
$P(O\text{-}p\text{-}ClC_6H_4)_3$	128	4.9	13.3
$P(O\text{-}n\text{-}Bu)_3$	112	4.5	4.3
$P(O\text{-}p\text{-}PhC_6H_4)_3$	128	3.9	5.7
$P(O\text{-}o,o\text{-}Me_2C_6H_3)_3$	190	3.4	0.9
$P(O\text{-}o\text{-}PhC_6H_4)_3$	152	2.8	1.1
$P(n\text{-}Bu)_3$	132	1.2	2.4
$P(O\text{-}p\text{-}MeOC_6H_4)_3$	128	1	4.9

[a] Reaction conditions: 10:1 PR_3 to Rh ratio, 80–100 psig, 90 °C.

fragmentation and catalyst deactivation. The low linear to branched selectivity for the very bulky $P(O\text{-}o,o\text{-}Me_2C_6H_3)_3$ ligand probably results from phosphite dissociation to form small amounts of very active $HRh(CO)_4$ that hydroformylates with low regioselectivity. Under the proper conditions, phosphite ligands produce extremely active rhodium catalysts (see Section 2.7). Unfortunately, phosphite ligands are also the most susceptible to rhodium-induced fragmentations. New developments in the exploration of catalytic intermediates by in situ high pressure IR (HP-IR) techniques have been reported by Kamer and coworkers.[29] The hydroformylation of 1-alkenes with phosphite-supported rhodium complexes was studied in situ with a rapid-scan IR technique. The predominant species in this reaction was identified as $RhC(O)R(CO)_3L$(L = 2-*tert*-butyl-4-methylphenylphosphite). Labeling experiments were carried out where it was possible to study the individual elementary steps in the catalytic cycle.

Chelating phosphines (*see* ***Coordination & Organometallic Chemistry: Principles***) have interesting effects on hydroformylation. $R_2P(CH_2)_xPR_2$ (x = 2–4) ligands with alkyl or aryl substituents generally form very poor hydroformylation catalysts that give low rates and selectivities, as well as extensive alkene isomerization and hydrogenation side reactions. However, several investigations have shown that chelating phosphines with large bite angles ($\beta_n \sim 100–130°$) (*see Bite Angle*) can influence the activity and selectivity in rhodium-catalyzed hydroformylation reactions. van Leeuwen and coworkers have discovered that by increasing the bite angle of the bisphosphine ligand in complexes of the general formula $[RhL_2(CO)_2]$ (L_2 = bisphosphine), the steric bulk at the metal increases and this ultimately leads to the preferential formation of the linear aldehyde.[30] Xantphos-type ligands ((**1**), natural $\beta_n \sim 102–123°$) have been crucial in the study of bite angle effects on the activity and selectivity of hydroformylation reactions. Ligands such as DPB-xantphos (**2**) and POP-xantphos (**3**) have shown good activity for the selective rhodium-catalyzed hydroformylation of internal alkenes to linear aldehydes.

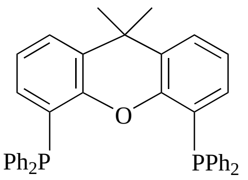

(**1**)

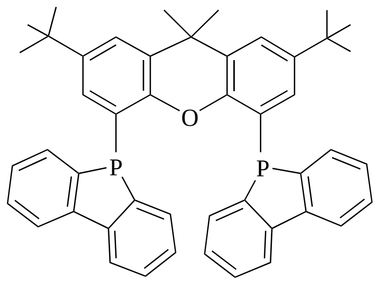

(**2**)

Stereoselectivity in hydroformylation reactions, as a result of the supporting ligand set (e.g. large bite angle diphosphines or chiral diphosphines) or by stereocontrol of the substrate has also been discussed by Breit.[31] Rhodium complexes supported by large bite angle diphosphines such as bisbi, biphephos and xantphos, shown in Scheme 10, are now well-established

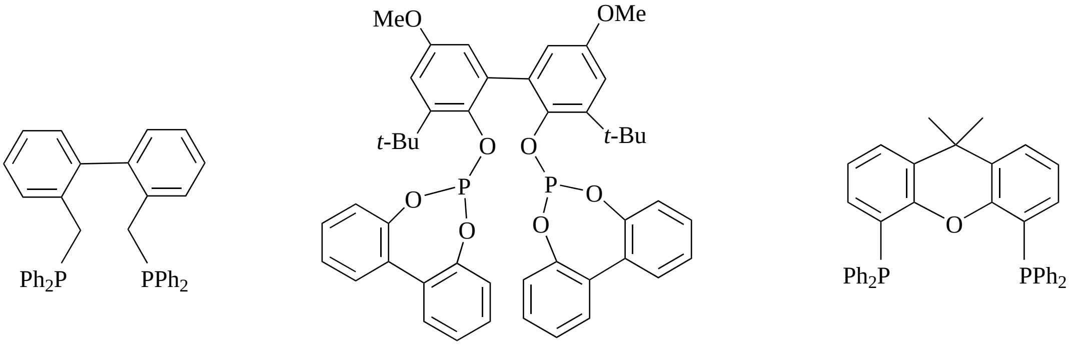

Bisbi
linear:branched
66:1 (1-hexene)

Biphephos
linear:branched
>40:1 (various substrates)

Xantphos
linear:branched
53:1 (1-octene)

Scheme 10

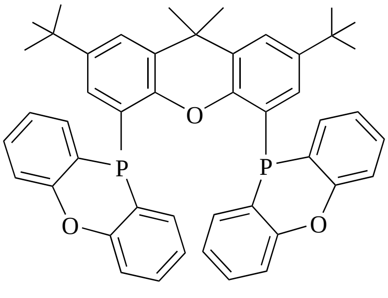

(**3**)

systems for the hydroformylation of olefins yielding high regioselectivity for the formation of the linear isomer. In order to prepare chiral products via hydroformylation reactions, branched products are essential, so a successful catalyst for asymmetric hydroformylation must therefore show simultaneously excellent regiocontrol as well as stereocontrol. Although systems involving substrate-based stereocontrol or catalyst-directing groups have been successful, additional research will be necessary for the development of target-oriented synthetic systems.

An integrated molecular orbital/molecular mechanics method (IMOMM) was utilized to explore trends in regioselectivity for rhodium-catalyzed hydroformylation supported by xantphos-type ligands.**[32]** A key intermediate in the reaction, [RhH(CO)(alkene)(diphosphine)], was studied through eight possible reaction pathways and corresponding transition states for alkene insertion. By canceling the effects of the phenyl substituents on the ligand, it was discovered that the nonbonding interactions between the diphenylphosphino substituents and the substrate affect the regioselectivity of the reaction. Orbital effects, or the bite angle, have an overall smaller direct influence in this area.

Unruh and Christenson studied the unusual chelating phosphine ligand 1,1′-bis(diphenylphosphino)ferrocene and found several interesting effects on Rh-catalyzed hydroformylation.**[33]** The effect of excess ligand on rate and selectivity is shown in Table 4.

Table 4 Rates and regioselectivities for the hydroformylation of 1-hexene using Rh(acac)$(CO)_2$ with 1,1′-(Ph_2P)ferrocene[a]

P_2:Rh ratio	1.0	1.25	1.5	2.0	3.0
Linear: branched ratio	2.2	2.8	5.2	5.2	5.2
k_{obs} (h^{-1} mM Rh^{-1})	5.8	3.1	1.4	1.5	1.5

[a]Reaction conditions: 165 psig, 110 °C, 1:1 H_2/CO.

This effect was interpreted as implying that three phosphine ligands needed to be coordinated to the rhodium center during the coordination of the alkene and insertion into the Rh–H bond to form the linear alkyl. Species (**4**) was proposed to explain the optimum 1.5:1 ligand to rhodium ratio for the higher selectivity. The rate and selectivity was also found to increase as electron-withdrawing substituents were added to the *para* positions on the phenyl rings of the 1,1′-bis(diphenylphosphino)ferrocene ligands. Going from H to CF_3 groups caused the rate to almost double and increased the selectivity from 5.4:1 to 11.4:1.

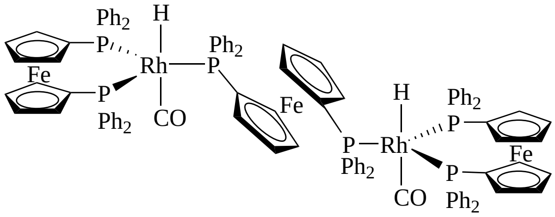

(**4**)

Matsumoto and Tamura (at Kuraray Co.) have demonstrated that the combination of simple bis(diphenylphosphino)alkane ligands and PPh_3 has a very positive effect on catalyst stability and the reduction of unwanted side reactions.**[34]** This is most evident in the hydroformylation of a reactive alkene substrate such as allyl alcohol. The use of $HRh(CO)(PPh_3)_2$ in the presence of excess PPh_3 leads to relatively rapid catalyst deactivation to unidentified species. The addition of just over 1 equivalent of dppb, for example, leads to a stable, active hydroformylation catalyst.**[35]** Use of dppb either by itself, or in quantities higher than 2 equivalents, leads to catalyst deactivation and/or poor activities and selectivities. ARCO Chemical Co. licensed the Kuraray technology to build the first commercial plant (1990) for the hydroformylation of allyl alcohol to produce 1,4-butanediol (Scheme 11).

It is not exactly understood how the mixed ligand Rh/dppb/PPh_3 catalyst system functions. Matsumoto proposed that the arm-on, arm-off equilibrium shown in Scheme 12 is operational. A species such as (**5**) would function much like a normal $HRh(CO)(PPh_3)_2$ catalyst, but the ability to reform the chelate to form a slightly more electron-rich complex (**6**) would tend to inhibit alkene isomerization and/or degradation reactions which require 16e unsaturated species. ^{31}P NMR studies of Rh/chelating phosphine complexes indicate that a variety of species can form, the most dominant of which are

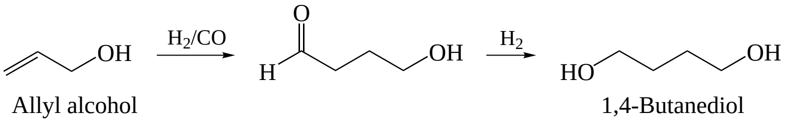

Scheme 11

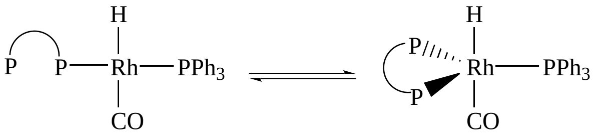

(**5**) (**6**)

Scheme 12

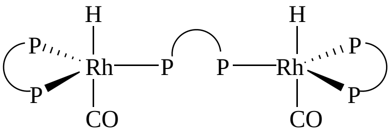

(**7**)

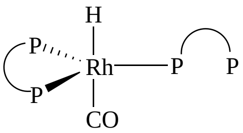

(**8**)

$HRh(CO)(\eta^2\text{-}P_2)(PPh_3)$ (**6**), $HRh(CO)(\eta^2\text{-}P_2)(\mu\text{-}P_2)RhH(\eta^2\text{-}P_2)(CO)$ (**7**), and $HRh(CO)(\eta^2\text{-}P_2)(\eta^1\text{-}P_2)$ (**8**).[36]

One important variant of Rh/PPh_3 catalysis is the water-soluble catalyst system developed by Kuntz at Rhone-Poulenc. By using a sulfonated PPh_3 ligand, $P(C_6H_4\text{-}m\text{-}SO_3^-Na^+)_3$ (tppts), a highly water-soluble rhodium catalyst is generated, $HRh(CO)(tppts)_3$. In aqueous solution, the catalyst essentially has a −9 charge, making it totally insoluble in all but the most polar organic solvents. Excess phosphine ligand is required for good regioselectivities, as with conventional Rh/PPh_3 catalysts, but somewhat lower concentrations are generally required. Shorter chain alkenes (C_2–C_6) are water soluble enough that migration into the aqueous catalyst phase occurs to give hydroformylation. Remigration of the aldehyde product back into the more soluble organic phase allows easy separation of product from catalyst. Rather high linear to branched regioselectivities of 16–18:1 for propylene can be obtained via this water-soluble catalyst. Rates are somewhat slower than with conventional Rh/PPh_3 catalysts owing to lower alkene concentrations in the water phase. The process is limited, of course, to the shorter chain alkenes that have some appreciable water solubility. Alkenes higher than 1-heptane are not soluble enough in water to use this catalyst system. Ruhrchemie–Hoechst currently operates several hydroformylation plants based on this water-soluble rhodium-catalyst technology. The large natural bite angle diphosphine ligand, xantphos, has been modified to yield a water-soluble version, $2,7\text{-bis}(SO_3Na)$-xantphos.[37] The rhodium-catalyzed hydroformylation of propene, 1-hexene, and 4-styrene supported by this ligand has been reported by van Leeuwen and coworkers. This system was found to be active and highly regioselective for the formation of linear products.

Rh/PPh_3-catalyzed hydroformylation is responsible for just over 50% of all oxo alcohols produced. Propylene is the largest single alkene hydroformylated to produce butylaldehyde, which can be hydrogenated to produce butanol, or dimerized by an aldol condensation and then hydrogenated to form 2-ethyl-1-hexanol (Scheme 13), the largest single product produced by hydroformylation (over 2.3 billion kg a year). 2-Ethyl-1-hexanol is usually reacted with phthalic anhydride to produce dialkyl phthalic esters that are used as plasticizers to keep poly(vinyl chloride) plastics soft and flexible.

2.5 Platinum–Tin Phosphine Catalysts

Although rhodium and cobalt complexes are the only ones used in industrial hydroformylation, the next most studied transition metal catalyst involves the use of mixed platinum/phosphine/$SnCl_2$ complexes (*see* ***Platinum: Organometallic Chemistry***). In 1975, Hsu and Orchin[38] reported that $HPt(SnCl_3)(CO)(PPh_3)_2$ gave high selectivity to linear alkenes. The hydroformylation of 1-pentene, for example, gave a 19:1 linear to branched aldehyde product ratio at 100 °C and 3000 psi.

Schwager and Knifton patented a $PtCl_2/SnCl_2/PPh_3$ catalyst system in 1973 and published a paper on it in 1976.[39] They reported that the most effective catalyst composition contained $5SnCl_2$, $2PPh_3$, and $1PtCl_2$. Temperatures greater than 100 °C led to excessive alkene isomerization, while partial CO pressures greater than $\approx$750 psig caused a fairly dramatic drop in reaction rate. Partial H_2 pressures greater than $\approx$750 psig increase the amount of aldehyde hydrogenation to alcohol, which leads to deactivation of the catalyst. The very negative effect of alcohol is due to its preferential coordination to $SnCl_2$, removing it from the Pt center and leading to catalyst deactivation. Polar solvents also have a negative effect on the rate of catalysis, presumably for similar reasons. Solvents with intermediate polarity, such as acetophenone, methyl ethyl ketone, or methyl isobutyl ketone, work the best.

The active hydroformylation catalyst is believed to be the square-planar 16e complex $HPt(SnCl_3)(CO)(PPh_3)$ and one proposed mechanism is shown in Scheme 13. Although the general mechanism closely follows the fundamental steps seen for Rh/PPh_3 catalysts (see Scheme 7), the general rate equation (equation 6) indicates that there are certainly some differences. The $SnCl_2$ can react with one of the chlorides to form a

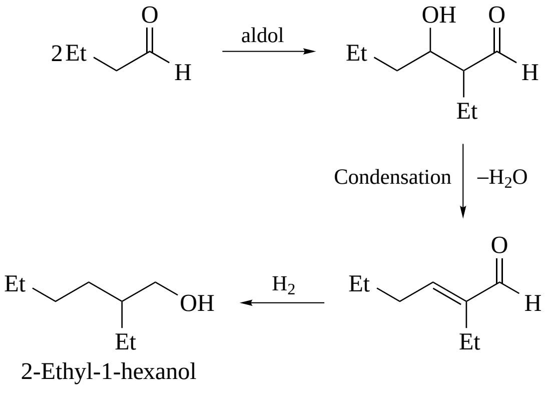

Scheme 13

coordinated $SnCl_3^-$ ligand. The tin is not needed for alkene insertion into the Pt–H bond, nor for CO insertion into the resulting alkyl to generate the acyl species. $SnCl_2$ is needed, however, for H_2 addition to the Pt center and elimination of the product aldehyde. The first few steps in Scheme 13 could, therefore, be written without the $SnCl_3$ ligand. The role of the $SnCl_3$ ligand is believed to be the removal of electron density from the Pt center to help dissociate a CO ligand from an 18e saturated five-coordinate species, such as $Pt(acyl)(Cl)(CO)(PPh_3)_2$. This would open up a coordination site to allow H_2 oxidative addition to the Pt center and subsequent elimination of aldehyde product.

$$\frac{\mathrm{d(aldehyde)}}{\mathrm{d}t} = k[\mathrm{alkene}][\mathrm{Pt}]^{1.5}[\mathrm{H_2}][\mathrm{CO}]^{-0.5} \qquad (6)$$

Although the $Pt/Sn/PPh_3$ catalyst system has been described as ‘highly active’, this activity is relative to that of Pt catalysts without $SnCl_2$, which are extremely slow. Hydroformylation rates for $Pt/Sn/PPh_3$ range from about 25 to 50 turnovers/h for 1-alkenes at 70 °C and 1500 psi. This rate can be compared to Rh/PPh_3, which produces 500 turnovers/h with 1-hexene giving a linear to branched aldehyde product ratio of 17:1 at 90 psig and 90 °C.

Interest in Pt/Sn hydroformylation arose from Stille’s asymmetric hydroformylation with chiral chelating phosphine ligands that gave >96% enantiomeric excess (*ee*) for the branched aldehyde products of substrates such as vinyl arenes and vinyl acetate (*see* ***Asymmetric Synthesis by Homogeneous Catalysis***). Unfortunately, the very low rates, poor branched to linear selectivities, and need for an aldehyde-trapping agent limited the commercial appeal of this catalyst. Note that this platinum catalyst uses an optically active-chelating phosphine, which implies that both phosphines can remain coordinated during the catalytic cycle, unlike that shown in Scheme 14.

More recently, an excellent review of sulfur-containing ligands in a variety of homogeneously catalyzed reactions, including platinum–tin hydroformylation, was published by Claver and coworkers and so this area will not be discussed here.**[40]** The development of amine and arsine analogues of xantphos-type ligands and their application in platinum–tin catalyzed hydroformylation has been reported by van Leeuwen and coworkers.**[41]** The amine-based ligands do not exhibit good activity probably due to the electron-donating capability of the diphenylamine group. The arsine-based systems, however, show comparable activities to xantphos-supported systems due to the formation of $[(ligand)Rh(CO)_2H]$ and $[(ligand)Rh(CO)_2]_2$ complexes. In the case of Pt–Sn catalyzed hydroformylation of 1-octene under mild conditions, xantarsine and the mixed phosphine–arsine xantphosarsine ligands (**9**) exhibit superior activity and selectivity compared to xantphos. A comparison of results for platinum–tin and rhodium-catalyzed reactions with various ligands is shown in Table 5.

Table 5 Hydroformylation of 1-octene with rhodium and platinum–tin complexes supported by amine, arsine and phosphine ligands[a]

Metal/Ligand	Natural bite angle, $\beta_n{}^b$ (°)	TOF	Linear:branched ratio
[Rh]/PP	110.1	240	50
[Rh]/NN		90	3.0
[Rh]/AsAs	112.9	500	2.9
[Rh]/AsP	111.4	84	8.9
[Pt–Sn]/PP		18	230
[Pt–Sn]/NN		<1	1.9
[Pt–Sn]/AsAs		210	>250
[Pt–Sn]/AsP		350	200

[a] Reaction conditions: 5:1 ligand to Rh, 20 bar, 1:1 CO/H_2, 80 °C; 2:2:1 ligand:$SnCl_2$:Pt, 40 bar, 1:1 CO/H_2, 60 °C. [b] Natural bite angle for xantamine, xantarsine and xantphos ligands.

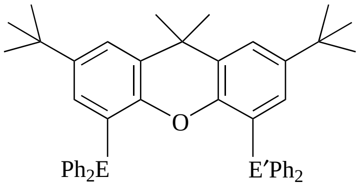

E, E′ = P,P; N,N; As,As; N,P; As,P

(**9**)

Parahydrogen has been utilized as a mechanistic probe in a number of reactions involving hydrogen. The application of parahydrogen-induced polarization (PHIP) in hydroformylation has been reported by Eisenberg and coworkers.**[42]** Hydroformylation of 1-hexene in the presence of *cis*-$[PtCl_2(CO)(PPh_3)]$-$SnCl_2$ using parahydrogen yields the expected aldehyde product in which the aldehydic resonance exhibits net emission in the ^1H NMR spectrum. This is the first observation of a PHIP effect for a single-proton transfer process.

2.6 Polymetallic Catalysts

There have been numerous reports on dimer and cluster catalysis for hydroformylation. Indeed, it was realized early on that cobalt– and rhodium–carbonyl dimers and clusters were viable catalyst precursors for modified or unmodified hydroformylation catalysts. Muetterties proposed the cluster-surface analogy, which stated that molecular metal clusters may be reasonable models of heterogeneous metal surfaces in catalysis (*see* ***Polynuclear Organometallic Cluster Complexes*** and ***Dinuclear Organometallic Cluster Complexes***).**[43]** It was recognized that on metal surfaces, cooperativity between two or more metal centers in activating substrates and in doing catalysis often played an important factor in the catalytic activity of heterogeneous catalysts.

This proposal ignited a worldwide effort by transition metal dimer and cluster chemists to show that polymetallic systems could be effective homogeneous catalysts. Pittman and

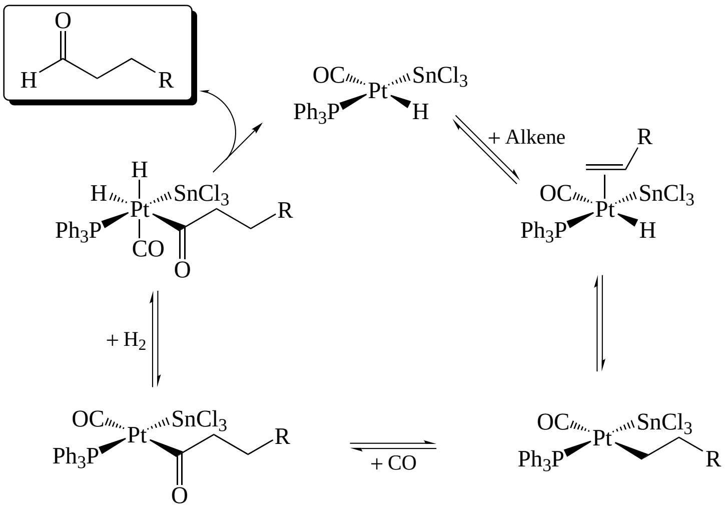

Scheme 14

coworkers reported that 1-pentene could be hydroformylated by the intact cobalt clusters (**10**).[44]

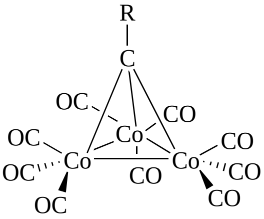

(**10**)

These clusters gave linear to branched aldehyde ratios of between 1 and 5:1 (≈2.5 being typical) at temperatures of 90–150 °C and pressures of 400–1100 psi. The highest linear aldehyde regioselectivities were found, as with monometallic cobalt catalysts, at lower temperatures and higher pressures. The intact clusters could be isolated in near-quantitative yields after the catalysis. One important piece of evidence that fragmentation to $HCo(CO)_4$ was not occurring was obtained from the influence of phosphine ligands on the chemoselectivity of the catalysis. The addition of 2–4 equivalents of PPh_3 improved the stability of the cluster (similar to the monometallic catalysts), but did not increase hydrogenation activity to produce alcohol products, quite unlike monometallic $HCo(CO)_3(PR_3)$ catalysts.[45] Recent high-pressure IR studies of phosphine-substituted analogs of (**7**) show that there is no observable cluster fragmentation under catalytic conditions (150 °C, 600 psi), even over extended periods of time (2 days).[46]

Sanger and coworkers reported an unusual effect of certain bisphosphine ligands, $Ph_2P(CH_2)_nPPh_2$, on the activity of $HRh(CO)(PPh_3)_2$ hydroformylation catalysts.[47] The addition of 0.25 equivalents of $Ph_2P(CH_2)_nPPh_2$ ($n = 2–4$) per equivalent of $HRh(CO)(PPh_3)_2$ caused an increase in the catalytic activity of 90–150%. Addition of more than 0.3 equivalents, however, caused a decrease in the activity relative to the starting $HRh(CO)(PPh_3)_2$ catalyst. Di- and polyphosphine-bridged rhodium species, such as (**11**) and (**12**), were spectroscopically identified at about the same time.

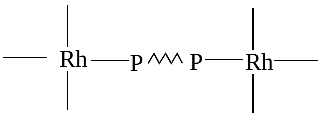

(**11**)

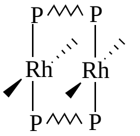

(**12**)

This observation led to the proposal that tethering two rhodium centers together via the bisphosphine ligands was producing some sort of bimetallic cooperativity between the two metal centers. An intramolecular hydride transfer, analogous to the intermolecular hydride transfer proposed by Heck (Scheme 1), enhanced by the proximity of the two metal centers, seemed a very likely possibility.

Fragmentation has been a major and continuing problem in polymetallic catalyst systems. Longoni and coworkers reported in 1984 that the $Co_2Rh_2(CO)_{12}$ mixed-metal cluster was more active than either the parent $Co_4(CO)_{12}$ or $Rh_4(CO)_{12}$ cluster species.[48] This higher activity was proposed to be caused by heterobimetallic cooperativity between the Co and Rh centers in the cluster. Garland, however, showed that the higher activity of the $Co_2Rh_2(CO)_{12}$ mixed-metal cluster was simply due to the more facile fragmentation of this cluster into reactive $HRh(CO)_4$ monometallic catalyst species.[49]

Hidai and coworkers in the mid-1980s also observed a ‘cooperative’ mixed-metal effect for $Co_2(CO)_8$ and $Ru_3(CO)_{12}$ cluster mixtures.[50] They observed a rather dramatic 27-fold increase in the rate for the hydroformylation of cyclohexene with a 9.9:1 Ru:Co ratio relative to $Co_2(CO)_8$ alone. More modest rate increases ($\approx$3 times at an optimum Ru:Co ratio of 1:1) were seen for the hydroformylation of 1-hexene. The linear to branched aldehyde product ratio, however, was the same as for $Co_2(CO)_8$. Discrete Co/Ru clusters, however, were not proposed. Hidai suggested instead that the clusters fragmented, and that the Heck bimetallic intermolecular hydride transfer mechanism (see Scheme 1) was responsible for the rate increases. $[HRu(CO)_4]^-$ has been shown to react much more readily with (acyl)$Co(CO)_4$ to eliminate aldehyde than $HCo(CO)_4$, probably because it is more nucleophilic.[51] Ru is also believed to activate H_2 more readily than cobalt. Thus, it was proposed that the Ru/Co cooperativity was in the form of an intermolecular hydride transfer to facilitate the elimination of aldehyde product.

One cluster system that has given very high product regioselectivities is $[HRu_3(CO)_{11}]^-$, reported by Süss–Fink and coworkers.[52] This cluster catalyst has linear to branched aldehyde regioselectivities of up to 70:1 for the hydroformylation of propylene. The very high selectivity, coupled with the fact that monometallic Ru hydroformylation catalysts do not have high product regioselectivities, strongly points to the presence of intact clusters performing the catalysis. One can then ask whether the hydroformylation is occurring only on a single-metal center, or whether one is having bi- or polymetallic cooperativity in the catalysis. Süss–Fink has discussed the possibility of bimetallic cooperativity, but strong evidence either way has not been found. Unfortunately, the activity of this cluster catalyst is extremely low (e.g. only 50 turnovers over the course of 66 h at 10 bar H_2/CO/propylene and 70 °C in diglyme), limiting its practical appeal.

A bimetallic hydroformylation catalyst that has attracted interest is the thiolate-bridged rhodium complex $Rh_2(\mu\text{-}SR)_2(CO)_2(PR_3)_2$ studied by Kalck.[53] This complex is a rather active hydroformylation catalyst for 1-alkenes, giving rates that are faster than $HRh(CO)(PPh_3)_2$. (Kalck has claimed that $Rh_2(\mu\text{-}SR)_2(CO)_2(PR_3)_2$ is four times faster than $HRh(CO)(PPh_3)_2$, but no excess PPh_3 was used for $HRh(CO)(PPh_3)_2$; this probably leads to deactivation of the monometallic catalyst by PPh_3 fragmentation.) Reaction conditions are typically mild for a Rh-based catalyst: 5 bar 1:1 H_2/CO and 80 °C. IR and ^{31}P NMR studies of the catalyst under hydroformylation conditions only show the presence of $Rh_2(\mu\text{-}SR)_2(CO)_2(PR_3)_2$ or $Rh_2(\mu\text{-}SR)_2(CO)_4$. Some excess PPh_3 is needed to keep the bimetallic catalyst in the $Rh_2(\mu\text{-}SR)_2(CO)_2(PR_3)_2$ state, since the tetracarbonyl-substituted bimetallic species $Rh_2(\mu\text{-}SR)_2(CO)_4$ is inactive for hydroformylation under mild conditions. The apparent high activity of this bimetallic catalyst, coupled with the lack of observable fragmentation reactions, led Kalck to propose the bimetallic mechanism shown in Scheme 15. The mechanism relies on several intramolecular hydride transfers, the first which leads to formation of the Rh–alkyl complex, the second transfer assisting in the elimination of aldehyde product. Ab initio molecular orbital studies have been performed on this system, providing some support for the various mechanistic steps.[54]

There are, however, a number of experimental observations on this bimetallic catalyst that could indicate that fragmentation to generate monometallic catalyst species is occurring. Foremost is that the selectivity of $Rh_2(\mu\text{-}SR)_2(CO)_2(PR_3)_2$ is essentially the same as that seen for monometallic Rh/PPh_3 catalysts. Furthermore, the effect on rate and regioselectivity of adding excess PPh_3 to the bimetallic catalyst almost exactly parallels the monometallic rhodium catalyst. There is a catalytic induction period for $Rh_2(\mu\text{-}SR)_2(CO)_2(PR_3)_2$ that would be consistent with the need to wait for fragmentation to generate monometallic complexes. Kalck has observed that when the two dimer complexes $Rh_2(\mu\text{-}pz)_2(CO)_2(PR_3)_2$ (pz = pyrazolate) and $Rh_2(\mu\text{-}SR)_2(CO)_2(PR_3)_2$ are mixed together, the mixed-bridge bimetallic complex *cis*-$Rh_2(\mu\text{-}pz)(\mu\text{-}SR)(CO)_2(PR_3)_2$ is slowly produced. This observation implies that some sort of dissociative/reassociative equilibrium process may be taking place.

Another bimetallic rhodium complex that may provide an indisputable example of bimetallic cooperativity in hydroformylation catalysis has been reported by Stanley and coworkers.[55] They designed a novel binucleating tetraphosphine ligand (et,ph-P4; (**13r**), (**13m**)) that can both bridge and chelate two transition metal centers, producing bimetallic complexes that only have a single, very conformationally flexible bridging group.

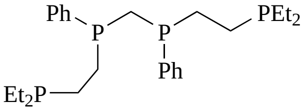

racemic-et,ph-P4
(**13r**)

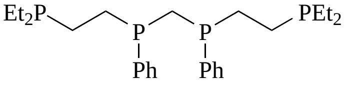

meso-et,ph-P4
(**13m**)

It was found that [*racemic*-$Rh_2(nbd)_2$(et,ph-P4)]$(BF_4)_2$ (nbd = norbornadiene) was a catalyst precursor to a highly active and regioselective hydroformylation catalyst for 1-alkenes under mild conditions. The bimetallic catalyst gave hydroformylation rates for 1-hexene that were $\approx$40% faster than the Rh/PPh_3 monometallic catalyst, and a linear to branched aldehyde regioselectivity of 28:1, relative to 17:1 for $HRh(CO)(PPh_3)_2$ with 0.82 M PPh_3 (conditions: 90 °C, 90 psig 1:1 H_2/CO). Since neither the *rac*-$Rh_2(nbd)_2$(et,ph-P4)$^{2+}$ precursor complex, nor the proposed active catalyst species *rac*-$Rh_2H_2(CO)_2$(et,ph-P4), have a Rh–Rh bond it was fairly straightforward to prepare mono- and bimetallic model systems to test whether the two metal centers were working independently or if the complex was fragmenting to generate active monometallic species. The hydroformylation activity of a series of monometallic complexes (**14**) and spaced bimetallic complexes (**15**) and (**16**) were studied. These were

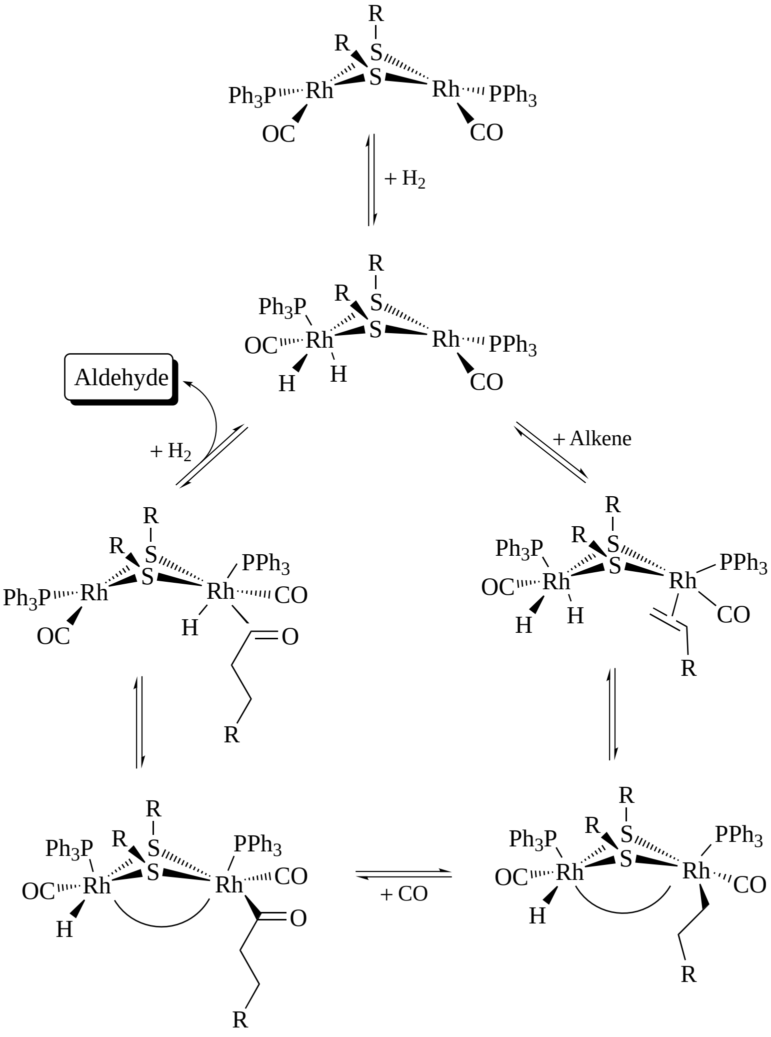
R
R
S
S
Ph3P
Rh
Rh
PPh3
OC
CO
+ H2
Aldehyde
OC
H
H
+ H2
+ Alkene
PPh3
CO
H
O
R
+ CO

Scheme 15

all found to be very poor hydroformylation catalysts, giving extremely low rates and selectivities.

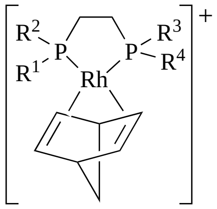
R2
R1
P
Rh
P
R3
R4
+

(14)

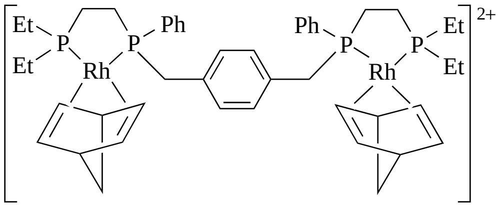
Et
Et
P
Rh
P
Ph
Ph
P
Rh
P
Et
Et
2+

(15)

This led Stanley to propose the bimetallic cooperativity mechanism shown in Scheme 16. The key bimetallic cooperativity step involves rotation about the central bridging methylene group to give a H^-/CO double-bridged intermediate (or transition state) species, which directly leads to an intramolecular hydride transfer to the acyl-coordinated rhodium center. Reductive elimination of the aldehyde product forms the Rh–Rh bonded dimer species shown at the top of the cycle. H_2 addition regenerates the nonmetal-bonded bimetallic catalyst *rac*-$Rh_2H_2(CO)_2$(et,ph-P4). A key kinetic and mechanistic prediction from this bimetallic mechanism is that if alkenes add to both rhodium centers within the same time period, there will be no hydride to transfer from

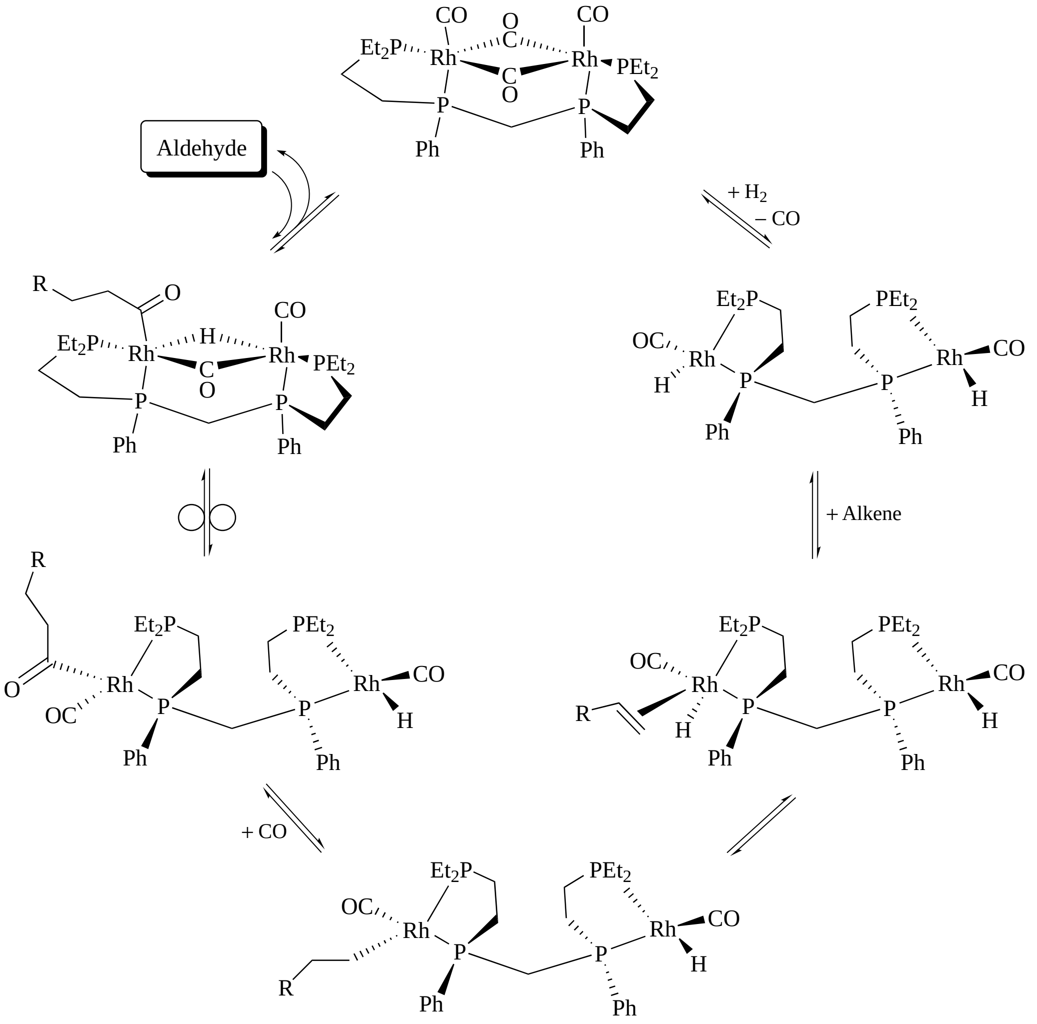

Scheme 16

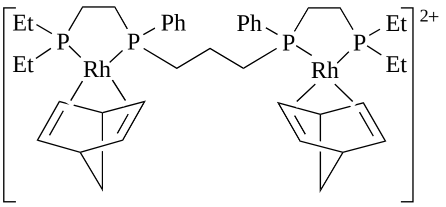

(**16**)

one rhodium center to the other. Thus, the catalyst should be inhibited by high concentrations of alkene. This is indeed the case and represents another relatively dramatic difference between this bimetallic catalyst and monometallic Rh/PPh_3 catalysts.

The rhodium-catalyzed hydroformylation of 1-hexene using a polar-phase solvent system (30% water by volume in acetone) has resulted in improvements in rate and chemoselectivity for catalysts supported by the tetraphosphine ligand et,ph-P4.[56] A cationic rhodium dimer comprising this ligand, $[rac\text{-}Rh_2H_2(\mu\text{-}CO)_2(CO)_4(\text{et,ph-P4})]^{2+}$, is shown to be an active catalyst for this reaction. A turnover frequency (TOF) of $73\,\mathrm{min}^{-1}$ and a chemoselectivity of 33:1 (linear:branched product) were found for this dimer with virtually no side-product formation (*cf.* pure acetone system: TOF $20\,\mathrm{min}^{-1}$, 25:1 l:b; side-product formation: 2.5% isomerization and 3.4% hydrogenation). The water is believed to prevent the dissociation of the phosphine, which would lead to deactivation of the catalyst, but since many higher alkenes and some aldehydes are not water soluble, this efficient reaction seems somewhat limited in scope.

The synergistic effect often observed in bimetallic systems was further explored by Garland and coworkers.[57] The hydroformylation of 3,3-dimethylbut-1-ene to form 4,4-dimethylpentanal in >95% selectivity at room temperature with $[Rh_4(CO)_{12}]$-$[Mn_2(CO)_{10}/HMn(CO)_5]$ as catalyst co-precursors was investigated using in situ FT-IR spectroscopic techniques and kinetic studies revealing evidence of a bimetallic catalytic binuclear elimination reaction (CBER).

Only the monometallic complexes, $RCORh(CO)_4$, $Rh_4(CO)_{12}$, $Rh_6(CO)_{16}$, $HMn(CO)_5$ and $Mn_2(CO)_{10}$, were observed during the reaction. In addition, the kinetic data is consistent with a unicyclic catalytic reaction mechanism (i.e. mononuclear intermediates, equations 7 and 8). Product formation is most probably due to interactions between a rhodium-acyl intermediate, for example, $RCORh(CO)_4$, and a hydrido-manganese species:

$$HMn(CO)_4 + RCORh(CO)_3 \longrightarrow RCHO + RhMn(CO)_7 \qquad (7)$$

$$HMn(CO)_5 + RCORh(CO)_4 \longrightarrow RCHO + RhMn(CO)_8 \qquad (8)$$

The [Rh–Mn] bimetallic system exhibits higher activity for hydroformylation ($\approx$500% higher) compared to the rhodium-only system. The presence of the manganese is responsible for a decrease in the induction period and prevents deactivation via cluster formation.

2.7 Novel Catalyst and Solvent Systems

New monodentate and bidentate phosphorus amidite (**17a, b**) and phosphinite ligands (**18a, b**) have been synthesized and utilized as supporting ligands in the rhodium-catalyzed hydroformylation of 1-octene in order to study electronic influences on the activity and selectivity of the reaction.[58] Monodentate ligands gave rise to systems with a moderate selectivity for linear product while catalysts supported with ligands with high π-acidity resulted in an increase in reaction rate. Reactions supported by the bidentate amidite ligand gave both high activity and regioselectivity for linear aldehyde (l:b $\sim$ 100:1) and modest selectivity for isomerization (7%).

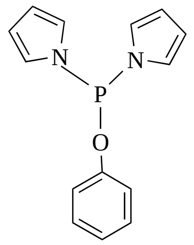
(**17a**)

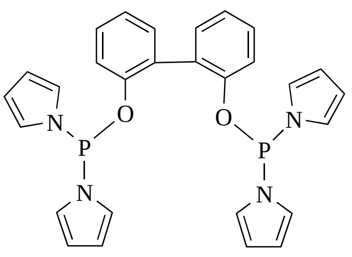
(**17b**)

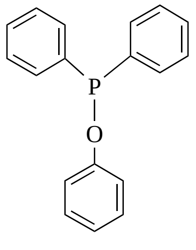
(**18a**)

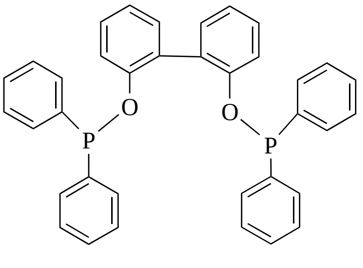
(**18b**)

As a further development in the exploration of the role of solvent in hydroformylation systems, the use of supercritical carbon dioxide ($scCO_2$), ionic liquids and fluorous systems has been reported. A review by Jessop, Ikariya, and Noyori presents information about the utility of $scCO_2$ in a variety of homogeneous reactions.[59]

Both modified and unmodified rhodium catalysts have shown good activity and selectivity for the hydroformylation of 1-octene in $scCO_2$.[60] With respect to the unmodified catalyst, higher reaction rates can be achieved compared to organic solvents or liquid CO_2 under similar conditions. These modified systems exhibit higher regioselectivities compared to conventional solvent systems.

The hydroformylation of 1-hexene by supported ionic liquid catalysis (SILC) was recently reported by researchers at ExxonMobil.[61] In this system, the active catalyst $HRh(CO)(tppti)_3$ (tppti = tri(m-sulfonyl)triphenyl phosphine tris(1-butyl-3-methyl-imidazolium)) is contained within the ionic liquid phase while excess tppti ligand is immobilized in the support material. TOF values of $65\,min^{-1}$ were obtained with silc while an unsupported biphasic ionic liquid medium gave TOF values of $23\,min^{-1}$.

The utility of a biphasic fluorous system with $Rh(acac)(CO)_2/P(C_6H_4\text{-}4\text{-}OCH_2C_7F_{15})_3$ as the catalyst precursor in the hydroformylation of 1-octene has been reported by Bultó and coworkers.[62] In this system, selectivities of 99% and regioselectivities for the linear aldehyde up to linear/branched = 2.8 were achieved with TOF values of $380\,h^{-1}$. Although loss of rhodium was observed after the first run, the system could be recycled twice without diminishing activity or selectivity.

2.8 Silylformylation

In 1989, Matsuda[63] and Ojima[64] independently reported a new hybrid reaction for alkynes that combined *Hydrosilation* (*see* ***Hydrosilation Catalysis***) and hydroformylation catalysis. This reaction produces 3-silyl-2-alkenals and is called silylformylation (see Scheme 17). Matsuda used $Rh_4(CO)_{12}$ as the catalyst, and $HSiPhMe_2$ was used as the hydrogen source instead of H_2. Typical reaction conditions were 100 °C and 150–450 psig CO and rather high catalyst activity was seen. The regioselectivity strongly favored silyl group addition to the carbon of the alkyne that was the least hindered or substituted. Thus, when $R^2 = H$, only one product was formed, usually in high yields. The Z:E *Regioselectivity* was also generally very good. Very bulky substituent groups on the alkyne can block catalysis.

Ojima used $Rh_4(CO)_{12}$ and the heterometallic catalyst $Co_2Rh_2(CO)_{12}$ (which forms $CoRh(CO)_7$ under the catalytic conditions and is believed to be the actual catalyst) for the silylformylation of 1-hexyne with a variety of $HSiR_3$ reagents. Although the reaction could be performed under ambient conditions, higher-product yields were obtained under 150 psig of CO. It was also found that $Co_2Rh_2(CO)_{12}$ gave

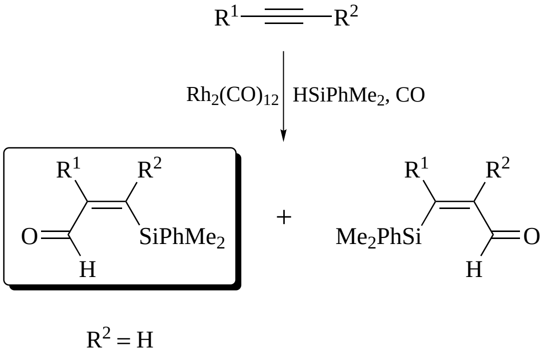
R¹—≡—R²
Rh₂(CO)₁₂
HSiPhMe₂, CO
R¹
R²
O
SiPhMe₂
H
+
R¹
R²
Me₂PhSi
O
H
R² = H

Scheme 17

higher yields (93–100%) of silylformylated products relative to $Rh_4(CO)_{12}$. When $HSi(OMe)_3$ was used as the silane, only hydrosilylation was seen for the $Rh_4(CO)_{12}$, while $Co_2Rh_2(CO)_{12}$ gave some (20–40%) of the silylformylation product. Only (*Z*)-1-silyl-2-formyl structures (**19**) were found.

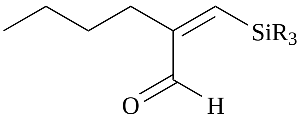

(**19**)

As monometallic Rh complexes also catalyze this reaction (although sometimes much more slowly) under conditions where clusters are unlikely to form, it appears that only a single-metal center is really required for this reaction. Ojima's $CoRh(CO)_7$ catalyst has been studied in considerable detail for the hydroformylation of fluoroalkenes,**[65]** and it has been concluded that although the active catalyst is $CoRh(CO)_7$, only the rhodium center is actively involved in the catalysis. A monometallic mechanism, patterned after hydroformylation, is shown in Scheme 18.

Note that in order to obtain the high regioselectivities observed for this catalytic process, the silyl group must transfer first to the terminal, less-hindered carbon center of the alkyne. If hydride transferred first, one would expect to see considerably poorer regioselectivities (see Section 2.3).

The silylformylation of alkenes to produce enol silyl ethers by $[IrCl(CO)_3]_n$ or $Ir_4(CO)_{12}$ has been reported by Murai and coworkers (equation 9).**[66]**

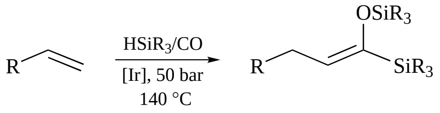
R
HSiR₃/CO
[Ir], 50 bar
140 °C
R
OSiR₃
SiR₃

(9)

In this case, alkene insertion into the Ir–H bond is likely to occur first, producing a linear alkyl species. CO insertion would produce an acyl species, which would then be followed by reductive elimination of the acylsilane product. Enolization, followed by rapid reaction of $HSiR_3$ with the OH group, traps out the enol silyl ether. The H_2 produced from this silylation step is used to hydrogenate some of the starting alkene. Thus, the maximum yield will generally be only 66% of the enol silyl ether product. The enol silyl ethers can be readily converted into silyl ketones (equation 10).

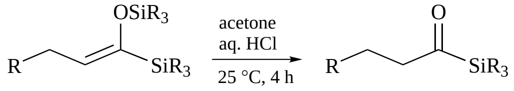
R
OSiR₃
SiR₃
acetone
aq. HCl
25 °C, 4 h
R
O
SiR₃

(10)

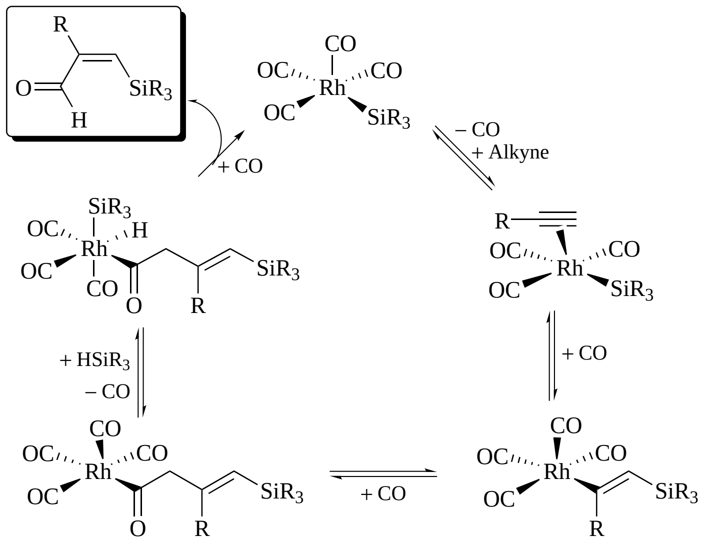
R
O
SiR₃
H
CO
OC
CO
Rh
OC
SiR₃
+ CO
− CO
+ Alkyne
SiR₃
OC
H
Rh
OC
CO
O
R
SiR₃
R
OC
CO
Rh
OC
SiR₃
+ HSiR₃
− CO
+ CO
CO
OC
CO
Rh
OC
O
R
SiR₃
+ CO
CO
OC
CO
Rh
OC
R
SiR₃

Scheme 18

The tandem silylformylation-allylsilylation of a diallylsilyl ether has been reported by Leighton, using [Rh(acac)(CO)$_2$] as the catalyst (equation 11).[67] This method was optimized and extended to propargylic systems where good diastereoselectivity can be achieved using the isopropyl derivative. A mechanism is proposed for the stereoselectivity involving coordination of the silicon by both of the oxygen atoms (equation 12).

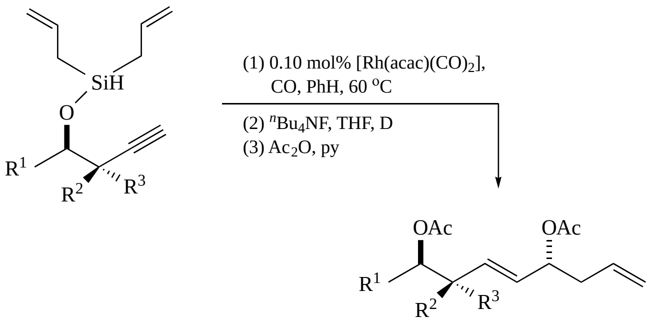

(11)

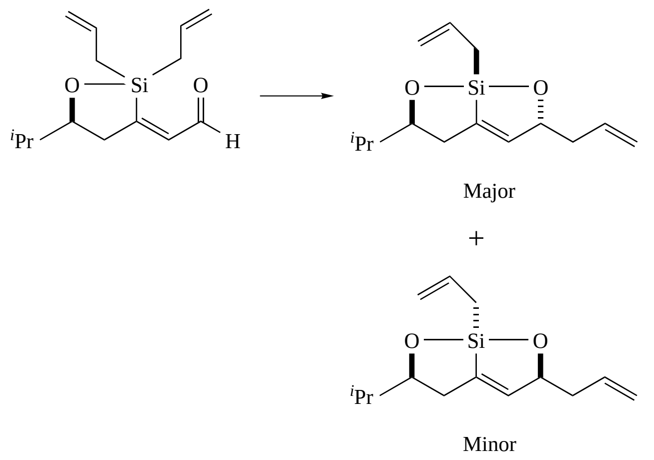

(12)

3 CARBOXYLIC ACIDS, ESTERS, AND ACYL HALIDES

The production of carboxylic acids via carbonylation catalysis is the second most important industrial homogeneous group of processes. Reppe developed most of the basic carbonylation chemistry in the 1930s and 1940s. The first commercial carbonylation process was the stoichiometric Ni(CO)$_4$-based hydroxycarbonylation of acetylene to give acrylic acid (see Section 3.5 for details). This discovery has since evolved into a true Ni-catalyzed process, used mainly by BASF. The introduction of rhodium catalysts in the 1970s revolutionized carboxylic acid production, particularly for acetic acid, much in the same way that Rh/PPh$_3$ catalysts changed the importance of hydroformylation catalysis.

3.1 Monsanto Acetic Acid Process

The second largest homogeneous catalytic industrial process is the carbonylation of methanol to produce acetic acid. Prior to 1970, acetic acid was made using cobalt catalysts (BASF process), requiring rather severe conditions. In 1970, Monsanto commercialized a rhodium–carbonyl iodide catalyst that is commonly called the Monsanto Acetic Acid Process (although in 1986, Monsanto sold the acetic acid plant and technology to British Petroleum). As with hydroformylation catalysis, rhodium is 10^3 to 10^4 times more active than the corresponding cobalt catalyst, which means that much lower CO pressures and moderately lower temperatures are required. Perhaps most importantly, the rhodium catalyst gives extremely high selectivities to acetic acid (see Table 6).[68]

The mechanism has been extensively studied by Forster and coworkers[69] at Monsanto and is shown in Scheme 19. It is actually a double catalytic cycle involving the HI-catalyzed conversion of MeOH to MeI and H_2O at the beginning of the Rh-catalyzed carbonylation reaction, and regeneration of HI at the end of the Rh cycle by hydrolysis of the acyl iodide.

The reaction rate is independent of CO pressure and is first-order in both rhodium and MeI. The rate-determining step is the oxidative addition of MeI to the $[Rh(CO)_2I_2]^-$ catalyst. Thus, the production of MeI from methanol, catalyzed by HI, is critically important. Iodide ligands are considered to be quite important in this reaction due to the HI-catalyzed conversion of MeOH to MeI and their good donor abilities on the Rh center. The negative charge on the $[Rh(CO)_2I_2]^-$ catalyst is believed to be critical in assisting the oxidative addition of MeI to the rhodium center. The resulting alkyl species, $[Rh(CO)_2(Me)I_3]^-$, is extremely reactive towards CO insertion to form the acyl complex.

Efforts to optimize rhodium-based systems for methanol carbonylation led to the development of new supporting ligands containing phosphorus and sulfur donor atoms, both thiolates and thioethers, such as those used in the preparation of complexes (**20**) and (**21**). Ligands such as 2-diphenylphosphinothiolate have been shown to give rise to complexes that exhibit higher activities, up to four times faster, for the carbonylation of methanol compared to $[Rh(CO)_2I_2]^-$.[70,71]

Zoeller and coworkers at Eastman Chemical Company Research Laboratories have reported an efficient system for the carbonylation of ethylene based on a iodide-promoted

Table 6 Comparison of cobalt- and rhodium-catalyzed carbonylation of methanol to acetic acid

Conditions	Cobalt	Rhodium
Concentration	$\approx 10^{-1}$ M	$\approx 10^{-3}$ M
Temperature	≈230 °C	≈180 °C
Pressure	500–700 atm	30–40 atm
Selectivity	90%	>99%
H_2 effect	CH_4, CH_3CHO, EtOH by-products	No effect

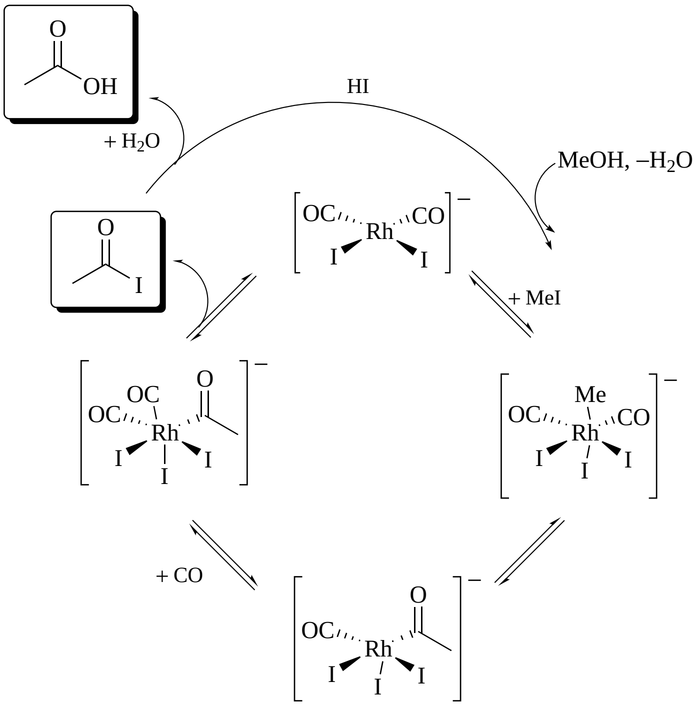
O
OH
HI
+ H₂O
MeOH, –H₂O
O
I
OC
CO
Rh
I
I
–
+ MeI
OC
O
OC
Rh
I
I
I
–
Me
OC
Rh
CO
I
I
I
–
+ CO
O
OC
Rh
I
I
I
–

Scheme 19

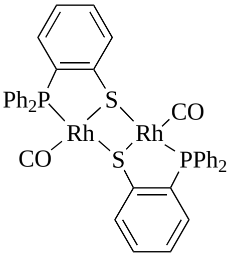
Ph₂P
S
CO
Rh
Rh
CO
S
PPh₂

(**20**)

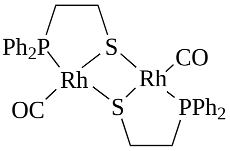
Ph₂P
S
CO
Rh
Rh
OC
S
PPh₂

(**21**)

$[Mo(CO)_6]$ complex.[72] The molybdenum intermediates were studied using in situ IR as part of an extensive mechanistic investigation. The following intermediates were identified in the reaction mixture: $[Mo(CO)_6]$, $[Mo(CO)_5I]^-$ and $[Mo(CO)_4I_3]^-$. Hydrogen, which at low concentrations increases the rate of the reaction, was found to reduce $[Mo(CO)_4I_3]^-$ to the zero-valent complex, thus regenerating the catalyst.[73]

3.2 Tennessee Eastman Acetic Anhydride Process

A very closely related process is the Tennessee Eastman (Kodak) carbonylation of methyl acetate to produce acetic anhydride.[74] The rhodium-catalyzed portion of the mechanism is the same as shown in Scheme 19. Differences occur in the iodide-promoted pre- and post-rhodium reactions shown in Scheme 20.

One pathway involves reaction of methyl acetate with HI to produce MeI and acetic acid. The MeI is carbonylated by $[Rh(CO)_2I_2]^-$ to give acyl iodide, which can then react with acetic acid to produce acetic anhydride and regenerate HI.

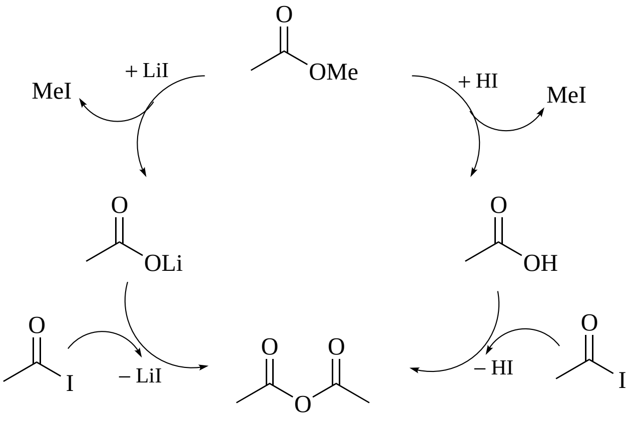
O
OMe
+ LiI
MeI
+ HI
MeI
O
OLi
O
OH
O
I
– LiI
O
O
O
– HI
O
I

Scheme 20

Alternatively, LiI can react with methyl acetate to give MeI and Li acetate. Carbonylation of MeI, again by $[Rh(CO)_2I_2]^-$, produces acyl iodide, which can react with lithium acetate to produce acetic anhydride and LiI. The importance of LiI is seen by the fact that at high lithium concentrations the rate of the catalysis is first-order with respect to MeI and rhodium concentrations. This observation, once again, is consistent with a rate-determining oxidative addition of MeI to the rhodium catalyst. At low lithium concentrations the rate approaches zero order in rhodium and methyl iodide, indicating that formation of methyl iodide from reaction of iodide and methyl acetate is now the rate-limiting step. Thus, the lithium iodide plays a very important role in the catalysis. Lithium is the most effective counter cation, with sodium being approximately 2.5 times slower.

The main difference between the Monsanto acetic acid process and Tennessee Eastman acetic anhydride process is the presence of water in the acetic acid process, which produces HI and acetic acid. In both reactions, a small amount of H_2 is added to the CO stream to act as a reducing agent to keep the catalyst in the more active Rh^I oxidation state. An engineering problem with both processes is the highly corrosive nature of the HI/iodide mixture, requiring the use of special chemically resistant alloys, pumps, and seals.

3.3 The BP Cativa™ Process

For approximately 30 years, the most successful industrial process for the carbonylation of methanol relied on an iodide-promoted rhodium catalyst. This technology, originally developed by Monsanto and acquired by BP Chemicals in 1986, is responsible for the majority of the acetic acid synthesized industrially. Since then, the most important development in industrial carbonylation chemistry is the Cativa™ process, announced by BP Chemicals in 1996.[75]

The Cativa™ process is based on a promoted iridium catalyst, and offers a considerable improvement over the rhodium-based system as a result of increased catalyst stability at lower water concentrations, decreased by-product formation, higher rates of carbonylation, high selectivity ($>99\%$ based upon methanol), and improved yields on carbon monoxide.[76] This is a more cost-effective process for methanol carbonylation owing to lower energy consumption and fewer purification requirements. Implementation of this new process has now been achieved in four plants worldwide.

Although the carbonylation of methanol using an iodide-promoted iridium complex was first reported by Monsanto researchers Roth and Paulik[77] in 1968, and its mechanism studied by Forster[78] and others, it was the rhodium system that was initially developed for commercialization. A more complex mechanism for iridium, involving both anionic and neutral intermediates was discovered, but it would take over twenty years to commercialize an iridium-based system for methanol carbonylation (Scheme 21). In the Cativa™ process, the iridium complex is promoted by two distinct classes of compounds. These comprise iodide complexes of transition and main group metals, such as zinc, cadmium, mercury, indium, and gallium and transition metal carbonyl complexes such as tungsten, rhenium, ruthenium, and osmium. A synergistic effect between the promoters and iodide salts has also been observed at low water concentrations.

Model studies[76] in aprotic solvents have shown that oxidative addition is 120 times faster with iridium complexes than with the corresponding rhodium complexes while the migratory insertion rate is higher for rhodium by a factor of 10^5 at 100 °C than iridium. The migratory insertion step, which is rate-determining in the Cativa™ process, is enhanced by the use of promoters, thus achieving a higher reaction rate. Batch autoclave studies were carried out to explore the effect of pCO, water, methyl iodide, and methyl acetate concentrations on the reaction system. In addition, spectroscopic studies have identified the key intermediate in the catalytic cycle as $[Ir(CO)_2I_3Me]^-$. The Sheffield University research group headed by Maitlis and Haynes, in collaboration with BP Chemicals, has published a comparison of both systems, where differences in the stability of this key intermediate, $[M(CO)_2I_3Me]^-$ ($M = Rh, Ir$), are crucial to the reaction.[79] The increased stability of the iridium complex is related to the stronger metal–carbon bond typically seen for iridium compared to rhodium. Additional corroboration was obtained from a static and dynamic density functional theory study of the migratory insertion step in methanol carbonylation, $[M(CO)_2I_3(CH_3)]^-$ to $[M(CO)I_3(COCH_3)]^-$ ($M = Rh, Ir$), reported by Ziegler and coworkers.[80]

In order to more fully understand the mechanism for the promotion of carbonylation in the Cativa™ process, a recent comprehensive study utilizing spectroscopic methods and ab initio calculations was carried out to explore the role of the promoters.[81] The acceleration of the migratory insertion step is the result of iodide abstraction from the iridium center in *fac,cis*-$[Ir(CO)_2I_3Me]^-$ by the promoters to yield the neutral species $[Ir(CO)_3I_2Me]$ in the presence of CO. It was determined that the migratory insertion of carbon monoxide in $[Ir(CO)_3I_2Me]$ is ≈ 700 times faster than for the anionic species $[Ir(CO)_2I_3Me]^-$.

3.4 Homologation of Carboxylic Acids

In 1981, Texaco announced the ruthenium/H_2/CO-catalyzed homologation of carboxylic acids. Homologation refers to a chain-extension reaction that increases the carbon number of the carboxylic acid (*see Homologation Reactions*). The particular reaction that was initially studied was the conversion of acetic acid to propionic acid. The proposed mechanism shown in Scheme 22 is based on a Ru^{II}/Ru^{IV} cycle, similar to that suggested by Knifton and coworkers at Texaco.

The reaction conditions are somewhat more severe relative to the rhodium-catalyzed acetic acid process: >200 °C and 100–250 bar 1:1 H_2/CO. The mechanism is not fully

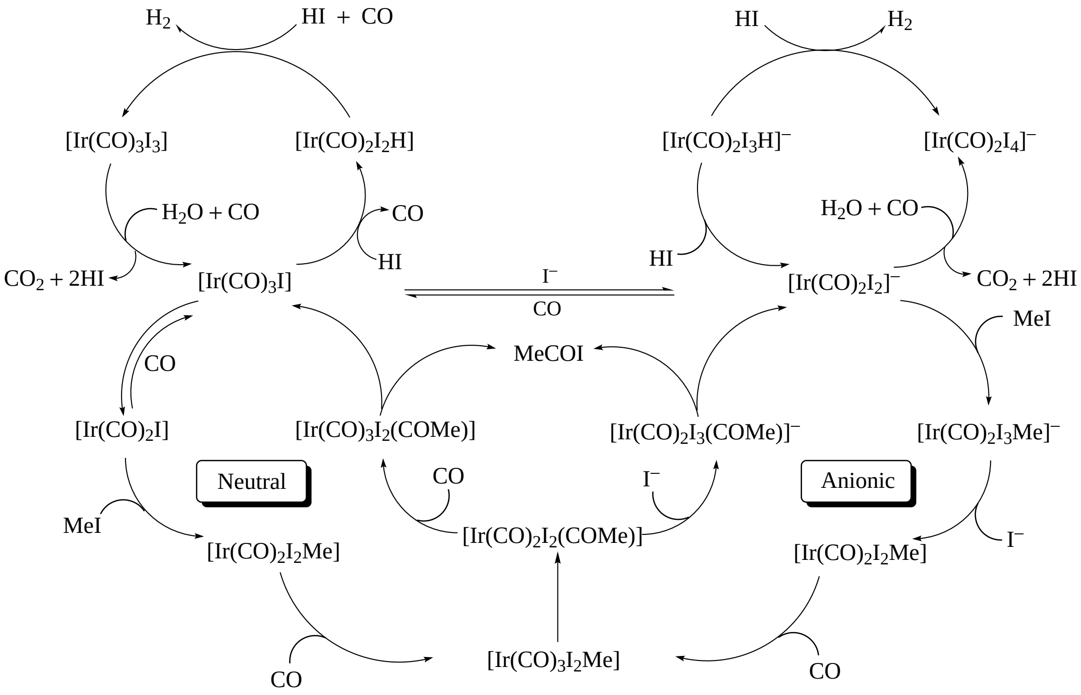
H2
HI + CO
HI
H2
[Ir(CO)3I3]
[Ir(CO)2I2H]
[Ir(CO)2I3H]⁻
[Ir(CO)2I4]⁻
H2O + CO
CO
HI
H2O + CO
CO2 + 2HI
[Ir(CO)3I]
HI
I⁻
CO
[Ir(CO)2I2]⁻
CO2 + 2HI
MeI
CO
MeCOI
[Ir(CO)2I]
[Ir(CO)3I2(COMe)]
[Ir(CO)2I3(COMe)]⁻
[Ir(CO)2I3Me]⁻
Neutral
CO
I⁻
Anionic
MeI
[Ir(CO)2I2(COMe)]
I⁻
[Ir(CO)2I2Me]
[Ir(CO)2I2Me]
CO
[Ir(CO)3I2Me]
CO

Organic reactions

$$MeOH + HI \longrightarrow MeI + H_2O$$

$$MeCOI + H_2O \longrightarrow MeCOOH + HI$$

Scheme 21

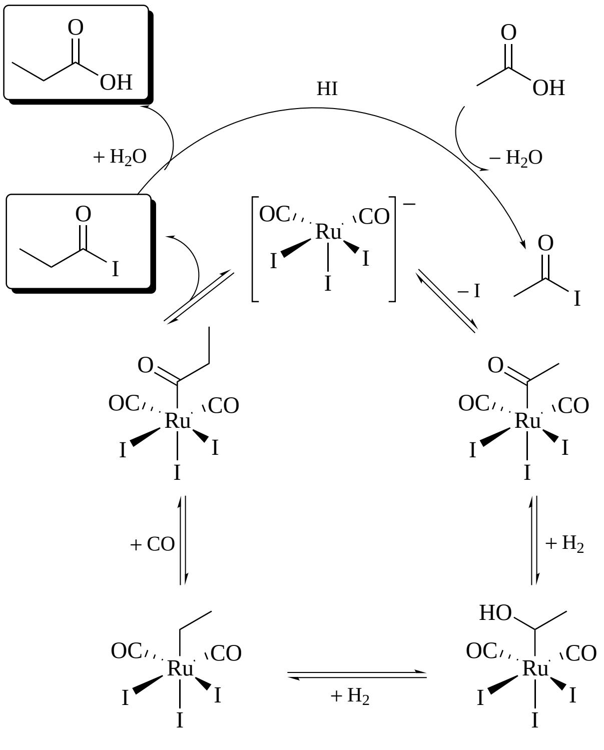
O
OH
HI
O
OH
+ H2O
− H2O
O
I
OC
CO
Ru
I
I
I
−
O
I
− I
O
OC
CO
Ru
I
I
I
O
OC
CO
Ru
I
I
I
+ CO
+ H2
OC
CO
Ru
I
I
I
+ H2
HO
OC
CO
Ru
I
I
I

Scheme 22

understood, because of the many-sided equilibria present and the difficulty of mechanistic studies under the higher pressures required. Labeling studies have confirmed that the carbonyl group in the carboxylic acid product does indeed come from CO insertion into an alkyl species. Ruthenium is well-known to heterolytically activate H_2 (to give H^- on the metal and free H^+), and this cleavage may well be the route taken here. Protonation of the oxygen atom of the carbonyl group in conjunction with a hydride transfer to the α-carbon would lead one nicely to the proposed Ru–CH(OH)CH_3 intermediate. Repeating this same process would then give the Ru–CH_2CH_3 alkyl species.

Interestingly, in spite of the fact that two equivalents of H_2 are formally required for a one-carbon atom homologation, the optimum yield of propionic acid occurs for a 1:1 H_2/CO ratio. The additional hydrogen needed undoubtedly comes from a Ru-catalyzed *Water Gas Reaction* that converts some CO and H_2O into CO_2 and H_2. CO_2 is one of the side products observed in this reaction. Additional homologation steps occur at higher temperatures and pressures. This homologation reaction also appears to be quite general for higher-chain acids as the starting materials.

The potential industrial significance of this catalytic reaction lies in the fact that acetic acid is readily synthesized from *Synthesis Gas* (via methanol). The ability to homologate acetic acid to higher carbon chain acids means that industry would not have to be dependent on petroleum feedstocks for longer chain carboxylic acid syntheses. The relatively good hydrogenation ability of Ru, however, lowers the total selectivity of the reaction by giving ethanol, ethane, and propane as side products, along with ethyl acetate and ethyl propionate ester products. Linear acids, however, are the dominant products, with only traces of chain branching observed.

3.5 The Hydrocarboxylation of Alkenes and Alkynes

The reaction of an alkene (or alkyne), CO, and H_2O to directly produce a carboxylic acid is called Reppe carbonylation chemistry or, more recently, hydrocarboxylation (*see Reppe Reaction*). An excellent review of palladium-catalyzed Reppe carbonylation systems has been published recently by Kiss,[82] and coverage of this important material will not be repeated here. This catalytic reaction has been known for quite some time, although the stoichiometric $Ni(CO)_4$-based carbonylation of acetylene was the first commercial carbonylation process implemented (equation 13). The extreme toxicity of $Ni(CO)_4$, however, has limited practical applications (*see* ***Nickel: Organometallic Chemistry***). Co, Rh, and Pd catalysts have certainly replaced $Ni(CO)_4$ in smaller-scale laboratory reactions, though for historical reasons a number of the fundamental mechanisms discussed in this section are based on $Ni(CO)_4$.

$$4HC{\equiv}CH + 4H_2O + Ni(CO)_4 + 2HCl \longrightarrow$$
$$4H_2C{=}CHCO_2H + NiCl_2 + H_2 \qquad (13)$$

The Ni-catalyzed production of acrylic acid from acetylene produces 320 million kg year^{-1}. The BASF process operates at 40–55 bar and 180–204 °C using a $NiBr_2$/Cu halide catalyst in THF solution. The details of the catalytic mechanism are not fully understood, but the core nickel-catalyzed cycle is shown in Scheme 23.

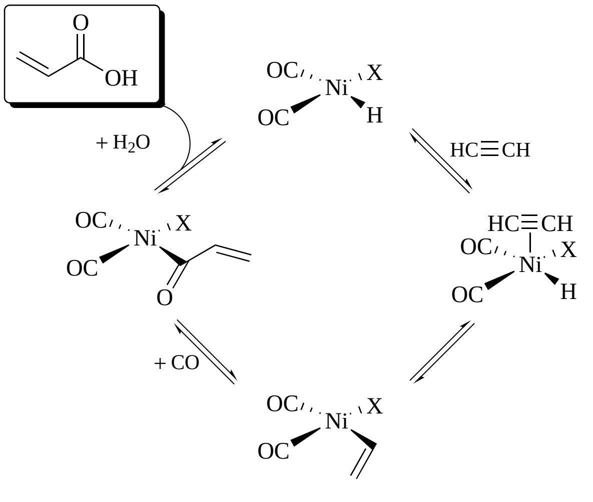

Scheme 23

An interesting variant of the above reaction occurs when allylic derivatives (halides, ethers, alcohols, etc.) are present as well. 2,5-Dienoic acids are catalytically produced in high yields under ambient conditions.[83,84]

$HCo(CO)_4$ will also catalyze the hydrocarboxylation of acetylene to produce acrylic acid, but under higher pressures (100–200 bar, 100 °C) an efficient second hydroxycarboxylation occurs to produce succinic acid in over 80% yield (equation 14).

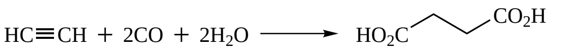

(14)

The $HCo(CO)_4$-catalyzed hydrocarboxylation of alkenes has also been known for a long time. The mechanism is analogous to that presented for hydroformylation (Scheme 1), except that H_2O is used instead of H_2. Hydrocarboxylation is generally slower than hydroformylation, and it is believed that the concentrations of the intermediate species are quite low relative to those seen for hydroformylation. Pyridine has a rate-enhancing effect that is believed to be due to the facile cleavage of the (acyl)$Co(CO)_4$ intermediate. This reaction forms [pyridine–acyl]$^+$ $[Co(CO)_4]^-$, which is more rapidly hydrolyzed by water to form the product carboxylic acid and $HCo(CO)_4$.

The hydrocarboxylation reactions discussed above have been proposed to involve direct addition of water to the metal center prior to elimination of the product, analogous to the oxidative addition of hydrogen to a metal center at the end of a hydroformylation catalytic cycle. Another class of hydrocarboxylation reactions is more analogous to the halide-promoted Monsanto acetic acid process, where one has a reductive elimination of an acyl halide species that is rapidly hydrolyzed with free water to generate the carboxylic acid and HX.

One of the first mechanistic proposals for the hydrocarboxylation of alkenes catalyzed by nickel–carbonyl complexes came from Heck in 1963 and is shown in Scheme 24.[85] An alternate possibility suggested by Heck was that HX could add to the alkene, producing an alkyl halide that would then undergo an oxidative addition to the metal center, analogous to the acetic acid mechanism (Scheme 19). Studies of Rh- and Ir-catalyzed hydrocarboxylation reactions have demonstrated that for these metals, the HX addition mechanism, shown in Scheme 24, dominates with ethylene or other short-chain alkene substrates.[86] Once again, HI is the best promoter for this catalytic reaction as long as there are not any other ligands present that are susceptible to acid attack (e.g. phosphines).

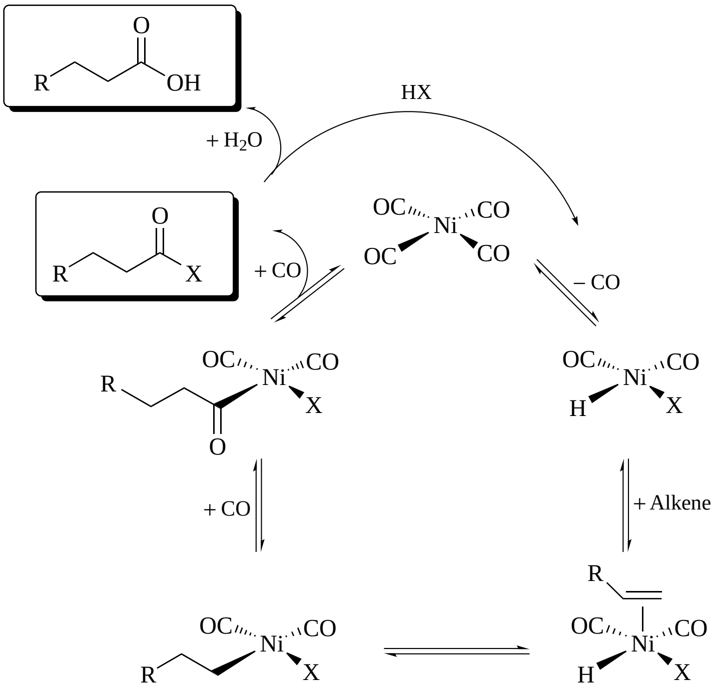

Scheme 24

Hydrocarboxylation reactions generally do not have very high regioselectivities when carried out with C_4 or higher alkenes, due to alkene isomerization side reactions catalyzed by both acid and metal. Thus, many of the reactions done industrially involve substrates such as acetylene and ethylene where isomerization side reactions will not present any problems.

The regioselectivity of the palladium-catalyzed hydrocarboxylation of styrene can be controlled by variation of the phosphine ligand set.[87] For monodentate phosphines, the cone angle (θ) is an important consideration, whereas in the case of chelating diphosphines the bite angle (β_n) is a controlling factor for the selectivity of the reaction. Palladium complexes comprising basic monophosphines such as PMe_3 show no activity for the hydroxycarbonylation of styrene whereas 98% conversion and regioselectivities of up to 84% for the branched isomer can be achieved with palladium complexes supported by PPh_3 (equation 15). A preference for the formation of the linear isomer is observed when diphosphines are employed in the reaction, although higher temperatures and pressures are required to achieve similar activities to the corresponding monodentate systems (Table 7). Chelating diphosphines with bite angles ~102° have exhibited the best activities for this reaction (95–99% conversion), while those with small bite angles ~90° tend to give low conversions (5–28%). By modifying the supporting ligand set and adjusting reaction conditions, it may be possible to influence the regioselectivity of the reaction to yield either mainly branched or mainly linear product.

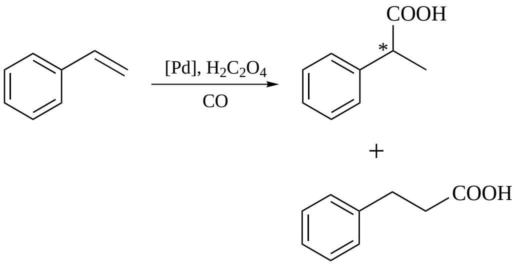

(15)

3.6 Carboxylic Acids from Aldehydes: Amidocarbonylation

Oxidation of aldehyde products produced from hydroformylation is a major industrial route to carboxylic acids. The Hoechst–Celanese Corporation, for example, produces considerable quantities of linear C_7 and C_9 carboxylic acids from the Rh/PPh_3-catalyzed hydroformylation of 1-hexene and 1-octene.

Another route to carboxylic acids from aldehyde products (once again, generally produced via hydroformylation catalysis) was discovered by Wakamatsu and coworkers. They reported the carbonylation of aldehydes and primary organic amides to produce *N*-acylamino acids (equation 16).[88] The reaction is efficiently catalyzed by $HCo(CO)_4$ at 100 °C and 140 bar of 3:2 H_2/CO (hydrogen is needed to help stabilize $HCo(CO)_4$). Yields of over 90% of the appropriate

Table 7 Hydrocarboxylation of styrene with $[PdCl_2(PhCN)_2]$ supported by monophosphines or diphosphines[a]

Phosphine	θ or $\beta_n{}^b$(°)	% Conversion	Branched:linear ratio
PPh_3	145	96	84:16
$P(p\text{-Tol})_3$	145	98	69:31
$PPh_2(o\text{-Tol})$	161	76	100:0
dppe	78[a]	5	47:53
DPEphos	102[a]	99	14:86
Xantphos	110[a]	99	19:81

[a]Reaction conditions: 4:1 monophosphine to Pd, 30 bar CO, 100 °C; 10:1 diphosphine to Pd, 75 bar CO, 150 °C. [b]Calculated bite angle.

N-acylamino acid can be obtained. This reaction has subsequently been referred to as amidocarbonylation and offers a viable alternative to the conventional Strecker reaction (which uses HCN and NH_3) for preparing α-amino acids from aldehydes.

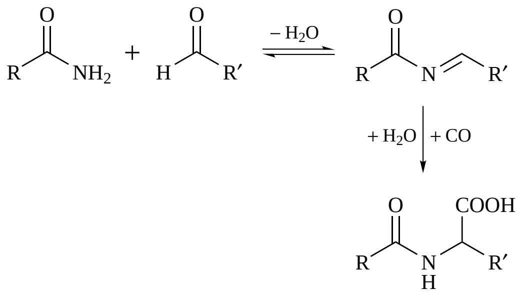

(16)

There has been considerable interest from both academics and industry in this reaction since 1980. There are a wide number of uses for the amido acid products: surface-active agents and specialty surfactants ($C_{10}-C_{16}$ amido acids), intermediates for aspartame sweeteners (phenylalanine), food additives (monosodium glutamate), and chelating agents (iminoacetic acid and polyamido acids). Knifton (Texaco) has done extensive studies of this reaction,[89] as have Ojima and coworkers.[90]

The proposed mechanism is shown in Scheme 25.[91] The coupling of this reaction with hydroformylation, for example, allows the conversion of an alkene directly into an N-acetyl product. Thus, the reaction of trifluoropropylene and acetamide produces N-acetyltrifluoronorvaline in 80% yield with 96% selectivity.

3.7 Carboxylic Acids from Organic Halides

Palladium-catalyzed carbonylation reactions have assumed increasing importance over the last 30 years, particularly for smaller-scale laboratory and fine chemical syntheses (*see* ***Palladium: Organometallic Chemistry***). There is an enormous amount of work on palladium-catalyzed reactions, and it would be impossible to cite many specific examples. It is possible, however, to generalize the mechanism for producing carboxylic acids, esters, amides, and so on from organic halides as shown in Scheme 26. The catalysis starts with a Pd^0 phosphine complex that dissociates a PPh_3 to open up a coordination site in order to oxidatively add the organic halide. Pd^0 species are often electron-rich and reactive enough to undergo an oxidative addition to an aryl halide. Coordination of CO, followed by an alkyl migration, produces the acyl complex, which can react with a variety of reactants to produce the product of choice. Not shown in Scheme 26 is that the acyl complex will react with H_2 to eliminate aldehyde products.

Carbonylation of aryl bromides with palladium catalysts in aqueous solutions to produce carboxylic acids is a general reaction. Typical reaction conditions are 100–130 °C, 3 bar of CO, 2–36-h reaction time using a $PdCl_2(PPh_3)_2/PPh_3$ catalyst (0.1–1 mol%). A base, such as an amine, is needed in slightly greater than stoichiometric quantities to trap out the HX acid produced in the reaction. The presence of an acetamido group ortho to the bromide significantly accelerates the reaction. Yields can be quite good, and there are usually no selectivity problems with these types of oxidative addition reactions. One example reaction is shown in equation (17).

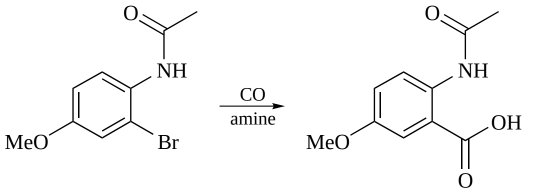

(17)

Amides and esters are formed in good yields through reaction of a primary or secondary amine or alcohol with the Pd–acyl complex. Amine reactions are, in general, more rapid and give better yields of products compared to the alcohol analogs. Interestingly, α-ketoamides can be formed under the proper conditions (equation 18). The use of alkyl- or alkylarylphosphine ligands, higher CO pressures (10 bar), and lower temperatures (room temperature) favor the double carbonylation. Long reaction times are often required, but high yields can be obtained in many cases. The mechanistic details of this reaction are not fully understood, but it is probably not a double CO insertion. Rather, it is believed that reductive elimination occurs from a double acyl species such as (**22**).

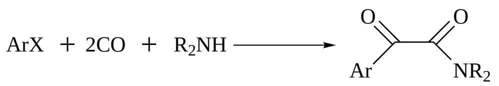

(18)

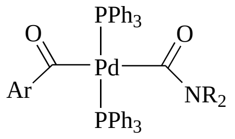

(**22**)

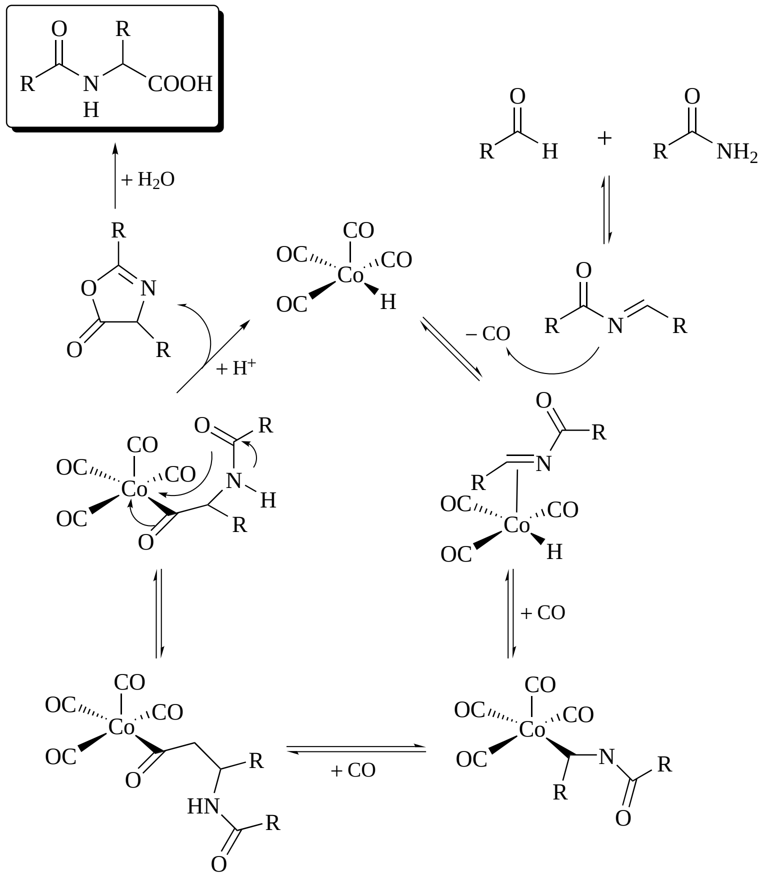

Scheme 25

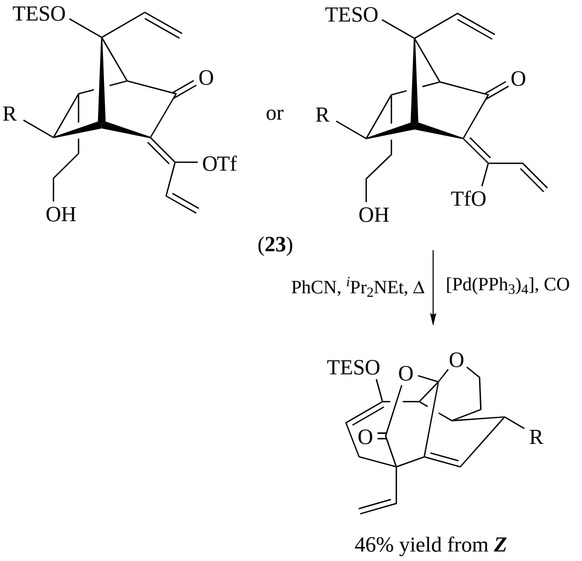

(**23**)

(19)

46% yield from ***Z***
56% yield from ***E***

An interesting example of the use of catalytic carbonylation in the total synthesis of natural products has been reported by Leighton and Bio.[92] The carbonylation of a Z-tetrasubstituted enol triflate by a tandem carbonylation–Cope rearrangement reaction to yield the CP core structure is shown in equation (19). Surprisingly, both the E and Z isomers of (**23**) are effective precursors in this transformation using a palladium–phosphine complex, possibly through an allylic intermediate.

A pyridine-2-carboxylato (N–O) complex of palladium(II) with a labile tosylato ligand has been shown to act as an efficient carbonylation catalyst for a series of alcohols and olefins.[93] The catalyst precursor, [Pd(N–O)(OTs)(PPh$_3$)] (**24**), in conjunction with promoters (e.g. LiI, LiCl, TsOH), is active for the carbonylation of primary, secondary and tertiary alcohols as well as functionalized terminal olefins with good selectivity and turnover frequency. This reaction has been further discussed in a report dealing with the kinetic modeling of this and other catalytic-carbonylation reactions.

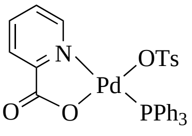

(**24**)

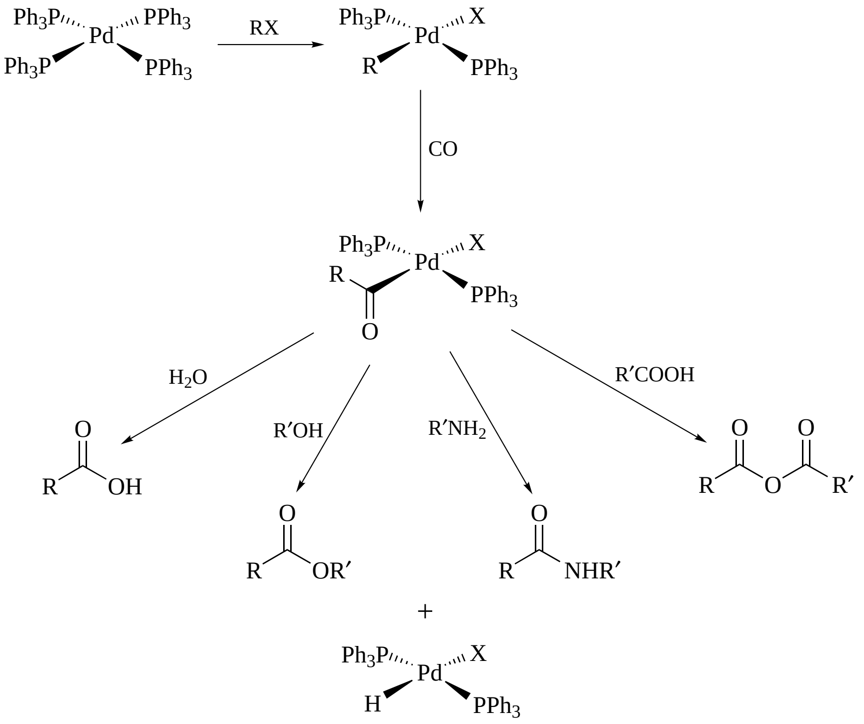

Scheme 26

The kinetic modeling study of 1-(4-isobutylphenyl)ethanol (IBPE) carbonylation using a homogeneous palladium complex has been reported by Chaudhari.[94] The three key steps (formation of the active substrate; formation of the active catalyst; catalytic carbonylation of active substrate) were studied in detail. The average carbonylation rate depends on several factors, so a dynamic analysis, where the concentrations of both the catalyst species and the intermediates were varied, was carried out.

A two-phase system for the carbonylation of benzyl alcohol using a water-soluble palladium complex supported by trisulfonated triphenylphosphine ligands (tppts = $P(C_6H_4\text{-}m\text{-}SO_3Na)_3$) and a Brønsted acid cocatalyst has been reported by Sheldon and coworkers.[95] The complex, $[Pd(tppts)_3]$ is an effective carbonylation catalyst for benzyl alcohol under mild conditions (100 °C; tppts/Pd molar ratio: 12; TsOH/substrate: 2). The only product obtained is phenylacetic acid in 77% yield with ≈100% selectivity. This system has also been applied to the carbonylation of IBPE to yield ibuprofen, which is currently prepared industrially using a palladium/triphenylphosphine-supported catalyst in organic solvents. Although the selectivities are lower for the biphasic system at this point, it is possible that further optimization of the biphasic system will bring the selectivities up to current industrial levels in the future.

The catalytic silylative carbonylation of aryl iodides using a bimetallic catalyst system, $[PdCl_2(PPh_3)_2\text{-}Co_2(CO)_8]$, has been reported by Hidai and coworkers.[96] The carbonylation of 4-iodotoluene (*p*-TolI) in the presence of carbon monoxide, triethylsilane, and the bimetallic [Pd–Co] system gave rise to *p*-$TolCH_2OSiEt_3$ (76% yield, 85% conversion). Upon addition of triethylamine, however, the product distribution changed to yield 1,2-di(*p*-tolyl)-1,2-bis(triethylsiloxy)ethane as the major product (57% yield, 70% conversion), along with *p*-$TolCH_2OSiEt_3$ and *p*-tolualdehyde as minor products. Neither metal complex was an active catalyst on its own, therefore a synergistic effect is clearly at work here. The corresponding PCy_3-supported palladium complex is active in the hydroformylation of internal alkynes, although higher activity can be achieved with the bimetallic system $[PdCl_2(PCy_3)_2\text{-}Co_2(CO)_8]$. The authors suggest a mechanism that involves two separate but linked catalytic cycles, each based upon one of the two metals.

4 KETONES

4.1 Ketones from Alkenes and Alkynes

Ketones are sometimes seen as by-products in hydroformylation, particularly when the alkene concentration is very high and the H_2/CO pressure is low. This product is most favored for ethylene (producing diethyl ketone), but yields drop-off quickly with higher-chain alkenes. It turns out that there are actually few good catalytic routes to acyclic ketones from alkenes or alkynes. One of the best examples involves the reaction of butadiene with CO, an alkyl halide, and base, which is catalyzed by $[Co(CO)_4]^-$.[97] The proposed mechanism is shown in Scheme 27. The reaction is highly regio- and stereospecific, with the acyl group always being added to the least-substituted carbon of the least-substituted double bond. The *trans*-acyl diene is the only product formed.

α,β-Unsaturated ketones can be obtained from the $Rh_4(CO)_{12}$-catalyzed reaction of alkynes and alkenes (equation 20). Terminal alkynes react with particularly high regio- and stereospecificity to give *trans*-α, β-unsaturated ketones.[98]

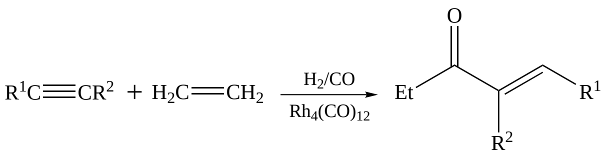

(20)

One of the more exciting developments in the catalytic production of ketones was the work of Sen on the Pd^{II}-catalyzed production of polyketones from ethylene and CO (equation 21).[99] Sen used $[Pd(MeCN)_3(PPh_3)]^{2+}$ as the catalyst and proposed that the mechanism consisted of the initial formation of some sort of Pd–H complex ($CHCl_3$ was used as the solvent) which inserts ethylene to produce a Pd–alkyl species. Carbonylation then occurs to produce a Pd–acyl complex. The rate-determining step is believed to be coordination and insertion of ethylene into the Pd–acyl moiety to produce $Pd–CH_2CH_2(CO)CH_2CH_3$. Alternating CO and ethylene insertions lead to a polyketone. β-Hydride elimination terminates the chain-growth process.

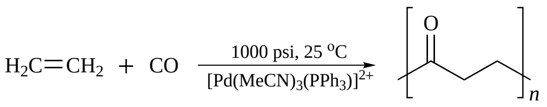

(21)

The cationic nature of the Pd catalyst is believed to be quite important to prevent CO and ethylene from binding too strongly to the metal center. Use of more basic phosphines leads to catalyst deactivation, consistent with this observation. Brookhart and coworkers have described a better characterized, highly active 'living catalyst' that can be used on a variety of alkenes to produce high molecular weight polyketones (20 000 to 60 000) with a very narrow polydispersity of 1.08.[100] The catalyst precursor used was $[Pd(Me)(MeCN)(N_2)]^+$ (N_2 = bipyridine or phenanthroline), and the active catalyst species in solution is believed to be $[Pd(acyl)(CO)(N_2)]^+$. Once again, the rate-determining step was identified as the alkene insertion into the Pd–acyl species.

There are a few more catalytic routes to cyclic ketones known, usually involving alkynes and cobalt or rhodium carbonyl catalysts. Spirocyclopentanones can be prepared in high yields according to equation (22).[101]

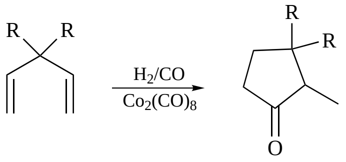

(22)

Pauson and Khand discovered the very important class of alkyne/alkene/CO cyclization catalytic reactions catalyzed, once again, by $Co_2(CO)_8$ (*see Pauson–Khand Reaction*).[102] This reaction produces α,β-unsaturated cyclopentanones (equation 23). With unstrained alkenes the reaction works best in a stoichiometric setting, but with strained alkenes like norbornadiene the reaction can be made catalytic. These reactions have been fairly extensively studied, and the reaction proceeds through an alkyne-bridged $Co_2(CO)_6$ dimer species. Unsymmetrical alkynes lead to mixtures of the various substituted α,β-unsaturated cyclopentanone products.

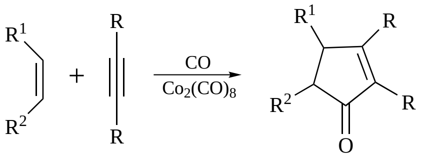

(23)

A Pauson–Khand type reaction of enynes, where the CO source is an aldehyde, has been reported by Morimoto and coworkers.[103] This CO-transfer carbonylation system was carried out with monomeric or dimeric rhodium complexes supported by monodentate or chelating phosphine ligands (e.g. $[RhCl(cod)]_2$/dppe or dppp; $[RhCl(CO)PPh_3]$). This reaction is successful for a series of enynes and aldehydes (Scheme 28).

The area of double carbonylation has been recently reviewed by des Abbayes and Salaün.[104] Both stoichiometric and catalytic systems are surveyed, covering monometallic complexes of Co, Pd, Fe and Ni, although the main emphasis is on catalytic monometallic systems of Co and Pd with a variety of substrates (amines, alcohols, organic halides). A general scheme for the double carbonylation of organic halides with a palladium is shown below (Scheme 29).

5 LACTONES AND LACTAMS

The importance of lactone and lactam rings in biological systems has prompted considerable interest in their stoichiometric and catalytic preparation (*see* ***Organic Synthesis using Transition Metal Carbonyl Complexes*** and ***Organic Synthesis using Transition Metal Complexes Containing π-Bonded Ligands***). One of the simplest reactions is the production of four-membered lactones from ethylene, CO, and water, catalyzed by $PdCl_2$ (equation 24). Stoichiometric amounts of

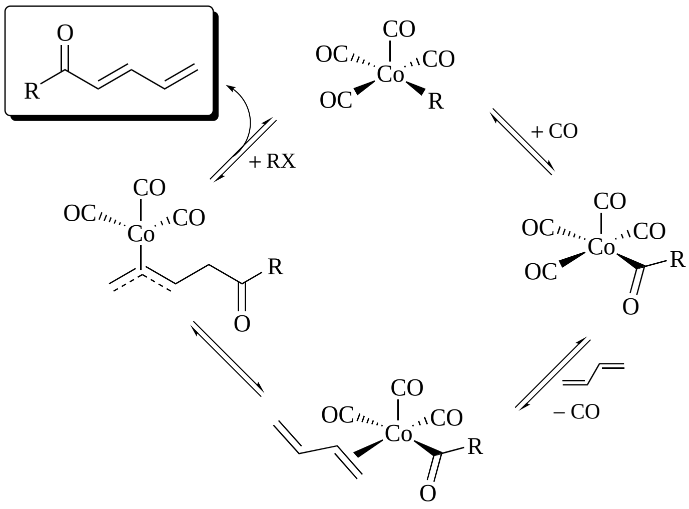

Scheme 27

$CuCl_2$ need to be used to reoxidize the Pd^0 back to Pd^{II}. The carbonylation of halide-containing alcohols is a better reaction as it takes place under mild conditions and often in good yields (equation 25).

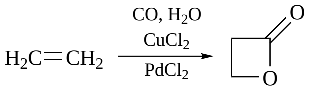

(24)

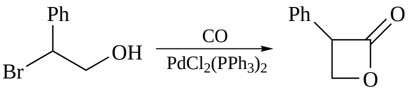

(25)

There has been more interest in the five-membered ring systems which, as one might expect, generally give better yields. A general synthesis for aryl lactones with five- through seven-membered rings is shown in equation (26). By using a primary or secondary amine, instead of an alcohol functional group, the analogous lactams can be prepared. As with the acyclic syntheses, the lactam preparations are somewhat more facile and give generally better yields.

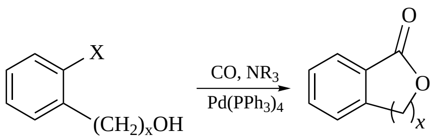

(26)

The cyclocarbonylation of vinylic halides (usually the bromide or iodide) is another route to lactones and lactams. 1,2-Substituted vinyl compounds produce lactones where the double bond is incorporated into the ring (equation 27), while 1,1-substituted vinyl substrates give an *exo* double bond (equation 28). The 1,2-substituted vinyl reactions can be run under ambient conditions (24–72 h), producing high yields of products. The 1,1-vinyl substrates require higher temperatures and pressures (70 °C, 30 psi) for the cyclocarbonylation reaction.

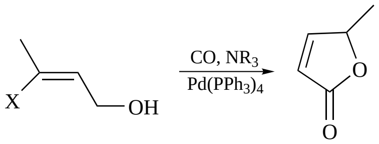

(27)

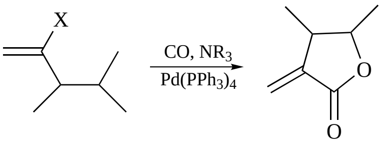

(28)

Alkyne alcohols can be cyclocarbonylated to produce lactones (equation 29). A $PdCl_2/P(n\text{-Bu})_3/SnCl_2$ catalyst system has been shown to be quite efficient for this reaction at 75 °C and 8 bar CO pressure.[105]

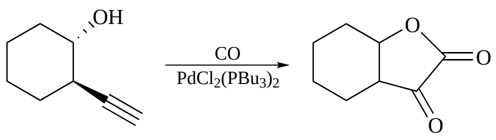

(29)

The proposed mechanism for this reaction is shown in Scheme 30. Coordination of the alcohol OH group to the Pd^{II} center causes deprotonation to produce the alkoxide-coordinated species. CO insertion produces the alkoxyacyl species, which reacts with the alkyne group to produce the cyclized vinyl–Pd species, which is then protonated off the Pd center.

Pd will catalyze the ring expansion of azirines with CO to form bicyclic β-lactams under mild conditions (equation 30). The Pd catalyst seems to always produce the bicyclic complex shown in equation (30). $Rh_2(CO)_4Cl_2$,

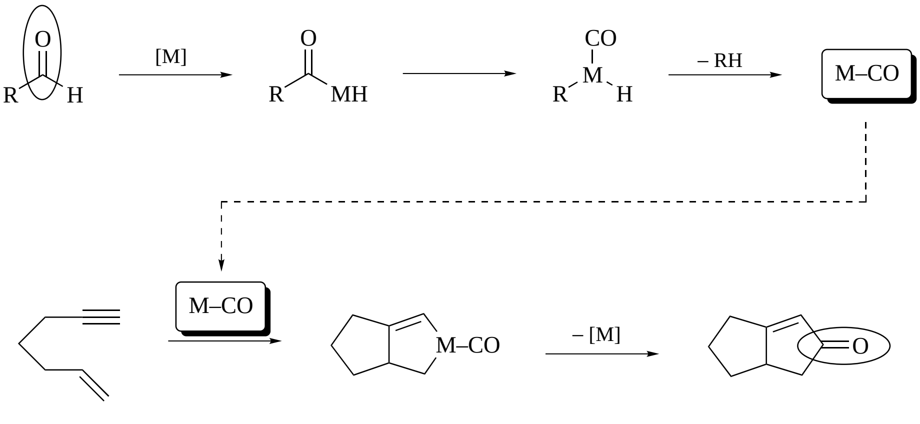
[M]
– RH
M–CO
M–CO
M–CO
– [M]

Scheme 28

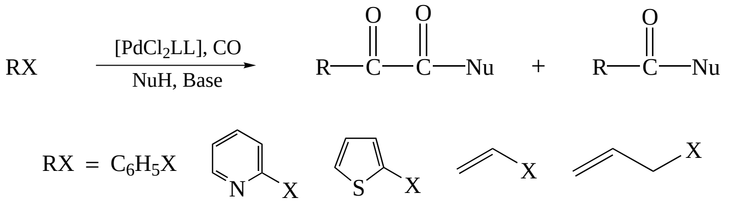
RX
[PdCl2LL], CO
NuH, Base
R—C—C—Nu
+
R—C—Nu
RX = C6H5X
N
X
S
X
X
X

NuH = R′$_2$NH, R′OH

L = phosphine

Scheme 29

however, will regioselectively ring-expand 2-arylaziridines to the monocyclic four-membered lactam (equation 31). None of the isomeric lactam is produced in the rhodium-catalyzed reaction.[106]

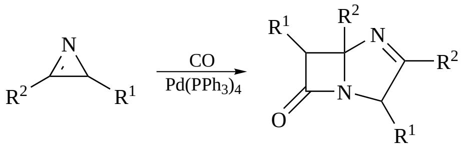
N
R2
R1
CO
Pd(PPh3)4
R1
R2
N
R2
N
O
R1

(30)

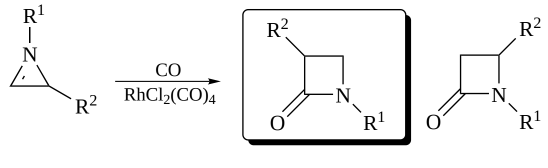
R1
N
R2
CO
RhCl2(CO)4
R2
O
N
R1
R2
O
N
R1

(31)

Finally, ring-expanding carbonylation reactions using cobalt have been reported by various groups. In the first of these, the synthesis of 4,5-dihydro-1,3-oxazin-6-ones by a ring-expanding carbonylation reaction of 2-aryl-2-oxazolines with a cobalt catalyst has been reported by Xu and Jia.[107] This is the first example of the application of catalytic carbonylation to 2-oxazolines leading to the synthesis of an important intermediate in peptide synthesis (equation 32). On the basis of ^{1}H NMR experiments, the catalyst, $BnCo(CO)_4$ (Bn = benzyl), is believed to dissociate the benzyl group to generate a $Co(CO)_4$ radical as the active catalyst.

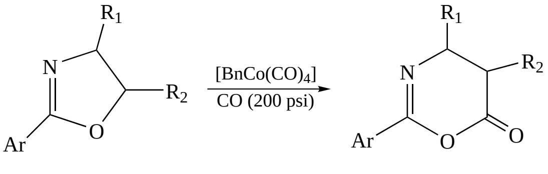
R1
N
R2
Ar
O
[BnCo(CO)4]
CO (200 psi)
R1
N
R2
Ar
O
O

(32)

R_1 = H, Me; R_2 = H, Me, Ph
Ar = Ph, *m*-F-Ph, *p*-tolyl, *o*-tolyl, thiophen-2-yl, furan-2-yl

This area has been further advanced by Coates and coworkers.[108] The synthesis of succinic anhydrides by *β*-lactone carbonylation using a Lewis acidic cation in conjunction with an anionic cobalt carbonyl complex has been reported (equation 33).

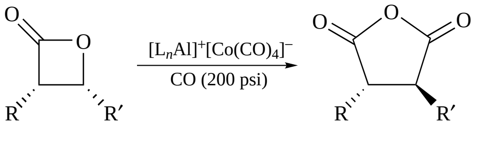
O
O
R
R′
[LnAl]+[Co(CO)4]−
CO (200 psi)
O
O
O
R
R′

(33)

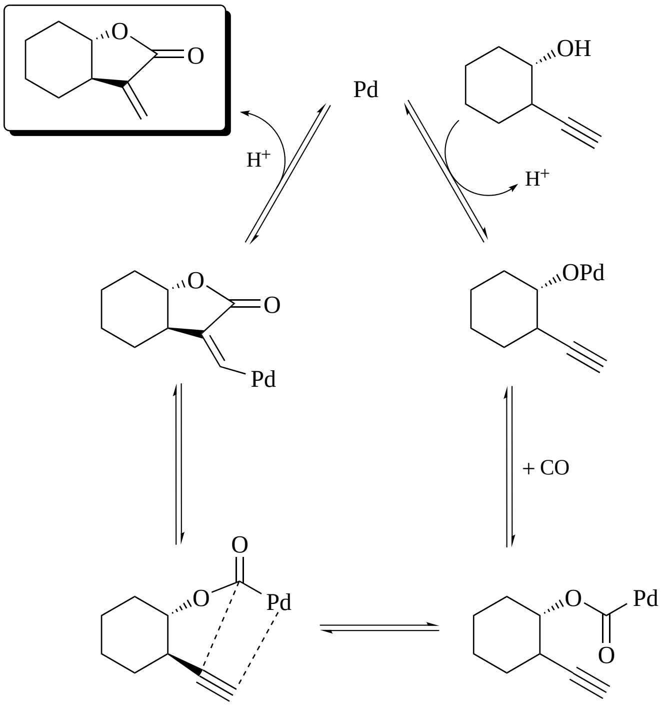

Scheme 30

6 RELATED ARTICLES

Asymmetric Synthesis by Homogeneous Catalysis; Cobalt: Organometallic Chemistry; Coordination Chemistry: History; Decarbonylation Catalysis; Dinuclear Organometallic Cluster Complexes; Electronic Structure of Organometallic Compounds; High Pressure Synthesis of Solids; Hydride Complexes of the Transition Metals; Hydrocyanation by Homogeneous Catalysis; Hydrogenation & Isomerization of Alkenes; Hydrosilation Catalysis; Mechanisms of Reaction of Organometallic Complexes; Nickel: Organometallic Chemistry; Organic Synthesis using Transition Metal Carbonyl Complexes; Organic Synthesis using Transition Metal Complexes Containing π-Bonded Ligands; P-donor Ligands; Palladium: Organometallic Chemistry; Phosphorus: Organophosphorus Chemistry; Platinum: Organometallic Chemistry; Polynuclear Organometallic Cluster Complexes; Rhodium: Organometallic Chemistry; Supported Organotransition Metal Compounds.

7 REFERENCES

1. B. Cornils, ‘Hydroformylation’, A. Mullen, ‘Reppe Chemistry’, and A. Mullen, Ring Closure Reactions with CO, in ‘New Syntheses with Carbon Monoxide’, ed. J. Falbe, Springer-Verlag, Berlin, 1980.
2. M. Beller, B. Cornils, C. D. Frohning, and C. W. Kohlpaintner, *J. Mol. Catal. A*, 1995, **104**, 17.
3. P. W. N. M. van Leeuwen and C. Claver, ‘Rhodium Catalyzed Hydroformylation’, Kluwer Academic Publishers, Dordrecht, 2000.
4. I. Ojima, ed., ‘Catalytic Asymmetric Synthesis’. 2nd edn., Wiley-VCH, New York, 2000.
5. B. Cornils and W. A. Herrmann, eds, ‘Applied Homogeneous Catalysis with Organometallic Compounds’, 2nd edn., Wiley-VCH, Weinheim, 2002.
6. F. Ungváry, *Coord. Chem. Rev.*, 2004, **248**, 867.
7. R. F. Heck, ‘Palladium Reagents in Organic Synthesis’, Academic Press, San Diego, CA, 1985.
8. J. J. McKetta and W. A. Cunningham, eds, ‘Encyclopedia of Chemical Processing and Design’, Marcel Dekker, New York, 1990.
9. B. Cornils and W. A. Herrmann, *J. Catal.*, 2003, **216**, 23.
10. D. S. Breslow and R. F. Heck, *Chem. Ind. (London)*, 1960, 467.
11. R. F. Heck and D. S. Breslow, *J. Am. Chem. Soc*, 1961, **83**, 4023.
12. R. Wyman, *J. Organomet. Chem.*, 1974, **66**, C23.
13. M. F. Mirbach, *J. Organomet. Chem.*, 1984, **265**, 205.
14. W. R. Moser, in ‘ACS Advances in Chemistry Series’, eds. W. R. Moser and D. W. Slocum, American Chemical Society, Washington, DC, 1992, Vol. 230, Chap. 1, p. 14.

15. P. Pino, in ‘Organic Syntheses via Metal Carbonyls’, eds. I. Wender and P. Pino, Wiley, New York, 1977, Vol. 2.
16. B. Fell, W. Rupilius, and F. Asinger, *Tetrahedron Lett.*, 1968, 3261.
17. M. Bianchi, F. Paicenti, P. Frediani, and U. Matteoli, *J. Organomet. Chem.*, 1977, **137**, 361.
18. B. L. Haymore, A. van Asselt, and G. R. Beck, *Ann. N.Y. Acad. Sci.*, 1984, **415**, 159.
19. L. H. Slaugh and R. D. Mullineaux, *J. Organomet. Chem.*, 1968, **13**, 469.
20. M. Garland and G. Bor, *Inorg. Chem.*, 1989, **28**, 410.
21. M. Garland and P. Pino, *Organometallics*, 1991, **10**, 1693.
22. R. L. Pruett and J. A. Smith, *J. Org. Chem.*, 1969, **34**, 327.
23. R. V. Kastrup, J. S. Merola, and A. A. Oswald, in ‘ACS Advances in Chemistry Series’, eds. E. L. Alyea and D. W. Meek, American Chemical Society, Washington, DC, 1982 Vol. 196, Chap. 3, p. 43.
24. W. R. Moser, C. J. Papile, D. A. Brannon, R. A. Duwell, and S. J. Weininger, *J. Mol. Catal.*, 1987, **41**, 271.
25. C. A. Tolman and J. W. Faller, in ‘Homogeneous Catalysis with Metal Phosphine Complexes’, ed. L. H. Pignolet, Plenum Press, New York, 1983, Chap. 2, p. 93.
26. A. G. Abatjoglou, E. Billig, and D. R. Bryant, *Organometallics*, 1984, **3**, 923.
27. M. Lewin, Z. Aizenshtat, and J. Blum, *J. Organomet. Chem.*, 1980, **184**, 255.
28. W. R. Moser, C. J. Papile, and S. J. Weininger, *J. Mol. Catal.*, 1987, **41**, 293.
29. P. C. J. Kamer, A. van Rooy, G. C. Schoemaker, and P. W. N. M. van Leeuwen, *Coord. Chem. Rev.*, 2004, **248**, 2409.
30. Z. Freixa and P. W. N. M. van Leeuwen, *J. Chem. Soc., Dalton Trans.*, 2003, 1890.
31. B. Breit, *Acc. Chem. Res.*, 2003, **36**, 264.
32. J. J. Carbó, F. Maseras, C. Bo, and P. W. N. M. Leeuwen, *J. Am. Chem. Soc.*, 2001, **123**, 7630.
33. J. D. Unruh and J. R. Christenson, *J. Mol. Catal.*, 1982, **14**, 19.
34. M. Matsumoto and M. Tamura, *J. Mol. Catal.*, 1982, **16**, 209.
35. M. Matsumoto and M. Tamura, *J. Mol. Catal.*, 1982, **16**, 195.
36. O. R. Hughes and D. A. Young, *J. Am. Chem. Soc.*, 1981, **103**, 6636.
37. M. C. Goedheijt, P. C. J. Kamer, and P. W. N. M. van-Leeuwen, *J. Mol. Catal. A*, 1998, **134**, 243.
38. C. Hsu and M. Orchin, *J. Am. Chem. Soc.*, 1975, **97**, 3553.
39. I. Schwager and J. F. Knifton, *J. Catal.*, 1976, **45**, 256.
40. J. C. Bayón, C. Claver, and A. M. Masdeu-Bultó, *Coord. Chem. Rev.*, 1999, **193–195**, 73.
41. L. A. van der Veen, P. K. Keeven, P. C. J. Kamer, and P. W. N. M. van Leeuwen, *J. Chem. Soc., Dalton Trans.*, 2000, 2105.
42. A. B. Permin and R. Eisenberg, *J. Am. Chem. Soc.*, 2002, **124**, 12406.
43. E. L. Muetterties, *Bull. Soc. Chim. Belg.*, 1975, **84**, 959.
44. R. C. Ryan, C. U. Pittman, Jr, and J. P. O’Connor, *J. Am. Chem. Soc.*, 1977, **99**, 1986.
45. C. U. Pittman, Jr, G. M. Wilemon, W. D. Wilson, and R. C. Ryan, *Angew. Chem., Int. Ed. Engl.*, 1980, **19**, 478.
46. M.-J. Don and M. G. Richmond, *J. Mol. Catal.*, 1992, **73**, 181.
47. A. R. Sanger, in ‘Homogeneous Catalysis with Metal Phosphine Complexes’, ed. L. H. Pignolet, Plenum Press, New York, 1983, Chap. 6, p. 228.
48. A. Ceriotti, L. Garlaschilli, G. Longoni, M. C. Malatesta, D. Strumolo, A. Fumagalli, and S. Martinengo, *J. Mol. Catal.*, 1984, **24**, 309.
49. M. Garland, *Organometallics*, 1993, **12**, 535.
50. M. Hidai, A. Fukuoka, Y. Koyasu, and Y. Uchida, *J. Mol. Catal.*, 1986, **35**, 29.
51. Y. Koyasu, A. Fukuoka, Y. Uchida, and M. Hidai, *Chem. Lett.*, 1985, 1083.
52. G. Süss-Fink and G. F. Schmidt, *J. Mol. Catal.*, 1987, **42**, 361.
53. P. Kalck, *Polyhedron*, 1988, **7**, 2441.
54. A. Dedieu, P. Escaffre, J. M. Frances, P. Kalck, and A. Thorez, *Nouv. J. Chim.*, 1986, **10**, 631.
55. M. E. Broussard, B. Juma, S. G. Train, W.-J. Peng, S. A. Laneman, and G. G. Stanley, *Science*, 1993, **260**, 1784.
56. D. A. Aubry, N. N. Bridges, K. Ezell, and G. G. Stanley, *J. Am. Chem. Soc.*, 2003, **125**, 11180.
57. C. Li, E. Widjaja, and M. Garland, *J. Am. Chem. Soc.*, 2003, **125**, 5540.
58. S. C. Van der Slot, J. Duran, J. Luten, P. C. J. Kamer, and P. W. N. M. van Leeuwen, *Organometallics*, 2002, **21**, 3873.
59. P. G. Jessop, T. Ikariya, and R. Noyori, *Chem. Rev.*, 1999, **99**, 475.
60. D. Koch and W. J. Leitner, *Am. Chem. Soc.*, 1998, **120**, 13398.
61. C. P. Mehnert, R. A. Cook, N. C. Dispenziere, and M. Afeworki, *J. Am. Chem. Soc.*, 2002, **124**, 12932.
62. A. Aghmiz, C. Claver, A. M. Masdeu-Bultó, D. Maillard, and D. Sinou, *J. Mol. Catal. A*, 2004, **208**, 97.
63. I. Matsuda, A. Oriso, S. Sato, and Y. Izumi, *J. Am. Chem. Soc.*, 1989, **111**, 2332.
64. I. Ojima, P. Ingallina, R. J. Donovan, and N. Clos, *Organometallics*, 1991, **10**, 38.
65. I. Ojima, M. Okabe, K. Kato, H. B. Kwon, and I. Horváth, *J. Am. Chem. Soc.*, 1988, **110**, 150.
66. N. Chatani, S. Ikeda, K. Ohe, and S. Murai, *J. Am. Chem. Soc.*, 1992, **114**, 9710.
67. S. J. O’Malley and J. L. Leighton, *Angew. Chem., Int. Ed. Engl.*, 2001, **40**, 2915.
68. D. Forster and T. W. Dekleva, *J. Chem. Educ.*, 1986, **63**, 204.
69. D. Forster, *J. Am. Chem. Soc.*, 1976, **98**, 846.

70. J. R. Dilworth, J. R. Miller, N. Wheatley, M. J. Baker, and J. G. Sunley, *J. Chem. Soc., Chem. Commun.*, 1995, 1579.
71. J. R. Dilworth, *Coord. Chem. Rev.*, 1996, **154**, 163.
72. J. R. Zoeller, E. M. Blakely, R. M. Moncier, and T. J. Dickson, *Catal. Today*, 1997, **36**, 227.
73. J. R. Zoeller, N. L. Buchanan, T. J. Dickson, and K. K. Ramming, *Catal. Today*, 1999, **49**, 431.
74. S. W. Polichnowski, *J. Chem. Educ.*, 1986, **63**, 206.
75. R. Stevenson, *Chem. Br*, 1996, 7.
76. G. J. Sunley and D. J. Watson, *Catal. Today*, 2000, **58**, 293.
77. F. E. Paulik and J. F. Roth, *J. Chem. Soc., Chem. Commun.*, 1968, 1578.
78. D. Forster, *J. Chem. Soc., Dalton Trans.*, 1979, 1639.
79. P. M. Maitlis, A. Haynes, G. J. Sunley, and M. J. Howard, *J. Chem. Soc., Dalton Trans.*, 1996, 2187.
80. M. Cheong, R. Schmid, and T. Ziegler, *Organometallics*, 2000, **19**, 1973.
81. A. Haynes, P. M. Maitlis, G. E. Morris, G. J. Sunley, H. Adams, P. W. Badger, C. M. Bowers, D. B. Cook, P. I. P. Elliott, T. Ghaffar, H. Green, T. R. Griffin, M. Payne, J. M. Pearson, M. J. Taylor, P. W. Vickers, and R. J. Watt, *J. Am. Chem. Soc.*, 2004, **126**, 2847.
82. G. Kiss, *Chem. Rev.*, 2001, **101**, 3435.
83. L. Cassar, G. P. Chiusoli, and F. Guerrieri, *Synthesis*, 1973, 509.
84. G. P. Chiusoli, *Acc. Chem. Res.*, 1973, **6**, 422.
85. R. F. Heck, *J. Am. Chem. Soc.*, 1963, **85**, 2013.
86. D. Forster, A. Hershman, and D. E. Morris, *Catal. Rev. – Sci. Eng.*, 1981, **23**, 89.
87. I. del Río, N. Ruiz, C. Claver, L. A. van der Veen, and P. W. N. M. van Leeuwen, *J. Mol. Catal. A*, 2000, **161**, 39.
88. H. Wakamatsu, J. Uda, and N. Yamakami, *Chem. Commun.*, 1971, 1540.
89. J. J. Lin and J. F. Knifton, in ‘ACS Advances in Chemistry Series’, eds. W. R. Moser and D. W. Slocum, American Chemical Society, Washington, DC, 1992, Vol. 230, Chap. 16, p. 235.
90. I. Ojima, *Chem. Rev.*, 1988, **88**, 1011.
91. J.-J. Parnaud, G. Campari, and P. Pino, *J. Mol. Catal.*, 1979, **6**, 341.
92. M. M. Bio and J. L. Leighton, *Org. Lett.*, 2000, **18**, 2905.
93. S. Jayasree, A. Seayad, and R. V. Chaudhari, *Org. Lett.*, 2000, **2**, 203.
94. R. V. Chaudhari, S. Jayasree, and A. Seayad, *Catal. Today*, 2001, **66**, 371.
95. G. Verspui, G. Papadogianakis, and R. A. Sheldon, *Catal. Today*, 1998, **42**, 449.
96. Y. Ishii and M. Hidai, *Catal. Today*, 2001, **66**, 53.
97. R. F. Heck, *J. Am. Chem. Soc.*, 1963, **85**, 3381.
98. P. Hong, T. Mise, and H. Yamazaki, *J. Organomet. Chem.*, 1987, **334**, 129.
99. A. Sen and T.-W. Lai, *Organometallics*, 1984, **3**, 866.
100. M. Brookhart, F. C. Rix, and J. M. DeSimone, *J. Am. Chem. Soc.*, 1992, **114**, 5894.
101. P. Eilbracht, M. Acker, and W. Totzauer, *Chem. Ber.*, 1983, **116**, 238.
102. D. C. Billington and P. L. Pauson, *Organometallics*, 1982, **1**, 1560.
103. T. Morimoto, K. Fuji, K. Tsutsumi, and K. Kakiuchi, *J. Am. Chem. Soc.*, 2002, **124**, 3806.
104. H. des Abbayes and J.-Y. Salaün, *J. Chem. Soc., Dalton Trans.*, 2003, 1041.
105. T. F. Murray, E. G. Samsel, V. Varma, and J. R. Norton, *J. Am. Chem. Soc.*, 1981, **103**, 7520.
106. H. Alper, F. Urso, and D. J. H. Smith, *J. Am. Chem. Soc.*, 1983, **105**, 6737.
107. H. Xu and L. Jia, *Org. Lett.*, 2003, **5**, 1575.
108. Y. D. Y. L. Getzler, V. Kundnani, E. B. Lobkovsky, and G. W. Coates, *J. Am. Chem. Soc.*, 2004, **126**, 6842.

Cation-activated Enzymes

Jenny P. Glusker
The Fox Chase Cancer Center, Philadelphia, PA, USA

1 Introduction 1
2 Characteristics of Metal Ions Common in Cells 2
3 Control of Cation Concentrations in Cells 3
4 Sodium- and Potassium-activated Enzymes 4
5 Magnesium- and Calcium-activated Enzymes 7
6 Summary 8
7 Related Articles 8
8 References 8

Abbreviations

PDB = Protein Data bank; PLP = pyridoxal 5′-phosphate; *E. coli* = *Escherichia coli*.

1 INTRODUCTION

Cation-activated enzymes are those that require a cation for maximal activity but for which that cation is generally not a direct component of the enzyme reaction mechanism. They were originally identified by Evans and Sorger in a study of activation of enzymes by monovalent metal cations.[1] These activating cations convert the enzyme to a form with enhanced catalytic activity. When a cation is part of the enzyme mechanism, its requirement is essential and no reaction occurs in its absence. On the other hand, if the enzyme is cation-activated, the presence of the cation merely increases the activity of the enzyme from a finite value, that is, the enzyme generally works (but not as well) in the absence of the activating cation.[2] A simple example, to be described here, is provided by the activation of pyruvate kinase by potassium ions that bind 6–8 Å from the active site of the enzyme.[3] Reviews on aspects of the subject of cation-activated enzymes by Suelter,[2] Woehl and Dunn,[4] and Larsen and Reed[5] are highly recommended.

The cations involved in such activation are usually metal ions or ammonium ions. Metal ions are generally utilized by enzymes for a variety of reasons, of which the most important are to maintain the stereochemistry of the active sites of the enzymes, and to aid in electrophilic catalysis and electron-transfer reactions. Metal ions that serve a cation-activating function in enzymes may be classified as cofactors because they generally act by binding at sites distinctly separate from the catalytic site. This type of modulation of protein function by cations can therefore be considered to be the result of allosteric (‘other site’) interactions wherein binding to one site affects the properties of a distant site in the enzyme (possibly the active site). The cation, on binding, therefore acts as an allosteric effector, and converts the enzyme from a fairly inactive conformation to a conformation that manifests appreciably increased catalytic activity.[4]

Monovalent metal ions generally bind oxygen atoms that are found in the carboxylate groups of aspartate or glutamate, the hydroxyl groups of threonine or serine, or the main-chain carbonyl groups of a protein. If the metal ions bind directly to the substrate, they may serve to position it for action. They can also act to stabilize some feature of the protein structure.[1] For example, many enzymes have ‘open’ and ‘closed’ conformations, thereby controlling the access of substrate to the active site. Activating cations may assist in such control, perhaps modulating the conformational transition between open and closed conformations.

Identification of activating cations is often fraught with problems. It was pointed out by Markham that ‘A difficulty in assessing the literature on monovalent cation activation of any enzyme is that potentially interacting ions are commonly present as counterions to the substrates and as buffer components’.[6] This means that it is important to note if specific precautions were taken to control the ionic environment of the enzyme during study before concluding that the enzyme is cation-activated in vivo. Recent X-ray crystallographic studies of enzymes have provided much of the structural evidence we have for cation activation by monovalent cations. The location of the cation in the enzyme and its relationship to the active site are found by this method. Such monovalent cations are less likely than divalent ions to be directly involved in catalytic mechanisms and therefore their activating ability can be identified more readily. There are, however, problems since ions such as Na^+ are not appreciably better X-ray scatterers than are water molecules (since the power of an atom to scatter X-rays depends on its atomic number, water 10, Na^+ 10, $NH_4{}^+$ 11). For example, ammonium ions are commonly used in crystallization of mother liquors. However, ammonium ions are difficult to identify except in very high-resolution structures or those determined by neutron diffraction, where hydrogen atoms can be located, and therefore ammonium ions differentiated from water molecules and sodium ions. A method for identifying Na^+ sites in proteins, involving valence calculations based on interatomic distances, has been proposed by Nayal and Di Cera.[7]

The activating cation presumably acts by helping the protein to maintain a productive conformation, and examples are provided by structural studies of enzymes that exhibit this property. Pauling suggested that complementarity between the structure of the enzyme active site and the transition state of the reaction is responsible for the lowering of activation energies of enzyme-catalyzed reactions.[8] Cation activation may aid this by ensuring that the active site has the correct three-dimensional structure for as good complementarity as is possible, given the amino acid sequence of the enzyme. The activation may be accomplished by binding of the cation directly to the substrate, or binding at a distant site. All gradations of these possibilities are encountered in structural studies. Woehl and Dunn[4] characterized two types of mechanisms of cation activation of enzymes: those in which the cation plays a static structural role and, on binding, activates by stabilizing the conformation of the enzyme that is catalytically active, and those in which the cation plays a dynamic role and, on binding, selectively acts to assist those enzyme conformational transitions that can lead to complementarity between the active site and the transition state of the reaction to be catalyzed. Thus if a cation binds selectively to the conformation of the enzyme that is complementary to the transition state structure for an important step in the reaction being catalyzed, then activation will occur. For example, Wells and Di Cera[9] suggest that when sodium binds to human α-thrombin, an enzyme that it activates, there is a significant change in protein conformation. Woehl and Dunn[4] remark that 'activation by such mechanisms represents the fine-tuning of highly evolved catalysts. Because Na^+ and K^+ are ubiquitous in biological milieu, there is logic to the evolution of enzyme systems that take advantage of the presence of these metal ions as activating cofactors'.

2 CHARACTERISTICS OF METAL IONS COMMON IN CELLS

Many cations are available for activation of enzymes. Among the most abundant in the body are the four cations Na^+, K^+, Mg^{2+}, and Ca^{2+}. They are found in living cells and extracellular fluids at millimolar concentrations. For Na^+ and Ca^{2+}, the concentrations are intermediate between those in seawater and those in freshwater. Potassium ions are present in high concentrations in the cell (95% of the total potassium ions in the body are intracellular), and magnesium ions are found in about the same concentration in both cells and the extracellular fluids around them. Cation-activated enzymes that are found within cells (where the K^+ concentration is greater than that of Na^+) generally utilize K^+, while those outside the cell (where the Na^+ concentration is greater than the K^+ concentration) utilize Na^+. For example, as will be described later, while most monovalent cation-activated enzymes prefer K^+ to Na^+, the blood-clotting enzyme, thrombin, which is an extracellular enzyme, prefers Na^+. Woehl and Dunn point out that the dissociation constants for Na^+ and K^+ binding are well below the physiological concentration of these ions.[4] This means that the binding sites for activating cations are saturated and their existence is 'a permanent feature of catalysis.' In general, it is found that activating properties are maintained if K^+ is replaced by $NH_4{}^+$ and Rb^+. The replacement is poor for an exchange with Na^+ and succeeds in maintaining activating properties rarely, if at all, when K^+ is exchanged for Li^+.[1]

Biological effects are different for Na^+ and K^+. The smaller ionic radius and therefore higher charge density on Na^+ gives this ion a more favorable hydration free energy. The strength of the ligand field at the metal site and the ionic radius of the metal ion can provide part of the basis for selectivity in the metal ion binding to proteins. The four cations Na^+, K^+, Mg^{2+}, and Ca^{2+} are simple, each with a single oxidation state (+1 or +2). They lack easily excitable, unshared valence electrons. They bind ligands by electrostatic interactions rather than other types of binding and they are classified as 'hard', because they are not readily polarized and are deformed only with difficulty (*see* ***Hard & Soft Acids and Bases***).[10] They tend to bind to 'hard' ligands, notably those containing oxygen atoms. Ligands bind these cations less readily by way of nitrogen atoms and very rarely, if at all, by way of 'soft' sulfur atoms. Ammonium ions are the same size as Rb^+, similar to K^+. The monovalent cations have weak positive charges and therefore would be expected to be more readily controlled. They are frequently found near divalent cations, often with bridging ligands. The positive charge of K^+ in peroxidases may exert an electrostatic effect that can influence the redox properties of a distant center.

Metal ions lose water from their hydration spheres when they bind to complexing agents or to biological macromolecules. The strength of binding of a monovalent metal ion to a site on a protein molecule is determined by the competition between water molecules and metal ions for the site. Selectivity will occur as a result of ionic size and the strength and nature of the attractive forces in the protein site. For example, a large rigid cavity for binding would favor a large cation, particularly if the directionalities of unpaired electrons in the cavity were appropriate for binding that metal ion. Furthermore, shielding of the cavity from a solvent would also be advantageous.

The four ions have different sizes, as shown in Table 1. Of these, magnesium is the smallest. In addition, the coordination numbers of these cations, that is, the number of liganding atoms that can pack around the cation in the first coordination sphere vary, ranging from six for magnesium to higher values and near eight for potassium. Na^+ and K^+, however, have only a weak tendency to form complexes. On the other hand, Mg^{2+} and Ca^{2+} have moderate tendencies to complex formation, particularly magnesium that has a high charge-to-radius value (the highest of any biologically important cation). They are therefore utilized to an advantage in the action of many enzymes.

Proteins bind these four cations with strengths that depend on the size of the cation and its charge. The higher the charge, the better the cation binds; the binding of potassium and sodium ions is poorer than that of magnesium and calcium ions. The size is also important and a protein often provides a pocket of the correct size so that it can distinguish between

Table 1 Sizes and charge-to-radius ratios of cations[11–13]

Cation	Ionic radius (Å)	Charge-to-radius ratio	Metal-oxygen distance (Å)	Average coordination number
Mg^{2+}	0.65	3.1	1.95	6.0
Ca^{2+}	0.99	2.0	2.25	6.4
Na^+	0.95	1.1	2.23	7.3
K^+	1.33	0.8	2.46	7.9

the two types of cations. It is shown in Table 1 that each of the four cations has very different characteristics with respect to size and charge, and these differences are utilized effectively by enzymes. For example, in pyruvate kinase there are two types of cation-binding sites. One binds cations smaller than Mn^{2+} (Mg^{2+}, Ni^{2+}, Co^{2+}, and Zn^{2+}), as for example, at the ATP-binding site, while the other binds larger cations (Ca^{2+}, Cd^{2+}, K^+) at the substrate-binding site.

Magnesium has a much higher affinity for water than do the other three cations. It is found in many crystal structures as Mg^{2+} $(H_2O)_6$, that is, octahedrally surrounded by six water molecules. Its high affinity for phosphate groups is often commented on in texts, and its complex with ATP (Mg-ATP) is a very important component of many enzymatic reactions. Surprisingly, however, in the crystal structure of $Mg_3(PO_4)_2{\cdot}22H_2O$ there are no $Mg{\cdots}O{-}P$ interactions, but each magnesium and each phosphate ion are surrounded by water molecules.[14] From this, it may be inferred that magnesium prefers to bind water molecules over phosphate groups. Since magnesium shows such a partiality for water, it is not surprising that it has a slower rate of water exchange than do the other three cations (10^{-6} s compared with 10^{-7} to 10^{-10} s for sodium, potassium, and calcium ions).

It is found, from crystal-structure determinations, that Na^+ and K^+ do not have spatial restraints on the coordination of ligands in the way that Ca^{2+} and Mg^{2+} do. Therefore, when monovalent cations bind functional groups on a protein, they do not tend to reorganize those groups in the way that divalent metal cations will. This was shown by an analysis of the manner by which cations bind to carboxylate groups in crystal structures.[15] It was found that sodium and potassium ions bind both in the plane of the carboxylate group and around it, out of the plane. On the other hand, magnesium and calcium ions tend to bind only in the plane of the carboxyl group. Of these two, in general, only calcium ions share the two oxygen atoms of the carboxylate group equally. This latter ability may explain the tendency of calcium ions to cross-link proteins (via carboxyl groups, as in blood clotting), while magnesium does not. In addition, the binding of ligands to magnesium ions is almost invariably octahedral and rigid. By contrast, calcium, sodium, and potassium ions, with more variable coordination numbers, show more flexibility in the geometry of ligand binding than do magnesium ions.

3 CONTROL OF CATION CONCENTRATIONS IN CELLS

The four cations Na^+, K^+, Mg^{2+}, and Ca^{2+}, while abundant in the body, are controlled by it. All the processes and their controls whereby animals maintain their internal biochemistry in a uniform and stable manner are described by the term ‘homeostasis’ (*see* ***Metallochaperones & Metal Ion Homeostasis***). These processes comprise the basis of life, and the maintenance of the size of a cell is very important so that it does not dry out or become so full of material that it swells and eventually bursts. This maintenance is done by control of the movement of ions in and out of the cell. The movement of water molecules across membranes that are permeable to water but not to solute (dissolved materials) is called osmosis. Water moves to the side of the membrane with the lower concentration of water (higher solute concentration), thereby diluting the solute.

In order to maintain the cytoplasmic concentrations of Na^+ below and K^+ above those in the extracellular fluid, it is advantageous to have active transport, that is, a process requiring energy. Active transport requires a coupled input of energy and this is the method needed in the cell because the flow of cations is from lower to higher concentrations, the opposite of that for passive transport. Sodium ions have to be pumped out of the cell in spite of the fact that their concentration is higher outside the cell than within it. There is also a steep chemical gradient to be overcome when pumping potassium ions into the cell. The system that controls cation concentrations by active transport is called a pump, and the pump that controls the balance of sodium and potassium ions is called a ‘sodium pump’, the (Na^+, K^+)-ATPase. When a cell swells, the pump is activated.

The (Na^+, K^+)-ATPase is a mammalian enzyme that pumps sodium ions out of the cell and potassium ions into the cell. It requires Mg^{2+}, which acts as a substrate and as a regulator. The energy for this process of pumping ions against the electrochemical gradient is obtained from the free energy of hydrolysis of ATP (12 kcal of energy liberated for every mole of ATP converted to ADP). The net result is that three sodium ions are eliminated from the cell for every two potassium ions that are brought into it.

Calcium ions are also transported into the cell by a pump, which is a Ca^{2+}-dependent ATPase. This pump is necessary because the calcium ion concentration is four orders of magnitude higher outside than inside living cells. Calmodulin regulates the level of calcium ions and hence the calcium pump. When the calcium concentration decreases, calcium is dissociated from calmodulin and the calcium pump is inactivated. The structure of such a pump from the sarcoplasmic reticulum is reported at 8 Å resolution.[16,17] This pump couples ATP hydrolysis with cation transport. The protein contains 10 transmembrane helices. A distinct cavity was located that led to the putative calcium-binding site, suggesting a path for a calcium passage.

The control of K^+ is illustrated by the 3.2 Å crystal structure of a potassium channel.[18] This allows potassium ions but not sodium ions to diffuse through a lipid bilayer that they would not normally permeate. An X-ray diffraction analysis has shown that the channel resembles an 'inverted tepee' or cone with the wide part opening to the outside of the cell membrane. This wide part is, however, almost filled by membrane-spanning α-helices that provide dipoles that aid K^+ movement through the channel and a 'selectivity filter' that provides a narrow opening with a diameter adjusted to favor K^+ and repel Na^+. As K^+ enters, it is dehydrated and coordinates to main-chain carbonyl groups. The pore is long enough to accommodate two K^+ that repel each other so that the inner one progresses into a wider aqueous chamber and on to the interior of the cell.

4 SODIUM- AND POTASSIUM-ACTIVATED ENZYMES

The crystal structures of several sodium- and potassium-activated enzymes have now been determined and the position of the monovalent cation established. Structural data are listed in the Protein Data Bank (PDB).[19] They provide a clue (but not an absolute proof) to their location within the enzyme on activation. Further biochemical studies may be necessary to verify this finding. Some examples of these structures are presented here. The first example (thrombin) is a sodium-activated enzyme, but the others are potassium-activated enzymes.

4.1 Thrombin

Thrombin, the final enzyme in the coagulation cascade, is a serine protease that causes blood clotting. It cleaves and converts fibrinogen to an insoluble fibrin clot so that wound repair can commence. It can also behave as an anticoagulant when protein C is brought into the picture. The enzyme cleaves at specific arginine residues aided in its selectivity by nearby sites on the enzyme. Human α-thrombin is a sodium-activated enzyme, in that its activity is greatly increased in the presence of Na^+. Wells and Di Cera[9] point out that the blood stream concentrations are higher for Na^+ than K^+ and that thrombin has adjusted to this environment. The binding of monovalent cations has been shown spectroscopically to facilitate a change in the conformation of the enzyme. Na^+ switches the enzyme between two conformational states, one of which activates fibrinogen and the other cleaves protein C. This function is referred to as an allosteric switch because the Na^+ converts the thrombin from a slow (Na^+-free) form that cleaves protein C to a fast (Na^+-bound) form that enhances substrate binding and fibrinogen cleavage.[20] Both forms are normally found in the blood because the Na^+ concentration is not high enough to saturate the site. A decrease in Na^+ reduces fibrinogen cleavage and therefore slows the clotting time.

Thrombin binds sodium better than potassium. The cation is bound by backbone carbonyl groups of Arg221a and Lys224 and by four buried water molecules.[21,22] One water molecule connects the sodium ion to OD2 of Asp819; this accounts for the primary specificity of the enzyme. When sodium is released, Asp819 reorients and this perturbation extends to the catalytic site.

It is not necessarily the strength of monovalent cation binding that determines the activating ability. This was demonstrated by Di Cera and coworkers.[23] They were able to convert thrombin from a sodium-specific enzyme to a potassium-specific enzyme. This was done by site-directed mutagenesis by redesigning a loop in the backbone that defines the geometry near the cation-binding site and controls access to it. They found, however, that, while the mutant enzyme bound K^+ better than Na^+, it was still preferentially activated by K^+ rather than Na^+.

4.2 2,2-Dialkylglycine Decarboxylase

This enzyme catalyzes a decarboxylation and transamination converting 2,2-dialkylglycine with pyruvate into a ketone, L-alanine, and carbon dioxide. It is activated by K^+ and inhibited by Na^+ and Li^+. The enzyme has a structure made up of a dimer of dimers. The catalytic site is near the interface between monomers of the dimeric unit and involves residues from both subunits.[24–26] There are two monovalent cation sites per monomer, one structural and the other regulatory. The regulatory K^+ causes changes in the active site, especially near Ser80 and Tyr301. Crystal structures have been reported, one with K^+ and Na^+, another with two Na^+ in the metal ion sites and the results were compared. Hohenester showed that Li^+ behaves like Na^+, while Rb^+ behaves like K^+. When potassium is replaced by sodium, the link to Ser80 is lost and its hydroxyl group is replaced by water. This change is caused by the ion size and coordination number. It results in a large change in conformation and a change at the catalytic site. Na^+ or Li^+ binding at the regulatory site is strongly inhibitory because of insertion of extra water molecules as metal ion ligands.

4.3 Pyruvate Kinase

Pyruvate kinase catalyzes the conversion of phosphoenolpyruvate and ADP to pyruvate and ATP. A proton is taken up in the reaction. The enzyme binds one K^+ and two Mg^{2+} ions. The 2.9 Å crystal structure shows that the K^+ interacts directly with the migrating phosphoryl group and indirectly with residues in the active site.[27,28] Activity with Na^+ is about 9% that of K^+. Figure 1 shows the geometry of the active site. Oxalyl phosphate is a substrate for pyruvate kinase and the ATP-oxalate complex (shown in the figure) is the product of the reaction. Each oxygen atom of the γ-ATP interacts with a metal ion, and it is possible that this prepares the phosphorus for nucleophilic attack. One oxygen atom of the oxalate is 3 Å from the γ-phosphorus of ATP, and is in position for an in-line transfer of the phosphoryl group from ATP to oxalate. This alignment is aided by the metal ion binding.

Many pyruvate kinases show the active-site geometry illustrated in Figure 1, but others, such as those from *Escherichia coli* and *Corynebacterium glutamicum* do not require monovalent cations for activation. In these, Glu117 in the K^+ binding site is replaced by lysine. This lysine behaves as an ‘internal monovalent cation’, that is, a tethered ammonium ion, for which the single positive charge takes the place of K^+.[29] Significantly, this experiment provides confirmation of the activation site of K^+.

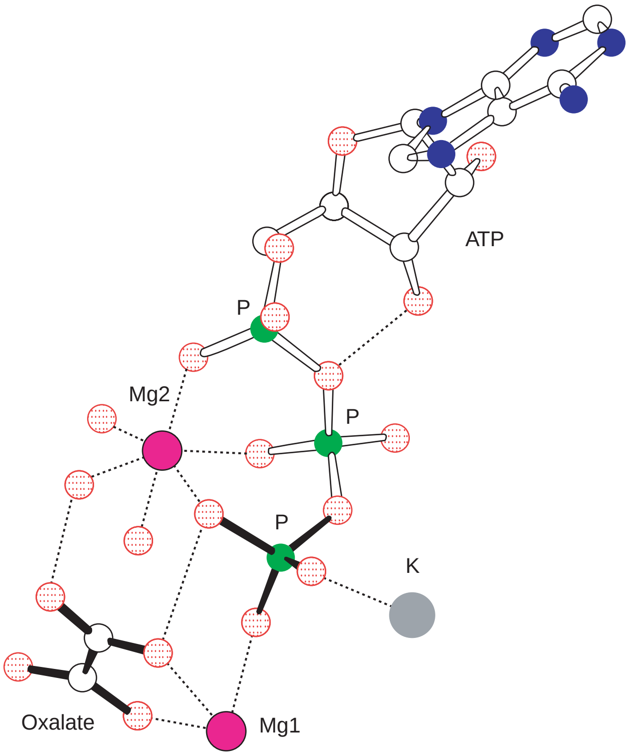

Figure 1 The active site of pyruvate kinase, drawn from PDB file 1A49, showing bound Mg^{2+}, K^+, ATP, and oxalate.[28] The bonds of the oxalate and the γ-phosphate of ATP are black. Mg1 is coordinated by two oxygen atoms of oxalate, one of the γ-phosphate of ATP, oxygen atoms of Glu271 and Asp295, and one water molecule. Mg2 is coordinated by three oxygen atoms of ATP and three water molecules. K is coordinated to the carbonyl group of Thr113, Ser76, Asp112, Asn74, the γ-phosphate of ATP (as shown), and a water molecule. Note that the K^+ interacts with a substrate. In this and Figure 2, drawn with the program ICRVIEW,[54] atoms of O are stippled, of N are filled, and of C are open

4.4 Diol Dehydrase

Diol dehydrase is a bacterial enzyme that catalyzes the dehydration of 1,2-diols to aldehydes. The structure at 2.1 Å showed that the enzyme binds K^+.[30,31] The K^+ has seven ligands: the two hydroxyl groups of the substrate, propane-1,2-diol, and five oxygen atoms of active-site residues. It is thought that the K^+ positions the substrate within the active-site cavity and also provides space between radical intermediates and amino acid residues in the active site, thereby protecting the enzyme from radical attack. The K^+ may also participate in the migration of the hydroxyl group on C2 to C1 of the radical form of 1,2-propanediol. The structure of glycerol dehydrase has approximately the same features.[32]

4.5 Inosine Monophosphate Dehydrogenase

In inosine monophosphate dehydrogenase, the monovalent metal ion accelerates the hydride transfer step of the reaction with apparently few other effects on the enzyme structure. Probably the monovalent cation is involved in helping position the nicotinamide cofactor. The active site and location of the potassium ion are shown in Figure 2.[33] Mycophenolic acid in this diagram is an inhibitor that is thought to lock inosine monophosphate into the active site, as shown. Note the large distance between the inhibitor (in the active site) and the K^+.

4.6 Tryptophanase

This enzyme cleaves L-tryptophan to give indole, pyruvate, and ammonia by β-elimination and deamination. It is activated by various monovalent cations, especially ammonium ions ($NH_4^+ > K^+ > Cs^+ > Na^+ > Li^+$).[4] The enzyme is a tetramer. Its catalytic sites, as well as the K^+-binding sites, lie

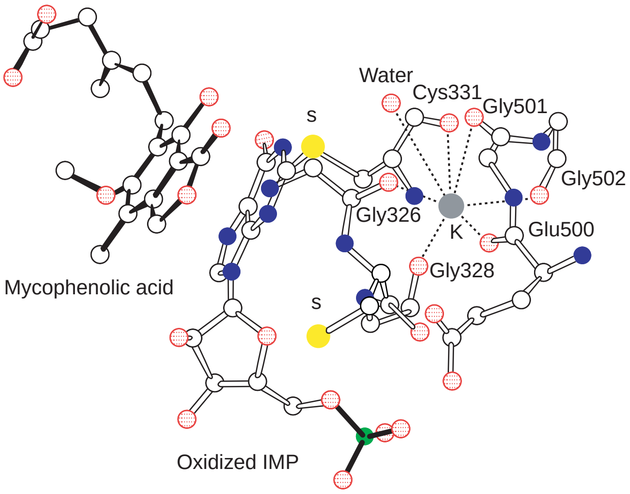

Figure 2 The active site of inosine monophosphate dehydrogenase, drawn from PDB file 1JR1.[33] This shows the inhibitor mycophenolic acid at the active site, stacking against PLP. The K^+ site is distant from the active site

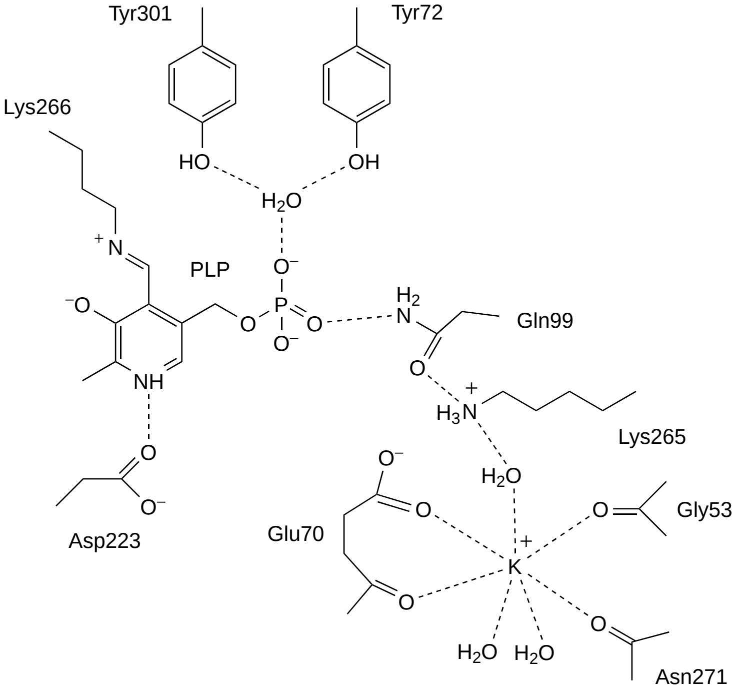

Figure 3 Diagram of the active site of tryptophanase[34] showing the large distance between the K^+ and the active site. The distance between K^+ and N1 of PLP is 15.5 Å

at the interface of two subunits.[34,35] The crystal structure at 2.1 Å resolution shows that the K^+ site is about 6 Å from the active site and 18 Å from the nearest pyridoxal 5′-phosphate (PLP, vitamin B_6) ring.[34] The K^+ is bound to the enzyme by backbone carbonyl oxygen atoms of Gly53, Glu70, and Asn71, a side-chain carboxylate group from the same Glu70 and three water molecules; Glu70 is in a different subunit from the other protein ligands. This is diagrammed in Figure 3. In this way, both the K^+ and the PLP contribute to the stability of the catalytic dimer. It appears that K^+ binding stabilizes the ground state of the quinonoidal form of the PLP-enzyme complex and lowers the activation energy for a subsequent α-proton abstracting step, that is, the conversion of an external aldimine Schiff base to the quinonoid form. By contrast, Na^+ does not behave in this way, which may explain why it is less efficient at activating. This is in line with spectroscopic evidence. A bound coenzyme gives a spectrum with peaks at 337 and 420 nm. In the presence of K^+, this spectrum changes with pH, but not in the presence of Na^+.[35] Tyrosine phenol-lyase cleaves L-tyrosine to give phenol, pyruvate, and an ammonium ion. This enzyme is like tryptophanase.[36] The metal ions add to subunit interactions and in the absence of metal the enzyme dissociates to monomers.

4.7 Tryptophan Synthase

Tryptophan synthase catalyzes the last two reactions in the biosynthesis of L-tryptophan. This enzyme needs a monovalent cation for activity. K^+ does not play a direct role in binding the substrate or cofactor but changes some side-chain orientations. The α-subunit cleaves 3-indole-D-glycerol 3′-phosphate to α-glycerolphosphate and indole. The β-subunit replaces the β-hydroxyl of L-serine by indole to form L-tryptophan. In the reaction, the α-subunit catalyzes the conversion of 1-(indol-3-yl)glycerol 3-phosphate to indole and glyceraldehyde 3-phosphate. The indole then migrates to the β-subunit where, with serine in the presence of pyridoxal 5′-phosphate, it is converted to tryptophan. The crystal structure of tryptophan synthase at 2.8 Å resolution showed that the active sites of the α- and β-subunits are about 25 Å apart.[37,38] The two sites are connected by a largely hydrophobic intramolecular tunnel with dimensions sufficiently large to accommodate up to four molecules of indole. It was found from further studies that the tunnel could be blocked by the side chain of Phe280. It appears that various monovalent cations cause movements of Phe280 out of the tunnel, implying that Phe280 can act as a gate to control passage through the tunnel.

4.8 Other Potassium-activated Enzymes

Many crystal structures of other potassium-activated enzymes have been reported. They generally require a divalent cation and are activated by a monovalent cation that also binds. Such enzymes include amylase,[39] which has a unique Ca–Na–Ca trinuclear center, *S*-adenosylmethionine synthetase,[40] *E. coli* methionine aminopeptidase[41] in which the K^+ is 13 Å from a dinuclear metal center and rhodanese,[42] Class II fructose 1,6-bisphosphate aldolase,[43,44] ascorbate peroxidase that contains a K^+ cation that has a profound influence on the redox properties of the heme group,[45] and cytochrome P450$_{cam}$ that binds camphor more readily when K^+ is present, possibly due to stabilization of the environment of Tyr96.[46] In carbamoyl phosphate synthetase, which also requires K^+, Glu214 bridges the K^+ and ADP forming a 'K loop' that allows communication from K^+ to the active site via the carboxylate of this glutamic acid.[47] In the heat-shock protein Hsc70, two potassium ions are bound in the nucleotide-binding site.[48]

5 MAGNESIUM- AND CALCIUM-ACTIVATED ENZYMES

Activation by divalent cations is more difficult to assess because divalent cations are often integral parts of the enzyme mechanism. Some of the guidelines for determining whether a cation activates enzymes were given above. About 60–65% of total body magnesium is in bone and 27% in muscle. The remaining is in living cells and extracellular fluids. The insolubility of calcium phosphate has meant that calcium is unsuitable as an intracellular cation. This leaves magnesium as the major intracellular ion for the complexation of phosphate. Magnesium ions are used as cofactors in phosphate transfer, to carry out the transfer of substituted phosphoric acids. Examples are provided by kinases (that transfer phosphoryl groups between ATP and a metabolite), synthetases, and phosphatases. They also catalyze the transfer of acyl groups, hydration-dehydration or tautomeric reactions, carbonyl addition reactions, and dehydrogenases. Magnesium with its double positive charge neutralizes anionic centers in proteins, particularly phosphate and carboxylate groups. Magnesium ions are smaller than calcium ions and bind with a coordination number that is generally six, while the coordination number of calcium is seven or eight. Thus, Mg^{2+} can fit in Ca^{2+} holes, but the opposite is not true. Often calcium binds both oxygen atoms of a carboxylate group (bidentate binding), but when magnesium takes its place only one of the oxygen atoms is bound to the metal ion.

5.1 Magnesium

The features of magnesium ions that are of particular significance are their strong affinity for water and their rigid octahedral coordination sphere which suggest they may be used to deliberately prevent motion in certain regions of the enzyme system and also to orient functional groups as needed for catalysis.[49] Magnesium shields the negative charges of the phosphate groups because otherwise these charges would tend to repel the electron pairs of the attacking nucleophile, especially those with anionic character. DNA polymerase requires magnesium to provide the proper conformation of the arriving nucleotide triphosphate for incorporation into nascent DNA in a 5′ to 3′ direction. When magnesium is replaced by manganese, there is an increase in the speed of replication and a decrease in the precision of the operation. Thus, nature has opted for magnesium throughout nucleic acid enzymology to maximize fidelity at the expense of speed in transmitting the genetic code.

The function of magnesium in enzyme activity may either be to form a complex with the substrate, as in the magnesium-ATP complex formed in creatine kinase and phosphofructokinase, or to bind to the enzyme and either produce an allosteric activation or play a direct role in catalysis. If an enzyme is known to utilize a nucleotide as one of its substrates, it can be assumed that magnesium is also required for catalysis. The magnesium ion possibly acts as an electrostatic shield. The enzyme pyruvate kinase, described earlier, and shown in Figure 1, requires both magnesium and potassium ions for maximal activity.

5.2 Alkaline Phosphatase

One example of a magnesium-activated enzyme is *E. coli* alkaline phosphatase. This is a zinc-binding enzyme with a high pH optimum (hence the name) that catalyzes phosphoryl transfer to various alcohols. When a phosphomonoester binds to the active site, a serine hydroxyl group (Ser102) is phosphorylated and the product alcohol leaves. The enzyme binds one magnesium and two zinc ions per active site.[50] A crystal structure shows the phosphate group bound by arginine and the two zinc ions. The magnesium ion is bound to Asp51, Glu322, Thr155, and three water molecules. Both zinc ions bind to the phosphate group and one (Zn2) also binds to Asp51. Lys328 is constrained by Asp153, which binds to a magnesium-bound water molecule. The importance of Asp153 is evident. Replacement of this aspartate by histidine (Asp153His) is found to give an enzyme that binds three zinc ions, no magnesium.[51] This third site (Zn3) is tetrahedral rather than octahedral as found when magnesium is present. The result is that Zn3 is bound by Asp51, Glu322, Thr155, and His153 but the link of Asp51 to Zn2 is lost, as is the constraint of Lys328 by Asp153. Therefore Lys328 binds to the phosphate, and the hydroxyl group of Ser102 interacts with Zn2. This means that the all-important Ser102 has decreased activity as a nucleophile as a result of the mutation, and the resulting enzyme (Asp153His) is inactive. However, when excess magnesium is added it regains activity. In this example, the activating power of magnesium is evident.

5.3 Klenow Fragment of DNA Polymerase

In the Klenow fragment of DNA polymerase I (the 3′,5′-exonuclease), two metal ions are used.[52] One stabilizes the transient pentacovalent species and the leaving of a 3′ oxyanion (Mg^{2+}), and the other facilitates the formation of an attacking water molecule or hydroxyl group (Zn^{2+}).

5.4 Calcium (*See Calcium-binding Proteins*)

Ninety-nine percent of the calcium and 85% of the phosphorus in the body are found in bones, mostly a poorly crystalline hydroxyapatite $Ca_{10}(PO_4)_6(OH)_2$. In addition, calcium is involved in blood coagulation and is an intermediary factor between impulses and muscle contraction. Calcium has an activating effect on enzymes such as phosphorylase kinase and pyruvate dehydrogenase (lipoamide)-phosphatase.

In small organic structures, the coordination number of calcium varies from 6 to 10. The geometry of this coordination varies from octahedra (6) to pentagonal bipyramids (7) to square antiprisms (8), possibly with additional capping ligands (9 and 10). Two types of calcium-binding proteins have been identified. The first group contains enzymes stabilized by calcium ions that may even be used in catalysis. The second group contains proteins that bind calcium reversibly and modulate the action of other enzymes. The calcium-binding group in this case is generally a helix-loop-helix structure (referred to as the EF hand).[53] The motif can be thought of, in terms of a right hand, as an index finger representing the E-helix, a curved second finger, the loop, and a thumb the F-helix. Such EF hands have a well-conserved calcium-binding site. In each EF hand, there are seven oxygen atoms around the calcium ion with an octahedral arrangement and one carboxyl group contributing two oxygen atoms (bidentate).

6 SUMMARY

The significant theme in the action of cation-activated enzymes is the control that the cations have on the action of the enzyme. This subject needs more study with the hope that the information gained may help us understand how we can harness and control in more detail the action of certain enzymes. The role of potassium has been stressed here because so much recent structural work has clarified the binding sites and indicated possible modes of action. Overall, the action of such cations is due to their electric charge (which aids the chemistry of the mechanism), their size (which affects coordination geometry), and the geometry of their first coordination sphere (which affects their power to orient functional groups as required for catalysis). The borderline between those cation-binding enzymes that are activated by the cation and those that use the cation as an essential component of the reaction is not clear, especially when the ‘activating cation’ is divalent. Further structural and biochemical studies will clarify this subject.

7 RELATED ARTICLES

Biomineralization; Calcium-binding Proteins; Metal Ion Toxicity; Metal-mediated Protein Modification; Metalloregulation; Nucleic Acid–Metal Ion Interactions; Nutritional Aspects of Metals & Trace Elements.

8 REFERENCES

1. H. J. Evans and G. J. Sorger, *Annu. Rev. Plant Physiol.*, 1966, **17**, 47.
2. C. H. Suelter, *Science*, 1970, **168**, 789.
3. P. D. Boyer, H. A. Lardy, and P. H. Phillips, *J. Biol. Chem.*, 1942, **146**, 673.
4. E. U. Woehl and M. F. Dunn, *Coord. Chem. Rev.*, 1995, **144**, 147.
5. T. M. Larsen and G. H. Reed, Interaction of Sodium and Potassium with Proteins, in ‘Handbook on Metalloproteins’, I. Bertini, A. Sigel and H. Sigel eds., Marcel Dekker, Inc, New York, Basel, 2001, p. 9.
6. G. D. Markham, Monovalent Cation Activation of IMP Dehydrogenase, ‘Inosine Monophosphate Dehydrogenase: A Major Therapeutic Target’, K. W. Pankiewicz and B. M. Goldstein eds., ACS Symposium, series 839, Washington, DC, 2003, p. 169.
7. M. Nayal and E. Di Cera, *J. Mol. Biol.*, 1996, **256**, 228.
8. L. Pauling, *Chem. Eng. News*, 1946, **24**, 1375.
9. C. M. Wells and E. Di Cera, *Biochemistry*, 1992, **31**, 11721.
10. R. G. Pearson, *J. Amer. Chem. Soc.*, 1963, **85**, 3533.
11. R. D. Shannon, *Acta Cryst.*, 1976, **A32**, 751.
12. I. D. Brown, *Acta Cryst.*, 1988, **B44**, 545.
13. J. P. Glusker, *Adv. Protein Chem.*, 1991, **42**, 1.
14. L. W. Schroeder, M. Mathew, and W. E. Brown, *J. Phys. Chem.*, 1978, **82**, 2335.
15. C. J. Carrell, H. L. Carrell, J. Erlebacher, and J. P. Glusker, *J. Am. Chem. Soc.*, 1988, **110**, 8651.
16. P. Zhang, C. Toyoshima, K. Yonekura, N. M. Green, and D. L. Stokes, *Nature*, 1998, **392**, 835.

17. A. N. Martonosi and S. Pikula, *Acta Biochim. Pol.*, 2003, **50**, 337.
18. D. A. Doyle, J. M. Cabral, R. A. Pfuetzner, A. Kuo, J. M. Gulbis, S. L. Cohen, B. T. Chait, and R. MacKinnon, *Science*, 1998, **280**, 69.
19. F. C. Bernstein, T. F. Koetzle, G. J. Williams, E. E. Meyer, M. D. Brice, J. R. Rodgers, O. Kennard, T. Shimanouchi, and M. Tasumi, *J. Mol. Biol.*, 1977, **112**, 535.
20. E. Di Cera, *Chest*, 2003, **124**, 11S.
21. W. Bode, D. Turk, and A. Karshikov, *Protein Sci.*, 1992, **1**, 426.
22. E. Di Cera, E. R. Guinto, A. Vindigni, Q. D. Dang, Y. M. Ayala, M. Wuyi, and A. Tulinsky, *J. Biol. Chem.*, 1995, **270**, 22089.
23. S. Prasad, K. J. Wright, D. B. Roy, L. A. Bush, A. M. Cantwell, and E. Di Cera, *Proc. Natl. Acad. Sci. USA*, 2003, **100**, 13785.
24. E. Hohenester, J. W. Keller, and J. N. Jansonius, *Biochemistry*, 1994, **33**, 13561.
25. M. D. Toney, E. Hohenester, S. W. Cowan, and J. N. Jansonius, *Science*, 1993, **261**, 756.
26. M. D. Toney, E. Hohenester, J. W. Keller, and J. N. Jansonius, *J. Mol. Biol.*, 1995, **245**, 151.
27. T. M. Larsen, L. T. Laughlin, H. M. Holden, I. Rayment, and G. H. Reed, *Biochemistry*, 1994, **33**, 6301.
28. T. M. Larsen, M. M. Benning, I. Rayment, and G. H. Reed, *Biochemistry*, 1998, **37**, 6247.
29. L. T. Laughlin and G. H. Reed, *Arch. Biochem. Biophys.*, 1997, **348**, 262.
30. N. Shibata, J. Masuda, T. Tobimatsu, T. Toraya, K. Suto, Y. Morimoto, and N. Yasuoka, *Structure*, 1999, **7**, 997.
31. J. Masuda, N. Shibata, Y. Morimoto, T. Toraya, and N. Yasuoka, *Structure*, 2001, **8**, 775.
32. M. Yamanishi, M. Yunoki, H. Sato, J. Matsui, A. Dokiya, Y. Iuchi, K. Oe, K. Suto, N. Shibata, Y. Morimoto, N. Yasuoka, and T. Toraya, *Eur. J. Biochem.*, 2002, **269**, 4484.
33. M. D. Sintchak, M. A. Fleming, O. Futer, S. A. Raybuck, S. P. Chambers, P. R. Caron, M. A. Murdo, and K. P. Wilson, *Cell*, 1996, **85**, 921.
34. M. N. Isupov, A. A. Antson, E. J. Dodson, G. G. Dodson, I. S. Dementieva, L. N. Zakomirdina, K. S. Wilson, Z. Dauter, A. A. Lebedev, and E. H. Harutyunyan, *J. Mol. Biol.*, 1998, **276**, 603.
35. R. S. Phillips, I. Richter, P. Gollnick, P. Brzovic, and M. F. Dunn, *J. Biol. Chem.*, 1991, **266**, 18642.
36. A. A. Antson, T. V. Demidkina, P. Gollnick, Z. Dauter, R. L. von Tersch, J. Long, S. N. Berezhnoy, R. S. Phillips, E. H. Harutyunyan, and K. S. Wilson, *Biochemistry*, 1993, **32**, 4195.
37. S. Rhee, K. D. Parris, S. A. Ahmed, E. W. Miles, and D. R. Davies, *Biochemistry*, 1996, **35**, 4211.
38. C. C. Hyde, S. A. Ahmed, E. A. Padlan, E. W. Miles, and D. R. Davies, *J. Biol. Chem.*, 1988, **263**, 17857.
39. M. Machius, N. Declerck, R. Huber, and G. Wiegand, *Structure*, 1998, **6**, 281.
40. F. Takasugawa, S. Kamitori, and G. D. Markham, *J. Biol. Chem.*, 1996, **35**, 2586.
41. W. T. Lowther, A. M. Orville, D. T. Madden, S. Lim, D. H. Rich, and B. W. Matthews, *Biochemistry*, 1999, **38**, 7678.
42. L. J. Lijk, C. A. Trofs, K. H. Kalk, M. C. H. De Maeyer, and W. G. J. Hol, *Eur. J. Biochem.*, 1984, **142**, 399.
43. D. R. Hall, L. E. Kemp, G. A. Leonard, K. Marshall, A. Berry, and W. N. Hunter, *Acta Cryst.*, 2003, **D59**, 611.
44. V. Villeret, S. Huang, H. J. Fromm, and W. N. Lipscomb, *Proc. Natl. Acad. Sci. USA*, 1995, **92**, 8916.
45. W. R. Patterson and T. L. Poulos, *Biochemistry*, 1995, **34**, 4331.
46. M. Vidakovic, S. G. Sligar, H. Li, and T. L. Poulos, *Biochemistry*, 1998, **37**, 9211.
47. J. B. Thoden, F. M. Raushel, M. M. Benning, I. Rayment, and H. M. Holden, *Acta Cryst.*, 1999, **D55**, 8.
48. S. M. Wilbanks and D. B. McKay, *J. Biol. Chem.*, 1995, **270**, 2251.
49. C. W. Bock, A. K. Katz, and J. P. Glusker, *J. Amer. Chem. Soc.*, 1995, **117**, 3754.
50. E. E. Kim and H. W. Wyckoff, *J. Mol. Biol.*, 1991, **218**, 449.
51. J. E. Murphy, X. Xu, and E. R. Kantrowitz, *J. Biol. Chem.*, 1993, **268**, 21497.
52. L. S. Beese and T. A. Steitz, *EMBO J.*, 1991, **10**, 15.
53. R. H. Kretsinger, *Annu. Rev. Biochemistry*, 1976, **45**, 239.
54. J. Erlebacher and H. L. Carrell, ‘ICRVIEW. Computer graphics program’, from The Institute for Cancer Research, Fox Chase Cancer Center, Philadelphia, PA, 1992.

Acknowledgment

This work was supported by grants CA10925 and CA06927 from the National Institutes of Health and by an appropriation from the Commonwealth of Pennsylvania. I thank Dr. G. D. Markham for helpful discussions.

Chalcogenides: Solid-state Chemistry

Mercouri G. Kanatzidis
Michigan State University, East Lansing, MI, USA

Based in part on the article Chalcogenides: Solid State Chemistry by Patricia M. Keane which appeared in the Encyclopedia of Inorganic Chemistry, First Edition.

1 Introduction 1
2 Binary Compounds 1
3 Ternary Compounds 5
4 Quaternary Compounds 25
5 Concluding Remarks 35
6 References 35

1 INTRODUCTION

The class of chalcogenide compounds is large and its members contain combinations of various elements with the chalcogens, that is, sulfur, selenium, and tellurium. Oxygen is not included because it has a distinct and vast chemistry of its own and it must be dealt with separately. Solid-state chalcogenides generally refer to those compounds whose structure involves extended frameworks and it is to be distinguished from another class of chalcogenide compounds that involves discrete molecular species. This section aims to introduce the reader to solid-state chalcogenides with particular emphasis given to the developments of the last decade. It is not meant to be an exhaustive review article but an entry point to this area of inorganic chemistry. Therefore many interesting results will be left out. Several important review articles have appeared on the subject which, when taken collectively, capture most of the research activity of the last decade.[1–6]

There exist large structural and chemical differences between the class of oxides that is huge and the smaller class of chalcogenides. Why are oxides different from chalcogenides? Part of the answer lies in the ability of the oxide ion (O^{2-}) to adopt almost any M–O–M angle from very small (e.g. 80 deg) to 180 deg. In contrast, the chalcogenide ions (Q^{2-}) do not, and prefer a much smaller range of M–Q–M angles. This can be explained by the more extensive hybridization of s-p orbitals in S, Se, and Te relative to those of oxygen. In oxygen, s-p mixing does not occur readily because of the large energy gap between the two orbital levels. In the heavier congeners, the s-p levels come increasingly closer in energy to give rise to strong sp^3 hybridization and more rigid angular requirements.

As we move down group 16, the elements acquire an increasing tendency to catenate, that is, to form homoatomic bonds creating chains. This results not only in rings or chains in the several elemental forms known, but also in the polychalcogenide $Q_n{}^{2-}$ ($Q = S$, Se, Te; $n = 2-7$) ions that can exist in solution or in the solid-state.[7–9] The fascination of chemists with the chalcogen group has many reasons, not the least of which is the ability to form intriguing polyanions and polycations.

Sulfur and selenium have several allotropic forms with the rings of S_8 and Se_8 being the most known. Tellurium is polymeric with no known allotropes. The discovery of the cyclo-octatellurium ring (Te_8) in Cs_3Te_{22},[10] represented a landmark in chalcogen chemistry as it completed the chalcogen series S_8, Se_8, and Te_8. Indeed, Te_8 has the expected puckered ring structure. Although not a true allotrope, since it coexists with other components in Cs_3Te_{22}, Te_8 has been a missing species and had caused chemists to wonder about its stability.

Chalcogenides of the transition and main group metals can exhibit useful physical and chemical properties that are intellectually stimulating, scientifically interesting, and often useful for applications in a variety of technological fields. Some examples include optical information storage devices,[11] thermoelectric devices,[12–14] radiation detectors,[15] nonlinear optics,[16] thin film electronics,[17] solar energy conversion devices,[18] catalysis,[19] spintronics,[20] and even superconductivity.[21] Binary and ternary chalcogenides have been more extensively investigated than quaternary chalcogenides however the latter also exhibit interesting properties. Not surprisingly, therefore, during the last decade the chemistry of quaternary chalcogenides has witnessed the largest growth.[22] Indeed, we have seen an impressive expansion in solid-state chalcogenide chemistry with emphasis in materials with new compositions and structure types. In this regard, the emergence of novel synthetic methodologies such as flux and solventothermal techniques has played a major role. Unfortunately, the physical properties of many of these new chalcogenide materials have not yet been investigated.

In this article, we will present selected developments in chalcogenide solid-state chemistry of the past decade. We will begin from the simple binary systems and evolve towards more complex systems.

2 BINARY COMPOUNDS

The binary group of compounds can be divided into three major subgroups (a) alkali and alkaline earth metal chalco- and polychalcogenides, (b) valence-precise metal chalcogenides, and (c) metal-rich chalcogenides.

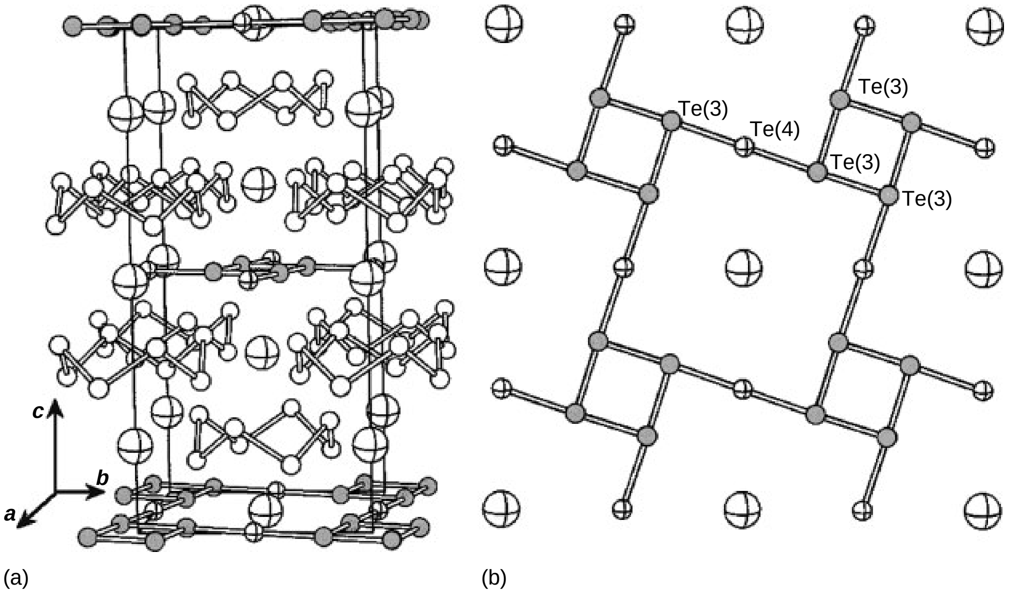

Figure 1 (a) Structure of Cs_3Te_{22} (b) The layer of $[Te_6]_n{}^{3-}$

2.1 Alkali and Alkaline Earth Metal Chalco- and Polychalcogenides A_xQ_y(A = Alkali Metal, Alkaline Earth Metal)

One of the most interesting binaries described is Cs_3Te_{22}, which was prepared solventothermally.[10,23] It contains the long time elusive Te_8 ring, which is trapped for the first time inside the crystal lattice. This has been the missing member of the well-known series of S_8 and Se_8 which in chemistry textbooks has been described as too unstable to exist. One way the Te_8 rings are stabilized in the structure is by acting as crown-ether type ligands on the Cs cations forming $(Te_8)_2Cs$ sandwiches. In addition to the Te_8 ring molecule, Cs_3Te_{22} contains the unusual infinite layer of $[Te_6]_n{}^{3-}$, a perfectly flat arrangement of Te atoms shown in Figure 1. The bond lengths in the flat layer range from 3.002(2) to 3.077(2) Å. The electronic structure of this network has been studied in detail.[24]

Along the same lines, the synthesis of Cs_2Te_{13} and Cs_4Te_{28}, tellurium-rich compounds[25] via a methanolothermal route is noteworthy. These systems are thought to be intermediates to Cs_3Te_{22}. The longest isolated tellurium anionic chain can be found in Cs_2Te_{13} (Figure 2). The bond lengths in the $[Te_{13}]^{2-}$ chain range from 2.755(2) to 2.910(2) Å and this is within the range of normal Te–Te bonds. The chains are connected in corrugated sheets via Te$\cdots$Te interactions of 3.18 and 3.26 Å to form ladders of Te_4 rectangles and chair-shaped Te_6 rings.

Another interesting binary compound is $RbTe_6$, the structure of which has the slab of $[Te_6]^{1-}$ polyanions.[26] The layers contain fused Te_6 rings with a chair conformation, which are connected via four Te–Te bonds into a layer structure (Figure 3). A T-type geometry is adopted by the resulting $TeTe_3$ units.

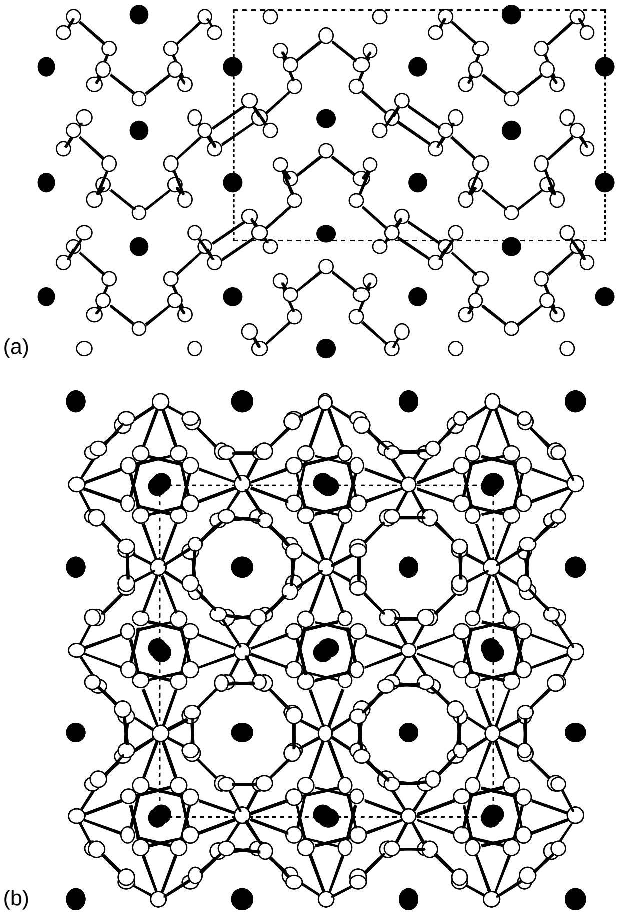

Figure 2 The structures of Cs_2Te_{13} (a) and Cs_4Te_{28} (b). Cs atoms are black solid circles

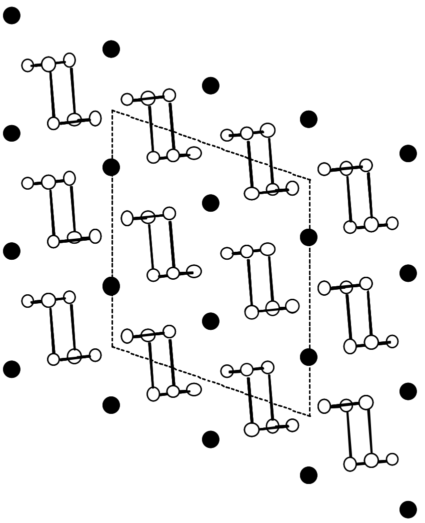

Figure 3 The structure of $RbTe_6$. The Te_6 rings are interacting via short Te–Te contacts to form a network

2.2 M_xQ_y (Valence-precise Metal Chalcogenides)

In this class of binary compounds, a new tetragonal form of boron sulfide B_2S_3 prepared by high-pressure synthesis is noteworthy. Remarkably, instead of a simple structure related to that of normal ambient pressure form of B_2S_3, it contains two kinds of supertetrahedra built up from 20 and 34 adamantane-type superclusters to form an elaborate three-dimensional framework (Figure 4).[27] These supertetrahedra are linked to each other in a unique way forming an interpenetrating zinc-blende-type structure. This compound is a wide band-gap semiconductor with an energy gap of 3.7 eV.

Another binary highlight is the $EuSe_2$ which was prepared in a Li_2Se_x flux.[28] $EuSe_2$ adopts the same structure as that of SrS_2 and $BaTe_2$ ($CuAl_2$ type) and has Eu^{2+} and $Se_2{}^{2-}$ ions. Looking down the b-axis (Figure 5), one can see the layers of Se stitched together by eight-coordinate Eu atoms. Looking down the c-axis in Figure 5, one can see rows of diselenide dumbbells. These rows are packed together in a staggered fashion and run parallel to the c-axis, separated by rows of Eu atoms. Each Eu atom is bonded to eight Se atoms in a square antiprismatic coordination. The diselenide dumbbell sits inside of a rectangular, parallelepiped pocket, shown in Figure 5. The structure of $EuSe_2$ is closely related to that of the ternary $KCeSe_4$, which is also tetragonal.[29] We can view the latter compound as deriving from $EuSe_2$ by substituting two Eu^{2+} ions with a K^+ and Ce^{3+} ion respectively. $EuSe_2$ is a semiconductor, with a well-defined energy gap, E_g, of 1.43 eV. It also behaves as a bulk antiferromagnet with a metamagnetic transition below 8 K.

2.3 M_xQ_y (Metal-rich Chalcogenides)

Metal-rich chalcogenides are those that contain enough metal atoms to form M–M bonds. These are regarded as reduced compounds with metals in very low oxidation states. Most of the metal-rich chalcogenide chemistry in the past decade had to do with early transition and rare earth element chemistry. Important in stabilizing these structures is an extensive array of M–M bonding distances. In general, it is not possible to predict the unusual compositions and structures of these compounds. Successful high temperature routes to metal-rich lanthanide chalcogenides have been developed, and for this the use of tantalum (or niobium) containers has made a great deal of difference. If glass or silica tubes are used to carry out these reactions the most common products are the REQ and RE_3Q_4 (RE = rare earth element) compounds. The metal-rich RE-Q systems are interesting species not only because of their novel compositions and structures, but also because of the localized 4f core electrons which can lead to novel electronic properties.

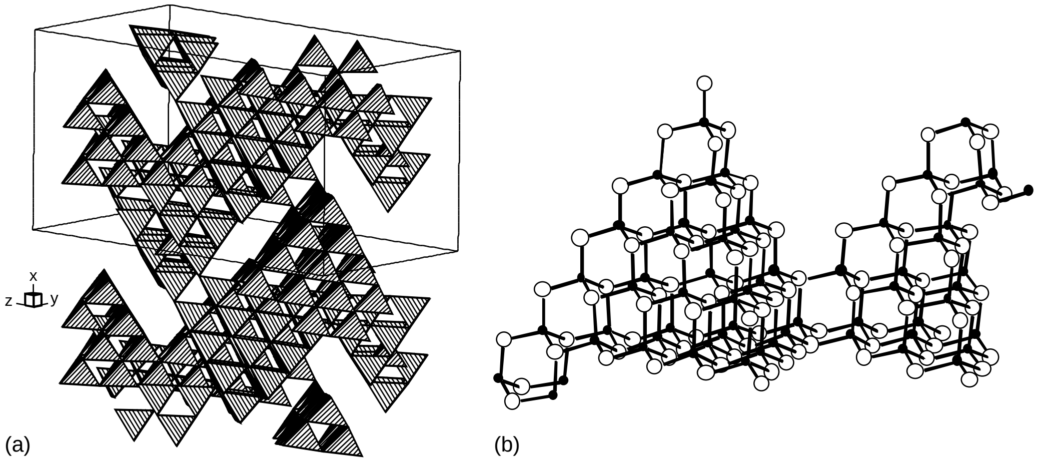

Figure 4 The structure of the high-pressure form of B_2S_3. (a) A polyhedral representation of the three-dimensional framework (b) an excised fragment from the structure showing the adamantane-type superclusters

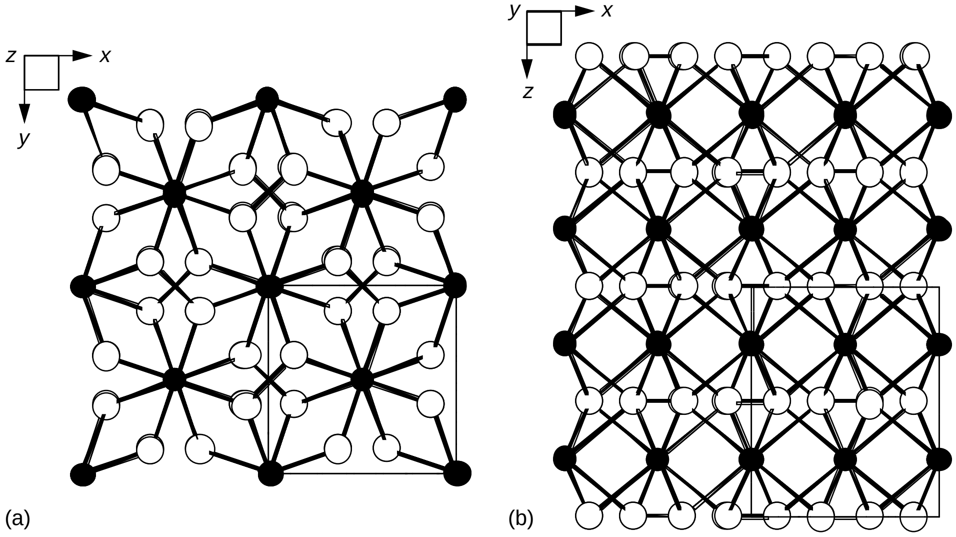

Figure 5 The structure of $EuSe_2$ viewed down (a) the *c*- and (b) the *b*-axis direction. Black atoms are Eu

There exists a remarkable range of compositions and structures, even among the M_2Q examples[30] ($M = Sc$, Ti, Zr, Hf, Nb, Ta; $Q = S$, Se, Te) and also rare earth analogs such as Dy_2Te. The building blocks observed in these structures are metal–metal bonded chains and sheets separated by Q^{2-} anions. It is an interesting example of a binary compound that shows condensed metal polyhedra in a metal-rich but in a relatively electron-poor environment. These compounds obtain their stability from a subtle synergism of metal–chalcogen and extended metal–metal bonding. Sc_2Te adopts a new structure-type with chains of condensed metal clusters.[31]

The structure of Sc_2Te contains two types of interconnected metal units separated by telluride in mono-, bi-, and tricapped trigonal prisms of metal: zigzag Sc4 chains and centrosymmetric 10-member condensed chains or ribbons that contain a spread of Sc–Sc distances (Figure 6). The more complex metal chain can be described geometrically starting with a pair of single chains of infinite trans-edge-sharing distorted octahedra that have been fused at Sc6-Sc6. As one moves from Sc to group 4 and lanthanide analogs, there are some appreciable differences because of significant changes in the metal's classical radius as well as orbital size and bond strength.

The electron-richer α-Ti_2Se[32] and Zr_2Te[33] also adopt the Sc_2Te-type structure, and increased bonding is evident in these phases. Since Zr and Sc have almost the same atomic radii, the contribution of crystal packing effects to bonding differences in Zr_2Te and Sc_2Te is small. So any differences in bonding can be attributed to other factors, such as the number of valence electrons. Theoretical studies of the bonding in Zr_2Te and Sc_2Te based on extended Hückel calculations indicate that M–Te bonding is comparable in the two compounds, whereas M–M bonding is reduced from a three-dimensional network in Zr_2Te to quasi-one-dimensional units in Sc_2Te. Despite the stability of the Sc_2Te structure-type with respect to variations in the valence electron concentration available for M–M bond formation and its adoption by Zr_2Te, it is interesting that the analogous Zr_2Se and Hf_2Te, adopt distinct types of structures.[34]

The early transition metals and rare earth elements exhibit a metal-rich chemistry that is often surprising in its structural and

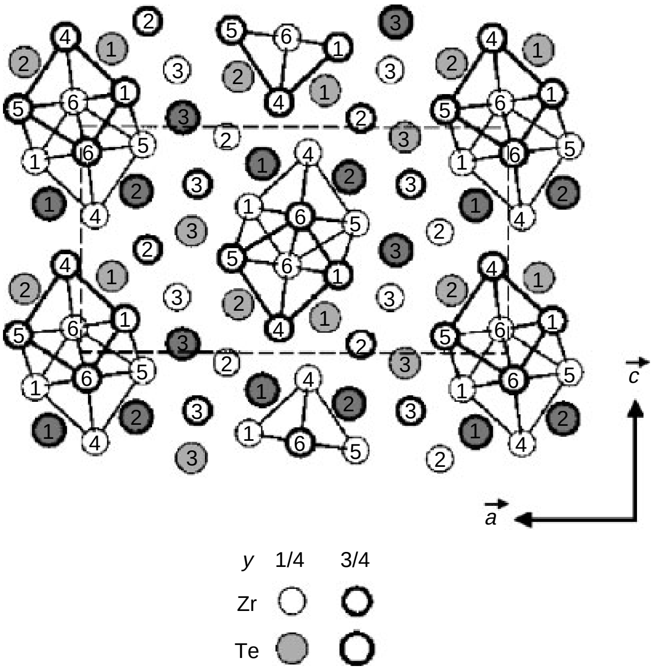

Figure 6 The structure of Sc_2Te. Some M–M bonds have been omitted for clarity

physical aspects. The fertile nature of this area is illustrated by the discovery of several interesting binary compounds within the past decade. The factors controlling the structural anisotropy of a new class of tetragonal layered compounds that includes Ta_2Se, $Ta_{2-x}Nb_xS$, Hf_3Te_2, and the ternary ZrZTe (Z = Si, Ge, Sn) have been discussed.[35] Examples of reduced binary chalcogenides of the earlier transition metals include M_8Te_3 (M = Sc, Y),[36] Sc_9Te_2,[37] Ti_8Q_3 (Q = S, Se),[38] Lu_8Te,[39] Lu_7Te,[39] $Ti_{11}Se_4$,[40] Zr_3Te, Zr_5Te_6,[41] ZrTe,[42] Hf_2Te,[34] Hf_3Te_2,[43] $Nb_{21}S_8$,[44] Ta_2Se,[45] $Ta_{97}Te_{60}$,[46] $Ta_{181}Te_{112}$,[47] and Ti_9Se_2.[48] Of these, the phases Ti_9Se_2, $Ti_{11}Se_4$, Hf_3Te_2, Ta_2Se, and the tantalum tellurides account for new, previously unknown structure types. The more metal-rich chalcogenides generally contain more condensed metal substructures, often in the form of corrugated sheets composed of condensed octahedra that are separated by chalcogen atoms. Hf_3Te_2 and Ta_2Se represent layered materials with bcc-like metal stacks coated on both sides with chalcogen atoms. Lu_8Te and Lu_7Te represent an extreme example of a metal-rich phase which can be regarded as novel substitutional derivatives of lutetium metal. Another very metal-rich phase is Sc_9Te_2 which shows a two-dimensional distortion wave.

Differences in the cohesive energy between Nb and Ta give rise to the formation of a bundle of (Nb, Ta)-rich sulfides without counterparts in the corresponding binary M–S systems. The phase richest in metal of this class has been identified as $Nb_xTa_{7-x}S_2$.[49] $(Nb, Ta)_7S_2$ is an excellent example of a mixed niobium–tantalum-rich sulfide without counterpart in the adjoining binary systems. Its structure differs markedly from those of the known binary sulfides. $(Nb, Ta)_7S_2$ forms a structure of its own type comprising distorted M_{13} icosahedra. The structure of $(Nb, Ta)_7S_2$ is composed of six crystallographic inequivalent atoms: Ta(1), M(1)–M(4) with M representing Nb or Ta, and S(1). Ta(1), M(2) and M(4) lie in mirror planes at $y = 1/4$ and $3/4$. The other atoms occupy general sites. Figure 7 shows a projection of the structure onto the *bc* plane. $Nb_xTa_{7-x}S_2$ forms a unique pentagonal antiprismatic columnar structure which – as opposed to the related structures of the Ta-rich sulfides – contains one additional metal site at which Nb accumulates. This facilitates an energetically favorable partial segregation of Nb outside the metallic columnar core.

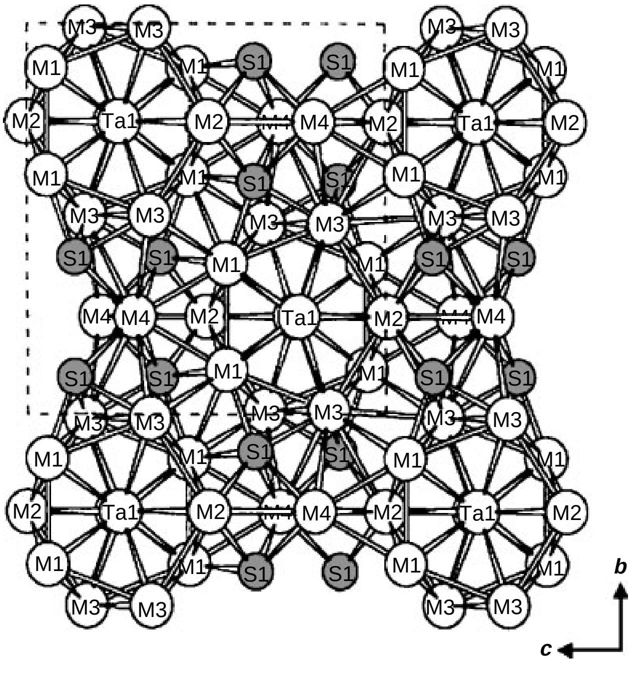

Figure 7 The structure of $Nb_{2.73}Ta_{4.23}S_2$ projected down the a-axis. (Reprinted from Ref. 49. © 2002, with permission from Elsevier)

The chemistry and metal–metal bonding is further enriched and enlarged by the addition of late transition metals that stabilize new metal frameworks (see below).

3 TERNARY COMPOUNDS

The ternary group of compounds can be divided into three major subgroups (a) alkali and alkaline earth metal chalco- and polychalcogenides, (b) valence-precise metal chalcogenides, and (c) metal-rich chalcogenides.

3.1 Compounds with Alkali and Alkaline Earth Metals

This subclass has seen rapid growth during the past decade. Compounds in this category can be conveniently viewed as pseudo-binary networks of metal chalcogenide anions which are charge-balanced with electropositive alkali or alkaline earth cations. The interactions between the electropositive cations and the $[M_xQ_y]^{n-}$ macro-anions are generally regarded to be electrostatic in nature. These compounds are normally prepared by direct combination reactions of simpler reagents, via the solventothermal method or by the polychalcogenide flux technique. The rationale behind the solventothermal method or alkali polychalcogenide flux technique has been explained in detail earlier.[4,5,50,51] Intercalation and ion-exchange chemistry as well as electrochemistry are also useful in preparing compounds at low temperatures that may not be accessible at higher temperatures.

Topotactic ion-exchange reactions can be used to prepare metastable materials. The use of alkali halides to form other alkali metal ternary chalcogenides has been used widely. The formation of other alkali topotactic derivatives from KBi_3S_5[52,53] is an example of such chemistry (equation 1).

$$KBi_3S_5 + x\text{s-AI} \longrightarrow ABi_3S_5 + KI \qquad (1)$$

$$A = \text{alkali metal}$$

The KBi_3S_5 possesses an open framework composed of edge-sharing BiS_6 octahedra to form large parallel tunnels

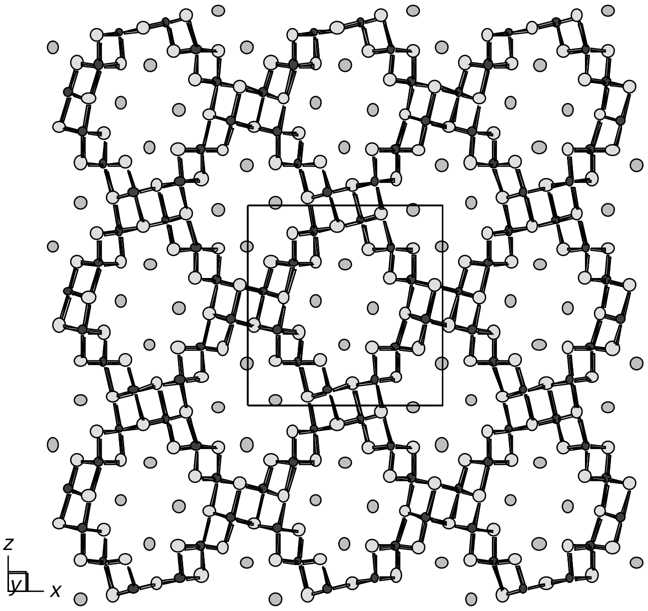

Figure 8 Structure of KBi_3S_5 with its large tunnels viewed down the large tunnels

which are occupied by K^+ ions fractionally distributed over several sites (Figure 8). The S···S distances across the channel range from 9.45–14.02 Å. The K^+ ions in KBi_3S_5 undergo one-dimensional diffusion along the large tunnels. As a result, KBi_3S_5 exhibits facile topotactic ion-exchange with various halides such as LiI, NaI, RbCl, and NH_4I. The resulting isostructural compounds, for example, $LiBi_3S_5$, $NaBi_3S_5$, and so on, cannot be prepared directly. This approach to new compositions though well-known has not been fully exploited. KBi_3S_5 is one of the early examples of a microporous, semiconducting nonoxidic framework. More information on ternary Bi compounds will be presented later.

The compounds $K_{1.10}Zr_2Se_6$, $Rb_{0.86}Zr_2Se_6$ and $Cs_{0.80}Zr_2Se_6$ were obtained by allowing mixtures of A_2Se (A = K, Rb, Cs), Zr and Se to react at 850 °C.[54] They have complex anionic layers $[Zr_2Se_6]^{x-}$ with intercalated alkali cations. The layers are built from $[ZrSe_3]$ trigonal prismatic columns, which are connected side by side by additional inter-column Zr–Se contacts, yielding an eightfold coordination for the Zr atoms. The structure is very similar to that of $ZrSe_3$ (Figure 9). In previous work in the 1970s and 1980s, $ZrSe_3$ was chemically and electrochemically intercalated with Li and Na but the structures of the products remained unknown owing to the absence of single crystals. The $A_xZr_2Se_6$ (A = K, Rb, Cs) compounds are bona-fide intercalation derivatives of $ZrSe_3$ and the fact that they were obtained in a single crystal form is significant. For the first time, the structural details of the intercalated forms are revealed and can now be compared to those of pristine $ZrSe_3$ and understood. For example, the Se–Se bond lengths are significantly altered, indicating a reduction of the Se–Se bond order owing to the electron transfer from the alkali metal.

In the early part of the periodic table, the infinite chain compounds $Cs_4Ti_3Se_{13}$, $Rb_4Ti_3S_{14}$, $Cs_4Ti_3S_{14}$, $Rb_4Hf_3S_{14}$, $Rb_4Zr_3Se_{14}$, $Cs_4Zr_3Se_{14}$, and $Cs_4Hf_3Se_{14}$ tend to be rather stable and are noteworthy.[55]

Interesting ternary chalcogenides have been prepared employing electrochemical methods via anodic dissolution of copper or silver electrodes at low temperatures.[56] For example, the series of $KCu_{7-x}S_4$ ($0 < x < 0.34$) was prepared in an ethylenediamine solution of polysulfide K_2S_x (x = 5, 6) electrolytes. Single crystal structure analysis confirmed the once ambiguous space group of these compounds and showed that the KCu_7S_4 phase which exhibits an unusual insulator-to-metal transition is non-stoichiometric.[57] The structure

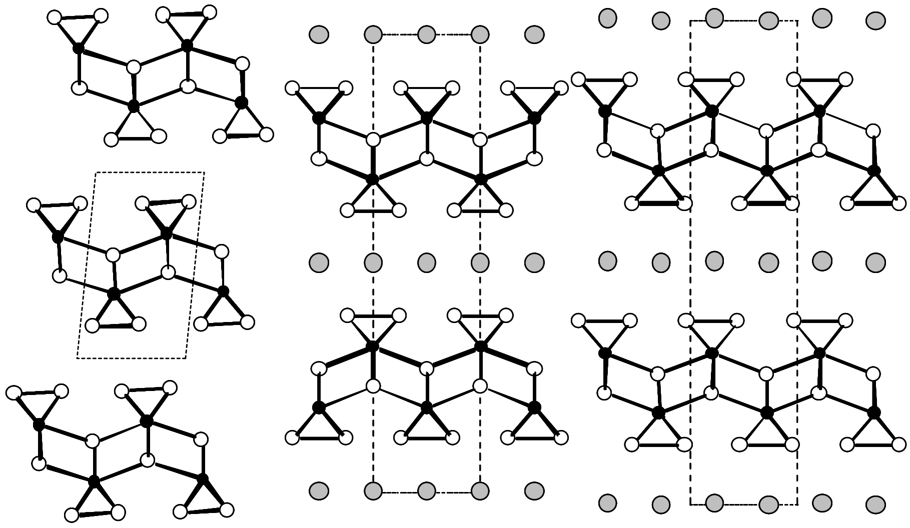

Figure 9 Comparison of the structure of $ZrSe_3$ and two intercalated versions $Rb_{0.86}Zr_2Se_6$ and $Cs_{0.80}Zr_2Se_6$

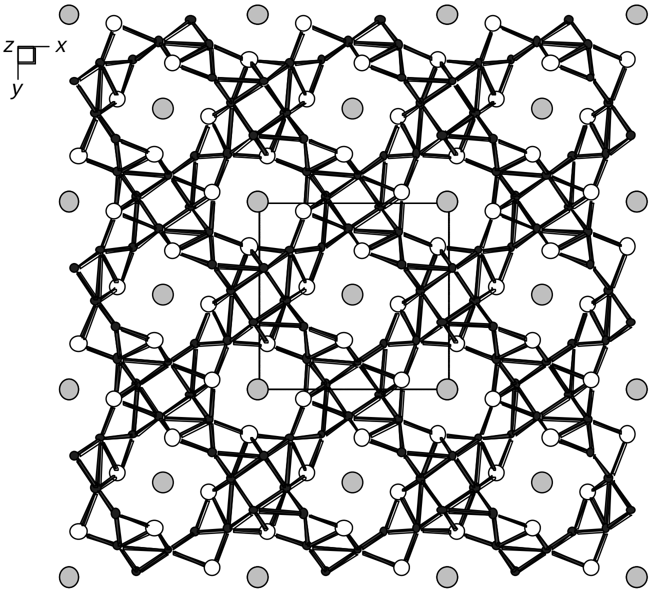

Figure 10 The structure of $KCu_{7-x}S_4$

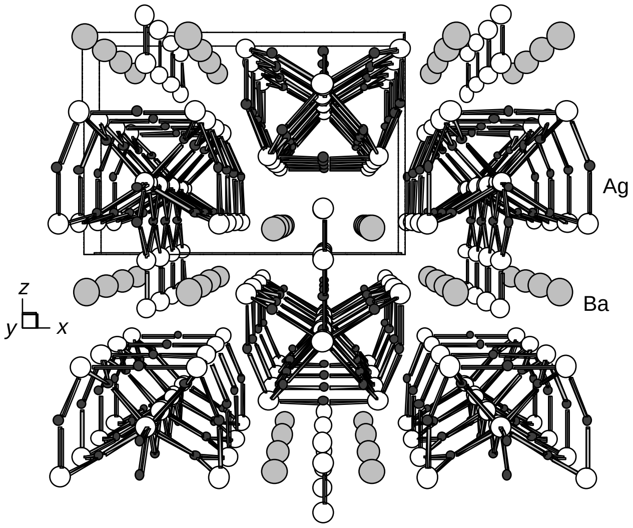

Figure 11 The $Ba_2Ag_8S_7$ structure projected on the *ac* plane. The S atoms are open circles. Ag atoms are small black circles

consists of quasi-one-dimensional Cu_4S_4 columns interlinked by tetrahedral copper chains (Figure 10). There are likely significant Cu–Cu interactions in the structure as several of the Cu–Cu distances are less than 2.8 Å. The $KCu_{7-x}S_4$ series exhibits complicated structure patterns with regard to the ordering of the Cu^+ cation along the tetrahedral chain. The nonstoichiometry and cation ordering are likely responsible for the anomalies observed in transport properties.

Crystals of $Ba_2Ag_8S_7$ were grown in a two-electrode cell from a BaS_3/ethylenediamine solution.**[58]** In the pseudo-one-dimensional structure columns of ${}^1_\infty[Ag_8S_7]$ are stacked head-to-tail in a stingray pattern to create voids where the barium atoms reside (Figure 11). The Ag atoms adopt both linear and trigonal planar coordination geometry. The isolation of this compound underscores the utility of the electrochemical method for controlled synthesis of reduced polychalcogenide phases.

$NaCu_4S_4$ was prepared in a polysulfide flux and has a two-dimensional Cu/S framework of trigonal symmetry.**[59]** Anionic $[Cu_4(S_2)(S)_2]^-$ layers, which contain both $S_2{}^{2-}$ and S^{2-}, alternate with charge-compensating Na^+ ions. The structure of the $[Cu_4(S_2)(S)_2]^-$ slab is composed of a Cu_2S_2 layer of anti-GaS structure-type sandwiched between two BN-type CuS layers (see Figure 12). The connections are made via Cu–S bonds involving metal atoms from the anti-GaS type layer and sulfur atoms from the slightly puckered BN-type layers. The structure of $NaCu_4S_4$ is akin to that of CuS itself in that in the binary solid the anti-GaS type Cu_2S_2 layers alternate with the BN-type CuS layers forming an infinite stack along the *c*-axis. In $NaCu_4S_4$ every other anti-GaS layer is missing and replaced by a layer of Na atoms. The formal oxidation states of $NaCu_4S_4$ do not balance unless we invoke mixed valency. If all monosulfides and disulfides are considered as 2−, then the charges on the metal become $Na(Cu^{1+})_2(Cu^{2+})(S_2)S_2$. In general a Cu^{2+}/S^{2-} bonding combination is considered thermodynamically favorable and is spontaneously susceptible

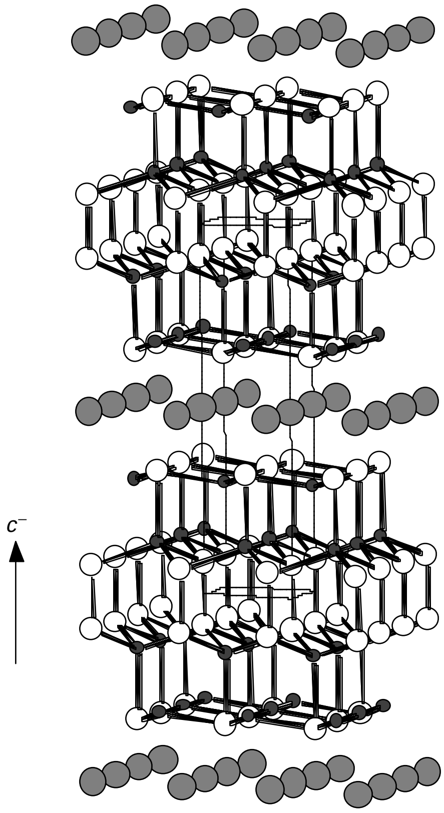

Figure 12 The layered structure of $NaCu_4S_4$. The S atoms are open circles. Cu atoms are small black circles

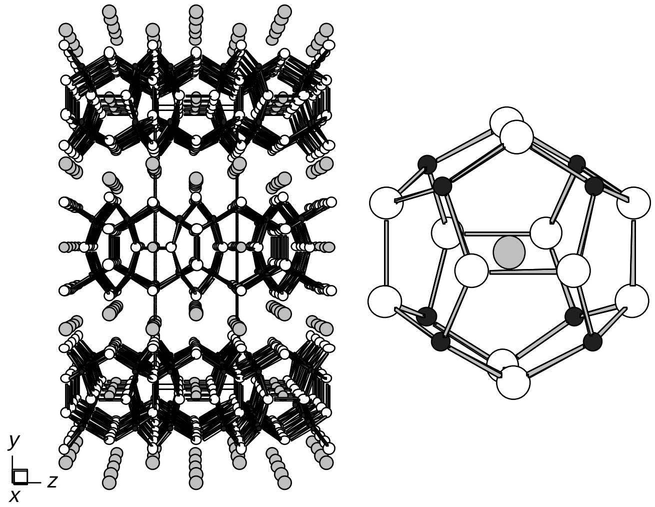

Figure 13 The layered structure of $A_2BaCu_8Te_{10}$. The $[Cu_8Te_{12}]$ pentagonal dodecahedral cage-cluster with Ba atoms inside. The Te atoms are open circles. Cu atoms are small black circles

to internal electron transfer giving Cu^{+}/S^{1-}. The S^{1-} species is considered a radical. Therefore, the metals should be taken as 1+ giving mixed valency at the sulfide side which manifests itself as holes in the sulfur-based valence band. As a result $NaCu_4S_4$ is p-type metallic.

The reactivity of copper in molten alkali polytelluride salts leads to a number of interesting compounds including $K_2Cu_5Te_5$,[60] $K_4Cu_8Te_{11}$,[61] $A_3Cu_8Te_{10}$,[62] $A_2BaCu_8Te_{10}$ (A = Rb, Cs) whose characteristic structural feature is the pentagonal dodecahedral $[Cu_8Te_{12}]$ cluster.[62] $A_3Cu_8Te_{10}$ and $A_2BaCu_8Te_{10}$ are isostructural and contain the same layered Cu/Te framework built from fused $[Cu_8Te_{12}]$ pentagonal dodecahedral cage-clusters (Figure 13). The quaternary phase derives from the ternary one by a substitution of a single A^{+} ion for a Ba^{2+} ion. The structure is layered and consists of condensed pentagonal dodecahedral clusters sharing Te–Te edges. Each $Cu_8(Te_2)_6$ dodecahedral cluster endohedrally encapsulates an alkali or Ba^{2+} ion. The $Cu_8(Te_2)_6$ cluster is also the building block of $K_4Cu_8Te_{11}$ (Figure 14). This compound has a Cu/Te framework with large tunnels running parallel to *b*-axis, which are filled with K^{+} ions. This framework is assembled from fused and linked $[Cu_8Te_{12}]$ clusters. $A_3Cu_8Te_{10}$ is mixed valence compound and exhibits metallic properties, whereas $K_4Cu_8Te_{11}$ and $A_2BaCu_8Te_{10}$ are narrow band-gap semiconductors.

The $K_2Cu_2Te_5$ forms under solventothermal conditions.[63] It contains a three-dimensional framework with the primary

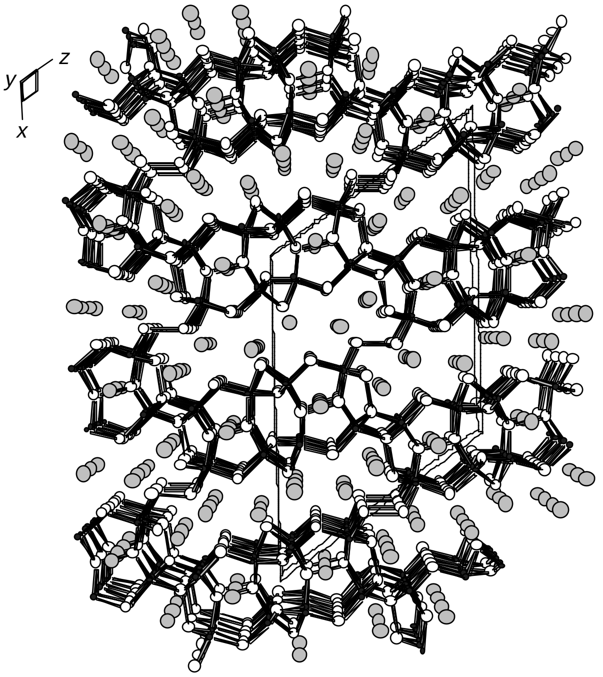

Figure 14 The tunnel framework structure of $K_4Cu_8Te_{11}$. The Te atoms are open circles. Cu atoms are small black circles

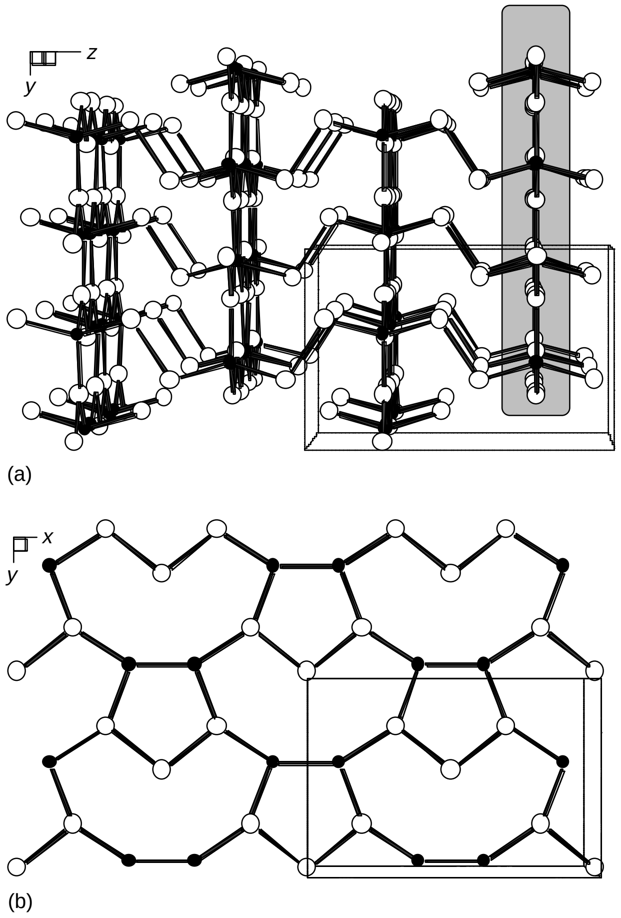

Figure 15 (a) The structure of $K_2Cu_2Te_5$ with the K atoms omitted. (b) The $Cu_2(Te_3)$ layers (indicated in the shaded boxed area in (a)) showing the linking modes of the Te_3^{2-} units. The Te atoms are open circles. Cu atoms are small black circles

building blocks being Te_2^{2-} and Te_3^{2-} fragments linking tetrahedral Cu^+ centers (Figure 15(a)). The framework can be viewed as $Cu_2(Te_3)$ layers that are linked by interlayer Te_2^{2-} units (Figure 15(b)). This generates small open channels that are occupied by the K^+ cations.

Systematic studies on selenoborates containing a B_{12} cluster entity and alkali metal cations led to the new crystalline phases $A_8[B_{12}(BSe_3)_6]$ (A = K, Rb, Cs)[64] and $Rb_4Hg_2[B_{12}(BSe_3)_6]$[65] which consist of a icosahedral B_{12} cluster completely saturated with trigonal-planar BSe_3 units and alkali metal counterions. These B-rich chalcogenoborates were prepared in a solid-state reaction from potassium selenide, amorphous boron, and selenium in evacuated carbon coated silica tubes at a temperature of 850 °C. The structure contains the first example of a B_{12} icosahedron completely saturated with chalcogen ligands (Figure 16). Six trigonal-planar selenoborate entities that function as bidentate ligands complete the B_{12} icosahedron to form a persubstituted closo-dodecaborate ion. The closo-cluster contains $2n + 2$ binding electrons for the B_{12} unit and therefore obeys Wade's rules for cluster compounds.

Other new compounds of boron with extended structures include $Rb_2B_2Se_7$, $Tl_2B_2Se_7$, $Cs_3B_3Se_{10}$, and $Tl_3B_3Se_{10}$, which contain infinite chains,[66] as well as BaB_2Se_6 and $Ba_2B_4Se_{13}$, which contain layers.[67]

From the reaction of Au with alkali metal polysulfide liquids, LiAuS and NaAuS were discovered.[68] Both compounds contain infinite one-dimensional $(AuS)_n{}^{n-}$ chains, featuring alternating sulfide anions and linear coordinated Au centers. In LiAuS, the chains are zigzag and fully extended and they pack in mutually perpendicular sets. In NaAuS, the same chains coil in an unusual fashion so that they become interwoven to form layers reminiscent of 'chicken-wire' (Figure 17). This novel coiling mode allows Au–Au contacts to form, which help to stabilize the structure.

The thioaurates $Rb_4Au_6S_5$ and $Cs_4Au_6S_5$ were prepared by allowing Rb_2S and Cs_2S, respectively, to react with stoichiometric amounts of gold and sulfur at 500 °C.[69] Though both thioaurates are characterized by essentially linear chalcogen coordination of the Au atoms, the topology of the complex anions formed is entirely different (Figure 18). $Rb_4Au_6S_5$ contains discrete anionic clusters $[Au_6S_5]^{4-}$ of trigonal bipyramidal shape with μ_3-S on the apices and μ_2-S forming in the equatorial plane. The Au atoms in the cluster form a trigonal prism with the shortest Au–Au contacts of 3.163 Å. The Cs compound, however, possesses corrugated layers of $[Au_6S_5]^{4-}$, consisting of condensed $Au_{12}S_{12}$ rings with μ_3-S at the nodal positions.

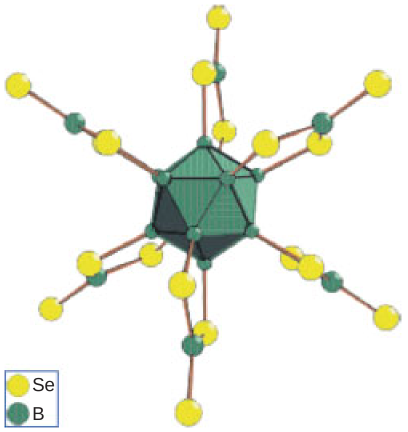

Figure 16 Structure of the $[B_{12}(BSe_3)_6]^{8-}$ ion in $Cs_8[B_{12}(BSe_3)_6]$

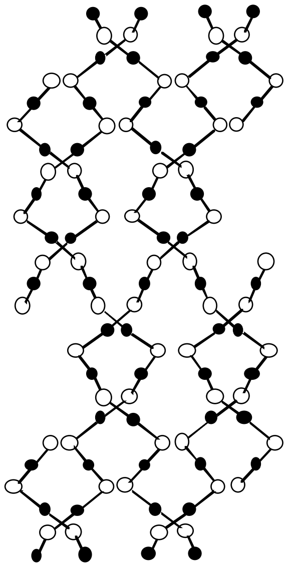

Figure 17 A section of a layer in the structure of NaAuS

Another interesting gold compound is $Cs_2Au_2Se_3$ which was obtained by allowing a stoichiometric mixture of Cs_2Se, Au, and Se to react at 670 K.[70] The characteristic structural feature of $Cs_2Au_2Se_3$ is the infinite helical anionic chains of $[AuSeAuSe_2]^{2-}$ (Figure 19). Au···Au contacts of 3.200 Å are formed within the chains. Other gold compounds worth mentioning here are $KAuS_5$, $KAuSe_5$, $CsAuSe_3$,[71] Na_5AuSe_{12},[72] and Li_3AuS_2.[73]

A fascinating set of compounds was generated by 'breaking up' the CdS (or CdSe, CdTe) lattice with A_2Q equivalents. The compounds $K_2Cd_2S_3$,[74] $A_2Cd_3Q_4$,[75,76] $Na_6Cd_7S_{10}$,[77] and $A_2Cd_3Te_4$[75,78] possess $[Cd_xQ_y]^{z-}$ networks that are low dimensional compared to that of diamond-like CdQ. The $K_2Cd_2S_3$ framework is assembled from $Cd_4S_6{}^{4-}$ clusters that are arranged in three dimensions to form K^+-filled channels running parallel to the crystallographic c-axis (Figure 20). $K_2Cd_2S_3$ is a semiconductor with a band gap of ~ 2.89 eV. The material photoluminesces at room temperature.

$Na_6Cd_7S_{10}$ has a three-dimensional framework in which Cd^{2+} tetrahedra are arranged to form four different channels running parallel to the crystallographic b-axis. Two types of channels, formed from the stacking of Cd_6S_6 and Cd_8S_8 rings,

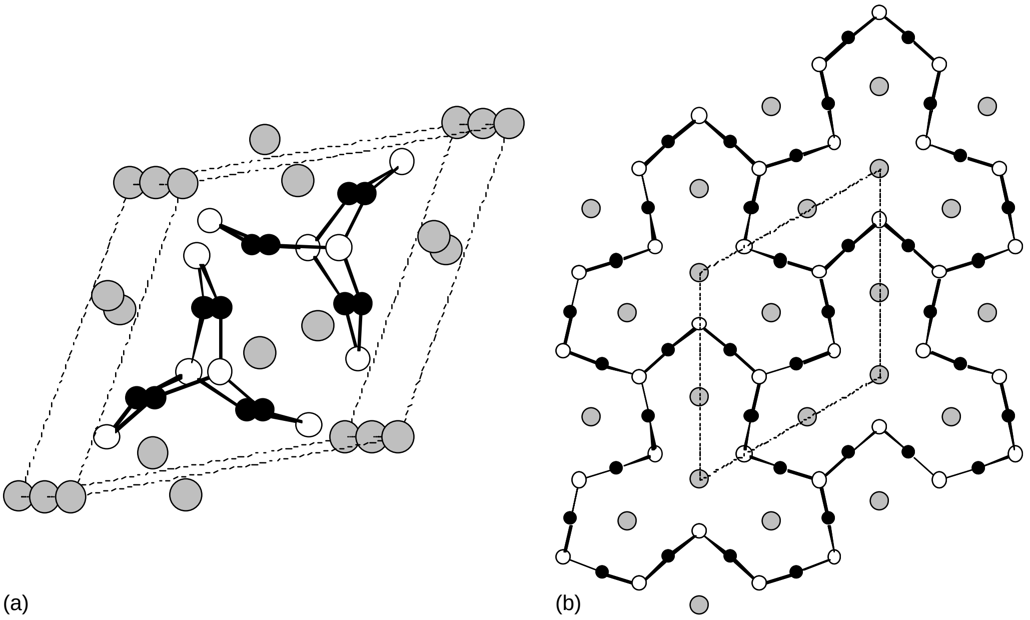

Figure 18 The structure of (a) $Rb_4Au_6S_5$ and (b) $Cs_4Au_6S_5$

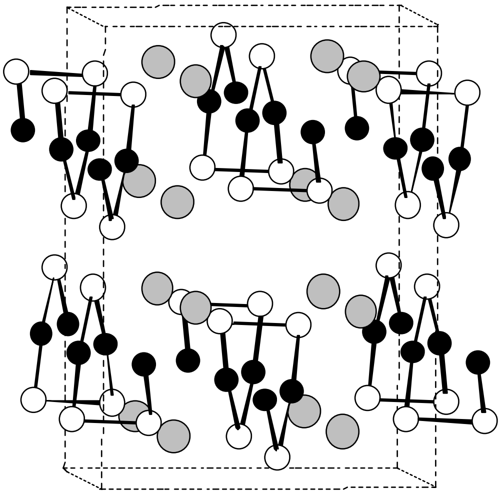

Figure 19 The structure of $Cs_2Au_2Se_3$

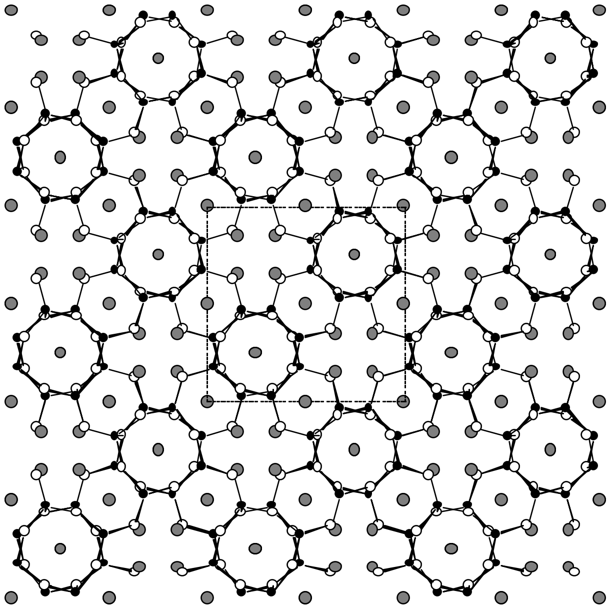

Figure 20 The framework structure of $K_2Cd_2S_3$

respectively, are filled with Na^+ cations, while two smaller channels (stacks of Cd_2S_2 and Cd_3S_3 rings) are devoid of Na^+ (Figure 21). $Na_6Cd_7S_{10}$ is a semiconductor with a room temperature band gap of 2.62 eV.

The isomorphous, layered $A_2Cd_3S_4$, $A_2Cd_3Se_4$,(A = K, Rb) and $K_2Cd_3Te_4$ feature $(Cd_3Q_4)_n{}^{2n-}$ layers separated with A^+ cations. The layers are composed of $(Cd_3Q_4)^{2-}$ units shaped as truncated cubes (Figure 22). The compounds are semiconductors with energy band gaps of 2.75, 2.92, 2.36, 2.37, and 2.26 eV respectively and also display strong photoluminescence. The structure and properties of these compounds have been compared with those of the three-dimensional binary parent phases CdS, CdSe, and CdTe, as well as those of the nanometer-sized CdQ clusters. A conceptual context has been presented to connect all these different ternary and binary compounds as shown in Figure 23:

A layered mercury telluride, $Rb_2Hg_3Te_4$, was discovered during an exploration of hydro(solvo)thermal synthesis of tellurides at temperatures somewhat above the boiling

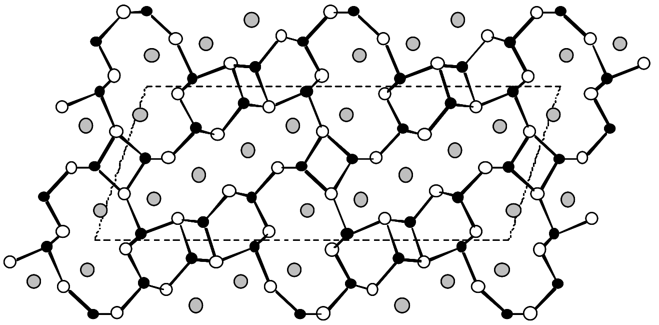

Figure 21 The structure of $Na_6Cd_7S_{10}$

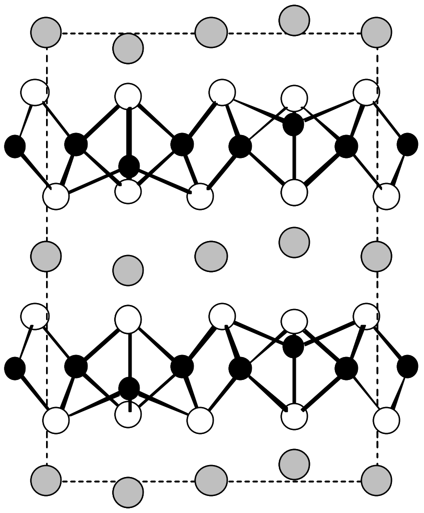

Figure 22 The structure of $A_2Cd_3Q_4$

point of ethylenediamine.[79] The structure contains slabs of $[Hg_3Te_4]^{2-}$ which are separated by the Rb^+ counterions (Figure 24). The interlayer Te–Te distances imply weak van der Waals interactions. The $^{2}_{\infty}[Hg_3Te_4{}^{2-}]$ layer is formed by interconnecting six- and eight-membered rings of alternating mercury and tellurium atoms, Hg_3Te_3, and Hg_4Te_4 (Figure 25). $Rb_2Hg_3Te_4$ is the first two-dimensional mercury telluride prepared by an unconventional low-temperature technique.

This stoichiometry ($A_2Hg_3Q_4$, where A = alkali metal, Q = S, Se) has several analogs. These are $K_2Hg_3S_4$,[80] $K_2Hg_3Se_4$,[80] $Cs_2Hg_3Se_4$,[4] and $Na_2Hg_3S_4$.[81] The first three are isostructural and contain chains of $^{1}_{\infty}[Hg_3Q_4{}^{2-}]$. They are closely related to that of the Te analog. The sulfide and selenide analogs are more one-dimensional in nature, whereas the bigger tellurium atoms reach to connect the chains forming slabs. $Na_2Hg_3S_4$ features highly corrugated layers based on 16-membered rings formed by alternating mercury and sulfur atoms.

The compounds AIn_3S_5 (A = Rb, Cs)[82] represent new ternary chalcogenides on the quasi binary section A_2S-In_2S_3 with the two binary phases in a molar ratio of 1:3. The indium atoms are coordinated by sulfur atoms with tetrahedral as well as octahedral arrangement, while the coordination numbers

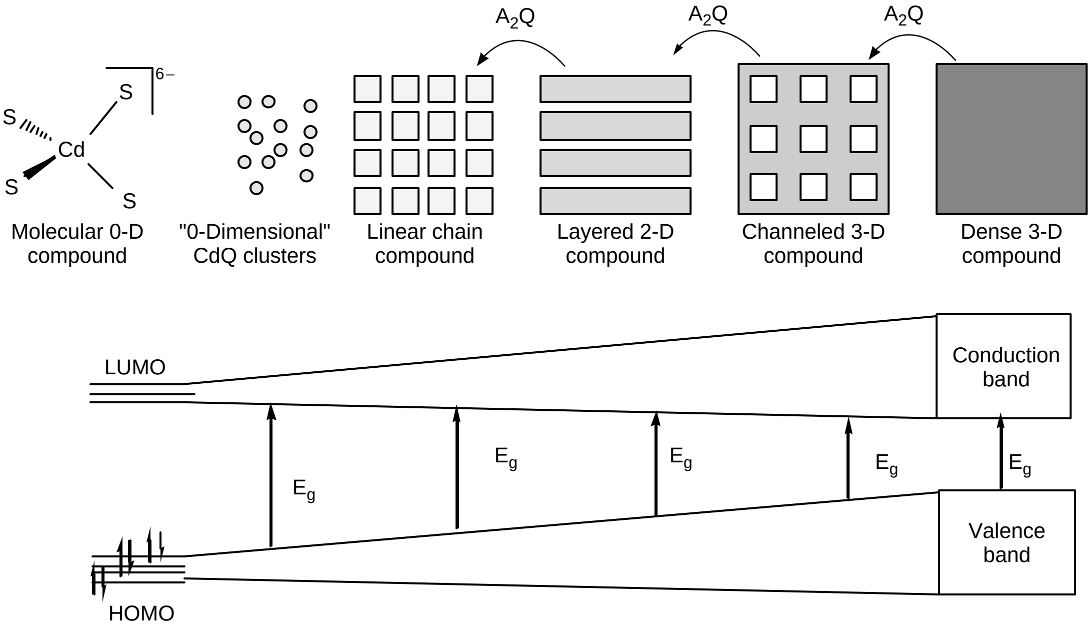
A2Q
A2Q
A2Q
6−
S
S
Cd
S
S
Molecular 0-D compound
"0-Dimensional" CdQ clusters
Linear chain compound
Layered 2-D compound
Channeled 3-D compound
Dense 3-D compound
LUMO
Conduction band
Eg
Eg
Eg
Eg
Eg
Valence band
HOMO

Figure 23 Structural evolution to lower dimensional structures in a A_2Q/MQ systems with increasing A_2Q/MQ ratio. The most dense and highest dimensionality exists in the MQ itself and the least in the compound that forms with the highest possible A_2Q/MQ ratio giving molecular $[MQ_n]^{z-}$ species

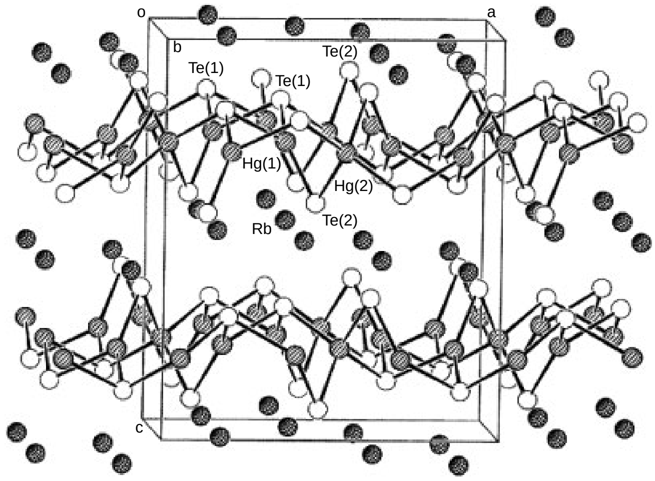

Figure 24 The layered structure of $Rb_2Hg_3Te_4$

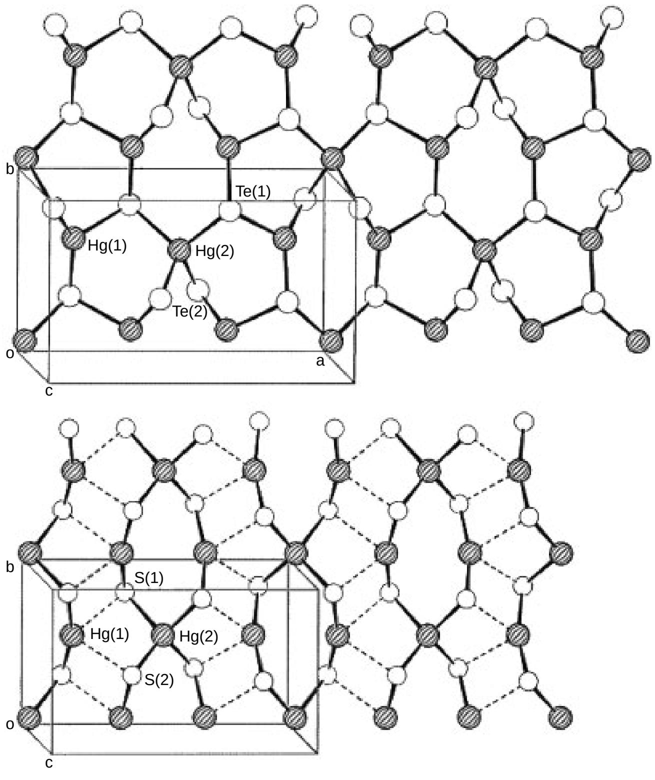

Figure 25 Comparison of the related structures of $Rb_2Hg_3Te_4$ and $K_2Hg_3Se_4$

of the two crystallographically independent A atoms are nine and ten (Figure 26). A special feature of these solids is the slightly distorted joint cubic close packed arrangement of the sulfur and alkali metal atoms.

Thallium is of comparable size and has the same charge as K^+ and Rb^+ and often behaves like an alkali metal.

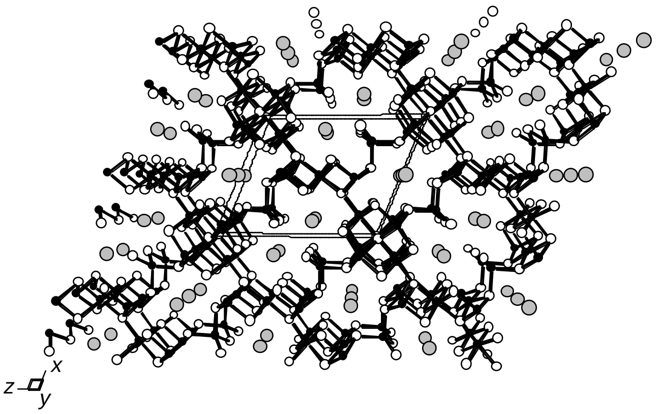

Figure 26 The structure of AIn_3S_5 (A = Rb, Cs)

New phases with indium have been reported such as $TlIn_5S_8$, $TlIn_3S_5$, $TlInS_2$, Tl_3InS_3, $TlIn_5S_6$, and $Tl_3In_5S_8$.[83] All compounds contain Tl^+ ions in a characteristic ‘lone pair coordination’ of S^{2-} ions. In atoms, however, they occur with the oxidation numbers +2 (formal In dumbbells with covalent In–In bonding) and +3 (with In^{3+} in tetrahedral and octahedral coordination of S^{2-}). Chemical preparation, crystal chemistry, and general properties of the ternary solids have been described.

Crystalline semiconducting sulfide and selenide zeolite analogs were synthesized that possess four-connected, three-dimensional tetrahedral networks built from tetravalent ($M^{4+} = Ge^{4+}$ or Sn^{4+}) and trivalent ($M^{3+} = Ga^{3+}$ or In^{3+}) cations.[84] These followed the reports of ternary In/S open framework materials whose anionic part was charge-balanced with various organic cations.[85] Also hydrothermal conditions give a series of compounds with the framework of $(M_4In_{16}S_{33})^{10-}$ (M = Mn, Co, Zn, Cd) which contain supertetrahedral clusters.[86] These materials are microporous and contain so-called supertetrahedra as their building blocks. These materials exhibit framework topologies with pore sizes ranging from 12 to 24 tetrahedral atoms, high surface area, high framework charge density and ion-exchange capacity, and tunable electronic and optical properties.

An interesting series of three-dimensional sulfides and selenides containing highly mobile alkali metal cations as charge-balancing extra-framework cations has been described.[87] Such crystalline inorganic chalcogenides integrate zeolite-like architecture with high anionic framework polarizability and high concentrations of mobile cations. Such structural features are particularly desirable for the development of fast-ion conductors. These materials demonstrate high ionic conductivity (up to 1.8×10^{-2} $S\,cm^{-1}$) at room temperature and moderate to high humidity. To make very open tetrahedral chalcogenido materials, three conditions seem to be required: (i) the building units should be supertetrahedra, (ii) the nets should have large cavities even in their contracted forms, and (iii) the nets should not interpenetrate.

A fascinating ternary compound is $Cs_2Sn_3S_7{\cdot}1/2S_8$, which was synthesized by reacting Sn with a Cs_2S_x flux at temperatures from 400–500 °C.[88] $Cs_2Sn_3S_7$ $1/2S_8$ encapsulates S_8 molecules in much the same way Cs_3Te_{22} encapsulates Te_8 molecules. The structure has an extended framework of $[Sn_3S_7]^{2-}$ anionic layers which possess large open rings (Figure 27). As these layers stack along the c direction, the large open rings are aligned forming channels. Cs^+ cations are located between the layers and S_8 molecules are found to occupy the space within the channels and also interacting with the Cs^+ cations. The $[Sn_3S_7]^{2-}$ layer has been crystallized with a number of other counterions but none of these analogs encapsulates sulfur or other neutral molecules.[89,90] In addition, several selenium analogs are also known.[91]

An interesting example of a compound is Cs_2SnTe_4 prepared by the methanolothermal reaction of Cs_2CO_3 with Sn and Te at 190 °C,[92] The crystal structure contains chain anions $[SnTe_4]^{2-}$ in which individual $SnTe_4$ tetrahedra are linked via Te–Te bonds of length 2.814(3) Å. Weak Te···Te secondary bonds of length 3.631(3)–3.663(3) Å connect neighboring chains into a framework structure. Nine Te atoms from three chain anions participate in the coordination sphere of the cesium cation. Apparently, the highly basic environment created by the presence of $[CO_3]^{2-}$ ions resulted in excess polytelluride ions most likely via a disproportionation reaction of elemental Te.

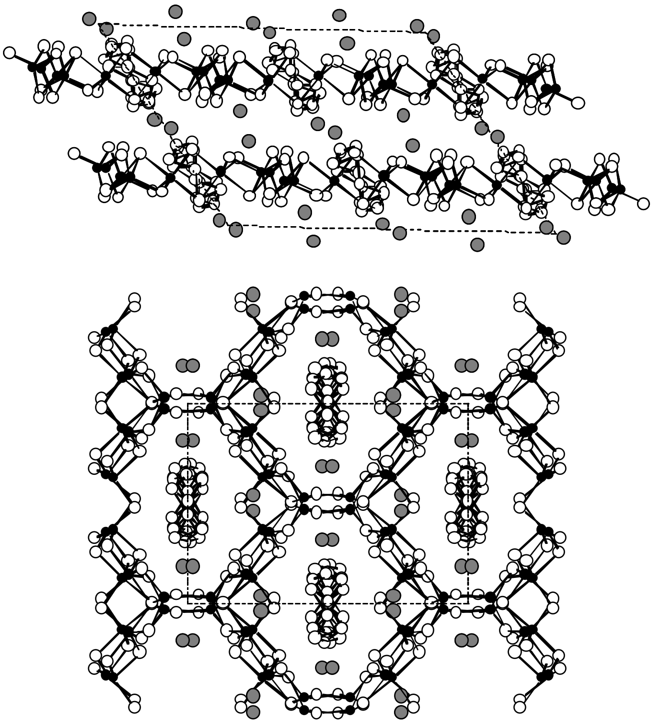

Figure 27 The structure of $Cs_2Sn_3S_7$ $1/2S_8$

Bismuth chalcogenide compounds have been investigated extensively because of their relevance as thermoelectric materials. As a result a large variety of them was discovered and shown to posses a fascinating array of structural arrangements. Some interesting phases are KBi_3S_5, $RbBi_3Se_5$,[93] $KBi_{6.33}S_{10}$,[94] $K_2Bi_8Q_{13}$ (Q = S, Se)[95] and $Cs_3Bi_7Se_{12}$.[96] These compounds belong to the general family of compounds $(A_2Q)_n(Bi_2Q_3)_m$ (A = alkali metal; Q = S, Se). Structurally, they can be thought of as an intimate composite of two different structure types interconnected to form a 3D network. They have three-dimensional structures made up of modular fragments that connect to form tunnels filled with K^+ cations.

The $[Bi_{6.33}S_{10}]^-$ framework is made of edge-sharing BiS_6 octahedra in a structure that is very similar to that of the mineral cosalite ($Pb_2Bi_2S_5$) (Figure 28). A key feature of this and other structures of this type is the occurrence of mixed occupancy sites between K and Bi in the structures. The mixed occupancy between nonisoelectronic elements can influence the electrical properties of these materials. These sites tend to be the high coordination sites (coordination number >6). The structure of $K_2Bi_8S_{13}$ is a three-dimensional assembly made up of Bi_2Te_3-, NaCl-, and CdI_2-type infinite rod shaped blocks (Figure 29(a)).

$K_2Bi_8Se_{13}$ comes in two modifications α- and β- in two structure types and represents an example where similar building blocks combine to give compounds with the same stoichiometry but different architecture.[97] α-$K_2Bi_8Se_{13}$ consists of Bi_2Te_3-, CdI_2-, and Sb_2Se_3-type rod fragments. β-$K_2Bi_8Se_{13}$ is isostructural to $K_2Bi_8S_{13}$. Overall, the structure of β-$K_2Bi_8Se_{13}$ is slightly denser, because in the latter 25% of the Bi atoms are found in a trigonal pyramidal geometry, while in the former all Bi atoms are in an octahedral or higher coordination geometry (see Figure 29(b)). Other related compounds include, $K_{2.5}Bi_{8.5}Se_{14}$, $Rb_2Bi_8Se_{13}$,[98] $K_{1+x}M_{4-2x}M'_{7+x}Se_{15}$ (A = K, Rb; M = Pb, Sn; M′ = Bi, Sb),[99] and so on.[100]

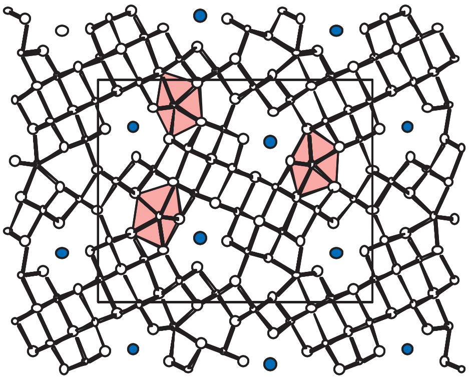

Figure 28 The structure of $KBi_{6.33}S_{10}$ (cosalite type). The shaded areas are the site of extensive K/Bi mixed occupancy

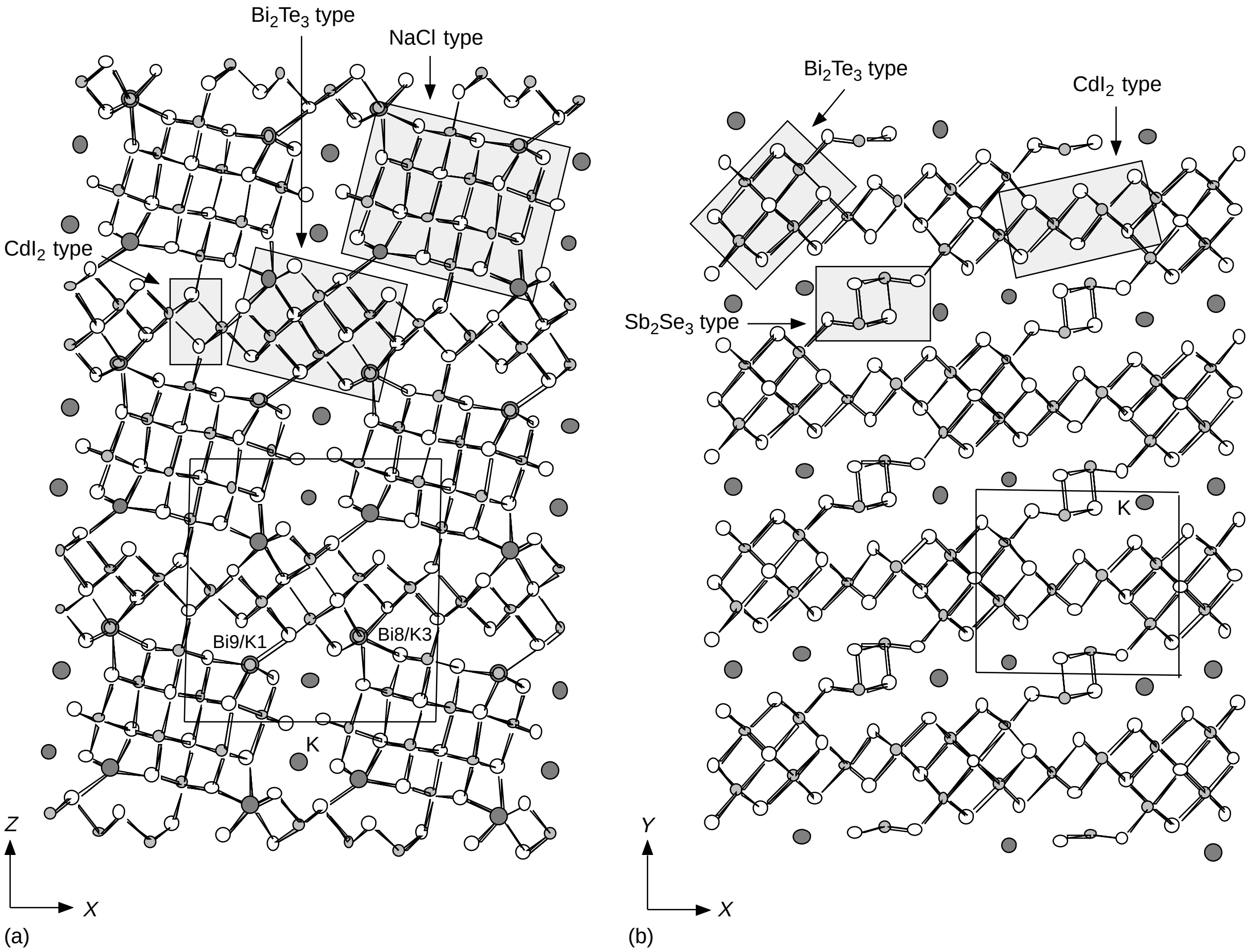

Figure 29 (a) The structure of β-$K_2Bi_8Se_{13}$. (b) The structure of α-$K_2Bi_8Se_{13}$. The modular fragments of the structure are related to the Bi_2Te_3 and CdI_2 structures are shown

$Cs_3Bi_7Se_{12}$ is a fascinating example of a layered compound which undergoes stepwise redox-induced oxidative coupling of its layers to convert to a three-dimensional structure. It is capable of two successive, single crystal to single crystal oxidative transformations. These processes convert the original 2D framework to another 2D′ framework and finally to a 3D framework. Well-defined solid-state processes of this type, besides being spectacular, are of fundamental importance in chemistry because they could provide basic systems for mechanistic studies. $Cs_3Bi_7Se_{12}$ has a layered structure made of Bi_2Te_3-type blocks (Figure 30(a)). A key characteristic of the structure is that adjacent slabs come in close, nonbonding contact by rows of Se(4) atoms. $Cs_3Bi_7Se_{12}$ can be oxidized topotactically to give $Cs_2Bi_7Se_{12}$ (Figure 30(b)). Remarkably, $Cs_2Bi_7Se_{12}$ also oxidizes topotactically to give $CsBi_7Se_{12}$ (Figure 30(c)). The structure has essentially the same $[Bi_7Se_{12}]^{3-}$ framework only now the original layers are all linked with a new set of Se(4)-Se(4) bonds forming a truly 3D framework. The $Se_2{}^{2-}$ groups act as the pillars between the original layers. $CsBi_7Se_{12}$ contains only 1/3 of the original Cs atoms present in Cs_3Bi_7 Se_{12} and because of all the void space now created they show a rather diffuse character (i.e. high temperature factors).

A rather unusual compound is $BaBiTe_3$, which is in fact a polytelluride (i.e. contains Te−Te bonds).[101] Its structure is layered with $[BiTe_3]^{2-}$ slabs alternating with Ba cations (Figure 31). The presence of Te–Te bonds form zigzag Te chains arranged in ribbons. The flat Te ribbons alternate between NaCl-type Bi–Te blocks.

Finally, the layered anisotropic phase $CsBi_4Te_6$ has been of interest because of its enhanced thermoelectric properties. Its structure is composed of anionic $[Bi_4Te_6]$ layers alternating with layers of Cs^+ ions (see Figure 32).[102–104] The average oxidation state of Bi is less than three with some of the Bi atoms forming Bi–Bi bonds. The presence of such bonds is very unusual in bismuth chalcogenide chemistry and it is not clear at the moment whether they play a role in the enhanced thermoelectric properties of the material. The Bi coordination geometry is octahedral. This material has strong anisotropic electrical transport and thermal transport properties.

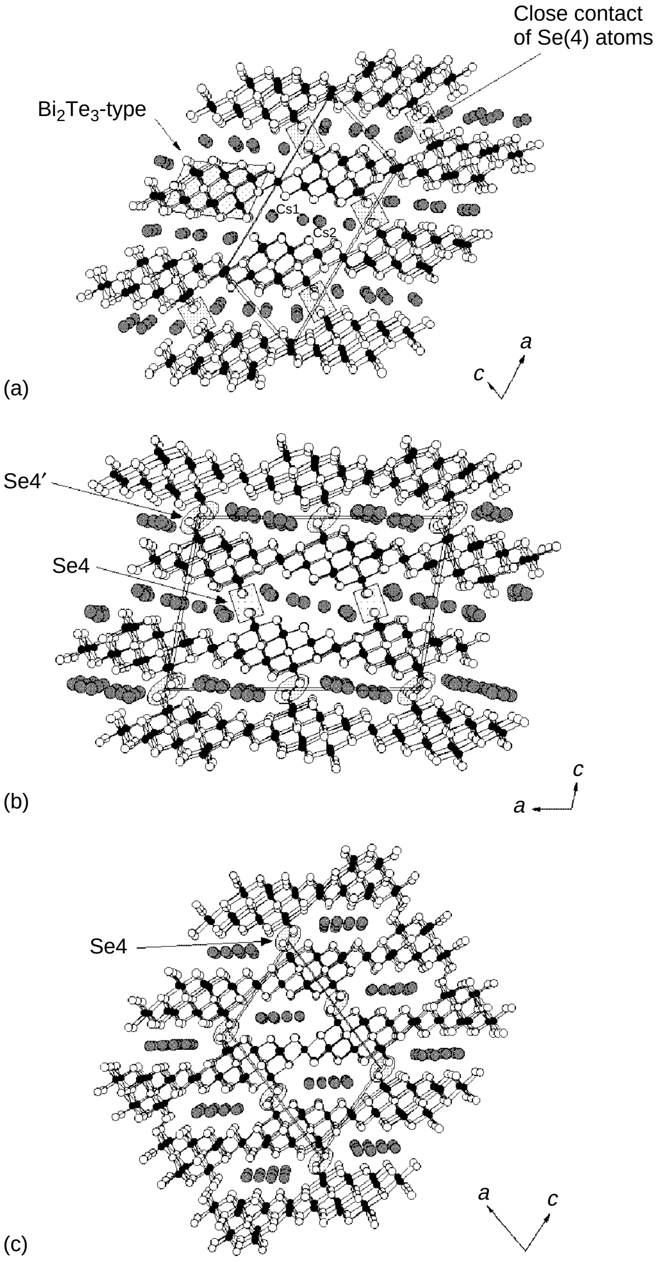

Figure 30 Projection down the *b*-axis of the structure of (a) $Cs_3Bi_7Se_{12}$, (b) $Cs_2Bi_7Se_{12}$, (c) $CsBi_7Se_{12}$. The square-like shaded areas indicate the Se(4)-Se(4) contacts while the oval ones the Se(4)′-Se(4)′ bonds in $Cs_2Bi_7Se_{12}$ and the Se(4)-Se(4) bonds in $CsBi_7Se_{12}$

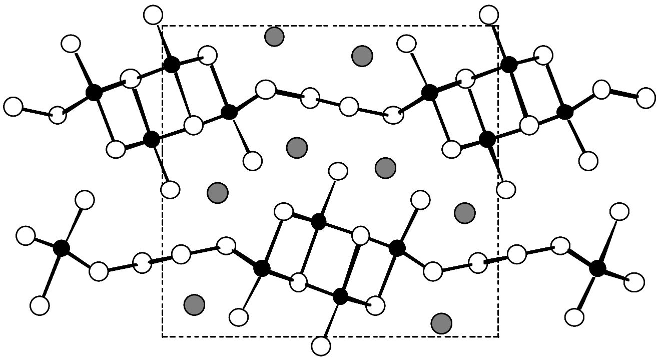

Figure 31 The layered structure of $BaBiTe_3$. Te atoms are in open circles

A large number of ternary systems have been prepared via solventothermal techniques. Hydrothermal and in general solventothermal synthesis has played a major role in expanding the scope of solid-state chemistry of a large number of compound classes including the chalcogenides. Some of the most interesting structural motifs and compositions in chalcogenides have formed under solventothermal conditions. Solventothermal synthesis involves reactions in a closed container with solvent added and the temperature taken above the boiling point of the solvent. The temperature need not be near the supercritical point. Even at a few degrees above boiling, the solubility, mobility, and reactivity of species changes substantially and promotes reactions that may not otherwise proceed. This leads to stabilization of a variety of novel materials. Under these relatively mild conditions intact molecular building blocks such as rings and chains can self-organize to a fascinating variety of chalcogeno-anions, whose dimensionality can be influenced by the choice of suitable structure-directing agents such as alkali metal or organic cations.

A novel layered Rb–Pd polyselenide has been synthesized by methanothermal reaction of Pd^{2+} with $Se_x{}^{2-}$ (from $Se^{2-}+$ Se) in the presence of Rb_2CO_3. $Rb_2[Pd(Se_4)_2]{\cdot}Se_8$ reveals a unique structure with infinite $[Pd(Se_4)_2]^{2-}$ sheet polyanions acting as a host for neutral Se_8 rings. The black shiny rectangular crystals of $Rb_2[Pd(Se_4)_2]{\cdot}Se_8$ are insoluble in H_2O and common organic solvents. The $[Pd(Se_4)_2]^{2-}$ sheet anion contains Pd^{2+} ions with a distorted square planar coordination geometry to four terminal Se atoms of $Se_4{}^{2-}$ chains. The cocrystallized neutral Se_8 rings have a crown-like conformation as known from the elemental Se_8 forms (Figure 33). Through coordination to Rb^+ ions, they build $[Rb(Se_8)^+]_n$ 'cationic chains' running in the *c* direction.

3.2 Valence-precise Metal Chalcogenides. Ternary Phases M/M/Q

This group of ternary chalcogenides contains metals other than from group 1 and 2. It is also a large group and only a small fraction will be highlighted. A fascinating set of compounds worth mentioning here is the family $Bi_2M_4Q_8$ (M = Al, Ga; Q = S, Se).**105** Although this set might also belong to the metal-rich chalcogenide section we chose to place it here for convenience. They possess a tetragonal structure shown in Figure 34 with the rare Bi–Bi dimeric unit (Bi–Bi 3.142 Å) which was also found in $CsBi_4Te_6$ described above. The structure is tetragonal and related to the TlSe type

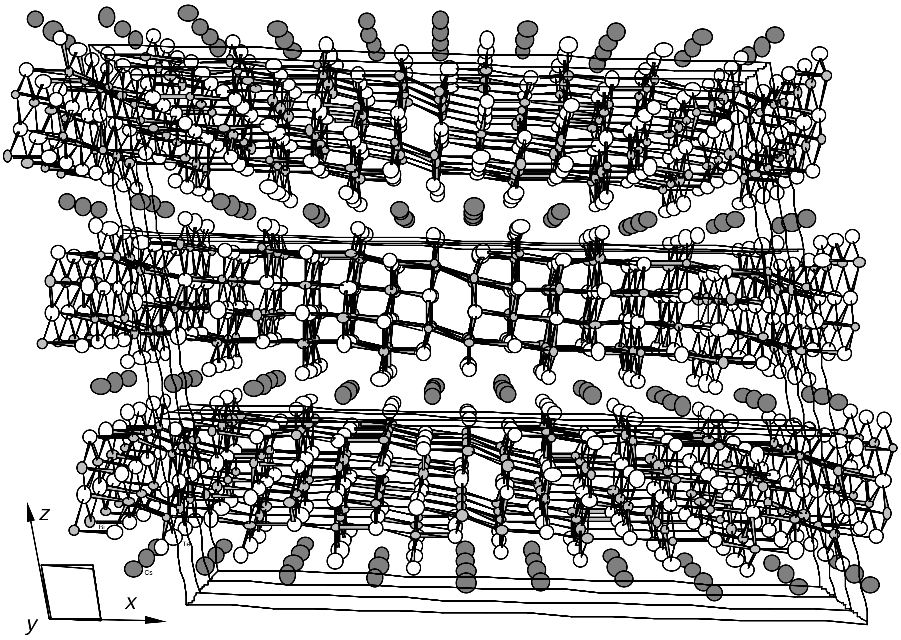

Figure 32 The layered structure of $\mathrm{CsBi_4Te_6}$

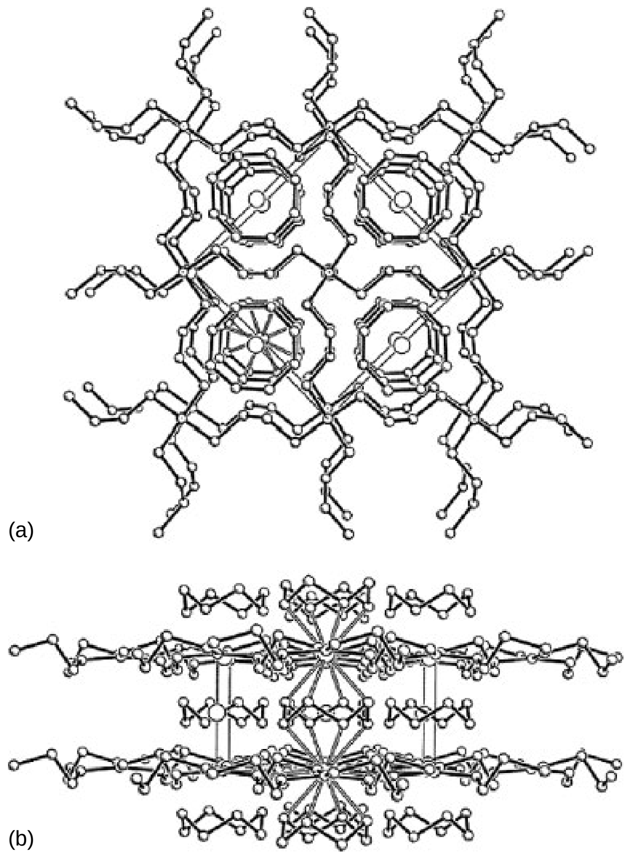

Figure 33 The structure of $\mathrm{Rb_2[Pd(Se_4)_2]{\cdot}Se_8}$ viewed down the (a) [001] and (b) [010] directions. The $[\mathrm{Rb(Se_8)}^{+}]_n$ chains pass through large rectangular rings of the 2D $[\mathrm{Pd(Se_4)_2}]^{2-}$ sheet and run along the c-axis

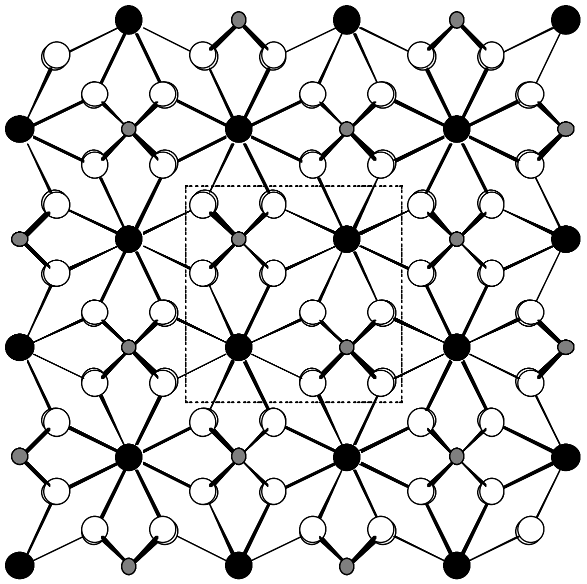

Figure 34 The tetragonal structure of $\mathrm{Bi_2M_4Q_8}$ (M = Al, Ga; Q = S, Se) viewed down the c-axis

with the Bi–Bi dimers running parallel to the c-axis inside infinite columns made of stacked square antiprisms (sap) of chalcogen atoms. The group 13 atoms Al (or Ga) occupy tetrahedral sites in the structure. The relationship to TlSe is as follows: TlSe = $\mathrm{Tl^{sap}}_4\mathrm{Tl^{tet}}_4\mathrm{Se}_8$, (two type of thallium atoms are square antiprismatic and tetrahedral). In this formulation the $\mathrm{Bi_2M_4Q_8}$ can be written as $(\mathrm{Bi}_{2\square 2})^{\mathrm{sap}}\mathrm{Al^{tet}}_4\mathrm{Q}_8$. These compounds are semiconductors with an electrical conductivity varying depending primarily on Q.

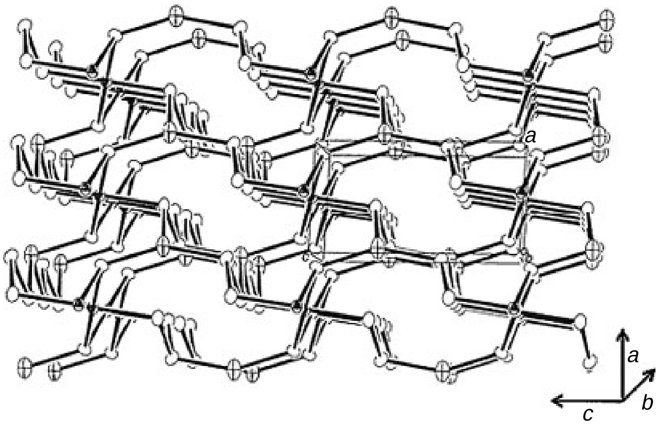

Figure 35 The three-dimensional framework of $AuCuSe_4$ looking down the *b*-axis. Shaded octant ellipsoid, Au; crossed ellipsoid, Cu; boundary ellipsoids, Se

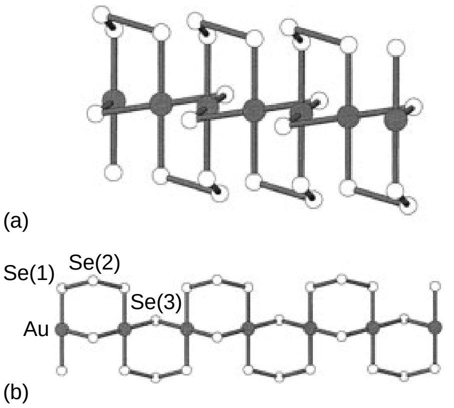

Figure 36 Two side views of the hypothetical $[Au(Se_3)Se]_n{}^{n-}$ chain running parallel to the *b*-axis with atom labeling scheme

An interesting ternary polychalcogenide phase is $AuCuSe_4$, which possesses a unique three-dimensional covalent framework (see Figure 35).[106] As revealed by the local metal coordination, this is formally a Au^{3+}/Cu^{+} compound with $Se_3{}^{2-}$ and Se^{2-} fragments. The structure can be regarded as made from one-dimensional $[Au(Se_3)Se]_n{}^{n-}$ chains linked by Cu^{+} atoms. Two views of the $[Au(Se_3)Se]_n{}^{n-}$ chain are shown in Figure 36. The structure is clearly anisotropic. Two views of the $[Au(Se_3)Se]_n{}^{n-}$ chain are shown in Figure 36. In this chain, the $Se_3{}^{2-}$ ligands bridge the Au atoms via their terminal Se(1), which spans the Au–Au distance of 3.7234(7) Å. The square planar coordination of Au atoms is completed by the bridging, Se(3). The chains are centrosymmetric and run parallel to the crystallographic *b*-axis.

$AuCrS_2$ was prepared from a mixture of Au, Cr, and S powder.[107] $AuCrS_2$ is a layered compound composed of CdI_2 -type layers and Au ions which reside in the interlayer regions. The Au atoms are linearly coordinated with two sulfide atoms, one from each $[CrS_2]^{1-}$ layer, thus acting as linking points between layers (Figure 37). This motif is very similar to that found in the $CuGaO_2$ structure-type and a related structure was determined for Ag_xMoS_2.[108] The magnetic susceptibility of $AuCrS_2$ follows the Curie−Weiss law above 150 K, and it becomes antiferromagnetic with Neel temperature at 55 K.

The $MREQ_2$ phases include $CuRES_2$, (RE = La, Nd, Sm, Gd, Dy, Ho, Yb, Lu, Y).[109–112] The structure of $CuLaS_2$ is made of a three-dimensional framework of $[LaS_2]^{-}$ with Cu^{+} ions occupying tetrahedral sites in it (Figure 38). Alternatively, it can be described as comprising of layers of $[CuS_2]^{3-}$ linked by La^{3+} atoms. The coordination environment of the RE atoms is monocapped trigonal prismatic. These compounds are p-type semiconductors with wide band gaps. The $YCuS_2$ also forms but its structure is different. It too is made of a three-dimensional framework of $[YS_2]^{-}$ with Cu^{+} ions occupying tetrahedral sites in it. The CuS_4 tetrahedra form chains along the *c*-axis and these chains fill the tunnels in the $[YS_2]^{-}$ framework. The coordination environment of the Y atoms is octahedral (Figure 39).

When the coinage metal is silver the compounds $REAgS_2$ (RE = Sm, Gd-Yb, Y),[113] $REAgSe_2$ (all RE except Pm and Eu), and $REAgTe_2$ (RE = Gd, Dy-Er, Y) have been described. $ErAgSe_2$ and $REAgS_2$ (RE = Gd, Ho, Yb)[114] have been studied by single crystal X-ray diffraction methods. $ErAgSe_2$ has a low and a high temperature form. The high temperature form adopts the NaCl structure with Ag and Er randomly distributed over the cation sites, whereas the low-temperature version has an orthorhombic distorted NaCl structure with ordered Er and Ag atoms (Figure 40). Both Ag and Er atoms have octahedral coordination. The structure of the $REAgS_2$ (RE = Gd, Ho) is a superstructure of the RES (NaCl) type with one-half of the RE cations replaced with Ag. The Ag atom is in a severely distorted octahedral environment with two short, three intermediate, and one long Ag–S bond.

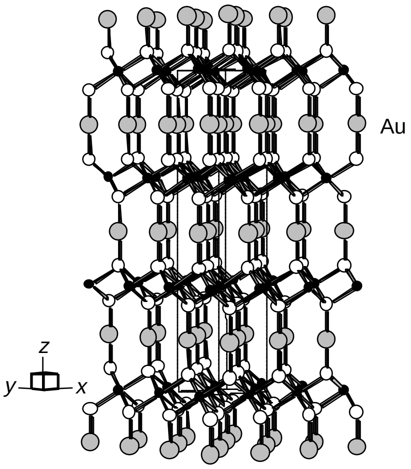

Figure 37 The structure of $AuCrS_2$

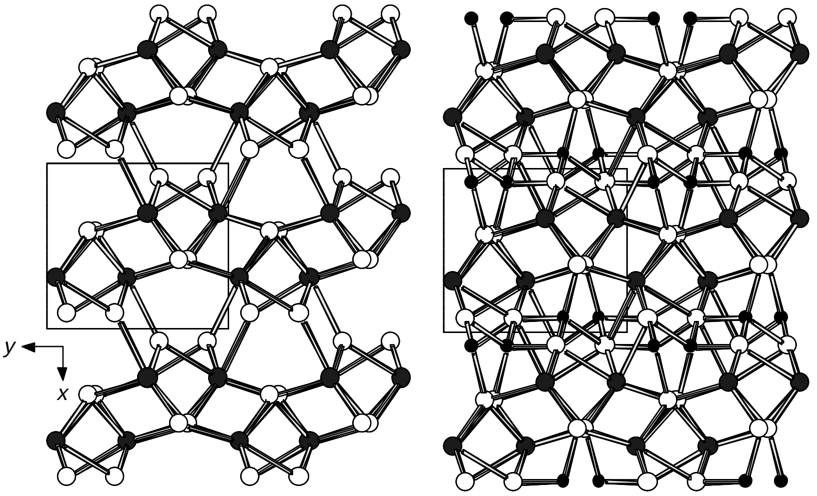

Figure 38 The $LaCuS_2$ structure-type in two perspectives. On the left the Cu atoms were omitted to highlight the 'LaS_2' framework. Large black spheres represent RE, intermediate-size black spheres represent M, and small black spheres represent Q atoms. The unit cell is outlined here and in most succeeding figures

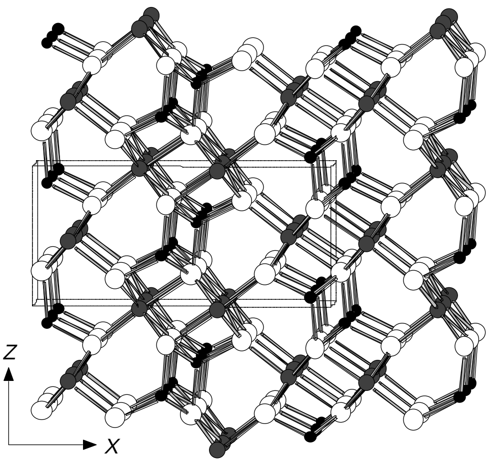

Figure 39 $YCuS_2$ structure. Open circles are S atoms and small black circles are Cu atoms

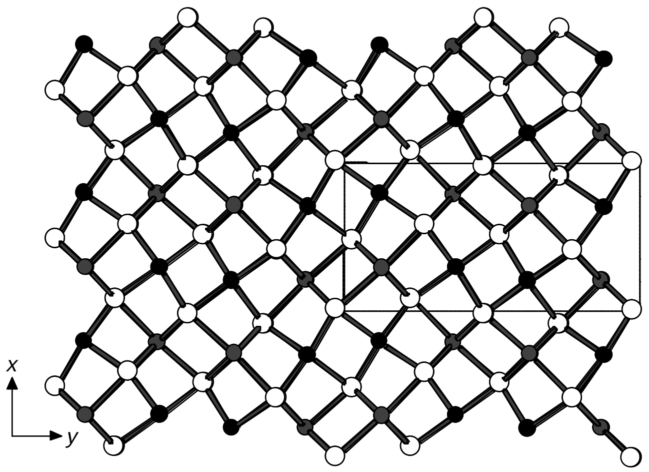

Figure 40 View of the structure of $ErAgSe_2$ along the *c*-axis

The combination of the soft transition metals such as Cu with hard lanthanide elements can give rise to interesting compounds as, for example, $CuSm_3Se_6$. The crystal structure of $CuSm_3Se_4[Se_2]$ contains both mono- (Se^{2-}) and diselenide anions ($[Se_2]^{2-}$) (Figure 41).[115] The latter are surrounded by six Sm^{3+} cations. If the diselenide units serve as one fragment, they form irregular $\{[Se_2]Sm_6\}^{16+}$ octahedra, which produce chains running along [010]. Together with $[SeSm_4]^{10+}$ tetrahedra, they build up a two-dimensional layer parallel to (001) according to $^2_\infty\{(Sm_3Se[Se_2])^{5+}\}$. Vertex-, edge-, and face-shared $[CuSe_4]^{7-}$ tetrahedra compose chains running along [010] as well. A three-dimensional network is created by stacking $\{(Sm_3Se[Se_2])^{5+}\}$ layers and $\{(CuSe_3)^{5-}\}$ chains parallel to (001) (Figure 42).

3.3 Metal-rich Chalcogenides

Similar to the metal-rich binary chalcogenides ternary metal-rich systems are also of growing interest. It has been demonstrated that strong early-late transition metal intermetallic bonding in combination with late transition metals can lead to an expanding class of compounds that includes members such as Hf_8MTe_6 (M = Mn, Fe, Co, Ni, Ru),[116] Hf_5MTe_3 (M = Fe, Co),[117] Nb_4MTe_4 (M = Al, Si, Cr–Ni),[118] Zr_6MTe_2 (M = Mn, Fe, Co, Ni, Ru, Pt),[119] Dy_6MTe_2 (M = Fe, Co, Ni),[120] $Sc_{14}M_3Te_8$ (M = Ru, Os),[121] $Ta_{1.09}Fe_{2.39}Te_4$,[122] $Ta_2M_3Q_5$ (M = Ni, Pd; Q = Se, Te)[123–125] and $Er_7Ni_2Te_2$.[126] Many of these compounds are known to crystallize in the ordered variant of the Fe_2P structure-type known as the Zr_6CoAl_2 type.[127] Here, the unit cell of Fe_2P

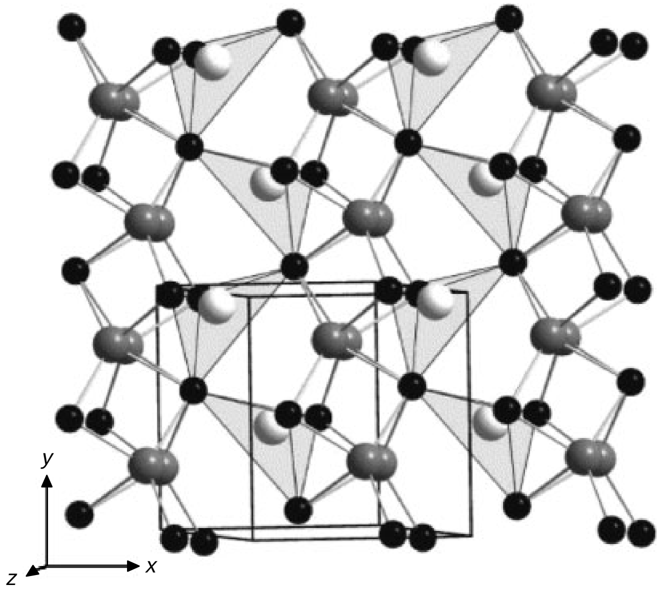

Figure 41 The structure of $\mathrm{CuSm_3Se_6}$. $\mathrm{Sm^{3+}}$: black, $\mathrm{Se^{2-}}$: white, $\mathrm{[Se_2]^{2-}}$: gray; $\{\mathrm{[Se_2]Sm_6}\}^{16+}$ octahedra are marked by bonds, whereas the $\mathrm{[SeSm_4]^{10+}}$ tetrahedra appear as closed polyhedra

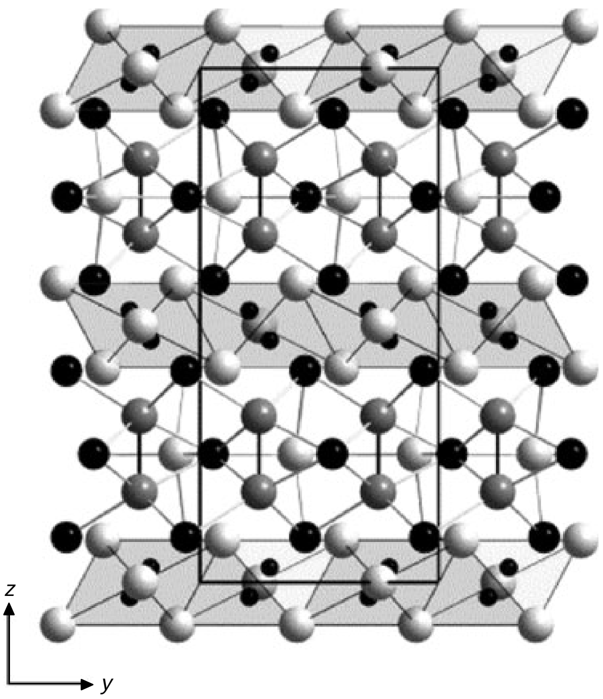

Figure 42 Stacking of ${}^{1}_{\infty}\{(\mathrm{CuSe_3})^{5-}\}$ chains and ${}^{2}_{\infty}\{(\mathrm{Sm_3Se[Se_2]})^{5+}\}$ layers parallel to (001); $\mathrm{Cu^+}$: small black, $\mathrm{Sm^{3+}}$: large black, $\mathrm{Se^{2-}}$: open, $\mathrm{[Se_2]^{2-}}$: gray spheres

is tripled, with the early transition metal on the iron positions and the late transition metal and main group element ordered between the two independent phosphorus sites.

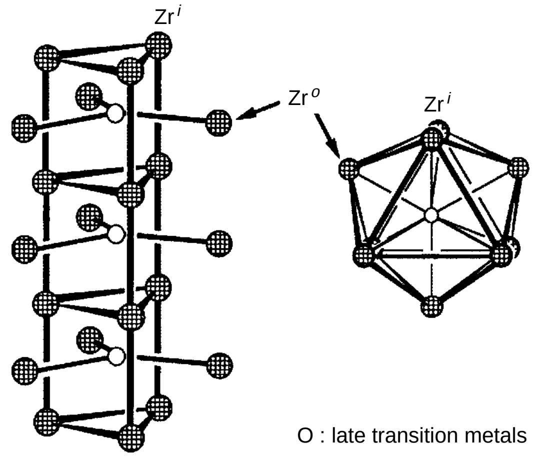

Figure 43 The infinite trigonal prismatic column found in metal-rich chalcogenides with the $\mathrm{Zr_6CoAl_2}$-structure type

A structural motif in the chemistry of more metal-rich compounds is the M-centered tricapped trigonal prismatic column (M-centered tetrakaidecahedron) shown in Figure 43. In this structural building block, late transition metals (M) are surrounded by nine early transition metals (Nb, Ta, Hf) that serve as vertices of the surrounding tetrakaidecahedron. Such tricapped trigonal prisms are observed in $\mathrm{Hf_8MTe_6}$ (M = Fe, Co, Ni) and $\mathrm{Hf_5MTe_3}$ (M = Fe, Co, Ni). Similarly, chains of condensed, M-centered square antiprisms are found in $\mathrm{Ta_4MTe_4}$ and $\mathrm{Nb_4MTe_4}$ (M = Al, Si, Cr–Ni). As with the metal-rich binaries bonding in these extended metal-linked networks is often discussed with particular emphasis on localized bonding descriptions for metal–metal bonds. Such descriptions give a reasonable understanding of otherwise anomalous properties and help unify the boundary between ‘‘metallic’’ and ‘‘covalent’’ bonding concepts.

The $\mathrm{Sc_6MTe_2}$ and $\mathrm{Zr_6MTe_2}$ (M = Mn, Fe, Co, Ni) belong to the $\mathrm{Zr_6CoAl_2}$-structure type (Figure 44). The late transition metals Mn–Ni center the tricapped trigonal prisms of Zr that stack and share faces along the *c*-axis to form linear chains. The tricapped trigonal prismatic chains are interconnected via Zr–Zr bonds. The condensation of $\mathrm{Zr_9Fe}$ polyhedra is achieved by sharing of triangular $\mathrm{Zr_3}$ faces.

Interestingly, the smaller sized sulfide and selenide, analogs of the $\mathrm{Zr_6MQ_2}$ composition have different structures than the telluride one (Figure 45). The larger Te atoms naturally adopt a higher coordination number (nine-coordinate in this compound), and the wide open channels in the $\mathrm{Zr_6FeTe_2}$ structure are the result. In $\mathrm{Zr_6Fe}_{1-x}\mathrm{Q}_{2+x}$, the structure rearranges to offer smaller seven- and eight-coordinate chalcogen sites, while retaining characteristic chains. In accordance with the closer Fe–Q size match for Q = S, Se is the fact that $\mathrm{Zr_6FeTe_2}$ is stoichiometric whereas the $\mathrm{Zr_6Fe}_{1-x}\mathrm{Q}_{2+x}$ phases exhibit noticeable phase width. Unlike the regular Zr tetrakaidecahedra in $\mathrm{Zr_6FeTe_2}$, those in both $\mathrm{Zr_6Fe_{0.6}Se_{2.4}}$ and $\mathrm{Zr_6Fe_{0.57}S_{2.43}}$ are appreciably distorted.

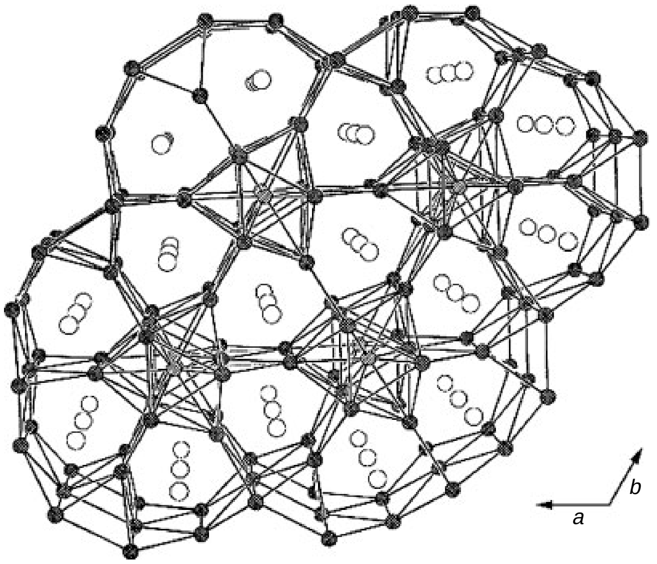

Figure 44 Approximate (001) projection of the Zr_6FeTe_2 structures. The zirconium, iron, and tellurium atoms are shown as cross-hatched, hatched, and open circles, respectively. Bonds shown indicate the Zr–Zr and Zr–Fe contacts

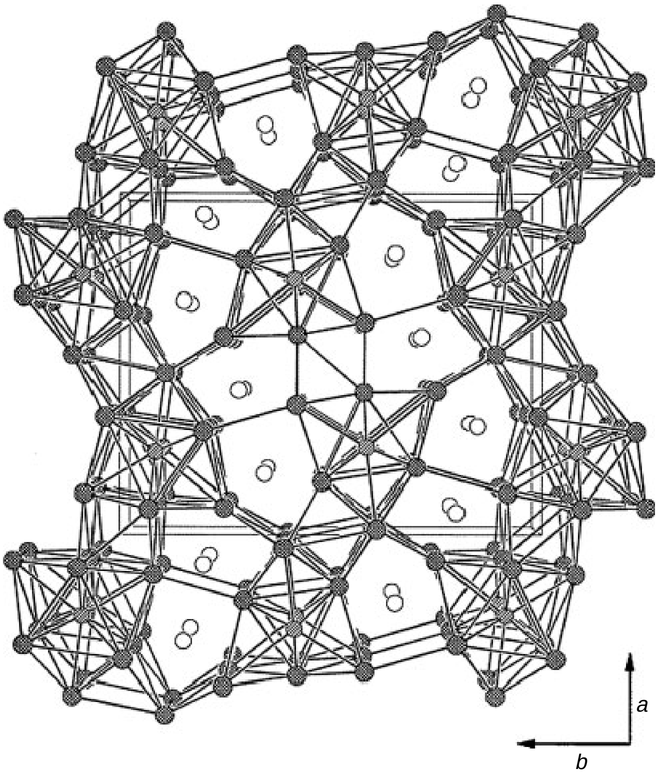

Figure 45 Projection of the $Zr_6Fe_{1-x}Q_{2+x}$ (Q = S, Se) structures down the [001] direction. Zirconium, iron, and chalcogen atoms are shown as cross-hatched, hatched, and open circles, respectively. Bonds shown indicate the Zr–Zr and Zr–Fe contacts

The compounds Sc_6AgTe_2, $Sc_6Cu_{0.80}Te_{2.20}$ and Sc_6CdTe_2, have similar stoichiometry to those described above but possess a different structural motif,**[128]** that is, isotypic with Sc_6PdTe_2. The structure can be viewed as heterometal sheets lying parallel to the *b*-*c* planes that are separated by isolated tellurium atoms. These sheets can also be viewed as a polymerization of two different types of metal chains in Sc_2Te (blades and zigzag chains) by heterometal (M) replacements of some intervening tellurium atoms, The new Sc_6CuTe_2 and Sc_6AgTe_2 are isostructural with Sc_6PdTe_2. The Sc_6AgTe_2 structure viewed along the short *b*-axis is given in Figure 46. The structure can be described as the result of a polymerization of two kinds of scandium metal chains, which were formerly described in Sc_2Te (see above) as separate double octahedral chains or blades (blue) and zigzag chains (black), via displacement of the Te1 atom by a strongly bonding heterometal Ag, and so on. The resulting condensed heterometal sheets are separated by isolated Te atoms (red) along the *a*-axis.

$Er_7Ni_2Te_2$ is the most metal-rich of the ternary rare earth chalcogenides. The structure is shown in Figure 47. The basic structural unit is a distorted, Ni-centered, tricapped trigonal prism of Er that is fused with similar prisms by sharing the Er_3 triangular bases to form an infinite $^1_\infty[(Er_3Er_{3/2}Er_{3/2})Ni]$ chain that propagates along the *b*-axis. These infinite chains are condensed to form corrugated layers across the *bc* plane by sharing Er zigzag chains, which are composed of capping

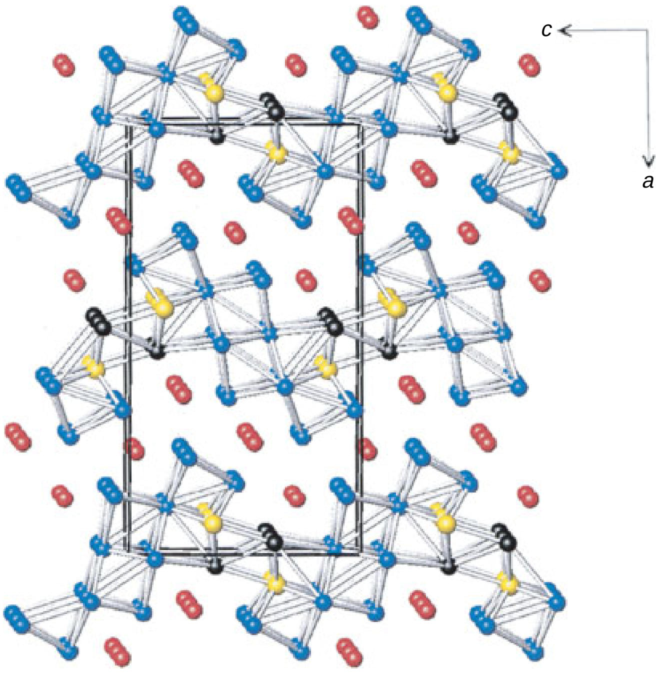

Figure 46 Unit cell of Sc_6AgTe_2. The blue atoms are Sc in the blade unit, the dark atoms are Sc4 that form the zigzag chains, the yellow atoms are silver, and red atoms are tellurium. The structure is infinite along the view direction

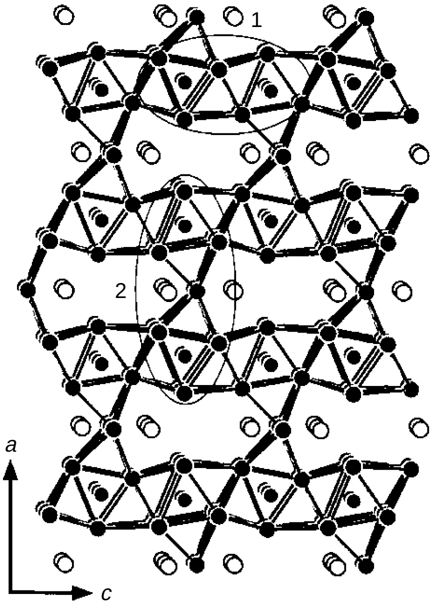

Figure 47 The $Er_7Ni_2Te_2$ structure. Er and Ni atoms are shown as dark circles with and without bonds, respectively. Te atoms are open circles. Er–Te and Er–Ni bonds are not shown for clarity. Circled regions 1 and 2 are depicted below

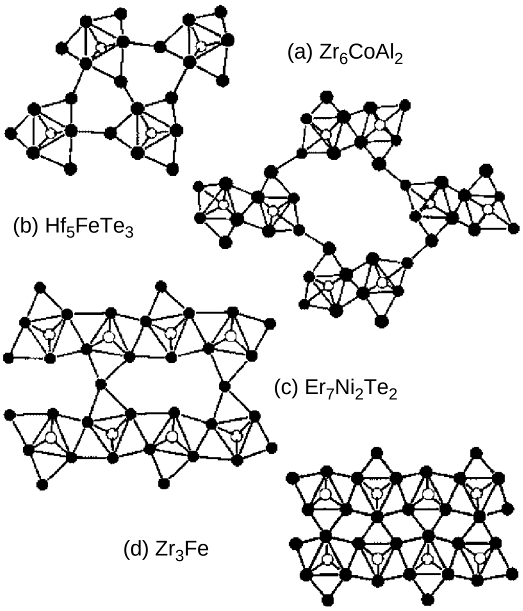

Figure 48 Arrangements of trigonal prismatic building blocks into (a) single chains in the Zr_6CoAl_2 structure, (b) double chains in the Hf_5FeTe_3 structure, (c) layers in the $Er_7Ni_2Te_2$ structure, and (d) a 3-D network in the Zr_3Fe structure. Early transition metals are shown as larger circles, and late transition metals are smaller. Some metal–metal bonds are omitted for clarity

Er atoms on one TTP and inner Er on the adjacent TTP (see region 1 in Figure 47). Finally, vertex condensation forms links between individual layers that result in the overall structure (see region 2 in Figure 47). Tellurium atoms reside between the metal–metal bonded layers, on *bc*-planes.

There is a structural relationship between $Er_7Ni_2Te_2$ and three other structures: Zr_6CoAl_2-type (e.g. Zr_6MTe_2, Sc_6MTe_2, Gd_6MTe_2), Hf_5FeTe_3, and Zr_3Fe. All can be constructed using centered transition metal trigonal prisms as fundamental building blocks, but with different condensation schemes (Figure 48). In the Zr_6CoAl_2-type structure, bonding between the capping and apical atoms of adjacent trigonal prisms interconnects single trigonal prismatic columns. In Hf_5FeTe_3, double chains are formed by edge condensation of single chains, and the double chains are then stitched together into a 3D network by forming longer bonds between the capping atoms not involved in condensation. Formation of condensed intermetallic layers becomes characteristic in the $Er_7Ni_2Te_2$ structure. Successive layers are shifted relative to one another along the *c* direction and are linked together by sharing capping atoms such that Te atoms are accommodated at two chemically inequivalent sites between the layers. A similar but more symmetrical layer architecture exists in Zr_3Fe, which in turn is a hexagonal-close-packing example in metals. Adjacent layers in the Zr_3Fe structure stack vertically, sharing one Zr atom in every trigonal prismatic unit. This 3D network is even more condensed owing to the formation of extensive Zr–Zr bonds between the layers (Figure 48(d)).

The $Sc_{14}M_3Te_8$ (M = Ru, Os) phases represent yet another structure-type among metal-rich ternary chalcogenides. In this motif, scandium atoms define infinite chains of alternate trans-face-sharing cubes and pairs of square antiprisms in which each polyhedron is also centered by an M atom (M = Ru, Os). These chains are further linked into a three-dimensional (3D) structure by $Sc(Te_2Te_{4/2})$ octahedra through strong Sc–Te interactions. A projection of the $Sc_{14}Ru_3Te_8$ structure is shown in Figure 49. Scandium metal plays two roles: one as Sc_3 in chains of individual octahedral complexes $[Sc(Te_2Te_{4/2})]$ centered at $^1/_2, 0, z$, and so on. The second role is seen in a side view in Figure 50 where Sc atoms define infinite columns of confacial clusters, each centered by a Ru or Os atom. In these columns, are found square antiprismatic units that share faces. Each metal unit is connected to four Te-rich bridging chains built of $Sc(3)Te_6$ octahedra to complete the 3D structure. The Te atoms have trigonal prismatic and pentagonal bipyramidal configurations, respectively. Physical property measurements show that $Sc_{14}Ru_3Te_8$ is metallic and Pauli-paramagnetic, consistent with the results of extended Hückel band structure calculations. The Sc–M and Sc–Te interactions are major.

The presence of early transition metals or rare earth elements is not necessary for the stabilization of metal-rich compounds. This is shown by the metal-rich nickel–tin sulfides Ni_6SnS_2 and $Ni_9Sn_2S_2$, which were found during investigations of phase relations in the ternary Ni–Sn–S

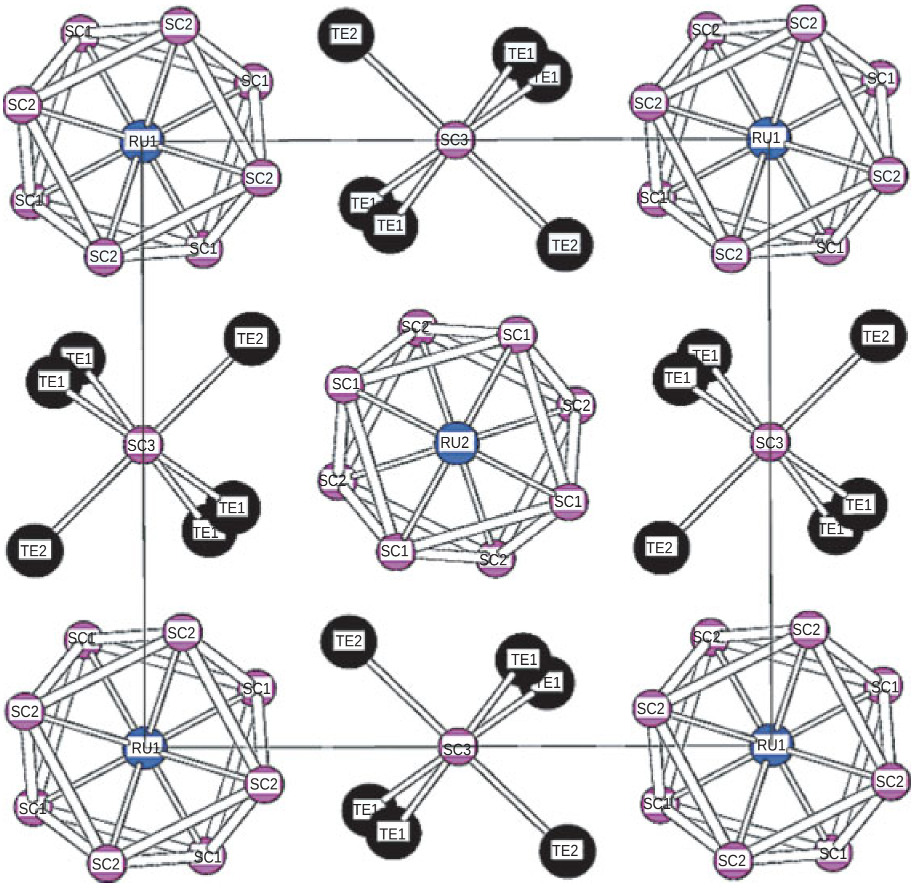
SC1
SC2
SC1
SC2
RU1
SC2
SC1
SC2
SC1
TE2
TE1
TE1
SC3
TE1
TE1
TE2
SC2
SC2
SC1
SC2
RU1
SC2
SC1
SC2
SC1
TE1
TE1
TE2
SC2
SC1
SC1
SC2
RU2
SC2
SC1
SC1
SC2
SC3
TE1
TE1
TE2
TE1
TE1
TE2
SC3
TE1
TE1
TE2

Figure 49 Projection of the unit cell of $Sc_{13.2}Ru_3Te_8$. The confacial Sc-based cubes and antiprisms centered by Ru are clearly seen. Sc3 atoms center infinite chains of edge-sharing $\{ScTe_6\}_n$ octahedra

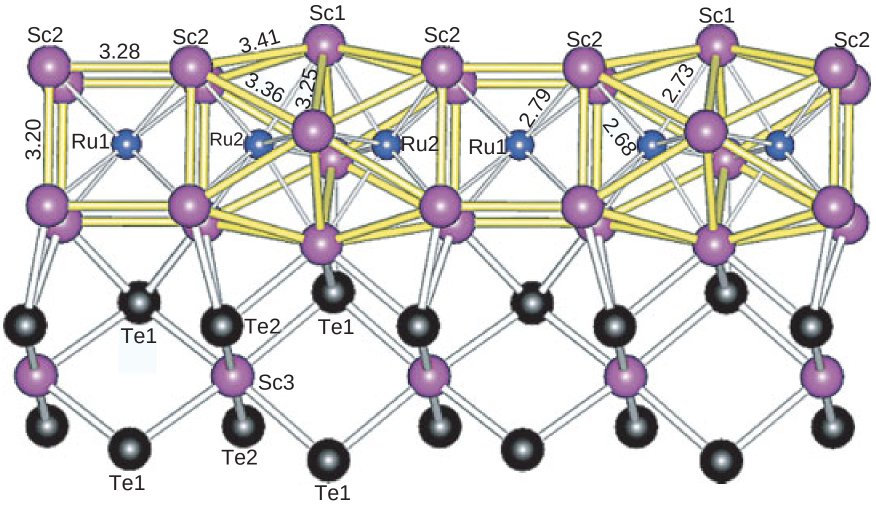
Sc2
3.28
Sc2
3.41
Sc1
Sc2
Sc2
Sc1
Sc2
3.20
3.36
3.25
2.79
2.73
2.68
Ru1
Ru2
Ru2
Ru1
Te1
Te2
Te1
Sc3
Te2
Te1
Te1

Figure 50 Segment of condensed $\{Sc_4Ru\}_n$ infinite chain of trans-face-sharing cubic (Sc1) and square antiprismatic (Sc1 and Sc2) polyhedra centered by Ru1 and Ru2, respectively. Distances are in Å

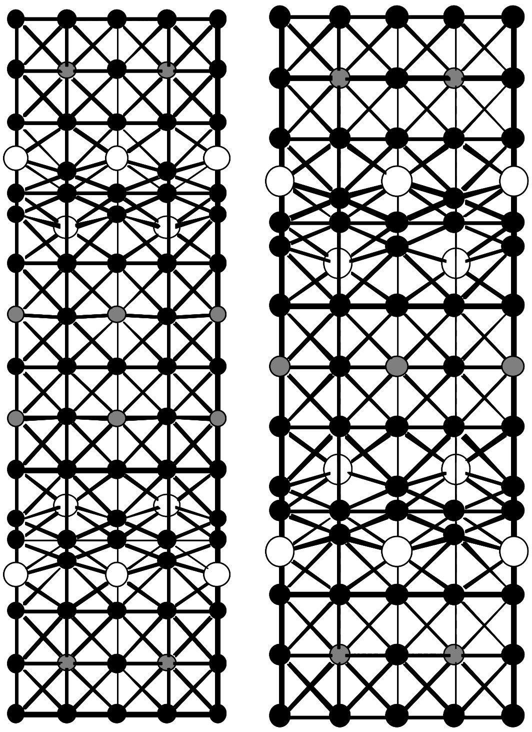

Figure 51 The structures of Ni_6SnS_2 and $Ni_9Sn_2S_2$

system at 540 °C.[129] Their crystal structures are tetragonal and represent a new structure-type that can be considered as assembled from bimetallic nickel–tin and nickel–sulfide slabs alternating along the crystallographic c-axis (Figure 51). Band structure calculations showed the bonding within the bimetallic slabs to have a delocalized, multicenter nature, typical for metallic systems, yet the bonding between nickel and sulfur is predominantly classical.

3.4 Misfit Compounds

A peculiar class is that of misfit layer compounds that can be viewed as stage composites of the type $[(MQ)_m]_{1+x}(TQ_2)_n$. The MQ part is an approximate tetragonal layer often called the Q-sublattice (not to be confused with the chalcogen atoms) and the TQ_2 sublattice is a hexagonal layer called the H-part. They are called misfit because the periodicities of the MQ and TQ_2 parts do not match exactly. That is, compounds are characterized by their incommensurate structures built from an alternate stacking of two different layered entities (sublattices Q and H), giving them a composite character (i.e. intergrowth compounds). Members of this class have been reported for T = Ti, Nb, or Ta and M = Sn, Pb, Sb, Bi, or rare earth elements. For example, the structure of $(LaSe)_{1.14}(NbSe_2)_2$ or '$LaNb_2Se_5$' contains double 2H-$NbSe_2$ slabs separated by rock salt LaSe layers as shown in Figure 52. The compound $(PbS)_{1.14}(NbS_2)_2$ is polytropic adopting orthorhombic and monoclinic modifications.

Incommensurability comes from the mismatch between periodicities of the two entities, along one direction. Their general formulation is defined and now well admitted as $[(MQ)_m]_{1+x}(TQ_2)_n$, with $m = 1$, 1.5, 2 and $n = 1$, 2, 3, the $1 + x$ value being related to the incommensurability. Such a formulation clearly indicates the composite nature of the compounds, with (MQ) and (TQ_2) sublattices that are of rock salt type structure for (MQ) (double-layer-thick for $m = 1$, or three-layer-thick for $m = 1.5$) and of CdI_2 type structure for (TQ_2) (T = Ti, V, Cr, i.e. an octahedral coordination) or NbS_2 (T = Nb, Ta, i.e. a trigonal prismatic coordination)

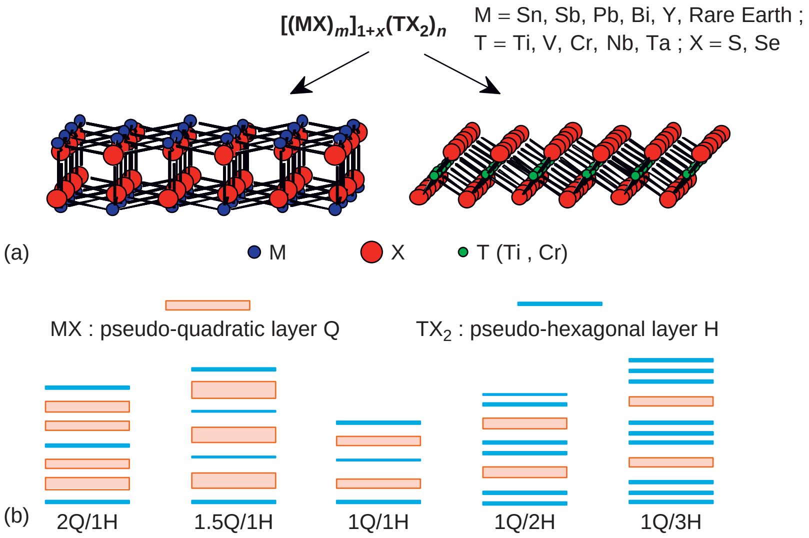
$[(MX)_m]_{1+x}(TX_2)_n$
M = Sn, Sb, Pb, Bi, Y, Rare Earth ;
T = Ti, V, Cr, Nb, Ta ; X = S, Se
(a)
● M
● X
● T (Ti , Cr)
MX : pseudo-quadratic layer Q
TX_2 : pseudo-hexagonal layer H
(b)
2Q/1H
1.5Q/1H
1Q/1H
1Q/2H
1Q/3H

Figure 52 (a) The MQ and TQ_2 parts of a misfit layer compound. (b) Different stacking motifs between the so-called quadratic and hexagonal slabs

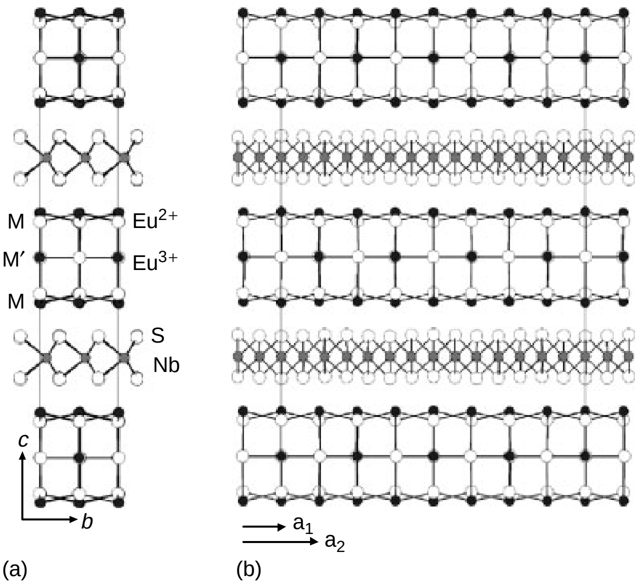

Figure 53 Projection of the structure of $[(EuS)_{1.5}]_{1.15}NbS_2$ (a) onto the (b, c) plane and (b) onto the (a, c) plane. This drawing was done for the commensurate approximation of 4/7

(Figure 53(a)). Abbreviated labeling 'Q' for MQ (= pseudo quadratic symmetry) and 'H' for TQ_2 (= pseudo Hexagonal symmetry) is typically used in this class. According to the combination of m and n values, one gets a variety of alternating sequences that are shown in Figure 53(b), with some respective referenced compounds.[130,131]

The $[(MQ)]_{1+x}(TQ_2)_2$ family has $n = 2$ and features a van der Waals gap between the two adjacent (TQ_2) slabs. Because the van der Waals gaps between the double MS_2 slabs are empty, the compounds can be exfoliated and intercalated in analogy to the parent MS_2 compounds. The octahedral holes in the van der Waals gap of monoclinic $(PbS)_{1.14}(NbS_2)_2$ are partially occupied by additional Nb. Thus, for the parent binary TQ_2 compounds tetrahedral and/or octahedral vacant sites within the gap are available for metal intercalation (donor species) as for instance, alkali metals[132] or transition metals such as Mn, Fe, Co.[133] One could also say that the [MQ] slab is, in itself, an intercalated entity (donor species) between two TQ_2 slabs. The crystal chemistry of the ternary misfit chalcogenides is similar to that of their parent binary chalcogenides, and this is reinforced by the phenomenon of polytypism which is occurring for both families.[134,135] Examples of Q-multilayered derivatives where $m = 2$, is $[(\{Pb_{1-x}Sb_x\}S)_2]_{1.14}(NbS_2)$ with $x \approx 0.2$.[136]

The issue of stability of these phases was not answered in the early studies. Only after a large number of misfit compounds was synthesized and studied did it become apparent that the key factor for the stability of these phases is a mechanism of charge transfer between the Q and H sublattices. The Q-part plays the role of electron donor and the H-part that of acceptor.[137,138] This hypothesis was of course envisioned, since the beginning, when a trivalent M metal was present (e.g. the rare earth elements), just considering the Q-part as $M^{3+} + Q^{2-} \rightarrow 1e^-$ to be transferred to the H-part. But the situation with a divalent M metal atom (e.g. Pb, Sn) has been 'resolved' later, after very precise chemical analyses were performed. It was found that a partial substitution of M^{2+} by T^{4+} took place in the Q-part, giving an excess of positive charges that must be equilibrated within the H-part as a reduction from T^{4+} to T^{3+}.[139] The analysis also indicated the presence of M-vacancies within the Q-part, specifically when $T = V$, Cr; this was illustrated for $[Gd_{1.16}\square_{0.11}S_{1.27}](CrS_2)$.[140] Thus, including the vacancies (□) in the composition leads to an almost exact charge equilibrium: the electronic transfer from the [GdS] to the $[CrS_2]$ slab is such that no excess electrons exist, and then the +3 oxidation state for Cr is stabilized.

Special attention has to be given to the case of 1.5-Q type misfit phases. For these phases, the Q-part is three-layer-thick, which implies two different coordination polyhedrons around the M/M′ metal atoms (Figure 53). Within the central layer, the M′ atom is octahedrally coordinated with X atoms, while the two external layers are concerned with M atoms surrounded by five X atoms within the Q-part and, in addition, two or three X atoms from the H-part. An example of this is provided with $[(EuS)_{1.5}]_{1.15}(NbS_2)$. It has to be noted that the charge transfer is established by the presence of Eu^{3+} (M′-site) while Eu^{2+} cations are attached to the external M-sites (see Figure 53). The mixed valence state for Eu was confirmed by Mössbauer spectroscopy.[141] Another example can be given with the Pb^{2+}/Fe^{3+} couple, that is, with $M \neq M'$. The 'classical type m = 1' for the Eu-derivative, $(EuS)_{1.173}(NbS_2)$, has been recently characterized; a mixed valence state for Eu, that is, Eu^{2+}/Eu^{3+} with a ratio close to 40/60, was demonstrated. However, in this compound, Eu^{2+} and Eu^{3+} ions occupy the same crystallographic site.[142]

Owing to the marked lamellar character of these phases, their physical properties are very anisotropic, and this anisotropy can be tuned by varying the mQ/nH ratio. It can be roughly said that transport properties are attributed to the H-part, while magnetic properties are related to the Q-part (when M = rare earth except La), or the H-part when T = Cr, or both parts together. About transport properties, an insulating behavior is found if T = Cr, or a semiconducting one with T = V[143] or a metallic one when T = Ti, Nb, or Ta.[144] A superconducting state was reported for the $[PbSe]_{1.14}(NbSe_2)_n$ series with $n = 1, 2, 3$.[145] A superconducting transition at a temperature as high as 5.3 K was observed for $[LaSe]_{1.14}(NbSe_2)_2$.[146] A complex behavior for electrical and/or magnetic properties is often present in relation with the modulated nature of both sublattices, which modulation results from the mutual interaction between sublattices. It is important to elucidate the details of the structures of these unusual compounds using sophisticated crystallographic methods such as the superspace approach.[147,148]

4 QUATERNARY COMPOUNDS

The number of quaternary phases has expanded dramatically in the past decade as interest in structural and compositional diversity in chalcogenides has increased. The majority of compounds has included alkali metal and alkaline earth metals which are in general associated with a ternary $[M_xM'_yQ_z]^{n-}$ covalently bonded framework. The selection of M and M′ is often a lanthanide/transition metal pair or a transition/main-group element pair. In the latter case, many of the compounds can also be conveniently considered as salts of various chalcometallate anions (e.g. $[PQ_4]^{3-}$, $[SnQ_4]^{4-}$ etc.) with different metals. As in the case of the ternary phases, the quaternary compounds also are generally prepared by direct combination reactions of simpler reagents or via solventothermal and polychalcogenide flux methodologies.

4.1 Alkali Metal Containing Quaternary Compounds

One permutation that has proven productive is the combination of lanthanides with late transition metals. From the reaction of the elemental copper and either lanthanides or actinides in molten alkali metal/polychalcogenide salts, several new quaternary phases have been discovered. Specifically, these phases are $ACuRE_2Q_6$ (where A = K, M = La, Q = S; A = Cs, M = Ce, Q = S; or A = K, M = Ce, Q = Se),**[149,150]** $ACuREQ_3$ (where A = Cs, RE = lanthanide or actinide, Q = S, Se)**[151]** and the structurally related $BaREMQ_3$ (RE = rare earth, M = coinage metal, Q = Se or Te),**[152]** ARE_2CuQ_4 (Q = S, Se),**[153]** $ARE_2Cu_3Q_5$, $ARE_2Ag_3Q_5$,**[154]** and $KCuCeTe_4$.**[155]** Other notable quaternary phases include $Rb_2Gd_4Cu_4S_9$, $Ba_4RE_2Cd_3S_{10}$ (RE = Sm, Gd, Tb),**[156]** $K_2Ag_3CeTe_4$,**[157]** $A_3RE_4Cu_5Te_{10}$ (A = alkali; RE = Sm, Gd, Er, Nd, Gd),**[158]** $CsGdZnSe_3$, and $BaGdCuSe_3$,**[159]** $Rb_2Cu_3CeTe_5$.**[160]** The class of rare earth transition metal chalcogenides has been recently reviewed.**[2]** In addition, the subclass of quaternary compounds with rareearth transition metal chalcogenides featuring square Te-based nets has also been reviewed.**[161]** Examples of square net compounds are $KCuCeTe_4$, $K_{2.5}Ag_{4.5}Ce_2Te_9$, and $KCuEuTe_2$; Section 4.2.

In $ACuM_2Q_6$, the lanthanides bond to a mixture of mono- and disulfides in a bicapped trigonal prismatic geometry; these polyhedra subsequently connect in two dimensions, forming layers equivalent to those seen in the $ZrSe_3$ structure-type with Cu^+ atoms residing in tetrahedral sites within the layers and alkali cations in the interlayer gallery.**[162]** A view of the structure of the orthorhombic compounds is given in Figure 54. The rare earth atoms are coordinated by a bicapped trigonal prism of Q atoms made of two $(Q_2)^{2-}$ units forming the short sides of the prism and four Q^{2-} ions at the apex and capping positions.

The compounds of the formula $ACuMQ_3$ also possess a layered structure.**[149]** Here the $[MQ_6]$ octahedral units form corrugated, two-dimensional sheets via edge-sharing in the first dimension and corner-sharing in the second. Cu cations are coordinated to tetrahedral sites in the folds of the corrugations, and alkali cations are again in the intergallery region. In the structure of the $ACuMQ_3$ phases, the f-block metal is coordinated to an octahedron of monochalcogenides. These $[MQ_6]$ units share edges with each other, forming one-dimensional chains parallel to the *a*-axis. These chains of octahedra are further connected through corner-sharing into a corrugated two-dimensional sheet (see Figure 55). The overall anionic network remains layered as the Cu^+ cations occupy tetrahedral sites in the folds of the layers of octahedra and so provide no extra dimensionality to the framework. The alkali metal cations reside within the interlayer galleries. If the Cu^+ were to be ignored, the remaining atoms would possess the anti-Pd_3Te_2 structure-type in which the Te atoms occupy both the octahedral sites and the interlayer gallery positions.

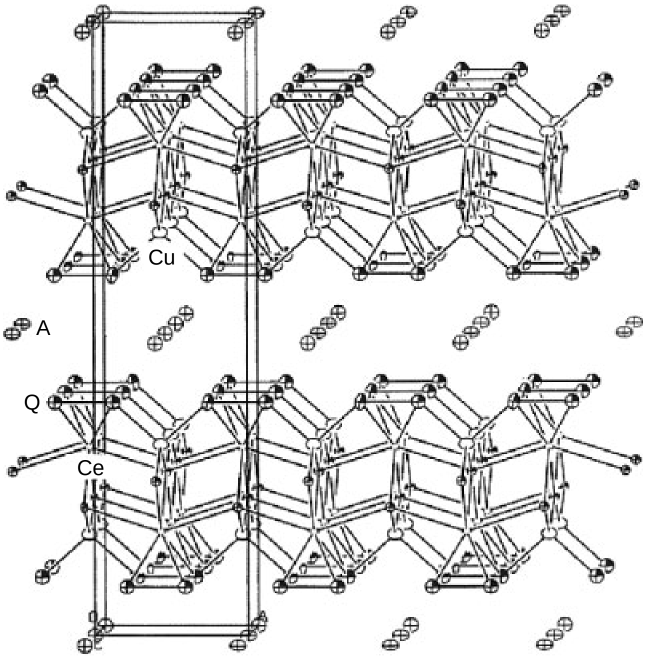

Figure 54 Extended structure of the orthorhombic form of $ACuCe_2Q_6$ as seen down the *a*-axis (circles with nonshaded octants, A; large open circles, Cu; small open circles, Ce; circles with shaded octants, Q)

The group of $ACuMQ_3$ compounds are members of a larger family that includes other members such as $CsCeCuS_3$, $CsGdZnSe_3$, $BaRECuQ_3$,**[152]** $BaREAgQ_3$.**[163]**

The ARE_2CuQ_4 family includes KGd_2CuS_4, $RbNd_2CuS_4$, $RbSm_2CuS_4$, $RbSm_2CuSe_4$, $RbGd_2CuSe_4$, $RbDy_2CuSe_4$, $CsLa_2CuSe_4$, and $CsSm_2CuSe_4$.**[164]** This structure-type has a three-dimensional tunnel framework (see Figure 56). The tunnels are 10-membered pentagonal rings that are large enough in cross section to accommodate a single eight-coordinate A atom. The three-dimensional anionic framework is built from REQ_6 octahedra and CuQ_4 tetrahedra. The RE/Q fragments in these compounds consist of distorted

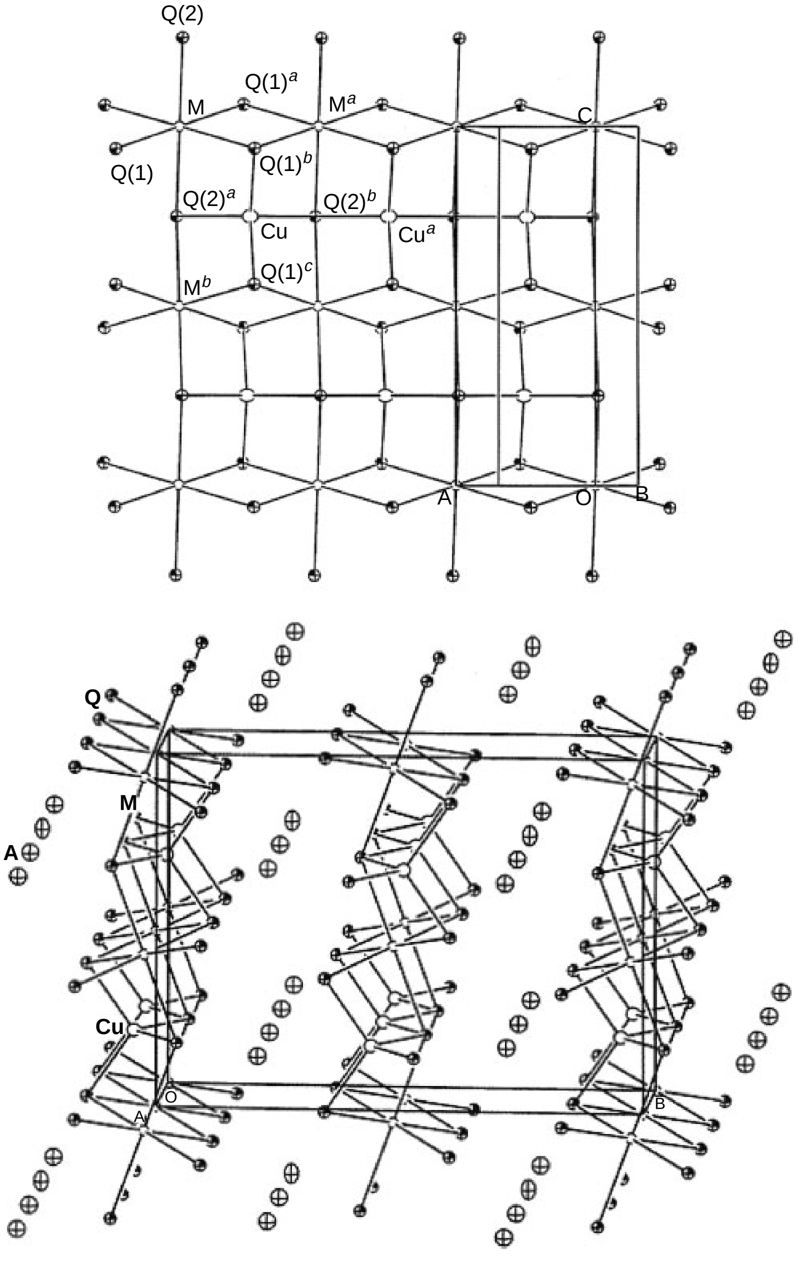

Figure 55 (a) View perpendicular to a single anionic layer of the $ACuMQ_3$ structure-type. (b) The $ACuMQ_3$ structure-type ($A = Cs$, $M = Ce$, $Q = S$; or $A = K$, $M = U$, $Q = Se$) as seen down the a-axis, parallel to the anionic layers (circles with nonshaded octants, A; large open circles, Cu; small open circles, M; circles with shaded octants, Q)

$^{2}_{\infty}[RE_2Q_5{}^{4-}]$ layers that are built from the REQ_6 octahedra sharing edges parallel to the a-axis to form chains. The chains are connected through vertex-sharing of Q atoms to form layers. The $^{2}_{\infty}[RE_2Q_5{}^{4-}]$ layers are connected by the octahedra in one layer sharing edges with octahedra in adjacent layers to form the three-dimensional framework.

The $ARE_2Cu_3Q_5$ and $ARE_2Ag_3Q_5$, compounds include $RbEr_2Cu_3S_5$,[153] $CsGd_2Ag_3Se_5$,[153] $CsTb_2Ag_3Se_5$,[153] and $RbSm_2Ag_3Se_5$.[154] The phases adopt a three-dimensional tunnel structure (Figure 57). The tunnels are 10-membered pentagonal rings consisting of six Cu–Q bonds and four RE-Q bonds that are large enough in cross section to accommodate a single eight-coordinate A atom. These AQ_8 polyhedra share triangular faces along the a-axis. The three-dimensional anionic framework is built from REQ_6 octahedra and CuQ_4 tetrahedra. The RE/Q fragments in these compounds consist of distorted $^{2}_{\infty}[RE_2Q_5{}^{4-}]$ layers that are built from the REQ_6 octahedra sharing edges parallel to the a-axis to form chains. The chains connect through vertex-sharing of Q atoms to form layers. The MQ_4 tetrahedra share vertices and edges

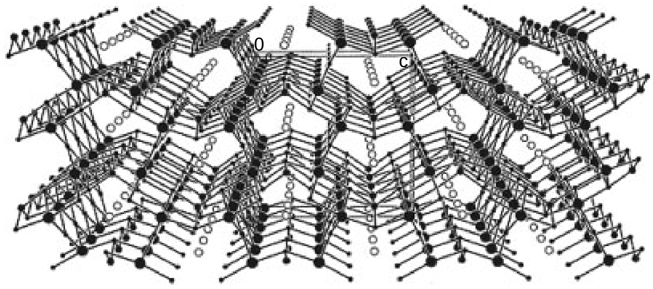

Figure 56 The tunnel motif of the ARE_2CuQ_4 group of phases. (Reprinted with permission from Ref. 2. © 2002 American Chemical Society)

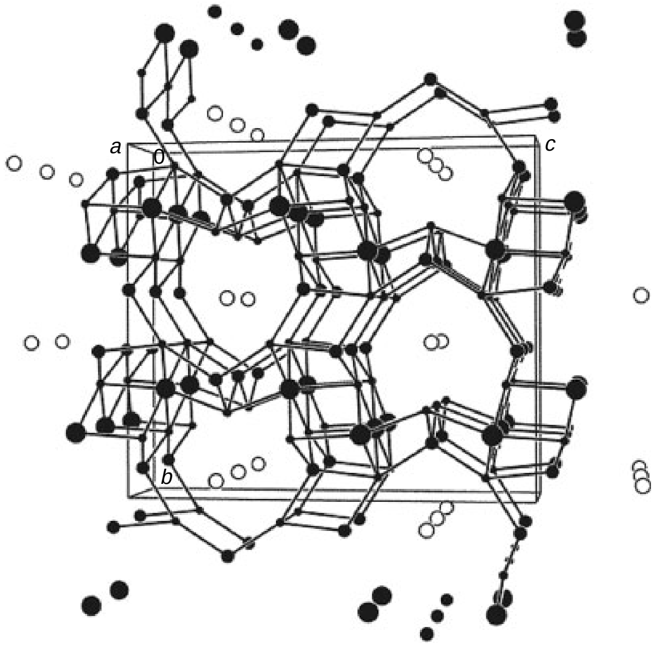

Figure 57 The framework structure adopted by the $ARE_2Cu_3Q_5$ and $ARE_2Ag_3Q_5$, compounds. Large black spheres are RE atoms. Small black spheres are Q atoms

to form two-dimensional layers that connect to form the tunnel structure.

Some of the telluride compounds, such as $KCuCeTe_4$, $K_{2.5}Ag_{4.5}Ce_2Te_9$, $KCuEuTe_2$, and $Na_{0.2}Ag_{2.8}EuTe_2$, contain the interesting structural feature that is defined by a square net of Te atoms. This net is a monoatomic layer of Te atoms with equal Te–Te bond distances in the squares of $\sim$3.1 Å. These distances are both curious and unusual in that they do not represent normal bonds. In addition, formal integer oxidation states cannot be assigned to these Te atoms and thus these compounds are considered ‘nonclassical’. The chemical, physical, and electronic properties of these compounds are largely decided by these square nets, and by their interaction with the remaining part of the structure. It can be a challenge to understand the properties of these compounds because the observed crystal structures are not consistent with the measured properties. The equality of Te–Te distance of $\sim$3.1 Å in the square net is at first intriguing but a more careful look in the diffraction properties of these materials reveals that there are extensive modulations in these nets that they are easy to miss. Both electron diffraction and X-ray diffraction experiments show the extent of these modulations (superstructures exist in the nets) and indicate that the square nets of Te atoms are actually distorted and the observation of the ‘novel’ distances of $\sim$3.1 Å are an artifact of averaging. Some of these distortions have been elucidated. This class of rare earth chalcogenide compounds has been described in a recent review.**[161]**

One case in point is that the tetragonal structure of $K_{0.33}Ba_{0.67}AgTe_2$,**[165]** obtained by conventional crystallography, is inconsistent with its semiconducting behavior. This is because conventional crystallography gives only an average structure, which shows a perfect square Te-net. In reality, this compound possesses an incommensurately modulated structure which was solved within a (3 + 1)D higher dimensional crystallographic formalism.**[166]** These types of structures need to be tackled with higher-dimensional crystallographic techniques (super space group approach), which at this stage makes their full structural characterization far from routine. The compound was shown to crystallize in the monoclinic symmetry, $P2_1(\alpha 0\gamma)$ super-space group in a symmetry different from that reported for the average structure (tetragonal) or that assumed from electron diffraction measurements (orthorhombic). The results are rather intriguing because the Te-net in this compound shows two different distortions at the same time. One distortion features only $Te_3{}^{2-}$ fragments, while the other has both $Te_5{}^{2-}$ and Te^{2-} ions. The two distortions alternate in a wave-like fashion (see Figure 58). This is the first time two different distortion motifs were found to coexist.

The structure of $K_{2.5}Ag_{4.5}Ce_2Te_9$ is shown in Figure 59. The $K_{2.5}Ag_{4.5}Ce_2Te_9$ is an intergrowth compound between two components $K_{2.5}Ag_{4.5}Te_3$ and $CeTe_3$ and can also be described as $(K_{2.5}Ag_{4.5}Te_3)(CeTe_3)_2$. There are Te nets in both components. In the $K_{2.5}Ag_{4.5}Te_3$ section, only Te^{2-} ions with no distortions exist; however, the atoms in the Te-net of the $CeTe_3$ section have an average formal charge < -2 and generate incommensurate modulations (see electron diffraction pattern in Figure 59). The nature of these modulations is currently an active area of research. It is anticipated that full structural characterization of these fascinating distortions will be accomplished within the next decade.

4.2 Polychalcogenide, Chalcophosphate and Related Fluxes

The application of salt fluxes in the synthesis of new solid-state compounds has witnessed significant development in the past decade. Particularly important has been the

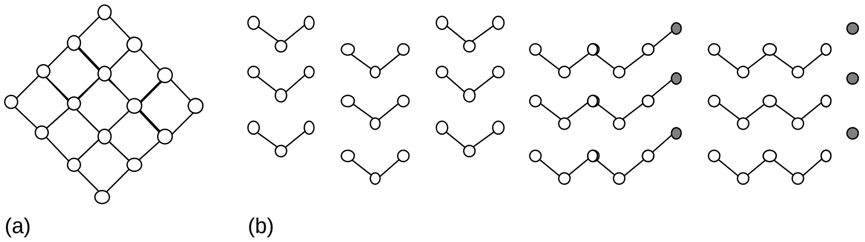

Figure 58 Striking difference between (a) the structure of the square Te-net determined by conventional crystallography (average tetragonal structure) which predicts a metallic compound and (b) the structure of the incommensurately modulated Te-net determined by higher dimensional crystallography. Two motifs are observed: Te groups with a 'V' shape and Te groups with a 'W' shape. Occasionally, as the motif changes from V to W, the lone Te atom (black dots) found between two W motifs is at a distance slightly shorter than 3.1 Å of a W motif (one such example is observed in the figure). This structure explains the narrow band gap semiconductor behavior of this compound

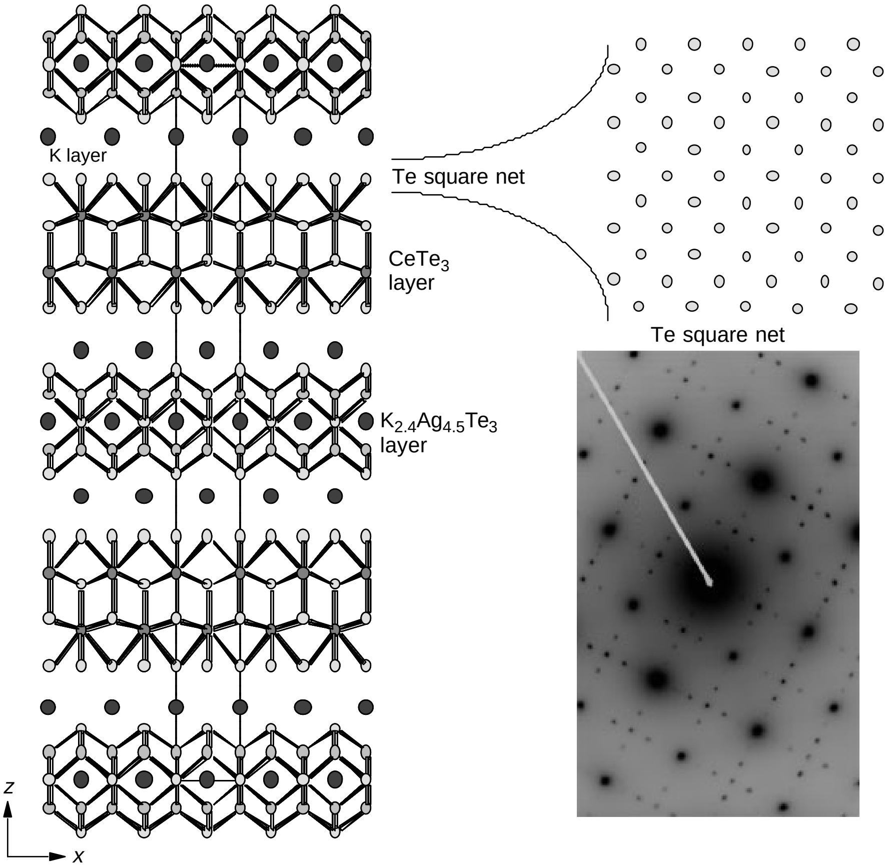

Figure 59 The structure of $K_{2.5}Ag_{4.5}Ce_2Te_9$ and representative electron diffraction pattern with the e-beam perpendicular to the square Te-net. The weak supercell spots appear between the strong subcell reflections

emergence of the molten polychalcogenide flux methodology in the exploratory synthesis of complex chalcogenides. This approach to new chalcogenides has been developed and brought to the main stream of inorganic chemistry methodology mainly in our laboratories. This method of synthesis and exploration has simplified access to low and intermediate temperatures (160–600 °C) and contributed to the discovery of some very interesting materials. In many cases, the compounds stabilized under polychalcogenide flux conditions are only kinetically stable and cannot be synthesized at higher temperatures. Lower temperatures, coupled with the presence of a liquid, also make possible the use of molecular assemblies as building blocks for incorporation into solid-state structures, and consequently the construction of complex multinary solids.

An excellent way to search for new solid-state materials is the use of molten salts as solvents in which to carry out exploratory synthetic reactions. For the discovery of chalcogenide materials, the use of alkali metal polychalcogenides, of the type A_2Q_x (A = alkali metal, Q = chalcogenide) as solvents, is very appropriate as we and others have demonstrated already. As solvents for intermediate temperature reactions, A_2Q_x salts are especially well-suited because the melting points range between the extremes of K_2S at about 850 °C to K_2S_4 at 145 °C, with the majority of compositions melting at < 300 °C. The polytelluride versions melt between 300–500 °C. Low melting, A_2Q_x fluxes remain nonvolatile over a wide temperature range, and so once above the melting point, reaction temperatures can be varied considerably without concern for solvent loss. Polychalcogenide fluxes are highly reactive towards metals because they are very strong oxidants. Reactions between metals and molten A_2Q_x are performed in situ.

The polychalcogenide salts can be made by allowing stoichiometric amounts of elemental chalcogenide to react an with alkali metal in liquid NH_3 at −70 °C or by direct combination reactions between the alkali metal and the chalcogen. In the latter case, care must be taken to avoid explosions owing to the highly exothermic nature of the reaction. To synthesize new compounds, one or more metals are added directly to the A_2Q_x/Q reaction mixture and heated in a sealed Pyrex or quartz container. Crystalline products either precipitate from the melt or form on slow cooling of the melt, depending on the specific stoichiometric and processing conditions. Presumably, the nucleated species are in equilibrium with the soluble intermediates, especially if the flux is present in excess, and hence a solvation/reprecipitation effect (often referred to as the mineralizer effect) occurs. This aids in the growth of high quality single crystals because the flux can redissolve small or poorly formed crystallites and then reprecipitate the species onto larger, well-formed crystals. The advantage of the flux method is that one allows the system to end up where it wants in the kinetic or thermodynamic sense without attempting to force upon it a certain stoichiometry or structure. Provided the temperature and time are appropriate, the reaction system has all the ingredients to form a new phase. The benefit of this becomes apparent from the unsual compositions often found for the new materials which most certainly could not have been predicted a priori.

Chalcophosphates are compounds that contain phosphorus and chalcogen atoms in which phosphorus is oxidized and there exists at least one P–Q bond, where Q = S or Se. To date, there are no examples with Q = Te. There exists a wonderful structural diversity among these compounds due primarily to the various $[P_yQ_z]^{n-}$ building blocks that can be stabilized and their fascinating variety of binding modes. In addition to their rich structural chemistry, several of these phases possess interesting ion-exchange, intercalation, magnetic, electrical, and optical properties. Therefore, it is important to inquire about chalcophosphates, develop their syntheses and explore their properties.

4.2.1 Chalcometallate Salts

By chalcometallate compounds we mean those that are based on complex anions of the type $[M_xQ_y]^{z-}$ where M is a high oxidation state metal or metalloid and Q is a chalcogen. The most well-known chalcometallate anions are $[PQ_4]^{3-}$, $[P_2Q_6]^{4-}$, $[GeQ_4]^{4-}$, $[SnQ_4]^{4-}$, $[AsQ_3]^{3-}$, and $[SbQ_3]^{3-}$, but a large variety of others also exist. These anions can be regarded as building blocks for constructing ternary and quaternary chalcogenide frameworks. They can form in situ during synthesis or be introduced in the reaction as their alkali metal salts. When combined with various metal cations, these anions can lead to an astonishing variety of compositions and structural arrangements.

A convenient way to stabilize these anions and make them available for reaction is through a flux methodology. This approach to new metal chalcogenides has simplified access to low and intermediate temperatures (160–600 °C) and contributed to the discovery of many fascinating solid-state materials. Lower temperatures, coupled with the presence of a flux, also make possible the use of molecular assemblies as building blocks for incorporation into solid-state structures.

When using the flux approach, the best way to generate chalcometallate anions such as $[PQ_4]^{3-}$, $[P_2Q_6]^{4-}$, $[GeQ_4]^{4-}$, $[SnQ_4]^{4-}$, $[AsQ_3]^{3-}$, and $[SbQ_3]^{3-}$ is to introduce P, Ge, Sn, As, or Sb in the appropriate amount into the A_2Q_x melt. For example, the polychalcophosphate fluxes form by simple in situ fusion of $A_2Q/P_2Q_5/Q$, (Q = S, Se) (see equation (2)). The acid/base characteristics of the $A_x[P_yQ_z]$ fluxes are very different from those of A_2Q_x fluxes in that they tend to be more basic. The relatively good solubility properties of $A_x[P_yQ_z]$ salts in water and polar organic solvents allow for easy isolation of products.

$$\left(\frac{x}{2}\right) A_2Q + \left(\frac{y}{2}\right) P_2Q_5 + zQ \xrightarrow{T > 300\,^\circ C} A_x[P_yQ_{x+y+z}]$$

$$\text{(A = alkali metal)} \qquad (2)$$

In these melts, various $[P_yQ_z]^{n-}$ species are solubilized in excess polychalcogenide flux. The melting points of $A_xP_yQ_z$ are in the intermediate temperature range 300–400 °C, making possible the synthesis of even metastable phases. The existence of various $[P_yQ_z]^{n-}$ species in the melt is influenced by the $A_xP_yQ_z$ composition. Their exact distribution as a function of composition, however, is not well-known; however, one can reasonably speculate the equilibria shown in Figure 60. Recognizing that there are such equilibria that can be controlled is important because flux composition determines the product outcome. Similar considerations apply for the $[GeQ_4]^{4-}$, $[SnQ_4]^{4-}$, $[AsQ_3]^{3-}$, and $[SbQ_3]^{3-}$ anions.

Although early investigations concentrated on the reactivity of Bi, almost all elements have good reactivity in them, as

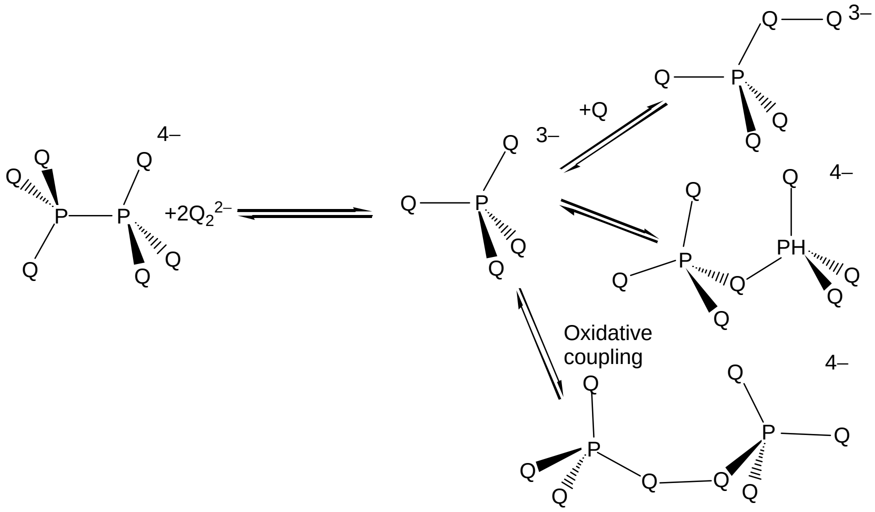

Figure 60 Possible chalcophosphate anion equilibria present in alkali metal polychalcogenide fluxes

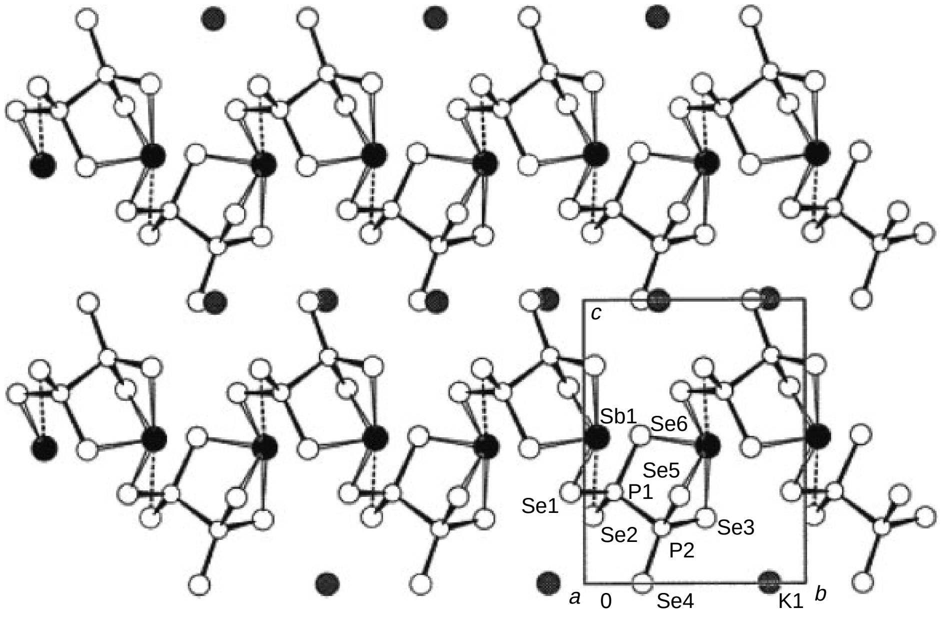

Figure 61 View of β-$KSbP_2Se_6$ perpendicular to the screw axis. The weak interchain bond is emphasized with a dashed line

has been demonstrated for a large fraction of the metallic elements. Many quaternary chalcophosphate compounds have been generated in this fashion including $ABiP_2S_7$ (A = K, Rb),[167] $A_3M(PS_4)_2$ (A = K, Rb, Cs; M = Sb, Bi),[168] $Cs_3Bi_2(PS_4)_3$, and $Na_{0.16}Bi_{1.28}P_2S_6$, α-, β-KMP_2Se_6 (M = Sb, Bi),[169] $A_2MP_2Se_6$ (A = K, Rb, Cs; M = Pd, Zn, Cd, Hg),[170] $APdPS_4$,(A = Na, K, Rb),[171] $K_2PdP_2S_6$,[172] $Cs_2PdP_2Se_6$,[172] $Rb_8Hg_4(Se_2)_2(PSe_4)$,[173] Tl_2AuPS_4,[173] $KAu_5P_2S_8$,[174] $K_4In_2(PSe_5)_2(P_2Se_6)$,[175] $Rb_4Ti_2(P_2Se_7)(P_2Se_9)_2$,[176] $Na_{1.5}Pb_{0.75}PSe_4$, $K_3RuP_5Se_{10}$,[177] $K_3Cu_3P_3Se_9$,[178] $Cs_2CuP_3S_9$,[179] $KInP_2Se_6$,[180] $NaCrP_2S_6$, $ANb_2P_2S_{12}$ (A = K, Rb, Cs),[181] K_2AuPS_4[182] and $A_2AuP_2Se_6$ (A = K, Rb).[182]

The new quaternary niobium thiophosphates $ANb_2P_2S_{12}$ (A = K, Rb, Cs) form by allowing Nb metal, A_2S, P_2S_5, and S to react at 600–700 °C. They crystallize as ‘stuffed’ variants of the tetragonal $TaPS_6$ structure-type. Their structures are based on double helices formed from interpenetrating, noninteracting spiral chains of binuclear $[Nb_2S_{12}]$ cluster units and $[PS_4]$ thiophosphate groups. The cavities and tunnels, which are formed by the helical chains, are filled with A^+ ions. Temperature-dependent conductivity studies reveal thermally activated electrical transport behavior. $ANb_2P_2S_{12}$ may be considered a chalcogenide analogue of metal phosphate bronzes.

The α-, β-KMP$_2$Se$_6$ (M = Sb, Bi) set presents an interesting case of thermodynamically metastable acentric compounds which were found to crystallize in the polar chiral space group $P2_1$, even though they are built up from the centrosymmetric, 'ethane-like' (P$_2$Se$_6$)$^{4-}$ group. These are kinetic crystallization products that transform to the more thermodynamically stable α-KMP$_2$Se$_6$ (M = Sb, Bi)[183] structure upon extended exposure to elevated temperature. The β-KSbP$_2$Se$_6$ has a pseudo-one-dimensional structure containing Sb^{3+} tri-coordinated by one (P$_2$Se$_6$)$^{4-}$ unit (see Figure 61). β-KSbP$_2$Se$_6$ crystallizes as a single phase by heating an amorphous precursor of the same composition to slightly above the glass transition temperature. At temperatures above 250 °C, β-KSbP$_2$Se$_6$ transforms slowly to α-KSbP$_2$Se$_6$. In other words, there are three states to this composition, amorphous, α-, and β-, and therefore it might be possible to utilize the unique transformation properties of the KSbP$_2$Se$_6$ system in a three-state logic gate.

The compound K$_3$RuP$_5$Se$_{10}$ forms from the reaction of Ru with a molten mixture of K$_2$Se/P$_2$Se$_5$/Se at 490 °C. It is a unique compound in that it is the first chalcophosphate to feature direct metal-phosphorus Ru–P bonds. It has infinite chains of [Ru(P$_2$Se$_6$)(P$_3$Se$_4$)$^-$] separated by K$^+$ cations (Figure 62). The chains have the polymeric [P$_3$Se$_4$$^-$] unit that contains P^{2+} and P^{3+} atoms, which is the backbone upon which each chain is built. Every P atom of this unit makes metal-phosphorus bonds with a Ru^{2+} center. The latter completes its *fac* octahedral coordination with three Se ligands that belong to [P$_2$Se$_6$]$^{4-}$ units. This M–P bonding is very much analogous to the bonding encountered in conventional M/phosphine complexes.

A number of lanthanide, actinide, and related compounds have been synthesized as well. A$_3$REP$_2$Se$_8$,[184] and A$_2$REP$_2$Se$_7$ (A = Rb, Cs; RE = Ce, Gd), K$_3$CeP$_2$S$_8$,[185] KREP$_2$Se$_6$ (RE = Y, La, Ce, Pr, Gd),[186,187] Rb$_4$U$_4$(Se)$_2$(Se$_2$)$_4$(PSe$_4$)$_4$,[188] K$_3$La(PSe$_4$)$_2$, K$_4$La$_{0.67}$(PSe$_4$)$_2$, K$_2$La(P$_2$Se$_6$)$_{0.5}$(PSe$_4$),[189] NaREP$_2$S$_6$,(RE = Yb, Sm),[190] KSmP$_2$S$_7$,[190] LiEuPSe$_4$ and KEuPSe$_4$,[191] NaCeP$_2$Se$_6$, Cu$_{0.4}$Ce$_{1.2}$P$_2$ Se$_6$, and the incommensurately modulated AgCeP$_2$Se$_6$.[192]

Actinide compounds have been prepared as well including Cs$_8$U$_5$(P$_3$S$_{10}$)$_2$(PS$_4$)$_6$,[193] K$_{10}$Th$_3$(P$_2$S$_7$)$_4$(PS$_4$)$_2$, and A$_5$An(PS$_4$)$_3$, (A = K, Rb, Cs; An = U, Th), K$_2$UP$_3$Se$_9$,[194] A$_2$ThP$_3$Se$_9$ (A = K, Rb),[195] and Cs$_4$Th$_2$P$_5$Se$_{17}$, and A$_{11}$U$_7$(PS$_4$)$_{13}$ (A = K, Rb).[196] Particularly interesting are the radioactive plutonium compounds KPuP$_2$S$_7$ and K$_3$PuP$_2$S$_8$.[197]

The LiEuPSe$_4$ structure is three-dimensional and composed of EuSe$_8$ distorted square antiprisms and PSe$_4$ tetrahedral building blocks that create tunnels, running down the a-axis, in which the Li ions reside. The Li ions are in a highly distorted tetrahedral coordination (Figure 63(a)).

The structure of KEuPSe$_4$ has two-dimensional character. Looking down the a-axis in Figure 63(b), one can see layers of [EuPSe$_4$]$_n$$^{n-}$ separated by K$^+$ cations that have a distorted bicapped trigonal prismatic coordination. The layers are composed of wedge-like EuSe$_6$ trigonal prisms and PSe$_4$ tetrahedral units. Each Eu is connected to four PSe$_4$ tetrahedral units. With two of the tetrahedra it shares an edge; with the other two it shares only corners. The EuSe$_6$ trigonal prisms share rectangular edges in such a way that the trigonal faces of the prisms (i.e. the wedges) point alternately up as they form parallel chains along the b-axis. The PSe$_4$ tetrahedra connect these chains along the a-axis by sharing their edges with the rectangular faces of the trigonal prisms and the opposite edges. KEuPSe$_4$ is closely related to CsPbPSe$_4$.[198]

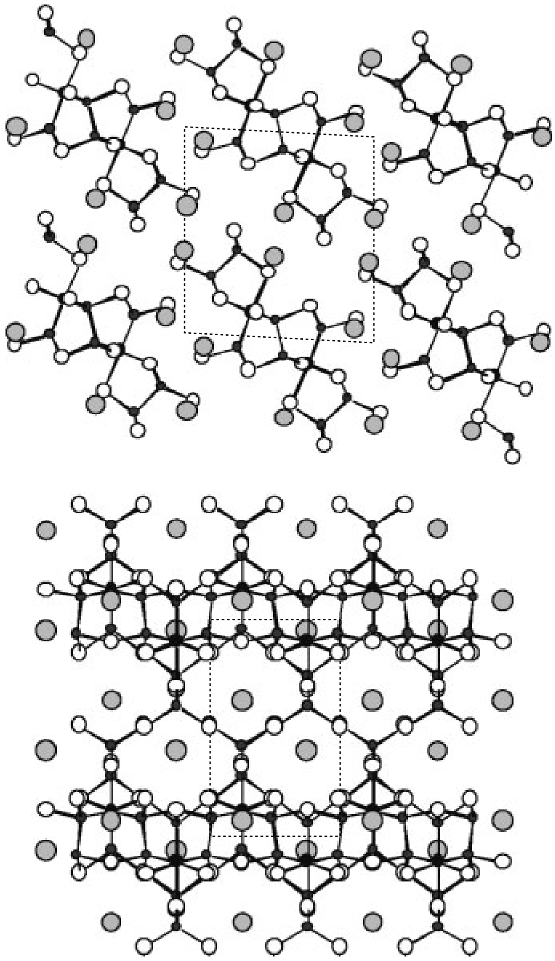
Figure 62 Two views of the low dimensional structure of the K$_3$RuP$_5$Se$_{10}$

The K$_{11}$U$_7$(PS$_4$)$_{13}$ features an interesting tunnel framework composed of eight interlocking uranium U$_7$(PS$_4$)$_{13}$ screw helices, with alkali metal cations residing inside the framework channels. The uranium atoms are coordinated in a bi- or tricapped trigonal prismatic fashion. The screw helices are built up from uranium atoms interconnected by PS$_4$, tetrahedral units.

Finally, the first series of plutonium thiophosphates has been identified and described. It appears that the chemistry of plutonium is neither similar to that of U nor any of the rareearth

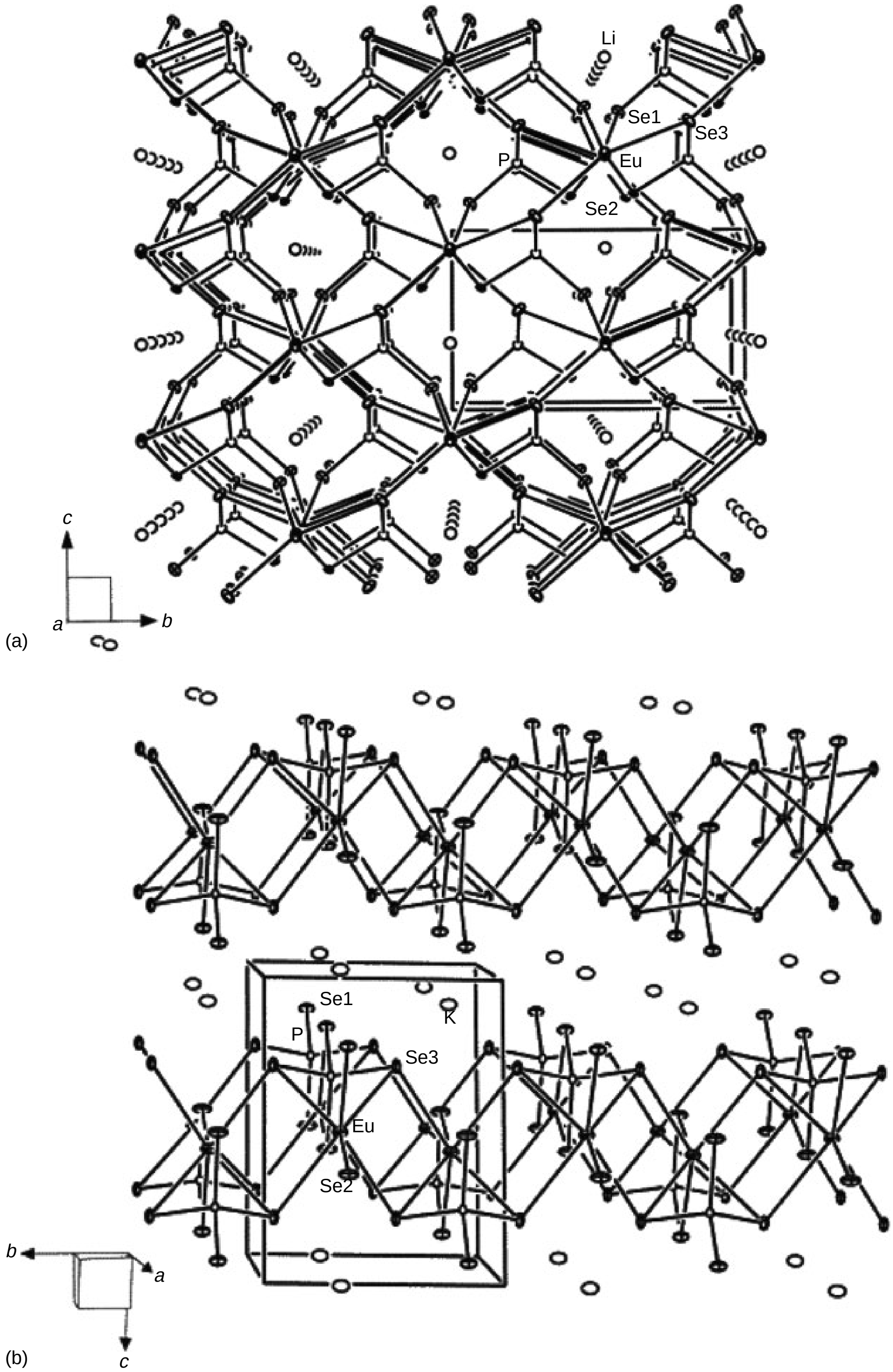
Li
Se1
Se3
P
Eu
Se2
c
a
b
(a)
Se1
P
K
Se3
Eu
Se2
b
a
c
(b)

Figure 63 (a) The structure of $LiEuPSe_4$ viewed down the a-axis with thermal vibrational (80%) ellipsoids. This view shows the $^{1}_{\infty}[EuPSe_4]^-$ framework that creates tunnels for the Li ions to reside. (b) The structure of $KEuPSe_4$

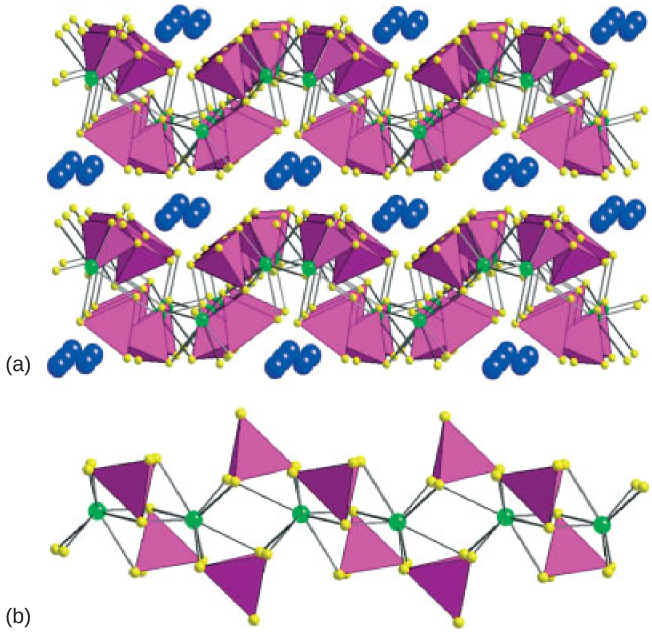

Figure 64 The structure of (a) $KPuP_2S_7$ and (b) $K_3PuP_2S_8$

element compounds. The $KPuP_2S_7$ and $K_3PuP_2S_8$ possess layered and chain-like structures, respectively (Figure 64).

The flux chemistry can be easily adapted for chalcogermanate and -stannate chemistry as well as chalcoantimonate and arsenate chemistry. The compounds $Na_8Pb_2[Ge_2S_6]_2$, $Na_8Sn_2[Ge_2S_6]_2$,[199] K_2MnSnS_4,[200] α-, β-$A_2Hg_3M_2S_8$ ($A = K$, Cs, Rb; $M = Sn$, Ge),[201,202] $ASmGeSe_4$ ($A = K$, Rb, Cs)[203] $A_{0.5}Pb_{1.75}GeS_4$ ($A = Li$, Na),[204] Li_2PbGeS_4 and Li_2EuGeS_4,[205] K_2EuMSe_5 and $KEuMS_4$ ($M = Si$, Ge),[206] the chalcoantimonates A_2AuSbS_4 ($A = Rb$, Cs),[207] $K_2Gd_2Sb_2Se_9$[208] and $K_2La_2Sb_2S_9$, $Ba_3Sb_{4.66}S_{10}$,[209] $Ba_{2.62}Pb_{1.38}Sb_4S_{10}$, K_2AuAsS_4, $KSnAsS_5$ and $K_2SnAs_2S_6$, have been synthesized using the flux protocol.

The α-, β-$A_2Hg_3M_2S_8$ ($A = K$, Rb; $M = Ge$, Sn) are closely related phases discovered using the alkali polychalcogenide flux method. They present structure types with a polar noncentrosymmetric character and strong nonlinear second-harmonic generation (SHG) properties. The polar character of the structure of α-$K_2Hg_3Ge_2S_8$ is evident when viewed down the b-axis (see Figure 65). The structure can be described in terms of a three-dimensional covalent anionic $[Hg_3Ge_2S_8]^{2-}$ framework filled with K^+ ions. The

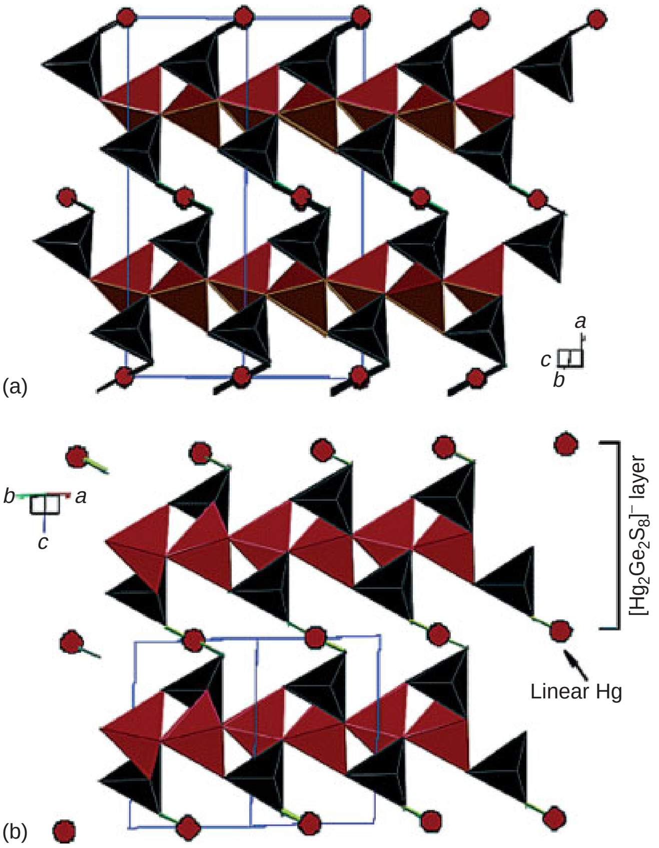

Figure 65 Polyhedral representation of the structure of (a) α-$K_2Hg_3Ge_2S_8$ and (b) β-$K_2Hg_3Ge_2S_8$ showing the bridging role of the linearly coordinated Hg atoms

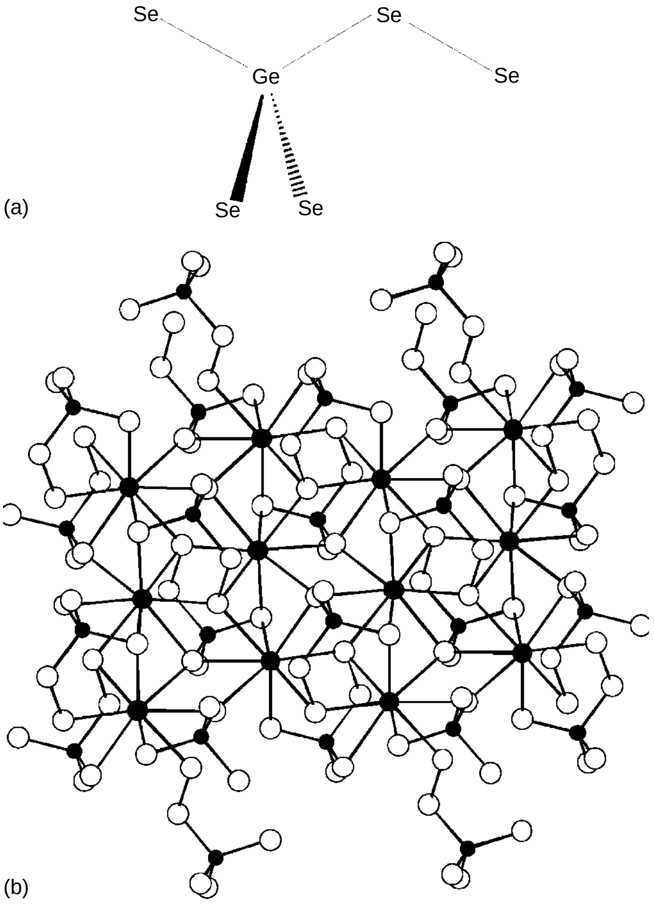

Figure 66 (a) The $(GeSe_5)^{4-}$ unit and (b) the $[EuSiSe_5]^{2-}$ framework

framework can be viewed as slabs of $[Hg_2Ge_2S_8]^{4-}$ linked by linear Hg(1) atoms. There are two types of Hg^{2+} atoms, a highly distorted tetrahedral [Hg(2) ‘seesaw-shaped’ HgS_4] and a linearly coordinated Hg(1) atom. The β-form is similar but it differs in how the linear Hg atoms link the $[Hg_2Ge_2S_8]^{4-}$ slabs (Figure 65).

The compounds $K_2EuSiSe_5$, $K_2EuGeSe_5$ are isostructural and they have a layered structure in which 9-coordinate Eu(II) atoms are linked into a layer by $(GeSe_5)^{4-}$ units. The $(GeSe_5)^{4-}$ unit, shown in Figure 66(a), is a Ge(IV) tetrahedron with one of its arms being a diselenide $(Se_2)^{2-}$ unit. It is isoelectronic to the $[PSe_5]^{3-}$ unit observed in thiophosphate chemistry. Five different $(GeSe_5)^{4-}$ units are coordinated to each europium atom. Two units are bound to europium with one selenium atom, two units are bound with two selenium atoms, and the fifth $(GeSe_5)^{4-}$ unit is bound to europium with three of its selenium atoms. Each $(GeSe_5)^{4-}$ unit links four different Eu^{2+} atoms within a layer as seen in Figure 66(b).

A classical example of reactivity of main group metal in thioarsenate melts and how Lewis flux basicity affects the chemistry is that of Sn. Low Lewis basicity fluxes favor the formation of $KSnAsS_5$, and as the basicity increases (e.g. by adding more K_2S) the reaction lead to layered $K_2SnAs_2S_6$ instead.**[210]** The former compound has infinite chains and the rare pyramidal β-$[AsS_4]^{3-}$ ligand (Figure 67(a)). The key unit in the chain is a centrosymmetric $[Sn(AsS_2(S_2))]_2$ dimeric core that propagates down the chain with bridging μ_2-S^{2-} ions. The pyramidal β-$[AsS_4]^{3-}$ anion features the As^{3+} ion and a disulfide unit, and it is very different from the well-known As^{5+} species α-$[AsS_4]^{3-}$. All three terminal sulfur atoms are involved in binding the two Sn^{4+} ions. The terminal atom, S(1), of the disulfide group serves to bridge the Sn atoms in the core (Figure 67(b)). This pyramidal unit is to be contrasted with the highly symmetrical tetrahedral α-$[AsS_4]^{3-}$ anion, which is formally an As^{5+} species and isostructural to the more familiar $[PS_4]^{3-}$ anion. Therefore, we see here a drastic departure of the thioarsenate flux chemistry from that of the thiophosphate which is attributed to the electronegativity difference in the two elements. It is possible that the two isomers are in fact in equilibrium with each other. Presumably, this equilibrium would be sensitive to the basicity of the flux which to a large extent is controlled by the formal $K_2S/As_2S_3/S$ ratio, and by the nature of the alkali ion. Thus, by controlling such equilibria in the flux, one could favor different thioarsenate anions to produce different outcomes.

The $K_2SnAs_2S_6$ compound is trigonal with layers consisting of SnS_6 octahedra and $[AsS_3]^{3-}$ pyramids (Figure 68). The layers are separated by seven coordinate K^+ ions. Topologically, the structure is TiS_2-type with Sn^{4+} cations in the octahedral Ti positions and $[AsS_3]^{3-}$ anions at

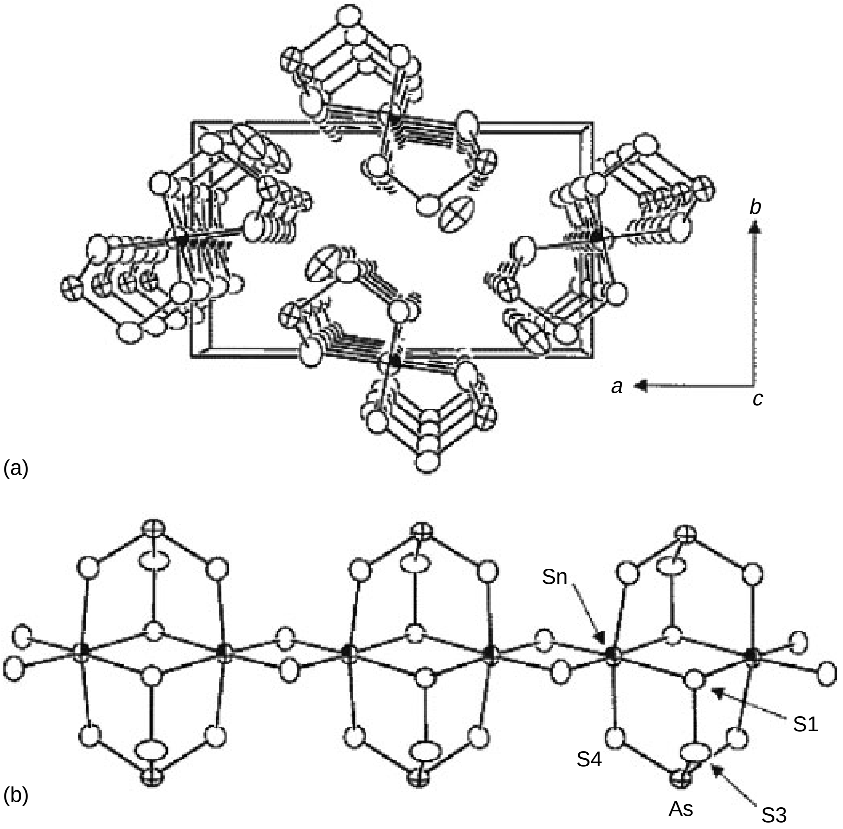

Figure 67 (a) The structure of $KSnAsS_5$ looking down the c-axis (b) A single chain of $KSnAsS_5$

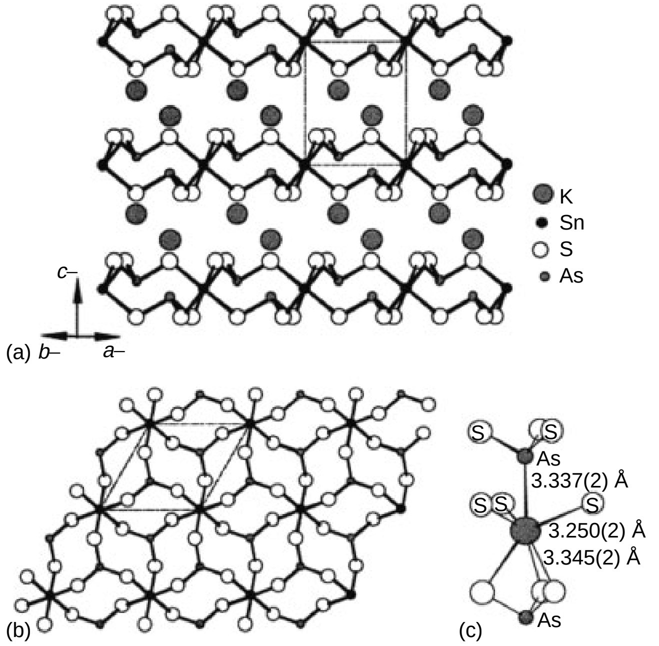

Figure 68 (a) Structure of $K_2SnAs_2S_6$ looking down the *c*-axis. Large gray circles between the layers are K^+ ions. Small black circles are Sn atoms, small gray circles are As atoms, and open circles are sulfur atoms. (b) Single layer of $[SnAs_2S_6]^{2-}$ with the eight member –S–Sn–S–As–S–Sn–S–As–rings. (c) Local coordination environment of K ions with bond lengths and apparent bonding interaction of the As atom with the K ion at 3.337(2) Å is shown

the pyramidal S positions. However, the $[AsS_3]^{3-}$ pyramids are inverted in a way that the As^{3+} atoms of a $[AsS_3]^{3-}$ anion on the topside of a $[SnAs_2S_6]^{2-}$ slab lie toward the slab's interior so that the lone electron pair is directed to the bottom side (Figure 68). This 'expanded TiS_2' structure creates large rings in the layers that dominate the two-dimensional network. Noteworthy is the unusual and surprising interaction at 3.337(2) Å between K^+ ions in the layers and the As atom of a $[AsS_3]^{3-}$ ligand, which in fact lies on the opposite side of the $[SnAs_2S_6]^{2-}$ slab (Figure 68(c)). This is possible because of the inverted nature of the $[AsS_3]^{3-}$ anion.

5 CONCLUDING REMARKS

The highly diverse class of solid-state chalcogenides marks an important area of inorganic chemistry. Its importance stems from multiple perspectives, including its role in being part of the foundation on which inorganic chemistry advances, its role as a basis for compounds with exceptional structural as well as physical properties, and finally its capacity to provide materials of technological relevance. The last two aspects were not touched upon in this article for reasons of space. Undoubtedly, a remarkable diversity in structure, composition, and properties exists in chalcogenide systems. Thanks to exploratory synthesis, a wealth of new materials is becoming available for study and investigation. Most of these could not have been anticipated prior to their synthesis. The rich chemistry that still lies within the less explored systems presages similar exciting materials discoveries in future investigations.

6 REFERENCES

1. B. W. Eichhorn, *Prog. Inorg. Chem.*, 1994, **42**, 139.
2. K. Mitchell and J. A. Ibers, *Chem. Rev.*, 2002, **102**, 1929.
3. W. S. Sheldrick and M. Wachhold, *Coord. Chem. Rev.*, 1998, **176**, 211.
4. M. G. Kanatzidis and A. C. Sutorik, *Prog. Inorg. Chem.*, 1995, **43**, 151.
5. M. G. Kanatzidis, *Curr. Opin. Solid State Mater. Sci.*, 1997, **2**, 139.
6. P. Bottcher and T. Doert, *Phosphorus Sulfur Silicon Relat. Elem. B*, 1998, **136**, 255.
7. M. G. Kanatzidis and S. P. Huang, *Coord. Chem. Rev.*, 1994, **130**, 509.
8. G. Parkin, *Prog. Inorg. Chem.*, 1998, **47**, 1.
9. K. W. Kim and M. G. Kanatzidis, *J. Am. Chem. Soc.*, 1998, **120**, 8124.
10. S. Sheldrick and M. Wachhold, *Angew. Chem. Int. Ed. Engl.*, 1995, **34**, 450.
11. T. Ohta, *J. Optoelectron Adv. Mat.*, 2001, **3**, 609. 15.
12. D.-Y. Chung, S. Jobic, T. Hogan, C. R. Kannewurf, R. Brec, R. J. Rouxel, and M. G. Kanatzidis, *J. Am. Chem. Soc.*, 1997, **119**, 2505.
13. D. M. Rowe ed., 'CRC Handbook of Thermoelectrics', CRC Press, Boca Raton, FL, 1995.
14. D.-Y. Chung, T. Hogan, P. Brazis, M. Rocci-Lane, C. R. Kannewurf, M. Bastea, C. Uher, and M. G. Kanatzidis, *Science*, 2000, **287**, 1024.
15. A. Rogalski, *Prog. Quant. Electron.*, 2003, **27**(2–3), 59.
16. V. V. Badikov, V. I. Chizhikov, V. V. Efimenko, T. D. Efimenko, V. L. Panyutin, G. S. Shevyrdyaeva, and S. I. Scherbakov, *Opt. Mater.*, 2003, **23**, 575.
17. D. B. Mitzi, L. L. Kosbar, C. E. Murray, M. Copel, and A. Afzali, *Nature*, 2004, **428**, 299.
18. A. Romeo, A. Terheggen, D. Abou-Ras, D. L. Batzner, F. J. Haug, M. Kalin, D. Rudmann, and A. N. Tiwari, *Prog. Photovoltaics*, 2004, **12**, 93.
19. E. J. M. Hensen and J. A. R. van Veen, *Catal. Today*, 2003, **86**, 87.
20. Y. J. Zhao and A. Zunger, *Phys. Rev. B*, 2004, **69**, Art. No. 075208.
21. I. B. Shirotani, *Chem. Soc. Jpn.*, 2003, **76**, 1291.

22. For developments in previous decades see Encyclopedia last editions.
23. F. Boucher and R. Rousseau, *Inorg. Chem.*, 1998, **37**, 2351.
24. Q. Liu, N. Goldberg, and R. Hoffmann, *Chem. – Eur. J.,* 1996, **2**, 390.
25. W. S. Sheldrick and M. Wachhold, *Chem. Commun.*, 1996, **5**, 607.
26. W. S. Sheldrick and B. Schaaf, *Z. Naturforsch. B*, 1994, **49**, 993.
27. T. Sasaki, H. Takizawa, K. Uhedaa, T. Yamashita, and T. Endo, *J. Solid State Chem.*, 2002, **166**, 164.
28. J. A. Aitken, J. A. Cowen, and M. G. Kanatzidis, *Chem. Mater.*, 1998, **10**, 3928.
29. A. C. Sutorik and M. G. Kanatzidis, *Chem. Mater.*, 1997, **9**, 387.
30. T. E. Weirich, R. Poettgen, and A. Z. Simon, *Kristallografiya*, 1996, **211**, 928.
31. P. A. Maggard and J. D. Corbett, *Angew. Chem., Int. Ed. Engl.*, 1997, **36**, 1974.
32. T. E. Weirich, X. Zou, R. Ramlau, A. Simon, G. L. Cascarano, C. Giacovazzo, and S. Hovmoller, *Acta Crystallogr.*, 2000, **A56**, 29.
33. G. Örlygsson and B. Harbrecht, *Inorg. Chem.*, 1999, **38**, 3377.
34. B. Harbrecht, M. Conrad, and T. Degen *et al.*, *J. Alloys Compd.*, 1997, **255**, 178.
35. T. Hughbanks, *J. Alloys Compd.*, 1995, **229**, 40.
36. P. A. Maggard and J. D. Corbett, *Inorg. Chem.*, 1998, **37**, 814.
37. P. A. Maggard and J. D. Corbett, *J. Am. Chem. Soc.*, 2000, **122**, 838.
38. T. E. Weirich, R. Pöttgen, and A. Simon, *Z. Kristallogr.*, 1996, **211**, 929.
39. L. Chen and J. D. Corbett, *J. Am. Chem. Soc.*, 2003, **125**, 7794.
40. T. E. Weirich, R. Ramlau, A. Simon, S. Hovmoller, and X. Zou, *Nature*, 1996, **382**, 144.
41. G. Orlygsson and B. Harbrecht, *Chem. – Eur. J.*, 2000, **6**, 4170.
42. G. Orlygsson and B. Harbrecht, *J. Am. Chem. Soc.*, 2001, **123**, 4168.
43. R. L. Abdon and T. Hughbanks, *Angew. Chem., Int. Ed. Engl.*, 1994, **33**, 2328.
44. M. Kockerling, D. Johrendt, and E. W. Finckh, *J. Am. Chem. Soc.*, 1998, **120**, 12297.
45. B. Harbrecht, T. Degen, and M. Conrad, *J. Alloys Compd.*, 1997, **246**, 37.
46. M. Conrad and B. Harbrecht, *Chem. – Eur. J.*, 2002, **8**(14), 3094.
47. M. Conrad, F. Krumeich, and C. Reich *et al.*, *Mater. Sci. Eng. A-Struct.*, 2000, **294**, 7.
48. T. E. Weirich and A. Simon, and R. Poetgen *Z. Anorg. Allg. Chem.*, 1996, **622**, 630.
49. S. Debus and B. Harbrecht, *J. Alloys Compd.*, 2002, **338**, 253.
50. M. G. Kanatzidis and B. K. Das, *Comments Inorg. Chem.*, 1999, **21**, 29.
51. J. A. Cody, M. F. Mansuetto, and M. A. Pell *et al.*, *J. Alloys Compd.*, 1995, **219**, 59.
52. T. J. McCarthy, T. A. Tanzer, and M. G. Kanatzidis, *J. Am. Chem. Soc.*, 1995, **117**, 1294.
53. K. Chondroudis and M. G. Kanatzidis, *J. Solid State Chem.*, 1998, **136**, 328.
54. K. O. Klepp, N. A. Harringer, and A. Kolb, *Z. Naturforsch. Sect. B-A, J. Chem. Sci.*, 2002, **57**(11), 1265.
55. F. O. Huang and J. A. Ibers, *Inorg. Chem.*, 2001, **40**(10), 2346.
56. H. Li, R. Mackay, S. J. Hwu, Y. K. Kuo, M. J. Skove, Y. Yokota, and T. Ohtani, *Chem. Mater.*, 1998, **10**(10), 3172.
57. Y.-K. Kuo, M. J. Skove, D. T. Verebelyi, H. Li. R. Mackay, S.-J. Hwu, M.-H. Whangbo, and J. W. Brill, *Phys. Rev. B*, 1998, **57**, 3315.
58. H. Li and S. J. Hwu, *Angew. Chem. Int. Ed. Engl.*, 1999, **38**(20), 3067.
59. X. Zhang, T. Hogan, C. R. Kannewurf, and M. G. Kanatzidis, *J. Am. Chem. Soc.*, 1996, **118**, 693.
60. Y. Park, D. C. DeGroot, J. L. Schindler, C. R. Kannewurf, and M. G. Kanatzidis, *Angew. Chem., Int. Ed. Engl.*, 1991, **30**, 1325.
61. Y. Park and M. G. Kanatzidis, *Chem. Mater.*, 1991, **3**, 781.
62. X. Zhang, Y. Park, T. Hogan, J. L. Schindler, C. R. Kannewurf, S. Seong, T. Albright, and M. G. Kanatzidis, *J. Am. Chem. Soc.*, 1995, **117**, 10300.
63. X. Chen, X. Huang, and J. Li, *Inorg. Chem.*, 2001, **40**, 1341.
64. J. Küper, O. Conrad, and B. Krebs, *Angew. Chem., Int. Ed. Engl.*, 1997, **36**, 1903.
65. A. Lindemann, J. Kuchinke, and B. Krebs, *Z. Anorg. Allg. Chem.*, 1999, **625**, 1165.
66. A. Lindemann, J. Küper, C. Jansen, J. Kuchinke, C. Köster, A. Hammerschmidt, M. Döch, T. Pruß, and B. Krebs, *Z. Anorg. Allg. Chem.*, 2001, **627**, 419.
67. A. Hammerschmidt, A. Lindemann, M. Döch, C. Köster, and B. Krebs, *Z. Anorg. Allg. Chem.*, 2002, **628**, 1561.
68. E. A. Axtell, J. H. Liao, and M. G. Kanatzidis, *Inorg. Chem.*, 1998, **37**, 5583.
69. K. O. Klepp and C. Weithaler, *J. Alloys Compd.*, 1996, **243**, 12.
70. K. O. Klepp and C. Weithaler, *Eur. J. Solid State Inorg. Chem.*, 1998, **35**, 101.
71. Y. Park and M. G. Kanatzidis, *J. Alloys Compd.*, 1997, **257**, 137.
72. K. O. Klepp, C. Weithaler, and M. Sing, *J. Alloys Compd.*, 1998, **269**, 92.
73. F. Q. Huang, Y. T. Yang, C. Flaschenriem, and J. A. Ibers, *Inorg. Chem.*, 2001, **40**, 1397.
74. E. A. Axtell, J. H. Liao, Z. Pikramenou, Y. Park, and M. G. Kanatzidis, *J. Am. Chem. Soc.*, 1993, **115**, 12191.

75. E. A. Axtell III, J.-H. Liao, Z. Pikramenou, and M. G. Kanatzidis, *Chem. – Eur. J.*, 1996, **2**, 656.
76. G. C. Papavassiliou, I. B. Koutselas, G. A. Mousdis, E. A. Axtell, and M. G. Kanatzidis, *High Technol.*, 2000, **81**, 97.
77. E. A. Axtell and M. G. Kanatzidis, *Chem. Mater.*, 1996, **8**, 1350.
78. A. A. Narducci and J. A. Ibers, *J. Alloys Compd.*, 2000, **306**, 170.
79. J. Li, Z. Chen, K. C. Lam, S. Mulley, and D. M. Proserpio, *Inorg. Chem.*, 1997, **36**, 684.
80. M. G. Kanatzidis and Y. Park, *Chem. Mater.*, 1990, **2**, 99.
81. K. O. Klepp, *J. Alloys Compd.*, 1992, **182**, 281.
82. H. J. Deiseroth, C. Reiner, M. Schlosser, and L. Kienle, *Z. Anorg. Allg. Chem.*, 2002, **628**, 1641.
83. H. J. Deiseroth and R. Walther, *Z. Anorg. Allg. Chem.*, 1996, **622**, 611.
84. N. F. Zheng, X. G. Bu, B. Wang, and P. Y. Feng, *Science*, 2002, **298**, 2366.
85. H. Li, A. Laine, M. O'Keeffe, and O. M. Yaghi, *Science*, 1999, **283**, 1145.
86. C. Wang, Y. Q. Li, X. H. Bu, N. F. Zheng, O. Zivkovic, C. S. Yang, and P. Y. Feng, *J. Am. Chem. Soc.*, 2001, **123**, 11506.
87. N. F. Zheng, X. H. Bu, and P. Y. Feng, *Nature*, 2003, **426**, 428.
88. G. A. Mariking and M. G. Kanatzidis, *Chem. Mater.*, 1995, **7**, 1915.
89. W. S. Sheldrick and H.-G. Braunbeck, *Z. Anorg. Allg. Chem.*, 1993, **619**, 1300.
90. J. B. Parise, Y. Ko, J. Rijssenbeek, D. M. Nellis, K. Tan, and S. Koch, *J. Chem. Soc., Chem. Commun.*, 1994, 527.
91. W. S. Sheldrick and H.-G. Braunbeck, *Z. Anorg. Allg. Chem.*, 1993, **619**, 1300.
92. W. S. Sheldrick and B. Schaaf, *Z. Naturforsch. GA*, 1994, **49**, 57.
93. L. Iordanidis, D. Bilc, S. D. Mahanti, and M. G. Kanatzidis, *J. Am. Chem. Soc.*, 2003, **125**, 13741.
94. D.-Y. Chung, K.-S. Choi, L. Iordanidis, J. L. Schindler, P. W. Brazis, C. R. Kannewurf, B. Chen, S. Hu, C. Uher, and M. G. Kanatzidis, *Chem. Mater.*, 1997, **9**, 3060.
95. M. G. Kanatzidis, T. J. McCarthy, T. A. Tanzer, L.-H. Chen, L. Iordanidis, T. Hogan, C. R. Kannewurf, C. Uher, and B. Chen, *Chem. Mater.*, 1996, **8**, 1465.
96. L. Iordanidis and M. G. Kanatzidis, *J. Am. Chem. Soc.*, 2000, **122**, 8319.
97. D.-Y. Chung, K.-S. Choi, L. Iordanidis, J. L. Schindler, P. W. Brazis, C. R. Kannewurf, B. Chen, S. Hu, C. Uher, and M. G. Kanatzidis, *Chem. Mater.*, 1997, **9**, 3060.
98. L. Iordanidis, P. W. Brazis, T. Kyratsi, J. Ireland, M. Lane, C. R. Kannewurf, W. Chen, J. S. Dyck, C. Uher, N. A. Ghelani, T. Hogan, and M. G. Kanatzidis, *Chem. Mater.*, 2001, **13**, 622.
99. K.-S. Choi, D.-Y. Chung, A. Mrotzek, P. Brazis, C. R. Kannewurf, C. Uher, W. Chen, T. Hogan, and M. G. Kanatzidis, *Chem. Mater.*, 2001, **13**, 756.
100. A. Mrotzek and M. G. Kanatzidis, *Acc. Chem. Res.*, 2003, **36**, 111.
101. D.-Y. Chung, S. Jobic, T. Hogan, C. R. Kannewurf, R. Brec, J. Rouxel, and M. G. Kanatzidis, *J. Am. Chem. Soc.*, 1997, **119**, 2505.
102. D.-Y. Chung, T. Hogan, J. L. Schindler, L. Iordanidis, P. W. Brazis, C. R. Kannewurf, B. Chen, C. Uher and M. G. Kanatzidis, *Proceedings of the 7th International Conference on Thermoelectrics*, 1997, Dresden, Germany.
103. J. L. Schindler, T. P. Hogan, P. W. Brazis, C. R. Kannewurf, D.-Y. Chung, and M. G. Kanatzidis, Thermoelectric Materials-New Directions and Approaches, in 'Materials Research Society Symposium Proceedings', eds. M. G. Kanatzidis, H. Lyon, G. Mahan, and T. Tritt, 1997, Vol. 478, p. 327.
104. D.-Y. Chung, T. Hogan, M. Rocci-Lane, P. Brazis, J. R. Ireland, C. R. Kannewurf, M. Bastea, C. Uher, and M. G. Kanatzidis, *J. Am. Chem. Soc.*, 2004, **126**, 6414.
105. H. Kalpen, W. Hoenle, M. Somer, U. Schwarz, K. Peters, H. G. von Schnering, and R. Blachnik, *Z. Anorg. Allg. Chem.*, 1998, **624**, 1137.
106. Y. Park and M. G. Kanatzidis, *Inorg. Chem.*, 2001, **40**, 5913.
107. H. Fukuoka, S. Sakashita, and S. Yamanaka, *J. Solid State Chem.*, 1999, **148**, 487.
108. S.-J. Hwang, V. Petkov, K. K. Rangan, S. Shastri, and M. G. Kanatzidis, *J. Phys. Chem. B*, 2002, **106**, 12453.
109. I. Ijjaali, K. Mitchell, and J. A. Ibers, *J. Solid State Chem.*, 2004, **177**, 760.
110. P. Lauxmann and T. Schleid, *Z. Anorg. Allg. Chem.*, 2000, **626**, 1608.
111. P. Lauxmann, S. Strobel, and T. Schleid, *Z. Anorg. Allg. Chem.*, 2002, **628**, 2403.
112. J. Llanos, C. Mujica, V. Sanchez, W. Schnelle, and R. Cardoso-Gil, *J. Solid State Chem.*, 2004, **177**, 1388.
113. A. Van der Lee, R. Van de Belt, and G. A. Wiegers, *J. Alloys Compd.*, 1992, **178**, 57.
114. Marek. Duczmal and Stefan. Pokrzywnicki, *J. Alloys Compd.*, 2001, **323**, 513.
115. S. Strobel and T. Schleid, *J. Solid State Chem.*, 2003, **171**, 424.
116. R. L. Abdon and T. Hughbanks, *Chem. Mater.*, 1994, **6**, 424.
117. R. L. Abdon and T. Hughbanks, *J. Am. Chem. Soc.*, 1995, **117**, 10035.
118. J. Neuhausen, E. W. Finckh, and W. Tremel, *Chem. Ber.*, 1995, **128**, 569.
119. C. C. Wang and T. Hughbanks, *Inorg. Chem.*, 1996, **35**, 6987.
120. N. Bestaoui, P. S. Herle, and J. D. Corbett, *J. Solid State Chem.*, 2000, **155**, 9.
121. L. Chen and J. D. Corbett, *J. Am. Chem. Soc.*, 2003, **125**, 1170.

122. J. Neuhausen and W. Tremel, *J. Alloys Compd.*, 1994, **204**, 215.

123. J. Neuhausen, R. K. Kremer, and W. Tremel, *Proc. Soft Chem. Routes New Mater.*, 1994, **152–3**, 383.

124. W. Tremel, *Angew. Chem., Int. Ed. Engl.*, 1991, **30**, 840.

125. W. Tremel, *Angew. Chem., Int. Ed. Engl.*, 1993, **32**, 1752.

126. F. Meng and T. Hughbanks, *Inorg. Chem.*, 2001, **40**, 2482.

127. P. A. Maggard and J. D. Corbett, *Inorg. Chem.*, 2000, **39**, 4143.

128. L. Chen and J. D. Corbett, *Inorg. Chem.*, 2002, **41**, 2146.

129. A. I. Baranov, A. A. Isaeva, L. Kloo, and B. A. Popovkin, *Inorg. Chem.*, 2003, **42**, 6667.

130. G. A. Wiegers and A. Meerschaut, 'Materials Science Forum', ed. A. Meerschaut,Trans Tech Publication, 1992, Vol. 100–101, p. 101.

131. G. A. Wiegers, *Prog. Solid State Chem.*, 1996, **24**, 1.

132. P. Lavela, J. Morales, and J. L. Tirado, *J. Solid State Chem.*, 1996, **124**, 238.

133. C. Michioka and K. Suzuki, *Phys. Rev. B*, 1999, **60**, 12941.

134. S. van Smaalen and J. L. de Boer, *Phys. Rev. B*, 1992, **46**, 2750.

135. C. Auriel, A. Meerschaut, and J. Rouxel, *Mater. Res. Bull.*, 1993, **28**, 675.

136. A. Lafond, A. Nader, Y. Moëlo, A. Meerschaut, A. Briggs, S. Perrin, P. Monceau, and J. Rouxel, *J. Alloys Compd.*, 1997, **261**, 114.

137. G. A. Wiegers, *J. Alloys Compd.*, 1995, **2219**, 152.

138. A. Meerschaut, Y. Moëlo, L. Cario, A. Lafond, and C. Deudon, *Mol. Cryst. Liq. Cryst.*, 2000, **341**, 1.

139. Y. Moëlo, A. Meerschaut, J. Rouxel, and C. Auriel, *Chem. Mater.*, 1995, **7**, 1759.

140. J. Rouxel, Y. Moëlo, A. Lafond, F. J. Di Salvo, A. Meerschaut, and R. Roesky, *Inorg. Chem.*, 1994, **33**, 3358.

141. L. Cario, A. Lafond, P. Palvadeau, C. Deudon, and A. Meerschaut, *J. Solid State Chem.*, 1999, **147**, 58.

142. L. Cario, P. Palvadeau, A. Lafond, C. Deudon, Y. Moëlo, B. Corraze, and A. Meerschaut, *Chem. Mater.*, 2003, **15**, 943.

143. T. Nishikawa, Y. Yasui, Y. Kobayashi, and M. Sato, *Physica C*, 1996, **263**, 554.

144. W. Y. Zhou, A. Meetsma, J. L. de Boer, and G. A. Wiegers, *J. Alloys Compd.*, 1996, **223**, 80.

145. Y. Oosawa, Y. Gotoh, J. Akimoto, T. Tsunoda, M. Sohma, and M. Onoda, *Jpn. J. Appl. Phys.*, 1992, **31**, L1096.

146. J. Kacmarcik, P. Szabo, P. Samuely, A. Briggs, A. G. M. Jansen, and A. Meerschaut, *Physica B*, 2000, **284–288**, 961.

147. S. van Smaalen, *Cryst. Rev.*, 1995, **4**, 79.

148. V. Petricek and M. Dusek, 'A Crystallographic Computing System; Institute of Physics', Academy of Sciences of the Czech Republic, Praha, 2000.

149. A. C. Sutorik, J. Albritton-Thomas, T. Hogan, C. R. Kannewurf, and M. G. Kanatzidis, *Chem. Mater.*, 1996, **8**, 751.

150. Y. Klawitter, C. Nather, I. Jess, W. Bensch, and M. G. Kanatzidis, *Solid State Sci.*, 1999, **1**, 421.

151. K. Mitchell, F. Q. Huang, and A. D. McFarland *et al.*, *Inorg. Chem.*, 2003, **42**, 4109.

152. Y. T. Yang and J. A. Ibers, *J. Solid State Chem.*, 1999, **147**, 366.

153. F. Q. Huang and J. A. Ibers, *J. Solid State Chem.*, 2001, **158**, 299.

154. F. Q. Huang and J. A. Ibers, *J. Solid State Chem.*, 2000, **151**, 317.

155. R. Patschke, J. Heising, and M. G. Kanatzidis *et al.*, *Chem. Mater.*, 1998, **10**, 695.

156. Y. T. Yang and J. A. Ibers, *J. Solid State Chem.*, 2000, **149**, 384.

157. R. Patschke, P. Brazis, and C. R. Kannewurf *et al.*, *Inorg. Chem.*, 1998, **37**, 6562.

158. F. Q. Huang and J. A. Ibers, *J. Solid State Chem.*, 2001, **160**, 409.

159. F. Q. Huang, K. Mitchell, and J. A. Ibers, *Inorg. Chem.*, 2001, **40**, 5123.

160. R. Patschke, P. Brazis, and C. R. Kannewurf *et al.*, *J. Mater. Chem.*, 1998, **8**, 2587.

161. R. Patschke and M. G. Kanatzidis, *Phys. Chem. Chem. Phys.*, 2002, **4**(14), 3266.

162. A. C. Sutorik, J. Albritton-Thomas, C. R. Kannewurf, and M. G. Kanatzidis, *J. Am. Chem. Soc.*, 1994, **116**, 7706.

163. P. Wu, A. E. Christuk, and J. A. Ibers, *J. Solid State Chem.*, 1994, **110**, 337.

164. P. Stoll, P. Dürichen, C. Näther, and W. Bensch, *Z. Anorg. Allg. Chem.*, 1998, **624**, 1807.

165. X. Zhang, J. Li, B. Foran, H.-Y. Guo, T. Hogan, C. R. Kannewurf, and M. G. Kanatzidis, *J. Am. Chem. Soc.*, 1995, **117**, 10513.

166. O. Gourdon, J. Hanko, F. Boucher, V. Petricek, M.-H. Whangbo, M. G. Kanatzidis, and M. Evain, *Inorg. Chem.*, 2000, **39**, 1398.

167. T. J. McCarthy and M. G. Kanatzidis, *Chem. Mater.*, 1993, **5**, 1061.

168. T. J. McCarthy and M. G. Kanatzidis, *J. Alloys Compd.*, 1996, **236**, 70.

169. J. D. Breshears and M. G. Kanatzidis, *J. Am. Chem. Soc.*, 2000, **122**, 7839.

170. K. Chondroudis and M. G. Kanatzidis, *J. Solid State Chem.*, 1998, **138**, 321.

171. S. Coste, J. Hanko, M. Bujoli-Doeuff, G. Louarn, M. Evain, R. Brec, B. Alonso, S. Jobic, and M. G. Kanatzidis, *J. Solid State Chem.*, 2003, **175**, 133.

172. K. Chondroudis, M. G. Kanatzidis, J. Sayettat, S. Jobic, and R. Brec, *Inorg. Chem.*, 1997, **36**, 5859.

173. K. Chondroudis and M. G. Kanatzidis, *Chem. Commun.*, 1997, 401.

174. S. Loken and W. Tremel, *Eur. J. Inorg. Chem.*, 1998, **2**, 283.

175. K. Chondroudis and M. G. Kanatzidis, *J. Solid State Chem.*, 1998, **136**, 79.

176. K. Chondroudis and M. G. Kanatzidis, *Inorg. Chem.*, 1995, **34**, 5401.

177. K. Chondroudis and M. G. Kanatzidis, *Angew. Chem., Int. Ed. Engl.*, 1997, **36**, 1324.

178. P. K. Dorhout and T. M. Malo, *Z. Anorg. Allg. Chem.*, 1996, **622**, 385.

179. J. A. Hanko and M. G. Kanatzidis, *J. Solid State Chem.*, 2000, **151**, 326.

180. S. Coste, E. Kopnin, M. Evain, S. Jobic, R. Brec, K. Chondroudis, and M. G. Kanatzidis, *Solid State Sci.*, 2002, **4**, 709.

181. C. Gieck, V. Derstroff, T. Block, C. Felser, G. Regelsky, O. Jepsen, V. Ksenofontov, P. Gutlich, H. Eckert, and W. Tremel, *Chem. – A Eur. J.*, 2004, **10**, 382.

182. K. Chondroudis, J. A. Hanko, and M. G. Kanatzidis, *Inorg. Chem.*, 1997, **36**,, 2623.

183. T. J. McCarthy and M. G. Kanatzidis, *J. Chem. Soc., Chem. Commun.*, 1994, 1089.

184. K. Chondroudis and M. G. Kanatzidis, *Inorg. Chem.*, 1998, **37**, 3792.

185. G. Gauthier, S. Jobic, and R. Brec *et al*., *Inorg. Chem.*, 1998, **37**, 2332.

186. J. H. Chen and P. K. Dorhout, *Inorg. Chem.*, 1995, **34**, 5705.

187. J. H. Chen, P. K. Dorhout, and J. E. Ostenson, *Inorg. Chem.*, 1996, **35**, 5627.

188. K. Chondroudis and M. G. Kanatzidis, *J. Am. Chem. Soc.*, 1997, **119**, 2574.

189. C. R. Evenson and P. K. Dorhout, *Inorg. Chem.*, 2001, **40**, 2875.

190. E. Y. Goh, E. J. Kim, and S. J. Kim, *J. Solid State Chem.*, 2001, **160**, 195.

191. J. A. Aitken, K. Chondroudis, V. G. Young, and M. G. Kanatzidis, *Inorg. Chem.*, 2000, **39**, 1525.

192. J. A. Aitken, M. Evain, L. Iordanidis, and M. G. Kanatzidis, *Inorg. Chem.*, 2002, **41**, 180.

193. R. F. Hess, K. D. Abney, and J. L. Burris *et al*., *Inorg. Chem.*, 2001, **40**, 2851.

194. K. Chondroudis and M. G. Kanatzidis, *C. R. Acad. Sci. Paris*, 1996, **322**, Serie IIb, 887.

195. P. M. B. Piccoli, K. D. Abney, and J. R. Schoonover *et al*., *Inorg. Chem.*, 2000, **39**, 2970.

196. C. Gieck and W. Tremel, *Chem. – Eur. J.*, 2002, **8**, 2980.

197. R. F. Hess, P. L. Gordon, C. D. Tait, K. D. Abney, and P. K. Dorhout, *J. Am. Chem. Soc.*, 2002, **124**, 1327.

198. K. Chondroudis, T. J. McCarthy, and M. G. Kanatzidis, *Inorg. Chem.*, 1996, **35**, 840.

199. G. A. Marking and M. G. Kanatzidis, *J. Alloys Compd.*, 1997, **259**, 122.

200. G. D. Albertelli, J. A. Cowen, C. N. Hoff, T. A. Kaplan, S. D. Mahanti, J. H. Liao, and M. G. Kanatzidis, *Phys. Rev. B*, 1997, **55**, 11056.

201. G. A. Marking, J. A. Hanko, and M. G. Kanatzidis, *Chem. Mater.*, 1998, **10**, 1191.

202. J.-H. Liao, G. M. Marking, K. F. Hsu, Y. Matsushita, M. D. Ewbank, R. Borwick, P. Cunningham, M. J. Rosker, and M. G. Kanatzidis, *J. Am. Chem. Soc.*, 2003, **125**, 9484.

203. B. R. Martin and P. K. Dorhout, *Inorg. Chem.*, 2004, **43**, 385.

204. J. A. Aitken, G. A. Marking, and M. Evain *et al*., *J. Solid State Chem.*, 2000, **153**, 158.

205. J. A. Aitken, P. Larson, S. D. Mahanti, and M. G. Kanatzidis, *Chem. Mater.*, (Article); 2001, **13**, 4714.

206. C. R. Evenson and P. K. Dorhout, *Inorg. Chem.*, 2001, **40**, 2409.

207. J. A. Hanko and M. G. Kanatzidis, *J. Alloys Compd.*, 1998, **280**, 71.

208. K. S. Choi, Jason. A. Hanko, and M. G. Kanatzidis, *J. Solid State Chem.*, 1999, **147**, 309.

209. K.-S. Choi and M. G. Kanatzidis, *Inorg. Chem.*, 2000, **39**, 5655.

210. R. G. Iyer and M. G. Kanatzidis, *Inorg. Chem.*, 2002, **41**, 3605.

Acknowledgment

I thank Dr. Alain Meerschaut for providing material regarding the misfit compounds. I also thank the National Science Foundation for generous support.

Chlorine, Bromine, Iodine, & Astatine: Inorganic Chemistry

Jian-Ping Lang
Suzhou University, Suzhou, China

Based in part on the article Chlorine, Bromine, Iodine, & Astatine: Inorganic Chemistry by Jacob Shamir which appeared in the Encyclopedia of Inorganic Chemistry, First Edition.

1 Introduction 1
2 Atomic Structure 1
3 Molecular Properties 2
4 Halogen Compounds 5
5 Interhalogen Compounds 6
6 Hydrogen Halides 12
7 Halogen Oxides 13
8 Organic Polyvalent Halogen Derivatives 19
9 Related Articles 20
10 References 20

1 INTRODUCTION

The elements of group 17, fluorine, chlorine, bromine, iodine, and astatine, are collectively called the halogens and these are the most representative nonmetals in the periodic table (*see* ***Periodic Table: Trends in the Properties of the Elements***). The nonmetallic feature is indicated by the high value of the ionization potentials of the halogens, which are only 1–4 eV lower than those of the corresponding noble gas atoms. As a result, the halogens are extremely electronegative with strong electron affinities. Many general references are available and we list only a few.[1–4] The name ‘halogen’, based on a Greek word, is intended to describe the ability of these elements to combine directly with metals to form salts.

The diatomic nature of the elemental halogens clearly indicates their nonmetallic nature. Only hydrogen, nitrogen, and oxygen share this property under normal conditions. The increase of the boiling points, melting points, and volatility of the halogens are compatible with the increase in the van der Waals’ forces with advancing size and *Polarizability* of the atoms and molecules.

Everyday uses of halogens or their compounds are well known, such as the use of chlorine in purifying drinking water, the use of iodine as an antiseptic, and the use of bromine in photographic films as the compound silver bromide.

The title of this article includes all the halogens except the first: fluorine (*see* ***Fluorine: Inorganic Chemistry***). Although the halogens form a remarkable homologous series, certain discontinuities are evident. Principal among these is the exceptional nature of fluorine and its chemically reactive compounds. It has, therefore, become customary to separate the discussion of fluorine chemistry from the rest of the halogens and treat this as a separate subject.

2 ATOMIC STRUCTURE

Some atomic properties are summarized in Table 1 and these are further discussed in the sections that follow.

2.1 Electronic Configuration

The electronic configuration of the halogen atoms in their ground state is ns^2np^5, just one electron short of the corresponding noble gas electronic configuration with the so-called inert octet. This electronic structure makes the halogens extremely powerful electron acceptors with the highest electron affinities of all atomic elements (*see Electron Affinity*). Consequently, the ionization potentials of the halogens are the highest known, except for the noble gases (*see Ionization Potential*). As a result, the dominant feature of the halogens is the ease with which their atoms accept an electron, forming either a uninegative anion X^-, or a single covalent bond –X. The compounds formed therefore range from ionic salts at one extreme to covalent molecules at the other.

In addition to the possibility of forming monoatomic anions at the -1 valency state or monovalent covalent bonds, the halogens can also form bridges between two other atoms, in a manner similar to hydrogen bonding, through the formation of covalent bonds with the two-bridged atoms. Many halogen compounds exist, in which the central halogen has a formal oxidation state of $+1$, $+3$, $+5$, and $+7$, as in the oxyhalogen species, and some cationic species are also known.

2.2 Stable Isotopes

Several chlorine isotopes exist with mass numbers ranging between 32 and 40. The two stable isotopes are ^{35}Cl and ^{37}Cl with natural abundances of 75.77% and 24.23% respectively, while the others are radioactive. Bromine also has two stable isotopes, ^{79}Br and ^{81}Br, with natural abundances of 50.69% and 49.31% respectively, while the others are radioactive. Iodine has only one stable isotope, ^{127}I, and numerous radioactive ones are known. Astatine is known only as its radioisotope (*see Radioactive Decay*).

Radioisotopes of the halogens have found uses in studies of exchange reactions and reaction mechanisms. A radioactive iodine isotope is used in medical diagnostics.

Table 1 Atomic properties of the halogens

Property	Cl	Br	I	At
Atomic number	17	35	53	85
Atomic weight	35.453	79.904	126.9045	209.99
Ionization energy ($kJ\,mol^{-1}$)	1255.7	1142.7	1008.7	(926)

2.3 Magnetic Moments

The fluorine atom has a nuclear spin number of 1/2, similar to that of hydrogen, and is therefore suitable for NMR measurements, giving narrow lines. The other halogens have nuclear spin numbers $>1/2$ (3/2 for chlorine and bromine, 5/2 for iodine), and so are unsuitable for NMR studies.

3 MOLECULAR PROPERTIES

3.1 Occurrence

Chlorine was the first halogen to be isolated and sodium chloride, common salt, has been known from early times as being essential to the human diet; as such it has been mentioned in the Bible. Aqua regia, a mixture of hydrochloric and nitric acids, has been known since the thirteenth century as a liquid for dissolving the very inert metal, gold. The ancient color mentioned in the Bible as purple has been identified as a brominated organic compound, namely 6,6-dibromoindigo, which used to be extracted from a small snail.

Since the halogens are very reactive, they are never found in nature as free elements. However, they are widespread and abundant in the form of salts, mostly containing the halide anion. Large quantities of NaCl and KCl are found in pure form as mineral deposits and can be mined directly. However, larger quantities are dissolved in water, as in oceans, inland seas, lakes, and brines (e.g. the Great Salt Lake of Utah and the Dead Sea in Israel). The liquid sources are usually concentrated by solar evaporation and the concentrated brines are then processed to obtain the salts present. Iodine is found in the sea as the iodide and also in Chile as an iodate salt, $IO_3{}^-$. Chlorine is the 20th most abundant element in crystal rocks, bromine the 46th, and iodine the 60th.

3.2 Production and Uses

Chlorine can be obtained in the laboratory by oxidation of HCl with a strong oxidizer such as manganese dioxide (equation 1). The industrial production of chlorine is a major section of the heavy chemical industry and is based on electrolytic oxidation of the chloride anion. Chlorine, sodium hydroxide, and hydrogen are produced by the electrolysis of aqueous solutions of sodium chloride (equation 2), whereas in the electrolysis of the molten NaCl salt, the coproduct is sodium metal, rather than sodium hydroxide. The old Deacon process was based on the copper-catalyzed reaction (equation 3). This has been made more efficient by passing HCl over CuO at 200 °C to give $CuCl_2$ and H_2O after which $CuCl_2$ at 300 °C is treated with O_2.

$$MnO_2 + 4HX \longrightarrow MnCl_2 + X_2 + 2H_2O \ (X = Cl, Br) \qquad (1)$$

$$Cl^- + H_2O \longrightarrow OH^- + \tfrac{1}{2}Cl_2 + \tfrac{1}{2}H_2 \qquad (2)$$

$$2HCl + \tfrac{1}{2}O_2 \longrightarrow Cl_2 + H_2O \qquad (3)$$

The main uses of chlorine are the following: (1) the production of chloro-organic compounds, such as vinyl chloride and ethylene dichloride for the plastics industry, as solvents, refrigerants, insecticides, and dyes (about 70%); (2) as a bleaching agent of paper, pulp, and textiles, and the disinfection of water supplies (about 20%); and (3) for the production of a large variety of inorganic chemicals, particularly covalent compounds.

Bromine can be obtained by oxidation of HBr with manganese dioxide (equation 1) or nitric acid. Industrially, bromine is produced by oxidation of the bromide anion with elemental Cl_2 (equation 4). Elemental Br_2 is then blown out of the solution by passing steam or air through it. The vapor is then condensed or fixed chemically and finally purified.

$$2Br^- + Cl_2 \longrightarrow Br_2 + 2Cl^- \qquad (4)$$

The industrial use of bromine was dominated by the production of ethylene dibromide as a valuable additive to gasoline to act as a scavenger for lead in the antiknock additive tetraethyllead. Now that the use of Et_4Pb in gasoline has been reduced, this consumption of bromine has also been reduced. The pesticide industry uses large quantities of bromine, and an increasing demand also exists in fire-retardant materials such as fibers and wood. A well-known use of bromine is as AgBr in the photographic industry.

Iodine is produced by similar methods, namely, oxidation of the iodide anion from brines by chlorine. However, iodine is also produced in a reductive process by reacting $NaIO_3$, extracted from the natural source of Chilean saltpeter, with sodium hydrogen sulfite. The pentavalent iodine is reduced to iodide (equation 5), which is then treated and oxidized with a sufficient amount of the mother liquor to liberate elemental iodine (equation 5). In contrast to chlorine and bromine, which have large industrial uses, iodine has no predominant commercial use.

$$[IO_3]^- + 3[HSO_3]^- \longrightarrow I^- + 3[HSO_4]^- \qquad (5)$$

$$5I^- + [IO_3]^- + 6H^+ \longrightarrow 3I_2 + 3H_2O \qquad (6)$$

The artificial radioactive element astatine is prepared by bombarding bismuth metal or bismuth oxide by α particles, producing 20 isotopes. Among them, the longest-living species are ^{210}At (8.3 h) and ^{211}At (7.2 h). The astatine is separated from the bismuth source either by distillation or by extraction. In the first method, on the basis of the high volatility of astatine, the reaction takes place in a current of nitrogen or in vacuo, by heating the source to 300–600 °C. The astatine is then condensed on a cold surface. In the extraction process, the bismuth source is dissolved in perchloric acid containing some iodine that serves as a carrier of the astatine. The bismuth is then precipitated as a phosphate and the remaining liquid can serve as an aqueous solution of astatine iodide, AtI.

3.3 Physical Properties

The halogens are volatile, diatomic elements whose color increases with increasing atomic numbers. Chlorine is a yellow–green gas at room temperature, bromine is a dark red liquid, and iodine is a lustrous, black, crystalline solid with a high vapor pressure that sublimes easily.

Although the thermodynamically stable form of the halogens is as diatomic molecules, these can easily dissociate into halogen atoms by using various techniques such as thermal dissociation at elevated temperatures, discharge reactions by electrodes, microwave, or photochemical reactions. In an electrical discharge at ambient temperatures and gas pressures of less than 1 mmHg, the degree of atomization can be 10–40%. In many organic halogenation processes, it is assumed that the reactions involve atomic halogen and the property of photodissociation is actually used in some organic halogenations.

The enthalpy of dissociation decreases as the mass number increases along the series. However, there exists a discontinuity (the value for F_2 is similar to that of I_2), and thus there is an increase when going from F_2 to Cl_2. This trend is also observed in other groups of the periodic table. In groups 15 and 16, the single bonds of the first elements in those groups, N–N in hydrazine and O–O in peroxides, are weaker than those of the following heavier elements, P–P and S–S, respectively. Some of these properties are summarized in Table 2.

3.4 Bonding in Diatomic Molecules

The bonding in the diatomic halogen molecules can be described in terms of simple ***Molecular Orbital Theory***, as depending on the balance between six electrons in bonding orbitals ($\sigma_g^2\pi_u^4$) and four in antibonding orbitals (π_g^4). This fits a diamagnetic ground state with a bond order of unity.

Table 2 Physical properties of the molecular halogens

Property	Cl_2	Br_2	I_2
Melting point (°C)	−101.0	−7.25	113.6
Boiling point (°C)	−34.9	59.5	185.2
H_{dissoc} (kJ mol^{-1})	242.58	192.77	151.10
Vibrational frequency (cm^{-1})	$^{35}Cl_2$ 559.72	$^{79}Br\,^{81}Br$ 324.24	$^{127}I_2$ 214.52

The electronic spectra of the halogens arise from absorption bands corresponding to the electronic transitions, in which an electron is excited from the antibonding π_g to the antibonding σ_u orbital (equation 6). The separation between these two orbitals decreases as the atomic number of the halogen increases.

$$\sigma_g^2\pi_u^4\pi_g^4 \longrightarrow \sigma_g^2\pi_u^4\pi_g^3\sigma_u^1 \qquad (7)$$

3.5 Solution and Charge-transfer Complexes

The halogens are soluble in numerous solvents, although their great chemical reactivity can cause solvolysis or halogenation of the solvent to take place.

Chlorine is moderately soluble in, but reactive with, water. It can form a gas hydrate $Cl_2{\cdot}7.3H_2O$ from Cl_2 on aqueous $CaCl_2$ at 0 °C. Bromine is also soluble in H_2O; it gives a crystalline hydrate, which appears to have a unique, noncubic structure, with a formula of $Br_2{\cdot}7.9H_2O$. In addition, 16 different crystals of distinct compositions ($Br_2{\cdot}8.62H_2O$ to $Br_2{\cdot}10.68H_2O$) and morphologies**5** show that there is just a single, tetragonal structure as proposed in 1963.

Iodine dissolves only slightly in water but its solubility can be increased in aqueous iodide solutions as a result of the formation of polyiodides (equation 8).

$$I_2 + I^- \longrightarrow [I_3]^- \qquad (8)$$

Iodine is also readily soluble in a variety of organic solvents, such as EtOH, CCl_4, benzene, and others. The color of these solutions depends on the solvent type. Solutions in strong donors such as alcohols, ethers, or amines are deep brown with maximum absorbance in the visible region of 450–480 nm. In aliphatic halocarbons, such as $CHCl_3$ or CCl_4, the color is violet with maximum absorbance in the region of 520–540 nm, whereas in aromatic hydrocarbons, such as benzene or toluene, the color is pink or reddish brown with maximum absorbance in the region of 490–510 nm.

It is assumed that the weak donor–acceptor interactions which form charge-transfer complexes $L \rightarrow X{-}X$ between the donor solvent and the halogen acceptor are the source of the different optical transitions. The existence of the vacant antibonding σ_u orbital in the halogen furnishes their acceptor capacity and allows a donor molecule to transfer charge to the halogen molecule. The acceptance of electrons in the antibonding orbital weakens the intramolecular X–X bond, which can even dissociate in extreme cases. With the increase of the $D \rightarrow A$ bond strength, the intramolecular bond of the halogen molecule becomes attenuated. In a notable case, of the complex $2C_5H_5N{\cdot}I_2$, the weakening of the I–I bond is so great as to break the covalent bond and to form the ionic complex $[(C_5H_5N)_2I]^+\,[I_3]^-$.

Two kinds of donors can be considered: (1) σ-donors that possess nonbonding electrons, such as various nitrogen bases (e.g. amines, pyridines, and nitriles), oxygen bases (e.g. alcohols, ethers, and carbonyl compounds), and organic sulfides and selenides, forming $\sigma-\sigma$ complexes; (2) π-donors in which the donor function is performed by bonding π-orbitals such as in aromatic compounds (e.g. benzene and polycyclic aromatics), forming $\sigma-\pi$ complexes.

Numerous solid complexes, as chains or sheets, have been crystallized from brown solutions of iodine, whether from σ-donors (particularly from those which have two coordination sites, such as the two separate oxygens in dioxane or one coordination atom with several nonbonding electron pairs of the oxygen of the carbonyl group in ketones), or from π-donors such as benzene. A well-known complex is the blue-colored starch–iodine, which serves as an analytical identification for iodine. Other examples are those of I_2/acridine dimers. $[(\text{acridine}\cdot I_2)_2]I_2$ adopts a zigzag shape (Figure 1), whilst those of the 9-chloroacridine analogue adopt a ‘C’ shape in the solid state and are decomposed by the loss of two I_2 molecules to generate $[(\text{9-Cl-acridine})_2I_2]$, which consists of two 9-Cl-acridine molecules bridged through N···I charge-transfer interactions with a single I_2 molecule.[6]

Cl_2 and Br_2, as well as ICl and IBr, have been found to behave similarly to I_2. For example, the interaction between *N*-methylbenzothiazole-2-selone with sulfuryl chloride in the solid state results in molecules of mbts·Cl_2. In the solid state, these T-shaped molecules interact via Cl···Cl intermolecular contacts to generate an extended structure of interlocking molecules with a zipper-like arrangement.[7] The low-temperature single-crystal structure of $C_6H_6\cdot Br_2$ and $MeC_6H_5\cdot Br_2$ revealed a localized form of bonding rather than the coaxial structure reported previously. The Br_2 molecule is oriented essentially perpendicular to the aromatic ring and is located at the rim of the molecule as shown in Figure 2.

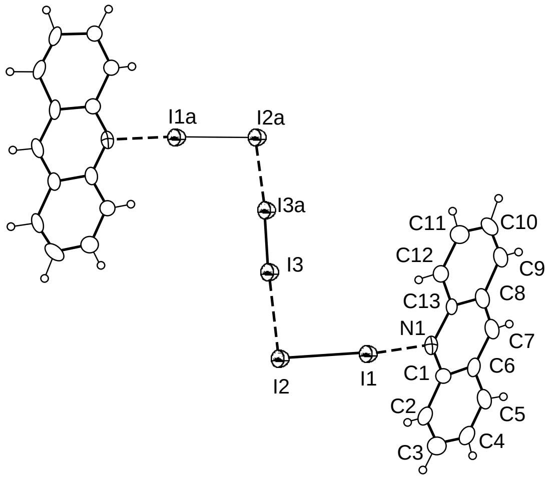

Figure 1 A perspective view of the Zigzag conformation of the $[(\text{aridine}\cdot I_2)_2]I_2$ dimer. (Reproduced by permission of Wiley-VCH)

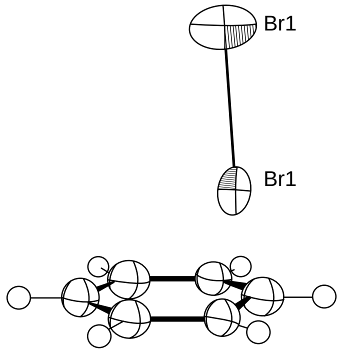

Figure 2 A view of the $C_6H_6\cdot Br_2$. (Ref. 8. Reproduced by permission of The Royal Society of Chemistry)

By considering all the Br···C distances, the interaction is interpreted as having a hapticity of 1.5, that is, it lies half-way between over-atom (η^1) and over-bond (η^2) for $C_6H_6\cdot Br_2$, whilst in $MeC_6H_5\cdot Br_2$, preference is shown for an over-bond interaction ($\eta = 1.7-1.86$) centered on the *ortho*- and *para*-carbons.[8]

Two intercalation compounds, CsF·Br_2 and 2CsF·Br_2, were isolated from the reaction of CsF with Br_2. In the 1:1 compound, X-ray analysis revealed eclipsed Cs···F layers (Cs^+ positioned above Cs^+), whereas the layers in the 2:1 compound are staggered. In both compounds, the Br–Br distance is larger than that for free gaseous bromine, suggesting some charge transfer from fluoride to bromine.[9]

The structurally characterized charge-transfer complexes between Ph_3PS and ICl/IBr consist of discrete molecular units with linear S···I–Cl/Br interactions.[10]

Although charge transfers generally involve organics, halogen adducts of metal complexes are known. An example is that the reaction of the metal-based Lewis acid $[Rh_2(O_2CCF_3)_4]$ system with I_2 results in a bridging coordination mode for iodine. As shown in Figure 3, in the solid state, dimeric rhodium complexes are linked together in a zigzag chain by interacting with neutral I_2 molecules, in which each I_2 molecule is believed to be functioning as an electron-pair donor to the rhodium atoms.[11] The reaction of $[NBu_4][PtX_3(CO)]$ (X =

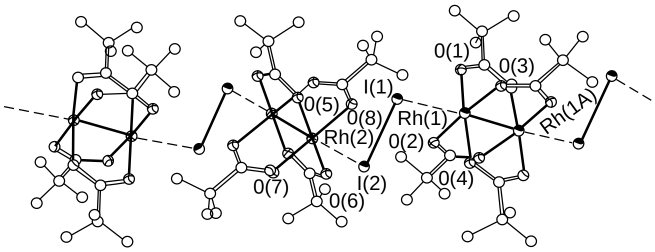

Figure 3 A view of the $[Rh_2(O_2CCF_3)_4]_2\cdot I_2$. (Reproduced by permission of Wiley-VCH)

Cl, Br) with dibromine gave rise to the platinum(IV) salts $[NBu_4]_2[Pt_2Br_{10}]\cdot(Br_2)_7$ and $[NBu_4]_2[PtBr_4Cl_2]\cdot(Br_2)_6$, which in the solid state form a polymeric network of bromine–bromine interactions.[12]

The relative acceptor strengths of the halogens and diatomic interhalogens to a given donor is: $ICl > BrCl > IBr > I_2 > Br_2 > Cl_2$. Similarly, the donor capacity to a given halogen is: benzene $<$ polyalkylbenzenes $\sim$ alkyl iodides $\sim$ alcohols $\sim$ ethers $\sim$ ketones $<$ organic sulfides $<$ organic selenides $<$ amines. Many organic halogenation reactions are explained on the basis of the presence of intermediates of halogen charge-transfer complexes.

3.6 Biological Action of Halogens

As vapors, all the halogens are highly irritating and react with the respiratory system, mucous membranes, eyes, and lungs. Exposure to high concentrations can be fatal.[13] This is true more for chlorine and bromine than for iodine, which is less volatile; in World War I, chlorine was used as an agent in chemical warfare.

4 HALOGEN COMPOUNDS

A majority of the halides of the pretransition metals in groups 1 and 2 of the periodic table, as well as those of the lanthanides and actinides at the valence states of +2 and +3, are usually ionic compounds, whereas the nonmetals and metals with valency states ≥3 are usually covalent halides.

4.1 Ionic Halides

In general, the greater the difference in electronegativity between the element and the halogen, the greater will be the charge separation and the better will be the ionic model. On the other hand, with an increase in the formal charge on the central atom or with a decreasing electronegativity difference, the better will be the covalent model.

The ionic halides, such as those of groups 1 and 2, exist as involatile solids with a three-dimensional lattice, whereas the semiionic halides, such as those of groups 11 and 12, form layers and chain structures.

In a series of the more ionic halides with the same metal, the melting and boiling points decrease with the increasing atomic number of halogen, following the sequence $MF_n > MCl_n > MBr_n > MI_n$; in a covalent series this sequence will be reversed: $MI_n > MBr_n > MCl_n > MF_n$.

Ionic halides dissolve easily in polar coordinating solvents with a high dielectric constant, such as water, whereas the covalent halides dissolve better in nonpolar, organic solvents.

Halide anions can also react with covalent halides to form complexed anionic species.

4.2 Covalent Halides

Covalent halides can be prepared by various synthetic routes. The simplest are direct reactions of elemental halogens (equation 9), or hydrogen halides with elements (equation 10) or oxides (equation 11). In other processes, the oxides are reacted with a halogen halide in the presence of carbon to combine with the oxygen (equation 12) or other reactive carbon–halides (equation 13). Exchange of halogens can also take place (equations 14–16). Anhydrous halides can also be obtained by dehydration of metal halide hydrates, using reactants such as thionyl halide, which react with the hydrated water (equation 17).

$$M + X_2 \longrightarrow MX_2 \tag{9}$$

$$2M + 2HX \longrightarrow 2MX + H_2 \tag{10}$$

$$MO + 2HX \longrightarrow MX_2 + H_2O \tag{11}$$

$$Ta_2O_5 + 5C + 10Br_2 \xrightarrow{>460\,^\circ C} 2TaBr_5 + 5COBr_2 \tag{12}$$

$$Nb_2O_5 + 5CBr_4 \xrightarrow{370\,^\circ C} 2NbBr_5 + 5COBr_2 \tag{13}$$

$$FeCl_3 + xs\ BBr_3 \longrightarrow FeBr_3 + BCl_3 \tag{14}$$

$$MCl_3 + xs\ 3HBr \longrightarrow MBr_3 + 3HCl \tag{15}$$

$$3TaCl_5 + xs\ 5AlI_3 \longrightarrow 3TaI_5 + 5AlCl_3 \tag{16}$$

$$MCl_x\cdot yH_2O + ySOCl_2 \longrightarrow MCl_x + ySO_2 + 2yHCl \tag{17}$$

In general, with the same central atom, the covalency of the corresponding halides will decrease with a decreasing halogen mass, namely, $MI_n > MBr_n > MCl_n$, as a result of the decrease of the polarizability, which is greatest in iodine and least in chlorine. The covalent halides have lower melting and boiling points than related ionic halides with isoelectronic central elements.

Usually, covalent halides hydrolyze in aqueous solutions forming oxides or hydroxides, but many transition element halides form ionic hydrates.

4.3 Covalent Polymeric Halides

The odd coordination numbers 1, 3, and 5 are not as stable as the even coordination numbers 2, 4, and 6 (*see* ***Coordination Numbers & Geometries***). Therefore, binary covalent halides of group 13 and 15 elements, MX_3 and MX_5, tend to dimerize into M_2X_6 (**1**) and M_2X_{10} (**2**), the central atoms having coordination numbers of four or six, respectively. In these dimers, halogen-bridging bonds exist in addition to the terminal halogen bonding.

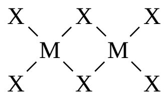

(1)

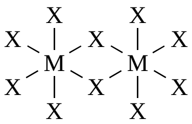

(2)

Although the vapor of phosphorous pentachloride is a covalent compound, in the solid phase it exists as a complexed ionic salt, in which both ions have a high degree of symmetry, the cation being tetracoordinated and the anion hexacoordinated (equation 18).

$$(\mathrm{PCl_5})_2 \longrightarrow [\mathrm{PCl_4}]^+[\mathrm{PCl_6}]^- \tag{18}$$

In contrast to fluorine, which can form binary fluorides in very high oxidation states such as six, even seven, and perhaps eight (*see* ***Fluorine: Inorganic Chemistry***), few hexahalides are known for the other halogens; there are three chlorides, $\mathrm{WCl_6}$, $\mathrm{ReCl_6}$, and $\mathrm{UCl_6}$, and only one bromide, $\mathrm{WBr_6}$.

4.4 Halide Complexes

Covalent mono-, tri-, tetra-, and pentavalent halides tend to form anionic complexes with coordination numbers of two (equation 19), four (equations 20 and 21), and six (equations 22 and 23). Such reactions take place mostly through the addition of halide anions.

$$\mathrm{AgCl} + \mathrm{Cl^-} \longrightarrow [\mathrm{AgCl_2}]^- \tag{19}$$

$$\mathrm{Al_2Cl_6} + 2\mathrm{Cl^-} \longrightarrow 2[\mathrm{AlCl_4}]^- \tag{20}$$

$$\mathrm{HgI_2} + 2\mathrm{I^-} \longrightarrow [\mathrm{HgI_4}]^{2-} \tag{21}$$

$$\mathrm{SnBr_4} + 2\mathrm{Br^-} \longrightarrow [\mathrm{SnBr_6}]^{2-} \tag{22}$$

$$\mathrm{SbCl_5} + \mathrm{Cl^-} \longrightarrow [\mathrm{SbCl_6}]^- \tag{23}$$

Some liquid covalent halides can act as nonaqueous solvents[14] based on Lewis acid–base behavior, according to the donor–acceptor definition. The self-dissociated ions consist of a cation formed by subtraction of a halide ion from the neutral compound, while the anion is formed by its addition (equation 24). Salts derived from such covalent halides can be considered as titration products of the parent acidic and basic compounds (equations 25 and 26). In such cases, both the cation and the anion usually possess a stable coordination number with a high geometrical symmetry.

$$2\mathrm{MX}_n \longrightarrow [\mathrm{MX}_{n-1}]^+ + [\mathrm{MX}_{n+1}]^- \tag{24}$$

$$\mathrm{PCl_5} + \mathrm{SbCl_5} \longrightarrow [\mathrm{PCl_4}]^+[\mathrm{SbCl_6}]^- \tag{25}$$

$$\mathrm{PBr_5} + \mathrm{BBr_3} \longrightarrow [\mathrm{PBr_4}]^+[\mathrm{BBr_4}]^- \tag{26}$$

4.5 Molecular Structures and its Determination

The geometric structure of the covalent binary halides, whether neutral or complexed ions, can be explained on the basis of the Nyholm–Gillespie rules known as the Valence Shell Electron Pair Repulsion Model (VSEPR) theory; the geometrical arrangements of the bonds around an atom in a species depends on the total number of electron pairs in the valence shell of the central atom, including both bonding pairs and nonbonding (unshared) pairs. The electron pairs in the valence shell adopt the arrangement that maximizes the distance between any two pairs, thereby decreasing their electrostatic interaction.

Table 3 Stereochemistry of halogen compounds[a]

Number	Geometry (symmetry)	Coordination examples
1 $\mathrm{AXE_3}$	Diatomic unit	$\mathrm{X_2}$, HX, XY
2 $\mathrm{AX_2E_3}$	Linear ($D_{\infty h}$)	$[\mathrm{X_3}]^-$, $[\mathrm{XY_2}]^-$, $[\mathrm{XYZ}]^-$
$\mathrm{AX_2E_2}$	Angular (C_{2v})	$[\mathrm{XY_2}]^+$, $\mathrm{XO_2}$, $[\mathrm{XO_2}]^-$
3 $\mathrm{AX_3E}$	Trigonal pyramid (C_{3v})	$\mathrm{PCl_3}$, $[\mathrm{XO_3}]^-$
$\mathrm{AX_3}$	Trigonal planar (D_{3h})	$\mathrm{BCl_3}$
$\mathrm{AX_3E_2}$	T-shaped, trigonal bipyramid with two vacant equatorial sites (C_{2v})	$\mathrm{XF_3}$, $\mathrm{RICl_2}$
4 $\mathrm{AX_4}$	Tetrahedral unit (T_d)	$\mathrm{SnCl_4}$, $[\mathrm{XO_4}]^-$, $\mathrm{FClO_3}$
$\mathrm{AX_4E_2}$	Square-planar unit (D_{4h})	$[\mathrm{XY_4}]^-$, $\mathrm{I_2Cl_6}$
$\mathrm{AX_3E_1}$	Trigonal bipyramid with one vacant equatorial site (C_{2v})	$\mathrm{XF_4}^+$, $[\mathrm{XO_2F_2}]^-$
5 $\mathrm{AX_5E}$	Square pyramid (C_{4v})	$\mathrm{XF_5}$
$\mathrm{AX_5}$	Trigonal bipyramid (D_{3h})	$[\mathrm{SnCl_5}]^-$, $\mathrm{F_3ClO_2}$
6 $\mathrm{AX_6}$	Octahedral unit (O_h)	$[\mathrm{XF_6}]^+$, $[\mathrm{PCl_6}]^-$
$\mathrm{AX_6E}$	Distorted octahedron	$[\mathrm{XF_6}]^-$
7 $\mathrm{AX_7}$	Pentagonal bipyramid (D_{5h})	$\mathrm{IF_7}$

[a] E = nonbonding electron pair.

Experimentally, the structures are determined by the use of various physical methods such as vibrational spectroscopy, both in the Raman and IR, NMR, or diffraction methods. Other accepted physical measurements, such as conductivity, cryoscopy, magnetic properties, electronic spectra in the UV and visible ranges, nuclear quadrupole resonance (NQR), and Mössbauer spectroscopy have also been applied. Table 3 summarizes various geometric structures found in halogen compounds, coordination numbers, bonding and nonbonding electronic arrangements, and symmetries.

5 INTERHALOGEN COMPOUNDS[15,16]

All halogens can combine with each other to form interhalogen compounds with compositions XY, $\mathrm{XY_3}$, $\mathrm{XY_5}$, and $\mathrm{XY_7}$. The central halogen, X, is always the heavier and less electronegative one and, therefore, no interhalogen exists in which fluorine is the central atom. All interhalogens XY_n, in which $n > 1$ are halogen fluorides, XF_n, except for $\mathrm{ICl_3}$, which exists only as the solid dimer $\mathrm{I_2Cl_6}$. On the other hand, compounds XY exist in which Y = F, Cl, and Br. $\mathrm{IF_7}$ is the only compound with this high coordination number, whereas XY, $\mathrm{XF_3}$, and $\mathrm{XF_5}$ compounds exist with X = Cl, Br, and I.

5.1 Preparation of Interhalogens

Most preparations take place by direct reaction of the two elements to form binary interhalogens (equations 27 and 28). Since the reactions between the same pair of halogens are equilibria, interhalogens with different compositions can be formed, depending on the working conditions such as relative concentrations, temperature, and pressure (equations 29–32).

$$I_2 + Br_2 \longrightarrow 2IBr \tag{27}$$

$$I_2 + 3Cl_2 \longrightarrow I_2Cl_6 \tag{28}$$

$$X_2 + 3F_2 \xrightarrow{200-300\,^\circ\mathrm{C}} 2XF_3 (X = Cl, Br) \tag{29}$$

$$I_2 + 3F_2 \xrightarrow{-78\,^\circ\mathrm{C}} 2IF_3 \tag{30}$$

$$Cl_2 + \text{xs } F_2 \xrightarrow[250\,\mathrm{atm}]{350\,^\circ\mathrm{C}} 2ClF_5 \tag{31}$$

$$I_2 + 5F_2 \xrightarrow{25\,^\circ\mathrm{C}} 2IF_5 \tag{32}$$

The compound BrF can be prepared by fluorinating bromine not with elemental fluorine but with a higher bromine fluoride in a disproportionation reaction (equations 33 and 34). Fluorination of halides (equation 35) instead of elemental halogen is sometimes preferable, leading to purer products. Interhalogen compounds also include astatine ones such as AtCl, AtBr, and AtI.

$$Br_2 + BrF_3 \longrightarrow 3BrF \tag{33}$$

$$2Br_2 + BrF_5 \longrightarrow 5BrF \tag{34}$$

$$KI + 4F_2 \longrightarrow KF + IF_7 \tag{35}$$

The interhalogens, particularly the halogen fluorides, are chemically very reactive materials and hydrolyze easily. The handling and manipulation of these, their derivatives, and cationic or anionic species have to be performed using the safety precautions customary in fluorine chemistry (exclusion of moisture and air, and in vacuum lines constructed from materials that are resistant to fluorine). The properties of the interhalogens are intermediate between those of their parent halogens, and some physical properties are summarized in Table 4.

5.1.1 *Diatomic Interhalogens XY*

All six possible interhalogens of this type exist. Out of these, the gaseous ClF is very stable, ICl and IBr are moderately stable and are pure crystalline materials at room temperature, whereas BrCl dissociates easily and reversibly into its elements (equation 36); BrF and IF disproportionate into a higher fluoride and Br_2 or I_2 (equation 37). IBr, a solid resulting from direct combination of the elements, is endothermic and extensively dissociated in the vapor. The structure of ClF, determined at – 188 °C, represents the only example of a halogen monofluoride structure. The structure is not like α- or β-ICl or IBr. The ClF molecules form infinite planar ribbons characterized by very short intermolecular Cl···Cl contacts [3.070(1) Å].[17]

Table 4 Physical properties of the interhalogens

Compound	Mp (°C)	Bp (°C)	Form at room temp.
ClF	−155.6	−100.1	Colorless gas
BrF	−33	20	Pale brown gas
BrCl	−66	5	Red-brown gas
ICl	27.2	100	Ruby red crystals
IBr	41	116	Black crystals
ClF_3	−76.3	11.8	Colorless gas/liquid
BrF_3	8.8	125.8	Straw-colored liquid
I_2Cl_6	101	Dissociates	Bright yellow solid
ClF_5	−103	−13.1	Colorless gas
BrF_5	−60.5	41.3	Colorless liquid
IF_5	9.4	104.5	Colorless liquid
IF_7	6.5	4.8	Colorless gas

$$2BrCl \xrightarrow[25\,^\circ\mathrm{C}]{CCl_4} Br_2 + Cl_2 \qquad K = 0.145 \tag{36}$$

$$3XF \longrightarrow XF_3 + X_2 \qquad (X = Br, I) \tag{37}$$

The chemical reactivities of the interhalogens are usually characterized by halogenation by the more electronegative element (equations 38 and 39). Sometimes, both halogens act as halogenation agents to form bonds with the same compound (equations 40–43).

$$W + 6ClF \longrightarrow WF_6 + 3Cl_2 \tag{38}$$

$$Se + 4ClF \longrightarrow SeF_4 + 2Cl_2 \tag{39}$$

$$CO + ClF \longrightarrow COFCl \tag{40}$$

$$RCN + 2ClF \longrightarrow RCF_2NCl_2 \tag{41}$$

$$SO_3 + ClF \longrightarrow ClOSO_2F \tag{42}$$

$$SF_4 + ClF \longrightarrow SF_5Cl \tag{43}$$

The interhalogens AtI, AtBr, and AtCl can also be formed by direct reaction of astatine with iodine, bromine, and chlorine respectively; excess of the lighter halogen can be pumped off in vacuo.

5.1.2 *Halogen Fluorides XF_3, XF_5, and IF_7*

Four tetraatomic interhalogens are known, namely, ClF_3, BrF_3, IF_3, and ICl_3, which is actually the solid dimer I_2Cl_6.

ClF_3 and BrF_3 are well-characterized volatile molecular liquids with a T-shaped structure (**3**). However, the related ICl_3 exists only as the solid dimer I_2Cl_6 with a planar structure (**4**) containing four terminal I–Cl bonds and two bridging I–Cl–I bonds with differing bond distances. The halogen fluorides are extremely powerful fluorinating agents. In particular, ClF_3 acts as such even at room temperature, while reacting elemental fluorine, under similar conditions, may require some preheating. This extreme reactivity of ClF_3 seems to result from the fact that it is in equilibrium with the dissociated species, ClF, and fluorine atoms, the fluorine radicals being more reactive than molecular fluorine itself (equation 44).

$$\mathrm{ClF_3 \longrightarrow ClF + 2F} \tag{44}$$

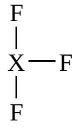

(**3**)

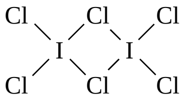

(**4**)

As shown in Figure 4, IF_3 has a polymeric structure based on planar T-shaped molecules [F–I–F = 160.3(2)°]. Intermolecular interactions to two adjacent molecules occur, which result in an unusual planar pentagonal coordination geometry around the iodine atom; this is quite unlike that seen for BrF_3 or ClF_3.[18]

All the halogens form hexaatomic halogen fluorides ClF_5, BrF_5, and IF_5, with a square pyramidal structure of C_{4v} symmetry, but IF_7 is the only one known with the highest coordination number of seven. This latter compound has a pentagonal bipyramidal structure with D_{5h} symmetry. All the halogen fluorides are very vigorous fluorinating agents, the least of them being IF_5. The order of reactivity is approximately $ClF_3 > ClF_5 > BrF_5 > IF_7 > ClF > BrF_3 > IF_5 > BrF > IF_3 > IF$.

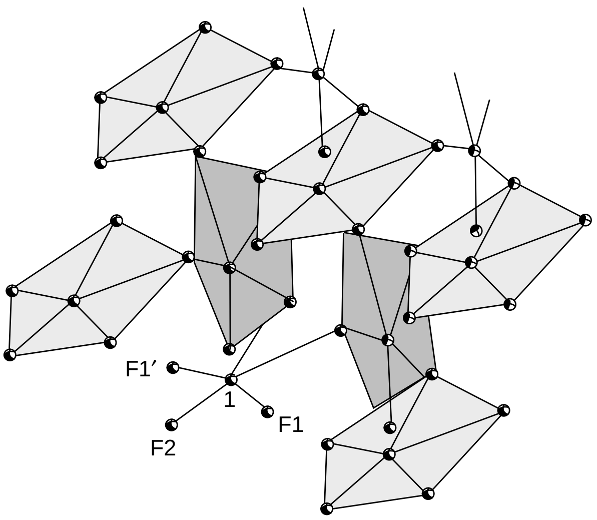

Figure 4 A view of the solid-state structure of IF_3 showing the intermolecular contacts resulting in a planar pentagonal geometry around each iodine center. (Reproduced by permission of Wiley-VCH)

5.2 Polyhalogen Cations[19–21]

Cation formation is not restricted, as normally observed, to association with metallic species. It can also occur among nonmetals and even the most typical ones such as halogens or interhalogens, which are usually more noted for halide and polyhalide anion formation.

There are two kinds of polyhalogen cations. The isopolyhalogen cations contain several atoms of the same halogen, whereas the heteropolyhalogen cations contain several atoms of at least two different halogens.

The formation of these cations can be considered as being derived from the self-ionic dissociation of the neutral halogens or interhalogens (equation 45). As with the interhalogens, the central atom is always the heavier and less electronegative one, even if this causes an unsymmetrical structure such as Cl–Cl–F (instead of Cl–F–Cl; equation 46). Sometimes the derived cation becomes polymerized, as in $[I_3Cl_2]^+$, which is a derivative of ICl (equation 47). In the case of elemental halogens, several ionic equilibria are possible, and different isopolyhalogen cations can be obtained from the same halogen (equations 48–50) depending on reaction conditions such as the acidity of the reactants. All the different varieties of such cations have been synthesized, characterized, and studied.

$$\mathrm{2XY}_n \longrightarrow [\mathrm{XY}_{n-1}]^+ + [\mathrm{XY}_{n+1}]^- \tag{45}$$

$$\mathrm{3ClF \longrightarrow [Cl\text{-}Cl\text{-}F]^+ + [F\text{-}Cl\text{-}F]^-} \tag{46}$$

$$\mathrm{4ICl \longrightarrow [I_3Cl_2]^+ + [ICl_2]^-} \tag{47}$$

$$\mathrm{3X_2 \longrightarrow [X_3]^+ + [X_3]^-} \tag{48}$$

$$\mathrm{4X_2 \longrightarrow [X_5]^+ + [X_3]^-} \tag{49}$$

$$\mathrm{5X_2 \longrightarrow 2[X_2]^+ + 2[X_3]^-} \tag{50}$$

5.2.1 Preparation of Polyhalogen Cations

On the basis of self-ionic dissociation, these compounds can be prepared by acid–base reactions. Heteropolyhalogen cations are usually prepared by reacting the parent compound with a Lewis acid (equation 51) in which XY_n = interhalogen and MY_m = Lewis acid, for example, halides of B, Al, P, As, and Sb, and so on (equations 52 and 53). Such reactions can be performed by direct interaction of the reactants with an excess of the more volatile reactant, which can then be pumped off, after completion of the reaction, leaving behind the pure product. Sometimes it is preferable to perform such reactions in solution, such as in anhydrous hydrogen fluoride (AHF), and pump off the solvent at the end of the reaction.

$$\mathrm{XY}_n + \mathrm{MY}_m \longrightarrow [\mathrm{XY}_{n-1}]^+ + [\mathrm{MY}_{m+1}]^- \tag{51}$$

$$\mathrm{ICl_3 + AlCl_3 \longrightarrow [ICl_2]^+[AlCl_4]^-} \tag{52}$$

$$\mathrm{BrF_5 + AsF_5 \longrightarrow [BrF_4]^+[AsF_6]^-} \tag{53}$$

Another synthetic route is the oxidative process, which is mostly applied to the formation of isopolyhalogen cations from elemental halogens or from diatomic interhalogens. An oxidizer is required in addition to the Lewis acid (equations 54–58), but sometimes the Lewis acid itself can also serve as an oxidizing agent (equations 59 and 60). Some heteropolyhalogen cations can also be obtained by oxidation reactions (equation 61).

$$7I_2 + KIO_3 + 8AlCl_3 \longrightarrow 5[I_3]^+[AlCl_4]^- \tag{54}$$

$$X_2 + S_2O_6F_2 \xrightarrow{\text{in HSO}_3\text{F}} \xrightarrow{\text{SbF}_5} [X_3]^+[Sb_3F_{16}]^- \tag{55}$$

$$Cl_2 + ClF + AsF_5 \xrightarrow{-78\,^\circ\text{C}} [Cl_3]^+[AsF_6]^- \tag{56}$$

$$\tfrac{3}{2}Br_2 + [O_2]^+[AsF_6]^- \longrightarrow [Br_3]^+[AsF_6]^- + O_2 \tag{57}$$

$$Au(s) + 4BrSO_3F \longrightarrow [Br_3]^+[Au(SO_3F)_4]^- + \tfrac{1}{2}Br_2 \tag{58}$$

$$3I_2 + 3MF_5 \longrightarrow 2[I_3]^+[MF_6]^- + MF_3\ (M = As, Sb) \tag{59}$$

$$2I_2 + \text{xs } SbF_5 \longrightarrow 2[I_3]^+[Sb_2F_{11}]^- \tag{60}$$

$$I_2 + 2SbCl_5 + \text{xs } Cl_2 \longrightarrow 2[ICl_2]^+[SbCl_6]^- \tag{61}$$

Polyhalogen cations in solution can also be prepared in oxidative liquids such as sulfuric acid, oleum, or fluorosulfonic acid. The most common isopolyhalogen cations are $[X_3]^+$ and the higher oxidized ones $[X_2]^+$, although additional species such as $[X_5]^+$ and $[X_4]^{2+}$ have also been identified, with the $[I_7]^+$ ion being possible but uncertain. The preparation of the more highly oxidized cations $[X_2]^+$ requires stronger acidic conditions than the less oxidized $[X_3]^+$ types. All triatomic polyhalogen cations ($[X_3]^+$, $[XY_2]^+$) have a bent structure (**5**) with C_{2v} symmetry, while $[X_5]^+$ ions have planar, trans Z-type structures. For the $[I_2]^+$ ion, dimerization occurs to give a brown diamagnetic $[I_4]^{2+}$ ion when solutions are cooled. Salts containing this cation, for example, $[I_4{}^{2+}][AsF_6{}^-]_2$ have been isolated. This weak dimerization may be due to the overlap of half-filled p* orbitals on the two $[I_2]^+$ units.

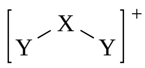

(**5**)

It is interesting to note that oxidation reactions (equations 62–73) can produce heteropolyhalogen cations such as $[IBr_2]^+$, $[ClF_6]^+$, and $[BrF_6]^+$, although their parent interhalogens, IBr_3, ClF_7, and BrF_7, have never been isolated.

$$[Br_3]^+[Au(SO_3F)_4]^- + Br_2 \longrightarrow [Br_5]^+[Au(SO_3F)_4]^- \tag{62}$$

$$8Br_2 + 3[XeF]^+[AsF_6]^- \longrightarrow 3[Br_5]^+[AsF_6]^- + 3Xe + BrF_3 \tag{63}$$

$$2I_2 + ICl + AlCl_3 \longrightarrow [I_5]^+[AlCl_4]^- \tag{64}$$

$$2ClF + AsF_5 \longrightarrow [FCl_2]^+[AsF_6]^- \tag{65}$$

$$I_2Cl_6 + 2SbCl_5 \longrightarrow 2[ICl_2]^+[SbCl_6]^- \tag{66}$$

$$ClF_3 + AsF_5 \longrightarrow [ClF_2]^+[AsF_6]^- \tag{67}$$

$$Br_2 + IOSO_2F \longrightarrow [IBr_2]^+[SO_3F]^- \tag{68}$$

$$BrF_5 + 2SbF_5 \longrightarrow [BrF_4]^+[Sb_2F_{11}]^- \tag{69}$$

$$ClF_5 + PtF_6 \longrightarrow [ClF_6]^+[PtF_6]^- \tag{70}$$

$$2ClF_5 + 2PtF_6 \longrightarrow [ClF_6]^+[PtF_6]^- + [ClF_4]^+[PtF_6]^- \tag{71}$$

$$BrF_5 + [KrF]^+[AsF_6]^- \longrightarrow [BrF_6]^+[AsF_6]^- + Kr \tag{72}$$

$$IF_7 + BrF_3 \longrightarrow [IF_6]^+[BF_4]^- \tag{73}$$

Heteropolyhalogen cations with coordination numbers ≥4 exist only with fluorine ligands, namely, $[XF_4]^+$ and $[XF_6]^+$ (X = Cl, Br, and I). The pentaatomic polyhalogen cations $[XF_4]^+$ have a pseudo-trigonal bipyramidal structure (**6**) with C_{2v} symmetry, two fluorines being in the axial positions and two others in the equatorial triangular plane.

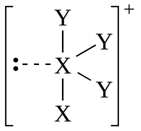

(**6**)

The structure of $[ClF_4]^+$ $[SbF_6]^-$ has a pseudo-trigonal bipyramidal geometry for the cation with two longer, more ionic, axial bonds and two shorter equatorial bonds. A pseudo-octahedral arrangement around the central chlorine atom results from interactions between the chlorine and neighboring fluorides of two adjacent $[SbF_6]^-$ anions to produce an infinite zigzag chain of alternating $[ClF_4]^+$ and $[SbF_6]^-$ moieties (Figure 5).[22] In the cases of $[BrF_4]^+$ and $[IF_4]^+$, they adopt a trigonal bipyramidal shape with one equatorial site occupied

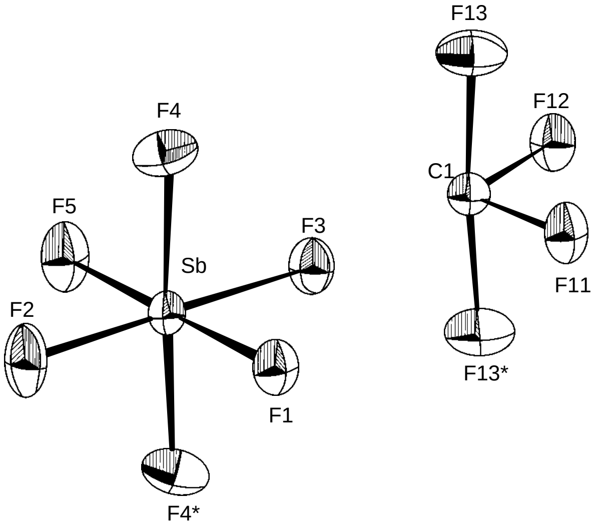

Figure 5 A view of the solid-state structure of $[ClF_4]^+$ $[SbF_6]^-$. (Reprinted with permission from Ref. 22. © 2001 American Chemcial Society)

by a lone pair of electrons. However, strong anion–cation interactions in $[BrF_4]^+$ $[Sb_2F_{11}]^-$ result in an infinite zigzag chain and distortion of the equatorial F–Br–F bond angle. In comparison, for $[IF_4]^+$ $[SbF_6]^-$, an infinite polymeric sheet motif is observed owing to four short I···F interactions, which results in a compression of the axial F–I–F angle.[23] The heptaatomic cations $[XF_6]^+$ are octahedral (O_h symmetry).

5.3 Polyhalide Anions[16,24–26]

A large number of polyhalide anions $[X_mY_nZ_p]^-$ exist in which $m + n + p = 3, 5, 7, 9$, and so on. Each of the numbers m, n, or p can equal 0. Thus, polyhalide anions can exist as isopolyhalide anions such as $[X_3]^-$, $[X_5]^-$, and $[X_7]^-$, or as binary or ternary heteropolyhalide types.

5.3.1 *Preparation of Polyhalide Anions*

The isopolyhalide anions can be prepared by reacting elemental halogen with the same monoatomic halide (equation 74). As mentioned before, polyhalide anions are the counterions of the self-dissociation process of interhalogens, and as such their preparation can take place by reacting an interhalogen with a Lewis base (equations 75–77). Some heteropolyhalides can be prepared by oxidation of simple halide anions (equations 78 and 79). The unique $[IF_8]^-$ anion can be made as its Me_4N^+ salt by interaction of IF_7 with Me_4NF in MeCN.

$$X_2 + X^- \longrightarrow [X_3]^- \qquad (74)$$

$$[Et_4N]^+Cl^- + ICl_3 \longrightarrow [Et_4N]^+[ICl_4]^- \qquad (75)$$

$$KF + BrF_3 \longrightarrow K^+[BrF_4]^- \qquad (76)$$

$$MCl + 2F_2 \longrightarrow M^+[ClF_4]^- (M = K, Rb, Cs) \qquad (77)$$

$$6MCl + xs\ 8BrF_3 \longrightarrow 6M^+[BrF_4]^- + 3Cl_2 + Br_2 (M = K, Ag, \tfrac{1}{2}Ba) \qquad (78)$$

$$IF_7 + Me_4NF \longrightarrow [Me_4N]^+[IF_8]^- \qquad (79)$$

In all the heteropolyhalide anions, the central atom is always the heavier and least electronegative halogen. Although three reactions (equations 80–82) with different starting anions can occur, a single anionic product, $[ICl_2]^-$, is obtained and no isomers are identified. The structure of $[PPh_4][ICl_2]$ shows an anion that is symmetric and nearly linear [Cl–I–Cl = 178.10(6)°].[27]

$$KI + Cl_2 \longrightarrow K^+[ICl_2]^- \qquad (80)$$

$$PBr_5 + IBr \longrightarrow [PBr_4]^+[IBr_2]^- \qquad (81)$$

$$K^+[ICl_4]^- + KI \longrightarrow 2K^+[ICl_2]^- \qquad (82)$$

Astatine interhalogens AtY (Y = Br and I) also react with I^-, Br^-, and Cl^- to form heteropolyhalide anions (equation 83).

$$AtY + X^- \longrightarrow [AtYX]^- (X = I, Br, Cl; Y = Br, Cl) \qquad (83)$$

The triatomic polyhalide anions have a linear structure (**7**), the pentaatomic ones $[XY_4]^-$ are square planar (**8**) with a D_{4h} symmetry, while the heptaatomic $[XF_6]^-$ have a distorted octahedral structure. The $[IF_8]^-$ ion has a square antiprismatic structure.

$$[Y{-}X{-}Y]^-$$

(**7**)

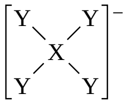

(**8**)

5.3.2 *Stability*

A solid polyhalide salt with the structure M^+ $[X_mY_nZ_p]^-$ tends to dissociate into a simple monohalide derivative of the cation M^+ with the most electronegative halogen, and a neutral halogen or interhalogen.

The stability of various polyhalide compounds with the same cation are as follows: $[I_3]^- > [IBr_2]^- > [ICl_2]^- > [I_2Br]^- > [Br_3]^- > [BrCl_2]^- > [Br_2Cl]^-$. The most stable compounds are those with iodine at the center. Similarly, the symmetric anions are more stable than the asymmetric ones, $[Cl–Br–Cl]^- > [Br–Br–Cl]^-$.

It is well known that a wide range of polyhalides exist for iodine, and most of these can be considered as arising from combinations of I_2, I^-, and $[I_3]^-$. Linear $[I_3]^-$ anions have been identified in numerous compounds such as $Co(C_6H_{12}S_3)(I_3)_2$,[28] $[Pr^nMe_2PhN](I_3)$,[29] and $Ag([18]aneS_6)(I_3)$.[30] The $[I_4]^{2-}$ anions are present in $[Cr(NH_3)_6](I_3)(I_4)$[31] and $[NH_4]_2[(AuI_4)AuI_2(\mu\text{-}I_4)]$.[32]

The V-shaped pentaiodide anions in $[\{Rh(\mu\text{-pz})I(CO)(PMe_2Ph)\}_2][I_5]$,[33] $[(Bu_3PSe)_2I][I_5]$,[34] $[C_{19}H_{16}FeNS][I_5]$,[35] and $[EtMe_3N][I_5]$[36] form extended polymeric layers, while $[EtMePh_2N][I_5]$ is of the rare isolated types.[37]

The anionic networks identified for $(DMFc)_4(I_{26})$[38] and $Ag([18aneS_6])(I_7)$,[30] despite the significantly different empirical compositions, are quite similar. For the former (Figure 6), the network may be derived from a primitive cubic lattice of iodide ions with I_2 bridges on all edges by systematically removing 1/12 of the I_2 molecules, while for the latter the iodide ions occupy the lattice points of a primitive rhombohedral lattice with I_2 bridges along all edges.

Cations embedded in a three-dimensional polyiodide network of cages of $[I_5]^-$ ions and diiodine molecules are presented in $[RhCl_2(C_{12}H_{24}S_4)](I_5)\cdot I_2$.[39] In $[Pr^iMe_2PhN](I_8)$, the anion is best described as $[I_{16}]^{2-}$, which is present as 14-membered rings, catenated by diiodine molecules, and linked into layers with 10-membered and types of 14-membered rings.[30] In $[Pd_2Cl_2([18aneN_2S_4])_{1.5}I_5(I_3)_2$, infinite chains of

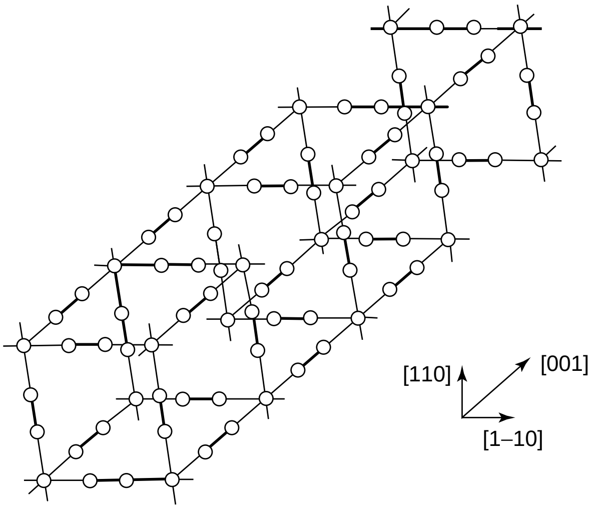

Figure 6 Primitive cubic lattice of iodide ions bridged by I_2 molecules in $(\text{DMFc})_4(I_{26})$. (Reproduced by permission of Wiley-VCH)

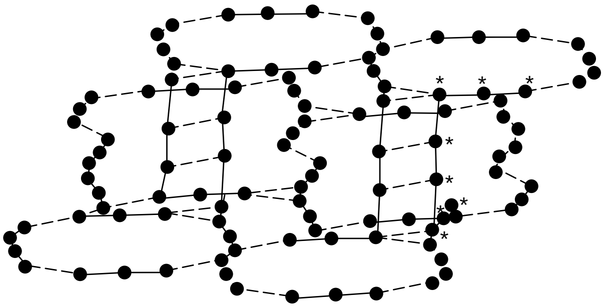

Figure 7 Anionic matrix in $[\text{Pd}_2\text{Cl}_2([18]\text{aneN}_2\text{S}_4)]_{1.5}I_5(I_3)_2$ (dicationic chains run through vertical channels). Starred atoms represent one $[I_8]^{2-}$ unit. (Reproduced by permission of Wiley-VCH)

binuclear cations are embedded in a matrix of the anions (Figure 7).[40]

Regular anionic shapes are present in the solid-state structures of $[(\text{Crypt-2,2,2})\text{H}_2](I_8)$, $[\text{Ni(phen)}_3](I_8)\cdot 2\text{CHCl}_3$, and bis(*N*-methylurotropinium)octaiodide, but that in bis(N-methylurotropinium)octaiodide represents a new configuration, which is somewhere between $(I_3{}^-\cdot I_2\cdot I_3{}^-)$ and broken $(I_3{}^-, I_5{}^-)$.[41]

Nonaiodides are very rare, but two, as $[\text{Pr}^i\text{Me}_2\text{PhN}]^+$[29] and $[\text{K}([15]\text{aneO}_5)]^+$[40] salts, have been structurally characterized. The anion in the former contains 14-membered rings tied by two iodine bridges into 10-membered rings, while that in the latter is best described as an $[I_3{}^-\cdot(I_2)_3]$ charge-transfer complex.

Meanwhile, $[I_{10}]^{2-}$ anions have been structurally characterized as counterions to a $[\text{Cd}(12\text{-crown-}4)_2]^{2+}$ complex cation. This anion, which adopts a twisted ring conformation, is composed of two triiodide ions linked by two I_2 molecules.[42]

As shown in Figure 8, the $[I_{11}]^-$ anion in $[([16]\text{aneS}_4)\text{MIM}([16]\text{aneS}_4)]I_{11}$ can be described either as two $[I_5]^-$ groups linked via an iodide ion or two $[I_3]^-$ groups and two iodine molecules linked via an iodide ion, that form a 14-membered polyiodide ring (9.66 × 12.64 Å) around the complex cation with the metal-bridging iodide at the center of the ring; these rings also link into an infinite two-dimensional sheet. This compound represents the first synthesis of a cyclic polyhalide array in which the complex cation acts as a template.[43]

The dodecaiodide dianion in $[\text{Ag}_2([15]\text{aneS}_5)_2](I_{12})$ is described as a charge-transfer complex $[(I^-)_2\cdot(I_2)_5]$ bound to the cation by Ag–I bonds with weak I···S interactions combining to build up an extended three-dimensional, spiral superstructure.[30] In marked contrast, the same anion in bis[potassium(dibenzo-18-crown-6)] dodecaiodide nearly a discrete entity $(I_2\cdot I_3{}^-\cdot I_2\cdot I_3{}^-\cdot I_2)$.[44] In $[\text{Cu(Dafone)}_3](I_{12})$, iodine–iodine interactions assemble novel, planar, $[I_{12}]^{2-}$ anions into a network around the strained tris-chelate complex of Cu(II).[45]

The $[I_{13}]^{3-}$ anion in $[\text{Me}_2\text{Ph}_2\text{N}]_3I_{13}$ consists of zigzag chains of iodide ions and iodine molecules, in which the iodide ions are coordinated to $[I_5]^-$ groups. The $[I_{16}]^{2-}$ anion in $[\text{Me}_2\text{Ph}_2\text{N}]_2I_{16}$ consists of two $[I_7]^-$ groups bridged by an iodine molecule.[46]

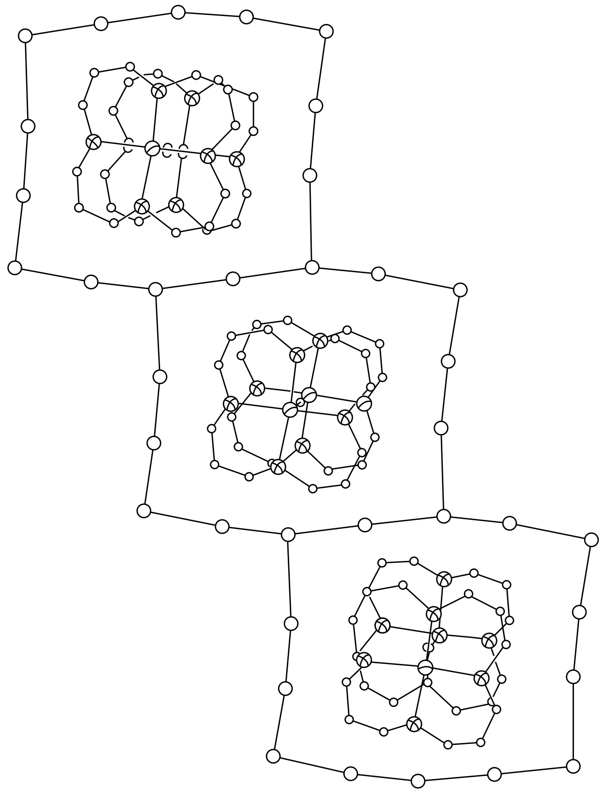

Figure 8 Perspective view of $[([16]\text{aneS}_4)\text{PdIPd}([16]\text{aneS}_4)][I_5]_2I$. (Ref. 43. Reproduced by permission of The Royal Society of Chemistry)

The $[I_{22}]^{4-}$ anion in $[MePh_3P]_4I_{22}$ consists of two L-shaped $[I_5]^-$ units bridged by an iodine molecule and completed by two end-on $[I_5]^-$ groups.[47]

Much larger iodine catenates are obtained when metal iodides are present; the reaction of TlI with $(Me_3S)I_7$ resulted in a number of species from which $(Me_3S)_3I_{26}$ has been structurally characterized, and shown to be of $[I_5]^-$ and $[I_7]^-$ anions with intercalated iodine molecules.[48] A mixture is identified in $[Me_3PNHPMe_3]_4(I_{28})$, the linear $[I_3]^-$, the Z-shaped $[I_8]^{2-}$, and the zigzag chains of $[I_{14}]^{4-}$.[49] In $[Cp_2Fe]_3[I_{29}]$, the most iodine-rich polyiodide, the ferrocenium cations, are made to interact in the cavities of an anionic three-dimensional network cage structure described by the formula $[\{(I_5{}^-)_{1/2}\cdot I_2\}\cdot\{(I_{12}{}^{2-})_{1/2}\cdot I_2\}\cdot I_2]$.[50]

Discrete linear symmetric $[ICl_2]^-$ anions have been reported in $[H_2Phen][ICl_2]Cl$[51] and $[Hphen]_2[ICl_2][I_2Cl]$.[52] For later, the columnar stacking of cations produces cavities for the $[ICl_2]^-$ anions and channels in which the polyanionic $[I_2Cl]^-$ chains are found. Unremarkable anionic geometries are reported in $[Pd(C_6H_{12}S_3)_2](IBr_2)$, $[Pd(C_{10}H_{20}S_4)](IBr_2)$,[53] and $[Cs(18\text{-crown-}6)](ICl_2)$.[54]

The structure of $[PPh_4][I_3Br_4]$, derived from the reaction of $[PPh_4]Br$ with IBr, has a seven-membered polybromide $[I_3Br_4]^-$ with a distorted C_{3v} symmetry, which is best described as a bromide coordinated to three IBr units via the iodine atoms.[55]

6 HYDROGEN HALIDES

The name hydrogen halides, HX, is used for the anhydrous compounds, whereas their aqueous solutions are called hydrohalic acids. In their anhydrous condition, these are molecular compounds, whereas solutions in water bring about ionic dissociation to give the protonated solvent and the halide anion (equation 84).

$$HX + H_2O \longrightarrow [H_3O]^+ + X^- \qquad (84)$$

Hydrogen chloride is produced industrially on a huge scale and is used as the anhydrous gas as well as a hydrochloric acid in aqueous solution. Several industrial routes to synthesize HCl are in use: (1) direct burning of hydrogen in chlorine, which results in a very pure product (equation 85); (2) reaction of an inorganic metal halide with a less volatile protic acid, such as sulfuric acid, to form the more volatile hydrogen halide (equation 86) and (3) as a by-product of the chlorination of hydrocarbons (equation 87).

$$H_2 + Cl_2 \longrightarrow 2HCl \qquad (85)$$

$$NaCl + H_2SO_4 \longrightarrow NaHSO_4 + HCl \qquad (86a)$$

$$NaCl + NaHSO_4 \longrightarrow Na_2SO_4 + HCl \qquad (86b)$$

$$RH + Cl_2 \longrightarrow RCl + HCl \qquad (87)$$

Similar reactions lead to the formation of HBr and HI. The latter can also be prepared by reacting the element with phosphorus and water (equation 88, X = Br or I).

$$2P + 6H_2O + 3X_2 \longrightarrow 6HX + 2H_3PO_3 \qquad (88)$$

Isotopic variants of the hydrohalides, such as with deuterium and tritium, can be prepared by hydrolytic reactions of covalent halides such as PX_3, PX_5, $AlCl_3$, and PhCOCl with D_2O or T_2O (equation 89).

$$PhCOX + D_2O \longrightarrow DX + PhCO_2D \qquad (89)$$

6.1 Physical Properties of Hydrogen Halides

Whereas the heavier HX are diatomic gases at room temperature, HF is a volatile liquid boiling at 19.5 °C. This exceptional property of HF is explained on the basis of its polymeric structure $(HF)_x$, due to the very strong F–H–F hydrogen bonding (*see **Fluorine: Inorganic Chemistry***). The order of the boiling and melting points of the hydrogen halides is $HF > HCl < HBr < HI$. This trend also exists for the group 16 and 15 hydrides, namely, $H_2O > H_2S < H_2Se < H_2Te$ and $NH_3 > PH_3 < AsH_3 < SbH_3$. This is in contrast to the properties of the hydrides of group 14, in which the order is as expected, that is, $CH_4 < SiH_4 < GeH_4 < SnH_4$. The discontinuity results from the fact that hydrogen bonds can be formed easily with the lighter elements, F, O, and N. Some physical properties of the hydrogen halides are summarized in Table 5. All are colorless, fume easily with moist air, and have penetrating odors.

6.2 Nonaqueous Solvents[56]

Except for hydrogen fluoride, the hydrogen halides have only a limited use as nonaqueous solvents. AHF plays an important role as a nonaqueous solvent[57] in fluorine chemistry, and it also serves as an important liquid medium for numerous synthetic preparations. It is easily handled owing to its boiling point (19.5 °C) being close to ambient temperature, and is a liquid under its own vapor pressure; it has a long liquid range of about 100 °C, has low viscosity, and a high dielectric constant. The physical properties of AHF therefore make it an excellent solvent for both inorganic polar solutes as well as organic nonpolar solutes, compounds, and even biological materials.

Table 5 Physical properties of the hydrogen halides

Property	HF	HCl	HBr	HI
Melting point (°C)	−83.4	−114.7	−88.6	−51
Boiling point (°C)	19.5	−84.2	−67.1	−35.1
Liquid range (°C)	102.9	30.5	21.5	15.9
Dielectric constant	84 (0 °C)	9.28 (−95 °C)	7.0 (−85 °C)	3.39 (−50 °C)

The properties of all other hydrogen halides are far removed from those of AHF and, therefore, their use as nonaqueous solvents is rather limited. Nevertheless, they are used for physical studies of solutions and for some synthetic purposes, such as in the formation of salts with HCl_2^- or BCl_4^- and related anions. Anhydrous HX can be considered to undergo self-ionization (equation 90) and can therefore be used to perform reactions of an acid–base nature, and solvolytic and redox reactions (equations 91–93).

$$3HX \longrightarrow [H_2X]^+ + [HX_2]^- \tag{90}$$

$$SbF_3 + 3HCl \longrightarrow SbCl_3 + 3HF \tag{91}$$

$$I^- + 2Cl_2 \longrightarrow [ICl_4]^- \tag{92}$$

$$PCl_3 + X_2 + HCl \longrightarrow [PCl_3X]^+ + [HClX]^- (X = Cl, Br) \tag{93}$$

6.3 Hydrohalic Acids

Hydrohalides dissolve easily in water to form hydrohalic acids and undergo virtually complete ionic dissociation (equation 84). All the hydrohalic acids, except HF, are very strong acids. Although AHF is one of the most acidic liquids, as measured by its Hammett function, hydrofluoric acid is a weak acid.

Hydrochloric acid is of great importance and is widely used in industrial processes. The largest use is in the metallurgical industry for the pickling of metals to remove oxide scales. Other uses include the production of inorganic halides from metals, oxides or carbonates, extraction of metals from ores in metallurgical processes, and various organic reactions.

Hydrobromic acid is used in the production of inorganic bromides as well as in organic brominations, particularly in the production of pesticides. Some physical properties of the hydrohalide acids are summarized in Table 6.

6.4 Biological Action

In addition to their action on the respiratory system and attacking the mucous membrane and skin, a major hazard of concentrated hydrohalic acids is direct contact with the skin, causing chemical burns. Some of these compounds, however, are important in biochemical processes. The hydrochloric acid in the stomach, for example, is extremely important in the digestive system, and iodine is of importance in thyroid function.

Table 6 Physical properties of hydrogen halides in aqueous solution

Property	HF	HCl	HBr	HI
Solubility in water (g/100 g soln at 1 atm and 0 °C)	all proportions	45.15	68.85	71
pK_a for acid	3.2	−7	<−7	<−7
Azeotrope				
Boiling point at 1 atm (°C)	112	108.58	124.3	126.7
Solubility (g/100 g solution)	38	20.22	47.63	56.7

7 HALOGEN OXIDES

A large number of binary halogen oxides are known, from shock-sensitive liquids to rather stable solids. Similarly, a large number of oxoacids and oxoacid salts are also known.

Most halogen oxides are not very stable and decompose easily. This stems from the fact that the number of electrons in these molecules is an odd number. Therefore, the ions formed by the addition of an electron, whether in oxoacids or in oxoacid salts, are more stable.

Dichlorine oxide, Cl_2O, is best prepared on a laboratory scale by reacting chlorine with mercury oxide (equation 94). On an industrial scale, it can be prepared by reacting chlorine with moist carbonate (equation 95). This oxide is readily soluble in water to form hypochlorous acid (equation 96). Its salts, the hypochlorites, are quite stable and are used in the textile industries and to bleach wood pulp. The low-temperature crystal structure of Cl_2O reveals an essentially molecular structure [d(O–Cl) = 1.7092(4) Å] with weak secondary interactions [d(O···Cl) = 2.7986(4) Å] affording a distorted tetrahedral coordination around the O atom.[58]

$$2Cl_2 + 2HgO \longrightarrow HgCl_2{\cdot}HgO + Cl_2O \tag{94}$$

$$2Cl_2 + 2Na_2CO_3 + H_2O \longrightarrow 2NaHCO_3 + 2NaCl + Cl_2O \tag{95}$$

$$Cl_2O + H_2O \longrightarrow 2HOCl \tag{96}$$

Cl_2O_3, generated in the reaction of ClO with ClO_2, has a relatively short lifetime and is not expected to be an important reservoir for ClO_x.[59]

Chlorine dioxide, ClO_2, is a stable oxide and can be prepared by reducing chlorates (equation 97) or in reaction with moist oxalic acid (equation 98). Chlorine dioxide is a strong oxidizing agent toward both organic and inorganic materials.

$$[ClO_3]^- + Cl^- + 2H^+ \longrightarrow ClO_2 + \tfrac{1}{2}Cl_2 + H_2O \tag{97}$$

$$[ClO_3]^- + [C_2O_4]^{2-} \longrightarrow ClO_2 \tag{98}$$

Dichlorine hexoxide, Cl_2O_6, is best made by ozonolysis of ClO_2 (equation 99). It is assumed to be an ionic compound in the solid state, $[ClO_2]^+ [ClO_4]^-$.

$$2ClO_2 + 2O_3 \longrightarrow Cl_2O_6 + 2O_2 \tag{99}$$

The most stable oxide is dichlorine heptoxide, Cl_2O_7, the anhydride of perchloric acid, $HClO_4$. It can be obtained by dehydration of that acid with H_3PO_4 at 10 °C, followed by low-temperature distillation at low pressure. Dissolution in water or alkali again produces the acid or perchlorates respectively. Table 7 summarizes some physical properties of the chlorine oxides. The ClO_4 radical is generated by thermal decomposition of Cl_2O_6 or Cl_2O_7 in Ar or Ne. It has a lifetime of only a few milliseconds but could be obtained in a matrix at low temperature and characterized by IR and UV/VIS specptroscopies, and indicates a dynamic Jahn–Teller effect.[60]

Bromine forms oxides such as Br_2O, Br_2O_3, and BrO_2, and these are less well characterized than for chlorine. They are stable at low temperatures but unstable at room temperature. For example, compound Br_2O_3 (synthesized from Br_2 and O_3) has been shown to form as an orange crystalline solid and on further ozonization to give a colorless oxide, which does not contain the colored O–Br(I) unit. It is insoluble in CH_2Cl_2, unlike Br_2O_3, and decomposes above $-40\,°C$. However, it can be crystallized from propionitrile as $Br_2O_5\cdot(EtCN)_3$ and the structure determination shows symmetric $O_2Br–O–BrO_2$ to be present. The molecule has terminal bonds (1.62 Å), which are shorter than the bridging ones (1.87–1.89 Å). The bond angle at the bridging oxygen atom is 121°. This study brings into doubt the existence of Br_2O_4, which has a Raman spectrum very similar to that of Br_2O_3.[61] The gas-phase FTIR spectra of two important bromine-containing species, OBrO and Br_2O, have been reported.[62] The hydrolysis of $BrOTeF_5$ offers a new route to Br_2O. X-ray analysis shows that the compound is bent [114.2(2)°] with strong Br$\cdots$Br interactions in the solid state resulting in chains.[63]

For the bromine oxides, the realization that the only well-characterized compounds use all the possible combinations of the only basic units in this area (i.e. terminal OBr and pyramidal $O–BrO_2$ in Br–O–Br, $Br–O–BrO_2$ and $O_2Br–O–BrO_2$) suggests that new homoleptic bromine oxides are likely to be even less stable than these derivatives.[64]

Iodine forms the most stable of all halogen oxides, I_2O_5, which exists as white, hygroscopic crystals. It can be prepared by dehydration of iodic acid, HIO_3, at 200 °C in a stream of air. It can also be prepared by direct interaction of iodine and oxygen in a glow discharge. I_2O_5 dissolves easily in water to form the parent compound (iodic acid). It can oxidize various inorganic chemicals and is one of the few agents that oxidizes carbon monoxide completely at room temperature (equation 100). This reaction is used to analyze the concentration of CO in air or in gaseous mixtures.

$$5CO + I_2O_5 \longrightarrow 5CO_2 + I_2 \qquad (100)$$

Table 7 Physical properties of the chlorine oxides

Compound	Mp (°C)	Bp (°C)	Form at room temp.
Cl_2O	−120.6	2.0	Yellow–brown gas
ClO_2	−59	11	Yellow–green gas
$ClOClO_3$	−117	44.5	Pale yellow liquid
Cl_2O_6	3.5	203	Dark red liquid
Cl_2O_7	−91.5	81	Colorless liquid

$(IO)_2SO_4$ has been shown to hydrolyze to a powder formulated as I_2O_4, which is monoclinic and thought to have a one-dimensional structure comprising alternating oxygen-bridged iodine(I) and iodine(V) units $–I–O–IO_2–O–(I–O–IO_2–O)_n–I–O–IO_2–O–$. It decomposes on heating to I_2O_5 and I_2 (equations 101 and 102).[65]

$$4(IO)_2SO_4 + 4H_2O \longrightarrow 4H_2SO_4 + I_2 + 3I_2O_4 \qquad (101)$$

$$5I_2O_4 \longrightarrow I_2 + 4I_2O_5 \qquad (102)$$

Reaction of H_5IO_6 with H_2SO_4 results in IO_3, whose structure consists of I_4O_{12} units (two IO_6 octahedra sharing an edge and two pyramidal IO_3 groups sharing two vertices with the double octahedron) linked through I$\cdots$O bridges, and may be considered to be the mixed anhydride of H_5IO_6 and HIO_3.[66]

7.1 Halogen Oxide Cations

Reacting halogen oxides with Lewis acids or dissolving them in superacids such as fluorosulfonic acid or persulfuric acid produces the halogen oxide cation $[ClO_2]^+$, as in $[ClO_2]^+$ $[SO_3F]^-$, $[ClO_2]^+$ $[SbF_6]^-$, and $[ClO_2]^+$ $[BF_4]^-$. Other cations have also been identified, such as $[ClO]^+$. The reaction of Cl_2 with $[O_2]^+$ $[SbF_6]^-$ forms $[Cl_2O_2]^+$ $[SbF_6]^-$ or $[Cl_2O_2]^+$ $[Sb_2F_{11}]^-$ (Figure 9).[67] In the reaction of iodine oxide with SO_3 or $S_2O_6F_2$, the cation $[IO_2]^+$ is formed, but when dissolved in concentrated sulfuric acid the reduced $[IO]^+$ cation is formed. Whereas the chlorine oxide cations are discrete ions, the iodine oxide species appear to be polymerized, with I–O–I bridging networks, cross-linked to the anions.

7.2 Halogen Oxide Fluorides

Halogen oxides can be reacted with fluorine or halogen fluoride to form halogen fluoride oxides, F_nXO_m. Similar to the halogen fluorides, the central atom is always that of the

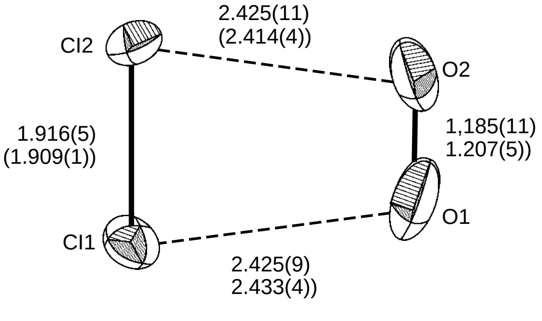

Figure 9 The $[Cl_2O_2]^+$ cation in $[Cl_2O_2][SbF_6]$. The cation in $[Cl_2O_2][Sb_2F_{11}]$ is practically identical and the bond length data (in Å) for it are given in parentheses. (Reprinted with permission from Ref. 67. © 2001 American Chemcial Society)

heavier halogen bonded directly to fluorine and to oxygen. Halogen oxide fluorides can be considered to undergo self-ionization, similar to interhalogens (equation 103), and can thus react with Lewis acids and bases to form the appropriate salts.

$$2F_mXO_n \longrightarrow [F_{m-1}XO_n]^+ + [F_{m+1}XO_n]^- \qquad (103)$$

These compounds range from the thermally unstable FClO to the rather chemically inert perchloryl fluoride $FClO_3$. The structure and properties of this family of compounds resemble those of the halogen fluorides. Therefore, they have to be handled with the same care as elemental fluorine and its chemically reactive fluorides. The halogen oxide fluorides can be prepared by fluorination of halogen oxides with elemental fluorine or with halogen fluoride.

Of the six possible chlorine oxide fluorides,[68] five have been identified. Reacting chlorine nitrate with fluorine at low temperature (equation 104) gives F_3ClO in high yield. Fluorination of a chlorate with chlorine trifluoride at room temperature produces $FClO_2$ (equation 105). The stable colorless gas $FClO_3$ can be prepared by fluorination of potassium chlorate at −40 °C with elemental fluorine. It is best prepared, in a 97% yield on an industrial scale, by fluorination of perchlorate with antimony pentafluoride or with superacid (a mixture of SbF_5 and fluorosulfonic acid, $HOSO_2F$) (equation 106). $FClO_3$ is a rather inert compound, particularly at room temperature.

$$ClONO_2 + 2F_2 \xrightarrow[>80\%]{-35\,^\circ C} F_3ClO + FNO_2 \qquad (104)$$

$$6NaClO_3 + 4ClF_3 \longrightarrow 6FClO_2 + 6NaF + 2Cl_2 + 3O_2 \qquad (105)$$

$$KClO_4 \xrightarrow{HOSO_2F/SbF_5} FClO_3 \qquad (106)$$

F_3ClO decomposes at 300 °C to chlorine trifluoride and oxygen (equation 107), whereas at room temperature this decomposition is rather slow, being increased by heating or by UV light. Similarly, $FClO_2$ decomposes to chlorine fluoride and oxygen (equation 108). These compounds can therefore serve either as fluorinating or oxidizing agents.

$$F_3ClO \longrightarrow ClF_3 + \tfrac{1}{2}O_2 \qquad (107)$$

$$FClO_2 \longrightarrow ClF + O_2 \qquad (108)$$

$FClO_3$ is considered to be chemically inert and yet it can be used in organic reactions to introduce either fluorine or the ClO_3 group, and it is used for selective fluorination. In spite of its so-called inertness, the handling of this reagent requires use of the safety precautions customary for fluorine chemistry and it should not be dealt with lightly.

The related bromine compounds are fewer than for chlorine and are more reactive. Of the bromine compounds, the most stable is $BrClO_3$, which can be prepared by fluorination of perbromate with AsF_5 or BrF_5 (equation 109).

$$KBrO_4 + 2AsF_5 + 3HF \longrightarrow FBrO_3 + [H_3O]^+[AsF_6]^- + KAsF_6 \qquad (109)$$

The related iodine compounds are more stable at the higher oxidation states, +5 and +7, of the central iodine, for example, as the pentavalent FIO_2 and F_3IO compounds, and the heptavalent FIO_3, F_3IO_2, and F_5IO compounds. Similar to the iodine oxides, these also form polymers through oxygen bridging. Reacting diiodine pentoxide with fluorine produces FIO_2 (equation 110), but dissolving that same compound in IF_5 yields F_3IO (equation 111). The stable FIO_3 can be prepared by reacting periodic acid with fluorine in AHF solution. Some physical properties of halogen oxide fluorides are listed in Table 8. The structure of IO_2F has an alternating axial–equatorial-linked trigonal-bipyramidal arrangement. The equatorial plane contains the two I=O bonds [1.805(6) and 1.773(6) Å] with the apical positions being occupied by one fluorine and one oxygen substituent I–F = 1.903(5) and I–O = 2.226(6) Å] (Figure 10).[69] The structures of $ClOF_3$ and $BrOF_3$ have been determined and both show the trigonal bipyramidal geometry around the central halogen atom with two axial fluoride ligands. Interestingly, the structure of $ClOF_3$ is described as tubelike stacking of pseudo-hexagonal, eight-membered rings in which the different ‘tubes’ are weakly interconnected, giving rise to a formal coordination number of seven to each chlorine atom.[70]

Compounds containing iodine in two different oxidation states are rare, comproportionation often occurring to give the more stable oxidation state compound. $[Cl_2IOI(O)F_2]$ is the first example of iodine oxofluoride chloride with mixed valency iodine atoms. The structure of this compound is of two linked trigonal bipyramidal iodine centers, one formally +III, the other +V, linked by an oxygen bridge.[71]

$$I_2O_5 + F_2 \xrightarrow{HF/20\,^\circ C} 2FIO_2 + \frac{1}{2}O_2 \qquad (110)$$

$$I_2O_5 + 3IF_5 \xrightarrow{105\,^\circ C} 5F_3IO \qquad (111)$$

Table 8 Physical properties of the halogen oxide fluorides

Compound	Mp (°C)	Bp (°C)	Form at room temp.
F_3ClO	−43	28	Stable, colorless gas
$FClO_2$	−115	−6	Stable, colorless gas
$FClO_3$	−147.8	−46.7	Stable, colorless gas
F_3ClO_2	−81.2	−21.6	Stable, colorless gas
$FBrO_3$	−110	2.4	Stable, colorless gas
FIO_2	>200	–	Colorless polymeric solid
F_3IO	–	–	Colorless crystals
FIO_3	100 (decomposes)	–	White crystalline solid

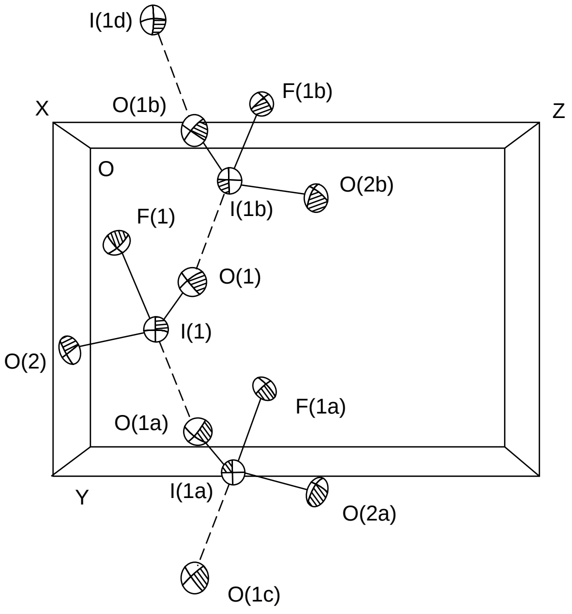

Figure 10 View of the solid-state structure of IO_2F, showing the interactions between adjacent molecules. (Reprinted with permission from Ref. 69. © 2001 American Chemcial Society)

7.3 Oxoacids and Oxoacid Salts[68]

The oxoacids and their salts are very stable, in contrast to the lack of stability of the halogen oxides themselves. A large number of these acids exist at the representative oxidation states of the halogens, namely, +1, +3, +5, and +7. Even perbromic acid, $HBrO_4$, has been synthesized by fluorination of bromates.

7.3.1 Hypohalous Acids and Hypohalites

The easiest preparation of aqueous solutions of the hypohalous acids is to dissolve the appropriate halogen in water (equation 112).

$$X_2 + H_2O \longrightarrow HOX + H^+ + X^- \qquad (112)$$

The addition of silver or mercury oxide precipitates the metal halide, leaving behind the aqueous solution, which is very reactive and is used for bleaching and sterilizing purposes. Solutions of hypohalites can be made by introducing the appropriate halogen into basic solutions (equation 113), but these will also contain some halide anions. To obtain pure hypochlorites, it is necessary to carefully neutralize pure hypochlorous acid. The most stable hypochlorites are those of Li, Ca, Sr, and Ba, although some others are also known but are not as stable, or are not sufficiently pure.

$$X_2 + 2OH^- \longrightarrow OX^- + X^- + H_2O \qquad (113)$$

Hydrated hypobromites are also known, for example, $NaOBr{\cdot}xH_2O$ and $KOBr{\cdot}3H_2O$, which can be crystallized from concentrated basic solutions into which bromine has been introduced; these solids decompose above 0 °C. No hypoiodites are known.

The hypohalites and their parent acids decompose to release oxygen (equation 114) and thus serve as very strong oxidizers in inorganic and organic chemistry. The hypohalites oxidize oxalates to carbon dioxide, nitrites to nitrates, sulfites to sulfates, divalent manganese to permanganate, halides to halates, and ketones to carboxylic acids, and so on.

$$2HOX \longrightarrow O_2 + 2H^+ + 2X^- \qquad (114)$$

In addition to the existence of ionic hypohalites, molecular hypohalites are also known such as $ClONO_2$ and $ClOClO_3$ with the ClO–group.

7.3.2 Halous Acids and Halites

This group of compounds is the least stable of the various oxoacids and oxoacid salts, and is restricted to chlorous acid and its salts. Barium chlorite is prepared by reacting ClO_2 with a basic solution in the presence of H_2O_2, which serves as a reducing agent (equation 115). Adding dilute sulfuric acid to a suspension of $Ba(ClO_2)_2$ forms chlorous acid (equation 116).

$$Ba(OH)_2 + H_2O_2 + 2ClO_2 \longrightarrow Ba(ClO_2)_2 + H_2O + O_2 \qquad (115)$$

$$Ba(ClO_2)_2 + H_2SO_4 \longrightarrow 2HClO_2 + BaSO_4 \qquad (116)$$

Anhydrous $NaClO_2$ crystallizes out of solution above room temperature and serves as an oxidizing agent toward malodorous and toxic organic compounds.

Although bromous acid itself is unknown, $Ba(BrO_2)_2$ and the corresponding strontium salt can be prepared by treating hypobromite with Br_2 in strongly basic solutions at 0 °C, followed by slow evaporation.

7.3.3 Halic Acids and Halates

Introducing a halogen into a hot basic solution causes a disproportionation process. Part of the halogen is reduced to the halide anion and another part of it is oxidized to the halate anion (equation 117).

$$3X_2 + 6OH^- \longrightarrow [XO_3]^- + 5X^- + 3H_2O \qquad (117)$$

Chlorate is the most important halate and is produced, on an industrial scale, by electrolysis of a halide solution in a diaphragmless cell, which promotes efficient mixing. This arrangement allows the chlorine produced at the anode to react with the hydroxyl anion at the cathode, forming the hypochlorous anion, which is then further oxidized to chlorate, whether by oxidation at the anode or through

$$Cl^- \longrightarrow \frac{1}{2}Cl_2 + e^- \text{ (anode)}$$

$$H_2O + e^- \longrightarrow OH^- + \frac{1}{2}H_2 \text{ (cathode)}$$

$$Cl_2 + 2OH^- \longrightarrow OCl^- + Cl^- + H_2O$$

$$OCl^- + 2H_2O \longrightarrow [ClO_3]^- + 2H_2 \text{ (anode)}$$

$$OCl^- \longrightarrow [ClO_3]^- + 2Cl^-$$

Scheme 1

disproportionation (Scheme 1). Bromates and iodates are also produced industrially but to a lesser extent.

The pure halic acids are produced by adding sulfuric acid to an aqueous solution of the appropriate barium salt and precipitating insoluble barium sulfate (equation 118).

$$Ba(XO_3)_2 + H_2SO_4 \longrightarrow 2HXO_3 + BaSO_4 \qquad (118)$$

All the halogens form halic acids in aqueous solution, which can be concentrated to about 40–50% when evaporated by heating carefully under reduced pressure. At higher concentrations, these disproportionate into perchloric acid, whereas the bromate decomposes to bromine and oxygen. Both chloric and bromic are strong acids in aqueous solution ($pK_a \leq 0$), whereas iodic acid is slightly weaker ($pK_a = 0.804$).

All the halates decompose on heating, usually above their melting point. In the presence of a transition metal catalyst such as MnO_2, the decomposition of $KClO_3$ to chloride and oxygen starts at 70 °C and is the source of pure oxygen in laboratory preparation. In a series of the halates with the same cation, the thermal stability decreases in the sequence of $[IO_3]^- > [ClO_3]^- > [BrO_3]^-$. Potassium chlorate is used in the mixture of 'safety' matches, in pyrotechnic formulations, and as intermediates in the production of perchlorates.

The oxidation of a halide anion with its own halate is sometimes quantitative and is used in the quantitative analysis of bromide and iodide (equation 119).

$$[XO_3]^- + 5X^- + 6H^+ \longrightarrow 3X_2 + 3H_2O \qquad (119)$$

A spectacular kinetic effect, known as the 'chemical clock', has been observed when an acidified sulfite solution is reacted with iodate in the presence of the starch indicator for elemental iodine, in which the color of the iodine complex alternately appears and disappears (Scheme 2.) Over the years, many more oscillating clocks like this have been discovered.

$$[IO_3]^- + 3[SO_3]^{2-} \longrightarrow I^- + 3[SO_4]_2^-$$

$$5I^- + [IO_3]^- + 6H^+ \longrightarrow 3I_2 + 3H_2O$$

$$3I_2 + 3[SO_3]^{2-} \longrightarrow 6I^- + 6H^+ + 3[SO_4]^{2-}$$

Scheme 2

7.3.4 Perhalic Acids and Perhalates

These compounds of the various halogens differ in their structure and properties and will therefore be treated separately.

The most stable chlorine compounds are the halides with the lowest oxidation state, −1, or the perhalates with the highest, +7. Perchloric acid and its salts are the most stable among the oxohalogen compounds. Aqueous solutions of perchlorates are not notable oxidizing agents at room temperature, but on heating become vigorous and even violent oxidants. Therefore special care has to be taken when handling these materials, particularly avoiding the presence of oxidizable materials, since explosions can take place.

Sodium perchlorate is produced industrially by electrolytic oxidation of $NaClO_3$. Perchloric acid is prepared by reacting a sodium or barium salt with concentrated HCl, filtering off the chloride, and concentrating the filtrate by distillation. The anhydrous acid can be obtained by low-pressure distillation in an all-glass apparatus in the presence of sulfuric acid, which combines with the rest of the water.

Pure perchloric acid is a colorless, hygroscopic, and shock-sensitive liquid. Although the anhydrous acid is a covalent compound, $HOClO_3$, the hydrates are considered to be ionic: $[H(H_2O)_n]^+$ $[ClO_4]^-$ ($n = 1$, 2, and 3). Hydration does not increase the coordination number of the chlorine atom above four, which is in contrast to a periodic acid having a coordination number of six (discussed later).

Anhydrous perchloric acid is a powerful oxidizing agent that reacts explosively with many organic and inorganic materials. On decomposition, various gaseous products are formed. However, aqueous solutions of perchloric acid are not oxidizing at room temperature. This is explained on the basis of kinetic activation barriers. Most metals form perchlorate salts, and even molecular compounds, such as NO and NO_2, also react with it to form ionic compounds such as $[NO]^+$ $[ClO_4]^-$. Ammonium perchlorate is used as a solid-fuel propellant, particularly in missiles. Potassium perchlorate is also used in pyrotechnic formulations such as fireworks and flares.

The perchlorate anion has long been considered as a noncoordinating ligand and has therefore been used in the preparation of 'inert' ionic solutions of constant ionic strength for physicochemical measurements. However, although this anion is definitely less coordinating than H_2O, it can be monodentate, bridging bidentate, or chelating bidentate. This is illustrated by structures of compounds such as $(CH_3)_3SnClO_4$, $Co(MeSC_2H_4SMe)_2(ClO_4)_2$, $(Ph_3BiOBiPh_3)(ClO_4)_2$, $Sb_2Cl_6(OH)(O)(ClO_4)$, and Ti $(ClO_4)_4$.

The existence of perbromic acid and perbromates were once considered an impossibility on the basis of thermodynamic considerations. Recently, however, these have been prepared on a regular laboratory scale. Perbromic acid or perbromates are synthesized by oxidation of BrO_3^- electrolytically or by fluorination of bromate with elemental fluorine (equation 120) or other strong fluorination agents such as XeF_2 (equation 121).

$$[BrO_3]^- + F_2 + 2OH^- \longrightarrow [BrO_4]^- + 2F^- + H_2O \qquad (120)$$

$$[BrO_3]^- + XeF_2 + H_2O \longrightarrow [BrO_4]^- + Xe + 2HF \qquad (121)$$

Salts such as $KBrO_4$ (dec. ~275 °C) and NH_4BrO_4 (dec. ~170 °C) are fairly stable thermally and isomorphorus with their perchlorate analogues. However, potassium perbromate is thermodynamically less stable than both the corresponding perchlorate and periodate analogues.

At least four series of periodates interconnected in aqueous solution by a complex series of equilibriums are known. All these are derived from the parent acid H_5IO_6 through deprotonation, dehydration, and aggregation; some are listed in Table 9.

The industrial preparation is based on electrolytic oxidation (equation 122) or with chlorine (equation 123).

$$[IO_3]^- + 6OH^- - 2e^- \longrightarrow [IO_6]^{5-} + 3H_2O \qquad (122)$$

$$[IO_3]^- + 6OH^- + Cl_2 \longrightarrow [IO_6]^{5-} + 2Cl^- + 3H_2O \qquad (123)$$

The polymeric structure of the various iodine compounds is achieved through oxygen bridging between iodine atoms. Being a multibasic acid, partial neutralization of the hydrogens by metal ions is possible, the rest of the hydrogens being retained as hydroxyl groups, such as in $Na_3IO_4(OH)_2$, which is a sodium salt of dihydrogen orthoperiodate.

Aqueous solutions of the periodic acid can be obtained by adding concentrated nitric acid to barium periodate. White crystals of H_5IO_6 can be obtained from these solutions, and heating to 120 °C yields a polymerized form of $H_7I_3O_{14}$. This compound in the solid state is a stoichiometric $H_5IO_6 \cdot 2HIO_4$ phase.[72] Spectroscopic and structural studies on $[Me_4N]^+[IO_4]^-$ confirm Pauling's 1930 proposal that the phase change in this system is due to the onset of free ion rotation and is not caused by positional disorder of the rotational oscillation axes.[73] In the room temperature structure (Phase II), the disordered $[IO_4]^-$ anion undergoes free rotation about one of the I–O bonds (Figure 11), while in the Phase III structure (determined at – 30 °C), the $[IO_4]^-$ anion is ordered. When heating to 100 °C at reduced pressure, it causes dehydration and forms HIO_4. Periodates are very potent oxidation agents and in acid solution can oxidize divalent manganese quantitatively from Mn^{II} to the heptavalent $[MnO_4]^-$. It is also used in organic chemistry for oxidation purposes. Periodates can act as ligands in the formation of complexes of transition metals in which the octahedral $[IO_6]^{5-}$ serves as a bidentate ligand. $[H_4I_2O_{10}]^{2-}$ anions in magnesium tetrahydrogen decaoxodiiodate $\{MgH_4I_2O_{10} \cdot 6H_2O\}$ connected the $[Mg(H_2O)_6]^{2+}$ cations via a network of hydrogen bonds.[74] A single-crystal X-ray study indicates that this represents the first example of a chelating I_2O_{12} unit coordinating via vertices to give I_2InO_{12} chains.[75]

Table 9 Periodic acids

Formula	Name	Relation to H_5IO_6
H_5IO_6	Orthoperiodic	Parent
HIO_4	Periodic	H_5IO_6–$2H_2O$
'H_3IO_5'	Mesoperiodic	$2H_5IO_6$–$2H_2O$
$H_7I_3O_{14}$	Triperiodic	$3H_5IO_6$–$4H_2O$

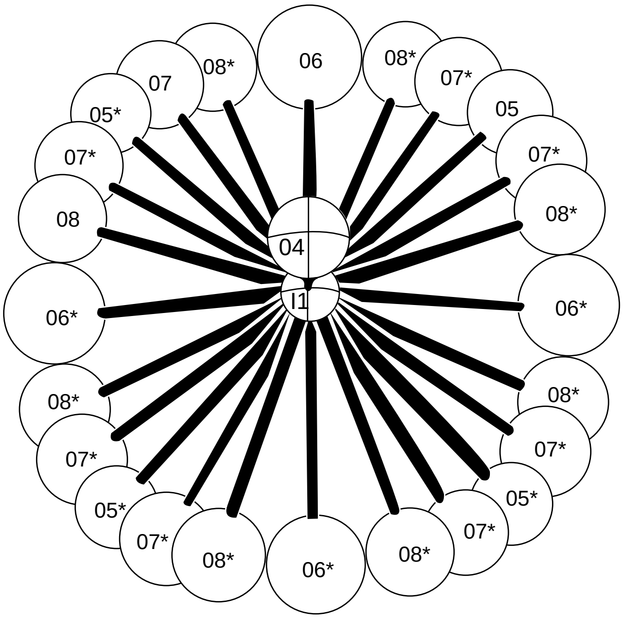

Figure 11 An ORTEP drawing of a single disordered $[IO_4]^-$ anion showing a detailed view of the rotational disorder about one I–O axis. (Reprinted with permission from Ref. 73. © 2001 American Chemcial Society)

7.4 Halogen Derivatives of Oxoacids

All halogens react to form compounds in which the halogen is bound through an oxygen atom in an oxoacid, and not directly to the central atom, for example, $XOClO_3$, $XOSO_2F$, and $XONO_2$ (X = F, Cl, Br, and I). Some trivalent halogen compounds are also known, such as $X(ONO_2)_3$ and $X(OSO_2F)_3$ (X = Br and I). In general, the thermal stability decreases with the increase of the atomic number of the halogen. They all decompose easily and violent reactions may occur. Of the halogen nitrates, fluorine nitrate is the most stable. The halogen fluorosulfates are among the more stable of the oxoacid derivatives.

8 ORGANIC POLYVALENT HALOGEN DERIVATIVES

The intention is not to cover the vast halo-organic chemistry in this context, but only organic polyvalent halogen compounds that are actually limited to derivatives with iodine (I), iodine (III), and iodine (V), though evidence for the divalent $L_2I^{\bullet}$ radical was obtained by the hemolytic cleavage of I–O bonds during thermolysis of *tert*-butyl-peroxyiodanes.**[76]**

8.1 Monovalent Iodine

Although Br^+ has been postulated to occur in reactions of Br_2, the evidence is usually only kinetic. However, the solvated linear ions $[L_2Br]^+$ and $[L_2I]^+$, where L may be pyridine, MeCN, quinuclidine, and so on are known.**[77]** The oxidants $[I(MeCN)_2]^+$ $[UF_6]^-$ can be prepared from reactions of UF_6 with 1/2 equiv of I_2 in MeCN. But Br^+ is too electrophilic to exist in MeCN. The reaction in liquid SO_2 gives a 95% yield of the salt $[I(MeCN)]^+$ $[AsF_6]^-$.**[78]**

8.2 Trivalent Iodine

Trivalent iodine compounds can be divided into the following categories: (1) with one carbon−iodine bond, such as in iodo salts, RIX_2, and iodoso compounds, RIO; (2) with two carbon−iodine bonds on the same iodine, such as RR′IX; and (3) with three carbon−iodine bonds on the same iodine, such as Ph_3I.

8.2.1 Iodo Disalts

Aromatic iodo disalts, $ArIX_2$, can be prepared by passing chlorine into an organic solution of an aryl iodide, ArI (equation 124). On standing, the material decomposes into HCl and a chlorine-substituted aromatic part (equation 125).

$$\mathrm{ArI} + \mathrm{Cl_2} \longrightarrow \mathrm{ArICl_2} \quad (124)$$

$$\mathrm{C_6H_5ICl_2} \longrightarrow p\text{-}\mathrm{ClC_6H_4I} + \mathrm{HCl} \quad (125)$$

Iodobenzene dichloride can be used as a mild chlorinating agent in organic synthesis. From vibrational spectroscopy,**[79]** it seems that the $ArICl_2$ has a T-shaped structure in which the Cl–I–Cl is linear and the phenyl group is perpendicular to it. Such a structure could be attributed to a partially ionic compound with the halide part being an anion, $[Cl–I–Cl]^-$, and the phenyl unit more positively charged. This physical structure has also been established by X-ray data.

Perfluoroalkyl iododifluorides can be prepared with halogen fluorides (equation 126). Using an excess of halogen fluoride, the iodotetrafluoride is obtained (equation 127).

$$\mathrm{R_fI} + \mathrm{XF}_n \longrightarrow \mathrm{R_fIF_2} \quad (126)$$

$$\mathrm{R_fI} + \mathrm{xs\ XF}_n \longrightarrow \mathrm{R_fIF_4} \quad (127)$$

Dissolving an $ArICl_2$ in basic solution forms the iodoso compound, ArIO (equation 128). Another synthetic procedure to obtain iodoso compounds is by direct oxidation of ArI with ozone, fuming nitric acid, or $KMnO_4$.

$$\mathrm{ArICl_2} + \mathrm{OH^-} \longrightarrow \mathrm{ArIO} \quad (128)$$

$ArI(OAc)_2$ can be crystallized from a solution of either $ArICl_2$ or ArIO in acetic acid. $ArI(ONO_2)_2$ can be obtained by reacting silver nitrate with a solution of those iodine compounds in acetonitrile.

8.2.2 Diorganohalonium Compounds

Diaryliodonium compounds can be prepared by acid-catalyzed condensation of iodoso aryls with another aryl molecule (equation 129). Another method is the use of iodine trichloride in reaction with organometallic compounds (equations 130 and 131). $RICl_2$ may be prepared by direct chlorination of RI (R = CF_3CH_2, $CHF_2(CF_2)_5CH_2$) and these materials can be used to chlorinate iodobenzene to give the less hydrolytically stable compound $PhICl_2$.**[80]**

$$\mathrm{ArIO} + \mathrm{Ar'H} \xrightarrow{\mathrm{HX}} \mathrm{ArAr'IX} + \mathrm{H_2O} \quad (129)$$

$$\mathrm{Ar_2Hg} + \mathrm{ICl_3} \longrightarrow \mathrm{Ar_2ICl} \quad (130)$$

$$\mathrm{CF_3CH_2I} + \mathrm{Cl_2} \longrightarrow \mathrm{CF_3CH_2ICl_2} \quad (131)$$

Diaryliodonium compounds are good arylating agents, introducing a second aryl group where one already exists (equation 132).

$$\mathrm{Ph_2ICl} + \mathrm{PhOH} \longrightarrow \mathrm{Ph_2O} + \mathrm{PhI} + \mathrm{HCl} \quad (132)$$

Among the compounds in which I^{3+} is combined with oxoanions are $I(OSO_2F)_3$, $I(NO_3)_3$, $I(OCOCH_3)_3$, IPO_4, and $I(OClO_3)_3$ (equations 133−137). These compounds contain essentially covalent I–O bonds. Preparative routes are shown as followings. These compounds are very sensitive to moisture and are not stable much above room temperature. They are hydrolyzed with disproportion of the I^{3+}, as shown for IPO_4 (equation 138).

$$2\mathrm{I_2} + 3\mathrm{AgClO_4} \longrightarrow \mathrm{I(OClO_3)_3} + 3\mathrm{AgI} \quad (133)$$

$$\mathrm{I_2} + 6\mathrm{ClOClO_3} \longrightarrow 2\mathrm{I(OClO_3)_3} + 3\mathrm{Cl_2} \quad (134)$$

$$\mathrm{CsI} + 4\mathrm{ClOClO_3} \longrightarrow \mathrm{Cs[I(OClO_3)_4]} + 2\mathrm{Cl_2} \quad (135)$$

$$\mathrm{I_2} + \mathrm{HNO_3(fuming)} + \mathrm{(CH_3CO)_2O} \longrightarrow \mathrm{I(OCOCH_3)_3} \quad (136)$$

$$\mathrm{I_2} + \mathrm{HNO_3(conc)} \longrightarrow \mathrm{IPO_4} \quad (137)$$

$$5\mathrm{IPO_4} + 9\mathrm{H_2O} \longrightarrow \mathrm{I_2} + \mathrm{HNO_3} + 5\mathrm{H_3PO_4} \quad (138)$$

The structure of $I(OCOMe)_3$ is T-shaped as expected with three primary I–O–C bonds and longer I–O interactions. In $[Bu_4N][I(OTeF_5)_4]$, the anion has a square IO_4 unit.

8.3 Pentavalent Iodine

Iodooxo compounds are formed through the disproportionation of iodoso compounds (equation 139). These can also be prepared by oxidation of iodoso compounds with aqueous hypochlorite solution. In the solid state, these are rather unstable and detonate on heating or shock. They hydrolyze in water to form a base (equation 140), which, in a cold alkaline solution, can form a diphenyliodyl hydroxide (equation 138).

$$2\mathrm{ArIO} \longrightarrow \mathrm{ArIO_2} + \mathrm{ArI} \qquad (139)$$

$$\mathrm{ArIO_2} + 2\mathrm{H_2O} \longrightarrow [\mathrm{H_3O}]^+ + [\mathrm{ArIO_2(OH)}]^- \qquad (140)$$

$$2[\mathrm{PhIO_2(OH)}]^- \longrightarrow [\mathrm{Ph_2IO}]^+[\mathrm{OH}]^- + [\mathrm{IO_3}]^- + \mathrm{OH}^- \qquad (141)$$

Adding acetic or trifluoroacetic acid to such a solution forms the salts of these acids. From such salts, other diphenyliodyl salts can be obtained, such as $[\mathrm{Ph_2IO}]^+\mathrm{X}^-$ ($\mathrm{X} = \mathrm{F}$, Cl, Br, $\mathrm{IO_3}$). The structures of these compounds have been determined by IR spectra to be ionic. The iodine (V) compound with a chelating polydentate nitrogen ligand, $[\mathrm{PhI(O)(2,2'\text{-}bipy)}](\mathrm{Otf})_2$ has been reported.**[81]** The use of $\mathrm{I_2O_5}$ and $\mathrm{HIO_3}$ has been demonstrated for the mild and atom-efficient dehydrogenation of a wide range of substrates. When either of these compounds are added to DMSO, 1:1 complexes (**3** and **4**) are formed, which are mild and efficient oxidants and can be used for dehydrogenation of aldehydes and ketones.**[82]** Reacting $\mathrm{ArIO_2}$ with AHF or with $\mathrm{SF_4}$ can yield fluoro derivatives such as $\mathrm{ArIOF_2}$ and $\mathrm{ArIF_4}$ respectively.

9 RELATED ARTICLES

Fluorine: Inorganic Chemistry; Hypervalent Compounds; Periodic Table: Trends in the Properties of the Elements.

10 REFERENCES

1. A. J. Downs and C. J. Adams, in ‘Comprehensive Inorganic Chemistry’, eds. J. C. Bailar Jr, H. J. Emeleus, R. Nyholm, and A. F. Trotman-Dickenson, Pergamon Press, Oxford, 1973, Vol. 2, Chap. 26.
2. V. Gutmann, ed., ‘Halogen Chemistry’, Academic Press, New York, 1967, Vols. 1–3.
3. N. N. Greenwood and A. Earnshaw, ‘Chemistry of the Elements’, Pergamon Press, Oxford, 1984, Chap. 17, p. 920.
4. F. A. Cotton, G. Wilkinson, C. A. Murillo, and M. Bochmann, ‘Advanced Inorganic Chemistry’, 6th edn., Wiley-Interscience, New York, 1999, Part 2, p. 547.
5. G. D. Enright, C. I. Ratcliffe, and J. A. Ripneester, *J. Am. Chem. Soc.*, 1997, **119**, 11481.
6. E. L. Rimer, R. D. Bailey, T. W. Hanks, and W. T. Pennington, *Chem. Eur. J.*, 2000, **6**, 4071.
7. P. D. Boyle, S. E. Davidson, S. M. Godfrey, and R. G. Pritchard, *Inorg. Chim. Acta*, 2001, **325**, 211.
8. V. A. Vasiyev, S. V. Lindeman, and J. K. Kochi, *Chem. Commun.*, 2001, 909.
9. T. Drews, R. Marx, and K. Seppelt, *Chem. Eur. J.*, 1996, **2**, 1303.
10. M. Acra, D. A. Devillanova, A. Garau, F. Isaia, V. Lippolis, G. Verani, and F. Demartin, *Z. Anorg. Allg. Chem.*, 1998, **624**, 745.
11. F. A. Cotton, E. V. Dikarev, and M. A. Petruhina, *Angew. Chem., Int. Ed.*, 2000, **39**, 2362.
12. M. Berkei, J. F. Bickley, B. T. Heaton, and A. Steiner, *Chem. Commun.*, 2002, 2180.
13. M. B. Jacobs, ‘The Analytical Toxicology of Industrial Poisons’, Interscience, New York, 1967.
14. D. S. Payne, in ‘Non-aqueous Solvent Systems’, ed. T. C. Waddington, Academic Press, London, 1965, Chap. 8, p. 301.
15. L. Stein, in ‘Halogen Chemistry’, ed. V. Gutmann, Academic Press, New York, 1967, Vol. 1, p. 133.
16. H. Meinert, *Z. Chem.*, 1967, **7**, 41.
17. R. Boese, A. D. Boese, D. Blaser, M. Yu. Antipin, A. Ellern, and K. Seppelt, *Angew. Chem. Int. Ed.*, 1997, **36**, 1489.
18. S. Hoyer and K. Seppelt, *Angew. Chem. Int. Ed.*, 2000, **39**, 1448.
19. J. Shamir, *Struct. Bonding*, 1979, **37**, 141.
20. R. J. Gillespie and M. J. Morton, *Q. Rev. Chem. Soc.*, 1971, **25**, 553.
21. B. D. Stepin, *Russ. Chem. Rev.*, 1987, **56**, 726.
22. K. O. Christe, X. Zhang, J. A. Sheehy, and R. Bau, *J. Am. Chem. Soc.*, 2001, **123**, 6338.
23. A. Vij, F. S. Tham, V. Vij, W. W. Wilson, and K. O. Christe, *Inorg. Chem.*, 2002, **41**, 6397.
24. J. Shamir, *Israel J. Chem.*, 1978, **17**, 37.
25. A. I. Popov, in ‘Halogen Chemistry’, ed. V. Gutmann, Academic Press, New York, 1967, Vol. 1, p. 225.
26. A. A. Opalovskii, *Russ. Chem. Rev.*, 1967, **36**, 711.
27. R. Minkwitz and M. Berkei, *Z. Naturforsch, Teil B*, 2001, **56**, 39.
28. A. J. Blake, V. Lippolis, S. Parsons, and M. Schröder, *Acta Crystallogr., Sect. C*, 1998, **54**, 293.
29. K. F. Tebbe and R. Loukili, *Z. Anorg. Allg. Chem.*, 1998, **624**, 1175.
30. A. J. Blake, R. O. Gould, W. S. Li, V. Lippolis, S. Parsons, C. Radek, and M. Schröder, *Inorg. Chem.*, 1998, **37**, 5070.
31. L. J. Farrugia, N. C. Norman, and N. L. Pickett, *Acta Crystallogr., Sect. C*, 1998, **54**, 476.
32. E. S. Lang and J. Strahle, *Z. Anorg. Allg. Chem.*, 1996, **622**, 1323.

33. C. Tejel, M. Bordonaba, M. A. Ciriano, A. J. Edwards, W. Clegg, and F. J. Lahoz, *Inorg. Chem.*, 1999, **38**, 1108.

34. E. Seppela, F. Ruthe, J. Feske, W. W. DuMont, and P. G. Jones, *Chem. Commun.*, 1999, 1471.

35. R. Richter, O. Seidelmann, and L. Beyer, *Z. Anorg. Allg. Chem.*, 1999, **625**, 511.

36. R. Loukili and K. F. Tebbe, *Z. Anorg. Allg. Chem.*, 1999, **625**, 650.

37. K. F. Tebbe and R. Louklli, *Z. Anorg. Allg. Chem.*, 1999, **625**, 820.

38. K. F. Tebbe and R. Louklli, *Z. Anorg. Allg. Chem.*, 1998, **624**, 671.

39. A. J. Blake, W. S. Li, V. Lippolis, and M. Schröder, *Acta Crystallogr., Sect. C*, 1998, **54**, 1410.

40. A. J. Blake, R. O. Gould, W. S. Li, V. Lippolis, S. Parsons, C. Radek, and M. Schröder, *Angew. Chem. Int. Ed.*, 1998, **37**, 293.

41. A. Grafe-Kavoosian, S. Nafepour, K. Nagel, and K. F. Tebbe, *Z. Naturforsch., Teil B*, 1998, **53**, 641.

42. C. Wieczorrek, *Acta crystallogr., Sect. C*, 2000, **56**, 1082.

43. A. J. Blake, V. Lippolis, S. Parsons, and M. Schröder, *Chem. Commun.*, 1996, 2207.

44. K. F. Tebbe and M. Essawi, *Z. Anorg. Allg. Chem.*, 1998, **624**, 1046.

45. S. Menon and M. V. Rajasekharan, *Inorg. Chem.*, 1997, **36**, 4983.

46. K. F. Tebbe and T. Gilles, *Z. Anorg. Allg. Chem.*, 1996, **622**, 138.

47. K. F. Tebbe and T. Farida, *Z. Naturforsch., Teil B*, 1995, **50**, 1440.

48. P. H. Svensson, G. Raud, and L. Kloo, *Eur. J. Inorg. Chem.*, 2000, 1275.

49. T. Grob, F. Weller, and K. Dehnicke, *Z. Naturforsch., Teil B*, 1998, **53**, 552.

50. K. F. Tebbe and R. Buchem, *Angew. Chem., Int. Ed.*, 1997, **36**, 1345.

51. Y. Q. Wang, Z. M. Wang, C. S. Liao, and C. H. Yan, *Acta Crystallogr., Sect. C*, 1999, **55**, 1503.

52. C. T. McElroy, C. A. McLinden, and J. C. Schmeck, *Angew. Chem. Int. Ed.*, 1999, **38**, 2594.

53. A. J. Blake, L. M. Gibby, R. O. Dould, V. Lippolis, S. Parsons, and M. Schröder, *Acta Crystallogr., Sect. C*, 1998, **53**, 295.

54. M. El Essawii, K. F. Tebbe, *Z. Naturforsch., Teil B*, 1998, **53**, 263.

55. R. Minkwitz, M. Berkei, and R. Ludwig, *Inorg. Chem.*, 2001, **40**, 25.

56. M. E. Peach and T. C. Waddington, in 'Non-aqueous Solvent Systems', ed. T. C. Waddington, Academic Press, London, 1965, Chap. 3, p. 83.

57. H. H. Hyman and J. J. Katz, in 'Non-aqueous Solvent Systems', ed. T. C. Waddington, Academic Press, London, 1965, Chap. 2, p. 47.

58. R. Minkwitz, R. Bochler, and H. Borrmann, *Z. Kristallogr.*, 1998, **213**, 237.

59. M. H. Harwood, D. M. Rowley, R. A. Freshwater, R. A. Cox, and R. L. Jones, *J. Chem. Soc., Faraday Trans.*, 1995, **91**, 4189.

60. H. Grothe and H. Willner, *Angew. Chem., Int. Ed.*, 1996, **35**, 768.

61. D. Leopold and K. Seppelt, *Angew. Chem. Int. Ed.*, 1994, **33**, 975.

62. L. T. Chu and Z. Li, *Chem. Phys. Lett.*, 2000, **330**, 68.

63. I. C. Hwang, R. Kuschel, and K. Seppelt, *Z. Anorg. Allg. Chem.*, 1997, **623**, 379.

64. K. Seppelt, *Acc. Chem. Res.*, 1997, **30**, 111.

65. H. Fjellvag and A. Kjekshus, *Acta Chem. Scand.*, 1994, **48**, 815.

66. T. Kraft and M. Jansen, *J. Am. Chem. Soc.*, 1995, **117**, 6795.

67. T. Drews, W. Koch, and K. Seppelt, *J. Am Chem. Soc.*, 1999, **121**, 4379.

68. F. Solymosi, 'Structure and Stability of Salts of the Halogen Oxyacids in the Solid Phase', Wiley, New York, 1978.

69. R. Minkwitz, M. Berkei, and R. Ludwig, *Inorg. Chem.*, 2001, **40**, 6493.

70. A. Ellern, J. A. Boatz, K. O. Christe, T. Drews, and K. Seppelt, *Z. Anorg. Allg. Chem.*, 2002, **628**, 1991.

71. R. Minkwitz and M. Berkei, *Eur. J. Inorg. Chem.*, 2001, 457.

72. T. Kraft and M. Jansen, *Angew. Chem. Int. Ed.*, 1997, **36**, 1753.

73. R. I. Wagner, R. Bau, R. Z. Gnann, P. F. Hjones, and K. O. Christe, *Inorg. Chem.*, 1997, **36**, 2564.

74. R. Nagel, M. Botova, G. Pracht, E. Suchanek, M. M. Maneva, and H. D. Lutz, *Z. Naturforsch., Teil B*, 1999, **54**, 999.

75. A. L. Hector, W. Levason, and M. Webster, *J. Chem. Soc., Dalton Trans.*, 1998, 3463.

76. D. Dolenc and B. P. Plesnicar, *J. Am. Chem. Soc.*, 1997, **119**, 2628.

77. W. S. Hua, S. I. Ajiboye, G. Haining, L. McGhee, R. D. Peacock, G. Peattie, R. M. Siddique, J. M. Winfield, *J. Chem. Soc., Dalton Trans.*, 1995, 3837.

78. P. K. Gowik and T. M. Klapotke, *J. Chem. Soc., Chem. Commun.*, 1990, 1433.

79. A. Loewenschuss, R. J. Mureinik, and J. Shamir, *Spectrochim. Acta*, 1977, **33A**, 183.

80. V. Montannari, D. D. desMarteau, and W. T. Pennington, *J. Mol. Struct.*, 2000, **550**, 337.

81. V. V. Zhdankin, A. Y. Koposov, and N. V. Yashin, *Tetrahedron Lett.*, 2002, **43**, 5735.

82. K. C. Nicolaon, T. Montagnon, and P. S. Baran, *Angew. Chem. Int. Ed.*, 2002, **43**, 5735.

Chromium: Biological Relevance

John B. Vincent
The University of Alabama, Tuscaloosa, AL, USA

1 Introduction 1
2 Glucose Tolerance Factor 1
3 Chromodulin (Low-molecular-weight Chromium-binding Substance) 1
4 Chromium Picolinate and Toxicity 3
5 Chromium Therapeutic Agents and Type 2 Diabetes 4
6 Chromate Toxicity 4
7 Related Articles 5
8 References 5

1 INTRODUCTION

Of the transition elements proposed to be an essential trace element for mammals, Cr is probably the least understood. The evidence for an essential role for Cr is suggestive,[1] but not conclusive. Four lines of evidence are usually used in support of an essential role. The first evidence comes from studies in the 1990s of rats fed a purified, Cr-deficient diet (33 ng Cr/g diet). In glucose tolerance tests, these rats had elevated insulin areas compared to controls, suggesting the onset of insulin resistance.[2] Unfortunately, similar studies before 1990, including the classic studies by Mertz that originally led to the proposal that Cr was essential, have methodological problems that hinder interpretation.[1] Second, Cr absorption by humans is inversely proportional to intake, suggesting that intake is regulated.[3] However, this is not the case for rats.[4] Next, five cases of Cr deficiency in humans have been reported.[5] The subjects were all on total parenteral nutrition (TPN), developed symptoms similar to those of type 2 diabetes, and did not respond to insulin treatment. However, the symptoms were reversed upon the addition of Cr to the TPN. The limited number of patients, the range of blood Cr concentrations of patients, and the varying symptoms have led to questions about these cases.[6] Finally, urinary Cr loss is directly related to blood serum insulin concentrations.[7] Increases in serum insulin (as would result from increases in serum glucose) result in increases in urinary Cr excretion. Similarly, conditions that alter glucose metabolism (such as type 2 diabetes) alter urinary Cr output. Thus, a relationship appears to exist between glucose metabolism, insulin levels, and Cr mobilization in the body.[8] Fortunately, Cr deficiency is difficult to develop. Recently, the Food and Nutrition Board of the National Academy of Sciences has lowered the daily adequate intake (AI) of Cr from 50–200 µg to 25 µg for women and 35 µg for men.[9] These values reflect the average daily intake of Cr for Americans,[3] suggesting that few Americans have Cr-deficient diets. Nutritional studies have been hampered by the lack of a biomarker for Cr status. While Cr as the chromic ion may be essential, Cr in the 6+ oxidation state, in contrast, is a potent carcinogen and is present in the environment primarily as a result of human activity.

2 GLUCOSE TOLERANCE FACTOR

For Cr to be essential, chromic ions presumably must bind to some biomolecule(s) and the resulting complex must have an inherent function. The first Cr-containing species to be proposed as this molecule was glucose tolerance factor (GTF).[10] GTF was originally extracted from porcine kidney powder and Brewer's yeast and was the subject of considerable research in the 1960s and 1970s. The species was believed to be a complex of nicotinate and amino acids and to bind to insulin, enhancing insulin's binding to the insulin receptor. However, since this time, several groups have separated the Cr-containing species in the yeast extracts from the insulin-stimulating factor, and GTF has been shown to be an artifact of its isolation procedure. Recently, a suggestion has been made to drop the use of the term GTF.[1]

3 CHROMODULIN (LOW-MOLECULAR-WEIGHT CHROMIUM-BINDING SUBSTANCE)

The best candidate for a biologically active form of Cr is the oligopeptide chromodulin, formerly known as low-molecular-weight Cr-binding substance (LMWCr). Yamamoto, Wada, and coworkers have demonstrated that isolated rat adipocytes in the presence of chromodulin and insulin display an increased ability to metabolize glucose; this increase occurs without a change in the insulin concentration required for half-maximal stimulation,[11,12] suggesting a role for chromodulin inside the insulin-sensitive cells after insulin binds externally to the insulin receptor.[13] The stimulation of glucose metabolism by chromodulin is proportional to its chromium content.[14]

Chromodulin is a naturally occurring oligopeptide composed of glycine, cysteine, aspartate, and glutamate with the carboxylates comprising more than half of the total amino acid residues.[12,14] The lack of a published sequence is a matter of concern. Despite its small size, the molecule has been shown to tightly bind four equivalents of chromic ions. The binding is quite tight ($K \sim 10^{21}\,M^{-4}$) and highly cooperative (Hill coefficient 3.47).[15] Spectroscopic studies suggest that the chromic ions comprise an anion-bridged multinuclear assembly supported by carboxylates from the oligopeptide.[16] Three of the Cr centers are arranged in an unsymmetric trinuclear assembly with the fourth mononuclear center in close proximity.[17] As holochromodulin can be prepared simply by addition of chromic ions to solutions of apochromodulin, these anionic bridges are probably hydroxide ions.[13,18,19] To date, the oligopeptide has been isolated and purified from mammalian liver (rabbit and bovine)[12,14] and kidney (porcine).[20] A related Cr-containing oligopeptide from bovine colostrum is composed of the same amino acids but in distinctly different ratios and also stimulates insulin-dependent glucose metabolism in rat adipocytes.[12] The significance of these differences remains unexplored, and the possibility that several low-molecular-weight, carboxylate-rich peptides exist for the binding of Cr is in need of investigation. Chromodulin appears to be maintained in the cytosol[21] and nucleus[22] of insulin-sensitive cells in the apo form. The oligopeptide is isolated as the holo-oligopeptide (so that it may be followed in the purification schemes by its Cr content), which means that an in vivo or in vitro Cr-loading step is required.[12,14] This observation and others have resulted in the suggestion that chromodulin may play a role in Cr detoxification; however, injection of chromic ions or chromate into mice does not stimulate the production of apochromodulin.[21] Thus, while chromodulin does carry Cr into the urine after intake of large dosages of Cr^{III} or Cr^{VI} and can serve to efficiently remove Cr,[22] the suggested detoxification role of chromodulin is unlikely to be its primary function.

Because the primary events between insulin binding to its receptor and glucose transport are signal transduction events, a role for chromodulin in these events has been probed. Chromodulin activates the tyrosine kinase activity of insulin-activated insulin receptor[18] and activates a membrane phosphotyrosine phosphatase in adipocyte membranes.[19] The addition of bovine liver chromodulin to rat adipocytic membranes in the presence of insulin results in a concentration-dependent eightfold stimulation of insulin-dependent protein tyrosine kinase activity (while no activation

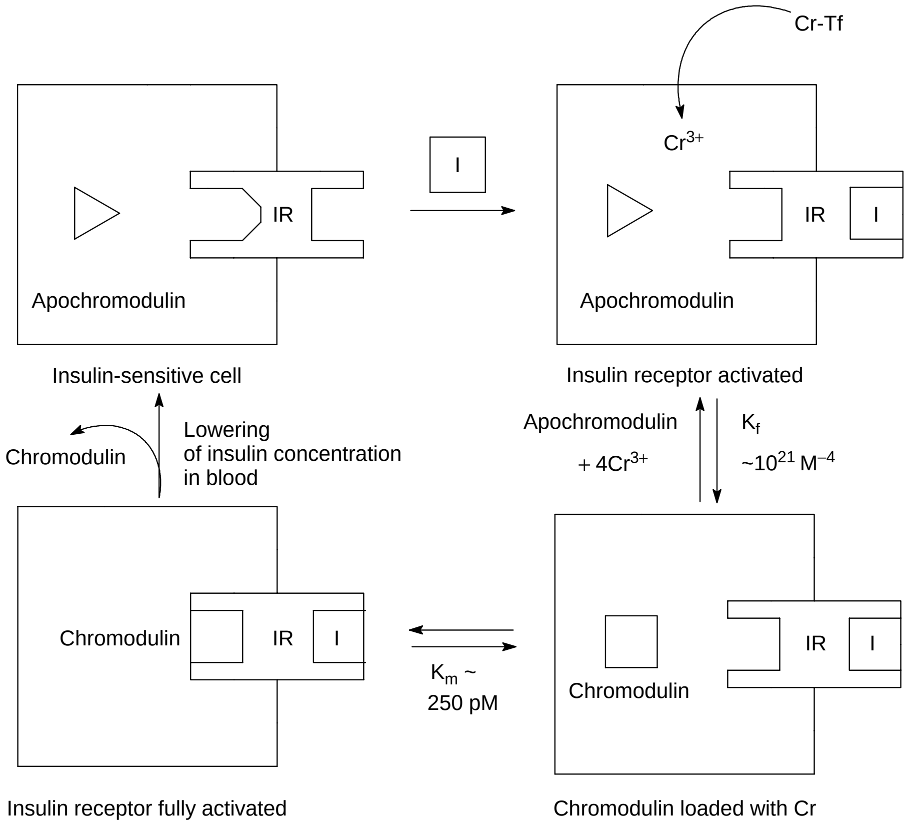
Cr-Tf
I
Cr^{3+}
IR
IR
I
Apochromodulin
Apochromodulin
Insulin-sensitive cell
Insulin receptor activated
Chromodulin
Lowering of insulin concentration in blood
Apochromodulin + $4Cr^{3+}$
K_f ~$10^{21}\,M^{-4}$
Chromodulin
IR
I
K_m ~ 250 pM
IR
I
Chromodulin
Insulin receptor fully activated
Chromodulin loaded with Cr

Figure 1 Proposed mechanism for the activation of insulin receptor kinase activity by chromodulin. The inactive form of insulin receptor (IR) is converted to the active form by binding insulin (I). This triggers a movement of Cr (in the form of Cr-transferrin, Cr-Tf) from the blood into cells, which in turn results in the binding of Cr to apochromodulin (triangle). Finally, holochromodulin (square) binds to insulin receptor, further activating the receptor's kinase activity. When the insulin concentration drops, holochromodulin is released from the cell to relieve its effects. (Ref. 1. Reproduced by permission of Elsevier)

of kinase activity is observed in the absence of insulin) with a dissociation constant of approximately 875 pM.[18] Blocking the insulin-binding site on the external α subunit results in the loss of the ability to activate insulin receptor kinase activity.[16] Isolated rat insulin receptor's kinase activity is activated by bovine chromodulin in the presence of insulin by approximately sevenfold, conclusively demonstrating that the receptor is the site of interaction with chromodulin. Similarly, studies with a catalytically active fragment (residues 941–1343) of the β subunit of human insulin receptor reveal that chromodulin can stimulate the kinase activity threefold. Thus, chromodulin appears to bind at or near the kinase active site.[23] Cr plays a crucial role in the activation of insulin receptor kinase activity by chromodulin.[18] Apochromodulin does not activate the receptor's insulin-dependent tyrosine kinase activity. However, titration of apochromodulin with chromic ions results in the total restoration of the ability to activate kinase activity; $\sim$ 4 chromic ions per oligopeptide are required for maximal activity, consistent with the number of Cr bound to an isolated holochromodulin. This reconstitution of chromodulin's activation potential is specific to Cr. Transition metal ions other than Cr that are commonly associated with biological systems are ineffective in potentiating the ability of apochromodulin to activate kinase activity. Thus, the ability of chromodulin to potentiate the effects of insulin is specific to Cr and is directly dependent on the Cr content of chromodulin.

On the basis of these results, chromodulin has been proposed to function as part of a unique autoamplification system for insulin signaling (Figure 1).[24] In this mechanism, apochromodulin is stored in insulin-sensitive cells. In response to increases in blood insulin concentrations, insulin binds to its receptor, bringing about a conformation change that results in the autophosphorylation of tyrosine residues on the internal side of the receptor. This transforms the receptor into an active kinase and transmits the signal from insulin into the cell. In response to insulin, Cr, stored in the blood plasma bound to the iron-transport protein transferrin (*see* ***Iron Proteins for Storage & Transport & their Synthetic Analogs***), is moved from the blood into cells via endocytosis.[25] The Cr flux results in loading of apochromodulin with Cr. The holochromodulin then binds to the insulin receptor, presumably assisting to maintain the receptor in its active conformation, amplifying its kinase activity. When insulin signaling is to be turned off, a drop in blood insulin levels facilitates relaxation of the conformation of the receptor, and the holochromodulin is excreted from the cell into the blood. Ultimately, chromodulin is excreted in the urine. The basis of the name chromodulin is the similarity of the proposed mechanism to that of the calcium-binding protein calmodulin.[26] Both bind four equivalents of metal ions in response to a metal ion flux; however, the four Ca ions that bind to the larger protein calmodulin rest in mononuclear sites. Both holoproteins selectively bind to kinases and phosphatases, stimulating their activity.

4 CHROMIUM PICOLINATE AND TOXICITY

After the first studies that suggested the nutritional supplement chromium picolinate, $[Cr(pic)_3]$, could have potentially beneficial effects on body mass and composition appeared in 1989,[27] the nutritional supplement has become amazingly popular; products containing the supplement generated nearly one-half billion dollars in sales in 1999, making the mineral supplement second only to Ca supplements.[28] Yet, studies of $[Cr(pic)_3]$ on healthy individuals since the initial reports have failed to support the early findings. This has resulted in a 'high degree of politicization and polarization apparent in this field... characterized by unproven claims and counterclaims and suspicion among investigators. Concerns about possible commercial interest have naturally emerged.'[29] Recent review articles[1,30–33] and meta-analyses[34–36] have concluded that the supplement has no demonstrated effects (body mass, body composition, or plasma glucose and insulin concentrations) on healthy individuals, even when taken in combination with an exercise program. Yet, six years after the initial report of potentially beneficial effects from $[Cr(pic)_3]$ supplementation, Wetterhahn and coworkers first reported potential concerns over the use of $[Cr(pic)_3]$.[37] The compound generated clastogenic damage in a Chinese hamster ovary (CHO) cell model. Stohs and coworkers have demonstrated similar damage and oxidative damage in murine macrophages.[38,39] Stearns, in continuing work with the CHO model, has observed mitochondrial damage and apoptosis generated by the supplement[40] and has reported that the supplement is mutagenic.[41]

The effects have been postulated to arise from the released picolinate ligand[37,40] or from reactive oxygen species catalytically generated by the intact complex.[15,42] Physiologically relevant concentrations of Cr as $[Cr(pic)_3]$ (e.g. 120 nM) and of biological reducing agents such as ascorbic acid and thiols resulted in catalytic production of reactive oxygen species, which cleaved DNA.[15,42] Most forms of Cr^{III} do not generate such species in the absence of a strong oxidant such as peroxide.[43] Hence, these studies are consistent with investigations that demonstrated that mutagenic forms of Cr^{III} possessed chelating ligands containing pyridine-type nitrogens or other imine nitrogens coordinated to the metal and generated reactive oxygen species.[44] Consequently, for this mechanism to lead to significant cell damage, $[Cr(pic)_3]$ needs to enter cells intact and remain intact long enough to produce a significant quantity of reactive oxygen species. Recently, $[Cr(pic)_3]$ has been shown to be able to rapidly pass from the bloodstream and enter cells intact, although the lifetime of the complex in cells is short.[45] In hepatocytes, Cr from [Cr(pic)$_3$] first appears in the nucleus and mitochondria, then the cytosol, and finally the lysosomes and microsomes; however, the complex has no propensity to bind to DNA. Kelley and coworkers have found that hepatocyte microsomes can catalytically modify the picolinate ligands, which would result in Cr release.[46]

Isolated incidents of deleterious effects of [Cr(pic)$_3$] supplementation have been reported.[30] The nature of these incidents makes their significance difficult to ascertain. In contrast, Anderson *et al.*[47] fed rats diets containing up to 100-mg Cr as [Cr(pic)$_3$] per kg diet for 24 weeks; no acute toxic effects were observed. No toxic effects of [Cr(pic)$_3$] supplementation were noted in any of the studies from the review articles mentioned previously, which combined monitored hundreds of subjects.[1,30] No study has yet to examine the effects, positive or negative, of the long-term use of [Cr(pic)$_3$]. Animal studies looking for DNA damage and oxidative damage have started to appear. No effect on 5-hydroxymethyl uracil levels have been observed in 10 obese women who were given 400-μg [Cr(pic)$_3$] (50-μg Cr) per day for 8 weeks.[48] In contrast, rats given [Cr(pic)$_3$] daily by intravenous injection for 60 days have elevated levels of urinary 8-hydroxydeoxyguanosine and peroxidized lipids.[49] Potentially deleterious in vivo effects of [Cr(pic)$_3$] have recently been examined using *Drosophila melanogaster*.[50] [Cr(pic)$_3$], but not CrCl$_3$, at levels of 260-μg Cr/kg food or less were found to lower the success rate of pupation and eclosion and to arrest development of pupae in a concentration-dependent fashion. X-linked lethal analysis indicated that the supplement greatly enhances the rate of appearance of lethal mutations and of dominant female sterility.

5 CHROMIUM THERAPEUTIC AGENTS AND TYPE 2 DIABETES

While Cr supplementation of the diet of healthy humans appears to have no statistically significant effects, the effects of Cr on type 2 diabetic subjects are still an area of debate. The administration of pharmacological, rather than nutritional, amounts of Cr could potentially result in beneficial effects, especially for subjects with altered metabolisms that could potentially lead to altered Cr status. A recent meta-analysis of studies with diabetic subjects revealed that the combined data from all placebo-controlled studies but one, the largest study, indicated no effect from Cr administration.[35] The largest study by Anderson and coworkers gave 155 subjects in China 0-, 200-, or 1000-μg Cr daily for 4 months.[51] At the highest Cr dosage, subjects had reduced fasting serum glucose, insulin, and total cholesterol and lower 2-h insulin and glucose concentrations after a glucose challenge. Subjects also possessed lower HbA$_{1c}$ levels. Anderson has reviewed studies on the effects of Cr administration on type 2 diabetics;[52,53] only studies using $\leq$200-μg Cr daily reported no effects from supplementation, suggesting that larger quantities of Cr are required for beneficial effects on type 2 diabetics. Significantly, the studies using $>$200-μg Cr per day are supported by studies on model rats.[54–56] Thus, continued rat and human studies are required to further elucidate the potential use of Cr administration as an adjuvant therapy for type 2 diabetes.

The existence of a multinuclear Cr^{III} carboxylate assembly in an active biomolecule has spurred an interest in the synthesis and characterization of multinuclear oxo(hydroxo)-bridged Cr^{III} carboxylate assemblies.[1] Well-characterized, water-soluble assemblies have been tested for the ability to stimulate insulin receptor's tyrosine kinase ability in a fashion similar to chromodulin. The trinuclear cation $[\mathrm{Cr}_3^{III}\mathrm{O}(\mathrm{O}_2\mathrm{CCH}_2\mathrm{CH}_3)_6(\mathrm{H}_2\mathrm{O})_3]^+$ was found in vitro to mimic the ability of chromodulin to stimulate this activity.[23] The biomimetic cation remains intact after injection into the bloodstream and is taken up by cells intact.[57,58] After 24 weeks of intravenous administration (0–20-μg Cr/kg body mass) in healthy rats, the cation resulted in a concentration-dependent lowering of levels of fasting blood plasma LDL cholesterol, total cholesterol, triglycerides, and insulin and of two-hour plasma insulin and glucose levels after a glucose challenge.[54] Zucker obese rats (a model of the early stages of type 2 diabetes) after 24 weeks of supplementation (20μg kg^{-1}) had lower fasting plasma total, HDL, and LDL cholesterol; triglycerides; and insulin levels and lower two-hour plasma insulin levels. The lowering of plasma insulin concentrations with little effect on glucose concentrations suggests that the cation increases insulin sensitivity.

6 CHROMATE TOXICITY

Given its similarity to HPO$_4{}^{2-}$ and SO$_4{}^{2-}$, chromate, [Cr^{VI}O$_4$]$^{2-}$, is able to travel via nonspecific anion transporters across the plasma membrane. Once inside a cell, cellular enzymatic and other systems are capable of reducing the chromate to Cr^{V}, Cr^{IV}, and Cr^{III} species, which are generally nondiffusing and thus trapped inside the cells. The mechanisms of these processes have been a subject of intense research[59,60] as they are directly related to the carcinogenicity and mutagenicity of Cr^{VI} (recently brought to public attention by the movie *Erin Brockovich*). Cr^{VI} is a potent carcinogen when inhaled, although the potential carcinogenicity when taken orally is currently actively debated. In cells, cysteine, glutathione, and ascorbate are probably significant players in chromate reduction. Most recent studies have focused on Cr^{V} as the species primarily responsible for carcinogenic effects. The involvement of Cr^{V} carbohydrate complexes in chromate-derived DNA damage has been proposed;[60] however, further research is required to establish their significance. The ultimate reduction product, Cr^{III}, accumulates in the nucleus of cells and may form DNA protein and other cross-links; the deleterious potential of these cross-links is uncertain.

7 RELATED ARTICLES

Chromium: Inorganic & Coordination Chemistry; Nutritional Aspects of Metals & Trace Elements.

8 REFERENCES

1. J. B. Vincent, *Polyhedron*, 2001, **20**, 1.
2. J. S. Striffler, J. S. Law, M. M. Polansky, S. J. Bhathena, and R. A. Anderson, *Metabolism*, 1995, **44**, 1314.
3. R. A. Anderson and A. S. Kovlosky, *Am. J. Clin. Nutr.*, 1985, **41**, 1177.
4. R. A. Anderson and M. M. Polansky, *Biol. Trace Elem. Res.*, 1995, **50**, 97.
5. K. N. Jeejeebhoy, *Nutr. Rev.*, 1999, **57**, 329.
6. D. N. Stearns, *Biofactors*, 2000, **11**, 149.
7. B. W. Morris, S. MacNeil, K. Stanley, T. A. Gray, and R. Fraser, *J. Endocrinol.*, 1993, **139**, 339.
8. B. W. Morris, S. MacNeil, C. A. Hardisty, S. Heller, C. Burgin, and T. A. Gray, *J. Trace Elem. Med. Biol.*, 1999, **13**, 57.
9. P. Trumbo, A. A. Yates, S. Schlickek, and M. Poos, *J. Am. Diet. Assoc.*, 2001, **101**, 294.
10. W. Mertz, *Nutr. Rev.*, 1975, **33**, 129.
11. A. Yamamoto, O. Wada, and H. Suzuki, *J. Nutr.*, 1988, **118**, 39.
12. A. Yamamoto, O. Wada, and T. Ono, *Eur. J. Biochem.*, 1987, **165**, 627.
13. J. B. Vincent, *J. Nutr.*, 1994, **124**, 117.
14. A. Yamamoto, O. Wada, and S. Manabe, *Biochem. Biophys. Res. Commun.*, 1989, **163**, 89.
15. Y. Sun, J. Ramirez, S. A. Woski, and J. B. Vincent, *J. Biol. Inorg. Chem.*, 2000, **5**, 129.
16. C. M. Davis and J. B. Vincent, *Arch. Biochem. Biophys.*, 1997, **339**, 335.
17. L. Jacquamet, Y. Sun, J. Hatfield, W. Gu, S. P. Cramer, G. A. Lorigan, J. B. Vincent, and J.-M. Latour, *J. Am. Chem. Soc.*, 2003, **125**, 774.
18. C. M. Davis and J. B. Vincent, *Biochemistry*, 1997, **36**, 4382.
19. C. M. Davis, K. H. Sumrall, and J. B. Vincent, *Biochemistry*, 1996, **35**, 12963.
20. K. H. Sumrall and J. B. Vincent, *Polyhedron*, 1997, **16**, 4171.
21. A. Yamamoto, O. Wada, and T. Ono, *J. Inorg. Biochem.*, 1984, **22**, 91.
22. B. J. Clodfelder, J. Emamaullee, D. D. D. Hepburn, N. E. Chakov, H. S. Nettles, and J. B. Vincent, *J. Biol. Inorg. Chem.*, 2001, **6**, 608.
23. C. M. Davis, A. C. Royer, and J. B. Vincent, *Inorg. Chem.*, 1997, **36**, 5316.
24. J. B. Vincent, *Acc. Chem. Res.*, 2000, **33**, 503.
25. J. B. Vincent, *J. Nutr.*, 2000, **130**, 715.
26. W. E. Meador, A. R. Means, and F. A. Quiocho, *Science*, 1992, **257**, 1251.
27. G. W. Evans, *Int. J. Biosoc. Med. Res.*, 1989, **11**, 163.
28. F. Mirasol, *Chem. Market Rep.* 2000, **257**, 2000.
29. M. K. Hellerstein, *Nutr. Rev.*, 1998, **56**, 302.
30. J. B. Vincent, *Sports Med.*, 2003, **33**, 213.
31. R. B. Kreider, *Sports Med.*, 1999, **27**, 97.
32. P. M. Clarkson, *Sports Med.*, 1997, **23**, 341.
33. H. C. Lukaski, *Annu. Rev. Nutr.*, 1999, **19**, 279.
34. S. L. Nissen and R. L. Sharp, *J. Appl. Physiol.*, 2003, **94**, 651.
35. M. D. Althius, N. E. Jordan, E. A. Ludington, and J. T. Wittes, *Am. J. Clin. Nutr.*, 2002, **76**, 148.
36. M. H. Pittler, C. Stevinson, and E. Ernst, *Int. J. Obes.*, 2003, **27**, 522.
37. D. M. Stearns, J. P. Wise Sr., S. R. Patierno, and K. E. Wetterhahn, *FASEB J.* 1995, **9**, 1643.
38. D. Bagchi, M. Bagchi, J. Balmoori, X. Ye, and S. J. Stohs, *Res. Commun. Mol. Pathol. Pharmacol.*, 1997, **97**, 335.
39. D. Bagchi, S. J. Stohs, B. W. Downs, M. Bagchi, and H. G. Preuss, *Toxicology*, 2002, **180**, 5.
40. K. R. Manygoats, M. Yazzie, and D. M. Stearns, *J. Biol. Inorg. Chem.*, 2002, **7**, 791.
41. D. M. Stearns, S. M. Silveira, K. K. Wolf, and A. M. Luke, *Mutat. Res.*, 2002, **513**, 135.
42. J. K. Speetjens, R. A. Collins, J. B. Vincent, and S. A. Woski, *Chem. Res. Toxicol.*, 1999, **12**, 483.
43. J. K. Speetjens, A. Parand, M. W. Crowder, J. B. Vincent, and S. A. Woski, *Polyhedron*, 1999, **18**, 2617.
44. K. D. Sugden, R. D. Geer, and S. G. Rogers, *Biochemistry*, 1992, **31**, 11626.
45. D. D. D. Hepburn and J. B. Vincent, *J. Inorg. Biochem.*, 2003, **94**, 86.
46. S. A. Kareus, C. Kelley, H. S. Walton, and P. C. Sinclair, *J. Hazard. Mater.*, 2001, **B84**, 163.
47. R. A. Anderson, N. A. Bryden, and M. M. Polansky, *J. Am. Coll. Nutr.*, 1997, **16**, 273.
48. I. Kato, J. H. Vogelman, V. Dilman, J. Karkoszka, K. Frenkel, N. P. Durr, N. Orentreich, and P. Toniolo, *Eur. J. Epidemiol.*, 1998, **14**, 621.
49. D. D. D. Hepburn, J. M. Burney, S. A. Woski, and J. B. Vincent, *Polyhedron*, 2003, **22**, 455.
50. D. D. D. Hepburn, J. Xiao, S. Bindom, J. B. Vincent, and J. O'Donnell, *Proc. Natl. Acad. Sci. U.S.A.*, 2003, **100**, 3766.

51. R. A. Anderson, N. C. Cheng, N. A. Bryden, M. M. Polansky, N. Cheng, J. Chi, and J. Feng, *Diabetes*, 1997, **46**, 1786.
52. R. A. Anderson, *J. Am. Coll. Nutr.*, 1998, **17**, 548.
53. R. A. Anderson, *Diabetes Metab. (Paris)*, 2000, **26**, 22.
54. Y. Sun, B. J. Clodfelder, A. A. Shute, T. Irvin, and J. B. Vincent, *J. Biol. Inorg. Chem.*, 2002, **7**, 852.
55. Y. Sun, K. Mallya, J. Ramirez, and J. B. Vincent, *J. Biol. Inorg. Chem.*, 1999, **4**, 838.
56. W. T. Cefalu, Z. Q. Wang, X. H. Zhang, L. C. Baldor, and J. C. Russell, *J. Nutr.*, 2002, **132**, 1107.
57. A. A. Shute and J. B. Vincent, *J. Inorg. Biochem.*, 2002, **89**, 272.
58. A. A. Shute and J. B. Vincent, *Polyhedron*, 2001, **20**, 2241.
59. A. Levina, R. Codd, C. T. Dillion, and P. A. Lay, *Prog. Inorg. Chem.*, 2003, **51**, 145.
60. R. Codd, C. T. Dillion, A. Levina, and P. A. Lay, *Coord. Chem. Rev.*, 2001, **216–217**, 533.

Chromium: Inorganic & Coordination Chemistry

Klaus H. Theopold
University of Delaware, Newark, DE, USA

1	Introduction	1
2	The Element	1
3	Binary Compounds and Simple Salts	3
4	Coordination Compounds	5
5	Cr−Cr Bonds	12
6	Related Articles	13
7	References	13

Abbreviations

mhp = deprotonated 6-methyl-2-hydroxypyridine; THT = tetrahydrothiophene.

1 INTRODUCTION

The transition metal chromium has played a prominent role in the development of inorganic chemistry. Discovered in 1797 by the French chemist Louis N. Vauquelin in the rare mineral crocoite ($PbCrO_4$), it was named for the varied colors of its compounds (chroma ($\chi\rho\omega\mu\alpha$) = color). Chromium compounds exist in an unusually large number of formal oxidation states (−IV to +VI) (*see Oxidation Number*); however, only the +II to +VI states are accessible in water. Hexavalent chromium is a powerful oxidant and the use of chromium-based oxidants in organic synthesis[1–3] goes back well over a century (witness the Etard reaction of alkylbenzenes with chromyl chloride (CrO_2Cl_2), which was first described in 1880). Chromium(II), on the other hand, is strongly reducing, and by far the most stable oxidation state of the element is +III, giving rise to an extensive series of stable inorganic compounds.

The remarkable chemical and configurational stability of octahedral Cr^{III} complexes (*see Octahedral*) was responsible for their role in the groundbreaking work of Alfred Werner, the father of modern coordination chemistry (*see* ***Coordination Chemistry: History***). In the twentieth century, the same properties led to their use in studies of the reaction mechanisms of metal complexes. In recent years, the chemistry of the chromium−carbon bond has been the most active area of research in chromium chemistry (*see* ***Chromium: Organometallic Chemistry***), motivated in part by its importance in catalytic processes (notably ethylene polymerization).

2 THE ELEMENT

2.1 Occurrence

The only chromium ore of practical importance is chromite, a black spinel of the idealized composition $FeCr_2O_4$; in practice, it contains varying amounts of MgO, Al_2O_3, and SiO_2. Major producers of chromite include South Africa, Kazakhstan, India, and Turkey. Since 1900, the production of chromite has doubled roughly every decade, reaching an estimated 14.2 million tons in 1998. Chromium is more rarely found as the mineral crocoite ($PbCrO_4$) and minor amounts of the element occur in many other minerals. Traces of chromium ions are responsible for the color of emeralds ($Be_3Al_2Si_6O_{18}$) and rubies (Al_2O_3). At an average concentration of 100 ppm in the earth's crust, chromium ranks 21st in elemental abundance; its typical level in seawater is ca. 2×10^{-4} ppm.

2.2 Production and Uses[4]

The greater part (ca. 85%) of chromite ore production is reduced by heating with coal to give 'ferrochrome', used in the manufacture of alloy steels. Pure chromium metal for use in iron-free alloys and metal-containing ceramics is produced by reduction of Cr_2O_3. Common reducing agents are aluminum, carbon, or silicon. Another process involves the electrolysis of chrome alum ($NH_4Cr(SO_4)_2 \cdot 12H_2O$) solutions. CrO_3 solutions are employed in electroplating of chromium on other metals to impart wear resistance and for decorative purposes.

Less than 15% of the ore is transformed into chromium compounds, principally chromates, dichromates, chromium(VI) oxide, chromium(III) oxide, and so on. Alkaline oxidative roasting of chromite in rotary kilns yields sodium chromate (see equation 1), which is leached out with water and typically converted into sodium dichromate with sulfuric acid (equation 2) or carbon dioxide (equation 3). Further treatment of sodium dichromate with sulfuric acid yields chromium(VI) oxide ('chromic acid'), while its reduction (with carbon, sulfur, or ammonium salts) produces chromium(III) oxide. Finally, basic chromium(III) salts, for example $Cr(OH)SO_4$, which are used as tanning agents for animal hides, also result from reduction of sodium dichromate. Heterogeneous chromium catalysts are used for the polymerization of ethylene.

$$4FeCr_2O_4 + 4Na_2CO_3 + 7O_2 \xrightarrow{>1000\,^\circ C} 8Na_2CrO_4 + 2Fe_2O_3 + 8O_2 \quad (1)$$

$$2Na_2CrO_4 + H_2SO_4 \longrightarrow Na_2Cr_2O_7 + Na_2SO_4 + H_2O \quad (2)$$

$$2Na_2CrO_4 + H_2O + 2CO_2 \longrightarrow Na_2Cr_2O_7 + 2NaHCO_3 \quad (3)$$

2.3 Atomic Properties[5–7]

Chromium has the atomic number 24. Of the 13 known isotopes (mass numbers 45–57), four are stable, giving chromium the relative atomic mass 51.9961 ($^{12}C = 12.0000$). Table 1 lists the properties of some isotopes. ^{53}Cr may be used for NMR spectroscopy;[8] however, its relative receptivity (8.62×10^{-5}, $^{1}H = 1.00$), quadrupole moment ($4.1 \times 10^{-30}\,m^2$), and low resonance frequency (16.956 MHz, $^{1}H = 300$ MHz) pose experimental difficulties. Radioactive ^{51}Cr is used in medical tracer studies.

Chromium atoms have the ground-state electronic configuration $[Ar]3d^5 4s^1$, giving rise to the term symbol $^7S_3$. Its *Electron Affinity* is 64.3 kJ mol^{-1} (0.67 eV) and its first through sixth ionization potentials are 652.7 (6.764), 1592 (16.50), 2987 (30.95), 4740 (49.12), 6690 (69.33), and 8738 (90.55) kJ mol^{-1} (eV), respectively (*see Ionization Potential*).

2.4 Physical Properties

Solid chromium adopts a body-centered cubic structure and crystallizes in the space group *Im*3*m* with $a = 288.46$ pm; its density is 7.19 g cm^{-3} (at 293 K). The metal melts at 2130 (±20) K and boils at 2945 K; the corresponding enthalpies are $\Delta H_{\text{fusion}} = 15.3$ kJ mol^{-1} and $\Delta H_{\text{vap}} = 348.78$ kJ mol^{-1}. Values of various thermodynamic functions are listed in Table 2. Some other values are: thermal conductivity: 93.7 W m^{-1} K^{-1} (at 300 K), electrical resistivity: $12.7 \times 10^{-8}\,\Omega$ m (at 273 K), magnetic susceptibility: $+3.5 \times 10^{-6}$ cm^3 g^{-1} (ambient temperature), and linear coefficient of thermal expansion: 6.2×10^{-6} K^{-1}.

Table 1 Properties of chromium isotopes

Isotope	Atomic mass	Abundance (%)	Half-life	Decay mode	Nuclear spin
^{48}Cr			23 h	EC	
^{49}Cr			41.9 minutes	β^-	5/2
^{50}Cr	49.946046	4.35	Stable		–
^{51}Cr	50.944768		27.7 days	EC	7/2
^{52}Cr	51.940509	83.79	Stable		–
^{53}Cr	52.940651	9.50	Stable		3/2
^{54}Cr	53.938882	2.36	Stable		–
^{55}Cr			3.5 minutes	β^-	
^{56}Cr			5.9 minutes	β^-	

Table 2 Thermodynamic properties of chromium[a]

State	$\Delta H_f°$ (kJ mol^{-1})	$\Delta G_f°$ (kJ mol^{-1})	$S°$ (J K^{-1} mol^{-1})	C_p (J K^{-1} mol^{-1})
Solid	0.0	0.0	23.47	23.35
Gas	396.6	351.8	174.50	20.79

[a] $T = 298.15$ K; $P = 10^5$ Pa.

2.5 Chemical Properties

Chromium is fairly resistant to ordinary corrosive agents. However, at elevated temperatures it reacts with many elements, including the halogens, oxygen and sulfur, nitrogen, carbon, and boron. It dissolves readily in dilute HCl or H_2SO_4, but not in nitric acid, phosphoric acid, or even aqua regia. The oxidizing acids are thought to passivate the metal surface by formation of a thin protective oxide layer. Under certain conditions, this passivation layer may be formed and destroyed periodically, leading to oscillations in the hydrogen evolution upon dissolution of the metal. Nonpassivated chromium is a strong reducing agent; see equations (4) and (5).

$$Cr^{2+}(aq) + 2e^- \rightleftharpoons Cr(s) \qquad E° = -0.91\,V \tag{4}$$

$$Cr^{3+}(aq) + 3e^- \rightleftharpoons Cr(s) \qquad E° = -0.74\,V \tag{5}$$

The most common oxidation states of chromium in inorganic compounds are +II, +III, and +VI. By comparison, there are few stable compounds of tetravalent or pentavalent chromium; these oxidation states are largely represented by reactive intermediates in redox reactions. π-Acid ligands like CO (*see π-Acid Ligand*) stabilize chromium in very low formal oxidation states (down to −IV!). Table 3 lists oxidations states and coordination environments for representative chromium compounds.

2.6 Biological Properties[9–11]

Chromium(VI) compounds (e.g. dichromates, chromic acid, etc.) have long been known as skin irritants. Indeed, chromium has been shown to be one of the most important causes of occupational contact dermatitis. There is also strong evidence that chromium(VI) compounds are carcinogenic. Most of the available data comes from studies of occupationally exposed groups. There are no data linking cancer with chromium in the general environment.

Chromium(III), on the other hand, is an essential trace metal in mammalian nutrition, aiding in the metabolism of glucose (*see* ***Nutritional Aspects of Metals & Trace Elements***). The ‘adequate intake’ of chromium has been estimated as 25–35 µg day^{-1}. The ‘glucose tolerance factor’ (GTF) is a chromium containing extract of brewer’s yeast, which enhances the action of insulin. There is no evidence for any toxic effects of Cr^{III}.

Table 3 Formal oxidation states and stereochemistry of chromium compounds

Oxidation state	Coordination number	Coordination geometry	Examples
Cr^{-IV}	?	?	$Na_4[Cr(CO)_4]$
Cr^{-II}	?	?	$Na_2[Cr(CO)_5]$
Cr^{-I}	6	Octahedral	$Na_2[Cr_2(CO)_{10}]$
Cr^{0}	6	Octahedral	$Cr(CO)_6$, $Cr(bipy)_3$
Cr^{I}	6	Octahedral	$[Cr(NCR)_6]^+$
Cr^{II}	4	Square planar	$Cr(O_2CCF_3)_2(Me_2py)_2$
	4	Tetrahedral	$CrCl_2(MeCN)_2$
	4	Cis-divacant octahedral	$Tp^{t\text{Bu},\text{Me}}CrCl$
	4	Trigonal pyramidal	$[Na(THF)_2(N_3N)Cr]$
	5	Trigonal bipyramidal	$[CrBr\{N(CH_2CH_2NMe_2)_2\}_3]^+$
	6	Octahedral	$CrCl_2$, $[Cr(en)_3]^{2+}$
	7	Capped trigonal prism	$[Cr(CO)(diars)_2X]^+$
Cr^{III}	3	Trigonal planar	$Cr\{N(SiMe_3)_2\}_3$
	4	Tetrahedral	$[CrCl_4]^-$
	5	Trigonal bipyramidal	$CrCl_3(NMe_3)_2$
	6	Octahedral	$[Cr(NH_3)_6]^{3+}$, $[Cr(CN)_6]^-$
Cr^{IV}	4	Tetrahedral	$Cr(NEt_2)_4$, $Cr(O\text{-}t\text{-}Bu)_4$
	6	Octahedral	$[CrF_6]^{2-}$
	8	Dodecahedral	$CrH_4(dmpe)_2$
Cr^{V}	4	Tetrahedral	$[CrO_4]^{3-}$
	5	Square pyramidal	$[CrOCl_4]^-$
	6	Octahedral	$[CrOCl_5]^{2-}$
	8	Dodecahedral	$[Cr(\eta^2\text{-}O_2)_4]^{3-}$
Cr^{VI}	4	Tetrahedral	$[CrO_4]^{2-}$, CrO_2Cl_2

3 BINARY COMPOUNDS AND SIMPLE SALTS

3.1 Hydrides

The solubility of hydrogen in chromium metal increases with temperature. The existence of two discrete hydrides of stoichiometry CrH and CrH_2 with different structures had been suggested in the older literature; however, the existence of the latter was called into question. Recent experiments involving the reaction of Cr atoms with H_2 and *Matrix Isolation* of the products have provided spectroscopic evidence for the molecules CrH and CrH_2. Species with higher hydrogen content are now thought to be dihydrogen complexes, for example, $(H_2)CrH$, $(H_2)CrH_2$, and $(H_2)_2CrH_2$.[12]

3.2 Compounds with Elements of Groups 13–15

Chromium borides have been prepared by heating mixtures of chromium and boron or Cr_2O_3 and boron; another preparation employed electrolysis of molten oxides of both elements. A number of phases have been identified; their compositions are Cr_4B, Cr_2B, Cr_5B_3, CrB, Cr_2B_3, Cr_3B_4, and CrB_2 (*see* ***Borides: Solid-state Chemistry***).[13] Crystals of several phases have been grown from high-temperature Al solutions.[14] The chromium borides are refractory materials with high melting points and metallic character, for example, they exhibit electrical conductivity. They are resistant to chemical attack.

Chromium carbides have been produced by melting mixtures of chromium and graphite under vacuum or by heating Cr_2O_3 with C. Chromium metal reacts with CH_4 at 600–800 °C, forming carbides and H_2. Three different compounds have been identified, namely, $Cr_{23}C_6$, Cr_7C_3, and Cr_3C_2 (*see* ***Carbides: Transition Metal Solid-state Chemistry***). They are very hard and high melting.

Chromium silicides have been isolated, inter alia, from melts of chromium/silicon mixtures, from the reduction of Cr_2O_3/SiO_2 mixtures (e.g. with Al), and from the electrolysis of Na_2SiF_6/CrF_2 melts. Tentatively identified compounds include Cr_3Si, Cr_2Si, Cr_5Si_3, Cr_3Si_2, CrSi, and $CrSi_2$. All of these appear metallic and conduct electricity. They are hard and brittle, have high melting points, and are resistant to attack by acids.

Chromium nitrides have been prepared by several routes: heating of chromium metal in N_2, reaction of chromium borides with NH_3, and heating of $CrCl_3$ in gaseous NH_3. The two stable nitrides have the composition Cr_2N and CrN (*see* ***Nitrides: Transition Metal Solid-state Chemistry***). At very high temperatures, both decompose into the constituent elements (CrN, >1425 °C; Cr_2N, >700 °C). CrN is very stable chemically, while Cr_2N dissolves in dilute acid with liberation of H_2.

The chromium phosphides Cr_3P, Cr_2P, CrP, Cr_2P_3, and CrP_2 have been described in the literature (*see* ***Phosphides:***

Solid-state Chemistry). They were prepared by direct reaction of the elements.

3.3 Oxides and Sulfides

Of the chromium oxides, only Cr_2O_3, CrO_2, and CrO_3 are of significance.

Chromium(III) oxide (Cr_2O_3) is produced commercially by reduction of CrO_3. Other preparations include burning of chromium metal in O_2, thermal decomposition of CrO_3 or $(NH_4)_2Cr_2O_7$, and heating of the hydrous oxide ($Cr_2O_3{\cdot}nH_2O$) obtained by adding hydroxide to aqueous solutions of Cr^{III} ion. When prepared in the latter way, it is reactive and amphoteric (*see Amphoterism*); dissolution in acid reforms the purple $[Cr(OH_2)_6]^{3+}$ ion ($Cr^{III}(aq)$), while treatment with base yields dark green 'chromite' solutions, that is $[Cr(OH)_6]^{3-}$. Cr_2O_3 is a green solid, which begins to decompose before it reaches its melting point (ca. 2435 °C). It adopts the corundum structure, that is, a hexagonally close-packed array of oxide ions with two-thirds of the octahedral holes occupied by Cr^{III} ions (*see Close Packing*). It is a semiconductor (conductivity: $10^{-6}-10^{-7}\ \Omega^{-1}\ cm^{-1}$) and an antiferromagnet with a Néel temperature of ca. 50 °C.

Chromium(IV) oxide (CrO_2) is formed as an intermediate in the thermal decomposition of CrO_3. It is commercially prepared by hydrothermal treatment ($T = 250-500\,°C$, $P = 50-3000$ atm) of CrO_3. CrO_2 is a brown–black solid that decomposes to Cr_2O_3 upon heating to 250–500 °C. It has the rutile structure (slightly distorted hexagonal close packing of oxide ions with one half of the octahedral holes filled by Cr^{IV} ions). It exhibits metallic conductance and is ferromagnetic (*see Ferromagnetism*); the latter property leads to its use in magnetic recording tapes.

Chromium(VI) oxide (CrO_3, 'chromic acid') is made by treatment of dichromate (e.g. $Na_2Cr_2O_7$) with sulfuric acid. It is an orange–red solid with a melting point of only 197 °C. Upon heating it slowly loses oxygen, eventually yielding Cr_2O_3. The structure of the rather covalent oxide consists of chains of corner-sharing tetrahedra (*see Tetrahedral*). CrO_3 reacts vigorously with organic substances; it is widely used as an oxidant in synthetic organic chemistry.**[1,2]**

CrO_3 dissolves in base, forming yellow solutions of the tetrahedral chromate ion ($CrO_4{}^{2-}$) (**1**). Chromate is a weak base; upon lowering of the pH it forms $HCrO_4{}^-$ (pK_a 6.49) and eventually H_2CrO_4 (pK_a 0.74). The latter species are in equilibrium with the orange dichromate ion ($Cr_2O_7{}^{2-}$) (**2**) (equation 6). In strongly acidic media, further polymerization yields tri- and tetrachromates ($Cr_3O_{10}{}^{2-}$ and $Cr_4O_{13}{}^{2-}$), short chains of corner-sharing tetrahedra anticipating the structure of the end member CrO_3. A comparison of structural data for a series of mono- and polychromates showed a smooth correlation of the Cr–O distances with increasing degree of polymerization.**[15]** By comparison with the heavier Group 6 elements (Mo, W), chromium shows little tendency for the formation of ***Polyoxometalates***. This is probably due to its smaller size, favoring four over six coordination, and to the relative strength of the Cr=O multiple bond. Acidic dichromate solutions are strongly oxidizing. The nonhygroscopic $K_2Cr_2O_7$ has been used extensively as a standard reagent in redox titrations.

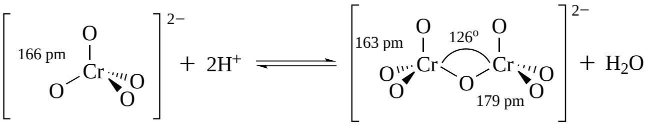

(**1**) (**2**)

(6)

Reduction of $CrO_4{}^{2-}$ (chromates(VI)) yields $CrO_4{}^{3-}$ ions (chromates(V)), which can be isolated in the form of their alkali metal and alkaline-earth metal salts, for example, Na_3CrO_4 and $Ba_3(CrO_4)_2$. The black or blue paramagnetic salts contain isolated CrO_4 tetrahedra and are hygroscopic; upon dissolution in water they disproportionate to Cr^{III} and Cr^{VI}.

Further reduction produces $CrO_4{}^{4-}$, an isolated tetrahedral anion found for example in the deep green Na_4CrO_4. The d^2 configuration of the Cr^{IV} ion gives rise to *Paramagnetism* consistent with two unpaired electrons.

The sulfide ion stabilizes chromium in its lower oxidation states. Thus, both Cr_2S_3 and CrS exist, but a chromium(VI) trisulfide does not. Heating of Cr_2S_3 causes decomposition, leading to CrS by way of a number of phases of intermediate composition. Both Cr_2S_3 and CrS are semiconductors and exhibit magnetic ordering; some of the other sulfides exhibit metallic character.

Several selenides and tellurides of chromium are also known; their stoichiometries parallel those of the sulfides.

3.4 Halides and Oxyhalides

The known halides of chromium are listed in Table 4 with some of their physical properties. The instability of a hexavalent chromium halide is noteworthy. The higher halides are prepared by direct reaction of the metal with the

Table 4 Chromium halides

Fluorides	Chlorides	Bromides	Iodides
'CrF_6'?			
CrF_5 red, mp 30 °C			
CrF_4 colorless, mp 277 °C	$CrCl_4$ gas phase only	$CrBr_4$ gas phase only	
CrF_3 green, mp 1404 °C	$CrCl_3$ violet, mp 1150 °C	$CrBr_3$ dark green, mp 1130 °C	CrI_3 black, mp >600 °C
CrF_2 green, mp 894 °C	$CrCl_2$ white, mp 824 °C	$CrBr_2$ white, mp 842 °C	CrI_2 red–brown, mp 868 °C

appropriate halogen. The chromium(II) halides are obtained by reduction of the trihalides with H_2 or by heating of the metal with HX.

A volatile yellow compound of the composition CrF_6 has been reported; however, those claims have been disputed.[16] Recent computational studies tend toward supporting the existence of the hexafluoride,[17] but definitive experimental work is still missing. Treatment of chromium with fluorine yields CrF_5, even at high temperatures (400 °C). CrF_5 is a sticky red solid with a vapor pressure of 3.3 mbar (330 Pa) at 20 °C. Gaseous CrF_5 is yellow and exhibits no tendency toward disproportionation up to 100 °C. It reacts rapidly with moisture, producing among others $CrOF_4$ and CrO_2F_2. The molecular structure of CrF_5 is a distorted trigonal bipyramid. In the solid state, it polymerizes by formation of fluoride bridges. CrF_4 has been prepared by fluorination of Cr, CrF_3, or $CrCl_3$, and by reaction of CrF_5 with Cl_2. It has been described as brown, dark green, ‘bluish’, and finally colorless (in a Ne matrix). In the gas phase, it adopts a regular tetrahedral structure (Cr–F, 170.6(2) pm).[18] CrF_3 is a nonvolatile green solid, which is best prepared by the reaction of $CrCl_3$ with HF at 500 °C. Its structure consists of hexagonally close-packed fluoride ions with chromium in octahedral coordination. Light green CrF_2 may be prepared by reduction of CrF_3 with hydrogen at 400 °C or by treatment of $CrCl_2$ with HF. It features a Jahn–Teller distorted rutile structure with chromium–fluorine distances of 200 and 243 pm.

The chromium chloride in the highest oxidation state is $CrCl_4$. This is not a stable compound under ordinary conditions; however, it may be produced by evaporation of anhydrous $CrCl_3$ at ca. 560 °C and trapped in an argon matrix. Its IR spectrum indicates a tetrahedral structure. Further heating of $CrCl_3$ yields molecular $CrCl_3$ at ca. 600 °C (trigonal planar) and finally $CrCl_2$ molecules at 780 °C (linear).[19] Probably the most important chromium halide is the violet $CrCl_3$, the starting material for much of synthetic chromium chemistry. In the solid state, it adopts an unusual layered structure consisting of a cubic close packing of chloride ions with two-thirds of the octahedral holes adjacent to every other anion layer occupied by chromium atoms. Pure $CrCl_3$ does not dissolve in water. However, addition of traces of reducing agents or Cr^{II} results in ready dissolution; this is thought to be due to electron transfer catalysis, that is, reduction of substitutionally inert Cr^{III} on the crystal surface to labile Cr^{II}, which readily dissolves and, in turn, functions as a reducing agent for further Cr^{III}. The same effect is used to practical advantage in the preparation of $CrCl_3(THF)_3$, a useful precursor for organometallic chromium compounds, which is prepared by Soxhlet extraction of $CrCl_3$ (with a little Zn metal added) with tetrahydrofuran (THF). Treatment of Cr metal with HCl or H_2 reduction of $CrCl_3$ (both at ca. 600 °C) yields colorless $CrCl_2$. The dichloride readily dissolves in water, yielding dark blue solutions of the strongly reducing Cr^{2+}(aq) ion.

Like the tetrachloride, $CrBr_4$ exists only in the gas phase. CrI_4 is not known. The structures and properties of the lower bromides and iodides parallel those of the corresponding chlorides.

Table 5 Oxyhalides of chromium

Fluorides	Chlorides	Bromides
$CrOF_4$ red, mp 55 °C		
CrO_2F_2 violet, mp 32 °C	CrO_2Cl_2 red, mp −96.5 °C, bp 117 °C	CrO_2Br_2 red
$CrOF_3$ purple, dec. 500 °C	$CrOCl_3$ dark red	
$CrOF_2$ brown – black		

The known oxyhalides of chromium are listed in Table 5 with some of their physical properties.[20] Only chromyl chloride (CrO_2Cl_2) (**3**) is of practical importance. The red liquid is prepared by treatment of CrO_3 with HCl or by heating a mixture of $K_2Cr_2O_7$ and KCl with concentrated H_2SO_4 (the latter reaction is the basis for a qualitative test for chloride). Chlorochromic acid ($CrO_2(OH)Cl$) is formed as an intermediate in these reactions; its salts can be isolated as crystalline solids. Chromyl chloride is light sensitive and, like all oxyhalides of chromium, easily hydrolyzed by water. It is also an extremely strong oxidant, reacting vigorously with many organic compounds. It adopts a pseudo-tetrahedral structure, with the O–Cr–O angle (108.5°) being smaller than the Cl–Cr–Cl angle (113°). The latter fact is in contradiction to the tenets of valence shell electron pair repulsion (VSEPR) theory. Numerous derivatives of chromyl chloride of the type CrO_2X_2 ($X = NO_3, ClO_4$, OAc, OR, N_3, etc.) are known. The electronic and vibrational spectroscopy of Cr^{VI} compounds, and chromyl derivatives in particular, has been reviewed.[21]

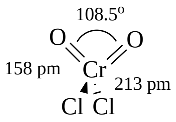

(**3**)

4 COORDINATION COMPOUNDS

4.1 Overview

Chromium complexes exist in a very wide range of formal oxidation states (−IV to +VI). The extremely low ones are stabilized by π-acid ligands, notably carbon monoxide; these are described in the article on organometallic compounds (*see **Chromium: Organometallic Chemistry***). The extensive coordination chemistry of Cr^{II} spans coordination numbers 3–7, but is dominated by octahedral complexes. Complexes of divalent chromium are usually strongly reducing and are often susceptible to air oxidation. By far the largest number of coordination compounds of chromium exists in the +III oxidation state. Commonly octahedral, they are substitution inert and often easily synthesized. In mononuclear complexes, the d^3 electronic configuration (t_{2g}^3) gives rise to spin-only magnetic moments (3.87 μ_B), but in polynuclear complexes, antiferromagnetic coupling between the Cr^{III} ions results in lower values (*see **Magnetism of Transition Metal Ions***). The electronic spectra and the photochemistry of trivalent chromium have been studied extensively. The oxidation states +IV and +V have attracted some attention recently. However, these oxidation states must still be considered unusual in the context of chromium chemistry. Finally, Cr^{VI} is a common and important oxidation state of this element, although the number of coordination compounds representing it is rather limited. The notion of a true Cr^{6+} ion is, of course, unrealistic, and the chemistry of Cr^{VI} is marked by strong *Covalent Bonds* to oxygen and halogens. These compounds are strong oxidants. By comparison to the heavier elements in group 6 (Mo, W), chromium shows much less tendency toward *Cluster* formation.

A comprehensive treatise of the coordination chemistry of chromium**[22]** is available.

4.2 Oxidation States 0 and I

Reduction of common chromium salts ($CrCl_3$, $CrCl_2$, $Cr_2(OAc)_4$) in the presence of chelating nitrogen heterocycles like bipy and phen provides access to formally neutral Cr^0 complexes $Cr(L–L)_3$ as well as salts of the type $[Cr(L–L)_3]X$ (L–L = bipy, phen; X = I, ClO_4). $[Cr(bipy)_3]$ is a black solid; its molecular structure is a trigonally distorted octahedron (Cr–N, 208 pm; N–Cr–N, 74.7°). Owing to the high ligand field strength of the nitrogen ligands, and as shown by their *Diamagnetism*, the $Cr(L–L)_3$ complexes adopt low-spin configurations (t_{2g}^6) (*see High-spin & Low-spin Compounds*). $[Cr(bipy)_3]X$ has an effective magnetic moment of 2.07 μ_B, consistent with one unpaired electron (t_{2g}^5). In solution, it exhibits an electron spin resonance (ESR) spectrum at $g = 1.9971$ with hyperfine splitting to both ^{53}Cr and ^{14}N evident. Electrochemical experiments in aprotic solvents (MeCN) show reversible redox processes involving $[Cr(L–L)_3]$ ions containing chromium in the oxidation states –I, 0, I, II, and III. The half-wave potential for the $[Cr(bipy)_3]^+/Cr(bipy)_3$ couple lies at −1.28 V versus the Ag/AgCl electrode.

Highly reduced chromium binds dinitrogen, for example in *trans*-$[Cr(dmpe)_2(N_2)_2]$ (**4**). Its crystal structure shows linearly bound N_2 ligands (Cr–N, 187.4 pm, N–N, 112.2 pm) and relatively short Cr–P distances (Cr–P_{av}, 229.6 pm). The related $Cr(dmpe)_3$ exhibits similarly short Cr–P bonds (231.7 pm). These short Cr–P distances are thought to be due to *π–Back Bonding* to the phosphine ligand. Both $Cr(dmpe)_3$ and $Cr[P(OMe)_3]_6$ were prepared by metal vapor synthesis (*see **Metal Vapor Synthesis of Transition Metal Compounds***). The same technique may also be used to prepare the fluorophosphine complexes $Cr(PF_3)_6$ and $Cr[(PF_2)_2NR]_3$. The phosphine complexes are all diamagnetic and colorless or yellow, indicating large ligand field splittings.

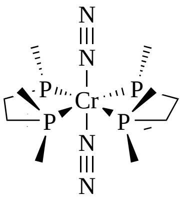

(**4**)

There are Cr^0 and Cr^I complexes of both aryl and alkyl isocyanides (RNC) as well as cyanides; because of their Cr–C linkages, these are described elsewhere (*see **Chromium: Organometallic Chemistry***).

4.3 Oxidation State II

The coordination chemistry of Cr^{II} can be subdivided into the realm of mononuclear coordination compounds, which can be derived (at least formally) from the blue $[Cr(OH_2)_6]^{2+}$ ion, and the chemistry of metal–metal bonded species (analogs of $Cr_2(OAc)_4$). Most of the former are octahedral high-spin complexes with distinct tetragonal distortions caused by the *Jahn–Teller Effect*. With strong-field ligands, low-spin octahedral complexes are formed, and there are also some four-coordinate complexes of various coordination geometries. The metal–metal bonded species are described in Section 5.

4.3.1 Hydride and Halide Ligands

Cr^{II} hydrides without Cr–C bonds are restricted to the seven-coordinate $[H_2Cr\{P(OMe)_3\}_5]$ and $[HCr\{(Me_2PCH_2)_3CMe\}_2]^+BEt_4^-$. The former complex results from oxidative addition of H_2 to $[Cr\{P(OMe)_3\}_6]$, while the latter was isolated from a reaction of $[CrCl_3\{(Me_2PCH_2)_3CMe\}]$ with $LiHBEt_3$. Both are diamagnetic molecules and their NMR spectra indicate fluxional behavior (*see Fluxional Molecule*).

The anhydrous halides CrX_2 (X = F, Cl, Br, I) were described earlier (Section 3.4). Through formal addition of halide ions, various halochromates(II) can be formed. These feature complex ions of the types CrX_3^-, CrX_4^{2-}, CrX_5^{3-}, and CrX_6^{4-}. These, when they contain fluoride ion, are, for example, the light blue $MCrF_3$ (M = Na, K, Rb, NH_4), dark blue Na_2CrF_4, or $MCrF_4$ (M = Ca, Sr, Ba), and Ba_2CrF_6. Most of these compounds contain six-coordinate Cr^{II}. All are more or less paramagnetic, because of the high-spin d^4 configuration ($t_{2g}^3e_g^1$); thus $KCrF_3$ has $\mu_{eff} = 4.9\,\mu_B$ and Na_2CrF_4 has $\mu_{eff} = 4.8\,\mu_B$. There is evidence for magnetic coupling at low temperatures. Among the corresponding chloro- and bromochromates(II), the tetrahalochromates M_2CrX_4 (M = alkali metal, organic cations; X = Cl, Br) especially have been the subject of detailed structural and magnetic studies, because some of these materials show weak ferromagnetic coupling. While the overwhelming majority of magnetically coupled transition metal complexes exhibit *Antiferromagnetism*, ferromagnetic coupling is rare and of great interest for the preparation of novel magnetic materials (*see* ***Magnetism of Extended Arrays in Inorganic Solids***).

The colorless alkali metal salts adopt a distorted K_2NiF_4 structure, containing layers of tetragonally distorted $CrCl_6$ octahedra held together by the M^+ ions. At room temperature their effective magnetic moments slightly exceed the spin-only values; upon lowering the temperature, they rise (to ca. $9\,\mu_B$ per Cr atom at 90 K). Curie temperatures between 40 and 75 K have been found. Some of the tetrahalochromates(II) are antiferromagnets. For example, the structure of $[NMe_2H_2]_2[CrCl_4]$ contains isolated $[Cr_3Cl_{12}]^{6-}$ units (**5**) in which three distorted $CrCl_6$ octahedra are joined via shared trigonal faces to form a linear chain of three chromium atoms.

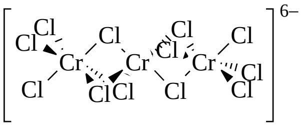

(**5**)

4.3.2 Oxygen and Sulfur Ligands

Solutions of the bright blue $[Cr(OH_2)_6]^{2+}$ ion can be prepared by dissolution of pure chromium metal in mineral acids or by reduction of Cr^{III} with exclusion of oxygen. Cr^{II}(aq) is a strong reducing agent (see equation 4) and has long been used in mechanistic investigations of electron transfer reactions; more recently it has also found applications as a reducing agent in synthetic organic chemistry. Even in the absence of O_2, aqueous Cr^{II} solutions slowly decompose with liberation of H_2; this reaction is catalyzed by various impurities. The electronic spectrum of the $[Cr(OH_2)_6]^{2+}$ ion exhibits a broad asymmetric absorption at $14\,000\,cm^{-1}$ and a weaker shoulder at $9500\,cm^{-1}$, features that are consistent with a tetragonally distorted octahedral complex. While the crystal structure of the $[Cr(OH_2)_6]^{2+}$ ion is not known, the structure of the closely related $Cr(OH_2)_4(SO_4)$ has been determined. The complex features *trans* sulfato oxygens with rather long bond distances (Cr–O, 242–246 pm) and four equatorial water oxygens with normal bond distances (Cr–O, 203–205 pm). This tetragonal elongation is the expected Jahn–Teller distortion.

Cr^{II} alkoxides $[Cr(OR)_2]$ are conveniently prepared by alcoholysis of chromium amides, for example $[Cr\{N(SiMe_3)_2\}_2(THF)_2]$. The alkoxides with bulky substituents are appreciably soluble in organic solvents, but those of primary alcohols are insoluble polymers. The wide variety of substituents gives rise to considerable structural complexity. In donor solvents such as THF, solvent adducts of the type $[Cr(OR)_2(THF)_2]$ are formed. They probably adopt square-planar geometries with *trans*-OR groups, as has been shown for $[(2,6\text{-}(t\text{-}Bu)_2\text{-}4\text{-}MeC_6H_2O)Cr(THF)_2]$.**[23]** The complex $[Li(THF)_2]\ [Cr\{OC(t\text{-}Bu)_3\}_2Cl]$ features an unusual T-shaped geometry (**6**).

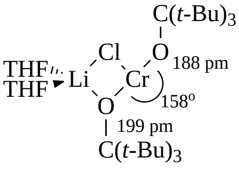

(**6**)

$Cr(acac)_2$ is a yellow paramagnetic solid with an effective magnetic moment ($4.99\,\mu_B$), consistent with a high-spin d^4 electronic configuration. Its crystal structure shows chromium coordinated by four oxygen atoms in a plane ($Cr–O_{av}$, 198 pm) and two long intermolecular contacts between the metal atom and the methine carbons of neighboring molecules (Cr–C, 305 pm), giving chromium a severely distorted octahedral coordination environment. A few other β-diketonates of Cr^{II} have been prepared.

A number of adducts of chromium(II) halides with oxygen-containing donor molecules have been characterized. They have the composition $CrX_2(L)_2$, where X = Cl, Br, I and L = THF, urea, biuret, dimethylsulfoxide (DMSO), phosphine oxide, arsine oxide, and so on. Most are blue high-spin molecules ($\mu_{eff} = 4.4–5.0\,\mu_B$). Pale-green $[CrCl_2(THF)_2]$ loses one equivalent of THF in vacuo, thereby yielding colorless $[CrCl_2(THF)]$, which is a useful synthetic precursor for nonaqueous Cr^{II} chemistry.

Sulfur-based Cr^{II} coordination compounds include a series of dithiocarbamates of the type $[Cr(S_2CNR_2)_2]$ (R = Me, Et or $R_2 = C_4H_8$), which are antiferromagnetically coupled. The diethyl-substituted compound is an S-bridged dimer, making chromium five-coordinate. Square-planar Cr^{II} coordinated by sulfur occurs in the violet $[NEt_4]_2[Cr(S_2C_2H_4)_2]$. Finally, *Thiourea* and its derivatives form adducts with Cr^{II} halides, which are similar to the adducts with O-donors mentioned above.

4.3.3 Nitrogen and Phosphorus Ligands

Ammonia deprotonates $[Cr(OH_2)_6]^{2+}$, resulting in precipitation of brown Cr^{II} hydroxide. However, treatment of solid halides CrX_2 or ethanol solutions of hydrated CrX_2 with NH_3 gas yields blue diammines $[Cr(NH_3)_2X_2]$, violet pentammines $[Cr(NH_3)_5X]X$, and greenish-gray hexammines $[Cr(NH_3)_6]X_2$. Their magnetic behavior is that expected of high-spin complexes. Spectroscopic measurements and comparative X-ray powder diffraction studies are consistent with Jahn–Teller distorted octahedral structures.

Substitution of various chelating bi- and polydentate amines, for example, en, 1,3-diaminopropane, dien, trien, and so on, in nonaqueous media yields an extensive series of octahedral amine complexes, which range in color from blue to purple. Their effective magnetic moments ($4.7-4.9\,\mu_B$) and electronic spectra are best explained assuming tetragonally distorted octahedral geometries.

Nitrogen heterocycles, either monodentate or incorporated into chelating ligands, form many Cr^{II} complexes. Most common among these are compounds containing pyridine and its derivatives. Complexes of the types $[Cr(py)_4X_2]$ and $[Cr(py)_6]X_2$ are all high spin and their spectra show the usual pattern of distorted octahedral coordination of Cr^{II}. Analogous complexes have been prepared with pyrazoles and imidazoles. With the introduction of bidentate heterocyclic ligands (bipy, phen, etc.), the spin state eventually changes to low spin. Thus halide-bridged $[Cr(bipy)Cl_2]$ is high spin, but $[Cr(bipy)_2Cl_2]$ and $[Cr(bipy)_3]Cl_2$ are low-spin complexes ($t_{2g}{}^4$, $\mu_{eff} = 3.0\,\mu_B$). Polypyrazolylborate ligands (also called *scorpionates*) have attracted increasing attention recently.**[24]** Cr^{II} complexes of such ligands include $[Cr(HBpz_3)_2]$ and $[Cr(Bpz_4)_2]$, which are both high-spin, distorted octahedral complexes. More sterically hindered tris(pyrazolyl)borates facilitate isolation of four-coordinate (e.g. cis-divacant octahedral $Tp^{t\mathrm{Bu,Me}}CrCl$) and five-coordinate (e.g. trigonal bipyramidal $Tp^{t\mathrm{Bu,Me}}Cr(L)Cl$) complexes. Use of bidentate pyrazolylborates, as in $[Cr(H_2Bpz_2)_2]$ and $[Cr(Et_2Bpz_2)_2]$, yields square-planar Cr^{II} complexes, for example (**7**).

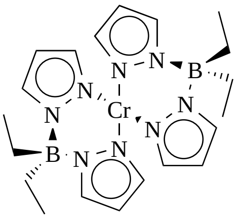

(**7**)

Aliphatic phosphines add to CrX_2 (X = Cl, Br), yielding adducts of uncertain composition, for example $[Cr(PR_3)_nX_2]$ ($n = 1-3$). With chelating diphosphines, for example dmpe, well-characterized six-coordinate complexes have been prepared. The latter have low-spin electronic configurations. A spin-crossover situation has been found in the complex $[Cr(depe)_2I_2]$ (depe = 1,2-bis(diethylphospino)ethane).**[25]** At ca. 170 K, this trans octahedral complex exhibits a discontinuous spin transition from $S = 1$ ($2.8\,\mu_B$) to $S = 2$ ($4.8\,\mu_B$).

Certain quadridentate tripod ligands featuring phosphine donors stabilize five-coordinate Cr^{II}. Examples of these are the cations $[Cr\{P(CH_2CH_2PPh_2)_3\}X]^+$, $[Cr\{N(CH_2CH_2PR_2)\}X]^+$ (R = Cy, Ph), and the N analogs $[Cr\{N(CH_2CH_2NR_2)\}X]^+$ (R = Me, Et). These complexes are thought to adopt trigonal bipyramidal structures in which the coordinated halide occupies an axial position.

4.4 Oxidation State III

Central to the coordination chemistry of Cr^{III} is six coordination in an essentially octahedral arrangement of ligands, because of the large ligand field stabilization energy of the d^3 configuration in this geometry. There are thousands of mononuclear Cr^{III} complexes, which exhibit effective magnetic moments close to or slightly below the spin-only value ($S = 3/2$, $3.88\,\mu_B$). There are also a large number of Cr^{III} *Polynuclear Complexes*, for example those with bridging hydroxide ligands, in which exchange coupling of the spins results in lower moments. The electronic spectra of Cr^{III} complexes are well understood. Consultation of the corresponding *Tanabe–Sugano Diagram* predicts three spin-allowed transitions, namely, ${}^4A_{2g} \rightarrow {}^4T_{2g}(F)$, ${}^4A_{2g} \rightarrow {}^4T_{1g}(F)$, and ${}^4A_{2g} \rightarrow {}^4T_{1g}(P)$, and three bands have indeed been found for many complexes. The lowest energy transition is a direct measure of the ligand field splitting (10 Dq or Δ_0); for the $[Cr(OH_2)_6]^{3+}$ ion, this transition lies at ca. $18\,000\ cm^{-1}$. The photochemistry of Cr^{III} complexes has been studied in some detail and a recent review is available.**[26]**

The reactivity of Cr^{III} complexes is marked by very slow *Ligand Substitution* reactions, resulting in unusual configurational stability. Many chiral complexes have been resolved. There has been a recent resurgence of interest in organochromium(III) complexes, owing to the importance of chromium in catalytic processes (*see* ***Chromium: Organometallic Chemistry***).

4.4.1 *Hydride and Halide Ligands*

The only known mononuclear Cr^{III} hydride is the recently described $[Li(THF)\{N(CH_2CH_2NSiMe_3)_3\}CrH]$, a trigonal bipyramidal molecule with a calculated $D_{Cr\text{–}H}$ of $297\ kJ\,mol^{-1}$.**[27]**

The simple halides (CrX_3) were described in Section 3.4. Addition of further halide ions generates ions of the compositions $[CrX_4]^-$ and $[CrX_6]^{3-}$. An example of the former is $K[CrF_4]$; its crystal structure consists of anionic columns of joined octahedra. The chromium atoms are weakly coupled antiferromagnetically. The highly symmetric $[CrF_6]^{3-}$ and $[CrCl_6]^{3-}$ ions have been the subject of many theoretical and experimental studies, owing to their perceived simplicity. Another set of heavily studied compounds are the dinuclear $[Cr_2X_9]^{3-}$ ions (**8**). Their structures consist of two octahedra sharing a trigonal face, that is, there are three bridging and six terminal halide ligands. The metal ions are weakly coupled ($J = 0-16\ cm^{-1}$). The Cr–Cr distances range from 277 to 400 pm and metal–metal bonding has been ruled out on the basis of spectroscopic and structural evidence. The chromium atoms are displaced from the centers of the octahedra formed by the halide ions, such that the Cr–Cr distance is increased. The interactions of adjacent Cr^{III} ions have indeed been called *repulsive*. This is in contrast to the isostructural Mo and W compounds, which show evidence for metal–metal bonding.

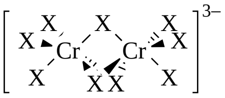

(**8**)

4.4.2 Oxygen and Sulfur Ligands

The violet hexaaquo ion $[Cr(OH_2)_6]^{3+}$ is a regular octahedron with Cr–O distances in the range 191.5–199.1 pm, depending on the particular compound used for the structure determination. EXAFS measurements on dilute solutions have provided information about the second hydration shell; it appears to contain an average of 13.5 water molecules at a Cr–O distance of 402(2) pm.[28]

The Cr^{III}(aq) ion occurs, for example, in $[Cr(OH_2)_6]Cl_3$ and in the chrome alums, $MCr(SO_4)\cdot 12H_2O$. There are several stable isomers of the chloride; among these the dark green *trans*-$[CrCl_2(OH_2)_4]Cl\cdot 2H_2O$ is the commercially available salt.

The rate of exchange of water with $[Cr(OH_2)_6]^{3+}$ is extremely slow ($k = 4.5 \times 10^{-7}\,s^{-1}$ at ambient temperature). Extensive mechanistic and kinetic studies suggest that this reaction proceeds by an I_a mechanism, that is, associative interchange. The aquo ion is fairly acidic (equation 7) and the resulting hydroxo complex dimerizes to the doubly bridged $[(H_2O)_4Cr(\mu\text{-}OH)_2Cr(OH_2)_4]^{4+}$, a weakly coupled antiferromagnet. Addition of base sets off a stepwise polymerization yielding various hydroxy complexes of higher nuclearity; some of these have been isolated by ion-exchange chromatography.

$$[Cr(OH_2)_6]^{3+} \underset{+H^+}{\overset{-H^+}{\rightleftharpoons}} [Cr(OH_2)_5(OH)]^{2+} \qquad pK_a = 4$$

$$\rightleftharpoons [(H_2O)_4Cr(\mu\text{-}OH)_2Cr(OH_2)_4]^{4+} \qquad (7)$$

Refluxing of $CrCl_3(THF)_3$ in anhydrous alcohols yielded purple insoluble solids, which were formulated as $[Cr(ROH)_nCl_3]$ adducts (R = Me, Et, *i*-Pr, *n*-Bu, *n*-hexyl). Various alkoxides of Cr^{III} have been prepared; they have been reviewed in detail.[29] Extreme steric congestion is likely to be responsible for the distorted tetrahedral coordination geometry exhibited by $Li[Cr\{OCH(t\text{-}Bu)_2\}_4]\cdot THF$.[30]

Many acetylacetonate complexes and related β-diketonates of Cr^{III} have been made over the years. Many of these are rather volatile, a property that has been exploited for the separation of isomers by gas chromatography and for gas-phase structure determinations by electron diffraction. Owing to its stability and solubility in organic solvents, paramagnetic $[Cr(acac)_3]$ has been used as a relaxation agent in ^{13}C NMR spectroscopy. Electrophilic substitutions at the coordinated diketonato ring are facile, and this has been taken as an evidence of an aromatic nature.

Attempts to prepare Cr^{III} acetate typically lead to trinuclear complexes of the familiar 'basic carboxylate' type (**9**). Three acetate bridged chromium ions share one central oxide ion, and the remaining sixth coordination site of every chromium is occupied by water or other ligands. A large variety of these complexes, differing in the associated ligands, the nature of the carboxylate, the counterion, and even the oxidation state, have been prepared and their physical properties studied. Especially their magnetic exchange interactions have been the subject of much controversy.

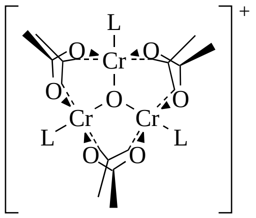

(**9**)

Oxalate (ox, $C_2O_4{}^{2-}$) complexes of Cr^{III} have been known since the very beginning of coordination chemistry. Thus, the resolution of chiral $[Cr(ox)_3]^{3-}$ with strychninium counterion by Werner in 1912 produced the first optically active anionic coordination compound. There also exists a series of bis(oxalato) complexes of the type $[Cr(ox)_2X_2]^{2+/0}$, where X can be any of a variety of neutral donors (e.g. H_2O, NH_3, etc.) or anionic ligands (e.g. SCN^-, $N_3{}^-$, etc.). These compounds have been used to study the mechanism of cis/trans isomerization and racemization of optically active octahedral coordination compounds.

Several dioxygen complexes of chromium featuring superoxide ($O_2{}^-$) bound to Cr^{III} can be made by exposure of Cr^{II} precursors to O_2.[31] The first structurally characterized example of such an adduct – that is, $[Tp^{t\text{Bu},\text{Me}}Cr(pz'H)(O_2)]^+$ – interestingly features the rare 'side-on' bonding mode of the superoxide ligand.[32]

Other oxygen-based donor molecules that form Cr^{III} complexes include THF (e.g. the synthetically useful $[Cr(THF)_3Cl_3]$), urea ($[Cr\{OC(NH_2)_2\}_6]^{3+}$), sulfoxides (e.g. $[Cr(DMSO)_6]X_3$), amides (e.g. $[Cr(DMF)_6]X_3$), N-oxides, and phosphine oxides.

Introduction of sulfur ligands into the coordination sphere of aqueous Cr^{III} has been accomplished by oxidation of Cr^{II}(aq) with various sulfur-containing oxidants. There resulted a series of complexes of the composition $[Cr(SR)(H_2O)_5]^{2+}$ (R = H, alkyl, aryl). They all ultimately suffer substitution of the sulfur ligand by water, that is, ‘aquation’. In nonaqueous media, a number of thiolato complexes ($[Cr(SR)_3]$, R = Me, Et, Ph, Bz) and thioether adducts of Cr^{III} halides ($[CrX_3(L)_3]$, X = Cl, Br; L = THT, SMe_2, SEt_2) have been prepared and characterized. There are also many complexes containing bidentate sulfur ligands such as dithiocarbamates, 1,3-dithiodiketonates, 1,2-dithiolates, and so on.

4.4.3 Nitrogen and Phosphorus Ligands

Cr^{III} complexes of ammonia and amines (both mono- and polydentate) exist in overwhelming numbers. Representatives of this class of compounds were among the first coordination compounds to be studied by Werner and his contemporaries. The early work (prior to 1970) on amine complexes has been reviewed comprehensively.[33] Typical complexes include $[CrA_6]^{3+}$ (A = NH_3, amine) and a wide variety of mixed ligand systems of the type $[CrA_{6-(n+m)}L_nX_m]^{(3-m)+}$ (L = neutral donor ligand, e.g. H_2O; X = monoanionic ligand, e.g. halide). Molecular orbital studies confirm that the $[Cr(NH_3)_6]^{3+}$ ion does not feature π-bonding with the NH_3 ligands. Because of the kinetic inertness of Cr^{III} complexes, isomers of various kinds are commonly observed and can be isolated and characterized. In neutral or basic media, mixed ammine/aquo complexes form dimers and polynuclear species with oxo and hydroxo bridges. The simplest of these are the blue ‘basic rhodo’ ion (**10**) and the red ‘acid rhodo’ complex (**11**). Complexes with two or three bridging ligands (e.g. μ-hydroxides) are also very common. The Cr^{III} ions in these complexes are invariably coupled antiferromagnetically. Much effort has been expended in trying to correlate the exchange constant J with structural parameters.[34] While it is generally accepted that the coupling in edge-bridged bioctahedra (two bridging ligands) is mediated by the bridging ligands, a direct correlation between J and the metal–metal distance of face-sharing d^3–d^3 systems (three bridging ligands) has also been proposed.[35]

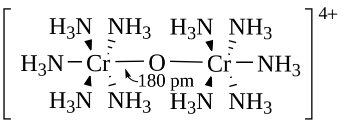

(**10**)

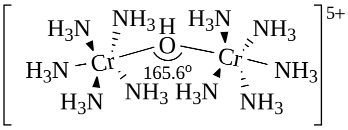

(**11**)

Nitrogen heterocycles also form an extensive series of Cr^{III} complexes, adding a π-bonding contribution to the metal–ligand bond. Complexes of this type include those containing pyridine and its derivatives, imidazoles, pyrazines, and pyrazoles. They are all six-coordinate octahedral species. $[Cr(bipy)_3]^{3+}$, the most oxidized member of an electron transfer series extending to $[Cr(bipy)_3]^{3-}$, is an example with a chelating ligand. A detailed study of its crystal structure and spectroscopic properties has been carried out.[36] *Porphyrin* ligands fall in this category also, and while they support chromium in the oxidation states +II to +V, Cr^{III} porphyrins are the most common ones. For example, [(TPP)CrCl] is soluble in toluene only in the presence of donor molecules, giving the expected six-coordinate [(TPP)Cr(L)Cl]. Remarkably, the sixth ligand is fairly labile and is substituted rapidly, in contrast to the typically slow ligand-substitution reactions of other Cr^{III} complexes. Finally, reports on poly(pyrazolyl)borate complexes of Cr^{III} are still relatively rare, despite the recent surge of interest in these ligands.[24]

Amide complexes of trivalent chromium constitute some of the rare exceptions from octahedral coordination. Largely because of steric constraints, there are examples of three- and four-coordinate complexes. Both $[Cr\{N(i\text{-}Pr)_2\}_3]$ and $[Cr(N\{SiMe_3)_2\}_3]$ (**12**) are monomeric in solution and in the solid state and have effective magnetic moments consistent with three unpaired electrons ($\mu_{eff} = 3.8\,\mu_B$). Their crystal structures feature trigonal planar CrN_3 moieties as well as planar $CrNR_2$ units. The latter observation, in concert with short Cr–N bonds, suggests strong ligand-to-metal π-donation. Sterically less demanding amides (NMe_2, NEt_2) lead to dimerization via bridging amido groups and thus tetrahedral coordination of Cr^{III}. The dimers disproportionate, thereby providing access to Cr^{IV} amides $[Cr(NR_2)_4]$. A four-coordinate Cr^{III} complex with the unusual trigonal monopyramidal geometry is formed by a chelating tris-amido ligand.[37]

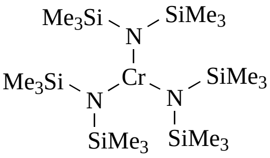

(**12**)

The unusual solid phase $Ca_3[CrN_3]$ contains sheets of trigonal planar $[CrN_3]^{6-}$ units with short Cr–N bonds (Cr–N, 186.4, 176.6 pm). The effective magnetic moment of 1.86 μ_B implies a low-spin configuration, unprecedented for a Cr^{III} complex.[38]

The hard Cr^{III} ion does not favor soft ligands such as phosphines and arsines. Nevertheless, phosphine adducts of the trihalides have been prepared, for example by displacement of THF from $CrCl_3(THF)_3$. Long Cr–P distances in crystallographically characterized molecules (ca. 247 pm) underscore the weakness of the bonds.

4.5 Oxidation State IV

There is no aqueous coordination chemistry of Cr^{IV}, except for unstable intermediates in reductions of Cr^{VI} species. However, the number of stable Cr^{IV} complexes prepared in nonprotic media is rapidly growing.

4.5.1 Hydrides and Halides

Hydrogenation of $[Cr(dmpe)_2(N_2)_2]$ yielded the hydride complex $[Cr(dmpe)_2H_4]$ (**13**). This unique eight-coordinate Cr^{IV} complex is diamagnetic and adopts a *Dodecahedral* structure with an average Cr–P distance of 225.5 pm and $Cr–H_{av} = 157$ pm. A more recent example is $[N(CH_2CH_2NSiMe_3)_3CrH]$.[27]

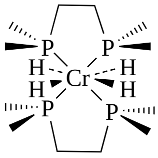

(**13**)

The fluorides CrF_4 and $CrOF_2$ were mentioned earlier (Section 3.4). The salts of the hexafluorochromate(IV) ion, that is, $[CrF_6]^{2-}$, are made by fluorinating $CrCl_3$/MCl mixtures. There are also the pentafluorochromates(IV) $M[CrF_5]$ (M = K, Rb, Cs) and the heptafluorochromates(IV) $M_3[CrF_7]$ (M = Rb, Cs). All of the above contain octahedral CrF_6 units, despite their different stoichiometries.

4.5.2 Oxygen Ligands

Besides the oxide CrO_2 and the chromates(IV) (see Section 3.3), there exists a number of Cr^{IV} alkoxides $[Cr(OR)_4]$ derived from tertiary alcohols. These are volatile blue liquids or low-melting solids with effective magnetic moments of ca. 2.8 μ_B. The crystal structure of $[Cr\{OCH(t\text{-}Bu)_2\}_4]$ has been determined and confirms the tetrahedral coordination geometry of chromium. The short Cr–O distances (177.3 pm) indicate significant ligand–metal π-donation.

4.5.3 Nitrogen Ligands

Certain Cr^{III} amides disproportionate upon heating and yield volatile Cr^{IV} derivatives of the type $[Cr(NR_2)_4]$ (R = Et, Pr). Their magnetic moments and electronic spectra are fully consistent with tetrahedral structures. Reaction with tertiary alcohols yields the tetraalkoxides described above and insertions of CO_2 or CS_2 yield Cr^{III} carbamates and dithiocarbamates, respectively.

Cr^{II} porphyrin complexes react with O_2 to form stable oxochromium(IV) species. For example, the red [(TPP)CrO] contains a five-coordinate Cr^{IV} displaced out of the porphyrin plane toward the oxygen atom (Cr–O, 157.2 pm). There are also a few Cr^{IV} scorpionates featuring terminally bound oxo ligands. The most recent of these is paramagnetic $[Tp^{tBu,Me}Cr(pz'H)(O)]BARF$ (Cr–O, 160.2 pm), which abstracts weakly bound hydrogen atoms from hydrocarbons.[39]

4.6 Oxidation State V[40]

Cr^V coordination chemistry is still very rare. Reduction of Cr^{VI} species gives rise to unstable Cr^V intermediates, which can be detected by ESR spectroscopy. Stable compounds of Cr^V are found mostly with halides or oxygen-based ligands.

4.6.1 Halide Ligands

Aside from CrF_5, there is the hexafluorochromate(V) ion in the brick-red complexes $Cs[CrF_6]$ and $NO_2[CrF_6]$. The oxyhalides $CrOX_3$ (X = F, Cl) form a number of adducts with halide ions, namely, oxotetrahalochromates(V) of the composition $[CrOX_4]^-$ and oxopentahalochromates(V) of the type $[CrOX_5]^{2-}$. The crystal structure of $AsPh_4[CrOCl_4]$ shows the presence of five-coordinate chromium in a square pyramidal arrangement (Cr–O, 151.9 pm; Cr–Cl, 224.0 pm). $CrOCl_3$ also adds amines, for example, to give $[CrOCl_3(bipy)]$.

4.6.2 Oxygen Ligands

Chromate(V) was mentioned earlier. Treatment of basic $[CrO_4]^{3-}$ solutions with 30% H_2O_2 yields the moderately stable peroxide ion $[Cr(O_2)_4]^{3-}$. The crystal structure of the representative $K_3[Cr(O_2)_4]$ has been determined; the Cr^V-containing anion features side-on bound peroxide ligands (O–O, 149 pm) and a distorted dodecahedral coordination geometry. The red–brown salt is paramagnetic with $\mu_{eff} = 2.94\,\mu_B$.

The reduction of Cr^{VI} with certain tertiary α-hydroxycarboxylic acids has yielded Cr^V complexes, which are stable in aqueous solution. The structure of $K[OCr(O_2CC(Et)(Me)O)_2]$ (**14**) showed a distorted square pyramid with a short apical Cr–O double bond (155.4 pm). The facile preparation and stability of these complexes have led to their use in the study of the mechanism of oxidations involving Cr^V.[41] A similar complex containing two perfluoropinacolate ligands has also been prepared.

4.6.3 Nitrogen Ligands

Chlorination of $[Cr(N\text{-}t\text{-}Bu)_2Cl_2]$ has yielded the imido complex $[Cr(N\text{-}t\text{-}Bu)Cl_3]$, a green oil. It adds donor

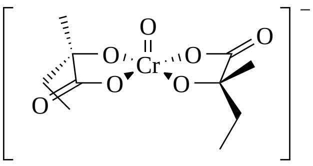

(**14**)

ligands to form a series of adducts of the composition $[Cr(N\text{-}t\text{-}Bu)Cl_3(L)_2]$ (L = THF, 1/2 DME, PR_3, NCR, X^-) as well as derivatives resulting from substitution of halide.

Porphyrin ligands also allow the preparation of Cr^V complexes. For example, reaction of [(TPP)CrCl] with iodosylbenzene provides [(TPP)Cr(O)Cl], a six-coordinate complex, which is stable in solution for several hours. Its reaction with alkenes involves oxygen atom transfer and yields alcohols and epoxides.**[42]** Another Cr^V porphyrin complex is the nitride [(TPP)CrN]. A crystal-structure determination has confirmed the square pyramidal structure with a very short bond distance to the apical nitrido ligand (Cr–N, 156.5 pm).

Cr^{III} salen also reacts with iodosylbenzene and yields cationic Cr^V oxo complexes. These catalyze oxygen atom transfer to alkenes.**[43]**

4.7 Oxidation State VI

The extremely oxidizing nature of Cr^{VI} makes its coordination chemistry rather limited, as most potential ligands suffer oxidation by the metal and reduce it to a lower oxidation state. For the same reason, various forms of Cr^{VI} serve an important role as oxidants in organic chemistry. Most Cr^{VI} compounds contain halide and oxygen ligands.

4.7.1 Halide and Oxygen Ligands

With the fluoride CrF_6 still in doubt (see Section 3.4), the only certain Cr^{VI} halo complexes are the oxyhalides. The neutral compounds are listed in Table 5. A large number of chromyl compounds (CrO_2X_2) are known, in which X can be a wide variety of anionic groups, for example, NO_3, ClO_4, FSO_3, OAc, N_3, O_2CR, and so on. The structure of $CrO_2(NO_3)_2$ has been determined by electron diffraction; it was described as a severely distorted octahedron with two single bonds and two partial bonds to NO_3-type oxygens.**[44]** Chromyl compounds generally hydrolyze rapidly to chromate and the corresponding acid.

CrO_3 adds pyridine to yield $[CrO_3(py)]$ and $[CrO_3(py)_2]$. With alcohols it forms chromate esters, $CrO_2(OR)_2$. Some of these are unstable, for example $CrO_2(OSiMe_3)_2$ has been reported to explode upon distillation, but $CrO_2(OCPh_3)_2$ has been structurally characterized by X-ray diffraction. Addition of halide ion to CrO_3 yields the trioxohalochromates $[CrO_3X]^-$ (X = F, Cl), and $[CrO_4F]^-$ and $[CrO_2F_4]^{2-}$ have also been described.

Reaction of acidic dichromate solutions with H_2O_2 produces a blue compound, which can be extracted into ether. Upon coordination of various donors complexes of the composition $[CrO(O_2)_2(L)]$ (L = H_2O, py (**15**), Et_2O, etc.) can be isolated. These six-coordinate molecules adopt roughly pentagonal pyramidal structures and contain two side-on bound peroxide ligands. Deprotonation of $[CrO(O_2)_2(OH_2)]$ yields the ion $[CrO(O_2)_2(OH)]^-$, which may be isolated in the form of violet explosive salts. Related to the latter are the blue peroxohalochromates, $Ph_3AsMe[CrO(O_2)_2X]$ (X = Cl, Br).

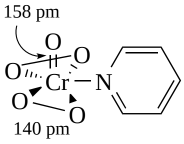

(**15**)

4.7.2 Nitrogen Ligands

Imido ligands can substitute for oxo ligands in Cr^{VI} complexes. Thus reaction of CrO_3 with $NH(t\text{-}Bu)(SiMe_3)$ yields $[Cr(N\text{-}t\text{-}Bu)_2(OSiMe_3)_2]$. Similarly, $[Cr(N\text{-}t\text{-}Bu)_2Cl_2]$, $[Cr(N\text{-}t\text{-}Bu)_2(NH\text{-}t\text{-}Bu)_2]$, and even the chromate analog $Li_2[Cr(N\text{-}t\text{-}Bu)_4]$ have been prepared.**[45]** $[Cr(N\text{-}t\text{-}Bu)_2Cl_2]$ even forms five-coordinate adducts with phosphine ligands; the crystal structure of $[Cr(N\text{-}t\text{-}Bu)_2Cl_2(PMe_2Ph)]$ revealed a trigonal bipyramidal molecule with the phosphine (Cr–P, 239.2 pm) and one chloride in the axial positions. Clearly, nitrogen to chromium π-donation strongly attenuates the oxidizing character of Cr^{VI}.

5 Cr–Cr BONDS[46]

The properties of chromium(II) acetate hydrate, which was first reported in 1844, set it apart from conventional Cr^{II} coordination compounds. Its red color, near diamagnetism (the weak residual paramagnetism corresponding to $\mu_{\text{eff}} = 0.3-0.7\,\mu_B$ is usually attributed to Cr^{III} impurities), and the binuclear structure (**16**) all raise the issue of metal–metal bonding. Cotton *et al.* have prepared and structurally characterized a large number of related molecules, containing carboxylates or other binucleating ligands. While the carboxylate dimers are almost always axially ligated, judicious choice of bridging ligands yields molecules featuring five-coordinate Cr^{II} (including the other chromium atom). The Cr–Cr distances cover a wide range from 183 to 255 pm, depending on the nature of the bridging ligands and the presence of axial ligands. On the basis of these observations, a quadruple bond between the Cr^{II} atoms (consisting of one σ, two degenerate π, and one δ contribution) has been assigned to these dimers.

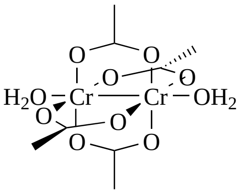

(**16**)

The Cr–Cr distances depend primarily on the presence or absence of axial ligands. Without the latter, Cr–Cr distances below 190 pm are observed and this has led to the designation of 'supershort' Cr–Cr bonds. An electron diffraction study of unligated $[Cr_2(OAc)_4]$ in the gas phase showed a Cr–Cr distance of 196 pm, contrasting with distances in excess of 230 pm for ligated carboxylates in the solid state. The only unligated carboxylate dimer to be crystallographically characterized is $[Cr(O_2C\text{-}2,4,6\text{-}{}^iPr_3C_6H_2)_4]$, with a Cr–Cr distance of 197 pm.**47** The metal–metal distances generally decrease with increasing basicity of the bridging ligand, and, in the presence of axial ligands, the Cr–Cr distances decrease with increasing donor strength of the ligand. Thus, there is a roughly inverse correlation between the Cr–Cr and Cr–L distances of a series of adducts of the type $[Cr_2(O_2CR)_4(L)_2]$. There is an even better inverse correlation, however, between the Cr–Cr distance and the 'pyramidality' of the CrX_4 units, that is, the Cr–Cr–X angle, where X=O of carboxylate, and so on. *Extended Hückel Molecular Orbital Theory* suggests a strengthening of the σ- and π-components of the metal–metal bond as a reason for this effect.**48** In an attempt to compare metal–metal bonds to other covalent bonds, Cotton has introduced the 'formal shortness ratio' (FSR). The FSR for $[Cr_2(2\text{-MeO-5-MeC}_6H_3)_4]$, the compound with the shortest known metal–metal distance, is 0.767, which is even shorter than the FSR for N_2 (0.786).

The photoelectron spectra of Cr–Cr bonded dimers exhibit valence electron ionization energies as low as 6.70 eV, presumably because of electron ejection from the δ-molecular orbital. However, the ionizations from the different M–M bonding MOs cannot always be resolved, and their energies remain uncertain. The electronic spectra exhibit their lowest energy transition at ca. 20 000 cm^{-1}, and this has been assigned to the $\delta \rightarrow \delta^*$ transition. The earlier assignment of the M–M stretching mode of $[Cr_2(mhp)_4]$ at 556 cm^{-1} has been questioned and is now believed to occur at 340 or 400 cm^{-1}.**49** The dissociation constant for $[Cr_2(OAc)_4(OH_2)_2]$ into monomeric Cr^{II} complexes has been measured in acetic acid/water mixtures; K_D ranged from 7×10^{-7} M ($[H_2O] = 8.32$ M) to 4.5×10^{-5} M (pure water).**50**

While the short Cr–Cr distances themselves are unambiguous, the strength of the attendant metal–metal bond has been the subject of some debate. It now seems that the earlier estimate of the bond dissociation energy of a Cr–Cr quadruple bond of 205 kJ mol^{-1} is probably unrealistically high. Indeed, it has been suggested that 'Cr–Cr quadruple bonds may in fact be just artifacts of the bridging ability of the ligands, able to impose both a dinuclear structure and close proximity between the two metals'.**51** However, there exists at least one example of a macrocyclic Cr^{II} complex that has no bridging ligands and clearly features a Cr–Cr bond (Cr–Cr, 209.6 pm, $\mu_{eff} = 0.7\,\mu_B$).**52** There are also several organometallic Cr^{II} (and even Cr^{III}) derivatives that exhibit short Cr–Cr contacts and low effective magnetic moments (*see* ***Chromium: Organometallic Chemistry***). Thus, metal–metal bonding does occur in chromium chemistry, but it is clearly of less consequence than for the heavier elements of this group (Mo, W).

6 RELATED ARTICLES

Chromium: Organometallic Chemistry; Coordination & Organometallic Chemistry: Principles Magnetism of Transition Metal Ions; Metal Ion Toxicity; Nutritional Aspects of Metals & Trace Elements; Oxidation Catalysis by Transition Metal Complexes.

7 REFERENCES

1. G. Cainelli and G. Cardillo, 'Chromium Oxidations in Organic Chemistry', Springer Publishing, Berlin, 1984.
2. S. O. Badanyan, T. T. Minasyan, and S. K. Vardapetyan, *Russ. Chem. Rev. (Engl. Transl.)*, 1987, **56**, 740.
3. J. Muzart, *Chem. Rev.*, 1992, **92**, 113.
4. W. Büchner, 'Industrial Inorganic Chemistry', VCH Publishers, New York, 1989, p. 255.
5. J. Emsley, 'The Elements', 2nd edn., Clarendon Press, Oxford, 1991, p. 52.
6. C. L. Rollinson, in 'Comprehensive Inorganic Chemistry', eds. J. C. Bailar Jr, H. J. Emeléus, R. Nyholm, and A. F. Trotman-Dickenson, Pergamon Press, Oxford, 1973, Vol. 3, Chap. 36, p. 623.
7. 'Gmelins Handbuch der Anorganischen Chemie, Chrom', Teil A, Lieferung 1 und 2, Verlag Chemie, Weinheim, 1963.
8. C. Brevard, P. S. Pregosin, and R. Thouvenot, *Stud. Inorg. Chem.*, 1991, **13**, 59.
9. D. Burrows, 'Chromium: Metabolism and Toxicity', CRC Press, Boca Raton, FL. 1983.
10. S. A. Katz and H. Salem, 'The Biological and Environmental Chemistry of Chromium', VCH Publishers, New York, 1994.
11. A. Levina, R. Codd, C. T. Dillon, and P. A. Lay, Chromium in biology: toxicology and nutritional aspects, in 'Progress in

Inorganic Chemistry', ed. K. D. Karlin, John Wiley & Sons, New York, 2003, Vol. 51, p. 145.

12. X. Wang and L. Andrews, *J. Phys. Chem. A*, 2003, **107**, 570.
13. 'Gmelins Handbuch der Anorganischen Chemie, Chrom', Teil B, Verlag Chemie, Weinheim, 1962.
14. S. Okada, K. Kudou, K. Iizumi, K. Kudaka, I. Higashi, and T. Lundström, *J. Cryst. Growth*, 1996, **166**, 429.
15. M. R. Pressprich, R. D. Willet, R. D. Poshusta, S. C. Saunders, H. B. Davis, and G. L. Gard, *Inorg. Chem.*, 1988, **27**, 260.
16. E. Jacob and E. Willner, *Chem. Ber.*, 1990, **123**, 1319.
17. T. V. Russo, R. L. Martin, and J. P. Hay, *J. Chem. Phys.*, 1995, **102**, 8023.
18. L. Hedberg, K. Hedberg, G. L. Gard, and J. O. Udeaja, *Acta Chem. Scand.*, 1988, **A42**, 318.
19. J. S. Ogden and R. S. Wyatt, *J. Chem. Soc., Dalton Trans.*, 1987, 859.
20. B. B. Ebbinghaus, *Combust. Flame*, 1995, **101**, 311.
21. M. Cieslak-Golonka, *Coord. Chem. Rev.*, 1991, **109**, 223.
22. P. A. Lay, A. Levina, in 'Comprehensive Coordination Chemistry II', eds. J. A. McCleverty & T. J. Meyer, Elsevier, 2004, Vol. 4, p. 313.
23. J. J. H. Edema, S. Gambarotta, F. van Bolhuis, W. J. J. Smeets, and A. L. Spek, *Inorg. Chem.*, 1989, **28**, 1407.
24. S. Trofimenko, 'Scorpionates', Imperial College Press, London, 1999.
25. D. M. Halepoto, D. G. L. Holt, L. F. Larkworthy, G. J. Leigh, D. C. Povey, and G. W. Smith, *J. Chem. Soc., Chem. Commun.*, 1989, 1322.
26. G. Irwin and A. D. Kirk, *Coord. Chem. Rev*, 2001, **211**, 25.
27. A. Filippou, S. Schneider, and G. Schnakenburg, *Angew. Chem., Int. Ed. Engl.*, 2003, **42**, 4486.
28. A. Muñoz-Paez and E. S. Marcos, *J. Am. Chem. Soc.*, 1992, **114**, 6931.
29. D. C. Bradley, R. C. Mehrotra, and D. P. Gaur, 'Metal Alkoxides', Academic Press, London, 1978.
30. M. Bochmann, G. Wilkinson, G. B. Young, M. B. Hursthouse, and K. M. Abdul Malik, *J. Chem. Soc., Dalton Trans.*, 1980, 1863.
31. M. H. Dickmann and M. T. Pope, *Chem. Rev.*, 1994, **94**, 569.
32. K. Qin, C. D. Incarvito, A. L. Rheingold, and K. H. Theopold, *Angew. Chem., Int. Ed. Engl.*, 2002, **41**, 2333.
33. C. S. Garner and D. A. House, *Transition Met. Chem.*, 1970, **6**, 59.
34. C. J. Cairns and D. H. Busch, *Coord. Chem. Rev.*, 1986, **69**, 1.
35. A. Niemann, U. Bossek, K. Wieghardt, C. Butzlaff, A. X. Trautwein, and B. Nuber, *Angew. Chem., Int. Ed. Engl.*, 1992, **31**, 311.
36. A. Hauser, M. Mäder, W. T. Robinson, R. Murugesan, and J. Ferguson, *Inorg. Chem.*, 1987, **26**, 1331.
37. C. C. Cummins, J. Lee, R. R. Schrock, and W. M. Davis, *Angew. Chem.*, 1992, **104**, 1510; *Angew. Chem., Int. Ed. Engl.*, 1992, **31**, 1501.
38. D. A. Vennos, M. E. Badding, and F. J. DiSalvo, *Inorg. Chem.*, 1990, **29**, 4059.
39. K. Qin, C. D. Incarvito, A. L. Rheingold, and K. H. Theopold, *J. Am. Chem. Soc.*, 2002, **124**, 14008.
40. M. Mitewa and P. R. Bontchev, *Coord. Chem. Rev.*, 1985, **61**, 241.
41. E. S. Gould, *Acc. Chem. Res.*, 1986, **19**, 66.
42. J. M. Garrison and T. C. Bruice, *J. Am. Chem. Soc.*, 1989, **111**, 191.
43. E. G. Samsel, K. Srinivasan, and J. K. Kochi, *J. Am. Chem. Soc.*, 1985, **107**, 7607; K. Srinivasan and J. K. Kochi, *Inorg. Chem.*, 1985, **24**, 4671.
44. C. J. Marsden, K. Hedberg, M. M. Ludwig, and G. L. Gard, *Inorg. Chem.*, 1991, **30**, 4761.
45. A. A. Danopoulos, W.-H. Leung, G. Wilkinson, B. Hussain-Bates, and M. B. Hursthouse, *Polyhedron*, 1990, **9**, 2625.
46. F. A. Cotton and R. A. Walton, 'Multiple Bonds between Metal Atoms', 2nd edn., Oxford University Press, Oxford, 1993, chap. 4.
47. F. A. Cotton, E. A. Hillard, C. A. Murillo, and H.-C. Zhou, *J. Am. Chem. Soc.*, 2000, **122**, 416.
48. J. Losada, S. Alvarez, J. J. Novoa, F. Mota, R. Hoffmann, and J. Silvestre, *J. Am. Chem. Soc.*, 1990, **112**, 8998.
49. M. C. Manning and W. C. Trogler, *J. Am. Chem. Soc.*, 1983, **105**, 5311.
50. L. M. Wilson and R. D. Cannon, *Inorg. Chem.*, 1988, **27**, 2382.
51. J. J. H. Edema and S. Gambarotta, *Comments Inorg. Chem.*, 1991, **11**, 195; F. A. Cotton, J. Czuchajowska, and X. Feng, *Inorg. Chem.*, 1990, **29**, 4329.
52. J. J. H. Edema, S. Gambarotta, P. van der Sluis, W. J. J. Smeets, and A. L. Spek, *Inorg. Chem.*, 1989, **28**, 3784.

Acknowledgment

Our investigation of chromium compounds has been supported for many years by the U.S. National Science Foundation, as well as by the Chevron Chemical Co. and its successor, the Chevron Phillips Chemical Co. We thank these organizations for their support.

Chromium: Organometallic Chemistry

Klaus H. Theopold & Robin R. Kucharczyk
University of Delaware, Newark, DE, USA

1	Introduction	1
2	Highly Reduced Chromium Organometallics	1
3	Chromium(0) Organometallics	2
4	Chromium(I) Organometallics	4
5	Chromium(II) Organometallics	6
6	Chromium(III) Organometallics	10
7	Chromium(IV) Organometallics	13
8	Chromium(V) Organometallics	15
9	Chromium(VI) Organometallics	15
10	Related Articles	15
11	References	16

1 INTRODUCTION

The organometallic chemistry of chromium originated with a pair of early discoveries implying the intermediacy of organochromium compounds. In 1866, Berthelot[1] found that acetylene was reduced to ethylene by salts of chromium(II). Forty eight years later, in 1914 Bennett and Turner[2] reported the coupling of aryl groups derived from *Grignard Reagents* in the presence of chromium(III). It was not until 1957, however, that Anet and Leblanc[3] prepared the first pure σ-bonded organochromium compound, $[PhCH_2Cr(H_2O)_5]^{2+}$, and Herwig and Zeiss[4] synthesized $Ph_3Cr(THF)_3$.

Organochromium species containing π-bonded ligands were first prepared by Hein as early as 1919, but were not definitively characterized for another 35 years. Hein[5] reported on the reaction of PhMgBr with $CrCl_3$ to give ‘Chromorganoverbindungen’; this synthesis was reproduced by Zeiss and Tsutsui[6] in 1954, at which time they identified the products as bis(arene)chromium cations. Shortly thereafter, Fischer and Hafner[7] published their route to neutral bis(benzene)chromium. This early work has been chronicled, most recently by Seyferth.[8]

The diverse chemistry of chromium carbonyl complexes has its origin in the discovery of $Cr(CO)_6$ in 1926 by Job and Cassal.[9] Early developments in this area included the preparation of the $(\eta^6\text{-arene})Cr(CO)_3$ family of organometallics by Nicholls and Whiting in 1959,[10] the synthesis of the first structurally characterized carbene complex by Fischer and Maasböl (1965),[11,12] and a subsequent report from Fischer’s laboratory describing *trans*-halogeno(phenylcarbyne)tetracarbonylchromium.[13]

Finally, the history of the chromium–carbon bond would not be complete without mention of the first homoleptic tetraalkyl, $Cr(CH_2SiMe_3)_4$, prepared by Wilkinson and his colleagues in 1970.[14] By this time, organochromium chemistry had become firmly established in the landscape of organometallic chemistry, and since then a vast array of molecules in oxidation states ranging from −IV to +VI has been reported in the chemical literature. Today, organochromium chemistry remains an area of vigorous research, as chemists seek more stereoselective (arene)chromium reagents, more efficient polymerization catalysts, and novel molecules in unusual oxidation states. This article summarizes the relevant chemistry, with emphasis on recent developments of interest. It is organized by the increasing formal oxidation state of the metal. Di- and polynuclear compounds are not explicitly covered here, but can be found in ***Dinuclear Organometallic Cluster Complexes*** and ***Polynuclear Organometallic Cluster Complexes***. A book devoted solely to the organometallic chemistry of chromium was published in 1975.[15] More recent comprehensive reviews are available,[16,17] and synthetic procedures have been summarized very recently.[18,19]

2 HIGHLY REDUCED CHROMIUM ORGANOMETALLICS

The most familiar compounds containing chromium in negative oxidation states are the binary carbonyl anions, also called carbonylmetallates.[20] $[Cr(CO)_5]^{2-}$ has been known for some time, having been first prepared via alkali metal reduction of $Cr(CO)_6$ in liquid ammonia.[21] Refinements of this basic methodology[22,23] have allowed for quantitative synthesis. The monomeric binary carbonyl anion $[Cr(CO)_5]^-$ can be generated electrochemically; its lifetime, however, is only a few seconds.[24] A remarkable ‘superreduced’ carbonylmetallate, $[Cr(CO)_4]^{4-}$, is obtained cleanly and in high yield from the reduction of the (tetracarbonyl)chromium(0) complex of tetramethylethylenediamine (equation 1).[25] The success of this reaction is attributed to ‘reductive labilization’, whereby preferential loss of the poorest acceptor ligand occurs upon reduction.

$$(TMEDA)Cr(CO)_4 + 4Na \xrightarrow{NH_3(l)} Na_4(Cr(CO)_4 + TMEDA \qquad (1)$$

$[Cr(CO)_5]^{2-}$ is a light yellow, extremely air-sensitive powder. *Back Bonding* to the carbonyls is extensive here, and is reflected in the median value of υ_{CO}, 1750 cm^{-1}.[23] This dianion is a strong base, a good nucleophile, and a powerful reducing agent (equations 2–4).[23,26,27]

$$2[Cr(CO)_5]^{2-} + 3H_2O \longrightarrow [HCr_2(CO)_{10}]^- + H_2 + 3OH^- \qquad (2)$$

$$[Cr(CO)_5]^{2-} + CN^- + 2H_2O \longrightarrow [Cr(CO)_5CN]^- + 2OH^- + H_2 \quad (3)$$

$$[Cr(CO)_5]^{2-} + Cl_2CS \longrightarrow 2Cl^- + Cr(CO)_5(CS) \quad (4)$$

Yellow pyrophoric $[Cr(CO)_4]^{4-}$ gives an IR spectrum consistent with its structure and with a *Formal Oxidation State* of -4: the most intense carbonyl band appears at 1462 cm^{-1}. Reaction with three equivalents of Ph_3SnCl in two steps yields $[(Ph_3Sn)_3Cr(CO)_4]^-$, the first seven-coordinate chromium compound with exclusively monodentate ligands. More efficient is the synthesis of $[(Ph_3Sn)_2Cr(CO)_4]^{2-}$ from $(TMEDA)Cr(CO)_4$ and Ph_3SnLi, followed by addition of Ph_3SnCl. These moderately air-sensitive organometallics can be isolated as their Et_4N^+ salts. A single-crystal X-ray study of the tris(triphenyltin) anion confirmed the presence of heptacoordinate chromium.[28] The tetraanion also reacts with NH_4Cl to give $Cr(CO)_4(NH_3)_2$ (rather than the anticipated $[H_3Cr(CO)_4]^-$), and with excess MeCN to give $[H_2Cr(CO)_8]^{2-}$. Further information on the reactivity of these carbonylmetallates and their derivatives can be found in a review article describing these compounds.[29]

Substituted compounds of chromium in negative oxidation states are also known. Two apparent examples are $[(\eta^6\text{-}C_6H_6)Cr(CO)_3]^{2-}$ and $[(bipy)Cr(CO)_4]^-$.[30,31] An EPR spectrum of the latter compound, however, indicated that the unpaired electron resides within the aromatic ring; this result implies that chromium is actually in the zero oxidation state, bound to $(bipy)^-$.[23] Finally, potassium reduction of $Cr(\eta^6\text{-}C_6H_6)_2$ yielded the corresponding radical anion $[Cr(\eta^6\text{-}C_6H_6)_2]^-$, a Cr(-I) compound without any carbonyl ligands, which was characterized by ESR spectroscopy.[32]

3 CHROMIUM(0) ORGANOMETALLICS

This section highlights some of the significant features of chromium(0) carbonyls and of the chemistry of this oxidation state. Further information can be found in the articles ***Carbonyl Complexes of the Transition Metals*** and ***Organic Synthesis using Transition Metal Carbonyl Complexes***, and in the review literature.[15,16]

3.1 Chromium Hexacarbonyl

This colorless, volatile, and air-stable solid is the starting material for synthesis of many Cr^0 derivatives. Commercially available, it is seldom synthesized; however, *Reductive Carbonylation* (e.g. equation 5) gives higher yields and is more reliable than other methods. $Cr(CO)_6$ melts at 130 °C, sublimes at room temperature in vacuo, and dissolves slightly in organic solvents. It exhibits perfect octahedral symmetry, as determined by electron and neutron diffraction and X-ray crystallography. The IR spectrum of this material in CCl_4 shows a single sharp band at 1984 cm^{-1}.

$$CrCl_3 + xsCO + LiAlH_4 \xrightarrow{Et_2O} Cr(CO)_6 \quad (5)$$

$$Cr(CO)_6 \xrightarrow{h\nu} Cr(CO)_5 + CO \quad (6)$$

Chromium hexacarbonyl is extremely photolabile (equation 6); therefore photochemical substitution is an efficient means of preparing derivatives.[33] Oxidation of the Cr^0 center requires nitric or sulfuric acid, or chlorine. Alternatively, some ligands induce complete carbonyl dissociation with concomitant oxidation, for example, acetylacetonate. Chemical reduction with alkali or alkaline-earth metals or electrochemical reduction proceeds in two-electron steps with loss of two CO molecules to first give $[Cr_2(CO)_{10}]^{2-}$ and then $[Cr(CO)_5]^{2-}$. Nucleophilic attack at CO generates a number of stable (Nu = R) and unstable (Nu = N_3, OH, H, NEt_2) products. The stable $[(OC)_5CrCOR]^-$ ion is a carbene precursor.

3.2 Substituted Chromium(0) Carbonyls Without Carbon Ligands[34]

The derivatives of chromium hexacarbonyl, $Cr(CO)_{6-x}(L)_x$, make up the single largest class of organochromium compounds, and a substantial number of these are Cr^0 compounds as well. The most common synthetic route involves direct reaction of $Cr(CO)_6$ and x L, but displacement of a weakly bound ligand from a carbonyl derivative is also frequently employed. Carbonyl dissociation is usually promoted with heating or UV irradiation.

The rare chromium carbonyl fluoride $[Cr(CO)_5F]^-$ can be prepared oxidatively or by substitution; it is stable in air for short periods. Protonation of $[Cr(CO)_5]^{2-}$ with methanol yields the carbonyl hydride $[HCr(CO)_5]^-$,[35] isolable as the Et_4N^+ or Ph_4As^+ salt. Its hydride resonance in the ^1H NMR spectrum is located at -7.0 ppm. Since σ-donor nitrogen ligands lack the acceptor ability of CO, an ability that minimizes the buildup of electron density on chromium trisubstitution is the maximum extent of reaction observed, for example, between $Cr(CO)_6$ and NH_3. Nucleophilic attack of an azide at a carbonyl carbon of $Cr(CO)_6$ gives an isocyanate following a Curtius-type degradation (Scheme 1). (Ammine)pentacarbonylchromium undergoes a condensation reaction with acetone in the presence of a drying agent to give the (ketimine)pentacarbonyl compound.

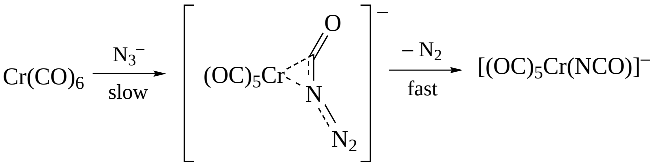

Scheme 1

$Cr(CO)_5(THF)$, an O-donor derivative, is synthetically useful as a source of the unsaturated fragment $Cr(CO)_5$, as the weakly bound cyclic ether is easily dissociated or displaced.[36] By contrast, phosphines (PR_3), phosphites ($P(OR)_3$), phosphorus halides (PX_3), phosphorus amines ($P(NR_2)_3$), phosphinites ($PR_2(OR)$), and phosphonites ($PR(OR)_2$) are σ-donor/π-acceptor ligands that readily substitute for THF, forming stable derivatives. The better π-acceptors, $P(OR)_3$ and PF_3, can form the homoleptic compounds $Cr\{P(OR)_3\}_6$ and $Cr(PF_3)_6$. A vast number of Cr^0 complexes containing carbonyl and phosphorus ligands can be found in the literature;[37,38] the reader is referred to these sources for information on specific complexes, syntheses, and reactions. Forcing conditions are necessary to form carbonyl compounds of the remaining group 15 ligands. As with the phosphorus derivatives, polydentate ligands and unusual compounds have been reported, for example, Scheme 2. An X-ray crystallographic structure revealed very short As=Cr bonds in this molecule, that is, 2.38 Å.

The nitrosonium ion[39] and the alkyl- and aryldiazonium ions[40] are π-acceptor ligands that are isoelectronic with carbon monoxide. Other π-acceptors are characterized by the α-diimine moiety; these include the stabilizing ligands bipy, phen, and terpy. Mononitrosyl complexes of chromium(0) have been known for some time (Scheme 3);[41] recently renewed interest in (nitrosyl)chromium species has led to the development of routes to $(\eta^5\text{-}C_5H_5)Cr(NO)_2X$ ($X = CH_2SiMe_3$, Cl, Me, FPF_5) and $[(\eta^5\text{-}C_5H_5)Cr(NO)_2L]^+$ ($L = PPh_3$, NCR, CNR, py, H_2NAr). A recent review of organometallic metal-NO complexes, including chromium compounds, is available.[42] The first thionitrosyl complex has been prepared using the novel reagent $N_3S_3Cl_3$ with $[(\eta^5\text{-}C_5H_5)Cr(CO)_3]^-$.[43] On the basis of CO stretching frequencies, it is likely that NS is even superior to NO as a π-acceptor. Other Cr^0 complexes containing sulfur, as well as selenium and tellurium ligands, have been described.[16,17]

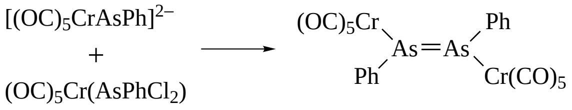

Scheme 2

3.3 Substituted Chromium(0) Carbonyls with σ-donor Carbon Ligands

Among the types of complexes found here are formyl, acyl, alkyl, and aryl carbonyls, carbonyl cyanides,[44] carbonyl isocyanides and acetylides,[45] and thiocarbonyl and selenocarbonyl complexes.[46] Of the greatest significance, however, are the chromium carbenes, for example, $(CO)_5Cr{=}C(OR)R'$. This chemistry has been thoroughly reviewed;[47] nevertheless, these compounds will be briefly discussed here.

The first carbene compound to be well characterized was prepared in 1966 and was one of many *Fischer-Type Carbene Complexes* to be reported (see equation 7). Fischer carbenes are characterized by heteroatom substituents at the carbene carbon, stabilization by a low-valent metal center, and a partial positive charge at the carbene carbon. In contrast, *Schrock-Type Carbene Complexes*, or alkylidenes,[48] that have alkyl substituents, are found on metal centers in higher oxidation states, and are nucleophilic at carbon. Many Fischer carbenes are known for chromium, whereas chromium alkylidenes are much less common. Monohalocarbenes of chromium, for example, $(OC)_5Cr{=}C(F)NEt_2$, have also been extensively investigated.[49] Two carbene reactions of note for their application to organic synthesis are the cycloaddition of alkenes with carbene complexes and the reaction of aromatic carbenes with alkynes to yield complexed naphthols (the 'Dötz reaction').[50]

$$Cr(CO)_6 \xrightarrow{PhLi} [(OC)_5C{=}C(O)Ph]^- \xrightarrow{MeI} (OC)_5Cr{=}C(OMe)Ph \quad (7)$$

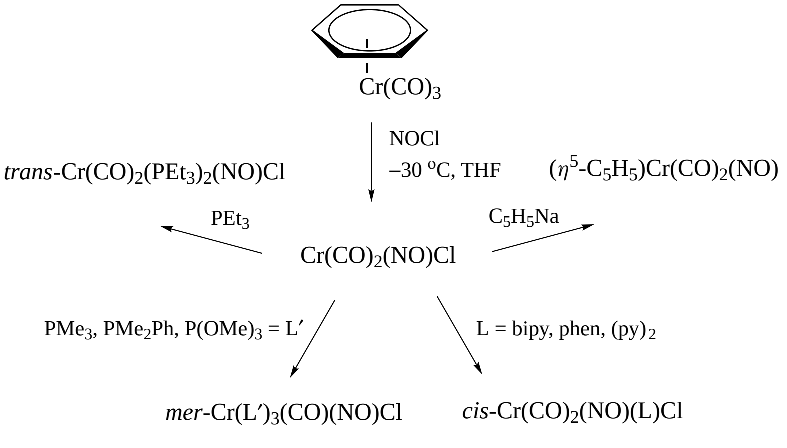

Scheme 3

4 CHROMIUM(I) ORGANOMETALLICS

4.1 Carbonyl Compounds of Chromium(I)

Almost all of the organochromium(I) compounds to be discussed in this section have a *Seventeen Electron Configuration*; that is, they are electron-deficient metallaradicals. In view of the π-acidity of the CO ligand, one would expect the more stable carbonyl species to possess one or more σ-donor ligands to compensate for the electron deficiency at chromium and the acceptor nature of the carbonyls. By this argument, $Cr(CO)_6{}^+$,[51] produced electrochemically from $Cr(CO)_6$, should be among the least stable examples of a chromium(I) carbonyl; in fact, it has a half-life of only seconds at room temperature. Pentacarbonyl halides, $Cr(CO)_5X$ ($X = F$, Cl, Br, I),[52] can be obtained via electrochemical oxidation of the corresponding anions; oxidative cleavage of $[Cr_2(CO)_{10}]^{2-}$ by I_2 constitutes an alternative route to the iodide, which in the solid state decomposes only slowly at 25 °C. The iodide also serves as the starting material for syntheses of other Cr^I derivatives (see equations 8 and 9). By contrast, the fluoride has a lifetime of minutes when in solution at ambient temperature.

$$Cr(CO)_5I + CN^- \longrightarrow Cr(CO)_5CN + I^- \quad (8)$$

$$Cr(CO)_5I + 4NH_3 \longrightarrow [Cr(CO)_2(NH_3)_4]I + 3CO \quad (9)$$

Tetracarbonyl cations $[Cr(CO)_4(L_2)]^+$, where L_2 represents arylphosphines, alkyl, or aryl phosphites, or a bidentate ligand with phosphorus or arsenic donor atoms, have been produced by both chemical and electrochemical means. However, only one of these complexes, namely, *trans*-$[Cr(CO)_4(PPh_3)_2]^+$, is stable enough to be isolated as the perchlorate salt.[53] Exposure to light and moisture produces *trans*-$Cr(CO)_4(PPh_3)_2$ via disproportionation. Just as easily isolated, but somewhat less sensitive, are the $[Cr(CO)_3(PR_3)_3]^+$ cations.[54] Oxidation with a silver ion or NO^+ converts the *fac*-($R_3 = Me_2Ph$, $(OMe)_3$) and *mer*-($R_3 = (OMe)_3$, $(OMe)_2Ph$, $(OPh)_3$) complexes into Cr^I products with mer structures. Light and heat promote the formation of reduced *mer*-$Cr(CO)_3(PR_3)_3$. These tetra(carbonyl) and tri(carbonyl) cations have been the subject of ESR spectroscopy and theoretical study.[55]

Tricarbonyl complexes of the tridentate ligand hydridotris(1-pyrazolyl)borate (Tp) and its 3,5-dimethyl analogue (Tp*), as well as of tetrakis(1-pyrazolyl)borate (Tp′), have been reported recently.[56] Each is prepared from the corresponding anion by oxidation with a ferricinium ion. Ligand substitution on $TpCr(CO)_3$ yields a phosphine derivative, $TpCr(CO)_2(PMe_3)$. Interestingly, $TpCr(CO)_3$ does not react with other, larger phosphines, while $Tp^*Cr(CO)_3$ is evidently too sterically hindered to undergo phosphine substitution at all. Although all four compounds are readily oxidized, they can be stored for several days at room temperature if kept under an inert atmosphere. EPR spectra of the Tp and Tp* tricarbonyls have been obtained at 5 K. The extremely low temperature was necessary in order to lower the C_{3v} symmetry of the chromium centers, breaking the associated orbital degeneracies so that spectral resonances could be observed. Not unexpectedly, the EPR spectra of the $Tp'Cr(CO)_3$ and $TpCr(CO)_2(PMe_3)$ complexes could be obtained at much higher temperatures (120 and 225 K respectively) because of their relatively lower symmetries.

The oxidation of substituted dicarbonyl complexes of chromium(I) featuring the bidentate ligands dppm and dppe has been examined. Chromium(0) starting materials, $Cr(CO)_2(dppm)_2$ and $Cr(CO)_2(dppe)_2$, both with cis carbonyl configurations, were oxidized to trans cations $[Cr(CO)_2(dppm)_2]^+$ and $[Cr(CO)_2(dppe)_2]^+$; chemical and electrochemical methods were employed. Chemical oxidation of the dppm compound proved more facile than that of the dppe analogue; this had been predicted on the basis of electrochemical studies. The dicarbonyl hydride, $[Cr^{II}(CO)_2(dppm)_2H]^+$, was isolated from the oxidation reaction of $[Cr(CO)_2(dppm)_2]$ with $O_2/HClO_4$, while the same reaction conditions oxidized the neutral dppe complex to the cation.

4.2 Cyclopentadienyl Compounds of Chromium(I)

Most of the (cyclopentadienyl)chromium(I) compounds found in the literature are of three types: nitrosyl complexes, both neutral and cationic, unsymmetrical sandwich complexes, and carbonyl complexes. Representative nitrosyl-containing molecules include $(\eta^5\text{-}C_5H_5)Cr(NO)(L)Cl$ ($L = py$, PR_3, $AsPh_3$, CNR, etc.), $(\eta^5\text{-}C_5H_5)Cr(NO)(PPh_3)CH_2SiMe_3$, $[(\eta^5\text{-}C_5H_5)Cr(NO)(L_2)]$ PF_6 ($L_2 = $ bipy, phen), and $[(\eta^5\text{-}C_5H_5)Cr(NO)(NCMe)_2]$ PF_6.[42] Although structurally and electronically similar, the two neutral compounds are prepared via dissimilar routes; this is also true of the cations. The chlorodinitrosyl complex $(\eta^5\text{-}C_5H_5)Cr(NO)_2Cl$ undergoes ligand substitution with strong Lewis bases to form the Cr^I mononitrosyls with liberation of NO. On the other hand, mononitrosyl $(\eta^5\text{-}C_5H_5)Cr(NO)(PPh_3)I$, a chromium(I) nitrosyl itself, serves as the synthetic precursor for the (trimethylsilyl)methyl species; ligand exchange being effected with Me_3SiCH_2MgCl (Scheme 4).

Noteworthy is the fact that these neutral nitrosyls, including the precursor iodide, are chiral by virtue of having four unique ligands bound to chromium. Reaction of bipy or phen with $[(\eta^5\text{-}C_5H_5)Cr(NO)_2(MeCN)]PF_6$ at 100 °C results in displacement of MeCN and one NO

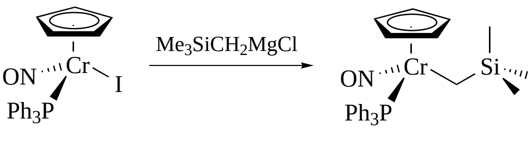

Scheme 4

group by the incoming bidentate ligand. Finally, cleavage of a nitrosyl iodide dimer, $[(\eta^5\text{-}C_5H_5)Cr(NO)I]_2$, with $AgPF_6$ in MeCN affords the nitrosylbis(acetonitrile) cation. These four compounds exhibit a range of stabilities. $[(\eta^5\text{-}C_5H_5)Cr(NO)_2L_2]$ PF_6 is extremely robust, while the bis(acetonitrile) cation and the chloronitrosyl complex can be handled briefly in air as solids. Magnetic moments are appropriate for d^5 low-spin systems: $1.47–1.96\,\mu_B$ (spin-only value $= 1.73\,\mu_B$). Structure determinations carried out on $(\eta^5\text{-}C_5H_5)Cr(NO)(PPh_3)CH_2SiMe_3$ and on $[(\eta^5\text{-}C_5H_5)Cr(NO)(NCCH_3)_2]PF_6$ revealed a three-legged *Piano Stool Structure* for both with no geometric distortions attributable to the effects of the unpaired electron in these metallaradicals. Studies of the reactivity of the trimethylsilylmethyl cation provided routes to two novel compounds. Treatment with NO, NO^+, and $2HSnPh_3$ led to isolation of $(\eta^5\text{-}C_5H_5)Cr(NO)_2CH_2SiMe_3$, $[(\eta^5\text{-}C_5H_5)Cr(NO)_2(PPh_3)]PF_6$, and $(\eta^5\text{-}C_5H_5)Cr(NO)(PPh_3)(SnPh_3)H$ (see Section 5.2).

Among the 17-electron species are those in which the *Cyclopentadienyl* ligand and a cyclic triene or arene form an unsymmetrical sandwich complex. The most familiar example, $(\eta^5\text{-}C_5H_5)Cr(\eta^6\text{-}C_6H_6)$,**[57]** is synthesized from $CrCl_3$, either C_5H_5MgBr or NaC_5H_5, and PhMgBr. Very reactive, it does not undergo Friedel–Crafts acylation but rather a ring expansion (Scheme 5), yielding $[(\eta^5\text{-}C_5H_5)Cr(\eta^7\text{-}C_7H_6R)]^+$. In the presence of cycloheptatriene and $AlCl_3$ or azulene and $BF_3{\cdot}Me_2O$, arene replacement occurs to give $[\eta^5\text{-}C_5H_5)Cr(\eta^7\text{-}C_7H_7)]^+$ and $[(\eta^5\text{-}C_5H_5)Cr(\eta^7\text{-azulenium})]^+$, respectively. Its permethylated analogue, $(\eta^5\text{-}C_5Me_5)Cr(\eta^6\text{-}C_6Me_6)$, has been obtained from the thermal reaction of dimeric $[(\eta^5\text{-}C_5Me_5)Cr(\mu\text{-}Cl)Me]_2$ and excess 2-butyne.**[58]** Photolysis of a mixture of $(\eta^5\text{-}C_5H_5)CrCl_2{\cdot}THF$, *i*-PrMgBr, and cycloheptatriene yields the $(\eta^6\text{-}C_7H_8)$ sandwich; air oxidation converts this to the cationic cycloheptatrienyl complex. Substitution of 1,3,5-cyclooctatriene or cyclooctatetraene in this preparation gives the analogous $(\eta^6\text{-}C_8H_{10})$ and $(\eta^6\text{-}C_8H_8)$ products. The latter can be protonated and reacted with R^- ($R = H$, Me), forming $(\eta^5\text{-}C_5H_5)Cr(7\text{-R-}1,3,5\text{-cyclooctatriene})$.

Recent interest in metal-centered radicals**[59,60]** has prompted numerous studies of the 17-electron monomers $(\eta^5\text{-}C_5H_5)Cr(CO)_3$ and $(\eta^5\text{-}C_5Me_5)Cr(CO)_3$, present to various extents at ambient temperature via dissociation of the parent dimers (e. g. equation 10).**[61]**

$$[(\eta^5\text{-}C_5H_5)Cr(CO)_3]_2 \rightleftharpoons 2(\eta^5\text{-}C_5H_5Cr(CO)_3) \qquad (10)$$

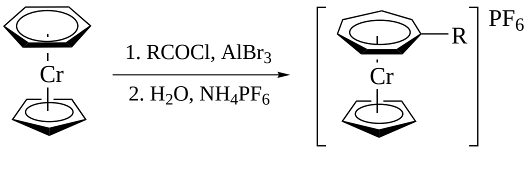

Scheme 5

That the chemistry of $[(\eta^5\text{-}C_5H_5)Cr(CO)_3]_2$ reflects the reactivity of the monomer can be seen in the products of atom abstraction, ligand substitution, and disproportionation reactions. A number of phosphine derivatives have been prepared; however, only $(\eta^5\text{-}C_5H_5)Cr(CO)_2PPh_3$ was sufficiently robust to be isolated in a crystalline form and fully characterized. In addition, dppm, dppe, and dppb gave stable disproportionation products. A comparative study of the analogous $(\eta^5\text{-}C_5Me_5)$ dimer and monomer revealed a longer, weaker Cr–Cr bond than is present in the cyclopentadienyl dimer;**[62]** reactivity toward *t*-BuNC and smaller phosphines (e.g. PMe_3 and $P(OMe)_3$), yielding very air sensitive, thermally labile derivatives, and participation in atom abstraction reactions to form labile halo, hydrido, alkyl, and tributyltin compounds of $(\eta^5\text{-}C_5Me_5)Cr(CO)_3$. Crystal-structure determinations have been carried out on $(\eta^5\text{-}C_5Me_5)Cr(CO)_2PPh_3$ and on $(\eta^5\text{-}C_5Me_5)Cr(CO)_2PMe_3$. Both exhibit monomeric three-legged piano-stool structures. The unusually small OC–Cr–CO bond angles, 80.9 °C and 79.9 °C, respectively, contrast with the approximate value of 90 °C for similar *Eighteen Electron Compounds* and are believed to represent a deformation associated with location of the electron 'hole' between the carbonyl ligands.

4.3 Arene, Bis(Arene), and Other π-ligand Compounds of Chromium(I)

Monoarene complexes of the form $[(\eta^6\text{-}C_6R_6)Cr(CO)_2L]^+$ ($R = H$, Me; $L = CO$, PR_3) may be prepared from the corresponding 18-electron species via chemical or electrochemical oxidation. The (benzene)tricarbonyl chromium cation is of limited stability; however, substituted arene complexes, for example, $[(\text{hexaethylbenzene})Cr(CO)_3]^+$, exhibit appreciable lifetimes on the cyclic voltammetric timescale.**[63]** Substantially more robust are the dicarbonyl cations $[(\eta^6\text{-}C_6Me_6)Cr(CO)_2L]^+$ ($L = PPh_3$, $PMePh_2$, PMe_2Ph), $[(\eta^6\text{-biphenyl})Cr(CO)_2PPh_3]^+$, and $[(\eta^6\text{-}C_6Me_6)Cr(CO)_2(RC{\equiv}CR)]^+$ ($R = Ph$, $4\text{-}MeOC_6H_4$).

Unlike bis(benzene)chromium itself, the bis(benzene)chromium cation and its numerous substituted analogues are air stable as solids and in solution. Three of these compounds, $[(\eta^6\text{-benzene})_2Cr]^+$, $[(\eta^6\text{-benzene})(\eta^6\text{-biphenyl})Cr]^+$, and $[(\eta^6\text{-biphenyl})_2Cr]^+$, were isolated by Hein during his historic work with 'Chromorganoverbindungen' in 1919.**[5]** Crystal structures feature eclipsed arene rings, and magnetic moments lie within the range $1.70–1.80\,\mu_B$.**[15]** These cations are derived from oxidation of $(\eta^6\text{-arene})_2Cr$. Alkyl and aryl halides, RX, oxidize bis(arene) complexes with the formation of $R{\cdot}$, which subsequently abstracts hydrogen, disproportionates, or dimerizes. Halogen oxidation is also effective in some cases. Most reactions of $[(\eta^6\text{-arene})_2Cr]^+$ are reductive in nature or decompose the molecule. Acid-promoted and oxidative routes to the free arene are also known.

5 CHROMIUM(II) ORGANOMETALLICS

5.1 Mono-, Di-, and Poly(organo)chromium(II) Compounds

Significantly fewer complexes of these types are known for chromium(II) than for chromium(III). Solvated species are of the general formula $\mathrm{R}_n\mathrm{CrCl}_{2-n}\mathrm{S}_x$ and can be prepared directly from $\mathrm{CrX_2}$ or $\mathrm{CrX_2(THF)_2}$ (X = Cl, Br) and one or two equivalents of Grignard reagents. Only two mono(organo) compounds, (1-naphthyl)CrBr(THF) and its 1-(2-methyl)naphthyl analog, have been prepared in this manner. The only other RCrClS_x complex, a mesityl chloride, was obtained via ligand exchange between solvated bis(mesityl)chromium and $\mathrm{CrCl_2}$.

In contrast, numerous examples of $\mathrm{R_2CrS}_x$ have been synthesized by the Grignard route, for example, $\mathrm{(mesityl)_2CrS}_x$ ($\mathrm{S}_x = \mathrm{(THF)_3}$ or (THF)(bipy)), $\mathrm{(Ph)_2Cr(bipy)_2}$, and ($o$-anisyl)$_2$Cr(bipy)$_2$. One finds that substitution of an N- or P-donor ligand for THF in these molecules stabilizes them considerably. For example, $\mathrm{(Ph)_2Cr(THF)}_n$ is an unstable brown solution at temperatures of −30 °C and above, whereas the bipy solvate is an isolable blue solid. Alternatives to the Grignard route include reaction with lithium reagents (equation 11) or thermal transformations of tri(organo)chromium(III) species and metal poly(organo)chromates (equation 12).

$$\mathrm{CrCl_2(THF)_2} \xrightarrow[-70\,^\circ\mathrm{C}]{2\mathrm{PhLi}} \mathrm{Ph_2Cr(THF)}_n \xrightarrow{2\mathrm{bipy}} \mathrm{Ph_2Cr(bipy)_2} \tag{11}$$

$$\mathrm{Ph_2Cr^{III}(CHPh_2)(THF)}_n \xrightarrow[\mathrm{bipy}]{\Delta,\ \mathrm{THF}} \mathrm{Ph_2Cr^{II}(bipy)_2} + \mathrm{Ph_2CH}\bullet \tag{12}$$

Chromium(II) polyorganochromates, $\mathrm{M_2CrR_4}$, exist as monomers and as dimers; the latter are discussed in ***Dinuclear Organometallic Cluster Complexes***. Reaction of appropriate lithium reagents with $\mathrm{CrBr_2(THF)_2}$ yields the three complexes $\mathrm{Li_2[Cr(}$*N*-methylpyrrolyl$\mathrm{)_4](THF)_3}$, $\mathrm{Li_2[CrPh_4](THF)_4}$, and $\mathrm{Li_2[Cr(mesityl)_4](THF)_4}$. The tetraphenyl compound may also be prepared from PhLi and $\mathrm{(Ph)_2CHCr(Ph)_2(THF)}_n$. Reversible cleavage of the chromium−chromium quadruple bond of $\mathrm{[Cr_2Me_8][Li(L)]_4}$ (L = THF, $\mathrm{Et_2O}$) gives the high-spin species $\mathrm{Li_2CrMe_4}$.**[64]** Cleavage is achieved by replacing the Lewis base coordinated to the lithium with TMEDA. Alternatively, the compound can be synthesized from $\mathrm{CrCl_2(THF)_2}$ and four equivalents of MeLi in $\mathrm{Et_2O}$ with an excess of TMEDA present (Scheme 6). Analogous complexes $\mathrm{(TMEDA)CrR_2}$ (R = $\mathrm{CH_2Ph}$, $\mathrm{CH_2CMe_3}$, $\mathrm{CH_2C(Ph)Me_2}$) have been prepared as well.**[65]**

As a rule, these compounds are very sensitive to oxygen and water. The solvated compounds tend to lose solvent molecules in vacuo. Magnetic measurements reveal the presence of high-spin and low-spin $\mathrm{Cr^{II}}$ species within this group. $\mathrm{(Mesityl)_2Cr(THF)_3}$ has an associated magnetic moment of 4.82 μ_B, the spin-only value for a system with four unpaired electrons being 4.9 μ_B. These values can be compared with the value of 3.22 μ_B for $\mathrm{(Ph)_2Cr(bipy)_2}$, which is indicative of a system with only two electrons unpaired (spin-only value = 2.8 μ_B). Little is known about the chemistry of these organochromium(II) compounds. Most have been shown to react with $\mathrm{HgCl_2}$ to give RHgCl and $\mathrm{Hg_2Cl_2}$, and to undergo the same Cr–C bond cleavage in the presence of $\mathrm{I_2}$. Hydrolysis and oxidation are two other reactions reported for some complexes.

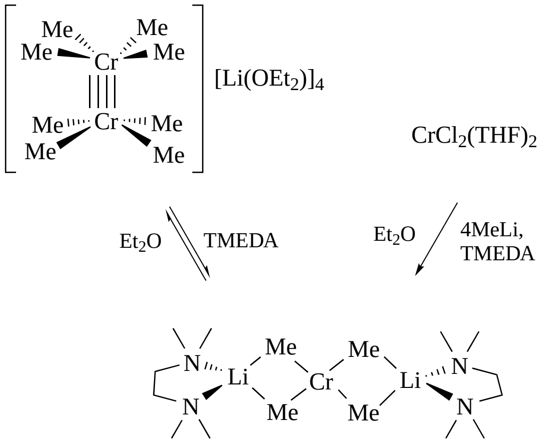

Scheme 6

5.2 Chromium(II) Hydrides

The majority of compounds in this family can be described by the formula $(\eta^5\text{-}\mathrm{C_5R_5})\mathrm{CrL_1L_2L_3H}$, where R = H or Me and $\mathrm{L_1{-}L_3}$ represent some combination of three carbonyl and/or phosphine ligands (*see* ***Hydride Complexes of the Transition Metals***). The most familiar hydride, $(\eta^5\text{-}\mathrm{C_5H_5})\mathrm{Cr(CO)_3H}$, is obtained from the reaction of chromocene with CO and $\mathrm{H_2}$. Addition of cyclopentadiene to $\mathrm{(MeCN)_3Cr(CO)_3}$ also affords the desired product, as does the synthesis from $\mathrm{Cr(CO)_6}$ and a metal cyclopentadienide followed by protonation. A weak acid, this thermally unstable species readily loses a molecule of hydrogen en route to reversible formation of the dimer $[(\eta^5\text{-}\mathrm{C_5H_5})\mathrm{Cr(CO)_3}]_2$. Reactions include carboxylation in the presence of $\mathrm{BF_3{\cdot}Me_2O}$ to give $[(\eta^5\text{-}\mathrm{C_5H_5})\mathrm{Cr(CO)_4}]\mathrm{BF_4}$ and preparation of compounds containing chromium−metal bonds. This hydride is also known to be an active catalyst for the hydrogenation of conjugated dienes, for example, isoprene; however, the $(\eta^6\text{-arene})\mathrm{Cr(CO)_3}$ system exhibits far greater stereoselectivity.

The $(\eta^5\text{-}\mathrm{C_5Me_5})$ analogue of $(\eta^5\text{-}\mathrm{C_5H_5})\mathrm{Cr(CO)_3H}$ was first identified in 1983,**[66]** but no details of its preparation or characterization were mentioned. A subsequent report described several synthetic routes: from $[(\eta^5\text{-}\mathrm{C_5Me_5})\mathrm{Cr(CO)_2}]_2$ and moist $\mathrm{LiPF_6}$ in $\mathrm{CH_2Cl_2}$ or $\mathrm{H_2O}$ in toluene, from treatment of $[(\eta^5\text{-}\mathrm{C_5Me_5})\mathrm{Cr(CO)_3}]\mathrm{Na}$ with acetic acid, and from

$(MeCN)_3Cr(CO)_3$ and C_5Me_5H.[67] It is also formed in the reaction of (η^5-C_5Me_5)$Cr(CO)_3$ with H_2S, the other products being (η^5-C_5Me_5)$Cr(CO)_3SH$ and [(η^5-C_5Me_5)$Cr(CO)_2$]$_2$(μ-S).[68] (η^5-C_5Me_5)$Cr(CO)_3H$ is a sublimable, air-sensitive crystalline solid. Solutions turn dark red when exposed to air or O_2, indicative of the presence of an unidentified transient species, which decomposes in the absence of O_2.

The hydride (η^5-C_5H_5)$Cr(P(OMe)_3)_3H$ has been prepared quantitatively from (η^5-C_5H_5)$CrCl_2$(THF), $NaBH_4$, and excess $P(OMe)_3$. Treatment of this product with CO results in a single substitution, and (η^5-C_5H_5)$Cr(P(OMe)_3)_2(CO)H$ forms. Reaction with CCl_4 oxidizes the chromium center, giving (η^5-C_5H_5)$CrCl_2(P(OMe)_3)$. Nitrosylation yields one of two products, monomeric (η^5-C_5H_5)$Cr(P(OMe)_3)_2NO$ or the hydride-bridged dimer {(η^5-C_5H_5)$Cr(NO)_2$}$_2$(μ_2-H).

The substituted hydride (η^5-C_5R_5)$Cr(CO)_2$(CDPP)H (R = H, Me; CDPP = cyclohexyldiphenylphosphine) was one of several products formed following substitution of phosphine for carbonyl in the 17-electron moiety (η^5-C_5R_5)$Cr(CO)_3$. This complex could also be synthesized by refluxing the chromium tricarbonyl dimer and CDPP in ethanol. Crystallographic analysis revealed a four-legged piano-stool structure with cis carbonyl ligands.

The first hydrido nitrosyl compound to be isolated, (η^5-C_5H_5)$Cr(NO)(PPh_3)(SnPh_3)H$, was derived from (η^5-C_5H_5)$Cr(NO)(PPh_3)(CH_2SiMe_3)$ and two equivalents of $HSnPh_3$. Its chemistry is yet to be investigated.

Other Cr^{II} hydrides of interest include (η^5-C_8H_{11})$Cr(PF_3)_3H$ and (η^6-C_6H_6)$Cr(CO)_2(SiCl_3)H$. The former complex was obtained in 2% yield upon cocondensation of chromium vapor, cyclooctadiene, and PF_3; its structure was verified crystallographically.[69] Although the hydridic hydrogen was not located, its ^1H NMR signal was observed. Of mechanistic significance is the fact that this molecule is structurally equivalent to an intermediate in the interconversion of (1,3-) and (1,5-cyclooctadiene)$Cr(PF_3)_3$ by the π-allylhydrido mechanism (Scheme 7). Preparation of the latter involves UV irradiation of a mixture of (η^6-C_6H_6)$Cr(CO)_3$ and $HSiCl_3$; IR spectral evidence indicates a distorted square-pyramidal structure with an apical arene ligand and cis carbonyls.

In this context, the tetranuclear hydride clusters [(η^5-C_5Me_5)Cr(μ-H)]$_4$ and [(η^5-C_5Me_4Et)Cr(μ-H)]$_4$ should be mentioned; they adopt a cubane-type structure and exhibit antiferromagnetic coupling between the Cr^{II} centers.[70]

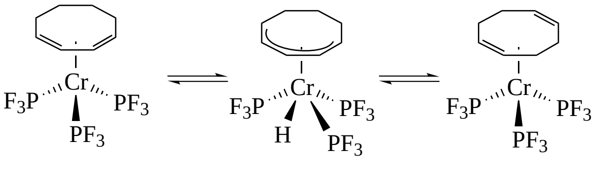

Scheme 7

Interestingly, the isotopomers (η^5-C_5Me_4Et)$_4Cr_4$(μ-H)$_x$(m-D)$_{4-x}$ exhibit extremely large isotope effects on the ^{13}C NMR chemical shifts of the cyclopentadienyl ligands ($\Delta\delta = 0.37-3.06$ ppm per H/D substitution). This effect has been used to measure the barrier for the exchange of the hydride ligands ($\Delta G^{\ddagger} = 12$ kcal mol^{-1}).[71] Further addition at H_2 at high pressure produced the hydride cluster (η^5-C_5Me_4Et)$_4Cr_4$(μ-H)$_7$, which was structurally characterized by neutron diffraction. This mixed-valent ($Cr^{III}{}_3Cr^{II}$) molecule has a spin state of $S = 7/2$.[72]

5.3 Carbonyl Compounds of Chromium(II)

This section describes chromium(II) species with two or more carbon monoxide ligands; (cyclopentadienyl)chromium carbonyls are presented separately (Section 5.4). An unusual seven-coordinate cation, $[Cr(CO)_2(diars)_2X]^+$ (X = Br, I), was prepared via oxidation of the precursor $Cr(CO)_2(diars)_2$ with X_2. This complex is an 18-electron, diamagnetic halide salt. An excess of X_2 does not oxidize it to Cr^{III}; instead, only the trihalide salt is isolated. $[Cr(CO)_4(SnPh_3)_3]^-$, a heptacoordinate anion, is the product of the reaction of *cis*-$[Cr(CO)_4(SnPh_3)_2]^{2-}$ with one equivalent of $SnPh_3Cl$. The first thermally stable chromium carbonyl species with seven monodentate ligands, it is subject to loss of a triphenylstannyl group via reduction or bond heterolysis. Electrochemical oxidation of $Cr(CO)_5X$ (X = Cl, Br, I) generated the halopentacarbonyl cations $[Cr(CO)_5X]^+$ at −75 °C. The room-temperature instability of these species, as well as the potentials required for their formation, were shown to account for the inability to produce $[Cr(CO)_5X]^+$ previously by chemical means. Finally, a bis(trichlorosilyl) complex, (η^6-C_6H_6)$Cr(CO)_2(SiCl_3)_2$, was obtained from the photolysis of (η^6-C_6H_6)$Cr(CO)_3$ in the presence of excess $HSiCl_3$.

5.4 (η^5-cyclopentadienyl)chromium(II) Carbonyl Compounds

Chromium compounds of this type feature one to four carbonyls and one or more ancillary ligands, as seen, for example, in (η^5-C_5H_5)$Cr(CO)_2$(η^3-allyl). A general synthesis for allyl complexes of this type, including the aforementioned parent complex has just been published.[73] Alternatively, the reaction of butadiene with [(η^5-C_5H_5)$Cr(CO)_3$]$_2$ in the presence of mercury yields the η^3-C_4H_7 crotyl derivative in a photolytic preparation. (η^5-C_5H_5)$Cr(CO)_2$(η^3-C_5H_7) forms as a by-product of the reaction of (η^5-C_5H_5)$_2$Cr with CO and H_2 to give (η^5-C_5H_5)$Cr(CO)_3H$. The latter two allyls were initially formulated as (η^4-cyclopentadiene)$Cr^0(CO)_2$(η^4-diene) (diene = C_4H_6, C_5H_6), but their true structures were later established by ^1H NMR studies. Photolysis of solutions containing (η^5-C_5H_5)$Cr(CO)_3Me$ and PR_3 (R = Ph, OMe) leads to isolation of (η^5-C_5H_5)$Cr(CO)_2(PPh_3)Me$, (η^5-C_5H_5)$Cr(CO)_2(PPh_3)COMe$, and $(\eta^5\text{-C}_5\text{H}_5)\text{Cr(CO)(P(OMe)}_3)_2\text{Me}$ as air-sensitive crystalline solids. Trimethyl phosphite complexes analogous to the two obtained with PPh_3 can be prepared using one equivalent of the reagent; these are sufficiently robust to undergo spectroscopic characterization, but too unstable to separate and crystallize. The acetyl species are thought to form from the attack of a photochemically activated methyl group on a *cis*-CO ligand. Other (dicarbonyl)phosphine compounds that have been reported include *trans*-$(\eta^5\text{-C}_5\text{H}_5)\text{Cr(CO)}_2(\text{PMe}_2\text{Ph})(\text{PCl}_2)$[74] and $(\eta^5\text{-C}_5\text{H}_5)\text{Cr(CO)}_2(\text{PR}_3)\text{Et}$ (R = OMe, OEt).

Chromium(II) compounds of the form $(\eta^5\text{-C}_5\text{H}_5)\text{Cr(CO)}_3\text{X}$ are numerous. The ligand X may be a halide or alkyl, or may be derived from a main-group or transition-series element. Table 1 lists some of these molecules and their syntheses. As a rule, these seven-coordinate complexes exhibit greater thermal instability and air sensitivity than their molybdenum and tungsten congeners. Most will decompose at ambient temperature, even in an inert atmosphere, and rapidly if exposed to oxygen. The compounds $(\eta^5\text{-C}_5\text{H}_5)\text{Cr(CO)}_3\text{X}$ (X = (triars)Cu, $\eta^1\text{-CH}_2\text{CH=CH}_2$, CH_2Ph, CH_2CN, $\text{CH}_2\text{CO}_2\text{Et}$, or $\text{CH(CO}_2\text{Me)}_2$) were all identified in solution on the basis of spectral data, but were too unstable to be isolated. Similar properties were observed for $(\eta^5\text{-C}_5\text{Me}_5)\text{Cr(CO)}_3\text{X}$ (X = I, Br, Cl, Me, Bn, $\eta^1\text{-C}_3\text{H}_5$, or SnBu_3). The examples in Table 1, however, are all stable solids, and most are crystalline.

The tetracarbonyl cation $[(\eta^5\text{-C}_5\text{H}_5)\text{Cr(CO)}_4]^+$ is the product of the reaction of $(\eta^5\text{-C}_5\text{H}_5)\text{Cr(CO)}_3\text{H}$ with CO in the presence of $\text{BF}_3{\cdot}\text{Me}_2\text{O}$. The moisture-sensitive product is isolated as the tetrafluoroborate salt.

5.5 Chromocene

Chromocene, bis(η^5-cyclopentadienyl)chromium, is most easily prepared by reacting a halide of chromium(II) with NaC_5H_5.[19] Other less efficient methods, for example, pyrolysis and vapor-phase reaction, are described elsewhere. Chromocene is a volatile and reactive solid with a magnetic moment of 3.27 μ_B. Comparison of this value with the spin-only value, 2.83 μ_B, suggests the presence of a significant orbital contribution. An electron diffraction study favors eclipsed cyclopentadienyl rings in $(\eta^5\text{-C}_5\text{H}_5)_2\text{Cr}$ (D_{5d} symmetry); however, a staggered configuration (D_{5h} symmetry) remains plausible, particularly in view of the low-barrier-to-ring rotation ($<3.8\,\text{kJ mol}^{-1}$).

The chromocene molecule undergoes reaction with a wide variety of substrates; these processes have been recently summarized.[75] Transformations of note include the exchange of cyclopentadienyl rings between $(\eta^5\text{-C}_5\text{H}_5)_2\text{Cr}$ and $\text{Li(C}_5\text{D}_5)$, providing a straightforward synthesis of the deuterated compound, the reaction with cold deoxygenated HBF_4 to form $[(\eta^5\text{-C}_5\text{H}_5)\text{Cr(OH}_2)_3]\text{BF}_4$, and the elimination of one aromatic ring with the cleavage of a second in the generation of binuclear $[(\eta^5\text{-C}_5\text{H}_5)\text{Cr}]_2(\mu_2,\eta^4,\eta^4\text{-C}_8\text{H}_8)$ from chromocene and $\text{Na}_2\text{C}_8\text{H}_8$.

While not catalytically active itself, chromocene deposited on silica yields a highly active catalyst, known as the Union Carbide catalyst, for the polymerization of ethylene.[76] It is thought that $(\eta^5\text{-C}_5\text{H}_5)\text{Cr}$ moieties on the silica surface constitute the active sites for polyethylene synthesis. This catalyst's high hydrogen response allows for the synthesis of polymers having a wide range of molecular weights via adjustment of the hydrogen-to-ethylene ratio. For a given ratio, however, a relatively narrow molecular weight distribution is obtained. In spite of vigorous research spanning 30 years,[77–79] many other features of this catalytic reaction, for example, the mechanism of initiation and the oxidation state of the active chromium species, remain controversial, and so studies of the chromocene–silica system and of potential model compounds continue.

5.6 Derivatives and Analogs of Chromocene

The substituted derivatives $(\eta^5\text{-C}_5\text{H}_5)_2\text{CrL}_n$ are generated from the direct reaction of chromocene with L. In

Table 1 Tricarbonyl derivatives $(\eta^5\text{-C}_5\text{H}_5)\text{Cr(CO)}_3\text{X}$

X	Synthesis	Comments
X (X = Br, I)	$\text{Hg}[(\eta^5\text{-C}_5\text{H}_5)\text{Cr(CO)}_3]_2 + \text{X}_2$	Cl_2 gives product with no CO ligands
R (R = Me, Et)	$[(\eta^5\text{-C}_5\text{H}_5)\text{Cr(CO)}_3]^- + \text{RI}$	Identity of Et compound questioned
$\text{CH}_2\text{CO}_2\text{Me}$	$[(\eta^5\text{-C}_5\text{H}_5)\text{Cr(CO)}_3]_2 + \text{BrCH}_2\text{CO}_2\text{Me}$	
PCl_2	$[(\eta^5\text{-C}_5\text{H}_5)\text{Cr(CO)}_3]^- + \text{PCl}_3$	Conversion to P(=S)Cl_2 compound increases stability
$\text{PO(CMe}_2)_2\text{O}$	$[(\eta^5\text{-C}_5\text{H}_5)\text{Cr(CO)}_3]^- + \text{ClPO(CMe}_2)_2\text{O}$	Dioxaphospholane ligand
AsMe_2	$[(\eta^5\text{-C}_5\text{H}_5)\text{Cr(CO)}_3]^- + \text{Me}_2\text{AsCl}$	Quite stable; As can be quaternized with MeI
SiH_3	$[(\eta^5\text{-C}_5\text{H}_5)\text{Cr(CO)}_3]^- + \text{H}_3\text{SiBr}$	No solvent used; first silyl complex of this type
SnMe_3	$(\eta^5\text{-C}_5\text{H}_5)\text{Cr(CO)}_3\text{H} + \text{Me}_3\text{SnNMe}_2$	CO atmosphere
	$(\text{CH}_3\text{CN})_3\text{Cr(CO)}_3 + (\eta^5\text{-C}_5\text{H}_5)\text{SnMe}_3$	CO atmosphere
MPh_3 (M = Ge, Sn, Pb)	$[(\eta^5\text{-C}_5\text{H}_5)\text{Cr(CO)}_3]^- + \text{Ph}_3\text{MCl}$	Stability: Pb<Ge, Sn
AuPPh_3	$(\eta^5\text{-C}_5\text{H}_5)\text{Cr(CO)}_3\text{H} + \text{Ph}_3\text{PAuCl}$	Diamagnetic
HgX (X = Cl, Br, I)	$\text{Hg}[(\eta^5\text{-C}_5\text{H}_5)\text{Cr(CO)}_3]_2 + \text{HgX}_2$	

this way, compounds with L_n = CO, $(NH_3)_4$, $(NH_3)_9$, and (η^2-$F_3CC{\equiv}CCF_3$) have been prepared.[75] None of these adducts, however, persist at temperatures greater than −20 °C. Thermally stable aminates, (η^5-$C_5H_5)_2Cr(RNH_2)_x$ (R = Et, Pr, Bu, $CH_2{=}CHCH_2$; x = 4.5−5.5), form at 25 °C upon exposure of chromocene to the vapors of primary linear amines; like the carbonylation and ammoniations just mentioned, this reaction is reversible. The first irreversible adduct formation was observed with an N-heterocyclic carbene, to give (η^5-C_5H_5)Cr(η^1-$C(NAr)_2C_2H_2$)(η^1-C_5H_5).[80] Other examples of thermally stable, irreversibly formed derivatives of this type contain an ansa-chromocene ligands. This tetramethylethylene-bridged chromocene carbonyl complex, $[Me_4C_2(C_5H_4)]_2Cr(CO)$, is the product of the reaction of the bis-Grignard reagent $Me_4C_2(C_5H_4MgCl)_2{\cdot}4THF$ with $CrCl_2{\cdot}THF$ in a CO atmosphere.[81] While extremely air sensitive, this substance is sufficiently robust to be sublimed at 60−70 °C. Similarly, adducts of the type [*trans*-1,2-(3,4-$(CH_3O)_2C_6H_3)_2C_2H_2\{\eta^5$-$C_5H_4\}_2$]Cr(L) (L = CO, CNR) and $Me_2Si(\eta^5$-$C_5Me_4)_2Cr(CO)$ have been reported.[82,83] At elevated CO pressures, $[Me_4C_2(C_5H_4)]_2Cr(CO)$ and (η^5-$C_5H_5)_2Cr(CO)$ react reversibly to give dicarbonyl species with concomitant $\eta^5 \rightarrow \eta^3$ slippage of one of the cyclopentadienyl rings (Scheme 8). Surprisingly, even a ligand-free ansa-chromocene, namely, $Me_2Si(\eta^5$-$C_5Me_4)_2Cr$, has now been prepared and structurally characterized.[84]

The known chromocene analogues feature substituted cyclopentadienyl rings and/or other anionic ligands with pentahapto coordination. (η^5-$C_5Me_5)_2Cr$ is efficiently prepared from $[C_5Me_5]Na$ and $Cr_2(OAc)_4$.[85] This volatile, air-sensitive solid is an extremely potent reducing agent ($E_{>1/2}$ = −1.04 V), forming mildly air-sensitive $[(\eta^5$-$C_5Me_5)_2Cr]^+$ in the presence of water, ammonium ion, or ferricinium ion. By contrast, chromocene is inert to water and decomposed by $[(\eta^5$-$C_5H_5)_2Fe]^+$; chromocinium salts are extremely air sensitive, even pyrophoric (see Section 6.9). Complexes with monosubstituted and perdeuterated cyclopentadienyl rings have also been reported. Octaisopropylchromocene undergoes a low-spin/high-spin transition with increasing temperature.[86]

Structurally similar to and isoelectronic with chromocene are (η^5-indenyl$)_2$Cr (now known to have a dinuclear structure)[87] (η^5-fluorenyl$)_2$Cr, and [η^5-(9-methyl)fluorenyl$]_2$Cr, (η^5-$C_8H_{11})_2Cr$, $\{[(3)$-1,6-$C_2B_{10}H_{12}]_2Cr\}^{2-}$, ($\eta^5$-pentadienyl$)_2$Cr, and ($\eta^5$-$C_5R_5$)Cr($\eta^5$-pentadienyl) (R = H, Me). Control of the spin state by sterically enforced rotational orientation of the ligands has been noted in substituted bis(indenyl)chromium complexes.[88] Supported indenyl, fluorenyl, and pentadienyl derivatives function as Union Carbide-type catalysts, catalyzing the polymerization of ethylene. Oxidation of the air-stable bis(metallocarborane)chromium by chemical or electrochemical means yields the stable Cr^{III} anion. Bis(pentadienyl) compounds undergo 'naked metal' reactions analogous to those of $Ni(allyl)_2$, yielding homoleptic bisphosphines and isocyanides. By contrast, the half-open chromocenes, whose pentadienyl ligands adopt the η^5-S (sickle) coordination mode, form 18-electron adducts with CO, PF_3, RNC, $PPhMe_2$, and other two-electron donor ligands.[89]

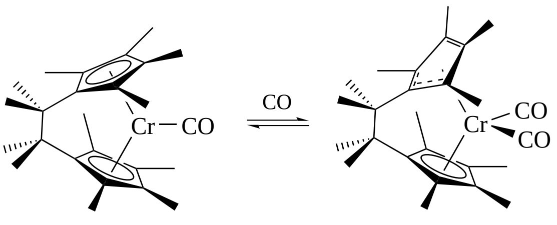

Scheme 8

5.7 Miscellaneous Compounds of Chromium(II)

The CrR_2 fragment figures prominently in this group of molecules. A thermally stable complex formulated as $Cr(CH_2SiMe_3)_2$ was obtained from the interaction of Me_3SiCH_2Li with excess $CrCl_2$ or $CrCl_3$. Its true tetrameric structure, $Cr_4(CH_2SiMe_3)_8$, was later revealed by X-ray crystallography.[90] Treatment of *trans*-$CrCl_2(dmpe)_2$ with two equivalents of MeLi yields the 16-electron trans dimethyl complex, $CrMe_2(dmpe)_2$.[91] Related (dialkyl)bisphosphine compounds with a rare square-planar geometry, *cis*-CrR_2(dippe) (R = Me_3CCH_2, Me_3SiCH_2, or 1,3,5-$Me_3C_6H_2$; dippe = 1,2-bis(diisopropylphosphinoethane)) are synthesized by alkylation of dimeric $[CrCl_2(dippe)]_2$. An X-ray study showed extremely long Cr–P bonds in these molecules, a consequence of their high-spin d^4 chromium centers ($\mu = 4.9\ \mu_B$), the trans influence of R, and the steric requirements of the R groups and phosphine. All of these dmpe and dippe products are air and moisture sensitive; in spite of their electron-deficient configuration, none are agostic (*see Agostic Bonding*). As ethylene polymerization catalysts, the dippe compounds demonstrate little activity, which may imply that low-valent Cr^{II} centers are not the active sites in chromium-based catalytic processes.

(η^5-C_5Me_5)Cr(dmpe)Me is derived from the chemical reduction of its Cr^{III} analogue with Na/Hg. Air sensitive but thermally stable, its magnetic moment, 2.79 μ_B, is compatible with a low-spin d^4 configuration.[92] Attempts to perform similar chemistry on $[(\eta^5$-$C_5Me_5)Cr(dmpe)R]^+$ (R = Et, other alkyls) were unsuccessful. This Cr^{II} complex reacted with ethylene at room temperature, but facile β-elimination prevented the formation of a polymer. That its isostructural Cr^{III} analog polymerized ethylene at 90 °C implies that chromium(III) is the more suitable oxidation state for catalysis, at least in this system. Reaction of the ethylene polymerization catalyst $[(\eta^5$-$C_5Me_5)CrMe(THF)_2]BPh_4$ with styrene gave (η^5-C_5Me_5)Cr(η^6-Ph-BPh_3), a Cr^{II} sandwich compound incorporating one of the rings of the 'noninteracting' BPh_4^- counterion.

Alkylation of the dinuclear chloride precursor $[(\eta^5$-$C_5Me_5)Cr(\mu$-$Cl)]_2$ yields a series of alkyl bridged chromium(II) alkyls of the constitution $[(\eta^5$-$C_5Me_5)Cr(\mu$-$R)]_2$

(R = Me, Et, *n*-Bu, CH_2SiMe_3, Ph). They feature short Cr–Cr distances (∼2.26 Å), low effective magnetic moments, and attenuated reactivity, all consistent with strong metal–metal bonding.**[93]** Steric saturation of chromium with a sterically encumbered tris(pyrazolyl)borate ligand (i. e. $Tp^{t\text{-Bu,Me}}$ = hydrotris(3-*tert*-butyl-5-methylpyrazolyl)borate), on the other hand, facilitates the preparation of mononuclear, coordinatively unsaturated alkyls. $Tp^{t\text{-Bu,Me}}CrR$ (R = Cl, Et, Ph, CH_2SiMe_3) adopt cis divacant octahedral structures and high-spin configurations with four unpaired electrons.**[94]** Notably, these four-coordinate 12-electron species do not react with ethylene. However, $Tp^{t\text{-Bu,Me}}CrPh$ undergoes a clean reaction with O_2, producing the paramagnetic Cr^{IV} complex $Tp^{t\text{-Bu,Me}}Cr(O)OPh$ via an observable Cr(III) superoxide intermediate.**[95]**

6 CHROMIUM(III) ORGANOMETALLICS

6.1 Neutral Solvated Mono(Organo)chromium(III) Compounds

Complexes in this class can be represented by the general formula $RCrCl_2S_n$, and numerous routes to their preparation are known. Reaction of a Grignard reagent or $CrR_3(THF)_n$ with $CrCl_3(THF)_3$ at the appropriate temperature gives the desired product. Organoaluminum reagents and the diphenylmethyl anion add to $CrCl_3$, giving the monoalkylated species as well. Benzyl derivatives $RC_6H_4CH_2CrCl_2(py)_3$ are generated cleanly from $RC_6H_4CH_2Cl$ (R = H, *o*-Cl, *p*-Cl) and $CrCl_2(py)_2$. Related dithiocarbamates and acetylacetonates can also be synthesized. Molecules of $RCrCl_2S_n$ typically contain a phenyl, benzyl, or an *n*-alkyl R group and THF or pyridine as solvate, but more unusual molecules such as $(C_3F_7)CrCl_2L_n$ (L_n = $(py)_3$, $(bipy)_2$, $(phen)_2$, terpy) are also known. The N-donor solvate ligands are particularly good at stabilizing the chromium–carbon bond in these otherwise unstable molecules.

These d^3 systems can be characterized by their magnetic moments, which fall in the range 3.6–4.0 μ_B (spin-only value = 3.87 μ_B), and by a sensitivity to temperature, oxygen, and moisture. They react with $HgCl_2$ to give RHgCl and Cr^{III}; thermally induced homolysis of the Cr–C bond leads to $CrCl_2$ and various organic species. $RCrCl_2(THF)_3$ (R = Me, Et, *n*-Pr, *i*-Bu) is also reported to catalyze ethylene polymerization under mild conditions.**[96]**

6.2 Solvated Mono(Organo)chromium(III) Aquo Cations[97,98]

The general formula $[RCr(OH_2)_5]^{2+}$ describes this group of complexes. Reaction of an alkyl halide with chromium(II) perchlorate in perchloric acid yields these pentaaquo cations; a similar synthesis employs the isomeric bromoalkylpyridinium bromides. Oxidation of Cr^{II} salts by hydroperoxides and peroxides gives cationic products, as does the hydrolysis of $RCrCl_2S_n$. Finally, the interaction of Cr^{II} and alkylbis(dimethylglyoximato)cobalt also provides $[RCr(OH_2)_5]^{2+}$. Most of these processes involve the generation of a free radical and its subsequent attack on chromium(II).

Solutions of these cations have been prepared for numerous ligands R, including $CHCl_2$, CF_3, CH_2OH, $C(Me)_2OH$, and η^5-C_5H_5, but few have been isolated as solids. Like $RCrCl_2S_n$, these compounds are temperature and oxygen sensitive. In the presence of acid or mercury(II), Cr–R bond cleavage occurs to give RH or RHgCl. Oxidative cleavage generates the aldehyde, RCHO. Reactions with metal salts, organic halides, and halogens are also known.

6.3 Solvated Di(Organo)chromium(III) Compounds

Complexes of chromium(III) bearing two alkyl ligands assume one of two forms, R_2CrClS_n or $[R_2Cr(\text{bidentate ligand})_2]^+$. Examples of the neutral species are known for R = *n*-alkyl, *i*-alkyl, and cyclohexyl, with THF as a solvate. A related species is $Cr(n\text{-alkyl})_2Cl(Me_2PCH_2)_3CMe$, in which a tripod ligand functions in the stabilizing role of solvate.**[99]** Preparations include reaction of a polyphenylchromate, $M_x[Cr(C_6H_5)_{x+3}]$, with $CrCl_3(THF)_3$ in DME, addition of Grignard reagent to a mixture of $CrBr_2(THF)_2$ and bidentate ligand, followed by air oxidation, and thermal rearrangement and hydrolysis of a tri(organo)chromium(III) complex, R_3Cr(bidentate ligand) (THF).

The di(organo) neutral species are oxygen and water sensitive; they react with $HgCl_2$ and I_2, and like their mono(organo) analogs they are reported to possess catalytic activity. The cations, on the other hand, are stabilized by the chelation of bipy or phen, and so are unaffected by air and water but do react with $HgCl_2$. X-ray structural analyses of several $[R_2Cr(bipy)_2]I$ complexes indicate a cis arrangement of R ligands in these octahedral molecules.

6.4 Solvated and Unsolvated Tri(Organo)chromium(III) Compounds

Compounds R_3CrS_n comprise the largest class of solvated chromium(III) organometallics. The most simple and efficient synthetic route entails the addition of Grignard or lithium reagents to $CrCl_3$. A myriad of complexes (R = alkyl, aryl, vinyl, benzyl, naphthyl, styryl, cyclohexyl, etc.) have been prepared in this way. The phenyl compound, and perhaps others, can be produced in high yield from the reaction of $Li_3[CrPh_6]$ with $CrCl_3$ in THF. Exchange of the customary THF solvate for bipy or phen yields more stable products; phosphines can also be employed here. A few R_3Cr compounds do not require solvent stabilization;

among these are $(CH_2{=}CHCH_2)_3Cr$, $(CH_2{=}C(Me)CH_2)_3Cr$, $(MeCH{=}CHCH_2)_3Cr$, (1-norcamphyl)$_3$Cr, and $[(Me_3Si)_2CH]_3Cr$.**[100]**

The R_3CrS_n triaryl derivatives are generally stable at room temperature, whereas their alkyl analogs must often be isolated and handled at low temperature. All undergo thermal fragmentations and rearrangements under appropriate conditions. The Cr–C bond of a triaryl complex homolyzes to give the arene and the biaryl; alternatively, a σ-to-π rearrangement occurs and bis(π-arene)chromium forms. Fragmentation via reductive dimerization to give butadienes is observed in triallyl and vinyl species. Trialkyl compounds are characterized by homolytic Cr−C bond cleavage and by α- and *β-Hydride Elimination*, the products being alkanes, alkenes, and chromium hydrides. The molecule $[t\text{-}BuSi(CH_2PMe_2)_3]Cr(n\text{-}Bu)_3$ demonstrates an extraordinary stability for a 15-electron trialkyl: its decomposition requires a temperature of 95 °C (Scheme 9). This resistance to β-elimination is attributed to the kinetically inert d^3 configuration and the chelating tripod phosphine ligand, the ‘arms’ of which are less likely to dissociate for entropic reasons.**[101]** While R_3Cr and R_3CrS_n do not themselves affect alkene isomerization or catalytic hydrogenation, their chromium-based fragmentation products have been shown to isomerize alkenes and act as hydrogenation catalysts. In addition, triallylchromium is known to function as a catalyst for the polymerization and oligomerization of butadiene and other unsaturated molecules.

The R_3CrS_n and R_3Cr complexes exhibit magnetic moments that are in the range expected for chromium(III): 3.53−3.98 μ_B. They react readily with $HgCl_2$ and I_2; most are sensitive to oxygen and moisture. The chemistry of these compounds with unsaturated substrates is extensive, and is described in detail elsewhere.

6.5 Lithium and Sodium Poly(Organo)chromates

Representatives of this class of chromium(III) complexes can be described by the general formula $M_n[CrR_{n+3}]$ ($n = 1-3$). Hexaorganochromium compounds are prepared from an appropriate lithium reagent and $CrCl_3$ (stoichiometric ratio >6:1). Two other pathways are available for synthesis of the hexaphenylchromate: reaction of stoichiometric PhLi with $CrBr_3$, $CrCl_3(py)_3$, or $Cr(acac)_3$, and treatment of Cr^{II} salts with a significant excess of the lithium reagent. $M_2[CrR_5]$ is apparently only known for R = Ph; a steric strain in $M_3[CrPh_6]$ causes the extrusion of MPh to leave this pentaphenylchromate. Solvents like THF or DME facilitate the process. Treatment of $CrCl_3(THF)_3$ with PhNa in ether constitutes a formal synthesis. Tetra(organo)chromates $M[CrR_4]$ are also known for R = aryl and are obtained from the reaction of $CrCl_2$, CrR_2, or $CrCl_3$ with RLi. Penta- and hexaphenylchromates will also combine with $CrCl_3$ to give tetraphenylchromates if DME is available to stabilize the products. The first structurally characterized representative is $Li(THF)_4[Cr(C_6Cl_5)_4]$. It adopts a pseudooctahedral geometry, including two Cr–Cl interactions besides the four covalent Cr–C bonds.**[74]**

Of these three types of poly(organo)chromate anions, only the hexaorgano species tolerates a variety of ligand types bound to chromium. Hexamethylchromate has been reported,**[102]** as well as an unusual spirocyclic compound, $Li_3[Cr(1,4\text{-}C_4H_8)_3]\ (Et_2O)_{2.5}$. Notable polyaryls include the tris(2,2′-biphenyl) compound and the hydride $Li_3[CrH(Ph)_5](Et_2O)_3$. Collectively, poly(organo)chromates are thermally stable, but exceedingly sensitive to oxygen, water, and protic media. An exception is found in the tetra(organo)chromates, which tend to form chromium(II) dimers with loss of R−R. Both Cr^{II} and Cr^{III} species are formed in the reactions of these compounds, which include fragmentation and ligand replacement.

X-ray crystal structures of $Li_3[CrMe_6](dioxane)_3$ and of $Na_2[CrPh_5](Et_2O)_3(THF)$ have been determined. The latter is a distorted trigonal bipyramid; the former is octahedral, with a remarkably long Cr–C bond distances (average = 2.300(15) Å).

6.6 Solvated Mono(η^5-cyclopentadienyl)chromium Compounds

These solvent-stabilized half-sandwich complexes, of the general formula $(\eta^5\text{-}C_5H_5)CrX_2S$, are customarily prepared by the addition of S (S = THF, dioxane, Ph_3P) to ‘$(\eta^5\text{-}C_5H_5)CrX_2$’ (X = Br, I) or $[(\eta^5\text{-}C_5H_5)_2Cr]\ [(\eta^5\text{-}C_5H_5)CrY_3]$ (Y = Cl, Br, I, $O(O{=}C)CF_3$). The dihalide starting material is generated from the action of the appropriate allyl halide on $[(\eta^5\text{-}C_5H_5)Cr(CO)_2]_2$; the ionic complex forms upon treatment of chromocene with CCl_4, CF_3CO_2H, or HX. Pyridine-solvated compounds are easily prepared in one step from chromocene and pyridinium tribromide or iodide. Reaction of the hydride

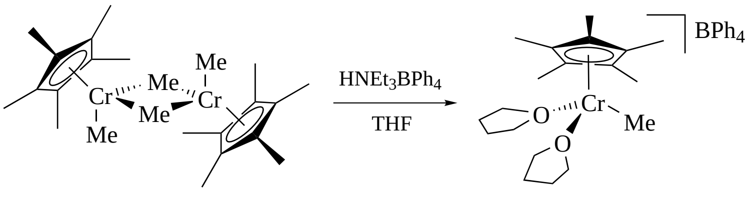

Scheme 9

$(\eta^5\text{-}C_5H_5)CrH\{P(OMe)_3\}_3$ with CCl_4 yields the phosphite-stabilized compound $(\eta^5\text{-}C_5H_5)CrCl_2\{P(OMe)_3\}$. Analogous THF-solvated $(\eta^5\text{-}C_5Me_5)CrX_2S$ species have been reported for X = Cl, Br, and I; however, their syntheses differ significantly. Besides solvent ligand exchange, two other reactions of these air-sensitive organometallics have been studied. $(\eta^5\text{-}C_5R_5)CrX_2(THF)$ (R = H, X = Br, I; R = Me, X = Cl, Br, I) dimerizes upon heating to give $[(\eta^5\text{-}C_5R_5)CrX_2]_2$. Finally, the hydride $(\eta^5\text{-}C_5H_5)CrH\{P(OMe)_3\}_3$, the starting material for the preparation of $(\eta^5\text{-}C_5H_5)CrCl_2\{P(OMe)_3\}$ (see above), is itself obtained from $(\eta^5\text{-}C_5H_5)CrCl_2(THF)$, $NaBH_4$, and $P(OMe)_3$.

6.7 Miscellaneous Unsolvated Mono(η^5-cyclopentadienyl)chromium Compounds

The unsolvated form of the dichloride described in the previous section may be synthesized from chromocene and hexachlorocyclopentadiene or gaseous HCl,[103] whereas the bromide is best obtained by removal of the solvate from $(\eta^5\text{-}C_5H_5)CrX_2(THF)$ in vacuo. The iodide is only available as crude '$(\eta^5\text{-}C_5H_5)CrI_2$' from the reaction of C_3H_5I with $[(\eta^5\text{-}C_5H_5)Cr(CO)_2]_2$. Trichloride anions, $[(\eta^5\text{-}C_5R_5)CrX_3]^-$ (R = H, X = Cl, Br, I; R = Me, X = I), result when HX is added to $(\eta_5\text{-}C_5R_5)_2Cr$, followed by NH_4X. The lithium salt of the trichloro anion has been crystallographically characterized. Treatment of $Cr(acac)_3$ with C_5H_5MgBr leads to formation of $(\eta^5\text{-}C_5H_5)CrBr(acac)$.

An unprecedented insertion of nitrile into the chromium–alkyl bonds of dimers $[(\eta^5\text{-}C_5Me_5)Cr(\mu\text{-}Cl)R]_2$ led to the formation of the mononuclear β-diketiminato species $(\eta^5\text{-}C_5Me_5)Cr\{[HNC(R)]_2CR'\}Cl$ (R = Me, Et; R′ = H, Me).[104] This unusual reactivity has been attributed to the relatively high oxidation state and coordinative unsaturation of the starting dimers and intermediates. Similar to the β-diketiminato complex in structure are $(\eta^5\text{-}C_5Me_5)Cr\{[OC(Me)_2]_2CH_2\}py$, featuring a chelating bis(alkoxide) ligand, and $(\eta^5\text{-}C_5Me_5)\overline{Cr[OC(Me)_2CHC(Me)O}]py$, whose bidentate ligand is a doubly deprotonated β-hydroxy ketone.[105] These molecules are the products of the reactions of $(\eta^5\text{-}C_5Me_5)Cr(R)_2py$ (R = Me or O-*t*-Bu, respectively) with acetone.

6.8 Mono(η^5-cyclopentadienyl)chromium Alkyl Compounds

This class of organometallics originates from chemistry of the chromium–carbon bond developed only within the last two decades.[105,106] Illustrative of this fact is the observation that a comprehensive reference published in 1982 makes no mention of compounds of chromium(III) bearing both cyclopentadienyl and alkyl ligands.[16] Within this class are found mono-, di-, and trialkyl complexes of $(\eta^5\text{-}C_5H_5)$ and $(\eta^5\text{-}C_5Me_5)$; these will be examined in turn. Much of the interest in these compounds centers on their role as catalysts for the polymerization, oligomerization, and selective trimerization of ethylene.

Monoalkyls of the form $(\eta^5\text{-}C_5R_5)Cr(R')(L)Cl$ (R = H, R′ = Me or Et, L = py, PPh_3, Cl^-; R = Me, R′ = Me or Et, L = py, PMe_3, 3,5-lutidine) are prepared by cleavage of the dimers $[(\eta^5\text{-}C_5R_5)Cr(R')(\mu\text{-}Cl)]_2$ with the appropriate nucleophile, L. Cationic monoalkyls, $[(\eta^5\text{-}C_5Me_5)CrL_2R]X$ (L = py, PMe_3, THF, MeCN, 3,5-lutidine; L_2 = dmpe, dppe, bipy; R = Me, Et), are derived from the same pentamethylcyclopentadienyl dimer or from $(\eta^5\text{-}C_5Me_5)Cr(R')(L)Cl$ upon treatment with $TlPF_6$ in the presence of L. An alternative preparation of the bis(THF)(methyl) cation involves protonation of $[(\eta^5\text{-}C_5Me_5)Cr(Me)(\mu\text{-}Me)]_2$ with $HNEt_3BPh_4$ in THF (Scheme 9).

Monomers and dimers can also serve as starting materials for the synthesis of the dialkyls $(\eta^5\text{-}C_5R_5)Cr(R'_2)L$ (R = H, R′ = Me, Bn, CH_2SiMe_3, L = PMe_3, PEt_3; R = Me, R′ = Me, L = PMe_3, py, THF). Treatment of $(\eta^5\text{-}C_5R_5)CrCl_2(PR_3)$ with two equivalents of alkyllithium or a Grignard reagent gives the desired product, as does the cleavage of $[(\eta^5\text{-}C_5Me_5)Cr(Me)(\mu\text{-}Cl)]_2$ with alkyllithium in the presence of L. $(\eta^5\text{-}C_5Me_5)Cr(Me)_2py$ can also be obtained from the addition of py to dimeric $[(\eta^5\text{-}C_5Me_5)Cr(Me)(\mu\text{-}Me)]_2$.

A particular subset of these ligated dialkyls are those in which the ligand is tethered to the cyclopentadienyl ligand. Thus, chromacyclopentane and cycloheptane derivatives stabilized by the $(\eta^5;\eta^1\text{-}Me_4C_5CH_2CH_2NMe_2)$ ligand have been prepared and their reactivity supports the intermediacy of such metallacycles in the catalytic trimerization of ethylene.[107] A variety of donor-ligand-substituted cyclopentadienylchromium(III) complexes with amino and phosphino substituents has been prepared and screened for an ethylene polymerization activity.[108,109]

Two other interesting cyclopentadienyl alkyls are $(\eta^5\text{-}C_5Me_5)Cr(CH_2SiMe_3)_2$ and $[(\eta^5\text{-}C_5Me_5)_2Cr_2(\eta^1\text{-}CH_2Ph)(\mu\text{-}\eta^3:\eta^6\text{-}CH_2Ph)]$. The former is an unusual 13-electron species whose coordinative unsaturation makes it an extremely effective catalyst for ethylene polymerization, and which exhibits a rich thermal decomposition chemistry.[110] The latter, a mixed-valent complex exhibits ferromagnetic coupling between the two chromium atoms and is a catalyst for the polymerization of ethylene as well.[111]

Compounds in this class are characterized by thermal stability, crystallinity, and sensitivity to air and moisture. Most possess 15-electron configurations and pseudooctahedral coordination spheres. The isolation of ethyl derivatives demonstrates that β-elimination is not facile in these Cr^{III} alkyls.[105] Also, evidence for agostic interactions is lacking. While the reactivity of the neutral complexes is limited to ligand exchange, alkylation, and dimer formation, cationic $[(\eta^5\text{-}C_5Me_5)CrL_2R]X$ is recognized as an efficient ethylene polymerization catalyst, particularly where L = THF, R = Me, and X = BPh_4. The PF_6^- analog is equally reactive; however, it is prone to decomposition by abstraction of fluoride from the counterion and chloride from the CH_2Cl_2 solvent, yielding polynuclear chromium complexes held together by fluoride bridges. The most reactive of these cationic alkyls is the exceedingly labile $[(\eta^5\text{-}C_5Me_5)Cr(OEt_2)_2CH_2SiMe_3][B(3,6\text{-}(CF_3)_2C_6H_3)_4]$;[112] it even oligomerizes propene, despite the well-established selectivity of CpCr-catalysts for insertion of ethylene over α-olefins.[113]

6.9 Chromocinium Derivatives and Analogs

The chromocinium ion, $[(\eta^5\text{-}C_5H_5)_2Cr]^+$, results from the oxidation of chromocene by chemical or electrochemical means. Allyl iodide is an efficient oxidant; however, the pyrophoric iodide product is best converted to the BPh_4^- salt or the reineckate, $[Cr(SCN)_4(NH_3)_2]^-$, for ease of handling. In addition, the reactions of $[(\eta^5\text{-}C_5H_5)Cr(CO)_3]_2$ with CCl_4 or HX (X = Br, I) and with chromocene generate the ion as $[(\eta^5\text{-}C_5H_5)_2Cr][(\eta^5\text{-}C_5H_5)CrX_3]$ and $[(\eta^5\text{-}C_5H_5)Cr][(\eta^5\text{-}C_5H_5)Cr(CO)_3]$, respectively. Treatment of $CrBr_3$ with C_5H_5Li gives $(\eta^5\text{-}C_5H_5)_2CrBr$. Electrochemical oxidation occurs reversibly with a half-wave potential of $-0.67\,V$. Chromocinium prepared by this route is stable in solution as the PF_6^- salt.

The decamethylchromocinium ion, $[(\eta^5\text{-}C_5Me_5)_2Cr]^+$, has been isolated as the iodide from chromocene and HI. Further reaction with HI forms the salt of the complex anion $[(\eta^5\text{-}C_5Me_5)_2Cr][(\eta^5\text{-}C_5Me_5)CrI_3]$.

There exist analogs of the chromocinium ion in which the cyclopentadienyl rings are partly or wholly replaced by dianionic carborane ligands. Dicarbollide ions $[(3)\text{-}1,2\text{-}C_2B_9H_9R_2]^{2-}$ ($R_2 = H_2$, HMe, Me_2, HPh) and $[(3)\text{-}1,7\text{-}C_2B_9H_{11}]^{2-}$ react with $CrCl_3$ to give $\{[(3)\text{-}1,2\text{-}C_2B_9H_9R_2]_2Cr\}^-$ and $\{[(3)\text{-}1,7\text{-}C_2B_9H_{11}]_2Cr\}^-$. If the reaction is carried out in the presence of $C_5H_5^-$, one obtains the neutral mixed-sandwich complexes $(\eta^5\text{-}C_5H_5)Cr[(3)\text{-}1,2\text{-}C_2B_9H_9R_2]$ and $(\eta^5\text{-}C_5H_5)Cr[(3)\text{-}1,7\text{-}C_2B_9H_{11}]$. The chromium(III) metallacarborane $[(1,6\text{-}C_2B_{10}H_{12})_2Cr]$ has been prepared by chemical (Ag^+, H_2O_2) or electrochemical oxidation of its Cr^{II} precursor. These dicarbollyl derivatives of Cr^{III} are stable in air and can be recrystallized from aqueous solutions, and are unaffected by acid. They do, however, decompose in the presence of an aqueous base. Electrochemical data indicate that reduction is not reversible in these complexes. A crystal-structure determination has been carried out on the cesium salt of $\{[(3)\text{-}1,2\text{-}C_2B_9H_9(Me)_2]_2Cr\}^-$. Related to these sandwich compounds is trianionic $[(B_{10}H_{10}CH)_2Cr]^{3-}$, which exhibits similar properties and reactivity.

6.10 Other Chromium(III) Organometallics

The search for chromium-based olefin polymerization catalysts has led to the exploration of chromium alkyls with a wide variety of ancillary ligands other than cyclopentadienyls.[114] For example, N,N'-disubstituted β-diketiminato (i.e. 'nacnac') complexes of chromium have been alkylated and shown to catalyze ethylene polymerization.[115,116] Specifically, the cationic complex $[(2,6\text{-}i\text{-}PrPh)_2nacnacCr(OEt_2)Me][B(3,6\text{-}(CF_3)_2C_6H_3)_4]$ catalyzes the polymerization of ethylene in the absence of any activators or cocatalysts and produces polyethylene of extremely narrow polydispersity.[117] Another set of ligands used to stabilize Cr^{III} alkyls are the N-substituted 1,3,5-triazacyclohexanes, for example, in $\{(i\text{-}Pr)_3N_3(CH_2)_3\}Cr(CH_2SiMe_3)_2Cl$.[118] Oxidation of square-planar Cr^{II} precursors containing a tridentate aminophosphine ligand with alkyl halides gives alkyls of the type $Cr(R)X[N(SiMe_2CH_2PPh_2)_2]$ and $Cr(R)X[N(SiMe_2CH_2PPh_2)_2]$ (R = Me, CH_2SiMe_3; X = Cl, Br, I). These compounds are unusual examples of five-coordinate Cr^{III} complexes.[119]

7 CHROMIUM(IV) ORGANOMETALLICS

7.1 Tetraorganochromium Compounds

The majority of chromium(IV) organometallics belong to the family of homoleptic tetraalkyls and tetraaryls. These compounds are generally prepared by one of two synthetic routes. In the first, the chromium(III) precursor $CrCl_3(THF)_3$ is reacted with four equivalents of alkyl- or aryllithium. If the reaction is performed in pentane or ether, a disproportionation reaction occurs and the tetrasubstituted product forms directly. In THF, however, the reaction yields $Li[CrR_4]$, which gives CrR_4 upon oxidation; substitution of Grignard reagents for alkyllithiums gives comparable results in some cases. Direct conversion to CrR_4 also occurs via the second route, in which $Cr(O\text{-}t\text{-}Bu)_4$ and four equivalents of alkyllithium are combined in pentane.

Table 2 lists representative homoleptic tetraalkyls and aryls. Like all σ-bonded transition metal alkyls, these compounds are subject to decomposition via a variety of routes. The absence of β-hydrogen atoms in many of these molecules, however, eliminates potential decomposition pathways involving β-hydride eliminations, thereby enhancing the thermal stability of these species. In other tetraalkyls, β-hydrogens are present but geometric or steric factors impede the concerted elimination or abstraction process. An obvious example is tetrakis(l-norbornyl)chromium, which will not eliminate to give the bridgehead alkene. In spite of these sources of stabilization, chromium–carbon bond homolysis remains a feasible fragmentation pathway.

General features of each molecule in Table 2 include a magnetic moment of $2.6\text{–}3.0\,\mu_B$, appropriate for a Cr^{IV} complex with two unpaired electrons, and tetrahedral coordination; the crystal structures of $Cr(CH_2SiMe_3)_4$ and $Cr(CH_2CMe_3)_4$

Table 2 Homoleptic tetra(organo)chromium(IV) compounds

Compound	Preparation[a]	Comments
$Cr(CH_2SiMe_3)_4$	1, 2	Purple–red crystals; thermally stable
$CrMe_4$	3	Maroon oil; stable at −78 °C
Cr(1-norbornyl)$_4$	1	Red–brown crystals; thermally stable
Cr(*t*-Bu)$_4$	1, 3	Dark red crystals; thermally stable
Cr(mesityl)$_4$	4	Dark brown crystals; thermally stable
Cr(cyclohexyl)$_4$	2	Dark red crystals; thermally stable
$Cr(C(Ph){=}CMe_2)_4$	1	Green crystals; thermally stable
Cr(*n*-Bu)$_4$	3	Red solution; stable at 0 °C

[a] Key to preparation: 1 = $CrCl_3(THF)_3 + 4RLi$, 2 = $CrCl_3(THF)_3 + 4RMgX$, 3 = $Cr(O\text{-}t\text{-}Bu)_4 + 4RLi$, 4 = (a) $Ar_3Cr + ArLi$, (b) air oxidation.

have recently been determined.[120] As a rule, these compounds show limited reactivity, and this is particularly the case for those in which the metal center is effectively shielded by bulky alkyl groups. However, supported tetraalkyls, for example, $Cr(CH_2SiMe_3)_4$ or $Cr(CH_2CMe_3)_4$ on an inorganic oxide carrier, function as very active catalysts for ethylene polymerization. A detailed 'surface organometallic' study of the reaction of these two compounds with silica showed the formation of surface bound bis(alkyl)chromium fragments, for example, $(\equiv SiO)_2Cr(CH_2CMe_3)_2$, which was transformed into alkylidene $(\equiv SiO)_2Cr(=CHCMe_3)$ upon heating. The latter species initiated the polymerization of ethylene.[121]

7.2 Chromium Carbonyl Carbynes[122]

An attempt to replace the methoxy group of $(CO)_5Cr(=C(Ph)OMe)$ with a halide (from BX_3) led to the unanticipated formation of the first carbyne complex (*see Carbyne Complexes*). This synthetic method, cleavage of a carbene substituent by a Lewis acid, remains a good general route to these organometallics. Initially, the Lewis acid coordinates strongly to an oxygen-, nitrogen-, or sulfur-containing group present on the carbene. The weakened carbene carbon–heteroatom bond then breaks, and a transient halocarbene intermediate forms. This decomposes to a cationic carbyne whose halide counterion displaces the trans carbonyl to yield the neutral product. However, if the carbene is substituted in the trans position with a good σ-donor such as a phosphine, the cationic carbyne species is charge stabilized and can be isolated.

Crystal-structure determinations performed on chromium carbonyl carbynes indicate an average Cr–C bond length of 1.70 Å, ca. 0.2 Å shorter than the average Cr–C(carbonyl) distance. An exception is seen in $X(CO)_4Cr{\equiv}C\text{-}NR_2$, in which the Cr–C bond is somewhat longer and the C–N bond somewhat shorter than expected. These findings are consistent with the presence of some double bond character. The Cr≡C–R bond angle is customarily very close to linear, but structures bent up to 12° are known. Chromium carbonyl carbynes are frequently employed as starting materials for the synthesis of carbenes inaccessible by standard routes. Other reactions include carbonyl substitution and oxidative decomposition, thermal coupling of carbynes to yield alkynes, and transfer of carbyne ligands to cobalt to form (μ_3-methylidyne)nonacarbonyl tricobalt complexes.

7.3 Chromocene Derivatives and Other Compounds of Chromium(IV)

A series of reports[123] describes a number of substituted chromocene derivatives obtained from the oxidative addition of sulfur, selenium, and halogen reagents to $(\eta^5\text{-}C_5H_5)_2Cr$. Air-stable $(\eta^5\text{-}C_5H_5)_2Cr(NCY)(YCN)$ and $(\eta^5\text{-}C_5H_5)_2Cr(CN)(NCY)$ (Y = S, Se) were produced in the reactions of chromocene with $(YNC)_2$ and $Y(CN)_2$ respectively. Addition of HN_3 and CNN_3 to $(\eta^5\text{-}C_5H_5)_2Cr$ gave rise to $(\eta^5\text{-}C_5H_5)_2Cr(N_3)_2$ with release of H_2, and to $(\eta^5\text{-}C_5H_5)_2Cr(CN)(N_3)$, while treatment of $(\eta^5\text{-}C_5H_5)_2Cr$ with IX (X = Cl, Br) gave $(\eta^5\text{-}C_5H_5)_2CrIX$. Notably, none of these compounds have been structurally characterized.

There are now also some ansa-chromocene derivatives that feature tetravalent chromium. The first of these was the diamagnetic hydride $[Me_4C_2(\eta^5\text{-}C_5H_4)_2Cr(CO)H][B(3,5\text{-}(CF_3)_2C_6H_3)_4]$[124] that was observed as a metastable intermediate in the protonation of $Me_4C_2(C_5H_4)_2Cr(CO)$. More recently, the stable cyanide $[Me_4C_2(\eta^5\text{-}C_5H_4)\{\eta^5\text{-}C_5H_3B(C_6F_5)_3\}Cr(CN)CNXyl]$ has been structurally characterized.[125]

A triamidoamine ligand $((N_3N)^{3-} = ((Me_3SiNCH_2CH_2)_3N)^{3-})$ has facilitated the preparation of a new class of chromium(IV) organometallics. Alkyls $(N_3N)CrR$ (R = Me, *n*-Bu) as well as the hydride $(N_3N)CrH$ have been characterized by X-ray diffraction.[126] The five-coordinate molecules adopt high-spin d^2 configuration.

Other chromium(IV) organometallics include $K_3[Cr(O_2)_2(CN)_3]$ and 1,1′-*commo*-$Cr[(2,3\text{-}SiMe_3)_2\text{-}2,3\text{-}C_2B_4H_4]_2$. The latter is a diamagnetic carborane sandwich complex. Diamagnetism has also been claimed for the compounds $(\eta^5\text{-}C_5Me_5)Cr(Cl)(Br)Me$ and $(\eta^5\text{-}C_5Me_5)Cr(OPh)_2Me$.

8 CHROMIUM(V) ORGANOMETALLICS

Few organochromium compounds possessing the d^1 configuration are known. $(\eta^5\text{-}C_5Me_5)CrOBr_2$ was obtained from the reaction of $[(\eta^5\text{-}C_5Me_5)Cr(Br)(\mu\text{-}Br)]_2$ with O_2.[127] Its cyclopentadienyl analog was synthesized from chromocene and Br_2 followed by O_2. These compounds possess the expected piano-stool geometry and are metastable, reverting easily to the starting materials. The electrophilic oxygen ligand of $(\eta^5\text{-}C_5Me_5)CrOBr_2$ is, however, readily transferred to phosphines; catalytic oxygenation occurs in the presence of O_2 and excess phosphine. $(\eta^5\text{-}C_5H_5)CrOBr_2$ is even more reactive, transferring its oxygen to both phosphines and sulfides (equation 13).

$$2(\eta^5\text{-}C_5Me_5)Cr(O)Br_2 \xrightarrow{PR_3} [(\eta^5\text{-}C_5Me_5)Cr(Br)(\mu\text{-}Br)]_2 + 2O{=}PR_3 \quad (13)$$

The corresponding chloro derivatives, that is, Cp^*CrOCl_2 and $CpCrOCl_2$, were reported more recently.[128] Both were prepared by oxidation of Cr(III) precursors with O_2, and they too engage in O-atom transfer chemistry; $CpCrOCl_2$ is particularly noteworthy for transferring oxygen to a variety of olefins. These reactions feature a change of spin state along the reaction pathway, and the corresponding potential energy surfaces and their ‘minimum energy crossing point’ (MECP) have been characterized computationally.

The first oxoalkyl of chromium(V), $(\eta^5\text{-}C_5Me_5)CrO(Me)_2$, was prepared via oxygen transfer from trimethylamine *N*-oxide to the Cr^{III} precursor $(\eta^5\text{-}C_5Me_5)Cr(py)Me_2$.[129] Its effective magnetic moment at 285 K, 1.76 μ_B, is consistent with the presence of pentavalent chromium. At ambient temperature and pressure, this complex does not function as an ethylene polymerization catalyst; however, it does react with the starting material to give the Cr^{IV} dimer $[(\eta^5\text{-}C_5Me_5)Cr(Me)_2]_2(\mu_2\text{-}O)$. Another chromium(V) alkyl, namely, dinuclear $[Cp^*Cr(O)Me]_2(\mu\text{-}O)$, was produced by the reaction of $[Cp^*Cr(\mu\text{-}Me)]_2$ with O_2.

9 CHROMIUM(VI) ORGANOMETALLICS

The majority of d^0 organochromium species feature a bis(imido)chromium moiety. The compounds $Cr(=N\text{-}t\text{-}Bu)_2(Ar)_2$ (Ar = mesityl, 2,6-xylyl), prepared from $Cr(=N\text{-}t\text{-}Bu)_2(OSiMe_3)_2$ and two equivalents of the appropriate Grignard reagent, were the first organometallic complexes of chromium(VI) to appear in the literature.[129] Their stability has been attributed to the steric protection afforded to the metal center and amido nitrogens by the aromatic ligands’ ortho methyl groups. The dimesityl compound does, however, undergo *CO Insertion* to give the unusual bis-acyl $Cr(=N\text{-}t\text{-}Bu)_2(COC_6H_2Me_3)_2$; this thermally eliminates the amide $HN(t\text{-}Bu)COC_6H_2Me_3$. *t*-Butyl isocyanide also inserts into the chromium–carbon bond of the mesityl complex, but only a single insertion is observed, and $Cr(=N\text{-}t\text{-}Bu)_2\{\eta^2\text{-}[t\text{-}BuN{=}C(C_6H_2Me_3)]\}(C_6H_2Me_3)$ is formed. An η^2-aminoacyl is also the product of the reaction between $Cr(=N\text{-}t\text{-}Bu)_2Cl_2(t\text{-}BuNC)$ and methyllithium. Presumably, methyl replaces one of the chlorides, then migrates to the isocyanide carbon to give $Cr(=N\text{-}t\text{-}Bu)_2\{[\eta^2\text{-}[t\text{-}BuN{=}C(Me)]\}Cl]$.

The first report of a chromium(VI) alkyl described the synthesis of $Cr(=N\text{-}t\text{-}Bu)_2R_2$ (R = CH_2SiMe_3, CH_2CMe_3, CH_2CMe_2Ph) via alkylation of $Cr(=N\text{-}t\text{-}Bu)_2X_2$ (X = Cl, Br) with RMgCl or R_2Zn.[130] Although coordinatively unsaturated, these complexes do not bind a fifth ligand, nor is there evidence for agostic interactions between the alkyl α-methylene groups and chromium. They also do not react to form alkylidenes. Novel monomeric cyclopentadienyl compounds of chromium(VI), $(\eta^5\text{-}C_5H_5)Cr(=N\text{-}t\text{-}Bu)_2X$ (X = Br, Cl), were prepared from $Cr(=N\text{-}t\text{-}Bu)_2(py)X_2$ and $Mg(\eta^5\text{-}C_5H_5)_2(THF)_{2.5}$. These halides could be alkylated to give $(\eta^5\text{-}C_5H_5)Cr(=N\text{-}t\text{-}Bu)_2R$ (R = Me, CH_2SiMe_3, CH_2CMe_3, CH_2CMe_2Ph).

The analogous arylimido species $Cr(=N\text{-}2,6\text{-}i\text{-}PrC_6H_3)_2Cl_2$ gives rise to the structurally characterized dialkyl $Cr(=N\text{-}2,6\text{-}i\text{-}PrC_6H_3)_2(CH_2CMe_3)_2$. The latter undergoes α-elimination and generates Cr(VI) alkylidenes of the type $Cr(=N\text{-}2,6\text{-}i\text{-}PrC_6H_3)_2(=CHMe_3)(L)$ (L = THF, PMe_3).[131] Surprisingly, these alkylidenes do not react with alkenes.

Treatment of several of the imido alkyls described above with borate activators (e. g. $[Ph_3C][B(C_6F_5)_4]$ or $[PhNMe_2H][B(C_6F_5)_4]$) generated ethylene polymerization catalysts.[132] However, the hexavalent nature of the active catalysts has been questioned based on density functional calculations on model systems.[133]

A monomeric oxoalkyl of chromium(VI), $(\eta^5\text{-}C_5Me_5)CrO_2Me$, has been obtained from the oxidation of $(\eta^5\text{-}C_5Me_5)Cr(py)Me_2$ with O_2.[134] In C_6D_6 solution, it slowly decomposes over a period of weeks; in addition, it fails to polymerize ethylene or undergo methanolysis of the chromium–carbon bond. $(\eta^5\text{-}C_5Me_5)CrO_2Me$ does, however, oxidize PPh_3 with concomitant formation of the chromium(V) dimer $[(\eta^5\text{-}C_5Me_5)Cr(O)(Me)]_2(\mu_2\text{-}O)$. Another set of formally hexavalent cyclopentadienyl chromium compounds are aminocarbyne complexes like $[(\eta^5\text{-}C_5H_5)Cr(\equiv Ci\text{-}Pr_2)(Br)(CNt\text{-}Bu)_2]\ PF_6$ and $[(\eta^5\text{-}C_5Me_5)Cr(\equiv Ci\text{-}Pr_2)(CNt\text{-}Bu)_3](PF_6)_2$.[135]

Finally, the nitrido alkyl $NCr(CH_2SiMe_2Ph)(Ni\text{-}Pr_2)_2$ has been structurally characterized,[136] and the related dialkyl $NCr(CH_2SiMe_3)_2(Ni\text{-}Pr_2)$ has been shown to insert *tert*-butylisonitrile.[137]

10 RELATED ARTICLES

Carbonyl Complexes of the Transition Metals; Chromium: Inorganic & Coordination Chemistry; Dinuclear

Organometallic Cluster Complexes; Magnetism of Transition Metal Ions; Oligomerization & Polymerization by Homogeneous Catalysis; Organic Synthesis using Transition Metal Carbonyl Complexes; Organic Synthesis using Transition Metal Complexes Containing π-Bonded Ligands; Paramagnetic Organometallic Complexes; Polynuclear Organometallic Cluster Complexes; Supported Organotransition Metal Compounds.

11 REFERENCES

1. M. Berthelot, *Ann. Chim. Phys.*, 1866, **9**, 401.
2. G. M. Bennett and E. E. Turner, *J. Chem. Soc.*, 1914, **105**, 1057.
3. F. A. L. Anet and E. Leblanc, *J. Am. Chem. Soc.*, 1957, **79**, 2649.
4. W. Herwig and H. H. Zeiss, *J. Am. Chem. Soc.*, 1957, **79**, 6561.
5. F. Hein, *Ber. Dtsch. Chem. Ges.*, 1919, **52**, 195.
6. H. H. Zeiss and M. Tsutsui, *J. Am. Chem. Soc.*, 1957, **79**, 3062.
7. E. O. Fischer and W. Hafner, *Z. Naturforsch. B*, 1955, **10**, 665.
8. D. Seyferth, *Organometallics*, 2002, **21**, 1520, 2800.
9. A. Job and A. Cassal, *Compt. Rend.*, 1926, **183**, 392.
10. B. Nicholls and M. Whiting, *J. Chem. Soc.*, 1959, 551.
11. E. O. Fischer and A. Maasböl, *Angew. Chem., Int. Ed. Engl.*, 1964, **3**, 580.
12. E. O. Fischer and A. Maasböl, *Chem. Ber.*, 1967, 2445.
13. E. O. Fischer, G. Kreis, C. G. Kreiter, J. Müller, G. Huttner, and H. Lorenz, *Angew. Chem., Int. Ed. Engl.*, 1973, **12**, 564.
14. G. Yagupsky, W. Mowat, A. Shortland, and G. Wilkinson, *Chem. Commun.*, 1970, 1369.
15. R. P. A. Sneeden, ‘Organochromium Compounds’, Academic Press, New York, 1975.
16. S. W. Kirtley, in ‘Comprehensive Organometallic Chemistry’, eds. G. Wilkinson, F. G. A. Stone, and E. W. Abel, Pergamon Press, Oxford, 1982, Vol. 3, Chap. 26.1, p. 784.
17. M. J. Winter, in ‘Comprehensive Organometallic Chemistry II’, eds. E. W. Abel, F. G. A. Stone, and G. Wilkinson, Pergamon Press, Oxford, 1995, Vol. 5, Chap. 3, p. 156.
18. K. H. Theopold, A. Mommertz, and B. A. Salisbury, in ‘Science of Synthesis’, ed. T. Imamoto, Thieme, Stuttgart, 2003, Vol. 2, p. 229.
19. R. Poli and K. M. Smith, in ‘Science of Synthesis’, ed. T. Imamoto, Thieme, Stuttgart, 2003, Vol. 2, p. 283.
20. J. E. Ellis, *Organometallics*, 2003, **22**, 3322.
21. H. Behrens and R. Weber, *Z. Anorg. Allg. Chem.*, 1957, **291**, 122.
22. E. Lindner, H. Behrens, and D. Uhlig, *Z. Naturforsch. B*, 1973, **28**, 276.
23. J. E. Ellis, S. G. Hentges, D. G. Kalina, and G. P. Hagen, *J. Organomet. Chem.*, 1975, **97**, 79.
24. C. J. Pickett and D. Pletcher, *J. Chem. Soc., Dalton Trans.*, 1976, 749.
25. J. E. Ellis, C. P. Parnell, and G. P. Hagen, *J. Am. Chem. Soc.*, 1978, **100**, 3605.
26. H. Behrens and W. Klek, *Z. Anorg. Allg. Chem.*, 1957, **292**, 151.
27. B. D. Dombeck and R. J. Angelici, *J. Am. Chem. Soc.*, 1973, **95**, 7516.
28. J. T. Lin, G. P. Hagen, and J. E. Ellis, *Organometallics*, 1984, **3**, 1288.
29. J. E. Ellis, *Adv. Organomet. Chem.*, 1990, **31**, 1.
30. R. D. Rieke, J. S. Arney, W. E. Rich, B. R. Willeford Jr, and B. S. Poliner, *J. Am. Chem. Soc.*, 1975, **97**, 5951.
31. Y. Kalzu and H. Kobayashi, *Bull. Chem. Soc. Jpn.*, 1972, **45**, 470.
32. C. Elschenbroich, E. Bilger, and J. Koch, *J. Am. Chem. Soc.*, 1984, **106**, 4297.
33. G. L. Geoffroy and M. S. Wrighton, ‘Organometallic Photochemistry’, Academic Press, New York, 1979.
34. G. R. Dobson, I. W. Stolz, and R. K. Sheline, *Adv. Inorg. Chem. Radiochem.*, 1966, **8**, 1.
35. M. Y. Darensbourg and J. C. Deaton, *Inorg. Chem.*, 1981, **20**, 1644.
36. W. Strohmeier and K. Gerlach, *Chem. Ber.*, 1961, **94**, 398.
37. C. A., McAuliffe ed., ‘Transition Metal Complexes of Phosphorus, Arsenic, and Antimony’, Macmillan, New York, 1973.
38. C. A. McAuliffe and W. Levanson, ‘Phosphine, Arsine, and Stibine Complexes of the Transition Elements’, Elsevier, New York, 1979.
39. J. A. McCleverty, *Chem. Rev.*, 1979, **79**, 53.
40. D. Sutton, *Chem. Soc. Rev.*, 1975, **4**, 443.
41. M. Herberhold and W. Bernhagen, *Angew. Chem., Int. Ed. Engl.*, 1976, **15**, 617.
42. T. W. Hayton, P. Legzdins, and W. B. Sharp, *Chem. Rev.*, 2002, **102**, 935.
43. B. W. S. Kolthammer and P. Legzdins, *J. Am. Chem. Soc.*, 1978, **100**, 2247.
44. A. G. Sharpe, ‘The Chemistry of Cyano Complexes of the Transition Metals’, Academic Press, London, 1976.
45. L. Malatesta and F. Bonati, ‘Isocyanide Complexes of Metals’, Wiley, New York, 1969.
46. P. V. Yaneff, *Coord. Chem. Rev.*, 1977, **23**, 183.
47. K. H. Dötz, H. Fischer, P. Hofmann, F. R. Kreissl, U. Schubert, and K. Weiss, ‘Transition Metal Carbene Complexes’, Verlag Chemie, Deerfield Beach, FL, 1983.
48. A. Aguero and J. A. Osborn, *New J. Chem.*, 1988, **12**, 111.

49. P. J. Brothers and W. R. Roper, *Chem. Rev.*, 1988, **88**, 1293.
50. K. H. Dötz and P. Tomuschat, *Chem. Soc. Rev.*, 1999, **28**, 187.
51. R. N. Bagchi, A. M. Bond, R. Colton, D. L. Luscombe, and J. E. Moir, *J. Am. Chem. Soc.*, 1986, **108**, 3352.
52. A. M. Bond, J. A. Bowden, and R. Colton, *Inorg. Chem.*, 1974, **13**, 602.
53. R. N. Bagchi, A. M. Bond, G. Brain, R. Colton, T. L. E. Henderson, and J. E. Kevekordes, *Organometallics*, 1984, **3**, 4.
54. A. M. Bond, S. W. Carr, and R. Colton, *Inorg. Chem.*, 1984, **23**, 2343.
55. D. A. Cummings, J. McMaster, A. L. Rieger, and P. H. Rieger, *Organometallics*, 1997, **16**, 4362.
56. J. H. MacNeil, W. C. Watkins, M. C. Baird, and K. F. Preston, *Organometallics*, 1992, **11**, 2761.
57. E. Fischer and H. P. Kögler, *Z. Naturforsch. B*, 1958, **13**, 197.
58. D. S. Richeson, J. F. Mitchell, and K. H. Theopold, *Organometallics*, 1989, **8**, 2570.
59. M. C. Baird, *Chem. Rev.*, 1988, **88**, 1217.
60. D. A. Sweigart, *Adv. Organomet. Chem.*, 1996, **40**, 171.
61. S. J. McLain, *J. Am. Chem. Soc.*, 1988, **110**, 643.
62. D. C. Woska, Y. P. Ni, and B. B. Wayland, *Inorg Chem.*, 1999, **38**, 4135.
63. K. M. Doxsee, R. H. Grubbs, and F. C. Anson, *J. Am. Chem. Soc.*, 1984, **106**, 7819.
64. S. Hao, S. Gambarotta, and C. Bensimon, *J. Am. Chem. Soc.*, 1992, **114**, 3556.
65. S. K. Hao, J. I. Song, P. Berno, and S. Gambarotta, *Organometallics*, 1994, **13**, 1326.
66. H. G. Alt, K. A. Mahmoud, and A. J. Rest, *Angew. Chem., Int. Ed. Engl.*, 1983, **22**, 544.
67. D. Wormsbächer, K. M. Nicholas, and A. L. Rheingold, *J. Chem. Soc., Chem. Commun.*, 1985, 721.
68. K. B. Kapps, A. Bauer, T. D. Ju, C. D. Hoff, *Inorg. Chem.*, 1999, **38**, 6130.
69. E. A. Koerner von Gustorf, O. Jaenicke, O. Wolfbeis, and C. R. Eady, *Angew. Chem., Int. Ed. Engl.*, 1975, **14**, 278.
70. R. A. Heintz, B. S. Haggerty, H. Wan, A. L. Rheingold, and K. H. Theopold, *Angew. Chem., Int. Ed. Engl.*, 1992, **31**, 1077.
71. R. A. Heintz, T. G. Neiss, and K. H. Theopold, *Angew. Chem., Int. Ed. Engl.*, 1994, **33**, 2326.
72. R. A. Heintz, T. F. Koetzle, R. L. Ostrander, A. L. Rheingold, K. H. Theopold, and P. Wu, *Nature*, 1995, **378**, 359.
73. D. W. Norman, M. J. Ferguson, and J. M. Stryker, *Organometallics*, 2004, **23**, 2015.
74. P. J. Alonso, L. R. Falvello, J. Fornies, M. A. Garcia-Nonforte, A. Martin, B. Menjon, and G. Rodriguez, *Chem. Commun.*, 1998, 1721.
75. J. Kalousova, J. Holecek, J. Votinsky, and L. Benes, *Z. Chem.*, 1983, **23**, 327.
76. F. J. Karol, G. L. Karapinka, C. Wu, A. W. Dow, R. N. Johnson, and W. L. Carrick, *J. Polym. Sci., Part A-1*, 1972, **10**, 2621.
77. A. Zecchina, G. Spoto, and S. Bordiga, *Faraday Discuss. Chem. Soc.*, 1989, **87**, 149.
78. S.-L. Fu and J. H. Lunsford, *Langmuir*, 1990, **6**, 1774.
79. S.-L. Fu and J. H. Lunsford, *Langmuir*, 1991, **7**, 1179.
80. C. D. Abernethy, J. A. Clyburne, A. C. Jason, A. H. Cowley, and R. A. Jones, *J. Am. Chem. Soc.*, 1999, **121**, 2329.
81. H. Schwemlein, L. Zsolnai, G. Huttner, and H. H. Brintzinger, *J. Organomet. Chem.*, 1983, **256**, 285.
82. G. J. Matare, D. M. Foo, K. M. Kane, R. Zehnder, M. Wagener, P. J. Shapiro, T. Concolino, and A. L. Rheingold, *Organometallics*, 2000, **19**, 1534.
83. F. Schaper, M. Rentzsch, M.-H. Prosenc, U. Rief, K. Schmidt, and H.-H. Brintzinger, *J. Organomet. Chem.*, 1997, **534**, 67.
84. F. Schaper, O. Wrobel, R. Schwoerer, and H.-H. Brintzinger, *Organometallics*, 2004, **23**, 3552.
85. J. L. Robbins, N. Edelstein, B. Spencer, and J. C. Smart, *J. Am. Chem. Soc.*, 1982, **104**, 1882.
86. H. Sitzmann, M. Schaer, E. Dormann, and M. Kelemen, *Z. Anorg. Allg. Chem.*, 1997, **623**, 1850.
87. O. Heinemann, P. W. Jolly, C. Krüger, and G. P. J. Verhovnik, *Organometallics*, 1996, **15**, 5462.
88. E. D. Brady, J. S. Overby, M. B. Meredith, A. B. Mussman, M. A. Cohn, and T. P. Hanusa, *J. Am. Chem. Soc.*, 2002, **124**, 9556.
89. J. W. Freeman, N. C. Hallinan, A. M. Arif, R. W. Gedridge, R. D. Ernst, and F. Basolo, *J. Am. Chem. Soc.*, 1991, **113**, 6509.
90. P. D. Smith and E. T. Hsieh, *US Pat.* 4 587 227 1986.
91. G. S. Girolami, G. Wilkinson, A. M. R. Galas, M. Thornton-Pett, and M. B. Hursthouse, *J. Chem. Soc., Dalton Trans.*, 1985, 1339.
92. B. J. Thomas, S. K. Noh, G. K. Schulte, S. C. Sendlinger, and K. H. Theopold, *J. Am. Chem. Soc.*, 1991, **113**, 893.
93. R. A. Heintz, R. L. Ostrander, A. L. Rheingold, and K. H. Theopold, *J. Am. Chem. Soc.*, 1994, **116**, 11387.
94. J. L. Kersten, R. R. Kucharczyk, G. P. A. Yap, A. L. Rheingold, and K. H. Theopold, *Chem. – Eur. J.*, 1997, **3**, 1668.
95. A. Hess, M. R. Hörz, L. M. Liable-Sands, D. C. Lindner, A. L. Rheingold, and K. H. Theopold, *Angew. Chem., Int. Ed. Engl.*, 1999, **38**, 166.
96. K. Nishimura, H. Kuribayashi, A. Yamamoto, and S. Ikeda, *J. Organomet. Chem.*, 1972, **37**, 317.
97. J. H. Espenson, *Adv. Inorg. Bioinorg. Mech.*, 1982, **1**, 1.
98. J. H. Espenson, *Acc. Chem. Res.*, 1992, **25**, 222.
99. E. G. Thaler, K. Folting, J. C. Huffman, and K. G. Caulton, *J. Organomet. Chem.*, 1989, **376**, 343.
100. G. K. Barker, M. F. Lappert, and J. A. K. Howard, *J. Chem. Soc., Dalton Trans.*, 1978, 734.

101. T. G. Gardner and G. S. Girolami, *J. Chem. Soc., Chem. Commun.*, 1987, 1758.
102. E. Kurras and J. Otto, *J. Organomet. Chem.*, 1965, **4**, 114, references therein.
103. K. Angermund, A. Döhring, P. W. Jolly, C. Krüger, and C. C. Romão, *Organometallics*, 1986, **5**, 1268.
104. D. S. Richeson, J. F. Mitchell, and K. H. Theopold, *J. Am. Chem. Soc.*, 1987, **109**, 5868.
105. K. H. Theopold, *Acc. Chem. Res.*, 1990, **23**, 263.
106. P. W. Jolly, *Acc. Chem. Res.*, 1996, **29**, 544.
107. R. Emrich, O. Heinemann, P. W. Jolly, C. Krüger, and G. P. J. Verhovnik, *Organometallics*, 1997, **16**, 1511.
108. A. Döhring, J. Gohre, and P. W. Jolly, *Organometallics*, 2000, **19**, 388.
109. A. Döhring, V. R. Jensen, and P. W. Jolly, *Organometallics*, 2001, **20**, 2234.
110. R. A. Heintz, S. Leelasubcharoen, L. M. Liable-Sands, A. L. Rheingold, and K. H. Theopold, *Organometallics*, 1998, **17**, 5477.
111. G. Bhandari, A. L. Rheingold, and K. H. Theopold, *Chem. – Eur. J.*, 1995, **1**, 199.
112. P. A. White, J. Calabrese, and K. H. Theopold, *Organometallics*, 1996, **15**, 5473.
113. C. W. Hoganson, D. J. Doren, and K. H. Theopold, *Macromolecules*, 2004, **37**, 566.
114. G. J. P. Britovsek, V. C. Gibson, and D. F. Wass, *Angew. Chem., Int. Ed. Engl.*, 1999, **38**, 428.
115. W.-K. Kim, M. J. Fevola, L. M. Liable-Sands, A. L. Rheingold, and K. H. Theopold, *Organometallics*, 1998, **17**, 4541.
116. V. C. Gibson, P. J. Maddox, C. Newton, C. Redshaw, G. A. Solan, A. J. P. White, and D. J. Williams, *Chem. Commun.*, 1998, 1651.
117. K. H. Theopold, L. A. MacAdams, C. Puttnual, G. P. Buffone, and A. L. Rheingold, *Polym. Mater. Sci. Eng.*, 2002, **86**, 310.
118. R. D. Köhn, D. Smith, D. Lilge, S. Mihan, F. Molnar, and M. Prinz, *ACS Sym. Ser.*, 2003, **857**, 88.
119. M. D. Fryzuk, D. B. Leznoff, S. J. Rettig, and V. G. Young, *J. Chem. Soc., Dalton Trans.*, 1999, 147.
120. C. Schulzke, D. Enright, H. Sugiyama, G. LeBlanc, S. Gambarotta, G. P. A. Yap, L. K. Thompson, D. R. Wilso, and R. Duchateau, *Organometallics*, 2002, **21**, 3810.
121. S. L. Scott, J. A. N. Ajjou, *Chem. Eng. Sci.*, 2001, **56**, 4155.
122. H. Fischer, ‘Carbyne Complexes’, VCH, Weinheim, 1988.
123. M. Morán, *Transition Met. Chem.*, 1981, **6**, 173.
124. D. M. J. Foo, P.-J. Sinnema, B. Twamley, and P. J. Shapiro, *Organometallics*, 2002, **21**, 1005.
125. P.-J. Sinnema, J. Nairn, R. Zehnder, P. J. Shapiro, B. Twamley, and A. Blumenfeld, *Chem. Commun.*, 2004, 110.
126. A. C. Filippou, S. Schneider, and G. Schnakenburg, *Angew. Chem., Int. Ed. Engl.*, 2003, **42**, 4486.
127. D. B. Morse, T. B. Rauchfuss, and S. R. Wilson, *J. Am. Chem. Soc.*, 1988, **110**, 8234.
128. J. S. Hess, S. Leelasubcharoen, A. L. Rheingold, D. J. Doren, and K. H. Theopold, *J. Am. Chem. Soc.*, 2002, **124**, 2454.
129. M. B. Hursthouse, M. Motevalli, A. C. Sullivan, and G. Wilkinson, *J. Chem. Soc., Chem. Commun.*, 1986, 1398.
130. N. Meijboom, C. J. Schaverien, and A. G. Orpen, *Organometallics*, 1990, **9**, 774.
131. M. P. Coles, V. C. Gibson, W. Clegg, M. R. J. Elsegood, and P. A. Porrelli, *Chem. Commun.*, 1996, 1963.
132. M. P. Coles, C. I. Dalby, V. C. Gibson, W. Clegg, and M. R. J. Elsegood, *Chem. Commun.*, 1995, 1709.
133. V. R. Jensen and K. J. Borve, *Chem. Commun.*, 2002, 542.
134. S. K. Noh, R. A. Heintz, B. S. Haggerty, A. L. Rheingold, and K. H. Theopold, *J. Am. Chem. Soc.*, 1992, **114**, 1892.
135. A. C. Filippou, B. Lungwitz, K. M. A. Wanninger, and E. Herdtweck, *Angew. Chem., Int. Ed. Engl.*, 1995, **34**, 924.
136. A. L. Odom and C. C. Cummins, *Organometallics*, 1996, **15**, 898.
137. A. L. Odom and C. C. Cummins, *Polyhedron*, 1998, **17**, 675.

Acknowledgment

Our investigation of organochromium compounds has been supported for many years by the U. S. National Science Foundation, as well as by the Chevron Chemical Co. and its successor, the Chevron Phillips Chemical Co. We thank these organizations for their support.

Cobalt: B_{12} Enzymes & Coenzymes

Bernhard Kräutler
University of Innsbruck, Innsbruck, Austria

1 Introduction 1
2 B_{12} Coenzymes 1
3 B_{12} Enzymes 10
4 Related Articles 17
5 References 17

Glossary

Base-off: nucleotide function not coordinated to a cobalt center in a complete corrin
Base-on: nucleotide function coordinated to a cobalt center in a complete corrin
Complete corrin: a cobamide with an appended nucleotide base
Ileum: last part of the small intestine
Incomplete corrin: a cobyrinic acid derivative lacking a nucleotide base
Pernicious anemia: microscopic abnormalities of blood and bone marrow correlating with B_{12}-deficiency

1 INTRODUCTION

Vitamin B_{12} (**1**) was discovered some 55 years ago as the (extrinsic) 'antipernicious anemia factor,' important for human and animal metabolism.[1] The cobalt complex (**1**) was structurally characterized by X-ray analysis in the laboratory of D.C. Hodgkin.[2,3] In these studies, the unique buildup of the 'tetrapyrrolic' corrin ligand and the intramolecularly coordinating 'pseudo-nucleotide' function of the vitamin were discovered.[2]

The unusual nature of the red cobalt complex (**1**) induced considerable activity in the field of coordination chemistry: vitamin B_{12} derivatives were found to represent unique examples of kinetically labile Co^{III} complexes, the analysis of whose 'model type' coordination chemistry itself proved to be of particular value.[4] Interestingly, for the transition metal cobalt, no other cofactor function has been clearly established, except for that in the B_{12}-derivatives.[5]

The complex and novel structure of the corrin ligand prompted a series of early investigations of its chemistry,[4,6] and the partial synthesis of vitamin B_{12} was achieved from the B_{12}-degradation product cobyric acid (**2**)[6] (Figure 1; for the nomenclature of the B_{12}-derivatives, see Kräutler[7]).

About 40 years ago, coenzyme B_{12} (adenosylcobalamin, (**3**)) was discovered by Barker *et al.*, and its organometallic nature was revealed by X-ray analysis in the laboratory of D. C. Hodgkin.[2,3] The partial syntheses of the coenzyme (**3**), of methylcobalamin (**4**), and of other organometallic B_{12}-derivatives from vitamin B_{12} were rapidly developed by Smith *et al.* and Bernhauer *et al.*; later on, methylcobalamin (**4**) was also found in human serum.[6]

The unmatched complex structure of the 'low-molecular weight' natural product vitamin B_{12} posed a challenge to synthetic chemistry, which was met in the early 1970s by Eschenmoser[8] and by Woodward[9] and their coworkers. The biosynthesis of the structure of natural cobalt-corrins is no less intricate[10,11] and facets of its pathways still remain to be uncovered (see section 2.3).

The metabolically important functions of the B_{12}-derivatives are directly concerned either with enzymatically controlled organometallic reactions involving protein-bound adenosylcobamides (such as coenzyme B_{12}, (**3**)), or methyl-Co^{III}-corrinoids (such as methylcobalamin, (**4**)), or with enzyme-controlled redox reactions. Studies on the underlying biologically relevant organometallic chemistry of the B_{12}-coenzymes in homogeneous (protic) solution, as well as the characterization of the enzymatic processes themselves have attracted considerable interest.[12–14]

Subsequent to the original quest for vitamin B_{12} (**1**), driven by medicinal purposes mainly, further investigations on the natural corrinoids laid bare the central roles of the B_{12}-coenzymes in the metabolism of microorganisms, in particular.[6,7] These 'primitive' organisms uniquely possess the capacity to build up the complex B_{12} structure in nature,[10,11,13,14] in which they may vary the constitution of the nucleotide function in a species-specific way (Figure 2).[6,13] The cobalt-corrins, in turn, have been proposed to be structural and functional remnants of 'early' (primitive) forms of life,[15] where presumably, central metabolic processes could rely considerably on organometallic chemistry at cobalt and nickel centers.[5]

2 B_{12} COENZYMES

The coenzyme B_{12} molecule consists of several unique structural units: the corrin ligand, the intramolecularly coordinating nucleotide function, the corrin-bound Co^{III}-ion, and the organometallically bound 5′-deoxyadenosyl ligand (Figure 3).[3] The cyanide derivative, vitamin B_{12} (**1**), is an isolation artifact that appears not to have a physiological role itself.[15]

Coenzyme B_{12} (**3**) and vitamin B_{12} (**1**) are thus representatives of the nucleotide-containing 'complete corrins'. Removal

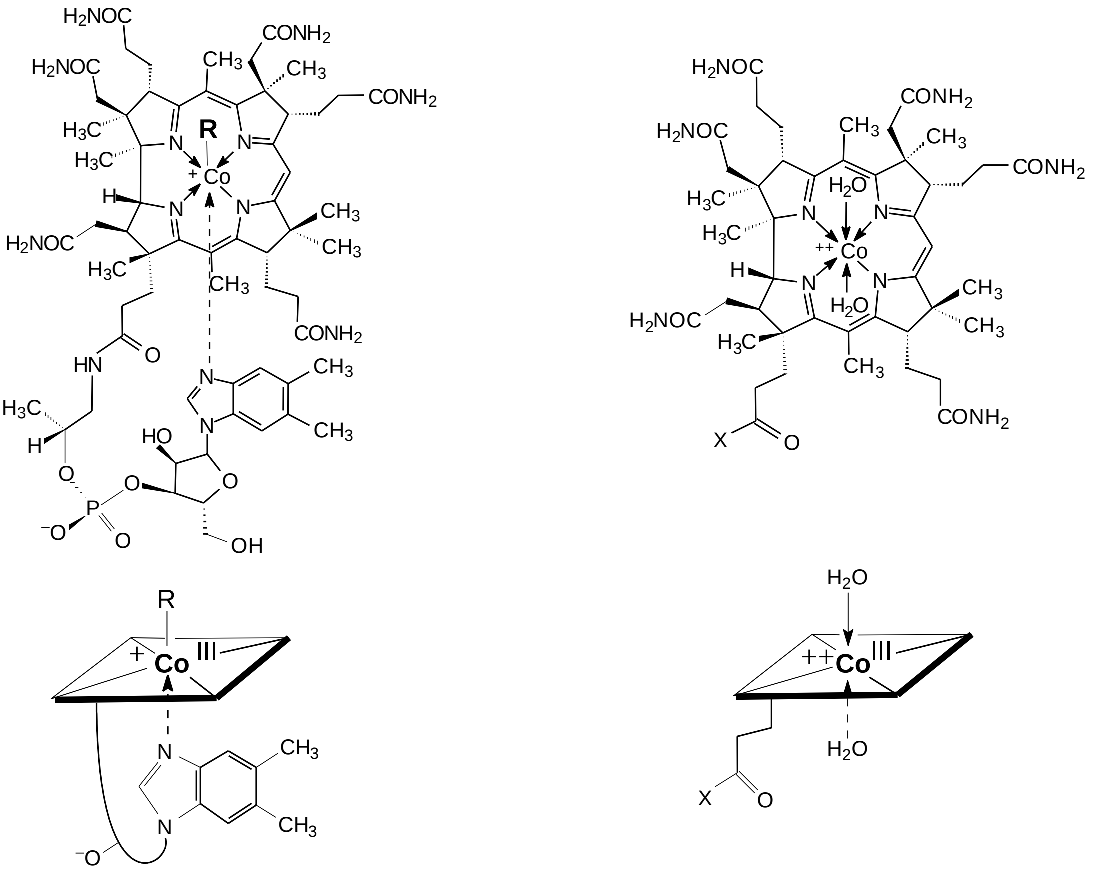

R = CN; cyanocobalamin (vitamin B_{12}, **1**)
R = 5′-adenosyl; adenosylcobalamin (coenzyme B_{12}, **3**)
R = CH_3; methylcobalamin (**4**)

X = OH; diaqua-Co^{III}-cobyric acid (**2**)
X = $NHCH_2CH(CH_3)OH$; diaqua-Co^{III}-cobinamide
X = $NHCH_2CH(CH_3)OPO_2$ (D O^3 ribofuranosyl); diaqua-Co^{III}-cobamid

Figure 1 Representative structural formulae and corresponding symbols of cobalamins([5′,6′-dimethylbenzimidazolyl]cobamides, (a)) and of diaquo-Co^{III} forms of incomplete corrins (b)

of the nucleotide function leads to ‘incomplete corrins’, such as the cobinamides (Figure 1).

2.1 Structure and Bonding in Corrins

2.1.1 Co^{III}-corrins

Early structural investigations have been concerned mostly with the (diamagnetic) Co^{III}-corrins.[2,3] Throughout, the corrin-bound Co^{III} center (a d^6 ion) is found to carry two axial ligands (pseudooctahedral hexacoordination); the existence[16] of (diamagnetic) five-coordinate alkyl-Co^{III}-corrins lacks convincing experimental support. In the base-on form of the complete corrins, the ‘lower’ axial position (α-position) is occupied by the nucleotide base. The sixth ligand, for example, a methyl group in methylcobalamin (**4**), then sits in the ‘upper’ position (β-position).

The corrins are related to the natural porphyrins by both their structure[17] and their biosynthesis.[10,11] Besides its linearly conjugated chromophoric system that comprises the four inner nitrogen centers, the corrin ligand exhibits a uniquely functionalized periphery and a saturated and direct trans junction between the two ‘western’ reduced pyrrole rings; the (15-membered inner ring of the) corrin ligand provides a coordination hole smaller than that of the (16-membered inner ring of the) porphyrins[17] and is inherently nonplanar (Figure 3).[2,3]

The remarkable ‘nucleotide loop’, which contains an unusual α-configured nucleotide function, forms a nearly strain-free 19-membered ring[17] to allow for coordination of the nucleotide base to the lower side of the corrin-bound metal center (base-on forms).[2,3] Protonation at the nitrogen atom of the nucleotide base (in some cases, mere solvolysis) leads to the base-off form (Figure 4).

The β-ligands in natural corrinoid cofactors are either organometallically bound 5′-adenosyl or methyl groups, or else an aquo or a cyano ligand is found in the isolation forms (where the latter two may be artifacts of the isolation conditions).[15]

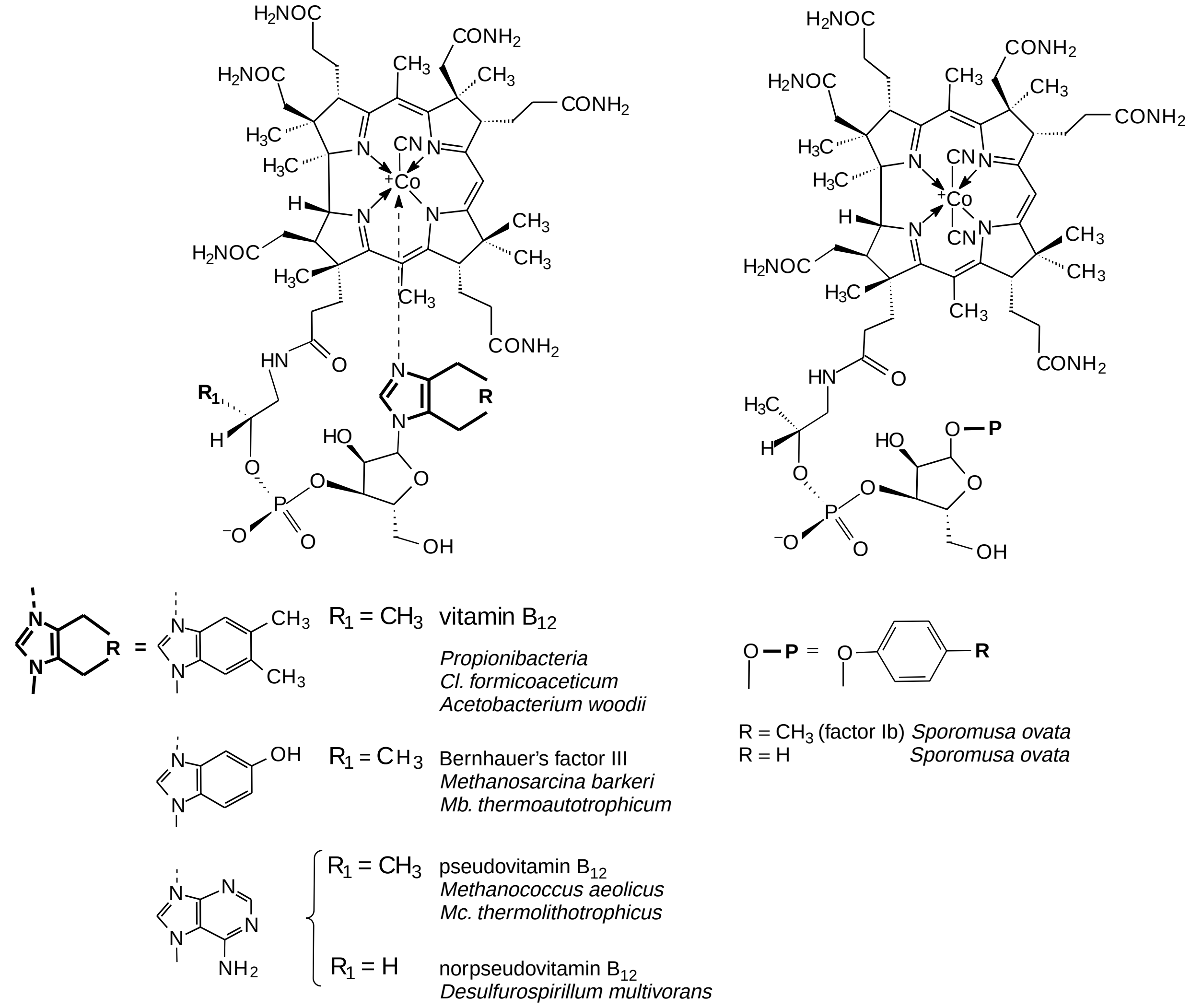
H2NOC
CONH2
CH3
CN
+Co
HN
O
R1
H
O
P
−O
HO
OH
R
O—P
R1 = CH3 vitamin B12
Propionibacteria
Cl. formicoaceticum
Acetobacterium woodii
R1 = CH3 Bernhauer's factor III
Methanosarcina barkeri
Mb. thermoautotrophicum
R1 = CH3 pseudovitamin B12
Methanococcus aeolicus
Mc. thermolithotrophicus
R1 = H norpseudovitamin B12
Desulfurospirillum multivorans
R = CH3 (factor Ib) Sporomusa ovata
R = H Sporomusa ovata
NH2
OH

Figure 2 Representative structural formulae of CN–Co^{III} forms of complete corrins containing different nucleotide bases, as isolated from specific bacterial sources

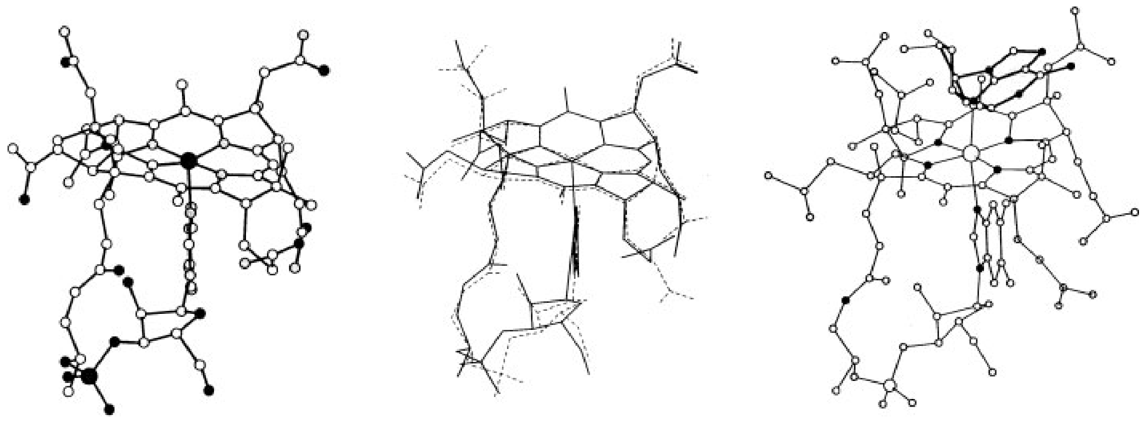
(a) (b) (c)

Figure 3 Three-dimensional structures in the crystal of Co^{II}-cobalamin ((**5**), (a)) and of coenzyme B_{12} ((**3**), (c)) according to X-ray analysis and superposition of the structure of the Co^{III}-corrin part of coenzyme (**3**) and that of the Co^{II}-corrin (**5**) (b)

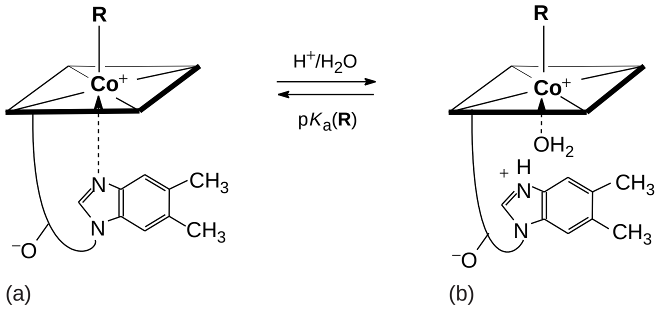

Figure 4 Symbolic representation of base-on form (a) and protonated base-off form (b) of cobalamins: (**1**) Co–R=Co^{III}–CN, $pK_a = 0.10$;[18] (**3**) Co–R=Co^{III}-5′-adenosyl, $pK_a = 3.67$;[18] (**4**) Co–R = Co^{III}–CH_3, $pK_a = 2.89$;[18] (**5**) Co–R=Co^{II}, pK_a = ca. 2.9;[19] (**7**) Co–R=Co^{III}–H_2O', $pK_a = -2.13$[18]

The corrin ligand and the basic motif of the nucleotide chain are widely conserved structural units in the natural corrins. Norpseudovitamin B_{12} (**8**) is the first example of a natural corrinoid with a modified isopropanolamine linker: it is (the isolation form of) the cofactor of perchloroethene-dehalogenase in an obligate anaerobe.[20] The nucleotide bases (a 5,6-dimethylbenzimidazole in the cobalamins) of natural complete corrins from different bacterial sources also exhibit variability in their constitution (Figure 2).[13]

Most of the X-ray analytical studies on Co^{III}-corrins were concerned with the bonding of the axial ligands and their effect on (1) the lengths of the axial (Co–N)- and (Co–ligand)-bonds, as well as on (2) the extent of nonplanarity of the corrin ligand:[3] the latter structural feature has been called the 'upwards-folding of the corrin – ligand', which is represented by the angle between the planes through the inner atoms of the northern and of the southern ligand halves.[3,21] This 'upwards-folding of the corrin ligand' was proposed to be a biologically relevant, particular ability of the corrin ligand to respond to the steric demands of the axial ligands[22] (but see below). Data of incomplete Co^{III}-corrins[3] indeed point to lesser nonplanarity of the corrin ring in the absence of a coordinating bulky base. The 'folding of the corrin ligand' also is smaller (11.7°) in Coα-imidazolyl-Coβ-cyanocobamide than in vitamin B_{12} (17.7°), in support of the proposed mechanical effect of the steric bulk of the nucleotide base.[2,3,23]

2.1.2 *Co^{II}-corrins*

For the paramagnetic (low-spin) Co^{II}-corrins, all available evidence points to a predominantly pentacoordinated Co^{II}-center.[4] The X-ray structures of two paramagnetic Co^{II}-corrins confirmed this to be the case in the crystal[3,24,25] and two-dimensional EPR-spectroscopy, in frozen solution.[26] In the crystal, the structure of Co^{II}-cobalamin (B_{12r}, (**5**)) was found to differ little from that of the 'complete' corrin moiety of alkyl-Co^{III}-cobalamins, such as coenzyme B_{12} (**3**) and methylcobalamin (**4**)[3,27,28] (Figure 3). In particular, the 'folding' of the corrin ligand (16.3° in (**5**)), as well as the positioning of the nucleotide base with respect to the corrin ligand, were found to be surprisingly similar in the three structures (folding in (**3**): 13.3°; in (**4**): 15.8°).[27] A complex of Co^{II}-cobalamin with molecular oxygen, shown to form in preparations of corrinoid enzymes upon exposure to air, could also be formed reversibly in the crystal, where it was studied by X-ray analysis.[29]

2.1.3 *Co^{I}-corrins*

So far, for the highly oxygen-sensitive Co^{I}-forms of cobalt-corrinoids (such as Co^{I}-cobalamin, (**6**)), information from X-ray analysis on their three-dimensional structure is not available. However, in these strongly nucleophilic,[30] highly reduced[19] cobalt complexes, the diamagnetic Co^{I}-center (a d^8 metal ion, isoelectronic with a Ni^{II}-ion) presumably is ligated by the corrin ligand only, in a tetracoordinated, nearly square-planar fashion.[4,19,31] As a consequence, the Co^{I}-forms of complete corrins would have to be base-off, that is, the nucleotide function would not be attached to the central cobalt ion.

2.2 Spectroscopy

Qualitative information on the structure of the colored corrinoids in solution can be extracted rapidly from UV/Vis and CD spectra; most of the spectroscopic features can be rationalized nowadays by comparison with theoretically calculated spectra.[4,32] For more precise constitutional information, some of the newly developed methods of mass spectrometry allow the analysis even of the involatile B_{12}-derivatives.[33] Modern one-and two-dimensional proton, carbon, nitrogen, and phosphorus NMR spectroscopy has proven a powerful instrument for the delineation of the structure of diamagnetic cobalt-corrins in solution.[34–36] ESR-spectroscopy has given important information on paramagnetic corrinoid Co^{II}-complexes,[26,37] whether in frozen solutions or bound in corrinoid enzymes. X-ray adsorption fine spectroscopy (EXAFS) spectroscopy and vibrational (IR and Raman) spectroscopy are other spectroscopic techniques used more frequently now in the B_{12} field.[38,39]

2.3 Synthesis and Biosynthesis of Corrins

The preparation of corrins[8] and the total synthesis of vitamin B_{12} was achieved in the 1970s in the laboratories of Eschenmoser[8] and Woodward[9] as a climax in synthetic chemistry. Indeed, once made accessible by laboratory synthesis, the corrin ring structure proved to be accessible on various oxidation levels by an array of ring closure reactions conceived for their possible biosynthetic model

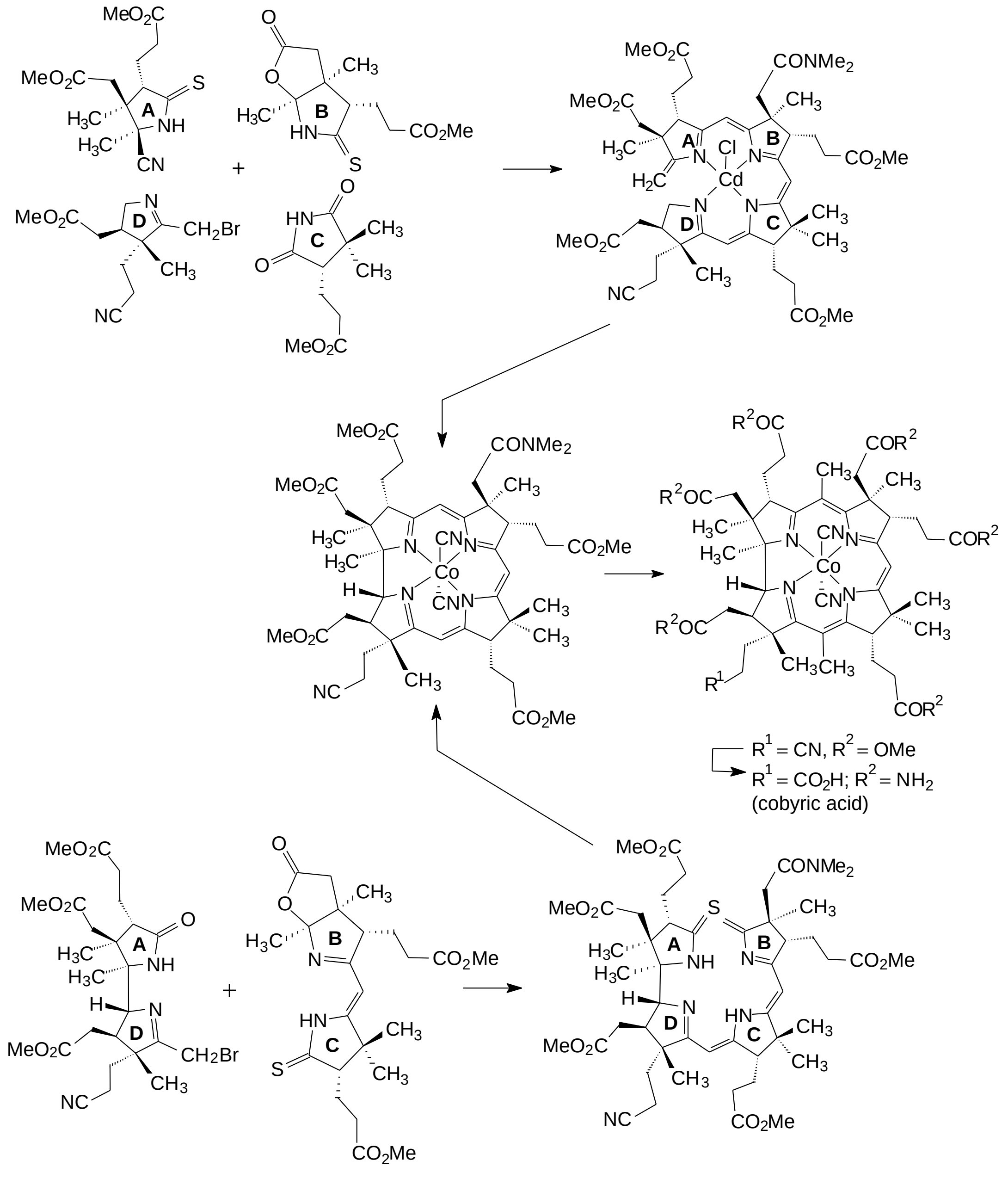

Figure 5 Outline of the total synthesis of cobyric acid (Figure 1) on the way to vitamin B_{12}: top: the ETH approach via an A/D ring closure of the corrin ring system; bottom: the Harvard/ETH approach via an A/B ring closure

character.[8,17] For the unique preparative conquest of the vitamin B_{12}-structure by abiotic synthesis,[8,9] the B_{12}-precursor cobyric acid (**2**) was first synthesized specifically (Figure 5) and then the attachment of the nucleotide chain was carried out by methods known from earlier work.[6,7] More recently, the regiospecific attachment of the nucleotide chain to an undifferentiated cobyrinate was also achieved in the laboratory of Eschenmoser, in support of his proposal of a 'preenzymatic' pathway to the B_{12}-structure.[17] For the insertion of cobalt into the corrin ligand, several methods are known, based on Co^{II} chemistry;[4] the removal of a cobalt ion from an intact natural corrinoid so far has not been successful.[40]

The natural corrinoids are made exclusively by microorganisms, which are also exploited on a large scale for the industrial production of vitamin B_{12}.[6,41] The biosynthesis of the corrin ligand branches off from that of the other porphinoids at their common tetrapyrrolic intermediate, uroporphyrinogen III, and has been studied both in aerobic and in anaerobic microorganisms[10,11] (Figure 6). The 'corrin pathway' separates with the sequential incorporation of (some of) the seven

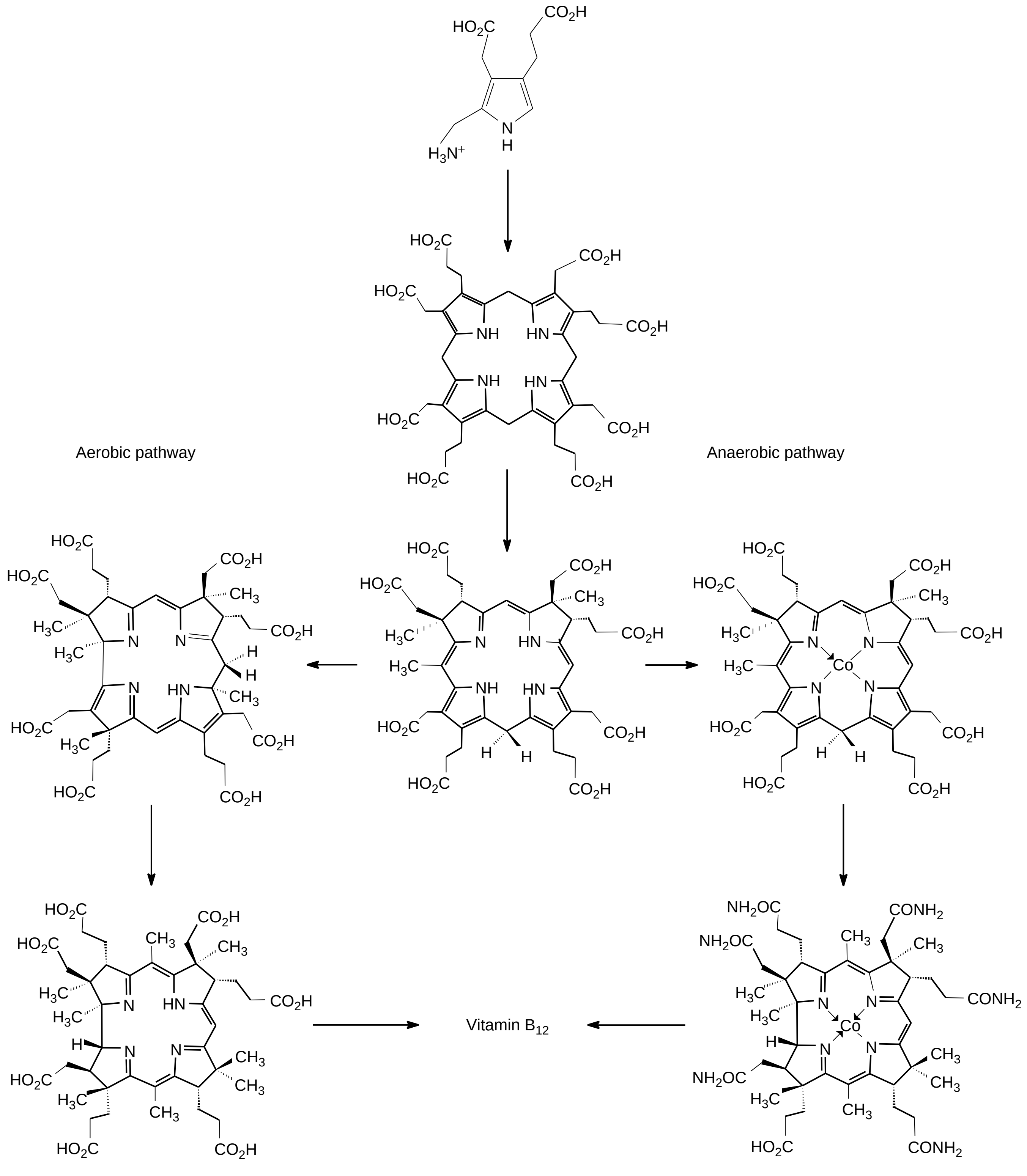
Aerobic pathway
Anaerobic pathway
Vitamin B_{12}

Figure 6 Outline and some central intermediates in the two main known pathways of the biosynthesis of vitamin B_{12}, the ‘aerobic path’ (left) and the ‘anaerobic path’ (right)

'extra' methyl groups into the reduced ligand. In the 'aerobic pathway,'[10,42] the metal-free hydrogenocobyrinic acid is produced first. The biological insertion of the cobalt ion thus occurs at a 'late' stage of a partially amidated form to lead to the 'incomplete' corrinoid cobyric acid, eventually. The nucleotide loop is finally built, starting with cobalt-adenosylated cobyric acid (5′-adenosylcobyrate).[6,43] In the 'anaerobic pathway', enzymatic insertion of the cobalt ion takes place much earlier, at the stage of the 'dimethylated' factor III. The bound cobalt ion is believed to assist the ring contraction and redox steps encountered in this biosynthetic path to cobyric acid.[11,44]

2.4 Organometallic B_{12} Derivatives

Most metabolic functions of the corrinoids are associated with their capacity for organometallic chemistry,[12–14] discovered together with the structure of coenzyme B_{12}.[2,3] The standard procedures for the synthesis of organometallic B_{12}-derivatives involve the alkylation of the corresponding highly nucleophilic Co^I-corrins with alkyl halides, alkyl tosylates, and so on.[19,45] In less well-investigated ways, organocorrinoids also can be prepared by the reaction of the radicaloid Co^{II}-corrins with radicals[46,47] or by alkylation with nucleophilic alkylating agents of the electrophilic Co^{III}-corrins.[48]

The 'super-nucleophilic' Co^I-corrins[19,30] can be prepared in situ by electrochemical or chemical reduction of B_{12};[4,19] the alkylation reaction is carried out in deoxygenated (aqueous or nonaqueous) solution. In general, the alkylation occurs with high diastereoselectivity on one side, at the 'upper' β-face.[6,49] Friedrich and coworkers noticed the formation of a second set of organocorrinoids, suggested to be the isomeric structures with the alkyl group bound at the 'lower' α-face. The organocorrinoids with a β-alkyl group are thermodynamically preferred in aqueous media.[6] The selective formation of organocorrins with an α-alkyl group thus has to be interpreted in terms of a kinetically controlled alkylation reaction.[4,48–50]

Two major mechanisms have to be taken into consideration for the alkylation of Co^I-corrins.[4,45,48–51] The 'classical' mechanism of a bimolecular nucleophilic substitution reaction at carbon (the Co^I-corrin acts as a nucleophile) leads to β-alkylated Co^{III}-corrins with high diastereoselectivity.[49] Secondly, an electron transfer-induced radical process (where the Co^I-corrin acts as a one-electron reducing agent) may also lead to cobalt alkylation. The observed formation of incomplete α-alkylated Co^{III}-corrins under kinetically controlled conditions has been proposed to occur via this path.[46,49] The high nucleophilic reactivity of Co^I-corrins and their diastereoselective nucleophilic reaction on the ('upper') β-face are not increased by the nucleotide function on the ('lower') α-face; rather they appear to be an inherent reactivity of the corrin-bound tetracoordinate Co^I-center.[46,52] Among the organometallic B_{12} derivatives prepared to date, neopentylcobalamin, benzylcobalamin, and dimethylmalonylcobalamin have particularly weak Co–C bonds and have served as models for thermally labile, homolytically cleaving organocobalamins.[53–55]

The major biosynthetic paths for the formation of adenosylcobamides (such as (**3**)) and of methylcobamides (such as (**4**)) proceed stereospecifically by alkylation (via nucleophilic attack) of enzyme-bound Co^I-cobamides with adenosine-5′-triphosphate (ATP) and with N^5-methyltetra-hydropterins or S-adenosylmethionine (SAM), respectively.[56,57]

Organocorrinoids are sensitive to visible light and can be photochemically dealkylated (typically via Co^{II}-corrins and alkyl radicals).[58,59] One-electron reduction of alkyl-Co^{III}-corrins produces short-lived alkyl-Co^{II}-corrins that rapidly cleave their organometallic bond with an alternative formation of Co^I-corrin and alkyl radical fragments or of Co^{II}-corrin and an alkyl anion.[19,51,60] However, electrochemical reduction of organo-Co^{III}-corrins in general occurs with a more negative half-wave potential than the reduction of Co^{II}-corrins (to Co^I-corrins); for this reason, the alkyl-Co^{III}-corrins can be prepared from and are in general stable in the presence of Co^I-corrins.[19,51]

2.4.1 Coenzyme B_{12}

The original crystal structure of coenzyme B_{12} was reexamined by X-ray (and neutron) diffraction analysis[3,27] and by NMR spectroscopy.[61] These latter spectroscopic investigations indicate that the organometallically bound deoxyadenosyl group of the coenzyme molecule is not conformationally fixed, but exists in (at least) two conformations around the Co–C bond. The lengths of the bonds to the two axially coordinated ligand atoms (Co–C $= 2.00$ Å; Co–N $= 2.24$ Å)[3,27] are longer than in the other organocobalamins studied by X-ray analysis.[2] The angle Co–Cα–Cβ ($= 124.4°$) is unusually large for a saturated carbon, possibly the indication of steric strain in this organometallic B_{12} derivative.[2]

The nucleotide base can be acidolytically decoordinated ($pK_a = 3.67$)[18] with relative ease. More slowly (and under more acidic conditions), the organometallically bound deoxyadenosyl group is cleaved by heterolytic decomposition.[62,63]

The strength of the Co–C bond of coenzyme B_{12} (**3**) has been estimated in the laboratories of Halpern[12] and of Finke[64,65] to be ca. $30\,\mathrm{kcal\,mol^{-1}}$ from a series of kinetic analyses of its thermal decomposition in aqueous and nonaqueous solutions. The original estimates for the homolytic (Co–C)-bond dissociation energy were $26 \pm 2\,\mathrm{kcal\,mol^{-1}}$;[12] and $30 \pm 2\,\mathrm{kcal\,mol^{-1}}$.[64] Complications in these investigations were caused by (1) the presence of the base-off form of (**3**) and (2) cage effects had to be taken into account for the quantitative analysis of such bond-dissociation processes.[65,66]

In some cases, the base-on forms of organocobalamins decompose considerably faster than their (protonated) base-off forms or the corresponding (incomplete) organocobinamides,[53–55] and this was considered to be valid in a more general sense.[64] However, the thermal decomposition of 5′-adenosyl-cobinamide at 110 °C in water at pH 7 ($k = 1.2 \times 10^{-5}\,s^{-1}$) is only 20 times slower than the decomposition of the coenzyme (**3**) ($k = 2.6 \times 10^{-4}\,s^{-1}$)[67] under the same conditions. Contribution of the nucleotide coordination to the activation of coenzyme B_{12} toward homolysis of the Co–C bond should, therefore, be correspondingly small. Indeed, on the basis of available thermodynamic data concerning the nucleotide coordination in the coenzyme (**3**) and in the homolysis product Co^{II}-cobalamin (**5**), the homolytic bond strength of the cobinamide was estimated earlier to be only ca. 0.7 kcal mol^{-1} higher than that of coenzyme B_{12}.[68]

2.4.2 *Methylcobalamin and Other Methyl-Co^{III}-corrins*

The structure of methylcobalamin (**4**) is available from X-ray analysis and NMR spectroscopy.[3,28,34,69] Both axial bonds (Co–C = 1.99 Å and Co–N = 2.19 Å) are shorter in methylcobalamin than in coenzyme B_{12}. The ‘upwards-folding’ is stronger than in coenzyme B_{12} (15.8° vs. 13.3°).[3] The homolytic (Co–C)-bond dissociation energy of methylcobalamin (**4**) has been estimated from the kinetics of its thermal decomposition at elevated temperature to be ca. 37 ± 3 kcal mol^{-1}.[60] Not unexpectedly, the Co–C bond of (**4**) is considerably more resistant to homolysis than that of coenzyme B_{12}.

The cobalt-bound methyl group of (**4**) is not readily removed by acid. Treatment of (**4**) with acid in aqueous solution leads to proteolytic decoordination of the nucleotide base ($pK_a = 2.9$).[18] The cobalt-bound methyl group of methyl-Co^{III}-corrins can be abstracted (1) by nucleophiles, such as thiol(ate)s,[54,70,71] (2) by radicaloid species, such as other Co^{II}-corrins,[68] or (3) by electrophilic species, such as Hg^{II}-ions.[72] A reversible and rapid methyl-group transfer occurs in deoxygenated aqueous solution between methyl-Co^{III}-corrins and Co^{I}-corrins.[15] From the pair, methyl-Co^{III}-cobinamide and Co^{I}-cobalamin (**6**), methylcobalamin (**4**) and Co^{I}-cobinamide are generated and prevail at equilibrium. Accordingly, the nucleotide coordination in (**4**) stabilizes it against abstraction of the cobalt-bound methyl group by nucleophiles (by ca. 4 kcal mol^{-1}; ca. 17 kJ mol^{-1}),[15,68] whereas it activates (**4**) for the abstraction of the cobalt-bound methyl group by electrophiles.[73] In addition, as a result of methyl-group transfer equilibria between (**4**) and incomplete Co^{II}-corrins, the nucleotide coordination was found to hardly influence (thermodynamically) the homolytic bond strength of the Co–C bond in (**4**).[15,45,68] The reversible methyl-group transfer reaction between methylcobalamin (**4**) and Co^{II}-cobinamide, to give Co^{II}-cobalamin and Coβ-methyl cobinamide respectively, and the reverse reaction were studied at temperatures between 5 and 60 °C in deoxygenated aqueous solutions, and the equilibrium was characterized ($K(20\,°C) = 0.56$, $\Delta H_0 = 2.5 \pm 0.5$ kcal mol^{-1}, and $\Delta S_0 = 7.1 \pm 0.1$ kcal mol^{-1}; Figure 7).[68]

In view of the coordination pattern in protein-bound methylcobalamin (see below), the thermodynamic studies on the effect of the coordination of the dimethylbenzimidazole base to the α-side of the cobalt center on the homolytic and heterolytic (Coβ-C)-bond dissociation energy in (**4**) (thermodynamic effect of the trans ligand or ‘trans influence’) were extended to corresponding investigations with Coβ-methyl-imidazolylcobamides, such as (**9**), where imidazole replaces the dimethylbenzimidazole: these studies showed this change of the nature of the axial base to have little effect on the two relevant bond-dissociation energies of the corresponding methylcobamide.[74]

2.5 B_{12} Coenzymes as Enzyme-bound Cofactors

2.5.1 *Coenzyme B_{12} and Adenosylcobamides as Cofactors*

The biologically relevant reactivity of coenzyme B_{12} is associated with the homolysis of its Co–C bond, as well as with the recombination of the products of homolysis (Figure 8).[12,15] The remarkable structural similarity between the corrinoid homolysis fragment Co^{II}-cobalamin and the Co^{III}-corrin part of coenzyme B_{12} contributes to lowering

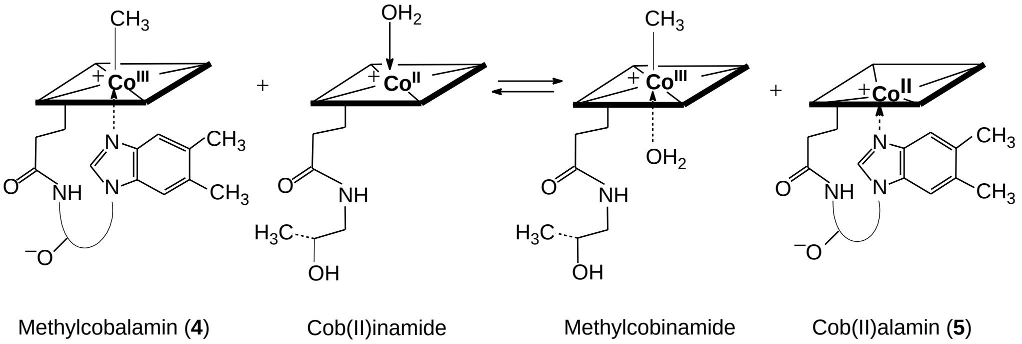

Figure 7 Schematic representation of the methyl-group equilibrium between methylcobalamin (**4**), Co^{II}-cobinamide, Co^{II}-cobalamin (**5**), and Coβ-methylcobinamide

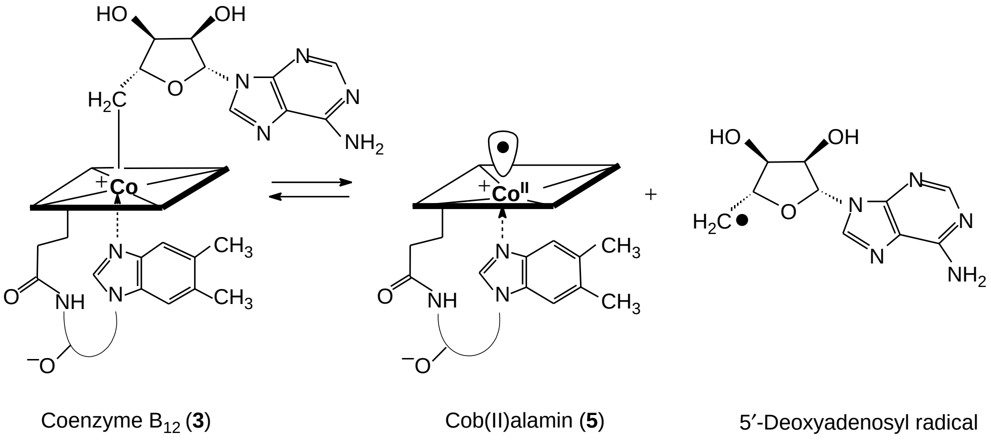

Figure 8 Illustration depicting the reversible homolysis of the Co–C bond, the biologically relevant reactivity of coenzyme B_{12} (**3**)

the activation barrier in both directions (and recombination occurs at (nearly) diffusion-controlled rates in homogeneous solution[58,59]).[25]

The role of coenzyme B_{12} as cofactor of enzymatic rearrangement reactions requires the (reversible) formation of the 5′-adenosyl radical by homolysis of the organometallic bond of (**3**) (estimated bond-dissociation energy ca. 30 kcal mol^{-1};[12,72]) to be accelerated there by a factor of $10^{12\pm1}$.[65,75]

In spite of the available crystallographic information on a series of coenzyme B_{12}-dependent enzymes (see below),[13,14] the 'activation' of the protein-bound coenzyme B_{12} toward (Co–C)-bond homolysis is still an unsolved matter.[76,77] The replacement of the dimethylbenzimidazole base by an imidazole, as observed in some (but not all) coenzyme B_{12}-dependent enzymes,[13,14] appears not to be a major factor contributing to the rate enhancement of the (Co–C)-bond homolysis. The presently available structural data on coenzyme B_{12}-dependent enzymes support the general validity of the 'mechanochemical model' (see below).[12–14] However, instead of an 'upwards conformational distortion' of the corrin ring,[12,22,78] or of a movement of the benzimidazole base toward the corrin ring,[79] 'strong binding of the separated Co^{II}-corrin and adenosyl fragments to the protein'[25] may enhance protein and substrate induced separation of the homolysis fragments and labilize the organometallic bond of the bound coenzyme B_{12}.[15] X-ray analysis of Co^{II}-cobalamin (**5**) was instrumental in contributing to this problem, as it indicated a little structural difference between this Co^{II}-corrin and the Co^{III}-cobamide-moiety of coenzyme B_{12}.[25]

2.5.2 *Methylcobalamin and Methylcobamides*

The cofactor role of the methylcorrinoids is based on enzymatic methyl-group transfer reactions. Formation of a methylcorrin by the methylation of an enzyme-bound Co^{I}-corrin and its subsequent demethylation by thiol(ate)s or other nucleophiles appear to be the two crucial steps of the known catalytic cycles. Heterolytic formation and cleavage of the Co^{III}-methyl bond in nucleophilic substitution reactions can be considered to be the main biologically relevant reactivity of the methylcorrinoids, such as methylcobalamin (**4**).[13,14,57] In such heterolytic reactions, the arrangement of the nucleotide loop with respect to the metal center could be inferred to change considerably the reactivity in methyl-group transfer reactions (as coordination would be intact in the methyl-Co^{III}-corrin,[46] but absent in the Co^{I}-corrins;[22,56] Figure 9): A weakening of the nucleotide coordination by interaction with a protein thus destabilizes the more oxidized state of the methyl-Co^{III}-corrinoid (with respect to that of the Co^{I}-corrin) and, in turn, activates the demethylation of the methyl-Co^{III}-corrin by a nucleophile.[80]

Similar to the situation with coenzyme B_{12}-dependent enzymes, recent pioneering crystallographic studies on methionine synthase have considerably clarified the structural aspects of enzymatic methyl-group transfer, involving protein-bound 'complete' methylcorrinoids.[57] There the coordinating

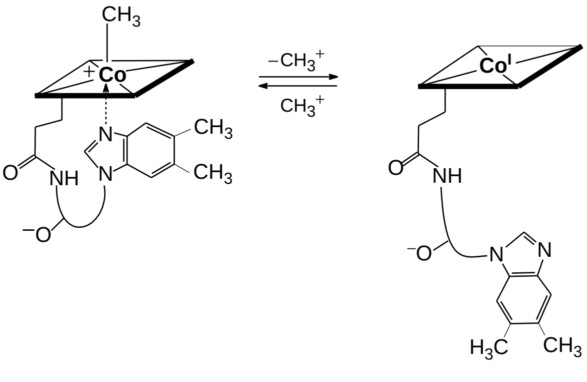

Figure 9 Symbolic illustration depicting the major structural changes occurring in heterolytic Co-demethylation and Co-methylation reactions of the cobalamins (**4**) and (**6**)

nucleotide was first recognized to be replaced by a histidine (to give a 'center' form of the bound (**4**)).[81,82] While the axial base coordination clearly helps to 'tune' the strength of the Co–C bond in heterolytic reactions of protein-bound methylcorrinoids,[13,57,68] the better dynamic binding of the center form of (**4**) in methionine synthase appears to be another important and necessary contributor to this enzyme's catalytic capacity, by allowing it access to the required modular structural changes.[68,83]

2.5.3 *Co^{II}-cobalamin and Co^{II}-cobamides*

The pertinent structural data indicate the arrangement of the nucleotide loop to change little with respect to the metal center in homolytic (Co–C)-bond dissociation reactions, but to vary considerably in one-electron redox reactions involving Co^{II}- and Co^{I}-corrins.[19] In a protein, weakening of the nucleotide coordination thus destabilizes the more oxidized state of the Co^{II}-corrinoid with respect to that of the Co^{I}-corrin and, in turn, activates its reduction to a Co^{I}-corrin by a one-electron reducing agent. In several cobalamin-dependent methyltransferases (see below), the nucleotide coordination is noticeably weakened (or inhibited) by the interactions of the bound corrin with the apoenzyme, and 'tuning' of the reactivity of the protein-bound corrinoid cofactors by control of the intramolecular nucleotide coordination was shown to be relevant.[57,84]

In dehalogenating enzymes of anaerobic microorganisms, corrinoid cofactors have a newly discovered further role in the redox catalysis of the energy conserving dehalogenation of chloro(hydro)carbon compounds ('dehalorespiration'), and the specific redox properties of the protein-bound unusual corrinoids are of particular current interest.[20,85]

3 B_{12} ENZYMES

Aside from the B_{12}-binding and transporting proteins, three major classes of corrinoid enzymes are known: methyltransferases, coenzyme B_{12} utilizing enzymes, and corrinoid dehalogenases. The coenzyme B_{12} utilizing enzymes can be classified further as carbon skeleton mutases, dehydratases, deaminases, and ribonucleotide reductase. Members of all classes of the B_{12}-enzymes are important in microorganisms. In human and animal metabolism B_{12}-binding proteins, the methyl transferase methionine synthase and methylmalonyl-CoA-mutase (MMCM) play essential roles.[13,14,45]

3.1 B_{12}-binding Proteins

B_{12}-binding (and B_{12}-transporting) proteins are important in human, animal, and bacterial metabolism, where they function as extracellular, membrane-bound, and intracellular proteins.[6,86,87] Lack of the B_{12}-binding (extracellular) protein 'intrinsic factor' and, as a consequence, a disorder in the uptake of vitamin B_{12}-derivatives from the nutrition, is recognized to be the most widely distributed cause for 'pernicious anemia'.[88,89]

The human B_{12}-binder intrinsic factor is a glycoprotein of ca. 44 kDa, with a high binding constant (in 1:1 complexes) for vitamin B_{12} (**1**) and other cobalamins. The intrinsic factor is secreted by cells of the gastric mucosa and specifically binds cobalamins and carries them to the ileum. There the ileum receptor protein accepts the corrinoid from the intrinsic factor complex and transports it further across the intestinal epithelial absorptive cell.[86,88] The cobalamins then appear to be bound to transcobalamin II and transported in the blood in this way to membrane-bound transcobalamin/corrin receptor proteins of the specific cells.[6,86,87]

3.2 Methyltransferases

The catalysis of the transfer of a methyl group is an important role of enzyme-bound vitamin B_{12} derivatives in human, animal, and bacterial metabolism.[13,14] The known enzyme-controlled methyl group-transfer reactions are key steps in the cobamide-dependent methylations of homocysteine to methionine, in the metabolic formation of methane from other C_1-compounds in methanogenic bacteria, and in the fixation of carbon dioxide via the acetyl coenzyme A pathway of some bacterial autotrophs (Figure 10).[13,14]

The catalytically active, protein-bound corrinoids involved in such enzymatic methyl-group transfer steps are Co^{I}-corrins (such as Co^{I}-cobalamin, (**6**)) and methyl-Co^{III}-corrins (such as methylcobalamin, (**4**)), which are now indicated to be 'base-off' in these enzymes, that is, with the nucleotide base uncoordinated.[57,84]

3.2.1 *Methionine Synthase*

The cobalamin-dependent formation of methionine by methylation of homocysteine is an important enzymatic process in human, animal, and bacterial metabolisms.[13,14,57] The catalysis of the methyl-group transfer and the role of enzyme-bound cobalt-corrinoids in cobalamin-dependent methionine synthase have been well studied for the enzyme from *Escherichia coli*.[57] (Figure 11). This cobalamin-dependent methionine synthase consists of a single polypeptide chain (about 123 kDa) and binds methylcobalamin in a center form.[81,82] Catalysis of the methyl transport occurs with a maximum turnover of ca. 20 s^{-1}, by an 'ordered sequential mechanism' involving two steps mainly: (1) From bound methylcobalamin, the cobalt-bound methyl group is abstracted by the thiol of homocysteine, with formation of methionine and of an enzyme-bound Co^{I}-cobalamin. (2) This highly nucleophilic enzyme-bound Co^{I}-corrin then abstracts the methyl group of (mono- or polyglutamate forms of)

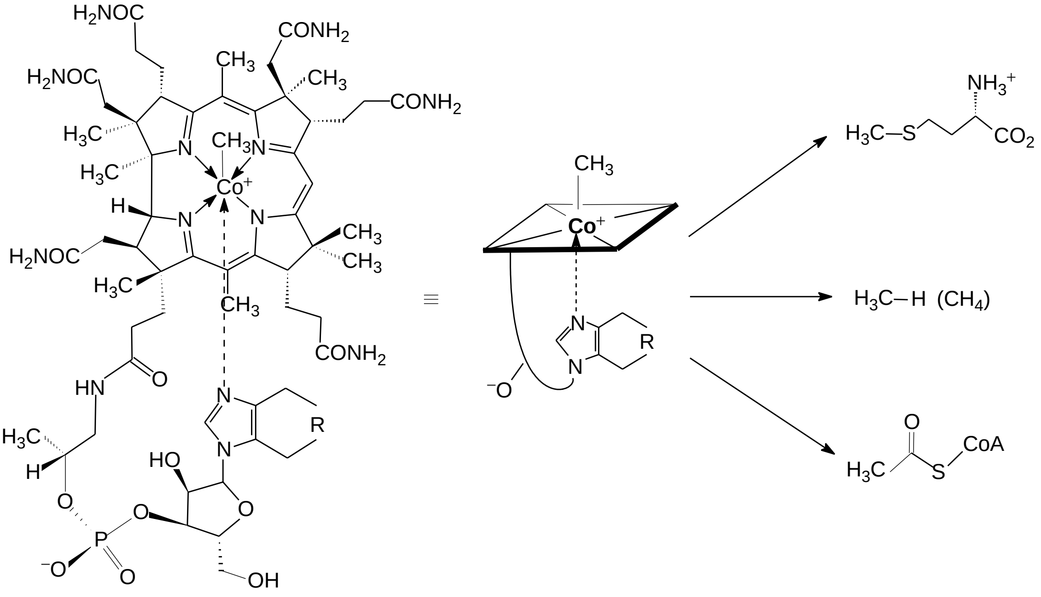
H2NOC
CONH2
CH3
CH3
CONH2
Co+
CH3
R
HN
O
HO
OH
P
≡
H3C–S
NH3+
CO2
H3C–H (CH4)
CoA
S

Figure 10 Methylcorrinoids as the source of a methyl group in the biosynthesis of methionine from homocysteine (top), of methane (middle), and of the acetyl group of acetyl coenzyme A (bottom)

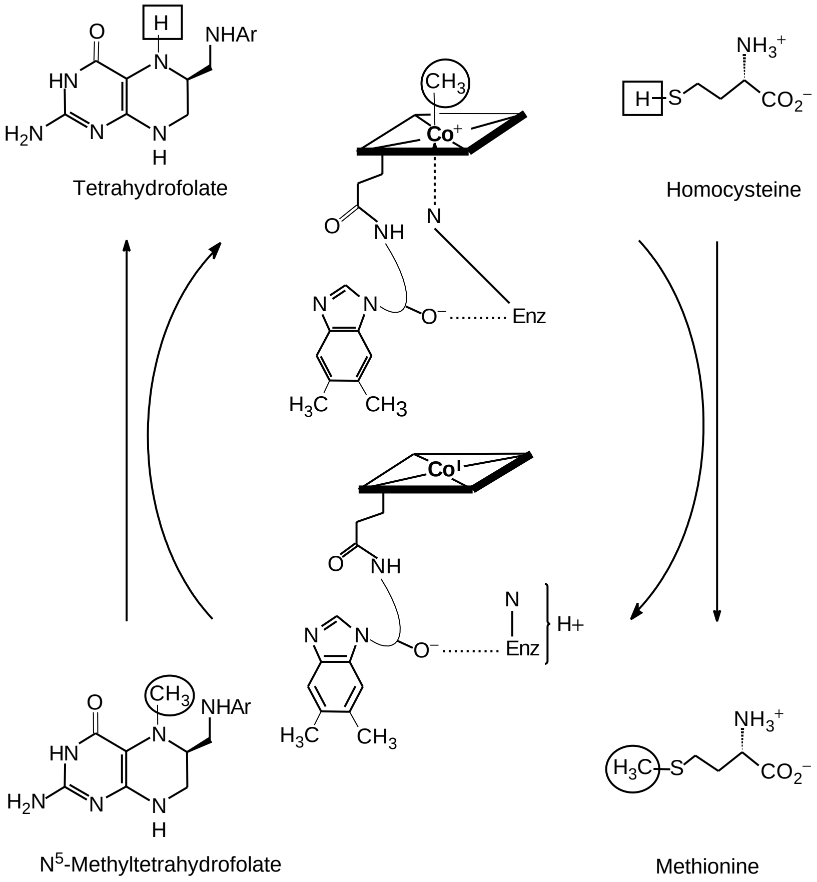
H
NHAr
Tetrahydrofolate
CH3
Co+
Enz
H+
CoI
Homocysteine
NH3+
CO2−
H3C
CH3
N5-Methyltetrahydrofolate
Methionine

Figure 11 Schematic illustration of the cobalamin-dependent enzymatic biosynthesis of methionine via methyl-group transfer from N^5-methyltetrahydrofolate to homocysteine

N^5-protonated N^5-methyltetrahydrofolate to reconstitute the bound methyl-Co^{III}-corrinoid. The transfer of the methyl group takes place with overall retention of configuration (indicating two nucleophilic substitutions, each with stereochemical inversion), formally involving the transfer of a methyl cation.[57]

The half-wave potential for the enzyme-bound Co^{II}/Co^{I}-cobalamin couple of the methionine synthase from *E. coli* at 526 mV versus SHE is about 80 mV lower than that of the Co^{II}/Co^{I}-cobalamin couple in neutral aqueous solution.[19] Access to the catalytic cycle of the enzyme by one-electron reduction of Co^{II}-cobalamin (and reactivation upon occasional adventitious formation of Co^{II}-cobalamin) is indicated to be accomplished by a unique mechanism. The (thermodynamically unfavorable) reduction with intermediate formation of the enzyme-bound Co^{I}-cobalamin is driven by a rapid methylation of the highly reduced Co^{I}-center of the reduced corrin with *S*-adenosylmethionine.[57] The modular nature of methionine synthase allows for the control of the methyl-group transfer processes by modulating and alternating conformational equilibria.[57,90,91]

3.2.2 *Corrinoid Enzymes in Bacterial Acetate Metabolism*

In bacterial metabolism, corrinoids related to methylcobalamin hold an essential position also as functional intermediates in autotrophic fixation of carbon dioxide via acetyl coenzyme A.[84,90] In Wood's group, the acetogen *Clostridium thermoaceticum* was analyzed particularly thoroughly for this new way of carbon dioxide fixation,[90,92] but the latter was found to operate also in a variety of other acetogenic, as well as in methanogenic, sulfur-metabolizing, and sulfate-reducing bacteria.[93] In the course of the assembly of acetyl coenzyme A from carbon dioxide in the carbon monoxide dehydrogenase/acetyl coenzyme A synthase complex, the cobalt-bound methyl group of a methylcorrinoid and carbon monoxide (from the reduction of carbon dioxide) combine to give the acetyl group of acetyl coenzyme A.[90] The function of the enzyme-bound corrinoid concerns the catalysis of a methyl-group transfer via two nucleophilic substitution steps from an N^5-methyltetrahydropterin to the as yet unidentified nucleophilic acceptor on the acetyl coenzyme A synthase subunit. The acetyl group is then assembled from the two C_1 fragments and without direct cooperation of a corrinoid (carbonylation of an enzyme-bound methyl-Co^{III}-corrinoid[94] has been shown to be highly unlikely).[90] The available crystal structures of the carbon monoxide dehydrogenase/acetyl coenzyme A synthase complex[95,96] indicate either a nickel[96] or a copper-center[95] at the active site cluster.

In acetate-catabolizing methanogens, enzyme-bound methylcorrinoids are also indicated to serve as intermediates in methyl-group transport. There, methane and carbon dioxide are formed from acetic acid (via acetyl coenzyme A, whose acetyl group is split into carbon monoxide and a corrin-bound methyl group). Accordingly, the methyl-group transport in this path of acetate degradation would have to work in the reverse sense, compared to the situation in the bacterial assembly of acetyl coenzyme A.[97,98]

3.2.3 *Corrinoid Enzymes in Bacterial Methanogenesis*

In other forms of bacterial methanogenesis, methyl-Co^{III}-corrinoids also perform an essential function as cofactors in enzymatic methyl-group transfer. Previously, enzyme-bound methyl-Co^{III}-corrinoids were suspected to directly provide access to methane (via protonation of their cobalt-bound methyl group).[99] Nowadays, the methyl-Co^{III}-corrinoids are recognized to act more indirectly in methanogenesis, as intermediates in methyl-group transport. The role of the terminal methyl-carrier in the formation of methane in methanogens is assigned to the porphinoid nickel complex coenzyme F430,[100] structurally characterized in Eschenmoser's group.[101] Enzyme-bound corrinoids are found, for example, to serve as methyl-group carriers between an N^5-methyltetrahydropterin and the thiol coenzyme M (i.e. in a function related to their role in the methylation of homocysteine to methionine; see Figure 11).[102]

3.3 Coenzyme B_{12} Utilizing Enzymes

About 10 coenzyme B_{12}-dependent enzymes are now known (reviewed in References 13,14, and 76 see Table 1): four carbon skeleton mutases (methylmalonyl-CoA mutase (MMCM),[103] glutamate mutase (GM),[104,105] methylene glutarate mutase (MGM),[104] isobutyryl-CoA mutase (ICM)[106]), diol dehydratase (DD),[107] glycerol dehydratase,[107] ethanolamine ammonia lyase (EAL),[108] two amino mutases,[109] and B_{12}-dependent ribonucleotide reductase.[110] The coenzyme B_{12}-dependent enzymes are unevenly distributed in the living world, and MMCM is the only enzyme that is also indispensable in human metabolism.[103]

The known coenzyme B_{12}-dependent enzymes all perform chemical transformations in enzymatic radical reactions that are difficult to achieve by typical 'organic' reactions. Homolytic cleavage of the Co–C bond of the protein-bound coenzyme B_{12} (**3**) to a 5′-deoxy-5′-adenosyl radical (**9**) and cob(II)alamin (**5**) is the entry to reversible H-abstraction reactions involving the 5′-position of the radical (**9**). Indeed, homolysis of the Co–C bond is the thermally most easily achieved transformation of coenzyme B_{12} (**3**) in neutral aqueous solution (with a homolytic (Co–C)-BDE of about 30 kcal mol^{-1};[12,65]). However, to be relevant for the observed rates of catalysis by the coenzyme B_{12}-dependent enzymes, the homolysis of the Co–C bond of the protein-bound coenzyme (**3**) needs to be accelerated by a factor of about 10^{12}, in the presence of a substrate.[12,65] Coenzyme B_{12} might then be considered, first of all, to be a structurally sophisticated, reversible source for an alkyl radical, whose Co–C bond is labilized in the protein-bound state[12] (Figure 8), and the first major task of the

Table 1 Coenzyme B_{12} catalyzed enzymatic reactions involving natural substrates

(*R*)-methylmalonyl-CoA/succinyl-CoA[103,111]	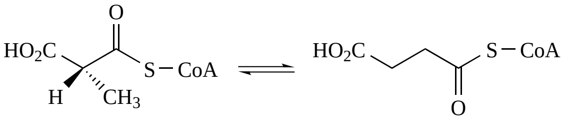
(*S*)-glutamic acid/(2*S*,3*S*)-methylaspartic acid[104,105]	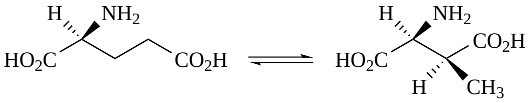
2-methyleneglutarate/(*R*)-3-methylitaconate[104]	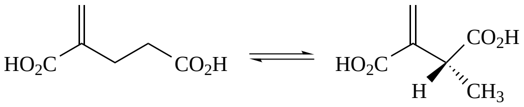
isobutyryl-CoA/*n*-butyryl-CoA[106]	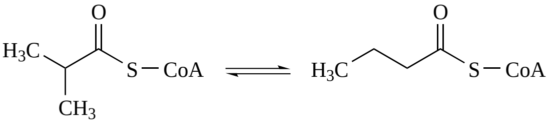
D-ornithine/(2*R*,4*S*)-2,4-diaminovaleric acid[109]	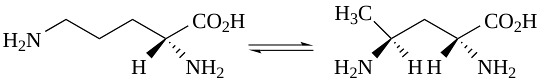
D-(α)-lysine/2,5-diaminohexanoic acid[109]	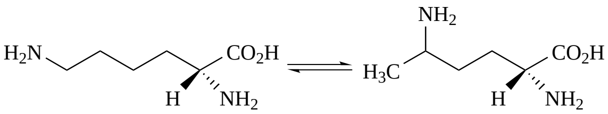
L-(β)-lysine/(3*S*,5*S*)-3,5-diaminohexanoic acid[109]	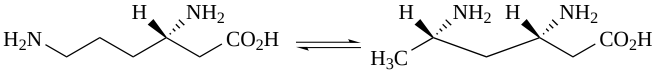
1,2-propanediol/propanal (R = CH_3)[107] glycerol/3-hydroxypropanal (R = CH_2OH)[107]	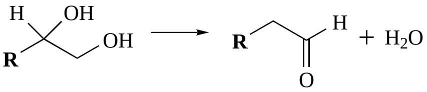
ethanolamine/acetaldehyde[108]	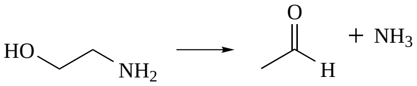
ribonucleotide/2′-deoxyribonucleotide[110,112]	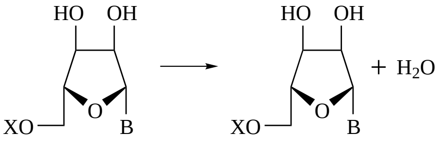 B = nucleotide base, X = diphosphate or triphosphate group

enzyme concerns the 'activation' of coenzyme B_{12} (**3**) and the reversible generation of the 5′-deoxy-5′-adenosyl radical (**9**).

The coenzyme B_{12}-dependent enzymes all rely upon the reactivity of bound organic radicals that are formed (directly or indirectly) by a H-atom abstraction by the 5′-deoxy-5′-adenosyl radical (**9**). In these enzymatic reactions, the radical (**9**) is the established reactive partner in the proper enzymatic radical reaction, so that AdoCbl (**3**) should be looked at as a 'precatalyst' (or catalyst precursor[15]). Tight control of the reactivity and correct mutual orientation of (**9**) and of the substrate for H-atom transfer must be advantageous,[113] but means of (further) activation of the catalyst (**9**) by the protein environment can hardly be recognized. A similar situation presumably also prevails in other enzymatic radical reactions involving protein-bound (**9**) not derived from AdoCbl (**3**)[109] or peptidic radicals.[110] Organometallic B_{12} species, in which (the putative) organic radicals are bound to the corrin-bound cobalt center via a Co–C_β bond, are now considered unlikely as (kinetically competent) intermediates in the rearrangements catalyzed by B_{12}-dependent enzymes.

3.3.1 *Carbon Skeleton Mutases*

In the four known carbon skeleton rearrangement reactions catalyzed by coenzyme B_{12}-dependent mutases, two vicinal groups (a hydrogen atom and an organic substituent) exchange their positions in a (pseudo)intramolecular fashion.[76] The B_{12} cofactor is bound in a 'base-off/His-on' constitution and at an interface between two modules, called the B_{12}-binding and the substrate activating domains (or subunits). Indeed, the B_{12}-binding domains in MMCM and MGM (and even of MetH) and the B_{12}-binding subunits in GM and ICM exhibit considerable mutual sequence homology. This homology does not extend to the other coenzyme B_{12}-dependent enzymes or to the substrate-binding domains of the carbon skeleton mutases.[114]

Methylmalonyl-CoA-mutase. MMCM interconverts *R*-methylmalonyl-CoA and succinyl-CoA in a carbon skeleton rearrangement reaction (Figure 12).[103] Binding of the substrate labilizes the Co–C bond toward homolysis (because of a decrease of the enthalpy of activation by about 16 kcal mol^{-1}) and triggers the homolysis of the Co–C bond of the bound adenosyl-corrinoid.[115] The radical (**9**) then abstracts an H atom from the methyl group of the enzyme-bound methylmalonyl-CoA. H-atom abstraction is accompanied by a large deuterium isotope effect of the (substrate) H atoms, and has been suggested to occur by tunneling and to be coupled kinetically to the homolysis step.[116] H-atom abstraction gives the 2′-methylmalon-2′-yl-CoA radical that rearranges rapidly to the succin-3-yl-CoA radical.[103] The rearrangement has been suggested to occur intramolecularly and involve the stage (formally) of a substituted cyclopropyloxyl radical, as no evidence for a fragmentation mechanism in model experiments has been seen. The radical rearrangement is also suggested to occur without noticeable participation of the bound cob(II)alamin, that is, the corrinoid is merely a 'spectator'.[117] The radical rearrangement step appears to be critically controlled by the interactions with the apoenzyme[118] and is assisted by an H-bond to His244 in the substrate activating domain of the enzyme. Mutation of His244 of MMCM reduced the rate of the rearrangement reaction by about 10^3-fold.[118] The succin-3-yl-CoA radical (resulting from the rearrangement) is suggested to reabstract an H atom from 5′-deoxyadenosine to give succinyl-CoA, and the 5′-deoxyadenosyl radical (**9**), that recombines with cob(II)alamin to give the enzyme-bound coenzyme B_{12} (**3**).

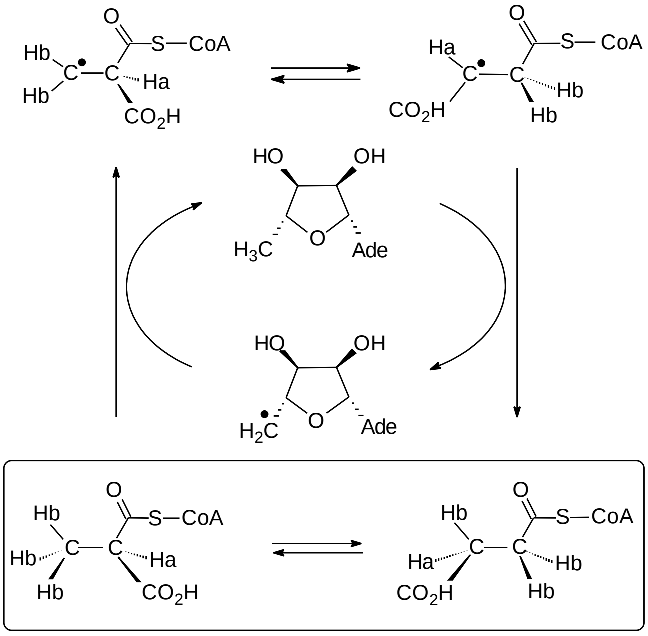

Figure 12 Illustration showing a possible mechanism of the coenzyme B_{12}-catalyzed rearrangement of (*R*)-methylmalonyl-CoA to succinyl-CoA[103]

X-ray analysis of MMCM provided the first crystal structure of a coenzyme B_{12}-dependent enzyme.[82,111,119] This study concerned the 150 kDa heterodimeric MMCM from *Propioni bacterium shermanii* and showed the B_{12} cofactor to be bound 'base-off/His-on'. The α-side of the corrin-bound cobalt center was coordinated to the histidine of a His-Asp-Lys triad as the 'regulatory' unit. The nucleotide tail of the bound corrinoid was tightly inserted into the protein, similar to the situation in MetH. The crystal structure revealed a rather 'flat' corrin ligand with a 'ligand-folding' comparable to that in the imidazolylcobamides,[23,74] without significant 'upwards conformational distortion' of the corrin. The pseudosubstrate used, dethiacoenzyme A, is bound tightly in a funnel provided by the 'substrate-binding' domain of the α-chain. A significant direct interaction between the rearranging substrate's reactive centers and the corrinoid cofactor is made unlikely by the crystal structure.[82,111,119]

MMCM was also investigated in a substrate-free form, which revealed considerable opening of the substrate-binding TIM barrel, indicating an intriguing conformational reorganization by the substrate binding.[119] In this crystal, coenzyme B_{12} (**2**) was found to be bound 'base-off/His-on' again, and to be largely intact, with the adenosine still bound to cobalt, but rotated away from its position in the crystal structure of (**3**) (above ring C of the corrin ligand) and toward a position above ring B. In a further crystal analysis of MMCM, this time with pseudosubstrates bound, the adenosyl group of the bound coenzyme AdoCbl (**3**) was again found to be repositioned (presumably with the help of the bound substrate), indicating the organometallic group to be particularly strained or to be detached from the cobalt center.[111,120] The data suggest substrate binding to assist the labilization of the Co–C bond by squeezing the adenosyl group off the cobalt-corrin.[82,120]

Glutamate mutase. GM from *Clostridium tetanomorphum* was the first enzyme discovered (around 1960) to be dependent upon a B_{12}-coenzyme. GM catalyzes the reversible rearrangement between (*S*)-glutamate and (2*S*,3*S*)-3-methylaspartate (where equilibrium favors glutamate by about 10).[104,105,114,121] GM has also been studied extensively in *Clostridium cochlearium*, but other microorganisms are suspected to have enzymes with GM activity as well.[104]

The functional GM proteins from *Cl. tetanomorphum* and from *Cl. cochlearium* are homologous heterotetramers ($\varepsilon_2\sigma_2$, about 140 kDa) consisting of a pair of smaller B_{12}-binding subunits (σ) and larger substrate-binding subunits (ε), and they contain two molecules of adenosyl-cobamide.[114,121] The cofactors from the two clostridia were identified as pseudocoenzyme B_{12} (Co$_\beta$-adenosyl-adeninyl-cobamide) and adenosyl-factor A (Co$_\beta$-adenosyl-2′-methyladeninyl-cobamide),[122] but coenzyme B_{12} (**3**) also is a cofactor.[104] Binding of the substrate triggers homolysis of the Co–C bond of the adenosyl-cobamide cofactor. Similar to the situation with MMCM, H-atom abstraction and homolysis of bound AdoCbl, which give the radical (**9**), are kinetically coupled processes, and a presteady state D-isotope effect of about 30 is observed.[123] The rearrangement reaction catalyzed by GM (in the 'reverse' direction) is initiated by the abstraction of an H atom from the bound substrate, that is, from the methyl group of enzyme-bound methyl aspartate, followed by a rearrangement of the 3-methylaspart-3′-yl radical to the glutam-4-yl radical.[104,114] The radical rearrangement of GM is suggested to take place via a fragmentation/recombination mechanism that involves acrylate as a fragment.[121] The glutam-4-yl radical is then suggested to reabstract an H atom from 5′-deoxyadenosine to give the rearrangement product, (*S*)-glutamate, and the 5′-deoxyadenosyl radical that recombines with cob(II)alamin (**5**) to give enzyme-bound (**3**). The radicals are indicated to be bound to the protein via several H bonds. The rearrangement step appears to be critically controlled by the interactions with the apoenzyme and seems to occur without noticeable participation of the bound cob(II)alamin, that is, the corrinoid is merely a 'spectator'.[116]

Crystallographic studies with GM from *Cl. cochlearium* have provided a detailed structural picture of the enzyme, in which the corrinoid cofactor is bound 'base-off/His-on' again and at the interface between the subunits σ and ε.[105] The cobalt-coordinating histidine is part of an H-bonded 'regulatory' His-Asp-Ser triad. Detailed analysis of GM with the bound coenzyme B_{12} (**3**) revealed the position of the ribose part of the 5′-deoxyadenosyl moiety to be disordered and to be present in two conformations, related to each other by a pseudo-rotation of the furanose ring. One of these structures places the 5′-methylene group of the adenosine close to the position of the corrin-bound cobalt center, but at a distance of about 3.1 Å, and thus appears to have features expected for the direct product of the homolysis of the Co–C bond of the bound cofactor (**3**). In the other conformation, the 5′-methylene carbon is at a distance of about 4.5 Å from the metal center and is displaced toward the substrate-binding site, as if in van der Waals contact with the bound substrate. In this way, GM achieves a controlled and energetically facile transposition of the 5′-radical center from cobalt to the substrate.[105]

The solution structures of the (roughly 15 kDa) B_{12}-binding σ-subunits of GM from *Cl. tetanomorphum*[124] and of *Cl. cochlearium* were analyzed by heteronuclear NMR spectroscopy.[125] These studies provided the first structure of a cofactor-free B_{12}-binding protein and indicated the latter to be largely preorganized for B_{12}-binding and to be structured similarly in solution as in the crystal of the holo-enzyme. However, the apo-protein was seen to contain a flexible loop and a 'nascent' helix, both suggested to become structured only upon binding of the corrinoid.[126] A model for the events in binding of the 'base-off/His-on' form of the B_{12}-cofactor by the σ-subunit could be derived. According to this model, the nucleotide tail of the 'base-off' form of the adenosyl-corrinoid is trapped first and the attached nucleotide moiety stabilizes the protein. Indeed, the natural cobamide cofactors of the two clostridia are adeninyl-cobamides, such as pseudocoenzyme B_{12} (Co$_\beta$-adenosyl-adeninyl-cobamide), for which the 'base-off' form predominates in aqueous solution.[127] By contrast, in aqueous solution AdoCbl (**3**) prefers to be in the 'base-on' form (with only about 1% of the 'base-off'-form).[4,18]

Other B_{12}-dependent carbon skeleton mutases. Besides MMCM and GM, two other B_{12}-dependent carbon skeleton mutases are known. These are (1) methylene glutarate mutase (MGM), which catalyzes the reversible interconversion of 2-methylene-glutarate and R-3-methylitaconate as part of a degradative path of nicotinic acid in *Clostridium barkeri*[104,121] and (2) ICM, which catalyzes the reversible rearrangement of isobutyryl-CoA and *n*-butyryl-CoA, an isomerization that is relevant in the course of the biosynthesis of polyketide antibiotics.[106] This coenzyme B_{12}-dependent isomerase is observed in species of the gram-positive bacteria *Streptomyces*[106] and appears to be distributed over a wide range of microorganisms.

3.3.2 *Diol Dehydratases, Glycerol Dehydratase, and Ethanolamine Ammonia Lyase*

Diol dehydratases and glycerol dehydratase. DD and glycerol dehydratase are isofunctional enzymes that catalyze the dehydration of propane-1,2-diol, ethane-1,2-diol, and glycerol to propanal, acetaldehyde, and 3-hydroxypropanal respectively (other glycols can be dehydrated in an analogous fashion).[77,107] DD uses adenosylcobamides (such as AdoCbl, (**3**)) as cofactors and catalyzes the dehydration of 1,2-diols via a (pseudo)intramolecular H-transfer involving the 5′-position of the organometallic cofactor (for reviews see[107,128]). In contrast to the B_{12}-dependent carbon skeleton mutases, the cofactor in these dehydratases is bound in a (conventional) 'base-on' form and the protein sequence of DD lacks the diagnostic 'B_{12}-binding' (Gly-X-X-His-X-Asp)-sequence motif.[128] B_{12}-binding in a 'base-on' form was made likely by ESR-investigations of DD[129] and was finally confirmed by X-ray analysis.[107,130] In addition, in the active site of DD of *Klebsiella oxytoca* a potassium ion is bound (together with the substrate propane-1,2-diol) to which a role as a Lewis acid in the radical rearrangement reaction has been ascribed.[130] The AdoCbl-catalyzed reaction again is based on a substrate-assisted homolysis of the Co–C bond of the corrinoid cofactor and formation of the 5′-deoxy-5′-adenosyl radical (**9**) and cob(II)alamin (**5**), as indicated by rapid kinetic studies by ESR- and UV/Vis-spectroscopic means.[128] In DD, the radical (**9**) then abstracts a H atom from the C-1 position of propane-1,2-diol, followed by 1,2-migration of the hydroxy group vicinal to the radical site (Figure 13). The migration of the hydroxyl group is suggested to be assisted by the potassium ion and by H-bonding with protic residues of the protein.[128] The (formal) product of the isomerization is a 1,1-diol (or the hydrate of the aldehyde propanal). The propanal isolated from ^{18}O-labeled (*S*)-propane-1,2-diol still is ^{18}O-labeled, while unlabeled propanal is obtained from ^{18}O-labeled (*R*)-propane-1,2-diol.[131]

The crystal structure of DD (from *Kl. oxytoca*) was solved as the complex with vitamin B_{12} (**1**) and (*S*)-propane-1,2-diol.[107,130] It showed the corrinoid to be bound at an interdomain-interface (of the B_{12}-binding β-subunit and of the substrate-binding α-subunit) and confirmed the ‘base-on’ nature of the bound corrinoid. The crystal structure showed the corrin-bound cobalt ion to be (largely) pentacoordinated, with an axial Co–N_α bond with 2.5 Å length, and the diol substrate to be ligating the potassium ion, which is situated at a distance of 11.7 Å from the cobalt center of the corrinoid.[130] The diol substrate is also bound via a tight net of H bonds to polar protein residues at an observed distance of more than 7 Å from the corrin-bound cobalt ion.[130] These observations excluded direct contacts of reaction intermediates with the cobalt center of the cofactor. Analysis of the crystal structure of DD reconstituted with the coenzyme B_{12} analogue 5-adeninyl-pentyl-cobalamin revealed the binding of an analogue of AdoCbl (**3**) to DD, in which a flexible pentamethylene unit links an adenine function to the cobalt center, similar to the ribose in the adenosyl ligand.[132] Together with earlier structure-function studies of a variety of other analogues of coenzyme B_{12} (**3**), this study supported the view of an effective adenine-binding pocket in the ‘substrate binding’ α-subunit. The observed binding of the adenine moiety of 5-adeninyl-pentyl-cobalamin indicates buildup of a strain in the adenosyl-cobamide cofactor as a means of activation toward homolysis of its Co–C bond.

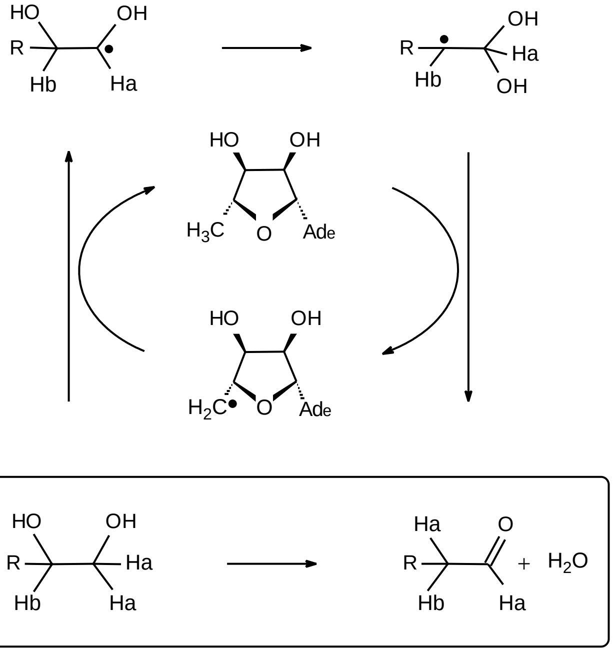

Figure 13 Illustration showing a possible mechanism of the coenzyme B_{12}-catalyzed diol dehydration

Ethanolamine ammonia lyase. EAL converts ethanolamine to acetaldehyde, with loss of ammonia.[108,133] EAL depends upon adenosylcobamides, such as coenzyme B_{12} (**3**), but a range of other adenosylcobamides are also accepted as cofactors, while cobalamins with β-ligands other than the 5′-deoxy-5′-adenosyl group (of AdoCbl) are inhibitors. Active EAL is multimeric and has an apparent molecular mass of about 560–600 kDa. Similar to the mechanism of DD, a radical mechanism is proposed for the isomerization of the vicinal amino-alcohol substrates (ethanolamine, (*R*)- and (*S*)-aminopropanol) by EAL, starting with the abstraction of an H atom from the C-1 position of the substrates.[134]

B_{12}-dependent amino mutases. Two coenzyme B_{12}-dependent amino mutases have been characterized, both of which catalyze the migration of ω-amino groups to the ($\omega - 1$) position in diamino-acids with the help of (**2**) and pyridoxal-phosphate as cofactors:[109] (1) Ornithine-4,5-aminomutase catalyzes the migration of the terminal amino group of D-ornithine to the 4-position, to give (2*R*,4*S*)-diaminovaleric acid (Table 1). The migration of the amino group is achieved in a radical reaction, which requires the pyridoxal cofactor PLP, to assist the migration by forming a Schiff’s base involving the migrating amino function. (2) D-lysine/L-β-lysine 5,6-aminomutase catalyzes the isomerization of D-lysine to 2,5-diaminohexanoic acid and of L-β-lysine to (3*S*,5*S*)-3,5-diaminohexanoic acid via a mechanism suggested to be similar to that of D-ornithine amino mutase. However, the related isomerization of L-α-lysine to L-β-lysine is catalyzed by lysine-2,3-aminomutase, which is an amino mutase that is independent of coenzyme B_{12} (**2**).[109]

3.3.3 *B_{12}-dependent Ribonucleotide Reductase*

In all organisms, the ribonucleotide reductases play essential roles in the biosynthesis of DNA by catalyzing the reduction of nucleoside di- or triphosphates to the corresponding 2′-deoxynucleotides.[110,112] The ribonucleotide reductase (RNR) from *Lactobacillus leichmanii* belongs to the class II ribonucleotide reductases, which make use of adenosylcobamides, such as coenzyme B_{12} (**3**), to initiate the radical reaction.[112,135]

RNR uses nucleoside triphosphates (NTPs) as substrates and 2′-deoxynucleoside triphosphates (dNTPs) as allosteric effectors.[110] In RNR, the 'B_{12}-binding motif', the (Gly-X-X-His-X-Asp)-sequence, is absent and the corrinoid cofactor binds in a 'base-on'-form.[136] Homolytic (Co–C)-bond cleavage of AdoCbl (**3**) is known to be accelerated by about10^{11}-fold in RNR.[137] The free enthalpy of activation of AdoCbl, when bound to GTP-activated but substrate-free RNR, was determined to be lowered in the enzyme by about $13-15$ kcal mol^{-1}compared to the value for the homolysis of AdoCbl in aqueous solution.[137] In RNR, a protein centered thiyl radical, which is generated from the homolysis of the Co–C bond of the bound coenzyme (**3**), induces the radical reactions that formally lead to the reductive substitution by hydrogen of the 2′-hydroxyl group of the ribonucleotide. The thiyl radical then abstracts the H atom at C-3′ of the bound substrate to induce the reductive dehydration of the bound NTP to a dNTP, which involves the oxidation of the thiol groups of two cysteines (suggested to be C-119 and C-419) to a disulfide bridge.

The crystal structures of dGTP-free AdoCbl-dependent RNR in the apo-form complexed with Co_β-adeninylpentyl-cobalamin (a structural analog of AdoCbl (**3**), see e.g.[132]) confirmed the 'base-on' nature of the bound corrinoid, deduced from ESR data earlier.[136] In crystalline RNR, the crucial cysteine is at a distance of about 10 Å from the cobalt(II) center of the bound corrinoid, and in a region of space that is also well conserved in the three classes of RNRs.[138]

4 RELATED ARTICLES

Bonding Energetics of Organometallic Compounds; Cobalt: Inorganic & Coordination Chemistry; Cobalt: Organometallic Chemistry; Mechanisms of Reaction of Organometallic Complexes.

5 REFERENCES

1. K. Folkers, in 'B_{12}', ed. D. Dolphin, Wiley, New York, 1982, Vol. I, p. 1.
2. J. P. Glusker, in 'B_{12}', ed. D. Dolphin, Wiley, New York, 1982, Vol. I, p. 24.
3. C. Kratky and B. Kräutler, in 'Chemistry and Biochemistry of B_{12}', ed. R. Banerjee, Wiley, New York, 1999, p. 9.
4. J. M. Pratt, 'Inorganic Chemistry of Vitamin B_{12}', Academic Press, New York, 1972.
5. J. J. R. Frausto da Silva and R. J. P. Williams, 'The Biological Chemistry of the Elements', Clarendon Press, Oxford, 1991, p. 400.
6. W. Friedrich, 'Vitamins', de Gruyter, Berlin, 1988, p. 839.
7. B. Kräutler, in 'Vitamin B_{12} and B_{12}-Proteins', eds. B. Kräutler, D. Arigoni, and B. T. Golding, Wiley-VCH, Weinheim, 1998, p. 517.
8. A. Eschenmoser and C. Wintner, *Science*, 1977, **196**, 1410.
9. R. B. Woodward, in 'Vitamin B_{12}', 4th Intl. Symposium, eds. B. Zagalak and W. Friedrich, de Gruyter, Berlin, 1979, p. 37.
10. A. R. Battersby, in 'Vitamin B_{12} and B_{12}-proteins', eds. B. Kräutler, D. Arigoni, and B. T. Golding, Wiley-VCH, Weinheim, 1998, p. 47.
11. A. I. Scott, in 'Vitamin B_{12} and B_{12}-proteins', eds. B. Kräutler, D. Arigoni, and B. T. Golding, Wiley-VCH, Weinheim, 1998, p. 81.
12. J. Halpern, *Science*, 1985, **227**, 869.
13. B. Kräutler, D. Arigoni, and B. T. Golding, 'Vitamin B_{12} and B_{12}-Proteins', Wiley-VCH, Weinheim, 1998.
14. R. Banerjee, 'Chemistry and Biochemistry of B_{12}', Wiley, New York, 1999.
15. B. Kräutler, in 'Vitamin B_{12} and B_{12}-proteins', eds. B. Kräutler, D. Arigoni, and B. T. Golding, Wiley-VCH, Weinheim, 1998, p. 3.
16. J. M. Pratt, in 'Chemistry and Biochemistry of B_{12}', ed. R. Banerjee, Wiley, New York, 1999, p. 113.
17. A. Eschenmoser, *Angew. Chem.*, 1988, **100**, 5; *Angew. Chem., Int. Ed Engl.*, 1988, **27**, 5.
18. K. L. Brown, J. M. Hakimi, and D. W. Jacobsen, *J. Am. Chem. Soc.*, 1984, **106**, 7894.
19. (a) D. Lexa and J. M. Saveant, *Acc. Chem. Res.*, 1983, **16**, 235; (b) B. Kräutler, in 'Chemistry and Biochemistry of B_{12}', ed. R. Banerjee, Wiley, New York, 1999, p. 315.
20. B. Kräutler, W. Fieber, S. Ostermann, M. Fasching, K.-H. Ongania, K. Gruber, C. Kratky, C. Mikl, A. Siebert, and G. Diekert, *Helv. Chim. Acta*, 2003, **89**, 3698.
21. V. B. Pett, M. N. Liebman, P. Murray-Rust, K. Prasad, and J. P. Glusker, *J. Am. Chem. Soc.*, 1987, **109**, 3207.
22. M. K. Geno and J. Halpern, *J. Am. Chem. Soc.*, 1987, **109**, 1238.
23. B. Kräutler, R. Konrat, E. Stupperich, G. Färber, K. Gruber, and C. Kratky, *Inorg. Chem.*, 1994, **33**, 4128.
24. B. Kräutler, W. Keller, M. Hughes, C. Caderas, and C. Kratky, *J. Chem. Soc., Chem. Commun.*, 1987, 1678.
25. B. Kräutler, W. Keller, and C. Kratky, *J. Am. Chem. Soc.*, 1989, **111**, 8936.
26. S. van Doorslaer, G. Jeschke, B. Epel, D. Goldfarb, R.-A. Eichel, B. Kräutler, and A. Schweiger, *J. Am. Chem. Soc.*, 2003, **125**, 5915.

27. H. F. J. Savage, P. F. Lindley, J. L. Finney, and P. A. Timms, *Acta Crystallogr.*, 1987, **B43**, 296.
28. M. Rossi, J. P. Glusker, L. Randaccio, M. F. Summers, P. J. Toscano, and L. G. Marzilli, *J. Am. Chem. Soc.*, 1985, **109**, 1729.
29. E. Hohenester, C. Kratky, and B. Kräutler, *J. Am. Chem. Soc.*, 1991, **113**, 4523.
30. G. N. Schrauzer, E. Deutsch, and R. J. Windgassen, *J. Am. Chem. Soc.*, 1968, **90**, 2441.
31. L. Walder, G. Rytz, U. Vägeli, R. Scheffold, and P. Engel, *Helv. Chim. Acta*, 1984, **67**, 1801.
32. T. A. Stich, A. J. Brooks, N. R. Buan, and T. Brunold, *J. Am. Chem. Soc.*, 2003, **125**, 5897.
33. H. M. Schiebel and H.-R. Schulten, *Mass Spectrom. Rev.*, 1986, **5**, 249.
34. R. Konrat, M. Tollinger, and B. Kräutler, in ‘Vitamin B_{12} and B_{12}-proteins’, eds. B. Kräutler, D. Arigoni, and B. T. Golding, Wiley-VCH, Weinheim, 1998, p. 349.
35. K. L. Brown, in ‘Chemistry and Biochemistry of B_{12}’, ed. R. Banerjee, Wiley, New York, 1999, p. 197.
36. R. Konrat, M. Tollinger, G. Kontaxis, and B. Kräutler, *Chem. Monthly*, 1999, **130**, 961.
37. G. Gerfen, in ‘Chemistry and Biochemistry of B_{12}’, ed. R. Banerjee, Wiley, New York, 1999, p. 165.
38. M. R. Chance, in ‘Chemistry and Biochemistry of B_{12}’, ed. R. Banerjee, Wiley, New York, 1999, p. 43.
39. S. Hirota and L. G. Marzilli, in ‘Chemistry and Biochemistry of B_{12}’, ed. R. Banerjee, Wiley, New York, 1999, p. 239.
40. N. J. Lewis, R. Nussberger, B. Kräutler, and A. Eschenmoser, *Angew. Chem.*, 1983, **95**, 744; *Angew. Chem., Int. Ed. Engl.*, 1983, **22**, 736.
41. J. Florent and L. Ninet, in ‘Microbial Technology’, eds. H. J. Pepples, and D. Perlman, Academic Press, New York, 1979, Vol. I, p. 479.
42. D. Thibaut, L. Debussche, and F. Blanche, *Proc. Natl. Acad. Sci. U.S.A.*, 1990, **87**, 8795.
43. J. Escalante-Semerena, in ‘Chemistry and Biochemistry of B_{12}’, ed. R. Banerjee, Wiley, New York, 1999, p. 577.
44. I. A. Scott, C. A. Roessner, and P. J. Santander, in ‘Chemistry and Biochemistry of B_{12}’, ed. R. Banerjee, Wiley, New York, 1999, p. 537.
45. B. Kräutler and S. Ostermann, in ‘The Porphyrin Handbook’, eds. K. M. Kadish, K. M. Smith, and R. Guilard, Academic Press, San Diego, 2003, Vol. 11, p. 227.
46. B. Kräutler, in ‘The Biological Alkylation of Heavy Elements’, eds. P. J. Craig and F. Glockling, Royal Society of Chemistry, London, 1988, p. 31.
47. M. Puchberger, R. Konrat, B. Kräutler, U. Wagner, and C. Kratky, *Helv. Chim. Acta*, 2003, **86**, 145.
48. J. Halpern, in ‘B_{12}’, ed. D. Dolphin, Wiley, New York, 1982, Vol. I, p. 501.
49. B. Kräutler and C. Caderas, *Helv. Chim. Acta*, 1984, **67**, 1891.
50. K. L. Brown, L. Zhou, D. Zhao, S. Cheng, and X. Zou, in ‘Vitamin B_{12} and B_{12}-proteins’, eds. B. Kräutler, D. Arigoni, and B. T. Golding, Wiley-VCH, Weinheim, 1998, p. 417.
51. L. Walder, R. Scheffold, R. Walder, and D. L. Zhou, *Helv. Chim. Acta*, 1992, **75**, 995.
52. J. S. Dorweiler, R. G. Matthews, and R. G. Finke, *Inorg. Chem.*, 2002, **24**, 6217.
53. J. G. Grate and G. N. Schrauzer, *J. Am. Chem. Soc.*, 1979, **101**, 4601.
54. J. M. Pratt, in ‘Chemistry and Biochemistry of B_{12}’, ed. R. Banerjee, Wiley, New York, 1999, p. 73.
55. H. Mosimann and B. Kräutler, *Angew. Chem., Int. Ed. Engl.*, 2000, **39**, 393.
56. R. J. Parry, J. M. Ostrander, and I. Y. Arzu, *J. Am. Chem. Soc.*, 1985, **107**, 2190.
57. R. G. Matthews, *Acc. Chem. Res.*, 2001, **34**, 681.
58. A. G. Cole, L. M. Yoder, J. J. Shiang, N. A. Anderson, L. A. Walker II, M. M. Banaszak Holl, and R. J. Sension, *J. Am. Chem. Soc.*, 2002, **124**, 434.
59. J. F. Endicott and T. L. Netzel, *J. Am. Chem. Soc.*, 1979, **101**, 4000.
60. B. D. Martin and R. G. Finke, *J. Am. Chem. Soc.*, 1992, **114**, 585.
61. M. F. Summers, L. G. Marzilli, and A. Bax, *J. Am. Chem. Soc.*, 1986, **108**, 4285.
62. B. Kräutler, in ‘Organic Reactivity: Physical and Biological Aspects (Proceedings of the 4th European Symposium on Organic Reactivity)’, eds. B. T. Golding, R. J. Griffin, and H. Maskill, Royal Society of Chemistry, London, 1995, p. 209.
63. M. P. Jensen and J. Halpern, *J. Am. Chem. Soc.*, 1999, **1218**, 21810.
64. B. P. Hay and R. G. Finke, *J. Am. Chem. Soc.*, 1986, **108**, 4820.
65. R. G. Finke, in ‘Vitamin B_{12} and B_{12}-proteins’, eds. B. Kräutler, D. Arigoni, and B. T. Golding, Wiley-VCH, Weinheim, 1998, p. 383.
66. T. N. König, B. P. Hay, and R. G. Finke, *Polyhedron*, 1988, **7**, 1499.
67. B. P. Hay and R. G. Finke, *J. Am. Chem. Soc.*, 1987, **109**, 8012.
68. B. Kräutler, *Helv. Chim. Acta*, 1987, **70**, 1268.
69. M. Tollinger, R. Konrat, and B. Kräutler, *Helv. Chim. Acta*, 1999, **82**, 1596.
70. H. P. C. Hogenkamp, G. T. Bratt, and S. Sun, *Biochemistry*, 1985, **24**, 6428.
71. P. R. Norris and J. M. Pratt, *Biofactors*, 1996, **5**, 240.
72. F. E. Brinckman and G. J. Olson, in ‘The Biological Alkylation of Heavy Elements’, eds. P. J. Craig, and F. Glockling, Royal Society of Chemistry, London, 1988, p. 168.
73. Y. T. Fanchiang, G. T. Bratt, and H. P. C. Hogenkamp, *Proc. Natl. Acad. Sci. U.S.A.*, 1984, **81**, 2698.

74. M. Fasching, W. Schmidt, B. Kräutler, E. Stupperich, A. Schmidt, and C. Kratky, *Helv. Chim. Acta*, 2000, **83**, 2295.
75. R. G. Finke, in 'Molecular Mechanisms in Bioorganic Processes', eds. C. Bleasdale and B. T. Golding, Royal Society of Chemistry, London, 1990, p. 244.
76. R. Banerjee, *Chem. Rev.*, 2003, **103**, 2083.
77. T. Toraya, *Chem. Rev.*, 2003, **103**, 2095.
78. J. Halpern, S. H. Kim, and T. W. Leung, *J. Am. Chem. Soc.*, 1984, **106**, 8317.
79. N. Bresciani-Pahor, M. Forcolin, L. G. Marzilli, L. Randaccio, M. F. Summers, and P. J. Toscano, *Coord. Chem. Rev.*, 1985, **63**, 1.
80. B. Kräutler, in 'Proceedings of the Royal Swedish Academy of Sciences Nobel Symposia: Carbon dioxide fixation and reduction in biological and model systems', eds. G. Schneider and C. I. Branden, Oxford University Press, 1994, p. 83.
81. C. L. Drennan, S. Huang, J. T. Drummond, R. G. Matthews, and M. L. Ludwig, *Science*, 1994, **266**, 1669.
82. M. L. Ludwig and P. Evans, in 'Chemistry and Biochemistry of B_{12}', ed. R. Banerjee, Wiley, New York, 1999, p. 595.
83. V. Bandarian, K. A. Pattridge, B. W. Lennon, D. P. Huddler, R. G. Matthews, and M. L. Ludwig, *Nat. Struct. Biol.*, 2002, **9**, 53.
84. S. W. Ragsdale, *CRC Crit. Rev. Biochem. Mol. Biol.*, 1991, **26**, 261.
85. G. Wolfarth and G. Diekert, in 'Chemistry and Biochemistry of B_{12}', ed. R. Banerjee, Wiley, New York, 1999, p. 871.
86. E. Nexø, in 'Vitamin B_{12} and B_{12}-Proteins', eds. B. Kräutler, D. Arigoni, and B. T. Golding, Wiley-VCH, Weinheim, 1998, p. 461.
87. D. H. Alpers and G. J. Russel-Jones, in 'Chemistry and Biochemistry of B_{12}', ed. R. Banerjee, Wiley, New York, 1999, p. 411.
88. S. P. Stabler, in 'Chemistry and Biochemistry of B_{12}', ed. R. Banerjee, Wiley, New York, 1999, p. 343.
89. L. Ellenbogen and B. A. Cooper, in 'Handbook of Vitamins, Nutritional and Clinical Aspects', ed. L. J. Machlin, Dekker, New York, 1984, p. 491.
90. S. W. Ragsdale and M. Kumar, *Chem. Rev.*, 1996, **96**, 2515.
91. V. Bandarian, M. L. Ludwig, and R. G. Matthews, *Proc. Natl. Acad. Sci. U.S.A.*, 2003, **100**, 8156.
92. H. G. Wood, S. W. Ragsdale, and E. Pezacka, *FEMS Microbiol. Rev.*, 1986, **39**, 345.
93. R. K. Thauer, *Eur. J. Biochem.*, 1988, **176**, 497.
94. B. Kräutler, *Helv. Chim. Acta*, 1984, **67**, 1053.
95. T. I. Doukov, T. M. Iverson, J. Seravalli, S. W. Ragsdale, and C. L. Drennan, *Science*, 2002, **298**, 567.
96. C. Darnault, A. Volbeda, E. J. Kim, P. Legrand, X. Vernède, P. A. Lindahl, and J. C. Fontecilla-Camps, *Nat. Struct. Biol.*, 2003, **10**, 271.
97. J. Vorholt, J. Kunow, K. O. Stetter, and R. K. Thauer, *Arch. Microbiol.*, 1995, **163**, 112.
98. R. S. Wolfe, in 'The Molecular Basis of Bacterial Metabolism', eds. G. Hauska and R. K. Thauer, Springer Verlag, Berlin, 1990, p. 1.
99. J. M. Poston, K. Kuratomi, and E. R. Stadtman, *Ann. N.Y. Acad. Sci.*, 1964, **112**, 804.
100. U. Ermler, W. Grabarse, S. Shima, M. Goubeaud, and R. K. Thauer, *Science*, 1997, **278**, 1457.
101. A. Eschenmoser, *Ann. N.Y. Acad. Sci.*, 1986, **471**, 108.
102. L. Chistoserdova, J. A. Vorholt, R. K. Thauer, and M. E. Lidstrom, *Science*, 1998, **281**, 99.
103. R. Banerjee and S. Chowdhury, in 'Chemistry and Biochemistry of B_{12}', ed. R. Banerjee, Wiley, New York, 1999, p. 70.
104. W. Buckel, G. Bröker, H. Bothe, A. J. Pierik, and B. T. Golding, in 'Chemistry and Biochemistry of B_{12}', ed. R. Banerjee, Wiley, New York, 1999, p. 7577.
105. C. Kratky and K. Gruber, *Curr. Opin. Chem. Biol.*, 2002, **6**, 598.
106. K. Zerbe-Burckhardt, A. Ratnatilleke, J. W. Vrijbloed, and J. A. Robinson, in 'Chemistry and Biochemistry of B_{12}', ed. R. Banerjee, Wiley, New York, 1999, p. 859.
107. T. Toraya, in 'Chemistry and Biochemistry of B_{12}', ed. R. Banerjee, Wiley, New York, 1999, p. 783.
108. V. Bandarian and G. H. Reed, in 'Chemistry and Biochemistry of B_{12}', ed. R. Banerjee, Wiley, New York, 1999, p. 811.
109. P. A. Frey and C. H. Chang, in 'Chemistry and Biochemistry of B_{12}', ed. R. Banerjee, Wiley, New York, 1999, p. 835.
110. J. Stubbe, S. Licht, G. Gerfen, D. Silva, and S. Booker, in 'Vitamin B_{12} and B_{12}-proteins', eds. B. Kräutler, D. Arigoni, and B. T. Golding, Wiley-VCH, Weinheim, 1998, p. 321.
111. K. Gruber and C. Kratky, in 'Handbook of Metalloproteins', eds. A. Messerschmidt, R. Huber, T. Poulos, and K. Wieghart, John Wiley, Chichester, 2001, p. 995.
112. J. Stubbe and W. A. van der Donk, *Chem. Rev.*, 1998, **98**, 705.
113. J. Rétey, *Angew. Chem., Int. Ed. Engl.*, 1990, **29**, 355.
114. E. N. G. Marsh, *Bioorg. Chem.*, 2000, **28**, 176.
115. S. Chowdhury and R. Banerjee, *Biochemistry*, 2000, **39**, 7998.
116. S. Chowdhury and R. Banerjee, *J. Am. Chem. Soc.*, 2000, **122**, 5417.
117. B. T. Golding, R. J. Anderson, S. Ashwell, C. H. Edwards, I. Garnett, F. Kroll, and W. Buckel, in 'Vitamin B_{12} and B_{12}-proteins', eds. B. Kräutler, D. Arigoni, and B. T. Golding, Wiley-VCH, Weinheim, 1998, p. 201.
118. N. H. Thomä, P. R. Evans, and P. F. Leadley, *Biochemistry*, 2000, **39**, 9213.
119. F. Mancia and P. R. Evans, *Structure*, 1998, **6**, 711.
120. F. Mancia, G. A. Smith, and P. R. Evans, *Biochemistry*, 1999, **38**, 7999.
121. W. Buckel and B. T. Golding, *Chem. Soc. Rev. (London)*, 1996, **25**, 329.

122. B. Hoffmann, M. Oberhuber, E. Stupperich, H. Bothe, W. Buckel, R. Konrat, and B. Kräutler, *J. Bacteriol.*, 2000, **182**, 4773.

123. E. N. G. Marsh and D. P. Ballou, *Biochemistry*, 1998, **37**, 11864.

124. M. Tollinger, R. Konrat, B. H. Hilbert, E. N. G. Marsh, and B. Kräutler, *Structure*, 1998, **6**, 1021.

125. B. Hoffmann, R. Konrat, H. Bothe, W. Buckel, and B. Kräutler, *Eur. J. Biochem.*, 1999, **263**, 178.

126. M. Tollinger, C. Eichmüller, R. Konrat, M. S. Huhta, E. N. G. Marsh, and B. Kräutler, *J. Mol. Biol.*, 2001, **309**, 777.

127. W. Fieber, B. Hoffmann, W. Schmidt, E. Stupperich, R. Konrat, and B. Kräutler, *Helv. Chim. Acta*, 2002, **85**, 927.

128. T. Toraya, *Cell. Mol. Life Sci.*, 2000, **57**, 106.

129. A. Abend, R. Nitsche, V. Bandarian, E. Stupperich, and J. Rétey, *Angew. Chem., Int. Ed. Engl.*, 1998, **37**, 625.

130. N. Shibata, J. Masuda, T. Tobimatsu, T. Toraya, K. Suto, Y. Morimoto, and N. Yasuoka, *Structure*, 1999, **7**, 997.

131. J. Rétey, A. Umani-Rouchi, J. Seibl, and D. Arigoni, *Experientia*, 1966, **22**, 502.

132. J. Masuda, N. Shibata, Y. Morimoto, T. Toraya, and N. Yasuoka, *Structure*, 2000, **8**, 775.

133. B. M. Babior, in 'B_{12}', ed. D. Dolphin, John Wiley, New York, 1982, Vol II, p. 263.

134. K. Warncke, J. C. Schmidt, and S.-C. Ke, *J. Am. Chem. Soc.*, 1999, **121**, 10522.

135. J. Stubbe, *Curr. Opin. Struct. Biol.*, 2000, **10**, 1373.

136. C. C. Lawrence, G. J. Gerfen, V. Samano, R. Nitsche, M. J. Robins, J. Rétey, and J. Stubbe, *J. Biol. Chem.*, 1999, **274**, 7039.

137. S. S. Licht, C. C. Lawrence, and J. Stubbe, *Biochemistry*, 1999, **38**, 1234.

138. M. D. Sintchak, G. Arjara, B. A. Kellogg, J. Stubbe, and C. D. Drennan, *Nat. Struct. Biol.*, 2002, **9**, 293.

Acknowledgment

I am grateful to the Austrian National Science Foundation (Projects 13595 and 17221) and to the European Commission (Project HPRN-CT-2002-00195) for continuous financial support of our research in the B_{12} area.

Cobalt: Inorganic & Coordination Chemistry

Allan G. Blackman
University of Otago, Dunedin, New Zealand

Based in part on the article Cobalt: Inorganic & Coordination Chemistry by David A. Buckingham which appeared in the Encyclopedia of Inorganic Chemistry, First Edition.

1	Introduction	1
2	The Element	1
3	General Chemistry	4
4	Salts and Other Simple Compounds	7
5	Coordination Complexes	8
6	Concluding Remarks	21
7	Related Articles	22
8	References	22

Abbreviations

18S6 = hexathia-18-crown-6; 9S3 = 1,4,7-trithiacyclononane; 2=phos = *cis*-(bis(diphenylphosphino)ethene); acac = acetylacetonate anion; bipy = 2,2′-bipyridine; cyclam = 1,4,8,11-tetraazacyclotetradecane; bzacen = N,N'-ethylenebis(benzoylacetoniminide); cyclen = 1,4,7,10-tetraaza cyclododecane; diphos = o-phenylenebis(dimethylphos phine); dmvi = dimethylviolurate anion; DNPP = 2,4-dinitrophenylphosphate; dppe = bis(diphenylphosphino)ethane; Hedta = ethylenediaminetetraacetic acid trianion; his = histidine monoanion; MAS = magic angle spinning; Me_3TACN = 1,4,7-Me_3-1,4,7-triazacyclononane; Me_6tren = tris(2-dimethylaminoethyl)amine; mmtp = 1,1,1-tris(dimethylphosphinomethyl)ethane; N-Mecyclen = 1-methyl-1,4,7,10-tetraazacyclododecane; nor = norbornyl; NP_3 = tris(2-(diphenylphosphino)ethyl)amine; OEC = octaethylcorrole trianion; ox = oxalic acid dianion; PP_3 = tris(2-(diphenylphosphino)ethyl)phosphine; salen = bis(salicylaldehyde)ethylenediimine; tepa = tris(2-pyridylethyl)amine; terpy = 2,2′:6′,2″-terpyridine; tetraen = tetraethylenepenta amine; tmen = 2,3-dimethylbutane-2,3-diamine; trien = triethylenetetraamine; triphos = 1,1,1-tris(diphenylphosphinomethyl)ethane; ttn = 2,5,8-trithianonane.

1 INTRODUCTION

'. . . we invite the attention of chemists to a class of salts which for beauty of form and color, and for abstract theoretical interest, are almost unequaled either among organic or inorganic compounds.' So wrote Wolcott Gibbs and Frederick Genth in their classic discourse 'Researches of the ammonia-cobalt bases,' published in 1856.[1] Since this time, cobalt has become arguably the most important transition metal in the development of modern coordination chemistry. The Swiss chemist Alfred Werner (1866–1919) was awarded the Nobel Prize in 1913 'in recognition of his work on the linkage of atoms in molecules by which he has thrown new light on earlier investigations and opened up new fields of research especially in inorganic chemistry' and he has often (quite correctly) been termed 'the father of modern coordination chemistry.' It is thanks to his extensive work on complexes of Co(III) that we now understand the concepts of oxidation state (*see Oxidation Number*) and coordination number (or primary and secondary valence as they were termed by Werner). His work also lies as the forefront of our understanding of inorganic stereochemistry (*see Stereochemistry*), and his studies of optically active Co(III) complexes in particular were crucial to the development of modern structural coordination chemistry. In recognition of his importance in chemistry, Co(III) am(m)ine complexes are often called *Werner complexes* (*see Werner Complexes*). Complexes of Co(III) have also been central to studies aimed at determining the mechanisms of ligand substitution (*see Ligand Substitution*) and electron transfer in coordination complexes, as exemplified in the work of the 1983 Nobel Laureate Henry Taube. In addition to the interest in its coordination complexes, cobalt finds many uses in industry, in areas as diverse as pigments, magnets, catalysts, superalloys, and batteries. ^{60}Co is an important isotope in radiotherapy, while the cobalamins constitute an important class of biological compounds. A comprehensive treatment of the chemistry of cobalt is beyond the scope of this article, and the following pages, of necessity, provide only a brief outline of some of the more interesting and important aspects of the inorganic and coordination chemistry of cobalt. The interested reader is referred to more detailed treatments of this extensive topic.[2–5]

2 THE ELEMENT

2.1 History

Cobalt ores were used by the ancient Egyptians to color glass and pottery blue, and a piece of such glass found in the tomb of Pharaoh Tutankhamen dates knowledge of cobalt to at least 1300 B.C.E. Cobalt ores were also used to color Chinese pottery from the Tang (600–900 C.E.) and Ming (1350–1650 C.E.) dynasties. Elemental cobalt was first isolated by the Swedish chemist Georg Brandt in 1735, while studying a dark blue ore obtained from a local copper mine, but it was to be another 45 years before Bergman proved that cobalt was indeed a new element. The name 'cobalt' derives from the German word ‘Kobald,’ meaning ‘goblin,’ which appears to have been given originally by miners in Saxony; silver mines in this region contained significant amounts of the ore smaltite ($CoAs_2$), and their attempts to smelt this led to the production of foul-smelling and toxic arsenic species. Such problems were blamed on ‘die Kobalde’. Espionage provided one of the earliest documented uses of cobalt compounds, with a mixture of cobalt chloride, glycerine, and water being used as an invisible ink by the Paris-based American agent Silas Deane in 1776–1777.

2.2 Abundance and Distribution

Cobalt ranks number 33 in abundance of the elements in the earth’s crust, which contains on average 20-µg Co/g, although soil levels of up to 2000-µg Co/g are found in Zaire and New Zealand. Significant deposits of cobalt are found in Canada, Russia, Zambia, and Congo, with these countries accounting for approximately 65% of the current total world supply. Smaller deposits are found in Cuba, New Caledonia, and Australia. Cobalt does not exist as the free metal in nature, but occurs in approximately 200 ores, of which smaltite ($CoAs_2$), cobaltite (CoAsS), and linnaeite (Co_3S_4) are commercially important.

2.3 Isolation and Uses

Cobalt sulfide and arsenide ores are often found mixed with those of nickel and copper. The mixed ore is roasted with Na_2CO_3 and KNO_3, which removes part of the sulfur and arsenic as volatile species. The residue contains the metal oxides, as well as sulfate and arsenate, and the latter are removed by leaching with water. The metal oxide mixture is then dissolved in hot HCl or H_2SO_4, and the individual metal oxides are fractionally precipitated using $Ca(OH)_2$ and NaOCl. This process gives the mixed valent oxide Co_3O_4, which is then reduced to the metal by treatment with charcoal.

Table 1 gives data on the current world production of cobalt. In 2002, approximately 50% of cobalt produced worldwide was a by-product of nickel refining, while some 18% was obtained from refining secondary products and scrap metal. Newfound ore deposits in Australia and Africa are expected to add significantly to world production, with six new refining operations having been commissioned in these areas between 1999 and 2001. As can be seen in Table 2, the major use of cobalt is as a component of superalloys, which are designed for use at elevated temperatures.

Table 1 Current world production of cobalt (2002)[3]

Country	Mined	Refined	Approximate refined quantity (tonne)
Australia	Yes	Yes	3900
Belgium	No	Yes	1200
Botswana	Yes	–	–
Brazil	Yes	Yes	950
Canada	Yes	Yes	4500
China	Yes	Yes	1800
Cuba	Yes	–	–
Finland	–	Yes	8000
France	–	Yes	200
India	–	Yes	250
Japan	–	Yes	350
Morocco	Yes	Yes	1200
New Caledonia	Yes	–	–
Norway	–	Yes	4000
Russia	Yes	Yes	4500
South Africa	Yes	Yes	400
Democratic Republic of Congo	Yes	Yes	3500
Uganda	–	Yes	400
Zambia	Yes	Yes	6000

Table 2 Estimated industrial usage of cobalt by area[3]

Use	%
Superalloys	25.5
Hardfacing and other alloys	7.0
Magnets	8.0
Hard materials – carbides, diamond tooling	15.5
Catalysts	9.8
Colors – glass, enamels, plastics, ceramics, artist’s colors, fabrics	11.6
Feedstuffs, anodizing, recording, electrolysis, Cu electrowinning	5.1
Batteries	8.5
Tyre adhesives, soaps, driers (paint/ink)	9.0

2.4 Properties

Table 3 gives the important properties of elemental cobalt. The metal itself is lustrous and silvery-blue at room temperature, and exists in two allotropic forms (*see Allotrope*), α and β. The α-form has a hexagonal closest-packed structure and exists below 417 °C, while the β-form exhibits a face-centered cubic arrangement. Interconversion between the two forms is slow, and may account, in part, for the variability in reported physical data for the metal. The metal is ferromagnetic (*see Ferromagnetism*) at room temperature and has the highest known Curie temperature (*see Curie Temperature*) of all elements (1121 °C). Addition of small amounts of cobalt to iron can increase the already large saturation magnetization of iron, and the Co/Fe alloy containing 35 wt% Co shows a maximum saturation magnetization of 2.45 T. Cobalt has only one naturally occurring isotope, ^{59}Co, and, consequently, the atomic mass of cobalt is known to high precision (58.933200(2)). A list of the known isotopes of cobalt is given in Table 4. The ^{59}Co isotope is NMR-active, and its high abundance results in a sensitivity of 0.28 relative to the ^{1}H nucleus. However, the ^{59}Co nucleus is quadrupolar (*see Quadrupolar*) with a spin of 7/2, and broad NMR

Table 3 Properties of cobalt

Property	Value
Atomic number	27
Atomic mass	58.933200(2)
Electronic configuration	$[Ar]3d^7 4s^2$
Electronegativity (Pauling)	1.88
Metal–metal distance in elemental Co (pm)	250
Ionic radius (pm)	
Co(IV)	53
Co(III)	54.5 (LS) 61(HS)
Co(II)	65.1 (LS) 74.5 (HS)
Melting point (°C)	1495
Boiling point (°C)	2927
ΔH_{fus} (kJ mol^{-1})	16.3
ΔH_{vap} (kJ mol^{-1})	382
ΔH_f (monatomic gas) (kJ mol^{-1})	425 ± 17
Density (g cm^{-3})	8.90 (20 °C)
Electrical resistivity ($\mu\Omega$ cm)	6.24
Curie temperature (°C)	1121
Molar volume (cm^3)	6.67
Ionization energy (kJ mol^{-1})	
First	760.4
Second	1648

peaks are often obtained for all but very high symmetry compounds. Despite this, ^{59}Co NMR is now routinely used for the characterization of cobalt compounds both in solution and in the solid state. As can be seen in Table 5, the chemical shift range for Co(III) complexes in solution is large and the signal linewidths vary over at least three orders of magnitude, correlating well with values of T_1 and T_2. Solid-state spectra can be obtained from single crystals and both static and MAS polycrystalline samples. Extensive collections of chemical shift data are available.[6–8] Solid-state ^{59}Co NMR has afforded substantial insight into the electronic structure of Co-containing molecules. For example, studies of several cobalamins, cobaloximes (*see Cobaloxime*), and cobalt porphyrins (*see Porphyrin*) have shown that cobaloximes ($\delta \sim 3200–5300$ ppm) display similar chemical shifts to the cobalamins ($\delta \sim 4300–4800$ ppm), and are thus better models of these biological compounds than the porphyrins ($\delta \sim 8200–9200$ ppm). The sensitivity of the solid-state technique is attested to by the observation that the four crystallographically nonequivalent Co sites in $[Co(NH_3)_6]Cl_3$ can be distinguished by ^{59}Co NMR. While ^{59}Co is the only naturally occurring isotope, some artificial isotopes of Co have important uses. ^{59}Co can be converted to the longest-lived ($t_{1/2} = 5.3$ years) radioactive isotope ^{60}Co by irradiation with thermal neutrons. The ^{60}Co nucleus emits 1.17- and 1.33-MeV γ-rays, and is widely used as a radiotheraputic agent in nuclear medicine. It is also used as a γ-source for food irradiation and industrial radiography. The ^{57}Co isotope finds use as an indirect source of photons for ^{57}Fe Mössbauer spectroscopy; it decays by electron capture to give an excited-state ^{57}Fe nucleus, which emits a 14.4-keV γ-ray on relaxing to the ground state.

Table 4 Isotopes of cobalt

Mass number	Half-life	Primary decay mode
49	<35 ns	Unknown
50	44 ms	Electron capture
51	>200 ns	Electron capture
52	0.115 s	Electron capture
53	0.240 s	Electron capture
53m	0.247 s	Electron capture
54	0.19323 s	Electron capture
54m	1.48 min	Electron capture
55	17.53 h	Electron capture
56	77.233 days	Electron capture
57	271.74 days	Electron capture
58	70.86 days	Electron capture
58m	9.04 h	Isomeric transition
59	Stable	
60	1925.3 days	β^-
60m	10.467 min	Isomeric transition
61	1.650 h	β^-
62	1.50 min	β^-
62m	13.91 min	β^-
63	27.4 s	β^-
64	0.30 s	β^-
65	1.20 s	β^-
66	0.233 s	β^-
67	0.42 s	β^-
68	0.199 s	β^-
69	0.27 s	β^-
70	0.15 s	β^-
71	0.21 s	β^-
72	0.09 s	β^-
73	>150 ns	β^-
74	>150 ns	β^-
75	>150 ns	β^-

Table 5 ^{59}Co NMR data for some Co(III) complexes at 294 K[9]

Complex	δ_{iso} (ppm)	$\Delta\nu_{1/2}$ (Hz)
$K_3[Co(CN)_6]^a$	− 1	6.5
$[Co(NH_3)_6]Cl_3$	8076	126
$[Co(NH_3)_5(NO_2)]Cl_2$	7565	166
$[Co(acac)_3]$	12570	190
$[Co(sepulchrate)]Cl_3$	6931	244
trans-$[Co(NH_3)_4(NO_2)_2]NO_3$	7157	440
cis-$[Co(NH_3)_4(NO_2)_2]NO_3$	7227	434
fac-$[Co(CN)_3(NH_3)_3]$	3289	417
$[Co(NH_3)_5CO_3]NO_3 \cdot 1/2H_2O$	9053	1265
cis-$[Co(NH_3)_4CO_3]NO_3$	9662	1300
$[Co(NH_3)_5Cl]Cl_2$	8793	2021
Na[Co(edta)]	10 237	2641

^{a}Spectra were acquired in D_2O and are referenced to aqueous 1.0 M $K_3[Co(CN)_6]$.

2.5 Chemical Reactivity

Elemental cobalt is relatively unreactive in air at ambient temperature, although the finely divided metal is pyrophoric. Cobalt is oxidized on heating in the presence of oxygen to give

Co_3O_4, which then gives CoO at temperatures above 900 °C. CoO can also be formed directly by treatment of cobalt with steam at red heat. Simple Co(II) salts having the formula $CoX_2{\cdot}nH_2O$ may be prepared by treatment of the metal with the appropriate mineral acid, while the anhydrous salts $CoCl_2$, $CoBr_2$, and CoI_2 can be prepared by direct treatment of the metal with Cl_2, Br_2, or I_2 at elevated temperatures. Reaction of the metal with F_2 gives the Co(III) salt CoF_3. The metal is unreactive toward both H_2 (although ternary hydrides such as Mg_2CoH_5 do exist) and N_2, but combines with carbon, sulfur, phosphorus, arsenic, boron, and silicon on heating to form binary compounds (*see Binary Compounds*).

3 GENERAL CHEMISTRY

3.1 Overview and Aqueous Chemistry

Simple cobalt salts most commonly contain the metal in the +2 oxidation state. Higher oxidation state compounds, especially those containing the metal in the +4 and +5 oxidation state, are rare, and are usually stabilized by the presence of fluorine or oxygen atoms. Simple salts of Co(III) include CoF_3 and CoO(OH). The yellow hexafluorocobaltate(IV) anion has been reported in Cs_2CoF_6, obtained by fluorination of Cs_2CoCl_4 or $Cs_2Co(SO_4)_2$ at 300 °C.[10] Co(IV) is also present in red–brown Ba_2CoO_4, while both Na_3CoO_4 and K_3CoO_4 contain Co(V), seemingly the highest known oxidation state of cobalt. These high-valent compounds have attracted surprisingly little attention since the initial reports of their syntheses and they remain to be completely characterized. There are very few simple compounds containing cobalt in oxidation states lower than +2. The black–red mixed-valence Co(II,I) oxide $Rb_5Co_2O_4$ contains Co(I) in discrete linear $[O–Co–O]^{3-}$ units, similar to those found in the Co(I) oxides K_3CoO_2 and $Na_5[CoO_2]CO_3$,[11] while Co(I) is also found in the nitride Ba[CoN].

The range and distribution of oxidation states in cobalt complexes differ substantially from those found in simple binary and ternary cobalt compounds. Cobalt complexes containing the metal ion in all oxidation states from −1 to +5 are known, with Co(III) complexes being the most numerous. The lower oxidation states are dominated by organometallic complexes (*see* ***Coordination Numbers & Geometries***), although the coordination chemistry of Co(I) is being increasingly explored. Commercially available Co(II) species of the formula $CoX_2{\cdot}4H_2O$ or $CoX_2{\cdot}6H_2O$ generally serve as starting materials for the synthesis of most cobalt coordination complexes, while treatment of commercially available $CoCO_3{\cdot}xH_2O$ with the appropriate acid allows the synthesis of Co(II) salts of most anions. Dissolution of these Co(II) salts in aqueous solution yields the octahedral hexaaquacobalt(II) ion $[Co(OH_2)_6]^{2+}$, which is pale pink in color ($\lambda_{max} \sim 510$ nm). Such solutions are stable to aerial oxidation, and are feebly acidic owing to the equilibrium shown in equation (1) (*see Acidity Constants*).

$$[Co(H_2O)_6]^{2+} + H_2O \rightleftharpoons [Co(H_2O)_5(OH)]^{+} + H_3O^{+} \qquad (1)$$

Increasing the pH of solutions of $[Co(OH_2)_6]^{2+}$ leads to the precipitation of amphoteric $Co(OH)_2$ at around pH 11. This exists in two forms, pink and blue, and redissolves on addition of further base to give blue solutions containing the tetrahedral species $[Co(OH)_3(OH_2)]^{-}$ and $[Co(OH)_4]^{2-}$.[12] The blue ($\lambda_{max} = 605$ nm, 401 nm) hexaaquacobalt(III) ion $[Co(OH_2)_6]^{3+}$, by contrast, is highly oxidizing and can only be obtained in strongly acidic solution. The cation is usually prepared by electrochemical oxidation of acidic ($HClO_4$, HNO_3, or H_2SO_4, $[H_3O^+] \geq 4$ M) solutions of $[Co(OH_2)_6]^{2+}$ at 0 °C using a Pt electrode. The high reactivity of $[Co(OH_2)_6]^{3+}$ makes the study of its solution chemistry difficult. While $[Co(OH_2)_6]^{3+}$ is undoubtedly more acidic than $[Co(OH_2)_6]^{2+}$, its exact pK_a is uncertain, with estimates ranging from 0.66 to >2.3. Kinetic studies of the oxidation of a number of organic and inorganic substrates by solutions of $[Co(OH_2)_6]^{3+}$ have shown that $[Co(OH_2)_5OH]^{2+}$ is significantly more reactive than the hexaaqua species in such reactions.

Standard reduction potentials ($E°$) for a variety of Co(III) complexes are given in Table 6, and these data clearly show the enormous stabilization of the +3 oxidation state relative to the +2 as the ligands are changed from O- to N-donors. Thus, while $[Co(OH_2)_6]^{3+}$ is strongly oxidizing ($E° = 1.83$ V), $[Co(NH_3)_6]^{3+}$ is stable to reduction in aqueous solution ($E° = 0.11$ V). Co(III) complexes containing am(m)ine ligands (*see* ***Ammonia & N-donor Ligands***) are also unusual amongst the first-row transition metal ions in that they are comparatively inert to ligand exchange and display an enormous range of rates for such reactions, as shown in Table 7 (*see Ligand Substitution*); for example, $[Co(NH_3)_5OClO_3]^{2+}$ has a half-life in 1.0 M $HClO_4$ of ~7 s, while the half-life for hydrolysis of $[Co(NH_3)_6]^{3+}$ in aqueous solution at pH 1 is of the order of 3800 years. Of the first-row transition metals, only complexes of Cr(III) display comparable (although somewhat more rapid) rates of ligand exchange. This combination of favorable thermodynamic and kinetic factors allows for facile synthesis of Co(III) am(m)ine complexes and the number of such complexes is legion. The first synthesis of a Co(III)

Table 6 Standard reduction potentials (vs SHE) for some Co(III) complexes

Couple	E° (V)
$[Co(H_2O)_6]^{3+} + e^- \rightarrow [Co(H_2O)_6]^{2+}$	1.83
$[Co(C_2O_4)_3]^{3-} + e^- \rightarrow [Co(C_2O_4)_3]^{4-}$	0.57
$[Co(edta)]^{-} + e^- \rightarrow [Co(edta)]^{2-}$	0.37
$[Co(bipy)_3]^{3+} + e^- \rightarrow [Co(bipy)_3]^{2+}$	0.31
$[Co(en)_3]^{3+} + e^- \rightarrow [Co(en)_3]^{2+}$	0.18
$[Co(NH_3)_6]^{3+} + e^- \rightarrow [Co(NH_3)_6]^{2+}$	0.11

Table 7 Rate data for hydrolysis of some Co(III) complexes[13]

Complex	k (s^{-1})
$[Co(NH_3)_5OClO_3]^{2+}$	1.0×10^{-1}
$[Co(NH_3)_5OC(CH_3)_2]^{2+}$	4.1×10^{-2}
$[Co(NH_3)_5O_2SC_4H_8]^{3+}$	3.1×10^{-2}
$[Co(NH_3)_5OSO_2CF_3]^{2+}$	2.6×10^{-2}
$[Co(NH_3)_5OSO_3F]^{2+}$	2.2×10^{-2}
$[Co(NH_3)_5OHCH(CH_3)_2]^{3+}$	3.5×10^{-4}
$[Co(NH_3)_5OP(OCH_3)_3]^{3+}$	2.5×10^{-4}
$[Co(NH_3)_5OSO_2CH_3]^{2+}$	2.0×10^{-4}
$[Co(NH_3)_5OS(CH_3)_2]^{3+}$	2.2×10^{-5}
$[Co(NH_3)_5OH_2]^{3+}$	5.9×10^{-6}
$[Co(NH_3)_5O_2CCH_3]^{2+}$	2.7×10^{-8}
$[Co(NH_3)_6]^{3+}$	5.8×10^{-12}

complex is generally attributed to B.M. Tassaert who, in 1798, observed that aqueous mixtures containing cobalt(II) chloride and ammonia underwent slow oxidation in air to give brown solutions, and this principle is still used today in the synthesis of Co(III) am(m)ine complexes. Synthesis of such complexes is usually achieved by air oxidation of an aqueous solution containing a Co(II) salt and either ammonia or an amine, while other commonly used oxidants include H_2O_2 and PbO_2. The Co(III) species $Co(acac)_3$, $Na_3[Co(NO_2)_6]$, and $Na_3[Co(O_2CO)_3]\cdot 3H_2O$ have also found use in the synthesis of Co(III) complexes; although formally kinetically inert to ligand substitution, all contain ligands that are acid labile (*see Labile*) and treatment with a protonated amine can give the Co(III) amine complex directly. While the synthesis of Co(II) complexes generally involves simple mixing of the ligand and a suitable Co(II) salt, the synthesis of Co(II) am(m)ine complexes must usually be carried out under an inert atmosphere, so as to preclude facile oxidation to Co(III).

Complexes of Co(III) are probably the most studied of any transition metal, and an extensive literature pertaining to their synthesis, structure, reactivity, and reaction kinetics exists.

3.2 Preparative Methods

A selection of articles detailing synthetic methods used for the preparation of cobalt compounds and complexes and a list of useful starting materials for such syntheses are available.[14]

3.3 Structures

The Cambridge Structural Database[15] contains X-ray crystallographic data for all reported compounds and complexes of cobalt that contain carbon (*see X-ray Crystallography*). The November 2002 version of this database lists 10 403 structures containing cobalt, with the earliest, the Co(II) complex of the phthalocyaninate dianion, dating back to 1936.[16] The Inorganic Crystal Structure Database[17] contains structural data for cobalt compounds not containing C–C or C–H bonds, and lists 2569 structures containing cobalt. Notably, several structural determinations of $[Co(NH_3)_6]^{3+}$ salts dating from the 1920s are reported.

3.4 Stereochemistry, Spectra and Magnetism

Co(III) complexes usually have a d^6 low-spin electronic configuration, and are almost exclusively six-coordinate, with octahedral (*see Octahedral*) or distorted octahedral geometries. Examples of high-spin six-coordinate Co(III) complexes are rare, and of necessity involve very weak field ligands. Examples include $[CoF_6]^{3-}$ and $[CoF_3(H_2O)_3]$. Although uncommon, square-planar (*see Square Planar*) Co(III) can be stabilized through judicious choice of ligand and complexes such as (**1**) and (**2**), which contain deprotonated amide ligands (*see Amide (Amido) Complexes*) crystallize from solution showing no close axial contacts.[18,19] The four-coordinate Co(III) complex (**3**) shows a significant distortion toward tetrahedral (*see Tetrahedral*) geometry, with a twist angle between the troponiminate rings of 41°.[20]

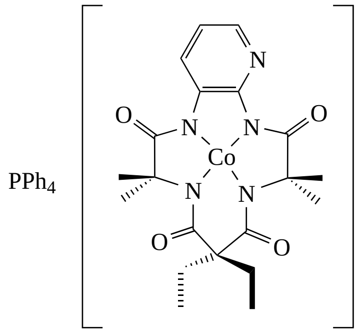

(**1**)

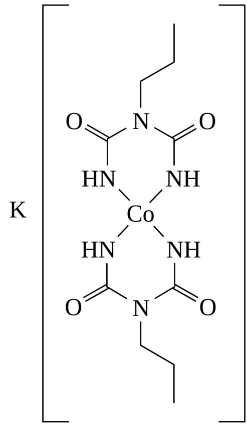

(**2**)

A number of five-coordinate Co(III) complexes have also been crystallographically characterized, with the corrole complex (**4**)[21] and the thiolate complex (**5**)[22] providing

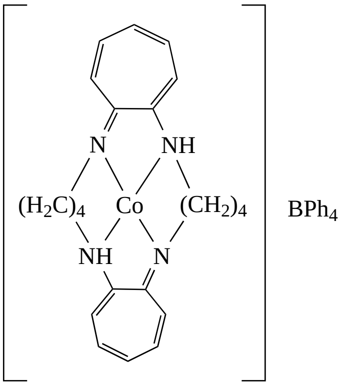

(**3**)

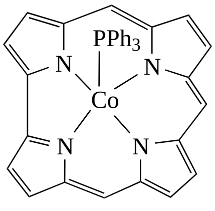

(**4**)

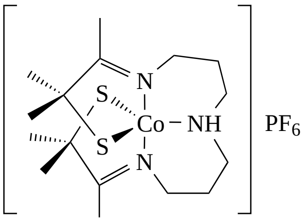

(**5**)

examples of these. Seven-coordinate Co(III) occurs in $[Co(H_2O)(Hedta)]\cdot 2H_2O$,**[23]** while the small size of the Co^{3+} ion appears to preclude the formation of any higher coordinate complexes. Three-coordinate Co(III) complexes have also been reported.**[24]**

The low-spin (*see High-spin & Low-spin Compounds*) electronic configuration of typical octahedral Co(III) complexes results in a $t_{2g}{}^6e_g{}^0$ electronic configuration and a corresponding $^1A_{1g}$ ground state. Two spin-allowed transitions, $^1T_{1g} \leftarrow {}^1A_{1g}$ and $^1T_{2g} \leftarrow {}^1A_{1g}$, are usually observed in the visible region of the spectrum. Such transitions are responsible for the wide variety of colors exhibited by Co(III) complexes, which literally span the entire spectrum of visible colors from red $[Co(NH_3)_5NCO]^{2+}$ to violet *cis*-$[Co(en)_2Cl_2]^+$. In fact, Co(III) complexes were originally named according to their colors. Thus, golden yellow $[Co(NH_3)_6]Cl_3$, purple $[Co(NH_3)_5Cl]Cl$, and green *trans*-$[Co(NH_3)_4Cl_2]Cl$ were named luteocobaltic chloride, purpureocobaltic chloride, and praseocobaltic chloride respectively. Lower-symmetry Co(III) complexes exhibit different spectral characteristics. In particular, geometric isomers of the type *cis*- and *trans*-$[CoA_4B_2]^{n+}$ display very different visible spectra, owing to a pronounced splitting of the $^1T_{1g}$ state in the trans isomer, which is absent in the cis. The centrosymmetric trans isomer also displays less intense absorption bands, and assignments of cis and trans isomers can thus often be made on the basis of the UV/vis spectrum. The magnetic behavior of low-spin octahedral Co(III) complexes is not noteworthy, as they are formally diamagnetic (*see Diamagnetism*). However, such complexes can display temperature-independent paramagnetism (TIP) (*see Paramagnetism*) through mixing of the excited $^1T_{1g}$ state with the $^1A_{1g}$ ground state. Four- and five-coordinate Co(III) complexes are paramagnetic, generally displaying magnetic moments ranging from 3.1 to 3.6 BM.**[25,26]**

The Co(II) oxidation state is unique in that it is the only commonly occurring example of a d^7 electron configuration. Co(II) complexes are generally six- or four-coordinate, often high spin (*see High-spin & Low-spin Compounds*), and predominantly adopt distorted octahedral or tetrahedral geometries. Low-spin Co(II) complexes are rare, and generally contain strong-field ligands; $[Co(CN)_5]^{3-}$ is a notable example. Spin-crossover behavior has been observed in a number of Co(II) complexes, with $[Co(terpy)_2]X_2$ complexes ($X = ClO_4{}^-$, Cl^-, NCS^-, Br^-) for example, exhibiting anion-dependent magnetic moments ranging from 2.96 BM ($X = Br^-$) to 4.65 BM ($X = ClO_4{}^-$) at room temperature. Some square-planar Co(II) complexes containing phthalocyanine, porphyrin and macrocyclic (*see Macrocycle*) ligands are known, and examples of both square pyramidal (*see Square Pyramidal*) ($[Co(CN)_5]^{3-}$) and trigonal bipyramidal (*see Trigonal Prism*) ($[Co(Me_6tren)Br]^+$) geometries have been found in five-coordinate complexes. Octahedral and tetrahedral Co(II) complexes are often in equilibrium, and the interconversion between octahedral pink $[Co(OH_2)_6]^{2+}$ and tetrahedral blue $[CoCl_4]^{2-}$ (equation 2) is the basis of both the well-known children's 'weather forecasting' toy that turns pink in humid conditions and blue on dry days, and the blue to pink color change in self-indicating silica gel drying agents.

$$[Co(H_2O)_6]^{2+} + 4Cl^- \longrightarrow [CoCl_4]^{2-} + 6H_2O \qquad (2)$$

Seven-coordinate Co(II) complexes are known,**[27–29]** and eight-coordinate Co(II) is found in both $(Ph_4As)_2[Co(O_2NO)_4]$**[30]** and the diazapyridinophane complex $[CoL_2]BPh_4\cdot Et_2O$ (L = (**6**)).**[31]** The three-coordinate β-diketiminate complexes (**7**) and (**8**) are also known.**[32,33]**

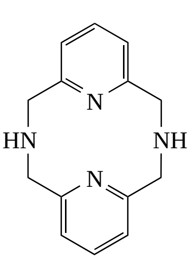

(**6**)

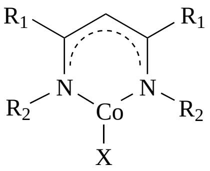

(**7**) R_1 = *t*-Bu, R_2 = 2,6-diisopropylbenzene, X = Cl

(**8**) R_1 = Me, R_2 = 2,6-diisopropylbenzene, X = $N(SiMe_3)_2$

More tetrahedral complexes of Co(II) are known than for any other transition metal ion, because, at least in part, of the fact that the crystal field stabilization energy (*see Crystal Field Stabilization Energy*) difference between the octahedral and tetrahedral geometries is small for a high-spin d^7 electron configuration. The polarizibility (*see Polarizability*) of the ligand also appears to be important in determining the stereochemistry of the complex; complexes of ligands containing soft donor atoms (P, S, As, aromatic N) are often tetrahedral, while O- and amine N-donor ligands usually give octahedral complexes. Octahedral high-spin Co(II) complexes have a $t_{2g}{}^5$ $e_g{}^2$ electronic configuration and a corresponding $^4T_{1g}$ ground state. They are often pink to violet in color and show absorbance maxima around 500 nm, owing to the transition $^4T_{1g}(P) \leftarrow {}^4T_{1g}$ (F). The lower-energy transitions $^4A_{2g}(F) \leftarrow {}^4T_{1g}$ (F) and $^4T_{2g}(F) \leftarrow {}^4T_{1g}$ (F) can also be observed, the former as a shoulder on the main visible band and the latter in the near infrared. Tetrahedral high-spin Co(II) complexes ($e^4t_2^3$) have a $^4A_2$ ground state and their usual intense blue color results from the transition $^4T_1(P) \leftarrow {}^4A_2(F)$. Two lower-energy transitions, $^4T_1(F) \leftarrow {}^4A_2(F)$ and $^4T_2(F) \leftarrow {}^4A_2(F)$, occur in the infrared. The magnetic behavior of Co(II) complexes has been extensively studied. Monomeric high-spin octahedral complexes have orbital contributions to their magnetic moment, owing to the T ground term, with values between 4.8 and 5.2 BM typically observed at room temperature. Tetrahedral complexes have magnetic moments in the range 4.4–4.8 BM, with a TIP component arising from mixing of the $^4T_2(F)$ level into the $^4A_2$ ground state.

3.5 Analysis

Many methods for the qualitative and quantitative analysis of cobalt have been reported. The classic qualitative test for Co(II) salts in solution involves formation of the blue $[Co(SCN)_4]^{2-}$ complex anion by addition of NH_4SCN to the neutral or mildly acidic test solution (the Vogel reaction). Shaking the resulting solution with a small volume of amyl alcohol results in a blue coloration of the organic (top) layer. Interference from Fe(III) can be avoided by prior addition of fluoride to give colorless $FeF_6{}^{3-}$, or reduction to Fe(II) with ascorbic acid. Addition of ammonium sulfide to a neutral or alkaline solution containing Co(II) ions gives a black precipitate of CoS, which is insoluble in dilute HCl and dilute acetic acid. Co(II) salts also give a yellow–brown precipitate with rubeanic acid and a deep red coloration with nitroso-R-salt reagent. Quantitative gravimetric tests for cobalt include precipitation with α-nitroso-β-napthol reagent and subsequent conversion to elemental cobalt, and precipitation of blue $Co[Hg(SCN)_4]$ following addition of $HgCl_2$ and NH_4NCS to a neutral solution containing the Co(II) salt. Potentiometric titrations with edta or cyanide can also be used for analysis of Co(II).

4 SALTS AND OTHER SIMPLE COMPOUNDS

4.1 Oxides, Hydroxides, Oxyanions, Sulfides

Only two pure oxides have been characterized unequivocally. CoO can be prepared from the metal as described in Section 2.5, and also by heating Co(II) salts (hydroxide, carbonate, nitrate) in the absence of air. CoO is antiferromagnetic (*see Antiferromagnetism*), with a Néel Point of ~290 K, and above this temperature exhibits a NaCl-type structure (space group $Fm3m$). Synchrotron powder diffraction studies have, however, shown that CoO has a monoclinic structure (space group $C2/m$) below the Neel point.**[34]** The mixed valent oxide Co_3O_4 ($Co^{II}Co_2{}^{III}O_4$) has a spinel-type structure, with the Co(II) ions occupying tetrahedral sites and the Co(III) ions occupying octahedral sites. Both Co_2O_3 and CoO_2 have been reported, but their purity is doubtful. Cobalt(II) hydroxide, $Co(OH)_2$, can be prepared as described in Section 3.1. The hydroxide is usually pink (octahedral) but a blue tetrahedral form can be obtained by slow precipitation at temperatures below 0 °C. $Co(OH)_3$ has been reported, but appears to be poorly characterized. Oxidation of $Co(OH)_2$ gives the dark brown Co(III) oxide hydroxide CoO(OH). Cobalt forms a number of ternary oxo compounds, although those containing Co(IV) and Co(V) remain to be fully characterized. Impure Na_3CoO_4 can be prepared by heating Co_3O_4 with Na_2O at 450 °C under 100 atm pressure of O_2, while K_3CoO_4 has been reported from the reaction of the nonstoichiometric oxides $KO_{1.7}$ and $CoO_{\sim 1.5}$ at 460 to 550° in an O_2 atmosphere (0.5–1 atm.) for 6 to 23 h. Ba_2CoO_4 is prepared from a mixture of $Ba(OH)_2$ and $Co(OH)_2$ at 1150 °C. Other known oxo species include $Na_5[CoO_2]CO_3$, $Rb_2Co_2O_3$, $LaCoO_3$, $LiCoO_2$, K_2CoO_2, and $Na_{10}Co_4O_9$. Of the numerous cobalt sulfides reported, CoS_2 (pyrite structure), Co_3S_4 (spinel structure), cobalt-deficient $Co_{1-x}S$ (NiAs structure), and Co_9S_8 have been well characterized, while laser ablation of cobalt sulfide yields 83 gaseous ions ranging from $CoS_2{}^-$ to $Co_{38}S_{24}{}^-$.**[35]**

4.2 Halides

The only known halides containing Co(III) and Co(IV) are the fluorides. CoF_4 is formed in low yield in the gas phase by the reaction of CoF_3 with TbF_4 over the temperature range 620 to 720 K,[36] while brown CoF_3 can be prepared by treatment of $CoCl_2$ with F_2 at 250 °C or from the reaction of elemental cobalt with ClF_3. The crystal structure of CoF_3 (space group $R\bar{3}c$) shows corner-sharing CoF_6 octahedra in which each cobalt ion is equidistant from six fluoride ions.[37] The anhydrous dihalides $CoCl_2$ and $CoBr_2$ can be prepared by reaction of the elements, while CoF_2 is prepared from the reaction of either CoO or $CoCl_2$ with HF, and CoI_2 results from the action of HI on the metal. The dihalides adopt the rutile (CoF_2), $CdCl_2$ ($CoCl_2$), and CdI_2 ($CoBr_2$, CoI_2) structures, in which the metal ions have a coordination number of 6 in all cases. The hydrated versions of the dihalides are well known, and are used extensively as starting materials for the synthesis of cobalt complexes. CoF and CoCl have been identified in the gas phase, and the latter can be stabilized in water clusters for several seconds under ultrahigh vacuum.[38] No authenticated examples of cobalt oxohalides have been reported.

5 COORDINATION COMPLEXES

5.1 Low Oxidation States: Co^{-I}, Co^0, Co^I

The low oxidation state chemistry of cobalt is dominated by organometallic complexes containing C-donor ligands (*see* ***Coordination Numbers & Geometries***), and ‘classical’ coordination complexes containing cobalt in oxidation states lower than +2 are comparatively rare. Despite this, the Co(I) oxidation state is important in vitamin B_{12} chemistry, where the blue–green vitamin B_{12s} contains five-coordinate Co(I) in a square pyramidal N_5 coordination environment. Extensive studies of this and a wide variety of Schiff-base (*see Schiff Base*), macrocyclic, and porphyrin model compounds have shown that these Co(I) species behave as ‘supernucleophiles’; they undergo facile alkylation by oxidative addition (*see Oxidative Addition*) to give Co(III) alkyl compounds, and can liberate H_2 from water. Details of this chemistry are outlined elsewhere in this volume (*see* ***Cobalt: Organometallic Chemistry***). Co(I) has a d^8 electron configuration and its complexes might be expected to favor a square-planar geometry, as found for complexes of the isoelectronic metal ions Ni^{2+}, Pd^{2+}, and Pt^{2+}. In practice, however, a variety of stereochemistries are found for Co(I) complexes, and five-coordinate geometries appear to be favored, as these lead to a formal 18-electron count (*see Eighteen Electron Compounds*). The Co(I) ion appears to be appreciably softer than its more highly charged congeners, preferring aromatic N-donor ligands over aliphatic, and there is an extensive chemistry of Co(I) with phosphorus donor ligands. Nearly all complexes of Co(I) are unstable with respect to oxidation in air, and must therefore be prepared and handled under an inert atmosphere.

5.1.1 Aliphatic Amine Ligands

In contrast to the higher oxidation states, the chemistry of Co(I) with aliphatic amine ligands is virtually nonexistent. Simple homoleptic (*see Homoleptic Compound*) Co(I) complexes of ligands such as ammonia or ethylenediamine are unknown, and Co(I) complexes of saturated N-containing macrocycles appear to be very unstable. A rare example of a Co(I) complex containing only nonaromatic N-donor ligands is found in the square-planar complex $(AsPh_4)[Co(s\text{-}disn)_2]$ (**9**). The unusually short Co–N bonds (1.831(2) Å) in this complex are thought to result from extensive charge delocalization over the entire molecule.[39]

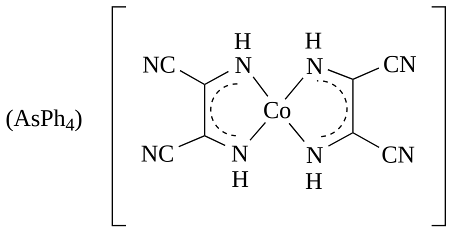

(**9**)

5.1.2 Aromatic Amine Ligands

The dark blue Co(I) complex $[Co(bipy)_3](ClO_4)$ can be prepared by reduction of $[Co(bipy)_3](ClO_4)_3{\cdot}3H_2O$ by $NaBH_4$ in aqueous ethanol under an inert atmosphere. It is stable in ethanol solution in the absence of oxygen. The analogous dark brown 1,10-phenanthroline complex can be prepared in a similar fashion from $[Co(phen)_3](ClO_4)_2$. The crystal structure of $[Co(bipy)_3]Cl{\cdot}H_2O$ shows the Co(I) ion in a distorted octahedral environment with an average Co–N distance of 2.115 Å. This compares with values of 2.130 and 1.932 Å in the analogous Co(II) and Co(III) complexes $[Co(bipy)_3]Cl_2{\cdot}2H_2O{\cdot}EtOH$ and $[Co(bipy)_3][Fe(CN)_6]{\cdot}8H_2O$ respectively. The $[Co(bipy)_3]^+$ ion is an excellent reducing agent, and can reduce water to H_2, CO_2 to CO, and phenylacetylene to styrene. $E°$ values (*see Redox Potential*) for the $[Co(bipy)_3]^{2+}/[Co(bipy)_3]^+$ couple ranging from −0.95 to −1.37 V versus SCE have been reported. The Co(0) species $[Co(bipy)_3]$ is known, and electrochemical evidence for the formation of $[Co(bipy)_3]^-$ by the two-electron reduction of $[Co(bipy)_3]^+$ in DMF has been obtained, but a solid compound has not been isolated. The $E°$ value for this $[Co(bipy)_3]^+/[Co(bipy)_3]^-$ couple has been estimated as −1.94 V versus SCE. The four-coordinate species $[Co(bipy)_2]$ and $[Co(bipy)_2]^+$ are both known, as is the homoleptic pyridine species $[Co(py)_6]BPh_4$. This latter compound was the first example of a Co(I) compound containing a monodentate N-donor ligand, and was originally synthesized from an organometallic Co(I) complex by dissolution in pyridine. However, a more convenient synthesis involves photoreduction of a pyridine solution of $[Co(py)_6](BPh_4)_2$.[40] Pyridine-containing tripodal ligands (*see Tripodal Ligand*) can also stabilize the Co(I) oxidation state. Thus, the approximately octahedral complex $[CoL_2]Br{\cdot}H_2O$ (L = tris(2-pyridyl)methane) can be synthesized using preparative electrochemical reduction of $[CoL_2]Br_2$ in dry ethanol/acetonitrile under argon. X-ray crystallographic analysis shows an average Co–N bond length of 2.111 Å in the Co(I) cation, approximately equal to that found in the $[CoL_2]^{2+}$ cation (2.109 Å) and significantly longer than in the Co(III) cation (1.95 Å).[41]

5.1.3 Macrocyclic, Schiff-base, and Porphyrin Ligands

Macrocyclic square-planar complexes containing Co(I) have been extensively studied as catalysts for the photo- and electrocatalytic reduction of water and carbon dioxide. Studies of the Co(I) complexes of a number of cyclam derivatives have shown that the equilibrium constants for CO_2 binding increase as the Co(II)/(I) redox potential becomes more negative, with binding constants up to $\sim 10^6\ M^{-1}$ measured. Steric factors are also important in determining the magnitude of the binding constant.[42] Co(I) complexes of the acyclic Schiff-base ligand salen and its derivatives also show a propensity to bind CO_2 in the presence of an alkali metal cation. X-ray structural data for the propyl salen derivative show that the CO_2 binds to the metal through the carbon atom, as shown in Figure 1, and the oxygen atoms interact with the alkali metal cation.

Some Co(I) macrocyclic complexes have been implicated in C–H activation reactions. The observation of N–H exchange with solvent CD_3CN in solutions of Co(I) cyclam derivatives has been interpreted as evidence for C–H activation by a mechanism involving oxidative addition of CD_3CN to the Co(I) center.[43] Co(I) Schiff-base complexes have been proposed to be important intermediates in ethene polymerization. Treatment of Co(II) complexes containing 2,6-bis(imino)pyridyl ligands with MAO leads to highly active catalysts for the polymerization of ethene, and square-planar Co(I) complexes are thought to be involved in the polymerization reaction.[44,45] The Schiff-base ligands used are noninnocent, but a detailed study has shown that reduction of the Co(II) bis-ligand complex leads to an authentic Co(I) complex, rather than a ligand radical species.[46] Co(I) complexes of porphyrin and porphyrin-derived ligands are well known, and can be prepared by chemical and electrochemical reduction of the Co(II) or Co(III) porphyrin species. The complexes are low spin and show no evidence of axial ligand coordination in the solid state.

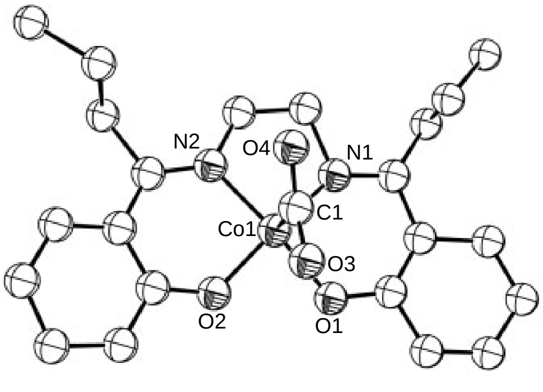

Figure 1 X-ray structure showing the coordination sphere of the Co(I) ion in $[Co(n\text{-}Pr\text{-salen})(CO_2)K(THF)]n$

5.1.4 Phosphorus Ligands

The majority of nonorganometallic Co(I) complexes contain P-donor ligands, presumably because of the π-acceptor (*see π-Acid Ligand*) character of such ligands. Reaction of $[(PP_3)CoH]$ with $MeOSO_2CF_3$ in THF under N_2 gives uncharacterized solution species, which then react with added elemental phosphorus (P_4) to give the trigonal bipyramidal $[(PP_3)M(\eta^1\text{-}P_4)]^+$ cation (**10**), in which the tetrahedral P_4 molecule is bound end-on to the metal ion. This complex decomposes above −40 °C.[47]

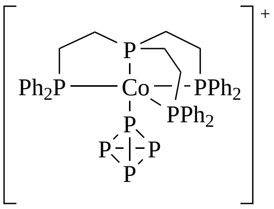

(**10**)

Several complexes containing the *cyclo*-P_3 unit as a ligand are also known. The diamagnetic, air-stable parent complex $[Co(triphos)P_3]$ can be prepared by reaction of $Co(BF_4)_2{\cdot}6H_2O$ with an equimolar amount of the triphos ligand and excess white phosphorus at 50 °C under an inert atmosphere. The *cyclo*-P_3 unit in this complex is appreciably nucleophilic and may be protonated and alkylated. It can also coordinate to other metal ions in a variety of ways; the symmetrical dimer $[\{Co(triphos)\}_2\mu(\eta^3\text{-}P_3)](BPh_4)_2$ and analogous mixed Co/Fe, Co/Ni, and Co/Rh dimers contain a bridging η^3P_3 unit (*see Hapticity*), while both η^2 and η^1 bridging modes are also known. $[Co(triphos)P_2S]$ and $[Co(triphos)P_2Se]$ can be prepared using the above synthetic method with P_4S_3 or P_4Se_3 in place of white phosphorus, and the P_2S unit can also bridge in an η^2 fashion to other metal ions.

A number of simple four-coordinate Co(I) species containing monodentate phosphine ligands are known. Complexes such as $[Co(PPh_3)_3X]$ (X = Cl, Br, I) were first prepared by reduction (electrochemical, $NaBH_4$, or powdered Zn) of an ethanol solution containing a Co(II) salt and a monodentate arylphosphine ligand.[48] Subsequent work extended the series of complexes to include alkylphosphine ligands.[49] The complexes are paramagnetic, implying an unusual tetrahedral, rather than square-planar, geometry about the d^8 metal ion, and this has been confirmed by X-ray structural analysis of compounds such as $[Co(PMe_3)_4](BF_4)$, $[Co(PMe_3)_3Cl]$, $[Co(PMe_3)_3I]$, $[Co(PPh_3)_3OSiMe_3]$, $[Co(PPh_3)_3OPh]$, and $[Co(PPh_3)_3Cl]$. The 17-electron Co(0) species $[Co(PPh_3)_4]$ and $[Co(PMe_3)_4]$ can be prepared by reduction of anhydrous $CoCl_2$ with sodium amalgam or magnesium in the presence of the appropriate phosphine. These complexes have a distorted tetrahedral structure and are excellent nucleophiles, undergoing a variety of oxidative addition and dimerization reactions. The dark brown $[Co(PMe_3)_4]$ has found use in polypeptide synthesis, as an initiator for polymerization of $\alpha-$amino acid$-$N-carboxyanhydrides[50] and can also mediate aldol-type reactions.[51] Low-temperature reduction of $[Co(PMe_3)_4]$ by alkali metals leads to the powerfully reducing Co(−I) species $[Co(PMe_3)_4]^-$; its reduction potential of $\geq -2.5\,V$ makes this one of the strongest reducing agents known. Dinitrogen complexes (*see Dinitrogen & Dinitrogen Complexes*) of Co(−I) containing monodentate phosphine ligands can also be prepared. $K[Co(PMe_3)_3N_2]$ is formed spontaneously from a THF or Et_2O solution of $K[Co(PMe_3)_3L]$ (L = propene, cyclopentene) under 1 bar pressure of N_2, and this propensity to bind nitrogen often necessitates the use of Ar as an inert atmosphere for the study of low-valent Co-phosphine complexes. The X-ray crystal structure of $K[Co(PMe_3)_3N_2]$ shows a tetrahedral ligand geometry around the d^{10} metal ion.

The behavior of the monodentate phosphine complexes is mirrored in those containing multidentate phosphine ligands, and Co(I), Co(0) and Co(−I) species containing such ligands are all known. Thus, $[Co(dppe)_2]BF_4$ can be prepared by Zn reduction of the Co(II) species $[Co(dppe)_2CH_3CN](BF_4)_2$, while the hydride complex $[Co(dppe)_2H]$ is obtained if $NaBH_4$ is used as the reductant.[52] In contrast to the homoleptic monodentate phosphine compounds however, $[Co(dppe)_2]X$ complexes ($X = ClO_4$, BF_4) are diamagnetic, and hence square planar, both in solution and in the solid state. The paramagnetic Co(0) complex $[Co(dppe)_2]$ can be prepared by Na reduction of $[Co(dppe)_2Br_2]$ and the deep red Co(−I) complex $[K(18\text{-crown-}6)(THF)_2][K(18\text{-crown-}6)][Co(dppe)_2]_2$ has been isolated from the reaction of $[Co(\eta^4\text{-anthracene})_2]^-$ with dppe in THF. X-ray structural analysis shows a slightly distorted tetrahedral geometry around the metal ion, with average Co–P bond lengths of 2.109 Å (Figure 2).

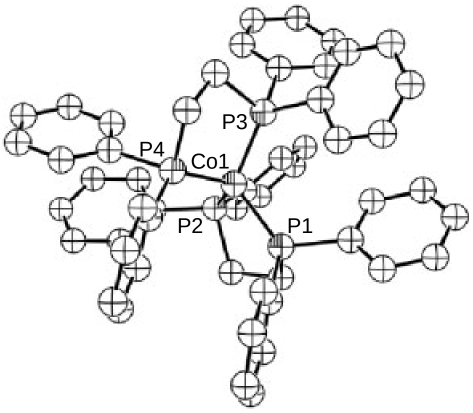

Figure 2 Diagram of the anion of $[K(18\text{-crown-}6)(THF)_2][K(18\text{-crown-}6)][Co(dppe)_2]_2$

Five-coordinate complexes of Co(I) are relatively common, and this can be rationalized on the basis of the 18-electron rule, which is satisfied by this coordination number for the d^8 metal center. Hence, tetrahedral Co(I) phosphine complexes tend to react readily with an additional ligand to give five-coordinate species, with addition of hydride and carbon monoxide ligands being particularly common. Mention must also be made of the planar Co(I) phosphine complex $[Co(2{=}phos)_2]BF_4$, which reacts irreversibly with dioxygen to give the mononuclear pseudo trigonal bipyramidal peroxo complex (*see Peroxo Complexes*) $[Co(O_2)(2{=}phos)_2]BF_4\cdot 2C_6H_6$ (**11**).[53]

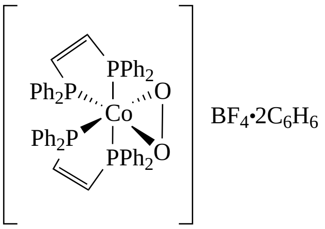

(**11**)

Five-coordinate metal centers are commonly found in complexes containing tripodal phosphine ligands. Thus, the ligand PP_3 enforces a trigonal bipyramidal geometry in the dark green halide complexes $[Co(PP_3)Cl]$, $[Co(PP_3)Br]$, and $[Co(PP_3)I]$, and red $[Co(PP_3)NCS]$. These are low spin and are prepared by $NaBH_4$ reduction of a $CH_2Cl_2/EtOH$ solution of the appropriate Co(II) salt and the ligand at room temperature. The halides can be displaced by other P-donor ligands and complexes such as $[Co(PP_3)\{P(OMe)_3\}]BF_4$, $[Co(PP_3)PEt_3]AsF_6$, and $[Co(PP_3)PPhMe_2]AsF_6$ can be prepared by this method. The five-coordinate hydride complex $[Co(PP_3)H]\cdot 0.5(CH_3)_2CO$ can be prepared by reduction of a mixture of $Co(BF_4)_2\cdot 6H_2O$ and PP_3 with excess $NaBH_4$ in EtOH/acetone, and a crystal structure shows a regular trigonal bipyramidal geometry about the Co(I) ion. The hydride ligand can be protonated with CF_3SO_3H in THF solution to yield the dihydrogen complex $[Co(PP_3)(H_2)]PF_6$, which is stable for days in the solid state, and also in solution under argon. This complex can also be prepared directly by treatment of $[Co(PP_3)H]$ with CF_3SO_3Me to generate the 16-electron fragment $[Co(PP_3)]^+$, which then reacts with $H_2(g)$. This fragment can also react with $N_2(g)$ to give the dinitrogen complex $[Co(PP_3)N_2]PF_6$. The mixed-donor tripodal ligand NP_3 also forms a diamagnetic trigonal bipyramidal hydride complex $[Co(NP_3)H]$. However, the $[Co(NP_3)X]$ complexes ($X = Cl$, Br, I, NCS) are paramagnetic, with magnetic moments corresponding to two unpaired electrons, and the crystal structure of $[Co(NP_3)Br]$ confirms hypodentate coordination of the tripodal ligand, with the tertiary nitrogen atom not coordinated to the cobalt ion (Figure 3). Co(I) thus adopts a tetrahedral geometry in these compounds, with the rearrangement to the five-coordinate species being symmetry-forbidden.

Phosphite ligands are also common in low-valent cobalt chemistry. Co(I), Co(0), and Co(−I) complexes containing these ligands are known, and this is nicely illustrated by the series of compounds $[Co\{P(OMe)_3\}_4]^+$, $[Co\{P(OMe)_3\}_4]$, and $[Co\{P(OMe)_3\}_4]^-$. The blue complex $[Co\{P(OMe)_3\}_4]PF_6$ is obtained from the propylene complex $[Co\{P(OMe)_3\}_4(C_3H_6)]PF_6$ in vacuum at room temperature. It is highly reactive, and forms $[Co\{P(OMe)_3\}_5]^+$ quantitatively on treatment with $P(OMe)_3$. Neutral $[Co\{P(OMe)_3\}_4]$ can be isolated from decomposition of a low-valent cobalt phosphite salt and exhibits an EPR spectrum (*see Electron Paramagnetic Resonance*) consistent with C_{3v} symmetry. The 'superreduced' complex $K[Co\{P(OMe)_3\}_4]$ was originally obtained as an insoluble material from the reaction of the hydride complex $[CoH\{P(OMe)_3\}_4]$ with KH. Treatment of the potassium salt with cryptand 222 (*see Cryptands & Cryptates*) gives the soluble species $[K\text{-}(222)][Co\{P(OMe)_3\}_4]$, the X-ray structural characterization of which shows a near-perfect tetrahedral geometry about the Co(−I) ion. The strongly reducing nature of this complex is evidenced by the reduction potential for the $[Co\{P(OMe)_3\}_4]/[Co\{P(OMe)_3\}_4]^-$ couple of −1.77 V versus Fc^+/Fc.**54** The influence of phosphite ligands in stabilizing the Co(I) oxidation state is illustrated by the fact that addition of trimethylphosphite to a solution of the Co(II) complex of the macrocyclic ligand (**12**) makes the Co(II)/(I) reduction potential less negative by 0.24 V. The dark green high-spin [Co(**12**){$P(OMe)_3$}] complex (Figure 4) was isolated following controlled potential electrolysis, and X-ray structural analysis confirmed an unusual pentagonal pyramidal structure.**55**

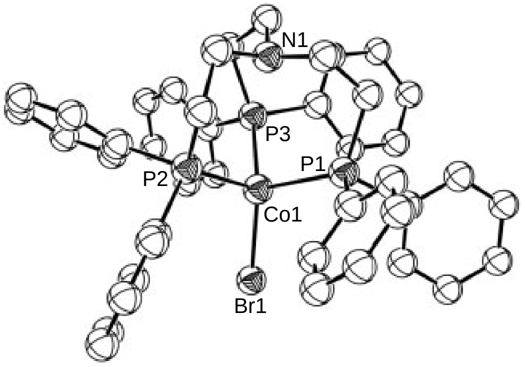

Figure 3 Structural diagram of $[Co(NP_3)Br]$ showing the noncoordinated tertiary N atom

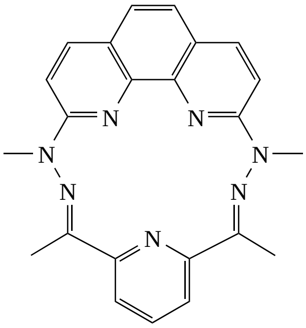

(**12**)

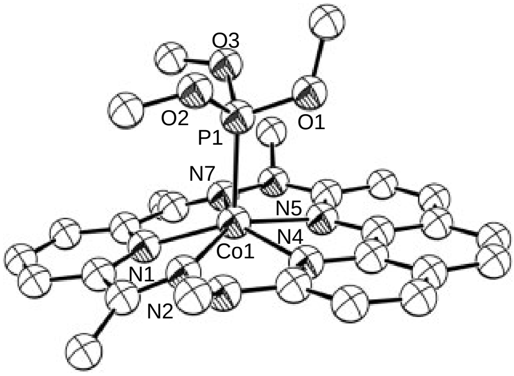

Figure 4 Structural diagram of [Co(**12**){$P(OMe)_3$}]

5.2 Co(II) Complexes

Complexes of Co(II) can be easily prepared by mixing solutions of a commercially available Co(II) salt with the appropriate ligand in a noncoordinating solvent. The complexes may be isolated by concentrating the mixture to effect crystallization, or, in the case of cationic and anionic complexes, addition of a suitable counterion to precipitate the product, and subsequent crystallization. Reactions can often be carried out in air without the need for an inert atmosphere, although such precautions are generally warranted in the syntheses of Co(II) amine complexes, which can often undergo facile air oxidation. Reactions of the Co(II) precursors with added ligand are generally rapid, owing to the lability of Co(II) complexes. Such lability is demonstrated by the rate of water exchange (*see Water Exchange*) in the $[Co(H_2O)_6]^{2+}$ ion, with rate constants for this process of the order of $3 \times 10^6\ s^{-1}$ having been measured using ultrasound absorption and ^{17}O NMR spectroscopy. Likewise, rate constants for the reaction of $[Co(OH_2)_6]^{2+}$ with various anionic and neutral ligands range from 10^4 to $10^8\ M^{-1}\ s^{-1}$, with those for the

Table 8 Rate data for the complexation reaction of $[Co(H_2O)_6]^{2+}$ with various ligands[12]

Ligand	k ($M^{-1}\ s^{-1}$)
$HP_2O_7{}^{3-}$	9.3×10^7
ATP^{4-}	9.2×10^7
$Hedta^{3-}$	4.0×10^6
H_2O	3.2×10^6
NH_3	9.5×10^5
Phen	1.2×10^5
Bipy	6.3×10^4

anionic ligands being larger (Table 8). A $\Delta V^{\ddagger}$ value (*see Activation Volume*) of $(+6.1 \pm 0.2)\ cm^3\ mol^{-1}$ obtained for the water exchange reaction is consistent with a dissociative mechanism for this process, and similar positive values have been obtained for other solvent exchange reactions in $[CoL_6]^{2+}$ complexes (L = MeOH, MeCN, DMF), as well as for the reaction of $[Co(OH_2)_6]^{2+}$ with a number of ligands, pointing to a common dissociative mechanism for substitution reactions at a Co(II) center. Octahedral (high-spin) and tetrahedral geometries predominate for Co(II) complexes, and in the case of such compounds as $[Co(Me_2SO)_6](CoCl_4)$ and $[Co(EtOH)_6](CoBr_4)$, both the geometries are found in a single species. Homoleptic octahedral high-spin Co(II) complexes often display tetragonal distortions, owing to the Jahn–Teller effect (*see Jahn–Teller Effect*), but these effects are usually nowhere near as pronounced as those found in Cu(II) complexes. For example, the axial and equatorial Co–O bond lengths in $[Co(OH_2)_6](p\text{-}CH_3C_6H_4SO_3)_2$ differ by only 0.024 to 0.028 Å, with an axial compression observed in this case.[56] A similar axial compression is seen in the $[Co(EtOH)_6]^{2+}$ cation of $CoCl_2{\cdot}2.5EtOH$ (actually $[Co(EtOH)_6][Cl_3CoClCo(EtOH)_4ClCoCl_3]$), with the axial Co–O bond lengths being 0.013 Å shorter than the equatorial.[57] However, the Jahn–Teller effect is not manifested in all high-spin octahedral Co(II) complexes. For example, all Co–O bond lengths in the homoleptic species $[Co(THF)_6](Co(THF)I_3)_2{\cdot}THF$ and $[Co(Me_2SO)_6](I_4)$ are identical.[58,59] The effect should theoretically be more pronounced in low-spin octahedral Co(II) complexes, but well-characterized examples of these are few. The phosphine complex $[Co(mmtp)_2]^{2+}$ (**13**)[60,61] displays rapid Co^{3+}/Co^{2+} electron self-exchange kinetics, consistent with a low-spin formulation for the Co(II) complex, while *trans*-$[Co(diphos)_2Cl_2]$[62] exhibits a magnetic moment of 1.97 BM. Neither complex has been structurally characterized.

A series of low-spin tris chelate complexes containing bidentate 2-(arylazo)pyridine derivatives has been prepared,[63] while X-ray structural characterization of the complex $[Co(dmvi)_2(phen)]{\cdot}2CHCl_3$ (**14**) showed a pronounced elongation of the Co–O bonds relative to the low-spin Fe(II) complex (2.17 vs 1.98 Å, respectively), consistent with an axial Jahn–Teller distortion.[64]

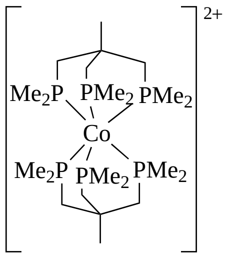

(**13**)

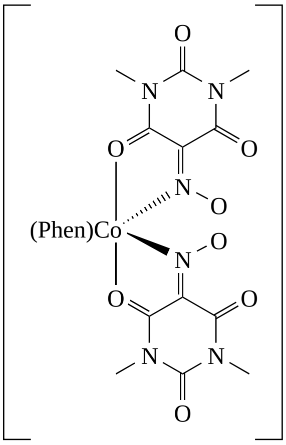

(**14**)

Surprisingly, the best-characterized examples of low-spin octahedral Co(II) are found in complexes containing thioether ligands. Purple $[Co(9S3)_2](BF_4)_2$ (Figure 5) has a magnetic moment of 1.71 BM, which is temperature independent down to 77 K, and its crystal structure shows two Co–S bonds to be substantially (0.12Å) shorter than the remaining four.[65] The opposite situation is seen in $[Co(9S3)_2](I_3)_2$, where an axial elongation results in two long (2.4088 Å) and four short (2.2742 and 2.2959 Å) bonds.[66] Macrocyclic $[Co(18S6)](picrate)_2$ (Figure 6) and acylic $[Co(ttn)_2](BF_4)_2$ (Figure 7) also show elongation of the axial bonds, magnetic moments of 1.81 and 1.78 BM respectively, and EPR behavior consistent with a d_{z^2} ground state. Significantly, these complexes are stable to air oxidation. They do, however, undergo reversible electrochemical oxidation, consistent with no change of spin state during the redox process.[67]

Tetrahedral complexes of Co(II) often contain ligands having soft donor atoms, while square-planar geometries are usually only found in complexes containing rigid multidentate ligands such as porphyrins and Schiff-base species, which contain a square-planar arrangement of donor atoms. Such complexes are often low spin. Polymeric Co(II) complexes are quite common in the solid state, especially complexes containing chloride and bromide ligands, through which bridging can occur. Thus, the complex $[Co(py)_2Cl_2]$ exists as a blue tetrahedral monomer, and as a violet octahedral polymer, with bridging chloride ligands (*see Bridging Ligand*).

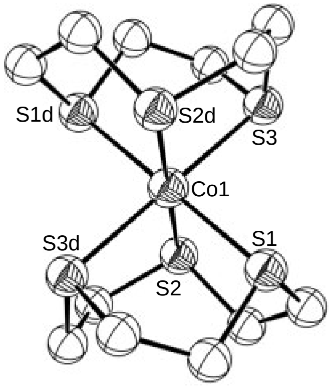

Figure 5 Structural diagram of the cation of $[Co(9S3)_2](BF_4)_2$

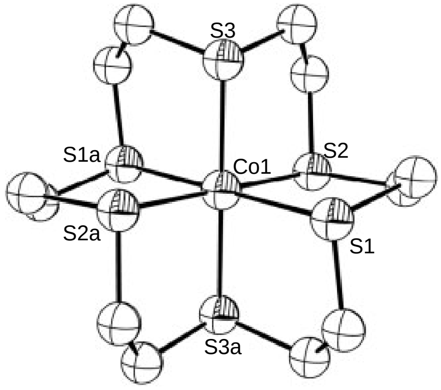

Figure 6 Structural diagram of the cation of $[Co(18S6)](picrate)_2$

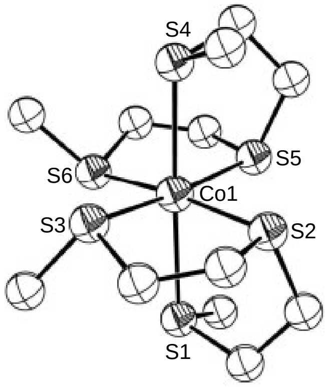

Figure 7 Structural diagram of the cation of $[Co(ttn)_2](BF_4)_2$

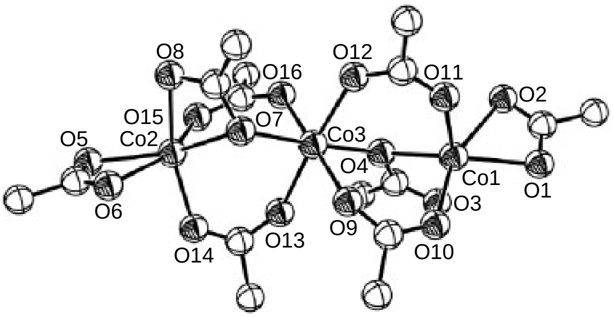

Figure 8 Structural diagram of the anion of $(NEt_4)_2[Co_3(O_2CCH_3)_8]$

5.2.1 *Carboxylate Ligands*

Given the propensity of carboxylate ligands to form polynuclear complexes, it is somewhat surprising that commercially available $Co(O_2CCH_3)_2{\cdot}4H_2O$ is monomeric. The structure consists of a six-coordinate, approximately octahedral, Co(II) ion coordinated to two trans monodentate acetate ligands and four equatorial waters, with extensive intramolecular and intermolecular hydrogen bonding (*see Hydrogen Bonding*).**[68,69]** Similar monomeric structures have been observed for a variety of $Co(O_2CR)_2{\cdot}4H_2O$ compounds. Slow crystallization of $Co(O_2CCH_3)_2{\cdot}4H_2O$ from acetic acid gives polymeric $Co(O_2CCH_3)_2{\cdot}2H_2O$, which contains two different types of bridging acetate ligands as well as a bridging water ligand, with a distorted octahedral geometry about the Co ions.**[70]** The unusual anion $[Co_3(O_2CCH_3)_8]^{3-}$, which contains a linear arrangement of three six-coordinate Co(II) ions and three different types of acetate coordination ($\mu_1\mu_2$, $\mu_1\eta_1$, and chelating) has also been structurally characterized in the salt $(NEt_4)_2[Co_3(O_2CCH_3)_8]$ (Figure 8).**[71]**

$Co(O_2CH)_2{\cdot}2H_2O$ is polymeric, with octahedral Co ions and monodentate bridging formate ions,**[72]** while polymeric anhydrous $Co(O_2CC_6H_5)_2$ contains both bridging and chelating benzoate ligands coordinated to octahedral Co(II) centers.**[73]** Discrete high-nuclearity complexes containing carboxylate ligands can be readily prepared, and complexes containing up to 13 Co(II) centers have been characterized.**[74]** $Co(O_2CCH_3){\cdot}4H_2O$ is used extensively as a catalyst in a number of industrial oxidations, most notably the synthesis of terephthalic acid from *p*-xylene in the presence of $Mn(O_2CCH_3){\cdot}4H_2O$ and HBr. Co(II) complexes such as cobalt oleate, cobalt ethylhexanoate, and cobalt linoleate, containing higher-molecular-weight carboxylate ligands, are used to accelerate drying in oil-based paints, varnishes, and inks.

5.2.2 *Heterocyclic Ligands*

Co(II) complexes containing polypyridyl ligands have attracted attention due to their unusual spin properties. Magnetic susceptibility measurements of a number of black and brown $[Co(terpy)_2]X_2$ complexes ($X = Cl^-$, Br^-, I^-, NO_3^-) over the temperature range 4.2 to 293 K show a decrease in magnetic moment from ∼3 to ∼1.9 BM as the temperature is lowered, consistent with a transition from a 70:30 mixture of low-spin/high-spin forms at room temperature to pure low spin at the lowest temperatures studied. The transition is gradual, in contrast to the abrupt changes seen in Fe(III)/(II) spin-crossover species. The red perchlorate salt behaves differently, exhibiting magnetic moments of 4.2 BM at room temperature and 3.5 BM at 4.2 K, and is thus predominantly high spin over the entire temperature range.**[75]** Room-temperature crystal structures of $[Co(terpy)_2](ClO_4)_2 \cdot 1/2H_2O$ and $[Co(terpy)_2]Br_2 \cdot 3H_2O$ ($\mu_{eff} = 2.94$ BM) show a shorter average Co–N bond length in the bromide salt, consistent with a greater proportion of low-spin molecules in this salt, although the exact extent of the structural difference between the high- and low-spin forms could not be determined because of both forms being disordered in the structure.**[76]** A higher proportion of the low-spin form is seen when the terpy complex (nitrate salt) is prepared in Zeolite Y,**[77]** and $[Co(bpy)_3]^{2+}$ also displays a thermal high-spin/low-spin interconversion when encapsulated in Zeolite Y, even though the free ion shows no evidence of a spin equilibrium at any temperature or with any counterion.**[78]** This behavior is thought to stem from the near-octahedral geometry imposed on the complex by the zeolite, in contrast to the trigonal prismatic distorted geometry adopted by the free complex.**[79]** The interconversion between the high- and low-spin forms of $[Co(terpy)_2]^{2+}$ is extremely rapid, as might be expected from a spin state change involving only one electron, with a relaxation time of less than 2 to 15 ns suggested by Raman laser T-jump and ultrasonic absorption experiments.**[80,81]**

5.2.3 Oxygen Carrier Complexes

In 1933, Pfeiffer and Tsumaki reported that a solid sample of the red square-planar Co(II) complex [Co(salen)] (**15**) slowly turned black on exposure to air for several days. Tsumaki later showed that the color change was due to coordination of dioxygen and that this process could be reversed by heating the solid compound in a stream of CO_2.

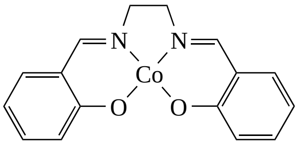

(**15**)

Since this time, a variety of Co(II) complexes have been found to reversibly bind dioxygen, and complexes containing salen and other Schiff-base ligands have been extensively studied. Such complexes have been found to act as catalysts in the oxygenation of a variety of organic substrates by oxygen and hydroperoxides. These complexes bind oxygen reversibly both in solution and in the solid state in ratios of 1 or 0.5 mol of O_2 per mole of complex to give mononuclear species with a terminal O_2-derived ligand or binuclear species with a bridging O_2-derived ligand respectively, depending on the nature of the Schiff-base ligand. The oxygenation reactions are generally rapid, with rate constants for O_2 binding between 10^6 and $10^8\ M^{-1}\ s^{-1}$ having been measured. The complexes slowly lose O_2-binding capacity, and this is thought to be due to ligand oxidation reactions. The first structurally characterized examples of oxygenated Schiff-base species, $\{[Co(salen)]_2(O_2)(dmf)_2\}$**[82]** and $\{[Co(3\text{-fluorosalen})]_2(O_2)(H_2O)\}_2$,**[83]** contained bridging O_2-derived ligands, with O–O distances of 1.339 (6) and 1.308 (28) Å respectively, consistent with a superoxo (*see Superoxide*) formulation for the O_2 bridge. Structural analysis of the monomeric species $[Co(bzacen)(py)(O_2)]$ (**16**) showed a six-coordinate Co ion and an O_2-derived ligand bound in a bent (Co–O–O = 126(2)°) monodentate fashion, with an O–O distance of 1.26(4) Å, again consistent with a superoxide formulation.**[84]** The ν(O–O) frequency of 1128 cm^{-1} also supports this assignment.

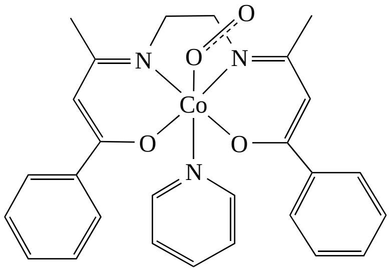

(**16**)

The exact nature of the metal–ligand interaction in these complexes has been the subject of intense debate, but it now appears generally accepted that significant electron transfer from Co to O_2 occurs on binding of the ligand and that the unpaired electron is located primarily on the ligand in both mononuclear and dinuclear species. Several non-Schiff-base complexes have also been found to bind dioxygen, most notably the amino acid complex $[Co(his)_2]$, which binds dioxygen reversibly in aqueous solution. The tris(3-*tert*-butyl-5-methylpyrazolyl)borate complex $Tp'Co(O_2)$ (Figure 9), which is formulated as a Co(II)-superoxo complex, contains a pseudotetrahedral Co ion coordinated to a side-on bound superoxide ligand. The O–O distance of 1.262(8)Å and the ν(O–O) frequency of 961 cm^{-1} is consistent with this formulation, while the magnetic moment of 3.88 BM at 298 K requires strong antiferromagnetic coupling between the metal and the superoxide ligand to give an $S = 1$ ground state with a large orbital component.**[85]** An unusual bis(μ-superoxo) complex containing a Tp′ ligand has also been characterized (Figure 10),**[86]** as has the mixed-valence Co(II)-Co(III) bis(μ-superoxo) complex (**17**) containing Me_3TACN.**[87]**

The dicobalt complex of the cryptand ligand O-BISTREN (**18**) displays reversible oxygenation in aqueous solution, with the maximum concentration of the oxygenated species being observed over the pH range 7.8 to 8.8. Purging

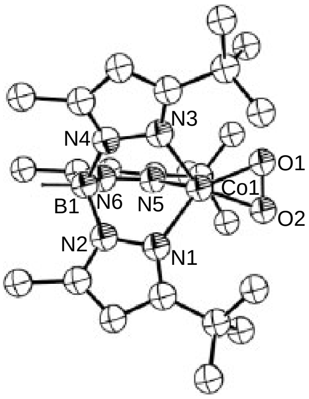

Figure 9 Structural diagram of [(HB(3-*t*-Bu-5-Mepz)$_3$)Co(O$_2$)]

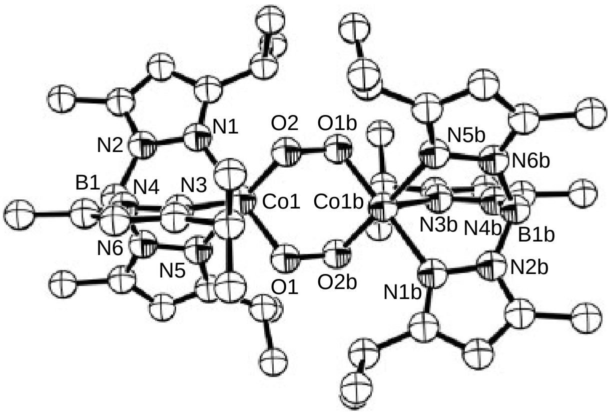

Figure 10 Structural diagram of [(HB(3-*i*-Pr-5-Mepz)$_3$)Co(O$_2$)]$_2$·2CH$_3$CN. Solvent molecules not shown

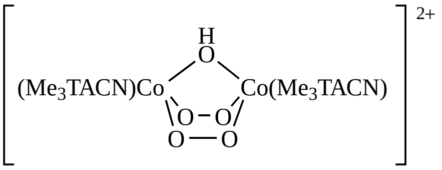

(**17**)

a solution of the oxygenated complex with N$_2$ regenerates the UV/vis spectrum of the starting material, which then reoxygenates on exposure to air. Heating the solution of the oxygenated complex to 75 °C also results in deoxygenation, and the oxygenated complex is regenerated on cooling. Irreversible degradation of the complex to what is thought to be a dicobalt(III) complex is observed above 90 °C.

5.3 Co(III) Complexes

Complexes of Co(III) are arguably the best studied of all transition metal complexes. They are easily prepared, generally from Co(II) precursors, they exhibit a huge variety of colors, they are usually air- and light-stable, and their relative inertness to ligand exchange allows purification by column chromatography and facilitates studies of these complexes in solution. The $t_{2g}{}^6e_g{}^0$ electron configuration means that these complexes are diamagnetic and allow NMR to be used as a tool for structural characterization, while their well-defined d-d bands in the UV/vis region provide a convenient spectroscopic handle for studies of their reactions in solution. Their slow rates of ligand exchange allow rate data for these reactions to be collected by conventional means using a variety of techniques, and also allow studies of the reactivity of coordinated ligands to be made. Co(III) is a prototypical 'hard' metal ion and generally binds aliphatic N- and O-donor ligands particularly well. However, there are many examples of stable complexes containing S-, As-, P- and even C-donor ligands. Despite its high oxidation state, Co(III) can bind quite strongly, reducing ligands such as thiolates, $H_2PO_2{}^-$, $H_2PO_3{}^-$, $NO_2{}^-$, $SO_3{}^{2-}$, and $S_2O_3{}^{2-}$ without undergoing internal redox reactions. Similarly, complexes containing strongly oxidizing ligands such as $MnO_4{}^-$ and $CrO_4{}^{2-}$ are stable.

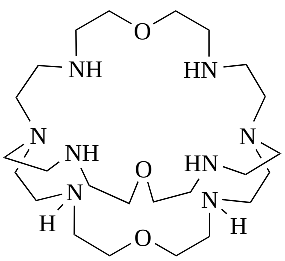

(**18**)

5.3.1 *Ammine and Amine Complexes*

The golden yellow $[Co(NH_3)_6]^{3+}$ cation can be prepared by air oxidation of an ammoniacal solution of Co(II) in the presence of charcoal. $[Co(NH_3)_6]Cl_3$ crystallizes in the monoclinic space group $C2/m$, and the X-ray structure shows four independent $[Co(NH_3)_6]^{3+}$ units, none of which display perfectly octahedral symmetry. Co–N bond lengths lie in the range 1.955 to 1.983 Å.**88** $[Co(NH_3)_6]^{3+}$ undergoes proton exchange even in mildly acidic solution via a mechanism involving deprotonation of the coordinated ammonia ligands, attesting to the enhanced acidity of these ligands on coordination to the 3+ metal center. This is further evidenced by the fact that treatment of $[Co(NH_3)_6](ClO_4)_3$ with KNH_2 in liquid ammonia at 100 °C gives the triply amido-bridged dimer $[(NH_3)_3Co(NH_2)_3Co(NH_3)_3](ClO_4)_3$ (**19**), which is stable in aqueous solution.

Literally hundreds of Co(III) complexes having the formula $[Co(NH_3)_5X]^{n+}$ have been reported, and there are few commonly available ligands that have not been coordinated to the $[Co(NH_3)_5]^{3+}$ moiety. The complexes span a vast range of reactivities in aqueous solution, from

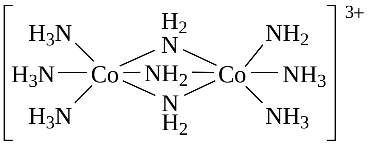

(**19**)

$[Co(NH_3)_5OClO_3]^{2+}$, which has a $t_{1/2}$ of 7 s for hydrolysis, to $[Co(NH_3)_6]^{3+}$, which has a half-life of thousands of years. $[Co(NH_3)_5X]^{n+}$ complexes can be synthesized from Co(II) starting materials, but are often more conveniently prepared from formally substitutionally inert $[Co(NH_3)_5X]^{n+}$ species containing X ligands that can be chemically labilized. Thus, treatment of $[Co(NH_3)_5Cl]^{2+}$ with either Ag^+ or Hg^{2+} in a noncoordinating solvent in the presence of the entering ligand has been used to prepare a large number of $[Co(NH_3)_5X]^{n+}$ complexes. Similarly, treatment of $[Co(NH_3)_5OCO_2]^+$ with acid or treatment of $[Co(NH_3)_5(N_3)]^{2+}$ with NO^+ in noncoordinating solvents generates very labile leaving groups, which can be easily replaced by a wide variety of entering ligands. Complexes such as $[Co(NH_3)_5OSO_2CF_3]^{2+}$ and $[Co(NH_3)_5OSMe_2]^{3+}$, which contain labile ligands, are also useful in synthesis. The mechanism of ligand substitution in $[Co(NH_3)_5X]^{n+}$, and numerous other Co(III) complexes, has been the topic of an enormous number of studies. The rates of hydrolysis of these complexes show significant dependence on the nature of the leaving group, while the rates of the reverse (anation) reactions are relatively insensitive to the identity of the entering ligand. These and other observations are consistent with a mechanism having dissociative character in which bond breaking to the leaving group is rate determining, although the question of whether a true five-coordinate intermediate is produced has yet to be conclusively answered. The rates of base hydrolysis of these and other similar Co(III) complexes show a first-order dependence on $[OH^-]$, which is consistent with am(m)ine deprotonation prior to loss of the leaving group. This has been termed the S_N1CB mechanism, and a review of the historical development of this chemistry is available.**89** Despite their apparent simplicity, much elegant chemistry has been carried out on $[Co(NH_3)_5X]^{n+}$ systems, and a selection of these studies are outlined below. The CN^- ligand binds to metal ions almost exclusively through the carbon atom, but the unusual N-bound isocyano complex $[Co(NH_3)_5NC]^{2+}$ can be formed through selenium extrusion from $[Co(NH_3)_5NCSe]^{2+}$ by treatment with CN^- in aqueous solution,**90** equation (3).

$$[(NH_3)_5CoNCSe]^{2+} + CN^- \longrightarrow [(NH_3)_5CoNC]^{2+} + SeCN^- \quad (3)$$

The thermal isomerization of the purple S-bound *trans*-$[Co(NH_3)_4(^{15}NH_3)SCN](N^{14}CS)_2$ complex (**20**) to the thermodynamically stable red N-bound isomer has been studied in the solid state (*see Ambidentate Ligand*), and the results are consistent with backside attack by ionic lattice thiocyanate as well as an intramolecular process. These results mirror those found in solution.**91**

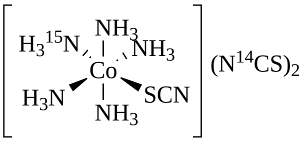

(**20**)

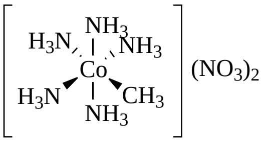

(**21**)

The remarkable complex $[Co(NH_3)_5CH_3](NO_3)_2$ (**21**), which could reasonably be called an organometallic Werner complex, can be prepared by air oxidation of an ammoniacal solution of Co(II) nitrate in the presence of methylhydrazine. The complex is stable in dilute aqueous ammonia solution for several months at 4 °C in the solid state.**92** The Co–C bond length is 1.980(2) Å, while the four cis Co–N bond lengths lie between 1.97 and 1.98 Å. The trans Co–N bond length of 2.1048(14) Å, shows the significant trans effect (*see Trans Effect*) exerted by the methyl ligand, and this is also manifested in the reactivity of $[Co(NH_3)_5CH_3]^{2+}$, which undergoes substitution of the normally inert ammonia ligands with remarkable ease.

The chelated phosphoramidate (**22**) is formed as an intermediate in the reaction of $[Co(NH_3)_5(DNPP)]^+$ in alkaline solution, through intramolecular nucleophilic attack of a deprotonated *cis*-ammine (Scheme 1).**93** Similar reactivity is observed in the monodentate pyruvate complex $[Co(NH_3)_5OC(O)C(O)CH_3]^{2+}$, where the imino carboxylate chelate (**23**) is formed at $pH > 12$.**94**

While a huge number of Co(III) ammine complexes have been prepared, there are markedly fewer Co(III) alkylamine complexes known, presumably due to the steric demands imposed by these larger ligands. Both $[Co(MeNH_2)_6]^{3+}$ and $[Co(NH_2OH)_6]^{3+}$ are known, and a small number of $[Co(RNH_2)_5X]^{n+}$ (R = Me, Et, Pr, Bu, *iso*-Bu) complexes have been prepared. The ethylenediamine (en) ligand (1,2-diaminoethane) occupies an important position in the development of coordination chemistry and a vast number of Co(III) complexes containing this ligand are known. In the majority of cases, the ethylenediamine ligand coordinates as a bidentate chelate, but complexes such as *cis*-$[Co(en)_2(enH)Cl](Cl)(ZnCl_4)$**95** (**24**) and $[Co(NH_3)_5(enH)]Cl_4$**96** (**25**) contain rare examples of monodentate ethylenediamine (*see Chelate Effect*).

The golden yellow $[Co(en)_3]^{3+}$ can exist as Δ and Λ enantiomers, and each chelate ring can adopt a δ- or λ-conformation. The enantiomers can be separated by crystallization using a chiral anion such as *d*-tartrate.

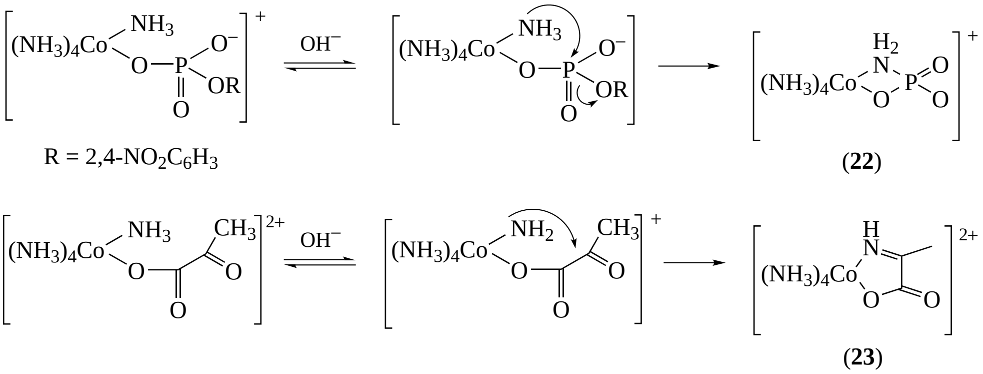

Scheme 1 Intramolecular reactions of pentaammine Co(III) complexes

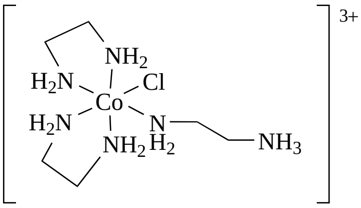

(**24**)

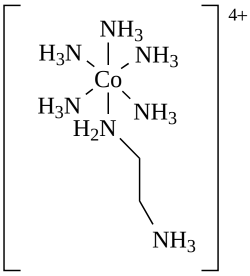

(**25**)

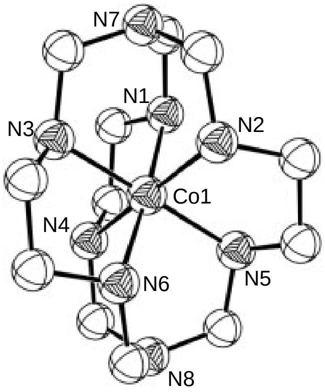

Figure 11 Structural diagram of the $[Co(sep)]^{3+}$ cation

Δ- and Λ-$[Co(en)_3]^{3+}$ undergo enantioselective binding with nucleotides, and the Δ isomer has been found to bind more strongly than the Λ to the major groove of the dodecanucleotide d(CAATCCGGATTG)$_2$. Co(III) complexes of a large number of bidentate diamine ligands such as 1,2-diaminopropane, 2,3-diaminobutane, 1,3-diaminopropane, and 1,2-diaminocyclohexane have been prepared and studied and a comprehensive review of their chemistry is available.[97] It is worth noting that $[Co(\pm\text{-1,2-diaminopropane})_3]^{3+}$, an apparently simple tris chelate complex, has a staggering 48 possible isomeric forms, comprising enantiomeric pairs, ring conformational isomers, and configurational isomers resulting from the relative positions of the methyl groups. The $[Co(en)_3]^{3+}$ ion has been used as a template for the synthesis of a large number of cage compounds. The first of these was prepared by treatment of Λ-$[Co(en)_3]^{3+}$ with HCHO and NH_3 at room temperature to give the sepulchrate $[Co(sep)]Cl_3{\cdot}H_2O$ in >95% yield (Figure 11).[98] The reaction is stereospecific, and gives only one out of a possible 16 isomers. The mechanism of formation is complex, and involves initial deprotonation of a coordinated ethylenediamine $-NH_2$ group and subsequent condensation with HCHO to give the imine, which then reacts with NH_3. This process is repeated until deprotonation of all six nitrogen atoms has occurred and the cage is formed. Reduction of the complex with zinc dust in mildly acidic conditions gives the Co(II) complex, which, remarkably, retains its absolute configuration and shows no exchange with added $^{60}Co^{2+}$ over one day.

Replacement of NH_3 with CH_3NO_2 in the reaction mixture leads to the production of the nitro-substituted C-capped 'sarcophagine' cage $[Co(diNOsar)]Cl_3{\cdot}H_2O$, which was originally prepared on a 156-g scale! The parent complex $[Co(sar)]Cl_3$ can be obtained following reduction to the diamine, nitrosation in the presence of Cl^-, and reductive dehalogenation. A large number of cages having a variety of capping substituents have been prepared, and the carbon bridgehead atoms can be replaced by N, P, P(O), and As. The Co(II) sarcophagine complexes are again kinetically inert, and resolved $[Co(sar)]^{2+}$ does not racemize in solution over 2 h. The metal ion can, however, be removed under forcing conditions, either in concentrated HCl at 130 °C in a sealed tube or by treatment with NaCN at 65 °C for 6 h in aqueous solution.

$[Co(en)_2X_2]^{n+}$ can exist as geometric isomers in cis and trans forms, with the violet *cis*-$[Co(en)_2Cl_2]^+$ and green *trans*-$[Co(en)_2Cl_2]^+$ cations being the textbook examples. The cis forms of $[Co(en)_2X_2]^{n+}$ complexes can also exist as enantiomers. The $[Co(en)_2]^{3+}$ moiety has been used as a combined protecting and activating group in peptide synthesis reactions, where reaction of $[Co(en)_2AAOMe]^{2+}$ complexes with an amino acid ester rapidly gives the coordinated peptide (Scheme 2). These reactions proceed with high retention of stereochemistry, and the coordinated peptide can be removed from the metal center by chemical or electrochemical reduction of the complex.**[99]**

The chemistry of Co(III) complexes of polyamine ligands has been extensively studied. Linear polyamines containing three or more N atoms give rise to numerous isomers on coordination to Co(III), due to the many possible ways of folding the ligand about the metal ion, and the differing possible orientations of protons on the secondary N atoms. For example, there are 9 possible isomers of the $[Co(trien)Cl_2]^+$ cation and 15 possible isomers of $[Co(tetraen)X]^{n+}$ systems. A significant body of meticulous work concerning the separation and characterization of such isomers exists and has contributed much to our ideas of inorganic stereochemistry. Crucial to much of this work has been the use of ion-exchange chromatography (*see Ion Exchange*) to effect separation of isomers, and this technique is now an indispensable part of Co(III) chemistry. Tripodal tetraamine ligands (*see Tetradentate Ligand*) such as tris(2-aminoethyl)amine (tren) and tris(3-aminopropyl)amine (trpn) have fewer isomeric possibilities on coordination to Co(III) than their linear tetraamine counterparts, although geometric isomers occur through the inequivalence of the remaining two coordination sites, and this property has been used in studies of $[Co(tren)XY]^{n+}$ complexes in particular to elucidate the amount of stereochemical change in anation and hydrolysis reactions. Co(III) complexes of the type $[Co(N)_4(OH/H)(OH/H)]^{+/2+/3+}$, where $(N)_4$ is a tripodal or macrocyclic tetraamine ligand, have been found to be efficient agents for the hydrolysis of phosphate esters, nitriles, polyphosphates, organic esters, and amides, with maximum rates found at around neutral pH values. The pentadentate ligand (*see Pentadentate Ligand*) trenen (**26**) is difficult to prepare by conventional routes, but the intramolecular condensation reaction of $[Co(tren)Cl(NH_2CH_2CHO)]^{2+}$ (**27**) under alkaline conditions and subsequent BH_4^- reduction of the resulting imine gives $[Co(trenen)Cl]^{2+}$ (**28**) in excellent yield (Scheme 3).

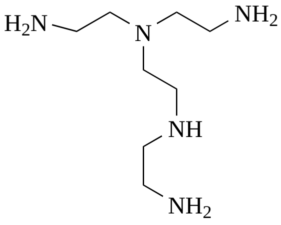

(**26**)

Co(III) complexes of macrocyclic amine ligands are well known, and such complexes display some interesting chemistry. The secondary N–H protons in $[Co(cyclen)XY]^{n+}$ complexes are remarkably acidic due at least in part to the high formal charge on the metal ion, and as a result, proton exchange occurs with great ease. This has significant effects on the reactivity of such complexes. For example, the carbonato chelate $[Co(cyclen)O_2CO]^+$ (**29**)

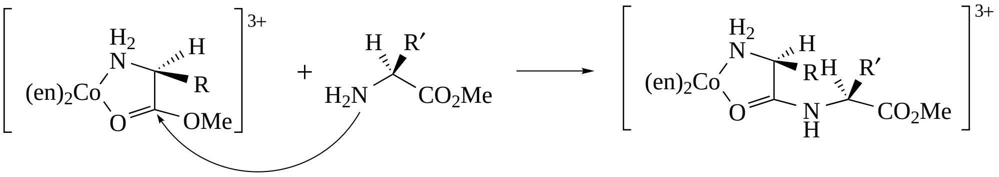

Scheme 2 Co(III)-promoted peptide synthesis

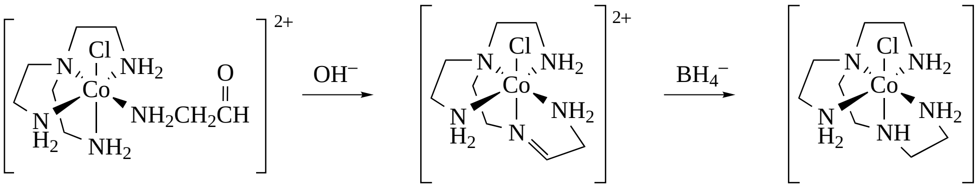

(**27**) (**28**)

Scheme 3 Intramolecular synthesis of the trenen ligand undergoes base-catalyzed ring opening in 1.0 M OH^- at least 1000 times more rapidly than either $[Co(tren)O_2CO]^+$ or $[Co(en)_2O_2CO]^+$, and this has been attributed to the higher concentration of N–H deprotonated species in the cyclen complex. Spectrophotometric evidence for the participation of singly deprotonated complexes in the ring-opening reaction has been obtained, while kinetic data are also consistent with the involvement of doubly N–H deprotonated species in the hydrolysis of the resulting monodentate carbonate complex.

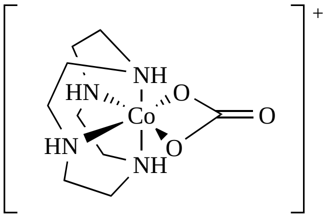

(**29**)

The highly acidic nature of Co(III) cyclen complexes is confirmed by the measured pK_a values for $[Co(cyclen)en]^{3+}$ and $[Co(cyclen)tn]^{3+}$ of 12.92 and 12.21 respectively, with deprotonation giving a color change from orange to red.**100** Co(III) cyclen complexes also offer isomeric possibilities with respect to the syn or anti configuration of the equatorial N–H protons relative to the remaining two coordination sites in the complex. These isomers can be fully characterized in solution using nOe and COSY ^{1}H NMR spectroscopy, and the substitution-inert nature of the Co(III) center has allowed them to be separated by ion-exchange chromatography, crystallized, and characterized by X-ray crystallography.**101** Co(III) complexes containing predominantly monodentate aromatic amine ligands are much less numerous than their ammine counterparts. $[Co(py)_6]^{3+}$ is unknown, although the $[Co(imH)]^{3+}$ ion has been reported, and there are no reported $[Co(py)_5X]^{n+}$ complexes. Green *trans*-$[Co(py)_4Cl_2]Cl{\cdot}6H_2O$ can be prepared by liquid chlorine oxidation of a methanolic solution containing pyridine and anhydrous $CoCl_2$,**102** and has proved to be a useful starting material for the synthesis of a variety of Co(III) complexes.**103** The $[Co(py)_4O_2CO]^+$ ion shows extraordinary stability in acidic solution, with its UV/vis spectrum remaining essentially unchanged over 2 h in 1 M HCl at room temperature. Use of more concentrated acids leads to an eventual decarboxylation, but this is immediately followed by rapid reduction to Co(II) species. Similar behavior has been observed in acidic solutions containing the $[Co(tepa)O_2CO]^+$ ion, and the unusual chelated bicarbonate complex $[Co(tepa)O_2COH](ClO_4)_2{\cdot}3H_2O$ (Figure 12) can be crystallized from 2.7 M $HClO_4$ solution. The reasons for the stability of these complexes in acidic solution and for the reduction of the hydrolysis product are not immediately apparent, but the presence of pyridyl ligands is a requirement for such behavior.

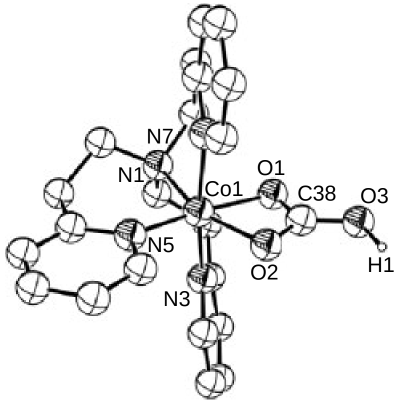

Figure 12 Structural diagram of the $[Co(tepa)O_2COH]^{2+}$ cation

5.3.2 O-donor Ligands

There are few examples of Co(III) complexes that contain solely O-donor ligands, and these almost invariably have limited stability in aqueous solution. Ironically, their very instability makes them ideal candidates as starting materials for the synthesis of other Co(III) complexes, and $Na_3[Co(O_2CO)_3]{\cdot}3H_2O$, $K_3[Co(ox)_3]$, $Co(acac)_3$, and $Na_3[Co(NO_2)_6]$ have all proven useful in this respect. One of the earliest characterized examples of a Co(III) ion with complete O-ligation was the tetrameric complex $[Co\{Co(OH)_2(NH_3)_4\}_3]Br_6$ (**30**), first prepared by Jørgensen. This was resolved into its enantiomers by Werner, and in so doing, he showed conclusively that optical activity was not a phenomenon associated solely with carbon.

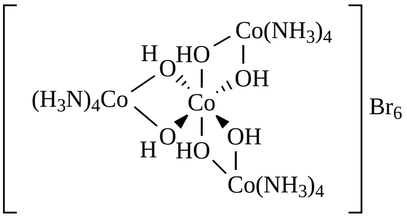

(**30**)

Co(III) carboxylate complexes can be prepared by oxidation of a Co(II) carboxylate with oxygen, ozone, and peracids, and these have been widely used as homogeneous catalysts for the oxidation of a wide variety of organic substrates. Despite this, the exact structures of these complexes remain unknown. The dark green solution obtained on oxidation of cobalt(II) acetate in acetic acid is thought to primarily contain the trinuclear μ_3-oxo (*see μ-Oxo Bridge*) complex $[Co_3O(OAc)_6(HOAc)_3]^+$, although this has yet to be confirmed by X-ray structural analysis of the solid obtained on removal of the solvent. Evidence for the presence of a trinuclear mixed-valence $Co(III)_2Co(II)$

species and a hydroxo-bridged dimer $[Co_2(OAc)_4(OH)_2]$ has also been obtained. However, the dark red–brown complex $[Co_3O(OAc)_6(py)_3](ClO_4)\cdot H_2O$ has been shown by X-ray crystallography to adopt a triangular structure (Figure 13).[104]

Tetranuclear Co(III) carboxylate complexes having the formula $[Co_4O_4(O_2CR)_2(bpy)_4](ClO_4)_2$ have been prepared and characterized. These are built around a central cubane-type $[Co_4O_4]^{4+}$ core (Figure 14) and, most interestingly, exhibit a reversible one-electron oxidation to give what are formally $Co(III)_3Co(IV)$ species.[105]

A large number of high-nuclearity Co(III) and mixed-valence Co(III)Co(II) carboxylate-based species containing up to 13 cobalt ions are known, and a review of these is available.[74] The unusual polynuclear chemistry of Co(III) carboxylates is not mirrored in Co(III) complexes of other oxoanions (*see Oxoanion*); these are generally mononuclear, and with the homoleptic exceptions described at the beginning of this section, usually contain N-based ancillary ligands. Complexes such as $[Co(en)_2O_2CO]^+$ and $[Co(en)_2O_2PO_2]$ containing chelated oxoanions are well known, despite the distortion from octahedral geometry caused by the presence of the four-membered chelate ring (O–Co–O angles of 68.39° and 75.74° respectively).[106,107] The acid hydrolysis of chelated carbonate in a variety of $[Co(L)_nO_2CO]^+$ complexes is a well-studied reaction. A detailed spectrophotometric study of the acid hydrolysis of the $[Co(en)_2O_2CO]^+$ ion showed biphasic kinetics corresponding to consecutive first-order processes involving chelate ring opening and subsequent hydrolysis of the monodentate bicarbonate ion. Protonation of the chelated carbonate is significant, with K_a for the bicarbonate chelate being $\sim 1\,M$.[108] A subsequent study of a variety of $[Co(L)_nO_2CO]^+$ complexes rationalized the large variation in acid hydrolysis rates with changing L (approximately seven orders of magnitude) in terms of the differing ability of the complexes to transfer the proton on the exo-oxygen to an endo (coordinated) oxygen atom, thus effecting ring opening, as the rates for hydrolysis of the monodentate bicarbonate were fairly constant over the range of complexes studied.[109] Somewhat surprisingly, $[Co(en)_2O_2SO_2]^+$ is unknown, with attempted syntheses of this giving the bis-monodentate sulfato bridged dimer $[(en)_2Co(OS(O)_2O)_2Co(en)_2]^{2+}$,[110] and the first crystallographically characterized example of a chelated Co(III) sulfato complex, $[Co(trpn)O_2SO_2]ClO_4\cdot H_2O$, has been reported only relatively recently.[111] Chelated nitrate is found in the unusual tris chelate $[Co(O_2NO)_3]$[112] and doubly chelated phosphate acts as a bridging ligand in $[(trpn)CoO_2PO_2Co(trpn)](ClO_4)_3\cdot 3H_2O$.[113] There are a vast number of Co(III) complexes containing monodentate oxoanion ligands as diverse as NO^-, NO_2^-, SO_3^{2-}, $S_2O_3^{2-}$, ReO_4^-, ClO_4^-, and $CF_3SO_3^-$. The isomeric nitrite complexes $[Co(NH_3)_5ONO]^{2+}$ (pink) and $[Co(NH_3)_5NO_2]^{2+}$ (yellow) provided the first examples of linkage isomers (*see Linkage Isomerism*) in coordination chemistry, and the spontaneous isomerization of the O-bound nitrito to the N-bound nitro complex has been well studied both in solution and in the solid state, with an intramolecular mechanism being proposed in both cases. The reverse reaction can be photochemically induced, and again occurs via an intramolecular mechanism. Similar linkage isomerism has been seen in complexes containing $S_2O_3^{2-}$ (O-bound to S-bound), sulfinate (S-bound to O-bound), sulfamate (N-bound to O-bound) and SO_3^{2-} (O-bound to S-bound) ligands. Coordination of water to a Co(III) center increases its acidity significantly and such aqua complexes typically have pK_a values ranging from 5 to 8. The resulting hydroxo complexes are potent nucleophiles toward a variety of organic and inorganic substrates. Of particular interest in this respect are complexes containing two cis-disposed aquo ligands; monodeprotonation of these gives cis-aqua/hydroxy complexes, which have been found to be efficient agents for the remarkably rapid stoichiometric hydrolysis of phosphate esters, polyphosphates, organic esters, nitriles, and amides around neutral pH values. Such reactions proceed at least in part via an intramolecular mechanism involving initial coordination of the substrate to the Co(III) center followed by intramolecular nucleophilic

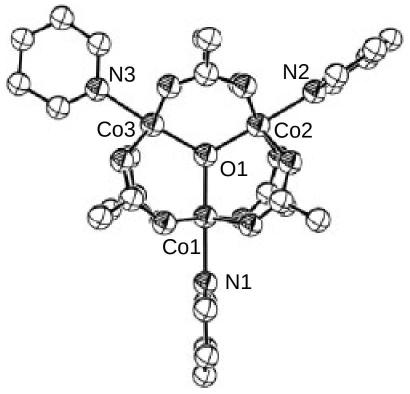

Figure 13 Structural diagram of the cation of $[Co_3O(OAc)_6(py)_3](ClO_4)\cdot H_2O$

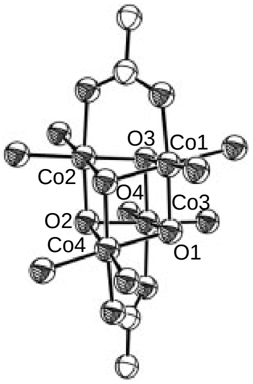

Figure 14 Structural diagram showing the coordination environment of the Co ions in the cation of $[Co_4O_4(O_2CC_6H_4NO_2)_2(bpy)_4](ClO_4)_3$

attack of the coordinated hydroxide. Given the normally slow rates of ligand exchange in Co(III) complexes, such rapid reactions might be considered anomalous. However, ^{17}O NMR studies of water exchange rates in a number of $[Co(N)_4(OH/H)(OH/H)]^{+/2+/3+}$ complexes ($(N)_4 =$ tren, cyclen, N-Mecyclen) have shown that, whereas the diaqua and dihydroxo complexes undergo relatively slow exchange with solvent water ($k_{ex} \sim 10^{-7}–10^{-4}\,s^{-1}$), the aquahydroxy complexes react approximately five orders of magnitude more rapidly ($k_{ex} \sim 10^{-2}–10^{1}\,s^{-1}$), thus allowing rapid anation of these species. This remarkable reactivity difference has been ascribed to the ability of the complex to partially transfer a proton to the departing hydroxide ligand in the transition state for Co–OH bond cleavage, and the cyclen complexes are particularly efficient in this respect.**[114]** Neutral O-donor ligands such as alcohols, ketones, esters, and ethers are generally poor ligands toward Co(III) and such ligands are usually rapidly replaced by water in aqueous solution.

5.4 Co(IV) and Co(V) Complexes

Although both the alkyl complex $[Co(nor)_4]$ (Figure 15)**[115]** and the hydride complex $[Co(C_5Me_5)(Si(H)Ph_2)_2(H)_2]$ (Figure 16)**[116]** offer well-characterized examples of organometallic Co(IV) and Co(V) complexes, the situation with ‘classical’ coordination complexes is much less clear.

The majority of reported Co complexes in oxidation states higher than 3+ contain noninnocent ligands, and this hence renders the assignment of metal oxidation state difficult. This problem has existed since Werner’s time; indeed, he initially formulated the superoxo-bridged dimers $[(NH_3)_4Co(O_2)(NH_2)Co(NH_3)_4]^{4+}$ and $[(en)_2Co(O_2)(NH_2)Co(en)_2]^{4+}$ as mixed-valence peroxo-bridged Co(III)/(IV) complexes. One-electron oxidation of the unusual square-planar Co(III) complex (**31**) using Ce(IV) gives a deep blue low-spin species. This is soluble and stable in benzene, and exhibits a reversible one-electron reduction at 1.26 V versus NHE. EPR data indicate that the unpaired electron is located primarily on the metal center, although Co(II) resonance contributors are also possible, owing to the presence of the noninnocent diaminobenzene fragment.**[117]**

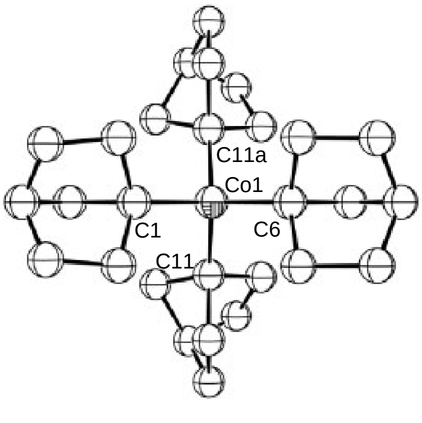

Figure 15 Structural diagram of the organometallic Co(IV) complex $[Co(nor)_4]$

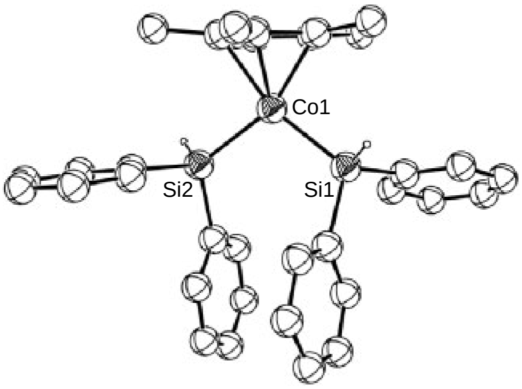

Figure 16 Structural diagram of the organometallic Co(V) complex $[Co(C_5Me_5)(Si(H)Ph_2)_2(H)_2]$. Hydride ligands bound to the Co are not shown

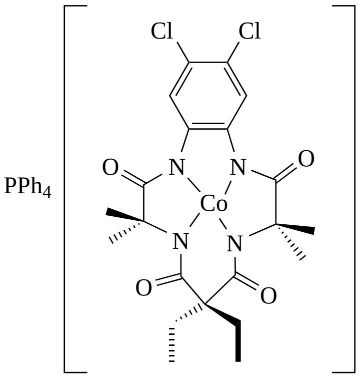

(**31**)

The corrole complex $[Co(OEC)(C_6H_5)]$, which was originally formulated as a Co(IV) complex,**[118]** has since been shown to have significant spin density on both the metal ion and the corrole ligand,**[119]** while EPR data collected on electrochemically generated $[Co(S_2CNR_2)_3]^+$ complexes ($R = Et$, cyclohexyl) are consistent with a Co(IV) formulation.**[120]** Obviously, the stabilization of highly oxidizing Co(IV) and Co(V) complexes remains a challenge for synthetic chemists.

6 CONCLUDING REMARKS

‘. . . we desire to state our conviction that the subject is by no means exhausted, but that on the contrary there is scarcely a single point which will not amply repay a more extended study'.[1] The words of Gibbs and Genth are as true today as they were in the mid-nineteenth century. Similarly, Werner's influence extends even into the twenty-first century, with a paper published in 2001 (coauthored by Werner!) reporting the crystallographic characterization of $[(NH_3)_3Co(\mu\text{-}OH)(\mu\text{-}O_2)(\mu\text{-}NH_2)Co(NH_3)_3](NO_3)_3\cdot1.25H_2O$ (**32**), using crystals prepared in Werner's laboratory around 1909.[121] This represents the first crystallographically characterized example of a triply bridged transition metal complex containing O_2^-, NH_2, and OH bridges.

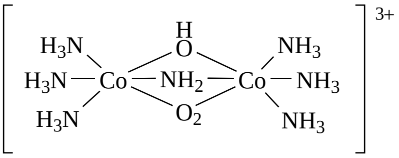

(**32**)

Cobalt chemistry, nowadays, might be regarded by some as unfashionable but its importance, both historical and current, is undeniable, as demonstrated by the work outlined in this chapter. Cobalt will always retain its capacity to surprise, as evidenced by the recent serendipitous isolation of both $[Co(tmen)(OH_2)(H)](NO_3)(ClO_4)\cdot C_2H_5OH$ (**33**), a hydride complex that can be recrystallized from 5 M aqueous $HClO_4$[122] and (**34**), a carbanionic perchlorato complex isolated from aqueous solution.[123] We await further developments in cobalt chemistry with interest.

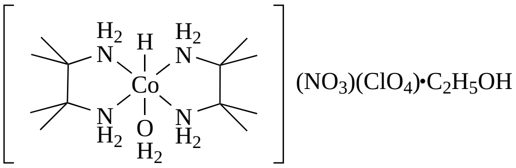

(**33**)

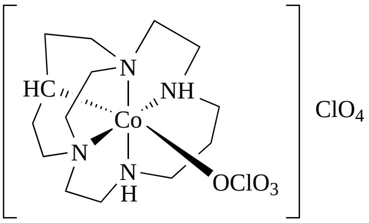

(**34**)

7 RELATED ARTICLES

Ammonia & N-donor Ligands; Cobalt: Organometallic Chemistry; Coordination Numbers & Geometries; Coordination & Organometallic Chemistry: Principles; Ligand Field Theory & Spectra; Magnetism of Transition Metal Ions; P-donor Ligands; Water & O-donor Ligands.

8 REFERENCES

1. W. Gibbs and F. A. Genth, in 'Smithsonian Contributions to Knowledge', The Smithsonian Institution, Washington, DC, 1856, Vol. 9, Article 5, p. 1.
2. D. A. Buckingham and C. R. Clark, Cobalt, in 'Comprehensive Coordination Chemistry', eds. G. Wilkinson, R. D. Gillard, and J. A. McCleverty, Pergamon Press, Oxford, 1987, Vol. 4, p. 635.
3. B. Clark, 'Cobalt Facts', The Cobalt Development Institute, Guilford, 2002.
4. P. V. Bernhardt and G. A. Lawrance, Cobalt, in 'Comprehensive Coordination Chemistry II', eds. J. A. McCleverty and T. J. Meyer, Elsevier Pergamon, Amsterdam, 2004, Vol. 6, p. 1.
5. J. D. Donaldson, Cobalt and cobalt compounds, in 'Ullmann's Encylcopedia of Industrial Chemistry', Wiley-VCH, Weinheim, 2000, Online Version, DOI: 10.1002/14356007.a07_281.
6. J. C. C. Chan and S. C. F. Au-Yeung, in 'Annual Reports on NMR Spectroscopy', ed. G. A. Webb, Academic Press, San Diego, CA, 2000, Vol. 41, p. 1.
7. P. S. Pregosin, in 'Transition Metal Nuclear Magnetic Resonance', ed. P. S. Pregosin, Elsevier, Amsterdam, 1991, p. 144.
8. R. J. Goodfellow, in 'Multinuclear NMR', ed. J. Mason, Plenum Publishing, New York, 1987, p. 521.
9. C. W. Kirby, C. M. Puranda, and W. P. Power, *J. Phys. Chem.*, 1996, **100**, 14618.
10. R. Hoppe, *Recl. Trav. Chim. Pays-Bas*, 1956, **75**, 569.
11. F. Bernhardt and R. Hoppe, *Z. Anorg. Allg. Chem.*, 1993, **619**, 540.
12. D. T. Richens, 'The Chemistry of Aqua Ions', John Wiley & Sons, Chichester, 1997, Chap. 9.
13. N. E. Dixon, W. G. Jackson, M. J. Lancaster, G. A. Lawrance, and A. M. Sargeson, *Inorg. Chem.*, 1981, **20**, 470.
14. D. A. Buckingham, Cobalt: Inorganic & coordination chemistry, in 'Encyclopedia of Inorganic Chemistry', ed. R. B. King, Wiley-VCH, Weinheim, 1994, p. 712.
15. Cambridge Structural Database, Version 5.24, November 2002, http://www.ccdc.cam.ac.uk/prods/csd/csd.html.
16. R. P. Linstead and J. M. Robertson, *J. Chem. Soc.*, 1936, 1736.
17. Inorganic Crystal Structural Database, Version 1.2.0, 2002, http://www.stn-international.de/stndatabases/databases/icsd.html.
18. C. P. Horwitz, S. W. Gordon-Wylie, Y. Leychkis, D. M. Flynn, S. T. Weintraub, G. R. Clark, and T. J. Collins, *J. Phys. Chem. B*, 2001, **105**, 8821.

19. J. J. Bour, P. T. Beurskens, and J. J. Steggarda, *J. Chem. Soc., Chem. Commun.*, 1972, 221.
20. L. H. Doerrer, M. T. Bautista, and S. J. Lippard, *Inorg. Chem.*, 1997, **36**, 3578.
21. P. B. Hitchcock and G. M. McLaughlin, *J. Chem. Soc., Dalton Trans.*, 1976, 1927.
22. I. Kung, D. Schweitzer, J. Shearer, W. D. Taylor, H. L. Jackson, S. Lovell, and J. A. Kovacs, *J. Am. Chem. Soc.*, 2000, **122**, 8299.
23. J. D. Zubkowski, D. L. Perry, E. J. Valente, and S. Lott, *Inorg. Chem.*, 1995, **34**, 6409.
24. J. J. Ellison, P. P. Power, and S. C. Shoner, *J. Am. Chem. Soc.*, 1989, **111**, 8044.
25. M. Langkjaer, E. Larsen, and S. Larsen, *Acta Chem. Scand.*, 1985, **A39**, 187.
26. N. A. Bailey, E. D. McKenzie, and J. M. Worthington, *J. Chem. Soc., Dalton Trans.*, 1977, 763.
27. D. Belletti, M. Carcelli, C. Pelizzi, and G. Pelizzi, *J. Crystallogr. Spectrosc. Res.*, 1992, **22**, 185.
28. C. Pelizzi, G. Pelizzi, and F. Vitali, *Transition Met. Chem.*, 1986, **11**, 401.
29. E. M. Holt, N. W. Alcock, R. R. Hendrixson, G. D. Malpass, R. G. Ghirardelli, and R. A. Palmer, *Acta Crystallogr.*, 1981, **B37**, 1080.
30. J. G. Bergman and F. A. Cotton, *Inorg. Chem.*, 1966, **5**, 1208.
31. W. O. Koch, J. T. Kaiser, and H.-J. Kruger, *Chem. Commun.*, 1997, 2237.
32. P. L. Holland, T. R. Cundari, L. L. Perez, N. A. Eckert, and R. J. Lachicotte, *J. Am. Chem. Soc.*, 2002, **124**, 14416.
33. A. Panda, M. Stender, R. J. Wright, M. M. Olmstead, P. Klavins, and P. P. Power, *Inorg. Chem.*, 2002, **41**, 3909.
34. W. Jauch, M. Reehuis, H. J. Bleif, F. Kubanek, and P. Pattison, *Phys. Rev. B*, 2001, **64**, 052102-1.
35. J. El Nakat, K. J. Fisher, I. G. Dance, and G. D. Willett, *Inorg. Chem.*, 1993, **32**, 1931.
36. J. V. Rau, S. N. Cesaro, N. S. Chilingarov, and G. Balducci, *Inorg. Chem.*, 1999, **38**, 5695.
37. M. A. Hepworth, K. H. Jack, R. D. Peacock, and G. J. Westland, *Acta Crystallogr.*, 1957, **10**, 63.
38. B. S. Fox, O. P. Balaj, I. Balteanu, M. K. Beyer, and V. E. Bondybey, *J. Am. Chem. Soc.*, 2002, **124**, 172.
39. S. M. Peng, D. S. Liaw, Y. Wang, and A. Simon, *Angew. Chem., Int. Ed. Engl.*, 1985, **24**, 210.
40. P. Biagini, T. Funaioli, A. Juris, and G. Fachinetti, *J. Organomet. Chem.*, 1990, **390**, C61.
41. K. R. Adam, P. A. Anderson, T. Astley, I. M. Atkinson, J. M. Charnock, C. D. Garner, J. M. Gulbis, T. W. Hambley, M. A. Hitchman, F. R. Keene, and E. R. T. Tiekink, *J. Chem. Soc., Dalton Trans.*, 1997, 519.
42. M. H. Schmidt, G. M. Miskelly, and N. S. Lewis, *J. Am. Chem. Soc.*, 1990, **112**, 3420.
43. E. Fujita and C. Creutz, *Inorg. Chem.*, 1994, **33**, 1729.
44. G. J. P. Britovsek, M. Bruce, V. C. Gibson, B. S. Kimberley, P. J. Maddox, S. Mastroianni, S. J. McTavish, C. Redshaw, G. A. Solan, S. Stroemberg, A. J. P. White, and D. J. Williams, *J. Am. Chem. Soc.*, 1999, **121**, 8728.
45. V. C. Gibson, M. J. Humphries, K. P. Tellmann, D. F. Wass, A. J. P. White, and D. J. Williams, *Chem. Commun.*, 2001, 2252.
46. B. De Bruin, E. Bill, E. Bothe, T. Weyhermueller, and K. Wieghardt, *Inorg. Chem.*, 2000, **39**, 2936.
47. M. Di Vaira, M. P. Ehses, M. Peruzzini, and P. Stoppioni, *Eur. J. Solid State Inorg. Chem.*, 2000, 2193.
48. M. Aresta, M. Rossi, and A. Sacco, *Inorg. Chim. Acta*, 1969, **3**, 227.
49. H. F. Klein and H. H. Karsch, *Inorg. Chem.*, 1975, **14**, 473.
50. T. J. Deming and S. A. Curtin, *J. Am. Chem. Soc.*, 2000, **122**, 5710.
51. F. Orsini, *J. Org. Chem.*, 1997, **62**, 1159.
52. R. Ciancanelli, B. C. Noll, D. L. DuBois, and M. Rakowski DuBois, *J. Am. Chem. Soc.*, 2002, **124**, 2984.
53. N. W. Terry, E. L. Amma, and L. Vaska, *J. Am. Chem. Soc.*, 1972, **94**, 653.
54. J. D. Protasiewicz and K. H. Theopold, *Inorg. Chem.*, 1988, **27**, 1133.
55. C. W. G. Ansell, J. Lewis, M. C. Liptrot, P. R. Raithby, and M. Schroeder, *J. Chem. Soc., Dalton Trans.*, 1982, 1593.
56. S. Cabaleiro-Martinez, J. Castro, J. Romero, J. A. Garcia-Vazquez, and A. Sousa, *Acta Crystallogr.*, 2000, **C56**, e249.
57. I. Bkouche-Waksman and P. L'Haridon, *Acta Crystallogr.*, 1977, **B33**, 11.
58. J. J. Schneider, R. Goddard, and C. Kruger, *Z. Naturforsch. B*, 1995, **50**, 448.
59. V. V. Tkachev, E. A. Lavrent'eva, O. S. Rosschupkina, I. P. Lavrent'ev, and L. Y. Atovmyan, *Koord. Khim.*, 1994, **20**, 674.
60. S. Iwatsuki, H. Kato, K. Obeyama, S. Funahashi, N. Koshino, K. Kashiwabara, T. Suzuki, and H. D. Takagi, *Inorg. Chem. Commun.*, 2000, **3**, 501.
61. S. Iwatsuki, K. Obeyama, N. Koshino, S. Funahashi, K. Kashiwabara, T. Suzuki, and H. D. Takagi, *Can. J. Chem.*, 2001, **79**, 1344.
62. L. F. Warren and M. A. Bennett, *J. Am. Chem. Soc.*, 1974, **96**, 3340.
63. B. K. Santra and G. K. Lahiri, *J. Chem. Soc., Dalton Trans.*, 1998, 139.
64. J. Faus, M. Julve, F. Lloret, and M. C. Munoz, *Inorg. Chem.*, 1993, **32**, 2013.
65. W. N. Setzer, C. A. Ogle, G. S. Wilson, and R. S. Glass, *Inorg. Chem.*, 1983, **22**, 266.
66. A. J. Blake, V. Lippolis, S. Parsons, and M. Schroder, *Acta Crystallogr.*, 1998, **C54**, 293.

67. J. A. Hartman, E. J. Hintsa, and S. R. Cooper, *J. Am. Chem. Soc.*, 1986, **108**, 1208.
68. B. Nicolai, G. J. Kearley, M. R. Johnson, F. Fillaux, and E. Suard, *J. Chem. Phys.*, 1998, **109**, 9062.
69. J. N. Van Niekerk and F. R. L. Schoening, *Acta Crystallogr.*, 1953, **6**, 609.
70. X.-D. Jiao, I. A. Guzei, and J. H. Espenson, *Z. Kristallogr.*, 2000, **215**, 173.
71. R. A. Reynolds, W. R. Dunham, and D. Coucouvanis, *Inorg. Chem.*, 1998, **37**, 1232.
72. A. Kaufman, C. Afshar, M. Rossi, D. E. Zacharias, and J. P. Glusker, *Struct. Chem.*, 1993, **4**, 191.
73. M. Spohn and J. Straehle, *Z. Naturforsch. B*, 1988, **43**, 540.
74. R. E. P. Winpenny, *Adv. Inorg. Chem.*, 2001, **52**, 1.
75. S. Kremer, W. Henke, and D. Reinen, *Inorg. Chem.*, 1982, **21**, 3013.
76. W. Henke and S. Kremer, *Inorg. Chim. Acta*, 1982, **65**, L115.
77. K. Mizuno, S. Imamura, and J. H. Lunsford, *Inorg. Chem.*, 1984, **23**, 3510.
78. S. K. Tiwary and S. Vasudevan, *Chem. Phys. Lett.*, 1997, **277**, 84.
79. S. K. Tiwary and S. Vasudevan, *Inorg. Chem.*, 1998, **37**, 5239.
80. J. K. Beattie, R. A. Binstead, M. T. Kelso, P. Del Favero, T. G. Dewey, and D. H. Turner, *Inorg. Chim. Acta*, 1995, **235**, 245.
81. J. K. Beattie, *Adv. Inorg. Chem.*, 1988, **32**, 1.
82. M. Calligaris, G. Nardin, L. Randaccio, and A. Ripamonti, *J. Chem. Soc. A*, 1970, 1069.
83. B.-C. Wang and W. P. Schaefer, *Science*, 1969, **166**, 1404.
84. G. A. Rodley and W. T. Robinson, *Nature*, 1972, **235**, 438.
85. J. W. Egan, B. S. Haggerty, A. L. Rheingold, S. C. Sendlinger, and K. H. Theopold, *J. Am. Chem. Soc.*, 1990, **112**, 2445.
86. O. M. Reinaud, G. P. A. Yap, A. L. Rheingold, and K. H. Theopold, *Angew. Chem., Int. Ed. Engl.*, 1995, **34**, 2051.
87. Y. Hayashi, M. Obata, M. Suzuki, and A. Uehara, *Chem. Lett.*, 1997, 1255.
88. G. J. Kruger and E. C. Reynhardt, *Acta Crystallogr.*, 1978, **B34**, 915.
89. W. G. Jackson, *Inorg. React. Mech.*, 2002, **4**, 1.
90. W. G. Jackson and A. F. M. M. Rahman, *Inorg. Chem.*, 1990, **29**, 3247.
91. D. A. Buckingham, Linkage isomerism of thiocyanate bonded to cobalt(III), in ‘Coordination Chemistry, A Century of Progress’, ACS Symposium Series 565, ed. G. B. Morgan Kaufmann, American Chemical Society, Washington, DC, 1994, p. 256.
92. P. Kofod, *Inorg. Chem.*, 1995, **34**, 2768.
93. P. Hendry and A. M. Sargeson, *Inorg. Chem.*, 1986, **25**, 865.
94. J. M. Harrowfield and A. M. Sargeson, *J. Am. Chem. Soc.*, 1974, **96**, 2634.
95. D. A. House and P. J. Steel, *Inorg. Chim. Acta*, 1999, **288**, 53.
96. R. L. Fanshawe, A. Mobinikhaledi, C. R. Clark, and A. G. Blackman, *Inorg. Chim. Acta*, 2000, **307**, 26.
97. P. Hendry and A. Ludi, *Adv. Inorg. Chem.*, 1990, **35**, 117.
98. I. I. Creaser, J. M. Harrowfield, A. J. Herlt, A. M. Sargeson, J. Springborg, R. J. Geue, and M. R. Snow, *J. Am. Chem. Soc.*, 1977, **99**, 3181.
99. R. J. Browne, D. A. Buckingham, C. R. Clark, and P. A. Sutton, *Adv. Inorg. Chem.*, 2000, **49**, 307.
100. A. J. Clarkson, D. A. Buckingham, A. J. Rogers, A. G. Blackman, and C. R. Clark, *Inorg. Chem.*, 2000, **39**, 4769.
101. D. A. Buckingham, C. R. Clark, A. J. Rogers, and J. Simpson, *Inorg. Chem.*, 1995, **34**, 3646.
102. J. Glerup, C. E. Schaffer, and J. Springborg, *Acta Chem. Scand.*, 1978, **A32**, 673.
103. W. L. Purcell, *Inorg. Chem.*, 1986, **25**, 4068.
104. J. K. Beattie, T. W. Hambley, J. A. Klepetko, A. F. Masters, and P. Turner, *Polyhedron*, 1996, **15**, 2141.
105. K. Dimitrou, A. D. Brown, G. Christou, T. E. Concolino, and A. L. Rheingold, *Chem. Commun.*, 2001, 1284.
106. H.-M. Hu, H.-S. Sun, C.-Y. Duan, Q. Zhao, X.-Z. You, Z.-Y. Zhou, and X.-G. Zhou, *Acta Crystallogr.*, 1997, **C53**, 1014.
107. B. Anderson, R. M. Milburn, J. M. Harrowfield, G. B. Robertson, and A. M. Sargeson, *J. Am. Chem. Soc.*, 1977, **99**, 2652.
108. D. A. Buckingham and C. R. Clark, *Inorg. Chem.*, 1993, **32**, 5405.
109. D. A. Buckingham and C. R. Clark, *Inorg. Chem.*, 1994, **33**, 6171.
110. D. A. Buckingham, C. R. Clark, J. Simpson, and W. T. Robinson, *Inorg. Chem.*, 1988, **27**, 3544.
111. M. Banaszczyk, J. J. Lee, and F. M. Menger, *Inorg. Chem.*, 1991, **30**, 1972.
112. J. Hilton and S. C. Wallwork, *Chem. Commun.*, 1968, 871.
113. J. A. Connolly, M. Banaszczyk, R. C. Hynes, and J. Chin, *Inorg. Chem.*, 1994, **33**, 665.
114. N. E. Brasch, D. A. Buckingham, C. R. Clark, and A. J. Rogers, *Inorg. Chem.*, 1998, **37**, 4865.
115. E. K. Byrne, D. S. Richeson, and K. H. Theopold, *J. Chem. Soc., Chem. Commun.*, 1986, 1491.
116. M. Brookhart, B. E. Grant, C. P. Lenges, M. H. Prosenc, and P. S. White, *Angew. Chem., Int. Ed. Engl.*, 2000, **39**, 1676.
117. T. J. Collins, R. D. Powell, C. Slebodnick, and E. S. Uffelman, *J. Am. Chem. Soc.*, 1991, **113**, 8419.
118. S. Will, J. Lex, E. Vogel, V. A. Adamian, E. Van Caemelbecke, and K. M. Kadish, *Inorg. Chem.*, 1996, **35**, 5577.

119. J. Harmer, S. Van Doorslaer, I. Gromov, M. Broering, G. Jeschke, and A. Schweiger, *J. Phys. Chem. B*, 2002, **106**, 2801.
120. R. D. Webster, G. A. Heath, and A. M. Bond, *J. Chem. Soc., Dalton Trans.*, 2001, 3189.
121. B. Spingler, M. Scanavy-Grigorieff, A. Werner, H. Berke, and S. J. Lippard, *Inorg. Chem.*, 2001, **40**, 1065.
122. A. F. M. M. Rahman, W. G. Jackson, A. C. Willis, and A. D. Rae, *Chem. Commun.*, 2003, 2748.
123. X. Zhou, A. L. Day, A. C. Willis, and W. G. Jackson, *Chem. Commun.*, 2003, 2386.

Acknowledgment

I wish to dedicate this article to David A. Buckingham and Charles R. Clark, two doyens of cobalt chemistry, in gratitude for initiating and fostering my interest in this subject.

Cobalt: Organometallic Chemistry

Keith T. Quisenberry & Timothy P. Hanusa
Vanderbilt University, Nashville, TN, USA

Based in part on the article Cobalt: Organometallic Chemistry by Ulrich Koelle which appeared in the Encyclopedia of Inorganic Chemistry, First Edition.

1	Introduction	1
2	Cobalt Carbonyls	1
3	Alkyl Complexes	13
4	Alkene and Allyl Complexes	16
5	Cyclopentadienyl Complexes	19
6	Cyclobutadiene and Arene Complexes	24
7	Cobaltocene and Cobaltocene Derivatives	26
8	Complexes with Boracyclic Ligands	29
9	CpCo Half-sandwich Complexes	31
10	Cobalt Carborane Complexes	34
11	Related Articles	34
12	References	35

Abbreviations

allyl = η^3-C_3R_5; arene = η^6-C_6R_6; BTSA = Bis(trimethylsilyl)acetylene; cyclopentadienyl = η^5-C_5R_5; cbd = Cyclobutadiene; cod = Cyclooctadiene; DFT = Density functional theory; dmg = Dimethylglyoximate; MO = Molecular orbital; nb = Norbornyl (bicyclo[2.2.1]hept-1-yl); OAc = CH_3COO^-; tim = 2,3,9,10-tetramethyl-1,4,8,11-tetraazacyclotetradeca-1,3,8,10-tetraene.

1 INTRODUCTION

From the time of Alfred Werner, the coordination chemistry of cobalt has been dominated by the synthesis and reactions of octahedral Co^{III} complexes (*see* ***Coordination Chemistry: History***). In contrast, the organometallic chemistry of cobalt displays a great diversity of structures and oxidation states. In addition, the transition from organometallic to pure coordination chemistry, that is, the change from a set of π-acceptor (*see π-Acid Ligand*) to σ-donor ligands (*see σ-Donor*), is smoother for cobalt than for its neighboring elements of the same period. For example, organometallic complexes in higher oxidation states, in particular Co^{III}, are more common than the rare examples found with manganese, iron, and nickel, and are encountered not only with strong σ-donors such as alkyl (*see Alkyl Complexes*) and hydride (*see Hydrides*), but also with the harder halide ligands. This trend is also valid for Co^{II} organometallic complexes (*see Organometallic Complexes*).

Owing to the odd number of valence electrons in the element (nine), the formal oxidation state +I is prominent in the organometallic chemistry of cobalt, as documented by the vast diversity of complexes of the type $CpCoL_2$ (Section 5). A particular feature of cobalt organometallic chemistry is the relative abundance of low oxidation state (i.e. −I) complexes, not only with carbonyl but also with phosphine (Section 5.1.3) and alkene ligands (*see Alkene Complexes*) (Section 5.1.2). Co^{II} is confined to sandwich complexes (*see Sandwich Compound*), mostly of the bis(cyclopentadienyl) type, and to a few mono- and dinuclear $CpCo^{II}$ half-sandwich complexes. More abundant are $CpCo^{III}$ half-sandwich complexes. This class of compound is closest to analogous rhodium complexes, although the coordination chemistry of cobalt and rhodium is more similar than is the organometallic chemistry of these metals.

A general introduction and overview of the organometallic chemistry of cobalt is intended in this article. In each section, a description of a few basic types of complexes is presented. These compounds have played a major role in developing the scope of the known organometallic chemistry of cobalt. Proceeding from these basic complexes as a starting point, more specialized compounds (which are treated and understood as derivatives) will be described. Special emphasis is placed on complexes and reactions that have opened or may open new synthetic transformations of organic molecules. Early reviews of the organometallic chemistry of cobalt can be found in the treatise by White[1] and in the articles in *Comprehensive Organometallic Chemistry*;[2] the latter have been updated.[3]

2 COBALT CARBONYLS

2.1 $Co_2(CO)_8$

Together with $Ni(CO)_4$ and $Fe(CO)_5$, dicobaltoctacarbonyl, $Co_2(CO)_8$ (**1**), was among the earliest metal carbonyls (*see Metal Carbonyls*) to be detected and characterized by Mond and coworkers.[4,5] It was prepared from finely divided metal (or by hydrogen reduction of the oxide, CoO) in a Cu-lined autoclave made from Ni steel at 150 °C and a CO pressure of 30–40 bar. Other preparations employ reductive carbonylation of cobalt salts, mainly $Co(OAc)_2$, or the carbonylation of an alkaline cobalt cyanide solution.[6] The acetate salt is also the common precursor for $Co_2(CO)_8$ or $Co(CO)_4H$ in the Co-catalyzed hydroformylation (*see Hydroformylation*) process (Section '$HCo(CO)_4$ in Hydroformylation Reactions').

Among the earliest known reactions of $Co_2(CO)_8$ was oxidation to Co^{II} salts by halogens with liberation of CO (a method used as an analytical tool to determine its molecular composition), slow air oxidation of the solid to give a violet basic carbonate and, noticeably, controlled thermal decomposition. Though molecular weight measurements in benzene indicated the formula $Co_2(CO)_8$, the orange compound was formulated as the radical $Co(CO)_4$. As with other metal carbonyls, the discoverers of $Co_2(CO)_8$ were puzzled by its properties and composition, which did not fit into the accepted concepts of chemical bonding at the time. An X-ray structure determination of crystals of (**1**) and its subsequent IR investigation in solution have disclosed three different structures: a C_{2v} isomer (**1a**) with two bridging CO groups in the solid state, a D_{3d} isomer (**1b**), and another isomer (**1c**) of unknown structure (possibly of D_{2d} point symmetry) in solution (Figure 1).

The structure of $Co_2(CO)_8$ has been investigated with computational techniques. In one study, 19 homoleptic binary carbonyls were probed using Density functional theory (DFT) methods; theoretical structures of C_{2v}, D_{3d}, and D_{2d} symmetries were found as energetic minima in agreement with experimental data.[7]

2.1.1 *Substitution at $Co_2(CO)_8$*

Despite the relatively low bond energy of the Co–CO bond in $Co_2(CO)_8$ ($92\,\mathrm{kJ\,mol^{-1}}$, the same strength as in $Ni(CO)_4$, cf. $Fe(CO)_5$ at $156\,\mathrm{kJ\,mol^{-1}}$), CO substitution in $Co_2(CO)_8$ is complicated by the interference of valence disproportionation (*see Disproportionation*). CO substitution to give a monosubstituted complex has been observed with a few donor ligands such as PPh_3 and $AsPh_3$ in nonpolar solvents. The kinetics of the reaction between $Co_2(CO)_8$ and $AsPh_3$ are zero order in ligand and first order in metal carbonyl. From other characteristics of the reaction, such as noninterference of O_2 and a rate very close to the one found for ^{13}CO exchange under the same conditions, a dissociative mechanism with rate-determining CO dissociation (*see Dissociation*) followed by fast recombination with the ligand (equations 1 and 2) was concluded.[8]

$$Co_2(CO)_8 \rightleftharpoons Co_2(CO)_7 + CO \quad (1)$$

$$Co_2(CO)_7 + L \rightleftharpoons Co_2(CO)_7L \quad (2)$$

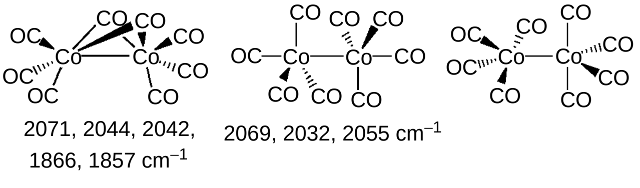

(**1a**) C_{2v} (**1b**) D_{3d} (**1c**) D_{2d}

Figure 1 Possible structures of $Co_2(CO)_8$

The addition of strongly basic phosphines in polar solvents give the ionic products $[Co^I(CO)_3(PR_3)_2][Co(CO)_4]$ (see below). Valence disproportionation in the presence of these ligands generates Co^I and Co^{-I} instead of Co^{II} and Co^{-I}, as is the case with only σ-donor ligands. Cations $[Co(CO)_{5-n}L_n]^+$ ($n = 1, 2, \ldots$) of coordination number five and trigonal bipyramidal structure (*see Trigonal Bipyramidal*) are known with many different substituents, and can be isolated from the above reactions by metathesis with suitable anions, such as BPh_4^-. Heating of the ion pair $[Co(CO)_3(PR_3)_2][Co(CO)_4]$ effects symmetrization with loss of CO to give the covalent disubstitution products $Co_2(CO)_6(PR_3)_2$ (equation 3). The PR_3 ligands in these hexacarbonyls occupy axial positions in what is probably a D_{3d} structure. Depending on the size of the ligands, non-bridged and bridged forms are in equilibrium in solution as judged from IR spectral bands; however, non-bridged forms predominate. One substituted dicobalt carbonyl complex synthesized in this manner is $Co_2(CO)_6(TPPTS)_2$ ($TPPTS = P\{m\text{-}C_6H_4SO_3Na\}_3$).[9]

$$[Co_2(CO)_3L_2][Co(CO)_4] \xrightarrow{\text{heat}} Co_2(CO)_6L_2 + CO \quad (3)$$

The mechanism for the formation of the ion pair $[Co(CO)_3L_2][Co(CO)_4]$ has been investigated in detail with $L = P(n\text{-Bu})_3$ and was found to be extremely complicated. Mixed reaction orders, between 1 and 1.5 in $Co_2(CO)_8$ and 0.3 to 0.6 in L, which depend not only on the ligand chosen but also on concentrations and temperature, show that a number of parallel reaction routes are followed where one or the other pathway has preponderance. The principal scheme, however, given by equations (4–10), is initiated by cleavage of a dinuclear species (equation 5) to start a radical chain (*see Radicals*).

$$Co_2(CO)_8 + L \longrightarrow Co_2(CO)_8L \quad (4)$$

$$Co_2(CO)_8L \longrightarrow Co(CO)_3L + Co(CO)_4 + CO \quad (5)$$

$$Co(CO)_3L + Co_2(CO)_8 \longrightarrow [Co(CO)_3L]^+[Co(CO)_4]^- + Co(CO)_4 \quad (6)$$

$$Co(CO)_3L^+ + L \longrightarrow Co(CO)_3L_2{}^+ \quad (7)$$

$$Co(CO)_3L_2{}^+ + Co(CO)_4{}^- \longrightarrow [Co(CO)_3L_2]^+[Co(CO)_4]^- \quad (8)$$

$$Co(CO)_4 \longrightarrow Co(CO)_3 + CO \quad (9)$$

$$Co(CO)_3 + L \longrightarrow Co(CO)_3L \quad (10)$$

Since the overall reaction proceeds under conditions where no $Co(CO)_4$ radicals from $Co_2(CO)_8$ cleavage can be detected, splitting of the dinuclear species $Co_2(CO)_8L$, which is formed in a rapid preequilibrium (equation 4), is responsible for radical formation during the induction period. The important step for the formation of the observed products is then outer-sphere electron transfer (*see Outer-sphere Reaction*) as depicted in equation (6). This requires the $Co(CO)_3L$ radical to act as a reducing agent towards $Co_2(CO)_8$. Since, from electrochemistry and pulse radiolysis of $Co_2(CO)_8$, it can be inferred that the cleavage of the Co–Co bond in the dimeric carbonyl requires transfer of just a single electron, and dissociation of the radical monoanion ($Co_2(CO)_{8-n}L_n^-$) is very fast, the electron transfer could even be driven slightly uphill by the follow-up reaction. This mechanistic scheme requires further that reaction of $Co(CO)_3L^+$ with L to form $Co(CO)_3L_2^+$ is faster than reaction with $Co(CO)_4^-$.[10]

This trend is reasonable in view of the coordinatively unsaturated (*see Coordinative Saturation & Unsaturation*) nature of $Co(CO)_3L^+$ (16-electron count) and the much higher concentration of L in solution as compared to that of $Co(CO)_4^-$. Recombination reactions, for example between $Co(CO)_3L$ and $Co(CO)_4$, or of $Co(CO)_3L$ with itself, that would lead to $Co_2(CO)_7L$ and symmetric $Co_2(CO)_6L_2$, respectively, are kinetically fast ($k_{\text{dim}} \sim 10^7 - 10^8\ M^{-1}\,s^{-1}$). However, they are less important owing to the low steady-state concentration of the radicals. Simulation of this mechanistic scheme with insertion of reasonable second-order rate constants results in a rate constant k_{12} for dissociation of $Co(CO)_4$, the step that drives the radical chain after the induction period, of about $10^6\ s^{-1}$ (or greater) and a rate for electron transfer, k_9, of about $10^8\ s^{-1}$ (*see Kinetic Methods*).

Higher substitution products of $Co_2(CO)_8$ are available through CO dissociation followed by ligand association, as described in equations (1) and (2). However, in cases where valence disproportionation (*see Disproportionation*) has occurred, valence conproportionation can also result in more substituted complexes (equations 11 and 12). Reduction of a cation solution of $Co(CO)_3L_2^+$ results in a two-electron reduction from the cation to the monoanion, which combines with excess cation in solution with loss of CO to form the product. An example that has been obtained by this procedure is $Co_2(CO)_4(PMe_3)_4$.[11] The preparation of these highly substituted species proves that the Co–Co bond is retained upon phosphine substitution.

$$Co(CO)_3L_2^+ \longrightarrow Co(CO)_2L_2^- + CO \qquad (11)$$

$$Co(CO)_3L_2^+ + Co(CO)_2L_2^- \longrightarrow Co_2(CO)_4L_4 + CO \qquad (12)$$

2.1.2 *Reaction of $Co_2(CO)_8$*

$Co_2(CO)_8$ has been used in numerous reactions in addition to the plethora of substitution reactions that it undergoes with phosphines, nitrosyls, alkynes, and so forth. Many of these substituted carbonyl complexes and their reactions have been discussed elsewhere in this report. One area in which $Co_2(CO)_8$ has received much attention is catalysis; two classes of catalytic reactions of which $Co_2(CO)_8$ plays a major role are hydroformylation (*see Hydroformylation*) and Pauson–Khand cycloaddition (*see Pauson–Khand Reaction*).

Hydroformylation. $Co_2(CO)_8$ is used as a catalytic precursor to convert alkenes to aldehydes in hydroformylation reactions (equation 13). Aldehydes can be further reduced to produce alcohols. The addition of CO to an alkene is called an ‘oxo’ process (*see Oxo Process*). Hydroformylation products and subsequent derivatives provide chemical components for many industries including polymer manufacture. More than four million tons of aldehydes are made annually, making hydroformylation one of the largest scale applications of homogeneous catalysis (*see Catalysis*). When substituted silanes are used instead of H_2, silyl enol ethers are obtained. The active catalytic species in hydroformylation is $HCo(CO)_4$ (Section ‘General and Acid Properties’), and the mechanism is discussed in section ‘$HCo(CO)_4$ in Hydroformylation Reactions’.

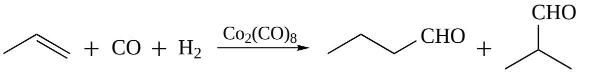

(13)

Substituted cobalt carbonyls of the type $Co_2(CO)_6L_2$ have also been compared to binary cobalt carbonyls as hydroformylation catalysts for linear aldehydes. One study compared four $Co_2(CO)_6L_2$ complexes (L = tertiary phosphines with functionalized alkyl groups) to the well-known complexes $Co_2(CO)_6(P\{n\text{-}Bu\}_3)_2$ and $Co_2(CO)_8$.[12] The bulky phosphine substituent $P(CH_2CH_2CH_2OCH_2CH_2)_3$ showed lower activity than the others, but analogous selectivity.

Pauson–Khand Cycloaddition. Pauson–Khand cycloaddition (*see Pauson–Khand Reaction*) is a cobalt-mediated method to prepare cyclopentenone from the cyclization of an alkyne with an alkene and CO (equation 14). This method is widely used to produce cyclic ketones. Originally, stoichiometric amounts of $Co_2(CO)_8$ were used in these reactions with the cobalt carbonyl being the CO source. However, it was shown that a strict temperature profile and high-purity reagents allowed the use of catalytic amounts of $Co_2(CO)_8$ for reactions with 1 atm of CO.[13] Currently, there is intense interest in developing catalytic cobalt starting materials for use in Pauson–Khand reactions.

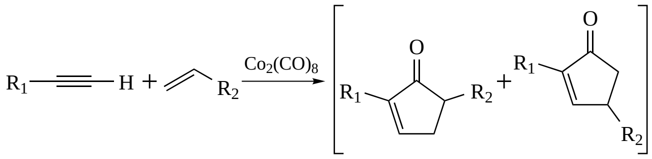

(14)

The mechanism is believed to begin with dissociation of CO, leaving $Co_2(CO)_6$ as the active catalyst. This carbonyl species adds an alkyne, forming a tetrahedrane complex (Section 2.4.1). Insertion of the alkene, upon CO loss, followed by CO insertion and reductive elimination from one of the Co units results in a cyclopentenone. Dissociation of the cyclopentenone from the other Co unit regenerates $Co_2(CO)_6$ (Scheme 1).

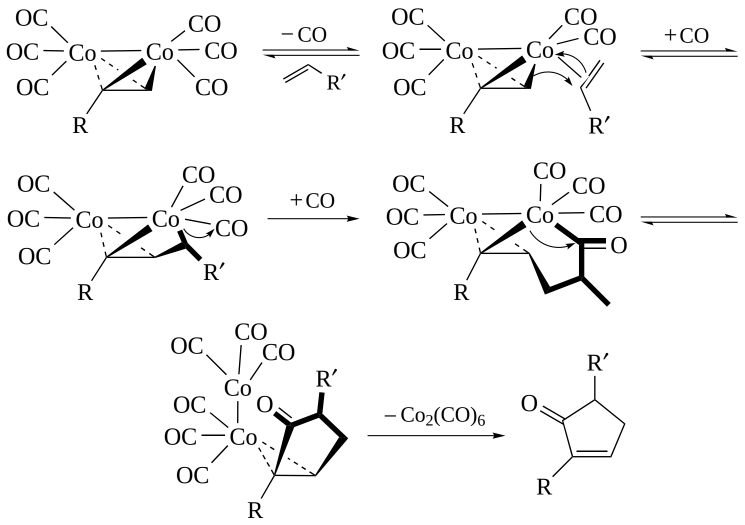

Scheme 1

Steric differences have been shown to affect the regiochemistry of cyclization, as the CO inserts in the α-position of the larger alkynyl substituent. However, theoretical studies on dicobalt hexacarbonyl alkyne complexes have suggested that electronic differences in alkyne substituents may also exert control over the regiochemistry of cyclization.[14,15] Calculations have also provided information on geometries and configurational stabilities of these complexes.

Reactions as described in Scheme 1 are intermolecular (*see Intermolecular*) reactions. An unusual example is the synthesis of 2-phenylcyclopentenone from phenylacetylene and ethane.[16] In this reaction, the substrate ethylene was also the solvent because the reaction was run in supercritical ethylene.

In addition to intermolecular cyclization products, Pauson–Khand reactions can also occur intramolecularly (*see Intramolecular*) to give cyclopentenones. One example of this is the conversion of a cyclic ketone into a functionalized polycyclic system (equation 15).[17]

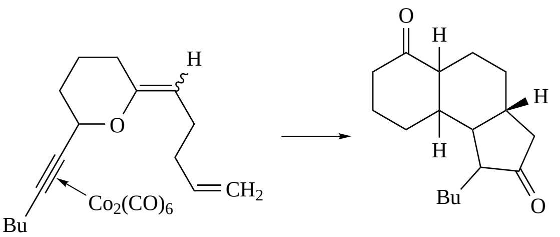

(15)

Many variations on this reaction have been studied over the last several years including use of $Co_2(CO)_8$ on a solid support to accelerate reaction rates,[18] the use of microwave radiation,[19] and the use of ionic liquids as solvents.[20] Asymmetric synthesis has also been given close attention.[21]

2.2 Mononuclear Cobalt Carbonyl Derivatives

2.2.1 $Co(CO)_4$

Depending on the wavelength of radiation used, irradiation of $Co_2(CO)_8$ produces either CO dissociation (at 250 nm) or cleavage into $Co(CO)_4$ radicals (at 360 nm). The radical $Co(CO)_4$ (**2**) itself has been detected by its Raman, infrared, UV–vis, and EPR (*see Electron Paramagnetic Resonance*) spectra.[22] It can be found by EPR when (**1**) is heated and sublimed on a 77 K cold finger in the EPR cavity, or it can be generated in a matrix at low temperature either by photolysis of (**1**) or by the metal vapor technique (*see **Metal Vapor Synthesis of Transition Metal Compounds***).

These methods have produced the full range of fragments from CoCO to $Co(CO)_4$, which could be identified through their IR absorptions. Addition products have been generated, not only with the usual spin traps, but also with dioxygen. In the latter case, a matrix-stabilized trigonal bipyramidal (*see Trigonal Bipyramidal*) adduct $O_2Co(CO)_4$ has been detected. Most significantly, the formation of radical (**2**) is detected with EPR in hexane solution above 120 °C under pressure, thereby indicating the start of thermal dissociation of (**1**) under these conditions. Solutions of (**1**) at ambient temperature are EPR silent and no direct proof for any detectable concentration of (**2**) has been given. Furthermore, reactions like the one between $Co_2(CO)_8$ and CCl_4 giving $Co(CO)_4Cl$ and $Co(CO)_4CCl_3$ are characteristic of radical intermediates. However, it has been shown that dimeric metal carbonyls, including the cyclopentadienyl derivatives $[CpM(CO)_3]_2$ (M = Cr, Mo, W) and $[CpM(CO)_2]_2$ (M = Fe, Ru), undergo fairly rapid redistribution reactions in benzene solution to form equilibrium mixtures of the homo- and heteronuclear dimers (equations 16 and 17).[23] This reaction is most easily explained through the presence of monomeric radicals, albeit in very low concentration.

$$Co_2(CO)_8 + Mn_2(CO)_{10} \rightleftharpoons 2(CO)_4Co–Mn(CO)_5 \quad (16)$$

$$Co_2(CO)_8 + [CpFe(CO)_2]_2 \rightleftharpoons 2(CO)_4Co–Fe(CO)_2Cp \quad (17)$$

CO substitution in heteronuclear cobalt carbonyl complexes has also been studied. Several phosphines were used in exchange reactions with CO in the complex $CpMo(CO)_3–Co(CO)_4$. Both a CO dissociative pathway, leading to substitution, and a radical chain pathway, initiated by associative attack of the phosphine and subsequent disproportionation (*see Disproportionation*), were found depending on reaction conditions (thermal or photochemical treatment) and the basicity and sterics of the phosphine ligands. As seen in substitution reactions with $Co_2(CO)_8$, strongly basic phosphines add to the complex via disproportionation, while less basic phosphines add via substitution. However, the metal centers help determine where the phosphine adds because the rates of substitution on each metal center differ depending on which pathway, dissociative or radical chain, is operative.[23,24]

A unique air-stable 19-electron derivative (*see Nineteen Electron Configuration*) of (**2**) was obtained with the ligand bis(diphenylphosphino)maleic anhydride. DFT calculations on this system predict that the spin density should reside on the ring. Experimental data support this prediction, as a large hyperfine coupling to P and a small hyperfine coupling to cobalt indicate that the odd electron delocalizes over the dppm unit (Figure 2) (*see* ***Paramagnetic Organometallic Complexes***).[25]

Electrochemical experiments on bidentate phosphorus ligands indicate that ligands with reduction potentials more positive than −1 V (versus SCE) form long-lived 19-electron species with cobalt carbonyls, whereas ligands with more negative potentials form reactive species. For example, with a reduction potential of −0.7 V, bis(diphenylphosphino)maleic anhydride was expected to form a stable species with cobalt carbonyls, a prediction confirmed by its synthesis.[26]

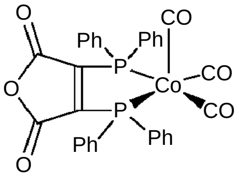

$g_{iso} = 2.0041$

$A_P = 11.11$ G, $A_{Co} = 1.4$ G

$\mu_{eff} = 2.04$ BM

$\nu_{CO} = 2015–2075$ cm^{-1}

Figure 2 Structure of $(dppm)Co(CO)_3$

2.2.2 *HCo(CO)₄*

General and Acid Properties. The carbonyl hydride $HCo(CO)_4$ (**3**) is formed in situ from $Co_2(CO)_8$ and H_2 in hydroformylation mixtures or by acidification of the anion $Co(CO)_4^-$ with a strong acid. The $Co(CO)_4^-$ anion is easily made by reduction of $Co_2(CO)_8$. Interestingly, if $Co_2(CO)_8$ is dissolved in strong acids under a CO atmosphere, the positively charged $[Co(CO)_4]^+$ cation is formed instead.[27]

$HCo(CO)_4$ is a volatile, very toxic liquid with an extremely unpleasant odor. It is rather unstable as a pure material, decomposing into $Co_2(CO)_8$ and H_2 below room temperature. The equilibria between $Co_2(CO)_8$ and $HCo(CO)_4$ under different H_2 pressures have been studied. Dilute solutions are more stable, from which observation of a second-order decomposition pathway has been concluded. However, very pure, colorless samples of (**3**) are much more stable, and $Co_2(CO)_8$ acts as a catalyst for the decomposition of (**3**). Since this decomposition follows a rate law of half-order in $Co_2(CO)_8$, the radical $Co(CO)_4$ is invoked as the active species in the decomposition process according to equations (18–21). From electron diffraction measurements, the geometry of (**3**) is trigonal bipyramidal (*see Trigonal Bipyramidal*), with hydrogen occupying an axial position.

$$HCo(CO)_4 + Co(CO)_3 \longrightarrow HCo_2(CO)_7 \quad (18)$$

$$HCo_2(CO)_7 + HCo(CO)_4 \longrightarrow H_2Co_2(CO)_7 + Co(CO)_4\cdot \quad (19)$$

$$H_2Co_2(CO)_7 \longrightarrow H_2 + Co_2(CO)_7 \quad (20)$$

$$Co_2(CO)_7 + Co(CO)_4 \longrightarrow Co(CO)_3 + Co_2(CO)_8 \quad (21)$$

$HCo(CO)_4$ is soluble in water to the extent of 5.6×10^{-2} M. It titrates as a strong mineral acid in water and deprotonation in methanol suggests a pK_a value around −4. The reason for the very high acidity of (**3**) may stem from the extra stabilization of the anion (**2**$^-$) owing to its d^{10} configuration.

High pressure NMR experiments performed over a temperature range of 80–200 °C in supercritical CO_2 showed that a hydride ligand transfer reaction between $HCo(CO)_4$ and $Co_2(CO)_8$ results in cobalt–metal exchange between $HCo(CO)_4$ and $Co_2(CO)_8$ (equation 22). A hydride transfer reaction between $HCo(CO)_4$ and $HMn(CO)_5$ is also evident; however, manganese exchange does not occur between $HMn(CO)_5$ and $Mn_2(CO)_{10}$ or $MnCo(CO)_9$. The lack of manganese exchange does not support an oxidative addition (*see Oxidative Addition*) reaction mechanism for the heterometallic hydride transfer, so the mechanism is regarded as a hydrogen atom transfer between $Co(CO)_4$ and $Mn(CO)_5$ radicals (equation 23).[28]

$$H^*Co(CO)_4 + Co_2(CO)_8 \rightleftharpoons HCo(CO)_4 + Co^*Co(CO)_8 \quad (22)$$

$$^*HMn(CO)_5 + HCo(CO)_4 \rightleftharpoons HMn(CO)_5 + {}^*HCo(CO)_4 \quad (23)$$

The majority of homoleptic carbonyls and many other derivatives can be formed with PF_3 ligands instead of CO.[29] In many instances, CO is exchanged by PF_3 under pressure. In contrast to the elusive nature of (**3**), its PF_3 analog $HCo(PF_3)_4$ is of very high thermal stability and does not decompose below 250 °C. Its acid–base properties seem to resemble those of the carbonyl hydride, however.

$HCo(CO)_4$ in Hydroformylation Reactions. As previously mentioned, $HCo(CO)_4$ is a key intermediate in the homogeneous hydroformylation of alkenes with CO/H_2 to aldehydes. Using $HCo(CO)_4$ as the CO component, hydroformylation can be made stoichiometric when run under N_2 as an inert atmosphere.

The coordinatively unsaturated species that adds to the alkene is believed to be the product of CO dissociation from $HCo(CO)_4$ (**3**), since the overall reaction is retarded by high CO pressure, and dissociation of CO from (**3**) or a phosphine substitution product (equation 24) is probably the rate-determining step. After alkene addition to $HCo(CO)_3$, CO adds to the metal center only to form a corresponding acyl via migratory insertion (*see Migratory Insertion*). Addition of H_2, followed by heterolytic cleavage, results in the product aldehyde and regeneration of the catalyst (Scheme 2).[30]

$$HCo(CO)_3P \rightleftharpoons HCo(CO)_2P + CO \qquad (24)$$

It was found in hydroformylation studies that sterically more demanding substituents such as phosphines (e.g. $P(n\text{-}Bu)_3$) influence the *n*/*iso* ratio of the final aldehyde in favor of the straight chain *n*-aldehydes, which are more valuable products from an industrial point of view. The reason seems to be the different migratory ability of terminal versus internal intermediate alkyl complexes (Scheme 3).[31] This finding has stimulated extensive synthetic activity in the area of the substituted carbonyls $Co_2(CO)_{8-n}(PR_3)_n$ and $HCo(CO)_{4-n}(PR_3)_n$ as well as the model intermediates $RCo(CO)_{4-n}(PR_3)_n$. Owing to its acidic properties, (**3**) adds to dienes yielding allyl complexes (equation 25), which are also intermediates in the hydrogenation of alkenes catalyzed by (**3**).

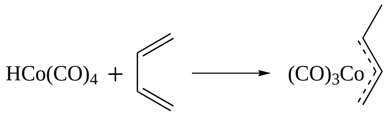

(25)

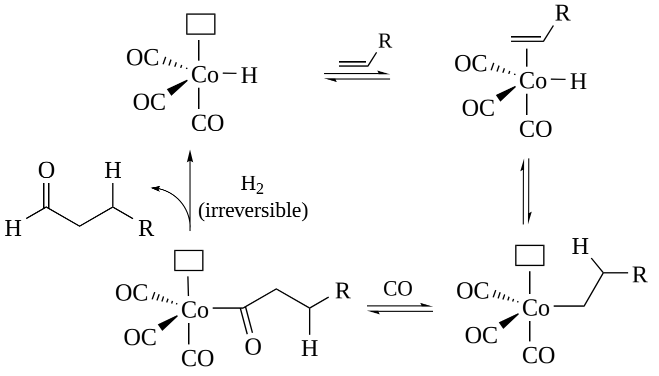

Scheme 2

2.2.3 $Co(CO)_4^-$

General Characteristics. In accordance with the high tendency for formation of $Co(CO)_4^-$ ($\mathbf{2}^-$) and the acidity of (**3**), the former compound behaves in many respects as a pseudohalide (*see Pseudohalide*). Relative rates of electrophilic substitution with MeI and MeOTs classify ($\mathbf{2}^-$) as a hard and relatively weak nucleophile (*see **Hard & Soft Acids and Bases***). Compounds of the type $RCo(CO)_4$ are prepared by two different methods: reaction of an electrophilic halide, sulfate, or tosylate (RX) with ($\mathbf{2}^-$), or reaction of $HCo(CO)_4$ with alkenes. Simple alkyl derivatives have low stability; nevertheless, many studies have been conducted in which species have been identified as $RCo(CO)_4$ intermediates. Apart from alkyl and aryl derivatives, for example $MeCo(CO)_4$ and $PhCo(CO)_4$, ($\mathbf{2}^-$) forms derivatives with main group residues R_3E^{IV} and R_2E^{V} and with the main group metals Zn, Cd, and Hg as well as with transition metals, as shown by examples in Scheme 4. Co–E bonding in these compounds appears to be predominantly covalent. The bond distances can be long, and consequently, the coordination number of Co can be high.

Among the numerous substitution products of the complexes $HCo(CO)_4$, $RCo(CO)_4$, and $XCo(CO)_4$, those with phosphines are particularly abundant. Accessible by either gradual photochemical or thermal substitution of CO for phosphine, these compounds can also be obtained in a

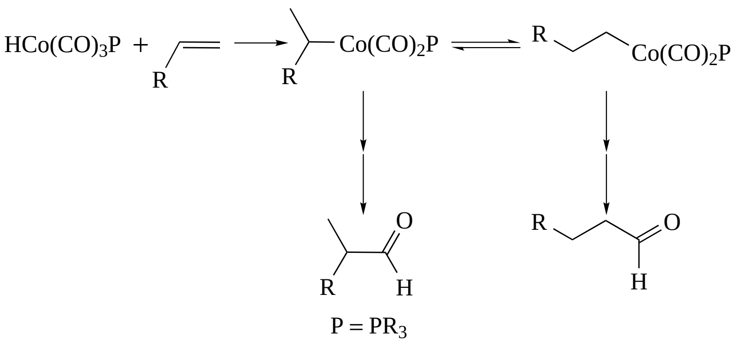

Scheme 3

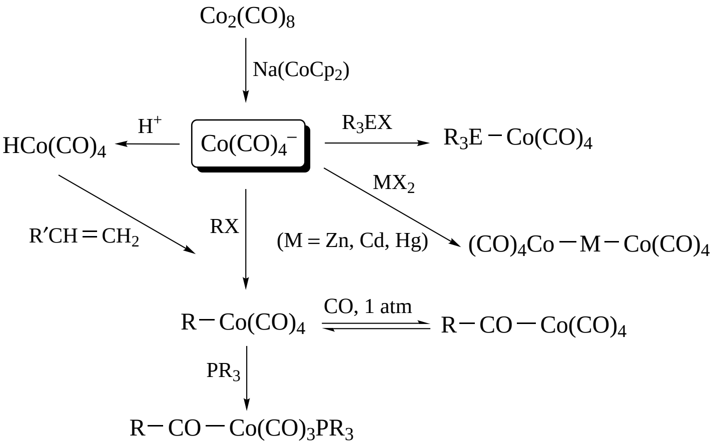

Scheme 4

reverse fashion by reaction of $CoCl_2$ with the appropriate phosphine to give cobalt chlorophosphine complexes that can be carbonylated with CO. Dissociative CO loss is probably the crucial step by which decomposition is initiated.

Molecular orbital (MO) calculations on $MeCo(CO)_4$ place a negative charge on the methyl carbon atom with polarization of the Co–Me bond. Substitution of CO ligands withdraws electron density from the alkyl carbon atom and delivers electron density to the metal, thus stabilizing the Co–C bond.

Insertion of CO into $RCo(CO)_4$ to give acyl complexes is facile (*see* ***Mechanisms of Reaction of Organometallic Complexes***). This reaction proceeds at 1 atm of CO at ambient temperature. The alkyl–acyl equilibrium lies far towards the acyl complex. The activation energy for the process has been calculated by MO methods to be about $85\,\mathrm{kJ\,mol^{-1}}$ (*see* ***Molecular Orbital Theory***). Thus, $RCo(CO)_4$ complexes can only be obtained under conditions of low CO pressure, which in turn opens the way for CO dissociative decomposition. Cobalt acyl complexes can be derivatized in several ways to form various products (Scheme 5).

Many industrially important catalytic processes use alkyl and acyl cobalt carbonyl complexes, which can be synthesized from (**2**$^-$). Acyl complexes produced after formation of the cobalt–carbon bond can be transformed in different ways to produce hydrocarbons, carbonyl compounds, or carboxylic acid derivatives. Interconversion of alkyl and acyl moieties results from carbonylation/decarbonylation reactions in which strong electron-withdrawing groups stabilize an alkyl product. The use of perfluorinated groups also gives enhanced stability to the complexes. One such stabilized species is the pentafluorophenylcobalt tricarbonyl triphenylphosphine complex, $C_6F_5Co(CO)_3P(C_6H_5)_3$ (Figure 3).**[32]**

Use of $Co(CO)_4^-$ in Organic Syntheses. The synthetic potential provided by the various methods for formation, modification, and cleavage of the Co–C bond with the aid of $Co(CO)_4^-$ has been exploited, in a way similar to that done with the Fe congener $Fe(CO)_4^{2-}$ (or $FeH(CO)_4^-$), in versatile stoichiometric and catalytic reactions (*see* ***Iron: Organometallic Chemistry***).

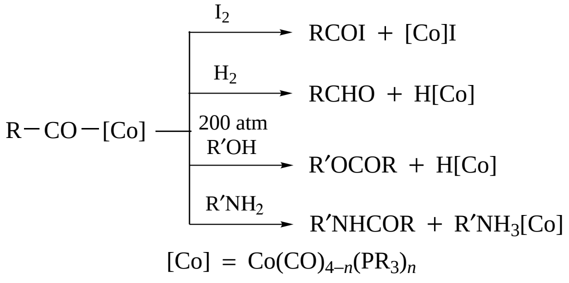

Scheme 5

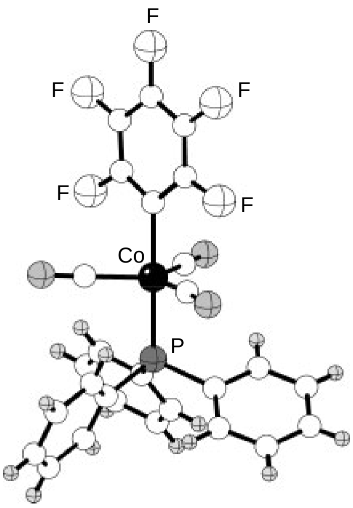

Figure 3 Structure of $C_6F_5Co(CO)_3P(C_6H_5)_3$

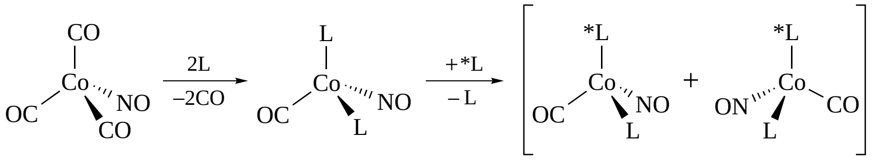

Scheme 6

The tetracarbonylate (**2**$^-$) is the driving nucleophile (*see Nucleophile*) in many applications. A procedure by which it can be transferred into a nonpolar organic phase with the aid of a phase transfer agent such as $BnNEt_3Cl$ created the possibility of conducting these reactions at or slightly above room temperature (equations 26–28).

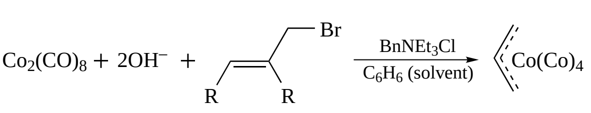

(26)

$$PhCH_2Cl + Co_2(CO)_8/OH^- \xrightarrow[C_6H_6(solvent)]{BnNEt_3Cl} PhCH_2CO_2H \tag{27}$$

$$Co(CO)_4{}^- + MeI + Co \xrightarrow[C_6H_6(solvent)]{BnNEt_3Cl} MeCO\text{–}Co(CO)_4 \tag{28}$$

2.2.4 Nitrosyl–Carbonyl Complexes

As a metal containing an odd number of valence electrons, cobalt is prone to form mononuclear NO complexes (*see Nitrosyl Complexes*) derived from carbonyls or substituted carbonyls by ligand substitution. The simplest of these compounds, $Co(CO)_3NO$ (**4**), is a dark red liquid at ambient temperature that slowly decomposes in air. Electron diffraction has confirmed its C_{3v} structure with a linear NO group. Compared to the different structural isomers of $Co_2(CO)_8$, the CO stretching vibrations are at higher frequency, indicating less back bonding (*see Back Bonding*) from cobalt into CO. The NO stretch is found in the range where such bonds for linear NO groups usually appear ($1650–1900\,cm^{-1}$). Substitution of the CO ligands of (**4**) leads to the derivatives $Co(CO)_{3-n}L_nNO$ ($n = 1, 2, 3$), with L being primarily phosphines.

Compound (**4**) reacts with halides, preferably their alkylammonium salts, in acetone or DME with exchange of one CO for a halide, giving anionic complexes of the type $Co(CO)_2(NO)X^-$ (X = Cl, Br, I, CN) (equation 29). Owing to the high charge density at the metal, these anions can act as sources for the hyponitrous ion, NO^-, which is transferred in nucleophilic substitutions at activated (benzyl) halides, giving aldoximes (e.g. PhCH=NOH from $PhCH_2Y$) (equation 30).[33]

$$Co(CO)_3NO + NR_4X \xrightarrow{DMF} Co(CO)_2(NO)X^- + CO$$
$$X = Cl, Br, I, CN \tag{29}$$

$$Co(CO)_2(NO)X^- + PhCH_2Y \longrightarrow \frac{1}{2}Co^{2+} + X^- + Y^- + \frac{1}{2}[Co(CO)_4] + PhCH{=}NOH \tag{30}$$

Optically active organometallic complexes have been used to study stereochemical reactions. Substituted cobalt nitrosyl complexes are interesting chiral (*see Chiral*) complexes because they exhibit tetrahedral structures, whereas most optically active organometallic complexes are half-sandwich structures with octahedral geometries. Diastereomeric cobalt complexes of the type Co(CO)(NO)(L)(*L) (L = phosphite or phosphane; *L = optically active phosphane or isocyanide) have been synthesized from (**4**) via substitution (Scheme 6).[34]

2.3 Higher Nuclearity Clusters and Cluster Anions

As noted in early reports, (**1**) undergoes thermal loss of CO at 60 °C (Scheme 7) to give the black, very air-sensitive ‘tricarbonyl $Co(CO)_3$’, subsequently recognized as the tetranuclear carbonyl $Co_4(CO)_{12}$ (**5**) with one $Co(CO)_3$ group on top of a Co_3 triangle built from three $Co(CO)_2$ groups with three edge-bridging carbonyls. Thermodynamic decomposition parameters have been calculated for this pathway under vacuum.[35]

Further heating leads to complete decomposition, since the third binary carbonyl of Co, $Co_6(CO)_{16}$ (**6**), decomposes at about the same temperature as (**5**) (110–120 °C). The hexacobalt cluster is obtained along with some (**5**) by $FeCl_3$ oxidation of the anions $Co_6(CO)_{15}{}^{2-}$ or $Co_6(CO)_{14}{}^{4-}$. No higher binary carbonyls of cobalt are known, but many heteroclusters and homometallic cluster anions of higher nuclearity have been prepared; $[Co_{10}N_2(CO)_9(\mu\text{-}CO)_{10}]^{4-}$ (Figure 4), a metal cage constructed from three condensed trigonal prisms, is an example of a homometallic cobalt cluster tetraanion.[36]

Reduction of (**5**) with alkali metal forms the green cluster anion $Co_6(CO)_{15}{}^{2-}$, which can be further reduced to the red dianion $Co_6(CO)_{14}{}^{4-}$, and isolated as a potassium salt. The latter cluster anion is an early example of the expanding family of highly reduced transition metal carbonyls, for example $Na_3Co(CO)_3$,[37] where up to two CO groups are replaced by two electrons each. $Co_6(CO)_{15}{}^{2-}$ is also the main product from valence disproportionation of $Co_2(CO)_8$ in ethanol. Oxidation (or acidification) of the cluster anions gives $Co_6(CO)_{16}$.

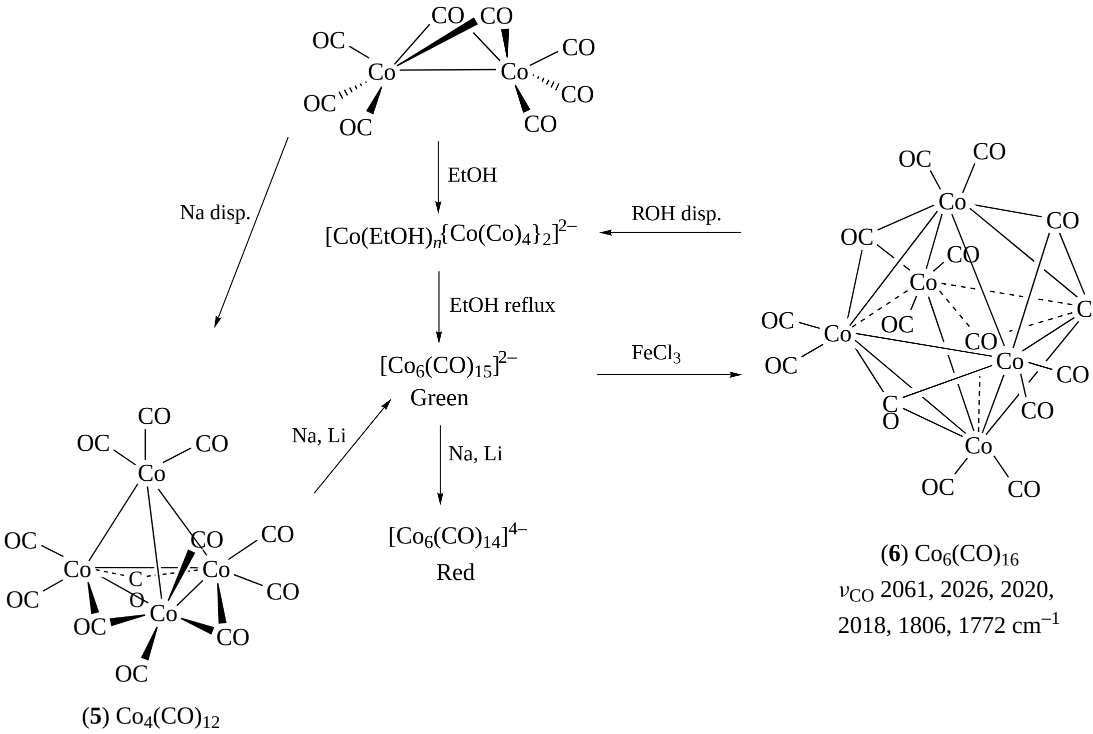
Na disp.
EtOH
$[Co(EtOH)_n\{Co(Co)_4\}_2]^{2-}$
ROH disp.
EtOH reflux
$[Co_6(CO)_{15}]^{2-}$
Green
FeCl$_3$
Na, Li
Na, Li
$[Co_6(CO)_{14}]^{4-}$
Red

(**6**) $Co_6(CO)_{16}$
ν_{CO} 2061, 2026, 2020,
2018, 1806, 1772 cm^{-1}

(**5**) $Co_4(CO)_{12}$

Scheme 7

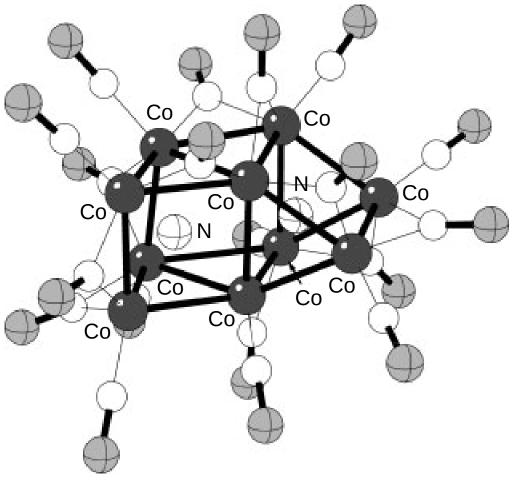
Co
Co
Co
Co
N
Co
Co
N
Co
Co
Co
Co
Co
Co

Figure 4 Structure of $[Co_{10}N_2(CO)_9(\mu\text{-}CO)_{10}]^{4-}$

2.4 Complexes with a Tetrahedrane Skeleton

Two classes of complexes are derived from $Co_4(CO)_{12}$ by replacement of one or two $Co(CO)_3$ groups by the isolobal (*see Isolobal Analogy*) RC unit, leading to cluster types $(RC\equiv CR)Co_2(CO)_6$ (**7**) and $RCCo_3(CO)_9$ (**8**). Both classes of compounds have an abundant variety of derivatives with widely differing R groups and hetero functions, and they exhibit a rich and extended chemistry (Scheme 8).

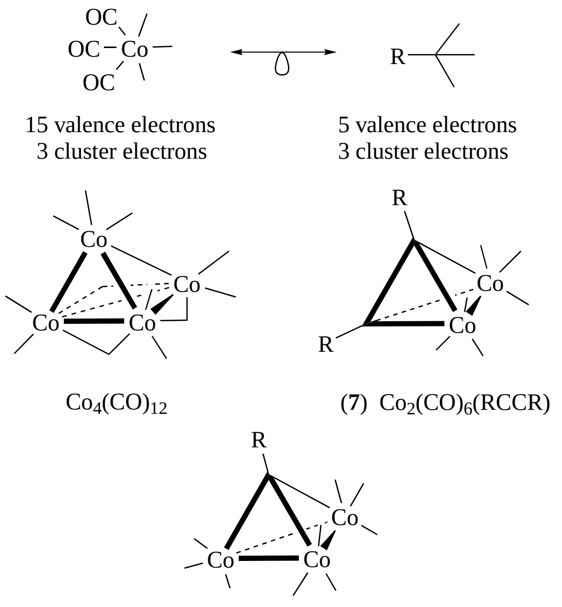
15 valence electrons
3 cluster electrons
5 valence electrons
3 cluster electrons
$Co_4(CO)_{12}$

(**7**) $Co_2(CO)_6(RCCR)$

(**8**) $Co_3(CO)_9CR$

Scheme 8

2.4.1 *$Co_2(CO)_6(\mu_2\text{-}RC\equiv CR)$*

Two-carbon, two-cobalt tetrahedranes $(RC\equiv CR)Co_2(CO)_6$ (**7**) are formed with great ease from $Co_2(CO)_8$ and the respective acetylenes. R groups on the alkyne comprise the usual alkyl, aryl, CF_3 and CO_2Me substituents, but they can also be functionalized organics such as NEt_2 or organometallics like ferrocene (*see Ferrocene*). The structure of these dinuclear compounds resembles a doubly bridged form of $Co_2(CO)_8$, in which the two bridging CO groups are replaced by the alkyne, which is arranged perpendicular to the Co–Co axis (Figure 5). A lowering of the C≡C stretching frequency from values of 2140–2300 cm^{-1} in the free alkyne to 1400–1630 cm^{-1} in the coordinated alkyne is observed. Carbon–carbon distances in the coordinated alkyne are in the range 1.32–1.37 Å, in accordance with a formal C=C double bond. The Co–Co bond, ranging from 2.45 to 2.49 Å, is shortened in comparison to that in $Co_2(CO)_8$ (2.52 Å).

According to an early computational study, bonding in μ-alkyne complexes is mainly through stabilization of the acetylene π*-orbitals by interaction with the dimetal fragment. An electron flow of one electron from an alkyne π-orbital to each cobalt, and back-bonding (*see Back Bonding*) of one d orbital per cobalt into an alkyne π*-orbital accounts for the C–C bond lengthening for the bending of the substituents from the C–C vector, typically by 140°.

Complexes containing terminal alkynes undergo rearrangement to the corresponding tricobalt clusters (**8**) (Section 2.4.2) when refluxed with mineral acid in methanol. This variety of complex is also formed directly under these conditions from $Co_2(CO)_8$ and excess alkyne. (equation 31).

$$Co_2(CO)_8 + RCCR\ (excess) \longrightarrow CO_3(CO)_9CR\ (\mathbf{8}) \qquad (31)$$

When compounds (**7**) were heated with alkyne in excess, two types of complexes, both involving alkyne coupling, are formed. A compound with the stoichiometry $Co_2(CO)_4(C_4R_2CO)_2$, formed mainly from terminal alkynes having one bulky substituent R, represents derivatives of $Co_2(CO)_8$ where two CO groups at either metal are replaced by a cyclopentadienone ligand. This compound type represents one of the many instances where alkynes combine with CO in the presence of a transition metal fragment to yield mostly cyclopentadienones, often complexed to the metal; this cycloaddition reaction is similar to the Pauson–Khand scheme except for the use of an alkyne in place on an alkene (see also Section 5.1.4 and Scheme 26). The reaction eventually proceeds further to liberate an arene. Thus, from the use of *t*-BuC≡CH, the alkyne trimerization product 1,2,4-tri-*t*-Bu-benzene was isolated.

Under more forcing conditions, that is, enhanced CO pressure, the complexed alkyne can combine with excess CO, giving lactones that are bound to the $Co_2(CO)_6$ moiety via a bridging methylidene group (Scheme 9).

At higher temperatures (100–160 °C), alkynes, in particular, those featuring electron-withdrawing R groups, form a different type of complex (Scheme 10). These consist of two metal–metal bonded $Co(CO)_3$ units that are also linked through a chain made up of three alkyne units. Under these more severe conditions, this complex type is also formed from $Co_2(CO)_8$ and the alkyne; at lower temperature, the reaction of $Co_4(CO)_{12}$ and the alkyne suffices. The cobalt moieties are bound to either part of this six-carbon chain in an allylic fashion and, in addition, to the terminal carbon

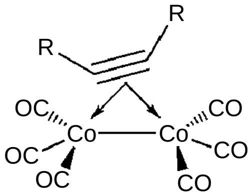

Figure 5 Schematic structure of $(RC{\equiv}CR)Co_2(CO)_6$

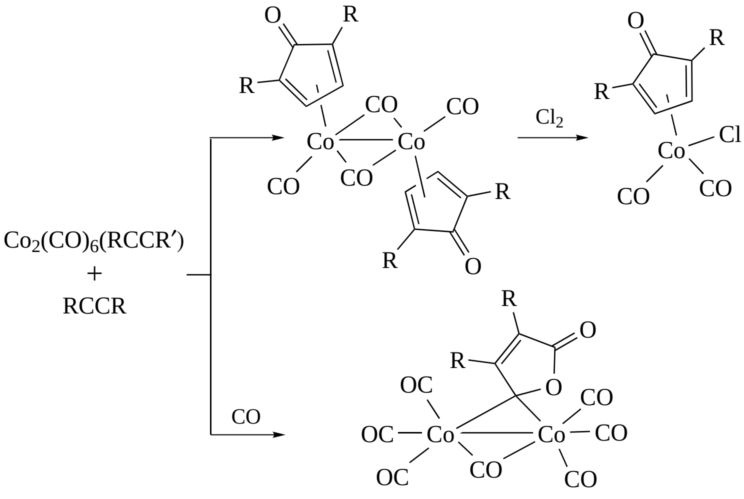

Scheme 9

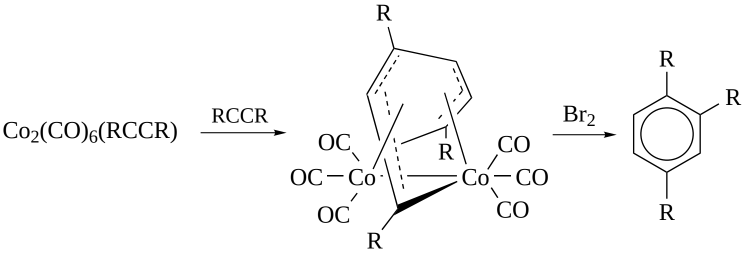

Scheme 10

atoms by a σ-bond. The carbon chain becomes a double four-electron ligand where two planar allyl parts are joined by a carbon–carbon single bond. These so-called 'flyover' complexes are represented by $Co_2(CO)_3(PPh_3)\{\mu$-$C(SiMe_3)=CH–CH=C(SiMe_3)–CH=C(SiMe_3)\}$ (Figure 6);[38] similar 'flyover' complexes are known with a variety of bimetal units.

Interestingly, these flyover complexes can be degraded and release substituted benzenes by thermal decomposition or oxidation of the metal fragment with halogens. The position of the R groups in the flyover complex, in the cases where they have been located, corresponds to their position in the benzene formed, thus proving ring closure between terminal carbon atoms. Even the product derived from t-BuC≡CH with three t-Bu groups at carbons 1, 3, and 6 in the complex is degraded to give the sterically constrained 1,2,4-tri-t-Bu-benzene. Consequently, the flyover complex is an important model intermediate in dicobalt-catalyzed alkyne trimerization (*see Cyclodimerization & -trimerization Reactions*), which has been shown to proceed at many different organometallic cobalt residues (Section 5.1.4). Note that substituted benzenes along with cyclopentadienones have also been formed in the thermal decomposition of (**7**).

Biologically Significant Reactions of $Co_2(CO)_6$ (μ_2-RC≡CR). Many dicobalt carbonyls with complexed alkynes have been used in natural product synthesis. In one study, $Co_2(CO)_6(\mu_2\text{-RC≡CR})$ complexes were shown to play an important role as stable intermediates for the construction of the antitumor enediyne agents dynemicin, calicheamiin, esperamicin, and neocarzinostatin.[39] The same type of cobalt complex was also involved in the syntheses of ingenol[40] and ciguatoxin.[41]

The $Co_2(CO)_6(\mu_2\text{-RC≡CR})$ complexes themselves can be biologically active; some exhibit antitumor activity exceeding that of cis-platin.[42] The first organometallic derivative of 11b-ethynylestradiol has also been synthesized; it incorporates the $Co_2(CO)_6(\mu_2\text{-RC≡CR})$ moiety and is a potential high-affinity estrogen receptor marker.[43]

2.4.2 Formation and Properties of $(CO)_9Co_3CR(= [Co_3C]R, 8)$

Geometrical parameters (from an X-ray structure determination) of a common derivative, the methyl compound $[Co_3C]CH_3$, are given in Figure 7. This class of complex can formally be generated by removing the apical $Co(CO)_3$ group from $Co_4(CO)_{12}$ and substituting for it a carbyne moiety RC (Scheme 8).[44] Electrochemistry of the tricobalt cluster has revealed a reversible one-electron reduction at about −0.4 V (vs. Ag/AgCl) to form stable radical anions.[45]

Although derivatives of (**8**) are formed in many different reactions, rational syntheses usually begin with trihalocarbons and $Co_2(CO)_8$ as reagents.[46] Bromoform gives the hydrocarbon $[Co_3C]H$, whereas CCl_4 yields $[Co_3C]Cl$.[47]

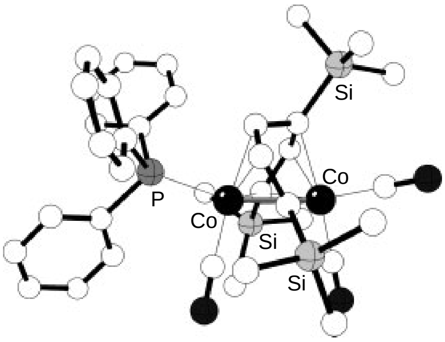

Figure 6 Structure of $Co_2(CO)_3(PPh_3)\{\mu$-$C(SiMe_3)=CH–CH=C(SiMe_3)–CH=C(SiMe_3)\}$

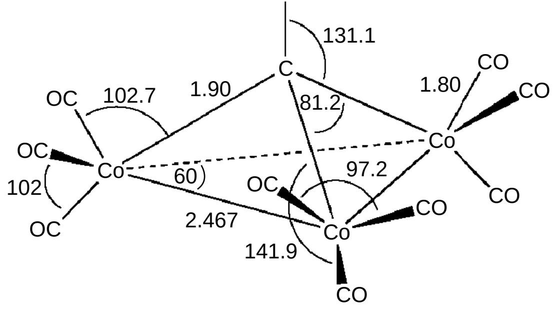

Figure 7 Structural parameters in $Co_3(CO)_9CMe$

The chloro derivative $[Co_3C]Cl$ can be used for Friedel–Crafts electrophilic aromatic substitution,**48** showing the electrophilic nature (*see Electrophile*) of the cation $[Co_3C]^+$. Apart from hydrogen and halogen, many other functionalities (R) are tolerated on the halocarbon X_3CR in the synthesis of organic derivatives $[Co_3C]R$. Dehalogenation of $[Co_3C]Cl$ with $AsPh_3$ at 100 °C gives a dimer (equation 32).

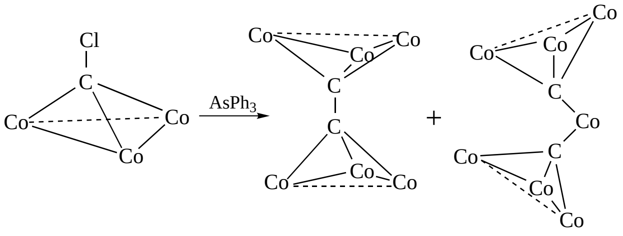

(32)

The steric properties of the $(CO)_9Co_3$ core are such that the apical carbon group is highly shielded by six of the nine CO groups pointing towards the apex. Substitutions at the carbon atom of $[Co_3C]$ are therefore subject to severe steric hindrance. With respect to its electronic properties, $[Co_3C]$ seems to be a strongly electron-releasing group. This effect is indicated by the facile formation of the black, isolable acylium cation formed from an acid or ester, for example, with HPF_6 in propionic anhydride (equation 33).

$$[Co_3C]CO_2R + HPF_6 \longrightarrow [Co_3C]CO^+PF_6^- + ROH$$
$$[Co_3C] = Co_3(CO)_9C \qquad (33)$$

Ketones of the type $[Co_3C]COR$ show very low carbonyl stretching frequencies in the IR (*see Infrared Reflection Adsorption Spectroscopy*) ($1560-1654\,cm^{-1}$), indicating a high degree of polarization of the C≡O bond, and are thus very reactive as carbonyl compounds. They are susceptible to acidic hydrogenation with CF_3CO_2H/Et_3SiH and produce hydrocarbon derivatives in up to 90% yield (equation 34).

$$[Co_3C]COR + CF_3CO_2H + 2Et_3SiH$$
$$\longrightarrow [Co_3C]CH_2R + CF_3CO_2SiEt_3 + Et_3SiOH \qquad (34)$$

The carbonyl activation by $[Co_3C]$ allows ketones $[Co_3C]COR$ to be hydrosilylated (*see Hydrosilation*), without catalyst under mild conditions, to silyl ethers $[Co_3C]CH(OSiEt_3)R$, whose acid hydrolysis gives the corresponding alcohols $[Co_3C]CH(OH)R$. These alcohols in turn are the sources for $[Co_3C]$ stabilized carbocations $[Co_3C]CRH^+$ (equation 35).

$$[Co_3C]CHROH + HPF_6 \xrightarrow{-H_2O} [Co_3C]CHR^+PF_6^- \qquad (35)$$

Aryl groups bound to $[Co_3C]$ as $[Co_3C]$-aryl are activated in the *para* position for electrophilic substitution (*see Electrophilic Reaction*). From the ν_{CO} of $1685\,cm^{-1}$ for *p*-$[Co_3C]$-C_6H_4COMe, a Hammett σ-constant of -0.35 was estimated for $[Co_3C]$, which is nearly equivalent to that for an OH group. The ^{13}C chemical shift of the apical carbon appears at $\delta 300$ ppm (in $[Co_3C]CH(OH)C_9H_{19}$) and shifts to 255–275 ppm in the carbonium ions. This region is outside the range for carbon in organic compounds and is found typically in carbyne complexes (*see Carbyne Complexes*) ($X(CO)_4M{\equiv}CR$). This similarity leads one to consider the $[Co_3C]$ core as a triply bridging carbyne.

2.4.3 Heteroatom Derivatives of $Co_3(CO)_9CR$

The apical carbon fragment of $[Co_3C]R$ complexes can be replaced by heteroatoms or heterofunctional groups. Clusters containing RSi, RGe, and RSn in place of RC have all been studied. Group 15 analogs (Scheme 11) can be prepared in which from one to three $Co(CO)_3$ groups in $Co_4(CO)_{12}$ are replaced by P, As, or Sb, and nearly the complete series has been synthesized. Surprisingly, derivatives $Co_3(CO)_9E$ with one ‘heterovertex’ appear to be the least stable. Thus $Co_3(CO)_9P$ has only been detected in solution by its IR

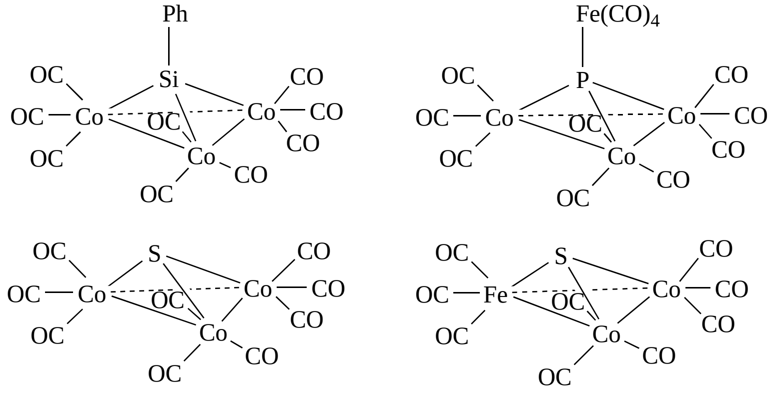

Scheme 11

absorbances (in comparison to the better studied As congener) and is further stabilized by coordination to a $Fe(CO)_4$ group. In contrast, derivatives $Co_2(CO)_6E_2$, formally containing the coordination stabilized E=E molecules, are all known, as are the tetrahedranes $Co(CO)_3E_3$, which are stable compounds that can be sublimed and recrystallized without decomposition.

Since an unsubstituted group 16 atom contributes four electrons (one more than RC) the resulting $(CO)_9Co_3E$ (E = S, Se, Te) complexes are paramagnetic. The odd electron resides in an a_2 orbital in the M–M–M plane and is metal–metal antibonding (*see Antibonding*). The effect has been substantiated by X-ray structures of $(CO)_9Co_3S$ and $(CO)_9Co_2FeS$,[49] the latter being diamagnetic and isoelectronic with $(CO)_9Co_3S^+$. In the paramagnetic cluster, a Co–Co distance elongated by some 0.1 Å relative to Co–Co distances in diamagnetic clusters is observed.

2.4.4 Cp and Arene Derivatives

Pseudotetrahedral cyclopentadienyl derivatives that retain the metal-core bonding scheme commonly feature the Co_3Cp_3 moiety. Since each CpCo unit contributes one electron fewer than does $(CO)_3Co$, stability requires that the apical group should be a six-electron ligand. Complexes that meet this requirement are of composition Cp_3Co_3(arene), and are prepared thermally from $CpCo(C_2H_4)_2$ (Section 5.1.2). The synthesis is only successful if the arene bears a vinyl group.[50]

The vinyl substituent is needed to anchor the first $CpCo(C_2H_4)$ group, which then can form Co–Co bonds with two other CpCo fragments to yield the final complex. The arene ligand is oriented so that the C–C bonds eclipse the cobalt atoms. Crystallographic studies show a Kekulé-type (threefold) distortion in the arene ring; the bonding asymmetry is emphasized by a hindered rotation of the arene ring around the Co–Co–Co triangle that is observed with NMR spectroscopy (Scheme 12).

Additional tetrahedrane clusters are formed when vertices in $Co_4(CO)_{12}$ are substituted with isolobal (*see Isolobal Analogy*) (or nonisolobal) metal fragments. In this category are the mixed Co–Rh and Co–Ir carbonyl complexes, which can be formed from the reaction of $M_4(CO)_{12}$ (M = Rh, Ir) and $Co_2(CO)_8$. For example, $Co_3Rh(CO)_{12}$, which has been used as a hydroformylation catalyst precursor, is prepared in this way.[51] Furthermore, since the $Co(CO)_3$ group is isolobal to a Co(arene) fragment, a series of substitutionally related polynuclear cobalt complexes is conceivable (Scheme 13), some of which have been identified from the metal vapor reaction of cobalt atoms with a toluene matrix in the presence of an alkyne.[52]

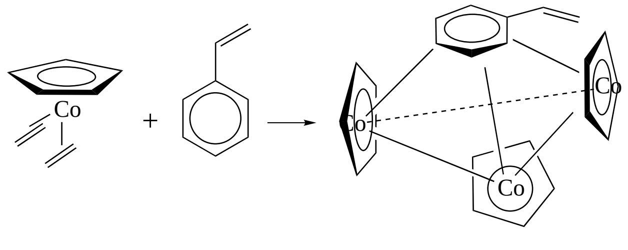

Scheme 12

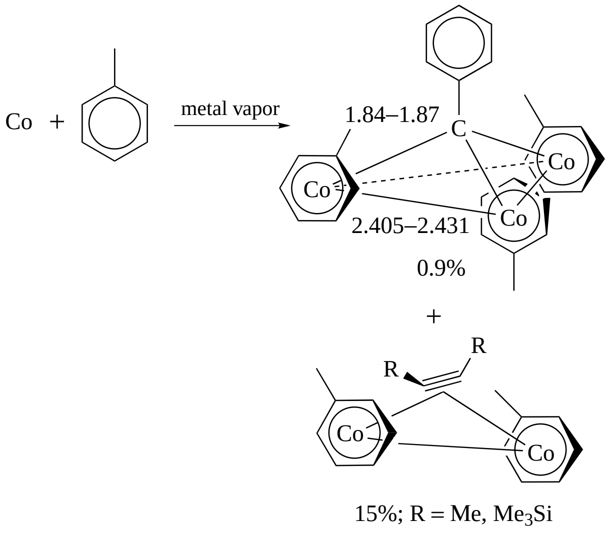

Scheme 13

2.5 Triangular Co_3 Clusters

The homoleptic carbonyl (*see Homoleptic Compound*) $Co_3(CO)_9$ is not known, but a few substituted derivatives have appeared in the literature. The best characterized cluster seems to be $Co_3(CO)_9H$, which is found in 10% yield as a decarbonylation product of $Co_3(CO)_{10}H$ ($[Co_3C]OH$). The X-ray structure has disclosed a regular triangle with three bridging and six terminal CO groups. The hydrogen atom was not located in the diffraction study.

Similar compounds of formula $[Co(CO)_2P(n\text{-}Bu)_3]_3$ have been isolated from stoichiometric hydroformylation of α-alkenes with $HCo(CO)_3P(n\text{-}Bu)_3$, where only hydrogen but no CO is present. Susceptibility measurements (*see Magnetic Susceptibility*) showed Curie–Weiss behavior with magnetic moments between 2.86 and 3.10 BM, appropriate for two unpaired electrons. Chemically or spectroscopically, hydrogen could not be located, but one additional hydrogen atom is needed to explain the observed magnetism and suggested structure (*see* ***Paramagnetic Organometallic Complexes***).

3 ALKYL COMPLEXES

3.1 $RCoL_4$

Only one example is known of a binary homoleptic (*see Homoleptic Compound*) cobalt alkyl compound, $Co(nb)_4$

(nb = norbornyl, bicyclo[2.2.1]heptyl) (Section 3.4). Otherwise, Co–alkyl σ-bonds are found combined with various alkenic and cycloalkenic ligands, in cobaltacarbocycles, and in $CpCo^{III}$ complexes, and will be treated in the respective sections. In addition to $Co(nb)_4$, two groups of alkyl compounds will be presented in this section: complexes of the type $RCo(PR'_3)_n$, and the monoalkyl derivatives of the so-called 'cobalamines' and 'cobaloximes', Schiff base (*see Schiff Base*) and glyoxime-derived coordination compounds of Co, respectively. Cobalt–cyano complexes are described elsewhere (*see* ***Cyanide Complexes of the Transition Metals***) and will not be covered here.

As noted above, σ-carbon complexes derived from $HCo(CO)_4$ are of low thermal stability and most of the isolated examples contain phosphine and phosphite ligands. Thus $Co(PMe_3)_4{}^-$ is readily alkylated by MeI to $MeCo(PMe_3)_4$. With excess MeI, oxidative addition with loss of one phosphine to $Me_2CoI(PMe_3)_3$ is found. Higher alkyls are subject to β-elimination (*see β-Elimination*).

The composition $MeCo(PR_3)_4$ is realized, apart from PMe_3, with various phosphines. The PPh_3 complex, however, has a lower coordination number, that is, $MeCo(PPh_3)_3$ is found in the solid, but it partially dissociates in solution into $MeCo(PPh_3)_2$, reminiscent of the behavior of $RhCl(PPh_3)_3$ (*see Wilkinson's Catalyst*). In protic solvents, this compound decomposes by proton abstraction, releasing methane, and this observation may explain its ability to effect aldol condensation of certain ketones (acetone and methyl ethyl ketone) in an aprotic solvent (equation 36).

$$MeCo(PPh_3)_{2,3} + RCH_2COR \longrightarrow CH_4 + Co(PPh_3)_3{}^+ + RCHCOR^- \qquad (36)$$

3.2 $Co^{II}$and Co^{III}Alkyl Complexes

Co^{II} alkyl complexes are represented by some $Co(Ar)_2(PR_3)_2$ and anionic acetylides $Co(C{\equiv}CR)_4{}^{2-}$ and $Co(C{\equiv}CR)_6{}^{4-}$; the latter complexes are closely related to Co^{II} cyano complexes (*see* ***Cyanide Complexes of the Transition Metals***). Chelating ligands have also been used in the synthesis of cobalt alkyl complexes. Cobalt(II) halides react with $LiN(SiMe_2CH_2PPh_2)_2$ to form the high-spin (d^7) tetrahedral complex $Co(X)N(SiMe_2CH_2PPh_2)_2$ (X = Cl, Br, I). These blue coordination complexes can be alkylated via salt metathesis, producing orange organometallic complexes (e.g. $Co(Me)N(SiMe_2CH_2PPh_2)_2$). The color change is indicative of both a geometry change (tetrahedral to square planar) and a spin state change from high-spin ($3.89\mu_B$, three unpaired electrons) to low-spin ($1.9–2.2\mu_B$, one unpaired electron).[53]

A considerable number of organo Co^{III} complexes of general formula $CoR_2L_2L'_2$, have been prepared, where L and L′ are acac, PR'_3, or bipy, and R is mostly Me but is Et in a few cases. The synthetic approach involves the reaction of $Co(acac)_3$ and R_2AlOR for acac derivatives, or the reaction of $CoCl_2$ with the ligand bipy and/or phosphine, the halocarbon, and $NaBH_4$. In these complexes, the R groups are either mutually trans, or trans to a hard σ-ligand (halide, ammine, acac), but not *trans* to a phosphine, owing to the strong labilizing effect of an alkyl group on a π-acceptor ligand trans to it (*see Trans Effect*).

3.3 Alkylcobaloximes and Cobalamins

A class of organocobalt complexes built from cobalt complexed in a square-planar geometry (*see Square Planar*) with a tetradentate ligand (*see Tetradentate Ligand*) is depicted in Scheme 14. Several tetradentate ligands have been studied including salen, a modified bis(dimethylglyoximate), in which the O–H–O bridge is replaced by F_2BO_2 or $–(CH_2)_3–$, and a variety of tetraaza macrocycles including porphyrin. An additional axial base such as a phosphine, pyridine, or most significantly, water is complexed to the cobalt (III) center resulting in complexes of the type $Co^{III}L_4(B)^+$. These complexes have been shown to accommodate an alkyl or other σ-carbon ligand trans to the axial base as the sixth ligand of an octahedral Co^{III} complex.

Cobalamins consist of a cobalt central atom, a substituted corrin ring that binds in a tetradentate fashion, a benzimidazole base that is linked to a pyrrole moiety of the corrin ring, and an axial ligand. The identity of the axial ligand can vary, but it can be a carbon-bound ligand. Vitamin B_{12} (*see* ***Cobalt: B_{12} Enzymes & Coenzymes***) is a cyanocobalamin, and an adenosyl group as the axial ligand makes the complex coenzyme B_{12}. Cobalamins are examples of naturally occurring organometallic compounds, and coenzyme B_{12} was the first recognized example of a biological organometallic

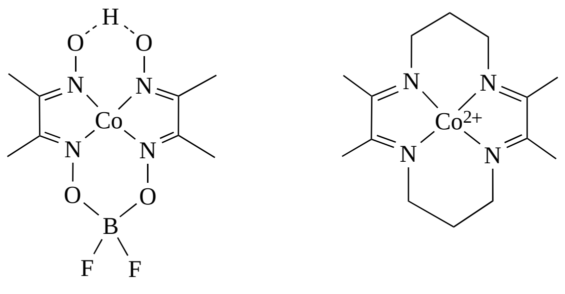
Co(dmgH)(dmBF) $[Co(tim)]^{2+}$

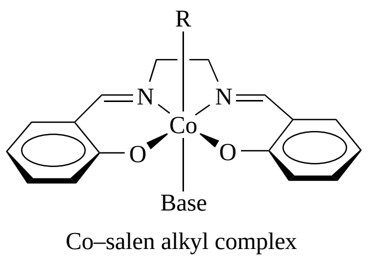
Co–salen alkyl complex

Scheme 14

compound. Methylcobalamins also play a role in biology, where they are found in microorganisms and can release methane at temperatures above 180 °C or methylate mercury in the environment.

Three methods of Co–C bond cleavage have been proposed to occur in cobalamins (Scheme 15). Heat or photochemical irradiation can induce homolysis of the Co–C bond with a consequent one-electron reduction of cobalt. Nucleophilic attack on the methyl group can occur, resulting in reduction of Co^{III} to Co^{I}. Electrophilic attack (e.g. mercury methylation) can also occur, where the methyl group is transferred as a carbanion.**[54]**

Cobaloximes have been studied as model systems for cobalamins. In the square pyramidal cobaloximes, CoL_4(Base), cobalt is known in three oxidation states (Co^{III}, Co^{II}, and Co^{I}), where the latter are monoanions in cases when the L_4 system is a dianion (as in bisglyoximates). Redox potentials interrelating the oxidation states as a function of the ligand and the axial base have been extensively investigated. Redox potentials become increasingly negative in the sequence H_2O > phosphine > pyridine. The Co^{II} complexes are square pyramidal (*see Square Pyramidal*) low-spin d^7 species, and the Co^{I} complexes (d^8) have the same geometry with two electrons in a nonbonding or weakly antibonding d_{z^2} orbital, a fact that makes them strong nucleophiles (*see Nucleophile*). Co^{III} cobaloximes react with hydrogen in alkaline solution to give hydrides. Some of the compounds reversibly bind O_2.

Alkylcobaloximes, $RCo^{III}L_4(B)$, are of interest as B_{12} cofactor model compounds and have been generated in many different ways from Co^{III}, Co^{II}, or Co^{I} precursors (Schemes 16 and 17). Co^{III} complexes featuring axial halide ligands are susceptible to alkylation by nucleophiles, for example, Grignard reagents (*see Grignard Reagents*) and other organometals. Alkenes and alkyls insert into the corresponding hydrides, and hydroxo complexes react with even weakly acidic CH functionalities by water elimination and formation of a Co–carbon bond. Co^{II} complexes react with activated halides in a two-step oxidative addition (*see Oxidative Addition*) through an intermediate radical (cf. Section 7.1).

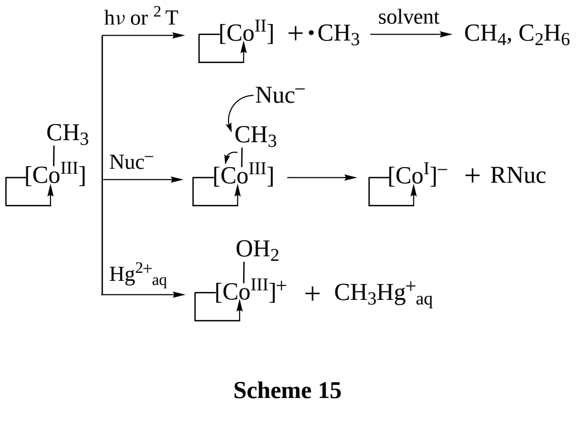

Scheme 15

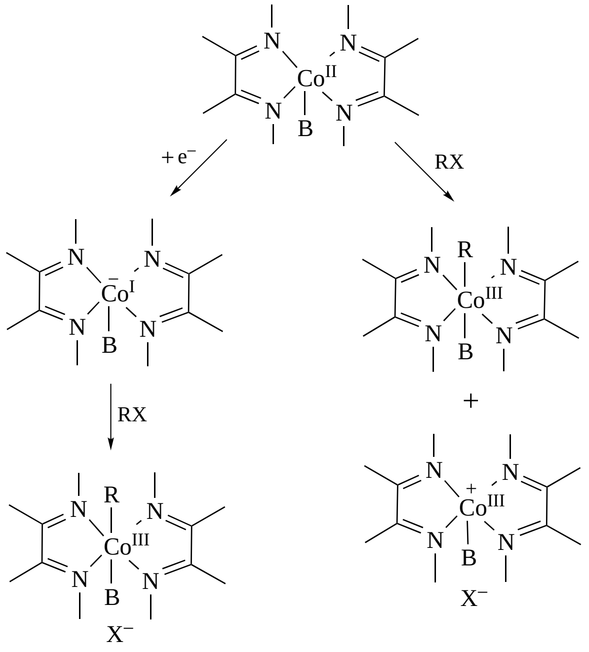

Scheme 16

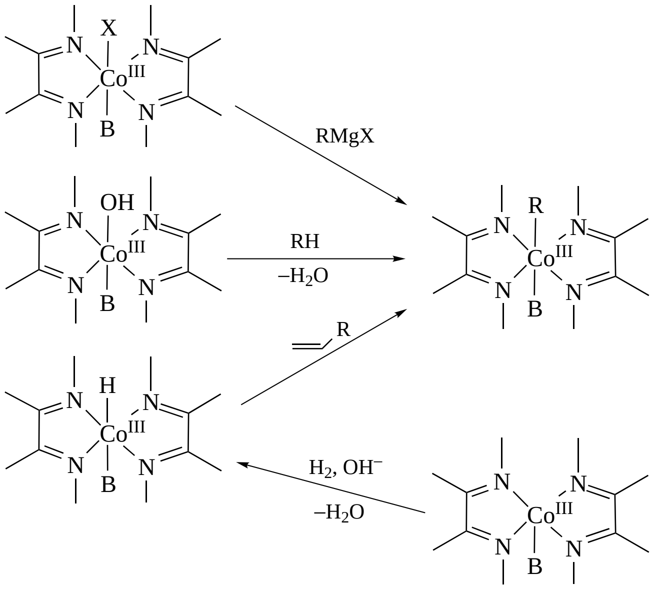

Scheme 17

A general route for synthesizing a great variety of cobaloximes is by reaction of Co^{I} complexes with electrophiles. Co^{I} precursors are generated by reduction of Co^{II} or Co^{III} electrochemically, by Na/Hg, or with borohydride. The reaction has been extensively investigated and rates have been compared with those found for various organic nucleophiles. It was found that Co^{I} cobaloximes are among the strongest nucleophiles known, and have been termed ‘supernucleophiles’ for that reason. These Co^{I} cobaloximes can undergo oxidative addition of alkyl halides to form Co^{III}–alkyl bonds. An organometallic compound with the longest known n-alkyl chain has been synthesized and characterized using a cobaloxime reagent.[55]

A significant observation for cobaloximes as B_{12} models was the reduction of $MeCo^{III}L_4(B)$ by $Cr(aq)^{2+}$, which gave $Co^{II}L_4(B)$ and $Cr(Me)(aq)^{2+}$ (equation 37). These products are indicative of an inner-sphere (*see Inner-sphere Reaction*) electron transfer with Me as the bridging ligand. This result has promoted further studies, notably methyl transfer between cobaloximes and nickel tetraazacycle complexes, which provides a possible model for the methylcobalamin alkylation of CO hydrogenase.[56]

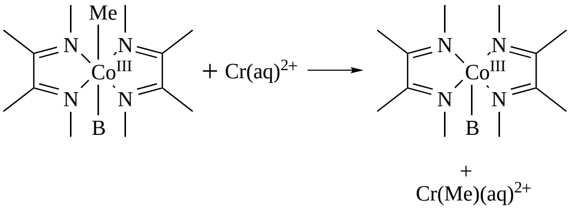

(37)

3.4 CoR_4

$Co(nb)_4$ is a unique compound formed from $CoCl_2$ and Li(nb) in THF. The somewhat surprising formal oxidation state of Co^{IV} is believed to stem from the intermediate hydrolysis of $Co(nb)_3^-$ to the hydride $HCo(nb)_3$, which on repeating the same sequence of reactions would give $H_2Co(nb)_4$; subsequent evolution of H_2 gives the stable alkyl complex. An X-ray structure (Figure 8) of a single crystal obtained by slow oxidation of the anion $Co(nb)_4^-$ shows, apart from some disorder of the Norbornyl (nb) ligands around the threefold axis, the expected D_{2d} geometry with two larger (114°) and two smaller (108°) C–Co–C angles and rather short Co–C bond lengths of 1.92 Å (mean).[57] The susceptibility of the compound was measured between 1.7 and 299 K and gave Curie–Weiss behavior with $\mu_{\text{eff}} = 1.89$ BM, that is, one unpaired electron that indicates a low-spin tetrahedral d^5 complex. $Co(nb)_4$ is the only known example of a low-spin tetrahedral complex.

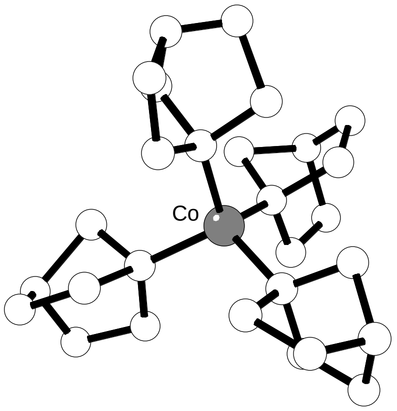

Figure 8 Structure of $Co(nb)_4$

4 ALKENE AND ALLYL COMPLEXES

Alkene complexes of cobalt generally have to be stabilized by CO, phosphine, or phosphite supporting ligands or contain a CpCo moiety. Homoleptic alkene ligands cannot match the electronic requirements of a single d^9 metal atom, but this is not the case for allyl ligands. The orbital energies of the cobalt 3d and 4s/4p atomic orbitals lie considerably above the filled π and somewhat below the π^* level of an unconjugated alkene, so that an alkene would act primarily as an electron acceptor to cobalt.

4.1 Matrix and Metal Vapor Reactions

Study of the interaction of metal atoms with ethylene in a noble gas matrix has led to the identification of a number of species, mostly by absorption spectra. They have been assigned formulas such as $Co(C_2H_4)$, $Co_2(C_2H_4)$, and $Co_2(C_2H_4)_2$. These species decompose at about 35 K.

Condensation of cobalt atoms into an ethylene matrix at 77 K yields $Co(C_2H_4)_3$, which decomposes at about 210 K. Reaction of this complex with phosphine ligands gives the more stable, neutral, paramagnetic complexes $Co(PR_3)_3(C_2H_4)$. Even more resistant to thermal decomposition is the green paramagnetic tris(norbornene) complex $Co(C_7H_{10})_3$, which decomposes at 258 K. This complex can be stabilized, and is similar to the green paramagnetic compound $Co(C_7H_{10})(PR_3)_3$. $Co(cod)_2$, obtained by the metal vapor technique in the same way, is not a stable compound and has been characterized by a variety of in situ reactions, such as reaction with cyclopentadiene to give CoCp(cod). Thus, these alkene complexes, though not isolated and characterized as pure compounds, can nevertheless, serve as starting materials for a variety of transformations (*see* ***Metal Vapor Synthesis of Transition Metal Compounds***).

4.2 Cyclooctadiene Complexes

The hydride $Co(cod)_2H$ was prepared by Wilke from AlR_2H and $Co(acac)_3$ (equation 38). It forms black, air-sensitive crystals of unknown structure that ignite spontaneously in air. An equilibrium between a cyclooctadiene/cyclooctenyl form (**9a**) and a bisalkene hydride (**9b**) in solution is inferred from chemical reactions of the compound (Scheme 18).

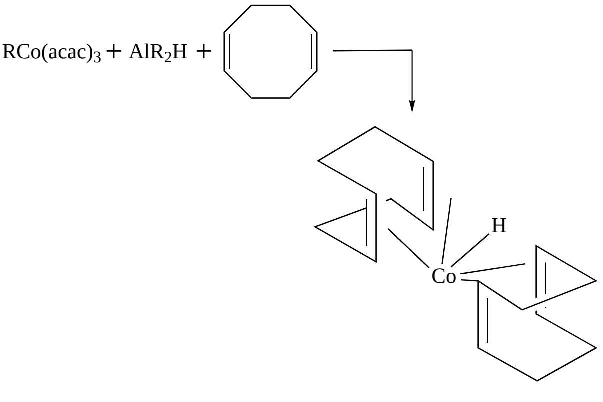

(38)

A different synthetic approach, namely, Na reduction of $CoCl_2$ in the presence of cyclooctadiene (cod) in a THF/pyridine mixture (equation 39),[58] gives a 16-electron complex (**10**) of identical composition, which is the conjugate analog of (**9a**), containing a π-cyclooctenyl ligand. Compound (**10**) is considerably more stable towards heat and air than is (**9**). It has also been observed as a by-product when excess $AlHR_2$ was employed in the synthesis of (**9**).

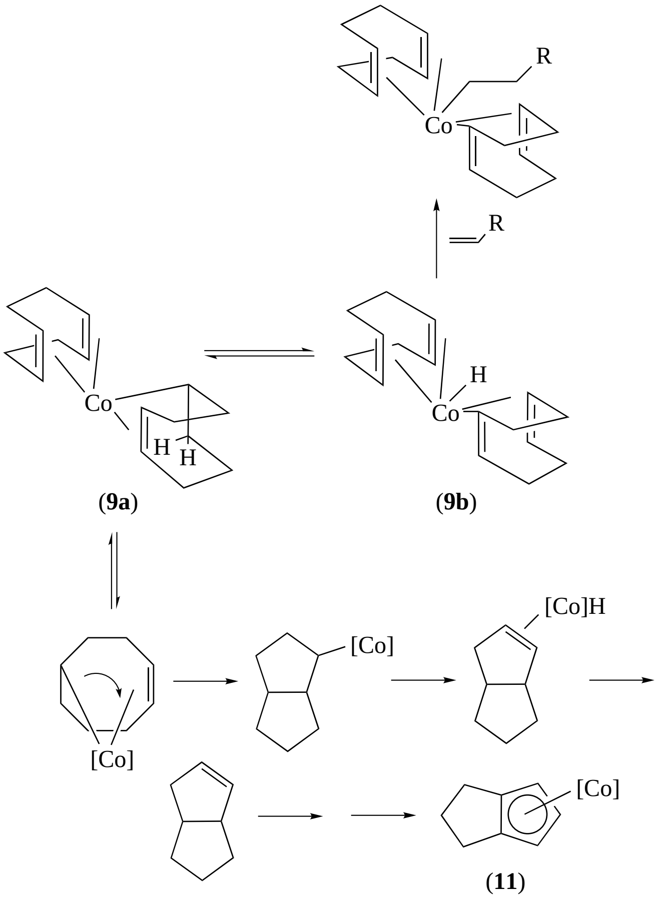

Scheme 18

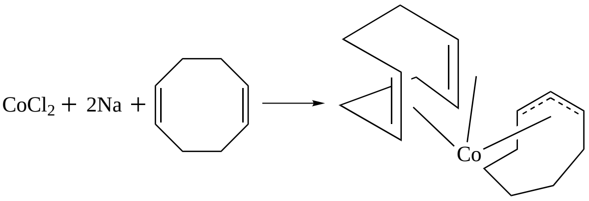

(39)

(**10**)

Reaction of (**9**) with $AlH(i\text{-}Bu)_2$ liberates cyclooctene, but at 40 °C it slowly isomerizes thermally in solution to the stable CpCo derivative (**11**) (Scheme 18). In the presence of excess cod, this latter complex is converted catalytically to tetrahydropentalene. Ring contraction to the pentalenyl system can be understood as an intraligand reductive elimination (*see Reductive Elimination*), the driving force of which may be coordination of cobalt to the double bond of free cod in solution. In the catalytic cycle some (**10**) is formed.

Many organometallic complexes use cod as a ligand because it can be easily substituted. For that reason, many cobalt cyclooctadiene complexes are important in catalytic reactions, particularly when used with cyclopentadienyl in complexes (Section 5.1.2).[59,60]

4.3 (Allyl)cobalt Complexes

4.3.1 Synthesis and Properties

The homoleptic complex $Co(\eta^3\text{-}C_3H_5)_3$ (**12**) obeys the 18-electron rule (*see Eighteen Electron Compounds*) and could be expected to be stable by analogy to the abundant allyl chemistry of Ni. The compound has been prepared from $Co(acac)_3$ and C_3H_5MgCl (equation 40) or, alternatively, from $CoCl_2$ and C_3H_5MgCl/C_3H_5Cl (equation 41) in about 50% yield.[61] The latter method has also furnished a number of substituted allyl derivatives. Despite its favored electron count, complex (**12**) decomposes in solution around −60 °C, and the pure crystalline solid decomposes spontaneously in an inert atmosphere at −20 °C. The solid ignites spontaneously in air (cf. $Co(allyl)_2(ethylene)Li$, Section 5.1.2).

$$\mathrm{Co(acac)_3 + 3(allyl)MgX \longrightarrow Co(allyl)_3 + 3MgX(acac)} \qquad (40)$$

$$\mathrm{2CoX_2 + 5(allyl)MgX + allylX \longrightarrow 2Co(allyl)_3 + 5MgX_2} \qquad (41)$$

Mass spectra of (**12**) show loss of allyl and of hydrogen as main fragmentation patterns. The ^1H NMR spectrum consists of three independent allyl (AA′MM′X) patterns for three chemically inequivalent allyl groups. A structure compatible with this symmetry (C_s) is depicted in Figure 9. It is based on a trigonal prism with allyl groups along the three parallel edges (an attempted X-ray structure determination was thwarted by extensive disorder).

The main reaction modes of (**12**) are reductive elimination (*see Reductive Elimination*) with C–C coupling to diallyl (1,5-hexadiene) (equation 42), or nucleophilic displacement

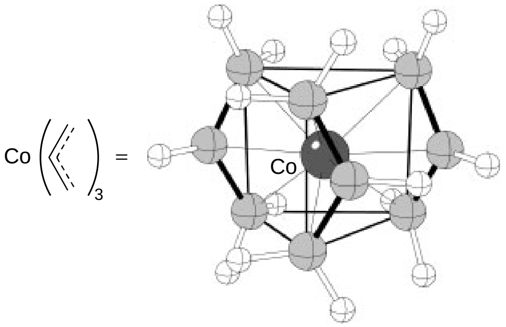

Figure 9 Geometrical arrangement of allyl groups in Co(allyl)$_3$

of one allyl group. Thus, with two-electron ligands, the displacement of two basal allyl groups and addition of three ligands gives Co(allyl)L$_3$. For substituted allyl ligands, it can be shown that the reaction proceeds with retention of the *syn/anti* conformation at the remaining allyl group, which can be used to determine the *syn/anti* distribution in the original tris(allyl) complex. Electrophiles selectively attack the edge-bound allyl, which is displaced in the form of C_3H_5X (equation 43) or C_3H_6 (equation 44) to give a thermally labile bis(allyl) halide complex, Co(allyl)$_2$X. Because of their low solubility, these cobalt complexes are presumed to be dimeric.

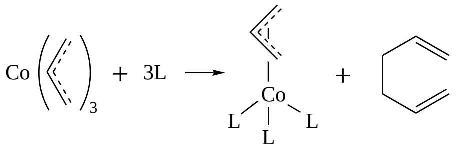

(42)

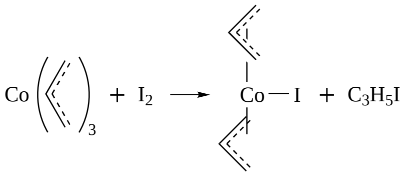

(43)

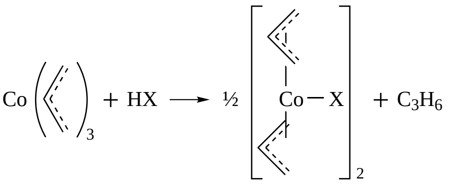

(44)

Recently, the synthesis and characterization of the only known homoleptic bis(allyl)cobalt complex has been reported.[62] The bulky bis(1,3-trimethylsilyl)allyl ligand has been shown to increase the thermal stability of allyl compounds, and examples of first-row transition metal complexes, for which no unsubstituted analogs exist, have been prepared with this ligand.[63] The formally 15-electron species [1,3-(SiMe$_3$)$_2$C$_3$H$_3$]$_2$Co is an air- and moisture-sensitive solid. The η^3-allyl ligands are in a staggered arrangement about the metal center, and the trimethylsilyl moieties are in a *syn-anti* arrangement on each allyl ligand (Figure 10). The range of Co–C bond distances in this complex (1.996–2.096 Å) suggests that the steric encumbrance (*see Steric Effect*) of the ligands leads to bond lengthening (cf. 1.918–1.948 Å in (η^3-C$_3$H$_5$)(η^5-Me$_5$C$_5$)Co).

4.3.2 Reactions of (Allyl)Co Complexes

A versatile application of Co(allyl)$_3$ has been found in its reaction with butadiene, which effects catalytic dimerization under very mild conditions. Individual reaction steps are reproduced in Scheme 19. These reactions lead to the isolated and structurally characterized complex (**13**) as the true catalyst. Scheme 19 is in fact a collection of all the classical steps involved in homogeneous transition metal C–C bond-forming reactions. The first step consists of replacement of two allyl groups by butadiene, which is reductively eliminated as diallyl, similar to what has been found with cod and with other two- or four-electron ligands.

Co(allyl)(butadiene) (**14**) has been identified by NMR at −40 °C. A crucial step is insertion of butadiene into a Co–allyl bond forming (**15**), which occurs if the temperature is raised to −15 °C. Transfer of one hydrogen from the coordinated heptadienyl to a coordinated butadiene gives (**16**). A second insertion of another molecule of butadiene into the new Co–allyl bond generates a 3-methylheptadienyl complex (**17**), and a final molecule of butadiene liberates heptatriene from the metal to give (**13**).

The 3-methylheptadienyl complex (**13**) is the active catalytic species in butadiene dimerization. The two dimers formed are 2-methylheptatriene and octatriene in a 9:1 ratio, depending on conditions. Attack of the incoming butadiene on C-1 or C-3 of the methylallyl complex (**17**) determines product formation.

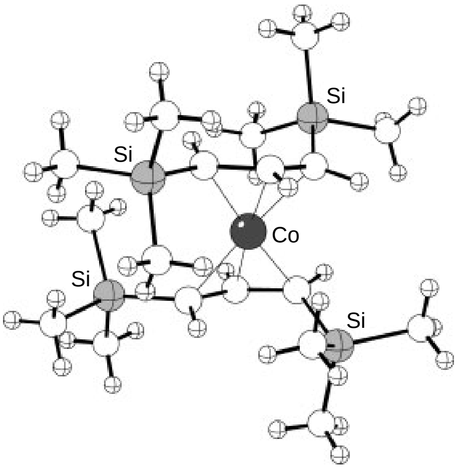

Figure 10 Structure of [1,3-(SiMe$_3$)$_2$C$_3$H$_3$]$_2$Co

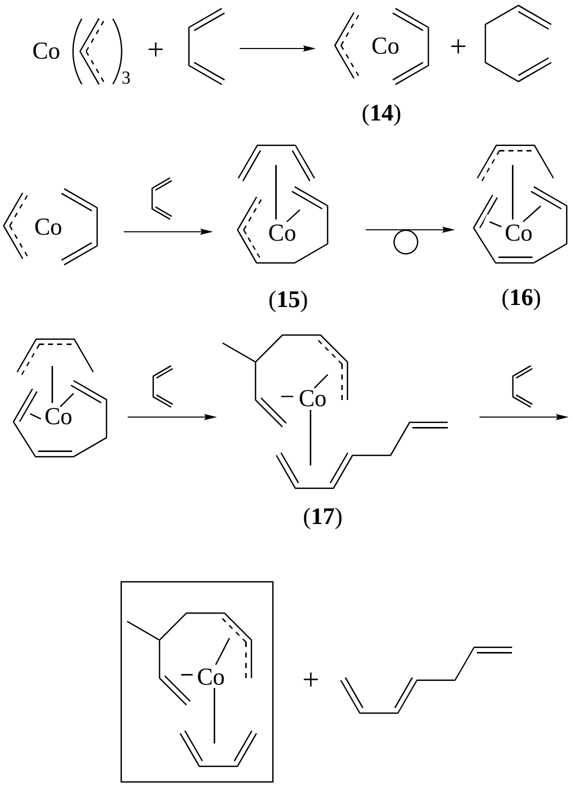

Scheme 19

5 CYCLOPENTADIENYL COMPLEXES

Cyclopentadienyl complexes of cobalt exist mainly in three oxidation states – Co^I, Co^{II}, and Co^{III}. Co^I is represented by complexes of the type $CpCoL_2$, where L is CO, alkene, alkyne, or phosphine. Apart from derivatives of cobaltocene, half-sandwich complexes (*see Half-sandwich Complexes*) $(CpCoX)_2$ or CpCoLX with cobalt in oxidation state II are known. $CpCo^{III}$ occurs in various $CpCoL_nX_m$ compositions (Section 9.2).

5.1 $CpCoL_2$

5.1.1 *$CpCo(CO)_2$*

$CpCo(CO)_2$ (**18**) is obtained on heating cobaltocene under CO or by heating $Co_2(CO)_8$ with cyclopentadiene. Since the latter reaction works with substituted cyclopentadienes as well, a variety of substitution products are easily accessible. $CpCo(CO)_2$ is a dark red, air- and light-sensitive oil (mp −22 °C) with a musty odor. The crystal structure has been determined and shows a conformation with one CO eclipsed by a Cp edge, whereas the Cp* derivative has a different conformation with the CO–Co–CO plane parallel to one side of the Cp ring. The latter was first obtained from C_5Me_5COMe and $Co_2(CO)_8$, but it can be prepared more conveniently by reaction of Cp*H with $Co_2(CO)_8$, or via CO substitution on Cp*Co half-sandwich complexes (Section 9.1).

Complex (**18**) is commercially available and has been used extensively for the preparation of CpCo complexes. The CO ligands are substituted thermally or photochemically under conditions similar to those required for the substitution of $Fe(CO)_5$ (i.e. at about 100–120 °C). The products formed from irradiation of (**18**) under different conditions are depicted in Scheme 20.

A complex reaction pathway occurs owing to the existence of two different oligomers of CpCo(CO) and the transient nature of most of the reaction products. When irradiated at low temperature in THF under an inert atmosphere, (**18**) gives the dimeric monocarbonyl $[CpCo(CO)]_2$ (**19**), which reverts to (**18**) when CO is admitted.[**64**] In contrast, irradiation in a closed system at 5 °C in toluene gives an equilibrium mixture with $(CpCo)_2(CO)_3$ (**20**) as a major component that can be isolated as crystals on cooling. Since the CO liberated in forming (**20**) is still present in this system, conversion to (**20**) is incomplete. When redissolved at room temperature, (**20**) forms green $(CpCo(CO))_3$ (**21**) and (**18**). On heating, (**21**) converts to black $(CpCo)_4(CO)_2$ (**22**) and (**18**).[**65**]

Another route to CpCo carbonyls is by reduction. A mixture of (**19**) and (**21**) has been obtained by reduction of (**23**) in toluene. The anion ($\mathbf{19}^-$) is obtained by Na/Hg reduction of (**18**) in THF. If the process is followed by cyclic voltammetry, a reversible reduction is observed. The anion $CpCo(CO)_2{}^-$ either loses a Cp^- ligand or forms the corresponding dimer. Loss of Cp^- is preferred if the complex is stabilized through substitution by electron-withdrawing groups.

The Co–Co distance of this dimer is 2.36 and 2.37 Å, respectively, in the two independent molecules of the unit cell. This distance is consistent with a bond order greater than 1 and is shorter than in any of the known cluster molecules with a formal Co–Co single bond (all have Co–Co distances around 2.45–2.52 Å). The EPR spectrum of ($\mathbf{19}^-$) shows a symmetric 15-line pattern, indicating equal coupling of the odd electron to either cobalt nucleus ($I = 7/2$). EPR studies of the related complex $CpCo(CO)_2{}^-$ indicate that the odd electron in this complex also resides on the cobalt center. However, DFT studies indicate that the odd electron in this complex is approximately evenly distributed over cobalt metal, the Cp ring, and the CO ligands; this discrepancy stems from the neglect of spin polarization when calculating atomic orbital spin populations from EPR hyperfine coupling constants (*see Electron Paramagnetic Resonance*).[**66**]

The hapticity of the Cp ring in $CpCo(CO)_2{}^-$ has been the topic of much debate. If an associative mechanism for substitution is followed, a hapticity (*see Hapticity*) of η^3 from ring slippage would result in a 19-electron intermediate and 17-electron product, while a hapticity of η^5 would result in a more unstable 21-electron intermediate. However, it has been shown that CO substitution follows a dissociative mechanism

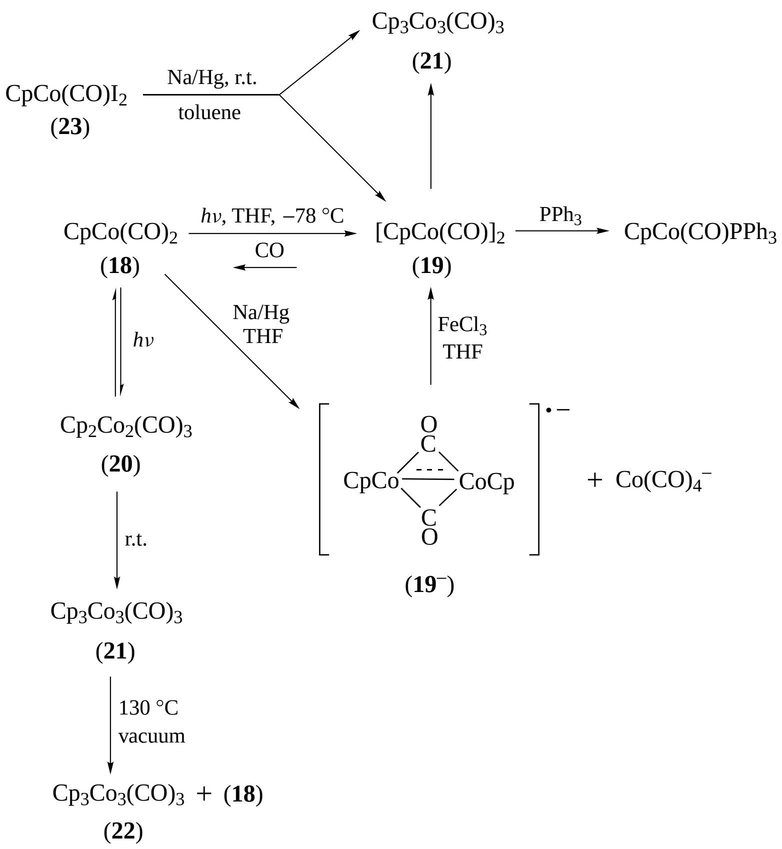

Scheme 20

for this complex, and several experimental and theoretical studies have added credibility to the argument of $CpCo(CO)_2^-$ possessing an η^5-Cp ligand. It is now generally accepted that $CpCo(CO)_2^-$ is a 19-electron complex with an η^5-Cp moiety.[64]

A different product of the series, $Cp_3Co_3(CO)_2$, has been obtained from the reaction of (**18**) and $CpCo(C_2H_4)_2$ (**24**). It is not stable in solution and can be isolated only because it precipitates out as it is being formed. It has 46 valence electrons, which is two electrons short of the requirement for a 5-vertex *closo* structure (*see Closo Cluster*). At room temperature, the solution magnetic moment of $\mu_{\text{eff}} = 3.0 \pm 0.2$ BM (Evans method) indicates a triplet; however, solid-state susceptibility measurements at 100 K show it to be diamagnetic. The structural determination disclosed a trigonal bipyramidal motif (D_{3h}, threefold crystallographic axis).[65] Like $Cp_3Co_3(CO)_3$, it converts in solution into (**18**) and (**22**).

Most of the unsaturated CpCo carbonyls are active catalysts in alkyne oligomerization (Section 5.1.4), as CO can be displaced for alkynes. In addition to cyclization reactions, CpCo(CO) complexes have been studied as C–H bond activators. Bergman determined that, unlike the corresponding rhodium and iridium complexes, CpCo(CO) is unreactive toward C–H activation.[67] Theoretical studies were used to probe the inability of CpCo(CO) to activate alkanes, and it was determined that a triplet ground state is responsible for the inertness of CpCo(CO) toward methane insertion.[68]

Thermal substitution of $CpCo(CO)_2$ with alkenes, phosphines, and other two-electron ligands has furnished many more $CpCoL_2$ variants. Mention should be made of nitrosyl complexes (*see Nitrosyl Complexes*), as migratory insertion of NO into cobalt–carbon bonds is an area of interest. The addition of phosphines to $CpCo(NO)CH_3$ results in a nitrosyl insertion product (equation 45). An intramolecular insertion followed by phosphine addition (mechanism 1) was proposed for the reaction; this mechanism is similar to the one for CO insertion (Scheme 21). However, the versatility of NO (a 3-electron linear ligand or a one-electron bent ligand) could allow NO insertion after phosphine addition (mechanism 2). Ab initio and DFT studies show that NO insertion is the rate-determining step for both mechanisms, and insertion with phosphine association (mechanism 1) occurs with lower activation energy of 10–20 kcal mol^{-1}.[69]

$$CpCo(NO)(CH_3) + PPh_3 \longrightarrow CpCo(PPh_3)(N(O)CH_3) \qquad (45)$$

5.1.2 *CpCo(alkene)$_2$ and CpCo(diene)*

Complexes of composition $CpCo(alkene)_2$ and CpCo (diene) are easily formed by different routes and have

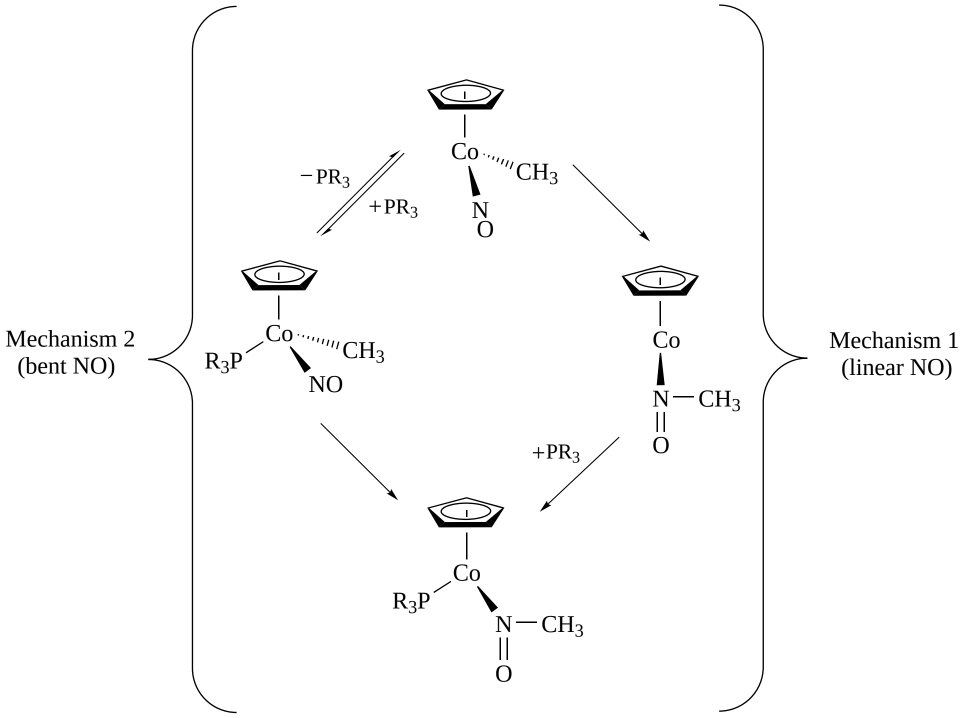
Co
CH3
N
O
− PR3
+PR3
Mechanism 2
(bent NO)
R3P
Co
CH3
NO
Mechanism 1
(linear NO)
Co
N — CH3
O
+PR3
R3P
Co
N — CH3
O

Scheme 21

played important roles in a variety of applications. Cycloalkene ligands are generated directly from cobaltocene, for example, $CpCo(C_5H_6)$, by addition of hydride to the cobaltocenium ion. All common alkenes and dienes (ethylene, butadiene, cyclodienes, cyclotrienes, cod, norbornadiene, cyclooctatetraene, and many others) have been coordinated to a CpCo moiety. A general route for the preparation of these compounds is substitution of $CpCo(CO)_2$ or reductive cleavage of cobaltocene in the presence of an alkene.

A one-electron reduction of cobaltocene (Section 7.1) transforms the sandwich complex into a 20-electron anion of low stability, the principal decomposition path being cleavage into Cp^- and a neutral CpCo fragment. This fragment can form derivatives upon addition of alkenes with alkali metals (Scheme 22). The reaction using potassium has produced the thermally unstable ethylene complex $CpCo(C_2H_4)_2$ (**24**), which dissociates ethylene above room temperature and is now generally employed as a source for the CpCo fragment. This method can generate CpCo under much milder conditions than if it were generated from the dicarbonyl (**18**).

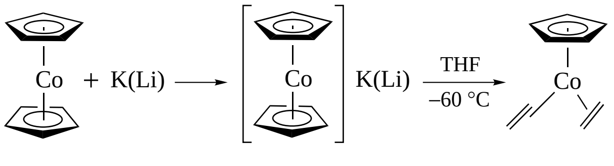
Co
+ K(Li)
Co
K(Li)
THF
−60 °C
Co

Scheme 22

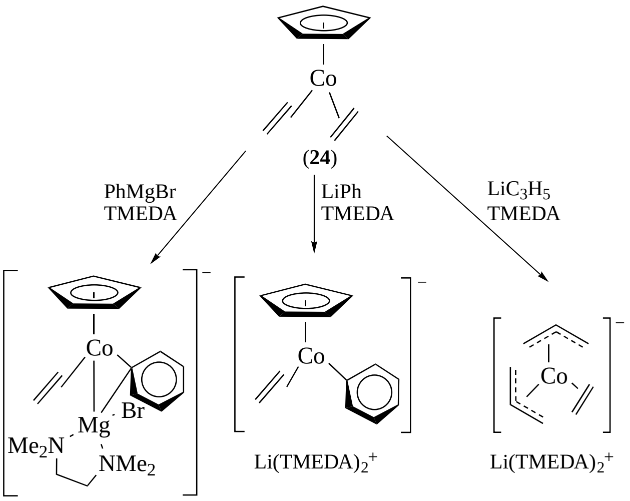
Co
(24)
PhMgBr
TMEDA
LiPh
TMEDA
LiC3H5
TMEDA
Co
Mg
Br
Me2N
NMe2
Co
Li(TMEDA)2+
Co
Li(TMEDA)2+

Scheme 23

The bis(ethylene) complex (**24**) can be derivatized in several ways (Scheme 23). The product isolated from PhMgBr and (**24**), after addition of TMEDA, has been characterized by X-ray diffraction and can be viewed as an alkene complex in which an ethylene molecule is replaced by a Mg–Ph bond of the Grignard reagent (*see Grignard Reagents*). Thus, the phenyl ring is coordinated to cobalt via a σ-bond and has interaction with magnesium; the magnesium center is bound to cobalt as well.

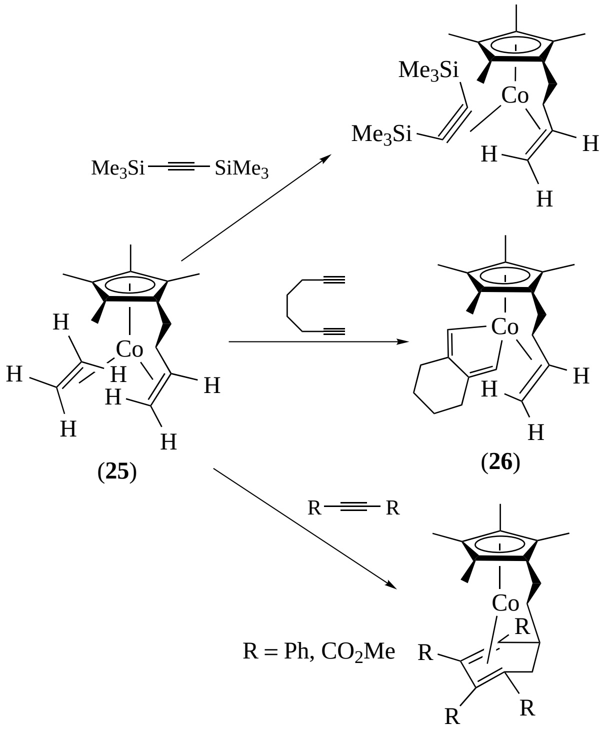

Scheme 24

Whereas Mg(allyl)Br gives a similar product, Li(allyl) instead replaces the Cp and one ethylene and forms anionic $Co(allyl)_2(ethylene)^-$. Note that this anion is related to tris(allyl)cobalt; it is much more stable as an ionic compound and can be isolated conveniently at ambient temperature.[70] The pentamethyl analog of (**24**), $Cp^*Co(C_2H_4)_2$, is best prepared by amalgam reduction of $[Cp^*CoBr]_2$ (Section 9.1) in the presence of ethylene.

In the intriguing derivative (**25**) of (**24**), one ethylene ligand is linked through a carbon bridge to a Cp* ring (Scheme 24). A $(CH_2)_2$ bridge has proved to be the best size with which to stabilize the coordinated alkene by the chelate effect (*see Chelate Effect*). The ethylene unbridged in (**25**) is more labile than is the pendant one, and as a consequence, facile monosubstitution occurs with many two-electron ligands, including alkynes. Cyclization (Section 5.1.4) can occur with alkynes and the pendant ethylene to form a pendant cyclohexadiene. Reaction intermediates of alkyne oligomerization at Co can be detected during this reaction sequence, as is demonstrated by the isolation of the stable cobaltacyclopentadiene (**26**).[71]

5.1.3 *Cyclopentadienyl Cobalt Phosphine and Related Complexes*

Among the wide variety of known $CpCoL_2$ complexes, the mono- or bis(phosphine) complexes bear special mention. If the phosphine has bulky substituents, such as PPh_3, there will be one labile PPh_3 ligand that dissociates easily, thereby liberating a coordination site accessible to smaller molecules. With the Cp* ligand, in fact, a bis PPh_3 complex is no longer formed. This reactivity has been exploited in studies concerned with alkyne oligomerization at a cobalt center (Section 5.1.4). Conversely, the metal becomes a strong Lewis base and readily reacts with protons, alkyl halides, and even mild electrophiles (*see Electrophile*) if phosphines with electron-donating substituents (e.g. PMe_3) are introduced.

As has been shown and comprehensively reviewed,[72] many d^8 $CpCoL_2$ complexes are readily protonated at the metal. Protonation (*see Protonation*) does not lead to simple products with $L = CO$, however, and requires strong acids for L = alkene. If both L ligands are phosphines, protonation can be effected with relatively mild acids such as NH_4^+ in an organic solvent to give salts of the cations $CpCo(PR_3)_2H^+$; $CpCo(PMe_3)_2$ is protonated even by methanol. These protonated complexes are decomposed on electrochemical reduction into the neutral cobalt complexes $CpCo(PR_3)_2$ and hydrogen at mild potential, depending on the phosphine.

Complexes of the type $CpCo(PR_3)_2$ are alkylated at the metal with small alkyl halides to give $CpCo(PR_3)_2R^+$ (Scheme 25). Bulky halides produce ring-substituted hydrido cations instead, explained by attack of the electrophile from the *exo* site followed by ring-to-metal proton transfer. This reaction could be electrophilic addition (*see Electrophilic Reaction*), $S_{E}1$, or more probably radical addition initiated by electron transfer similar to the RX reaction of cobaltocene (Section 7.1). Since the oxidation potential of $CpCo(P(alkyl)_3)_2$ is more negative than that of cobaltocene, this latter mechanism is very plausible.

The use of Cp rings with pendant phosphines in $CpCoL_2$ complexes has also been reviewed.[73] Carbonyl complexes of this type $(Cp'Co(CO)_2)$ lose CO at room temperature to afford pendant phosphane adducts (equation 46). The chelated phosphane can then be uncoordinated with ligands such as cod; substitution of cod (Section 5.1.4) with alkynes allows the cobalt complex to participate in cyclization reactions (Scheme 26).

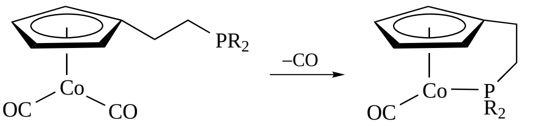

(46)

5.1.4 *Cyclopentadienyl Cobalt Alkyne Complexes*

Many of the complexes discussed in the previous sections are catalysts for alkyne oligomerization. In fact, alkyne dimerization and trimerization (*see Cyclodimerization & -trimerization Reactions*) at a cobalt center is recognized as one of the most synthetically useful catalytic reactions mediated by a homogeneous transition metal complex. The cobalt complexes most useful and extensively studied are $CpCoL_2$, where L is CO, alkene, diene, or phosphine. The complex types

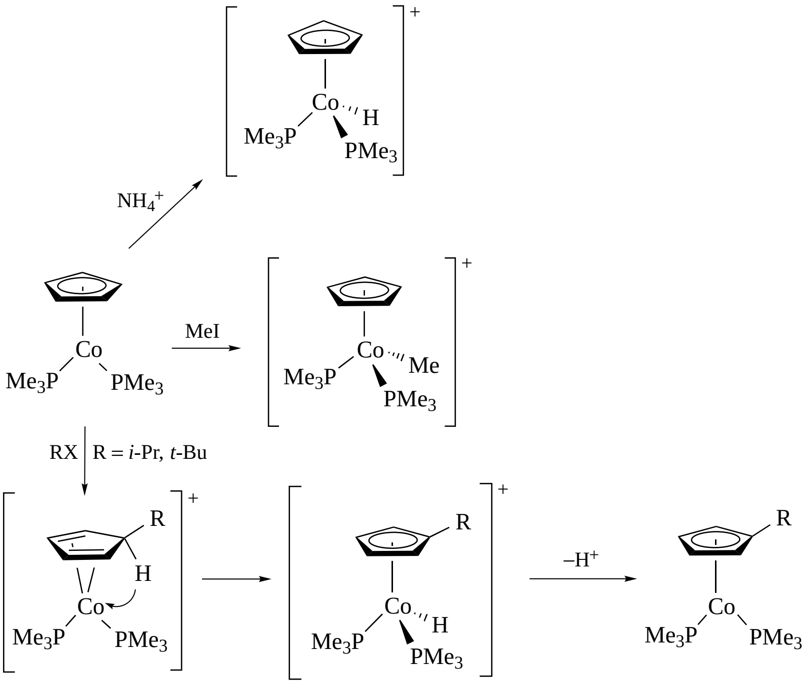

Scheme 25

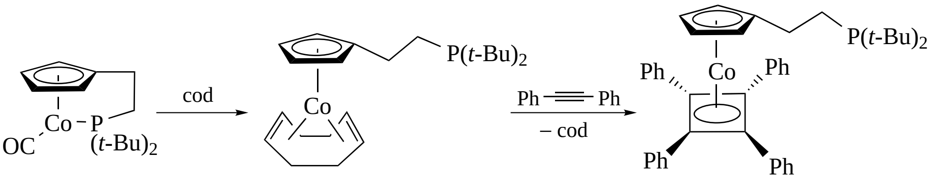

Scheme 26

have their specific applications as catalysts. CpCo(diene) and CpCo(alkene) complexes are used for co-trimerization of alkynes with a nitrile to give substituted pyridines, while the carbonyl complex is used for the $2 + 2$ cycloaddition of linked acetylenes. The phosphine complexes are mainly used for mechanistic studies.

The main reaction modes and products that are formed from reaction of $CpCoL_2$ and an alkyne are depicted in Scheme 27. If $CpCo(PPh_3)_2$ is treated with polar alkynes under ambient conditions, a monosubstitution product (**27**) can be isolated. Another isolable product is a cobaltacyclopentadiene (**28**) and, in certain instances, the dinuclear cobaltole complex (**29**) is formed, which has many analogs in the chemistry of $Fe(CO)_3$ and other 14-electron fragments. The cyclobutadiene complex (**30**) is the direct product from collapse of (**28**) and is of high kinetic and thermodynamic stability. In catalytic cycles, (**30**) is inactive. If the ligand L in (**28**) is a third molecule of alkyne, insertion of the latter forms the arene (**31**).

Since a CpCo(arene) is a 20-electron complex, it will not generally be stable; however, it will easily undergo displacement of the arene by new alkyne to regenerate (**27**). An alkene can be incorporated into the organic ligand either by adding to the alkene directly or by starting from CpCo(alkene)L. Addition of an alkyne now results in the formation of cyclohexadiene, which remains complexed to CpCo as in (**32**) (see also Scheme 24); consequently, the reaction cannot be catalytic in this case. If L = CO, complexes containing a cyclopentadienone ligand (**33**) are frequently encountered.

An important and extensively investigated application of CpCo complex chemistry is the catalyzed synthesis of pyridines from alkynes and nitriles.**[74]** Dissociation of the L ligands liberates the CpCo fragment to react with alkyne to form a cobaltacyclopentadiene complex. The nitrile coordinates to this intermediate and subsequently undergoes insertion to form a seven-membered cobaltacycle. Reductive coupling gives pyridine and reforms CpCo. Asymmetric alkynes add to the carbon with the bulkier substituent adjacent to the nitrile carbon.

Cyclobutadiene complexes are formed preferentially if cyclic dialkynes are treated with $CpCo(CO)_2$. Depending

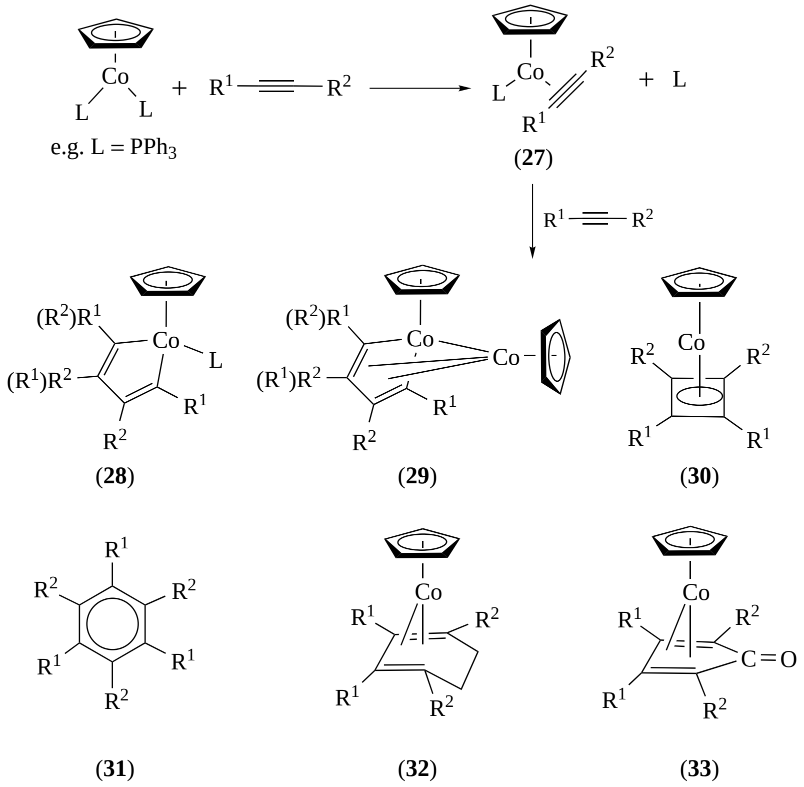
Co
L
L
e.g. L = PPh3
+
R1
R2
Co
L
R2
R1
+ L
(27)
R1
R2
(R2)R1
Co
L
(R1)R2
R1
R2
(28)
(R2)R1
Co
Co
(R1)R2
R1
R2
(29)
R2
Co
R2
R1
R1
(30)
R1
R2
R2
R1
R1
R2
(31)
Co
R1
R2
R1
R2
(32)
Co
R1
R2
C=O
R1
R2
(33)

Scheme 27

on the ring size, either intramolecular cyclization to form a tricyclic CpCo cyclobutadiene complex (equation 47) or intermolecular cyclization combining two different rings through a cyclobutadiene (equation 48) can occur. An intramolecular pathway requires rings of 10 to 12 carbon atoms, whereas intramolecular double cyclization is no longer feasible with an eight-carbon cyclic dialkyne. In this case, the cyclobutadiene product is formed by intermolecular cyclization. This latter product then can undergo a second $2 + 2$ cycloaddition at the opposite end of the molecule to give a 'superphane' having two CpCo cyclobutadiene units linked in a paracyclophane-like manner.**[75]** The free hydrocarbon can be liberated from the metals by Ce^{4+} oxidation (however, the expected double $2 + 2$ cycloaddition of two cyclobutadienes in the free superphane to yield an all edge-bridged cubane does not take place). Reaction of CpCo(cbd) with nitrile to give pyridine, as well as related reactions, proved that under appropriate conditions the Cyclobutadiene (cbd) complex, once formed, can undergo ring opening or insert again (equation 49).

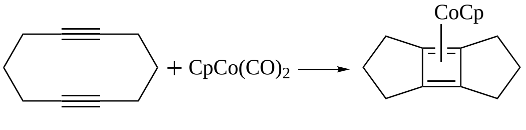
+ CpCo(CO)2
CoCp

(47)

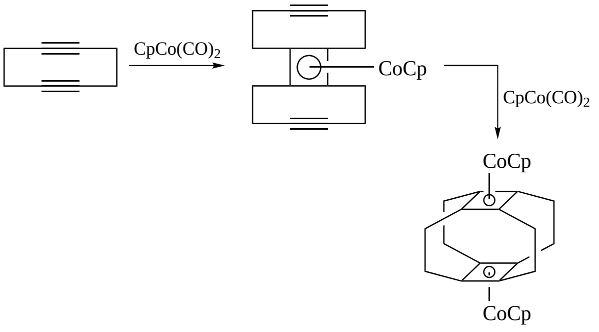
CpCo(CO)2
CoCp
CpCo(CO)2
CoCp
CoCp

(48)

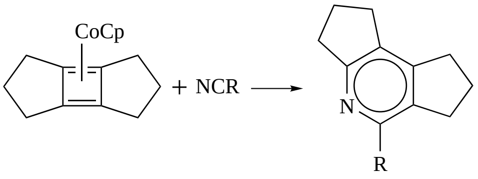

(49)

6 CYCLOBUTADIENE AND ARENE COMPLEXES

6.1 Cyclobutadiene Complexes

The majority of cobalt cbd complexes are of the type CpCo(cbd) (**34**). Cbd derivatives of $Co_2(CO)_8$, that is, (cbd)$Co_2(CO)_4$ (**35**), and (cbd)$Co(CO)_2X$ (**36**) are also known. The preparation of (**36**) is achieved by halogen cleavage from (**35**). Complex (**35**) is accessible along the common routes for the preparation of cbd complexes,[76] that is, (i) ligand transfer from a Ni or Pd complex, and (ii) reaction of (2^-) with 1,2-dichlorobutene. An elegant method for the preparation of the tetramethylcyclobutadiene derivative of (**36**) has made use of Hogeveen's complex, which is formed from 2-butyne and $AlCl_3$ in dichloromethane (equation 50). Carbonyl cations (cbd)$Co(CO)_3^+$ easily exchange CO for donor ligands (equation 51) and are susceptible to nucleophilic attack at the cbd ring.[77]

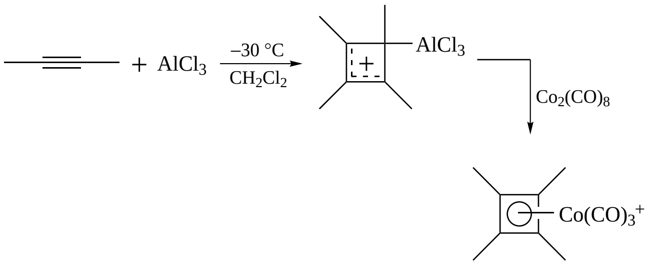

(50)

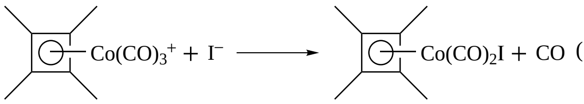

(51)

Complexes of type (**34**) are obtained from many different alkynes and suitable $CpCoL_2$ precursors, as detailed in the foregoing section. Early workers studied the reaction between CpCo(diene) or $CpCo(CO)_2$ with phenylacetylenes, which gives the respective phenylcyclobutadiene complexes. The tetracyclone complex is a major reaction product when carbonyls are employed. Complexes of type (**34**) have exceptional stability and normally do not react by substitution of the cbd ring. However, the cbd ligand can undergo electrophilic substitution if free positions are available on the ring. Thus, CpCo(cbd) was the only $CpCoL_2$ compound that was found to be inactive in the Co-mediated pyridine synthesis.[78]

Even as CpCo(cbd) can be viewed as the 18-electron analog of cobaltocene (Section 7.1), the cationic complexes Co(arene)(cbd)$^+$ are analogs of the cobaltocenium ion. They can be prepared from either $C_4Ph_4Co(CO)_2Br$ or $C_4Me_4Co(CO)_2I$ and a broad variety of arenes in the presence of $AlCl_3$ to give phenyl- or methyl-substituted sandwich complexes, respectively (equation 52).[77] Homogeneous reduction of (arene)Co(C_4Ph_4)$^+$ with CpFe(HMB) (HMB = hexamethylbenzene) gives the neutral 19-electron sandwich complex (arene)Co(C_4Ph_4). It shows the characteristic reactivity for 19-electron sandwich complexes, for example oxidative addition (*see Oxidative Addition*) of mild electrophiles such as MeI (Section 7.1).

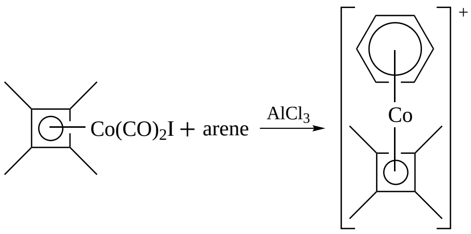

(52)

6.2 Arene Complexes

Cationic sandwich complexes of the type CpCo(arene)$^{2+}$ were first prepared by hydride abstraction from cyclohexadienyl cations (Section 7.1). They are accessible in broader variation from the reaction of CpCoX half-sandwich complexes with arene in the presence of $AlCl_3$. Their electrochemical reductions to the corresponding 19-electron monocations and to 20-electron neutral complexes have been studied.[79] The stability of electron-rich sandwich complexes increases with increasing alkyl substitution in either ring despite the more negative redox potential; mass spectrometry studies of bond dissociation energies of (arene)Co$^+$ complexes corroborate these results.[80] However, neutral sandwich complexes are not very stable in the polar solvents necessary for the reduction of mono- or dications and have been isolated only from alkyne trimerization with CpCo precursors in nonpolar solvents (Section 5.1.4).

Co arene chemistry has been expanded by the preparation of a number of (arene)Co(η^4-diene)$^+$ and (arene)Co(η^1,η^2-enyl) complexes starting from (**10**).[81] Hydrogenation of (**10**) in the presence of an arene and a base (piperidine or quinuclidine for obvious stabilization of coordinatively unsaturated cobalt intermediates) gives cyclooctenyl complexes (**37**) (equation 53). This reaction occurs with a large number of arenes; even C_6F_6 gives an η^6-arene complex. The resulting complexes (**37**) are moderately active catalysts in the pyridine synthesis from alkynes and nitriles (Section 5.1.4).

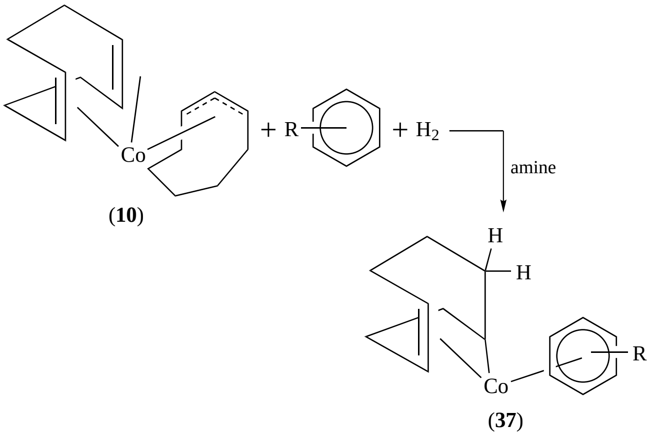

(53)

Another preparation method for (arene)Co(η^4-diene)$^+$ complexes is the reaction of dienes with 20-electron

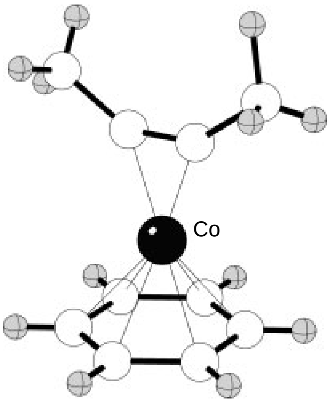

Figure 11 Structure of benzene(butyne)cobalt complex

bis(arene)Co$^+$ complexes (equation 54). Arene displacement can occur in polar media with a variety of dienes – cyclohexadiene, cycloheptadiene, cod, and norbornadiene. The resulting 18-electron cationic complexes can be electrochemically reduced to 19-electron neutral radicals. EPR studies have shown that these complexes to have a ground state similar to those of $[\mathrm{CpCoL_2}]^-$ analogs.**[82]**

$$[(\mathrm{arene})_2\mathrm{Co}]^+ + \mathrm{diene} \longrightarrow [(\mathrm{arene})\mathrm{Co}(\eta^4\text{-diene})]^+ + \mathrm{arene} \quad (54)$$

Cobalt-arene complexes can also be synthesized from metal vapor reactions. For example, $(\eta^6\text{-C}_6\text{H}_5\text{Me})\text{Co}(\text{C}_6\text{F}_5)_2$ is made at low temperature and low pressure conditions (equation 55).

A remarkable cobalt-arene complex was also isolated from the metal vapor reaction of cobalt atoms with toluene (Scheme 13) and subsequent addition of an alkyne (acetylene, butyne, or BTSA).**[52]** According to EPR spectra, compounds of the type (toluene)Co(alkyne) are 19-electron complexes of near-axial symmetry where the alkyne acts as a four-electron ligand on the cobalt atom. The methyl derivative has been structurally characterized with Co–C$_{\text{alkyne}}$ distances of 1.88 and 1.90 Å, and a C≡C distance of 1.254 Å (Figure 11).

$$2\mathrm{Co} + 2\mathrm{C_6F_5Br} + \mathrm{C_6H_5Me} \xrightarrow{-190\,^\circ\mathrm{C},\ 10^{-5}\ \mathrm{torr}} (\eta^6\text{-C}_6\text{H}_5\text{Me})\text{Co}(\text{C}_6\text{F}_5)_2 + \text{CoBr}_2 \quad (55)$$

7 COBALTOCENE AND COBALTOCENE DERIVATIVES

7.1 Cobaltocene

7.1.1 Synthesis and Properties

The compound $(\mathrm{C_5H_5})_2\mathrm{Co}$ ($\mathrm{Cp_2Co}$) (**38**) was one of the earliest examples of transition metal sandwich compounds to be synthesized (*see Cobaltocene*). In fact, the cation (**38**$^+$) was prepared in 1952, a year before the neutral metallocene. The sandwich compound (**38**) (equation 56) was first prepared from the cobalt hexammine complex $\mathrm{Co(NH_3)_6(C_5H_5)_2}$ that lost ammonia under high vacuum. Subsequently, many different preparations, starting from $\mathrm{CoX_2}$, or diverse complex cobalt salts and either NaCp, MgXCp, TlCp, or CpH/KOH in THF, were employed. A recommended procedure that gives high and reliable yields of (**38**) is the reaction of $\mathrm{CoCl_2}$ with NaCp in THF,**[83]** which is basically equation (56) performed in one step. Under an inert atmosphere, the compound is indefinitely stable.

$$\mathrm{Co(NH_3)_6Cl_2} + 2\mathrm{NaCp} \longrightarrow \mathrm{Co(NH_3)_6(Cp)_2} \xrightarrow{\text{heat}} \mathrm{Cp_2Co} + 6\mathrm{NH_3} \quad (56)$$

Compound (**38**) crystallizes with a unit cell isomorphous with that of ferrocene; there is a smooth variation of the cell parameters along the series from ferrocene, cobaltocene, and nickelocene. A crystal structure determined at two different temperatures, 100 and 297 K,**[84]** indicated that one ring is rotated by 22 and 34°, respectively. Occupancy for this second orientation was 10% at 100 K and 20% at 297 K. Moreover, one ring is tilted with respect to the other by 6° in the 100 K structure and 3° in the 297 K structure and slipped (parallel distance of the two ring centers) by 0.231 and 0.162 Å, respectively. Owing to this ring slip, Co–C distances are unequal in the molecule.

Whereas ferrocene (*see Ferrocene*) is an 18-electron complex with filled bonding and nonbonding orbitals, cobaltocene has 19 electrons with the extra electron residing in an e^*_{1g} antibonding orbital (*see Antibonding*) and is thus paramagnetic. This antibonding orbital occupancy weakens the Co–C$_{\text{ring}}$ bonds and results in longer metal–carbon distances than in ferrocene, but shorter distances than in the 20-electron complex nickelocene (*see Nickelocene*).

The dynamic Jahn–Teller effect (*see Jahn–Teller Effect*) has been investigated in metallocenes by means of experimental and DFT methods. A sandwich complex with an orbitally degenerate ground state (only ^{2}E states are known for orbitally degenerate sandwich molecules) lifts the degeneracy through vibrational modes in the ring plane that have the same symmetry as the degenerate MOs. Cobaltocene and various substituted cobaltocenes have played an important role in understanding the effects of electronic configuration and MO levels in the bonding characteristics and chemical reactivities of metallocenes.**[85]**

Redox potentials of cobaltocene and substituted cobaltocenes (Section 7.3) have been determined; for the reduction of cobaltocenium to cobaltocene, a potential of −0.95 V (vs. SCE) in acetonitrile or −0.86 V (vs. SCE) in $\mathrm{CH_2Cl_2}$ was measured (−1.35 V vs. the ferrocene/ferrocenium couple in aprotic solvents). The large potential difference between oxidation of ferrocene and cobaltocene is intriguing, since it is related in a simple fashion to the difference in the HOMO–LUMO gap in these two sandwich complexes. At a more negative potential (-1.88 V vs. SCE in acetonitrile, -2.30 V vs. Fc/Fc^+), a cobaltocenate anion has been detected electrochemically.[86,87] This species is short-lived in polar solvents but has some stability in dry ether solvents, such as DME. Reduction to cobaltocenate plays an important role in the reductive cleavage of cobaltocene (Section 7.1.2). Redox potentials of Cp_2Co^{2+} (3.15 V vs. SCE) and Cp_2Co^{2-} (-3.1 V vs. SCE) have also been obtained from oxidation of cobaltocenium and reduction of cobaltocenate; owing to the extreme potentials needed for these systems, liquid sulfur dioxide was used for its low nucleophilicity and tetrahydrofuran was used for its low electrophilicity.[88]

7.1.2 Reactions of Cobaltocene

Cobaltocene is stable as a monomer under all conditions, showing no tendency to dimerize, as does the rhodium congener rhodocene. Cobaltocenium salts are easily prepared by several routes, including mild oxidation of cobaltocene, and are stable as cations. However, neutral electron-rich monomers are no longer stable if the aromaticity of one of the Cp rings is perturbed by interposed CH_2 groups (e.g. CpCo(cyclohexadienyl)). Dimerization of a C–C bond adjacent to the π-system frequently occurs (Scheme 28). The process can be followed electrochemically on reduction of the $CpCo(\eta^5\text{-L})^+$ cation to the neutral sandwich, which then dimerizes. Logically, the same dimerization is observed with so-called 'half-open' cobaltocene, that is, a bis(pentadienyl)cobalt, which has one pentadienyl (*see Pentadienyl Ligand*) and one pentadiene ligand linked to a second unit through a terminal carbon.[89]

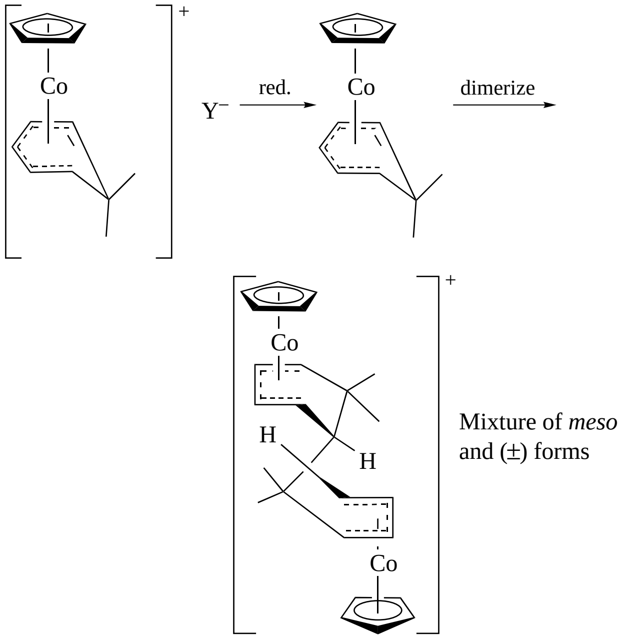

Mixture of *meso* and (±) forms

Scheme 28

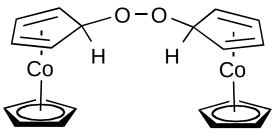

Figure 12 Structure of $[CpCo(\eta^4\text{-}C_5H_5)]_2(\mu\text{-}O_2)$

At low temperature, (**38**) reacts with stoichiometric O_2 to form a transient diamagnetic adduct (**38**)–O_2–(**38**) (Figure 12) from which oxygen can be transferred to α-diketones.[90] A similar dimer has been observed in which two molecules of (**38**) are linked via an acetylene bridge, that is, (**38**)–C≡C–(**38**).

Because of facile oxidation, there is no possibility for electrophilic substitution (*see Electrophilic Reaction*) at cobaltocene. On the other hand, owing to its positive charge, the cobaltocenium ion is deactivated towards electrophilic substitution. Thus, apart from simple electron-transfer oxidation, one of the most important reactions undergone by cobaltocene is a two-step oxidative addition, as depicted in equations (57) and (58).

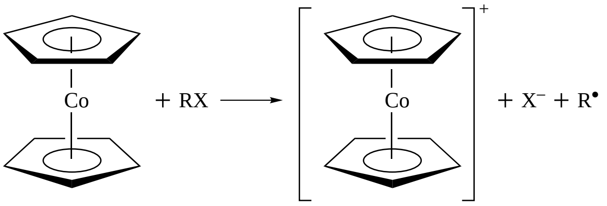

(57)

(**38**) (**38**$^+$)

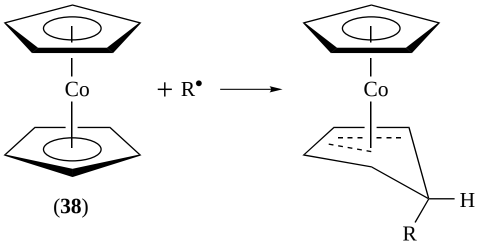

(58)

(**38**)

The mechanism of this reaction has been investigated in some detail.[90] RX must be an activated halide, such as a benzyl halide, α-halo ether, or a 1,1-dihalocarbon where at least one of the halides is Br or I. Simple halocarbons do not react, nor does methylene chloride. Reaction with chloroform is slow, while reaction with carbon tetrachloride is instantaneous at room temperature. The (pseudo) first-order rate constant is linearly correlated to the polarographic reduction potential of the halide; thus electron transfer from (**38**) to RX (equation 57) is the rate-determining step, followed by rapid cleavage of the RX^- radical anion into R• and X^-.

When the electrophile is a dihaloalkane R–CHXY, the ensuing *exo*-halomethyl derivative (**39**) undergoes a metal-assisted solvolytic ring-expansion reaction in polar solvents to give an *endo*-R-cyclohexadienyl(cyclopentadienyl)Co cation (**40**) (equation 59). This reaction is highly stereoselective, leading preferentially to the *endo*-R derivative.

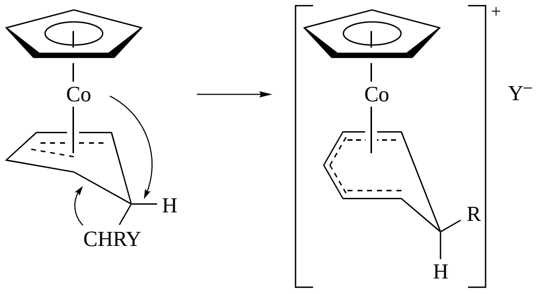

(59)

(**39**) (**40**)

A transformation of some synthetic versatility is the oxidation of methyl groups in a methylcobaltocenium salt by MnO_4^- to give the respective carboxylic acid. In this way, mono- and dicarboxylatocobaltocenium salts have been prepared. These acids can be further functionalized and used as receptors for the selective recognition of anion guest species.[91] A pyrrole-functionalized cobaltocenium salt has also been electropolymerized on an electrode surface; this system displays anion sensing in solution and when immobilized.[92]

Methyl groups in the cobaltocenium ion are sufficiently acidic to be deprotonated by strong bases. The ensuing fulvene complexes are not isolated, but can be alkylated in situ with alkyl iodide. Starting from pentamethylcobaltocenium, derivatives which bear five or 10 alkyl, benzyl, or other functionalized organic groups have been prepared (Scheme 29).[93]

An intriguing reaction of cobaltocene involves protonic acids as reagents, which in the case of a noncoordinating anion, gives (38^+) and hydrogen in a very clean reaction. Cobaltocene is a one-electron reducing agent, which makes the overall reaction a non-complementary electron transfer. Thus, a kinetic barrier is expected, although the redox potential indicates the reaction is highly favorable.[94]

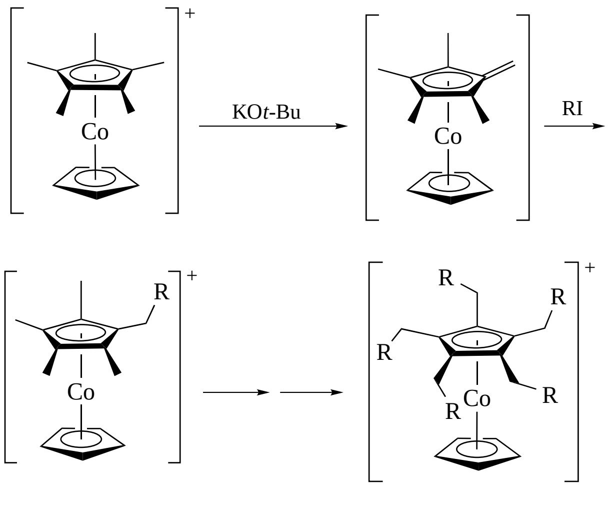

Scheme 29

7.2 Permethylated Cobaltocene

Permethylated Cp derivatives (Cp*) have proven to be valuable not only in metallocene chemistry, but also in the chemistry of half-sandwich complexes. Pentamethylcyclopentadiene is stable as a monomer and is a considerably weaker CH acid than cyclopentadiene. It can be converted into the anion by alkali metals (in ammonia) or more conveniently by *n*-BuLi. The Cp* anion is a strong base, but a poor nucleophile. The methyl groups strengthen the electron-donating ability of the ligand, which in turn augments the reducing properties of the permethylated cobaltocene (**41**); the redox potential is 0.6 V more negative in comparison to unsubstituted cobaltocene.[90]

Reactivity of (**41**) is largely analogous to that of (**38**) despite steric shielding by the methyl groups. As expected from the more negative redox potential, reactivity towards electrophiles is enhanced. Thus (**41**) reacts with alkyl and aryl monohalides such as PhI as in equations (57–59), where (**38**) has been found to be unreactive. A further difference lies in the orientation of the group R in solvolytic ring expansion of the *exo*-CHYR derivatives of (**38**) and (**41**) (equation 59); the group R in the methylated cyclohexadienyl complex now has an *exo* orientation, which stems from the steric influence of methyl groups on the rings.

7.3 Other Cp analogs

Several other derivatives of cobaltocene have been synthesized and studied. Heavily substituted cobaltocenes have been made with triisopropyl- (Cp^{3i}) and tetraisapropyl (Cp^{4i}) cyclopentadienyl ligands from alkali metal Cp salts and $CoCl_2$. These ‘encapsulated’ complexes exhibit exceptional stability with $(Cp^{4i})_2Co$ (Figure 13) being stable in air indefinitely. These complexes can be chemically oxidized with ammonium salts, although steric hindrance of the rings impedes the process. Interestingly, cyclic voltammetric data show the oxidation potentials of $(Cp^{3i})_2Co$ and $(Cp^{4i})_2Co$ to be virtually identical (−1.15 V and −1.14 V vs. SCE).[95]

Other derivatives such as CpCo(indenyl) and $Co(indenyl)_2$ have been prepared.[96] These compounds exhibit properties similar to that of cobaltocene but are of lower thermal stability. There have been numerous studies of linked metallocenes with a focus on the nature of metal–metal interactions.[97] The bis(fulvalene)dicobalt complex was found to be diamagnetic, either because of direct metal–metal coupling or by electron coupling through the linked five-membered ring (Scheme 30).

Isolobal replacement of the exocyclic methylene group of fulvene with a cobalt fragment generates cobaltafulvenes;

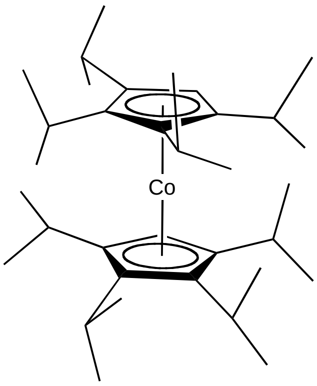

Figure 13 Structure of $(Cp^{4i})_2Co$

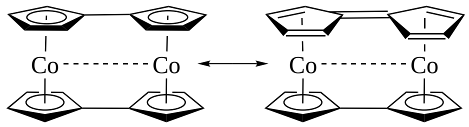

Scheme 30

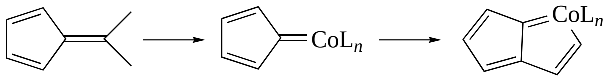

Scheme 31

these complexes can be further reacted with substituted alkynes to form cobaltapentalenes (Scheme 31). Dicobalt complexes of metallafulvenes and metallapentalenes can be prepared in this manner. The mechanism for the synthesis of cobaltapentalenes begins with oxidative addition of an alkyne to the cobalt atom of a cobaltafulvene (**42**) followed by nucleophilic attack of the acetylide on the fulvene system; a 1,3-hydrogen shift converts the metallabicyclic ring system to the cobaltapentalene (**43**) (Scheme 32).[98]

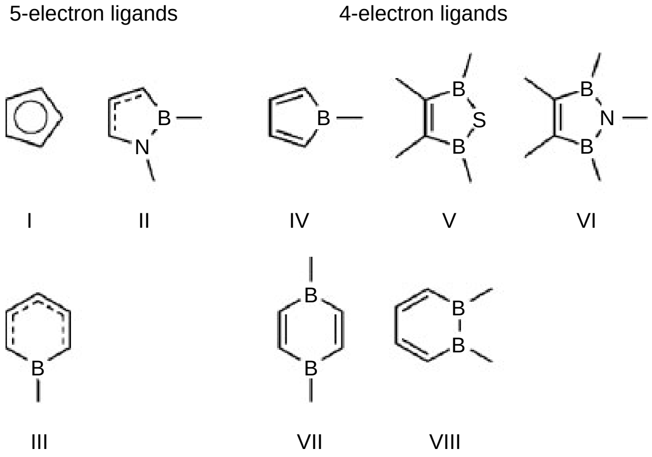

Figure 14 Boracyclic ligands used in cobalt sandwich complexes

8 COMPLEXES WITH BORACYCLIC LIGANDS

Cobalt does not complex to any group 15 or 16 heterocycles such as pyridine, pyrroline, or even thiophene. It appears that these electron-rich rings will not stabilize the metal as π-ligands and prefer to complex as σ-ligands. In contrast, a variety of cobalt sandwich complexes containing a boracyclic ring ligand have been prepared and studied because these complexes are isoelectronic with either cobaltocene, its cation, or analogs of CpCo(cyclobutadiene) (Figure 14). Boracycles are good ligands for cobalt in a sandwich complex because an electropositive atom incorporated in a π-cyclic ring will stabilize an electron-rich central metal.[99]

8.1 Borabenzene Complexes

One of the most intensely studied boracyclic compound is the borabenzene ligand synthesized by Herberich and coworkers.[100] Bis- and monoborabenzene cobalt sandwich complexes were first obtained by treating cobaltocene with boron trihalides BX_3 ($R = Cl$, Br) or alkyl/arylboron dihalides ($R =$ alkyl, aryl) as outlined in

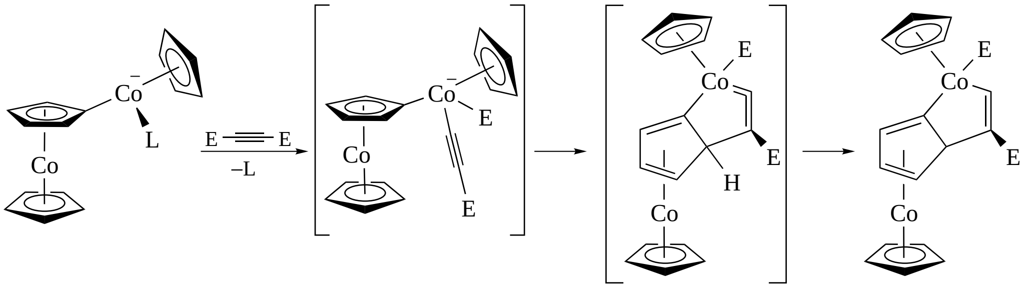

(**42**) (**43**)

Scheme 32

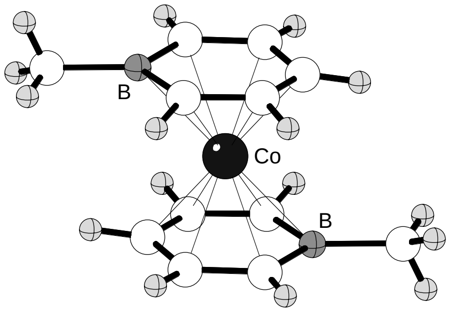

Figure 15 Molecular structure of $Co(C_5H_5BMe)_2$

Scheme 33. The first intermediate in this reaction, the *exo*-haloborylcyclopentadiene(cyclopentadienyl)cobalt (**44**) cannot be isolated because the solvolytic ring expansion to the (1-boratacyclohexadienyl)(cyclopentadienyl)cobalt cation ($\mathbf{45}^+$) occurs spontaneously, even in nonpolar solvents. The boracyclic cation ($\mathbf{45}^+$) is reduced by excess cobaltocene, and the neutral complex (**45**) can undergo the same reaction cycle, leading finally to the bisborabenzene complex (**46**).

A single-crystal X-ray structural determination of $Co(C_5H_5BMe)_2$ (Figure 15) revealed a planar sandwich where the cobalt atom is displaced towards C(4) by 0.28 Å. The Co–B distance of 2.283(5) Å is considered a bonding distance. The upfield shift of the ^{11}B NMR signal and the diminished nucleophilicity of the boron atom are consistent with this interpretation.

Redox properties of (borabenzene)cobalt complexes have been investigated electrochemically.**[101]** The reduction potentials are displaced uniformly to more positive values by about 0.5 V per borabenzene ligand. The existence of the relatively stable anion $Co(C_5H_5BPh)_2^-$ ($\mathbf{46}^-$), isolated as the PPh_4^+ salt, is a consequence of the positively displaced redox potentials; this complex undergoes electrophilic addition to give neutral sandwich complexes with one boratacyclohexadiene ligand. This anion is one of the few isolable 20-electron sandwich complexes of cobalt (see Section 5.1.4).

8.2 Aza- and Thiaborolene Complexes

A heterocycle ligand isoelectronic with cyclopentadiene is the azaborolinene ring for which the 1,2-isomer (II, Figure 14) is accessible and has been complexed to Co.**[102]** Sandwich compounds $Co(C_3H_3BRNR')_2$ were prepared from the free ligand C_3H_4BRNR' by metal vapor synthesis. Since the ligand has no plane of symmetry perpendicular to the ring plane, two diastereoisomers (a d,l-pair and a *meso* form) are formed having different orientations of the rings. The molecular structure is a sandwich molecule with a *trans* orientation of N and B, respectively, at either ring. Perturbation in the bonding exists between cobalt and the azaborolide ligand; the electron-rich cobalt is displaced from the ring centroid, resulting in shortened Co–C distances and longer Co–heteroatom distances. The neutral complex can be oxidized by ferrocenium ion to give a diamagnetic cation corresponding to cobaltocenium. Mixed ring cobalt complexes have also been prepared with azaborolides and CpCo species.

Aza- and thiadiborolene complexes derived from V and VI are closely related by symmetry and electron distribution, but the thia heterocycle exhibits better complexing properties. Complexes of the type CpCoL, where $L = C_2Et_2(BMe)S(BMe)$ or $C_2Et_2(BMe)(NMe)(BMe)$, have been prepared by heating the free ligand with $CpCo(CO)_2$. The

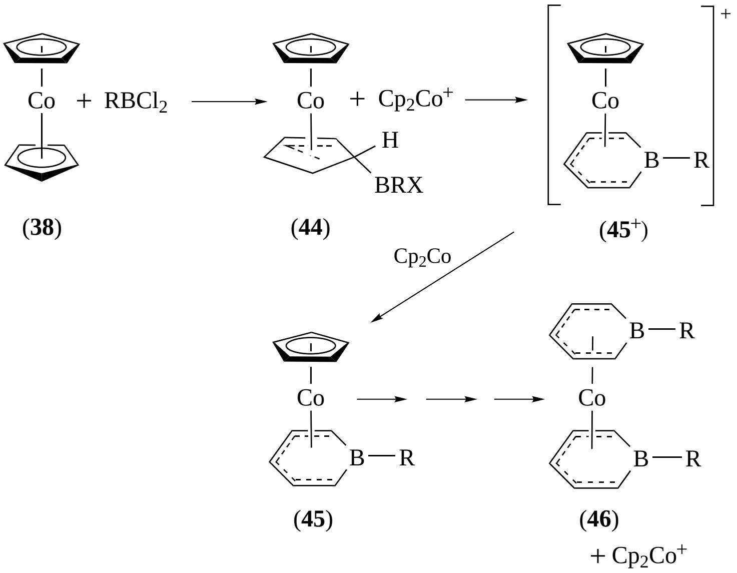

Scheme 33

dimeric carbonyl $[LCo(CO)(\mu\text{-}CO)]_2(Co\text{–}Co)$ is obtained as a by-product.

8.3 Borole Complexes

The four-electron boracycles IV, VII, and VIII (Figure 14) have been complexed to cobalt in sandwich structures. The type of complex formed with these ligands is CpCoL; these are electronic analogs of CpCo(diene) or CpCo(cyclobutadiene), respectively (Sections 5.1.2 and 6.1).

Borole (IV in Figure 14) has been used to synthesize a plethora of sandwich and half-sandwich structures; it is the bora analog of cyclopentadiene. Borole is an antiaromatic system (*see Antiaromatic Compound*), and only the blue pentaphenyl derivative has been prepared.[103] The general route to borole complexes consists of complexation under dehydrogenation of 2- or 3-borolenes, which are prepared from $[Mg(butadiene)]_x$ and RBX_2. Thus, the heating of either isomer of borolene with $Co_2(CO)_8$ produces $[(borole)Co(CO)_2]_2$ (**47**) (equation 60) from which further cobalt borole complexes are prepared (equation 61). CpCo(borole) (**48**) can be made from (**47**) by Cp transfer from the labile 20-electron nickelocene (equation 61). Pyrolysis of (**48**) at 160–180 °C gives a triple-decker complex (**49**) in nearly quantitative yield, which in turn can be cleaved by Cp^- into (**48**) and the bis(borole)cobaltate anion ($\mathbf{50}^-$) (Scheme 34).

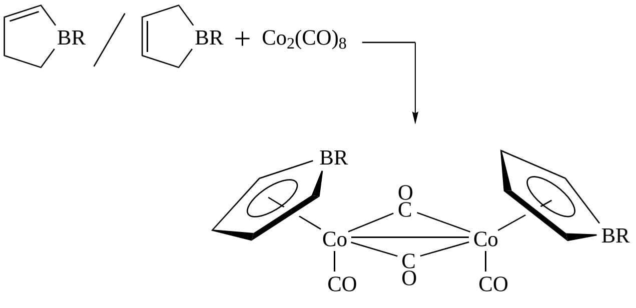

(**47**)

(60)

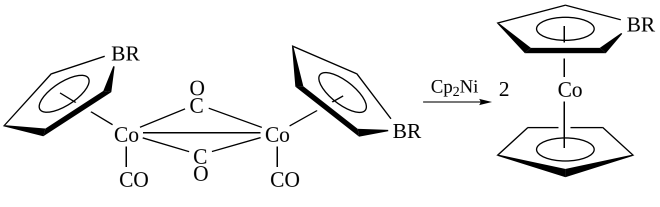

(**47**) (**48**)

(61)

This chemistry is analogous to that of $Co(diene)_2^-$ (Section 5.1.2), but boracyclic complexes are stabilized relative to anionic alkene complexes. Thus, bis(borole)cobaltate is stable in water at pH > 6 and can be precipitated as a NMe_4^+ salt. Electrophilic substitution of (**48**) occurs exclusively at the 2-position of the boracyclic ring.[103]

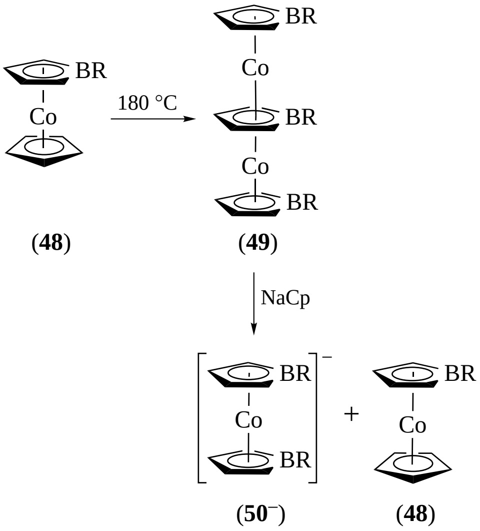

Scheme 34

9 CpCo HALF-SANDWICH COMPLEXES

9.1 Derivatives of $CpCo^{II}$

A few half-sandwich complexes containing a $CpCo^{II}$ unit are known; some of them are of synthetic utility and will be discussed below. The $[CpCo(CO)]_2^-$ anion ($\mathbf{19}^-$) can be methylated with MeI to give a dimethyl derivative, $[CpCoMe(CO)]_2$. This complex decomposes to produce acetone in high yield, a reaction that is reminiscent of the use of $Fe(CO)_4H^-$ in the carbonylation (*see Carbonylation*) of alkyl halides.

Dinuclear complexes $[CpCo(PR_2)]_2$ or $[CpCo(SR)]_2$ are prepared from $CpCo(CO)_2$ (**18**) or cobaltocene (**38**) with phosphines PR_2H, sulfides RSH, or disulfides RSSR, respectively. They are diamagnetic, puckered molecules having a Co–Co single bond (2.56 Å in $[CpCo(PPh_2)]_2$). Electrophiles or π-acceptor ligands (*see π-Acid Ligand*) add to the Co–Co bond to afford dinuclear Co^{III} complexes. Phosphine complexes, such as $CpCo(PPh_3)_2$, are much more stable thermally as the 17-electron cation $[CpCo(PPh_3)_2]^+$. The latter is readily isolated with various anions.[104]

Substituted cyclopentadienyl ligands have also been used to synthesize half-sandwich complexes of cobalt. For example, if $(C_5R_4H)Li$ ($R = {}^i Pr$; $Cp^{4i}Li$) is treated with $CoCl_2$ in a 1:1 ratio at – 20 °C, the half-sandwich complex $[Cp^{4i}CoCl]_2$ (**51a**) is produced in excellent yield (equation 62). A similar type of complex with amide bridging groups (**52**) is formed from $[Co(NH_3)_6](BF_4)_2$ and LiCp* (equation 63). The product complexes are paramagnetic at ambient temperature and show antiferromagnetic coupling (*see Antiferromagnetism*) when cooled below 100 K, although the coupling is weaker in the tetraisopropyl species.[105] These dimers are EPR silent, but in solvents more polar than hydrocarbons, a certain fraction of a monomeric complex Cp*CoX(S) (S = solvent) is found in equilibrium with the dimer; the monomer was identified by a hyperfine coupling to one cobalt and with EPR parameters very similar to characterized mononuclear species (see below). With donor ligands, these dimers are cleaved into stable monomers (**53**), for example, Cp*Co(pyridine)Cl and Cp*Co(PMe$_3$)Cl (Scheme 35).

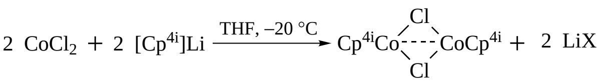

$$2\ \mathrm{CoCl_2} + 2\ [\mathrm{Cp^{4i}}]\mathrm{Li} \xrightarrow{\text{THF, }-20\,^{\circ}\text{C}} \mathrm{Cp^{4i}Co}\overset{\mathrm{Cl}}{\underset{\mathrm{Cl}}{\cdots}}\mathrm{CoCp^{4i}} + 2\ \mathrm{LiX} \qquad (62)$$

(**51a**)

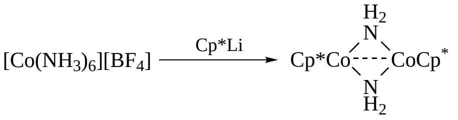

$$[\mathrm{Co(NH_3)_6}][\mathrm{BF_4}] \xrightarrow{\text{Cp*Li}} \mathrm{Cp^{*}Co}\overset{\mathrm{NH_2}}{\underset{\mathrm{NH_2}}{\cdots}}\mathrm{CoCp^{*}} \qquad (63)$$

(**52**)

The dinuclear halides (**51**) are starting materials for a great variety of synthetic transformations, some of which are depicted in Scheme 35, giving either Cp*Co$^{\mathrm{I}}$ derivatives by reduction or valence disproportionation upon reaction with acceptor ligands, or Cp*Co$^{\mathrm{III}}$ complexes by valence disproportionation or oxidation (equation 64 and Scheme 35). Many of these reactions are analogous to those that occur with the unsubstituted CpCo moiety.

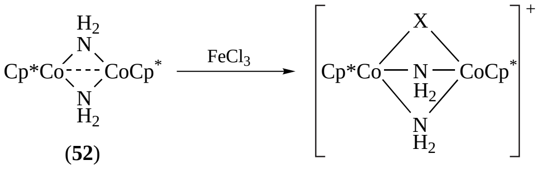

(64)

9.2 Derivatives of CpCo$^{\mathrm{III}}$

The organometallic chemistry of cobalt in oxidation state III is more extensive than that of iron and nickel. This observation is certainly connected to the high stability of octahedral Co$^{\mathrm{III}}$ coordination complexes. These compounds are of types I–V as depicted in Figure 16.

The use of a Cp* or other alkylated Cp ligand instead of unsubstituted Cp in CpCo$^{\mathrm{III}}$ chemistry is preferred for two reasons. First, there is less of a tendency to form oligomers and polymers with type I and III compounds, which ensures higher solubility; secondly, there seems to be a favorable electronic effect. Electron-donating alkyl groups on the Cp

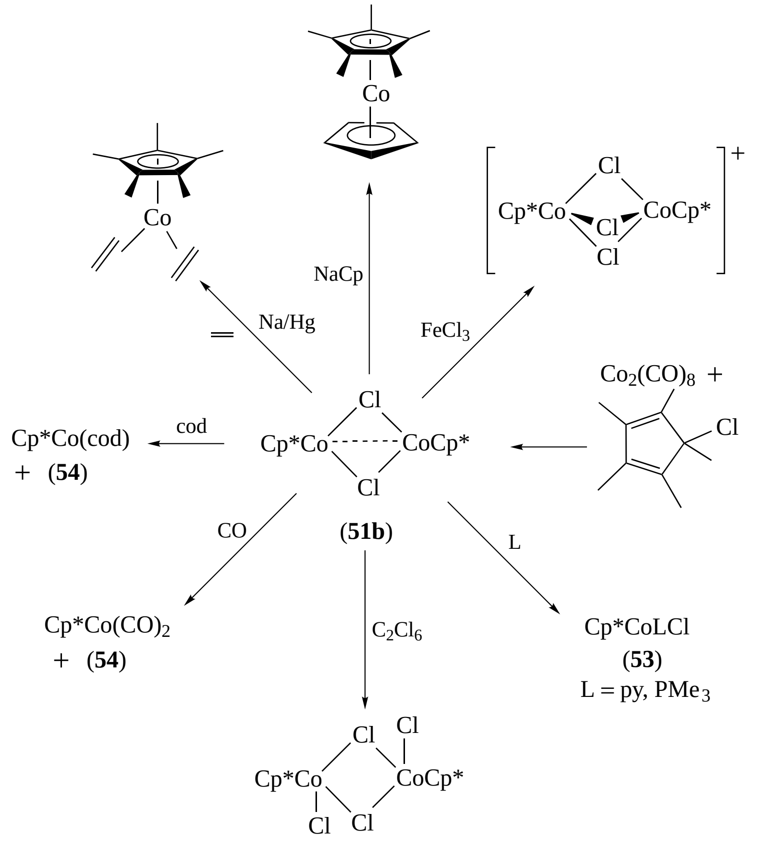

Scheme 35

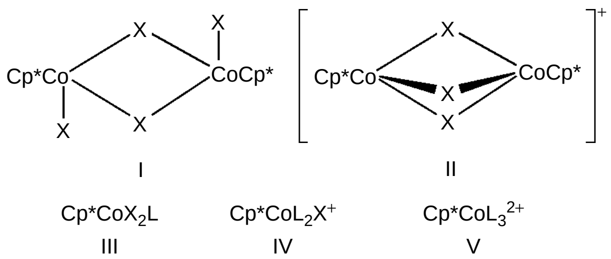

Figure 16 Co(III) octahedral complex types

ring tend to stabilize Co^{III} in its complexes. Addition of oxoanions (RCO_2^-, SO_4^{2-}), THF, water, or primary amines to $CpCo(NCMe)_3^{2+}$ causes rapid disproportionation, leading finally to Co^{2+} and Cp_2Co^+,**[106]** whereas Cp*Co derivatives with many kinds of hard σ-donor ligands have been isolated.

Cp derivatives of types III and IV containing soft donor or acceptor ligands, L, have been known for a long time. The only Cp derivative known of type I is the iodo complex $(CpCoI_2)_n$, which is formed from $CpCo(CO)_2$ and I_2. It is rather insoluble and is probably polymeric, but it reacts with strong nucleophiles and can be transformed into more soluble derivatives of type III with donor bases.

Cp^*CoX_2 complexes are known with X = Cl, Br, or I. They are soluble in organic solvents of medium polarity and are dimeric.**[107]** $[Cp^*CoCl_2]_2$ (**54**) is prepared from $[Cp^*CoCl]_2$ by disproportionation or by selective oxidation with C_2Cl_6 (Scheme 35). It is of limited stability and slowly decomposes even below room temperature into $CoCl_2$ and $(Cp^*)_x$. It is easily cleaved by donor ligands into complexes of type III–V and can serve as the starting material for many different kinds of Cp*Co complexes owing to its substitutional lability.

As an example, spontaneous hydrolysis gives the aqua ion $Cp^*Co(H_2O)_3^{2+}$, which can be derivatized as shown in Scheme 36. In this way, a series of complexes with ligands ranging from I (e.g. $[Cp^*CoI_2]_2$) to CN (e.g. $Cp^*Co(CN)_3^-$) with O-, N-, and S-donor atoms can be prepared. The ligand series essentially covers the whole spectrochemical series (*see Spectrochemical Series*), and a regular shift of the two absorption bands in the visible region characteristic for octahedral Co^{III} complexes ($^1A \rightarrow {}^1T_1$ and $^1A \rightarrow {}^1T_2$ descendants) is seen from about 700 nm in the iodide complex to 320 nm in the cyanide complex, with concomitant color change from green to blue, mauve, red, and yellow, providing a unique visualization of the spectrochemical series through a range of analogous complexes.**[108]**

A further derivative of type V should be mentioned, where L is $P(OR)_2O$ or PR_2O. The phosphonate group is formally uninegative; thus $CpCo[P(OR)_2O]_3^-$ (**55**) is a monoanion. This anion functions as a tridentate (*see Tridentate Ligand*) chelating ligand through the oxygen atoms, and it imposes a weak ligand field (*see* ***Ligand Field Theory & Spectra***) and low nephelauxetic parameter (*see Nephelauxetic Effect*) on the complexed central metal with a high binding constant. Complexes of the types $[CpCo[P(OR)_2O]_3]_2M$ and $[CpCo[P(OR)_2O]_3]\,ML_n$ have been prepared where M can be a p- or a d-block metal and ML_n any of a number of common transition organometallic fragments ($M(CO)_n$ or $CpM(CO)_n$, e.g.).**[109]**

The first compound of this type that was obtained was the cobalt complex $\{[CpCo[P(OR)_2O]_3]_2Co\}^+$ (**56**) (Scheme 37) of Co^{III}. It is formed when cobaltocene is treated with $P(OR)_3$ at about 120 °C in a reaction that comprises substitution of a Cp by $P(OR)_3$ followed by a triple Arbuzov rearrangement (*see Arbuzov Rearrangement*) and complexation of the cobalt ion liberated during the reaction. When (**56**) is treated with cyanide, the central cobalt ion is extracted as $Co(CN)_6^{3-}$, thereby liberating the free ligand (**55**) (Scheme 37).**[110]** Remarkably, the very inert cobalt atom incorporated in the

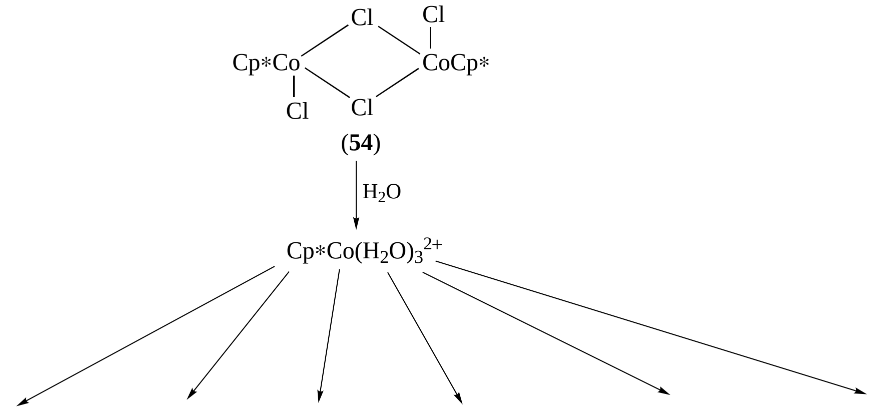

	$[Cp^*CoI_2]_2$	$[Cp^*Co(N_3)_2]_2$	$Cp^*Co(acac)Cl$	$Cp^*Co(bipy)(H_2O)^{2+}$	$Cp^*Co(NO_2)_3^-$	$Cp^*Co(CN)_3^-$
λ_{max}(nm):	720	615	610	530	490	382
Color:	green	green	blue	mauve	red	yellow

Scheme 36

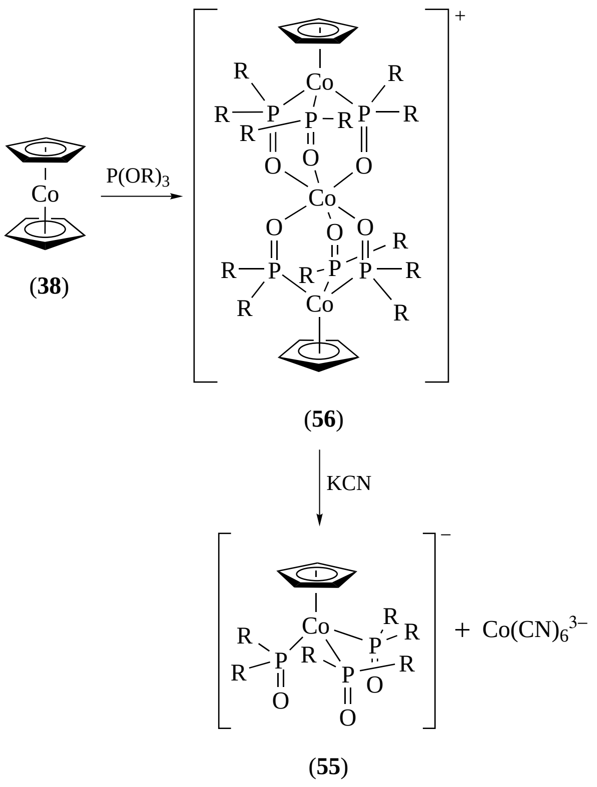

Scheme 37

tripodal complex (**55**) is not abstracted by this procedure. This tripodal ligand, despite its hard donor properties, has been proven to stabilize transition metal fragments in low as well as in high oxidation states. Its position at the left end (weak ligand) of the spectrochemical series (*see Spectrochemical Series*) is indicated by the observation of a low spin–high spin equilibrium in (**56**), where the exact value for the equilibrium constant at a given temperature depends on the group R. The central cobalt in (**56**) is thus one of the very few examples of high-spin Co^{III}.

10 COBALT CARBORANE COMPLEXES

Boron adopts a wide variety of cluster geometries because it has only three valence electrons; many stable architectures of boranes (*see* ***Boron: Organoboranes***) and carboranes (*see* ***Boron: Polyhedral Carboranes***) have been synthesized.**111** It has long been recognized that $B_9C_2H_{11}^{2-}$ acts as an analog of Cp (and especially Cp*) in many transition metal complexes, and can be used to form metallacarboranes (*see* ***Boron: Metallacarbaboranes***) including cobaltacarboranes.**112** The complex $(Et_3NH)[3,3'\text{-}Co(1,2\text{-}C_2B_9H_{11})_2]$ was one of the first metallacarboranes to be synthesized and structurally characterized (Figure 17).**113**

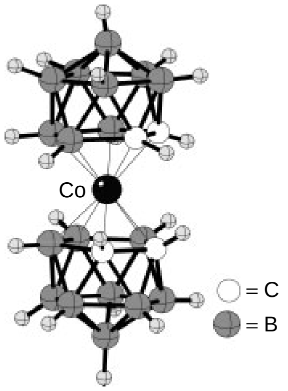

Figure 17 Structure of $[3,3'\text{-}Co(1,2\text{-}C_2B_9H_{11})_2]^-$

Cobaltacarboranes have been shown to be useful as extraction agents for ions, and competitive extractions have been conducted with ions associated with dyes used in photometric determinations of bases.**114** Lipophilic moieties can be substituted on cobaltacarboranes to allow efficient extraction of radioactive metal ions such as ^{90}Sr, ^{137}Cs, and ^{152} Eu in water at low pH.**115**

Cobaltacarboranes also have been used in sensor technology. The sandwich complex $[Co(B_9C_2H_{11})_2]^-$ can be used as a lipophilic coreceptor instead of tetraarylborate ion additives in ion selective electrodes, producing electrodes that are more selective for specific alkali metal ions.**116**

As carboranes are chemically stable and exhibit low toxicity to humans, biomedical applications of carborane systems, including cobaltacarboranes, have slowly emerged. The boron isotope ^{10}B accounts for about 20% of boron in nature, and it has the ability to capture a slow neutron and release an α-particle (equation 65). This reaction, if conducted in live tissue, will kill the immediate cell, but not its neighbors. Although early studies were done with toxic boron compounds, carboranes, with their low toxicities and high boron content, have been proven to be good substrates for boron capture neutron therapy (BCNT).**111** Cobaltacarboranes have been employed in radioimmunodetection and radioimmunotherapy as well.**117**

$$^{10}B + {}^{1}n \longrightarrow {}^{4}He + {}^{7}Li \tag{65}$$

11 RELATED ARTICLES

Carbonylation Processes by Homogeneous Catalysis; Coordination Chemistry: History; Coordination Numbers & Geometries; Iron: Organometallic Chemistry; Manganese: Organometallic Chemistry; Nickel: Organometallic Chemistry; Rhodium: Organometallic Chemistry.

12 REFERENCES

1. C. White, ‘Organometallic Compounds of Cobalt, Rhodium, and Iridium’, Chapman and Hall, New York, 1985.
2. R. D. W. Kemmitt and D. R. Russell, in ‘Comprehensive Organometallic Chemistry’, eds. G. Wilkinson, F. G. A. Stone, and E. W. Abel, Pergamon Press, Oxford, 1982, Vol. 5, Chap. 34, p. 1.
3. R. L. Sweany, in ‘Comprehensive Organometallic Chemistry-II’, eds. G. Wilkinson, F. G. A. Stone, and E. W. Abel, Pergamon, Oxford, 1995, Vol. 8, Chap. 1, p. 1.
4. L. Mond, H. Hirtz, and D. M. Cowap, *Chem. News*, 1908, **98**, 165.
5. L. Mond, H. Hirtz, and D. M. Cowap, *J. Chem. Soc.*, 1910, **97**, 798.
6. P. Gilmont and A. A. Blanchard, *Inorg. Synth.*, 1946, **2**, 238.
7. J. P. Kenny, R. B. King, and H. F. Schaefer III, *Inorg. Chem.*, 2001, **40**, 900.
8. M. Absi-Halabi, J. D. Atwood, N. P. Forbus, and T. L. Brown, *J. Am. Chem. Soc.*, 1980, **102**, 6248.
9. T. Bartik, B. Bartik, B. E. Hanson, K. H. Whitmire, and I. Guo, *Inorg. Chem.*, 1993, **32**, 5833.
10. N. P. Forbus, R. Oteiza, S. G. Smith, and T. L. Brown, *J. Organomet. Chem.*, 1980, **193**, C71.
11. R. Poilblanc and D. Montauzon, *J. Organomet. Chem.*, 1975, **93**, 397.
12. L. Rosi, A. Bini, P. Frediani, M. Bianchi, and A. Salvini, *J. Mol. Catal.*, 1996, **112**, 367.
13. D. B. Belanger, D. J. R. O’Mahony, and T. Livinghouse, *Tetrahedron Lett.*, 1998, **39**, 7637.
14. F. Robert, A. Milet, Y. Gimbert, D. Konya, and A. E. Greene, *J. Am. Chem. Soc.*, 2001, **123**, 5396.
15. T. J. M. de Bruin, A. Milet, F. Robert, Y. Gimbert, and A. E. Greene, *J. Am. Chem. Soc.*, 2001, **123**, 7184.
16. N. Jeong and S. H. Hwang, *Angew. Chem., Int. Ed. Engl.*, 2000, **39**, 636.
17. D. R. Carbery, N. D. Miller, and J. P. A. Harrity, *Chem. Commun.*, 2002, 1546.
18. M. Kurhinen and T. A. Pakkanen, *Langmuir*, 2000, **16**, 2658.
19. S. Fischer, U. Groth, M. Jung, and A. Schneider, *Synlett*, 2002, 2023.
20. A. Becheanu and S. Laschat, *Synlett*, 2002, 1865.
21. M. Guenter and H.-J. Gais, *J. Org. Chem.*, 2003, **68**, 8037.
22. R. Tuba and F. Ungvary, *Inorg. Chim. Acta*, 2002, **334**, 308.
23. X. Song and T. L. Brown, *Inorg. Chim. Acta*, 1996, **242**, 271.
24. X. Song and T. L. Brown, *Organometallics*, 1995, **14**, 1478.
25. D. A. Braden and D. R. Tyler, *Organometallics*, 2000, **19**, 3762.
26. R. Meyer, D. M. Schut, K. J. Keana, and D. R. Tyler, *Inorg. Chim. Acta*, 1995, **240**, 405.
27. Q. Xu, Si. Inoue, Y. Souma, and H. Nakatani, *J. Organomet. Chem.*, 2000, **606**, 147.
28. R. J. Klingler and J. W. Rathke, *J. Am. Chem. Soc.*, 1994, **116**, 4772.
29. T. Kruck, *Angew. Chem., Int. Ed. Engl.*, 1967, **6**, 53.
30. R. H. Crabtree, ‘The Organometallic Chemistry of the Transition Metals’, Wiley, New York, 2001.
31. M. Orchin, *Acc. Chem. Res.*, 1981, **14**, 259.
32. S. L. Gipson, L. A. Bryson, and K. K. Klausmeyer, *Inorg. Chim. Acta*, 2002, **340**, 221.
33. H. Schumann, M. Meissner, and H. J. Kroth, *Z. Naturforsch., B: Chem. Sci.*, 1978, **33B**, 1489.
34. H. Brunner, P. Faustmann, and B. Nuber, *J. Organomet. Chem.*, 1998, **556**, 129.
35. R. Tannenbaum and G. Bor, *J. Organomet. Chem.*, 1999, **586**, 18.
36. A. Fumagalli, S. Martinengo, M. Tasselli, G. Ciani, P. Macchi, and A. Sironi, *Inorg. Chem.*, 1998, **37**, 2826.
37. J. E. Ellis, *Adv. Organomet. Chem.*, 1990, **31**, 1.
38. F.-E. Hong, J.-Y. Wu, Y.-C. Huang, C.-K. Hung, H.-M. Gau, and C. C. Lin, *J. Organomet. Chem.*, 1999, **580**, 98.
39. P. Magnus, *Tetrahedron*, 1994, **50**, 1397.
40. T. Nakamura, T. Matsui, K. Tanino, and I. Kuwajima, *J. Org. Chem.*, 1997, **62**, 3032.
41. T.-Z. Liu and M. Isobe, *Synlett*, 2000, 266.
42. K. Schmidt, M. Jung, R. Keilitz, B. Schnurr, and R. Gust, *Inorg. Chim. Acta*, 2000, **306**, 6.
43. D. Osella, G. Cavigiolio, M. Vincenti, A. Vessieres, I. Laios, G. Leclercq, E. Napolitano, R. Fiaschi, and G. Jaouen, *J. Organomet. Chem.*, 2000, **596**, 242.
44. D. Seyferth, *Adv. Organomet. Chem.*, 1976, **14**, 97.
45. A. M. Bond, B. M. Peake, B. H. Robinson, J. Simpson, and D. J. Watson, *Inorg. Chem.*, 1977, **16**, 410.
46. T. Sugihara and M. Yamaguchi, *J. Am. Chem. Soc.*, 1998, **120**, 10782.
47. D. Seyferth, C. N. Rudie, J. S. Merola, and D. H. Berry, *J. Organomet. Chem.*, 1980, **187**, 91.
48. R. Dolby and B. H. Robinson, *J. Chem. Soc., Dalton Trans.*, 1973, 1794.
49. C. H. Wei and L. F. Dahl, *Inorg. Chem.*, 1967, **6**, 1229.
50. H. Wadepohl, K. Buchner, M. Herrmann, and H. Pritzkow, *J. Organomet. Chem.*, 1999, **573**, 22.
51. L. Huang, *J. Mol. Catal.*, 1997, **125**, 47.
52. L. Vasquez, H. Pritzkow, and U. Zenneck, *Angew. Chem., Int. Ed. Engl.*, 1988, **27**, 705.
53. M. D. Fryzuk, D. B. Leznoff, R. C. Thompson, and S. J. Rettig, *J. Am. Chem. Soc.*, 1998, **120**, 10126.
54. C. Elschenbroich and A. Salzer, ‘Organometallics: A Concise Introduction’, VCH Publishers, New York, 1992.

55. E. J. Starr, S. A. Bourne, M. R. Caira, and J. R. Moss, *J. Organomet. Chem.*, 1995, **490**, C20.
56. M. S. Ram and C. G. Riordan, *J. Am. Chem. Soc.*, 1995, **117**, 2365.
57. E. K. Byrne, D. S. Richeson, and K. H. Theopold, *J. Chem. Soc., Chem. Commun.*, 1986, 1491.
58. S. Otsuka and M. Rossi, *J. Chem. Soc. A*, 1969, **3**, 497.
59. M. Costa, E. Dalcanale, F. S. Dias, C. Graiff, A. Tiripicchio, and L. Bigliardi, *J. Organomet. Chem.*, 2001, **619**, 179.
60. J. A. K. du Plessis and J. S. Viljoen, *J. Mol. Catal.*, 1995, **99**, 71.
61. H. Boennemann, C. Grard, W. Kopp, W. Pump, K. Tanaka, and G. Wilke, *Angew. Chem.*, 1973, **85**, 1024.
62. J. D. Smith, K. T. Quisenberry, T. P. Hanusa, and W. W. Brennessel, *Acta Crystallogr., Sect. C*, 2004, **60**, m507.
63. J. D. Smith, T. P. Hanusa, and V. G. Young Jr, *J. Am. Chem. Soc.*, 2001, **123**, 6455.
64. J. M. Campbell, A. A. Martel, S. P. Chen, and I. M. Waller, *J. Am. Chem. Soc.*, 1997, **119**, 4678.
65. H. Wadepohl and S. Gebert, *Coord. Chem. Rev.*, 1995, **143**, 535.
66. D. A. Braden and D. R. Tyler, *J. Am. Chem. Soc.*, 1998, **120**, 942.
67. A. A. Bengali, R. G. Bergman, and C. B. Moore, *J. Am. Chem. Soc.*, 1995, **117**, 3879.
68. P. E. M. Siegbahn, *J. Am. Chem. Soc.*, 1996, **118**, 1487.
69. S. Niu, M. B. Hall, and G. ten Brinke, *J. Am. Chem. Soc.*, 1997, **119**, 3077.
70. K. Jonas, G. Koepe, and C. Kruger, *Angew. Chem., Int. Ed. Engl.*, 1986, **25**, 923.
71. H.-W. Fruhauf, *Chem. Rev*, 1997, **97**, 523.
72. H. Werner, *Angew. Chem., Int. Ed. Engl.*, 1983, **22**, 927.
73. H. Butenschoen, *Chem. Rev.*, 2000, **100**, 1527.
74. L. S. Hegedus, ‘Transition Metals in the Synthesis of Complex Organic Molecules’, University Science Books, Mill Valley, 1994.
75. R. Gleiter and D. Kratz, *Acc. Chem. Res.*, 1993, **26**, 311.
76. P. K. Baker and H. Silgram, *Trends Organometallic Chem.*, 1999, **3**, 21.
77. A. R. Kudinov, E. V. Mutseneck, and D. A. Loginov, *Coord. Chem. Rev.*, 2004, **248**, 571.
78. H. Bonnemann and W. Brijoux, *Synth. Methods Organomet. Inorg. Chem.*, 2002, **10**, 149.
79. U. Koelle, B. Fuss, M. V. Rajasekharan, B. L. Ramakrishna, J. H. Ammeter, and M. C. Boehm, *J. Am. Chem. Soc.*, 1984, **106**, 4152.
80. K. Schroeter, R. Wesendrup, and H. Schwarz, *Eur. J. Org. Chem.*, 1998, 565.
81. H. Boennemann, R. Goddard, J. Grub, R. Mynott, E. Raabe, and S. Wendel, *Organometallics*, 1989, **8**, 1941.
82. J. M. Mevs and W. E. Geiger, *Organometallics*, 1996, **15**, 2350.
83. I. Omae, ‘Applications of Organometallic Compounds’, John Wiley & Sons, New York, 1998.
84. M. Y. Antipin, R. Boese, N. Augart, and G. Schmid, *Struct. Chem.*, 1993, **4**, 91.
85. Z.-F. Xu, Y. Xie, W.-L. Feng, and H. F. Schaefer III, *J. Phys. Chem. A*, 2003, **107**, 2716.
86. W. E. Geiger Jr, *J. Am. Chem. Soc.*, 1974, **96**, 2632.
87. R. S. Stojanovic and A. M. Bond, *Anal. Chem.*, 1993, **65**, 56.
88. A. J. Bard, E. Garcia, S. Kukharenko, and V. V. Strelets, *Inorg. Chem.*, 1993, **32**, 3528.
89. K. E. Torraca and L. McElwee-White, *Coord. Chem. Rev.*, 2000, 206.
90. N. J. Long, ‘Metallocenes: An Introduction to Sandwich Complexes’, Blackwell Science, London, 1998.
91. P. D. Beer, *Acc. Chem. Res.*, 1998, **31**, 71.
92. I. del Peso, B. Alonso, F. Lobete, C. M. Casado, I. Cuadrado, and J. Losada del Barrio, *Inorg. Chem. Commun.*, 2002, **5**, 288.
93. B. Gloaguen and D. Astruc, *J. Am. Chem. Soc.*, 1990, **112**, 4607.
94. U. Koelle, P. P. Infelta, and M. Graetzel, *Inorg. Chem.*, 1988, **27**, 879.
95. D. J. Burkey, M. L. Hays, R. E. Duderstadt, and T. P. Hanusa, *Organometallics*, 1997, **16**, 1465.
96. S. A. Westcott, A. K. Kakkar, G. Stringer, N. J. Taylor, and T. B. Marder, *J. Organomet. Chem.*, 1990, **394**, 777.
97. S. Barlow and D. O’Hare, *Chem. Rev.*, 1997, **97**, 637.
98. H. Wadepohl, Cobaltafulvenes and Cobaltapentalenes: Highly Polar Metallacyclic II-Systems with Unusual Properties, in ‘Unusual Structures and Physical Properties in Organometallic Chemistry’, eds. M. Gielen, R. Willem, and B. Wrackmeyer, John Wiley & Sons, West Sussex, 2002.
99. G. E. Herberich, Boron Rings Ligated to Metals, in ‘Comprehensive Organometallic Chemistry-II’, eds. G. Wilkinson, F. G. A. Stone, and E. W. Abel, Pergamon Press, Oxford, 1995, Vol. 1, Chap. 5, p. 197.
100. G. E. Herberich and H. Ohst, *Adv. Organomet. Chem.*, 1986, **25**, 199.
101. U. Koelle, *J. Organomet. Chem.*, 1978, **152**, 225.
102. G. Schmid, Two Adjacent Heteroatoms with at Least One Boron, in ‘Comprehensive Heterocyclic Chemistry-II’, eds. A. R. Katritzky, C. W. Rees, and E. F. V. Scriven, New York, 1996, Vol. 3, Chap. 3.17, p. 739.
103. G. Varvounis, Boroles, in ‘Comprehensive Heterocyclic Chemistry-II’, eds. A. R. Katritzky, C. W. Rees, and E. F. V. Scriven, New York, 1996, Vol. 2, Chap. 2.18, p. 919.
104. U. Koelle and S. Paul, *Inorg. Chem.*, 1986, **25**, 2689.
105. F. Baumann, E. Dormann, Y. Ehleiter, W. Kaim, J. Karcher, M. Kelemen, R. Krammer, D. Saurenz, D. Stalke, C. Wachter,

G. Wolmershauser, and H. Sitzmann, *J. Organomet. Chem.*, 1999, **587**, 267.

106. U. Koelle, *J. Organomet. Chem.*, 1980, **184**, 379.
107. J. J. Schneider, R. Goddard, and C. Krueger, *Z. Naturforsch., B: Chem. Sci.*, 1995, **50**, 448.
108. U. Koelle and B. Fuss, *Chem. Ber.*, 1984, **117**, 753.
109. M. Akita, D.-q. Ma, S. Hikichi, and Y. Moro-oka, *J. Chem. Soc., Dalton Trans.*, 1999, 987.
110. W. Klaui, *Angew. Chem., Int. Ed. Engl.*, 1990, **29**, 627.
111. R. N. Grimes, *J. Chem. Educ.*, 2004, **81**, 657.
112. T. P. Hanusa, *Polyhedron*, 1982, **1**, 663.
113. I. B. Sivaev and V. I. Bregadze, *Collect. Czech. Chem. Commun.*, 1999, **64**, 783.
114. O. Navratil, Z. Skalican, Z. Kobiha, and E. Halamek, *Collect. Czech. Chem. Commun.*, 1998, **63**, 967.
115. C. Vinas, S. Gomez, J. Bertan, J. Texidor, J. F. Dozol, and H. Rouquette, *Inorg. Chem.*, 1998, **37**, 3640.
116. M. Krondak, R. Volf, and V. Kral, *Collect. Czech. Chem. Commun.*, 2001, **66**, 66.
117. D. E. Harwell, J. Nabakka, C. B. Knobler, and M. F. Hawthorne, *Can. J. Chem.*, 1995, **73**, 1044.

Coordination Chemistry: History

George B. Kauffman
California State University, Fresno, CA, USA

1 Introduction 1
2 Historically Important Coordination Compounds 1
3 Some Pre-Werner Theories of Coordination Compounds 3
4 Werner's Coordination Theory and his Controversy with JØrgensen 5
5 Twentieth-century Developments 11
6 Other Developments 16
7 Related Articles 22
8 References 22

1 INTRODUCTION

Coordination chemistry deals with a wide variety of substances and reactions (*see* ***Coordination & Organometallic Chemistry: Principles***). This discussion of its history is confined to the major discoveries, both experimental and theoretical, in the evolution of the discipline, and many interesting but minor events must necessarily be omitted. In view of Alfred Werner's central role in the field, considerable space is allotted to his monumental achievements, but contributions of lesser-known pioneers will also be included.

In this broad chronological survey, some of the most historically significant coordination compounds are first discussed, along with several pre-Werner theories of their formation and constitution, followed by Werner's theory and his most important discoveries. This article concludes with a brief consideration of discoveries and developments from Werner's time through 2003.**[1–5]**

2 HISTORICALLY IMPORTANT COORDINATION COMPOUNDS

The development of our knowledge of coordination compounds has been a very slow, gradual, and cumulative process.

2.1 Alizarin

The earliest known coordination compound is possibly bright red alizarin dye, a calcium aluminum chelate compound of hydroxyanthraquinone. Clay was the source of the calcium and aluminum ions; the hydroxyanthraquinone was obtained from the roots of the madder plant. Although the origin of this dye is shrouded in antiquity, it was first used in India and by ancient Persians and Egyptians, long before it was used by the Greeks and Romans. It may have been used to dye Joseph's biblical 'coat of many colors' (Genesis 37:3).

Herodotus (ca. 450 BC) mentioned alizarin, and it may have been the dye that Alexander the Great used in winning a battle against a much larger Persian army 120 years later. Alexander dyed his soldiers' clothing with bloodlike splotches, enticing the Persians into attacking what they believed was a demoralized force of wounded men, possibly the first recorded example of chemical camouflage. Alizarin was used to dye the British 'redcoats', making it an integral part of American Revolutionary history.

2.2 The Tetraamminecopper(II) Ion

In 1597, the German physician and alchemist Andreas Libavius (ca. 1540–1616) reported that *aqua calcis* (lime water or saturated $Ca(OH)_2$ solution) containing *sal ammoniac* (NH_4Cl) becomes blue in contact with brass (an alloy of copper and zinc), probably the first scientifically recorded observation of a completely inorganic coordination compound; in this case the familiar tetraamminecopper(II) ion, $[Cu(NH_3)_4]^{2+}$ (*see* ***Copper: Inorganic & Coordination Chemistry***).

2.3 Prussian Blue

Prussian Blue, potassium iron(III) hexacyanoferrate(II) ($KCN{\cdot}Fe(CN)_2{\cdot}Fe(CN)_3$), was first obtained accidentally in 1704 by a manufacturer of artists' colors from Berlin named Diesbach (*see* ***Iron: Inorganic & Coordination Chemistry*** and ***Mixed Valence Compounds***). This dark blue substance precipitated from an iron-containing solution when he added an alkali that he had obtained from the wandering German alchemist Johann Conrad Dippel. In 1710, it was first described as a nontoxic pigment for oil colors. Its method of preparation was not given, probably because Diesbach wanted to sell his discovery, but a recipe for the substance appeared in Latin in 1724. Ferrocyanides (hexacyanoferrates(II)) probably antedate Diesbach's discovery because materials containing iron, potash, and nitrogenous matter such as blood or animal hooves were most likely to have been heated together in earlier times. They may possibly be the first known examples of coordination compounds containing transition metal carbon bonds (organometallic compounds) because they contain Fe–CN bonds (*see Organometallic Complexes*).

2.4 The Hexaamminecobalt(III) Ion

Many historians credit the discovery of the first metal – ammine to Citizen (Citoyen) Tassaert, a Parisian chemist about whom virtually nothing is known, not even his first name. Some of them imply or state that he was the first to prepare the parent compound from which all cobalt–ammines may be considered to be derived, hexaamminecobalt(III) chloride, $[Co(NH_3)_6]Cl_3$ (*see* ***Cobalt: Inorganic & Coordination Chemistry***). However, Tassaert, in 1798, only reported the brownish mahogany color of a solution formed by adding excess aqueous ammonia to a cobalt chloride or cobalt nitrate solution, and he failed to isolate any compounds or pursue his accidental discovery.

2.5 Vauquelin's Salt and Magnus' Green Salt

In 1813, the pink compound tetraamminepalladium(II) tetrachloropalladate(II), ($[Pd(NH_3)_4][PdCl_4]$), was discovered by Louis-Nicolas Vauquelin (1763–1829). Known as Vauquelin's Salt, it contains coordinated palladium in both the cation and the anion. In 1828, the corresponding platinum compound ($[Pt(NH_3)_4][PtCl_4]$) was discovered by Heinrich Gustav Magnus (1802–1870). The first platinum–ammine to be discovered, it is known as Magnus' Green Salt. Both Vauquelin's Salt and Magnus' Green Salt differ markedly in color from their constituent ions, which indicates the presence of an interaction between the cationic metal atom and the anionic metal atom. They are 'polymerization isomers' of the *cis* and *trans* isomers of the diamminedichloro complexes of the corresponding metals (see Section 2.8).

2.6 Gmelin's Compounds

Some authorities consider the reddish yellow hexaamminecobalt(III) oxalate ($[Co(NH_3)_6]_2(C_2O_4)_3$), described in 1822 by Leopold Gmelin (1788–1853), to be the first metal–ammine to be isolated in the solid state. Other historically significant coordination compounds discovered by Gmelin include a number of double salts: potassium ferricyanide (potassium hexacyanoferrate(III), $K_3[Fe(CN)_6]$), the cobalticyanides (hexacyanocobaltates(III), $M_3[Co(CN)_6]$), and the platinocyanides (tetracyanoplatinates(II), $M_2[Pt(CN)_4]$).

2.7 Zeise's Salt

This compound, potassium trichloro(ethylene)platinate(II) monohydrate ($K[PtCl_3(C_2H_4)]\cdot H_2O$), has played an important role in both inorganic and organic bonding theory. Discovered in 1827 by William Christoffer Zeise (1789–1847),[6] it was the first organometallic compound containing an unsaturated organic ligand, and its discovery later led to the preparation and characterization of many other platinum–alkene compounds. Its structure and bonding only began to be understood after Kealy and Pauson (1951)[7] in the United States and Miller *et al.* (1952)[8] in England prepared and characterized the first 'sandwich' compound, ferrocene (bis(cyclopentadienyl)iron(II)).

2.8 Peyrone's Salt and Reiset's Second Chloride

Two significant isomeric platinum(II) complexes were discovered in the same year, 1844. Although both possess the same formula ($PtCl_2(NH_3)_2$), they differ in physical and chemical properties and represent the simplest, best, and longest known case of stereoisomeric platinum compounds. One isomer (platosemidiammine chloride or Peyrone's Salt) was prepared by the action of aqueous ammonia on potassium tetrachloroplatinate(II), while the other (platosammine chloride or Reiset's Second Chloride) was prepared by Jules Reiset (1818–1896) by the action of heat or concentrated hydrochloric acid on tetraammineplatinum(II) chloride. In his first paper on the coordination theory,[9] Werner used these compounds, which he rightly considered to be geometric isomers, to assign a square-planar configuration to platinum(II) compounds. Il'ya Il'ich Chernyaev's trans effect[10] (1926) (see Section 5.7) explained the reactions involved in the preparation of these isomers in a generalized form.

2.9 Gibbs and Genth's Researches

During the first half of the nineteenth century, there were few other investigations of cobalt–ammonia compounds except for Gmelin's work. The existence of well-defined, crystalline cobalt–ammine salts was first recognized by Frederick Augustus Genth (1820–1893)[11] in 1847 at the University of Marburg. Before completing his analysis of his new compounds, he emigrated from Germany to the United States. It was 1851 before he published his results in German in an obscure Philadelphia journal for German physicians.

Genth described salts of two cations, roseocobalt (pentaammineaquacobalt(III)) and luteocobalt (hexaamminecobalt(III)). Although several similar compounds of platinum had been prepared in Europe before this, Genth's work drew attention to the neglected field of coordination compounds. In 1852, Oliver Wolcott Gibbs (1822–1908) began a collaboration with Genth, which has become famous in the annals of coordination chemistry. In November 1852, Gibbs made his first original contribution to this field by discovering a new cobalt–ammonia cation, xanthocobalt (pentaamminenitrocobalt(III)), which he obtained by passing oxides of nitrogen into solutions of Genth's compounds.

In 1856, Gibbs and Genth published their results in a 67-page monograph,[12] describing in detail the preparation, properties, analytical data, and reactions of 35 salts of four cobalt–ammine cations: (1) Genth's roseocobalt or pentaammineaquacobalt(III) ($[Co(NH_3)_5H_2O]X_3$); (2) purpureocobalt or pentaamminechlorocobalt(III) ($[CoCl(NH_3)_5]X_2$); (3) Genth's luteocobalt or hexaamminecobalt(III) ([Co

$(NH_3)_6]X_3$); and (4) Gibbs' xanthocobalt or pentaamminenitrocobalt(III) ($[CoNO_2(NH_3)_5]X_2$). Roseo and purpureo compounds were clearly differentiated for the first time, although Gibbs and Genth erroneously supposed them to be isomeric. They correctly predicted the existence of coordination compounds in which one or more equivalents of ammonia are replaced by an equal number of equivalents of an organic amine, as well as compounds with other metals in place of cobalt. Their experimental results link Libavius', Diesbach's, and Tassaert's primitive, qualitative observations to the most recent sophisticated, quantitative, contemporary studies.

3 SOME PRE-WERNER THEORIES OF COORDINATION COMPOUNDS

Because sufficient experimental data must be accumulated before attempts can be made to explain them and to predict new phenomena, theories usually lag behind practice. During the first half of the nineteenth century, discoveries of coordination compounds were few, sporadic, and often accidental. Only after Gibbs and Genth's work did chemists devote themselves to systematic studies of these compounds. It might therefore be expected that few theories of coordination compounds would be proposed until late in the second half of the nineteenth century. In fact, theories were devised promptly because of the great importance of coordination compounds to the general problem of chemical bonding.

3.1 Graham's Ammonium Theory (1837)

As more coordination compounds were discovered, theories to explain their constitution were proposed.[13–15] Thomas Graham (1805–1869) proposed the first theory of metal–ammines, the ammonium theory, in which metal–ammines are considered to be substituted ammonium compounds. He explained the constitution of compounds such as diamminecopper(II) chloride by the formula shown in structure (**1**).

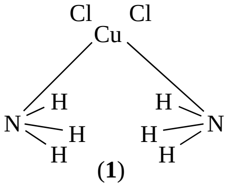

(**1**)

He suggested that two hydrogen atoms, one from each ammonia molecule, were displaced by the copper atom, and he viewed the salt as a 'chloride of cuprammonium' similar to the 'chloride of ammonium', thus explaining the strong retention of the ammonia in the compound. Graham's theory is very similar to the modern Lewis acid–base explanation for the formation of coordinate covalent bonds. Although it could be applied only when the number of ammonia molecules in the coordination compound equaled the electrovalence of the metal, it attained a fair degree of success, largely because of modifications proposed by chemists such as Gerhardt, Wurtz, Reiset, von Hofmann, and Weltzien.

3.2 Berzelius' Conjugate Theory (1841)

In his conjugate theory, which used terms and ideas (*corps copulés*) borrowed from Gerhardt, Jöns Jacob Berzelius (1779–1848) viewed metal–ammines as conjugated or copulated compounds consisting of ammonia and a conjugate or copula.[16] The conjugate cannot be removed by reaction with an acid, and it neither decreases nor increases the saturation capacity of a base, that is, a metal conjugated with ammonia can still combine with other substances.

Berzelius introduced his theory of copulae to make his electrochemical theory (1811) compatible with newly discovered organic compounds, but with time the supporters of his theory were outnumbered by its opponents. Increasingly complicated and improbable formulas became necessary to reconcile the theory with experimental facts. In many cases, Berzelius' device of regarding some compounds as conjugated species bore little resemblance to reality. Claus (1854) and Blomstrand (1869) tried to revive and modify Berzelius' ideas, but otherwise his theory was of little value.

3.3 Claus'Ammonia Theory (1854)

In 1854, Carl Ernst Claus (1796–1864), a professor of Chemistry at the University of Kazan and the discoverer of ruthenium (also known by the Russian name of Karl Karlovich Klaus), rejected the ammonium theory and proposed a return to Berzelius' view of complexes as conjugated compounds. He compared the platinum–ammines with metal oxides, rather than with ammonium salts or ammonium hydroxide. He called the coordinated ammonia molecule 'passive, in contrast to the active, alkaline state in the ammonium salts, where it can easily be detected and replaced by other bases'.

Claus's ideas were summarized in his paper of 1856:[17] (1) 'If several equivalents of ammonia (from two to six) combine with an equivalent of certain metal chlorides, neutral substances are formed, in which the basic property of ammonia has been destroyed, and simultaneously the ammonia can be neither detected by the usual methods nor be eliminated by double decomposition.' (2) 'If the chlorine in these compounds is replaced by oxygen, strong bases are obtained, whose saturation capacity is always determined by the oxygen equivalents contained in them but not by the number of equivalents of ammonia present in them.' (3) 'The number of equivalents of ammonia entering into these substances is not a random one; as is evident from a number of facts, it is determined by the number of equivalents of water contained in the hydrates of the metal oxides that can enter into such compounds along with the ammonia.'

Claus's first idea was attacked by Carl Weltzien (1813–1870), who considered the term 'passive' to be indefinite and confusing. Weltzien, one of the leading proponents of the rival ammonium theory, insisted that every part of a molecule affects every other part and therefore no part can be considered passive. Hugo Schiff (1834–1915) attacked not only Claus's first idea but also his second. Schiff pointed out that the oxides of the metal–ammines are much stronger bases than the metal oxides themselves. This criticism seems to imply that Schiff was confusing the strength of a base, that is, the hydroxide ion concentration of its solution, with its saturation capacity, that is, the number of equivalents of acid with which it could combine. Claus's third idea, the close parallel between metal salt hydrates and metal–ammines, was attacked on the grounds that many hydrates were known for which corresponding ammines were unknown. Claus's third idea foreshadows Werner's concepts of the coordination number, and of the transition series between metal–ammines and metal salt hydrates. All three ideas reappeared in a modified form almost four decades later in Werner's coordination theory.

3.4 Constant Valency and Kekulé's 'Molecular Compounds'

When Claus proposed his ammonia theory, the valence concept was being developed by several chemists, especially, Kekulé, Frankland, Williamson, Odling, Kolbe, and Couper. The main difficulty lay in applying valence to *all* types of chemical compounds, and one of the principal controversies involved the question of whether a given element could possess more than one valence. Because coordination compounds pose several fundamental problems of constitution, they soon became involved in the question of variable versus constant valence.[18]

Although most of the valence theory pioneers readily admitted the possibility of variable valence, August Kekulé (1829–1896) adhered rigidly to the principle of constant valence. Despite the overwhelming amount of data that accumulated to contradict this view, he maintained that atomicity (valence) was 'a fundamental property of the atom that is just as constant and unchangeable as the atomic weight itself.' However, this principle's simplicity was more than outweighed by the complicated, unrealistic formulas required to maintain it. Eventually, Kekulé stood alone in defending it.

Kekulé tried to buttress his theory of constant valence by dividing compounds into 'atomic compounds' and 'molecular compounds': 'Compounds in which all the elements are held together by the affinities of the atoms that mutually saturate one another could be called *atomic compounds*. They are the only ones that can exist in the vapor state. We must distinguish a second category of compounds that I shall designate *molecular compounds*.'

Because for Kekulé the valence of nitrogen, phosphorus, and cobalt was invariably three and that of copper was invariably two, he considered phosphorus(V) chloride, ammonium chloride, copper(II) sulfate pentahydrate, and hexaamminecobalt(III) chloride as 'molecular compounds' with the formulas $PCl_3{\cdot}Cl_2$, $NH_3{\cdot}HCl$, $CuSO_4{\cdot}5H_2O$, and $CoCl_3{\cdot}6NH_3$, respectively. His artificial dichotomy of compounds into 'atomic compounds', obeying the rules of classical valence theory, and 'molecular compounds', not obeying these rules, possessed, at most, limited value as a formal classification. It failed to explain the nature or operation of the forces involved in forming 'molecular compounds' except to assume that they were acting between molecules rather than atoms. The forces acting between molecules were supposedly weaker than those acting between atoms. Therefore, Kekulé assumed that the resulting 'molecular compounds' would be less stable than 'atomic compounds'. Some substances of limited thermal stability cited by Kekulé as 'molecular compounds', for example, phosphorus(V) chloride, ammonium chloride, and copper(II) sulfate pentahydrate, did decompose in the vapor state, but this was a relative rather than an absolute phenomenon. In time, many chemists considered Kekulé's classification meaningless.

Kekulé's instability criterion, however, failed completely for many coordination compounds. Although they were extremely resistant to heat and chemical reagents, he was forced to consider them 'molecular compounds'. Hexaamminecobalt(III) chloride, for example, contains ammonia, yet it does not evolve ammonia on mild heating, and it fails to react with acids to form ammonium salts. Furthermore, adding a base to its aqueous solution does not precipitate hydrated cobalt(III) hydroxide.

3.5 The Blomstrand–Jørgensen Chain Theory

While Kekulé dealt with coordination compounds by relegating them to the limbo of 'molecular compounds', other chemists elaborated theories explaining their constitution and properties. The most widely accepted and successful of these pre-Werner theories was the so-called chain theory,[19] proposed by Christian Wilhelm Blomstrand (1826–1897),[20] and modified by Sophus Mads Jørgensen (1837–1914).[21] Werner's ideas triumphed eventually, but Jørgensen's experiments have proven completely reliable. They provided the experimental foundation not only for the chain theory but for Werner's coordination theory as well.[22]

During the latter half of the nineteenth century, organic chemistry exerted a great influence on other branches of the science. According to Blomstrand, ammonia molecules could link together as $-NH_3-$ chains, analogous to $-CH_2-$ chains in hydrocarbons. Although nitrogen can form at most four bonds, these chains involved 'quinquevalent' nitrogen, a concept that was quite common in Blomstrand's time.

The length of the chain, that is, the number of ammonia molecules associated with the metal, depended on the metal and its valence. This was later explained far better by Werner's coordination number. Jørgensen accounted for differing reactivities of atoms and groups. He called halogen atoms that could not be precipitated immediately by silver nitrate 'nearer' and considered them as bonded directly to the metal atom; he called halogen atoms that could be precipitated immediately by silver nitrate 'farther' and considered them as bonded through the ammonia chains. Werner later explained these two types of bonding more satisfactorily by the terms 'nonionogenic' and 'ionogenic', respectively, and by his concepts of inner and outer spheres of coordination. In spite of its limitations, the chain theory correlated much empirical data.

In 1883, Jørgensen reported that tertiary amines form compounds analogous to metal–ammines. Because tertiary amines contain no replaceable hydrogen, Jørgensen's discovery eliminated Graham's ammonium theory (Section 3.1) from serious consideration, leaving the chain theory and Kekulé's concept of 'molecular compounds' in the running. In Werner's words, Kekulé's dichotomy merely 'substituted a beautiful word for a confused concept'. Therefore, for almost a quarter of a century, until displaced by Werner's coordination theory, the chain theory became the most popular and satisfactory explanation of metal–ammines.

Jørgensen did not create a new theory of his own, but he logically and consistently extended and modified Blomstrand's chain theory to interpret the many new series of complexes that he, Jørgensen, had discovered. In 1893, Alfred Werner (1866–1919)[1,23] challenged this theory with a revolutionary new theory. According to Werner's own admission, it was based on Jørgensen's painstaking experimental data. In fact, Jørgensen's own work bore the seeds of the chain theory's destruction; some of Jørgensen's compounds later were crucial in Werner's proof of his coordination theory.

4 WERNER'S COORDINATION THEORY AND HIS CONTROVERSY WITH JØRGENSEN

4.1 Werner's Coordination Theory

In a classic example of the 'flash of genius', Alfred Werner, a 26-year-old *Privat-Dozent* at the University of Zürich, awoke at 2 A.M. one night in late 1892. In a dream, he had solved the riddle of the constitution of 'molecular compounds'. Writing furiously and without interruption, by 5 P.M. of the following day he had finished his most famous paper, 'Beitrag zur Konstitution anorganischer Verbindungen' (Contribution to the Constitution of Inorganic Compounds).[1,9]

Werner's theory abruptly broke with classical theories of valence and structure, postulating two types of valence: primary or ionizable valence (Hauptvalenz) and secondary or nonionizable valence (Nebenvalenz). Every metal in a given oxidation state (primary valence) also has a fixed coordination number (a specific number of secondary valences that must be satisfied). Primary valences can be satisfied only by anions, but secondary valences can be satisfied by anions and neutral molecules. Secondary valences are directed in space around the central metal atom. The combined aggregate forms a 'complex', which usually exists as a discrete unit in solution. The most common configurations are octahedral (coordination number six) and square planar or tetrahedral (coordination number four). Werner's view of the two types of linkage, 'ionogenic' (ionizable) and 'nonionogenic' (nonionizable), clarified ideas of chemical bonding, a generation before Kossel's and Lewis's views (1916) led to present concepts of ionic and covalent bonding, respectively.

The following comparison between the chain theory and the coordination theory will be limited to the most common type of complexes, octahedral (hexacovalent) cobalt(III)–ammines, but Werner used similar arguments to prove the constitution and configuration of compounds of the coordination number four. This survey includes only the most important aspects of the Werner–Jørgensen controversy. It is arranged according to compound type, that is, in a logical rather than strictly chronological order. Type MA_6, in which the coordination number of the central metal atom is satisfied by six ammonia molecules, is considered first. These ammonia molecules are then replaced one at a time with other groups.[22,24,25]

In examining the comparative successes of the chain theory and the coordination theory in explaining known facts and predicting new ones, the metal–ammines will be considered under two aspects: (1) *constitution* (the manner of bonding of the constituent atoms and groups) and (2) *configuration* (the spatial arrangement of these atoms and groups).

4.2 Constitution of Cobalt–ammines

4.2.1 Hexaammines (Type MA_6)

In solution, all the chlorine in luteo cobaltic chloride ($[Co(NH_3)_6]Cl_3$, hexaamminecobalt(III) chloride) is immediately precipitated by silver nitrate. None of its ammonia is removed by treatment with hydrochloric acid at 100 °C. Sulfuric acid does not remove any ammonia but yields $Co_2(SO_4)_3{\cdot}12NH_3$, that is, the chlorine atoms are replaced by sulfate groups.[26] Some sort of very stable metal–ammonia bonding but much less stable metal–chlorine bonding is obviously indicated.

Heating removes one-sixth of the ammonia, and only two-thirds of the chlorine in the resulting purpureo cobaltic chloride ($[CoCl(NH_3)_5]Cl_2$) is precipitable by silver nitrate. Considering that halogen atoms bonded to the metal atom through other groups such as ammonia are precipitable by silver nitrate, while those bonded directly to the metal atom are not, Jørgensen proposed formula (**2**) for the luteo salt.

Jørgensen's (**3**) and Werner's (**4**) structures are both compatible with the experimental observations (for simplicity,

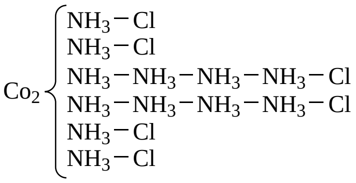

(**2**)

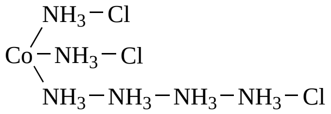

$[Co(NH_3)_6]Cl_3$

Jørgensen
(**3**)

Werner
(**4**)

monomeric formulas are used for this discussion although they were not used by Jørgensen until 1890). However, Jørgensen regarded the chlorine atoms as attached to the metal atom through ammonia molecules, whereas Werner regarded them as ionogenic and outside the coordination sphere. Werner regarded the central metal atom and the ammonia molecules as comprising a discrete unit, a complex cation. This structure should yield four ions in solution, a fact later confirmed by Werner and Miolati's conductance studies.[27,28]

4.2.2 *Pentaammines (Type MA_5B)*

These compounds can be regarded as luteo salts in which another group has replaced one-sixth of the ammonia molecules. This type can be subdivided into several series, depending on the replacing group. Pentaammines in which the replacing group is sulfate, nitrate, oxalate, or a halogen are called purpureo salts. Ammonia is not evolved even on heating purpureo cobaltic chloride ($[CoCl(NH_3)_5]Cl_2$) to 100 °C, evidence that the ammonia molecules are strongly bonded to the cobalt atom. Jørgensen reported that cold concentrated sulfuric acid does not react with the ammonia in the salt but yields the compound $[CoCl(NH_3)_5]SO_4$, which gives no immediate precipitate with silver nitrate, although it contains chlorine. Furthermore, he found that only two-thirds of the chlorine in the original salt is immediately precipitated by silver nitrate, while the remaining third is precipitated only on long boiling.

In order to account for this difference in reactivity, Jørgensen proposed, as Werner did after him, that the 'unreactive' or 'masked' chlorine is bonded directly to the metal atom. The structures that they proposed, (**5**) and (**6**), are both compatible with the experimental facts but again differ in the mode of attachment of the 'reactive' chlorine atoms. Jørgensen considered these atoms as linked to the metal atom through ammonia molecules, whereas Werner considered them as not linked to any particular atom but attracted by electrostatic forces to the complex cation as a whole. According to Werner's structure, a solution of purpureo cobaltic chloride should furnish three ions, a fact confirmed by conductance studies.[27,28] The roseopentammines (aquapentaammines, $[M(NH_3)_5H_2O]X_3$), and the isomeric xantho and isoxantho salts (nitropentaammines and nitritopentaammines, $[MNO_2(NH_3)_5]X_2$ and $[MONO(NH_3)_5]X_2$) were other pentaammine series over whose structures Jørgensen and Werner disagreed.[12,28,29]

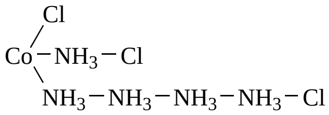

$[CoCl(NH_3)_5]Cl_2$

Jørgensen
(**5**)

Werner
(**6**)

4.2.3 *Tetraammines (Type MA_4B_2)*

These compounds can be regarded as luteo salts in which other groups have replaced one-third of the ammonia. Both the Blomstrand–Jørgensen (**7**) and Werner (**8**) formulas predicted two ions for this type of compound, a fact confirmed by conductance studies.[27,28] The stereoisomerism of these compounds is discussed in Section 4.3.

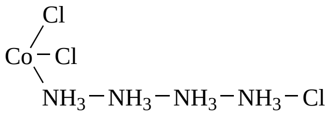

$[CoCl_2(NH_3)_4]Cl$

Jørgensen
(**7**)

Werner
(**8**)

4.2.4 *Triammines (Type MA_3B_3)*

These compounds can be regarded as luteo salts in which other groups have replaced one-half of the ammonia. Although Jørgensen's and Werner's formulations for hexaammines, pentaammines, and tetraammines were compatible with the experimental facts, allowing two rival hypotheses to coexist for a time, the scales began to tip in favor of Werner's theory as additional experimental evidence accumulated.

As negative groups such as chlorine atoms successively replace ammonia molecules in a hexaammine, they enter the coordination sphere and become nonionic or 'masked'. The ionic character of the compounds predicted by the two theories is in complete agreement with the replacement of the first two ammonia molecules. However, the ionic character of the resulting compounds (**9**) and (**10**) differs radically according to the two theories when the third ammonia molecule is replaced. The formulas and predicted numbers of ions for the transition series $[Co(NH_3)_6](NO_2)_3$-$K_3[Co(NO_2)_6]$ according to the two theories are compared in Table 1, and Figure 1 shows the results of Werner's study of conductances carried out in collaboration with his friend and former fellow student Arturo Miolati (1869–1956), the first experimental work published in support of his coordination theory.

Table 1 A Comparison of Blomstrand–Jørgensen's Chain Theory with Werner's Coordination Theory. (Ref. 2b. Reproduced by permission of Dover Publications, Inc.)

	Blomstrand–Jørgensen		Werner	
Class of compound	Formula	No. of ions	Formula	No. of ions
Hexaammines MA_6	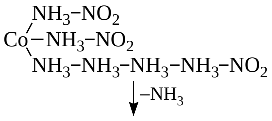 $\begin{array}{l}\quad NH_3{-}NO_2\\ Co{-}NH_3{-}NO_2\\ \quad NH_3{-}NH_3{-}NH_3{-}NH_3{-}NO_2\end{array}$ $\downarrow -NH_3$	4	$[Co(NH_3)_6](NO_2)_3$ $\downarrow -NH_3$	4
Pentaammines MA_5B	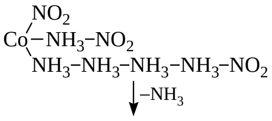 $\begin{array}{l}\quad NO_2\\ Co{-}NH_3{-}NO_2\\ \quad NH_3{-}NH_3{-}NH_3{-}NH_3{-}NO_2\end{array}$ $\downarrow -NH_3$	3	$[CoNO_2(NH_3)_5](NO_2)_2$ $\downarrow -NH_3$	3
Tetraammines MA_4B_2	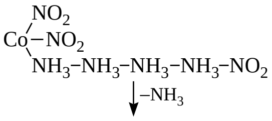 $\begin{array}{l}\quad NO_2\\ Co{-}NO_2\\ \quad NH_3{-}NH_3{-}NH_3{-}NH_3{-}NO_2\end{array}$ $\downarrow -NH_3$	2	$[Co(NO_2)_2(NH_3)_4]NO_2$ $\downarrow -NH_3$	2
Triammines MA_3B_3	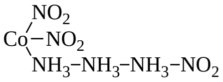 $\begin{array}{l}\quad NO_2\\ Co{-}NO_2\\ \quad NH_3{-}NH_3{-}NH_3{-}NO_2\end{array}$	2	$[Co(NO_2)_3(NH_3)_3]$ $\downarrow -NH_3$	0
Diammines MA_2B_4	Unaccountable	–	$K[Co(NO_2)_4(NH_3)_2]$ $\downarrow -NH_3$	2
Monoammines MAB_5	Unaccountable	–	Unknown for Cobalt $\downarrow -NH_3$	(3)
Double Salts MB_6	Unaccountable	–	$K_3[Co(NO_2)_6]$	4

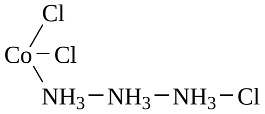

$\begin{array}{l}\quad Cl\\ Co{-}Cl\\ \quad NH_3{-}NH_3{-}NH_3{-}Cl\end{array}$

Two ions

Jørgensen

(**9**)

$[CoCl_3(NH_3)_3]^0$

Nonelectrolyte

Werner

(**10**)

Werner and Miolati's first publication on this subject[27] showed that the molecular conductances (μ) of coordination compounds decrease as molecules of ammonia are successively replaced by acid residues (negative groups or anions). For cobalt(III) salts, μ for luteo salts (hexaammines) $>$ μ for purpureo salts (acidopentaammines) $>$ μ for praseo salts (diacidotetraammines). The conductance decreases almost to zero for the triacidotriammine $Co(NO_2)_3(NH_3)_3$ and then increases for tetraacidodiammines, in which the complex behaves as an anion. Werner and Miolati used these measurements to determine the number of ions in cobalt(III) and platinum(II) and -(IV) complexes, which supported the coordination theory and also elucidated the process of dissociation of salts in aqueous solution and the progress of aquation reactions.

Werner and Miolati's second article on conductances of complexes[28] showed a complete agreement in magnitude, variation, and pattern between their experimentally measured conductances and those predicted by the coordination theory. For example, the experimentally measured conductances for the $[Co(NH_3)_6]Cl_3-K_3[Co(NO_2)_6]$ transition series (Figure 1) agreed completely with the numbers of ions predicted by the coordination theory (Table 1), and were also concordant with the number of 'masked' and 'unmasked' acid radicals. The Werner theory also explained anionic complexes and demonstrated the existence of a continuous transition series (Übergangsreihe) between metal–ammines (MA_6) and double salts (MB_6), an area in which the Blomstrand–Jørgensen theory was unable to complete.

4.3 Configuration of Cobalt(III)–Ammines

The technique of 'isomer counting' used by Werner to prove the configuration of cobalt–ammines and other complexes did not originate with him,[25] but had been used earlier by Wilhelm Körner for benzene derivatives in 1874, and was also suggested by Jacobus Henricus van't Hoff in 1875. However, the technique of comparing the number and type of isomers actually prepared with the number and type theoretically predicted for different configurations probably attained its zenith with Werner. Not only did he use this method to discredit completely the chain theory but also to

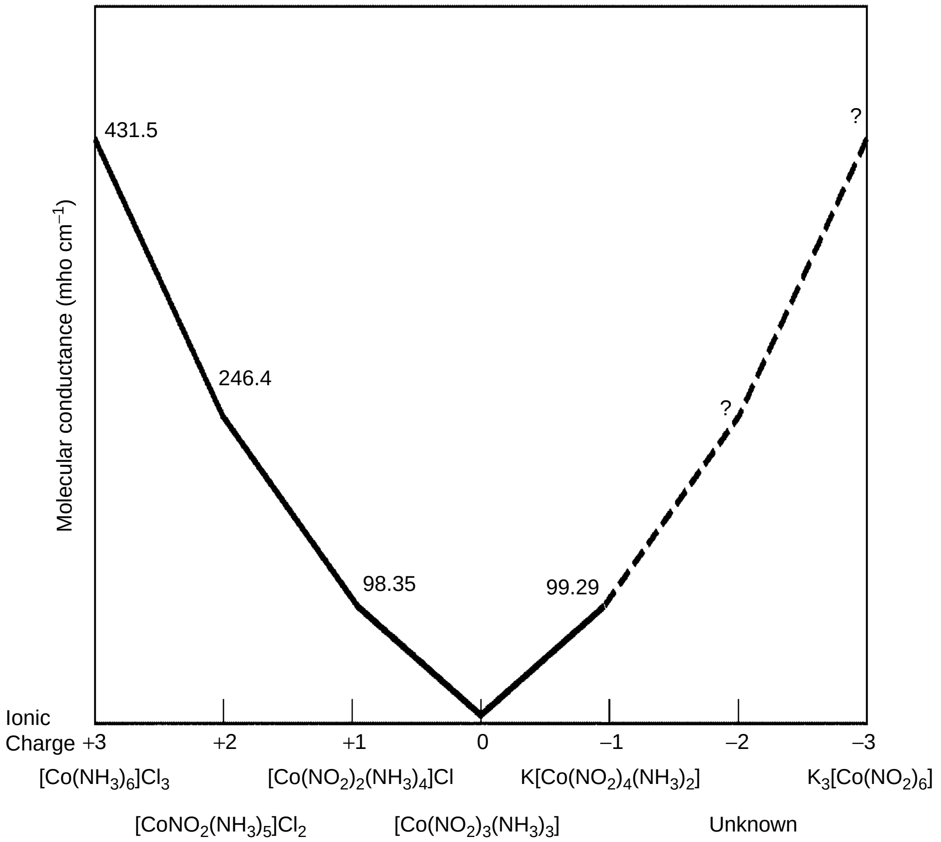

Figure 1 Conductances of cobalt(III) coordination compounds. (Ref. 28. Reproduced by permission of Dover Publications, Inc.)

demonstrate unequivocally an octahedral configuration for cobalt(III) rather than any other symmetrical arrangement, for example, hexagonal planar or trigonal prismatic. Werner's method is summarized in Figure 2 and Table 2. Werner's proof of the configuration of cobalt–ammines involves two types of stereoisomerism, geometric and optical.

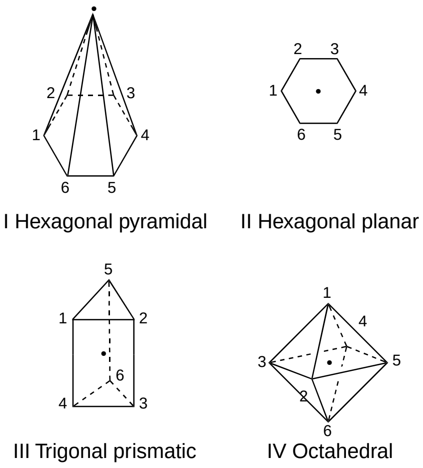

Figure 2 Configurational possibilities for coordination number 6

4.3.1 Geometric Isomerism[11,22,25,30]

Werner and his students prepared and characterized, in most cases for the first time, geometric isomers of 53 series of cobalt and chromium complexes.[30] Comparing columns IV and V of Table 2 shows that, in most cases, the number and type of isomers prepared agrees with the expectations for the octahedral configuration. However, there were a few exceptions; it took Werner more than 20 years to accumulate a definitive proof for his structural ideas. For example, the best-known case of geometric (*cis–trans*) isomerism was observed by Jørgensen (1889), not among simple tetraammines MA_4B_2 but among salts $M(\overline{AA})_2B_2$, in which the four ammonia molecules had been replaced by two molecules of a chelating ligand, ethylenediamine (en), that is, among the praseo (green) and violeo (violet) salts of formula $CoCl_3{\cdot}2en$. Jørgensen ascribed the difference in color to *structural* isomerism connected with the linking of the two ethylenediamine molecules, while Werner considered the salts *stereoisomers*, compounds with the same atoms and bonds but differing only in the orientation of these atoms and bonds in space (Figure 3).

If, as Werner insisted, this isomerism were only a geometric consequence of the octahedral structure, it should also be observed among simple tetraammines MA_4B_2,

Table 2 Proof of configuration for coordination number 6 by 'Isomer Counting'. (Ref. 2b. Reproduced by permission of Dover Publications, Inc.)

	Theoretically predicted isomers					
Compound type[a]	I hexagonal pyramidal	II hexagonal planar (a special case of I)	III trigonal prismatic	IV octahedral	Experimentally found isomers	Result
MA_6	One form only	One form only	One form only	One form only	One form only	None
MA_5B	One form only	One form only	One form only	One form only	One form only	None
$M(\overline{AA})B_4$	One form only	One form only	Two geometric	One form only	One form only	Provisionally eliminates trigonal prismatic (III)
MA_4B_2	Three geometric (1,2; 1,3; 1,4)	Three geometric (1,2; 1,3; 1,4)	Three geometric (1,2; 1,3; 1,4)	Two geometric (1,2 *cis*; 1,6 *trans*)	Two or less geometric	Provisionally proves octahedral (IV); discovered 1907
MA_3B_3	Three geometric (1,2,3; 1,2,4; 1,3,5)	Three geometric (1,2,3; 1,2,4; 1,3,5)	Three geometric (1,2,3; 1,2,5; 1,2,6)	Two geometric (1,2,3 *facial*; 1,2,6 *peripheral*)	Two or less geometric	Provisionally proves octahedral (IV)
$M(\overline{AA})_2B_2$ or $M(\overline{AA})_2BC$	Two geometric	Two geometric	Four geometric, one of which is asymmetric	Two geometric (1,2 *cis*; 1,2 *trans*), the first of which is asymmetric	Two geometric (1,2 *cis*; 1,6 *trans*), the first of which was resolved	Unequivocally proves octahedral (IV); discovered 1911
$M(\overline{AA})_3$	One form only	One form only	Two geometric	One asymmetric pair	One pair optical resolved	Unequivocally proves octahedral (IV); discovered 1912

[a] $\overline{AA}$ represents a symmetrical bidentate (chelate) ligand. Such ligands coordinate at two adjacent positions. They can span *cis* positions but not *trans* positions.

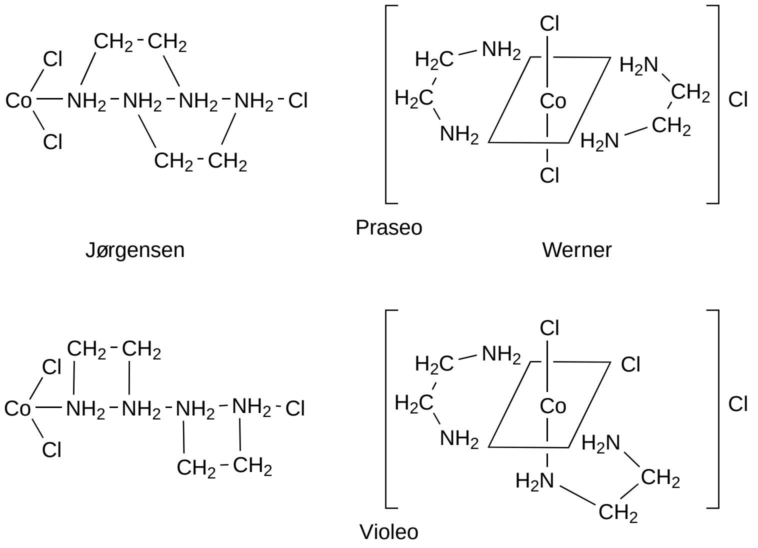

Figure 3 Jørgensen's and Werner's formulas for praseo and violeo ethylenediamine isomers

which do not contain ethylenediamine. However, compounds $[CoCl_2(NH_3)_4]X$ were known in only one series (praseo, green).[12] Jørgensen, a confirmed empiricist, appropriately criticized Werner's theory for implying the existence of unknown compounds. It was only in 1907 that Werner finally prepared the unstable violeo tetraammines, *cis*-$[CoCl_2(NH_3)_4]X$,[31] which are a necessary consequence of his theory but not of Jørgensen's (Figure 4).

4.3.2 Optical Isomerism

Although Werner's discovery of violeo salts proved that Jørgensen's views were incorrect, Werner's preparation of two, and only two, isomers of $[CoCl_2(NH_3)_4]X$ salts and many other MA_4B_2 compounds was insufficient to prove conclusively his octahedral configuration. In spite of this 'negative' evidence, one could argue that failure to isolate a third isomer does not prove its nonexistence. The 'positive' proof chosen by Werner involved resolving certain types of asymmetric coordination compounds containing chelate groups into optical isomers.[32] Comparison of column V with columns I–IV in Table 2 shows that Werner's empirical results agree with the predictions for the octahedral configuration.

Werner recognized in 1899 that resolving optical isomers of certain types of coordination compounds containing chelate groups (which can span *cis* positions only) could provide the 'positive' proof that he sought. After many unsuccessful attempts, he and his American student Victor L. King (1886–1958) resolved *cis*-amminechlorobis(ethylenediamine)cobalt(III) salts with silver d-α-bromocamphor-π-sulfonate, which proved that cobalt(III) has an octahedral configuration (Figure 5).[33]

The resolution of optically active coordination compounds brought the coordination theory widespread recognition and Werner the 1913 Nobel Prize in chemistry.[34] However, at that time, optical activity was almost always connected with carbon atoms, and some of Werner's contemporaries argued that the optical activity of the numerous mononuclear and polynuclear coordination compounds that he resolved[35] was due to the organic chelate groups present, even though all these symmetrical ligands were optically inactive. Werner's 1914 resolution of completely carbon-free coordination compounds, the tris[tetraammine-μ-dihydroxocobalt(III)]cobalt(III) salts (**11**),[36] first prepared by Jørgensen, finally silenced his opponents. These salts are

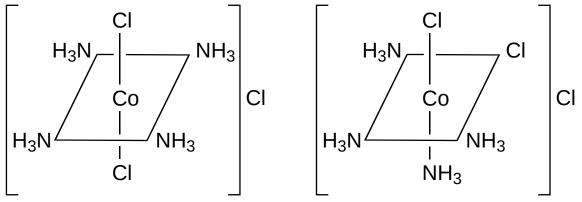
Praseo (*trans*: 1,6)
Gibbs and Genth (1857)

Violeo (*cis*: 1,2)
Werner (1907)

Figure 4 Ammonia praseo and violeo isomers

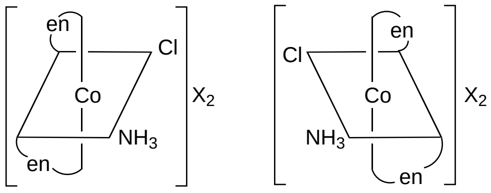

Figure 5 Optical antipodes of *cis*-$[CoCl(NH_3)(en)_2]X_2$

$M(\overline{AA})_3$ compounds, in which $(\overline{AA})$ is the inorganic bidentate ligand (**12**).

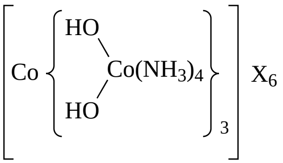

(**11**)

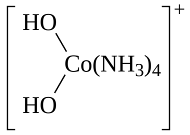

(**12**)

In his doctoral dissertation (1890),[37] Werner had ascribed the geometric isomerism of oximes to the tetrahedral configuration of the nitrogen atom, thus destroying the carbon atom's monopoly on geometric isomerism. Now, at the peak of his career, he demonstrated that the tetrahedron had no monopoly on optical isomerism, thus attaining a major goal by proving that stereochemistry is a general phenomenon not limited to carbon compounds, and that no fundamental difference exists between organic and inorganic compounds. Werner's structural views were later confirmed by X-ray diffraction studies (see Section 5.5), but despite determinations by more *direct* modern techniques; Werner's classical determinations of configuration by simple *indirect* methods remain a monument to his intuitive vision, experimental skill, and inflexible tenacity.

5 TWENTIETH-CENTURY DEVELOPMENTS

5.1 Inner Complexes: Ley and Bruni (1904)

With few exceptions, Werner's coordination theory[9] was accepted by most chemists, and most twentieth-century contributions have been developments, extensions, or confirmations of it rather than ideas incompatible with or opposed to it. One of the earliest of these post-Werner developments is the concept of inner complex salts.[38]

Metal chelates were known in the late-nineteenth century, but the first person to recognize clearly the significance and consequences of cyclic structure in coordination compounds was Heinrich Ley (1872–1938), a German chemist. In 1904, using observations of color, transference, and distribution experiments, and determinations of molecular weight and electrical conductance, he explained the constitution of copper glycinate and similar compounds. He used Werner's primary valence (Hauptvalenz) and secondary valence[38,39] (Nebenvalenz) concepts to show that these compounds are not ordinary salts or even ordinary complex salts but a type of metal chelate, an inner metal complex salt (inneres Metallkomplexsalz) (**13**), in which each chelate ligand is bonded to the central metal ion by both a primary valence and a secondary valence, forming a ring. In the same year, Giuseppe Bruni and C. Fornara proposed a similar formula for copper glycinate.

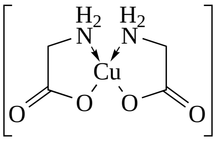

(**13**) Bis(glycinato)copper(II)

5.2 Cyclic Bonding and Stability: Chugaev's Rule of Rings (1906)

Chugaev's so-called rule of rings is closely related to Ley's concept of inner complexes. For a molecule with two potential coordinating groups (e.g. a diamine, $NH_2(CH_2)_nNH_2$, or an amino acid, $NH_2(CH_2)_nCO_2H$) to function as a chelate group, it must form a ring of low strain. According to Baeyer's strain theory (1885), five- and six-membered rings are the most stable, while four-membered rings are less stable and three-membered rings are unstable. In 1906, Lev Aleksandrovich Chugaev (1873–1922), Professor of Chemistry at St. Petersburg University, showed that these relationships among organic compounds are applicable to coordination compounds. Chugaev's rule of rings served as a basis not only for his own stereochemical research but also for that of others, for example, A. A. Grinberg's method for determining the configuration of Pt^{II} complexes by reaction with oxalic acid (1931) involves the stability of a five-membered ring. By comparing the ability of Co^{III}, Ni^{II}, and Pt^{II} to form chelates with various diamines, Chugaev also demonstrated the stability of pentatomic and hexatomic ring systems.[40]

5.3 Alternative Theories of Coordination Compounds

5.3.1 *Friend (1908)*

In 1908, the English chemist John Albert Newton Friend (1881–1966) criticized Werner's theory and suggested an alternative explanation for coordination compounds. According to Friend, classical valency theory was unable to explain why the valency of most elements apparently varies, why electropositive elements combine readily with electronegative elements to form the most stable compounds, why electropositive and electronegative elements combine with themselves and with other elements of the same sign to form stable molecules, and why molecules can combine with other molecules to form very stable coordination compounds. Friend postulated three kinds of valency: (1) free positive, (2) free negative, and (3) residual or latent valency. Residual valency referred to positive and negative valencies that differ from free valencies in that they can only function in pairs of equal and opposite sign. Free valencies correspond to Werner's primary valences and his latent valencies to Werner's secondary valences, with certain differences in the second case.

In a 1908 article[41] Friend criticized Werner's theory, differentiated between his latent valencies and Werner's secondary valences, and applied his valency theory to ammonium salts, metal–ammines, and halide ‘double salts’. For hexacoordinate central atoms, he suggested that a ‘hexatomic shell’ forms around the metal with all the elements or groups joined *together* by latent valencies and not necessarily to the metal itself. In 1916, he applied his theory to hexaamminecobalt(III), pentaamminechlorocobalt(III), and tetraamminedichlorocobalt(III) chlorides, and he emphasized four differences between his theory and Werner’s.[42]

5.3.2 Briggs

In 1908, the English chemist Samuel Henry Clifford Briggs (1880–1935) proposed formulas for complexes that he claimed agreed with experimental data and showed how the affinities of the atoms are disposed in the molecule.[43] He did not claim to be proposing a new theory of valence. Like Werner, he thought that ‘a totally comprehensive and satisfactory theory of valence will not be possible until we have a much more complete knowledge of the constitution of molecular compounds, and also of the nature of chemical affinity, than we possess today’. He later (1917) reinterpreted his formulas in terms of the electronic theory of valence, differentiated between what he called primary and secondary affinity (similar to Werner’s primary and secondary valences), and proposed three different types of chemical combinations.

5.3.3 Povarnin (1915)

In five papers (1915), the Russian chemist Georgi Georgievich Povarnin (1880–1946) attacked Werner’s theory because: (1) it required two kinds of valences, with a further differentiation of groups into ‘ionogens’ and ‘nonionogens’, three varieties of affinity bonds in all; (2) it required a distinction between atomic and molecular compounds; (3) it assumed that whereas the number of an element’s principal valences depended on its position in the periodic table, the number of its secondary valences did not; (4) prediction of the number of possible isomers was difficult in many cases; and (5) it explained only the structure of the inner sphere where atoms or groups are linked directly to the central atom but failed to explain how this sphere was joined to the outer sphere where union with the central atom occurred through other atoms.[44]

To overcome these objections, Povarnin proposed a theory of polar affinities. He suggested that atoms themselves were complex systems of positive and negative affinities in unequal amounts; an element was positive when the positive charge exceeded the negative, and negative when the reverse was true. He thus considered the classical valence unit to be composed of two polar charges not identical in absolute magnitude. He suggested that bonds between atoms have the power to oscillate and that atoms tend to form four- or six-membered rings.

5.3.4 Pfeiffer (1920)

Even Paul Pfeiffer (1875–1951), Werner’s former student, onetime ‘chief of staff’ at the University of Zürich, and the man who first applied coordination theory to crystal structures (see Section 5.4), proposed modifications of Werner’s theory. In 1920, Pfeiffer applied his principle of ‘affinity adjustment of the valencies’ to answer certain shortcomings of Werner’s theory. He considered ionizable radicals or atoms in the outer sphere as combined with the entire complex radical rather than attached to the central atom or any of its associated molecules, and he applied this idea to organic molecular compounds. His modifications, however, are not to be interpreted as attacks on Werner’s ideas.

5.4 Pfeiffer’s ‘Crystals as Molecular Compounds’ (1915)

Werner failed to recognize that polynuclear coordination compounds[45] represent a transition between mononuclear complexes and the infinite structure of the crystal lattice. However, Paul Pfeiffer, Paul Niggli (1888–1953), and others reported crystal structures agreeing with Werner’s coordination theory, as revealed by the new X-ray diffraction technique.[46]

Pfeiffer applied Werner’s coordination theory to new areas. He regarded crystals as very high-molecular-weight coordination compounds, in which atoms act as coordination centers, about which further atoms group themselves in specific symmetrical relationships.[47] He proposed that they obey the same structural chemical and steric laws as coordination compounds and that atoms or groups of atoms in crystals are held together by the same chemical forces operating among coordination compounds.

Pfeiffer regarded sodium chloride as a highmolecular–weight coordination compound $(NaCl)_n$ constructed of equal numbers of $[NaCl_6]$ and $[ClNa_6]$ units. The difference between primary valences and secondary valences disappears in crystals of symmetrical compounds. He demonstrated that, in other crystals, coordination centers can be groups of atoms as well as single atoms, and that coordination numbers as high as 12 must sometimes be considered. He proposed that, in crystals of simple organic molecular compounds of type AB, each constituent acts as a coordination center; AB_6 and BA_6 units interpenetrate exactly as in sodium chloride.

5.5 Configurational Determination by X-ray Diffraction

5.5.1 Wyckoff and Posnjak (1921)

Pfeiffer’s application of Werner’s theory to crystals and the advent of new experimental techniques led a number of scientists in various countries to use X-ray diffraction to determine crystal structures of coordination compounds. American chemist Ralph W. G. Wyckoff (1897–1994) ‘chose ammonium hexachloroplatinate(IV) as a crystal that should provide a clear-cut test of Werner coordination',[48] and, together with Eugen Posnjak (1888–1949), he published the first experimental crystallographic study of a coordination compound[49] (*see* ***Platinum: Inorganic & Coordination Chemistry***). According to Wyckoff, 'All six chlorine atoms in $(NH_4)_2PtCl_6$... were crystallographically identical. They were equally distant from the metal atom, and hence there was no difference in the bonds they formed with it. Furthermore, chlorines were found to be at the corners of a regular octahedron having the platinum atom at its center. A more complete agreement with the predictions of the Werner theory could scarcely have been imagined.'[48]

Other scientists soon used X-ray diffraction to confirm the octahedral configuration of the six halogen atoms in similar hexacoordinate complexes. Wyckoff also confirmed Werner's view that the molecules of water and of ammonia in most crystalline hydrates and ammines are associated with the metallic atom in the same way as the coordinated atoms and radicals in a complex anion. Since the early 1920s, the structures of numerous coordination compounds of various coordination numbers have been determined by X-ray diffraction.

5.5.2 Dickinson (1922)

Less than a year after Wyckoff and Posnjak determined the octahedral configuration for platinum(IV) (coordination number six), Roscoe Gilkey Dickinson (1894–1945) used the same technique to confirm Werner's predicted planar configuration for platinum(II) (coordination number four)[50] (*see* ***Platinum: Inorganic & Coordination Chemistry***). After determining the crystal structure of ammonium hexachlorostannate(IV), $(NH_4)_2[SnCl_6]$ (isomorphous with Wyckoff and Posnjak's $(NH_4)_2[PtCl_6]$), Dickinson determined the crystal structures of potassium tetrachloroplatinate(II), $K_2[PtCl_4]$, and potassium and ammonium tetrachloropalladates(II), $K_2[PdCl_4]$ and $(NH_4)_2[PdCl_4]$ (*see* ***Palladium: Inorganic & Coordination Chemistry***), and found each platinum or palladium atom to be surrounded by four equivalent and equidistant chlorine atoms in a plane. The ammonia molecules in $[Pt(NH_3)_4]Cl_2$ show a similar structure.

The crystal structures of numerous other complexes of various coordination numbers have been determined, completely and *directly* confirming Werner's earlier *indirect* configurational proofs by the preparation of isomers and resolution of optically active compounds (see Section 4). Today, the terminology and concepts of coordination chemistry are universally used in crystallography.

5.6 Sidgwick's Effective Atomic Number Concept (1923)

In 1923, Nevil Vincent Sidgwick (1873–1952) and Thomas Martin Lowry (1874–1936) made the first attempts to interpret Werner's views on an electronic basis. Sidgwick tried to explain the coordination number according to the sizes of the subgroups of electrons in the Bohr atom,[51] and he systematized coordination numbers in his 'effective atomic number' (EAN) concept. He regarded ligands as Lewis bases that donate electrons (usually one pair per ligand) to the metal ion, which consequently acts as a Lewis acid. By this process, ions add electrons until the EAN (sum of the electrons on the metal ion and the electrons donated by the ligand) of the next noble gas is reached. This EAN rule is still of importance; although some elements obey it, there are many important stable exceptions. However, it is very useful as a predictive rule for organometallic compounds (*see* ***Carbonyl Complexes of the Transition Metals***). Finally, it is of historical significance in being the result of the first attempt to explain Werner's coordination theory in terms of electronic structure.

5.7 Chernyaev's Trans Effect (1926)

Just as substitution reactions in organic chemistry do not occur in a random manner, those among coordination compounds are not random. However, the general principles concerning the directive influences of coordinated ligands were not proposed until the late 1920s; they were deduced from reactions of platinum(II) complexes.

These compounds were among the earliest known complexes. Werner cited the well-known regularities in their substitution reactions to assign *cis* and *trans* configurations to platinum(II) complexes, which he rightly regarded as square planar.[9] On the basis of their substitution reactions, Werner assigned platosemidiammine chloride (Peyrone's Salt) and platosammine chloride (Reiset's Second Chloride), both with the formula $PtCl_2(NH_3)_2$ (see Section 2.8), the configurations of structure (**14**).

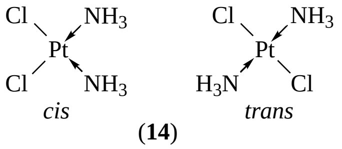

cis *trans*

(**14**)

The preparations of both these compounds involve directive influences, the syntheses being known as Peyrone's reaction and Jørgensen's reaction, respectively. They were said to exemplify Peyrone's rule (*cis* orientation) and Jørgensen's rule (*trans* orientation) (see Scheme 1).

In 1893, the Russian chemist Nikolai Semenovich Kurnakov (1860–1941) observed a third important regularity. During a study of the substitution of ligands by thiourea and thioacetamide, he found a replacement of all the ligands of the *cis* compound but only of the acid radicals of the *trans* compound (Scheme 2). Because the two isomers yield different products, this reaction (Kurnakov's reaction or Kurnakov's test) has been used to differentiate *cis* from *trans* isomers of platinum(II) or palladium(II). It was crucial in

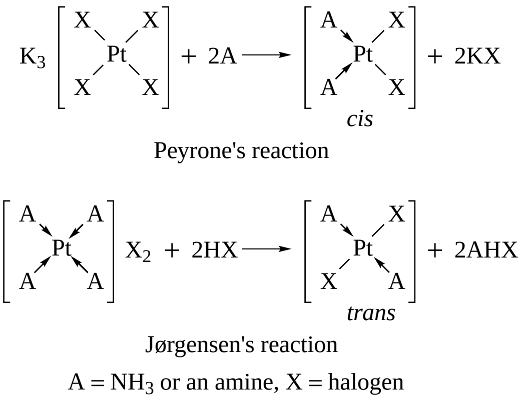

Scheme 1

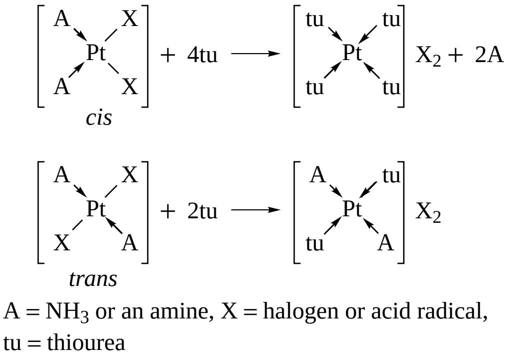

Scheme 2

Werner's proof of the square-planar configuration[9] of Pt^{II}, as well as in Chernyaev's formulation of the trans effect.[10]

Werner recognized the principle of 'trans elimination' in 1893,[9] but it was only in 1926 that the Russian chemist Il'ya Il'ich Chernyaev (1893–1966) enunciated his trans effect describing the influence of a coordinated ligand on the ease of preparing compounds in which the group trans to it had been replaced.[10] According to Chernyaev, a negative group coordinated to a metal atom loosens the bond of any group trans to it. Thus Peyrone's, Jørgensen's, and Kurnakov's reactions are all specialized cases of Chernyaev's more general directive influence.

Chernyaev also studied substitution reactions of chromium, cobalt, tellurium, and osmium complexes, and he reported that the trans effect of atoms is inversely proportional to their metallic character (directly proportional to their electronegativities). Electronegative ligands, for example, NO_2^-, NCS^-, F^-, Cl^-, Br^-, and I^-, have a greater 'trans influence' than neutral ligands, for example, NH_3, ammines, or H_2O. His original trans-directing series has now been extended to include additional ligands: $CN^- \sim CO \sim C_2H_4 \sim NO > CH_3^- \sim SC(NH_2)_2 \sim SR_2 \sim PR_3 > SO_3H^- > NO_2^- \sim I^- \sim SCN^- > Br^- > Cl^- > C_5H_5N > RNH_2 \sim NH_3 > OH^- > H_2O$.

5.8 Proof of the Square-planar Configuration for Platinum(II): Mills and Quibell (1935)

The octahedral configuration of cobalt(III) and platinum(IV) (coordination number six) was proven in three ways: (1) chemical evidence such as 'isomer counting' and transformation reactions (see Section 4.3); (2) resolution of selected compounds (see Section 4.3); and (3) X-ray diffraction studies (see Section 5.5). The first two methods were pursued successfully, largely by Werner.

The square-planar configuration of platinum(II) was proven by the same methods but with a different chronology and a difference in interpretation of the resolutions. Three symmetrical configurations for the coordination number four are theoretically possible (see Figure 6).

The square-pyramidal configuration has never been observed experimentally. Although theoretically possible, it is considered unlikely and is usually eliminated from active consideration in stereochemical work. The method is summarized in Table 3.

Because only a few platinum(II) and palladium(II) isomers were known and similar isomerism among other elements was not discovered for a number of years, Werner's square-planar configuration (1893)[9] was increasingly questioned as time went by, and other proposals were made to account for the structures of these compounds. For example, several workers claimed to have isolated more than two isomers for compounds of type MA_2B_2, which would eliminate a square-planar configuration although it is also not compatible with either the tetrahedral or square-pyramidal arrangements. Also, others claimed to have resolved tetracoordinate platinum(II) complexes of type $M(\overline{AB})_2$, a fact inexplicable by the square-planar configuration.

Dickinson's X-ray diffraction proof of a square-planar arrangement of chloride ions around the central metal atoms in $K_2[PtCl_4]$, $K_2[PdCl_4]$, and $(NH_4)_2[PdCl_4]$ (see Section 5.5.2) was confirmed by additional X-ray structural studies of other compounds. Linus Pauling explained the square-planar structure of platinum(II) and palladium(II) compounds on a theoretical basis and predicted a similar configuration for diamagnetic compounds of nickel(II), gold(III), copper(III), and silver(III).

In 1928, Chernyaev used his trans effect to confirm the square-planar configuration for platinum(II) by preparing the three theoretically possible geometric isomers of a compound of type MABCD (**15**). The occurrence of three

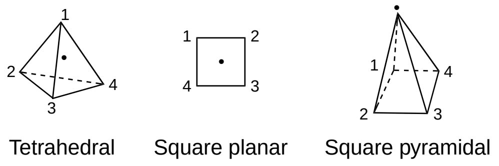

Figure 6 Theoretically possible symmetrical configurations for coordination number 4

Table 3 Proof of configuration for coordination number 4 by 'Isomer Counting'. (Ref. 2c. Reproduced by permission of Dover Publications, Inc.)

	Theoretically predicted isomers			
Compound type[a]	I tetrahedral	II square-planar (a special case of III)	III square-pyramidal	Conclusions
MA_4	One form only	One form only	One form only	None possible
MA_3B	One form only	One form only	One form only	None possible
MA_2B_2	One form only	Two geometric (1,2 *cis*; 1,3 *trans*)	Two geometric (1,2 *cis*; 1,3 *trans*)	More than one isomer would eliminate I and prove II or III
MA_2BC	One form only	Two geometric (1,2 *cis*; 1,3 *trans*)	Two geometric (1,2 *cis*; 1,3 *trans*); *cis* is asymmetric	More than one isomer would eliminate I; resolution of *cis* isomer would prove III
MABCD	One asymmetric pair	Three geometric (1,2,3,4; 1,2,4,3; 1,3,2,4)	Three geometric (1,2,3,4; 1,2,4,3; 1,3,2,4); each consists of an asymmetric pair	Optical isomerism without geometric isomerism would prove I; geometric isomerism without optical isomerism would prove II; both optical isomerism and geometric isomerism would prove III
$M(\overline{AA})_2$	One form only	One form only	One form only	None possible
$M(\overline{AB})_2$	One asymmetric pair	Two geometric (1,2; 4,3 *cis*; 1,2; 3,4 *trans*)	Two geometric (1,2; 4,3 *cis*; 1,2; 3,4 *trans*) *trans* is asymmetric	Optical isomerism without geometric isomerism would prove I; geometric isomerism without optical isomerism would prove II; both optical isomerism and geometric isomerism would prove III
$M(\overline{AA})CD$	One form only	One form only	One asymmetric pair	Two isomers would indicate that both I and II exist; resolution would indicate III
$M(\overline{AA})CD$	One asymmetric pair	Two geometric	Two geometric; each consists of an asymmetric pair	One resolvable form would indicate I; two nonresolvable isomers would indicate II; two resolvable isomers would indicate III

[a] $\overline{AA}$ represents a symmetrical bidentate (chelate) ligand, which can span *cis* positions but not *trans* positions. $\overline{AB}$ represents an unsymmetrical bidentate (chelate) ligand, which can span *cis* positions but not *trans* positions.

geometric isomers eliminated the tetrahedral arrangement but did not absolutely rule out the square-pyramidal configuration (Table 3). One could still argue that each of Chernyaev's isomers consists of an asymmetric pair but that he was unable to resolve them. Because it is impossible to prove a negative proposition, another problem of 'negative' evidence similar to that which Werner had faced (see Section 4.3) had again arisen.

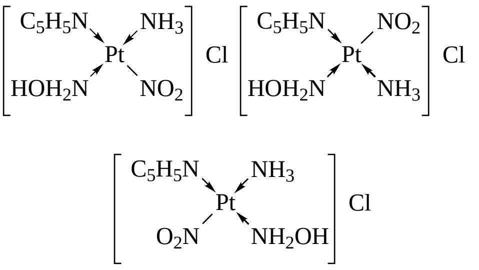

(**15**)

In 1934 and 1937, Harry D. K. Drew *et al.* tried to solve the problem by preparing isomers of compound types $M(\overline{AA})CD$ and $M(\overline{AB})CD$ (see Table 3). For the symmetrical chelate group he chose ethylenediamine and, for the unsymmetrical one, isobutylenediamine (1,2-diamino-2-methylpropane). As an example of the first type complex, he obtained one and only one form of (**16**). For the second type complex, he obtained the two geometric isomers (**17**). His experimental data agreed with the square-planar configuration; he did not consider the square-pyramidal configuration.

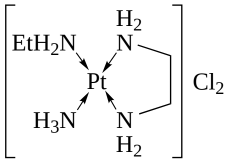

(**16**)

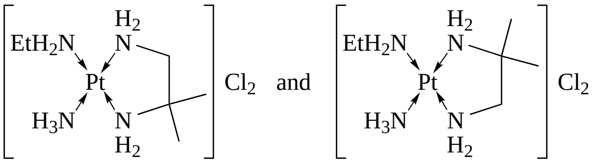

(**17**)

As Werner, a generation before, had realized that successful resolution of coordination compounds would offer a 'positive' proof that hexacoordinate cobalt(III) possesses an octahedral configuration, the English chemist William Hobson Mills (1873–1959) realized that resolution of a certain type of bisbidentate complex of platinum(II) would permit a definite decision to be made between the planar and tetrahedral configurations. In 1935, Mills and Thomas Henry Hall Quibell (1907–1997) prepared dichloro(1,2-diamino-2-methylpropane)platinum(II) by the reaction of isobutylenediamine with potassium tetrachloroplatinate(II) (Scheme 3).[52]

By reacting *meso*-1,2-diphenylethylenediamine (stilbenediamine) with this compound, they obtained (1,2-diamino-2-methylpropane)(*meso*-1,2-diamino-1,2-diphenylethane)platinum(II) chloride (**18**). If the arrangement of the bonds around the platinum atom were tetrahedral, the chelate rings would lie in planes perpendicular to each other, a configuration with a median plane of symmetry that could not give rise to optical isomerism. However, if the two chelate rings were coplanar, the cation would be disymmetric, and optical isomerism would be possible.

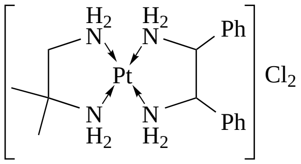

(**18**)

Mills and Quibell resolved the compound into stable enantiomorphs using diacetyl-*d*-tartaric anhydride as the resolving agent. Because simple complexes such as $[(en)Pt(bn)]Cl_2$ (en = ethylenediamine and bn = isobutylenediamine) have never been resolved, there is no evidence favoring the square-pyramidal configuration. Mills and Quibell's resolution eliminated the tetrahedral configuration and offered unequivocal proof for the planar configuration of platinum(II). In 1939, A. G. Lidstone and Mills resolved the corresponding palladium(II) compound by the same method. By this time, other stereochemical and crystallographic evidence for the configuration of platinum(II) and palladium(II) existed, but Mills' resolutions afforded ingenious, elegant, and entirely independent proofs.

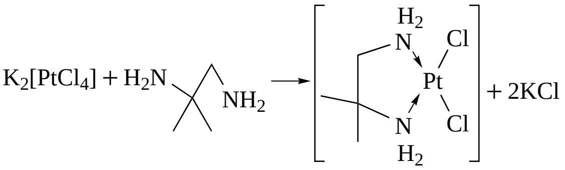

Scheme 3

6 OTHER DEVELOPMENTS

In his 1965 book *History of the Concept of Valency to 1930*, W. G. Palmer stated that it is 'yet too early to assess the very rapid developments since 1930 in a just historical perspective'. The same can be said about coordination chemistry. For this reason and because of space limitations, this historical account of coordination chemistry must close at this point. In general, research, discoveries, and innovations in the field since the 1930s have taken place at an ever-accelerating rate.

Despite the guiding star of Werner's coordination theory, classical coordination chemistry was largely empirical. Modern coordination chemistry has been characterized by increased emphasis on comprehensive theories of chemical bonding that have served to integrate and explain the large amount of experimental data. The valence bond (VB) theory of coordination was developed by Linus Pauling and John C. Slater from Gilbert Newton Lewis's covalent model (1916). Closely related to theories of hybridization and resonance, this theory was the first successful application of the electronic theory of valence to coordination compounds. From the early 1930s to the early 1950s, virtually all coordination phenomena were interpreted in its terms. It gave simple and satisfactory answers to geometric and magnetic susceptibility questions, with which chemists were then concerned.

Walther Kossel's ionic model (1916) was revitalized and developed into the crystal field theory (CFT) of coordination by Hans Bethe and John H. Van Vleck. Although used to some extent by physicists as early as the 1930s, it was not generally accepted by chemists until the 1950s. When modified to include some degree of covalence, CFT is usually known as ligand field theory (LFT) or adjusted crystal field theory (ACFT), and is currently the best and most popular method for treating spectra and other properties quantitatively. A simpler electrostatic theory is the valence shell electron pair repulsion (VSEPR) theory of directed valency, proposed in 1957 by Ronald J. Gillespie and the late Ronald S. Nyholm. Both the VB theory and CFT are only simplifications of the more general, but more complicated, molecular orbital (MO) theory, which today offers the best interpretation of the properties of coordination compounds. In the future, these theories will probably be modified, or even totally new ones may arise.

Another characteristic of modern coordination chemistry is the increasing reliance upon physicochemical methods unknown to Werner and his contemporaries. Simultaneously with an introduction of these newer techniques, emphasis shifted from preoccupation with qualitative studies of structure and stereochemistry to quantitative studies of thermodynamics, kinetics, and reaction mechanisms. Some areas of current research interest include unusual ligands, oxidation states and coordination numbers, solid-state chemistry, photochemistry, relationship between structure and reactivity, variable oxidation state, chelates, heteropoly complexes, organometallic

Table 4 Some historically significant events in coordination chemistry

Date	Chemist(s)	Event
1838	J. Gros	Gros's Salt, *trans*-$[PtCl_2(NH_3)_4]Cl_2$
1852	Edmond Fremy	Color nomenclature
1852	O. Wolcott Gibbs	Pentaamminenitrocobalt(III) salts $[CoNO_2(NH_3)_5]X_2$
1853	Wilhelm Hittorf	Transference number determination: first method of studying complexes in solution
1863	Discovered by J. Morland (1860); investigated by A. Reinecke (1863)	Reinecke's Salt, NH_4 *trans*-$[Cr(SCN)_4(NH_3)_2]$
1866	O. L. Erdmann	Erdmann's Trinitrite; Gibbs's Salt, $[Co(NO_2)_3(NH_3)_3]$
1870	Per Theodor Cleve	Cleve's Salt, *cis*-$[PtCl_4(NH_3)_2]$
1890	Ludwig Mond, C. Langer, and F. Quincke	Nickel tetracarbonyl (the first metal carbonyl)
1893	Alfred Werner	Coordination theory
1897	Alfred Werner	Nomenclature of coordination compounds
1904	Alfred Werner	*Lehrbuch der Stereochemie*
1905	Alfred Werner	*Neuere Anschauungen auf dem Gebiete der anorganischen Chemie*
1905	H. Grossmann	Use of high ionic strength medium for studying complex constants
1905	Lev Aleksandrovich Chugaev	Dimethylglyoximate test for nickel (first organic spot test reagent for a metal ion)
1907	L. A. Chugaev and V. Sokolov	First coordination compound containing an asymmetric ligand; stereospecificity
1908	Marcel Delépine	Metal dithiocarbamates
1915	L. A. Chugaev and N. A. Vladimirov	Chugaev's Salt, $[PtCl(NH_3)_5]Cl_3$
1916	Walther Kossel	First calculation of energy of a complex by electrostatic model
1918	Hans Hürlimann	Stereospecificity
1919	Fritz Hein	First arene complex
1921	Marcel Delépine	Active racemates
1925	Paul Job	Determination of stability constants by method of continuous variations
1926	Johannes Nicolaus Brønsted	S_N1CB mechanism (substitution, nucleophilic, first order, conjugate base)
1927–1931	E. U. Condon, W. Heitler, F. London, Linus Pauling, and J. C. Slater	VB theory and orbital hybridization
1929	J. Forestier	Antiarthritic gold compounds
1929–1932	Hans Bethe (1929), R. S. Mulliken (1932), and John H. Van Vleck (1932)	CFT (ligand field theory)
1931	Paul Pfeiffer	The Pfeiffer effect
1932	Jannik Bjerrum	Square-pyramidal $[Cu(NH_3)_5]^{2+}$
1933	P. Pfeiffer, E. Breith, E. Lubbe, and T. Tsumaki	Oxygen-carrying chelate bis(salicylaldehyde)ethylenediiminecobalt(II)
1933	Frederick G. Mann	Resolution of Na *cis*-$[Rh(H_2O)_2(SO_2(NH_2)_2)_2]$ (second completely inorganic coordination compound to be resolved)
1934	John C. Bailar, Jr and Robert W. Auten	Optical inversion in reactions of cobalt complexes (inorganic Walden inversion)
1934	Reginald P. Linstead	Iron(II) and copper(II) phthalocyanines
1935	K. A. Jensen	Dipole moments to determine structures of Pt^{II} isomers
1937	H. A. Jahn and Edward Teller	Jahn–Teller Effect
1938	T. Tsumaki	Explanation of oxygen-carrying chelates
1938	R. Tsuchida	Spectrochemical series of ligands
1939	Linus Pauling	*The Nature of the Chemical Bond*
1940	John H. Van Vleck and R. Finkelstein	First application of electrostatic model to absorption bands of the ruby
1940	Nevil Vincent Sidgwick and H. M. Powell	Nonbonding pairs of electrons and stereochemistry
1941	Jannik Bjerrum	Theory of the reversible step reactions
1943	R. P. Rây and N. K. Dutt	Tetragonal twist mechanism
1946	Gerold Schwarzenbach	Ethylenediaminetetraacetate in complexometric titrations
1948	H. Irving and R. J. P. Williams	Stability order of complexes
1950	J. Chatt and R. G. Wilkins	$Pt(C_2H_4)_2Cl_2$ (first example of two C=C bonds on one metal atom)
1951	John W. Irvine, Jr and Geoffrey Wilkinson	$[Ni(PX_3)_4]$ (where X = F, Cl, or Br)
1951	T. J. Kealey and P. L. Pauson (1951); S. A. Miller, J. A. Tebboth, and J. F. Tremaine (1952)	Discovery of bis(cyclopentadienyl)iron(II), later called ferrocene
1952	R. B. Woodward, Geoffrey Wilkinson, M. Rosenblum, and M. C. Whiting	Recognition of structure, aromatic properties, and proposal of name 'ferrocene'
1952	Henry Taube	Inner and outer orbital complexes

Table 4 cont'd

Date	Chemist(s)	Event
1952	Max Wolfsberg and L. Helmholz	Molecular orbital model applied to transition metal complexes
1954	Yukito Tanabe and Satoru Sugano	Calculation of energy level diagrams for octahedral d-group complexes
1954	Geoffrey Wilkinson	Lanthanum cyclopentadienides
1955	E. O. Fischer and W. Hafner	Bisbenzenechromium(0)
1955	Geoffrey Wilkinson and J. M. Birmingham	Biscyclopentadienylrhenium hydride
1955	Y. Saito, K. Nakatsu, M. Shiro, and H. Kuroya	Absolute configuration of
1955	J. Chatt, L. A. Duncanson, and L. M. Venanzi; L. E. Orgel	π Bonding theory of the trans effect
1956	L. N. Essen and A. D. Gel'man	Synthesis of $[Pt(I)(Br)(NO_2)(Cl)(NH_3)(py)]$ (only example of MABCDEF)
1956	Dorothy Crowfoot Hodgkin	Crystal structure of the cobalt(III) complex of vitamin B_{12}
1957	Jack Bobinski, Marvin Fein, and Nathan Mayes	First carborane (1-isopropenylcarborane)
1957	Ronald S. Nyholm and Ronald J. Gillespie	Valence shell electron pair repulsion (VSEPR) approach to structure
1958	Claus E. Schäffer and Christian Klixbüll Jørgensen	Nephelauxetic series (interelectronic repulsion) of central atoms and ligands
1958	S. Ahrland, J. Chatt, and N. R. Davies	Systematization of donor atom coordination tendencies of metal ions
1958	John C. Bailar, Jr.	Trigonal twist mechanism
1959	Elias J. Corey and John C. Bailar, Jr.	Conformational analysis of coordination compounds
1959	W. H. Zachariasen and H. A. Plettinger	Hexagonal bipyramidal 8-coordination, $[UO_2(OCOMe)_3]^-$
1959	F. G. A. Stone	First cyclooctatetraene complexes
1959	Leo H. Sommer	First resolution of optically active silicon compounds
1960	Anthony R. Pitochelli and M. Frederick Hawthorne	Icosahedral $B_{12}H_{12}{}^{2-}$
1960	Stanley Kirschner	Resolution and structure proof of a hexacoordinate silicon complex
1960	Robert B. Woodward *et al.*	Proof of structure of chlorophyll by total synthesis
1960	R. A. Marcus	Outer-sphere electron transfer theory
1960–1967	John C. Bailar, Jr., M. J. S. Crespi, and John Geldard	Action of biological systems on optically active complexes
1961	Christian Klixbüll Jørgensen	Optical electronegativities from electron transfer spectra
1962	R. E. Sievers, R. W. Moshier, and M. L. Morris	Resolution of chromium hexafluoride acetylacetonate by gas chromatography
1962	Neil Bartlett	Synthesis of $Xe[PtF_6]$
1962	Fred Basolo and G. S. Hammaker	Linkage isomerism, nitritopentaammines of Rh^{III}, Ir^{III}, and Pt^{IV}
1963	Lauri Vaska	Reversible reaction of $[IrCl(CO)(Ph_3P)_2]$ with molecular oxygen
1963	Lawrence F. Dahl *et al.*	First metal carbonyl containing a metal cluster
1963	Ralph G. Pearson	Hard and soft acids and bases
1965	B. Rosenberg, L. Van Camp, and T. Krigas	Biological effects of platinum complexes
1965	Richard Eisenberg and J. A. Ibers	Trigonal prismatic coordination compounds
1965	A. D. Allen and C. V. Senoff	First metal complex with molecular nitrogen
1965	Cooper H. Langford and Harry B. Gray	σ Bonding theory of the trans effect
1965	Henry Taube	Proof of inner-sphere mechanism $[CoCl(NH_3)_5]^{2+} + Cr^{2+} \rightarrow [CrCl(NH_3)_5]^{2+} + Co^{2+}$
1965	David L. Kepert	Calculations of shape of 6-coordinate complexes
1965	I. I. Chernyaev, L. S. Korablena, and G. S. Muraveiskaya	Optically active complexes with only unidentate ligands
1965	M. F. Hawthorne, D. C. Young, and P. A. Wegner	First metallocarborane
1965	F. Albert Cotton and Charles B. Harris	Dinuclear metal clusters, $[Re_2Cl_8]^{2-}$
1966	Geoffrey Wilkinson	Homogeneous hydrogenation of alkenes by $(Ph_3P)_3RhCl$ (Wilkinson's catalyst)
1966	Stanley Kirschner	Anticancer activity of coordination compounds
1966	Swiatoslaw (Jerry) Trofimenko	'Scorpionates' – anionic tris(pyrazolyl)borates and related tripodal ligands
1967	Jack M. Williams	Hydrated proton $[H_5O_2]^+$ in $[CoCl_2(en)_2]Cl \cdot HCl \cdot H_2O$
1967	C. J. Pedersen	Crown ethers (complexes with planar, macrocyclic ligands)
1967	James A. Ibers and Derek J. Hodgson	Structure of $[Ir(NO)(CO)(Ph_3P)_2Cl]^+$ showing bent $M–NO^-$ bond

(cont'd overleaf)

Table 4 cont'd

Date	Chemist(s)	Event
1968	Andrew Streitwieser, Jr. and Ulrich Müller-Westerhoff	Bis(cyclooctatetraene)uranium(IV), in which π-molecular orbitals share electrons with uranium f-orbitals
1969	Dale K. Cabbiness and Dale W. Margerum	Recognition and naming of the macrocyclic effect
1969	D. Brown, J. F. Easey, and C. E. F. Rickard	Cubic 8-coordination, $Na_3[PaF_8]$
1969	Eugene E. van Tamelen *et al.*	Nitrogen fixation with titanium(II) alcoholate
1969	James P. Collman	Interconvertibility of linear and bent modes of NO coordination
1970	I.H. Sabherval and Anton B. Burg	Synthesis of $Co(NO)_3$
1970	D. A. Owen and M. Frederick Hawthorne	Carborane–transition metal chelate complexes
1970	Jean-Marie Lehn *et al.*	Cryptand metal complexes
1971	Rachel Countryman and W. S. McDonald	Cubic 8-coordination, $[NEt_4][U(SCN)_8]$
1971–1974	P. W. R. Confield and P. G. Eller (1971); P. H. Davis, R. L. Belford, and I. C. Paul (1973); N. C. Baenziger, K. M. Dittemore, and J. R. Doyle (1974); J. A. Tiethof, A. T. Hetey, and Devon W. Meek (1974)	Planar 3-coordination, $[(Me_3PS)_3Cu]ClO_4$, $(Ph_3P)_2CuBr$, $(Ph_3P)_2AuCl$, and $(Me_3PS)_3Cu$
1973	James P. Collman and S. R. Winter	First stable formyl complex, $(CO)_4Fe(CHO)^-$
1973	G. L. Simon and Lawrence F. Dahl	First 'naked' phosphorus complex
1973	Ernst Otto Fischer and Geoffrey Wilkinson	Nobel Chemistry Prize 'for their pioneering work, performed independently, on the chemistry of the organometallic so-called sandwich compounds
1974	James P. Collman *et al.*	Picket fence porphyrin
1974	James L. Dye *et al.*	Cryptated sodium cation and sodium anion
1974	Lawrence F. Dahl	Platinum carbonyl cluster dianions ('tinker toy' construction) with trigonal prismatic configuration
1974–1975	N. J. de Stephano, D. K. Johnson, and L. M. Venanzi (1974); Isao Mochida, J. Arthur Mattern, and John C. Bailar, Jr. (1975)	Trans spanning ligands in planar complexes
1975	C. M. Lukehart, G. P. Torrence, and J. V. Zerle	Diacetylmetallate anions
1976	E. C. Baker *et al.*	Lanthanide and actinide organometallics
1976	Loren D. Lower and Lawrence F. Dahl	Cube-shaped metal-cluster compound, $Ni_8(CO)_8(PPh_3)_6$, the first transition metal analog of cubane
1976	Earl L. Muetterties *et al.*	Metal clusters as homogeneous catalysts for reduction of carbon monoxide in Fischer-Tropsch reaction
1976	David G. Whitten *et al.*	Photoinduced electron transfer to produce hydrogen and oxygen from water using tris(2,2'-bipyridine)ruthenium(II) ion
1977	James P. Collman	Synthesis and characterization of a 'face-to-face' iron(II)-porphyrin compound
1977	David Dolphin and Brian James	Ru(II)-porphyrin complex acting as oxygen carrier at room temperature
1978	R. D. Gillard and F. L. Wimmer	Third resolution of a completely inorganic complex, $[Pt(S_5)_3]^{2-}$
1978	Alan M. Sargeson *et al.*	Sepulchrate complex completely encapsulates the metal
1978	Kenneth O. Hodgson, Richard H. Holm, *et al.*	EXAFS (extended X-ray absorption fine structure) study of structure of FeMo protein component of nitrogenase
1979	Satoru Shimba, Shuhei Fujinami, and Muraji Shibata	Fourth and fifth resolutions of completely inorganic complexes, *cis,cis,cis*-$[Co(CN)_2(NH_3)_2(H_2O)_2]^+$ and *cis,cis,cis*-$[Co(NO_2)_2(NH_3)_2(H_2O)_2]^+$
1979	Alan M. Sargeson	Caged metal ions (macrocycles in three dimensions)
1979	Stephen J. Lippard	Reaction of *cis*- and *trans*-$[PtCl_2(NH_3)_2]$ with DNA still attached to nucleosome core particle
1979	Duward F. Shriver *et al.*	Reduction of carbon monoxide to methane by protonation of a polynuclear metal carbonyl anion, $[Fe_4(CO)_{13}]^{2-}$
1979	Petra Köpf-Maier	Metallocene dihalides, especially titanocene dichloride, as antitumor drugs
1980	Milenko ãelap	Resolution of $W(OCOC_5H_4N)_2(ONC_9H_4Cl_2)_2$, the first resolution of an 8-coordinate compound
1980	Brice Bosnich *et al.*	Chiral rhodium complexes that are highly stereoselective catalysts
1980	Roger Y. Tsien	Fluorescent indicators/sensors for intracellular calcium
1980	K. Barry Sharpless and Tsutomu Katsuki	Titanium-catalyzed asymmetric epoxidation

Table 4 cont'd

Date	Chemist(s)	Event
1981	R. N. Shchelokov and V. E. Karasev	Introduction of Eu(III) complexes into polymeric matrix permits preparation of light transducers for greenhouses
1981	Thomas J. Meyer	First experimental observation of proton-coupled electron transfer
1982	Gregory J. Kubas	First complex of molecular hydrogen
1982	Harry B. Gray	Experimental demonstration of long-range electron tunneling in proteins (Ru-cytochrome c)
1982	Carlo Floriani	Reversible addition of CO_2 to bifunctional metal complexes containing acidic and basic sites
1983	Brian M. Hoffman	Electron tunneling in hybrid hemoglobins
1983	George McLendon *et al.*	Electron tunneling in a physiological heme-protein complex
1983	Thomas J. Meyer	First well-defined molecular catalyst for water oxidation
1984	Robert G. Bergman; William A. G. Graham	Oxidative addition of alkanes by iridium complexes
1984	Patricia L. Watson; Tobin J. Marks	Oxidative addition of alkanes by lanthanide and actinide compounds, respectively
1984	Duward F. Shriver; Harry R. Allcock	Inorganic ion-conducting solids
1985	Kenneth N. Raymond	New class of macrocyclic polycatecholates
1986	William C. Trogler	$[Pt(H)Cl\{P(CH_3)_3\}_2]$ as homogeneous catalyst for addition of water to terminal olefins in anti-Markovnikov manner
1986	Tobin J. Marks	Selective binding of $(\eta^5\text{-}C_5H_5)_2VCl_2$ to phosphate groups of DNA
1986	Karl O. Christe	Chemical synthesis of fluorine by reaction of SbF_5 with K_2MnF_6
1986	James L. Dye	$[NaC]^+$ and $[CsC]^+$ salts (C = 18-crown-6 ether)
1987	Wolfgang A. Herrmann	Organometallic compounds of rhenium(VII)
1987	Thomas G. Richmond	Facile chelate-assisted C–F bond cleavage at tungsten(0)
1987	M. Frederick Hawthorne	Macrocyclic carbaborane derivatives with bound chlorine
1987	Donald J. Cram, Jean-Marie Lehn, and Charles J. Pedersen	Nobel Chemistry Prize 'for their development and use of molecules with structure-specific interactions of high selectivity'
1988	Jonathan L. Sessler	Porphin-like macrocyclic ligand with 5 nitrogen atoms coordinated to a cadmium atom
1988	C. Frank Shaw III	Protein chemistry of antiarthritic gold(I) complexes
1988	G. M. Larin and B. B. Umarov	Super hyperfine structure (SHFS) from ligand atoms not bonded to central metal atom show unpaired electron of metal atom is delocalized over peripheral atom of chelate ligands
1989	Dieter Otto Sellmann	Iron-diazene complex as model for enzymatic nitrogen fixation
1989	Jean-Pierre Sauvage	Molecular trefoil knots
1990	Richard H. Holm	Substitution of other metals for iron in iron−sulfur clusters $[MoFe_3S_4]^{n+}$ and ($[Fe_{18}S_{30}]^{10-}$ containing two Na atoms)
1990	Dimitri Coucouvanis	Substitution of other metals for iron in iron−sulfur clusters ($[Mo_2Fe_6S_6]^{n+}$)
1990	Stephen J. Lippard	Molecular 'ferric wheel', $[Fe(OCH_3)_2(O_2CCH_2Cl)]_{10}$
1990	G. Attillio Ardizzoia	Ring-shaped $[Cu_8(C_5N_2H_7)_8(OH)_8]$ can substitute alcohols for hydroxides and can catalytically oxidize CO to CO_2
1990	Richard G. Finke	(1,5-cyclooctadienyl)iridium$[P_2W_{12}Nb_3O_{62}]^{8-}$ catalytically reduces cyclohexene to cyclohexane
1990	Jon A. Zubieta and Qin Chen	Polyoxovanadate, $[V_6O_{13}\{O_2NC(CH_2O)_3\}_2]^{2-}$, bonds organic fragments to a structure resembling a metal oxide
1990	Rafaele Acerete	$Na_{20}[P_6W_{18}O_{79}]$, first phosphotungstate proved to have a P:W ratio of 1:3
1990	Robert Haushalter	Heteropoly molybdophosphate containing 35% empty space reversibly absorbs 12% water by weight without changes in crystal structure
1991	Jay Winkler	Flash-quench method for measurements of electron tunneling over long distances
1991	M. Fujita	Molecular squares
1991	Wolfgang Saak and Siegfried Pohl	Self-assembly of $[Fe_3Ni_5S_6I_8]^{4-}$ cluster
1991	L. Jos de Jongh, Fokko N, Mulder, Timeke A. Stegink, and Roger C. Thiel	Mössbauer spectroscopy of Günter Schmid's platinum clusters shows that 147-atom cluster shows metallic behavior
1991−1992	Alan F. Williams, Claude Piguet, and Gerald Bernardelli	$[Co_2L_3]^{4+}$ (L = bis[1-methyl-2-(6′-methyl-2′-pyridyl)benzimidazol-5-yl]methane), similar to helical DNA and RNA structure
1992	Douglas C. Rees	X-ray diffraction determination of structure of metal centers in the two component proteins of nitrogenase
1992	Song-ping Huang and Mercouri G. Klanatzidis	Synthesis of cryptand $[NaAu_{12}\,Se_8]^{3-}$

(cont'd overleaf)

Table 4 cont'd

Date	Chemist(s)	Event
1992	Boon K. Teo and Hong Zhang	Polyicosahedron of Ag and Au atoms with two trapped Au atoms
1992	Karl S. Hagen	Macrobicyclic diaza hexaoxa cryptand
1993	Amilra Prasanna de Silva	Molecular logic gates and computation
1993	Vincenzo Balzani, Sebastiano Campagna, and Gianfranco Denti	1,090-atom dendrimer containing 22 Ru atoms, believed to be largest transition metal complex of its kind
1993	Jean-Marie Lehn	Ru-(bipyridyl) complex that acts as a molecular 'switch'
1993	Walter Leitner	Synthesis of formic acid from CO_2 and H_2 with Rh-based catalyst
1993	Dieter Fenske	Properties of Cu_{146} $Se_{73}[P(C_6H_5)_3]_{30}$ cluster like those in bulk Cu_2 Se
1994	Isabelle M. L. Billas, A. Châtelain, and Walt A. de Heer	Development of magnetic properties with cluster size in Fe, Co, and Ni clusters
1995	Craig L. Hill and Xuan Zhang	'Smart' catalyst, complex polyanion cluster α-$[(CoII)PW_{11}O_{39}]^{5-}$ assembles itself from four precursor species
1995	P. Andrew Karplus	Structure of Ni-containing metalloenzyme urease by X-ray crystallography
1995	Christopher C. Cummins	$Mo(NRAr)_3$ amide complexes react with N_2 to yield $(NRAr)_3MoN$ nitrido complexes as result of $N\equiv N$ bond cleavage
1995	Christopher C. Cummins and Richard R. Schrock	First Mo and W complexes containing $M\equiv P$ bonds
1995	Gerard Parkin	First complex with indium multiple bond ($In=Se$)
1996	Douglas C. Rees	Structure of metalloenzyme DMSO reductase in oxidized and reduced form
1996	Hubert Schmidbauer	Structure of pair of Ag(I) and Au(I) complexes showing that Au is smaller than Ag
1996	John A. Gladysz	Linear chain of 20 carbon atoms (C_{20}) capped at both ends with organometallic Rh-containing groups (longest carbon chain with metals at each end)
1996	Gregory J. Kubas	Stable Pt complexes with chlorocarbon, bromocarbon, and iodocarbon ligands
1996	Roeland Nolte	Micrometer-sized 'wheels' composed of connected molecules of Pd-porphyrin complex
1996	Christopher C. Cummins	Transition metal complexes cleave N_2 triple bond
1996	Robert F. Curl, Jr., Harold W. Kroto, and Richard E. Smalley	Nobel Chemistry Prize 'for their discovery of fullerenes'
1997	Günter Wächtershäuser and Claudia Huber	Primordial model for reductive acetyl-coenzyme pathway found in living organisms
1997	John A. Gladysz and István Horváth	$RhCl\{P(CH_2CH_2(CF_2)_5CF_3)_3\}_3$ catalyst in fluorocarbon solvents for transformations of organic compounds
1997	Gianluca Pozzi	Cobalt porphyrin-based catalyst with perfluoroalkyl groups bonded to porphyrin
1997	Christopher A. Reed and Peter D. W. Boyd	Compound with bond between metal atom and C–H bond of a free alkane
1997	Gregory H. Robinson	$Na_2[ArGa{=}GaAr]$ ($Ar = 2,6$-disubstituted phenyl group) contains unprecedented $Ga\equiv Ga$ triple bond
1997	Karl W. Klinkhammer	Molecular orbital study of Robinson's compound
1997	John G. Brennan	New ways of synthesizing cluster compounds of samarium
1998	Daniel Stack	Cu complex that reproduces the essential reactivity of galactose oxidase
1998	Carlo Floriani *et al.*	Nitrogen fixation by stepwise reduction of N_2 to form nitride dimer complex $Nb_2(\mu\text{-}N_2)Na_2(thf)_{12}$
1998	Masanobu Hidai, Yoshiaki Nishibayashi, and Shotaro Iwai	Nitrogen fixation by reaction of tungsten complex bonded to a N_2 molecule
1998	Graham E. Ball	Rh–C_5H_5 complex – first characterization of compound with metal–alkane bonding
1998	Jim A. Thomas	Self-assembly of a molecular cube
1999	Pat Holland and William B. Tolman	Synthesis of a trigonal Cu(II) complex, a blue copper synthetic analogue
2001	Harry B. Gray	Electron tunneling in heme-protein single crystals
2001	Remir G. Kostyanovsky *et al.*	Wedekind-Fock-Havinga salt as first object for absolute asymmetric synthesis
2001	William S. Knowles and Ryoji Noyori; K. Barry Sharpless	Nobel Chemistry Prize 'for their work on chirally catalyzed hydrogenation reactions; [and] for his work on chirally catalyzed oxidation reactions', respectively
2001	Thomas J. Meyer	Localized-to-delocalized transition in mixed-valence chemistry
2002	F. Albert Cotton and Carlos A. Murillo	Ditungsten paddlewheel complex, a powerful reductant
2002	Stephen D. Kinrade, Ashley Gillson, and Christopher T. G. Knight	First direct evidence for production of organosilicate complex by a living system
2002	K. Barry Sharpless *et al.*	*In situ* click chemistry
2002	Douglas C. Rees	Previously unrecognized atom – possibly nitrogen – coordinated to six iron atoms in MoFe protein of metalloenzyme nitrogenase
2002	Bruce E. Bursten *et al.*	First noble gas-actinide complexes

Table 4 cont'd

Date	Chemist(s)	Event
2002	Kenneth S. Suslick, Steven C. Zimmerman, *et al.*	Zeolite-like metalloporphyrin that adsorbs and desorbs compounds with high selectivity for size, shape, and functional group
2002	Omar M. Yaghi *et al.*	'Isoreticular metal-organic frameworks' with lowest densities and highest methane storage capacities
2002	Harry C. Dorn *et al.*	First organic derivative of a C_{80} metallofullerene
2003	Lawrence Que	Synthesis of a nonheme ferryl complex, an analogue of nonheme iron oxygenase active intermediates
2003	Paul E. Kruger	'Trinity helix', ligand with C_2 symmetry used to prepare metallohelicates
2003	Glenn Millhauser and Stanley B. Prusiner	Prion protein binds five Cu(II) ions
2003	Piet W. N. M. van Leeuwen *et al.*	SPANphos, a C_2 symmetric trans-coordinating diphophane ligand
2003	Dmitry V. Yandulov and Richard R. Schrock	Catalytic reduction of dinitrogen to ammonia at a single Mo center
2003	Paul Smith *et al.*	Stable, soluble semiconductor, $[Pt(NH_2dmoc)_4][PtCl_4]$ (dmoc = dimethyloctane)
2003	Bradley D. Smith	Coordination compound as apoptosis chemosensor
2003	Chad A. Mirkin and Nathan C. Gianneschi	Supramolecular allosteric catalyst
2003	Bryan W. Eichhorn; Manfred Scheer, Junfeng Bai, and Alexandria V. Virovets; Achim Müller	Inorganic fullerene-like molecules

compounds such as metallocenes and π-aromatic complexes with 'sandwich structures', compounds with metal–metal bonds (metal clusters), clathrates, fluxional coordination compounds, borane complexes, macrocyclic and stereochemically nonrigid ligands, and nitrogen- and oxygen-containing complexes. Many biologically active compounds are complexes, and even the simpler types of complexes have served as model compounds in investigating bodily processes. In fact, the new field of bioinorganic chemistry is concerned largely with coordination compounds.

It is difficult, if not impossible, to predict the future of coordination chemistry, an exciting research field in which the solution to any given problem usually opens up a number of new research avenues and poses newer and more challenging problems. If its past history gives any indication of its future course, the continued success, expansion, and vitality of coordination chemistry remain assured.

The chronological list in Table 4 of some historically significant events in coordination chemistry is intended to supplement the more detailed previous historical survey. Being illustrative rather than exhaustive, it is necessarily incomplete, for many other valuable contributions have not been included because of lack of space.

7 RELATED ARTICLES

Carbonyl Complexes of the Transition Metals; Coordination Numbers & Geometries; Coordination & Organometallic Chemistry: Principles; Diffraction Methods in Inorganic Chemistry; Molecular Orbital Theory.

8 REFERENCES

1. G. B. Kauffman, 'Alfred Werner: Founder of Coordination Chemistry', Springer-Verlag, Berlin, 1966.
2. G. B. Kauffman, (a) 'Classics in Coordination Chemistry, Part I: The Selected Papers of Alfred Werner', Dover, New York, 1968; (b) 'Part II: Selected Papers (1798–1899)', 1976; (c) 'Part III: Twentieth-Century Papers (1904–1935)', 1978.
3. G. B. Kauffman, 'Inorganic Coordination Compounds', Heyden, London, 1981.
4. G. B. Kauffman, in 'Comprehensive Coordination Chemistry', eds. G. Wilkinson, R. D. Gillard, and J. A. McCleverty, Pergamon Press, Oxford, 1987, Chap. 1.1.
5. J. C. Bailar Jr, in 'Comprehensive Coordination Chemistry', eds. G. Wilkinson, R. D. Gillard, and J. A. McCleverty, Pergamon, Oxford, 1987, Chap. 1.2.
6. W. C. Zeise, *Pogg. Ann. Phys. Chem.*, 1827, **9**, 632; 1831, **21**, 497; For a discussion and annotated English translation of the second article, see G. B. Kauffman, 'Part II: Selected Papers (1798–1899)', Dover, New York, 1976, p. 17.
7. T. J. Kealy and P. L. Pauson, *Nature (London)*, 1951, **168**, 1639; For a brief discussion of the discovery of ferrocene, see G. B. Kauffman, *J. Chem. Educ.*, 1983, **60**, 185.
8. S. A. Miller, J. A. Tebboth, and J. F. Tremaine, *J. Chem. Soc.*, 1952, 632.
9. A. Werner, *Z. Anorg. Chem.*, 1893, **3**, 267; For a discussion and annotated English translation, see G. B. Kauffman, 'Classics in Coordination Chemistry, Part I: The Selected Papers of Alfred Werner', Dover, New York, 1968, p. 5.
10. I. I. Chernyaev, *Izv. Inst. Izuch. Plat. Drugikh Blagorodn. Met.*, 1926, **4**, 243; For a discussion and annotated English translation, see G. B. Kauffman, 'Part III: Twentieth-Century

Papers (1904–1935)', Dover, New York, 1978, p. 143; See also G. B. Kauffman, 'Inorganic Coordination Compounds', Heyden, London, 1981, p. 158.

11. G. B. Kauffman, *Isis*, 1977, **68**, 392; G. B. Kauffman, 'Inorganic Coordination Compounds', Heyden, London, 1981, p. 64.
12. W. Gibbs and F. A. Genth, 'Researches on the Ammonia-Cobalt Bases', Smithsonian Institution, Washington, DC, 1856; reprinted in *Am. J. Sci.*, 1856, series [2], **23**, 235, 248, 319; 1857, [2]**24**, 86.
13. G. B. Kauffman, *J. Chem. Educ.*, 1974, **51**, 522; G. B. Kauffman, 'Inorganic Coordination Compounds', Heyden, London, 1981, p. 69.
14. F. Reitzenstein, *Z. Anorg. Chem.*, 1898, **18**, 152.
15. J. C. Bailar Jr, in 'The Chemistry of the Coordination Compounds', ed. J. C. Bailar Jr, Reinhold, New York, 1956, Chap. 2.
16. G. B. Kauffman, 'Part II: Selected Papers (1798–1899)', Dover, New York, 1976, p. 47; G. B. Kauffman, 'Inorganic Coordination Compounds', Heyden, London, 1981, p. 72.
17. C. Claus, *Ann. Chem.*, 1856, **98**, 317; For an annotated English translation, see G. B. Kauffman, 'Part II: Selected Papers (1798–1899)', Dover, New York, 1976, p. 52; See also G. B. Kauffman, 'Inorganic Coordination Compounds', Heyden, London, 1981, p. 74.
18. G. B. Kauffman, *J. Chem. Educ.*, 1972, **49**, 813; G. B. Kauffman, 'Part II: Selected Papers (1798–1899)', Dover, New York, 1976, p. 69; G. B. Kauffman, 'Inorganic Coordination Compounds', Heyden, London, 1981, p. 76.
19. C. W. Blomstrand, *Ber.*, 1871, **4**, 40; For a discussion and annotated English translation, see G. B. Kauffman, 'Part II: Selected Papers (1798–1899)', Dover, New York, 1976, p. 71; and G. B. Kauffman, 'Inorganic Coordination Compounds', Heyden, London, 1981, p. 81.
20. G. B. Kauffman, in 'Dictionary of Scientific Biography', ed. C. C. Gillispie, Scribner, New York, 1970, Vol. 2, p. 199; *Ann. Sci.*, 1975, **32**, 12; *Centaurus*, 1977, **21**, 44.
21. G. B. Kauffman, in 'Dictionary of Scientific Biography', ed. C. C. Gillispie, Scribner, New York, 1973, Vol. 7, p. 179.
22. G. B. Kauffman, *J. Chem. Educ.*, 1959, **36**, 521; *Chymia*, 1960, **6**, 180; G. B. Kauffman, 'Part II: Selected Papers (1798–1899)', Dover, New York, 1976, p. 92; G. B. Kauffman, 'Inorganic Coordination Compounds', Heyden, London, 1981, p. 81.
23. G. B. Kauffman, in 'Dictionary of Scientific Biography', ed. C. C. Gillispie, Scribner, New York, 1976, Vol. 14, p. 264.
24. G. B. Kauffman, *Chemistry*, 1966, **39**,(12), 14.
25. G. B. Kauffman, *Educ. Chem.*, 1967, **4**,(1), 11; G. B. Kauffman, 'Part II: Selected Papers (1798–1899)', Dover, New York, 1976, p. 93; G. B. Kauffman, 'Inorganic Coordination Compounds', Heyden, London, 1981, Chap. 6.
26. S. M. Jørgensen, *Z. Anorg. Chem.*, 1899, **19**, 78, 109; For a discussion and annotated English translation of the second article, see G. B. Kauffman, 'Part II: Selected Papers (1798–1899)', Dover, New York, 1976, p. 92.
27. A. Werner and A. Miolati, *Z. Phys. Chem.*, 1893, **12**, 35; For a discussion and annotated English translation, see G. B. Kauffman, 'Classics in Coordination Chemistry, Part I: The Selected Papers of Alfred Werner', Dover, New York, 1968, p. 89.
28. A. Werner and A. Miolati, *Z. Phys. Chem.*, 1894, **14**, 506; For a discussion and annotated English translation, see G. B. Kauffman, 'Classics in Coordination Chemistry, Part I: The Selected Papers of Alfred Werner', Dover, New York, 1968, p. 117.
29. G. B. Kauffman, *Coord. Chem. Rev.*, 1973, **11**, 161.
30. G. B. Kauffman, *Coord. Chem. Rev.*, 1975, **15**, 1.
31. A. Werner, *Ber.*, 1907, **40**, 4817; For a discussion and annotated English translation, see G. B. Kauffman, 'Classics in Coordination Chemistry, Part I: The Selected Papers of Alfred Werner', Dover, New York, 1968, p. 141.
32. G. B. Kauffman, in 'Van't Hoff-Le Bel Centennial', ed. O. B. Ramsay, American Chemical Society, Washington, DC, 1975, p. 126; *Isis*, 1975, **65**, 38.
33. A. Werner and V. L. King, *Ber.*, 1911, **44**, 1887; For a discussion and annotated English translation, see G. B. Kauffman, 'Classics in Coordination Chemistry, Part I: The Selected Papers of Alfred Werner', Dover, New York, 1968, p. 155; See also V. L. King, *J. Chem. Educ.*, 1942, **19**, 345.
34. A. Werner, in 'Les Prix Nobel en 1913', Norstedt, Stockholm, 1914; For an English translation see 'Nobel Lectures in Chemistry, 1901–1921', Nobel Foundation, Elsevier, Amsterdam, 1966, p. 253.
35. G. B. Kauffman, *Coord. Chem. Rev.*, 1974, **12**, 105.
36. A. Werner, *Ber.*, 1914, **47**, 3087; For a discussion and annotated English translation, see G. B. Kauffman, 'Classics in Coordination Chemistry, Part I: The Selected Papers of Alfred Werner', Dover, New York, 1968, p. 175.
37. A. Hantzsch and A. Werner, *Ber.*, 1890, **23**, 11; For a discussion and annotated English translation, see G. B. Kauffman, *J. Chem. Educ.*, 1966, **43**, 155.
38. G. B. Kauffman, *J. Chem. Educ.*, 1973, **50**, 693.
39. H. Ley, *Z. Elektrochem.*, 1904, **10**, 954; For an annotated English translation, see G. B. Kauffman, *J. Chem. Educ.*, 1973, **50**, 698; G. B. Kauffman, 'Part III: Twentieth-Century Papers (1904–1935)', Dover, New York, 1978, p. 5; G. B. Kauffman, 'Inorganic Coordination Compounds', Heyden, London, 1981, p. 137.
40. L. A. Chugaev, *Ber.*, 1906, **39**, 3190; *J. Prakt. Chem.*, 1907, series [2] **75**, 153; For an annotated English translation of the second article, see G. B. Kauffman, 'Part III: Twentieth-Century Papers (1904–1935)', Dover, New York, 1978, p. 26.
41. J. A. N. Friend, *J. Chem. Soc.*, 1908, **93**, 1006; reprinted with annotations in G. B. Kauffman, 'Part III: Twentieth-Century Papers (1904–1935)', Dover, New York, 1978, p. 52.
42. J. A. N. Friend, *J. Chem. Soc.*, 1916, **109**, 715; reprinted with annotations in G. B. Kauffman, 'Part III: Twentieth-Century Papers (1904–1935)', Dover, New York, 1978, p. 60.

43. S. H. C. Briggs, *J. Chem. Soc.*, 1908, **93**, 1564; G. B. Kauffman, ‘Part III: Twentieth-Century Papers (1904–1935)’, Dover, New York, 1978, p. 46; G. B. Kauffman, ‘Inorganic Coordination Compounds’, Heyden, London, 1981, p. 147.
44. G. Povarnin, *J. Russ. Phys. Chem. Soc.*, 1915, **47**, 217, 501, 989, 1787, 2073; G. B. Kauffman, ‘Part III: Twentieth-Century Papers (1904–1935)’, Dover, New York, 1978, p. 48; G. B. Kauffman, ‘Inorganic Coordination Compounds’, Heyden, London, 1981, p. 148.
45. G. B. Kauffman, *Coord. Chem. Rev.*, 1973, **9**, 339.
46. G. B. Kauffman, *J. Chem. Educ.*, 1973, **50**, 277.
47. P. Pfeiffer, *Z. Anorg. Chem.*, 1915, **92**, 376; For a discussion and annotated English translation, see G. B. Kauffman, ‘Part III: Twentieth-Century Papers (1904–1935)’, Dover, New York, 1978, p. 74; See also G. B. Kauffman, ‘Inorganic Coordination Compounds’, Heyden, London, 1981, p. 150.
48. R. W. G. Wyckoff, in ‘Werner Centennial’, ed. G. B. Kauffman, American Chemical Society, Washington, DC, 1967, p. 114.
49. R. W. G. Wyckoff and E. Posnjak, *J. Am. Chem. Soc.*, 1921, **43**, 2292; reprinted with annotations and discussion in G. B. Kauffman, ‘Part III: Twentieth-Century Papers (1904–1935)’, Dover, New York, 1978, p. 85; See also G. B. Kauffman, ‘Inorganic Coordination Compounds’, Heyden, London, 1981, p. 151.
50. R. G. Dickinson, *J. Am. Chem. Soc.*, 1922, **44**, 2404; reprinted with annotations and discussion in G. B. Kauffman, ‘Part III: Twentieth-Century Papers (1904–1935)’, Dover, New York, 1978, p. 112; See also G. B. Kauffman, ‘Inorganic Coordination Compounds’, Heyden, London, 1981, p. 153.
51. N. V. Sidgwick, *J. Chem. Soc.*, 1923, **123**, 725; reprinted with annotations and discussion in G. B. Kauffman, ‘Part III: Twentieth-Century Papers (1904–1935)’, Dover, New York, 1978, p. 127; See also G. B. Kauffman, ‘Inorganic Coordination Compounds’, Heyden, London, 1981, p. 155.
52. W. H. Mills and T. H. H. Quibell, *J. Chem. Soc.*, 1935, 221; reprinted with annotations and discussion in G. B. Kauffman, ‘Part III: Twentieth-Century Papers (1904–1935)’, Dover, New York, 1978, p. 206; See also G. B. Kauffman, ‘Inorganic Coordination Compounds’, Heyden, London, 1981, p. 162.

Coordination Numbers & Geometries

Brian W. Clare & David L. Kepert
University of Western Australia, Nedlands, Australia

1	Introduction	1
2	Five-coordinate Compounds	1
3	Six-coordinate Compounds	3
4	Seven-coordinate Compounds	6
5	Eight-coordinate Compounds	8
6	Nine-coordinate Compounds	9
7	Ten-coordinate Compounds	10
8	Twelve-coordinate Compounds	10
9	Further Reading	11
10	References	11

1 INTRODUCTION

A very convenient and widely used method for depicting the 3D structure of molecules AX_n is to imagine that the X atoms are situated at the vertices of various polyhedra centered on atom A.[1,2] In the two most common geometries (i) the arrangement of four groups about a central atom is tetrahedral, as was independently proposed for carbon by van't Hoff and Le Bel in 1874,[3] and (ii) as Werner proposed some 20 years later in 1893, six groups are commonly arranged about a metal atom at the vertices of an octahedron.[4] In some cases, isomers are possible. Thus optical isomers can be obtained when the molecule has no plane of symmetry, for example when four different groups are attached to a tetrahedral carbon atom, [Cabcd], which shows that the molecular rearrangement of such structures must be very slow. Similarly, the ability to isolate optical and geometrical isomers for complexes such as $[Co(NH_2CH_2CH_2NH_2)_2Cl_2]^+$ shows that rearrangement is again very slow.

This structural rigidity of the tetrahedron and octahedron arises from the transition states for rearrangement being substantially disfavored relative to the ground state. Steric repulsion between the ligands is an important component. Five-, seven-, eight-, and nine-coordination geometries tend to be substantially less rigid, and different structural isomers of the same composition cannot be isolated. The relative energy required to convert from one polyhedron into another of the same coordination number can be estimated from the ligand–ligand repulsion energies using an empirical force law (Table 1).[5]

Well-defined rigid stereochemistries may be obtained for all coordination numbers, however, in one of two ways. (i) With the exception of the tetrahedron and octahedron, most polyhedra have different types of vertex, and for complexes of the type [M(unidentate $A)_x$(unidentate $B)_y$] the sorting of the different ligands into the appropriate polyhedral vertices may stabilize a preferred structure. In general, it is found that charged ligands such as halide, and more particularly the more highly charged oxide, sulfide, and nitride, occupy the sterically less crowded vertices, in contrast to uncharged ligands which occupy the remaining sites. It is also found that for complexes of the lighter elements of lower coordination numbers that contain stereochemically active nonbonding pairs of electrons, these lone pairs also occupy the sterically less hindered sites. (ii) Complexes containing chelate groups may also have rigid stereochemistries. For bidentate ligands it is useful to define the geometry of the chelate ring in terms of a 'normalized bite' b, defined as the distance between the donor atoms divided by the metal–ligand distance.

2 FIVE-COORDINATE COMPOUNDS

The starting point for five-coordination is to consider the trigonal bipyramid and the square pyramid and the relation between them.[1,2,6] A twofold axis passes through the metal atom M and the donor atom E, the other four atoms lying on a pair of vertical mirror planes (see Figure 1). The angles between this axis and the metal–ligand bonds to the pairs of atoms AC and BD are defined by ϕ_A and ϕ_B, respectively. Neither the square pyramid nor the trigonal bipyramid is the same as those defined in classical geometry, which have equal edge lengths. The square pyramid with equal edge lengths is half an octahedron with $\phi_A = \phi_B = 90.0°$, but in real molecules the more open space created by the square face relative to the triangular faces is partially closed by increasing ϕ_A and ϕ_B to $\sim 100°$. This results in the basal sites becoming more sterically hindered than the axial site. The regular trigonal bipyramid formed from equilateral triangles would have the metal–ligand bond lengths in the triangular plane approximately 30% shorter than the metal–axial ligand bonds. The triangular plane therefore expands, making all bond lengths more nearly equal, with the consequence that the equatorial sites are less sterically crowded with only two close neighbors, compared with three for the axial sites.

There is no potential energy barrier between the square pyramid at $\phi_A = \phi_B \approx 100°$ and the two slightly more stable trigonal bipyramids at $\phi_A = 90$, $\phi_B = 120°$ and $\phi_A = 120$, $\phi_B = 90°$. Movement along this 'reaction coordinate' connecting the two trigonal bipyramids is usually described as *Berry Pseudorotation*.[7] Any one of the three equatorial site of the trigonal bipyramid can become the apical site of a square pyramid and so repetition of this process scrambles all atom sites.

Table 1 Differences in repulsion energy coefficients, $10^3\Delta X$, corresponding to polyhedral rearrangements of $[\mathrm{M(ligand)}_n]$

n	Rearrangement	$10^3\Delta X$
4	Tetrahedron → Square	215
5	Trigonal bipyramid → Square pyramid	13
6	Octahedron → Trigonal prism	388
7	Capped octahedron → Capped trigonal prism	1
	Capped octahedron → Pentagonal bipyramid	36
8	Square antiprism → Dodecahedron	60
9	Tricapped trigonal prism → Capped square antiprism	12
10	Bicapped square antiprism → Sphenocorona	25
	Bicapped square antiprism → Trirhombohedron	26
11	Edge-coalesced icosahedron → Capped pentagonal antiprism	9
12	Icosahedron → Bicapped pentagonal prism	2397

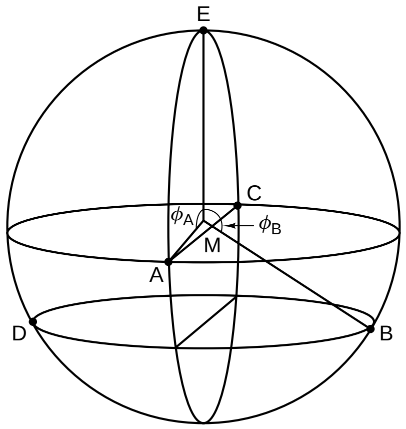

Figure 1 General stereochemistry for $[\mathrm{M(unidentate)_5}]$

Table 2 Stereochemical parameters for examples of $[\mathrm{M(unidentate)_5}]$ complexes[1,2,8]

Complex	ϕ_A (°)	ϕ_B (°)
$(\mathrm{PhCH_2NMe_3})[\mathrm{SiF_5}]$	90.3	121.2
$[\mathrm{SbPh_5}]\cdot0.5\mathrm{C_6H_{12}}$	90.3	119.2
$(\mathrm{PCl_4})[\mathrm{SnCl_5}]$	90.2	117.8
$[\mathrm{Sb(C_6H_4Me)_5}]$	91.1	114.9
$[\mathrm{Co(MeC_5H_4NO)_5}](\mathrm{ClO_4})_2$	93.0	114.0
$[\mathrm{SbPh_5}]$	98.3	105.4
$[\mathrm{Mg(Me_3AsO)_5}](\mathrm{ClO_4})_2$	99.8	107.6
$[\mathrm{Mg(Me_3PO)_5}](\mathrm{ClO_4})_2$	99.9	106.4
$(\mathrm{Et_4N})_2[\mathrm{InCl_5}]$	103.0	104.7

Table 3 Examples of trigonal bipyramidal molecules with charged ligands, X, occupying trigonal planar sites[2]

$[\mathrm{MX(ligand)_4}]$	$[\mathrm{MX_2(ligand)_3}]$	$[\mathrm{MX_3(ligand)_2}]$
$[\mathrm{NiBr(PMe_3)_4}](\mathrm{BF_4})$	$[\mathrm{NiBr_2(PMe_3)_3}]$	$[\mathrm{CoCl_3(PEt_3)_2}]$
$[\mathrm{Ni(CH_3)(PMe_3)_4}](\mathrm{BPh_4})$	$[\mathrm{NiI_2\{P(OMe)_3\}_3}]$	$[\mathrm{AlCl_3(thf)_2}]$

Structurally characterized molecules with five identical ligands cover the complete range from the pure trigonal bipyramid ($\phi_A = 90$, $\phi_B = 120°$) to the pure square pyramid ($\phi_A = \phi_B \approx 100°$), some simple examples being shown in Table 2. Whether a compound is near the trigonal bipyramid or near the square pyramid may often be attributed to crystal-packing forces. For example, the structure of $\mathrm{SbPh_5}$ is near the square pyramid whereas the solvate $\mathrm{SbPh_5}\cdot0.5\mathrm{C_6H_{12}}$ is near the trigonal bipyramid. In molecules near the trigonal bipyramidal end of the range the axial bonds are about 5% longer than the equatorial bonds, whereas for molecules near the square pyramid the axial bond is about 4% shorter than the four basal bonds.

Many five-coordinate molecules exhibit very rapid intramolecular rearrangements, leading to all five ligands being equivalent over the NMR timescale.[1,2,5] For example, the ^{19}F NMR spectrum of $\mathrm{PF_5}$ shows all fluorine atoms equivalent over the temperature range 60 to $-197\,°$C. Proton NMR studies on $\mathrm{SbMe_5}$ in carbon disulfide down to about $-100\,°$C also show the presence of only one type of methyl group. The ^{13}C NMR spectra of $[\mathrm{Fe(CO)_5}]$ and $[\mathrm{Fe(CNBu)_5}]$ show only a single resonance at temperatures as low as -170 and $-80\,°$C, respectively. Both the ^{19}F NMR and ^{31}P NMR studies of $[\mathrm{Fe(PF_3)_5}]$, $[\mathrm{Ru(PF_3)_5}]$, and $[\mathrm{Os(PF_3)_5}]$ down to $-160\,°$C in $\mathrm{CHClF_2}$ show all ligands are equivalent.

When there is a mixture of different types of ligand, a more well-defined structure is usually observed. In general, charged ligands such as halides require more space about the central atom than do uncharged ligands and occupy the less sterically hindered axial site of a square pyramid or the trigonal planar sites of a trigonal bipyramid, examples being shown in Table 3. The dominant stereochemistry for monooxo complexes is the axially substituted square pyramid, examples including $[\mathrm{ReOCl_4}]$ and $[\mathrm{MOCl_4}]^-$ (M = Cr, Mo, W) as well as the nitrido complexes $[\mathrm{MNCl_4}]^-$ (M = Mo, Tc, Re, Ru, Os).[1]

For compounds containing a lone pair, this occupies one of the three trigonal sites of a trigonal bipyramid,[2] as in $\mathrm{Rb[Bi(:)(SCN)_4]}$ and $[\mathrm{Te(:)Ph_4}]$. The trifluoro complexes $\mathrm{ClF_3}$ and $\mathrm{XeF_3}^+$ are T-shaped but can be considered as trigonal bipyramidal if the two nonbonding lone pairs are considered.[2] Likewise, linear trihalide ions such as $\mathrm{I_3}^-$ can be regarded as trigonal bipyramidal with three nonbonding pairs of electrons in the three equatorial sites.[2]

The edge lengths for a trigonal bipyramid, square pyramid, and intermediate structures vary from $1.73r$ for the edges linking the equatorial sites of a trigonal bipyramid to $1.39r$ for the edges linking the basal sites of a square pyramid, where r is the metal–ligand distance. The introduction of chelating ligands of fixed normalized bite influences the structure obtained, the simplest examples being of the type $[\mathrm{M(bidentate)_2(unidentate)}]$. Complexes with bidentate ligands of small bite, as in $[\mathrm{Fe(S_2CNR_2)_2X}]$ ($b = 1.24$)[9] are close to square pyramidal, whereas complexes with a larger bite, for example $[\mathrm{P(O_2C_6H_4)_2X}]$ ($b \approx 1.42$)[1] have stereochemistries intermediate between a square pyramid and a trigonal bipyramid (X $=$ halide, alkyl, etc.). Superimposed on this effect of normalized bite upon stereochemistry is that due to the unidentate ligand necessarily being different to the bidentate ligands. Thus complexes containing O^{2-} as the unidentate ligand have structures close to square pyramids at all values of the normalized bite, as in $[\mathrm{V(MeCOCHCOMe)_2O}]$ ($b = 1.38$)[10] and $[\mathrm{V(S_2CNEt_2)_2O}]$ ($b = 1.21$).[11] A number of compounds of the p-block elements containing two bidentate ligands can be considered as trigonal bipyramidal if a nonbonding pair of electrons occupies an equatorial site, as in $[\mathrm{Pb(RCOCHCOR)_2}(\mathbf{:})]$ and $[\mathrm{Sn(S_2CNR_2)_2}(\mathbf{:})]$.[1]

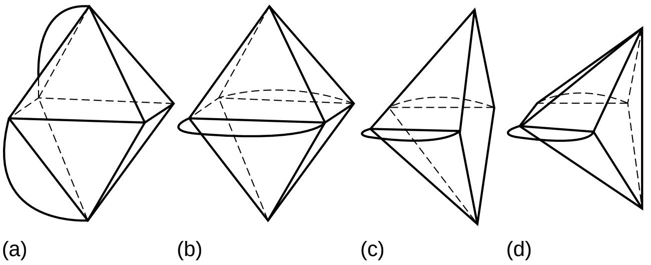

Figure 2 Stereochemistries of $[\mathrm{M(bidentate)_2(unidentate)_2}]$: (a) *cis* octahedral; (b) *trans* octahedral; (c), (d) skew-trapezoidal bipyramidal

3 SIX-COORDINATE COMPOUNDS[1,2,12]

3.1 $[\mathrm{M(unidentate)_6}]$

The octahedron is the dominant stereochemistry for complexes containing six unidentate ligands. For complexes containing two ligands different from the other four, the rigid nature of the octahedron is illustrated by the ability to separate both *cis* and *trans* isomers. When one pair of ligands is grossly different to the other four, the *trans* structure is more stable. An important example is the dioxo complexes as in the uranyl complexes $[\mathrm{UO_2X_4}]^{2-}$.[2] Other examples of *trans*-dioxo complexes are $[\mathrm{ReO_2py_4}]^+$, $[\mathrm{ReO_2(CN)_4}]^{3-}$, and $[\mathrm{MoO_2(CN)_4}]^{4-}$.[2] However, complexes containing two different unidentate ligands in addition to O^{2-} may be either *cis* or *trans*.

Compounds containing two nonbonding pairs of electrons and four unidentate ligands are invariably observed to be square planar, as in $[\mathrm{Te^{II}(ligand)_4}(\mathbf{:})_2]^{2+}$, $[\mathrm{I^{III}Cl_4}(\mathbf{:})_2]^-$, and $[\mathrm{Xe^{IV}F_4}(\mathbf{:})_2]$.[2]

A second-order Jahn–Teller effect leads to a trigonal prismatic structure being preferred for some d^0 $\mathrm{ML_6}$ species, such as $\mathrm{WMe_6}$. This illustrates the role of electronic effects in determining coordination geometry.

3.2 $[\mathrm{M(bidentate)_2(unidentate)_2}]$

Complexes containing two bidentate and two unidentate ligands may be either *cis* or *trans* octahedral, but it is important to note that both structures show very large distortions as the size of the chelate rings is reduced; the *trans* structure turns into the skew-trapezoidal bipyramidal structure (Figure 2).

For a normalized bite of $b = 2^{1/2}$, the *cis* and *trans* structures have the same energy, but as the normalized bite is reduced the *cis* structure becomes more stable. A survey[1] of all structurally characterized compounds showed that for $b > \sim 1.3$ there were an approximately equal number of *cis* and *trans* structures, but for four-membered chelate rings with $b < \sim 1.2$ there was a strong preference for the *cis* structure.

Reduction in size of the chelate rings in *cis*-$[\mathrm{M(bidentate)_2(unidentate)_2}]$, as in $[\mathrm{Mo(S_2CNEt_2)_2O_2}]$,[13] is accompanied by a substantial rotation of the bidentate ligands about the twofold axis of the molecule, relative to the $\mathrm{MoO_2}$ plane: $\theta_A = 15°$, $\theta_B = -60°$ (Figure 3). At the same time the bonding of the bidentate ligand becomes significantly unsymmetrical with the metal ligand bond *cis* to both unidentate ligands becoming shorter than the metal–sulfur bond to the other end of the bidentate ligand: (M–A)/(M–B) $= 0.93$.

The *trans* structure of $[\mathrm{M(bidentate)_2(unidentate)_2}]$ with five- or six-membered chelate rings and relatively large normalized bites ($b \approx 1.2-1.5$) are normally undistorted. For four-membered chelate rings with $b < \sim 1.2$, however, the plane formed by the two bidentate ligands becomes a trapezoid (Figure 2). The unidentate ligands are simultaneously skewed toward (Figure 2(c)) or even past (Figure 2(d)) the long edge of the trapezoid. The bonding of the bidentate ligand becomes grossly unsymmetrical, the end nearer the unidentate ligands becoming sterically very crowded.

Important examples of this skew trapezoidal bipyramid structure are the dialkyltin complexes with four-membered

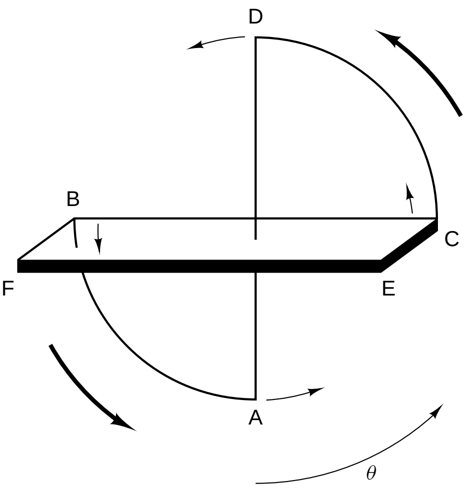

Figure 3 Distortion in *cis*-$[\mathrm{M(bidentate)_2(unidentate)_2}]$ as the size of the chelate ring is reduced. The bidentate ligands are rotated in an anticlockwise direction to higher θ relative to the $\mathrm{M(unidentate)_2}$ plane

chelate rings. Structural parameters for typical examples are given in Figure 4, together with the undistorted $[Sn(MeCOCHCOMe)_2Me_2]$ for comparison. A notable feature of these structures is the very unsymmetrical bonding of the bidentate ligands, one bond being 20–35% longer than the other. Similar skew-trapezoidal bipyramidal structures are observed for dialkylgermanium[14] and -lead[15] complexes.

Selenium(II) and tellurium(II) xanthates, dithiocarbamates, and related molecules have planar trapezoidal structures with the *trans* sites apparently occupied by lone pairs of electrons. Detailed parameters for a typical structure, $[Te(S_2COMe)_2(\mathbf{:})_2]$,[16] are shown in Figure 5.

3.3 [M(bidentate)$_3$]

The stereochemistries of complexes of the type [M(bidentate)$_3$] occupy an important place in inorganic

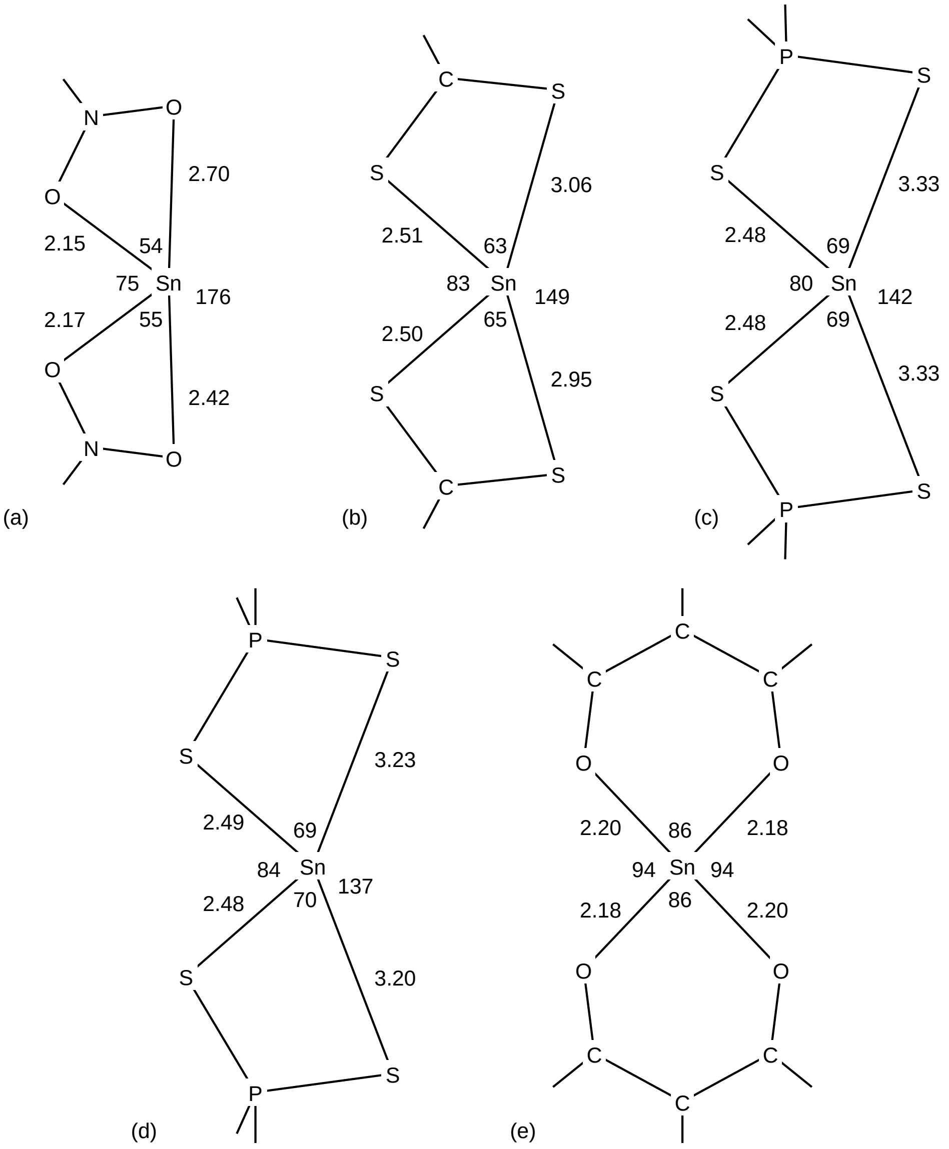

N
O
O
2.70
2.15
54
75
Sn
176
2.17
55
O
2.42
N
O
(a)
C
S
S
3.06
2.51
63
83
Sn
149
65
2.50
S
2.95
C
S
(b)
P
S
S
3.33
2.48
69
80
Sn
142
2.48
69
S
3.33
P
S
(c)
P
S
S
3.23
2.49
69
84
Sn
137
2.48
70
S
3.20
P
S
(d)
C
C
C
O
O
2.20
86
2.18
94
Sn
94
2.18
86
2.20
O
O
C
C
C
(e)

Figure 4 Geometries, in degrees and Å, of the Sn(bidentate)$_2$ plane in [Sn(bidentate)$_2$(alkyl)$_2$]. The alkyl groups above and below the plane are skewed towards the long edge of the Sn(bidentate)$_2$ trapezoid:

		b	C–Sn–C(°)
(a)	$[Sn(NO_3)_2Me_2]$[14]	0.92	144
(b)	$[Sn(S_2CNMe_2)_2Me_2]$[15]	1.06	136
(c)	$[Sn(S_2PMe_2)_2Me_2]$[16]	1.13	123
(d)	$[Sn\{S_2P(OEt)_2\}Ph_2]$[17]	1.14	135
(e)	$[Sn(MeCOCHCOMe)_2Me_2]$[18]	1.36	180

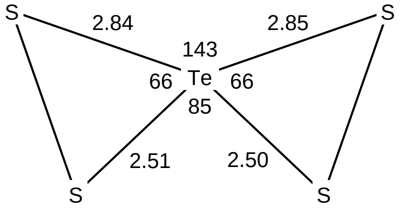

Figure 5 Geometry, in degrees and Å, of $[Te(S_2COMe)_2(:)_2]$

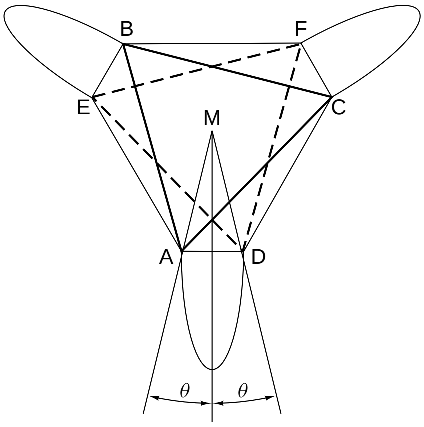

Figure 6 General stereochemistry for $[M(bidentate)_3]$

chemistry. The general stereochemistry is shown in Figure 6, viewed down the threefold axis. The stereochemistry is defined by the normalized bite b of the bidentate ligands and the angle of twist θ between the upper and lower triangular faces. The regular octahedron corresponds to $b = 2^{1/2}$ and $\theta = 30°$. The trigonal prism is the eclipsed arrangement with $\theta = 0$.

A theoretical dependence of θ upon b is shown by the line in Figure 7. For $b = 2^{1/2}$ the regular octahedron at $\theta = 30°$ is as expected, but as b is progressively decreased θ also progressively decreases until a trigonal prism is formed. The overwhelming majority of tris(bidentate) complexes have structures intermediate between the octahedron and trigonal prism. The structures are indicated in Figure 7.[1] (Dithiolate molecules, $[M(S_2C_2R_2)_3]^{x-}$, are not included in Figure 7 as many have structures much closer to the trigonal prism than would be expected.[2]) Figure 8 displays some of the data in Figure 7, but is now restricted to complexes of the first-row transition elements from chromium to copper to avoid large variations in the size of the central atom.

To a first approximation the ligands divide into three groups. The first group is contained within the limits $b = 1.37_5$ to $b = 1.50$ and consists of those ligands that form six-membered chelate rings, such as acetylacetonate and trimethylenediamine. The second group is contained within the limits $b = 1.25$ to $b = 1.37_5$ and contains the complexes with five-membered chelate rings, such as *o*-phenanthroline and ethylenediamine. The third group is contained within $b = 1.05$ to $b = 1.25$ and contains the complexes with four-membered rings, such as nitrate and dithiocarbamates. This strikingly simple and important correlation is further illustrated in Figure 9 with three representative examples: $[Co(MeCOCHCOMe)_3]$,[17] $[Co(NH_2CH_2CH_2NH_2)_3]^{3+}$,[1] and $[Co(NO_3)_3]$.[18]

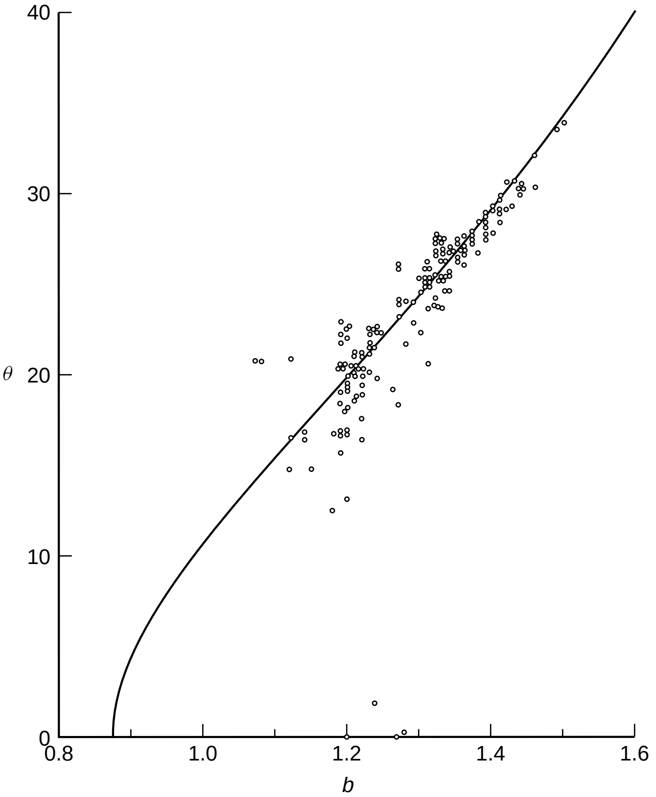

Figure 7 Angle of twist, θ (degrees), and normalized bite, b, for complexes of the type $[M(bidentate)_3]$. A theoretical curve is also shown

Further subdivisions can be made according to the size of the nonmetal atoms in the chelate ring. For example, the four-membered chelate ring group may be divided into four subgroups. The subgroup containing ligands of lowest normalized bite ($b = 1.05–1.12_5$) consists of $(PhN_3Ph)^-$ and NO_3^-, where three small second-row elements complete the chelate ring. There are no known examples of the second subgroup. The third subgroup of normalized bite 1.17–1.25 contains ligands with one second-row element and two larger elements in the chelate ring, such as the dithiocarbamates and xanthates. The fourth subgroup contains the dithiophosphates with three large ring atoms, and this subgroup intrudes into the group containing the five-membered chelate rings. A comparison of the ring geometries of $[Co(NO_3)_3]$,[18] $[Co(S_2COEt)_3]$,[19] and $[Co\{S_2P(OMe)_2\}_3]$[20] is shown in Figure 10.

Unusually large normalized bites may be achieved with five-membered chelate rings by again incorporating large

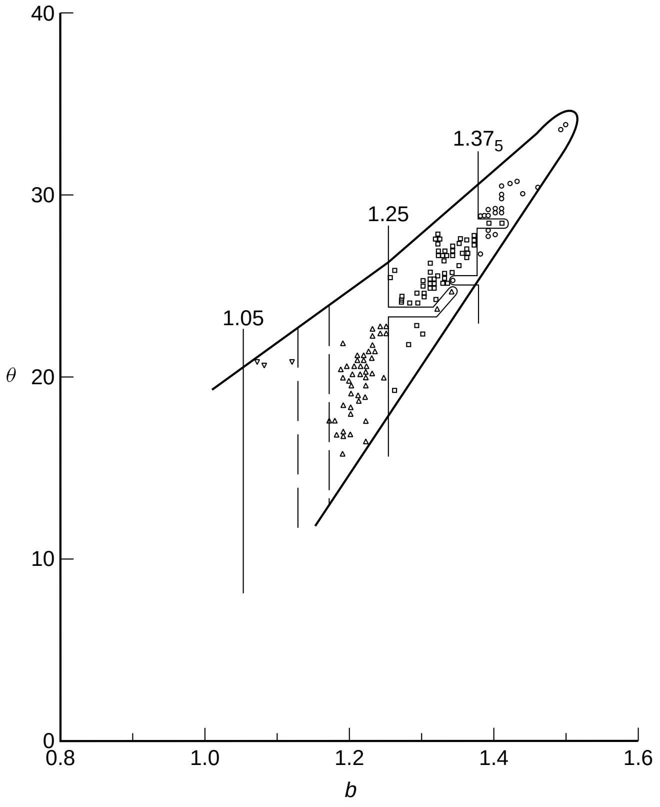

Figure 8 Angle of twist, θ (degrees), and normalized bite, b, for complexes of the type [M(bidentate)$_3$] (M = Cr, Mn, Fe, Co, Ni, Cu)

atoms into the ring. The intrusion of the five-membered ring region into the six-membered ring region in Figure 8 is due to a dithiooxalate complex containing two sulfur atoms in the chelate ring, all other five-membered rings in Figure 8 containing only carbon, nitrogen, and oxygen atoms. Comparative ring geometries in $[Co(C_2O_4)_3]^{3-}$[21] and $[Co(S_2C_2O_2)_3]^{3-}$[22] are also shown in Figure 10.

The size of the metal atom is also important in determining the normalized bite, the smaller normalized bites being obtained with the larger metal atoms. Thus the lowest normalized bite for a six-membered ring containing a transition metal ion is that observed for $[Sc(MeCOCHCOMe)_3]$[23] in which the normalized bite of 1.31 is similar to complexes of the other transition metals containing five-membered chelate rings. Similarly, the lowest normalized bite for a transition metal complex containing a five-membered ring is $b = 1.20$, observed for the tropolonate complex $[Sc(O_2C_7H_5)_3]$.[24]

4 SEVEN-COORDINATE COMPOUNDS

The starting point for the consideration of seven coordination is three structures with very similar stabilities: the pentagonal bipyramid, capped octahedron, and capped

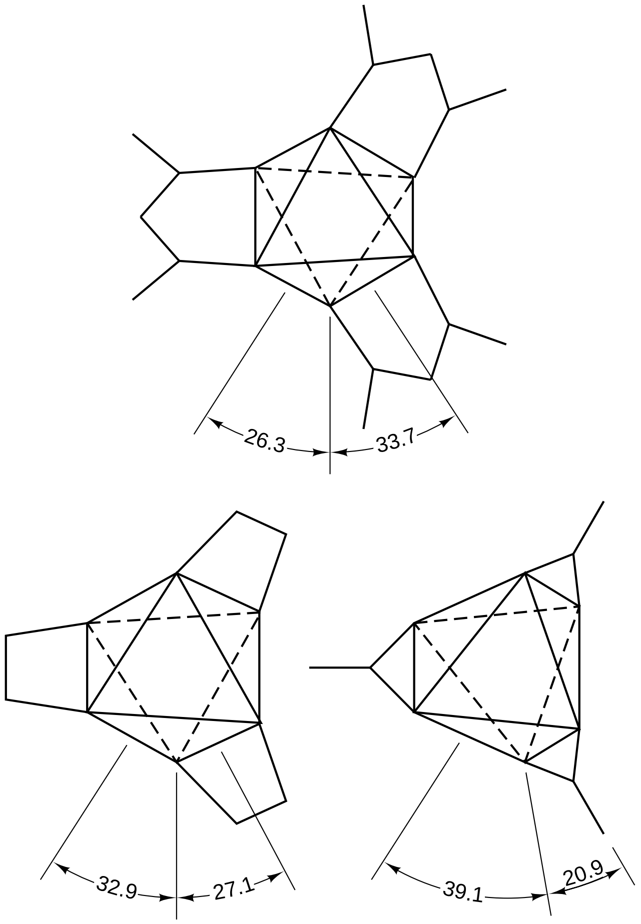

Figure 9 $[Co(acac)_3]$, $[Co(en)_3]^{3+}$, and $[Co(NO_3)_3]$

trigonal prism (Figure 11).[1,2,25] There are no potential energy barriers between these polyhedra and a range of structures is expected. For example, moving one of the equatorial atoms of the pentagonal bipyramid (starred in Figure 11) downward forms a capped octahedron with the starred atom as the capping atom. Further movement in the same direction forms a capped trigonal prism. The mirror plane in the plane of the page is retained.

Structurally characterized molecules with seven identical ligands are restricted mainly to some fluoro complexes $[MF_7]^{x-}$, aqua complexes $[M(H_2O)_7]^{2+}$, isonitrile complexes $[M(CNR)_7]^{2+}$, and cyanide complexes $[M(CN)_7]^{x-}$. The stereochemistries are distorted along the long ‘reaction coordinate’ connecting the capped trigonal prism and the pentagonal bipyramid. The X-ray data on IF_7[2] and $[TeF_7]^{-}$[26] are not sufficient to establish the precise stereochemistry. The NMR spectra show rapid intramolecular rearrangement. The anions in $K_2[NbF_7]$ and $K_2[TaF_7]$ are intermediate between a capped octahedron and a capped trigonal prism.[27]

In the calcium polyiodide compound $[Ca(H_2O)_7](I_{10})$ the stereochemistry appears to be intermediate between a capped octahedron and a pentagonal bipyramid, whereas

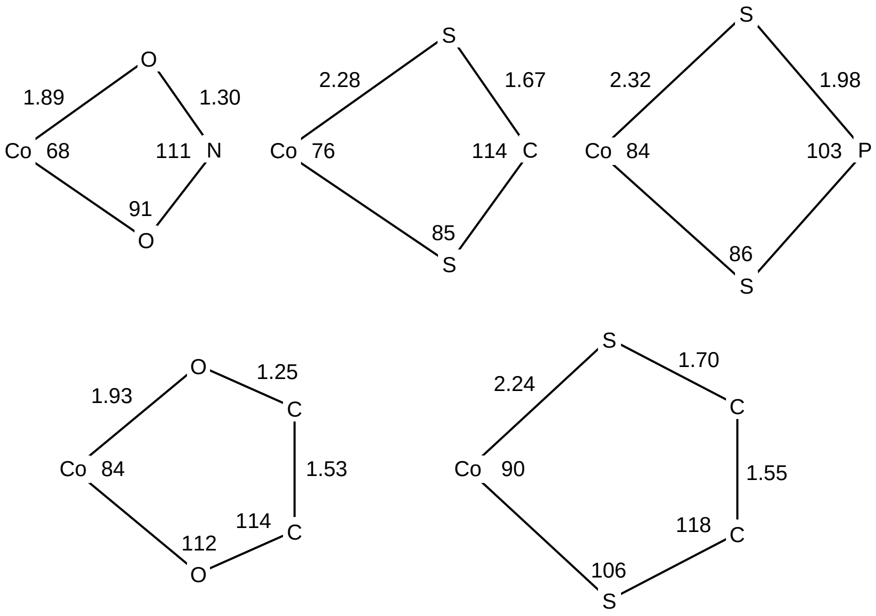

Figure 10 Ring geometries, in degrees and Å, in: $[Co(NO_3)_3]$, $[Co(S_2COEt)_3]$, $[Co\{S_2P(OMe)_2\}_3]$, $[Co(C_2O_4)_3]^{3-}$, and $[Co(S_2C_2O_2)_3]^{3-}$

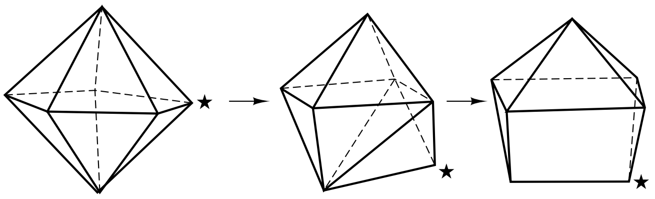

Figure 11 The pentagonal bipyramid, capped octahedron, and capped trigonal prism

$[Sr(H_2O)_7](I_{12})$ and $[Ca(H_2O)_7]_2[Cd_6Cl_{16}(H_2O)_2]\cdot H_2O$ contain capped trigonal prismatic cations.[2]

A close approximation to a capped trigonal prism is observed for $[Mo(CNBu)_7](PF_6)_2$. However, the closely related compounds $[Cr(CNBu)_7](PF_6)_2$, $[Mo(CNPh)_7](PF_6)_2$, $[Mo(CNMe)_7](BF_4)_2$, and $[W(CNBu)_7](W_6O_{19})$ lie further towards capped octahedra than capped trigonal prisms.[2] Solutions of $[Mo(CNBu)_7]^{2+}$ yield only a single ^{13}C NMR signal even down to $-135\,°C$, confirming the expected stereochemical nonrigidity.[2]

The structures of $K_4[V(CN)_7]\cdot 2H_2O$, $K_5[Mo(CN)_7]\cdot H_2O$, $Na_5[Mo(CN)_7]\cdot 10H_2O$ and $K_4[Re(CN)_7]\cdot 2H_2O$ are close to pentagonal bipyramids.[2]

As for five coordination, a mixture of unidentate ligands may lead to more well-defined stereochemistries due to the different types of polyhedral vertices available and the different spatial requirements of the different ligands. For example, the sterically least hindered sites in these structures are the axial sites of a pentagonal bipyramid as these are the only ones with no neighboring ligands having ligand–metal–ligand angles less than 90°. As expected, the O^{2-} ligand occupies this site and forces this structure in $Na_3[NbOF_6]$[28] and a range of uranyl complexes such as $[UO_2(OSMe_2)_5](ClO_4)_2$.[29] Likewise, a planar pentagonal arrangement of fluorine atoms is observed in $(Me_4N)[XeF_5(:)_2]$ with the pentagonal bipyramidal structure presumably completed by the two lone pairs of electrons.[30]

Well-defined stereochemistries may also be obtained by replacing the unidentate ligands with chelate groups which have a relatively fixed normalized bite. For example, ligands of very small normalized bite occupy one of the pentagonal edges of the pentagonal bipyramid, these being the shortest edges available among the seven-coordinate polyhedra. Examples include peroxo complexes with three-membered chelate rings, $[Ti(O_2)F_5]^{3-}$[31] and $[Cr(O_2)_2(CN)_3]^{3-}$,[32] and a number of complexes with four membered chelate rings, $[Cd(NO_3)_2py_3]$[33] and $[Hg(O_2CCF_3)_2py_3]$.[34] This dependence of structure upon size of the chelate ring is also illustrated by a group of molybdenum and tungsten carbonyl iodides.[35] A complex containing a four-membered chelating phosphine, $[W(Ph_2PCH_2PPh_2)I_2(CO)_3]$, has the pentagonal bipyramidal structure as above, whereas complexes containing larger rings, $[Mo(Ph_2PCH_2CH_2PPh_2)I_2(CO)_3]$ and $[Mo(Ph_2PCH_2CH_2CH_2PPh_2)I_2(CO)_3]$, have capped trigonal prismatic structures.

For complexes containing larger bidentate ligands which can wrap around the metal atom in a variety of stereochemistries, the structure is dependent upon both the size of the chelate ring and the nature of the unidentate ligands. A particularly well-studied group of complexes is of the type [M(bidentate)$_3$(unidentate)].[2] Uncharged unidentate ligands form two types of structure. The first is a capped octahedron with the unidentate ligand in the capping site and the three bidentate ligands forming a three-bladed propeller as in [M(bidentate)$_3$], examples including [$Tc(S_2COBu)_3(PPh_3)$],[36] [$Ho(PhCOCH_2COPh)_3(H_2O)$],[37] and [$Y(PhCOCH_2COMe)_3(H_2O)$].[38] The second structure approximates to a capped trigonal prism and is observed for [$Dy(BuCOCH_2COBu)_3(H_2O)$], [$Lu(C_3F_7COCH_2COBu)_3(H_2O)$], and [$Yb(MeCOCH_2COMe)_3(H_2O)$].[2] Charged unidentate ligands, on the other hand, form a structure which approximates to a pentagonal bipyramid but is distorted by the constraints of the bidentate ligands to be intermediate between a pentagonal bipyramid and a capped trigonal prism. Examples include [$Nb(S_2CNEt_2)_3O$],[39] [$V(S_2CNEt_2)_3O$],[39] $(NH_4)_3[Nb(C_2O_4)_3O]\cdot H_2O$,[40] and [$Zr(MeCOCHCOMe)_3Cl$].[41]

5 EIGHT-COORDINATE COMPOUNDS

The starting point for the consideration of eight coordination is the square antiprism and the triangular dodecahedron (Figure 12).[1,2,42] The square antiprism is usually slightly more stable than the dodecahedron and is more commonly observed.

The ideal square antiprism has all edge lengths equal but, because the square faces are larger than the triangular faces, the structure distorts slightly by decreasing the size of the square faces, in an analogous way to the distortion observed in square pyramidal molecules. This distortion is measured by a decrease in the angle α, the angle the eight metal–ligand bonds make with the fourfold axis, from the idealized 59.3° to about 57° (Table 4).

The dodecahedron has one set of four donor atoms necessarily different from the other set of four, labeled A and B, respectively, in Figure 12. A useful way of viewing the dodecahedron is to consider it as two interpenetrating and mutually orthogonal planar trapezoids, BAAB (Figure 12).

Table 4 Square antiprismatic [M(unidentate)$_8$] Molecules[2,43,44]

Complex	α (°)
$H_4[W(CN)_8]\cdot 6H_2O$	57.6
$Na_3[W(CN)_8]\cdot 4H_2O$	59.1
$H_4[W(CN)_8]\cdot 4HCl\cdot 12H_2O$	56.1
$[Nd(ONC_5H_5)_8](ClO_4)_3$	56.1
$[Nd(ONC_5H_4Me)_8](CF_3SO_3)_3$	54.4
$[NO(NOF)_2][IF_8]$	57.6
$[Sr(H_2O)_8](AgI_2)_2$	58.2
$[Cu(H_2O)_6]_2[ZrF_8]$	57.1
$Cs_4[U(NCS)_8]$	56.7

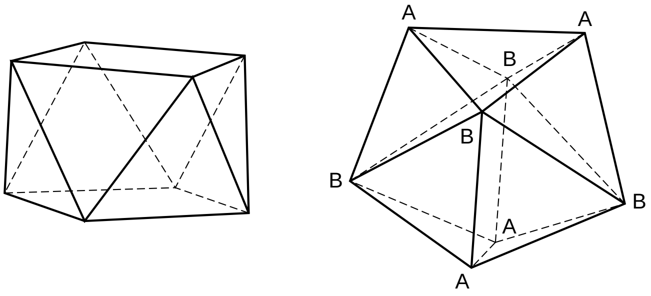

Figure 12 The square antiprism and dodecahedron

The B–B edges are approximately 25% longer than the A–A and A–B edges so that the B sites, which consequently have only three close neighbors, are sterically less crowded than the A sites. Examples of dodecahedral structures include $K_4[Mo(CN)_8]\cdot 2H_2O$,[45] $(Bu_4N)_3[Mo(CN)_8]$,[46] $[Gd(H_2O)_8]Cl_3\cdot 2C_{10}H_8N_2$, and $[Y(H_2O)_8]Cl_3\cdot 2C_{10}H_8N_2$.[47]

The square antiprism can be converted to the dodecahedron by creasing along a diagonal of each square face so that it becomes the B–B edge of a dodecahedron. Conversely, the dodecahedron in Figure 12 is converted to a square antiprism by forming square faces from two ABAB pairs of triangular faces. There is no potential energy barrier to this interconversion and intermediate structures are also possible, as observed for $(Et_3NH)_2(H_3O)_2[Mo(CN)_8]$.[48] As indicated above, the structures of $[M(CN)_8]^{x-}$ ($x = 3, 4$; M = Mo, W) may be square antiprismatic, dodecahedral, or intermediate. In solution, only a single ^{13}C NMR signal is observed for $[Mo(CN)_8]^{4-}$ at temperatures as low as −165 °C, consistent with very rapid intramolecular rearrangement.[49]

For complexes with a mixture of different ligands, the dodecahedron with its two different types of ligand site is generally favored. Charged ligands such as halide preferentially occupy the B sites of a dodecahedron, as observed for $[UCl(DMF)_7]_2[UO_2Cl_4]_3$,[50] $[UCl_4(MeCN)_4]$,[51] $[ThCl_4(OSPh_2)_4]$,[52] and $[ThBr_4(THF)_4]$.[53] On the other hand, $[EuCl_2(H_2O)_6]Cl$[54] and $[U(NCS)_4\{OP(NMe_2)_3\}_4]$[55] retain the square antiprismatic structure.

A preference by charged ligands to occupy the B sites of a dodecahedron is also indicated for complexes containing two bidentate ligands, as in $[WCl_4(Me_2PCH_2CH_2PMe_2)_2]$,[56] $[ThCl_4\{OP(NMe_2)_2OP(NMe_2)_2O\}_2]$,[57] and a series of diarsine complexes $[MX_4\{C_6H_4(AsMe_2)_2\}_2]^{x+}$, where M is Ti^{IV}, Nb^{IV}, Nb^{V}, etc. and X is Cl or Br.[58–60]

The influence the size of the chelate ring has upon the stereochemistry around the metal atom is clearly shown by complexes of the type [M(bidentate)$_4$]. Bidentate ligands of small normalized bite form dodecahedral structures, in which each of the BAAB trapezoids is formed from a pair of ligands (Figure 13). There are numerous examples of this structure with three- and four-membered chelate rings such as peroxide, nitrate, acetate, xanthate, and dithiocarbamate

(Table 5). Larger rings form an intermediate structure which can be represented as a square antiprism with the bidentate ligands spanning the square edges, but which is frequently distorted due to a creasing of the square faces as has been noted above, and alternative descriptions of the structure may be preferred (Figure 13). This structure is commonly observed for six-membered chelate rings such as the acetylacetonates of the lanthanide and actinide elements (Table 5). Ligands of intermediate size, such as the five-membered chelate rings oxalate and tropolate, and four-membered chelate rings containing large atoms such as dithiophosphate, may have either of the above structures, or an intermediate structure. The largest normalized bites are obtained with a combination of six-membered rings and smaller (than lanthanides or actinides) metal atoms, as in [Nb(BuCOCHCOBu)$_4$], which has a square antiprismatic structure in which the bidentate ligands span the triangular edges to form a four-bladed propeller (Figure 13, Table 5). As for the octahedron–trigonal prism correlation found for [M(bidentate)$_3$], the angle of twist between the two square faces is dependent upon the size of the chelate ring; in this case $b = 1.28$ and $\theta = 24°$.

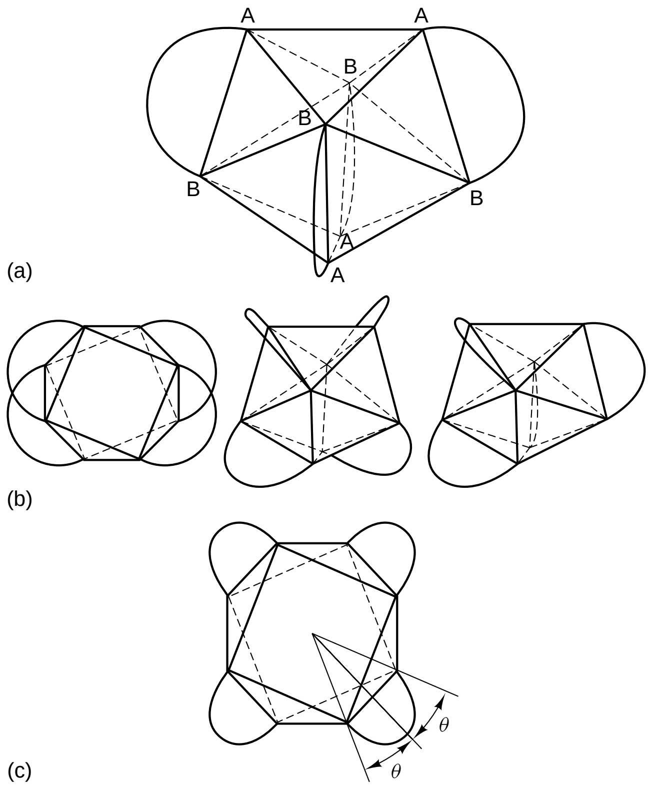

Figure 13 Stereochemistries of [M(bidentate)$_4$]. (a): the dodecahedron observed for low values of *b*. (b): alternative depictions of the intermediate structure observed for intermediate values of *b*. (c): the square antiprismatic structure observed for large values of *b*

Table 5 Stereochemistries and chelate ring size for examples of complexes of the type [M(bidentate)$_4$]**[2,61]**

Ring size	Complex	Stereochemistry
3	$K_3[Cr(O_2)_4]$	Dodecahedron
3	$[Zn(NH_3)_4][Mo(O_2)_4]$	Dodecahedron
4	$[Sn(NO_3)_4]$	Dodecahedron
4	$[Ti(NO_3)_4]$	Dodecahedron
4	$[Sn(O_2CMe)_4]$	Dodecahedron
4	$(Et_4N)[Bi(S_2COEt)_4]$	Dodecahedron
4	$[Ti(S_2CNEt_2)_4]$	Dodecahedron
4	$[Mo(S_2CNEt_2)_4]Cl$	Dodecahedron
4	$[Th(S_2PMe_2)_4]$	Dodecahedron
4	$(Ph_4P)[Pr(S_2PMe_2)_4]$	Intermediate
5	$[Hf(O_2C_7H_5)_4]\cdot DMF$	Dodecahedron
5	$Na_4[Zr(C_2O_4)_4]\cdot 3H_2O$	Distorted dodecahedron
6	$[U(PhCOCHCOPh)_4]$	Intermediate
6	$[Zr(MeCOCHCOMe)_4]$	Intermediate
6	$[Sm(NH_2CONHCONH_2)_4](NO_3)_3$	Intermediate
6	$[Nb(BuCOCHCOBu)_4]$	Square antiprism

6 NINE-COORDINATE COMPOUNDS

The two important stereochemistries for nine coordination**[1,2,62]** are the capped square antiprism and the slightly more stable tricapped trigonal prism (Figure 14). The tricapped trigonal prism can be converted to the capped square antiprism by converting two of the capping atoms and the two intervening prism atoms into a square. There is no potential energy barrier to this interconversion and repetition scrambles all nine atoms.

The most important structurally characterized compounds containing nine equivalent unidentate ligands are the aqua lanthanoid complexes $[Ln(H_2O)_9]^{3+}$.**[2,63]** In these compounds the capping atoms are more sterically hindered than the prism atoms and the metal–capping atom bond lengths are larger than the metal–prismatic atom bond lengths. As the size of the metal atom decreases, all three capping atoms are further squeezed out so that the 9-coordinate structure approaches a $(6 + 3)$-coordinate structure rather than an 8-coordinate

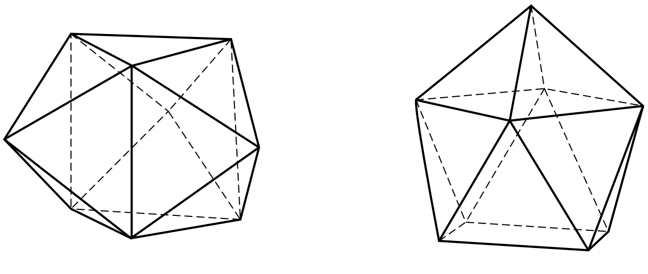

Figure 14 The tricapped trigonal prism and capped square antiprism

structure. For example:

	$M–O_{cap}$	$M–O_{prism}$	$(M–O_{cap})/(M–O_{prism})$
$[La(H_2O)_9](CF_3SO_3)_3$	2.62 Å	2.52 Å	1.04
$[Gd(H_2O)_9](CF_3SO_3)_3$	2.55	2.40	1.06
$[Lu(H_2O)_9](CF_3SO_3)_3$	2.50	2.29	1.09

The tricapped trigonal prismatic structure is retained in a series of trinitrato complexes such as $[Ln(NO_3)_3(H_2O)_3]$**[2,64]** in which bidentate nitrates span the capping and prism sites with retention of threefold symmetry. The angle of twist between the two triangles spanned by the three bidentate ligands is ~46°, in good agreement with theory; compare with $[M(bidentate)_3]$ and the capped octahedral $[M(bidentate)_3(unidentate)]$. Each bidentate ligand is unsymmetrically bonded as expected, $(M–O_{cap})/(M–O_{prism}) \approx 1.05$.

The most symmetrical way four equivalent bidentate ligands can be wrapped around a nine-coordinate metal atom is to form a capped square antiprism with the bidentate ligands linking the two square faces of the antiprism to form a four-bladed propeller with the unidentate ligand capping one square face. This structure is observed for $[Th(CF_3COCHCOCH_3)_4(H_2O)]$.**[65]** The angle of twist between the two square faces of 42° is as expected for the normalized bite of $b = 1.15$. In the capped square antiprism the four atoms forming the capped face are sterically less crowded than the four atoms forming the uncapped face, and this is reflected in the Th–O bond lengths of 2.39 and 2.46 Å, respectively.

7 TEN-COORDINATE COMPOUNDS[1,2,62]

There is, as yet, no structurally characterized compound containing ten unidentate ligands. Nevertheless, the geometry of these hypothetical compounds is a useful introduction to the stereochemistry of known ten-coordinate compounds containing chelate groups, such as $[M(bidentate)_5]$.

Three structures can be envisaged for ten coordination: the bicapped square antiprism, sphenocorona, and trirhombohedron (Figure 15).

The two most important structures for $[M(bidentate)_5]$ are shown in Figure 16, drawn as idealized bicapped square antiprisms. Isomer I is possible at all values of the normalized bite whereas isomer II is expected only for larger chelate rings. A number of lanthanoid and actinoid complexes with four-membered nitrate or carbonate rings, $[M^{III}(NO_3)_5]^{2-}$ and $[M^{IV}(CO_3)_5]^{6-}$, have structure I. The only monomeric molecule in which structure II is observed is $[Ba(MeCONHCOMe)_5](ClO_4)_2$ with six-membered chelate rings.

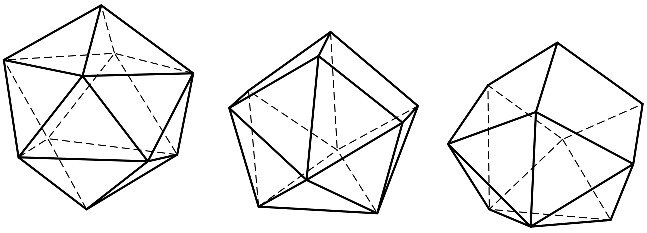

Figure 15 The bicapped square antiprism, sphenocorona, and trirhombohedron

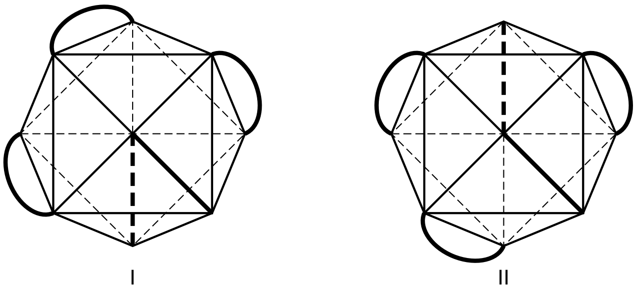

Figure 16 Bicapped square antiprismatic isomers of $[M(bidentate)_5]$

8 TWELVE-COORDINATE COMPOUNDS[1,2,62]

The tetrahedron, octahedron, and icosahedron are the three polyhedra formed from equivalent triangular faces, and these rigid, close packed structures dominate the stereochemistries for coordination numbers four, six, and twelve, respectively.

As for ten coordination, there are no twelve-coordinate complexes containing only unidentate ligands. The most common twelve-coordinate molecules are of the type $[M(bidentate)_6]$. Three structural isomers may be formed by wrapping six bidentate ligands along the edges of an icosahedron (Figure 17). Isomer III is less stable than the other two and is not observed. Isomer I is observed for a number of hexanitrato complexes, for example $[La(NO_3)_6]^{3-}$ and $[Th(NO_3)_6]^{2-}$. Isomer II has been observed for the naphthyridine complex $[Pr(napy)_6]^{3+}$.

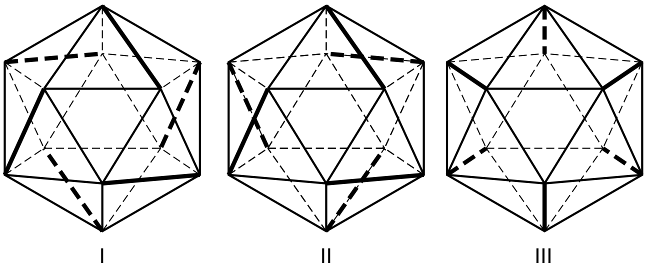

Figure 17 Icosahedral isomers of $[M(bidentate)_6]$

9 FURTHER READING

J. Hilton, E. K. Nunn, and S. C. Wallwork, *J. Chem. Soc., Dalton Trans.*, 1973, 173.

T. Kimura, N. Yasuoko, N. Kasai, and M. Kukuda, *Bull. Chem. Soc. Jpn.*, 1972, **45**, 1649.

B. W. Liebich and M. Tomassini, *Acta Crystallogr.*, 1978, **B34**, 944.

G. A. Miller and E. O. Schlemper, *Inorg. Chem.*, 1973, **12**, 677.

K. C. Mollog, M. B. Hossain, D. van der Helm, J. J. Zuckerman, and F. P. Mullins, *Inorg. Chem.*, 1981, **20**, 2172.

10 REFERENCES

1. D. L. Kepert, ‘Inorganic Stereochemistry’, Springer-Verlag, Berlin, 1982.
2. D. L. Kepert, in ‘Comprehensive Coordination Chemistry’, eds. G. Wilkinson, R. D. Gillard, and J. A. McCleverty, Pergamon Press, Oxford, 1987, Vol. 1, Chap. 2, p. 31.
3. J. R. Partington, ‘A History of Chemistry’, Macmillan, London, 1964, Vol. 4, p. 755.
4. A. Werner, *Z. Anorg. Chem.*, 1893, **3**, 267; G. B. Kauffman, ‘Classics in Coordination Chemistry, Part I: The Selected Papers of Alfred Werner’, Dover, New York, 1968.
5. B. W. Clare, M. C. Favas, D. L. Kepert, and A. S. May, *Adv. Dynamic Stereochem.*, 1985, **1**, 1.
6. M. C. Favas and D. L. Kepert, *Prog. Inorg. Chem.*, 1980, **27**, 325.
7. R. S. Berry, *J. Chem. Phys.*, 1960, **32**, 933.
8. D. Schomburg and R. Krebs, *Inorg. Chem.*, 1984, **23**, 1378.
9. D. L. Kepert, C. L. Raston, A. H. White, and D. Petridis, *J. Chem. Soc., Dalton Trans.*, 1980, 1921.
10. P. K. Hon, R. L. Belford, and C. E. Pfluger, *J. Chem. Phys.*, 1965, **43**, 3111.
11. K. Henrick, C. L. Raston, and A. H. White, *J. Chem. Soc., Dalton Trans.*, 1976, 26.
12. D. L. Kepert, *Prog. Inorg. Chem.*, 1977, **23**, 1.
13. A. Kopwillem, *Acta Chem. Scand.*, 1972, **26**, 2941.
14. R. K. Chadha, J. E. Drake, and A. B. Sarker, *Inorg. Chem.*, 1986, **25**, 2201.
15. M. G. Begley, C. Gaffney, P. G. Harrison, and A. Steel, *J. Organomet. Chem.*, 1985, **289**, 281.
16. H. Graver and S. Husebye, *Acta Chem. Scand.*, 1975, **A29**, 14.
17. G. J. Kruger and E. C. Reynhardt, *Acta Crystallogr.*, 1974, **B30**, 822.
18. J. Hilton and S. C. Wallwork, *Chem. Commun.*, 1968, 871.
19. S. Merlino, *Acta Crystallogr.*, 1969, **B25**, 2270.
20. J. F. McConnell and A. Schwartz, *Acta Crystallogr.*, 1972, **B28**, 1546.
21. K. R. Butler and M. R. Snow, *J. Chem. Soc. (A)*, 1971, 565.
22. K. R. Butler and M. R. Snow, *Acta Crystallogr.*, 1975, **B31**, 354.
23. T. J. Anderson, M. A. Neuman, and G. A. Melson, *Inorg. Chem.*, 1973, **12**, 927.
24. T. J. Anderson, M. A. Neuman, and G. A. Melson, *Inorg. Chem.*, 1974, **13**, 158.
25. D. L. Kepert, *Prog. Inorg. Chem.*, 1979, **25**, 41.
26. A. R. Mahjoub, T. Drews, and K. Seppelt, *Angew. Chem., Int. Ed. Engl.*, 1992, **31**, 1036.
27. M. C. Favas, J. M. Harrowfield, D. L. Kepert, B. W. Skelton, L. M. Vitolo, and A. H. White, *Aust. J. Chem.*, 1992, **45**, 1547.
28. R. Stomberg, *Acta Chem. Scand.*, 1983, **A37**, 453.
29. J. M. Harrowfield, D. L. Kepert, J. M. Patrick, A. H. White, and S. F. Lincoln, *J. Chem. Soc., Dalton Trans.*, 1983, 393.
30. K. O. Christe, E. C. Curtis, D. A. Dixon, H. P. Mercier, J. C. P. Sanders, and G. J. Schrobilgen, *J. Am. Chem. Soc.*, 1991, **113**, 3351.
31. R. Schmidt and G. Pausewang, *Z. Anorg. Allg. Chem.*, 1989, **575**, 197.
32. R. Stomberg, *Arkiv. Kemi.*, 1965, **23**, 401.
33. A. F. Cameron, D. W. Taylor, and R. H. Nuttall, *J. Chem. Soc., Dalton Trans.*, 1972, 1608.
34. J. Halfpenny and R. W. H. Small, *Acta Crystallogr.*, 1978, **B34**, 3758.
35. R. M. Foy, D. L. Kepert, C. L. Raston, and A. H. White, *J. Chem. Soc., Dalton Trans.*, 1980, 440.
36. T. Nicholson, J. Thornback, L. O’Connell, G. Morgan, A. Davison, and A. G. Jones, *Inorg. Chem.*, 1990, **29**, 89.
37. A. Zalkin, D. H. Templeton, and D. G. Karraker, *Inorg. Chem.*, 1969, **8**, 2680.
38. F. A. Cotton and P. Legzdins, *Inorg. Chem.*, 1968, **7**, 1777.
39. J. C. Dewan, D. L. Kepert, E. N. Maslen, C. L. Raston, D. Taylor, and A. H. White, *J. Chem. Soc., Dalton Trans.*, 1973, 2082.
40. G. Mathern and R. Weiss, *Acta Crystallogr.*, 1971, **B27**, 1610.
41. R. B. VonDreele, J. J. Stezowski, and R. C. Fay, *J. Am. Chem. Soc.*, 1971, **93**, 2887.
42. D. L. Kepert, *Prog. Inorg. Chem.*, 1978, **24**, 179.
43. C. A. Fantin, L. B. Zinner, G. Vicentini, C. Rodellas, and L. Niinisto, *Acta Chem. Scand.*, 1987, **A41**, 259.
44. A.-R. Mahjoub and K. Seppelt, *Angew. Chem., Int. Ed. Engl.*, 1991, **30**, 876.
45. J. L. Hoard, T. A. Hamor, and M. D. Glick, *J. Am. Chem. Soc.*, 1968, **90**, 3177.
46. B. J. Corden, J. A. Cunningham, and R. Eisenberg, *Inorg. Chem.*, 1970, **9**, 356.
47. M. Bukowska-Strzyzewska and A. Tosic, *Acta Crystallogr.*, 1982, **B38**, 950.
48. J. G. Leipoldt, S. S. Basson, and L. D. C. Bok, *Inorg. Chim. Acta*, 1980, **44**, L99.

49. E. L. Muetterties, *Inorg. Chem.*, 1973, **12**, 1963.
50. D. L. Kepert, J. M. Patrick, and A. H. White, *J. Chem. Soc., Dalton Trans.*, 1983, 381.
51. G. Van den Bossche, J. Rebizant, M. R. Spirlet, and J. Goffart, *Acta Crystallogr.*, 1986, **C42**, 1478.
52. C. E. F. Rickard and D. C. Woollard, *Acta Crystallogr.*, 1980, **B36**, 292.
53. D. L. Clark, T. M. Frankcom, M. M. Miller, and J. G. Watkin, *Inorg. Chem.*, 1992, **31**, 1628.
54. D. L. Kepert, J. M. Patrick, and A. H. White, *Aust. J. Chem.*, 1983, **36**, 477.
55. D. L. Kepert, J. M. Patrick, and A. H. White, *J. Chem. Soc., Dalton Trans.*, 1983, 385.
56. V. Saboonchian, G. Wilkinson, B. Hussain-Bates, and M. B. Hursthouse, *Polyhedron*, 1991, **10**, 595.
57. D. L. Kepert, J. M. Patrick, and A. H. White, *J. Chem. Soc., Dalton Trans.*, 1983, 559.
58. R. J. H. Clark, J. Lewis, R. S. Nyholm, P. Pauling, and G. B. Robertson, *Nature*, 1961, **192**, 222.
59. J. C. Dewan, D. L. Kepert, C. L. Raston, and A. H. White, *J. Chem. Soc., Dalton Trans.*, 1975, 2031.
60. D. L. Kepert, B. W. Skelton, and A. H. White, *J. Chem. Soc., Dalton Trans.*, 1981, 652.
61. S. F. Haddad, *Acta Crystallogr.*, 1987, **C43**, 1882.
62. M. C. Favas and D. L. Kepert, *Prog. Inorg. Chem.*, 1981, **28**, 309.
63. J. M. Harrowfield, D. L. Kepert, J. M. Patrick, and A. H. White, *Aust. J. Chem.*, 1983, **36**, 483.
64. H. Jacobsen and G. Meyer, *Z. Anorg. Allg. Chem.*, 1992, **615**, 16.
65. T. W. Hambley, D. L. Kepert, C. L. Raston, and A. H. White, *Aust. J. Chem.*, 1978, **31**, 2635.

Coordination & Organometallic Chemistry: Principles

Robert H. Crabtree
Yale University, New Haven, CT, USA

1	Introduction	1
2	Werner Complexes	1
3	The Trans Effect	2
4	Soft versus Hard Ligands	3
5	The Crystal Field	3
6	The Ligand Field	5
7	Back Bonding	6
8	Electroneutrality	8
9	Types of Ligands	9
10	The Eighteen Electron Rule and its Limitations	10
11	Oxidation State	13
12	Coordination Number	13
13	Effects of Complexation	14
14	Effects of Changing Metal	15
15	Other Properties of Coordination Compounds	15
16	Related Articles	16
17	References	16

1 INTRODUCTION

This article is adapted with permission from the first two chapters of the author's book *Organometallic Chemistry of the Transition Metals*.[1c] Several other useful texts are also available on organometallic and coordination chemistry.[1] Transition metal ions can bind ligands (*see Ligand*), L to give a coordination compound, or complex (*see Coordination Complexes*) ML_n, as in the familiar aqua ions $[M(OH_2)_6]^{2+}$ ($M = V$, Cr, Mn, Fe, Co, or Ni) where O is considered the donor atom. Where the ligands have only N, O, or halide donor atoms, the complexes are considered to be classical coordination compounds. On the other hand, complexes with any C-donor ligands or hydrides are usually considered as being organometallic compounds. Organometallic species tend to be more covalent, and the metal is often more reduced than in other coordination compounds. Typical ligands which usually bind to metals in their lower oxidation states are CO, alkenes, and arenes, for example, $Mo(CO)_6$, $(C_6H_6)Cr(CO)_3$, or $Pt(C_2H_4)_3$. Apart from these inner-sphere complexes, outer-sphere complexes also exist, for example, in which a counterion is associated with the inner-sphere complex in an ion pair.

2 WERNER COMPLEXES[2]

The simplest metal–ligand bond is perhaps $L_nM{-}NH_3$, where an ammonia binds to a metal fragment. This fragment will usually have other ligands, represented here by L_n. The bond consists of the lone pairs of electrons present in free NH_3 that are donated to the metal to form the complex. The metal is a polyvalent Lewis acid capable of accepting the lone pairs of several ligands, L, which act as Lewis bases.

The most common type of complex is ML_6, which adopts an octahedral coordination geometry (**1**),[1,2] based on one of the Pythagorean regular solids. The ligands occupy the six vertices of the octahedron, which allows them to minimize their M–L bonding distances while maximizing their L$\cdots$L nonbonding distances. From the point of view of the coordination chemist, it is perhaps unfortunate that Pythagoras decided to name his solids after the number of faces ($octa$ = eight) rather than the number of vertices. After (**1**), ML_4 and ML_5 are the next most common types (*see* ***Coordination Numbers & Geometries***).

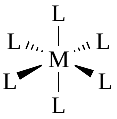

(**1**)

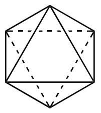

Octahedron

The assembly of metal and ligands that we call a complex may have a net charge, in which case it is a complex ion (e.g. $[PtCl_4]^{2-}$). Together with the counterions, we have a complex salt (e.g. $K_2[PtCl_4]$). In some cases both the cation and the anion may be complex, as in Magnus's green salt, $[Pt(NH_3)_4][PtCl_4]$. Square brackets are used to enclose the individual complex molecules or ions where necessary to avoid ambiguity. Those ligands with more than one lone pair can donate one to each of two or more metal ions to give polynuclear complexes, such as the orange crystalline compound (**2**) ($L = PR_3$). The bridging group is represented in formulae by using the Greek letter μ, as in $[Ru_2(\mu\text{-}Cl)_3(PR_3)_6]^+$. Note how (**2**) can be considered as two octahedral fragments sharing the face that contains the three chloride bridges.

Other ligands can have more than one donor atom; an example is ethylenediamine ($NH_2CH_2CH_2NH_2$, often abbreviated as en). Such ligands most commonly donate both lone pairs to the same metal to give a ring compound known as a chelate (*see Chelating Ligands* and *Chelate Effect*). A typical example of such a complex is (**3**).

The early Russian investigator Chugaev first drew attention to the fact that chelating ligands are much less easily displaced

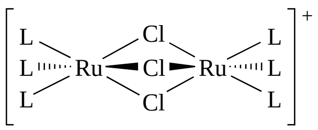

(**2**)

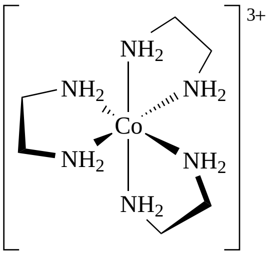

(**3**)

from a complex than are monodentate ligands of the same type. The reason is illustrated in equation (1).

$$[M(NH_3)_6]^{n+} + 3\ en \rightleftharpoons [M(en)_3]^{n+} + 6NH_3 \qquad (1)$$

Formation of the chelate releases six NH_3 molecules so that the total number of particles increases from four to seven. This creates entropy, and so favors the chelate form. Each chelate ring usually leads to an additional factor of about 10^5 in the equilibrium constant for reactions like equation (1). Equilibrium constants for complex formation are usually called formation constants; the higher the value the more stable the complex.

Not only does chelation make the complex more stable, but it also forces the donor atoms to take up adjacent or cis sites in the resulting complex. Equation (2) shows how displacement of a chelating carbonate ion gives the unusual *cis* dichloride product instead of the thermodynamically more stable trans dichloride. Polydentate chelating ligands with three or more donor atoms also exist. Macrocyclic ligands, such as (**4**) and (**5**), confer an additional increment in the formation constant (the macrocyclic effect); they have been given trivial names, such as ‘cryptates’ (**4**) and ‘sepulchrates’ (**5**).[1]

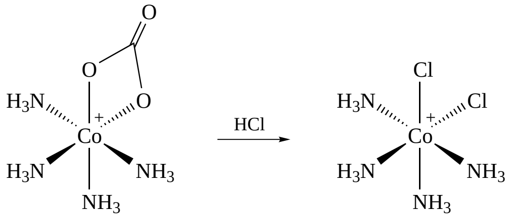

(2)

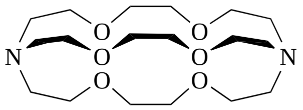

(**4**)

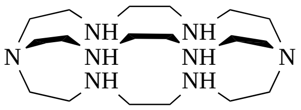

(**5**)

Ligands such as nitrite can have isomers (linkage isomers; see *Linkage Isomerism*), in which the metal is bound via N in one case (M–NO_2) or O (M–ONO) in the other. Complexes such as $[Co(en)_2XY]^{n+}$ can have optical isomers (**6**) and (**7**), as a result of the absence of a plane of symmetry. Some have very large optical rotations: Werner’s complex (**8**), which is unusual in containing only inorganic elements, has the extraordinarily high specific rotation of 36 000°, and required 1000 recrystallizations to resolve.

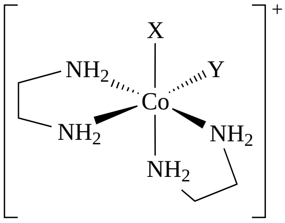

(**6**)

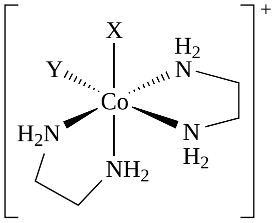

(**7**)

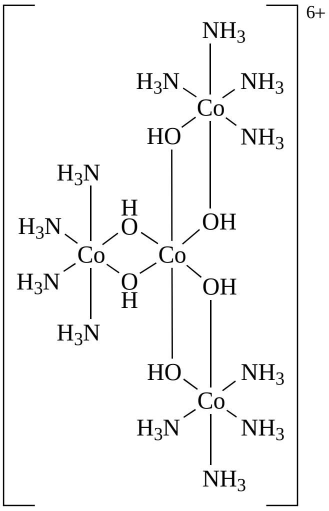

(**8**)

3 THE TRANS EFFECT

In the 1920s, Chernaev discovered that certain ligands facilitate the departure of a second ligand *trans* to the first, and their replacement or substitution by an external ligand (*see Ligand Substitution*). Ligands that are more effective at this labilization are said to have a higher *trans effect*. The effect is most marked in substitution on Pt^{II}, and the highest trans effect ligands either form unusually strong σ-bonds, such as H^-, Me^-, or $SnCl_3^-$, or unusually strong π-bonds, such as CO, C_2H_4, and thiourea ($(NH_2)_2CS$, a ligand often represented as tu). The same ligands also weaken the trans M–L bonds in the ground state, as shown by a lengthening of the M–L distances found by X-ray crystallography, or by some spectroscopic measure, such as the M–L coupling constant in the NMR, or the ν(M–L) stretching frequency in the IR spectrum. A change in the ground-state thermodynamic properties, such as these, is usually termed the *Trans Influence* to distinguish it from the parallel effect on the properties of the transition state for the substitution reaction, which is the trans effect proper, and refers to differences in *rates* of substitution and is therefore a result of a change in the energy difference between the ground state and transition state for the reaction. A classic system in which trans effects are very marked is PtL_4^{2+}, in which Pt^{II} adopts the square-planar geometry (**9**), a square with the metal at the center.

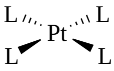

(**9**)

An important application of the trans effect is the synthesis of specific isomers of coordination compounds. Equations (3) and (4) show how the cis and trans isomers of $Pt(NH_3)_2Cl_2$ can be prepared selectively by taking advantage of the trans effect order Cl > NH_3. This example is also of practical interest because the cis isomer is an important antitumor drug, but the trans isomer is ineffective. In each case the first step of the substitution can give only one isomer. In equation (3) the cis isomer is formed in the second step because the Cl trans to Cl is more labile than the Cl trans to the lower trans effect ligand, ammonia. On the other hand, in equation (4) the first Cl to substitute labilizes the ammonia trans to itself to give the trans dichloride as final product.

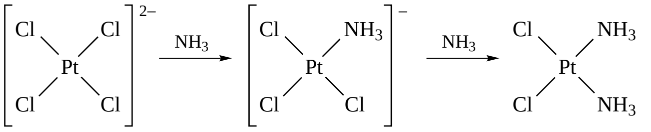

(3)

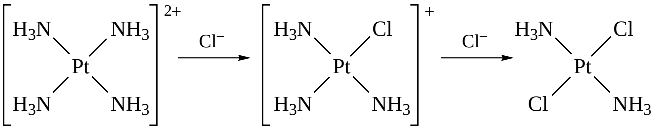

(4)

4 SOFT VERSUS HARD LIGANDS

Chatt[3a] pointed out in the 1950s that most metal ions in their usual oxidation states tend to bind saturated ligands such as NH_3, H_2O, or F^-. These are now[3b] called *hard* metals by allusion to their low polarizability. On the other hand, a small group of ions, including the platinum metals, Ag^+, Hg^{2+}, and a few others, form stronger complexes with unsaturated or polarizable ligands, such as Br^-, I^-, PPh_3, or C_2H_4 (now called *soft*; see *Hard & Soft Acid–Base Theory*). Soft ligands either have donor atoms from the second or subsequent rows of the periodic table (e.g. Br^-, PPh_3, or Me_2S), or they have double or triple bonds (ethylene, acetylene, benzene). We now know that essentially all the transition metals can become soft if they are reduced to a sufficiently low valence state. The peculiarity of the small group of metals identified by Chatt is that they normally occur in low oxidation states, and so had long been known to form soft complexes. Table 1 shows some formation constants that illustrate the differences. The reason that low oxidation state metals tend to bind soft ligands is that these metals have excess electron density by virtue of their reduced state. They therefore avoid strong donor ligands, but prefer ligands with which they can form covalencies, and that have available empty orbitals into which they can donate some of their excess electron density (see Section 7). High oxidation state metals, on the other hand, are short of electron density and require good donor ligands.

5 THE CRYSTAL FIELD

An important advance in understanding the spectra, structure, and magnetism of transition metal complexes is provided by the crystal field (CF) model (*see Crystal Field Theory*). The d orbitals of the metal are assumed to be affected by the presence of the ligands, which are considered to act simply as negative charges. For a free metal ion isolated in space, the d orbitals are degenerate (have the same energy). As the ligands L approach the metal from the six octahedral directions $\pm x$, $\pm y$, and $\pm z$, the d orbitals take the form shown in Figure 1. Those d orbitals that point toward the L groups ($d_{x^2-y^2}$ and d_{z^2}) are destabilized by the negative charge of the ligands and move to higher energy. Those that point away from L (d_{xy}, d_{yz}, and d_{xz}) are less destabilized. The pair of orbitals that are most strongly destabilized are often identified by their symmetry label, e_g, or simply as d_σ, because they point along the M–L σ-bonding directions. The three more stable orbitals have the label t_{2g}, or simply d_π; these point away from the ligand directions but can form π bonds with

Table 1 Hard and soft acids and bases: some formation constants[a]

	Ligand			
Metal ion	F^-	Cl^-	Br^-	I^-
H^+	3	−7	−9	−9.5
Zn^{2+}	0.7	−0.2	−0.6	−1.3
Cu^{2+}	1.2	0.05	−0.03	–
Hg^{2+}	1.03	6.74	8.94	12.87

[a] The values are the negative logarithms of the equilibrium constant for $[M{\cdot}aq]^{n+} + L = [ML{\cdot}aq]^{(n-1)+}$, and show how H^+ and Zn^{2+} are hard acids, forming stronger complexes with F^- than with Cl^-, Br^-, or I^-. Cu^{2+} is a borderline case, and Hg^{2+} is a very soft acid, forming much stronger complexes with the more polarizable halide ions.

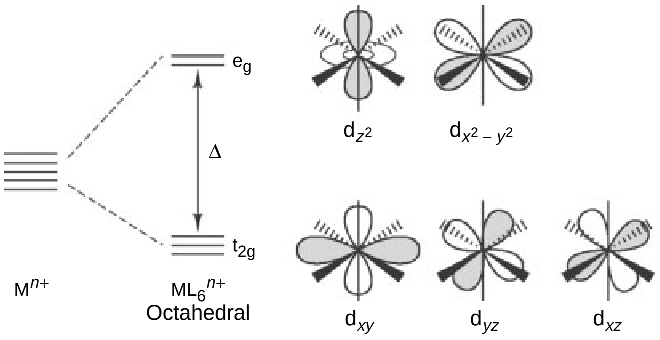

Figure 1 The effect on the d orbitals of bringing up six ligands along the $\pm x$, $\pm y$, and $\pm z$ directions. In this figure, shading represents the symmetry (not the occupation) of the d orbitals; shaded parts have the same sign of Ψ

the ligands. The magnitude of the energy difference between the d_σ and d_π set, usually called the CF splitting, and labeled Δ (or sometimes $10Dq$) depends on the value of the effective negative charge and therefore on the nature of the ligands.

The metal ion Werner studied, Co^{3+}, has a strong preference for the octahedral geometry because it has a d^6 configuration. Six electrons just fill the three low-lying d_π orbitals of the CF diagram, and leave the d_σ empty. This is a particularly stable arrangement and other d^6 metals (Mo^0, Re^I, Fe^{II}, Ir^{III}, and Pt^{IV}) also show a very strong preference for the octahedral geometry. In spite of the high tendency to spin pair the electrons in the d^6 configuration (to give the low-spin form $t_{2g}^6e_g^0$; *see High-spin & Low-spin Compounds*), if the crystal field splitting is small enough, then the electrons may rearrange to give the high-spin form $t_{2g}^4e_g^2$. The high-spin form has all the spins aligned, as prescribed for the free ion by Hund's rule and shown in Figure 2. The high-spin form is favored because fewer electrons are paired up in the same orbitals and so electron–electron repulsions are reduced. On the other hand, if Δ becomes large enough, then the energy gained by dropping from the e_g to the t_{2g} level will be big enough to drive the electrons into pairing up in spite of e–e repulsions. The spin state of the complex can usually be determined by measuring the magnetic moment of the complex. This is done by placing a sample of the complex in a magnetic field gradient. In the low-spin form of a d^6 ion the molecule is diamagnetic (*see Diamagnetism*), that is to say it is very weakly repelled by the field. This behavior is exactly the same as is found for the vast majority of organic compounds, which are also spin paired. On the other hand, the high-spin form is paramagnetic (*see Paramagnetism*), in which case it is attracted into the field. The complex does not itself form a permanent magnet as does a piece of iron or nickel (this property is called *Ferromagnetism*), because the spins are not aligned in the crystal in the absence of an external field, but they do respond to the external field by lining up together when placed in an external magnetic field in order to measure the magnetic moment.

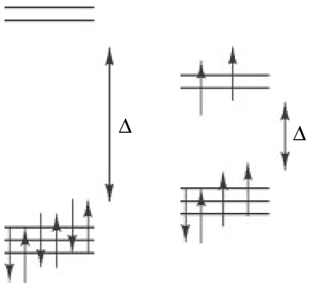

Figure 2 In a d^6 metal ion, both low- and high-spin complexes are possible, depending on the value of Δ. A high Δ leads to the low-spin form

The great majority of organometallic complexes are diamagnetic, because Δ is usually large in these complexes, favoring electron configurations that completely fill the low-lying levels. Paramagnetic organometallic species are becoming more common, however. This is always the case for molecules like $V(CO)_6$ that have an uneven number of electrons. For molecules with an even number of electrons, a high-spin configuration is more likely for the first-row metals, where Δ tends to be smaller than in the later rows. Paramagnetic centers are present in many metalloenzymes that involve organometallic intermediates, such as hydrogenase and CO dehydrogenase.

Sometimes the low- and high-spin forms of a metal complex have almost exactly the same energy. Each state can now be populated, and the relative populations of the two states vary with temperature; this happens for $Fe(S_2CNEt_2)_3$, for example. When two metals are present in the same complex, each having one unpaired electron, they may show singlet (↑↓) or triplet (↑↑) behavior. This depend on the strength of the coupling between the spins; once again, spin equilibria can occur.**4** It is now recognized that spin state crossings may occur in the course of chemical reactions of metal complexes, leading to unexpected pathways and abnormal kinetics. Even diamagnetic species can react via paramagnetic spin states.

In an octahedral d^7 ion, we are obliged to place one electron in the higher-energy d_σ level to give the configuration $t_{2g}^6e_g^1$, and this will normally make the complex paramagnetic (Figure 3). The net stabilization, often termed the crystal field stabilization energy or CFSE, of such a system will also be less than for d^6 (low spin), where we can put all the electrons into the more stable t_{2g} level. This is reflected in the chemistry of d^7 ions (e.g. Co^{II}), which, as long as they remain octahedral, are more reactive than their d^6 analogues. For example, they undergo ligand dissociation much more readily. The reason is that the d_σ levels are really M–L σ-antibonding in character, as we see later. Werner was able to study his chemistry with Co^{III} because the ligands tend to stay put. This is why Co^{III} and other d^6 ions are often referred to as coordinatively inert (*see Coordinatively Inert & Labile Complexes*); d^3 ions like Cr^{III} are also coordinatively inert because the t_{2g} level is now exactly half filled, another favorable situation. On

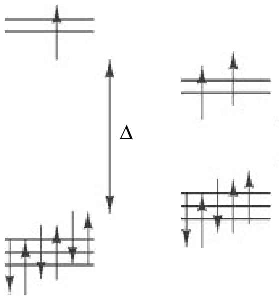

Figure 3 A d^7 ion is paramagnetic even in the low-spin form

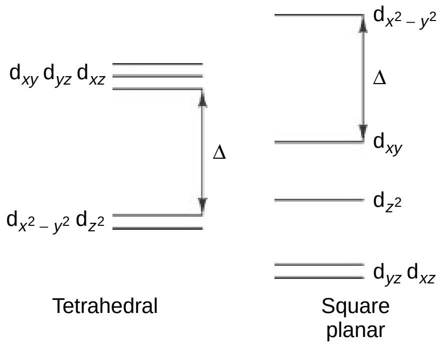

Figure 4 Crystal field splitting patterns for the common coordination geometries: tetrahedral and square planar. For the square-planar arrangement, the z-axis is conventionally taken to be perpendicular to the square plane

the other hand, Co^{II} and other non-d^6 and -d^3 ions can be coordinatively labile.

The colors of transition metal ions often arise from the absorption of light that corresponds to the d_π to d_σ energy gap, Δ. The spectrum of the complex can then give a direct measure of this gap, and therefore of the CF strength. So-called high-field ligands (*see Ligand Field Theory*) such as thiourea, CO, and C_2H_4 give rise to a large value of Δ. Low-field ligands such as H_2O or NH_3 can give such a low Δ that the spin pairing is lost and even the d^6 configuration can become paramagnetic (Figure 2, right). This rarely occurs for organometallic ligands, since they tend to induce a large Δ splitting, and are therefore high-field ligands. Other important CF splitting patterns are shown in Figure 4. For the same ligand set the tetrahedral splitting parameter is smaller than that for the octahedral geometry by a factor of 2/3, because we now have only four ligands, not six, and so the chance of having a high-spin species is larger. The ordering of the levels is also reversed, three going up and only two down in energy. This is because the d_{xy}, d_{yz}, and d_{xz} orbitals now point toward, and the $d_{x^2-y^2}$ and d_{z^2} orbitals away from the ligands. d^{10} ions (e.g. Zn^{II}, Pt^0, Cu^I) are often tetrahedral. The square-planar splitting pattern is also shown. This geometry tends to be adopted by d^8 ions such as Au^{III}, Ni^{II}, Pd^{II}, or Pt^{II}, and Rh^I or Ir^I, in which case the complex is diamagnetic; it is also common for paramagnetic d^9 ions, for example Cu^{II}.

5.1 Electron Transfer

A very important feature of Werner complexes is the ease with which they can undergo electron transfer (ET) reactions[**5**] in which they are reduced or oxidized by one or more electrons. This can completely change the properties of the complex. A classic case is Co^{III}, which as a d^6 metal is coordinatively inert but on reduction the coordinatively labile d^7 Co^{II} state is formed. The work of Taube[**5a**] showed how certain electron-transfer reactions occur between two separate complexes (outer-sphere reactions), while others take place through a bridging ligand (inner-sphere type). This was most elegantly shown by experiments in which the bridging group was transferred from one coordinatively inert metal, which becomes labile in the redox process to a second metal, initially labile but which becomes inert in the redox process. The rate of outer-sphere ET reactions is often well predicted by Marcus-Hush theory,[**6**] which relates k_{12}, the rate of reaction between A_{red} and B_{ox}, to the equilibrium constant for the reaction (K_{12}) and the rates for the degenerate exchanges between A_{red} and A_{ox} (k_{11}) and between B_{red} and B_{ox} (k_{22}). The form of the equation which is most often used is shown in equation (5).

$$k_{12} = [k_{11}k_{22}K_{12}]^{1/2} \tag{5}$$

This is very similar in principle to a free energy relationship, such as the Hammett equation in organic chemistry. Normally the reaction rate goes up as the driving force goes up. Under certain special circumstances the rate reaches a maximum and begins to fall at very high driving force; the existence of this 'Marcus inverted region[**7**]' has been confirmed in several systems. This is fully covered in the article (*see* ***Electron Transfer in Coordination Compounds***) as well as in all standard textbooks of inorganic chemistry. ET can also occur in electrochemical processes (*see* ***Electrochemistry: Applications in Inorganic Chemistry***) and in photochemical processes (*see* ***Photochemistry of Transition Metal Complexes***).

6 THE LIGAND FIELD

The CF picture gives a useful understanding of coordination chemistry and one that is widely used for qualitative discussions. A more sophisticated version of this approach, LF theory (*see* ***Ligand Field Theory & Spectra***), which is really a conventional molecular orbital (or MO) picture, can be used for more accurate electronic structure calculations. In the CF model (Figure 5) we consider the s, the three p, and the five d orbitals of the valence shell of the isolated ion as well

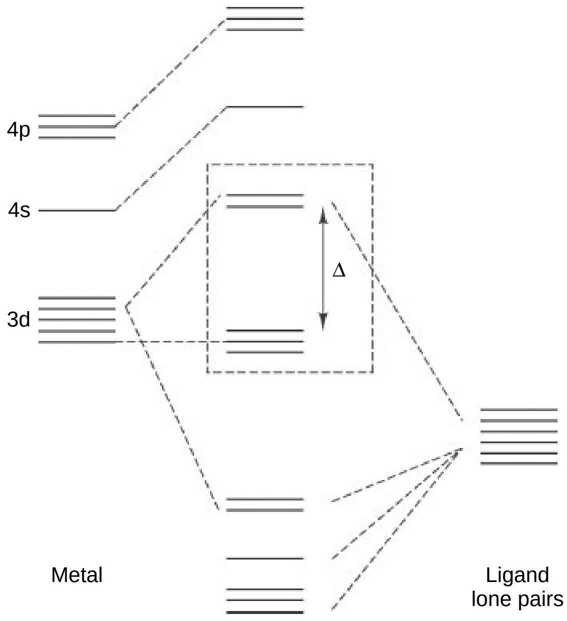

Figure 5 The molecular orbital or ligand field picture of metal–ligand bonding in an ML_6 complex. Compare this picture with Figure 1 to see how the octahedral crystal field splitting pattern (in the box) is still present in the MO model

as the six lone-pair orbitals of a set of pure σ donor ligands in an octahedron around the metal. Six of the metal orbitals, the s, the three p, and the two d_σ, which we will call the dsp_σ set, find symmetry matches in the six ligand orbitals. In combining the six metal orbitals with the six ligand orbitals, we make a bonding set of six (the M–L σ bonds) which are stabilized, and an antibonding set of six (the M–L σ^* levels) which are destabilized when the six L groups approach to bonding distance. The remaining three d orbitals, the d_π set, do not find a match among the ligand orbitals and remain nonbonding. In a d^6 ion we have six electrons from Co^{3+} and 12 electrons from the ligands, giving 18 in all. This means that all the levels up to and including the d_π set are filled, and the M–L σ^* levels remain unfilled. Note that we can identify the familiar CF splitting pattern in the d_π and two of the M–L σ^* levels. The Δ splitting will increase as the strength of the M–L σ bonds increase. The bond strength is the analog of the effective charge in the CF model. In the LF picture, high-field ligands are ones that form strong σ bonds. We can now see that a d_σ orbital is better described in the CF picture as an M–L σ-antibonding orbital, d_{σ^*}.

The L lone pairs start out in free L as pure ligand electrons but become bonding electron pairs shared between L and M when the M–L σ bonds are formed; these are the six lowest orbitals in Figure 5 and are always completely filled (12 electrons). Each M–L σ-bonding MO is formed by the combination of the ligand lone pair, L(σ), with M(d_σ) and has both metal and ligand character, but L(σ) predominates. Any MO will more closely resemble the parent atomic orbital (AO) which lies closest in energy to it, and L(σ) almost always lies below M(d_σ) and therefore closer to the M–L σ-bonding orbitals. This means that electrons which were purely L lone pairs in the free ligand gain some metal character in the complex; in other words the L(σ) lone pairs are partially transferred to the metal. As L becomes more basic, the energy of the L(σ) orbital increases, and the extent of ET will increase.

7 BACK BONDING

Ligands like NH_3 are good σ-donors but are not significant π-acceptors. CO, in contrast, is an example of a good π-acceptor, sometimes also called a π-acid ligand. Such ligands are of very great importance in organometallic chemistry. They tend to be very high-field ligands and form strong M–L bonds. All have empty orbitals of the correct symmetry to overlap with a filled d_π orbital of the metal. In the case of CO, this acceptor orbital is the CO π^*. Figure 6 shows how overlap takes place to form the M–C π-bond. It may seem paradoxical that an antibonding orbital like the π^*(CO) can form a bond, but this orbital is only antibonding with respect to C and O; it can still be bonding with respect to M and C.

We can make the LF diagram of Figure 5 appropriate for the case of $W(CO)_6$ by including the π^* levels of CO (Figure 7). The d_π set of levels still find no match with the six CO(σ) orbitals, which are lone pairs on C. They do interact strongly with the empty CO π^* levels. Since the M(d_π) set are filled in this d^6 complex, the result is that d_π electrons that were metal-centered now spend some of their time on the ligands: this means that the metal has donated some electron density to the ligands. This is called *Back Bonding* and is a key feature of M–L bonds where L is an unsaturated molecule.

As antibonding orbitals, these π^* levels are high in energy, but they are able to stabilize the d_π set as shown in Figure 7. This has two important consequences. First, the LF splitting parameter Δ rises, explaining why π-bonding ligands have such a strong LF. Secondly, back bonding allows electron density on the metal to make its way back to the ligands. This in turn allows low-valent or zerovalent metals to form complexes. Such metals are in a reduced state, and already have a high electron density (they are said to be very electron rich; *see Electron Rich Compound*). They cannot accept

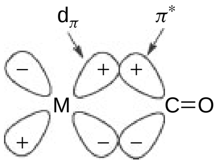

Figure 6 The overlap between a filled metal d_π orbital and an empty CO π^* orbital to give the π component of the M–CO bond. The plus and minus signs refer to the symmetry

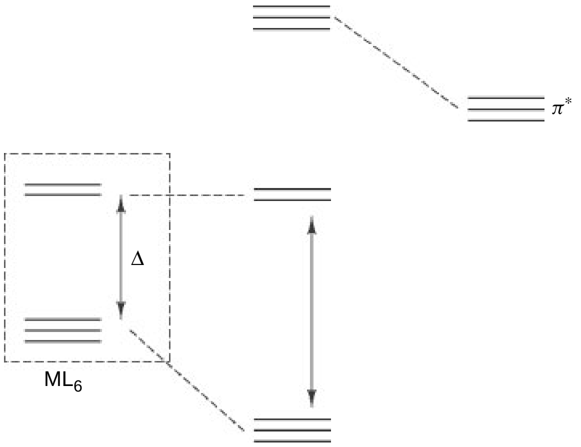

Figure 7 The effect of 'turning on' the π interaction between a π-acceptor ligand and the metal. The unoccupied, and relatively unstable, π* orbitals of the ligand are shown on the right. Their effect is to stabilize the filled d_π orbitals of the complex and so increase Δ

further electrons from pure σ-donors; this is why $W(NH_3)_6$ is not a stable compound. By back bonding, the metal can relieve itself of some of this excess electron density. In $W(CO)_6$, back bonding is so effective that the compound is air stable and relatively unreactive; the CO groups have so stabilized the electrons that they have no tendency to be abstracted by an oxidizing agent. In $W(PMe_3)_6$ by contrast, back bonding is inefficient and the compound is very air sensitive and reactive.

Spectroscopic and theoretical studies show that for CO this π back donation is usually comparable to or greater than the CO-to-metal electron donation that constitutes the σ-bond. One of the most direct arguments is structural. The M=C bond in metal carbonyls is usually substantially shorter than an M–C single bond. This is easiest to test when both types of bond are present in the same complex, such as $CpMo(CO)_3Me$, where M–C is 2.38 Å, and M=CO is 1.99 Å. We have to remember that a putative M–CO single bond would be shorter than 2.38 Å by about 0.07 Å, to allow for the higher s-character (and therefore shorter bond length) of the sp hybrid on CO compared to the sp^3 hybrid of the methyl group. The remaining shortening of 0.32 Å is still substantial.

If CO were bound to the metal by its carbon lone pair, nonbonding with respect to CO, then the ν(CO) frequency in the complex would be very little different from that in free CO. BH_3, which is as pure a σ-acceptor as will bind to CO, shows a slight shift of ν(CO) to higher energy: free CO, 2149 cm^{-1}; H_3B–CO, 2178 cm^{-1}. Metal complexes, in contrast, show ν(CO) coordination shifts of hundreds of wave numbers to lower energy, consistent with the weakening of the C=O bond that would be expected if the π* orbital were being filled by back donation (e.g. $Cr(CO)_6$, $\nu(CO) = 2000\,cm^{-1}$). Not only is there a coordination shift, but the shift is larger in cases where we would expect stronger back donation and vice versa. A net positive charge raises ν(CO), and a net negative charge lowers it (e.g. $V(CO)_6{}^-$, 1860 cm^{-1}; $Mn(CO)_6{}^+$, 2090 cm^{-1}). The effect of replacing three π-acceptor COs by the three pure σ-donor nitrogens of the dien ligand ($H_2NCH_2CH_2NHCH_2CH_2\ NH_2$) is almost as great as changing the net charge by one unit (e.g. $Cr(dien)(CO)_3$, 1880 cm^{-1}). This makes ν(CO) a good indicator of how electron rich a metal is, and it often correlates well with other ways of estimating electron-rich character, such as the ease of removing an electron.[4]

Series of compounds such as $V(CO)_6{}^-$, $Cr(CO)_6$, and $Mn(CO)_6{}^+$ are said to be *Isoelectronic* complexes because they have the same number of electrons distributed in very similar structures. Isoelectronic ligands are CO and NO^+ or CO and CN^-, for example. Strictly speaking, CO and CS are not isoelectronic, but as the difference between O and S lies in the number of core levels (the valence shell being the same), the term isoelectronic is often extended to cover such pairs. A comparison of isoelectronic complexes or ligands can be useful in making analogies and understanding trends.[8]

The dipole moments of a variety of coordination compounds show that the bond dipole moments of the M–L bonds of most σ-donor ligands are about 4 D, with the donor atom positive. In contrast, metal carbonyls show an M–C bond moment which is essentially zero because the M → L back donation compensates for L → M direct donation plus the enhanced polarization of CO on binding. Formation of the M–CO bond weakens the C–O bond relative to free CO because a π* orbital on CO is now partly filled by back donation. This will still lead to a stable complex as long as the energy gained from the M–C bond exceeds the loss in C–O. Bond weakening within L on binding to a metal is a common feature in many M–L systems.

7.1 Frontier Orbitals

The picture sketched above for CO holds with slight modifications for a whole series of π-acceptor (or soft) ligands, such as alkenes, alkynes, arenes, carbenes, carbynes, NO, N_2, and PF_3. Each of these ligands has a filled orbital that acts as a σ -donor and an empty orbital that acts as a π-acceptor. These orbitals are almost always the highest occupied (*HOMO*) and lowest unoccupied molecular orbitals (*LUMO*) of L, respectively. The HOMO of L is a donor to the LUMO of the metal, which is normally d_σ. The LUMO of the ligand accepts back donation from a filled d_π orbital of the metal. The HOMO and LUMO of each fragment are the so-called *Frontier Orbitals,* and it is nearly always the case that these dominate the bonding. The HOMO of each fragment, M and L, is usually closest in energy to the LUMO of the partner fragment than to any other vacant orbital of the partner. Strong bonding is therefore expected if the *HOMO–LUMO Gap* of both partners is small. A small HOMO–LUMO gap usually makes a ligand soft, because it is a good π-acceptor.

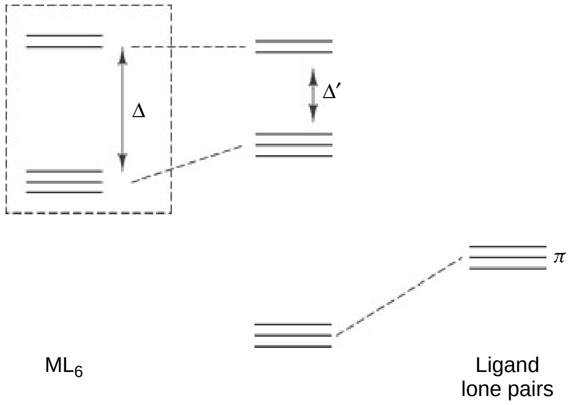

Figure 8 The effect of ‘turning on’ the π interaction between a π-donor ligand and the metal. The occupied, and relatively stable, lone pair (π) orbitals of the ligand are shown on the right. Their effect is to destabilize the filled d_π orbitals of the complex and so decrease Δ

7.2 π-Donor Ligands

Ligands such as OR^-, F^-, and Cl^- are π-donors as a result of the lone pairs that are left after one lone pair has formed the M–L σ-bond. Instead of stabilizing the d_π electrons in a d^6 complex as does a π-acceptor, these electrons are now destabilized by what is effectively a repulsion between two filled orbitals. This lowers Δ, as shown in Figure 8, and leads to a weaker M–L bond than in the π-acceptor case. Lone pairs on electronegative atoms, such as Cl and O, are much more stable than the $M(d_\pi)$ level and this is why they are lower in Figure 8 than are the π^* orbitals in Figure 7. A d^0 complex, in contrast, readily binds π-donor ligands, as in $Ti(OMe)_4$ or $[TiF_6]^{2-}$ because the empty d_π orbitals are now available for π-bonding.

8 ELECTRONEUTRALITY

In 1948, Pauling[9] proposed the powerful *Electroneutrality* principle. This says that the atoms in molecules arrange themselves so that their net charges fall within rather narrow limits, from about $+1$ to -1 overall. In fact, the range for any given element is likely to be narrower than this, and will tend toward a preferred charge, which will differ according to the electronegativity of the element concerned. The nonmetals, such as C, N, or O, will tend to be closer to -1, and the metals such as Li, Mg, and Fe, will tend to be closer to $+1$. This implies that as far as electroneutrality arguments go, an element will bond best to other elements which have complementary preferred charges. In this way, each can satisfy the other. An electropositive element will prefer an electronegative one, for example, NaCl, TiO_2, and elements with an intermediate electronegativity will tend to prefer each other, for example, HgS, Au metal. An isolated Co^{3+} ion is not an electroneutral species, as it has an excessively high positive charge. In its compounds it will therefore seek good electron donors as ligands, such as O^{2-} in Co_2O_3, or NH_3 in the amine complexes. On the other hand, an isolated W^0 atom is too electron rich for its electronegativity, so it will prefer net electron attracting ligands such as CO.

There is a deeper reason why the d orbitals of transition metals are only available for back donation in electron-rich complexes. Co^{III}, for example, has a filled d_π level, but it does not bind CO because it is too low in energy and therefore not sufficiently basic. The reason is that the s, p, and d orbitals respond differently to a change in the charge on the metal. If the metal is in a high oxidation state, like Co^{III}, then there are three electron ‘holes’ in the valence shell compared with the neutral atom. This means that the valence shell of the ion is positive with respect to the situation in the atom. Since d orbitals tend to have their maximum electron density far away from the nucleus (because they have two planar nodes), p orbitals reach their maximum somewhat closer to the nucleus (one planar node), and s orbitals reach their maximum at the nucleus (no planar nodes), the orbitals will be less sensitive to the 3+ change in the net charge that took place on going from Co^0 to Co^{III}, in the order $d > p > s$. In other words, the d orbitals will be much more strongly stabilized than the others on going from the atom to the ion. This is why the atomic electron configuration for the transition metals involves s orbital occupation, for example, Co is d^7s^2, but the configuration of the ion is d^6, not d^4s^2. On the other hand, the more electron rich (i.e. the more reduced, or low oxidation state) the metal complex, the less positive will be the charge on the metal. This will destabilize the d orbitals and make them more available for back donation.

We also alter the orbital energies as we go from left to right in the transition series. For each step to the right, a proton is added to the nucleus. This extra positive charge stabilizes all the orbitals. The earlier metals are the more electropositive because it is easier to remove electrons from their less-stable energy levels. The sensitivity of the orbitals to this change is different from what we saw above. This time the order is $d \sim s > p$ because the s orbital, having a maximum electron density at the nucleus, is more stabilized by the extra protons that we add for each step to the right in the periodic table, than are the p orbitals, that have a planar node at the nucleus. The d orbitals are stabilized because of their lower principal quantum number (e.g. 3d versus 4s and 4p for Fe). The special property of the transition metals is that three types of orbital are in the valence shell, neither too stable nor too unstable to contribute significantly to the bonding. Metal carbonyls, for example, are only stable for groups 4–10 because CO requires d orbital participation to bind effectively. For the same reason, d^0 metals form carbonyls with very low stability, and in the later d^{10} metals, the d orbitals become too stable to back donate and carbonyls are rare.

Finally, as we go down a group from the first-row transition element to the second row, the outer valence electrons become more and more shielded from the nucleus by the extra shell of electrons that has been added. They are therefore more easily lost, and the heavier element tends to be the more basic and more electronegative, and forms more stable high oxidation state complexes. This trend also extends to the third row, but as the f electrons that were added to build up the lanthanide elements are not as effective as s, p, or even d electrons in shielding the valence electrons from the nucleus, there is a smaller change on going from the second- to the third-row element than was the case for moving from the first row to the second. Compare, for example, Cr^{VI} in Na_2CrO_4 and Mn^{VII} in $KMnO_4$, which are unstable and make good oxidizing agents, with their stable analogues in the second and third rows, Na_2MoO_4, Na_2WO_4, and $KReO_4$. Similarly, the increase in covalent radii is larger on going from the first to the second row than it is on going from the second to the third. This is termed the 'Lanthanide Contraction'; it arises because the f-block elements occur between the second and third rows of the transition metals. These add 14 additional protons to the nucleus, while adding 14 f-electrons that poorly shield the additional nuclear charge, thus increasing the stability of the electrons in later elements.

Another aspect of electroneutrality is that ionic compounds with excessively high positive or negative charges are not normally formed. The great majority of compounds are neutral, net charges of ±1 are not uncommon, but net ionic charges of ±2 or greater are increasingly rare unless there is some special reason to expect them, such as the presence of several metals to share the ionic charge.

9 TYPES OF LIGANDS

Most ligands form the M–L σ-bond by using a lone pair, that is, a pair of electrons which are nonbonding in the free ligand. For ligands which have them, lone pairs are often the HOMO and the most basic electrons in the molecule. Classical Werner coordination complexes always involve lone-pair donor ligands. There are two other types of ligand found in organometallic compounds, of which C_2H_4 and H_2 are typical examples.

Ethylene is an example of a molecule that has no lone pairs, yet it binds strongly to low-valent metals. In this case the HOMO is the C=C π-bond and it is these electrons that form the M–L σ-bond, as shown in Figure 9(a). The arrow marked '1' represents the π-bonding electron pair of ethylene being donated to the metal. There is also a back bonding component (marked '2') where the π^* orbital of ethylene plays the role of acceptor. Since the C=C π-bond lies above and below the molecular plane, the metal has to bind out of the plane where the electrons are. This type of binding is sometimes represented as (η^2-C_2H_4), where η represents the hapticity of the ligand, defined as the number of atoms in the ligand bonded to the metal.

Molecular hydrogen has neither a lone pair nor a π-bond, yet it also binds as an intact molecule to metals in such complexes as the Kubas**10** complex, $[W(\eta^2\text{-}H_2)(CO)_3L_2]$. The only available electron pair is the H–H σ-bond and this becomes the donor ('3' in Figure 9(b)). Back donation in this case ('4' in Figure 9(b)) is accepted by the $H_2\sigma^*$ orbital. The metal binds side-on to H_2 to maximize σ- and π-overlap (equation 6). Related *σ-Complexes***11** are formed with C–H, Si–H, B–H, and M–H bonds. In general, the basicity of electron pairs decreases in the order: lone pairs > π-bonding pairs > σ-bonding pairs, because taking part in a bond stabilizes electrons. The usual order of binding ability is therefore: lone-pair donor > π-bond donor > σ-bond donor.

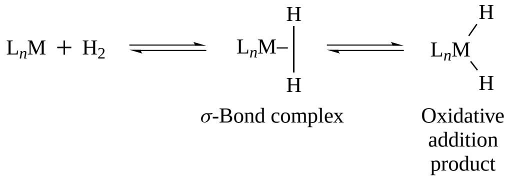

$$L_nM + H_2 \rightleftharpoons L_nM\text{–}\begin{matrix}H\\ |\\ H\end{matrix} \rightleftharpoons L_nM\begin{matrix}H\\ \\ H\end{matrix} \qquad (6)$$

σ-Bond complex

Oxidative addition product

For lone-pair donors the M–L π-bond can have two electrons (2e) and be attractive, as we saw for CO (Figures 6 and 7) or 4e and be repulsive, as is the case for F^- (Figure 8). For the more weakly binding σ- and π-bond donors, the M–L π-bond is nearly always attractive because if it were not, L would not bind strongly enough to form an isolable complex. In the π-bond a $M(d_\pi)$ electron pair is donated to an empty antibonding orbital of the ligand, usually a π^* for π-bond donors and a σ^* for σ-bond donors (Figure 9). In the case of a π-bond donor like ethylene, this back bonding weakens the C=C π-bond but does not break it because C_2H_4 is still held together by strong C–C and C–H σ-bonds which are not involved in M–L bond formation. The C=C distance of 1.32 Å in free ethylene is only lengthened to 1.35–1.5 Å in the complex.

For σ-bond donors such as H_2, forming the M–L σ-bond partially depletes the H–H σ-bond because electrons that were fully engaged in keeping the two H atoms together in free H_2 are now also delocalized over the metal (hence the name 2-electron–3-center bond for this type of interaction). Back bonding into the H–H σ^* causes additional weakening of

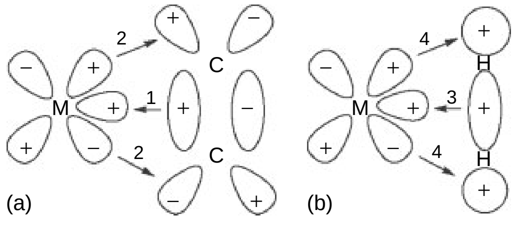

Figure 9 The bonding of a typical π-ligand, ethylene

the H–H σ-bond. Free H_2 has an H–H distance of 0.74 Å, but the H–H distances in H_2 complexes go all the way from 0.82 to 1.5 Å. Eventually the H–H bond breaks and a dihydride is formed (equation 6); this is called the *Oxidative Addition*. Formation of a σ-bond complex can be thought of as an incomplete oxidative addition. Table 2 classifies common ligands by the nature of the M–L σ- and π-bonds.

Some ligands have several types of electron pair available for bonding. For example, aldehydes (**10**) have the C=O π-bond and lone pairs on the oxygen. When they act as π-bond donors, aldehydes bind side-on (**11**) like ethylene; when they act as lone-pair donors, they bind end-on (**12**). Sometimes an equilibrium is found (equation 7) but strongly π-donor metals favor (**11**) and strong σ-acceptors favor (**12**). Alkenes have both a C=C π-bond and C–H σ-bonds. Gladysz[12] has shown how metals can move from one face of a C=C bond to the other via intermediate binding to the C–H bond (equation 8).

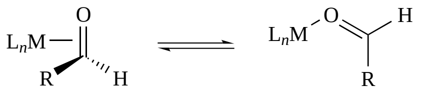

(**11**) (**12**) (7)

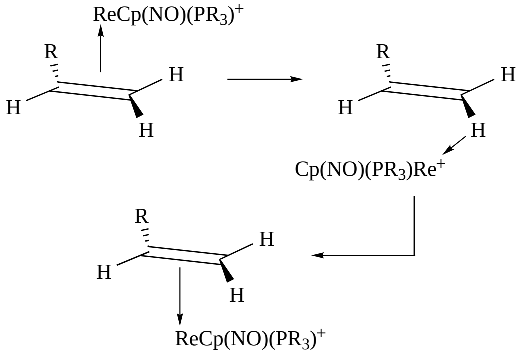

(8)

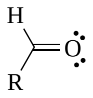

(**10**)

The $\{(NH_3)_5Os^{II}\}^{2+}$ fragment in equation (9) is a strong π-donor because NH_3 is strongly σ-donor but not a π-acceptor ligand, and it prefers to bind to one C=C bond of aniline. Oxidation to Os^{III} causes a sharp fall-off in π-donor power because the extra positive charge stabilizes the d orbitals, and the complex rearranges to the N-bound aniline form.[13] This illustrates how the electronic character of a metal can be altered by choosing the ligand set and oxidation state.

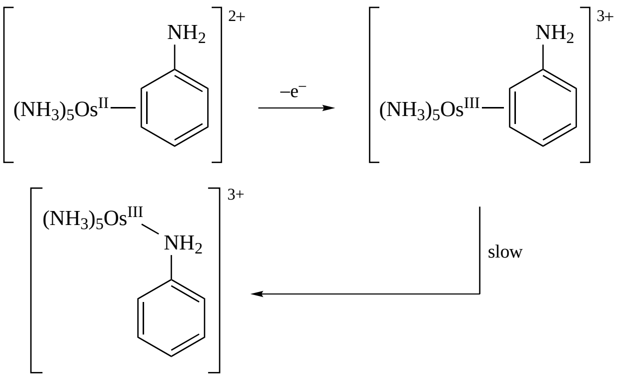

(9)

Table 2 Types of ligands

Type	Examples
Lone-pair donors	NH_3, H_2O, PPh_3, CO, Cl^-, CH_3^-, H^-
π-Bond donors	η^2-C_2H_4, η^6-C_6H_6, η^4-C_4H_6
σ-Bond donors	η^2-H_2, η^2-R_3C–H, η^2-R_3Si–H

10 THE EIGHTEEN ELECTRON RULE AND ITS LIMITATIONS

The 18e rule[14] is a way to help decide whether a given d-block transition metal organometallic complex is likely to be stable. In carbon chemistry, CH_5 with a pentavalent carbon is not stable, but CH_4 with its octet is stable. Carbon therefore follows an 8e rule which corresponds to carbon using its s and three p orbitals to form four filled bonding orbitals and four unfilled antibonding orbitals. On the covalent model we can consider that of the eight bonding electrons, four come from carbon and one each comes from the four H substituents. We can therefore think of each H atom as being a 1e ligand to carbon. The same applies to a transition metal but the target electron count is now 18.

We can also assign an oxidation state to a metal in a complex much as we can assign a formal oxidation state to carbon in an organic molecule by artificially dissecting it into ions. In doing this, each electron pair in any bond is assigned to the most electronegative of the two atoms or groups that constitute the bond. For methane, this dissection gives $C^{4-} + 4H^+$, carbon being the more electronegative element. This makes methane an 8e compound with an oxidation state of C^{-IV}. The net electron count is invariant whether we adopt the covalent (4e{C atom} + 4 × 1e{4H atoms} = 8e), or ionic models (8e{C^{4-}ion} + 4 × 0e{$4H^+$ions} = 8e). In the 18e rule, which applies to many low-valent transition metal complexes, the metal now uses nine orbitals: one s and three p orbitals, as before, but now also five d orbitals. Only a limited number of combinations of metal and ligand will be able to attain the 18e count. Figure 5 shows that 18e will fill the MO diagram of the complex ML_6 up to the d_π level, and leave the d_σ orbitals empty. The resulting configuration is analogous to the closed shell present in the group 18 elements and is therefore called the *noble gas configuration*. Each AO on the metal that remains nonbonding will clearly give rise to one MO in the complex; each AO that interacts with a ligand orbital will give rise to one bonding MO, which will be filled in the complex, and one antibonding MO, that will normally be empty. Our nine metal orbitals will therefore give rise to nine low-lying orbitals in the complex and to fill these we will need 18 electrons.

Table 3 shows how the first-row carbonyls mostly follow the 18e rule. Each metal contributes the same number of electrons as its group number, and each CO contributes 2e for its lone pair. π Back bonding makes no difference to the electron count for the metal. In the free atom it had one AO for each pair of d_π electrons it uses for back bonding; in the complex it still has one filled MO, but now delocalized over metal and ligands.

In cases where we start with an odd number of electrons on the metal, we can never reach an even number, 18, by adding 2e ligands like CO. In such cases, M–M bonds are often formed; for example, $Mn_2(CO)_{10}$ achieves 18e because two 17e $Mn(CO)_5$ units combine. For the 17e fragment $Co(CO)_4$, dimerization also takes place via a metal–metal bond, but a pair of COs also move into bridging positions. It makes no difference to the electron count whether a CO bridges or not, because the bridging CO is a 1e ligand to each metal, so an M–M bond is still required to attain 18e. The even-electron metals are able to achieve 18e without M–M bond formation, and in each case they do so by binding the appropriate number of COs; the odd-electron metals need to form M–M bonds.

In Table 4 we see some of the common ligands and their electron counts on the ionic and covalent models. In the former, we dissect an M–X bond into M^+ and X^- and in the latter model into M• and X• radicals. The symbol L is commonly used to signify a neutral ligand, which can be lone-pair donors (such as CO or NH_3), π-bond donors (such as C_2H_4), or σ-bond donors (such as H_2), which are all 2e ligands on both models. The symbol X refers to ligands such as H, Cl, or Me, which are 1e X ligands on the covalent model and 2e X^- ligands on the ionic model. In the covalent model we regard them as 1e $X^\bullet$ radicals bonding to the neutral metal atom; in the ionic model we regard them as 2e X^- anions bonding to the M^+ cation. Green has developed a useful extension of this nomenclature by which more complicated ligands can be classified. For example, benzene (**13**) can be considered as a combination of three C=C ligands, and therefore as L_3. The allyl group can be considered as a combination of an alkyl and a C=C group. The two canonical forms (**14**) and (**15**) show how we can consider allyl groups in which all three carbons are bound to the metal as LX ligands. This can also be represented in the delocalized form as (**16**). In such a case the hapticity of the ligand, the number of ligand atoms bound to the metal, is 3 and so (**17**), referred to as bis-π-allylnickel in the older literature, is now known as bis-η^3-allylnickel, or $[Ni(\eta^3\text{-}C_3H_5)_2]$. Occasionally the letter h is used instead of η and sometimes η is used without a superscript as a synonym for the older form, π. The electron count of the η^3 form of the allyl group is 3e on the covalent model and 4e on the ionic model, as suggested by the LX label. The advantage of the LX label is that those who follow the covalent model will translate LX as meaning a 3e ligand, and the devotees of the ionic model will translate LX as meaning a 4e ligand.

Table 3 The first-row carbonyls

$V(CO)_6$	17e; $V(CO)_6{}^-$ also stable
$Cr(CO)_6$	
$(CO)_5Mn–Mn(CO)_5$	The M–M bond contributes 1e to each metal; all the CO groups are terminal
$Fe(CO)_5$	
$(CO)_3Co(\mu\text{-}CO)_2Co(CO)_3$	A μ-CO contributes 1e to each metal and there is also an M–M bond
$Ni(CO)_4$	

Table 4 Common ligands and their electron counts

Ligand	Type	Covalent model	Ionic model
Me, Cl, Ph, Cl, η^1-allyl, NO (bent)[a]	X	1e	2e
Lone-pair donors: CO, NH_3	L	2e	2e
π-Bond donors: C_2H_4	L	2e	2e
σ-Bond donors: (H_2)	L	2e	2e
η^3-Allyl, η^3-acetate	LX	3e	4e
NO (linear)[a]	LX	3e	2e
η^4-Butadiene	L_2[b]	4e	4e
η^5-Cp	L_2X	5e	6e
η^6-Benzene	L_3	6e	6e

[a] Linear NO is considered as NO^+ on the ionic model. [b] The alternative LX_2 structure sometimes adopted gives the same electron count.

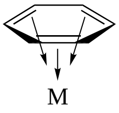

(**13**)

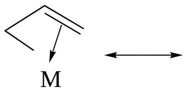

(**14**)

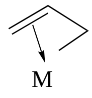

(**15**)

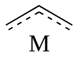

(**16**)

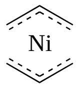

(**17**)

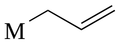

(**18**)

There is also a second way (**18**) that the allyl group can bind: this is the η^1-allyl or σ-allyl form. In this bonding mode the allyl behaves as an X-type ligand, like a methyl group, and is therefore a 1e ligand on the covalent model and a 2e ligand on the ionic model. Some examples of electron counting, such as (**21–23**), are shown in Figure 10. Note the dissection into atoms and radicals in the covalent model and into ions in the ionic model.

Bridging ligands are very common in coordination chemistry and their presence is symbolized by the prefix μ. Bridging ligands are usually counted as follows. First, we will look at bridging halide. This carries a lone pair, which is donated to the second metal in forming the bridge. An L_nMCl

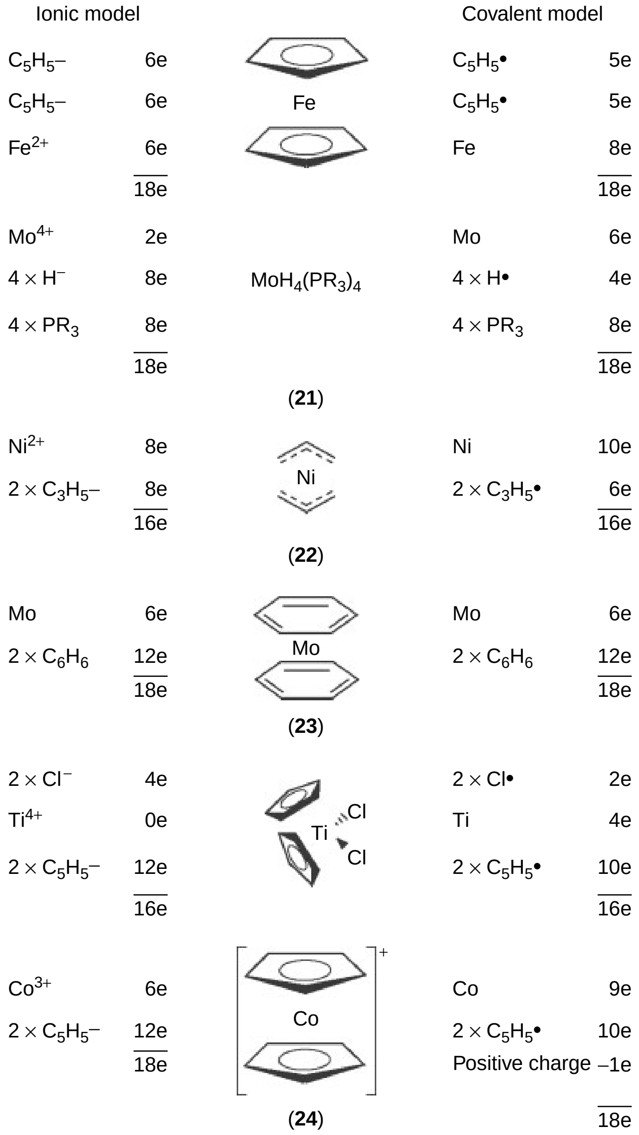

Figure 10 Electron counting on the covalent and ionic models. For (**24**), note the adjustment to account for the positive ionic charge on the complex as a whole; for anions, the net charge is added to the total

group is effectively acting as a ligand to the second metal. If $ML_n = M'L_n$ then the two bonds to Cl are indistinguishable by resonance between (**19**) and (**20**) (equation 10).

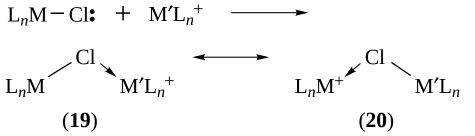

(**19**) (**20**) (10)

As shown in (**25**) and (**26**), M–X signifies a normal covalent bond but L → M is used for the coordinate bond, as an indication that both electrons are regarded as originating from the ligand L. For complex ions we have to adjust for the net ionic charge in making the electron count. For example, $CoCp_2^+$ (**24** in Figure 10) is counted on the covalent model as $9 + 10 - 1 = 18$e. Electron counting can be summarized by equation (11), which shows the electron count for a generalized complex $[MX_aL_b]^{c+}$, where N is the group number of the metal (and therefore the number of electrons in the neutral M atom):

$$\text{electron count} = N + a + 2b - c \tag{11}$$

$M \leftarrow L$ (**25**) $M{-}X$ (**26**)

10.1 Limitations of the Eighteen Electron Rule

There are many cases in which the electron count for a stable complex is not 18 (e.g. $MeTiCl_3$, 8e; Me_2NbCl_3, 10e; WMe_6, 12e; $Pt(PCy_3)_2$, 14e; $[M(H_2O)_6]^{2+}$ (M = V, 15e; Cr, 16e; Mn, 17e; Fe, 18e); $CoCp_2$, 19e; $NiCp_2$, 20e). The rule works best for hydrides and carbonyls, because these are sterically small, high-field ligands. Being small, as many will generally bind as are required to achieve 18e. As high-field ligands, Δ for the complex will be large. This will mean that the d_{σ^*} orbitals, which would be filled if the metal had more than 18e, are high in energy and therefore poor acceptors. On the other hand, the d_π orbitals, which would have to give up electrons if the molecule had less than 18e, are low in energy thanks to π-bonding by CO (or, in the case of H, thanks to the very strong σ-bond and the absence of repulsive π-interactions with any lone pairs). The d_π level is therefore a good acceptor and, to be stable, a complex must have this level filled (otherwise the electrophilic metal will gain electrons by binding more CO, or the solvent or some functional group in the ligands until the 18e configuration is attained). M–M bonded compounds also tend to obey the rule.

Conversely, the rule works least well for high-valent metals with weak-field ligands. In the hexaaqua ions $M(H_2O)_6{}^{2+}$ (M = V, Cr, Mn, Fe, Co, Ni), the structure is the same whatever the electron count of the metal and so must be dictated by the fact that six H_2O molecules fit well around a metal ion. H_2O has two lone pairs, one of which it uses to form a σ-bond. This leaves one remaining on the ligand, which acts as a π-donor to the metal and so lowers Δ; H_2O is therefore a weak-field ligand. If Δ is small, then the tendency to adopt the 18e configuration is also small because it is easy to add electrons to the low-lying d_{σ^*}, or to remove them from the high-lying d_π.

An important class of complexes follow a 16e, rather than an 18e, rule, because one of the nine orbitals is very high-lying and is usually empty. This can happen for the d^8 metals of groups 8–11 (Table 5). Group 8 shows the least, and group 11 the highest, tendency to become 16e. When these metals are 16e, they normally adopt the square-planar geometry, which makes the $d_{x^2-y^2}$ orbital very high in energy. To go to an 18e species the metal has to rehybridize to

Table 5 The d^9 metals which can adopt a 16e configuration

Group	8^a	9^b	10	11
	Fe^0	Co^I	Ni^{II}	Cu^{IIIc}
	Ru^0	Rh^I	Pd^{II}	–
	Os^0	Ir^I	Pt^{II}	Au^{III}

[a]These metals prefer 18e to 16e. [b]The 16e configuration is more often seen, but 18e complexes are common. [c]A rare oxidation state.

give a trigonal bipyramidal geometry, so as to direct the empty orbital toward the incoming fifth ligand and lower its energy. Some examples of 16e complexes of this sort are $RhClL_3$, $IrCl(CO)L_2$, $PdCl_2L_2$, $[PtCl_4]^{2-}$, and $[AuMe_4]^-$ ($L = t$-phosphine).

The smaller metal clusters, such as $Os_3(CO)_{12}$, often obey the 18e rule for each metal, but for clusters of six metals or more there are deviations, for which special cluster counting rules have been devised.**[1c]** The rule is not useful for main group elements (e.g. $ZnMe_2$, 14e; $MeHg(bipy)^+$, 16e; $[I(py)_2]^+$, 20e; $[SbF_6]^-$, 22e; IF_7, 24e). The lanthanides and actinides have seven f orbitals to fill before they even start on the d orbitals, and so they are essentially never able to bind a sufficient number of ligands to raise the electron count to the $s^2p^6d^{10}f^{14}$ or 32e configuration of the appropriate noble gas (e.g. $U(cot)_2$, 22e; Cp_2LuMe, 28e). This means that the stoichiometry of the complex tends to be decided by steric saturation of the space around the metal. Paramagnetic complexes (e.g. $V(CO)_6$, 17e; Cp_2Fe^+, 17e; Cp_2Ni, 20e) do not generally obey the 18e rule. Some of these have reactions in which they attain an 18e configuration, for example, the 19e $CpFe(\eta^6$-arene) is a powerful 1e donor.**[10]**

Electron counting in metal clusters uses Wade's rule (*see Ligand Field Theory*).

11 OXIDATION STATE

The oxidation state of a metal in a complex is simply the charge that the metal would have on the ionic model. In practice, all we have to do for a neutral complex is to count the number of X ligands. For example, Cp_2Fe has two L_2X ligands and so can be represented as MX_2L_4; this means that the oxidation state (OS) is 2+, so Cp_2Fe is said to be Fe^{II}. For a complex ion we need also to take account of the net charge, as shown for $[MX_aL_b]^{c+}$ in equation (11). For example, Cp_2Fe^+ is Fe^{III} and $[W(CO)_5]^{2-}$ is W^{-II}. Once we have the oxidation state, we can immediately obtain the corresponding d^n configuration. This is simply the number of d electrons that would be present in the free metal ion which corresponds to the oxidation state we have assigned. For Cp_2Fe^+ the OS is Fe^{III}, which corresponds to the Fe^{3+} ion. The iron atom, being in group 8, has 8e, and so the ion has $8 - 3 = 5$e. Cp_2Fe^+ is therefore said to be a d^5 complex. Equations (12) and (13) give the value of n in a general form. The significance of the d^n configuration is that it tells us how to fill up the CF diagrams we saw in Section 4. For example, the odd number for Cp_2Fe^+ implies paramagnetism because in a mononuclear complex we cannot pair five electrons, whatever the d orbital splitting.

$$\mathrm{OS} = c + a \tag{12}$$

$$n = N - (c + a) = N - c - a \tag{13}$$

11.1 Ambiguous Oxidation States

There are many situations in which the formal oxidation state is ambiguous and cannot be specified. Any organometallic fragment that has several resonance forms that contribute to a comparable extent to the real structure can be affected. For example, this is the case for the resonance forms (**27**) and (**28**) in butadiene complexes. One structure is L_2 (or π_2), the other LX_2 (or $\pi\sigma_2$). The binding of butadiene as (**27**) leaves the oxidation state of the metal unchanged, but as (**28**) it becomes more positive by two units. On the covalent model, each gives exactly the same electron count: 4e. On the ionic model, the count changes by 2e (**27**, 4e; **28**, 6e) but this is compensated by a 2e 'oxidation' of the metal. In the case of $W(butadiene)_3$, we can attribute any even oxidation state between W^0 and W^{VI} to the molecule by counting one or more of the ligands as LX_2, rather than L_2. To avoid misunderstandings it is therefore necessary to specify the resonance form to which the formal oxidation state applies. For neutral ligands like butadiene the neutral L_2 form is generally used because this is the stable form of the ligand in the free state. Yet crystal structural studies show that the ligand can in reality more closely resemble (**28**) rather than (**27**). Clearly, we can place no reliance on the formal oxidation state to tell us about the real charge on the metal in $W(butadiene)_3$. In spite of its ambiguities, the oxidation state convention is almost universally used in classifying organometallic complexes.

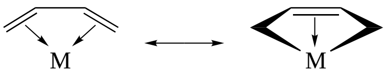

(**27**) (**28**)

One very useful generalization is that the oxidation state of a complex can never be higher than the group number of the transition metal involved. Ti can have no higher oxidation state than Ti^{IV}, for example. This is because Ti has only four valence electrons with which to form bonds and $TiMe_6$ cannot exist.

12 COORDINATION NUMBER

The coordination number (CN) of a complex is easily defined in cases in which the ligands are all monodentate;

it is simply the number of ligands present (e.g. $[PtCl_4]^{2-}$, CN = 4; $W(CO)_6$, CN = 6). A useful generalization is that the coordination number cannot exceed nine for the transition metals. This is because the metal only has nine valence orbitals, and each ligand will need its own orbital. In most cases the CN will be less than nine, and some of the nine orbitals will either be lone pairs on the metal or engaged in back bonding.

$$\text{Coordination number: } \mathrm{CN} = a + b \leq 9 \tag{14}$$

$$\text{Electron count:} N + a + 2b - c = 18 \tag{15}$$

$$\text{Oxidation state:} \quad \mathrm{OS} = a + c \leq N \tag{16}$$

Each coordination number has one or more coordination geometries associated with it. The most common are: CN = 4, tetrahedral and square planar; CN = 5, trigonal bipyramidal and square pyramidal; CN = 6, octahedral. The article (*see* ***Coordination Numbers & Geometries***) should be consulted for other examples. In order to reach the maximum coordination number for d-block metals of nine, we need relatively small ligands, for example $[ReH_9]^{2-}$. Coordination numbers lower than four tend to be found with bulky ligands, which cannot bind in greater number without prohibitive steric interference between the ligands, for example $Pt(PCy_3)_2$.

Unfortunately, the definition of coordination number is less clear-cut for organometallic species, such as Cp_2Fe. Is this molecule two-coordinate (there are two ligands), or six-coordinate (there are six electron pairs involved in metal–ligand bonding), or ten-coordinate (the 10 C atoms are all within bonding distance of the metal)? Most often it is the second definition that is used, which is equivalent to adding up the number of L's and X's from all the ligands.

Equations (14–17) summarize the different counting rules as applied to our generalized d-block transition metal complex $[MX_aL_b]^{c+}$, where N is the Group number, and n is the d^n configuration.

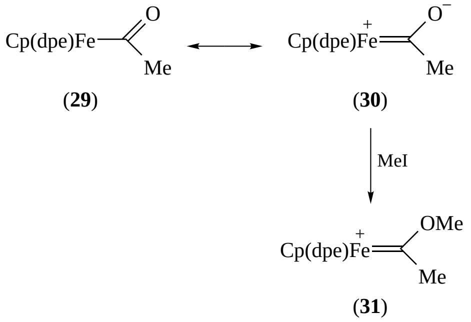

(17)

(**29**) (**30**)

(18)

(**31**)

13 EFFECTS OF COMPLEXATION

Much of the interest and importance of coordination chemistry comes from the fact that the chemical character of many ligands is profoundly modified on binding to the metal. For the typical range of metal fragments L_nM, there is a smooth gradation of properties from strongly σ-acceptor to strongly π-basic. A typical unsaturated ligand Q will be depleted of charge and made more electrophilic by a σ-acceptor L_nM fragment, and be made to accept electrons and therefore become more nucleophilic for a π-basic L_nM fragment. As an example, water is made more acidic by 4–6 pK units on binding to a divalent metal ion. As another example, free benzene is very resistant to attack by nucleophiles, but reacts readily with electrophiles. In the complex $(C_6H_6)Cr(CO)_3$, in contrast, the $Cr(CO)_3$ fragment is a good acceptor, by virtue of its three CO ligands, and so depletes the electron density on the aromatic ring. This makes it susceptible to nucleophilic attack, but resistant to electrophilic attack. A factor that increases the electrophilic character of the ligands is a net positive charge on the complex, e.g. $[Ru(\eta^6\text{-}C_6H_6)_2]^{2+}$. On the other hand, both Cp groups and phosphines are strong donors, and so the acetyl group in (**29**) in equation (18) is very largely in the carbene form shown in (**30**). It is subject to electrophilic attack to give (**31**).

There is a third important situation that we need to consider. If the metal fragment is somewhere in the middle of the range of electronic properties mentioned above, and is both a σ-acceptor and a π-donor, then it might be thought that the unsaturated ligand would differ little in its chemical character from the situation in the free state. In fact, the ligand can still be strongly activated by polarization (*see Polarizability*). This is because the σ-donation from the ligand to the metal usually depletes the electron density of one atom or set of atoms in the ligand, but π-back donation from the metal raises the electron density on a different set of atoms. For example, in the case of molecular nitrogen N_2, σ-donation to the metal comes from a lone pair on the nitrogen directly bonded to the metal. The back bonding from the metal goes into a π^* orbital which is delocalized over both nitrogens. This means that the nitrogen directly bound to the metal tends to become positively charged, and the terminal nitrogen negatively charged on binding (see (**32**)).

$$\mathrm{M}\text{—}\mathrm{N}^{\delta+}{=}\mathrm{N}^{\delta-}$$

(**32**)

This polarization activates the coordinated N_2 toward chemical reactions, such as protonation at the terminal nitrogen and nucleophilic attack at the vicinal nitrogen; the free ligand is, of course, notably unreactive. If a ligand is normally reactive toward, say, nucleophiles, we can deactivate it by binding to a nucleophilic metal. The metal can then be thought of as acting as a protecting group. A ligand that is inert toward nucleophilic attack can be activated by binding to an electrophilic metal.

13.1 Free ≠ Bound

The bound form of a given ligand is usually very different in properties compared to the same ligand in the free state. A knowledge of the behavior of carbenes, dienes, and so on, can be misleading in trying to understand the chemistry of their complexes. For example, one of the most notable features of diene chemistry is their reaction with dienophiles in the Diels–Alder reaction. Dienes coordinated in the η^4-fashion do not give this reaction. In a sense, we might consider that the complex is already a Diels–Alder adduct, with the metal as the dienophile.

Not only are the properties of ligands altered by binding, so are the properties of the metal ions. For example, Co^{III} is very strongly oxidizing in a simple compound such as the acetate. We know from Werner's work that most of this oxidizing power can be quenched by binding ammonia to the Co^{III} ion. The $Co(NH_3)_6{}^{3+}$ ion lacks the severe electron deficiency of the acetate as a result of the presence of six strong σ-donor ligands. Molybdenum atoms are strongly reducing, yet $Mo(CO)_6$ is an air-stable compound with only modest reducing properties.

Finally, it is important to remember that donor and acceptor are relative terms. If we take a complex L_nM–H, in which the hydride ligand bears no strong positive or negative charge, then we can consider the complex as arising from $L_nM^+ + H^-$, $L_nM\bullet + H\bullet$, or $L_nM^- + H^+$. We would have to regard H^- as a strong donor to L_nM^+, H^+ as a strong acceptor from L_nM^-, and H• as being neither with respect to $L_nM\bullet$. Normally the ionic model is assumed and the first type of dissection is implied.

14 EFFECTS OF CHANGING METAL

Changing the metal has an important effect on the properties of the resulting complexes. So great are the differences that it is not unusual for a single research group to confine itself to one part of the periodic table. As we move from left to right, the electronegativity of the elements increases substantially. This means that the orbitals in which the electrons are located start out relatively high in energy and fall steadily as we go to the right. Table 6 shows the Pauling electronegativities of the transition elements. The early transition metals are electropositive and so readily lose all their valence electrons. These elements are therefore often found in the highest permissible oxidation state, for example, d^0 Zr^{IV} and Ta^V. Lower oxidation states, such as d^2 Zr^{II} and Ta^{III}, are very easily oxidized, because the two d electrons are in an orbital of relatively high energy, and therefore easily lost. These systems can be very air sensitive. Not only are they easily lost to an oxidizing agent, they also have a strong tendency to be lost to the π^* orbitals of an unsaturated ligand in back donation. This makes d^2 early metal ions very π-basic and able to bind π-ligands strongly with the effects we saw earlier. Ligands like CO, C_6H_6, and C_2H_4, which require back bonding for stability, will tend to bind only weakly, if at all, to d^0 metals.

Table 6 The Pauling electronegativities of the transition elements[a]

Sc	Ti	V	Cr	Mn	Fe	Co	Ni	Cu
1.3	1.5	1.6	1.6	1.6	1.8	1.9	1.9	1.9
Y	Zr	Nb	Mo	Tc	Ru	Rh	Pd	Ag
1.2	1.3	1.6	2.1	1.9	2.2	2.3	2.2	1.9
La	Hf	Ta	W	Re	Os	Ir	Pt	Au
1.1	1.3	1.5	2.3	1.9	2.2	2.2	2.3	2.5

[a] Lanthanides and actinides: 1.1–1.3. The electronegativities of important ligand atoms are: H, 2.2; C, 2.5; N, 3.0; O, 3.4; F, 4; Si, 1.9; P, 2.2; S, 2.6; Cl, 3.1; Br, 2.9; I, 2.6. Effective electronegativities of all elements are altered by their substituents; for example, the electronegativities estimated for an alkyl C, a vinyl C, and a propynyl C are 2.5, 2.75, and 3.3, respectively.

Late metals, in contrast, are relatively electronegative, so they tend to retain their valence electrons. The low oxidation states, such as d^8 Pd^{II}, tend to be stable, and the higher ones, such as d^6 Pd^{IV}, often find ways to return to Pd^{II}, that is, are oxidizing. Back donation is not so marked as with the early metals and so any unsaturated ligand attached to the weak π-donor Pd^{II} accumulates a positive charge. This makes the ligand subject to attack by nucleophiles, Nu^-, and is the basis for important applications in organic synthesis.

A net anionic charge on a complex, for example, $[Mo(CO)_5]^{2-}$, or the presence of donor ligands, for example, PR_3 or Cp, tends to enhance the π-basicity of the metal. Conversely, a net positive charge or the presence of π-acceptor ligands, such as NO or CO, will tend to diminish the π-basicity of the metal. The size of the effects produced can be estimated from the ν(CO) frequency changes in a series of CO complexes as shown in Table 7. The effect of net charge is surprisingly large.

First-row metals have lower M–L bond strengths and CF splittings compared with their second- and third-row analogues. They are more likely to undergo 1e redox changes rather than the 2e changes often associated with the second and third rows. Finally, the first-row metals do not attain high oxidation states so easily as the second and especially the third row. Mn^V, Mn^{VI}, and Mn^{VII} (e.g. $MnO_4{}^-$) are rare and usually highly oxidizing; Re^V and Re^{VII} are not unusual and the complexes are not strongly oxidizing.

15 OTHER PROPERTIES OF COORDINATION COMPOUNDS

Other aspects of coordination and organometallic chemistry, such as ET and catalysis, are dealt with under these headings.

Table 7 Effects of changing metal, net charge, and ligands on the π-basicity of a metal, as measured by the ν(CO) values in the IR spectrum

Changing metal					
$V(CO)_6$	$Cr(CO)_6$	$Mn_2(CO)_{10}$	$Fe(CO)_5$	$Co_2(CO)_8$	$Ni(CO)_4$
1976	2000	2013(av)[a]	2023(av)[a]	2044(av)[b]	2057
Changing net ionic charge					
$[Ti(CO)_6]^{2-}$	$[V(CO)_6]^{-}$	$Cr(CO)_6$	$[Mn(CO)_6]^{+}$		
1747[c]	1860[d]	2000	2090		
Replacing π-acceptor CO groups by non-π-acceptor amines					
$[Mn(CO)_6]^{+}$	$[(MeNH_2)Mn(CO)_5]^{+}$	$[(en)Mn(CO)_4]^{+}$	$[(dien)Mn(CO)_3]^{+}$		
2090	2043(av)	2000(av)	1960		

[a] Several bands are seen; average ν(CO) reported. [b] Of isomer without bridging CO groups. [c] This value is extremely low, well into the bridging CO region. [d] The IR bands of this species may be lowered by coordination of the countercation to the CO oxygen.

16 RELATED ARTICLES

Coordination Chemistry: History; Coordination Numbers & Geometries; Ligand Field Theory & Spectra.

17 REFERENCES

1. (a) J. A. McCleverty and T. J. Meyer eds, 'Comprehensive Coordination Chemistry', From biology to nanotechnology, Pergamon, Oxford, 2003, Vol. 2; (b) C. E. Constable, 'Metals and Ligand Reactivity: An Introduction to the Organic Chemistry of Metal Complexes', VCH, Weinheim, New York, 1996; (c) R. H. Crabtree, 'Organometallic Chemistry of the Transition Metals', 4th edn., Wiley, New York, 2005; (d) G. B. Kauffman, 'Inorganic Coordination Compounds', Wiley, New York, 1981.
2. A. M. Sargeson, *Pure Appl. Chem.*, 1984, **56**, 1603.
3. (a) S. Ahrland, J. Chatt, and N. R. Davies, *Q. Rev. Chem. Soc.*, 1958, **12**, 265; (b) R. G. Pearson, *J. Chem. Educ.*, 1987, **64**, 561.
4. V. Guillaume, V. Mahias, A. Mari, and C. Lapinte, *Organometallics*, 2000, **19**, 1422; R. Poli, *Acc. Chem. Res.*, 1997, **30**, 494.
5. (a) H. Taube, *Adv. Chem. Ser.*, 1997, **253**, 1, refs. cited; (b) P. F. Barbara and T. J. Meyer, and M. A. Ratner, *J. Phys. Chem.*, 1996, **100**, 13148.
6. T. W. Swaddle, *Inorg. Chem.*, 1990, **29**, 5017.
7. P. Suppan, *Top. Curr. Chem.*, 1992, **163**, 95.
8. A. J. Ashe, H. Yang, X. D. Fang, and J. W. Kampf, *Organometallics*, 2002, **21**, 4578; S. Y. Liu, M. M. C. Lo, and G. C. Fu, *Angew. Chem. Int. Ed. Engl.*, **41**, 2002, 174.
9. L. Pauling, *J. Chem. Soc.*, 1948, 1461.
10. G. J. Kubas, R. R. Ryan, and D. A. Wrobleski, *J. Am. Chem. Soc.*, 1986, **108**, 1339; G. J. Kubas, 'Metal-dihydrogen and σ-bond Complexes', Kluwer Academic, New York, 2001.
11. R. H. Crabtree, *Angew. Chem., Int. Ed. Engl.*, 1993, **32**, 789.
12. T. S. Peng and J. A. Gladysz, *J. Am. Chem. Soc.*, 1992, **114**, 4174.
13. H. Taube, *Pure Appl. Chem.*, 1991, **63**, 651.
14. C. Tolman, *Chem. Soc. Rev.*, 1972, **1**, 337.

Copper: Hemocyanin/ Tyrosinase Models

Jason Shearer & Kenneth D. Karlin
Johns Hopkins University, Baltimore, MD, USA

Based in part on the article Copper: Hemocyanin/Tyrosinase Models by Nobumasa Kitajima which appeared in the Encyclopedia of Inorganic Chemistry, First Edition.

1 Introduction 1
2 Structure of Cu_2^{II}–O_2 Adducts 2
3 Formation of Cu_2^{II}–$O_2{}^{2-}$ Adducts 5
4 Oxidation Reactions 6
5 Future Directions/Summary 8
6 Related Articles 8
7 References 8

Glossary

bis-μ-oxo complex: a metal complex containing at least two metals and two oxo (O^{2-}) ligands where the oxo ligands bridge between the metal centers

μ-η^2:η^2-peroxo: a side-on bridging (μ) peroxo ligand in which both oxygen atoms are symmetrically ligated to the same metal center

μ-peroxo complex: polynuclear metal complexes in which at least two metal ions are bridged with a peroxide ligand ($O_2{}^{2-}$)

Abbreviations

Co = Catechol oxidase; Hc = Hemocyanin; Tyr = Tyrosinase; MePy2 = *N*,*N*-bis(2-pyridylethyl)methylamine; TACN = 1,3,5-triazocyclononane; TMPA = Tris[(2-pyridyl) methyl]amine; XYL-O = α,α'-bis[*N*,*N*-bis(2-pyridylethyl) amino]-*m*-xylene-2-olate; XYL = α,α'-bis[*N*,*N*-bis(2-pyridylethyl)amino]-*m*-xylene; XYL-R = *Meta* substituted α,α'-bis[*N*,*N*-bis(2-pyridylethyl)amino]-*m*-xylene; N3 = *N*,*N*,*N'*,*N'*-Tetrakis-(2-pyridin-2-yl-ethyl)-propane-1,2-diamine; N4 = *N*,*N*,*N'*,*N'*-Tetrakis-(2-pyridin-2-yl-ethyl)-butane-1,2-diamine; N5 = *N*,*N*,*N'*,*N'*-Tetrakis-(2-pyridin-2-yl-ethyl)-pentane-1,2-diamine; $HB(3,5\text{-}Pr_2pz)_3$ = Hydrotris(3, 5-diisopropyl-1-pyrazolyl) borate; XAS = X-ray absorption spectroscopy; EXAFS = Extended X-ray absorption fine structure; rR = resonance Raman.

1 INTRODUCTION

Copper is a ubiquitous transition metal that is involved in a number of metabolic pathways including those involving dioxygen processing.[1–5] One of the best characterized and most extensively studied biological motifs for copper is the coupled dinuclear copper center, which is found in enzymes such as hemocyanin (Hc),[1,2] tyrosinase (Tyr)[1,2] and catechol oxidase (Co) (*see* ***Copper Proteins with Dinuclear Active Sites***).[6] Hc is a dioxygen carrier protein in mollusks and anthropods, whereas Tyr and Co perform oxidation reactions. Tyr *ortho*-hydroxylates phenols to give *ortho*-catechols, while Co performs the oxidation of *ortho*-catechols to *ortho*-quinones. X-ray crystal structures have been solved for both Hc and Co in various states of oxidation and activity. In Hc's fully reduced form (redHc), the active site is characterized by an unbridged Cu_2^I moiety with a $Cu^I\cdots Cu^I$ separation of $\sim$4.5 Å.[7] Each copper(I) cation is coordinated by three imidazole ligands from histidine (His) protein residues, forming a pseudo-trigonal coordination geometry about copper (Figure 1). Upon exposure to dioxygen (forming oxyHc), the two Cu^I centers bind and reduce O_2, producing a μ-η^2:η^2-peroxo (bridging side-on) ligand, that is, a $Cu_2^{II}(O_2{}^{2-})$ core. The $Cu\cdots Cu$ distance shortens to $\sim$3.5 Å (Figure 1). In Hc, the reversible binding and reduction of dioxygen to peroxide is responsible for its blood O_2-transporting activity. Although no crystal structure has been elucidated for Tyr and no oxyCo X-ray structure is available,[6] the nearly identical spectroscopic properties of oxyHc, oxyTyr, and oxyCo suggest similar active-site structures.[1,2] This implies that the $Cu_2^{II}(O_2{}^{2-})$ core is not only a competent oxidant (in Co), but an oxygenating agent (monooxygenase) in Tyr.

The oxy form of these O_2-binding dinuclear copper centers is characterized by a number of distinct spectroscopic signatures. The electronic absorption spectrum contains two intense charge transfer bands in the visible region, at $\sim$350 nm ($\varepsilon \sim 20\,000\ M^{-1}\ cm^{-1}$) and $\sim$570 nm ($\varepsilon \sim 1000\ M^{-1}\ cm^{-1}$).[8] Strong magnetic coupling ($-2J > 600\ cm^{-1}$) between the two Cu^{II} centers is also observed, which results in a diamagnetic behavior, and hence no EPR signal. It should be pointed out that the inactive met forms of these enzymes (produced by F^-, $N_3{}^-$, and SCN^- coordination to the oxidized copper ions) also display similar characteristics. These met forms were previously the best spectroscopically characterized forms, and represented a major thrust in early synthetic modeling endeavors.[8,9] Since most of the recent modeling work in this field has been aimed at mimicking the oxy form of the enzymes, this review will focus exclusively on this aspect. In addition to these two (above) physical properties, resonance Raman (rR) studies on oxyHc have shown that the $Cu_2^{II}(O_2{}^{2-})$ core displays an exceptionally low O–O stretching frequency of $\sim$750 cm^{-1}, compared with a $\upsilon_{O\text{–}O}$ of 800–900 cm^{-1} normally displayed by transition metal peroxo complexes. In addition, rR studies have also elucidated a symmetrical binding mode for the peroxo moiety (based

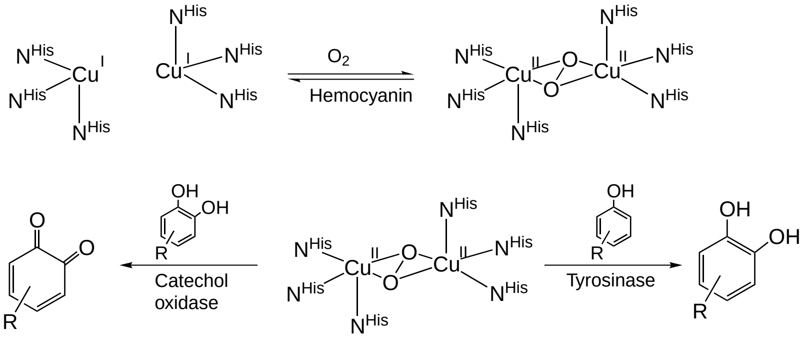

Figure 1 Schematic representation of the dioxygen binding dinuclear copper enzymes Hemocyanin (Hc), Tyrosinase (Tyr), and Catechol oxidase (Co)

on using mixed ^{18}O–^{16}O gas experiments to generate the peroxo form) many years before the structure of oxyHc was crystallographically determined.

The remainder of this review will concentrate on synthetic models for the dioxygen bound forms of these enzymes. Synthetic modeling endeavors have been of fundamental importance in elucidating structural information concerning hemocyanin peroxo coordination (prior to the elucidation of the structure for oxyHc), the mechanism of the hydroxylation of tyrosine by Tyr, and in gaining insight into Co activity. Many detailed reviews have been written on specific aspects of this field.[5,10–17] We will be giving a general overview of this field, highlighting major advances made in the past, as well as directions this field may be taking in the future. There are far too many important contributions in this field to be adequately covered in the space provided, therefore only prototypical systems are highlighted. To add coherence, we will be focusing mainly on copper–dioxygen adduct structure, formation, and reactivity.

2 STRUCTURE OF Cu_2^{II}–O_2 ADDUCTS

Early endeavors in the late 1970s into modeling Hc's ability to bind dioxygen and form a μ-peroxo-Cu_2^{II} species met with little success.[18] Although the formation of such species was indirectly suggested, the extreme thermal sensitivity of these complexes made isolation difficult. Thus definitive evidence (e.g. vibrational, electronic absorption, and structural data) was lacking. It was only with advances in low–temperature spectroscopic techniques (e.g. better laser sources for rR studies, CCD detectors for rR and crystallographic studies, and improved optics for X-ray absorption studies), coupled with a better understanding of how to handle these generally thermally unstable has allowed for an explosion in the number of Cu-peroxo species has been reported. Generation of $Cu_2(O_2)$ species is usually performed at low temperatures (< -40 °C) in weakly coordinating solvents such as THF and CH_2Cl_2 by exposing solutions of discrete Cu^I complexes to dioxygen.[10]

An early successful example of generation and subsequent spectroscopic study of a dioxygen adduct of a dicopper(I) complex was reported in 1984 by Karlin and coworkers, where dioxygen was shown to bind quasireversibly to the dinuclear Cu^I complex $[Cu_2^I(XYL\text{-}O)]^+$ (Figure 2a).[19–21] This complex, which contains a bridging phenoxo ligand, formed $[Cu_2^{II}(XYL\text{-}O)(O_2{}^{2-})]^+$ (**1**) upon exposure to dioxygen. It was thought that this complex would be a good mimic for Hc based on the initial formulation of the active site of oxyHc from early rR and XAS work, which suggested the protein contained a bridging oxygen ligand (such as a tyrosine, see Figure 2(b)) and may bind dioxygen in either a μ-1,1 or μ-1,2 fashion. EXAFS studies demonstrated a Cu···Cu separation

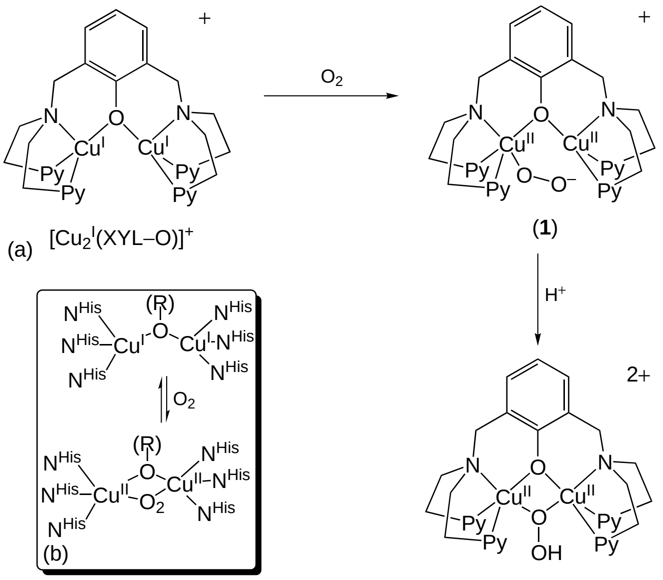

Figure 2 (a) Formation of peroxo species $[Cu_2^{II}(XYL\text{-}O)(O_2{}^{2-})]^+$ (**1**) and its protonation to a hydroperoxo complex, by O_2 reaction with $[Cu_2^I(XYL\text{-}O)]^+$. (b) An earlier description for O_2-binding in Hc

of ~3.3 Å for (**1**),[22] which was consistent with what had been reported for oxyHc. However, the $\nu_{\text{O–O}}$ stretching frequency ($803\,\text{cm}^{-1}$) and an inconsistent electronic absorption spectrum ($\lambda = 505$ nm ($\varepsilon = 6300\,\text{M}^{-1}\,\text{cm}^{-1}$), 610 nm ($2400\,\text{M}^{-1}\,\text{cm}^{-1}$)) suggested the binding mode of $\text{O}_2{}^{2-}$ was not similar to that found in the enzyme. Mixed isotope rR spectroscopic studies[23] demonstrated that the peroxo ligand was in an unsymmetric coordination environment, possibly binding end-on to one copper ion (Figure 2a), and hence inconsistent with data reported for the enzymes. Upon exposure of (**1**) to a proton source, a bridging hydroperoxo species is formed (Figure 2).[24] EXAFS measurements[24] demonstrate a short Cu···Cu separation of 3.0 Å, which is consistent with a μ-1,1 binding mode of OOH, but is significantly shorter than that reported for the oxy forms of the enzymes. In addition to shedding light on possible active-site structures of oxyHc, study and characterization of these complexes also demonstrated the feasibility of preparing and manipulating dinuclear copper–dioxygen adducts.

The first crystallographically characterized peroxo-containing model for oxyHc was originally reported by Karlin, and resulted from dioxygen binding to the tetradentate Cu^{I} center of $[\text{Cu}^{\text{I}}(\text{TMPA})]^{+}$, forming the purple $[\{\text{Cu}^{\text{II}}(\text{TMPA})\}_2(\text{O}_2)]^{2+}$ complex (**2**, Figure 3); the crystal structure of (**2**) was obtained in 1988, and featured a *trans*-μ-1,2 peroxo ligand coordination.[25,26] Although the Cu^{II} centers were strongly magnetically coupled ($-2J > 600\,\text{cm}^{-1}$), the electronic absorption spectrum ($\lambda = 440$ (2000), 525 (11500), and 590 nm (7600)) and relatively high-energy $\nu_{\text{O–O}}$ stretching frequency ($834\,\text{cm}^{-1}$) were significantly different from the corresponding properties of oxyHc, strongly suggesting the peroxo binding mode was not the same.

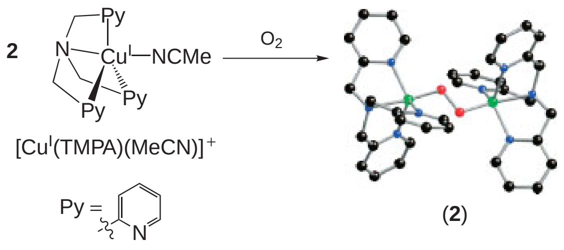

Figure 3 Crystal structure of $[\{\text{Cu}^{\text{II}}(\text{TMPA})\}_2(\text{O}_2{}^{2-})]^{2+}$ (**2**) resulting from the reaction of $[\text{Cu}^{\text{I}}(\text{TMPA})(\text{MeCN})]^{+}$ and dioxygen at low temperature

This dioxygen binding mode (end–on) seems to be the preferred one when Cu is placed in a tetradentate ligand environment; however, recent studies have suggested this is not a steadfast rule.[10,27] Although apparently not a biologically relevant binding mode for $\text{O}_2{}^{2-}$ at dinuclear copper centers, complex (**2**) (and derivatives thereof)[16] have been exceptionally important in determining the fundamental dioxygen chemistry of Cu^{I} complexes. A good number of *trans*-μ-1,2 peroxo complexes have since been generated.[10,28]

Aliphatically tethered dinuclear Cu^{I} complexes, where the metal center was bound to tri- and tetradentate ligands, were prepared by Karlin and coworkers (tridentates; Figure 4a), and demonstrated reversible O_2 binding at low temperatures.[16,29] Tolman and coworkers more recently reported on the preparation of Cu^{I} complexes contained in tethered TACN ligands (Figure 4b).[17] In the case of the dinuclear complexes with tridentate ligand donors for each copper ion ($[\text{Cu}^{\text{I}}_2(\text{Nn})]^{2+}$ (**3**)), it was suggested by low-temperature solution EXAFS that the peroxo ligand bridged the metal centers in a side–on fashion.[22,29] The spectroscopic properties were consistent with those of oxyHc, with an intense charge transfer band in the UV/Vis region at ~350 nm ($\varepsilon \sim 20\,000\,\text{M}^{-1}\,\text{cm}^{-1}$), and rR spectroscopy showed a range for $\nu_{\text{O–O}}$ between $760–730\,\text{cm}^{-1}$.[30] The shorter tether was found to impose a structural constraint about the $\text{Cu}^{\text{II}}_2\text{O}_2{}^{2-}$ core and according to EXAFS data, causes a distortion or 'butterflying', so that the peroxo ligand moves out of the Cu_2O_2 plane (based on Cu···Cu separations, Figure 4c).[29,30] This butterflying causes

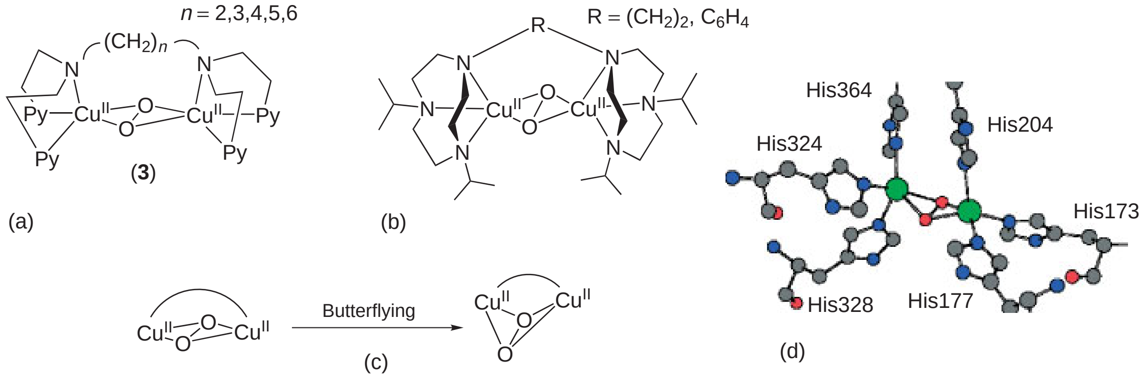

Figure 4 Aliphatically tethered Cu^{II}_2-peroxo complexes (a) and (b). Figure 4(c) depicts the distortion, or butterflying, of the $\text{Cu}_2\text{O}_2{}^{2-}$ core facilitated by the ligand constraints the aliphatic tether imposes on the copper complex. Figure 4(d) depicts the structure of oxyHc from *Limulus polyphemus*, which shows some degree of butterflying of the $\text{Cu}_2\text{O}_2{}^{2-}$ core

a strengthening of the O–O bond (i.e. higher O–O stretching frequencies indicating less O_2 bond activation), and has interesting consequences concerning dioxygen binding and reactivity of the peroxo core, namely that the Cu_2O_2 core is a poorer oxidant compared to the planar arrangement.[30] Available crystallographic data for oxyHc from *Limulus polyphemus* and *Octopus doflenini* suggest there is some butterflying of the O_2^{2-} ligand from the central core (see Figure 4(d)).[31] In dinuclear complexes possessing untethered tridentate Cu moieties, ligand constraints are less severe, allowing for planar μ-η^2:η^2-peroxo coordination, low ν_{O-O} values, and resulting exogenous substrate oxidation reactions (see further discussion below).

A major advance in Hc modeling chemistry was made in 1989 from the group of the late N. Kitajima when he reported on the preparation of a Cu^I complex where copper is contained in a tridentate trispyrazolyl-borate ligand environment.[32,33] Similar to the chemistry of (**1**), (**2**), and (**3**), dioxygen binds quasireversibly to the Cu^I center at low temperatures, forming a $Cu^{II}_2(O_2^{2-})$ species. The spectroscopic properties of the dioxygen adduct $[\{Cu^{II}[HB(3,5\text{-}i\text{-}Pr_2pz)_3]\}_2(O_2^{2-})]$ (**4**, Figure 5) very closely matched that of oxyHc ($\nu_{O-O} = 741\ cm^{-1}$; $\lambda_{max} = 349$ (21000) and 551 nm (790); $-2J > 800\ cm^{-1}$). Crystallographic studies on (**4**) demonstrated a side–on binding mode for the peroxo–ligand, with a Cu···Cu separation of 3.56 Å, nearly identical to the Cu···Cu distance in the enzyme as determined by EXAFS at that time, and an O–O bond distance of 1.41 Å. All of this evidence strongly suggested a similar coordination geometry for the $Cu^{II}_2(O_2^{2-})$ core in the enzyme. This was confirmed when the 2.4 Å resolution crystal structure of oxyHc was solved (see above). The work demonstrates the potential power of bioinorganic modeling, as coordination chemistry studies (employing a non-biologically relevant ligand) yielded a new compound that allowed the (correct) prediction of an important biological structure.

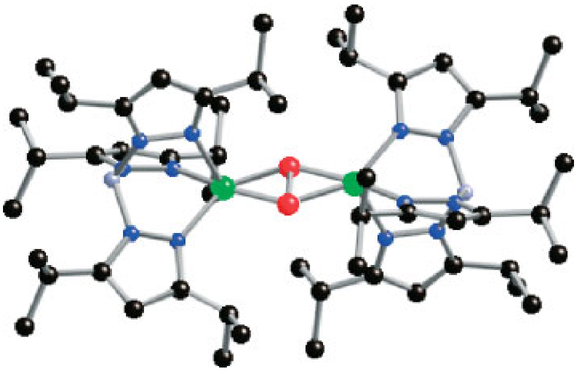

(**4**)

Figure 5 Crystal structure of the Kitajima/Fujisawa side-on peroxo complex $[\{Cu^{II}[HB(3,5\text{-}i\text{-}Pr_2pz)_3]\}_2(O_2^{2-})]$ (**4**)

Independent work by Tolman and Stack in the mid- and late-1990s, using cyclic and linear bi/tridentate amine-based ligands, demonstrated that the side–on peroxo ligand in $Cu^{II}_2(O_2^{2-})$ complexes can be in equilibrium with its Cu^{III}_2-bis-μ-oxo isomer (Figure 6).[10,17] This has also been supported by work performed by Karlin and Itoh using bi/tridentate pyridyl amine ligands (Figure 6).[34,35] It has been found that copper complex attributes such as ligand electronics, changes in counterion, ligand steric bulk, along with a solvent change, can influence the equilibrium position and interconversion of the Cu^{II}_2 (peroxo) and Cu^{III}_2(bis-μ-oxo) forms. The breadth of work concerning this field is far too great to be done justice here, so we will only briefly touch upon this subject, and point to relevant reviews.[10–13,17] Upon interconversion from the side-on peroxo to the bis-μ-oxo form, a change in structure is noted, with a breaking of the

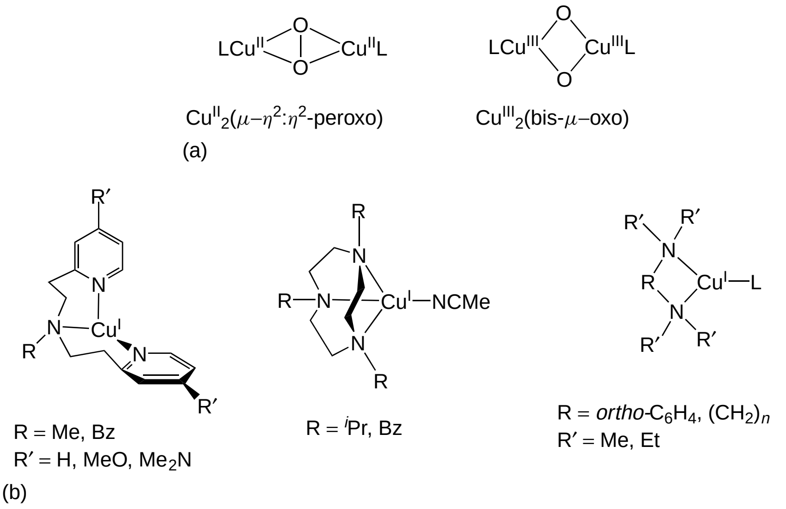

Figure 6 Depiction of the changes involved in core interconversion between Cu^{II}_2(μ-η^2-η^2-peroxo) and Cu^{III}_2(bis-μ-oxo) isomers (a), and representations of Cu^I complexes capable of forming Cu^{III}_2(bis-μ-oxo) upon exposure to dioxygen (b)

O–O bond followed by elongation of the O· · ·O distance to ∼2.3 Å, and a contraction of the Cu· · ·Cu distance to between 2.7–2.9 Å. The electronic absorption spectrum is also altered with the disappearance of the charge transfer peak at ∼350 nm and the appearance of two intense peaks at 300 and ∼400 nm. Breaking of the O–O bond is also evident by rR studies where the characteristic $\nu_{\text{O–O}}$ frequency at ∼750 cm^{-1} is lost, and a Cu–O vibration at ∼600 cm^{-1} appears. Variations do occur. Core interconversion may also have important consequences concerning subsequent substrate reactivity (see Section 4). It has yet to be determined if the Cu_2^{III}(bis-μ-oxo) core is a biologically relevant O_2-binding mode.

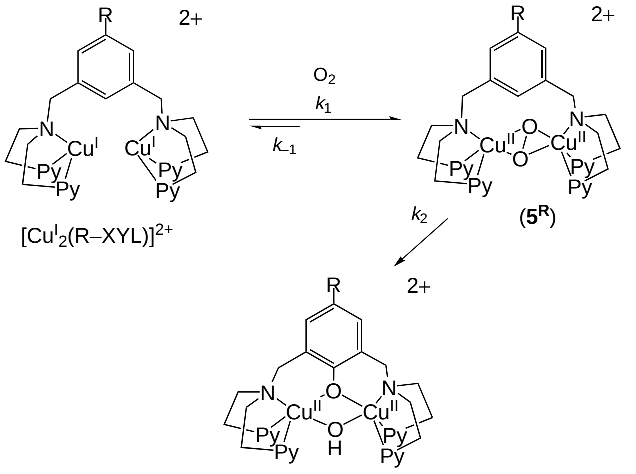

Figure 7 Formation of side-on peroxo intermediate $[\text{Cu}_2^{\text{II}}(\text{R-XYL})(\text{O}_2{}^{2-})]^{2+}$ (**5$^{\text{R}}$**) from O_2-reaction with $[\text{Cu}_2^{\text{I}}(\text{R-XYL})]^{2+}$, followed by oxygenation of the arene bridge

3 FORMATION OF Cu_2^{II}–$\text{O}_2{}^{2-}$ ADDUCTS

As stated previously, early work into the direct observation of unstable Cu_2^{II}–$\text{O}_2{}^{2-}$ species met with little success. These species were often postulated based on both chemical logic, as well as limited kinetic information, but direct evidence pointing to the presence of such complexes was lacking. This situation changed in the mid-1980s in large part due to the utilization of low-temperature (−40 to −105 °C) stopped-flow spectroscopy where direct observation of spectroscopically identifiable copper–dioxygen intermediates was possible.[5,16] This has allowed for the direct observation of a number of elementary steps in the formation and subsequent reactions of these complexes.

One of the first model systems to undergo detailed low-temperature kinetic studies was the $[\text{Cu}_2^{\text{I}}(\text{R-XYL})]^{2+}$ system of Karlin (Figure 7).[16,36] $[\text{Cu}_2^{\text{I}}(\text{R-XYL})]^{2+}$ (where R = NO$_2$, H, F, and ^{t}Bu) will bind O$_2$ at low temperatures, forming $[\text{Cu}_2^{\text{II}}(\text{R-XYL})(\text{O}_2)]^{2+}$ (**5$^{\text{R}}$**), which contains a bridging side-on peroxo ligand. Complexes (**5$^{\text{R}}$**) will then further react with itself performing an oxygenation reaction, similar to Tyr (*vide infra*). Stopped-flow measurements of (**5$^{\text{R}}$**) formation at 183 K demonstrate quasireversible binding of dioxygen with k_{on} values ranging between 470 M^{-1} s^{-1} (R = ^{t}Bu) to 7.2 M^{-1} s^{-1} (R = F) and k_{off} values varying from 1.5×10^{-6} s^{-1} (R = F) to 2.1×10^{-5} s^{-1} (R = NO$_2$).[5,16] Dioxygen binding is characterized by low activation enthalpies which are partially offset by unfavorable entropy terms ($\Delta S^{\ddagger} \sim -40$ cal mol^{-1} K^{-1}). At higher temperatures, the unfavorable ΔS° precludes observation of Cu$^{\text{I}}$ dioxygen adduct formation. This appears to be a general finding for copper–dioxygen chemistry; $\text{Cu}_2^{\text{II}}(\text{O}_2{}^{2-})$ formation is driven by and favorable enthalpies, but at high temperature unfavorable entropies dominate.[16]

Another hallmark of $\text{Cu}_2^{\text{II}}(\mu\text{-}\eta^2{:}\eta^2$ peroxo) formation appears to be the fact that a Cu$^{\text{II}}$-superoxo complex is initially formed, which then reacts with another Cu$^{\text{I}}$ complex forming the corresponding Cu_2^{II}-peroxo species.[16,29] This was always suspected; however, direct observation of a superoxo intermediate during the O$_2$-binding process was lacking. For example, the oxidation of (**3**) (Figure 4) and subsequent formation of $[\text{Cu}_2^{\text{II}}(\text{Nn})(\text{O}_2)]^{2+}$ follows an overall quasireversible second order process.[33] However, the enthalpies of activation are very low and in some cases negative, indicative of a pre-equilibrium step involving the formation of Cu$^{\text{II}}$–O$_2{}^{-}$· · ·Cu$^{\text{I}}$ species followed by a 'closing' step that forms the Cu_2^{II}-peroxo products (Figure 8a). Cu$^{\text{II}}$-superoxo formation can in fact be directly observed using $[\text{Cu}^{\text{I}}(\text{TMPA})(\text{L})]^{+}$ (L = RCN or CO; Figure 8b). In a coordinating solvent (such as EtCN), formation of a $[\text{Cu}^{\text{II}}(\text{TMPA})(\text{O}_2{}^{-})]^{+}$ can be observed by low-temperature stopped-flow measurements,[16,37] while a flash photolysis study involving $[\text{Cu}^{\text{I}}(\text{tmpa})(\text{CO})]^{+}$ in a weakly coordinating solvent demonstrated superoxo formation following photodissociation of the CO ligand.[38] These results are supported by the work of Kitajima/Fujisawa[39,40] and Tolman,[41,42] who have isolated and characterized Cu$^{\text{II}}$-superoxo complexes bound in a side-on fashion. In other ligand systems, particularly tetradentate, there is also ample kinetic and spectroscopic evidence for Cu$^{\text{II}}$-superoxo complexes which are intermediates on the way towards dinuclear peroxo-dicopper(II) formation.[16,28,37,43,44]

The kinetics of Cu$_2$(O$_2$) adduct formation was also followed utilizing Tolman's $[\text{Cu}^{\text{I}}(i\text{-Pr}_3\text{TACN})]^{+}$ (**6$^{i\text{Pr}}$**) systems.[11,17,45] Oxygenation of (**6$^{i\text{Pr}}$**) in acetone affords a Cu$_2$-dioxygen adduct, which has been identified as being a mixture of peroxo/bis-μ-oxo complexes (Figure 9). The formation of the Cu_2^{II}-peroxo complex occurs in parallel with Cu_2^{III}-bis-μ-oxo formation, implying a rapid equilibrium involving peroxo/oxo core interconversion. It is unknown if one forms prior to the other, but see further discussions in recent reviews.[10,11]

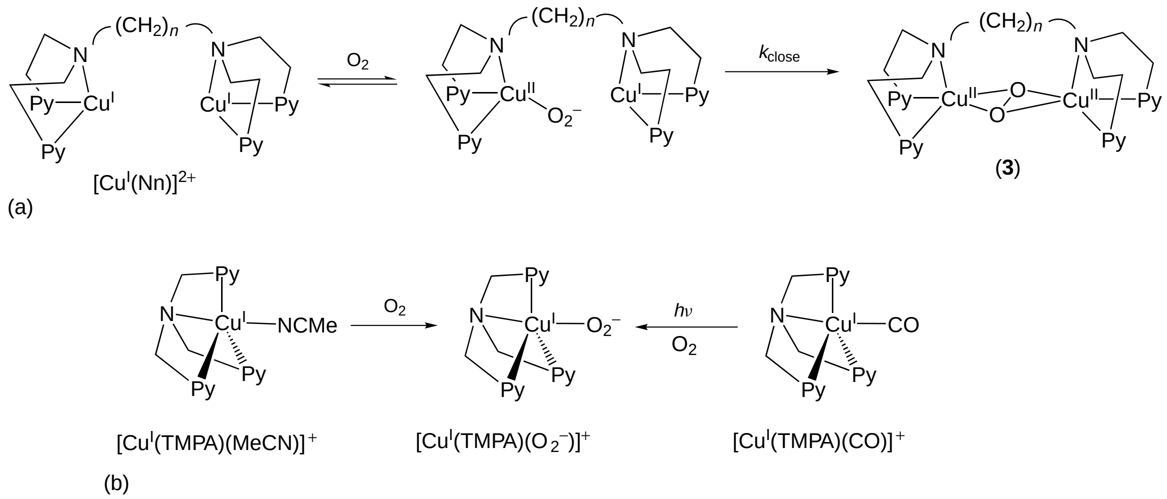

Figure 8 Formation of an initial superoxo species has been long suspected in the formation of Cu_2^{II}-peroxo species. For example the formation of (**3**) from $[Cu_2^{I}(Nn)]^{2+}$ proceeds with a very low (and sometimes negative) activation enthalpy, suggestive of the formation of an initial species $Cu^{II}–O_2^{-}\cdots Cu^{I}$ (a). Direct observation of such an intermediate came from dioxygen reactivity studies with $[Cu^I(TMPA)]^+$ complexes (b)

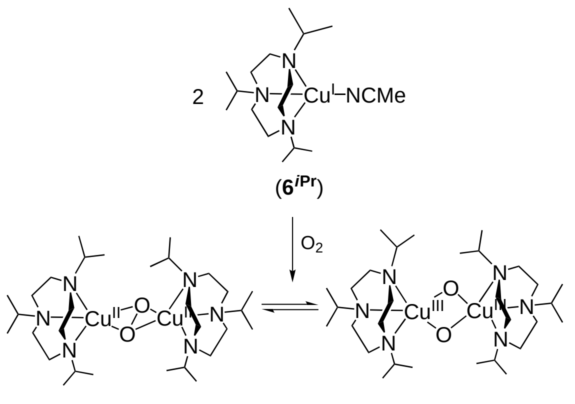

Figure 9 Oxygenation of $[Cu^I(i\text{-}Pr_3TACN)(MeCN)]^+$ (**6^{iPr}**) in acetone leads to both the corresponding peroxo and oxo-species, apparently in concert, suggesting a rapid equilibrium exists between bis-μ-oxo and μ-η^2:η^2-peroxo complexes

4 OXIDATION REACTIONS

Much of the current research performed in the field of modeling these biological dinuclear copper centers now focuses on the generation of complexes that can perform substrate oxidation reactions.[11,12] Of key interest is not only determining the identity of the reactive species in oxyCo and oxyTyr (i.e. $Cu_2^{II}(O_2{}^{2-})$ vs. $Cu_2^{III}(O^{2-})_2$), but also the detailed mechanism(s) of substrate oxidations. The best studied of the substrate oxidations is the hydroxylation of arenes by $Cu_2^{II}(O_2{}^{2-})$ species. In 1984, Karlin and coworker described the ligand hydroxylation reaction of $[Cu_2^{II}(R\text{-}XYL)(O_2{}^{2-})]^{2+}$ (**5^R**, Figure 7).[46] By varying the R-group *para* to the site of oxygenation, reaction rates (k_2) could be modulated.[5,16,36] It was determined that as R became more electrondonating, the rates of the oxygenation step increased. This is strong evidence in favor of an electrophilic attack of the peroxo moiety on the arene ring. In other words, hydroxylations appear to occur *via* an electrophilic aromatic substitution from $Cu_2^{II}(\mu\text{-}\eta^2{:}\eta^2$ peroxo) complexes. This is supported by the recent work of Itoh.[11,47,48]

In 2001, Itoh and coworkers reexplored the mechanism of *ortho*-phenol hydroxylations using $[\{Cu^{II}(L^{PY2})\}_2(O_2)]^{2+}$ (**7**, Figure 10).[47] This complex contains a deutero-benzylamine moiety, and can undergo ligand auto-oxidation, forming benzaldehyde, through a proton-coupled electron transfer (PCET) reaction with the μ-η^2:η^2 peroxo ligand. Perdeuteration of the methylene linker affords a relatively kinetically stable complex, which allows for the monitoring of exogenous substrate oxidations. When (**7**) is exposed to cold (−95 °C) acetone solutions of the lithium salts of *para*-substituted phenolates, clean conversion to the corresponding *o*-catechols is observed. Deuterium kinetic isotope effects (KIEs) for these hydroxylation reactions of ~1.0 are observed, which is consistent with an electrophilic attack of the peroxo ligand on the arene ring. An electrophilic aromatic substitution is also consistent with the observation that lithium *p*-methoxy-phenolate reacts substantially faster with (**7**) than lithium *p*-chloro-phenolate. Furthermore, a plot of observed reaction rates vs. *p*-chloro-phenolate concentration demonstrated that substrate coordination to the metal center is occurring prior to hydroxylation, and thus may be an important feature in these phenolate *o*-hydroxylation reactions.

Recently the oxidative coupling of *para*-substituted phenols was investigated by Itoh using both (**7**) and $[\{Cu^{III}(L^{PY1})(O^{2-})_2\}_2]^{2+}$ (**8**, Figure 10).[49] This allowed for the direct comparison of the reactivity of a Cu_2^{II} μ-η^2:η^2 peroxo

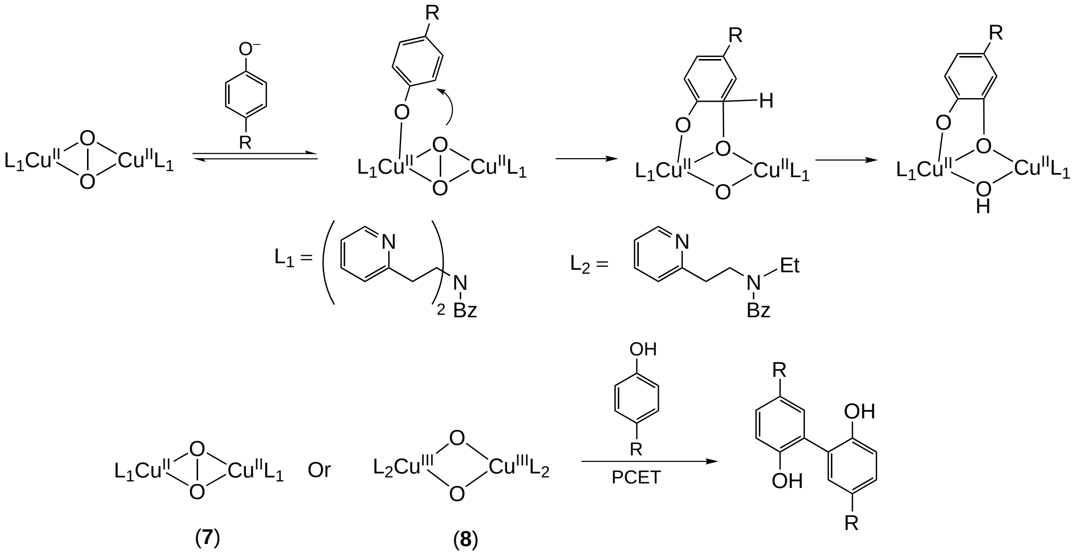
L1CuII O O CuIIL1
O−
R
R
O
L1CuII O O CuIIL1
R
O
H
L1CuII O O CuIIL1
R
O
L1CuII O O CuIIL1
H
L1 =
N
N
2 Bz
L2 =
N
N
Et
Bz
L1CuII O O CuIIL1
Or
L2CuIII O O CuIIIL2
OH
R
PCET
R
OH
OH
R

(7) (8)

Figure 10 Reactions of phenolates with μ-η^2:η^2-peroxo complex (**7**) yields an *ortho*-hydroxylation reaction reminiscent of Tyr, while reactions of phenols by both (**7**) and bis-μ-oxo complex (**8**) results in *ortho*-phenol coupled dimers through an apparent PCET pathway

complex and a structurally related Cu_2^{III} μ-bis-oxo complex. Determination of differential reactivity between peroxo and bis-μ-oxo complexes is currently where considerable effort in this field is being directed. In the case of phenol (vs. phenolate) oxidations, pre-coordination of substrate to the copper center is less likely (owing to lack of the anionic phenolate). Furthermore, the phenol contains only a moderately strong O–H bond ($\sim$90 kcal mol^{-1}), which opens up the possibility of an O–H bond homolysis through a hydrogen atom transfer (HAT) pathway (Figure 10). However, it was suggested that both (**7**) and (**8**) will couple phenols through a PCET pathway, as opposed to a HAT pathway (i.e. the electron- and proton transfer steps are kinetically resolvable). This is in contrast to ligand hydroxylation reactions of Tolmans derivatized TACN systems (vide infra).

$[\{Cu^{III}(Bz_3\text{-TACN})\}_2(O^{2-})]^{2+}$ (**9**, Figure 11) is a Cu_2^{III} (bis-μ-oxo) complex, and will undergo auto-oxidation forming benzaldehyde, following oxidative N-dealkylation of the TACN ligand.[50–52] Labeling studies with ^{18}O demonstrate the oxygen source comes from the bis-μ-oxo moiety, and experiments with deuterated ligand lead to large observable KIEs (>24) at −40 °C. This is indicative of a rate-limiting C–H bond homolysis occurring through a HAT pathway. Unlike the phenol oxidative couplings of Itoh's system, the

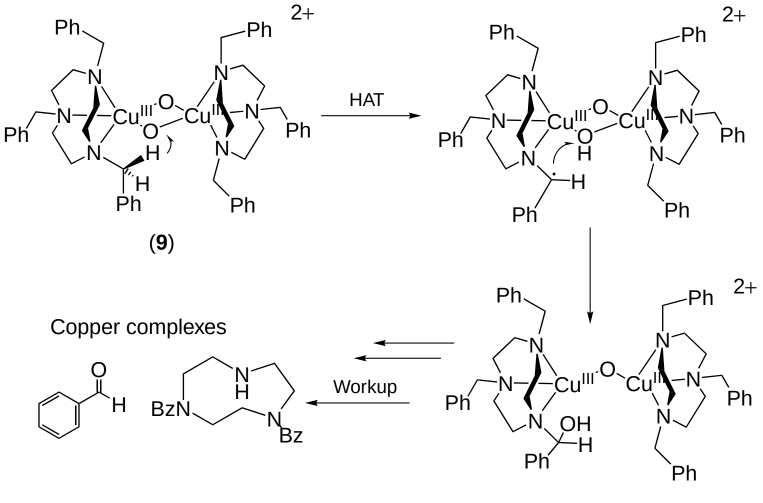
Ph
Ph
2+
Ph
N
N
CuIII
O
O
CuIII
N
Ph
N
N
H
H
Ph
N
Ph
HAT
Ph
Ph
2+
Ph
N
N
CuIII
O
O
CuIII
N
Ph
N
H
H
N
Ph
Ph
Ph
Ph
2+
Ph
N
N
CuIII
O
CuIII
N
Ph
N
OH
H
N
Ph
Ph
Copper complexes
O
H
BzN
N
H
N
Bz
Workup

(9)

Figure 11 Cu_2^{III}(bis-μ-oxo) complex $[\{Cu^{III}(Bz_3\text{-TACN})\}_2\,(O^{2-})_2]^{2+}$ (**9**) will undergo an auto-oxidation resulting in ligand N-dealkylation of a benzyl group, forming benzaldehyde, presumably through a HAT pathway

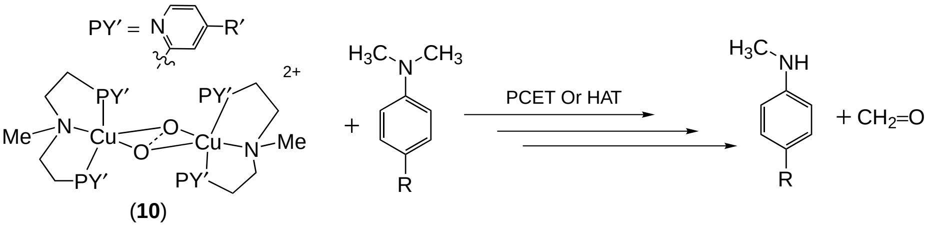

Figure 12 $[\{Cu^{II}(MePY2)^{R'}\}_2(O_2)]^{2+}$ (**10**), which exists as a mixture of both bis-μ-oxo and μ-η^2:η^2-peroxo complexes in solution, will oxidatively N-dealkylate *para*-substituted dimethylanilines through either a PCET or a HAT pathway

TACN ligands of Tolman are not easily oxidizable (due to unfavorable redox potentials), which may make a formal ET event unlikely. Molecular orbital calculations also suggest that a HAT pathway is much more likely than PCET with this system.**[12]** The wavefunction for the oxo acceptor orbital is of the proper energy and symmetry to accept the hydrogen atom from the ligand. If one considers the three-dimensional structure of (**9**), it appears the hydrogen that is being abstracted is in an optimal position to be transferred to the oxo-ligand. All of this strongly supports a HAT pathway for intramolecular ligand oxidation by (**9**).**[11]**

In an attempt to address the PCET versus HAT issue, Shearer, Karlin, and coworkers investigated the mechanism of dimethylaniline oxidations by $[\{Cu(MePy2)^R\}_2(O_2)]^{2+}$ (**10**, Figure 12).**[53]** Here, the complexes are not pure peroxo or bis-μ-oxo complexes, but instead are mixtures. The R'-*para* pyridyl ligand donor substituent produces more of the bis-μ-oxo tautomer as the R' group is made more electron donating (7–30% bis-μ-oxo).**[54]** Based upon comparisons of both intra- vs intermolecular KIEs and KIE profiles of *para*-substituted dimethylaniline oxidations (R-DMA, Figure 12), it was determined that both PCET and HAT reactions occur. For the more easily oxidizable R-DMAs, a PCET reaction is preferred, while for the more difficult to oxidize R-DMAs a HAT pathway is favored. Also, it was observed that the more bis-μ-oxo isomer that is in solution, the more likely it is that a HAT reaction will occur.

5 FUTURE DIRECTIONS/SUMMARY

Since the structures and spectroscopic correlations for both oxy and red forms of Hc, Co, and Tyr are well understood, much of the future synthetic modeling work will focus on the reactivity of Cu_2O_2 species. Tyr activity, *o*-phenol hydroxylation, seems to occur via an electrophilic aromatic substitution, but the broader scope of reaction for side-on μ-η^2:η^2-peroxodicopper(II) complexes should be further explored. Much remains to be accomplished in determining the detailed mechanism of catechol oxidase catalysis (i.e. HAT vs. PCET). The differential reactivity of peroxo versus bis-μ-oxo tautomers is still largely unknown. Although there is as yet no evidence that the Cu_2^{III}(bis-μ-oxo) core is found in nature, it could be present in low concentrations (and thus undetectable), yet still be important from a mechanistic point of view. Also, the structure of particulate methane monooxygenase has yet to be elucidated, and this enzyme may contain the Cu_2^{III}(bis-μ-oxo) moiety or related structure, possibly within a trinuclear copper center.**[55,56]**

6 RELATED ARTICLES

Copper Proteins: Oxidases; Copper Proteins with Dinuclear Active Sites; Cytochrome Oxidase.

7 REFERENCES

1. E. I. Solomon, P. Chen, M. Metz, S.-K. Lee, and A. E. Palmer, *Angew. Chem., Int. Ed. Engl.*, 2001, **40**, 4570.
2. E. I. Solomon, U. M. Sundaram, and T. E. Machonkin, *Chem. Rev.*, 1996, **96**, 2563.
3. J. P. Klinman, *Chem. Rev.*, 1996, **96**, 2541.
4. C. X. Zhang, H.-C. Liang, K. J. Humphreys, and K. D. Karlin, in 'Copper-Dioxygen Complexes and Their Roles in Biomimetic Oxidation Reactions', ed. L. Simandi, Dordrecht, 2003.
5. K. D. Karlin and A. D. Zuberbühler, in 'Formation, Structure and Reactivity of Copper Dioxygen Complexes', ed. J. Reedijk and E. Bouwman, Marcel Dekker New York, 1999.
6. C. Gerdemann, C. Eicken, and B. Krebs, *Acc. Chem. Res.*, 2002, **35**, 183.
7. K. A. Magnus, H. Ton-That, and J. E. Carpenter, *Chem. Rev.*, 1994, **94**, 727.
8. N. Kitajima, *Encyclopedia of Inorganic Chemistry*, 1997, **2**, 822.
9. N. Kitajima, *Adv. Inorg. Chem.*, 1992, **39**, 1.
10. L. M. Mirica, X. Ottenwaelder, and T. D. P. Stack, *Chem. Rev.*, 2004, **104**, 1013.
11. E. A. Lewis and B. Tolman William, *Chem. Rev.*, 2004, **104**, 1047.

12. L. Que Jr and W. B. Tolman, *Angew. Chem., Int. Ed. Engl.*, 2002, **41**, 1114.
13. T. D. P. Stack, *Dalton Trans.*, 2003, 1881.
14. N. Kitajima and Y. Moro-oka, *Chem. Rev.*, 1994, **94**, 737.
15. K. D. Karlin and Z. Tyeklár, 'Bioinorganic Chemistry of Copper', Chapman & Hall, New York, 1993.
16. K. D. Karlin, S. Kaderli, and A. D. Zuberbühler, *Acc. Chem. Res.*, 1997, **30**, 139.
17. W. B. Tolman, *Acc. Chem. Res.*, 1997, **30**, 227.
18. K. D. Karlin and Y. Gultneh, *Prog. Inorg. Chem.*, 1987, **35**, 219.
19. Z. Tyeklár and K. D. Karlin, *Acc. Chem. Res.*, 1989, **22**, 241.
20. K. D. Karlin, R. W. Cruse, Y. Gultneh, J. C. Hayes, and J. Zubieta, *J. Am. Chem. Soc.*, 1984, **106**, 3372.
21. K. D. Karlin, R. W. Cruse, Y. Gultneh, A. Farooq, J. C. Hayes, and J. Zubieta, *J. Am. Chem. Soc.*, 1987, **109**, 2668.
22. N. J. Blackburn, R. W. Strange, A. Farooq, M. S. Haka, and K. D. Karlin, *J. Am. Chem. Soc.*, 1988, **110**, 4263.
23. J. E. Pate, R. W. Cruse, K. D. Karlin, and E. I. Solomon, *J. Am. Chem. Soc.*, 1987, **109**, 2624.
24. K. D. Karlin, P. Ghosh, R. W. Cruse, A. Farooq, Y. Gultneh, R. R. Jacobson, N. J. Blackburn, R. W. Strange, and J. Zubieta, *J. Am. Chem. Soc*, 1988, **110**, 6769.
25. Z. Tyeklár, R. R. Jacobson, N. Wei, N. N. Murthy, J. Zubieta, and K. D. Karlin, *J. Am. Chem. Soc.*, 1993, **115**, 2677.
26. R. R. Jacobson, Z. Tyeklár, K. D. Karlin, S. Liu, and J. Zubieta, *J. Am. Chem. Soc.*, 1988, **110**, 3690.
27. H. Hayashi, S. Fujinami, S. Nagatomo, S. Ogo, M. Suzuki, A. Uehara, Y. Watanabe, and T. Kitagawa, *J. Am. Chem. Soc.*, 2000, **122**, 2124.
28. K. Komiyama, H. Furutachi, S. Nagatomo, A. Hashimoto, H. Hayashi, S. Fujinami, M. Suzuki, and T. Kitagawa, *Bull. Chem. Soc. Jpn.*, 2004, **77**, 59.
29. H.-C. Liang, K. D. Karlin, R. Dyson, S. Kaderli, B. Jung, and A. D. Zuberbühler, *Inorg. Chem.*, 2000, **39**, 5884.
30. E. Pidcock, H. V. Obias, M. Abe, H.-C. Liang, K. D. Karlin, and E. I. Solomon, *J. Am. Chem. Soc.*, 1999, **121**, 1299.
31. K. A. Magnus, B. Hazes, H. Ton-That, C. Bonaventura, J. Bonaventura, and W. G. J. Hol, *Proteins: Struct., Funct., Genet.*, 1994, **19**, 302.
32. N. Kitajima, K. Fujisawa, C. Fujimoto, Y. Moro-oka, S. Hashimoto, T. Kitagawa, K. Toriumi, K. Tasumi, and A. Nakamura, *J. Am. Chem. Soc.*, 1992, **114**, 1277.
33. N. Kitajima, K. Fujisawa, Y. Moro-oka, and K. Toriumi, *J. Am. Chem. Soc.*, 1989, **111**, 8975.
34. C. X. Zhang, H.-C. Liang, E.-i. Kim, J. Shearer, M. E. Helton, E. Kim, S. Kaderli, C. D. Incarvito, A. D. Zuberbühler, A. L. Rheingold, and K. D. Karlin, *J. Am Chem. Soc.*, 2003, **125**, 634.
35. S. Itoh, M. Taki, H. Nakao, P. L. Holland, W. B. Tolman, L. Que Jr, and S. Fukuzumi, *Angew. Chem., Int. Ed. Engl.*, 2000, **39**, 398.
36. K. D. Karlin, M. S. Nasir, B. I. Cohen, R. W. Cruse, S. Kaderli, and A. D. Zuberbühler, *J. Am. Chem. Soc.*, 1994, **116**, 1324.
37. C. X. Zhang, S. Kaderli, M. Costas, E.-i. Kim, Y.-M. Neuhold, K. D. Karlin, and A. D. Zuberbühler, *Inorg. Chem.*, 2003, **42**, 1807.
38. H. C. Fry, D. V. Scaltrito, K. D. Karlin, and G. J. Meyer, *J. Am Chem. Soc.*, 2003, **125**, 11866.
39. K. Fujusawa, M. Tanaka, Y. Moro-oka, and N. Kitajima, *J. Am. Chem. Soc.*, 1994, **116**, 12079.
40. P. Chen, D. E. Root, C. Campochiaro, K. Fujisawa, and E. I. Solomon, *J. Am. Chem. Soc.*, 2003, **125**, 466.
41. D. J. E. Spencer, N. W. Aboelella, A. M. Reynolds, P. L. Holland, and W. B. Tolman, *J. Am Chem. Soc.*, 2002, **124**, 2108.
42. N. W. Aboelella, E. A. Lewis, A. M. Reynolds, W. W. Brennessel, C. J. Cramer, and W. B. Tolman, *J. Am. Chem. Soc.*, 2002, **124**, 10660.
43. B. A. Jazdzewski, A. M. Reynolds, P. L. Holland, V. G. Young, S. Kaderli, A. D. Zuberbuehler, and W. B. Tolman, *J. Biol. Inorg. Chem.*, 2003, **8**, 381.
44. M. Weitzer, S. Schindler, G. Brehm, S. Schneider, E. Hoermann, B. Jung, S. Kaderli, and A. D. Zuberbuehler, *Inorg. Chem.*, 2003, **42**, 1800.
45. J. A. Halfen, S. Mahapatra, E. C. Wilkinson, S. Kaderli, V. G. Young Jr, L. Que Jr, A. D. Zuberbühler, and W. B. Tolman, *Science*, 1996, **271**, 1397.
46. K. D. Karlin, Y. Gultneh, J. C. Hayes, R. W. Cruse, J. W. McKown, J. P. Hutchinson, and J. Zubieta, *J. Am. Chem. Soc.*, 1984, **106**, 2121.
47. S. Itoh, H. Kumei, M. Taki, S. Nagatomo, T. Kitagawa, and S. Fukuzumi, *J. Am. Chem. Soc.*, 2001, **123**, 6708.
48. S.-i. Yamazaki and S. Itoh, *J. Am. Chem. Soc.*, 2003, **125**, 13034.
49. T. Osako, K. Ohkubo, M. Taki, Y. Tachi, S. Fukuzumi, and S. Itoh, *J. Am. Chem. Soc.*, 2003, **125**, 11027.
50. S. Mahapatra, J. A. Halfen, and W. B. Tolman, *J. Am. Chem. Soc.*, 1996, **118**, 11575.
51. S. Mahapatra, J. A. Halfen, E. C. Wilkinson, G. Pan, X. Wang, V. G. Young Jr, C. J. Cramer, L. Que Jr, and W. B. Tolman, *J. Am. Chem. Soc.*, 1996, **118**, 11555.
52. S. Mahapatra, V. G. Young Jr, S. Kaderli, A. D. Zuberbühler, and W. B. Tolman, *Angew. Chem., Int. Ed. Engl.*, 1997, **36**, 130.
53. J. Shearer, C. X. Zhang, L. Q. Hatcher, and K. D. Karlin, *J. Am. Chem. Soc.*, 2003, **125**, 12670.
54. M. J. Henson, M. A. Vance, C. X. Zhang, H.-C. Liang, K. D. Karlin, and E. I. Solomon, *J. Am. Chem. Soc.*, 2003, **125**, 5186.
55. R. L. Lieberman, D. B. Shrestha, P. E. Doan, B. M. Hoffman, T. L. Stemmler, and A. C. Rosenzweig, *Proc. Natl. Acad. Sci. U.S.A.*, 2003, **100**, 3820.
56. S. S. F. Yu, L.-Y. Wu, K. H. C. Chen, W.-I. Luo, D.-S. Huang, and S. I. Chan, *J. Biol. Chem.*, 2003, **278**, 40658.

Copper: Inorganic & Coordination Chemistry

Rebecca R. Conry
Colby College, Waterville, ME, USA

Based in part on the article Copper: Inorganic & Coordination Chemistry by Rebecca R. Conry & Kenneth D. Karlin which appeared in the Encyclopedia of Inorganic Chemistry, First Edition.

1	Introduction	1
2	History	1
3	Occurrence	2
4	Production and Uses	2
5	Properties of the Metal	5
6	Reactions of the Metal	7
7	Usual Oxidation States and Stereochemistries	7
8	Binary and Other Simple Compounds	7
9	Coordination Compounds	12
10	Copper in Biology	16
11	Related Articles	17
12	References	17

1 INTRODUCTION

Copper (Figure 1) is among the 25 most abundant elements in the earth's crust, occurring at an average of about 50–100 g ton^{-1}. Copper metal has played an important role in human technological, industrial, and cultural development since primitive times. Thus, along with iron and gold, copper was one of the first metals used widely, because copper could be found in its native elemental form plus it could be easily hammered into tools and weapons. The metal and its alloys have subsequently been employed in a wide variety of applications because they exhibit a number of useful qualities such as ductility, malleability, strength, corrosion resistance, and high thermal and electrical conductivity, combined with an attractive appearance. One of the most widespread and long-standing uses of copper is for monetary purposes; thus, it is known as a coinage metal along with its fellow d-block triad members silver and gold. Copper is also an essential trace element nutritionally, being among the most abundant metals in the human body, although it is toxic to humans in large quantities (*see* ***Metal Ion Toxicity***).

Copper exhibits a rich coordination chemistry, primarily in the monovalent (+1) and divalent (+2) oxidation states. Compounds of copper have been used extensively in a wide range of practical applications, including as catalysts in both homogeneous and heterogeneous reactions, as fungicides, pesticides, and wood preservatives, as pigments for paints and glasses, and in the so-called high-temperature superconductors (*see* ***Superconductivity***).

2 HISTORY

Copper metal has been recognized and used extensively since prehistoric times (Scheme 1), probably beginning around 5000 B.C., or even somewhat earlier. The word copper and the symbol Cu are derived from *cuprum*, which is believed to have evolved from *aes cyprium* (the metal of Cyprus). The copper mine on the Island of Cyprus supplied most of the metal for the Romans from about 2500 B.C., although it is now uncertain whether Cyprus was named for the metal or vice versa.[1]

Initially the metal was mined and used primitively in weapons, tools, and, presumably, currency; this period in a civilization's evolutionary period is often referred to as the Copper Age. In ancient times, primary copper-mining sites were located in Sinai, Cyprus, Syria, Caucusus, Afghanistan, Macedonia, Iberia, and Central Europe.[2] Later, progression to the so-called Bronze Age occurred with progresses in metallurgy including the discovery that bronze, an alloy of copper with tin (an alloy is a homogeneous mixture of a metallic element and one or more other elements and is commonly made by adding the alloying element to the molten metal) first used around 2500 B.C., is stronger than copper metal alone. Brass, the alloy of copper and zinc that also imparts greater strength than pure copper, was probably developed some time later, perhaps around 300 A.D.

Significantly, copper was detected in plants and animals in the early to mid-1800s. The discoveries related to electricity that followed in the nineteenth century promoted the development of important new uses for copper metal. During approximately the same time period the ascent of the copper industry in the United States began, initially in Connecticut, then primarily in the Upper Peninsula of Michigan, and finally in the west (Arizona, Utah, Montana, New Mexico, and Nevada). The world production of mined copper ore exceeded 5 million tons by the 1960s, at that time led by the United States, which has since been overtaken by Chile. Other major producers include the former Soviet Union, Canada, China, and Zambia. There have been some recent periodic reductions in copper production due to the successful development of other competitive substitute materials, including aluminum, steel, and plastics, combined with the rising costs of the large open-pit mining operations now needed to isolate significant quantities of copper ore.

A major scientific breakthrough in the area of material science involving copper occurred in late 1986 and early 1987: the discovery of the so-called high-temperature cuprate superconductors (*see* ***Superconductivity***). These copper-oxide containing materials hold the record for the highest transition temperature (T_c, the temperature at which all resistance to electricity is lost), currently 133 K, which is significant

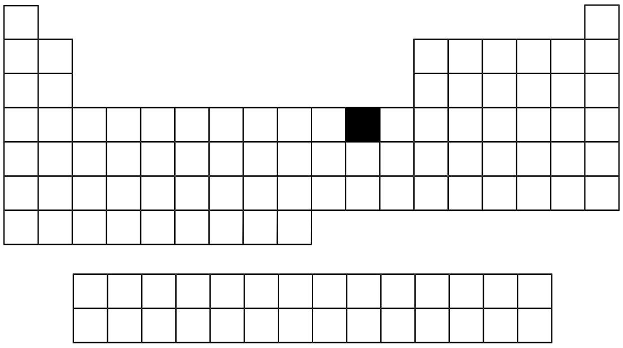

Figure 1 The place where copper is found in the conventional version of the periodic table

because liquid nitrogen can be used as the coolant to reach that temperature (77 K), instead of the much more expensive liquid helium coolant that was previously required.[3] Two-dimensional $Cu^{II}O_2$ planes might be (or might not be[4]) responsible for the superconductivity, thus, the magnetic properties (*see* ***Magnetism of Extended Arrays in Inorganic Solids***) of cuprates (*see* ***Magnetic Oxides***) have been extensively studied, for instance, for $CuGeO_3$.[5]

3 OCCURRENCE

Copper deposits are widely distributed over many parts of the world. Copper occurs at an average of 68 ppm in the earth's crust, 0.003 ppm in seawater, 0.7 ppm in the sun, and 1.0 ppm in the human body.[6] At one time native copper deposits (i.e. occurring as the metal) were relatively common, but now they are found infrequently. Native copper frequently contains small amounts of Ag, Be, Hg, As, and Sb impurities.[7] The present primary source of copper is the mineral ores (Table 1; Figure 2), combinations of copper cations and other ions, most commonly sulfur, iron, carbon, and/or oxygen. Although more than 150 copper minerals have been identified, much of the mined copper is composed of chalcopyrite, followed by chalcocite (Figure 3). About 90% of the known reserves are found in North America (Rocky Mountain and Great Basin areas and central Canada), South America (western slopes of the Andes in Peru and Chile) and the upper Katango region of the Congo plus the adjacent Copperbelt region of Zambia. The largest known deposit is at Chuquicamata, Chile.

4 PRODUCTION AND USES

4.1 Production

The world production of mined copper ore was 8 million metric tons in 1993; the major contributors were: Chile, 22%;

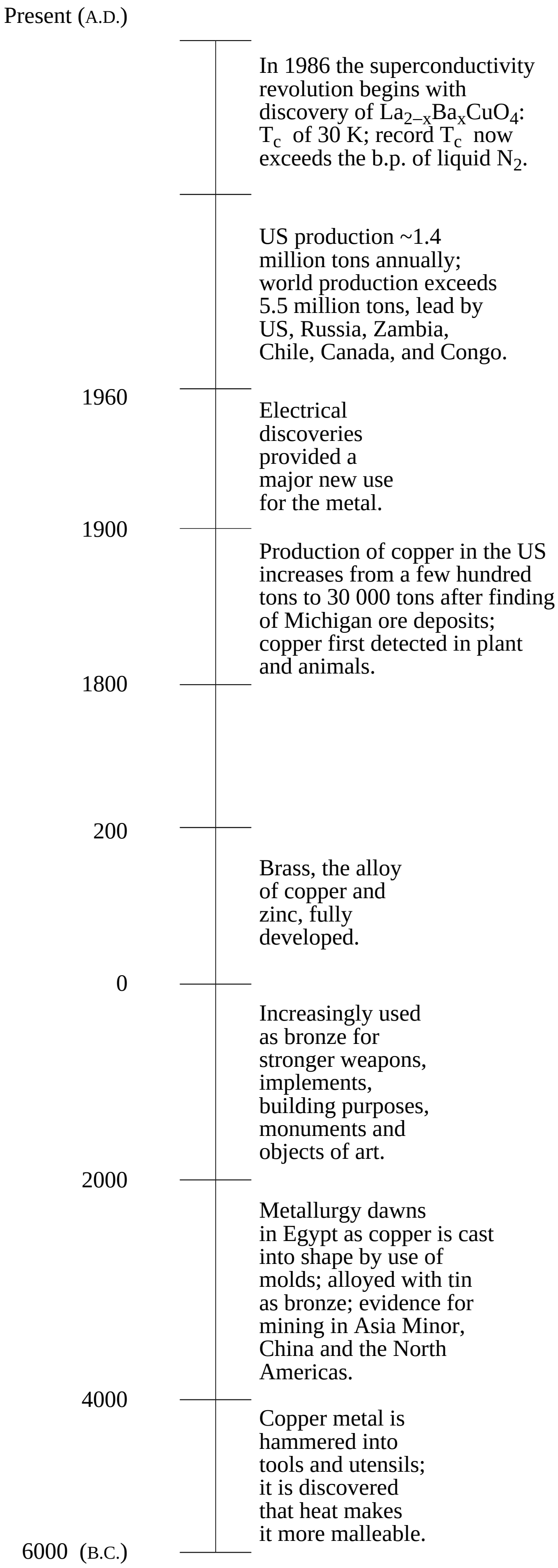
Present (A.D.)
In 1986 the superconductivity revolution begins with discovery of $La_{2-x}Ba_xCuO_4$: T_c of 30 K; record T_c now exceeds the b.p. of liquid N_2.
US production ~1.4 million tons annually; world production exceeds 5.5 million tons, lead by US, Russia, Zambia, Chile, Canada, and Congo.
1960
Electrical discoveries provided a major new use for the metal.
1900
Production of copper in the US increases from a few hundred tons to 30 000 tons after finding of Michigan ore deposits; copper first detected in plant and animals.
1800
200
Brass, the alloy of copper and zinc, fully developed.
0
Increasingly used as bronze for stronger weapons, implements, building purposes, monuments and objects of art.
2000
Metallurgy dawns in Egypt as copper is cast into shape by use of molds; alloyed with tin as bronze; evidence for mining in Asia Minor, China and the North Americas.
4000
Copper metal is hammered into tools and utensils; it is discovered that heat makes it more malleable.
6000 (B.C.)

Scheme 1 An approximate timeline of copper history

Table 1 Principal copper-containing minerals[a]

Name	Chemical Formula	% Cu	Color	Specific gravity
Native elemental copper	Cu	100	Light red metallic	8.9
Sulfides				
Chalcopyrite[b] (copper pyrite)	$CuFeS_2$	34.5	Yellow metallic	4.2
Chalcocite[b] (copper glance)	Cu_2S	79.8	Dark gray	5.7
Bornite[b]	Cu_5FeS_4	63.3	Bronze-brown	5.1
Covellite (indigo copper)[b]	CuS	66.5	Indigo blue	4.7
Tennantite[b]	$Cu_{12}As_4S_{13}$	51.6	Steel-gray	4.7
Tetrahedrite (grey copper)[b]	$Cu_{12}Sb_4S_{13}$	45.8	Steel-gray	4.9
Enargite	Cu_3AsS_4	48.4	Violet-tinted gray	4.4
Oxides				
Cuprite[b]	Cu_2O	88.8	Red	6.1
Tenorite	CuO	79.9	Gray to black	6.0
Carbonates				
Malachite[b]	$Cu_2CO_3(OH)_2$	57.3	Green	4.0
Azurite (chessylite)[b]	$Cu_3(CO_3)_2(OH)_2$	55.1	Sky blue	3.8
Silicate				
Chrysocolla[b]	$\sim Cu_4H_4Si_4O_{10}(OH)_8$	36.0	Blue-green	2.2
Sulfates				
Brochantite	$Cu_4SO_4(OH)_6$	56.2	Emerald green	3.9
Antlerite	$Cu_3SO_4(OH)_4$	54.0	Green	3.9
Halide				
Atacamite	$Cu_2(OH)_3Cl$	59.5	Dark green	3.8

[a]Reference: R. Dud'a and L. Rejl, 'Minerals of the World', Arch Cape Press, New York, 1989. [b]Most abundant copper-containing mineral ores.

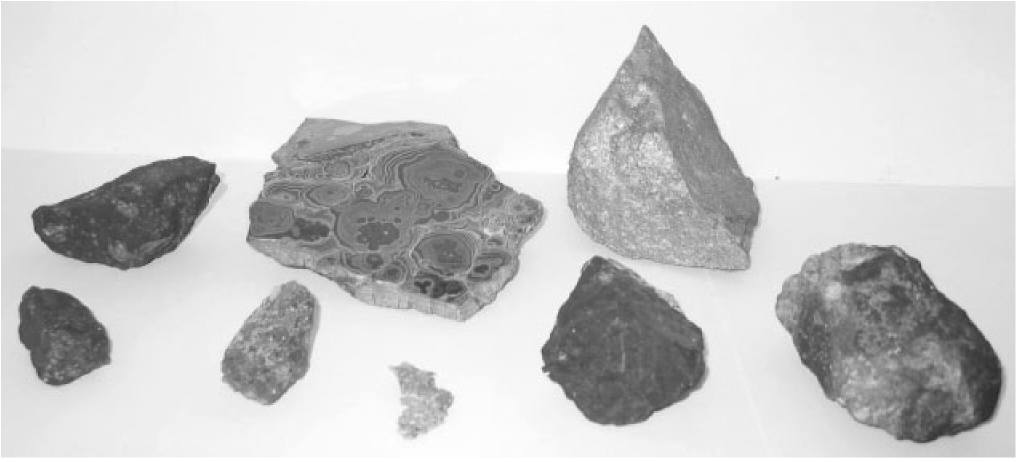

Figure 2 Copper minerals and native copper; from right to left: bornite (front and back); mixed malachite and azurite (front and back); native copper (front); covellite (front); chalcopyrite (back); and chalcocite

USA (primarily Arizona, New Mexico, and Utah), 20%; the former Soviet Union, 9%; Canada, 8%; China 8%; and Zambia, 5%. Presently, recycled scrap metal, or secondary copper, contributes an additional 25–35% to this yearly output. Open-pit strip mining yields most of the copper ore, which is typically 0.4–1% in copper. Underground methods are used for deeper, vein-type deposits that have a significantly higher copper content (needed to offset the increased mining costs).

4.2 Refining

The refining process[8] typically begins with crushing of the ores, then concentration by froth-flotation, which yields material that is typically 15–20% Cu. The main impurity in these concentrates is iron; however, nickel, gold, and silver are often present, along with traces of zinc, selenium, arsenic, antimony, tellurium, cobalt, tin, and lead. Silica (sand) is

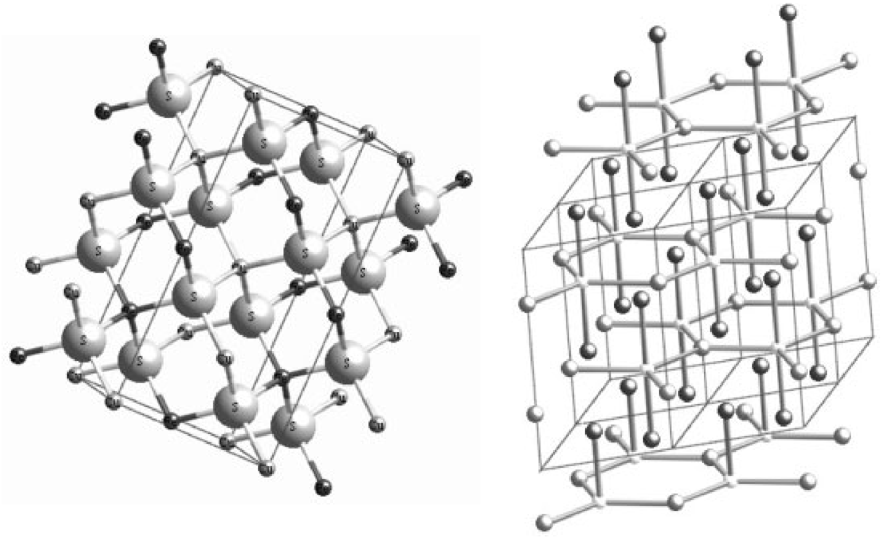
(a) (b)

Figure 3 Depictions of the solid-state structures of the minerals (a) chalcopyrite the largest spheres represent sulfide ions and the smaller spheres represent copper and iron centers, represented by lighter and darker gray spheres, respectively and (b) chalcocite the lightest spheres represent sulfide ions and the darker spheres represent the two unique copper positions shown in approximately averaged positions drawn with CrystalMaker 6.1 software

added to the concentrates in a reverberatory furnace so that the mixture can be heated to 1400–1450 °C to make a melt. Roasting with added air converts most of the iron to its oxide (equation 1 or 2), which reacts with silica to form an iron silicate slag (equation 3). This slag spontaneously separates into upper layer and lower layers. The upper layer is periodically removed to give a liquid matte that is largely Cu_2S and FeS. This liquid matte is placed in a converter with more silica, and additional air is forced through it. In a similar fashion, this transforms the remaining FeS first to FeO (equation 2) and then to slag (equation 3). The Cu_2S is partially transformed to Cu_2O (equation 4), which reacts with any remaining FeS (equation 5). Finally, metallic or blister copper is produced (equation 6 and 7). The name blister copper derives from its blistered appearance that is caused by the bubbling of the SO_2 through the melt. This copper product is approximately 98–99% pure and can be further purified by fire refining (similar to the process described above), electrolysis, and/or by zone refining. The electrolytic process uses impure copper as an anode with a purified copper cathode in a solution containing H_2SO_4 and $CuSO_4$ electrolytes. The electrolysis deposits quite pure (~99.95%) copper on the cathode. Further purification, to 99.9999% purity, can be accomplished by zone refining, if needed. Commercially significant amounts of by-products are produced in copper refining, including silver, molybdenum, selenium, tellurium, gold, and sulfuric acid.

$$2CuFeS_2 + O_2 \longrightarrow Cu_2S + 2FeO + 3SO_2 \quad (1)$$

$$2FeS + 3O_2 \longrightarrow 2FeO + 2SO_2 \quad (2)$$

$$FeO + SiO_2 \longrightarrow Fe_2(SiO_3)_3 \quad (3)$$

$$2Cu_2S + 3O_2 \longrightarrow 2Cu_2O + 2SO_2 \quad (4)$$

$$Cu_2O + FeS \longrightarrow Cu_2S + FeO \quad (5)$$

$$Cu_2S + O_2 \longrightarrow 2Cu + SO_2 \quad (6)$$

$$2Cu_2O + Cu_2S \longrightarrow 6Cu + SO_2 \quad (7)$$

Copper can also be extracted from the ores using wet processes. Examples of such processes include leaching with dilute sulfuric acid solutions, or the use of solutions containing chelating ligands.

4.3 Uses

Copper is one of the few common metals for which commercial applications use greater amounts of the pure metal than its alloys. The major uses of copper are: building construction (roofing parts, gutters) and plumbing installations (valves, pipe fittings); electrical and electronic products (wire, motors, generators, transformers, switchgears, switchboards, telephone wire, and cable); industrial machinery and equipment; transportation (in automobile pumps, compressors, radiators, heaters, and defrosters as well as in airplane and train parts); household appliances (refrigerators, washing machines, air-conditioners, radios, television sets), and other consumer-related products including cookware, art, and jewelry (some of these items are shown in Figure 4). In addition, copper is part of nearly all coinage alloys, and semiconductor companies have begun to use copper in the production of various devices.[9]

Over 1000 alloys of copper have been studied; each alloy displays slightly different properties than pure copper metal.

Figure 4 A few of the many common objects made from copper metal

The most important ones are probably brass (Cu/Zn) and bronze (Cu/Sn). Bronze is generally a stronger material than brass, however, tin is more expensive than zinc and the electrical and thermal conductivities of brass are larger than those of bronze. An excellent example of how the properties of an alloy change with composition is provided by brasses: the 90/10 (%Cu/%Zn) brass is rich bronze in color, the 85/15 brass is golden, the 70/30 brass is yellow, and the 60/40 brass is reddish yellow. Brass is used for industrial applications, plumbing fixtures, and decorative items such as lamps because it is stronger, more corrosion resistant, and more easily machined than copper itself while having an appearance that is similar to gold but being much less expensive. Some other alloys of copper worth mentioning include: the so-called nickel silver (55–65% Cu, 10–18% Ni, 17–27% Zn, and sometimes Fe, Pb, and Mn); the very corrosion resistant Monel metal (Cu/Ni usually 60/40); aluminum bronzes (Cu/Al); phosphor bronze (Cu with 1.25–10% Sn, 0.35% P); and beryllium copper (~2% Be). The addition of silicon to copper also confers enhanced strength.**[10]**

5 PROPERTIES OF THE METAL

Copper metal crystallizes with a close-packed, face-centered cubic structure (Figure 5). Pure copper metal has a reddish gold to orange color and is nonmagnetic, relatively dense, and resists wear well. The color of copper metal is due to the excitation of electrons from the filled d band to the s-p conduction band by the absorption of visible light corresponding to blue and green wavelengths (but not orange or red). Copper is highly valued for its strength, malleability, ductility, and corrosion resistance. However, the most important property of bulk copper (see Table 2) is probably its very high electrical conductivity (for metals the conductivity on the basis of a unit volume at room temperature is only exceeded by silver), which is, in fact, used as an international standard (the electrical conductivity of a 1.00-m long copper bar weighing 1.00 g at 20.0 °C is defined as 100% conductivity). Similarly, the very high thermal conductivity of copper leads to many of its commercial applications and again is also only exceeded by the thermal conductivity of silver. Another widely exploited trait of copper is its resistance to oxidation while carrying or storing water, for which the antibacterial properties of copper are also useful.

Both of the naturally occurring isotopes of copper are active in nuclear magnetic resonance (NMR) spectroscopy but are quadrupolar nuclei, both with $I = 3/2$ (Table 3). Copper NMR studies have been limited because most have been restricted to complexes of the Cu^{I} oxidation state since they are diamagnetic. In addition, the fairly large quadrupole moment for the more abundant ^{63}Cu restricts studies to complexes with nearly perfectly symmetrical environments; small distortions broaden the signal, often making it unobservable. Fewer NMR studies been reported using the second isotope, ^{65}Cu. This is because, even though it has a similar quadrupole moment, it has not only less than half the natural abundance but it also has a lower receptivity. The tetrakis(acetonitrile) complex, $[Cu(CH_3CN)_4]^+$, has most often been used as the reference (defined as 0 ppm) for the ^{63}Cu NMR studies to date.**[11]** A range of about 500 ppm has been observed for $[Cu(L)_4]^+$ complexes (e.g. for $L = P(O\text{-alkyl})_3$, 70–90 ppm; L = pyridine, 110 ppm; $L = PMe_2Ph$, 250 ppm; $L = CN^-$, 480 ppm) with linewidths ranging from 100 to 3000 Hz. Solid state $^{63,65}Cu$ NMR experiments on cuprates have also been reported.**[12,13]**

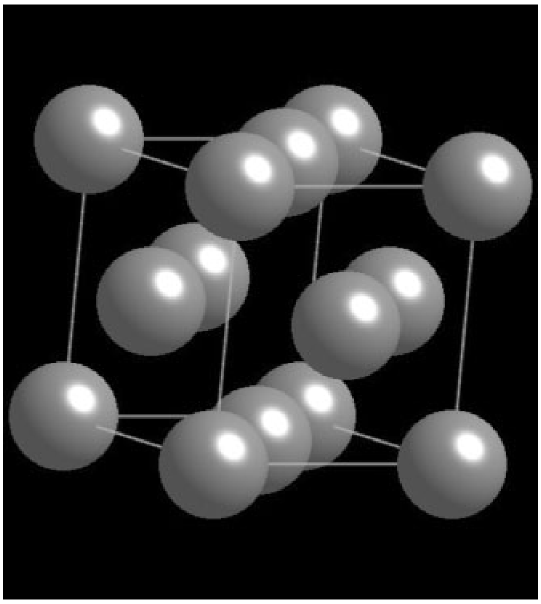

Figure 5 The face-centered cubic, close-packed solid-state structure of copper metal

Table 2 Properties of copper metal

Atomic number	29
Atomic weight	63.546
Electronic configuration	$1s^2 2s^2 2p^6 3s^2 3p^6 3d^{10} 4s^1$
Melting point	1083 °C
Boiling point	2573 °C
Crystal structure	*Fm3m*, face-centered cubic, $a = 3.615$ Å
Density	$8.95\ \mathrm{g\,cm^{-3}}$ at 20 °C; $7.94\ \mathrm{g\,mL^{-1}}$ at m.p.
Electronegativity	1.90 (Pauling); 1.75 (Allred–Rochow)
Mass magnetic susceptibility (as a solid)	$-1.081 \times 10^{-9}\ \mathrm{kg^{-1}\,m^3}$
Ionic radius (Pauling)	0.96 Å ($\mathrm{Cu^I}$); 0.73 Å ($\mathrm{Cu^{II}}$)
Atomic radius; covalent radius	1.278 Å; 1.17 Å
Vapor pressure	5.05×10^{-2} Pa (at the melting point)
Standard reduction potentials	$+0.520$ V for $\mathrm{Cu^+ + e^- \longrightarrow Cu}$ $+0.341$ V for $\mathrm{Cu^{2+} + 2e^- \longrightarrow Cu}$ $+0.159$ V for $\mathrm{Cu^{2+} + e^- \longrightarrow Cu^+}$
Ionization potential (1st)	7.725 Ev
Electron affinity	$\mathrm{M \longrightarrow M^-}$ $118.3\ \mathrm{kJ\,mol^{-1}}$
Ionization energies $\mathrm{M \longrightarrow M^+}$	$745.4\ \mathrm{kJ\,mol^{-1}}$
$\mathrm{M^+ \longrightarrow M^{2+}}$	$1958\ \mathrm{kJ\,mol^{-1}}$
$\mathrm{M^{2+} \longrightarrow M^{3+}}$	$3554\ \mathrm{kJ\,mol^{-1}}$
$\mathrm{M^{3+} \longrightarrow M^{4+}}$	$5326\ \mathrm{kJ\,mol^{-1}}$
Electrical resistivity	1.675×10^{-6} ohm-cm (20 °C)
Thermal conductivity	$4.01\ \mathrm{w\,cm^{-1}\,{}^\circ C^{-1}}$ (25 °C)
Specific heat	$0.3845\ \mathrm{J\,g^{-1}\,{}^\circ C^{-1}}$ (25 °C)
Effective nuclear charge	4.20 (Slater); 5.84 (Clementi); 8.07 (Froese–Fischer)
$\Delta H_{\mathrm{fusion}}$	$13.0\ \mathrm{kJ\,mol^{-1}}$
ΔH_{vap}	$306.7\ \mathrm{kJ\,mol^{-1}}$
Coefficient of linear thermal expansion	$16.5 \times 10^{-6}\ \mathrm{cm\,cm^{-1}\,{}^\circ C^{-1}}$ (25 °C)
Electron (or photoelectron) work function ϕ	4.65 eV
Elastic modulus in tension	17 000 000 psi (annealed)
Poisson's ratio	0.33
Tensile strength	32 000–37 000 psi (annealed) 55 000–61 000 psi (drawn)
Yield strength	4600–12 000 psi (0.5% extension of annealed) 50 000–55 000 psi (0.5% extension of drawn)
Elongation, % in 2 in.	46 (annealed)
Reduction of area, %	48 (annealed)
Electrical conductivity	101.8% (annealed)
Brinell hardness number	43 (annealed); 103 (hard rolled)
Surface tension	$1104\ \mathrm{dynes\,cm^{-1}}$ at 1150 °C
Viscosity	0.0341 cgs units at 1145 °C
Solidification shrinkage	4.92%
Hall effect	-5.24×10^{-4} V; 3000 to 8116 gauss
Velocity of sound	$12\,700\ \mathrm{ft\,s^{-1}}$ at 20 °C

Table 3 NMR Properties of the naturally occurring copper isotopes

NMR property	$^{63}\mathrm{Cu}$	$^{65}\mathrm{Cu}$
Abundance	69.17%	30.83%
Relative Sensitivity ($^1\mathrm{H} = 1.00$)	9.31×10^{-2}	0.11
Receptivity ($^{13}\mathrm{C} = 1.00$)	365	201
Magnetogyric ratio (rad $\mathrm{T^{-1}s^{-1}}$)	7.0965×10^7	7.6018×10^7
Quadrupole moment ($\mathrm{m^2}$)	-0.211×10^{-28}	-0.195×10^{-28}
Frequency ($^1\mathrm{H} = 100$ Hz; 2.3488 T) in Hz	26.505	28.394

The two naturally occurring isotopes of copper are stable to nuclear decay. Nine synthetic radioisotopes have been reported (^{59}Cu, ^{60}Cu, ^{61}Cu, ^{62}Cu, ^{64}Cu, ^{66}Cu, ^{67}Cu, ^{68}Cu, ^{69}Cu) with half-lives of those nuclides ranging from 31 s (^{68}Cu) to 2.58 days (^{67}Cu).**[6]** One isotope has been used for medical diagnostic purposes (*see* ***Metal-based Imaging Agents***) to scan the brain and to study Wilson's disease. This isotope, ^{64}Cu, has a half-life of 12.7 h (decay modes: β^- at 0.571 MeV, β^+ at 0.657 MeV, and γ at 1.34 MeV) and is usually administered as copper$^{\mathrm{II}}$ acetate (orally or intravenously for Wilson's disease studies) or copper$^{\mathrm{II}}$ versenate (intravenously for brain scans).**[14]**

6 REACTIONS OF THE METAL

Metallic copper is stable indefinitely in pure dry air at room temperature, but forms a superficial protective green coating or patina of hydroxo carbonates and hydroxo sulfates in the atmosphere. Copper is attacked more readily by some other oxidants, including elemental sulfur and halogens. In the absence of air, copper metal does not react with nonoxidizing acids, as it is below hydrogen in the electromotive or activity series. However, copper metal dissolves in hot concentrated sulfuric acid and both dilute and concentrated nitric acid (and acidic solutions of thiourea). Copper also dissolves in aqueous ammonia or cyanide solutions in the presence of dioxygen or, more readily, when hydrogen peroxide is added.

7 USUAL OXIDATION STATES AND STEREOCHEMISTRIES

Copper complexes are known in oxidation states ranging from 0 to $+4$, although the $+2$ (cupric) and the $+1$ (cuprous) oxidation states are by far the most common, with the divalent state predominating. Only a relatively small number of Cu^{III} complexes have been characterized and the Cu^0 and Cu^{IV} oxidation states are extremely rare. A few mixed valence (*see* ***Mixed Valence Compounds***) polynuclear species have also been isolated; examples include a Cu^I/Cu^{II} species[15] and a Cu^{II}/Cu^{III} catenane.[16] The coordination numbers and geometries (*see* ***Coordination Numbers & Geometries***) of copper complexes vary with oxidation state. Thus, the majority of the characterized Cu^{III} complexes are square planar and diamagnetic, as is common for late transition metals with d^8 electronic configurations.

For the spherically symmetric Cu^I d^{10} ion, the common geometries are two-coordinate linear, three-coordinate trigonal planar, and four-coordinate tetrahedral. Some distortions from these ideal geometries are observed, particularly with chelating ligands; a fairly small number of pentacoordinate Cu^I complexes have been isolated and characterized as well. Cu^I compounds are diamagnetic and colorless, except where the color results from charge-transfer bands[17] or a counterion. Cu^I complexes are often fairly readily oxidized to Cu^{II} compounds; the electron-transfer kinetics of several systems have been studied.[18]

The d^9 Cu^{II} ion is commonly found in a tetragonal coordination environment, with four shorter equatorial bonds and another one or two longer axial bonds[19] or less frequently with two shorter axial bonds and four longer equatorial bonds,[20] although four-coordinate tetrahedral and planar complexes are also known, for instance, the $CuCl_4{}^{2-}$ ion, which has crystallized in geometries ranging from square planar (usually green) to almost ideal tetrahedral (usually orange).[21] Additionally, five-coordinate trigonal bipyramidal to square-planar complexes have been reported, as well as a small number of three-, seven-, and eight-coordinate complexes. Most of the Cu^{II} compounds are blue or green in color because of d–d absorptions in the 600–900 nm region; exceptions generally also have charge-transfer bands tailing into the visible, causing a red or brown appearance. Magnetic moments of monomeric Cu^{II} complexes are typically found in the range 1.75–2.20 BM (Bohr magnetons; *see* ***Magnetism of Transition Metal Ions***), consistent with one unpaired electron.

Since the Cu^{II} ion is smaller and more highly charged or harder (*see* ***Hard & Soft Acids and Bases***) than the Cu^I ion, it interacts more strongly with water molecules – the result being that the Cu^{II} ion is more stable in aqueous solutions than the Cu^I ion (in spite of the stable d^{10} configuration for Cu^I). Thus, water does not sufficiently stabilize the Cu^I ion; it is unstable toward disproportionation to Cu^0 and Cu^{II} in solution (which is usually a fast process for soluble compounds that produce the Cu^I ion in solution). However, the stability of Cu^I relative to Cu^{II} is easily altered, such that the presence of softer ligands will stabilize Cu^I (e.g. sulfur donors, unsaturated nitrogen donors, etc.). For example, the Cu^I ion is effectively solvated by CH_3CN,[22] which makes the resulting complex stable toward disproportionation (in acetonitrile Cu^{II} and Cu comproportionate to Cu^I) as well as to molecular oxygen in CH_3CN solution (as the oxidation of Cu^I by O_2 generally requires an open coordination site). There are other strategies to obtain water-stable and -soluble Cu^I complexes, for instance, by the coordination of the copper ion to a softer ligand that also incorporates very polar or charged peripheral functional groups.[23]

8 BINARY AND OTHER SIMPLE COMPOUNDS

Copper compounds containing carbon-bound ligands, such as cyanide, carbon monoxide, alkyls, and so on are covered elsewhere (*see* ***Copper: Organometallic Chemistry***).

8.1 Hydrides (*see also Hydride Complexes of the Transition Metals*)

The high-temperature reaction of Cu and H_2 yields CuH, which has been studied spectroscopically in the gas phase; the reddish-brown precipitate obtained when aqueous $CuSO_4$ is reduced by hypophosphorous acid (H_3PO_2) is probably also largely CuH.[24] CuH_2 is not isolable, as it appears to be a higher energy species than $Cu + H_2$.[25] The Cu^{II} cationic hydride $[CuH]^+$ has been observed by using a guided ion beam approach to study the reaction of Cu^+ and H_2.[24] The tetrahedral $Cu^IH_4{}^{3-}$ anion was found in the product from the reaction of a Ba/Cu alloy with H_2.[26] Matrix-isolation techniques combined with laser-ablated $Cu + H_2$ reactions appear to have formed several copper hydrides, including CuH and $CuH_2{}^-$.[27,28]

8.2 Halides

CuCl and CuBr can be synthesized by boiling an acidic solution of the Cu^{II} halide with an excess of copper metal; dilution causes precipitation of white CuCl or pale yellow to white CuBr, which are polymeric even in the vapor state (as a solid, CuCl crystallizes as the zinc blende structure with regular tetrahedral $CuCl_4$ centers, linked by bridging chlorides). Binary $copper^{I}$ compounds with very hard fluoride ligands are not known, undoubtedly because CuF is unstable to disproportionation to form CuF_2 and Cu.**[29]**

The $copper^{II}$ dihalide complexes CuX_2 (X = F, C, Br) can be synthesized from the elements. The white ionic CuF_2 compound has a tetragonally distorted octahedral structure about the copper ion with extensive bridging fluoride ligands. Anhydrous $CuCl_2$ and $CuBr_2$ are more covalent yellow-brown and black compounds, respectively, that are polymers of planar CuX_4 units with shared edges. Monomeric $CuCl_2$ and $CuBr_2$ exist in the gas phase at high temperatures; for example, $CuCl_2$ has been studied spectroscopically at 1000 °C in the presence of Cl_2 (to prevent decomposition to CuCl and Cl_2).**[30]** Binary $copper^{II}$ compounds with very soft iodide ligands are not known; by simply adding I^- to a solution of Cu^{2+}, CuI and I_2 are quickly formed. This reaction can be used for the volumetric analysis of Cu^{2+} in solution by titrating the I_2 produced with sodium thiosulfate (equation 8). Hydrates of the dihalides (F, Cl, Br) are common, easily prepared from aqueous haloacids, and contain coordinated water molecules.

$$2Na_2S_2O_3 + I_2 \longrightarrow Na_2S_4O_6 + 2NaI \tag{8}$$

Copper chloride complexes can be used as catalysts in a number of organic reactions. Examples include the Wacker process, which is the oxidization of ethylene to acetaldehyde by oxygen and aqueous Cu^{II} and Pd^{II} precatalysts (or, alternatively using iron catalysts)**[31]** plus the synthesis of acrylonitrile from acetylene and hydrogen cyanide using CuCl. Cuprous chloride has also been used as a desulfurizing and

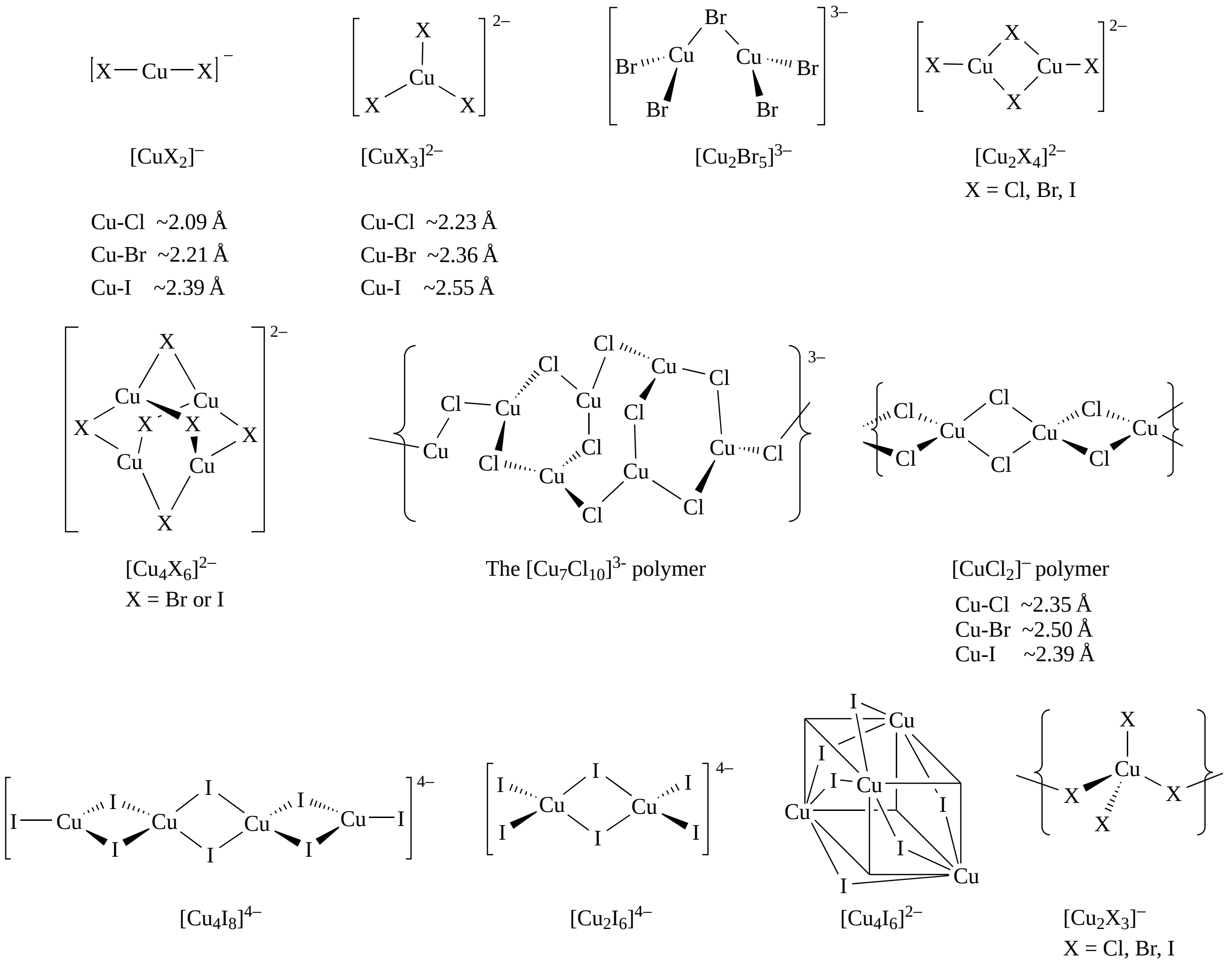

Scheme 2 Structures of selected anionic $copper^{I}$ halides

decolorizing agent in the petroleum industry; cupric chloride as a fixative in the dyeing and printing of textiles plus as a disinfectant, feed additive, and pigment for glass and ceramics.

Only the examination of only a few anionic cuprous halide[32] complexes (Scheme 2) is needed to clearly illustrate the geometric preferences of the Cu^I ion.[33,34] Thus, $[CuX_2]^-$ exhibits a linear structure. Trigonal-planar CuX_3 triangles are quite common, Examples include the complexes $[CuX_3]^{2-}$ and $[Cu_2Br_5]^{3-}$; the latter ion has two $CuBr_3$ triangles linked through a bridging bromide and that are folded to give a Cu–Br–Cu angle of about 73°; $[Cu_2X_4]^{2-}$, where the two of these triangles share one side; and $[Cu_4Cl_6]^{2-}$, where four $CuCl_3$ triangles have common vertices. Tetrahedral copper centers are found frequently, such as in the dimeric complex $[Cu_2I_6]^{4-}$ as well as in the tetranuclear $[Cu_4I_8]^{4-}$ complex (that also contains trigonal-planar copper centers). Polymeric copper halides are also common; examples are $[Cu_7Cl_{10}]^{3-}$ and $[Cu_2X_3]^-$. In addition, many stoichiometries can exist in more than one form depending on the nature of the counterion; for instance, $[CuCl_2]^{2-}$ is a discrete, linear monomer only with large cations, otherwise it is a linked tetrahedral polymer. Unlike the smaller halide ligands, the iodide ion can form more open structures with Cu^I ions, such as the cubane-type structure seen for $[Cu_4I_6]^{2-}$, which has a Cu_4 tetrahedron with six I^- ions bridging the Cu_2 edges.

Similarly, the cupric ion also has distinct coordination geometry preferences, which are seen when a few of the Cu^{II} halide complexes are examined (Scheme 3).[35] The Cu^{II}

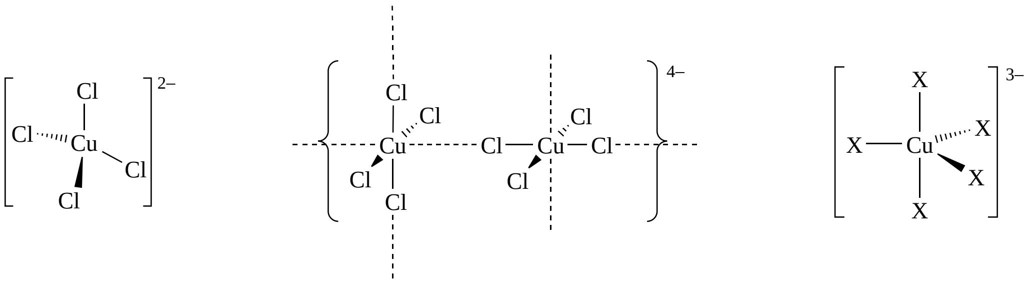

$[CuCl_4]^{2-}$ $[CuCl_4]^{2-}$ polymer $[CuX_5]^{3-}$
X = Cl, Br

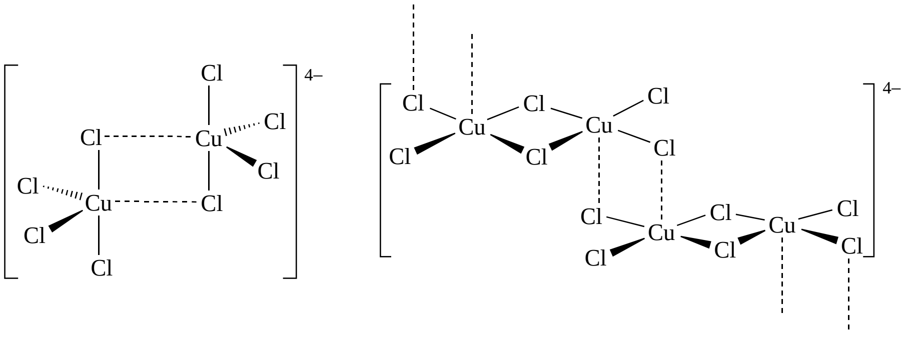

The $[Cu_2Cl_8]^{4-}$ dimer Stacking of $Cu_2Cl_6{}^{2-}$ ions in $Me_2NH_2CuCl_3$

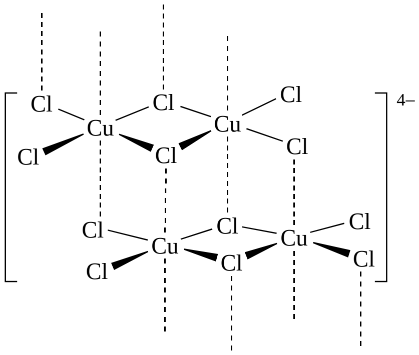

The stacking of $Cu_2Cl_6{}^{2-}$ ions in $KCuCl_3$ and NH_4CuCl_3

Scheme 3 Typical Cu^{II} anionic halides coordination numbers are often higher than those seen for Cu^{I}, typically from four to six, and the structures are usually distorted from ideal geometries due to the Jahn-Teller effect. Complexes with the formula $[CuCl_3]^-$ usually exist as recognizable $[Cu_2Cl_6]^{2-}$ dimers which stack in various ways, and the discrete dianion $[CuCl_4]^{2-}$ has been seen in a range of structures from tetrahedral to square planar to a polymeric form.[21] Again, the structures of the complexes are very dependent on the nature of the counterion. The polymeric form of $[CuCl_4]^{2-}$ stoichiometry comprises tetragonally elongated octahedra that are linked to create infinite layers. The pentahalide complexes $[CuX_5]^{3-}$ ($X = Cl$, Br) have a trigonal bipyramidal structure when large cations force it to be monomeric. The high-valent anionic copper-fluoride compounds, M_3CuF_6 and M_2CuF_6 ($M =$ alkali metal), can be synthesized by the high-pressure fluorination of mixtures containing the proper ratio of MCl and CuCl. The pale-green K_3CuF_6 compound is paramagnetic (two unpaired electrons) and exhibits an octahedral geometry about the copper ion; the brick-red compound Cs_2CuF_6 is an example of a complex containing the rare Cu^{IV} oxidation state. A crystal structure containing a three-coordinate Cu^{II} complex ion with isolated $[CuX_3]^-$ ($X =$ mixed Cl and Br) species was recently reported.[36]

8.3 Hydroxides

CuOH has been studied spectroscopically and theoretically.[37] The binary Cu^{II} hydroxide complex exists as either a gelatinous green-blue material with variable water content (probably with coordination to both OH^- and H_2O ligands), or as a pale-blue crystalline material of $Cu(OH)_2$ stoichiometry (Figure 6) isolated upon adding a base to a Cu^{II} solution at room temperature. The synthesis can be slightly modified to yield colloids or nanowires.[38] The Cu^{II} complex $Ba_2[Cu(OH)_6]$ has also been reported,[39] as well as the dark blue anions $[Cu(OH)_4]^{2-}$ and $[Cu(OH)_6]^{4-}$ which are formed in concentrated alkali metal hydroxide solutions.

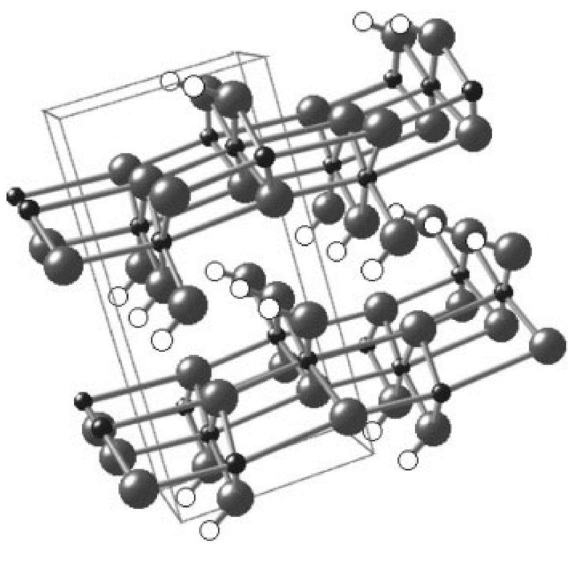

Figure 6 The structure of $Cu(OH)_2$

8.4 Oxides

The Cu^{I} oxide is more stable than the Cu^{II} oxide; thus the reaction of copper metal and oxygen yields black CuO initially when heated gently, but this compound is converted to red Cu_2O during longer reaction times and/or at higher temperatures. Yellow to reddish Cu_2O (the color depends on the particle size) can also be conveniently prepared by the reduction of a Cu^{II} salt using hydrazine or a sugar in aqueous alkaline solution; this is the basis for Fehling's test for sugars and other reducing agents. The compound Cu_2O has two-coordinate linear CuO_2 centers;[40] X-ray and electron diffraction techniques and electronic-structure calculations for Cu_2O are interpreted to indicate Cu–Cu bonding in the solid state for this compound.[41,42] Cuprous oxide is used as a red pigment in some paints, glasses, porcelain glazes, and ceramics and has been used as a fungicide. CuO is best prepared by pyrolysis of the Cu^{II} nitrate or other oxo salts; it is sometimes used as a black surface coating in solar-energy collecting devices because a thin layer transmits infrared radiation but not shorter wavelength radiation. Upon heating a mixture of K_2O and Cu_2O, the nearly colorless KCuO compound is prepared; this compound contains $[Cu_4O_4]^{4-}$ rings with coplanar Cu atoms. The Cu^{II} oxides M_2CuO_3 ($M =$ Ba or Sr) contain linked CuO_4 planar units. The bluish Cu^{III} complex, $MCuO_2$ ($M =$ alkali metal), can be made from CuO and MO_2 in an oxygen atmosphere; it is a low-spin, diamagnetic square-planar complex as one might predict for such a d^8 metal center. A high-pressure synthesis and an oxidizing agent were required to make Sr_2GaCuO_5, which contains only Cu^{III} ions.[43]

8.5 Sulfides, Selenides, and Tellurides

The binary Cu^{I} sulfide is more stable than the Cu^{II} compound of empirical formula CuS, which is actually better formulated as $Cu_2Cu^{II}(S_2)S$;[44] $NaCu_4S_4$ has a related structure to CuS.[45] Cu_2S can be prepared by heating copper and sulfur (or H_2S) in the absence of air or by heating CuS in a stream of hydrogen gas. CuS is produced as a black, insoluble colloidal precipitate by the action of H_2S on an aqueous solution of Cu^{II} ion, which can be dissolved by the addition of Na_2S because of the formation of $[CuS_2]^{2-}$. Cuprous sulfide is used in solar cells (or ternary chalcopyrites such as $CuInS_2$[46]), electrodes, and certain solid lubricants. The selenides and tellurides, CuX, Cu_2X, MCuX, MCu_3X ($M =$ Na, K; $X =$ Se, Te), and $K_4Cu_8Te_{11}$ are also known, some of which are superconductors. The polytelluride complex $K_2Cu_2(Te_2)(Te_3)$

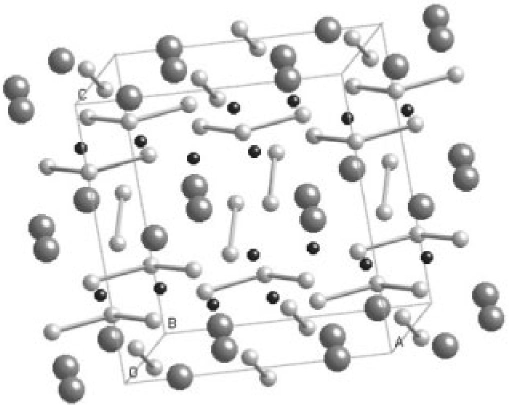

Figure 7 The solid-state structure of $K_2Cu_2(Te_2)(Te_3)$ which exhibits alternating $Cu_2(Te_3)$ planes with potassium ions with $Te_2{}^{2-}$ ion containing planes. Copper centers are shown as black spheres, tellurium atoms are nearly white, and potassium ions are gray and only bonds between Te atoms are shown to aid visualization

crystallizes (Figure 7) with four Te atoms coordinated to each Cu center in an approximately tetrahedral array with Cu ions paired up and displaying short Cu−Cu distances of 2.574(3) Å.**[47]** The nonclassical $[CuTe_7]^{3-}$ anion has been crystallized and studied theoretically.**[48]**

8.6 Sulfates

The Cu^I sulfate complex, Cu_2SO_4, can be prepared from $copper^I$ oxide (equation 9). This compound must be stored in dry conditions because moisture causes the compound to disproportionate to Cu and $CuSO_4$. The very stable Cu^{II} sulfate pentahydrate compound $CuSO_4{\cdot}5H_2O$, often called blue vitriol for its bright blue color, is the copper compound used commercially in the greatest quantity. This compound is formed in the reaction of CuO and sulfuric acid and is widely utilized for electroplating processes, as a fungicide and an algaecide, as a component of fertilizers, plus as a starting material to synthesize other copper compounds. The biuret test for proteins involves the addition of $CuSO_4{\cdot}5H_2O$ to a basic solution potentially containing protein; the hydroxide ions hydrolyze the protein at least partially to form fragments that coordinate to the Cu^{II} ion to give a characteristic violet-purple color. The solid-state structure of crystalline $CuSO_4{\cdot}5H_2O$ has four water ligands coordinated to the Cu^{II} ion in the equatorial plane and two axially bound monodentate sulfate groups, giving an overall elongated-octahedral geometry about the Cu center. The fifth water molecule is hydrogen bonded in the lattice between the bridging sulfate groups and one of the coordinated waters. Upon heating, $CuSO_4{\cdot}5H_2O$ loses water, first to give the trihydrate, then the monohydrate, and finally (above about 200 °C) producing the white anhydrous compound $CuSO_4$, which eliminates SO_3 above about 700 °C to form CuO.

$$Cu_2O + Me_2SO_4 \longrightarrow Cu_2SO_4 + Me_2O \qquad (9)$$

8.7 Nitrates

The binary Cu^I nitrate $CuNO_3$ compound is not known. The hydrated Cu^{II} nitrate complex, $Cu(NO_3)_2(H_2O)_2{\cdot}1/2H_2O$, has an unsymmetrically coordinated bidentate nitrato group; it cannot be fully dehydrated to the anhydrous Cu^{II} nitrate without decomposition. The anhydrous compound $Cu(NO_3)_2$ is instead prepared by the dissolution of copper metal in an ethyl acetate solution of N_2O_4 from which the salt $Cu(NO_3)_2{\cdot}N_2O_4$ is crystallized (which is probably formulated $[NO^+][Cu(NO_3)_3{}^-]$).**[49]** Finally, this salt is gently heated to yield the blue sublimable compound $Cu(NO_3)_2$, which exists as a gaseous monomeric planar complex with chelated nitrate ligands or as a solid with an infinite array of Cu^{II} ions linked by nitrate groups. Cupric nitrate has been used in light-sensitive reproductive papers and as a polishing/coloring reagent for iron and copper items.

8.8 Nitrites

$Copper^I$ nitrites are unknown, in contrast to Cu^{II}, for which more than one stoichiometry has been found. In $[Cu(NO_2)_6]^{4-}$ all the nitrite ligands are N-bound (nitro groups). In contrast, the structure of the complex $K_3[Cu(NO_2)_5]$ contains all possible $NO_2{}^-$ binding modes to a single metal center, including N-bound, symmetrical bidentate O-bound, and unsymmetrical monodentate binding through only one O-atom. The complex ion $[Cu(NO_2)_4]^{2-}$ in one system has been found to contain O-bound nitrite groups.**[50]**

8.9 Phosphates

In the Cu^{II} compound $Cu_3(PO_4)_2$, the bridging phosphate group interacts with seven (!) different copper centers; three of the phosphate oxygen atoms bridge two copper centers with the other oxygen coordinated to only one copper ion.**[51]** The anionic $[CuPO_4]^-$ compounds exhibit extensive Cu–O interactions as well, which vary with factors such as the associated cation.**[51]** The crystal structures of the pyrophosphate-containing compounds $Cs_2Cu_7(P_2O_7)_4{\cdot}6CsCl$ and $Cs_2Cu_5(P_2O_7)_3{\cdot}3CsCl$ contain square-planar CuO_4 units in open-framework structures.**[52]** Square planar, trigonal bipyramidal, and distorted octahedral geometries are found for the copper ions in mixed strontium-copper phosphate structures.**[53]** Three polymorphs for the structure of $copper^{II}$ hypophosphite, $Cu(H_2PO_2)_2$, have been reported.**[54]**

8.10 Carbonates

Binary copper carbonate complexes are apparently not known; however, the basic carbonates malachite, $Cu_2(OH)_2CO_3$, and azurite, $Cu_3(CO_3)_2(OH)_2$, occur naturally. The complex ion $[Cu(CO_3)_2]^{2-}$ contains a bridging carbonate ligand that is bound in a monodentate fashion to each copper ion; the hydrated species, $Na_2Cu(CO_3)_2 \cdot 3H_2O$, is also known. Cupric carbonate ($Cu_2(OH)_2CO_3$) is prepared by the reaction of sodium carbonate and copper sulfate; this compound is used as a coloring agent and, after reaction with arsenic to form the poisonous acetate cupric arsenite compound $Cu(C_2H_3O_2)_2 \cdot 3Cu(AsO_2)_2$, a wood preservative and insecticide commonly known as Paris green.

8.11 Acetates

Cu^I acetate is a white crystalline air- and moisture-sensitive compound formed by the reduction of anhydrous Cu^{II} acetate with copper metal in pyridine or acetonitrile solvent. Cu^{II} acetate is usually found as the dimeric dihydrate complex, $Cu_2(CH_3COO)_4 \cdot 2H_2O$, which has been used as a starting compound in the sol-gel synthesis of CuO thin films.[55] The Cu^{II} ion in the crystal structure of $Cu_2(CH_3COO)_4 \cdot 2H_2O$ is approximately square pyramidal in geometry (Figure 8) with four bridging acetate ligands and a water ligand in the axial position.[56] The Cu–Cu distance of 2.64 Å in this complex, along with the fairly high magnetic moment (1.4 BM per Cu at 25 °C; compare to the spin-only value of 1.73 BM; *see* ***Magnetism of Transition Metal Ions***) suggest that there is not a formal Cu–Cu bond, although there is weak antiferromagnetic coupling. The sodium salt of the monomeric Cu^{II} tetraacetate complex crystallizes with monodentate acetate groups and a square-planar geometry about the Cu ion.[57]

8.12 Alkoxides

Copper^I alkoxide complexes are typically yellow in color and are made from Cu^I starting materials, for example, in the metathesis reaction shown in equation (10). Cu^IOR complexes are generally soluble in etheral solvents and some are sublimable; exceptions are polymeric complexes such as the methoxide. The triphenylmethoxocopper^I complex crystallizes as a tetramer with alkoxo bridges and the *tert*-butoxocopper^I complex crystallizes as two polymorphs, a similar tetranuclear structure plus a unique octanuclear form.[58] Cu^IOR complexes are generally reactive. Thus, Cu^IOR complexes metallate acidic hydrocarbons such as in terminal acetylenes, and will react with organic halides to give ether products, plus they will react with carbon dioxide and secondary amines to yield carbamate products.[49]

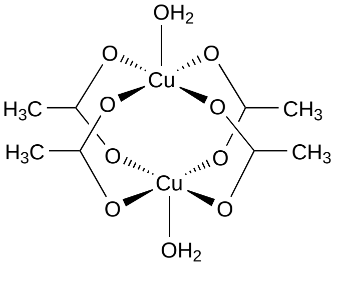

Figure 8 A depiction of the structure of $Cu_2(CH_3COO)_4 \cdot 2H_2O$

$$\mathrm{CuCl + LiOR \longrightarrow LiCl + CuOR} \tag{10}$$

8.13 Other Compounds

The anhydrous Cu^I sulfite complex is not known; however, hydrated species can be prepared, including the pale-yellow $Cu_2SO_3 \cdot 1/2H_2O$ compound (known as Etard's salt) and the mixed sulfites NH_4CuSO_3 and $NaCuSO_3 \cdot 6H_2O$. The blue hydrated Cu^{II} ion $[Cu(H_2O)_6]^{2+}$ is formed when the Cu^{II} hydroxide, carbonate, sulfate, or nitrate binary compounds are dissolved in water. The coordinated water ligands can be substituted for ammonia molecules; thus, equilibrium solutions of mixed aqua/ammine complexes are formed in aqueous ammonia. The average stoichiometry depends on the ammonia concentration; in concentrated ammonia solutions $[Cu(NH_3)_4]^{2+}$ is probably the predominant species, although $[Cu(NH_3)_6]^{2+}$ can been prepared in liquid ammonia and must be stored under an ammonia atmosphere to prevent decomposition. The perchlorate Cu^{II} complex $Cu(ClO_4)_2$ is known; spectroscopic results are consistent with the presence of two types of coordinated bidentate perchlorate groups. In addition, the orange perchlorate-containing complex $ClO_2Cu(ClO_4)_3$ is an isolable intermediate in the synthesis of the blue-white $Cu(ClO_4)_2$ and $Cu(ClO_4)_2 \cdot 2H_2O$.[59] The copper triflate compounds $Cu^{II}(CF_3SO_3)_2$ and $Cu^I(CF_3SO_3)C_6H_6$ have been used as starting materials for the synthesis of a number of compounds. Cu^I complexes with NO, Ar, and Xe have been studied in the gas phase.[60]

9 COORDINATION COMPOUNDS

Owing to limitations on the size of this article, plus the large number of Cu^I and Cu^{II} complexes that have been reported, only a general overview of the extensive coordination chemistry of copper can be presented with only a few of the typical and unusual complexes described. More extensive[39,61] and limited timeframe reviews[62–69] are available. Many of the homoleptic complex ions are covered along with the binary compounds in the above sections. In addition, organometallic complexes, containing C-bound ligands, are covered in another chapter (*see* ***Copper: Organometallic Chemistry***).

9.1 Copper^0

No structurally characterized discrete Cu^0 complexes are known. A few species have been observed in the gas phase, or at very low temperatures using matrix-isolation techniques, including polynuclear copper species such as Cu_2 and Cu_3 and several copper–carbon monoxide and copper-ethylene species. There have also been reports of reactive species thought to contain zerovalent copper,[70] and several clusters or other species where, arguably, some of the Cu is present in the Cu^0 oxidation state.[71]

9.2 Copper^I

The Cu^I ion is classified as a soft acid (*see* ***Hard & Soft Acids and Bases***), which predicts reasonably well the types of ligands that will be most stabilizing and are, thus, commonly observed in Cu^I complexes. The preference of Cu^I for softer ligands is quite apparent in the homoleptic complexes, for instance the halides discussed above. Polynuclear compounds are quite commonly seen in the chemistry of Cu^I. Thus, the solid-state structure cannot be reliably predicted from the reaction stoichiometry or from the empirical formula of the resulting compound. The careful selection of ligands, for instance, an appropriate macrocyclic ligand can ensure the formation of a mononuclear complex if one is desired.

9.2.1 Hydrogen Ligands

Complexes of Cu^I with hydride (*see* ***Hydride Complexes of the Transition Metals***) and other H-donating ligands are fairly rare; most of the reported examples contain phosphine coligands. For example, the stable, readily prepared copper borohydride complex, $Cu(BH_4)(PPh_3)_2$, contains a coordinated BH_4^- group (*see* ***Boron Hydrides***) and has been found to be a very selective reducing agent, for instance, in reducing acid chlorides to the corresponding aldehydes.[72] Similarly, the hexameric species $[H_6Cu_6(PPh_3)_6]$, which contains bridging hydride ligands, has been found to be a good reagent for reductive organic transformations, such as the conversion of α,β-unsaturated carbonyl compounds to saturated carbonyl compounds.[73] In addition, the in situ preparation of phosphine-ligated ‘CuH’ has been utilized for organic synthetic reactions.[74]

9.2.2 Halide Ligands

As predicted by the soft nature of Cu^I, very few examples of fluoride-coordination are known, and the ones that have been reported typically have additional Cu^I-stabilizing ligands, such as $[Cu(PPh_3)_3F]$. Coordination of a fluoride-containing anion, such as BF_4^- is, perhaps, more common, for instance, in the phosphine complex $[Cu(PPh_3)_3(FBF_3)]$. A completely different situation is seen for the chloride ion, in that both extensive Cu^I homoleptic compounds are known (see above) as well as complexes containing mixed chloride/other donor ligands. A fair number of bromide and iodide compounds have been prepared as well, although not nearly as many as ones containing chloride ligands. This is presumably not due to the lack of stability of those species, but rather because of choices made by researchers considering factors such as the availability of literature starting material preparations, cost, and desired reactivity.

9.2.3 Nitrogen Ligands

A variety of different nitrogen ligands (*see* ***Ammonia & N-donor Ligands***) have been used to synthesize Cu^I complexes. Monovalent complexes with exclusively saturated N-donor ligands are known, but are generally less stable than analogous complexes with unsaturated or aromatic nitrogen-containing ligands. Thus, the ammine complex $[Cu(NH_3)_2]^+$ can be prepared, but it is less stable than the analogous Cu^I complex with imidazole donors. In addition, accounts of Cu^I complexes with chelating nitrogen ligands outnumber those involving monodentate nitrogen ligands. $Cu(LBF_2)(CO)$ [L = difluoro-3,3′-(trimethylenedinitrilo)bis(2-butanone oximato)borate; Figure 9(a)][75] is an example of the rare, but growing number of five-coordinate Cu^I complexes. Nitrogen-ligated Cu^I complexes have also been studied for their photochemical (*see* ***Photochemistry of Transition Metal Complexes***) properties,[76] including their long-lived excited states.[77] A number of tris(pyrazolyl)hydroborate-ligated[78] Cu^I complexes have been prepared and crystallographically characterized, such as the complex shown in Figure 9(b).[79]

9.2.4 Phosphine, Arsine, and Stibine Ligands

Phosphorus is one of the best soft donor atoms for Cu^I; thus many Cu^I-phosphine complexes have been reported, including ones with other ligands that by themselves would be unlikely to sufficiently stabilize Cu^I. By far, most of the known complexes involve monodentate phosphine ligands. As one goes down the nitrogen family, progressively fewer complexes have been characterized, such that substantially less arsine-coordinated complexes have been reported and there are only a handful of stibine species.

9.2.5 Oxygen Ligands

The actual number of reported Cu^I complexes with oxygen-donor ligands (*see* ***Water & O-donor Ligands***) is much smaller than for complexes containing other kinds of ligands, such as those with halide and/or pnictogen donor atoms, but, nevertheless, a wide range of ligand types is represented. A fair number of complexes containing coordinated oxyanions can be prepared; for instance, see the sections above on sulfate, phosphate, acetate, and alkoxide ligands. Some of the

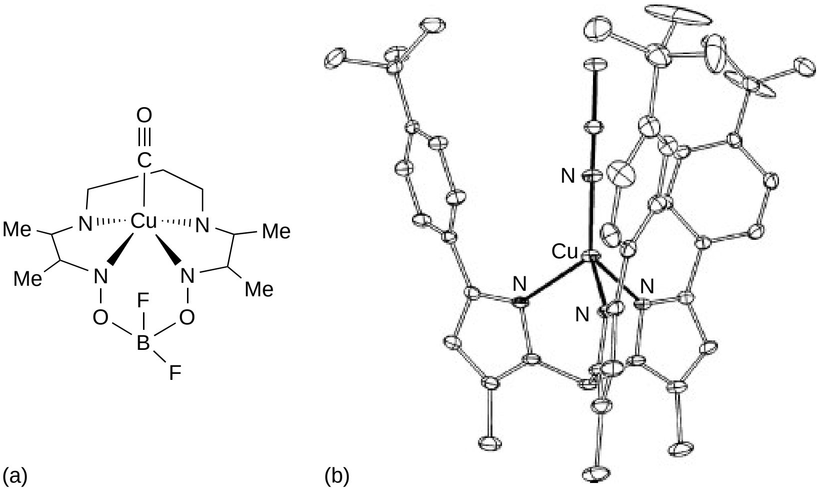

Figure 9 An example of a five-coordinate Cu^{I} complex (a) and a copper acetonitrile complex with a substituted tris(pyrazolyl) hydroborate ligand (b)

ligands that are unknown in homoleptic compounds can be found in complexes with other Cu^{I}-stabilizing coligands, for instance, H_2O in $[Cu(1,4\text{-oxathiane})_3(OH_2)]BF_4$ and nitrate in $[Cu(PPh_3)_2(NO_3)]$.

9.2.6 *Sulfur, Selenium, and Tellurium Ligands*

There is extensive Cu^{I} chemistry with the soft sulfur-donor ligands (*see* ***S-donor Ligands***). Thus, the addition of Me_2S to a solution of Cu^{II} forms a Cu^{I} species. A variety of sulfur-containing ligands and kinds of complexes can be found, for instance, monodentate ligation in trigonal planar $[Cu(\text{tetraethylenethiourea})_3]SO_4$, extensive bridging in $(Ph_4P)_2[Cu_4(SPh)_6]$, the polysulfide anion as in the aggregate $(Ph_4P)_2[Cu_6(S_4)_3(S_5)]$, and the macrocyclic $[Cu(15\text{-ane-}S_5)]^+$. Selenium- and tellurium-containing Cu^{I} complexes are also known, but are not nearly as abundant as sulfur-ligated compounds; examples are the cluster compound $Cu_{12}(P_2Se_6)\{Se_2P(OCH_2CH_3)_2\}_8$ which contains trigonal-planar $CuSe_3$ and tetrahedral $CuSe_4$ groups as well a number of short Cu−Cu distances in the solid state[80] and polynuclear compounds containing Cu^{I} and halide ions plus a chelating phosphine-selenide ligand.[81]

9.3 Copper^{II}

The Cu^{II} ion is classified as a borderline hard acid (*see* ***Hard & Soft Acids and Bases***); thus, its coordination chemistry is dominated by nitrogen- and oxygen-donating ligands, followed by chloride and sulfur-containing species. Similar to the situation seen for Cu^{I}, ligands not normally associated with Cu^{II} can often be found in the presence of Cu^{II} stabilizing coligands. More crystal structures of Cu^{II} complexes have been reported than for any other transition metal ion.[20]

9.3.1 *Hydrogen Ligands*

Although virtually unknown in Cu^{II} chemistry, Cu-hydride species have been suggested as reactive intermediates in hydrogenation reactions.[82]

9.3.2 *Halide Ligands*

Copper-fluoro complexes are more frequently encountered for the Cu^{II} ion than for the Cu^{I} ion, although not to the extent one might predict. Fluoride bound in a monodentate fashion is extremely rare, while bridging fluoride ligands and coordinated F-containing anions, such as BF_4^- and PF_6^-, are more common. Similar to that found for Cu^{I}, chloride is found extensively in Cu^{II} chemistry, followed distantly by bromide. Iodide coordination to Cu^{II} is, as one might expect, limited; seen only in complexes such as [Cu(bipy)I]I. The section on binary and simple compounds above also discusses a number of Cu^{II} halide compounds.

9.3.3 *Phosphine, Arsine, and Stibine Ligands*

These soft ligands are very rarely isolated in Cu^{II} complexes, however, they can occur with Cu^{II} stabilizing ligands, such as in the tetraacetate dimer $[Cu_2(O_2CMe)_4(PPh_3)_2]$.

9.3.4 *Nitrogen and Oxygen Ligands*

Nitrogen- (*see* ***Ammonia & N-donor Ligands***) and oxygen-donor (*see* ***Water & O-donor Ligands***) ligands are very prevalent in Cu^{II} chemistry and cover a wide range of ligand types, for example, N-donor ligands include saturated amines like ammonia and ethylene diamine, nitro groups (N-bound NO_2), azides, nitrogen-bound cyanates, and aromatic

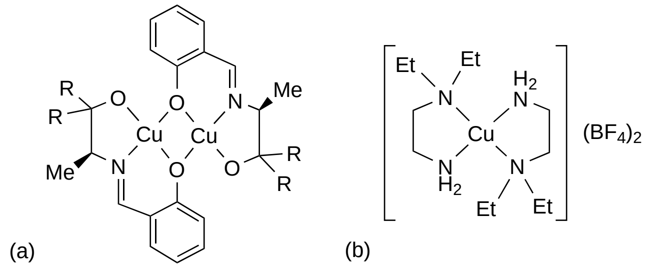

Figure 10 (a) A dimeric Cu^{II} complex with mixed oxygen/nitrogen ligation that is used as an asymmetric cyclopropanation precatalyst (R = bulky substituted phenyl group). (b) A thermochromic complex that is red at lower temperatures and is purple at higher temperatures

amines such as the pyridines and imidazoles. Chelated groups are also very commonly seen. The Cu^{II} complex with a N/O-mixed donor ligand (*see* ***Mixed Donor Ligands***) shown in Figure 10(a) has been used as an asymmetric cyclopropanation**[83]** precatalyst.**[84]** The monomeric nitrogen-ligated complex shown in Figure 10(b) is interesting because it exhibits thermochromic behavior; at lower temperatures the complex is red and square planar about the Cu^{II} center while at higher temperatures the complex converts to a purple tetrahedral form.**[85]** Nitrogen-ligated copper, for example, complexes with N-alkylated triazacyclononane ligands have been used to model the dioxygen activation (*see* ***Dioxygen & Related Ligands***) chemistry of copper-containing metalloproteins (*see* ***Copper: Hemocyanin/Tyrosinase Models***),**[86]** as hydrolysis and aziridination**[87]** catalysts, and as DNA cleavage agents.**[88]**

9.3.5 Sulfur Ligands

A fair number of Cu^{II} complexes with sulfur ligands (*see* ***S-donor Ligands***) are known, dominated by dimercaptomaleonitrile and thiocarbamate-type ligands. Simple sulfides as ligands are observed almost exclusively in mixed N/S donor chelating ligands. In addition, the coordination of Cu^{II} to other miscellaneous sulfur donors, such as bridging thiolate (e.g. PhS^-) and SCN^- ligands, is known.

9.4 Copper^{III}

Copper^{III} complexes are most frequently prepared by oxidation of Cu^I and Cu^{II} complexes, initially accomplished with various chemical oxidizing agents, including aqueous hypochlorite (ClO^-), chlorine or fluorine gas, alkaline persulfate $[(S_2O_8)^{2-}]$ solutions, and oxidizing oxyanions such as $TeO_6{}^{6-}$ and $IO_6{}^{5-}$. Thus, this is how the pale-green octahedral paramagnetic $K_3[CuF_6]$ complex as well as the square-planar diamagnetic $Cs[CsF_4]$ fluoride complex were synthesized. The first crystal structure of a Cu^{III} complex was that of $Na_3KH_3[Cu(IO_6)_2]\cdot 14H_2O$. This complex exhibits a square-based pyramidal structure, in which the copper ion is chelated to two oxygen atoms on each of the IO_6 groups and is also coordinated to one of the water molecules with a long Cu−O bond.**[89]** Owing to the number of protons and water molecules in this complex, some questioned the oxidation state assignment, even though the complex was diamagnetic. However, the diamagnetic purple macrocyclic complex, (Figure 11) formed by the condensation of oxalodihydrazide and acetaldehyde in the presence of Cu^{II} ions, was crystallographically characterized and found to contain a similar square pyramidal structure,**[90]** leaving little question that both complexes contain Cu^{III}. A Cu^{III} complex of a doubly N-confused porphyrin was isolated from the reaction of Cu^{II} acetate and the porphyrin starting material.**[91]**

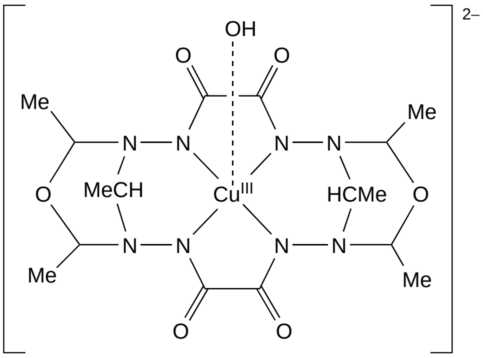

Figure 11 An example of a Cu^{III} complex that has been structurally characterized

A more recent preparative method for Cu^{III} complexes is the use of electrochemical oxidation techniques. Oxygen, nitrogen, and sulfur ligands dominate the latest Cu^{III} complexes, which include various nitrogen macrocycle and dithiolate ligands as well as an unusual carborane complex.**[92]** A number of Cu^{III} peptide (*see also* ***Peptide–Metal Interactions***) complexes have synthesized and characterized;**[93]** these are coordinated and stabilized by deprotonated amide groups and are usually made by oxidizing Cu^{II} precursors by bulk electrolysis in a flow cell. The crystal structure of the tripeptide complex $Cu^{III}(H_{-2}Aib_3)\cdot 2H_2O\cdot 1.5NaClO_4$ ($H_{-2}Aib_3 = \alpha$-aminoisobutyryl-α-aminoisobutyryl-α-aminoisobutyric acid) contains a square-planar Cu^{III} center with the Cu–N and Cu–O bonds observed to be 0.12−0.17 Å shorter than those in analogous Cu^{II} complexes.

9.5 Copper^{IV}

The few reported Cu^{IV} compounds all contain the two most electronegative elements as ligands. The most completely characterized Cu^{IV} complex is probably the paramagnetic, presumably octahedral complex $[CuF_6]^{2-}$.**[94]** Some Cu^{IV} centers are believed to be present in $BaCuO_{2.63}$, which is made by heating $BaCuO_2$ in the presence of oxygen.[95] In addition, the CuO_2 species formed in the reaction of copper metal with dioxygen has been studied spectroscopically using matrix-isolation techniques and is believed to contain linear copper-dioxo [Cu-$(O^{2-})_2$] rather than copper peroxide [Cu-$(O_2{}^{2-})$] ligation.[96]

10 COPPER IN BIOLOGY

The use of copper bracelets and ointments for the treatment of conditions such as arthritis has been part of folk medicine for a long time. Copper-containing intrauterine contraceptive devices (IUDs) have been used for more than 30 years; the increased copper concentration in the uterus resulting from the IUD appears to be toxic to sperm, inhibiting fertilization. Traces of copper are needed for the normal growth, development, and function of all life forms.[97] Copper is the third most abundant trace element in the body. In fact, the overall concentration of copper in living organisms is fairly consistent (about 0.5–3 ppm), except for in shellfish and nuts (higher) plus some microorganisms (variable). The distribution in a particular organism varies from one part to another; in plants the highest concentration is found in the seeds and in humans in the kidney, liver, brain, heart, skeleton, hair, and nails contain the most copper.

Many copper-containing metalloproteins have been identified[97,98] [some are mentioned below in passing; for more information see the articles on copper proteins (*see* ***Copper: Hemocyanin/Tyrosinase Models***; ***Copper Proteins with Dinuclear Active Sites***; ***Copper Proteins: Oxidases***; ***Copper Proteins with Type 1 Sites***; ***Cytochrome Oxidase***; ***Copper Proteins with Type 2 Sites***, and ***Copper Enzymes in Denitrification***)], these proteins carry out a number of fairly diverse functions. Thus, copper centers take an electron-transfer role in cytochrome *c* oxidase (part of the respiratory electron transport chain in most cells, contains two different copper sites), plastocyanin (part of photosystem II in plants and green algae) as well as in azurin and stellocyanin. The dinuclear copper active site in hemocyanin functions as the dioxygen (*see* ***Dioxygen & Related Ligands***) carrier for arthropods and molluscs, instead of the iron-containing hemoglobin and myoglobin biomolecules found in other species (*see* ***Iron: Heme Proteins & Dioxygen Transport & Storage***). Several copper proteins act as oxidases: laccase, ascorbate oxidase, and cytochrome *c* oxidase (reducing O_2 to H_2O); amine oxidase and galactose oxidase (reducing O_2 to H_2O_2) plus tyrosinase, the particulate membrane-bound form of methane monooxygenase, plus dopamine β-hydroxylase and peptidyl α -amidating monooxygenase (monooxygenases). In addition, there are copper-containing reductases: nitrite reductase and nitrous oxide reductase (in bacterial denitrification) and superoxide dismutase (contains both copper and zinc). There is also a relationship between copper and iron metabolism. Thus, the blue plasma copper protein ceruloplasmin is a ferroxidase, which converts Fe^{II} to Fe^{III} for binding to transferrin (*see* ***Iron Proteins for Storage & Transport & their Synthetic Analogs***). As a result of this relationship, a low copper intake can result in anemia, probably by lowering the copper ferroxidase activity.[99]

There are at least five major components of the blood plasma to which copper is known to be associated. These include ceruloplasmin (a fairly abundant glycoprotein containing the largest proportion of copper ion in most animals and humans); albumin (contains a single high-affinity copper-binding site); ferroxidase II and transcuprein (nonceruloplasmin, nonalbumin proteins); and small molecules in the plasma such as amino acids and small peptides. Within vertebrate cells there appear to be at least three proteins that contain copper; two of them, cytochrome *c* oxidase and superoxide dismutase, are described briefly above. The third, the metallothioneins (*see* ***Metallothioneins***), are small, cysteine-rich metal-binding proteins, which appear to serve in the regulation and detoxification of a number of metal ions including copper.

Copper is an essential trace nutrient, but large quantities (typically grams) are toxic (*see also* ***Metal Ion Toxicity***) to humans.[100] About 2–5 mg of copper is absorbed per day from the diet, primarily by the small intestine with 6–13% of the average daily intake coming from drinking water. Other factors influence the efficiency of copper uptake, such as the amount of fiber, zinc, and ascorbic acid in the diet.[99] Nearly all copper excretion occurs in the bile in a form that prevents reabsorption in nearly the same quantity as that taken in; the biological half-life of copper ranges from about 2 to 4 weeks. Copper deficiency can occur if there is insufficient nutritional copper and leads to low blood cell counts and osteopenia (low bone density/poor bone formation, between normal levels and osteoporosis). However, copper deficiency is rarely observed in developed countries except in individuals who have had a large segment of their bowel removed (or bypassed), or in infants given homemade formulas that are lacking in copper. Seldom are symptoms of severe deficiency observed like those seen in the genetic disorder, Menkes' disease.[101] This disease primarily occurs in boys since it is X-linked (a recessive defect in the ATP7A gene) and is usually apparent at birth, or within 2 to 3 months. The babies may be born prematurely and have unusual facial appearances and hair (kinky and colorless, or with the appearance of steel wool), plus have brain damage that results in mental retardation. Other characteristic symptoms include seizures, stunted growth, failure to thrive, subnormal body temperatures, a higher occurrence of aortic abnormalities such as blockages or aneurisms, and weakened bones that more easily fracture. Unfortunately, progressive neurological deterioration usually occurs until death, typically at six months to three years of age.[99,102] The severe prenatal brain damage that had already occurred often makes postnatal copper therapy ineffective, except in a milder form called occipital hormone syndrome. Phase II clinical trials are under way for copper-histidine injections (*see* ***Metal-based Drugs***); at this time it appears that this therapy may be useful for some, but not all, Menkes' disease patients, especially when started as early as possible (including possibly before birth).

Acute copper poisoning can be fatal and has been seen after the ingestion of grams of copper from contaminated water (the U.S. Environmental Protection Agency has set a limit of $1.3\,\mathrm{mg\,L^{-1}}$ for drinking water), during hemodialysis, or in farm workers using copper sulfate as a fungicide. This condition is rare and is sometimes self-limiting, because the resulting nausea, vomiting, and diarrhea can purge the system of moderate amounts of excess copper. Copper toxicosis syndromes have been identified in some infants whose formulas were stored, prepared, and/or heated in copper or brass pots. Some believe that the afflicted infants were heterozygotes for Wilson's disease (see below), thus, would not exhibit medical problems with normal copper intakes, only with consistently elevated levels.

Chronic copper toxicity is found in some individuals; the accumulation damages the liver and then the nervous system and other organs. The primary, relatively rare disorder is called Wilson's disease,[103] which is an autosomal recessive genetic disorder caused by mutations in the ATP7B gene. This condition is usually diagnosed in children to young adults with liver disease and/or neurological problems and arises from the body's failure to excrete copper in the bile. Wilson's disease is treatable with anticopper agents including zinc acetate (Galzin™; *see* ***Metal-based Drugs***) which blocks copper absorption and has the lowest rate of side effects, or *D*-penicillamine (Cuprimine, Depen), or trientine (Syprine; the hydrochloride salt of N,N'-bis(2-aminoethyl)-1,2-ethanediamine) to chelate and remove the excess copper, combined with a low copper diet. Tetrathiomolybdate (*see* ***Metal-based Drugs***) is also being investigated to treat Wilson's disease and is currently in phase III clinical trials.

The role of copper in other disease states is being investigated. For Alzheimer's disease studies, it has been found that the amyloid precursor protein interacts with copper to produce increased oxidant damage, and trace amounts of copper promote the precipitation of the amyloid β protein. In familial myotrophic lateral sclerosis about a quarter of the cases are caused by inherited dominant mutations in the Cu/Zn superoxide dismutase that probably result in abnormal Cu binding and the generation of reactive oxygen species. Copper has also been proposed to be involved in prion metabolism and function; however, whether or not this implicates copper in the prion diseases is unclear at this time.[102]

The lowering of copper levels appears to produce antiangiogenesis (inhibition of blood vessel growth and proliferation) and, thus, is being probed for its potential anticancer effects. In addition, since fibrotic and inflammatory cytokines have been found to be copper dependent, copper-lowering therapy is being investigated in the treatment of diseases involving fibrosis and inflammation, for instance, pulmonary fibrosis and cirrhosis.[102] Thus, the copper-lowering agent tetrathiomolybdate is currently involved in several clinical trials (most Phase II at this time) for a variety of cancers, idiopathic pulmonary fibrosis, schleroderma, primary biliary cirrhosis, and psoriasis.

11 RELATED ARTICLES

Copper Enzymes in Denitrification; Copper: Hemocyanin/Tyrosinase Models; Copper: Organometallic Chemistry; Copper Proteins: Oxidases; Copper Proteins with Dinuclear Active Sites; Copper Proteins with Type 1 Sites; Superconductivity.

12 REFERENCES

1. M. E. Weeks, 'Discovery of the Elements', 6th edn., Journal of Chemical Education, Easton, PA, 1960.
2. 'Copper Through the Ages', Copper Development Association, London, 1937.
3. F. J. Owens and C. P. Poole Jr, 'The New Superconductors', Plenum, New York, 1996.
4. J. D. Dow and D. R. Harshman, *J. Phys. Chem. Solids*, 2002, **63**, 2309.
5. K. Uchinokura, *J. Phys. Condens. Matter*, 2002, **14**, R195.
6. 2005, http://www.webelements.com/.
7. C. Klein, and C. S. Hurlbut Jr 'Manual of Mineralogy', 21st edn.; Wiley, New York, 1993.
8. R. R. Moskalyk and A. M. Alfantazi, *Miner. Eng.*, 2003, **16**, 893.
9. P. Singer, *Semicond. Int.*, 2002, 46.
10. 2005, http://www.matweb.com/reference/copper-alloys.asp.
11. J. K. Irangu and R. B. Jordan, *Inorg. Chem.*, 2003, 3934.
12. N. J. Curro, *J. Phys. Chem. Solids*, 2002, **63**, 2181.
13. B. Grévin, Y. Berthier, G. Collin, and P. Mendels, *Phys. Rev. Lett.*, 1998, **80**, 2405.
14. M. J., O'Neil, ed. 'The Merck Index', 13th edn., Merck, Whitehouse Station, NJ, 2001.
15. R. Ahlrichs, C. E. Anson, D. Fenske, O. Hampe, A. Rothenberger, and M. Sierka, *Angew. Chem., Int. Ed. Engl.*, 2003, **42**, 4036.
16. M. E. Padilla-Tosta, O. D. Fox, M. G. B. Drew, and P. D. Beer, *Angew. Chem., Int. Ed. Engl.*, 2001, **40**, 4235.
17. M. Melnik, L. Macaskova, and C. E. Holloway, *Coord. Chem. Rev.*, 1993, **126**, 71.

18. Q. Yu, C. A. Salhi, E. A. Ambundo, M. J. Heeg, L. A. Ochrymowycz, and D. B. Rorabacher, *J. Am. Chem. Soc.*, 2001, **123**, 5720.
19. I. Persson, P. Persson, M. Sandström, and A.-S. Ullström, *J. Chem. Soc. Dalton Trans.*, 2002, 1256.
20. M. A. Halcrow, *Dalton Trans.*, 2003, 4375.
21. S. Keinan and D. Avnir, *Inorg. Chem.*, 2001, **40**, 318.
22. P. Kamau and R. B. Jordan, *Inorg. Chem.*, 2001, **40**, 3879.
23. F. Tisato, F. Refosco, G. Bandoli, G. Pilloni, and B. Corain, *Inorg. Chem.*, 2001, **40**, 1394.
24. A. Dedieu, ed., 'Transition Metal Hydrides', VCH, New York, 1992.
25. H. Smithson, C. A. Marianetti, D. Morgan, A. Van der Ven, A. Predith, and G. Ceder, *Phys. Rev. B*, 2002, **66**, 144107.
26. R. B. King, *Coord. Chem. Rev.*, 2000, **200–202**, 813.
27. X. Wang, L. Andrews, L. Manceron, and C. Marsden, *J. Phys. Chem. A*, 2003, **107**, 8492.
28. L. Andrews and X. Wang, *J. Am. Chem. Soc.*, 2003, **125**, 11751.
29. T. Söhnel, H. Hermann, and P. Schwerdtfeger, *Angew. Chem., Int. Ed. Engl.*, 2001, **40**, 4382.
30. J. T. Hougen, G. E. Leroi, and T. C. James, *J. Chem. Phys.*, 1961, **34**, 1670.
31. C. N. Satterfield, 'Heterogeneous Catalysis in Industrial Practice', 2nd edn., McGraw-Hill, New York, 1991.
32. L. Subramanian and R. Hoffmann, *Inorg. Chem.*, 1992, **31**, 1021.
33. S. Jagner and G. Helgesson, *Adv. Inorg. Chem*, 1991, **37**, 1.
34. J. A. Tossell and D. J. Vaughan, *Inorg. Chem.*, 1981, **20**, 3333.
35. D. W. Smith, *Coord. Chem. Rev.*, 1976, **21**, 93.
36. C. Hasselgren, S. Jagner, and I. Dance, *Chem. Eur. J.*, 2002, **8**, 1269.
37. S. Ikeda, T. Nakajima, and K. Hirao, *Molec. Phys.*, 2003, **101**, 105.
38. W. Wang, C. Lan, Y. Li, K. Hong, and G. Wang, *Chem. Phys. Lett.*, 2002, **366**, 220.
39. B. J. Hathaway, in 'Comprehensive Coordination Chemistry', eds. G. Wilkinson, R. D. Gillard, and J. A. McCleverty, Pergamon, New York, 1987, p. 533.
40. A. F. Wells, 'Structural Inorganic Chemistry', Clarendon Press, Oxford, 1984.
41. A. Buljan, M. Llunell, E. Ruiz, and P. Alemany, *Chem. Mater.*, 2001, **13**, 338.
42. J. M. Zuo, M. Kim, M. O'Keeffe, and J. C. H. Spence, *Nature*, 1999, **401**, 49.
43. M. L. Ruiz-González, C. Prieto, J. Alonso, J. Ramírez-Castellanos, and J. M. González-Calbet, *Chem. Mater.*, 2002, **14**, 2055.
44. N. N. Greenwood and A. Earnshaw, 'Chemistry of the Elements', 2nd edn., Butterworth Heinemann, Boston, 1997.
45. X. Zhang, M. G. Kanatzidis, T. Hogan, and C. R. Kannewurf, *J. Am. Chem. Soc.*, 1996, **118**, 693.
46. K. K. Banger, J. Cowen, and A. F. Hepp, *Chem. Mater.*, 2001, **13**, 3827.
47. X. Chen, X. Huang, and J. Li, *Inorg. Chem.*, 2001, **40**, 1341.
48. P. Sekar, F. P. Arnold, and J. A. Ibers Jr *Inorg. Chem.*, 2002, **41**, 577.
49. F. A. Cotton, G. Wilkinson, C. A. Murillo, and M. Bochmann, 'Advanced Inorganic Chemistry', 6th edn., Wiley, New York, 1999.
50. A. J. Blake, S. J. Hill, and P. Hubberstey, *Chem. Commun.*, 1998, 1587.
51. B. J. Hathaway, in 'Comprehensive Coordination Chemistry', eds. G. Wilkinson, R. D. Gillard, and J. A. McCleverty, Pergamon, New York, 1987, p. 413.
52. Q. Huang and S.-J. Hwu, *Inorg. Chem.*, 2003, **42**, 655.
53. A. A. Belik, A. P. Malakho, B. I. Lazoryak, and S. S. Khasanov, *J. Solid State Chem.*, 2002, **163**, 121.
54. D. Y. Naumov, M. I. Naumova, N. V. Kuratieva, E. V. Boldyreva, and J. A. K. Howard, *Acta Cryst.*, 2002, **C58**, i55.
55. L. Armelao, D. Barreca, M. Bertapelle, G. Bottaro, C. Sada, and E. Tondello, *Thin Solid Films*, 2003, **442**, 48.
56. O. W. Kolling and J. L. Lambert, *Inorg. Chem.*, 1964, **3**, 202.
57. A. C. Warden, M. T. W. Hearn, and L. Spiccia, *Inorg. Chem.*, 2003, **42**, 7037.
58. M. Hå kansson, C. Lopes, and S. Jagner, *Inorg. Chim. Acta*, 2000, **304**, 178.
59. J.-L. Pascal, J. Potier, and C. S. Zhang, *J. Chem. Soc. Dalton Trans.*, 1985, 297. references therein.
60. K. Koszinowski, D. Schröder, H. Schwarz, M. C. Holthausen, J. Sauer, H. Koizumi, and P. B. Armentrout, *Inorg. Chem.*, 2002, **41**, 5882.
61. R. Mukherjee, in 'Comprehensive Coordination Chemistry II', eds. J. A. McCleverty and T. J. Meyer, Elsevier, New York, 2004, p. 747.
62. D. R. Smith, *Coord. Chem. Rev.*, 1997, **164**, 575.
63. D. R. Smith, *Coord. Chem. Rev.*, 1998, **172**, 457.
64. D. W. Smith, *Annu. Rep. Prog. Chem., Sect. A*, 1998, **94**, 233.
65. D. W. Smith, *Annu. Rep. Prog. Chem., Sect. A*, 1999, **95**, 189.
66. D. W. Smith, *Annu. Rep. Prog. Chem., Sect. A*, 2000, **96**, 255.
67. D. W. Smith, *Annu. Rep. Prog. Chem., Sect. A*, 2001, **97**, 217.

68. D. W. Smith, *Annu. Rep. Prog. Chem., Sect. A*, 2002, **98**, 213.
69. D. W. Smith, *Annu. Rep. Prog. Chem., Sect. A*, 2003, **99**, 221.
70. R. D. Rieke, M. S. Sell, W. R. Klein, T.-A. Chen, J. D. Brown, and M. V. Hanson, in 'Active Metals', ed. A. Fürstner, VCH, New York, 1996, p. 1.
71. L. Balogh and D. A. Tomalia, *J. Am. Chem. Soc.*, 1998, 7355.
72. A. Mortreux, F. Petit, eds. 'Industrial Applications of Homogeneous Catalysis'; D. Reidel: Boston, 1988.
73. W. S. Mohoney, D. M. Brestensky, and J. M. Stryker, *J. Am. Chem. Soc.*, 1988, **110**, 291.
74. B. H. Lipshutz, K. Noson, W. Chrisman, and A. Lower, *J. Am. Chem. Soc.*, 2003, **125**, 8779.
75. R. R. Gagné, J. L. Allison, R. S. Gall, and C. A. Koval, *J. Am. Chem. Soc.*, 1977, **99**, 7170.
76. N. Armaroli, *Chem. Soc. Rev.*, 2001, **30**, 113.
77. D. G. Cuttell, S.-M. Kuang, P. E. Fanwick, D. R. McMillin, and R. A. Walton, *J. Am. Chem. Soc.*, 2002, **124**, 6.
78. S. Trofimenko, 'Scorpionates – The Coordination Chemistry of Polypyrazolylborate Ligands', Imperial College Press, London, 1999.
79. R. R. Conry, G. Ji, and A. A. Tipton, *Inorg. Chem.*, 1999, **38**, 906. references therein.
80. C. W. Liu, H.-C. Chen, J. C. Wang, and T.-C. Keng, *Angew. Chem., Int. Ed. Engl.*, 2001, **40**, 2342.
81. L. T. S. Rimple, A. Castineiras, P. Turner, *Inorg. Chem.* 2003, **42**, 4731.
82. B. R. James, 'Homogeneous Hydrogenation', Wiley-Interscience, New York, 1973.
83. M. P. Doyle, M. A. McKervey, and T. Ye, 'Modern Catalytic Methods for Organic Synthesis with Diazo Compounds', Wiley-Interscience, New York, 1999.
84. T. Aratoni, *Pure Appl. Chem.*, 1985, **57**, 1839.
85. K. Takahashi, R. Nakajima, G. Zhong-ze, H. Yoshiki, A. Fujishima, and O. Sato, *Chem. Commun.*, 2002, 1578.
86. P. L. Holland and W. B. Tolman, *Coord. Chem. Rev.*, 1999, **190–192**, 855.
87. T. Rovis and D. A. Evans, *Prog. Inorg. Chem.*, 2001, **50**, 1.
88. K. M. Deck, T. A. Tseng, and J. N. Burstyn, *Inorg. Chem.*, 2002, **41**, 669.
89. I. Hadinec, L. Jensovsky, A. Linek, and V. Synecek, *Naturwissenschaften*, 1960, **47**, 377.
90. G. R. Clark, B. W. Skelton, and T. N. Waters, *J. Chem. Soc., Chem. Commun.*, 1972, 1163.
91. H. Furuta, H. Maeda, and A. Osuka, *J. Am. Chem. Soc.*, 2000, **122**, 803.
92. R. M. Wing, *J. Am. Chem. Soc.*, 1968, **90**, 4828.
93. D. W. Margerum, W. M. Scheper, M. R. McDonald, F. C. Fredericks, L. Wang, and H. D. Lee, in 'Bioinorganic Chemistry of Copper', eds. K. D. Karlin, and Z. Tyeklár, Chapman & Hall, New York, 1993, p. 213.
94. W. Harnischmacher and R. Hoppe, *Angew. Chem., Int. Ed. Engl.*, 1973, **12**, 582.
95. M. Arjomand and D. J. Machin, *J. Chem. Soc., Dalton Trans.*, 1975, 1061.
96. V. E. Bondybey and J. H. English, *J. Phys. Chem.*, 1984, **88**, 2247.
97. M. C. Linder, 'Biochemistry of Copper', Plenum, New York, 1991.
98. E. T. Adman, *Adv. Protein Chem.*, 1991, **42**, 145.
99. R. M. LLanos and J. F. B. Mercer, *DNA Cell. Biol*, 2002, **21**, 259.
100. D. G. Barceloux, *Clin. Toxicol.*, 1999, **37**, 217.
101. 2005, http://www.menkessyndrome.com/index.html.
102. G. J. Brewer, *Curr. Opin. Cell Biol.*, 2003, **7**, 207.
103. 2005, http://www.wilsonsdisease.org/.

Copper: Organometallic Chemistry

Bruce H. Lipshutz & Steven S. Pfeiffer
University of California, Santa Barbara, CA, USA

Based in part on the article Copper: Organometallic Chemistry by Bruce H. Lipshutz & Michael R. Wood which appeared in the Encyclopedia of Inorganic Chemistry, First Edition.

1 Introduction 1
2 Copper-catalyzed Cross-couplings 1
3 Asymmetric Catalysis with Cu(I) 3
4 Oxidation & Cyclization Reactions 5
5 Cyanocuprate Technology 7
6 Spectroscopic & Structural Studies 9
7 Mechanistic Advances 11
8 Related Articles 13
9 References 13

Glossary

Carbocupration: addition of the elements of copper and carbon across a C–C triple bond
Cyanocuprates: RCu(CN)Li, $R_2Cu(CN)Li_2/[R_2Cu]^-[Li_2CN]^+$
Gilman cuprate: R_2CuLi
Phosphine Ligands: species coordinated *via* phosphorus to copper in this case

Abbreviations

LO cuprate = A lower order cuprate; HO cuprate = A higher order cuprate; R_r = A residual or nontransferable ligand; R_t = A transferable ligand; hfa = Hexafluoroacetylacetone; acac = Acetylacetonate; EWG = Electron-withdrawing group; TfO = Trifluoromethylsulfonyloxy (triflate).

1 INTRODUCTION

Roughly 10 years ago, the discussion on copper chemistry in this *Encyclopedia* focused mainly on reactions and physical organic studies of ‘organocuprates’, or copper(I) *ate* (i.e. salt) complexes. In general, these highly valued, extensively utilized reagents ‘R_2CuLi’ are prepared in the traditional Gilman fashion (from 2RLi + CuX), or *via* ligand exchange with other organometallics (e.g. stannanes, zirconocenes, etc.). They continue to serve synthetic practitioners who have come to rely on their ability to mainly effect substitution, conjugate addition, and to a lesser extent, carbocupration reactions (Scheme 1).

Implied in the stoichiometry of their preparation is the full equivalent of transition metal relative to substrate. Indeed, to this day, cuprates tend to be used in excess in most smaller scale reactions. Over the past decade, however, there has been a noticeable shift toward development of methodology catalytic in Cu(I). The rationale behind the emphasis is in line with the times; that is, environmental concerns have come to the fore, placing implied limits on the extent of transition metal usage. Therefore, notwithstanding favorable economic factors associated with copper, it being a ‘base’ rather than ‘precious’ metal, much effort has been devoted toward copper-catalyzed reactions, including cross-couplings to arrive at C–N, C–O, and C–H, in addition to C–C bonds. Moreover, tremendous strides have been made in asymmetric versions of perhaps the most fundamental of cuprate reactions: 1,4-additions to Michael acceptors.

A wealth of new and valuable structural information on cuprates has appeared in the recent literature. The importance of ligands on copper, which impact residues on the metal undergoing transfer to a substrate, are better understood, as are the locations of counterions ‘X’ that derive from the starting copper(I) salts (‘CuX’). Advances in technology have translated into opportunities for carrying out highly sophisticated spectral and computational studies that have provided much insight regarding the mechanistic pathways that account for these important synthetic processes.

2 COPPER-CATALYZED CROSS-COUPLINGS

Copper salts have become crucial additives for bond forming reactions between carbon and heteroatoms such as N, O, S, or P. While many involve a transmetalation (*see Transmetalation*) step from Pd, Ni, Sn, B, Te, Se, Mg, and so on, several of these cross-coupling (*see Coupling*) reactions occur with copper as the only metal present. Typically, a (bidentate) ligand is used for stabilization of a copper-containing intermediate, while enhancing reactivity of the copper catalyst.

Extensive progress has been made over the past decade in C–N bond formations, including amines,**[1]** heteroaromatics,**[2]** amides,**[3]** oxazolidinones,**[4]** aziridines,**[5]** azodicarboxylates,**[6]** and hydroxylamines.**[7]** A variety of carbon-based substrates such as aryl and vinyl halides, alkenes, alkynes, enols, and nitroaromatics may serve as reaction partners (Scheme 2). The standard coupling reaction requires, in addition to a Cu(I) or Cu(II) source (e.g. CuCN, CuI, $Cu(OTf)_2$, $Cu(OAc)_2$, etc.), a base (e.g. Et_3N, K_2CO_3, Cs_2CO_3, K_3PO_4, or 2,6-lutidine), and a solvent (e.g. PhMe, dioxane, DME, CH_2Cl_2, THF, DMF), with reaction temperatures ranging from 23 to 110 °C. 1,2-Diamino ligands have been shown to aid in the amidation

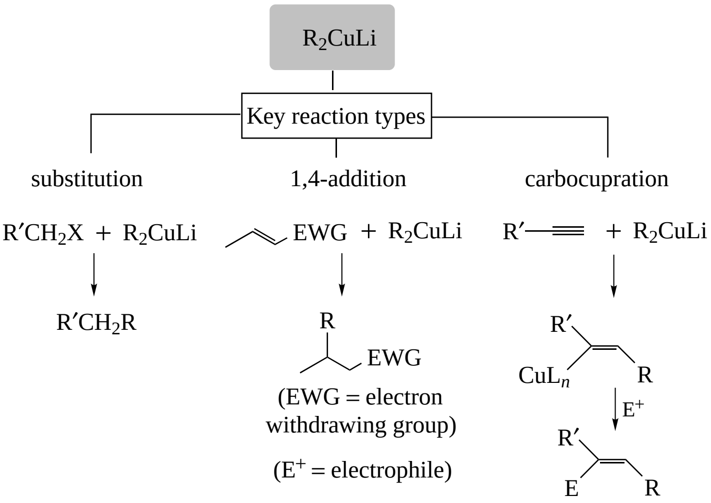
R2CuLi
Key reaction types
substitution
1,4-addition
carbocupration
R′CH2X + R2CuLi
EWG + R2CuLi
R′ + R2CuLi
R′CH2R
R
EWG
(EWG = electron withdrawing group)
(E+ = electrophile)
R′
CuLn
R
E+
R′
E
R

Scheme 1

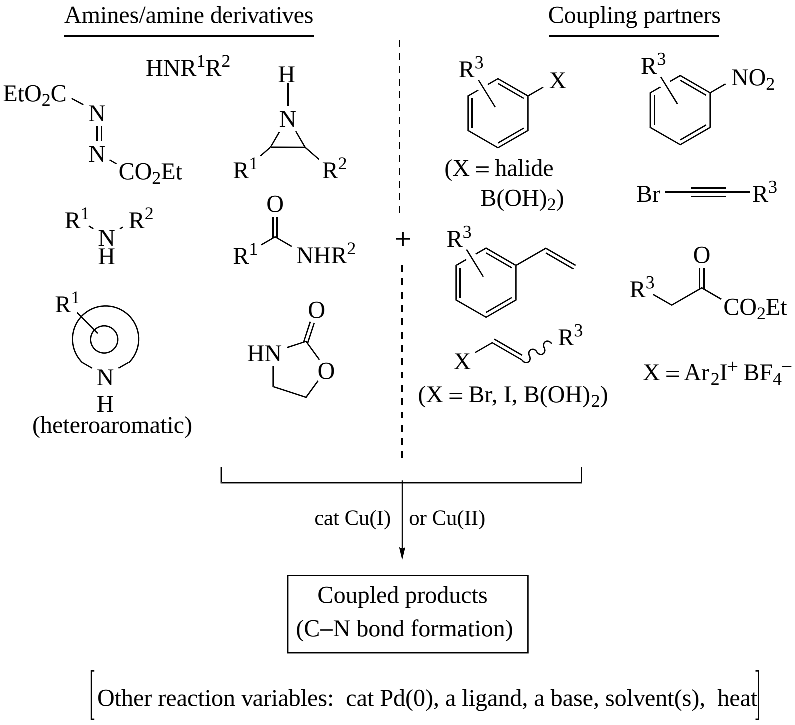
Amines/amine derivatives
Coupling partners
HNR1R2
EtO2C
N
N
CO2Et
H
N
R1
R2
R1
R2
N
H
O
R1
NHR2
R1
N
H
(heteroaromatic)
O
HN
O
+
R3
X
(X = halide
B(OH)2)
R3
NO2
Br
R3
R3
O
R3
CO2Et
X
R3
(X = Br, I, B(OH)2)
X = Ar2I+ BF4−
cat Cu(I)
or Cu(II)
Coupled products
(C–N bond formation)
Other reaction variables: cat Pd(0), a ligand, a base, solvent(s), heat

Scheme 2

process, although use of an external ligand does not seem to be a general requirement for aminations.[3c]

As with C–N couplings, C–O, C–S, and C–P bond formations also require a Cu(I) or Cu(II) source, a base, and solvent, with reaction temperatures ranging from 45 to 195°C. Typically the couplings (*see Coupling*) are performed with aryl/vinyl boronic acids[8] and aryl iodides (Scheme 3). Use of microwave technology allows for aryl thioether formation between aryl bromides and thiophenols.[9] Inclusion of external ligands is not required for coupling, although several have been used to presumably assist with solubility/stability of the catalyst.[10]

Nonracemic binaphthol (BINOL) ligands are heavily utilized in asymmetric synthesis. They can be readily fashioned from 2-naphthol precursors employing Cu(I) or Cu(II) salts. With either an external source of chirality (e.g. 1,5-diaza-*cis*-decalin, **1**),[11] or an internal chiral center (e.g. as in the proline-derived amide **2**),[12] derivatives substituted at the key 3- and 3′-sites are realized under mild conditions with ee’s (*see Enantioselectivity*) up to 94%.

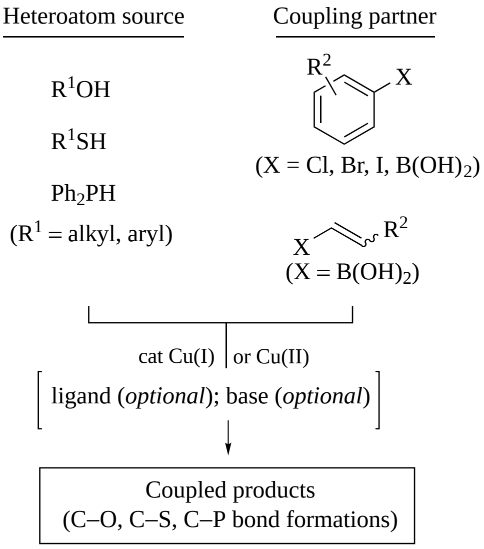
Heteroatom source
Coupling partner
R1OH
R1SH
Ph2PH
(R1 = alkyl, aryl)
R2
X
(X = Cl, Br, I, B(OH)2)
X
R2
(X = B(OH)2)
cat Cu(I)
or Cu(II)
ligand (optional); base (optional)
Coupled products
(C–O, C–S, C–P bond formations)

Scheme 3

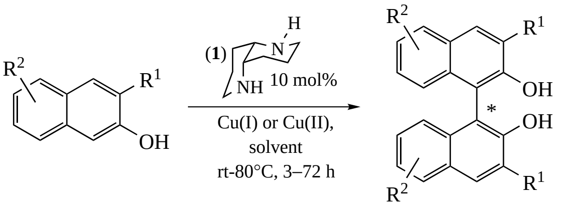
R2
R1
OH
(1)
H
N
NH
10 mol%
Cu(I) or Cu(II),
solvent
rt-80°C, 3–72 h
R2
R1
OH
*
OH
R2
R1

(1)

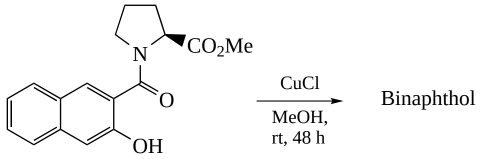
N
CO2Me
O
OH
CuCl
MeOH,
rt, 48 h
Binaphthol

(**2**)

(2)

Other especially useful C–C coupling reactions wherein copper functions as the only metal catalyst present include (**1**) alkynes with acid chlorides (equation 3);[13] (**2**) alkynes with other alkynes (Glaser couplings; equation 4);[14] and (**3**) Grignard reagents with alkyl fluorides (equation 5).[15] Notably, copper mediated couplings of C_{sp3}-fluorine bonds with alkyl or aryl Grignards (*see Grignard Reagents*) indicate that usually inert fluorinated compounds can be functionalized using copper-based organometallic chemistry.

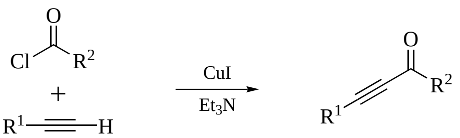
O
Cl
R2
+
R1
H
CuI
Et3N
O
R2
R1

(3)

$$R^1—≡—H + R^2—≡—H \xrightarrow[\text{EtNH}_2\text{, MeOH}]{\text{CuCl, NH}_2\text{OH}} R^1—≡—≡—R^2 \qquad (4)$$

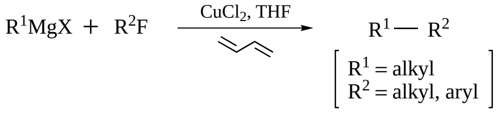
R1MgX + R2F
CuCl2, THF
R1— R2
R1 = alkyl
R2 = alkyl, aryl

(5)

Much effort has gone into further development of Sonogashira couplings (*see Sonogashira Coupling*) between an alkyne and an aryl or vinyl halide. These palladium or nickel mediated reactions call for catalytic copper as an important additive. Variations on this theme have expanded the substrate pool to include aryl/vinyl/alkyl halides,[16] allenes,[17] and vinyl selenides/tellurides[18] as coupling partners with alkynes. Thus, in addition to the presence of a palladium catalyst (Pd(0) or Pd(II)), copper salts such as CuCl, $CuBr{\cdot}SMe_2$, CuI, Cu(3-methylsalicylate), $CuOP(O)Ph_2$, and $CuCl_2$ have all found use. As in traditional Sonogashira reactions, an amine base (e.g. pyrrolidine, diisopropylamine, or Et_3N) is required. Solvents can also vary, such as toluene, MeOH, CH_2Cl_2, or THF, and in some cases, the amine itself can be used as the medium.

Several related cross-couplings that involve both catalytic levels of Pd and Cu have also been reported, such as Heck-like reactions (*see Heck Reaction*) of vinyl esters with arylstannanes (equation 6),[19] aryl selenenylations between $Bu_3SnSeAr$ and aryl halides (equation 7),[20] and thioarene or thioester couplings to aryl, vinyl, or alkyl stannanes (equation 8).[21]

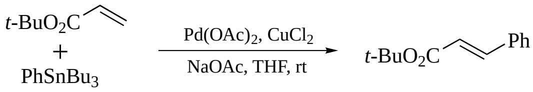
t-BuO2C
+
PhSnBu3
Pd(OAc)2, CuCl2
NaOAc, THF, rt
t-BuO2C
Ph

(6)

$$\text{ArBr} + \text{4-FC}_6\text{H}_4\text{SeSnBu}_3 \xrightarrow[\text{1, 10-phenanthroline}]{\text{CuI, DMF, 110 °C}} \text{4-FC}_6\text{H}_4\text{SeAr} \qquad (7)$$

$$R^1SR^2 + Bu_3SnR^3 \xrightarrow[\text{cat Pd(0), THF or DME, }\sim 50\,°\text{C}]{\text{CuMeSal, CuBr·SMe}_2\text{, or CuOP(O)Ph}_2} R^1 - R^3 \qquad (8)$$

$$\left[\begin{array}{l} R^1 = \text{Ar, HetAr, COR}^4 \\ R^2 = \text{Me, } p\text{-tolyl} \\ R^3 = \text{Ar, HetAr, vinyl} \end{array}\right]$$

3 ASYMMETRIC CATALYSIS WITH Cu(I)

For effective use of catalytic copper in asymmetric reactions, there are many variables that must be controlled: solvents, that impact aggregation state, gegenion Lewis acidity (*see Lewis Acids & Bases*) in solution, that can greatly affect rates of couplings; the stoichiometric organometallic source of the residue to be transferred *via* copper, that must be relatively unreactive to avoid a competitive background reaction thereby reducing observed levels of induction; and the most critical parameter, the choice of chiral ligand, for given the facility with which groups on copper exchange between metal centers, chelation control is crucial for success.

Most of the focus has been on asymmetric conjugate additions to unsaturated ketones.[22] A combination of copper salt (usually copper triflate, Cu(OTf)$_2$), a dialkylzinc reagent (*see* ***Zinc: Organometallic Chemistry***) (which reduces Cu(II) to Cu(I) in situ and supplies the group to be transferred to the substrate), and a nonracemic ligand (which is usually a mono- or bidentate phosphine) is common, such reactions oftentimes being run in toluene or CH_2Cl_2 and can lead to very high facial selectivities. Model substrates tend to be cyclohexenone and chalcone, representative of cyclic and acyclic enones, respectively.

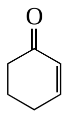

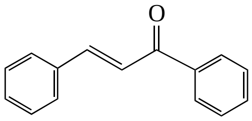

chalcone

Ligands such as phosphoramidite (**3**) and TADDOLs (**4**) have proven to be remarkably discriminating in their reactions of cyclic cases. Due to interconversion between s-cis and s-trans conformers, acyclic systems have been far more challenging. Here, optically pure peptidic phosphines (e.g. **5**) deliver products of 1,4-additions in good yields and high enantioselectivities (equation 9).

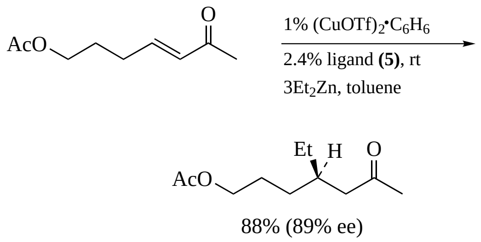
AcO
O
1% (CuOTf)2•C6H6
2.4% ligand (5), rt
3Et2Zn, toluene
AcO
Et H O
88% (89% ee)

(9)

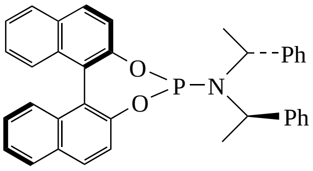

(**3**)

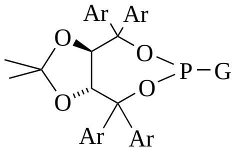
Ar Ar
O
O
O
O
P G
Ar Ar

(**4**) G = OR, NR$_2$

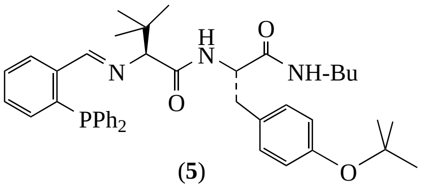
N
H
N
O
O
NH-Bu
PPh2
O

(**5**)

An alternate strategy to control absolute stereochemistry at a β-site to a carbonyl calls for asymmetric addition of a copper hydride (i.e. CuH)[23] to a β,β-disubstituted carbonyl

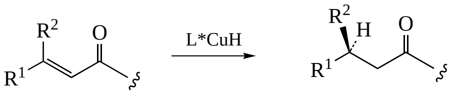
R2 O
R1
L*CuH
R2 H O
R1

(10)

array (equation 10). With the advent of extremely powerful biaryl bis-phosphine ligands, such as Roche's BIPHEP (e.g. **6**),[24a] Takasago's SEGPHOS (e.g. **7**),[24b] and Solvias' JOSIPHOS (e.g. **8**)[24c] series, many substrate types can now be reduced in very high ee's. Thus, in the presence of *in situ* generated CuH (from CuCl + NaO-*t*-Bu, with a silane as the stoichiometric source of hydride), the ligated CuH reduces aryl ketones (with BIPHEP or SEGPHOS),[25a] cyclic enones (with SEGPHOS),[25b] acyclic enones (with JOSIPHOS),[25c] and enoates and unsaturated lactones (with SEGPHOS and JOSIPHOS).[25d] Particularly noteworthy is the case of aryl imines (**9**), which afford nonracemic benzylic amines at ambient temperatures (equation 11).[25e]

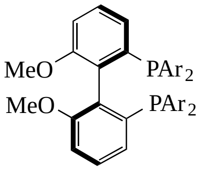
MeO
PAr2
MeO
PAr2

(**6**)

Roche's (*R*)-BIPHEP series

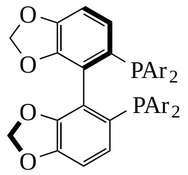
O
O
PAr2
O
O
PAr2

(**7**)

Takasago's (*R*)-SEGPHOS series

(Ar = Ph, substituted Ph)

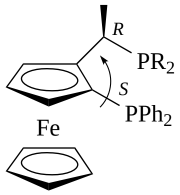
R
PR2
S
PPh2
Fe

(**8**)

Solvias' *R,S*-JOSIPHOS series

(R = *t*-Bu, Cy, etc..)

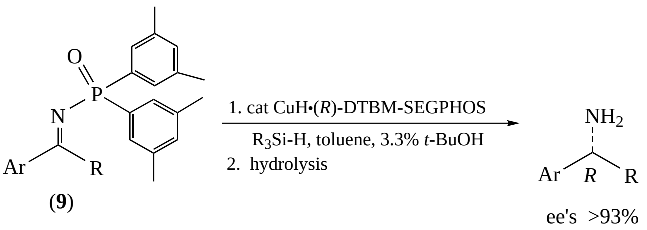
O
P
N
Ar R
1. cat CuH•(R)-DTBM-SEGPHOS
R3Si-H, toluene, 3.3% t-BuOH
2. hydrolysis
NH2
Ar R R
ee's >93%

(**9**)

(11)

Great strides in asymmetric allylic alkylations have been made very recently, with Cu(I) playing a key role. Not surprisingly, the ligand, to a far greater extent than the other reaction variables, determines the extent of success as measured by observed ee's. Allylic halides, including cinnamates generalized by (**10**), react with Grignards (*see Grignard Reagents*) in the presence of copper thiophenecarboxylate (CuTC) and phosphoramidite ligand (**11**).[26a] The regioselectivity (*see Regioselectivity*) (S_N2':S_N2) is usually high, and ee's in the >90% range are to be expected (equation 12).

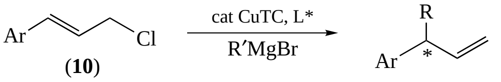
Ar
Cl
(10)
cat CuTC, L*
R′MgBr
R
Ar
*

(12)

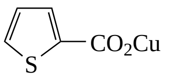

CuTC

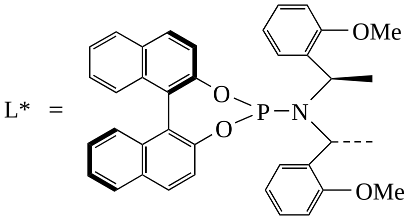
L* =
OMe
O
O
P
N
OMe

(**11**)

Related allylic systems, such as enoates (**12**) bearing a phosphate leaving group are susceptible to copper-catalyzed S_N2' reactions.[26b] Employing copper triflate and a dialkylzinc, peptidic ligand (**13**) is especially effective at inducing asymmetry at the newly created stereogenic carbon α to the ester in (**14**) (equation 13).

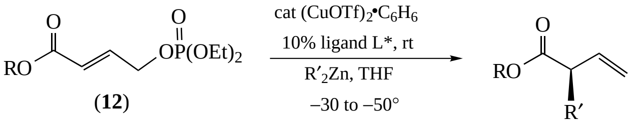
O
RO
O
OP(OEt)2
(12)
cat (CuOTf)2•C6H6
10% ligand L*, rt
R′2Zn, THF
−30 to −50°
O
RO
R′

(**14**) ee's 87–97%

(13)

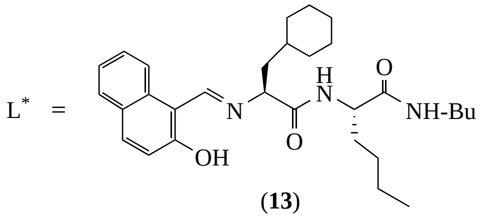
L* =
N
O
H
N
O
NH-Bu
OH

(**13**)

4 OXIDATION & CYCLIZATION REACTIONS

4.1 Oxidations

Oftentimes, a transition metal catalyst is needed to effect an oxidation at carbon. Both Cu(I) and Cu(II) complexes have gained recent recognition as catalysts for this purpose because of their minimal cost and relatively low toxicity. In the presence of a co-oxidant and a stabilizing ligand, oxidations of alcohols, hydroquinones, olefins, and simple hydrocarbons can be accomplished under mild conditions. Oxidants, such as TEMPO,[27] peroxides (e.g. H_2O_2, t-BuOOH),[28] or O_2[29] assist in the conversion of alcohols (**15**) to aldehydes (**16**) or ketones (**17**) in media that ranges from H_2O to biphasic fluorous in nature, and have been accomplished as well even without solvent. These oxidations are typically performed at somewhat elevated temperatures and use a variety of copper sources (e.g. CuCl, CuBr·SMe_2, $CuCl_2$, $Cu(NO_3)_2$). Nitrogen-based bidentate salen-type ligands (**18–21**) play a key role owing to their stabilizing influence on copper during these reactions, which are typically high-yielding (>90%).

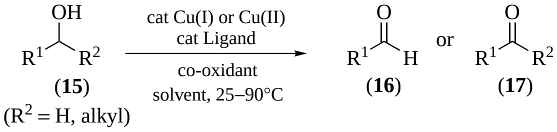
OH
R1
R2
(15)
(R2 = H, alkyl)
cat Cu(I) or Cu(II)
cat Ligand
co-oxidant
solvent, 25–90°C
O
R1
H
(16)
or
O
R1
R2
(17)

(14)

Ligands

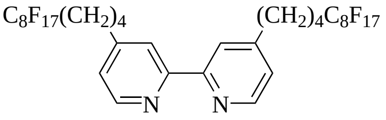
C8F17(CH2)4
(CH2)4C8F17
N
N

(**18**)

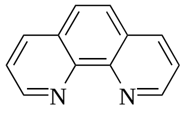

(**19**)

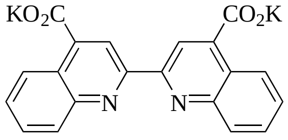
KO2C
CO2K
N
N

(**20**)

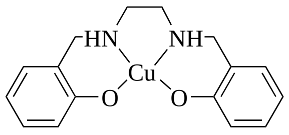

(**21**)

Oxidation of a phenol to the corresponding p-quinone using a copper catalyst takes place at room temperature under similar conditions as those used for alcohol oxidation, with O_2 as oxidant. Likewise, hydroquinones (**22**) can be transformed to 3-alkoxy-p-quinones (**23**) when reacted in the presence of an alcohol.[30] In the case of 4-substituted phenols (**24**), polymer-based catalysts composed of ligands (e.g. PVBPy) that chelate copper have been used at elevated temperatures to selectively oxidize a benzylic carbon to yield 4-hydroxybenzaldehydes (**25**) in good yields.[31]

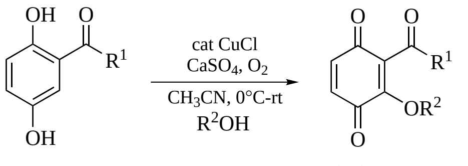
OH
O
R1
OH
cat CuCl
CaSO4, O2
CH3CN, 0°C-rt
R2OH
O
O
R1
OR2
O

(15)

(**22**) (**23**) 71–88%

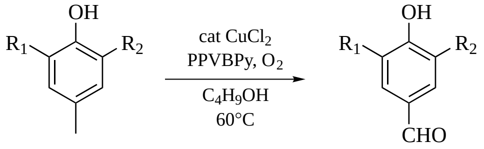
OH
R1
R2
cat CuCl2
PPVBPy, O2
C4H9OH
60°C
OH
R1
R2
CHO

(**24**) (**25**) 47–94% (16)

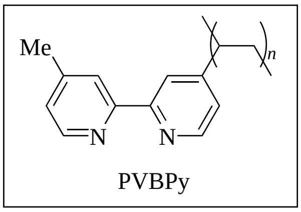

PVBPy

Copper catalysts, such as $Cu(CH_3CN)_4PF_6$ and $Cu(BF_4)_2\cdot nH_2O$, have also found utility in the epoxidation of olefins using MCPBA or O_2 as the stoichiometric oxidant.[32,33] Oxidations of C–N and C–H bonds are also successfully carried out under such catalytic conditions. For example, aldehydes are readily converted in one pot to the corresponding nitriles, by way of the initially formed imine, upon treatment with ammonia and aqueous hydrogen peroxide with CuCl or $CuCl_2$ as catalyst.[34] Primary amines are converted to nitriles, and secondary amines to imines, when treated with Cu(I) or Cu(II) catalysts and O_2 as oxidant.[35] Oxidation of a C–H bond is much more difficult, although such processes are of increasing importance in organic chemistry. Typically, expensive ruthenium, or toxic iron complexes are used, although $Cu(OH)_2$, $Cu(OAc)_2$, and $CuCl_2$/18-crown-6 show considerable promise as alternatives.[36] Turnover numbers (TON) on the order of 27 000 were reported for the $Cu(OAc)_2$ catalyzed oxidation of cyclohexane to cyclohexanol and cyclohexanone (∼1:1) with O_2 as oxidant.[36] C–H oxidation can also occur *via* transient metal carbene complex insertion. Recently, $Tp^{Ms}Cu$ (**26**) and ethyl diazoacetate (as the carbene source) were shown to activate cycloalkanes and cyclic ethers to afford substituted carbo- and heterocycles, respectively,[37] highlighting useful chemistry on very basic starting materials (equation 17).

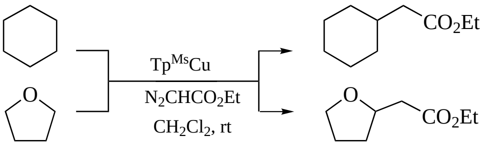
O
TpMsCu
N2CHCO2Et
CH2Cl2, rt
CO2Et
O
CO2Et

(17)

4.2 Cyclizations

Cyclization reactions, where Cu(II) serves as a Lewis acid, have been utilized in the formation of substituted indoles (**28**) from 2-ethynylaniline derivatives (**27**).[38] The combination of isocyanates (**29**) and allylic carbonates (**30**) also leads to substituted indoles (**31**), in this case relying on both catalytic amounts of Pd(0) and Cu(I).[39] Here, a π-allylpalladium intermediate between the metal and allylic fragment, is followed by insertion into the isocyanate. Proposed Lewis acid complexation of the alkyne by CuCl and ultimately reductive elimination (*see Reductive Elimination*) from palladium provides 2,3-disubstituted indoles.

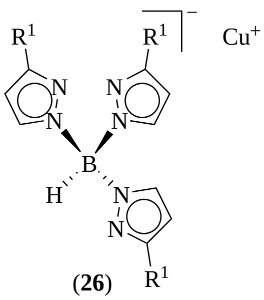
R1
R1
−
Cu+
N
N
N
N
B
H
N
N
R1

(**26**)

$Tp^{Ms}Cu$

$R^1 = 2,4,6\text{-}Me_3C_6H_2$

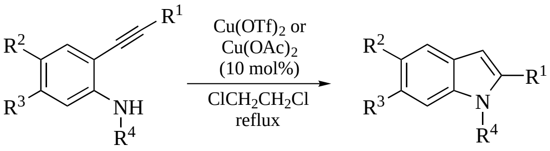
R1
R2
R3
NH
R4
Cu(OTf)2 or
Cu(OAc)2
(10 mol%)
ClCH2CH2Cl
reflux
R2
R3
R1
N
R4

(**27**) (**28**) 9–95% (18)

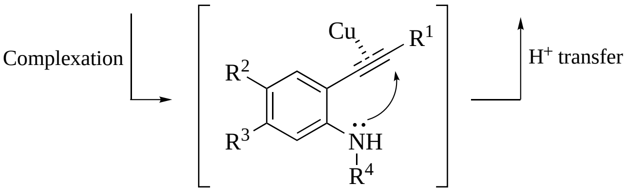
Complexation
Cu
R1
R2
R3
NH
R4
H+ transfer

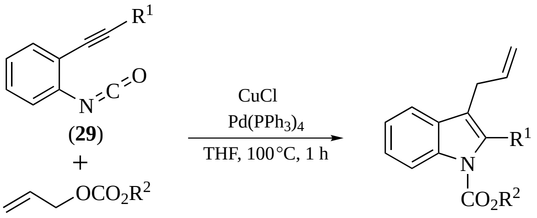
R1
N
C
O
(29)
+
OCO2R2
CuCl
Pd(PPh3)4
THF, 100°C, 1 h
R1
N
CO2R2

(**30**) (**31**) (19)

Cu(I)-mediated cyclizations to substituted isoquinolines (**34**),[40] or their monocyclic pyridyl analogs, take place in one pot following a Pd/Cu catalyzed Sonogashira coupling (*see Sonogashira Coupling*) between an aryl halide (**32**) and alkyne (**33**).

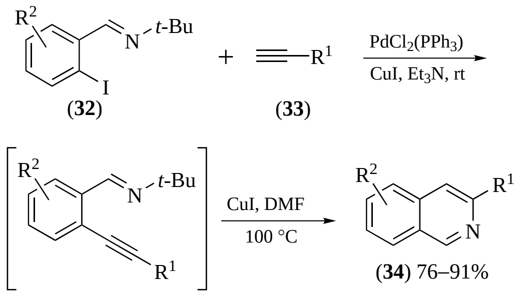

(**32**) (**33**) (**34**) 76–91%

(20)

Various imidazo[1,5-a]imidazoles (**35**), imidazo[1,5-a] pyridines (**36**), and imidazo[5,1-a]isoquinolines (**37**), important ligands or precursors to pharmaceuticals,[41] can be constructed *via* copper-catalyzed heterocyclization of Schiff's bases. A stepwise cycloaddition between azides and terminal alkynes is also catalyzed by copper salts in what has now been termed 'click' chemistry, producing 1,4-disubstituted triazoles (**38**) in excellent yields.[42]

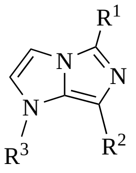

(**35**)

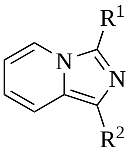

(**36**)

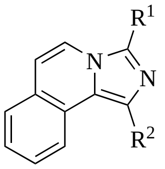

(**37**)

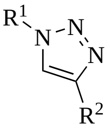

(**38**)

As an alternative to radical cyclizations induced by tin reagents (e.g. R_3SnX) that typically require elevated temperatures for activation, bidentate ligated CuCl leads to ring formations at ambient temperatures (as with **39** to **41** and **40** to **42**).[43,44]

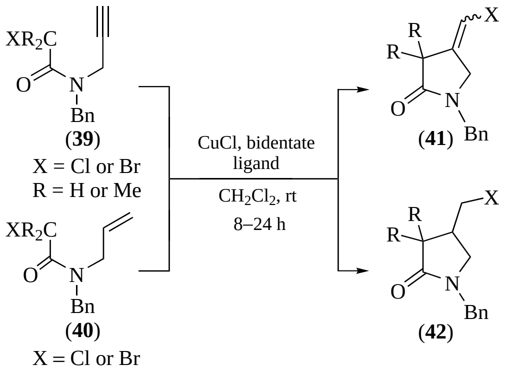

(**39**)
X = Cl or Br
R = H or Me

(**40**)
X = Cl or Br
R = F or Cl

(**41**) (**42**)

(21)

Insertion by copper(II) into a diazo derivative such as (**43**), thus forming an intermediate metallocarbene, leads to cyclized products with high stereoselectivity (e.g. **44**; after decarboxylation).[45] Diazo ketone (**45**) produced quinolizidines (**46**) and (**47**), which arise from initial metallocarbene formation, nitrogen ylide formation, and lastly, a ring-expanding 1,2-shift to complete the cyclization.

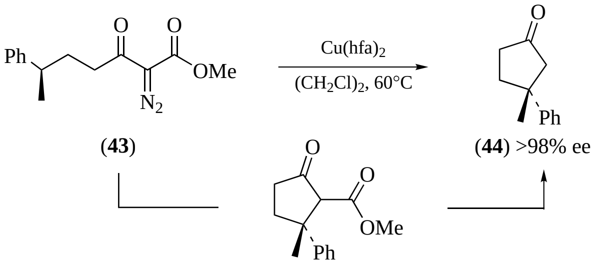

(**43**) (**44**) >98% ee

(22)

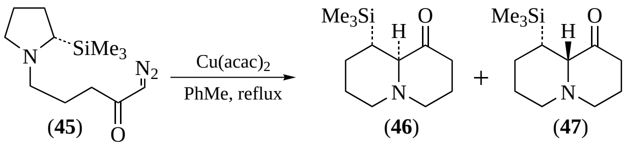

(**45**) (**46**) (**47**)

(2:1; 71% & 63% ee)

(23)

5 CYANOCUPRATE TECHNOLOGY

The lively debate that took place in print throughout the 1990s regarding the structure of cyanocuprates (*see* ***Cyanide Complexes of the Transition Metals***) (i.e. lower order (LO) monoanionic reagents $RCu(CN)Li$ and $R_2CuLi \cdot LiCN$ *vs.* higher order (HO) dianionic cyanocuprates $R_2Cu(CN)Li_2$; Scheme 4 and vide infra)[46] had little impact on their already widespread use in synthesis. While reliance on stoichiometric cuprates, whether cyano ligand-containing or otherwise, is still commonplace in organic synthesis, academicians are the main consumers of these synthetic developments as new processes only truly catalytic in transition metal stand a chance at acceptance in industrial circles.

Use of CuCN in catalytic fashion implies that another organometallic must be present bearing the desired transferable ligand (in quantities equivalent to the educt). Upon transmetalation, a complicated mix of reagents may well result, the total composition of which is likely to be unknown. For example, when solubilized catalytic $CuCN \cdot 2LiCl$[47] is added to a preformed mixed organozinc reagent (**48**) (Scheme 5), the presumed ligand exchange occurs to afford a copper(I) species which is ultimately followed by alkylation, for example by vinyl triflate (**49**). What is the nature of the copper reagent doing the chemistry? If the cyanide ligand remains on copper, then a LO cyanocuprate is formed (**50**), with a gegenion of ill-defined nature (is it the R_rZn^+, and/or the Li^+ in the pot from the $CuCN \cdot LiCl$ used to solubilize the copper(I) salt?). With excess mixed reagent R_tR_rZn (e.g. **48**) present relative to CuCN, does the CN group reside within the cluster but not on copper, forming a 'Gilman-like' species $R_2Cu^- \cdot M_2CN^+$? Related questions apply to the case of catalytic CuCN plus Grignard reagents (*see Grignard Reagents*),

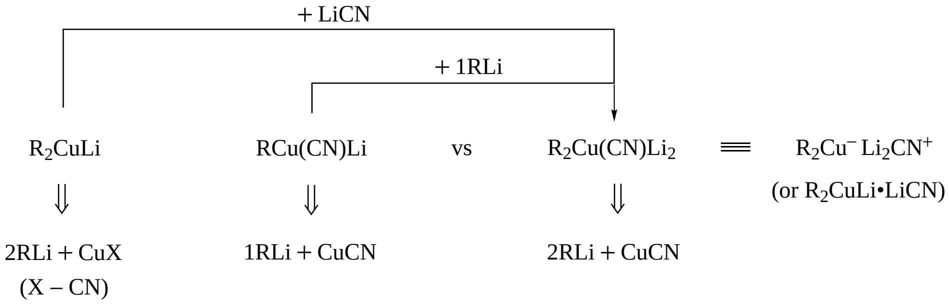
+ LiCN
+ 1RLi
R2CuLi
RCu(CN)Li
vs
R2Cu(CN)Li2
R2Cu− Li2CN+
(or R2CuLi•LiCN)
2RLi + CuX
(X – CN)
1RLi + CuCN
2RLi + CuCN

Scheme 4

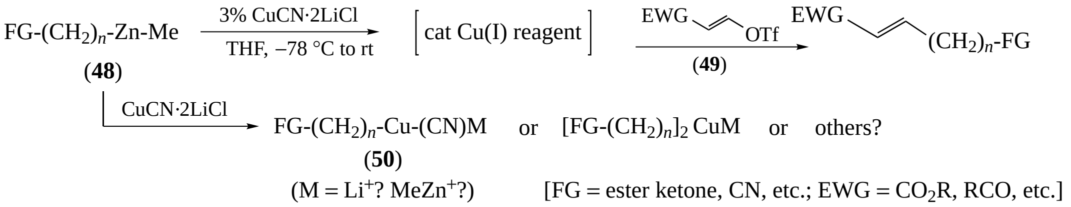
FG-(CH2)n-Zn-Me
(48)
3% CuCN·2LiCl
THF, −78 °C to rt
cat Cu(I) reagent
EWG
OTf
(49)
EWG
(CH2)n-FG
CuCN·2LiCl
FG-(CH2)n-Cu-(CN)M
or
[FG-(CH2)n]2 CuM
or
others?
(50)
(M = Li+? MeZn+?)
[FG = ester ketone, CN, etc.; EWG = CO2R, RCO, etc.]

Scheme 5

the precise nature of the species involved here as well is far from certain. Nonetheless, highly selective and mild couplings can be carried out, as represented by the functionalization of β-lactam (**51**) to derivative (**52**) (equation 24).[48a]

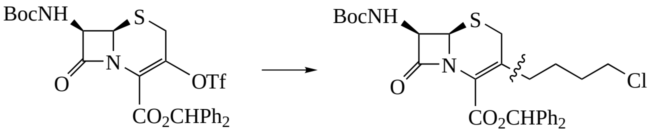
BocNH
S
N
O
OTf
CO2CHPh2
BocNH
S
N
O
Cl
CO2CHPh2

(**51**) (**52**) 86%

(24)

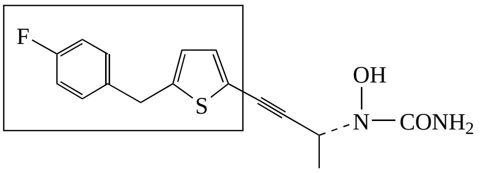
F
S
OH
N
CONH2

(**53**) ABT-761

While such questions of reagent composition remain, advances on the synthetic front have responded to the challenges of minimizing levels of copper required, whether in the form of a salt (CuCN), a halocuprate ($CuCN{\cdot}2LiCl$ = (Cl)Cu(CN)Li), or as a cuprate (RCu(CN)Li or '$R_2Cu(CN)Li_2$'). Thus, in addition to the example above (equation 24), functionalized aryl Grignard reagents undergo alkylations with primary iodides and benzylic bromides mediated by CuCN (equation 25).[48b] The latter give rise to the diarylmethane (or diheteroarylmethane) subunit, a common theme found in many active pharmaceuticals, such as with ABT-761 (**53**), a very potent 5-lipoxygenase inhibitor.[48c]

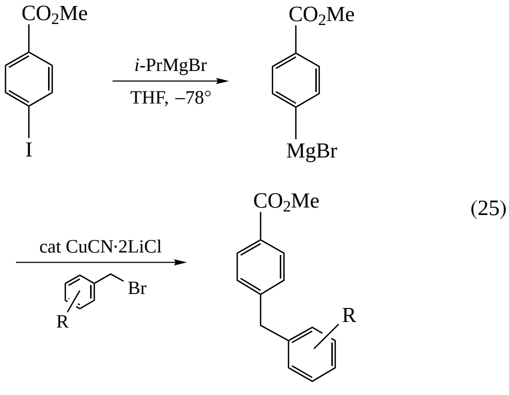
CO2Me
I
i-PrMgBr
THF, −78°
CO2Me
MgBr
cat CuCN·2LiCl
Br
R
CO2Me
R

(ca. 60%)

(25)

Transmetalations (*see Transmetalation*) between various organometallics (e.g. vinyl zirconocenes, stannanes, tellurides, alanes, etc.) and HO cyanocuprates, as discussed previously,[49] generate stoichiometric mixed cuprates that are well-behaved; they transfer the desired residue R_t and usually afford good yields. The problem, again, is that they rely on stoichiometric copper. To derive the benefits of HO cyanocuprate chemistry while 'downsizing' copper,[50] an organometallic 'shuttle' was developed that supplies R_rLi so as to maintain copper at the far more reactive *ate* stage.[51a] Thus, using only a few percent $Me_2Cu(CN)Li_2$ along with zincate Me_3ZnLi as a relatively unreactive source of MeLi, vinyl zirconocenes can now be added in a conjugate manner to enones (Scheme 6). The presumed sequence calls for step (1): conversion of the initially formed vinyl zirconocene (**54**) to its methylated

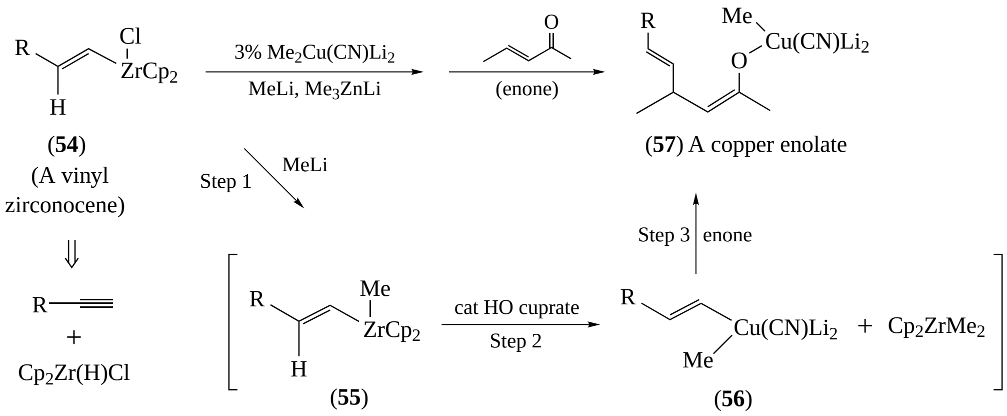
(54) (A vinyl zirconocene)
3% Me2Cu(CN)Li2
MeLi, Me3ZnLi
(enone)
(57) A copper enolate
Step 1 MeLi
Step 3 enone
cat HO cuprate
Step 2
R—≡ + Cp2Zr(H)Cl
(55)
(56)
Cu(CN)Li2 + Cp2ZrMe2

Scheme 6

derivative (**55**) with MeLi; step (2): transmetalation from Zr to Cu, where a methyl moiety goes to Zr in return for the vinyl residue going to copper; step (3): the mixed cuprate (**56**) adds and transfers the vinyl reside to the enone to give the transient copper enolate (**57**). In step (4), Me_3ZnLi, presumably exchanges readily with the weak Cu–O bond in (**57**), providing the elements of MeLi and thereby reforming the catalytic species $Me_2Cu(CN)Li_2$ for recycling (Scheme 7). The by-product Me_2Zn remains associated with oxygen as the resulting zinc enolate (**58**).**[51b]**

Once the zinc enolate has accumulated, it can be used further in a net ‘3-component coupling’, which has been found advantageous for quick entries to prostaglandins (e.g. equation 26).**[51c]**

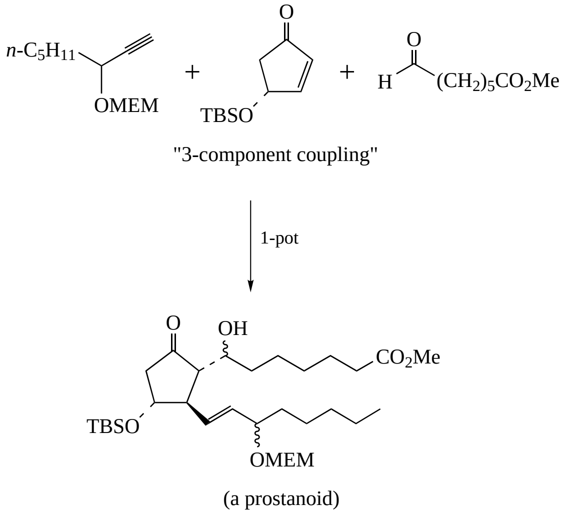
n-C5H11
OMEM
TBSO
H
(CH2)5CO2Me
"3-component coupling"
1-pot
OH
CO2Me
TBSO
OMEM
(a prostanoid)

(26)

The concept of using mixed zincates to moderate the reactivity of organolithiums in solutions containing catalytic copper species can be extended to other organometallics. Transfer of a silyl group such a $PhMe_2Si$, well known to be a hydroxyl surrogate, has been routinely delivered to substrates stoichiometrically *via* the corresponding cuprate. Masking $PhMe_2SiLi$ within the mixed zincate $PhMe_2Si{-}ZnMe_2Li$, however, and using only 3% of a simple HO dimethylcyanocuprate leads to silyl ligand exchange between zinc and copper, ultimately delivering the desired silyl residue to various electrophilic coupling partners (equation 27).**[52]** In the case of enones, although these 1,4-additions go very smoothly at low temperatures, inclusion of catalytic amounts of $Sc(OTf)_3$ leads to extremely rapid conjugate additions.

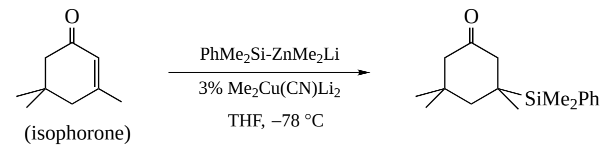
(isophorone)
PhMe2Si-ZnMe2Li
3% Me2Cu(CN)Li2
THF, −78 °C
SiMe2Ph

$$\boxed{\begin{array}{c} PhMe_2Si\text{-}ZnMe_2Li \\ \Downarrow \\ PhMe_2SiLi + ZnMe_2 \end{array}}$$

Additive	Time	Yield(%)
None	2.5 h	90
5% $Sc(OTf)_3$	5 min	81

(27)

6 SPECTROSCOPIC & STRUCTURAL STUDIES

As previously mentioned**[49]** and remains true today, NMR spectroscopy is the primary tool for accessing information regarding the composition of cuprates in solution. Advancements in NMR technology of late have encouraged highly sophisticated labeling experiments, leading to a far better appreciation for cuprate structure and mechanism. Some of the recent NMR work has focused on cuprate complexation of enones and/or enoates, but most has been in direct response to the controversial ‘higher order’/‘lower order’ debate in the literature regarding the structure of cyanocuprates. Excellent reviews on this subject are now available.**[53]**

^{15}N NMR spectroscopy has been applied to cyanocuprates $BuCu(C^{15}N)^6Li$ and $Bu_2Cu^6Li\cdot{}^6LiCN$, both reagents derived from labeled *n*-butyllithium and copper cyanide.**[54]** In this study, ^6Li and ^{15}N NMR spectra were obtained in THF-d_8 and Et_2O-d_{10} at −80 °C for cuprates with a lithium:copper ratio of

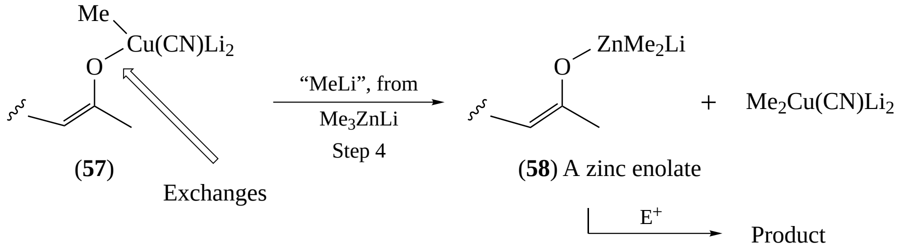

Scheme 7

1:1, 1.3:1, and 2:1. That no $^{6}LiC^{15}N$ or ^{6}Li-^{15}N couplings were observed in any of the cuprate mixtures strongly suggests that CN is not bound to copper. From these data and associated calculated cyanide IR stretching frequencies, several cyclic arrays for 'higher order' cyanocuprates were proposed (**59**–**61**), with structure (**59**) being energetically favored.

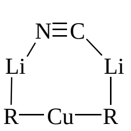

(**59**)

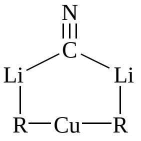

(**60**)

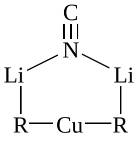

(**61**)

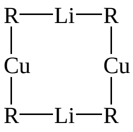

(**62**), A Gilman cuprate

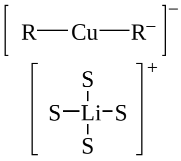

(**63**)

The coupling patterns of ^{1}H and ^{1}H-coupled ^{13}C NMR spectra of ^{13}C-labeled cuprates Me_2CuLi, Me_3CuLi_2, and $Me_2Cu(CN)Li_2$ in THF were compared. It was found that Me_3CuLi_2 and $Me_2Cu(CN)Li_2$ behave like that of Me_2CuLi.[55] However, no coupling was observed for the cyanide ligand (*see Cyanides*) in $Me_2Cu(CN)Li_2$. Heteronuclear Overhouser effect spectroscopy (HOESY) was also used to analyze lithium's connectivity in these cuprates. Doubly labeled MeLi (^{13}C and ^{6}Li) served as the precursor to each cuprate, which yielded ^{6}Li–^{1}H and ^{6}Li–^{13}C HOESY spectra. The HOESY spectra showed a correlation between lithium and the protons; however, no correlation was seen between lithium and carbon thus indicating that Li^{+} is mainly localized apart from anionic copper in these species.[56]

$^{1}H,^{6}Li$ HOESY NMR techniques likewise led to the hypothesis that contact ion pairs (CIPs, **59** and **62**) and/or solvent-separated ion pairs (SSIPs, **63**) are present for cyanocuprates in solution.[57] Both MeCu(CN)Li and *t*-$Bu_2CuLi{\cdot}LiCN$ appear to be monomeric SSIP in THF owing to the strong solvating effects of this solvent on lithium atoms. This is also evident from the HOESY spectra by the lack of dipolar interactions between lithium and the organocopper species. $^{1}H,^{6}Li$ HOESY spectra conducted in Et_2O for these same two cuprates, however, show a definite dipolar interaction, indicating a CIP. For $Me_2CuLi{\cdot}LiCN$ and $[(Me_3Si)CH_2]_2CuLi$[58a] a temperature-dependent equilibrium was detected in THF between SSIPs and CIPs which helps to explain the relative reactivity of various cuprates in different solvents, and in the presence of additives.[52] Cuprates formed in the presence of crown ethers (*see Crown Ethers*) lead to SSIP's and are much less reactive toward 1,2- and 1,4-additions, indicating that cuprates which are able to form CIPs (i.e. dimers) are the reactive species in addition reactions.[58] Further studies on $Me_2CuLi{\cdot}LiCN$ and Me_2CuLi using SYM-BREAK-NOE/ROE-HSQC NMR experiments have shown that these two cuprates have homodimeric structures (similar to **62**) in Et_2O through ^{1}H–^{1}H dipolar interactions and $^{1}H,^{6}Li$ HOE spectra.[58]

Several new structures of organocopper and cuprate reagents have been provided by X-ray crystallography. Complex (**64**), containing a CuX:CuR ratio of 2:1, crystallizes as a six-membered ring containing three copper atoms, two bromines, and an *ipso* carbon of the Mes* group.[59] A homoleptic organocopper tetramer $[Cu_4(viph)_4]$ (viph = *o*-vinylphenyl, **65**) has been prepared which further supports the square-planar nature of organocopper species fundamental to copper chemistry.[60]

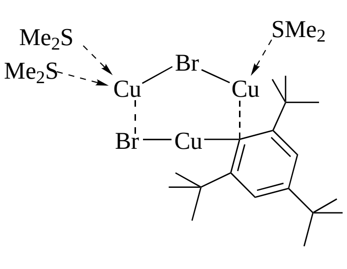

(**64**)

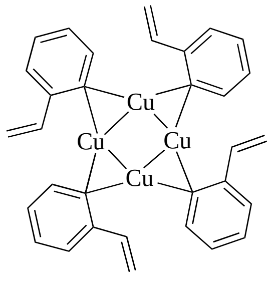

(**65**)

The crystal structure of an aryl cyanocuprate $[Li(THF)_2\{Cu(CN)C_6H_3\text{-}2,6\text{-}Trip_2\}]_2$ (**66**) (Trip = $\text{-}C_6H_2\text{-}2,4,6\text{-}i\text{-}Pr_3$) revealed a LO species with cyanide bridging both copper and lithium atoms.[61] Cyanocuprate (**67**), isolated from Et_2O rather than THF, likewise shows a LO nature, while (**68**)

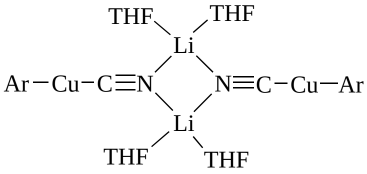
(**66**)

(from CuCN and 2t-BuLi) clearly reveals the expected linear arrangement of the two alkyl groups on copper(I), with the cyano group sequestered by two lithium ions. The same linear array is found in diaryl cuprate (**69**), where the tertiary benzylic amine functions as an internal chelating agent for Li^+ and is thus, ionic in nature. This species is representative of those typically abbreviated as $[R_2Cu]^-$ $[LiCNLi]^+$.[62]

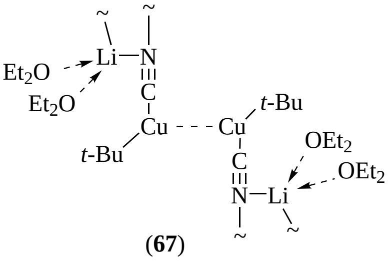
(**67**)

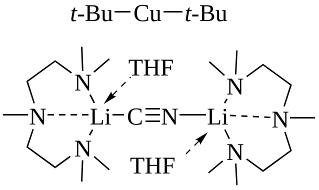
(**68**)

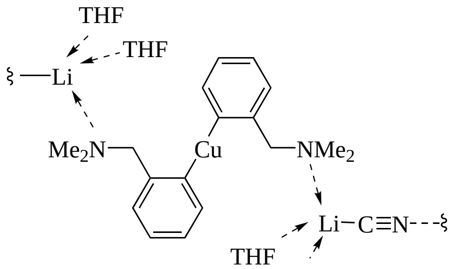
(**69**)

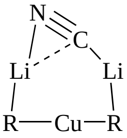
(**70**)

Several other techniques have been used to determine the structure or aggregation state of organocuprates. Cryoscopic studies in THF found that discrete monomeric species were formed when RLi (R = Me, t-Bu) was added to CuCN in various ratios.[63] A dimeric species resulted, however, when PhLi was used for cuprate formation. X-ray absorption spectroscopy (XAS) was utilized in an investigation of CuI- and CuCN-based dimethyl cuprates.[64] Both extended X-ray absorption fine structure (EXAFS, *see Extended X-ray Absorption Fine Structure*) and X-ray absorption near edge structure (XANES, *see XANES*) indicated that dimethyl cuprates Me_2CuLi and '$Me_2Cu(CN)Li_2$' are two-coordinate, and hence, cyanide does not reside on copper. In a separate but related study using XAS, it was found that dimethyl cuprates formed from CuI are dimeric (i.e. $[Me_2CuLi]_2$) in Et_2O and Me_2S.[65] Electrospray mass spectrometry[66] suggests that several cuprate complexes are present in solution, many of which cannot be detected on the NMR timescale.

With advances in computational chemistry, many theoretical studies addressing structural aspects of organocuprates have been undertaken. Calculations using density functional theory (DFT)[67] or at the MP2/II perturbation level,[68] indicate that 'higher order' cuprates are structurally along the lines of (**61**) and (**70**), respectively. The latter study used XANES and EXAFS spectroscopic data to support their theoretical cuprate structure.[68] A recent report on organocuprate structures and energies using the B3LYP and MP2 methods found that while MP2 structural calculations correlated well with X-ray data, the B3LYP method was superior for reaction pathway studies of organocopper intermediates.[69]

Computational investigations on linear $(CH_3)_2Cu^-$ indicate that the HOMO (*see HOMO*) $Cu(s + d_{z^2})$ and $C(s + p)$ orbitals are involved in cuprate S_N2 alkylation reactions. Bent carbon–copper bonds allow $Cu(d_{xz})$ and $C(s + p)$ orbitals to mix, thus forming a HOMO that can interact with π^* orbitals of alkynes and alkenes.[53] Related studies suggest that dialkylcuprates of type (R_2Cu^-) act as metal centered nucleophiles owing to their high lying d orbitals versus carbon-based alkyl nucleophiles, which explains their S_N2/1,4-addition capabilities.[70]

A chemical reactivity scale has been created to reflect electron transfer abilities of various methylcopper reagents in conjugate additions, using trimethylethylene-1,1,2-tricarboxylate as acceptor.[71] The reported order is; $Me_3CuLi_2 > Me_2CuLi \gg Me_2Cu(CN)Li_2 > MeCu > MeCu(CN)Li$. The corresponding butyl cuprates are more able to effect electron transfer, the order found to be: $Bu_2CuLi > BuCu(CN)Li \approx Bu_2Cu(CN)Li_2 > BuCu$, in this case using 3-cyclopropyl-2-methoxycarbonyl-3-phenyl-2-propenoate as substrate.[71]

7 MECHANISTIC ADVANCES

Although organocuprate chemistry has already celebrated its 50th year since the discovery by Gilman,[72] the mechanisms by which transformations of organocopper reagents take place are still not fully understood. Significant progress, however, in particular from theoretical treatments, has been made.[73]

Cuprate conjugate addition to α,β-unsaturated carbonyl compounds involves an initial π-complexation of the α,β-unsaturated double or triple bond by copper followed by an oxidative addition (*see Oxidative Addition*) resulting in a

σ-Cu(III) species that reductively eliminates (*see Reductive Elimination*) to yield the conjugate addition product. From low temperature NMR techniques, π-complexation can be observed for enones, ynoates, as well as for their more highly conjugated analogs.**74** ^{13}C-NMR studies show that complexation is reversible, where the C2 and C3 carbons of α,β-unsaturated carbonyl systems shift upfield due to rehybridization of the sp^2 to sp^3–like carbons, and downfield for sp to sp^2–like atoms as a direct result of d-π^*-complexation by copper at low temperatures.**75** Typically, a downfield shift for a carbonyl carbon is also observed and is associated with complexation of oxygen with lithium ion within the cuprate.**75** Through rapid-injection NMR experiments at $-100\,^\circ$C of $Me_2CuLi{\cdot}LiX$ ($X = I$ or CN) and 2-cyclohexenone, significant enolate character of the π-complex was postulated and rate of formation data suggest a two-step process is involved in π-complex formation.**76**

Ynoates in the presence of $Me_2CuLi{\cdot}LiI$ show syn-addition of the cuprate followed by a rapid isomerization of a lithium allenolate to the Z-substituted alkene.**74** Removing LiI can decelerate E- to Z-alkene isomerization, and the allenoate can be trapped by TMSCl if present in the reaction mixture.

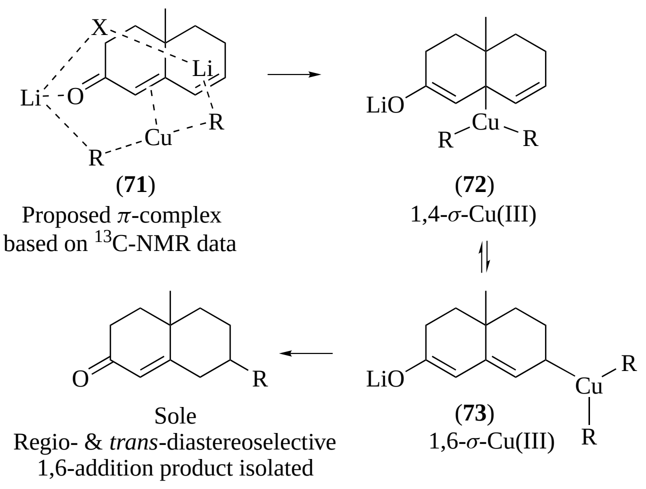

Scheme 8

A cyclic dienone also showed a characteristic C2–C3^{13}C-NMR shift due to π-complexation (*cf.* **71**; Scheme 8).**74** The 1,4- and 1,6-σ-Cu(III) species (**72**) and (**73**), respectively, are proposed to be in equilibrium, and *via* kinetic measurements, the suggested rate-determining step of conjugate addition involves an intramolecular π-complex rearrangement.**75** An extensive ^{13}C-labeled 1-D and 2-D-NMR study of 1,6-addition to an ynenone supports π-complex formation and shows that the C-Cu–C orientation must distort from the typical square-planar conformation in order to react.**74**

Computational work applied to cuprates has provided plausible pathways for conjugate addition to enones (e.g. 5-methylcyclohexenone; Scheme 9), S$_N$2 alkylations, and carbometalation reactions. It has been hypothesized that the copper(I) anion donates electron density to a substrate enone, thus aiding in Cu(III) intermediate formation.**53** The role of the lithium atom as a Lewis acid is essential in cuprate additions, whereas non-Lewis acidic (*see Lewis Acids & Bases*) TMSCl is believed to lower the energy of the final C–C bond forming step *via* stable silyl enol ether formation, or acting as a stabilizer in the transition state leading to the π-complex.**77** Calculations also indicate that nontransferable 'dummy' ligands on the metal accelerate reductive elimination of a Cu(III) intermediate, enhancing reactivity of the cuprate by simultaneously binding to Cu and Li.**53** Through B3LYP density functional calculations, reductive elimination (*see Reductive Elimination*) of a π-allylcopper(III) species leading to C–C bond formation occurs *via* a π-allyl enyl[$\sigma+\pi$]-type transition state, instead of through a simpler σ-allylcopper(III) intermediate. Electronic effects on a substituted π-allylcopper(III) species account for the regioselectivity of reductive elimination, which also correlates well with Hammett σ_p^+ constants.**78**

Theoretical studies on S$_N$2 alkylations of cyanocuprates with alkyl halides or epoxides indicate electronic as well as structural effects are due to the presence of the $[Li_2CN]^+$ cation, leading to increased reactivity of 'higher order' cuprates as compared to 'lower order' Gilman reagents (Scheme 10).**53** Bridging by this cation is important in cuprate alkylations, as is solvent polarity and coordination ability. Calculations show that geometry and transition state energy are not affected by a solvated copper atom, although solvent does participate following alkylation. Without solvent, the S$_N$2

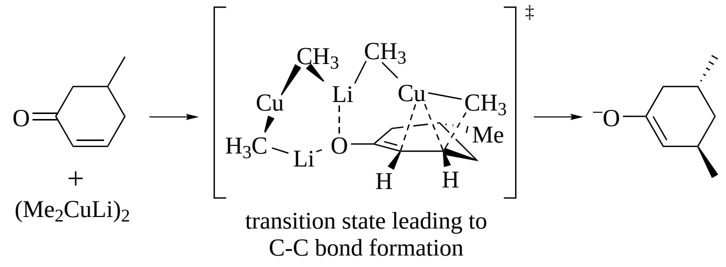

Scheme 9

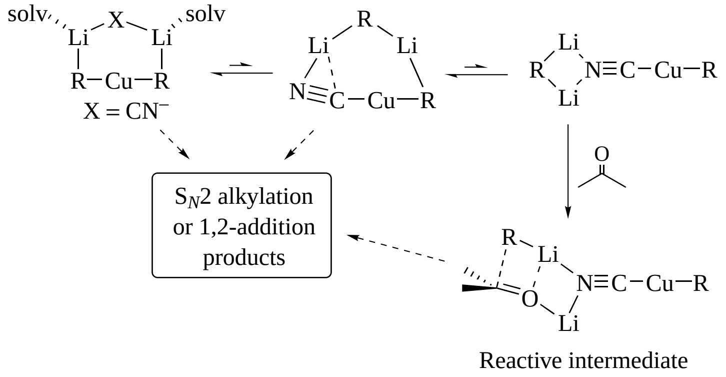
solv
X
solv
Li
Li
R−Cu−R
X = CN−
R
Li
Li
N≡C−Cu−R
Li
R
N≡C−Cu−R
Li
O
SN2 alkylation
or 1,2-addition
products
R
Li
N≡C−Cu−R
O
Li
Reactive intermediate

Scheme 10

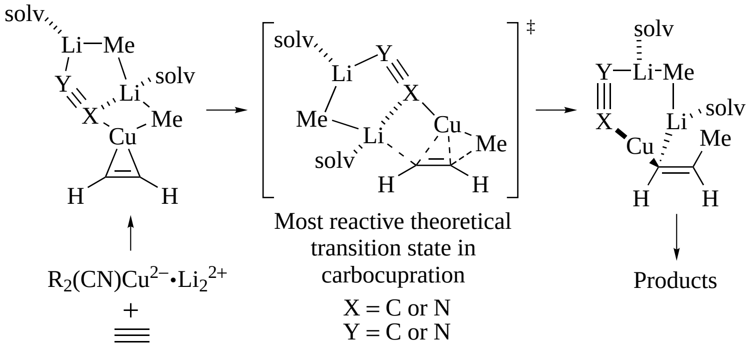
solv
Li−Me
Y
Li
solv
X
Me
Cu
H
H
R2(CN)Cu2−•Li22+
+
solv
Y
Li
X
Me
Li
Cu
Me
solv
H
H
‡
Most reactive theoretical
transition state in
carbocupration
X = C or N
Y = C or N
solv
Y−Li-Me
X
Li
solv
Cu
Me
H
H
Products

Scheme 11

alkylation involves the nucleophilic Cu(d_{z^2}) and $H_3C(2s + 2p)$ orbitals of the cuprate, where cleavage of the C–LG (LG = leaving group) bond is the rate-determining step.[53]

Computational investigations on carbocupration of acetylene indicate that negative charge transfer occurs from copper to the acetylene unit (Scheme 11). Lithium atom participation in this reaction is similar to that in conjugate addition to an enone, where Li^+ stabilizes negative charge buildup in the alkyne and facilitates electron flow from copper.[53] Molecular orbital (*see Molecular Orbitals*) analysis of Me_2Cu^- addition to acetylene (π^*-orbital) shows that the Cu($3d_{xz}$) orbital back donation is responsible for the nucleophilicity of organocuprates.[79] It has also been suggested that cyanide on copper (i.e. R(CN)CuLi·LiR) in the carbocupration is a more reactive species than when it is associated with lithium (i.e. $R_2CuLi{\cdot}LiCN$), and that both complexes are present in solution according to high-level calculations.[53]

8 RELATED ARTICLES

Alkali Metals: Organometallic Chemistry; Copper: Inorganic & Coordination Chemistry; Cyanide Complexes of the Transition Metals; Palladium: Organometallic Chemistry; Silicon: Organosilicon Chemistry; Tin: Organometallic Chemistry; Zinc: Organometallic Chemistry; Zirconium & Hafnium: Organometallic Chemistry.

9 REFERENCES

1. V. I. Timokhin, N. R. Anastasi, and S. S. Stahl, *J. Am. Chem. Soc.*, 2003, **124**, 12996; T. D. Quach, and R. A. Batey, *Org. Lett.*, 2003, **5**, 4397; Y. Imada, M. Yuasa, I. Nakamura, and S.-I. Murahashi, *J. Org. Chem.*, 1994, **59**, 2282; S.-K. Kang, S.-H. Lee, and D. Lee, *Synlett*, 2000, 1022; D. Ma and C. Xia, *Org. Lett.*, 2001, **3**, 2583; J. C. Antilla, *Org. Lett.*, 2001, **3**, 2077.
2. T. Zhou and Z.-C. Chen, *Heteroat. Chem.*, 2002, **13**, 617; J. P. Collman, M. Zhong, L. Zeng, and S. Costanzo, *J. Org. Chem.*, 2001, **66**, 1528.
3. a) P. Y. S. Lam, G. Vincent, C. G. Clark, S. Deudon, and P. K. Jadhav, *Tetrahedron Lett.*, 2001, **42**, 3415; R. Shen and J. A. Porco, *Org. Lett.*, 2000, **2**, 1333; A. Klapars, X. Huang, and S. L. Buchwald, *J. Am. Chem. Soc.*, 2002, **124**, 7421.

4. A. Padwa, K. R. Crawford, P. Rashatasakhon, and M. Rose, *J. Org. Chem.*, 2003, **68**, 2609; M. O. Frederick, J. A. Mulder, M. R. Tracey, R. P. Hsuang, J. Huang, K. C. M. Kurtz, L. Shen, and C. J. Douglas, *J. Am. Chem. Soc.*, 2003, **125**, 2368.
5. M. Sasaki, S. Dalili, and A. K. Yudin, *J. Org. Chem.*, 2003, **68**, 2045.
6. K. Juhl and K. A. Jørgensen, *J. Am. Chem. Soc.*, 2002, **124**, 2420; S. Kobayashi, Y. Yamashita, and H. Ishitani, *Chem. Lett.*, 1999, 307.
7. C.-M. Ho and T.-C. Lau, *New J. Chem.*, 2000, **24**, 859; S. Seko, K. Miyake, and N. Kawamura, *J. Chem. Soc., Perkin Trans. 1*, 1999, 1437.
8. C. Savarin, J. Srogl, and L. S. Liebeskind, *Org. Lett.*, 2002, **4**, 4309; P. Y. S. Lam, G. Vincent, D. Bonne, and C. G. Clark, *Tetrahedron Lett.*, 2003, **44**, 4927.
9. Y.-J. Wu and H. He, *Synlett*, 2003, 1789.
10. M. Wolter, G. Nordmann, G. E. Job, and S. L. Buchwald, *Org. Lett.*, 2002, **4**, 973; R. K. Gujadhur, C. G. Bates, and D. Venkataraman, *Org. Lett.*, 2001, **3**, 4315; J. M. Baskin and Z. Wang, *Org. Lett.*, 2002, **4**, 4423; F. Y. Kwong and S. L. Buchwald, *Org. Lett.*, 2002, **4**, 3517.
11. X. Li, J. B. Hewgley, C. A. Mulrooney, J. Yang, and M. C. Kozlowski, *J. Org. Chem.*, 2003, **68**, 5500.
12. Z.-Q. Xin, C.-S. Da, S.-L. Dong, D.-X. Liu, J. Wei, and R. Wang, *Tetrahedron: Asymmetry*, 2002, **13**, 1937.
13. C. Chowdhury and N. G. Kundu, *Tetrahedron Lett.*, 1996, **37**, 7323.
14. B. W. Gung and G. Kumi, *J. Org. Chem.*, 2003, **68**, 5956.
15. J. Terao, A. Ikumi, H. Kuniyasu, and N. Kambe, *J. Am. Chem. Soc.*, 2003, **125**, 5646.
16. M. Eckhardt and G. C. Fu, *J. Am. Chem. Soc.*, 2003, **125**, 13642.
17. D. Bruyere, R. Grigg, J. Hinsley, R. K. Hussain, S. Korn, C. O. De La Cierva, V. Sridharan, and J. Wang, *Tetrahedron Lett.*, 2003, **44**, 8669.
18. C. C. Silveira, A. L. Braga, A. S. Vieira, and G. Zeni, *J. Org. Chem.*, 2003, **68**, 662.
19. J. P. Parrish, Y. C. Jung, S. Shin, and K. W. Jung, *J. Org. Chem.*, 2002, **67**, 7127.
20. I. P. Beletskaya, A. S. Sigeev, A. S. Peregudov, and P. V. Petrovskii, *Tetrahedron Lett.*, 2003, **44**, 7039.
21. F.-A. Alphonse, F. Suzenet, A. Keromnes, B. Lebret, and G. Guillaumet, *Org. Lett.*, 2003, **5**, 803; R. Wittenberg, J. Srogl, M. Egi, and L. S. Liebeskind, *Org. Lett.*, 2003, **5**, 3033, and references therein.
22. A. Alexakis and C. Benhaim, *Eur. J. Org. Chem.*, 2002, 3221.
23. B. H. Lipshutz, in ‘Modern Organocopper Chemistry’, ed. N. Krause, Wiley-VCH, Weinheim, 2002, p. 167.
24. (a) R. Schmid, E. A. Broger, M. Cereghetti, Y. Crameri, J. Foricher, M. Lalonde, R. K. Muller, M. Scalone, G. Schoettel, and U. Zutter, *Pure Appl. Chem.*, 1996, **68**, 131; (b) T. Saito, T. Yokozawa, T. Ishizaki, T. Moroi, N. Sayo, T. Miura, and H. Kumobayashi, *Adv. Synth. Catal.*, 2001, **343**, 264; (c) H.-U. Blaser, W. Brieden, B. Pugin, F. Spindler, M. Studer, and A. Togni, *Top. Catal.*, 2002, **19**, 3.
25. (a) B. H. Lipshutz, K. Noson, W. Chrisman, and A. Lower, *J. Am. Chem. Soc.*, 2003, **125**, 8779; (b) B. H. Lipshutz, J. M. Servesko, T. B. Petersen, P. P. Papa, and A. Lover, *Org. Lett.*, 2004, **6**, 1273; (c) B. H. Lipshutz and J. M. Servesko, *Angew. Chem., Int. Ed. Engl.*, 2003, **41**, 4789; (d) B. H. Lipshutz, J. M. Servesko, and B. R. Taft, *J. Am. Chem. Soc.*, 2004, **126**, 8352; (e) B. H. Lipshutz and H. Shimizu, *Angew. Chem., Int. Ed. Engl.*, 2004, **42**, 2227.
26. (a) K. Tissot-Croset, D. Polet, and A. Alexakis, *Angew. Chem., Int. Ed. Engl.*, 2004, **42**, 2426; M. Pineschi, *New J. Chem.*, 2004, **28**, 657; (b) K. E. Murphy and A. Hoveyda, *J. Am. Chem. Soc.*, 2003, **125**, 4690.
27. G. Ragagnin, B. Betzemeier, S. Quici, and P. Knochel, *Tetrahedron*, 2002, **58**, 3985; P. Gamez, I. W. C. E. Arends, J. Reedijk, and R. A. Sheldon, *Chem. Commun.*, 2003, 2414.
28. S. Velusamy and T. Punniyamurthy, *Eur. J. Org. Chem.*, 2003, 3913; G. Ferguson and A. N. Ajjou, *Tetrahedron Lett.*, 2003, **44**, 9139.
29. I. E. Markó, P. R. Giles, M. Tsukazaki, S. M. Brown, and C. J. Urch, *Science*, 1996, **274**, 2044.
30. P. Capdevielle and M. Maumy, *Tetrahedron*, 2001, **57**, 379.
31. K. Takaki, Y. Shimasaki, T. Shishido, and K. Takehira, *Bull. Chem. Soc. Jpn.*, 2002, **75**, 311.
32. M. B. Andrus and B. W. Poehlein, *Tetrahedron Lett.*, 2000, **41**, 1013.
33. a) G. Rousselet, C. Chassagnard, P. Capdevielle, and M. Maumy, *Tetrahedron Lett.*, 1996, **37**, 8497; b) J. Barluenga, H. Vazquez-Villa, A. Ballesteros, and J. M. González, *Org. Lett.*, 2002, **4**, 2817.
34. M. B. Erman, J. W. Snow, and M. J. Williams, *Tetrahedron Lett.*, 2000, **41**, 6749.
35. Y. Maeda, T. Nishimura, and S. Uemura, *Bull. Chem. Soc. Jpn.*, 2003, **76**, 2399.
36. S.-I. Murahashi, N. Komiya, Y. Hayashi, and T. Kumano, *Pure Appl. Chem.*, 2001, **73**, 311.
37. M. M. Diaz-Requejo, T. R. Belderrain, M. C. Nicasio, S. Trofimenko, and P. J. Perez, *J. Am. Chem. Soc.*, 2002, **124**, 896.
38. K. Hiroya, S. Itoh, M. Ozawa, Y. Kanamori, and T. Sakamoto, *Tetrahedron Lett.*, 2002, **43**, 1277.
39. S. Kamijo and Y. Yamamoto, *Angew. Chem., Int. Ed. Engl.*, 2002, **41**, 3230.
40. K. R. Roesch and R. C. Larock, *Org. Lett.*, 1999, **1**, 553.
41. M. E. Bluhm, M. Ciesielski, H. Görls, and M. Döring, *Angew. Chem., Int. Ed. Engl.*, 2002, **41**, 2962.
42. V. V. Rostovtsev, L. G. Green, V. V. Fokin, and K. B. Sharpless, *Angew. Chem., Int. Ed. Engl.*, 2002, **41**, 2596.
43. A. J. Clark, G. M. Battle, and A. Bridge, *Tetrahedron Lett.*, 2001, **42**, 1999.

44. H. Nagashima, Y. Isono, and S.-I. Iwamatsu, *J. Org. Chem.*, 2001, **66**, 315.
45. P. Müller and C. Boléa, *Helv. Chim. Acta*, 2002, **85**, 483.
46. N. Krause, *Angew. Chem., Int. Ed. Engl.*, 1999, **38**, 79.
47. P. Knochel, M. C. P. Yeh, S. C. Berk, and J. Talbert, *J. Org. Chem.*, 1988, **53**, 2390.
48. (a) B. H. Lipshutz and R. W. Vivian, *Tetrahedron Lett.*, 1999, **40**, 2871; (b) W. Dohle, D. M. Lindsay, and P. Knochel, *Org. Lett.*, 2001, **3**, 2871; (c) Y.-Y. Ku, R. R. Patel, and D. P. Sawick, *Tetrahedron Lett.*, 1996, **37**, 1949.
49. B. H. Lipshutz and M. R. Wood, Copper: Organometallic Chemistry, in 'Encyclopedia of Inorganic Chemistry', ed. R. B. King, John Wiley & Sons, West Sussex, 1994.
50. B. H. Lipshutz, *Acc. Chem. Res.*, 1997, **30**, 277.
51. (a) B. H. Lipshutz and M. R. Wood, *J. Am. Chem. Soc.*, 1993, **115**, 12625; (b) B. H. Lipshutz and M. R. Wood, *Tetrahedron Lett.*, 1994, **35**, 6433; (c) B. H. Lipshutz and M. R. Wood, *J. Am. Chem. Soc.*, 1994, **116**, 11689.
52. B. H. Lipshutz, J. A. Sclafani, and T. Takanami, *J. Am. Chem. Soc.*, 1998, **120**, 4021.
53. E. Nakamura and N. Yoshikai, *Bull. Chem. Soc. Jpn.*, 2004, **77**, 1, See references therein.
54. S. H. Bertz, K. Nilsson, O. Davidsson, and J. P. Snyder, *Angew. Chem., Int. Ed. Engl.*, 1998, **37**, 314.
55. T. A. Mobley, F. Müller, and S. Berger, *J. Am. Chem. Soc.*, 1998, **120**, 1333.
56. R. M. Gschwind, P. R. Rajamohanan, M. John, and G. Boche, *Organometallics*, 2000, **19**, 2868.
57. M. John, C. Auel, C. Behrens, M. Marsch, K. Harms, F. Bosold, R. M. Gschwind, P. R. Rajamohanan, and G. Boche, *Chem. – Eur. J.*, 2000, **6**, 3060.
58. a) R. M. Gschwind, X. Xie, P. R. Rajamohanan, C. Auel, and G. Boche, *J. Am. Chem. Soc.*, 2001, **123**, 7299; b) The contact ion pair (CIP) hypothesis is also supported by a reaction profile study conducted by Bertz that showed R_2CuLi reacted faster in Et_2O than THF with various enones.
59. C.-S. Hwang, M. M. Olmstead, X. He, and P. P. Power, *J. Chem. Soc., Dalton Trans.*, 1998, 2599.
60. H. Eriksson, M. Örtendahl, and M. HÅkansson, *Organometallics*, 1996, **15**, 4823.
61. C.-S. Hwang and P. P. Power, *J. Am. Chem. Soc.*, 1998, **120**, 6409.
62. C. M. P. Kronenburg, J. T. B. H. Jastrzebski, A. L. Spek, and G. van Koten, *J. Am. Chem. Soc.*, 1998, **120**, 9688.
63. A. Gerold, J. T. B. H. Jastrzebski, C. M. P. Kronenburg, N. Krause, and G. van Koten, *Angew. Chem., Int. Ed. Engl.*, 1997, **36**, 755.
64. T. M. Barnhart, H. Huang, and J. E. Penner-Hahn, *J. Org. Chem.*, 1995, **60**, 4310.
65. H. Huang, C. H. Liang, and J. E. Penner-Hahn, *Angew. Chem., Int. Ed. Engl.*, 1998, **37**, 1564.
66. B. H. Lipshutz, J. Keith, and D. J. Buzard, *Organometallics*, 1999, **18**, 1571, and references therein.
67. J. P. Snyder and S. H. Bertz, *J. Org. Chem.*, 1995, **60**, 4312.
68. T. L. Stemmler, T. M. Barnhart, J. E. Penner-Hahn, C. E. Tucker, P. Knochel, M. Böhme, and G. Frenking, *J. Am. Chem. Soc.*, 1995, **117**, 12489.
69. M. Yamanaka, A. Inagaki, and E. Nakamura, *J. Comput. Chem.*, 2003, **24**, 1401.
70. S. Mori, A. Hirai, M. Nakamura, and E. Nakamura, *Tetrahedron*, 2000, **56**, 2805.
71. Y. Chounan, H. Horino, T. Ibuka, and Y. Yamamoto, *Bull. Chem. Soc. Jpn.*, 1997, **70**, 1953.
72. H. Gilman, R. G. Jones, and L. A. Woods, *J. Org. Chem.*, 1952, **17**, 1630.
73. S. Woodward, *Chem. Soc. Rev.*, 2000, **29**, 393, and references therein.
74. a) K. Nilsson, C. Ullenius, and N. Krause, *J. Am. Chem. Soc.*, 1996, **118**, 4194; b) M. Uerdingen and N. Krause, *Tetrahedron*, 2000, **56**, 2799; c) J. Canisius, T. A. Mobley, S. Berger, and N. Krause, *Chem. – Eur. J.*, 2001, **7**, 2671, and references therein.
75. J. Canisius, A. Gerold, and N. Krause, *Angew. Chem., Int. Ed. Engl.*, 1999, **38**, 1644.
76. S. H. Bertz, C. M. Carlin, D. A. Deadwyler, M. D. Murphy, C. A. Ogle, and P. H. Seagle, *J. Am. Chem. Soc.*, 2002, **124**, 13650.
77. S. Mori and E. Nakamura, *Chem. – Eur. J.*, 1999, **5**, 1534; B. H. Lipshutz, D. H. Aue, and B. James, *Tetrahedron Lett.*, 1996, **37**, 8471.
78. M. Yamanaka, S. Kato, and E. Nakamura, *J. Am. Chem. Soc.*, 2004, **126**, 6287.
79. S. Mori and E. Nakamura, *THEOCHEM*, 1999, **461–462**, 167.

Copper Proteins with Dinuclear Active Sites

Heinz Decker
Institute for Molecular Biophysics, Johannes Gutenberg University, Mainz, Germany

Based in part on the article Copper Proteins with Dinuclear Active Sites by Konrad Lerch which appeared in the Encyclopedia of Inorganic Chemistry, First Edition.

1 Introduction 1
2 Dinuclear Copper Site 1
3 Type 3 Copper Family 3
4 Phenoloxidase 9
5 Phenoloxidase Activity of Hemocyanin 10
6 References 12

1 INTRODUCTION

This review is based on a former one from K. Lerch[1] in a previous edition of this work. While that article summarized the results up to 1995, this article will be focused on the time after and concentrate more on the structural features and less on the spectroscopic ones. Nevertheless, some former but updated parts of Lerch's review will be included without special indications. In addition, the selection of references can only be very limited and some important ones may not be included.

During the last twenty years, it became obvious that quite a few proteins belong to the protein family designated as 'copper proteins with dinuclear active sites'. As described previously,[1] the first of these proteins were discovered during the nineteenth century: the respiratory protein hemocyanin and the enzyme tyrosinase. In 1878, Fredericq[2] described a colorless protein in the blood of the mollusc *Octopus vulgaris*, which turned deep blue in the presence of air. He introduced the name hemocyanin (Hc) derived from the greek words $\alpha`\iota\mu\alpha$ (blood) and $\kappa\upsilon\nu\alpha\nu o\zeta$ (blue). The enzyme tyrosinase (Ty) was discovered in 1895 by Bertrand and Bourquelot[3] who demonstrated that the darkening of certain varieties of mushrooms is due to the oxidation of the aromatic amino acid tyrosine. The identification of Hc and Ty as copper proteins, however, took place several decades later. In 1928, Redfield[4] showed that Hc's both from arthropods and molluscs bind one molecule of oxygen per two copper atoms. A few years later, the same stoichiometry was found for the binding of carbon monoxide.[5] In 1937, Kubowitz[6] observed a linear relationship between the copper content and enzymatic activity of potato Ty. The most highly purified enzyme had a copper content of 0.2% and the activity was inhibited by cyanide, diethyldithiocarbamate, and carbon monoxide. He showed that the copper was essential for catalytic activity by removing it reversibly with cyanide. Moreover, the substrate-reduced enzyme was found to bind carbon monoxide with the same stoichiometry reported earlier for Hc. Thus, Kubowitz was the first to realize a clear relationship between the two copper proteins Hc and Ty.

These pioneering studies on Hc and Ty were followed by a period in which the two proteins were investigated extensively in terms of their protein architecture and oxygen binding (Hc) and catalytic activity (Ty).[7–12] In the 1970s, the relationship of the two copper proteins was further corroborated by numerous spectroscopic studies showing unequivocally the dinuclear nature of their copper active sites. Several reviews have appeared on the chemical and spectroscopic properties of the unique dinuclear copper complex.[13–20] Since about 1980 to now many dozens of sequences of type 3 copper proteins were solved from many different sources, shedding new light on the evolution of this diverse class of copper proteins.[19–28] It turned out that not only hemocyanins, tyrosinases, catecholoxidases, but also pseudohemocyanins, cryptocyanins, and hexamerins belong to this family.[29–31] The three latter ones, however, have lost the ability to bind copper. In addition, complete gene sequences were published.[32,33] Several high resolution 3-D structures based on crystals and electron microscopy also became available.[34–43] During the last few years, it was unequivocally demonstrated that hemocyanins can be converted to enzymes exhibiting phenoloxidase activity.[44–51] As a result of these studies, a rather detailed picture of the molecular and copper active-site structures of Hc and Ty became available. Various review articles on copper proteins with dinuclear sites were published since 1995.[25–28,51–57] In addition, recent developments on this topic were presented at a recent international conference in Mainz in fall of 2003 being published in a special issue of Micron 2004, 35, Volumes 1 and 2.

2 DINUCLEAR COPPER SITE

The active site of type 3 copper proteins consists of two copper atoms. Each of them is bound by three histidines provided by an antiparallel alpha-helix pair (Figure 1). Cu-A denotes the copper-binding site closer to the N-terminus, whereas Cu-B is the copper-binding site closer to the C-terminus. According to crystal structures of arthropod[34–38] and mollusc[39,40] hemocyanins, the coppers bind a dioxygen molecule in the same way as a peroxide in $\mu{:}\eta^2\text{-}\eta^2$ side-on coordination between the coppers (Figure 1) and as found in a synthetic dicopper complex.[58] The binding of dioxygen as a peroxide results in a change of valency of the two copper atoms from Cu(I) to Cu(II).

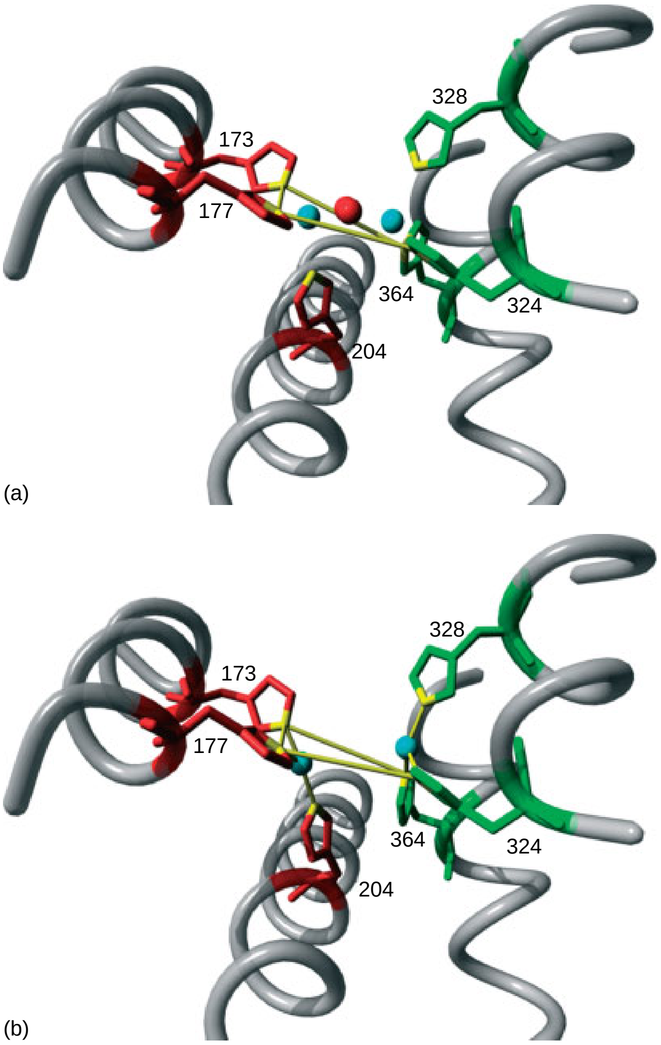

Figure 1 Oxy (a) and deoxy (b) states of the active sites of subunit II of *Limulus polyphemus* hemocyanin. The three histidines coordinating Cu-A are colored red, those coordinating Cu-B green. The two copper atoms are colored blue and oxygen red. Yellow lines connect the four histidines forming the plane on which the coppers and the dioxygen are often discussed to be placed. Two axial histidines are perpendicularly oriented to this plane: His204 coordinates the Cu-A site, His328 the Cu-B site. The channel to the surface for substrates to the active sites is located on the top of the active sites

Various spectroscopic methods applied to hemocyanin and phenoloxidases strongly favored a very similar oxy-structure of the active site for many years.[1] In addition, the X-ray data and sequences of type 3 copper proteins reveal that two different classes exist, which differ in their Cu-A and Cu-B[28] environment. While the Cu-B environment remains more or less unchanged, the environment of Cu-A is different in arthropod and mollusc (Figures 1, 2). As in mollusc Hc and catecholoxidase, one helix binding the copper atom is shorter. One of the Cu-A coordinating histidines is located at the end of an alpha-helix (His109 (*Ipomea*), His2563 (*Octopus*), His61 (*Rapana*)) and is stabilized by a conserved covalent bond to a cysteine,[39–41,59,60] a bond that is very seldom observed in nature (Figure 2).

During the late 1970s, Solomon and collaborators prepared and extensively characterized a series of derivatives leading to models of the copper active-site structure and it function that are summarized in several articles.[61–63] While decades ago the end-on coordination was favored when interpreting the spectra, now great effort is applied to interpreting the spectra on the basis of the results of the recently resolved X-ray structure,[63–67] which clearly show that dioxygen is bound in a side-on coordination between the two copper atoms.[38,39] Several other contributions in this book will focus this point (*see* ***Copper: Hemocyanin/Tyrosinase Models***).

Hemocyanins and tyrosinase can exists in various states, the oxy-state (dioxygen is bound between the two copper atoms), deoxy-state (no dioxygen is bound), apo-state (no copper is bound) and met-state (the two copper atoms are bridged by a hydroxyl group). The former article by Lerch[1] reviewed the met and apo forms intensively. However, some features of the oxy and deoxy structures should be mentioned.

Oxy-form. While deoxygenated hemocyanin can bind dioxygen reversibly as a peroxide, oxy-Ty is only formed after treatment of met-Ty with reducing agents (hydrogen peroxide, a number of different reducing agents, such as hydroxylamine, ascorbic acid, sodium dithionite, sodium borohydride, and *o*-diphenols) in the presence of molecular oxygen. However, the molecular reason is not known yet owing to the lack of any structure of a tyrosinase.

Because of the highly unusual and unique spectral features of oxy-Hc's and Ty's, these forms have been studied in great detail by many different groups: Resonance Raman Spectroscopy has shown that, in oxy-Hc's and oxy-Ty, dioxygen is bound as peroxide to the dinuclear site. All data imply that the two copper ions are in the copper(II) oxidation state, which was confirmed by XAS studies. Like the met forms, oxy-Hc's and Ty's are EPR nondetectable and show strong antiferromagnetic coupling between the two Cu(II) ions ($2J > 600\,\mathrm{cm}^{-1}$), as demonstrated by magnetic susceptibility studies. The large coupling requires orbital overlap between the two Cu(II) ions, which based on a Cu–Cu distance of <3.6 Å from EXAFS measurements, must involve a superexchange pathway through a bridging ligand, which, however, was not found yet within a distance of 0.5–0.7 nm. Oxy-Hc and oxy-Ty are characterized by unique spectral features. The absorption spectrum shows two bands at <590 nm ($\varepsilon < 1000\,\mathrm{M}^{-1}\,\mathrm{cm}^{-1}$) and an extremely intense transition at <345 nm ($\varepsilon < 18–20\,000\,\mathrm{M}^{-1}\,\mathrm{cm}^{-1}$). The CD spectrum shows in addition to the intense transition at 345 nm a positive band at <520 nm. These absorption and CD bands are absent in the met forms and hence have been assigned as peroxide-to-Cu(II) charge-transfer transitions.

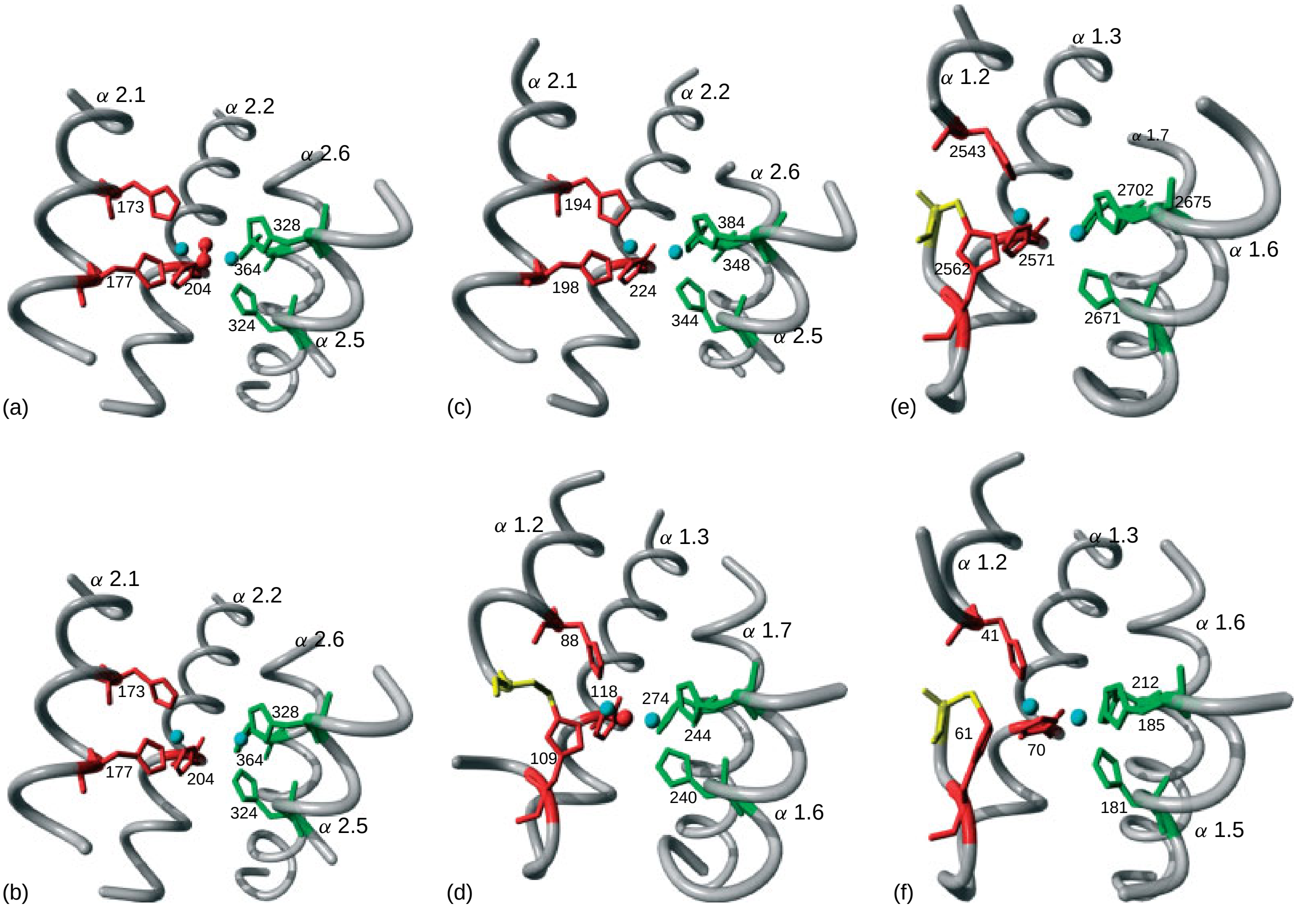

Figure 2 Active sites of hemocyanins from horseshoe crab *L. polyphemus* (a: oxy; b: deoxy), spiny lobster *Panulirus interruptus* (c), sweet potato *Ipomoea batatas* (d), *Octopus dofleini* (e), *Rapana thomasiana* (f). Cleary the four alpha-helix bundle motif with the metal center can be seen. The three histidines coordinating Cu-A are colored red, those coordinating Cu-B green. The two copper atoms are colored blue and oxygen red. The cysteines binding covalently a histidine at the Cu-A site are colored yellow. In the case of *Ipomoea*, a water molecule connects the two copper atoms

At the same time when the first X-ray structure of an oxy-hemocyanin was published[38] a side-on peroxo complex has successfully been prepared by Kitajima's group, which was commonly accepted but after strong discussions.[58] This complex was found to be diamagnetic and showed spectral features remarkably similar to those of oxy-Hc's and Ty's. These also include the unusually low peroxo O–O stretching frequencies ($<750\,\mathrm{cm}^{-1}$) that appear to be characteristic for the μ:η^2-η^2 structure. Finally, the side-on peroxo structure is also consistent with theoretical studies of different copper−peroxide complexes.

Deoxy-form. The deoxy-forms of Hc's and Ty's are colorless and EPR silent. In agreement with XAS studies, both coppers are present in oxidation state +I. The X-ray structure of *P. interruptus* deoxy-Hc showed that the two $\mathrm{Cu^I}$ ions are separated by <3.6 Å, which is in agreement with EXAFS studies of deoxy-Hc indicating most probably a 3,3-coordination of the coppers, which is also in agreement with the data from X-ray structural analysis. A thorough analysis of the electronic structure of the deoxy structure is presented by Solomon *et al*.[61]

3 TYPE 3 COPPER FAMILY

Provided here is only a short overview of type 3 copper proteins.

3.1 Hemocyanin

Hc's are very large oxygen-binding copper proteins freely dissolved in the hemolymph of many invertebrates of the two phyla of Arthropoda and Mollusca. Hemocyanin accounts for up to 80−98% of the total protein in the hemolymph. A more detailed description of the distribution of Hc's in Arthropoda and Mollusca can be found in reviews.[23,27,28,52,53,68,69]

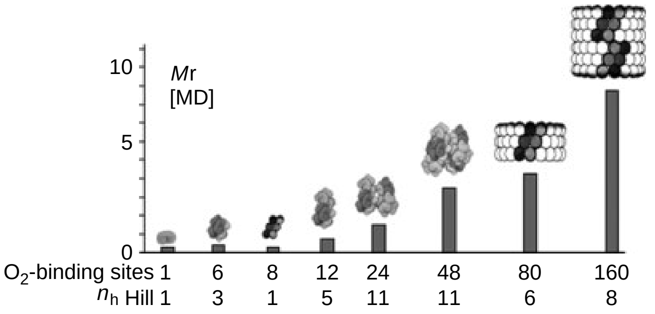

Figure 3 Hierarchies in the structures of hemocyanins from arthropods and molluscs. A kidney shaped arthropod subunit (Mr ~ 72 kDa) binds one molecule of dioxygen. Depending on the species, the subunits associate to 1 × 6, 2 × 6, 4 × 6, 6 × 6 and 8 × 6-meric hemocyanins found freely dissolved in the hemolymph. A molluscan hemocyanin subunit (Mr ~ 400 kDa) folds into eight functional units each carrying one active site (two cannot be seen being hidden in the interior of the cylinder). Ten of these subunits form cylinders. Depending on the species, decamers or didecamers are found. Thus, hemocyanins can bind up to 160 dioxygen molecules with a cooperativity n_h of over 11

To summarize, ultrastructural studies (ultracentrifugation, electron microscopy, small-angle X-ray scattering, immunochemistry, analysis of sequences and genes) have revealed that Hc's from the two phyla have unique and completely different quaternary structures[18,37–43,69–78] (Figure 3). Thus, arthropodan Hc's typically consist of hexamers (Mr 400–450 000) or multihexamers (2·6, 4·6, 6·6, and 8·6). From protein chemical studies, it has been found that the subunit Mr is about 75 000, consistent with the presence of one dinuclear copper activesite per polypeptide chain. Numerous studies have also indicated a widespread subunit heterogeneity in arthropodan Hc's. Molluscan Hc's consist of 10 or 20 large subunits (Mr 350–450 000), which form a hollow cylinder with Mr up to ca. 8–9·10^6 Daltons. Proteolytic digestion of the purified proteins showed that the subunits are composed of seven or eight oxygen-binding functional units with an Mr of ca. 45 000–55 000. These results are again in agreement with one dinuclear copper active site per functional unit (FU). Like arthropodan Hc's, molluscan Hc's also show substantial heterogeneity both on the subunit and the functional unit levels, being essential for the self-assembly process to yield species-dependent oligomers and being essential to develop cooperativity and allostery.[79]

3.1.1 Arthropod hemocyanins

Primary structure of hemocyanins. Many hemocyanin subunits were sequenced and analyzed (see latest reviews of Burmester and coworkers[23,24,68,69]). However, only for a few Hcs are all subunits composing the native structure sequenced. In most cases, a sequence identity of only about 30% is found between the subunit types of native hemocyanins within one species as well as when compared with those from different species. Most conserved is domain II carrying the active site. These sets of data allow the study of evolution of hemocyanins within a species and between species as well.

A few completely sequenced hemocyanins should be discussed: The 6-mer from the spiny lobster *P. interruptus* (Figure 4) consists of three different subunits a, b, c.[80,81] The hemocyanin of the European spiny lobster *Panulirus elephas* (synonym: *Panulirus vulgaris*) is also a hexamer composed by four closely related but distinct subunits.[82] Assuming a constant evolution rate, the *P. elephas* hemocyanin subunits emerged from a single hemocyanin gene around 25 million years ago. The alpha-type hemocyanins of *P. elephas* and the American spiny lobster *P. interruptus* split around 100 million years ago. This is about five times older than the assumed divergence time of the species and suggests that the genera may have split with the formation of the Atlantic Ocean.

The 4 × 6-meric tarantula Hc from *Eurypelma californicum* consists of 7 different subunit types.[83] In contrast to crustacean hemocyanin, the chelicerate hemocyanin subunit lost the alpha 1.2 helix (Figure 4, 5d, e), which then allows the assembly of larger hemocyanins than hexamers.[18,69,70] Each hexamer contains subunit a, d, e, f and g. The sixth position is taken by subunit b or c. Thus, the smallest structurally identical units are the 2 × 6-meric half-molecules, which dimerize

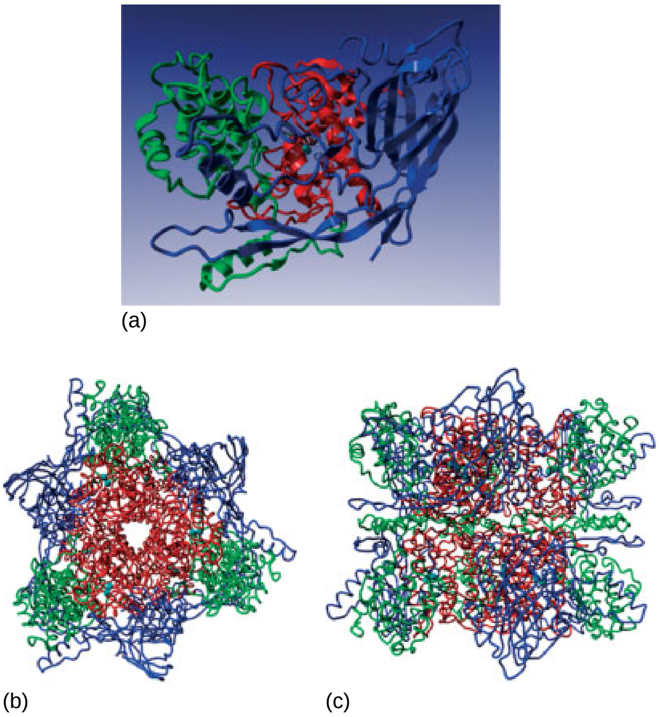

Figure 4 Structures of a crustacean hemocyanin subunit and the hexamer (*P. interruptus*). The three domains are colored differently (green: I; red: II; blue: III). Alpha-helix 1,2 will be missing in the chelicerate subunit compared to a crustacean subunit (a). The top view shows the threefold symmetry along the central channel (b), the side view (c) shows that the two trimers are isologously dimerized

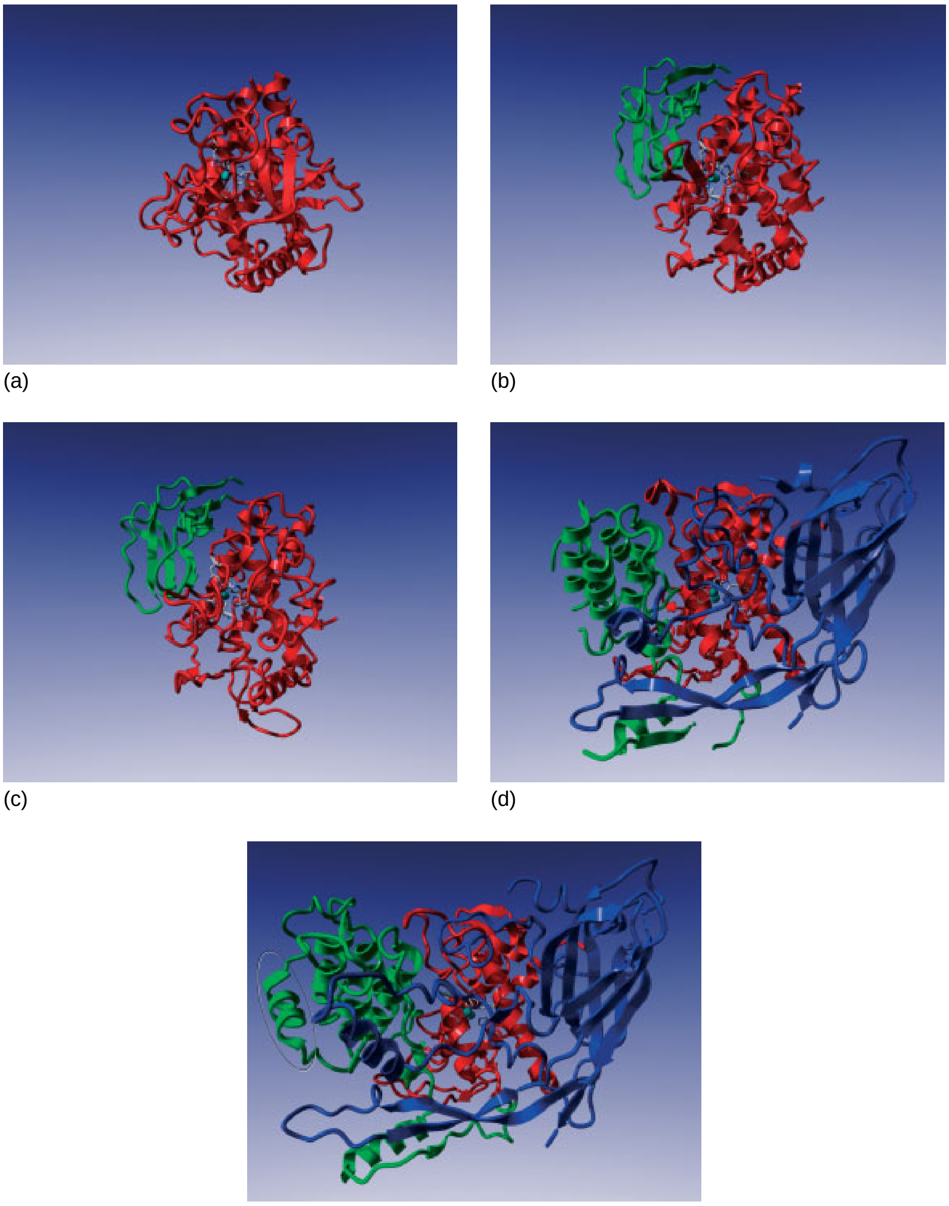

(a) (b) (c) (d) (e)

Figure 5 Comparison of the tertiary structures of a catecholoxidase from a sweet potato *Ipomea* sp. (a), functional units of molluscan hemocyanins (*O. dofleini* (b) and *R. thomasiana* (c)) and arthropod hemocyanin subunits from *L. polyphemus* (d) and *P. interruptus* (e). All structures are centered with respect to domain II (red) carrying the active site, domain I is colored green, domain III blue. The histidines are colored gray. In the *Limulus structure* (d) the alpha 1,3 helix is missing compared to the *Panulirus* (e) structure (ellipse)

isologously by forming two noncovalent bonds between the two subunits b and c.

Six distinct hemocyanin subunits were also identified in the red-legged golden orb-web spider *Nephila inaurata madagascariensis*.**[84]** The complete cDNA sequences of six subunits were obtained that corresponded to a-, b-, d-, e-, f-, and g-type subunits of the tarantula hemocyanin from *E. californicum*. A thorough evaluation of sequence comparisons revealed that subunit type a diverged first, followed by the common branch of the dimer-forming b and c subunits, while subunits d and f, as well as subunits e and g form common branches.**[84]**

Although being intensively investigated, only very few subunit types were sequenced of the 4 × 6-meric scorpion Hc (*Androctonus australis*, subunit Aa6 of eight subunit types**[85]**), and the 8 × 6-meric horseshoe crab (*L. polyphemus*, subunit II of more than ten subunit types**[86]**).

Scorpions and orthognath spiders, which possess highly conserved 4 × 6-mer hemocyanins, seem to possess at least six distinct subunit types (termed a to g). But many ‘modern’ entelegyne spiders such as *Cupiennius salei* differ from the standard arachnid scheme and have 2 × 6-mer hemocyanins. Six distinct subunit types (1 through 6) and three additional allelic sequences were identified.[87] Each 1 × 6-mer half-molecule most likely is composed of subunits 1–6, with subunit 1 linking the two hexamers via a disulfide bridge located in a C-terminal extension.

Insect hemocyanin. In the phyla Arthropoda, one class, the insects, are thought not to have oxygen carriers such as hemocyanins, since the oxygen supply by trachea is very effective. However, recently some hemocyanins were also detected in insects. An embryonic hemolymph protein (EHP) was found being expressed during early stages of development in the grasshopper embryo. EHP is a 78-kDa soluble protein present initially in the yolk sac content, and later in the embryonic hemolymph. Peptide sequencing was used to identify it being related to cheliceratan hemocyanins and prophenol oxidases and was therefore proposed to function as an oxygen carrier or storage protein during embryonic development.[88] Just recently in the hemolymph of nymphs and adults of the stonefly *Perla marginata*, a hexameric Hc was identified, which consists of two distinct subunit types of 659 and 655 amino acids. This Hc displays a cooperative oxygen binding with a moderately high oxygen affinity.[89]

Myriapod hemocyanin. The presence of hemocyanins in the diplopod Myriapoda was reported during the last few years, demonstrating that these proteins are more widespread among the Arthropoda than previously thought.[90–92] The hemocyanin of *Spirostreptus* sp.(Diplopoda: Spirostreptidae) is composed of two immunologically distinct subunits in the 75-kDa range that are most likely arranged in a 36-mer (6 × 6) native molecule. *Spirostreptus* hemocyanin is structurally similar to the single known hemocyanin from the myriapod taxon, *Scutigera coleoptrata* (Chilopoda), indicating a rather conservative architecture of the myriapod hemocyanins.[92] The 6 × 6-mer is composed of four distinct subunit types that are 49.5–55.5% identical. The cDNA of a fifth, highly diverged, putative hemocyanin subunit was identified that is not included in the native 6 × 6-mer hemocyanin. Phylogenetic analyses show that myriapod hemocyanins are monophyletic, but at least three distinct subunit types evolved before the separation of the Chilopoda and Diplopoda more than 420 million years ago.[92]

Hc related proteins in Arthropods. Some members of the type 3 copper protein family are closely related to hemocyanins and phenoloxidases but lost the ability to bind oxygen any more. In most cases they are known as pseudohemocyanins, hexamerins, and hexamerin receptors. In the case of cryptocyanin, three of the six highly conserved copper-binding histidine residues of hemocyanin are lacking.[93] The concentration of cryptocyanin in the hemolymph is closely coordinated with the molt cycle and reaches levels higher than hemocyanin during premolt.[94] A nonrespiratory pseudohemocyanin PHc of *Homarus americanus* consists of two different subunit types of 660 and 661 amino acids, respectively, that share a 94.4% sequence identity. Here only one of the histidines was mutated that coordinates the copper atom at the active site. It should be pointed out that Hc and PHc are synthesized in different tissues in the same species. Whereas *Homarus* hemocyanin is produced in the hepatopancreas, PHc is synthesized by the ovaries and the heart tissue.[94]

Evolution. Based on over 100 sequences of hemocyanins and related phenoloxidases, hypotheses for the evolution of this protein family were suggested.[23–25,28,95] Based on thorough investigations and analysis of the data by Burmester and coauthors the following scenario is proposed for the evolution of type 3 copper proteins in arthropods: Within the arthropod hemocyanin superfamily, the phenoloxidase probably emerged early in evolution. The respiratory hemocyanins evolved from these enzymes before the radiation of the extant euarthropodan subphyla. The results were consistent and indicated the separation of the cheliceratan and crustacean hemocyanins close to 600 MYA. The different subunit types of the multihexameric cheliceratan hemocyanin have a rather conservative structure and diversified in the arachnidan stemline between 550 and 450 MYA. By contrast, the separation of the crustacean (malacostracan) hemocyanin subunits probably occurred only about 200 MYA. The nonrespiratory pseudohemocyanins evolved within the Decapoda about 215 MYA. The insect hemocyanins and storage hexamerins emerged independently from the crustacean hemocyanins. The time of divergence of the insect proteins from the malacostracan hemocyanins was estimated to be about 430–440 MYA, providing support for the notion that the Hexapoda evolved from the same crustacean lineage as the Malacostraca.

Occurrence of hemocyanin related proteins in organisms. While textbooks tell that Hcs occur only in arthropods and molluscs, recently Hcs were also found in other phyla. The velvet worms (*Onychophora*) are considered living fossils and are closely related to the Euarthropoda. Onychophora possess a tracheal system for respiratory function, thus oxygen transport proteins have been considered unnecessary. In the hemolymph of the *Epiperipatus sp.* (Onychophora: Peripatidae), an arthropod-type hemocyanin was found, demonstrating that such proteins exist outside the Euarthropoda.[96]

Although four hemoglobin genes are present in the tunicate Ciona, two cDNA sequences from Ciona encoding for 794 and 775 amino acids have been identified to belong to the arthropod hemocyanin superfamily.[97] All amino acids required for oxygen binding and other structurally important residues are conserved. However, phylogenetic analyses and mRNA expression data suggest that the Ciona hemocyanin-like proteins rather act as phenoloxidases, possibly involved in humoral immune response. Based on these surprising results, it can be deduced that the hemocyanin superfamily emerged before the Protostomia and Deuterostomia diverged and support the idea that respiratory hemocyanins evolved from ancestors with an enzymatic function such as phenoloxidases.

3.1.2 *Molluscan hemocyanin*

Some subunits of mollusc hemocyanins were also completely sequenced. The first completely sequenced subunit of a mollusc hemocyanin subunit was that from *O. dofleini*.**[60]** The protein subunit has 2896 amino acids and contains seven functional units with *M*r of about 45 000–55 000, each carrying two sets of three invariant histidine residues constituting the binding sites (A and B) for two copper atoms. An accompanying paper**[39]** presents the structure of a functional unit (Odg). This allowed the organization of the long sequence. The sequences of the seven units exhibit high similarity, averaging about 40% identity, with a concentration of conserved sequences in the region surrounding the copper-binding sites. The sequences around the B-site show significant homology to the sequences of arthropod hemocyanins. A number of putative N-linked carbohydrate binding sites can be recognized in the sequence. In contrast to this hemocyanin, the hemocyanin subunit from the gastropod *Haliotis tuberculata* HtH1 folds into eight FUs, a-h.**[32,33]** With 3404 amino acids (392 kDa) it is the largest polypeptide sequence ever obtained for a respiratory protein. The cDNA comprises 10 758 base pairs and includes the coding regions for a short signal peptide, the eight different functional units, a 3′-untranslated region of 478 base pairs, and a poly(A) tail. The predicted protein contains 13 potential sites for N-linked carbohydrates (one for HtH1-a, none for HtH1-c, and two each for the other six functional units). Multiple sequence alignments show that the fragment HtH1-abcdefg is structurally equivalent to the seven-FU subunit from *Octopus* hemocyanin. However, an additional FU h is fused at the C-terminus. The gene organization of two molluscan hemocyanins has been resolved and discussed thoroughly.**[33]**

3.1.3 *Stability*

The quaternary structures of Hc's are strongly dependent on pH and the presence or absence of divalent cations such as Ca^{2+} or Mg^{2+}. Thus, most arthropodan Hc's can be dissociated to functional units by simply raising the pH above 9 with the concomitant removal of divalent cations by chelating agents (e.g. EDTA). This dissociation can be reversed by dropping the pH and/or addition of divalent cations (>10 mM). A very similar behavior is also observed for Hc's from molluscs. Hc's from both phyla typically exhibit cooperative oxygen binding. The extent of cooperativity is dependent upon several parameters such as pH, temperature, and the presence of divalent cations such as Ca^{2+} and Mg^{2+}.**[93,94,98]**

The observed heterogeneity can be ascribed to the fact that Hc's are glycoproteins.**[99–101]** Typically, molluscan Hc's have a carbohydrate content of 8–10%, compared to 1–4% for arthropodan Hc's.

3.2 X-ray Structures of Hemocyanins

Several X-ray structures of hemocyanins and of one catecholoxidase were solved during the last decade. The main features are presented in Figure 5.

Hc from the spiny lobster *P. interruptus* consists of a single hexamer with a *M*r of ca. 460 000 (Figure 4, 6). Using monoclinic crystals grown at pH 4.5 (one hexamer per asymmetric unit), Hol and his associates have successfully

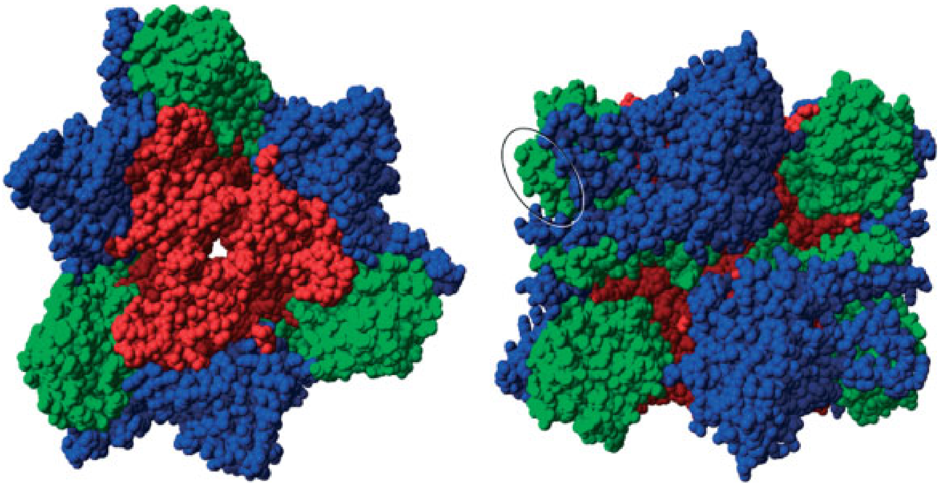

Figure 6 Top and side view of the hexameric structure of *P. interruptus* hemocyanin. The three domains of the six subunits are colored green (I), red (II), and blue (III). The six domains II (red) form the central channel. Alpha-helix 1.2 is marked by an ellipse

solved the 3-D structure at atomic resolution.[34] Recently, the structure has been refined to 3.2 Å using restrained least-squares procedures.

The crystal structure studied is that of the deoxy-form, as was shown by spectroscopic techniques (copper X-ray absorption spectroscopy, UV–visible spectroscopy, and electron paramagnetic resonance). The polypeptide chain of a subunit of *P. interruptus* Hc is folded into an irregular ellipsoid with three distinct domains. Domain I (comprising 175 amino acid residues) consists of seven helices and two beta-strands, one of which forms a beta-sheet with two strands from the third domain. The second domain (comprising residues 176–398) is also mainly helical and globular. The oxygen-binding site is located in the center of this domain surrounded by four helices: 2.1, 2.2, 2.5, and 2.6. The two copper ions (Cu-A and Cu-B) are each ligated by three histidines, which originate from the four helices. Two of the ligands of Cu-A and Cu-B come from successive turns of helix 2.1 and 2.5, respectively. The third ligand of each copper is provided by the remaining two helices. The helical pair consisting of 2.1 and 2.2 (Cu-A) is related to the helical pair 2.5 and 2.6 by an internal pseudo-twofold symmetry.[102] Three histidines (His194 and 198 of Cu-A and His344 of Cu-B) are tightly bound with N_ε–Cu distances smaller than 2 Å. A slightly less tightly bound ligand, His348, is found at a distance of 2.1 Å to Cu–B. The N_ε atoms of the four histidines together with the Cu-A and Cu-B are approximately arranged in a plane. His224 and His384 are located perpendicular to this plane, at opposite sides, with Cu–N_ε distances of ca. 2.7 Å to the two copper ions. The average Cu–Cu distance of the six subunits in deoxy-Hc is 3.54 Å, in good agreement with the value obtained by EXAFS.

The third domain (comprising residues 399–657) consists of a seven-stranded beta-barrel with two long loops. These loops function as arms holding the three domains together. The beta-barrel of domain 3 was found to be structurally very similar to those of Cu, Zn-superoxide dismutase and the immunoglobulin domains.

Hc from Limulus polyphemus Subunit II. In a recent study by Magnus and associates,[36,37] subunit II from *L. polyphemus* Hc was crystallized in the oxygenated and deoxygenated forms. The blue oxygenated crystals were found to contain one subunit of *M*r of 73 000 per asymmetric unit. The present model of the *L. polyphemus* crystal structure is based on X-ray data at 2.4 Å resolution (Figure 1). In the deoxy structure, two histidines each are bound to Cu-A (N1 and N2) and Cu-B (N5 and N6) at a distance between 2.0 and 2.1 Å. The other two histidines (N3 and N4) are located perpendicular to the equatorial plane formed by the other four histidines, and at opposite sides to the plane formed by N1, N2, N3, N4, Cu-A, and Cu-B. The Cu–N distances are 2.4 Å for both histidines. The two oxygen atoms of molecular oxygen are clearly distinguishable in the active site as two extra electron density peaks. The dioxygen molecule is bound in the $\mu{:}\eta^2\text{-}\eta^2$ conformation with regard to the copper atoms. The Cu–Cu distance in oxy-Hc from *L. polyphemus* is 3.6 Å, in good agreement with the values measured by EXAFS spectroscopy of arthropod and mollusc hemocyanins.[103] The O–O distance of 1.4 Å is in the range typically found for a peroxide ion bound to a transition metal ion. Finally, no evidence for an endogenous bridging ligand was found from the map as predicted from the spectroscopical analysis. The closest nonprotein electron density peak at ca. 4–5 Å from the copper ions was suggested to be a water molecule or a hydroxide ion.

Comparing this structure with the deoxy-homohexamer of *Limulus* subunit II,[37] three main structural movements can be observed during the deoxygenation. The distance between the two copper atoms enlarges to 4.2 Å, a rotation of the first domain with respect to the other three domains by 8° is observed and the highly conserved Phe49 is withdrawn from the active site by about 3 Å.[36,37] A metal ion such as calcium is supposed to be located at the concave site of domain III.

Molluscan hemocyanins. Two FUs from molluscan hemocyanins were resolved, the oxy-form of *O. dofleini* Hc FU g[39] (Figure 5b) and the deoxy-form of *R. thomasiana* Hc (Figure 5c[40]). Each FU consists of two domains. The N-terminal domain II carries the active site with a four alpha-helix bundle folding motif with two copper atoms. The C-terminal domain III replaces topologically the domain I in arthropod subunits and looks like a squeezed beta-barrel. Although the *Rapana* structure is not resolved as well as the *Octopus* FU, two different conformations can be deduced. In the oxy FU of *Octopus* hemocyanin, domain III covers the entrance to the active site completely while in the deoxy-form this domain is shifted a few degrees so that the channel to the active site becomes completely uncovered.

Catechol oxidase from sweet potato. Only one structure of a-phenoloxidase is available yet: the crystal structure of a catecholoxidase from sweet potato (*I. batatas*; the met form and with a bound inhibitor) was recently presented[41] (Figure 5a). This catecholoxidase is more similar to mollusc hemocyanin with respect to sequence similarity (about 25%) and the active site (Figure 2d).[26,41,104–107] As in mollusc hemocyanin in catecholoxidase one of the Cu-A coordinating histidines is covalently linked to a cysteine, a bond that is very seldom seen in nature (Figure 2d, yellow). This monomeric catecholoxidase seems to be only capable to catalyze the oxidation of diphenols. In contrast to mollusc hemocyanins, purified catecholoxidase from *I. batatas* consists of only one monomer with an open entrance to the active site in the activated form.[41] A part of the C-terminal sequence is not resolved yet and is absent in the activated form. Comparing similar sequences of catecholoxidase and mollusc hemocyanins, a homology modeling of the C-terminal sequence revealed that it most likely covers the entrance to the active site[106,107] supporting the hypothesis of an oxygenation-dependent conformational transition of the C-terminal domain.

4 PHENOLOXIDASE

Tyrosinase catalyzes two reactions, the hydroxylation of phenolic compounds in ortho-position (cresolase activity) and subsequently the oxidation of the diphenolic products (catecholase activity).[2–4] Tyrosinase as well as another enzyme that catalyzes only the oxidation reaction, catecholoxidase (EC 1.10.3.1), belongs to the group of phenoloxidases. The monooxygenase nature of Ty was established by Mason and coworkers[8] in a pioneering study using ^{18}O-labeled oxygen. The two-electron donor required in the hydroxylation reaction is the *o*-diphenol, which is generated internally from the monophenol substrate.

The presence of phenoloxidase in all phyla of living organisms demonstrates that their origin is very early in the history of life.[23,24,28] It is involved in the biosynthesis of melanins and other polyphenolic compounds. Depending on the species, phenoloxidases are involved in the primary immune response, wound healing, sclerotization, and coloring processes. In mammals, L-tyrosine is the initial substrate in the pathway leading to the final products of black–brown eumelanins, red–yellow pheomelanins, or a mixture of pheo- and eumelanins.[1,108]

Ty initiates melanin synthesis by the hydroxylation of L-tyrosine to 3,4-dihydroxyphenylalanine (Dopa) and the oxidation of dopa to dopaquinone. In the presence of L-cysteine, dopaquinone rapidly combines with the thiol group to form cysteinyldopas, which undergo nonenzymatic conversion and polymerization to pheomelanin via benzothiazine intermediates.[1] In the absence of thiol groups, dopaquinone very rapidly undergoes conversion to dopachrome, which is transformed to 5,6-dihydroxyindole-2-carboxylic acid (DHICA) by dopachrome tautomerase. Alternatively, dopachrome is converted nonenzymatically to 5,6-dihydroxyindole (DHI). Oxidation of DHICA and DHI to the corresponding quinones and subsequent polymerization leads to eumelanins. It is still questionable if Ty is involved in this step.

Depending on the source of the enzyme, the Mr's vary between 29 000 and 450 000 with subunit Mr's from 29 000 to 67 000. To date, the enzyme from the bacterium *Streptomyces glaucescens* was found to have the smallest functional unit with one copper pair per polypeptide chain of 29 000. Ty's from microorganisms and plants are generally present as soluble proteins; in contrast, those from mammals are bound to specific organelles (melanosomes) in cells termed melanocytes.

In contrast to Hc's, which can be easily purified in large amounts, Ty's are present in low concentrations in all organisms studied. Furthermore, they are difficult to obtain in pure form owing to pigment contamination and the occurrence of multiple forms. It is therefore not surprising that, to date, Ty from only one species (*Neurospora crassa*) has been sequenced by classical protein chemical means. With the advent of recombinant DNA technology, however, several amino acid sequences have become available recently.[1] These include Ty's from the bacteria *S. glaucescens* and *Streptomyces antibioticus* as well as mouse and man. All Ty molecules sequenced so far are single-chain proteins with calculated Mr's of 30 900 (273 amino acid residues) for *S. glaucescens* and *S. antibioticus*, 46000 (407 amino acid residues) for *N. crassa*, 57 900 (480 amino acid residues) and 58 550 (515 amino acid residues) for mouse, and 58 000 (515 amino acid residues) and 62 600 (548 amino acid residues) for man.

Amino acid sequence comparison of the different Ty's shows that they are structurally related. The sequence identity is 24% between bacterial and fungal Ty and 26% between mouse and *N. crassa* Ty. A comparison of all three types of Ty (bacterial, fungal, and mammalian) reveals a sequence identity of only 8.7%.

Although many phenoloxidases are described in arthropods, only very few are proven to be tyrosinases such as those from *Pacifastacus leniusculus*,[109] *Astacus leptodactylus*,[110] and *P. elephas*.[110]

As already known at the time when Lerch wrote his review,[1] mammalian Ty's (mouse and man) are synthesized as proforms containing a typical signal peptide at the amino-terminal ends. This peptide is required for the translocation of the molecule into the melanosomes, the sites of melanin biosynthesis. In addition, mammalian Ty's are glycosylated (5–6 putative glycosylation sites) and are rather rich in cysteine. From 17 residues, 10 are clustered within the first 100 amino acid residues and 5 are found in the middle of the molecule. In the form of disulfides these residues contribute significantly to the unusually high resistance of mammalian Tys towards digestion by proteases. Nevertheless, still no structure is available although structural features were deduced from comparisons with hemocyanins.[111] In addition, a recent paper describes catalase and peroxygenase activities of tyrosinases.[112]

The field of phenoloxidases is absolutely unclear with respect to the structure. Mammalian tyrosinases have transmembrane parts and are glycosylated,[111] in arthropods they are freely soluble.[110] The aggregation is unclear as well. In mammals and prokaryotes, tyrosinases seem to be monomers,[111] in arthropods they occur as hexamers and look like hemocyanins.[110] The fact that not much knowledge is available on the structure and function of tyrosinases is surprising especially since tyrosinases are of major concern in medical and cosmetic research.

Copper-binding Regions of Hemocyanins and Tyrosinases. In the previous review by Lerch,[1] the similar copper centers of hemocyanins and phenoloxidases were thoroughly discussed on the basis of sequence comparisons. Thus, the surroundings of Cu-A and Cu-B are different as already discussed in this report. Nevertheless, it should be pointed out that the tertiary structure of the various domains of hemocyanins and phenoloxidases are very similar and in most sections superimposable although the sequence identity is less than 30%.

Comparing the most conserved parts, the active site, reveals two different types of type 3 copper proteins, an arthropod hemocyanin-like one and a molluscan hemocyanin-like one. While the Cu-B site is highly conserved in both types, the Cu-A site differs. In the case of molluscan hemocyanins, one helix is too short for stabilizing the important histidine complexing Cu-A so that it has to be tied down by an unusual His–Cys bond as shown in Figure 2 (d–f).

5 PHENOLOXIDASE ACTIVITY OF HEMOCYANIN

The obvious structural similarity between hemocyanins and phenoloxidases is also supported by the fact that for almost all hemocyanins a-phenoloxidase activity can be induced by detergents or proteases as discussed in previous papers.[54,55] In most cases, especially in crustaceans, the activity is very weak.[113]

However, in some chelicerates, strong phenoloxidase activities have persisted in hemocyanins to date. Tarantula hemocyanin from *E. californicum* is very much comparable to phenoloxidases based on activation mechanism, substrate specificity, and inhibition.[45] The same holds for the hemocyanins from the horseshoe crabs *L. polyphemus* and *Tachypleus tridentatus*.[47,50] All three are ancient chelicerate species and unlike in more modern crustaceans, myriapods, and insects, no phenoloxidases have been found in their hemolymph to date. Thus, it may be that the hemocyanin fulfills the functions of the phenoloxidase in these chelicerates.

Activation of hemocyanins. Recently, quite a few papers reported the conversion of the oxygen-binding function of hemocyanins to phenoloxidase activity, that is, the conversion of the oxygen carrier hemocyanin into an enzyme.[44–51,114] These groups confirm older observations, which were hardly trusted for many years.[115,116] Many hemocyanin subunits can be activated by in vitro effectors, which are normally used for denaturation.[113] During this unfolding, access to the active site for phenolic substrates will be possible for a short period before the structure will be destroyed completely. This would explain that all subunits from crustacean hemocyanins show catecholoxidase activity in native PAGE. Meanwhile different ways of activation of hemocyanins are accepted and summarized in various articles.[26,28,54,55]

One way for activation to occur is the induction by in vivo factors. The inactive prophenoloxidase from hemocytes can be activated by a defense cascade. The defense cascade of insects and crustaceans, however, is different from that of the horseshoe crab *L. polyphemus* and most likely from chelicerates in general. Nagai and Kawabata[50,51] reported a clotting enzyme from the horseshoe crab *T. tridentatus*, that converts hemocyanins to phenoloxidase by forming a complex with a stoichiometry of 1:1 without proteolytic cleavage.

Activation mechanism. What happens during activation in hemocyanins and how can we use them as model systems to understand tyrosinase/catecholoxidase activity? Arthropod and mollusc hemocyanins have to be considered separately, although the processes are similar.

Here, I would like to present our hypothesis on the activation as published in various articles:[26,45,47,54,55] The activation of an arthropod hemocyanin opens a large entrance for phenolic substances to the active site by removal of an N-terminal peptide cleaved at a similar position as in prophenoloxidase of arthropods. This pulls a phenylalanine out of the substrate-binding pocket, which is highly conserved among hemocyanins and phenoloxidases. In the case of the horseshoe crab *L. polyphemus* hemocyanin it is Phe49 (Figure 7). As a result, a channel is opened and the dinuclear copper active site becomes accessible also to nongaseous bulky phenolic substrates. A phenolic substrate can be modelled into this pocket exactly like Phe49 from *Limulus* hemocyanin (Figure 8). This hypothesis is supported by a synthesized inhibitor of phenoloxidase activity carrying a phenylalanine that takes the position of Phe49. Phenylalanine is an ideal amino acid in this respect since it is inert with respect to any enzymatic activity at the active site. The flexibility of the substrates is constrained by hydrophobic interactions between its phenyl ring and the axial His328 on Cu-B and a Thr351 residue next to Cu-A in the *Limulus* structure. The phenyl ring of the substrate is almost perpendicular to the Cu-O_2-Cu plane, with close contacts of its hydroxyl group to Cu-A and of its ortho-position to one of the two oxygen atoms of the dioxygen ligand. This suggests bonding to Cu-A, in agreement with earlier concepts assuming direct coordination of the phenolic substrate to one Cu center, preferably Cu-A. Consequently, the vicinity of the ortho-position of the aromatic ring to dioxygen then allows the hydroxylation reaction.

Independent of in vivo or in vitro activation, the opening of the entrance by pulling out the placeholder Phe49 seems to be crucial and is achieved by proteolysis or a conformational transition of the first domain carrying Phe49.

A similar substrate-binding pocket was identified for molluscan hemocyanins, which was not surprising since the active site of mollusc hemocyanins and that of arthropod hemocyanins and catecholoxidases are very similar. Therefore, we proposed the following mechanism for the activation of the molluscan hemocyanin based on the recently solved X-ray structure of a functional unit of the hemocyanin from the molluscan *O. dofleini*.[39] The C-terminal domain covers the entrance to the active site located on the N-terminal site by sticking Leu2830 into the entrance door. Detergents

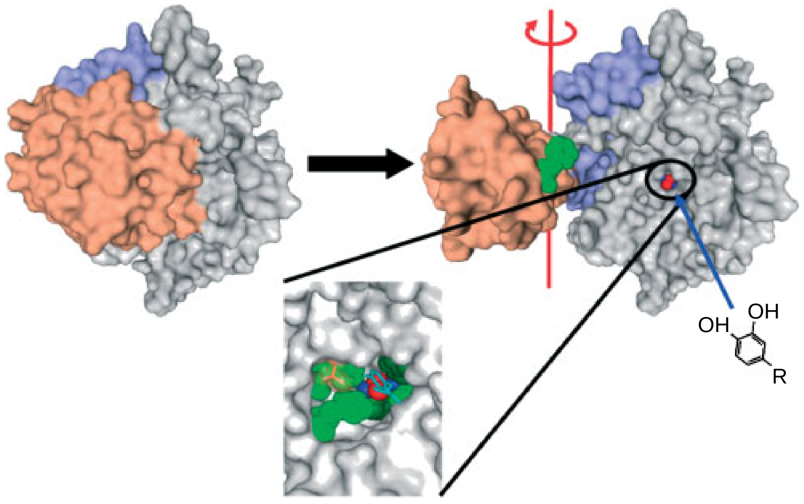

(a) inactive (b) active

Figure 7 Scheme of the activation of the phenoloxidase activity of hemocyanins. A part of domain I (brown) is turned away together with the conserved Phe49 (green). This opens a view into the active site, which is enlarged. The copper atoms are colored blue, the oxygen red, a hypothetical substrate light blue. The amino acids forming the channel are drawn green[55]

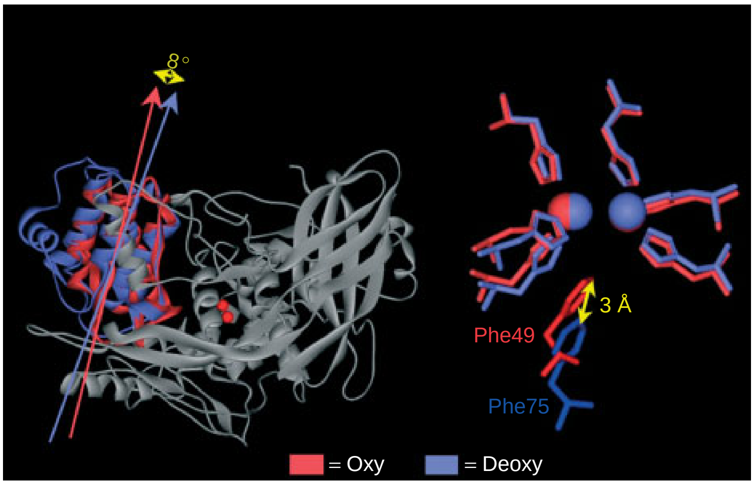

(a) Movement of domain 1 (b) Active site

Figure 8 Proposed mechanism of phenoloxidase activity in arthropod hemocyanins based on two X-ray structures of the oxy- and deoxy-forms of the *Limulus* subunit II[55]

might disrupt these interactions to open the entrance to the active site by tilting upward the compact β-rich domain. Thus, Leu2830 will also be pulled out from the substrate-binding pocket opening an access route to the active site. This also can be accomplished by a conformational transition deduced for the two resolved functional unit structures, the one being in the oxy-state (*O. dofleini*) and the other being in the deoxy-state (*R. thomasiana*).[40] In the latter state, an open channel to the active site becomes visible. In addition, the hypothesis of a conformational transition may explain the pH-dependent activation of *O. vulgaris* hemocyanin.

This idea agrees well with a similar hypothesis presented for the solved structure of the catecholoxidase from *I. batatas*[41] after superimposing the C-terminal sequence, which is not structurally resolved, on the known structure of the *Octopus* FU.[26,106,107] Here a leucine residue, Leu439 in *Ipomoea* catecholoxidase, corresponds to Leu2830 in *Octopus* hemocyanin, which blocks the entrance.

Are hemocyanins tyrosinases or catecholoxidases?. All crustacean hemocyanins seem to exhibit only catecholoxidase activity. Only two hemocyanins from chelicerates, the

4 × 6-meric hemocyanins of the tarantula *E. californicum* and scorpion *Pandinus imperator*, seem to hydroxylate tyramine after proper activation.[45] However, further experiments are in progress to reveal the mechanism.

Evolution of two phenoloxidases, an arthropod and molluscan type. A close relationship between phenoloxidase and hemocyanin was deduced based on their similar sequences, physico-chemical properties and similar functions. But sequence comparisons also revealed that there is not a common phenoloxidase type: the enzymes found in animals, plants, and fungi are different with respect to their sequences, size, glycosylation, and activation. Two different types of tyrosinases can be distinguished based on their sequences, structure, and function. One type (*m*-phenoloxidase) is more related to molluscan hemocyanin with respect to the active site. The other type (a-phenoloxidase), which is very similar to arthropod hemocyanins, is found in arthropods together with hemocyanins (Figure 9).[54,55]

Comparison of the arrangements of the domains within an arthropod hemocyanin subunit and the functional unit of a molluscan hemocyanin also suggests two different types of phenoloxidases, the a-phenoloxidase and the *m*-phenoloxidase. Cleavages of the N-terminal domain of a-phenoloxidase and the C-terminal domain of m-phenoloxidase open the entrances to the active sites for bulky substrates. The key amino acids are indicated in Figure 9.

Reaction mechanism of phenoloxidases. Although no structure of any tyrosinase or an oxy-catecholoxidase is available, similar spectroscopic features indicate similar active sites compared with hemocyanins as discussed above and summarized in various reviews and other articles. In addition, several models about the chemistry of the two reactions were presented based on synthetic tyrosinases being published recently. Only a few are mentioned.[61–67,117–121] However, this part is not the focus of this article but will be discussed in other contributions in great detail. Nevertheless, it should be noted that most presented models are based on synthetic copper compounds in order to mimic the catecholoxidase and cresolase activity. However, they do not respect the influence of the protein matrix. No particular electronic interactions between the copper atoms, the dioxygen, and the amino acids are discussed owing to the lack of any structure. Although when steric hindrance is discussed, it should be remembered that the protein structure limits the degree of orientation of the substrates at the active site and therefore limits the proposals on the chemistry of catalysis.[117] Thus, as long as there is no structure available for tyrosinases or for the oxy-catecholoxidase, the chemical description of the catalysis still remains a hypothesis as presented in the previous article of Lerch.[1]

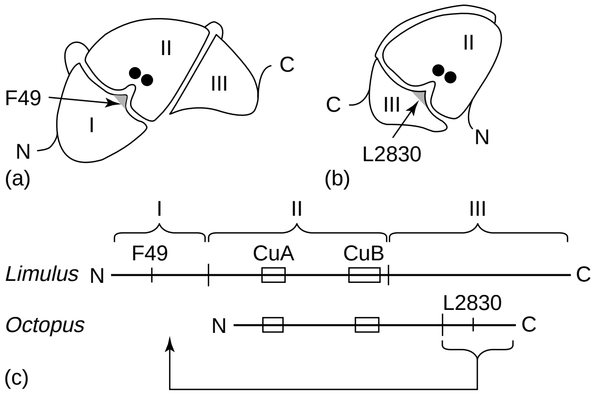

Figure 9 The orientation of the domains from an arthropod and a functional unit from a molluscan hemocyanin are compared. In the first case (a) F49 in the N-terminal domain blocks the entrance to the active site, in the latter one (b) L2830 located in the C-terminal domain[55]

6 REFERENCES

1. K. Lerch, ‘Encyclopedia of Inorganic Chemistry’, 1st edn., 1994, p. 850.
2. M. L. Fredericq, *C. R. Hebd. Séances, Acad. Sci. Paris*, 1878, **87**, 996.
3. E. Bourquelot and G. Bertrand, *Comput. Rend. Soc. Biol.*, 1895, **47**, 582.
4. A. C. Redfield, T. Coolidge, and H. Montgomery, *J. Biol. Chem.*, 1928, **76**, 197.
5. R. W. Root, *J. Biol. Chem.*, 1934, **104**, 239.
6. F. Kubowitz, *Biochem. Z.*, 1938, **299**, 32.
7. J. M. Nelson and C. R. Dawson, *Adv. Enzymol.*, 1944, **4**, 99.
8. H. S. Mason, *Adv. Enzymol.*, 1955, **16**, 105.
9. H. S. Mason, *Annu. Rev. Biochem.*, 1965, **34**, 595.
10. W. H. Vanneste and A. Zuberbühler, in ‘Molecular Mechanisms of Oxygen Activation’, ed. O. Hayaishi, Academic Press, New York, 1974, Chap. 9, p. 371.
11. F. Ghiretti, in ‘The Oxygenases’, ed. O. Hayaishi, Academic Press, New York, 1962, p. 517.
12. K. E. Van Holde and E. F. J. van Bruggen, in ‘Subunits in Biological Systems’, eds. S. N. Timasheff and G. D. Fasman, Dekker, New York, 1971, p. 1.
13. R. Lontie and R. Witters, in ‘Inorganic Biochemistry’, ed. G. Eichhorn, Elsevier, Amsterdam, 1973, Vol. 1, p. 344.
14. K. Lerch, in ‘Metal Ions in Biological Systems’, ed. H. Sigel, Dekker, New York, 1981, Vol. 13, p. 143.
15. E. I. Solomon, in ‘Copper Proteins’, ed. T. G. Spiro, Wiley, New York, 1981, Vol. 3, p. 41.
16. K. Lerch, *Mol. Cell. Biochem.*, 1983, **52**, 125.
17. E. I. Solomon, K. W. Penfield, and D. E. Wilcox, *Struct. Bonding (Berlin)*, 1983, **53**, 1.

18. B. Linzen, N. M. Soeter, A. F. Riggs, H. J. Schneider, W. Schartau, M. D. Moore, E. Yokata, P. Q. Behrens, H. Nakashima, T. Tagaki, T. Nemoto, J. M. Vereijken, H. J. Bak, J. J. Beintema, A. Volbeda, W. P. Gaykema, and W. G. J. Hol, *Science*, 1985, **229**, 519.
19. K. Lerch, in 'Advances in Pigment Cell Research', ed. J. Bagnara, Liss, New York, 1988, p. 85.
20. K. Lerch and U. A. Germann, in 'Oxidases and Related Redox Systems', eds. T. E. King, H. S. Mason, and M. Morrison, Liss, New York, 1988, p. 331.
21. G. Müller, S. Ruppert, E. Schmid, and G. Schütz, *EMBO J.*, 1988, **7**, 2723.
22. V. J. Hearing and M. Jiménez, *Pigment Cell Res.*, 1989, **2**, 75.
23. T. Burmester, *Mol. Biol. Evol.*, 2001, **2**, 184.
24. T. Burmester, *J. Comput. Phys.*, 2002, **2**, 95.
25. H. Decker and N. Terwilliger, *J. Exp. Biol.*, 2000, **12**, 1777.
26. H. Decker and F. Tuczek, *Trends Biochem. Sci.*, 2000, **25**, 392.
27. N. Terwilliger, *J. Exp. Biol.*, 1998, **201**, 1085.
28. K. van Holde, K. Miller, and H. Decker, *J. Biol. Chem.*, 2001, **276**, 15563.
29. N. B. Terwilliger, L. Dangott, and M. Ryan, *Proc. Natl. Acad. Sci. U.S.A.*, 1999, **96**, 2013.
30. T. Burmester, *J. Biol. Chem.*, 1999, **274**, 13217.
31. T. Burmester, H. C. Massey Jr, S. O. Zakharkin, and H. Benes, *J. Mol. Evol.*, 1998, **47**, 93.
32. B. Lieb, B. Altenhein, and J. Markl, *J. Biol. Chem.*, 2000, **275**, 5675.
33. B. Lieb, B. Altenhein, J. Markl, A. Vincent, E. van Olden, K. E. van Holde, and K. I. Miller, *Proc. Natl. Acad. Sci. U.S.A.*, 2001, **98**, 4546.
34. W. P. J. Gaykema, W. G. J. Hol, J. M. Vereijken, N. M. Soeter, H. J. Bak, and J. J. Beintema, *Nature*, 1984, **309**, 23.
35. A. Volbeda and W. G. J. Hol, *J. Mol. Biol.*, 1989, **209**, 249.
36. K. Magnus and H. Ton-That, *J. Inorg. Biochem.*, 1992, **47**, 20.
37. B. Hazes, K. Magnus, C. Bonaventura, J. Bonaventura, Z. Dauter, K. Kalk, and W. Hol, *Protein Sci.*, 1993, **2**, 597.
38. K. Magnus, B. Hazes, H. Ton-That, C. Bonavenura, J. Bonaventura, and W. Hol, *Proteins*, 1994, **19**, 302.
39. M. Cuff, K. Miller, K. van Holde, and W. Hendrickson, *J. Mol. Biol.*, 1998, **278**, 855.
40. M. Perbandt, E. Guthohrlein, W. Rypniewski, K. Idakieva, S. Stoeva, W. Voelter, N. Genov, and C. Betzel, *Biochemistry*, 2003, **42**, 6341.
41. T. Klabunde, C. Eicken, J. Sacchettini, and B. Krebs, *Nat. Struct. Biol.*, 1998, **5**, 1084.
42. E. V. Orlova, P. Dube, J. R. Harris, E. Beckman, F. Zemlin, J. Markl, and M. van Heel, *J. Mol. Biol.*, 1997, **271**, 417.
43. U. Meissner, M. Stohr, K. Kusche, T. Burmester, H. Stark, J. R. Harris, E. V. Orlova, and J. Markl, *J. Mol. Biol.*, 2003, **325**, 99.
44. T. Zlateva, P. Di Muro, B. Salvato, and M. Beltramini, *FEBS Lett.*, 1996, **384**, 251.
45. H. Decker and T. Rimke, *J. Biol. Chem.*, 1998, **273**, 25889.
46. B. Salvato, M. Santamaria, M. Beltramini, G. Alzuet, and L. Casella, *Biochemistry*, 1998, **37**(40), 14065.
47. H. Decker, M. Ryan, E. Jaenicke, and N. Terwilliger, *J. Biol. Chem.*, 2001, **276**, 17796.
48. D. D. Pless, M. B. Aguilar, A. Falcon, E. Lozano-Alvarez, and E. P. Heimer de la Cotera, *Arch. Biochem. Biophys.*, 2003, **409**, 402.
49. S. Y. Lee, B. L. Lee, and K. Söderhäll, *J. Biol. Chem.*, 2003, **278**, 7927.
50. T. Nagai and S. Kawabata, *J. Biol. Chem.*, 2000, **275**, 29264.
51. T. Nagai, T. Osaki, and S. Kawabata, *J. Biol. Chem.*, 2001, **276**, 27166.
52. K. E. van Holde and K. I. Miller, *Adv. Biochem.*, 1995, **47**, 1.
53. J. Markl and H. Decker, *Adv. Comp. Environ. Physiol.*, 1992, **13**, 325.
54. H. Decker and E. Jaenicke, *Dev. Comp. Immunol.*, 2004, **28**, 673.
55. E. Jaenicke and H. Decker, *ChemBioChem.*, 2004, **5**, 163.
56. C. van Gelder, W. Flurkey, and H. Wichers, *Phytochemistry*, 1997, **45**, 1309.
57. A. Sanchez-Ferrer, J. Rodriguez-Lopez, F. Garcia-Canovas, and F. Garcia-Carmona, *Biochim. Biophys. Acta*, 1995, **1247**, 1.
58. N. Kitajima and Y. Moro-oka, *Chem. Rev.*, 1994, **94**, 737.
59. R. Drexel, S. Siegmund, H. J. Schneider, B. Linzen, C. Gielens, G. Preaux, R. Lontie, J. Kellermann, and F. Lottspeich, *Biol. Chem. Hoppe-Seyler*, 1987, **368**, 617.
60. K. I. Miller, M. E. Cuff, W. F. Lang, P. Varga-Weisz, K. G. Field, and K. E. van Holde, *J. Mol. Biol.*, 1998, **278**(4), 827.
61. E. I. Solomon, F. Tuczek, D. E. Root, and C. A. Brown, *Chem. Rev.*, 1994, **94**, 827.
62. E. I. Solomon, U. Sundaram, and T. E. Machonkin, *Chem. Rev.*, 1996, **96**, 2563.
63. E. I. Solomon, P. Chen, M. Metz, S. K. Lee, and A. E. Palmer, *Angew. Chem., Int. Ed. Engl.*, 2001, **40**, 4570.
64. P. Chen and E. I. Solomon, *Proc. Natl. Acad. Sci. U.S.A.*, 2004, **101**, 13105.
65. P. Chen, K. Fujisawa, M. E. Helton, K. D. Karlin, and E. I. Solomon, *J. Am. Chem. Soc.*, 2003, **125**, 6394.
66. P. E. Siegbahn, *J. Biol. Inorg. Chem.*, 2004, **9**, 577.
67. P. E. Siegbahn, *J. Biol. Inorg. Chem.*, 2003, **8**, 577.
68. T. Burmester, *Micron*, 2004, **35**, 121.
69. F. de Haas and E. F. van Bruggen, *J. Mol. Biol.*, 1994, **237**, 464.
70. M. van Heel and P. Dube, *Micron*, 1994, **25**, 387.
71. F. de Haas, J. F. L. van Breemen, E. J. Boekema, W. Keegstra, and E. F. J. van Bruggen, *Ultramicroscopy*, 1993, **49**, 426.

72. H. Decker, H. Hartmann, R. Sterner, E. Schwarz, and I. Pilz, *FEBS Lett.*, 1996, **393**, 226.
73. H. Hartmann, B. Lohkamp, N. Hellmann, and H. Decker, *J. Biol. Chem.*, 2001, **276**, 19954.
74. H. Hartmann, A. Bongers, and H. Decker, *J. Biol. Chem.*, 2004, **279**, 2841.
75. H. Hartmann and H. Decker, in 'Methods in Enzymology – Energetics of Biological Macromolecules', eds. J. M. Holt, M. L. Johnson, and G. K. Ackers, Academic Press, 2004, Vol. 379, p. 81.
76. I. Micetic and B. Salvato, *Micron*, 2004, **35**(1–2), 17.
77. F. Spinozzi, E. Maccioni, C. V. Teixeira, H. Amenitsch, R. Favilla, M. Goldoni, P. Di Muro, B. Salvato, P. Mariani, and M. Beltramini, *Biophys. J.*, 2003, **85**, 2661.
78. E. Borghi, P. L. Solari, M. Beltramini, L. Bubacco, P. Di Muro, and B. Salvato, *Biophys. J.*, 2002, **82**, 3254.
79. H. Decker, A. Savel-Niemann, D. Korschenhausen, E. Eckerskorn, and J. Markl, *Biol. Chem. Hoppe-Seyler*, 1989, **370**, 511.
80. P. A. Jekel, B. Neuteboom, and J. J. Beintema, *Comp. Biochem. Physiol. B, Biochem. Mol. Biol.*, 1996, **115**, 243.
81. P. A. Jekel, H. J. Bak, N. M. Soeter, J. M. Vereijken, and J. J. Beintema, *Eur. J. Biochem.*, 1988, **178**, 403.
82. K. Kusche, A. Hembach, C. Milke, and T. Burmester, *J. Comp. Physiol. [B]*, 2003, **173**, 319.
83. R. Voit, G. Feldmaier-Fuchs, T. Schweikardt, H. Decker, and T. Burmester, *J. Biol. Chem.*, 2000, **275**, 39339.
84. A. Averdam, J. Markl, and T. Burmester, *Eur. J. Biochem.*, 2003, **270**(16), 3432.
85. A. Buzy, J. Gagnon, J. Lamy, P. Thibault, E. Forest, and G. Hudry-Clergeon, *Eur. J. Biochem.*, 1995, **233**, 93.
86. H. Nakashima, P. Q. Behrens, M. D. Moore, E. Yokota, and A. F. Riggs, *J. Biol. Chem.*, 1986, **261**, 10526.
87. P. Ballweber, J. Markl, and T. Burmester, *J. Biol. Chem.*, 2002, **277**, 14451.
88. D. Sanchez, M. D. Ganfornina, G. Gutierrez, and M. J. Bastiani, *Mol. Biol. Evol.*, 1998, **15**, 415.
89. S. Hagner-Holler, A. Schoen, W. Erker, J. H. Marden, R. Rupprecht, H. Decker, and T. Burmester, *Proc. Natl. Acad. Sci. U.S.A.*, 2004, **101**, 871.
90. E. Jaenicke, H. Decker, W. Gebauer, J. Markl, and T. Burmester, *J. Biol. Chem.*, 1999, **274**, 29071.
91. K. Kusche and T. Burmester, *Mol. Biol. Evol.*, 2001, **18**, 1566.
92. K. Kusche, A. Hembach, S. Hagner-Holler, W. Gebauer, and T. Burmester, *Eur. J. Biochem.*, 2003, **270**, 2860.
93. R. Hübler, B. Fertl, N. Hellmann, and H. Decker, *Biochim. Biophys. Acta*, 1998, **1383**, 327.
94. R. Favilla, M. Goldoni, A. Mazzini, P. Di Muro, B. Salvato, and M. Beltramini, *Biochim. Biophys. Acta*, 2002, **1597**, 42.
95. T. Burmester, *Micron*, 2004, **35**(1–2), 121.
96. K. Kusche, H. Ruhberg, and T. Burmester, *Proc. Natl. Acad. Sci. U.S.A.*, 2002, **99**, 10545.
97. A. Immesberger and T. Burmester, *J. Comp. Physiol. [B]*, 2004, **174**, 169.
98. R. Favilla, M. Goldoni, F. Del Signore, P. Di Muro, B. Salvato, and M. Beltramini, *Biochim. Biophys. Acta*, 2002, **1597**, 51.
99. P. Dolashka-Angelova, A. Beck, A. Dolashki, S. Stevanovicd, M. Beltramini, B. Salvato, R. Hristova, L. Velkova, and W. Voelter, *Micron*, 2004, **35**, 101.
100. C. Gielens, N. De Geest, F. Compernolle, and G. Preaux, *Micron*, 2004, **35**, 99.
101. T. Kurokawa, M. Wuhrer, G. Lochnit, H. Geyer, J. Markl, and R. Geyer, *Eur. J. Biochem.*, 2002, **9**(22), 5459.
102. A. Volbeda and W. G. Hol, *J. Mol. Biol.*, 1989, **206**(3), 531.
103. A. Sabatucci, I. Ascone, L. Bubacco, M. Beltramini, D. Muro, and B. Salvato, *J. Biol. Inorg. Chem.*, 2002, **7**, 120.
104. C. Eicken, B. Krebs and J. C. Sacchettini, *Curr. Opin. Struct. Biol.*, 1999, **9**, 677.
105. C. Eicken, C. Gerdemann, and B. Krebs, in 'Catechol oxidase. Handbook of Metalloproteins', eds. A. Messerschmidt, R. Huber, T. Poulos, and K. Wieghardt, John Wiley & Sons, Chichester, 2001.
106. C. Gerdemann, C. Eicken, H. J. Galla, and B. Krebs, *J. Inorg. Biochem.*, 2002, **89**, 155.
107. C. Eicken, C. Gerdemann, and B. Krebs, *Acc. Chem. Res.*, 2002, **35**, 183.
108. M. Sugumaran, *Pigment Cell Res.*, 2002, **15**(1), 2.
109. A. Aspan, T. S. Huang, L. Cerenius, and K. Söderhäll, *Proc. Natl. Acad. Sci. U.S.A.*, 1995, **92**(4), 939.
110. E. Jaenicke and H. Decker, *Biochem. J.*, 2003, **371**, 515.
111. J. C. Garcia-Borron and F. Solano, *Pigment Cell Res.*, 2002, **15**, 162.
112. S. Yamazaki, C. Morioka, and S. Itoh, *Biochemistry*, 2004, **43**, 11546.
113. E. Jaenicke and H. Decker, *Micron*, 2004, **35**, 89.
114. S. Y. Lee, B. L. Lee, and K. Söderhäll, *Biochem. Biophys. Res. Commun.*, 2004, **322**(2), 490.
115. A. Nakahara, S. Suzuki, and J. Kino, *Life Chem. Rep.*, 1983, Suppl. 1, 319.
116. B. Salvato, G. Jori, A. Piazzese, F. Ghiretti, N. Beltramini, and K. Lerch, *Life Chem. Rep.*, 1983, Suppl. 1, 313.
117. H. Decker, R. Dillinger, and F. Tuczek, *Angew. Chem., Int. Ed. Engl.*, 2000, **39**, 1591.
118. A. Granata, E. Monzani, and L. Casella, *J. Biol. Inorg. Chem.*, 2004, **9**(7), 903.
119. L. Casella, A. Granata, E. Monzani, R. Pievo, L. Pattarello, and L. Bubacco, *Micron*, 2004, **35**(1–2), 141.

120. G. Battaini, E. Monzani, L. Casella, E. Lonardi, A. W. Tepper, G. W. Canters, and L. Bubacco, *J. Biol. Chem.*, 2002, **277**(47), 44606.
121. A. W. Tepper, L. Bubacco, and G. W. Canters, *J. Biol. Chem.*, 2004, **279**(14), 13425.

Acknowledgments

This work was financed by the DFG. The figures were provided by Thorsten Schweikardt.

Copper Proteins: Oxidases

Christopher S. Stoj & Daniel J. Kosman
The University at Buffalo, Buffalo, NY, USA

1 Introduction 1
2 Structural Genomics 2
3 Oxidases: Laccases and Ascorbate Oxidase 7
4 Ferroxidases: Ceruloplasmin and the Fet3 Protein 13
5 Bacterial Oxidases, Copper Resistance, and Metallo-oxidation 21
6 Related Articles 24
7 References 24

Abbreviations

AO = Ascorbate oxidase; (h)Cp = (human) Ceruloplasmin; CT = Charge transfer; Hp = Hephaestin; GPI = Glycosylphosphatidylinositol; Lac = Laccase; MCO = Multicopper oxidase; T1(2,3)D = Type 1 depleted (and/or type 2 or type 3); Tf = Transferrin.

1 INTRODUCTION

Here we summarize the structures and functions of the class of copper enzymes known as multicopper oxidases (MCOs). These copper enzymes are characterized by containing three types of copper prosthetic groups. These three types, themselves distinguished by specific electronic and ligand coordination features, are: type 1 Cu(II), often referred to as a 'blue' copper due to its intense absorption at ~600 nm (*see* ***Copper Proteins with Type 1 Sites***); type 2 Cu(II), whose electronic structure is comparable to that of simple, square-planar Cu(II) complexes (*see* ***Copper Proteins with Type 2 Sites***); and type 3, binuclear Cu(II)–Cu(II), whose diamagnetism and strong absorption at ~330 nm is due to efficient spin (charge) transfer involving an oxygen atom (or OH) that bridges the Cu(II) pair (*see* ***Copper: Hemocyanin/Tyrosinase Models*** and ***Copper Proteins with Dinuclear Active Sites***). Thus, multicopper oxidases are unique in that they possess each of the three spectrally distinct types of copper sites found in biology.[1–4]

The three copper sites – which represent a total of four one-electron acceptors – place the multicopper oxidases in the small family of enzymes that can couple the oxidation of four equivalents of a one-electron reducing substrate to the four-electron reduction of dioxygen to $2H_2O$. The other members of this family are the heme-containing terminal oxidases (*see* ***Cytochrome Oxidase***), whose exergonic turnover of O_2 is typically linked to an endergonic process, thus transforming the oxidation-reduction free energy released into a more biologically usable form.[5] The multicopper oxidases differ in this respect, playing roles that more closely conform to ones in intermediary metabolism on the one hand, and in metal resistance on the other.

The copper prosthetic groups common to the multicopper oxidases result from another feature shared among the eukaryotic members, that is, their synthesis and processing in the cell's vesicular trafficking pathway. It is in these membrane-continuous compartments that the newly synthesized apoprotein acquires the four copper atoms. Some of these eukaryotic oxidases are synthesized fully within the lumen of these compartments (they are not membrane-bound) and so are secreted from the cell as soluble proteins, whereas other members have an encoded transmembrane domain and thus, as mature proteins, associate with either the plasma membrane or, in fungi, with the vacuolar membrane as well. In partial contrast, all of the known prokaryotic oxidases are soluble, secreted proteins, taking up residence in the bacterial periplasmic space, the compartment between the inner and outer membranes that characterize this organismal superkingdom. 'Where' in the bacterial cell the apoprotein obtains its prosthetic group copper atoms is not known. Teleologically, the ultimate cellular locale of any of the multicopper oxidases is integral to the physiologic function of each.

In fact, multicopper oxidases do appear to fall into two functional classes. That is, although all multicopper oxidases use aromatic phenols and amines as reducing substrate (e.g. dimethoxyphenol, hydroquinone, phenylenediamine), a few exhibit an equally robust activity towards Fe^{2+}, and, in an increasing number of cases, towards Cu^{1+} and/or Mn^{2+}, as well. This latter select group is therefore known more precisely as ferroxidases, or, even more broadly, as metallo-oxidases. These include ceruloplasmin (Cp), Fet3p, and CueO, but, as summarized in the next section, it is likely that several other ferroxidases (metallo-oxidases) exist in both pro- and eukaryotic genomes. What is also becoming clear is that these enzymes, particularly those with metallo-oxidase activity, are linked to severe and eventually lethal disorders of metal metabolism. Thus, aside from providing us with a 'primer' on the properties of the 'types' of copper found in biology, these proteins also offer insights into fundamental aspects of the biology of at least three of the nutritionally essential, but potentially cytotoxic, first-row transition metals (*see* ***Metal-related Diseases of Genetic Origin***). The reader is encouraged to review the first edition of the Encyclopedia for references to the earlier literature on the members of the multicopper oxidase family.[6] The review of much of that literature will not be duplicated here.

2 STRUCTURAL GENOMICS

2.1 Structural Signatures: Sequence and Copper-site Properties

MCOs possess a fairly easily recognizable sequence motif pattern that includes four elements that together comprise the copper-binding sites in the protein. The first two such elements are HXH motifs located within the first one-quarter of the protein sequence, typically separated by ca. 50 residues. Some examples are shown in Figure 1(a). There is a pattern within these two motifs, also, namely, the 'X' in the first is most commonly a bulky nonpolar residue (V, W, or F) while the 'X' in the second is a residue generally found in turns, for example, P, G, or S. The third motif is an HXYHZH sequence that is found in the carboxyl-terminal quarter of the protein. Again, within this motif there is a clear pattern in which X is a residue found in a bend, most commonly P (occasionally T); and Y and Z are bulky nonpolar residues, for example, L, I, and F. Although not part of the coordination spheres of any of the four copper atoms in the MCO, the four residues carboxyl-terminal to this third motif are also strongly conserved with GHXF seen in ca. 80% of ORFs that likely encode MCO proteins.

The last motif, HCHXYZH, resides 60–90 residues carboxyl-terminal to the third one and, except in the case of those MCOs that are type 1 membrane proteins (with a carboxyl-terminal transmembrane domain), is found within 30–50 residues of the C-terminus. Although there is no pattern to the 'XYZ' in this motif, two features are conserved to either side of it. First, the three residues immediately amino-terminal to the HCH element are typically nonpolar with W as a highly conserved $n-3$ residue. Second, the residue in the $n+5$ position relative to the carboxyl-terminal H is either M or L/F in $>90\%$ of MCO sequences. The significance of this second conserved feature is that the sulfide –S– of an M at this position occupies a fourth coordination site in the distorted tetrahedral ligand field (alternatively described as trigonal pyramidal) of the type 1 Cu(II) in those proteins with that sequence. In some cases, the limited S → Cu CT from this thioether group appears to modulate the redox potential of the coordinated Cu(II).[3,4,7–10]

The four motifs described fold into a canonical MCO ligation scheme for each protein's four copper atoms. In Figure 1, this fold is illustrated in two ways. The first, Figure 1(a), illustrates the characteristic fold via alignments of four members of the protein family; these alignments are presented in terms of the four sequence motifs summarized above. The sequence spacing of the ligands in each motif is highlighted in this presentation. For example, note that the type 2, type 3 trinuclear cluster is assembled from four sets of HXH elements, one from each of the four conserved motifs. Also, note that the type 2, type 3 coordination spheres are assembled via what appears to be a nucleotide sequence duplication. So, as illustrated for hCp in Figure 1(b), the first three H residues (from motifs 1 and 2) provide one 'side' of the trinuclear cluster while the last two H residues of motif 3 and the first of motif 4 assemble to constitute the other 'side'. The binuclear, type 3 and 'blue' type 1 Cu(II) sites share a similar clustering of ligands within the sequence via the HCH triad that is the most representative of the multicopper oxidase sequence homologies. As discussed below, the backbone within this HCH motif that links the type 1 cysteine residue to these two histidine ligands – one each at each of the two type 3 Cu(II) sites – is likely to provide the route of the intramolecular electron transfer from the T1 Cu to the T3 binuclear cluster during substrate turnover. That is, in all MCOs, the intermolecular electron transfer from reducing substate to enzyme occurs at the type 1 Cu(II) while the electron transfers to dioxygen occur at the trinuclear cluster. The H ← C → H provides the extension cords that couple these two redox processes.[1,2,4]

As noted in the next section, MCOs are encoded in the genomes of organisms in all three superkingdoms – Archaea, Bacteria, and Eukarya. This identification is based on the presence of the four motifs summarized above. However, there are striking differences among this collection of nearly 600 proteins. For example, their size varies from ∼400 to over 1800 residues. As implied, some are soluble proteins, while others are type 1 membrane proteins with carboxyl-terminal 'extensions' that tether the MCO domain to the luminal face of a cell compartment or to the extracellular surface of the plasma membrane. Less obvious in the primary sequence are those protein folds that confer the specificity that some MCOs have for bulky aromatic phenols and amines and other MCOs have for low-valent first-row transition metals like Mn^{2+}, Fe^{2+}, and Cu^{1+}. Lastly, there are a few MCOs in which the order of the four motifs in the primary sequence are 'inverted' so that the HXYHZH and HCHXYZH motifs are encoded to the amino-terminal side of the two HXH ones. One of these bacterial proteins, the mnxG protein from *Bacillus* sp. strain SG-1, is a manganous oxidase;[11,12] an MCO from *Nitrosomonas europaea* (a chemolithoautotroph that can obtain all of its energy from the oxidation of ammonia to nitrite) is proposed to have the same metallo-oxidase specificity[13] as is the CumA protein from *Pseudomonas putida*.[14,15] These and other prokaryotic MCOs will be reviewed in Section 5.

Multicopper oxidases owe their characteristic and striking 'sky blue' color (captured in 'ceruloplasmin', from the Latin *caeruleus*, or deep blue (azure) sky) to the type 1 Cu(II) that all possess. The ligand field at type 1 Cu(II) can be qualitatively described as distorted tetrahedral or better, perhaps, as trigonal (bi)pyramidal even if the coordination sphere lacks ligands at one or both of the apical positions.[1,3,10,16] Type 1 Cu(II) that have an apical ligand (the Sδ of Met), as in plastocyanin (a simple blue copper electron-transfer protein, *see* ***Copper Proteins with Type 1 Sites***) conform more closely to tetrahedral geometry. 'Loss' of this apical ligand, as in *Trametes versicolor* Lac, for example, results in the Cu moving down into the 'equatorial' ligand plane, resulting

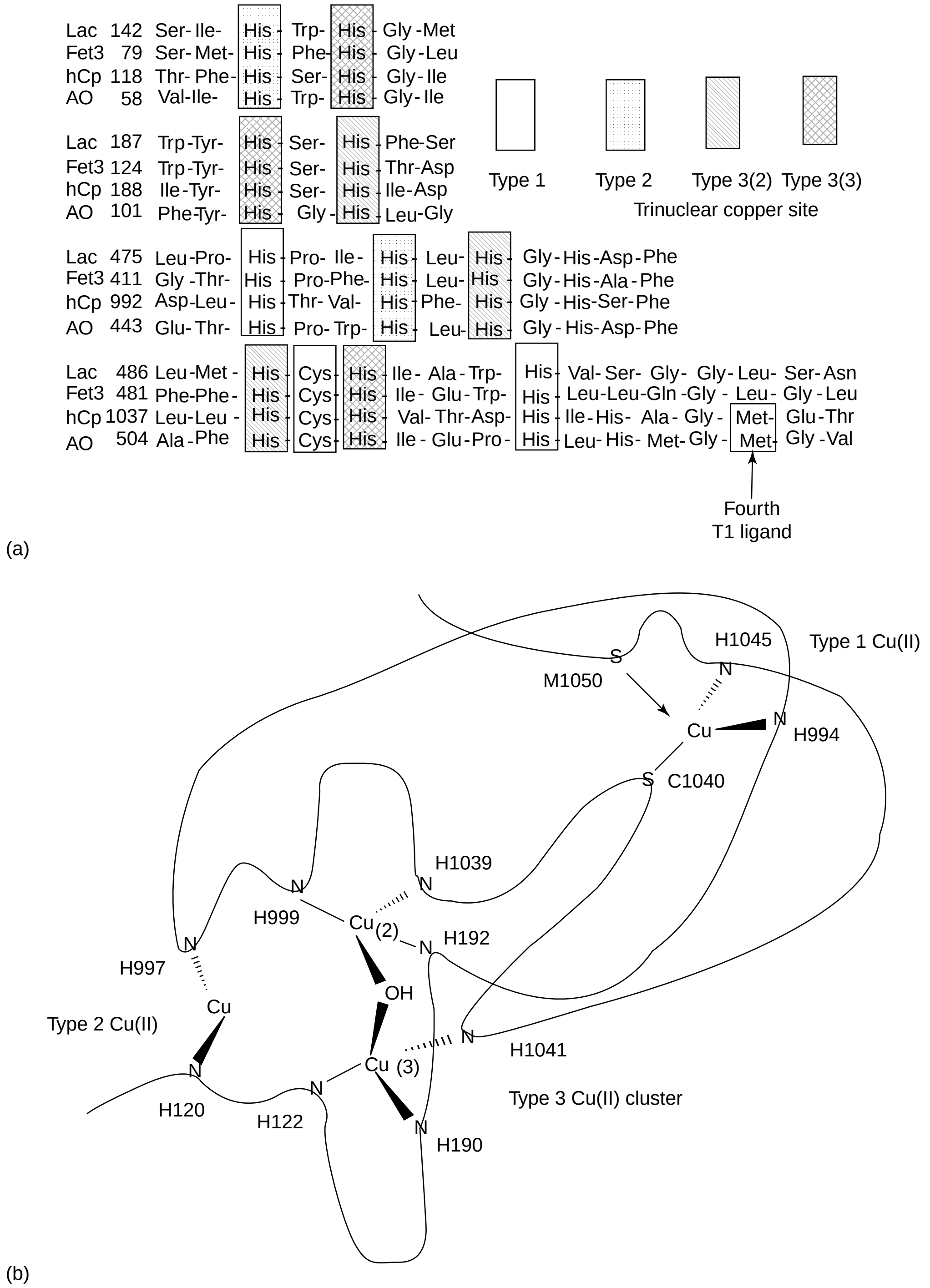
Lac 142 Ser-Ile-His-Trp-His-Gly-Met
Fet3 79 Ser-Met-His-Phe-His-Gly-Leu
hCp 118 Thr-Phe-His-Ser-His-Gly-Ile
AO 58 Val-Ile-His-Trp-His-Gly-Ile
Lac 187 Trp-Tyr-His-Ser-His-Phe-Ser
Fet3 124 Trp-Tyr-His-Ser-His-Thr-Asp
hCp 188 Ile-Tyr-His-Ser-His-Ile-Asp
AO 101 Phe-Tyr-His-Gly-His-Leu-Gly
Lac 475 Leu-Pro-His-Pro-Ile-His-Leu-His-Gly-His-Asp-Phe
Fet3 411 Gly-Thr-His-Pro-Phe-His-Leu-His-Gly-His-Ala-Phe
hCp 992 Asp-Leu-His-Thr-Val-His-Phe-His-Gly-His-Ser-Phe
AO 443 Glu-Thr-His-Pro-Trp-His-Leu-His-Gly-His-Asp-Phe
Lac 486 Leu-Met-His-Cys-His-Ile-Ala-Trp-His-Val-Ser-Gly-Gly-Leu-Ser-Asn
Fet3 481 Phe-Phe-His-Cys-His-Ile-Glu-Trp-His-Leu-Leu-Gln-Gly-Leu-Gly-Leu
hCp 1037 Leu-Leu-His-Cys-His-Val-Thr-Asp-His-Ile-His-Ala-Gly-Met-Glu-Thr
AO 504 Ala-Phe-His-Cys-His-Ile-Glu-Pro-His-Leu-His-Met-Gly-Met-Gly-Val
Type 1
Type 2
Type 3(2)
Type 3(3)
Trinuclear copper site
Fourth T1 ligand
(a)
Type 1 Cu(II)
H1045
N
M1050
S
Cu
N
H994
S
C1040
H1039
N
N
H999
Cu(2)
N
H192
H997
N
OH
Cu
Type 2 Cu(II)
N
H1041
Cu (3)
N
N
H120
H122
N
H190
Type 3 Cu(II) cluster
(b)

Figure 1 (a) The four signature Cu-binding sequence elements are aligned for four MCOs. The copper site associated with each ligand is indicated. (b) A strand diagram shows the connectivity of the copper-binding elements in hCp

in a geometry that more closely conforms to slightly distorted trigonal planar. These geometries are illustrated in Figure 2 (adapted from Reference 17).

These two geometries as in Pc and Lac correspond to the state energies illustrated in Figure 3.[17] The qualitative difference between the two ligand fields is the presence of the bonding orbital localized on the Sδ of the apical Met in the case of Pc. The most significant quantitative difference between the two geometries, a difference that corresponds to the removal of this ligand and the 'relaxation' to the trigonal planar geometry in *T. versicolor* Lac, is the decrease in the energy of the d_{z^2} orbital on this Cu atom. The highest energy

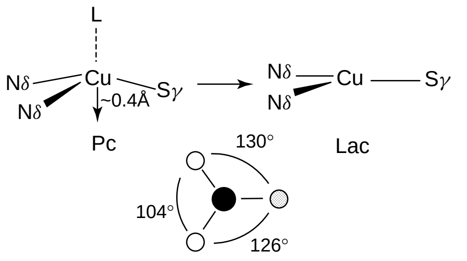

Figure 2 Ligand geometries in Pc (with fourth, apical ligand −S−from Met) and a Lac lacking this ligand. (Reprinted with permission from Ref. 17. © 1999 American Chemical Society)

orbital in either case is the $d_{x^2-y^2}$ one (thus defining the ground state) whose lobes usually lie along the bonds to ligands in the xy plane. However, the two spectral and, therefore, electronic features that characterize a type 1 Cu(II) site indicate that the $d_{x^2-y^2}$ orbital is rotated in this plane such that the Cu–Sγ (Cys) bond lies between and not aligned with the $d_{x^2-y^2}$ electron density (Figure 3). The first of these spectroscopic features is the intense $S_{cys}\pi \rightarrow$ Cu $d_{x^2-y^2}$ charge-transfer band observed at ∼600 nm.[3,4,10,17] The strength of this charge transfer can only be accounted for by significant overlap between the S_{cys} p-π orbital and the lobes of the Cu $d_{x^2-y^2}$ one. These lobes would have diminishing probability at the S_{cys} p-π orbital if they were oriented along and orthogonal to the Cu–S bond. Second, the π-type S_{cys}, Cu $d_{x^2-y^2}$ interaction leads to covalency in the Cu–S bond, and thus to significant transfer of unpaired spin density to the S. The result is a reduction in electron spin-orbit coupling (with the electron delocalized to the less anisotropic S-centered orbitals) and thus in the deviation of the electron's g value from that of a 'free' electron. In addition, the net unpaired spin at the Cu is reduced so as to decrease the Cu nuclear hyperfine coupling as well. Thus, type 1 Cu(II) in proteins exhibits smaller g and A values; the latter are most commonly in the range of $80-90 \times 10^{-4}\,\mathrm{cm}^{-1}$ (Table 1).[1,3,10]

Spectrally, the type 2 Cu(II) in multicopper oxidases is typical of this class of protein copper sites in that it exhibits the very weak absorbance in the far visible due to forbidden d–d transitions ($\sim 100\,\mathrm{M}^{-1}\,\mathrm{cm}^{-1}$) and the spin Hamiltonian parameters of normal, tetragonally distorted square-planar Cu(II). The relatively larger g and A values show the unpaired electron strongly localized on the copper atom. In particular, $A_{||}$ for type 2 Cu(II) is in the range of $160-200 \times 10^{-4}\,\mathrm{cm}^{-1}$.[1,3] The larger hyperfine coupling means that the type 2 Cu(II) alone contributes to the low field region of the EPR spectrum (g value equivalent >2.3) with its $m_s = -3/2$ transition typically centered at ∼2750 G (at

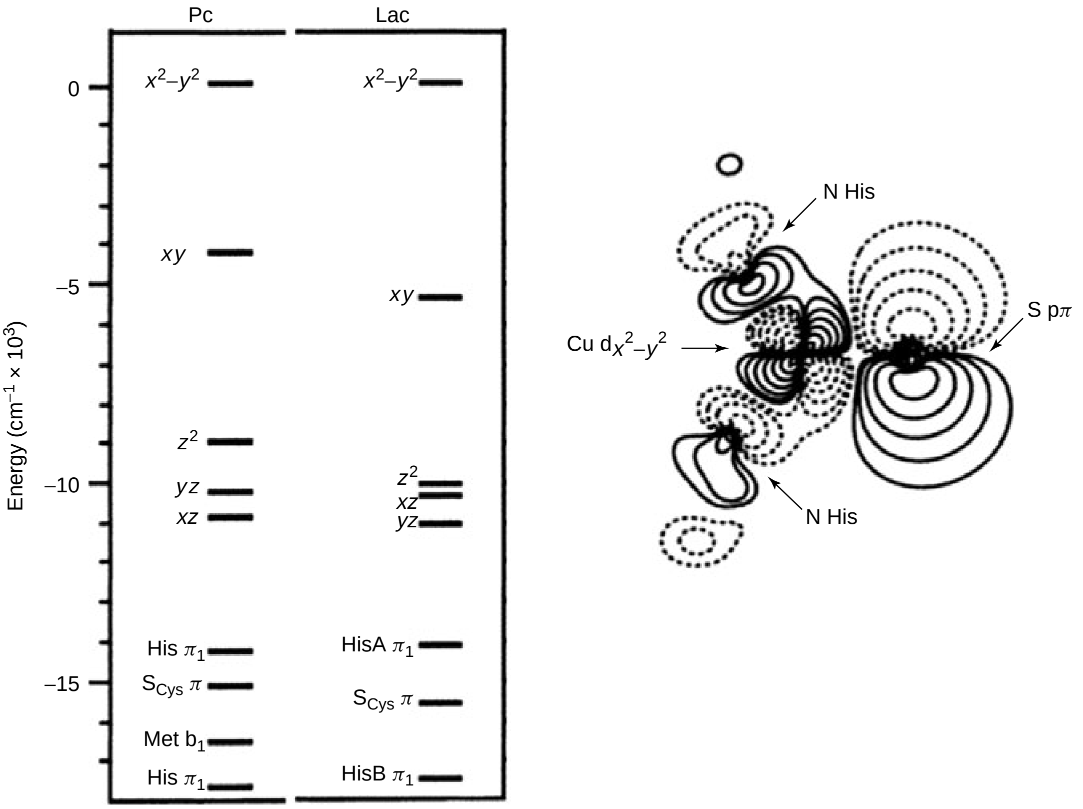

Figure 3 Orbital energy diagram for the two T1 ligand fields and the ground-state HOMO. (Reprinted with permission from Ref. 17. © 1999 American Chemical Society)

Table 1 Physico-chemical data for representative MCOs

MCO^a	E°	T3 λ (ε)	T1 λ (ε)	T1 $g_{\parallel}$	A ($g_{\parallel}$)	T2 $g_{\perp}$	A ($g_{\perp}$)
Tv Lac (F)	0.79	330 (4.0)	613 (4.0)	2.194	90	2.248	182
Tv Lac (M)	0.68	330 (3.3)	600 (4.3)	2.214	78	2.248	183
Rv Lac (M)	0.44	330 (5.0)	607 (5.5)	2.300	39	2.24	182
C. p. AO (M)	0.34	nd	610 (5.0)	2.227	56	2.242	199
Sc Fet3p	0.43	330 (5.0)	607 (5.5)	2.202	88	2.240	195

^{a}Apical 'ligand' at T1 Cu. Units are: E°, V; λ, nm; ε, $mM^{-1}\,cm^{-1}$; A, (value) × $10^{-4}\,cm^{-1}$; nd, not determined.

9.5 GHz). The spectral similarity between the type 2 Cu(II) in MCOs and in other mononuclear type 2 Cu(II) proteins is somewhat surprising since the coordination in the former is different than in the latter. While type 2 Cu(II) is most commonly characterized by a four-coordinate, tetragonally distorted square-planar ligand field (with, in some cases, some rhombic distortion also), the MCO type 1 Cu(II) is coordinated by two protein His residues and a solvent H_2O only.[1,3] The ligand field associated with this coordination is not directly obvious; that is, among other uncertainties, whether the H_2O is an equatorial or an axial ligand has not been established. In AO, the Cu–O distance is 2.02–2.03 Å,[18,19] whereas in *T. versicolor* Lac it is 2.3–2.9 Å.[20,21] The shorter distance is consistent with equatorial ligation, while the longer distances are what one might expect for an apical ligand. In both structures, the His–Cu–His bond angles are very close to 180°, however, suggesting that they could be trans ligands in a square planer ligand field.[18–21] This appears to be the case and will be considered again below.

The type 3 binuclear Cu(II) pair in an MCO is characteristic of this type of copper site in biology. First, both copper atoms are ligated by three protein side chains each; all six are His residues. Five of the imidazoles coordinate the Cu(II) atoms via the Nε2 nitrogens while the sixth His does so via Nδ1. This coordination pattern is a conserved feature of the MCO structure.[18,20–24] Second, the two Cu(II) are bridged by an oxygen atom, probably as OH^-. This bridge is the distinguishing feature of type 3 Cu(II) generally because it provides a superexchange pathway that couples the unpaired electron density on the two cupric ions rendering the type 3 site diamagnetic.[1] Another spectral signature of this coupling is a strong O → Cu CT transition at ca. 330 nm ($\varepsilon = 3-5000\,M^{-1}\,cm^{-1}$). The binuclear cluster exhibits a relatively strong d–d transition at ca. 750 nm as well.[1,25]

Functionally, the most significant feature of MCOs is the spatial relationship of the type 2 and type 3 copper atoms: atom-to-atom distance, they form a near isosceles triangle of ~3.5–4.5 Å on a side.[18,20–24] Together with the relatively 'under-ligated' nature of all three copper atoms, particularly the type 2 copper, this feature provides for the docking and ligation of dioxygen to the trinuclear copper cluster, most probably bridging the type 2 and one of the type 3 copper atoms during O_2 turnover (reviewed in Reference 2). The cluster structure is illustrated in the polypeptide strand topology rendering shown in Figure 1(b).

2.2 MCO Species Distribution and Differences

The sequences listed in Figure 4 provide a fair representation of MCO homologues that are archived at www.sanger.ac.uk/Software/Pfam (keyword, 'multicopper

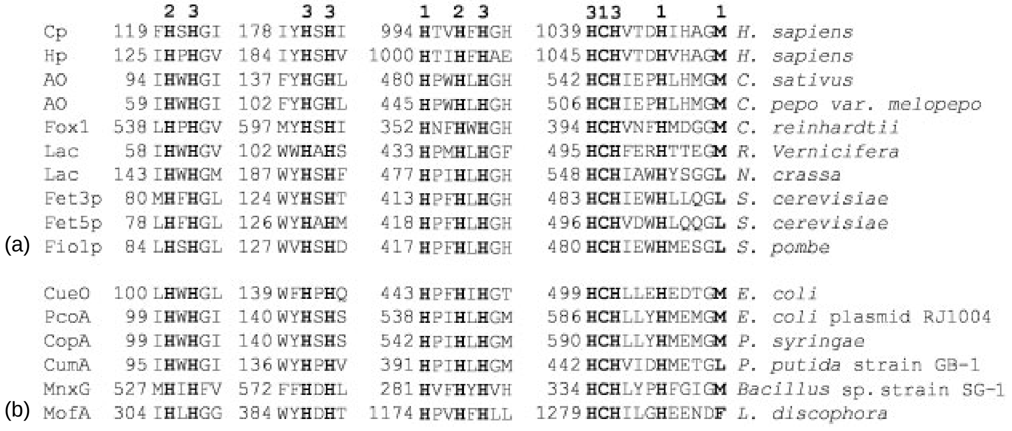

```
              2 3         3 3           1  2 3          313   1     1
    Cp     119 FHSHGI  178 IYHSHI    994 HTVHFHGH  1039 HCHVTDHIHAGM H. sapiens
    Hp     125 IHPHGV  184 IYHSHV   1000 HTIHFHAE  1045 HCHVTDHVHAGM H. sapiens
    AO      94 IHWHGI  137 FYHGHL    480 HPWHLHGH   542 HCHIEPHLHMGM C. sativus
    AO      59 IHWHGI  102 FYHGHL    445 HPWHLHGH   506 HCHIEPHLHMGM C. pepo var. melopepo
    Fox1   538 LHPHGV  597 MYHSHI    352 HNFHWHGH   394 HCHVNFHMDGGM C. reinhardtii
    Lac     58 IHWHGV  102 WWHAHS    433 HPMHLHGF   495 HCHFERHTTEGM R. Vernicifera
    Lac    143 IHWHGM  187 WYHSHF    477 HPIHLHGH   548 HCHIAWHYSGGL N. crassa
    Fet3p   80 MHFHGL  124 WYHSHT    413 HPFHLHGH   483 HCHIEWHLLQGL S. cerevisiae
    Fet5p   78 LHFHGL  126 WYHAHM    418 HPFHLHGH   496 HCHVDWHLQQGL S. cerevisiae
(a) Fio1p   84 LHSHGL  127 WVHSHD    417 HPFHLHGH   480 HCHIEWHMESGL S. pombe

    CueO   100 LHWHGL  139 WFHPHQ    443 HPFHIHGT   499 HCHLLEHEDTGM E. coli
    PcoA    99 IHWHGI  140 WYHSHS    538 HPIHLHGM   586 HCHLLYHMEMGM E. coli plasmid RJ1004
    CopA    99 IHWHGI  140 WYHSHS    542 HPIHLHGM   590 HCHLLYHMEMGM P. syringae
    CumA    95 IHWHGI  136 WYHPHV    391 HPIHLHGM   442 HCHVIDHMETGL P. putida strain GB-1
    MnxG   527 MHIHFV  572 FFHDHL    281 HVFHYHVH   334 HCHLYPHFGIGM Bacillus sp. strain SG-1
(b) MofA   304 IHLHGG  384 WYHDHT   1174 HPVHFHLL  1279 HCHILGHEENDF L. discophora
```

Figure 4 Four Cu-binding motifs in representative MCOs from Eukarya (a) and Bacteria (b)

oxidase'), the 'Pfam' web site.[26] This database of protein family alignments catalogues 534 putative MCOs; excluding a number of entries, such as blood coagulation factor VIII, that are not, in fact, MCOs, leaves >400 family members. Of these, most are distributed between eukaryotes (55%) and bacteria (40%), with the few remaining found among archea (one representative) or unclassified organisms. The single largest group identifiable in this sequence database are the laccases; among metazoa, however, the largest group includes ceruloplasmin-like proteins. In addition, MCOs are found in many eukarya that contain encoded transmembrane domains making them likely integral membrane proteins. Otherwise, as a family, MCOs are 'soluble' proteins.

As discussed in more detail below, all relevant differences among MCOs are not readily discerned from sequence database information alone. One such difference that can be deduced from sequence is the presence of a transmembrane domain, for example, thus distinguishing ceruloplasmin from hephaestin in mammalian genomes. MCO size also correlates with a recognizable difference in MCO tertiary structure; as noted below, most MCOs are proteins of ca. 600 residues with three-domain repeats, while a few – like Cp and Hp – are proteins of ca. 1200 residues with six domain repeats. However, a Blast search using a 'laccase' as the query sequence generates a list of subject sequences comparable to one generated by using AO as query, or using a fungal ferroxidase like Fet3p (although the 'Expect' values do differ to some extent). Species origin most commonly defines function: a secreted MCO in a fungus or a woody plant is presumed to be a laccase, one in a leafy plant an AO. At this point, there are not enough structural, that is, crystallographic data to provide the prediction algorithm(s) correlating MCO sequence to MCO structure and function. For example, an aromatic phenol/amine binding surface in an MCO could be predicted given sufficient structural data on a number of known laccase proteins. Such differences are known among the MCOs, but we now have only one or a few examples of three eukaryotic MCO types: one AO, one ferroxidase, and three laccases.

2.3 Bioinorganic Chemistry – MCO Models

Of specific relevance to MCOs are biomimetics that attempt to reproduce the intramolecular electron transfer between a type 1 site and a bi- or trinuclear copper cluster, or model the trinuclear cluster itself. Three recent reports exemplify these attempts. Lever and his coworkers synthesized the tetracopper assembly shown in Figure 5(a) and demonstrated that it was reduced stepwise by 3e$^-$: $\{\mathrm{Cu(II)}\text{–}\mathrm{Cu_2(II,II)}\text{–}\mathrm{Cu(II)}\} \rightarrow \{\mathrm{Cu(I)}\text{–}\mathrm{Cu_2(II,II)}\text{–}\mathrm{Cu(II)}\} \rightarrow \{\mathrm{Cu(I)}\text{–}\mathrm{Cu_2(II,II)}\text{–}\mathrm{Cu(I)}\}/\{\mathrm{Cu(I)}\text{–}\mathrm{Cu_2(I,II)}\text{–}\mathrm{Cu(II)}\} \rightarrow \{\mathrm{Cu(I)}\text{–}\mathrm{Cu_2(I,II)}\text{–}\mathrm{Cu(I)}\}$.[27] Figure 5(b) illustrates the polarogram for this reduction. EPR spectra were consistent with the reduction scheme proposed and indicated that the last of these 1e$^-$ electron transfers was associated with the reduction potential of -0.42 V. In summary, this complex did appear to mimic the intramolecular electron transfer from a mono- to a binuclear copper-site characteristic of the MCOs.

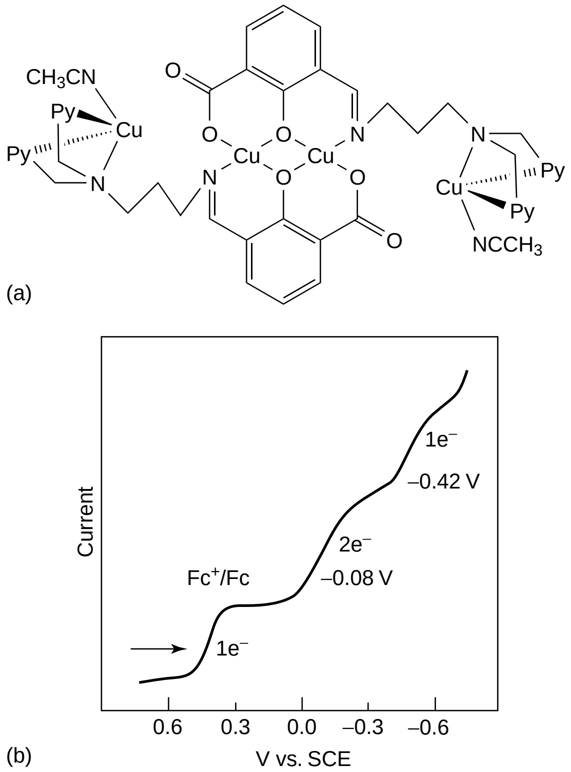

Figure 5 T1,T3 biomimetic (a) and its 3e$^-$ polarogram (b) that indicates T1 → T3 intramolecular electron transfer. (Reprinted with permission from Ref. 27. © 1999 American Chemical Society)

Tolman and Lee constructed a type 1-like site linked to a type 2-like site and investigated the potential for intramolecular electron transfer between the two.[28] Their coordination scheme is illustrated in Figure 6(a); the structure of their complex in shown in Figure 6(b). Cyclic voltammetry showed the two Cu(II) atoms to undergo quasi-reversible, independent reduction with $E_{1/2}$ values consistent with the two copper atoms' coordination: -0.911 V for the CuSR site, -0.112 V for the CuPyr one. These studies did not address the question of intramolecular electron transfer between the two sites, however.

Chakravarty and his coworkers prepared a pseudo-trinuclear cluster mimic, pseudo because all three Cu are O-bridged (Figure 7);[29] in the trinuclear cluster found in an MCO, only the type 3 Cu(II) are oxygen-bridged (*cf* Figure 1(b)). Magnetic susceptibility measurements confirmed that all three Cu(II) in this model are exchange-coupled, albeit with a set of two J values (for example, for complex **1**, the values were -82.7 and $-73\,\mathrm{cm^{-1}}$). The synthetic methodology employed offers some promise for fine-tuning the structural features of such complexes to provide more relevant biomimetics of the MCO bi- or trinuclear cluster. The challenge in exploiting bioinorganic approaches in MCO research will be to define precise questions about MCO

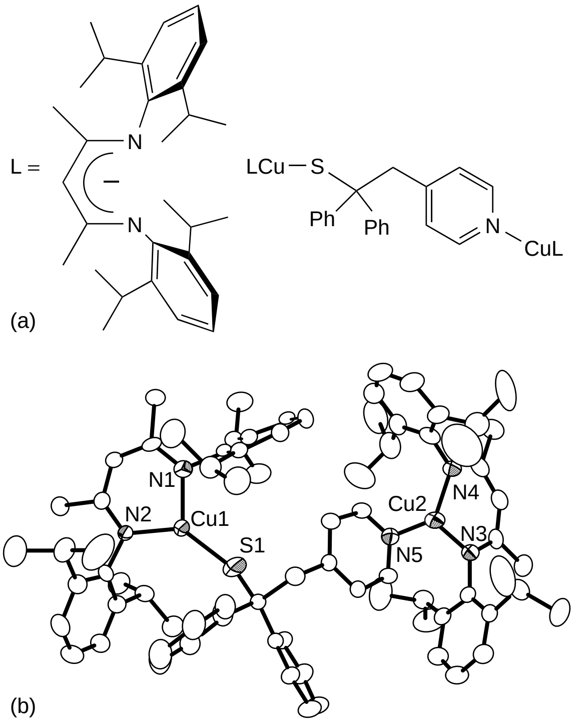

Figure 6 Model (a) and structure (b) of a T1,T2 coupled biomimetic. The E° values reflected the ligand field differences at the two Cu; intramolecular electron transfer was not demonstrated[28]

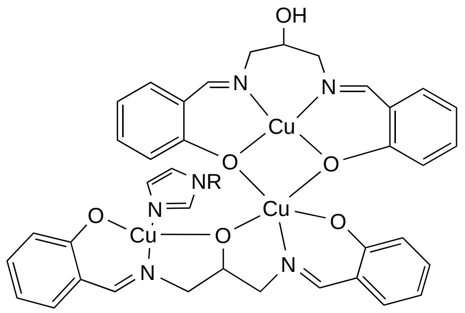

[R = H, 1; Me, 2]

Figure 7 Pseudo-trinuclear biomimetic in which the three Cu(II) are exchanged-coupled. This is not a true trinuclear model since all three Cu(II) are oxygen-bridged[29]

chemistry that can be productively if not uniquely examined by study of small molecule biomimetics.

3 OXIDASES: LACCASES AND ASCORBATE OXIDASE

3.1 Laccases

Three of the five crystal structures of eukaryotic MCOs archived in the PDB are of laccases: from *Coprinus cinereus* (1A65[30] and 1HFU[31]); from *Melanocarpus albomyces* (1GWO);[32] and from *T. versicolor* (1GYC[21] and 1KYA[20]). The structure of *Cc* Lac is of a type 2-depleted form (T2D, hereafter) which not only lacks the information about the ligation of this copper atom but, because of the absence of this prosthetic group, the ligation at the type 3 site is also changed. In addition to this structural information, Lac has been the most intensively studied of the MCOs, particularly by spectral techniques that can elucidate both the physical and electronic structure of copper sites in proteins: EXAFS, EPR, and MCD, in particular.

3.1.1 Structure

Of the three Lac structures, two contain the full complement of four copper atoms. Although the third – of *C. cinereus* – lacks the type 2 Cu(II), it is overall similar to the other two, and all provide a view of the canonical tripartite cupredoxin (or plastocyanin) fold that characterizes the MCOs that contain ∼500–600 amino acid residues. This fold is found in all of the small blue copper electron transport proteins (*see* ***Copper Proteins with Type 1 Sites***) and is described as a member of the 'Greek-key' connectivity pattern family found in biology.[33] Greek keys are β-barrel tertiary folds, a fold which, in the case of the cupredoxin domain, consists of 8 strands and that, unlike many other Greek-key folds that are composed of exclusively antiparallel sheet, include two that form parallel H-bonds with their neighboring strands. The cupredoxin fold, typically containing 125–150 residues, is diagrammed in Figure 8(a). As noted above, the simplest MCOs are assembled from three cupredoxin domains. Thus, the MCO fold clearly arises from a gene 'triplication' in which the three folding elements, domains

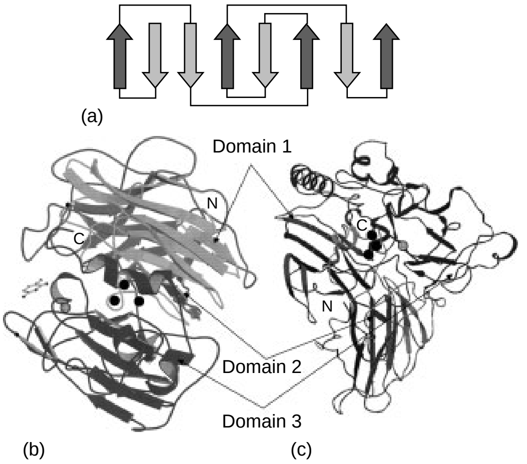

Figure 8 The connectivity of the cupredoxin fold in shown in (a); the ribbon diagrams of *Tv*[20] and *Ma*[32] Lac are shown in (b) and (c), respectively. (Reproduced by permission of Nature (Y-hotlink www.nature.com))

1, 2, and 3 (or a, b, and c) conform to the first, second and third one-third of the protein sequence. Thus, the MCOs are modular proteins as is illustrated by the ribbon diagrams for *T. versicolor* and *M. albomyces* laccases shown in Figure 8(b)[20] and (c),[32] respectively. As an indication of the conservation of the MCO fold is that the striking structural similarity between these two laccases evident in the two ribbon diagrams obtains despite the fact that as products of different fungal divisions – *Basidiomycota* and *Ascomycota*, respectively – the two laccases share less than 30% sequence identity.

The type 1 Cu in the three laccases crystallized (and in AO and hCp, also) is located in the third cupredoxin domain; as discussed above, all of the ligands to the type 1 copper are found in the carboxyl-terminal region of the MCO sequence, the region that folds into domain 3. The trinuclear cluster is composed of ligands from both the first and third regions of the primary sequence (*cf* Figure 1) and is therefore found at the interface between domains 1 and 3 in the structure (Figure 8(b) and 8(c)). This general fold in relation to the coordination fields of the three copper sites is common to all MCOs characterized structurally; sequence homology and other biophysical studies suggest strongly that it represents the 'MCO' fold in general, although there are some intriguing exceptions. Another relatively rare difference found is additional gene duplication giving rise to 6 rather than 3 cupredoxin domains as in hCp.[34] The Cp family members have >1100 residues; size appears to be a legitimate predictor of whether an encoded MCO homolog is composed of 3 or 6 cupredoxin domains as discussed below.

3.1.2 Type 1 Copper-site Coordination and Properties

In MCOs, the type 1 Cu inner coordination sphere can come with or without a Met whose thioether sulfur atom occupies the apical coordination site at this copper (below); archived Lac sequences divide roughly 50:50 in this respect. If the Met is absent, the coordination of the type 1 copper is trigonal planar in geometry as illustrated for *T. versicolor* Lac in Figure 9(a);[20] the spectral properties of *T. versicolor* Lac were summarized in Table 1. The ligand, 2,5-xylidine (a substrate analogue), is present in the structure (Figure 9(a)). The structure suggests that amino group H-bonding to the protein contributes to ligand binding and indicates that a typical aryl phenol substrate would bind similarly via the D206 carboxylate and the H458 Nε2 hydrogen. The latter interaction would provide the initial electron matrix coupling element in the intermolecular electron transfer from reducing substrate to the type 1 Cu(II). Electron transfer in MCO reactivity is discussed more fully below.

The relative specificity that laccases have for bulky aromatic (poly) phenols and amines is due not only to the H-bond Network. The type 1 site associated with these H-bonds lies at the base of a shallow cavity that is lined with nonpolar side chains, or the nonpolar aliphatic carbon skeleton of a polar one, for example, Q and K. The binding cavities of two laccases (superimposed) are shown in Figure 9(b).[20] As discussed below, those MCOs that exhibit a strong specificity for Fe^{2+} as substrate – the ferroxidases – have a substrate binding site that differs in two respects from the laccase one: the ferroxidase site is spatially more constrained and it

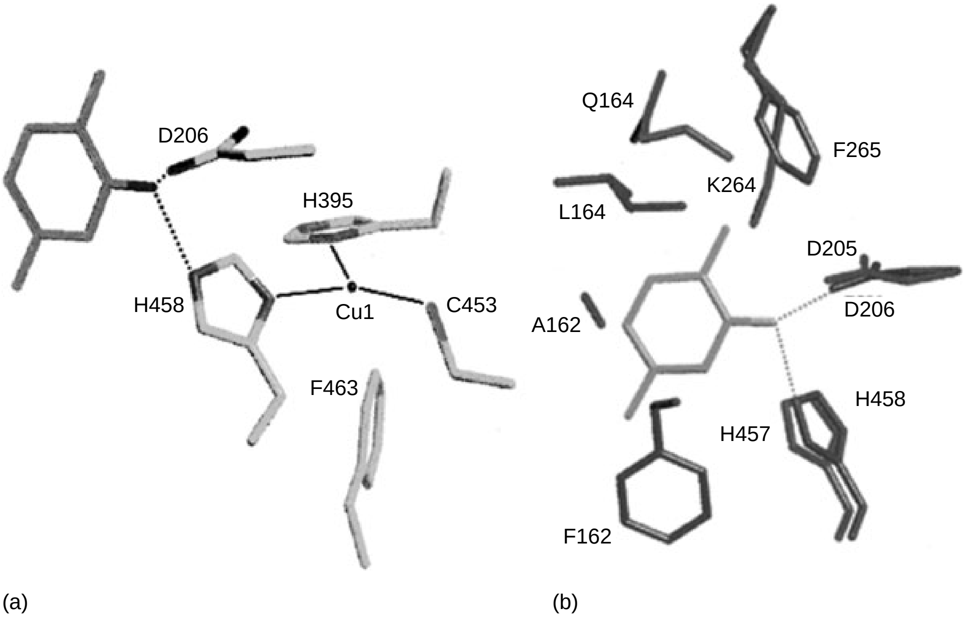

Figure 9 The T1 Cu site in *Tv* lac with H-bonding to substrate analog, 2,5-xylindine (a); the overall substrate binding cavity is illustrated in (b) for *Tv*[20] and *Ma*[32] laccases. (Reprinted with permission from Ref. 20. © 2002 American Chemical Society)

displays an overall net negative electrostatic surface rather than a nonpolar one (see below).

The redox potential of the type 1 Cu(II) in MCOs has been a subject of much examination since E°_{type1} provides the driving force for oxidation of a given reducing substrate. Also, despite the fact that all type 1 sites possess a 2 His, 1 Cys ligand field, and exhibit essentially the same (quantitatively) 600 nm $S_{\text{cys}}\pi \rightarrow \text{Cu } d_{x^2-y^2}$ charge-transfer band, the reduction potentials for these sites vary from 0.34 V in *Cp* ascorbate oxidase to 0.79 V in *Tv* laccase (Table 1). In comparison to the reduction potentials of type 1 sites in simple mononuclear blue copper proteins, the T1 sites in MCOs, except T1 Cu in ascorbate oxidase, are significantly higher. A major contributor to setting the reduction potential of this Cu(II) is likely to be the fourth, axial ligand. As implied above, the presence (or absence) of this ligand can be deduced from the sequence in that it is encoded five residues carboxyl-terminal to the HCHxxxH sequence that essentially defines these oxidases (*cf* Figures 1 and 4). This Met is present in many if not most of the metazoan MCOs that are likely to be ferroxidases (e.g. Cp and Hp in mammals, MCOs encoded in the *Drosophila* genome) but in none of the known or likely fungal ferroxidases. Most if not all of the bacterial MCO genes encode this Met. There is no correlation between substrate specificity (physiologic function?) and the presence of this methionine ligand.

Solomon and his coworkers have examined the relationships between type 1 site ligation, electronic structure, and reduction potential in some detail, making use of site-directed mutagenesis to test the role of the Sδ of Met as an axial ligand directly.[8,9,17] Indeed, the electronic structure of the type 1 Cu(II) in the F463M mutant of *Polyporous pinsitus* laccase (F463 in this laccase is equivalent to F463 illustrated in the structure of *T. versicolor* laccase in Figure 6) was intermediate between that of the parental wild-type laccase and plastocyanin. This relationship is evident in the absorbance and MCD envelopes centered at 15 000 cm^{-1} (600 nm) due the $S_{\text{cys}}\pi \rightarrow \text{Cu } d_{x^2-y^2}$ charge transfer (Figure 10).[17] The former has been deconvoluted into seven bands that were assigned to the transitions associated with the ligand field diagram shown in Figure 3.

The relative intensities in absorbance versus MCD of bands 4 and 6 are the most informative about how axial ligation changes the electronic structure of the type 1 Cu(II). MCD depends on the magnitude of spin-orbit coupling, therefore, transitions centered on Cu(II) (greater coupling) will have greater MCD intensity. In contrast, absorbance correlates with charge transfer from ligand to metal; as noted above with respect to type 1 Cu(II) *g* values, the shift of spin density from Cu to S reduces spin-orbit coupling, and, therefore the intensity of an associated MCD transition. The 'conversion' of the laccase type 1 Cu(II) into a more plastocyanin-like one in the F463M mutant is strikingly evident in the MCD spectrum. The spectra were used to calculate the oscillator strengths of the various bands that were summed to give a total oscillator strength for the three proteins. The values ranged from 0.1046 to 0.1096 for wild-type fungal laccases, but was 0.1032 for the F463M mutant and for Pc was 0.0824. Since oscillator strength of a ligand-to-metal charge-transfer transition is directly proportional to the strength of the metal-ligand bond, the relative values indicate that axial ligation of the Met Sδ lowers the covalency of the Cu–S$_{\text{cys}}$ bond. However, covalency alone does not determine the overall bonding and electronic structure of the MCO type 1 site since

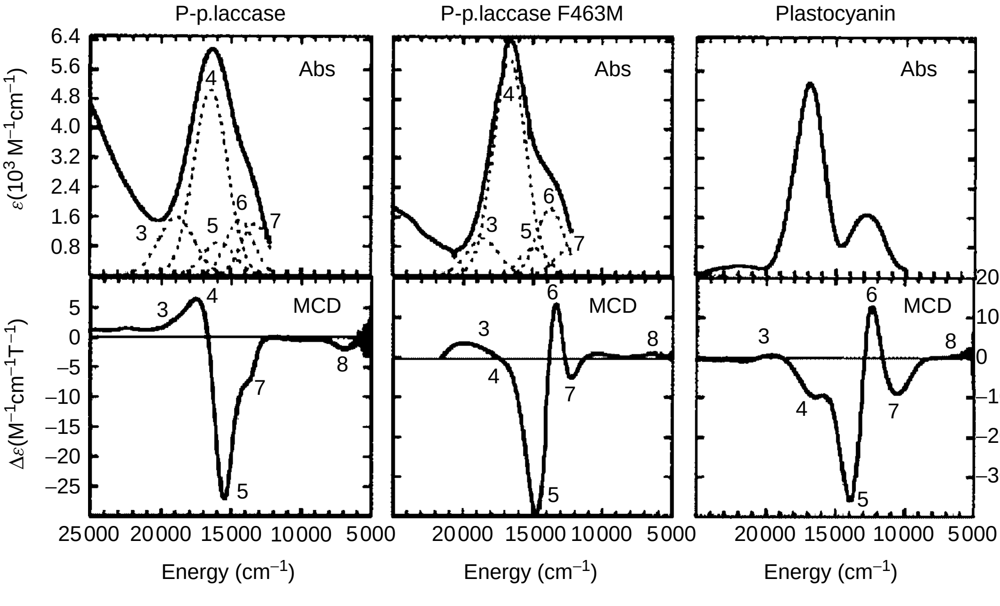

Figure 10 Absorbance and MCD spectra of three T1 Cu(II) sites with deconvolution of the absorbance spectrum into the individual transitions as indicated. (Reprinted with permission from Ref. 17. © 1999 American Chemical Society)

the type 1 Cu(II) in the F463M mutant is *not* equivalent to that in Pc. This conclusion is illustrated further by the fact that while the F463M substitution reduced the type 1 Cu(II) reduction potential from 780 to 680 mV, the E° value for the mutant remained 300 mV higher than that in Pc. Clearly, there are other factors that together, quantitatively, contribute more to the 'tuning' of type 1 Cu E° than does the absence or presence of axial ligation by Met. These additional factors have not been delineated. Note that there is a relative lack of spectral and structural information about laccases that likely have Met, thioether coordination at their type 1 sites, for example, *Rhus vernicifera* laccase, whose kinetic properties have been much studied (below).

3.1.3 Dioxygen Turnover at the Trinuclear Cluster

The mechanism of dioxygen reduction at the trinuclear cluster in MCO catalysis has been a strong focus for research on this class of copper oxidases.**[1,2]** Dioxygen reduction has been most thoroughly investigated in *Rhus* laccase (a plant laccase, from the Japanese lacquer tree).**[35–38]** The primary reason for using *Rhus* Lac is the availability of a metal-substituted form the enzyme, a T1Hg form, in which the type 1 Cu has been replaced by a redox-inert Hg^{2+} ion. T1Hg enzyme is inactive in turnover, but the fully, three-electron reduced form does react with O_2 forming a reduced oxygen, peroxy intermediate, whose properties have been well-characterized. The properties of the adduct that forms upon the binding of H_2O_2 to the fully oxidized T1Hg protein have also been thoroughly examined. In addition, the true 'native' intermediate that forms when fully reduced native laccase is mixed with O_2 has been studied by spectral and kinetic means. As a result of these several investigations, a molecular mechanism has been proposed for the reduction of O_2 to H_2O by MCOs. This mechanism is illustrated in Figure 11.**[2,17]**

The salient features of the proposed mechanism are as follows. First, the 'resting' fully oxidized enzyme does not appear to be a kinetically competent enzyme form during turnover since its formation from the native intermediate ($0.034\,s^{-1}$) is at most 1/30th the turnover number for laccase with a typical substrate (e.g. phenylenediamine). A 'ball-park' value for k_{cat} – $100\,s^{-1}$ – is given in Figure 11 for illustration. In any event, under pseudo-first-order conditions (e.g. mM [**S**] or more) the steady-state level of E_{ox} would be diminishingly small given the relative rates of formation and reduction of

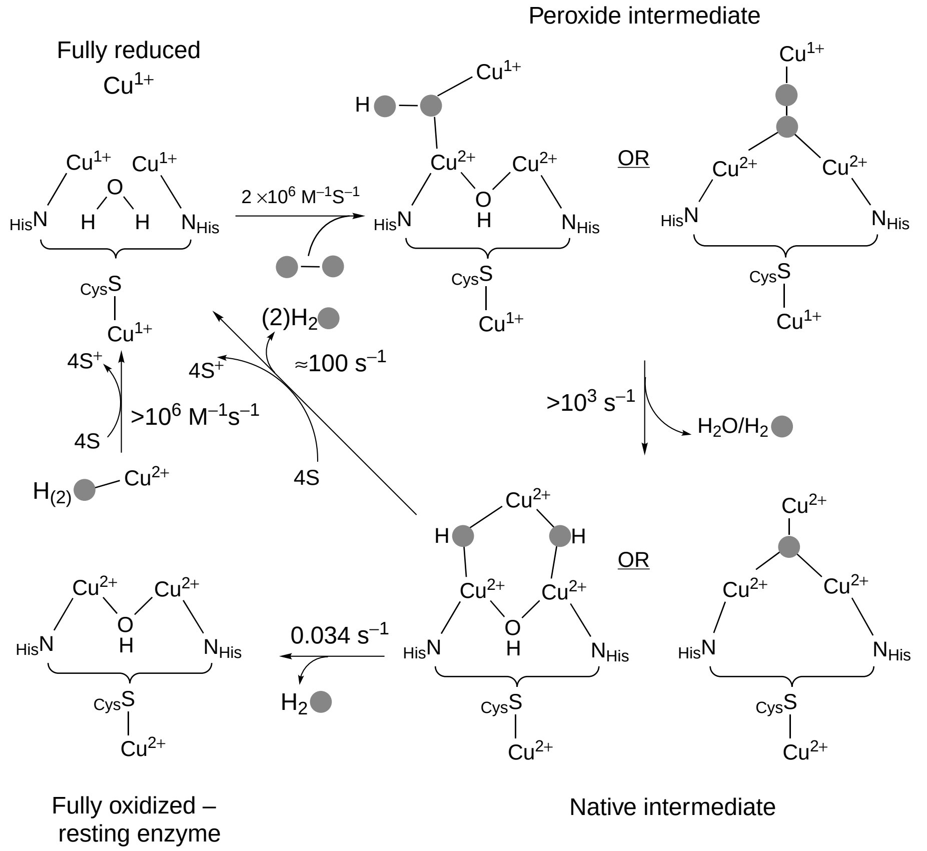

Figure 11 Reaction scheme for MCO dioxygen turnover based on spectral and kinetic data for *Rv* lac. (Reprinted with permission from Ref. 17. © 1999 American Chemical Society)

the ‘resting’ fully oxidized protein. Instead, the rate-limiting step in turnover is the four-electron reduction of the native intermediate. Since, as noted, the reduction per se does not represent a significant fraction of the energy barrier to this reductive turnover process, this step must involve ligand reorganization/displacement and/or proton transfers. These presumably would be associated with the protonation of the O^{2-} species tethered to the trinuclear cluster (Figure 11) and the release of H_2O. Indeed, the pH dependence of turnover and of the rate of decay of the peroxide intermediate reveal a dependence on the conjugate acid form of a group with pK_a values of 5.9 (turnover),[39] and 5.8 (intermediate decay).[37] On the other hand, whereas a kinetic solvent isotope effect (KSIE) of 2.12 was measured in turnover,[39] the KSIE for intermediate decay was 0.89.[37] A KSIE less than 1.0 represents an inverse effect and can indicate that the proton (deuteron) involved is bound more tightly in the transition state in comparison to the reactant state. Thus, although both turnover and intermediate decay exhibit the same pH dependence, the different KSIE values could indicate that the proton transfers involved in the two reactions are not precisely the same, that is, that two different free-energy surfaces are involved.

The two models for both the peroxide and native intermediates shown in Figure 11 are based on a variety of spectral evidence the most compelling of which is provided by the power-saturation behavior of the native intermediate’s EPR spectrum and its EXAFS. Figure 12 compares the X-band EPR spectra of the native intermediate at 77 K (A) with that of the resting oxidized protein (B).[38] The spectra show that in the intermediate, the type 1 copper is fully oxidized, but the type 2 copper is effectively diamagnetic, either reduced or spin-coupled. The saturation behavior of this spin system at 10 °K (C and D) reveals the presence of a broad, rhombic signal centered around 4000 G, a feature apparent only as the axial T1 Cu(II) transition saturates. The saturation behavior of the rhombic signal yielded a value of $P_{1/2} > 25$ mW, nearly 100-fold greater than for the T1 Cu(II). In a magnetically isolated protein matrix, the dominant electron spin relaxation mechanism is likely to be coupling with a low-lying excited state in the spin manifold such that $\ln P_{1/2} \propto -\Delta/k_B \cdot T$, where Δ is the energy gap between the ground and the excited state in cm^{-1}. Evaluating the relaxation as a function of temperature yields Δ; based on this Orbach analysis,[40] the native intermediate has a low-lying excited state at $\sim$140 cm^{-1}.[38]

The origin of the excited state was inferred from EXAFS analysis that provided a structural model for the Cu atoms in the intermediate. The ‘result’ of any EXAFS experiment is a best-fit based on evaluation of several possible models; Figure 13 gives the best-fit.[38] The primary difference in the underlying model and all others tested was the inclusion of 1 to 1.5 Cu–Cu interactions at 3.3 Å. This corresponds to two or three bridging interactions in the trinuclear cluster, with the former possibility yielding a more favorable σ^2 value. However, the EPR data, which show that the trinuclear cluster is ‘spin-frustrated’, requires that the three Cu(II) must be spin-exchange coupled via a set of equivalent bridges, that is, as in the two models illustrated in Figure 11. In the first, both oxygen atoms remain as bridges (shown between the two type 3 Cu atoms and the type 2 one); in the second, one of the oxygen atoms has debound (as H_2O) with the second remaining as a single μ_3-oxo bridge. Note that decay of the peroxide to the native intermediate exhibits an oxygen isotope effect, $k(^{16}O_2)/k(^{18}O_2) = 1.11$,[37] a value that strongly

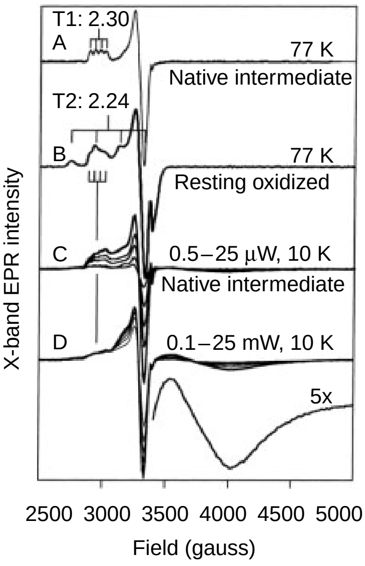

Figure 12 cwEPR spectra and saturation behavior of various forms of *Rv* Lac that show the unusual T2 Cu(II) signal and its relaxation in the native intermediate. (Reprinted with permission from Ref. 38. © 2002 American Chemical Society)

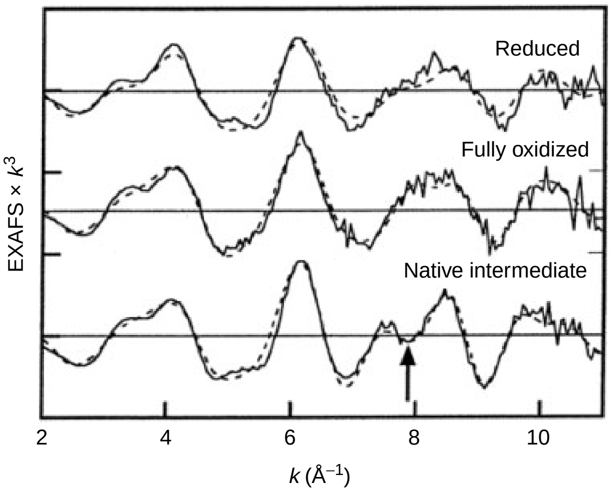

Figure 13 EXAFS of the *Rv* forms represented in Figure 12; the feature at $\sim 8\,\text{Å}^{-1}$ is assigned to a Cu–Cu interaction unique to the native intermediate. (Reprinted with permission from Ref. 38. © 2002 American Chemical Society)

indicates that in this process, the dioxygen bond is cleaved, as illustrated in Figure 11. Furthermore, the fact that all four copper atoms are in the cupric state indicates that O_2 has been converted to O^{2-} as in both suggested models.

The rate constants and the associated free-energy surfaces available to the peroxide and native intermediates deserve comment since they differ overall by nearly 10^5 (or ca. 7 kcal mol^{-1} in absolute value). Given the relatively electroneutral nature of electron transfers between the copper sites (the E° values for the three sites differ overall by only 60 mV), the differences in rate in the first instance reflect the difference in the E° value for $1e^-$ versus $2e^-$ reduction of dioxygen (leading to the peroxy intermediate) and peroxide (leading to the native intermediate). Second, the differences reflect the 'work' available from the favorable $4e^-$ reduction that drives the turnover from native intermediate to fully reduced enzyme primed, now, to react with O_2. This latter process, $k \approx 100\,s^{-1}$ (compare to $k = 0.34\,s^{-1}$ for decay of the native intermediate to fully oxidized enzyme), is functionally equivalent to the reductive release of Fe^{2+} from Fe^{3+}·transferrin catalyzed by the membrane metalloreductase, Dcytb; in both cases, the lower valent metal species is more loosely coordinating. Whereas Fe^{2+} dissociates in the latter case, in MCO turnover the bound water(s) dissociate.

The overall reaction mechanism for MCO catalysis reflects the electron stoichiometry associated with the lowest free-energy surface.[2] For dioxygen, the surface is given by $2e^{-1}$ transfers as is strikingly demonstrated by the 1 versus $2e^-$ reduction of peroxide. With $E° = 0.38\,V$ for the T1 and T2 copper atoms, and for the $1e^-$ reduction of H_2O_2 to $H_2O + HO\bullet$, there is no driving force for a $1e^-$ reaction. In contrast, the $E° = 1.37\,V$ for reduction of H_2O_2 to $2H_2O$ provides a strong driving force for the $2e^-$ process, a difference illustrated by the Morse potential energy surfaces in Figure 14.[2] The Morse potentials predict that the $\Delta\Delta G^‡$ for the $2e^-$ versus $1e^-$ reduction of peroxide is ca. -10 kcal mol^{-1}, consistent with the kinetic data shown in (Figure 11). The argument for the $2e^-$ mechanism is basically teleologic: given all the atom rearrangements, there is a large Franck–Condon barrier between H_2O_2 and $2H_2O$; the only compensating driving force large enough to overcome this barrier is from $2e^-$ reduction.

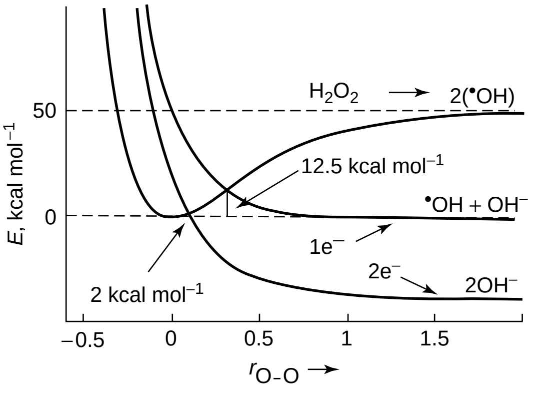

Figure 14 Morse potentials for $1e^-$ and $2e^-$ H_2O_2 reduction illustrating the ~10 kcal mol^{-1} more favorable $\Delta G^‡$ for the latter.[2] (Reproduced by permission of Wiley-VCH)

3.2 Ascorbate Oxidase

Functionally, ascorbate oxidase is a specialized laccase in that it exhibits specificity for dihydroascorbic acid as reducing substrate whereas laccases turn over a wide range of bulky aromatic phenols and amines. Also, AO appears confined to plants whereas laccases are widely dispersed in both plants and fungi. This suggests that AO is associated with the cellular differentiation that distinguishes higher from lower eukaryotes, and/or with the development of plants specifically. However, the few studies on the expression pattern of AO in plants, for example, in cultured tobacco,[41] have not clarified AO's biological role. One hypothesis, that has not been thoroughly tested, is that the AO, de/dihydroascorbate system functions in plants to maintain cell redox balance as the glutathione reductase, GSH/GSSG system does in other eukaryotes.[42]

AO was the first of the MCOs to be crystallized and characterized by X-ray diffraction.[18,19,43] Of continuing relevance are the structures of the azide- and peroxide-bound forms of the trinuclear cluster that have informed our understanding of ligation at this MCO copper site.[19] For example, the native, oxidized trinuclear cluster is pictured in Figure 15(a); of interest here is the solvent water coordinated in what is an apparent trigonal planar geometry of the type 2 Cu(II) (the type 2 Cu is designated Cu4 in the coordinate file). However, the two protein His ligands are fully trans indicating the type 2 Cu(II) could have a square-planar geometry with one open equatorial coordination site. However, the crystal structure does not define nor determine the electronic ground state. An alternative, albeit less probable interpretation of T2 Cu(II) ligation geometry is that the H_2O is apically coordinated and that there are two open equatorial sites. The oxygen bridging the binuclear Cu atoms, Cu2, and Cu3, is also clearly defined in the electron density map. Upon reduction of the cluster (not shown) or upon peroxide binding to the cluster (Figure 15b), the bridging oxygen is lost with the peroxide bound in an end-on fashion to Cu2. The loss of the bridging oxygen (in either case) results in Cu2 and Cu3 moving apart, from 3.7 to 4.8 Å in the peroxide-bound form. The other significant change is in the relationship of the type 2 Cu(II) to the type 3 copper atoms; whereas the Cu4 ↔ Cu3 distance remains essentially unchanged at 3.7 Å, the Cu4 ↔ Cu2 distance increases to 4.5 Å, undoubtedly due to the change in the ligand field at Cu2 due to peroxide coordination. Qualitatively and quantitatively similar structural changes occur upon N_3^- binding to Cu2,

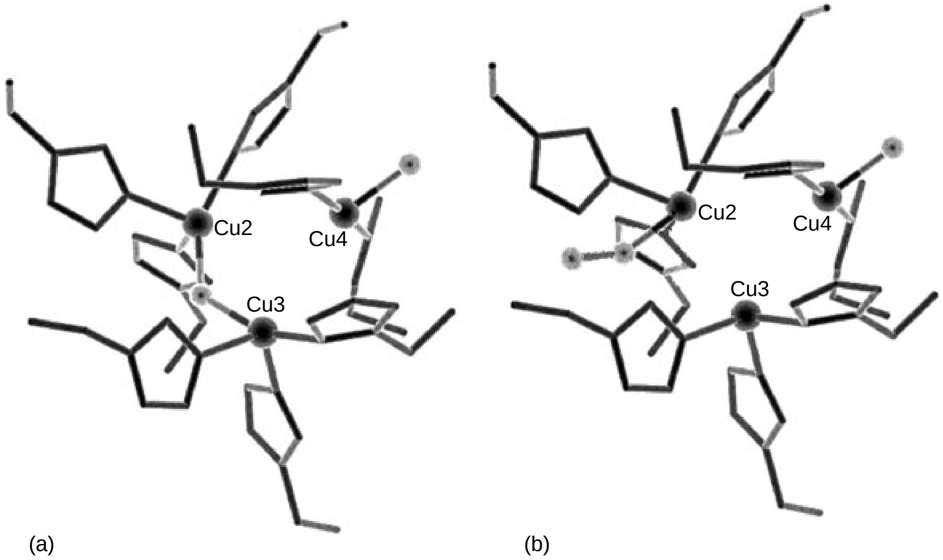

Figure 15 Trinuclear cluster in AO (a) and the AO, peroxide adduct (b)[19]

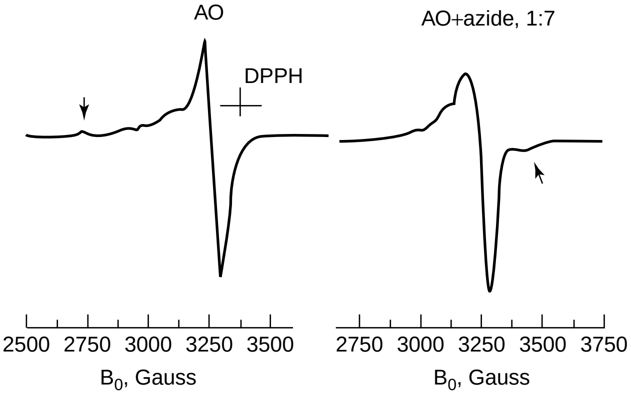

Figure 16 cwEPR spectra of AO and AO, azide adduct[44]

indicating that these structures reflect the basic coordination chemistry at the MCO trinuclear cluster.

The structural changes are reflected in electronic ones as well. The differences in the X-band cwEPR spectrum of AO and the AO-azide adduct illustrate one such change (Figure 16).[44] The spectra, recorded at 14 K, show that upon N_3^- binding, the normal T2 Cu(II) low field transition in $A_{||}$ decreases and a broad signal between 3000–3200 G appears ($g \approx 1.97$), but only below 40 K. A new T2 signal centered at 2860 G appears, also, but this signal is observed only above 40 K. The temperature and power-saturation dependence of the low g value signal suggests that it arises from an $S = 1$ spin system, likely to be a dipolar-coupled Cu(II) pair. This inference is fully consistent with the structure determined for the azide (and peroxide) AO adducts in which the two type 3 Cu(II), while not bridged (and thereby exchange-coupled), certainly could be spin-coupled through-space. That the T2 Cu(II) spin Hamiltonian in the azide adduct is perturbed is also consistent with the adduct's structure. First, the native trinuclear cluster is symmetric while in the adduct, the T3 Cu2 'moves away' from the T2 Cu4 by ca. 0.7 Å. In addition, the T3 Cu(II) atoms are no longer antiferromagnetically coupled. Both the perturbed T2 Cu(II) and the $g \approx 1.97$, $S = 1$ T3 Cu(II) spin systems exhibit an increased spin-lattice relaxation rate consistent with these structural and electronic changes. Finally, the results support the model for dioxygen reduction at the trinuclear cluster (Figure 11) in that they show that a potentially bidentate ligand binds end-on to only Cu2 in the cluster. Either form of the peroxide intermediate in Figure 11 would be compatible with this ligation scheme. What is missing, of course, from the structural and EPR studies is the mixed-valent state of the cluster suggested by kinetic and other spectral data in which the type 2 copper is present as Cu(I). Perhaps the more exchange-labile lower valent state of the T2 copper allows for the system to sample the Cu2-Cu4 bridged forms shown in the model; a ~4.5 Å spacing of Cu2 and Cu4 as in the peroxide adduct would be compatible with either the μ-1,1-hydroperoxide or μ_3 $(\eta^1)_3$ bridging modes illustrated. However, explicit correlations between static and kinetic experiments like those briefly summarized here have not been thoroughly explored.

4 FERROXIDASES: CERULOPLASMIN AND THE Fet3 PROTEIN

4.1 Background – The Copper, Iron Connection

Over fifty years ago, nutritional studies in swine and sheep demonstrated that copper deficiency correlated to the symptoms of iron deficiency in iron-replete animals.[45] This physiological correlation was subsequently extended to a biochemical one, namely, that the apparent iron-deficient state was linked to the decline in serum oxidase activity due to a blue, copper-containing protein, ceruloplasmin.[46] In the 1960s and 70s, Earl Frieden and his coworkers established that ceruloplasmin had a strong kinetic specificity for Fe^{2+} as substrate and proposed that the physiologic dependence that normal iron metabolism had on copper status was due to the role that Cp played in the efficient trafficking of iron – as Fe^{3+} – to apotransferrin (Tf) (*see* ***Iron Proteins for Storage & Transport & their Synthetic Analogs***).[47,48] Hence, Cp was described as a ferroxidase, a specialized member of the MCO family.

Biochemical support for this hypothesis was difficult to obtain. For example, if Cp 'catalytically' traffics Fe^{3+} to *apo*Tf then the transfer 'catalysis' should be kinetically demonstrable. The reactions involved are complex, however:[49]

$$\mathrm{Fe_{(aq)}}^{2+} \longrightarrow \mathrm{Fe_{(aq)}}^{3+} + e^- \qquad (k_1)$$

$$\mathrm{Fe_{(aq)}}^{3+} + apo\mathrm{Tf} \longrightarrow \mathrm{Tf{\cdot}Fe^{3+}} \qquad (k_2)$$

$$\mathrm{Fe_{(aq)}}^{3+} + \mathrm{H_2O} \longrightarrow \mathrm{Fe(OH)}_n \qquad (k_3)$$

$$\mathrm{Fe_{(aq)}}^{2+} + \mathrm{Cp} \longrightarrow \mathrm{Fe_{(Cp)}}^{3+} \qquad (k_4)$$

$$\mathrm{Fe_{(Cp)}}^{3+} + apo\mathrm{Tf} \longrightarrow \mathrm{Tf{\cdot}Fe^{3+}} \qquad (k_5)$$

The first two reactions lead to formation of $\mathrm{Tf{\cdot}Fe^{3+}}$ via the autooxidation of 'free' ferrous iron (k_1). However, the hydrolysis of $\mathrm{Fe_{(aq)}}^{3+}$ (k_3) competes with the binding of $\mathrm{Fe_{(aq)}}^{3+}$ to *apo*Tf (k_2), reducing the observed rate of formation of $\mathrm{Tf{\cdot}Fe^{3+}}$. Thus, irrespective of the rate of Fe^{3+} binding to *apo*Tf, there are two barriers that rate-limit the formation of *holo*Tf: the rate of autooxidation of Fe^{2+}, and the partitioning of Fe^{3+} between binding and hydrolysis. Cp could 'catalyze' the binding reaction in two ways: 1) increasing the rate of oxidation (ferroxidation) and/or 2) by reducing or eliminating the competition from hydrolysis.

The first of these effects is easily demonstrated independent of iron trafficking to *apo*Tf. For example, given the strongly limited concentration of free oxygen in the presence of hemoglobin ($<10\,\mu\mathrm{M}$ in plasma), the pseudo-first-order rate of autooxidation of Fe^{2+} at physiologic pH is $\sim 0.1\,\mathrm{min}^{-1}$. With a K_M for $O_2 \sim 1\,\mu\mathrm{M}$, hCp functions close to its V_{max} for ferroxidation under physiologic conditions and can turn over 100-fold more Fe^{2+} than would autooxidization.[50] Such 'catalysis' is required given the daily iron turnover in humans of *ca* 700 µmol. The question of competition from the hydrolysis 'side reaction' is more difficult to address experimentally. Experiments in which the rate of accumulation of $\mathrm{Tf{\cdot}Fe^{3+}}$ was enhanced by inclusion of Cp in the binding reaction mixture do not by themselves confirm a mechanism.[49] However, the fact that enhancement occurs only when the binding reaction is initiated with the addition of Fe^{2+} (and not when Fe^{3+} is added to Cp and *apo*Tf) suggests that Cp-generated Fe^{3+} is a 'preferred' Tf substrate ligand. Also, the combination of Cp and *apo*Tf stimulates release of ^{59}Fe from mammalian cells (with the formation of $^{59}\mathrm{Fe{\cdot}Tf}$). That neither Cp alone, nor Tf alone, stimulates ^{59}Fe release suggests the two proteins function synergistically in this iron trafficking but does not indicate how they do so.[51]

However, the link between the ferroxidase activity of an MCO and iron homeostasis has been put on firm ground due to genetic studies in yeast and normal and transgenic animals over the past decade.[52,53] First, the identification of a family of fungal ferroxidases that are required for normal iron trafficking in their respective organisms – the Fet3p family of proteins – has provided a biochemical model system in which to study if not establish how a ferroxidase enzyme can 'channel' Fe^{3+} within an iron trafficking pathway, for example, as in the formation of $\mathrm{Tf{\cdot}Fe^{3+}}$ from $\mathrm{Fe_{(aq)}}^{2+}$ and *apo*Tf as above. In fungi, and most likely in plants also, these ferroxidases are part of an enzyme-iron permease complex that transports iron across a membrane.[53,54] Second, genetic studies in animals have revealed the presence of additional members of the mammalian ferroxidase family, one of which – hephaestin – like the Fet3 protein, is required for membrane iron transport.[55] Thus, irrespective of the role that Cp might play in iron loading of *apo*Tf, there is a superabundance of data that the iron oxidase activity of the ferroxidases is not a curiosity and that the ferroxidases are aptly named.

4.2 Ceruloplasmin

4.2.1 Protein Properties, Synthesis, and Processing

Human ceruloplasmin (hCp) is an encoded 1065 residue protein, calculated $M_r = 122\,205$ Da. The preprotein contains a 19-residue signal sequence that targets it to the endoplasmic reticulum during synthesis; this sequence is cleaved during processing leaving a mature protein of 1046 residues.[52] Note that all reference to residue number in this chapter is based on the encoded protein and not on the sequence of the mature protein even if this sequence is known precisely from experiment. As are all of the eukaryotic MCOs, hCp and its mammalian homo- and orthologues are glycoproteins; mature hCp is ca. 10% w/w N-linked carbohydrate. In addition to the signal sequence cleavage and glycosylation, Cp also obtains its prosthetic group copper atoms during its processing in the vesicular protein trafficking pathway. This copper addition appears to occur relatively late in this pathway, in what is commonly referred to as the trans-Golgi network that includes vesicles targeted for fusion with the plasma membrane (and in fungi, the vacuolar membrane, as well).

The copper content of this compartment is maintained by one or two P-type ATP-utilizing copper pumps. These two proteins are known by their association with two disorders of human copper metabolism, the Menkes (MNK) and Wilson (WND) proteins, and genetically as ATP7A and ATP7B, respectively (*see* ***Metal-related Diseases of Genetic***

Origin).[56,57] These pumps, in turn, are ‘supplied’ with copper, as Cu(I), by the cytoplasmic copper chaperone, the product of the human HAH1 gene (*see* ***Metallochaperones & Metal Ion Homeostasis***). This chaperone is also commonly known at Atox1, the product of the mouse ATX1 gene. The latter designation followed from the original isolation of this locus, in yeast, where it was given the designation *ATX1* for antioxidant protein 1.[56] The point to be made here is that the fully metallated Cp, or of any eukaryotic MCO, is the product of a true metabolic or processing pathway that involves two separate compartments and at least two copper trafficking activities. A last subtle point is that the copper ‘substrate’ for this trafficking is very clearly Cu^{1+}; data below will indicate that this is likely to be the state of the copper in the newly mature MCO.

4.2.2 Structure, Specificity, and Electron-transfer Mechanism

As noted above, hCp represents the ‘duplicated’ MCO family, those MCOs that contain >1000 residues and, therefore, possess a tertiary fold consisting of six cupredoxin domains.[34] What is unusual about Cp is the presence of three type 1 Cu sites; that is, whereas in the other MCOs, the first two of the three cupredoxin domains ‘lost’ the type 1 ligands found in the third, carboxyl-terminal one, in Cp, these motifs are retained in three of the six, in domains 2, 4 and 6. The relationship of these three type 1 Cu sites to the trinuclear center (found at the interface of domains 1 and 6, not 1 and 3 as in the three-domain MCOs) is shown in Figure 17.[24] The type 1 Cu in domain 6 is ∼13 Å from this cluster; the distance from the cluster of the other two are ∼22 (domain 2) and ∼30 Å (domain 4), respectively. On the other hand, the three putative type 1 sites form a near isosceles triangle, ∼18 Å on a side.

One of these type 1 copper atoms is redox inert and, with a reduction potential of ∼1.0 V, is in a permanently reduced site. The redox properties of this site were deduced from a combination of chemical assay for Cu(I) using biquinoline and XAS.[58] The copper K-edge XAS for Cu(I) exhibits a distinctive feature at 8983 eV; the peroxide-oxidized Cp retains ∼12% of the intensity of this edge absorption observed in the fully reduced protein. The biquinoline assay indicates that ∼20% of the total copper in this oxidized Cp is present as Cu(I). These values indicate that of the six copper atoms/molecule detected in Cp by chemical solution, one of them is present as Cu(I). Since three of the others can be accounted for as part of the trinuclear cluster, and two as ‘normal’ type 1 Cu(II) based on absorption at 608 nm and spin quantification by cwEPR, this reduced Cu(I) must be at one of the type 1 sites predicted by sequence (Figures 1 and 4) and confirmed crystallographically.[24,59] Kinetic analyses indicate that the two redox-active blue sites are competent in enzyme turnover of reducing agent and dioxygen. Again, note that Cp (and its paralogue, hephaestin) is the only known MCO that is a ‘dimer of trimers’; that is, Cp has two of the prototypical plastocyanin ‘triplets’ characteristic of all MCOs.

The specificity of Cp for Fe^{2+} as substrate appears to derive from two structural features.[59] First, the cavity that rings the ferroxidase-active type 1 Cu(II) atoms noted above presents an overall negatively charged electrostatic surface to bulk solvent. Second, there appear to be two specific binding sites for Fe^{2+} and Fe^{3+} and other comparably sized and charged first-row transition metals (e.g. Co^{3+}, Cu^{2+}) that are found associated with this anionic surface. These two sites are shown in Figure 18; metal soaking and subsequent crystallographic difference analyses indicate that these sites in domains 4 and 6 only are occupied.[59] Distinct functions for the two sites are indicated in the figure. The ferroxidase site directly adjacent to the type 1 Cu(II) is where Fe^{2+} is oxidized by electron transfer to the Cu(II) via one or both the metal’s two His ligands. Following metallo-oxidation, the higher valent species is suggested to migrate to the distal, ‘holding’ site. The fate of the Fe^{3+} product at this site has not been established, for example, whether it dissociates or is trafficked directly to transferrin. In simple turnover, it clearly equilibrates with bulk solvent.

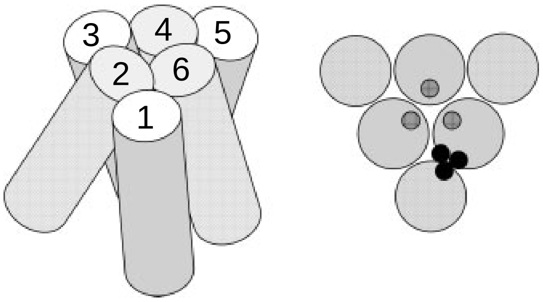

Figure 17 Domain organization in hCp illustrates the pattern for six-domain MCOs. Note the three T1 sites; the two in domains 4 and 6 are redox active, the one in domain 2 is permanently reduced

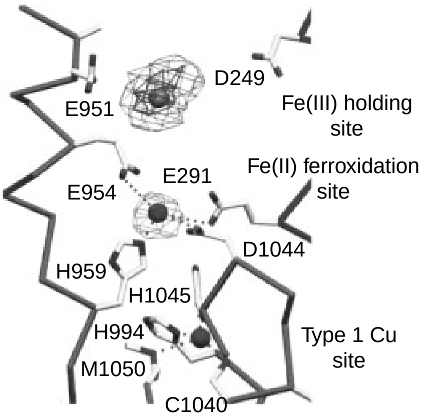

Figure 18 Fe(II) ferroxidation and Fe(III) holding sites at the T1 Cu site in hCp. (Reprinted from Ref. 59. © 1997 Society of Biological Inorganic Chemistry)

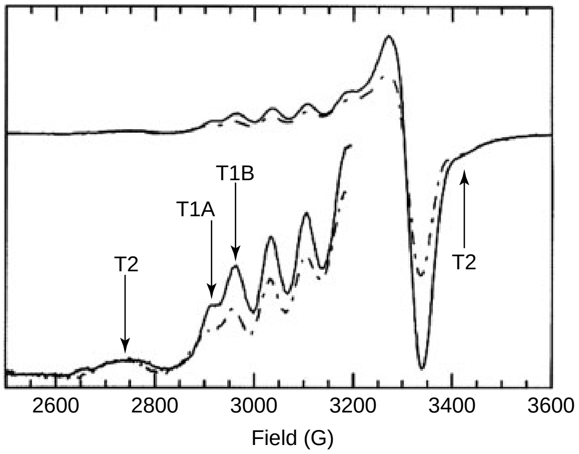

Figure 19 cwEPR spectrum of 'oxidation' product from the reaction of fully reduced hCp with O_2 showing that two T1 Cu atoms share one 'hole'. (Reprinted with permission from Ref. 60. © 2000 American Chemical Society)

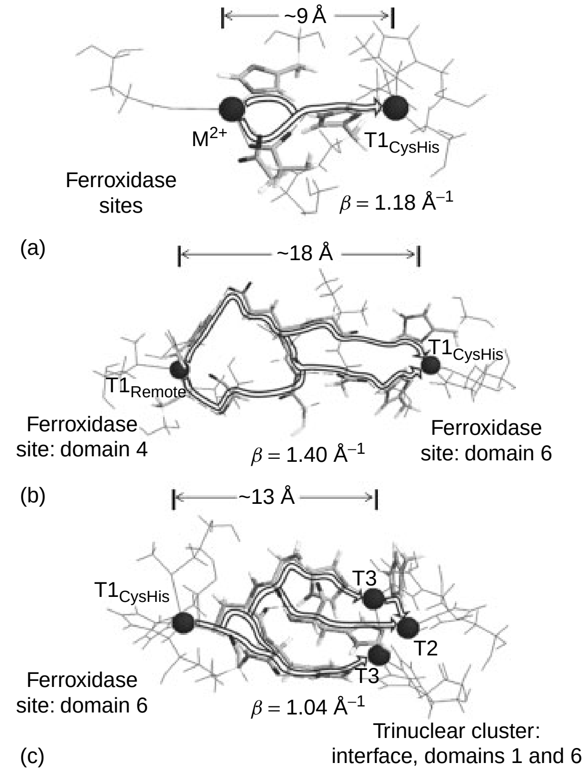
~9 Å
M2+
T1CysHis
Ferroxidase sites
β = 1.18 Å−1
(a)
~18 Å
T1CysHis
T1Remote
Ferroxidase site: domain 4
β = 1.40 Å−1
Ferroxidase site: domain 6
(b)
~13 Å
T1CysHis
T3
T2
T3
Ferroxidase site: domain 6
β = 1.04 Å−1
Trinuclear cluster: interface, domains 1 and 6
(c)

Figure 20 Intramolecular electron-transfer pathways in hCp with the coupling decay value, β, for each. (Reprinted with permission from Ref. 60. © 2000 American Chemical Society)

The Cp system is the most thoroughly examined with regards to the intramolecular electron transfers that couple ferroxidation to dioxygen reduction. Figure 19 demonstrates several things about this redox system.[60] The solid lined spectrum is that of fully oxidized Cp in which 5 of the six copper atoms are present as Cu(II); this includes two of the three Cu at the putative type 1 sites. The spectrum shows clearly the different spin Hamiltonian parameters for these two sites; spin quantification shows that they each contain one spin-equivalent. The $m_s = -3/2$ Cu hyperfine line due to the single type 2 Cu(II) is also apparent in this oxidized sample; it, too, represents one spin-equivalent. If fully reduced protein is reoxidized by O_2, the spectrum given by the dashed line is obtained. Whereas the type 2 Cu(II) is clearly fully oxidized, the two type 1 Cu are not. Spin quantification shows that, in effect, they are sharing one 'hole', and one electron. Since fully reduced Cp has five redox-available electrons while dioxygen reduction requires only four, this leaves one electron 'on' the enzyme. The spectrum in Figure 19 demonstrates that this electron is shared by the two type 1 copper atoms.

This result indicates that the type 1 sites in domains 4 and 6 (based on the fact that metal binding is observed at these sites crystallographically) are both ferroxidase-active in turnover. The reduction-oxidation result above suggests that an electron transferred to one of these copper atoms is 'shared' with the other. Based on kinetic studies, the lower limit of this intramolecular electron transfer is $150\,\mathrm{s}^{-1}$ but is likely to be as much as ten times this value. A calculation of this rate based on the Pathways program developed by Beratan and Onuchic[61] gives a value of $1500\,\mathrm{s}^{-1}$. This program generates a value for the electronic coupling matrix element, H_{AB}, that in simple Marcus theory is given by the product of a single scalable factor, β, times the distance between the electron transfer sites. The program assigns different 'efficiencies' to electron transfer through covalent bonds of different types, H-bonds, and through-space 'jumps'; input for this program is a protein structure coordinate file with protons added as needed to complete putative H-bonds (*see* ***Electron Transfer Reactions: Theory*** and ***Long-range Electron Transfer in Biology***). The results of this modeling are illustrated in Figure 20 for the three electron-transfer steps that kinetic analyses suggest for the Cp-catalyzed turnover of Fe^{2+} and O_2. The computed values of the coupling decay, β, are given; these give an estimate of the 'conductance' of the putative electron-transfer pathways indicated in the figure.[60]

4.2.3 *The GPI-ceruloplasmin Isoform and Hephaestin*

Cp is a soluble protein, secreted by mammalian cells into the plasma or interstitial space.[52] However, in some cells (neuronal, visual), alternative splicing of the nascent Cp transcript produces an mRNA that is translated into a Cp protein with a carboxyl-terminal extension that is substrate for the addition of a glycosylphosphatidylinositol (GPI) tag.[62] This tag leads to the insertion of this Cp form into the inner surface of the vesicular membrane that encloses this Cp processing pathway. Upon fusion of this vesicle with the plasma membrane, the Cp becomes tethered to the outer surface of the cell. Metazoan genomes also encode a Cp-like protein that contains a carboxyl-terminal transmembrane domain; in mammals, this is hephaestin.**[63]** Like the GPI-Cp protein, Hp is found tethered to the inner surface of the vesicular membrane, or to the outside of the cell. Either enzyme is thus positioned to act on Fe^{2+} that is found in these two environments.

GPI-Cp is linked to neuronal cell homeostasis, probably by preventing the abnormal accumulation of Fe^{2+} (and, perhaps, Cu^{1+}).**[64]** Loss of Cp activity in neurons correlates with a variety of degenerative diseases of the nervous system with an underlying pathophysiology that involves iron deposition and oxidative damage.**[52]** Given the known pro-oxidant activity of low-valent metal ions like Fe^{2+} and Cu^{1+}, Cp could suppress this pathophysiology simply by lowering these ions' steady-state level, or by coupling this oxidation to the trafficking of iron out of 'harms way', for example, by catalyzing its transfer to transferrin. Cp also could work by assisting in the membrane transport of iron; this suggestion is based on the known role that hephaestin plays in iron transport in the epithelial cells in the intestine,**[63]** and that fungal ferroxidases play in the uptake of iron in those organisms (below). Hephaestin is expressed in the intestine, and together with a divalent metal ion transporter, Ireg1,**[65]** is required for the export of iron across the epithelial lining of this tissue into the circulation. The coupling of the activities of Hp and Ireg1 in this iron trafficking process is not understood, but most certainly involves the ferroxidase activity that Hp has.**[66]** This coupling is characteristic also of high affinity iron uptake in fungi, as discussed below.

4.3 Fungal Ferroxidases – The Fet3 Protein from *Saccharomyces cerevisiae*

4.3.1 Protein Properties, Synthesis, and Processing

All fungal genomes archived encode at least one MCO of *ca* 700 residues that contains a carboxyl-terminal transmembrane domain; this is in addition to the laccase(s) that many also produce. Most if not all of these membrane-associated MCOs are ferroxidases, and, like Cp and Hp, play an essential role in the iron metabolism of these fungi. Three of these were represented in the sequences given in Figure 4 (Fet3p, Fet5p and Fio1). Of these proteins, the most thoroughly characterized representative is the Fet3p protein from baker's yeast, *Saccharomyces cerevisiae*.**[53,54]**

Fet3p is produced as a 636 residue preprotein that is processed first by cleavage of a 20-residue signal sequence that targets the nascent polypeptide to the endoplasmic reticulum. The mature protein is highly glycosylated; there are as many as 13 potential N-linked glycosylation sites within the sequence. The apoprotein is metallated in what is termed the trans-Golgi network, a series of vesicular compartments that connect the Golgi apparatus to the plasma membrane, or, in yeast, to the vacuole as well. Insertion of the protein's four copper atoms requires three membrane functions in these vesicles: acidification due to a H^{+}-ATPase; Cl^{-} trafficking due to a chloride pump; and the fungal homologue to the mammalian copper pumps, ATP7A/B, the Ccc2p protein.**[56]** Yeast deficient in any one of these three actitivies produce only the apo form of Fet3p. These yeast mutants, like those that are mutant in the Fet3p gene itself or those that are in a copper-deficient state, exhibit a strong iron deficiency owing to a lack of high affinity iron uptake. This metabolic coupling of an MCO with normal iron trafficking was and is the most compelling data relevant to the molecular mechanism of the 'copper-iron' connection in biology (*see* ***Nutritional Aspects of Metals & Trace Elements*** and ***Metallochaperones & Metal Ion Homeostasis***).

This iron deficiency is due to the fact that Fet3p likely forms a complex with the high affinity iron permease, Ftr1p, in the yeast plasma membrane.**[54]** In this complex, Fet3p oxidizes Fe^{2+} produced by a plasma membrane metalloreductase (the Fre1p protein in yeast, comparable to the Dcytb protein in mammalian cells**[66]**) to Fe^{3+} in the ferroxidase reaction; the Fe^{3+} is substrate for iron uptake through Ftr1p. The obligatory coupling of the ferroxidation and uptake processes suggests that Fet3p-produced Fe^{3+} is trafficked directly to Ftr1p in a nondissociative ligand-exchange reaction much as Cu^{1+} traffics between copper chaperone and target protein (*see* ***Metallochaperones & Metal Ion Homeostasis***).**[56,67]** This direct solute transfer in a metabolic pathway is termed 'channeling' and is common when the solute transferred is likely to undergo an undesirable side reaction if it equilibrates with bulk solvent.**[68]** In the case of Fe^{3+}, one such reaction would be hydrolysis, as outlined above in regards to the role of Cp in Fe^{3+} transfer to transferrin.

4.3.2 Spectral Properties

The Fet3p system has been exploited to produce mutant MCO forms that lack one or more of the copper atoms so as to isolate the spectral and functional properties of the remaining sites.**[53]** Chemical means had been used to produce metal-substituted (T1Hg forms) and metal-deficient forms (T2 depleted) of Lac and AO. With Fet3p, site-directed mutagenesis afforded T1D, T2D and, for the first time, T1D/T2D MCO protein without the use of possibly damaging chemical treatments.**[25]** Figure 21 illustrates the T1 and trinuclear cluster sites in Fet3p (panels A and B, respectively) and the amino acid substitutions that were made to produce these copper-site depleted mutants (the double mutant contained both C484S and H81N substitutions). The X-band cwEPR and near UV–vis spectra for wild-type Fet3p and these mutant proteins are shown in Figure 22. The spectral values corresponding to these spectra were given in Table 1.

Both the EPR and UV–vis spectra demonstrate two features of this system. First, they show that the remaining Cu(II) sites in mutant proteins lacking either the T1 or T2 Cu(II), or both, exhibit the same spectral properties that obtain in the wild-type protein. Second, sequentially depleting the protein of Cu(II) atoms allows the direct assignment of these spectral

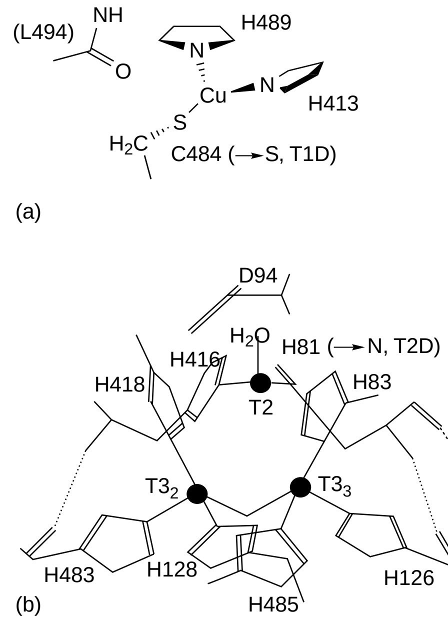

Figure 21 T1 Cu (a) and trinuclear cluster (b) of Fet3p indicating substitutions leading to site-depleted protein forms

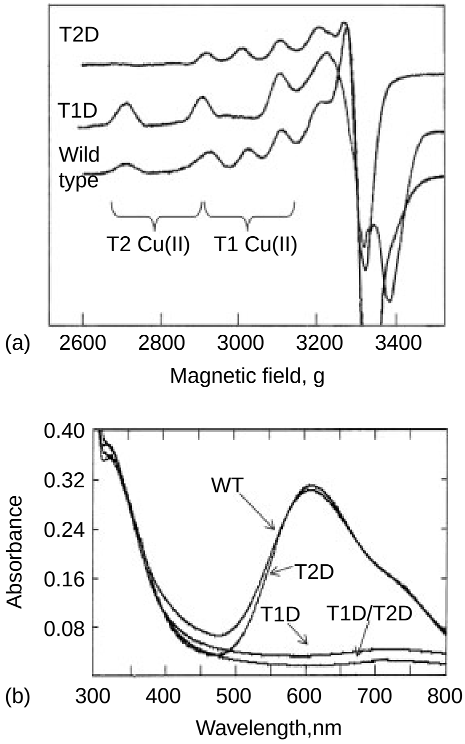

Figure 22 cwEPR (a) and absorbance spectra (b) of wild type and site-depleted forms of Fet3p.[53] (Reprinted with permission from Ref. 25. © 2000 American Chemical Society)

values to specific Cu(II) atoms. This is most obvious in the UV–vis spectra: the shoulder at 330 nm is clearly from the T3 binuclear cluster while the broad absorbance at ~720 nm persists in the T1D/T2D mutant indicating that it, too, comes from the T3 site.

The double mutant was most useful in examining the EXAFS of the binuclear cluster in an MCO, spectrally isolated for the first time in this mutant; the experimental and fitted spectra for the oxidized and reduced clusters in Fet3p(T1D/T2D) are shown in Figure 23 a and b, respectively. Some of the parameters used to construct the fits are shown in the model in Figure 23(c). The three principal insights provided by these fits, as illustrated in this model, are: 1) a bridging O is clearly distinguished in the oxidized T3 site that is absent in the reduced form: 2) upon reduction, the Cu–Cu backscatterer detected in the oxidized site is reduced or absent, likely due to the two Cu(I) moving apart; and 3) an

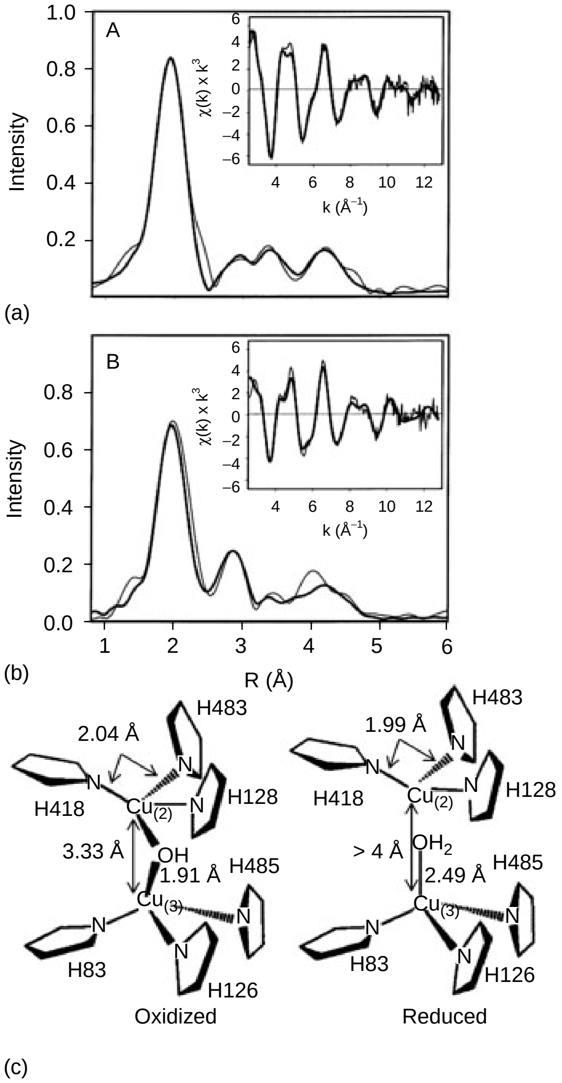

Figure 23 EXAFS of oxidized (a) and reduced (b) T3 site in Fet3p. The fits shown are illustrated by the model of the binuclear site shown in c.[53] (Reprinted with permission from Ref. 25. © 2000 American Chemical Society)

additional O/N is fit in the EXAFS of the reduced site, that, at 2.49 Å, is dissimilar to the coordinating imidazole nitrogen atoms. These changes upon reduction of the type 3 site in Fet3p deduced from the EXAFS data parallel those observed crystallographically upon reduction of AO.[19] Specifically, upon reduction, the bridging O in AO is lost and the type 3 Cu–Cu distance increases from 3.7 to 5.1 Å. Furthermore, the coordination geometry of the two Cu atoms differ, much as they do in the model of the reduced type 3 cluster in Fet3p shown in Figure 23(c). This difference could be due to the H_2O molecule apically coordinated to one of the Cu(I). This Cu atom, designated $Cu_{(3)}$, remains somewhat tetragonal because of this water coordination, while the other, $Cu_{(2)}$, becomes more trigonal planar in geometry.

4.3.3 Structure-function Relationships

The utility of yeast as a genetic and recombinant protein system is exemplified also by the several structure-function studies on the Fet3p protein. In addition to those studies that targeted copper-site ligands (above) are those that probed for amino acid residues required for oxidase activity or for substrate specificity, that is, specificity for Fe^{2+} as reducing substrate. Enzyme turnover involves three electron-transfer steps: to the type 1 Cu(II) from the reducing substrate; intramolecular electron transfer from the type 1 Cu(I) to the trinuclear cluster; and electron transfer from the cluster to dioxygen. In regards to the first of these electron-transfer steps, it is likely that the coupling pathway from substrate to Cu(II) is via the coordinating histidine imidazole homologous to H1045 in hCp and H489 in Fet3p (*cf* Figures 1 and 21). Depending upon the solvent exposure of this NHε2, the coupling is direct (as in the laccases) or indirect, as in hCp. This difference in solvent exposure is illustrated in Figure 24; the Connolly (water-accessible) surfaces for *C. cinereus* laccase (1A65, Figure 24a) and hCp (1KCW, Figure 24b) are shown (images generated using InsightII software from Molecular Dynamics). Whereas the NH is fully exposed to solvent in Lac, it is ~9 Å beneath the surface in hCp. One cannot directly correlate the extent of solvent accessibility of this His with electron-transfer rate since, according to the Marcus formulation, this rate depends on the driving force ($\Delta E°$) and steric and 'binding' terms (S and K_A, respectively), as well as on the electronic coupling matrix element and reorganization energy (which is likely to be roughly the same for all MCOs). However, with a large organic reductant like hydroquinone as substrate, T1 Cu(II) reduction in Lac is 500-fold faster than in hCp.[69] This difference is not due to a difference in $\Delta E°$ since the two T1 Cu(II) have essentially the same redox potential (~440 mV); thus, in this case, the rate difference could be due to a physical interaction of this substrate with Lac in comparison to the electron transfer-productive interaction with hCp. Indeed, as noted, crystallographic studies have demonstrated the Lac does have a shallow binding site for bulky aromatics where the substrate binding site is more constrained. Since this histidine coupling element is also a copper ligand, mutagenesis cannot be used to test its role in electron transfer; as outlined above, substitution at this ligand results in the production of a stable T1D protein.

However, substrate specificity at the T1 copper can be probed by site-directed mutagenesis; in particular, this approach has been used to identify residues that confer the Fe^{2+} specificity characteristic of ferroxidases. The acidic (negative) patch adjacent to the T1 copper in hCp has been noted; two of the residues implicated in this Fe^{2+} site are E954 and H959 (*cf* Figure 18). Mauk and coworkers demonstrated that the E954A/H959A hCp double mutant lost 50% of its ferroxidase activity while retaining full activity towards *o*-dianisidine.[70] Although not directly measuring the increase in K_m for Fe^{2+} that would be expected if these residues were part of the specificity site, these experiments did provide evidence in support of this model.

There is no structure of Fet3p (or of any other fungal ferroxidase) on which to base such structure-activity studies; on the other hand, the plethora of fungal Fet3p homologues

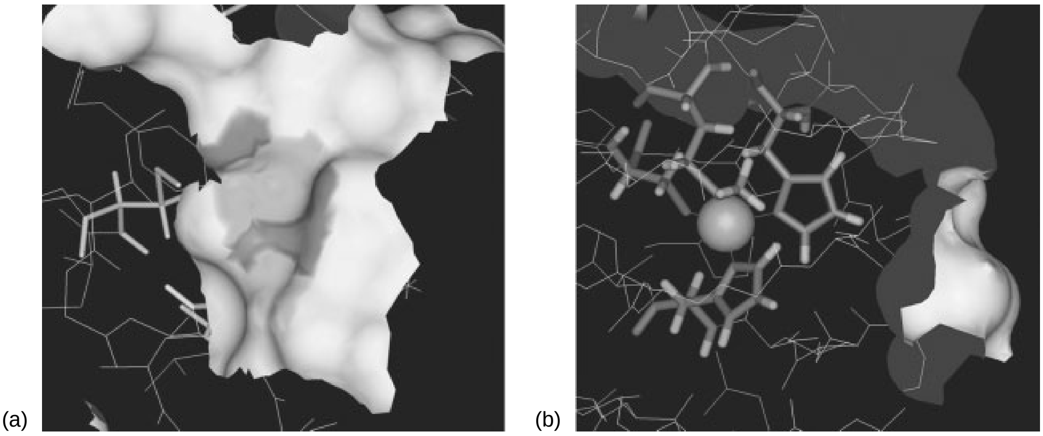

Figure 24 Connolly surfaces of *Cc* Lac (a) and hCp (b) illustrating solvent exposure of the T1 site

provides a wealth of sequence data on which to make well-educated guesses as to which sequence motifs might distinguish a ferroxidase from other fungal MCOs. Two such studies have identified E185 and Y354 as residues that contribute to the specific binding of Fe^{2+} in Fet3p turnover of O_2.[71,72] This conclusion was based on three- to tenfold increases in K_M for Fe^{2+} in E185A and Y354A mutants. A D278A mutant also exhibited a specific twofold increase in this value suggesting that this residue contributed to Fe^{2+} binding as well. All three residues are conserved among the fungal 'ferroxidases', but their specific roles in catalysis have only been tested in *S. cerevisiae* Fet3p.

The binding of Fe^{2+} at E185 has been demonstrated directly by use of low temperature (LT) MCD.[73] High spin, non-heme Fe^{2+} has a $^5T_{2g}$ ground state; spin-allowed electronic transitions are to the ^5E_g state, which is at $10\,Dq$.[74] With common biological ligands like N and O, $10\,Dq \approx 10\,000\,\text{cm}^{-1}$. The splitting of these ground and excited states is sensitive to coordination number and distortion from pure octahedral symmetry; Solomon and his coworkers have correlated calculated and measured splittings with well-characterized coordination complexes, for example, octahedral, square pyramidal, and trigonal bipyramidal.[74] Octahedral complexes exhibit two overlapping transitions centered at ca. $10\,000\,\text{cm}^{-1}$ whereas the latter five-coordinate geometry alone gives rise to a single Fe^{2+} LT MCD transition between 8500 and $10\,000\,\text{cm}^{-1}$. The LT MCD spectrum of a 1:1 Fe^{2+}:Fet3p mixture exhibits a broad transition at $8900\,\text{cm}^{-1}$ (Figure 25, WT).[73] One equivalent of Fe^{2+} experiences an equivalent ligand field in the presence of the Fet3pE185D mutant (Figure 25, E185D). In contrast, in the presence of Fet3pE185A, added Fe^{2+} experiences a ligand field equivalent to that in buffer alone, with a transition energy shifted up to $9700\,\text{cm}^{-1}$ (Figure 25, E185A). Variable temperature variable field (VTVF) analyses of this MCD transition, and a comparable one observed for Fe^{2+} in the presence of hCp, indicate that the ferroxidase Fe^{2+} binding sites in both proteins are most likely distorted octahedral in geometry; irrespective of the precise geometry, however, in Fet3p, E185 is part of this coordination sphere.

Possible catalysis by protein groups of dioxygen turnover at the trinuclear cluster has been examined in Fet3p also.[75] As noted above, both turnover and intermediate decay in laccase catalysis exhibit a descending pH dependence ($pK_a = 5.8$) and a KSIE that indicate an enzyme-derived H^+ is transferred during O–O bond cleavage. A similar pH dependence of intermediate decay has been determined for Fet3p(T1D) (see Figure 21(a) for structure) as shown in Figure 26. The enzyme group responsible for the acid catalysis indicated is likely the carboxylic acid group on a Asp residue adjacent to the type 2 site that is conserved in all MCOs; in Fet3p, this is D94 as shown in Figure 21(b) in a model based on the *Tv* Lac structure. The structure-activity relationship suggested by the pH and isotope studies has been tested in Fet3p by substitution of this residue by Glu, Asn, and Ala. Whereas the D94E mutant is fully wild type in activity, the other two mutants are catalytically inert. The absorbance and cwEPR properties of all three Cu(II) sites in these three mutants are quantitatively wild type consistent with the hypothesis that the D94 side chain interacts with some part of the substrate during turnover and not with any one of copper atoms in the trinuclear cluster in the free enzyme.

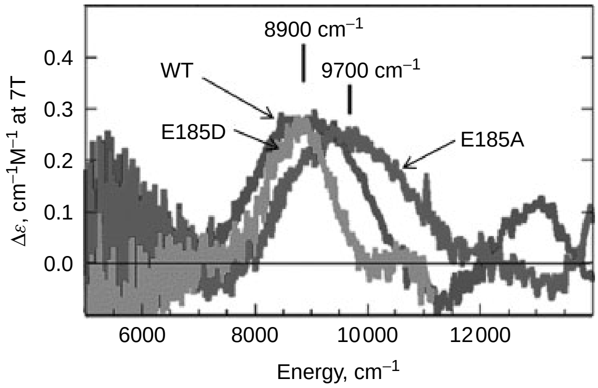

Figure 25 LT MCD spectra of wild type and E185 mutant forms of Fet3p in the presence of one equivalent of Fe^{2+}. (Reprinted with permission from Ref. 73. © 2004 American Chemical Society)

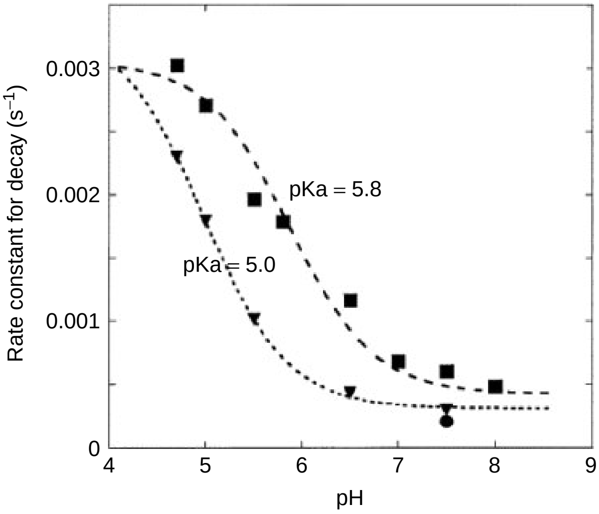

Figure 26 Acid catalysis of decay of peroxide intermediate in *Rv* Lac (squares) and Fet3p (triangles). (Reprinted with permission from Ref. 75. © 2002 American Chemical Society)

One unexpected finding came from these studies on Fet3p mutants. The strategy employed to produce these proteins was to 'engineer-out' the carboxyl-terminal transmembrane domain of the native protein so that following synthesis and processing, the Fet3p species produced was secreted from

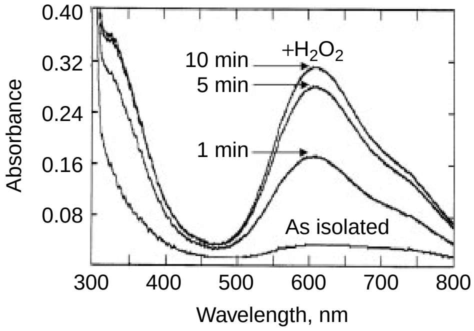

Figure 27 T2D Fet3p is fully reduced when isolated but readily reoxidizes with H_2O_2 indicating that Cu(I) is the valence of Cu trafficked to apoprotein

the cell into the growth medium; from there it was easily purified.[76] As for all MCOs, solutions (at $>100\,\mu M$) and crystals of the secreted Fet3p are azure-blue. In contrast, Fet3p forms that have oxidation-inert trinuclear clusters are colorless. These include Fet3pT2D, for example. In the protein secreted from the cell, the type 1 copper is present as Cu(I), and because electrons flow from the type 1 to the type 3 binuclear Cu pair, this cluster is also stably reduced. All three Cu are stably reduced because, lacking the type 2 Cu to supply the critical O_2-cleaving electron (in going from the peroxide to the native intermediate, Figure 11), this reduced protein cannot turn over. The reduced sites can be oxidized by peroxide or other oxidants, demonstrating, after this reaction, that these remaining sites are otherwise 'wild type'. This story is illustrated by the spectra in Figure 27. This result indicates that copper is inserted into the *apo*-Fet3p as Cu(I). This inference is fully consistent with the overall model of copper uptake and trafficking that has evolved from the study of the transporter, copper chaperone, and copper pump involved, Ctr1p, Atx1p, and Ccc2p, respectively (in yeast).[56] All three copper processing proteins handle Cu(I) in a series of transfer reactions, that, in the case of the transfer from Atx1p to Ccc2p, is a nondissociative, ligand-exchange process in which the Cu(I) does not equilibrate with bulk solvent.[56,67] The nonblue, Fet3pT2D that is secreted from the yeast cell is the end-product of this cuprous ion trafficking pathway (*see* ***Metallochaperones & Metal Ion Homeostasis***).

5 BACTERIAL OXIDASES, COPPER RESISTANCE, AND METALLO-OXIDATION

5.1 The PcoA/CueO Protein Family

Free-living organisms tend to be highly adaptable to relatively precipitous changes in their environments. In bacteria, this adaptation is often due to the acquisition of episomally encoded enzymatic activities; penicillin resistance due to β-lactamase inhibitors is a well-known example. Resistance to metal ions that at some level of exposure are toxic is another, albeit less well advertised one. In *E. coli*, this resistance is due in part to the *pco* metabolic pathway encoded on plasmid pRJ1004[77] while in *Pseudomonas syringae* the homologous *cop* system is encoded on plasmid pPT23D.[78] Among the enzymes found in this pathway is an MCO that in *E. coli* is known as the PcoA protein; an homologous CopA protein is found in *P. syringae* (not to be confused with the chromosomally encoded CopA Cu-ATPase in *E. coli*). Although the spectral and chemical properties of these proteins have not been determined, they are suggested to act to both sequester copper [perhaps as Cu(I)] and catalyze the oxidation of Cu(I) to Cu(II).[23,78,79]

Their metallo-oxidase activity is inferred from two facts. First, the bacterial chromosome also encodes an MCO that has been linked to copper resistance, also. In *E. coli*, this is the CueO protein (previously YacK), but similar MCOs have been identified in all bacterial genomes archived, including that of *Pseudomonas aeruginosa*. That these proteins are MCOs is indicated by their oxidase activity (e.g. towards aromatic phenols and amines), and, in the case of CueO, by extensive biophysical studies including X-ray crystallography.[23,80] The second fact is that PcoA can partially complement the absence of CueO in regards to the copper sensitivity of a Δ*cueO Pseudomonas* mutant strain indicating that PcoA exhibits CueO-like activity.[78] What this physiological activity is, however, has not been directly demonstrated. The hypothesis is that these proteins act as cuprous oxidases, reducing the steady-state level of the redox-active, Cu(I), a known pro-oxidant. There are no enzymatic activity data with either enzyme that support this hypothesis; their correlation with bacterial copper resistance is the only observation that does. However, one aspect of the structure of CueO that is consistent with a role in Cu(I) binding, at least, is the presence of a Met-rich region that is absent in the 'classic' MCO. This motif, that roughly starts at the beginning of the third cupredoxin domain, is shown below in its entirety although there is no evidence that this whole element is required for function.

$^{355}\underline{\mathrm{M}}\mathrm{DPML}\underline{\mathrm{D}}$ MMGMQMLMEK YGDQAMAGMD
HSQMMGHMGH GNMNHM^{396}

However, an equivalent Met-rich sequence is found in tens of bacterial PcoA homologues indicating that whatever this motif's function, it could be highly conserved. A related Met-rich sequence is found in the much smaller PcoC protein that a variety of spectral studies have shown binds Cu(I)[81] and Cu(II).[82]

This region is illustrated in Figure 28 that gives several views of the structure of CueO.[23,80] The significant difference in the structure of CueO in comparison to that of AO or Lac, for example, is the helix that 'covers' access to the

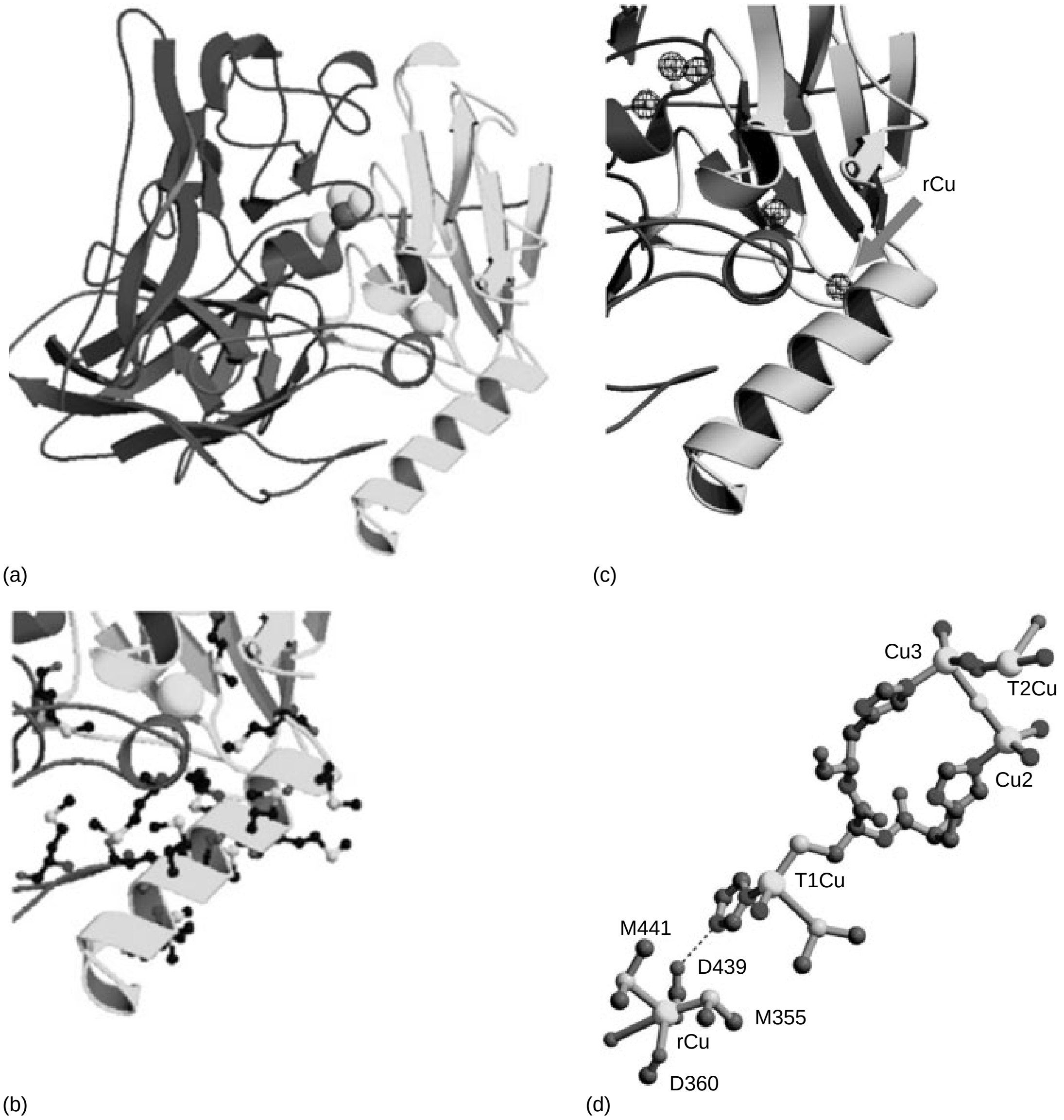

Figure 28 Views of the Met-rich, Cu-binding site adjacent to the T1 copper in CueO (S. A. Roberts, A. Weichsel, G. Grass, K. Thakali, J. T. Hazzard, G. Tollin, C. Rensing, and W. R. Montfort, Proc. Natl. Acad. Sci. USA, 2002, 99, 2766–2771. © 2002 National Academy of Sciences, USA)

T1 site (Figure 28a). An expanded view of this Met-rich helix is shown in Figure 28(b). Although copper binding to this region in CueO has not been demonstrated spectrally (e.g. by EXAFS), a 'labile' copper is observed bound in CueO crystals soaked with $CuCl_2$. The difference Fourier that identifies this Cu is shown in Figure 28(c). The binding of this Cu(II) (precisely, the redox state of the copper atom is not known, however) is specific, involving ligation to two Met thioether S atoms, and two Asp carboxylates. One of these carboxylates appears H-bonded to the (noncoordinating) NHε2 of H443 at the type 1 Cu site in CueO. This H-bonding network is shown in Figure 28(d); it provides an attractive electronic matrix coupling pathway for electron transfer into the type 1 Cu(II) although that analysis has not been reported. Note that only two of the four ligands to this labile Cu come from the Met-rich motif noted above – M355 and D360 (highlighted) – and neither of these residues is actually in the helix that restricts solvent exposure of the type 1 site (Figure 28). Furthermore, the other two ligands come from a ^{438}GDMM^{441} motif that is part of a subsequent strand of β-sheet. In other words, the structural genomics of the bacterial MCOs and their relationship to the structure-function relationships in other copper-handling proteins remain to be fully elucidated.

However, cupric ion does stimulate the oxidase activity of CueO with a kinetic K_M for this dissociable Cu(II) of 0.16 mM.**[78]** Structure-activity studies on CueO mutants confirm that this activation is likely due to Cu(II) binding at the Met-rich region. Substitution at any one of the Cu-binding residues seen in the structure (Figure 28d) increased the Cu(II) K_M; most striking are the 10- and 500-fold increases seen in the D360A and M355L mutants, respectively.**[80]** While these studies clearly demonstrate Cu-binding to this region in CueO – and likely, therefore, to the same region in the other 'Met-rich' homologues – and demonstrate the catalytic activation associated with this Cu-binding, they do not resolve the question of the physiological substrate specificity and function of these bacterial MCOs. There is some evidence that these MCOs may target phenolic siderophores such as enterobactin,**[83]** although the physiological outcome of that reaction remains obscure.

On the other hand, the *P. aeroginosa* MCO exhibits a molecular activity (k_{cat}) with Fe^{2+} as substrate of $\sim 10\,\mathrm{min}^{-1}$, similar to the rate measured for Fet3p. In addition, deletion of the gene encoding this MCO reduced bacterial iron uptake by ca. 70%. The data suggest that this MCO is involved in iron uptake via its ferroxidase activity much as Fet3p functions in yeast. In contrast to data reported in *E. coli*, the *P. aeruginosa* MCO was not required for copper resistance.**[84]** Indeed, CueO does have an activity towards Fe^{2+} that is comparable to its oxidase activity,**[83]** so it and the other bacterial MCOs could be involved in iron acquisition as well. The significance of this possibility is the known correlation between iron availability and bacterial pathogenicity.**[85]** The bacterial MCO could be a critical element in this correlation. Clearly, the role of bacterial MCOs in the metabolism of copper and iron remains to be fully understood.

5.2 MCOs As Metallo-oxidases: Metabolism and Resistance

However, there is evidence that MCOs do have oxidase activity towards low-valent metal ions other than Fe^{2+}, specifically, Mn^{2+} and Cu^{1+}. Furthermore, this activity does correlate with a specific aspect of metal metabolism. In the case of phylogenetically distinct bacteria, an MCO with Mn^{2+} oxidase activity is likely involved in the remarkable resistance bacterial spores have towards environmental insults. The mnxG protein in the spore coat of *Bacillus* strains and the cumA protein in the plasma membrane of *Pseudomonas* strains oxidize environmental Mn^{2+} to form $Mn^{III/IV}$ oxides that precipitate on the cell surface, eventually encrusting the organism. This oxidation has been demonstrated histochemically (e.g. formation of the brown Mn oxides on bacterial colonies on plates or associated with MCO protein bands in acrylamide gels) but the proteins have not been characterized in vitro. However, one curious aspect of the *Bacillus* mnxG protein (but not the *Pseudomonas* cumA one) is that the cupredoxin domains are in the 'order' 2-3-1. If the chain-fold in mnxG is equivalent to that found in the 'normal' MCO, this sequence (shown below) places the trinuclear cluster between the 2nd and 3rd cupredoxin domains (rather than the 1st and 3rd ones) and the overall relationship between the copper clusters would be the mirror image of that illustrated in the several MCO structures above. The MCO from *Nitrosomonas europaea* (which, in addition, appears to have six cupredoxin domains) has a similar 'inverted' domain structure;**[13]** both sequences are illustrated below.

mnxG protein	*Nitrosomonas europaea* MCO
^{281}HVFHYH	^{451}HVFHLH
^{334}HCHLYPH	^{521}HCHLYPH
^{528}HIH	^{877}HIH
^{574}HDH	^{998}HDH

The Fox1 protein from the blue-green algae, *Chlamydomonas reinhardtii*, a plant homologue of the Fet3p ferroxidase involved in iron uptake, has a similarly inverted domain pattern (*cf* Figure 4).**[86]** None of these 'unusual' MCOs have been chemically characterized.

Although the cuprous oxidase activity proposed for the bacterial copper resistance MCOs has not been demonstrated (above), it has been for the yeast ferroxidase, Fet3p, and for the human ferroxidase, hCp.**[87]** The cuprous oxidase and ferroxidase activities of the two enzymes are comparable with K_M values for Cu^{1+} as substrate $\sim 35\,\mu M$ in comparison to the $\sim 5\,\mu M$ value with Fe^{2+} as substrate. The k_{cat} values with the two substrates are nearly the same. In yeast, this cuprous oxidase activity does correlate with copper resistance. For example, yeast deficient in Fet3p are two- to threefold more sensitive to copper added to the medium as Cu^{2+}. This sensitivity is suppressed if the plasma membrane metalloreductase, Fre1p, is also absent indicating that the toxic species is Cu^{1+}. The protection towards copper afforded by Fet3p is likely to be the maintenance of a low steady-state concentration of Cu^{1+} at the plasma membrane due to the enzyme's cuprous oxidase activity. hCp reasonably plays a similar role in mammalian cell copper homeostasis, although this inference has not been experimentally tested. Putting metal ion speciation aside, one might assume that any metal with a reduction potential low enough to provide an adequate driving force for the reduction of the type 1 Cu(II) – for most MCOs this would be $<400\,\mathrm{mV}$ or so – would support MCO-catalyzed O_2 turnover. This would include Fe^{2+} and Cu^{1+} in many ligand environments, as well as Mn^{2+}. The question then becomes what other Marcus factors serve as 'specificity' elements in the substrate selectivity exhibited by an MCO. In the end, MCO substrate specificity centers on the same questions about the origin of efficient electron transfer that have engaged bioinorganic chemists for the past two decades.

6 RELATED ARTICLES

Copper: Hemocyanin/Tyrosinase Models; Copper Proteins with Dinuclear Active Sites; Copper Proteins with Type 1 Sites; Copper Proteins with Type 2 Sites; Cytochrome Oxidase; Electron Transfer Reactions: Theory; Long-range Electron Transfer in Biology; Metal Ion Toxicity; Metal-related Diseases of Genetic Origin; Metallochaperones & Metal Ion Homeostasis; Nutritional Aspects of Metals & Trace Elements.

7 REFERENCES

1. E. I. Solomon, U. M. Sundaram, and T. E. Machonkin, *Chem. Rev.*, 1996, **96**, 2563.
2. E. I. Solomon, P. Chen, M. Metz, S. K. Lee, and A. E. Palmer, *Angew. Chem., Int. Ed. Engl.*, 2001, **40**, 4570.
3. E. I. Solomon, R. K. Szilagyi, S. D. George, and L. Basumallick, *Chem. Rev.*, 2004, **104**, 419.
4. R. K. Szilagyi and E. I. Solomon, *Curr. Opin. Chem. Biol.*, 2002, **6**, 250.
5. S. Ferguson-Miller and G. T. Babcock, *Chem. Rev.*, 1996, **96**, 2889.
6. D. R. McMillin, C. Peyratout, and C. Miller, Copper Proteins: Oxidases, in ‘Encyclopedia of Inorganic Chemistry’, ed. R. B. King, John Wiley & Sons, New York, 1994, p. 869.
7. F. Xu, W. Shin, S. H. Brown, J. A. Wahleithner, U. M. Sundaram, and E. I. Solomon, *Biochim. Biophys. Acta*, 1996, **1292**, 303.
8. F. Xu, R. M. Berka, J. A. Wahleithner, B. A. Nelson, J. R. Shuster, S. H. Brown, A. E. Palmer, and E. I. Solomon, *Biochem. J.*, 1998, **334**, 63.
9. F. Xu, A. E. Palmer, D. S. Yaver, R. M. Berka, G. A. Gambetta, S. H. Brown, and E. I. Solomon, *J. Biol. Chem.*, 1999, **274**, 12372.
10. E. I. Solomon, K. W. Penfield, A. A. Gewirth, M. D. Lowery, S. E. Shadle, J. A. Guckert, and L. B. LaCroix, *Inorg. Chem. Acta*, 1996, **243**, 67.
11. C. A. Francis, K. L. Casciotti, and B. M. Tebo, *Arch. Microbiol.*, 2002, **178**, 450.
12. C. A. Francis and B. M. Tebo, *Appl. Environ. Microbiol.*, 2002, **68**, 874.
13. P. Chain, J. Lamerdin, F. Larimer, W. Regala, V. Lao, M. Land, L. Hauser, A. Hooper, M. Klotz, J. Norton, L. Sayavedra-Soto, D. Arciero, N. Hommes, M. Whittaker, and D. Arp, *J. Bacteriol.*, 2003, **185**, 2759.
14. C. A. Francis and B. M. Tebo, *Appl. Environ. Microbiol.*, 2001, **67**, 4272.
15. G. J. Brouwers, J. P. de Vrind, P. L. Corstjens, P. Cornelis, C. Baysse, and E. W. de Vrind-de Jong, *Appl. Environ. Microbiol.*, 1999, **65**, 1762.
16. D. W. Randall, D. R. Gamelin, L. B. LaCroix, and E. I. Solomon, *J. Biol. Inorg. Chem.*, 2000, **5**, 16.
17. A. E. Palmer, D. W. Randall, X. Feng, and E. I. Solomon, *J. Am. Chem. Soc.*, 1999, **121**, 7138.
18. A. Messerschmidt, R. Ladenstein, R. Huber, M. Bolognesi, L. Avigliano, R. Petruzzelli, A. Rossi, and A. Finazzi-Agró, *J. Mol. Biol.*, 1992, **224**, 179.
19. A. Messerschimidt, H. Luecke, and R. Huber, *J. Mol. Biol.*, 1993, **230**, 997.
20. T. Bertrand, C. Jolivalt, P. Briozzo, E. Caminade, N. Joly, C. Madzak, and C. Mougin, *Biochemistry*, 2002, **41**, 7325.
21. K. Piontek, M. Antorini, and T. Choinowski, *J. Biol. Chem.*, 2002, **277**, 37663.
22. F. J. Enguita, L. O. Martins, A. O. Henriques, and M. A. Carrondo, *J. Biol. Chem.*, 2003, **278**, 19416.
23. S. A. Roberts, A. Weichsel, G. Grass, K. Thakali, J. T. Hazzard, G. Tollin, C. Rensing, and W. R. Montfort, *Proc. Natl. Acad. Sci. U.S.A.*, 2002, **99**, 2766.
24. I. Zaitseva, V. Zaitsev, G. Card, K. Moshkov, B. Bax, A. Ralph, and P. Lindley, *J. Biol. Inorg. Chem.*, 1996, **1**, 15.
25. N. J. Blackburn, M. Ralle, R. Hassett, and D. J. Kosman, *Biochemistry*, 2000, **39**, 2316.
26. A. Bateman, E. Birney, L. Cerruti, R. Durbin, L. Etwiller, S. R. Eddy, S. Griffiths-Jones, K. L. Howe, M. Marshall, and E. L. Sonnhammer, *Nucleic Acids Res.*, 2002, **30**, 276.
27. S. Yamanaka, H. Okawa, K. Motoda. Ki, M. Yonemura, D. E. Fenton, M. Ebadi, and A. B. Lever, *Inorg. Chem.*, 1999, **38**, 1825.
28. W. Z. Lee and W. B. Tolman, *Inorg. Chem.*, 2002, **41**, 5656.
29. A. Mukherjee, I. Rudra, S. G. Naik, S. Ramasesha, M. Nethaji, and A. R. Chakravarty, *Inorg. Chem.*, 2003, **42**, 5660.
30. V. Ducros, A. M. Brzozowski, K. S. Wilson, S. H. Brown, P. Ostergaard, P. Schneider, D. S. Yaver, A. H. Pedersen, and G. J. Davies, *Nat. Struct. Biol.*, 1998, **5**, 310.
31. V. Ducros, A. M. Brzozowski, K. S. Wilson, P. Ostergaard, P. Schneider, A. Svendson, and G. J. Davies, *Acta Crystallogr. D Biol. Crystallogr.*, 2001, **57**, 333.
32. N. Hakulinen, L. L. Kiiskinen, K. Kruus, M. Saloheimo, A. Paananen, A. Koivula, and J. Rouvinen, *Nat. Struct. Biol.*, 2002, **9**, 601.
33. M. E. Murphy, P. F. Lindley, and E. T. Adman, *Protein Sci.*, 1997, **6**, 761.
34. K. Nakamura, T. Kawabata, K. Yura, and N. Go, *FEBS Lett.*, 2003, **553**, 239.
35. W. Shin, U. M. Sundaram, J. L. Cole, H. H. Zhang, B. Hedman, K. O. Hodgson, and E. I. Solomon, *J. Am. Chem. Soc.*, 1996, **118**, 3202.
36. U. M. Sundaram, H. H. Zhang, B. Hedman, K. O. Hodgson, and E. I. Solomon, *J. Am. Chem. Soc.*, 1997, **119**, 12525.

37. A. E. Palmer, S. K. Lee, and E. I. Solomon, *J. Am. Chem. Soc.*, 2001, **123**, 6591.
38. S. K. Lee, S. D. George, W. E. Antholine, B. Hedman, K. O. Hodgson, and E. I. Solomon, *J. Am. Chem. Soc.*, 2002, **124**, 6180.
39. G. B. Koudelka, F. B. Hansen, and M. J. Ettinger, *J. Biol. Chem.*, 1985, **260**, 15561.
40. S. Chakravarty and R. Orbach, *Phys. Rev. Lett.*, 1990, **64**, 224.
41. C. Pignocchi, J. M. Fletcher, J. E. Wilkinson, J. D. Barnes, and C. H. Foyer, *Plant Physiol.*, 2003, **132**, 1631.
42. M. Sanmartin, P. A. Drogoudi, T. Lyons, I. Pateraki, J. Barnes, and A. K. Kanellis, *Planta*, 2003, **216**, 918.
43. A. Messerschmidt, W. Steigemann, R. Huber, G. Lang, and P. M. H. Kroneck, *Eur. J. Biochem.*, 1992, **209**, 597.
44. I. Gromov, A. Marchesini, O. Farver, I. Pecht, and D. Goldfarb, *Eur. J. Biochem.*, 1999, **266**, 820.
45. M. E. Lahey, M. S. Gubler, G. E. Chase, G. E. Cartwright, and M. M. Wintrobe, *Blood*, 1952, **7**, 1053.
46. G. R. Lee, S. Nacht, J. N. Lukens, and G. E. Cartwright, *J. Clin. Invest.*, 1968, **47**, 2058.
47. E. Frieden and S. Osaki, *Adv. Exp. Med. Biol.*, 1974, **48**, 235.
48. E. Frieden and H. S. Hsieh, *Adv. Exp. Med. Biol.*, 1976, **74**, 505.
49. M. V. Chidambaram, G. Barnes, and E. Frieden, *FEBS Lett.*, 1983, **159**, 137.
50. S. Osaki, D. A. Johnson, and E. Frieden, *J. Biol. Chem.*, 1966, **241**, 2746.
51. J. Sarkar, V. Seshadri, N. A. Tripoulas, M. E. Ketterer, and P. L. Fox, *J. Biol. Chem.*, 2003, **278**, 44018.
52. N. E. Hellman and J. D. Gitlin, *Annu. Rev. Nutr.*, 2002, **22**, 439.
53. D. J. Kosman, Fet3p, Ceruloplasmin, and the Role of Copper in Iron Metabolism, in ‘Advances in Protein Chemistry’, eds. J. S. Valentine and E. Gralla, Elsevier, New York, 2002, p. 221.
54. D. J. Kosman, *Mol. Microbiol.*, 2003, **47**, 1185.
55. C. D. Vulpe, Y. M. Kuo, T. L. Murphy, L. Cowley, C. Askwith, N. Libina, J. Gitschier, and G. J. Anderson, *Nat. Genet.*, 1999, **21**, 195.
56. D. L. Huffman and T. V. O’Halloran, *Annu. Rev. Biochem.*, 2001, **70**, 677.
57. E. D. Harris, *Annu. Rev. Nutr.*, 2000, **20**, 291.
58. T. E. Machonkin, H. H. Zhang, B. Hedman, K. O. Hodgson, and E. I. Solomon, *Biochemistry*, 1998, **37**, 9570.
59. P. F. Lindley, G. Card, I. Zaitseva, V. Zaitsev, B. Reinhammar, E. Selin-Lindgren, and K. Yoshida, *J. Biol. Inorg. Chem.*, 1997, **2**, 454.
60. T. E. Machonkin and E. I. Solomon, *J. Am. Chem. Soc.*, 2000, **122**, 12547.
61. J. N. Onuchic, D. N. Beratan, J. R. Winkler, and H. B. Gray, *Annu. Rev. Biophys. Biomol. Struct.*, 1992, **21**, 349.
62. B. N. Patel, R. J. Dunn, and S. David, *J. Biol. Chem.*, 2000, **275**, 4305.
63. D. M. Frazer, C. D. Vulpe, A. T. McKie, S. J. Wilins, D. Trinder, G. J. Cleghorn, and G. J. Anderson, *Am. J. Physiol.*, 2001, **281**, G931.
64. B. N. Patel, R. J. Dunn, S. Y. Jeong, Q. Zhu, J.-P. Julien, and S. David, *J. Neurosci.*, 2002, **22**, 6578.
65. A. T. McKie, G. O. Latunde-Dada, S. Miret, J. A. McGregor, G. J. Anderson, C. D. Vulpe, J. M. Wrigglesworth, and R. J. Simpson, *Biochem. Soc. Trans.*, 2002, **30**, 722.
66. S. Miret, R. J. Simpson, and A. T. McKie, *Annu. Rev. Nutr.*, 2003, **23**, 283.
67. A. C. Rosenzweig, *Acc. Chem. Res.*, 2001, **34**, 119.
68. K. S. Anderson, *Methods Enzymol.*, 1999, **308**, 111.
69. T. E. Machonkin, L. Quintanar, A. E. Palmer, R. Hassett, S. Severance, D. J. Kosman, and E. I. Solomon, *J. Am. Chem. Soc.*, 2001, **123**, 5507.
70. M. A. Brown, L. M. Stenberg, and A. G. Mauk, *FEBS Lett.*, 2002, **520**, 8.
71. M. C. Bonaccorsi di Patti, M. R. Felice, A. P. Camuti, A. Lania, and G. Musci, *FEBS Lett.*, 2000, **472**, 283.
72. T.-P. Wang, L. Quintanar, S. Severance, E. I. Solomon, and D. J. Kosman, *J. Biol. Inorg. Chem.*, 2003, **8**, 611.
73. L. Quintanar, G. Gebhard, T.-P. Wang, D. J. Kosman, and E. I. Solomon, *J. Am. Chem. Soc.*, 2004, **126**, 6579.
74. E. I. Solomon, T. C. Brunold, M. I. Davis, J. N. Kemsley, S.-K. Lee, N. Lehnert, F. Neese, A. J. Skulan, Y.-S. Yang, and J. Zhou, *Chem. Rev.*, 2000, **100**, 235.
75. A. E. Palmer, L. Quintanar, S. Severance, T. P. Wang, D. J. Kosman, and E. I. Solomon, *Biochemistry*, 2002, **41**, 6438.
76. R. F. Hassett, D. S. Yuan, and D. J. Kosman, *J. Biol. Chem.*, 1998, **273**, 23274.
77. N. L. Brown, S. R. Barrett, J. Camakaris, B. T. Lee, and D. A. Rouch, *Mol. Microbiol.*, 1995, **17**, 1153.
78. S. M. Lee, G. Grass, C. Rensing, S. R. Barrett, C. J. Yates, J. V. Stoyanov, and N. L. Brown, *Biochem. Biophys. Res. Commun.*, 2002, **295**, 616.
79. F. W. Outten, D. L. Huffman, J. A. Hale, and T. V. O’Halloran, *J. Biol. Chem.*, 2001, **276**, 30670.
80. S. A. Roberts, G. F. Wildner, G. Grass, A. Weichsel, A. Ambrus, C. Rensing, and W. R. Montfort, *J. Biol. Chem.*, 2003, **278**, 31958.
81. K. Peariso, D. L. Huffman, J. E. Penner-Hahn, and T. V. O’Halloran, *J. Am. Chem. Soc.*, 2003, **125**, 342.
82. D. L. Huffman, J. Huyett, F. W. Outten, P. E. Doan, L. A. Finney, B. M. Hoffman, and T. V. O’Halloran, *Biochemistry*, 2002, **41**, 10046.
83. C. Kim, W. W. Lorenz, J. T. Hoopes, and J. F. Dean, *J. Bacteriol.*, 2001, **183**, 4866.

84. W. M. Huston, M. P. Jennings, and A. G. McEwan, *Mol. Microbiol.*, 2002, **45**, 1741.

85. C. Ratledge and L. G. Dover, *Annu. Rev. Microbiol.*, 2000, **54**, 881.

86. S. La. Fontaine, J. M. Quinn, S. S. Nakamoto, M. D. Page, V. Gohre, J. L. Moseley, J. Kropat, and S. Merchant, *Eukaryot. Cell*, 2002, **1**, 736.

87. C. Stoj and D. J. Kosman, *FEBS Lett.*, 2003, **554**, 422.

Copper Proteins with Type 1 Sites

P. John Hart,[1] Aram. M. Nersissian[2] & Serena DeBeer George[3]

[1]University of Texas, Health Science Center, San Antonio, TX, USA
[2]Occidental College, Los Angeles, CA, USA
[3]Stanford University, Stanford, CA, USA

Based in part on the article Copper Proteins with Type 1 Sites by Edward N. Baker which appeared in the Encyclopedia of Inorganic Chemistry, First Edition.

1 Introduction 1
2 Occurrence, Classification, and Biological Roles 2
3 Structural Biology and Bonding 5
4 Spectroscopy and Electronic Structure 15
5 Correlations to Function 19
6 Related Articles 23
7 References 24

Glossary

β-barrel: a roughly cylindrical arrangement of strands in a protein
Resolution (in Å): the minimum interplanar spacing of reflections used in single-crystal diffraction analyses

Abbreviations

P. aer. = *Pseudomonas aeruginosa*; *A. den.* = *Alcaligenes denitrificans*; MCD = magnetic circular dichroism; EPR = electron paramagnetic resonance; XAS = X-ray absorption spectroscopy; NMR = nuclear magnetic resonance; EXAFS = extended X-ray absorption fine structure.

1 INTRODUCTION

Type 1 or 'blue' copper proteins were among the first to be isolated and as such, they have played a long-standing and distinguished role in the development of bioinorganic chemistry. Proteins of the type 1 class are defined as containing a copper-binding site with the following properties: (1) an intense blue color in the Cu(II) oxidation state which results from a strong visible absorption near 600 nm; (2) a small hyperfine coupling constant in the EPR (electron paramagnetic resonance) spectrum, and (3) a relatively high redox potential when compared with values found for 'typical' copper complexes. The unique characteristics of type 1 copper proteins have also been a major driving force in the development of the 'entatic' or 'rack' concept in metalloproteins[1,2] (reviewed in,[3–5] *see* ***Long-range Electron Transfer in Biology***), which states that the blue copper coordination is not dictated by the presence of the metal ion *per se*, but is instead predetermined by the energetic constraints of the polypeptide that forces a geometry that effectively accommodates both Cu(I) and Cu(II) coordination states. This coordination geometry is believed to confer distinct functional advantages, particularly in long-range electron-transfer processes. Given the above, it is not surprising that extensive chemical and physical approaches have been directed toward a comprehensive understanding of the properties of the type 1 copper site over the last 35 years.

Type 1 copper sites are found in both small, single copper-containing proteins as well as in larger, multicopper-containing proteins. The latter, in addition to their blue copper sites, contain other copper atoms with different characteristics that leads to the classification of their sites as type 1, type 2, or type 3[6,7] (*see* ***Copper Proteins with Type 2 Sites***; ***Copper Proteins with Dinuclear Active Sites***; ***Copper Proteins: Oxidases***). This general review will focus primarily on the small, single polypeptide blue copper proteins that contain only type 1 copper. Their simplicity and small size have made them amenable to structural analyses as well as attractive targets for mutagenesis studies. Because they also serve as models for the blue copper sites found in the more complex multicopper proteins, the spectroscopic properties of the type 1 sites will on occasion be compared to those found in nitrite reductase or laccase. The first part of this review provides an inventory of the occurrence, distribution, and classification of blue copper proteins based on analyses of genomic and expressed sequence tag data. The second part provides information on the overall architecture of these proteins as well as an inventory of the three-dimensional structures of blue copper proteins as determined by X-ray crystallography and nuclear magnetic resonance (NMR) spectroscopy. The last part discusses the electronic, spectroscopic, and electron-transfer properties of these proteins.

A number of excellent reviews on this subject are available. Some are general, covering biological, chemical, and physical aspects[8–16] while others concentrate on structure,[17] spectroscopy,[18,19] or electron transfer.[20,21] A short, very readable review by Gray and colleagues[5] is particularly recommended to the general reader.

2 OCCURRENCE, CLASSIFICATION, AND BIOLOGICAL ROLES

2.1 Overview

Blue copper proteins have been purified and biochemically characterized from *Archaea*, *Bacteria*, and *Eukarya*. Such ubiquitous distribution suggests an important ancient role. A survey of sequence databases reveals genes encoding blue copper proteins that display characteristics often quite different from those of well-studied canonical (traditional) blue copper proteins. For example, there are modular proteins where the domains that bind type 1 copper are fused with structurally distinct and evolutionarily unrelated sequence motifs (Figure 1). While these additional domains do not usually contribute directly to the function of a blue copper protein, they do so indirectly by facilitating protein translocation to a specific cellular compartment. Together, these blue copper proteins can be combined into a large superfamily which can be subdivided into three classes as described below.

Proteins of the first class are composed of only a single type 1 copper-binding domain in their mature form. They are known as cupredoxins after the suggestion by Adman that they function analogously to the iron-containing ferredoxins.[12] These include plastocyanin, azurin, pseudoazurin, amicyanin, auracyanin, rusticyanin, halocyanin, and sulfocyanin. The second class includes multidomain blue copper proteins, which are composed exclusively of two (nitrite reductases), three (laccases and ascorbate oxidase), or six (ceruloplasmin and hephaestin) domains. The proteins of the third class display a mosaic/chimeric domain organization in which the blue copper domains are fused with structurally unrelated sequence motifs. These include plant stellacyanins, uclacyanins, and dicyanins. The proteins in the first and third classes are the focus of this review. The proteins in the second class are discussed elsewhere (*see* ***Copper Proteins: Oxidases***).

2.2 Copper-binding Site and Sequence Characteristics

The copper ion is bound to the protein via imidazole nitrogens from two His residues and a thiolate from a Cys residue, which form a pseudotrigonal plane. These three equatorial ligands are found in all naturally occurring type 1 sites. In most cases, a fourth ligand coordinates the copper ion in an axial position, pulling it out of the pseudotrigonal plane. The nature of this axial interaction is partially responsible for the subtle differences in the electronic structure of blue copper sites and for the tuning of their redox potentials, which range from +165 mV to +800 mV (see Section 5.1). The vast majority of blue copper sites have a weakly coordinated thioether from a Met residue or more rarely, a strongly coordinated oxygen from a Gln side chain. However, amino acid sequence alignments indicate that in some instances the protein does not provide any ligating residue at the axial position. In these cases, the noncoordinating amino acid is a Leu, Phe, Ile or Val.

Three of the four copper ligands, His, Cys, and the axial ligand, are located together at the C-terminus in the copper-binding loop (Figures 1 and 3). The fourth ligand, also His, is approximately 40-amino acids N-terminal of this triad. The length (determined by the number of amino acids separating ligating residues) and the composition of the copper-binding loop are important indications for the phylogenetic relationships between blue copper proteins (see Section 3.5.3).

2.3 Subcellular Localization and Function

All type 1 copper proteins, with the exception of plastocyanin, possess an ∼20-amino acid N-terminal signal peptide (Figure 1). These peptides help the proteins translocate

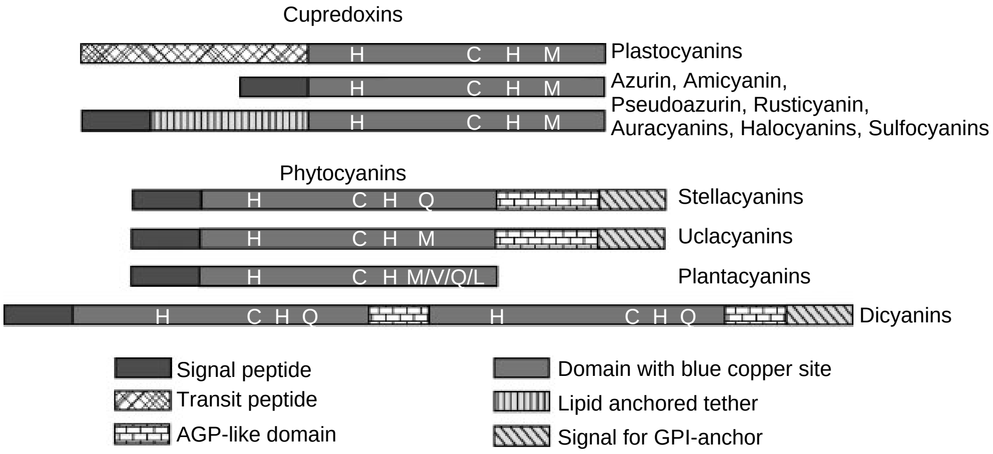

Figure 1 Domain organization of the precursors of type 1 copper proteins in the cupredoxin and phytocyanin families. Positions of copper ligands are indicated by single letter codes

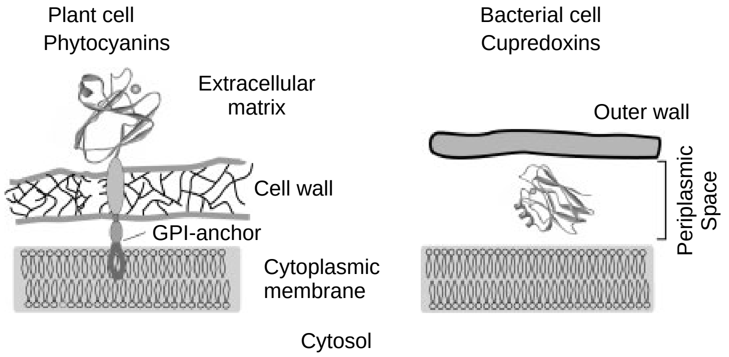

Figure 2 Localization of phytocyanins and cupredoxins in plants and bacteria

across the bacterial cytoplasmic membrane into the periplasmic space (Figure 2). In eukaryotes, the signal peptides target blue copper proteins to the endoplasmic reticulum where they enter the secretory pathway that subsequently directs them into the extracellular milieu. Plant plastocyanins are targeted to the chloroplast. Although most cupredoxins are freely diffusible, some of them are attached to the cell surface via an N-terminal lipid modified anchor. Those with an additional C-terminal hydrophobic sequence (a signal for covalent modification with a glycosylphosphatidylinositol, GPI, moiety) are also anchored to the cell surface (Figure 2).

Not surprisingly, the proteins harboring type 1 copper sites are involved in a diverse array of vital cellular processes. They are crucial components of (1) the electron-transfer chains used in bacterial energy conversion; (2) the photosynthetic apparatus in plants, cyanobacteria, and algae; and (3) the plant-defense response against attacking pathogens.

2.4 Cupredoxins

Cupredoxins are found primarily in *Bacteria* and in *Archaea*. None have been identified in vertebrates, nematodes, insects or unicellular eukaryotes, but they do exist in plants. Where their function has been established, they act as freely diffusible electron-shuttle proteins in a variety of electron-transfer chains for energy conversion.

2.4.1 Plastocyanin

Plastocyanins are the most widely studied cupredoxins. They are one of the most abundant copper proteins in plant photosynthetic tissues.[22] Plant plastocyanins have an intricate evolutionary history because of their ancient bacterial origin. It is currently well accepted that plants diverged from the main eukaryotic domain into a separate lineage when the unicellular, oxygen respiring common ancestor of the eukaryotes incorporated a prokaryotic endosymbiont, the cyanobacterial chloroplast.

Plant plastocyanins are synthesized in the cytosol as 160–170-amino acid precursor polypeptides consisting of a 60–70-residue transit peptide followed by a 97–99-amino acid mature protein.[23] The transit peptide imports the precursor plastocyanin molecule across the chloroplast envelope and thylakoid membranes to its final destination in the thylakoid lumen, where it shuttles electrons by accepting them from the membrane bound cytochrome f (cyt f) of the cyt $b6/f$ complex and donating them to the photooxidized reaction center P700+ of photosystem I. Cyanobacterial plastocyanins use an ~30-amino acid leader sequence for thylakoid membrane translocation. Currently, there are more than 100 plant and cyanobacterial plastocyanin sequences that are available either by direct protein sequencing or deduced from the nucleotide sequences of their genes.

2.4.2 Azurin

The amino acid sequence of azurin from *Pseudomonas fluorescens* was reported in 1964,[24] one of only a few dozen protein sequences available in the mid-1960s. Currently, more than thirty sequences of azurins are available. The azurin gene was one of the first cupredoxins to be cloned in 1987,[25] which led to the generation of mutant proteins. This made azurin an attractive model system for redesigning blue copper sites[15] and the information gained from these mutagenesis studies has had a significant impact on our understanding of many of their properties. Azurin has also been extensively applied as a useful model protein for characterizing long-range electron-transfer processes within a polypeptide matrix.[21] The redox partners of azurin remain largely unknown, although it has been implicated in anaerobic nitrite respiration.

2.4.3 Pseudoazurin and Amicyanin

Pseudoazurins are found in bacteria which under limited oxygen conditions are capable of using nitrate/nitrite as an energy source. They are key components of the electron-transfer chain that sequentially reduces NO_3^-/NO_2^- to molecular nitrogen. Pseudoazurin donates electrons to another blue copper protein, nitrite reductase. However, the biological electron donor of pseudoazurin has not yet been identified.

Amicyanin is found in methylotrophic bacteria that can use methylated amines as an energy source. The inactivation of the amicyanin gene in *Paracoccus denitrificans* results in complete loss of its ability to grow on methylamine,[26] a direct indication that amicyanin is a key component of the methylamine driven electron-transfer chain. Amicyanin accepts an electron from methylamine dehydrogenase and transfers it to a *c*-type cytochrome (see Section 5.4.5). Currently, more than a dozen amicyanin and pseudoazurin sequences are available.

2.4.4 *Rusticyanin*

Rusticyanin is found in *Thiobacillus ferrooxidans*, an acidophilic, chemolithotrophic sulfur bacterium utilizing Fe^{2+} and reduced sulfur compounds as its sole energy source.[27] *T. ferrooxidans* does not produce rusticyanin when grown on reduced sulfur. Similar to other substrate-inducible cupredoxins, the rusticyanin gene is activated when soluble iron is present in the media. Little is known about its redox partners and it should be noted that rusticyanin itself does not carry out Fe^{2+} oxidation. Other iron-oxidizing bacteria, for example, *Leptospirillum ferrooxidans*, produce a cytochrome which substitutes rusticyanin functionally. To date *T. ferrooxidans* remains the only source for rusticyanin.

2.4.5 *Halocyanin and Sulfocyanin*

Halocyanin and sulfocyanin are archaebacterial cupredoxins that are attached to peripheral membranes through a lipid anchor at their N-terminus. Halocyanin was the first cupredoxin purified from an archaeon, haloalkaliphilic *Natronobacterium pharaonis*.[28] These cells live in high pH (around 10–11) and in extreme salinity (30%) environments. The presence of the blue copper protein, sulfocyanin in *Sulfolobus acidocaldarius* was first predicted from its gene sequence.[29] It has been subsequently purified as a recombinant protein and shown to bind a single copper ion with spectroscopic properties typical for a blue copper site.[30]

The sequences of halocyanin and sulfocyanin, deduced from their gene sequences, have unusually long N-terminal extensions. These extensions feature a hydrophobic signal peptide which is followed by a segment that in the case of halocyanin has an Asn-Gly doublet occurring consecutively seven times.[31] In sulfocyanin, this segment is rich in Ser residues. It is believed that these extensions are covalently modified by a lipid moiety which anchors the proteins to the cell membrane.

The function of these proteins is not known. The sulfocyanin gene is positioned in the same operon with the components of the respiratory electron-transfer chain, and it therefore has been implicated as a direct electron donor for the Cu_A-containing terminal oxidase.[32]

2.4.6 *Auracyanin*

Two distinct cupredoxins labeled auracyanin A and B have been characterized from the gliding thermophilic photosynthetic bacterium *Chloroflexus aurantiacus*,[33] which is only distantly related to other photosynthetic organisms and appears to have acquired its photosynthetic capabilities by lateral gene transfer. The two forms of auracyanin are distinctly different from each other with respect to their amino acid sequences and the spectroscopic properties of their blue copper sites. In addition, auracyanin B is glycosylated while auracyanin A is not.

Like halocyanin and sulfocyanin, auracyanin B has an N-terminal extension that is thought to anchor the protein to the cell membrane. In contrast to those proteins, however, this extension is rich in Pro, Ala, and Thr residues. In auracyanin A, they are Gly residues.[34]

Numerous other putative members of the cupredoxin family can be identified in the GenBank database (http://www.ncbi.nlm.nih.gov). Many of these sequences display remote similarities to other cupredoxins and they therefore cannot be attributed to any of the above described traditional groups.

2.5 Phytocyanins

Phytocyanins are plant-specific proteins distinctly different from plastocyanins, azurins, and other cupredoxins of archaeal and bacterial origin with respect to sequence, structure, and function. Phytocyanins constitute one of the largest gene families in plants. For example, rice and *Arabidopsis thaliana* house, respectively, 57 and 39 distinct phytocyanin genes. More than 300 full-length sequences of phytocyanin precursors deduced from either genomic DNA or cDNA are currently available. Phytocyanins are further classified into three subfamilies: stellacyanins, plantacyanins, and uclacyanins.[16] This classification is based (1) on their spectroscopic properties, (2) on precursor as well as mature protein domain organization, and (3) on identity or availability of residues that are involved in blue copper binding.

With the exception of the plantacyanins, phytocyanins are chimeric proteins in their mature forms. They are composed of two structurally distinct sequence motifs, a 100–109-amino acid blue copper domain followed by a domain that varies in length between 30–220 amino acids, lacks any obvious consensus sequence, but resembles heavily glycosylated arabinogalactan proteins (AGP). Where such AGP domains are present, they are followed by a hydrophobic sequence predicted to provide a signal for the attachment of a GPI moiety, which anchors the protein to the cell surface (Figure 2). This cell-surface attachment of phytocyanins via a GPI anchor has been demonstrated experimentally.[35] Intriguingly, stellacyanin, umecyanin, and mavicyanin have also been purified from plant tissues as soluble proteins, indicating that phytocyanins may be freed from their GPI anchors and released into the extracellular matrix.

2.5.1 Stellacyanins and Uclacyanins

Stellacyanin from the Japanese lacquer tree *Rhus vernicifera* was one of the first blue copper proteins to be described in the literature.[36] Because of its unusual spectroscopic and sequence characteristics, it has been the subject of thorough biochemical and biophysical studies. *R. vernicifera* stellacyanin possesses a Gln residue at the position of the axial Met found in all other blue copper proteins known at that time.[37] Proteins displaying spectroscopic properties similar to those of *R. vernicifera* stellacyanin have been subsequently purified from horseradish (umecyanin),[38] zucchini (mavicyanin),[39] cucumber,[40] and spinach.[41] Their sequences also feature a Gln residue at the position of the axial ligand (Figure 1). In contrast, uclacyanins have a Met residue, which is one of the main features that differentiate them from stellacyanins. Stellacyanins and uclacyanins display identical domain organization, where in their mature form they consist of both copper-binding domain and an AGP-like domain. Both subfamilies have GPI-anchoring signals in their precursors and carry several N-linked glycosylation sites in their copper-binding domains through Asn residues, as well as numerous O-linked glycosylation sites in their AGP-like domains through hydroxyproline, Ser, and Thr residues. There are five different stellacyanin genes in *Arabidopsis*, while rice has only three. In contrast, the rice genome contains twenty-one uclacyanin genes. *Arabidopsis* has eight, one of which (UCC1), has been expressed and purified from *Escherichia coli* and is the only uclacyanin for which the copper-binding abilities and spectroscopic properties have been reported.[16]

2.5.2 Plantacyanin

First isolated from cucumber in 1974,[42] plantacyanins have since been characterized from various other plant species. They are single-domain proteins in their mature form and neither an AGP-like domain nor a GPI-anchoring signal are found in their precursors (Figure 1). Most plantacyanins are strongly basic proteins with an isoelectric point around 10. However, there are examples displaying neutral or extremely negative surface charge characteristics with isoelectric points ranging between 4.5 and 8. Plantacyanins demonstrate relatively high-sequence identity and similar spectroscopic properties to stellacyanins, although they generally utilize a Met residue as the axial ligand. There are several exceptions where plantacyanins have Gln, Leu, or Val residues at this position. For instance, tomato plantacyanin has a Val (see Section 3.5.2). Such diversity in isoelectric points and ligand environment in plantacyanin subfamily has been previously documented for multicopper oxidase laccases. Although plantacyanins have been purified from cucumber and spinach as nonglycosylated proteins, there are some examples with a single N-linked glycosylation site.

Plantacyanin is represented in the *Arabidopsis* genome by a single gene, while rice has nine. Multiple plantacyanin sequences can also be identified in plant species such as wheat, barley, and maize. Spinach plantacyanin is 91-amino acids long and is perhaps the smallest blue copper protein known.

Domains with high-sequence identity to phytocyanins are also found in a recently identified novel class of blue copper proteins in which two such domains are fused together into a single polypeptide. One of them, dicyanin, was identified in tomato and is composed of two stellacyanin-like domains, both of which feature a blue copper-binding site with two $(His)_2$,(Cys)(Gln) ligand sets (Figure 1). These fused domains display 45–60% sequence identity with each other as well as with stellacyanins. Similar to the known mature stellacyanin sequences, both domains are followed by a 35-amino acid AGP-like domain. The dicyanin precursor harbors an N-terminal signal peptide and contains an additional C-terminal GPI-anchoring signal, suggesting that these proteins follow the same posttranslational secretory pathway as the phytocyanins.

It is also important to note that plants house a large group of phytocyanin-related proteins (22 and 24 in *Arabidopsis* and rice, respectively) that have extensive sequence identity and identical domain architecture to the stellacyanins and uclacyanins but lack the copper-ligating amino acid residues that are crucial for the formation of the type 1 copper site.[16] These copper-free proteins, known as early nodulins, share a common ancestor with metazoan ephrins, which are involved in multiple aspects of embryonal development.[43,44]

3 STRUCTURAL BIOLOGY AND BONDING

3.1 Historical Development

Although proteins containing type 1 copper-binding sites were first discovered in the early 1960s, the three-dimensional structures of these molecules remained unknown until 1978 when the structures of both plastocyanin and azurin were first determined using single-crystal X-ray diffraction methods.[45,46] In the interim, however, multiple spectroscopic approaches were employed in an effort to delineate the nature and determinants of the blue copper site.[45,47] The intense visible absorption at ~600 nm and narrow EPR hyperfine splitting suggested a distorted tetrahedral geometry, but the exact identity of the ligand set remained somewhat controversial. Evidence suggested there was likely a highly polarizable ligand, probably the thiolate sulfur of a Cys residue. Mercurials (which are known to be thiol-specific reagents) were shown to prevent the binding of

Cu(II) to apo-plastocyanin and subsequent metal-substitution experiments strongly suggested that the ~600-nm band in the visible spectrum comes from an $S_{thiolate} \rightarrow Cu(II)$ charge-transfer.[48,49] In addition, NMR proton exchange studies by Markley and colleagues on both copper-bound and copper-free (apo) forms of spinach plastocyanin strongly suggested the presence of two His (imidazole) ligands.[50] By the time the plastocyanin and azurin crystal structures appeared, it had become generally accepted that the type 1 copper-binding site consisted of a distorted tetrahedral arrangement of two His ligands and one Cys ligand [$(His)_2Cys$], plus an unknown fourth ligand which might be Met. The fact that sequence analysis of all plastocyanins and azurins revealed a single conserved Met along with one conserved Cys and two conserved His further supported this view.[51]

3.2 Three-dimensional Structural Analyses

At this writing, the three-dimensional structures of eight different naturally occurring type 1 copper proteins are known. These include the cupredoxins plastocyanin at 1.33 Å resolution (pdb code 1PLC), azurin at 1.8 Å (pdb code 2AZA), pseudoazurin at 1.55 Å (pdb code 1PAZ), amicyanin at 1.3 Å (pdb code 1AAC), auracyanin at 1.55 Å (pdb code 1QHQ), rusticyanin at 1.9 Å (pdb code 1RCY), and the phytocyanins cucumber basic protein at 1.8 Å (pdb code 2CBP), and stellacyanin at 1.6 Å (pdb code 1JER) Atomic coordinates for these and all other single-domain type 1 copper proteins are available from the Research Collaboratory for Structural Bioinformatics (RCSB) Protein Data Bank (PDB) and can be accessed online at www.rcsb.org/pdb/.

A keyword search will provide access to coordinate sets from all species that are currently available as well as various site-directed mutants, type 1 copper proteins substituted with metals other than copper, and ruthenated blue copper protein derivatives. Table 1 provides a summary (with references) of the structures of blue copper-binding domains elucidated using X-ray crystallography and NMR spectroscopy.

The crystal structures of these native proteins have been refined to high resolution by macromolecular standards. They remain, however, far from the atomic resolution limits of small-molecule crystal structures. Even so, there have now been enough independent structure analyses to establish the error level in the crystallographic analyses reasonably well. Guss *et al*. were particularly attentive to the question of accuracy in their analyses of various plastocyanin structures. The error in the 1.33 Å oxidized poplar plastocyanin is estimated, from comparison of models, as 0.1 Å in atomic positions, 0.04 Å in copper–ligand bond lengths, and 2.5° in copper-bond angles.[57] Comparison of poplar and algal plastocyanin indicates an error in the latter of 0.15 Å in atomic positions and 0.07 Å in copper–ligand bond lengths.[54] With regard to azurin, both *Alcaligenes denitrificans* (*A. den.)* and *Pseudomonas aeruginosa* (*P. aer*.) crystal structures have multiple copies of the azurin molecule in the asymmetric unit. This allows comparisons of these independent copies and the derivation of an error level of 0.1–0.15 Å in atomic positions generally, 0.05–0.07 Å in copper–ligand bond lengths, and 3–5° in copper-bond angles.[77,89,103]

3.3 General Structural Organization

The type 1 copper proteins discussed here are small, single polypeptide chains of 91–155 residues. They all possess a similar topological architecture that has been described as a Greek key β-barrel or β-sandwich. The barrel or sandwich is normally composed of eight parallel or antiparallel β-strands which are divided into two β-sheets (Figure 3). Amicyanin and auracyanin have β-barrels comprised of nine β-strands, while the rusticyanin β-barrel has thirteen β-strands. The β-sheets in all structures come together to bury apolar residues at the heart of the sandwich. This simple, stable structural module has been adopted and modified by a variety of other proteins including the multicopper oxidases, ascorbate oxidase, laccase, ceruloplasmin, and Fet3p (*see* ***Copper Proteins: Oxidases***) as well as proteins that do not bind type 1 copper, including immunoglobulin variable domain and copper-zinc superoxide dismutase (*see* ***Copper Proteins with Type 2 Sites***).

Although the β-barrel structure is common to all type 1 copper proteins whose structures have been determined to date (Figure 4), the regularity of the strands, the extent of hydrogen bonding between them, and the lengths of the loops that connect them vary from one protein to another. These structural variations, together with amino acid sequence differences and the presence (or absence) of various extensions to the blue copper-binding domain, differentiate the various proteins (see Section 2 above).

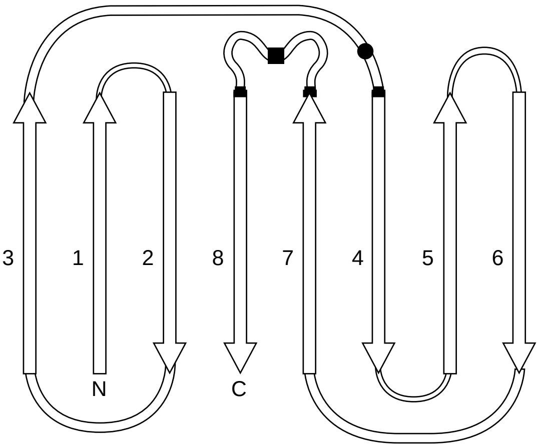

Figure 3 Topology diagram showing the connectivity of the eight extended polypeptide strands which make up the β-barrel in type 1 copper proteins. The locations of the common copper ligands and the carbonyl oxygen in azurin are shown as filled circles and squares

Table 1 Structures of type 1 copper proteins

Protein	Source	Meth	Oxi.	Å	PDB	Ref.
Plastocyanin	*C. reinhardtii*	X-ray	CuII	1.50	2PLT	52
Plastocyanin	*D. crassirhizoma*	X-ray	CuI	1.80	1KDI	53
Plastocyanin	*D. crassirhizoma*	X-ray	CuII	1.70	1KDJ	53
Plastocyanin	*E. prolifera*	X-ray	CuII	1.80	7PCY	54
Plastocyanin	*P. laminosum*	X-ray	CuII	2.80	1BAW	55
Plastocyanin 21–25 Disulfide Bridge	*P. nigra*	X-ray	CuI	1.60	1JXG	56
Plastocyanin pH 6.0	*P. nigra*	X-ray	CuII	1.33	1PLC	57
Plastocyanin 173 °K	*P. nigra*	X-ray	CuII	1.60	1PNC	58
Plastocyanin 173 °K	*P. nigra*	X-ray	CuII	1.60	1PND	58
Plastocyanin pH 6.0	*P. nigra*	X-ray	Apo	1.80	2PCY	59
Plastocyanin	*P. nigra*	X-ray	HgII	1.90	3PCY	60
Plastocyanin pH 7.8 Cross-Linked w/Gluteraldehyde	*P. nigra*	X-ray	CuI	2.15	4PCY	61
Plastocyanin pH 7.0	*P. nigra*	X-ray	CuI	1.80	5PCY	61
Plastocyanin pH 3.8	*P. nigra*	X-ray	CuI	1.90	6PCY	61
Plastocyanin G8D	*S. oleracea*	X-ray	CuII	1.70	1AG6	62
Plastocyanin G8D/L12E	*S. oleracea*	X-ray	CuII	2.00	1OOW	63
Plastocyanin	*S. pratensis*	X-ray	CuII	2.00	1BYO	64
Plastocyanin E43K/D44K	*S. pratensis*	X-ray	CuII	1.75	1BYP	65
Plastocyanin	*Synechococcus* sp.	X-ray	CuII	1.90	1BXU	65
Plastocyanin	*Synechococcus* sp.	X-ray	CuI	1.80	1BXV	65
Plastocyanin A42D/D47P/A63L	*Synechocystis* PCC6803	X-ray	CuII	2.15	1PCS	66
Plastocyanin	*U. pertusa*	X-ray	CuII	1.60	1IUZ	67
Plastocyanin	*A. variabilis*	NMR	CuII		1FA4	68
Plastocyanin	*A. variabilis*	NMR	?		1NIN	69
Plastocyanin	*P. crispum*	NMR	CuI		1PLA	70
Plastocyanin	*P. crispum*	NMR	CuI		1PLB	70
Plastocyanin T2S	*P. hollandica*	NMR	CuI		1B3I	71
Plastocyanin T2S	*P. hollandica*	NMR	CuI		2B3I	71
Plastocyanin	*P. vulgaris*	NMR	CuI		9PCY	72
Plastocyanin	*S. obliquus*	NMR	?		Unavail	73
Plastocyanin	*Synechocystis* sp. Pcc6803	NMR	CuII		1J5C	74
Plastocyanin	*Synechocystis* sp. Pcc6803	NMR	CuII		1J5D	74
Plastocyanin	*Synechocystis* sp. Pcc6803	NMR	CuI		1JXD	75
Plastocyanin	*Synechocystis* sp. Pcc6803	NMR	CuI		1JXF	75
Azurin M121H, pH 6.5, 16 °C	*A. den.*	X-ray	CuII	1.89	1A4A	76
Azurin M121H, pH 6.5, −180 °C	*A. den.*	X-ray	CuII	1.91	1A4B	76
Azurin M121H, pH 3.5, −180 °C	*A. den.*	X-ray	CuII	2.45	1A4C	76
Azurin	*A. den.*	X-ray	CuII	1.80	2AZA	77
Azurin II	*A. xylosoxidans*	X-ray	CuII	1.75	1DYZ	78
Azurin II	*A. xylosoxidans*	X-ray	CuI	1.75	1DZ0	79
Azurin I	*A. xylosoxidans*	X-ray	CuII	2.45	1RKR	79
Azurin	*A. xylosoxydans*	X-ray	Apo	1.80	1AIZ	80
Azurin	*A. xylosoxydans*	X-ray	Apo	2.20	1AZB	80
Azurin	*A. xylosoxydans*	X-ray	Apo	1.80	1AZC	80
Azurin M121Q	*A. xylosoxydans*	X-ray	CuII	1.94	1URI	81
Azurin Isomer-2	*Methylomonas* sp. J	X-ray	CuII	1.60	1CUO	82
Azurin C113D	*P. aer.*	X-ray	CuII	2.40	1AG0	83
Azurin F114A	*P. aer.*	X-ray	CuII	2.60	1AZN	84
Azurin N47D	*P. aer.*	X-ray	CuII	2.40	1AZR	85
Azurin	*P. aer.*	X-ray	CuII	2.70	1AZU	86
Azurin	*P. aer.*	X-ray	CuII	2.30	1BEX	87
Azurin 113–118 TFPGHS to SELCGINH	*P. aer.*	X-ray	CuII	1.65	1CC3	88
Azurin pH 5.5	*P. aer.*	X-ray	CuII	2.00	1E5Y	89
Azurin pH 9.0	*P. aer.*	X-ray	CuII	2.00	1E5Z	89
Azurin	*P. aer.*	X-ray	Apo	1.85	1E65	90
Azurin	*P. aer.*	X-ray	Zn	2.14	1E67	91
Azurin M121E	*P. aer.*	X-ray	CuII	2.30	1ETJ	92
Azurin C3A/C26A	*P. aer.*	X-ray	CuII	2.00	1EZL	93
Azurin C3S/S100P	*P. aer.*	X-ray	CuII	1.80	1GR7	94
Azurin Q107H	*P. aer.*	X-ray	CuII	1.80	1I53	95

(cont’d overleaf)

Table 1 cont’d

Protein	Source	Meth	Oxi.	Å	PDB	Ref.
Azurin I7S/P110S.	*P. aer.*	X-ray	CuII	2.20	1ILS	96
Azurin I7S/P110S	*P. aer.*	X-ray	CuII	2.30	1ILU	96
Azurin Dimer	*P. aer.*	X-ray	CuII	2.00	1JVL	97
Azurin Dimer	*P. aer.*	X-ray	CuII	2.75	1JVO	97
Azurin Ru(Bpy)2(Im) (His83)	*P. aer.*	X-ray	CuII	1.60	1JZE	98
Azurin Ru(Tpy) (Phen) (His83)	*P. aer.*	X-ray	CuII	1.50	1JZF	98
Azurin Ru(Tpy) (Phen) (His83)	*P. aer.*	X-ray	CuI	1.40	1JZG	98
Azurin Ru(Tpy) (Phen) (His83)	*P. aer.*	X-ray	CuII	1.70	1JZH	98
Azurin Re(Phen) (Co)3(His83)	*P. aer.*	X-ray	CuII	1.62	1JZI	99
Azurin Os(Bpy)2(Im) (His83)	*P. aer.*	X-ray	CuII	1.80	1JZJ	98
Azurin W48M	*P. aer.*	X-ray	NiII	2.20	1NZR	100
Azurin Re(Phen) (CO)3(His107) W48F/Y72F/ H83Q/Y108W	*P. aer.*	X-ray	CuI	1.90	1R1C	101
Azurin	*P. aer.*	X-ray	CoII	1.90	1VLX	102
Azurin H35Q/H35L	*P. aer.*	X-ray	CuII	1.90	2AZU	103
Azurin M121A	*P. aer.*	X-ray	CuII	2.20	2TSA	104
Azurin M121A-Azide	*P. aer.*	X-ray	CuII	2.30	2TSB	104
Azurin H35Q/H35L	*P. aer.*	X-ray	CuII	2.10	3AZU	103
Azurin pH 5.5	*P. aer.*	X-ray	CuII	1.90	4AZU	89
Azurin pH 9.0	*P. aer.*	X-ray	CuII	1.90	5AZU	89
Azurin	*P. fluorescens*	X-ray	CuII	2.05	1JOI	105
Azurin	*P. putida*	X-ray	CuII	1.92	1NOW	106
Azurin	*P. putida*	X-ray	CuII	1.60	1NWP	106
Pseudoazurin	*A. cycloclastes*	X-ray	CuII	1.35	1BQK	107
Pseudoazurin	*A. cycloclastes*	X-ray	CuI	1.60	1BQR	107
Pseudoazurin	*A. cycloclastes*	X-ray	CuII	1.54	1ZIA	108
Pseudoazurin	*A. cycloclastes*	X-ray	CuI	2.00	1ZIB	108
Pseudoazurin	*A. faecalis*	X-ray	CuII	1.55	1PAZ	109
Pseudoazurin pH 7.8	*A. faecalis*	X-ray	CuI	1.80	1PZA	110
Pseudoazurin pH 4.4	*A. faecalis*	X-ray	CuII	1.80	1PZB	110
Pseudoazurin	*A. faecalis*	X-ray	Apo	1.85	1PZC	110
Pseudoazurin	*A. faecalis*	X-ray	CuI	1.73	3PAZ	111
Pseudoazurin P80A	*A. faecalis*	X-ray	CuII	1.76	4PAZ	111
Pseudoazurin P80A	*A. faecalis*	X-ray	CuI	1.76	5PAZ	111
Pseudoazurin P80I	*A. faecalis*	X-ray	CuII	1.91	6PAZ	111
Pseudoazurin P80I	*A. faecalis*	X-ray	CuI	2.00	7PAZ	111
Pseudoazurin	*A. faecalis*	X-ray	CuII	1.60	8PAZ	111
Pseudoazurin pH 6.8	*M. extorquens*	X-ray	CuII	1.50	1PMY	112
Pseudoazurin	*P. denitrificans*	X-ray	CuII	2.50	1ADW	n/a
Amicyanin	*P. denitrificans*	X-ray	CuII	1.31	1AAC	113
Amicyanin	*P. denitrificans*	X-ray	Apo	1.80	1AAJ	113
Amicyanin	*P. denitrificans*	X-ray	CuII	2.00	1AAN	113
Amicyanin complex	*P. denitrificans*	X-ray	CuII	2.50	1MDA	114
Amicyanin complex	*P. denitrificans*	X-ray	CuII	2.25	1MG2	115
Amicyanin complex	*P. denitrificans*	X-ray	CuII	2.40	1MG3	116
Amicyanin complex	*P. denitrificans*	X-ray	CuII	2.40	2MTA	116
Amicyanin pH 4.4	*P. denitrificans*	X-ray	CuI	1.30	1BXA	113
Amicyanin pH 7.7	*P. denitrificans*	X-ray	CuI	1.30	2RAC	114
Amicyanin	*P. versutus*	X-ray	CuII	2.15	1ID2	117
Plantacyanin	*S. oleracea*	X-ray	CuI	2.05	1F56	118
Cucumber Basic Protein	*C. sativus*	X-ray	CuII	1.80	2CBP	119
Stellacyanin, pH 7.0	*C. sativus*	X-ray	CuII	1.60	1JER	120
Auracyanin	*C. aurantiacus*	X-ray	CuII	1.55	1QHQ	121
Auracyanin B	*C. aurantiacus*	X-ray	CuII	1.90	1OV8	122
Rusticyanin	*T. ferrooxidans*	X-ray	CuI	1.90	1A3Z	123
Rusticyanin	*T. ferrooxidans*	X-ray	CuI	2.10	1A8Z	124
Rusticyanin	*T. ferrooxidans*	X-ray	CuII	1.50	1E30	125
Rusticyanin S86D/M148L	*T. ferrooxidans*	X-ray	CuII	1.65	1GY1	126
Rusticyanin M148L	*T. ferrooxidans*	X-ray	CuII	1.82	1GY2	126
Rusticyanin	*T. ferrooxidans*	X-ray	CuII	1.90	1RCY	123
Rusticyanin	*T. ferrooxidans*	NMR	CuI		1CUR	127

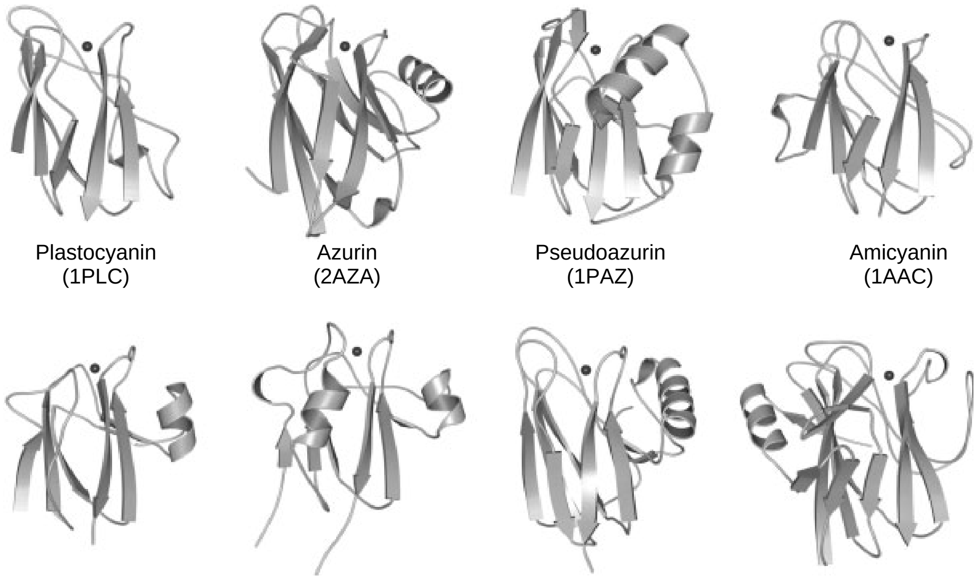
Plastocyanin (1PLC)
Azurin (2AZA)
Pseudoazurin (1PAZ)
Amicyanin (1AAC)
Cucumber Basic Protein (Plantacyanin) (2CBP)
Stellacyanin (1 JER)
Auracyanin (1QHQ)
Rusticyanin (1RCY)

Figure 4 Polypeptide folding for eight type 1 copper proteins. In each case, the copper lies between loops at the ‘northern’ end of the β-barrel

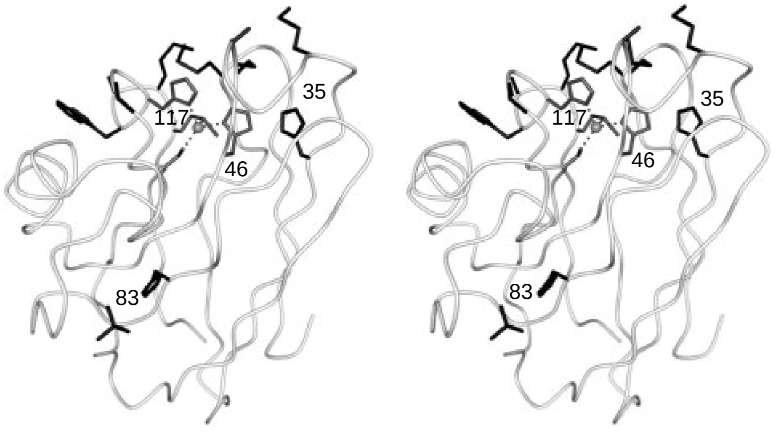

Figure 5 Stereo image of *A. den.* azurin showing (thick lines) the side chains of the hydrophobic patch (top), the His ligands 46 and 117, the conserved nonligating His residues, 35 and 83, and the bound SO_4^{2-} ion

Following the convention of Freeman and colleagues first used in the description of plastocyanin, the copper-binding site is said to be located at the ‘northern’ end of the molecule. Figure 4 shows that the copper ion is bound in a cavity formed by the loop elements that connect the β-strands. These loop elements and their hydrogen-bonding patterns are conserved across the family and they also provide the amino acid side chains that act as ligands to the copper ion (Figure 3). The extensive hydrogen bonding and copper–ligand interactions tend to make the northern end the most rigid part of the molecule.[77]

A feature that appears to be common to several of the proteins is a hydrophobic surface patch at the northern end (Figure 5), comprising some 5–10 apolar amino acid side chains which surround the exposed edge of one of the two copper-bound His ligands. In many other respects, however, the surfaces of the proteins are highly variable which probably reflects differing specificity in the recognition of electron-transfer partners in the different organisms.

3.4 Polypeptide Chain Variations

Plastocyanin (97–105 residues) represents the nearly minimal structural module for binding type 1 copper. The N-terminus is at the beginning of strand 1 of the barrel and the

C-terminus is at the end of strand 8. Seven of the eight strands are extended in a β-conformation (the other, strand 5, is less regular with several kinks and one α-helical turn and does not participate in the β-sheet hydrogen bonding), and the loops between strands are all relatively short.

Azurin (128–129 residues) has a more regular β-barrel than plastocyanin. All eight of the strands are extended and incorporated in the β-sheet hydrogen bonding.[77] Relative to plastocyanin, however, azurin has approximately 30 extra residues which are accommodated in two regions, the loops joining strands 3 and 4 and strands 4 and 5. The 3–4 loop is at the 'northern' end of the molecule, to one side of the copper site. The expansion of this loop by ~5 residues contributes to the somewhat more buried copper site in azurin and is probably responsible for the closer approach of a peptide carbonyl oxygen to the copper (see Section 3.5.2). The 4–5 loop in azurin contains ~15 extra amino acids compared with that in plastocyanin which creates an extra 'flap' on the azurin surface, made up of a three-turn α-helix and a series of tight turns. This 'flap' is an appendage on the surface of the barrel. It does not disturb the β-sheet structure or the copper site although it does help create a slightly larger hydrophobic patch at the northern end of the protein and it covers a region which forms an acidic patch in plastocyanin (see Section 5.4.3).

Pseudoazurin (123–124 residues) closely resembles plastocyanin in many respects. It has a minimal β-barrel with short connecting loops. Strand 5 contains fewer residues than the equivalent strand in plastocyanin, however, as it has a regular, extended β-structure without the extra kinks and loops of plastocyanin. The major difference is the presence of an extra 25 residues at the C-terminal end of the polypeptide chain; these form two α-helices which pack on the surface of the β-barrel in a location adjacent to but structurally distinct from the 'flap' in azurin.

The structure of amicyanin (99–106 residues) also more closely resembles that of plastocyanin than azurin as shown by both sequence comparisons[128] and the crystal-structure data.[113,115] It has short connecting loops and no 'flap'. Strand 5 is shorter and more regular than that in plastocyanin. Amicyanin, however, has an extension at the N-terminal end of the polypeptide chain (rather than the C-terminus as in pseudoazurin); the extra ~20 amino acids form a ninth β-strand which extends the β-barrel by hydrogen bonding to the exposed edge of one of the two β-sheets (i.e. to strand 6 in Figure 3).

Plantacyanins, such as cucumber basic protein (96 residues) and the plantacyanins from spinach (91 residues) and tomato (95 residues), have a somewhat less regular β-barrel, but with no external appendages. Part of strand 1 and all of strand 2 have irregular conformations with kinks and turns, and strands 4 and 5 are twisted out from the general orientation of the β-barrel; thus the structure, although it consists of eight strands, more closely resembles two 3-strand β-sheets packed together. This twisted barrel conformation is stabilized by a disulfide bond at the northern end of the molecule between Cys residues of the 4–5 and 7–8 loops. The presence of this disulfide bond is one of the factors that distinguishes phytocyanins from other blue copper proteins.

Cucumber stellacyanin (110 residues in soluble form) is much more similar to plantacyanins than any of the other blue copper proteins described above. It possesses a 5-residue insertion that creates a larger 1–2 loop as well as a two-turn α-helix that is absent in CBP. Unlike the soluble blue copper-binding domains described above, however, mature cucumber stellacyanin contains a C-terminal AGP-like domain that may help the protein to be integrated into the cell wall. TheN- and C-terminii are both longer than those found in plantacyanins like CBP (Figure 4). Thus, its function may be different than those freely diffusible proteins thought to be involved in long-range electron-transfer reactions.

Auracyanin (140 residues) is much more similar to azurin structurally than the other blue copper proteins except that it has an additional N-terminal β-strand that hydrogen bonds to strand 6, giving the barrel a total of nine strands. The positions of the 'flaps' are also similar in azurin and auracyanin, although the position of the α-helix differs slightly.

Rusticyanin (155 residues) has a similar topology to azurin except that the core of the molecule is a β-sandwich of two mixed β-sheets, one of six and one of seven strands. Rusticyanin contains a substantial N-terminal extension relative to azurin that includes a β-strand followed by an α-helix followed by two β-strands that are connected by a β-hairpin. Thus, the fourth β-strand in rusticyanin corresponds to the first in azurin. The 'flap' in rusticyanin is in a structurally analogous position to that in azurin, except that it does not contain an α-helix.

3.5 The Type 1 Copper Site

High-resolution crystallographic studies of type 1 copper proteins supplemented by EXAFS (extended X-ray absorption fine structure) data and analyses of sequence conservation show that the archetypal type 1 copper site has certain constant features. There exist several excellent reviews.[16,17,19] For reference, the copper sites in plastocyanin, azurin, tomato plantacyanin, and cucumber stellacyanin are shown in Figure 6.

3.5.1 The Basic Trigonal N_2S^- Ligand Set

The copper atom is coordinated to three equatorial ligands, two imidazole nitrogens and one thiolate sulfur, in an approximate trigonal planar arrangement. Bond lengths are 1.9–2.2 Å (Table 2A) and bond angles irregular, ranging from ~97° to 138° (Table 2B). The three ligands are His 37, Cys 84, and His 87 in poplar plastocyanin; His 46, Cys 112, and His 117 in *P. aer*. azurin; His 39, Cys 79, and His 84 in tomato plantacyanin; and His 46, Cys 89, and His 94 in cucumber stellacyanin (Figure 6). The same equatorial N_2S^- ligand set is found in all type 1 copper proteins characterized

Table 2 Type 1 copper site geometry

Protein	PC	AZ	PAZ	AMI	CBP	CST	AUR	RST
pdb code	1PLC	1JZF	1PAZ	1AAC	2CBP	2JER	1QHQ	1RCY
Resolution (Å)	1.33	1.5	1.55	1.31	1.80	1.20	1.55	1.90
A. Copper–ligand bond distances (Å)[a]								
Cu–N_1	1.91	2.02	2.16	1.95	1.93	2.05	2.02	2.04
Cu–N_2	2.06	2.08	2.12	2.03	1.95	2.01	2.03	1.89
Cu–S_1	2.07	2.21	2.16	2.11	2.16	2.18	2.19	2.26
Cu–S_2	2.82	3.32	2.76	2.90	2.61		2.84	2.88
Cu–O		2.60						
Cu–Gln						2.36		
B. Bond angles around copper (deg.)								
S_1–Cu–N_1	132	132	136	136	138	133	137	128
S_1–Cu–N_2	121	123	112	112	110	121	117	119
N_1–Cu–N_2	97	105	100	104	99	99	101	105
S_2–Cu–N_1	89	72	87	85	83		80	85
S_2–Cu–N_2	101	85	112	100	112		105	106
S_2–Cu–S_1	110	110	108	111	111		106	105
Gln–Cu–N_1						93		
Gln–Cu–N_2						96		
Gln–Cu–S_1						106		
O–Cu–N_1		80						
O–Cu–N_2		92						
O–Cu–S_1		97						
O–Cu–S_2		150						

[a] Ligands identified as in Figure 6.

to date. The geometry is highly conserved. The Cu–N bond lengths at ~2.0 Å are normal for imidazole ligands, but the Cu–S(thiolate) bond is short, at 2.07–2.26 Å. This short Cu–S bond is a key feature of the blue copper site. The bond angles within the pseudotrigonal plane average 101°, 117°, and 134° in the eight oxidized structures (plastocyanin, azurin, pseudoazurin, amicyanin, cucumber basic protein, cucumber stellacyanin, auracyanin, and rusticyanin), determined at resolutions better than 2.0 Å, with rms deviations of 2.5°, 4.1°, and 2.8°. The thiolate sulfur geometry is also highly conserved; the Cu–Sγ–Cβ–Cα and Sγ–Cβ–Cα–N dihedral angles are always near 180°, so that the Cu–Sγ bond is coplanar with the Cys side chain atoms and part of the polypeptide backbone.[129]

3.5.2 Axial Interactions

In addition to the equatorial ligating interactions, longer axial interactions with the copper are made by other groups which can vary among different type 1 copper proteins. In poplar plastocyanin, Met 92 provides a fourth ligand, through its thioether sulfur, although at a much longer distance (2.82 Å) than the other three ligands. It thus completes an N_2SS^- ligand set with a distorted tetrahedral or trigonal pyramidal geometry, in which the copper atom is displaced 0.36 Å from the N_2S^- plane towards the thioether S ligand (Figure 6a). (Note that the displacement in a regular tetrahedron would be ~0.7 Å.).

In *P. aer.* azurin there are two long axial approaches, one from the thioether sulfur of Met 121, equivalent to Met 92 in poplar plastocyanin, and the other from the peptide carbonyl oxygen of Gly 45 (Figure 6b). Their distances from the copper are 3.3 and 2.6 Å, respectively. In this Cu–O interaction, the oxygen is buried in a nonpolar environment with no other possible partner for polar interactions and the geometry is right for interaction with an oxygen lone pair.[77] Thus, the azurin geometry may best be described as distorted trigonal bipyramidal. The copper accordingly lies almost directly in the trigonal N_2S^- plane.

Cucumber basic protein, amicyanin, auracyanin, and rusticyanin more closely resemble plastocyanin than azurin in their copper sites. The axial Cu–S(Met) distances are all similar to that seen in plastocyanin (CBP has the shortest Cu–S(Met) distance at ~2.6 Å); the copper atom is displaced ~0.2–0.4 Å out of the N_2S^- plane towards the S(Met) ligand, giving a distorted tetrahedral or trigonal pyramidal geometry, and the carbonyl oxygen equivalent to that in azurin is much farther away (~3.8 Å). The lack of a Cu–O interaction in these proteins and in plastocyanin may result from a shortened 3–4 loop. Tomato plantacyanin contains a Val residue at the axial ligand position and thus possesses only the N_2S^- ligand set (Figure 6c).

Stellacyanin contains no Met and before its structure was known, it was speculated that sulfur from a disulfide bond binds to copper in place of the Met ligand.[130] Sequence alignments (Figure 1), model building based on the highly homologous cucumber basic protein structure, and physicochemical arguments all suggested, however, that the amide group of a Gln side chain takes the

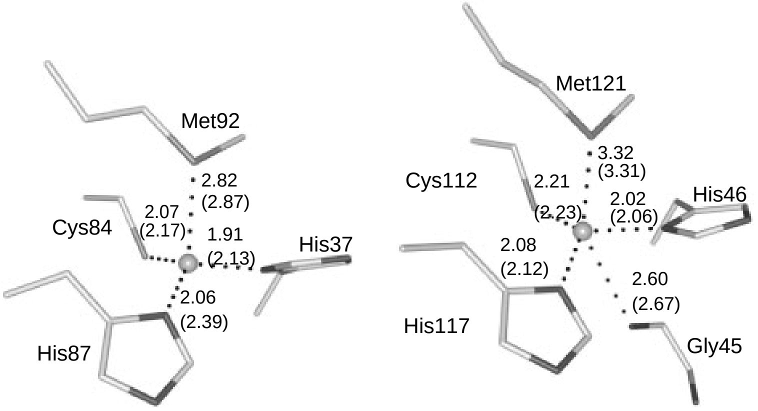

(a) Plastocyanin
1PLC (5PCY)

(b) Azurin
1JZF (1JZG)

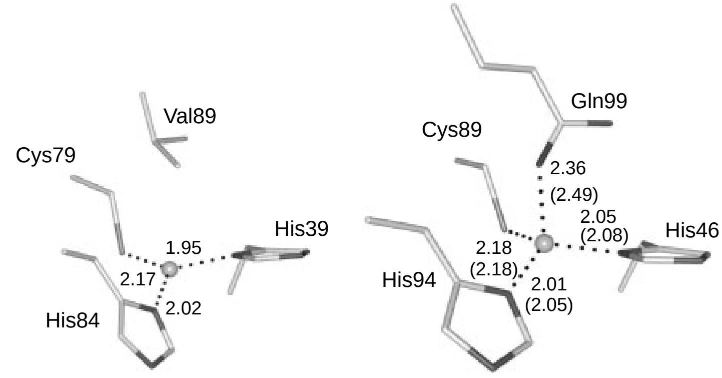

(c) Plantacyanin
to be deposited

(d) Stellacyanin
to be deposited

Figure 6 Copper sites in (a) poplar plastocyanin, (b) *A. den.* azurin, (c) tomato plantacyanin, and (d) cucumber stellacyanin. Distances are for the oxidized form, with those for the reduced form in parentheses

place of Met in the coordination sphere.[131] This is indeed the case, as was observed in the crystal structure of cucumber stellacyanin[120] which is found to have a short Cu–O–(Gln) bond of 2.21 Å in the 1.6 Å structure and 2.36 Å in the newly refined 1.2 Å structure. This bond lengthens to 2.5 Å in the structure of the reduced protein at 1.45 Å resolution (Figure 6d). The spectroscopic properties of cucumber stellacyanin are nearly identical to that of the protein from *Rhus vernicifera*.[132]

3.5.3 Copper-binding Loops

The copper ligands are contributed by two loops of polypeptide chain (Figure 3). The first His ligand and the peptide carbonyl oxygen (where this is close enough to be considered a ligand) are at the end of the loop joining β-strands, 3 and 4 (or the structurally analogous strands in amicyanin, auracyanin, and rusticyanin); in fact the His can be considered the first residue of strand 4. The three remaining ligands belong to the loop joining strands 7 and 8 (or their structural analogs). The Cys is the last residue of strand 7, the second His is in the middle of the loop, and the Met (Gln) is the first residue of strand 8. The 7–8 loop also plays a critical part in forming one wall of the copper-binding cleft and in contributing side chains to the hydrophobic patch surrounding the second His. Many of the functional variations between different type 1 copper proteins can be traced to variations in this loop.

The 3–4 loop is clearly shorter in plastocyanin, pseudoazurin, and amicyanin than in azurin, auracyanin, and rusticyanin, and shorter still in cucumber basic protein, tomato plantacyanin, and cucumber stellacyanin. The azurin, auracyanin, and rusticyanin copper sites are correspondingly the most buried and cucumber basic protein, spinach plantacyanin, tomato plantacyanin, and cucumber stellacyanin are the most exposed. Azurin may also be the only one with a fifth, carbonyl oxygen, although this atom in auracyanin resides ~3.5 Å from the copper ion. The number of residues between the Cys and His, and His and Met ligands in the 7–8 loop varies from two to four; amicyanin has the minimal number, with two sets of two, which may increase the exposure of its copper site. All, with the exception of cucumber stellacyanin, have a Pro somewhere between the Cys and His ligands, which may lend some rigidity; the location of this residue, however, affects the interactions with the thiolate sulfur (see below).

3.5.4 *Thiolate Geometry*

A notable feature of the Cys ligand is that its thiolate sulfur is involved in hydrogen bonding, just as the sulfur ligands are in the iron–sulfur proteins (*see* ***Iron–Sulfur Proteins***). In azurin, cucumber stellacyanin, auracyanin, and rusticyanin, the thiolate sulfur has four bonds in an almost perfect tetrahedral arrangement (Figure 7): two covalent bonds and two N–H–S hydrogen bonds (the latter unequivocally establish the sulfur as thiolate). The two N–H–S interactions at ∼3.5 Å come from the peptide NH groups adjacent to the first His ligand, and from NH groups found in the 7–8 loop. The latter interaction, in which the sulfur receives a hydrogen bond from the NH of the next-but-one residue (S_n–HN_{n+2}) is of a type particularly common in the iron–sulfur proteins. Such an interaction does not occur in plastocyanin as Pro 86, two removed from Cys 84, has no NH. Pseudoazurin and amicyanin also have only one N–H–S bond for the same reason. Cucumber basic protein is somewhat of an outlier, having only very weak N–H–S interactions at distances of 3.7–3.8 Å.

The strong conservation of the short Cu–S bond and the dihedral angles involving the thiolate sulfur (see Section 3.5.1) are also key features with important implications for the spectroscopic properties of the type 1 copper site.

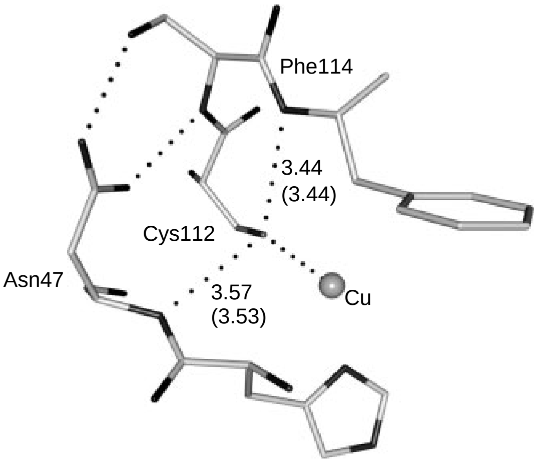

Figure 7 Cysteine ligand environment in *A. den.* azurin showing the two N–H–S hydrogen bonds. Distances are for the oxidized protein, with those for the reduced form in parentheses. Also shown are the hydrogen bonds made by the conserved Asn 47, which help constrain the copper site

3.5.5 *Constraints on the Copper Site*

The copper site is highly constrained by the surrounding protein structure. The Cys ligand is hydrogen-bonded as described above and the first His ligand binds to copper through Nδ1 and is hydrogen-bonded to a main-chain carbonyl oxygen through Nε2. In amicyanin, this His is hydrogen-bonded to the side chain of Glu 49; in rusticyanin, to the side chain of Asn 80; in the phytocyanins it is hydrogen-bonded to a water molecule. The second His is not hydrogen-bonded to any protein atom, but packs against other residues of the hydrophobic patch and is also hydrogen-bonded to a water molecule; the latter is further hydrogen-bonded to other protein atoms and is probably present in solution as well as in the crystal.[133] The Met (Gln) ligand always packs against an aromatic side chain (Phe, Tyr, or Trp). The orientation of the carbonyl oxygen in azurin is controlled by the secondary structure and by its packing against Phe 114. In cucumber stellacyanin, the orientation of the Gln side chain can be inferred by its proximity to Trp 13, where the nonligating atom points into the negatively charged 'hole' formed by the π electrons of the Trp 13 ring. A Trp 13/ε-oxygen ring face interaction would be electrostatically unfavorable and therefore it was suggested that the ε-oxygen was coordinated to the copper ion.[120]

Outside the immediate copper ligands there are further constraints on the site. In particular, the Asn residue which immediately follows the first His (Asn 38 in plastocyanin, Asn 47 in azurin) makes multiple hydrogen bonds, two of them to the residue which follows the Cys ligand (85 in plastocyanin, 113 in azurin); the latter is generally conserved as Ser or Thr. Thus the Asn side chain, which is conserved in most type 1 copper proteins (rusticyanin has a serine), helps to tie the two copper-binding loops together. The mutation of the Asn side chain to a Leu, which has no hydrogen-bonding capability, drastically lowers stability.[134]

These and other hydrogen bonds and hydrophobic interactions at the 'northern' end of the molecule around the copper site make this the most rigid part of the molecule.[77] This particularly applies to azurin, auracyanin, and rusticyanin, with the most buried copper sites and least to the phytocyanins, where the sites are much more exposed.

3.6 EXAFS Studies

Both protein crystallography and EXAFS data have been important in obtaining insight into the changes which occur upon reduction of the blue copper site. As noted below, while providing very limited angular information, EXAFS has the advantage of providing much more accurate metal–ligand distances. Studies on the oxidized and reduced forms of plastocyanins and azurins show that on average, the Cu–N(His) and Cu–S(Cys) bond lengths increase by ∼0.06 Å and ∼0.08 Å upon reduction (Table 3, adapted from[19] and references therein). Note that these changes are based on

Table 3 Summary of published EXAFS data for oxidized and reduced plastocyanins and azurins[19]

	Poplar plastocyanin		*P. vulgaris* plastocyanin		*S. oleracea* plastocyanin		*P. aer.* azurin	
Oxidation state	ox	red	ox	red	ox	red	ox	red
pH	6.0	7.0	–	–	5.5	5.5	5.5	5.5
2 Cu–N (His)	1.98	1.96/2.01	1.97	2.05	1.94/2.02	1.96/2.11	1.95	2.00
1 Cu–S (Cys)	2.08	2.19	2.11	2.22	2.09	2.15	2.14	2.21
1 Cu–S (Met)	2.76	2.86	2.66	–	2.90	–	–	–

EXAFS studies of plastocyanin at pH 6.0–7.0 and therefore do not reflect the more dramatic changes which occur in plastocyanin at low pH. The small changes in distance are consistent with the results obtained by protein crystallography. In addition, protein crystallography indicates that only limited angular changes occur upon reduction of the blue site. These small changes in the active site structure upon reduction are important in maintaining a low reorganization energy, which is critical to the electron-transfer function of these sites (*see* ***Long-range Electron Transfer in Biology***).

EXAFS results also provided the first measure of the short Cu–S(thiolate) distance in blue copper proteins[135] and have been used extensively to measure structural changes under varied conditions.[136–140] It has also been an important technique for examining systematic changes upon point mutation of the protein,[140–143] and is of particular utility when the proteins cannot be crystallized or when the changes that occur are within the error limits of protein crystallography. It should be noted that EXAFS results have historically not been able to determine contributions from the long Cu–S(Met).[144] Even the short axial Cu–O(Gln) bond in stellacyanin has proven questionable to determine by EXAFS due to correlated parameters;[137] however, it should be noted that conflicting reports exist.[136,139,145] These differences have been attributed to the method of analysis, in particular whether multiple scattering contributions from the His rings, which would occur at a similar distance, were included in the analyses.[19]

3.7 Effects of Copper Removal

A fundamental premise of the entatic state concept is that the metal simply fits into a site that is preformed by the protein and determined by the many interactions which stabilize the protein structure. This idea has been tested by crystallographic studies of apo-forms of azurin, plastocyanin, pseudoazurin and amicyanin.

The structure of apo-plastocyanin was the first to demonstrate that the geometry of the copper site is indeed created by the polypeptide.[59] The polypeptide conformation itself is essentially unchanged by copper removal, the rms deviation between oxidized and apo structures, for all main-chain atoms, being only 0.12 Å. Only minor changes occur in the copper-binding site; His 37, Cys 84, and Met 92 all move inward slightly (0.1–0.3 Å) and the largest change is a rotation of the imidazole ring of His 87. This led to the suggestion of a ‘rotating-door’ mechanism for the incorporation of copper, in which the metal binds to Nδ1 of His 87 in its ‘out’ conformer, after which the imidazole ring rotates to carry the bound copper in.[59] As with plastocyanin, the structures of apo-pseudoazurin and apo-amicyanin are practically identical to the metal-loaded forms.[113,146]

For apo-azurin different results have been obtained for the *A. den*. and *P. aer*. proteins. For *A. den*. apo-azurin, both the polypeptide structure and the copper site remain unchanged.[80] The ligand residues simply move very slightly (0.1–0.2 Å) inwards toward the site vacated by copper. In the *P. aer*. apo-azurin crystal structure,[90] there are four independent molecules in the asymmetric unit, and these show two different conformations. Two molecules are unchanged as for *A. den*. azurin, but the other two show a local rearrangement at the copper site. The second His ligand, His 117, moves outwards by ∼1.6 Å and an accompanying movement of His 46 by ∼0.6 Å allows the incorporation of a water molecule near the position vacated by copper. The movement suggests that a slightly different mechanism of copper insertion/removal may be operative for azurin: instead of a rotation of the imidazole ring, which is inhibited by the tighter packing of neighboring side chains compared with plastocyanin, a twist of the polypeptide backbone carries the His 117 side chain outwards. These results suggest that in solution an equilibrium exists between the two structural forms of the apoprotein.[90]

3.8 Metal Substitution

The substitution of other metal ions for copper has played an important role in spectroscopic studies of the type 1 copper proteins. For example, Mn(II), Co(II), and Ni(II) derivatives proved useful in analyzing their electronic absorption spectra[9,48] and Cd(II) substitution has been used to examine the metal binding sites through ^{113}Cd NMR spectroscopy.[148]

Five crystallographic analyses have provided direct information on the effects of metal substitution, with replacement of Cu(II) by Hg(II) in plastocyanin, and by Zn(II), Cd(II), and Co(II) in azurin (Table 4). In each case, the metal does occupy the Cu(II) site and changes in the overall protein structure are minimal. There are, however, differences that appear to depend on the type of

Table 4 Bond length (Å) in metal-substituted type 1 proteins

	PCY[a]		*A. den* AZ[b]		*P. aer.* AZ[c]			
Bond	Cu(II)	Hg(II)[d]	Cu(II)	Cd(II)[e]	Cu(II)	Zn(II)[f]	Ni(II)[g]	Co(II)[h]
M–N_1	1.91	2.34	2.08	2.25	2.08	2.01	2.23	2.32
M–N_2	2.06	2.36	2.00	2.21	2.01	2.07	2.22	2.25
M–S_1	2.07	2.38	2.15	2.38	2.24	2.30	2.39	2.20
M–S_2	2.82	3.02	3.11	3.23	3.15	3.40	3.30	3.49
M–O			3.13	2.76	2.97	2.32	2.46	2.15

[a] 1PCY; [b] 2AZA; [c] 4AZU (average distances, multiple molecules in asymmetric unit); [d] 3PCY [e] 1AIZ; [f,g] from reference (5) (average distances, multiple molecules in asymmetric unit); [h] 1VLX from reference (5) (average distances, multiple molecules in asymmetric unit).

site provided by each protein and the particular metal ion chosen. In Hg(II)-substituted plastocyanin the coordination is essentially unchanged, with small protein movements allowing the three strong bonds to be lengthened to ∼2.35 Å, typical for Hg(II).[60] In Cd(II)-substituted azurin,[149] the polypeptide structure is again unchanged but the interaction of Cd(II) with the carbonyl–oxygen ligand is strengthened compared with Cu(II); the decrease of 0.4 Å in the M–O bond length is achieved by small movements, both of the metal towards the oxygen and of the oxygen towards the metal. The latter occurs through a slight twist of the Gly 45–His 46 peptide unit. In Zn(II), Ni(II), and Co(II)-azurin,[5,91] this process is continued further such that the Zn, Ni, and Co atoms make a strong bond with the oxygen ligand and the geometry is now best described as flattened tetrahedral.

The implications are that the binding site has limited flexibility. Very little movement of the three principal equatorial ligands occurs, but small displacements of the metal atom and the weaker axial ligands can occur. This is particularly the case in azurin where involvement of a peptide carbonyl oxygen in the binding site allows some movement by local twisting of a single peptide unit. The five-coordinate site may also allow more variation than the four-coordinate site in plastocyanin. Coordination preferences of the metal also have some influence, as the changes in Zn and Co azurins presumably represent a preference for tetrahedral coordination over trigonal bipyramidal, and for bonding to a carbonyl oxygen over a thioether sulfur.

3.9 The Type 1 Copper Site and the Entatic State Concept

The structural results described above give strong support for the ideas implicit in the entatic state concept of Vallee and Williams[2] and the related concept of ‘rack-induced bonding’ (*see* ***Long-range Electron Transfer in Biology***).[150] As applied to electron-transfer proteins, this proposes that the metal center has a geometry which is a compromise between the normal preferences of the two valence states, in this case Cu(I) and Cu(II). This geometry is stabilized by the constraints imposed by the secondary and tertiary structures of the protein.

In all the type 1 copper proteins examined crystallographically to date, the same approximately trigonal arrangement of three strongly bound ligands, two His and one Cys, is found. This is responsible for the strong conservation of the ‘unusual’ physicochemical properties of the blue copper site (see Section 4). With two minor qualifications, the geometrical arrangement remains the same in the absence of the metal or when a different metal is substituted for copper. The minor qualifications are that a mechanism must exist for incorporation of copper into the apoprotein (one His ligand can move to achieve this), and that substitution of a different metal, for example, Zn(II) or Cd(II) in azurin, can lead to small movements in the more weakly bound axial ligands.

Description of the site in terms of a classic coordination geometry is difficult and can be misleading. In most of the proteins, the coordination geometry could be described as distorted tetrahedral or trigonal pyramidal, but in azurin distorted trigonal bipyramidal or trigonal seems more appropriate, while stellacyanin and tomato plantacyanin have copper coordination geometries that are best described by tetrahedral and trigonal planar, respectively. On balance, the description as a distorted trigonal site with weaker axial interactions is to be preferred. The site can thus be seen as a compromise between the coordination preferences of Cu(I) and Cu(II) in terms of both ligands (mixture of S and N) and geometry [intermediate between trigonal, common for Cu(I), and trigonal bipyramidal, appropriate for Cu(II)], with a bias toward Cu(I) which explains the relatively high redox potential. The functional implications are seen in the minimal structural change accompanying the change of oxidation state, implying that the native type 1 site is optimized for rapid electron transfer by providing a very low-activation energy barrier.

4 SPECTROSCOPY AND ELECTRONIC STRUCTURE

The active sites of oxidized blue copper proteins are characterized by unique features relative to those of normal Cu(II) complexes. These features include an intense absorption

Table 5 EPR and resonance Raman parameters for blue copper sites

	EPR parameters		Resonance Raman
	$g_{\parallel}$	$A_{\parallel}$ ($\times 10^{-4}$ cm^{-1})	⟨Cu–S⟩ (cm^{-1})
Plastocyanin	2.23	63	403
Cucumber basic	2.21	57	394
R. s. nitrite reductase	2.19	73	383
P. p. laccase	2.19	90	413
Cucumber stellacyanin	2.29	35	386

Table 6 Dependence of E°; on the axial ligand in blue Cu proteins[19]

	Axial ligand and E° (mV)		
	Phe/Leu/Thr	Met	Gln
Fungal laccase	+770	+680	–
Azurin	+412	+310	+285
Cuc. stellacyanin	+580	+420	+260
Nitrite reductase	+354	+247	–
Rusticyanin	+800	+667	+563
Mavicyanin	–	+400	+213
Amicyanin	–	+250	+165

at ~600 nm ($\varepsilon \approx 5000\,\mathrm{cm}^{-1}\,\mathrm{M}^{-1}$), an unusually small $A_{\parallel}$ value in the EPR spectrum ($A_{\parallel} \leq 100 \times 10^{-4}$ cm^{-1}, Table 5), and a high-reduction potential ($E° > 150$ mV vs. NHE (normal hydrogen electrode), Table 6). Efforts to obtain a detailed understanding of these unique characteristics and their relation to function have resulted in numerous experimental and theoretical studies. Reviews are available.[3,19,52,151–155] Insight into the electronic structure of blue copper proteins has been obtained through a combination of optical spectroscopy, EPR, resonance Raman, X-ray absorption spectroscopy (XAS), and density functional calculations. In this section, the spectroscopic results and theoretical calculations are discussed in relation to the 'classic' blue copper sites found in plastocyanins and azurins, and then extended to the 'perturbed' blue copper sites. For the purpose of discussing the spectroscopy, the perturbed sites are divided into 3 main classes:[19] (1) those sites having the same S(Met), S(Cys), N(His)$_2$ ligand set as plastocyanin and azurin, but exhibiting a tetragonal distortion of the ligand field (e.g. cucumber basic protein[118] and nitrite reductase[156] (*see* ***Copper Enzymes in Denitrification***)); (2) sites in which the axial S(Met) is replaced by a stronger field ligand (e.g. O(Gln) in stellacyanin);[120] and (3) sites in which the S(Met) is replaced by a Leu, Phe, Ile or Val as in the plant and fungal laccases[16,157] (*see* ***Copper Proteins: Oxidases***) and tomato plantacyanin,[16] and hence no axial ligand is provided by the protein. It should be noted that laccases and nitrite reductases are not single-domain mononuclear blue copper proteins. However, a discussion of their spectroscopic features is included in order to cover the full range of perturbations within blue copper sites. The correlations between the electronic structure and the function of blue copper sites are discussed in Section 5.

4.1 Electronic Absorption Spectroscopy

Possibly the most striking feature of oxidized blue copper proteins is the intense absorption band at ~600 nm which gives rise to the deep blue color (Figure 8). It is now well-established that this absorption band results from a ligand-to-metal charge transfer (LMCT) from the S(Cys)$\pi \rightarrow$ Cu 3d$_{x^2-y^2}$ orbital, while a weak feature to slightly higher energy (~530 nm) corresponds to the S(Cys)$\sigma \rightarrow$ Cu 3d$_{x^2-y^2}$ transition.[19,153,158,159] This assignment is inverted relative to that of normal Cu(II) complexes, which exhibit weak π charge transfer (CT) transitions and intense σ CT transitions. This assignment was first made by Solomon and coworkers on the basis of a combination of low-temperature absorption and magnetic circular dichroism (MCD) data.[159] Examination of the low-temperature MCD (LT-MCD) to absorption ratios allows for the assignment of bands as either CT (which will be intense in the absorption spectrum, but weak in the MCD spectrum) or d → d bands (which will be weak in the absorption spectrum, but intense in the MCD spectrum). Using this methodology, the absorption bands at ~430 nm and 465 nm were assigned as S(Met) → Cu and N(His) → Cu CT bands, respectively. The four absorption bands between 650–1050 nm were assigned as ligand field (LF, or d → d) transitions. A detailed description of this analysis is available.[159]

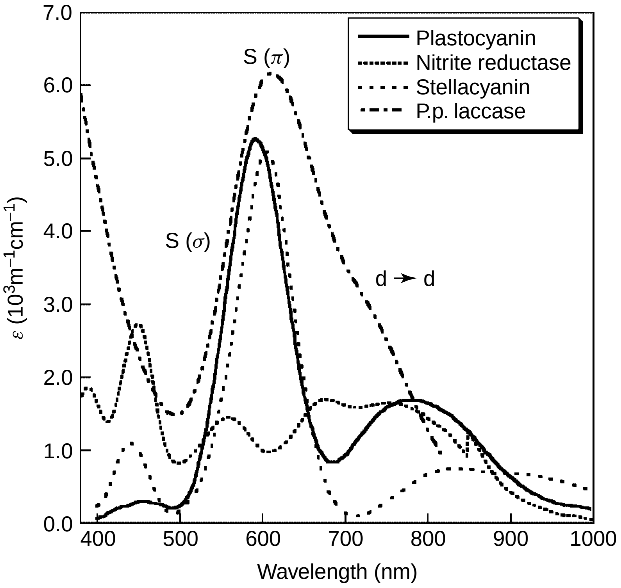

Figure 8 Low-temperature absorption spectra of plastocyanin, nitrite reductase, cucumber stellacyanin, and P. p. laccase

With a more detailed understanding of the electronic spectra of classic blue copper proteins, the analysis can then be extended to the perturbed blue copper sites. First, it is useful to examine the absorption spectra of cucumber basic protein and R.s. nitrite reductase, which have the same ligand set as plastocyanin, but exhibit altered spectral features.**[160]** Both of these proteins exhibit an increase in the ratio of the σ:π CT bands (with a greater change for nitrite reductase than for cucumber basic protein, data for R.s. nitrite reductase are shown in Figure 8) indicating that $3d_{x^2-y^2}$ orbital is rotating from a π to a more σ bonding interaction with the highest-occupied molecular orbital (HOMO).**[161]** In addition LT-MCD data show that the LF transitions have shifted to higher energy, indicating that this spectral change reflects a tetragonal distortion of the site, which is consistent with the changes observed by protein crystallography. It is also important to note that going from plastocyanin to cucumber basic protein to nitrite reductase, the Cu–S(Met) bond length decreases while the Cu–S(Cys) bond length increases, which together result in a tetragonal distortion of the site. The correlated geometric and electronic perturbation of these sites has been termed '*the coupled distortion*'.**[19]** In contrast, for sites with no axial ligand, the ratio of the σ:π CT bands is similar to that in plastocyanin indicating that the site remains trigonal, while the d → d bands shifts to higher energy, indicating an increase in the LF**[141,162,163]** (Figure 8). For the blue copper site in stellacyanin, the absorption pattern remains weak σ /intense π (Figure 8), again indicating that the site is not tetragonally distorted.**[164]** The LF transitions decrease in energy, consistent with a slightly more tetrahedral site relative to plastocyanin.

4.2 EPR

Like normal tetragonal Cu(II) complexes, blue copper sites show $g_{\parallel} > g_{\perp} > 2.0023$, indicating $3d_{x^2-y^2}$ ground state. However, the EPR spectra of blue copper sites are characterized by an extremely small $A_{\parallel}$ values ($A_{\parallel} \leq 100 \times 10^{-4}\,\text{cm}^{-1}$, Table 5) relative to those of 'normal' copper complexes. This small hyperfine was originally attributed to either covalency,**[165]** which would decrease the hyperfine coupling through delocalization of the unpaired copper electron spin onto the sulfur and thus decrease the interaction of the unpaired electron with the copper nuclear spin; or to $4p_z$ mixing into the $3d_{x^2-y^2}$ orbital,**[166–168]** which, due to the opposition of the $4p_z$ spin dipolar contribution with the $3d_{x^2-y^2}$ orbital, would also reduce the coupling between the unpaired electron and the copper nuclear spin. Through an elegant polarized Cu K-edge XAS study, it was demonstrated that the origin of the small $A_{\parallel}$ hyperfine coupling was in fact due to the highly covalent Cu–S(Cys) bond.**[169]** In a Cu K-edge, the intense edge jump is due to an electric dipole allowed 1s → 4p transition. At a lower energy of ~8979 eV is a pre-edge feature that is due to a 1s → 3d transition. An s → d transition is formally electric dipole forbidden, and hence the primary mechanism for pre-edge intensity is mixing of 4p character into the 3d orbitals giving this transition electric dipole allowed character. Solution data of plastocyanin shows a pre-edge peak, indicating that there is 4p mixing into the $3d_{x^2-y^2}$ orbital, although it does not show whether this originates from $4p_z$ or $4p_{x,y}$ mixing. By orienting a single crystal of plastocyanin along the electronic z-axis, it was shown that there was no intensity in the pre-edge feature, indicating no $4p_z$ mixing. In contrast, the y-polarized data demonstrated pre-edge intensity, indicating that this feature in solution plastocyanin is due to $4p_{x,y}$ mixing into the $3d_{x^2-y^2}$ orbital. Hence, these results provided experimental evidence that the small $A_{\parallel}$ hyperfine coupling in the EPR spectra of blue copper proteins is due to the highly covalent nature of this site.

The classic blue copper sites in plastocyanin and azurin exhibit essentially identical EPR spectra, with approximately axial ($g_x \approx g_y$) EPR signals.**[160]** This argues that the long ~3.0 Cu–O Å carbonyl oxygen makes little contribution to the electronic structure of azurin, consistent with other spectroscopy and the fact that the relatively compact O 2p orbitals would be expected to have little contribution to bonding at this distance.**[154]** On the basis of EPR, the perturbed blue copper sites can be divided into 2 classes: (1) those which exhibit a rhombic EPR signal (i.e. $\Delta g_{\perp} = g_x - g_y > 0.01$, as in cucumber basic protein, nitrite reductase and stellacyanin, Figure 9)**[159,160]** and (2) those which are perturbed, but still exhibit an axial EPR signal, for example, the T1 site in fungal laccase (Figure 9) (*see* ***Copper Proteins: Oxidases***) and tomato plantacyanin. It has been shown that the rhombic distortions are linked to stronger interactions by the axial ligand, as originally proposed by Gewirth**[170]** and later confirmed by subsequent structural data.**[53,120,156]** In cases where no axial ligand is provided by the protein (e.g. tomato plantacyanin and the T1 site in fungal laccase), a rhombic distortion does not occur.**[162]**

4.3 Resonance Raman

Resonance Raman spectroscopy has been used extensively as a method to probe the Cu–S(Cys) stretching frequency in blue copper proteins.**[160,171–173]** Laser excitation into the S(Cys) → Cu(II) CT band leads to enhancement of vibrational bands associated with the Cu–S(Cys) moiety. These bands also show a large S- and Cu- isotope shift, a high-resonance Raman intensity, and are associated with the generation of combination bands. For the classic blue copper sites found in plastocyanin, the effective Cu–S stretching frequency is $403\,\text{cm}^{-1}$ (Figure 10, Table 5).**[173]** In contrast, the perturbed blue copper sites in cucumber basic protein and nitrite reductase have effective Cu–S stretching frequencies of ~$394\,\text{cm}^{-1}$ and $383\,\text{cm}^{-1}$,**[147,160]** respectively, indicating a significant weakening of the Cu–S(Cys) bond (Figure 10, Table 5). The effective Cu–S stretching frequency of stellacyanin also similarly decreases to ~$386\,\text{cm}^{-1}$.**[141]** In contrast, the effective Cu–S stretching frequency for

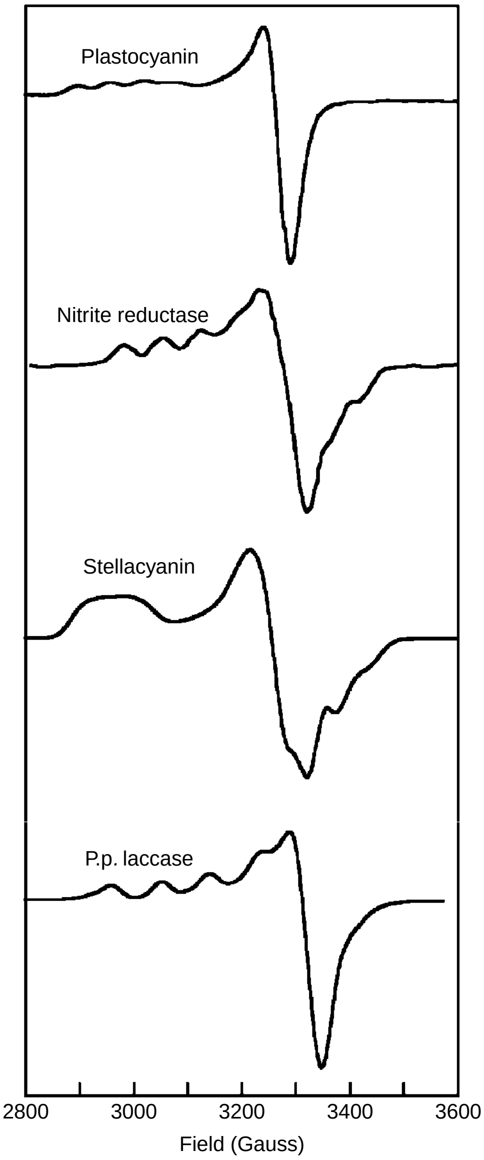

Figure 9 EPR spectra of plastocyanin, nitrite reductase, cucumber stellacyanin, and P. p. laccase

the T1 sites in fungal laccases (*see* ***Copper Proteins: Oxidases***) increase,[162] indicating a stronger Cu–S(Cys) bond. By using the intensity-weighted average of the Cu–S stretching frequencies, and applying Badger's rule, resonance Raman can be used as a sensitive indicator of the relative Cu–S(Cys) bond lengths. These data have been successfully correlated with the results of EXAFS and provide experimental evidence that the strength of the axial ligand inversely effects the strength of the Cu–S(thiolate) bond.[141]

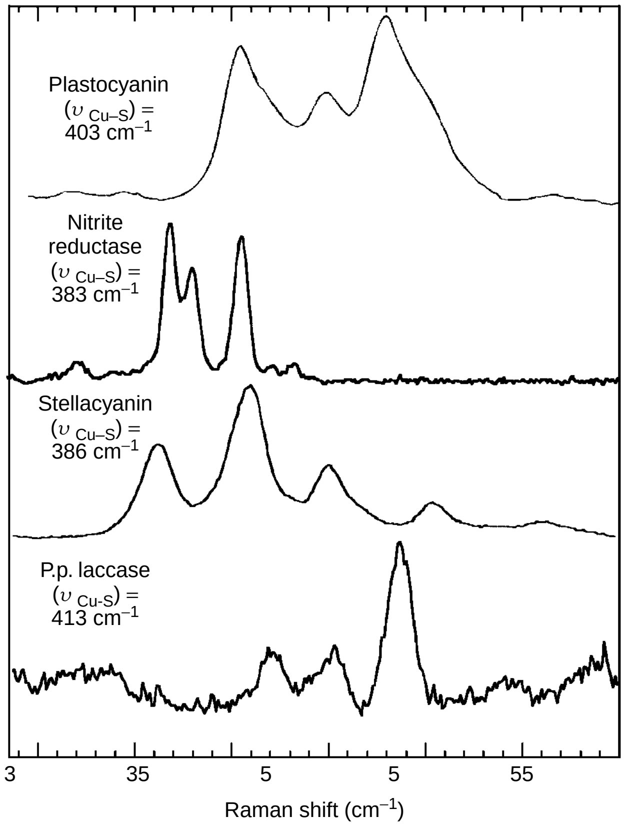

Figure 10 Resonance Raman spectra of plastocyanin, nitrite reductase, cucumber stellacyanin, and P. p. laccase

In addition to providing a sensitive probe of Cu–S bonding, resonance Raman data have also been used to obtain an experimental measure of the reorganization energy in plastocyanin and azurin. Through an excited distortion analysis, Loppnow and coworkers have obtained a measure of the inner-sphere reorganization energies of 0.26 and 0.19 eV for plastocyanin and azurin, respectively.[174,175] The relation of these values to the electron-transfer function of these sites is discussed further in Section 5 (*also see* ***Long-range Electron Transfer in Biology***).

4.4 Copper L-edge and Sulfur K-edge XAS

Combined X-ray absorption spectroscopic studies at the copper L-edge and the sulfur K-edge (S K-edge) have been important in experimentally defining the electronic structure of the classic blue copper site in plastocyanin.[169,176] The Cu L-edge results from an electric dipole allowed Cu 2p → Cu $3d_{x^2-y^2}$ transition. Since the transition is localized on the Cu, the resultant intensity reflects the amount of Cu character in the HOMO. By using D_{4h}-$CuCl_4$ as a well-defined reference with 61% Cu character, the Cu 3d character in the HOMO of plastocyanin was determined to be ~41%. The S K-edge provides complementary information to the Cu L-edge. A S K-edge corresponds to a transition from the S 1s → S 4p orbital. When sulfur is bound to an open-shell metal (such as Cu(II)), a pre-edge feature will occur, which corresponds to a S 1s transition to the orbital formed by interaction of the Cu $3d_{x^2-y^2}$ and the S 3p orbitals. The intensity of this pre-edge is dependent on the strength of the covalent interaction between the S and the Cu. Using these methods, the S 3p character in the $3d_{x^2-y^2}$ orbital of plastocyanin was found to be ~38%. However, it should be noted that more recent S K-edge XAS studies on azurin indicate ~45% S 3p character.[141]

It should also be noted that S K-edge studies have been extended to perturbed blue copper sites. Analysis of the S K-edge pre-edge intensity for nitrite reductase is similar to that determined for plastocyanin.[161] However, this is believed to reflect a contribution from both the S(Cys) and the S(Met) due to the tetragonal distortion of the site (note, in plastocyanin, only the S(Cys) has overlap with the $3d_{x^2-y^2}$ orbital and therefore the S(Met) does not contribute to pre-edge intensity). Systematic studies on a series of stellacyanin axial mutants show the effect of the axial ligand on the second and third class of perturbed blue copper sites;[141] upon strengthening the axial ligand, the Cu–S(Cys) covalency decreases and upon weakening the axial ligand, the Cu–S(Cys) covalency increases.

4.5 Electronic Structure Calculations

Calculations have provided general insight into the electronic structure of blue copper sites. Early studies using self-consistent field Xα calculations[159,160] overestimated the ground-state covalency of plastocyanin; hence, the Xα atomic sphere radii were adjusted to fit the experimental EPR g-values. The resulting calculational wave function was in good agreement with spectroscopic results, including the very covalent Cu–S(thiolate) bond, the Cu 3d character in the HOMO, and the orientation of the Cu $3d_{x^2-y^2}$ orbital. More recent calculations have shown qualitatively similar descriptions of plastocyanin, reproducing the Cu–S(thiolate) π bonding interaction in the HOMO, however, the sulfur 3p character in the HOMO shows a large dependence on the functional used.[19,177–180] Here it should be emphasized that spectroscopic results have provided a very detailed description of the electronic structure of blue copper sites, which have been important for the calibration of electronic-structure calculations.[19,181]

5 CORRELATIONS TO FUNCTION

Blue copper proteins are involved in electron transfer (ET) reactions in organisms ranging from bacteria to humans. In order to understand the contribution of the electronic structure to the ET function of these sites, it is useful to examine the three primary terms that contribute to the rate of ET, as described by the semi-classical Marcus equation (1) (*see also* ***Long-range Electron Transfer in Biology***).

$$k_{ET} = \left(\frac{\pi}{\hbar^2\lambda k_B T}\right)^{1/2} (H_{AB})^2 \exp\left[\frac{-(\Delta E^\circ + \lambda)^2}{4\lambda k_B T}\right] \quad (1)$$

Here ΔE° is the difference in reduction potential between the donor and acceptor sites (i.e. the driving force), H_{AB} is the donor–acceptor electron coupling, and λ is the reorganization energy required for electron transfer. The rate is maximized when H_{AB} is large and λ is small. The reduction potential of the site is dictated by the biological function and therefore must be within the range of the donor and acceptors.[5]

5.1 Reduction Potentials (E°)

The reduction potentials for classic blue sites (165–800 mV) span a wide range, but are all higher than that of an aqueous Cu(I)/Cu(II) couple (~150 mV). The reduction potential results from both the protein environment and the geometric and electronic structure of the blue site. In order to obtain an estimate of the contribution from the protein environment, it is useful to compare geometrically and electronically similar blue copper sites within different protein environments. Table 6 ([19] and references therein) shows that S(Met) axially ligated blue proteins have reduction potentials that span a range of 250–680 mV; blue sites with an axial O(Gln) span a range of 165–563 mV; and blue sites with nonligating axial amino acids have reduction potentials in the 354–800 mV range.

This indicates that factors such as local dipoles, hydrogen bonding, and solvent exposure can make significant contributions to the reduction potential. By examining mutants in which the axial ligand is systematically varied within an otherwise fixed protein environment (as shown in Table 6), the contribution of the axial ligand to the reduction potential can be assessed. On the basis of systematic point mutations within numerous blue copper proteins, it is estimated that a O(Gln) to S(Met) or S(Met) to Phe/Leu/Thr mutation contributes ~+100 mV to the redox potential. Hence, the axial ligand can provide a means of tuning the potential of the blue copper site to a biologically relevant range.

5.2 Electron Matrix Coupling Element (H_{AB})

The rate of electron transfer through a protein is dependent on the electron coupling matrix element, $H_{AB}\cdot H_{AB}$ is dependent on the distance an electron must travel between the donor and acceptor sites (the shorter the distance, the better the coupling and the larger the value of H_{AB}) and on the covalency of ligand–metal bonds (the higher the covalency, the larger the value of H_{AB}).[182–184] In plastocyanin, there are two ET sites on the surface of the protein; one located ~5 Å from the copper and the other located ~13 Å from the copper. Despite the large difference in the length of these ET pathways, the ET rates are similar.[185] This is attributed to the increase in covalent coupling in the longer pathway, which goes through the Cu–S(Cys) bond.[183] Figure 11 shows that the shorter pathway goes through the Cu–N(His) bond, which is an order of magnitude less covalent than the Cu–S(Cys) bond.[169,186] This

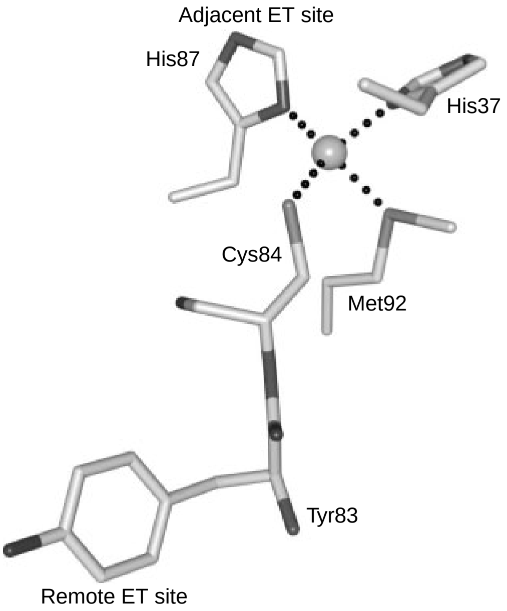

Figure 11 Proposed electron-transfer pathways to the remote and adjacent electron-transfer sites in plastocyanin. Structure from PDB, 1PLC

clearly demonstrates the importance of the highly covalent Cu–S(Cys) bond to the ET function of these sites.

5.3 Reorganization Energy (λ)

In addition to good donor–acceptor coupling, it is also important to minimize the reorganization energy (λ), in order to maximize the rate of ET. For aqueous Cu(II)/Cu(I) redox couples, λ is large owing to significant structural changes that typically occur between different redox states of copper-model complexes. For example, $[Cu(phen)_2]^{2+/+}$ has a λ_{total} of 2.4 eV.[187] In contrast, studies on ruthenium modified azurins and plastocyanins have shown λ_{total} is ∼0.7–1.2 eV.[188–190] This decrease in reorganization energy is generally attributed to protein-enforced constraints and will have contribution from both inner- and outer-sphere reorganization energies. Estimates of the inner-sphere reorganization energy have been obtained from differences in oxidized and reduced crystal structures (0.6–0.8 eV),[191] resonance Raman distortion data (0.2–0.5 eV),[174,175] and calculations (0.6–0.7 eV).[192] In all cases, the values are lower than that obtained for a copper-tetramine complex, where λ_{inner} has been calculated as ∼1.4 eV.[193] The decrease in λ_{inner} in blue copper proteins has been attributed to the lack of a Jahn–Teller distorting force, which eliminates a large angular change upon oxidation.[19]

5.4 Electron Transfer With Other Proteins

The type 1 copper proteins participate in electron-transfer reactions with a wide variety of partners, including inorganic complexes such as $[Fe(CN)_6]^{3-}$ and $[Co(phen)_3]^{3+}$, small molecules such as flavins and ascorbate, and redox proteins such as cytochromes, oxidases, and reductases. They also participate in electron self-exchange reactions. Much of the experimental data relates to plastocyanin, whose physiological electron-transfer partners, cyt *f* and P700, are clearly established. This work has been reviewed.[20] In other studies, the type 1 copper proteins have been used as models to address the mechanisms of long-range electron transfer in proteins generally (*see* ***Long-range Electron Transfer in Biology***).[98,194]

5.4.1 General Considerations

The rates of electron transfer fall within the stopped-flow range for both inorganic and protein redox agents.[20] In some cases, for example, in the reaction of $[Co(phen)_3]^{3+}$ with plastocyanin, saturation kinetics are observed, implying the formation of a stable precursor complex; an equilibrium constant of 340 has been estimated at pH 7.5.[20] This is attributed to the electrostatic interaction of the highly positive Co(III) complex with the negative patch of plastocyanin (see below). Positively charged redox inactive complexes also bind at this site. In contrast, negatively charged complexes do not show saturation behavior with plastocyanin nor do most redox reagents with the other type 1 copper proteins. Although encounter complexes must be formed, their association is generally weak; the equilibrium constant for the formation of the complex between azurin and cytochrome *c*-551, for example, is 6.7 in 0.01 M phosphate, pH 7.0 at 293 K.[195] Under these conditions the kinetics can be analyzed in terms of Marcus theory.[99,195]

Electron self-exchange rates are rapid, for example, $\sim 10^6\,M^{-1}\,s^{-1}$ for azurin and $\sim 10^5\,M^{-1}\,s^{-1}$ for amicyanin, but substantially lower for plastocyanin ($<3 \times 10^3\,M^{-1}\,s^{-1}$).[13] The lower value for plastocyanin probably reflects repulsion owing to its high negative charge. These self-exchange rates compare with the very much lower value of $\sim 10^{-5}\,M^{-1}\,s^{-1}$ estimated for the aqueous Cu(I)/Cu(II) couple.[13] The difference presumably arises from the high reorganization energy of the latter, where the two species have very different geometries compared with the minimal structural change in the proteins (see Section 3.6).

Both rate constants and equilibrium constants tend to be influenced by pH and ionic strength, depending on the importance of electrostatic interactions. For French bean plastocyanin, no saturation behavior is seen for $[Co(phen)_3]^{3+}$ at high ionic strength, but stronger association develops in low salt. These effects and competition behavior with highly charged redox inactive complexes[20] give clues to the nature of the binding sites used by different reactants.

5.4.2 Binding Sites and Electron-transfer Pathways

Many of the type 1 copper proteins appear to have a common surface feature, that is, a hydrophobic patch at the

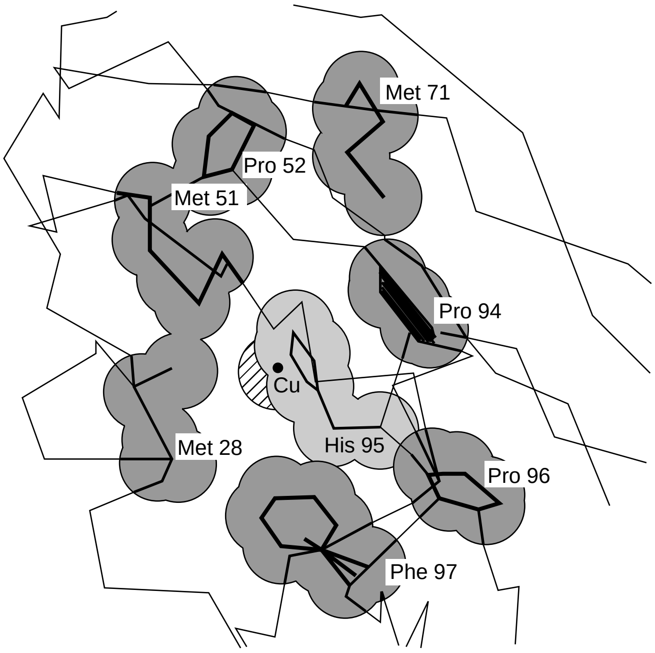

Figure 12 Hydrophobic patch surrounding the exposed edge of the His ligand, His 95, in amicyanin. (Reprinted with permission from Ref. 115. © 1992 American Chemical Society)

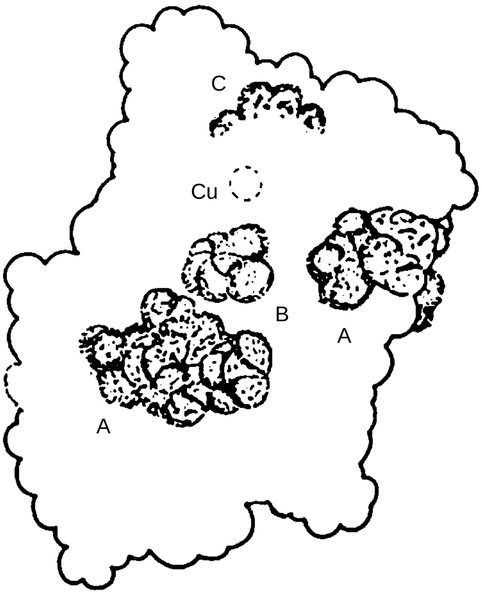

Figure 13 Location of the acidic patch (A) in plastocyanin around Tyr 83 (B). The copper atom and the second His ligand (C), which is located in the center of the hydrophobic patch, are also shown. (Ref. 20. Reproduced by permission of Springer-Verlag)

‘northern’ end of the molecule, surrounding the exposed edge of the imidazole ring of the second His ligand (Figure 12). The extent of the hydrophobic patch and the exposure of the His ligand vary somewhat from one protein to another, with azurin, auracyanin, and rusticyanin the least exposed, most hydrophobic and the phytocyanins the most exposed, least hydrophobic. While the hydrophobic patch is one clear candidate for a redox binding site, the rest of the surface varies considerably from one protein to another and binding sites are thus also likely to vary.

5.4.3 *Plastocyanin*

The 3D structure of plastocyanin reveals two potential binding sites on the molecular surface (Figure 13). The closest to the copper is the hydrophobic patch around His 87; the copper atom lies ∼6 Å below this patch. The second potential binding site is the so-called *acidic patch*. This comprises two groups of acidic residues, 42–45 and 59–61, on either side of the surface-exposed side chain of Tyr 83; the latter is invariant in most all plastocyanins (some algal plastocyanins have Phe and plastocyanin from *Gleobacter violaceus* has Asn) and appeals as a likely participant in an electron-transfer pathway. This site is on the side of the β-barrel structure, some 15–20 Å from the copper site. It is a feature which appears to be shared by the plastocyanins and cucumber stellacyanin, and only universally by the plant plastocyanins, since the equivalent residues on the algal protein from *Anabaena variabilis* are no longer acidic.

NMR line broadening has been used to identify the binding sites for inorganic complexes, with the acidic patch implicated as the binding site for positively charged reagents and the hydrophobic patch and His 87 as the preferred site for neutral and negatively charged species.[14,20] Chemical modifications at the acidic patch inhibit the reaction of plastocyanin with cyt f, but not that with P700, implying that the acidic patch and Tyr 83 form the binding site for cyt f, and another site, presumably the hydrophobic patch, binds with P700 of the photosynthetic reaction center.[14] Conclusive evidence seems to have finally come from mutagenesis experiments, in which mutants of pea plastocyanin have shown that the side chain of Tyr 83, at the center of the acidic patch, is directly involved in binding to cyt f, and forms part of the main route of electron transfer to the copper.[196] Likewise, mutation of Leu 12 in the hydrophobic patch implicates this region in binding to Photosystem I.[197] Additional studies support these observations.[198–201] The crystal structure for cyt f[202] has led to a suggested model for the plastocyanin–cyt f interaction which has been further modeled by paramagnetic NMR and restrained rigid-body molecular dynamics.[203] The optimal orientation of the two proteins demonstrates the interaction of oppositely charged residues in plastocyanin and cyt f, but also showed hydrophobic interactions at the copper and heme sites necessary for electron transfer. The suggestion is that long-range electrostatic forces guide the proteins to an initial encounter complex followed by rearrangement to form a complex optimal for electron transfer and stabilized by short-range interactions.

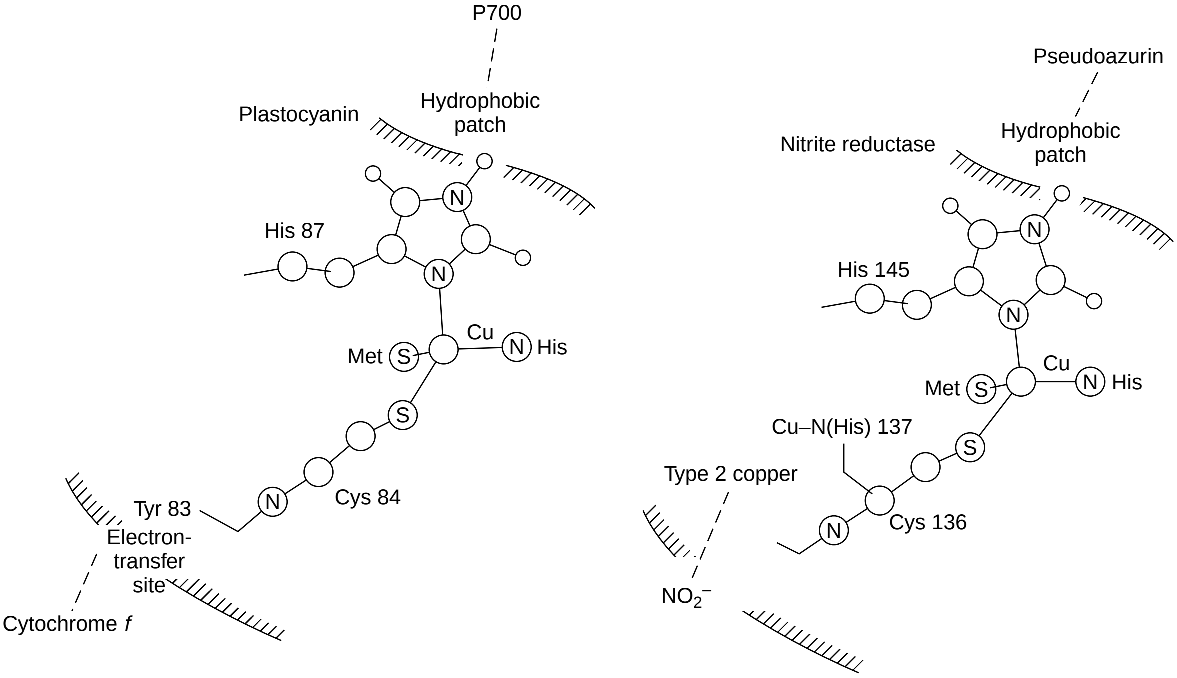

Figure 14 Similarity between the putative electron-transfer routes to and from the type 1 copper sites in plastocyanin and nitrite reductase. (Reproduced with permission of Chapman and Hall from J. Sanders–Loehr, in 'Bioinorganic Chemistry of Copper', ed. K.D. Karlin and Z. Tyeklar, 1993, p. 51)[172]

One intriguing feature of the Tyr 83 site is its similarity to the electron-transfer route in ascorbate oxidase (*see* ***Copper Proteins: Oxidases***) and nitrite reductase. In both of the latter, a His ligand belonging to the type 2 site immediately precedes the Cys ligand of the type 1 site, while in plastocyanin, Tyr 83 immediately precedes Cys 84, the Cys ligand of its type 1 copper site. This suggests the possibility of a common through-bond mechanism (Figure 14).

5.4.4 Azurin

The physiological electron-transfer partners for azurin are less well proven, although they are believed to be a small *c*-type cytochrome (cytochrome *c*-551 (*see* ***Iron: Heme Proteins & Electron Transport***) for *P. aer.* azurin) and a nitrite reductase. As in the plastocyanin case, numerous studies with inorganic redox agents have been carried out in attempts to identify binding sites and electron-transfer pathways.[12] Two conserved His residues, 35 and 83, have been implicated[10] but the evidence is not conclusive and relevance to the physiological (protein) electron-transfer partners is not established. The 3-D structure of *A. den.* azurin shows a SO_4^{2-} ion bound to His 83[77] (Figure 5) suggesting it as a possible binding site for anionic redox reagents. His 83 sits in a shallow depression between the 'flap' (which buries the region equivalent to the acidic patch in plastocyanin) and the main body of the molecule; its location is thus somewhat analogous to the acidic patch.

More attention has been focused on His 35 because of the pH-dependent conformational change which perturbs this residue and apparently influences redox activity by *P. aer.* azurin,[12] and because a nearby region becomes labeled with Cr(III) following the reduction of azurin with Cr(II).[204] These experiments suggested the 'His 35 patch' as a possible redox site. The 3-D structure of azurin shows no obvious binding region near His 35, however,[77] and mutagenesis of this residue in *P. aer.* azurin indicates that it is not involved in electron transfer with either cytochrome *c*-551 or nitrite reductase. Instead, these proteins apparently use the same mechanism and presumably the same site as is involved in the electron self-exchange reaction.[195]

There is now conclusive evidence that it is the hydrophobic patch which is the site of the electron self-exchange reaction in azurin.[195] Mutation of Met 44 in the hydrophobic patch of *P. aer.* azurin to Lys does not change the 3-D structure or spectral properties significantly but does drastically affect electron transfer. At pH 5, where Lys is protonated, the electron self-exchange rate is reduced more than 1000-fold, whereas at higher pH, as Lys becomes deprotonated and more hydrophobic, the rate approaches the native rate of $\sim 10^6\,M^{-1}\,s^{-1}$. The crystal structures of azurin, in fact, provides a model for protein–protein complexes utilizing the hydrophobic patch. In both *A. den.* azurin[77] and *P. aer.* azurin,[103] pairs of molecules dock together through their hydrophobic patches (Figure 15) in such a way that the outer edges of the two His 117 side chains are ~ 7 Å apart. This

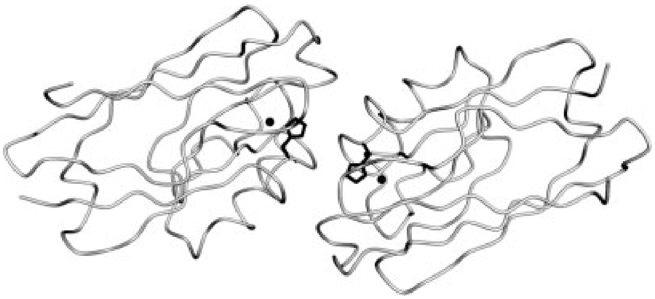

Figure 15 Interaction between two azurin molecules in crystals of *A. den.* azurin. The hydrophobic patches are docked with the two His 117 ligands (thick lines) ~7 Å apart

distance is compatible with the observed rates of electron self-exchange assuming the electron is transferred from one Cu to the other via the two-coordinated imidazole rings. In *P. aer.* azurin, there is the added suggestion that a pair of water molecules, one hydrogen-bonded to each His side chain, may further facilitate the process.[103] With respect to the cytochrome *c*-551 and nitrite reductase from *P. aer.*, the 3-D structure of the latter is not known, but cytochrome *c*-551 does have a hydrophobic patch surrounding the heme edge through which association with the hydrophobic patch of azurin could occur.[195]

5.4.5 An Electron-transfer Complex of Amicyanin

The most spectacular illustration of the importance of the hydrophobic patch in the type 1 copper proteins is provided by the crystal structure of a complex between amicyanin and its electron-transfer partners methylamine dehydrogenase (MADH) and cytochrome *c*-551.[205] As in the other type 1 proteins, amicyanin has a hydrophobic patch comprising some 7 hydrophobic side chains surrounding the exposed edge of the copper-bound His 95 (analogous to His 87 in plastocyanin and His 117 in azurin) (Figure 16). In the complex, this docks with a hydrophobic surface on MADH containing about 12 nonpolar or neutral side chains, including Trp 108, which is part of the tryptophan tryptophylquinone (TTQ) cofactor. The indole ring of Trp 108 approaches within 5.4 Å of the imidazole ring of His 95, such that electron transfer from the *o*-quinone ring of Trp 57 in the TTQ cofactor, through Trp 107, to His 95 in amicyanin, and then to the copper can be readily envisaged.

5.4.6 Electron Transfer in Modified Type 1 Proteins

Ruthenium, osmium, and rhenium complexes have been used to define electron-transfer rates over defined distances and pathways (*see* ***Iron: Heme Proteins & Electron Transport***; ***Long-range Electron Transfer in Biology***).[98,194] They can be attached to external His residues by displacement of its aqua ligand, and are particularly useful because of their redox potentials and inertness to substitution. For azurin, His 83, 11.8 Å from the copper, is an ideal site for derivatization with these reagents. Rates of reduction of Os(III), Ru(III) and Re(I)* by Cu(I) in His 83-modified *P. aer.* azurin have been measured in single crystals where the protein conformation and surface solvation are defined by high-resolution X-ray crystallography. The time constants for electron tunneling in crystals are roughly what they are in solution suggesting very similar protein structures in the two states. The high-resolution structures of the oxidized (1.5 Å) and reduced (1.4 Å) states confirm that there are only very small changes in copper coordination accompany reduction. Both the driving force and temperature effects on Cu(I) → Ru(III), Os(III), and Re(I)* electron-transfer rates were examined. The reorganization energy for the electron transfer falls in the range of 0.6–0.8 eV, which agrees with that determined experimentally in solution. This work suggests that outer-sphere protein reorganization is the dominant component required for electron tunneling.

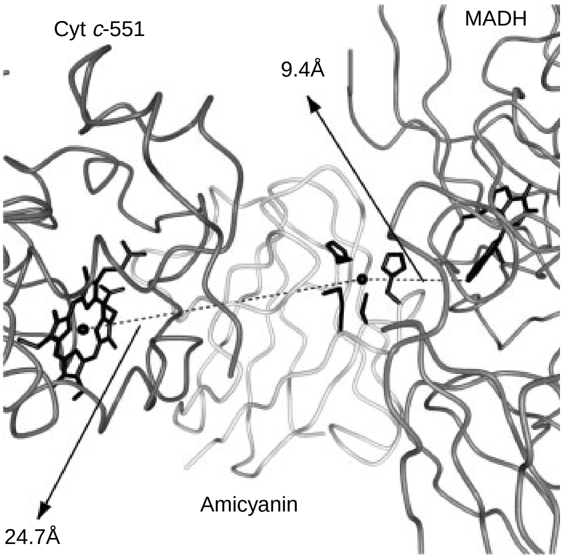

Figure 16 Structure of the ternary electron-transfer complex of MADH, amicyanin, and cytochrome *c*-551 (pdb code 2MTA). The copper atom of amicyanin is ~9.4 Å from the edge of Trp 108 in the electron donor MADH and ~24.7 Å from the electron acceptor iron atom in cytochrome *c*-551

6 RELATED ARTICLES

Copper Enzymes in Denitrification; Copper: Hemocyanin/Tyrosinase Models; Copper Proteins: Oxidases; Copper Proteins with Dinuclear Active Sites; Copper Proteins with Type 2 Sites; Iron–Sulfur Proteins; Metallochaperones & Metal Ion Homeostasis; Zinc Enzymes.

7 REFERENCES

1. B. G. Malmström, in ‘Oxidases and Related Redox Systems’, eds. T. E. King, H. S. Mason, and M. Morrison, Wiley, New York, 1964, p. 207.
2. B. L. Vallee and R. J. Williams, *Proc. Natl. Acad. Sci. U.S.A.*, 1968, **59**, 498.
3. B. G. Malmström, *Eur. J. Biochem.*, 1994, **223**, 711.
4. R. J. Williams, *Eur. J. Biochem.*, 1995, **234**, 363.
5. H. B. Gray, B. G. Malmström, and R. J. Williams, *J. Biol. Inorg. Chem.*, 2000, **5**, 551.
6. R. Malkin and B. G. Malmström, *Adv.Enzymol. Relat. Areas Mol. Biol.*, 1970, **33**, 177.
7. B. G. Malmström, *Adv. Exp. Med. Biol.*, 1982, **148**, 87.
8. J. A. Fee, *Struct. Bonding (Berlin)*, 1975, **23**, 1.
9. H. B. Gray and E. I. Solomon, in ‘Copper Proteins’, ed. T. G. Spiro, Wiley, New York, 1981, Vol. 3, p. 1.
10. A. G. Lappin, in ‘Metal Ions in Biological Systems’, ed. H. Sigel, Marcel Dekker, New York, 1973, Vol. 13, p. 15.
11. L. Ryden, in ‘Copper Proteins and Copper Enzymes’, ed. R. Lontie, CRC Press, Boca Raton, FL, 1984, Vol. 1, p. 37.
12. E. T. Adman, in ‘Metalloproteins’, ed. P. M. Harrison, Macmillan, New York, 1985, Vol. 1, p. 1.
13. A. G. Sykes, *Adv. Inorg. Chem.*, 1991, **36**, 377.
14. S. K. Chapman, in ‘Perspectives in Bioinorganic Chemistry’, eds. R. W. Hay, J. R. Dilworth, and K. B. Nolan, JAI Press, London, 1991, Vol. 1, p. 95.
15. G. W. Canters and G. Gilardi, *FEBS Lett.*, 1993, **325**, 39.
16. A. M. Nersissian and E. L. Shipp, *Adv. Protein Chem.*, 2002, **60**, 271.
17. E. T. Adman, *Adv. Protein Chem.*, 1991, **42**, 145.
18. E. I. Solomon and K. W. Penfield, *Struct. Bonding (Berlin)*, 1983, **53**, 1.
19. E. I. Solomon, R. K. Szilagyi, S. DeBeer George, and L. Basumallick, *Chem. Rev.*, 2004, **104**, 419.
20. A. G. Sykes, *Struct. Bonding (Berlin)*, 1990, **75**, 175.
21. D. S. Wuttke and H. B. Gray, *Curr. Opin. Struct. Biol.*, 1993, **3**, 555.
22. J. Moseley, J. Quinn, M. Eriksson, and S. Merchant, *EMBO J.*, 2000, **19**, 2139.
23. S. Smeekens, M. Degroot, J. van Binsbergen, and P. Weisbeek, *Nature*, 1985, **317**, 456.
24. R. P. Ambler and L. H. Brown, *J. Mol. Biol.*, 1964, **65**, 825.
25. G. W. Canters, *FEBS Lett.*, 1987, **212**, 168.
26. R. J. van Spanning, C. W. Wansell, W. N. Reijnders, L. F. Oltmann, and A. H. Stouthamer, *FEBS Lett.*, 1990, **275**, 217.
27. D. E. Rawlings, *Hydrometallurgy*, 2001, **59**, 187.
28. B. Scharf and M. Engelhard, *Biochemistry*, 1993, **32**, 12894.
29. J. Castresana, M. Lubben, and M. Saraste, *J. Mol. Biol.*, 1995, **250**, 202.
30. L. Komorowski and G. Schafer, *FEBS Lett.*, 2001, **487**, 351.
31. S. Mattar, B. Scharf, S. B. Kent, K. Rodewald, D. Oesterhelt, and M. Engelhard, *J. Biol. Chem.*, 1994, **269**, 14939.
32. L. Komorowski, W. Verheyen, and G. Schafer, *Biol. Chem.*, 2002, **383**, 1791.
33. J. D. McManus, D. C. Brune, J. Han, J. Sanders-Loehr, T. E. Meyer, M. A. Cusanovich, G. Tollin, and R. E. Blankenship, *J. Biol. Chem.*, 1992, **267**, 6531.
34. G. Van Driessche, W. Hu, G. Van de Werken, F. Selvaraj, J. D. McManus, R. E. Blankenship, and J. J. Van Beeumen, *Protein Sci.*, 1999, **8**, 947.
35. G. H. H. Borner, K. S. Lilley, T. J. Stevens, and P. Dupree, *Plant Physiol.*, 2003, **132**, 568.
36. T. Omura, *J. Biochem. (Tokyo)*, 1961, **50**, 394.
37. C. Bergman, E. K. Gandvik, P. O. Nyman, and L. Strid, *Biochem. Biophys. Res. Commun.*, 1977, **77**, 1052.
38. K. G. Paul and T. Stigbrand, *Biochim. Biophys. Acta*, 1970, **221**, 255.
39. A. Marchesini, M. Minelli, H. Merkle, and P. M. Kroneck, *Eur. J. Biochem.*, 1979, **101**, 77.
40. V. T. Aikazyan and R. M. Nalbandyan, *FEBS Lett.*, 1979, **104**, 127.
41. L. K. Sarkissian and R. M. Nalbandyan, *Biosci. Rep.*, 1983, **3**, 915.
42. K. A. Markossian, V. T. Aikazyan, and R. M. Nalbandyan, *Biochim. Biophys. Acta*, 1974, **359**, 47.
43. J. Toth, T. Cutforth, A. D. Gelinas, K. A. Bethoney, J. Bard, and C. J. Harrison, *Dev. Cell*, 2001, **1**, 83.
44. J. P. Himanen, K. R. Rajashankar, M. Lackmann, C. A. Cowan, M. Henkemeyer, and D. B. Nikolov, *Nature*, 2001, **414**, 933.
45. P. M. Colman, H. C. Freeman, J. M. Guss, M. Murata, V. A. Norris, J. A. M. Ramshaw, and M. P. Venkatappa, *Nature*, 1978, **272**, 319.
46. E. T. Adman, R. E. Stenkamp, L. C. Sieker, and L. H. Jensen, *J. Mol. Biol.*, 1978, **123**, 35.
47. D. R. McMillin, *J. Chem. Educ.*, 1985, **62**, 997.
48. D. R. McMillin, R. C. Rosenberg, and H. B. Gray, *Proc. Natl. Acad. Sci. U.S.A.*, 1974, **71**, 4760.
49. R. J. P. Williams, *Inorg. Chim. Acta Rev.*, 1971, **5**, 137.
50. J. L. Markley, E. L. Ulrich, S. P. Berg, and D. W. Krogmann, *Biochemistry*, 1975, **14**, 4428.
51. L. Ryden and J. Lundgren, *Nature*, 1976, **261**, 344.
52. M. R. Redinbo and T. O. Yeates, *Acta. Crystallogr., Sect. D*, 1993, **49**, 375.
53. T. Kohzuma, T. Inoue, F. Yoshizaki, Y. Sasakawa, K. Onodera, S. Nagatomo, T. Kitagawa, S. Uzawa, Y. Isobe, Y. Sugimura, M. Gotowda, and Y. Kai, *J. Biol. Chem.*, 1999, **274**, 11817.

54. C. A. Collyer, J. M. Guss, Y. Sugimura, F. Yoshizaki, and H. C. Freeman, *J. Mol. Biol.*, 1990, **211**, 617.
55. C. S. Bond, D. S. Bendall, H. C. Freeman, J. M. Guss, C. J. Howe, M. J. Wagner, and M. C. Wilce, *Acta. Crystallogr., Sect. D*, 1999, **55**, 414.
56. M. Milani, L. Andolfi, S. Cannistraro, M. P. Verbeet, and M. Bolognesi, *Acta. Crystallogr., Sect. D*, 2001, **57**, 1735.
57. J. M. Guss, H. D. Bartunik, and H. C. Freeman, *Acta Crystallogr.*, 1992, **B48**, 790.
58. B. A. Fields, H. H. Bartsch, H. D. Bartunik, F. Cordes, J. M. Guss, and H. C. Freeman, *Acta. Crystallogr., Sect. D*, 1994, **50**, 709.
59. T. P. Garrett, D. J. Clingeleffer, J. M. Guss, S. J. Rogers, and H. C. Freeman, *J. Biol. Chem.*, 1984, **259**, 2822.
60. W. B. Church, J. M. Guss, J. J. Potter, and H. C. Freeman, *J. Biol. Chem.*, 1986, **261**, 234.
61. J. M. Guss, P. R. Harrowell, M. Murata, V. A. Norris, and H. C. Freeman, *J. Mol. Biol.*, 1986, **192**, 361.
62. Y. Xue, M. Okvist, O. Hansson, and S. Young, *Protein Sci.*, 1998, **7**, 2099.
63. H. Jansson, M. Okvist, F. Jacobson, M. Ejdeback, O. Hansson, and L. Sjolin, *Biochim. Biophys. Acta*, 2003, **1607**, 203.
64. H. Sugawara, T. Inoue, C. Li, M. Gotowda, T. Hibino, T. Takabe, and Y. Kai, *J. Biochem. (Tokyo)*, 1999, **125**, 899.
65. T. Inoue, H. Sugawara, S. Hamanaka, H. Tsukui, E. Suzuki, T. Kohzuma, and Y. Kai, *Biochemistry*, 1999, **38**, 6063.
66. A. Romero, B. De la Cerda, P. F. Varela, J. A. Navarro, M. Hervas, and M. A. De la Rosa, *J. Mol. Biol.*, 1998, **275**, 327.
67. N. Shibata, T. Inoue, C. Nagano, N. Nishio, T. Kohzuma, K. Onodera, F. Yoshizaki, Y. Sugimura, and Y. Kai, *J. Biol. Chem.*, 1999, **274**, 4225.
68. L. Ma, A. M. Jorgensen, G. O. Soerensen, J. Ulstrup, and J. J. Led, *J. Am. Chem. Soc.*, 2000, **122**, 9473.
69. U. Badsberg, A. M. Jorgensen, H. Gesmar, J. J. Led, J. M. Hammerstad, L. L. Jespersen, and J. Ulstrup, *Biochemistry*, 1996, **35**, 7021.
70. S. Bagby, P. C. Driscoll, T. S. Harvey, and H. A. Hill, *Biochemistry*, 1994, **33**, 6611.
71. C. R. Babu, B. F. Volkman, and G. S. Bullerjahn, *Biochemistry*, 1999, **38**, 4988.
72. J. M. Moore, C. A. Lepre, G. P. Gippert, W. J. Chazin, D. A. Case, and P. E. Wright, *J. Mol. Biol.*, 1991, **221**, 533.
73. J. M. Moore, W. J. Chazin, R. Powls, and P. E. Wright, *Biochemistry*, 1988, **27**, 7806.
74. I. Bertini, S. Ciurli, A. Dikiy, C. O. Fernandez, C. Luchinat, N. Safarov, S. Shumilin, and A. J. Vila, *J. Am. Chem. Soc.*, 2001, **123**, 2405.
75. I. Bertini, D. A. Bryant, S. Ciurli, A. Dikiy, C. O. Fernandez, C. Luchinat, N. Safarov, A. J. Vila, and J. Zhao, *J. Biol. Chem.*, 2001, **276**, 47217.
76. A. Messerschmidt, L. Prade, S. J. Kroes, J. Sanders-Loehr, R. Huber, and G. W. Canters, *Proc. Natl. Acad. Sci. U. S. A.*, 1998, **95**, 3443.
77. E. N. Baker, *J. Mol. Biol.*, 1988, **203**, 1071.
78. F. E. Dodd, Z. H. L. Abraham, R. R. Eady, and S. S. Hasnain, *Acta. Crystallogr., Sect. D*, 2000, **56**, 690.
79. C. Li, T. Inoue, M. Gotowda, S. Suzuki, K. Yamaguchi, K. Kunishige, and Y. Kai, *Acta. Crystallogr., Sect. D*, 1998, **54**, 347.
80. W. E. B. Shepard, R. L. Kingston, B. F. Anderson, and E. N. Baker, *Acta Crystallogr.*, 1993, **D49**, 331.
81. A. Romero, C. W. Hoitink, H. Nar, R. Huber, A. Messerschmidt, and G. W. Canters, *J. Mol. Biol.*, 1993, **229**, 1007.
82. T. Inoue, N. Nishio, K. Kanamoto, S. Suzuki, K. Yamaguchi, K. Kataoka, J. Tobari, and Y. Kai, *Acta. Crystallogr., Sect. D. Biol. Crystallogr.*, 1999, **55**, 307.
83. S. Faham, T. J. Mizoguchi, E. T. Adman, H. B. Gray, J. H. Richards, and D. C. Rees, *J. Biol. Inorg. Chem.*, 1997, **2**, 464.
84. L. C. Tsai, L. Sjolin, V. Langer, T. Pascher, and H. Nar, *Acta. Crystallogr., Sect. D*, 1995, **51**, 168.
85. L. Sjolin, L. C. Tsai, V. Langer, T. Pascher, G. Karlsson, M. Nordling, and H. Nar, *Acta. Crystallogr., Sect. D*, 1993, **49**, 449.
86. E. T. Adman and L. H. Jensen, *Isr. J. Chem.*, 1981, **21**, 8.
87. S. Faham, M. W. Day, W. B. Connick, B. R. Crane, A. J. Di Bilio, W. P. Schaefer, D. C. Rees, and H. B. Gray, *Acta. Crystallogr., Sect. D*, 1999, **55**, 379.
88. H. Robinson, M. C. Ang, Y.-G. Gao, M. T. Hay, Y. Lu, and A. H.-J. Wang, *Biochemistry*, 1999, **38**, 5677.
89. H. Nar, A. Messerschmidt, R. Huber, M. van de Kamp, and G. W. Canters, *J. Mol. Biol.*, 1991, **221**, 765.
90. H. Nar, A. Messerschmidt, M. Huber, M. van de Kamp, and G. W. Canters, *FEBS Lett.*, 1992, **306**, 119.
91. H. Nar, R. Huber, A. Messerschmidt, A. C. Filippou, M. Barth, M. Jaquinod, M. van de Kamp, and G. W. Canters, *Eur. J. Biochem.*, 1992, **205**, 1123.
92. B. G. Karlsson, L. C. Tsai, H. Nar, J. Sanders-Loehr, N. Bonander, V. Langer, and L. Sjolin, *Biochemistry*, 1997, **36**, 4089.
93. N. Bonander, J. Leckner, H. Guo, B. G. Karlsson, and L. Sjolin, *Eur. J. Biochem.*, 2000, **267**, 4511.
94. M. Okvist, N. Bonander, A. Sandberg, B. G. Karlsson, U. Krengel, Y. Xue, and L. Sjolin, *Biochim. Biophys. Acta*, 2002, **1596**, 336.
95. A. J. Di Bilio, B. R. Crane, W. A. Wehbi, C. N. Kiser, M. M. Abu-Omar, R. M. Carlos, J. H. Richards, J. R. Winkler, and H. B. Gray, *J. Am. Chem. Soc.*, 2001, **123**, 3181.

96. C. Hammann, A. Messerschmidt, R. Huber, H. Nar, G. Gilardi, and G. W. Canters, *J. Mol. Biol.*, 1996, **255**, 362.

97. M. C. Van Amsterdam, M. Ubbink, O. Einsle, A. Messerschmidt, A. Merli, D. Cavazzini, G. L. Rossi, and G. W. Canters, *Nat. Struct. Biol.*, 2002, **9**, 48.

98. B. R. Crane, A. J. Di Bilio, J. R. Winkler, and H. B. Gray, *J. Am. Chem. Soc.*, 2001, **123**, 11623.

99. R. A. Marcus and N. Sutin, *Biochim. Biophys. Acta*, 1985, **811**, 265.

100. L. C. Tsai, L. Sjolin, V. Langer, N. Bonander, B. G. Karlsson, T. Vanngard, C. Hammann, and H. Nar, *Acta. Crystallogr., Sect. D*, 1995, **51**, 711.

101. J. E. Miller, C. Gradinaru, B. R. Crane, A. J. Di Bilio, W. A. Wehbi, S. Un, J. R. Winkler, and H. B. Gray, *J. Am. Chem. Soc.*, 2003, **125**, 14220.

102. N. Bonander, T. Vanngard, L. C. Tsai, V. Langer, H. Nar, and L. Sjolin, *Proteins*, 1997, **27**, 385.

103. H. Nar, A. Messerschmidt, R. Huber, M. van de Kamp, and G. W. Canters, *J. Mol. Biol.*, 1991, **218**, 427.

104. L. C. Tsai, N. Bonander, K. Harata, G. Karlsson, T. Vanngard, V. Langer, and L. Sjolin, *Acta. Crystallogr., Sect. D*, 1996, **52**, 950.

105. W. Zhu, T. Dahms, K. Willis, A. G. Szabo, and X. Lee, *Arch. Biochem. Biophys.*, 1994, **308**, 469.

106. Z. W. Chen, M. J. Barber, W. S. McIntire, and F. S. Mathews, *Acta. Crystallogr., Sect. D*, 1998, **54**, 253.

107. T. Inoue, N. Nishio, S. Suzuki, K. Kataoka, T. Kohzuma, and Y. Kai, *J. Biol. Chem.*, 1999, **274**, 17845.

108. T. Inoue, N. Nishio, Y. Kai, S. Harada, Y. Ohshiro, S. Suzuki, T. Kohzuma, S. Shidara, and H. Iwasaki, *J. Biochem. (Tokyo)*, 1993, **114**, 761.

109. K. Petratos, Z. Dauter, and K. S. Wilson, *Acta. Crystallogr., Sect. B*, 1988, **44**, 628.

110. E. Vakoufari, K. S. Wilson, and K. Petratos, *FEBS Lett.*, 1994, **347**, 203.

111. C. A. Libey, M. Kukimoto, M. Nishiyama, S. Horinouchi, and E. T. Adman, *Biochemistry*, 1997, **36**, 13160.

112. T. Inoue, Y. Kai, S. Harada, N. Kasai, Y. Ohshiro, S. Suzuki, T. Kohzuma, and J. Tobari, *Acta. Crystallogr., Sect. D*, 1994, **50**, 317.

113. R. Durley, L. Chen, L. W. Lim, F. S. Mathews, and V. L. Davidson, *Protein Sci.*, 1993, **2**, 739.

114. Z. Zhu, L. M. Cunane, Z. Chen, R. C. Durley, F. S. Mathews, and V. L. Davidson, *Biochemistry*, 1998, **37**, 17128.

115. L. Chen, R. Durley, B. J. Poliks, K. Hamada, Z. Chen, F. S. Mathews, V. L. Davidson, Y. Satow, E. Huizinga, and F. M. Vellieux, *Biochemistry*, 1992, **31**, 4959.

116. D. Sun, Z. W. Chen, F. S. Mathews, and V. L. Davidson, *Biochemistry*, 2002, **41**, 13926.

117. A. Romero, H. Nar, R. Huber, A. Messerschmidt, A. P. Kalverda, G. W. Canters, R. Durley, and F. Mathews, *J. Mol. Biol.*, 1994, **236**, 1196.

118. J. M. Guss, E. A. Merritt, R. P. Phizackerley, and H. C. Freeman, *J. Mol. Biol.*, 1996, **262**, 686.

119. O. Einsle, Z. Mehrabian, R. Nalbandyan, and A. Messerschmidt, *J. Biol. Inorg. Chem.*, 2000, **5**, 666.

120. P. J. Hart, A. M. Nersissian, R. G. Herrmann, R. M. Nalbandyan, J. S. Valentine, and D. Eisenberg, *Protein Sci.*, 1996, **5**, 2175.

121. M. Lee, M. J. Maher, H. C. Freeman, and J. M. Guss, *Acta. Crystallogr., Sect. D*, 2003, **59**, 1545.

122. C. S. Bond, R. E. Blankenship, H. C. Freeman, J. M. Guss, M. Maher, F. Selvaraj, M. C. J. Wilce, and K. Willingham, *J. Mol. Biol.*, 2001, **306**, 47.

123. R. L. Walter, S. E. Ealick, A. M. Friedman, R. C. Blake II, P. Proctor, and M. Shoham, *J. Mol. Biol.*, 1996, **263**, 730.

124. I. Harvey, Q. Hao, E. M. Duke, W. J. Ingledew, and S. S. Hasnain, *Acta. Crystallogr., Sect. D*, 1998, **54**, 629.

125. J. F. Hall, L. D. Kanbi, R. W. Strange, and S. S. Hasnain, *Biochemistry*, 1999, **38**, 12675.

126. L. D. Kanbi, S. Antonyuk, M. A. Hough, J. F. Hall, F. E. Dodd, and S. S. Hasnain, *J. Mol. Biol.*, 2002, **320**, 263.

127. M. V. Botuyan, A. Toy-Palmer, J. Chung, R. C. Blake II, P. Beroza, D. A. Case, and H. J. Dyson, *J. Mol. Biol.*, 1996, **263**, 752.

128. J. Van Beeumen, S. Van Bun, G. W. Canters, A. Lommen, and C. Chothia, *J. Biol. Chem.*, 1991, **266**, 4869.

129. J. Han, E. T. Adman, T. Beppu, R. Codd, H. C. Freeman, L. L. Huq, T. M. Loehr, and J. Sanders-Loehr, *Biochemistry*, 1991, **30**, 10904.

130. S. Wherland, O. Farver, and I. Pecht, *J. Mol. Biol.*, 1988, **204**, 407.

131. B. A. Fields, J. M. Guss, and H. C. Freeman, *J. Mol. Biol.*, 1991, **222**, 1053.

132. A. M. Nersissian, Z. B. Mehrabian, R. M. Nalbandyan, P. J. Hart, G. Fraczkiewicz, R. S. Czernuszewicz, C. J. Bender, J. Peisach, R. G. Herrmann, and J. S. Valentine, *Protein Sci.*, 1996, **5**, 2184.

133. M. van de Kamp, G. W. Canters, S. S. Wijmenga, A. Lommen, C. W. Hilbers, H. Nar, A. Messerschmidt, and R. Huber, *Biochemistry*, 1992, **31**, 10194.

134. C. W. Hoitink and G. W. Canters, *J. Biol. Chem.*, 1992, **267**, 13836.

135. T. D. Tullius, P. Frank, and K. O. Hodgson, *Proc. Natl. Acad. Sci. U.S.A.*, 1978, **75**, 4069.

136. P. J. Ellis, Studies of Metalloproteins Using EXAFS and XRD, Thesis, University of Sydney, Sydney, 1995.

137. S. DeBeer, D. W. Randall, A. M. Nersissian, J. S. Valentine, B. Hedman, K. O. Hodgson, and E. I. Solomon, *J. Phys. Chem. B*, 2000, **104**, 10814.

138. S. DeBeer, P. Wittung-Stafshede, J. Leckner, G. Karlsson, J. R. Winkler, H. B. Gray, B. G. Malmström, E. I. Solomon, B. Hedman, and K. O. Hodgson, *Inorg. Chim. Acta.*, 2000, **297**, 278.

139. R. W. Strange, B. Reinhammer, L. M. Murphy, and S. S. Hasnain, *Biochemistry*, 1995, **34**, 220.

140. R. W. Strange, L. M. Murphy, B. G. Karlsson, B. Reinhammar, and S. S. Hasnain, *Biochemistry*, 1996, **35**, 16391.

141. S. DeBeer George, L. Basumallick, R. K. Szilagyi, D. W. Randall, M. G. Hill, A. M. Nersissian, J. S. Valentine, B. Hedman, K. O. Hodgson, and E. I. Solomon, *J. Am. Chem. Soc.*, 2003, **125**, 11314.

142. S. M. Berry, M. Ralle, D. L. Low, and N. J. Blackburn, *J. Am. Chem. Soc.*, 2003, **125**, 8760.

143. S. DeBeer, C. N. Kiser, G. A. Mines, J. H. Richards, H. B. Gray, E. I. Solomon, B. Hedman, and K. O. Hodgson, *Inorg. Chem.*, 1999, **38**, 433.

144. R. A. Scott, J. E. Hahn, S. Doniach, H. C. Freeman, and K. O. Hodgson, *J. Am. Chem. Soc.*, 1982, **104**, 5364.

145. L. M. Murphy, S. S. Hasnain, R. W. Strange, I. Harvey, and W. J. Ingledew, Xafs Studies on Blue Copper Proteins: The Effect of ph and Oxidation State Changes on the Copper Site, in ‘X-ray Absorption Fine Structure’, ed. S. S. Hasnain, Ellis Horwood, London, 1991, p. 152.

146. K. Petratos, M. Papadovasilaki, and Z. Dauter, *FEBS Lett.*, 1995, **368**, 432.

147. T. Sakurai, H. Okamoto, K. Kawahara, and A. Nakahara, *FEBS Lett.*, 1982, **147**, 220.

148. H. R. Engeseth, D. R. McMillin, and J. D. Otvos, *J. Biol. Chem.*, 1984, **259**, 4822.

149. E. N. Baker, *J. Inorg. Biochem.*, 1991, **43**, 162.

150. H. B. Gray and B. G. Malmström, *Comments Inorg. Chem.*, 1983, **2**, 202.

151. A. Messerschmidt, *Struct. Bonding*, 1998, **90**, 38.

152. E. N. Baker, in ‘Encyclopedia of Inorganic Chemistry’, Wiley, 1994, Vol. 1, p. 883.

153. E. I. Solomon, U. M. Sundaram, and T. E. Machonkin, *Chem. Rev.*, 1996, **96**, 2563.

154. D. W. Randall, D. R. Gamelin, L. B. LaCroix, and E. I. Solomon, *J. Biol. Inorg. Chem.*, 2000, **5**, 16.

155. R. J. P. Williams, *Eur. J. Biochem.*, 1995, **234**, 363.

156. E. T. Adman, J. W. Godden, and S. Turley, *J. Biol. Chem.*, 1995, **270**, 27458.

157. A. Messerschmidt ed., ‘Multicopper Oxidases’, World Scientific, Singapore, 1997, p. 23.

158. E. I. Solomon, K. W. Penfield, A. A. Gewirth, M. D. Lowery, S. E. Shadle, J. A. Guckert, and L. B. Lacroix, *Inorg. Chim. Acta*, 1996, **243**, 67.

159. A. A. Gewirth and E. I. Solomon, *J. Am. Chem. Soc.*, 1988, **110**, 3811.

160. J. Han, T. M. Loehr, Y. Lu, J. S. Valentine, B. A. Averill, and J. S. Loehr, *J. Am. Chem. Soc.*, 1993, **115**, 4256.

161. L. B. LaCroix, S. E. Shadle, Y. N. Wang, B. A. Averill, B. Hedman, K. O. Hodgson, and E. I. Solomon, *J. Am. Chem. Soc.*, 1996, **118**, 7755.

162. A. E. Palmer, D. W. Randall, F. Xu, and E. I. Solomon, *J. Am. Chem. Soc.*, 1999, **121**, 7138.

163. T. E. Machonkin, L. Quintanar, A. E. Palmer, R. Hassett, A. Severance, D. J. Kosman, and E. I. Solomon, *J. Am. Chem. Soc.*, 2001, **123**, 5507.

164. L. B. LaCroix, D. W. Randall, A. M. Nersissian, C. W. G. Hoitink, G. W. Canters, J. S. Valentine, and E. I. Solomon, *J. Am. Chem. Soc.*, 1998, **120**, 9621.

165. B. G. Malmström and T. Vanngard, *J. Mol. Biol.*, 1960, **2**, 118.

166. C. A. Bates, W. S. Moore, K. J. Standley, and K. W. H. Stevens, *Proc. Phys. Soc. London*, 1962, **79**, 73.

167. M. Sharnoff, *J. Chem. Phys.*, 1964, **42**, 3383.

168. A. S. Brill and G. R. Bryce, *J. Chem. Phys.*, 1968, **48**, 4398.

169. S. E. Shadle, J. E. Penner-Hahn, H. J. Schugar, B. Hedman, K. O. Hodgson, and E. I. Solomon, *J. Am. Chem. Soc.*, 1993, **115**, 767.

170. A. A. Gewirth, S. L. Cohen, H. J. Schugar, and E. I. Solomon, *Inorg. Chem.*, 1987, **26**, 1133.

171. T. G. Spiro and R. S. Czernuszewicz, *Methods Enzymol.*, 1995, **246**, 416.

172. J. Sanders-Loehr, in ‘Bioinorganic Chemistry of Copper’, eds. K. D. Karlin and Z. Tyeklar, Chapman & Hall, New York, 1993, p. 51.

173. E. Fraga and G. R. Loppnow, *J. Phy. Chem.*, 1998, **102**, 7659.

174. E. Fraga, M. A. Webb, and G. R. Loppnow, *J. Phys. Chem. B*, 1996, **100**, 3278.

175. M. A. Webb, C. M. Kwong, and G. R. Loppnow, *J. Phys. Chem. B*, 1997, **101**, 5062.

176. S. J. George, M. D. Lowery, E. I. Solomon, and S. P. Cramer, *J. Am. Chem. Soc.*, 1993, **115**, 2968.

177. S. Larsson, A. Broo, and L. Sjölin, *J. Phys. Chem.*, 1995, **99**, 4860.

178. K. Pierloot, J. O. A. DeKerpel, U. Ryde, and B. O. Roos, *J. Am. Chem. Soc.*, 1997, **119**, 218.

179. K. Pierloot, J. O. A. De Kerpel, U. Ryde, M. H. M. Olsson, and B. O. Roos, *J. Am. Chem. Soc.*, 1998, **120**, 13156.

180. R. K. Szilagyi, M. Metz, and E. I. Solomon, *J. Phys. Chem. A*, 2002, **106**, 2994.

181. R. K. Szilagyi and E. I. Solomon, *Curr. Opin. Chem. Biol.*, 2002, **6**, 250.

182. J. J. Regan, A. J. Di Bilio, R. Langen, L. K. Skov, J. R. Winkler, H. B. Gray, and J. N. Onuchic, *Chem. Biol.*, 1995, **2**, 489.

183. M. D. Lowery, J. A. Guckert, M. S. Gebhard, and E. I. Solomon, *J. Am. Chem. Soc.*, 1993, **115**, 3012.

184. M. D. Newton, *Chem. Rev.*, 1991, **91**, 767.

185. P. Kyritsis, L. G. Lundberg, M. Nordling, T. Vanngard, S. Young, N. P. Tompkins, and A. G. Sykes, *Chem. Commun.*, 1991, **20**, 1441.

186. M. M. Werst, C. E. Davoust, and B. M. Hoffman, *J. Am. Chem. Soc.*, 1991, **113**, 1533.
187. J. R. Winkler, P. Wittung-Stafshede, J. Leckner, B. G. Malmström, and H. B. Gray, *Proc. Natl. Acad. Sci. U.S.A.*, 1997, **94**, 4246.
188. A. J. Di Bilio, M. G. Hill, N. Bonander, B. G. Karlsson, R. M. Villahermosa, B. G. Malmström, J. R. Winkler, and H. B. Gray, *J. Am. Chem. Soc.*, 1997, **119**, 9921.
189. L. K. Skov, T. Pascher, J. R. Winkler, and H. B. Gray, *J. Am. Chem. Soc.*, 1998, **120**, 1102.
190. K. Sigfridsson, M. Ejdeback, M. Sundahl, and O. Hansson, *Arch. Biochem. Biophys.*, 1998, **351**, 197.
191. S. Larsson, *J. Chem. Soc., Faraday Trans. 2*, 1983, **79**, 1375.
192. U. Ryde and M. H. M. Olsson, *Int. J. Quantum Chem.*, 2001, **81**, 335.
193. M. H. M. Olsson, U. Ryde, and B. O. Roos, *Protein Sci.*, 1998, **7**, 2659.
194. H. B. Gray, *Chem. Soc. Rev.*, 1986, **15**, 17.
195. M. van de Kamp, M. C. Silvestrini, M. Brunori, J. Van Beeumen, F. C. Hali, and G. W. Canters, *Eur. J. Biochem.*, 1990, **194**, 109.
196. S. He, S. Modi, D. S. Bendall, and H. B. Gray, *EMBO J.*, 1991, **10**, 4011.
197. M. Nordling, K. Sigfridsson, S. Young, L. G. Lundberg, and O. Hansson, *FEBS Lett.*, 1991, **291**, 327.
198. X. Gong, J. Q. Wen, N. E. Fisher, S. Young, C. J. Howe, D. S. Bendall, and J. C. Gray, *Eur. J. Biochem.*, 2000, **267**, 3461.
199. X. Gong, J. Q. Wen, and J. C. Gray, *Eur. J. Biochem.*, 2000, **267**, 1732.
200. M. Ejdeback, A. Bergkvist, B. G. Karlsson, and M. Ubbink, *Biochemistry*, 2000, **39**, 5022.
201. A. Bergkvist, M. Ejdeback, M. Ubbink, and B. G. Karlsson, *Protein Sci.*, 2001, **10**, 2623.
202. S. E. Martinez, D. Huang, A. Szczepaniak, W. A. Cramer, and J. L. Smith, *Structure*, 1994, **2**, 95.
203. M. Ubbink, M. Ejdeback, B. G. Karlsson, and D. S. Bendall, *Structure*, 1998, **6**, 323.
204. O. Farver and I. Pecht, in ‘Copper Proteins’, ed. T. G. Spiro, Wiley, New York, 1981, Vol. 3, p. 151.
205. L. Chen, R. C. Durley, F. S. Mathews, and V. L. Davidson, *Science*, 1994, **264**, 86.

Acknowledgments

We thank Alex Taylor, and Stephen Holloway for help with the figures and Jennifer Elam and Lisa Whitson for unpublished work on cucumber stellacyanin and tomato plantacyanin, respectively. Funding support from the Robert A. Welch Foundation Grant AQ-1399 (PJH) is gratefully acknowledged. SSRL operations are funded by the Department of Energy, Office of Basic Energy Sciences. The Structural Molecular Biology program is supported by the National Institutes of Health, National Center for Research Resources, Biomedical Technology Program and by the Department of Energy, Office of Biological and Environmental Research.

Cyanide Complexes of the Transition Metals

Timothy P. Hanusa
Vanderbilt University, Nashville, TN, USA

Based in part on the article Cyanide Complexes of the Transition Metals by Timothy P. Hanusa & David J. Burkey which appeared in the Encyclopedia of Inorganic Chemistry, First Edition.

1 Introduction 1
2 The Cyanide Ion 1
3 Synthesis 3
4 Reactions 3
5 Physical Methods of Characterization 5
6 Structures 6
7 Applications 8
8 Related Articles 9
9 References 10

Glossary

Cyano metal complex: a metal complex that contains one or more bound cyanide ligands
Second Sphere Coordination: coordination of molecules in the layer just beyond the ligands bound to the metal center

Abbreviations

bpy = 2,2′-bipyridine; Cp* = η^5-C_5Me_5; Cp′ = η^5-C_5H_4Me; 18-Crown-6 = 1,4,7,10,13,16-hexaoxacyclooctadecane; crypt-2.2.2 = 1,7,13,16,21,24-hexaoxa-1,10-di-azabicyclo[8.8.8]hexacosane; dppe = 1,2-bis(diphenylphosphino)ethane $Ph_2PCH_2CH_2PPh_2$; dppm = bis(diphenylphosphino)methane $Ph_2PCH_2PPh_2$; DMSO = dimethyl sulfoxide $(CH_3)_2SO$; en = ethylenediamine $H_2NCH_2CH_2NH_2$; EXAFS = Extended X-Ray Absorption Fine Structure; HMTA = Hexamethylenetetramine $C_6H_{12}N_4$; Me_3tacn = *N*,*N*′,*N*″-trimethyl-1,4,7-triazacyclononane; PPN = bis(triphenylphosphine)iminium cation $(Ph_3P)_2N^+$; Tp′ = hydridotris(3,5-dimethylpyrazolyl)borate.

1 INTRODUCTION

The cyanide ion, CN^-, is one of the most common and longest-known ligands (*see Ligand*) in coordination chemistry. The first coordination compound to be synthesized was the cyano metal complex was Prussian blue, $[Fe_4\{Fe(CN)_6\}_3]$ (*see Prussian Blue*), made by the Berlin painter Diesbach in 1704. Much of our understanding of coordination chemistry can be attributed to research on cyano metal complexes (*see* ***Coordination & Organometallic Chemistry: Principles***).

Cyanide complexes are often compared to metal carbonyls (*see Metal Carbonyls*), and both cyanide and carbon monoxide, CO, can function as π-acid ligands (*see π-Acid Ligand*). Unlike CO, however, the cyanide ion possesses a negative charge, and can form very strong σ-bonds (*see σ-Bond*) with metal ions. This characteristic, along with other behavior such as the formation of a hydracid (HCN) and a dimer (cyanogen, $(CN)_2$), is reminiscent of halogen ligands; the cyanide ion has accordingly been described as a pseudohalide (*see Pseudohalide*). Cyano metal complexes in fact display some similarities to metal halide complexes, which has often led to their being classified as inorganic compounds. However, with very few exceptions, all cyanide complexes display metal-carbon interactions, a characteristic of organometallic compounds (*see Organometallic Complexes*). Comprehensive coverage of early cyano metal chemistry can be found in the classic monograph by Sharpe;**[1]** more recent reviews are available.**[2–5]**

2 THE CYANIDE ION

2.1 Properties of the Cyanide Ion

The cyanide ion is isoelectronic (*see Isoelectronic*) with CO, N_2 and NO^+, with an electronic configuration of $(1\sigma)^2(2\sigma)^2(3\sigma)^2(4\sigma)^2(1\pi)^4(5\sigma)^2$; this corresponds to a triple bond (one σ-bond (*see σ-Bond*) and two π-bonds (*see π-Bond*)) between the carbon and nitrogen atoms. A lone pair (*see Lone Pair*) of electrons is present on both atoms in CN^-. Calculations have indicated that the negative charge of the cyanide ion is shared approximately equally between the two atoms.**[6]** The carbon-nitrogen triple bond distance is 1.16 Å in the free cyanide ion; the fundamental vibrational frequency of the C≡N bond (aqueous solution) is 2080 cm^{-1}. The effective *Crystallographic Radius* of CN^-, as determined in cubic alkali metal cyanides, is 1.92 Å; this value is intermediate between those of chloride and bromide.

2.2 Cyanide Ion as a Ligand

When the cyanide ion binds to metal atoms through the lone pair (*see Lone Pair*) of electrons on the carbon atom (see Section 2.3), the resulting M–CN σ-bond (*see σ-Bond*)

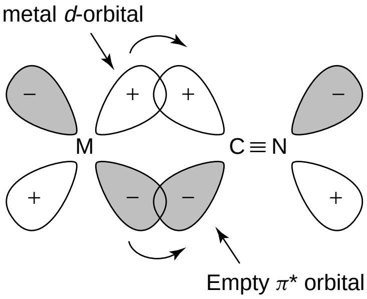

Figure 1 π-backbonding in the metal-cyanide bond

is one of the strongest metal-ligand bonds known (*see Bond Dissociation Energy*). The σ-donor (*see σ-Donor*) capacity of CN^- allows it to stabilize transition metals (*see Transition Metals*) with high oxidation numbers (*see Oxidation Number*). However, the cyanide ion also can function as a π-acid ligand (*see π-Acid Ligand*) (Figure 1), by accepting electron density from a filled metal d orbital (*see d-Orbitals*) into an empty antibonding orbital of the carbon-nitrogen bond. This allows CN^- to stabilize transition metals with low oxidation numbers (*see Oxidation Number*) as well; hence, cyano complexes can often be formed for several different oxidation states of a given metal. It should be stressed, however, that owing to the repulsive effect of its negative charge, the π-bonding (*see π-Bond*) capability of CN^- is considerably less than that of either CO or NO^+.

The bonding properties of CN^- make it a very strong-field ligand; it is one the highest in the spectrochemical series (*see Spectrochemical Series*). The strong-field character of CN^- is exemplified by its ability to form a low-spin (*see High-spin & Low-spin Compounds*) octahedral (*see Octahedral*) Fe^{II} complex, $[Fe(CN)_6]^{4-}$, and in its stabilization of a square-planar (*see Square Planar*) Co^{II} complex, $(PPN)_2[Co(CN)]_4$, with a d^7 configuration (*see Electron Configuration*).[7] The cyanide ion also exhibits a strong *trans* effect (*see Trans Effect*) and a large nephelauxetic effect (*see Nephelauxetic Effect*), indicative of the high degree of covalency in the metal-cyanide bond.

2.3 Binding Modes

Monodentate (*see Monodentate Ligand*) cyanide ligands almost always bind to the metal center through the carbon atom as in Figure 2(a); monodentate isocyano linkages 2(b) are known only in a few gas-phase species.[8] Cyanide also can act as a bridging, bidentate ligand (*see Bidentate Ligand*) through binding of the lone pair (*see Lone Pair*) of electrons on the nitrogen atom to another metal center. Usually, the cyanide ion bridges two metals in a linear fashion 2(c); this type of bridging cyanide is present in Prussian blue and several other polymeric (*see Polynuclear Complexes*) metal cyanides. Other CN^- bridging modes, although much less common, are known 2(d–h). Cyanide is capable of acting as a σ-π bridging ligand, as in 2(e); in complexes of this type, for example, (**1**), the bridging bond is formed by metal coordination to the π-bond (*see π-Bond*) of the cyanide.[9] Cyanide also can bond to metals with a single-atom bridging structure analogous to that seen in metal carbonyls, 2(f) and 2(g). In $Ru_2(F_5ap)_4(\mu\text{-}CN)_2$ (F_5ap) = 2-(2,3,4,5,6-pentafluoroanilino)pyridinate (**2**),[10] the carbon atoms of the cyanides bridge two Ru atoms, whereas in $[Ru_3(CO)_{10}\{(\mu\text{-}NC)MnCp(CO)_2\}]_2$ (**3**), the nitrogen atoms are bridging.[11]

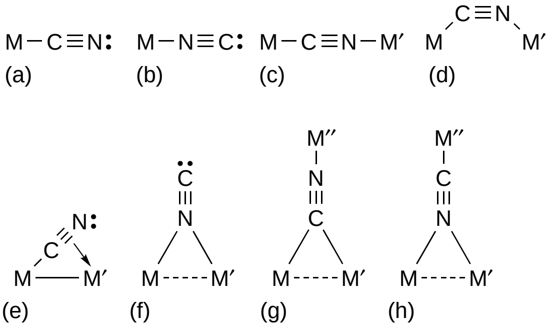

Figure 2 Metal-ligand binding modes found in cyanide complexes

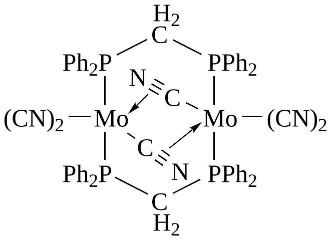

(**1**)

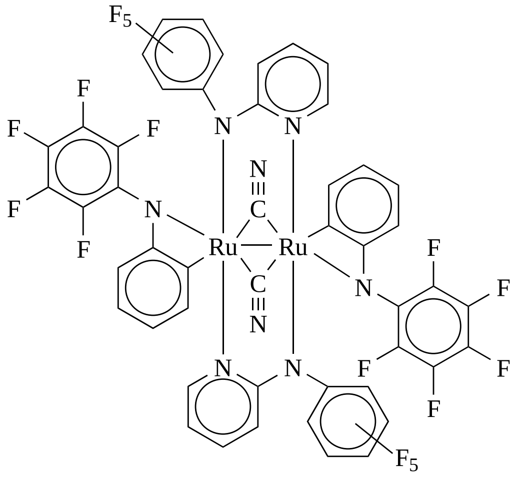

(**2**)

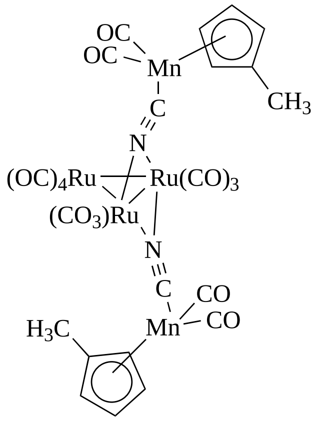

(**3**)

3 SYNTHESIS

3.1 Cyanide Substitution

Cyano metal complexes are commonly formed by the addition of an excess of cyanide ion (usually as an alkali metal salt) to a transition metal complex in water or a polar organic solvent (equation 1).**1** The completely cyanide-substituted metal complex is usually isolated from these reactions, although one or more steps in the reaction may be relatively slow. In certain cases, cyanide substitution is not complete, resulting in partially substituted cyano metal complexes; an example is the addition of CN^- to Pt^{II} alkyl compounds, from which $[PtR(CN)_3]^{2-}$ species are isolated.**12**

$$ML_n{}^{x+} + CN^-(\text{excess}) \xrightarrow{H_2O} [M(CN)_m]^{x-} + nL \qquad (1)$$

External oxidizing or reducing reagents are often used during CN^- substitution reactions to change the oxidation state of the metal in the cyano complex. Cyanide itself can act as a reducing agent in these reactions, as it is easily oxidized to cyanogen, $(CN)_2$, or cyanate, CNO^-.**1** Liquid ammonia is used as a solvent for the synthesis of hydrolytically unstable cyano complexes, such as those of Ti^{III} and the f-block metals (*see f-Block Metals*),**13** or to provide added solubility in the synthesis of Ag^I and Au^I cyanides.**14** In the case of the square-planar (*see Square Planar*) $[Pt(CN)_4]^{2-}$ complexes, partial oxidation with halogens produces the one-dimensional conducting salts $[Pt(CN)_4]X_{0.3}{\cdot}3H_2O$ (see Section 6.1).

3.2 Oxidative Addition

Cyano metal complexes can be formed by the oxidative addition (*see Oxidative Addition*) of cyanogen to a transition metal complex (equation 2).**15** The oxidative addition of $(CN)_2$ usually requires a low-valent, electron-rich metal center such as Ni^0, Pt^0, or Rh^I, and leads to *trans*-dicyanide complexes, unless steric crowding at the metal center enforces a *cis* geometry on the incoming cyanide ligands. HCN and cyanogen halides, XCN, have also been shown to add oxidatively to metal centers to give cyano metal complexes;**15** the oxidative addition of HCN to a metal center is believed to be a key step in the transition metal-catalyzed hydrocyanation (*see Hydrocyanation*) of alkenes (*see* ***Hydrocyanation by Homogeneous Catalysis***).

$$[Ni(CO)_2(PPh_3)_2] + (CN)_2 \longrightarrow [Ni(CN)_2(PPh_3)_2] + 2CO \qquad (2)$$

3.3 Indirect Synthesis of the Cyanide Ligand

There are cases in which a cyanide ligand is generated during a reaction to give a cyano metal complex. The addition of PMe_3 to an alkylruthenium nitrosyl complex results in a Ru-bound cyanide formed from the NO^+ and methyl ligands (equation 3).**16** Pyrazine and nitric acid are found to react in the presence of CuO to give a polymeric Cu^I cyanide complex; the coordinated cyanide is evidently generated by acid-catalyzed decomposition of the pyrazine (equation 4).**17** The reductive cleavage of the nitrogen-alkyl bond in isocyanide ligands (*see Isocyanide Ligands*), $-C{\equiv}NR$, is another indirect route to cyano metal complexes. The reaction of ruthenium carbonyl with *tert*-butylisocyanide under CO pressure produces a 1:1 mixture of *cis*- and *trans*-$[Ru(CN)_2(CN^tBu)_4]$; formally the isocyanide is converted into a cyano ligand, isobutene, and a proton; the latter is subsequently reduced to dihydrogen (equation 5).**18**

$$Cp^*Ru(NO)(CH_3)_2 + 2PMe_3 \xrightarrow[C_6H_6]{150\,^\circ C} Cp^*Ru(PMe_3)_2CN + CH_4 + H_2O \qquad (3)$$

$$CuO + pyz + HNO_3 \xrightarrow[2\text{ days}]{200\,^\circ C} Cu(CN)(pyz) + Cu(NO_2)_2(pyz) \qquad (4)$$

$$2Ru_3(CO)_{12} + 36{}^tBuNC \xrightarrow[-24\,CO]{} cis\text{-}[Ru(CN)_2(CN^tBu)_4] + trans\text{-}[Ru(CN)_2(CN^tBu)_4] + 12(H_3C)_2C \equiv CH_2 + 6H_2 \qquad (5)$$

4 REACTIONS

4.1 Electrochemistry

Cyano metal complexes undergo a variety of oxidation-reduction reactions. One of the most studied is the fast self-exchange reaction of the $[Fe(CN)_4]^{3/4-}$ anions; information from this research was instrumental in establishing the outer-sphere mechanism (*see Outer-sphere Reaction*) for transition metal oxidation-reduction reactions (*see* ***Electrochemistry: Applications in Inorganic Chemistry***). The nature of the solvent has a pronounced effect on the oxidation of $[Fe(CN)_6]^{4-}$; its rate of oxidation by O_2 is dramatically enhanced in electron-donor solvents. Conversely, the reduction of $[Et_4N]_3[Fe(CN)_4]$ becomes much more favorable on increasing the electron acceptor properties of the solvent.[19] Cyano metal complexes also can undergo inner-sphere redox reactions (*see Inner-sphere Reaction*); a classic illustration of the ligand interaction involved in such reactions is provided by the cyanide-bridged bimetallic complex $[(NC)_5Co^{III}(\mu\text{-}NC)Fe^{II}(CN)_5]^{6-}$, which can be isolated from the redox reaction of $[Co^{II}(CN)_5]^{3-}$ and $[Fe^{III}(CN)_6]^{3-}$.

In certain cases, a bound cyanide ligand can participate in an oxidation-reduction reaction. For example, the electroreduction of the complex *trans*-[Mo(CN)Cl(dppe)$_2$] in the presence of phenol reduces the cyanide ligand to the simplest aminocarbyne ligand, $\equiv CNH_2$, and gives *trans*-[(Mo$\equiv$CNH$_2$)Cl(dppe)$_2$]. The reduction of the cyanide is reversible, as oxidation of the aminocarbyne complex regenerates *trans*-[Mo(CN)Cl(dppe)$_2$].[20]

4.2 Substitution of Coordinated Cyanide

Owing to the strong σ-donor (*see σ-Donor*) properties of CN^-, only a few ligands are capable of directly replacing metal-bound cyanide: these include strong π-acids such as CO or NO^+, or aromatic N-donor chelating ligands (*see Chelating Ligands*) such as 2,2′-bipyridine or 1,10-phenanthroline.[21] For most substitution reactions of cyano metal complexes, photochemically induced dissociation of one or more of the CN^- ligands is needed (*see* ***Photochemistry of Transition Metal Complexes***). A substituted cyanide complex obtained in this manner is $[Cr(CN)_5(NH_3)]^{2-}$, synthesized by the irradiation of $[Cr(CN)_6]^{3-}$ in methanol, followed by addition of ammonia (Scheme 1).[22] Although they do not generally affect the absorption spectra of cyano metal complexes, the *Second Sphere Coordination* of polyammonium macrocyclic ligands can markedly suppress photochemically induced substitution reactions. This is exemplified in the decreased *Quantum Yield* of 0.10 mol/einstein for the photosolvation of the supramolecular polyammonium complex of $[Co(CN)_6]^{3-}$ (**4**), compared to a quantum yield of 0.30 for free $[Co(CN)_6]^{3-}$.[23] Hydrogen bonding (*see Hydrogen Bonding*) interactions with the cyanide ligands prevent their dissociation upon irradiation.

Protonation of a cyanide ligand (see Section 4.3) also can lead to enhanced rates of cyanide substitution, since this weakens the M–CN σ-bond. This is especially true for *trans* substituted cyano complexes, where the strong *trans* effect (*see Trans Effect*) of the cyanide ligands renders them more susceptible to protonation than in *cis* cyano complexes. As a result, *trans*-$[Cr(NH_3)_4(CN)_2]^+$, for example, undergoes a substitution reaction in acidic solution to give *trans*-$[Cr(NH_3)_4(H_2O)_2]^{3+}$ at a rate approximately 1000 times that of *cis*-$[Cr(H_2O)_4(CN)_2]^+$.[24]

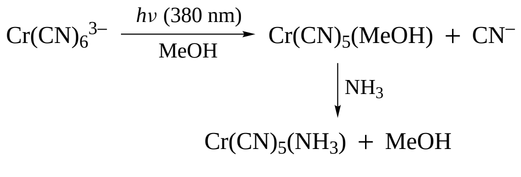

Scheme 1 Photochemically induced CN^- substitution reaction

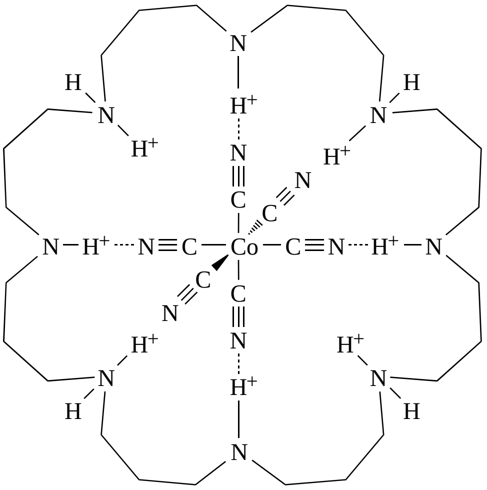

(**4**)

4.3 Addition to Coordinated Cyanide

The lone pair (*see Lone Pair*) of electrons on the nitrogen atom of bound cyanide can react with Lewis acids (*see Lewis Acids & Bases*) to form adducts of the type M–C $\equiv$N: $\rightarrow$ L. Often, strong Lewis acids such as BF_3 are used to generate complexes of this type (equation 6),[25] although weaker Lewis acids, such as Ph_3SnCl, also can form cyanide adducts (equation 7).[26] The binding of sterically bulky Lewis acids, such as BPh_3, to coordinated cyanide ligands is used to control regioselectivity (*see Regioselectivity*) in transition metal-catalyzed hydrocyanation (*see Hydrocyanation*) of alkenes.

$$\mathrm{Tp'(CO)(CN)W(PhC{\equiv}CMe) + BF_3{\bullet}Et_2O \xrightarrow{CH_2Cl_2} Tp'(CO)(CN{\cdot}BF_3)W(PhC{\equiv}CMe) + Et_2O} \qquad (6)$$

$$\mathrm{3Ph_3SnCl(in\ CH_3CN) + K_3[Fe(CN)_6]}(aq) \longrightarrow \mathrm{[(Ph_3Sn_3)Fe(CN)_6{\bullet}H_2O{\bullet}2CH_3CN]}_n + \mathrm{3KCl} \qquad (7)$$

Addition of an electrophile (*see Electrophile*) to metal-bound cyanides will often form an isocyanide ligand (*see Electrophile*), –C$\equiv$N–R. For example, the compound $[Fe\{P(OMe)_3\}(NO)_2(\eta^3\text{-}C_3H_4R)]$, which is a source of the allyl cation $(\eta^3\text{-}C_3H_4R)^+$, reacts with *trans*-[Mn(CN)(CO)(dppm)$_2$] to alkylate the cyanide, giving an allyl isocyanide ligand (equation 8).[2] The tungsten alkyne complexes Tp′(CO)(CN)W(RC≡CR′) (R = H, Ph; R′ = H, ^{n}Bu, Ph, Me) react with triflic acid or methyl triflate to form the corresponding hydrogen or methyl isocyanide complexes [Tp′(CO)(CN(H,Me))W(RC≡CR′)][O_3SCF_3] (equation 9).**[25]** Fluoroboric acid is exceptional in this regard, as the same tungsten complexes react with HBF_4 in CH_2Cl_2 solution to produce BF_3 adducts (equation 10), rather than the anticipated hydrogen isocyanide complexes.

$$\textit{trans}\text{-}[\mathrm{Mn(CN)(CO)(dppm)_2}] + [\mathrm{Fe\{P(OMe)_3\}(NO)_2(\eta^3\text{-}C_3H_4R)}][\mathrm{PF_6}] \xrightarrow{\text{THF}} \textit{trans}\text{-}[\mathrm{Mn(CO)(CNCH_2CH{=}CHR)(dppm)_2}][\mathrm{PF_6}]\cdot\mathrm{thf} \tag{8}$$

$$\mathrm{Tp'(CO)(CN)W(RC{\equiv}CR')} \xrightarrow[\mathrm{CH_2Cl_2}]{[\mathrm{Me}][\mathrm{O_3SCF_3}]} [\mathrm{Tp'(CO)(CNMe)W(RC{\equiv}CR')}][\mathrm{O_3SCF_3}] \tag{9}$$

$$\mathrm{Tp'(CO)(CN)W(RC{\equiv}CR')} \xrightarrow[\mathrm{CH_2Cl_2}]{\mathrm{HBF_4},\ 0\,^\circ\mathrm{C}} [\mathrm{Tp'(CO)(CNBF_3)W(RC{\equiv}CR')}][\mathrm{O_3SCF_3}] \tag{10}$$

5 PHYSICAL METHODS OF CHARACTERIZATION

5.1 Vibrational Spectroscopy

The characteristic absorption band in the vibrational spectroscopy of cyano metal complexes is the C≡N bond stretch, which occurs in the frequency range of approximately 1950 to 2250 cm^{-1}. Most other bands, notably the M–C bond stretch, occur at much lower wavenumbers (<600 cm^{-1}). Variations in the frequency of the C≡N bond stretching band have been used to probe the extent of metal−cyanide π-bonding; increased M–CN π-bonding decreases the strength of the C≡N bond, and therefore decreases ν(CN). For example, the C≡N stretching vibration in Fe[(CN)$_6$]$^{3-}$ occurs at 2135 cm^{-1}, whereas in [Fe(CN)$_6$]$^{4-}$, the same band is at 2098 cm^{-1}, indicative of stronger metal-cyanide π-bonding in the latter complex. Similarly, the increase in ν(CN) observed upon increasing the oxidation state of the metal (and thus decreasing the number of d electrons) has been attributed to a decrease in metal-cyanide π-bonding. It should be noted, however, that the shifts in ν(CN) due to varying degrees of π-bonding in cyano metal complexes are much smaller than the analogous shifts seen in metal carbonyls, since metal-cyanide π-bonding is weaker.

The CN$^-$ nitrogen lone pair (*see Lone Pair*) resides in a mostly C–N antibonding (*see Antibonding*) orbital; therefore, the involvement of the nitrogen lone pair of electrons in bonding increases the strength of the carbon-nitrogen bond, which results in an increase in ν(CN) for bridging cyanides. This is illustrated by the binding of BF_3 to the cyanide in Tp′(CO)(CN)W(PhC≡CMe) (equation 6, Section 4.3), which shifts the C≡N bond stretching frequency from 2110 to 2185 cm^{-1}.**[25]**

5.2 Diffraction Methods

X-ray diffraction has proven to be an invaluable tool for the determination of the solid-state structures of cyano metal complexes (*see* ***Diffraction Methods in Inorganic Chemistry***). Accurate data on bond distances and angles obtained from X-ray structural determinations have provided information on the bonding in cyano complexes, although interactions in the solid state can complicate interpretation of bond lengths. For example, the finding that in the solid state the Fe–C bond is shorter in the Fe$^{\mathrm{II}}$ complex Cs$_2$Mg[Fe(CN)$_6$] (1.90 Å) than in the *Isomorphous* Fe$^{\mathrm{III}}$ complex Cs$_2$Li[Fe(CN)$_6$] (1.93 Å) was taken as evidence of stronger metal-cyanide π-bonding in the [Fe$^{\mathrm{II}}$(CN)$_6$]$^{4-}$ ion.**[1]** However, the ferricyanide and ferrocyanide ions have been studied in solution with Extended X-Ray Absorption Fine Structure (EXAFS) spectroscopy (*see Extended X-ray Absorption Fine Structure*), and the Fe–C bond distance is found to increase by 0.03 Å on electroreduction of Fe$^{\mathrm{III}}$ to Fe$^{\mathrm{II}}$.**[27]** High precision charge-density X-ray diffraction and spin-polarized neutron diffraction (*see* ***Diffraction Methods in Inorganic Chemistry***) experiments on Cs$_2$K[Fe(CN)$_6$] were used to determine quantitatively the electron orbital populations of the Fe–CN bonds.**[28]**

A common problem encountered in X-ray structural studies of oligomeric cyano metal compounds is the inability to distinguish between the carbon and nitrogen atoms in linearly bridging cyanide ligands. This problem stems from the similar electron densities and metal bond distances for both the carbon and nitrogen atoms in a bridging cyanide ligand, although in certain cases, the symmetry of the lattice forces the cyanide to be crystallographically disordered over both bridging configurations.

5.3 NMR Spectroscopy

NMR spectroscopy (^{13}C and ^{15}N) is routinely used in the characterization of cyano metal complexes. The free CN$^-$ ion exhibits a ^{13}C NMR shift of δ 166.2, but the ^{13}C NMR shift in complexes is almost always upfield of this value; the ^{15}N shift is correspondingly downfield. Information on the rates of reactions for cyano metal complexes can be obtained from NMR studies; the self-exchange rates for electron transfer in the [Fe(CN)$_6$]$^{3-/4}$, [Ru(CN)$_6$]$^{3-/4-}$, [Os(CN)$_6$]$^{3-/4-}$, and [W(CN)$_8$]$^{3-/4-}$ couples have been determined by ^{13}C or ^{15}N NMR line-broadening techniques, but cation-catalyzed pathways dominate the observed rate constants. Experiments using sequestered K$^+$ (by either 18-crown-6 or crypt-2.2.2) found an exchange constant for [Fe(CN)$_6$]$^{3-/4-}$ of 2.4×10^2 L mol^{-1} s^{-1} (25 °C, ionic strength 0.2 mol L^{-1}); this is two orders of magnitude less than the frequently quoted value of $1.9 \times 10^4\ \mathrm{L\,mol^{-1}\,s^{-1}}$.**[29]** NMR measurements on the metal nucleus in cyanide complexes also can yield useful information. For example, variable temperature ^{95}Mo NMR studies indicate that the $[Mo(CN)_8]^{4-}$ ion, which exhibits several different geometries in the solid state (see Section 6.1), is dodecahedral (*see Dodecahedral*) in aqueous solution.**[30]** Additionally, solid-state ^{113}Cd NMR has proven useful in determining the orientation of bridging CN^- ligands in polymeric cadmium cyanide complexes in cases where X-ray structural data could not accomplish this.**[31]**

5.4 Other Methods

The energies of d-d electronic and metal-to-ligand charge transfer (*see Charge Transfer*) transitions that occur in transition metal-cyanide complexes can be determined by electronic spectroscopy (*see Electronic Spectroscopy*); this technique has also been used to measure reaction rates and to detect intermediates in reactions. *Mössbauer spectroscopy* has been used to determine the relative contribution of Fe–L σ- and π-bonding in a series of $[Fe(CN)_5L]^{n-}$ complexes, on the basis of the observed changes in *Isomer Shifts* and quadrupolar (*see Quadrupolar*) splitting.**[32]** The use of secondary-ion mass spectrometry (*see Mass Spectrometry*) has enabled the qualitative determination of the proton affinity and π-acceptor ability of CN^- in substituted cyanoruthenium complexes. Nitrogen-14 *Nuclear Quadrupole Resonance Spectroscopy* (NQR) has been used to determine the charge distribution in metal cyano complexes,**[33]** and to identify the binding mode (terminal vs. bridging) for CN^- by the evaluation of the *Nuclear Quadrupole Coupling Constant* for the nitrogen atom.**[34]**

6 STRUCTURES

6.1 Monomeric Cyano Metal Complexes

In most instances, rationalization of the geometries exhibited by monomeric cyano metal complexes is straightforward (*see* ***Coordination & Organometallic Chemistry: Principles***). All known six-coordinate metal-cyanide complexes have the expected octahedral geometry. Cyano metal complexes with the d^{10} metal centers Au^I and Ag^I are two-coordinate, that is, $[Au(CN)_2]^-$ and $[Ag(CN)_2]^-$, and have linear geometries. Four-coordinate cyano complexes are either tetrahedral (*see Tetrahedral*), when the metal center has a d^{10} configuration, or square-planar (*see Square Planar*) in complexes containing d^8 ions such as Ni^{2+}, Pd^{2+}, and Pt^{2+}. Often, the individual square-planar tetracyano metal ions stack so that the metal ions form one-dimensional infinite chains with metal–metal interactions; this is especially well-studied for the tetracyanoplatinate anion $[Pt(CN)_4]^{2-}$ and its derivatives. These chains can be straight, helical or zigzag in shape, and can possess uniform or staggered (short-long) intermolecular metal–metal distances. Partially oxidized tetracyanoplatinate chains, such as those found in the series of Krogmann salts (e.g., $Rb_2[Pt(CN)_4]Cl_{0.3}\cdot 3H_2O$, (**5**)), are examples of one-dimensional metallic conductors.**[35]**

For certain coordination numbers, the structures of cyano metal complexes show a surprising degree of variability. The complex $[Cr(en)_3][Ni(CN)_5]\cdot 1.5H_2O$ contains both square-pyramidal (*see Square Pyramidal*) and trigonal bipyramidal (*see Trigonal Bipyramidal*) $[Ni(CN)_5]^{3-}$ ions; desolvating the compound converts all the anions to the square-pyramidal geometry. The $[Mo(CN)_8]^{3-}$ and $[Mo(CN)_8]^{4-}$ anions have variable geometries in the solid state depending on the specific counterion present. The structure of the anions ranges from dodecahedral

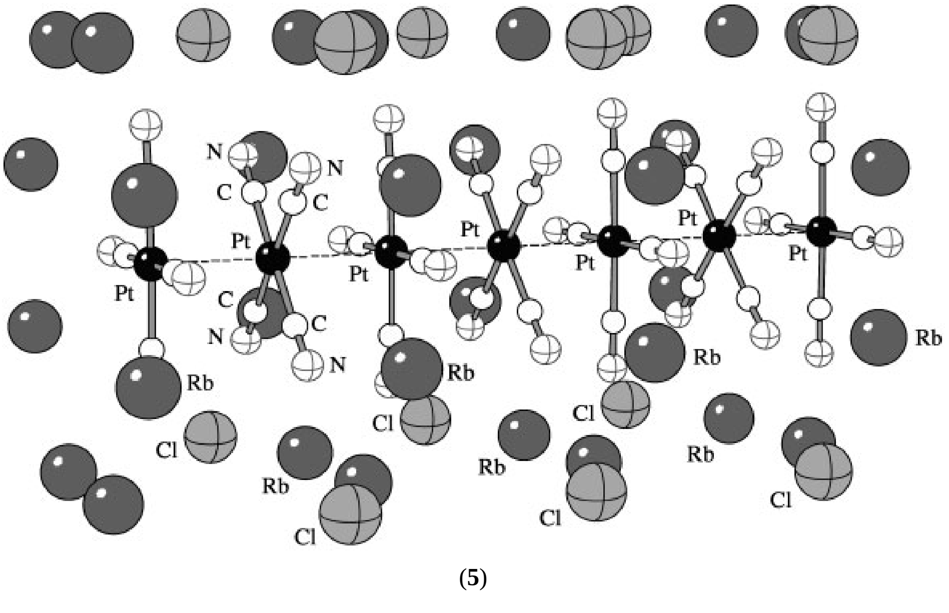

(**5**)

(*see Dodecahedral*) in $K_4[Mo(CN)_8]\cdot 2H_2O$, to square antiprismatic (*see Square Antiprism*) in $Na_3[Mo(CN)_8]\cdot 4H_2O$, to approximately bicapped-trigonal-prismatic (*see Trigonal Prism*) in $Cs_3[Mo(CN)_8]\cdot 2H_2O$.

6.2 Bridging Cyano Metal Complexes

One of the most distinctive features of the cyanide ligand is its ability to form a bridging M–CN–M′ bond between two metal centers. Consequently, cyanide has been increasingly used as a bridging ligand in the synthesis of discrete, molecular bi- and trimetallic mixed valence compounds (*see Mixed Valence Compounds, Classification*). A nine-membered ring is present in the trimeric compound $[Pd(dppe)(\mu\text{-}CN)]_3[ClO_4]_3$ (**6**),[36] and an unusual cyclic cluster, $[(CO)Pd(\mu\text{-}CN)Mn(Cp')(CO)_2]_4$ (**7**), was obtained by the reaction of the ‘cyanometallate ligand’ $[(CpMe)Mn(CO)_2(CN)]^-$ with a tetrameric palladium acetate cluster;[37] this ligand was used in the synthesis of the nitrogen-bridging CN^- compound (**3**) described in Section 2.3.

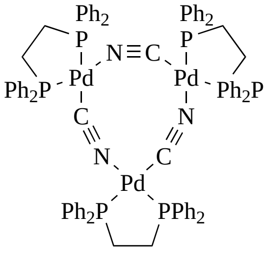

(**6**)

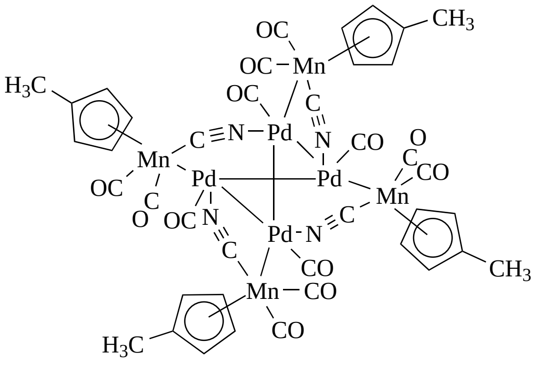

(**7**)

In some instances, the presence of templating ions strongly affects the nature of cage structures formed by bridging CN^- ligands. For example, reaction of $[Mo(Mes)(CO)_3]$ with $(Et_4N)CN$ in a 1:1 ratio generates $(Et_4N)_3[Mo_4(\mu\text{-}CN)_4(CO)_{12}(MeCN)_4]$, which contains a square 12-membered ring;[38] with excess cyanide in the presence of lithium or sodium as templating ions, the tetrahedral (*see Tetrahedral*) cyanometallates $(Et_4N)_5[(Li,Na)\{Mo_4(\mu\text{-}CN)_6(CO)_{12}\}]$ are formed (**8**).[39] Furthermore, addition of Cs^+ will convert the tetrahedral species into the cesium analogue of the less strained, trigonal-prismatic (*see Trigonal Prism*) cage $(Et_4N)_8K[Mo_6(\mu\text{-}CN)_9(CO)_{18}]$. The same trigonal-prismatic cage (**9**) will be formed if K^+ ion is used instead of Li^+ or Na^+ in the original reaction.[38] A boxlike aggregate forms from $[Cp^*Rh(CN)_3]^-$ and $[Mo(Mes)(CO)_3]$ in the presence of K^+ or Cs^+ (**10**).

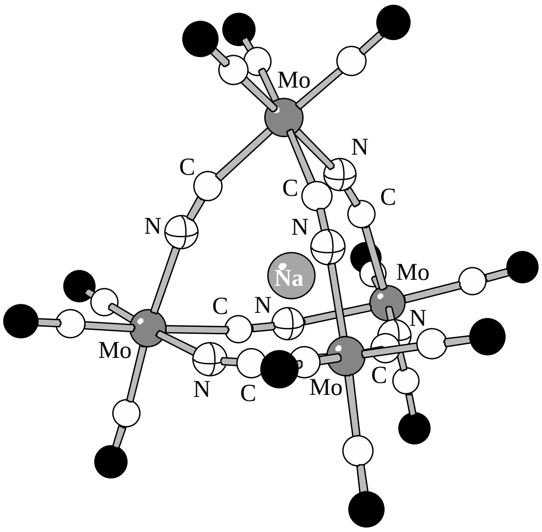

(**8**)

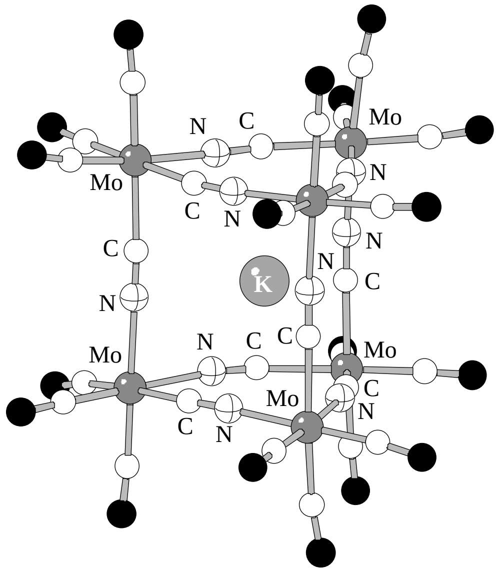

(**9**)

Even larger aggregates are known, such as $[Mn^{II}\{Mn^{II}(MeOH)_3\}_8(\mu\text{-}CN)_{30}\{Mo^{V}(CN)_3\}_6]\cdot 5MeOH\cdot 2H_2O$ (**11**), in which six Mo^V ions surround a central Mn^{II} ion, and the faces of the octahedron are capped by eight additional Mn^{II} ions, producing an approximate *Rhombododecahedron*.[40] The molecule has 51 unpaired electrons, and ferromagnetic coupling leads to an $S = 51/2$

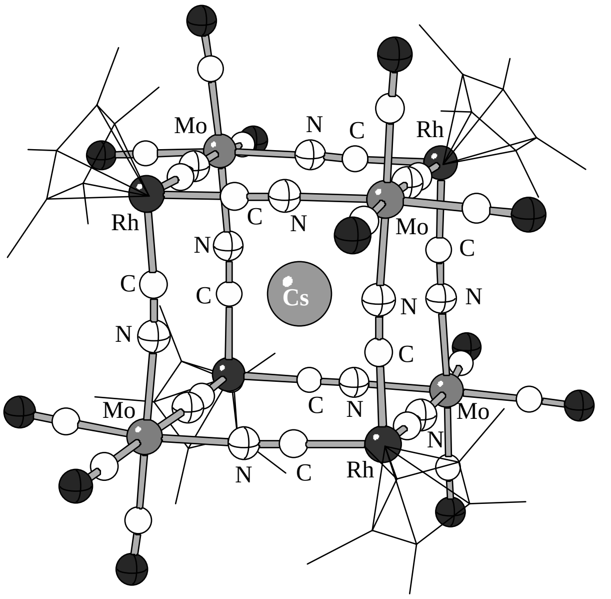
Mo
N
C
Rh
Rh
C
N
Mo
C
N
C
Cs
C
N
N
C
C
N
Mo
C
N
Mo
N
N
C
Rh

(**10**)

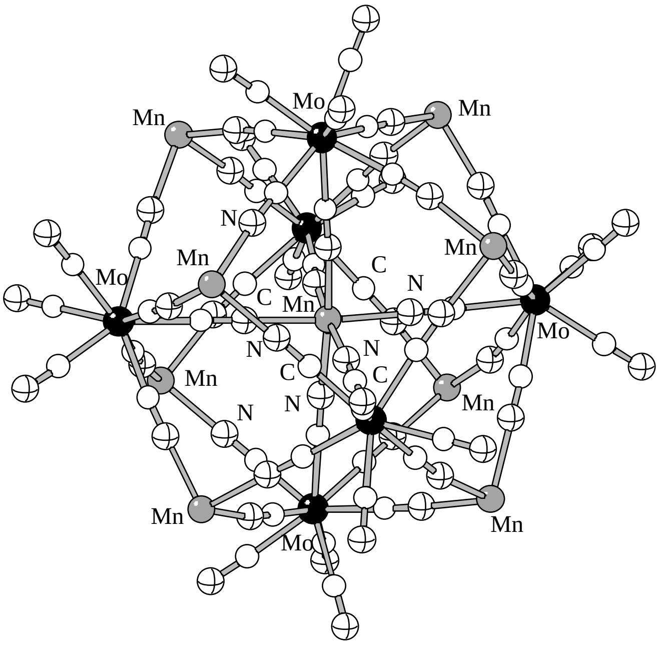
Mo
Mn
Mn
N
Mn
Mn
C
Mo
N
C
Mn
Mo
N
N
Mn
C
C
Mn
N
N
Mn
Mo
Mn

(**11**)

ground state. A double face-centered cubic aggregate, $[(Me_3tacn)_{14}Cr_{14}Ni_{13}(CN)_{48}]^{20+}$ (**12**), has been isolated from the reaction of $[(Me_3tacn)Cr(CN)_3]$ and NiI_2 in water.**41**

Unlike the discrete molecular complexes described above, many compounds with bridging cyanide ligands are three-dimensional coordination polymers. The classic example of this type of compound is Prussian blue, $[Fe_4\{Fe(CN)_6\}_3]\cdot xH_2O$ (**13**), whose intense color arises from an intervalence transfer transition (*see Intervalence Transfer Transition*) from low-spin Fe^{2+} to high-spin Fe^{3+} at 680 nm. Although long in dispute because of various amounts of water and/or potassium ions in different samples (potassium ions are present in 'soluble' Prussian blue, which is actually a colloidal dispersion), the generally accepted structure has a cubic face-centered lattice, with CN^- ligands on the edges of the cube bridging the iron cations. The iron centers have octahedral geometries with the Fe^{2+} ions ligated by six C-bonded cyanides and the Fe^{3+} ions by six N-bonded cyanides.**3** To achieve the 4:3 ratio of the iron atoms, one-fourth of the $[Fe(CN)_6]^{4-}$

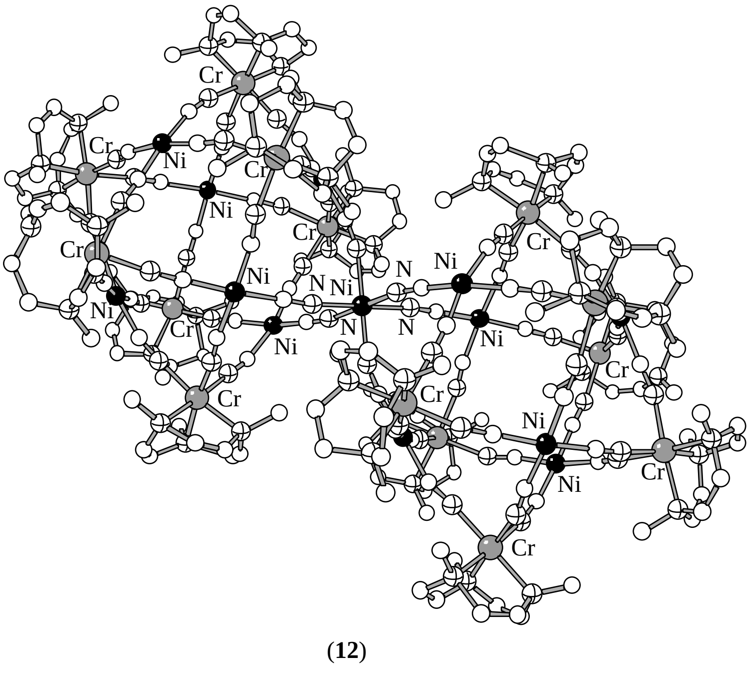
Cr
Cr
Ni
Cr
Ni
Cr
Cr
N
Ni
Ni
Cr
Ni
N
Ni
Ni
Ni
Cr
N
N
Ni
Cr
Cr
Cr
Ni
Ni
Cr
Cr

(**12**)

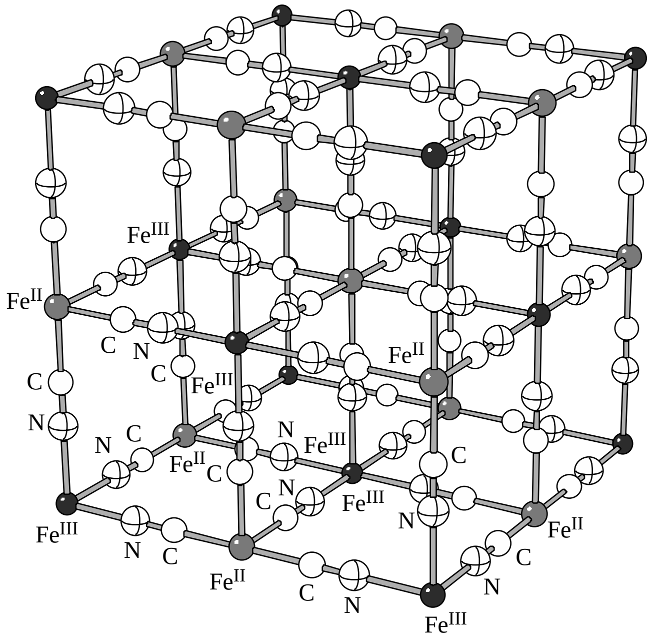

(**13**)

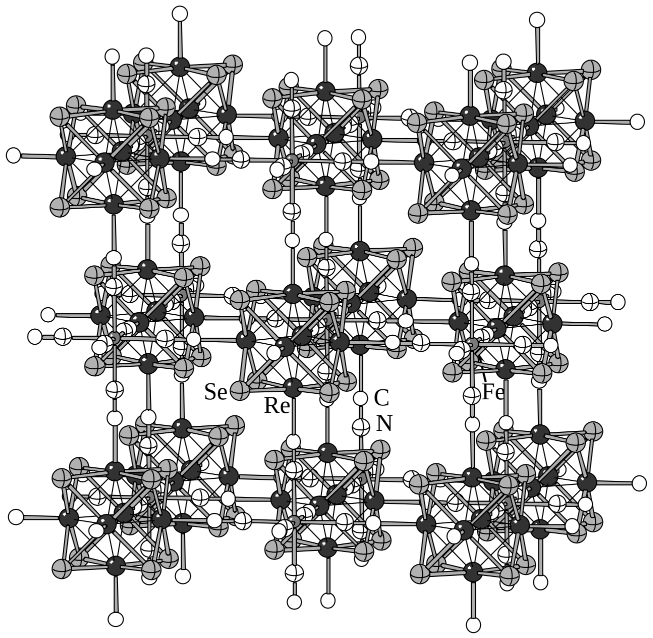

(**14**)

groups are absent from the lattice; the vacancies left by the cyanide ligands are occupied by coordinated water molecules.

A wide variety of other structural types is known for polymeric cyano complexes, some with high degrees of void space (>50%). These range from ‘expanded’ Prussian blues, in which octahedral $[Fe(CN)_6]^{4-}$ units are replaced with larger aggregates such as $[Re_6Se_8(CN)_6]^{4-}$ (**14**),**[42]** to the interpenetrating diamond-like frameworks of $[Cd(CN)_2]_n$, to the PtS-related structure of $[NMe_4][CuPt(CN)_4]$, which has large hexagonal and square channels.**[43]** Often, the structures of polymeric cyano complexes can be related to the structures of silicates and zeolites (*see* ***Zeolites***); in fact, complexes such as $Mg_3[Co(CN)_6]_2$ and $Zn[Fe(CN)_5NO]$ have been shown to be effective molecular sieves.**[44]** Cyano metal complexes also form an immense variety of clathrates (*see Clathrate*), examples being the so-called Hofmann-type clathrates $M(NH_3)_2M'(CN)_4\cdot(guest)_2$ (M = Mn, Fe, Co, Ni, Cu, Zn, Cd; M′ = Ni, Pd, Pt; guest = C_4H_5N, C_4H_4S, C_6H_6, $C_6H_5NH_2$), and ‘*Mineralomimetic*’ compounds with a β-cristobalite $Cd(CN)_2$ framework; the latter can be crystallized with a variety of hydrocarbon, chlorocarbon, and chlorofluorocarbon molecules in their structural cavities.**[45]**

7 APPLICATIONS

Historically, the major application of cyano metal complexes was Prussian blue’s use as a pigment in the painting, printing, and dyeing industries. Since the 1970s, however, organic pigments such as phthalocyanine blue have supplanted Prussian blue for some of these purposes. Prussian blue has been used as an oral drug to increase fecal excretion of cesium and thallium, and has been used to remediate nuclear wastes containing ^{137}Cs.

Prussian blue has been deposited in thin films on chemically modified electrodes. Such electrodes have been used for ion detection and for promoting electrocatalytic reactions. There has also been exploratory use of Prussian blue in batteries and photoelectrochemical cells.

Photoinduced electron transfer has been described in ‘antenna-sensitizer’ molecules, such as $[\{Ru(bpy)_2(CN)_2\}_2\text{-}Ru(bpyCOO)_2]^{2-}$, in which peripheral substituents absorb light energy and transfer it to a central component (**15**). Such molecules serve as sensitizers for TiO_2 in photovoltaic cells; some have been constructed that display promisingly high levels of solar energy collection and conversion.**[46]**

The ability of some porous cyanide complexes to serve as hosts for organic molecules has been noted above (see Section 6.2). A series of platinum compounds containing alternating anions ($[Pt(CN)_4]^{2-}$) and cations ($[Pt(CNR)_4]^{2+}$; R = *i*Pr, *c*-$C_{12}H_{23}$, *p*-$(C_2H_5)C_6H_4$) has been developed. These compounds undergo striking color changes on absorption of volatile organic compounds, and are being examined as chemical sensing agents.**[47]**

8 RELATED ARTICLES

Carbonyl Complexes of the Transition Metals; Coordination & Organometallic Chemistry: Principles; Hydrocyanation by Homogeneous Catalysis.

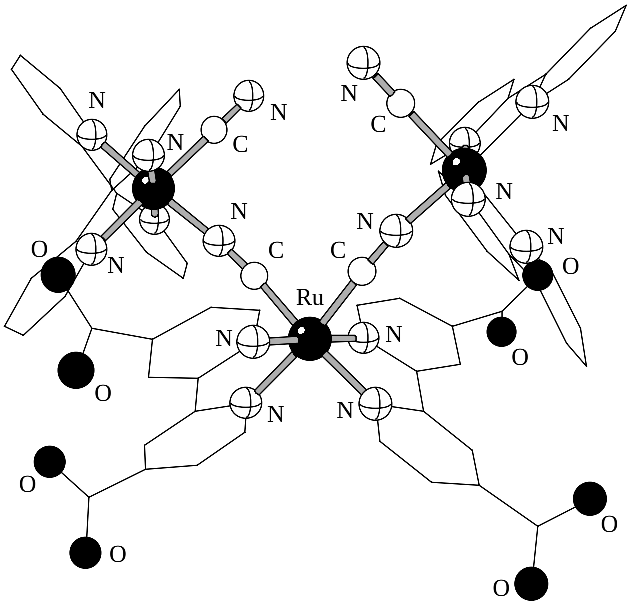

(**15**)

9 REFERENCES

1. A. G. Sharpe, 'The Chemistry of Cyano Complexes of the Transition Metals', Academic, London, 1976.
2. W. P. Fehlhammer and M. Fritz, *Chem. Rev.*, 1993, **93**, 1243.
3. K. R. Dunbar and R. A. Heintz, *Prog. Inorg. Chem.*, 1997, **45**, 283.
4. B. Sieklucka, *Prog. React. Kinet.*, 1999, **24**, 165.
5. J. Cernak, M. Orendac, I. Potocnak, J. Chomic, A. Orendacova, J. Skorsepa, and A. Feher, *Coord. Chem. Rev.*, 2002, **224**, 51.
6. J. P. Flament and M. Tadjeddine, *THEOCHEM*, 1995, **330**, 155.
7. S. J. Carter, B. M. Foxman, and L. S. Stuhl, *J. Am. Chem. Soc.*, 1986, **25**, 2888.
8. J. Lie and P. J. Dagdigian, *J. Chem. Phys.*, 2001, **114**, 2137.
9. P. S. Szalay and K. R. Dunbar, *Inorg. Chem. Commun.*, 2000, **3**, 49.
10. J. L. Bear, Y. Li, J. Cui, B. Han, E. Van Caemelbecke, T. Phan, and K. M. Kadish, *Inorg. Chem.*, 2000, **39**, 857.
11. B. Oswald, A. K. Powell, F. Rashwan, J. Heinze, and H. Vahrenkamp, *Chem. Ber.*, 1990, **123**, 243.
12. A. Y. C. Hung, J. C. Woolcock, M. F. Rettig, and R. M. Wing, *Inorg. Chem.*, 1992, **31**, 810.
13. A. M. Golub, H. Köhler, and V. V. Skopenko, in 'Chemistry of Pseudohalides', ed. R. J. H. Clark, Elsevier, Berlin, 1986.
14. P. Gans, J. B. Gill, and L. H. Johnson, *J. Chem. Soc., Dalton Trans.*, 1987, 673.
15. B. Corain, *Coord. Chem. Rev.*, 1982, **47**, 165.
16. J. Chang, M. D. Seidler, and R. G. Bergman, *J. Am. Chem. Soc.*, 1989, **111**, 3258.
17. R. Kuhlman, G. L. Schimek, and J. W. Kolis, *Polyhedron*, 1999, 1379.
18. D. Doennecke and W. Imhof, *Dalton Trans.*, 2003, 2737.
19. L. M. Baraldo, P. Forlano, A. R. Parise, L. D. Slep, and J. A. Olabe, *Coord. Chem. Rev.*, 2001, **219**, 881.
20. R. A. Michelin, A. J. L. Pombeiro, and M. F. C. Guedes da Silva, *Coord. Chem. Rev.*, 2001, **218**, 75.
21. A. G. Sharpe, 'The Chemistry of Cyano Complexes of the Transition Metals', Academic, London, 1976.
22. E. Zinato and P. Riccieri, *Coord. Chem. Rev.*, 2001, **211**, 5.
23. F. Pina and A. J. Parola, *Coord. Chem. Rev.*, 1999, **186**, 149.
24. E. Zinato, *Coord. Chem. Rev.*, 1994, **129**, 195.
25. D. S. Frohnapfel, S. Reinartz, P. S. White, and J. Templeton, *Organometallics*, 1998, **17**, 3759.
26. J. Lu, W. T. A. Harrison, and A. J. Jacobson, *Inorg. Chem.*, 1996, **35**, 4271.
27. L. R. Sharpe, W. R. Heineman, and R. C. Elder, *Chem. Rev.*, 1990, **90**, 705.
28. P. Day, C. D. Delfs, B. N. Figgis, P. A. Reynolds, and F. Tasset, *Mol. Phys.*, 1993, **78**, 769.
29. A. Zahl, R. van Eldik, and T. W. Swaddle, *Inorg. Chem.*, 2002, **41**, 757.
30. R. T. C. Brownlee, P. Shehan, and A. G. Wedd, *Inorg. Chem.*, 1987, **26**, 2022.
31. S. Nishikiori, C. I. Ratcliffe, and J. A. Ripmeester, *J. Am. Chem. Soc.*, 1992, **114**, 8590.
32. Sd. S. S. Borges, A. L. Coelho, I. S. Moreira, and M. A. B. de Araujo, *Polyhedron*, 1994, **13**, 1015.
33. J. Murgich, I. Bonalde, A. Diaz, and J. A. Abanero, *J. Mag. Res.*, 1991, **93**, 47.
34. J. Murgich and T. Oja, *J. Chem. Soc., Dalton Trans.*, 1987, 1637.
35. J. M. Williams, *Adv. Inorg. Chem. Radiochem.*, 1983, **26**, 235.
36. J. A. Davies, F. R. Hartley, S. G. Murray, and M. A. Pierce-Butler, *J. Chem. Soc., Dalton. Trans.*, 1983, 1305.
37. P. Braunstein, B. Oswald, A. Tiripicchio, and M. T. Camellini, *Angew. Chem., Int. Ed. Engl.*, 1990, **29**, 1140.
38. S. M. Contakes and T. B. Rauchfuss, *Angew. Chem., Int. Ed. Engl.*, 2000, **39**, 1984.
39. S. M. Contakes and T. B. Rauchfuss, *Chem. Commun.*, 2001, **39**, 553.
40. J. Larionova, M. Gross, M. Pilkington, H. Andres, H. Stoeckli-Evans, H. U. Gudel, and S. Decurtins, *Angew. Chem., Int. Ed. Engl.*, 2000, **39**, 1605.
41. J. J. Sokol, M. P. Shores, and J. R. Long, *Inorg. Chem.*, 2002, **41**, 3052.
42. M. V. Bennett, L. G. Beauvais, M. P. Shores, and J. R. Long, *J. Am. Chem. Soc.*, 2001, **123**, 8022.
43. M. O'Keeffe, M. Eddaoudi, H. L. Li, T. Reineke, and O. M. Yaghi, *J. Solid State Chem.*, 2000, **152**, 3.
44. J. Kuyper and G. Boxhoorn, *J. Catal.*, 1987, **105**, 163.

45. T. Iwamoto, S. Nishikiori, T. Kitazawa, and H. Yuge, *J. Chem. Soc. Dalton Trans.*, 1997, 4127.

46. K. Kalyanasundaram and M. Gratzel, *Coord. Chem. Rev.*, 1998, **177**, 347.

47. J. W. Grate, L. K. Moore, D. E. Janzen, D. J. Veltkamp, S. Kaganove, S. M. Drew, and K. R. Mann, *Chem. Mater.*, 2002, **14**, 1058.

Cytochrome Oxidase

Mårten Wikström
University of Helsinki, Helsinki, Finland

Based in part on the article Cytochrome Oxidase by Gerald T. Babcock which appeared in the Encyclopedia of Inorganic Chemistry, First Edition.

1	Introduction	1
2	Structure	2
3	Function	5
4	Conclusions	9
5	Related Articles	10
6	References	10

1 INTRODUCTION

In bacterial and eukaryotic (mitochondrial) cell respiration, strongly reducing electrons (~ -0.35 V) that derive from the oxidation of catabolically processed foodstuffs are transferred through a series of membrane-bound electron transfer proteins ultimately to dioxygen, reducing it to water (*see* ***Long-range Electron Transfer in Biology***; ***Iron: Heme Proteins & Electron Transport***). The redox cofactors that are involved in maintaining this current include flavins, iron-sulfur centers, quinones, copper centers, and heme groups (Figure 1). The redox potentials of these centers increase sequentially as electron transfer proceeds, leaving gaps of ca. 0.2–0.5 V, at which points the exergonic redox reaction is coupled to effective translocation of protons across the membrane. The net result of cell respiration is, therefore, the buildup and maintenance of an electrochemical proton gradient, which is subsequently used to synthesize adenosine triphosphate (ATP) from adenosine 5′-diphosphate (ADP) and inorganic phosphate (P_i), catalyzed by the proton-translocating ATP synthase complex in the same membrane[1] (Figure 2). Cell respiration is an efficient and chemically sophisticated mechanism for coupling exergonic redox chemistry, through the intermediacy of a proton gradient, to the energy-conserving formation of ATP (equation 1).

$$\text{Redox reactions} \longrightarrow \text{proton electrochemical gradient} \longrightarrow \text{ATP} \quad (1)$$

This sequence has been termed *the central dogma of bioenergetics* by analogy to the universal sequence of biological information transfer, DNA → RNA → proteins. Hydrolysis of ATP back to ADP and P_i is the common energy source for virtually all energy-requiring processes in the cell, such as mechanical work, active transport, and biosynthesis of macromolecules.

Molecular oxygen is the ultimate acceptor of the electrons. When constantly supplied, O_2 provides a high-potential electron sink that ensures overall exergonicity of some 1.2 eV of cell respiration. As a whole, the mitochondrial respiratory chain translocates 5 protons across the inner mitochondrial membrane per transferred electron, thereby creating an electrochemical proton gradient of ca. 0.2 V across it (Figure 1). It follows that, overall, the process of cell respiration can operate relatively close to thermodynamic equilibrium where the free energy of the driving redox reactions ($\sim$1.2 eV) closely matches the free energy of the generated proton gradient ($\sim$1.0 eV). This is quite different from photosynthetic energy transductions, where typically a large amount of solar light energy is lost as heat.

The O_2 reduction chemistry in solution takes place as shown in equation (2).

$$4e^- + 4H^+ + O_2 \longrightarrow 2\,H_2O \quad (2)$$

O_2 is chemically quite inert owing to its triplet ground state, but thermodynamically it is highly oxidizing ($E_{m,7} = 0.815$ V). This combination makes it highly fitted for its role in cell respiration, where its reduction requires activation at the bimetallic Fe[II]/Cu[I] active site of the respiratory enzyme, but also making transport of the inert O_2 molecule possible by the hemoglobin/myoglobin pathway before reaching the point of consumption in the cells[2] (*see* ***Iron: Heme Proteins & Dioxygen Transport & Storage***).

The molecular machinery that catalyzes the reaction in equation (2) is contained within the respiratory enzyme (Warburg's Atmungsferment), a complex membrane-spanning assembly of polypeptides also called *cytochrome oxidase*, Complex IV (Figure 1), or cytochrome aa_3. The latter terminology is based on the two A-type heme groups (*see* ***Iron Porphyrin Chemistry***) found in all mitochondrial cytochrome oxidases. In bacteria, the heme composition varies and hemes B and O are also encountered.[2] In addition, bacteria often express a quinol oxidase that is structurally and functionally homologous to cytochrome *c* oxidase, but utilizes a hydroquinone as electron donor. As shown in Figure 1, the immediate source of electrons to cytochrome *c* oxidase is the small, water-soluble hemoprotein, cytochrome *c*, from which the designation 'cytochrome oxidase' originated. In fact, cytochrome oxidase belongs to a large superfamily of structurally and functionally homologous enzymes, the 'heme-copper oxidases'.[3] The subscript '3' in cytochrome aa_3 is of historical origin and due to David Keilin, who named the O_2-binding heme 'a_3' to distinguish it from 'heme *a*', which does not bind ligands. Thus, for example, the major heme-copper oxidase in *E. coli*, which is a quinol oxidase, is called *cytochrome* bo_3 because it contains B (protoheme) and O type[4] hemes, of which the latter binds O_2.

As implied by the above description, cytochrome oxidase is the terminal member of the so-called respiratory chain and functionally located at the confluence of the electron current

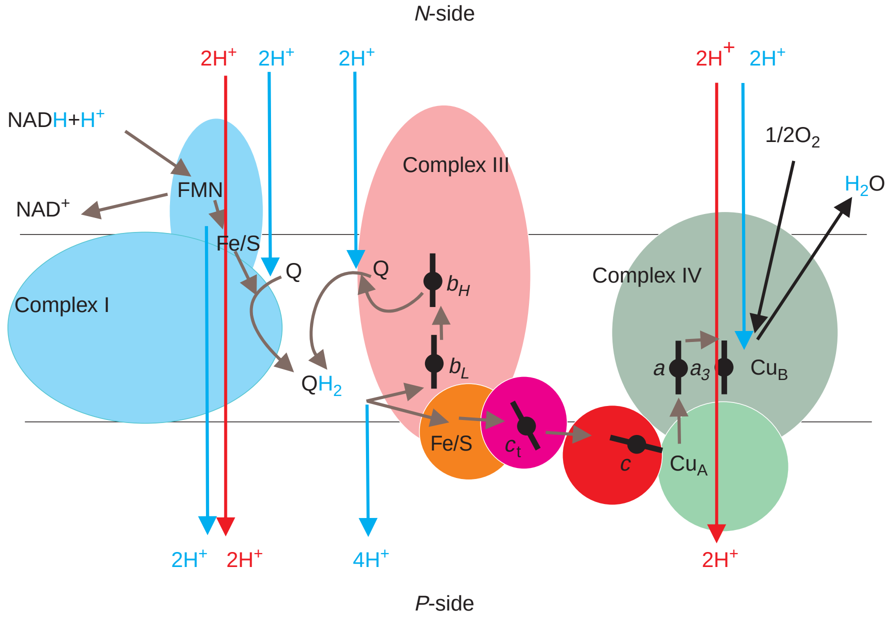

Figure 1 The mitochondrial respiratory chain. Electron transfer (brown arrows) between the three major membrane-bound complexes (I, III, and IV) is mediated by ubiquinone (Q/QH_2) and the peripheral protein cytochrome *c* (*c*). Transfer of protons linked to the redox chemistry is shown by blue arrows; red arrows denote proton translocation. NAD^+: nicotinamide adenine dinucleotide, FMN: flavin mononucleotide, Fe/S: iron-sulfur center; b_H, b_L, and c_1 are the heme centers in the cytochrome bc_1 complex (Complex III). Note the bifurcation of the electron transfer path on oxidation of QH_2 by the heme b_L – Fe/S center. Complex IV is the subject of this review. *N* and *P* denote the negatively and positively charged sides of the membrane, respectively

maintained by respiration, and of the oxygen current that in higher animals is initiated in the lungs, and sustained by the hemoglobin/myoglobin system.

The free energy drop in the cytochrome *c* oxidase reaction is greater than 0.5 eV. Rather than merely dissipating this free energy as heat, mechanisms have evolved within the heme-copper oxidases that provide for coupling electron transfer to proton translocation across the membrane,[2,5] as shown in Figure 1. The thermodynamically important charge-translocating stoichiometry in this process is *two* electrical charge equivalents per transferred electron. Thus, in order to describe the overall function in the membrane, equation (2) should be replaced by equation (3),

$$4e^-{}_{(P)} + 8H^+{}_{(N)} + O_2 \longrightarrow 4H^+{}_{(P)} + 2H_2O \qquad (3)$$

where ‘*N*’ and ‘*P*’ refer to the **n**egatively and **p**ositively charged sides of the inner mitochondrial or bacterial membrane. Note that the protons consumed in the reduction of O_2 to water (‘substrate’ protons) are specifically taken up from the inside of the membrane, while the electrons are donated by cytochrome *c* from the opposite side (Figure 1). This means that the redox chemistry is itself oriented with respect to the membrane and that it contributes to charge separation and therefore to energy conservation. Note also that in the quinol oxidases four additional protons per O_2, originating from the oxidation of hydroquinone, are released to the outside of the membrane.[6]

In summary, the heme-copper oxidases provide two crucial functions in cell respiration: O_2 activation/reduction and energy conservation by redox-linked proton translocation. Significant progress has been made in this field since the first edition of this series in the understanding of both structure and function. X-ray structures at atomic resolution have now been solved for several heme-copper oxidases,[7–12] and this has provided an important basis for further functional work. A summary of the recent advances that have been made in understanding the architecture of the heme-copper oxidases and their metal-containing active sites and a discussion of insights into the molecular mehanisms of operation are presented here with special emphasis on important issues that still remain to be solved.

2 STRUCTURE

2.1 Overall Structure

The mammalian cytochrome oxidase consists of 13 subunits, of which the three heaviest (subunits I, II, and III) are encoded in mitchondrial DNA. The additional 10 smaller subunits are encoded in nuclear DNA, and do not have counterparts in the bacterial enzymes. Their function is still mostly enigmatic, but many of them have been

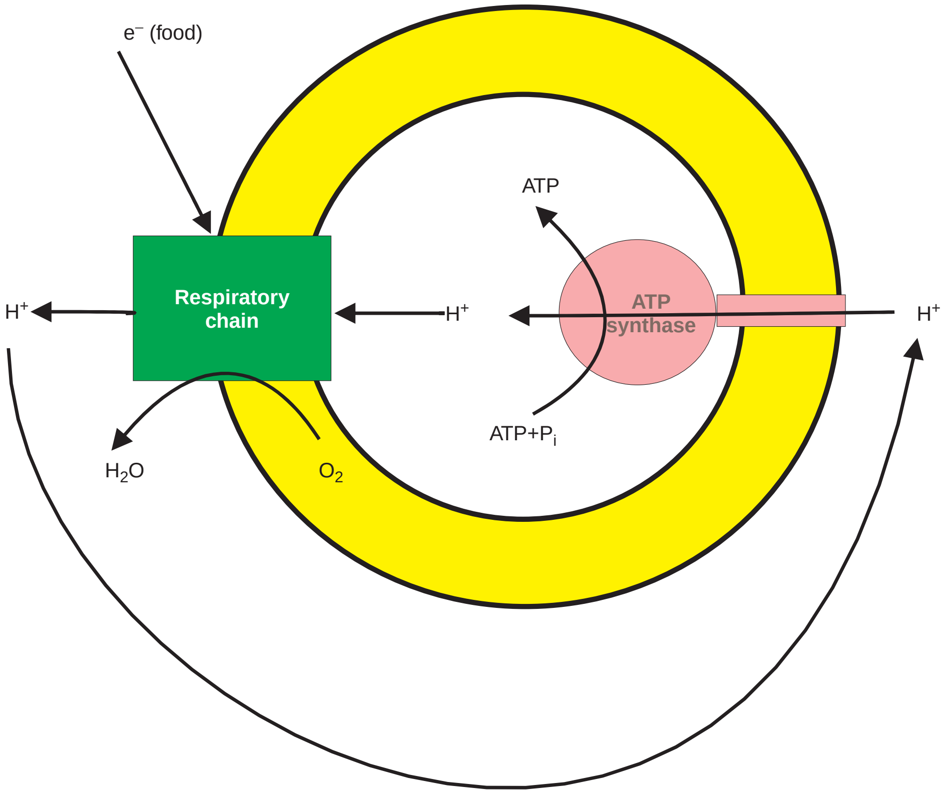

Figure 2 The chemiosmotic theory of respiration. The mitochondrial or bacterial membrane (yellow) provides resistance to proton conduction. The respiratory chain generates a proton electrochemical gradient across the membrane by redox-coupled proton translocation (Figure 1). This gradient is used as the driving force for synthesis of ATP, as catalyzed by the H^+-ATP synthase in the same membrane

implicated in enzyme regulation and/or assembly.[13,14] The bacterial oxidases are structurally much simpler, usually containing the homologs of subunits I, II, and III, although there are examples of distantly related heme-copper oxidases that only have the homolog of subunit I. Yet, the bacterial enzymes carry out both O_2 reduction and redox-linked proton translocation, usually with the same efficiency as the enzyme from mitochondria. Subunit I forms the functional core of the enzyme and invariably binds three redox-active metal centers, two hemes, and one copper ion (see Figure 3a and below). Subunit II forms a globular β-barrel structure on the P-side of the membrane that caps the domain in subunit I with the two heme groups, and is anchored to the membrane by two membrane-spanning helices. The β-structure entails most of the binding site for the electron donor, cytochrome c, and contains a fourth redox-active site, Cu_A, in most cytochrome c oxidases. The interaction of cytochrome c with the oxidase has been extensively studied and is mainly due to electrostatic interactions.[15] The Cu_A center is lacking from the quinol oxidases despite the presence of subunit II.[11] Subunit I from mitochondrial and some bacterial cytochrome c oxidases also comprises a Mg–binding site, which is absent from the quinol oxidases, and which lies near the interface between subunit I and the globular domain of subunit II.

Subunit III has no bound metal ions. Although it is the second-heaviest subunit, relatively little is known about its function. Its genetic deletion causes misassembly of the enzyme, while biochemical deletion decelerates proton transfer via the D-pathway (see below) in subunit I, and the subunit III-depleted enzyme becomes spontaneously inactivated after a number of turnovers, which is linked to loss of the Cu_B center.[16] A role of subunit III as an oxygen reservoir has also been proposed.[17,18]

2.2 Proton Transfer Pathways

As implied by equation (3), and by the location of the O_2 reduction site in the structure, proton transfer across the cytochrome oxidase protein is required for function, which necessitates proton-conducting pathways for three specific purposes, that is, to transfer the four ‘substrate’ protons from the N-side of the membrane into the site of O_2 reduction, for uptake of the four ‘pumped’ protons (per O_2 reduced) that are translocated across the membrane coupled to the redox reaction, and for release of these protons to the opposite side of the membrane (exit pathway). Site-directed mutagenesis data indicated the presence of two proton transfer pathways from the N-side of the membrane toward the binuclear heme

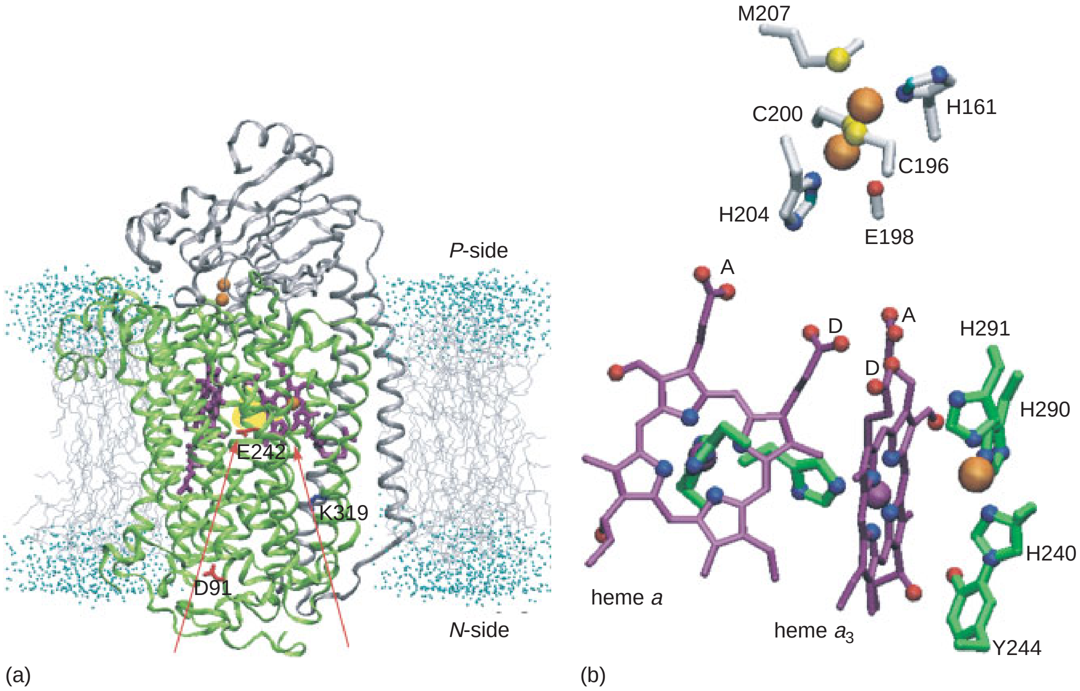

Figure 3 Cytochrome *c* oxidase structure (based on the structure of the enzyme from bovine heart mitochondria;[23] PDB code 1V54), modeled into a phospholipid membrane (gray) surrounded by water molecules (blue spheres) (Liisa Laakkonen, unpublished). (a) only subunits I (green) and II (gray) are shown. Hemes *a* (left) and a_3 (right) are shown in magenta, the copper ions (bimetallic Cu_A, and Cu_B near heme a_3) as orange spheres. Two proton transfer pathways in subunit I are indicated by red arrows, and some key residues in these pathways are indicated in red (D91 and E242 in the D-pathway) or blue (K319 in the K-pathway). A hydrophobic cavity between E242, the D-propionate of heme a_3, and the heme-copper site is indicated in yellow. *P* and *N* denote the positively and negatively charged sides of the membrane. (b) structure of the redox centers. Hemes and copper ions are colored as above. Oxygen: red; nitrogen: blue, sulfur, yellow. The bimetallic Cu_A (top) is coordinated by two histidines and two cysteines plus two weaker bonds to a methionine sulfur (M207) and a peptide oxygen (E198); all these residues are from subunit II. The A and D propionate groups of the hemes are labelled. The long hydroxyethyl farnesyl side chains of the hemes are truncated leaving only the hydroxyethyl group. The VMD program was used for the molecular graphics[29]

a_3-Cu_B site,[19] and the presence of these pathways was nicely corroborated and further specified by the crystal structures.

The so-called D-pathway in subunit I starts with a conserved aspartic acid near the *N*-side, and continues into the middle of the membrane domain with a series of hydrophilic amino acids and several bound water molecules (Figure 3a). The latter were predicted by computational methods[20,21] and were subsequently identified in the refined crystal structures.[9,12,22,23] The D-pathway proper ends at a conserved glutamic acid residue at the bottom of a hydrophobic cavity, still some 10 Å away from the site of O_2 reduction (Figure 3a). Further proton conductivity to the latter site is not evident from the crystal structures. The so-called K-pathway (mostly also in subunit I) is quite different. A conserved lysine residue either connects toward the *N*-side via a water molecule and a serine residue in subunit I (S255), or via a conserved glutamic acid residue (E62) in one of the membrane-spanning helices of subunit II. This pathway is lined by threonine and/or serine residues and appears to end at a key tyrosine moiety close to the O_2 reduction site (Figure 3a, b).

Based on the X-ray structure,[24] a third proton transfer pathway (the H-pathway) was suggested by Yoshikawa and coworkers to be involved in proton pumping. This structure extends from the *N*- to the *P*-side of the membrane, passing close to the heme *a* site at its formyl substituent, and a conserved arginine residue with strong contact to the formyl. Mutagenesis of residues in this pathway in the bacterial enzymes do not, however, cause changes in proton transfer activity or efficiency of proton translocation.[25] Yet, a recent study employing an ingenious hybridization of bovine heart and human cytochrome oxidase reports that mutation of an aspartic acid residue in this pathway (which is absent in the bacterial enzymes) leads to loss of proton pumping.[23] Hence, the role of this pathway has been reopened, as well as the question of whether different proton translocation mechanisms might be operable in mitochondria and bacteria. In the present author's opinion, the latter seems improbable in view of the very high degree of conservation of the subunit I structure between bacteria and mitochondria (see also below).

Identification of the exit pathway of the pumped protons is much poorer. Experimental evidence has suggested that it starts from a domain that includes the D-propionate of heme a_3 (Figure 3b) and its ion pair, a conserved arginine.[26,27]

However, the domain on the *P*-side of the propionate/arginine pair is rich in hydrophilic residues and water molecules, making it difficult to identify a unique proton exit path based on the structure.

2.3 Structure of Redox-active Metal Centers

Subunit I entails the functonally most important redox sites, which are conserved among all heme-copper oxidases (Figure 3b). A binuclear heme-copper site, where the Fe–Cu distance is <5 Å is the site of O_2 binding and reduction. The copper ion (Cu_B) is located on the distal side of the heme; it has three histidine ligands plus an OH^- or aquo ligand in some states of the catalytic cycle, as demonstrated by EXAFS and ENDOR spectroscopy.[28] Site-directed mutagenesis data had correctly predicted the histidine ligands of the heme *a*, heme a_3, and Cu_B centers.[2] The oxygen-binding heme is usually high spin, six-coordinate, with a histidine as the proximal axial ligand, and magnetically coupled to Cu_B (*see* ***Iron Porphyrin Chemistry***; ***Magnetism of Transition Metal Ions***). The distal Fe ligand is possibly a water molecule, or a hydroxide anion in some low-spin states (see below). Upon reduction of this heme it assumes a five-coordinate, high-spin geometry. The second heme group (heme *a* in the mitochondrial enzyme) lies very close to heme a_3, nearly at van der Waals contact and almost at a right angle (Figure 3). Heme *a* (hemes *b* or *o* in some bacteria) is low spin and six-coordinate with histidines as axial ligands.[2]

The optical and magnetic resonance properties of the Cu_A center were long noted to be unusual. The reason for this is now understood: the center consists of two adjacent Cu ions. Five of the 6 metal ligands were correctly predicted by mutagenesis data, as summarized before.[2] The structure of the Cu_A center (Figure 3b) is reminiscent of binuclear iron-sulfur centers where Fe is replaced by Cu and inorganic sulfur by cysteine sulfur.[18] Cu_A functions as a single electron transfer center where the only accessible redox states are formally Cu[I]Cu[I] (reduced) and Cu[II]Cu[I] (oxidized), the latter having the unique EPR signature.

3 FUNCTION

3.1 Electron Transfer Processes

As summarized earlier,[2] there is consensus with regard to the sequence of electron transfer in cytochrome oxidase. The Cu_A center is the initial acceptor of electrons from cytochrome *c* ($k \sim 3 \times 10^8\,M^{-1}s^{-1}$). This electron transfer depends crucially on a conserved tryptophan residue in subunit II ca. 5 Å away from the Cu_A center.[15] Then follows fast electron equilibration between Cu_A and the low-spin heme ($k_f \sim 10^4\,s^{-1}$; $k_r \sim 5 \times 10^3\,s^{-1}$, k_f and k_r denoting the forward and backward rate constants). Babcock[2] concluded that the low-spin heme acts as an ‘electron-queuing’ point for controlled electron injection into the binuclear heme a_3-Cu_B center, and although there are unsolved questions with regard to this property, it is still considered valid and will be given special attention in this review.

In its purest form, electron transfer between the low-spin heme and the binuclear heme-copper center may be studied following photolysis of CO from heme a_3 in ‘mixed-valence’ enzyme, where the binuclear site is reduced and heme *a* and Cu_A are oxidized. Several groups have described the ensuing electron equilibration with heme *a* as a process with a 3-μ s time constant.[30] This reaction is independent of pH and unaffected by exchanging water with deuterium oxide, and hence apparently due to pure electron transfer. However, according to the empirical electron tunneling theory of Dutton *et al*.[31] the electron transfer rate at the very short heme–heme distance should be three orders of magnitude faster, that is, in the nanosecond regime (*see* ***Long-range Electron Transfer in Biology***). Likewise, recent extended Hückel level calculations[32] have suggested a maximum rate of $3 \times 10^8\,s^{-1}$. Although experimental evidence for such fast electron transfer has been presented,[33] it has been disputed[34] and the issue remains open.

3.2 Dioxygen Binding and Reduction

The flow-flash technique of Gibson and Greenwood[35] and its low-temperature counterpart pioneered by Chance,[36] in conjunction with a variety of spectroscopic techniques, have continued to provide important new insights in the mechanism of O_2 reduction. The structure of some of the central intermediates in the process have been revised since the last edition of this review (Figure 4).

Photodissociation of CO (‘flash’) from the reduced enzyme after mixing with O_2 (‘flow’) in the dark has been the main method of initiating the reaction. Some concern has been voiced as to the possibility that this technique might introduce artifacts due to CO, but results using a rapid O_2 mixing system without CO have confirmed the applicability of the ‘flow/flash’ technique.[37] Yet, it has been shown by infrared spectroscopy that upon photolysis, the heme a_3-bound CO is first transferred in less than a picosecond to the nearby Cu_B, to which it remains bound for about a microsecond at room temperature[38] before diffusing out of the enzyme, as also verified by EXAFS data.[39]

Two experimental starting conditions are often employed, *viz*. the fully reduced and the ‘mixed-valence’ enzyme (Figure 4). Though not shown here, the first observed event upon the enzyme’s reaction with O_2 is a transient (ca. 2 μs) weak ($K_d \sim 8$ mM) binding of the incoming dioxygen to Cu_B, which might be limited by the dissociation of CO from the copper ion.[40] This and related phenomena have lent credit to the idea of a ‘ligand shuttle[41]’ where the incoming O_2 molecule must transiently replace any ligand that might

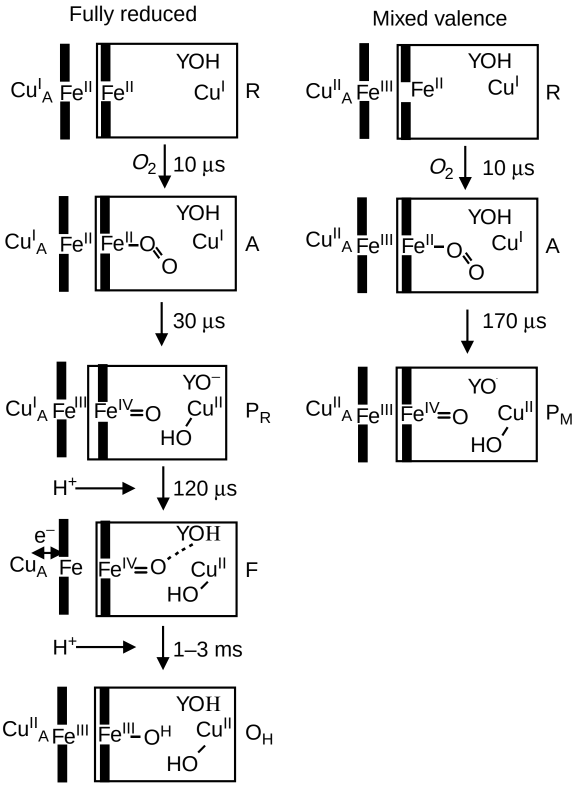
Fully reduced
Mixed valence
YOH
Cu^I_A Fe^II Fe^II Cu^I R
Cu^II_A Fe^III Fe^II Cu^I R
O2 10 µs
O2 10 µs
Cu^I_A Fe^II Fe^II–O–O Cu^I A
Cu^II_A Fe^III Fe^II–O–O Cu^I A
30 µs
170 µs
YO⁻
Cu^I_A Fe^III Fe^IV=O Cu^II HO P_R
YO
Cu^II_A Fe^III Fe^IV=O Cu^II HO P_M
H⁺
120 µs
e⁻
Cu_A Fe Fe^IV=O Cu^II HO F
H⁺
1–3 ms
Cu^II_A Fe^III Fe^III–OH Cu^II HO O_H

Figure 4 Oxidation of reduced cytochrome *c* oxidase by O_2. Tentative structures of intermediate states observed when starting the reaction from fully reduced or 'mixed-valence' enzyme. The rectangle denotes the heme a_3-copper B site, where Y is tyrosine-244 covalently bonded to the copper ligand H240 (Figure 3b). The formal redox states of heme *a* and the Cu_A center are shown on the left side of the rectangle

occupy the fourth coordination site of Cu_B[I] before binding to heme iron. Next, the heme a_3-O_2 adduct is formed (Chance's Compound A)[36] in ca. 8-µs at room temperature, as shown by both optical and Raman spectroscopy.[2] The binding of O_2 to the heme iron is surprisingly weak ($K_d \sim 0.25$ mM) considering that the Michaelis constant (K_M) is less than 1 µM. This high operational affinity for O_2 is very important *in vivo* because the rate of cell respiration must be sufficient even at the low local tissue concentrations of O_2. On the other hand, a high binding affinity would require energy expenditure that would lessen the free energy available for ATP synthesis. In cytochrome oxidase, the low K_M is instead secured by fast O_2 diffusion into the binding site (ca. $3 \times 10^8\ s^{-1}M^{-1}$), most likely via a distinct route in the protein,[17,21] and by kinetic trapping of the bound O_2 by electron transfer,[36,42] which is much faster than the rate of enzyme turnover. The latter is usually limited by the rate of electron delivery from earlier parts of the respiratory chain.

In the mixed-valence enzyme, O_2 binding and formation of Compound **A** is followed by a single reaction, as distinguished by optical and Raman spectroscopy (Figure 4).[2] This is the ca. 200-µs formation of Chance's 'Compound C,'[36] which has a prominent absorption band at 607 nm and a red-shifted Soret spectrum, relative to the fully oxidized enzyme. This species, also called the $\mathbf{P_M}$ state of the binuclear heme-copper site, was originally suggested to have a ferric **p**eroxide-cupric structure[2,43] consistent with the observations that the same state may be formed by treating the oxidized enzyme with a ferric/cupric binuclear site with hydrogen peroxide, or by withdrawing two reducing equivalents from this ferric/cupric site by an energy-dependent reversal of the reaction in mitochondria. In the last decade it has become clear, however, mainly from two sets of ingenious experiments, that heme a_3 is not in a peroxy form in the $\mathbf{P_M}$ intermediate. The Raman studies by Kitagawa and coworkers[44] using oxygen isotope-labelled O_2 showed that the O–O bond is already broken in the $\mathbf{P_M}$ state, and these data strongly suggested a ferryl heme-iron structure (Fe=O) (*see* ***Iron Porphyrin Chemistry***). In agreement with this, the experiment of Fabian *et al.*,[45] also using isotope-labelled O_2, showed that one of the two oxygen atoms could be recovered from water when the enzyme reached the $\mathbf{P_M}$ state, again indicating scission of the O–O bond at the $\mathbf{P_M}$ level of the reaction. Actually, already much earlier Weng and Baker[46] had insightfully pointed out the likelihood of a ferryl heme in $\mathbf{P_M}$ because the Soret spectrum of this compound is very similar to that of the the **F** state of the bimetallic center that is encountered later in the catalytic cycle, and which was correctly interpreted as such from the early optical and redox titration data with mitochondria.[43]

Since the O–O bond is broken in the EPR-silent $\mathbf{P_M}$, state, four redox equivalents must have been transferred to effectively reduce dioxygen to two oxygenous entities equivalent to water in the redox sense. Oxidation of ferrous to ferryl heme-iron accounts for two electrons, copper oxidation to cupric for one, but the source of the fourth electron equivalent is not obvious. Much interest has been raised toward a conserved tyrosine residue in the binuclear site that is uniquely covalently bonded to one of the three histidine ligands of Cu_B (Figure 3b).[12,24,47] The major proposal is that this tyrosine is the source of the fourth electron (and a proton), forming a neutral tyrosine radical in the $\mathbf{P_M}$ state.[48,49] This was supported by the experimental work of Proshlyakov *et al.*,[50] who showed specific reactivity of the tyrosine toward iodide in the $\mathbf{P_M}$ state, and this view has also been suported by DFT calculations.[51] The alternatives are a heme Fe[V]=O state (*see* ***Iron Porphyrin Chemistry***), suggested by Kitagawa *et al.*,[52] a Cu_B[III] state, for which there is no precedent in biology, however, or that the electron donor may be another amino acid than tyrosine. At any rate, the majority view at this time is that the $\mathbf{P_M}$ intermediate has the structure Fe[IV]=O; Cu_B[II]-OH; tyr-$O^{\cdot}$.

The above findings entail a fundamental piece of information. After binding to the reduced heme-copper site, dioxygen is fully reduced in the next reaction step to metal-bound oxide and hydroxide by electron and proton transfers within the site itself. From measurements of transmembrane electrical potential in liposomes inlaid with the enzyme, it can be concluded that this reaction is indeed not coupled to generation of proton electrochemical potential.[53] Even very small movements of charged particles (protons) in a direction perpendicular to the membrane would have been detected with this technique. Formation of $\mathbf{P_M}$ thus precedes the steps in the catalytic cycle that conserve energy. This reaction transfers the high redox potential (electron affinity) of the O_2/H_2O redox couple to the enzyme's heme-copper site to yield at least two highly oxidizing species, ferryl heme iron and the tyrosine radical. Subsequent electron transfer from cytochrome *c* to these centers is thus exergonic and linked to uphill proton translocation and charge separation across the membrane. This insight also explains why the catalytic cycle can be readily reversed when driven by a high proton electrochemical gradient in intact mitochondria, from the oxidized ferric cupric state ($\mathbf{O_H}$, Figure 5) back to the $\mathbf{P_M}$ state, but not further to evolve O_2.[43]

When the fully reduced enzyme is allowed to react with O_2, a more complicated sequence of events ensues (Figure 4),[2] since now electrons are available also in the heme *a* and Cu_A centers. After formation of the O_2 adduct (compound A), the next step is a ca. 30-µs event which involves electron transfer from the low spin heme to the binuclear site. As reported by Morgan *et al.*,[54] the optical spectrum of the state formed is indistingishable from that of $\mathbf{P_M}$ if the absorption change owing to oxidation of heme *a* is accounted for. In contrast, Einarsdóttir *et al.*[55] have claimed that the spectrum of this $\mathbf{P_R}$ state formed from the fully **r**educed enzyme is different from that of $\mathbf{P_M}$, and that $\mathbf{P_R}$ does not represent a structurally homogeneous entity, but rather a mixture of **P** and **F** states. In their alternative branched reaction mechanism, the **A** state decays in part into what we call $\mathbf{P_R}$ here, and in part into state **F** with net uptake of a proton. However, such early proton uptake disagrees with time-resolved measurements of membrane potential, which is not generated during the conversion of **A** to $\mathbf{P_R}$.[53] Moreover, contrary to Ref. 54, there is indeed resonance Raman evidence[44,52] for $\mathbf{P_R}$ formation ($\nu_{\text{Fe=O}} = 804\,\text{cm}^{-1}$) before **F** ($\nu_{\text{Fe=O}} = 785\,\text{cm}^{-1}$) when the fully reduced enzyme reacts with O_2. Morgan *et al.*[56] showed that $\mathbf{P_R}$ is the state that exhibits an unusual EPR signal from Cu_B[II], indicating an interaction with another paramagnetic center nearby, the ferryl heme iron.[57] Thus, $\mathbf{P_R}$ may have the structure Fe[IV]=O; Cu_B[II]-OH^-; tyr-O^- (Figure 4). It decomposes spontaneously in ca. 60–100 µs (depending on the source of the enzyme) to the ferryl-cupric state **F**, without further electron transfer into the binuclear center, but with net uptake of one proton.[2] Thus $\mathbf{P_R}$ and **F** are equivalent electronically, but the latter has one more proton taken up via the D-pathway, probably to protonate the tyrosinate, as recent FTIR experiments have suggested (P.R. Rich, personal communication).

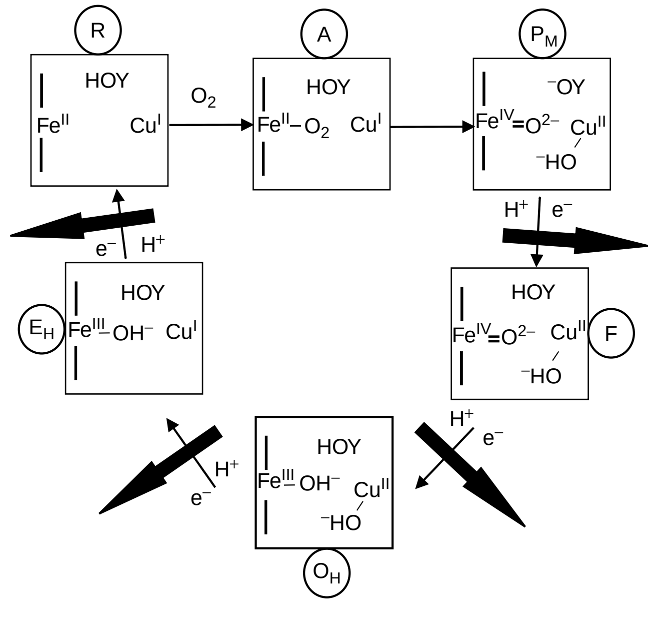

Figure 5 The catalytic cycle and its linkage to proton translocation. States **R** through $\mathbf{O_H}$ are equivalent to those in Figure 4. Large arrows denote translocation of one proton across the membrane (proton pumping). For details, see the text

While the binuclear site has very similar Soret band spectra in states $\mathbf{P_M}$, $\mathbf{P_R}$, and **F**, they differ considerably in the Q band (*see **Iron Porphyrin Chemistry***). Thus both $\mathbf{P_R}$ and $\mathbf{P_M}$ show a prominent sharp absorption maximum at 607 nm with high absorptivity, whereas **F** has a broad maximum at 580 nm with a much lower extinction coefficient. This difference, like the $20\,\text{cm}^{-1}$ difference in $\nu_{\text{Fe=O}}$ observed in Raman experiments, may be due to a different hydrogen-bonding pattern on the distal side of the heme[44,49] caused by the additional proton present in **F**. There may be stronger hydrogen bonding to the ferryl oxygen in **F** relative to **P**, which would be consistent with the lower $\nu_{\text{Fe=O}}$ as well as with its larger shift on substituting D_2O for H_2O. Additional hydrogen bonding in **F** may either be due to an aquo ligand of Cu_B (which is OH^- in **P**), or to protonation of the tyrosine, which may donate a hydrogen bond to Fe=O via a water molecule within the site (Figure 4). Such distal hydrogen bonding in **F** may induce strain that compromises an otherwise axial symmetry of the Fe=O structure in **P**, which could explain the large spectral perturbation of the Q band.

The electron originally at Cu_A becomes equilibrated approx. equally between heme *a* and Cu_A with the same kinetics as the **F** state is formed (Figure 4). This electron is finally transferred to the binuclear site, together with uptake of another proton via the D-pathway, and the **O** state is formed in ca. 2–3 ms. Different forms of the **O** state that differ in spectroscopic and kinetic parameters have long been described in the literature,[58,59] but the structural basis for these differences remains unclear. Most recently Verkhovsky *et al.*[60] reported a distinct difference in function, where reduction of the enzyme in state **O** was coupled to proton translocation only when such reduction followed immediately after oxidation of the reduced enzyme by O_2. The structure of the binuclear site in state **O** is thus of great interest. Resonance Raman data have shown iron-bound hydroxide in recently oxidized enzyme.[44,61] Thus, a possible structure for this state is Fe[III]-OH$^-$; Cu$_B$[II]-OH$^-$; tyr-OH, which has also been supported by *ab initio* calculations.[62] Re-reduction of heme a_3 and Cu$_B$ in the **O** state to form state **R** is known to be associated with net uptake of approx. two protons (Figure 5).[63]

3.3 Proton Pumping and Protonation of the Binuclear Site

The scheme of the catalytic cycle depicted here (Figure 5) is by no means proven correct in all respects. For example, the site that accepts the substrate proton (*e.g.* tyrosinate or hydroxy-ligand of Cu$_B$) is still uncertain. Notwithstanding this uncertainty, the catalytic scheme in Figure 5 has been drawn to follow two key principles: first, proton translocation (see below) is driven by uptake of a substrate proton to the binuclear site,[64,65] and second, translocation of one proton occurs in association with each one of the four electron transfers to the binuclear site.[60,66] These two principles dictate that the protonatable oxygenous sites that are formed as a result of O–O bond splitting (ferryl oxygen, Cu-bound hydroxide, tyrosine radical), and which together will take up four protons in the complete cycle, will take up one proton at each single electron transfer step. This principle differs from the proposed mechanisms of Michel[67] and Popovic and Stuchebrukhov,[68] in which proton translocation does not occur in association with the first (**O** → **E**) or second (**E** → **R**) electron transfer, respectively, but in both cases only *after* the **R** state has reacted with O$_2$. In both these proposed models the binuclear center is already fully protonated in the **E** state, that is, prematurely relative to the principles outlined above. A remaining distal OH$^-$ ligand on heme a_3 in the **E** state (Figure 5) is, however, consistent with recent results of Brzezinski *et al.*,[69] who showed that the conversion of **R** back to **E** in the isolated enzyme at high pH is associated with release of one proton that most likely derives from a water molecule cordinated to heme a_3, forming a low-spin ferric hydroxide species that was detected by EPR. The structure **O$_H$** for the oxidized site in Figure 5 is metastable,[60,66] and almost certainly different from the structure of the oxidized enzyme as isolated, which is also supported by *ab initio* calculations.[62] The exact changes that occur on relaxation of the metastable **O$_H$** state are unknown to date, however, and this is another important issue that remains to be solved, not least because it may highlight the structural requirements of active proton translocation.

3.4 Proton Translocation Mechanisms

Several details of the proton translocation mechanism have been revealed since the previous edition of this series. Thus, the proton transfer pathways have been elucidated (see above), and near consensus has been reached that all protons that are pumped across the membrane will pass through the D-pathway (but see Ref. 23). However, as discussed above, there is not yet consensus with respect to the identity of the reactions in the catalytic cycle that are coupled to proton translocation. Major uncertainties start when considering the fate of the protons beyond the glutamic acid in the D-pathway. Also, the ‘pump element’ that links proton translocation to electron transfer remains to be identified. In the histidine cycle type of mechanism[7,64] a dissociable histidine ligand of Cu$_B$ was proposed to be the ‘pump element’. This proposal was based on the notion that all four proton-pumping steps in the catalytic cycle would occur in the **P** → **F** and **F** → **O** steps, as suggested by the dependence of the **P** ↔ **F** and **F** ↔ **O** equilibria on the [ATP]/[ADP]$\cdot$[P$_i$] ratio in mitochondria at a high electrochemical proton gradient.[70] However, subsequent kinetic data with cytochrome oxidase incorporated in vesicles showed unequivocally that this is not the case, but that one proton is pumped during each of these steps.[60,66] It is still not fully understood why the mitochondrial experiments overestimated the charge translocaton stoichiometry. One possibility suggested by Michel[67] is significant proton leaks across the mitochondrial membrane at the high proton electrochemical potential employed. This would compromise the assumption of near equilibrium in the system and cause artifactually high charge translocation stoichiometries.

It is known that the D-pathway transfers the pumped protons, but it also transfers substrate protons to be consumed at the binuclear site, at least those consumed during the **P$_M$** → **F** → **O$_H$** reactions.[71,72] Mutation of the lysine in the K-pathway (Figure 3a) hardly affects these reactions, but strongly inhibits reduction of heme a_3 and blocks the reversal of the **E** → **R** reaction step.[73] Measurements of charge translocation in reconstituted oxidase vesicles suggested that also the **O$_H$** → **E$_H$** reaction is blocked by this mutation.[74,75] One important problem, already alluded to, is indeed why two proton transfer pathways are required, especially since the two do not discriminate between pumped and substrate protons, as first assumed.[7]

Iwata *et al.*[7] suggested that the D-propionate of heme a_3 may provide the entry into the proton exit pathway of proton pumping, and this has received experimental support.[26,27] Tsukihara *et al.*[23] (supporting information) and Popovic and Stuchebrukhov[68] criticized this proposal on the basis of the strong ion pair formed between this propionate and a conserved arginine. However, a proton-accepting role of the propionate may be transient and dependent on fluctuations of the arginine-propionate structure.[76,77] The problem remains that both substrate and pumped protons must be transferred through the D-pathway via the glutamic acid, which calls for a molecular ‘switch’ that transfers the proton from the glutamic acid in a controlled fashion, either to be pumped or to be consumed. There are, however, at least two possible scenarios where a redox state dependent switch may not be required. If the first proton taken up is transferred to the pump rather than to the binuclear site purely for thermodynamic reasons (*i.e.* if the pK_a of the former is much higher),[78] no switching function is necessary. Alternatively, if the first proton is transferred to the binuclear site (having the highest pK_a), and this causes a conformational change that raises the pK_a of a pump site, the next proton will automatically be transferred to be pumped.[77]

The model by Siegbahn *et al.*[78] proposed the key 'pump element' to be the A-propionate of heme a_3 (Figure 3b), which according to their DFT calculations can have a higher proton affinity than the binuclear site itself. However, one experimental drawback of this model is the finding that mutations of the conserved aspartic acid that strongly interacts with this propionate has little effect on enzyme activity, and no effect on the efficiency of proton pumping.[79,80] The model by Brzezinski and Larsson[77] attributes a conformational change and a concomitant rise in the pK_a of the propionate/arginine pair to the deprotonation of glutamic acid when its proton is delivered to the binuclear center. However, such a key role of the glutamic acid carboxyl group is difficult to reconcile with proton pumping by some of the more distanty related heme-copper oxidases in which a tyrosine residue has replaced the glutamate.[81,82] Of course, here we assume again that the same mechanism of proton translocaton is shared by all heme-copper oxidases.

The model recently proposed by Popovic and Stuchebrukhov[68] was based on electrostatic calculations and claimed H291 to be the 'pump element'. H291 is one of the ligands of Cu_B (Figure 3b), and was proposed to be deprotonated at the Nδ1 position when the binuclear center is oxidized, or when it receives a proton.[68] Apart from the deviation of this model from the two basic principles outlined above, it stands in contrast to the electrostatic calculations by Kannt *et al.*[83] according to which the Cu_B ligands H291 and H290 are neutral (*i.e.* singly protonated) even in the fully oxidized enzyme.

As already discussed, the model proposed by Tsukihara *et al.*[23] depends on the so-scalled H-pathway of proton transfer and on the function of an aspartic acid that is not conserved in the bacterial oxidases. This model also depends crucially on the formyl group and on the hydroxyethyl farnesyl side chain of heme *a*. Many proton-pumping bacterial oxidases, such as cytochrome bo_3 from *E. coli*, have replaced heme *a* with a protoheme (heme B) that lacks both the formyl and the farnesyl side chain. Therefore, this model is restricted to heme *a* – containing oxidases, and implies different mechanisms of proton translocation in different members of the heme-copper oxidase superfamily.

Yoshikawa *et al.*[18] made the important statement that 'the role of heme *a* may be the biggest mystery in the structure and function of cytochrome *c* oxidase'. It is indeed not at all obvious why all heme-copper oxidases have a low-spin heme group very close to the binuclear heme-copper site, especially since direct electron transfer from Cu_A to that site (if it occurred) would take place across almost the same distance. In the cytochrome *c* oxidases such direct electron transfer is effectively prevented, perhaps due to the bound Mg, the coordination sphere of which lies on the shortest path between Cu_A and heme a_3. The Mg site is indeed lacking from the quinol oxidases, which also lack Cu_A, and where electrons from a bound quinol on the back of the low-spin heme are transferred via that heme group to the binuclear site.[11]

The enigmatic role of heme *a* may also be related in an interesting way to Babcock's important conclusion[2] that it is an 'electron-queuing' point, and that further electron transfer to the binuclear center is strictly controlled by proton uptake.[84] It occurred to us[76] that this queuing function, as well as the unique positioning of heme *a* in the structure, may provide the key to the proton-pumping mechanism. An electron that is 'queuing' at heme *a* will induce an electric field between this heme and the binuclear center, parallel to the membane. Such a field may have the effect of orienting water molecules in the hydrophobic cavity between the glutamic acid and the binuclear site (Figure 3a), and thus provide a redox state-controlled switch between proton pumping and proton consumption. The short distance between the two hemes, their position relative to the membrane, the proton-donating glutamic acid, the proton-accepting propionate, and the hydrophobic cavity between them are all prerequisites of this proposed mechanism.[76] In some ways this structure is reminiscent of that between the proton-donating D96 and the proton-accepting Schiff's base in the light-driven proton pump, bacteriorhodopsin.[85] Also in this latter case there is a hydrophobic cavity between proton donor and acceptor, which contains an array of water molecules that carries the proton across the 10 Å distance.[86] In cytochrome oxidase the role of the water molecules may be more intricate, however, because they may provide strictly redox state-controlled proton-conducting Grotthuss 'wires'[87,88] for proton translocation and consumption.[76]

4 CONCLUSIONS

The fundamental role of aerobic respiration for all higher organisms and for several prokaryotes has conferred specific characteristics on cytochrome oxidase, and on the large family of heme-copper oxidases more generally. Many of these characteristics have been revealed since the last edition of this series. The crystal structures of several heme-copper oxidases have been solved, generally confirming the coordination of the redox centers that had been worked out by site-directed mutagenesis combined with spectroscopic and other biophysical techniques. However, for example, the relative positioning of the two heme groups in the structure was not anticipated. The unique capability of catalyzing safe reduction of dioxygen to water is now fairly well understood mechanistically. In a single fast reaction step the weakly but rapidly bound O_2 is trapped by accepting four electrons locally from within the active site itself in a reaction that is much faster than turnover, therefore allowing fast cell respiration even at low O_2 concentrations. This step is not coupled to energy transduction, but is designed to transfer the oxidizing potential of O_2 to the active site without spending energy on O_2 binding. As a result, the active site becomes highly oxidizing, and thereby poised to accept electrons in the four discrete reaction steps that follow. As pointed out by Babcock,[2] the strategy is strict proton control of these latter steps, which allows buildup of intermediates, and gives the opportunity to study catalysis and energy transduction in cytochrome oxidase by a variety of time-resolved biophysical techniques. But more important, the control by proton transfer has profound mechanistic implications because it allows coupling of the electron transfers to proton translocation. In cytochrome oxidase these single electron transfers are each coupled to translocation of *two* electrical charge equivalents whereby the energy transduction efficiency per electron is twice that encountered in photosynthetic reaction centers or in the cytochrome bc_1 complex, which operate according to Mitchell's redox loop principle.[1] Athough many mechanistic models have been presented, as discussed above, it is still not fully understood how this fundamental difference in function is resolved mechanistically.

5 RELATED ARTICLES

Dioxygen & Related Ligands; Iron: Heme Proteins & Dioxygen Transport & Storage; Iron: Heme Proteins, Peroxidases, Catalases & Catalase-peroxidases; Iron Porphyrin Chemistry; Long-range Electron Transfer in Biology.

6 REFERENCES

1. P. Mitchell, *Biol. Rev.*, 1976, **41**, 445.
2. G. T. Babcock, Cytochrome Oxidase, in 'Encyclopedia of Inorganic Chemistry', ed. R. B. King, John Wiley & Sons, Chichester, 1994, Vol. 2, p. 950.
3. M. Saraste, L. Holm, L. Lemieux, M. Lübben, and J. van der Oost, *Biochem. Soc. Trans.*, 1991, **19**, 608.
4. W. Wu, C. K. Chang, C. Varotsis, G. T. Babcock, A. Puustinen, and M. Wikström, *J. Am. Chem. Soc.*, 1992, **114**, 1182.
5. M. Wikström, *Nature*, 1977, **266**, 271.
6. A. Puustinen, M. Finel, M. Virkki, and M. Wikström, *FEBS Lett.*, 1989, **249**, 163.
7. S. Iwata, C. Ostermeier, B. Ludwig, and H. Michel, *Nature*, 1995, **376**, 660.
8. T. Tsukihara, H. Aoyama, E. Yamashita, T. Tomikazi, H. Yamaguchi, K. Shinzawa-Itoh, R. Nakashima, R. Yaono, and S. Yoshikawa, *Science*, 1995, **269**, 1069.
9. M. Svensson-Ek, J. Abramson, G. Larsson, S. Törnroth, P. Brzezinski, and S. Iwata, *J. Mol. Biol.*, 2002, **321**, 329.
10. T. Soulimane, G. Buse, G. P. Bourenkov, H. D. Bartunik, R. Huber, and M. E. Than, *EMBO J.*, 2000, **19**, 1766.
11. J. Abramson, S. Riistama, G. Larsson, A. Jasaitis, M. Svensson-Ek, L. Laakkonen, A. Puustinen, S. Iwata, and M. Wikström, *Nat. Struct. Biol.*, 2000, **7**, 910.
12. C. Ostermeier, A. Harrenga, U. Ermler, and H. Michel, *Proc. Natl. Acad. Sci. U.S.A.*, 1997, **94**, 10547.
13. B. Kadenbach, *Biochim. Biophys. Acta*, 2003, **1604**, 77.
14. R. O. Poyton and J. E. McEwen, *Ann Rev. Biochem.*, 1996, **65**, 563.
15. O. Maneg, F. Malatesta, B. Ludwig, and V. Drosou, *Biochim. Biophys. Acta*, 2004, **1655**, 274 (available at www.sciencedirect.com).
16. J. P. Hosler, *Biochim. Biophys. Acta*, 2004, **1655**, 332 (available online www.sciencedirect.com).
17. S. Riistama, A. Puustinen, A. Garcia-Horsman, S. Iwata, H. Michel, and M. Wikström, *Biochim. Biophys. Acta*, 1996, **1275**, 1.
18. S. Yoshikawa, K. Shinzawa-Itoh, and T. Tsukihara, *J. Bioenerg. Biomembr.*, 1998, **30**, 7.
19. P. Brzezinski and P. Ädelroth, *J. Bioenerg. Biomembr.*, 1998, **30**, 99.
20. S. Riistama, G. Hummer, A. Puustinen, B. R. Dyer, W. H. Woodruff, and M. Wikström, *FEBS Lett.*, 1997, **414**, 275.
21. I. Hofacker and K. Schulten, *Proteins*, 1998, **30**, 100.
22. E. Olkhova, M. C. Hutter, M. A. Lill, V. Helms, and H. Michel, *Biophys. J.*, 2004, **86**, 1873.
23. T. Tsukihara, K. Shimokata, Y. Katayama, H. Shimada, K. Muramoto, H. Aoyama, M. Mochizuki, K. Shinzawa-Itoh, E. Yamashita, M. Yao, Y. Ishimura, and S. Yoshikawa, *Proc. Natl. Acad. Sci. U.S.A.*, 2003, **100**, 15304.
24. S. Yoshikawa, K. Shinzawa-Itoh, R. Nakashima, R. Yaono, E. Yamashita, N. Inoue, M. Yao, M. J. Fei, C. P. Libeu, T. Mizushima, H. Yamaguchi, T. Tomizaki, and T. Tsukihara, *Science*, 1998, **280**, 1723.
25. H. M. Lee, T. K. Das, D. L. Rousseau, D. Mills, S. Ferguson-Miller, and R. B. Gennis, *Biochemistry*, 2000, **39**, 2989.
26. A. Puustinen and M. Wikström, *Proc. Natl. Acad. Sci. U.S.A.*, 1999, **96**, 35.
27. D. A. Mills and S. Ferguson-Miller, *Biochim. Biophys. Acta*, 2002, **1555**, 96.
28. Y. C. Fann, I. Ahmed, N. J. Blackburn, J. S. Boswell, M. L. Verkhovskaya, B. M. Hoffman, and M. Wikström, *Biochemistry*, 1995, **34**, 10245.
29. W. Humphrey, A. Dalke, and K. Schulten, *J. Mol. Graphics*, 1996, **14**, 33.

30. Ó. Einarsdóttir, K. E. Georgiadis, and A. Sucheta, *Biochemistry*, 1995, **34**, 496.

31. C. C. Page, C. C. Moser, X. Chen, and P. L. Dutton, *Nature*, 1999, **402**, 47.

32. M. L. Tan, I. Balabin, and J. N. Onuchic, *Biophys. J.*, 2004, **86**, 1813.

33. M. I. Verkhovsky, A. Jasaitis, and M. Wikström, *Biochim. Biophys. Acta*, 2001, **1506**, 143.

34. A. Namslauer, M. Brändén, and P. Brzezinski, *Biochemistry*, 2002, **41**, 10370.

35. Q. H. Gibson and C. Greenwood, *Biochem. J.*, 1963, **86**, 541.

36. B. Chance, C. Saronio, and J. S. Leigh, Jr, *J. Biol. Chem.*, 1975, **250**, 9226.

37. S. Takahashi, Y.-s. Ching, J. Wang, and D. L. Rousseau, *J. Biol. Chem.*, 1995, **270**, 8405.

38. W. H. Woodruff, Ó. Einarsdóttir, R. B. Dyer, K. A. Bagley, G. Palmer, S. J. Atherton, R. A. Goldbeck, T. D. Dawes, and D. S. Kliger, *Proc. Natl. Acad. Sci. U.S.A.*, 1991, **88**, 2588.

39. M. Ralle, M. L. Verkhovskaya, J. E. Morgan, M. I. Verkhovsky, M. Wikström, and N. J. Blackburn, *Biochemistry*, 1999, **38**, 7185.

40. J. A. Bailey, C. A. James, and W. H. Woodruff, *Biochem. Biophys. Res. Commun.*, 1996, **220**, 1055.

41. W. H. Woodruff, *J. Bioenerg. Biomembr.*, 1993, **25**, 177.

42. M. I. Verkhovsky, J. E. Morgan, A. Puustinen, and M. Wikström, *Nature*, 1996, **380**, 268.

43. M. Wikström, *Proc. Natl. Acad. Sci. U.S.A.*, 1981, **78**, 4051.

44. T. Ogura and T. Kitagawa, *Biochim. Biophys. Acta*, 2004, **1655**, 290 (available at www.sciencedirect.com).

45. M. Fabian, W. W. Wong, R. B. Gennis, and G. Palmer, *Proc. Natl. Acad. Sci. U.S.A.*, 1999, **96**, 13114.

46. L. Weng and G. M. Baker, *Biochemistry*, 1991, **30**, 5727.

47. G. Buse, T. Soulimane, M. Dewor, H. E. Meyer, and M. Blüggel, *Protein Sci.*, 1999, **8**, 985.

48. R. B. Gennis, *Biochim. Biophys. Acta*, 1998, **1365**, 241.

49. D. A. Proshlyakov, M. A. Pressler, and G. T. Babcock, *Proc. Natl. Acad. Sci. U.S.A.*, 1998, **95**, 8020.

50. D. A. Proshlyakov, M. A. Pressler, C. DeMaso, J. F. Leykam, D. L. DeWitt, and G. T. Babcock, *Science*, 2000, **290**, 1588.

51. M. R. A. Blomberg, P. E. M. Siegbahn, G. T. Babcock, and M. Wikström, *J. Am. Chem. Soc.*, 2000, **122**, 12848.

52. T. Kitagawa and T. Ogura, *Prog. Inorg. Chem.*, 1997, **45**, 431.

53. A. Jasaitis, M. I. Verkhovsky, J. E. Morgan, M. L. Verkhovskaya, and M. Wikström, *Biochemistry*, 1999, **38**, 2697.

54. J. E. Morgan, M. I. Verkhovsky, and M. Wikström, *Biochemistry*, 1996, **35**, 12235.

55. Ó. Einarsdóttir and I. Szundi, *Biochim. Biophys. Acta*, 2004, **1655**, 263 (available at www.sciencedirect.com).

56. J. E. Morgan, M. I. Verkhovsky, G. Palmer, and M. Wikström, *Biochemistry*, 2001, **40**, 6882.

57. Ö. Hansson, B. Karlsson, R. Aasa, T. Vänngård, and B. G. Malmström, *EMBO J.*, 1982, **1**, 1295.

58. M. T. Wilson, J. Peterson, E. Antonini, M. Brunori, A. Colosimo, and J. Wyman, *Proc. Natl. Acad. Sci. U.S.A.*, 1981, **78**, 7115.

59. G. W. Brudvig, T. H. Stevens, R. H. Morse, and S. I. Chan, *Biochemistry*, 1981, **20**, 3912.

60. M. I. Verkhovsky, A. Jasaitis, M. L. Verkhovskaya, J. E. Morgan, and M. Wikström, *Nature*, 1999, **400**, 480.

61. S. Han, Y.-C. Chin, and D. L. Rousseau, *Nature*, 1990, **348**, 89.

62. D. M. Moore and T. J. Martinez, *J. Phys. Chem.*, 2000, **104**, 2367.

63. R. Mitchell and P. R. Rich, *Biochim. Biophys. Acta*, 1994, **1186**, 19.

64. J. E. Morgan, M. I. Verkhovsky, and M. Wikström, *J. Bioenerg. Biomembr.*, 1994, **26**, 599.

65. P. R. Rich, *Aust. J. Plant. Physiol.*, 1995, **22**, 479.

66. D. Bloch, I. Belevich, A. Jasaitis, C. Ribacka, A. Puustinen, M. I. Verkhovsky, and M. Wikström, *Proc. Natl. Acad. Sci. U.S.A.*, 2004, **101**, 529.

67. H. Michel, *Biochemistry*, 1999, **38**, 15129.

68. D. M. Popovic and A. A. Stuchebrukhov, *J. Am. Chem. Soc.*, 2004, **126**, 1858.

69. M. Bränden, A. Namslauer, Ö. Hansson, R. Aasa, and P. Brzezinski, *Biochemistry*, 2003, **42**, 13178.

70. M. Wikström, *Nature*, 1989, **338**, 776.

71. A. A. Konstantinov, S. Siletsky, D. Mitchell, A. Kaulen, and R. B. Gennis, *Proc. Natl. Acad. Sci. U.S.A.*, 1997, **94**, 9085.

72. P. Ädelroth, R. B. Gennis, and P. Brzezinski, *Biochemistry*, 1998, **37**, 2470.

73. M. Bränden, F. Thomson, R. B. Gennis, and P. Brzezinski, *Biochemistry*, 2002, **41**, 10794.

74. M. Ruitenberg, A. Kannt, E. Bamberg, B. Ludwig, H. Michel, and K. Fendler, *Proc. Natl. Acad. Sci. U.S.A.*, 2000, **97**, 4632.

75. M. I. Verkhovsky, A. Tuukkanen, C. Backgren, A. Puustinen, and M. Wikström, *Biochemistry*, 2001, **40**, 7077.

76. M. Wikström, M. I. Verkhovsky, and G. Hummer, *Biochim. Biophys. Acta*, 2003, **1604**, 61.

77. P. Brzezinski and G. Larsson, *Biochim. Biophys. Acta*, 2003, **1605**, 1.

78. P. E. M. Siegbahn, M. R. A. Blomberg, and M. L. Blomberg, *J. Phys. Chem. B*, 2003, **107**, 10946.

79. J. W. Thomas, A. Puustinen, J. O. Alben, R. B. Gennis, and M. Wikström, *Biochemistry*, 1993, **32**, 10923.

80. J. Qian, W. Shi, M. Pressler, C. Hoganson, D. Mills, G. T. Babcock, and S. Ferguson-Miller, *Biochemistry*, 1997, **36**, 2539.

81. M. M. Pereira, M. L. Verkhovskaya, M. Texeira, and M. I. Verkhovsky, *Biochemistry*, 2000, **39**, 6336.

82. C. Backgren, G. Hummer, M. Wikström, and A. Puustinen, *Biochemistry*, 2000, **39**, 7863.

83. A. Kannt, C. R. D. Lancaster, and H. Michel, *Biophys J.*, 1998, **74**, 708.

84. M. I. Verkhovsky, J. E. Morgan, and M. Wikström, *Biochemistry*, 1995, **34**, 7483.

85. M. Wikström, *Curr. Opin. Struct. Biol.*, 1998, **8**, 480.

86. Y.-S. Lee and M. Krauss, *J. Am. Chem. Soc.*, 2004, **126**, 2225.

87. N. Agmon, *Chem. Phys. Lett.*, 1995, **244**, 456.

88. J. F. Nagle and H. J. Morowitz, *Proc. Natl. Acad. Sci. U.S.A.*, 1978, **75**, 298.

Acknowledgments

This work was supported by grants from the Academy of Finland (program 44 895), Biocentrum Helsinki, and the Sigrid Jusélius Foundation. Dr. Liisa Laakkonen is acknowledged for producing Figure 2.

This article is dedicated to the memory of Gerald T. Babcock (1946–2000), who wrote the earlier version in the previous edition of this series,[2] of which this is an update. Amino acid residues are abbreviated by the one-letter code, and their numbering follows that of cytochrome *c* oxidase from bovine heart.

Decarbonylation Catalysis

Fred H. Jardine
Washington State University, Pullman, WA, USA

1 Introduction 1
2 Scope of the Reaction 1
3 Decarbonylation of Acid Halides 2
4 Aldehyde Decarbonylation 4
5 Related Articles 6
6 References 6

Glossary

Acyl complex: a complex containing the grouping M−COR, where R is an alkyl or aryl group
Anti-Bredt alkene: a polycyclic alkene that contravenes Bredt's rules by having a C=C bond attached to a bridgehead carbon atom
Deuterioaldehyde: a compound of the general formula RC^2HO
Hofmann elimination: loss of a proton leading preferentially to the alkene carrying the smaller number of alkyl groups (cf. Saytzeff elimination below)
Isotopic scrambling: random incorporation of an isotopic substituent (usually deuterium) during a reaction
Kinetic isotope effect: the ratio $k\mathrm{H}/k\mathrm{D}$ of the rates of reaction of the normal substrate and the deuterated substrate. If a bond to deuterium is broken in the rate-determining step, the ratio is usually greater than 1
Saytzeff elimination: loss of a proton leading preferentially to the alkene carrying the larger number of alkyl groups (cf. Hofmann elimination above)

1 INTRODUCTION

The decarbonylation of carboxylic acid halides or aldehydes by complexes of the platinum group metals represents a modern, convenient method of descending a homologous series. Acid halides are particularly useful starting materials since most are decarbonylated to alkenes, while the major product from an aldehyde is the alkane. The utility of the reaction is increased by the fact that chiral groups retain their configuration throughout the reaction. If the reactants are scrupulously dried, decarbonylation of deuterioaldehydes represents a means of specifically labeling the product with deuterium at the site of the original formyl substituent.

The reactions may be carried out either stoichiometrically or catalytically. Normally, economy dictates that the reaction is carried out catalytically at temperatures between 150 and 200 °C. Addition of a carbonyl acceptor permits the catalytic reaction to be carried out at room temperature with simple substrates.

The first stage in the reaction is oxidative addition of the acyl compound, RCOX (X = H, halide) to the low-valent, coordinatively unsaturated metal complex (*see Oxidative Addition*). The acyl complex so formed rearranges to an alkyl carbonyl complex, which subsequently undergoes *reductive elimination* of the products. The carbonyl group abstracted from the organic substrate is incorporated in the resulting transition metal carbonyl complex. If the substrate or an added reagent displaces the carbonyl ligand from its complex, then the reaction is catalytic.

2 SCOPE OF THE REACTION

Many transition metal carbonyl complexes have been prepared, often inadvertently, by allowing a metal halide or polyhalometallate to react with a ligand in an organic solvent with carbon−oxygen bonds. Indeed, carbonyl abstraction is an important synthetic route to *trans*-$[\mathrm{MCl(CO)(PPh_3)_2}]$ (M = Rh, Ir) or $[\mathrm{OsHX(CO)(ZPh_3)_3}]$ (X = Cl, Br; Z = P, As) and related osmium(II) complexes.

Other carbonyl complexes can be obtained from the reactions between existing complexes and organic solvents, which incorporate oxygen. Thus, *mer*-$[\mathrm{ReCl_3(PMe_2Ph)_3}]$ abstracts carbon monoxide from refluxing dimethylaminoethanol to form *trans*-$[\mathrm{ReCl(CO)(PMe_2Ph)_4}]$. The *mer*-tribromo complex reacts analogously with formic acid.

Since these initial discoveries, it has been found that a wide variety of substrates can be decarbonylated by transition metal complexes. Rhodium complexes are the most widely used since their products are usually the very stable *trans*-$[\mathrm{RhCl(CO)L_2}]$ complexes.

Acyldiphenylphosphines, aromatic ketoalkynes, allylic alcohols, metal carbonyl complexes, or acid anhydrides can be decarbonylated by $[\mathrm{RhCl(PPh_3)_3}]$, while α, β- and certain other diketo compounds are semi-decarbonylated by this complex (Scheme 1). Many binary transition metal carbonyl complexes undergo metathetical reactions with $[\mathrm{RhCl(PPh_3)_3}]$. These metathetical reactions also occur if $[\mathrm{RhCl(PPh_3)_3}]$ is used to decarbonylate acyl carbonyl complexes since ^{13}CO labeling of the acyl ligand has shown that a carbonyl ligand is abstracted. The product, $[(\eta^5\text{-}\mathrm{C_5H_5})\mathrm{Fe(CO)(COMe)PPh_3}]$, arises from a triphenylphosphine attack on the intermediate $(\eta^5\text{-}\mathrm{C_5H_5})\mathrm{Fe(CO)(COMe)}$ before it can rearrange to the methyl complex.[1]

Many of the above reactions are stoichiometric, which greatly limits their applicability because of the high cost of platinum metals. Fortunately the decarbonylation of

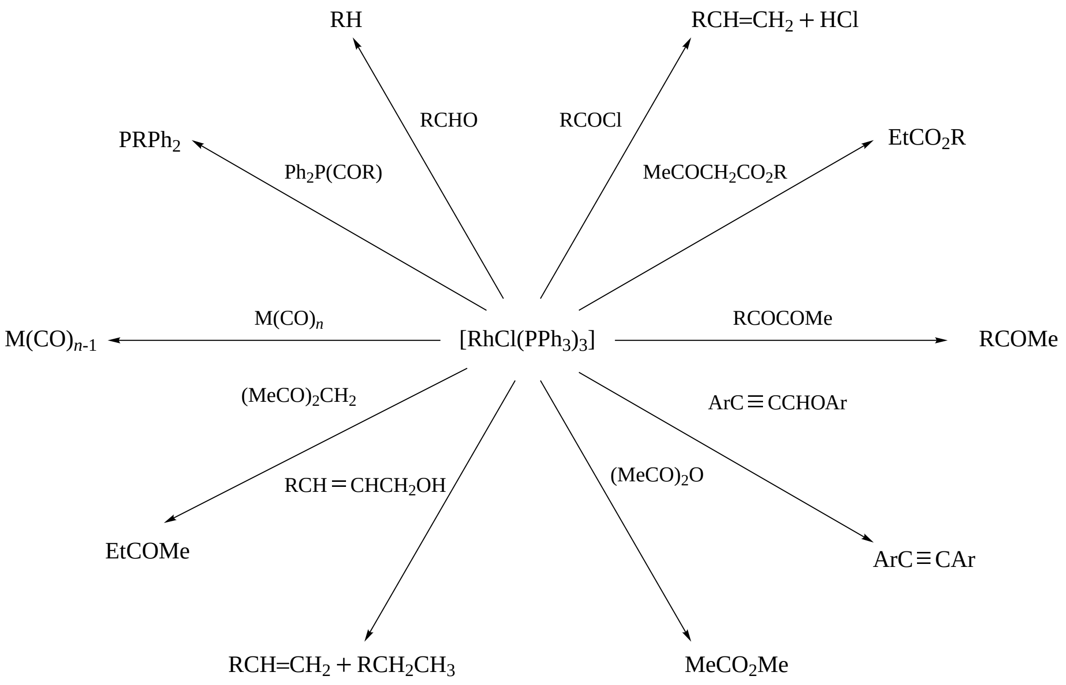
RH
RCH=CH2 + HCl
PRPh2
RCHO
RCOCl
EtCO2R
Ph2P(COR)
MeCOCH2CO2R
M(CO)n-1
M(CO)n
[RhCl(PPh3)3]
RCOCOMe
RCOMe
(MeCO)2CH2
ArC≡CCHOAr
RCH=CHCH2OH
(MeCO)2O
EtCOMe
ArC≡CAr
RCH=CH2 + RCH2CH3
MeCO2Me

Scheme 1

aldehydes and acid chlorides is catalytic at the high temperatures required to decompose *trans*-[RhCl(CO)(PPh_3)$_2$]. Palladium(0) complexes also act as catalysts in the decarbonylation of acyl or aroyl cyanides at somewhat lower temperatures.[2]

3 DECARBONYLATION OF ACID HALIDES

These decarbonylation reactions can be either stoichiometric[3] or catalytic.[4] The latter reactions are carried out at high temperatures in high-boiling, inert solvents such as benzyl chloride. The high temperatures are required to eliminate CO from the *trans*-[RhCl(CO)(PPh_3)$_2$] initially formed in these reactions. Other than this essential regeneration of the intermediate RhCl(PPh_3)$_2$, there is little reason to suppose that there are significant differences between the stoichiometric and catalytic reactions.

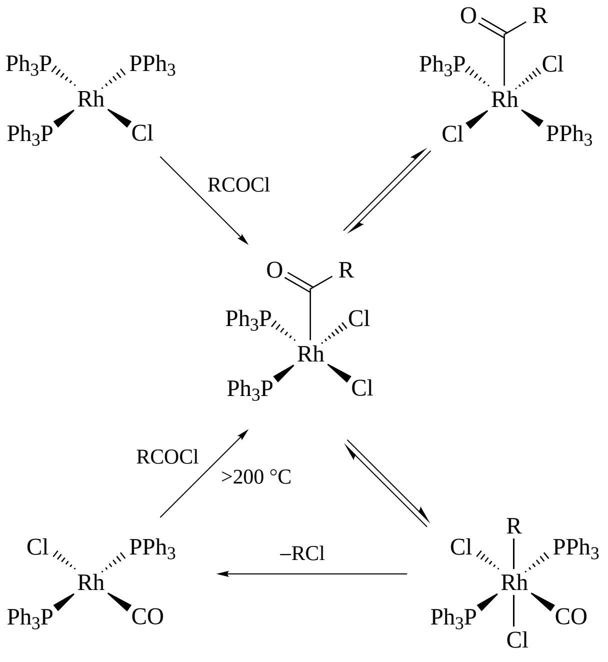
Ph3P
PPh3
Rh
Ph3P
Cl
O
R
Ph3P
Cl
Rh
Cl
PPh3
RCOCl
O
R
Ph3P
Cl
Rh
Ph3P
Cl
RCOCl
>200 °C
Cl
PPh3
Rh
Ph3P
CO
–RCl
R
Cl
PPh3
Rh
Ph3P
CO
Cl

Scheme 2

The catalytic cycle is shown in Scheme 2. The first step is the two-fragment oxidative addition of acid halide to *trans*-[RhCl(CO)(PPh_3)$_2$]. It has been demonstrated that the initial pentacoordinate acylrhodium(III) product is square pyramidal with cis basal triphenylphosphine ligands. This isomerizes to a more stable square-pyramidal complex with trans basal triphenylphosphine ligands. In both complexes, the apex of the pyramid is occupied by the acyl group. However, it has been clearly shown that only the cis square-pyramidal isomer undergoes alkyl migration to the vacant site on rhodium in the next step of the catalytic cycle.[5] It is now generally agreed that the migration of chiral alkyl groups takes place with retention of configuration.

The decarbonylation is completed by a reductive elimination reaction. The exact form of this reaction is determined by the nature of the alkyl group. The alternatives available are reductive elimination of chloroalkane, or reductive elimination of HCl and release of alkene. The first process is restricted to aryl groups and those alkyl groups that contain no β-hydrogen atoms. The elimination again occurs with retention of configuration if a chiral alkyl group is present.

This duality is entirely analogous to that found in the decarbonylation of aroyl or acyl cyanides by $[Pd(PPh_3)_4]$ as shown in equations (1) and (2).[2]

$$\text{ArCOCN} \xrightarrow{[\text{Pd(PPh}_3)_4]} \text{ArCN} + \text{CO} \qquad (1)$$

$$\text{RCH}_2\text{CH}_2\text{COCN} \xrightarrow{[\text{Pd(PPh}_3)_4]} \text{RCH}_2\text{CH}_2\text{CN} + \text{RCH{=}CHCN} \qquad (2)$$

That alkenes are formed from those alkyl groups containing a β-hydrogen atom strongly implies that the mechanism of alkene formation involves a β-hydride abstraction step. There is a very pronounced kinetic isotope effect when $C_6D_5CD_2CH_2COCl$ is decarbonylated, which indicates that not only does a β-deuteride abstraction take place but that it is also rate determining. Further evidence for the participation of a β-hydride abstraction comes from the decarbonylation of *erythro*- or *threo*-2,3-diphenylbutanoyl chloride, where the former yields the (E)-alkene and the latter the (Z)-isomer.

However, in other instances, postelimination reactions can change the nature of the products. The main difficulty arises from the readdition of the alkene initially produced to the hydrido complex. This can result in isotopic scrambling or isomerization of the alkene upon reelimination. The formation of internal alkene products from the $[Pd(PPh_3)_4]$-catalyzed decarbonylation of acyl cyanides (equation 2) may also arise from postelimination reactions between the alkene and $[PdH(CN)(CO)(PPh_3)_n]$ initially formed. The importance of this reaction in isomerizing the anti-Bredt alkenes[6] formed by the catalytic decarbonylation of 3-chlorocarbonyltricyclo[5.3.1.0^{3,7}]undecane is shown in Scheme 3.

If the influence of these posteliminations can be minimized, it is possible to show that Saytzeff rather than Hofmann elimination takes place. The preference for hydrogen abstraction is tertiary > secondary > primary.[8]

Both pre- and postelimination reactions conspire to frustrate attempts to determine if the rhodium complex retains its original chloro ligand throughout the catalytic cycle. Experiments employing $[RhCl(PPh_3)_3]$ in the catalytic decarbonylation of aroyl fluorides are not very successful. The reaction soon ceases, implying that halo ligand exchange has taken place and that fluoro complexes do not catalyze

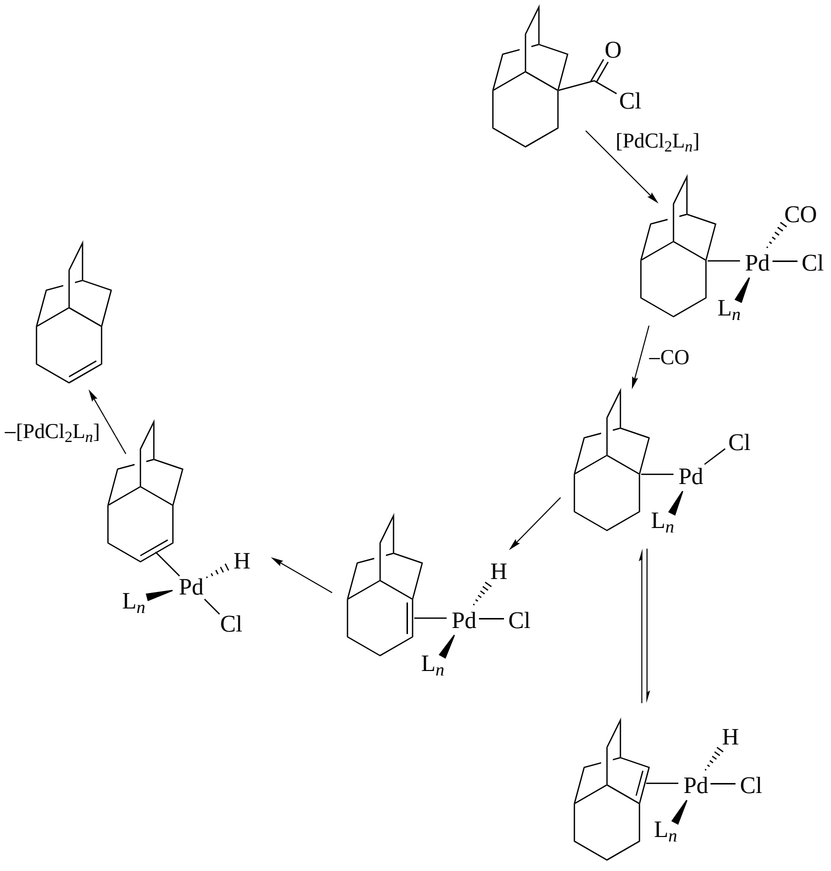

Scheme 3

the decarbonylation reaction. Neither aroyl bromides nor iodides poison the catalyst in this way, but anomalous products are sometimes obtained from the decarbonylation of 2-iodobenzoyl halides because of the participation of benzyne intermediates.

Generally, the products formed by the catalytic decarbonylations of acid halides are easily predicted. Some of the few instances where this is not the case are the decarbonylations of pent-3-enoyl or 2-methylbut-3-enoyl chlorides. Here the formation of η^3-allyl complexes after decarbonylation results in several products being formed.**[7]**

4 ALDEHYDE DECARBONYLATION

The $[RhCl(PPh_3)_3]$ catalyzed decarbonylations of aldehydes proceed in an entirely analogous manner to acyl halide decarbonylations, the first stage being the oxidative addition of aldehyde to a coordinatively unsaturated rhodium complex (Scheme 4). The acyl ligand then undergoes an alkyl group migration in which the configuration of the latter is retained. The reaction is completed either by reductive elimination of alkane or by β-hydride abstraction from the alkyl group and elimination of alkene. The final inorganic product is *trans*-$[RhCl(CO)(PPh_3)_2]$.

The reaction is catalytic at high temperatures, but some thermolysis of many aldehydes occurs under these conditions. In the past, several attempts have been made to persuade the catalytic reaction to take place at lower temperatures. It is normally necessary to heat the reaction mixture to >150 °C in order to release carbon monoxide from *trans*-$[RhCl(CO)(PPh_3)_2]$. If the catalytic complex is replaced with [RhCl(CO)(dppp)], decarbonylation takes place at lower temperatures since the CO ligand is trans to phosphorus, not Cl, in this complex, and so the M–CO bond is more labile.

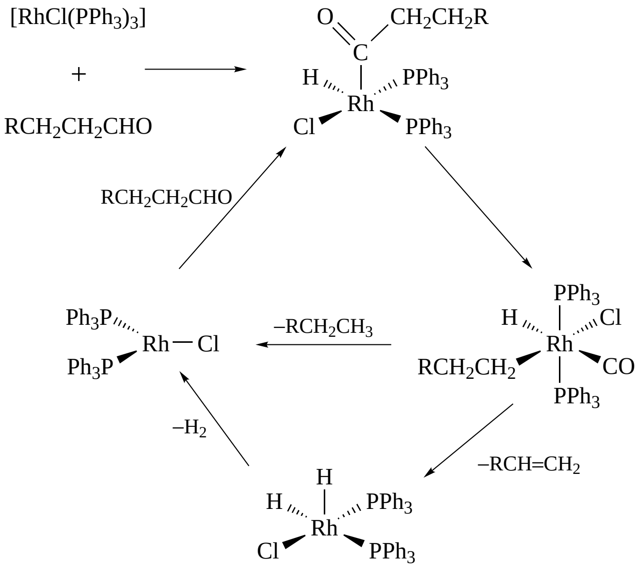

Scheme 4

Employing a stoichiometric quantity of diphenylphosphoryl azide as a carbon monoxide receptor allows the reaction to proceed at a lower temperature. The azide reacts with *trans*-$[RhCl(CO)(PPh_3)_2]$ to form a cyanate at room temperature. Alkene formation is suppressed when this reagent is employed, but higher aldehydes are not decarbonylated in its presence.**[9]**

Provided care is taken to avoid exchange with water, a kinetic isotope effect is noted when CDO groups are decarbonylated. This indicates that the rate-determining step of the reaction is the scission of the C–D bond. Deuteration studies have also shown that decarbonylation of RCDO yields RD.**[10]** Further, decarbonylation of Ar^1CDO and Ar^2CHO mixtures yields only Ar^1D and Ar^2H.**[11]**

The formation of alkene from eligible substrates is not so pronounced as in the decarbonylation of acyl halides. Usually about 10% of alkene is obtained from alkyl intermediates bearing a β-hydrogen atom. The β-hydride abstraction reaction requires a vacant site on the catalyst to accept the abstracted hydrogen. The very low yields of alkenes found when diphenylphosphoryl azide is added to the reaction mixture suggest that this reagent also acts as a ligand and occupies the vacant coordination site required for hydrogen abstraction.

The decarbonylation reaction is not confined to aldehydes, but also embraces those compounds that have aldehyde tautomers. Thus, both carbohydrates and allylic alcohols can be decarbonylated. When glucose is allowed to react with *trans*-$[RhCl(CO)(PPh_3)_2]$ in N-methylpyrrolidin-2-one, decarbonylation occurs and arabinitol is formed with retention of configuration. The decarbonylation of fructose to arabinitol is complicated by the simultaneous dehydration to furfuryl alcohol, which is the major product. Analogous reactions occur with lower carbohydrates; in the limit, glycolaldehyde is decarbonylated to methanol. Aldose derivatives can also be converted to their C_{n-1} analogues, but the yields are only about half of those obtained with the parent aldoses. Disaccharides usually give better yields.**[12]**

The formation of both erythro and threo products from suitable allylic alcohols containing CD_2OH groups implies that an η^3-allylic mechanism is involved in their decomposition (equation 3).

Not all decarbonylations give the expected product,**[10,12]** and the relative yields are influenced by the rhodium catalyst employed. Chlorotris(triphenylphosphine)rhodium(I) rapidly and selectively decarbonylated the *endo*-norbornene isomer shown in equation (4) to form a tricycline product, but $[Rh(dppp)_2]Cl$ additionally forms an isomeric alkene. In the case of the corresponding exo-isomer (equation 5), $[RhCl(PPh_3)_3]$ is the less selective catalyst.**[13]** It was also found that $[Rh(dppp)_2]Cl$ was a superior catalyst in bringing about the double decarbonylation shown in equation (6).[14]

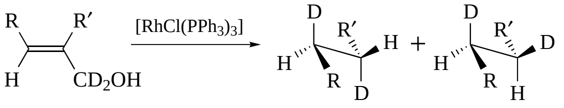

R
R′
H
CD2OH
[RhCl(PPh3)3]
D
R′
H
H
R
D
+
D
R′
D
H
R
H

(3)

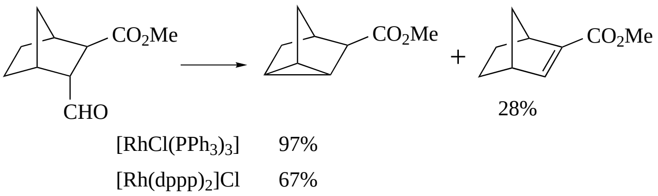

CO2Me
CHO
CO2Me
+
CO2Me
28%
[RhCl(PPh3)3] 97%
[Rh(dppp)2]Cl 67%

(4)

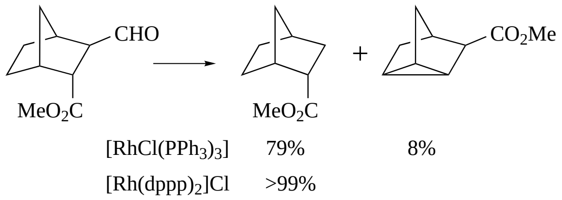

CHO
MeO2C
MeO2C
+
CO2Me
[RhCl(PPh3)3] 79% 8%
[Rh(dppp)2]Cl >99%

(5)

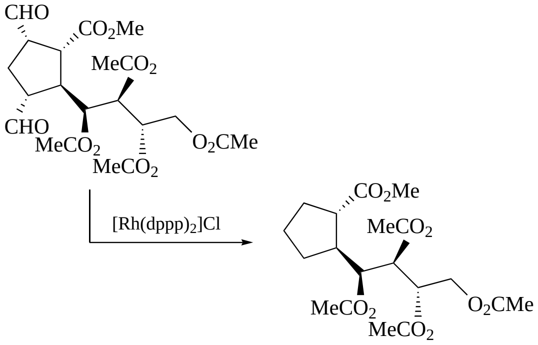

CHO
CO2Me
MeCO2
CHO
MeCO2
MeCO2
O2CMe
[Rh(dppp)2]Cl
CO2Me
MeCO2
MeCO2
MeCO2
O2CMe

(6)

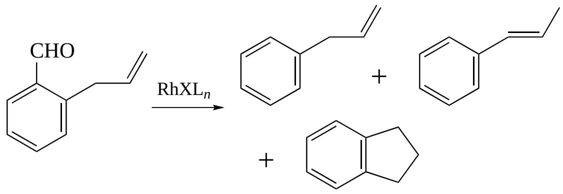

(7)

It was noted in Section 3 that unsaturated acyl halides often formed anomalous products. This tendency is even more pronounced in the case of aldehydes. The decarbonylation of 2-allylbenzaldehyde gives a high yield of indan, and very little allylbenzene is formed (equation 7). Some of the latter product is isomerized to prop-2-enylbenzene. The highest yield of indan occurs when the reaction is catalyzed by $[RhCl(PPh_3)_2]_2$ because no triphenylphosphine is released as it would be from *trans*-$[RhCl(CO)(PPh_3)_2]$. This allows indan formation to take place by utilizing the vacant coordination site on the monomer. Conversely, addition of PPh_3 to the mixture suppresses both indan formation and isomerization,

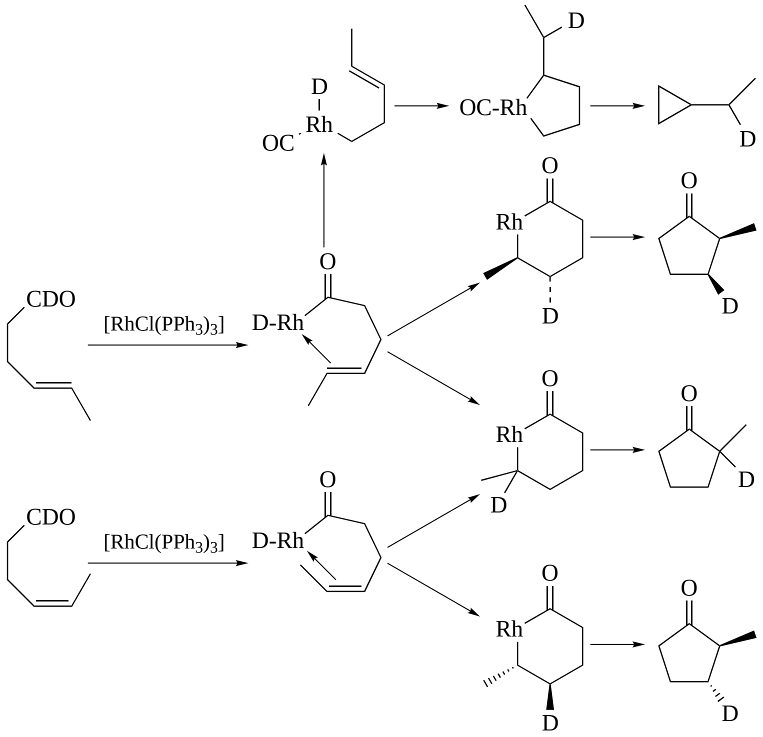

D
Rh
OC
OC-Rh
D
D
O
Rh
D
O
D
CDO
[RhCl(PPh3)3]
D-Rh
O
O
Rh
D
O
D
CDO
[RhCl(PPh3)3]
D-Rh
O
O
Rh
D
O
D

Scheme 5

showing the importance of the vacant site on the catalyst for both these reactions.[15]

Considerable information about the course of aldehyde decarbonylations has been gleaned from the decarbonylations of alk-4-enals. Pent-4-enals form cyclopentanones in high yield in decarbonylations catalyzed by $[RhCl(PPh_3)_3]$. The major product from the decarbonylation of hex-4-enal is 2-methylcyclopentanone. As shown in Scheme 5, the cyclization reaction requires a vacant site on rhodium. The other products result from decarbonylation of the unsaturated acyl before cyclization can take place. In these cases, there is competition between addition of deuterium to C-1 of the alkenyl ligand or its addition to the alkene bond and the formation of an unstable metallocycle.[16]

Again the best catalyst for the cyclization is $[RhCl(PPh_3)_2]_2$, which does not release PPh_3 during the reaction. Conversely, low yields of cyclopentanone are obtained in the presence of added PPh_3 or dppe, which competitively coordinate to the vacant site required in the cyclization reaction.

In the analogous stoichiometric reaction, Milstein has correlated the yields of but-1-ene and *trans*-$[RhCl(CO)(PMe_3)_2]$.[17] It has also been reported that oct-6-enal can be cyclized to cyclohexanol.

However, cyclic ketones can themselves be decarbonylated by $[RhCl(PPh_3)_3]$ in high-boiling solvents. There appears to be no correlation with ring size since both 3-hexadecylcyclobutanone and cyclododecanone can be decarbonylated.[18]

5 RELATED ARTICLES

Palladium: Inorganic & Coordination Chemistry; Rhodium: Inorganic & Coordination Chemistry.

6 REFERENCES

1. F. H. Jardine, *Prog. Inorg. Chem.*, 1981, **28**, 63.
2. S.-I. Murahashi, T. Naota, and N. Nakajima, *J. Org. Chem.*, 1986, **51**, 898.
3. J. Tsuji and K. Ohno, *J. Am. Chem. Soc.*, 1966, **88**, 3452.
4. K. Ohno and J. Tsuji, *J. Am. Chem. Soc.*, 1968, **90**, 99.
5. J. A. Kampmeier and T. Z. Liu, *Inorg. Chem.*, 1989, **28**, 2228.
6. K. Hori, M. Ando, N. Takaishi, and Y. Inamoto, *Tetrahedron Lett.*, 1986, **27**, 4615.
7. J. A. Kampmeier and T. Z. Liu, *Organometallics*, 1989, **8**, 2742.
8. J. K. Stille, M. T. Regan, R. W. Fries, F. Huang, and T. McCarley, *Adv. Chem. Ser.*, 1974, **132**, 181.
9. J. M. O'Connor and J. Ma, *J. Org. Chem.*, 1992, **57**, 5075.
10. W. von E. Doering, J. L. Ekmanis, K. D. Belfield, F. G. Klärner, and B. Krawczyk, *J. Am. Chem. Soc.*, 2001, **123**, 5532.
11. J. A. Kampmeier, S. H. Harris, and D. K. Wedegaertner, *J. Org. Chem.*, 1980, **45**, 315.
12. M. A. Andrews and S. A. Klaeren, *Chem. Commun. (Cambridge)*, 1988 1266.
13. D. Horton and T. Usui, *Carbohydr. Res.*, 1991, **216**, 33.
14. D. Horton and T. Usui, *Carbohydr. Res.*, 1991, **216**, 51.
15. J. A. Kampmeier, S. H. Harris, and I. Mergelsberg, *J. Org. Chem.*, 1984, **49**, 621.
16. R. E. Campbell, C. F. Lochow, K. P. Vora, and R. G. Miller, *J. Am. Chem. Soc.*, 1980, **102**, 5824.
17. D. Milstein, *Chem. Commun. (Cambridge)*, 1982, 1357.
18. M. Murakami, H. Amii, K. Shigeto, and Y. Ito, *J. Am. Chem. Soc.*, 1996, **118**, 8285.

Defects in Solids

Richard J. D. Tilley
University of Cardiff, Cardiff, UK

1	Introduction	1
2	Defects and the Composition of Solids	1
3	Defects in Stoichiometric Materials	2
4	Defects and Nonstoichiometry	5
5	Defect Chemistry	6
6	Grossly Nonstoichiometric Crystals	10
7	Point Defect Clusters	11
8	Extended Defects	13
9	Combinations of Defects	17
10	Defect Elimination and Assimilation: Modulated Structures	17
11	Related Articles	19
12	References	19

1 INTRODUCTION

Defects play an important part in both the chemical and physical behavior of solids and much of modern science and technology centers upon the exploitation or suppression of the properties that defects confer upon a solid. The chemical and physical aspects of a defect are intimately connected, but for simplicity, defects are often portrayed as influencing only chemical or physical properties. Thus, defects such as dislocations, which have a profound effect upon the mechanical properties of a solid, also influence chemical properties such as rates of dissolution and reaction, although these chemical aspects are not always mentioned. Similarly, defects that can be considered as more chemical in nature, such as impurity atoms, have profound effects on the physical properties of materials, as witnessed by 'doped' semiconductors (*see* ***Semiconductors***; ***Semiconductor Interfaces***).

The concept of a defect has undergone considerable evolution over the course of the last century. The simplest notion of a defect is a mistake at normal atom site in a solid. These structurally simple defects are called point defects. Not long after the recognition of point defects, the concept of linear defects, dislocations, was invoked to explain the mechanical properties of metals. In later years, it became apparent that planar defects, including surfaces, and volume defects such as rods, tubes, or precipitates, also have important roles to play in influencing the physical and chemical properties of the host matrix. More recently, it has become apparent that interactions between point defects are of considerable importance, and the simple model of isolated point defects is often inadequate with respect to prediction of the structural, chemical, or physical properties of solids.

Besides the multiplicity of defects that can be envisaged there is a wide range of host solid phases within which such defects can reside. The differences between an alloy, a metallic sulphide, a crystalline fluoride or a silicate glass are significant from both a chemical or physical viewpoint. By default, defects have come to be associated with crystalline solids. This is because a crystal has a regular repetition of atoms throughout its volume. A disturbance of this regularity then constitutes the defect. In this sense, the nature of a defect in, for example, a glass, is difficult to picture.

In this entry, the principal *chemical* features of defect populations (defect chemistry) will be described from the restricted viewpoint of crystalline inorganic solids. The influence of defects upon mechanical properties will be excluded and defects that may have greatest relevance to physical properties will be treated from the point of view of chemical importance. Defects in molecular crystals and amorphous and glassy solids will be omitted (*see* ***Noncrystalline Solids***), as will the important areas of alloys (*see* ***Alloys***), thin films (*see* ***Thin Film Synthesis of Solids***), and carbon nanotubes and related nanoparticles (*see* ***Carbon: Fullerenes***). References to the literature before 1994 are to be found in the corresponding article in the first edition of this Encyclopedia.[1]

There have been two significant changes in the decade since this latter publication. There has been a rapid expansion in computational studies of defects, mirroring the accelerating improvement in computer hardware and software, which are covered in detail elsewhere (*see* ***Solids: Computer Modeling***).[2,3] In addition to calculations of point defect energies, calculations have been applied to the study of defect clusters, the assessment of the most favorable sites for metal insertion into a host structure, defect migration paths, the structure of 'active sites' on heterogeneous catalysts (*see* ***Heterogeneous Catalysis by Metals***; ***Oxide Catalysts in Solid-state Chemistry***), and the calculation of the properties of surfaces and of thin films.

Within recent years, it has been realized, by virtue of increasing sophistication in structure determination, especially that provided by transmission electron microscopy, that many systems that were once described as containing high defect populations are, in fact, defect free. The structure is continuously modulated to remove the necessity for defects. This remarkable change of viewpoint is briefly reviewed in the final section of this article.

2 DEFECTS AND THE COMPOSITION OF SOLIDS

During the latter part of the nineteenth century and the early years of the twentieth century, there was considerable controversy over the composition of chemical compounds. It was clear that some solids, especially metallic alloys (*see*

Alloys), had a variable composition, despite the fact that the material seemed to retain its chemical integrity. Experimental data was less clear-cut about the composition of nonmetallic solids. Although some of these seemed to be rather like alloys and show a composition range, many others had, as far as could be detected at this epoch, no composition range at all.

For the development of chemistry, it was inevitable that the idea that compounds had a fixed composition came to the fore. Most compounds that could be easily investigated were molecular in nature, with fixed compositions, and fitted this concept perfectly. The alloys and other inconvenient solids were pushed to one side of traditional chemical studies, and ended up in technological disciplines such as metallurgy. There was a tacit recognition that simple chemical valence ideas did not apply to metals.

The increasing use of single-crystal X-ray diffraction for structural analysis (*see* ***Diffraction Methods in Inorganic Chemistry***) and powder X-ray diffraction for phase analysis (*see* ***Solids: Characterization by Powder Diffraction***), during the middle years of the last century, began to clarify matters. The definition of a chemical compound then became associated with that of a solid with a known crystal structure. In terms of this approach, it was proved that many metallic systems could retain the same crystal structure over wide composition ranges, while others, showed no tendency to composition variation. Inorganic solids were similarly disparate. Many seemed to possess no significant composition range at all, and these came to be called stoichiometric compounds. Others, just as clearly, appeared to retain the same crystal structure over wide composition ranges, and these became known as nonstoichiometric compounds.

The cause of nonstoichiometry was initially attributed to the presence of point defects in a structure. It was recognised that all ionic solids should, in principle, possess a composition range by virtue of a population of point defects.[4] Those solids with a vanishing composition range make up the stoichiometric compounds, and those with a measurable composition range are the nonstoichiometric compounds. The structural nature of the defects in a crystal is more complex. Defects interrupt the regularity of the surrounding crystal structure and give rise to stress fields, resulting in local strain. When defect density is small, a population of isolated point defects may provide a sound structural model for the interpretation of properties. However, as the defect density increases, strain can often be reduced by the association of defects, so that isolated point defects, as such, become replaced with clusters or extended defects. When stoichiometry is altered, electronic interactions can also occur, often greatly outweighing the stress, leading to point defect interaction. In many cases, the interaction energies are of the same order of magnitude as thermal energy. Thus, at low temperatures, defects tend to order. This ordering, particularly when promoted by long annealing times, can result in the formation of new structures in which the defects are eliminated. Intermediate stages of ordering are also common, in which clusters or aggregates of defects, exist. In both of these cases, the ordering may be lost at high temperatures. In such cases the low-temperature structure, which may be defect free or contain extended defects, is transformed into one in which a population of noninteracting point defects becomes a reasonable structural model. In the sections that follow, the temperature variation will not be repetitively stressed, but one should always be aware that defect structures investigated at room temperature may not occur in materials at high temperatures.

3 DEFECTS IN STOICHIOMETRIC MATERIALS

First approaches to the quantitative understanding of defects in stoichiometric crystals were published in the early years of the last century by Frenkel in Russia and Schottky in Germany. These workers described the statistical thermodynamics of solids in terms of the atomic occupancies of the various crystallographic sites available in the structure. Two noninteracting defect types were envisaged. Interstitial defects consisted of atoms that had been displaced from their correct positions into normally unoccupied positions, namely, interstitial sites. Vacancies were positions that should have been occupied but were not.

3.1 Monoatomic Solids

A monatomic crystal such as silicon can contain vacancies at normally occupied atomic positions, and interstitial atoms, called self-interstitials, at normally unoccupied sites in the

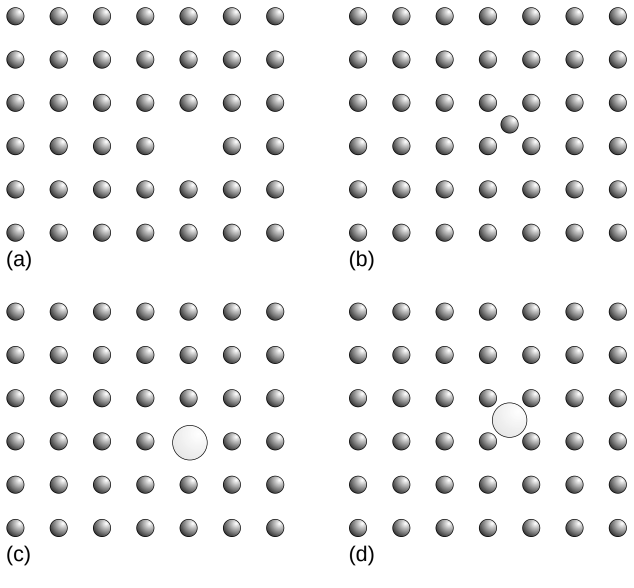

Figure 1 Idealised representations of point defects in a monatomic crystal. (a) vacancy, (b) (self) interstitial, (c) substitutional impurity or dopant, (d) interstitial impurity or dopant

solid (Figure 1(a), (b)). The Gibbs energy of a crystal containing a small number of these defects is lower than that of a perfect crystal, mainly owing to the entropy of the defect populations. Thus, a population of point defects is to be expected in a crystal, and such defects are called intrinsic defects. This defect population can be treated as a chemical equilibrium, and written:

$$\text{null} \rightleftharpoons \text{vacancy} \tag{1}$$

The law of mass action in its simplest form, with concentrations instead of activities, can be applied if there is no interaction between the defects, to give an expression for the equilibrium constant, K_v:

$$K_v = \frac{n_v}{N} = \exp\left[\frac{-\Delta G_v}{RT}\right]$$

$$n_v = N\exp\left[\frac{-\Delta G_v}{RT}\right]$$

where n_v is the number of vacant sites per unit volume in a crystal, N is the total number of sites per unit volume and ΔG_v is the molar Gibbs energy of formation of the vacancies, R is the gas constant, and T the absolute temperature. The Gibbs energy, ΔG_v, is often replaced by the enthalpy of vacancy formation, ΔH_v.

A similar equation holds for the relationship between the number of self-interstitials and the equilibrium constant, K_i. The creation of a self-interstitial on one of N^* possible interstitial sites leaves a vacancy on one of the N normal lattice sites:

$$\text{null} \rightleftharpoons \text{interstitial} + \text{vacancy} \tag{2}$$

$$K_i = \left(\frac{n_i}{N^*}\right)\left(\frac{n_v}{N}\right) = \exp\left[\frac{-\Delta G_i}{RT}\right]$$

As the number of interstitials and vacancies is the same, $n_i = n_v$, and:

$$n_i = \sqrt{NN^*}\exp\left[\frac{-\Delta G_i}{2RT}\right]$$

where ΔG_i is the molar Gibbs energy of formation of the self-interstitials. The Gibbs energy, ΔG_i, is often replaced by the enthalpy of interstitial formation, ΔH_i.

Under normal circumstances, both of these equilibria operate concurrently, and both types of defect are present in the crystal. However, it is often possible to assume that the only defect of importance is that with the lowest formation energy.

3.2 Impurities and Solid Solutions

Impurities are invariably present in solids, and in low concentrations, they may form point defects. The impurity atom can occupy atom sites normally occupied by the parent atoms, to form substitutional point defects, or can occupy interstitial sites, to form interstitial point defects (Figure 1(c), (d)).

If two solids have the same or very similar structures, and the component atoms have similar sizes, extensive substitutional solid solutions form. In the case of nonmetallic solids, oxidation number is important, since charge balance must be preserved over the composition range of the solid solution. Which atoms are regarded as the defects and which the matrix, will depend upon their relative concentration. For example, the corundum structure oxides Al_2O_3 and Cr_2O_3 form a continuous solid solution of formula $Al_{2-x}Cr_xO_3$, $(0 < x < 2)$, in which Al^{3+} cations in the structure are gradually replaced by Cr^{3+} cations. In solids with several atomic constituents, solid solution formation may be restricted to one of the component atoms, as in the pyrochlore structure oxides $Bi_2TlPb_2O_7$, and $Tl_2Pb_2O_7$, which form a continuous solid solution with a formula $Bi_{2-x}Tl_xPb_2O_7$, $(0 < x < 2)$. In cases where the atoms sizes differ sufficiently, only partial solid solution ranges occur, for example, $Sr_{1-x}Ca_xCuO_2$, $(0 < x < 0.6)$.

The physical and chemical properties of such solid solutions can vary in a dramatic fashion. In the $Bi_{2-x}Tl_xPb_2O_7$ system, for example, $Bi_2TlPb_2O_7$ is a red insulator while $Tl_2Pb_2O_7$ is black and shows metallic properties. The solid solution changes smoothly from insulating to metallic in its behavior. The bonding implications of these changes are of considerable chemical interest.

3.3 Balanced Populations of Point Defects

Balanced populations of point defects do not alter the anion to cation ratio, or overall stoichiometry of the crystal. In addition, the numbers of such defects must be such as to maintain charge neutrality. Calculations similar to those for monatomic solids show that the free energy of crystals containing such balanced populations of point defects is lower than that for a defect-free crystal, and these defects are also intrinsic defects, occurring in pure crystals under equilibrium conditions at all temperatures above 0 K. Two important examples of such balanced point defect populations have been described.

3.3.1 Schottky Defects

Balanced populations of vacancies on both the cation and anion sites in a crystal are known as Schottky defects. For example, if the crystal has a formula MX, then the number of cation vacancies must be equal to the number of anion vacancies, in order to maintain electrical neutrality. In such a crystal, a Schottky defect consists of 1 cation vacancy and 1 anion vacancy, although these need not be geometrically close together (Figure 2(a)). In a crystal of formula MX_2, there needs to be twice as many anion vacancies as cation vacancies. Similar considerations apply to compounds with other compositions. As with monatomic solids, this defect population can be treated as a chemical equilibrium. For a crystal of composition *MX*:

$$\text{null} \rightleftharpoons \text{cation vacancy} + \text{anion vacancy} \qquad (3)$$

If there is no interaction between the defects, the law of mass action in its simplest form, with concentrations instead of activities, yields an expression for the equilibrium constant, K_S:

$$K_S = \left(\frac{n_{cv}}{N}\right)\left(\frac{n_{av}}{N}\right) = \exp\left[\frac{-\Delta G_S}{RT}\right]$$

where n_{cv} is the number of cation vacancies and n_{av} the number of anion vacancies per unit volume, N the number of cation or anion sites per unit volume in the crystal, ΔG_S is the molar Gibbs energy of formation of the Schottky defects, R is the gas constant, and T the absolute temperature. Because n_{cv} is equal to n_{av} and to the number of Schottky defects present, n_S:

$$n_{cv} = n_{av} = n_S = N \exp\left[\frac{-\Delta G_S}{2RT}\right]$$

The Gibbs energy, ΔG_S, is often replaced by the enthalpy of Schottky defect formation, ΔH_S.

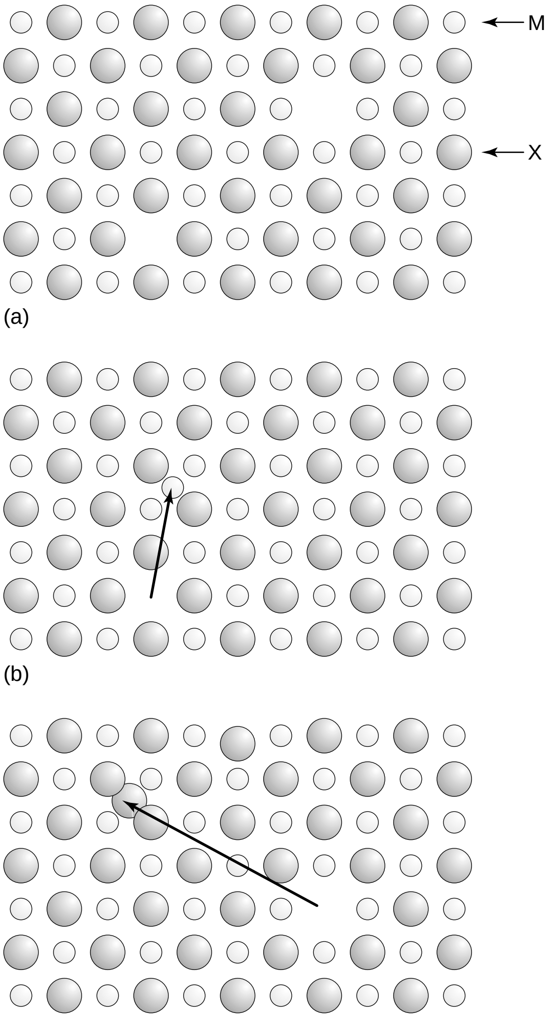

Figure 2 Idealised representation of balanced point defects in an ionic crystal of formula *MX*. (a) Schottky defects, (b) Frenkel defects on cation sites, (c) Frenkel defects on anion sites

3.3.2 Frenkel Defects

A population of vacancies on one subset of atoms created by displacing some atoms into normally unoccupied interstitial sites constitute a second arrangement of paired point defects, termed Frenkel defects (Figure 2(b), (c)). Because one species of atom or ion is simply being redistributed in the crystal, charge balance is not an issue. A Frenkel defect in a crystal of formula *MX* consists of one interstitial cation plus one cation vacancy, or one interstitial anion plus one anion vacancy. Equally, a Frenkel defect in a crystal of formula MX_2 can consist of one interstitial cation plus one cation vacancy, or one interstitial anion plus one anion vacancy. As with the other point defects, it is found that the free energy of a crystal is lowered by the presence of Frenkel defects and so a population of these intrinsic defects is to be expected at temperatures above 0 K. The calculation of the number of Frenkel defects in a crystal can proceed along lines parallel to those for Schottky defects. The appropriate chemical equilibrium for cation defects is:

$$\text{null} \rightleftharpoons \text{cation vacancy} + \text{cation interstitial} \qquad (4)$$

The equilibrium constant, K_{cF}, is given by:

$$K_{cF} = \left(\frac{n_{cv}}{N}\right)\left(\frac{n_{ci}}{N^*}\right) = \exp\left[\frac{-\Delta G_{cF}}{RT}\right]$$

where n_{cv} is the number of cation vacancies and n_{ci} the number of cation interstitials per unit volume, N the number of occupied cation sites per unit volume that support Frenkel defects, N^* the number of available interstitial sites per unit volume, ΔG_{cF} is the molar Gibbs energy of formation of the cation Frenkel defects, R is the gas constant, and T the absolute temperature. Because n_{cv} is equal to n_{ci} and to the number of Frenkel defects present, n_F:

$$n_{cv} = n_{ci} = n_{cF} = \sqrt{NN^*} \exp\left[\frac{-\Delta G_{cF}}{2RT}\right]$$

The Gibbs energy, ΔG_{cF}, is often replaced by the enthalpy of Frenkel defect formation, ΔH_{cF}.

A similar equation can be written for Frenkel defects on the anion positions:

$$\text{null} \rightleftharpoons \text{anion vacancy} + \text{anion interstitial} \qquad (5)$$

leading to:

$$n_{av} = n_{ai} = n_{aF} = \sqrt{NN^*} \exp\left[\frac{-\Delta G_{aF}}{2RT}\right]$$

where ΔG_{aF} is the molar Gibbs energy of formation of the anion defects.

3.3.3 Total Defect Populations

The defect equilibria represented by equations (3), (4), and (5) operate simultaneously. However, the defect formation energies generally differ considerably, and it is a reasonable approximation to assume that the only defect type of importance is that with the lowest formation energy. This may change with temperature.

3.4 Disordered Cation Compounds

Disordered cation compounds, also called superionic conductors (*see* ***Ionic Conductors***), are a group of materials that can be thought of as containing very high concentrations of cation Frenkel defects. The prototype material is silver iodide. The low-temperature polymorph, β-AgI, is a normal compound, but the high-temperature form, α-AgI, which is stable above 147 °C, possesses an unusually high ionic conductivity for a pure, stoichiometric phase. The structures of both α- and β-AgI derive from a body-centered cubic sublattice of iodine atoms. Within the unit cell, there are 6 octahedral, 12 tetrahedral, and 24 trigonal sites available for cation occupation. In the β polymorph, the two silver atoms per unit cell exclusively occupy two of the tetrahedral positions. In the α form, studies show that the Ag^+ ions are randomly distributed over the 12 tetrahedral positions, leading to the concept of a molten sublattice of Ag^+ ions moving like a liquid through a fixed matrix of I^- ions.

A number of other materials show similar behavior. At low temperatures, the compounds are normal and defect free while at some higher temperature all or part of the metal atom array becomes mobile with cations able to freely move over some or all of the various allowed cation sites in the unit cell. For example, the compound Ag_3CuS_2 has a distorted body-centered cubic packing of sulphur atoms with Ag atoms in distorted octahedral or tetrahedral sites and Cu atoms in linear coordination at room temperature. The cation structure disorders at 117 °C, leading to a high Ag^+ conductivity. The crystal structure of the closely related compound CuAgS shows that the sulphur atoms form a slightly distorted hexagonal close-packed array, in which the copper atoms are located. The Ag ions lie between the sulphur–copper layers. These Ag^+ ions show a progressively greater anisotropic thermal motion as the temperature rises, until, above 93 °C, they are essentially completely mobile, leading to extremely high silver ion conductivity. In the compound $Rb_4Cu_{16}I_{7+x}Cl_{13-x}$, $(-0.2 < x < 0.5)$, the 16 Cu atoms can occupy any one of 56 possible positions. The occupancy varies with temperature, and above room temperature, the phase shows high solid-state conductivity, in this case owing to mobile Cu^{2+} ions (*see* ***Halides: Solid-state Chemistry***).

4 DEFECTS AND NONSTOICHIOMETRY

4.1 Unbalanced Point Defect Populations

If cations or anions in a lattice are replaced by others that have a different valence, or alternatively if interstitial atoms or ions are added to the structure without compensating populations of vacancies, the composition of the crystal must change. Variable populations of such defects will lead to composition ranges of the solid phase and to additional electronic or optical properties. At low concentrations, these defects can be conveniently considered as point defects distributed at random throughout the structure. As the number of defects increases, interactions will lead to the formation of clusters or extended defects.

A number of materials show small but measurable departures from stoichiometry, which can be attributed to an unbalanced population of point defects. The best known of these compounds are probably the transition metal compounds with the halite (rocksalt) structure,**[5]** typified by NiO and CoO. However, a large number of other materials also fall into this class, for example, ZnO, CdO, Cu_2O, V_2O_3, VO_2, and NbO_2, and ternary oxides such as $BaTiO_3$. In some of these phases, the limited composition range spans both sides of the stoichiometric composition; NbO_2, for instance, has a reported composition range of from $NbO_{1.9975}$ to $NbO_{2.003}$. In others, the materials have a composition range only on one side of the stoichiometric composition. Cobalt oxide, CoO has a reported composition range from approximately $Co_{0.99}O$ to $Co_{1.00}O$ while for CdO the composition ranges from $Cd_{1.00}O$ to approximately $Cd_{1.0005}O$.

The nature of the defects is often difficult to ascertain. Nickel and cobalt monoxides are considered to accommodate composition changes by way of a population of vacancies on the normally occupied metal positions, while in the isostructural CdO the metal excess is usually considered to arise from interstitial Cd atoms.

4.2 Color Centers

When electrons or holes are trapped at defects in a solid, both the electronic and the optical properties are modified. Such composite defects are called color centers. Large numbers of these defects have been characterized, and the term includes defects that have absorption maxima outside the visible spectrum. The expression *color center* is thus used in a generic sense to refer to defects and associated trapped electrons or holes that interact with electromagnetic radiation.

Many different types of high-energy radiation and chemical treatment will cause color centers to form in a crystal. Regardless of the method of formation, the color produced in any particular crystal is always the same.

4.2.1 Electron-excess Centers

The best-known electron-excess center, the F-center, consists of an anion vacancy plus a trapped electron. The defect arises in crystals that are slightly nonstoichiometric and contain a small excess of metal. F-centers were originally characterized in the alkali halides, the color being indicative of the host structure and not the excess metal. Thus, F-centers in sodium chloride are always yellow–orange, irrespective of whether the excess metal is sodium or another alkali metal. Similar metal excess F-centers exist in a rare blue-purple ‘Blue John’ form of fluorite, CaF_2, and bright red nonstoichiometric ZnO, containing small quantities of interstitial Zn atoms. Centers can exist that are capable of trapping more than one electron, leading to a multiplicity of related defects.

4.2.2 Hole-excess Centers

One of the commonest forms of hole-excess center imparts color to the minerals smoky quartz and amethyst. These minerals are forms of silica, containing aluminium as an impurity. The Al^{3+} substitutes for Si^{4+}, and to preserve charge neutrality equal amounts of H^+ are incorporated into the crystal. The smoky purple color arises in the electron deficient $[AlO_4]^{4-}$ group. It is formed when an electron is liberated from a neutral $[AlO_4]^{5-}$ group by ionising radiation is trapped on one of the H^+ ions present. Other hole centers have been described in a variety of crystals.

5 DEFECT CHEMISTRY

5.1 Kröger-Vink Notation: Defect Nomenclature

In order to describe the consequences of point defect populations, a notation is required analogous to that used in chemical equations. The most widely employed system is the Kröger-Vink notation, the principal features of which follow.

Vacancies Vacancies (empty *atom* sites) are indicated by the symbols V_M and V_X for metal, M, and nonmetal, X, sites respectively. Where confusion may occur with the atom vanadium, the symbol for a vacancy is written *Va*. Vacancies are created by the removal of neutral atoms from the crystal. This rule also applies to ionic solids. For example, in ionic NiO, V_{Ni} would imply the removal of a Ni^{2+} cation together with two electrons, that is, a neutral Ni atom. Similarly, V_O indicates a vacancy in the oxygen sublattice, and implies removal of an O^{2-} anion from the crystal together with the subsequent addition of two electrons to the crystal.

Interstitial atoms Interstitial atoms are denoted by M_i and X_i for metals and anions respectively. Interstitial atoms are regarded as neutral additives. Hence K_i represents an interstitial potassium atom, not an ion, in a crystal.

Impurity atoms Neutral impurity atoms are given their normal chemical symbol and the site occupied is written as a subscript. Thus, an Mg atom on a Ni site in NiO would be written as Mg_{Ni}. The same nomenclature is used if an atom in a crystal occupies the wrong site. Thus it is possible for M atoms to be on X sites, written as M_X, or X atoms to be on M sites, written as X_M. A potassium atom on a bromine site in KBr would be written as K_{Br}.

Associated defects Point defects that are associated or clustered are indicated by enclosing the components of such a group in parenthesis. For example, $(V_M V_X)$ would represent a defect in which two vacancies are associated as a vacancy pair.

Electrons and holes Free electrons are denoted by the symbol e', where the superscript $'$ represents the negative charge on the electron. Free holes are denoted by the symbol $h^{\bullet}$, where the positive charge is represented by the superscript $\bullet$.

Charges on defects Atomic defects may carry a charge, and in ionic crystals, this may be considered the normal state of affairs. The Kröger-Vink notation bypasses the problem of deciding on the real charges on defects by considering only effective charges on defects. The effective charge is the charge that the defect has with respect to the normal crystal structure. For example, a vacancy in the NaCl structure at a sodium position will have an effective charge of -1 relative to that normally encountered at that position. In order to distinguish effective charges from real charges, the superscript $'$ is used for each unit of negative charge and the superscript $\bullet$ is used for each unit of positive charge. Hence a vacancy at a sodium site in ionic NaCl would be written as V'_{Na} and a vacancy at a chlorine site would be written $V^{\bullet}_{Cl}$. The same principle applies to the other atomic defects mentioned. Thus $Zn_i^{2\bullet}$ would indicate a Zn^{2+} ion at an interstitial site that is normally unoccupied and hence without any preexisting charge. Similarly, substitution of a divalent ion such as Ca^{2+} for monovalent Na^+ gives a local electronic charge augmented by one extra positive unit, which is then represented as $Ca^{\bullet}_{Na}$. When a defect bears no effective charge and the situation needs to be emphasised, the superscript x is used, that is, K^{x}_{Na}.

The main features of the notation are summarised in Table 1.

5.2 Reaction Equations

The chemical accounting system that equations represent can be modified to take defect populations into account by using the following rules.

1. The number of metal atom sites must always be in the correct proportion to the number of nonmetal atom sites

Table 1 Summary of the Kröger–Vink notation

Type of defect	Notation
Nonmetal vacancy at nonmetal site	V_X
Metal vacancy at metal site	V_M
Interstitial metal	M_i
Interstitial nonmetal	X_i
Impurity metal (A) at metal site	A_M
Impurity nonmetal (Y) at nonmetal site	Y_X
Neutral vacancies	V_M^x, V_X^x
Nonmetal vacancy with effective positive charge	$V_X^\bullet$
Metal vacancy with effective negative charge	V_M'
Metal interstitial with effective positive charge	$M_i^\bullet$
Nonmetal interstitial with effective negative charge	X_i'
Free electron[a]	e'
Free positive hole[a]	$h\bullet$

[a] Concentrations of these defects are frequently designated by n and p, respectively.

in the crystal. As long as this proportion is maintained, the total number of sites can vary, since this simply corresponds to more or less substance present. If the crystal contains vacancies, these must also be counted in the total number of sites. Interstitial atoms do not occupy normal sites and so are not relevant when this rule is being applied.

2. The total number of atoms on both sides of the equation must be equal.
3. The crystal must always be electrically neutral. This means not only that the total charge on one side of the equation must be equal to the total charge on the other side, but also that the sum of the charges on each side of the equation must equal zero. In this assessment, both effective and real charges must be counted if both sorts are present.
4. Only neutral atoms are involved in chemical reactions. After reaction, neutral atoms can dissociate into charged species if this is thought to represent the real situation in the crystal.

As an example, consider the reactions that can occur when ZrO_2 is allowed to react with CaO to produce calcia-stabilised zirconia. In ZrO_2, there are twice as many anion sites as there are cation sites. Suppose that the Ca atoms are located on normal cation sites. Since the Ca atom is neutral, the effective charge at the site will be 4′ with respect to the charge normally encountered at a Zr^{4+} ion. In order to comply with rule (1), two anion sites must be created per added Ca atom. It is reasonable to place the oxygen atom from the CaO in one of these sites. The oxygen atom is neutral and carries an effective positive charge of 2•. The other site remains vacant, and carries an effective positive charge of 2•. The reaction equation is given by:

$$\mathrm{CaO(s)} \xrightarrow{\mathrm{ZrO_2}} \mathrm{Ca}_{\mathrm{Zr}}^{4'} + \mathrm{V}_{\mathrm{O}}^{2\bullet} + \mathrm{O}_{\mathrm{O}}^{2\bullet} \tag{6}$$

If it is thought that the compound is ionic, charge redistribution is allowed:

$$\mathrm{Ca}_{\mathrm{Zr}}^{4'} + \mathrm{V}_{\mathrm{O}}^{2\bullet} + \mathrm{O}_{\mathrm{O}}^{2\bullet} \xrightarrow{\mathrm{ZrO_2}} \mathrm{Ca}_{\mathrm{Zr}}^{2'} + \mathrm{V}_{\mathrm{O}}^{2\bullet} + \mathrm{O}_{\mathrm{O}}^{\mathrm{x}} \tag{7}$$

In this equation, the substitutional calcium defect is now Ca^{2+}, (written $Ca_{Zr}^{2'}$), and the added oxygen is O^{2-} (written O_O^x to emphasise this), and no longer a defect in the structure.

5.3 The Thermodynamics of Defect Populations

If macroscopic thermodynamics are applied to materials containing a population of defects, particularly nonstoichiometric compounds, the defects themselves do not enter into the thermodynamic expressions in an explicit way. However, it is possible to construct a statistical thermodynamic formalism that will predict the shape of the free energy-temperature-composition curve for any phase containing defects. The simplest approach is to assume that the point defects are noninteracting species, distributed at random in the crystal, and that the defect energies are constant and not a function either of concentration or of temperature. In this case, reaction equations similar to those described above, equations (6) and (7), can be used within a normal thermodynamic framework to deduce the way in which defect populations respond to changes in external variables.

To illustrate this approach, consider an anion-deficient oxide, MO_x. The appropriate defect chemical equation to describe this process could be, for example, equation (8).

$$\mathrm{O_O} + 2M_{\mathrm{M}} \rightleftharpoons \mathrm{V}_{\mathrm{O}}^{2\bullet} + 2M_{\mathrm{M}}' + \tfrac{1}{2}\mathrm{O_2(g)} \tag{8}$$

This describes the situation where oxygen is lost from the crystal, and the surplus electrons, two per lost oxygen, reside on separate metal atoms in the crystal. In formal ionic terms, two M^{2+} cations are transformed to M^+ cations. In semiconductor terms, two electrons are trapped on separate M^{2+} cations. Chemically this process may be considered as equivalent to doping of MO with M_2O. The law of mass action, applied in its simplest form with concentrations instead of activities, in view of the supposed noninteraction of the defects, then gives an expression for the equilibrium constant, (9):

$$\mathrm{K} = [\mathrm{V}_{\mathrm{O}}^{2\bullet}][\mathrm{M}_{\mathrm{M}}']^2 \mathrm{p}_{\mathrm{O_2}}^{1/2} \tag{9}$$

For each vacancy two metal defects are created, hence

$$[\mathrm{M}_{\mathrm{M}}'] = 2[\mathrm{V}_{\mathrm{O}}^{2\bullet}] \tag{10}$$

and:

$$\mathrm{K} = 4[\mathrm{V}_{\mathrm{O}}^{2\bullet}]^3 \mathrm{p}_{\mathrm{O_2}}^{1/2} \tag{11}$$

The composition of the oxide, x in $M\mathrm{O}_x$, depends upon the oxygen partial pressure via the relationship:

$$x \propto [\mathrm{V_O^{2\bullet}}] \propto \mathrm{p}_{\mathrm{O_2}}^{-1/6} \tag{12}$$

In those cases where the trapped electrons are freed by thermal energy, making the compound into an n-type semiconductor, the electronic conductivity, σ_n, follows the relationship:

$$\sigma_\mathrm{n} \propto \mathrm{p}_{\mathrm{O_2}}^{-1/6} \tag{13}$$

In general, for an anion-deficient (n-type) semiconducting oxide:

$$\sigma_\mathrm{n} \propto x \propto [\mathrm{V_O^{2\bullet}}] \propto \mathrm{p}_{\mathrm{O_2}}^{-1/m} \tag{14}$$

where m is a theoretically an integer, usually 4 or 6. Experimentally m is usually found to take a value between 3 and 7.

Cation deficient oxides $M_{1-x}\mathrm{O}$ can be considered in the same way. An appropriate reaction equation could be:

$$2\mathrm{M_M} + \tfrac{1}{2}\mathrm{O_2(g)} \rightleftharpoons \mathrm{O_O} + \mathrm{V_M^{2'}} + 2\mathrm{M_M^\bullet} \tag{15}$$

In formal ionic terms, two M^{2+} cations are transformed to M^{3+} cations. In semiconductor terms, two holes are trapped on separate M^{2+} cations. Chemically this process may be considered as equivalent to doping of MO with $M_2\mathrm{O}_3$. If the holes are mobile, the oxide is a p-type semiconductor, with electronic conductivity σ_p, and it is possible to write:

$$\sigma_\mathrm{p} \propto x \propto [\mathrm{M_M^\bullet}] \propto \mathrm{p}_{\mathrm{O_2}}^{1/6} \tag{16}$$

In general, for a cation deficient (p-type) semiconducting oxide:

$$\sigma_\mathrm{p} \propto x \propto [\mathrm{M_M^\bullet}] \propto \mathrm{p}_{\mathrm{O_2}}^{+1/m} \tag{17}$$

where m is a theoretically an integer, usually 4 or 6. Experimentally m is usually found to take a value between 3 and 7.

5.4 Brouwer Diagrams

Defect populations and physical properties such as electronic conductivity can be altered and controlled by manipulation of the surrounding atmosphere. To specify the exact electronic conductivity of such a material, it is necessary to specify its chemical composition, the defect types and populations present, the temperature of the crystal and the surrounding partial pressures of all the constituents. It is extremely helpful if the defect concentrations can be displayed graphically as a function of some variable such as partial pressure of one of the components. A procedure introduced by G. Brouwer allows such figures to be compiled.

To construct such a diagram, a set of defect reaction equations similar to equations (6–17) is constructed, and expressions for the equilibrium constants of each are obtained. The assumption that the defects are noninteracting allows the law of mass action to be used in its simplest form with concentrations instead of activities. The logarithm of these expressions is obtained, and a graph is drawn of log[defect concentration] against an experimental variable such as the log[partial pressure] of the components. To simplify matters, only one defect reaction is considered to be dominant in any particular composition region; this being chosen from a knowledge of the chemical attributes of the system under consideration.

The procedure is best illustrated by an example. Suppose that a nonstoichiometric phase of composition MX can have an existence range, which spans both sides of the stoichiometric composition, $MX_{1.00}$. Assume that in this phase only vacancies are of importance, so that the stoichiometric composition will occur when the number of vacancies on the cation sublattice is exactly equal to the number of vacancies on the anion sublattice, which is, therefore, due to a population of Schottky defects. At other compositions, electrical neutrality is adjusted via mobile electrons or holes, leading to n-type or p-type semiconductivity. Thus there are four defects to consider, electrons, $\mathrm{e'}$, holes, $\mathrm{h^\bullet}$, vacancies on metal sites, $\mathrm{V_M}$, and vacancies on anion sites, $\mathrm{V_X}$. Finally, assume that the most important gaseous component is X_2 as is the case in most oxides, halides, and sulphides.

In order to construct the diagram there are three equilibria of importance.

1. creation and elimination of vacancies, as Schottky defects:

$$\mathrm{nul} \rightleftharpoons \mathrm{V_M^{2'}} + \mathrm{V_X^{2\bullet}}; \quad \mathrm{K_S} = [\mathrm{V_M^{2'}}][\mathrm{V_X^{2\bullet}}] \tag{18}$$

2. creation and elimination of electronic defects:

$$\mathrm{nul} \rightleftharpoons \mathrm{e'} + \mathrm{h^\bullet}; \quad \mathrm{K_e} = [\mathrm{e'}][\mathrm{h^\bullet}] \tag{19}$$

3. change of composition, by interaction with the gas phase to produce cation vacancies:

$$\tfrac{1}{2}\mathrm{X_2} \rightleftharpoons \mathrm{X_X} + \mathrm{V_M^{2'}} + 2\mathrm{h^\bullet}; \quad \mathrm{K_3} = [\mathrm{V_M^{2'}}][\mathrm{h^\bullet}]^2 \mathrm{p}_{\mathrm{X_2}}^{-1/2} \tag{20}$$

(A change in composition to produce anion vacancies:

$$\mathrm{X_X} \rightleftharpoons \tfrac{1}{2}\mathrm{X_2(g)} + \mathrm{V_X^{2\bullet}} + 2\mathrm{e'} \tag{20a}$$

is redundant.)

4. maintenance of electrical neutrality. Equations (20) and (20a) define the formation of charged species, so that the appropriate electroneutrality equation is:

$$2[\mathrm{V}_{\mathrm{M}}^{2\prime}] + [\mathrm{e}'] = 2[\mathrm{V}_{\mathrm{X}}^{2\bullet}] + [\mathrm{h}^{\bullet}] \qquad (21)$$

The four equations (19–21) are simplified using chemical intuition. For example, it is reasonable to suppose that at higher partial pressures of X_2 the number of anion vacancies and hence of electrons is unimportant. Equation (21) then becomes:

$$2[\mathrm{V}_{\mathrm{M}}^{2\prime}] = [\mathrm{h}^{\bullet}] \qquad (22)$$

This expression is used, via substitution into equations (18–20) to obtain expressions for the defect types in terms of the constants $\mathrm{K_S}$, $\mathrm{K_e}$, $\mathrm{K_3}$, and $\mathrm{p_{X_2}}$.

$$[\mathrm{V}_{\mathrm{M}}^{2\prime}] = \tfrac{1}{2}(2\mathrm{K}_3)^{1/3}\mathrm{p}_{\mathrm{X}_2}^{1/6} \qquad (23)$$

$$[\mathrm{V}_{\mathrm{X}}^{2\bullet}] = 2\mathrm{K_S}(2\mathrm{K}_3)^{-1/3}\mathrm{p}_{\mathrm{X}_2}^{-1/6} \qquad (24)$$

$$[\mathrm{h}^{\bullet}] = (2\mathrm{K}_3)^{1/3}\mathrm{p}_{\mathrm{X}_2}^{1/6} \qquad (25)$$

$$[\mathrm{e}'] = \mathrm{K_e}(2\mathrm{K}_3)^{-1/3}\mathrm{p}_{\mathrm{X}_2}^{-1/6} \qquad (26)$$

It is now possible to plot log[defect concentration] versus log[$\mathrm{p_{X_2}}$] as a set of four straight lines applicable to the high $\mathrm{p_{X_2}}$ region, as on the right hand region of Figure 3.

At moderate partial pressures of X_2, the assumption made above is replaced by the assumption that the crystal is an insulator and Schottky equilibrium is dominant. In this case:

$$[\mathrm{V}_{\mathrm{M}}^{2\prime}] = [\mathrm{V}_{\mathrm{X}}^{2\bullet}] \qquad (27)$$

This is equivalent to the assumption that $\mathrm{K_S}$ is a lot greater than $\mathrm{K_e}$. The original equations are now reworked with this substitution to yield:

$$[\mathrm{V}_{\mathrm{M}}^{2\prime}] = [\mathrm{V}_{\mathrm{X}}^{2\bullet}] = \mathrm{K}_{\mathrm{S}}^{1/2} \qquad (28)$$

$$[\mathrm{h}^{\bullet}] = \mathrm{K}_3^{1/2}\mathrm{K}_{\mathrm{S}}^{-1/4}\mathrm{p}_{\mathrm{X}_2}^{1/4} \qquad (29)$$

$$[\mathrm{e}'] = \mathrm{K_e}\mathrm{K}_{\mathrm{S}}^{1/4}\mathrm{K}_3^{-1/2}\mathrm{p}_{\mathrm{X}_2}^{-1/4} \qquad (30)$$

These are plotted to yield the middle part of Figure 3.

At lower partial pressures of X_2, it is more reasonable to consider that anion vacancies become dominant. The electroneutrality equation is now written as:

$$[\mathrm{e}'] = 2[\mathrm{V}_{\mathrm{X}}^{2\bullet}] \qquad (31)$$

Once again, a set of equations relating the defect concentrations to the partial pressure of X_2 and the equilibrium constants $\mathrm{K_S}$, $\mathrm{K_e}$, and $\mathrm{K_3}$ are written and plotted. The result is shown in the left hand part of Figure 3.

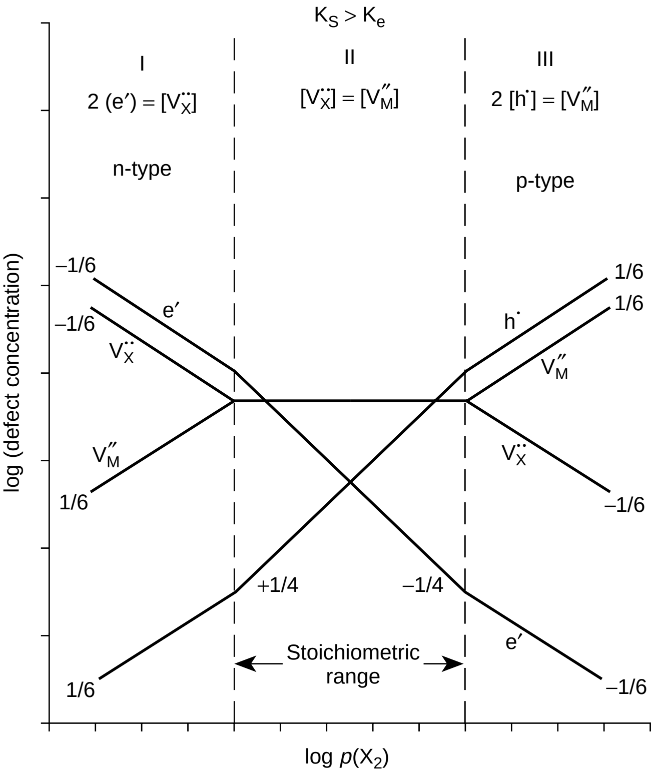

Figure 3 Brouwer diagram for a phase of approximate composition *MX* that responds to changes in composition by the electroneutrality conditions specified in the three regions I, II, III

The complete diagram shows three regions corresponding to low, medium, and high partial pressures of X_2 gas. It is apparent that the electron concentration starts high, in the n-type region I, and falls progressively to the p-type region III, while the hole concentration starts low in the n-type region I, and ends high in the p-type region III. The way in which the other defects vary in concentration is also readily determined from the figure. This variation gives a number of clues about the way in which the properties change as the partial pressure of X_2 and the composition alter. At the left, for example, there is high concentration of anion vacancies and so easy diffusion of anions is to be expected. Similarly, in region III we have a high concentration of cation vacancies, which would be expected to enhance cation diffusion.

The original assumption was that Schottky defect formation was preferred to the formation of electronic defects, and this is explicitly stated at the top of the figure. As Frenkel defect formation has been ignored altogether it is also possible to write $\mathrm{K_S} > \mathrm{K_e} \gg \mathrm{K_F}$, where $\mathrm{K_F}$ would represent the equilibrium constant for a reaction that formed Frenkel defects in *MX*. Figure 3 contains all the assumptions made, as well as the way in which defect concentrations vary. Moreover, it is easy to see what changes will take place if the relative values of $\mathrm{K_S}$ and $\mathrm{K_e}$ are altered, and the graphical representation is able to present trends in a lucid fashion.

6 GROSSLY NONSTOICHIOMETRIC CRYSTALS

Inorganic phases with broad composition ranges are called grossly nonstoichiometric phases, and considerable effort has been put into the clarification of the structure of these materials. The initial model for such materials is to suppose that they contain high populations of vacancies or interstitials, to make up the compositional imbalance. A few examples of this approach, from among the many in the literature, are chosen as illustrative. It is possible that the examples cited will be shown to have more complex defect structures in the future.

6.1 Point Defect Populations

The perovskite structure, adopted by many compounds of nominal formula ABX_3, in which A is a large cation and B a medium size, often transition metal, cation, and X an anion, is prone to wide ranges of stoichiometric variation. Of these, the oxides have been most studied. The formula can be modified by doping on both the A sites and B sites to produce a wide variety of nonstoichiometric phases. For example, the perovskite $LaCoO_3$ shows considerable oxygen loss when the La is partly replaced by Sr, in $La_{1-x}Sr_xCoO_{3-\delta}$. In this and related lanthanide containing compounds, the oxygen deficit is regarded as being due to a population of oxygen vacancies. At some compositions, it has been shown that a combined Ln/Sr and O/vacancy ordering occurs.**[6]** The same is true of Fe-containing perovskites such as $Ln_{1-x}Sr_xFeO_{3-\delta}$, in which a population of disordered oxygen vacancies is present. Many compounds show pronounced oxygen vacancy ordering. The extreme example is $Sr_2Fe_2O_5$, in which the ‘ordered oxygen vacancies’ are assimilated to give the brownmillerite structure. At high temperatures the oxygen vacancies disorder to form a defect perovskite structure.**[7]** The brownmillerite structure, as well as other ordered phases occur in the $(Ba_{1-x}La_x)_2In_2O_{5+x}$ phases.**[8]** The perovskites $LaMnO_{3+\delta}$ and related doped derivatives are reported as oxygen excess materials. This terminology is misleading, as the structure contains vacancies on both La and Mn sites, while the oxygen structure is intact.

The material β-alumina has an ideal formula $Na_2Al_{22}O_{34}$. The structure is composed of slabs of 4 oxygen layers in a cubic close-packed arrangement with a structure resembling that of spinel, $MgAl_2O_4$, linked by more open layers containing the Na^+ ions. At normal temperatures, the Na^+ ions are distributed at random over the many available sites between the spinel-like slabs, to form a quasi-liquid layer. The real composition is variable and the phase always contains an excess of alkali metal. To maintain neutrality, two possible defects can be envisaged to compensate for the alkali metal ions, Al^{3+} vacancies in the spinel sheets or interstitial O^{2-} ions in the open sodium containing layers. In β-alumina, it appears that interstitial oxygen ions are favored. In this phase, therefore, there are two unbalanced point defect populations, mobile Na^+ ions, over the stoichiometric requirement, and interstitial oxygen ions. At low temperatures, there is considerable evidence that these defects order.

A number of other β-alumina related phases have been prepared. In some of these the spinel blocks have an increased thickness, the so-called β', β'' and β''' phases, while in others, the Na or Al components have been replaced with similar species. Related structures, such as $BaMgAl_{11}O_{17}$ doped with Eu^{3+}, are widely used as phosphors. Crystal-structure studies on such materials show that the defects present depend sensitively upon both temperature and the constituents of the phase. Large replacement ions, lanthanide or alkali metals, tend to occupy the interlayer regions as interstitial defects, but surprisingly, some also enter the spinel blocks as substitutional defects, in association with oxide ion vacancies.**[9]** Smaller ions occupy the spinel blocks as substitutional point defects. The delicate balance between oxygen interlayer interstitials and spinel block cation vacancies varies with composition. These defect interactions can often be successfully explored by using simulation techniques.**[10]** Ordering occurs at lower temperatures (*see* ***Ionic Conductors***).

The crystal structure, microstructure, and defect structures found in the superconducting phase $YBa_2Cu_3O_{7-\delta}$ have been intensively investigated (*see* ***Superconductivity***). Chemically, the material is a grossly nonstoichiometric phase with a composition range from $YBa_2Cu_3O_6$ to $YBa_2Cu_3O_7$. The structure is built up from the sequence of planes [CuO_2-Y-CuO_2-BaO-CuO_x-BaO]. Composition variation is confined to the CuO_x planes, and oxygen is lost from Cu-O-Cu-O chains, which converts square-planar coordinated Cu to linear coordinated ions. In the range between approximately $YBa_2Cu_3O_7$ and $YBa_2Cu_3O_{6.8}$, the oxygen vacancies appear to be disordered, at least on a macroscopic scale, although long annealing times may allow ordering to occur. At greater degrees of reduction, this does take place, and a variety of ordered oxygen vacancy superstructures occur, notably at the compositions $YBa_2Cu_3O_{6.75}$ and $YBa_2Cu_3O_{6.5}$. It is possible that other patterns of order will appear under different conditions of preparation or in phases in which Y is replaced by other rare earths, or the Ba by other alkaline earths.

6.2 Interpolation

Interpolation or intercalation (*see* ***Intercalation Chemistry***) is said to occur when additional species are placed into a host structure to change either composition or properties. At one extreme, intercalation can refer to the insertion of guest molecules into cage structures such as that of the zeolites (*see* ***Zeolites***), or between the layers of laminated compounds such as the clays (*see* ***Silicon: Inorganic Chemistry***). At the other extreme, the insertion of small atoms such as C or N into metal phases to form interstitial alloys (*see* ***Alloys***; ***Carbides: Transition Metal Solid-state Chemistry***; ***Nitrides: Transition Metal Solid-state Chemistry***), is included in the category. A large variety of structures can be found in such materials, and in this section, a small number of examples relevant to defect chemistry are given.

The layer structure disulphides, such as $M_x\text{TiS}_2$ and $M_x\text{NbS}_2$, consist of layers of Ti or Nb in octahedral coordination, held together by weak bonds. Interpolation of metals between these layers is relatively easy, and materials such as Li_xTiS_2, in which the metal atoms are regarded as random interstitials, have been investigated as battery electrodes. Charge compensation is unnecessary, as extensive electron delocalization occurs. If the interpolated atoms are the same as those in the layers, Ti in TiS_2 for example, the composition can change from one stoichiometric extreme, TiS_2, to another, Ti_2S_2, (TiS). The interpolated atoms may be ordered to form intermediate phases such as Ti_8S_9, Ti_4S_5, Ti_3S_4, Ti_2S_3 and Ti_5S_8.

The perovskite-structure tungsten bronzes, which have a formula $M_x\text{WO}_3$, are formed by the reaction of metals with WO_3. The interpolated metal atoms occupy random cage sites between the corner-linked WO_6 octahedra that make up the WO_3 structure. The degree of filling is variable and the compounds have wide composition ranges. In the compound Li_xWO_3, x can vary continuously between the values of 0 and 0.5. For Na_xWO_3, x can vary between the limits of 0 and 0.11, and then from 0.41 to 0.95. The outer electrons of the interpolated atoms are delocalized, endowing the solids with metallic properties, and originally they were believed to be alloys, hence the name bronzes. The metallic nature of the materials obviates the need for counterdefects to maintain charge neutrality.

In addition to the perovskite-structure tungsten bronzes, two other tungsten bronze types exist that make use of interpolation to vary their compositions. These are both made up of corner-linked WO_6 octahedra, rearranged to form either pentagonal, square, or hexagonal tunnels. Variable filling of these tunnels by metal atoms gives rise to metallic materials with wide stoichiometry ranges. In the tetragonal tungsten bronze phases, the pentagonal and square tunnels in the structure are partly filled. These are typified by the compounds Pb_xWO_3 and Sn_xWO_3, in which x can take values of from approximately 0.16 to 0.26. The degree of interaction between the interpolated atoms is unclear, but ordering in the Pb_xWO_3 bronzes has recently been found to be a result of interactions between the interpolated Pb atoms with the underlying W atoms in the WO_6 framework, rather than due to a simple ordering of the interpolated atoms themselves.[11] Hexagonal tungsten bronzes contain large hexagonal tunnels that are partly occupied. The composition of the archetypal hexagonal tungsten bronze phase K_xWO_3 extends from $x = 0.19$ to $x = 0.33$.

The cathode material $\text{Li}_{1-x}\text{CoO}_2$ is an intercalation compound in which the Li^+ ions lie between layers of composition CoO_2. In theory, the composition range of the cathode material is from LiCoO_2 to CoO_2, that is, x varying from 1 to 0, the operational degree of nonstoichiometry is restricted, and x generally takes values in the range of 0 to about 0.45. Intercalation of lithium changes the layer stacking of the parent oxide framework. Cobalt oxide, CoO_2, is built of hexagonal close-packed (ABAB) layers of oxygen atoms, while LiCoO_2 has cubic (ABC) close packing. Intercalation is then accompanied by planar faulting in the matrix.

7 POINT DEFECT CLUSTERS

7.1 Crystals with Compositions Close to *MX*

Even when the departures from stoichiometry remain small, there are reasons for suspecting that the defect structures of nonstoichiometric phases are more complex than a picture of isolated point defects would suggest. Probably the best-documented example is that of Fe_xO, wüstite. This oxide exists over a composition range that varies from about $\text{Fe}_{0.89}\text{O}$ to $\text{Fe}_{0.96}\text{O}$ at approximately l300 K and that broadens with increasing temperature. Isolated iron vacancies are not present, but small groups of atoms and vacancies aggregate into elements of new structure, termed point defect clusters, which are distributed throughout the wüstite matrix (Figure 4). It is found that the clusters bear a strong resemblance to elements of Fe_3O_4, the next higher oxide to FeO. Structurally, therefore, the over-oxidised FeO can be regarded as a partly ordered assembly of fragments of the Fe_3O_4 (spinel) structure intergrown within the halite (NaCl) structure of FeO.

Many 3d-transition metal monoxides and sulphides show nonstoichiometric behavior. The high defect population is disordered at high temperature, but annealing usually produces a variety of phases containing ordered or partially ordered arrangements of defects. The nonstoichiometric oxides TiO and VO are typical examples. Samples cooled rapidly from high temperatures yield diffraction patterns that show diffuse scattering, indicative of short-range order and defect clustering. Slow cooling or annealing yields materials with complex arrangements of ordered metal and oxygen vacancies. A similar situation is found with the nonstoichiometric sulphides that lie near to the compositions FeS, ZrS, CrS, and the phases between digenite, (Cu_2S), and bornite, (Cu_5FeS_4). Under laboratory preparation conditions, diffraction patterns often show diffuse scattering indicative of defect clusters. Natural samples frequently reveal the presence of ordered superstructures.

7.2 Fluorite-related Structures

Compounds with structures related to that of fluorite, CaF_2 (*see* ***Fluorides: Solid-state Chemistry***), readily form solid solutions with other solids containing cations of a similar size to the fluorite host cation. Invariably the foreign cation substitutes for the host cation, and stoichiometric imbalance is taken up by the anion component of the crystal. The

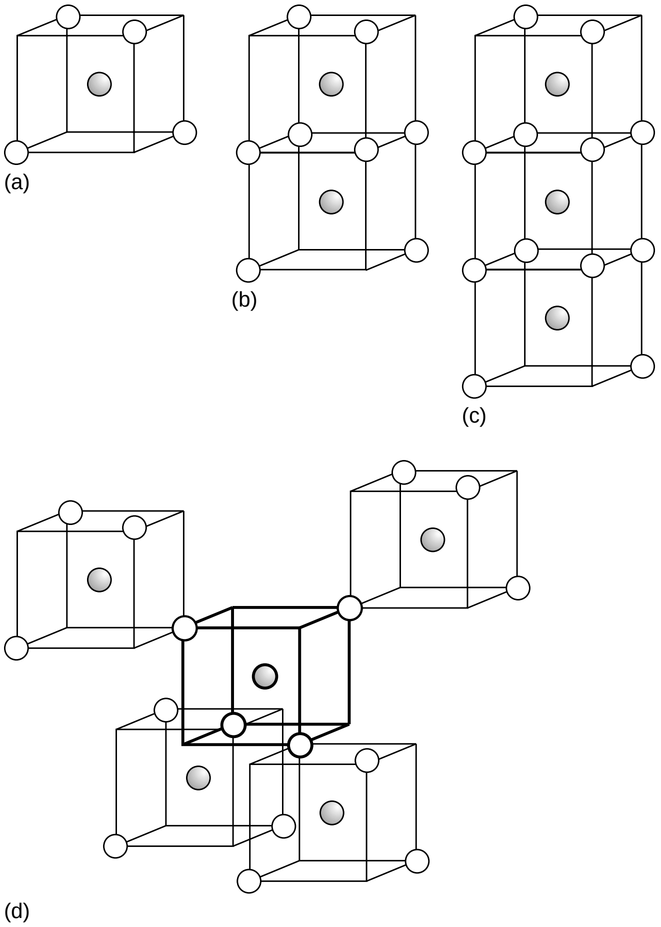

Figure 4 Point defect clusters in $Fe_{1-x}O$. The open circles represent cation vacancies and the shaded circles Fe^{3+} interstitials. The unmarked cube vertices are occupied by oxide ions. (a) 4:1 cluster, (b) 6:2 cluster, (c) 8:3 cluster, (d) 16:5 cluster. In (d), four 4:1 clusters are arranged tetrahedrally around a central cluster, drawn with heavy outline

resulting structures display considerable flexibility towards both an excess and deficiency of anions compared to the ideal composition MX_2. The real defect structure of many of these phases remains obscure.

7.2.1 Anion-deficient Structures

Anion-deficient structures can form by direct reduction of parent oxides, as with the lanthanide and actinide oxides PrO_2, CeO_2, TbO_2, UO_2 and PuO_2, among others (*see* ***Oxides: Solid-state Chemistry***). Reaction with lower valence compounds achieves the same result, as when ZrO_2, ThO_2 or HfO_2 are heated with Y_2O_3 or CaO. Notionally these phases contain anion vacancies. However, truly isolated vacancies have not been observed and structural rearrangements occur to form defect clusters. At lower temperatures, and within well-defined oxygen partial pressures regimes, these clusters are ordered. In this case, homologous series of phases may form, typified by the M_nO_{2n-2} oxides found in the Pr-O, Tb-O and Ce-O systems. In the Pr_nO_{2n-2} series, ($n = 7$, 9, 10, 11, 12), the defects appear to consist of pairs of anion vacancies oriented along a body diagonal of the fluorite-type cubic unit cell. Surrounding atoms relax to form a cluster with a composition of Pr_7O_{30}. Such clusters have been observed in the lanthanide oxides Pr_7O_{12}, Tb_7O_{12}, and in the ternary phases UY_6O_{12} and $Zr_{10}Sc_4O_{24}$. It has been suggested that the structures of all the Pr_nO_{2n-2} homologues are can be built from ordered arrangements of such clusters.

The structures of the defects in many anion-deficient fluorite structures are sensitive to composition. For example, in the Bi_2O_3-Nb_2O_5 and Bi_2O_3-Ta_2O_5 systems, MO_6 defect clusters have been identified at compositions close to Bi_2O_3, and pyrochlore-like M_4O_{18} clusters at greater Nb or Ta concentrations. Broadly speaking, modulated structures tend to form at lower defect populations (see Section 10) and defect clusters at higher defect populations.

7.2.2 Anion-excess Structures

The MX_{2+x} phases contain interstitial anions. As with the anion-deficient phases, these interstitials are not random point defects, but ordered or clustered. The earliest cluster geometry to be postulated was the [2:2:2] cluster in UO_{2+x}, the prototype anion-excess fluorite phase. The cluster is composed of 2 interstitial oxygen atoms displaced along $\langle 110 \rangle$, two interstitial oxygen atoms displaced along $\langle 111 \rangle$ in UO_{2+x} (Figure 5). Other cluster geometries have also been proposed in this oxide, and the defect structure of this well studied phase is still not completely resolved.

In many of the lanthanide oxyfluorides and related phases, different cluster geometries, (labelled [1:0:2], [1:0:3] and [1:0:4] in the above notation), are found. The type of cluster depends upon the size of the lanthanide present. Large cations, La–Nd, form only [1:0:3] clusters, while smaller cations, such as Sm, form [1:0:2] clusters, found in $SmO_{0.7}F_{1.6}$. In all of these systems, the cluster distribution seems to be a function of temperature.

A large number of anion-excess halides exist, especially fluorides formed by the reaction of M^{2+} difluorides with lanthanide and related trifluorides (*see* ***Fluorides: Solid-state Chemistry***). The archetypal system is CaF_2–YF_3, leading to phases $Ca_{1-x}Y_xF_{2+x}$. It is clear from diffraction data that defect clusters occur in these materials, and that at higher concentrations these order to produce a homologous series of phases. The nature of the clusters however has been difficult to determine. Earlier studies were interpreted in terms of pairs of anions, one 'interstitial' and one 'normal', aligned along the [110] direction. More recently, clusters that adopt geometries that are more complex have been suggested. In $Ca_{0.94}Y_{0.06}F_{2.06}$ and related phases, a cuboctahedral cluster is known to form. Different packing arrangements of these clusters lead to a homologous series of ordered phases of

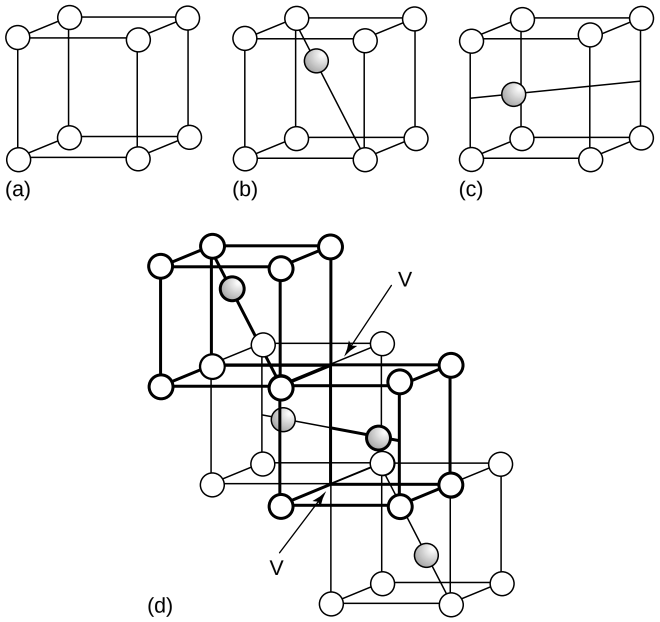

Figure 5 Defect cluster structures in UO_{2+x}. The parent structure is built from cubes with an oxygen ion at each corner (a), alternating with similar cubes containing a metal cation. Interstitial oxygen ions (dark circles), occupy empty cubes, but are displaced from the center along $\langle 111\rangle$ (b), or $\langle 110\rangle$ (c). The 2:2:2 cluster consists of four such cubes, two of which contain $\langle 111\rangle$ interstitial oxygen ions and two of which contain $\langle 110\rangle$ interstitial oxygen ions. The oxygen vacancies are marked V (d)

formula $M_{m-5}R_5X_{2m+5}$, where M is a divalent cation and R a trivalent cation. Examples of these phases are provided by the $m = 19$ member of the series, $Ca_{14}Y_5F_{43}$, the naturally occurring mineral tveitite, Ca_2YbF_7 and Ca_2LuF_7, which seem to be isostructural with the $m = 15$ phase Ca_2YF_7, ($Ca_{10}Y_5F_{35}$), and $Na_7Zr_6F_{31}$, which seems to be isostructural with the $m = 13$ phase, $Ca_8Y_5F_{31}$. Recent structural studies suggest that these defects may be best described in terms of modulated structures (see Section 10).

7.3 Microdomains

Statistical thermodynamic treatments of defect populations have lead to an explanation of existence of grossly nonstoichiometric crystals in terms of microdomains of ordered structure. The model considers that the nonstoichiometric matrix is made up of a mosaic of small regions of ordered defect-free structures, the microdomains. To account for stoichiometric variation, one can postulate that at least two microdomains with different compositions occur. However, compositional change might simply arise at the surface of the domain. For example, if there are compositionally identical microdomains, one of which is bounded by an anion surface and one by a cation surface, variation in the two populations can give rise to compositional variation. In a strict sense, as each microdomain is ordered, the concept of a 'defect' is redundant, except for the intermicrodomain boundaries. Nucleation concepts can be applied to derive the size of the microdomains as a function of the chemical potentials of the components. The results of the analysis suggest that the size of microdomains is small, and at one extreme, equivalent to defect clusters.

Microdomains within the perovskite-like slabs of layered perovskite phases in the Ba-Bi-O system illustrate these ideas.[12] The structures are layered perovskites with K_2NiF_4 related structures and gross changes in the Ba to Bi ratio are accommodated by the formation of a homologous series $Ba_{n+1}Bi_nO_{3n+1}$, made up of slabs of $BaBiO_3$ perovskite structure (see Section 8.4). In addition, subtle changes in the Ba to Bi ratio are accommodated by microdomains of ordered structure within the perovskite slabs themselves. These microdomains are ordered fragments of perovskite structure, and cation variation occurs at the interface between the microdomains in such a way that local excess or deficit of one cation over the other is accomplished.

Well-defined examples of microdomains are found in the $(1 - x)ZrO_2 - xLn_2O_3$ ($Ln = \mathrm{Ho}$, Dy, Tb, Gd) and $(1 - x)CeO_2 - xY_2O_3$ system. The dioxide adopts the fluorite structure and the sesquioxides the C-type structure. For many years, it was thought that a continuous solid solution fluorite structure forms across this whole composition range. This is not so. Close to the dioxide, the composition balance is achieved by a population of microdomains of 13 to 14 nm diameter. Near to the sesquioxide, ordered vacancy pairs occur in the fluorite matrix. These two regions are separated by a narrow two-phase region.[13]

8 EXTENDED DEFECTS

8.1 Extended Defects and Nonstoichiometry

The point defect clusters described in earlier sections can be legitimately termed extended defects. In this section, defects that are less easily considered in terms of point defects will be described. Perhaps the best known of these are the planar boundaries, the most abrupt example being the crystal surface itself (*see* ***Surfaces***; ***Semiconductor Interfaces***).

Isolated planar boundaries within a crystal will constitute extended defects. Some boundaries, such as certain configurations of antiphase boundaries and twin boundaries, do not change the overall composition of the crystal. However, coordination polyhedra and nearest neighbor geometry different from those in the bulk are found near the discontinuity. These may provide sites for unusual chemical reactions or introduce significant changes in the physical properties compared to the defect-free phase. Other boundaries may cause a change in composition. If such boundaries are present in variable numbers and distributed at random, the crystal will be operationally nonstoichiometric. If the defects order, a series of new phases will be generated, each with a definite composition and chemical formula. Each phase will be characterized by the separation between the ordered planar boundaries, which are no longer faults or defects, but integral structure elements.

Examples of such materials have been known for a number of years in the mineralogical field, where the terms ‘intergrowth phases’, ‘polysynthetic twinned phases’, ‘polysomatic phases’ and ‘tropochemical cell twinning’ have been applied to describe the structures.[14–16] In recent years, the application of electron microscopy has revealed the defect structures of vast numbers of phases containing extended defects. In this section, some well-characterized examples chosen are chosen for illustration.

8.2 Crystallographic Shear (CS) Phases

Crystallographic shear (CS) occurs mainly in the transition metal oxides WO_3, MoO_3, Nb_2O_5, and the rutile form of TiO_2 (*see* ***Oxides: Solid-state Chemistry***). Recently CS has been reported in an oxygen deficient perovskite, $PbMnO_{2.75}$.[17] A crystallographic shear plane is a planar fault that changes the anion to cation ratio without changing the shape of the anion coordination polyhedra surrounding the metal atoms significantly. In the oxides in which CS occurs, the metal coordination polyhedron is usually an octahedron of oxygen atoms. These are linked by corners or edges and corners to form rather open structures. On reduction, either by direct removal of oxygen or by reaction with lower valence compounds, the open structure collapses along specific crystallographic planes, the CS planes. The vector that describes the collapse, the CS vector, is equal to an oxygen–oxygen distance, and the operation effectively removes a complete plane of oxygen atoms from the structure. The lower oxides so produced are known as crystallographic shear phases, and CS families are known as homologous series. Disordered CS planes are known as Wadsley defects, both in the materials discussed in this section and in the block structures considered below.

The structurally simplest compounds that can be used to illustrate this process are the tungsten oxides. The structure of the parent oxide, WO_3, is made up of a three-dimensional array of corner-shared WO_6 octahedra (Figure 6(a)). Very slight reduction, to a composition of $WO_{2.9998}$, for example, results in a crystal containing a low concentration of planar faults randomly oriented on all possible {102} planes. The CS operation effectively eliminates a {102} plane of oxygen atoms from the structure. The defects consist of lamellae made up of blocks of four edge-shared octahedra in a normal WO_3-like matrix of corner-sharing octahedra (Figure 6(b)).

Continued reduction initially produces an increased density of disordered {102} CS planes, but as the composition approaches $WO_{2.97}$, they tend to become ordered. When the CS planes are perfectly ordered, the composition of the crystal is given by a formula W_nO_{3n-1}, where n is the number of octahedra separating the CS planes. An upper value of n is difficult to determine, owing to the coexistence of ordered and disordered CS planes, but a value of about 30 is reasonable, giving a composition of $WO_{2.9666}$. The lower limit of the {102} CS series corresponds to a formula of $W_{18}O_{53}$, with a composition of $WO_{2.9444}$.

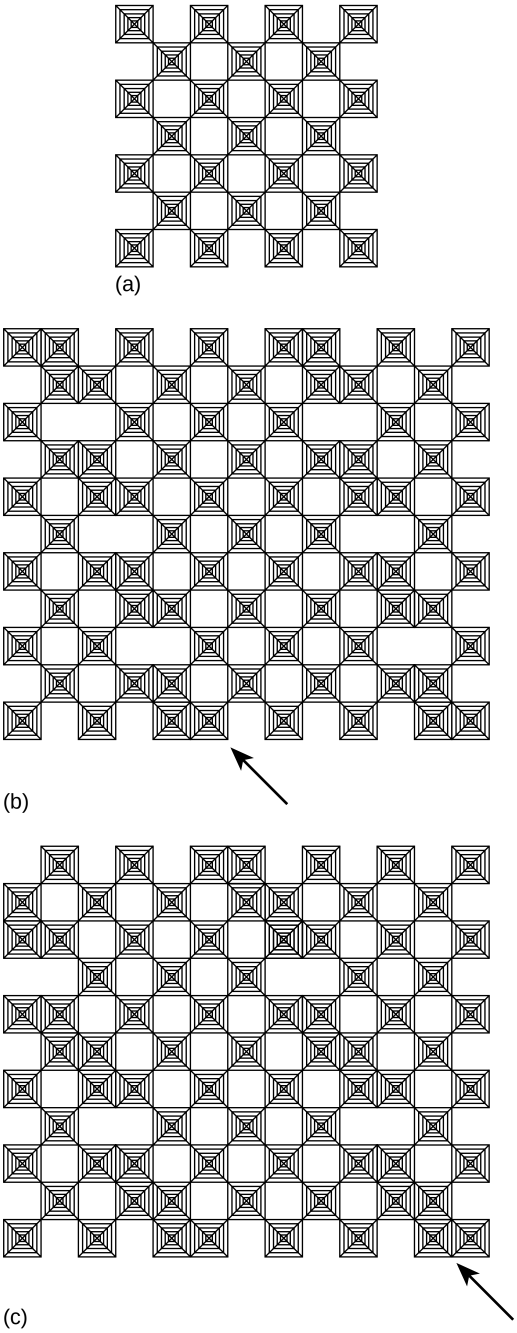

Figure 6 Crystallographic shear in WO_3 (a) the idealized structure of WO_3, drawn as corner-shared WO_6 octahedra, squares in projection (b) {102} CS planes (arrowed), consisting of blocks of four edge-shared octahedra (c) {103} CS planes (arrowed), consisting of blocks of six edge-shared octahedra

Further reduction, to take the composition below about $WO_{2.93}$, produces a different CS structure, in which blocks of six edge-shared octahedra form (Figure 6(c)). The CS planes lie on {103} planes, and are usually ordered, giving rise to the homologous series W_nO_{3n-2}. They occur within the approximate range $W_{25}O_{73}$, ($WO_{2.9200}$), to $WO_{16}O_{46}$, ($WO_{2.8750}$).

The reduction of the rutile form of TiO_2 is similar to that of WO_3. Small degrees of reduction are accommodated on {132} CS planes and ordered {132} phases occur at greater degrees of reduction, to form the homologous series Ti_nO_{2n-1}, with n taking values between approximately 15 to 37. Greater degrees of reduction use {121} planes, the changeover from {132} CS occurring at compositions between approximately $TiO_{1.93}$ and $TiO_{1.90}$. The {121} series also has the formula Ti_nO_{2n-1}, with n taking values between 4 and 9 or 10.

When reaction with other oxides is used to reduce the anion to cation ratio, CS families occur that are not found in the binary metal–oxygen systems, revealing that complex factors are involved in determining the planes upon which CS actually occurs. For example, when WO_3 is allowed to react with small amounts of Nb_2O_5 at temperatures above approximately 1250 °C, the CS planes lie on planes between {104}, with a series formula $(W, Nb)_nO_{3n-3}$, and {001}, with a series formula $(W, Nb)_nO_{3n-1}$. Reacting TiO_2 with between 0.7 and 6.5 mol% Li_2O produces a CS series in which the CS plane gradually changes from {021} to {051}.**[18]** If TiO_2 is allowed to react with Fe_2O_3, CS structures form on planes between {020} to {121}.

In any CS plane family, the amount of oxygen loss may be increased by decreasing the spacing between the defects or by changing their orientation. This is most easily understood by examples from the reduced tungsten oxides. Each block of four edge-sharing octahedra in a {102} CS plane eliminates one oxygen atom. Each block of six edge-sharing octahedra in a {103} CS plane eliminates two oxygen atoms, and so on. Rotation from {102} towards {103} at a constant CS plane spacing continuously increases the amount of oxygen lost. The initial step could be occasional insertion of blocks of six edge-sharing octahedra into a {102} CS plane. If these are ordered, the planes will take on indices somewhere between {102} and {103}. If disordered, the CS planes become curved or wavy. Continued interpolation of blocks of six edge-shared octahedra continues the reduction. Regions of such wavy CS planes lying between {104} and {001} are common in the Nb_2O_5-WO_3 system. Regions of well ordered CS planes with indices anywhere between {132}, at the oxygen rich end of the phase range to {121} at the oxygen poor end are found when rutile is reacted with Cr_2O_3 to produce a phase with a composition between approximately $(Ti,Cr)O_{1.93}$ and $(Ti,Cr)O_{1.90}$. Every composition prepared can have a different ordered arrangement of CS planes, with a definite spacing and CS orientation.

There are a number of uncertainties that remain concerning CS planes, notably the mechanism by which they form, and their stability relative to other defect populations. Electron microscopy has shown that CS planes can form extremely rapidly under the conditions holding during observation and that they extend along their length. This implies that the crystal can collapse directly to yield the fault plane. Other studies suggest that at high temperatures the predominant defect population consists of clusters of 'interstitials', which can be regarded either as CS plane nuclei or as point defect clusters. Although several mechanisms have been put forward to account for sideways movement of CS planes and hence lateral ordering, little direct evidence for how this takes place has been obtained.

8.3 Twinning

A twin plane in a crystal is a planar fault that acts as a mirror, in that the atoms on one side of the plane are mirrored in position with respect to those on the other. Not all twin planes produce composition changes, but some do. Many inorganic crystals prepared by conventional solid-state reactions, including sulphides such as In_2S_3, and oxides such as $Ca_3Mn_2O_7$ and $Ca_4Mn_3O_{10}$, are heavily twinned. These disordered boundaries constitute a high density of extended defects in the structures. They may form as a response to local compositional changes or in order to provide cation coordination polyhedra not available in the normal crystal.

When a twin plane introduces a composition change, a set of ordered twin planes would produce a new phase. Homologous series of phases will result if the spacing between the twin planes can take discrete values. Such phases, typified by lillianite, $Pb_3Bi_2S_6$, are found, for instance, in the PbS-Bi_2S_3 and PbS-Sb_2S_3 systems, and the phenomenon has been called tropochemical twinning.**[16]** When the twin planes are disordered, a nonstoichiometric phase with a measurable composition range will result. The resulting solid may be described as containing intergrowths of various members of the homologous series or as a twinned parent phase, depending upon the density of the faults.

Many structures can be thought of as built from twinned fragments within the unit cell. The phenomenon is referred to as chemical twinning (CT), or unit cell twinning. As the size of the twin fragments increases, different structure types arise, all related as in homologous series.

8.4 Planar Intergrowths

A large number of solids encompass a range of composition variation by way of intergrowth. In this situation, two (or more) crystalline materials with different compositions can interleave if they each have at least one structurally compatible crystallographic plane. The composition can vary from that of one of the parents to the other. When such intergrowths are perfectly ordered, no defects are present. However, disorder in the stacking of the different units naturally leads to a structure containing planar faults. Examples abound, including the hexagonal ferrites, in which different spinel-related slabs of structure coexist, extensive families of hexagonal perovskites, the $In_2O_3(ZnO)_n$ and related phases, and some polytypes.

For illustrative purposes, three perovskite related phases are described. Other examples are given in Sections 9 and 10.

K_2NiF_4-related structures, also called Ruddleston-Popper phases, are built of slabs of perovskite structure cut parallel to the (idealized) perovskite {100} planes united by way of lamellae of halite (NaCl) structure. The series formula for these compounds is $A_{n+1}B_nO_{3n+1}$ where A is a large cation, typically an alkali metal, alkaline earth or rare earth and B is a medium sized cation, typically a 3d transition metal cation. The first examples characterized were Sr_2TiO_4, $Sr_3Ti_2O_7$ and $Sr_4Ti_3O_9$, in which the perovskite slabs are derived from $SrTiO_3$ and the halite slabs from SrO.

Replacement of the halite layers in the above series by layers of composition Bi_2O_2 leads to a series of Aurivillius phases, with a general formula $(Bi_2O_2)(A_{n-1}B_nO_{3n+1})$, where A is a large cation, and B a medium sized cation. The best-known member of this series of phases is the ferroelectric $Bi_4Ti_3O_{12}$ in which $n = 3$ and A is Bi.

A third series of perovskite related intergrowths has a general formula $A_nB_nO_{3n+2}$, where A is a large cation, and B a medium sized cation, typified by the $(Na,Ca)_nNb_nO_{3n+2}$ series. The oxides are intergrowths of slabs of perovskite structure with the halite structure. They differ from the Ruddleston-Popper series in that the (idealized) perovskite slabs are sliced along {110} rather than {100}.

When prepared from mixed oxides, chemical homogeneity in these materials is hard to achieve. Under these circumstances, a variety of different n-values can be said to coincide in a crystal. The defects here are regarded as slabs of the halite type interspersed more or less at random in the perovskite-structure matrix.

8.5 Block Structures

The block structures are found in a group of niobium oxides (*see **Oxides: Solid-state Chemistry***), close in composition to Nb_2O_5. In the binary system, these oxides lie between the compositions $NbO_{2.5}$ and $NbO_{2.42}$, and in them two sets of CS planes intersect to divide the materials up into columns of corner-linked octahedra, with an NbO_3 stoichiometry. The columns, in projection, look like rectangular blocks, accounting for the common name of these materials. The phase range over which these structures occur is increased greatly by reacting Nb_2O_5 with other oxides, and it is possible to pass from phases with composition below $NbO_{2.5}$, formed by reaction with TiO_2, for example, to compositions above $NbO_{2.5}$, by reaction with oxides such as WO_3.

These changes of stoichiometry are brought about by changing the block sizes. Larger blocks push the overall stoichiometry towards MO_3 and smaller blocks towards MO_2. Composition change is thus achieved at the block periphery. Changes in local composition are taken care of by local rearrangements in the block sizes and the way in which they are packed together. Defects consisting of clusters or walls of inappropriate blocks are very common in these compounds.

An extensive family of 'tubular oxides' with formulae $(Bi_{2+x}Sr_{2-x}CuO_{6+\delta})_n(Sr_{8-y}Cu_6O_{16+z})$, with n taking integer values of between 4 and 7, are somewhat related to the block structures.[19] In these materials, walls of copper polyhedra form rectangular units containing perovskite-like structures. The arrangement of the rectangular units is very flexible, and defects very similar to those encountered in the block structures are common.

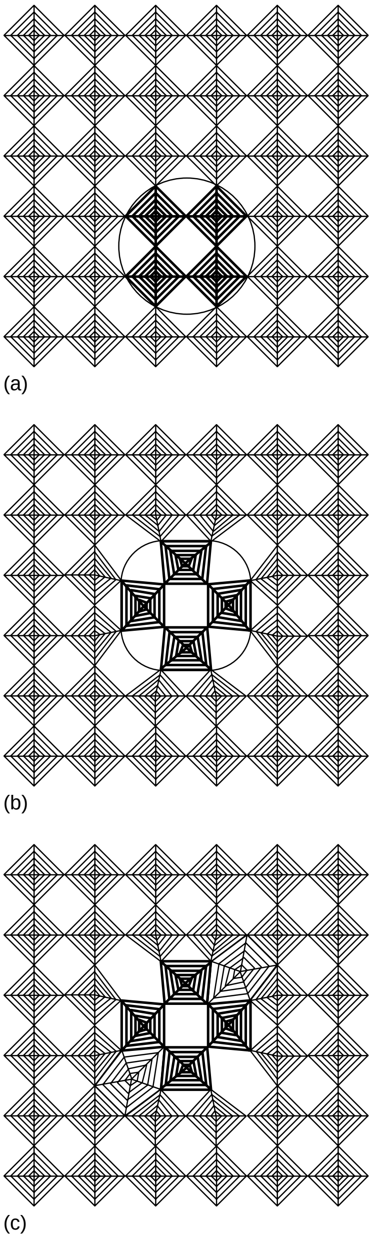
(a)

(b)

(c)

Figure 7 The generation of pentagonal columns in the WO_3 structure. Blocks of four octahedra, circled in (a), are rotated by 90° in (b) to produce four pentagonal tunnels. Filling of these tunnels by O-M-O chains produces pentagonal columns, two of which are shaded in (c)

8.6 Pentagonal Column and Related Phases

The extended defects just described are planar structures. An increasing number of solids are being described as made up of columnar elements of structure dispersed in a parent matrix. One of the best characterized of these materials are metal oxides that have, as their basic structural motif, the pentagonal column (PC). This unit consists of a ring of five MO_6 octahedra; the central pentagonal tunnel so formed being filled with an alternating chain of oxygen and metal atoms to form a pentagonal column (Figure 7). It is found that groups of PCs can coherently exist within a WO_3 or perovskite type of matrix. As a number of oxides adopt this structure or a distorted version of it, a wide range of PC phases can form. As in previous discussions, when the PC elements are perfectly ordered, one or more structurally related ordered phases such as Mo_5O_{14} or $Nb_{16}W_{18}O_{94}$ are generated. When the PC elements in the host structure are disordered, a nonstoichiometric compound is generated. Such disorder occurs, for example, when WO_3 is reacted with Nb_2O_5 for short periods at temperatures below about 1250 °C.

Walls of PC units can also intergrow with WO_3 to give ordered phases such as $U(Ta,W)_2O_8$ and others, which form in a number of U-W-M-O systems. Disordered materials in which the PC walls are unequally spaced are also common in samples prepared by solid-state synthesis.[20]

9 COMBINATIONS OF DEFECTS

In many crystals, several defect types contribute to the overall defect structure of the material. Three examples will be chosen as illustrative.

The intergrowth tungsten bronzes are typified by those found in the K_xWO_3 system. When the amount of potassium is less than the minimum needed to form the hexagonal tungsten bronze structure, $x < 0.19$, an intergrowth between the hexagonal tungsten bronze structure and WO_3 is found. The strips of hexagonal structure are normally two tunnels in width. Intergrowth tungsten bronzes are also known in other systems, including Rb-, Cs-, Ba-, Sn-, and Pb-WO_3. In the nonalkali metal intergrowth bronzes, single tunnels are preferred. In all these phases, the separation of the strips of hexagonal tunnels increases as the concentration of the large interpolated atoms decreases. Homologous series of compounds form when these are ordered. Defect structures consist of disorder in the disposition and widths of the lamellae of hexagonal tunnels and by the variable degree of filling of the hexagonal tunnels.

In the K_2NiF_4 series of phases described above, composition variation can take place by disorder in the width of the perovskite slabs, and the solid contains planar defects. In cases where the components of the intergrowth contain cations with a variable valence, additional defect structures can result. Many of these have been studied because of their physical properties, including $Sr_{n+1}V_nO_{3n+1-\delta}$ ($n = 1,2,3,\infty$), $La_2CuO_{4+\delta}$, $(La,Sr)_2CuO_{4+\delta}$, $La_2NiO_{4+\delta}$, $(La,Sr)_2NiO_{4+\delta}$ and phases in which the perovskite part of the structure contains Mn or Fe. In the oxygen rich compounds, the additional oxygen is in the form of interstitials. These oxygen defects are sometimes distributed at random, especially in the interlayer regions, while in some structures ordered arrangements have been reported. In phases that are oxygen poor, such as $Sr_2VO_{4-\delta}$ with δ taking values of 0.18, 0.29, 0.38, the oxygen deficit defects appear to be oxygen vacancies, which are distributed at random. In $LaSrNiO_{3.1}$ the oxygen vacancies appear to be ordered along one crystallographic direction. In $La_xSr_{2-x}FeO_{4\pm\delta}$, oxygen interstitials or oxygen vacancies, sometimes ordered, are found.

Unresolved complexity is found in the defect structures of the Bi and Tl containing superconducting oxides (*see* ***Superconductivity***). These compounds, closely related to the Aurivillius phases described above, form restricted homologous series, with formulae $TlBa_2Ca_{n-1}Cu_nO_{2n+3}$, $Tl_2Ba_2Ca_{n-1}Cu_nO_{2n+4}$ and $Bi_2Ba_2Ca_{n-1}Cu_nO_{2n+4}$ with $n =$ 1, 2 or 3. The Cu atoms are contained in perovskite-like sheets 1, 2, or 3 layers thick, joined by Bi–O or Tl–O layers. Crystals consist of intergrowths of more than one thickness of perovskite layer and planar defects are commonplace. Additionally, the variable valence of the Cu creates an oxygen vacancy population. The extent to which any oxygen defects can order is not yet clear, but it is becoming apparent that many are modulated structures (see Section 10).

10 DEFECT ELIMINATION AND ASSIMILATION: MODULATED STRUCTURES

In recent years, a rapidly increasing number of grossly nonstoichiometric solids have been characterized that are essentially free of macroscopic defect populations, owing to advances in crystallographic techniques.[21,22] In general, these materials have a (conventional) underlying structure and an additional component that is modulated in one, two, or three dimensions. It has been found that nonstoichiometry is accommodated by continuous adjustment of the modulated part of the structure. In cases in which the modulation period fits exactly with the underlying structure that is commensurate with it, a normal crystallographic phase forms. In cases where the modulation is not commensurate with the underlying structure, the phase is an incommensurately modulated phase. As the recognition of this class of materials is relatively new, the nomenclature is not yet stable,[23] and a variety of other terms, notably incommensurate structures, vernier structures, chimney-ladder structures, layer misfit structures, and infinitely adaptive structures are also current in the literature. Not all forms of modulation involve composition change, and only a small number of examples of modulated nonstoichiometric crystals are described here.

One of the prototypes of this behavior is the low-temperature form of tantalum pentoxide, L-Ta_2O_5. The structure of this phase is ill defined, even though it is a stoichiometric oxide, and the room temperature structure is a function of the prior thermal treatment temperature of the material. Reaction with other oxides, notably WO_3, ZrO_2 and Al_2O_3, gives rise to solids with a broad oxygen nonstoichiometry. However, each composition appears to generate a uniquely ordered structure, which have been termed *infinitely adaptive structures*.

The structures were originally described in terms of undulating chains of MO_7 pentagonal bipyramids, with a composition of M_3O_8. The cation coordination was described as a mixture of octahedral and pentagonal bipyramidal. Interstitial metal atoms situated in sites between sheets of pentagonal bipyramids were invoked to achieve the correct composition. It is now clear that the cations are in a hexagonal planar array and that the anion array is continuously modulated, and expands or contracts to fit the anion to cation ratio. In some places, the cation coordination is well represented by a pentagonal bipyramid, and in other places by an octahedron. Elsewhere the coordination polyhedra can be described as distorted variants of these.

Vernier structures have two interpenetrating substructures. One of these expands or contracts as a smooth function of composition, while the other remains relatively unchanged. Over much of the composition range, these are not in register, giving rise to an incommensurate structure with enormous ‘unit cells’. Typical of this group are the barium–iron sulphides of formula $Ba_xFe_2S_4$, with x taking values from 1.0 to approximately 1.25, as in, for example, $Ba_{1.1250}Fe_2S_4$, $Ba_9(Fe_2S_4)_8$. Across the composition range of these phases, the Ba atoms are distributed evenly between rods of composition Fe_2S_2. The density of packing of the Ba chains fluctuates as a smooth function of the composition. As with other metallic solids, charge compensation relied upon electron delocalization. The Sr_xTiS_3 phases, where x can vary between 1.05 and 1.22, seems to be structurally similar.

The misfit layer compounds are typified by materials with a formula $MS_{1+x}(TS_2)_m$, in which T is a transition metal atom, Ti, V, Cr, Nb, or Ta, and M is a large atom such as Sn, Pb, Bi, with stereochemically active electron lone pairs, or a lanthanide. The structures are built from S-T-S layers, in which the metal T takes trigonal-prismatic coordination. These layers are interleaved with layers of the halite structure, usually two or three atom layers in thickness, with composition MS_x. This leads to a chemical formula of $[MS_x]_n(TS_2)_m$, where n varies from approximately 1.08–1.24, and m takes values of 1–3, depending upon the nature of T and M. A typical example is the compound $[(Ln_{1/3}Sr_{2/3}S)_{1.5}]_{1.15}$ NbS_2. In all of the misfit layer compounds, the lattice parameter of the interpolated halite layers fit one lattice parameter of the TS_2 layer but not the other, so that in this direction, the match is irrational, and the MS_x layers are incommensurate with the (TS_2) layers in one direction. The nonstoichiometric variation of metal to sulphur ratio is not due to point defects or aggregates of these, but simply lies with the misfit between the two portions of the structure. Many other nonsulphide misfit layer structures are known.

The way in which the structures of nonstoichiometric phases have been revised, as better crystallographic techniques become available, is well illustrated the anion-excess fluorite-related systems. The prototypes of this family are formed in the YOF-YF_3 system, where it was originally believed that a solid solution existed over the approximate composition range $MX_{2.125}$ to $MX_{2.250}$. Careful powder X-ray diffraction replaced this idea with the idea that a homologous series of compounds with a general formula $Y_nO_{n-1}F_{n+2}$ might occur. Single-crystal studies refined the structures sufficiently for a vernier effect to be suggested. In this, the positions of the metal atoms were similar to those found in the fluorite parent structure. The anions were thought to take two forms, either as square nets, or as hexagonal nets. The square nets are identical to those found in the parent fluoride structure. The hexagonal nets are able to accommodate more anions per unit length that the square nets, so that as the anion stoichiometry changes, the ratio of the square to hexagonal nets alters. The coincidence of the anion and cation substructures (the pitch of the vernier), gave a measure of the unit cell of the phase. A similar evolution of understanding has occurred with $Nb_2Zr_{x-2}O_{2x+1}$, in which x takes values 7.1–12.0, (corresponding to $MX_{2.1409}$ to $MX_{2.0833}$) and $ZrO_{2-x}F_{2x}$.

The vernier model also turned out to be an approximation. It is now clear that although the metal atoms in these structures are similar to that found in the fluorite parent structure, the anion array is continuously modulated, and expands or contracts throughout the structure to fill the space optimally with respect to the chemical and crystallographic constraints that apply. Although for some modulation wavelengths the anion array is well described in terms of a square net or a hexagonal net, this is not universally correct, and the modulated description is a more accurate representation of the anion substructure.

Although modulation of the anion substructure occurs frequently in anion-excess fluorite structures, it may not be the unique mode of accommodating the stoichiometric imbalance. The phase $CeN_{0.222}O_{0.667}F_{1.333}$ prepared via shorter heating times produces a material that contains defect clusters. These are statistically distributed, in an anisotropic way, among the square anion-net planes of the parent fluorite structure. Long annealing of the sample causes these defect clusters to be assimilated into the structure.

Apart from annealing times, the structures described above are also sensitive to the preparation temperature. This is well illustrated by phases in the Bi_2O_3–TeO_2 system. At high temperatures, a nonstoichiometric anion-deficient fluorite structure seems to be stable between the composition limits Bi_2TeO_5 and $Bi_2Te_2O_7$, ($MO_{1.6667}$–$MO_{1.7500}$). This broad nonstoichiometric phase range transforms to a modulated structure at lower temperatures. In this phase, the metal atoms are in the normal fluorite array, and the anions form a modulated net that flexibly adapts to the overall cation to anion ratio. The defects that are responsible for the high-temperature phase have yet to be clarified.

There is little doubt that many materials that at present are described as containing ordered arrays of point or extended defects will be successfully described as notionally defect-free modulated structures. For example, the intergrowth Aurivillius phases, described as containing extended planar defects, have recently been described compactly as modulated structures.[24,25] The same formalism has been applied to hexagonal perovskite structures[26,27] and superconducting copper oxides.[28] Others will certainly follow.

11 RELATED ARTICLES

Alloys; Borates: Solid-state Chemistry; Carbides: Transition Metal Solid-state Chemistry; Chalcogenides: Solid-state Chemistry; Diffraction Methods in Inorganic Chemistry; Electronic Structure of Solids; Fluorides: Solid-state Chemistry; Halides: Solid-state Chemistry; Intercalation Chemistry; Ionic Conductors; Magnetic Oxides; Magnetism of Extended Arrays in Inorganic Solids; Nitrides: Transition Metal Solid-state Chemistry; Noncrystalline Solids; Oxide Catalysts in Solid-state Chemistry; Oxides: Solid-state Chemistry; Quasicrystals; Semiconductor Interfaces; Solids: Characterization by Powder Diffraction; Solids: Computer Modeling; Superconductivity; Surfaces.

12 REFERENCES

1. R. J. D. Tilley, Defects in Solids, in ‘Encyclopedia of Inorganic Chemistry’, 1st edn., John Wiley & Sons, Chichester, 1995, and references therein.
2. C. R. A. Catlow and G. D. Price, *Nature*, 1990, **347**, 243.
3. C. R. A. Catlow, J. D. Gale, and R. W. Grimes, *J. Solid State Chem.*, 1993, **106**, 13.
4. G. G. Libowitz, Defect Equilibria, in Solids, in ‘Treatise on Solid State Chemistry’, ed. N. B. Hannay, Plenum Press, New York, London, 1975, Vol. 1, Chap. 6, p. 335.
5. J. K. Burdett and J. F. Mitchell, *Prog. Solid State Chem.*, 1995, **23**, 131.
6. R. L. Withers, M. James, and D. J. Goosens, *J. Solid State Chem.*, 2003, **174**, 198.
7. J. Mizusaki, M. Okayasu, S. Yamauchi, and K. Fueki, *J. Solid State Chem.*, 1992, **99**, 166.
8. J. P. Hodges, S. Short, J. D. Jorgensen, X. Xiong, B. Dabrowski, S. M. Mini, and C. W. Kemball, *J. Solid State Chem.*, 2000, **151**, 190.
9. V. Pike, S. Patraw, A. L. Diaz, and B. G. DeBoer, *J. Solid State Chem.*, 2003, **173**, 359.
10. J.-G. Park and A. N. Cormac, *J. Solid State Chem.*, 1996, **121**, 278.
11. S. K. Haydon and D. A. Jefferson, *J. Solid State Chem.*, 2002, **168**, 306.
12. V. I. Nickolaichik, S. Amelinckx, L. A. Klinkova, N. V. Barkovskii, O. I. Lebedev, and G. Van Tendeloo, *J. Solid State Chem.*, 2002, **163**, 44.
13. R. L. Withers, J. G. Thompson, N. Gabbitas, R. L. Wallenberg, and T. R. Welberry, *J. Solid State Chem.*, 1995, **120**, 290.
14. D. R. Veblen, *Am. Mineral.*, 1991, **76**, 801.
15. D. R. Veblen, Electron Microscopy applied to Nonstoichiometry, Polysomatism and Replacement Reactions in Minerals, in ‘Reviews in Mineralogy’, ed. P. R. Buseck, Mineralogical Society of America, 1992, Chap. 6, p. 181.
16. Y. Takéuchi, ‘Tropochemical Cell-Twinning’, Terra Scientific, Tokyo, 1997.
17. P. C. Bougerol, M. F. Gorius, and I. E. Grey, *J. Solid State Chem.*, 2003, **169**, 131.
18. I. E. Grey, L. M. D. Cranswick, C. Li, L. A. Bursill, and J. L. Peng, *J. Solid State Chem.*, 1998, **138**, 74.
19. G. Van Tendeloo, B. Domengès, M. T. Caldes, M. Hervieu, and B. Raveau, *J. Solid State Chem.*, 1994, **112**, 161.
20. C. Askeljung and M. Sundberg, *J. Solid State Chem.*, 1999, **144**, 152.
21. R. L. Withers, S. Schmid, and J. G. Thompson, *Prog. Solid State Chem.*, 1998, **26**, 1.
22. G. A. Weigers, *Prog. Solid State Chem.*, 1996, **24**, 1.
23. G. Chapuis, M. Farkas Janhnke, J. M. Perez-Mato, M. Senechal, W. Steurer, C. Janot, D. Pandy, and A. Yamamoto, *Acta Crystallogr., Sect. A*, 1997, **53**, 95.
24. P. Boullay, G. Troillard, and D. Mercurio, *J. Solid State Chem.*, 2002, **164**, 252.
25. P. Boullay, G. Troillard, and D. Mercurio, *J. Solid State Chem.*, 2002, **164**, 261.
26. G. Troillard, N. Tènéze, P. Boullay, M. Manier, and D. Mercurio, *J. Solid State Chem.*, 2003, **173**, 91.
27. P. Boullay, N. Tènéze, G. Troillard, D. Mercurio, and J. M. Perez-Mato, *J. Solid State Chem.*, 2003, **174**, 209.
28. M. Huvé, G. Van Tendeloo, S. Amelinckx, M. Hervieu, and B. Raveau, *J. Solid State Chem.*, 1995, **120**, 332.

Dielectric Polarizabilities of Oxides & Fluorides

Robert D. Shannon
DuPont Company, Wilmington, DE, USA

1 Introduction 1
2 Polarizabilities of Simple Oxides 2
3 Ion Polarizabilities 2
4 Estimation of Dielectric Constants 6
5 References 7

1 INTRODUCTION

Dielectric polarizabilities are useful for prediction of dielectric constants of new materials and compounds whose dielectric constants have not been measured, and in calculations of energies of the formation and migration of defects.[1,2] In addition, deviations from the polarizability additivity rule are useful in understanding certain physical properties such as thermodynamic functions[3] and ionic and electronic conductivity.[4–6]

Polarizabilities measure the response of ions or atoms to an electric field. Electronic polarizabilities, α_e, arise from deformation of the electron cloud relative to the nucleus and are given by the Lorenz–Lorentz equation:[7,8]

$$\alpha_e = 1\, b \left[(V_m) \frac{(n^2 - 1)}{(n^2 + 2)} \right] \tag{1}$$

where V_m is the molar volume, n is the refractive index, and b is assumed to be $4\pi/3$. Ionic polarizabilities, α_i, which arise from relative movements of positive and negative ions in ionic or partly ionic crystals, cannot be calculated or measured directly.

Dielectric polarizabilities, α_D, defined by Roberts,[9] include both ionic and electronic components, and are related to the measured dielectric constant, κ', by the Clausius–Mosotti (C–M) equation:

$$\alpha_D = \alpha_e + \alpha_i = 1\, b \left[(V_m) \frac{(\kappa' - 1)}{(\kappa' + 2)} \right] \tag{2}$$

where κ', the real part of the complex dielectric constant, is measured in the range 1 kHz to 10 MHz.[9–11] Assumption of point dipole ions and cubic symmetry leads to $b = 4\pi/3$.[12,13] The Clausius–Mosotti equation is strictly valid only for compounds where the molecule or ion has cubic symmetry, but has been found to be approximately valid for a number of noncubic crystals.[9,10,14–18]

The molecular polarizability of a complex substance can be broken up into the molecular polarizabilities of simpler substances according to

$$\alpha(M_2M'X_4) = 2\alpha(MX) + \alpha(M'X_2) \tag{3}$$

This rule can be applied to both electronic and dielectric polarizabilities, but here we discuss the rule only insofar as it applies to dielectric polarizabilities. The molecular or oxide additivity rule has been applied to hydrates,[19,20] to the compounds $MTiO_3$ where M = Mg, Ca, Sr, and Ba,[21] to dolomite ($CaMg(CO_3)_2$), zircon ($ZrSiO_4$), and spinel ($MgAl_2O_4$),[22] to several titanates and zirconates and $KMgF_3$,[11] and to a variety of minerals.[14]

Molecular polarizabilities of complex substances can also be broken up into ion polarizabilities according to

$$\alpha(M_2M'X_4) = 2\alpha(M) + \alpha(M') + 4\alpha(X) \tag{4}$$

Sets of empirical electronic ion polarizabilities, α_e, were derived from the Lorenz–Lorentz relation and the additivity rule using the alkali halides and alkaline earth chalcogenides by many investigators[23–26] and using a variety of minerals by Lasaga and Cygan.[14] These polarizabilities were found to be useful in predicting refractive indices.

A set of 18 dielectric ion polarizabilities, α_D, derived from cubic compounds by Roberts,[9] assuming $\alpha_D(O^{2-}) = 2.387\,\text{Å}^3$ was found to give agreement between observed and calculated total compound polarizabilities of ∼5%. A second set of 11 dielectric ion polarizabilities was derived by Lasaga and Cygan,[14] assuming $\alpha_D(O^{2-}) = 2.37\,\text{Å}^3$ for application to minerals. Using these ion polarizabilities, agreement between observed and calculated total polarizabilities of 24 common minerals was ∼10% with some individual deviations as large as 20%.

Although molecular polarizabilities are known with precision, the apportionment between cation and anion polarizabilities is a difficult problem. This situation is analogous to the apportionment of cation and anion crystal radii. Roberts[9] arbitrarily assumed $\alpha_D(O^{2-}) = 2.387\,\text{Å}^3$ whereas Lasaga and Cygan[14] did not specify the source of their value of $2.37\,\text{Å}^3$.

Unlike studies on electronic polarizabilities, we have no calculated values of ion dielectric polarizabilities to rely on. One approach is to estimate a value for the maximum polarizability of oxygen. Thus, $\alpha_D(O^{2-})$ can be derived from an oxide whose total polarizability is contributed primarily by the polarizability of O^{2-}. Because B^{3+} has the lowest polarizability of the commonly occurring cations, the ideal choice would be B_2O_3. Using $\alpha_D(B_2O_3) = 6.15\,\text{Å}^3$ derived from Be_2BO_3OH, $CaB_2Si_2O_8$, $MgAlBO_4$, $Zn_4B_6O_{12}$, and BaB_2O_4,[17] we find $\alpha_D(O^{2-}) < 2.05\,\text{Å}^3$. The next most useful reliable compound is BeO. From BeO, we fix $\alpha_D(O^{2-})$ at a value which does not result in a negative cation polarizability, i.e. $\alpha_D(O^{2-}) < 2.213\,\text{Å}^3$.

Alternatively, we can assume the values of $\alpha_D(Be^{2+})$ and $\alpha_D(O^{2-})$ to be related by the r^3 law[27] ($\alpha \propto r^3$) using BeO and a variety of simple oxides with both 'bonded radii'[28] and crystal radii.[29] Using this scheme, $\alpha_D(O^{2-})$ varies from 1.97 Å^3(BeO) to 2.55 Å^3 (CaO) using bonded radii and 2.15 Å^3 (BeO) to 2.87 Å^3 (CaO) using crystal radii. Thus, using bonded radii we would choose a value of $\alpha_D(O^{2-}) = 2.0\text{–}2.5\,\text{Å}^3$. Using both criteria, we arrive at a value of $\alpha_D(O^{2-})$ between 2.0 and 2.3 Å^3. As for crystal radii, oxygen polarizability appears to depend on interatomic distance, but as we shall see, it is often convenient to assume a constant oxygen polarizability.

Most of the early studies of electronic polarizabilities assumed cation and anion polarizabilities that do not vary with the crystal environment. However, Tessman *et al.*[23] noted considerable variation of the oxide ion polarizability ($\alpha_e(O^{2-}) = 0.9\text{–}3.2\,\text{Å}^3$) and were able to correlate this variation with the volume occupied by the oxygen ion. Other investigators subsequently noted the dependence of experimental oxygen polarizabilities on their environment in the crystal.[30,31] Ruffa[32] concluded that anion polarizabilities were strongly increased as lattice interaction decreased, and Wilson and Curtis[24] found a significant dependence of anion polarizabilities on interatomic distances in alkali halides. Coker[25] found significant improvement in agreement between calculated and observed molar polarizabilities for alkali halides and alkaline earth chalcogenides when the anion polarizability was allowed to vary; large increases in anion polarizability were observed as the size of the cation was increased. More recently, Mahan,[33] in a theoretical study, found constant cation polarizabilities but concluded that anion polarizabilities are affected by their crystalline environment.

2 POLARIZABILITIES OF SIMPLE OXIDES

Oxide dielectric polarizabilities can be measured directly from dielectric constants of some of the simple oxides using the Clausius–Mosotti relation (equation 2) or derived indirectly from the dielectric constants of complex oxides and the oxide additivity rule (equation 3). Table 1 summarizes the accurately known values of oxide polarizabilities. These values can be used to check the oxide additivity rule.

Table 2 shows that agreements between observed dielectric polarizabilities and those calculated from the sum of the oxide polarizabilities according to equation (3) are typically 1%. This excellent agreement indicates that oxide polarizabilities can be used in conjunction with the C–M relationship to predict dielectric constants of many compounds.

Table 1 Mean dielectric constants and molar polarizabilities of simple oxides

Compound	$\langle \kappa' \rangle$	V_m (Å^3)	α_D (Å^3)^a
Li_2O	8.06	24.51	4.11
Na_2O	–	–	5.59 E
K_2O	–	–	10.91 E
BeO	7.16	13.79	2.213
MgO	9.830	18.69	3.331
CaO	11.95	27.83	5.22
SrO	14.5	33.16	6.48
BaO	31.1	42.48	9.22
ZnO	8.49	23.55	4.01
NiO	11.9	18.21	3.41
CoO	12.9	19.30	3.67
FeO	–	–	4.18 D
MnO	18.70	22.00	4.49
B_2O_3	–	–	6.15 D
Al_2O_3	10.126	42.45	7.627
Ga_2O_3	–	–	8.80 D
V_2O_3	–	–	8 E
Cr_2O_3	12.60	48.10	9.12
Fe_2O_3	–	–	10.5 D
In_2O_3	8.9	64.72	11.20
Sc_2O_3	13	59.64	11.39
Y_2O_3	11.4	74.50	13.81
Lu_2O_3	12.5	70.10	13.27
Er_2O_3	13.0	73.33	14.00
Ho_2O_3	13.1	74.57	14.2
Dy_2O_3	13.1	75.86	14.51
Tb_2O_3	13.3	77.19	14.81
Gd_2O_3	13.6	79.01	15.24
Eu_2O_3	13.9	80.05	15.50
Nd_2O_3	–	85.01	16.3 D
La_2O_3	–	–	17.7 D
Ce_2O_3	–	–	17.3 E
SiO_2	4.559	37.66	4.878
GeO_2	–	–	5.45 D
TiO_2	117	31.21	7.26
ZrO_2	–	35.1	7.30 D
P_2O_5	–	–	12.44 D
V_2O_5	–	–	15.8 D
H_2O (ice I)	3.2	32.15	3.25
H_2O (liquid)	4.2	29.8	3.5
CO_2 (solid)	1.70	73.04	4.52
CO_2 (liquid)	1.60	79.82	3.18

^{a}E = estimated: D = derived from complex oxides.

3 ION POLARIZABILITIES

According to equation (4), total molar dielectric polarizability of a compound can be calculated (α_{calc}) as a simple linear combination of individual ion polarizabilities, α(ion):

$$\alpha_{calc} = \sum_{I=1}^{N} n\,\alpha(\text{ion}) \tag{5}$$

Here, I varies over the total number (N) of types of ions (I) in the formula unit and n is the number of ions of type I

Table 2 Comparison of observed and calculated single crystal dielectric properties of well-behaved compounds

	Observed and calculated polarizabilities from oxide polarizabilities[a]			Observed and calculated dielectric constants from ion polarizabilities[b]		
Compound	α^{T}_{calc}	α^{T}_{obs}	Δ (%)	κ'_{calc}	κ'_{obs}	Δ (%)
Borates						
BaB_2O_4	15.37	14.44	−6.4	6.14	6.05	−1.6
$MgAlBO_4$	10.24	10.18	−0.6	8.16	8.07	−1.0
Be_2BO_3OH	–	8.80	–	4.71	4.82	+2.2
$CaB_2Si_2O_8$	21.13	21.29	+0.8	6.50	6.74	+3.6
$CaBSiO_4OH$	14.27	14.36	+0.6	7.36	7.34	+0.3
Aluminates						
$BeAl_2O_4$	9.84	9.87	+0.3	8.75	8.93	+2.0
$MgAl_2O_4$	10.96	11.10	+1.3	7.82	8.18	+4.4
$Y_3Al_5O_{12}$	39.79	39.38	−1.0	10.68	10.60	−0.8
$Lu_3Al_5O_{12}$	38.97	38.68	−0.7	11.15	10.87	−2.6
$Er_3Al_5O_{12}$	40.07	39.39	−1.7	10.95	10.90	−0.4
$Ho_3Al_5O_{12}$	39.56	39.70	+0.4	11.12	10.92	−1.7
$Dy_3Al_5O_{12}$	40.84	40.10	−1.8	11.23	11.07	−1.4
$Tb_3Al_5O_{12}$	41.28	40.52	−1.9	11.42	11.13	−2.6
$Y_{1.5}Er_{1.5}Al_5O_{12}$	39.93	39.42	−1.3	10.86	10.76	−0.9
$Y_3Sc_2Al_3O_{12}$:Nd	43.64	43.48	−0.4	12.25	12.20	−0.4
$Gd_3Sc_2Al_3O_{12}$:Nd,Cr	45.73	45.35	−0.8	12.53	12.71	+1.4
AlOOH	–	5.02	–	8.75	8.44	−3.7
Gallates						
$CoGa_2O_4$	12.48	12.63	+1.2	9.19	9.20	+0.1
$Ho_{3.06}Ga_{4.94}O_{12}$	43.55	43.90	+0.8	12.05	12.38	+2.7
$Dy_{3.05}Ga_{4.95}O_{12}$	43.91	44.15	+0.5	12.09	12.36	+2.2
$Tb_{3.04}Ga_{4.96}O_{12}$	44.33	44.49	+0.3	12.35	12.40	+0.4
$Gd_{3.03}Ga_{4.97}O_{12}$	44.96	44.61	−0.8	12.32	12.18	−1.1
$Eu_{3.02}Ga_{4.98}O_{12}$	45.32	45.18	−0.3	12.54	12.46	−0.6
$Sm_{3.02}Ga_{4.98}O_{12}$	45.6	45.59	0.0	12.91	12.55	−2.8
$Nd_{3.01}Ga_{4.99}O_{12}$	46.88	46.4	−1.0	12.90	12.58	−2.4
$Y_3Sc_2Ga_3O_{12}$	45.30	45.42	+0.3	12.51	12.94	+3.3
$Sm_3Sc_2Ga_3O_{12}$	48.10	48.72	+1.2	13.30	13.67	+2.7
$La_{2.37}Nd_{0.07}Lu_{2.54}Ga_{3.00}O_{12}$	51.80	52.70	+1.7	13.73	14.40	+4.6
Silicates						
Li_2SiO_3	8.99	9.23	+2.6	6.79	6.70	−1.3
Be_2SiO_4	9.31	9.35	+0.5	6.11	6.22	+1.8
Mg_2SiO_4	11.54	11.54	0.0	7.01	7.00	−0.1
Fe_2SiO_4	13.24	13.25	0.0	8.99	8.77	−2.5
Mn_2SiO_4	13.86	14.26	+2.8	9.12	9.31	+2.0
$ZrSiO_4$	12.16	12.12	−0.3	11.58	11.50	−0.7
$BeAlSiO_4OH$	12.11	12.16	+0.4	6.62	6.64	+0.3
Germanates						
$Ca_3Ga_2Ge_3O_{12}$	40.96	40.84	−0.3	10.28	9.73	−5.6
$Ca_{0.9}Y_{1.88}Mg_{2.27}Ge_3O_{12}$	41.74	42.11	+0.9	10.26	10.35	+0.9
$CaY_{1.96}Nd_{0.04}Zn_2Ge_3O_{12}$	43.61	43.93	+0.7	11.30	11.32	+0.2
$Nd_{2.95}Mg_{1.48}In_{0.68}Ge_{1.32}O_{12}$	47.42	47.34	−0.2	11.59	11.86	+2.2
Phosphates, arsenates, vanadates						
$AlPO_4$	10.03	10.0	−0.3	4.60	4.56	−0.8
AlP_3O_9	22.47	22.49	+0.1	5.20	5.18	−0.3
YPO_4	13.12	12.99	−1.0	10.93	10.70	−2.2
$NaBePO_4$	11.23	11.50	+2.4	6.04	6.37	+5.1
$LiAlPO_4OH$	13.30	13.32	+0.2	8.08	7.77	−4.1
NdP_5O_{14}	39.25	39.24	0.0	6.32	6.33	+0.1
$YAsO_4$	–	13.15	–	8.86	8.07	−9.7
$LuAsO_4$	–	13.46	–	9.80	10.0	+2.0
$SmAsO_4$	–	14.47	–	9.18	9.08	−1.1
YVO_4	14.80	14.94	+0.9	11.40	11.98	+4.8
$LuVO_4$	14.53	14.09	−3.1	12.65	10.93	−15.7
$NaCa_2Mg_2V_3O_{12}$	43.75	43.62	0.0	10.34	10.32	−0.2

[a]Using the C–M equation and oxide polarizabilities from Table 1. [b]Using the C–M equation and ion polarizabilities from column 2 of Table 3.

in the formula unit.[34] With sufficient measurements of α_{obs}, ion polarizabilities, $\alpha(\text{ion})$, can be used as a set of refinable parameters in a least squares procedure which minimizes the function:

$$\sum_{i=1}^{M} w_i(\alpha_{\text{obs}} - \alpha_{\text{calc}})^2 \tag{6}$$

Here i varies over the number of measurements of α_{obs} for a variety of compounds and $w_i = \sigma_i{}^{-2}$, where σ_i is the estimated % error in the experimental dielectric constant. In practice it is necessary to fix one polarizability, preferably in such a way that its errors do not seriously affect the overall errors of the other ions; we have arbitrarily assumed the value for $\alpha_{\text{D}}(\text{B}^{3+}) = 0.05\,\text{Å}^3$. This assumption results in $\alpha_{\text{D}}(\text{O}^{2-}) = 2.01\,\text{Å}^3$.

As discussed in Section 1, both theoretical and experimental oxygen electronic polarizabilities depend on their crystalline environments.[33,35–38] The fluoride ion polarizability is less dependent on near-neighbor distances than that of the oxide ion. An oxide ion polarizability dependence on V_{ox}, the volume occupied by the oxygen, is consistent with the concept of bonded radii devised by Gibbs and Boisen,[28] where anion radii vary with the bond length of the M–O bond and V_{ox} increases from $13.8\,\text{Å}^3$ in BeO to $27.8\,\text{Å}^3$ in CaO; $\alpha_{\text{D}}(\text{O}^{2-})$ increases from $1.94\,\text{Å}^3$ to $2.57\,\text{Å}^3$. The oxide radius in compounds containing Na–O bonds is 1.22 Å, whereas the oxide radius in compounds containing tetrahedral Si–O bonds is 0.95 Å. Thus, the concept of cation electronic polarizabilities that are constant and oxygen ion polarizabilities that vary approximately with lattice constant and oxygen molar volume is well established.

3.1 Oxygen Polarizability Independent of Oxygen Molar Volume

In one scheme, oxygen dielectric polarizabilities, $\alpha_{\text{D}}(\text{O}^{2-})$ are assumed not to depend on oxygen molar volume, V_{ox}. Dependence of $\alpha_{\text{D}}(\text{O}^{2-})$ on V_{ox}, as described by Tessman *et al.*,[23] shows up as greater deviations from additivity in compounds having larger interatomic distances and large oxygen molar volumes, such as SrO ($V_{\text{ox}} = 33.2\,\text{Å}^3$) and BaO ($V_{\text{ox}} = 42.4\,\text{Å}^3$). This scheme has the advantage of simplicity of application and is, in general, valid for most oxidic compounds which generally have $V_{\text{ox}} = 15–25\,\text{Å}^3$.

The results from least squares refinements of $\alpha_{\text{D}}(\text{ion})$ made using experimental polarizability data from 129 oxides and 25 fluorides[34] are given in Table 3. The second column in Table 3 was calculated by fixing the parameters m and N in equation (7) at 0.001 and 1.0, respectively. The polarizabilities listed in this column are recommended for use with most oxides and fluorides, and in particular, for calculation of dielectric constants.

Although ignoring the oxygen molar volume correction allows more rapid calculation of estimated dielectric constants, the additivity deviations (Δ) are larger for compounds such as SrO ($\Delta = -3.3\%$) and BaO ($\Delta = -8.6\%$) with $V_{\text{ox}} > 25\,\text{Å}^3$. Most of the calculated uncertainties in refined ion polarizabilities are small, i.e. $<0.01\,\text{Å}^3$. These uncertainties are unrealistically low; a more reasonable estimate of the uncertainty is $\sim 0.05\,\text{Å}^3$ for the smaller ions such as Al^{3+} and Si^{4+} and $\sim 0.1\,\text{Å}^3$ for larger ions such as Ca^{2+} and Y^{3+}. In cases such as Cs^+, Tl^+, Co^{2+}, Ni^{2+}, Cu^{2+}, Eu^{2+}, Sb^{3+}, Ce^{3+}, Ce^{4+}, Zr^{4+}, As^{5+}, V^{5+}, Sn^{4+}, U^{4+}, Th^{4+}, and Nb^{5+}, the uncertainties are larger because the ratio of the number of observed molar polarizabilities to refined ion polarizabilities is rather low and the observed total polarizabilities have larger errors. Figure 1 shows a periodic table of ion dielectric polarizabilities prepared from column 2 of Table 3.

3.2 Oxygen Polarizability Dependent on Oxygen Molar Volume

In a slightly more complex scheme, $\alpha_{\text{D}}(\text{O}^{2-})$ is assumed to depend exponentially on V_{ox}, the volume occupied by an oxide ion, as proposed by Bussmann *et al.*[39] The parameter V_{ox} is easily calculated for all compounds whose structure is known. Then

$$\alpha_{\text{D}}(\text{O}^{2-}) = \alpha_{\text{D}_0}(\text{O}^{2-}) + m(V_{\text{ox}}^N) \tag{7}$$

where $\alpha_{\text{D}}(\text{O}^{2-})$ = polarizability of oxygen in a compound having oxygen molar volume, V_{ox}; $\alpha_{\text{D}_0}(\text{O}^{2-})$ = polarizability of oxygen at an arbitrary value of V_{ox}; and m, N = parameters to be fitted. Polarizabilities of cations and F^- are presumed to be independent of the compound in which the ions are found.

Assuming a linear relationship between $\alpha_{\text{D}}(\text{O}^{2-})$ and V_{ox} ($N = 1.0$) (see equation 7), m refines to a value of 0.022. This results in a better fit for SrO ($\Delta = +1.5\%$) and BaO ($\Delta = -3.1\%$). Using the stronger dependence of $\alpha_{\text{D}}(\text{O}^{2-})$ on oxygen molar volume given by the exponential relation (equation 7) results in a refined value of $N = 2.0$. This results in a slightly worse overall fit between observed and calculated total polarizabilities, but the fit to SrO ($\Delta = +0.02\%$), BaO ($\Delta = -2.4\%$), and most rare earth oxides is somewhat better. This set of ion polarizabilities[34] is included in column 1 of Table 3 for use with compounds having $V_{\text{ox}} > 25\,\text{Å}^3$.

3.3 Comparison with Previous Sets of Ion Polarizabilities

The set of dielectric polarizabilities found in Table 3 appears to be significantly different from the sets of Roberts[9] and Lasaga and Cygan.[14] However, the differences arise primarily because of the large difference in $\alpha_{\text{D}}(\text{O}^{2-})$: $2.01\,\text{Å}^3$ (Table 3) vs. $2.387\,\text{Å}^{3}$[39] or $2.37\,\text{Å}^3$.[14] Roberts and Lasaga and Cygan chose these latter values because they had no

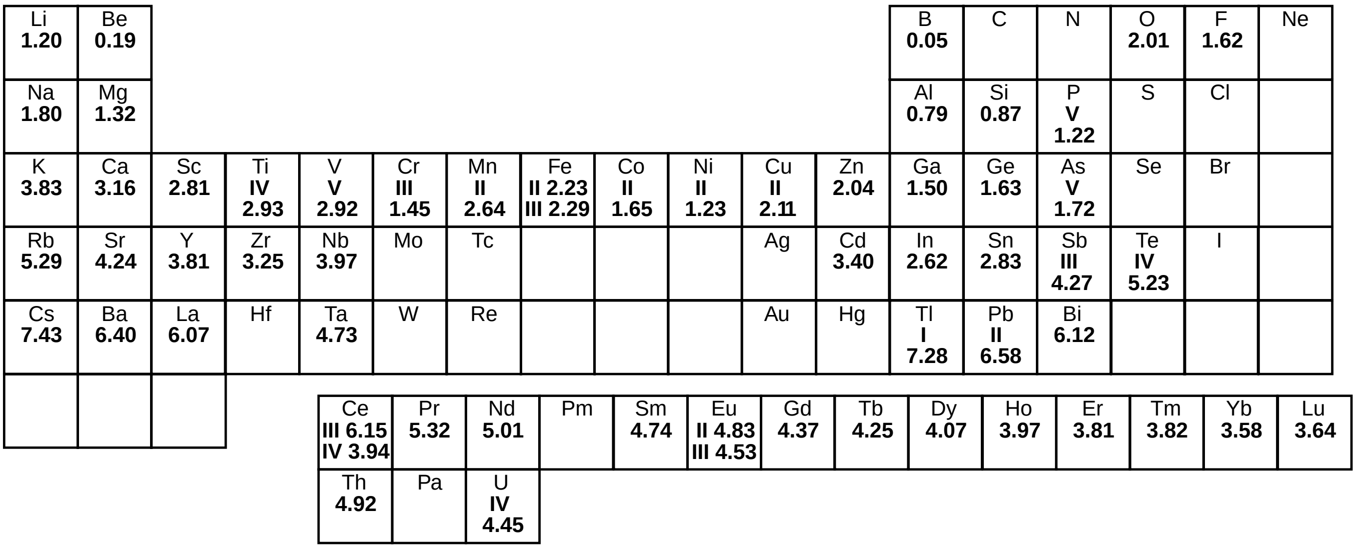

Li **1.20**	Be **0.19**											B **0.05**	C	N	O **2.01**	F **1.62**	Ne
Na **1.80**	Mg **1.32**											Al **0.79**	Si **0.87**	P **V** **1.22**	S	Cl	
K **3.83**	Ca **3.16**	Sc **2.81**	Ti **IV** **2.93**	V **V** **2.92**	Cr **III** **1.45**	Mn **II** **2.64**	Fe **II 2.23** **III 2.29**	Co **II** **1.65**	Ni **II** **1.23**	Cu **II** **2.11**	Zn **2.04**	Ga **1.50**	Ge **1.63**	As **V** **1.72**	Se	Br	
Rb **5.29**	Sr **4.24**	Y **3.81**	Zr **3.25**	Nb **3.97**	Mo	Tc				Ag	Cd **3.40**	In **2.62**	Sn **2.83**	Sb **III** **4.27**	Te **IV** **5.23**	I	
Cs **7.43**	Ba **6.40**	La **6.07**	Hf	Ta **4.73**	W	Re				Au	Hg	Tl **I** **7.28**	Pb **II** **6.58**	Bi **6.12**			

Ce **III 6.15** **IV 3.94**	Pr **5.32**	Nd **5.01**	Pm	Sm **4.74**	Eu **II 4.83** **III 4.53**	Gd **4.37**	Tb **4.25**	Dy **4.07**	Ho **3.97**	Er **3.81**	Tm **3.82**	Yb **3.58**	Lu **3.64**
Th **4.92**	Pa	U **IV** **4.45**											

Figure 1 Table of ion dielectric polarizabilities given in Å^3. (Reproduced by permission of the American Institute of Physics from R.D. Shannon.[34])

Table 3 Ion polarizabilities in oxides and fluorides

Ion	$m = 0.001$ $N = 2.00$ α_i (Å^3)	$m = 0.001$ $N = 1.00$ α_i (Å^3)	Ion	$m = 0.001$ $N = 2.00$ α_i (Å^3)	$m = 0.001$ $N = 1.00$ α_i (Å^3)
F^-	1.62	1.62	Lu^{3+}	3.65	3.64
O^{2-}	2.00	2.01	Yb^{3+}	3.55	3.58
OH^-	2.26	2.27	Tm^{3+}	3.78	3.82
Li^+	1.20	1.20	Er^{3+}	3.83	3.81
Na^+	1.80	1.80	Ho^{3+}	3.99	3.97
K^+	3.83	3.83	Dy^{3+}	4.10	4.07
Rb^+	5.29	5.29	Tb^{3+}	4.27	4.25
Cs^+	7.43	7.43	Gd^{3+}	4.38	4.37
Tl^+	7.28	7.28	Eu^{3+}	4.53	4.53
Be^{2+}	0.20	0.19	Sm^{3+}	4.74	4.74
Mg^{2+}	1.33	1.32	Nd^{3+}	5.01	5.01
Zn^{2+}	2.09	2.04	Pr^{3+}	5.31	5.32
Ni^{2+}	1.23	1.23	La^{3+}	6.03	6.07
Co^{2+}	1.66	1.65	Ce^{3+}	6.01	6.15
Fe^{2+}	2.23	2.23	Sb^{3+}	4.12	4.27
Cu^{2+}	2.11	2.11	Bi^{3+}	6.04	6.12
Mn^{2+}	2.64	2.64	Si^{4+}	0.88	0.87
Ca^{2+}	3.17	3.16	Ge^{4+}	1.59	1.63
Sr^{2+}	4.25	4.24	Ti^{4+}	2.94	2.93
Ba^{2+}	6.40	6.40	Sn^{4+}	2.84	2.83
Cd^{2+}	3.40	3.40	Zr^{4+}	3.25	3.25
Pb^{2+}	6.21	6.58	Ce^{4+}	3.94	3.94
Eu^{2+}	4.84	4.83	U^{4+}	4.45	4.45
B^{3+}	0.05	0.05	Th^{4+}	4.91	4.92
Al^{3+}	0.78	0.79	Te^{4+}	5.22	5.23
Ga^{3+}	1.50	1.50	P^{5+}	1.24	1.22
Cr^{3+}	1.45	1.45	As^{5+}	1.72	1.72
Fe^{3+}	2.28	2.29	V^{5+}	2.92	2.92
In^{3+}	2.62	2.62	Nb^{5+}	3.98	3.97
Sc^{3+}	2.80	2.81	Ta^{5+}	4.75	4.73
Y^{3+}	3.84	3.81			

data from borates or beryllates; use of $\alpha_D(O^{2-}) = 2.387\,\text{Å}^3$ results in negative polarizabilities for B^{3+} and Be^{2+}. The polarizabilities in Table 3 are more reliable because of the use of more accurate dielectric constants from a larger number of compounds involving more ions. The problem of relative values of cation and anion polarizabilities still remains, but based on the r^3 law and the concept of bonded radii the values obtained from the least squares procedure seem reasonable.

4 ESTIMATION OF DIELECTRIC CONSTANTS

Rewriting the C–M relation (equation 2) gives an expression for estimating the dielectric constant of a compound of known structure type:

$$\kappa' = \frac{(3V_m + 8\pi\alpha_D^T)}{(3V_m - 4\pi\alpha_D^T)} \tag{8}$$

where α_D^T = total dielectric polarizability. Total polarizabilities can be evaluated using either the oxide polarizabilities listed in Table 1 where they are available, or ion polarizabilities listed in Table 3. Table 2 compares the observed dielectric constants, κ'_{obs}, of a variety of borates, aluminates, gallates, silicates, germanates, phosphates, arsenates, and vanadates with the dielectric constants, κ'_{calc}, calculated from ion polarizabilities and equation (8). In general, the Clausius–Mosotti equation appears to allow estimation of mean dielectric constants of nonferroelectric oxides and fluorides having $V_{ox} < 25\,\text{Å}^3$ to within about 2% of their actual values.

Most nonferroelectric oxides and fluorides fall in this category of 'well-behaved' compounds, but some materials exhibit larger deviations.**[4,34]** Such deviations between observed and calculated dielectric constants can frequently be traced to factors which are known to increase κ': ionic or electronic conductivity, ferroelectric behavior, the presence of H_2O or CO_2 in channels or large cavities, or the presence of dipolar impurities other than H_2O. A further cause of large deviations from additivity is the presence of 'rattling' or 'compressed' cations having unusually large or small cation polarizabilities, respectively.

Table 4 illustrates examples of compounds showing substantial deviations of typical observed and calculated polarizabilities and dielectric constants. Poor agreement in the case of $KTiOPO_4$ is probably caused by motion of K ions which results in electrode polarization and consequent higher dielectric constants. Deviations from additivity occur even when the conductivity is negligible at room temperature.

Conductivity in $LiGaO_2$, $Ca_5(PO_4)_3F$, and PbF_2 occurs at high temperatures with the abnormally high polarizabilities, probably indicating residual cation or anion disorder present at room temperature. The deviation in PbF_2 is possibly caused by the disorder inherent in anion–Frenkel pairs. Dielectric constants of Fe_2SiO_4 (fayalite) vary widely. The example in

Table 4 Total polarizabilities and calculated dielectric constants of materials with large deviations from the additivity rule

Compound	$\langle\alpha^T_{obs}\rangle$	$\langle\alpha^T_{calc}\rangle$	δ (%)	$\langle\kappa'_{obs}\rangle$	$\langle\kappa'_{calc}\rangle$	δ (%)
Ionic and electronic conductors						
$KTiOPO_4$	20.6	18.9	+8.2	12.56	8.3	+34
$LiGaO_2$	7.0	6.7	+4.3	7.27	6.6	+9
$Ca_5(PO_4)_3F$	46.42	45.42	+2.2	9.67	8.85	+9
PbF_2	11.31	9.82	+13.2	29.3	10.3	+65
Fe_2SiO_4:Fe^{3+} (impure fayalite)	14.1	13.24	+6.3	14.1		
Dipolar impurities						
CaF_2:3% Er	6.90	6.48	+6.1	8.28	6.98	+16
SrF_2:1% Er	7.69	7.49	+2.6	6.90	6.48	+6
BaF_2:1% Er	10.34	9.63	+6.9	9.06	7.33	+19
Rattling cations						
$CaYAlO_4$	16.22	15.94	+1.7	19.67	16.7	+15
$LiAlSi_2O_6$	16.87	15.62	+7.4	8.96	7.38	+18
$K_{0.92}Na_{0.08}AlSi_3O_8$	25.61	23.77	+7.2	5.42	4.57	+13
$Mg_3Al_2Si_3O_{12}$	35.72	33.54	+6.1	12.20	9.19	+25
$CaAl_2Si_2O_8$	26.86	22.60	+15.8	7.14	4.70	+34
Epidote	42.73	38.40	+10.1	12.00	8.25	+31
$Ca_2Al_3Si_3O_{12}OH$	42.11	37.22	+11.6	11.80	8.00	+32
$Ca_2MgSi_2O_7$	27.90	23.53	+15.7	10.54	6.32	+23
$Ca_2ZnSi_2O_7$	28.03	24.21	+13.6	10.76	6.81	+24
Compressed cations						
$CaNdAlO_4$	16.84	17.18	−2.0	18.98	20.2	−7
$SrLaAlO_4$	18.07	19.14	−5.9	17.88	27.8	−55
$Ca_3Al_2Si_3O_{12}$	35.75	37.87	−5.9	8.71	10.5	−23

Table 4 is associated with high losses and the presence of Fe^{3+}, leading to space charge polarization.

The effect of RE^{3+}–F dipolar complexes on observed dielectric constants of RE-doped fluorites can be seen in Table 4. Polarizabilities and dielectric constants are elevated much more than would be anticipated from the introduction of the rare earth alone. For example, 1% ErF_3 substituted in BaF_2 raises the dielectric constant by 19%, compared to an expected reduction of $<0.5\%$.

Perhaps the most interesting deviations from additivity are associated with 'rattling' and 'compressed' cations. The 'rattling' cation effect has been described by Dunitz and Orgel**[40]** as a progressive 'loosening of the central cation at the center of its surrounding octahedron to off-center displacements characteristic of ferroelectric and antiferroelectric substances' as the size of the central cation in an octahedron decreases. Conversely, a 'tightening' of the central cation occurs as the size of the central cation in a polyhedron increases. In most structures, displacements of cations or anions result in polyhedral distortions. However, in certain structures, crystal symmetry prevents the distortion and the rattling cation phenomenon occurs. Table 4 shows examples of 'rattling' cations in $CaYAlO_4$, $LiAlSi_2O_6$ (spodumene), $K_{0.92}Na_{0.08}AlSi_3O_8$ (orthoclase), $Mg_3Al_2Si_3O_{12}$ (pyrope), $Ca_2Al_{2.5}Fe_{0.5}Si_3O_{12}OH$ (epidote), $Ca_2Al_3Si_3O_{12}OH$ (zoisite), $Ca_2MgSi_2O_7$ (akermannite), and $Ca_2ZnSi_2O_7$ (hardystonite).**[34]** Frequently associated with these large positive deviations of additivity are unusually large entropy and thermal vibration parameters, accompanied by smaller than normal apparent bond valences. Figure 2 shows the correlation between additivity deviations and apparent bond valence of the divalent ion in a series of silicate garnets of the type $M_3{}^{2+}M_2{}^{3+}Si_3O_{12}$. Figure 3 shows a similar plot for a series of melilite compositions of the type $M_2M'M''_2O_7$ where the apparent bond valences of the divalent M ions deviate significantly from the ideal value of 2.

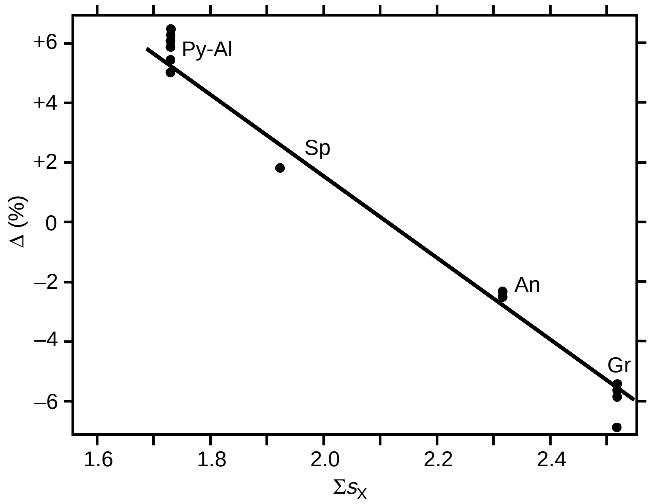

Figure 2 Deviations from the oxide additivity rule vs. apparent bond valence of the divalent ion in silicate garnets of the type $M_3M'_2Si_3O_{12}$. Py-Al = pyrope-almandine ($Mg_{2-x-y}Fe_xCa_yAl_2Si_3O_{12}$); Sp = spessartine ($Mn_3Al_2Si_3O_{12}$); An = andradite ($Ca_3Fe_2Si_3O_{12}$); Gr = grossular ($Ca_3Al_2Si_3O_{12}$). (Reproduced by permission of the Mineralogical Society of America from R.D. Shannon and G.R. Rossman, *Am. Mineral.*, **77**, 94)

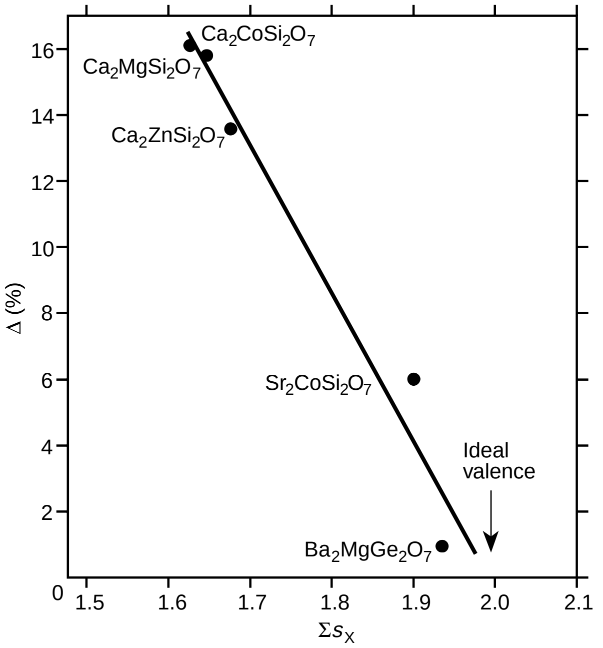

Figure 3 Deviations from the oxide additivity rule vs. apparent bond valence of the divalent M ions in a series of melilite compositions of the type $M_2M'M''_2O_7$. (Reprinted from R.D. Shannon, K. Iishi, T.H. Allikm, G.R. Rossman, and J. Liebertz, *Eur. J. Mineral.*, 1992, **4**, 1241. By permission of Schweizerbart'sche Verlagsbuchhandlung)

Examples of 'compressed' cations are Ca in $CaNdAlO_4$ and $Ca_3Al_2Si_3O_{12}$ (grossular) and Sr in $SrLaAlO_4$. Correspondingly, smaller than anticipated entropy in grossular and enhanced apparent bond valences of Ca and Sr in grossular, $CaYAlO_4$, and $SrLaAlO_4$ are observed.

5 REFERENCES

1. J. Yamashita and T. Kurosawa, *J. Phys. Soc. Jpn.*, 1954, **9**, 944.
2. A. C. Lasaga, *Am. Mineral.*, 1980, **65**, 1237.
3. R. D. Shannon and G. R. Rossman, *Am. Mineral.*, 1992, **77**, 94.
4. R. D. Shannon, 'NIST Special Publication', NIST, Washington, DC, 1991, No. 804, p. 457.
5. R. D. Shannon, M. A. Subramanian, S. Hosoya, and G. R. Rossman, *Phys. Chem. Mineral.*, 1991, **18**, 1.
6. R. D. Shannon and G. R. Rossman, *Phys. Chem. Mineral.*, 1992, **19**, 157.

7. L. Lorentz, *Annu. Phys. Chem.*, 1880, **11**, 70.
8. H. A. Lorenz, *Annu. Phys. Chem.*, 1880, **9**, 641.
9. R. Roberts, *Phys. Rev.*, 1949, **76**, 1215.
10. R. Roberts, *Phys. Rev.*, 1950, **77**, 258.
11. R. Roberts, *Phys. Rev.*, 1951, **81**, 865.
12. O. Anderson, *Fortschr. Mineral.*, 1974, **52**, 611.
13. J. Arndt and W. Hummel, *Phys. Chem. Mineral.*, 1988, **15**, 363.
14. A. C. Lasaga and R. T. Cygan, *Am. Mineral.*, 1982, **67**, 328.
15. R. D. Shannon, M. A. Subramanian, T. H. Allik, H. Kimura, M. R. Kokta, M. H. Randles, and G. R. Rossman, *J. Appl. Phys.*, 1990, **67**, 3798.
16. R. D. Shannon and M. A. Subramanian, *Phys. Chem. Mineral.*, 1989, **16**, 747.
17. R. D. Shannon, M. A. Subramanian, A. N. Mariano, T. E. Gier, and G. R. Rossman, *Am. Mineral.*, 1992, **77**, 101.
18. R. D. Shannon, R. A. Oswald, T. H. Allik, J. P. Damen, D. Mateika, B. A. Wechsler, and G. R. Rossman, *J. Solid State Chem.*, 1991, **95**, 313.
19. C. K. Cheng, *Phil. Mag.*, 1940, **30**, 505.
20. A. Heydweiller, *Z. Phys.*, 1920, **3**, 308.
21. G. H. Jonker and J. H. Van Santen, *Chem. Weekblad*, 1947, **43**, 672.
22. D. A. A. S. Rao Narayana, *Proc. Ind. Acad. Sci.*, 1949, **30A**, 317.
23. J. R. Tessman, A. H. Kahn, and W. Shockley, *Phys. Rev.*, 1953, **92**, 890.
24. J. N. Wilson and R. M. Curtis, *J. Phys. Chem.*, 1970, **74**, 187.
25. H. Coker, *J. Phys. Chem.*, 1976, **80**, 2078.
26. F. H. Claro, *Phys. Rev.*, 1978, **B18**, 7058.
27. J. Shanker, N. Kumar, and M. P. Verma, *Indian J. Pure Appl. Phys.*, 1973, **11**, 644.
28. G. V. Gibbs and M. B. Boisen, ‘Better Ceramics Through Chemistry II’, Materials Research Society, Pittsburgh, PA, 1986, p. 515.
29. R. D. Shannon, *Acta Crystallogr.*, 1976, **A32**, 751.
30. R. Kirsch, A. Gerard, and M. Wautelet, *J. Phys. C: Solid State Phys.*, 1974, **7**, 3633.
31. R. Migoni, H. Bilz, and D. Bauerle, *Phys. Rev. Lett.*, 1976, **37**, 1155.
32. A. R. Ruffa, *Phys. Rev.*, 1963, **130**, 1412.
33. G. D. Mahan, *Solid State Ionics*, 1980, **1**, 29.
34. R. D. Shannon, *J. Appl. Phys.*, 1993, **73**, 348.
35. P. W. Fowler and P. A. Madden, *J. Phys. Chem.*, 1984, **89**, 1035.
36. E. W. Pearson, M. D. Jackson, and R. G. Gordon, *J. Phys. Chem.*, 1984, **88**, 119.
37. P. W. Fowler and P. A. Madden, *Mol. Phys.*, 1983, **49**, 913.
38. P. W. Fowler and P. A. Madden, *Phys. Rev.*, 1984, **B29**, 1035.
39. A. Bussmann, H. Bilz, R. Roenspiess, and K. Schwarz, *Ferroelectrics*, 1980, **25**, 343.
40. J. D. Dunitz and L. E. Orgel, *Adv. Inorg. Chem. Radiochem.*, 1960, **2**, 1.

Diffraction Methods in Inorganic Chemistry

Judith A. K. Howard & Andrei S. Batsanov
University of Durham, Durham, UK

1 Introduction 1
2 Background to Diffraction Techniques 2
3 Applications of the Techniques 15
4 Interpretation of the Results 28
5 Conclusions 31
6 Related Articles 31
7 Further Reading 31
8 References 31

1 INTRODUCTION

Diffraction is a coherent scattering of waves (radiation) from an object, the size of which is comparable with the wavelength. The scattering must be elastic, that is, without a change of energy of the quantum and hence of the wavelength. In this case, the waves scattered from different parts of the object can interfere, in some directions reinforcing each other (when their phases coincide), in other directions canceling each other out (if the phases are opposite). Thus the diffraction pattern is a succession of peaks and troughs, from which one can extract information about the structure of the diffracting object. The sizes of atoms being of the order of 10^{-10} m, three types of radiation have comparable wavelengths: X rays, thermal neutrons, and electrons. Electron diffraction is widely used to determine the structures of molecules in gases, which give continuous diffraction patterns with relatively few features. Thus, only relatively simple molecules can be characterized. The crystal, on the other hand, is like a microscopic diffraction grating, with a long-range order (periodicity) of atoms and molecules in all three dimensions, therefore its diffraction pattern comprises a large number of sharp, well-separated peaks ('reflections'), carrying enough information to determine three-dimensional structures of even the most complex chemical species. This makes single-crystal diffraction methods (especially with X rays, which are the easiest to generate and detect) by far the most important technique for elucidating the structures, not only of inorganic solids, but also of molecular compounds generally. Neutron diffraction is even more informative than X ray, but the sources of neutrons are scarce and expensive. Electron diffraction is used mainly for structural studies of semicrystalline solids, textures, surface layers, contacts between phases and transitional structures, and so on.[1]

The importance of X-ray diffraction (XRD) in the history of chemistry is hard to overstate. When Laue's students Friedrich and Knipping first observed this effect in 1912,[2] the physical reality of atoms was still doubted; the diffraction photographs were the first *visible* proof of their existence. The structural chemistry of silicates, immensely important in mineralogy and geology, has been rationalized[3] entirely by X-ray crystallography: the classical chemical and spectroscopic analyses could do nothing with these insoluble materials. The chemistry of boranes and organometallic π-complexes after 1950 and of metal clusters since 1960s, with their repercussions in the theory of the chemical bond, were only possible because X-ray diffraction provided a ready technique for fast characterization of such compounds. In fact, the first cluster ($[Ta_6Cl_{12}]Cl_2 \cdot 7H_2O$) had been synthesized in 1907,[4] and the first d metal π-complex (Zeise's salt, $K[PtCl_3(H_2C{=}CH_2)]$) in 1827,[5] but the nature of either was not understood until the X-ray studies in 1950[6] and 1954,[7] respectively. The surprising structures of ferrocene and fullerene had been suggested by chemists' intuition, but X-ray studies provided the ultimate confirmation. Indeed, fullerene must have been produced by the ton in the late 19th century, when Voltaic arcs between carbon electrodes were the principal method of public lighting, but even had somebody managed to isolate it, there would have been no means of studying it at that time. Such achievements are possible, because in a good single-crystal X-ray diffraction experiment, the experimental observations outnumber the unknowns (atomic coordinates and vibrational parameters) by a factor of 10. In this, XRD is unique among physical methods, which often have more unknown than known parameters. Thus, XRD requires no a priori model to solve a structure and therefore can cope with a totally novel and unexpected product, while structure determination by spectroscopic methods relies basically on comparison with known 'fingerprints' for certain moieties, linkage types, and so on.

X-ray (as well as neutron) crystallographers elegantly exploited many technological and computational advances in the last decades. Before 1960, solving a structure of moderate complexity required months, sometimes years, of hard work. In the 1970s, automated diffractometers, (mainframe) computers, and new software reduced this time to weeks or even days, and X-ray crystallography evolved from the method of last resort to a routine technique of chemical analysis with affordable timescale. As such, X-ray diffraction became economically advantageous over more traditional methods, notwithstanding large capital investment in the equipment. Crucially, XRD requires very little material: a complete structure determination can be made with a crystal of 0.01 mg or less without necessarily destroying even that. Since the first edition of the EIC, massive replacement of point detectors with area detectors again reduced the duration of the experiment, from days to hours. With an exponential accumulation of structural results and emergence of online databases providing easy access to them,[8] it is now practical to obtain novel results (structural correlations)[9] by statistical analysis of the structures already known, rather than the experiment itself being the sole object of the research program (see Section 4).

This article is divided into three major sections: background to the techniques, their practical aspects, and inspection of the results. No attempt has been made to repeat the excellent textbooks, both classical and new, which expound the complete theory of X-ray or neutron diffraction and full details of the experimental techniques.[10–22] Our aim is to give the reader (an inorganic chemist) a general outlook of the subject, basic knowledge necessary to practice the techniques and to use and interpret the results intelligently (particularly in application to their own research), and a key for further reading of the extensive literature available.

2 BACKGROUND TO DIFFRACTION TECHNIQUES

2.1 Basics of Crystal Symmetry

A crystalline solid is one in which atoms and molecules (more strictly, the mean positions around which they thermally vibrate) form a regular three-dimensional array, corresponding to a free energy minimum of the crystalline state. It is always possible to select a small parallelepiped of the crystal space in such a way that repetitions (parallel translations) of this parallelepiped in all three dimensions will reproduce the entire crystal structure. This parallelepiped is called the unit cell and is defined by three noncoplanar vectors (**a, b, c**) forming its edges. These vectors are also the (smallest) translations by which the unit cell should be shifted to fill the whole crystal space. Thus, once we know the contents of one unit cell, we know the entire crystal structure. By convention, the positive directions of **a, b**, and **c** are chosen so as to make them a right-hand set. These directions are also chosen as the axes x, y, and z of the crystal coordinate system (Figure 1(a)). The scalar dimensions of the unit cell are described by three edge lengths (a, b, c) and three angles between them (α, β, γ). Note that a point (e.g. position of an atom) in a unit cell is described in crystallography by 'fractional coordinates', for example, each coordinate is given as a fraction of the lattice repeat (translation) in that direction.

Compared to the unit cell, a macroscopic crystal can be regarded as infinitely large. Thus, a NaCl crystal of 1 mm^3 contains 10^{19} unit cells. Ignoring its finiteness, each vertex of the unit cell and every one generated by translations are physically identical: the atomic environments and all physical properties at these points are the same. An (infinite) three-dimensional array of such points in space is called the crystal lattice. Note that the latter is only a mathematical device to describe the crystal's regularity and is *not* synonymous with the crystal structure itself, which is an array of physical objects (atoms and molecules). Thus, a lattice point need not (although in some structures *can*) coincide with the center of an atom or a molecule, and a molecule need not lie entirely within a 'box' of a unit cell, without being bisected by its face (boundary).

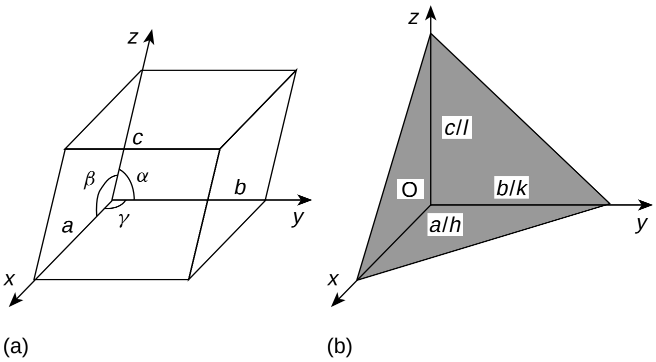

Figure 1 (a) Primitive unit cell showing its six defining parameters. (b) lattice, or Miller plane (*hkl*), O is the origin of the unit cell

A unit cell, as defined above, can be chosen in many different ways, but the meaningful choice is such as reflects the symmetry of the structure (e.g. a square prism for a structure having a fourfold axis), even if this means choosing *not* the smallest possible unit cell. For this reason, a unit cell can have lattice points not only in its vertices (primitive cell, denoted P) but besides also in its center (body-centered, or I), or in the center of each face (face-centered, F), or in the centers of two opposite faces (base-centered). The latter is denoted A, B, or C, depending on whether the centered faces are opposite to the lattice vectors **a**, **b**, or **c**, respectively. There are only seven different types of lattice symmetry, known as crystal systems, each corresponding to a distinct shape of the unit cell (Table 1). Taking into account all centering conditions compatible with each crystal system, there are 14 different types of lattices in all, known as Bravais lattices (Figure 2). A trigonal unit cell can contain two additional lattice points with the coordinates $\frac{1}{3}$, $\frac{2}{3}$, $\frac{2}{3}$ and $\frac{2}{3}$, $\frac{1}{3}$, $\frac{1}{3}$, but usually such a centered lattice is described by a geometrically equivalent primitive lattice, called rhombohedral (R), with the unit cell volume three times smaller.

A lattice plane is a plane passing through at least three noncolinear lattice points. The direction of such a plane is described by a set of three integers h, k, and l, written in parentheses as (*hkl*) and known as Miller indices (originally introduced[23] to describe external crystal faces, which must always be lattice planes). It means that the plane intersects the axes x, y, and z at the distances from the origin, equal to rational fractions of the corresponding unit cell parameters, that is, a/h, b/k, and c/l, respectively (Figure 1(b)). Miller indices should not be confused with those for crystallographic directions, given in square brackets as [uvw] and representing the vector $u\mathbf{a} + v\mathbf{b} + w\mathbf{c}$, radiating from the origin. A zone is defined as a set of lattice planes, whose intersections are all

Table 1 Relations between unit cell parameters and lattice symmetry

Crystal system	Bravais lattices	Unit cell constraints	Laue symmetry
1. Triclinic	*P*	$a \neq b \neq c, \alpha \neq \beta \neq \gamma$	$\bar{1}$
2. Monoclinic	*P*, *C*	$a \neq b \neq c, \alpha = \gamma = 90°, \beta > 90°$	2/*m*
3. Orthorhombic	*P*, *C*, *I*, *F*	$a \neq b \neq c, \alpha = \beta = \gamma = 90°$	*mmm*
4. Tetragonal	*P*, *I*	$a = b \neq c, \alpha = \beta = \gamma = 90°$	4/*m* or 4/*mmm*
5. Trigonal	*P*, *R*[a]	$a = b \neq c, \alpha = \beta = 90°, \gamma = 120°$	$\bar{3}$ or $\bar{3}m$
Rhombohedral[a]	*R*	$a = b = c, \alpha = \beta = \gamma < 120°$	Ditto
6. Hexagonal	*P*	$a = b \neq c, \alpha = \beta = 90°, \gamma = 120°$	6/*m* or 6/*mmm*
7. Cubic	*P*, *I*, *F*	$a = b = c, \alpha = \beta = \gamma = 90°$	$m\bar{3}$ or $m\bar{3}m$

[a] Alternative setting for centered trigonal lattices.

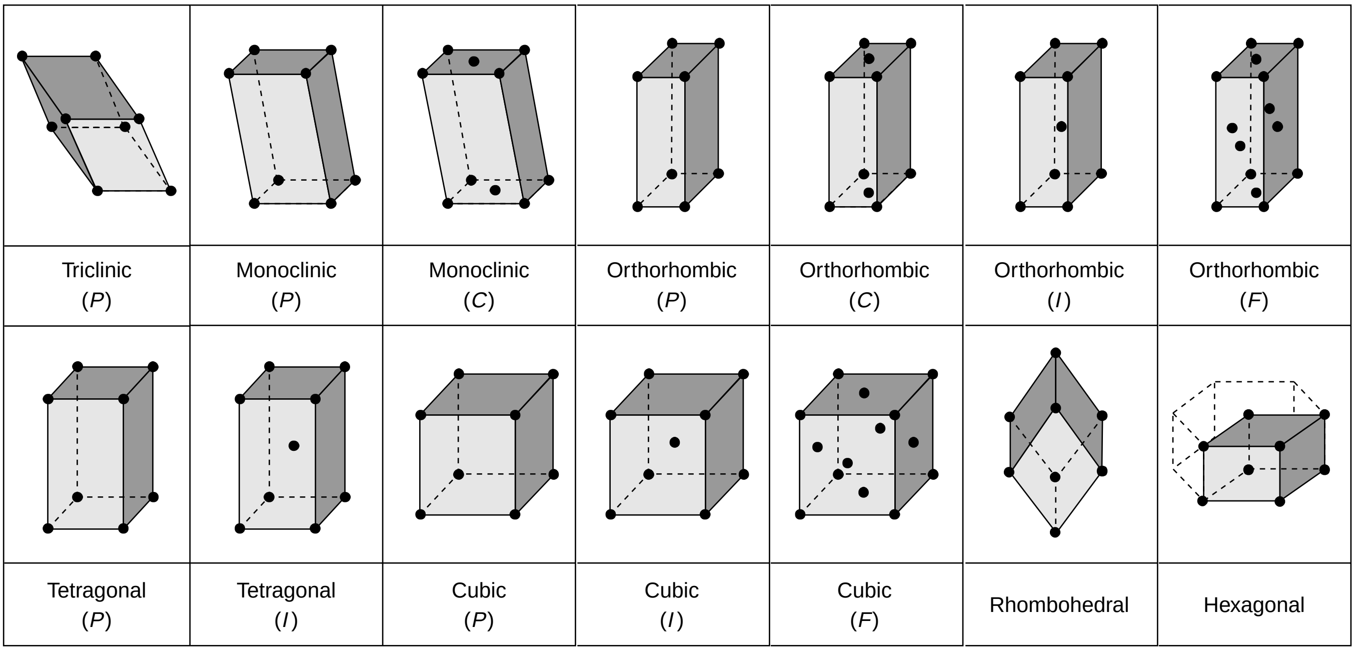
Triclinic (*P*)
Monoclinic (*P*)
Monoclinic (*C*)
Orthorhombic (*P*)
Orthorhombic (*C*)
Orthorhombic (*I*)
Orthorhombic (*F*)
Tetragonal (*P*)
Tetragonal (*I*)
Cubic (*P*)
Cubic (*I*)
Cubic (*F*)
Rhombohedral
Hexagonal

Figure 2 The 14 Bravais lattices

parallel. The common direction of these intersections is called the zone axis (Figure 3).

Symmetry operation is an operation transforming an object into an (apparently) identical one. Lattice translations are the symmetry operations present in any crystal structure by definition. Besides them, a structure may (or may not) have other symmetry operations, performed about a certain point, line or plane, which is called an element of symmetry. There are two types of symmetry operations: those which involve an overall shift (translation) and those which leave at least one point of an object unmoved. The latter operations can apply both to crystal structures and to finite, isolated objects. Repeating such operations two or several times will bring the object back to the original position. The following symmetry elements of this type can be found in crystals.

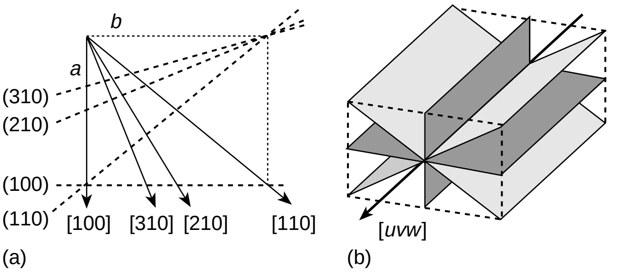
b
a
(310)
(210)
(100)
(110)
[100]
[310]
[210]
[110]
(a)
[*uvw*]
(b)

Figure 3 (a) Crystallographic directions (bold) and planes (dotted); (b) a zone of planes with its axis [*uvw*]

1. An *n*-fold rotation axis is a line, rotation about which through 360°/*n* leaves the object indistinguishable from the original. Only axes with $n = 2$, 3, 4, and 6 can be present in crystals, all others being incompatible with translational symmetry.

2. An inversion center, or center of symmetry (designated $\bar{1}$), is a point. If an object lies at a distance r from this point, its symmetry-related object lies at the same distance in the opposite direction. Thus, if a center of symmetry lies at the origin (0, 0, 0) of the unit cell, for each atom with coordinates x, y, z there will be an equivalent one with coordinates $-x, -y, -z$.
3. A mirror plane, designated by the letter m. For example, a mirror plane parallel to the xy plane and passing through the origin will convert an object at x, y, z into one at $-x, y, z$.
4. A rotatory-inversion axis combines a rotation around a line through 360°/n with inversion through a specific point on this line. Axes with $n = 3$, 4, or 6 (designated $\bar{3}$, $\bar{4}$, and $\bar{6}$) are possible in crystals, that with $n = 2$ is equivalent to a mirror plane, which is perpendicular to the twofold axis and passes through the inversion center.

These operations can be combined into 32 self-consistent sets, known as point groups. Because the outer form ('habit') of a crystal depends on the crystal structure, point groups describe all possible crystal forms, classified correspondingly into 32 crystal classes.

Symmetry operations which involve shifts, can apply *only* to regularly repeating infinite patterns, like crystal structures. A repeated application of such an operation brings the structure not to the original position, but to a different one, separated from the original by an integer number of lattice translations. There are two types of such ('translational') symmetry elements (see Table 2), besides primitive lattice translations **a**, **b**, **c**.

- Screw axes, designated by a number with a subscript (n_q), combine a rotation by 360°/n (see i) with a shift parallel to this axis and equal to the lattice repeat in this direction, multiplied by q/n. Screw axes possible in crystals are 2_1, 3_1, 3_2, 4_1, 4_2, 4_3, 6_1, 6_2, 6_3, 6_4, and 6_5. Note that the operations of axes 3_1 and 3_2, 4_1 and 4_3, 6_1 and 6_5, 6_2 and 6_4, respectively, are mirror images of each other. Such axes are called right-handed if $q < n/2$, left-handed if $q > n/2$, and without hand if $q = n/2$.
- Glide planes combine a reflection in a mirror plane with a shift parallel to this plane. They are called a, b, and c planes when the shift equals 1/2 of a cell edge (i.e. **a**/2, **b**/2, and **c**/2, respectively), n planes when it equals 1/2 of (any) face-diagonal or body-diagonal of the unit cell, and d (so-called 'diamond') planes when it equals 1/4 of such diagonal.

Note that rotation axes and translations are 'perfect symmetry elements': they transform an object into a perfectly identical one, while inversion centers and planes are 'imperfect': they change an asymmetric object (molecule) into one of different 'handedness' (an enantiomer).

There are 230 possible combinations of symmetry elements of types (i) to (vi) with lattice translations, called crystallographic space groups. They describe the symmetries of all crystal structures that can exist, although not all have been actually observed so far. A space group symbol includes a capital letter describing the lattice type, followed by the essential symmetry elements present. A comprehensive description of each space group can be found in Reference.[24]

Table 2 Systematic absences related to lattice centering and translational elements of symmetry

		Related translation	Ref- lections affected	Conditions for systematic absence
A-centered lattice			hkl	$k + l \neq 2n$
B-centered lattice			hkl	$h + l \neq 2n$
C-centered lattice			hkl	$h + k \neq 2n$
F-centered lattice			hkl	$h + k, k + l$, or $h + l \neq 2n$
I-centered lattice			hkl	$h + k + l \neq 2n$
R lattice on hexagonal axes				
obverse setting			hkl	$-h + k + l \neq 3n$
reverse setting			hkl	$h - k + l \neq 3n$
2-fold screw (2_1) ∥ to	x	$a/2$	$h00$	$h \neq 2n$
	y	$b/2$	$0k0$	$k \neq 2n$
	z	$c/2$	$00l$	$l \neq 2n$
3-fold screw (3_1, 3_2) ∥ to	z	$c/3$	$00l$	$l \neq 3n$
4-fold screw (4_1, 4_3) ∥ to	x	$a/4$	$h00$	$h \neq 4n$
	y	$b/4$	$0k0$	$k \neq 4n$
	z	$c/4$	$00l$	$l \neq 4n$
4-fold screw (4_2) ∥ to	x	$a/2$	$h00$	$h \neq 2n$
	y	$b/2$	$0k0$	$k \neq 2n$
	z	$c/2$	$00l$	$l \neq 2n$
6-fold screw (6_1, 6_5) ∥ to	z	$c/6$	$00l$	$l \neq 6n$
6-fold screw (6_2, 6_4) ∥ to	z	$c/3$	$00l$	$l \neq 3n$
6-fold screw (6_3) ∥ to	z	$c/2$	$00l$	$l \neq 2n$
a glide plane ⊥ to	y	$a/2$	$h0l$	$h \neq 2n$
	z	$a/2$	$hk0$	$h \neq 2n$
b glide plane ⊥ to	x	$b/2$	$0kl$	$k \neq 2n$
	z	$b/2$	$hk0$	$k \neq 2n$
c glide plane ⊥ to	x	$c/2$	$0kl$	$l \neq 2n$
	y	$c/2$	$h0l$	$l \neq 2n$
n glide plane ⊥ to	x	$(b + c)/2$	$0kl$	$k + l \neq 2n$
	y	$(a + c)/2$	$h0l$	$h + l \neq 2n$
	z	$(a + b)/2$	$hk0$	$h + k \neq 2n$
d glide plane ⊥ to	x	$(b \pm c)4$	$0kl$	$k + l \neq 4n$
	y	$(a \pm c)/4$	$h0l$	$h + l \neq 4n$
	z	$(a \pm b)/4$	$hk0$	$h + k \neq 4n$

2.2 Diffraction Summary

2.2.1 Directions of Diffracted Beams

X rays (electromagnetic waves) passing through crystal make electrons of atoms oscillate about their nuclei and become sources of secondary radiation of the same frequency. Thus X rays are scattered from electron clouds. In the process, the phase of the X-ray wave is altered by 180°, but because this change happens to *all* waves, it is ignored in the following treatment of diffraction geometry. Neutrons are scattered only by atomic nuclei, and electron beam by the electrostatic potential of atoms, which is contributed to by both nuclei and electrons, but mainly the latter.

Waves scattered from different parts of a crystal structure can reinforce each other only if they arrive in phase, that is, if their path lengths D differ by an integer number of wavelengths. This applies also to atoms separated by one lattice translation, and must be true in all three dimensions, therefore Laue (1912) derived the following conditions for X-ray diffraction:

$$\begin{aligned}\Delta D_1 &= \mathbf{a}(\mathbf{s}-\mathbf{s}_0) = a(\cos\alpha_n - \cos\alpha_0) = n_1\lambda\\ \Delta D_2 &= \mathbf{b}(\mathbf{s}-\mathbf{s}_0) = b(\cos\beta_n - \cos\beta_0) = n_2\lambda\\ \Delta D_3 &= \mathbf{c}(\mathbf{s}-\mathbf{s}_0) = c(\cos\gamma_n - \cos\gamma_0) = n_2\lambda \end{aligned}\tag{1}$$

where $\mathbf{s}_0$ and $\mathbf{s}$ are unit vectors along the directions of the incident and diffracted beams, n are integers (orders of diffraction), α, β, and γ are the angles between the incident beam (subscript 0) or the diffracted beam (subscript n) and the axes x, y, and z, respectively.

Bragg[25] in 1913 drastically simplified the picture, assuming that X rays are 'reflected' from a lattice plane as light is reflected from a mirror, the angle of incidence being equal to the angle of reflection, θ. A diffraction beam occurs only at certain θ values, when the waves reflected from all parallel planes are all in phase, that is, path differences between waves reflected from adjacent planes equal an integer number of wavelengths λ (Figure 4), as defined by Bragg's law:

$$n\lambda = 2d_{hkl}\sin\theta \tag{2}$$

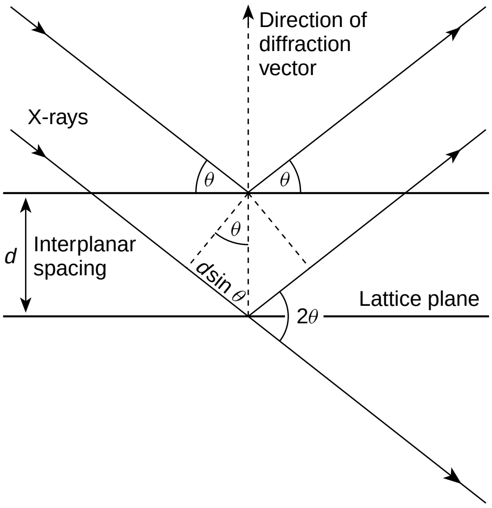

Figure 4 Bragg's law illustrated

Thus each diffracted beam is regarded as a 'reflection' from a plane with Miller indices (hkl) and is named by the same indices. Since d_{hkl} depends on the unit cell parameters, as $d_{hkl} = X/Y$, where

$$X = [1 - \cos^2\alpha - \cos^2\beta - \cos^2\gamma + 2\cos\alpha\cos\beta\cos\gamma]^{1/2} \tag{3}$$

$$\begin{aligned} Y = \Bigg[&\left(\frac{h}{a}\right)^2 \sin^2\alpha + \left(\frac{k}{b}\right)^2 \sin^2\beta + \left(\frac{l}{c}\right)^2 \sin^2\gamma\\ &-2\left(\frac{kl}{bc}\right)(\cos\alpha - \cos\beta\cos\gamma) - 2\left(\frac{lh}{ca}\right)(\cos\beta - \cos\alpha\cos\gamma)\\ &- 2\left(\frac{hk}{ab}\right)(\cos\gamma - \cos\beta\cos\alpha)\Bigg]^{1/2} \end{aligned}\tag{4}$$

it is possible to determine the unit cell if λ and the directions of several diffracted beams are known.

These and other calculations can be greatly simplified, using the concept of the reciprocal space[14] (which has the dimension of reciprocal length, Å^{-1}) and of reciprocal crystal lattice in this space. The reciprocal lattice vectors, $\mathbf{a}^*$, $\mathbf{b}^*$, and $\mathbf{c}^*$, are related to those of the direct lattice ($\mathbf{a}$, $\mathbf{b}$, and $\mathbf{c}$) by the relationships

$$\mathbf{a}\cdot\mathbf{a}^* = \mathbf{b}\cdot\mathbf{b}^* = \mathbf{c}\cdot\mathbf{c}^* = 1 \tag{5}$$

$$\mathbf{a}^*\cdot\mathbf{b} = \mathbf{a}^*\cdot\mathbf{c} = \mathbf{b}^*\cdot\mathbf{a} = \mathbf{b}^*\cdot\mathbf{c} = \mathbf{c}^*\cdot\mathbf{a} = \mathbf{c}^*\cdot\mathbf{b} = 0 \tag{6}$$

which means that $\mathbf{a}^*$ is perpendicular to the ($\mathbf{b}$, $\mathbf{c}$) plane, $\mathbf{b}^*$ to the ($\mathbf{a}$, $\mathbf{c}$) plane, and $\mathbf{c}^*$ to the ($\mathbf{a}$, $\mathbf{b}$) plane (see Figure 5). The full relationships for all lattice symmetries can be found elsewhere.[14,26] Each point of the reciprocal lattice corresponds to a certain Miller plane of the direct lattice and is designated by the same indices hkl. Note that it therefore corresponds also to a possible Bragg reflection, which makes this concept indispensable in interpreting diffraction patterns.

Another useful mathematical image in reciprocal space is the sphere of reflection, introduced by Paul Ewald and named after him.[27] The Ewald sphere (Figure 6(a)) has the diameter of 2/λ, coinciding with the direction of the incident beam (wavelength λ). The crystal (in direct space) is placed at the

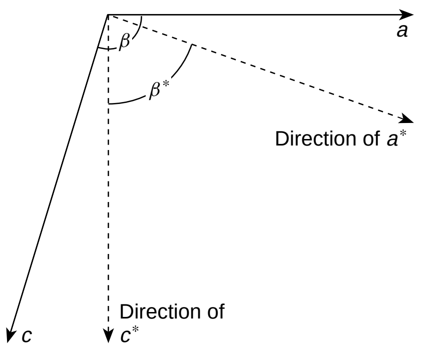

Figure 5 Relationship between reciprocal and direct lattices for a monoclinic unit cell; shown in the **ac** (≡ $\mathbf{a}^*\mathbf{c}^*$) plane

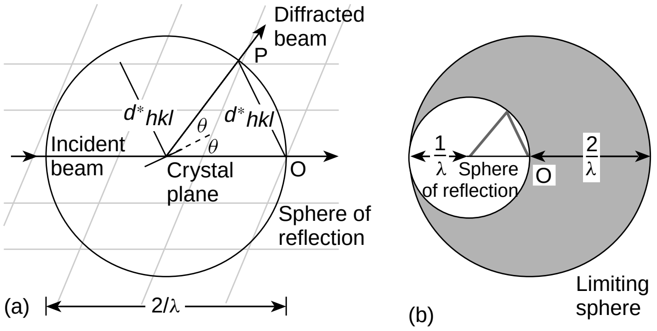

Figure 6 (a) The Ewald construction illustrated. (b) Limiting sphere and sphere of reflection

center C of the sphere. The corresponding reciprocal lattice, drawn at the same scale as the Ewald sphere, is placed with its origin O at the point where the incident beam emerges from the sphere. If the crystal is rotated, the reciprocal lattice also rotates around O. Whenever another reciprocal lattice point P with indices *hkl* touches the surface of the sphere, Bragg's law (and Laue conditions) are satisfied for the Miller plane with the same indices *hkl*, and a diffracted beam emerges in the *CP* direction. Note that although the number of the reciprocal lattice points is infinite, the number of observable reflections is limited to those points which can, in principle, pass through the Ewald sphere, that is, those lying within the radius of 2/λ from O (Figure 6(b)).

The alternative is to vary the size of the Ewald sphere (i.e. the wavelength) until it touches a reciprocal lattice point. In practice, this is achieved by using an incident beam of 'white radiation' with a continuous spectrum of wavelengths. Historically, this was the first X-ray technique (Laue method), later eclipsed by methods using monochromatic radiation but recently resurgent with the introduction of image plate detectors (see below).

2.2.2 *Intensities of Diffracted Beams*

From the unit cell dimension one can calculate the directions of a diffracted beam, but not its intensity, which depends on the types and positions of atoms in the cell. Inversely, these positions cannot be determined without the knowledge of intensities, except in a few simplest structures (e.g. NaCl), where all atoms occupy the lattice points. The intensity I_{hkl} of a reflection depends on many factors.[10,13] Thus, for X-ray diffraction,

$$I_{hkl} = \frac{e^4\,\Omega}{m^2c^4V} I_0\lambda^3 LPTE|F_{hkl}|^2 \qquad (7)$$

where I_0 is the intensity of the incident beam, Ω is the volume of the crystal, V the volume of the unit cell, e and m are the charge and mass of the scattering particle, in this case electron (that is why the contribution of nuclei, with much greater m, is negligible). L is the Lorentz factor,[28] accounting for the time needed for the reflection to pass through the Ewald sphere. P is the polarization factor. X rays produced by a (laboratory) source are not polarized, but they (like any electromagnetic radiation) undergo polarization when reflected. Thus if the primary beam is monochromatized by reflection from a crystal (see below), the radiation reaches the sample in a partially polarized state, which affects the intensity of the diffracted beam in a way dependent on the θ angle. Both L and P are dependent on θ and the precise geometry of the particular X-ray instrument. Together the modifications of the intensity data for these two effects are referred to as the 'Lp correction'.[29] The transmission factor T depends on the absorption of X rays in the crystal (see below). The extinction factor E accounts for two different effects: the diffracted beam being diffracted again in the crystal ('primary extinction') and the decrease of the incident beam intensity I_0 during its progress through the crystal, because some energy is taken away by the diffracted beam ('secondary extinction').[30]

But in the first place, I_{hkl} depends on the structure, that is, on the distribution of electron density in the unit cell. This dependence is represented by the structure factor F_{hkl} of a reflection,

$$F_{hkl} = \int_V \rho(xyz)\exp[2\pi i(hx + ky + lz)]\,\mathrm{d}V \qquad (8)$$

where ρ is the electron density at a point with the fractional coordinates x, y, z. Equation (8) can be drastically simplified if we present ρ not as a continuous function but as a superposition of atoms,

$$F_{hkl} = \sum_j f_j \exp[2\pi i(hx_j + ky_j + lz_j)] \qquad (9)$$

where f_j is the atomic scattering factor (form factor) for the j-th atom and x_j, y_j, z_j are the fractional coordinates of

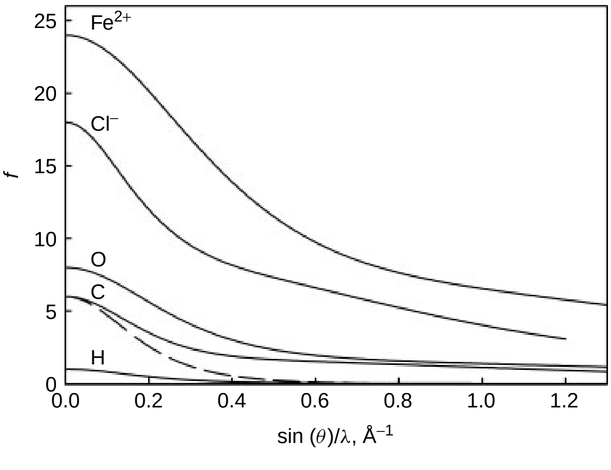

Figure 7 Variation of X-ray form factors, f, with sin θ/λ. Solid lines: stationary atoms, dashed line: C atom with $U = 0.1$ Å^2

this atom. For X-ray diffraction, f_j is not a constant but a function of $\sin\theta/\lambda$ (Figure 7), steadily decreasing from the maximum value equal to the total number of electrons in the atom and approaching zero at high $\sin\theta/\lambda$.[13] This dependence is due to the fact that the size of an electron cloud of an atom is comparable with the wavelength. By contrast, neutrons are scattered only by atomic nuclei, which can be regarded as point scatterers, and hence neutron equivalents of f_j, so-called scattering lengths b_j, are practically angle-independent.[21] The curves of f_j are presumed invariant for a given element in any structure and are calculated by means of quantum mechanics (Hartree-Fock theory),[31,32] presuming the atom to be isolated (ground state) and spherically symmetrical. This 'spherical-atom model' may look a rash, even absurd, simplification: we ignore the existence of chemical bonds in molecules or solids! However, for most practical purposes this approximation is sensible, because the maximum of the electron density peak of an atom (especially a heavy atom) is defined mainly by the core electrons, belonging to the closed inner electron shells, which are unaffected by bonding. The hydrogen atom, which lacks core electrons, is an exceptional case (see below). Only for the most ionic structures does it make sense to use f_j, calculated for ions, rather than neutral atoms (but still spherically symmetrical).

The structure factor is a complex number, expressing both the amplitude $|F_{hkl}|$ and the phase angle α_{hkl} of the scattered wave:

$$F_{hkl} = |F_{hkl}|\exp[i\alpha_{hkl}] = A_{hkl} + iB_{hkl} \tag{10}$$

$$A_{hkl} = \sum_j [f_j \cos 2\pi(hx_j + ky_j + lz_j)] \tag{11}$$

$$B_{hkl} = \sum_j [f_j \sin 2\pi(hx_j + ky_j + lz_j)] \tag{12}$$

$$\alpha_{hkl} = \tan^{-1}\left[\frac{B_{hkl}}{A_{hkl}}\right] \tag{13}$$

For a centrosymmetric structure, α_{hkl} can equal only 0 or 180° (i.e. F having signs $+$ or $-$, respectively), for a noncentrosymmetric structure it can have any value. Owing to the translational symmetry of crystals, $\rho(xyz)$ can be considered as a periodic function in three-dimensional space and expressed by the Fourier transform of equation (8),

$$\begin{aligned}\rho(xyz) &= \frac{1}{V}\sum_{hkl} F_{hkl}\exp[2\pi i(hx + ky + lz)] \\ &= \frac{1}{V}\sum_{hkl} |F_{hkl}|\exp[2\pi i(hx + ky + lz - \alpha_{hkl})]\end{aligned} \tag{14}$$

Thus if we know the moduli (amplitudes) and the phase angles of X-ray reflections, we can calculate the distribution of electron density in the unit cell, that is, find the atomic positions. Finding $|F_{hkl}|$ from I_{hkl} is straightforward, but the values of α_{hkl} are lost in all usual diffraction experiments.[33] Determining (reconstructing) phase angles remains the most difficult part of the structure solution.

The diffraction pattern of a crystal has its own symmetry (known as Laue symmetry), related to the symmetry of the structure, thus in the absence of systematic errors (particularly absorption), reflections with different, but related, indices should have equal intensities. According to Friedel's law,[34] the diffraction pattern of any crystal has a center of inversion, whether the crystal itself is centrosymmetric or not, that is, reflections with indices hkl and $\overline{hkl}$ ('Friedel equivalents') are equal. Therefore Laue symmetry is equal to the point-group symmetry of a crystal plus the inversion center (if it is not already present). There are 11 Laue symmetry classes. For example, if a crystal is monoclinic ($\beta \neq 90°$), then $I(hkl) = I(\overline{hkl}) = I(\bar{h}k\bar{l}) = I(h\bar{k}l) \neq I(\bar{h}kl)$. For an orthorhombic crystal, reflections hkl, $\bar{h}kl$, $h\bar{k}l$, $hk\bar{l}$ and their Friedel equivalents are equal. If by chance a monoclinic crystal has $\beta \approx 90°$, it can be mistaken for an orthorhombic, but Laue symmetry will show the error.

Friedel's law is valid only if every atom in the structure scatters X rays with the same phase change of 180°. However, if the frequency of the incident radiation is close to the natural absorption frequency of an atom, then an anomalous phase change occurs. Thus the atomic scattering factor, which has been regarded in equation (9) as a real number, is strictly a complex number of the form

$$f_j = f_o + \Delta f' + i\Delta f'' \tag{15}$$

where the real ($\Delta f'$) and imaginary ($\Delta f''$) correction terms are (unlike f_o) wavelength-dependent, but to a first approximation independent of θ (again unlike f_o). They are significant for heavy elements and particularly near the absorption edges, in which cases $I(hkl)$ and $I(\overline{hkl})$ of noncentrosymmetric crystals can be significantly different. Bijvoet was the first to show that this effect, known as anomalous scattering or anomalous dispersion, can be used to determine the absolute configuration of crystal structures and therefore of chiral molecules,[35] as well as to solve the phase problem for a noncentrosymmetric crystal.[36] The latter proved very useful for determining protein structures.[37] Since anomalous scattering is wavelength-dependent, so will be the reflection intensities of a protein crystal that contains anomalously scattering atoms naturally (e.g. Fe, Zn) or has them artificially introduced into the molecule (e.g. replacing Ca with Tb, S with Se). If the diffraction data at two or more different wavelengths are measured, phase angles can be determined either algebraically or by first locating the anomalously scattering atom by the anomalous difference Patterson method or second-generation direct methods. Although the idea of this 'multi-wavelength anomalous dispersion' (MAD) method has been suggested long ago,[38] it became widely practiced only in 1990s with the development of synchrotrons (where λ can be changed freely), as well as improved theory[39] and software.[40]

Anomalous scattering also occurs in neutron diffraction, several nuclei (^{113}Cd, ^{149}Sm, ^{151}Eu, ^{157}Gd, and ^{239}Pu) showing a large wavelength-dependent effect. It also has been used to solve the phase problem by MAD technique.[41]

Another manifestation of the crystal symmetry are systematic absences, or 'extinctions', of reflections that apparently satisfy Bragg's law. If the crystal lattice is not primitive, some reflections of the general type (i.e. with nonzero h, k, and l) are systematically absent. Specific absences along certain lattice directions indicate the existence of screw axes or glide planes in the crystal (Table 2). Systematic absences are valuable for determining the space group of a crystal. Because nontranslational elements of symmetry do not cause any systematic absences, only 63 out of 230 space groups can be unequivocally determined in this way. Additional information can be obtained from the distribution of reflection intensities, which is different for centrosymmetric and noncentrosymmetric structures, the former giving a relatively higher number of weak reflections than the former.[42] This method is fairly reliable but inconclusive, because of its probabilistic nature, and only a successful refinement of the structure gives the final proof of the correctness of the space group assignment.

2.2.3 Effects of Thermal Motion

The calculation of the structure factor in equation (8) assumes all atoms to be at rest in the positions corresponding to perfect crystal symmetry. In fact, atoms and molecules perform thermal vibrations and sometimes are statically disordered, that is, shifted from ideal positions, differently in different unit cells. Both effects disturb the long-range periodicity of a crystal and thus make it a poorer diffractor. Smearing of the electron distribution of an atom due to thermal vibration effectively reduces its scattering factor f_j, so that it drops faster with $\sin\theta/\lambda$ than the corresponding curve for a stationary atom (f_o), as shown in Figure 7. The decrease is described by an exponential temperature, or thermal, factor Q:

$$f_j = f_o Q = f_o \exp\left(-\frac{B\sin^2\theta}{\lambda^2}\right) \tag{16}$$

where B is related to the mean-square amplitude U of the atom's vibrations

$$B = 8\pi^2 U \qquad U = \overline{u}^2 \tag{17}$$

Here the atom is assumed to vibrate with isotropic amplitude in all directions. As atoms in crystals seldom have isotropic environment, their displacements can be better approximated[43] by an ellipsoid, that is, a symmetrical tensor **U** with six independent components U_{ij}:

$$\mathbf{U} = \begin{pmatrix} U_{11} & U_{12} & U_{13} \\ U_{12} & U_{22} & U_{23} \\ U_{13} & U_{23} & U_{33} \end{pmatrix} \tag{18}$$

such that the mean-square amplitude of vibration in a direction of a vector **l** with components l_1, l_2, l_3 is

$$\overline{u}^2 = \sum_{ij} U_{ij} l_i l_j \tag{19}$$

In this case the temperature factor also becomes anisotropic, that is, reflections are weakened unequally in different direction. Historically, three different representations of anisotropic temperature factor have been used in the literature,[32,44] namely,

$$Q = \exp[-(h^2\beta_{11} + k^2\beta_{22} + l^2\beta_{33} + 2hk\beta_{12} + 2hl\beta_{13} + 2kl\beta_{23})] \tag{20}$$

$$Q = \exp[-1/4\{h^2B_{11}(a^*)^2 + k^2B_{22}(b^*)^2 + l^2B_{33}(c^*)^2 + 2hkB_{12}a^*b^* + 2hlB_{13}a^*c^* + 2klB_{23}b^*c^*)] \tag{21}$$

$$Q = \exp[-2\pi^2\{h^2U_{11}(a^*)^2 + k^2U_{22}(b^*)^2 + l^2U_{33}(c^*)^2 + (2hkU_{12}a^*b^* + 2hlU_{13}a^*c^* + 2klU_{23}b^*c^*)] \tag{22}$$

Parameters B_{ij} and U_{ij}, like the isotropic temperature factor, are expressed in Å^2, while β_{ij} are dimensionless. The accepted standard now is to report U for the isotropic model (U_{iso}) and U_{ij} for the anisotropic one.[45]

At ambient temperature, it is usually impossible to discern the smearing caused by thermal vibrations (averaged over time) from that caused by static displacements of atoms (averaged over the whole crystal), and the 'vibrational parameters' in fact account for both. Therefore it is now recommended to use the term 'atomic displacement parameters' (ADP) instead. A diffraction study of the same structure at different temperatures, however, will show the difference: the genuine thermal vibrations diminish on cooling, but the ADP due to static disorder (e.g. in ferrocene[46]) will remain large.

The mathematics of the temperature factor are described fully elsewhere.[32,43] Some notes of caution are necessary. The terms 'temperature factor' and 'thermal vibration parameters' are often used as synonyms. In fact, the former applies to diffraction intensities (and reciprocal space) and the latter to actual atomic motion (and direct space). Both are expressed by tensors/ellipsoids, but these are Fourier images of one another. It also must be emphasized that *separate* components U_{ij} have no physical meaning on their own and cannot be directly compared.[47] Graphically, ADP are usually presented in the form of a 'thermal ellipsoid', defined as a surface, inside which the vibrating atom's center can be found with a certain probability.[48] Most commonly, the ellipsoids are drawn at a 50% probability level. Their shape provides a good visual indication of the anisotropy of thermal motion. The principal semiaxial lengths D of an ellipsoid are proportional to the root-mean-square displacement (RMSD) in the corresponding directions,

$$D_x = c\sqrt{\overline{u}_x^2},\ D_y = c\sqrt{\overline{u}_y^2},\ D_z = c\sqrt{\overline{u}_z^2} \tag{23}$$

(where $c = 1.5382$ for 50% probability), its dimensions in any other direction have no definite meaning. A surface

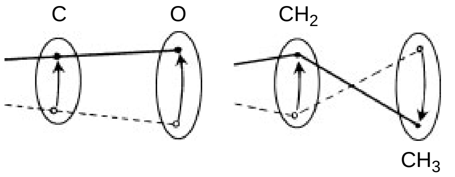

Figure 8 Vibrations of a rigid (CO) and a flexible (ethyl) groups: similar thermal ellipsoids can conceal different types of motion

duly representing RMSD components in all directions is not an ellipsoid but a quadric surface, resembling the shape of a peanut.[49] This presentation proved useful in analyzing thermal motion. A covalently bonded atom vibrates mainly in perpendicular direction to the bond. In a molecular crystals vibrations of a molecule as a whole are usually far more significant than intramolecular modes.

When atomic displacements are large, systematic errors can be introduced into the derived bond distances and angles associated with the strongly vibrating atom. Note that atomic motions discussed above are measured relative to the crystal lattice. Bragg reflections contain no information whatsoever about motion of atoms relative to each other. Knowing the ADP of two atoms, one cannot tell (without some external information) whether the atoms vibrate in phase or not (Figure 8). The measured bond lengths are in fact the distances between average positions of atoms. If, for example, atom A makes rotational oscillations (librations) around atom B as a center (Figure 9), its average position $\overline{A}$ lies inside the arc A′A″ and the bond AB is apparently shortened.[50] Although techniques[50,51] (and software[52]) for correcting these errors are available, they always require certain assumptions about correlations between atomic motions, that is, rigidity of the molecule or group under investigation. One must keep in mind that these assumptions originate from the model and not from the experiment.[53] Therefore the best way to avoid these systematic errors is to reduce the thermal motion itself, by carrying out the experiment at as low a temperature as possible. This is even more important in accurate electron density studies.[54,55] Only this way one can be certain that any anisotropy of electron distribution[56] is not caused either by inadequate corrections for all systematic errors or poor modeling of the displacement parameters.

2.3 Generation of X rays and Neutrons

2.3.1 Generation of X rays

X rays can be produced either (i) by sharp deceleration of fast-moving electrons, or (ii) by ionizing collisions of these electrons with atoms of a suitable (metallic) target. Process (i) gives a continuous ‘white’ spectrum (because the energy of a free electron is not quantized), whilst (ii) gives narrow *characteristic lines*. The latter occur when the energy of the colliding electron exceeds a certain limit (*threshold potential*), permitting it to knock another electron out of an interior electron shell of the atom. The vacancy created is then filled by a descent of an electron from a higher shell, and the released potential energy is emitted as nearly monochromatic radiation. The characteristic lines are called K, L, and M, after the electron shells (quantum numbers $n = 1$, 2, and 3) from which the electron is knocked out, with subscripts α or β indicating whether the vacancy is filled from the nearest shell or from the next higher one, respectively. Thus, the K_α line is emitted by a $L \rightarrow K$ transition and the K_β line by a $M \rightarrow K$ one. Because transition can occur from two electron configurations, slightly different in energy, both α and β lines are close doublets comprising $\alpha1$, $\alpha2$ and $\beta1$, $\beta2$ lines. The $\alpha1$ line is about twice as intense as $\alpha2$ and three to six times stronger than $\beta1$, whilst $\beta2$ is usually very weak. The characteristic wavelengths are constants of a given element. The lines commonly used in crystallography are Cu-K_α and Mo-K_α, with $\overline{\lambda}$ (the average λ of the $\alpha1$–$\alpha2$ doublet) of 1.54178 and 0.71073 Å, respectively. Radiations from Cr, Fe, Co, Ni, Ag, and W targets have limited application for special purposes.

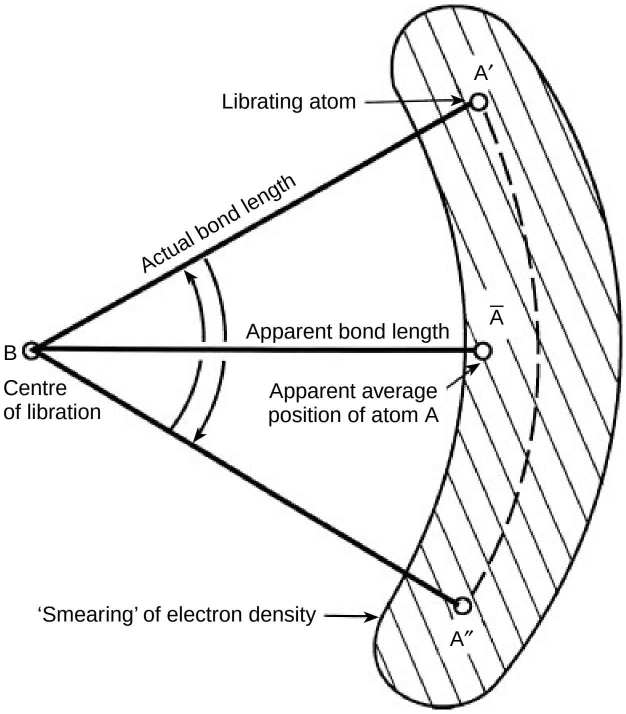

Figure 9 Apparent bond shortening in a librating group

The most common laboratory source of X rays is a sealed X-ray tube, that is, a glass (or ceramic) vessel with a metal base, in which under conditions of high vacuum a beam of electrons is created, accelerated by an electric potential of 30 to 60 kV and focused onto a target of one of the abovementioned metals, thereby producing X rays which leave the tube through a beryllium window. When electrons bombard the target, both processes (i) and (ii) take place, producing an X-ray spectrum such as shown in Figure 10(a). X rays are emitted randomly in all directions; however, diffraction experiments require a parallel beam of monochromatic (unless Laue method is used) radiation, preferably focused. Neither can be achieved, as in light optics, by prisms, lenses, and so on, because refractive indices of X-ray radiation for all materials are very close to 1 and practically independent from the wavelength. X rays of a required wavelength (strictly speaking, of a narrow range of wavelengths) are selected using a crystal-monochromator or a β-filter. The former is a crystal, oriented in such way that the Bragg condition is met for the wavelength of the K_α line and the direction of the diffracted beam of a *very strong* reflection pointing toward the sample. This beam is then effectively monochromatic. The common monochromator for laboratory X-ray sources is a specimen of pyrolytic (textured polycrystalline) graphite, which can convert up to 54% of the incident K_α radiation into the monochromatic beam, corresponding to the (0 0 2) Bragg reflection. For *single* crystals of LiF, quartz or Si this parameter (efficiency, or reflectivity) is much lower, for example, 9.4% for LiF, but the monochromaticity of the resulting beam is much better than for graphite. Therefore single-crystal monochromators are used with synchrotron X-ray sources (see below), where some loss of intensity is not a problem. Unfortunately, a monochromator tuned to a wavelength λ will let through also any λ/n, of which $\lambda/2$ is present in X-ray tube radiation, $\lambda/2$ and $\lambda/3$ in synchrotron radiation (SR).

Filter is a thin film of a metal immediately, or closely, preceding the target element in the periodic table, for example, Ni for Cu target, Zr for Mo target. Thus the absorption edge of the filter metal falls between the K_α and K_β lines and effectively removes the latter, but not the white radiation. Filters lose very little of the K_α intensity compared to monochromators, but are inferior to the latter in spectral purity of the resulting beam.

To obtain a parallel beam, the monochromated X rays are passed through a *collimator*, a long metallic tube containing slits with pinholes, which reduces the divergence of the beam and prevents X rays scattered from other parts of the device (secondary scattering) from reaching the detector. Furthermore, only 0.3% of the power of the tube goes into the energy of X rays, the rest into heating the target. Removal of this heat (by circulating water) sets the limit to the power and brilliance of an X-ray tube. These can be improved by an order of magnitude if a stationary target is replaced by a *rotating anode*, a fast-revolving cylinder or cone constantly placing under the electron beam a new area. The anode is rotated by a shaft, entering the tube body through a vacuum seal, and cooled by water running inside the shaft; therefore such tube and (unlike a sealed tube) requires constant vacuum-pumping and frequent maintenance.

Note that collimator does *not* make divergent X rays parallel and hence utilizes only a small fraction of the emitted radiation. The efficiency can be improved, if divergent X rays are concentrated and directed toward the sample. This can be done by *bent* crystal monochromators, or by concave mirrors utilizing total external reflection of X rays at very small incidence angles ($<0.1°$), known as ‘grazing incidence’. Both are commonly used with synchrotrons but seldom in laboratory devices. Recently this problem was addressed on a completely fresh basis, by means of polycapillary collimators, known also as ‘X-ray lenses’.**[57]** An X-ray lens is composed of a large number (up to millions) of tapered capillaries (hollow fibers), gently bent to achieve grazing incidence of X rays, which by successive total reflections at the inner walls are guided along the capillaries with a very small energy loss. The curvatures of the capillaries can be arranged such that a divergent beam emitted by the tube is concentrated into a quasi-parallel incident beam of much higher flux. With better utilization of X rays, the focal spot can be made much smaller but also more intense (heat removal being faster from a small spot), drastically reducing the electric power required. Thus, a 60 W microfocal X-ray generator (Bede Microsource®**[58]**) with X-ray lenses achieves higher brilliance than a conventional sealed X-ray tube of 2 kW power.

The most powerful sources of X-ray radiation are synchrotrons,**[59–61]** that is, accelerators of charged elementary particles operating in s stationary (storage-ring) mode. Within the ring electrons (or sometimes positrons) circulate with ultrarelativistic (close to the speed of light) velocity along a closed-loop orbit inside an evacuated ring chamber. The electron beam is guided along the loop by *bending magnets* (magnetic dipoles) placed at equal intervals along the ring. A turning of the electron trajectory, like electron deceleration (i) mentioned earlier, generates SR directed tangentially to the trajectory (and therefore already highly collinear). Depending on the energy of the electrons, SR can vary from microwave to γ-rays, including the entire X-ray range. Between the bending magnets the electron beam moves by a straight line, here it is focused by magnetic lenses, that is, magnetic quadrupoles or higher-order multipoles.

Currently there are about 40 operating SR sources worldwide, with another 10 under construction. The circumference of the ring varies from 65 to 1436 m. For example, the European Synchrotron Radiation Facility (ESRF) in Grenoble (France), opened in 1994, has the circumference of 844 m with 64 bending magnets and 27 straight sections, and the working energy of 6 GeV. The first-generation synchrotrons, built in 1960s, were intended for high-energy particle physics research, X rays being a ‘parasitic’ by-product, and had the brilliance of 10^9 to 10^{12} photon $\mathrm{s^{-1}\,mm^{-2}\,rad^{-2}}$ (0.1% BW)$^{-1}$. Synchrotrons of the second generation (built in 1980s) were often specialized for SR production (‘dedicated sources’). They achieved the brilliance of $10^{12}-10^{15}$, which in the third generation (1992–1999) was increased to $10^{18}-10^{23}$, thus exceeding the brilliance of conventional X-ray tubes by a factor of 10^8-10^{14}. The straight sections of third-generation synchrotrons are equipped with special magnetic devices (undulators and wrigglers, jointly known as insertion devices),

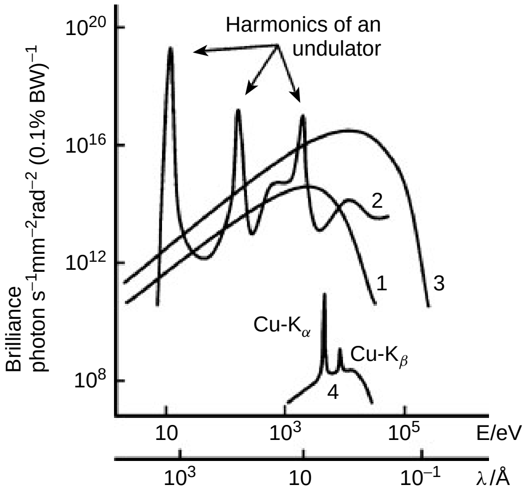

Figure 10 Spectral distribution of X-ray radiation generated by bending magnet (1), undulator (2) and wiggler (3) of a synchrotron and by a conventional X-ray tube with a Cu target. Brilliance and quantum energy are given on logarithmic scales. (Ref. 62. Reproduced by permission of Russian Academy of Science)

which cause the passing electrons' trajectory to oscillate, thus generating SR with enhanced characteristics. Particularly, the operational parameters of an undulator are chosen so as to achieve interference between the radiation emitted on adjacent curved sections of the electron trajectory. Consequently, the spectrum of undulator radiation shows a series of intensity maxima, known as undulator harmonics (Figure 10).

SR makes possible diffraction studies of much smaller or poorly diffracting crystals. It has also the advantage of easily tunable wavelength. However, owing to an imperfect vacuum inside the chamber, the electron beam, and hence the SR intensity, tend to decay with time (until a new portion of electrons is injected into the ring) and the observed reflection intensities must be corrected correspondingly.

2.3.2 Production of Neutron Beams

The practical neutron sources are nuclear fission reactors[62] and spallation facilities.[63,64] In the former, a thermal neutron is absorbed by a ^{235}U nucleus, which becomes excited and splits into medium-heavy nuclei with an emission of 2 to 5 fast neutrons, or on average 2.5 neutrons per fission, of which 1.5 are required to keep the chain reaction going. This leaves one usable neutron with the kinetic energy of about 2 MeV, while *ca.* 200 MeV are released as heat which has to be cooled away. For example, the High Flux Beam Reactor of the Institut Laue Langevin in Grenoble produces a flux density of approximately 1.5×10^{15} neutrons cm^{-2} at a thermal power of 62 MW. Usually the reactor operates in a 'steady state', producing a constant flux of neutrons, although some pulsed reactors have been constructed (IBR-2 in Russia).

Spallation is a process whereby a heavy metal target (of U, Ta or W) is bombarded by a stream of high-energy (typically 1 GeV) protons, accelerated in a proton synchrotron. A complex cascade of processes then yields ca. 20–25 neutrons per incident proton, besides other particles such as pions, muons, neutrinos, and protons. Most neutrons have energies of a few MeV, although for a small minority it can be as high as hundreds of MeV. While a spallation source is inferior to a fission reactor in the *total* output of neutrons, these are generated in a much smaller volume and therefore can give a more concentrated beam. Normally a spallation beam is pulsed (typical frequency 24 to 50 MHz) with the peak intensity comparable to that of a high-flux reactor. A continuous spallation source also exists (SINQ, Switzerland).

The energy E, wavelength λ and velocity v of a neutrons are related as

$$E = \frac{h^2}{2m\lambda^2} = \frac{C}{\lambda^2} \qquad \lambda = \frac{h}{mv} \qquad E = h\nu \tag{24}$$

where h is Planck's constant, m is the mass of a neutron (1.6749×10^{-27} kg) and $C = 81.799\,\mathrm{meV\,Å^{-2}}$. Neutrons are classified into cold ($E \leq 10\,\mathrm{meV}$), thermal ($E \approx 25\,\mathrm{meV}$), hot ($E \geq 100\,\mathrm{meV}$), and epithermal ($E > 0.6\,\mathrm{eV}$). Diffraction experiments (and most other solid-state studies) require thermal neutrons, which have wavelengths of 1.5–2.0 Å (and $v \approx 2200\,\mathrm{m\,s^{-1}}$). Therefore neutrons emitted from a reactor or a spallation source must be slowed down in a *moderator*, where they are brought into thermal equilibrium through inelastic collisions with light atoms (e.g. H, D, or Be) and acquire an energy spectrum approaching Maxwellian distribution (Figure 11). The distribution can be shifted to lower or higher energies by using a low-temperature moderator (e.g. a vessel with liquid CH_4, H_2 or D_2) or a high temperature

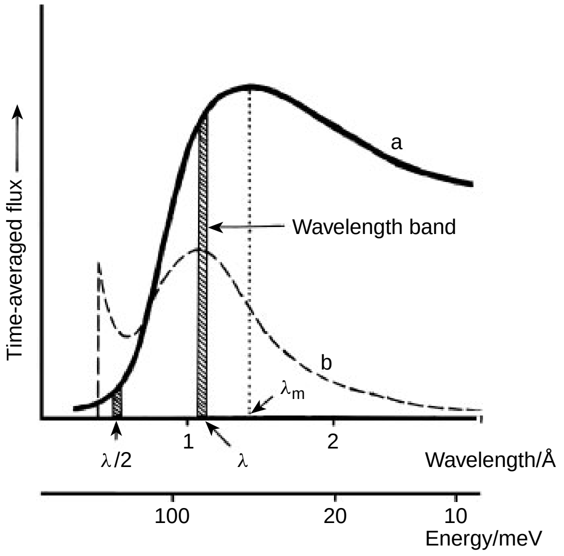

Figure 11 Spectral distribution of neutrons: (a) thermal neutrons from a moderator (showing the wavelength band isolated by monochromatization), (b) pulse spectrum in a TOF machine

one (e.g. a graphite block maintained at ca. 2000 K), known as ‘cold source’ and ‘hot source’, respectively.

Monochromatic neutron radiation is obtained using beryllium, copper or germanium single crystals as monochromators (in the same way as for X rays). Usually the wavelength extracted is chosen not at the intensity maximum (λ_m) but at $\lambda < \lambda_m$, in order to minimize $\lambda/2$ contamination (see Figure 11(a) and Section 2.3.1). In any case, monochromatization can utilize only 1% of thermal neutrons owing to their ‘white’, featureless spectrum; the rest are wasted. The alternative technique, similar to Laue method in X-ray diffraction, uses the widest possible range of λ, that is, the diameter of the Ewald sphere is varied to obtain a reflection. It requires distinguishing of neutrons of different wavelengths and knowledge of their spectral distribution, which is done in practice by sending short pulses of polychromatic radiation toward the sample by a long tube. As neutrons of different λ differ also in velocity (equations 24), they become segregated during the flight and can be identified according to the time of arrival to the detector. This method is therefore known as the ‘time-of-flight’ (TOF) technique.[63–65] The pulses can be obtained from a constant neutron source (a reactor) by interrupting the beam with a ‘chopper’, but the intrinsically pulsed (spallation) sources are most suitable for TOF experiments. In the latter case, the neutrons are moderated less (to avoid extending the time of the pulse) and retain a substantial higher-energy component (Figure 11(b)).

Neutron beams can be focused by mirrors or transmitted by long *curved* tubes (beam guides) using the effect of grazing reflection (see above) in both cases.

2.4 Detection of X rays and Neutrons

In a modern diffraction experiment it is necessary to measure both the directions of diffracted beams with the precision of a few hundredths of a degree *and* their intensities (which can vary by many orders of magnitude!) with the precision of about 1%. A good detector should have high spatial resolution, and be sensitive even to single quanta of diffracted radiation but also able to measure strongest reflections without ‘overflow’ or radiation damage. It should be a ‘proportional counter’, that is, with linear dependence between the beam intensity and the output signal in the whole range. This requires low inherent background (noise) and short dead time of the detector, whose behavior should be stable over time and uniform over its whole working area. Besides counting the *number* of radiation quanta, the detector should be able distinguish their energy (or λ), both to discriminate against parasitic radiation of different λ and to extract positive information in polychromatic methods (energy resolution, or spectral resolution). Finally, the output of a modern detector must be in electronic (digital) form, suitable for computer processing.

2.4.1 X-ray Detectors

The main classes of X-ray detectors are: (i) photographic films (plates), (ii) point detectors, and (iii) position-sensitive detectors (PSDs). AgBr based films react to X rays in much the same way as they do to light. They were used in the first X-ray diffraction experiment (1912) and remained the only practical means until the spread in 1960s and 70s of automated diffractometers equipped with scintillation detectors. A variety of X-ray methods (rotation, precession, and Weissenberg) and corresponding camera designs have been invented.[16–18] The reflection intensities were estimated by measuring the darkening of the film (optical density), at first visually and then by microdensitometers.[66] Photographic methods are slow and labor-intensive and have inherent problems of limited dynamic range and nonlinear response. Since ca. 1980, they have been used only for educational purposes and preliminary investigation of crystals, and recently have been superceded to a large extent even there by area detectors.

On the contrary, a point detector has a window ≤1° wide and therefore can measure diffraction intensity only in one direction (at a single point of the reciprocal space) at a time. Therefore, crystal and detector must be moved in a predetermined manner during the experiment. This is done by a four-circle diffractometer (Figure 12), an automated computer-controlled machine with four independently rotating axes (‘circles’). A goniometric head with the crystal attached is mounted on the shaft of the φ circle, whose carriage moves along the ring-like χ circle, the (imaginary) axis of which is always horizontal. This entire block is rotated on the vertical axis ω, while θ (or 2θ) axis moves the arm on which the detector is placed. All axes and the primary beam from the X-ray source intersect (with a precision of ≤0.02 mm) in the same point, called optical center of the diffractometer. The crystal, if properly aligned, remains centered in this point during any rotation. The ω and θ axes are driven by separate step-motors, while the φ and χ rotations are performed by one motor through two ring pinions located inside the χ circle and enclosing the φ shaft between them, so that an opposite rotation of the pinions spins the φ shaft and a similar rotation moves the φ carriage along the χ circle. All circles can be positioned with high precision, 0.01–0.02°.

In principle, rotations around *three* axis (one of them θ) would be sufficient to bring any lattice plane into an orientation satisfying the Bragg condition (see above) and to intercept the resulting diffracted beam with the detector. However, the fourth degree of freedom makes possible an ‘azimuthal scan’ of a reflection, during which the plane remains in a reflecting position but the crystal rotates around the normal to this plane (so-called ψ axis).

Alternatively, four-circle diffractometer can have a κ (kappa) geometry, in which the χ circle is replaced by two arcs, one of which (‘ω block’) rotates around the vertical ω axis and the other (‘κ block’) around the κ shaft, mounted on the ω block (Figure 12). The κ and ω axes always form the ‘magic angle’ $\alpha = 54°$. Note that in either geometry, every

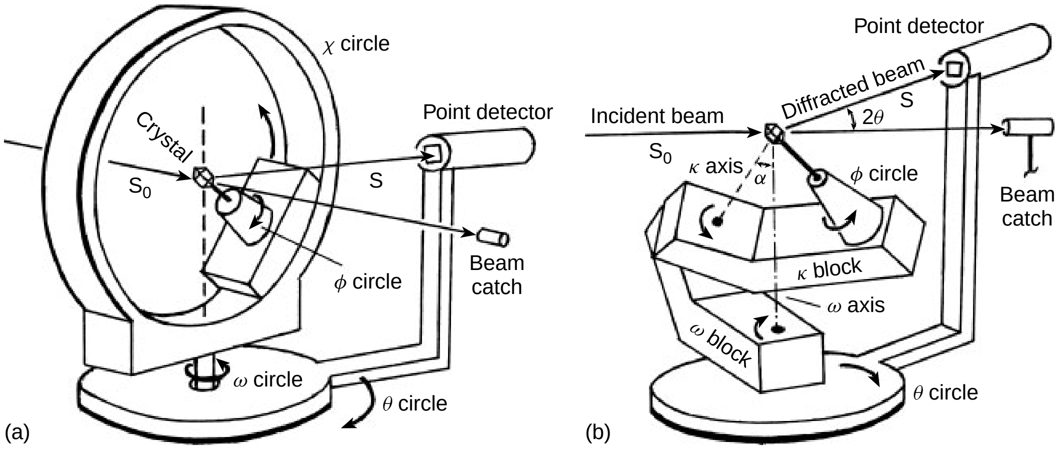

Figure 12 Scheme of a four-circle diffractometer: (a) conventional geometry, (b) κ (kappa) geometry

reflection must be brought into the horizontal (equatorial) plane, in which the counter moves.

Three successive generations of X-ray point detectors have been developed, namely,

- *Gas ionization counters* (classified into ionization chambers, proportional counters, and Geiger-Muller counters) consist of a chamber filled with gas (usually Ar or Xe) and containing a pair of electrodes with a potential difference. Ionizing the gas, X rays produce an electric discharge between the electrodes, proportional to the number and energy of the quanta. Historically the first point detector, which was mounted on a primitive hand-driven diffractometer, was used by Bragg in 1913. Ionization chambers are used today only for primary beam monitoring, being suitable for very high X-ray intensities.
- *Scintillation counters*, wherein X-ray quanta are absorbed in a fluorescent material (usually a Tl-doped NaI or CsI crystal, protected from outside by a Be foil) and converted into light (visible or UV) photons, which are converted into electric pulses and amplified by a photoelectronic multiplier tube, connected to the scintillator through a smear of optical grease. Their comprehensive description can be found in Reference.[15]
- *Solid-state (semiconductor) detectors* are similar in their operational principle to ionization chambers, with the gas replaced by a semiconductor crystal (e.g. silicon or germanium doped with lithium, high purity Ge, CdTe, or HgI_2) in which passing X-ray photons generate electron-hole pairs. This requires only a few eV (compared to tens of eV in a gas), hence such detectors have high sensitivity and energy resolution ca. 15 times higher than scintillation ones. They are closer to being ideally proportional counters than any other type.

Semiconductor detectors have supplanted all other point detectors during 1980s, soon to be superseded by *position-sensitive detectors* (PSDs) alias *area detectors*, which can measure simultaneously all diffracted beams reaching an extensive surface, thus combining greatly increased speed of the experiment with the visual obviousness of a diffraction photograph and the precision equal to (or higher than) that of a modern point detector. The earliest PSDs were developed (since 1970s) for neutron diffraction (see below)[67] and protein crystallography,[68] where respectively the scarcity of source time and the large size of unit cells (and hence of reflection numbers) made the slowness of measuring one reflection at a time particularly vexing. Operating a PSD requires much more complex data analysis and handy electronic storage of vast amounts of data, severely taxing the IT of the time. However, since the mid-1990s PSDs were applied increasingly to small-molecule X-ray crystallography and currently became standard laboratory devices, thanks to major advances in computer technology and recent tremendous decrease in data storage costs. Since the development impetus came from protein crystallography, all early X-ray PSDs were designed for Cu-K_α radiation, but in the last few years, instruments optimized for Mo-K_α radiation (which is normally used in inorganic X-ray crystallography) became commercially available.

The first practical PSDs were the multiwire proportional counter[69] and the television-camera area detector (TVD).[70] The former is a large flat gas-filled chamber, containing a planar anode sandwiched between two planar cathodes. The anode consists of an array of parallel wires, and one of the cathodes of similar wires at a right angle with the former. A passing X-ray photon ionizes the gas (Xe is used for Cu-K_α radiation) and causes an electric discharge between *certain wires*, whose intersection gives the place of its arrival. This method was never much used in X-ray chemical crystallography, but is important in neutron studies.

In a TVD, X rays are converted by a fluorescent phosphor (gadolinium oxysulfide or ZnS) into visible light, which is amplified by an image intensifier (essentially a second phosphor) and detected by the photocathode of a high

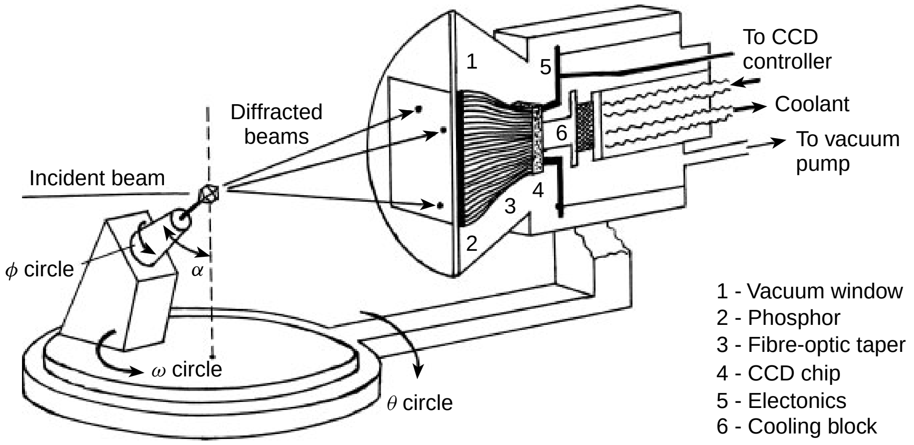

Figure 13 Scheme of a CCD area detector

sensitivity television camera. This scheme had been used in the single-crystal diffractometer FAST commercially manufactured by Enraf-Nonius in the 1990s, but was abandoned because image intensifiers proved expensive, delicate, and error-generating.

Today, two classes of PSD have proven their superiority and have practically replaced other detectors: imaging plates (IP)**[71]** and charge coupled devices (CCD).**[72]** IP's sensitive layer (ca. 150 µm thick) consists of a 'storage phosphor', that is, very fine particles (ca. 5 µm) of amorphous BaFBr or BaF(Br,I) doped with Eu^{2+}, bound by an organic binder. X rays 'photo-stimulate' the phosphor, by causing oxidation of Eu^{2+} to Eu^{3+}. The released photo-electrons are caught by halide vacancies and form color centers (so-called F-centers), which comprise a latent image of the diffraction pattern. This image can be displayed by irradiating the plate with a He–Ne laser beam, which causes an electron in a color center to reduce Eu^{3+} back to Eu^{2+}, with an emittance of blue (390 nm) fluorescent light (so-called poststimulated luminescence).

IPs possess all the advantages of photographic films, that is, high quantum efficiency, good linearity, and (being integrating devices) no dead time limitations. They are available in large sizes and relatively inexpensive. The spatial resolution (which depends on the size of the phosphor grains) is better than that in any other device currently available. The latent image can be stored for fairly long periods of time ($t_{1/2} \approx 10$ h), but usually the plate is processed immediately. In a read-out device, an IP is scanned, in a record-player like manner, by a fine laser beam and a photosensitive reading head. The image is then digitized and stored in computer memory. Then the IP is 'erased' by white light and is ready for repeated use. IPs are used with diffraction cameras, similar in geometry to the photographic ones, but the exposure time is incomparably shorter, usually seconds (although the reading-out process takes minutes).

CCD is a high-photosensitivity semiconductor chip, in which visible-light photons generate electron-hole pairs; the electrons are trapped in potential wells and then read out as electric current. CCDs were originally developed for astronomic observations and similar devices are now used in video cameras. The front of an X-ray CCD detector (Figure 13) is a thin protective layer of beryllium metal; behind it lies the phosphor of Tb-doped Gd_2O_2S, which transforms X rays into light photons. The light from different points of the phosphor sheet is conducted through a taper of optical fibers to the CCD chip of smaller area ('demagnification'). This process inevitably introduces spatial distortions, which must be calibrated on installation and whenever any alterations are made in the detector. In the latest generation of CCD detectors the taper is eliminated and the chip is connected directly to the phosphor. In the first commercially available X-ray CCD detectors, the chip had 1024 × 1024 sensitive points (pixels). Later this number was increased to 4096 × 4096. These detectors have efficient recording, a high dynamic range, and a read-out time measured in seconds. However, the CCD has high intrinsic noise owing to thermal excitation of electrons (even in the absence of any incident radiation) and therefore must be operated at low temperature (typically, 193 to 228 K) to achieve a low noise level. The next few years are likely to see the introduction of so-called 'pixel arrays', another form of solid-state detectors which should be able to record X rays directly, that is, without conversion into visible light, and over a larger area.

The use of area detectors requires much less crystal movement to access all reflections, hence the four-circle diffractometer geometry is no longer necessary. Thus, a CCD detector is usually mounted on a 2θ arm of a three-circle diffractometer, the χ circle is eliminated which inter alia gives considerably more freedom for attachments like low-temperature devices or high-pressure cells. Instead the φ block is mounted rigidly on the ω circle, so that the φ axis forms the 'magic' angle (54°) with the vertical. During a data collection, the reciprocal space is scanned by rotating the ω axis by a small constant steps (commonly, 0.3°), while other circles remaining stationary. During each step the detector accumulates the signal, which is then stored on a computer disk as a ‘frame’. The procedure (‘run’) can be repeated with the φ (and possibly 2θ) circle repositioned. The entire accessible area of the reciprocal space can be covered by a few such runs. When the crystal is mounted in a capillary (see below), it is preferable to perform φ scans while keeping the ω circle stationary.

2.4.2 Neutron Detectors

Neutrons are extremely penetrating and therefore both dangerous to personnel and difficult to detect. Neutron instruments are designed on broadly the same principles as their X-ray counterparts, but are of much greater size and bulk. This is largely due to the need of extensive shielding, in order to stop or slow down the fast neutrons and γ-rays. For shielding, the same materials are used as those employed in moderators or detectors. Cadmium metal captures neutrons very efficiently, but unfortunately produces equally dangerous γ-radiation in the process.

Unlike X rays, neutrons can be detected only by being ‘killed’, hence the detectors exploit certain neutron capture reactions. The early type of point detector was a gas-filled proportional counter containing pressurized ^{3}He or BF$_3$ enriched with ^{10}B, in which the absorbed neutron produces charged particles that ionize the gas. The emitted electrons are accelerated and in turn ionize more gas.**[15,62]** The charge obtained at the high-voltage anode wire is proportional to the reaction energy, which makes these counters extremely efficient for detecting thermal neutrons and discriminating against γ-radiation.

Scintillation detectors are composed of a glass or a plastic front plate loaded with ^{6}Li and ZnS. These absorb neutrons and in so doing create electronic excitations which decay through emitting light photons. The latter are channeled by light guides into photomultiplier tubes. Although they were originally introduced as point detectors, large scintillation detectors can be used as area detectors; with fast electronics, high count rates can be accommodated.**[67b]** This type of detector is particularly suited for neutron time-of-flight experiments with a pulsed source, and has found application at the ISIS neutron facility (Rutherford and Appleton Laboratory, Chilton, UK).

As already mentioned, area (or position sensitive) detectors were first developed for neutron crystallography, since neutrons are scarce and expensive and it is important both to shorten the experiment and to use all neutrons scattered by a sample in various directions, rather than waste all but one reflection at a time. Besides 2D scintillation detectors, there are ‘banana’ 1D multiwire detector**[67b]** and 2D detectors with two mutually perpendicular sets of parallel wires. The latter design is useful for time-of-flight experiments because of ideal time resolution: once an ionization discharge induces current in one or more wires, we instantly know both the place *and* time of its arrival.

3 APPLICATIONS OF THE TECHNIQUES

3.1 Choice of the Technique

The major decisions to be taken are the choice of single-crystal versus powder technique, of the radiation type, and of temperature. Of course, in practice this is often a matter of expediency rather than choice. Thus, all the techniques described above require single crystals. Obviously, if none are available but only microcrystalline powders, a powder diffraction method seems the only route to follow. Although significant advances are being made in solving crystal structures *ab initio* from powder data**[73]** (*see* ***Solids: Characterization by Powder Diffraction***), this route is much more expensive in human and computer time, limited in terms of the complexity of the structure (i.e. number of independent atoms) that can be solved, and less certain in outcome than the single-crystal technique, and should be resorted to only after all attempts to obtain a single crystal have failed.

Since neutrons are an infinitely more expensive and limited resource than X rays, all neutron beam allocation committees normally require that an X-ray determination of the structure has already been completed and that the experiment represents one of those tasks that can be solved *only* by neutron diffraction, such as

1. locating hydrogen atoms with precision, especially in the presence of heavy atoms (e.g. in transition metal hydrides);**[74]**
2. distinguishing between real crystal symmetry and pseudosymmetry created by the arrangement of heavy atoms;**[75]**
3. distinguishing between heavy elements with close atomic numbers;
4. studying magnetic properties of the materials (neutrons have a magnetic moment);**[76,77]**
5. studying structural dynamics, using inelastic scattering of neutrons (the latter exchanging energy with the structure);**[77,78]**
6. real-time studies of transient phenomena, for example, solid-state chemical reactions, phase transitions, and morphology transformations, and particularly of thermally stimulated processes (‘thermo-diffractometry’).**[62,64]**

Tasks 1–3 rely on the fact that neutron (unlike X-ray) scattering does not correlate directly with the atomic number and therefore heavy atoms no longer dominate the diffraction pattern; 4 and 5 also depend on intrinsic properties of thermal neutrons, but require special experimental settings, distinct from ordinary diffraction studies. Task 6 requires a combination of a high-flux neutron source *and* a PSD, so that a complete (powder) diffraction pattern can be recorded simultaneously within minutes.

In 1970s and 1980s, neutron diffraction was regarded an indispensable step in a charge density study, but this is no longer the case (see below).[52,54] Neutron radiation is also used for powder diffraction and Rietveld analysis[77] (*see* ***Solids: Characterization by Powder Diffraction***).

Another limitation of the neutron technique is that it generally requires much larger single crystals than X-ray studies, which are not always possible to grow. However, this is changing with the introduction of new generation of neutron area detectors.

X-ray SR, because of its high intensity, enables crystallographers to obtain meaningful data from samples which are too small or weakly diffracting to be studied with a laboratory source. However, synchrotron beamtime is also a scarce resource.

The choice of X-ray wavelength λ is guided by a number of (often conflicting) considerations. In laboratory conditions, this choice is usually restricted to two characteristic wavelengths, from X-ray tubes with Cu-anode (1.54178 Å) and Mo-anode (0.71073 Å). The intensity of X-ray scattering is proportional to λ^3 (equation 7), hence the former will give 10 times more diffracted intensity from the same sample. On the other hand, long-wavelength X rays are almost always absorbed more strongly than short-wavelength (except in the rare cases when the latter wavelength falls under the specific absorption band of some sample element). Not only does this reduce the overall intensity of the recorded reflections, but the *relative* intensities are distorted, sometimes drastically (if the crystal shape is very anisotropic and heavier elements are present). The latter can seriously hinder structure solution and refinement. Furthermore, the absorbed X-ray energy goes into heating the crystal and may cause its chemical deterioration.

A longer λ is preferable when unit the cell parameters are very large, in order to facilitate the resolution of adjacent reflections. This is one of the reasons why Cu radiation is preferable in protein crystallography, where the unit cell dimensions are generally large. In inorganic chemistry this problem seldom occurs, except for some metal clusters, which are unsuitable for Cu radiation anyway, owing to its strong absorption. On the other hand, the shorter the wavelength, the more reflections will appear on an area detector of a constant size, and the higher order of reflections can be measured with the same experimental setting.

Anomalous X-ray scattering (Section 2.2.2) is a specific property, but generally it increases with λ and with atomic number Z. The difference may be significant if an absolute configuration of the compound is to be determined. With Mo radiation, it is hopeless to attempt such determinations unless atoms with $Z \geq 15$ are present in the sample. With Cu radiation, even anomalous scattering of oxygen is sometimes sufficient to effect discrimination.

Finally, X rays of a certain λ can specifically excite X-ray luminescence of the sample. Thus, Cu-K_α line will excite iron atoms, and Mo-K_α those of yttrium, producing a strong parasitic background which (unlike Bragg scattering) *does not* decrease with the increase of the Bragg angle – a most unwelcome complication.

As for the choice of temperature, it is always preferable to collect X-ray diffraction experiments at as low temperature as possible, unless the sample undergoes a phase transition on cooling, resulting in its destruction or serious deterioration of quality. The advantages of low-temperature experiment[79] are numerous, including:

- it decreases the atomic vibrations, which both reduce diffraction intensities (especially at high Bragg angles) and cause systematic errors in observed bond distances (see Section 2.1.3);
- it reduces the thermal diffuse scattering (TDS) and extinction – sources of systematic errors in F_{hkl};
- it makes possible data collection from most crystals which would be unstable at room temperature, owing to radiation damage, chemical decomposition (even without irradiation), reactions with air and moisture, or solvent loss;
- it allows both positional (static) and thermal (dynamic) disorder to be more readily identified and modeled.

3.2 Nonambient Conditions

3.2.1 *Low Temperatures*

The standard device for maintaining the low temperature of the crystal during an X-ray diffraction experiment is an open flow nitrogen gas cryostat, which is required (i) to produce a stream of cold N_2 gas with constant temperature and flow rate, (ii) to convey it to the crystal without obstructing movements of the diffractometer circles, and (iii) to prevent ice forming upon the contact between the N_2 and warm outside air. The ice is highly undesirable, as it provides X-ray reflections of its own, and can damage the crystal and sometimes even the hardware.

In early designs of cryostats,[80,81] the cold gas was obtained by evaporating liquid nitrogen (by a boiling resistor) inside a pressurized Dewar vessel, transferred by an insulated pipe, and delivered through the nozzle placed within <1 cm from the crystal. Inside the pipe (usually just before the nozzle), there are an electric heater to regulate the stream temperature and a thermo-couple to measure it. Although such low-temperature attachments to X-ray diffractometers (Syntex, Enraf-Nonius) were produced since 1970s, smooth running thereof required constant efforts and engineering skills, and was done routinely only in a few laboratories. The main sources of trouble were fluctuations of the flow rate, frequent ice blockages, high consumption rate of liquid N_2 ($2-3\,\mathrm{l\,h^{-1}}$) and impossibility to refill the supply tank without interrupting the experiment. Furthermore, since the N_2 gas was warming up by 20 K or more in the long transfer pipes, the base temperature was impossible to achieve.

These problems were largely eliminated by the principally new Cryostream device,[82] which became commercially available in 1990 from Oxford Cryosystems. In it, liquid

N_2 was pumped from an unpressurized Dewar tank into an electric evaporator, converted there into nitrogen gas, cooled in a heat exchanger by a counterflow of liquid N_2 and delivered to the sample through a very short pipe. This device proved extremely reliable. The consumption of liquid N_2 is low ($0.6\,l\,h^{-1}$) and the supply tank can be refilled without stopping the experiment. Using a stream heater, the temperature can be regulated between 80 and 375 K with a stability of 0.1 K. Icing is efficiently prevented by surrounding the cold N_2 nozzle with an outer warmer one, which conveys dry air at room temperature. However, it is very important to avoid any turbulence between the two streams and between the cold stream and the crystal mount.

Since the Cryostream nozzle is stationary, the angle between the stream and the crystal mount changes as the diffractometer circles move. For a long time such an arrangement was regarded as highly undesirable, because it was a source of systematic errors. Therefore, in the low-temperature attachments to the Syntex (later Bruker) four-circle diffractometers, the nozzle is fixed to the χ circle and remains coaxial with the φ axis, whatever the circle movements. The gas is conveyed to the nozzle through a system of Dewar glass pipes with swivel joints, which provide reasonably free movement about all goniometer axes (but not as free as without them!). To prevent icing, an electrically heated conical deflector is placed below the crystal. However, it has been proven by experience that the advantages of the latter design are not substantial, and hardly compensate for the restricted circle movements and for the loss of cold at each of the swivel joints.

Most importantly, with the new cryostats the sample temperature can be regulated at will (while for the first generation, any alteration of the setting was most undesirable). Combined with the new means of fast and visual monitoring of the diffraction pattern, this opens unprecedented opportunities for in situ, real-time studies, for example of phase transitions.

Using these cryostats, it is possible to grow and study single crystals of substances which are liquid, or even gaseous, at room temperature.[83] The liquid/gas is sealed into a Lindemann tube, which is attached to a goniometric head. The sample is flush-cooled and freezes into a polycrystalline mass, then warmed up to the melting point, until all of it melts except a single powder grain, then very cautiously cooled again. Now the surviving grain serves as the nuclei, from which a single crystal is grown. Such experiments still require more-than-average dexterity and patience, but have been greatly simplified by new cryostats and area detectors.

3.2.2 Ultralow Temperatures

The absolute lower limit of cryostats using N_2 is its boiling point of 77 K. Lower temperatures can be obtained using helium as a cryogen, in the following two principally different schemes.

- Closed-circuit cryostats, for example, of the Displex type, were originally introduced for neutron diffraction studies,[84] but later were successfully applied for X-ray studies as well.[85] The crystal is enclosed by three successive thin-walled cans of beryllium metal, the interior of which is evacuated. Circulating He cryogen cools the copper block, on which the crystal is mounted upon a heat-conducting fiber, and hence the crystal itself. Temperatures down to 9 K have been achieved and maintained with high stability.[85] However, the device is large and heavy (several kg) – and it has to be mounted on the χ circle of a diffractometer. This does not matter for neutron diffractometers (which have to be massive anyway), but have precluded wide use of the closed-circuit scheme in X-ray diffractometry. Besides this, the beryllium metal of the cans (i) contributes strong parasitic diffraction, (ii) in nontransparent, hence the crystal has to centered ‘blindly’ according to the diffraction pattern, and (iii) is highly toxic.
- Open-circuit He cryostats work on the same principle as N_2 cryostats, that is, a stream of cold He gas is blown upon the crystal and then dissipated into the atmosphere.[86] The high cost of He made this scheme unthinkable until the duration of X-ray experiments was drastically reduced by the advent of area detectors, as well as made the access the sample easier (by eliminating the need for the χ circle). The first commercial device (Oxford HeliX, from Oxford Cryosystems) has recently emerged from the prototype stage.[87] It allows experiments at temperatures down to 30(1) K (Figure 14), while successfully addressing the problem of icing. It has the advantage of using He gas (ca. $2\,l\,h^{-1}$ at 200 bar) rather than liquid He, which is very expensive and difficult to handle. The cryostat comprises a small closed-cycle helium refrigerator which is used

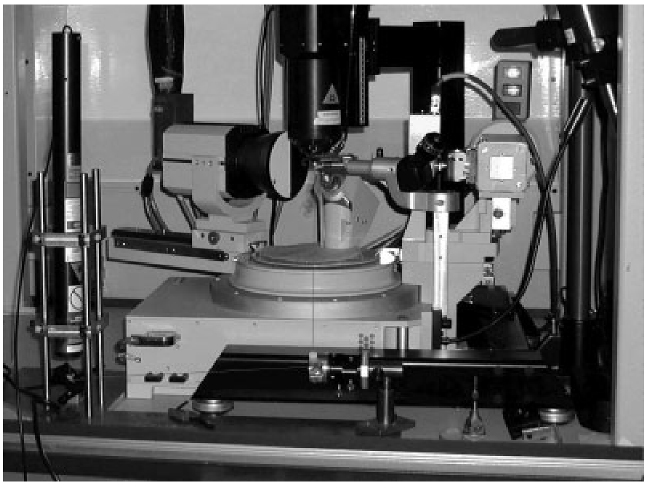

Figure 14 An experimental setting for single-crystal X-ray diffraction study at 30 K, showing a Bruker three-circle diffractometer with a SMART 1000 CCD area detector, a laser device for crystal irradiation and a HeliX open flow helium cryostat in action

to cool down a heating stage. He gas flowing around this stage is cooled down and finally released through a specially designed nozzle onto the sample.

The lowest possible temperatures are essential for

- charge density studies (Section 3.2.8);
- the studies of superconducting material, for most of which the T_c is well below 77 K.

Generally, access to the widest possible temperature range is vital for the study of new materials, where the detailed structure is unknown at certain critical temperatures directly related to changes in physical properties.

3.2.3 High Temperatures

High-temperature crystallography[81,88,89] is a very specialized area of research and will not be discussed here in detail. In the past decade, a large number of novel sophisticated single-crystal heaters[88,89] and corresponding crystal holders[90] have been described. Generally, single crystals can be heated up to ca. 900 °C using gas-flow heaters (either resistance- or combustion-heated) and above that limit by radiative heaters or laser heaters. Moderately high temperatures (up to 500 K) can also be achieved with standard nitrogen cryostats, which permit heating of the N_2 stream.

3.2.4 High Pressures

High-pressure crystallography generally, and diffraction studies (with both X rays and neutrons) particularly, is a nonroutine and traditionally highly specialized area of research, developed by several research groups around the world and (in part) closely associated with industrial, aerospace, and defense applications. X-ray diffraction studies began in 1935 with a modest pressure of 1 kbar (0.1 GPa) achieved between quartz anvils.[91] The real breakthrough came with the development of the diamond anvils cell (DAC)[92] which increased the pressure limit to 1 Mbar, and subsequently to 3 Mbar (300 GPa),[93] thus approaching the ultimate strength of diamond (gem grade). Although high-pressure diffraction is more often carried out on powders, highly sophisticated single-crystal techniques[93,94] have also been developed. In recent years this field has undergone explosive growth, owing to the new possibilities offered by better methods of generation and detection of X rays, and increasingly attracts the interest of the wider crystallographic community.

The operating principle of a DAC is elegantly simple (Figure 15). A gasket of metal foil (usually steel, W or Re) is placed between the diamond anvils. A hole drilled in the center of the gasket contains the sample immersed in a hydrostatic liquid. The anvils are mounted on beryllium (for X-ray transparency) back-plates, to which force is applied by an inflatable membrane, a level-arm mechanism or just by tightening screw-bolts. Thus a hydrostatic compression is achieved. Such cells can be operated also at high and low temperature, and are also suitable for spectroscopic studies, since diamond is an ideal transmitter of heat and of all types of radiation.

Unfortunately, the scale of the DAC is limited by the size of natural diamonds (which are also expensive and are prone to crack during loading). Hence, the higher the pressure, the smaller the volume to which it can be applied, which in the megabar range is already of the order of 0.001 mm^3. Furthermore, metallic parts of the cell greatly reduce the accessible part of the reciprocal space. Finally, both the incident and the diffracted beams have to pass through the whole thickness of the diamond, which both absorbs X rays

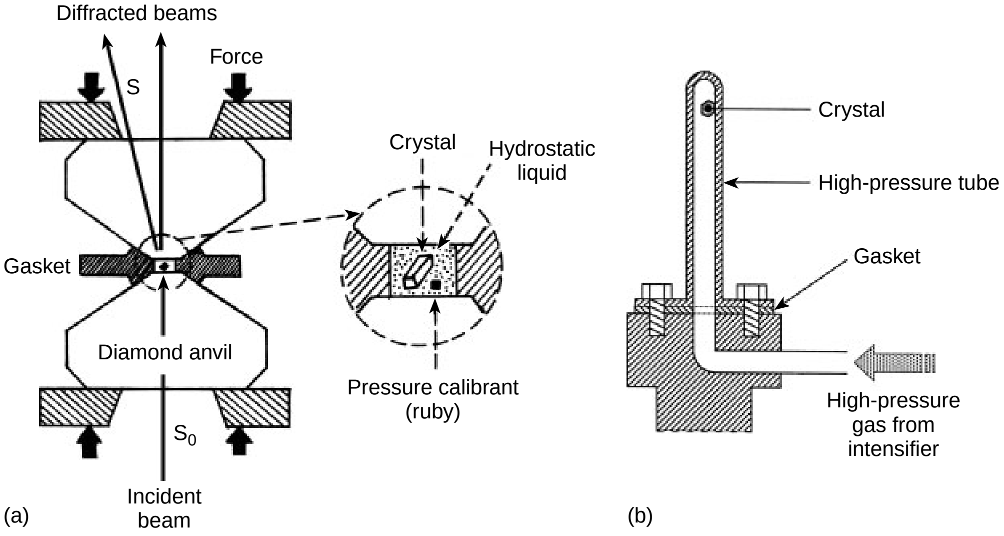

Figure 15 High-pressure cells for single-crystal X-ray studies: (a) diamond anvil cell, (b) gas pressure cell

and (being a single crystal) contributes *very* strong reflections of its own. Thus the experiment is far from trivial[95] and requires a strong X-ray beam and specialized software. In this respect, much can be expected from the novel sharp-focused Microsource X-ray sources (see Section 2.3.1).

The DAC is unsuitable for an ordinary neutron experiment, because the latter requires much larger samples. Alternative means of compression, such as liquid- and gas-pressure cells,[94] or even sapphire anvils (specially designed for use with He cryostats),[96] are but poor substitutes in the magnitudes of pressure. However, encouraging results[97] have been obtained by using DACs in conjunction with high-power neutron sources and optimizing the diffraction instrument itself.

Single-crystal diffraction studies at moderate pressures (2–3 kbar, with 5 kbar in prospect) can be carried out with a gas pressure cell, that is, a thin but strong tube of X-ray transparent material, for example, a laminated carbon composite (Figure 15). Such a cell is small enough to be mounted on an ordinary goniometer head, yet can accommodate much larger (and more easily mounted) crystals than a DAC. A similar device is being developed at the ISIS facility for neutron diffraction experiments.[98]

3.3 Conducting an X-ray Diffraction Study

A sufficiently detailed practical guide on this subject would run into many volumes, hence only the main points are summarized in this section, together with some ‘hints’ not always included into main textbooks. A routine X-ray crystallographic study comprise the following major steps:

1. grow good quality crystals;
2. select a suitable crystal, mount it on a diffractometer and optically center;
3. assess its ‘X-ray quality’ and find the (preliminary) crystal lattice;
4. choose measuring strategy and collect the intensity data;
5. reduce intensity data to structure factors F_{hkl};
6. solve the phase problem and find a model structure;
7. refine this model against observed structure factors;
8. calculate geometrical parameters of the structure and interpret them;
9. prepare the results for publication and/or deposit them at one of the databases.

It is noteworthy that area detectors require somewhat different strategies than point detectors; the differences are discussed below.

3.3.1 *Growing Crystals*

This step is surprisingly overlooked, in a sense ‘lost’ between crystallographers and synthetic chemists. One cannot emphasize too strongly that crystallographic results can be only as good as the crystals. Ii is also unfortunate that details are seldom published of exactly how the crystals were obtained, as this often requires much ingenuity or a lucky hit upon the right conditions. The remark ‘suitable crystals were obtained by slow evaporation’ is of no help to the reader.

Optimally, X-ray crystallography requires single crystals of a few tenths of a millimetre in size, which are not intergrown and which have grown *slowly* (they are usually of better quality). Neutron experiments generally require larger crystals; a decade ago ca. $5\,\mathrm{mm}^3$ was considered a standard size, but recent improvement of the technique make considerably smaller samples acceptable ($\leq 1\,\mathrm{mm}^3$).

In fact, extremely valuable information about different crystallization techniques can be found in the chemical literature.[99] Good crystals can be grown from gas phases (sublimation), melts, gels[100] and liquid solutions, the latter being by far the most common. Crystallization comprises two major stages, namely (a) nucleation and (b) growth of the resulting crystal seed into a substantial crystal. Nucleation is usually endothermic, hence it is better achieved by slow evaporation at elevated temperature than by slow cooling. It is often helped by ultrasound (that is the reason why scratching at the glass of the vessel may help) and affected considerably by mere traces of impurities (which may act both as inhibitors and accelerators). Hence extremely clean, or brand new, vessels are preferable.

On evaporation the solvent often creeps up the walls of a glass vessel, because the silicate OH-groups make glass hydrophilic. Therefore nucleation occurs outside the solution; this never gives good crystals and can be avoided by using polypropylene or Teflon vessels.

Note that *very few* seeds are required to grow good single crystals, and that massive seeding gives a crash precipitation of powder or poor crystals. Therefore it is advisable, after spontaneous crystallization sets in, to redissolve almost all the seeds and to leave the remaining few to grow, as close as possible to the point of thermodynamic equilibrium, beyond which the nuclei redissolve. Therefore crystallization from too concentrated solutions, that is, good solvents, should be avoided. It is better to use a solvent, or a mixture of solvents, in which the solute is less soluble.

It is helpful to avoid, as far as possible, the solvents (especially dichloromethane) and anions (e.g. perchlorate or triflate) that show a tendency to be disordered in the crystal structure.

3.3.2 *Choosing and Handling the Crystal*

Selection of the crystal is the crucial step of the whole study and the time spent on it is well spent. During data collection the crystal should remain within that inner part of the incident beam which has a uniform intensity distribution. Its diameter is smaller (80% at best) than the nominal diameter of the collimator. Thus in X-ray diffractometry a good working norm is for all dimensions of the crystal to be $\leq 0.5\,\mathrm{mm}$, and preferably as uniform as possible. For neutron experiments, the samples must be larger by one or two orders of magnitude, but the following comments concerning crystal quality apply to them also. With area detectors this requirement is not as strict with point detectors, if a sufficient redundancy of the data can be ensured to perform an empirical correction of the reflection intensities (see below). Larger crystals must be cut to size by a sharp scalpel blade (special diamond or sapphire blades are used for hard crystals). If thereupon they crumble and fall apart, they are probably aggregates of microcrystals that had grown deceptively into more or less 'regular' shape, but these will not give usable diffraction patterns. The way in which a (true) single crystal cleaves reflects its internal packing. For this reason, some crystals which grow as long thin needles or plates, respond to any attempt to cut them by cleaving in all directions except the necessary one. These have to be used as they are, or reduced by dissolving parts of them in a solvent.

On the other hand, the crystal must be big enough to provide sufficiently strong diffraction, but this depends also on the beam intensity, detector sensitivity, and crystal composition, and has to be learned by the rule-of-thumb. Thus, a crystal smaller than $0.001\,\mathrm{mm}^3$ and containing no atom heavier than oxygen seldom gives good data, while this size may be ideal for a crystal of a heavy metal cluster. Other things being equal, a crystal with larger unit cell dimensions diffracts more weakly, the density of lattice points in the Bragg plane being lower. If the crystal is strongly absorbing the X rays, its optimal diameter would be the inverse of the linear absorption coefficient μ, for example, if $\mu = 10\,\mathrm{mm}^{-1}$, the maximum optimal diameter would be 0.1 mm.

The crystal should have well defined faces and straight edges, with no reentrant angles and must be transparent, unless very darkly colored. The time-depending darkening or clouding of once shiny crystal faces, the loss of transparency, surface pitting, and 'auto-crumbling' are indicators that the crystal is chemically unstable toward air oxygen or moisture. Alternatively, many crystal structures incorporate solvent molecules, the gradual loss of which has a similar effect, that is, the crystal deteriorates in quality and finally turns polycrystalline or amorphous.

Several techniques exist for handling air-sensitive crystals. The highly sensitive ones are handled inside a laboratory glovebox (filled with a dry, inert gas) and sealed into a Lindemann tube, that is, a thin-walled glass capillary made of low-density, nonsilicate glass (which thus gives minimum parasitic X-ray scattering). In this case, careful preinspection of the crystal is almost impossible and its quality must be investigated subsequently using X-ray diffraction.

Crystals that are only moderately unstable can be handled using the 'oil drop' method,[101] which became popular in the last decade. This method is extremely convenient and easy, obviating the need for glove boxes and other complicated mounting devices. The crystals are prepared in a Schlenk vessel which is connected to an inert gas (N_2 or Ar) line, creating an excess pressure inside. Then it is possible to open the vessel without letting the air in and to reach the crystal with a spatula carrying a drop of the inert oil (polyfluorinated polyesters). The oil, which has exceptionally high surface tension, will coat the crystal and become an effective atmospheric seal. Then the crystal (under an oil drop) can be studied visually on a microscope slide (with the possibility to be cooled by dry ice), mounted onto a holder and thus transferred to the diffractometer, which is operating with a low-temperature device. On cooling, the oil, which solidifies at -30 to $-40\,^\circ\mathrm{C}$, will act as a glue.

Neither the inert atmosphere nor the oil, will prevent the crystal from losing any solvent of crystallization. In such a case, the crystal should be stored under its mother liquor and sealed into a Lindemann capillary together with a small amount of mother liquor, to maintain a high local vapor pressure of the solvent.

A number of 'home-grown' and commercially produced mounting devices exist,[79a] which allow manipulations of sensitive crystals under a stream of dry, possibly cold, N_2 gas, or even their transportation in a small Dewar vessel with liquid N_2 and direct transfer into the cold stream of the diffractometer cryostat.

The quality of a transparent crystal can be very efficiently checked using a polarizing microscope.[11] When the crystal is placed between two polarizing prisms with perpendicular polarizing directions, the background and all noncrystalline matter will remain dark, but the crystal itself will be illuminated owing to its birefringence. If the microscope slide is rotated, the crystal will be 'extinguished' every 90°. If parts of it do not extinguish simultaneously, or not at all, we are dealing with more than one crystal grown together. Note that crystals of trigonal, hexagonal, and tetragonal symmetry viewed along the major axis, and cubic crystals in any direction, behave like optically isotropic (amorphous) matter, that is, remain dark.

After a suitable crystal has been selected, it must be fixed securely (e.g. with epoxy resin) inside a Lindemann tube, or on the end of a glass fiber several mm long, which in turn is glued into a metal pip, which fits into the well at the top of a goniometer head. During the experiment the whole mounting must remain perfectly rigid lest a wandering crystal play havoc with the reflection intensities. Therefore one should avoid adhesives which do not set quickly and firmly. The glass fiber must be thick enough not to wobble during circle rotations or under the pressure of the N_2 stream, but its thickness and the amount of glue should not be excessive, because both will contribute to parasitic X-ray scattering and absorption. At low temperature, a human hair 2–3 mm long is preferable to glass fiber.

The goniometer head is mounted on the φ circle of the diffractometer. The head has three mutually orthogonal micrometric screws, which permit optical centering of the crystal in the center of rotation of all diffractometer axes. The crystal must not appear to precess at all when viewed through the telescope (or a video camera) mounted on the diffractometer, that is, it must not move away from the optical center when rotated around any axis. Good optical centering is often difficult with crystals mounted inside capillary tubes, or when working at low temperatures as ice starts to form on the crystal, the fiber, and the tube. Here the true center can be deduced from the X-ray scattering results.

3.3.3 Preliminary X-ray Investigation

With a point detector, it is impractical to scan the whole of the reciprocal space; X-ray intensity is measured only in the areas where the reflections are expected. Hence it is impossible even to begin data collection until the parameters of the crystal lattice *and* its orientation are known with precision. To determine them, a few sectors of the reciprocal space are scanned in a 'random search mode'. Once a high intensity is detected, the setting angles of the reflection are optimized by an iteration procedure, with the precision of 0.01° in ω, 0.04° in χ. Alternatively, the preliminary angles of a reflection can be determined from a Polaroid diffraction photograph and then refined. After 20 to 50 reflections (lattice points in the reciprocal space) are thus obtained, the autoindexing program will search for a set of three shortest vectors (reciprocal lattice translations, see Section 2.1) describing all these points.

Now we have two different coordinate systems. One, known as the 'laboratory axes', comprises three orthogonal axes of unit length, the directions of which are uniquely defined with respect to the axes of the diffractometer circles and the direction of the primary beam (although these conventions vary from one diffractometer type to another). A point in these coordinates is described by a vector **x**. The other system comprises three principal vectors of the reciprocal crystal lattice (see Section 2.1). In this system, a Bragg reflection is expressed by a vector **h** whose coordinates are the Miller indices *hkl* (Section 2.2.1). The relation $\mathbf{x} = \mathbf{Ah}$ between the two systems is defined by the *orientation matrix* (OM) **A**,

$$\mathbf{A} = \begin{pmatrix} a_x^* & b_x^* & c_x^* \\ a_y^* & b_y^* & c_y^* \\ a_z^* & b_z^* & c_z^* \end{pmatrix} \qquad (25)$$

The OM is pivotal to the data collection, because from it one can calculate diffractometer angles for each reflection.[102] After the autoindexing, the unit cell parameters and the OM are refined by least squares[103] against the setting angles of all available reflections. Then the lattice is transformed to the standard Bravais lattice in the standard setting. It is now possible to measure the intensity of any reflection in its precalculated position. A common approach is to find another 20 to 50 strong reflections with higher Bragg angle, and re-refine the unit cell and OM against them, with higher precision.

The real crystal, even of the best quality, is not the perfectly ordered array described in Section 2.1, but an assembly of microscopic crystalline 'blocks', the orientations of which differ by a small angle known as its 'mosaic spread'. Equation (2) is not satisfied for all of the blocks simultaneously, but under slightly different conditions. The same, of course, applies to the monochromator crystal, hence the λ in equation (2) is not a single value but varies in a certain range. The incident beam is not absolutely collinear, and the sample has finite size. Because of these and other factors, each reflection is not a geometrical point but a three-dimensional feature in the reciprocal space. The quality of the crystal can be assessed by scanning the profiles of several reflections. There are many different types of scans,[104] corresponding in fact to different directions in the reciprocal space (Figure 16). For example, if the ω circle (i.e. the crystal) is rotated by a certain angle while the 2θ circle (i.e. the counter) is simultaneously rotated by twice that angle (so-called $\omega/2\theta$ or $\theta/2\theta$ scan), the reflection is scanned along the line connecting its center with the lattice origin. If the ω circle is rotated and the counter remains stationary ('ω scan'), the reflection is scanned along an arc, the center of which is the origin. This scan, whereby blocks are passing through the Ewald sphere in succession, gives the most explicit indication of the crystal quality. A 'good' crystal must have a symmetric peak in any cross section (scan). A split peak indicates two slightly misoriented (intergrown) crystals, an exceedingly wide peak indicates a crystal of poor quality or one in the process of decomposition.

If the autoindexing fails, it is usually because (i) the reflections are too few, and more of them should be found

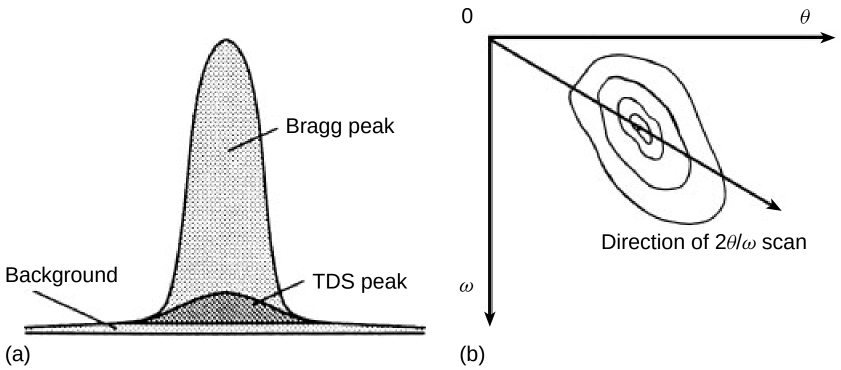

Figure 16 Schematic of a diffraction peak profile in one (a) and two (b) dimensions

and centered, (ii) the reflection set does not define a 3D picture, for example, all reciprocal lattice point lie in one plane, or (iii) the reflections belong to more than one crystal, grown together in the sample. In the latter case, autoindexing can apparently 'succeed', yielding a unit cell with unreasonably large dimensions (>50 Å). It is sometimes possible to 'deconvolute' the reflection set, that is, to identify which reflections belong to each of the crystals and index them separately. Nevertheless, determining the structure from such crystal is a task difficult and uncertain in outcome, which should be undertaken only if no truly single crystals can be obtained.

This illustrates the principal drawback of the point-detector instrument, that is, the operator cannot see the whole diffraction pattern but can only probe it at different points. For example, if the structure contains one outstandingly heavy atom with the coordinate $x = 0.5$, all reflections with the even index h will be systematically stronger than those with odd h. In this case, a random search may miss the latter reflections altogether and the cell parameter a that is found by the autoindexing will be half the value of the real one. The data collection routine based on such parameters will miss half of the reflections, without which it will be impossible to determine the structure.

With an area detector, the data collection consists of scanning all the accessible reciprocal space or a large part thereof, and we do not need the OM or any other information to begin it. However, it is always advisable to investigate the crystal quality at this stage, rather than risk wasting valuable instrument time on collecting worthless data. In this case, the autoindexing routine includes

- scanning through three narrow sectors of the reciprocal space, in mutually perpendicular directions;
- identifying strong reflections (peaks of intensity) and determining their weighted centers;
- finding the lattice vectors fitting the positions (setting angles) of these reflections;
- performing the least squares refinement of the lattice parameters and OM.

The unit cell thus obtained will be the smallest one fitting all the reflections, that is, a primitive triclinic one. The software will automatically investigate whether (i) the shape of the lattice does not correspond to a higher system (i.e. orthorhombic if all the unit cell angles are close to 90° within experimental errors) and (ii) the primitive lattice can be transformed (by linear combinations of the lattice vectors) into a centered lattice of higher symmetry, corresponding to one of the Bravais types. However, the suggested symmetry is based solely on the *shape* of the unit cell (which can be deceptive) and must be verified by comparing the intensities of the (supposedly) symmetrically related reflections, which are not yet available on this stage.

A failure of the autoindexing routine happens for the same reasons as described above and can be treated in a similar manner. The great advantage of the area detector is the possibility of constant visual monitoring of the *whole* diffraction pattern, as each frame is processed and displayed on a computer screen in real time, and previously recorded frames are stored in memory and can be recalled rapidly. The crystal quality can be assessed by investigating peak profiles in various directions. In this case, each peak is recorded as a *three-dimensional* intensity map, as it covers a number of CCD pixels in each frame (this gives two dimensions, x and y) and usually is present in a few adjacent frames (the third dimension, z). The software also can calculate the expected reflection positions on the detector and to compare them with the actual intensity at the spot; this greatly reduces the risk of mis-characterising the lattice.

Generally, an area detector permits one to check the sample quality much faster and more conclusively, because of easier visualization. Thus if a supposed single crystal gives a set of powder diffraction rings or an amorphous-state halo, the operator will see this immediately; it would take a lot of time and expertise to extract this from the results of a random search!

In any case, the unit cell found must be considered with common sense. It must always contain an integer number (Z) of formula units, and Z is related in certain ways to the crystal symmetry. Thus a triclinic crystal with the space group $P\overline{1}$ may have $Z = 1$ if the molecule lies at an inversion center, $Z = 2$ if the molecule has no crystallographic symmetry, $Z = 3$ for the (most unlikely) combination of the first two options, and $Z = 2n$ if there are n symmetrically independent molecules in the structure. Note that while (molecular) crystals with $n = 2$ are very common, those with $n > 4$ are extremely rare.

Thus it is easy to check whether the cell volume is compatible with the expected molecular formula, allowing 18 Å^3 per nonhydrogen atom. This rule is valid for a surprisingly wide range of organic, organometallic, and coordination compounds, although adjustments can be made for special cases (down to 14 Å^3 for fluorine and some highly condensed aromatics, up to 22.5 Å^3 for some organosilicon compounds). It is useful to check at this stage whether the structure has not been already determined, by searching the relevant database (see Section 4) for similar unit cell parameters.

The experiments with N_2 cryostats are usually run at temperatures between 100 and 170 K; the desire for the lowest possible temperature is balanced by the necessity to avoid icing. Such temperatures are almost always sufficient to prevent both the chemical (or photochemical) decomposition of the sample and the solvent loss. The choice between rapid (flash) and slow cooling depends on the nature of the sample. When the thermal expansion coefficient is likely to be high, as is usually the case with conformationally flexible molecules, slow cooling is preferable if the crystal stability permits it. On the other hand, flash-cooling is the only technique possible for protein crystals, because slow cooling will allow the crystallization water to form ice crystals, whereupon the protein itself will lose crystallinity.[105] In fact, most crystals survive sharp cooling, that is, being placed instantly under the cold stream of N_2. If the crystal cracks, turns polycrystalline (and opaque) or falls off the mount at this moment, this is usually because it has undergone a phase transition on cooling. During a transition into a phase of lower symmetry, a single crystal often becomes a twin (see Section 3.37) while remaining apparently intact; thus the sample that looked perfect during preliminary investigation (at room temperature!) gives an unindexable diffraction pattern. In such cases, one should determine the transition temperature (by a slow cooling) and perform the data collection at a slightly higher temperature, unless the transition itself is the object of the study.

3.3.4 Data Collection

Data collection on a point-detector diffractometer consists of scanning the reflections (at predetermined positions) in succession, by one of the scan modes described above, as well as measuring the background on both sides of every reflection. The $\omega/2\theta$ scan mode is preferable for good crystal with sharp peak profiles, ω mode for poorer quality crystals. In neutron experiments, a compromise $\omega/x\theta$ scan is used, where x equals 1 or it is variable. In order to attain the same statistical accuracy (e.g. 1%) for all reflections, weaker reflections are scanned more slowly than the strong ones. For a good structure determination, the diffraction data should extend at least to $\sin\theta/\lambda = 0.6$ Å^{-1}, that is, a complete set of reflections with $\theta_{\max} \geq 25°$ for Mo-K_α radiation, or $\theta_{\max} \geq 68°$ must be collected. Light-element molecular crystals at room temperature seldom diffract much beyond this limit, but minerals do. Cooling the sample tremendously increases high-angle diffraction, especially for molecular materials. Often only symmetrically independent ('unique'), rather than all reflections within the θ limit are measured, in order to shorten the experiment. The risk inherent in this strategy is that if the lattice symmetry has been overestimated on the previous step, for example, a monoclinic lattice with $\beta \approx 90°$ has been mistaken for an orthorhombic, the experiment will yield only a fraction (in this case, about half) of the real unique set. Such data is completely useless, and there is no way to repair the blunder except repeating the whole experiment.

The duration of the data collection is roughly proportional to the number of unique reflections, that is, basically to the volume of the asymmetric part of the unit cell. For a well-diffracting sample, a modern four-circle diffractometer can measure 80–150 reflections per hour, although the speed can be considerably lower for a weakly diffracting sample. Thus the whole experiment can take several days for a moderately complex structure. Data collection is highly automated; a small group of strong reflections (standard, or check reflections) is remeasured at regular intervals throughout the experiment, thus monitoring the possible radiation source instability, movement/misalignment of the crystal or its chemical or radiation decay. If the latter occurs, reflection intensities are corrected by scaling them against the intensities of the standard reflections.[104b]

With an area detector, the data collection time is proportional to the volume of the reciprocal space scanned (no matter how many reflections are present there) and hence independent of the unit cell size. The scan speed must be optimized according to the intensity of diffraction for each sample. Since all reflections, with widely varying intensities, are scanned with the same speed, it has to be a compromise speed. With too fast speed, weak reflections may have unacceptably low signal-to-noise ratio. With too slow speed (or too large crystal), the strongest reflections may overflow the charge-accumulating wells of the CCD, and their intensities will be underestimated. In this case, the offending frame has to be remeasured at a faster rate.

A standard data collection with a CCD does not exceed 6 to 10 h, or 1 day for the extremely weakly diffraction samples. Therefore, crystal decay is much less of a problem, it can be monitored by rescanning the first several (up to 50) frames at the end of the data collection and comparing the intensities of duplicate reflections.

With less time-pressure, it became the common strategy to collect much more than one unique set of data; often a full sphere of the reciprocal space is scanned. Having several symmetrical equivalents of each reflection, it is possible to make empirical corrections for absorption and some other systematic errors, and to obtain more realistic estimates of the estimated standard deviation (esd's) for individual reflections (important in crystallographic calculations). In fact, a high-redundancy data set usually gives much better results even without explicit corrections. It has been proven by experience that a given amount of diffractometer time is always better spent on measuring more unique sets than on measuring a single set slower.

3.3.5 Obtaining Structure Factors

The data needed for structure solution and refinement are moduli of the structure factors F_{hkl}. To obtain these from the raw intensity measurements, we need to

1. integrate the intensity over an entire reflection peak and subtract the background;
2. correct the integrated intensities I_{hkl} for the Lp factor (Section 2.2.2) and various systematic errors;
3. calculate $|F_{hkl}|$ as square roots of I_{hkl} and bring them to the absolute scale.

Step (a) is illustrated in Figure 16. In a reflection, the Bragg peak is superimposed upon the lower, but broader, peak of TDS which peaks at the same position, and the incoherent scattering which varies slowly and not periodically through reciprocal space. The latter can be subtracted, in the first approximation, as an averaged flat background, provided we know where the peak ends and the background begins! In one dimension (i.e. with point detectors), this is done either by assuming a constant width for all reflections, or by optimizing the width of each individual reflection by the following technique.[104c] The routine starts with an overestimate of the peak width and reduces it by successive steps, each time calculating the ratio of I integrated within the peakwidth to $\sigma(I)$ integrated outside it. The maximum $I/\sigma(I)$ corresponds to the 'true' width. A 3D equivalent of this procedure can be applied to area detector data.

A correction for TDS, that is, the inelastic phonon scattering,[44] is a difficult problem not yet satisfactorily solved. A proper correction can only be made[106] if the elastic constants of the crystal are known, although an empirical method has been suggested.[107] TDS is inversely correlated with the bulk modulus, thus for soft molecular crystals at room temperature it can be as high as 20–30% of the Bragg intensity, while a much smaller percentage for hard inorganic solids. The effect of no correction is to underestimate the ADP.[108] For neutrons, the problem is even more complicated since the TDS correction will depend on the neutron velocity relative to the velocity of sound in the crystal.[15,22,109]

Other systematic errors include absorption, extinction, and multiple reflection. *Absorption* effects and the required corrections are well understood. When a monochromatic beam of X rays or neutrons with incident intensity I_o passes through a crystal, the intensity is reduced exponentially

$$I = I_o \exp(-\mu t) \qquad (26)$$

where t is the beam path length (mm or cm) inside the crystal and μ is the linear absorption coefficient (measured in mm^{-1} or cm^{-1}), which can be calculated from the individual atomic absorption coefficients of the elements of the sample.[25] These coefficients are element-specific and depend on the wavelength λ, in different ways for X rays and neutrons.[110] In general, all mass atomic absorption coefficients (μ/ρ) are smaller for neutrons than X rays, which is fortuitous given the large samples required for the neutron diffraction experiments. In the range of λ used in crystallography, (μ/ρ) is the sum of two terms: (i) true absorption, due to the photoelectric effect for X rays and to nuclear capture processes for neutrons, and (ii) apparent absorption, due to both coherent and incoherent scattering. For X-ray diffraction the former predominates, while for neutrons the capture absorption varies with λ and can be less than the apparent absorption. The values for true absorption, as well as the incoherent absorption cross sections required to calculate (μ/ρ) for neutrons and tables of (μ/ρ) for X rays can be found elsewhere.[25,110]

Absorption correction can be based on an accurate description of the crystal shape in terms of Miller planes (faces), so that the t can be calculated for each incident and diffracted beam. The total absorption is then given by equation (27), where A is the absorption factor.

$$I = I_o \frac{1}{V} \int_v \exp(-\mu t)\,\mathrm{d}v = I_o A \qquad (27)$$

In the analytical method of absorption correction,[111] the integration required by equation (27) is performed by representing the crystal as a combination of several tetrahedra, but the standard technique is numerical or Gaussian integration.[112] When the crystal faces cannot be measured or the absorption coefficient is not well known, empirical or semiempirical methods can be used. On a four-circle diffractometer, it is possible to perform a 360° azimuthal scan of several reflections. The variation of intensity during the scan will define the dependence of absorption on the ψ angle,[113] which can then be applied to all data. With an area detector the azimuthal scan is impractical, but instead there is (due to high data redundancy) a sufficiently large number of Laue equivalents or even of identical reflections repeatedly measured, to derive a polynomial function describing absorption factors in various directions.[114] The latter method has an advantage of simultaneously correcting for the absorption by things other than the crystal (e.g. the glass fiber, glue, capillary) indeed, for any direction-dependent systematic error (e.g. due to parts of the crystal projecting out of the beam). It can be applied to strongly absorbing crystals *after* a numerical correction. A rather controversial program DIFABS is also styled as an 'empirical' absorption correction.[115] In fact, this program adjusts the observed data to minimize the angle-dependent differences between these and the model, during least squares refinement of the structure.

To assess whether an absorption correction is necessary, one should calculate the minimum and maximum μt values from the minimum and maximum crystal dimensions. If $\mu t_{\text{max}} < 2$, absorption is unlikely to be a problem. If $\mu t_{\text{max}} > 5$ or $\mu t_{\text{max}} - \mu t_{\text{min}} > 2$, an absorption correction is necessary, or there will be significant errors in U_{ij} (Section 2.1.3). For $\mu > 20\,\text{mm}^{-1}$, absorption correction is necessary even when the crystal shape is highly isotropic, indeed spherical, for although in a spherical sample t does not depend on the ψ angle, it does depend on θ. The traditional technique for very strongly absorbing materials (e.g. Pb, Hg, or W containing minerals) is to collect the data from a crystal which has been ground into a sphere. Absorption corrections for a sphere have been calculated analytically and tabulated once and for all.[32]

Extinction (see Section 2.2.2) is the phenomenon that reduces the observed intensity of the incident or diffracted beams by internal scattering and backscattering parallel to the incident beam direction. *Primary extinction* is assumed to take place when the different crystal blocks (domains) are sufficiently mutually misoriented that the reduction in intensity takes place only within each block. In *secondary extinction*, the size of the blocks is assumed to be so small that loss of intensity within each block is negligible. Instead, the reduction takes place by adjacent blocks scattering and rescattering the passing beam. It is an effect most commonly observed in strong X-ray reflections at low Bragg angle from crystals with low mosaic spread. An increase in mosaicity (i.e. deterioration of the crystal quality!) reduces any extinction effects. This can happen as a result of irradiation or of a thermal shock, that is, flash-cooling of the crystal, in which case the strong reflections will appear to increase in intensity relative to other reflections. However, the changes in intensity at lower temperatures are likely to mask this effect. Zachariasen's theory (1967)**[116]** has formed the basis for most extinction correction programs in common use.**[117]** These corrections are applied on the stage of structure refinement and not of data reduction, like most other corrections. Extinction effects are less with smaller crystals and shorter wavelengths, but such apparent 'remedies' are usually impractical or counterproductive.

Multiple reflection, or the Renninger effect,**[118]** occurs when more than one reciprocal lattice point simultaneously cross, or come very close to, the surface of the Ewald sphere. In this case, the once-scattered beam can be rescattered by the other plane(s) with a decrease of intensity. On the other hand, this process ('umwegangregung') can also enhance intensity, such that a reflection will appear to be present even when it should be forbidden by space group symmetry. This is a common enough source of ambiguity in space group determination from systematic absences, which can be resolved by measuring the same reflection (or its equivalent) at a different ψ angle where the multiple reflection will not occur. This effect is observed more frequently in high-symmetry lattices. In routine analyses it is largely ignored, although it can be corrected**[119]** when very accurate data are required, for example, in charge density studies.

To calculate equation (14) correctly, the structure factor magnitudes must be expressed on the absolute scale, that is, relative to the scattering factor of a single electron under the same conditions. In practice, the observed I_{hkl} and hence $|F_{hkl}|_{obs}$ values are on an arbitrary scale, depending on the crystal size, primary beam flux, photon-multiplying effect of the counter, and so on, which are in practice impossible to estimate. The scale factor K, required to bring $|F_{hkl}|_{obs}$ to the absolute scale, can be found by means of a so-called Wilson plot,**[120,121]** which gives also the overall temperature factor B (see below) of the structure

$$\ln\left(\frac{\Sigma|F_{hkl}|^2_{obs}}{\Sigma f^2}\right) = \ln K - 2B\frac{\sin^2\theta}{\lambda^2}, \tag{28}$$

since

$$K|F_{hkl}|^2_{obs} \approx \Sigma f^2 \exp\left[-2B\frac{\sin^2\theta}{\lambda^2}\right] \approx |F_{hkl}|^2 \tag{29}$$

The scale factor so obtained is very approximate; it is used only in the early stages of the structure solution and it is then refined, among other structural parameters, in the least squares procedure.

3.3.6 Structure Solution and Refinement

These, essentially computational, steps of the crystallographic study are treated extensively in many excellent textbooks and are only summarized here.

The phase problem can be solved, that is, phases of the scattered waves determined, either by Patterson function**[122]** or by direct methods.**[121,123]** The Patterson function P is a 'self-convolution' of the electron density ρ, and its magnitude at a point u, v, w can be obtained by multiplying $\rho\ (x, y, z)$ by $\rho\ (x+u, y+v, z+w)$ and summing these products for every point of the unit cell. In practice, it is calculated as

$$P(u,v,w) = \frac{1}{V}\sum_h\sum_k\sum_l |F_{hkl}|^2\cos 2\pi(hu+kv+lw) \tag{30}$$

This summation, known as the Patterson synthesis, has the same form as equation (14) for the electron density, but it contains no phase angle. Its coefficients are $|F_{hkl}|^2$, so that the unknown phases of F_{hkl} are irrelevant. When the structure contains two atoms (with atomic numbers Z_1 and Z_2) connected by a $[u, v, w]$ vector, the Patterson map has a peak at u, v, w, whose height is approximately proportional to Z_1Z_2. Thus the only prominent peaks correspond to the vectors connecting heavy atoms (this applies only to X ray and not neutron diffraction!), whose coordinates can be deduced from the peak positions, using the knowledge about various symmetry operations in the given space group. Even a single heavy atom, if it comprises a large fraction of the total scattering power, is sufficient to determine phases for a large number of the measured structure factors. It is quite common for more than 80% of the phasing to be correct, based only on one metal atom possessing 10% of the total scattering power. The Patterson method had only very limited application for structures of similar (light) atoms, so that in the past, heavy atoms (e.g. Br) had to be introduced into organic molecules to make the structure solution possible.

Fortunately the phases of structure factors are not independent but have certain relations to each other and to the magnitudes $|F_{hkl}|$, all of them being the consequences of the same electron density distribution. Therefore the phases can be derived from the magnitudes by mathematical techniques, collectively known as the *direct methods*. They rely on certain 'constraints' on the electron density, especially its being everywhere nonnegative and comprising discrete peaks (atoms). These assumptions were the basis of the Harker-Kasper inequalities,**[124]** from which the philosophy of the direct methods has grown.**[125]** All phase relations in the direct methods are essentially probabilistic (except those imposed by the space group symmetry, which are strict) and were originally based also on the assumption of equal atoms randomly distributed in the unit cell.**[126]** Direct methods first of all revolutionized the crystallography of light atom (organic) structures, making unnecessary the toil of 'heavy-atom' substitution. Today, the vast majority of crystal structures are solved by powerful 'descendants'**[127]** of these early ideas, including cluster-type organometallic complexes which are a far cry from the concept of 'equal atoms'.

Generally, direct methods require better data quality than the Patterson method, because phases of some reflections are used to derive other phases, and a single bad reflection can do much harm. Early direct methods used only the stronger reflections in the phasing equations; modern versions rely heavily on weaker data, which therefore must be measured carefully and not neglected, as has been the case quite often in the past. It can happen that not all necessary Bragg reflections are available, owing to poor crystal quality, restricted 2θ maximum, and so on. In this case, simply ignoring the missing reflections, that is, assuming them to have zero intensity, may generate false patterns. Since 1990s, the concept of maximum entropy[128] has been applied to this problem, with very impressive results.[129]

The Patterson or direct method solution will give a number of electron density peaks which can be identified as atoms of certain types. This is still a very crude model of the structure, which should be optimized by the *least squares* (*LS*) *refinement*[130,131] in the following way. Spherically symmetrical Hartree-Fock atoms are placed at the positions of the peaks and the coordinates (Section 2.2.2) and displacement parameters (Section 2.2.3) of these atoms are altered so as to minimize the function

$$M_1 = \Sigma w(|F_o| - |F_c|)^2 \tag{31}$$

$$M_2 = \Sigma w(F_o^2 - F_c^2)^2 \tag{32}$$

where F_o are the observed structure factors and F_c are those calculated from the current model according to equation (9), and weights w account for the fact that different reflections have been measured with unequal precision. The crystallographic community is still divided as to whether equation (31) or (32) represents a better way of refinement, and both (as well as refinement against I) are used in various software packages, but with good data the outcome is not substantially different. The commonly used and quoted single-value measures of how well the model fits the observations, are the so-called R-factors, or discrepancy factors. There are several forms of these, for example,

$$R = \frac{\Sigma||F_o| - |F_c||}{\Sigma|F_o|} \tag{33}$$

$$R_w = \frac{\Sigma w^{-1/2}||F_o| - |F_c||}{\Sigma w^{-1/2}|F_o|} \tag{34}$$

$$wR = \left\{\frac{\Sigma[w(F_o^2 - F_c^2)^2]}{[w(F_o^2)^2]}\right\}^{1/2} \tag{35}$$

R is traditionally established as *the* R-factor and accorded a (greatly exaggerated) reverence as the most important indicator of quality; R_w is known as the weighted R-factor and *wR* as the 'generalized R-factor' (also referred to as R' and R_g). For a good routine structure analysis, R value is expected to be 0.02 to 0.05 (2 to 5%); values between 5 and 10% may be acceptable but the model must be scrutinized carefully for possible errors (see below); $R > 10\%$ indicate serious problems. Note that *wR* is roughly twice the magnitude of R for the same data and model, simply because squares of any numbers differ more than the numbers themselves.

LS refinement is an iterational procedure, repeated in 'cycles' until the shifts of refined variables during the last cycle become insignificant. If the model is still incomplete (not all atoms have been located), an electron density map is calculated according to equation (14), atoms assigned to the revealed peaks and the refinement is repeated. In fact, a more revealing technique is to calculate not the full electron density map, but a 'difference' one, from which the already known atoms have been subtracted. The electron density map calculated after the final LS refinement, is known as the *residual density* map. For a good quality data sets and an adequate model, this map should be relatively featureless. For Period 2 elements the highest peaks should not exceed 0.2–0.3 eÅ^{-3}, although they can be higher for heavier elements.

Other variables refined in the LS procedure are the scale factor K (Section 3.3.5) always, atomic site occupancies in the cases of disorder and/or nonstoichiometric composition and the absolute structure parameter for noncentrosymmetric structures.[132] If the sample contains atoms with sufficiently strong anomalous scattering, the latter parameter indicates whether the assumed absolute structure of the crystal is right or wrong.

Modern programs for LS refinement[133] reached high degree of sophistication, permitting various types of constrained refinement (e.g. treating methyl or phenyl groups as rigid bodies), intelligently dealing with disorder, and so on. Work is currently in progress in several centers on the development of a new generation of truly intelligent, interactive programs. Nevertheless, there are many possible sources of errors in LS refinements (for practical advice see[131]), for example,

1. Insufficient data. A 'good' LS refinement requires at least 5, and preferably 10 reflections per refined variable. Each refined atom contributes three coordinates and 1 or 6 displacement parameters (in isotropic or anisotropic refinement, respectively);
2. Too weak data: background noise is comparable in intensity with the reflections;
3. Errors in the model, for example, attempting to refine an atom as a wrong element;
4. Unrecognized or incorrectly modeled disorder;
5. Wrong symmetry/space group;
6. Twinned crystal;
7. Modulated or incommensurate structure.

Twinning is one of the most common causes of failure in structure determinations. It is estimated that ca. 10% of all crystals submitted for X-ray analysis are twinned, and the proportion is much larger for high-symmetry structures (trigonal/hexagonal, tetragonal, and cubic). Twin[10,134] is a combination of two (or occasionally more) crystals, grown together in such way that they are related by some symmetry operation. This element (‘twin law’) is usually a rotation around some rational lattice direction in the direct space or in reciprocal space (the latter amounts to a reflection in a mirror plane in the direct space). The twin law may be such that the *positions* of all reflections from the two crystals coincide, so that the diffraction pattern seems ‘normal’ at the first glance (merohedral twin). However, as the reflection intensities are affected, the model cannot be found, or even if found, cannot be refined properly. Often R-factor cannot be reduced below 15–20%, even as the structural parameters are chemically meaningful, if imprecise. In the case of nonmerohedral twin, only some of the reflections coincide, or the overlap is imperfect.

Twinning usually occurs for good structural reasons, that is, when the symmetry of the crystal lattice (or its superlattice) is higher than the symmetry of the structure (e.g. when a monoclinic lattice has $\beta \approx 90°$) and the bonding interactions across the twin boundary are competitive in energy with those within a single crystal. Therefore twinning usually tends to affect *all* crystals of a given phase. Until recently, determining the structure of a twinned crystal was a highly specialized area, almost an art. In the last decade, it has been greatly facilitated through introduction of area detectors (visualizing the diffraction pattern is crucial here!) and development of efficient software,[135,136] specially designed for dealing with twins. This requires (i) indexing the diffraction patterns of a twinned crystal, (ii) determining the twin law, (iii) integrating the reflection intensities for each crystal separately, (iv) finding out, how the reflections overlap, and (v) refining the structure with the relative contributions of the components to the observed reflections refined among other LS variables.[137]

Modulation[138] is a perturbation of the crystal lattice which, unlike random perturbations due to thermal motion and static disorder, has regular character and therefore creates sharp diffraction peaks, usually as ‘satellites’ of ordinary reflections. The diffraction vector can be then expressed as (cf. Section 2.2.1)

$$Q = h\mathbf{a}^* + k\mathbf{b}^* + l\mathbf{c}^* + m\mathbf{q} = h\mathbf{a}^* + k\mathbf{b}^* + l\mathbf{c}^* + m(\alpha\mathbf{a}^* + \beta\mathbf{b}^* + \gamma\mathbf{c}) \tag{36}$$

The modulation is called commensurate if the coefficients α, β and γ are all rational, and incommensurate[138] if at least one of them is irrational. Effectively the crystal has two different periodicities. Since its discovery of this effect in 1927,[139] it remained one of the most difficult (and specialized) areas of diffraction studies. Recently it also experienced remarkable progress of understanding[140] and development of efficient programs.[141]

3.3.7 Charge Density Studies

In all the calculations described above, it has been assumed that the electron density in the crystal is well described by the superposition of isolated, ground-state (spherically symmetrical) atoms, and that the maxima of electron density coincide with the nuclear positions. This assumption, known as the independent-atom model (IAM) is, of course, only an approximation, albeit a remarkably good one. In the actual structure the atoms form chemical bonds, bear net electric charges, and lose spherical symmetry (e.g. through hybridization). Is it possible to go beyond the IAM and determine the actual distribution of electron density (ED), also called charge density? In principle, the possibility has been envisaged by Debye as early as 1915,[142] and practical attempts have been made since 1950s.[143] However, in practice the X-ray crystallography had neither experimental accuracy nor mathematical apparatus to deal with the problem until the 1970s. Since then, only a few hundreds of ED studies have been published, compared to hundreds of thousands of IAM structures – a clear indication of the difficulty of the task. It is not possible to give more than the briefest outline of this subject. For an introduction the reader is referred to the article by Coppens[144] and for a detailed description of the technique (for a practitioner) to two recent books.[55,145] Chemical applications of X-ray ED analysis[146] and ED studies of silica and silicates[147] have been reviewed extensively.

An ED study requires a complete set of intensity data, measured to a much higher Bragg angle ($\sin\theta/\lambda > 1.1\,\text{Å}^{-1}$, sometimes[148] up to $1.77\,\text{Å}^{-1}$) than is required for an IAM study, and with much more accuracy and precision. It is necessary to measure all symmetrical equivalents of each reflection, carefully address all possible sources of systematic errors, especially extinction and TDS. With a point detector, the data collection required many weeks or even months, but with an area detector (especially using SR) this time has been reduced to a few days, without any loss in precision.[148] There is an intrinsic difficulty to distinguish between the ED distribution of a stationary atom and an apparent ‘smearing’ of its ED from thermal motion, therefore the data must be collected at as low a temperature as possible.[79,85]

The results can be represented in different ways. The earliest approach was to calculate by a Fourier synthesis the total ED distribution and then to subtract from the latter the ED of the *promolecule*, that is, of isolated atoms, centered at the atomic nuclei positions. The latter can be determined directly by neutron diffraction (X–N method) or from high-order X-ray reflections (X–X$_{\text{ho}}$ method). The latter technique, which by now has practically supplanted the X–N method, makes use of the fact that valence electrons scatter X rays mainly at lower Bragg angles ($\sin\theta/\lambda < 0.7$ or $0.8\,\text{Å}^{-1}$) and thus the high-angle reflections are due mainly to the inner (core) electron shells, which remain unaffected by chemical bonding. The resulting *deformation electron density* maps give a rather crude picture of the chemical bonding, which can be made more informative if we subtract a correctly preoriented atom in a correct state of hybridization rather than a spherically symmetrical atom. The main disadvantage of this approach is that the ED map can be only as accurate as the assumed phases of the structure factors which are very difficult to determine, especially for noncentrosymmetric structures.

Alternatively, the deformation ED can be described by a series of multipoles, that is, spherical harmonic density functions, the parameters of which can be refined by the LS technique. The core ED is described as spherically symmetrical, using the so-called κ formalism. The κ parameter expresses the isotropic expansion ($\kappa > 1$) or contraction ($\kappa < 1$) of a valence shell as a whole. The higher-order multipoles describe the deviations of the ED from spherical symmetry.

Chemically relevant information can be obtained by the topological analysis of the ED distribution and of its Laplacian (second gradient),

$$\nabla^2\rho(\mathbf{r}) = \frac{\partial^2\rho(\mathbf{r})}{\partial x} + \frac{\partial^2\rho(\mathbf{r})}{\partial y} + \frac{\partial^2\rho(\mathbf{r})}{\partial z} \tag{37}$$

Such analysis can reveal bond paths (lines of maximum ED linking two atoms), exact location of the bond critical points, bond ellipticity (deviation from cylindrical symmetry), and so on. The 'real' atomic boundaries can be found and the effective atomic charges integrated.

The X-ray ED formalism, which is closely connected to the theory of atoms in molecules,[149] is still evolving and there are some unsolved problems. Thus, it appears that in simple inorganic structure the multipole model may be nonunique.[150]

4 INTERPRETATION OF THE RESULTS

4.1 Reading a Crystallographic Paper

The complete results of an ordinary (IAM) crystal structure determination comprise:

1. lattice type and symmetry, space group, and unit cell dimensions with the errors, that is, the esd's, of the latter;
2. other details of the structure itself and of the experimental technique, known (together with 1) as *crystal data*;
3. fractional coordinates of all atoms (with esd's);
4. ADP with esd's;
5. bond distances, bond angles, and torsion angles (with esd's);
6. observed and calculated structure factors.

Most papers in the chemical, biological, and material science literature reporting the results of crystal structure analyses include a section (or a footnote) listing the crystal data, which should indicate the quality of the crystal, the form of the experiment, the accuracy of the measurements, and the precision of the results. The journals all have slightly different requirements for the contents of this section; the list presented in Table 3 conforms to the most rigorous requirements of the International Union of Crystallography (IUCr) and its journal *Acta Crystallographica*. On the other extreme, the *minimum minimorum* of the structural information comprises 1 and 3. Parameters 5 can be always calculated from 3, although the esd of 5 can be only approximately estimated from those of 3.

In earlier years, all the parameters 1–6 were published for each crystal structure. With the exponential growth of the number of structures, the publication of structure factors has been discontinued about 1975, and today they are requested only by *Acta Crystallographica* and that only for refereeing purposes. ADP soon followed, unfortunately just at the time when their calculation was at last becoming reliable (see below). Then many journals resorted to deposition rather than publication of extensive tables of 3 and 5. With the recent development of the Internet, all data except 6 began to be published as electronic supplementary information. The archiving of crystallographic information has been greatly facilitated by the development (by IUCr) of the Crystallographic Information File (CIF) with its standardized, yet flexible, format.[151]

To read a structural paper intelligently, one must be able to appreciate various measures of the precision (i.e. the level of random errors) and accuracy (the absence of systematic errors) of a structure and be able to spot the warning signs that it may be incorrect.[131] There are three principal ways of assessing the structure 'quality' viz.

1. From the internal consistency of the X-ray data itself,[152] for example, the agreement between the intensities of symmetrically related reflections, which must be equivalent by definition. Also, the number of data should be sufficiently large (at least 5, or better 10 times the number of refined variables) for a stable LS refinement.
2. From various measures of agreement between observed and calculated data.[153] Of the overall 'residuals', or single-value measures of agreement, the most popular are various R-factors (equations (33–35)) and especially the traditional one expressed by equation (33). It is frequently the case that the R value is the only criterion taken into account by a nonspecialist. Unfortunately, it (and other R-factors) can be deceptive. In the first place R can always be reduced by omitting some part of the data (not necessarily of inferior quality!), but this can simultaneously increase the esd's in the positional and displacement parameters. Indeed, the latter can provide a complementary measure of quality. All R-factors can be manipulated to a considerable degree by changing the weighting scheme. A good additional indicator is the 'goodness of fit',

$$S = \left[\frac{\Sigma w(|F_o| - |F_c|)^2}{(m-n)}\right]^{-1/2} \tag{38}$$

where m is the number of observed reflections and n is the number of parameters refined. Theoretically S should equal 1 for a perfect structure with absolute weights

Table 3 Crystal data required by *Acta Crystallographica*, with additional explanatory comments

Formula	Refers to the molecule or the smallest chemical formula unit in continuous solids
Formula weight, M (a.u.)	Molecular weight for the formula above
Crystal system and space group	E.g. orthorhombic, *Pbca*
Unit cell dimensions	1 to 6 of the parameters a, b, c (Å), α, β, γ (°). How many depends on the crystal system, from cubic (1) to triclinic (6). Esd's are given in parentheses
Volume of unit cell, V (Å^3)	Calculated from cell parameters
Z	Number of formula units per unit cell
Measured density D_m	If measured, details of the method should be given, e.g. 'by flotation in ... '
Calculated density, D_x (g cm^{-3})	In Mg m^{-3} (= g cm^{-3}), calculated as $D_x = 1.661MZ/V$
Radiation type and wavelength	E.g. Mo-K_α, $\overline{\lambda} = 0.71073$Å; mean $\overline{\lambda}$ is given for the α_1/α_2 doublet
Number and θ range of reflections used to determine lattice parameters	E.g. 20, $10° < \theta < 20°$. Tens of reflections are usual for point-detector experiments, hundreds or thousands for area detectors
Linear absorption coefficient, μ	In mm^{-1}, not cm^{-1}; if large, absorption correction is necessary
Temperature of measurement, T	In K
Crystal shape, color, and size	E.g. Dark red, rectangular prism, $0.50 \times 0.34 \times 0.28$ mm
Diffractometer used	E.g., Bruker SMART 6000 CCD area detector diffractometer
Scan mode	E.g. ω scans
Standard reflection measurements	E.g. 3 standard reflections every 97 reflections, intensity decay: 5%; N/A to area detectors
Absorption correction applied	E.g. analytical, numerical, empirical via ψ-scans; max. and min. transmission factors T must be specified, $0 < T_{\mathrm{min}} < T_{\mathrm{max}} < 1$
Number of reflections	Total number of measured reflections; no of unique (independent) reflections after merging symmetrical equivalents; no of 'observed reflections' and the criterion for 'observed'; e.g '6896 measured refls., 4323 unique, 2544 observed refls. with $I > 2\sigma\ (I)$'
R_{int}	Discrepancy factor from merging equivalent reflections; expect $\leq$5% for good and $\leq$10% for weak data; if higher, absorption correction or crystal symmetry may be wrong
Maximum Bragg angle, θ_{max}	$\theta_{\mathrm{max}} \geq 25°$ for Mo-K_α, 68° for Cu-K_α required for a routine study
Range of indices h, k, l	E.g. $0 \leq h \leq 7$, $0 \leq k \leq 15$, $-18 \leq l \leq 18$; check for consistency with crystal symmetry (this corresponds to monoclinic), θ_{max} and a, b, c parameters
Type of refinement	On F, or F^2, or I
Numbers of reflections and variables in LS	Number of reflections in least squares refinement ($\leq$ number of unique reflections) must be $\geq$10 times the number of refined variables (in exceptional cases, $\geq$5 times)
Weighting scheme in LS refinement	E.g. $w = 1/[\sigma(F_o^2) + (0.045\mathrm{P})^2]$ where $\mathrm{P} = (F_o^2 + 2F_c^2)/3$
Treatment of hydrogen atoms	E.g. H-atom parameters constrained
Shift-to-error ratio, $(\Delta/\sigma)_{\mathrm{max}}$	Must be small in the last cycle of LS refinement, for example, 0.001; if ≥ 1, the refinement is unfinished or does not converge at all (disorder? wrong symmetry?)
Final values of R	Various R-factors are in use, typically quoted in *Acta Crystallographica* are the R (equation 33) for 'observed' data and wR (equation 35) for all data used in LS
Goodness of fit, S	According to equation 38; ideally ≈ 1, usually 0.8 to 2.5
Residual electron density, $\Delta\rho_{\mathrm{max,min}}$ (e Å^{-3})	Largest peak and 'hole' in the residual electron density map e.g. 0.25, −0.18; $\Delta\rho_{\mathrm{max}}$ should not exceed 0.2–0.4 for light elements, 1 for heavy ones, higher values indicate disorder, uncorrected absorption, twinned crystal

and without errors; in practice S varies from 0.8 to 2.5. More sophisticated indicators include the χ^2 distribution, normal probability plots, significance testing, and so on. They are particularly important in charge density studies. A 'noisy' residual electron density map also indicates disagreement between the data and the model.

3. From the absolute values and internal consistency of ADP, visualized as 'thermal (or displacement) ellipsoids'. These parameters, especially in anisotropic approximation, tend to act as 'sinks' for all kinds of random and (neglected) systematic errors. Thus, for a strongly absorbing crystal (in the absence of intensity correction) the thermal ellipsoids of all atoms will approximate the Fourier image of the crystal's outer shape. An unreasonably small or large ADP often indicates a wrongly assigned atomic type, with a too small or too large atomic number, respectively. Exceedingly elongated thermal ellipsoids usually signify static disorder rather than thermal vibrations, certainly so if the data has been collected at low temperature. Often, such disorder can be better approximated by two or more partially occupied positions for the atom in question. Covalent bonds usually remain 'rigid' (undeformed) during thermal vibrations, and in molecular crystals the vibrations of a molecule as a whole are far more important than intramolecular modes. Hence thermal ellipsoids are usually elongated in the direction perpendicular to the bonds, and the ellipsoids of adjacent atoms are similar (correlated). If this does not happen, or if anisotropic

ADP are 'non-positive definite', that is, they do not define an ellipsoid at all but an open surface, this usually indicates grossly erroneous data (e.g. due to twinning) or a wrong space group (e.g. a centrosymmetric structure is refined as noncentrosymmetric).

4. From comparison of the structure with chemically similar ones, that is, by spotting unusual bond distances or intermolecular contacts. An excellent standard for such comparison is provided by the tables of bond distances in organic[154] and inorganic or coordination[155] compounds, which have been compiled using the Cambridge Crystallographic Database (see below). These tables are also reproduced verbatim elsewhere.[32,156]

4.2 Crystallographic Databases

Today, the number of crystal structures in the public domain runs into hundreds of thousands, so that the traditional literature search has long since become impractical. Fortunately, a number of crystallographic databases are available,[8] which store all the published and some unpublished structures and provide very efficient access to this wealth of information.

The Cambridge Structural Database (CSD)[156,157] is the oldest (established in 1965) and probably the most widely used database for chemical crystallography, run by the Cambridge Crystallographic Data Centre (CCDC), Cambridge, UK. Although it stores only the structures which contain at least one 'organic' carbon atom (except biopolymers), in fact only about 50% of its contents are organic compounds proper. The rest are organometallic compounds (including transition metal carbonyl clusters), metal complexes with organic ligands (but without direct metal–carbon bonds) or even the structures of purely 'inorganic' molecules or ions with organic counterions or solvent molecules. Thus it is eminently relevant for inorganic structural chemistry.[158] Besides X ray and neutron single-crystal structures, the CSD includes powder diffraction studies which yield 3D atomic coordinates at least for all nonhydrogen atoms. The November 2004 release of the CSD contained 325 709 entries (cf. 109 000 in 1994) with ca. 24 000 added annually.

The CSD provides powerful search-and-retrieval methods,[159] which can be formulated in terms of

- text and numerical data items;
- two-dimensional chemical (sub)structures (chemical connectivity);
- an extensive range of three-dimensional geometrical parameters.

The results are presented in terms of bibliographic and chemical text, 2D chemical diagrams, 3D structure diagrams at the molecular or extended crystal structure levels, and also as tables of geometrical parameters for each located substructure or chemical fragment. The search query is via a menu-driven graphical interface and the graphical results obtained for any hit can be manipulated interactively too. The tables of user-defined geometrical parameters for a set of retrieved fragments can form the basis for a variety of data analysis methodologies. These can range from simple descriptive statistics,[160] that is, the mean values, medians, and estimated standard deviations, through correlation and regression methods, to the multivariate numerical techniques of principal component and clustering analysis.[161] These latter are designed to reduce the dimensionality of the problem and enable the user to locate and classify the configurational subgroups.

Besides its most obvious utility as a bibliographic source, the CSD enabled researchers to investigate many problems relevant to the nature of the chemical bonding and chemical reactivity. Thus, the so-called method of structure correlations[9,162] uses the geometries of a given chemical fragment in different environments within many crystal structures as static 'snapshots' of a chemical transformation, such as nucleophilic substitution, and thus to provide insight into the structural changes accompanying a chemical reaction. Principal component analysis has been used to show correlations between the structural parameters of the same molecular fragment in many different molecules. These structural results can be combined with kinetic information (vibrational force constants, activation energies, etc.) to model the energy surfaces involved in the formation and breaking of bonds in a reaction sequence. While accuracy is not crucial for the mapping of reaction pathways in which the changes in structure are much greater than the experimental errors, it is of considerable importance in structure–reactivity relationships. Here very small differences in structure can relate to large changes in activation energies and high precision structural data are essential. The structural data stored, and the molecular patterns extracted from them, are used in force field calculations and subsequent molecular mechanics procedures. Molecular modeling software relies upon the parameters so derived and 'modeling' has become a powerful predictive tool in many aspects of chemical research, finding wide applications in the pharmaceutical and agrochemical industries.

Another major area of CSD-based research is the supramolecular structural organization and crystal engineering,[163] and particularly the role of hydrogen bonding[164] in the solid state. Although the initial incentive came from biomolecular chemistry, the results are equally important for inorganic, organometallic, and polymeric materials.

Various more specific structural-chemical problems addressed successfully with the use of the CSD are too numerous to list. Inter alia, it was possible for the first time to clarify the stereochemistry of less common (and less regular) types of metal coordination, for example, with coordination numbers five[165] and seven.[161,166]

The Inorganic Crystal Structure Database (ICSD),[167] originally established at the University of Bonn and currently run by the Fachinformationszentrum, Karlsruhe (Germany), covers inorganic and mineral structures (64 848 structures in 2003, with ca. 3000 added annually). There is a small area of overlap between the CSD and ICSD, comprising 'molecular inorganics'. The methods of search, retrieval and analysis[168] in ICSD are similar to those of the CSD, except that in continuous (inorganic) solids it is inherently more difficult to define clearly the geometrical form and connectivities than in molecular crystals.

The Metals Crystallographic Data File (CRYSTMET)[169] covers metals, alloys, and intermetallides (77 242 entries in 2003, ca. 2500 added annually). It was started in 1960 in Los Alamos (USA), in 1974 has been transferred to the National Research Council of Canada and since 1996 is managed by Toth Information Systems (Ottawa, Canada). CRYSTMET contains the bibliographic and crystallographic data categories similar to CSD and ICSD, but formal connectivity is not applicable.

Biopolymer structures are stored at the Protein Data Bank (PDB),[170] founded in 1971 at Brookhaven National Laboratory (USA), and the Nucleic Acid Database (NDP),[171] both currently operated by Rutgers, the State University of New Jersey (USA). As of April 2004, the PDB contained 25 176 structures and NDP had 2379 structures.

Additionally there is the Crystal Data Identification File (CDIF), maintained by the US National Institute of Science and Technology, which stores unit cell parameters and crystal class information (determined by either single-crystal or powder diffraction) for all types of substances. The CDIF does not store any information on atomic positions, indeed it does not require the full structure to be known. Nevertheless, it provides a very useful preliminary check at the start of a 'new' structure analysis. Currently the CDIF contains ca. 237 000 entries, with a large backlog.

5 CONCLUSIONS

Since the first edition of this Encyclopedia (1994), the technique of single-crystal X-ray diffraction experiment underwent a major revolution, comparable to that occasioned by the replacement of diffractometers for photographic cameras about 1970. A routine X-ray data collection, which took many weeks with photographic films in 1965 and several days with a 4-circle diffractometer in 1970–1995, is now reduced to several hours. Furthermore, area detectors made feasible many experiments altogether impossible before, through higher sensitivity and the recording of the whole pattern. The technology for nonambient conditions has greatly improved; experiments at liquid nitrogen temperatures have become routine and those at liquid helium temperatures and at high pressures have ceased to be exotic. The improvement of software and computer facilities has greatly facilitated structure solution (particularly by direct methods) and charge density calculations; efficient programs for dealing with twinned crystals and incommensurate phases are being developed.

6 RELATED ARTICLES

Solids: Characterization by Powder Diffraction.

7 FURTHER READING

J. P. Glusker, M. Lewis, and M. Rossi, 'Crystal Structure Analysis for Chemists and Biologists', VCH, New York, 1994.

W. Massa, 'Crystal Structure Determination', 2nd edn., Springer-Verlag, Berlin-Dordrecht, 2004.

C. C. Wilson, 'Single Crystal Neutron Diffraction from Molecular Materials', World Scientific, Singapore, 1999, Vol. 1; 2000 Vol. 2.

8 REFERENCES

1. B. K. Vainshtein, 'Structure Analysis by Electron Diffraction', Pergamon Press, Oxford, 1964; D. L. Dorset, *Acta Crystallogr.*, 1996, **B52**, 753; D. L. Dorset, *Acta Crystallogr.*, 1998, **A54**, 750.
2. M. von Laue, *Phys. Z.*, 1913, **15**, 1075.
3. N. V. Belov, 'Chemistry of Large Cation Silicates', Consultants Bureau, New York, 1965.
4. M. C. Chabrie, *Compt. Rend.*, 1907, **144**, 804.
5. W. C. Zeise, *Ann. Phys. (Leipzig)*, 1827, **9**, 632.
6. H. S. Harned, L. Pauling, and R. B. Corey, *J. Am. Chem. Soc.*, 1950, **72**, 5477.
7. J. A. Wunderlich and D. P. Mellor, *Acta Crystallogr.*, 1954, **7**, 130.
8. F. H. Allen, *Acta Crystallogr.*, 1998, **A54**, 758.
9. H.-B. Bürgi and J. D. Dunitz eds, 'Structure Correlations', VCH, Weinheim, 1994, Vol. 1 and 2.
10. C. Giacovazzo, H. L. Monaco, D. Viterbo, F. Scordari, G. Gilli, G. Zanotti, and M. Catti, 'Fundamentals of Crystallography', Oxford University Press, Oxford, 1992.
11. C. W. Bunn, 'Chemical Crystallography: An Introduction to Optical and X-ray Methods', Clarendon Press, Oxford, 1961.
12. C. Hammond, 'The Basics of Crystallography and Diffraction', Oxford University Press, Oxford, 1997.
13. M. J. Buerger, 'Crystal Structure Analysis', Wiley, New York, 1960.
14. M. J. Buerger, 'X-ray Crystallography', Wiley, New York, 1962.

15. U. W. Arndt and B. T. M. Willis, ‘Single Crystal Diffractometry’, Cambridge University Press, Cambridge, 1966.
16. G. H. Stout and L. H. Jensen, ‘X-ray Structure Determination: A Practical Guide’, Macmillan, London, 1972.
17. D. McKie and C. McKie, ‘Essentials of Crystallography’, Blackwell Scientific, Oxford, 1986.
18. J. P. Glusker and K. N. Trueblood, ‘Crystal Structures Analysis’, Oxford University Press, Oxford, 1985.
19. M. M. Woolfson, ‘An Introduction to X-ray Crystallography’, 2nd edn., Cambridge University Press, 1997.
20. L. A. Aslanov, G. V. Fetisov, and J. A. K. Howard, ‘Crystallographic Instrumentation’, Oxford University Press, Oxford, 1998.
21. G. E. Bacon, ‘Neutron Diffraction’, 3rd edn., Oxford University Press, Oxford, 1975.
22. G. L. Squires, ‘Introduction to the Theory of Thermal Neutron Scattering’, 2nd edn., Dover Publications, Mineola, 1996.
23. W. H. Miller, ‘A Treatise on Crystallography’, J. & J.J. Deighton, Cambridge, 1839.
24. A. J. C. Wilson ed., ‘International Tables for X-ray Crystallography’, D. Reidel Publishing Company, Dordrecht, 1983, Vol. A.
25. W. H. Bragg and W. L. Bragg, *Proc. R. Soc. London, Ser. A*, 1913, **88**, 428.
26. U. Shmueli ed., ‘International Tables for X-ray Crystallography’, Kluwer, Dordrecht, 1993, Vol. B.
27. IUCr Monograph on Crystallography (2), ‘P.P. Ewald and his Dynamical Theory of X-ray Diffraction’, eds. D. J. W. Cruickshank, H. H. Juretschke, and N. Kato, Oxford University Press, 1992.
28. E. G. Cox and W. F. B. Shaw, *Proc. R. Soc. London, Ser. A*, 1930, **127**, 71.
29. M. J. Buerger, *Proc. Natl. Acad. Sci. U.S.A.*, 1940, **26**, 637; M. J. Buerger and G. E. Klein, *J. Appl. Physiol.*, 1945, **16**, 408.
30. W. H. Zachariasen, *Acta Crystallogr.*, 1967, **23**, 558; P. J. Becker and P. Coppens, *Acta Crystallogr.*, 1974, **A30**, 129; N. Kato, *Acta Crystallogr.*, 1976, **A32**, 453.
31. D. T. Cromer and J. B. Mann, *Acta Crystallogr.*, 1968, **A24**, 321.
32. (a) J. A. Ibers and W. C. Hamilton eds, ‘International Tables for X-ray Crystallography’, Kluwer, 1989, Vol. IV; (b) A. J. C. Wilson ed., ‘International Tables for X-ray Crystallography’, Kluwer, Dordrecht, 1992, Vol. C.
33. B. Post, *Acta Crystallogr.*, 1979, **A35**, 17; B. Post, *Acta Crystallogr.*, 1983, **A39**, 711.
34. G. Friedel, *Compt. Rend.*, 1913, **157**, 1533.
35. J. M. Bijvoet, *Proc. Koninkl. Ned. Acad. Wetensch.*, 1949, **B52**, 313; J. M. Bijvoet, A. F. Peerdeman, and A. J. van Bommel, *Nature (London)*, 1951, **168**, 271.
36. J. M. Bijvoet and A. F. Peerdeman, *Acta Crystallogr.*, 1956, **9**, 1012.
37. K. Moffat, *Nature (London)*, 1988, **336**, 422.
38. Y. Okaya and R. Pepinsky, *Phys. Rev.*, 1956, **103**, 1645.
39. J. Karle, *Int. J. Quant. Chem.*, 1980, **7**, 357; E. Fanchon, W. A. Hendrickson, *Acta Crystallogr.*, 1990, **A46**, 809.
40. G. M. Sheldrick, Z. Dauter, K. S. Wilson, H. Hope and L. C. Seiker, *Acta Crystallogr.*, 1993, **D49**, 18; G. M. Sheldrick, ‘Direct Methods for Solving Macromolecular Structures’, Dordrecht, Kluwer, 1998.
41. D. Dale and B. T. M. Willis, *AERE Rep.*, 1966, R5195; S. Ramaseshan, *Curr. Sci. Ind.*, 1966, **35**, 87; S. Ramaseshan, K. Ventakesan, and N. V. Mani, *Proc. Ind. Acad. Sci.*, 1957, **A46**, 95.
42. A. J. C. Wilson, *Acta Crystallogr.*, 1949, **2**, 318; A. J. C. Wilson, ed. ‘Structure and Statistics in Crystallography’, Adenine Press, Guilderland, NY, 1985.
43. D. W. J. Cruickshank, *Acta Crystallogr.*, 1956, **9**, 747.
44. B. T. M. Willis and A. W. Pryor, ‘Thermal Vibrations in Crystallography’, Cambridge University Press, Cambridge, 1975.
45. J. D. Dunitz, E. F. Maverick, and K. N. Trueblood, *Angew. Chem. Int. Ed. Engl.*, 1988, **27**, 880.
46. D. Braga, *Chem. Rev.*, 1992, **92**, 633; J. D. Dunitz, *Acta Crystallogr.*, 1995, **B51**, 619; C. P. Brock and Y. Fu, *Acta Crystallogr.*, 1997, **B53**, 928.
47. S. Cerrini, *Acta Crystallogr.*, 1971, **A27**, 130.
48. R. J. Nelmes, *Acta Crystallogr.*, 1969, **A25**, 523.
49. W. Hummel, A. Raselli, and H.-B. Burgi, *Acta Crystallogr.*, 1990, **B46**, 683.
50. D. W. J. Cruickshank, *Acta Crystallogr.*, 1956, **9**, 757; W. R. Busing and H. A. Levy, *Acta Crystallogr.*, 1964, **17**, 142.
51. V. Schomaker and K. N. Trueblood, *Acta Crystallogr.*, 1968, **B24**, 63.
52. A. L. Speck, ‘PLATON for Windows’, University of Utrecht, The Netherlands, 2002.
53. K. N. Trueblood, in ‘Accurate Molecular Structures’, eds. A. Domenicano and I. Hargittai, Oxford University Press, Oxford, 1992.
54. F. K. Larsen, in ‘The Applications of Charge Density Research to Chemistry and Drug Design’, eds. G. A. Jeffrey and J. F. Pinniella, Plenum Press, New York, 1991.
55. P. Coppens, ‘X-ray Charge Densities and Chemical Bonding’, Oxford University Press, Oxford, 1997.
56. F. L. Hirshfeld, *Isr. J. Chem.*, 1977, **16**, 198.
57. M. A. Kumachov and F. A. Komarov, *Phys. Rep.*, 1990, **5**, 289; V. A. Kogan and J. Bethke, *Mater. Sci. Forum*, 1998, **278–281**, 227; P. Scardi, S. Setti and M. Leoni, *Mater. Sci. Forum*, 2000, **321–324**, 162.
58. A. C. Bloomer and U. W. Arndt, *Acta Crystallogr.*, 1999, **D55**, 1672.
59. E.-E. Koch ed., ‘Handbook of Synchrotron Radiation’, North Holland, Amsterdam, 1983, Vol. 1; G. V. Marr ed.

1987, Vol. 2; G. B. Brown and D. E. Moncton, 1991, Vol. 3; S. Ebashi, M. Koch, and E. Rubenstein eds. 1991, Vol. 4.

60. P. Coppens, D. Cox, E. Vlieg, and I. K. Robinson, 'Synchrotron Radiation Crystallography', Academic Press, London, 1992; Ya. V. Zubavichus and Yu. L. Slovokhotov, *Russ. Chem. Rev.*, 2001, **70**, 373.
61. M. M. Harding, *Acta Crystallogr.*, 1995, **B51**, 432; H. Winick, *J. Synchr. Radiat.*, 1998, **5**, 168.
62. J. Baruchel, J. L. Hodeau, M. S. Lehmann, J. R. Regnard, and C. Schlenker eds, 'Neutron and Synchrotron Radiation for Condensed Matter Studies', Springer-Verlag, Berlin, 1993, Vol. 1.
63. C. G. Windsor, 'Pulsed Neutron Scattering', Taylor and Francis, London, 1981; 'Neutron Scattering at a Pulsed Source', eds. R. J. Newport, B. D. Rainford and R. Cywinski, Hilger, Bristol, 1988.
64. M. A. Carrondo and G. A. Jeffrey eds, 'Chemical Crystallography with Pulsed Neutron and Synchrotron X-Rays', NATO ASI Series C, 1987, Vol. 221.
65. C. C. Wilson and R. I. Smith, in 'Time-resolved Diffraction', eds. J. R. Helliwell, and P. M. Rentzepis, Oxford Science Publications, Oxford, 1997, p. 401.
66. A. J. Wonnacot and R. M. Barnett, in 'The Rotation Method in Crystallography', eds. U. W. Arndt and A. J. Wonnacot, North Holland, Amsterdam, 1977; B. W. Matthews, C. E. Klopfenstein and P. M. Colman, *J. Phys. E*, 1972, **5**, 353.
67. (a) J. L. Alberi, J. Fischer, V. Radeka, L. C. Rogers, and B. P. Schoenborn, *IEEE Trans. Nucl. Sci.*, 1975, **22**, 255; (b) 'Position Sensitive Detection of Thermal Neutrons', eds. P. Convert and J. Forsyth, Academic Press, London, 1983.
68. R. Hamlin, C. Cork, A. Howard, C. Nielsen, W. Vernon, D. Mathews, Ng. H. Xuong, and V. Perez-Mendez, *J. Appl. Crystallogr.*, 1981, **14**, 85.
69. R. Lewis, *J. Synchr. Radiat.*, 1994, **1**, 43.
70. U. W. Arndt and D. J. Gilmore, *J. Appl. Crystallogr.*, 1979, **12**, 1; U. W. Arndt, *J. Appl. Crystallogr.*, 1986, **19**, 145; S. J. Andrews, M. Z. Papiz, R. McMeeking, A. J. Blake, B. M. Lowe, K. R. Franklin, J. R. Helliwell, and M. M. Harding, *Acta Crystallogr.*, 1988, **B44**, 73.
71. Y. Amemiya, *J. Synchr. Radiat.*, 1995, **2**, 13.
72. M. W. Tate, E. F. Eikenberry, S. L. Barna, M. E. Wall, J. L. Lowrance, and S. M. Gruner, *J. Appl. Crystallogr.*, 1995, **28**, 196.
73. K. D. M. Harris and M. Tremayne, *Chem. Mater.*, 1996, **8**, 2554; V. K. Pecharsky and P. Y. Zavalij, 'Fundamentals of Powder Diffraction and Structural Characterization of Materials', Kluwer Academic Publishers, Dordrecht, 2003; K. D. M. Harris and E. Y. Cheung, *Chem. Soc. Rev.*, 2004, **33**, 526.
74. L. Brammer, J. A. K. Howard, O. Johnson, T. F. Koetzle, J. L. Spencer, and A. M. Stringer, *J. Chem. Soc., Chem. Commun.*, 1991, 241, refs. therein.
75. J. A. K. Howard, J. L. Spencer, and S. A. Mason, *Proc. R. Soc. London, Ser. A*, 1983, **A386**, 141; S. Teslic and T. Egami, *Acta Crystallogr.*, 1998, **B54**, 750.
76. P. J. Brown, J. Deportes, and K. R. A. Ziebeck, *J. Phys. I Fr.*, 1991, **1**, 1529; J. B. Forsyth, P. J. Brown, and B. M. Wanklyn, *J. Phys. C*, 1988, **21**, 2917; see also Annual Report, Institut Laue Langevin, 1992, 52.
77. B. T. M. Willis, *Acta Crystallogr.*, 1998, **A54**, 914.
78. F. Fillaux, J. Tomkinson, and J. Penfold, *Chem. Phys.*, 1988, **124**, 425; A. V. Belushkin, J. Tomkinson, and I. A. Shuvalov, ISIS Annual Report, 1991.
79. D. Stalke, *Chem. Soc. Rev.*, 1998, **27**, 171; A. E. Goeta and J. A. K. Howard, *Chem. Soc. Rev.*, 2004, **33**, 490.
80. F. van Bolhius, *J. Appl. Crystallogr.*, 1971, **4**, 263.
81. R. M. Hazen and L. W. Finger, 'Comparative Crystal Chemistry', John Wiley & Sons, New York, 1981.
82. J. Cosier and A. M. Glazer, *J. Appl. Crystallogr.*, 1986, **19**, 105.
83. L. N. Zakharov, M. Yu. Antipin, Yu. T. Struchkov, A. V. Gusev, A. M. Gubin, and N. V. Zhernikov, *Kristallografiya*, 1986, **31**, 171 (in Russian); H.-B. Bürgi, S. C. Capelli, A. E. Goeta, J. A. K. Howard, M. A. Spackman, and D. S. Yufit, *Chem. Eur. J.*, 2002, **8**, 3512.
84. J. R. Allibon, A. Filhol, M. S. Lehmann, S. A. Mason, and P. Simms, *J. Appl. Crystallogr.*, 1981, **14**, 326.
85. F. K. Larsen, *Acta Crystallogr.*, 1995, **B51**, 468; R. C. B. Copley, A. E. Goeta, C. W. Lehmann, J. C. Cole, D. S. Yufit, J. A. K. Howard, and J. M. Archer, *J. Appl. Crystallogr.*, 1997, **30**, 413.
86. T. Teng, W. Schildkamp, P. Dolmer, and K. Moffat, *J. Appl. Crysallogrt.*, 1994, **27**, 133; M. J. Hardie, K. Kirschbaum, A. Martin, and A. A. Pinkerton, T. Teng, W. Schildkamp, P. Dolmer, and K. Moffat, *J. Appl. Crysallogrt.*, 1998, **31**, 815; B. L. Hanson, A. Martin, J. M. Harp, D. A. Parrish, C. G. Bunick, K. Kirschbaum, A. A. Pinkerton, and G. J. Bunick, M. J. Hardie, K. Kirschbaum, A. Martin, and A. A. Pinkerton, T. Teng, W. Schildkamp, P. Dolmer, and K. Moffat, *J. Appl. Crysallogrt.*, 1999, **32**, 814.
87. A. E. Goeta, L. K. Thompson, C. L. Sheppard, S. S. Tandon, C. W. Lehmann, J. Cosier, C. Webster and J. A. K. Howard, *Acta Crystallogr.*, 1999, **C55**, 1243; M. A. Leech, N. K. Solanki, M. A. Halcrow, J. A. K. Howard, and S. Dahaoui, *Chem. Commun.*, 1999, 2245, see also www.Oxford-Cryosystems.co.uk/helix.
88. J. Schreuer, A. Baumgarte, and W. Steurer, *J. Appl. Crystallogr.*, 1997, **30**, 1162.
89. R. C. Peterson and H. Yang, *Rev. Mineral. Geochem.*, 2000, **41**, 425.
90. P. Delarue and M. Jannin, *J. Appl. Crystallogr.*, 1999, **32**, 824.
91. L. K. Frevel, *Rev. Sci. Instrum.*, 1935, **6**, 214.
92. A. W. Lawson and T. Y. Tang, *Rev. Sci. Instrum.*, 1950, **21**, 815; J. C. Jamieson, A. W. Lawson, and N. D. Nachtrieb, A. W. Lawson and T. Y. Tang, *Rev. Sci. Instrum.*, 1959, **30**,

1016; A. van Valkenburg, *Diamond Res.*, 1964, 17; L. Merrill and W. A. Bassett, *Rev. Sci. Instrum.*, 1974, **45**, 290.

93. M. I. Eremets, 'High Pressure Experimental Methods', Oxford University Press, Oxford, 1996.
94. R. M. Miletich, D. R. Allan, and W. F. Kuhs, *Rev. Miner. Geochem.*, 2000, **41**, 445.
95. R. J. Angel, R. T. Down, and L. W. Finger, *Rev. Miner. Geochem.*, 2000, **41**, 559.
96. I. N. Goncharenko, J. M. Mignot, and I. Mirabeau, *Neutron News*, 1996, **7**, 29; W. F. Kuhs, F. C. Bauer, R. Hausmann, H. Ahsbahs, R. Dorwarth, and K. Hölzer, *High Press. Res.*, 1996, **14**, 341.
97. R. J. Nelmes, J. S. Loveday, R. M. Wilson, W. G. Marshall, J. M. Besson, S. Klotz, G. Hamel, T. L. Aselage, and S. Hull, *Phys. Rev. Lett.*, 1995, **74**, 2268; J. B. Parise, J. S. Loveday, R. J. Nelmes, and H. Kagi, *Phys. Rev. Lett.*, 1999, **83**, 328; J. S. Loveday and R. J. Nelmes, *Phys. Rev. Lett.*, 1999, **83**, 4349.
98. M. J. Gutmann, D. A. Keen, and C. C. Wilson, *High Pressure Research*, 2003, **23**, 313.
99. H. E. Buckley, 'Crystal Growth', Wiley, London, 1951; P. G. Jones, *Chem. (Britain)*, 1981, **17**, 222; J. W. Mullin, 'Crystallization', Butterworth-Heinemann, Oxford, 1993; J. Hulliger, *Angew. Chem., Int. Ed. Engl.*, 1994, **33**, 143.
100. H. K. Henisch, 'Crystal Growth in Gels', Dover Publications, 1996.
101. T. Köttke and D. Stalke, *J. Appl. Crystallogr.*, 1993, **26**, 615.
102. W. R. Busing and H. A. Levy, *Acta Crystallogr.*, 1967, **22**, 457; W. Clegg, *J. Appl. Crystallogr.*, 1984, **17**, 334.
103. K. Tichy, *Acta Crystallogr.*, 1970, **A26**, 295.
104. (a) E. J. Gabe and Y. Le Page, in 'Computational Crystallography', ed. D. Sayre, Clarendon Press, Oxford, 1982; (b) R. H. Blessing, *Crystallogr. Rev.*, 1987, **1**, 3; (c) M. S. Lehmann and F. K. Larsen, *Acta Crystallogr.*, 1974, **A30**, 580.
105. E. F. Garman and T. R. Schneider, *J. Appl. Crystallogr.*, 1997, **30**, 211.
106. M. J. Cooper in 'Thermal Neutron Diffraction', ed. B. T. M. Willis, Oxford University Press, Oxford, 1970; M. J. Cooper and K. D. Rouse, *Acta Crystallogr.*, 1968, **A24**, 405; E. D. Stevens, M. J. Cooper and K. D. Rouse, *Acta Crystallogr.*, 1974, **A30**, 184; M. Sakata, A. W. Stevenson, and J. Harada, *J. Appl. Crystallogr.*, 1983, **16**, 156 and refs. therein.
107. R. H. Blessing, *Acta Crystallogr.*, 1984, **A40**, C156; A. I. Stash and V. E. Zavodnik, *Crystallogr. Rep.*, 1996, **41**, 404.
108. J. A. K. Duckworth, B. T. M. Willis, and G. S. Pawley, *Acta Crystallogr.*, 1969, **A25**, 482; J. A. K. Duckworth, B. T. M. Willis, and G. S. Pawley, *Acta Crystallogr.*, 1970, **A26**, 263.
109. B. T. M. Willis, *Acta Crystallogr.*, 1970, **A26**, 396.
110. S. F. Mughabghab, M. Divadeenam, and N. E. Holden, 'Neutron Cross Sections', Academic Press, New York, 1981, Vols. I and II; V. F. Sears, *Neutron News*, 1992, **3**, 26.
111. J. de Meulenaer and H. Tompa, *Acta Crystallogr.*, 1965, **19**, 1014.
112. P. Coppens, L. Leiserowitz, and D. Rabinovich, *Acta Crystallogr.*, 1965, **18**, 1035; K. D. Rouse, M. J. Cooper, E. J. York, and A. Chakera, *Acta Crystallogr.*, 1970, **A26**, 682; N. W. Alcock, G. S. Pawley, C. P. Rourke, and M. R. Levine, *Acta Crystallogr.*, 1972, **A28**, 440; P. Coppens, 'Crystallographic Computing', eds. F. R. Ahmed, S. R. Hall, and C. P. Huber, Munksgaard, Copenhagen, 1970.
113. A. C. T. North, D. C. Philips, and F. S. Mathews, *Acta Crystallogr.*, 1968, **A24**, 351; D. Schwarzenbach and H. D. Flack, *J. Appl. Crystallogr.*, 1989, **22**, 601; N. W. Alcock and P. J. Marks, *J. Appl. Crystallogr.*, 1994, **26**, 200.
114. R. H. Blessing, *Acta Crystallogr.*, 1995, **A51**, 33; L. Häming and G. M. Sheldrick, XVII IUCr Congress and General Assembly, Glasgow, 1999, Collected Abstracts, 206; G. M. Sheldrick, 'SADABS: Program for Scaling and Correction of Area Detector Data', University of Göttingen, Germany, 1996; SADABS, version 2.10, Bruker AXS, Madison, Wisconsin, WI, 2003.
115. N. Walker and D. Stuart, *Acta Crystallogr.*, 1983, **A39**, 158.
116. W. H. Zachariasen, *Acta Crystallogr.*, 1967, **23**, 558.
117. P. J. Becker and P. Coppens, *Acta Crystallogr.*, 1974, **A30**, 129; T. M. Sabine, R. B. von Dreele, and J.-E. Jorgenson, *Acta Crystallogr.*, 1988, **A44**, 374.
118. M. Renninger, *Z. Phys.*, 1937, **106**, 41; R. M. Moon and C. G. Shull, *Acta Crystallogr.*, 1964, **17**, 597.
119. P. Coppens, *Acta Crystallogr.*, 1968, **A24**, 253; K. Tanaka and Y. Saito, P. Coppens, *Acta Crystallogr.*, 1975, **A31**, 841; Y. Le Page and E. J. Gabe, K. Tanaka and Y. Saito, P. Coppens, *Acta Crystallogr.*, 1979, **A35**, 73; B. T. M. Willis, C. J. Carlile, R. C. Ward, W. I. David, and M. W. Johnson, *Europhys. Lett.*, 1986, **2**(10), 767.
120. A. J. C. Wilson, *Nature (London)*, 1942, **150**, 152.
121. G. Giacovazzo, 'Direct Phasing in Crystallography', Oxford University Press, Oxford, 1998.
122. A. L. Patterson, *Z. Krist.*, 1935, **A90**, 517; 'Patterson and Pattersons. Fifty Years of the Patterson Function', eds. J. P. Glusker, B. K. Patterson, and M. Rossi, Oxford University Press, Oxford, 1987.
123. M. M. Woolfson, *Acta Crystallogr.*, 1987, **A43**, 593 and refs. therein; G. Giacovazzo, 'Direct Methods in Crystallography', Academic Press, London, 1980.
124. D. Harker and J. S. Kasper, *Acta Crystallogr.*, 1948, **1**, 7.
125. J. Karle and H. A. Hauptman, *Acta Crystallogr.*, 1956, **9**, 635; J. Karle and I. L. Karle, *Acta Crystallogr.*, 1966, **21**, 849; G. Germain and M. M. Woolfson, *Acta Crystallogr.*, 1968, **B24**, 91; G. Germain, P. Main, and M. M. Woolfson, *Acta Crystallogr.*, 1971, **A24**, 368; G. Bricogne, *Acta Crystallogr.*, 1984, **A40**, 410; M. M. Woolfson and J. Yao, *Acta Crystallogr.*, 1990, **A46**, 409.
126. D. Sayre, *Acta Crystallogr.*, 1952, **5**, 60; W. Cochran, *Acta Crystallogr.*, 1952, **5**, 65.

127. G. M. Sheldrick, *Acta Crystallogr.*, 1990, **A46**, 467; A. Altomare, G. Cascarano, C. Giacovazzo, A. Guagliardi, M. C. Burla, G. Polidori, and M. Camalli, *J. Appl. Crystallogr.*, 1994, **27**, 435.
128. W. von der Linden, V. Dose, R. Fischer, and R. Preuss eds, ‘Maximum Entropy and Bayesian Methods’, Kluwer Academic Publishers, Dordrecht, 1998.
129. M. Sakata and M. Sato, *Acta Crystallogr.*, 1990, **A46**, 263; C. J. Gilmore, *Acta Crystallogr.*, 1996, **A52**, 561.
130. J. S. Rollett, in ‘Computational Crystallography’, ed. D. Sayer, Clarendon Press, Oxford, 1982; D. J. Watkin, in ‘Crystallographic Computing. 3. Data Collection, Structure Determination, Proteins and Data Bases’, eds. G. M. Sheldrick, C. Kruger, and R. J. Goddard, Clarendon Press, Oxford, 1985.
131. D. Watkin, *Acta Crystallogr.*, 1994, **A50**, 411; R. L. Harlow, *J. Res. Natl. Inst. Stand. Technol.*, 1996, **101**, 327.
132. H. D. Flack, *Acta Crystallogr.*, 1983, **A39**, 876; H. D. Flack and G. Bernardinelli, *J. Appl. Crystallogr.*, 2000, **33**, 1143 and refs therein.
133. G. M. Sheldrick, ‘SHELXTL-97’, University of Göttingen, Germany, 1997; SHELXTL: An Integrated System for Solving, Refining and Displaying Crystal Structures from Diffraction Data, version 6.12, Bruker AXS, Madison, Wisconsin, WI, 2001; D. J. Watkin, C. K. Prout, J. R. Carruthers, P. W. Betteridge, and R. I. Cooper, ‘CRYSTALS’, Issue 11, Chemical Crystallography Laboratory, University of Oxford, Oxford, 2002.
134. E. Koch, in ‘International Tables for X-ray Crystallography’, ed. A. J. C. Wilson, Kluwer, Dordrecht, 1992, Vol. C, p. 10.
135. Y. Le Page, *J. Appl. Crystallogr.*, 1982, **15**, 255; A. J. M. Duisenberg, *J. Appl. Crystallogr.*, 1992, **25**, 92; J. Schlessman and D. B. Litvin, *Acta Crystallogr.*, 1995, **A51**, 947.
136. R. A. Sparks, GEMINI, Bruker AXS, Madison, Wisconsin, WI, 1999, G. M. Sheldrick, TWINABS, Bruker AXS, Madison, Wisconsin, WI, 2002.
137. R. Herbst-Irmer and G. M. Sheldrick, *Acta Crystallogr.*, 1998, **B54**, 443; 2002, **B58**, 477.
138. S. van Smallen, *Crystallogr. Rev.*, 1995, **4**, 79.
139. U. Dehling, *Z. Kristallogr.*, 1927, **65**, 615.
140. J. Peterková, M. Dušek, and V. Petřiček, *Acta Crystallogr.*, 1998, **B54**, 809; M. Evain, F. Boucher, O. Gourdon, V. Petřiček, M. Dušek, and P. Bezdička, *Chem. Mater.*, 1998, **10**, 3068; S. van Smaalen, *Z. Kristallogr.*, 2004, **219**, 681.
141. V. Petřiček and M. Dušek, ‘The Crystallographic Computing System’, Institute of Physics, Praha, Czech Republic, 2000; M. Dušek, V. Petřiček, M. Wunschel, R. E. Dinnebier, and S. van Smaalen, *J. Appl. Crystallogr.*, 2001, **34**, 398; V. Petříček and M. Dušek, *Z. Kristallogr.*, 2004, **219**, 692.
142. P. Debye, *Ann. Phys.*, 1915, **46**, 809.
143. H. Witte and E. Wölfel, *Z. Phys. Chem. NF*, 1955, **3**, 296.
144. P. Coppens, *Acta Crystallogr.*, 1998, **A54**, 779.
145. V. G. Tsirel’son and R. P. Ozerov, ‘Electron Density and Bonding in Crystals’, Institute of Physics Publishing, Bristol, 1996.
146. T. S. Koritsanszky and P. Coppens, *Chem. Rev.*, 2001, **101**, 1583.
147. G. V. Gibbs, F. C. Hill, and M. B. Boisen Jr, *Phys. Chem. Miner.*, 1997, **24**, 167; E. L. Belokoneva, *Russ. Chem. Rev.*, 1999, **68**, 299.
148. A. Martin and A. A. Pinkerton, *Acta Crystallogr.*, 1998, **B54**, 471; B. B. Iversen, F. K. Larsen, A. A. Pinkerton, A. Martin, A. Darovsky, and P. A. Reynolds, *Acta Crystallogr.*, 1999, **B55**, 363.
149. R. W. F. Bader, ‘Atoms in Molecules: A Quantum Theory’, Clarendon Press, Oxford, 1990.
150. N. Pérès, A. Boukhris, M. Souhassou, G. Gavoille, and C. Lecomte, *Acta Crystallogr.*, 1999, **B55**, 1038.
151. S. R. Hall, F. H. Allen, and I. D. Brown, *Acta Crystallogr.*, 1991, **A47**, 655; B. McMahon, *Acta Crystallogr.*, 1993, **C49**, 418; S. R. Hall, *Acta Crystallogr.*, 1998, **A54**, 820; see also http://www.iucr.org/cif.
152. M. S. Weiss, *J. Appl. Crystallogr.*, 2001, **34**, 130.
153. G. J. Kleywegt, *Acta Crystallogr.*, 2000, **D56**, 249.
154. F. H. Allen, O. Kennard, D. G. Watson, L. Brammer, A. G. Orpen, and R. Taylor, *J. Chem. Soc., Perkin Trans. 2*, 1987, S1.
155. A. G. Orpen, L. Brammer, F. H. Allen, O. Kennard, D. G. Watson, and R. Taylor, *J. Chem. Soc., Dalton Trans.*, 1989, S1.
156. F. H. Allen, O. Kennard, and D. G. Watson, in H.-B. Bürgi and J. D. Dunitz eds, ‘Structure Correlations’, VCH, Weinheim, 1994, Vol. 1, p. 71.
157. F. H. Allen and O. Kennard, *Chemical Design Automation News*, 1993, **8**, 1; F. H. Allen, *Acta Crystallogr.*, 2002, **B58**, 380, see also http://www.ccdc.cam.ac.uk.
158. A. G. Orpen, *Acta Crystallogr.*, 2002, **B58**, 398.
159. F. H. Allen and R. Taylor, *Chem. Soc. Rev.*, 2004, **33**, 463.
160. R. Taylor and O. Kennard, *Acta Crystallogr.*, 1983, **B39**, 517; *J. Chem. Inform. Comput. Sci.*, 1986, **26**, 28.
161. (a) F. H. Allen, M. J. Doyle and R. Taylor, *Acta Crystallogr.*, 1991, **B47**, 29; (b) F. H. Allen, P. Bath, and P. Willett, *J. Chem. Inf. Comput. Sci.*, 1994, **35**, 261; (c) J.-W. Yao, R. C. B. Copley, J. A. K. Howard, F. H. Allen, and W. D. S. Motherwell, *Acta Crystallogr.*, 2001, **B57**, 251.
162. H.-B. Bürgi, *Acta Crystallogr.*, 1998, **A54**, 873.
163. G. R. Desiraju, ‘Crystal Engineering. The Design of Organic Solids’, Elsevier, Amsterdam, 1989; A. Nangia and G. R. Desiraju, *Acta Crystallogr.*, 1998, **A54**, 934; J. W. Steed and J. L. Atwood, ‘Supramolecular Chemistry’, John Wiley & Sons, Chichester, 2000.
164. G. A. Jeffrey, in ‘Accurate Molecular Structures’, eds. A. Domenicano and I. Hargittai, Oxford University Press,

Oxford, 1992; G. A. Jeffrey and W. Saenger, 'Hydrogen Bonding in Biological Systems', Springer-Verlag, Berlin, 1991; N. Shankland, A. J. Florence, and C. C. Wilson, *Acta Crystallogr.*, 1997, **B53**, 176; T. Steiner, *Angew. Chem. Int. Ed. Engl.*, 2002, **41**, 48.

165. T. P. E. auf der Heyde and H.-B. Bürgi, *Inorg. Chem.*, 1989, **28**, 3960.

166. J. A. K. Howard, R. C. B. Copley, J.-W. Yao, and F. H. Allen, *Chem. Commun.*, 1998, 2175.

167. G. Bergerhoff, R. Hundt, R. Sievers, and I. D. Brown, *J. Chem. Inf. Comput. Sci.*, 1983, **23**, 66; http://www.fiz-informationsdienste.de/en/DB/icsd.

168. U. D. Altermatt and I. D. Brown, *Acta Crystallogr.*, 1987, **A43**, 125; I. D. Brown, *J. Chem. Inf. Comput. Sci.*, 1989, **29**, 266.

169. CRYSTMET, Toth Information Systems Inc., 2045 Quincy Avenue, Gloucester, Ontario K1J 6B2, 2000, http://www.tothcanada.com.

170. F. C. Bernstein, T. F. Koetzle, G. J. B. Williams, E. F. Meyer, M. D. Brice, J. R. Rodgers, O. Kennard, T. Shimanouchi, and M. Tasumi, *J. Mol. Biol.*, 1977, **122**, 535; E. E. Abola, J. L. Sussman, J. Priluski, and N. O. Manning, *Methods Enzymol.*, 1997, **277**, 556; H. M. Berman, J. Westbrook, Z. Feng, G. Gilliland, T. N. Bhat, H. Weissig, I. N. Shindyalov, and P. E. Bourne, *Nucleic Acids Res.*, 2000, **28**, 235; see also http://www.rcsb.org/pdb/.

171. H. M. Berman, W. K. Olson, D. L. Beveridge, J. Westbrook, A. Gelbin, T. Demeny, S.-H. Hsieh, A. R. Srinivasan, and B. Schneider, *Biophys. J.*, 1992, **63**, 751; http://ndbserver.rutgers.edu/.

Dinuclear Organometallic Cluster Complexes

Gabor Kiss, James Eric McDonough, John J. Weir & Carl D. Hoff
University of Miami, Coral Gables, FL, USA

1 Introduction 1
2 Recent Developments and New Directions 1
3 Historical Background 5
4 Illustrative Examples of Metal–Metal Bonded Complexes 7
5 Literature Sources for Metal–Metal Bonded Complexes 15
6 Synthetic Methods 15
7 Reactions of Metal–Metal Bonded Complexes 19
8 Metal Dimers as Catalysts and Catalyst Precursors 22
9 Physical Properties of Metal–Metal Bonded Dimers 23
10 Related Articles 24
11 References 24

1 INTRODUCTION

Metals and metal–metal bonding hold a fascination for all chemists. Dimers are the simplest units that incorporate metal–metal bonds. They represent the next step in chemical complexity in going from monomers to clusters (*see* ***Polynuclear Organometallic Cluster Complexes***) and ultimately to surfaces as shown in equation (1).

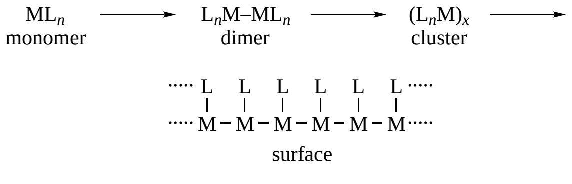

$$\underset{\text{monomer}}{ML_n} \longrightarrow \underset{\text{dimer}}{L_nM\text{–}ML_n} \longrightarrow \underset{\text{cluster}}{(L_nM)_x} \longrightarrow \underset{\text{surface}}{\cdots\begin{matrix} L & L & L & L & L & L \\ | & | & | & | & | & | \\ M- & M- & M- & M- & M- & M \end{matrix}\cdots}$$

(1)

All the complexes shown in equation (1) can undergo reactions such as ligand substitution (*see Ligand Substitution*) or oxidative addition (*see Oxidative Addition*), which reflect the character of the individual metal–ligand bonds. For metal–metal bonded complexes, reactions can occur at the following sites: (1) reaction at the coordinated ligand; (2) reaction at the metal–ligand bond; (3) reaction at the metal–metal bond.

The presence of a metal–metal bond not only introduces possibility (3) but can also modify the reactivities (1) and (2). The influence of metal–metal bonds on these types of reactivity is still being investigated, and this review is meant to be an illustrative introduction to metal–metal bonding in inorganic and organometallic dimers. Since the metal–metal bond of a dimeric complex provides the fundamental unit of more complex architectures, some discussion of clusters is also included.

2 RECENT DEVELOPMENTS AND NEW DIRECTIONS

The basic themes of metal–metal bonded dimers were established years ago and have remained largely unchanged. However, new aspects of metal–metal bonding have been discovered and in addition, application of metal–metal bonded complexes in other areas has grown. Important contributions in emerging fields such as nanomaterials, fullerene (*see* ***Carbon: Fullerenes***) chemistry, combinatorial catalytic research, molecular recognition, and dendrimers have all utilized metal–metal bonded complexes.

2.1 Electrical Conductivity and Related Physical Properties

An increasing area of interest and utilization of metal–metal bonded complexes is the area of electrical conduction at the molecular level. A prototypical complex is shown in Figure 1, which incorporates a diphosphine-bridged $Pt^I–Pt^I$ dimer**[1]** spliced to two linear acetylenic linkages terminated by ferrocenyl (*see Ferrocene*) groups as endcaps.

Electronic communication is deemed to be high in this complex, but much lower in a related gold-bridged system. The exact nature of what controls 'conductivity' or 'electronic communication' at the molecular level is far from being understood. Inroads in that area have been made as well, as discussed later, but advances in synthetic and structural chemistry continue to lead the way, as demonstrated by the complexes highlighted in this section.

The cluster $Ir_4(CO)_8(PMe_3)_4$ reacts with excess C_{60} to yield a square planer core of four Ir atoms.**[2]** Two of the Ir atoms in the Ir_4 fragment are linked simultaneously to the faces of two C_{60}'s, as shown in Figure 2.

In addition to electrical properties, the optical properties (*see* ***Luminescence Behavior & Photochemistry of Organotransition Metal Compounds***) of the metal–metal bonded unit have also received increased attention. 'Luminescence tribochromism' – light emission that occurs with mechanical grinding – has been displayed by a Au–Au dimeric complex where the monomeric unit with a Au–Au separation of 2.8797 Å arranges in a helical structure with alternating longer Au···Au distances as shown in Figure 3.**[3]**

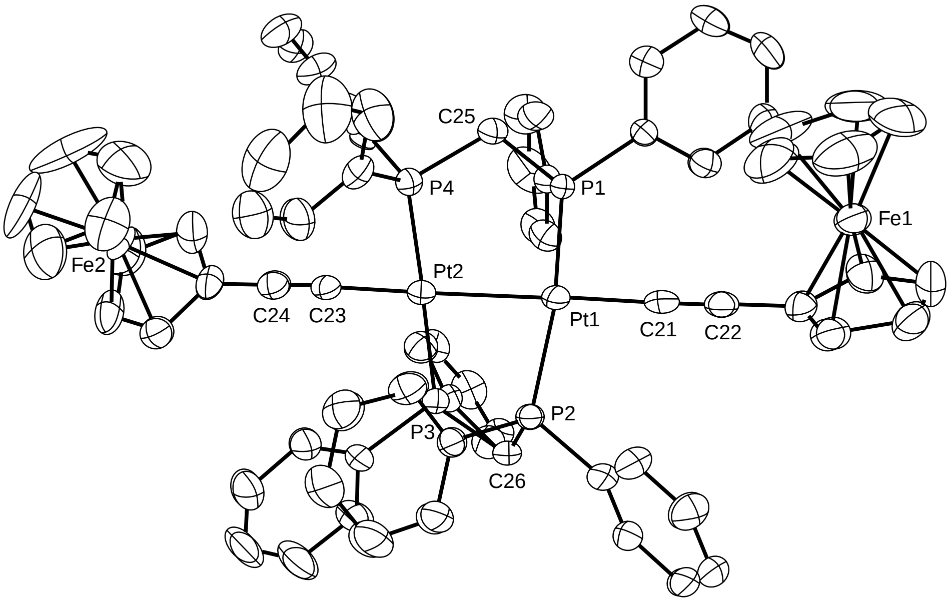
C25
P4
P1
Fe1
Fe2
Pt2
C24
C23
Pt1
C21
C22
P2
P3
C26

Figure 1 Chelating phosphine-bridged Pt(I)–Pt(I) metal–metal bonded dimer.[1] (Reprinted with permission from Ref. 1. © 2002 American Chemical Society)

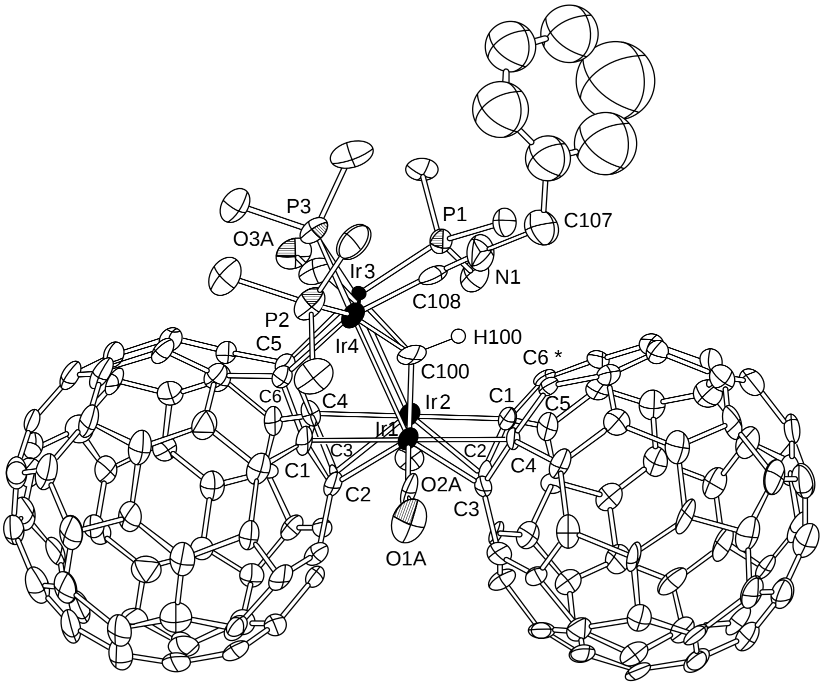
C107
P3
P1
O3A
Ir3
N1
C108
P2
H100
Ir4
C5
C6 *
C100
C6
C4
Ir2
C1
C5
Ir1
C3
C2
C4
C1
C2
O2A
C3
O1A

Figure 2 Coordination of two C_{60}'s to an Ir–Ir fragment, allowing a 'wide passage for interfullerene electronic interaction'.[2] (Reprinted with permission from Ref. 2. © 2003 American Chemical Society)

2.2 Supramolecular Complexes, Molecular Engineering, Dendrimers, Nanoparticles

Nanotechnology has seen an upsurge in development and in this area as well, metal–metal bonded complexes find a role. Manganese phosphide (*see* ***Phosphides: Solid-state Chemistry***) nanocrystals have recently been prepared utilizing $Mn_2(CO)_{10}$.[4] In this application, metal–metal bonded complexes are used as precursors to novel materials. A number of applications in which supramolecular architectures have

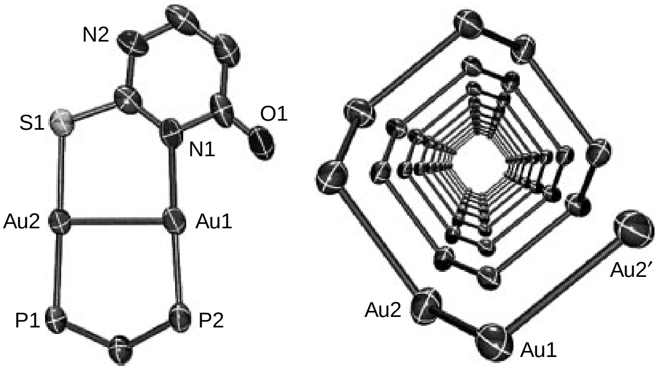

Figure 3 Au–Au dimeric unit[3] that crystallizes, producing a helical arrangement conducive to 'luminescence tribochromism'. (Reprinted with permission from Ref. 3. © 2003 American Chemical Society)

been assembled that incorporate, as part of the assembly, a metal–metal bonded subunit. The ability of these subunits to interact and the extent of these interactions remains an area of open investigation. Aspects of polymer formation incorporating metal–metal multiply bonded dimeric units have been explored and reviewed for one-dimensional polymers[5] and as supramolecular arrays.[6] Dimeric ruthenium complexes have been prepared that crystallize in square arrays, each containing four paramagnetic Ru–Ru dimers, as shown in Figure 4.

The entire crystal structure displays a supramolecular structure that is tetragonal, as shown in Figure 5.

Square-shaped channels in the crystal are occupied by solvent molecules. Further illustration of continued utilization of metal–metal bonded complexes in 'molecular engineering' type of applications is the dendrimer-like complex in Figure 6.

A novel one-dimensional helical polymer resembling DNA and composed of heterodinuclear subunits containing $\mathrm{Pt^{II}} \rightarrow \mathrm{Ag^{I}}$ dative bonds has been synthesized.[9] The design and utilization of supramolecular metal–metal bonded assemblies such as those shown above can be expected to be an area of intense research effort in the future (*see* ***Semiconductor Interfaces***).

2.3 Multiple Bonded Main Group–Main Group and Transition Metal–Main Group Complexes

A general resurgence in main group inorganic chemistry has led to a number of spectacular developments including

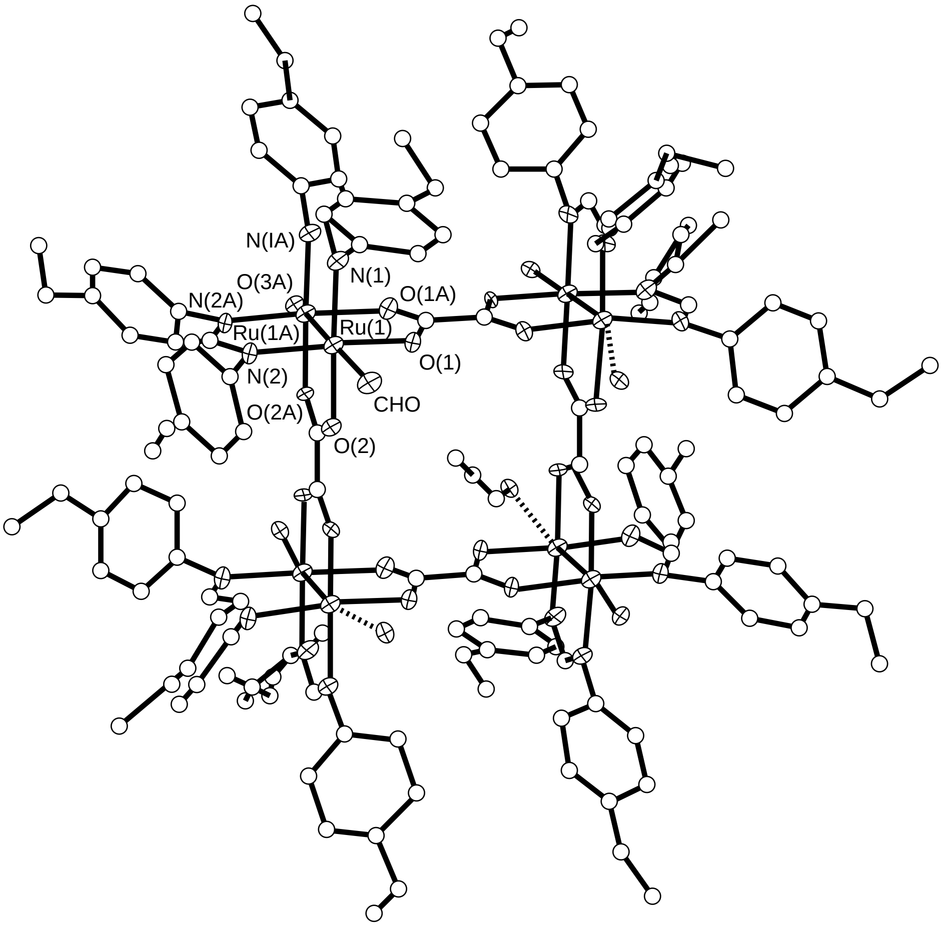

Figure 4 Tetrameric structure containing four Ru–Ru units. (Reprinted with permission from Ref. 7. © 2003 American Chemical Society)

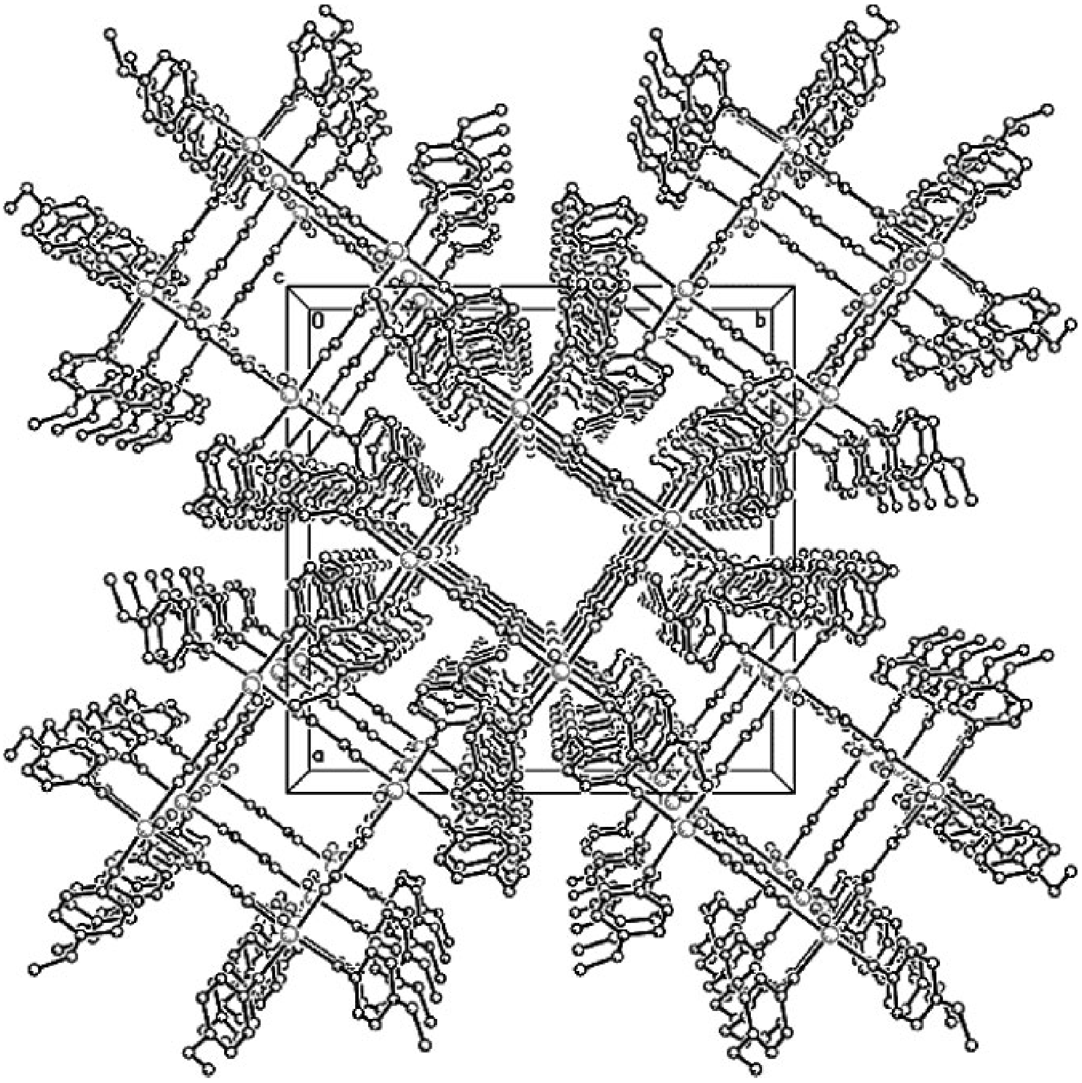

Figure 5 Figure showing supramolecular stacking of Ru–Ru complex from Figure 4. (Reprinted with permission from Ref. 7. © 2003 American Chemical Society)

synthesis of multiply bonded metal complexes. The concept of 'metalloaromaticity' and 'antiaromaticity' has been introduced for some of these complexes and is an area of current theoretical debate.[10] In addition to main group–main group multiple bonding, main group metal–transition-metal complexes with metal–metal bonds have also been prepared, as shown in Figure 7.

2.4 Theoretical Advances

The rapid advances in synthetic and structural chemistry of the metal–metal bond have inspired detailed theoretical investigation. Unlike main group elements such as carbon, transition metals can form a quadruple bond between two metal atoms. The quadruple bond consists of a single σ bond (overlap of two d_z2 orbitals), two degenerate π bonds (overlap of two d_{yz} orbitals and two d_{xz} orbitals), and a δ bond (overlap of two d_{xy} orbitals). The existence of a quadruple bond between two metal atoms was first recognized in 1964 when Cotton and coworkers[12] isolated the compound $[Re_2Cl_8]^{-2}$. Since then, many other compounds have been found containing a quadruple bond (such as $[Mo_2Cl_8]^{-4}$).

The bonding between two metals that contain a quadruple bond is largely due to the σ and π bond interactions. The δ bond contribution to the quadruple bond is small and is illustrated by the fact that the removal of a δ bond typically results in a bond lengthening of only 3%.[13] Also, in the compound $[Re_2Cl_8]^{-2}$ whose bond strength is $85 \pm 5\,\text{kcal mol}^{-1}$, only approximately $6\,\text{kcal mol}^{-1}$ is assigned to the δ bond[14] (which is comparable to a hydrogen bond). The strength of a δ bond depends on the amount of overlap existing between the two d_{xy} orbitals of the metals. Orbital overlap of the δ bond depends on a twist angle

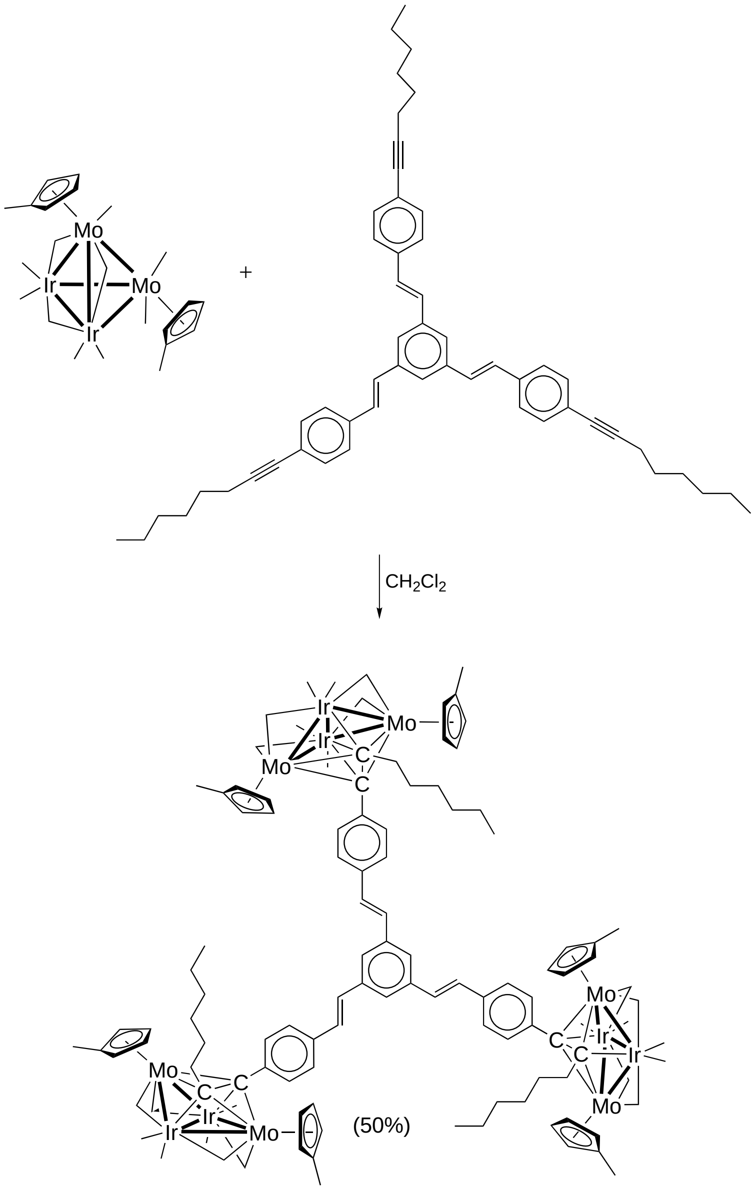

Figure 6 Preparation of bridging acetylene dendrimeric metal–metal bonded complexes. (Reprinted with permission from Ref. 8. © 2003 American Chemical Society)

between the two metals and can be varied because of steric factors of the ligand substituents. The weakening of the δ bond can be observed in several ways, such as by the lengthening of the M–M bond distance or by a decrease in the $\delta \rightarrow \delta^*$ transition.[15] It seems clear that a nearly continuous variation of bond orders can be developed for the M–M bond.[13,15–20]

3 HISTORICAL BACKGROUND

Although the first transition metal complex that we now know contains metal–metal bonds[21] was reported as early as 1844, the concept of metal–metal bonding became widely accepted only more than a century later, during the 1960s. The development of the chemistry of organometallic compounds with metal–metal bonds is intimately connected with metal carbonyl chemistry (*see* ***Carbonyl Complexes of the Transition Metals***) and homogeneous catalysis.[22–24] The first organometallic compound, which would later be shown to have a metal–metal bond, was $Co_2(CO)_8$, discovered by Mond in 1910. The successful use of this complex as the starting catalyst in hydroformylation (*see Hydroformylation*) was developed by Roelen in 1938 and would later have a tremendous impact on this area. The pioneering work of Hieber and his group during the 1930s led to the synthesis of numerous

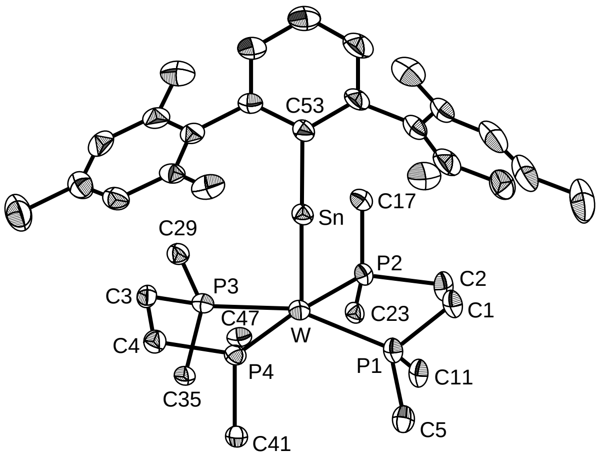

Figure 7 Complex with proposed Sn$\equiv$W bond. (Reprinted with permission from Ref. 11. © 2003 American Chemical Society). There is a long history of transition metal–main group–metal dimers, but multiple bonding between main group metals and transition metals is a new area

landmark complexes whose structures and chemistries would only later be shown to have metal–metal bonds.

The earliest structural proof[25] of a metal–metal bond in a complex was that of Hg_2Cl_2 in 1926, but this structure was considered something of an anomaly. The Swedish chemist Brosset published the structure of $K_3W_2Cl_9$ in 1935, and it showed clear evidence of a W–W bond.[21] The first organometallic complex proven to have a metal–metal bond was $Fe_2(CO)_9$. Its structure, determined in 1939 and reinvestigated more recently by Cotton,[26] shows an Fe–Fe distance of 2.46 Å. Since the metal–metal bond is supported by three bridging carbonyl ligands, it did not give definitive proof of the metal–metal interaction. The synthesis and later structural determinations of the complexes $Re_2(CO)_{10}$, $Mn_2(CO)_{10}$, and $[Cp(CO)_3Mo]_2$ provided the first unequivocal structural proofs of metal–metal bonding unsupported by bridging ligands (For leading references to these and related complexes, see Ref. 1 and also Ref. 27).[27]

The slow evolution of metal–metal bonding was greatly accelerated when Cotton and coworkers[12] published the X-ray structure of $Re_2Cl_8{}^{2-}$ in 1964. This complex with its quadruple metal–metal bond remains a landmark complex, and recently, its electronic structure and orbital energies in the gas phase were confirmed experimentally for the first time.[28] The first organometallic complexes showing multiple metal–metal bonds were prepared and characterized only a few years later by King and Bisnette.[29] The oil crisis in the mid-1970s induced a flurry of interest in homonuclear bimetallic transition metal complexes because of their potential application as catalysts or catalyst precursors. The concept of combining the activity of heterogeneous catalysts with the selectivity of homogeneous systems motivated the development of this chemistry. More recently, considerable interest has focused on the synthesis and chemistry of heteronuclear catalysts, in particular, early–late bimetallics. It is hoped that such complexes containing hard and soft metal centers in close proximity can activate organic substrates by combining the different reactivity of the two metal centers. Understanding the nature of the metal–metal bond has been a motivating factor for pure research in this area from the beginning. In spite of the large amount of work, the chemistry of metal–metal bonded complexes remains a vast frontier. In a review of this length, it is only possible to highlight principle features.

Transition metal complexes with metal–metal bonds have been divided into two general classes by Cotton and Wilkinson:[30] (1) high-valent halide complexes, such as $Re_2Cl_8{}^{2-}$ and (2) low-valent organometallic carbonyl complexes, such as $Mn_2(CO)_{10}$. This division held precedent for a long time since the groups of people working were largely different and used different approaches. In addition, the chemistry itself seemed to have different qualities. This distinction is no longer clear. Many researchers have made contributions to both classes, none more than Cotton himself. For example, the complex $[Re_2Cl_8]^{2-}$, one of the first halide types prepared, has an organometallic analog $[Re_2Me_8]^{2-}$ that was prepared some 14 years after the halide complex. According to all definitions, $[Re_2Me_8]^{2-}$ qualifies as an organometallic complex since it has direct bonds between organic groups and a metal. On the other hand, $Re_2(CO)_{10}$ is viewed in some strict definitions as not being organometallic since CO is 'inorganic carbon'. These semantic problems mask the more subtle questions of which complexes most resemble each other. The reactivity patterns of these compounds are a varied mosaic that crosses all boundaries. This review will focus on what are traditionally viewed as organometallic complexes but, where appropriate, inorganic complexes will be discussed as well. Related articles are also available to the reader (*see* ***Polynuclear Organometallic Cluster Complexes***; and ***Cluster Compounds: Inorganometallic Compounds Containing Transition Metal & Main Group Elements***).

The development of organic chemistry has been organized largely around the idea of 'functional groups'. Certainly, the metal–metal bond is one of the more important functional groups in inorganic chemistry. However, it must be recognized that there may be little in common between, for example, an iron–iron or a niobium–niobium bond. In addition, even for a given element, there is a range of oxidation states that display metal–metal bonding. For a given metal and a given oxidation state, variation of the ligand arrangement can be expected to cause changes in the character or, even possibly, the chemical reactivity of metal–metal bonds. Metal–metal bonds may show a continuous variation of reaction patterns, but at the time of writing this review, the principles guiding this field are still not completely known. Three quotations from the literature make this clear. The first is from a review of this field by Vahrenkamp[31] in 1978 regarding what is known about metal–metal bond complexes: 'So much that compounds containing metal–metal bonds have already been treated in about 70 reviews and monographs cited in this article. The other answer is: So little that the significance of metal–metal interactions is still uncertain even in the simplest compounds…'. The second is from a later review by Chisholm:[32] 'Are there simple chemical tests available to distinguish between M–M quadruple, triple, and double bonds based on reactivity? Some 20 years after the discovery of the M–M quadruple bond, the answer is still no!' The final quotation is taken from Cotton, Murillo, *et al.*[7] and points to the future: 'In short with the synthesis of **1**, **2**, and **3**, we have opened the door to the possibility of magnets and conductors built with metal–metal bonded subunits'.

This refers to complexes such as that shown in Figure 5. It shows both how much progress has been made in metal–metal bonded complexes and how much remains to be discovered.

4 ILLUSTRATIVE EXAMPLES OF METAL–METAL BONDED COMPLEXES

The range of metal–metal bonding as a function of ancillary ligands and oxidation state can be best illustrated by specific examples. The given examples are chosen primarily from molybdenum chemistry, but are indicative of general classes of metal–metal bonded complexes. With the possible exception of dinuclear ligand-bridged complexes of iron, there are probably more characterized metal–metal bonded dimers of molybdenum than of any other element. The reactions shown are meant to be illustrative of different methods of obtaining metal–metal bonds but may not represent optimum synthetic procedures. For detailed coverage, the next section provides additional review articles and monographs. The relation of some of these complexes to $Mo(CO)_6$ is shown in Scheme 1.

The present section begins with examples of metal–metal bonding in the absence of external ligands (gas-phase dimers, the solid state, and surfaces). These are covered since they represent metal–metal bonding in its simplest form. Study of the addition of organic ligands to these structures is an area of ever-increasing research activity. It continues on to complexes that are representative of broad classes of organometallic metal–metal bonding dimers.

4.1 'Naked Dimers', Mo_2 (g)

The simplest metal–metal bonded dimers occur in the gas phase in the absence of ligands. Pyrolysis of molybdenum metal at high temperatures in vacuum produces Mo (g) that is in equilibrium with the gas-phase dimer Mo_2 (g) (equation 2).

$$\cdots\text{Mo–Mo–Mo–Mo–Mo}\cdots \longrightarrow \underset{1.93\,\text{Å}}{\text{Mo=Mo(g)}} \rightleftharpoons 2\text{Mo} \quad (2)$$

The internuclear distance of 1.93 Å, is the shortest Mo–Mo distance observed to date. The net bond strength of 97 kcal mol^{-1} in this molecule[33] probably represents an upper limit for the Mo–Mo interaction in any environment. It seems unlikely, but not impossible, that some type of additional bridging ligand could be found to further strengthen/shorten this bond. To date, it does not appear to have been accomplished. This highlights the fact that, in spite of their importance, metal–metal bonds, even multiple ones, are not generally of exceptional strength.

In view of the tremendous amount of gas-phase chemistry that has been done with metal atoms and ions, the use of these 'naked dimers' as precursors to ligated metal–metal bonded complexes seems to be a field that could expand (equation 3).

$$\text{Mo=Mo} + n\text{L} \longrightarrow \text{L}_n\text{Mo=MoL}_n \quad (3)$$

Only scattered reports of studies of gas-phase reactions of dimers, such as that shown in equation (3), have appeared. There have been several reports in metal-atom chemistry of formation of dimeric complexes, but the mechanism of dimer formation is not known.

4.2 Metals, Colloids, Surfaces, and Mo(s)

Solid metals provide a benchmark for judging metal–metal bond distances and a rough guide to energetics and bond strengths. This is true, even though the metal–metal bond in bulk metals is best understood in terms of solid-state theory (*see* ***Surfaces*** and ***Electronic Structure of Solids***). The metal–metal bond in dimers and clusters is often cited as a model for metal–metal bonding in bulk metals or on surfaces. The reverse should also be considered: observations from surface and cluster chemistry could provide insight and perspective for dimers. There is probably a smooth transition in the nature of the metal–metal bond as the number of neighboring metal atoms increases. Recent results in the study of metallic colloids appear to indicate that when the cluster size begins to exceed 50 to 60 atoms, the electronic properties of some of the atoms in the center begin to approach those of bulk metals.

Work on metal dimers has been aimed at understanding the effects of adding or withdrawing electrons from the metal framework. In some cases, either addition or subtraction of electrons has been shown to apparently strengthen the bond. These, and related studies, could provide the framework for understanding bonding effects in more complex systems once allowance is made for the additional constraints placed on the system by the total lattice energy and framework.

For comparison to the properties of dimeric complexes, it is worth noting that the Mo–Mo distance in the bulk metal is 2.76 Å. The enthalpy of atomization of molybdenum is 157 kcal mol^{-1} (equation 4).

$$[\cdots\text{Mo–Mo–Mo–Mo–Mo}\cdots](\text{s}) \longrightarrow n\text{Mo(g)} \quad (4)$$

Molybdenum metal exists as either body-centered cubic (bcc) or hexagonal close-packed allotropes. In the bcc form,

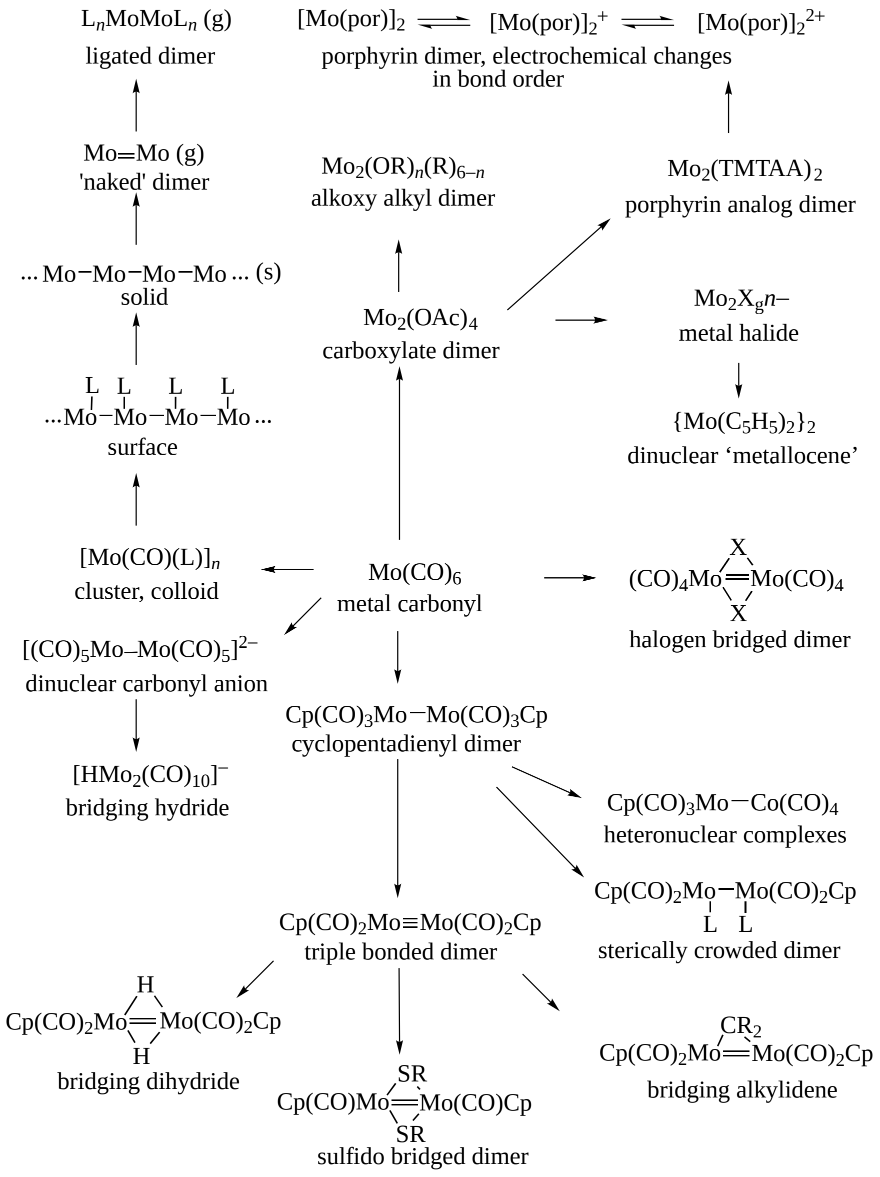
LnMoMoLn (g)
ligated dimer
[Mo(por)]2 ⇌ [Mo(por)]2+ ⇌ [Mo(por)]22+
porphyrin dimer, electrochemical changes in bond order
Mo=Mo (g)
'naked' dimer
Mo2(OR)n(R)6–n
alkoxy alkyl dimer
Mo2(TMTAA)2
porphyrin analog dimer
... Mo−Mo−Mo−Mo ... (s)
solid
Mo2(OAc)4
carboxylate dimer
Mo2Xgn–
metal halide
L L L L
...Mo−Mo−Mo−Mo...
surface
{Mo(C5H5)2}2
dinuclear 'metallocene'
[Mo(CO)(L)]n
cluster, colloid
Mo(CO)6
metal carbonyl
X
(CO)4Mo=Mo(CO)4
X
halogen bridged dimer
[(CO)5Mo–Mo(CO)5]2–
dinuclear carbonyl anion
Cp(CO)3Mo−Mo(CO)3Cp
cyclopentadienyl dimer
[HMo2(CO)10]–
bridging hydride
Cp(CO)3Mo−Co(CO)4
heteronuclear complexes
Cp(CO)2Mo−Mo(CO)2Cp
L L
sterically crowded dimer
Cp(CO)2Mo≡Mo(CO)2Cp
triple bonded dimer
H
Cp(CO)2Mo=Mo(CO)2Cp
H
bridging dihydride
CR2
Cp(CO)2Mo=Mo(CO)2Cp
bridging alkylidene
SR
Cp(CO)Mo=Mo(CO)Cp
SR
sulfido bridged dimer

Scheme 1 Flow chart for metal–metal bonded molybdenum complexes

it has a coordination number of eight. If a localized bond structure were imagined for this system, complete destruction of the lattice could correspond to breaking four bonds per metal atom, corresponding to an average value of approximately 40 kcal mol^{-1} for a single molybdenum–molybdenum bond. Whether such an approximation is valid or not, this is a reasonable estimate for the single bond strength in organometallic dimers of molybdenum (see Section 4.3). It is also nearly the same as the Mo–CO bond strength in $Mo(CO)_6$. The metal–metal bond strength (in the absence of steric repulsion) is often on the order of the metal–carbon monoxide bond strength for low-valent metals. For that reason, metal–metal bond cleavage is often competitive with ligand dissociation.

A second insight regarding bond strengths can be gained by comparing the enthalpies of atomization of $Cr = 95$, $Mo = 157$, and $W = 203\,kcal\,mol^{-1}$. Metal–metal bond strengths in dimeric complexes also increase when going from Cr to Mo to W. To date, information appears to support this trend for all transition metals.

In spite of considerable study, the effects of ligands on metal–metal bonding in dimeric complexes is not fully understood. Nevertheless, binding of bulky ligands in dimetallic complexes normally decreases the metal–metal bond strength for both enthalpic and entropic reasons. This would correspond in metal surfaces to the coverage of two adjacent sites at the metal, as shown in equation (5).

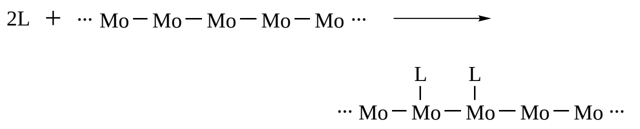

$$2L + \cdots \mathrm{Mo{-}Mo{-}Mo{-}Mo{-}Mo}\cdots \longrightarrow \cdots \mathrm{Mo}-\overset{L}{\overset{|}{\mathrm{Mo}}}-\overset{L}{\overset{|}{\mathrm{Mo}}}-\mathrm{Mo}-\mathrm{Mo}\cdots \qquad (5)$$

A recent monograph on the energetics of metal surfaces has appeared,[34] but at this time, it does not appear that the influence of ancillary ligands to either increase or decrease metal–metal bond strengths is well understood. In several cases now, it has been established in ‘molecular wire’ type complexes that mild oxidation or, in some cases, reduction can influence the M–M bond distances and strengths.[35] The goal in these complexes is to increase the metal–metal bond strength; however, in heterogeneous catalysis with metals, the goal might be to weaken the metal–metal bond. It, therefore, seems possible that at local kinks and ledges of a heterogeneous metal, changes in bond order may occur during surface redox reactions. This illustrates that principles learned from both disciplines (solid state and surface chemistry on the one hand and homogeneous discrete systems on the other) may be symbiotic.

Understanding the types of bonding involved in metal colloids (intermediates between surfaces and dimers) has been enhanced by a range of physical techniques. For example, EXAFS studies[36] of $Au_{55}(PPh_3)_{12}Cl_6$ indicate that the Au–Au distance is 2.803 Å, smaller than that found in bulk gold (2.878 Å). Thus, in this case, surprisingly, binding of ligands appears to shorten the metal–metal bonds in a surface-like environment. Several groups, most notably Schmidbauer, have extended the knowledge of the ‘aurophilic’ Au···Au interaction. (*see* ***Gold: Organometallic Chemistry***).

4.3 Metal Carbonyl Dimers, $Mo_2(CO)_{10}{}^{2-}$

One of the broadest and historically most important areas of dimetal chemistry is that of the simple carbonyl complexes (*see* ***Carbonyl Complexes of the Transition Metals***). As mentioned above, $Co_2(CO)_8$, $Fe_2(CO)_9$, and $Mn_2(CO)_{10}$ were among the first metal–metal bonded complexes characterized. To this day, these complexes continue to be involved in new chemistry, for example, $Co_2(CO)_8$ found recent use in a one-pot synthesis of ‘tricyclic δ-lactones’.[37] In the case of molybdenum, the zerovalent carbonyl is monomeric; however, reduction gives a dinuclear metal carbonyl dianion in which the metal is in the [−1] oxidation state (equation 6).

$$\mathrm{Mo(CO)_6} \xrightarrow{K} \mathrm{K_2[(CO)_5Mo{-}Mo(CO)_5]} \qquad (6)$$

$$d(\mathrm{Mo{-}Mo}) = 3.123\,\text{Å}$$

There are a number of metal carbonyl clusters, many of them anionic in nature. They range in size from dinuclear complexes, such as that shown above, to very large clusters and even charged colloidal particles.

In many cases, particularly for first-row metals, the metal–metal bonds are supported by bridging carbonyl ligands. The simplest case is $Co_2(CO)_8$, which exists as an equilibrium mixture of bridged and unbridged forms (equation 7).

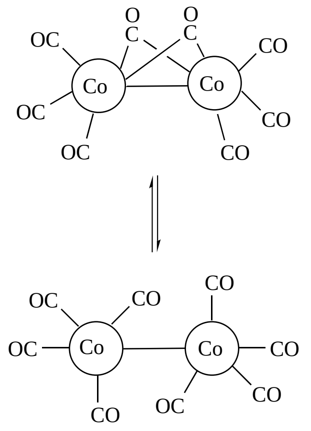

(7)

More complicated forms of CO bridging, which involve bonding through both the C and O atoms, also appear in metal–metal bonded compounds. For example, while $Mn_2(CO)_{10}$ does not have bridging CO ligands, substitution by the chelating phosphine ligand dppm (bis-diphenyl phosphino methane) proceeds as shown in equation (8). In this reaction, the phosphine-substituted metal–metal bonded dimer reversibly loses CO to produce a structure, which escapes coordinative unsaturation by having a π-CO interaction across the metal–metal bond.

$$\begin{array}{ccc} \mathrm{Mn_2(CO)_{10}} + 2\mathrm{dppm} & \longrightarrow & \mathrm{Mn_2(CO)_6(dppm)_2} \\ & & {\scriptstyle +\,\mathrm{CO}}\ \big\uparrow\!\big\downarrow\ {\scriptstyle -\,\mathrm{CO}} \\ & & \mathrm{Mn_2(CO)_4(\mu\text{-}CO)(dppm)_2} + \mathrm{CO} \end{array} \qquad (8)$$

A related reaction is shown for the molybdenum–niobium complex (equation 9). As described in a review by Horowitz and Shriver[38] on bridging carbonyl ligands, this complex is a rare example of a structure containing terminal, bridging, and π-bridging CO ligands. All such complexes, of necessity, include metal–metal bonding.

$$\mathrm{Cp_2Nb(BH_4)} + \mathrm{Et_3N} + \mathrm{RMo(CO)Cp} \longrightarrow$$

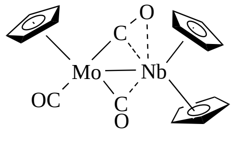

(9)

This two-site binding of ligands is one of the great potentials of dimetal complexes. The π-bridging CO in the complex cited above shows significant lengthening of the carbon–oxygen bond. The goal of such chemistry is activation or cleavage of CO. The binding interactions in such dimers are complex and not easily analyzed. For example, even if one knew the enthalpy of binding of the π-bridging CO, this value would be difficult to interpret since it involves at least four bonding interactions: weakening of the carbon–oxygen bond along with formation of metal–carbon and metal–oxygen bonds as well as changes in metal–metal bonding character. Clearly, delocalized molecular orbital theory is the best approach to understand the nature of bonding in such complicated situations.

4.4 Hydrido-bridged Carbonyls, $HMo_2(CO)_{10}^-$

An important class of metal–metal bonded dimers is the hydrido-bridged carbonyls (*see* ***Hydrides: Solid State Transition Metal Complexes***). These can be obtained through a number of reactions, most commonly, through protonation and direct reaction with hydrogen. Protonation of the metal carbonyl dianion $Mo_2(CO)_{10}^{2-}$ yields the complex shown in equation (10).

$$Mo_2(CO)_{10}^{2-} + H^+ \longrightarrow HMo_2(CO)_{10}^- \qquad d(\text{Mo–Mo}) = 3.41\,\text{Å} \tag{10}$$

Complexes of this type are found for anionic, neutral, and cationic metal carbonyl dimers. It is difficult to determine the extent of metal–metal bonding in these structures. The Mo–Mo bond distance in the protonated complex is quite long, almost beyond the limit of what is reasonable for metal–metal bonding. This complex is best viewed in terms of a three-center, two-electron bond similar to that found in B_2H_6 and other bridging borohydrides. Some metal–metal bonding character may be implied. The related complex, $H_2W_2(CO)_8^{2-}$, has a W–W bond length of 3.1 to 3.2 Å, which is indicative of a stronger W–W interaction.

In complexes of this type, the potential energy surface is probably ‘soft’, with the interplay of metal–metal, metal–hydrogen, and three-center forms of bonding close in energy. Thus, opening of the bridging structure to a linear bridging hydride is probably a low-energy process and could be the precursor to dissociation to a mononuclear metal hydride and a coordinatively unsaturated complex (equation 11).

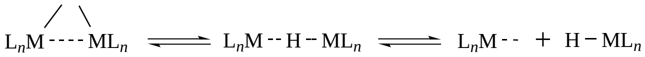

$$L_nM(\mu\text{-H})ML_n \rightleftharpoons L_nM\cdots H-ML_n \rightleftharpoons L_nM\cdots + H-ML_n \tag{11}$$

It should also be considered that, due to the high mobility of the H^- ligand, linear hydrido-bridged species might readily transform to transition states involving hydrido-bridged metal–metal bonded complexes.

In a novel use of photolytic addition of H_2 across the metal–metal multiple bond, the two-H-atom-bridged double-bonded complex**[39]** shown below has been prepared (equation 12).

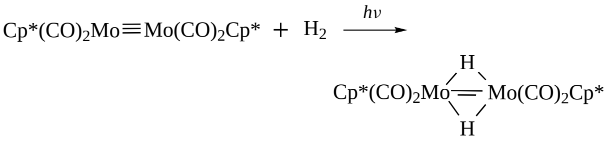

$$Cp^*(CO)_2Mo{\equiv}Mo(CO)_2Cp^* + H_2 \xrightarrow{h\nu} Cp^*(CO)_2Mo(\mu\text{-H})_2Mo(CO)_2Cp^* \tag{12}$$

For the analogous cyclopentadiene(*see Cyclopentadienyl*) derivative, prepared by a different route, the complex is unstable in solution and is believed to dissociate back to H_2 and the Mo–Mo triple-bonded complex. In view of the fact that many catalytic cycles utilize hydrogen, these types of complexes are important models. Interactions of dihydrogen leading to cleavage of the metal–metal bond are discussed in Section 7.1.4.

4.5 Halogeno-bridged Carbonyls, $[XMo(CO)_4]_2$

While bridging carbonyl and hydrido ligands are often present in metal–metal bonded dimers, halogens are probably the most common bridging ligands. Oxidation by halogens under controlled conditions leads to the Mo^I-bridged dimers as shown in equation (13).

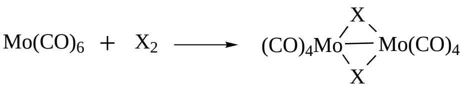

$$Mo(CO)_6 + X_2 \longrightarrow (CO)_4Mo(\mu\text{-X})_2Mo(CO)_4 \tag{13}$$

X = Cl, Br, I

In complexes such as $[XMo(CO)_4]_2$, where the metal–metal bond is held together by the equally strong or stronger bridging halide system, it is difficult to assess the strength of the metal–metal bond. The importance of metal–metal bonds in this type of complex is still disputed.

4.6 Cyclopentadienyl Metal Carbonyl Dimers, $Cp(CO)_3Mo–Mo(CO)_3Cp$

Aside from the carbonyl group, the Cp ligand and its analogs are probably the most common ligand systems in organometallic chemistry. This is also reflected in the large number of cyclopentadienyl metal carbonyl dimers and their derivatives that have been studied. For molybdenum, direct reaction of molybdenum hexacarbonyl and dicyclopentadiene is one of several routes to $[CpMo(CO)_3]_2$ (equation 14).

$$C_{10}H_{12} + Mo(CO)_6 \longrightarrow Cp(CO)_3Mo–Mo(CO)_3Cp \qquad d(\text{Mo–Mo}) = 3.235\,\text{Å} \tag{14}$$

A number of derivatives of this complex have been prepared (*see* ***Multi-Heme Cytochromes & Enzymes***). Substitution of carbonyl ligands by other donors, such as that shown in equation (15), gives rise to a wide range of complexes.

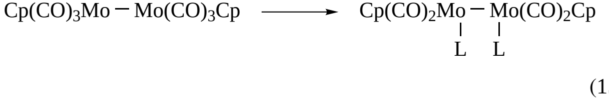

$$Cp(CO)_3Mo-Mo(CO)_3Cp \xrightarrow{2L} Cp(CO)_2(L)Mo-Mo(L)(CO)_2Cp \tag{15}$$

In addition to substitution of the carbonyl groups, changes in the cyclopentadienyl ring have also been extensively studied. The use of pentamethylcyclopentadiene led to formation of some of the first organometallic multiply bonded complexes as discussed in Section 4.8. The tris(pyrazolyl)borate ion (Tp^-, *see Tris(pyrazolyl)borates*) is a Cp analog.[40] It reacts with $Mo(CO)_6$ to yield the $TpMo(CO)_3^-$ anion. Oxidation yields the paramagnetic radical that shows no tendency to form a single metal–metal bond. Decarbonylation yields a triply bonded structure. These reactions are summarized in equation (16).

$$Tp^- + Mo(CO)_6 \longrightarrow TpMo(CO)_3^- \longrightarrow TpMo(CO)_3 \longrightarrow [Tp(CO)_2Mo]_2 \qquad (16)$$

$$d(\text{Mo–Mo}) = 2.507\,\text{Å}$$

4.7 'Tethered' Bridges, $[(Fulvalene)Mo(CO)_3]_2$, and Related Complexes

A number of ligands have been tethered to a cyclopentadienyl ring to prepare unique chelating ligands. In some cases, these have been extended to metal–metal bonded complexes. A good example is the work of Vollhardt and coworkers on fulvalene systems.[41] Complexes of this type are often more flexible than halide-bridged complexes; that is, the bridging ligand keeps the metal fragments in close proximity so that the metal–metal bond can be readily broken and reformed. Cleavage of the metal–metal bond will not result in disruption of individual metal–ligand bonds, as would be the case for many bridging ligands. One interesting reaction of the fulvalene–molybdenum complex produces the novel zwitterionic (*see Zwitterion*) structure shown in equation (17).

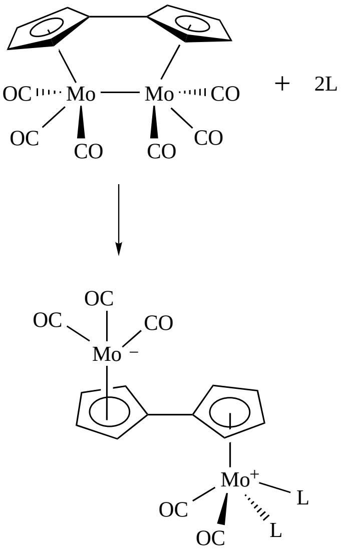

(17)

In addition to fulvalene complexes, other bridges such as the bis(dimethylsilylclopentadienyl) ligand have been used to bridge dinuclear complexes.[42] Other pendant groups have been attached to the cyclopentadienyl ligand, and these can lead to interesting complexes as well. The cyclopentadienyl phosphine system[43] shown in equation (18) is but one of the numerous examples.

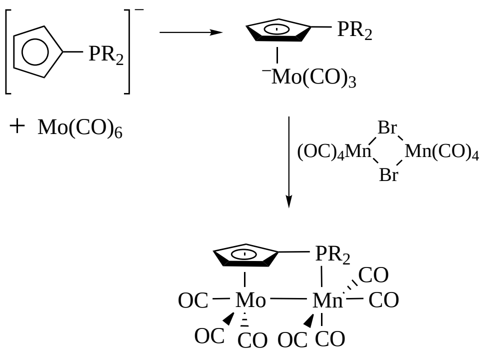

(18)

4.8 Multiple Bonded and 'Unsaturated' Dimers, $(C_5R_5)(CO)_2Mo{\equiv}Mo(CO)_2(C_5R_5)$

Some of the most interesting metal–metal bonded complexes contain multiple bonds. A good example[44] of this, and one of the first multiply bonded complexes formed, is the reaction of pentamethylcyclopentadiene with molybdenum carbonyl (equation 19).

$$Mo(CO)_6 + C_5Me_5H \longrightarrow Cp^*(CO)_3Mo{-}Mo(CO)_3Cp^* \underset{+2CO}{\overset{-2CO}{\rightleftharpoons}} Cp^*(CO)_2Mo{\equiv}Mo(CO)_2Cp^* \quad (Cp^* = \eta\text{-}C_5Me_5) \qquad (19)$$

Heating the single-bonded dimer causes loss of two moles of carbon monoxide to yield the triple-bonded dimer in a fully reversible reaction. Owing to the fact that the carbonyl groups in the triply bonded dimer are semibridging (*see Semibridging Carbonyl Ligand*), there can be some question about the true bond order in this dimer. A wide range of reactions are displayed by this and other 'coordinatively unsaturated' metal dimers (*see Coordinative Saturation & Unsaturation*). While the complex does obey the eighteen-electron rule (*see Effective Atomic Number Rule*) by adopting the triple bond and/or semibridging structure, the multiple metal–metal bond is relatively weak. Thus, it is somewhat like mononuclear complexes that have a vacant site at the metal, which is protected by an agostic bond (*see Agostic Bonding*). The operational difference here is that it is a two-center site, and thus capable of more complex reactions. A good example of this is coordination of acetylenes as well as the interconversions shown in equation (20).[45]

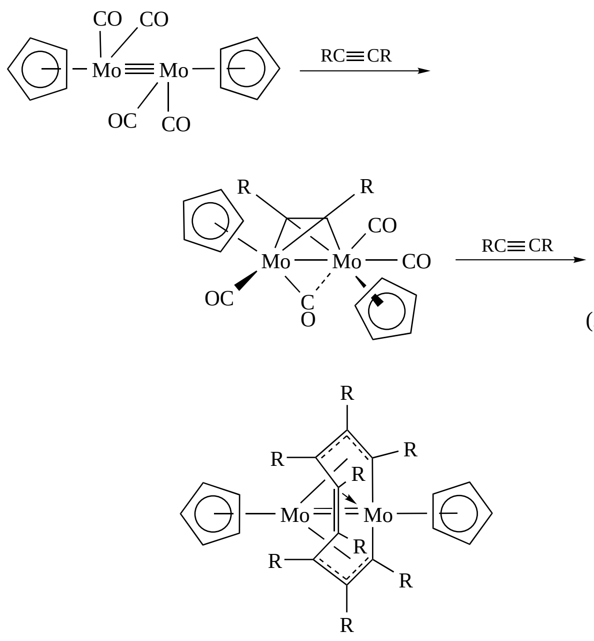
CO
CO
Mo
Mo
OC
CO
RC≡CR
R
R
CO
Mo
Mo
CO
OC
C
O
RC≡CR
R
R
R
R
Mo
Mo
R
R
R
R

(20)

Some coordinatively unsaturated metal dimers are not proposed to contain multiple bonds, for example, $CoRh(CO)_7$. This complex can be viewed as an analog of $Co_2(CO)_8$ in which one CO ligand has dissociated from the complex and the heavier congener Rh has replaced one of the Co atoms. The degree of interaction between the two metals is not clear in spite of the known structure. This complex can fragment,[46] but can also undergo addition reactions at the metal–metal bond, as shown in equations (21) and (22) respectively.

$$CoRh(CO)_7 + CO \rightleftharpoons CoRh(CO)_8 \qquad (21)$$

$$CoRh(CO)_7 + \tfrac{1}{2}H_2 \longrightarrow HCo(CO)_4 + \tfrac{1}{4}Rh_4(CO)_{12} \qquad (22)$$

4.9 Sulfur- and Selenium-bridged Dimers, [CpMo(ER)$_2$]$_2$

In addition to halogen-bridged dimers illustrated above, chalcogen-bridged dimers are another major category of organometallic metal–metal bonded dimers. For example, the complexes shown in equation (23) have been prepared and studied by several groups.

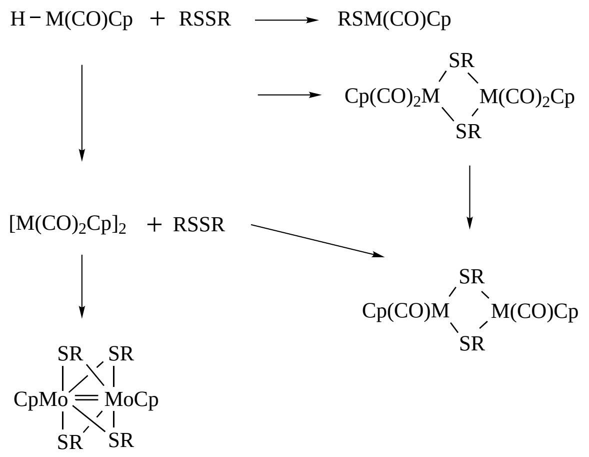
H−M(CO)Cp
+ RSSR
RSM(CO)Cp
SR
Cp(CO)2M
M(CO)2Cp
SR
[M(CO)2Cp]2
+ RSSR
SR
Cp(CO)M
M(CO)Cp
SR
SR
SR
CpMo
MoCp
SR
SR

(23)

In addition to thiolate-bridged dimers, sulfido complexes containing metal–metal bonds show related chemistry. Of particular interest are the products of reaction between $[(C_5R_5)(CO)_3Mo]_2$ and sulfur (equation 24). In complexes such as these, the ability to assign bond orders is no longer simple. The internuclear distances are supportive of metal–metal bonds for a majority of the complexes, but the exact bond orders are uncertain in some cases.

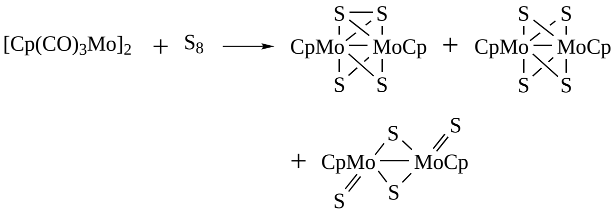
[Cp(CO)3Mo]2
+ S8
S
S
CpMo
MoCp
S
S
+
S
S
CpMo
MoCp
S
S
+
S
S
CpMo
MoCp
S
S

(24)

Bridging ligands are normally 'innocent' or 'spectators' and do not play an active role in chemical reactions. This is not always the case, however, particularly for coordinated sulfur. For example, reaction of the sulfur-bridged metal–metal bonded complexes with hydrogen, followed by reaction with acetylene, occurs at the sulfur, as investigated by Rakowski Dubois (equation 25).[47]

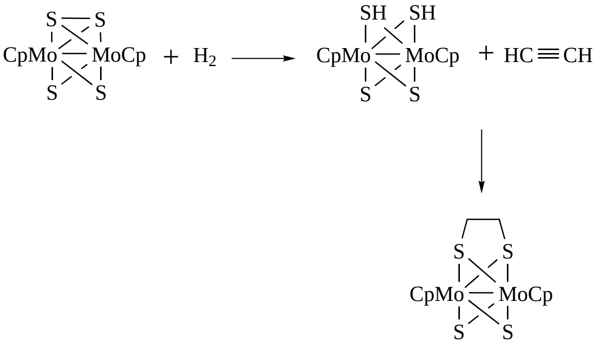
S
S
CpMo
MoCp
S
S
+ H2
SH
SH
CpMo
MoCp
S
S
+ HC≡CH
S
S
CpMo
MoCp
S
S

(25)

Kubas[48] discovered reactions of the Cp∗ dimers, which are part of a catalytic cycle for the hydrogenation of SO_2 (equation 26). The net reactions involve the coordinated sulfur and may or may not involve the metal atoms, which may be the true 'spectators' in this chemistry. This opens the possibility that the metal–metal bond serves to stabilize the reacting fragment without direct involvement in the chemistry. However, reaction could also occur at the metal–metal bond followed by transfer to the sulfide ligands. These types of multiple interactions give an added dimension, but also an added complexity, to metal–metal bonded chemistry with bridging functional ligands.

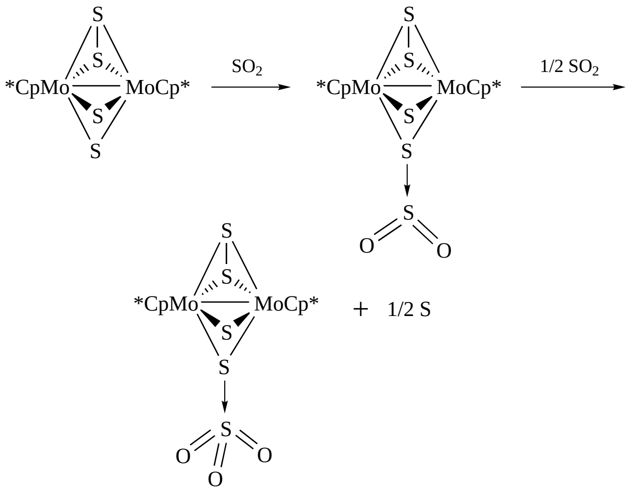

(26)

An interesting example[49] of sulfur-bridged systems is shown in equation (27). The disulfur-bridged dianion does not contain a metal bond. Chemical or electrochemical oxidation generates the neutral species that does have a metal–metal bond. This process of electrochemically induced changes in bond order will be discussed below for porphyrin complexes as well.

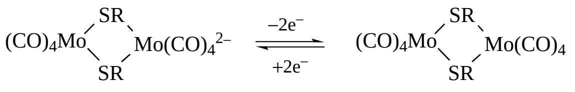

(27)

Increasingly, heavier congeners of sulfur have been investigated. For example, Adams has recently reported preparation, structure, and reactions of $CpMoMn(CO)_5(\mu\text{-}Se_2)$,[50] which contains a doubly bridging diselenido ligand in the heteronuclear Mo–Mn bonded complex.

4.10 Phosphorus and Nitrogen Ligand-bridged Dimers

There are a range of nitrido, phosphido, carbido, and related complexes with metal–metal bonds (*see* ***Cluster Compounds: Inorganometallic Compounds Containing Transition Metal & Main Group Elements***). They are not as common as the halogen- and chalcogen-bridged species described above. Carbido complexes are generally associated with higher-level clusters and are not discussed here (*see* ***Carbides: Transition Metal Solid-state Chemistry***). Reaction of the coordinated dinitrogen complex, shown in equation (28), with butylsilane results in cleavage of the nitrogen–nitrogen bond and in the formation of a bridged Ta–Ta bonded complex.[51]

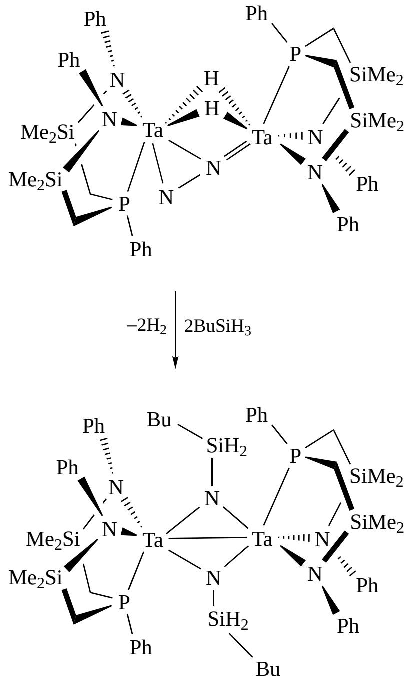

(28)

A range of chelating phosphine ligands with small 'bite' size have been shown to stabilize metal bonds. In addition to chelates, metal phosphido, amido, and even polyelemental derivatives exist. A range of truly novel complexes are known, such as the two products isolated in low yield in equation (29). The dimers retain metal–metal bonding and stabilize the coordinated P_2 and P_6 fragments.[52]

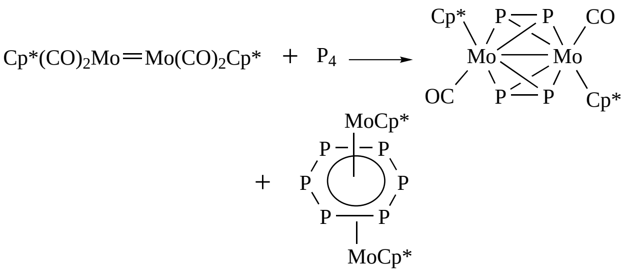

(29)

4.11 Hydrocarbon-bridged Metal–metal Bonded Dimers

Carbide-type ligands often hold together clusters of higher order but not dimers or trimers. However, a number of dimeric complexes are bridged by hydrocarbon ligands. These can be viewed as dimetallacycloalkanes or as bridging alkenes and more complicated species. The simplest form would be the metal–metal bonded complexes with bridging alkylidene (*see Alkylidene*) ligands. Several reviews have appeared regarding these complexes.[53] Reaction with diazoalkenes and the triple-bonded complex, shown in equation (30), leads to formation of bridging carbene (dimetallacyclopropane) structures.

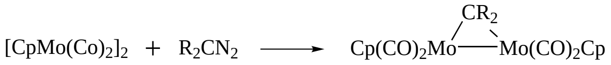

$$\mathrm{[CpMo(Co)_2]_2 + R_2CN_2 \longrightarrow Cp(CO)_2Mo\overset{CR_2}{-\!\!-\!\!-}Mo(CO)_2Cp} \tag{30}$$

Saturated alkanes can also bridge metals. Reaction of metal carbonyl anions[54] with dihaloalkanes has been widely investigated since the report of equation (31) by King. In most cases, a metal–metal bond is not formed. Bergman and coworkers[55] have prepared and done elegant studies on a series of cobalt complexes of the general form shown in equation (32) that do contain metal–metal bonds. A range of transformations and reaction pathways are available to these complexes.[56]

$$\mathrm{2NaFe(CO)_2Cp + I{-}(CH_2)_n{-}I \longrightarrow Cp(CO)_2Fe{-}(CH_2)_n{-}Fe(CO)_2Cp} \tag{31}$$

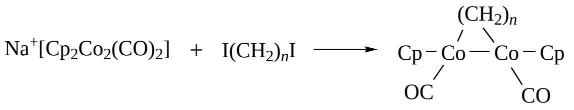

$$\mathrm{Na^+[Cp_2Co_2(CO)_2] + I(CH_2)_nI \longrightarrow \underset{OC}{Cp-Co}\overset{(CH_2)_n}{-}\underset{CO}{Co-Cp}} \tag{32}$$

4.12 Molybdenocene, π-bound Organic Ligand-bridged Dimers

In addition to monocyclopentadienyl dimers, various molybdenocene derivatives can form dimers, as shown in equation (33). This is one example of a vast range of organic ligands that bridge metal–metal bonded complexes.[57] Another example[58] is one of the several products obtained by reaction of diphenylacetylene and molybdenum carbonyl (equation 34).

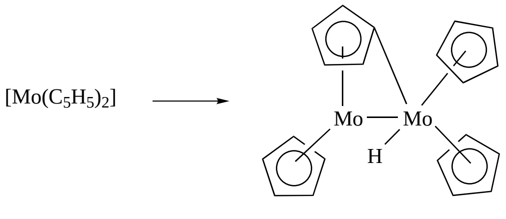

(33)

d(Mo–Mo) = 3.19 Å

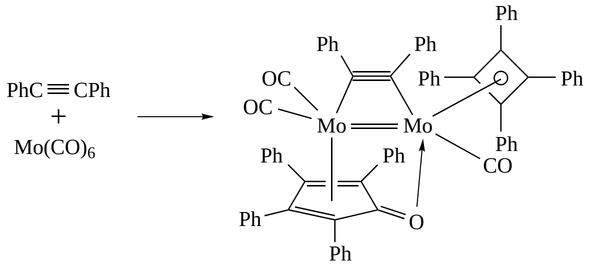

(34)

To some extent, these complexes fall into the category of tethered ligand systems. One difference is the ‘template’ effect: they are often assembled from simpler units as opposed to the use of preformed, designed, tethered ligands. Complexes prepared in this fashion contain oligomerized organic ligands whose color and spectra indicate the presence of metal–metal bonding. A novel azulene Ru–Ru system has been prepared by metal-mediated ligand assembly.[59] The detailed mechanisms for many of these reactions remain unknown.

4.13 Carboxylate-bridged Dimers $Mo_2(OAc)_4$ and Related Complexes

Oxidation of molybdenum hexacarbonyl with acetic acid produces the carboxylate-bridged quadruple-bonded dimers, as shown in equation (35). This complex can undergo a number of substitution reactions that leave the metal–metal bond intact.[60,61]

$$\mathrm{Mo(CO)_6 + HOAc \longrightarrow Mo_2(OAc)_4} \tag{35}$$

The carboxylate dimers resemble, in some ways, the dimeric alkoxides with multiple metal–metal bonds. This chemistry has been extensively developed by Chisholm and coworkers.[62,63] These complexes react with CO to cleave the metal–metal bond, as shown in equation (36).

$$\mathrm{2Mo_2(OR)_6 + 6CO \longrightarrow Mo(CO)_6 + 3Mo(OR)_4} \tag{36}$$

While the alkoxide derivatives are viewed primarily as inorganic dimers, they undergo reactions with a number of organic compounds. In addition, a number of mixed alkyl/alkoxide complexes have been prepared. For example, compare the Mo–Mo distances in two complexes: (1) alkoxy complex $Mo_2(OCH_2\text{-}t\text{-}Bu)_6$, d(Mo–Mo) = 2.222 Å; (2) alkoxy/alkyl complex $Mo_2(O\text{-}t\text{-}Bu)_2(CH_2SiMe_3)_4$, d(Mo–Mo) = 2.209 Å. There is a clear relation between these complexes. As mentioned in the introduction and as highlighted in Scheme 1, there is a full range of characteristic reactivities being developed for metal–metal bonded dimers.

Reactions of $Mo_2(NMe_2)_6$ with *p-tert*-butylcalix[4]arenes have generated Mo≡Mo complexes incorporating that functionality.[64]

4.14 Porphyrin and Related Model Systems

Owing to their relevance to biological chemistry, metalloporphyrin (*see Metalloprotein*) complexes and their analogs have been widely studied.[65] While most of these are mononuclear, a range of metal–metal bonded porphyrins and porphyrin-like complexes also exist. For example, the acetate groups of $Mo_2(OAc)_4$ (discussed in Section 4.13) can be replaced by the porphyrin-like ring with retention of the metal–metal bond (equation 37).[66]

$$Mo_2(OAc)_4 + 2Li_2TMTAA \longrightarrow (TMTAA)MoMo(TMTAA)$$

H_2TMAA =

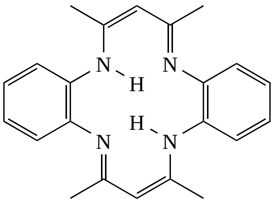

(37)

In keeping with the generally weaker bonds of first-row metals, the chromium complex in equation (38) has been shown[67] to reversibly bind pyridine with cleavage of the metal–metal bond.

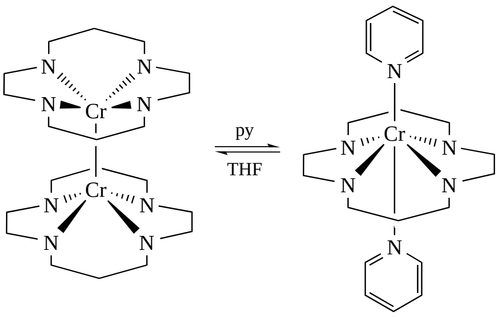

(38)

True porphyrin complexes also exist for molybdenum, and their chemistry has been explored by Collman and coworkers (equation 39). Oxidation of these complexes has been shown to increase the bond order from 2.0 to 3.0 for these redox-active systems.[68]

$$\underset{2.0}{[(OEP)M]_2} \longrightarrow \underset{2.5}{[(OEP)M]_2^{+}} \longrightarrow \underset{3.0}{[(OEP)M]_2^{2+}} \qquad (39)$$

A range of heteronuclear metal–metal bonded dimeric porphyrin complexes have also been prepared.[69]

4.15 Heteronuclear Complexes

The complexes discussed above have been primarily homonuclear; however, the range of complexes and their properties have been greatly expanded by work on heteronuclear dinuclear metal–metal bonded complexes (*see* ***Cluster Compounds: Inorganometallic Compounds Containing Transition Metal & Main Group Elements***). These complexes can involve all combinations of main group, transition metal (both early and late), and lanthanide (*see* ***Scandium, Yttrium & the Lanthanides: Organometallic Chemistry***) and actinide (*see* ***Actinides: Organometallic Chemistry***) complexes (equations 40–42).

$$[Mo(CO)_3Cp]_2 + Co_2(CO)_8 \longrightarrow 2Cp(CO)_3Mo–Co(CO)_4 \qquad (40)$$

$$3HMo(CO)_3Cp + Sn(Cp)_2 \longrightarrow HSn–[Mo(CO)_3Cp]_3 + 2CpH \qquad (41)$$

$$Cp_3U–NMe_2 + HFe(CO)_2Cp \longrightarrow Cp_3U–Fe(CO)_2Cp + HNMe_2 \qquad (42)$$

Particular areas of interest are the chemistry of early–late metal–metal bonded complexes,[70] main group metal–transition metal dimers,[71] transition metal carborane derivatives,[72] and lanthanide and actinide transition metal complexes.[73]

5 LITERATURE SOURCES FOR METAL–METAL BONDED COMPLEXES

The section above illustrated the range of metal–metal bonding complexes, highlighting organomolybdenum chemistry but with references to the general literature. In addition to computer-based literature searches, *Chemical Abstracts*, and Gmelin, another excellent source to bring the reader up to date is the Organometallic Chemistry volumes of Specialist Periodical Reports published by the Royal Society of Chemistry. Each year has sections on metal–metal bonds. An introduction and broad overview can be obtained from Cotton and Wilkinson's textbook on inorganic chemistry, which contains a chapter on metal–metal bonds.[30] Several texts on organometallic chemistry[74–76] also contain sections on metal–metal bonding. Listed in Table 1 are some additional references to introduce the reader to this area.

6 SYNTHETIC METHODS

A number of different routes are available for preparing metal–metal bonded dimers. The conditions used and the stability of the dimers produced vary widely. Some complexes such as $[CpW(CO)_3]_2$ are as air stable as solids and are only slowly oxidized in solution. Some, such as $[CpCr(CO)_3]_2$, are so air sensitive that they are pyrophoric when finely divided. Most of the complexes are intensely colored. The literature in this area is so vast that it is difficult to do more than just illustrate some of the proven techniques.

Table 1 Selected reviews on metal–metal bonded dimers

Chalcogen-bridged metal-carbonyl complexes[77]
Multiple bonding involving heavier group 3 elements Al, Ga, In, Tl[78]
'Very mixed' -metal carbonyl clusters[79]
Homometallic and heterometallic transition metal-allenyl complexes: synthesis, structure, and reactivity[80]
Multiple bonds involving aluminum and gallium atoms[81]
Organometallic chemistry of the lanthanides[82]
Bridged silylene and germylene complexes[83]
Transition metal-clusters in homogeneous catalysis[84]
Metal–metal bonded carbonyl dimers and clusters[85]
Group 6 metal chalcogenide cluster complexes[86]
Clusters and metal–metal bonded chains in molybdenum oxide systems[87]
Structure and reactivity of early-late heterobimetallic complexes[88]
Di- and polymetallic heteroatom stabilized (Fischer) metal carbene complexes[89]
Multiple bonds between metal atoms[90]
The influence of ligands on dirhodium(II) on reactivity and selectivity in metal carbene reactions[91]
Lanthanide-transition metal complexes: from ion pairs to extended arrays[92]
Supramolecular arrays based on dimetal building units[6]
One-dimensional polymers and mesogens incorporating multiple bonds between metal atoms[5]
The whole story of the two-electron bond, with the δ Bond as a paradigm[13]
From organotransition-metal chemistry towards molecular electronics: electronic communication between ligand-bridged metals[93]
Carbonylated nickel clusters: from molecules to metals[94]
Hydrocarbon bridged dinuclear bridged complexes.[95]
Heterobimetallic compounds linked by heterodifunctional ligands.[96]
General review on μ^2 bridging carbonyl systems in transition metal complexes.[97]
Multiple bonds between metal atoms.[98]
Mo–Mo bonded complexes.[99]
Introduction to metal–metal bonds; historical perspective.[100]
Multiple bonds in dimetal clusters.[101]
Macrocyclic ligands and metal–metal dimers.[102]
Structures of metal–metal bonded complexes with edge sharing bioctahedral geometries.[103]
Development of triple bonded Mo and W dimers, and the idea of an inorganic functional group.[104]
Metal–metal bonds and metal–carbon bonds in the chemistry of molybdenum and tungsten alkoxides.[105]
Chemistry of d^3–d^3 dimolybdenum and ditungsten complexes.[106]
Reactions of multiple bonded complexes.[107]
Bridging hydrocarbyl ligands in dinuclear systems.[108]
Compounds of the transition elements involving metal–metal bonds.[109]
Hydrocarbon or hydrocarbyl bridged dinuclear transition metal complexes.[110]
Dinuclear metallocenes.[111]
Photochemistry of metal–metal bonds.[112]
Metal–metal bond dinuclear complexes of early transition metals (groups 4 and 5).[113]
Heteronuclear complexes containing quadruple bonds.[114]
Dinuclear complexes with a common unsaturated ligand.[115]
Dinuclear iron carbonyl complexes with nitrogen containing bridges.[116]
Bridged homobimetallic complexes as models of dimetal active centers.[117]
Metal colloids and large clusters.[118]
Early–late heterobimetallics.[119]
Developments in the chemistry of multiply bonded dimetal complexes with bridging phosphine ligands.[120]
Metal–metal triple bonds.[121]

6.1 Nucleophilic Substitution

One of the most general methods of preparing metal–metal bonded organometallics is the reaction of metal carbonyl anions[54] with metal halides in a 'salt-elimination' reaction. The $Fe(CO)_2Cp^-$ anion has been widely used in reactions of this type (equation 43).

$$NaFe(CO)_2Cp + Cl\text{–}W(CO)_3Cp \longrightarrow Cp(CO)_2Fe\text{–}W(CO)_3Cp + NaCl \qquad (43)$$

The success of these reactions depends on the nucleophilicity of the anions used. Numerous accounts have discussed the basicity and the nucleophilicity of metal carbonyl anions and their influence on reactivity. Electrochemical studies (see Section 9.3) are particularly helpful in predicting the feasibility of reactions. The driving force for these reactions is often attributed to the precipitation of the insoluble salt. In spite of this, the free energies of reaction can be close to zero. In some cases, the metal–metal bond is cleaved by salts or an equilibrium is established (equation 44).[122]

$$\mathrm{Cp(CO)_3Mo{-}Mo(CO)_3Cp + KBr \longrightarrow KMo(CO)_3Cp + BrMo(CO)_3Cp} \tag{44}$$

In addition to displacement of halides, ligands can also be displaced by metal carbonyl anions, as shown in equation (45). These reactions need not be restricted to formation of dimers. Incorporation of the anions into existing polymetallic complexes has proven to be a general means of expanding the cluster size.

$$\mathrm{Na^+Co(CO)_4{}^- + Fe(CO)_5 \longrightarrow Na^+[(CO)_4Co{-}Fe(CO)_4]^- + CO} \tag{45}$$

Controlled reduction of carbonyls often leads to dinuclear compounds. This may involve attack by the reduced species on the unreacted starting material. The complex chemistry of iron carbonyls, going back to the pioneering work of Hieber and Hein, is a good example (equation 46).

$$\mathrm{Fe(CO)_5} \xrightarrow{\text{base, reducing agent}} \mathrm{Fe}_x\mathrm{(CO)}_y{}^{n-} \tag{46}$$

6.2 Elimination of Neutral Molecules

A second major route to metal–metal complexes, related to the 'salt-elimination' method described above, is elimination of neutral molecules with concurrent formation of metal–metal bonded complexes. Transition metal hydrides readily undergo these dinuclear reductive elimination reactions. The oxidative addition/reductive elimination (*see Oxidative Addition* and *Reductive Elimination*) reaction of molecular hydrogen is a key reaction in this area (equation 47).

$$\mathrm{2H{-}ML}_n \rightleftharpoons \mathrm{L}_n\mathrm{M{-}ML}_n + \mathrm{H_2} \tag{47}$$

Thermodynamically, the free energy of this reaction can be strongly negative (evolution of hydrogen to form metal–metal bond), near zero (equilibrium situation, good for a catalyst), or strongly positive (no formation of dimetallic complex, retention of metal hydride). Kinetically, the mechanism of loss of hydrogen is complex and radical intermediates are often implicated. This is reminiscent of main group metal hydride chemistry where, for example, formation of ditin complexes is catalyzed by free radical initiators, light, or trace metal catalysts (equation 48).

$$\mathrm{2R_3Sn{-}H \longrightarrow H_2 + R_3Sn{-}SnR_3} \tag{48}$$

In practice, it is often observed that *pure* metal hydrides reluctantly eliminate hydrogen to form dimetals. Trace impurities can generate autocatalytic reactions that rapidly evolve hydrogen. Elimination can occur between homonuclear metal compounds (equation 49) or in heteronuclear reactions (equation 50). It can also occur between main group metals and transition metals (equation 51). Under appropriate conditions, these reactions are often clean and can be used to readily generate the dinuclear complexes.

$$\mathrm{2H{-}Co(CO)_4 \longrightarrow H_2 + Co_2(CO)_8} \tag{49}$$

$$\mathrm{H{-}Co(CO)_4 + H{-}Mn(CO)_5 \longrightarrow H_2 + (CO)_4Co{-}Mn(CO)_5} \tag{50}$$

$$\mathrm{HSnR_3 + H{-}Mo(CO)_3Cp \longrightarrow R_3Sn{-}Mo(CO)_3Cp} \tag{51}$$

A related reaction is stoichiometric hydrogenation of dienes. For example, the complexes $\mathrm{[(C_5R_5)M(CO)_3]_2}$ (M = Cr, Mo, W) can be generated quantitatively[123] by the reaction of $\mathrm{H{-}M(CO)_3C_5R_5}$ with excess cyclohexadiene (equation 52).

$$\mathrm{2H{-}M(CO)_3C_5R_5 + 1,3\text{-}C_6H_8 \longrightarrow [M(CO)_3C_5H_5]_2 + C_6H_{10}} \tag{52}$$

Unlike reactions involving nucleophilic substitution that rely on polar solvents to achieve sufficient solubility of the reactants, eliminations and reactions based on hydrides have the advantage that the hydrides are often soluble in alkane or arene solvents and the dimetallic complexes are not. Thus, under favorable conditions the pure product crystallizes out of solution.

Reductive elimination of hydrocarbons or their derivatives is another viable route to metal–metal bonded systems. A good example is dinuclear reductive elimination, as studied by Bergman and coworkers (equation 53).[124] In this case, both the single and triple-bonded complexes are formed. Exposure to CO instantly converts the triple-bonded complex to the single-bonded one.

$$\begin{aligned}&\mathrm{HMo(CO)_3Cp + EtMo(CO)_3Cp \longrightarrow}\\ &\qquad\mathrm{EtC(O)H + Cp(CO)_3Mo{-}Mo(CO)_3Cp}\\ &\qquad\quad\mathrm{+\ Cp(CO_2)Mo{\equiv}Mo(CO)_2Cp}\end{aligned} \tag{53}$$

Elimination of hydrogen halides, particularly in the presence of base, is also a common reaction (equation 54). The actual mechanism of these reactions could involve nucleophilic displacement of halide by the metal carbonyl halide that is formed *in situ* from the hydride (equations 55 and 56).

$$\mathrm{H{-}ML}_n + \mathrm{X{-}ML}_n \xrightarrow{\text{base}} \mathrm{L}_n\mathrm{M{-}ML}_n + \mathrm{HX{\bullet}base} \tag{54}$$

$$\mathrm{H{-}ML}_n + \text{base} \rightleftharpoons \mathrm{ML}_n{}^- + \mathrm{B{-}H^+} \tag{55}$$

$$\mathrm{ML}_n{}^- + \mathrm{X{-}ML}_n \longrightarrow \mathrm{L}_n\mathrm{M{-}ML}_n + \mathrm{X^-} \tag{56}$$

Reaction of metal hydrides with metal–metal bonded complexes can result in transfer of hydrogen from one metal to another with concomitant formation of new metal–metal bonds (equation 57). For example, Markó and coworkers[125] have shown that the reactions in equation (58) occur.

$$\mathrm{2H{-}ML}_n + \mathrm{J}_n\mathrm{M'{-}MJ}_n \longrightarrow \mathrm{L}_n\mathrm{M{-}ML}_n + \mathrm{2H{-}M'J}_n \tag{57}$$

$$\mathrm{H{-}Co(CO)_4 + Mn_2(CO)_{10} \longrightarrow H{-}Mn(CO)_5 + (CO)_4Co{-}Mn(CO)_5} \tag{58}$$

Similar reactions can occur between radicals and hydrides and involve H-atom transfer, followed ultimately by formation of the most stable metal–metal bonded systems (equation 59). The mixed-metal complex formed slowly disproportionates (equation 60).

$$\mathrm{{\bullet}Cr(CO)_3C_5Me_5 + H{-}W(CO)_3C_5H_5 \longrightarrow H{-}Cr(CO)_3C_5Me_5 + \tfrac{1}{2}C_5Me_5(CO)_3Cr{-}W(CO)_3C_5H_5} \tag{59}$$

$$\mathrm{C_5H_5(CO)_3Cr{-}W(CO)_3C_5H_5 \longrightarrow {\bullet}Cr(CO)_3C_5Me_5 + \tfrac{1}{2}[W(CO)_3C_5H_5]_2} \tag{60}$$

It is common to observe both homonuclear and heteronuclear products since metathesis (*see Metathesis*) of metal–metal bonded complexes is a common reaction, as discussed in Section 6.6.

6.3 Condensation Reactions

Loss of a ligand from saturated metal complexes often generates highly reactive fragments. In the absence of other reaction pathways, these fragments can condense to metal–metal bonded dimers or higher-order clusters. The best example of this reaction is loss of carbon monoxide from metal carbonyls to yield dimers and clusters. For example, photogenerated $\mathrm{Fe(CO)_4}$ species readily react with $\mathrm{Fe(CO)_5}$ to yield $\mathrm{Fe_2(CO)_9}$ (equation 61).

$$\begin{tikzcd} \mathrm{Fe(CO)_5} \arrow[r] & \mathrm{CO + Fe(CO)_4 + Fe(CO)_5} \arrow[r] \arrow[d] & \mathrm{Fe_2(CO)_9} \\ & \frac{1}{3}\,\mathrm{Fe_3(CO)_{12}} & \end{tikzcd} \tag{61}$$

A competing reaction is trimerization to $\mathrm{Fe_3(CO)_{12}}$. This process can be reversible and the dimers or clusters are suitable ‘staging grounds’ for breakup of the clusters. These often lead to complex equilibria, which have been investigated by Bor and coworkers for a number of systems.[126]

6.4 Ligand Substitution on Existing Metal–Metal Frameworks

A general method of extending and changing the character of metal–metal bonds is by substitution of ligands. While this type of reaction does not generate new metal–metal bonds, it can be of use in modifying the properties and reactivities of existing metal–metal bonded complexes. In particular, where more sterically demanding ligands are incorporated, the metal–metal bond strength can be expected to change (equation 62).

$$\mathrm{Mn_2(CO)_{10} + 2PR_3 \longrightarrow (CO)_4(PR_3)Mn{-}Mn(PR_3)(CO)_4} \tag{62}$$

Replacement of the carbonyl ligand by the bulky phosphine ligands shown generally destabilizes the metal–metal bond. Kinetics of ligand substitution in dimers and clusters have been reviewed by Poe.[127]

6.5 Insertion Reactions

A number of species, such as Hg and $\mathrm{SnCl_2}$, insert into metal–metal bonded complexes to form metal–metal bonds (equations 63 and 64).

$$\mathrm{[Cp(CO)_2Fe]_2 + SnCl_2 \longrightarrow Cp(CO)_2Fe{-}SnCl_2{-}Fe(CO)_2Cp} \tag{63}$$

$$\mathrm{Co_2(CO)_8 + Hg \longrightarrow (CO)_4Co{-}Hg{-}Co(CO)_4} \tag{64}$$

The mechanisms of these reactions are probably complex but radical processes seem likely. The final products of insertion into the metal–metal bond are actually trinuclear species. Insertion into terminal metal–hydride or metal–alkyl bonds could, in principle, generate mixed-metal dimers. In practice, aside from insertion into the metal–halogen bond, such as that shown in equation (65), few such reactions have been reported.

$$\mathrm{X{-}Co(CO)_4 + Hg \longrightarrow X{-}Hg{-}Co(CO)_4} \tag{65}$$

6.6 Metathesis Reactions

A common reaction of metal–metal bonded complexes is σ-bond metathesis (*see σ-Bond Metathesis*), such as that shown in equation (66).

$$\mathrm{Co_2(CO)_8 + Mn_2(CO)_{10} \longrightarrow 2(CO)_4Co{-}Mn(CO)_5} \tag{66}$$

This type of reaction has been studied by Vahrenkamp in a classic paper in this field.[128] In the majority of cases, a nearly statistical distribution of products is formed. This result implies that in most cases, the heteronuclear complexes have bond strengths that are the average of the parent homonuclear complexes. This observation also carries implications about the ‘group electronegativity’ of the complexes studied. The original Pauling scale of electronegativity is based on experimental enthalpies of metathesis (equation 67). If the enthalpy of this reaction is zero, then the difference in electronegativity is also zero. Thus, the results of Vahrenkamp imply a similar electronegativity for the groups studied. This is not surprising since the study focused on relatively ‘soft’ metal carbonyl complexes. Exceptions to this could occur for crowded complexes where steric strain is reduced in the mixed dimer or where there are significant electronic differences between the two metals groups.

$$\text{A–A} + \text{B–B} \longrightarrow 2\text{A–B} \qquad (67)$$

A second type of metathesis reaction involves metals multiply bonded to nonmetals (equation 68). In one sense, this corresponds to a special case of dinuclear reductive elimination of neutral molecules in which multiply bonded species are involved. This reaction can occur in both directions. Multiply bonded metal–metal complexes can be cleaved by multiply bonded main group species.

$$\text{M}{\equiv}\text{C} + \text{M}{\equiv}\text{C} \longrightarrow \text{M}{\equiv}\text{M} + \text{C}{\equiv}\text{C} \qquad (68)$$

7 REACTIONS OF METAL–METAL BONDED COMPLEXES

Reactions of metal–metal bonded complexes can be divided into three categories: (1) cleavage of the metal–metal bond; (2) reduction in the metal–metal bond order (e.g. for multiply bonded metal species); and (3) retention of the metal–metal bond order. Dimers undergo a wide range of reactions, and it is only possible to illustrate some of them in the following sections.

7.1 Reactions that Cleave the Metal–metal Bond

7.1.1 Radical Formation

One characteristic reaction of metal–metal bonded complexes is cleavage to form radicals. In some cases, such as those shown in equations (69) and (70), an equilibrium has been shown to exist,[129–132] and the radical species in solution are readily detected spectroscopically.

$$[\text{C}_3\text{H}_5(\text{CO})_3\text{Fe}]_2 \rightleftharpoons 2\text{C}_3\text{H}_5(\text{CO})_3\text{Fe}\bullet \qquad (69)$$

$$[\text{C}_5\text{H}_5(\text{CO})_3\text{Cr}]_2 \rightleftharpoons 2\bullet\text{Cr(CO)}_3\text{C}_5\text{H}_5 \qquad (70)$$

In other cases, the radical species cannot be detected spectroscopically but kinetic evidences for their existence and their involvement in reaction pathways is convincing (equation 71). In the case of the Rh(OEP) complex, use of bulkier groups (such as mesityl) on the porphyrin ring decreases the metal–metal bond strength and radicals can be detected and characterized.[133]

$$[(\text{OEP})\text{Rh}]_2 \rightleftharpoons 2\text{Rh(OEP)}\bullet \qquad (71)$$

$$\text{OEP} = \text{octaethylporphyrin}$$

Wayland and coworkers[134] have recently prepared a novel diporphyrin linked dirhodium(II) bimetallo radical complex whose ligand parameters preclude a strong metal–metal interaction but allow binuclear activation of methane and methanol.

These reactions are important in that the 17-electron radicals produced may undergo ligand substitution or additional reactions and then recombine. The rates of radical recombination are generally fast, and approach diffusion-controlled limits. This is one of the mechanisms of ligand substitution of metal–metal bonded complexes that is discussed in Section 7.3.1.

7.1.2 Photochemical Disproportionation

The photochemistry of metal–metal bonded complexes has been the subject of several reviews[135,136] (*see* ***Luminescence Behavior & Photochemistry of Organotransition Metal Compounds*** and ***Photochemistry of Transition Metal Complexes: Theory***). Strong σ bonding to σ^* antibonding transitions are often observed in metal–metal bonded systems. These lead to photogenerated fragments that undergo reactions and may ultimately recombine (equation 72).

$$\text{Mn}_2(\text{CO})_{10} \xrightarrow{h\nu} 2\bullet\text{Mn(CO)}_5 \longrightarrow \bullet\text{Mn(CO)}_4(\text{L}) \longrightarrow \text{Mn}_2(\text{CO})_9(\text{L}) \qquad (72)$$

In many cases, parallel pathways exist for photochemical loss of ligands, particularly for CO. In addition, many of the radicals have appreciable lifetimes and can also undergo photochemical reactions. This type of reactivity can be used in designed synthesis and, possibly, photocatalysis. It also has to be guarded against since many metal–metal bonded complexes that are relatively stable, even in solutions in the presence of oxygen in the dark, are rapidly oxidized in the presence of stray light.

7.1.3 Disproportionation

In the presence of excess base, a number of metal carbonyl complexes disproportionate (equations 73 and 74).

$$\text{Co}_2(\text{CO})_8 + \text{B} \rightleftharpoons \text{CoB}_6{}^{2+}[\text{Co(CO)}_4]_2{}^{-} \qquad (73)$$

$$[\text{CpMo(CO)}_3]_2 + \text{diphos} \longrightarrow \text{CpMo(CO)}_2(\text{diphos})^{+} + \text{CpMo(CO)}_3{}^{-} \qquad (74)$$

These reactions are often reversible and depend on temperature, concentration, and nature of the base. In addition, since this reaction involves changing from a metal–metal bonded system that is soluble in organic solvents to an ionic complex that is water soluble, the solubility patterns change greatly. Phase transfer catalysis (*see Phase Transfer*

Catalyst)[137] of cobalt-carbonyl reactions can utilize the water solubility of the salt and the hydrocarbon solubility of the metal–metal dimer. Ion pairing is important in the disproportionated metal complexes, and traces of water in organic solvents can not only serve as catalysts for this reaction but can also influence the equilibrium position by stabilizing the ionic products.

7.1.4 H_2 Addition

Perhaps the most important metal–metal bonded reaction from the point of view of catalysis is addition of hydrogen. In spite of years of study, the exact mechanism of hydrogenation of even dicobalt octacarbonyl is not fully understood. Oxidative addition (*see Oxidative Addition*) of hydrogen to metal–metal bonds is generally slower than oxidative addition to mononuclear complexes that have vacant sites. Two principal mechanisms have been proposed in this chemistry. The first relies on cleavage of the metal–metal bond to generate radicals (equation 75). The second mechanism involves dissociation of CO to generate a coordinatively unsaturated complex that retains the metal–metal bond (equation 76). In spite of the apparent simplicity of these two possibilities, the reaction mechanism is unknown and it is likely that parallel reaction mechanisms occur.

$$\mathrm{Co_2(CO)_8} \rightleftharpoons \mathrm{2Co(CO)_4{\bullet}} + \mathrm{H_2} \longrightarrow \text{Products} \tag{75}$$

$$\mathrm{Co_2(CO)_8} \rightleftharpoons \mathrm{Co_2(CO)_7} + \mathrm{CO} + \mathrm{H_2} \longrightarrow \text{Products} \tag{76}$$

The conflict between the two general modes of reactivity of metal–metal bonded complexes (metal–metal or metal–ligand bond homolysis) is finely balanced and varies from complex to complex. The classic example in this field is illustrated by the chemistry of $M_2(CO)_{10}$ (M = Mn, Re). Using isotope labeling techniques, Muetterties and coworkers[138] were able to show definitively that in this system, it is the metal–ligand rather than the metal–metal bond that is cleaved in substitution and scrambling reactions. Phosphine substitution, however, can weaken the metal–metal bond and then, metal–metal bond cleavage becomes the favored reaction channel. Detailed kinetic study has shown that $C_5Me_5(CO)_3Cr–Cr(CO)_3C_5Me_5$ reacts with H_2 by dissociation to radicals, which then form a termolecular $Cr{\bullet}\cdots H_2 \cdots{\bullet}Cr$ transition state.[139] More complex modes of splitting of hydrogen have evolved. Heterolytic cleavage of H_2 by a W–Ru-bonded sulfido-bridged dimer occurs with net H^+ addition to a terminal W=O and H^- addition to Ru. During this process, the metal–metal bond is retained.[140]

7.1.5 Reduction

In most cases, the metal–metal bond is cleaved by reducing agents. Dilute sodium amalgam is often used to generate anion radicals from organometallic dimers (equation 77). In addition to Na/Hg, other reducing agents such as Na/benzophenone, or even other metal carbonyl anions, have been used to reduce a metal–metal bond.

$$\mathrm{Mn_2(CO)_{10}} + \mathrm{Na/Hg} \longrightarrow \mathrm{2NaMn(CO)_5} \tag{77}$$

7.1.6 Oxidation

Organometallic complexes of any type are thermodynamically unstable with respect to oxidation and this is true of metal–metal bonded complexes as well. Reaction with oxygen or chlorine will ultimately lead to the metal oxide or chloride. Milder oxidizing agents cleave the metal–metal bond selectively, leaving the other bonds intact. For example, reaction with iodine is often a fast, clean reaction (equation 78).

$$\mathrm{[Cp(CO)_3M]_2} + \mathrm{I_2} \longrightarrow \mathrm{2I{-}M(CO)_3Cp} \tag{78}$$

$$\mathrm{M} = \mathrm{Cr, Mo, W}$$

Related reactions using similar 'soft' oxidants, such as disulfides, are also common (equation 79).

$$\mathrm{[Cp(CO)_2Fe]_2} + \mathrm{RSSR} \longrightarrow \mathrm{RS{-}Fe(CO)_2Cp} \tag{79}$$

7.2 Reactions That Reduce the Metal–metal Bond Order

For metal–metal bonded complexes that contain multiple bonds, addition of ligands can reduce the bond order but does not have to destroy the metal–metal interaction entirely. The reactions shown below are written in the forward direction, which highlights addition reactions leading to a loss in multiple-bond character. It should be kept in mind that these are often in equilibria, and ligand elimination in the reverse direction can be a source of the multiply bonded species.

Addition of the ligand can occur at both metals, as shown in equations (80) and (81). Interestingly, addition of triphenylphosphine sulfide does not proceed to yield products on both metals but an unsymmetrical product is formed (equation 82).

$$\mathrm{M_2(OR)_6} + 2\mathrm{L} \rightleftharpoons \mathrm{M_2(OR)_6(L)_2} \tag{80}$$

$$\mathrm{L} = \text{P or N donor}$$

$$\mathrm{M} = \mathrm{Mo, W}$$

$$\mathrm{Cp(CO)_2M{=}M(CO)_2Cp} + 2\mathrm{L} \rightleftharpoons \mathrm{CpM(CO)_2(L)M{-}M(CO)_2(L)Cp}$$

$$\mathrm{L} = \mathrm{PR_3, CO} \tag{81}$$

$$\mathrm{M} = \mathrm{Cr, Mo, W}$$

$$\mathrm{Cp(CO)_2Mo{\equiv}Mo(CO)_2Cp} + 2\mathrm{L} \rightleftharpoons \mathrm{CpM(CO)(L)_2Mo{-}Mo(CO)_3Cp}$$

$$\mathrm{L} = \mathrm{PPh_3S} \tag{82}$$

A range of complicated reactions can occur between metal–metal multiply bonded complexes and ligands that also have multiple bonds. The reader is referred to the review by Curtis[44] for numerous examples. The triply bonded dimolybdenum carbonyl anion has been shown to undergo a range of reactions, as displayed in equation (83).[141]

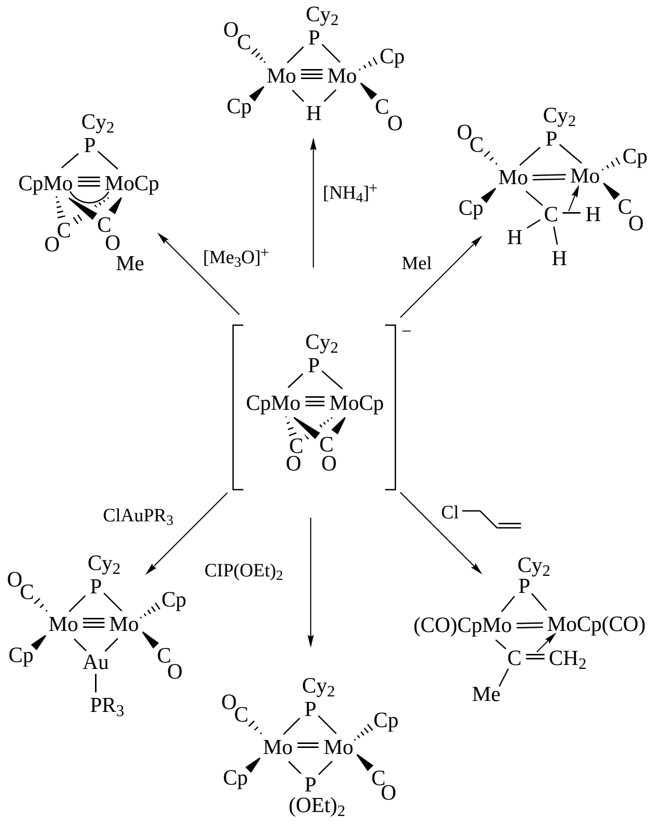

(83)

It is well known that the chlorine-bridged dimeric complex (which does not contain a metal bond) obtained from Wilkinson's catalyst can react via stepwise addition of H_2 to rhodium (equation 84) (*see* ***Rhodium: Organometallic Chemistry***).

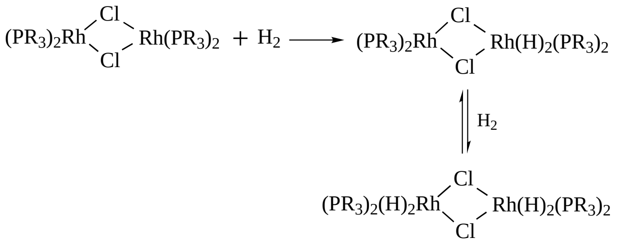

(84)

It is likely that metathesis reactions, such as those shown in equations (85) and (86), proceed through intermediates with reduced metal–metal bond order.

$$W_2(OR)_6 + RC{\equiv}CR \longrightarrow 2(RO)_3W{\equiv}CR \qquad (85)$$

$$W_2(OR)_6 + RC{\equiv}N \longrightarrow (RO)_3W{\equiv}N + (RO)_3W{\equiv}CR \qquad (86)$$

Addition of pyridine and acetylene results in generation and trapping of the complex shown in equation (87), which has a reduced bond order. In this complex, the acetylene bridges the two metals.[142] This type of chemistry was initially developed by Schrock and coworkers for alkyne metathesis (*see Alkyne Metathesis*) reactions[143] but has been subsequently developed by a number of other researchers.

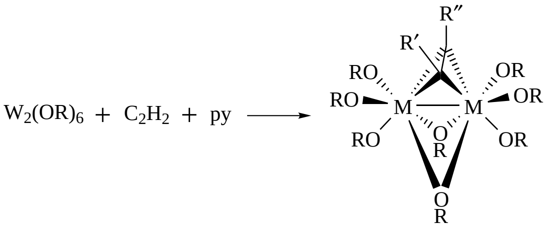

(87)

7.3 Reactions That Retain the Metal–metal Bond Order

7.3.1 Ligand Substitution Mechanisms for Dimers

The topic of ligand substitution was discussed above in the context of ways of generating different metal–metal bonded complexes from existing ones. Ligand substitution is one of the most fundamental reactions of mononuclear organometallic compounds. Ligand binding, transformation, and exchange are all key elements of catalytic cycles. For dinuclear complexes, ligand exchanges that take place while retaining the metal–metal bond occur by a range of mechanisms. This section will outline some of them. It is well to keep in mind that reaction mechanisms cannot be proven: evidence supporting them or ruling out other pathways is all that can be provided. There are a number of mechanisms for ligand substitution, and sometimes, it is difficult to tell the operational differences between them. Furthermore, where several mechanisms are possible, complexes can follow more than one reaction channel. Several groups (nitrosyl, indenyl) are known to accelerate reactivity by a change in the donor ability of the ligand at the transition state. Metal groups could play a similar role, but the influence of a second metal on ligand substitutions is still not well understood. In the discussion below, the complex $Mn_2(CO)_{10}$ is used to illustrate possible mechanisms.

Dissociative Loss of a Ligand Followed by Uptake of the New Ligand. In this type of mechanism, the metal–ligand bond is broken and the metal–metal bond remains intact (equation 88). It is expected to show an activation energy reflective of the metal–ligand bond strength. The proposed intermediate, $Mn_2(CO)_9$ in this example, could be partially stabilized by an increase in the Mn–Mn bond strength upon loss of CO. This might not be reflected in the transition state, however, since loss of ligand might precede any increase in metal–metal bonding. The major differences between substitution of the dimer and a comparable monomer would be (1) possible stabilization of the transition state via a partial multiple bond and (2) steric crowding in the ground state.

$$(CO)_5Mn\text{–}Mn(CO)_5 \longrightarrow CO + Mn_2(CO)_9 + L \longrightarrow Mn_2(CO)_9(L) \qquad (88)$$

Associative Ligand Displacement. In the same way that mononuclear complexes can undergo both associative and dissociative ligand displacement, dinuclear complexes can be expected to show the same type of behavior. These reactions would be expected to show more favorable enthalpies of activation than pure dissociative reactions but less favorable entropies of activation (equation 89).

$$Mn_2(CO)_{10}L \longrightarrow Mn_2(CO)_{10}(L) \longrightarrow Mn_2(CO)_9(L) + CO \qquad (89)$$

Owing to concentration effects, the solvent can also participate in this second order displacement, as shown in equation (90). The presence of a metal–metal bond may or may not stabilize such an associative transition state. Steric factors would probably argue against such stabilization, especially for first-row complexes.

$$\begin{tikzcd} Mn_2(CO)_{10} + S \arrow[r] & Mn_2(CO)_{10}(S) \arrow[r] & Mn_2(CO)_9(S) + CO \arrow[d] \\ & & Mn_2(CO)_9(L) \end{tikzcd} \qquad (90)$$

Cleavage of the Metal–metal Bond into Radical Fragments. In cases where the metal–metal bond is weaker than the metal–ligand bond, fragmentation of the complex into two radicals is preferred over ligand dissociation (equations 91–93).

$$(CO)_5Mn\text{–}Mn(CO)_5 \longrightarrow 2{\bullet}Mn(CO)_5 \qquad (91)$$

$${\bullet}Mn(CO)_5 + L \longrightarrow {\bullet}Mn(CO)_4L + CO \qquad (92)$$

$${\bullet}Mn(CO)_5 + {\bullet}Mn(CO)_4L \longrightarrow Mn_2(CO)_9L \qquad (93)$$

The 17-electron species (*see Seventeen Electron Configuration*) formed can undergo rapid substitution since associative pathways of low activation energy exist for them. Recombination of the substituted fragments can yield the monosubstituted, disubstituted, or more fully substituted complexes. The rate-determining step would be cleavage of the metal–metal bond since all other steps are relatively fast. This pathway may be preferred for photochemical substitution. Clearly, this pathway is not open to mononuclear analogs. The reactivity of low valent metal radical complexes has been reviewed.**[144]**

Cleavage of Metal–metal Bond to Ion Pairs. In polar solvents, heterolytic cleavage to anion/cation complexes is an equilibrium process. This can also be involved in substitution reactions in polar solvents (equations 94 and 95). Substitution at the cation is shown here since, for carbonyl ligands, due to a decrease in back bonding (*see Back Bonding*), the cationic carbonyl complexes often undergo more rapid substitution. Recombination by anion/cation pair annihilation will regenerate the metal–metal bonded complex. This process can yield polar metal–metal bonded complexes, referred to as ‘xenophilic’, between hard open-shell Werner-type complexes and softer metal carbonyl anions.**[145]**

$$(CO)_5Mn\text{–}Mn(CO)_5 + S \longrightarrow Mn(CO)_5(S)^+ + Mn(CO)_5{}^- \qquad (94)$$

$$Mn(CO)_5(S)^+ + L \longrightarrow Mn(CO)_5(L)^+ + Mn(CO)_5{}^- \longrightarrow Mn_2(CO)_9(L) \qquad (95)$$

Cleavage of the Metal–metal Bond to 17- and 19-electron Fragments. A final mechanistic possibility involves cleavage, either photochemically or thermally, of the metal–metal bond to 17- and 19-electron fragments (*see Nineteen Electron Configuration*). This is ligand induced and differs somewhat from the normal dissociative mechanism that generates 17-electron species. Initially, mechanisms involving 19-electron intermediates were met with skepticism. Evidence supporting them has grown to the point that they are now well accepted, particularly due to the work of Tyler and coworkers.**[146]**

7.3.2 *Reactions at Coordinated Ligands of Dimers*

For mononuclear complexes, reactions at coordinated ligands is a topic of major study, and numerous reviews and even books have been written on this topic.**[147]** At the time of writing this review, the authors could find no major review articles in this area for dinuclear compounds. The best examples are probably those on the reactions of coordinated molybdenum sulfides discussed earlier. A related observation is the reaction of metal carbonyls with Lewis acids. It has been observed by Shriver and coworkers**[38]** that carbonyl ligands bridging metal–metal bond atoms show increased tendency to coordinate Lewis acids (equation 96).

$$[Co(CO)_2Fe]_2 + Et_3Al \longrightarrow \qquad (96)$$

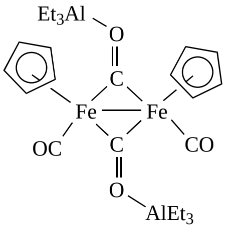

8 METAL DIMERS AS CATALYSTS AND CATALYST PRECURSORS

A principal motivation in the study of dinuclear organometallic complexes is the hope that they can accomplish catalytic reactions that are not achievable by mononuclear complexes. There are a number of cases where metal–metal complexes are catalysts precursors. The most famous is

Table 2 Processes that could be catalyzed by metal dimers and clusters[148]

Alkene isomerization
Alkene hydrogenation
Ketone hydrogenation
Hydrogenation of cyanides
Hydrogenation of nitro group
Alkyne hydrogenation
Aminomethylation
Water gas shift reaction
Reduction of CO and ketones
Hydroformylation
Fischer–Tropsch synthesis
Synthesis of methanol from CO
Hydrogenation of amides
Alkyne cyclization
Hydroxymethylation

dicobalt octacarbonyl, which can be used in the Oxo Process (*see Oxo Process*) but which is probably not itself involved in the catalytic cycle, except as a dead-end by-product of certain loops.

It should be kept in mind that it is often difficult to ascertain what the active catalyst is. There are, in fact, very few proven catalytic mechanisms where the structure of the actual catalyst is known with certainty. There are, to the author's knowledge, few, and possibly no, *proven* useful homogeneous catalytic processes that involve metal dimers *in the catalytic cycle*. In an excellent review on cluster catalysis, Muetterties[148] lists the following processes as metal-cluster-catalyzed reactions (see Table 2). This review also lists the important classes of metalloenzyme clusters; however, these compounds do not normally involve metal–metal bonds per se but are usually bridged by chalcogens, such as sulfur or oxygen donors.

For a dimer or cluster to be the active catalyst, it must survive the catalytic reaction conditions of the system. These are often high pressure and high temperature. At high temperatures, entropic factors will favor cleavage of the metal–metal bond into radical fragments. In view of the increase in metal–metal bond strength in going from first to second to third row metals (see below), the heavier congeners show the greatest promise for the development of robust dinuclear catalysts. In addition, high pressures of CO and H_2 or other reactants provide an additional pathway for decomposition. Bridging ligands (*see Bridging Ligand*) will increase the thermodynamic stability of the dimer or cluster in the face of these conditions. Thus, in general, the best prospects for genuine catalysis by homogeneous dimers and clusters is, under mild conditions and using either second or third row metals, preferably with bridging ligands. Photochemical activation, provided the metal–metal bond is not cleaved in the process, would also meet these conditions.

9 PHYSICAL PROPERTIES OF METAL–METAL BONDED DIMERS

9.1 Structural Studies

Definitive proof of metal–metal bonding usually relies on X-ray crystallography (*see* ***Diffraction Methods in Inorganic Chemistry***). Development of this field has accelerated greatly since the advent of modern structural techniques. This is such a widely used physical measurement that it is now considered routine.

While solid-state structures are readily generated by crystallography, evidence for structures in solution is usually generated by spectroscopic techniques. Rotation about the metal–metal bond of single-bonded dimers has been studied extensively by NMR and IR (*see* ***Structure & Property Maps for Inorganic Solids***). For example, the complex $[Mo(CO)_3Cp]_2$ exists as anti and gauche isomers that interconvert (equation 97).

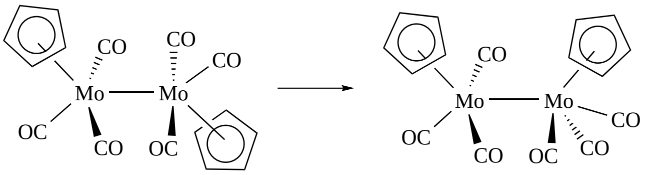

(97)

As the physical database increases, it can be expected that computer calculation of molecular conformations will play an increasing role in this chemistry. From the beginning, molecular orbital calculations have played a strong role in assessing the nature of the metal–metal bond. While molecular mechanics calculations have played a large role in organic chemistry and biochemistry, they have yet to play a prominent role in metal–metal bonded chemistry. It can be anticipated that this area will experience rapid development in the near future.

9.2 Spectroscopic Studies

The metal–metal bond is normally a strong chromophore, and nearly all metal–metal bonded dimers are strongly colored. Electronic transitions from bonding to antibonding orbitals are normally of low energy and have high extinction coefficients. The photochemistry of these complexes is discussed in several reviews.[135] The electronic transition in complexes such as that shown in equation (98) has been used to estimate that the strength of the δ-bond is on the order of $10\,\mathrm{kcal\,mol^{-1}}$.[149]

$$\mathrm{Re_2Cl_8}^{2-} \xrightarrow{h\nu} \text{excited state} \qquad (98)$$

Photoelectron spectroscopy (*see* ***Photoelectron Spectroscopy of Transition Metal Systems***) has also been applied to gain information about metal–metal bonding. For example, the metal–metal bonded complexes $M_2(OR)_6$ (M = Mo, W) show clearly defined ionizations attributed to the σ-orbital as well as to the π-orbital manifold.[150]

Finally, vibrational spectroscopy has been used to measure metal–metal force constants using both IR and Raman spectroscopy. In general, the metal–metal bond stretching frequencies are in the 100 to $500\,\mathrm{cm^{-1}}$ region and vibrational studies in this area are difficult to conduct. For that reason, this area of research is largely restricted to specialists. The reader is referred to literature treatment of this topic by Maslowsky[151] as well as the book on IR spectroscopy by Nakomoto.[152]

9.3 Electrochemical Studies

As discussed above, reduction of metal–metal bonded complexes is common, particularly for carbon monoxide–substituted complexes. The electrochemical potential of these reactions has been widely studied (*see* ***Electrochemistry: Applications in Inorganic Chemistry***). In addition, Meyer[153] has shown that the metal–metal bond strength can be estimated via electrochemical techniques. The results applied to $Mn_2(CO)_{10}$ are in agreement with values obtained by other methods and could provide a means of generating a wide range of metal–metal bond strengths. The legs of the electrochemical cycle are shown in equation (99).

$$\begin{tikzcd}
Mn_2(CO)_{10} \arrow[rr] \arrow[dr] & & 2{\bullet}Mn(CO)_5 \\
& 2Mn(CO)_5^- \arrow[ur] &
\end{tikzcd} \tag{99}$$

Concerted two-electron transfer and reversible metal–metal bond cleavage in phosphine-bridged dimers have been investigated, and extended Hückel molecular orbital calculations have shown that the redox-active orbital is a metal–metal antibonding orbital.[154] A Ru–Ru-bonded dimeric cation $[Ru(Cp)2]_2^{++}$ has been prepared and characterized electrochemically.[155] The electrochemistry of these dimers may give insight into more complex clusters and polymeric metals.

9.4 Thermochemical and Kinetic Studies

A key question in determining the thermodynamic stability of dimers and clusters is the strength of the metal–metal bond. This corresponds to the enthalpy of dissociation (step (i) in equation 100).

Table 3 Selected estimates of metal–metal bond dissociation enthalpies

Complex	D (kcal mol^{-1})
$[Cr(CO)_3C_5H_5]_2$[131]	15
$[Cr(CO)_3C_5Me_5]_2$[131]	14
$[Cr(CO)_2\{P(Ome)_3\}C_5H_5]_2$[131]	12
$[Mo(CO)_3C_5H_5]_2$[156]	33
$[W(CO)_3C_5H_5]_2$[157]	56
$Mn_2(CO)_{10}$[158]	38
$[Fe(CO)_2C_5H_5]_2$[159]	27
$[Fe(CO)_3(\eta\text{-}C_3H_5)]_2$[160]	14
$Hg[Cr(CO)_3C_5H_5]_2$[131]	20
$[Ru(OEP)]_2$[161]	17
$[Mo(CO)_2C_5H_5]_2$[162]	69
$Mo_2(O_2Cme)_4$[163]	77
$Mo_2(NMe_2)_6$[164]	95

$$L_nM\text{–}ML_n \underset{}{\overset{(i)}{\rightleftharpoons}} 2{\bullet}ML_n + 2S \overset{(ii)}{\rightleftharpoons} 2{\bullet}ML_n(S) \tag{100}$$

In view of the apparent propensity of 17-electron radicals to be in equilibrium with 19-electron adducts, it must always be considered, particularly in solvents such as THF or EtCN, that solvation of the radicals occurs. In view of the general increase in metal–ligand bond strength in going from first to second to third row transition metals, such solvent coordination would seem, most likely, to occur for the heavier analogs. It is difficult to determine whether the process involved in an apparent homolysis is only due to step (i) in equation (100) or due to additional solvolysis. The metal–metal bond strengths listed in Table 3 have been derived in various ways. These include kinetic values for enthalpies of activation, direct spectroscopic measurement of the monomer/dimer equilibrium, as well as more indirect thermochemical analysis. These are meant to provide only a rough guide, and the reader is referred to the original literature for more detailed treatment. One important point is that, in addition to enthalpic (bond strength) factors, the entropy of formation of metal–metal bonded complexes can vary significantly from that predicted on the basis of the Sakur–Tetrode equation alone. Thus, particularly for first-row metals, hindered rotation about the metal–metal and metal–ligand bonds can result in entropic forces that favor dissociation. This influence appears to be most severe for first-row metals due to the shorter metal–metal bond length.

10 RELATED ARTICLES

Cluster Compounds: Inorganometallic Compounds Containing Transition Metal & Main Group Elements; Polynuclear Organometallic Cluster Complexes.

11 REFERENCES

1. J. H. K. Yip, J. Wu, K. Y. Wong, K. P. Ho, C. S. N. Pun, and J. J. Vittal, *Organometallics*, 2002, **21**, 5292.
2. G. Lee, Y. J. Cho, B. K. Park, K. Lee, and J. T. Park, *J. Am. Chem. Soc.*, 2003, **125**, 13920.
3. Y. A. Lee and R. Eisenberg, *J. Am. Chem. Soc.*, 2003, **125**, 7778.
4. S. C. Perera, G. Tsoi, L. E. Enger, and S. L. Brock, *J. Am. Chem. Soc.*, 2003, **125**, 13960.
5. M. H. Chisholm, *Acc. Chem. Res.*, 2000, **33**, 53.
6. F. A. Cotton, C. Lin, and C. A. Murillo, *Acc. Chem. Res.*, 2001, **34**, 759.

7. P. Angaridis, J. F. Berry, F. A. Cotton, C. A. Murillo, and X. Wang, *J. Am. Chem. Soc.*, 2003, **125**, 10327.
8. N. T. Lucas, E. G. A. Notaras, M. P. Cifuentes, and M. G. Humphrey, *Organometallics*, 2003, **22**, 284.
9. T. Yamaguchi, F. Yamazaki, and T. Ito, *J. Am. Chem. Soc.*, 2001, **123**, 743.
10. S. K. Ritter, *Chem. Eng. News*, 2003, **81**(50), 23.
11. A. C. Fillipou, A. I. Philippopoulos, and G. Schnakenburg, *Organometallics*, 2003, **22**, 3339.
12. F. A. Cotton, N. F. Curtis, C. B. Harris, B. F. G. Johnson, S. J. Lippard, J. T. Mague, W. R. Robinson, and J. S. Wood, *Science*, 1964, **145**, 1305.
13. F. A. Cotton and D. G. Nocera, *Acc. Chem. Res.*, 2000, **33**, 483.
14. F. A. Cotton, *Pure Appl. Chem.*, 1992, **64**, 1383.
15. F. L. Campbell III, F. A. Cotton, and G. L. Powell, *Inorg. Chem.*, 1985, **24**, 177.
16. F. A. Cotton, C. Y. Liu, C. A. Murillo, D. Villagran, and X. Wang, *J. Am. Chem. Soc.*, 2003, **125**, 13564.
17. E. Alonso, J. M. Casea, F. A. Cotton, X. Feng, J. Fornies, C. Fortuno, and M. Tomas, *Inorg. Chem.*, 1999, **38**, 5034.
18. G. Estiu, F. Cukiernik, P. Maldivi, and O. Poizat, *Inorg. Chem.*, 1999, **38**, 3030.
19. I. Demachy, A. Lledos, and Y. Jean, *Inorg. Chem.*, 1999, **38**, 5443.
20. D. L. Lichtenberger, J. R. Pollard, M. A. Lynn, F. A. Cotton, and X. Feng, *J. Am. Chem. Soc.*, 2000, **122**, 3182.
21. F. A. Cotton, *J. Chem. Educ.*, 1983, **60**, 713.
22. W. A. Herrmann, *J. Organomet. Chem.*, 1990, **383**, 21.
23. H. Werner, *Angew. Chem., Int. Ed. Engl.*, 1990, **29**, 1077.
24. W. A. Herrmann, *Angew. Chem., Int. Ed. Engl.*, 1982, **21**, 117.
25. R. J. Havighurst, *J. Am. Chem. Soc.*, 1926, **48**, 2113.
26. F. A. Cotton, *Prog. Inorg. Chem.*, 1976, **21**, 1.
27. G. Wilkinson, F. G. A. Stone, and E. W. Abel eds., ‘Comprehensive Organometallic Chemistry’, 2nd edn., Pergamon Press, Oxford, 1995.
28. X. B. Wang and L. S. Wang, *J. Am. Chem. Soc.*, 2000, **122**, 2096.
29. R. B. King, *Coord. Chem. Rev.*, 1976, **20**, 155.
30. F. A. Cotton and G. Wilkinson, C. A. Murillo, M. Bochmann, ‘Advanced Inorganic Chemistry’, 6th edn., John Wiley & Sons, New York, 1999.
31. H. Vahrenkamp, *Angew. Chem., Int. Ed. Engl.*, 1978, **17**, 379.
32. M. H. Chisholm, *Angew. Chem., Int. Ed. Engl.*, 1986, **25**, 21.
33. S. K. Gupta, R. M. Atkins, and K. A. Gingerich, *Inorg. Chem.*, 1978, **17**, 3211.
34. E. Shustorovich ed., ‘Metal-Surface Reaction Energetics’, VCH Publishers, New York, 1991.
35. J. F. Berry, F. A. Cotton, L. M. Daniels, and C. A. Murillo, *J. Am. Chem. Soc.*, 2002, **124**, 3212.
36. G. Schmid, *Chem. Rev.*, 1992, **92**, 1709.
37. A. Odedra, C. J. Wu, R. J. Madhushaw, S. L. Wang, and R. S. Liu, *J. Am. Chem. Soc.*, 2003, **125**, 9610.
38. C. P. Horowitz and D. F. Shriver, *Adv. Organomet. Chem.*, 1984, **23**, 219.
39. H. G. Alt, K. A. Mahmoud, and A. J. Rest, *Angew. Chem., Int. Ed. Engl.*, 1983, **22**, 544.
40. S. Trofimenko, *Chem. Rev.*, 1993, **93**, 943.
41. M. Tilset and K. P. C. Vollhardt, *Organometallics*, 1985, **4**, 2230.
42. D. P. Klein, M. V. Ovchinnikov, A. Ellern, and R. J. Angelici, *Organometallics*, 2003, **22**, 3691.
43. R. M. Bullock and C. P. Casey, *Acc. Chem. Res.*, 1987, **20**, 167.
44. M. D. Curtis, *Polyhedron*, 1987, **6**, 759.
45. S. A. R. Knox, *J. Organomet. Chem.*, 1990, **400**, 255.
46. I. T. Horvath, G. Bor, M. Garland, and P. Pino, *Organometallics*, 1986, **5**, 1441.
47. M. R. Rakowski Dubois, *Chem. Rev.*, 1989, **89**, 1.
48. G. J. Kubas, R. R. Ryan, and K. A. Kubat-Martin, *J. Am. Chem. Soc.*, 1989, **111**, 7823.
49. D. A. Smith, B. Zhuang, W. E. Newton, J. W. McDonald, and F. A. Schultz, *Inorg. Chem.*, 1987, **26**, 2524.
50. R. D. Adams and O. S. Kwon, *Inorg. Chem.*, 2003, **42**, 6175.
51. M. D. Fryzuk, B. A. MacKay, and B. O. Patrick, *J. Am. Chem. Soc.*, 2003, **125**, 3234.
52. O. J. Scherer, H. Sitzmann, and G. Wolmershauser, *Angew. Chem., Int. Ed. Engl.*, 1985, **24**, 351.
53. J. Holton, M. F. Lappert, R. Pearce, and P. I. W. Yarrow, *Chem. Rev.*, 1983, **83**, 135.
54. R. B. King, *Acc. Chem. Res.*, 1970, **3**, 417.
55. G. K. Yang and R. G. Bergman, *J. Am. Chem. Soc.*, 1983, **105**, 6045.
56. C. P. Casey and J. D. Audett, *Chem. Rev.*, 1986, **86**, 339.
57. D. A. Lemonovskii and V. P. Fedin, *Russ. Chem. Rev.*, 1986, **55**, 127.
58. A. Efraty, J. A. Potenza, L. Zyontz, J. Daily, M. H. A. Huang, and B. Toby, *J. Organomet. Chem.*, 1978, **145**, 315.
59. J. A. Cabeza, I. del Ro, S. Garcia-Granda, L. Martinez-Mendez, M. Moreno, and V. Riera, *Organometallics*, 2003, **22**, 1164.
60. F. A. Cotton, *Polyhedron*, 1986, **5**, 3.
61. F. A. Cotton, *Polyhedron*, 1987, **6**, 667.
62. M. H. Chisholm, *Polyhedron*, 1983, **2**, 681.
63. M. H. Chisholm, *J. Organomet. Chem.*, 1990, **400**, 235.
64. M. H. Chisholm, K. Folting, W. E. Streib, and D. D. Wu, *Inorg. Chem.*, 1999, **38**, 5219.
65. P. J. Brothers and J. P. Collman, *Acc. Chem. Res.*, 1986, **19**, 209; C. D. Tait, J. M. Garner, J. P. Collman,

A. P. Sattelberger, and W. H. Woodruff, *J. Am. Chem. Soc.*, 1989, **111**, 9072.

66. F. A. Cotton and J. Czuchajowska, *Polyhedron*, 1990, **9**, 2553.
67. S. Hao, J. H. H. Edema, S. Gambarotta, and C. Bensimon, *Inorg. Chem.*, 1992, **31**, 2676.
68. C. D. Tait, J. M. Garner, J. P. Collman, A. P. Sattelberger, and W. H. Woodruff, *J. Am. Chem. Soc.*, 1989, **111**, 7806.
69. J. P. Collman, S. T. Harford, S. Franzen, A. P. Shreeve, and W. H. Woodruff, *Inorg. Chem.*, 1999, **38**, 2093.
70. D. W. Stephan, *Coord. Chem. Rev.*, 1989, **95**, 41.
71. M. J. Taylor, 'Metal to Metal Bonded State of the Main Group Elements', Academic Press, New York, 1975.
72. A. K. Saxena and N. S. Hosmane, *Chem. Rev.*, 1993, **93**, 1081.
73. M. A. Giardello, W. A. King, S. P. Nolan, M. Porchia, C. Sishta, and T. J. Marks, in 'Energetics of Organometallic Species', Kluwer Academic Publishers, Dordrecht, 1992 p. 35.
74. J. P. Collman, L. S. Hegedus, J. R. Norton, and R. G. Finke, 'Principles and Applications of Organotransition Metal Chemistry', University Science Books, Mill Valley, 1987.
75. R. E. Crabtree, 'The Organometallic Chemistry of the Transition Metals', 3rd edn., John Wiley & Sons, New York, 2001.
76. C. Elschenbroich and A. Salzer, 'Organometallics, A Concise Introduction', VCH Publishers, Weinheim, 1992.
77. P. Mathur, *Adv. Organomet. Chem.*, 1997, **41**, 243; This review highlights the fact that metal-metal bonding is well established in higher oxidation state complexes.
78. P. J. Brothers and P. P. Power, *Adv. Organomet. Chem.*, 1996, **39**, 1.
79. S. M. Waterman, N. T. Lucas, and M. G. Humphrey, *Adv. Organomet. Chem.*, 2001, **46**, 47.
80. S. Doherty, J. F. Corrigan, A. J. Cart, and E. Sappa, *Adv. Organomet. Chem.*, 1995, **37**, 39.
81. G. H. Robinson, *Adv. Organomet. Chem.*, 2001, **47**, 283.
82. C. J. Schaverien, *Adv. Organomet. Chem.*, 1996, **36**, 283.
83. H. Orino and H. Tobita, *Adv. Organomet. Chem.*, 1998, **42**, 223.
84. G. Suss-Fink and G. Meister, *Adv. Organomet. Chem.*, 1993, **35**, 41.
85. C. E. Housecroft 'Metal–Metal Bonded Carbonyl Dimers and Clusters', Oxford University Press, New York, 1996.
86. T. Saito, *Adv. Inorg. Chem.*, 1995, **44**, 45.
87. R. E. McCarley, 'Early Transition Metal Clusters with Pi-Donor Ligands', ed. H. Malcolm, Chisholm, VCH Publishers, New York, 1995.
88. N. Wheatley and P. Kalck, *Chem. Rev.*, 1999, **99**, 3379.
89. M. A. Sierra, *Chem. Rev.*, 2000, **100**, 3591.
90. F. A. Cotton and R. A. Walton, 'Multiple Bonds Between Metal Atoms', 2nd edn., Oxford University Press, Oxford, 1993.
91. M. P. Doyle and T. Ren, *Prog. Inorg. Chem.*, 2001, **49**, 113.
92. C. E. Plecnik, S. Liu, and S. G. Shore, *Acc. Chem. Res.*, 2003, **36**, 499.
93. D. Astruc, *Acc. Chem. Res.*, 1997, **30**, 383.
94. G. Pacchioni and N. Rosch, *Acc. Chem. Res.*, 1995, **28**, 390.
95. C. P. Casey and J. D. Audett, *Chem. Rev.*, 1986, **86**, 339.
96. R. M. Bullock and C. P. Casey, *Acc. Chem. Res.*, 1987, **20**, 167.
97. R. Colton and M. J. McCormick, *Coord. Chem. Rev.*, 1980, **31**, 1.
98. F. A. Cotton and R. A. Walton, 'Multiple Bonds between Metal Atoms', John Wiley & Sons, New York, 1982.
99. F. A. Cotton, *Polyhedron*, 1986, **5**, 3.
100. F. A. Cotton, *J. Chem. Educ.*, 1983, **60**, 713.
101. F. A. Cotton and R. A. Walton, *Struct. Bonding*, 1985, **62**, 1.
102. F. A. Cotton and J. Czuchajowska, *Polyhedron*, 1990, **9**, 2553.
103. F. A. Cotton, *Polyhedron*, 1987, **6**, 667.
104. M. H. Chisholm, *Angew. Chem., Int. Ed. Engl.*, 1986, **25**, 21.
105. M. H. Chisholm, *Polyhedron*, 1983, **2**, 681.
106. M. H. Chisholm, *J. Organomet. Chem.*, 1990, **400**, 235.
107. M. D. Curtis, *Polyhedron*, 1987, **6**, 759.
108. J. C. Jeffery and M. J. Went, *Polyhedron*, 1988, **7**, 775.
109. D. L. Kepert and K. Vrieze, 'Compounds of the Transition Elements Involving Metal–Metal Bonds', Pergamon Press, Oxford, 1973.
110. J. Holton, M. F. Lappert, R. Pearce, and P. I. W. Yarrow, *Chem. Rev.*, 1983, **83**, 135.
111. D. A. Lemonovskii and V. P. Fedin, *Russ. Chem. Rev.*, 1986, **55**, 127.
112. T. J. Meyer and J. V. Casper, *Chem. Rev.*, 1985, **85**, 187.
113. L. Messerle, *Chem. Rev.*, 1988, **88**, 1229.
114. R. H. Morris, *Polyhedron*, 1987, **6**, 793.
115. A. N. Nesmeyanov, M. I. Rybinskaya, L. V. Rybin, and V. S. Kaganovich, *J. Organomet. Chem.*, 1973, **47**, 1.
116. A. N. Nesmeyanov, M. I. Rybinskaya, and L. V. Rybin, *Russ. Chem. Rev.*, 1979, **48**, 213.
117. R. Poilblanc, *Inorg. Chim. Acta*, 1982, **62**, 75.
118. G. Schmid, *Chem. Rev.*, 1992, **92**, 1709.
119. D. W. Stephan, *Coord. Chem. Rev.*, 1989, **95**, 41.
120. A. C. Price and R. A. Walton, *Polyhedron*, 1987, **6**, 729.
121. R. A. Walton, *Isr. J. Chem.*, 1985, **25**, 196.
122. J. L. Hughey and T. J. Meyer, *Inorg. Chem.*, 1975, **14**, 947.
123. A. Miyake and H. Kondo, *Angew. Chem., Int. Ed. Engl.*, 1968, **7**, 631, 880.
124. W. D. Jones, J. M. Huggin, and R. G. Bergman, *J. Am. Chem. Soc.*, 1981, **103**, 4415.
125. I. Kovacs, A. Sisak, F. Ungvary, and L. Marko, *Organometallics*, 1989, **8**, 1873.
126. M. Garland, I. T. Horvath, G. Bor, and P. Pino, *Organometallics*, 1991, **10**, 559.

127. A. Poe, *Chem. Ber.*, 1983, **116**, 999.
128. T. Madach and H. Vahrenkamp, *Chem. Ber.*, 1980, **113**, 2675.
129. C. F. Putnik, J. J. Werner, G. D. Stucky, M. J. D'Aniello Jr, B. A. Sosinsky, J. F. Kirner, and E. L. Muetterties, *J. Am. Chem. Soc.*, 1978, **100**, 4107.
130. M. C. Baird, *Chem. Rev.*, 1988, **88**, 1217.
131. W. C. Watkins, T. Jaeger, C. E. Kidd, S. Fortier, M. C. Baird, G. Kiss, G. C. Roper, and C. D. Hoff, *J. Am. Chem. Soc.*, 1992, **114**, 5907.
132. S. J. McLain, *J. Am. Chem. Soc.*, 1988, **110**, 643.
133. B. B. Wayland, S. Ba, and A. E. Sherry, *J. Am. Chem. Soc.*, 1991, **113**, 5305.
134. W. Cui, P. Zhang, and B. B. Wayland, *J. Am. Chem. Soc.*, 2003, **125**, 4994.
135. A. E. Stiegman and D. Tyler, *Coord. Chem. Rev.*, 1985, **63**, 217.
136. T. J. Meyer and J. V. Casper, *Chem. Rev.*, 1985, **85**, 187.
137. H. Alper, *Adv. Organomet. Chem.*, 1981, **19**, 183.
138. N. J. Coville, A. M. Stolzenberg, and E. L. Muetterties, *J. Am. Chem. Soc.*, 1983, **105**, 2499.
139. K. B. Capps, A. Bauer, G. Kiss, and C. D. Hoff, *J. Organomet. Chem.*, 1999, **586**, 23.
140. Y. Ohki, N. Matsuura, T. Marumoto, H. Kawaguchi, and K. Tatsumi, *J. Am. Chem. Soc.*, 2003, **125**, 7978.
141. M. E. Garcia, S. Melon, A. Ramos, V. Riera, M. A. Ruiz, D. Belletti, C. Graiff, and A. Tiripicchio, *Organometallics*, 2003, **22**, 1983.
142. M. H. Chisholm, B. K. Conroy, B. W. Eichhorn, K. Folting, D. M. Hoffman, J. C. Huffman, and N. S. Marchant, *Polyhedron*, 1987, **6**, 783.
143. R. R. Schrock, *J. Organomet. Chem.*, 1986, **300**, 249.
144. C. D. Hoff, *Coord. Chem. Rev.*, 2000, **206**, 451.
145. K. Uehara, S. Hikichi, and M. Akita, *Organometallics*, 2001, **20**, 5002.
146. D. R. Tyler and F. Mao, *Coord. Chem. Rev.*, 1990, **97**, 119.
147. P. S. Braterman ed., 'Reactions of Coordinated Ligands', Plenum Press, New York, 1989 Vols. 1–3.
148. E. L. Muetterties and M. J. Krause, *Angew. Chem., Int. Ed. Engl.*, 1983, **22**, 135.
149. M. D. Hopkins, H. B. Gray, and V. M. Miskowski, *Polyhedron*, 1987, **6**, 705.
150. E. M. Kober and D. L. Lichtenberger, *J. Am. Chem. Soc.*, 1985, **107**, 7199.
151. E. Maslowsky, Jr, *Chem. Rev.*, 1971, **71**, 507.
152. K. Nakomoto, 'Infrared and Raman Spectra of Inorganic and Coordination Complexes', John Wiley & Sons, New York, 1978.
153. J. R. Pugh and T. J. Meyer, *J. Am. Chem. Soc.*, 1988, **110**, 8245.
154. D. Uhrhammer and F. A. Schultz, *J. Phys. Chem. A*, 2002, **106**, 11630.
155. S. Trupia, A. Nafady, and W. E. Geiger, *Inorg. Chem.*, 2003, **42**, 5480.
156. S. Amer, G. Kramer, and A. J. Poe, *J. Organomet. Chem.*, 1981, **209**, C28.
157. J. R. Krause and D. R. Bidinosti, *Can. J. Chem.*, 1975, **53**, 628.
158. J. L. Goodman, K. S. Peters, and V. Vaida, *Organometallics*, 1986, **5**, 815.
159. A. R. Cutler and M. Rosenblum, *J. Organomet. Chem.*, 1976, **120**, 87.
160. E. L. Muetterties, B. A. Sosinsky, and K. I. Zamaraev, *J. Am. Chem. Soc.*, 1975, **97**, 5299.
161. B. B. Wayland, *Polyhedron*, 1988, **7**, 1545.
162. S. P. Nolan, R. L. de la Vega, and C. C. Hoff, *Inorg. Chem.*, 1986, **25**, 4446.
163. K. J. Cavell, C. D. Garner, G. Pilcher, and S. Parkes, *J. Chem. Soc., Dalton Trans.*, 1979, 1714.
164. J. A. Connor, G. Pilcher, H. A. Skinner, M. H. Chisholm, and F. A. Cotton, *J. Am. Chem. Soc.*, 1978, **100**, 7738.

Dioxygen & Related Ligands

Prof. Rebecca R. Conry
Colby College, Waterville, ME, USA

Based in part on the article Dioxygen & Related Ligands by Rebecca R. Conry & Kenneth D. Karlin which appeared in the Encyclopedia of Inorganic Chemistry, First Edition.

1 Introduction 1
2 Properties of Dioxygen and Related Species 1
3 Transition Metal–Dioxygen Complexes Overview 2
4 Examples of Superoxo Complexes 3
5 Examples of Peroxo Complexes 5
6 Related Articles 7
7 References 7

1 INTRODUCTION

Dioxygen (O_2) constitutes 21% by volume (23% by weight) of the earth's atmosphere, plus a significant quantity of dioxygen is dissolved in surface waters. This ready availability, along with the properties of dioxygen (*see* ***Oxygen: Inorganic Chemistry***), especially its ability to accept electrons, is exploited by organisms that are dependent on O_2 for life. Thus, aerobic organisms have developed mechanisms to transport, store, and activate dioxygen (*see* ***Iron: Heme Proteins, Mono- & Dioxygenases*** and ***Copper Proteins: Oxidases***).[1] Nearly all of these mechanisms utilize proteins that incorporate one or more transition metals at their functional active sites, that is where O_2 binds and/or reacts. These metalloproteins contain one of several known metal–dioxygen interacting sites.[2,3] Examples include a single iron-heme center in hemoglobin and myoglobin (*see* ***Iron: Heme Proteins & Dioxygen Transport & Storage***), a dinuclear iron nonheme active site in hemerythrin, the dicopper-containing hemocyanin (*see* ***Copper Proteins with Dinuclear Active Sites***), and a heterodinuclear site in cytochrome *c* oxidase (*see* ***Copper Proteins: Oxidases***), which features both a heme-iron center as well as a nonheme copper center in its active site. Model complexes that mimic biological processes like dioxygen binding and activation (*see* ***Copper: Hemocyanin/Tyrosinase Models***, ***Iron: Models of Proteins with Dinuclear Active Sites***) can help us understand what might be occurring at the metal centers in those complicated biological systems, and can also be developed for practical applications, such as the separation of dioxygen from the air.[4] Transition-metal catalysts that use dioxygen or related species as an oxidant[5,6] are also involved in many industrial processes (*see* ***Oxidation Catalysis by Transition Metal Complexes***). The interaction of dioxygen with metals is important to these systems as well as to the development of O_2 sensors[7] plus fuel cells, batteries, and electrocatalysts (*see* ***Electrochemistry: Applications in Inorganic Chemistry***).[8] Therefore, it is not surprising that studies of the interaction and activation of dioxygen at metal sites have occupied and fascinated researchers for quite some time.

Metal–dioxygen adducts have been known for more than a hundred years, for example, in 1898, Werner and Mylius reported[9] the Co^{III} complex $[\{(NH_3)_5Co\}_2O_2]^{4+}$. Thirty-eight years later, a Pauling and Coryell paper[10] sparked considerable interest in metal–dioxygen binding; this paper concluded that 'the oxygen molecule undergoes a profound change in electronic structure on combination with hemoglobin.' Another milestone in metal–dioxygen chemistry was the discovery by Vaska of the 1:1 reversible oxygen carrier $IrCl(CO)(PPh_3)_2$ (Vaska's complex), because the resulting dioxygen complex was extremely stable compared to previously known dioxygen adducts and, thus, provided the first crystal structure of a dioxygen complex.[11] Most d-block metals have been found to bind dioxygen, resulting in complexes with a range of oxidation states (from I to VI) and d electron counts (from 0 to 9) and a variety of coordination modes of the dioxygen-derived ligand (discussed below).[12]

2 PROPERTIES OF DIOXYGEN AND RELATED SPECIES (*See also Oxygen: Inorganic Chemistry*)

Dioxygen is a paramagnetic molecule whose electronic ground state is a triplet ($^3\Sigma_g{}^-$) in which two unpaired electrons occupy degenerate antibonding orbitals ($2p\pi^*$). Dioxygen is considered to contain a formal oxygen–oxygen double bond (Table 1). Even though dioxygen is thermodynamically a powerful oxidant, it is kinetically fairly inert because, in order to conserve spin, its diradical character requires that it reacts with another radical (which often involves one or more highly endothermic steps) or forms a product that possesses a triplet ground state.[13] Owing to the rarity of the latter process, the major reactivity pathways of dioxygen usually involve radicals (for instance, by using transition metals with unpaired electrons) or require excitation to singlet oxygen (described below). In addition, dioxygen has a fairly low solubility in water (with a 1 atm or ~45 mmol dioxygen vapor phase, the solution concentration is about 1 mmol).

The first electronic excited state ($^1\Delta_g$) for O_2 is 23 kcal mol^{-1} above the ground state and is a singlet state (no unpaired electrons); the electronic configuration is the same as the ground state except that one of the two previously unpaired $2p\pi^*$ spins has been flipped and paired with the other one. This species, simply referred to as singlet oxygen,

Table 1 Information about dioxygen and related species

Species	Bond order	O–O distance (Å)	υ(O–O) (cm^{-1})	Bond energy (kcal mol^{-1})
Oxygenyl in $[O_2^+][AsF_6^-]$	2.5	1.12	1858	149.4
Triplet O_2 ($^3\Sigma_g^-$)	2	1.21	1555	117.2
Singlet O_2 ($^1\Delta_g$)	2	1.22	1484	94.7
Superoxide in $[K^+][O_2^-]$	1.5	1.34	1145	
Peroxide in $[Na^+]_2[O_2^{2-}]$	1	1.49	794	48.8
Peroxide in H_2O_2	1	1.46	880	34.3

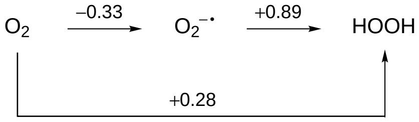

Figure 1 Standard reduction potentials for dioxygen species in water [1 atm O_2, pH 7, V vs. NHE]

has a half-life in water of about 2 µs and is very reactive. The enhanced reactivity of singlet oxygen versus ground-state oxygen is due to the fact that two of the barriers associated with the ground state have been overcome: the problem of matching electron spin is discussed above and the problem of adding an electron to an already occupied orbital is mentioned below. In fact, singlet oxygen has been estimated to be one volt more oxidizing than ground-state oxygen, which makes it more electrophilic and potentially useful, for instance, in chemical synthesis and wastewater treatment.**14** Most reactions of O_2 with transition metals use ground-state oxygen, although there have been some studies with singlet oxygen, which, in many cases, is quenched by the complex.

Simple reduction of dioxygen by one electron to produce the superoxide ion (O_2^-) is thermodynamically unfavorable (Figure 1); it requires adding an electron to a half-filled antibonding orbital. Reduction to peroxide (i.e. O_2^{2-}), however, is downhill, both from superoxide and dioxygen. Owing to the increased population of antibonding orbitals in reduced O_2 species, the O–O bond order decreases, the O–O distance increases, and the O–O stretch decreases compared to dioxygen (Table 1).

3 TRANSITION METAL–DIOXYGEN COMPLEXES OVERVIEW

The synthesis of transition metal–dioxygen complexes is often carried out by the addition of dioxygen to a precursor complex. Binding involves some shift of electron density from the metal to the O_2 ligand, generally regarded as resulting in either a superoxo (one-electron reduced or superoxide-like) or peroxo (two-electron reduced or peroxide-like) ligand when the O–O bond remains intact. Consistent with this, metal–O_2 complexes have also been synthesized from superoxide or peroxide sources.

Spectroscopic methods are used to decide whether the complex is best described as containing a superoxo or peroxo ligand. This is typically done by comparing the oxygen–oxygen vibration [υ(O–O)] obtained by infrared and/or Raman spectroscopies and/or the O–O distance, usually acquired from an X-ray crystallographic structure determination, to data for the ionic oxygen species (Table 1). There has been some discussion of this system and of assignment of oxidation states in metal–dioxygen complexes.**15**

A classification scheme devised by Vaska was used to describe the earliest dioxygen complexes: type I for superoxo and type II for peroxo, with the additional descriptors a and b to represent mononuclear and dinuclear binding, respectively. Because other binding modes are now known that cannot easily be distinguished using Vaska's system, an alternative more descriptive nomenclature has since been adapted (Figure 2). In this system, μ (mu) signifies a bridging dinuclear M_2O_2 (M = metal center) species with a numerical subscript added if the ligand bridges more than two metal centers, for example, μ_4 signifies bridging of the indicated ligand between four metal ions. In addition, the binding mode is delineated: η_1 (eta-one or monohaptic) indicates a monodentate O_2 (one oxygen atom is bound to one metal ion, sometimes referred to as *end-on coordination*) and η^2 (eta-two or dihaptic, sometimes called *side-on binding*) designates bidentate O_2 (both oxygen atoms are bound to the same metal center). The binding mode does not indicate the reduction state of the dioxygen ligand, for instance, both superoxo and peroxo η^2-O_2 and *trans*-μ-η^1:η^1-O_2 complexes have been reported (*trans* indicates that the two metal centers are diagonally located on opposite sides of the O_2 ligand and *cis* signifies that the metal centers are on the same side of the O_2 ligand). Therefore, superoxo or peroxo is also stated to fully describe the metal–dioxygen interaction in a complex.

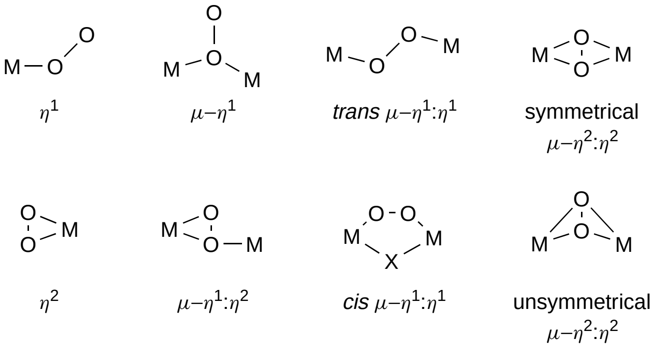

Figure 2 Mononuclear and dinuclear metal–dioxygen binding modes

In general, superoxide complexes exhibit υ(O–O) between about 960 and 1200 cm^{-1} and usually contain planar metal–O$_2$ units with O–O distances usually falling between about 1.20 and 1.35 Å, whereas peroxide complexes result in υ(O–O) between 650 and 950 cm^{-1} and typically have nonplanar metal–O$_2$ units with longer O–O distances, typically between ~1.38 and 1.55 Å, although there are a few exceptions to these generalities. Mononuclear superoxide and peroxide complexes usually give higher υ(O–O) values within those ranges and dinuclear dioxygen-containing complexes typically result in lower υ(O–O) values, with the μ-η^1:η^1 systems giving greater magnitude of υ(O–O) than the μ-η^2:η^2 systems.**16** For some time, all metal–dioxygen complexes were thought to exhibit υ(O–O) greater than 800 cm^{-1} and, in fact, most M–O$_2$ complexes do give υ(O–O) values above 800 cm^{-1}, with the notable exception of some μ-η^2:η^2-peroxo complexes (discussed in more detail below). In addition, an equilibrium between the μ-η^2:η^2-peroxo and bis(μ-oxo) species (equation 1) has been demonstrated in Cu$_2$O$_2$ complexes (discussed below).**17**

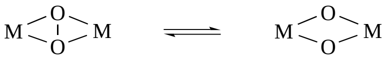

(1)

4 EXAMPLES OF SUPEROXO COMPLEXES

4.1 η^1-superoxo Complexes

Many of the structurally characterized η^1-superoxo complexes are cobalt containing, or are iron complexes with sterically hindering porphyrins. Co$^{\text{II}}$ compounds often react with dioxygen to form mononuclear superoxo complexes, although frequently further reaction occurs to form binuclear peroxo-bridged species.**18** Therefore, 1:1 adducts are often isolated by working quickly at low temperatures and/or at high dilution to prevent reaction with a second metal center. The typical O–O distances are from 1.21 to 1.35 Å, M–O–O angles from 115 to 135°, and υ(O–O) are of 1100 to 1220 cm^{-1}. Representative examples of this 'end-on' coordination mode include Fe(picket fence porphyrin)(MeIm)(O$_2$)**19** [picket fence porphyrin = *meso*-tetrakis(α, α, α, α-*ortho*-pivalamidophenyl); MeIm = 1-methyl-imidazole] and the superoxorhodium$^{\text{III}}$ complex containing an N$_4$-macrocyclic ligand shown in Figure 3,**20** plus a Cu$^{\text{II}}$ complex with a hydrogen-bonded superoxo ligand.**21** In addition, oxy-myoglobin and oxy-hemoglobin appear to have η^1–superoxo dioxygen ligands with O–O vibrations occurring at 1103 and 1132 cm^{-1}, respectively. Disorder of the dioxygen ligand is a common occurrence in crystal-structure determinations, especially with this type of dioxygen complex, and must be treated carefully or unrealistic O–O bond lengths may result (e.g. ≤1.10 Å). This binding mode is also found for some hydroperoxide or alkyl peroxide complexes.

4.2 η^2-superoxo Complexes

This binding mode for dioxygen complexes is almost invariably seen in complexes that also incorporate multidentate supporting ligands. Thus, this binding mode is found in the substituted tris(pyrazolyl)hydroborate (Tp) ligated Sm$^{\text{III}}$ and Co$^{\text{II}}$ complexes**22,23** shown in Figure 4 as well as in the Tp–Cr$^{\text{III}}$ and V$^{\text{V}}$ complexes that have been recently reported.**24,25** The Co$^{\text{II}}$ superoxo complex (Figure 4(b)) is generated by addition of dioxygen to a Co$^{\text{I}}$ dinitrogen precursor complex. Interestingly, this complex displays a υ(O–O) that is more consistent with a peroxo ligand, although the O–O

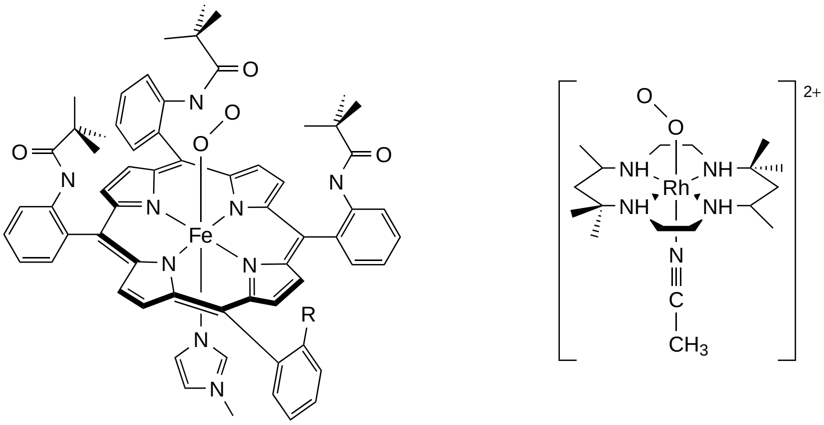

R = NC(O)C(CH$_3$)$_3$
O–O 1.24(8) Å
<Fe–O–O 136(4)°

O–O 1.306(5) Å
<Rh–O–O 115.3(3)°

Figure 3 Examples of η^1-superoxo complexes

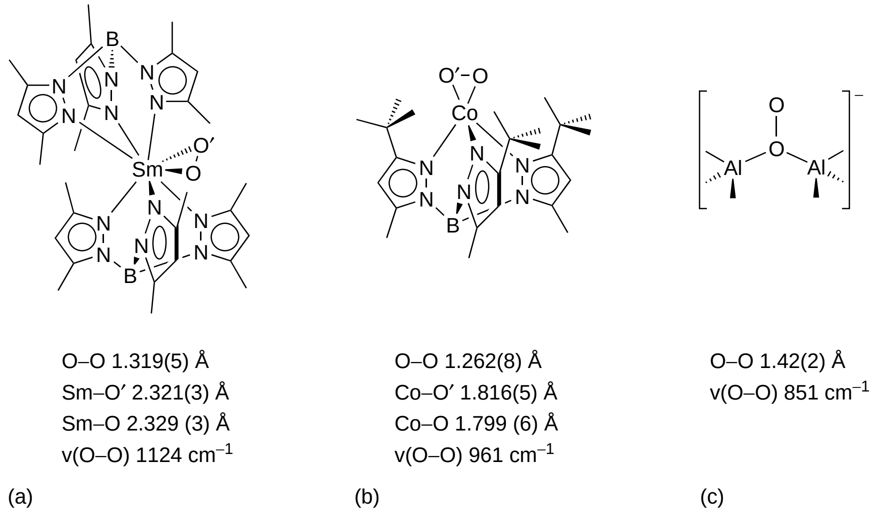

(a)
O–O 1.319(5) Å
Sm–O′ 2.321(3) Å
Sm–O 2.329 (3) Å
v(O–O) 1124 cm^{-1}

(b)
O–O 1.262(8) Å
Co–O′ 1.816(5) Å
Co–O 1.799 (6) Å
v(O–O) 961 cm^{-1}

(c)
O–O 1.42(2) Å
v(O–O) 851 cm^{-1}

Figure 4 Examples of η^2-superoxo complexes (a and b) a μ-η^1:η^1-superoxo complex (c)

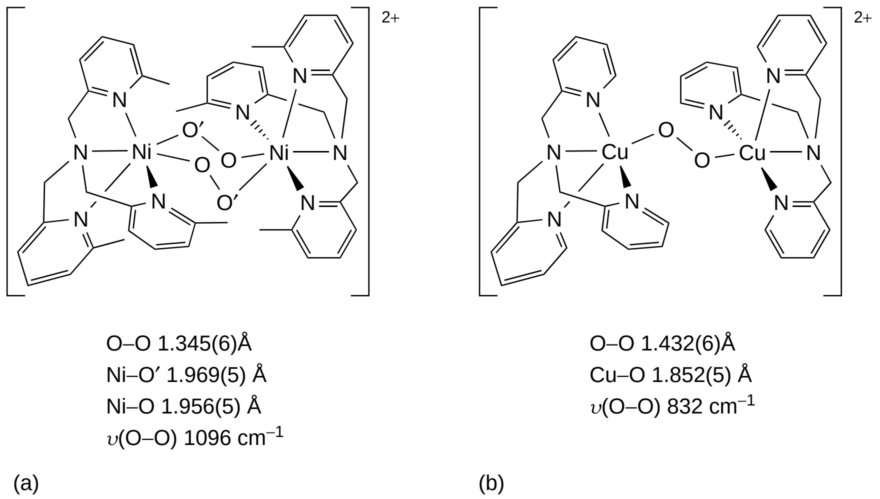

(a)
O–O 1.345(6)Å
Ni–O′ 1.969(5) Å
Ni–O 1.956(5) Å
υ(O–O) 1096 cm^{-1}

(b)
O–O 1.432(6)Å
Cu–O 1.852(5) Å
υ(O–O) 832 cm^{-1}

Figure 5 Examples of μ-η^1:η^1-O_2 complexes with similar ancillary ligands: Ni^{II}_2-bis(superoxo) complex (a) and Cu^{II}_2-peroxo complex (b)

distance is reasonable for a superoxo ligand. If the substituents on the Tp ligand directed at the cobalt ion are changed from *tert*-butyl to *iso*-propyl groups, a similar monomeric complex is formed that dimerizes to form a complex with two *trans*-μ-η^1:η^1 superoxo ligands.[23]

4.3 μ-η^1-superoxo Complexes

The μ-η^1-superoxo binding mode is uncommon, occurring in the aluminum compound $[(Me_3Al)_2O_2]^-$ shown in Figure 4(c).[26] The spectrochemical data for this compound fit a peroxo ligand instead of the superoxo ligand that it must be to make chemical sense, reminding us that oxidation states and levels of reduction are just bookkeeping and may be an oversimplification (or that this ligand is actually μ-OOH^-). This mode of bonding is more commonly seen for a different class of compounds where the dioxygen is protonated or alkylated (i.e. a bridging hydroperoxide or alkylperoxide ligand).

4.4 *Trans*-μ-η^1:η^1-superoxo Complexes

These are often referred to as *trans*-μ-1,2 complexes. The superoxo *trans*-μ-η^1:η^1-O_2 complexes typically give υ(O–O) in the range 1000 to 1100 cm^{-1} and O–O bond distances between 1.24 and 1.36 Å and the dioxygen moiety is generally planar (dihedral angle, $\Phi = 180°$). Examples are the tetrameric superoxo complex $[O_2\{Co(F{-}salen)(H_2O)\}_2]_2$ [F−salen = *N*,*N*′-ethylenebis(3-fluorosalicylideneiminato)] that has a dihedral angle of 122° and an O–O distance of 1.31 (3) Å and the Ni^{II}_2-bis(superoxo) complex shown in Figure 5 that was generated in an unusual reaction from a $Ni^{III}{}_2$-bis(μ-oxo)$_2$ complex.[27]

4.5 *Cis*-μ-η^1:η^1-superoxo Complexes

These complexes are doubly bridged, with an $O_2{}^-$ group as well as one or more other bridging ligands, often an amide ($NH_2{}^-$), hydroxo (OH^-), or alkoxo (OR^-, R = alkyl or aryl group) ligand. The O–O distances in these complexes are similar to those found in the corresponding *trans*-μ-η^1:η^1-superoxo complexes, with planar metal$_2$–superoxo groups ($\Phi = 0°$). Most of the reported *cis*-μ-η^1:η^1-superoxo complexes contain cobalt and interconversions between the superoxo and peroxo complexes have been reported (e.g. equation 2).[28]

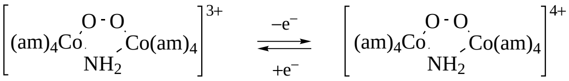

$$\left[(am)_4Co\overset{O-O}{\underset{NH_2}{\ }}Co(am)_4\right]^{3+} \underset{+e^-}{\overset{-e^-}{\rightleftharpoons}} \left[(am)_4Co\overset{O-O}{\underset{NH_2}{\ }}Co(am)_4\right]^{4+} \qquad (2)$$

cis μ–η^1:η^1 peroxo (am = amine ligand)

cis μ–η^1:η^1 superoxo

5 EXAMPLES OF PEROXO COMPLEXES

5.1 η^2-peroxo Complexes

This is a very common binding mode for transition metal complexes, found for a variety of metals including members of all three periods of d-block elements as well as early metals such as Ti, V, Nb, and Ta and late metals like Ir, Ni, Pd, and Pt. Usually, the coordination is not quite symmetrical, the M–O and M–O′ distances vary slightly, and the O–O′ bond length is in the range 1.40 to 1.50 Å. Typical examples include the peroxide complex *trans*-$Ir(O_2)Cl(CO(PPh_3))_2$,[11] which is derived from the simple addition of dioxygen to Vaska's compound, and the Mo^{IV} complex shown in Figure 6. A redetermination of an iridium structure lead to the conclusion that data yielding unusual or extreme O–O bond lengths have to be examined carefully.[29]

5.2 μ-η^1:η^2-peroxo Complexes

This is one of the rarer bonding modes for metal–dioxygen complexes, found in only a handful of cases, including the heterodinuclear complex[30] shown in Figure 6 that was synthesized to model the active site of cytochrome *c* oxidase (*see* ***Iron: Heme Proteins, Mono- & Dioxygenases***). In addition, *ab initio* calculations have suggested this binding mode for the peroxo species formed by the diiron containing enzyme, methane monooxygenase (*see* ***Iron Proteins with Dinuclear Active Sites***).[31]

5.3 *Trans*-μ-η^1:η^1-peroxo Complexes

Peroxo *trans*-μ-η^1:η^1-O_2 complexes typically have υ(O–O) between 790 and 885 cm^{-1} and O–O distances between 1.38 and 1.53 Å and have nonplanar, twisted metal$_2$-peroxo groups ($\Phi < 180°$). An example of a peroxo *trans*-μ-η^1:η^1 complex has been reported by Karlin and

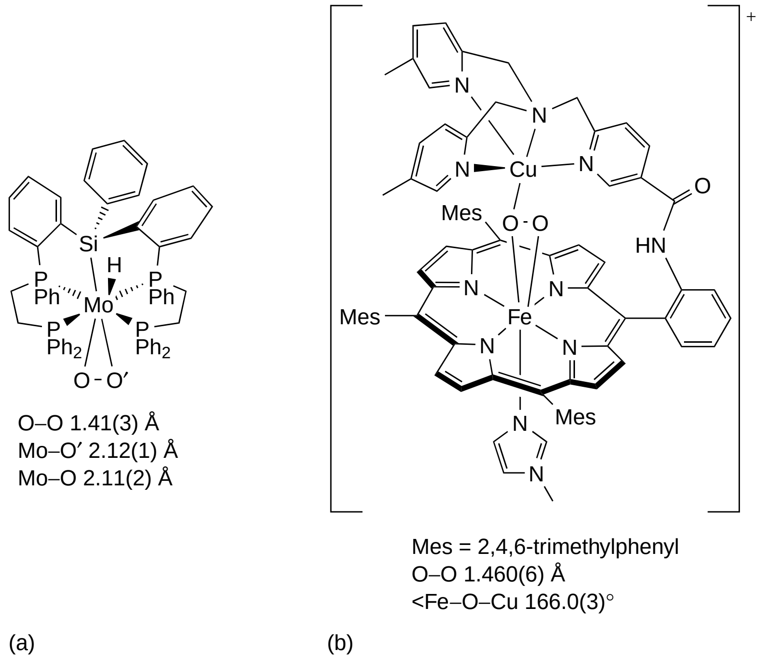

O–O 1.41(3) Å
Mo–O′ 2.12(1) Å
Mo–O 2.11(2) Å

Mes = 2,4,6-trimethylphenyl
O–O 1.460(6) Å
<Fe–O–Cu 166.0(3)°

(a) (b)

Figure 6 Examples of a η^2-peroxo complex (a) and a μ-η^2:η^1-peroxo complex (b)

coworkers.[2] This complex has a dihedral angle of 180° and is shown in Figure 5(b), next to a $\mathrm{Ni^{II}}$ *trans*-μ-η^1:η^1-superoxo complex (Figure 5(a)) with a similar ancillary ligand for easy comparison.

5.4 *Cis*-μ-η^1:η^1-peroxo Complexes

These complexes are usually doubly bridged, with an $O_2{}^{2-}$ ligand as well as another bridging group, which is frequently an amide, hydroxide, or alkoxide group. The O–O distances are similar to those found in the corresponding *trans*-μ-η^1:η^1-peroxo complexes, and the metal$_2$–peroxo group is nonplanar ($\Phi > 0°$). Most of the reported *cis*-μ-η^1:η^1-peroxo complexes contain cobalt, iron, or copper,[32] although an account has appeared of an interesting $\mathrm{Ir^{II}}$ complex (Figure 7(a)) with a peroxo ligand straddling an Ir–Ir bond.[33]

5.5 Symmetrical μ-η^2:η^2-peroxo Complexes

This is a fairly unusual binding mode for dioxygen, occurring in a few cases, including the Kitajima complex shown in Figure 7(b).[34] The O–O vibration for this complex is essentially identical to that found for the dioxygen-carrier protein oxy-hemocyanin [υ(O–O) 740 cm^{-1}] (*see* ***Copper Proteins with Dinuclear Active Sites***), which has also been found to contain a symmetrical μ-η^2:η^2-peroxo ligand.

Interestingly, an equilibrium between the μ-η^2:η^2-peroxo (**A**) and bis(μ-oxo) (**B**) species has been found to exist in Cu_2O_2 systems (Figure 8).[17] Structurally, the Cu–Cu distance is longer in **A** (∼3.6 Å) compared to **B** (∼2.8 Å), and there are notable spectroscopic differences for the two species. For example, **A** typically has a low υ(O–O) in the resonance Raman spectrum (∼750 cm^{-1}). In contrast, **B** gives a resonance Raman feature at ∼600 cm^{-1} that is assigned to be a symmetric vibration of the $Cu_2(\mu\text{-}O)_2$ core as the band shifts when ^{18}O is incorporated into the complex.[17] Whether **A** or **B** is favored appears to be strongly dependent on the size and orientation of the ligand substituents because **B** has a much more compact dicopper core that requires a closer approach of ligand groups.[35] There is also postulated to be an electronic effect that is not as important in determining the equilibrium position as the steric influence.[17] The oxo-containing compounds **B** are reactive, often displaying different reactivity than the peroxo-containing compounds **A**; however, the reactivity can also be similar to **B** and appears to depend on the choice and possible

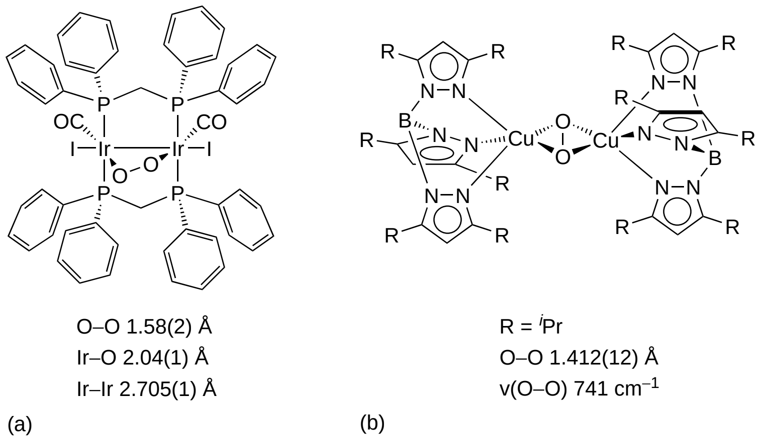

O–O 1.58(2) Å
Ir–O 2.04(1) Å
Ir–Ir 2.705(1) Å

R = ^{i}Pr
O–O 1.412(12) Å
v(O–O) 741 cm^{-1}

Figure 7 (a) A *cis*-μ-η^1:η^1-peroxo complex that also contains a metal–metal bond and (b) a symmetrical μ-η^2:η^2-peroxo model complex for the dioxygen-carrier hemocyanin

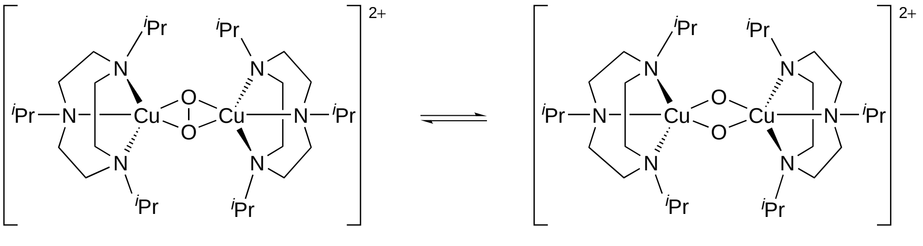

an example of a μ-η^2:η^2-peroxo compound **A**

an example of a bis(μ-oxo) compound **B**

Figure 8 An example of the equilibrium found between some μ-η^2:η^2-peroxo and bis(μ-oxo) species (^{i}Pr = –CH(CH$_3$)$_2$)

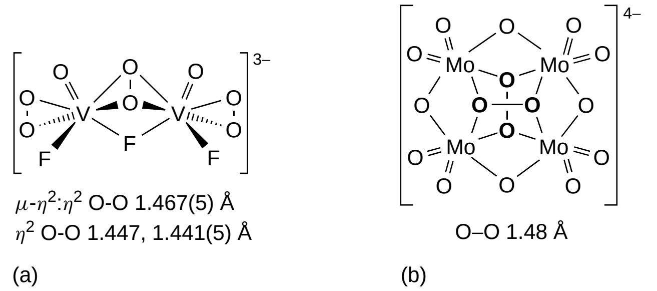

Figure 9 An unsymmetrical μ-η^2:η^2-peroxo complex (a) and a μ_4-peroxo complex (b)

relative orientations of potential substrates.[17] The fact that the reactivity of species **B** can resemble that of **A** means that some metalloenzymes, like tyrosinase (*see* ***Copper Proteins with Dinuclear Active Sites***), may form reactive species similar to **B** instead of **A**. The conversion of a dinuclear species complex to one containing two bridging oxo ligands has been suggested for other systems, including cobalt complexes,[16] as well as for diiron enzymes (*see* ***Iron Proteins with Dinuclear Active Sites***) that activate dioxygen, which appear to convert a peroxo-diiron species to a bis(μ-oxo) species, although the structure of the peroxo-diiron species is unknown.[36]

5.6 Unsymmetrical μ-η^2:η^2-peroxo Complexes

This is also an unusual type of dioxygen binding, occurring in the divanadium complex shown in Figure 9(a) (also contains η^2-peroxo ligands);[37] presumably, the μ-peroxo is found in an unsymmetrical configuration because of the presence of another bridging ligand.

5.7 Miscellaneous Peroxo Complexes

There are a few additional interesting complexes that contain peroxide ligands that do not fall into the categories given above. For instance, there are complexes where the peroxo ligand bridges four metal centers such as $[Mo_4O_8(\mu\text{-}O)_4(O_2)_2]^{4-}$ (Figure 9(b)), which was prepared by the reaction of K_2MoO_4 and H_2O_2 at neutral pH aqueous solution,[38] and two Cu_4O_2 complexes that have been crystallographically characterized.[39]

6 RELATED ARTICLES

Cobalt: Inorganic & Coordination Chemistry; Copper: Hemocyanin/Tyrosinase Models; Copper: Inorganic & Coordination Chemistry; Copper Proteins: Oxidases; Copper Proteins with Dinuclear Active Sites; Iron: Heme Proteins & Dioxygen Transport & Storage; Iron: Heme Proteins, Mono- & Dioxygenases; Iron: Models of Proteins with Dinuclear Active Sites; Iron Proteins with Dinuclear Active Sites; Manganese: The Oxygen-evolving Complex & Models; Oxidation Catalysis by Transition Metal Complexes; Oxygen: Inorganic Chemistry.

7 REFERENCES

1. R. H. Holm and E. I. Solomon, eds., *Chem. Rev.* 1996, **96**(7), Bioinorganic Enzymology Thematic Issue, 2237.
2. J. Reedijk, E. Bouwman eds., ‘Bioinorganic Catalysis’, Marcel Dekker, New York, 1999.
3. H. H. Thorp, V. L. Pecoraro eds., ‘Mechanistic Bioinorganic Chemistry’, American Chemical Society, Washington, DC, 1995, Advances in Chemistry Series Vol. 246.
4. G. Q. Li and R. Govind, *Ind. Eng. Chem. Res.*, 1994, **33**, 755.
5. L. I. Simándi ed., ‘Advances in Catalytic Activation of Dioxygen by Metal Complexes’, Kluwer, London, 2003, Catalysis by Metal Complexes Vol. 26.
6. B. Meunier ed., ‘Metal-oxo and Metal-peroxo Species in Catalytic Oxidations’, Springer, New York, 2000, Structure and Bonding Vol. 97.
7. A. Mills, *Platinum Metals Rev.*, 1997, **41**, 115.
8. F. C. Anson, C. Shi, and B. Steiger, *Acc. Chem. Res.*, 1997, **30**, 437.
9. A. Werner and A. Mylius, *Z. Anorg. Chem.*, 1898, **16**, 245.
10. L. Pauling and C. D. Coryell, *Proc. Natl. Acad. Sci. U.S.A.*, 1936, **22**, 210.
11. S. J. La Placa and J. A. Ibers, *J. Am. Chem. Soc.*, 1965, **87**, 2581.
12. I. M. Klotz and D. M. Kurtz Jr, eds., *Chem. Rev.* 1994, **94**(3), Metal-Dioxygen Complexes Thematic Issue, 567.
13. D. Schröder and H. Schwarz, ‘Essays in Contemporary Chemistry: From Moleculas Structure towards Biology’, eds. G. Quinkert and M. Volkan Kisakürek, VHCA, Zürich, Wiley/VCH, Weinheim, 2001, p. 131.
14. M. C. DeRosa and R. J. Crutchley, *Coord. Chem. Rev.*, 2002, **233–234**, 351.
15. L. Vaska, *Acc. Chem. Res.*, 1976, **9**, 175.
16. M. Akita and Y. Moro-oka, *Catal. Today*, 1998, **44**, 183.
17. P. L. Holland and W. B. Tolman, *Coord. Chem. Rev.*, 1999, **190–192**, 855.
18. C. Bianchini and R. W. Zoellner, *Adv. Inorg. Chem.*, 1997, **44**, 263.
19. R. S. Gall, J. F. Rogers, W. P. Schaefer, and G. G. Christoph, *J. Am. Chem. Soc.*, 1976, **98**, 5135.
20. A. Bakac and I. A. Guzei, *Inorg. Chem.*, 2000, **39**, 736.
21. M. Harata, K. Jitsukawa, H. Masuda, and H. Einaga, *J. Am. Chem. Soc.*, 1994, **116**, 10817.
22. X. Zhang, G. R. Loppnow, R. McDonald, and J. Takats, *J. Am. Chem. Soc.*, 1995, **117**, 7828.

23. S. Hikichi, M. Akita, and Y. Moro-oka, *Coord. Chem. Rev.*, 2000, **198**, 61.
24. K. Qin, C. D. Incarvito, A. L. Rheingold, and K. H. Theopold, *Angew. Chem., Int. Ed.*, 2002, **41**, 2333.
25. H. Kelm and H.-J. Krüger, *Angew. Chem., Int. Ed.*, 2001, **40**, 2344.
26. D. C. Hrncir, R. D. Rogers, and J. L. Atwood, *J. Am. Chem. Soc.*, 1981, **103**, 4277.
27. K. Shiren, S. Ogo, S. Fujinami, H. Hayashi, M. Suzuki, A. Uehara, Y. Watanabe, and Y. Moro-oka, *J. Am. Chem. Soc.*, 2000, **122**, 254.
28. S. Fallab and P. R. Mitchell, *Adv. Inorg. Bioinorg. Mech.*, 1984, **3**, 311.
29. M. J. Nolte, E. Singleton, and M. Laing, *J. Am. Chem. Soc.*, 1975, **97**, 6396.
30. T. Chishiro, Y. Shimazaki, F. Tani, Y. Tachi, Y. Naruta, S. Karasawa, S. Hayami, and Y. Maeda, *Angew. Chem., Int. Ed.*, 2003, **42**, 2788.
31. B. D. Dunietz, M. D. Beachy, Y. Cao, D. A. Whittington, S. J. Lippard, and R. A. Friesner, *J. Am. Chem. Soc.*, 2000, **122**, 2828.
32. M. Suzuki, H. Furutachi, and H. Okawa, *Coord. Chem. Rev.*, 2000, **200–202**, 105.
33. J. Xiao, B. D. Santarsiero, B. A. Vaartstra, and M. Cowie, *J. Am. Chem. Soc.*, 1993, **115**, 3212.
34. N. Kitajima and W. B. Tolman, *Prog. Inorg. Chem*, 1995, **43**, 419.
35. S. Itoh and S. Fukuzumi, *Bull. Chem. Soc. Jpn.*, 2002, **75**, 2081.
36. W. B. Tolman, L. Que Jr., *J. Chem. Soc., Dalton Trans.* 2002, 653.
37. A. E. Lapshin, Yu. I. Smolin, Yu. F. Shepelev, P. Schwendt, and D. Gyepesova, *Acta Crystallogr.*, 1990, **C46**, 1753.
38. R. Stomberg, L. Trysberg, and I. Larking, *Acta Chem. Scand.*, 1970, **24**, 2678.
39. S. Schindler, *Eur. J. Inorg. Chem.*, 2000, **2000**, 2311.

Electrochemistry: Applications in Inorganic Chemistry

H. Holden Thorp
University of North Carolina at Chapel Hill, Chapel Hill, NC, USA

Based in part on the article Electrochemistry: Applications in Inorganic Chemistry by Robert H. Crabtree which appeared in the Encyclopedia of Inorganic Chemistry, First Edition.

---

1 Introduction 1374
2 Fundamentals of Cyclic Voltammetry 1375
3 Computation of Redox Potentials in Solution 1376
4 Digital Simulation 1376
5 Molecular Electronics 1377
6 Related Articles 1377
7 References 1379

Abbreviations

E_p^{red} = Peak potential for reductive peak in cyclic voltammetry; E_p^{ox} = Peak potential for oxidative peak in cyclic voltammetry; I_p^{red} = Peak current for reductive peak in cyclic voltammetry; I_p^{ox} = Peak current for oxidative peak in cyclic voltammetry; $E_{1/2}$ = Average of E_p^{ox} and E_p^{red}; n = Number of electrons transferred for a particular voltammetric wave; A = Electrode area (in cm^2); D = Diffusion coefficient of redox analyte; ν = Scan rate; C = Bulk concentration; DFT = Density functional theory; bpy = 2,2′-bipyridine; dppz = Dipyridophenazine.

---

1 INTRODUCTION

Electrochemical methods are useful for the study of transition metal complexes because many electrochemical techniques, particularly voltammetric methods, provide information on both the energetics of redox reactions and the kinetics of electron transfers and coupled homogeneous reactions.[1–3] Electrochemical methods have therefore seen considerable application in determining redox potentials of new complexes and in evaluating chemical mechanisms of reactions initiated by an electron transfer.[4] Such systems are conveniently studied using simple, affordable potentiostats, and solid electrodes in single or multi-compartment cells. As such, electrochemical methods are generally part of the experimental repertoire of inorganic researchers (*see* ***Analytical Chemistry of the Transition Elements***).

The practice of electrochemistry by most inorganic chemists involves the use of techniques where current is measured as a function of applied potential. Generally referred to as 'voltammetric' methods, these approaches offer rich kinetic and thermodynamic information.[5] The most common technique, cyclic voltammetry, involves the linear variation of the applied potential at a given scan rate (generally in mV s^{-1}). After reaching a predetermined switching potential, the potential is returned to the starting point at the same rate. A plot of the current versus the applied potential produces a cyclic voltammogram. Note that most modern, digital potentiostats vary the potential in discrete increments, so the proper name for cyclic voltammetry is therefore cyclic staircase voltammetry, a subtlety often ignored in the literature. There are other types of waveforms that can be used to vary the potential and that provide advantages in data interpretation.[6] The discussion here will be limited to cyclic voltammetry, since it remains the primary method by which inorganic complexes are studied.[4] The reader is encouraged to explore other pulsed voltammetric methods to complement cyclic voltammetry.[6]

2 FUNDAMENTALS OF CYCLIC VOLTAMMETRY

Numerous excellent texts exist on the fundamentals of cyclic voltammetry.[1–3] The reader is referred especially to the recent text by Bond,[2] which provides an excellent treatment of fundamentals as well as applications. The important aspects of cyclic voltammetry are illustrated by the diagram shown in Figure 1 of a typical voltammogram of a soluble, reversible couple subjected to a linear potential sweep (and return scan) between applied voltages E_1 and E_2. The characteristic curve shown in Figure 1 provides peak potentials (E_p^{red} and E_p^{ox}) as well as peak currents (I_p^{ox} and I_p^{red}). Note that the diagram in Figure 1 utilizes a convention for plotting currents and potentials that shows positive potentials on the right and oxidative current up; other conventions are often used.

The four values obtained from the voltammogram provide three important insights that are readily visible in the idealized voltammogram:

1. The splitting between the E_p^{ox} and E_p^{red} values is 56/n mV where n is the number of electrons transferred.
2. The midpoint potential, $E_{1/2}$, is the average of the E_p^{ox} and E_p^{red} values and is generally very similar to the formal potential (E°) for the redox couple (the formal potential is different from $E_{1/2}$ only when the oxidized and reduced forms of the complex have different diffusion coefficients).

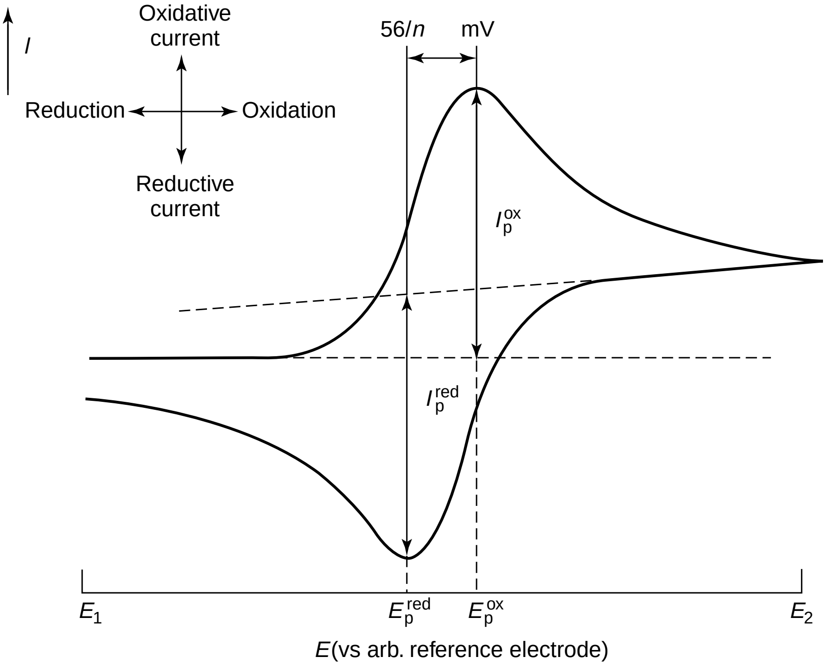

Figure 1 Typical cyclic voltammetric response. Indicated variables are described in the abbreviations section. (Reprinted from Ref. 2. © 1999, with permission from Elsevier)

3. The peak currents (I_p^{ox} and I_p^{red}) are equal for a reversible process, and at 25 °C are described by the Randles–Sevcik expression:

$$I_p^{ox} = -I_p^{red} = (2.69 \times 10^5)n^{3/2}AD^{1/2}\nu^{1/2}C \qquad (1)$$

where n is the number of electrons transferred, A is the electrode area (in cm^2), D is the diffusion coefficient of the oxidized form, ν is the scan rate (in $V\,s^{-1}$), and C is the bulk concentration of the oxidized form (in $mol\,cm^{-3}$).

Note that the conclusions derived above are for the idealized, reversible reaction and are subject to assumptions regarding kinetics, diffusion, and the presence of coupled chemical reactions.**[1–3]**

3 COMPUTATION OF REDOX POTENTIALS IN SOLUTION

Under appropriate conditions, analysis of cyclic voltammograms such as that shown in Figure 1 provide simple measures of the solution redox potentials of transition metal complexes, derived as $E_{1/2}$. Extensive tabulations of redox potentials are available,**[1,7]** and provide a key resource for inorganic chemistry. The correlation redox potentials with parameters such as ligand field strength, ligand hardness, and ionization energy of the transition metal forms an important theoretical framework for transition metal chemistry.

Recently, a number of efforts have sought to use new theoretical methods, particularly density functional theory (DFT), to predict redox potentials in solution. While considerable progress has been made toward predicting gas-phase ionization potentials,**[8]** the role of solvation and coupled chemical reactions are of high importance to solution chemists. Baik and Friesner have recently discussed the ability of new methods for incorporating solvation effects**[9]** into DFT calculations. Using these solvation methods, DFT calculations can be used to determine solution redox potentials to within 150 mV.**[10]**

3.1 Applications of Calculating Redox Potential

The ability to calculate redox potentials has powerful implications. For example, electrocatalytic reactions of metal complexes, such as $Ru(bpy)_3^{2+}$, with DNA nucleobases, such as guanine, provide a sensitive method for detection of nucleic acids on surfaces in electrochemical DNA chips (*see* ***Nucleic Acid–Metal Ion Interactions***).**[11,12]** In these reactions, voltammetric oxidation of $Ru(bpy)_3^{2+}$ to $Ru(bpy)_3^{3+}$ in the presence of guanine produces an enhancement in the oxidative current due to the reaction of Ru(III) with guanine (Figure 2).**[13]** On surfaces, the extent of electrocatalytic enhancement is indicative of the quantity of bound nucleic acid;**[14]** levels of DNA as low as 40 attomoles have been detected using related methods.**[15–17]**

One limitation of electrocatalytic detection for nucleic acid detection was its limitation to native guanine as an

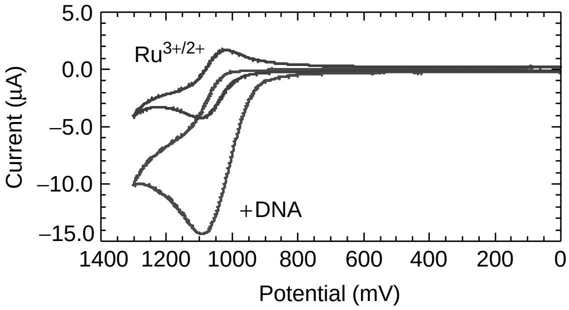

Figure 2 Cyclic voltammograms showing the response of $Ru(bpy)_3^{2+}$ both without and with DNA. The current enhancement in the presence of DNA arises from the catalytic oxidation of guanine by Ru(III) according to equations (2) and (3)

oxidizable nucleobase. The use of DFT calculations with modern solvation corrections was applied to the determination of solution redox potentials for a variety of native and synthetic nucleobases.[18] In addition to treating the solvation, reliable calculation of the redox potentials also required inclusion of deprotonation of the nucleobase radical (equation 3)[19,20] following oxidation:

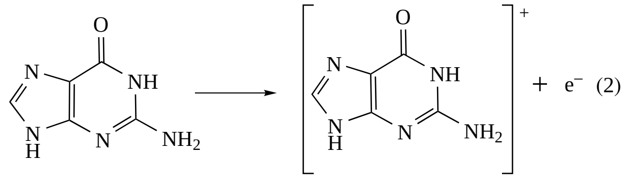

(2)

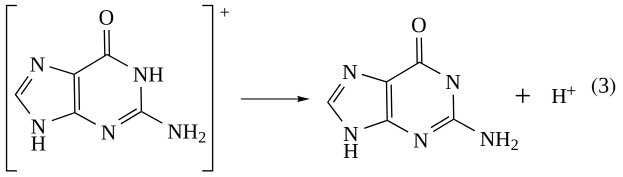

(3)

The inclusion of the solvation correction therefore led to two important insights. The first is on the role of the deprotonation in the electrocatalytic process.[19,20] The second was to modified nucleobases useful in sophisticated and sensitive schemes for nucleic acid detection.[15]

4 DIGITAL SIMULATION

Another key computational advance in electrochemistry has been the development of convenient programs for simulating voltammetric responses.[5,6] Such programs, which can be run on conventional personal computers, allow for determination of fundamental electrochemical parameters and reaction rates for coupled chemical reactions. Because of the prevalence of cyclic voltammetry, the majority of such applications are performed using DigiSim,[5] which calculates cyclic voltammetric responses. However, simulation packages are also available for pulsed voltammetry, which provide a useful complement.[6]

One of the earliest applications of digital simulation to inorganic chemistry was for analysis of isomerization of $CpCo(1,3\text{-}C_8H_8)$ to $CpCo(1,5\text{-}C_8H_8)$, which proceeds via a simple square scheme (Figure 3).[21] Because the 1,3 and 1,5 isomers have different $E_{1/2}$ values (−2.27 V and −2.51 V, respectively), resolution of the two species in voltammetric curves is possible. Variation of the scan rate produces different currents for the electrogenerated species based on

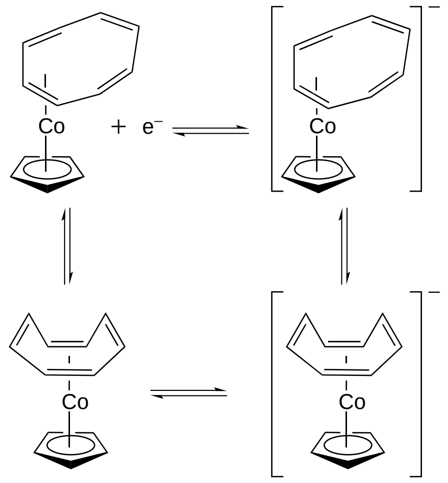

Figure 3 Isomerization of $CpCo(1,3\text{-}C_8H_8)$[21]

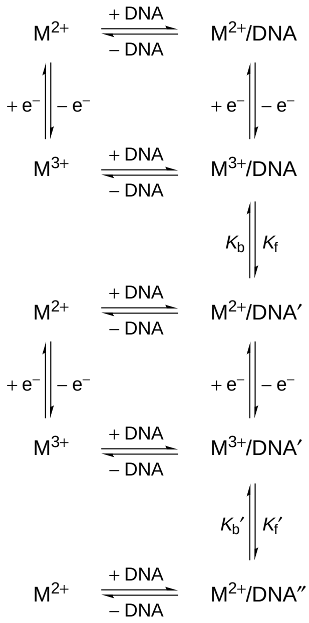

Figure 4 Multiple square schemes for electrocatalytic oxidation of DNA by $M(bpy)_3^{3+/2+}$ couples[24]

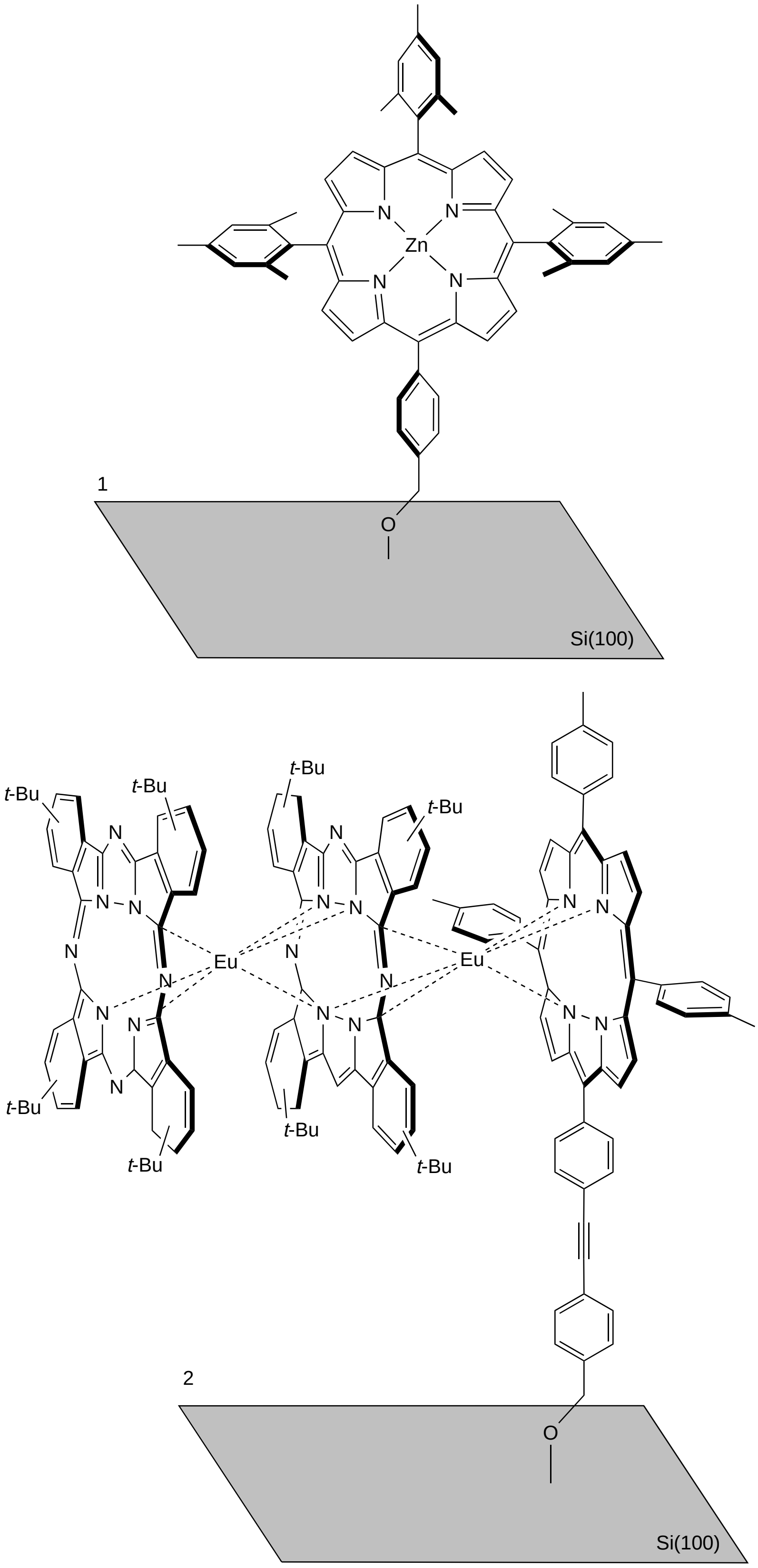
N
N
Zn
N
N
1
O
Si(100)
t-Bu
t-Bu
t-Bu
t-Bu
N
N
N
N
N
N
N
N
N
N
N
N
Eu
Eu
t-Bu
t-Bu
t-Bu
t-Bu
N
N
N
N
2
O
Si(100)

Figure 5 Remarkably stable porphyrin complexes for use in molecular electronics[34]

the time available for isomerization during the sweep. By simulating the generated curves using the input square scheme (Figure 3), characteristic voltammograms can be obtained. Simulation requires input of the fundamental electrochemical parameters as well as the equilibrium and rate constants for the isomerizations.**[21]** Similar applications to metal complex reactions are now routine using the DigiSim package have been performed, for example, on coupled proton-electron transfers in polyoxometallates (*see* ***Polyoxometalates***)**[22]** and on organometallic isomerizations (*see* ***Electronic Structure of Organometallic Compounds***).**[22]**

Digital simulations have been applied to numerous aspects of the oxidation of nucleic acids by polypyridyl complexes. The mechanistic scheme needed for such analysis is shown in Figure 4. In addition to the fundamental electrochemical parameters for the metal complex ($M^{3+/2+}$), numerous other parameters are required. The first is the diffusion coefficient of the DNA. These were determined by simulation of the normal pulse voltammetry of strongly binding metal complexes, such as $Os(bpy)_2(dppz)^{2+}$.**[23]** For more weakly binding complexes, which effect more efficient electrocatalysis, binding constants for each complex to DNA (the horizontal reactions in Figure 4) were also required (*see* ***Nucleic Acid–Metal Ion Interactions***).**[24]** With these parameters in hand, it was possible to determine the electron transfer rate constants (k_f, k_b) for oxidation of guanine by the bound metal, which were determined independently by stopped-flow analysis and compared favorably with values determined by simulation of cyclic voltammograms or square-wave voltammetry.**[13]** This methodology has since been applied to DNA oxidation using a number of complex systems, including high-viscosity solutions,**[25]** guanine tetrads,**[26]** and heterobinuclear complexes.**[27]**

5 MOLECULAR ELECTRONICS

The notion of using molecules as storage centers for electronic memory is seductive.**[28–30]** Use of molecules in memory clearly allows for extraordinary miniaturization, thereby permitting a high density of information storage.**[31]** Because of their capacity to store multiple electrons (bits) and to exhibit diverse stereochemistries, metal complexes are of particular interest.**[32,33]** One feature needed for a practical molecular memory is the ability of the redox functionality to sustain multiple read–write cycles, that is, to withstand multiple oxidations and reductions without decomposition. Such a consideration is a concern for metal complexes that are typically more stable in one redox form compared to the others.

Certain porphyrin complexes have been shown to be remarkably stable to redox cycling. The Zn and Eu complexes shown in Figure 5, can be attached to device-grade silicon surfaces and exhibit two or four reversible redox waves, respectively.**[34]** Remarkably, these systems are stable over as many as 10^{12} redox cycles, making them particularly suitable for stable storage devices.

6 RELATED ARTICLES

Electron Transfer in Coordination Compounds; Electron Transfer Reactions: Theory.

7 REFERENCES

1. A. J. Bard and L. R. Faulkner, 'Electrochemical Methods', John Wiley & Sons, New York, 1980.
2. A. M. Bond, 'Broadening Electrochemical Horizons: Principles and Illustration of Voltammetric and Related Techniques', Oxford University Press, Oxford, 2002.
3. D. Astruc, 'Electron Transfer and Radical Processes in Transition-Metal Complexes', VCH, New York, 1995.
4. A. A. Vlcek, *Coord. Chem. Rev.*, 2000, **200–202**, 979.
5. M. Rudolph, D. P. Reddy, and S. W. Feldberg, *Anal. Chem.*, 1994, **66**, 589a.
6. J. Osteryoung, *Acc. Chem. Res.*, 1993, **26**, 77.
7. A. J. Bard, R. Parsons, and J. Jordan, 'Standard Potentials in Aqueous Solution', Marcel Dekker, New York, 1985.
8. A. D. Becke, *J. Chem. Phys.*, 1993, **98**, 5648.
9. M. Friedrichs, R. H. Zhou, S. R. Edinger, and R. A. Friesner, *J. Phys. Chem. B*, 1999, **103**, 3057.
10. M.-H. Baik and R. A. Friesner, *J. Phys. Chem. A*, 2002, **106**, 7407.
11. N. Popovich and H. H. Thorp, *Interface*, 2002, **11**, 30.
12. M. J. Tarlov and A. B. Steel, in 'Biomolecular Films: Design, Function, and Applications', ed. J. F. Rusling, Marcel Dekker, New York, 2003, p. 545.
13. D. H. Johnston, K. C. Glasgow, and H. H. Thorp, *J. Am. Chem. Soc.*, 1995, **117**, 8933.
14. M. E. Napier and H. H. Thorp, *Langmuir*, 1997, **13**, 6342.
15. M. S. Gore, V. A. Szalai, P. A. Ropp, I. V. Yang, J. S. Silverman, and H. H. Thorp, *Anal. Chem.*, 2003, **75**, 6586.
16. P. M. Armistead and H. H. Thorp, *Anal. Chem.*, 2000, **72**, 3764.
17. L. Dennany, R. J. Forster, and J. F. Rusling, *J. Am. Chem. Soc.*, 2003, **125**, 5213.
18. M.-H. Baik, J. S. Silverman, I. V. Yang, P. A. Ropp, V. A. Szalai, W. Yang, and H. H. Thorp, *J. Phys. Chem. B*, 2001, **105**, 6537.
19. S. C. Weatherly, I. V. Yang, P. M. Armistead, and H. H. Thorp, *J. Phys. Chem. B*, 2003, **107**, 372.
20. S. C. Weatherly, I. V. Yang, and H. H. Thorp, *J. Am. Chem. Soc.*, 2001, **123**, 1236.

21. T. C. Richards and W. E. Geiger, *J. Am. Chem. Soc.*, 1994, **116**, 2028.
22. P. D. Prenzler, C. Boskovic, A. M. Bond, and A. G. Wedd, *Anal. Chem.*, 1999, **71**, 3650.
23. T. W. Welch, A. H. Corbett, and H. H. Thorp, *J. Phys. Chem.*, 1995, **99**, 11757.
24. T. W. Welch and H. H. Thorp, *J. Phys. Chem.*, 1996, **100**, 13829.
25. V. A. Szalai, J. Jayawickamarajah, and H. H. Thorp, *J. Phys. Chem. B*, 2002, **106**, 709.
26. V. A. Szalai and H. H. Thorp, *J. Am. Chem. Soc.*, 2000, **122**, 4524.
27. R. C. Holmberg and H. H. Thorp, *Anal. Chem.*, 2003, **75**, 1851.
28. A. Aviram and M. A. Ratner, *Chem. Phys. Lett.*, 1974, **29**, 277.
29. J. J. Hopfield, J. N. Onuchic, and D. N. Beratan, *Science*, 1988, **241**, 817.
30. M. J. Natan and M. S. Wrighton, *Prog. Inorg. Chem.*, 1989, **37**, 391.
31. J. R. Heath and M. A. Ratner, *Phys. Today*, 2003, **56**, 43.
32. W. Liang, M. P. Shores, M. Bockrath, J. R. Long, and H. Park, *Nature*, 2002, **417**, 725.
33. J. Park, A. N. Pasupathy, J. I. Goldsmith, C. Chang, Y. Yaish, J. R. Petta, M. Rinkoski, J. P. Sethna, H. D. Abruna, P. L. McEuen, and D. C. Ralph, *Nature*, 2002, **417**, 722.
34. Z. Liu, A. A. Yasseri, J. L. Lindsey, and D. F. Bocian, *Science*, 2003, **302**, 1543.

Electron Transfer in Coordination Compounds

John F. Endicott
Wayne State University, Detroit, MI, USA

1 Introduction 1
2 Electron-transfer Reaction Classes and Some Definitions 2
3 Experimental Techniques 3
4 Basic Concepts and Some Perturbation Theory-based Relationships of Electron-transfer Parameters 5
5 Experimental Observations at the Weakly-coupled Limit 12
6 Strongly Coupled, Bridged Electron-transfer Systems 15
7 Extensions and Applications 18
8 Related Articles 19
9 References 19

Abbreviations

bpy = 2,2′-Bipyridine; cp = Cyclopentadienyl; LMCT = Ligand to metal charge transfer; MLCT = Metal to ligand charge transfer; MMCT = Metal-to-metal charge transfer; SHO = Simple harmonic oscillator; N_4 = Tetraaza-macrocyclic ligand; S_4 = Tetrathiaether macrocyclic ligand.

1 INTRODUCTION

The transfer of a single electron between two chemical entities is the simplest of oxidation-reduction processes, but it is of central importance in vast areas of chemistry. Electron transfer processes constitute the fundamental steps in biological utilization of oxygen, in electrical conductivity, in oxidation–reduction reactions of organic and inorganic substrates, in many catalytic processes, in the transduction of the sun's energy by plants and by synthetic solar cells, and so on. The breadth and complexity of the subject is evident from the five volume handbook *Electron Transfer in Chemistry* (V. Balzani, Ed.),[1] published in 2001. The most fundamental principles that govern the efficiencies, the yields or the rates of electron-transfer processes are independent of the nature of the substrates. The properties of the substrates do dictate the conditions for applicability of those fundamental principles: that is, the boundary conditions and limiting forms of the theoretical models most suitable for the description of the electron-transfer processes vary from one area to another. Transition metal complexes have several unique features that must be considered in accounting for their patterns of electron-transfer reactivity; for example: (1) one-electron oxidation and reduction processes of nonradical species are commonplace; (2) one-electron oxidation and one-electron reduction of the complexes can occur at relatively mild potentials; (3) these complexes can have several electronic states with energies relatively near to those of the reacting species; (4) the number of electronic states and the energy differences between them can vary with changes of coordination sphere geometry and ligation; (5) the transition metal reaction centers can be shielded from the environment by the ligands, or the ligands may permit only a limited range of specific, molecular level reaction pathways. These properties contribute to the importance of transition metal electron-transfer processes in biological and catalytic systems, but they can lead to very complex models, or to models that are useful for one type of system that appear to be vastly different from those most useful for another. This article emphasizes the most basic, common features of electron-transfer reactions in coordination complexes. The modifications necessary to adapt standard approaches to electron-transfer reactivity to the specific requirements of selected, different reaction classes is noted.

The transfer of a single electron from one transition metal center to another is appropriately described as a nonradiative electronic relaxation process during which the locus of electron density is changed from a molecular orbital (MO) largely localized at a donor center in the initial state to a MO that is largely localized at an acceptor center in the final state. In an idealized limit, the donor (D) and acceptor (A) centers are each single transition metals. The MOs appropriate for describing the highest occupied molecular orbital (HOMO) or the lowest unoccupied molecular orbital (LUMO) of most complexes involve some contributions from several atoms; this is most notably an issue in the systematic discussion of bridged D/A complexes. The 'correct' MO descriptions of electron-transfer reactants and products are important concerns in the discussion of many contemporary issues, particularly those involving D/A electronic coupling, the adiabaticity of reactions, the contributions of anharmonicities of the potential energy (PE) surfaces, and so on.[2,3] This article takes a largely phenomenological approach and emphasizes simple limiting models of electron-transfer reactivity rather than detailed MO treatments. Details of theoretical approaches can be found in books by Kuznetsov[4,5] or by Kuznetsov and Ulstrup,[6] or in specialist monographs such as the two volumes of *Advances in Chemical Physics*, edited by Jortner,[7] or the volume edited by Kornyshev, Tosi, and Ulstrup.[8] Other specialized monographs and special issues of journals, sometimes based on symposia, may be consulted for a broad range of electron-transfer topics,[9–15] on heterogeneous photochemical electron transfer,[16] on photochemical and radiation chemical methods for study of electron transfer,[17] and on biological and biophysical aspects of electron transfer.[18–20] A useful chapter by Meyer and Taube[21] describes the evolution of electron-transfer studies of coordination complexes and the experimental bases for distinguishing between classes of electron-transfer reactions. A more recent chapter by Endicott[22] integrates spectroscopic and kinetic studies in an overview of electron transfer issues and problems.

The material presented in this article is partly organized around some concepts whose basis is discussed in Section 3 below. Most of these concepts have evolved to describe reactions in homogeneous solutions, and this is the focus of most of this article. Extensions to gas-phase, solid-state, biological, and heterogeneous reactions are very briefly considered.

2 ELECTRON-TRANSFER REACTION CLASSES AND SOME DEFINITIONS

It is useful to separate the information about electron-transfer reactions into classes in order to make their discussion tractable and to highlight the important distinctions. Bimolecular electron-transfer reactions in solution have been traditionally separated into two classes: (1) outer-sphere reactions, in which there is no significant chemical bonding between the reactants in the transition state (as in equation 1; in aqueous solution); and (2) inner-sphere reactions, in which some ligand is bonded to both the oxidant and reductant in the transition state (as is inferred from equation 2; in aqueous solution).[21,23–25] The second order rate constant for reaction 2 is several orders of magnitude larger than that for reaction 1, but the interpretation of this rate advantage is somewhat complicated by differences in the free energy change during the electron-transfer step. Studies of the analogous reactions of cobalt(III) and low-spin cobalt(II) complexes in which the amine (or imine) ligands are linked together in a tetraaza-macrocyclic ring (N_4) have demonstrated that, in the limit that there is no free energy change ($\Delta G^\circ_{\mathrm{DA}}$) accompanying electron transfer, the halide-bridged inner-sphere pathway for this class of complexes has about a million-fold rate advantage ($k_{\mathrm{is}}/k_{\mathrm{os}} \sim 10^6$), equations (3) and (4).[26] The size of $k_{\mathrm{is}}/k_{\mathrm{os}}$ appears to vary with the electronic structure of the reactants. This dramatic contrast in reactivity could originate from: (1) enhanced coupling of the donor and acceptor electronic wavefunctions mediated by the bridging ligand in the transition state; (2) smaller displacements of nuclei for the inner-sphere than for the outer-sphere pathway (for example, there is no net change of charge of the complexes for the inner-sphere reactions and one would expect a smaller solvent contribution to the activation energy); or (3) some combination of these. The role (or roles) of bridging ligands in mediating electron-transfer processes has been a major concern of the studies of electron-transfer processes.

$$\mathrm{Co(NH_3)_6}^{3+} + \mathrm{Cr(OH_2)_6}^{2+} + 6\mathrm{H}^+ \longrightarrow \mathrm{Co(OH_2)_6}^{2+} + \mathrm{Cr(OH_2)_6}^{3+} + 6\mathrm{NH_4}^+ \tag{1}$$

$$\mathrm{Co(NH_3)_5Cl}^{2+} + \mathrm{Cr(OH_2)_6}^{2+} + 5\mathrm{H}^+ \longrightarrow \mathrm{Co(OH_2)_6}^{2+} + \mathrm{Cr(OH_2)_5Cl}^{2+} + 5\mathrm{NH_4}^+ \tag{2}$$

$$\mathrm{Co(N_4)(OH_2)_2}^{3+} + \mathrm{Co({}^*N_4)(OH_2)_2}^{2+} \longrightarrow \mathrm{Co(N_4)(OH_2)_2}^{2+} + \mathrm{Co({}^*N_4)(OH_2)_2}^{3+} \tag{3}$$

$$\mathrm{Co(N_4)(OH_2)Cl}^{2+} + \mathrm{Co({}^*N_4)(OH_2)_2}^{2+} \longrightarrow \mathrm{Co(N_4)(OH_2)_2}^{2+} + \mathrm{Co({}^*N_4)(OH_2)Cl}^{2+} \tag{4}$$

The outer-sphere/inner-sphere classification is operationally useful in the context of bimolecular reactions, but it does not help much with the full range of electron-transfer behavior that has evolved over the past several decades. The definition of useful, general reaction classes for complexes in which the donor and acceptor are covalently linked is particularly difficult. Several classification schemes have been proposed.[21,22,27]

It is probably necessary to make a primary operational distinction of reaction classes based on the phase (or phases) of matter involved; thus: (1) homogeneous, liquid phase; (2) gas phase; (3) solid phase; (4) heterogeneous. A basic subclassification distinguishes between reactions in which the reactants are chemically different from the products, as in equations (1) and (2), and reactions in which the reactants and products involve the same chemical species, as in equations (3) and (4) when $(N_4) = ({}^*N_4)$. Equations (1) and (2) are examples of cross electron-transfer reactions (or cross-reactions), while equations (3) and (4) are examples of self-exchange electron-transfer reactions when $(N_4) = ({}^*N_4)$. More generally, subclassifications of the primary classes are commonly based on energy or free energy considerations such as:

a. Whether the reactions are activated by thermal or light energy.
b. Whether the standard free energy of the electron-transfer step, $\Delta G^\circ_{\mathrm{DA}}$, is different from zero (as in equations (1) and (2)) or equal to zero (as in equations (3) and (4) when $(N_4) = ({}^*N_4)$).
c. Whether the magnitude of $\Delta G^\circ_{\mathrm{DA}}$ is smaller than that of the reorganizational free energy, χ_r, (the 'Marcus normal region'), or whether $|\Delta G^\circ_{\mathrm{DA}}| > |\chi_r|$ (the 'Marcus inverted region').[28–30]

Classifications based on energy (or free energy) considerations are very fundamental and useful.

Classification can also be based on potential applications (devices, enzymatic reactions, etc.).

The principle focus of this article is on electron transfer between transition metal complexes in homogeneous liquid phase solutions. These span a very large range of energy regimes. It is frequently useful to distinguish between those electron-transfer processes that are 'weakly coupled' and those that are 'strongly coupled' based on the extent of mixing (or overlap) of the electronic orbitals of the donor and acceptor centers. The weaklycoupled classification includes most of the classical outer-sphere electron-transfer reactions, but it also includes many electron-transfer reactions of covalently linked complexes, many electron transport reactions of biological substrates, and so on. In the limit that the mixing of the donor and acceptor wave functions goes to zero, the interactions between donor and acceptor are called 'diabatic' (the term 'nonadiabatic' is often used for this limit); when the mixing is significant, the reactions are called 'adiabatic'. The simplest, basic theoretical models of electron-transfer processes are technically correct only for the diabatic limit. The reactions in this limit are described in terms of simple harmonic oscillator (sho) models of the nuclear motions that accompany the transfer of charge, and this leads to the well-known parabolic PE surfaces to describe the reactant and product states (the dashed-line curves in Figure 1). The models employed in the weakly coupled limit may be referred to as classical (e.g. the Marcus theory),[28,29,31,32] semiclassical[32,33] or quantum-mechanical,[34,35] but they are little modified from the limiting sho models. In the strongly coupled limit, the electron-transfer reactions are strongly adiabatic, and the theoretical sho descriptions of the reaction coordinate must be corrected, usually by means of perturbation theory, or completely new theoretical models developed. These concepts are conveniently illustrated with respect to a semiclassical expression for the bimolecular rate constant (equation 5).[32]

$$k_{\mathrm{et}}(b) = K_{\mathrm{A}}\kappa_{\mathrm{el}}\nu_{\mathrm{nu}}\kappa_{\mathrm{nu}} = K_{\mathrm{A}}k_{\mathrm{et}} \tag{5}$$

In equation (5), K_{A} is the equilibrium constant for the outer-sphere association of the donor and acceptor, κ_{el} is the electronic transmission coefficient (the probability that products form once the nuclear configuration of the transition state is achieved), ν_{nu} is the effective frequency for nuclear motion along the reaction coordinate in the neighborhood of the transition state, and the nuclear transmission coefficient κ_{nu} is the classical exponential function of the activation energy. The weak-coupling limit corresponds to the limit in which $\kappa_{\mathrm{el}} < 1$, and for the strong-coupling limit $\kappa_{\mathrm{el}} = 1$.

When the donor and acceptor are sufficiently close, as in an ion pair or in covalently linked complexes, electron transfer can be promoted by the absorption of light. An absorption band corresponding to the light induced electron transfer is usually called a 'charge transfer (CT) absorption band'. The molecular parameters that determine the CT absorptivity, bandwidth, and band shape are the same molecular parameters that determine the magnitude of the electron-transfer rate constant.[31,36,37] In the weak-coupling limit, the absorptivity of the CT absorption band is small (much less than $10^3\ \mathrm{M}^{-1}\ \mathrm{cm}^{-1}$); in the strong-coupling limit, the absorptivity of the CT absorption band is large (greater than, or equal to $10^3\ \mathrm{M}^{-1}\ \mathrm{cm}^{-1}$).

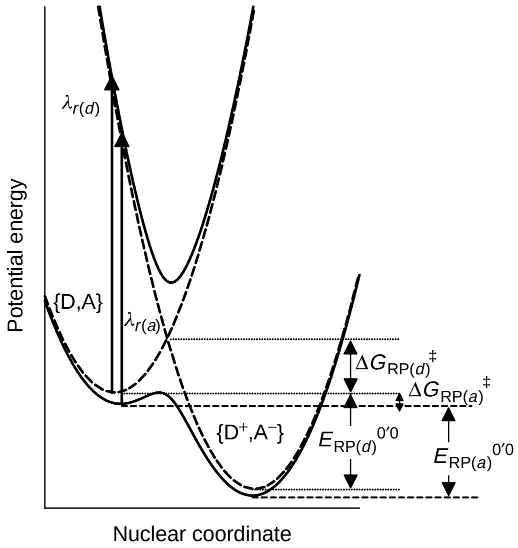
Potential energy
$\lambda_{r(d)}$
{D,A}
$\lambda_{r(a)}$
$\Delta G_{\mathrm{RP}(d)}{}^{\ddagger}$
$\Delta G_{\mathrm{RP}(a)}{}^{\ddagger}$
{D$^+$,A$^-$}
$E_{\mathrm{RP}(d)}{}^{0'0}$
$E_{\mathrm{RP}(a)}{}^{0'0}$
Nuclear coordinate

Figure 1 Illustrating diabatic (dashed lines) and adiabatic (solid lines) PE surfaces. The diabatic parameters are indicated with a subscript (d), the adiabatic parameters with a subscript (a)

3 EXPERIMENTAL TECHNIQUES

A large variety of experimental techniques is employed in the study of electron transfer phenomena. The technique employed depends on the type of substrate, the class of reaction and the aspect of electron-transfer behavior to be investigated. Only a brief summary is possible here. More detailed discussions may be found elsewhere.[1,17,38–41] The experimental techniques are organized in terms of the parameter to be measured in order to simplify discussion.

3.1 Rate Constant Determinations

The determination of reaction rate constants for cross-reactions is based on the time rate of change of concentration of a reactant and/or product (equation 6).

$$\mathrm{Rate} = -\frac{d[\mathrm{D}]}{dt} = K_{\mathrm{A}}k_{\mathrm{et}}[\mathrm{D}][\mathrm{A}] \tag{6}$$

Any technique that is sensitive to one or another of the reactant or product species may be employed. For relatively slow reactions (reaction lifetimes longer than a few ms), simple spectrophotometric, electrochemical, magnetic resonance, and so on techniques may be employed. In order to make useful determinations, the time for mixing the reactants and the instrumental response time must both be short compared to the reaction half-life (for a bimolecular reaction, $t_{1/2} \cong 0.69/\{K_{\mathrm{A}}k_{\mathrm{et}}[\mathit{excess\ reactant}]\}$). Reactions with shorter lifetimes ($10^{-3}\ \mathrm{s} > t_{1/2} > 10^{-15}\ \mathrm{s}$) can often be determined by spectral line broadening techniques at equilibrium, or by the photochemical or pulse-radiolytic generation of reactants for reactions with large equilibrium constants.

3.2 The Experimental Determination of Values of the Reactant Properties that Contribute to the Efficiency of Electron-transfer

Some of the key properties were introduced above; all will be discussed in more detail below. Quantities related to reaction energetics may all be expressed in terms of energies, as in potential energy diagrams, or in terms of free energies, as in equilibrium constants and differences in electrode potentials. Energy and free energy quantities should not be casually mixed. The differences in these expressions of reaction energetics are discussed in a later section.

a. The free energy of the electron-transfer step, $\Delta G^\circ_{\mathrm{DA}}$ (or electron-transfer energy, $E^{0'0}_{\mathrm{DA}}$). The problems in determining this parameter are nicely illustrated by reactions 1 and 2. Equations (1) and (2) represent overall reactions, each comprised of several elementary reaction steps: Association of reactants; electron transfer; dissociation of products; ligand substitution (hydrolysis). For reaction 1, the primary steps are illustrated in equations (7) and (8) (the curly brackets designate a contact ion pair).

$$\mathrm{Co(NH_3)_6}^{3+} + \mathrm{Cr(OH_2)_6}^{2+} \overset{K_\mathrm{A}}{\rightleftharpoons} \{\mathrm{Co(NH_3)_6}^{3+}, \mathrm{Cr(OH_2)_6}^{2+}\} \tag{7}$$

$$\{\mathrm{Co(NH_3)_6}^{3+}, \mathrm{Cr(OH_2)_6}^{2+}\} \xrightarrow{k_\mathrm{et}} \{\mathrm{Co(NH_3)_6}^{2+}, \mathrm{Cr(OH_2)_6}^{3+}\} \tag{8}$$

The parameter $\Delta G^\circ_{\mathrm{DA}}$ pertains to the reaction described in equation (8). Owing to the substitutional lability of $\mathrm{Co(NH_3)_6}^{2+}$, this is not directly measureable. When the electron transfer is not followed by rapid bond breaking or ligand substitution, $\Delta G^\circ_{\mathrm{DA}}$ may be determined from measured differences in electrode potentials for the two couples involved; this would be the case for the reaction in equation (3).

For some reactions, it is possible to infer the energy change for the electron-transfer step, $E^{0'0}_{\mathrm{DA}}$, from the energy and bandwidth of the fundamental vibronic component of the CT absorption or emission band; see the discussion below.

b. The solvent reorganizational free energy, χ_s (or the solvent reorganizational energy, λ_r). The electron-transfer process described by equation (8) involves a substantial change in the spatial distribution of charge. The solvation of the reactant and product species must be very different (at the minima of the respective PE surfaces). However, energy conservation requires that electron transfer in the transition state be modeled as the movement of an electron between two electronic configurations whose potential energies are equal. Thus, the reactants, {D, A}, and products, $\{\mathrm{D}^+, \mathrm{A}^-\}$, are generally assumed to have the same solvation free energy (or energy) at the transition state (this assumption depends on the independence of nuclear motions with different vibrational frequencies). The difference between the equilibrium solvation free energy of the reactants and the solvation free energy in the transition state is generally a significant contribution to the free energy of activation (or the energy barrier to the reaction). The corresponding reorganizational energy (or free energy) parameters are defined with respect to vertical energy differences between the reactant and product states as illustrated in Figure 1. For an electron transfer self-exchange reaction in the weakly coupled limit and for no differences in the molecular structures of reactants and products, the solvent reorganizational free energy is given by $\chi_\mathrm{s} = 4\Delta G^\ddagger_{\mathrm{DA}} = -4RT\ \ln[k_\mathrm{et}/A]$ (A is the product of several preexponential factors, see discussion below). The solvent reorganizational energy, λ_s, can, in principle, be inferred from the full width at half height, $\Delta\nu_{1/2}$, of the fundamental vibronic component of the CT absorption or emission; for a Gaussian band shape and if there are no other contributions to bandwidth.[31]

$$\Delta\nu_{1/2} \cong 4[RT\lambda_\mathrm{s} \ln 2]^{1/2} \tag{9}$$

The solvent contribution to the reorganizational free energy should be distinguished from the solvent reorganizational energy; the relationship between them is

$$\chi_\mathrm{s} = \lambda_\mathrm{s} + RT - T\Delta S_\mathrm{r} \tag{10}$$

There can be other significant contributions to the optical bandwidths; important among these are those that arise when the absorption (or emission) is solvent dependent and there is a distribution of solvation environments in solution or when there is a contribution from the thermal population of vibrational excited states (‘hot bands’). Such contributions necessitate an additional term (or terms) in equation (9), so that, in practice, this equation provides an upper limit for λ_s.

c. The reorganizational energy associated with differences in molecular geometry, λ_M. Any differences in molecular geometry (changes in bond lengths, angles, etc.) between the reactants and the products will also contribute to the electron-transfer reorganizational energy, λ_r. The vibrational quanta that are associated with these changes span a very wide range of frequencies for transition metal complexes, and their reorganizational energy contributions are usually separated into low-frequency ($h\nu_{\mathrm{l,M}} < 4RT$) and high-frequency ($h\nu_{\mathrm{h,M}} \geq 4RT$) vibrations. The contributions of low-frequency, molecular vibrational modes to λ_r are not usually distinguishable from the solvent contributions and they are combined into $\lambda_l = \lambda_{l,M} + \lambda_s$. Thus, the CT bandwidths, as in equation (9), reflect contributions of λ_l, not just those of λ_s.

The contributions of the high frequency vibrational modes to λ_r, hereafter written λ_h, appear as nuclear tunneling contributions to k_{et}, and as vibronic side bands in CT spectroscopy. The intensity of a vibronic side band relative to the intensity of the fundamental component is equal to $\lambda_h/h\nu_h$.[42] If the high frequency components can be resolved in the emission spectra, then λ_h can be determined and the nuclear tunneling contributions to k_{et} can be evaluated for each such component.[34,35]

d. The preexponential nuclear frequency term. This parameter is not readily measurable. It is usually calculated, based on sho arguments, from[43]

$$\nu_{nu}^2 = \frac{{\nu_l}^2\lambda_l + {\nu_h}^2\lambda_h}{\lambda_l + \lambda_h} \tag{11}$$

e. Electronic contributions.[2,3] These are usually formulated in terms of an electronic matrix element, $H_{RP} = \langle\psi_R^\circ|H'|\psi_P^\circ\rangle$, where ψ_R° and ψ_P° are the electronic wave functions for the diabatic states of the reactants and products, respectively, and H' is a Hamiltonian operator.[44] Obviously, electronic wavefunctions are not measurable. The matrix element is probably most often inferred from the properties of the CT absorption; it is sometimes inferred by fitting the value determined experimentally for a rate constant to some theoretical model.

The matrix element can be inferred from the deviations of observed properties from those expected of the reacting system in the diabatic limit. The size of those deviations tends to increase as a function of the fraction of an electron that is delocalized between donor and acceptor, $(H_{RP}/E_{RP}^\circ)^2$, where E_{RP}° is the vertical energy difference between the diabatic reactants and products states; $H_{RP}/E_{RP}^\circ = \alpha_{RP}$ is the coefficient for mixing ψ_R° and ψ_P°.

$$\psi_R = \frac{(\psi_R^\circ + \alpha_{RP}\psi_P^\circ)}{(1 + {\alpha_{RP}}^2)^{1/2}} \tag{12}$$

There are problems with all of these approaches, and the evaluation of H_{RP} by means of some combination of measurements is usually a good idea. The integrated intensity of an electronic absorption band is a function of the matrix element. Equation (13) expresses this relationship for a Gaussian-shaped absorption band.[31,44]

$$H_{RP} = \frac{0.0206}{r_{RP}}\left[\frac{(\varepsilon_{max}\Delta\nu_{1/2})h\nu_{max}}{g_o}\right]^{1/2} \tag{13}$$

The parameters in equation (13) are the molar absorptivity at the absorption maximum (ε_{max}), the full width at half height ($\Delta\nu_{1/2}$), the energy of the absorption maximum ($h\nu_{max}$), an orbital degeneracy factor (g_o; this is important only in comparisons involving different open shell systems) and a distance parameter (r_{RP}). The distance parameter can be interpreted as the distance between the center of charge in the ground and in the excited state.[44] In the diabatic limit (zero absorptivity!), r_{RP} can be taken to be the distance between the centers of the donor and acceptor moieties; otherwise, it is smaller than this distance and not readily measurable. A less ambiguous approach to inferring the matrix element from electronic absorption spectroscopy is based on the electric field dependence of the spectrum (electroabsorption spectroscopy).[45] This approach allows the experimental determination of both the difference of the ground and excited state molecular dipole moments ($\Delta\mu_{RP}$) and the electronic transition moment (M_{RP}), and[3,45,46]

$$H_{RP} = \frac{\left|\vec{M}_{RP}\right|}{[4{M_{RP}}^2 + \Delta{\mu_{RP}}^2]^{1/2}} E_{RP} \tag{14}$$

The electroabsorption technique involves the measurement of the changes in absorption spectra that result when very large electric fields (typically tens of thousands of volts) are applied to glassy solutions at very low temperatures. It has been used primarily for covalently linked donor–acceptor complexes that are in the strongly coupled regime.[45]

4 BASIC CONCEPTS AND SOME PERTURBATION THEORY-BASED RELATIONSHIPS OF ELECTRON-TRANSFER PARAMETERS

Some basic aspects of electron-transfer theory are necessary for discussing the important issues and for organizing general information. Some of the important concepts have been introduced in the preceding sections, and more extensive discussions may be found elsewhere.[2,3,6–8,31,32,37,47–49]

4.1 The InterRelationship of the Fundamental Electron-transfer Parameters of Spectroscopy and Kinetics

Treatments of radiative and nonradiative electron-transfer processes are conveniently formulated in terms of the probability of changing the electronic configuration from that of the initial state to that of the final state, P_{RP}.[33,36,50]

$$P_{RP}(\nu_{obs}) \propto \frac{{H_{iRP}}^2 f(\nu_{eff})}{(4\pi\chi_s k_B T)^{1/2}}(FC)_r \tag{15}$$

$$(FC)_r = \sum_j F_{j,h}[e^{-(G_j)^2/4RT\chi_s}] \tag{16}$$

$$F_{j,h} = {S_h}^j \frac{[\exp(-S_h)]}{j!}$$

$$S_h = \frac{\lambda_h}{h\nu_h} \tag{17}$$

Equations (15–17) are based on sho models; $f(\nu_{\mathrm{eff}})$ is an algebraic function that is different for light absorption, light emission, and nonradiative relaxation; the solvent reorganizational free energy, χ_{s} (rather than the reorganizational energy, λ_{s}), is used for consistency with $\Delta G^{\circ}_{\mathrm{RP}}$, the high frequency contribution is usually evaluated in terms of an energy contribution; FC is a 'Franck–Condon factor'. This equation differs only in detail from the expression for k_{et}, equation (5). For simplicity, this equation is written in terms of a single high frequency vibrational mode (ν_{h}) and it treats only the limit that $\kappa_{\mathrm{el}} \ll 1$. The transition probability is exponential in G_{j}^2, where

$$G_{\mathrm{j}}(r) = \Delta G^{\circ}_{\mathrm{RP}} + \chi_{\mathrm{s}} + jh\nu_{\mathrm{h}} + rh\nu_{\mathrm{obsd}} \tag{18}$$

Light absorption, light emission, and nonradiative electron-transfer rate constants differ in the last term of equation (18) (as well as in $f(\nu_{\mathrm{eff}})$; note that $\Delta G^{\circ}_{\mathrm{RP}}$ is positive for light absorption and negative for emission).

$$\left.\begin{array}{l} \mathrm{r} = -1 \text{ (light absorption)} \\ \mathrm{r} = 0 \text{ (nonradiative)} \\ \mathrm{r} = +1 \text{ (light emission)} \end{array}\right\} \tag{19}$$

The exponential factor of FC dominates equation (15). This feature simplifies much of the discussion. This exponential function is in Gaussian form, and it is the basis for a Gaussian analysis of absorption or emission spectra.[36,50] Equations (15–18) provide the basis for analyzing the absorption or emission spectral envelope by considering some range of values of light frequencies (ν_{obsd}), but the nonradiative rate constant corresponds to the zero-photon limit.[34,36]

Equation (15) is the basis for equation (9) and several other important relationships for electron-transfer systems. For very weak electronic coupling and when high frequency modes do not contribute, the energy of the absorption maximum corresponds to the maximum value of this term (note that the nuclei do not move during the optical transition).

$$h\nu_{\mathrm{max}}(\mathrm{abs}) = E_{\mathrm{RP}}{}^{0'0} + \lambda_{\mathrm{s}} + \cdots = |\Delta G^{\circ}_{\mathrm{DA}}| + \chi_{\mathrm{s}} + \cdots \tag{20}$$

The emission maximum is given by

$$h\nu_{\mathrm{max}}(\mathrm{emis}) = |\Delta G^{\circ}_{\mathrm{DA}}| - \chi_{\mathrm{s}} + \cdots \tag{21}$$

The pressure-volume work (equal to RT) for an optical transition is zero, so $|\Delta G^{\circ}_{\mathrm{RP}}| = (E^{00}_{\mathrm{RP}} - T\Delta S^{\circ}_{\mathrm{RP}})$ and $\chi_{\mathrm{s}} = (\lambda_{\mathrm{s}} - T\Delta S_{\mathrm{r}})$. A necessary condition for the equality in equation (20) is that

$$\Delta S^{\circ}_{\mathrm{RP}} \cong -\Delta S_{\mathrm{r}} \tag{22}$$

Equation (22) indicates that the entropy contribution to the reorganizational free energy cannot be neglected. For the electron-transfer rate constant, the free energy of activation is $\Delta G^{\ddagger}_{\mathrm{RP}} = [G_{\mathrm{j}}(r=0)]^2/4\chi_{\mathrm{s}}$, and the entropy of activation is usually expressed as

$$-\Delta S^{\ddagger}_{\mathrm{RP}} = \frac{\partial(\Delta G^{\ddagger}_{\mathrm{RP}})}{\partial T} \cong \frac{1}{4}\gamma^2 \Delta S_{\mathrm{r}} \tag{23}$$

where $\gamma = (\Delta G^{\circ}_{\mathrm{RP}} + \chi_{\mathrm{s}})/\chi_{\mathrm{s}}$. Equation (23) is useful for cross-reactions, but it neglects other terms. This is most evident for a self-exchange reaction ($\Delta S^{\circ}_{\mathrm{RP}} = 0$) since the equal PE of reactants and products implies that the donor and acceptor are equally solvated; this implies an entropy increase ($\Delta\sigma$) for the difference in solvation of the transition state and ground-state (for a self-exchange reaction of +3 and +2 ions in water this amounts to approximately 4–8 $\mathrm{J\,K^{-1}\,M^{-1}}$). An additional contribution to equation (23), $Rln(g_{\mathrm{s}}^{\ddagger}/g_{\mathrm{s}})$, arises from any difference in the spatial degeneracy of the ground and transition state; for a self-exchange reaction this contributes about 0.6 $\mathrm{J\,K^{-1}\,M^{-1}}$. Differences in the densities of vibrational states will also contribute in cross electron-transfer reactions. The activation enthalpy is

$$\Delta H^{\dagger}_{\mathrm{RP}} = \left(\frac{\partial\left(\dfrac{\Delta G_{\mathrm{RP}}}{T}\right)}{\partial\left(\dfrac{1}{T}\right)}\right) = \frac{E_{\mathrm{RP}}{}^{00}}{2}\gamma + \frac{\lambda_{\mathrm{s}}}{4}[2-\gamma](\gamma) \tag{24}$$

When high frequency vibrational modes contribute to the difference in excited state and ground-state geometry, then the CT absorption (or emission) envelope will include a series of peaks (a vibronic progression), differing in intensity (an effect of F_{j}, an expression based on the vibrational overlap integral), but each with a bandwidth given by equation (9). For a single contributing high frequency vibrational mode, the energies of the maxima in the absorption and emission spectra (at $j = 0, 1, 2, \ldots$) are given by

$$h\nu_{\mathrm{max}}(\mathrm{abs})_{\mathrm{j}} = |\Delta G^{\circ}_{\mathrm{RP}}| + \chi_{\mathrm{s}} + jh\nu_{\mathrm{h}} \ldots \tag{25}$$

$$h\nu_{\mathrm{max}}(\mathrm{emis})_{\mathrm{j}} = |\Delta G^{\circ}_{\mathrm{RP}}| - \chi_{\mathrm{s}} - jh\nu_{\mathrm{h}} \ldots \tag{26}$$

The peaks of a vibronic progression will only be resolved when $2\Delta\nu_{1/2} < h\nu_{\mathrm{h}}$; when $2\Delta\nu_{1/2} > h\nu_{\mathrm{h}}$, the vibronic components will be unresolved, but the spectral band may not have a Gaussian shape.

The contribution of high frequency vibrational modes to k_{et} is determined by their Boltzman populations when $|\Delta G^{\circ}_{\mathrm{RP}}/\chi_{\mathrm{s}}| < 1$. In the Marcus inverted region, where $|\Delta G^{\circ}_{\mathrm{RP}}/\chi_{\mathrm{s}}| > 1$, any high frequency vibrational modes that correlate with differences in reactant and product geometries can act (qualitatively) as if they are transient reaction products (technically, as acceptor modes; this is an implication of equation (18)). If there are significant differences in reactant and product molecular geometries that correlate with modes for which $h\nu_{\mathrm{h}} > 4k_{\mathrm{B}}T$, then the rate constant in the normal region is small relative to expectation based on the classical limit of a continuum of vibrational energies (or to very efficient energy exchange between all molecular and solvent vibrational modes), and nuclear tunneling factors become important.[3,32] Most electron transfer process are characterized by contributions from several high frequency vibrational modes. When this is the case, equation (15) should include a sum over the single ($j = 1$) and multiquantum ($j > 1$) contributions of these modes (h). The multiquantum contributions are analogous to the higher harmonics of a single mode and combination bands (simultaneous excitation of different modes) in infrared spectra; each vibronic component has the same bandwidth as the fundamental, so this is not a product of individual vibronic progressions. Equation (15) has far more parameters than can be determined in ordinary kinetic studies, and other types of measurement generally must supplement the kinetic data in order to establish the details of the reaction pathway.

For light absorption, equation (15) can be put into the form of equation (27).[36,50,51]

$$\varepsilon_{\nu_m} = \frac{8N\pi^3}{3000h^2 c\nu_m \ln 10}\,\frac{\eta H_{\mathrm{RP}}^2(\Delta\mu_{\mathrm{RP}})^2}{(4\pi\chi_{\mathrm{s}} k_{\mathrm{B}} T)^{1/2}}(\mathrm{FC})_{\mathrm{r}=-1} \qquad (27)$$

Equation (27) (N = Avagadro's number; η = refractive index; c = velocity of light) implies that $\Delta\mu_{\mathrm{RP}}$ and H_{RP} are constant over the absorption band (Condon approximation). A closely related expression, equation (28), can be used for the emission intensity.

$$I_{\nu_m} = \frac{64\pi^4}{3h^3c^3 \ln 10}\,\frac{\nu_m \eta^3 H_{\mathrm{RP}}^2(\Delta\mu_{\mathrm{RP}})^2}{(4\pi\chi_{\mathrm{s}} k_{\mathrm{B}} T)^{1/2}}(\mathrm{FC})_{\mathrm{r}=+1} \qquad (28)$$

The related expression for the electron-transfer rate constant is[33–36,52–55]

$$k_{\mathrm{et}} = \frac{2\pi^2}{h}\,\frac{H_{\mathrm{RP}}^2}{(\pi\chi_{\mathrm{s}} k_{\mathrm{B}} T)^{1/2}}(\mathrm{FC})_{\mathrm{r}=0} \qquad (29)$$

Equation (29) is for the weakly coupled, $\kappa_{\mathrm{el}} < 1$, or 'nonadiabatic' limit of equation (5). The connection to equation (5) is made clear by setting $\kappa_{\mathrm{nu}} = (\mathrm{FC})$ and

$$\kappa_{\mathrm{el}} \cong \left[\frac{(1 + h\nu_{\mathrm{nu}}\{\pi\chi_{\mathrm{s}} k_{\mathrm{B}} T\}^{1/2})}{2\pi^2 H_{\mathrm{DA}}^2}\right]^{-1} = [1 + \nu_{\mathrm{nu}}/\nu_{\mathrm{el}}]^{-1} \qquad (30)$$

In equation (30), ν_{el} is the frequency of electronic motion across the reaction coordinate near the transition state. Other expressions for κ_{el} have been proposed, for example, based on Landau–Zener approaches.[3,32,49]

4.2 Contributions to (FC) in the Weak-Coupling Limit

The important Franck–Condon contributions to k_{et} are $\Delta G^{\circ}_{\mathrm{RP}}$, χ_{l} and χ_{h} (and ν_{h}). The high frequency vibrational contributions can be described in terms of nuclear tunneling pathways, and they are very important for reactions in the Marcus inverted region (i.e. when $-\Delta G^{\circ}_{\mathrm{RP}} > \chi_{\mathrm{l}}$).

The general patterns of the energy contributions to (FC) are more easily discussed than the entropy contributions, and the energy contributions will be emphasized here. Equations (15–18) and (29) predict a complex dependence of k_{et} on the reaction driving force. In the diabatic limit this corresponds to variations in the intersections of the reactants and products PE surfaces with the differences in their PE minima; this is illustrated in Figure 2 for the diabatic (a) and weak-coupling (b) limits.

Marcus described the solvent reorganizational energy (λ_{s}) that accompanies the transfer of a charge of magnitude e in terms of the repolarization of a dielectric continuum (with index of refraction η and static dielectric constant D_{s}) around two spherical reactants with radii a and b, separated a distance d_{DA}.[28,29,32]

$$\lambda_{\mathrm{s}} = \mathrm{e}^2\left(\frac{1}{2a} + \frac{1}{2b} - \frac{1}{d_{\mathrm{DA}}}\right)\left(\frac{1}{\eta^2} + \frac{1}{\mathrm{D_s}}\right) \qquad (31)$$

The slope of a plot of λ_{s} versus. a^{-1} is expected to be $31.9 \times 10^5\ \mathrm{cm^{-1}\,pm^{-1}}$ for self-exchange reactions (for which $a = b$ and $d_{\mathrm{DA}} = 2a$). Equation (31) is expected to give the general pattern for solvational contributions to the reorganizational free energy, but it does not take account of entropy, specific solvational effects, the effect

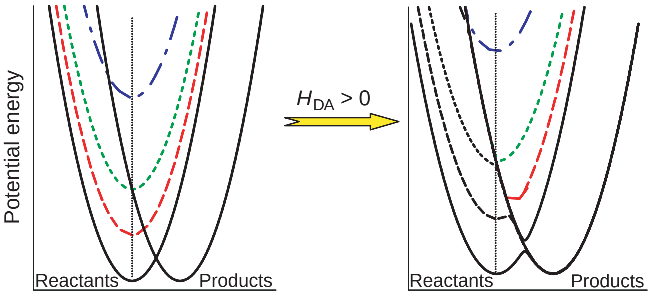

Nuclear coordinate.
(no configurational mixing)
(a)

Nuclear coordinate
(configurational mixing)
(b)

Figure 2 (a) Qualitative representation of the effects of differences in driving force on electron-transfer reactivity in the limit of no configurational mixing (diabatic limit): the black and red curves fall into the 'normal' region ($|\Delta G_{\mathrm{RP}}| < \chi_{\mathrm{r}}$); barrierless region ($|\Delta G_{\mathrm{RP}}| = \chi_{\mathrm{r}}$), green curve; and the 'inverted' region ($|\Delta G_{\mathrm{RP}}| > \chi_{\mathrm{r}}$), blue curve. The products curves are the same for each reaction represented. (b) Qualitative representation of the effects of configurational mixing on each of the cases considered in (a). The ground state (adiabatic reaction coordinate) is represented with a black curve for each different driving force; these curves all superimpose on the right-hand side for large displacements along the reaction coordinate. The electron-transfer excited states are color coded as in (a); these curves all superimpose on the left-hand side of the diabatic products parabola for small displacements along the reaction coordinate. The vertical dashed lines are drawn through the reactants PE minima of a nonspherical transition state or ambiguities about the donor–acceptor distance (see the discussion of equation 13).[56]

In the weak-coupling (sho) limit, the inner-sphere reorganizational contributions for a self-exchange reaction can be approximated by[28,29,32,43]

$$\lambda_{\mathrm{M}} = 2 \sum_{\mathrm{j}}^{\mathrm{bonds}} \frac{f_{\mathrm{D}(j)} f_{\mathrm{A}(j)}}{f_{\mathrm{D}(j)} + f_{\mathrm{A}(j)}} (\Delta d_{\mathrm{ML}(j)})^2 \tag{32}$$

The summation is over all bonds, the $f_{\mathrm{N(j)}}$ ($N = D$ or A) are local bond force constants (not normal mode force constants) for the j^{th} bond and $\Delta d_{\mathrm{ML(j)}}$ is the bond length difference of the j^{th} bond for the oxidant and reductant. When the molecular vibrational quanta are significantly smaller than 4RT, their contributions to λ_{M} will appear as contributions to λ_{l}, as noted above.

4.3 Contributions to (FC) in the Strong-Coupling Limit

Since the PE surfaces are anharmonic in this limit, the Franck–Condon contributions can be difficult to treat. The approaches to this limit can be separated into two classes: (a) perturbation theory corrections of the weak-coupling limit; and (b) quantum-mechanical calculations of the reaction coordinate. The latter tend to be done on a reaction-by-reaction basis; this makes it difficult to generalize. The perturbation theory approaches have the advantage that they make use of the parameters used in the weak-coupling limit, and this can provide useful insights into general trends and patterns.

In this limit, $\kappa_{\mathrm{el}} = 1$; however, configurational mixing of reactant and product PE surfaces results in a decrease of the activation free energy barrier to reaction and larger rate constants. When the distortions of the PE surfaces are not very large, the electron-transfer rate constant may be represented,

$$k_{\mathrm{et}} = \nu_{\mathrm{nu}} \kappa_{\mathrm{nu}} f_{\mathrm{ad}} \tag{33}$$

where $f_{\mathrm{ad}} > 1$ is an adiabatic correction factor and κ_{nu} is based the Franck–Condon factor for the weak-coupling limit. For a simple electron-transfer process $f_{\mathrm{ad}} \approx \exp[(H_{\mathrm{RP}} + \cdots)/RT]$, the higher order correction terms arise from the shifts of the adiabatic relative to the diabatic PE minima.

In the simplest model of the strong-coupling limit, one considers only the reactant and product electronic states; this is illustrated in Figures 1 and 2, and presumed in equation (33). This is a two state model, and two state models have been used extensively to describe electron-transfer systems.[57] In many strongly coupled electron-transfer systems, the donor and acceptor are linked by a bridging ligand, and the properties of the bridging ligand are very important in determining the extent of electronic mixing between D and A. In order to describe the systematic variations in the properties of such complexes, it is often necessary to consider the mixing of the donor with the bridging ligand, the acceptor with the bridging ligand and the effects of these configurational mixings on the overall D/A coupling.[22,58] When the relevant electronic features of the bridging ligand can be described in terms of a single electronic state (e.g. in terms of a single electron in the HOMO or in the LUMO of the ligand), then the appropriate model is a three-state model. If the bridging ligand electronic structure is best described in terms of several electronic states, then a correspondingly more complicated model may be used.

For the two state limit, assume that the minima of the diabatic PE surfaces differ in energy by $E_{\mathrm{RP}}(d)^{0'0}$ and that these minima are separated by an amount $x_{(d)}$ in some correlated nuclear coordinate. If the electronic matrix element that mixes the two states is H_{RP}, then the adiabatic energies of the electron-transfer states are the solutions of equation (34).

$$\begin{vmatrix} E^{0'0}_{\mathrm{RP}(d)} + \frac{1}{2} f (x - x_{(d)})^2 - \varepsilon & H_{\mathrm{RP}} \\ H_{\mathrm{RP}} & \frac{1}{2} f x^2 - \varepsilon \end{vmatrix} = 0 \tag{34}$$

If we set $\lambda_{r(d)} = 1/2 f (x_{(d)})^2$ and $y = (x/x_{(d)})$, then the solutions are given by equation (35),[59]

$$\begin{aligned} V^{\pm}(y) = {} & \frac{1}{2} E^{0'0}_{\mathrm{RP}(d)} + \lambda_{\mathrm{r}}^{\circ}(\frac{1}{2} - y + y^2) \\ & \pm \frac{1}{2}[(E^{0'0}_{\mathrm{RP}(d)} + \lambda_{r(d)} - 2\lambda_{r(d)} y)^2 + 4H_{\mathrm{RP}}^2]^{1/2} \end{aligned} \tag{35}$$

For $y = 0$ and $(E^{0'0}_{\mathrm{RP}(d)} + \lambda_{r(d)}) = E_{\mathrm{RP}}(d) \gg H_{\mathrm{RP}}$, one obtains for the upper surface[44]

$$V^{+}(x = 0) \cong E_{\mathrm{RP}(d)} + \frac{H_{\mathrm{RP}}^2}{E_{\mathrm{RP}(d)}} \tag{36}$$

and for the lower surface[44]

$$V^{-}(x = 0) = -\frac{H_{\mathrm{RP}}^2}{E_{\mathrm{RP}(d)}} = -\varepsilon_{\mathrm{RP}} \tag{37}$$

In addition to stabilization of the ground state and destabilization of the excited state (both by $\varepsilon_{\mathrm{RP}}$), the two state configurational mixing results in a shift of the reactants and products PE minima nearer to one another by approximately $2\alpha_{\mathrm{RP}}^2 x_{(d)}$. The correction for this shift results in small, higher order contributions to equations (36) and (37); when $E^{0'0}_{\mathrm{RP}}(d) = 0$, the vertical energy at the reactant PE minimum (the CT absorption maximum) is $h\nu_{\max}(CT, obsd) = \lambda_{r(d)}$. These energy relationships are illustrated in Figure 3.

Figure 1 illustrates the distortions of the PE surfaces that are characteristic of the strong-coupling limit; Figure 2(b) illustrates intermediate coupling. These distortions result in smaller reorganizational energies for this than for the diabatic ($H_{\mathrm{RP}} = 0$) limit. This effect can be estimated using the perturbation theory approach; thus, for $\alpha_{\mathrm{PR}} = H_{\mathrm{RP}}/E_{\mathrm{PR}}(d)$ ($E_{\mathrm{PR}}(d)$ is the vertical energy difference at the product PE minimum),[22,59–62]

$$\lambda_r \cong \lambda_{r(d)}[1 - 2(\alpha_{\mathrm{RP}}^2 + \alpha_{\mathrm{PR}}^2) + \cdots] \tag{38}$$

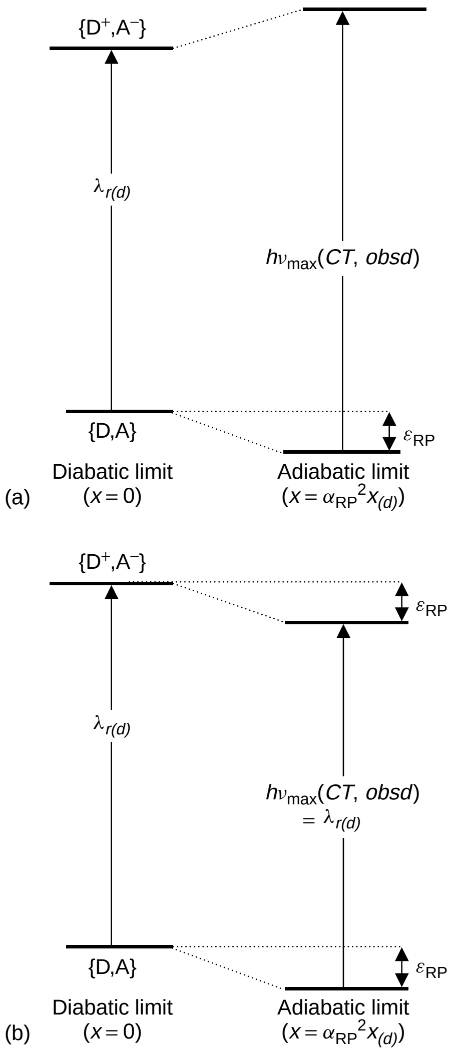

Figure 3 Qualitative two-state energy diagrams for a simple electron-transfer system (a) the limit in which there is no net free energy change for the reaction; (b) qualitatively illustrates the energy relations when the reaction is thermodynamically favorable

At the same level of approximation,

$$\Delta G^{\circ}_{\mathrm{RP}} = \Delta G^{\circ}_{\mathrm{RP}}(1 + \alpha^2_{\mathrm{RP}} + \alpha^2_{\mathrm{PR}}) \qquad (39)$$

4.4 Three-state Models and Superexchange Coupling[22]

The covalent linker of a donor and acceptor, in a {D-(B)-A}, complex can function simply as a spacer, separating the donor and acceptor, or it may contribute significantly to the electron-transfer process. The contributions of the ligand to the electron-transfer process can arise even when the actual transfer of charge to the bridging ligand is thermodynamically unfavorable. This effect can be approached as an extension of the configurational mixing issues discussed above.

Most of the studies of linked transition metal D/A complexes have employed bridging ligands that have relatively low-energy π-type LUMOs and metals in which the electron-transfer process involves $d\pi$-orbitals.[63,64] There are fewer studies of purely σ analogs, partly for reasons of complex instability. Some general features are characteristic of any type of bridging ligand.

The superexchange mechanism is commonly employed to describe bridging ligand mediated D/A electronic coupling.[2] The basic concepts involved in this approach can be traced back to the theory of magnetic interactions,[65] and the first application to electron-transfer processes is attributed to McConnell.[66] The approach is simply addressed in terms of a three-state system (see Figure 3): (a) ground (or reactant) state, {(D)-(B)-(A)}; (b) bridge or metal to ligand charge transfer (MLCT) state, {(D^+)-(B^-)-(A)}; and (c) the electron-transfer excited state (or product state), {(D^+)-(B)-(A^-)}. If H_{DA} is small or zero (no direct D/A overlap; the D and A subscripts are based on a localized configurational notation for the reactant and product states), then the bridge mediated coupling will be dominant. Electron transfer mediated by a bridging ligand MLCT state is typical of the majority of linked transition metal systems. The bridging ligand state could also be a ligand to metal charge transfer (LMCT) state, {(D)-(B^+)-(A^-)}; the formalisms differ only by a factor of two that arises when the bridging ligand orbital that mixes the electronic configurations is unoccupied and the acceptor orbital is half occupied.[58] These are commonly referred to as the ‘electron’ and ‘hole’ transfer formalisms, respectively. If the mixing coefficients for the donor and acceptor mixing with the bridging ligand are $\mathrm{H_{DB}/E_{DB}}$ and $\mathrm{H_{BA}/E_{BA}}$, respectively, then for MLCT mediation by the LUMO of single bridging moiety and for a filled donor orbital and half-filled acceptor orbital (as in a complex with a low-spin d^6-donor and d^5-acceptor),[2,58]

$$H_{\mathrm{DA}}^{\mathrm{spx}} = \frac{H_{\mathrm{DB}} H_{\mathrm{BA}}}{2E_{\mathrm{av}}} \qquad (40)$$

For a single interacting bridging unit and LMCT mediation of the electron transfer (vacant acceptor orbital),

$$H_{\mathrm{DA}}{}^{\mathrm{spx'}} = \frac{H_{\mathrm{AB}} H_{\mathrm{BD}}}{E_{\mathrm{av}}} \qquad (41)$$

The value of the energy parameter in the denominators of equations (40) and (41) is based on vertical energies, usually obtained from the charge transfer spectra of the metal complexes (equation 42).[2]

$$E_{\mathrm{av}} = \frac{2\mathrm{E_{DB}} E_{\mathrm{A\text{-}B}}}{(E_{\mathrm{DB}} + E_{\mathrm{A\text{-}B}})} \qquad (42)$$

For a chain of linkers ($\mathrm{B}^{(1)}$, $\mathrm{B}^{(2)}$, …, $\mathrm{B}^{(n)}$), when only the interactions between nearest neighbor moieties of the bridging ligand are considered, and for γ_{ij} the mixing coefficient between the ith and jth bridging ligand moieties, the D/A coupling matrix element is given by equation (43).[2,3,66]

$$H_{\mathrm{DA}} = \frac{H_{\mathrm{DB}^{(1)}}}{E_{\mathrm{DB}^{(1)}}}\left[\prod_{(i)=1}^{(i)=n-1}\gamma_{(i)(i+1)}\right]H_{\mathrm{B}^{(n)}\mathrm{A}} \qquad (43)$$

In the limit of an infinite chain of identical bridging ligand moieties, equation (43) takes the form of an exponential dependence on the geometrical distance between the donor and acceptor, d_{DA}.[2,3,66]

$$H_{\mathrm{DA}} = H_{\mathrm{DA}}(i=0)e^{-\beta d_{\mathrm{DA}}} \qquad (44)$$

An algebraically similar expression can be based on the overlap of spherical wavefunctions far from their nucleus of origin;[67] in this case β is an inverse orbital radius. The interpretation of β in a superexchange-based expression is more complicated.[3]

Equation (31) suggests that the solvent reorganizational energy should increase as the linker increases in length (i.e. for the linker length defined as $d_{\mathrm{L}} = [d_{\mathrm{DA}} - a - b]$). This can be a substantial effect, even if the linker does not otherwise affect the electron-transfer rate constant. One expects H_{RP} to decrease with distance (equation 44), so α_{DA}^2 decreases rapidly with d_{L} and any attenuation of χ_{s} due to the delocalization of electron density as in equation (38) will also decrease. The different distance dependencies of χ_{s} and H_{DA} make them difficult to resolve. A further complication is that the linker itself usually has dielectric properties (e.g. η and D_{s} in equation 31) that differ from those of the solvent. The increase of χ_{s} with d_{L} implied in equation (31) suggests that the bandwidth for absorption or emission should also increase with d_{L}; the maximum increase in $\Delta\nu_{1/2}$ is about 40%. There should be a correlated, systematic shift to higher energies of the electron-transfer absorption maxima of the linked complexes as d_{L} increases.

The differences between the observed electron-transfer parameters (χ_{r}, ΔG_{DA}, $h\nu_{\mathrm{max}}$, etc.) and their values for an appropriate reference, when the D/A electronic coupling is mediated by a bridging ligand, can provide useful information about the extent of configurational mixing between the donor and acceptor moieties with the bridging ligand.[68,69] When the direct coupling between the donor and acceptor can be neglected, as when they are far apart, the effect of the bridging ligand in mediating their coupling can be expressed as in equations (45–47).[2,44]

$$\psi_{\mathrm{R}} = \frac{[\psi_{\mathrm{R}(d)} + \alpha_{\mathrm{RB}}\psi_{\mathrm{B}(d)}]}{[1+\alpha_{\mathrm{RB}}^2]^{1/2}} \qquad (45)$$

$$\psi_{\mathrm{P}} = \frac{[\psi_{\mathrm{P}(d)} + \alpha_{\mathrm{BP}}\psi_{\mathrm{B}(d)}]}{[1+\alpha_{\mathrm{BP}}^2]^{1/2}} \qquad (46)$$

$$\psi_{\mathrm{B}} = \frac{[\psi_{\mathrm{B}(d)} - \alpha_{\mathrm{PB}}\psi_{\mathrm{B}(d)} - \alpha_{\mathrm{BR}}\psi_{\mathrm{B}(d)}]}{[1+\alpha_{\mathrm{PB}}^2 + \alpha_{\mathrm{BR}}^2]^{1/2}} \qquad (47)$$

The configurational mixing with the ligand reduces the energy of the ground state by $\varepsilon_{\mathrm{s}}(R) = H_{\mathrm{RB}}^2/E_{\mathrm{RB}}$, and that of the electron-transfer excited state by $\varepsilon_{\mathrm{s}}(P) = H_{\mathrm{BP}}^2/E_{\mathrm{PB}}$. Since $E_{\mathrm{RB}} > E_{\mathrm{PB}}$ (see Figure 4), the absorption maximum of the $D \rightarrow A$ electronic transition is shifted to lower energy,

$$h\nu_{\mathrm{max}}(\mathrm{D/A}) = h\nu_{\mathrm{max}}(\mathrm{ref}) + \varepsilon_{\mathrm{s}}(\mathrm{R}) - \varepsilon_{\mathrm{s}}(\mathrm{P}) \qquad (48)$$

The reference chosen for evaluating this shift should be a D/A complex in which there is no configurational mixing ($H_{\mathrm{DB}} = H_{\mathrm{AB}} = 0$), and evaluated for general conditions as in the system investigated. The shifts in the absorption maxima are a measure of the configurational mixing with the bridging ligand in strongly coupled systems. For a chemically symmetric system, $H_{\mathrm{RB}} = H_{\mathrm{PB}}$, and when no other factors contribute to the shifts in absorption maximum,

$$\Delta h\nu_{\mathrm{max}} = [h\nu_{\mathrm{max}}(\mathrm{D/A}) - h\nu_{\mathrm{max}}(\mathrm{ref})] = H_{\mathrm{RB}}{}^2\left(\frac{E_{\mathrm{RB}} - E_{\mathrm{PB}}}{E_{\mathrm{RB}}E_{\mathrm{PB}}}\right) \qquad (49)$$

Comparison of equation (41) with equation (49) indicates that in a simple, chemically symmetrical system (assuming one partly filled acceptor orbital, as in $\mathrm{Ru^{II}/Ru^{III}}$ couples), the shift of the absorption maximum should be closely related to

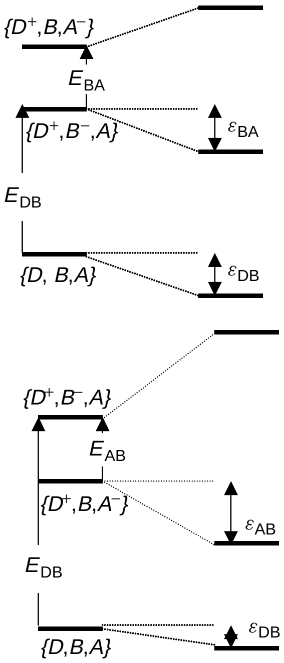

Figure 4 Qualitative three-state energy level diagrams. All energies are with respect to ground-state nuclear coordinates (vertical energies). The lower diagram illustrates the usual case in which a higher energy bridging ligand electronic state mediates the donor–acceptor coupling by means of configurational mixing. The upper diagram illustrates the limit in which the vertical energy of the bridging ligand electronic state is less than that of the electron-transfer excited state. Diabatic states on the left and adiabatic states on the right of each diagram

the single, linker MLCT excited state mediated superexchange coupling.[68,69]

$$\Delta h\nu_{\max} \cong 4H_{\mathrm{DA}}{}^{\mathrm{spx}}\left[\frac{E_{\mathrm{DA}}}{E_{\mathrm{DB}}+E_{\mathrm{AB}}}\right] \tag{50}$$

Appropriate parameters can often be inferred from the properties of related but separate donor and acceptor complexes, or from the extrapolation of the properties of a closely related series of linked complexes to the limit that $\alpha_{\mathrm{DA}}^2 = 0$.

4.5 Vibronic Coupling and the Mixing of Nuclear and Electronic Coordinates[48,70–72]

It is usually assumed that the electronic coupling matrix element is a constant across the reaction coordinate. Since the electronic wavefunction is a function of both the electronic and nuclear coordinates, even in the Born-Oppenheimer approximation, it is not surprising that in some systems the assumption that the nuclear and electronic coordinates are independent (the Condon approximation) is not appropriate. The most obvious example of the failure of this approximation is for a system in which the matrix element is dominated by superexchange contributions, since the vertical energies, E_{DB} and E_{BA}, vary with the nuclear coordinates. There are other, probably less obvious kinds of such vibronic coupling:

a. H_{DA} may be different in different vibrational states.
b. A change in the nuclear coordinates of the ligands of one of the reactants may be directly coupled with a change in the nuclear coordinates of the other reactant (e.g. for a mono-atomic bridge).
c. Electron delocalization between the donor, the acceptor, and/or the bridging ligand may lead to significant anharmonicities along the reaction coordinate that alter the reactant-bridging ligand interaction.
d. The timescale for electron transfer (i.e. $(\nu_{\mathrm{el}})^{-1}$) may be comparable to that for coupled nuclear vibrations (ν_{nu}^{-1}).
e. The timescale for electron transfer (i.e. $(\nu_{\mathrm{el}})^{-1}$) may be shorter than or equal to that for the relaxation of vibrational excited states (k_{vib}^{-1}) of the products.

Each of these effects may be referred to as 'vibronic coupling' even though the underlying physics and/or the experimental manifestations of the coupling are often different. Although, the issues related to vibronic coupling are very complicated, it is possible to get some insight into them from the consideration of some idealized, limiting cases:[22]

Case 1. A one-dimensional system in which the donor and acceptor differ only in the distances between metal and some nonbridging ligand(s),

$$[L\text{—}M^{II}]\text{-}B\text{-}[{}^{*}M^{III}\text{-}L] \rightleftarrows \{[L\leftrightsquigarrow M]\text{-}B\text{-}[{}^{*}M\leftrightsquigarrow L]^{\ddagger} \rightleftarrows [L\text{-}M^{III}]\text{-}B\text{-}[{}^{*}M^{II}\text{—}L] \tag{51}$$

A lengthening of a bond at one center and compression at the other accompanies the transfer of charge between metal centers. Simple vibronic models assume that the electron is equally distributed over the metals in the transition state, designated $\{\ldots\}^{\ddagger}$, or, alternatively, that the 'hopping frequency' (see equation 30) $\nu_{\mathrm{el}} > \nu_{\mathrm{ML}}, \nu_{*\mathrm{ML}}$ (note that in the transition state, $\nu_{\mathrm{ML}}^{\ddagger} = \nu_{*\mathrm{ML}}^{\ddagger}$ for the M–L stretches of the respective moieties for a symmetrical system). The classical, transition-state-based Marcus–Hush-type of models assume that the vibrations ν_{ML} and $\nu_{*\mathrm{ML}}$ are completely independent. In a simple vibronic model it is assumed that the compression of *[L–M]* and the extension of *[*M–L]* occur simultaneously along the electron-transfer coordinate. The transfer of electron density couples these vibrations of the donor and acceptor moieties. The nuclear coordinate implicated in this simple model is the antisymmetric combination of component stretching coordinates,[72] $r_{\mathrm{ML}}^{-} = (r_{\mathrm{ML}} - r_{*\mathrm{ML}})/2^{1/2}$. The corresponding vibration is $\nu_{\mathrm{ML}}^{-} = \nu_{\mathrm{ML}}^{\ddagger} - \delta_{\mathrm{ML}}$; where δ_{ML} is the coupling between the local bond stretches.

Case 2. For a reaction in which the donor and acceptor differ significantly in their distances to the bridging ligand,

$$[L\text{-}M^{II}]\text{—}B\text{-}[{}^{*}M^{III}\text{-}L] \rightleftarrows \{[L\text{-}M]\leftrightsquigarrow B\leftrightsquigarrow[{}^{*}M\text{-}L]^{\ddagger} \rightleftarrows [L\text{-}M^{III}]\text{-}B\text{—}[{}^{*}M^{II}\text{-}L] \tag{52}$$

The coupled nuclear motion is $r_{\mathrm{MB}}^{-} = (r_{\mathrm{MB}} - r_{*\mathrm{MB}})/2^{1/2}$, and $\nu_{\mathrm{MB}}^{-} = \nu_{\mathrm{MB}}^{\ddagger} - \delta_{\mathrm{MB}}$. This could be used as a model for reactions 2 and 4.

Case 3. The nuclear coordinates within the bridging ligand of the D/A complex may be different from those in the complexes with the metals in identical oxidation states.

$$\begin{tikzcd}
{[\mathrm{L{-}M^{II}}]\text{–}(\mathrm{B}\text{-}{}^{*}\mathrm{B})\text{–}[{}^{*}\mathrm{M^{II}{-}L}]} \arrow[r, "-\mathrm{e}"] & {[\mathrm{L{-}M^{II}}]\text{–}(\mathrm{B}\text{–}{}^{*}\mathrm{B})\text{–}[{}^{*}\mathrm{M^{III}{-}L}]} \arrow[d, "-\mathrm{e}"] \\
 & {[\mathrm{L{-}M^{III}}]\text{–}(\mathrm{B}\text{–}{}^{*}\mathrm{B})\text{–}[{}^{*}\mathrm{M^{III}{-}L}]}
\end{tikzcd} \tag{53}$$

This process and the symmetry of the system are both different from those of *Cases 1* and *2*. This corresponds to a system in which there is appreciable delocalization of electron density between the donor (acceptor) and the bridging ligand, the bridging ligand mediates donor–acceptor coupling and the bridging ligand distortion enhances the D/A coupling.

The coupling of the nuclear and electronic coordinates is probably not a major issue in the discussion of most outer-sphere electron-transfer reactions because: (1) the nuclear motions, or molecular vibrations, at the donor and acceptor centers are independent of one another; and (2) the D/A electronic coupling and the fraction of delocalized electron density are both small. One perspective on the classical, Marcus–Hush description of the electron-transfer reaction coordinate is that $\kappa_{\mathrm{el}} = 0$ for all nuclear coordinates except for those of the transition state, and that $\kappa_{\mathrm{el}} = 1$ at the transition state (a resonance condition). This description is conceptually useful since the nuclear motions are treated as random and independent at the donor and acceptor. A consequence of this independence of the nuclear motions is that when the reactant system is near to the transition state, a fluctuation in the positions of the nuclei that moves the system away from the product configuration is more probable than one that moves it towards that configuration. On the other hand, any coupled nuclear motions of the reactant system near to the transition state that correspond to nuclear motion across the reaction coordinate will tend to couple to the electronic distribution. This is especially possible for some bridging moieties that link the donor to the acceptor; for example, some vibrations of the bridge may be directly coupled to the electronic distribution between the donor and the acceptor.[73]

Finally, it is to be noted that configurational mixing-related anharmonicities of the PE surfaces have the effect of mixing the nuclear and electronic coordinates, even in the two state model (see equations 35–40). These anharmonicities must result in changes in the frequencies of some vibrational modes that are correlated with the reaction coordinate. The size of the anharmonic contribution increases with electron delocalization.

5 EXPERIMENTAL OBSERVATIONS AT THE WEAKLY-COUPLED LIMIT

Much of the pertinent information has been summarized previously, and the details can be found in the references cited in those summaries.[21,22,74]

5.1 A Summary of Outer-Sphere Electron-transfer Reactions

Overall, the outer-sphere electron-transfer reactions of transition metal complexes reactions are consistent with the expectations of the semiclassical Marcus–Hush theory.[3,21,22,25,32,43,57,71,75–78] For the most part, this agreement of theory with experimental observations is based on the correlations between different experimentally measured parameters (such as the variations of experimental rate constants with driving force, with different solvents, with the size or separation of donor and acceptor, with bond length changes, etc.). There are some notable exceptions. Many of these are for reactions involving a high-spin cobalt(II) complex among the reactants or the products,[79,80] and these deviations from expected behavior have usually been attributed to contributions from $\kappa_{\mathrm{el}} \ll 1$. Another class of notable exceptions is for reactions in the Marcus inverted region. Thus, the physical properties of the coordination complexes that influence the Franck–Condon parameters χ_{s} and $\Delta G^{\circ}_{\mathrm{RP}}$ alter the observed rate constants in a manner that is nearly quantitatively predictable from the semiclassical approaches when $|\Delta G^{\circ}_{\mathrm{RP}}| < \chi_{\mathrm{s}}$. Observations on the various contributing parameters are briefly summarized.

5.1.1 *Solvent reorganizational contributions*

In principle, the importance of the solvent contribution to the electron-transfer reorganizational energy should be most evident in a comparison of reaction rates in the presence to those in the absence of a solvent. Gas-phase electron-transfer reactions provide this contrast. There are important differences between solution and gas-phase reactions: (a) electrostatic interactions between reactants are far more important in the gas phase since solvent polarization tends to moderate these interactions in solution; (b) the translational energy difference that the reactants bring into the collision complex must be distributed over the internal degrees of freedom during the lifetime of the reactive collision; (c) in the absence of solvent, only the molecular geometry changes contribute to χ_{r}. Several useful studies have employed ion cyclotron resonance (ICR) spectroscopic techniques to study the gas-phase electron-transfer reactions of bis-cyclopentadienyl (Cp; Cp* designates the pentamethyl-cyclopentadienyl ligand) complexes,[81,82]

$$[\mathrm{M(Cp)_2}] + [\mathrm{M(^{*}Cp)_2}]^{+} \rightleftharpoons [\mathrm{M(Cp)_2}]^{+} + [\mathrm{M(^{*}Cp)_2}] \qquad (54)$$

Isotopic labeling of the Cp^{-} rings enables the study of self-exchange reactions using the ICR technique. The rate constants for the gas-phase reactions are close to the diffusion limit and about 10^{4} times larger than their solution phase equivalents. The slower solution reactions correspond to $\chi_{\mathrm{s}} \sim (12\ \text{to}\ 13) \times 10^{3}\,\mathrm{cm}^{-1}$.

The bimolecular self-exchange reactions of $\mathrm{Ru^{II}/Ru^{III}}$ complexes in aqueous solution involve the exchange of an electron between largely nonbonding orbitals so the accompanying changes in molecular geometry tend to be very small. Even when there are geometry differences between the two electron-transfer states, the metal–ligand vibrational quanta are small enough ($300–600\,\mathrm{cm}^{-1} < 4k_{\mathrm{B}}T$)[83] that the contributions of high frequency modes, χ_{M}, to χ_{r} are small. This makes these couples a convenient choice for examining the contributions of χ_{s} to k_{et}. The self-exchange rate constants for these complexes are relatively large,[21,22] and values of χ_{s} can be estimated from the experimental rate constants ($\chi_{\mathrm{r}} = 4\Delta G^{\ddagger}_{\mathrm{DA}}$) with only small corrections for χ_{M}. These estimates of χ_{s} for several ruthenium couples are summarized elsewhere,[22] and tend to increase with the inverse mean external radius of the complex (r^{-1}_{mean} in pm^{-1})[84] as expected from equation (31). They correlate well ($r^{2} = 0.99$ for the ammine-polypyridine complexes) with the reciprocal of the estimates of the mean external radius[84] of the complexes. The least squares fit (χ_{s} in units of $10^{3}\,\mathrm{cm}^{-1}$) of the observations for the ammine-polypyridine Ru(III)-(II) couples in aqueous solutions is[22]

$$\chi_s = \frac{(4570 \pm 2)}{r_{\text{mean}}} + (0.1 \pm 0.4) \qquad (55)$$

The slope of this correlation is about 50% larger than predicted by equation (31). This contrast may arise from an underestimate of the external radii of the complexes, or (more likely) some specific solvation effects and the inadequacies of the dielectric continuum model on which equation (31) is based. Equation (55) seems to be a good basis for estimating the contributions of χ_s, provided the same procedure is used to estimate r_{mean}.[84] Relatively elaborate solvation models, in which the solvent structure near to the reactants plays an important role, are being explored.[85]

5.1.2 *The intramolecular contributions, χ_M*

Among six-coordination complexes, the changes of metal–ligand bond length that accompany the transfer of an electron tend to be the largest for cobalt(III)-(II) couples. The self-exchange electron-transfer rate constants of a wide range of Co^{III}/Co^{II} complexes for which X-ray and/or solution EXAFS data are available is in agreement with equation (33) within the limits of the experimental uncertainties.[22]

5.1.3 *The purely electronic contributions, H_{RP}*

The contributions of (FC) to k_{et} tend to be very large, as noted above, and the exponential dependence of k_{et} on the experimental uncertainties in the determination of Franck–Condon parameters is often large enough to overwhelm the determination of H_{RP} from rate constant measurements. This has made systematic studies of this parameter difficult and controversial. That κ_{el} is less than unity for many reactions, particularly of Co^{III}/Co^{II} couples, has been demonstrated by the contrasting effects (compared to Ru^{III}/Ru^{II} couples) of purely electronic, ion-pair charge transfer perturbations of the rate constant (this is a superexchange contribution),[79] and by the complex dependencies of the electron-transfer rates of simple coordination complexes on the intensities of external magnetic fields.[86]

The simple self-exchange reaction in equation (56) has been extensively investigated.

$$[Fe(CN)_6]^{4-} + [{}^*Fe(CN)_6]^{3-} \rightleftharpoons [Fe(CN)_6]^{3-} + [{}^*Fe(CN)_6]^{4-} \qquad (56)$$

This reaction is strongly ‘catalyzed’ by cations; the uncatalyzed rate constant in aqueous solution (25 °C, $I = 0.2\,M$) is $K_A k_{et} = 2.2 \times 10^2\,M^{-1}\,s^{-1}$.[87,88] The {*[Fe(CN)*$_6]^{4-}$, *[Fe(CN)*$_6]^{3-}$} ion pair (see section 5.2, below) has been reported ($[K^+] = 2.5\,M$, ionic strength $\sim 10\,M$ and K_A determined as $0.05\,M^{-1}$) to have an absorption maximum at $12.2 \times 10^3\,cm^{-1}$ with $\varepsilon_{max} = 28\,cm^{-1}\,M^{-1}$ and $\Delta\nu_{1/2} = 7.9 \times 10^3\,cm^{-1}$.[89] Based on the ion-pair absorption spectrum and equation (13) (neglecting g_o), $H_{DA} = 116\,cm^{-1}$ ($\kappa_{el} \cong 0.5$).

Several studies of bimetallic complexes in which the donor and acceptor are linked across aliphatic chains have demonstrated that these are generally weakly coupled systems.[90–92] Studies of complexes linked by 1,2-bis(2,2′bipyridyl-4′-yl)ethane (bb; see Figure 5), indicate that these are good models of the precursor complexes for outer-sphere electron-transfer reactions of tris-bipyridyl complexes. A careful comparison of kinetic and spectroscopic data with computational studies has led to an estimate of $H_{RP} \cong 20\,cm^{-1}$ for the $[Fe(bb)_3Fe]^{5+}$ self-exchange electron transfer.[91] In a related cross-reaction, the Ru/bpy MLCT excited state of $[(bpy)_2Ru(bb)Co(bpy)_2]^{5+}$ is efficiently quenched by electron transfer to the cobalt center in several resolved steps, equations (57) and (58).[90]

$$[(bpy)_2Ru^{II}(bb)Co^{III}(bpy)_2]^{5+} + h\nu \longrightarrow [{}^3MLCT(bpy)_2Ru^{III}(bb)({}^2E)Co^{II}(bpy)_2]^{5+} \qquad (57)$$

$$[{}^3MLCT(bpy)_2Ru^{III}(bb)({}^2E)Co^{II}(bpy)_2]^{5+} \longrightarrow [(bpy)_2Ru^{III}(bb)({}^4T)Co^{II}(bpy)_2]^{5+} \qquad (58)$$

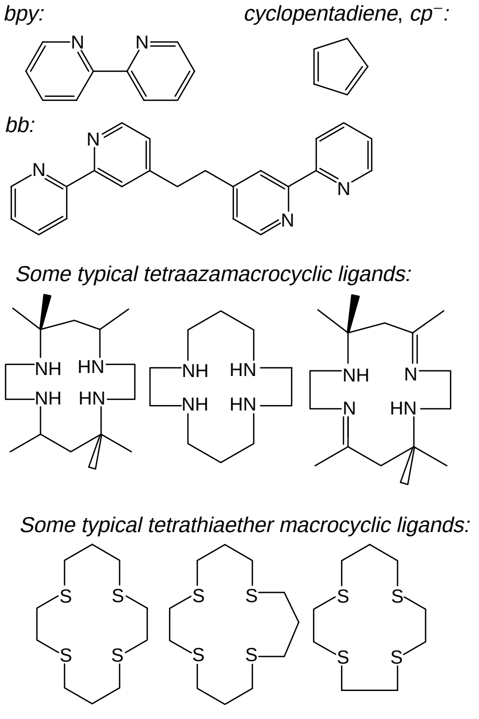
bpy:
cyclopentadiene, cp⁻:
N
N
bb:
N
N
N
N
Some typical tetraazamacrocyclic ligands:
NH HN
NH HN
NH HN
NH HN
NH N
N HN
Some typical tetrathiaether macrocyclic ligands:
S S
S S
S S
S S
S S
S S

Figure 5 Some ligands of coordination complexes used in studies of electron transfer. (Reprinted from Ref. 22, © 2004, with permission from Elsevier)

This is followed by very fast back electron transfer to regenerate the ground state.

$$[(bpy)_2Ru^{III}(bb)(^4T)Co^{II}(bpy)_2]^{5+} \longrightarrow [(bpy)_2Ru^{II}(bb)\,Co^{III}(bpy)_2]^{5+} \qquad (59)$$

The process in equation (59) was estimated to have $H_{RP} \cong 8\,cm^{-1}$ ($\kappa_{el} \approx 10^{-2}$).[90]

5.2 Correlations of Kinetic, Electrochemical, and Spectroscopic Parameters of Ion Pairs

Ion pairs of the type $\{ML_n^{z+}, {}^*MX_m^{y-}\}$ generally exhibit weak CT absorption bands. When self-exchange kinetic data and reduction potentials are available (or can be estimated) for the $ML_n^{z+}/ML_n^{(z-1)+}$ and $MX_m^{(y+1)-}/{}^*MX_m^{y-}$ couples, then the thermal parameters can be compared to the spectroscopic based on equation (20). In this limit, the free energy contribution can be approximated by the difference in the half-wave potentials of the donor and acceptor as in equation (60); $\Delta G^\circ_{RP} - F\Delta E_{1/2}$ ($F =$ Faraday's constant; in this limit, the correction for the difference in the species involved in light absorption and the electrochemical process, proportional to α^2_{RP}, is small).[22,93]

$$h\nu_{max}(abs) \cong F\Delta E_{1/2} + \chi_r + \cdots \qquad (60)$$

The ion-pair charge transfer absorption (IPCT) band maxima are combined with the electrochemical and kinetic data in Figure 6 to illustrate that equation (60) works very well, over nearly a 5-eV range, in the weak-coupling limit.[22] The reorganizational parameters for most of the cationic acceptors in the ion pairs in Figure 6 have been derived from rate constant data (those involving $[Co(NH_3)_6]^{3+}$ have been corrected for the estimated effects of κ_{el}),[22] the resulting parameters may contain a contribution from some additional factor such as $2RT\ln\kappa_{el}$; the deviations from the least squares correlation line average about $1600\,cm^{-1}$ for Ru complexes and about $2700\,cm^{-1}$ for Co complexes. The self-exchange and electrochemical reactions of many of these ion pairs involve high-spin Co^{II} complexes, while the spin-allowed IPCT transitions involve low-spin Co^{II}. That these cobalt ion pairs come close to the line of unit slope suggests that the reorganizational energy is smaller and the free energy change is larger for the couples involving low spin than for those involving high-spin Co^{II}, and that the differences are small on the ~5 eV scale of Figure 6. Some of the deviations may arise because this correlation combines data obtained independently in more than 40 different laboratories.[22]

The observations summarized in this subsection demonstrate that the magnitudes of solvational changes and geometrical differences dominate electron-transfer reactivity, and that these contributions to the Franck–Condon factor are readily interpreted and analyzed in the weak-coupling limit. Electron-transfer behavior in this weak-coupling limit constitutes a useful reference for evaluating the behavior of more complex systems. Thus, the deviations of the Franck–Condon parameters found for systems that fall into the strongly coupled limit can be evaluated with respect to representative systems in the weakly coupled limit.[22]

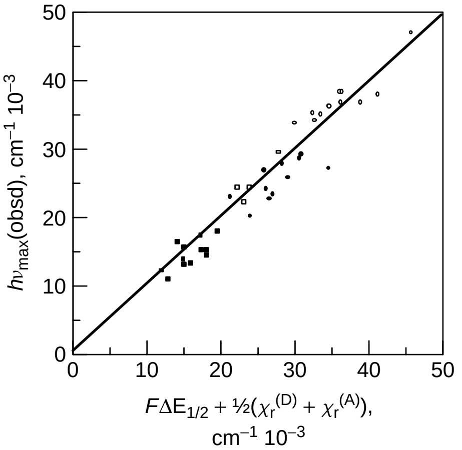

Figure 6 The correlation, based on equation (61), of the absorption maxima of ion-pair charge transfer transitions to the difference in reduction potentials and the average of the reorganizational energies of the constituent electron-transfer couples.[22] ■, Ru^{III} with $M(CN)_n{}^{k-}$; □, Ru^{III} with halides; ●, Co^{III} with $M(CN)_n{}^{k-}$; ○, Co^{III} with halides

5.3 Intermediates, Gated Electron-transfer and Vibrational Excited States

Electron-transfer processes that generate metastable 'intermediates' are frequently encountered in the reactions of transition metal donors and acceptors. Any initial reaction product is considered an intermediate in this context if its lifetime is long compared to the intrinsic lifetime of electron transfer (i.e. ν_{el}^{-1} in equation 30). Thus, low-energy electronic excited states are often important in the Marcus inverted region (e.g. see equations 57–59) because the electron-transfer rate in this region decreases rapidly with increasing driving force. When the reactants and products of a cross-reaction differ significantly in geometry, then the electron-transfer step may involve the formation of a product in a metastable geometry if the conformational equilibration (k_{conf}) of the products is slow.

Similarly, if the rate of vibrational relaxation (k_{vib}) is small compared to ν_{el}, then vibrational excited states of the products can act as intermediates in the electron-transfer process. Since vibrational modes with large quanta tend to relax more slowly than modes with small quanta, the role of high frequency vibrational modes in the Marcus inverted region can be interpreted as electron transfer to form a vibrationally excited intermediate with a net driving force of $(\Delta G^\circ_{RP} + jh\nu_h)$ (see equations 18 and 29). It should be noted that the lifetimes of the high frequency vibrational modes depend in large part on the rate of transfer of the excess energy to the solvent (or 'bath') modes and this is not easy to predict when there are specific solvation effects.

The generation of intermediates with the product electronic structure is only important when the relaxation (or equilibration) of these intermediates to the equilibrium geometry occurs more slowly than ν_{el}, and when the metastable product state is thermodynamically accessible and kinetically advantageous compared to direct generation of ground-state products from the reactants. The intervention of conformationally dictated pathways raises the possibility that protein conformational changes might enable the regulation of electron transfer in metallo-enzyme systems. Such 'gated' electron-transfer pathways have been explored theoretically.[94,95]

Rorabacher and coworkers have found that rate comparisons (based on a classical Marcus model) of the oxidations of $Cu^I(S_n)_{(j)}$ and reductions of $Cu^{II}(S_n)_{(j)}$ complexes, where $(S_n)_{(j)}$ is a polythiaether ligand, often suggest that these processes occur by means of different pathways. Since $Cu^{II}L$ and Cu^IL generally have very different equilibrium coordination geometries, these pathways have been associated with the generation of metastable $Cu^{II}L(Q)$ and $Cu^IL(P)$ intermediates, respectively. In principle, the reactivity associated with the resulting pathways can be interpreted in terms of self-exchange reactions that involve these intermediates: that is, the $Cu^{II}L(O)/Cu^IL(P)$ and the $Cu^{II}L(Q)/Cu^IL(R)$ self-exchange reactions, where $Cu^{II}L(O)$ and $Cu^IL(R)$ are the equilibrium species.[96] Self-exchange reactions may also proceed through metastable intermediates, although they need not be the same intermediates as in the cross-reactions. In the simplest limit, there is no direct electron exchange between $Cu^{II}L$ and Cu^IL and the intermediates are in equilibrium with the reactants. In this limit, the rate constants for electron transfer for the different pathways, $k_{et(a)}$ and $k_{et(b)}$, will be determined only by the solvent reorganizational energy, χ_s. Yu *et al.*[96] have observed that the variations in the observed self-exchange rate constants are very nearly accounted for by the variations in the equilibrium constants for formation of the intermediates. If the complexes are all about the same size (~440 pm), then from equation (56) $\chi_s \cong 10.5 \times 10^3\ \mathrm{cm}^{-1}$, and the observed (second order) self-exchange rate constant is given by equation (61).

$$K_A k_{et}(\mathrm{obsd}) = K_A \left[\frac{K_a}{1+K_a} + \frac{K_b}{1+K_b}\right] k_{et}(\mathrm{solv}) \qquad (61)$$

The value estimated for χ_s corresponds to $K_A k_{et}(\mathrm{solv}) \cong 3 \times 10^5\ \mathrm{M^{-1}\ s^{-1}}$. Only the values self-exchange rate constants for the $[Cu([14]aneS_4)]^{2+,+}$ and the $[Cu([15]aneS_4)]^{2+,+}$ couples are sufficiently different to infer an important contributions from intermediates. The equilibrium constants, $K_a = 4 \times 10^{-5}$ and $K_b = 0.02$, have been determined from rapid-sweep cyclic voltammetry for $[Cu([14]aneS_4)]^{2+,+}$.[96] For these values, $K_A k_{et}(\mathrm{solv}) = 4 \times 10^5\ \mathrm{M^{-1}\ s^{-1}}$, in excellent agreement with the estimate based on the solvent reorganizational energy for complex ions of this size.

The reactions of the $[Cu(S_n)_{(j)}]$ complexes appear to involve well-defined chemical intermediates, and reaction pathways involving these intermediates are important because they are thermodynamically accessible and because the direct conversion of the equilibrium reactant species to the equilibrium product species would involve a substantial reorganizational energy, χ_{RP}. The reorganizational energy, χ_{int}, for the reaction pathway involving the intermediate must be smaller than χ_{RP} for such an effect to be observed. In the $[Cu(S_n)_{(j)}]$ systems, this constraint can be interpreted in terms of significant molecular distortions (bond breaking, conformational changes, etc.) along the ground-state reaction coordinate, but only solvent reorganization along the reactant-intermediate reaction coordinate. This approach to the role of conformational intermediates presumes well-defined chemical species characterized by a local PE minimum.

6 STRONGLY COUPLED, BRIDGED ELECTRON-TRANSFER SYSTEMS

The literature on covalently linked transition metal donor and acceptor complexes is enormous.[1,11,12,21,58,63,64,74,97–103] Much of it is covered in the article on ***Mixed Valence Compounds***.

General matters of principle and the basic physics are the same as for the outer-sphere reactions. Figure 7 illustrates how increases in the configurational mixing can alter the reaction coordinate (or the reactants-products ground-state PE surface) for chemically degenerate, or mixed valence systems. This range of behavior is often classified as: (a) diabatic limit, Robin-Day class I; (b) delocalized limit, Robin-Day class III; (c) intermediate cases, Robin-Day class II[27] (see Figure 7). There is an intermediate situation in which the adiabatic ground-state PE surface cannot be approximated as a parabola, and this has sometimes been called class II-III[98,100] (see Figure 7).

There can be some significant deviations from the properties characteristic of the weak-coupling limit. For example, the Gaussian absorption band shapes expected based on equation (15) may not be appropriate. Those Gaussian shapes can be attributed to the projection of the ground-state vibrational wave packet onto the excited state PE surface.[50] When there is a very great deal of configurational mixing, as illustrated in Figure 7, the ground-state vibrational wave function and the resulting vibrational wave packet, may be better represented as a sum of Gaussian functions. This will lead to non-Gaussian absorption band shapes. Some of the other contrasts in properties can be attributed to the size of

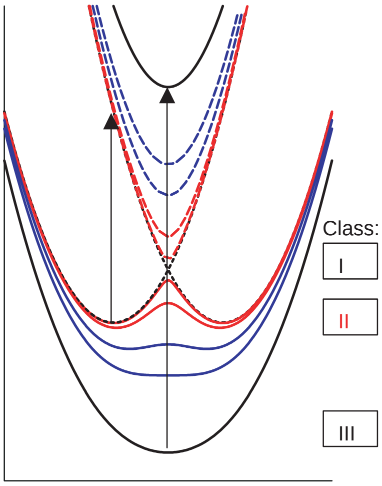

Figure 7 Qualitative effects of configurational mixing in the degenerate ($\Delta G^{\circ}_{\mathrm{RP}} = 0$) limit. The dashed black curves are for the diabatic limit. H_{RP} increases with the vertical distance of the center of the adiabatic curves from the crossing point of the diabatic curves; the separation of the ground and excited state adiabatic curves along a vertical line through this region is $2H_{\mathrm{RP}}$. The red curves correspond to mixed valence complexes with significant configurational mixing, but 'valence localized' reactant and product states ($H_{\mathrm{RP}} < \lambda_{\mathrm{r}}$); Robin-Day class II. The Robin-Day classifications are noted in the boxes on the right. The blue curves correspond to the intermediate situation that is not easily classified

the adiabatic correction factors and some issues are more important in bridged than in outer-sphere electron-transfer processes. A feature of bridged, strongly coupled complexes is that the electronic structure of the bridging ligand can contribute profoundly to their electron-transfer properties (see Section 4.4 and Figure 4, above). The interpolation between the diabatic limits and the adiabatic complexes is most often based on standard perturbation theory (see section 4.4 above). It is to be noted that these approaches are usually constructed, in terms of stationary state wave functions of the system, assuming vertical energies, fixed nuclei, and large differences in the vibrational and electron-transfer timescales. These assumptions are not always appropriate in the linked electron-transfer systems.[70,71,98,104–106]

The presence of a ligand bridging the donor to the acceptor can change many properties of the resulting complex relative to those of the appropriate diabatic limit. Typical changes are: (a) in the separation and orientation of donor and acceptor (from constraints imposed by the bridge); (b) stereochemically dictated differences in orbital overlap; (c) in solvation and ion-pairing; (d) configurational mixing of the bridging ligand orbitals with those of donor and/or acceptor; or (e) the bridge can directly participate in the electron-transfer process.

6.1 Complexes with Aromatic Bridging Ligands

A large number of complexes have been prepared in which the donor and acceptor are bridged by 4,4′-bipyridine and closely related ligands.[21,22,58,63,64] The values of H_{DA} estimated for these complexes are comparable to those of simple ion pairs, and the fraction of delocalized electron density, α^2_{DA}, is small.[22] Most of these complexes fit into the weakly coupled limit.

A wide range of range of electron-transfer behavior is exhibited by D/A systems that are classified as very strongly coupled. The properties of such systems have been extensively reviewed.[63,64,98,99] The Creutz–Taube ion, $[\{\mathrm{Ru(NH_3)_5}\}_2\mathrm{pz}]^{5+}$,[107] has an electron-transfer CT absorption band at $6.4 \times 10^3\,\mathrm{cm^{-1}}$ (absorptivity, in water, of $5 \times 10^3\,\mathrm{M^{-1}\,cm^{-1}}$; $\Delta\nu_{1/2} = 1400\,\mathrm{cm^{-1}}$), and it has been regarded as the prototype of a very strongly coupled D/A system. The electron transfer CT spectroscopy of related pyrazine-bridged bimetallic complexes range from that of $[\{\mathrm{Os(NH_3)_5}\}_2\mathrm{pz}]^{5+}$, which does not exhibit a clearly defined $\mathrm{Os^{II}/Os^{III}}$ absorption band,[108] to a pyrazine-bridged $\{(\mathrm{Ru_3})_2\mathrm{pz}\}$-cluster complex ($\mathrm{Ru_3} = [\mathrm{Ru_3}(\mu_3\text{-O})(\mu\text{-CH_3CO_2})_6(\mathrm{CO})(\mathrm{py})]^-$ for the $\mathrm{Ru^{II}/Ru^{II}/Ru^{III}}$, 'reduced' complex) in which a $12 \times 10^3\,\mathrm{cm^{-1}}$ absorption band with an absorptivity of $12200\,\mathrm{M^{-1}\,cm^{-1}}$ and $\Delta\nu_{1/2} = 3760\,\mathrm{cm^{-1}}$ (in dichloromethane) has been assigned as an metal-to-metal charge transfer (MMCT) absorption.[105] All of these pyrazine-bridged complexes have values of $\Delta E_{1/2}$ of several hundred meV, consistent with very strong electronic coupling.

For the diabatic limit one expects $h\nu_{\max}(\mathrm{abs}) \cong \chi_{\mathrm{s}} \cong 13 \times 10^3\,\mathrm{cm^{-1}}$ for the pentaammines (zero absorptivity and $\Delta\nu_{1/2} \sim 5400\,\mathrm{cm^{-1}}$);[22] since the $\mathrm{Ru_3}$ cluster complexes are larger and their net charges are smaller than those of the pentaammines, one expects that in the corresponding diabatic limit for the cluster complexes, $h\nu_{\max}(\mathrm{abs}) < 6.5 \times 10^3\,\mathrm{cm^{-1}}$ and $\Delta\nu_{1/2} < 3700\,\mathrm{cm^{-1}}$ (based on the dielectric properties of the solvents[109] and equations (20) and (31); based on equation (13), $H_{\mathrm{RP}} \sim 1500\,\mathrm{cm^{-1}}$). Equations (49) and (50) indicate that when the perturbing bridging ligand electronic state is higher in energy than the electron-transfer states, the electron-transfer excited state should decrease in energy as the configurational mixing increases. In a perturbation theory-based three-state model, the reverse is characteristic of a system in which the diabatic electron-transfer excited state is higher in energy than the configurationally mixed bridging ligand electronic state.

6.2 Cyanide and Di-Nitrogen Bridged Donor–Acceptor Complexes

Many mixed valence complexes with $\mathrm{N_2}$, or $\mathrm{CN^-}$ bridging ligands have been investigated. The cyanide bridge is the most versatile. These relatively simple ligands have cylindrical symmetry, they have a single, well-characterized intraligand vibrational mode and they have general molecular orbital properties analogous to the more complicated polypyridyl bridging ligands. These complexes illustrate many interesting issues of electron-transfer systems.

The $[(NH_3)_5M(NCM'(CN)_5)]^{n-}$ complexes are among the simplest of this class. Hupp and Barbara and their coworkers have extensively examined such complexes (with M = Ru or Os and M′ = Fe, Ru or Os).[110–112] The electronic coupling in These complexes typically exhibit an intense near-infrared M/M′ absorption and H_{DA} is of the order of $2 \times 10^3\,cm^{-1}$. One of the interesting characteristics of many of these complexes is that the photogenerated electron-transfer excited state returns to the ground state with a rate constant $k_{et} \approx 10^{13}\,s^{-1}$. This is faster than faster than the CN^- vibrational relaxation rate: the back electron-transfer occurs from an upper vibrational level of the electron-transfer excited state to form a ground state with vibrationally excited cyanides. This vibrational state-to-vibrational state electron-transfer process is not properly described in terms of electronic PE surfaces and the usual approaches to electron-transfer problems.

The donor–acceptor properties of complexes of the general stoichiometry $[(L)_nM(CNRu(NH_3)_5)_{(6-n)}]^{m+}$ ($n = 4$ or 5; L = a polypyridyl or am(m)ine nonbridging ligand; M = Fe, Ru, Os, Cr, Co, Rh) have also been reported.[68,113–117] One very striking feature of the CN^--bridged D/A complexes is that the CN stretch of a $(L)_nM(CNRu)$ moiety shift to lower frequency,[115–117] opposite to expectation for a bridging cyanide.[83] The size of this shift of ν_{CN} to lower frequencies in CN^--bridged D/A complexes, $\Delta\nu_{CN}$, is proportional to the oscillator strength of the Ru^{II}/M^{III} MM′CT absorption band,[115,116] and this suggests that the CN-nuclear coordinates (Q_{CN}) are a significant factor in determining the D/A electronic coupling. The shift in ν_{CN} appears to be a symmetry-dependent molecular, not a local $Ru^{II}(CN^-)$ Cr^{III}, coupling of electronic and nuclear properties. A vibronic model corresponding to vibronic coupling case 3 has been proposed to account for this behavior,[116,117] with

$$H_{DA} = H^{\circ}_{DA} + bQ_{CN} \tag{62}$$

Complexes with more than one cyanide, such as $[(L)_4M(CN)_2]^{p+}$, can function as bridging ligands. For a series of complexes of the type $[(NH_3)_5Ru^{II}\{(NC)(N_4)M^{III}(CN)\}Ru^{III}(NH_3)_5]^{6+}$, where (N_4) is a cyclic tetraamine, the Ru^{II}/Ru^{III} MMCT absorption band energies decrease in proportion to increasing absorptivity and decreasing energy of the Ru^{II}/M^{III} 'MLCT' absorption, as expected (equations 48 and 49), but the Ru^{II}/Ru^{III} MMCT absorptivities are nearly independent of the Ru^{II}/M^{III} MMCT absorption properties and weak ($\varepsilon_{max} \cong 120\,M^{-1}\,cm^{-1}$) contrary to expectation based on equation (41). Thus, it appears that superexchange coupling is 'turned off' for this type of bridging ligand.[68] This amounts to a vibronic selection rule for the electron-transfer absorption. If H°_{DA} in equation (62) is very small, then the Ru^{II}/M^{III} electronic coupling depends mostly on bQ_{CN}, and nuclei are configured for optimal electronic coupling (bQ_{CN} maximized) in the ground state of the complex; the C–N bridging Ru^{II} and M^{III} stretched; the cyanide bridging Ru^{III} and M^{III} compressed. In the excited state the oxidation states are reversed but the nuclei are fixed (for a vertical transition), and the coupling is minimized. This amounts to a phase restriction on electron transfer. It is relaxed in $[(py)_4Ru^{II}(CNRu^{II}(NH_3)_5)_2(CNRu^{III}(NH_3)_5)]^{5+}$ because the vertical energies of the (terminal–terminal) electron-transfer and Ru^{II}(central)-to-Ru^{III}(terminal) CT excited states are very similar, leading to appreciable excited state-excited state configurational mixing so that the $Ru^{II}(NH_3)_5 \rightarrow Ru^{III}(NH_3)_5$ MMCT transition is relatively intense ($\varepsilon_{max} = 1500\,M^{-1}\,cm^{-1}$).

The $[(NH_3)_5Ru^{II}\{(NC)(N_4)Cr^{III}(CN)\}Ru^{II}(NH_3)_5]^{6+}$ complexes are characterized by intense ($\sim 4000\,M^{-1}\,cm^{-1}/Ru^{II}$), Ru^{II}/Cr^{III} metal-to-metal CT absorption bands at approximately 500 nm.[114] The irradiation of these absorption bands of the complexes in 77 K DMSO/H_2O glassy solutions results in $Ru^{III}/Cr^{II} \rightarrow Ru^{II}/Cr^{III}$ electron-transfer emissions.[114] The emission bands have maxima at 850–775 nm (depending on N_4), are relatively broad ($\Delta\nu_{1/2} \approx 1000\,cm^{-1}$) and have roughly microsecond lifetimes. The emission energies are consistent with estimated electron-transfer parameters. These emission bands have relatively strong vibronic components with $h\nu_h \cong 400–500\,cm^{-1}$ (metal–ligand vibrations) and approximately $2000\,cm^{-1}$ (C≡N stretch), and much weaker N–H stretching and NH_2 deformation components (at ∼3100 and l600 cm^{-1}, respectively). The very large k_{NH}/k_{ND} isotope effects, in the range of 15–30, imply that the low-temperature excited state back electron transfer in these complexes is by means of a nuclear tunneling pathway mediated by the N–H stretch (the highest frequency vibrational modes). These complexes illustrate the electron-transfer behavior expected in the Marcus inverted region when thermally activated pathways are not accessible.

6.3 Complexes in Which the Donors and Acceptors are Bridged by a Single Atom

Although the reaction in equation (2) has long been a paradigm for efficient, single-atom-bridged electron-transfer reactions,[23] few simple model complexes exist that have a similarly linked donor and acceptor. A problem in such systems is that ligand-substitution rates tend to be very large when the d σ-orbitals are partly or fully occupied.[40]

Bimetallic complexes with a σ-bridging ligand between a transition metal donor and acceptor have been constructed by means of a of a pair of tetraaza-macrocyclic ligand complexes linked through carbon atoms of the macrocyclic rings to xylene, forming face-to-face bimetallic complexes. The $[L\{M^{II}(N_4)\}_2]^{4+}$ complexes have large ion-pair association constants with halides and they are potentially good models for σ-bridged donor–acceptor systems.[118]

Gamelin, *et al.*[73] characterized the oxy-bridged mixed valence $[\{(Me_3[9]aneN_3)Fe\}_2(OH)_3]^{2+}$ complex using a variety of spectroscopic and computational techniques. The $13.4 \times 10^3\,cm^{-1}$ MMCT absorption band has a non-Gaussian band shape and a $3.7 \times 10^3\,cm^{-1}$ bandwidth (300 K in a propionitrile/butyronitrile solvent). The iron atoms lie along the molecular 3-fold rotational axis and resonance Raman probing of the near-infrared MMCT absorption led to the conclusion that the electron density is delocalized between the iron atoms in this complex. The non-Gaussian band shape was attributed to anharmonicities in the excited state PE surface. The Fe–Fe electronic coupling was inferred to be mediated by Fe($d\pi$)–O–Fe(dσ) superexchange mechanism and H_{DA} was inferred to be a function of the Fe–Fe distance.

7 EXTENSIONS AND APPLICATIONS

There are many studies of the transfer of electrons from enzymes to substrates, across biological membranes, to (or from) electrodes from (or to) substrates, between adsorbed molecular dyes and semiconductor particles, within synthetic films and nano-scale arrays, within 'molecular wires', and so on. Only a few, general comments will be offered on these topics here. The basic physics of molecular electron transfer does not change with the scale of the system, as long as identifiable molecular moieties are present with at least partly localized electronic configurations. The nature of the properties observed, the experimental probes available, and the level of theoretical treatment that is useful may be very different. Different approaches, different limiting models are used for extended arrays (or lattices) of very strongly coupled moieties.

7.1 Electron Transfer in Biological Systems

Electron transfer is an essential component of energy transduction in biological systems. Elementary electron transport steps often involve donors and acceptors separated by cell membranes or protein structure. Multielectron processes are also important. Electron-transfer mechanisms in biological systems have provided challenges to the understanding of fundamental issues and inspirations for the design of efficient, synthetic catalytic systems and a large number of studies.[6,7,19,75,119–126] A combination of studies, employing synthetic 'model systems' that attempt to isolate and mimic selected aspects of the more complicated biological systems and chemical or genetic modification of key components of the biological systems, has been used to probe important features of biological electron-transfer behavior.

Issues related to the preferred pathways and the distance dependence of electron transfer in biological systems have been addressed by covalently linking electron-transfer donors or acceptors (e.g. a ruthenium complex) to specific sites (e.g. a histidine) of a protein or an enzyme.[124,126,127] The distance dependence of the electron-transfer rate constants is generally fitted to equation (44), with most values of β for proteins falling in the range of 1.0 to 1.3 Å $^{-1}$.[124] The protein in these experiments can be regarded as a huge, largely aliphatic bridging ligand, and in most cases it is possible to identify several feasible σ-bonded pathways for the coupling of the donor to the acceptor. A variation on the superexchange coupling model (see equation 43) has been used to identify the most likely of different possible pathways.[124,128–130] The size and flexibility of the protein makes it difficult to accurately define either a precise distance between the donor and acceptor, or a unique pathway.[127,129,131]

In related model complex studies, Isied and coworkers, have examined photo-induced (or pulse-radiolytically initiated) electron-transfer processes in which a polypyridine-ruthenium(II) complex is linked by means of a 4-carboxylato,4′-methyl,2,2′-bipyridine ligand and a polyproline chain to a $[\mathrm{Co(NH_3)_5}]^{3+}$ or $[(\text{-NH-py})\mathrm{Ru^{III}(NH_3)_5}]$ acceptor.[126] Chains composed of from zero to six cis-prolines have been examined. The apparent distance dependence of the electron-transfer rate constant, corrected for variations in the solvent reorganizational energy, seems to exhibit two types of distance dependence, $\beta \approx 0.7-1$ Å $^{-1}$ for short chains and $\beta \approx 0.3$ Å $^{-1}$ for long chains. A very detailed theoretical analysis of electron transfer in the complexes with four proline linkers has indicated that the electronic coupling is sensitive to conformational variations within the proline chain.[3]

When the appropriate equilibrium constants are not extremely small, direct electron (or hole) transfer to bridge units may occur and the electron (or hole) may then hop from moiety-to-moiety (randomly) along the bridge. When this happens, the electron-transfer rate will decrease only slowly with bridge length. This behavior has been treated in terms of standard nonadiabatic electron-transfer theory.[119]

When metallo-enzymes effect the oxidation or reduction of organic substrates or simple molecules such as H_2O, N_2 or O_2, they often function as multielectron donors or acceptors with two or more metals at the active site.[121–125,132,133] The electronic coupling between the metals is often accompanied by unique spectroscopic features such as electron spin–spin coupling.[73,134–137] The metal–metal electronic coupling may facilitate the multi-electron-transfer reactions with the substrates. In simpler molecular systems, two electron-transfer processes most often require substrate 'binding', as in an inner-sphere, group (or 'atom') transfer process.[138,139]

7.2 Complexes Containing Multiple Donors and/or Acceptors

Trimetallic complexes can be regarded as the first steps in the construction of nano-scale materials from simple molecular species. As the complex aggregates become larger, some of the factors dominating their electron-transfer properties may differ from the factors important in their bimetallic analogs. The observation of vibronic phase effects observed in the dicyano-complex-bridged $\mathrm{Ru(NH_3)_5}^{2+}$ /$\mathrm{Ru(NH_3)_5}^{3+}$ complexes may be a hint of this.

The issue of the 'wire-like' properties of arrays of metal complexes has been of some interest, has been reviewed recently.[140,141] See Volume 5 of the series *Electron Transfer in Chemistry*.[1,142,143]

7.3 Heterogeneous Electron-transfer Systems

Heterogeneous electron-transfer processes are important, they have been extensively studied and they span a wide range of phenomena. These include studies of electron transfer from (or to) molecular substrates within (or across) micelles and vesicles,[144] porous solid media,[145,146] layered materials,[147–149] and to (or from) semiconductors and electrodes.[150–156]

The study of heterogeneous systems in which a donor or acceptor is linked to the surface of a conductor or semiconductor has been of special interest when the electron injection into the semiconductor or electrode can be induced by light absorption of the linked dye molecule.[16,149,152,154,157–163] Grätzel and coworkers have used a ruthenium(II) complex linked to TiO_2 by means of a *bis*-carboxylato-bipyridine ligand to construct an efficient photocell.[16,152–154,157] Many details of the functioning of this photocell are not well understood, but it is based on efficient photo-induced injection of electrons, from the MLCT excited state, into the semiconductor. Femtosecond pump and probe experiments have demonstrated that at least some of the photoelectrons are injected within 50 ps of the MLCT excitation.[161,164] This is one of the fastest electron-transfer rates yet measured; it apparently occurs in competition with vibrational relaxation of the excited state.

8 RELATED ARTICLES

Electron Transfer Reactions: Theory; Long-range Electron Transfer in Biology; Mixed Valence Compounds; Molecular Orbital Theory; Oxidation Catalysis by Transition Metal Complexes; Photochemistry of Transition Metal Complexes; Photochemistry of Transition Metal Complexes: Theory.

9 REFERENCES

1. V. Balzani ed., 'Electron Transfer in Chemistry', Wiley-VCH, Weinheim, 2001.
2. M. D. Newton, *Chem. Rev.*, 1991, **91**, 767.
3. M. D. Newton, in 'Electron Transfer In Chemistry', ed. V. Balzani, Wiley-VCH, Weinheim, 2001, Vol. 1, p. 3.
4. A. M. Kuznetsov, 'Charge Transfer in Physics, Chemistry and Biology: Physical Mechanisms of Elementary Processes and an Introduction to the Theory', Gordon and Breach, New York, 1995.
5. A. M. Kuznetsov, 'Charge Transfer in Chemical Reaction Kinetics', Presses Polytechniques et Universitaires Romandes, Lausanne, 1997.
6. A. M. Kuznetsov and J. Ulstrup, 'Electron Transfer in Chemistry and Biology', Wiley-VCH, New York, 1998.
7. J. Jortner and M. Bixon, ed., *Adv. Chem. Phys.*, 1999, **B106**, 35.
8. A. A. Kornyshev, M. Tosi, and J. Ulstrup eds, 'Electron and Ion Transfer in Condensed Media', World Scientific, Singapore, 1997.
9. M. K. Johnson, R. B. King, D. M. Kurtz Jr, C. Kutal, M. L. Norton and R. A. Scott eds, 'Electron Transfer in Biology and the Solid State', ACS Advances in Chemistry Series, 228, American Chemical Society, Washington, 1989.
10. J. R. Bolton, N. Mataga and G. McLendon eds, 'Electron Transfer in Inorganic, Organic and Biological Systems', ACS Advances in Chemistry Series, 226, American Chemical Society, Washington, DC, 1991.
11. S. S. Isied ed., 'Electron Transfer Reactions', ACS Advances in Chemistry Series, 253, American Chemical Society, Washington, DC, 1997.
12. J. Jortner and M. A. Ratner eds, 'Molecular Electronics', Blackwell Science Ltd., Oxford, 1997.
13. T. J. Meyer and M. D. Newton eds, *Chem. Phys.*, 1993, **176**, 289.
14. M. A. Fox and M. Channon eds, 'Photoinduced Electron Transfer', Elsevier, Amsterdam, 1988.
15. G. J. Kavarnos, 'Fundamentals of Photoinduced Electron Transfer', VCH, New York, 1993.
16. M. Gratzel, 'Heterogeneous Photochemical Electron Transfer', CRC press, Boca Raton, FL, 1989.
17. J. N. Wishart and D. G. Nocera eds, 'Photochemistry and Radiation Chemistry: Complementary Methods for the Study of Electron Transfer', ACS Advances in Chemistry Series, 254, American Chemical Society, Washington, DC, 1998.
18. C. Nicolini ed, 'Biophysics of Electron Transfer and Molecular Bioelectronics', Plenum Press, New York, 1998.
19. G. W. Canters and E. Vijenboom eds, 'Biological Electron Transfer Chains: Genetics, Composition and Mode of Operation', Kluwer Academic Publishers, Dordrecht, 1998.
20. M. A. Fox, ed., *Chem. Rev.*, 1992, **92**, 365.
21. T. J. Meyer and H. Taube, in 'Comprehensive Coordination Chemistry', ed. G. Wilkinson, Pergamon, Oxford, 1987, Vol. 7, p. 331.
22. J. F. Endicott, in 'Comprehensive Coordination Chemistry II', eds. J. McCleverty and T. J. Meyer, Pergamon, Oxford, 2003, Vol. 7, p. 657.
23. H. Taube, H. Myers, and R. L. Rich, *J. Am. Chem. Soc.*, 1953, **75**, 4118.
24. H. Taube, *Can. J. Chem.*, 1959, **37**, 129.
25. R. D. Cannon, *Adv. Inorg. Chem. Radiochem.*, 1979, **21**, 179.

26. B. Durham, J. F. Endicott, C. L. Wong, and D. P. Rillema, *J. Am. Chem. Soc.*, 1979, **101**, 847.
27. M. B. Robin and P. Day, *Adv. Inorg. Chem. Radiochem.*, 1967, **10**, 247.
28. R. A. Marcus, *Discuss. Faraday Soc.*, 1960, **29**, 21.
29. R. A. Marcus, *Annu. Rev. Phys. Chem.*, 1964, **15**, 155.
30. R. A. Marcus, *J. Chem. Phys.*, 1965, **43**, 670.
31. N. S. Hush, *Prog. Inorg. Chem.*, 1968, **8**, 391.
32. M. D. Newton and N. Sutin, *Annu. Rev. Phys. Chem.*, 1984, **35**, 437.
33. N. Kestner, J. Logan, and J. Jortner, *J. Phys. Chem.*, 1974, **64**, 2148.
34. R. Englman and J. Jortner, *Mol. Phys.*, 1970, **18**, 145.
35. K. F. Freed and J. Jortner, *J. Chem. Phys.*, 1970, **52**, 6272.
36. I. R. Gould, D. Noukakis, G. J. Luis, R. H. Young, J. L. Goodman, and S. Farid, *Chem. Phys.*, 1993, **176**, 439.
37. D. V. Matyushov and G. A. Voth, in ‘Reviews in Computational Chemistry’, eds. K. B. Lipkowitz, and D. B. Boyd, Wiley-VCH, New York, 2002.
38. J. H. Espenson, ‘Chemical Kinetics and Reaction Mechanisms’, McGraw-Hill, New York, 1981.
39. P. Zuman and R. C. Patel, ‘Techniques in Organic Reaction Kinetics’, Wiley, New York, 1984.
40. R. G. Wilkins, ‘Kinetics and Mechanisms of Transition Metal Complexes’, 2nd edn., VCH, Weinheim, 1991.
41. J. N. Demas, ‘Excited State Lifetime Measurements’, Academic Press, New York, 1983.
42. T. C. Brunold and H. U. Gudel, in ‘Inorganic Electronic Structure and Spectroscopy’, eds. E. I. Solomon and A. B. P. Lever, Wiley-Interscience, New York, 1999, Vol. 1, p. 259.
43. N. Sutin, *Prog. Inorg. Chem.*, 1983, **30**, 441.
44. R. S. Mulliken and W. B. Person, ‘Molecular Complexes’, Wiley-Interscience, New York, 1967.
45. B. S. Brunschwig, C. Creutz, and N. Sutin, *Coord. Chem. Rev.*, 1998, **177**, 61.
46. J. R. Reimers and N. S. Hush, *J. Phys. Chem.*, 1991, **95**, 9773.
47. M. J. Ondrechen, S. Gozashiti, L. T. Zhang, and F. Zhou, in ‘Electron Transfer in Biology and the Solid State’, ACS Advances in Chemistry Series, 226, eds. M. K. Johnson, R. B. King, D. M. Kurtz Jr, C. Kutal, M. L. Norton, and R. A. Scott, American Chemical Society, Washington, DC, 1990, p. 225.
48. S. B. Piepho, E. R. Krausz, and P. N. Schatz, *J. Am. Chem. Soc.*, 1978, **100**, 2996.
49. H. Sumi, in ‘Electron Transfer in Chemistry’, ed. V. Balzani, Wiley-VCH, Weinheim, 2001, Vol. 1, p. 65.
50. A. B. Myers, *Acc. Chem. Res.*, 1998, **30**, 519.
51. J. V. Casper and T. J. Meyer, *Inorg. Chem.*, 1983, **22**, 2446.
52. D. Graff, J. P. Claude, and T. J. Meyer, in ‘Electron Transfer in Organometallic and Biochemistry’, ACS Advances in Chemistry Series 253, ed. S. S. Isied, American Chemical Society, Washington, DC, 1997, p. 183.
53. J. B. Birks, ‘Photophysics of Aromatic Molecules’, Wiley-Interscience, New York, 1970.
54. E. M. Kober, J. V. Casper, R. S. Lumpkin, and T. J. Meyer, *J. Phys. Chem.*, 1986, **90**, 3722.
55. M. Bixon, J. Jortner, J. Cortes, H. Heilte, and M. E. Michel-Beyerle, *J. Phys. Chem.*, 1994, **98**, 7289.
56. B. S. Brunschwig, S. Ehrenson, and N. Sutin, *J. Phys. Chem.*, 1986, **90**, 3657.
57. B. S. Brunschwig and N. Sutin, in ‘Electron Transfer in Chemistry’, ed. V. Balzani, Wiley-VCH, Weinheim, 2001, Vol. 2, p. 583.
58. C. Creutz, M. D. Newton, and N. Sutin, *Photochem. Photobiol., A: Chem.*, 1994, **82**, 47.
59. J. F. Endicott, M. J. Uddin, and H. B. Schlegel, *Res. Chem. Intermed.*, 2002, **28**, 761.
60. D. V. Matyushov and G. A. Voth, *J. Phys. Chem. A*, 2000, **104**, 6470.
61. D. V. Matyushov and M. D. Newton, *J. Phys. Chem. A*, 2001, **105**, 8516.
62. J. F. Endicott, H. B. Schegel, M. J. Uddin, and D. Senerivatne, *Coord. Chem. Rev.*, 2002, **229**, 95.
63. C. Creutz, *Prog. Inorg. Chem.*, 1983, **30**, 1.
64. R. Crutchley, *Adv. Inorg. Chem.*, 1994, **41**, 273.
65. P. W. Anderson, in ‘Magnetism’, eds. G. T. Rado and H. Suhl, Academic Press, New York, 1963.
66. H. M. McConnell, *J. Chem. Phys.*, 1961, **35**, 508.
67. D. L. Dexter, *Phys. Rev.*, 1962, **126**, 1962.
68. A. V. Macatangay, X. Song, and J. F. Endicott, *J. Phys. Chem.*, 1998, **102**, 7537.
69. A. V. Macatangay and J. F. Endicott, *Inorg. Chem.*, 2000, **39**, 437.
70. P. N. Schatz, in ‘Inorganic Electronic Structure and Spectroscopy’, eds. E. I. Solomon and A. B. P. Lever, Wiley, New York, 1999, Vol. 2, p. 175.
71. D. E. Richardson, in ‘Inorganic Electronic Structure and Spectroscopy’, eds. E. I. Solomon and A. B. P. Lever, Wiley, New York, 1999, Vol. 2, p. 131.
72. B. S. Tsukerblat, ‘Group Theory in Chemistry and Spectroscopy’, Academic, London, 1994.
73. D. R. Gamelin, E. L. Bominaar, C. Mathoniere, M. L. Kirk, J. J. Girerd, and E. I. Solomon, *Inorg. Chem.*, 1996, **35**, 4323.
74. R. D. Cannon, ‘Electron Transfer Reactions’, Butterworth, London, 1980.
75. P. F. Barbara, T. J. Meyer, and M. Ratner, *J. Phys. Chem.*, 1996, **100**, 13148.
76. B. S. Brunschwig and N. Sutin, *Coord. Chem. Rev.*, 1999, **187**, 233.
77. N. S. Hush, in ‘Mechanistic Aspects of Inorganic Reactions’, ACS Symposium Series eds. D. B. Rorabacher and

J. F. Endicott, American Chemical Society, Washington, DC, 1982, Vol. 198, p. 301.

78. N. Sutin, *Adv. Chem. Phys.*, 1999, **106**, 7.
79. J. F. Endicott, *Acc. Chem. Res.*, 1988, **21**, 59.
80. M. D. Newton, *J. Phys. Chem.*, 1991, **95**, 30.
81. D. E. Richardson, *J. Phys. Chem.*, 1986, **90**, 3697.
82. D. K. Phelps, J. R. Gord, B. S. Freiser, and M. J. Weaver, *J. Phys. Chem.*, 1991, **95**, 4338.
83. K. Nakamoto, 'Infrared and Raman Spectra of Inorganic and Coordination Compounds', Wiley, New York, 1997, Part B.
84. G. M. Brown and N. Sutin, *J. Am. Chem. Soc.*, 1979, **101**, 883.
85. R. M. Levy and E. Gallicchio, *Annu. Rev. Phys. Chem.*, 1998, **49**, 531.
86. G. Ferraudi, *Inorg. Chem.*, 2000, **39**, 2866.
87. R. J. Campion, C. F. Deck, P. King, and A. C. Wahl Jr, *Inorg. Chem.*, 1967, **6**, 672.
88. A. Zahl, R. van Eldik, and T. W. Swaddle, *Inorg. Chem.*, 2002, **41**, 757.
89. R. Billing and D. E. Khoshtariya, *Inorg. Chem.*, 1994, **33**, 4038.
90. X. Song, Y. Lei, S. Van Wallendel, M. W. Perkovic, D. C. Jackman, J. F. Endicott, and D. P. Rillema, *J. Phys. Chem.*, 1993, **97**, 3225.
91. C. M. Elliott, D. L. Derr, D. V. Matyushov, and M. D. Newton, *J. Am. Chem. Soc.*, 1998, **120**, 11714.
92. R. H. Schmehl, R. A. Auerbach, W. F. Wacholtz, C. M. Elliott, R. A. Freitag, and J. W. Merkert, *Inorg. Chem.*, 1986, **25**, 2440.
93. A. B. P. Lever and E. Dodsworth, in 'Electronic Structure and Spectroscopy of Inorganic Compounds', eds. A. B. P. Lever and E. I. Solomon, Wiley, New York, 1999, Vol. 2, p. 227.
94. B. M. Hoffman and M. A. Ratner, *J. Am. Chem. Soc.*, 1987, **109**, 6237.
95. B. S. Brunschwig and N. Sutin, *J. Am. Chem. Soc.*, 1989, **111**, 7454.
96. Q. Yu, C. A. Salhi, E. A. Ambundo, M. J. Heeg, L. A. Ochrymowycz, and D. B. Rorabacher, *J. Am. Chem. Soc.*, 2001, **123**, 5720.
97. P. Piotrowiak, *Chem. Soc. Rev.*, 1999, **28**, 143.
98. K. D. Demadis, C. M. Hartshorn, and T. J. Meyer, *Chem. Rev.*, 2001, **101**, 2655.
99. W. Kaim, A. Klein, and M. Glockle, *Acc. Chem. Res.*, 2000, **33**, 755.
100. B. S. Brunschwig, C. Creutz, and N. Sutin, *Chem. Soc. Rev.*, 2002, **31**, 168.
101. F. Scandola, C. Chiorboli, M. T. Indelli, and M. A. Rampi, in 'Electron Transfer in Chemistry', ed. V. Balzani, Wiley-VCH, Weinheim, 2001, Vol. 3, p. 337.
102. L. Fabbrizzi, M. Licchelli, and A. Taglietti, in 'Electron Transfer in Chemistry', ed. V. Balzani, Wiley-VCH, Weinheim, 2001, Vol. 3, p. 462.
103. D. Gust, T. A. Moore, and A. L. Moore, *Acc. Chem. Res.*, 2001, **34**, 40.
104. R. W. Wu, M. Poyraz, F. E. Sowrey, C. E. Anson, S. Wocadlo, A. K. Powell, U. A. Jayasooriya, and R. D. Cannon, *Inorg. Chem.*, 1998, **37**, 1913.
105. T. Ito, T. Hamaguchi, H. Nagino, T. Yamaguchi, H. Kido, I. S. Zavarine, T. Richmond, J. Washington, and C. P. Kubiak, *J. Am. Chem. Soc.*, 1999, **121**, 4625.
106. I. S. Zavarine, C. P. Kubiak, T. Yamaguchi, K. Ota, T. Matsui, and T. Ito, *Inorg. Chem.*, 2000, **39**, 2696.
107. C. Creutz and H. Taube, *J. Am. Chem. Soc.*, 1973, **95**, 1086.
108. P. A. Lay, R. H. Magnuson, and H. Taube, *Inorg. Chem.*, 1988, **27**, 2364.
109. A. B. P. Lever, 'Inorganic Electronic Spectroscopy', Elsevier, Amsterdam, 1984.
110. P. Kambhampati, D. H. Son, T. W. Kee, and P. F. Barbara, *J. Phys. Chem. A*, 2000, **104**, 10637.
111. D. H. Son, P. Kambhampati, T. W. Kee, and P. F. Barbara, *J. Phys. Chem. A*, 2002, **106**, 4591.
112. J. T. Hupp and R. T. Williams, *Acc. Chem. Res.*, 2001, **34**, 808.
113. C. A. Bignozzi, S. Roffia, and F. Scandola, *J. Am. Chem. Soc.*, 1985, **107**, 1644.
114. J. F. Endicott, P. G. McNamara, T. Buranda, and A. V. Macatangay, *Coord. Chem. Rev.*, 2000, **208**, 61.
115. A. V. Macatangay, S. E. Mazzetto, and J. F. Endicott, *Inorg. Chem.*, 1999, **38**, 5091.
116. M. A. Watzky, J. F. Endicott, X. Song, Y. Lei, and A. V. Macatangay, *Inorg. Chem.*, 1996, **35**, 3463.
117. M. A. Watzky, A. V. Macatangay, R. A. Van Camp, S. E. Mazzetto, X. Song, J. F. Endicott, and T. Buranda, *J. Phys. Chem.*, 1997, **101**, 8441.
118. M. Y. Udugala-Ganehenege, M. J. Heeg, L. M. Hyhroczuk, L. E. Wenger, and J. F. Endicott, *Inorg. Chem.*, 2001, **40**, 1614.
119. M. Bixon, B. Giese, S. Wessely, T. Langenbacher, M. E. Michel-Beyerle, and J. Jortner, *Proc. Natl. Acad. Sci. U.S.A.*, 1999, **96**, 11713.
120. F. D. Lewis, in 'Electron Transfer in Chemistry', ed. V. Balzani, Wiley-VCH, Weinheim, 2001, Vol. 3, p. 105.
121. B. G. Malmstrom, in 'Electron Transfer in Chemistry', ed. V. Balzani, Wiley-VCH, Weinheim, 2001, Vol. 3, p. 39.
122. A. E. Pond, A. P. Ledbetter, M. Sono, D. B. Goodin, and J. H. Dawson, in 'Electron Transfer in Chemistry', ed. V. Balzani, Wiley-VCH, Weinheim, 2001, *Vol 3*, p. 56.
123. C. C. Moser, C. C. Page, and P. L. Dutton, in 'Electron Transfer in Chemistry', ed. V. Balzani, Wiley-VCH, Weinheim, 2001, *Vol. 3*, p. 24.
124. H. B. Gray and J. B. Winkler, in 'Electron Transfer in Chemistry', ed. V. Balzani, Wiley-VCH, Weinheim, 2001, Vol. 3, p. 3.

125. E. I. Solomon, M. D. Lowery, J. A. Guckert, and J. A. Guckert, in 'ACS Advances in Chemistry Series: Electon Transfer Reactions', ed. S. S. Isied, American Chemical Society, Washington, DC, 1997, Vol 253, p. 317.
126. S. S. Isied, in 'Electron Transfer Reactions', ACS Advances in Chemistry Series, ed. S. S. Isied, American Chemical Society, Washington, DC, 1997, Vol. 253, p. 349.
127. B. Durham, P. P. Lian, S. Hahm, L. Long and F. Millett, in 'Electron Transfer in Biology and the Solid State', ACS Advances in Chemistry Series, 226, eds. M. K. Johnson, R. B. King, D. M. Kurtz Jr, C. Kutal, M. L. Norton and R. A. Scott, American Chemical Society, Washington, DC, 1990, p. 181.
128. D. N. Beratan, J. N. Betts, and J. N. Onuchic, *Science*, 1991, **252**, 1285.
129. S. S. Skourtis and D. N. Beratan, in 'Electron Transfer in Chemistry', ed. V. Balzani, Wiley-VCH, Weinheim, 2001, Vol. 1, p. 109.
130. J. J. Regen and J. N. Onuchic, *Adv. Chem. Phys.*, 1999, **107**, 497.
131. A. Warshel, *Acc. Chem. Res.*, 2002, **35**, 385.
132. A. E. Shilov, in 'Electron Transfer in Chemistry', ed. V. Balzani, Wiley-VCH, Weinheim, 2001, Vol. 2, p. 878.
133. C. E. Forde and R. H. Morris, in 'Electron Transfer in Chemistry', ed. V. Balzani, Wiley-VCH, Weinheim, 2001, Vol 2, p. 905.
134. I. V. Vonseggern, F. Tuczek, and W. Bensch, *Inorg. Chem.*, 1995, **34**, 5530.
135. E. I. Solomon, F. Tuczek, D. E. Root, and C. A. Brown, *Chem. Rev.*, 1994, **94**, 827.
136. E. I. Solomon and M. A. Hanson, in 'Inorganic Electronic Structure and Spectroscopy', eds. E. I. Solomon, and A. B. P. Lever, Wiley, New York, 1999, Vol. 2, p. 1.
137. T. C. Brunold, D. R. Gamelin, and E. L. Solomon, *J. Am. Chem. Soc.*, 2000, **122**, 8511.
138. H. Taube, in 'Mechanistic Aspects of Inorganic Reactions', ACS Symposium Series, eds. D. B. Rorabacher and J. F. Endicott, American Chemical Society, Washington, DC, 1982, Vol. 198, p. 151.
139. C. Creutz, in 'Electron Transfer Reactions' American Chemical Society Advances in Chemistry Series, ed. S. S. Isied, American Chemical Society, Washington, DC, 1997, Vol. 253, p. 151.
140. J. P. Launay and C. Coudret, in 'Electron Transfer in Chemistry', ed. V. Balzani, Wiley-VCH, Weinheim, 2001, Vol. 5, p. 3.
141. L. De Cola and P. Belser, in 'Electron Transfer in Chemistry', ed. V. Balzani, Wiley-VCH, Weinheim, 2001, Vol. 5, p. 97.
142. J. P. Sauvage and C. O. Dietrich-Buchecker eds, 'Catenanes, Rotaxanes and Knots', Wiley-VCH, Weinheim, 1999.
143. D. B. Ambabilino and J. F. Stoddart, *Chem. Rev.*, 1995, **95**, 2725.
144. J. K. Hurst and R. F. Khairutdinov, in 'Electron Transfer in Chemistry', ed. V. Balzani, Wiley-VCH, Weinheim, 2001, Vol. 4, p. 578.
145. A. S. Vaidyalingam, M. A. Coutant, and P. K. Dutta, in 'Electron Transfer in Chemistry', ed. V. Balzani, Wiley-VCH, Weinheim, 2001, Vol. 4, p. 412.
146. P. K. Dutta and M. Ledney, *Prog. Inorg. Chem.*, 1997, **44**, 209.
147. L. A. Vermeulen, *Prog. Inorg. Chem.*, 1997, **44**, 143.
148. V. Bhat and D. Kazunari, in 'Electron Transfer in Chemistry', ed. V. Balzani, Wiley-VCH, Weinheim, 2001, Vol. 4, p. 487.
149. R. S. Clegg and J. E. Hutchison, in 'Electron Transfer in Chemistry', ed. V. Balzani, Wiley-VCH, Weinheim, 2001, Vol. 4, p. 541.
150. P. Qu and G. J. Meyer, in 'Electron Transfer in Chemistry', ed. V. Balzani, Wiley-VCH, Weinheim, 2001, Vol. 4, p. 353.
151. C. A. Bignozzi, J. R. Schoonover, and F. Scandola, *Prog. Inorg. Chem.*, 1997, **44**, 1.
152. T. Gerfin, M. Gratzel, and L. Walder, *Prog. Inorg. Chem.*, 1997, **44**, 345.
153. A. Hagfeldt and M. Gratzel, *Acc. Chem. Res.*, 2000, **33**, 269.
154. M. Gratzel and J. E. Moser, in 'Electron Transfer in Chemistry', ed. V. Balzani, Wiley-VCH, Weinheim, 2001, Vol. 5, p. 589.
155. J. W. Turner and F. A. Schultz, *Coord. Chem. Rev.*, 2001, **219**, 81.
156. X. Y. Zhu, *Annu. Rev. Phys. Chem.*, 2002, **53**, 221.
157. M. K. Nazeeruddin, A. Kay, I. Rodicio, R. Humphrybaker, E. Muller, P. Liska, N. Vlachopoulos, and M. Gratzel, *J. Am. Chem. Soc.*, 1993, **115**, 6382.
158. P. V. Kamat, *Prog. Inorg. Chem.*, 1997, **44**, 273.
159. K. Rajeshwar, in 'Electron Transfer in Chemistry', ed. V. Balzani, Wiley-VCH, Weinheim, 2001, Vol. 5, p. 279.
160. N. S. Lewis, *J. Electroanal. Chem.*, 2001, **508**, 1.
161. T. Hannappel, B. Bernd, W. Storck, and F. Willig, *J. Phys. Chem. B*, 1997, **101**, 6799.
162. A. Meier, D. C. Selmarten, K. Seiemoneit, B. B. Smith, and A. J. Nozik, *J. Phys. Chem. B*, 1999, **103**, 2122.
163. J. B. Asbury, R. J. Ellingson, H. N. Ghosh, S. Ferrere, A. J. Nozik, and T. Q. Lian, *J. Phys. Chem. B*, 1999, **103**, 3110.
164. J. B. Asbury, R. J. Ellingson, H. N. Ghosh, S. Ferrere, A. J. Nozik, and T. Q. Lian, *J. Phys. Chem. B*, 1999, **103**, 3110.

Acknowledgment

Support from the Office of Basic Energy Sciences of the Department of Energy is gratefully acknowledged.

Electron Transfer Reactions: Theory

Dmitry Matyushov
Arizona State University, Tempe, AZ, USA

Based in part on the article Electron Transfer Reactions: Theory by Roderick D. Cannon which appeared in the Encyclopedia of Inorganic Chemistry, First Edition.

1	Introduction	1
2	The Electron-Transfer Process	2
3	The Marcus Theory	3
4	Microscopic Properties of Solvent Reorganization	5
5	The Cross Relation	5
6	Nonadiabatic Transfer	6
7	Connection with Optical Spectroscopy	6
8	State-to-state Theories	7
9	The Inverted Region	9
10	Beyond the Parabolas	9
11	Long-range and Bridged Electron Transfer	10
12	Solvent Dynamics	11
13	Effects of Pressure	12
14	Electron Transfer and Magnetism	12
15	Conclusions	13
16	Related Articles	13
17	Further Reading	13
18	References	14

1 INTRODUCTION

This article is concerned with reactions in which the net effect is transfer of one or more electrons, with little permanent rearrangement of the structures surrounding the donor and acceptor sites. Typical examples are the following: an outer-sphere reaction (equation 1), an inner-sphere reaction (equation 2) that involves direct bridging Cr–Cl–Cr in the transition state, and a two-electron reaction (equation 3) that could be classed as atom transfer, but is formally analogous to equation (2).

$$\mathrm{MnO_4^{-}} + {}^{*}\mathrm{MnO_4^{2-}} \longrightarrow \mathrm{MnO_4^{2-}} + {}^{*}\mathrm{MnO_4^{-}} \qquad (1)$$

$$[\mathrm{Cr(OH_2)_5Cl}]^{2+} + [{}^{*}\mathrm{Cr(OH_2)_6}]^{2+} \longrightarrow [\mathrm{Cr(OH_2)_6}]^{2+} + [{}^{*}\mathrm{Cr(OH_2)_5Cl}]^{2+} \qquad (2)$$

$$\mathrm{C_5H_5NO} + \mathrm{PPh_3} \longrightarrow \mathrm{C_5H_5N} + \mathrm{O} = \mathrm{PPh_3} \qquad (3)$$

Symmetrical reactions such as equations (1) and (2) are called self-exchange reactions, and are often abbreviated; for example, $\mathrm{MnO_4}^{-/2-}$ denotes equation (1). Excluded from this review are reactions such as $[\mathrm{Fe(OH_2)_6}]^{2+} + \mathrm{NO} \rightarrow [\mathrm{Fe(OH_2)_5NO}]^{2+} + \mathrm{H_2O}$, in which substantial charge transfer is believed to occur but the final oxidation states are not well defined, and reactions with drastic coordination changes such as reductive elimination and oxidative addition. Also excluded are noncomplementary reactions such as $\mathrm{Tl}^{3+} + 2\mathrm{Fe}^{2+} \rightarrow \mathrm{Tl}^{+} + 2\mathrm{Fe}^{3+}$, which involve more or less complicated reaction pathways, except insofar as the individual steps of such reactions include simple electron transfers of the type defined above.[1]

It is generally assumed that even the simplest reactions can be dissected into still smaller steps:

$$\mathrm{A^+ + Bs} \rightleftharpoons \mathrm{A^+ \cdots B} \qquad k_{\mathrm{ip}}, k_{\mathrm{pi}} \qquad (4a)$$

$$\mathrm{A^+ \cdots Bs} \rightleftharpoons \mathrm{A \cdots B^+} \qquad k_{\mathrm{ps}}, k_{\mathrm{sp}} \qquad (4b)$$

$$\mathrm{A \cdots B^+ s} \rightleftharpoons \mathrm{A + B^+} \qquad k_{\mathrm{sf}}, k_{\mathrm{fs}} \qquad (4c)$$

Here A, B denote the reacting centers and the superior plus signs denote the higher of the two oxidation states, regardless of the actual ionic charge. The letters i, p, s, and f, denote the initial, precursor, successor, and final states of the reacting system. Provided the two intermediates remain at low concentration throughout, the overall rate law is:

$$\mathrm{Rate} = -\frac{\mathrm{d}[\mathrm{A}^+]}{\mathrm{d}t} = k[\mathrm{A}^+][\mathrm{B}] \qquad (5)$$

where

$$k^{-1} = k_{\mathrm{ip}}{}^{-1} + (K_{\mathrm{ip}}k_{\mathrm{ps}})^{-1} + (K_{\mathrm{ip}}K_{\mathrm{ps}}k_{\mathrm{sf}})^{-1} \qquad (6)$$

where K_{ip} and K_{ps} are the equilibrium constants for equations (4a and b). Actual precursor and successor complexes have been detected in a number of cases, and various combinations of rate and equilibrium constants have been measured under favorable conditions, but the commonest case for reactions between separated complexes in solution is for equation (4b) to be rate determining, so that

$$k = K_{\mathrm{ip}}k_{\mathrm{ps}} \qquad (7)$$

and equations (4a) and (c) are diffusion controlled. A second important situation arises when the precursor complex can be synthesized and k_{ps} can be measured directly.[2] This has been done with complexes such as (**1**) in which by various means the extra electron is rapidly and selectively added to one of the two centers and then transfers intramolecularly to the other, and with quasi-symmetrical mixed-valence molecules such as (**2**) in which the two centers differ only by the number of electrons, as in a self-exchange reaction.

$[(\mathrm{H_3N})_5\mathrm{Co^{III}(pz)Ru^{II}(NH_3)_4SO_4}]^{3+}$
(1)

$[\mathrm{O_2NC_6H_4OC_6H_4NO_2}\bullet]^{-}$
(2)

The formulas quoted in this section have been used to estimate absolute rates of a considerable number of outer-sphere electron-transfer reactions. The reactions $\mathrm{Ru(OH_2)_6}^{3+/2+}$ and $\mathrm{Ru(NH_3)_6}^{3+/2+}$,[3] and $\mathrm{MnO_4}^{-/2}$,[4] are particularly well-studied examples. The dependence of rate on solvent polarity implied by equation (6) has proved more difficult to test and it has only recently become clear that some reactions, such as $[\mathrm{Ru(hfac)_3}]^{0/-}$, fit the equation well, while others, such as $[\mathrm{Mn(NC(C_6H_{11})_6)}]^{2+/+}$, do not.[5] The variation in polarity is usually achieved by using mixed solvents in varying proportions, and selective solvation by one component may be one reason for discrepancies.

2 THE ELECTRON-TRANSFER PROCESS

In equation (1) the precursor complex is a loose ion-pair of formula $[(\mathrm{MnO_4})^- \cdots (\mathrm{MnO_4})^{2-}]\cdot\mathrm{aq}$. The questions arise, why is the electron-transfer reaction not instantaneous, or why does the complex not adopt a stable symmetrical structure owing to resonance? That it does not do so is shown by the fact that the rate of reaction is less than the rate of diffusion-controlled encounter between the ions.[1] There are several other well-recognized chemical and physical analogs to electron transfer. (1) Electron transfer can be viewed as a radiationless transition of the precursor complex and it is well established that such processes can be slow. (2) If the complex were constrained to the symmetrical configuration, it would evidently change spontaneously to the less symmetrical form, and this recalls the Jahn–Taller effect, as in an octahedral copper(II) complex that tends to distort to a tetragonal configuration. (3) The localization of one extra electron on one side of the binuclear species is analogous to the localization of a solvated electron or polaron in a liquid or solid medium. The theories of all these effects have in fact been successfully adapted to electron-transfer kinetics. We begin here with the semiclassical two-state model of a mixed-valence dimer first outlined by Mayoh and Day.[6]

In a molecule $(\mathrm{A}\cdots\mathrm{B})^+$ the electronic wavefunctions can be written

$$\Psi_1 = \rho\phi_\mathrm{A} + \sqrt{(1-\rho^2)}\,\phi_\mathrm{B} \tag{8a}$$

$$\Psi_2 = \sqrt{(1-\rho^2)}\phi_\mathrm{A} - \rho\,\phi_\mathrm{B} \tag{8b}$$

so that $\rho = 0$ corresponds to a ground state with the electron localized on redox center B and an excited state with the electron localized on redox center A, and $\rho = 1$ corresponds to the reverse localization. Partial localization, with $0 < \rho < 1$, means electron densities of ρ^2 and $(1 - \rho^2)$ on the respective sites in the ground state, and vice versa in the excited state. Localization is due to differences in metal–ligand bonds and solvation, and the electron is trapped in a potential well, as shown in Figure 1. The curves drawn in Figure 1 show the potential energy of the electron as a function of position along the internuclear axis.

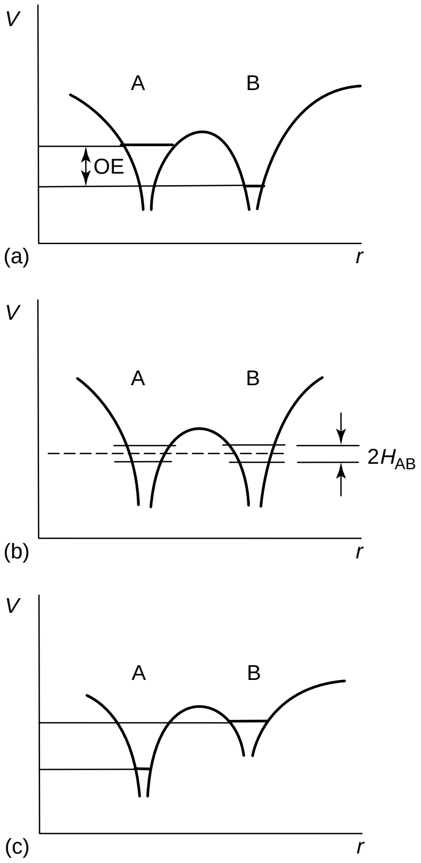

Figure 1 Potential wells for an electron trapped by polarization of solvent or ligand environment in a dinuclear complex $(\mathrm{A}\cdots\mathrm{B})^+$. V = electron potential energy, r = distance along the A–B axis. (a) Ground state $p(\mathrm{A}^+\cdots\mathrm{B})$ with electron localized mainly at site B, excited state s^* $(\mathrm{A}\cdots\mathrm{B}^-)$ with electron mainly transferred to site A. (b) The energy wells adjusted to equal 'depth' by solvent and ligand motion. The electron is delocalized with two energy levels separated by $2H_\mathrm{AB}$. (c) The reverse polarization, ground state $s(\mathrm{A}\cdots\mathrm{B}^+)$, excited state $p^*(\mathrm{A}^+\cdots\mathrm{B})$

In this model, electron transfer occurs when the potential wells change shape to the point where $\rho = 1/2$. The change comes about as a result of a suitable combination of adjustments of positions of ligand and solvent molecules. At this point the electron has, over time, an equal probability of being found on either site, and if the atomic positions continue to evolve in the same sense, the electron transfer goes to completion. Alternatively, if the electron were somehow constrained to one site and then released, it would oscillate between the two sites, or rather, its wavefunction would oscillate between the two forms ϕ_A and ϕ_B. The process whereby the electron passes from one potential well to the other is electron tunneling since in quantum mechanics it is not necessary for the electron to acquire the potential energy corresponding to the top of the barrier.

The energy gap between the donor and acceptor electronic states ΔE (Figure 1) defines the reaction coordinate $X = \Delta E$.

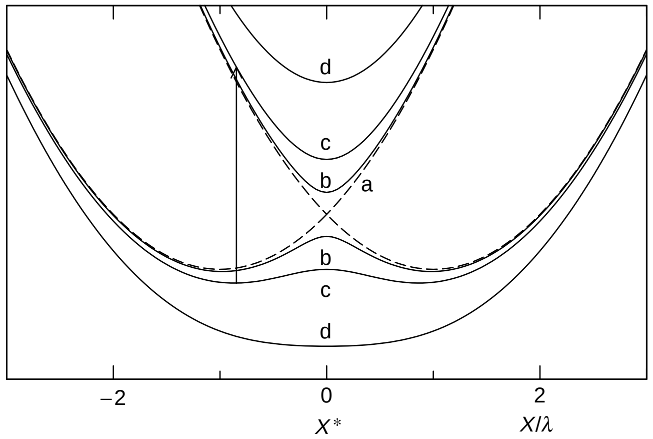

Figure 2 Potential curves for a mixed-valence dinuclear complex ($A^+\cdots A$) as functions of the energy gap reaction coordinate X. Broken lines (a), no electronic interaction; (b,b), (c,c), (d,d), successively stronger interactions, the last corresponding to $H_{AB} > \lambda/2$ (see text) so that the symmetrical structure is the most stable. The vertical arrow indicates an intervalence charge-transfer transition

The activated state $X^* = 0$ then corresponds to resonance of the donor and acceptor electronic levels at which electron tunneling may occur. The energy of the reacting system as a function of this coordinate is shown in Figure 2. The two intersecting curves (a) correspond to the fully localized wavefunctions ϕ_A, ϕ_B. The pairs of nonintersecting curves correspond to the mixed wavefunctions Ψ_1, Ψ_2, with different values of H_{AB}, the resonance integral or tunneling integral:

$$H_{AB} = \langle \phi_A | H | \phi_B \rangle \tag{9}$$

where H is the Hamiltonian of the dinucear complex $(A\cdots B)^+$. The separation between upper and lower curves at the point of resonance is $2H_{AB}$. The vertical arrow in Figure 2 also corresponds to an observable physical process, the optical transition whereby the electron localization is reversed, but by the Franck-Condon principle atomic positions remain unchanged. For larger values of H_{AB}, the lower curves take the form shown as (b) and (c), with two potential wells and a smooth energy barrier between them, and finally the single-well potential (d), in which the electron delocalized form is the stable form of the dinuclear complex.[6]

3 THE MARCUS THEORY

The model developed by Marcus[7] and Hush[8] assumes the transition state formalism

$$k_{ps} = \kappa_{el}\left(\frac{RT}{Lh}\right)\exp\left(\frac{-\Delta G^*}{RT}\right) \tag{10}$$

where ΔG^* is the free energy of formation of the transition state from the precursor complex, κ_{el} is the probability that the reactants, once assembled into this state, will go on to form products, and the other symbols have their usual meanings. The transition state is defined as the configuration at which the zero-order energy curves cross. Figure 3 shows the crossings of the curves for different values of the overall free energy change ΔG^o. Neglecting the resonance energy, and assuming that the curves are parabolic with equal curvature, the activation free energy is given by the Marcus equation:

$$\Delta G^* = \left(\frac{\lambda}{4}\right) 1 + \Delta G^o \tag{11}$$

where λ is the intrinsic free energy barrier. The arguments showing that free energy is the relevant parameter here are discussed by Marcus and Sutin.[9] When $\Delta G^o = 0$, λ is the work required to be done to move the electron from the precursor to successor electronic state without changing the ligand and solvent coordinates.

Reactions with κ_{el} significantly less than 1 are called nonadiabatic. Reactions with $\kappa_{el} \sim 1$ are adiabatic. A convenient notation due to Sutin is

$$k_{ps} = \nu_n \kappa_n \kappa_{el} \tag{12}$$

where ν_n is called the nuclear frequency factor and κ_n is the nuclear rearrangement factor $\exp(-\Delta G^*/RT)$.

All of the above applies to the intramolecular reaction (equation 4b). For the bimolecular process with second-order rate constant k (equation 5), we have

$$\begin{aligned} k &= K_{ip}k_{ps} = K_{ip}\kappa_{el}\left(\frac{RT}{Lh}\right)\exp\left(\frac{-\Delta G^*}{RT}\right) \\ &= Z\kappa_{el}\exp\left(\frac{-w}{RT}\right)\exp\left(\frac{-\Delta G^*}{RT}\right) \end{aligned} \tag{13}$$

where w, the work term, is the reversible work needed to bring the reactants from infinity to the appropriate distance, and Z is a second-order rate constant that can be interpreted as the specific rate of collisions between reactant molecules having the same size and shape as the reactants in question, in the same solvent, but with no mutual attractive or repulsive forces.

The importance of the work term is shown by the observation of chiral recognition in some electron-transfer reactions. Differences in the rate of reaction of different optical enantiomers of the same complex, with a common chiral complex, are attributed to differences in the preequilibrium constant K_{ip} rather than electronic effects.[10]

The reorganization energy is usually considered as the sum of intramolecular (‘in’) and solvent (‘out’) contributions:

$$\lambda = \lambda_{out} + \lambda_{in} \tag{14}$$

The intramolecular part is assumed to come from changes in bond length, that is, for a self-exchange reaction,

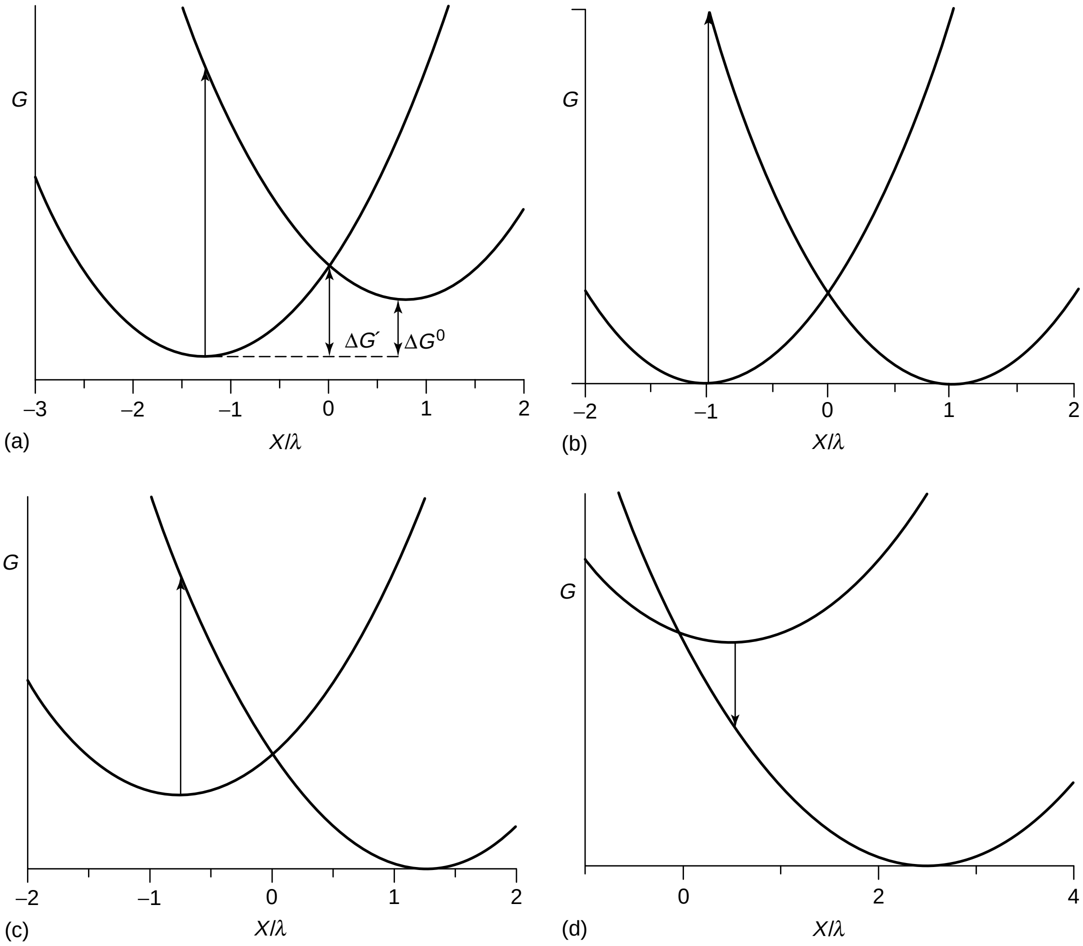

Figure 3 Plots of free energy of zero-order precursor and successor states versus reaction coordinate, for electron-transfer reactions $p(\mathrm{A}^{+}\cdots\mathrm{B}) \rightarrow s(\mathrm{A}\cdots\mathrm{B}^{+})$. (a) $\Delta G^{\mathrm{o}} > 0$; (b) $\Delta G^{\mathrm{o}} = 0$; (c) $0 > \Delta G^{\mathrm{o}} > -\lambda$; (d) $\Delta G^{\mathrm{o}} < -\lambda$. The upward-pointing arrows in (a), (b), and (c) indicate intervalence charge-transfer transitions; the downward-pointing arrow in (d) indicates a possible fluorescent transition from the precursor state $p(\mathrm{A}^{+}\cdots\mathrm{B})$

$\mathrm{ML_N}^{z+} + \mathrm{ML_N}^{(z-1)+}$

$$\lambda_{\mathrm{in}} = \left(\frac{LN}{2}\right)\left[\frac{f^{+}f^{-}}{(f^{+}+f^{-})}\right](\Delta r)^{2} \tag{15}$$

where f^{+} and f^{-} are the bond force constants in the higher and lower oxidation states and Δr the change in bond length. For the solvent part, the polarization of the solvent fluctuates on two distinct timescales. If the solvent is subject to an instantaneously applied electric field, the immediate response is well approximated by the so-called optical dielectric constant, $\varepsilon_{\mathrm{op}}$, equal to the square of the refractive index of the medium. The slow polarization that follows is due to the atoms and molecules moving to new (average) locations. The sum of these two responses is what is measured by the ordinary ‘static’ dielectric constant ε_{s}. An argument involving hypothetical reversible charging processes, due to Marcus,[7] and an argument involving hypothetical transfers of molecules between media, due to Hush,[8] lead to the same result, which (in Marcus’ formulation[1]) is

$$\lambda_{\mathrm{out}} = \left(\frac{L\varepsilon_0}{2}\right)(\varepsilon_{\mathrm{op}}{}^{-1} - \varepsilon_{\mathrm{s}}{}^{-1})\int_V (E_{\mathrm{c}}{}^{\mathrm{P}} - E_{\mathrm{c}}{}^{\mathrm{S}})^2 \mathrm{d}V \tag{16}$$

where $E_{\mathrm{c}}{}^{\mathrm{P}}$ and $E_{\mathrm{c}}{}^{\mathrm{S}}$ are the electrostatic fields due to the charges of the reactant ions in the precursor and successor complexes respectively, in a vacuum. The integral is taken over the volume occupied by the solvent. Applied to the case of two spherical reactants of radii a_1 and a_2, with central point charges, at distance R_{AB} apart, the formula integrates approximately to

$$\lambda_{\mathrm{out}} = \left(\frac{Le^2}{8\pi\varepsilon_0}\right)(\varepsilon_{\mathrm{op}}{}^{-1} - \varepsilon_{\mathrm{s}}{}^{-1})\left(\frac{1}{a_1} + \frac{1}{a_2} - \frac{2}{R_{\mathrm{AB}}}\right) \tag{17}$$

Refinements of this formula have been given that allow for ‘image forces’, for changes in radius during reaction,[1] and for cases where the shape of the precursor complex can be better described as an ellipsoid or a sphere[11–14] rather than two spheres at close distance.

For the work term between charged ions in a polar solvent, the Fuoss equation is often used, giving

$$K_{\mathrm{ip}} = \left(\frac{4}{3}\right)\pi a^3 L \exp\left(\frac{-z_1 z_2 s}{a}\right) \tag{18}$$

where z_1, z_2 are respective ionic charge numbers, a is the radius, and $s = e^2/4\pi\varepsilon_0\varepsilon_{\mathrm{s}}k_{\mathrm{B}}T$. (This constant has the value 6.94 Å for water at 25 °C.) For moderate ionic strength I, the extended Debye–Hückel formula leads to the modified Fuoss equation with $a(1+\kappa a)$ in place of a, where $\kappa = \sqrt{(8\pi LsI)}$.

4 MICROSCOPIC PROPERTIES OF SOLVENT REORGANIZATION

Dielectric continuum approximation for the solvent may work in some cases, but fails when microscopic nature of the solvent is involved in the reaction activation. Such examples include H bonding interaction with ligands such as NH_3 and CN^- where donation of a lone pair leads to donor–acceptor interactions.[3] Even in the absence of specific interactions, dielectric continuum models are not reliable in application to properties obtained as thermodynamic derivatives of the activation Gibbs energy, for instance, the entropy[4] and volume[5] of activation. Both these properties are much more affected by the local solvent structure of the solvent around the donor–acceptor pair than by the long-ranged dielectric response. When the Gibbs energy of reorganization is concerned, a linear trend of λ_{out} versus the Pekar factor $c_0 = \varepsilon_{op}{}^{-1} - \varepsilon_{\mathrm{s}}{}^{-1}$ predicted by equation (17) is often observed for a set of polar solvents.[15] However, there is one class of solvents for which the dielectric continuum approximation is completely inapplicable: nondipolar solvents. These solvents (e.g. benzene) lack any permanent dipole moment and possess only a quadrupole moment and higher multipolar moments. The existence of molecular quadrupole is not reflected by the macroscopic dielectric constant leading to $c_0 \rightarrow 0$ and, correspondingly, $\lambda \rightarrow 0$ for nondipolar solvents. In contrast, substantial reorganization energies are observed in experiment[16] and obtained from microscopic theories of solvent reorganization.[17]

5 THE CROSS RELATION

The above equations predict the absolute rates of electron-transfer reactions, but by far the most popular and useful aspect of the Marcus theory is comparison of rates of different, related reactions.

From equation (11) it follows directly that in a series of reactions, if the work terms and nonadiabaticity parameters are the same or similar, the rates will correlate with the thermodynamic driving force. For small differences, the relationship is linear:

$$\frac{\mathrm{d}\Delta G^{\#}}{\mathrm{d}\Delta G^{\mathrm{o}}} = \frac{\mathrm{d}\log k}{\mathrm{d}\log K} = \frac{1}{2} \tag{19}$$

where K is the equilibrium constant of the overall reaction (equations 4a–c), and for larger differences it is quadratic. In Figure 4 this is expressed as a plot of log k against $-\Delta G^{\mathrm{o}}$. Curve (a) represents the Marcus prediction. Curvature in the range of moderately negative ΔG^{o} has been verified many times.[1] The Marcus cross relation[18] expresses the rate constant in terms of those of the two self-exchange reactions involving the same couples:

$$\mathrm{A}^+ + \mathrm{B} \longrightarrow \mathrm{A} + \mathrm{B}^+ \qquad k_{12} \tag{20a}$$

$$\mathrm{A}^+ + \mathrm{A} \longrightarrow \mathrm{A} + \mathrm{A}^+ \qquad k_{11} \tag{20b}$$

$$\mathrm{B}^+ + \mathrm{B} \longrightarrow \mathrm{B} + \mathrm{B}^+ \qquad k_{22} \tag{20c}$$

In this context, equation (20a) is called the ‘cross reaction’. Assuming that the reorganization energies are related by

$$\lambda_{12} = \left(\frac{1}{2}\right)(\lambda_{11} + \lambda_{22}) \tag{21}$$

then substitution into equation (11), with the further condition that the work terms are small or cancel, gives

$$\log k_{12} = \left(\frac{1}{2}\right)\log(k_{11}k_{22}K_{12}f_{12}) \tag{22a}$$

$$\log f_{12} = \frac{(\log K_{12})^2}{4\log(k_{11}k_{22}/Z^2)} \tag{22b}$$

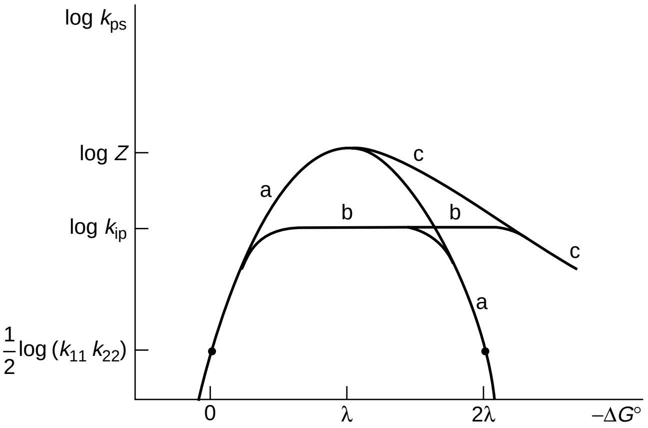

Figure 4 Variation of rate with standard free energy change: (a) as predicted by the classical Marcus equation; (b) with the higher rates limited by diffusion; (c) with nuclear tunneling in the range of highly negative ΔG^{o}

This result has been tested many times and often predicts values of k_{12} within a factor of two of the experimental result.[19] Deviations due to noncancellation of work terms are also understood,[1] and in some cases have actually been used to estimate the magnitude of the work terms, especially in nonaqueous systems where ionic interactions are strong.[20] Deviations due to nonadiabaticity (see next section) have also been proposed, but with less certainty.[21] When used in reverse to predict an unknown self-exchange rate constant k_{11} from known k_{22}, k_{12}, and K_{12}, the margin of error is greater because of the factor of 1/2 in equation (22a).

6 NONADIABATIC TRANSFER

As mentioned above, if the reactants are assembled with all nuclei in the positions required for the transition state, but the electron is artificially localized at one of the two sites, then released, it will oscillate between the sites. The probability κ_{el} of transfer thus depends on the time the reacting system spends in traversing this small region of reaction coordinate space, in relation to the frequency of oscillation of the wavefunction. Calculations developed by Landau and others give

$$k_{\mathrm{ps}} = \left(\frac{4\pi^2}{h}\right) H_{\mathrm{AB}}{}^2 (4\pi\lambda RT)^{-1/2} \exp\left(\frac{-\Delta G^*}{RT}\right) \tag{23}$$

The resonance integral in equation (23) can be obtained from experimental data using the Mulliken-Hush relation

$$H_{\mathrm{AB}} = \frac{\mu_{12}}{\Delta\mu_{\mathrm{AB}}}\,\Delta E_{12} \tag{24}$$

where μ_{12} is the transition dipole coupling the adiabatic states Ψ_1 and Ψ_2 separated by the adiabatic energy gap ΔE_{12}, and $\Delta\mu_{\mathrm{AB}}$ is the dipole moment change between the diabatic states A and B. For the case of a well-resolved intervalence band of Gaussian shape, the area of the band gives a measure of the transition dipole moment and hence the mixing parameter ρ (equation 8),[22,23] (the transition dipole moment (in D) can be defined in terms of the molar extinction coefficient by the following relation: $m_{12} = 9.585 \times 10^{-2}(\sqrt{n_D}/f(n_D))\left[\int \bar{\nu}\varepsilon(\bar{\nu})d\bar{\nu}\right]^{1/2}$, where n_D is the solvent refractive index, the function $f(n_D)$ accounts for the local field of the electronic polarization of the solvent, and $\bar{\nu}$ is the wave number (cm^{-1})).

Equations (23) and (24) presume a knowledge of the relevant electronic states, either the charge-localized diabatic states ϕ_{A} and ϕ_{B} or the adiabatic states Ψ_1 and Ψ_2 (equation 8). Typically, diabatic states are natural for studying electron transfer, whereas the adiabatic states are used for optical transitions. The generalized Mulliken-Hush approximation[24] adopts the definition of diabatic states that are diagonal with respect to the component of the dipole moment operator along the charge-transfer direction. The diabatic dipole moment shift is then given in terms of adiabatic parameters observable in optical experiment

$$\Delta\mu_{\mathrm{AB}} = [(\Delta\mu_{12})^2 + 4(\mu_{12})^2]^{1/2} \tag{25}$$

The calculation of H_{AB} according to equations (24) and (25) is in a good agreement with the corresponding values extracted from kinetic measurements at varying temperature.[25]

The present consensus is that most reactions of the outer-sphere type between simple metal complexes in solution are either weakly adiabatic or weakly nonadiabatic with κ_{el} in the range of perhaps 10^{-3} to 1; but that inner-sphere reactions are probably more adiabatic, and reactions such as equation (3) (above) are strongly adiabatic. Also, many electrochemical reactions proceeding via a direct contact between the reactant and the electrode are adiabatic.[26]

7 CONNECTION WITH OPTICAL SPECTROSCOPY

Spectroscopic charge transfer between the two centers of a mixed-valence or precursor complex, known as intervalence charge transfer,[2,22] has the energy E_{op} given by

$$E_{\mathrm{op}} = Lh\nu_{\mathrm{CT}} = \lambda + \Delta G^{\mathrm{o}}_{\mathrm{ps}} \tag{26}$$

From equations (11) and (24) we have

$$\Delta G^* = \frac{E_{\mathrm{op}}{}^2}{4(E_{\mathrm{op}} - \Delta G^{\mathrm{o}}_{\mathrm{ps}})} \tag{27}$$

and in the limit of $\Delta G^{\mathrm{o}}_{\mathrm{ps}} = 0$; in other words for intervalence transfer in a quasi-symmetrical mixed-valence complex, ‘Hush’s Law’:

$$\Delta G^* = \frac{E_{\mathrm{op}}}{4} \tag{28}$$

This relation relies on the fact that the entropy is unchanged in the Franck-Condon transition, so that the energy difference measured by optical transitions can be connected to the free energy difference for the activations barrier.[13,27] The conclusion, that the rate of a thermal electron-transfer reaction can be estimated from relatively simple spectroscopic data, is remarkable. But it has been pointed out that cases in which an optical and thermal electron transfer have actually been measured on precisely the same system, free of doubts over the assignments, are still very few.[28,29]

It is actually much easier to measure λ spectroscopically than kinetically. The Marcus-Hush model of charge-transfer transitions predicts two fundamental relations between the kinetic parameters and spectroscopic observables. The first relations is between the reorganization energy and the Stoke shift $h\nu_{\text{st}}$ equal to the difference in the first spectral moments for absorption and emission approximately equal to the corresponding maxima energies[30]

$$\lambda = \frac{h\nu_{\text{st}}}{2} \tag{29}$$

The second relation connects the intramolecular and solvent reorganization energies to the second spectral moments of absorption, $\langle(\delta\nu)^2\rangle_{\text{abs}}$, and emission, $\langle(\delta\nu)^2\rangle_{\text{abs}}$, spectral lines:[30]

$$L^2h^2\langle(\delta\nu)^2\rangle_{\text{abs/em}} = 2RT\lambda_{\text{out}} + Lh\nu\lambda_{\text{in}} \tag{30}$$

where ν is the characteristic frequency of bond vibrations. The dependence on the optical and static dielectric constants (equation 17, above) has been verified mainly by measurements of spectra of mixed-valence complexes in solution. Extrapolation of such data to the limit of $({\varepsilon_{\text{op}}}^{-1} - {\varepsilon_{\text{s}}}^{-1}) = 0$ also provides a way of separately measuring λ_{in} and λ_{out}.

The analytical expression for the upper and lower of each pair of energy curves in Figure 2 is:[1]

$$E = \left(\frac{\lambda}{4}\right)(x^2+1) \pm \left(\frac{1}{2}\right)[\lambda^2x^2 + 4H_{\text{AB}}^2]^{1/2} \tag{31}$$

where $x = X/\lambda$. Valence localization means that the lower curve has two minima and the criterion for this is $H_{\text{AB}} < \lambda/2$.[1] The energy curves shown in Figure 2 provide the semiclassical model of a dinuclear mixed-valence complex,[6] distinguishing Robin and Day Class I (distinct valencies with negligible interaction), Class III (indistinguishable metal centers with complete electron delocalization), and Class II (intermediate cases with structurally distinct centers but physical properties affected by the interaction).[31] As the limit of delocalization is approached, the minima also begin to be lowered in energy, and to become less separated on the horizontal axis. This corresponds to the onset of appreciable 'resonance stabilization' in the ground states of the precursor and successor complexes. A comprehensive discussion of the effect of tunneling and other factors on the character of the interaction in a well-studied series of ruthenium(III)–ruthenium(II) dimers has been given by Richardson and Taube.[32]

For all values of H_{AB} (within this first-order perturbation model), equation (27) remains valid, and also

$$\Delta G^* = \left(\frac{1}{4}\right)\lambda - H_{\text{AB}} + \frac{{H_{\text{AB}}}^2}{\lambda} \tag{32}$$

Analogous relationships have been derived and tested for trinuclear mixed-valence systems[33] such as the triangular-shaped $\text{Fe}^{\text{III,III,II}}$ complexes.[33c]

8 STATE-TO-STATE THEORIES

More rigorous treatments of nonadiabatic electron transfer have been developed by Levich, Van Duyne and Fischer, Hopfield, Jortner, and others.[34] These consider the full range of vibrational energy levels of the precursor and successor states, so that electron transfer is not restricted to the single crossing point of the zero-order curves (Figure 5). Transfer can occur between any two levels at the same energy, with a probability given by the overlap integral of the respective vibrational wavefunctions, the so-called Franck-Condon factor:

$$(\text{FC})_{ij} = \langle\chi^{\text{o}}_{\text{S}i}|\chi^{\text{o}}_{\text{P}j}\rangle \tag{33}$$

where $\chi^{\text{o}}_{\text{S}i}$ and $\chi^{\text{o}}_{\text{P}j}$ are vibrational wavefunctions of the precursor complex and successor complex in vibrational energy levels numbered i and j from their respective zero-point levels. The result can be expressed as

$$k_{\text{ps}} = \left(\frac{4\pi^2}{h}\right){H_{\text{AB}}}^2(\text{FCWD}) \tag{34}$$

where FCWD is the Franck-Condon weighted density of states:

$$\text{FCWD} = \sum_{i,j}\langle\chi^{\text{o}}_{\text{S}i}|\chi^{\text{o}}_{\text{P}j}\rangle^2 \exp\left(\frac{-E_{\text{R}j}}{k_{\text{B}}T}\right) \times \left[\sum_j \exp\left(\frac{-E_{\text{R}j}}{k_{\text{B}}T}\right)\right]^{-1} \delta(E_{\text{P}i} - E_{\text{R}j}) \tag{35}$$

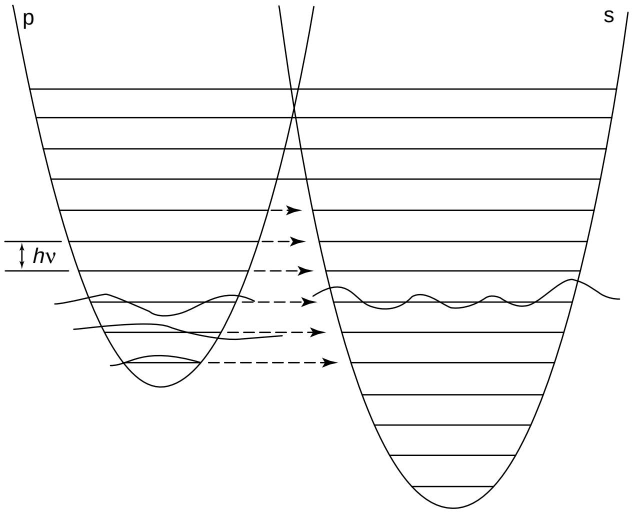

Figure 5 Potential energy curves for an electron-transfer reaction $p(\text{A}^+\cdots\text{B}) \rightarrow s(\text{A}\cdots\text{B}^+)$, showing vibrational quantization, assuming the same vibrational frequency ν in precursor and successor states. Some of the vibrational wavefunctions are indicated. The dotted arrows refer to electron transfer below the energy of the crossing of the two curves

the δ function indicating that the electron transfer can only take place with conservation of electronic energy. With the further simplifications that only one high-frequency mode ν effectively contributes to the electron transfer, and that the low-frequency solvent modes can treated by the Marcus-Hush model, this gives

$$k_{\text{ps}} = \left(\frac{4\pi^2}{h}\right) H_{\text{AB}}{}^2 (4\pi\lambda_{\text{out}} k_{\text{B}} T)^{-1/2} \times \sum_m \left[\frac{e^{-S} S^m}{m!}\right]\left[\exp - \frac{(\lambda_{\text{out}} + \Delta G^{\text{o}} + mh\nu)^2}{4\lambda_{\text{out}} k_{\text{B}} T}\right] \quad (36)$$

where $S = \lambda_{\text{in}}/h\nu$, which in the high-temperature limit reduces to the Marcus expression (equation 11). This type of model has been extensively used for the band-shape analysis of charge-transfer transitions with the goal of extracting the activation parameters from spectra.**[2]**

This approach makes it clear that electron transfer can occur at temperatures where the population of energy levels near the crossing point is negligible, and indeed the probability of transfer remains finite even at the limit of $T = 0$. In that limit, transfer is from the zero-point level of the precursor complex, and the activation energy is zero. Examples of activationless electron transfer at low temperature have indeed been reported, though it should be noted that there are sometimes difficulties of assignment. The most famous example is the cytochrome–chlorophyll transfer in the bacterium *Chromatium*. The facts are well attested, and the electron-transfer rate does tend to a low and temperature-independent value at low temperature, but detailed fitting to equations derived by Jortner does not yield a self-consistent model.**[35]** It is now considered that the implied nuclear frequency ν is too high to be physically reasonable, and an alternative suggestion (not necessarily the only possible one) is that two independent electron-transfer reactions take place with different activation energies. Other examples of efficient electron transfer at very low temperature (down to 10 K) have been reported, some of them in nonbiological systems,**[36]** and the whole area is still being debated.

Studies of the intervalence charge-transfer spectrum in solid-state inorganic materials and dinuclear mixed-valence complexes have given analogous information, less controversially. At low temperatures, the variation of spectral bandwidth is given by**[37]**

$$(\Delta v_{1/2})^2 (16 \ln 2)\lambda^2 (h\nu)^2 \coth\left(\frac{h\nu}{2k_{\text{B}}T}\right) \quad (37)$$

where $\Delta\nu_{1/2}$ is the full width at half-height. This has been verified experimentally in several cases, and reasonable values of the frequency have been found. For example, in the complex $[(\text{NC})_5\text{Fe}^{\text{III}}(\text{pz})\text{Fe}^{\text{II}}(\text{CN})_5]^{5-}$, Felix and Ludi estimated $\nu = 490\,\text{cm}^{-1}$, which is close to the average of the Fe–C stretch frequencies of the complexes $[\text{Fe}^{\text{III}}(\text{CN})_6]^{3-}$ and $[\text{Fe}^{\text{II}}(\text{CN})_6]^{4-}$.**[37b]**

The most thorough-going state-to-state treatment is due to Piepho, Krausz, and Schatz (PKS).**[38]** Adapted from previous work on the dynamic Jahn–Teller effect, it covers the full range from nonadiabatic to strongly adiabatic. One method of approach starts from the analytical expressions for the double-well and single-well potentials (see equation 27) and uses the fact that, for these particular wells, exact solutions of the time-dependent Schrödinger wave equation are available. The energy wells for the lower surface are highly anharmonic, and the lower levels are grouped in closely spaced pairs, as shown in Figure 6.

Although the eigenvalues can be calculated exactly for these complicated wells, the PKS theory in its preferred form proceeds differently. This is because in the first method the upper and lower potential curves are treated as independent, so that a vibrating system would always be confined to one or the other. At sufficiently high energy and for an appropriate set of coupling parameters it should be possible for a system to spend time on either surface. In general, just as a single quantum oscillator has nuclear coordinates concentrated around two positions, corresponding to the stationary positions of a classical oscillator, so a mixed-valence molecule, or precursor/successor reacting system has nuclear coordinates concentrated around four positions, which it visits randomly by a process of simultaneous electron and nuclear tunneling. As a general basis for the calculation therefore, the original parabolic, zero-order potential curves are used and energy levels and transition probabilities are calculated without reference to the double-well potential as such. The concept of activation energy is avoided, though it reappears in the final results in the sense of the temperature dependence of the calculated rate constant. Plots of rate versus temperature show the expected transition from activated to activationless transfer at low temperature.**[39]** Other parameters calculated from the model include degrees of electron delocalization in mixed-valence dimers,**[38]** band shapes of

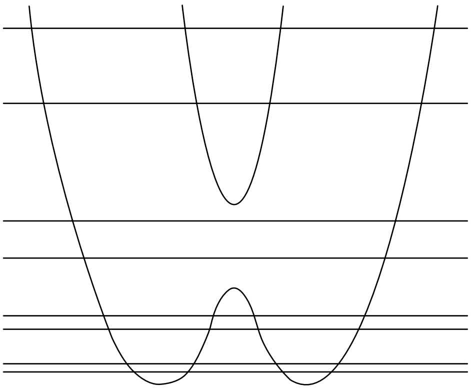

Figure 6 Potential curves for an electron transfer reaction $\text{p}(\text{A}^+ \cdots \text{A}) \rightarrow \text{s}(\text{A} \cdots \text{A}^+)$, or a mixed-valence molecule $(\text{A} \cdots \text{A})^+$, with moderately strong electronic interaction, showing the lowest vibrational states split by tunneling through the activation barrier (not to scale)

intervalence charge-transfer spectra,[40] low-energy tunneling transitions,[41] and more recently, intervalence charge-transfer spectra of two-electron mixed-valence systems with one-electron excited states, such as $\mathrm{Sb^{V}\cdots Sb^{III} \rightarrow Sb^{IV}\cdots Sb^{IV}}$.[42] The model has been applied to a series of ruthenium(III,II) complexes, calculating parameters such as the degree of valence localization, from the observed shapes of the intervalence charge-transfer bands.[43]

9 THE INVERTED REGION

A consequence of the Marcus-Hush model is the negative dependence of rate on total free energy change, when the latter is made highly negative. This corresponds to a crossing of the potential energy surfaces at the position shown in Figure 3(d). It is now accepted that the Marcus prediction is not likely to be followed in this highly negative range of ΔG^{o}. Two types of deviation have been discussed and can now be said to be understood.

Depending on the values of λ and w, the predicted maximum value of log k may exceed the diffusion-controlled limit for a bimolecular reaction. In that case, a flat-topped log $k - \Delta G^{\mathrm{o}}$ profile is expected (Figure 4, curve b), though this in itself would not preclude a descending regime at sufficiently negative ΔG^{o}.[44] Early attempts to probe the inverted region, using positively charged inorganic complexes in polar media, did indeed reach a plateau region, at the level predicted for diffusion control when due allowance was made for the work terms.

In the inverted region, electron is transferred to acceptor vibrational levels well below the classical crossing point. This transition requires almost no activation barrier and thus nuclear tunneling is more favored than thermal activation along the classical activation mechanism. Equation (36), when applied to this situation, leads to a decrease of log k with increasingly negative ΔG^{o}, but not such a rapid decrease as the Marcus equation (Figure 4, curve c). This prediction appears to be supported by a considerable number of experiments, all involving electron transfer in rigid systems (precursor complexes with stiff organic bridging groups),[45,46] and redox centers in biological molecules[46,47] and glasses.[48] Experiments involving bimolecular electron transfer in solution have been much less supportive. Even though the earliest convincing demonstration of inverted behavior, by Creutz and Sutin, involved inorganic complexes in solution,[49] the effects were small; and in some other systems involving excited states of organic molecules as reactants, over much longer ranges of ΔG^{o}, constant, diffusion-controlled rates have been found.[50]

The extreme case of inverted behavior comes, again, from spectroscopy. Figure 3(d) can be applied to the electronic states of a fluorescent molecule as functions of a molecular vibrational coordinate. Fluorescence corresponds to the downward vertical transition, but competing with this is the radiationless transition, which is essentially transfer of an electron between different orbitals through vibrational coupling. The probability of this electron transfer decreases with increasing energy separation of the curves according to the linear energy gap law:[2]

$$k_{\mathrm{ps}} \propto \exp\left[-S - \gamma\frac{|\Delta G^{\mathrm{o}} - \lambda_{\mathrm{out}}|}{h\nu}\right] \tag{38a}$$

$$\gamma = \ln\left(\frac{-\Delta G^{\mathrm{o}}}{\lambda_{\mathrm{out}}}\right) - 1 \tag{38b}$$

Most examples studied are organic molecules,[51] but an inorganic example is the nonradiative decay of the excited states of complexes such as $[\mathrm{Os(bipy)_3}]^{2+}$, assigned to electron transfer from the coordinated radical $(\mathrm{bipy})^{-}$ to $\mathrm{Os^{III}}$.[52]

10 BEYOND THE PARABOLAS

Figure 4 shows that there are several reasons contributing to the deviation of the energy gap law ($\log k_{\mathrm{ps}}$ vs $-\Delta G^{\mathrm{o}}$) from the inverted parabola of the Marcus-Hush theory. While the diffusion limit and effects of high-frequency vibrations can be sorted out, it is of fundamental interest whether the low-frequency nuclear modes follow the Gaussian statistics resulting in the picture of intersecting parabolas shown in Figure 3. This problem has been extensively studied in recent decades by computer simulations.[53] The quest for nonparabolicity effects predominantly aimed to understand the conditions at which linear solvation by the nuclear modes breaks down reflecting the onset of non-Gaussian statistics. It turned out, however, that solvation of fixed charges in high-temperature, dense molecular solvents is linear resulting in parabolic free energy surfaces for charge transfer.[53a] On the other hand, spectroscopic evidence indicates that relations between spectroscopic observables following from traditional theories may not stand the experimental test. An experimental test of the Marcus-Hush theory can be realized by combining equations (29) and (30). The resulting equation (39) contains only experimental observables

$$L^2h^2\langle(\delta\nu)^2\rangle_{\mathrm{abs/em}} \cong RTh\nu_{\mathrm{st}} + Lh\nu\lambda_{\mathrm{in}} \tag{39}$$

In Figure 7, the absorption and emission second spectral moments are plotted against the Stokes shift obtained for coumarin-153 optical dye in 40 molecular solvents of varying polarity.[16] The slopes of $\langle(\delta\nu)^2\rangle$ versus ν_{st} have opposite signs for absorption and emission transitions in contrast to the prediction of equation (39).

The understanding of optical experiments demonstrating different optical widths (second spectral moments) for absorption and emission spectral lines requires an extension of the Marcus-Hush model that would incorporate different reorganization energies for forward and backward charge transfers

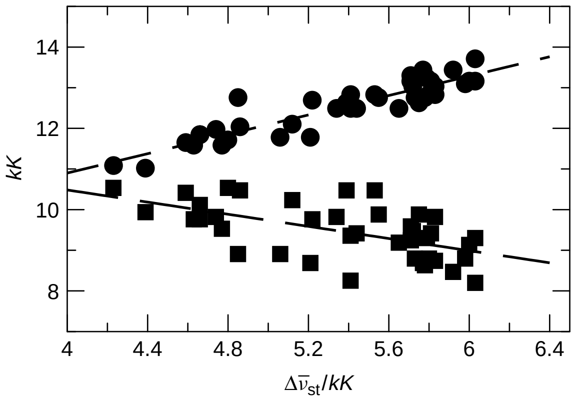

Figure 7 Absorption (circles) and emission (squares) widths $L^2h^2\langle(\delta\nu)^2\rangle/RT$ versus the Stokes shift for 40 molecular solvents according to Reynolds *et al.*[16] The dashed lines are regressions drawn as a guide for the eye. (Reprinted with permission from Ref. 16a, © 1996 American Chemical Society)

Q-model. Several physical reasons may be responsible for the difference in the reorganization energies; one of them is different polarizabilities of the $(A\cdots B)^+$ complex in the precursor and successor charge-transfer states. When $\lambda_p \neq \lambda_s$, the free energy of activation for the p → s transition changes from equation (11) to the following relation:[54]

$$\Delta G^* = |\alpha| \left(\sqrt{\left| \Delta G^o - \lambda_p \frac{\alpha^2}{1+\alpha} - \sqrt{|\alpha|\lambda_p} \right|} \right)^2 \tag{40}$$

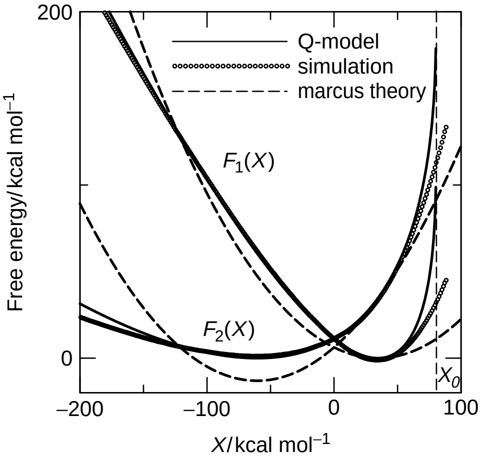

Figure 8 Free energy surfaces for the precursor and successor states of intramolecular electron transfer in a model charge-transfer system.[54] On the plot the dashed lines indicate the Marcus theory, circles are simulations, and solid lines refer to the Q-model. The vertical dashed line marked X_0 indicates the boundary of the energy gap fluctuation band predicted by the Q-model. (Reprinted with permission from Ref. 54, © 1989 American Chemical Society)

where α is the parameter on nonparabolicity of the free energy surfaces defined through the reorganization energies of the precursor and successor states

$$\alpha = \left(\sqrt[3]{\frac{\lambda_p}{\lambda_s}} - 1 \right)^{-1} \tag{41}$$

When $\lambda_p \rightarrow \lambda_s$, the parameter α tends to infinity and equation (40) transforms into the Marcus equation (11).

Figure 8 shows an example of free energy surfaces for a charge-transfer transition when both the charge distribution and dipolar polarizability are allowed to change. The results of analytical theory agree well with computer simulations.[54] Change in the polarizability in the course of charge transfer leads to a significant deviation of the free energy surfaces from parabolas.

11 LONG-RANGE AND BRIDGED ELECTRON TRANSFER

The internuclear distance R_{AB} enters into the expression for the rate constant in two main ways: through the effect on reorganization energy (equation 7), and the effect on the tunneling integral H_{AB}. The two are difficult to distinguish experimentally.[55,56]

Most interest has centered on the variation of H_{AB}, which certainly becomes dominant at long range. For nonadiabatic transfer, with donor and acceptor sites connected through space, H_{AB} falls off rapidly with distance and most theories lead to an exponential formula:

$$H_{AB} = H_{AB}{}^o \exp\left[\frac{-\beta(R_{AB} - R_{AB}{}^o)}{2} \right] \tag{42}$$

where R^o_{AB} is the closest possible distance and H^o_{AB} is the value of H_{AB} at that distance, the factor of 2 being included because of the squared term in equation (23), so that the rate constant varies as $\exp(-\beta R_{AB})$. Endicott has reviewed the theories and collected experimental estimates of β, mostly in the range 0.8 to 1.5. ***Electron Transfer in Coordination Compounds*** Through-space interaction actually occurs in the gas phase, and distances of 10 to 20 Å are involved.[1] In condensed systems the intervening medium cannot be ignored and this leads to consideration of the effects of bridging groups.[57]

It is clear that in a bridged electron-transfer reaction the nature of the bridging group can profoundly affect the rate. Two aspects of this are immediately obvious, though they require careful analysis before they can be identified quantitatively.[1,53] One is that in a bimolecular reaction the bridging group may simply draw the reacting centers closer together than they would otherwise be, and hence facilitate the reaction by increasing the direct electron tunneling parameter H_{AB}. The second is that, in a unimolecular or a bimolecular reaction, the strength of the metal–bridge bonds will affect the stabilities of both the final products and the transition state to different extents depending on the chemical nature of the metals and ligand atoms. When these effects have been correctly discounted, intrinsic differences between bridging groups still remain. In a series of bridging reactions such as equation (2), with different halogen atoms, rates increase in the order $F < Cl < Br < I$, and there is a sense in which the iodine atom is the best 'conductor' of electrons. Theories of bridging groups all focus on this aspect and are therefore concerned with the first-order rate constant, k_{ps}, for intramolecular electron transfer.

It is useful to distinguish between 'chemical' and 'resonance' electron transfer.[58,59] In chemical transfer the electron is actually transferred from donor to bridge, and then from bridge to acceptor, in two distinct reaction steps (or conversely, a positive hole is transferred in two steps). Resonance transfer is a single concerted step. Experimentally, some clear examples of chemical transfer are known.[1,58b] However, even in a concerted process the effectiveness of a bridge can depend on its ability to accept or donate a mobile electron and this is shown by the fact that a particular type of bridging group may be effective only when the donor and acceptor redox potentials lie in a certain range.[60] It is claimed, for example, that in long-range electron transfer in biological systems, aromatic residues are effective bridges only when the oxidizing centers have $E°$ more positive than ca. 0.8 V.[61]

Most theories assume the superexchange mechanism,[58–60] according to which the wavefunctions $\Psi_{1,2}$ are modified by mixing in those of an excited state consisting either of the electron transferred from atom B to a bridging atom or molecule X, or an electron transferred from the bridge to atom A^+, depending on the relative energies of the orbitals involved. (The superexchange contributions to the mechanism can then be called 'electron transfer' or 'hole transfer' respectively.[60]) First-order perturbation treatments are used involving the tunneling integrals H_{AX} and H_{BX}. Such integrals may be calculated theoretically or derived from spectroscopic measurements of the relevant charge transfers.

Even outer-sphere reactions can be treated as bridged, by invoking the tunneling integral for transfer between the contacting ligands or through solvent molecules.[62] Thus, Newton has concluded that for the $[Fe(OH_2)_6]^{3+/2+}$ exchange reaction, hole transfer prevails, but for the reaction $[Ru(NH_3)_5(py)]^{3+/2+}$, electron transfer is dominant as a result of metal-to-pyridine charge transfer in the ruthenium(II) complex. In the latter case, expressions were calculated for a pathway with the pyridine rings in face-to-face contact, overlapping in the vicinity of their remote (C-3) carbon atoms.[63] Using spectroscopic data, Endicott has estimated nonadiabaticity for a series of reactions of the type $[Co^{III}(NH_3)_5L]^{2+} +$ [Co(sepulchrate)]$^{2+}$ and obtained κ_{el} in the range 10^{-3} to 1, increasing along the series $L^- = CN^-$, Cl^-, Br^-, $N_3{}^-$.[64]

All these calculations aim to provide a revised value of the single electron tunneling integral H_{AB}, so they are restricted to cases of resonance transfer in which the electron spends little effective time actually residing on the bridge. Reimers and Hush have discussed the conditions under which this approach can be justified.[65] They have provided a more general formalism for a three-level electron-transfer system that spans the regime from chemical to resonance transfer. As expected, the most effective transfer is predicted when the three orbital energy levels, for the electron located on donor, bridge, or acceptor, are equal.

For strongly coupled systems, molecular orbital theories are appropriate. Burdett has considered the energetics of M–X–M complexes, both homovalent and mixed-valent, and the relative stability of symmetrical and unsymmetrical structures, such as the nearly symmetric bridging in 'ruthenium red' $[(H_3N)_5RuORu(en)_2ORu(NH_3)_5]^{6+}$, and the asymmetric Cr^{III}–F–Cr^{II} units in solid Cr_2F_5 and Pt–Br–Br units in linear platinum(IV)–platinum(II) compounds. The question here is the shape of the potential well (see Figure 2). Calculations of the amount of charge located on the bridge in the transition state are used to distinguish chemical from resonance transfer, and for the Cr^{III}–Cl–Cr^{II} system, the latter is preferred.[66]

In the bioinorganic field, interest centers on extremely long-range electron transfer, over distances up to 20 Å in protein media. ***Long-range Electron Transfer in Biology*** Rates have been measured both in natural molecules and in artificially modified systems with ruthenium(III/II) centers coordinated to nitrogen atoms of the protein chain. Gray, Williams, and others have argued that aromatic residues and other polarizable units strategically located on the electron-transfer 'pathway' can strongly influence the rate. The opposite view is taken by Dutton and coworkers, who maintain that distance is overwhelmingly important, and that the electronic part of the rate expression is adequately given by equation (35), with a decay constant β that varies little from one medium to another.[57b,c]

12 SOLVENT DYNAMICS

The transition state theory assumes that as the reacting species proceeds over the energy barrier, the medium adjusts rapidly enough to stay in equilibrium. Classical electron-transfer theory takes the first step away from this idea by distinguishing rapid and slow polarization due to electronic and atomic motion, respectively. More recently, as faster reactions have been studied, interest has turned to the effects of rates of motion of solvent molecules. It is still possible to retain the notion of the solvent as a continuum, by introducing polarizations that respond at different characteristic rates to an applied electric stimulus, in addition to the limiting fast and slow polarizations of the semiclassical model; or more generally by considering the dispersion of the relative permittivity over a spectrum of frequencies.

A model due to Debye that incorporates a single relaxation time τ_D gives

$$\varepsilon(\omega) = \varepsilon(\infty) + \frac{[\varepsilon(0) - \varepsilon(\infty)]}{(1 - i\omega\tau_D)} \tag{43}$$

where $\varepsilon(0)$ and $\varepsilon(\infty)$ are limiting relative permittivities at frequencies $\omega = 0$ and ∞ (replacing the previous ε_s and ε_{op}). The change in free energy of solvation of a dissolved species, in response to a sudden change in the charge distribution, is then given by an exponential function with time constant τ_L, the 'longitudinal' relaxation time, given by

$$\tau_L = \tau_D \frac{[\varepsilon(\infty)]}{[\varepsilon(0)]} \tag{44}$$

and more complicated expressions when processes with different time constants are involved.[67] Bulk dielectric loss measurements were the traditional method of measuring these times, but now microscopic techniques such as time-resolved emission spectroscopy are available.[68] The effect on the electron-transfer rate depends largely on the relaxation times compared with the nuclear vibration frequencies and resonant electron-transfer frequency in the transition state. In the last 10 years, there have been many detailed theoretical studies of these questions, and some good reviews.[17,69] Much of this work goes well beyond the continuum model and considers microscopic reorientation and translation motions of molecules in various regions of the solvation shell surrounding the reactants.[69d]

Hynes[67] uses the notion of 'friction' meaning that the motion of the reacting system along the reaction coordinate (Figure 3) is resisted by the solvent, and if the resistance is strong enough the motion may become a random process analogous to diffusion. As Endicott remarks in summary, 'this means that on the one hand, friction can lower the rate of reaction in the same way as nonadiabaticity, but on the other hand the effect of true nonadiabaticity [low κ_{el}] can be offset by the fact that the reacting system is forced to spend more time in the vicinity of the crossover point'. In one treatment, Hynes and coworkers have concluded that for nonadiabatic or weakly adiabatic electron transfer, if the solvent has a single relaxation time τ_d the rate constant k of equation (26) is changed to a new value k', given by

$$k' = (1 + 2\tau_d k)^{-1} k \tag{45}$$

To test these theories it is obviously necessary to concentrate on reactions that are both rapid and strongly controlled by solvent rather than intramolecular reorganization effects. Weaver and coworkers have measured self-exchange rates of metallocene couples such as $[Co(C_5H_5)_2]^{+/0}$ in various solvents and found that they can be rationalized on the basis of the measured relaxation times τ_L.[70]

There are a number of experimental systems for which the rate constant is higher than the frequency of longitudinal polarization relaxation. These systems indicate that here must be faster nuclear modes driving electron transfer. One possible source is the inertial component of solvent dynamics occurring on shorter timescales than diffusive polarization relaxation.[71] The participation of high-frequency vibrations rendering the reaction essentially barrierless is still another scenario.[72] Both mechanisms would obviate any correlation of the rate constant with the diffusional solvation timescale.

13 EFFECTS OF PRESSURE

Studies of reaction rates as a function of applied pressure lead to measures of the volume of activation $\Delta V^{\#}$, defined by

$$\Delta V^{\#} = -2.3RT \left(\frac{\partial \log k}{\partial P}\right)_{P=0} \tag{46}$$

Such measurements have been extremely useful in the study of substitution reactions, both organic and inorganic, and after a rather slow start, interest in pressure effects on electron transfer has now begun to pick up strongly. It is hoped among other things to obtain better evidence of adiabatic or nonadiabatic character in simple systems. Swaddle has discussed the factors that contribute to $\Delta V^{\#}$ in terms of the Marcus model.[73] He argues that since the tunneling integral H_{AB} is sensitive to distance, and since changes in pressure presumably directly affect the reaction distance in the transition state, there is a contribution due to nonadiabaticity. However, other systems have been less easy to interpret.[73,74] Once again, spectroscopy provides another approach. Intervalence charge-transfer spectra show small shifts with pressure, which have been interpreted as due in part to increases in the electron coupling,[75] though solvation changes are also a major factor.[14]

14 ELECTRON TRANSFER AND MAGNETISM

All one-electron transfers involve paramagnetic molecules, but this aspect was not much considered until recently. An early observation was that reactions between cobalt(III) and cobalt(II) complexes are often unexpectedly slow, and this is evidently related to the necessity of spin change from the $^1A_{1g}$ (low-spin d^6) cobalt(III) to the $^4T_{1g}$ (high-spin d^7) cobalt(II) state. Endicott and coworkers have provided, and analyzed, a mass of experimental data on this question.[76] The most recent discussion invokes spin–orbit coupling in the transition state.[77]

More recently, interest has centered on electron-transfer reactions in which both reacting centers are paramagnetic, before and after the reaction. Anderson and Hasegawa treated the complex $\mathrm{Mn^{III}}$–O–$\mathrm{Mn^{IV}}$ (a unit in the structures of certain mixed oxides) as a system with one mobile electron moving between two centers of local spin $S_1 = S_2 = 3/2$.[78] They pointed out that facile electron transfer requires the spins S_1 and S_2 to be parallel so that the mobile electron can couple parallel to both and so transfer without change of spin. The more common coupling scheme in a ligand-bridged paramagnetic complex is antiferromagnetic, and in that case electron transfer is spin forbidden. In other words, antiferromagnetic coupling favors localized mixed valency and slow electron transfer; ferromagnetic coupling favors delocalized mixed valency and rapid electron transfer. Examples of mixed-valence systems are known that support this view, including dinuclear molecular systems such as $\mathrm{Ni^{II}} \cdots \mathrm{Ni^{I}}$ (metal–metal bonded), delocalized and ferromagnetic; and $[(\mathrm{bipy})_2\mathrm{Mn^{IV}}(\mu\text{-O})_2\mathrm{Mn^{III}}(\mathrm{bipy})_2]^+$ (anion-bridged), localized and ferromagnetic.[79] Several groups of workers have discussed the electronic energy levels in such systems, as functions of appropriate coupling constants. Closest to the subject of this article are those in which vibronic coupling is included.[80] Girerd and coworkers have made detailed predictions of energy levels in some dinuclear mixed-valence iron(III)–iron(II) molecules.[81] They have calculated electronic energy levels as functions of reaction coordinates, as for example in Figure 9. The diagram can be compared directly with the one-electron case illustrated in Figure 2. In the case illustrated, the total spin can range overall integral values from 1/2 to 9/2, and the localized precursor/successor complex is antiferromagnetic, while the transition state for electron transfer is ferromagnetic. In other words, if spin is conserved throughout the electron-transfer reaction the activation energy will be high, but if a mechanism for spin change exists, the activation energy will be much lower.

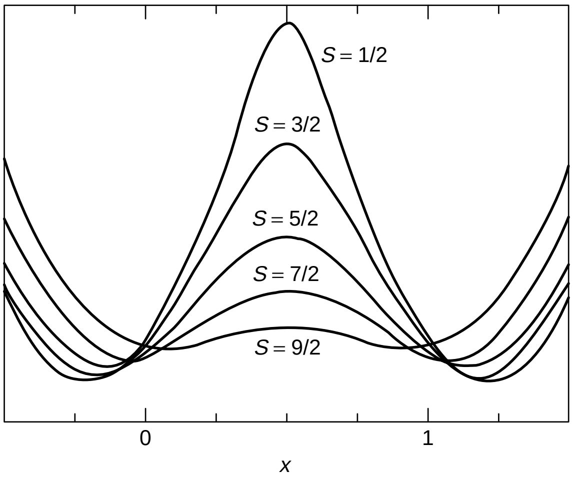

Figure 9 Potential energy curves for a mixed-valence iron(III,II) molecule, with various total spins S, and with coupling parameters such that the ordering of spin states is reversed in the electron-transfer transition state. (Reprinted with permission from Ref. 81, © 1990 American Chemical Society)

15 CONCLUSIONS

Perhaps unlike any other field of Chemistry the continuing progress in the understanding of the mechanisms and kinetics of electron-transfer reactions has been a result of fruitful collaboration between theory and experiment. The landmarks of experimental progress have been the discoveries of measurable self-exchange reactions, the bridging mechanism, long-lived precursor complexes, activationless transfer, and long-range electron transfer in solids and proteins. The theoretical predictions have lead to the recognition of the energy gap law, connection between spectroscopy and thermal activation, solvent dynamics control of transition rates, and the importance of inertial solvent dynamics. Electron transfer is only a part of many more complex mechanisms involved in reduction-oxidation reactions such as corrosion, dissociative electron-transfer reactions, atom transfer, proton-coupled electron transfer, and heterogeneous electrochemical reactions.[82] Intramolecular electron transfer is a promising line of approach to the synthesis of molecular electronic devices[83] and mimicking natural photosynthetic systems.[84] The rate of progress is healthy and there can be no doubt that electron-transfer studies will continue to be a leading edge of progress in chemistry for a long time to come.

16 RELATED ARTICLES

Electron Transfer in Coordination Compounds.

17 FURTHER READING

(a–c) R. D. Cannon, in ‘Inorganic Reaction Mechanisms’, Royal Society of Chemistry, London, 1977–1981, Vols. 5–7, Chap. 1; (d–g) R. D. Cannon, in ‘Mechanisms of Inorganic and Organometallic Reactions’, ed. M. V. Twigg, Plenum Press, New York, 1984–1988, Vols. 2–5, Chap. 1; (h) R. D. Cannon and J. F. Endicott, ‘Mechanisms of Inorganic and Organometallic Reactions’, ed. M. V. Twigg, Plenum Press, New York, 1989, Vol. 6; (i) J. F. Endicott, ‘Mechanisms of Inorganic and Organometallic Reactions’, ed. M. V. Twigg, Plenum Press, New York, 1991, Vol. 7.

A. Haim, *Inorg. Chem.*, 1968, **7**, 1475.

(a) N. Sutin, *Acc. Chem. Res.*, 1982, **15**, 275; (b) S. J. Lippard, *Prog. Inorg. Chem.*, 1983, **30**, 441; (c) M. D. Newton and N. Sutin, *Annu. Rev. Phys. Chem.*, 1984, **35**, 437; (d) R. A. Marcus and N. Sutin, *Biochim. Biophys. Acta*, 1985, **811**, 265; (e) T. Guarr and G. McLendon, *Coord. Chem. Rev.*, 1985, **68**, 1; (f) R. A. Marcus and N. Sutin, *Comments Inorg. Chem.*, 1986, **5**, 119; (g) M. K. Johnson, R. B. King, D. M. Kurtz, C. Kutal, M. L. Norton, and R. A. Scott, *Adv. Chem. Ser.*, 1990, **226**; (h) J. R. Bolton, N. Mataga, and G. McLendon, *Adv. Chem. Ser.*, 1991, **228**; (i) K. Prassides ed., ‘Mixed Valency Systems in Chemistry, Physics and Biology’, Kluwer, Dordrecht, 1991; (j) A. Müller, H. Ratajczak, W. Junger, and E. Diemann, ‘Electron and Proton Transfer in Chemistry and Biology’, Elsevier, Amsterdam, 1992.

18 REFERENCES

1. R. D. Cannon, ‘Electron Transfer Reactions’, Butterworth, London, 1980.
2. P. Chen and T. J. Meyer, *Chem. Rev.*, 1998, **98**, 1439.
3. J. C. Curtis, B. P. Sullivan, and T. J. Meyer, *Inorg. Chem.*, 1983, **22**, 224.
4. P. Vath, M. B. Zimmt, D. V. Matyushov, and G. A. Voth, *J. Phys. Chem. B*, 1999, **43**, 9130.
5. T. W. Swaddle, *Can. J. Chem.*, 1996, **74**, 631.
6. B. Mayoh and P. Day, *J. Am. Chem. Soc.*, 1972, **94**, 2885.
7. (a) R. A. Marcus, *J. Chem. Phys.*, 1956, **24**, 966; (b) R. A. Marcus, *J. Phys. Chem.*, 1986, **90**, 3460; (c) R. A. Marcus, *Rev. Mod. Phys.*, 1993, **65**, 599.
8. N. S. Hush, *Z. Elektrochem.*, 1957, **61**, 734; *J. Chem. Phys.*, 1958, **28**, 962; *Trans. Faraday Soc.*, 1961, **57**, 557.
9. R. A. Marcus and N. Sutin, *Comments Inorg. Chem.*, 1986, **5**, 119.
10. R. A. Marshall, T. P. Shields, and A. G. Lappin, *Adv. Chem. Ser.*, 1990, **226**, 237.
11. R. D. Cannon, *Chem. Phys. Lett.*, 1977, **49**, 299.
12. R. A. Marcus, *J. Chem. Phys.*, 1965, **43**, 1261.
13. B. S. Brunschwig, S. Ehrenson, and N. Sutin, *J. Phys. Chem.*, 1986, **90**, 3657.
14. N. A. Lewis and D. V. Taverner, *Adv. Chem. Ser.*, 1990, **226**, 197.
15. J. T. Hupp, Y. Dong, and R. L. Blackbourn, *J. Phys. Chem.*, 1993, **97**, 3278.
16. (a) L. Reynolds, J. A. Gardecki, S. J. V. Frankland, and M. Maroncelli, *J. Phys. Chem.*, 1996, **100**, 10337; (b) D. V. Matyushov and M. D. Newton, *J. Phys. Chem. A*, 2001, **105**, 8516.
17. F. O. Raineri and H. L. Friedman, *Adv. Chem. Phys.*, 1999, **107**, 81.
18. R. A. Marcus, *Discuss. Faraday Soc.*, 1960, **29**, 21.
19. S. F. Nelsen and J. R. Pladziewicz, *Acc. Chem. Res.*, 2002, **35**, 247.
20. R. A. Reed and R. W. Murray, *J. Phys. Chem.*, 1986, **90**, 3829.
21. M. Chou, C. Creutz, and N. Sutin, *J. Am. Chem. Soc.*, 1977, **99**, 5615.
22. G. C. Allen and N. S. Hush, *Prog. Inorg. Chem.*, 1967, **8**, 357; N. S. Hush, *Prog. Inorg. Chem.*, 1967, **8**, 391.
23. see D. V. Matyushov and G. A. Voth, in ‘Reviews in Computational Chemistry’, eds. K. B. Lipkowitz and D. B. Boyd, Wiley-VCH, Hoboken, New Jersey, 2002, Vol. 18.
24. M. D. Newton, *Adv. Chem. Phys.*, 1999, **106**, 303.
25. C. M. Elliott, D. L. Derr, D. V. Matyushov, and M. D. Newton, *J. Am. Chem. Soc.*, 1998, **120**, 11714.
26. W. Schmickler, ‘Interfacial Electrochemistry’, Oxford University Press, New York, 1996.
27. J. T. Hupp, E. M. Kober, G. A. Neyhart, and T. J. Meyer, in ‘Mixed Valency Systems in Chemistry, Physics and Biology’, ed. K. Prassides, Kluwer, Dordrecht, 1991, p. 51.
28. A. Haim, *Comments Inorg. Chem.*, 1985, **4**, 113.
29. D. Sun, S. V. Rosokha, and J. K. Kochi, *J. Am. Chem. Soc.*, 2004, **126**, 1388.
30. R. A. Marcus, *J. Phys. Chem.*, 1989, **93**, 3078.
31. M. B. Robin and P. Day, *Adv. Inorg. Chem. Radiochem.*, 1967, **10**, 247; P. Day, *Int. Rev. Phys. Chem.*, 1981, **1**, 149.
32. D. E. Richardson and H. Taube, *Coord. Chem. Rev.*, 1984, **60**, 107.
33. (a) J. P. Launay and F. Babonneau, *Chem. Phys.*, 1982, **67**, 295; (b) S. A. Borshch, I. N. Kotov, and I. B. Bersuker, *Chem. Phys. Lett.*, 1982, **89**, 381; (c) R. D. Cannon, L. Montri, D. B. Brown, K. M. Marshall, and C. M. Elliott, *J. Am. Chem. Soc.*, 1984, **106**, 381.
34. A convenient list is given by R. B. Miller, *Adv. Chem. Ser.*, 1991, **228**, notes 1–15.
35. M. Bixon and J. Jortner, *J. Phys. Chem.*, 1986, **90**, 3795.
36. (a) P. Chen, E. Danielson, and T. J. Meyer, *J. Phys. Chem.*, 1988, **92**, 3708; (b) M. R. Wasielewski, D. G. Johnson, W. A. Svec, K. M. Kersy, and D. W. Minsek, *J. Am. Chem. Soc.*, 1988, **110**, 7219.
37. (a) L. Atkinson and P. Day, *J. Chem. Soc. A*, 1969, 2423; (b) F. Felix and A. Ludi, *Inorg. Chem.*, 1978, **17**, 1782.
38. (a) S. B. Piepho, E. A. Krausz, and P. N. Schatz, *J. Am. Chem. Soc.*, 1978, **100**, 2991; (b) K. Y. Wong and P. N. Schatz, *Prog. Inorg. Chem.*, 1981, **28**, 369; (c) P. N. Schatz, in ‘Mixed Valency Systems in Chemistry, Physics and Biology’, ed. K. Prassides, Kluwer, Dordrecht, 1991, p. 7.
39. P. N. Schatz, in ‘Mixed Valence Compounds’, ed. D. B. Brown, D. Reidel, Dordrecht, 1980, p. 115; K. Y. Wong and P. N. Schatz, *Chem. Phys. Lett.*, 1980, **71**, 152.
40. K. Y. Wong, P. N. Schatz, and S. B. Piepho, *J. Am. Chem. Soc.*, 1979, **101**, 2793.
41. P. N. Schatz, S. B. Piepho, and E. R. Krausz, *Chem. Phys. Lett.*, 1978, **55**, 539; K. Y. Wong and P. N. Schatz, *Chem. Phys. Lett.*, 1984, **108**, 484.

42. K. Prassides, P. N. Schatz, K. Y. Wong, and P. Day, *J. Phys. Chem.*, 1986, **90**, 5588.
43. M. Tanner and A. Ludi, *Inorg. Chem.*, 1981, **20**, 2348.
44. B. Brunschwig and N. Sutin, *J. Am. Chem. Soc.*, 1978, **100**, 7568.
45. G. L. Closs, L. T. Calcaterra, N. J. Green, K. W. Penfield, and J. R. Miller, *J. Phys. Chem.*, 1986, **90**, 3673; S. S. Isied, *Adv. Chem. Ser.*, 1991, **228**, 229.
46. B. Bowler, A. L. Raphael, and H. B. Gray, *Prog. Inorg. Chem.*, 1990, **38**, 259; D. N. Beratan, J. N. Onuchic, J. R. Winkler, and H. B. Gray, *Science*, 1992, **258**, 1740.
47. M. R. Gunner, D. E. Robinson, and P. L. Dutton, *J. Phys. Chem.*, 1986, **90**, 3783; C. C. Moser, J. M. Keske, K. Warncke, and P. L. Dutton, ‘Electron and Proton Transfer in Chemistry and Biology’, Elsevier, Amsterdam, 1992, p. 111; C. C. Moser, J. M. Keske, K. Warncke, R. S. Farid, and P. L. Dutton, *Nature*, 1992, **355**, 796.
48. J. R. Miller, *Science*, 1975, **189**, 221; see further references listed in J. R. Miller, *Adv. Chem. Ser.*, 1991, **228**, 265; K. Y. Wong and P. N. Schatz, *Chem. Phys. Lett.*, 1980, **71**, 152.
49. C. Creutz and N. Sutin, *J. Am. Chem. Soc.*, 1977, **99**, 1.
50. D. Rehm and A. Weller, *Isr. J. Chem.*, 1970, **8**, 259.
51. W. Siebrand and D. F. Williams, *J. Chem. Phys.*, 1967, **46**, 403; for later references see C. Creutz and N. Sutin, *J. Am. Chem. Soc.*, 1977, **99**, 1.
52. E. M. Kober, J. V. Caspar, R. Lumpkin, and T. J. Meyer, *J. Phys. Chem.*, 1986, **90**, 3722.
53. (a) R. A. Kuharski, J. S. Bader, D. Chandler, M. Sprik, and M. L. Klein, *J. Chem. Phys.*, 1988, **89**, 3248; (b) E. Carter and J. T. Hynes, *J. Phys. Chem.*, 1989, **93**, 2184; (c) G. King and A. Warshel, *J. Chem. Phys.*, 1990, **93**, 8682; (d) M. Marchi, J. N. Gehlen, D. Chandler, and M. D. Newton, *J. Am. Chem. Soc.*, 1993, **115**, 4178.
54. D. W. Small, D. V. Matyushov, and G. A. Voth, *J. Am. Chem. Soc.*, 2003, **125**, 7470.
55. R. F. Khairutdinov, K. I. Zamaraev, and N. P. Zhandov, in ‘Comprehensive Chemical Kinetics’, ed. R. G. Compton, Elsevier, Amsterdam, 1989 Vol. 30.
56. K. Shiriwong, A. A. Voityuk, M. D. Newton, and N. Roesch, *J. Phys. Chem. B*, 2003, **107**, 2595.
57. (a) S. S. Skourtis and D. N. Beratan, *Adv. Chem. Phys.*, 1999, **106**, 377; (b) D. N. Beratan, J. N. Onuchic, J. R. Winkler, and H. B. Gray, *Science*, 1992, **258**, 1740; (c) C. C. Moser, J. M. Keske, K. Warncke, R. Farid, and P. L. Dutton, *Nature*, 1992, **355**, 796.
58. (a) H. Taube and E. S. Gould, *Acc. Chem. Res.*, 1969, **2**, 321; (b) J. Halpern and L. E. Orgel, *Discuss. Faraday Soc.*, 1960, **29**, 32.
59. M. Bixon and J. Jortner, *Adv. Chem. Phys.*, 1999, **106**, 35.
60. M. Newton, *Chem. Rev.*, 1991, **91**, 767.
61. R. J. P. Williams, *Adv. Chem. Ser.*, 1990, **226**, 3.
62. M. B. Zimmt and D. H. Waldeck, *J. Phys. Chem. A*, 2003, **107**, 3580.
63. M. D. Newton, *J. Phys. Chem.*, 1986, **90**, 3734.
64. J. F. Endicott and T. Ramaswami, *J. Phys. Chem.*, 1986, **90**, 3740.
65. J. R. Reimers and N. S. Hush, *Adv. Chem. Ser.*, 1990, **226**, 27.
66. J. K. Burdett, *Inorg. Chem.*, 1978, **17**, 2537.
67. J. T. Hynes, *J. Phys. Chem.*, 1986, **90**, 3701.
68. X. Zhang, M. Kozik, N. Sutin, and J. R. Winkler, *Adv. Chem. Ser.*, 1991, **228**, 247.
69. (a) W. Frauenfelder and P. G. Wolynes, *Science*, 1985, **89**, 5822; (b) J. T. Hynes, *Annu. Rev. Phys. Chem.*, 1985, **36**, 573; (c) M. Maroncelli, J. MacInnis, and G. R. Fleming, *Science*, 1989, **243**, 1674; (d) B. Bagchi and A. Chandra, *Adv. Chem. Phys.*, 1991, **80**, 1.
70. G. McManis and M. J. Weaver, *J. Chem. Phys.*, 1989, **90**, 912.
71. P. J. Reid, C. Silva, P. F. Barbara, L. Karki, and J. T. Hupp, *J. Phys. Chem.*, 1995, **99**, 2609.
72. B. Bagchi and N. Gayathri, *Adv. Chem. Phys.*, 1999, **107**, 1.
73. T. W. Swaddle, *Inorg. Chem.*, 1990, **29**, 5017.
74. M. Stabler, R. M. Nelson, W. F. Siam, J. P. Hunt, H. W. Dodgen, and S. Wherland, *Inorg. Chem.*, 1988, **27**, 2893.
75. W. S. Hammack, H. G. Drickamer, M. D. Lowery, and D. N. Hendrickson, *Chem. Phys. Lett.*, 1986, **132**, 231; *J. Phys. Chem.*, 1988, **92**, 1771.
76. J. F. Endicott, B. Durham, and K. Kumar, *Inorg. Chem.*, 1982, **21**, 2437; J. F. Endicott, *Acc. Chem. Res.*, 1988, **21**, 59.
77. M. D. Newton, *ACS Symp. Ser.*, 1989, **394**, 378.
78. P. W. Anderson and H. Hasegawa, *Phys. Rev.*, 1955, **100**, 675.
79. L. Sacconi, C. Mealli, and D. Gatteschi, *Inorg. Chem.*, 1974, **13**, 1985; P. M. Plaskin, R. C. Stoufer, M. Mathew, and C. Palenik, *J. Am. Chem. Soc.*, 1972, **94**, 2121.
80. G. Blondin, S. Borshch, and J.-J. Girerd, *Comments Inorg. Chem.*, 1993, **12**, 315; I. B. Bersuker and S. A. Borshch, *Adv. Chem. Phys.*, 1992, **81**, 703; see also references R. D. Cannon, in ‘Mechanisms of Inorganic and Organometallic Reactions’, ed. M. V. Twigg, Plenum Press, New York, 1984–1988, Vols. 2–5, Chap. 1.
81. G. Blondin and J.-J. Girerd, in ‘Mixed Valency Systems in Chemistry, Physics and Biology’, ed. K. Prassides, Kluwer, Dordrecht, 1991, p. 119; *Chem. Rev.*, 1990, **90**, 1359.
82. N. S. Hush, *J. Electroanal. Chem.*, 1999, **470**, 170.
83. M. A. Ratner and J. Jortner, in ‘Molecular Electronics’, eds. M. A. Ratner and J. Jortner, IUPAC, 1997.
84. M. R. Wasielewski, *Chem. Rev.*, 1992, **92**, 435.

Electronic Structure of Clusters

David J. Wales
University of Cambridge, Cambridge, UK

1 Introduction 1
2 Computational Approaches 1
3 Empirical Structure–Electron Count Correlations 2
4 Models of Cluster Bonding 3
5 Further Development of TSH Theory 8
6 Cluster Rearrangements 15
7 Related Articles 18
8 References 18

Glossary

Ab initio calculations: attempt to calculate from first principles, without use of empirical data, solutions to Schrödinger's equation
Deltahedron: a polyhedron with only triangular faces

Abbreviations

DFT = Density Functional Theory; DSD = Diamond-Square-Diamond; HOMO = Highest Occupied Molecular Orbital; IR = Irreducible Representation; LCAO = Linear Combination of Atomic Orbitals; Ph = Phenyl; PSEPT = Polyhedral Skeletal Electron Pair Theory; SCF = Self-Consistent-Field; SDDS = Square-Diamond, Diamond-Square; TSH = Tensor Surface Harmonic.

1 INTRODUCTION

The first problem encountered in writing an article of this kind lies in deciding what a *Cluster* actually is, and which sorts of cluster are relevant to the audience in question. The former problem may be addressed in terms of size or number of constituent atoms; for example, Sugano[1] considers a classification in terms of molecules, microclusters, and fine particles. On the other hand, Berry has distinguished clusters as 'finite aggregates whose composition can be changed by adding or taking away units of the species that comprise them. . . they are finite bits of what, in composition but not necessarily in structure, constitute a tiny sample of bulk material, but more than a single molecule or even two atoms or molecules'.[2] Here, we must recognize that the domain of cluster chemistry extends beyond systems such as boranes, carboranes, and transition metal carbonyls, which are generally considered to be the stuff of inorganic cluster chemistry.[1,3–5] These are certainly the molecules of primary interest here, but it would be shortsighted to ignore the connections between these species and clusters bound, for example, by van der Waals forces. There is often much to be learned from making such comparisons: for instance, we may find analogous structures and rearrangement mechanisms in clusters bound by quite different forces. The converse is also true, and a better understanding of the dynamics of small inert gas clusters has been achieved partly by the application of ideas that originated in inorganic chemistry concerning rearrangement mechanisms.[6]

To appreciate the ubiquity of clusters in chemistry and physics, one need only consult the proceedings of one of the biennial International Symposia on Small Particles and Inorganic Clusters (ISSPIC).[7] These volumes include species ranging from hydrocarbon polyhedra, such as dodecahedrane[8] (*see also Dodecahedral*), to large carbon clusters,[9] and from small inert gas clusters to colloidal metal particles containing thousands of atoms. These systems are of interest for a variety of reasons, such as the investigation of fundamental processes including melting and freezing, and can sometimes provide insight into the behavior of larger systems at a more tractable level. Furthermore, small clusters may exhibit properties that are unique to the intermediate size regime, which may be of technological importance.[10]

The principal subject of this contribution is the electronic structure of clusters, and so we shall mainly be concerned with molecules in which the interatomic forces cannot be well described by simple empirical potential energy functions. Hence, the following section provides an overview of the progress that has been made in performing quantum mechanical calculations for clusters. Major difficulties remain to be solved in this field, particularly with regard to systems containing *Transition Metals*. However, although accurate calculations are certainly important, there are various patterns concerning the correlation between structure and electron count, which require a more general explanation. The latter are considered in Section 3, and the various models that have been developed to explain them are reviewed in Section 4. One of these, Stone's Tensor Surface Harmonic (TSH) theory, is then developed in Section 5, and some further applications to cluster rearrangements are described in Section 6.

2 COMPUTATIONAL APPROACHES

It is certainly not the purpose of this section to describe the mechanics of ab initio quantum chemical calculations on clusters.[11] However, some understanding of the problems and achievements in this field is necessary to appreciate the simpler general models described in subsequent sections. Even if extensive and accurate calculations were possible for all the inorganic clusters of interest, the latter models would still be needed to explain the structural patterns that have been deciphered.

Most applications of ab initio quantum chemistry involve expanding the wavefunction using a basis set of atomic orbitals. As the many-body problem is not analytically tractable in either classical or quantum mechanics, we can never obtain the exact wavefunction. However, the variation principle**[12]** tells us that the more basis functions we use, the more accurate our calculation should become. Unfortunately, the computational cost of the most commonly employed self-consistent-field**[12]** (SCF) method increases roughly as N^4, where N is the number of basis orbitals. Hence, for clusters containing *Transition Metals*, for which even a minimal basis set of atomic orbitals requires many functions, the calculations rapidly become impossible. There is another problem as well: the usual Hartree–Fock SCF procedure neglects the instantaneous electron–electron interaction, replacing it instead with an average field**[12,13]** (*see Hartree–Fock Theory*). The error incurred by this treatment of the electron correlation problem generally becomes more significant for systems with low-lying electronic states, as are commonly found in transition metal compounds. Density functional theory**[14]** (DFT) can help deal with the correlation problem, but the reliability of such calculations is often subject to debate. This is particularly true for molecules containing heavy elements, where relativistic effects are also important.**[15]**

Given this background, it is not surprising that many different approaches, all introducing further approximations,**[16]** have been applied to inorganic clusters. The two most commonly encountered approaches in this area are the Extended Hückel**[17]** and Fenske–Hall**[18]** methods (*see also Extended Hückel Molecular Orbital Theory*). The former is the simplest approach, making use of empirical data, while the latter uses no experimental information, but instead approximates the quantum mechanical Hamiltonian so as to avoid many of the most time-consuming integrals. Despite the sweeping assumptions used in these methods,**[19]** they have often been found to give valuable insights, although DFT is now commonly used instead.

The early DFT studies of main group clusters by Jones and coworkers should be mentioned here.**[20]** However, as these are primarily concerned with clusters that are describable in terms of two-center, two-electron bonds, they will not be considered further. For similar reasons, no attempt will be made to survey the rapidly growing body of calculations on carbon–fullerene systems**[9]** (*see* ***Carbon: Fullerenes***). The σ-bonding framework of these molecules is again easily understood from the point of view of electron counting. Predicting for which geometries the delocalized π-system is especially favorable is a more interesting problem, but is beyond the scope of this review. Some other specific calculations on boranes, carboranes, metal, and silicon clusters will be considered in the following sections.

3 EMPIRICAL STRUCTURE–ELECTRON COUNT CORRELATIONS

With the explosion in size of the database of known cluster compounds, it is reassuring to note that a number of patterns were soon recognized and exploited by inorganic chemists. The most important relationships between geometry and the number of electrons in a cluster (‘electron-counting rules’, *see Counting Electrons*) are summarized in the Debor Principle**[21]** (or *Wade’s Rules*), Polyhedral Skeletal Electron Pair Theory**[22]** (PSEPT), and the Isolobal Principle.**[23]** These ‘rules’ (to which there are various exceptions) include three-connected clusters (By convention, the connectivity’ of a vertex is the number of nearest-neighbors in the cluster cage, not counting terminally bound ligands.), like prismane, deltahedral clusters (which have only triangular faces), such as *closo*-boranes; ‘naked’ clusters**[24]** like $Sn_5{}^{2-}$ and $Pb_5{}^{2-}$; clusters with interstitial atoms, fused molecules, which can be decomposed into deltahedra that share vertices, edges, or faces, and even large multispherical transition metal clusters. Much of the rest of this article is devoted to rationalizing these patterns, whose importance can perhaps be appreciated by the example of $Au_{13}Cl_2(PMe_2Ph)_{10}{}^{3+}$. This compound was successfully synthesized several years after the stability of gold clusters $Au_{13}(PR_3)_{12}{}^{5+}$ was predicted on the basis of simple bonding considerations.**[25]**

Some of the historical development of the electron-counting rules is summarized in a review by Mingos and Johnston;**[26]** here, we will concentrate on the patterns themselves, beginning with the simplest cases – more details can be found elsewhere.**[27]** The most straightforward clusters commonly encountered in inorganic chemistry are those that can be described by essentially localized two-center, two-electron bonds, where all the atoms obey an effective atomic number rule EAN Rule. For main group atoms, this means that each one is associated with 8 valence electrons to give an ‘inert gas configuration’; for *Transition Metals*, 18 electrons are usually required to do this. Hence, such clusters are associated with

$$\begin{aligned} N_e &= 8n - 2E \qquad \text{main group} \qquad \text{or} \\ N_e &= 18n - 2E \qquad \text{transition metal} \end{aligned} \tag{1}$$

where N_e is the number of valence electrons, n is the number of vertices in the cluster, and E is the number of two-center, two-electron bonds, or edges. For ring compounds, $E = n$ and hence $N_e = 6n/16n$ for main group/transition metal clusters. Three-connected *Polyhedral* systems, such as prismane, have $E = 3n/2$ so that $N_e = 5n/15n$. To cover mixed compounds, we note that replacement of a main group vertex atom by a transition metal should increase N_e by 10, while interstitial atoms are generally not associated with an increase in the number of occupied molecular orbitals,[27] and effectively act as electron donors. The relatively simple consequences of interchanging main group and transition metal atoms basically follow from the symmetries of the orbitals that these fragments provide for skeletal cluster bonding, as identified in the Isolobal Principle of Hoffmann and collaborators.[23]

Most clusters, however, cannot be described adequately in terms of two-center, two-electron bonds because the connectivity of the vertices exceeds the number of valence orbitals that are available for bonding. Early efforts to rationalize such systems, such as Lipscomb's styx approach[28] and Kettle's Topological Equivalent Orbital Method,[29] are described by Mingos and Johnston.[26] In these more difficult cases, the simple valence-bond picture is inappropriate; examples are deltahedral clusters composed of B−H vertices or conical $M(CO)_3$ fragments, both of which usually have only three orbitals available for skeletal bonding. Theoretical models for describing these systems will be discussed in the next section.

We find that four-connected clusters and *closo*-deltahedra have $N_e = 4n + 2/14n + 2$ for main group/transition metal clusters. *Closo*-deltahedra are clusters with entirely triangular faces; however, some four-connected clusters have one or more square faces.[27] When successive vertices are (notionally) removed from a *closo*-deltahedron, the resulting molecules are called nido, arachno, hypho, and so on. The Debor Principle[21] (or *Wade's Rules*) recognizes that the total number of valence electrons in such systems does not change, and in terms of the number of vertices remaining, n, this gives $N_e = 4n + 4/14n + 4$, $4n + 6/14n + 6, \ldots$ for main group/transition metal nido, arachno, ... clusters.

Most of the remaining patterns might be classified under the heading of 'condensation rules,' many of which were developed by Mingos and coworkers. The Capping Principle states that the number of skeletal bonding orbitals is unchanged when one face of a *Polyhedral* cluster is capped.[22,30] Hence, if the capping moiety is a conical $M(CO)_3$ fragment, then N_e increases by 12, this being the number of electrons in the nonbonding and metal−ligand bonding orbitals.[26] The Principle of Polyhedral Fusion deals with clusters that can be (notionally) decomposed into two polyhedra (A and B) that share a vertex, edge, or face.[31] In this case, N_e is usually equal to the sum of $N_e(A)$ and $N_e(B)$, regarded as complete, individual entities each containing copies of the fragments that are shared between them, minus the number of valence electrons expected for the shared unit.[26] The final one of these 'principles' is that of polyhedral inclusion, where high nuclearity multispherical systems are considered in terms of encapsulated polyhedra.[32] However, as a number of subcases must be considered for such systems, the reader is referred elsewhere for details.[27,32]

The remainder of this article is largely concerned with describing how some of the above observations can be rationalized using Stone's Tensor Surface Harmonic theory, and with the further implications of this model for dynamical processes such as cluster rearrangements. The number of example systems and electron count rationalizations will be kept relatively small in favor of explaining the theoretical foundations that underlie the method. Tables of examples and more detailed analyses of the various cases may be found elsewhere.[26,27]

4 MODELS OF CLUSTER BONDING

To achieve a general understanding of the patterns described in the previous section requires some sort of model for the energy of a cluster as a function of its geometry and the number of valence electrons. In this section, we focus upon the three most successful approaches, namely, jellium models, topological methods based upon graph theory, and Stone's Tensor Surface Harmonic (TSH) theory. In each case, the energetic problem is simplified by asking how many bonding, nonbonding, and antibonding orbitals are available for a given cluster geometry, and these orbitals may be delocalized, localized, or a mixture of both. In fact, TSH theory is more powerful than this, as it really defines an orbital transformation, which may be applied to the results of any calculation, as discussed below.

In each of the three approaches, we effectively guess the forms and energies of the solutions to the quantum mechanical many-body problem. Jellium models achieve this by solving a Schrödinger equation in which all the electron−electron and electron−nucleus interactions are replaced by a simple effective potential. The result is a set of spatially delocalized functions of increasing energy into which electrons are assigned by the usual Aufbau principle.[12] Although jellium methods are commonly found in the physics literature, they are of rather limited application in the present context, and are more appropriate for clusters of alkali or alkali earth metals, for which very large systems have been considered.

The topological or graph-theoretical approaches attempt to define the bonding and antibonding orbitals available to a cluster in terms of a sort of valence-bond description,[12] where hybridized atomic orbitals are directed in space to form either localized or multicenter functions. (*See also Hybridization*.) The analysis of a complex structure involving delocalized bonding may, however, require some seemingly subjective decisions about how the atomic orbitals overlap, where the multicenter bonds should be formed, and so forth.

How is it then, that organic chemists, armed only with pencil, paper, and some knowledge of basic molecular orbital theory and the Woodward–Hoffmann rules,[33] can often successfully predict the outcome of apparently complex organic reactions? The simple answer is that the bonding in such systems is generally rather easier to describe than in clusters, and relatively accurate calculations may often be used for guidance. However, with the advent of TSH theory, the inorganic chemist now has tools that are similar in many respects to those used in organic chemistry. The increased difficulty of the analysis in inorganic clusters may then be seen as a consequence of delocalization occurring in three dimensions, and of the presence of d valence atomic orbitals in *Transition Metals*.

TSH theory may be regarded as either a descent-in-symmetry approach, or, equivalently, as a method that exploits the existence of approximate quantum numbers in roughly spherical clusters. The idealized high-symmetry case in question is the free electron-on-a-sphere, for which the wavefunctions are the spherical harmonics, $Y_{LM}(\theta, \phi)$, and the angular momentum operators $\hat{L}^2$ and $\hat{L}_z$ have corresponding good quantum numbers L and M_L. In a finite cluster, the Hamiltonian has lower symmetry appropriate to the point group in question. TSH theory assumes that approximately good quantum numbers still exist for the angular momentum of an electron about the center of a roughly spherical cluster, and exploits this assumption to approximate the molecular orbitals. The resulting linear combinations of atomic orbitals (LCAOs) would be the true molecular orbitals of the cluster if it actually had spherical symmetry; they are known as cluster orbitals. (*See also LCAO Approximation*.) However, the usefulness of TSH theory goes beyond this construction, in providing a transformation of basis that may be applied to the results of any calculation in which identifiable atomic orbitals are used. Despite the fact that the ideal linear combinations of TSH theory actually mix in real clusters, it is often true that they are still recognizable. This is the essence of an approximate quantum number.

Before developing the TSH approach in Section 5 to explain some of the structure-electron count correlations described above, we will first consider the connections between the jellium, topological, and TSH methods in a little more detail. It is noteworthy that none of these models in their usual form includes any attempt to allow for electron correlation. Hence, it is important to ask, for example, why TSH theory can explain all the general structure-electron count correlations so successfully. The answer is presumably that the correlation energy is often not of primary importance in discriminating between different geometries with the same number of electrons. However, sometimes there exists more than one low-energy structure associated with a given electron count; in such cases, and in any case where the correlation energy exhibits a large variation with geometry, we should anticipate exceptions to the usual ‘rules’.

4.1 The Jellium Model

The jellium model was first developed by Knight *et al.*[34] to explain the ‘magic numbers’ observed in mass spectra of sodium and potassium clusters produced by supersonic expansion in molecular beams.[35] The method was adapted from nuclear physics, where ‘magic number’ nuclear states have been successfully explained.[36] If the potential energy vanishes inside a sphere and is infinite outside it, then the energetic ordering of the solutions to the resulting Schrödinger equation is

$$1\mathrm{s} < 2\mathrm{p} < 3\mathrm{d} < 2\mathrm{s} < 3\mathrm{f} < 3\mathrm{p} < 4\mathrm{g} < 4\mathrm{d} < 3\mathrm{s} < 5\mathrm{h}\ldots, \qquad (2)$$

where 3d, for example, has no radial nodes and two angular nodes and is fivefold degenerate. The notation is analogous to that used for atomic orbitals, though different from that used in some of the literature,[34] and seems appropriate in this context. The wavefunctions for any potential energy function that depends only upon the distance from a fixed origin may be written as a product of spherical harmonics[12] and functions that depend only upon the distance. Hence, the same degeneracies arise, because of the assumed spherical symmetry, as for an atom. It is noteworthy that differences in the order of these energy levels with a deep potential well only occur for relatively high-lying solutions.[37] Experimentally, peaks in the mass spectra of sodium and potassium clusters are indeed found for 8, 18, 20, 40, ... atoms, corresponding to completed electronic shells in the above scheme.[38]

Various refinements of the above model have been proposed; for example, using alternative spherical potentials or allowing for nonspherical perturbations,[39–40] and these can improve the agreement of the model with the abundance peaks observed in different experimental spectra. For small alkali metal clusters, the results are essentially equivalent to those obtained by TSH theory, for the simple reason that both approaches start from an assumption of zeroth-order spherical symmetry. This connection has been emphasized in two reviews,[40,41] and also holds to some extent when considerations of symmetry breaking are applied. This aspect is discussed further below. The same shell structure is also observed in simple Hückel calculations for alkali metals, again basically due to the symmetry of the systems considered.[42] However, the developments of TSH theory, below, and the assumptions made in the jellium model itself, should make it clear that the latter approach is only likely to be successful for alkali and perhaps alkali earth metals. For example, recent results for aluminium clusters have led to the suggestion that symmetry-breaking effects are more important in these systems.[43]

These conclusions are not unexpected. Firstly, the free-electron approximation works best for the alkali metals, with significant deviations for divalent and trivalent metals.[44] Secondly, the LCAO-MO TSH treatment requires a more complicated treatment of p and d orbitals, involving tensor spherical harmonics. The jellium model makes no allowance for these properties, and hence, the analogy to TSH theory breaks down here. An alternative way to think about this breakdown is in terms of the strength of the nonspherical potential due to the nuclei,[40,41] and its influence upon electrons that occupy effective single-particle states. As the orbital energy increases, so too does the de Broglie wavelength;[12] and the effect of the nonuniform distribution of nuclei becomes more significant. Splittings of the spherical symmetry degeneracies should therefore increase with the orbital energy, and will probably be greater for aluminium than, say, sodium, because for a given cluster geometry there are more valence electrons to accommodate. The former effect is apparent around the Highest Occupied Molecular Orbital HOMO and above in Hückel calculations on different cluster morphologies containing up to 1000 atoms.[45] One further viewpoint is obtained by considering the magnitude of matrix elements of the nuclear potential, expanded in terms of spherical harmonic components.[41]

Before leaving the jellium model, it seems appropriate to mention some results for sodium clusters of up to 22 000 atoms. The abundances observed can be explained in terms of the extra stability associated with both completed jellium shells (for less than about 3000 atoms) and with completed icosahedral or cuboctahedral geometric shells for larger sizes.[46] The results are especially interesting because of the observation of ‘supershells’ that occur because of an interference effect, which has been explained using semiclassical arguments.[47]

One further question that one might naturally ask of metal clusters is how large they need to be for bulk properties to manifest themselves.[48] However, as the answer to this question depends crucially upon the bulk property in question, and the answer is still somewhat subjective, such issues will not be pursued here.

4.2 Topological Approaches

In the most well-developed topological approach, the mechanics of algebraic graph theory[49] are applied to enumerate the bonding and antibonding orbitals of a given cluster. From the earliest work of King and Rouvray,[50] the method has been extended by King,[51] leading to a self-consistent framework for rationalizing the electron counts of many of the systems mentioned in Section 3, among others. Connections to TSH theory have been discussed in several studies.[27,52] Basically, the method analyzes structures in terms of edge-localized, face-localized, and core-delocalized bonds that arise in the middle of cluster polyhedra. Electron pairs are then assigned to the resulting bonding orbitals, rather like the construction of a valence-bond wavefunction[12] when multicenter orbitals are included as building blocks.

This approach is perhaps best illustrated by a simple example. Consider a deltahedral cluster where the vertex connectivity is greater than three, for example, $B_6H_6{}^{2-}$. One valence orbital per vertex is used to form a two-center, two-electron bond to a terminal ligand (hydrogen in this case), leaving three orbitals, which may be partitioned into two functions that are tangential to the sphere on which the vertex atoms lie, and one which points toward the center of the cluster. Rationalization of the cluster electron count ($N_e = 4n + 2$) proceeds as follows. We already have n bonding orbitals corresponding to B−H bonds in this example. Pairwise overlap of the $2n$ tangential orbitals then produces n bonding and n antibonding sets, while overlap of the inward-pointing hybrids gives rise to one particularly low-lying orbital,[51] giving a total of $2n + 1$ bonding orbitals, which are completely filled by $4n + 2$ electrons.

To describe edge-localized bonding, as in prismane, for example, the three valence orbitals left after terminal bonding are simply directed toward the three-neighboring vertices. This is not unreasonable, but for more complex systems, it may require some imagination to direct the various valence orbitals along edges, into faces or into cavities to obtain the required number of bonding orbitals. Furthermore, it can be a significant approximation to neglect mixing between the radial and tangential orbitals in some clusters.[53] The corresponding problem in TSH theory is the mixing of TSH σ- and π-type cluster orbitals, which is readily quantified by simply transforming the results of any MO calculation into a TSH theory cluster orbital basis (see below).

Teo’s topological approach also deserves mention in this section.[54] It combines Euler’s theorem with the idea of an effective atomic number rule for each cluster vertex, but involves a rather arbitrary parameter whose purpose is to correct for the formation of multicenter bonds.

4.3 Tensor Surface Harmonic (TSH) Theory

Stone’s TSH theory is framed within LCAO-MO theory, whose power was first demonstrated in the field of cluster chemistry by Longuet–Higgins and Roberts[55] in providing the first satisfactory analysis of icosahedral $B_{12}H_{12}{}^{2-}$. (*See also LCAO Approximation*.) Here, it is perhaps worth mentioning that the popular nomenclature for such species, that is, ‘electron deficient’, is a misnomer. Although there are certainly not enough valence electrons in the cluster for all the nearest-neighbor contacts to represent two-center, two-electron bonds, it is not the case that there are unoccupied bonding orbitals. On the contrary, all the bonding molecular orbitals are precisely filled, as we shall see. (*See also Electron Deficient Compound*).

The closest forerunner to TSH theory was due to Hoffmann, Ruedenberg, and Verkade.[56] These authors used spherical harmonics at the center of the cluster to generate linear combinations of orbitals with particular symmetry and nodal characteristics. The energy of these orbitals could then be estimated by the number of angular nodes in the parent spherical harmonic. For alkali metal clusters, one could actually produce the same answers for the symmetries of the bonding orbitals as for the spherical jellium model (above) or TSH theory. However, once again the method cannot work for systems, where p and d orbitals contribute to the bonding, because then there are valence orbitals that have intrinsic nodal planes containing the radius vector of the atom. Stone's principal contribution was to produce a remedy for this problem.[57]

Let us first consider how the π molecular orbitals of linear and cyclic conjugated polyenes may be obtained by a descent-in-symmetry approach. If the electrons moved in an average nuclear potential, the corresponding free-particle wavefunctions would be the solutions of the Schrödinger equation for a particle-in-a-box and a particle-on-a-ring, respectively. These are, of course, just sine and cosine functions,[12,27] and there are 'good' quantum numbers associated with the linear momentum and the angular momentum about the center of the ring, respectively. The corresponding linear combinations of p^{π} orbitals, which have the same transformation properties as the free-electron functions, are obtained by taking the coefficients to be the values of the latter functions evaluated at the atom positions.[27] In fact, if the boundary conditions are chosen appropriately, this procedure gives precisely the molecular orbitals of simple Hückel theory in both cases, as shown below. This result should not be taken to mean that TSH theory has its basis in Hückel theory. Rather, it is an illustration that the descent-in-symmetry results from the free-electron problem may be a very useful guide to the true LCAO-MO wavefunctions.

For a conjugated linear polyene with n atoms, it is not hard to show[27] that the normalized Hückel wavefunctions are given by

$$\psi_m = \sqrt{\frac{2}{n+1}} \sum_t p^{\pi}(t) \sin \frac{\pi t m}{n+1} \tag{3}$$

where $1 \le m \le n$ and $p^{\pi}(t)$ is the π orbital at atom t. The solutions of the Schrödinger equation for a free particle-in-a-box of length L are

$$\psi_m = \sqrt{\frac{2}{L}} \sin \frac{\pi x m}{L} \tag{4}$$

where $m > 0$. The (unnormalized) coefficients for each p^{π} orbital in the expansion are now obtained from the values of $\sin \pi x m/L$ at the atom positions if we identify x/L with $t/(n+1)$. For a cyclic polyene, the normalized Hückel wavefunctions are

$$\psi_{ms} = \sqrt{\frac{2}{n}} \sum_t p^{\pi}(t) \sin \frac{2\pi t m}{n} \quad \text{or}$$
$$\psi_{mc} = \sqrt{\frac{2}{n}} \sum_t p^{\pi}(t) \cos \frac{2\pi t m}{n} \tag{5}$$

while for a free particle-on-a-ring the wavefunctions may be written as

$$\psi_{ms} = \sqrt{\frac{1}{\pi}} \sin m\phi \quad \text{and} \quad \psi_{mc} = \sqrt{\frac{1}{\pi}} \cos m\phi \tag{6}$$

where ϕ is the angle that describes the particle's position on the ring. In this case, we may obtain the expansion coefficient for $p^{\pi}(t)$ from the above functions by setting $\phi = 2\pi t/n$.

Stone applied similar reasoning to the problem of a three-dimensional cluster. Here, the solutions of the corresponding free-particle problem for an electron-on-a-sphere are spherical harmonics.[12] These functions should be familiar because they also describe the angular properties of atomic orbitals.[27] Two quantum numbers, L and M, are associated with the spherical harmonics, $Y_{LM}(\theta, \phi)$, and these define the eigenvalues for the operators $\hat{L}^2$ and $\hat{L}_z$, which correspond to the square of the total orbital angular momentum and its projection on the z-axis, respectively. It is more convenient to use the real linear combinations of $Y_{LM}(\theta, \phi)$and $Y_{L-M}(\theta, \phi)$ (except when $M = 0$), and these are written as $Y_{LMc}(\theta, \phi)$ and $Y_{LMs}(\theta, \phi)$ because they are proportional to $\cos M\phi$ and $\sin M\phi$, respectively. Hence, the functions Y_{10}, Y_{11c}, and Y_{11s} are proportional to z, x, and y, respectively, as in p_z, p_x, and p_y atomic orbitals.

We now categorize the basis atomic orbitals in any, roughly spherical, cluster according to the number of nodal planes they possess that contain the radius vector. Hence, s atomic orbitals are classified as σ-type cluster orbitals, and so are p_z and d_{z^2} orbitals, where the local axes at each vertex are chosen with the x and y directions tangential to the surface of the sphere so that z points outwards along the radius vector. Radially directed hybrids, such as sp_z are also σ-type under this classification. Examples will be illustrated below. π-type cluster orbitals have one intrinsic nodal plane containing the radius vector, for example, p_x, p_y, d_{xz} and d_{yz} in the same axis system. d_{xy} and $d_{x^2-y^2}$ functions contain two such nodal planes, and are known as δ orbitals.[27,57]

A set of σ-type atomic orbitals transform amongst themselves under point group operations like scalar quantities. Hence, to construct descent-in-symmetry-type LCAO cluster orbitals, we simply follow the same reasoning as for the linear and cyclic polyenes, above, and define (unnormalized) σ-type cluster orbitals as

$$L_{\mu}^{\sigma} = \sum_t Y_{L\mu}(\theta_t, \phi_t)\sigma(t) \tag{7}$$

where $\mu = Mc$ or Ms, $\sigma(t)$ is a σ-type basis orbital at atom t and θ_t and ϕ_t are the angular coordinates of atom t. We write $S, P, D, \ldots$ when $L = 0, 1, 2, \ldots$, by analogy with atomic orbitals. This is as it should be, for our assumption that the orbital angular momentum of an electron about the center of the cluster provides approximate quantum numbers is not unlike describing the cluster as a pseudoatom.

σ-cluster orbitals transform like the parent spherical harmonics in any given point group, and these properties are easily determined from standard descent-in-symmetry tables.[58] Sometimes it may be more convenient to omit the μ subscripts from the cluster orbitals and give the transformation properties instead. For example, the six 2s orbitals in Li_6 form a basis for a representation that spans[12] $A_{1g} \oplus T_{1u} \oplus E_g$. When transforming to a basis of cluster orbitals, we generally start from functions with the smallest L and work up. In this case, the cluster orbitals are $S^\sigma(A_{1g})$, $P^\sigma(T_{1u})$, and $D^\sigma_{0,2c}(E_g)$ as illustrated in Figure 1, where the three $P^\sigma(T_{1u})$ functions transform like x, y, and z and correspond to the Y_{11c}, Y_{11s}, and Y_{10} spherical harmonics. Note that in this case, the energetic ordering is simply expected to follow the number of nodes in the cluster orbital.

π-type basis functions, however, transform like a set of unit vectors because the intrinsic nodal plane in each one defines a particular direction. Stone recognized that appropriate LCAO combinations may be formed using vector surface harmonics, which have both magnitude and direction at any given point in space. Hence, instead of LCAO expansion coefficients, which are just the values of spherical harmonics evaluated at the atom sites, the coefficients for π-type basis functions define not only an amplitude but also the *direction* in which the π-functions point.[27,57]

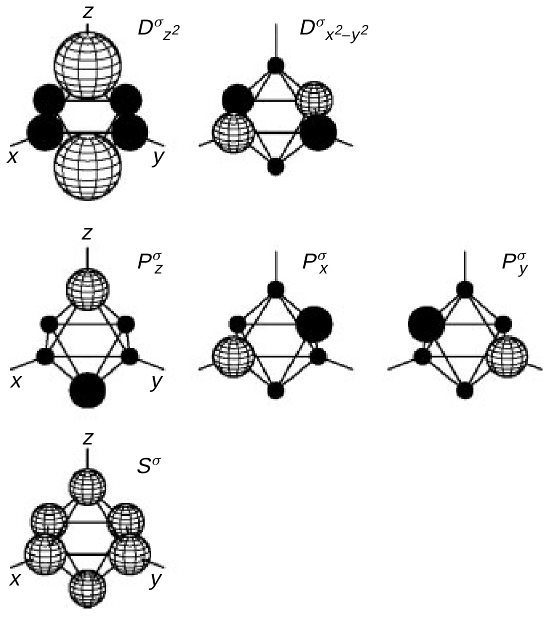

Figure 1 The (unnormalized) σ-cluster orbitals of an *Octahedral* cluster, such as Li_6 for which the basis functions are 2s orbitals.[27] The light and dark shading indicates the phase; the atoms are represented as small filled black circles. (This figure was produced using Mathematica 2.0 © Wolfram Research Inc., 1990.)

In fact, two types of vector function can be derived from the spherical harmonics, and these are defined by

$$\mathbf{V}_{LM} = \nabla Y_{LM} \quad \text{and} \quad \overline{\mathbf{V}}_{LM} = \mathbf{r} \times \mathbf{V}_{LM} = \mathbf{r} \times \nabla Y_{LM} \tag{8}$$

where $\times$ denotes the vector cross product and ∇ is the gradient operator, which is $(\partial/\partial x, \partial/\partial y, \partial/\partial z)$ in Cartesian coordinates. These vector functions are clearly orthogonal; $\mathbf{V}_{LM}$ has the same parity as the parent Y_{LM}; it is a *polar* (or even) vector surface harmonic. $\overline{\mathbf{V}}_{LM}$ has the opposite parity (i.e. it changes sign under inversion if L is even, and is unchanged if L is odd) and is an *axial* (or odd) vector surface harmonic. The first π-cluster orbitals are the P^π and $\overline{P}^\pi$ sets because the derivatives of $Y_{00}(\theta, \phi)$ are zero. We denote the even and odd sets generically by L^π and $\overline{L}^\pi$ respectively; the p^π cluster orbitals of an octahedron are given in Figure 7.

Linear combinations of radial p orbitals, or sp hybrids, may be used to construct σ-cluster orbitals as mentioned above. If we consider an n-vertex cluster, then there are $2n$ π-type p orbitals, that is, two at each vertex, and these correspond to the two independent directions at each site tangential to the surface of the sphere upon which all the atoms are assumed to lie. It is convenient to choose the two directions corresponding to the spherical polar coordinates θ and ϕ increasing, that is, along the unit vectors $\hat{\mathbf{e}}_\theta$ and $\hat{\mathbf{e}}_\phi$. Using the standard form for the gradient vector operator in spherical polars, this gives the two orthogonal vector functions

$$\begin{aligned} \mathbf{V}_{L\mu} &= \frac{\partial Y_{L\mu}}{\partial \theta}\hat{\mathbf{e}}_\theta + \frac{1}{\sin\theta}\frac{\partial Y_{L\mu}}{\partial \phi}\hat{\mathbf{e}}_\phi \quad \text{and} \\ \overline{\mathbf{V}}_{L\mu} &= -\frac{1}{\sin\theta}\frac{\partial Y_{L\mu}}{\partial \phi}\hat{\mathbf{e}}_\theta + \frac{\partial Y_{L\mu}}{\partial \theta}\hat{\mathbf{e}}_\phi \end{aligned} \tag{9}$$

The θ component of $\overline{\mathbf{V}}_{L\mu}$, written $\overline{V}^\theta_{L\mu}$, is the same as the negative of $V^\phi_{L\mu}$ while $\overline{V}^\phi_{L\mu} = V^\theta_{L\mu}$. Hence, odd π cluster orbitals may be obtained from their even partners by rotating the p orbital components through 90° about the radius vector. These cluster orbitals may be written as

$$\begin{aligned} L^\pi_\mu &= \sum_t \left(V^\theta_{L\mu}(t)\mathrm{p}^\theta(t) + V^\phi_{L\mu}(t)\mathrm{p}^\phi(t)\right) \quad \text{and} \\ \overline{L}^\pi_\mu &= \sum_t \left(\overline{V}^\theta_{L\mu}(t)\mathrm{p}^\theta(t) + \overline{V}^\phi_{L\mu}(t)\mathrm{p}^\phi(t)\right) \end{aligned} \tag{10}$$

where the functions are evaluated at the atom positions t as for the σ cluster orbitals. We could therefore sketch the π cluster orbitals from p^θ and p^ϕ orbitals at each vertex using the appropriate expansion coefficients. However, an alternative representation would take just one resultant p orbital, which is the superposition of these two, taking into account their relative weights in a given cluster orbital. This is just the same as choosing one p orbital at each site with the direction and magnitude of the tangential component of $\mathbf{V}_{L\mu}$ or $\overline{\mathbf{V}}_{L\mu}$

at that point. This fact was used to produce Figure 7 in Section 5.

As for σ cluster orbitals, the transformation of basis to give π cluster orbitals from π-type basis atomic orbitals is not unique. To define a transformation, we must first form and reduce the representation, $\Gamma_{\pi/\overline{\pi}}$, spanned by the $2n$ π orbitals of a given n-vertex cluster.[27] Conventionally, we start from $L = 1$, $M = 0$ and take the corresponding L_{μ}^{π} and $\overline{L}_{\mu}^{\pi}$ cluster orbitals until we have matched the irreducible representations contained in $\Gamma_{\pi/\overline{\pi}}$ in number and type. Usually, this gives a linearly independent set of cluster orbitals; if not, then functions of higher L or M with the appropriate symmetry are substituted to produce such a set. It is helpful to realize that L_{μ}^{π} orbitals transform in the same way as the parent $Y_{L\mu}(\theta, \phi)$ functions under operations of the point group; the corresponding odd functions $\overline{L}_{\mu}^{\pi}$ transform in the same way under pure rotations, but with a sign change under reflections, inversions, and rotation–reflections.[27] Detailed worked examples for the equilateral triangle and the octahedron may be found elsewhere.[27]

Transition metal clusters also have d_{xy} and $d_{x^2-y^2}$ atomic orbitals, which are classified as δ-type in TSH theory. To represent the transformation properties of these orbitals, we use second derivatives of the spherical harmonics, that is, tensor spherical harmonics – hence the name of the theory. As for the vector surface harmonics, there are again both odd and even δ cluster orbitals, denoted by $\overline{L}^{\delta}$ and L^{δ}, respectively. Usually, both sets are completely filled in transition metal clusters, and we will not consider their properties in any detail in this review. However, the cases of partial occupation are important and have been described in previous articles.[27,59]

Having provided an overview of the TSH theory cluster orbital transformation, it may be as well to emphasize once more the idea behind this approach, namely, to guess first approximations to the true molecular orbitals of the system. In this section, we have basically dealt with the mechanics of this transformation; to see how it leads to a general theoretical basis for structure-electron counting rules, we need to know the energies of the cluster orbitals. This problem is considered in the next section; for σ cluster orbitals, simple node-counting arguments suffice, while for clusters where π cluster orbitals are occupied, we must introduce the TSH theory ‘pairing principle’.

There are, however, some other useful applications due to Mingos and coworkers that are based upon or framed within TSH theory, but will not be dealt with here. For example, the TSH theory pairing theorem may be generalized and used to analyze nonbonding orbitals in hydrocarbon polyenes, coordination compounds, and clusters.[60] The ligand and central atom valence orbitals may be classified using TSH theory to analyze the bonding and the stereochemistries of coordination compounds.[61] Finally, an alternative transformation framework has been developed in terms of edge-localized and face-centered equivalent orbitals.[62]

5 FURTHER DEVELOPMENT OF TSH THEORY

5.1 Clusters Involving Only σ orbitals

5.1.1 Characteristics of σ cluster Orbitals

In clusters where the contributions of p and d atomic orbitals can be neglected, the bonding is especially simple. In such cases, we need to only consider σ cluster orbitals, whose energies are basically defined by node counting. For such systems, the same qualitative energy-level pattern often results as for jellium models, because the angular parts of the jellium wavefunctions are also spherical harmonics. Hence, the same ‘magic numbers’ for precisely filled electronic shells are also found, as mentioned in Section 4.1 above. The σ cluster orbitals for an octahedron were illustrated in Figure 1.

For a cluster with n vertices, the cluster orbital transformation involves n functions. For deltahedral geometries, it is generally not necessary to use the cluster orbitals from the set with $L + 1$ until all the $2L + 1$ members of the set based upon the spherical harmonics $Y_{L\mu}(\theta, \phi)$ have been used. However, this is not possible for all systems, such as three-connected structures and bipyramids.[27] For example, if all the atoms of a particular cluster happen to lie on nodal planes of one of the spherical harmonics, then no σ cluster orbital can be constructed from that function.

The energies of the L_{μ}^{σ} depend principally upon the value of L, because this defines the number of angular nodes. The nodeless S^{σ} orbital always lies lowest, followed by P^{σ}, D^{σ}, ..., and so forth. Furthermore, for a given value of L, the L^{σ} orbitals become more bonding as the number of atoms in the cluster increases, so long as all these atoms lie approximately on a single sphere.[57] The P^{σ} and D^{σ} orbitals usually become bonding when n is greater than about 6 and 16, respectively. Hence, filled bonding sets of orbitals are expected for 2 electrons, 8 electrons ($n > 6$), and 18 electrons ($n > 16$), and these correspond to the same ‘magic numbers’ for sodium clusters as predicted by the jellium model, above. However, in a finite cluster, the degeneracies associated with spherical symmetry are usually split, so this is by no means a complete explanation of why such magic number clusters are especially stable. Furthermore, one should really be more precise about whether it is kinetic or thermodynamic stability (or both) that is in question.

5.1.2 Splitting of σ cluster Orbitals

In radially bonded clusters, the bonding cluster orbital energy levels lie lower when the number of nearest neighbors per atom is maximized, and this usually corresponds to close-packed high-symmetry structures. However, in clusters that do not correspond to completely filled S^{σ}, P^{σ} and so on, shells, it may be more favorable for the cluster to distort and open up a significant *HOMO-LUMO* gap. The splittings induced by symmetry-lowering distortions of an L^{σ} shell follow an approximate center-of-gravity rule,**63** and so stabilization of the occupied orbitals and a large *HOMO-LUMO* gap are synonymous at this qualitative level of theory. The sense of the splitting (i.e. which orbitals are stabilized and which are destabilized) depends upon the way in which the cluster is distorted and can be analyzed rather like the splitting of atomic d orbitals in transition metal complexes.**64**

Two different classes of distortion may be recognized, namely oblate and prolate.**63** A prolate molecule, like CH_3F, has two equal principal moments of inertia, which are greater than the third, while an oblate molecule, like NH_3, has two equal moments of inertia, which are less than the third. In each case, the unique axis corresponds to a rotational axis of order 3 or more. The classification may be loosely extended to less symmetrical species, where two of the principal moments of inertia are similar and different from the third.

If applied with due caution, these ideas may provide useful insight. In any planar structure, the P_0^{σ} cluster orbital vanishes if the z axis is taken perpendicular to the plane, and we cannot apply the barycentre principle. In the triangle and square, the $P_{1c,1s}^{\sigma}$ orbitals are antibonding and nonbonding, respectively, and Na_3, Na_4, Li_3, Li_4 are all found to be planar, albeit relatively unsymmetrical, structures.**11** In nonplanar clusters with more than around 6 atoms, the $P_{1c,1s}^{\sigma}$ pair are expected to lie lower than P_0^{σ}, as shown in Figure 2. In agreement with this observation, both Na_6 and Li_6 exhibit a low-energy oblate geometry, that is, a capped pentagonal structure, as well as a planar raft, and both are favorable according to ab initio calculations.**11** In contrast, both Na_8 and Li_8 are calculated**11** to adopt tetracapped tetrahedral geometries, where the P^{σ} orbitals are all degenerate and precisely filled.

Similar considerations apply to gold clusters of the form $Au_m(PPh_3)_m^{x+}$, where the 5d orbitals may be treated as a closed shell in the first approximation, and bonding occurs principally through inwardly directed s/p_z σ hybrids.**65** For example, $Au_6(PPh_3)_6{}^{2+}$ has a D_{2h} pseudoprolate gold skeleton, in which the P_0^{σ} cluster orbital is preferentially stabilized. However, $Au_7(PPh_3)_7{}^{+}$ is an oblate pentagonal bipyramid, where the two $P_{1c,1s}^{\sigma}$ orbitals are occupied**27** (Figure 3).

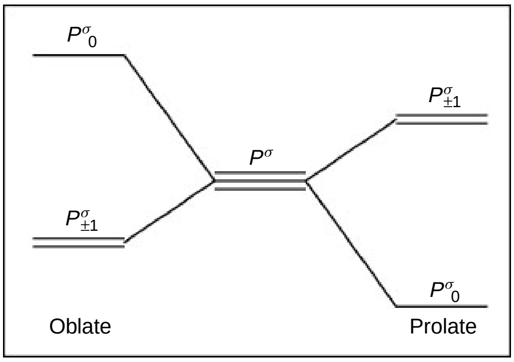

Figure 2 The idealized splitting of the P^{σ} orbitals in nonplanar oblate and prolate clusters

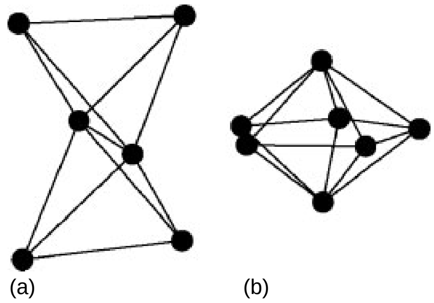

Figure 3 The gold skeletons of (a) $Au_6(PPh_3)_6{}^{2+}$ and (b) $Au_7(PPh_3)_7{}^{+}$

5.2 The TSH Pairing Principle

In most clusters, the bonding is more complicated than for the systems discussed in the previous section, because π-cluster orbitals must be considered. One simplification is obtained from an energy-pairing relation**57** between even cluster orbitals L_{μ}^{π} and their odd partners $\overline{L}_{\mu}^{\pi}$.

The idea of a pairing rule may be more familiar in the context of conjugated alternant hydrocarbons (which are defined as those containing no odd-membered rings). Coulson and Rushbrooke**66** showed that the Hückel molecular orbitals of such systems occur in pairs with energy $\alpha \pm \lambda\beta$, where α and β are the usual energetic parameters of *Hückel Theory*.**12** The LCAO coefficients of either of the partner orbitals may be obtained from the other by changing the signs of alternate coefficients.

The TSH theory pairing principle plays a similar role in cluster bonding. It can be shown that the energies of partner L_{μ}^{π} and $\overline{L}_{\mu}^{\pi}$ cluster orbitals have the same magnitude but opposite signs with respect to an origin at α. Several approximations are made in the proof,**27** for example, all the atoms are assumed to lie on a sphere, and the β parameters for π orbitals interacting in σ- and π-fashion are assumed to be the same. Neglect of nonnearest neighbors is not necessary, however.**27** The usefulness of this result is probably best illustrated by the detailed analysis of $B_6H_6{}^{2-}$ in the following section.

5.3 Bonding in Deltahedral Clusters

5.3.1 *Analysis of $B_6H_6{}^{2-}$*

As mentioned in Section 3, the deltahedral *closo*-boranes, $B_nH_n{}^{2-}$, and carboranes, $C_2B_{n-2}H_n$, have $4n + 2$ valence electrons. In this section, the presence of $2n + 1$ bonding molecular orbitals, of which $n + 1$ may be identified with skeletal bonding, is explained using TSH theory. The structures of the *closo*-boranes from $B_5H_5{}^{2-}$ to $B_{12}H_{12}{}^{2-}$ are illustrated in Figure 4 (*see also* ***Boron: Polyhedral Carboranes***).

$2n$ of the valence electrons are associated with n two-center, two-electron B−H bonds, and will not be considered further. In deltahedra, we generally find that all the even π cluster orbitals are bonding in character, and all their odd partners are therefore antibonding, by the pairing principle. The $n + 1$ skeletal bonding orbitals may be formally identified as S^σ and the n even L^π orbitals. However, the P^σ set may be bonding in character too, but these orbitals transform in the same way as the corresponding P^π orbitals, and hence the two sets mix to give strongly bonding and antibonding combinations. Because of this σ/π mixing, we are generally guaranteed to have $n + 1$ skeletal bonding orbitals in deltahedral clusters.

A detailed analysis of the bonding in $B_6H_6{}^{2-}$ should help illustrate exactly how the TSH approach is applied; the labelling scheme for this cluster is illustrated in Figure 5. The six σ cluster orbitals, $S^\sigma(A_{1g})$, $P^\sigma(T_{1u})$, and $D^\sigma(E_g)$, generated by the s orbitals in Li_6 or Na_6 were shown in Figure 1. For $B_6H_6{}^{2-}$, it is more appropriate to form radial sp_z hybrids from the outset, and use these as the basis for the B−H bonds and the L^σ cluster orbitals. The same linear combinations are generated, and these are shown for the inwardly directed sets in Figure 6. Explicitly, the linear combinations are

Orbital	LCAO form	Energy
$S_0^\sigma(A_{1g})$	$\sqrt{\frac{1}{6}}(\sigma(1) + \sigma(2) + \sigma(3)$ $+\sigma(4) + \sigma(5) + \sigma(6))$	$\alpha + 4\beta$
$P^\sigma_{0,1c,1s}(T_{1u})$	$\sqrt{\frac{1}{2}}(\sigma(1) - \sigma(6))$ $\sqrt{\frac{1}{2}}(\sigma(2) - \sigma(4))$ $\sqrt{\frac{1}{2}}(\sigma(3) - \sigma(5))$	α
$D^\sigma_{0,2c}(E_g)$	$\frac{1}{2}(\sigma(2) + \sigma(4) - \sigma(3) - \sigma(5))$ $\sqrt{\frac{1}{12}}(2\sigma(1) + 2\sigma(6) - \sigma(2)$ $-\sigma(3) - \sigma(4) - \sigma(5))$	$\alpha - 2\beta$

To form $P^\sigma_{1c} \equiv P^\sigma_z$, for example, we need only use the value of z at each vertex to obtain $P^\sigma_z \propto (\sigma(1) - \sigma(6))$. The energies have been evaluated in the Hückel approximation (*see Hückel Theory*), but this is simply to provide an idea of the bonding/antibonding character, and some more accurate calculations will be discussed below. (Note that the splitting obeys another center-of-gravity rule.) The normalization is simply $1/\sqrt{2}$, as overlap between the two σ orbitals has been neglected.[27]

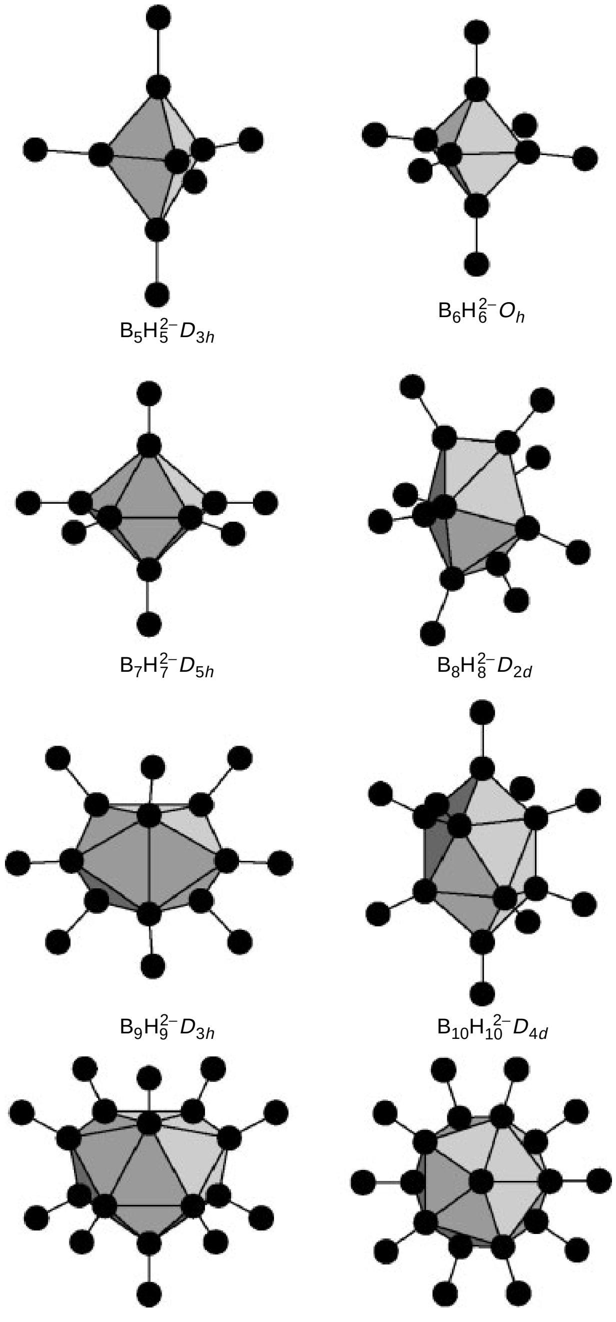

Figure 4 Structures of the *closo*-boranes from $B_5H_5{}^{2-}$ to $B_{12}H_{12}{}^{2-}$; these are the optimized geometries calculated with a minimal STO-3G basis. (This figure was produced using Mathematica 2.0 © Wolfram Research Inc., 1990.)

To find the linear combinations required for the π cluster orbitals, we must first form and reduce the representation spanned by the 12 tangential p^π atomic orbitals, $\Gamma_{\pi/\overline{\pi}}$. The result is[27] $\Gamma_{\pi/\overline{\pi}} = T_{1u} \oplus T_{1g} \oplus T_{2g} \oplus T_{2u}$, and the corresponding cluster orbitals are $P^\pi(T_{1u})$, $\overline{P}^\pi(T_{1g})$, $D^\pi_{1c,1s,2s}(T_{2g})$, and $\overline{D}^\pi_{1c,1s,2s}(T_{2u})$. Owing to the particular

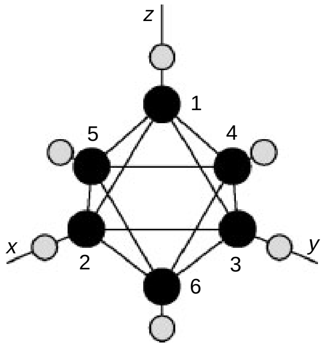

Figure 5 Structure and labeling scheme for the $B_6H_6{}^{2-}$ octahedron

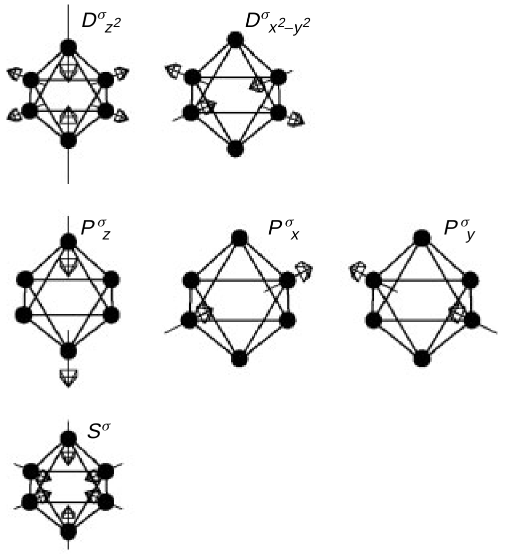

Figure 6 Unnormalized L^σ cluster orbitals for $B_6H_6{}^{2-}$ formed from inwardly pointing sp_z hybrids. Each arrow represents a hybrid valence orbital contribution to the molecular orbital in both magnitude and direction. (This figure was produced using Mathematica 2.0 © Wolfram Research Inc., 1990.)

symmetry of this cluster, it is quite convenient to express everything in Cartesian coordinates rather than spherical polars, that is, using p_x, p_y, and p_z instead of p^θ and p^ϕ. The only disadvantage is that the relationship between odd and even partner orbitals is more obvious when the latter basis functions are used, but this analysis may be found elsewhere.[27] In the following linear combinations, the x, y and z directions correspond to the global axes, as defined in Figure 5, not the local axes described previously. (Note that ∇z has no tangential components at vertices 1 and 6, and no radial components at the other atoms.) To form P_0^π, for example, we simply use the fact that $\nabla z = (0, 0, 1)$, so that $P_0^\pi = \frac{1}{2}(p_z(2) + p_z(3) + p_z(4) + p_z(5))$, where the normalization has been added as for the σ-cluster orbitals above. Hence, the full set of π orbitals is

Orbital	LCAO form	Energy
$P^{\pi}_{0,1c,1s}(T_{1u})$	$\frac{1}{2}(p_z(2) + p_z(3) + p_z(4) + p_z(5))$ $\frac{1}{2}(p_x(1) + p_x(6) + p_x(3) + p_x(5))$ $\frac{1}{2}(p_y(1) + p_y(6) + p_y(2) + p_y(4))$	$\alpha + 2\beta$
$\overline{P}^{\pi}_{0,1c,1s}(T_{1g})$	$\frac{1}{2}(-p_y(2) + p_x(3) + p_y(4) - p_x(5))$ $\frac{1}{2}(p_y(1) - p_y(6) - p_z(3) + p_z(5))$ $\frac{1}{2}(-p_x(1) + p_x(6) + p_z(2) - p_z(4))$	$\alpha - 2\beta$
$D^{\pi}_{1c,1s,2s}(T_{2g})$	$\frac{1}{2}(p_x(1) - p_x(6) + p_z(2) - p_z(4))$ $\frac{1}{2}(p_y(1) - p_y(6) - p_z(5) + p_z(3))$ $\frac{1}{2}(p_y(2) - p_y(4) - p_x(5) + p_x(3))$	$\alpha + 2\beta$
$\overline{D}^{\pi}_{1c,1s,2s}(T_{2u})$	$\frac{1}{2}(p_y(1) + p_y(6) - p_y(2) - p_y(4))$ $\frac{1}{2}(-p_x(1) - p_x(6) + p_x(5) + p_x(3))$ $\frac{1}{2}(p_z(2) + p_z(4) - p_z(5) - p_z(3))$	$\alpha - 2\beta$

Again, the Hückel energies are given simply as a guide to the bonding character and do not imply that the Hückel approximation must necessarily be used. (*See also Hückel Theory*.) These functions are illustrated in Figure 7; note that all of them contain nodes, but where these are only intrinsic to the atomic orbitals, they do not lead to antibonding interactions. The intrinsic nodes are not explicitly illustrated; they would, of course, bisect each arrow.

A qualitative energy-level diagram for the separate L^σ and L^π sets is shown in Figure 8. When the two sets are allowed to mix, we expect to find seven strongly bonding orbitals that may be written as $S^\sigma(A_{1g})$, $P^{\sigma/\pi}(T_{1u})$ and $D^\pi(T_{2g})$. To verify this result, one may perform any sort of standard MO calculation and transform to the cluster orbital basis.[27] For comparison, the energy-level spectrum resulting from a minimal basis set calculation is given in Figure 9. This analysis illustrates the general result that n-vertex deltahedra have $n + 1$ skeletal bonding orbitals, which may formally be identified with the S^σ and L^π cluster orbitals. Although the composition of the occupied orbitals may change when σ/π mixing is admitted, the symmetries of the occupied set do not.

5.3.2 *Symmetry-Forced Electron Count Deviations*

We may also use the TSH formalism to explain systematic deviations from the usual deltahedral electron count. Such cases arise when the two members of a pair of degenerate L^π orbitals are paired with one another, and must therefore both be nonbonding.[67] This will be the case in any cluster where $\Gamma_{\pi/\overline{\pi}}$ contains an odd number of E-type irreducible representations (IR's). Fowler[67] proved that any cluster with a rotation axis of order 3 or more, and a single vertex atom lying on that axis, would be forced to deviate from the usual skeletal electron count. These results were generalized by Johnston and Mingos,[68] who classified clusters as nonpolar, polar, or bipolar according to the number of atoms on the principal rotation axis, that is, 0, 1, or 2, respectively. For

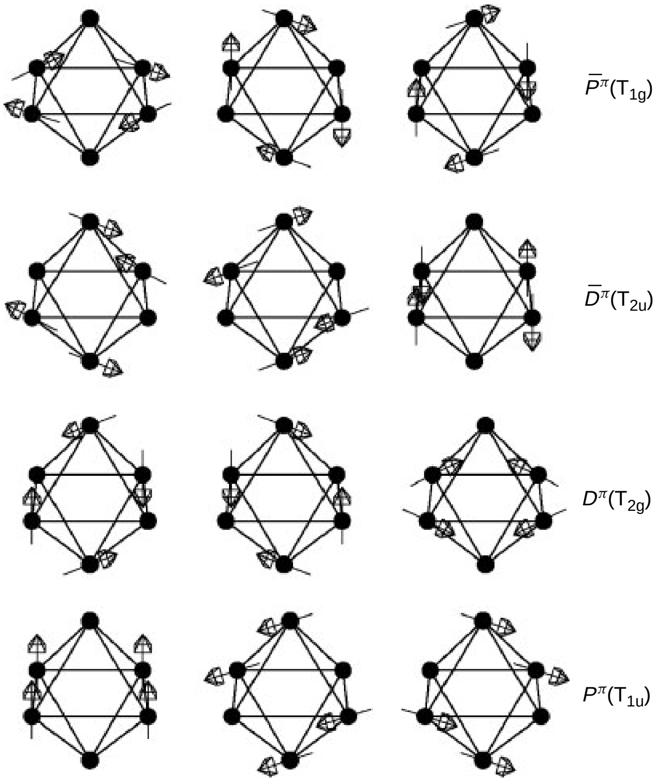

Figure 7 L^{π} cluster orbitals for $B_6H_6^{2-}$ formed from tangential p orbitals. Each arrow represents a p orbital contribution to the molecular orbital in both magnitude and direction, for example, all the arrow heads may be taken as the positive lobes. (This figure was produced using Mathematica 2.0 © Wolfram Research Inc., 1990.)

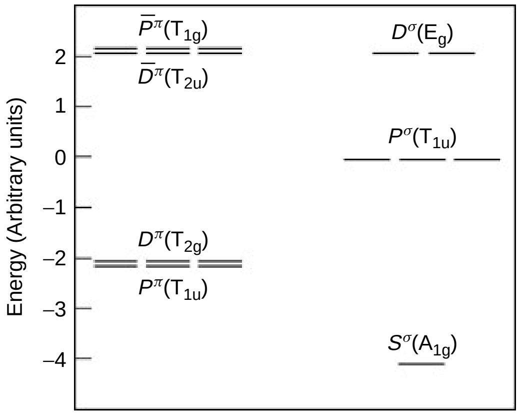

Figure 8 Qualitative energy-level diagram for the L^{σ} and L^{π} cluster orbitals of an octahedron, prior to mixing. The units are arbitrary, and the relative scales for the σ (right) and π (left) sets cannot be determined precisely without further calculation. $\overline{P}^{\pi}$ and $\overline{D}^{\pi}$ both lie at +2 units and P^{π} and D^{π} at −2 units

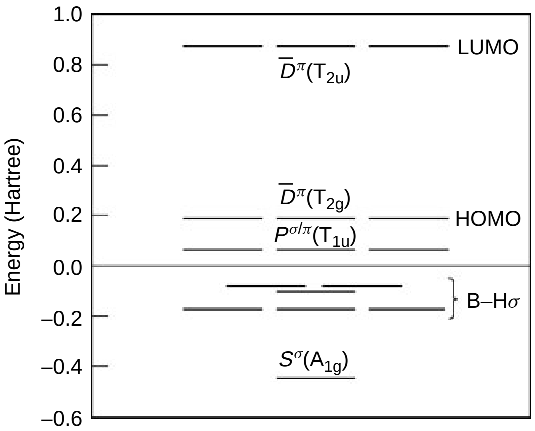

Figure 9 Energy-level diagram for $B_6H_6^{2-}$ calculated for the optimized geometry using a minimal STO-3G basis. The cluster orbitals have been picked out and labeled appropriately

polar deltahedral clusters, the principal axis can only have order 3, because all the faces must be triangular, and the axis passes through only one vertex, by definition. Hence, we expect deviations only for clusters with 3p + 1 vertices. In fact, axes of order 2 are possible for a polar deltahedron if an edge is bisected, as in $B_{11}H_{11}^{2-}$, and in such systems the *HOMO-LUMO* gap may be small, depending upon the splitting of the idealized *e* pair of frontier orbitals. When there is a threefold axis, the π orbitals of each set of three equivalent atoms span precisely two E-type IR's. However, the p^{π} orbitals of the unique vertex atom also span an E symmetry IR, giving 2p + 1 in total. Since all the even π cluster orbitals of E symmetry must find odd partners in this set, it follows that one pair must be paired with itself, and is therefore nonbonding[68] because of the energy-pairing principle described in Section 5.2. As this result depends critically upon the point group, it is hard to see how it could be derived by any other approach that does not consider symmetry explicitly.

Polar deltahedra with an approximately nonbonding *e* pair of orbitals might have either $4n$ or $4n + 4$ valence electrons, depending upon whether these orbitals are vacant or fully occupied. Here, as usual, we are assuming that intermediate occupation numbers would be unfavorable, since they would entail open shells and/or Jahn–Teller distortions. Both cases are known for $p = 1$, that is, $n = 4$ vertices, with B_4Cl_4 and P_4 tetrahedra having 8 and 12 skeletal valence electrons, respectively. The latter cluster can also be described in terms of two-center, two-electron edge-localized bonds, as discussed below. Examples for larger systems are found amongst the hypothetical *closo*-boranes investigated by Fowler;[67] some more complicated cases have also been considered and various examples are known for *Transition Metals*.[68,69]

In fact, it is also possible for nonpolar deltahedra to exhibit deviations from the usual electron-counting rules.[68] The D_{3h} tricapped trigonal prism provides an interesting example. In $B_9H_9^{2-}$ (see Figure 4), which has the usual

$n + 1 = 10$ skeletal electron pairs, the HOMO is actually odd in character ($\overline{F}{}_0^{\pi}$) and the *HOMO-LUMO* gap is rather small. Hence, it is perhaps not surprising that B_9Cl_9 and $Bi_9{}^{5+}$ have analogous structures, but 9 and 11 skeletal electron pairs, respectively.

5.3.3 *The closo, nido, arachno Debor Pattern*

TSH theory also provides an explanation for the number of bonding orbitals observed in related closo, nido, and arachno clusters.[21,57] Consider the notional formation of a nido cluster by removing a B−H vertex from a closo system. Now assume an idealized axial symmetry for the cluster such that the p^{π} orbitals of the vertex removed span an E-type IR. If the original closo cluster has a 'normal' electron count, that is, $n + 1$ skeletal bonding orbitals, then it must have been bipolar, that is, there were two vertices lying on the rotation axis on different sides of the cluster. It follows that the nido cluster is itself polar, and could exhibit n or $n + 2$ skeletal electron pairs, where n is now the number of vertices remaining in the nido cluster. Furthermore, the approximately nonbonding e pair of orbitals must have significant amplitude around the open face, because they would interact strongly with the corresponding orbitals of the missing vertex. Usually, the open face is protonated, thus stabilizing the frontier e pair and leading to $n + 2$ occupied skeletal orbitals that is, the same as in the parent closo cluster with $n + 1$ vertices. The loss of just one inwardly directed σ hybrid does not generally destabilize the S^{σ} orbital significantly.

An alternative explanation has been given within the topological graph-theoretical framework[50] using the 'Principle of Polyhedral Excision'. Here, it is argued that the atoms bordering each 'hole' left by removing a vertex would interact to give a core-type bonding orbital in addition to the usual core orbital and the n bonding orbitals resulting from pairwise overlap of the tangential orbitals at each vertex. However, this does not explain the presence of a nonbonding pair of e orbitals around the open face, which can be verified by calculation.

Of course, as with all these general structure-electron count correlation 'rules,' there is scope for deviation. For example, if the nido cluster does not have a threefold or higher-order axis (a higher-order axis is possible because the cluster is no longer deltahedral), then the idealized e pair will be split. The electron count will then depend upon the splitting, specific stabilization by protonation, and so on. Of course, as successive vertices are removed, the cluster may also deviate significantly from the assumed roughly spherical arrangement of atoms.

The TSH formalism may also be used to explain the electron counts of arachno clusters, why the 'missing' vertex in a nido cluster usually gives the largest possible open face, and why it appears to be most favorable to 'remove' two adjacent vertices to give an arachno cluster. Since the (possibly idealized) nonbonding e pair of orbitals has significant amplitude around the open face, each orbital must have a single nodal plane passing through this face. The consequent antibonding interactions are minimized if the open face is as large as possible, as then their contribution relative to the in-phase bonding interactions is minimized.[57] This also explains why neighboring vertices appear to be 'lost' to give arachno clusters. To rationalize the electron count of such an arachno cluster requires further idealizations.[57] The essential idea is that two e-type nonbonding pairs of orbitals are created; the details are omitted here.

5.4 Transition Metal Clusters

The analysis of these molecules is complicated by the presence of the d orbitals, which contribute one orbital of σ symmetry (d_{z^2} in local axes), two of π symmetry (d_{xz} and d_{yz}), and two of δ symmetry (d_{xy} and $d_{x^2-y^2}$). There are far more examples of deviations from the usual patterns in transition metal clusters than in main group clusters, and many of these must be treated specifically, although TSH theory may again provide a useful framework in which to perform the analysis. However, in this section the objective will simply be to understand the most common patterns, as set out in Section 3, which are typically found in clusters with π-acceptor ligands such as CO.

It is easiest to derive the number of inaccessible orbitals in this case, that is, the number of orbitals that are too high in energy to contain electrons, and we divide the ns, np, and $(n-1)$d orbitals (n here represents a principal quantum number, for example, 4s, 4p, 3d) into three sets. By suitable *Hybridization*, we may construct in-pointing and out-pointing σ and π orbitals, leaving one orbital of σ character and the two δ orbitals. The latter consist approximately of d_{z^2}, d_{xy}, and $d_{x^2-y^2}$, and are conveniently referred to as the 't_{2g}' set by analogy to the way they transform in *Octahedral* transition metal complexes. Similar divisions are made in the graph-theoretical approach.[51]

The t_{2g} set and the three out-pointing hybrids usually correlate formally with accessible orbitals, with varying ligand character, assuming that there are sufficient π-acceptor ligands to stabilize them. This is usually the case in clusters composed of so-called 'conical' $M(CO)_3$ vertices. However, deviations may occur for lower carbonyl to metal ratios. It follows that the detailed geometrical arrangement of the ligands is not of primary importance, so long as there are enough of them. This result is in agreement with the fluxionality commonly observed in transition metal carbonyls and with the view that the carbonyl arrangement is determined principally by packing considerations.[70] The remaining in-pointing σ and π orbitals then give rise to $n + 1$ bonding and $2n - 1$ antibonding orbitals, as discussed for main group deltahedral clusters in the preceding section. Indeed, this is actually the basis of the Isolobal Principle.[23] The antibonding orbitals are not stabilized by ligand interactions because they are inwardly directed, and hence they are termed 'inaccessible'. The result is $7n + 1$ accessible orbitals and $14n + 2$ valence electrons, in agreement with calculations by Lauher[71] and Ciani and Sironi.[72]

It is noteworthy that the δ orbitals are always considered to be accessible in this analysis, and need not be considered further. Of course, this assumption is not always true, but clusters where the δ orbitals need to be analyzed in detail will not be treated here.[27,73] Furthermore, since the only inaccessible orbitals arise from the inwardly directed σ and π interactions, the same analysis for symmetry-forced electron counts involving one additional occupied (or unoccupied) orbital holds.[68] Closo, nido, and arachno relationships follow by analogy so long as no additional inaccessible orbitals arise.

5.5 Bonding in Three-Connected Clusters

Here, we deal with clusters such as prismane, C_6H_6, and cubane C_8H_8, which can simply be described in terms of edge-localized two-center, two-electron bonds. Why, then, is it necessary to devote any space to such molecules? The answer is that it was not initially clear how TSH theory can rationalize the electron counts of these molecules. Of course, this is not entirely surprising, as the *Hybridization* patterns used in the TSH model are not well adapted to cover this situation. However, the correct answer can be obtained without abandoning the framework developed in the preceding sections.

The reason why the TSH analysis of deltahedral clusters, with $n + 1$ skeletal bonding orbitals, is inapplicable is that the L^{π} and $\overline{L}^{\pi}$ cluster orbitals are not necessarily bonding and antibonding, respectively, in three-connected clusters. This result is basically due to the low coordination number and the relatively sparse manner in which the vertices in three-connected structures cover a sphere.[52]

An n-vertex three-connected cluster has $3n/2$ edge-localized bonds, that is, $3n$ skeletal valence electrons rather than the $2n + 2$ found in deltahedra. Johnston and Mingos considered the $3n/2$ skeletal bonding orbitals in terms of linear combinations of the localized bonds, identifying $n/2 + 2$ combinations that are 'face-bonding' and $n - 2$ that are 'face-antibonding'.[74] The face-bonding combinations have all the localized bonds in phase around each face, the face-antibonding (or nonbonding) combinations do not, and lie somewhat higher in energy, though they are, of course, bonding overall. A TSH analysis[52,74] identifies the $n/2 + 2$ strongly bonding combinations as S^{σ} and $n/2 + 1$ members of the L^{π} set. The more weakly bonding skeletal orbitals then consist of the remaining $n/2 - 1$ L^{π} orbitals, and their parity-related $\overline{L}^{\pi}$ partners.

5.6 Additional Examples

There is space to provide only a very brief mention of how TSH theory is able to rationalize some of the other bonding patterns mentioned in Section 3. TSH analyses of the bonding in cylindrical clusters[75] and the hyper−closo versus iso−closo discussion[76] may also be found in the literature.

5.6.1 Interstitial Atoms

For larger clusters, the central cavity may be big enough to accommodate additional atoms. For example, the distance from the shell to the center of a cuboctahedral cluster is the same as the nearest-neighbor distance within the shell, and the cavity at the center of an *Octahedral* transition metal cluster is typically large enough to accommodate first-row main group atoms such as boron, carbon, or nitrogen. The valence orbitals of such interstitial atoms will generally mix with inwardly directed L^{σ} and L^{π} orbitals of the shell that have the same symmetry, leading to strongly bonding and antibonding combinations.

For a main group atom in a radially bonded cluster (see Section 5.1), the analysis is especially simple, as the s and p orbitals of the interstitial transform in the same way as the S^{σ} and P^{σ} cluster orbitals. The net result is that the original energy-level spectrum is reinforced, with more strongly bonding s/S^{σ} and p/P^{σ} in-phase combinations and additional inaccessible antibonding combinations, as shown in Figure 10. Hence, the interstitial atom effectively acts as an electron donor, without producing any new bonding orbitals, and therefore represents a possible remedy for 'electron deficiency'. (*See also Electron Deficient Compound*.) However, this does not mean that a large charge is necessarily associated with the interstitial atom. A simple example is Na_6Mg in which the magnesium atom occupies the central position in a sodium octahedron. This cluster has 8 valence electrons, completely filling the bonding s/S^{σ} and p/P^{σ} orbitals.[27]

The same pattern emerges in simple transition metal carbonyls[27] such as $Ru_6C(CO)_{16}{}^{2-}$, which has 86 valence electrons as does $Ru_6(CO)_{18}{}^{2-}$. Some more complicated

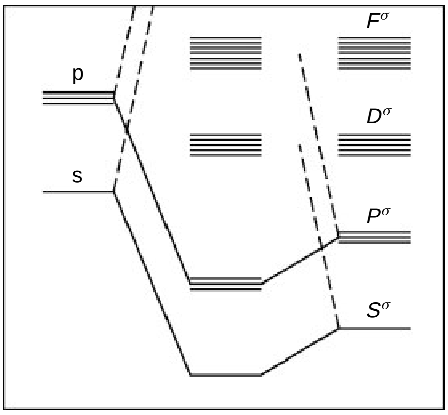

Figure 10 Schematic energy-level spectrum for a radially bonded cluster with a main group interstitial atom

examples[27] are provided by halide clusters with interstitial main group atoms, a wide variety of which have been characterized by Corbett and his coworkers.[77]

5.6.2 *The Capping,[22,30] Condensation,[31] and Inclusion[78] Principles*

Of these three 'Principles' mentioned in Section 3, the Capping Principle is the easiest to understand.[22,30] The others will only be mentioned briefly here; more details may be found elsewhere.[27] It should also be mentioned that King has proposed alternative visualizations of the bonding in such systems within his graph-theoretical approach.[51]

Consider a transition metal cluster that consists of an n-vertex deltahedron with m additional caps that are well separated so that they do not interact significantly with one another. Because the inaccessible orbitals of the deltahedron are all inwardly hybridized, they will only mix very weakly with orbitals on the capping atoms, and we do not expect to obtain any new bonding orbitals in this fashion. If the caps are also transition metal atoms, then we may again describe each one in terms of three inwardly directed orbitals (one σ plus two π), a 't_{2g}' set and three outward-pointing hybrids (again one σ plus two π). The six orbitals consisting of the t_{2g} set and the outward-pointing hybrids will be accessible, but the inward-pointing hybrids mix with orbitals of the n-vertex deltahedron, which have already been formally identified as accessible. Hence, the addition of a single capping atom generally increases the valence electron count by just 12. However, additional accessible orbitals can occur if there are inwardly pointing $\overline{L}^{\pi}$ orbitals generated by a set of capping atoms that are not matched in symmetry by any accessible orbitals of the inner sphere. The tricapped trigonal prism may be analyzed in this way.[27]

5.6.3 *Silicon Clusters*

A short discussion of the bonding in small silicon clusters will demonstrate how the TSH framework may be useful in considering the structures of less familiar molecules. These species have received much attention in recent years, partly because of the technological significance of silicon as a semiconductor. Calculational strategies fall into two camps, namely, ab initio quantum mechanical treatments of some kind and analyses that employ analytic empirical atom–atom potentials.[79]

Slee, Lin, and Mingos[80] have analyzed the geometries of small silicon clusters, exploiting a connection with the deltahedral boranes and carboranes. A silicon atom with an out-pointing lone pair and three in-pointing hybrids is isolobal to a B–H vertex. However, Si_n clusters have $4n$ valence electrons, two fewer than the corresponding boranes, $B_nH_n{}^{2-}$. Hence, we should not expect the two series of clusters to be isostructural, but it may be helpful to start from the corresponding borane deltahedron and consider how the structure might distort to destabilize one of the skeletal bonding orbitals.[80] Of course, Si_n clusters could adopt structures analogous to C_n, with two-center, two-electron bonds and delocalized π systems. However, this is probably not favorable because carbon is unusual in its ability to form strong π bonds. Silicon clusters therefore tend to exhibit delocalized bonding and higher coordination numbers.

The $P_z^{\sigma/\pi}$ orbital, where the z-direction defines the principal rotation axis of the cluster, may be destabilized by contraction along this axis.[80] The D_{3h} minimum-energy structure found for Si_5 in ab initio calculations by Raghavachari[81] may be viewed in this way as a squashed trigonal bipyramid. Alternatively, application of the Capping Principle discussed in the previous section shows that $2n$ skeletal electron pairs can also result through capping, and both Si_6 (capped trigonal bipyramid) and Si_{10} (tetracapped octahedron or trigonal prism[82]) appear to exploit this fact.

The empirical interatomic potentials cannot really account for the detailed geometries of clusters such as these, where the structure depends critically upon the molecular orbital spectrum. For example, a high binding energy has been predicted[83] for Si_{13} in a centered icosahedral geometry. However, the 52 valence electrons in this cluster would require 12 lone pair orbitals and 14 skeletal bonding orbitals to accommodate them, whereas the centered icosahedron has only 13 skeletal bonding orbitals. A distortion is therefore predictable, although $Si_{13}{}^{2+}$ might adopt a centered icosahedral geometry.

6 CLUSTER REARRANGEMENTS

Lipscomb[84] first proposed his diamond-square-diamond (DSD) mechanism for skeletal rearrangements in clusters in 1966, but in 1975 he commented that 'few reaction pathways in rearrangements of boron compounds are well understood'.[85] A general theory to rationalize the relative rearrangement rates of boranes and carboranes did not, in fact, emerge until 1987, when Wales and Stone[86] used TSH theory to deduce some orbital symmetry selection rules. An equivalent description was provided by Mingos and Johnston,[87] and subsequently the theory was further developed and various predictions made.[88] Combining the new theoretical tools provided by TSH theory with modern ab initio calculations now puts us in a significantly more optimistic position than in 1975.

In the DSD process (Figure 11), an edge common to two triangular faces breaks while a new edge is formed perpendicular to it. Hence, the idealized transition state geometry would have a square face. Degenerate rearrangements, in which the rearrangement leads to the same cluster skeleton, aside from possible permutations among atoms of the same element, are particularly important in small

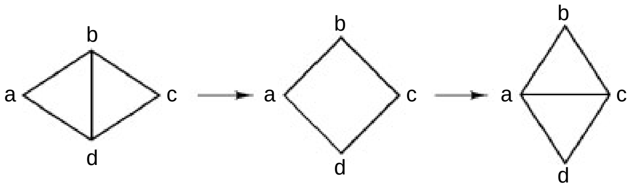

Figure 11 Lipscomb's DSD process

clusters where there may only be one stable minimum-energy structure. The boranes, and associated carboranes, provide a good example. King[89] used topological considerations to deduce which *closo*-boranes $B_nH_n{}^{2-}$ have geometrically possible single DSD processes available. If the connectivities of the vertices are α, β, γ, and δ, then a general DSD process may be written as $\alpha\beta(\gamma\delta)$, where the edge is broken between the vertices of connectivity α and β and made between the two with connectivities γ and δ.[89] For a degenerate single DSD process to be possible, there must therefore be vertices satisfying $\alpha + \beta = \gamma + \delta + 2$, and of the *closo*-boranes this condition is only satisfied for $B_5H_5{}^{2-}$, $B_8H_8{}^{2-}$, $B_9H_9{}^{2-}$ and $B_{11}H_{11}{}^{2-}$ (see Figure 4). However, of these four molecules only $B_8H_8{}^{2-}$ and $B_{11}H_{11}{}^{2-}$ appear to be readily fluxional;[86] in the other two clusters, the geometrically feasible single DSD process turns out to be 'forbidden' by orbital symmetry.[33] (*See also Fluxional Molecule*.)

Gimarc and Ott first noticed that the single DSD processes in $B_5H_5{}^{2-}$ and $B_9H_9{}^{2-}$ would result in crossings of filled and vacant molecular orbitals, and would therefore be expected to have high activation energy barriers.[90] (The hypothetical single DSD process in $B_5H_5{}^{2-}$ is, in fact, directly analogous to the *Berry Pseudorotation* in PCl_5.) Subsequent computational studies have confirmed the result[91] for $B_5H_5{}^{2-}$ (and the corresponding carborane) and suggest that the orbital symmetry–'allowed' double DSD process may account[92–93] for the experimental results obtained by Onak and coworkers for B, B′-disubstituted 2, 4–$C_2B_5H_7$ derivatives.[94] Group theoretical analysis framed within TSH theory leads to two important theorems that enable orbital crossings to be easily identified:[86,88]

(1) A crossing occurs if the proposed transition state has a single atom lying on a principal rotation axis of order 3 or more.
(2) A crossing also occurs if a mirror plane, which must pass through two atoms in the critical face, is retained throughout a DSD process.

Theorem 1 immediately reveals that the single DSD processes in $B_5H_5{}^{2-}$ and $B_9H_9{}^{2-}$ are forbidden. The result follows from the same considerations of nonbonding orbitals and symmetry-forced deviations in electron count that were discussed in Section 5.3.2. The polar transition state in question must have a nonbonding *e* pair of *Frontier Orbitals*, which are absent in the starting and finishing structures, and therefore correspond to an orbital crossing.

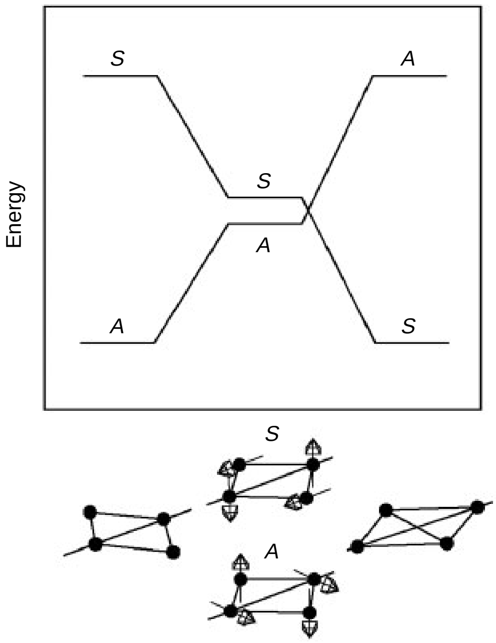

Figure 12 Splitting of the frontier orbitals in the open face of a DSD transition state. One function is symmetric (*S*) with respect to the conserved mirror plane, the other is antisymmetric (*A*). Their energies change in opposite senses and lead to an orbital crossing

Theorem 2 is a more subtle result of the TSH pairing principle, and may be deduced[88] by considering the number of occupied orbitals with a given parity under reflection. The frontier orbitals, which need not be strictly degenerate, are sketched in Figure 12. They have different parities under reflection through a mirror plane that includes either pair of opposite vertices. Hence, one orbital rises in energy and the other falls when the square face contracts along a diagonal, but the splitting is in the opposite sense for the other diagonal. If only a C_2 rotation axis is preserved throughout, then there is an avoided crossing, for the two frontier orbitals are both antisymmetric under this operation.[88]

Using the above results, and the premiss that double DSD processes are less favorable than single DSD processes, and so on, (on the grounds that a single DSD process produces the smallest structural perturbation), Wales and Stone were able to rationalize the available experimental evidence for borane and carborane rearrangement rates.[86] The archetypal single DSD mechanism in $B_8H_8{}^{2-}$ has since been studied by accurate ab initio calculations[95] and is shown in Figure 13. Calculations for $C_2B_4H_6$ have also characterized a high-energy rearrangement mechanism based upon 'local bond rotation'.[96] The case of icosahedral $B_{12}H_{12}{}^{2-}$ and the associated carboranes (of which there are three isomers) is also interesting. There is no geometrically

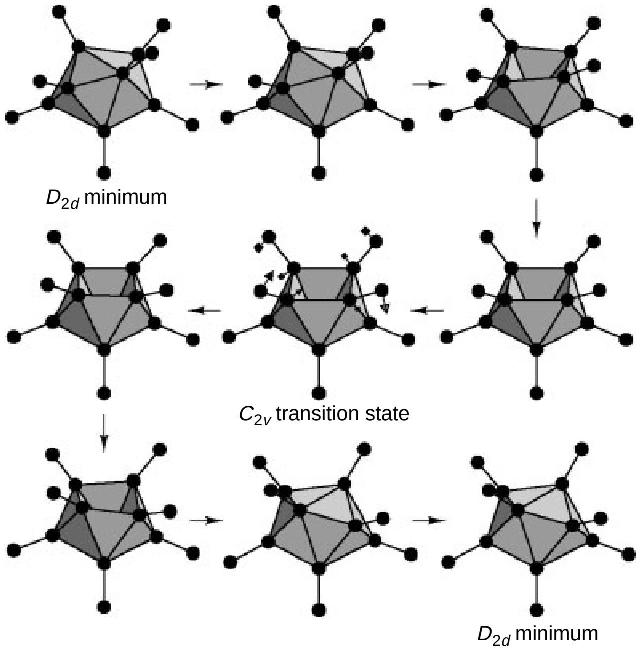

Figure 13 Calculated reaction mechanism for $B_8H_8{}^{2-}$. The arrows superimposed upon the transition state represent appropriately scaled normal mode displacements for the mode with the unique imaginary frequency. Structures were selected along the reaction path so as to include all three stationary points plus three geometries at regular intervals on either side of the transition state. The structures were triangulated using distance cutoffs of 2.1 Å. (This figure was produced using Mathematica 2.0 © Wolfram Research Inc., 1990.)

feasible single DSD process for this cluster, and earlier work[86] has shown that concerted hextuple and pentuple DSD processes are probably not responsible. Possible high-symmetry intermediates were investigated by Gimarc *et al.*,[97] but more recent results suggest that the interconversions probably occur via a complex series of rearrangements involving low-symmetry minima and transition states.[98] These pathways confirm previous suggestions made on the basis of orbital symmetry selection rules.[88] The highest barrier encountered on the pathway between the 1,2 and 1,7 carboranes involves a concerted double DSD process, as shown in Figure 14.

Of the other predictions concerning cluster rearrangement mechanisms using TSH theory, only one more will be mentioned here. This is the square-diamond, diamond-square (SDDS) mechanism that may occur in a cluster with a square face, such as square-based pyramidal $C_5H_5{}^+$. The TSH theory prediction is that a concerted mechanism should be orbital symmetry allowed if the edges that are made and broken lie in the same mirror plane. If one edge lies in a mirror plane and the other lies across it, then two crossings are predicted.[27,88] The mechanism is unlikely to occur in *nido*-boranes, because of the additional bridging hydrogen atoms around the open face; however, recent ab initio calculations[95] have confirmed that it does indeed occur in $C_5H_5{}^+$, as shown in Figure 15.

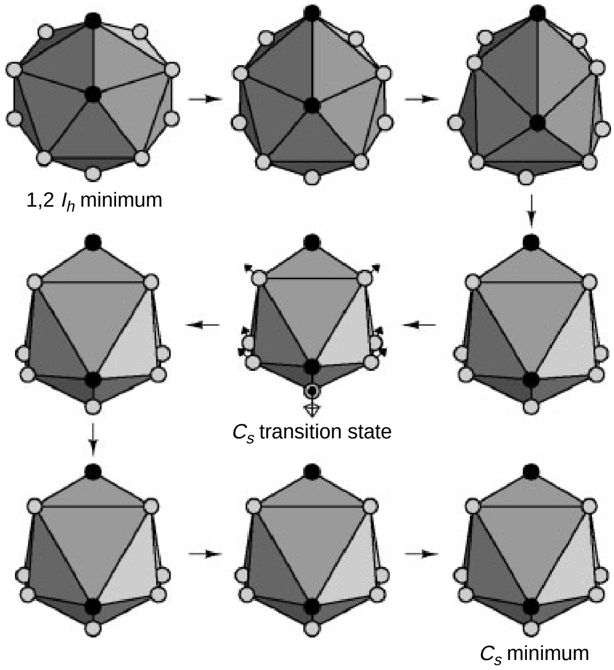

Figure 14 Concerted double DSD process (calculated at the SCF level with an STO-3G minimal basis set) linking 1, $2-C_2B_{10}H_{12}$ with C_{2v} symmetry to a high-energy local minimum with C_s symmetry. The diagram is arranged as for Figure 13 except that the terminal hydrogen atoms are omitted for clarity and the distance cutoff for triangulation is 2.8 Å. The calculated barriers are 311 and 13 kJ mol^{-1} for the forward and reverse processes, respectively. (This figure was produced using Mathematica 2.0 © Wolfram Research Inc., 1990.)

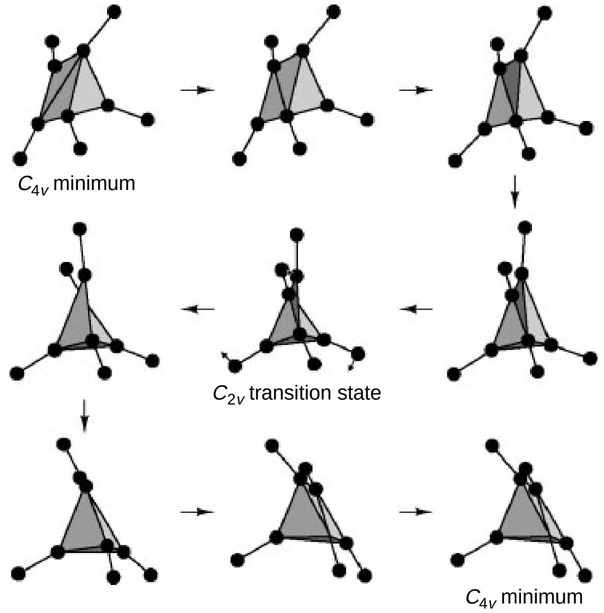

Figure 15 The SDDS rearrangement of square-based pyramidal $C_5H_5{}^+$, which proceeds through a C_{2v} symmetry transition state.[95] The diagram is arranged as for Figure 13 and the triangulation cutoff is 2.1 Å. (This figure was produced using Mathematica 2.0 © Wolfram Research Inc., 1990.)

7 RELATED ARTICLES

Boron: Polyhedral Carboranes; Carbon: Fullerenes.

8 REFERENCES

1. S. Sugano, ‘Microcluster Physics’, Springer-Verlag, Berlin, 1991.
2. R. S. Berry The Chemical Physics of Atomic and Molecular Clusters, in ‘Course CVII, Proceedings of the International School of Physics Enrico Fermi’, ed. G. Scoles, North-Holland, Amsterdam, 1990.
3. J. Luo, U. Landman, and J. Jortner, ‘Physics and Chemistry of Small Clusters’, Plenum Publishing, New York, 1987; S. Sugano, Y. Nishina, and S. Ohnishi eds, ‘Microclusters’, Springer-Verlag, Berlin, 1987; I. Prigogine and S. A. Rice (eds), *Adv. Chem. Phys.*, 1988, **70**, 75.
4. R. L. Johnston, ‘Atomic and molecular clusters’, Taylor and Francis, London and New York, 2002.
5. D. J. Wales, ‘Energy landscapes: applications to clusters, biomolecules and glasses’, Cambridge University Press, Cambridge, 2003.
6. D. J. Wales and R. S. Berry, *J. Chem. Phys.*, 1990, **92**, 4283.
7. For example, the proceedings of ISSPIC10 occupy volume 16 of Euro. Phys. J. D, 2001.
8. L. A. Paquette, *Acc. Chem. Res.*, 1971, **4**, 280.
9. H. W. Kroto, J. R. Heath, S. C. O’Brien, R. F. Curl, and R. E. Smalley, *Nature*, 1985, **318**, 162; H. W. Kroto, A. W. Allaf, and S. P. Balm, *Chem. Rev.*, 1991, **91**, 1213; R. F. Curl and R. E. Smalley, *Sci. Am.*, 1991, **265**, 54.
10. R. Whyman in ‘Transition Metal Clusters’, ed. B. F. G. Johnson, Wiley, New York, 1981, and references therein; A. B. Anderson, *J. Chem. Phys.*, 1976, **64**, 4046; J. F. Hamilton, *J. Vac. Sci. Technol.*, 1976, **13**, 319.
11. V. Boniačič-Koutecký, P. Fantucci, and J. Koutecký, *Chem. Rev.*, 1991, **91**, 1035.
12. See e.g. P. W. Atkins, ‘Molecular Quantum Mechanics’, 2nd edn., Oxford University Press, Oxford, 1983.
13. See e.g. A. Szabo and N. S. Ostland, ‘Modern Quantum Chemistry’, revised 1st edn., McGraw-Hill, New York, 1989.
14. P. Hohenberg and W. Kohn, *Phys. Rev. B*, 1964, **136**, 864; W. Kohn and L. J. Sham, *Phys. Rev. A*, 1965, **140**, 1133; R. Car and M. Parrinello, *Phys. Rev. Lett.*, 1985, **55**, 2471.
15. K. S. Pitzer, *Acc. Chem. Res.*, 1979, **12**, 271; P. Pyykko and J. Desclaux, *Acc. Chem. Res.*, 1979, **12**, 276.
16. B. J. Duke, *Chem. Soc. Spec. Rep.*, 1975, **2**, 159; M. C. Manning and W. C. Trogler, *Coord. Chem. Rev.*, 1981, **38**, 89.
17. R. Hoffmann, *J. Chem. Phys.*, 1963, **39**, 1397.
18. M. B. Hall and R. F. Fenske, *Inorg. Chem.*, 1972, **11**, 768.
19. R. G. Woolley *Inorg. Chem.*, 1985, **24**, 3519, 3525.
20. O. Gunnarsson and R. O. Jones, *Phys. Scr.*, 1980, **21**, 394; G. Seifert and R. O. Jones, *Z. Phys. D*, 1991, **20**, 77, and references therein.
21. R. E. Williams, *Adv. Inorg. Chem. Radiochem.*, 1976, **18**, 67; K. Wade, *J. Chem. Soc., Chem. Commun.*,, 1971, 792; K. Wade, *Adv. Inorg. Chem. Radiochem.*, 1976, **18**, 1; W. W. Rudolph, *Acc. Chem. Res.*, 1976, **9**, 446; D. M. P. Mingos, *Acc. Chem. Res.*, 1984, **17**, 311.
22. R. Mason, K. Thomas, and D. M. P. Mingos, *J. Am. Chem. Soc.*, 1973, **95**, 3802.
23. R. Hoffmann, *Angew. Chem., Int. Ed. Engl.*, 1982, **21**, 711.; M. Elian, M. M. L. Chen, R. Hoffmann, and D. M. P. Mingos, *Inorg. Chem.*, 1976, **15**, 1148.
24. J. D. Corbett, *Chem. Rev.*, 1985, **85**, 383.
25. C. E. Briant, B. R. C. Theobald, J. W. White, L. K. Bell, and D. M. P. Mingos, *J. Chem. Soc., Chem. Commun.*,, 1981, 201.
26. D. M. P. Mingos and R. L. Johnston, *Struct. Bonding*, 1987, **68**, 29.
27. D. M. P. Mingos and D. J. Wales, ‘Introduction to Cluster Chemistry’, Prentice-Hall, Englewood Cliffs, 1990.
28. W. N. Lipscomb, ‘Boron Hydrides’, Benjamin, New York, 1963; Good textbook descriptions of the styx approach may also be found in K. F. Purcell and J. C. Kotz, ‘Inorganic Chemistry’, Holt-Saunders, Philadelphia, International Edition 1977; E. L. Muetterties ed., ‘Boron Hydride Chemistry’, Academic Press, New York, 1975; C. E. Housecroft, ‘Boranes and Metalloboranes’, Ellis Horwood, Chichester, 1990.
29. S. F. A. Kettle and V. Tomlinson *J. Chem. Soc. A* 1969, 2002, 2007.
30. D. M. P. Mingos, *Nature*, 1972, **236**, 99; D. M. P. Mingos and M. I. Forsyth, *J. Chem. Soc., Dalton Trans.*, 1977, 610.
31. D. M. P. Mingos, *J. Chem. Soc., Chem. Commun.*, 1983, **706**,; D. M. P. Mingos and D. G. Evans, *J. Organomet. Chem.*, 1983, **251**, C13.
32. D. M. P. Mingos, *Chem. Soc. Rev.*, 1986, **15**, 31.
33. R. B. Woodward and R. Hoffmann, *Angew. Chem., Int. Ed. Engl.*, 1969, **8**, 781.
34. W. D. Knight, K. Clemenger, W. A. de Heer, W. A. Saunders, M. Y. Chou, and M. L. Cohen, *Phys. Rev. Lett.*, 1984, **52**, 2141.
35. W. D. Knight, W. A. de Heer, K. Clemenger, and W. A. Saunders, *Solid State Commun.*, 1985, **53**, 445.
36. R. D. Woods and D. S. Saxon, *Phys. Rev.*, 1954, **95**, 577.
37. L. D. Landau and E. M. Lifshitz, ‘Quantum Mechanics’, 3rd edn., Pergamon, Oxford, 1977.
38. A critical appraisal of the meaning of magic numbers in experimental mass spectra has been given by J. C. Phillips, *Chem. Rev.*, 1986, **86**, 619.
39. K. Clemenger, *Phys. Rev. B*, 1985, **32**, 1359.
40. D. M. P. Mingos, T. Slee, and Z. Lin, *Chem. Rev.*, 1990, **90**, 383.

41. D. J. Wales, D. M. P. Mingos, T. Slee, and Z. Lin, *Acc. Chem. Res.*, 1990, **23**, 17.

42. D. M. Lindsay, Y. Wang, and T. F. George, *J. Chem. Phys.*, 1987, **86**, 3500.

43. K. E. Schriver, J. L. Persson, E. C. Honea, and R. L. Whetten, *Phys. Rev. Lett.*, 1990, **64**, 2539; J. L. Persson, R. L. Whetten, H.-P. Cheng, and R. S. Berry, *Chem. Phys. Lett.*, 1991, **186**, 215.

44. See e.g. N. W. Ashcroft and N. D. Mermin, 'Solid State Physics', Holt-Saunders, Japan, 1976, International Edition.

45. J. Mansikka-aho, M. Manninen, and E. Hammerén, *Z. Phys. D*, 1991, **21**, 271.

46. T. P. Martin, T. Bergmann, H. Göhlich, and T. Lange, *Chem. Phys. Lett.*, 1990, **172**, 209; T. P. Martin, S. Bjørnholm, J. Borggreen, C. Bréchignac, Ph. Cahuzac, K. Hansen, and J. Pedersen, *Chem. Phys. Lett.*, 1991, **186**, 53; T. P. Martin, T. Bergmann, H. Göhlich, and T. Lange, *Z. Phys. D*, 1991, **19**, 25; H. Göhlich, T. Lange, T. Bergmann, U. Näher, and T. P. Martin, *Chem. Phys. Lett.*, 1991, **187**, 67; J. Pedersen, S. Bjørnholm, J. Borggree, K. Hansen, T. P. Martin, and H. D. Rasmussen, *Nature*, 1991, **353**, 733.

47. H. Nishioka, *Z. Phys. D*, 1991, **19**, 19.

48. J. Demuynck, M.-M. Rohmer, A. Stich, and A. Veillard, *J. Chem. Phys.*, 1981, **75**, 3443.

49. N. L. Biggs, 'Algebraic Graph Theory', Cambridge University Press, Cambridge, 1974.

50. R. B. King and D. H. Rouvray, *J. Am. Chem. Soc.*, 1977, **99**, 7834.

51. R. B. King, *Acc. Chem. Res.*, 1992, **25**, 247. references therein.

52. A. J. Stone and D. J. Wales, *Mol. Phys.*, 1987, **61**, 747.

53. R. B. King, *Inorg. Chem.*, 1988, **27**, 1941.

54. B. K. Teo, *Inorg. Chem.*, 1984, **23**, 1251, 1257.

55. H. C. Longuet-Higgins, *Q. Rev. Chem. Soc.*, 1957, **11**, 121; H. C. Longuet-Higgins and M. de V. Roberts, *Proc. R. Soc. A*, 1955, **230**, 110.

56. D. K. Hoffmann, K. Ruedenberg, and J. G. Verkade, *Struct. Bonding*, 1977, **33**, 57.

57. A. J. Stone, *Mol. Phys.*, 1980, **41**, 1339; *Inorg. Chem.*, 1981, **20**, 563; *Polyhedron*, 1984, **3**, 1299; A. J. Stone and M. J. Alderton, *Inorg. Chem.*, 1982, **21**, 2297.

58. For example, P. W. Atkins, M. S. Child, and C. S. G. Phillips, 'Tables for Group Theory', Oxford University Press, Oxford, 1986.

59. P. W. Fowler and A. Ceulemans, *Inorg. Chim. Acta*, 1985, **75**, 105.

60. D. M. P. Mingos and Z. Lin, *Struct. Bonding*, 1989, **71**, 1; *New. J. Chem.*, 1988, **12**, 787.

61. D. M. P. Mingos and J. C. Hawes, *Struct. Bonding*, 1985, **63**, 1; D. M. P. Mingos, *Pure Appl. Chem.*, 1987, **59**, 145.

62. R. L. Johnston, Z. Lin, and D. M. P. Mingos, *New J. Chem.*, 1989, **13**, 33.

63. D. J. Wales and D. M. P. Mingos, *Inorg. Chem.*, 1989, **28**, 2748.

64. F. A. Cotton and G. Wilkinson, 'Advanced Inorganic Chemistry', 4th edn., John Wiley and Sons, New York, 1980, p. 641.

65. D. M. P. Mingos *J. Chem. Soc., Dalton Trans.* 1976, 1163.

66. C. A. Coulson and S. Rushbrooke, *Proc. Cambridge. Philos. Soc.*, 1940, **36**, 193.

67. P. W. Fowler, *Polyhedron*, 1985, **4**, 2051.

68. R. L. Johnston and D. M. P. Mingos, *Polyhedron*, 1986, **12**, 2059; *J. Chem. Soc., Dalton. Trans.*, 1987, 647.

69. D. J. Wales and A. J. Stone, *Inorg. Chem.*, 1989, **28**, 3120.

70. B. F. G. Johnson, *J. Chem. Soc., Chem. Commun.*, 1976, 211; B. F. G. Johnson and R. E. Benfield, *J. Chem. Soc., Dalton. Trans.*, 1980, 1742.

71. J. W. Lauher, *J. Am. Chem. Soc.*, 1978, **100**, 5305; 1979, **101**, 2604.

72. G. Ciani and A. Sironi, *J. Organomet. Chem.*, 1980, **197**, 233.

73. R. L. Johnston and D. M. P. Mingos, *Inorg. Chem.*, 1986, **25**, 1661.

74. R. J. Johnston and D. M. P. Mingos, *J. Organomet. Chem.*, 1985, **280**, 407.

75. Z. Lin and D. M. P. Mingos, *J. Organomet. Chem.*, 1988, **339**, 367.

76. R. L. Johnston and D. M. P. Mingos, *Inorg. Chem.*, 1986, **25**, 3321.

77. R. P. Ziebarth and J. D. Corbett, *J. Am. Chem. Soc.*, 1988, **110**, 1132.

78. D. M. P. Mingos, *J. Chem. Soc., Chem. Commun.*, 1985, 1352; D. M. P. Mingos and Z. Lin, *J. Chem. Soc., Dalton. Trans.*, 1988, 1657.

79. References to both approaches are given in D. J. Wales and M. C. Waterworth, *J. Chem. Soc., Faraday Trans.*, 1992, **88**, 3409.

80. T. Slee, Z. Lin, and D. M. P. Mingos, *Inorg. Chem.*, 1989, **28**, 2256.

81. K. Raghavachari, *J. Chem. Phys.*, 1986, **84**, 5672.

82. K. Raghavachari and C. M. Rohlfing, *J. Chem. Phys.*, 1988, **89**, 2219.

83. J. R. Chelikowsky, K. M. Glassford, and J. C. Phillips, *Phys. Rev. B*, 1991, **44**, 1538.

84. W. N. Lipscomb, *Science (Washington DC)*, 1966, **153**, 373.

85. T. A. Halgren, I. M. Pepperberg, and W. N. Lipscomb, *J. Am. Chem. Soc.*, 1975, **97**, 1248.

86. D. J. Wales and A. J. Stone, *Inorg. Chem.*, 1987, **26**, 3845.

87. D. M. P. Mingos and R. L. Johnston, *Polyhedron*, 1988, **7**, 2437.

88. D. J. Wales, D. M. P. Mingos, and Z. Lin, *Inorg. Chem.*, 1989, **28**, 2754; D. J. Wales and D. M. P. Mingos, *Polyhedron*, 1989, **15**, 1933.

89. R. B. King, *Inorg. Chim. Acta.*, 1981, **49**, 237.

90. B. M. Gimarc and J. J. Ott, *Inorg. Chem.*, 1986, **25**, 83, 2708.

91. M. L. McKee, *J. Mol. Struct. (Theochem)*, 1988, **168**, 191.

92. M. L. McKee, *J. Am. Chem. Soc.*, 1988, **110**, 5317.
93. J. J. Ott, C. A. Brown, and B. M. Gimarc, *Inorg. Chem.*, 1989, **28**, 4269.
94. See W. Nam, Z. J. Abdou, H. Lee, T. Banuelos, and T. Onak, *Inorg. Chem.*, 1989, **28**, 669 references therein.
95. D. J. Wales and R. G. A. Bone, *J. Am. Chem. Soc.*, 1992, **114**, 539.
96. M. L. McKee, *J. Am. Chem. Soc.*, 1992, **114**, 879.
97. B. M. Gimarc, D. S. Warren, J. J. Ott, and C. Brown, *Inorg. Chem.*, 1991, **30**, 1598.
98. D. J. Wales, *J. Am. Chem. Soc.*, 1993, **115**, 1557.

Electronic Structure of Main-group Compounds

Gernot Frenking & Matthias Lein
Philipps-Universität Marburg, Marburg, Germany

Based in part on the article Electronic Structure of Main Group Compounds by Jeremy K. Burdett which appeared in the Encyclopedia of Inorganic Chemistry, First Edition.

1 Introduction 1
2 The Natural Bond Orbital Method 1
3 Energy Decomposition Analysis of the Chemical Bond 4
4 Molecular Orbital Models 10
5 The Valence Shell Electron-pair Repulsion Model and the Ligand Close-packing Model 18
6 Topological Analysis of the Electron Density Distribution 21
7 Chemical Bonding in Donor–Acceptor Complexes 23
8 Chemical Bonding of the Heavier Main-group Elements 24
9 References 27

1 INTRODUCTION

The electronic structure and bonding situation in main-group compounds is usually introduced and discussed in textbooks of inorganic chemistry with heuristic bonding models which have been proven to be helpful ordering schemes and to provide plausible explanations for the experimental findings. The most widely used approach for describing the electronic structure of molecules is the Lewis paradigm of electron-pair bonding, which was introduced into chemistry before quantum chemistry was developed.[1] A quantum theoretical reasoning of the Lewis electron-pair model was later suggested by Pauling who employed valence bond theory as a basis for chemical models.[2] A complimentary and equally important approach uses molecular orbitals for explaining the geometries and reactivities of molecules. Another frequently used concept is the valence shell electron-pair repulsion (VSEPR) model.[3] The advantage of the heuristic models is that the rather complicated molecular electronic structure that is determined by quantum theoretical laws of interatomic electrostatic interactions becomes expressed in terms of comparatively simple pictures and rules that are very useful for a qualitative interpretation of experimental observations. Chemistry would be a scientific pandemonium without the ordering power of chemical models.

Much effort has been devoted to the connection between the heuristic chemical models and the quantum theory of molecular electronic structure in theoretical chemistry in recent years. It is important to understand why and where the models are valid descriptions of experimental results and why and where they fail. It is also possible to examine the validity of the explanations that are given to understand the reactivity, geometry, and other properties of molecules. This article deals with important chemical models and recent quantum chemical studies, which shed light on the electronic structure and bonding situation in main-group compounds.

2 THE NATURAL BOND ORBITAL METHOD

The most popular and currently most widespread method that connects the qualitative Lewis model for writing molecular structures in terms of electron pairs with the results of quantum chemical calculations is the natural bond orbital (NBO) approach developed by Weinhold.[4] The NBO method is a charge partitioning analysis of the electronic structure that maximizes the electronic charge that can be localized in occupied orbitals that are either core orbitals, one-center (lone-pair) orbitals, or two-center (bonding) orbitals. A special option considers also delocalized three-center two-electron bonds. The set of occupied MOs indicates the best Lewis structure of the molecule. The remaining electrons, which cannot be localized into the three types of orbitals, occupy MOs, which are called Rydberg orbitals. The population of the usually weakly occupied Rydberg functions is a sensitive probe that shows how well the electronic structure of the molecule is described by the 'Lewis' occupied orbitals. A significant occupation of Rydberg orbitals suggests that the molecule has a nonclassical bonding situation, which should be described with more than one resonating Lewis structure. The NBO method also makes it possible to enforce a particular Lewis structure during the calculation. The comparison of the amount of localized electronic charge of a selected Lewis structure with the best (i.e. unconstrained) NBO solution indicates the weight of this structure.

The NBO method can be used for ab initio calculations at the HF and any correlated levels as well as for DFT methods. The results do not strongly depend on the size of the basis set, which is one reason that the NBO method has replaced the outdated Mulliken population analysis, for example, for the calculation of atomic partial charges. But there is a price that has to be paid for the advantages. Like any orbital-based method for partitioning the electronic charge into atomic and bonding domains, the choice of the selection procedure has some arbitrary character that needs to be known in order to judge the quality of the results.

The NBO method uses the one-electron density matrix, which can be obtained from any quantum chemical method as starting point for the partitioning procedure. The first step is the diagonalization of the one-center (atomic) blocks, which yields the pre-Natural Atomic Orbitals (pre-NAOs). This is a straightforward procedure. The second step is crucial in the NBO method. The pre-NAOs at the different atoms that are not orthogonal to each other are then orthogonalized yielding the natural atomic orbitals (NAOs). The pre-NAOs are first divided into two sets. One set consists of the strongly occupied minimal basis set, which describes the atomic electron density in the ground state. The other set consist of the remaining weakly occupied Rydberg orbitals. The subsequent sequence of orthogonalization steps treats the minimal functions and the Rydberg functions in different ways. The 'occupancy-weighted symmetric orthogonalization' (OWSO transformation), which was developed with the goal to preserve maximum resemblance of the NAOs with the pre-NAOs, strongly favors the minimal basis set in the description of the NAOs. Another reason for introducing the weighting factor was to ensure the stability of the orthogonalization procedure toward basis set enlargement. It is important to recognize that the weighting factor automatically disfavors atomic basis functions that are empty in the atomic ground state in the description of the chemical bond. Thus, the NBO method excludes a priori the outermost d orbitals of the heavier main-group elements and the outermost p orbitals of the transition metals from the valence space! Thus, the results of the NBO method cannot be used to investigate the question whether the d functions of main-group elements and the p functions of the TMs are true valence orbitals or polarization functions, because the answer is already enforced by the preselection of the orbitals belonging to the valence space in the occupancy-weighted orthogonalization.

The third step of the NBO algorithm is the calculation of the natural hybrid orbitals (NHOs), which form the two-center (sometimes three-center) NBOs. The density matrix in the NAO basis is first partitioned into one-center and two-center subblocks. Each one-center block is searched for NAOs, which have an occupancy ≥ 1.90 e. These one-center orbitals are labeled as core or valence lone-pair orbitals. The latter are deleted from the two-center subblocks, which are then orthogonalized (again via the OWSO transformation) yielding the final orthogonal set of NHOs. This leads to a set of N/2 (N being the number of electrons) NBOs. The search for NBOs is then repeated with lower occupancy thresholds than 1.90 e in steps of 0.1 e up to 1.50 e. The set of NBOs that accommodates most electrons is then given as the optimal Lewis structure of the molecule.

The information that becomes available from a NBO calculation shall be demonstrated by the analysis of the chemical bonds between carbon and hydrogen and the first-octal row elements Li–F. Table 1 gives the results for the C–H and C–E bonds of $H_3C\text{-}EH_n$ ($EH_n = H$, Li, BeH, BH_2, CH_3, NH_2, OH, F).

The calculated atomic partial charges agree with the expected trend, which follows the electronegativites of the atoms. The high occupation of the orbitals of the classical Lewis structures shows that the standard textbook description of the molecules $H_3C\text{-}EH_n$ as methyl substituted species having C–H, C–E, E–H single bonds and lone-pair orbitals at $EH_n = NH_2$, OH, F is a faithful representation of the electronic structure. The polarisation of the C-E ($E = Li$–F) bonds follows smoothly the trend of the electronegativity of atom E, that is, the bonds become more strongly polarized toward E when E becomes more electronegative. The hybridization of the C–H bond in CH_4 is perfectly sp^3 while the other C–E bonds deviate from this value. The %p character at the carbon end increases from boron to fluorine, which is in agreement with Bent's rule, which states that 'Atomic s character concentrates in orbitals directed towards electropositive substituents'.[5] However, the C–Be and C–Li bonds also have a very large %p character at carbon. This comes from the diffuse 2s orbitals of beryllium and particularly of lithium, which have large overlaps with the 2p AOs of carbon. The C–Li bond has the highest %p value at carbon while lithium has a nearly pure s AO in the C–Li bond. The beryllium atom is ∼sp-hybridized in the C–Be bond while the heavier atoms have a much higher p character. There is

Table 1 NBO analysis of $H_3C\text{-}EH_n$ ($EH_n = H$, Li, BeH, BH_2, CH_3, NH_2, OH, F) at B3LYP/6−31G(d)[a]

	Charges	C–E							C–H				
Molecule	$q(CH_3)/q(C)/q(E)$	occ.	%C	%E	%s(C)	%p(C)	%s(E)	%p(E)	occ.	%C	%H	%s(C)	%p(C)
CH_3–H	−0.23/−0.91/0.23	2.00	61.4	38.6	25.0	74.9	100.0	0.0					
CH_3–Li	−0.76/−1.38/0.76	2.00	88.4	11.6	17.7	82.3	92.4	6.2	2.00	60.3	39.7	27.5	72.4
CH_3–BeH	−0.72/−1.46/1.27	1.95	88.3	11.7	26.2	73.8	51.2	48.8	1.99	62.3	37.7	24.7	75.3
CH_3–BH_2[b]	−0.97/−1.07/0.49	2.00	67.8	32.2	32.0	68.0	34.0	65.9	1.95	62.6	37.4	22.1	77.9
CH_3–CH_3	0.0/−0.67/0.67	2.00	50.0	50.0	28.1	71.8	28.1	71.8	1.99	61.3	38.7	24.0	76.0
CH_3–NH_2[b]	0.15/−0.47/−0.89	2.00	40.7	59.3	24.9	75.0	30.9	69.1	1.99	60.6	39.4	25.2	74.7
CH_3–OH[b]	0.28/−0.30/−0.74	2.00	33.5	66.5	22.0	77.8	29.3	70.6	2.00	60.3	39.7	26.0	73.9
CH_3–F	0.38/−0.18/−0.38	2.00	28.0	72.0	19.9	79.9	26.3	73.6	2.00	59.8	40.2	26.8	73.2

[a] Partial charges q, occupation, polarisation, and hybridization of the C–E and C–H bonds. [b] Values for the C–H bond are averaged over the two symmetry nonequivalent C–H bonds.

Table 2 NBO analysis of group 13 Donor–acceptor complexes at MP2/6–31G(d)[a,b]

				D(*x*)–A(*y*)							
Molecule	$\Delta q(D \rightarrow A)$	$q_{D(x)}$	$q_{A(y)}$	%x	%s(*x*)	%p(*x*)	%d(*x*)	%s(*y*)	%p(*y*)	%d(*y*)	D_e
$F_3B–NH_3$	0.29	−1.03	+1.34	84.7	31.1	68.9	<0.1	20.0	79.4	0.6	23.5
$F_3B–CO$	0.03	+0.44	+1.47	100.0	76.4	23.5	<0.1	–	–	–	3.2
$F_3B–C(NH_2)_2$	0.44	+0.27	+1.20	74.8	39.2	60.7	<0.1	25.2	74.4	0.4	42.5
$F_3Al–NH_3$	0.13	−1.19	+1.99	93.8	23.0	77.0	<0.1	19.1	79.9	1.0	43.4
$F_3Al–CO$	0.13	+0.44	+1.97	92.8	64.3	35.7	<0.1	13.5	84.9	1.6	15.1
$F_3Al–C(NH_2)_2$	0.19	+0.06	+1.92	88.9	34.1	65.8	<0.1	21.8	76.4	1.8	58.0
$F_3Ga–NH_3$	0.15	−1.16	+1.87	93.1	20.2	79.8	<0.1	18.5	81.2	0.3	38.5
$F_3Ga–CO$	0.12	+0.45	+1.86	93.4	63.4	36.5	<0.1	12.2	87.1	0.7	12.5
$F_3Ga–C(NH_2)_2$	0.23	+0.08	+1.79	86.8	33.2	66.7	<0.1	23.4	75.6	1.0	59.5
$F_3In–NH_3$	0.12	−1.18	+1.98	94.2	20.1	79.9	<0.1	17.7	82.0	0.3	40.9
$F_3In–CO$	0.10	+0.43	+1.97	94.5	63.1	36.9	<0.1	12.3	87.7	0.0	14.2
$F_3In–C(NH_2)_2$	0.19	+0.06	+1.91	88.6	32.3	67.7	<0.1	22.8	77.2	0.1	60.1
$Cl_3B–NH_3$	0.38	−1.01	+0.23	80.2	35.4	64.6	<0.1	20.8	78.8	0.4	32.0
$Cl_3B–CO$	0.01	+0.43	+0.29	100.0	76.9	23.1	<0.1	–	–	–	2.3
$Cl_3B–C(NH_2)_2$	0.50	+0.28	+0.11	69.6	40.9	59.0	<0.1	25.5	74.3	0.2	59.7
$Cl_3Al–NH_3$	0.16	−1.18	+1.47	92.2	28.8	71.2	<0.1	19.3	79.6	1.1	44.1
$Cl_3Al–CO$	0.18	+0.48	+1.35	89.1	65.9	34.1	<0.1	13.7	84.7	1.6	14.2
$Cl_3Al–C(NH_2)_2$	0.26	+0.08	+1.39	85.9	36.8	63.1	<0.1	22.1	76.5	1.4	61.6
$Cl_3Ga–NH_3$	0.18	−1.15	+1.38	91.5	26.3	73.7	<0.1	18.0	81.7	0.2	35.4
$Cl_3Ga–CO$	0.17	+0.49	+1.29	90.5	65.5	34.5	<0.1	10.8	88.6	0.6	9.7
$Cl_3Ga–C(NH_2)_2$	0.30	+0.12	+1.30	84.1	36.0	64.0	<0.1	23.1	76.4	0.5	57.5
$Cl_3In–NH_3$	0.16	−1.16	+1.60	92.4	24.2	75.8	<0.1	17.1	82.8	0.1	38.7
$Cl_3In–CO$	0.15	+0.47	+1.53	91.8	64.4	35.6	<0.1	11.3	88.5	0.1	12.0
$Cl_3In–C(NH_2)_2$	0.28	+0.12	+1.50	85.4	34.4	65.6	<0.1	21.9	78.0	0.1	57.6

[a] Donor $\rightarrow$ acceptor charge donation $\Delta q(D \rightarrow A)$; partial atomic charges q of the donor atoms D(*x*) and acceptor atoms A(*y*); polarization of the donor–acceptor bond D(*x*)–A(*y*) in %x, hybridisation of the D(*x*)–A(*y*) bond; theoretically predicted bond dissociation energies D_e in kcal mol^{-1}.

[b] Reference 6.

little variation in the polarization and hybridization of the C–H bonds.

The NBO analysis may be used to address the question if a molecule should be written with a bonding line between two atoms or not. Table 2 shows the NBO results of donor–acceptor complexes of group-13 Lewis acids EF_3 and ECl_3 ($E = B$–In) with the Lewis bases NH_3, CO and $C(NH_2)_2$ as examples.**[6]** The NBO analysis suggests that the very weakly bonded complexes F_3BCO ($D_e = 3.2$ kcal mol^{-1}) and Cl_3BCO ($D_e = 2.3$ kcal mol^{-1}) should not be written with a bonding line between the donor and acceptor moiety but rather with a lone-pair orbital at CO. The NBO calculations of the remaining complexes of CO, which have bond dissociation energies between $D_e = 9.7$ kcal mol^{-1} and 15.1 kcal mol^{-1}, give E–CO bond orbitals that are highly polarized towards the carbon donor end (Table 2). The hybridization at the C(CO) atom in the donor–acceptor bonds is always $s > p$ while for the other donor molecules NH_3 and $C(NH_2)_2$ the hybridization at the donor atom is $s < p$.

There is no correlation between the polarization of the donor–acceptor bond and the bond strength. This becomes obvious, for example, by comparing the $F_3Ga–NH_3$ bond with $F_3Ga–CO$. The latter complex has a much weaker bond ($D_e = 12.5$ kcal mol^{-1}) than the former ($D_e = 38.5$ kcal mol^{-1}) but the donor–acceptor bonds are polarized to the same extent. There is also no correlation between the calculated charge transfer from the donor to the acceptor moiety. The charge transfer $\Delta q(D \rightarrow A)$ of the most strongly bonded complex $Cl_3Al–C(NH_2)_2$ ($D_e = 61.6$ kcal mol^{-1}) is only 0.26 e while the weaker bonded complex F_3B-NH_3 ($D_e = 23.5$ kcal mol^{-1}) has a charge transfer of 0.29 e.

Another important point concerns the calculated atomic charges at the donor and acceptor atom. Table 2 shows that the partial charges at the donor and acceptor atoms have positive values. A naive interpretation would suggest that there is Coulomb repulsion between the donor and acceptor atoms. This is not correct because even the positively charged donor atom carries an occupied lone-pair orbital, which is directed toward the acceptor atom. There is always a *local area of negative charge concentration at the overall positively charged donor atom* that yields strong *Coulomb attraction* with the positively charged acceptor atom. The nonspherical charge distribution at the bonded atoms becomes analyzed in paragraph 6, Topological Analysis of the Electron Density Distribution, using $Cl_3B–CO$ as an example. The energetic aspects of the interatomic interactions must be analyzed in order to understand the nature of the chemical bond. This will be shown in the next section.

3 ENERGY DECOMPOSITION ANALYSIS OF THE CHEMICAL BOND

Like the charge distribution in a molecule can be partitioned into domains that may be used for a chemically meaningful interpretation of the bonding situation, the electronic energy of a molecule can also be divided up into quantities that are helpful for an understanding of the molecular structure and reactivity. Because the geometry and reactivity of molecules are driven by the associated energy changes, it is even more important to understand the factors that make a molecular structure energetically favorable. The energy of a chemical bond has been the subject of theoretical research for a long time.

There are some fundamental concepts and quantities that are used by chemists to characterize a chemical bond. For example, a bond is considered as covalent when the attractive interactions arise from the mixing of the wave functions of the fragments, which yields a chemical bond. This type of chemical bonding is conceptually different from ionic bonding, which can be rationalized in terms of classical Coulomb attraction that arises when two charges of opposite sign attract each other. It is important to recognize the carrier of the charges, which are the electrons and protons but not the atoms. While the protons may be reasonably described as a point charge, the electronic charge distribution in a molecule is usually highly anisotropic, which means that a point charge description is not appropriate. Atomic partial charges may therefore be a misleading guide for estimating classical Coulomb interactions between atoms in a molecule. It is also important to recognize that ionic bonding and classical electrostatic attraction are not identical quantities. Theoretical studies have shown that there are strong classical electrostatic attractions between atoms in nonpolar bonds that are not ionic. This will be discussed in more detail below.

Covalent bonding is usually described in terms of orbital interactions. If the molecule has a mirror plane, the bonding orbitals have σ symmetry when they are symmetric with regard to the mirror plane, or they have π symmetry when they are antisymmetric. This definition leads to the familiar concept of single and multiple bonds in molecules. It must be emphasized that covalent and ionic interactions do not establish different types of elementary forces. The driving force of chemical bonding is electrostatic interaction. The difference is that covalent bonding is associated with quantum theoretical laws of electrostatic interactions whereas ionic bonding is associated with the classical description of electrostatic forces.

The question if the bonding interactions in a molecule are covalent or ionic (electrostatic) cannot be answered in a definite way neither by experiment nor by theory because covalency and ionicity are conceptual quantities but no observables. The same holds true for the strength and the existence of σ and π bonds. Any statement about single or multiple bond character in a molecule depends on the theoretical method that is used to analyze the electronic structure. The situation is easy for molecules such as ethylene or acetylene but for complicated bonding situations it can be more difficult to determine the multiplicity of a bond.

A powerful method that addresses both the question about the covalent and electrostatic character of a bond and the strength of the σ and π bonding contributions is the energy decomposition analysis (EDA), which was developed by Morokuma[7] and Ziegler.[8] The focus of the bonding analysis is the instantaneous interaction energy ΔE_{int} of a bond A – B, which is the energy difference between the molecule AB and the fragments A and B in the frozen geometry of the compound. Note that ΔE_{int} is not the same as the bond dissociation energy D_e. The difference between D_e and ΔE_{int} is the preparation energy of the fragments ΔE_{prep}, which is necessary to promote the fragments from their equilibrium geometry in the electronic ground state into the geometry and electronic state in the molecule:

$$-D_e = \Delta E_{int} + \Delta E_{prep} \qquad (1)$$

The advantage of using ΔE_{int} and not the bond dissociation energy as a starting point for a bonding analysis is that the actual interatomic interactions of the bond are considered. In the EDA, the bond formation A–B is considered to be the result of a three-step process for which individual energy terms are calculated, which can be interpreted in a physically meaningful way. In the first step, the fragments A and B with the frozen electron densities are superimposed in the geometry of A–B. This is a quasi-classical approach that gives the classical Coulomb interaction energy ΔE_{elstat}. The electronic structure that is yielded in the first step violates the Pauli principle, which states that two electrons having the same spin must not occupy the same region in space. The Pauli repulsion ΔE_{Pauli} between two electrons with the same spin (which is much stronger than the Coulomb repulsion at short distances) is calculated in the second step of the EDA. This is done by enforcing the wave function of the superimposed fragments to obey the Pauli principle by antisymmetrization and renormalization. The latter interaction is rather strong for most chemical bonds but its contribution to the interatomic interactions is frequently neglected in bonding models.

In the final step of the EDA, the wave function of the molecule relaxes to its optimal form yielding the orbital interaction term ΔE_{orb}. This term can be further partitioned into contributions by the orbitals belonging to different irreducible representations of the point group of the interacting system. Thus, it is possible to give energy contributions of the σ and π bonding contributions to a bond that has a mirror plane. More details about the EDA method in the framework of DFT can be found in a recent review article.[9]

$$\Delta E_{int} = \Delta E_{elstat} + \Delta E_{Pauli} + \Delta E_{orb} \qquad (2)$$

The calculated values for ΔE_{elstat} and ΔE_{orb} may be used to classify a bond in terms of electrostatic and covalent interactions, because the two terms are the attractive contributions to the chemical bond.[10] However, the orthodox view that nonpolar bonds such as the C–C bond in ethane are purely covalent must then be revised because the bonding contributions of ΔE_{elstat} are rather large.

3.1 Isoelectronic Diatomic Molecules N_2, CO, BF

Table 3 gives the EDA results for the isoelectronic diatomic molecules N_2, CO and BF.[11] The contribution of the electrostatic interaction $\Delta E_{elstat} = -308.5\,\text{kcal mol}^{-1}$ to the N–N bond is *larger* than the total interaction energy $\Delta E_{int} = -232.2\,\text{kcal mol}^{-1}$, which gives directly the bond dissociation energy because there is no relaxation energy of the fragments, that is, the nitrogen atoms. This result is surprising for most chemists, because the bonding in N_2 is usually considered to come from the σ and the degenerate π bonds. Table 3 shows that the bonding contributions from σ orbitals ($\Delta E_\sigma = -470.0\,\text{kcal mol}^{-1}$) and π orbitals ($\Delta E_\pi = -245.4\,\text{kcal mol}^{-1}$) are rather large, indeed. However, there is strong repulsion from the Pauli term ($\Delta E_{Pauli} = 791.7\,\text{kcal mol}^{-1}$), which compensates the attractive orbital interactions. If N_2 would be held together by classical electrostatic forces, the bond energy would be $\sim$450 kcal mol^{-1} at an equilibrium distance of $\sim$0.85 Å. This is shown in Figure 1, which displays the energy terms of N_2 as a function of the internuclear distance.

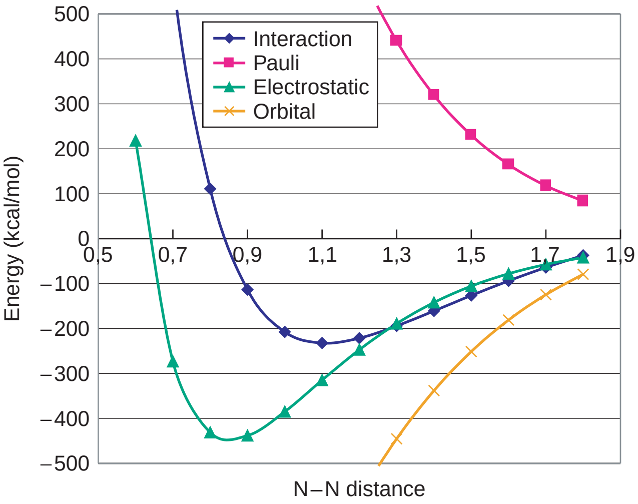

Figure 1 Energy contributions ΔE_{elstat}, ΔE_{Pauli} and ΔE_{orb} to the total interaction energy ΔE_{int} in N_2 as a function of N–N interatomic distance. (Ref. 11. Reproduced by permission of Springer Verlag)

The important role of quasi-classical electrostatic bonding in molecules has been recognized as early as 1974.[13] In 1986, Spackman and Maslen published the calculated results for 148 diatomic molecules, which showed that, in 147 diatomics, the ΔE_{elstat} term contributes a significant portion of the binding energy.[14] The only diatomic molecule among the 148 species where the electrostatic attraction is negligible is H_2. Dihydrogen is an atypical molecule for learning about the principal bonding contributions in a molecule.

It is well known that CO has a larger bond dissociation energy (BDE) than N_2. Table 3 shows that the attractive components of the C–O bonding energy ($\Delta E_{elstat} = -240.0\,\text{kcal mol}^{-1}$; $\Delta E_{orb} = -594.2\,\text{kcal mol}^{-1}$) are weaker than in N_2. The larger BDE of CO is caused by the weaker Pauli repulsion ($\Delta E_{Pauli} = 575.8\,\text{kcal mol}^{-1}$) compared with CO. This can be explained with the smaller orbital overlap in heteroatomic CO than in homoatomic N_2, which yields a smaller ΔE_{orb} term. But also the ΔE_{Pauli} term becomes smaller when there is less overlap! The EDA results also show that the π bonding in CO has nearly the same strength as the σ bonding that supports the Lewis structure (−)C≡O(+) with a triple bond as the most important one. BF, however, should be written with a single bond. Table 3 shows that the most important difference between BF and the isoelectronic diatomics N_2 and CO is the much weaker contribution of the π orbitals, which provide only 11.2% of the total orbital interaction term. If π bonding in BF would be as strong as in N_2 and CO, it would have an even bigger BDE.

Table 3 Energy partitioning analysis of the N–N, C–O and B–F bonds. Energy values are given in kcal mol^{-1}

	N_2	CO	BF
ΔE_{int}	−232.2	−258.4	−180.8
ΔE_{Pauli}	791.7	575.8	476.1
ΔE_{elstat}[a]	−308.5 (30.1%)	−240.0 (28.8%)	−210.5 (32.0%)
ΔE_{orb}[a]	−715.4 (69.9%)	−594.2 (71.2%)	−446.4 (68.0%)
ΔE_σ[b]	−470.0 (65.7%)	−301.7 (50.8%)	−396.4 (88.8%)
ΔE_π[b]	−245.4 (34.3%)	−292.5 (49.2%)	−50.0 (11.2%)
$-D_e$	−232.2	−258.4	−180.8
$-D_0$[c]	−228.8 [−225.0]	−255.4 [−255.7]	−178.9 [−179.9]

[a] The percentage values in parentheses give the contribution to the total attractive interactions $\Delta E_{elstat} + \Delta E_{orb}$. [b] The percentage values in parentheses give the contribution to the orbital interactions ΔE_{orb}. [c] Experimental values are given in brackets.[12]

3.2 Dihalogens $F_2 - I_2$

Table 4 gives the EDA results for the dihalogens E_2(E = F–I). The BDE of E_2 increases for the lighter elements except for F_2, which has a weaker bond energy than Cl_2. The standard textbook explanation for the relatively weak F–F bonding is given in terms of strong Pauli repulsion between the lone-pair electrons at the equilibrium distance of F_2, which is much shorter than that of Cl_2. However, also the radius of the valence orbitals of fluorine is much smaller than the radius of the chlorine valence orbitals because of the higher electronegativity of F. Inspection of the energy components to the interatomic interactions in E_2 (Table 4) shows that the absolute values of ΔE_{Pauli} and ΔE_{orb} increase from I_2 to F_2 but

Table 4 Energy partitioning analysis of the E–E Bond for E = F–I. Energy values are given in kcal mol^{-1}

	F_2	Cl_2	Br_2	I_2
ΔE_{int}	−47.4	−59.1	−47.8	−34.1
ΔE_{Pauli}	140.8	123.2	76.7	45.4
$\Delta E_{elstat}{}^{a}$	−38.2 (20.3%)	−44.1 (24.2%)	−31.9 (25.6%)	−19.8 (24.9%)
$\Delta E_{orb}{}^{a}$	−150.0 (79.7%)	−138.1 (75.8%)	−92.6 (74.4%)	−59.7 (75.1%)
$\Delta E_{\sigma}{}^{b}$	−144.6 (96.4%)	−123.8 (89.6%)	−85.9 (92.8%)	−59.4 (99.5%)
$\Delta E_{\pi}{}^{b}$	−5.4 (3.6%)	−14.3 (10.4%)	−6.7 (7.2%)	−0.3 (0.5%)
$-D_e$	−47.4	−59.1	−47.8	−34.1
$-D_0{}^{c}$	−46.0 [−36.9]	−58.3 [−57.2]	−47.4 [−45.4]	−33.8 [−35.6]

[a] The percentage values in parentheses give the contribution to the total attractive interactions $\Delta E_{elstat} + \Delta E_{orb}$. [b] The percentage values in parentheses give the contribution to the orbital interactions ΔE_{orb}. [c] Experimental values are given in brackets.[12]

Table 5 Energy partitioning analysis of the E–E bond for E = N–Bi. Energy values are given in kcal mol^{-1}

Variable	N_2	P_2	As_2	Sb_2	Bi_2
ΔE_{int}	−232.2	−109.2	−80.6	−54.4	−48.4
ΔE_{Pauli}	791.7	299.3	247.9	182.3	168.1
$\Delta E_{elstat}{}^{a}$	−308.5 (30.1%)	−175.8 (43.0%)	−160.5 (48.9%)	−131.5 (55.6%)	−126.3 (58.3%)
$\Delta E_{orb}{}^{a}$	−715.4 (69.9%)	−232.7 (57.0%)	−168.0 (51.1%)	−105.2 (44.4%)	−90.3 (41.7%)
$\Delta E_{\sigma}{}^{b}$	−470.0 (65.7%)	−140.1 (60.0%)	−105.1 (62.6%)	−69.9 (66.4%)	−61.2 (67.8%)
$\Delta E_{\pi}{}^{b}$	−245.4 (34.3%)	−92.6 (40.0%)	−62.9 (37.4%)	−35.3 (35.6%)	−29.1 (32.2%)
Overlap σ	0.18	0.30	0.32	0.34	0.34
Overlap π	0.37	0.30	0.28	0.24	0.24
$-D_e$	−232.2	−109.2	−80.6	−54.4	−48.4
$-D_o{}^{c}$	−228.8 [−225.0]	−108.1 [−116.1]	−80.0 [−91.3]	−54.0 [−71.3]	−48.1 [−47.0]

[a] The percentage values in parentheses give the contribution to the total attractive interactions $\Delta E_{elstat} + \Delta E_{orb}$. [b] The percentage values in parentheses give the contribution to the orbital interactions ΔE_{orb}. [c] Experimental values are given in brackets.[12]

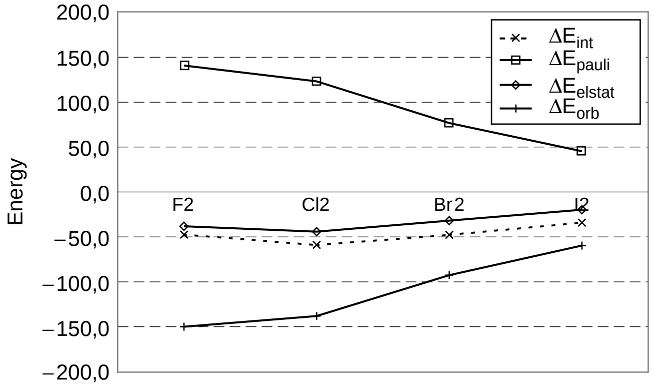

Figure 2 Energy contributions ΔE_{elstat}, ΔE_{Pauli} and ΔE_{orb} to the total interaction energy ΔE_{int} in the dihalogen molecules E_2 at the equilibrium bond length

the increase of the Pauli repulsion from Cl_2 to F_2 is not very steep. This becomes obvious from Figure 2, which displays a plot of the energy components and the total interaction energy from I_2 to F_2. The trend of ΔE_{Pauli} and ΔE_{orb} exhibits a regular behavior from the right to the left. What is unregular, however, is the trend of ΔE_{elstat}. The electrostatic attraction increases from iodine to chlorine, but then it decreases for fluorine. Figure 2 shows that the ΔE_{int} and ΔE_{elstat} correlate nicely over the whole range of dihalogen molecules. It becomes obvious from the EDA results that the weak bond of F_2 is *not* because the Pauli repulsion becomes very strong, but rather because the electrostatic attraction is unusually weak, weaker than in Cl_2. If the trend of ΔE_{elstat} would show a regular increase from Cl_2 to F_2, its value would be ∼56 kcal mol^{-1}, which would yield a total interaction energy of ∼65 kcal mol^{-1}.

3.3 Dipnicogens $N_2 - Bi_2$

Another set of diatomic molecules that reveals interesting information about the strength of π bonding in heavy main-group compounds is the pnicogen series E_2 (E = N–Bi). Table 5 shows the EDA results of the E–E bonding situation. The percentage contribution of the orbital interaction to the total bonding decreases from nitrogen to bismuth where only 41.7% of the attractive energy comes from ΔE_{orb}. The most important information concerns the strength of the σ and π bonding in the diatomics. Compounds with multiple bonds between heavy main-group elements are much less stable than molecules that have multiple bonds between first-octal row elements. It is sometimes stated that π bonding is weak in the former species because their bonds are longer than in the latter molecules. However, the π overlap between heavier main-group elements does not become much smaller when one goes down in the periodic table because the orbitals have also large radii.[15] The size of the overlap integral is not a reliable probe for estimating the strength of the orbital interactions because it does not give any information about the energy of the electrons that occupy the orbital.

Table 5 shows that the overlap integral of the σ orbitals in N_2 (0.18) is only about one half of the overlap of the π orbital (0.37). This is because the 2p(σ) AOs of the nitrogen atoms overlap at short distance partly in an antibonding fashion with each other. The binding contributions of the σ orbitals are still much larger than those of the π orbital because the 2s AOs of nitrogen are lower in energy and, therefore, contribute strongly to the attractive orbital term.

Table 5 shows also that the percentage contribution of ΔE_π to the orbital interaction term in P_2, As_2 and Sb_2 is even slightly higher than in N_2, and the relative π bonding in Bi_2 is not much smaller. The trend of the σ and π orbital overlap does not show the important energy contribution of the π orbitals although the size of the π orbital overlap remains quite large. Molecules with multiple bonds between heavier main-group elements are not intrinsically unstable because of weak π bonding. The electronic structure of heavy main-group molecules containing multiple bonds will be discussed below.

3.4 Single and Multiple Bonds in First-row Molecules $H_nE–EH_n$ (E = Li–F)

Table 6 gives the EDA results of a complete 'first-row sweep' of nonpolar single bonds $H_nE–EH_n$ (E = Li–F), which gives important information about the electronic structure and bonding situation in the molecules.[48] The covalent contribution decreases and the electrostatic bonding increases from F–F to HBe–BeH. The Li–Li bond is a special case as it is the dihydrogen bond H–H. The 2s orbital of Li is very diffuse, and the long Li–Li bond yields only a very weak electrostatic attraction (Table 6). Although the valence orbital of Li_2 is bonding, removal of one electron from the 3σ HOMO that leads to Li_2^+ gives a Li–Li bond that is stronger (33.2 kcal mol^{-1}) than in Li_2 (26.4 kcal mol^{-1}). The Pauli repulsion in Li_2 prevents shortening of the bond.[9] Removing one-electron reduces Pauli repulsion and the increase in electrostatic attraction at shorter distances compensates for the loss of orbital interaction. H_2 and Li_2 are atypical molecules for discussing the electronic structure of main-group compounds.

The contribution of π bonding interactions in classical multiple bonds to the bond strength becomes obvious from the EDA results of the HB=BH, $H_2C{=}CH_2$, HN=NH, and HC≡CH bonds, which are shown in Table 7.[48] The covalent contributions to the attractive interactions are stronger than the electrostatic contributions in the above molecules. The relative contribution of ΔE_π decreases for the double bonds in the order HB=BH > $H_2C{=}CH_2$ > HN=NH. The degenerate π bond in acetylene contributes 44.4% to the orbital interactions, which means that it is not much weaker than the σ bond. Note that the absolute values of ΔE_σ in acetylene (-215.5 kcal mol^{-1}) and ethylene (-212.2 kcal mol^{-1}) are nearly the same while ΔE_π in acetylene (-172.4 kcal mol^{-1}) is more than twice as strong as in ethylene (-79.2 kcal mol^{-1}).

3.5 Single Bonds in Group-14 Molecules $H_3E–EH_3$ (E = C–Pb)

Table 8 gives the EDA results for the heavy-atom analogs of ethane $H_3E–EH_3$ (E = Si–Pb).[48] The calculated data suggest that the nature of the E–E bonding changes little when one goes from carbon to the heavier group-14 atoms. The covalent contributions decrease slightly from C to Sn, but the changes are not very big. The increase of ΔE_{orb} from Sn to Pb is caused

Table 6 Energy decomposition analysis of the H_nE-EH_n single bond (E = Li–F) at BP86/TZ2P. Energy values in kcal mol^{-1}

	Li_2	Be_2H_2	B_2H_4	C_2H_6	N_2H_4	O_2H_2	F_2
Sym.	$D_{\infty h}$	$D_{\infty h}$	D_{2d}	D_{3d}	C_2	C_2	$D_{\infty h}$
ΔE_{int}	−20.6	−70.3	−114.5	−114.8	−76.8	−62.6	−52.8
ΔE_{Pauli}	1.9	41.1	161.7	201.6	407.9	384.6	145.8
ΔE_{elstat}[a]	−8.4 (37.3%)	−65.1 (58.4%)	−140.5 (50.9%)	−130.9 (41.4%)	−178.3 (36.8%)	−145.8 (32.6%)	−41.1 (20.7%)
ΔE_{orb}[a]	−14.1 (62.7%)	−46.3 (41.6%)	−135.7 (49.1%)	−185.5 (58.6%)	−306.4 (63.2%)	−301.4 (67.4%)	−157.5 (79.3%)
ΔE_σ[b]		−46.3 (100%)	−119.7 (88.2%)	−175.5 (94.6%)			−151.3 (96.1%)
ΔE_π[b]			−16.0 (11.8%)	−10.0 (5.4%)			−6.2 (3.9%)
ΔE_{prep}	0	1.6	6.1	21.7	4.2	3.2	0
$-D_e$	−20.6	−68.7	−108.4	−93.1	−72.6	−59.4	−52.8
$-D_0$[c]	−20.1 [−26.4]	−64.9 [−71.7][d]	−103.0 [−104.0][d]	−83.4 [−89.9]	−62.8 [−65.8]	−53.6 [−50.9]	−51.5 [−37.9]

[a] The percentage values in parentheses give the contribution to the total attractive interactions $\Delta E_{elstat} + \Delta E_{orb}$. [b] The percentage values in parentheses give the contribution to the orbital interactions ΔE_{orb}. [c] Experimental values are given in brackets.[12] [d] Theoretical value taken from high-level ab initio calculations.[16]

Table 7 Energy decomposition analysis of the HB=BH, $H_2C{=}CH_2$, *trans* NH=HN and HC≡CH Multiple bonds at BP86/TZ2P. Energy values in kcal mol^{-1}

	B_2H_2 ($D_{\infty h}$)	C_2H_4 (D_{2h})	*trans* N_2H_2 (D_{2h})	C_2H_2 ($D_{\infty h}$)
ΔE_{int}	−159.8	−191.1	−137.4	−280.0
ΔE_{Pauli}	116.3	281.9	599.4	255.4
ΔE_{elstat}[a]	−110.6 (40.1%)	−181.6 (38.4%)	−254.6 (34.6%)	−147.5 (27.6%)
ΔE_{orb}[a]	−165.5 (59.9%)	−291.4 (61.6%)	−482.2 (65.4%)	−387.9 (72.4%)
ΔE_{σ}[b]	−111.1 (67.1%)	−212.2 (72.8%)	−392.6 (81.4%)	−215.5 (55.6%)
ΔE_{π}[b]	−54.4 (32.9%)	−79.2 (27.2%)	−89.6 (18.6%)	−172.4 (44.4%)
ΔE_{prep}	4.4	12.9	5.6	32.8
$-D_e$	−155.4	−178.2	−131.8	−247.2
$-D_0$[c]	−149.8	−168.3 [−175.4]	−123.7 [−123.8]	−238.7 [−230.9]

[a] The percentage values in parentheses give the contribution to the total attractive interactions $\Delta E_{elstat} + \Delta E_{orb}$. [b] The percentage values in parentheses give the contribution to the orbital interactions ΔE_{orb}. [c] Experimental values are given in brackets.[12b,17]

Table 8 Energy decomposition analysis of the $H_3E{-}EH_3$ Single bond (E = C–Pb) at BP86/TZ2P. Energy values in kcal mol^{-1}

	C_2H_6	Si_2H_6	Ge_2H_6	Sn_2H_6	Pb_2H_6
Sym.	D_{3d}	D_{3d}	D_{3d}	D_{3d}	D_{3d}
ΔE_{int}	−114.8	−75.2	−69.7	−58.8	−48.2
ΔE_{Pauli}	201.6	101.2	114.4	98.3	84.0
ΔE_{elstat}[a]	−130.9 (41.4%)	−83.8 (47.5%)	−95.2 (51.7%)	−86.6 (55.1%)	−68.3 (51.7%)
ΔE_{orb}[a]	−185.5 (58.6%)	−92.6 (52.5%)	−88.9 (48.3%)	−70.5 (44.9%)	−63.9 (48.3%)
ΔE_{σ}[b]	−175.5 (94.6%)	−87.8 (94.8%)	−84.3 (94.8)	−67.5 (95.7%)	−61.2 (95.8%)
ΔE_{π}[b]	−10.0 (5.4%)	−4.8 (5.2%)	−4.6 (5.2%)	−3.0 (4.3%)	−2.7 (4.2%)
ΔE_{prep}	21.7	2.8	2.2	1.4	1.4
$-D_e$[c]	−93.1	−72.4	−67.5	−57.4	−46.8
$-D_0$[c]	−83.4 [−89.9]	−68.3 [−74.1]	−63.8 [−70.2][d]	−54.4	−43.6

[a] The percentage values in parentheses give the contribution to the total attractive interactions $\Delta E_{elstat} + \Delta E_{orb}$. [b] The percentage values in parentheses give the contribution to the orbital interactions ΔE_{orb}. [c] Experimental values are given in brackets.[12b] [d] Theoretical value taken from high-level ab initio calculations.[18]

by relativistic effects. The weaker bonds for heavier elements can be explained with the fact that the electrons in the ns and np valence orbitals are higher in energy when n becomes larger because they are farther away from the nucleus.

3.6 Chemical Bonding in XeF_6 and SF_6

The nature of the chemical bonding in noble gas compounds has been a challenge to chemical bonding theory since the first synthesis of a xenon compound by Neil Bartlett in 1962.[19] Textbooks of inorganic chemistry employ either resonance structures in terms of three-center four-electron bonds[20] or molecular orbital correlation diagrams, which are discussed in the following section for explaining the electronic structure in noble gas compounds. A particularly difficult case for qualitative models of the chemical bond is XeF_6.[21] The six unpaired electrons of the fluorine atoms yield six Xe–F σ bonds, which leaves two nonbonded electrons at xenon. If the latter electrons occupy the 6s orbital, it would become a stereochemically inactive electron pair and XeF_6 should have an octahedral geometry where only the 6p AOs of Xe are used for the bonds. Experimental studies have shown, however, that xenon hexafluoride has a fluxional structure based on a trigonally distorted octahedron.[22] High-level quantum chemical calculations suggest that the energy difference between the O_h form of XeF_6 and the distorted equilibrium geometry is very small (<2 kcal mol^{-1}).[21]

There are various ions valence-isoelectronic with XeF_6 like $ClF_6{}^{-}$, $BrF_6{}^{-}$, and $BiCl_6{}^{-}$, which have a regular octahedral structure, while others like $SeF_6{}^{2-}$ and $IF_6{}^{-}$ are trigonally distorted and still others like $SeCl_6{}^{2-}$, $SeBr_6{}^{2-}$, $TeCl_6{}^{2-}$, $TeBr_6{}^{2-}$, and $TeI_6{}^{2-}$ are either octahedral or distorted, depending on the counter ion. It becomes obvious that the equilibrium geometry of the above molecules is controlled by a very delicate balance of various competing effects. Simple explanations using qualitative models should be met with caution. The a posteriori rationalization of the distorted structures in terms of a stereochemically active electron pair as it is suggested by the VSEPR model has more a character of a tautology than a true explanation because the model does not say in the beginning if an electron lone pair is active or not.

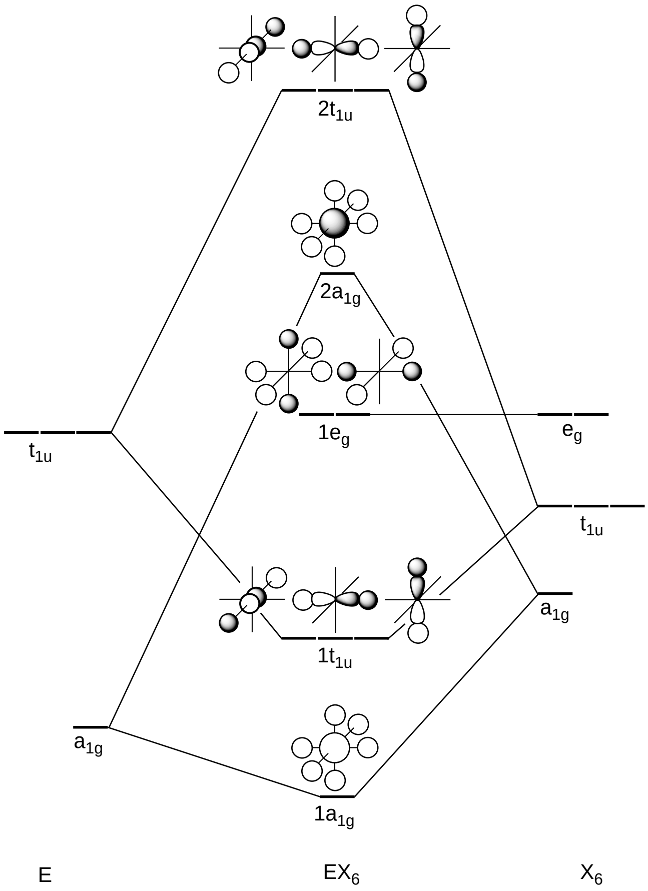

Figure 3 Orbital correlation diagram between a main-group atom E and six σ bonded ligands X in octahedral EX_6

Because the octahedral form of XeF_6 is only slightly higher in energy than the distorted equilibrium structure the O_h form may be used for the energy decomposition analysis. The results of the EDA calculations shall be used to compare the calculated orbital interactions with the qualitative MO model. Figure 3 shows a typical MO diagram for the σ orbital interactions in a molecule EX_6 in octahedral symmetry. π Orbitals between are not shown because in XeF_6 there are only Xe–F single bonds. The σ orbitals of the X_6 cage split in an octahedral field into three sets of a_{1g}, e_g, and t_{1u} symmetry. There are 14 electrons available for the σ bonding in XeF_6 (8 electrons from Xe and 1 electron from each F). Figure 3 shows that according to the aufbau principle, the 14 electrons occupy four sets of orbitals in the order $1a_{1g}$, $1t_{1u}$, e_g, and $2a_{1g}$ where the latter is the antibonding HOMO (Highest Occupied Molecular Orbital). The nonbonding e_g orbital is completely localized at the ligand atoms while the bonding contribution of the $1a_{1g}$ MO is compensated by the antibonding contribution of the $2a_{1g}$ MO. Thus, the MO correlation diagram suggests that the xenon−fluorine bonding in XeF_6 should mainly come from the t_{1u} (σ) orbital interactions. However, the MO correlation diagram is only a qualitative model. The strength of the orbital interactions can be quantitatively estimated through the EDA.

Table 9 shows that the latter prediction is supported by the EDA results as far as the contributions of the orbitals with different symmetry to the ΔE_{orb} term is concerned.**[50]** 90.4% of the latter come from the t_{1u} orbitals. The d orbitals of Xe do not play a role for the Xe–F bonds. The contributions of the e_g and t_{2g} orbital interactions are negligible. However, the EDA results show also that the attractive orbital interactions are compensated by the repulsive Pauli term. Xenon hexafluoride is stable because there is strong quasi-classical Coulomb attraction between Xe and F_6. The sum of the quantum theoretical expressions (ΔE_{orb} and ΔE_{Pauli}) is destabilizing.

The same valence orbital interaction diagram as for XeF_6 may also be used for a qualitative discussion of the sulfur−fluorine bonding in SF_6. The difference between the two molecules is that the antibonding HOMO of the former molecule is empty in SF_6. It may therefore be expected that the ΔE_{orb} term in SF_6 is more stabilizing than in XeF_6, and that the stabilizing contribution of the a_{1g} MOs should become larger in the former molecule than in the latter. Table 9 shows that this is indeed the case. The orbital interactions in SF_6 contribute 78.7% of the total attraction while in XeF_6 the ΔE_{Orb} term contributes only 69.3%. The strength of the a_{1g} orbital interactions in SF_6 is $-197.2\,\text{kcal mol}^{-1}$ while in XeF_6 it is only $-7.8\,\text{kcal mol}^{-1}$. The general picture of the bonding situation in SF_6 and XeF_6, which comes from the EDA results, is very similar though. The most important orbital interactions in both molecules come from the t_{1u} orbitals. The sum of ΔE_{Orb} and ΔE_{Pauli} in SF_6 is also repulsive. Without the significant stabilizing contribution of the classical Coloumb attraction ($-820.2\,\text{kcal mol}^{-1}$), sulfur hexafluoride would not be stable.

The distortion of some EX_6 molecules, which have 14 valence electrons from octahedral symmetry to C_{3v} or C_{2v},

Table 9 Energy decomposition analysis of SF_6 and XeF_6 using the fragments F_6 and E (E = S, Xe) at BP86/TZ2P. The energy values are given in kcal mol^{-1}

Term	S + F_6	Xe + F_6
ΔE_{int}	−674.1	−315.1
ΔE_{Pauli}	3192.9	1361.2
$\Delta E_{elstat}{}^a$	−847.6 (21.9%)	−516.5 (30.8%)
$\Delta E_{orb}{}^a$	−3019.4 (78.1%)	−1159.2 (69.2%)
$A_{1g}{}^b$	−207.2 (6.9%)	−7.2 (0.6%)
A_{1u}	0.0	0.0
A_{2g}	0.0	0.0
A_{2u}	0.0	0.0
$E_g{}^b$	−96.2 (3.2%)	−42.1 (3.6%)
E_u	0.0	0.0
$T_{1g}{}^b$	−6.7 (0.2%)	−6.1 (0.5%)
$T_{1u}{}^b$	−2624.3 (86.9%)	−1051.8 (90.7%)
$T_{2g}{}^b$	−69.5 (2.3%)	−35.6 (3.0%)
$T_{2u}{}^b$	−15.5 (0.5%)	−16.6 (1.4%)

[a] The value in parentheses gives the percentage contribution to the total attractive interactions. [b] The value in parentheses gives the percentage contribution to the total orbital interactions.

has been explained using MO models with the small energy gap between the $2a_{1g}$ HOMO and the $2t_{1u}$ LUMO (Figure 3), which makes the system prone to second-order Jahn–Teller distortion.[23] Like the VSEPR explanation in terms of stereochemically active lone pairs this is not a satisfactory explanation because there is no a priori information if a given HOMO–LUMO gap is small enough to yield a distortion from O_h symmetry. The MO model predicts correctly (as does the VSEPR model) that a 14-electron system like SF_6 has octahedral symmetry because the HOMO–LUMO gap between the $1e_g$ HOMO and the $2t_{1u}$ LUMO is much larger (Figure 3).

4 MOLECULAR ORBITAL MODELS

The last example XeF_6 in the section about the energy decomposition analysis introduced already the MO correlation model, which is a very powerful and widely used method for the explanation of the structure and reactivity of molecules. The MO models are based on the assumption that the geometry of a molecule and its reactivity are mainly determined by the molecular orbitals of appropriately chosen interacting fragments. In particular, the HOMO and LUMO (Lowest Unoccupied Molecular Orbital), which are called frontier orbitals, play an important and dominating role in the MO models. The frontier orbital theory has been developed by Fukui with the goal to explain the stereoselectivity of chemical reactions.[24] MO models can be used not only for explaining and predicting molecular properties in the electronic ground state, they are also useful for molecules in electronically excited states.

Walsh suggested already in 1953 that the energetic behavior of the HOMO on distortion determines the molecular geometry.[25] The generalizations concerning the shapes of molecules as a function of the number and arrangement of valence electrons are known as Walsh's rules. They are derived from MO diagrams (Walsh diagrams) where the orbitals in a reference geometry are correlated in energy with the orbitals in another geometry.[26] A related qualitative approach uses the orbitals of molecular fragments for the construction of the MOs of the whole molecule.[23] An example is shown in Figure 3 where the σ valence MOs of XeF_6 are built from the valence orbitals of Xe and F_6. The scope and limitations of the MO model shall be discussed in this section.

An important aspect of the MO model is the choice of the molecular orbitals that are used for discussing the properties of molecules. Early work considered either qualitative sketches of MOs or molecular orbitals, which came from EHT calculations. Later work used Hartree-Fock (HF) orbitals for the MO models. The latter have the disadvantage that the correlation energy is not considered although correlation effects can be very important for the structure and reactivity of molecules. The advent of DFT calculations introduced also the use of Kohn-Sham (KS) orbitals for MO models.[9] The advantage of KS orbitals is that correlation effects are intrinsically included in the orbital energy. In general, HF and KS orbitals have a similar shape and the energy ordering of the orbitals is in most cases the same, but the absolute values of the energy levels are quite different.

MO models may be used for molecules that have covalent bonds. Ionic bonds having little orbital overlap between the bonded atoms are less influenced by the stereochemical guidance of the valence orbitals. The geometry of ionic compounds is mainly determined by the electronic repulsion between the nonbonded atoms. A bonding model that considers the latter interaction as the dominant factor for determining molecular geometries is the VSEPR approach, which is discussed further below.

4.1 Walsh Diagrams for EH_2 and EX_2

Figure 4 shows the Walsh diagram for the energy changes of the valence orbitals on bending linear EH_2 (E = main-group element). The Walsh rules predict that molecules with 2 valence electrons such as LiH_2^+ have a bent geometry in the electronic ground state. Molecules with 3 and 4 valence electrons where the $1\sigma_u$ MO is singly or doubly occupied should be linear. Table 10 gives examples that support the Walsh rules. EH_2 molecules, which have 5 or 6 valence electrons, should be bent. The same holds true for systems with 7 or 8 electrons because the energy level of the $1b_1$ MO does not change when the molecule is bent, which means that the $2a_1$ MO determines the bond angle. Table 10 shows that the shapes of the EH_2 molecules are in agreement with predictions made by using the Walsh rules.

A strength of the Walsh diagrams is that predictions can also be made for geometries of molecules in electronically excited

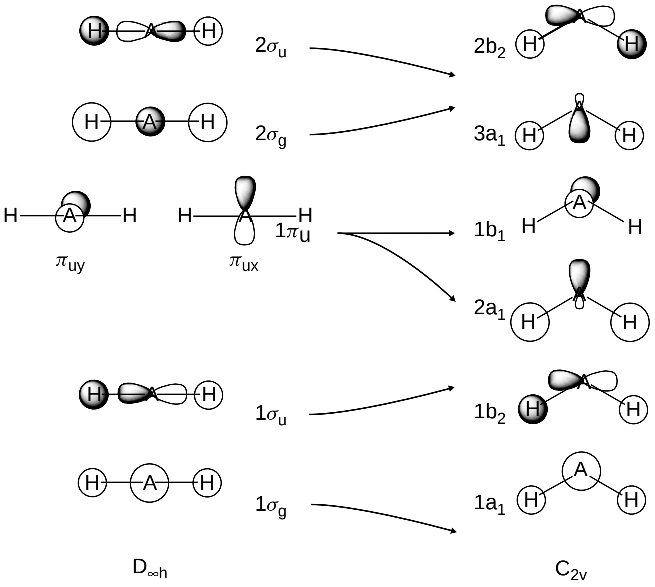

Figure 4 Qualitative MO correlation diagram for linear and bent AH_2 molecules. (Ref. 26. Reproduced by permission of Elsevier)

Table 10 The shape of AH_2 molecules predicted by Walsh rules[a]

AH_2	Number of valence electrons	Shape
LiH_2^+	2	bent
LiH_2, BeH_2^+	3	linear
BeH_2, BH_2^+	4	linear
BeH_2, AlH_2, CH_2^+	5	bent
CH_2, SiH_2, GeH_2, $BH_2NH_2^+$	6	bent
NH_2, PH_2, AsH_2, CH_2^-, OH_2^+, SH_2^+,	7	bent
H_2O, H_2S, H_2Se, H_2Te, NH_2^-, PH_2^-, H_2F^+	8	bent

[a] Reference 26.

states. An example is BH_2. The electronic configuration in the ground state is $(1a_1)^2(1b_2)^2(2a_1)^1$ yielding a bent geometry because the singly occupied $(2a_1)^1$ orbital becomes strongly stabilized upon bending (Figure 4). If the unpaired electron is excited to the stereochemically inactive $1b_1$ orbital, BH_2 in the $(1a_1)^2(1b_2)^2(1b_1)^1$ configuration becomes linear because the lower-lying $1b_2$ orbital becomes stabilized. Another example is the ground and first excited state of NH_2, which have the electron configurations $(1a_1)^2(1b_2)^2(2a_1)^2(1b_1)^1$ and $(1a_1)^2(1b_2)^2(2a_1)^1(1b_1)^2$. With only one electron in the $2a_1$ orbital, the molecule is less bent than in the ground state. The behavior of the energy levels of the MOs shown in Figure 4 upon bending makes it possible to predict qualitatively the geometry of EH_2 in any electronically excited state.

The Walsh diagram for the valence orbitals of EX_2 where E and X are main-group elements becomes a bit more complicated than for EH_2 (Figure 5). The predictions about the geometry of EX_2, which are made by looking at the energy change of the HOMO upon bending, are still in remarkably good agreement with experimental observations, but there are some exceptions (Table 11). The equilibrium geometries of the 12 electron compounds SiC_2 and CSi_2 and the 21 electron molecule ClF_2 are bent but the Walsh diagrams predict a linear structure.**[27]** It becomes obvious that the stereochemical influence of the orbitals that are energetically lower lying than the HOMO may not always be neglected. It is important to recognize that the molecular properties are determined by the interactions of all electrons and nuclei of the compound.

An interesting class of compounds EX_2 that shows the limitations of the MO model but also the pitfalls of the VSEPR approach described below are the alkaline earth dihalides where $E = Be - Ba$ and $X = F–I$. The Walsh rules predict that the 16 electron systems should have a linear geometry (Figure 5). The E–X bonds are highly polar because of the large differences between the electronegativities of E and X and thus, an ionic description of the bonding situation (X^-)-(A^{2+})-(X^-) might be more appropriate. The geometry may therefore be determined by the repulsion between the X^- anions, which, however, would also lead to the prediction that the alkaline earth dihalides should be linear. But high-level ab initio calculations show that some EX_2 molecules have a bent equilibrium geometry! Table 12 shows that bending occurs for the heavier earth alkaline species SrF_2, BaF_2, $BaCl_2$, and $BaBr_2$. The molecules CaX_2, SrX_2 ($X = Cl–I$) and BaI_2 are called quasilinear because the computed energy changes for angle deviation of 20° is $<1\,kcal\,mol^{-1}$.**[28]**

The electronic structures of a series of monomeric alkaline earth EX_2 compounds have been analyzed in order to explain the bent equilibrium geometry of some species. Several factors that have an influence on the bending angle could be identified. One factor is the core polarization of the positively charged metal cation by the negatively charged X^- atoms (Figure 6(a)), which allows stabilizing charge-dipole and dipole–dipole interactions in bent structures. Another factor that favors a

Table 11 The shape of AB_2 molecules predicted by Walsh rules[a]

AB_2	Number of Valence electrons	Shape
B_2C	10	linear
BC_2, BSi_2	11	linear
C_3, SiC_2[b], Si_2C[b]	12	linear
NC_2	13	linear
CN_2, C_2O	14	linear
BO_2, BS_2, CO_2^+, CS_2^+, N_3, N_2O	15	linear
CO_2, CS_2, CSe_2, BF_2^+, BO_2^-, CN_2^{2-}, N_3^-, NO_2^+, N_2O, N_2F^+	16	linear
BF_2, CO_2^-, NO_2, N_3^{2-}, SO_2^+	17	bent
CF_2, CBr_2, NO_2^-, O_3, SO_2, S_2O, S_3, SeO_2, SiF_2, GeF_2, ClO_2^+	18	bent
NF_2, NCl_2, PF_2, PCl_2, O_3^-, S_3^-, Se_3^-, SO_2^-, NO_2^{2-}, PO_2^{2-}, PS_2^{2-}, AsS_2^{2-}, FO_2, ClO_2	19	bent
OF_2, OCl_2, OBr_2, SF_2, SCl_2, Cl_3^+, Br_3^+, I_3^+, ClF_2^+, $ClBr_2^+$, BrF_2^+, Cl_2F^+, $BrCl_2^+$, ICl_2^+, Ibr_2^+, ClO_2^-, BrO_2^-, S_3^{2-}	20	bent
ClF_2, Cl_3, Br_3	21	linear
F_3^-, Cl_3^-, Br_3^-, I_3^-, ClF_2^-, $ClBr_2^-$, BrF_2^-, $BrCl_2^-$, BrI_2^-, ICl_2^-, IBr_2^-, KrF_2, XeF_2, $XeCl_2$	22	linear

[a] Reference 26. [b] Molecule is not linear.

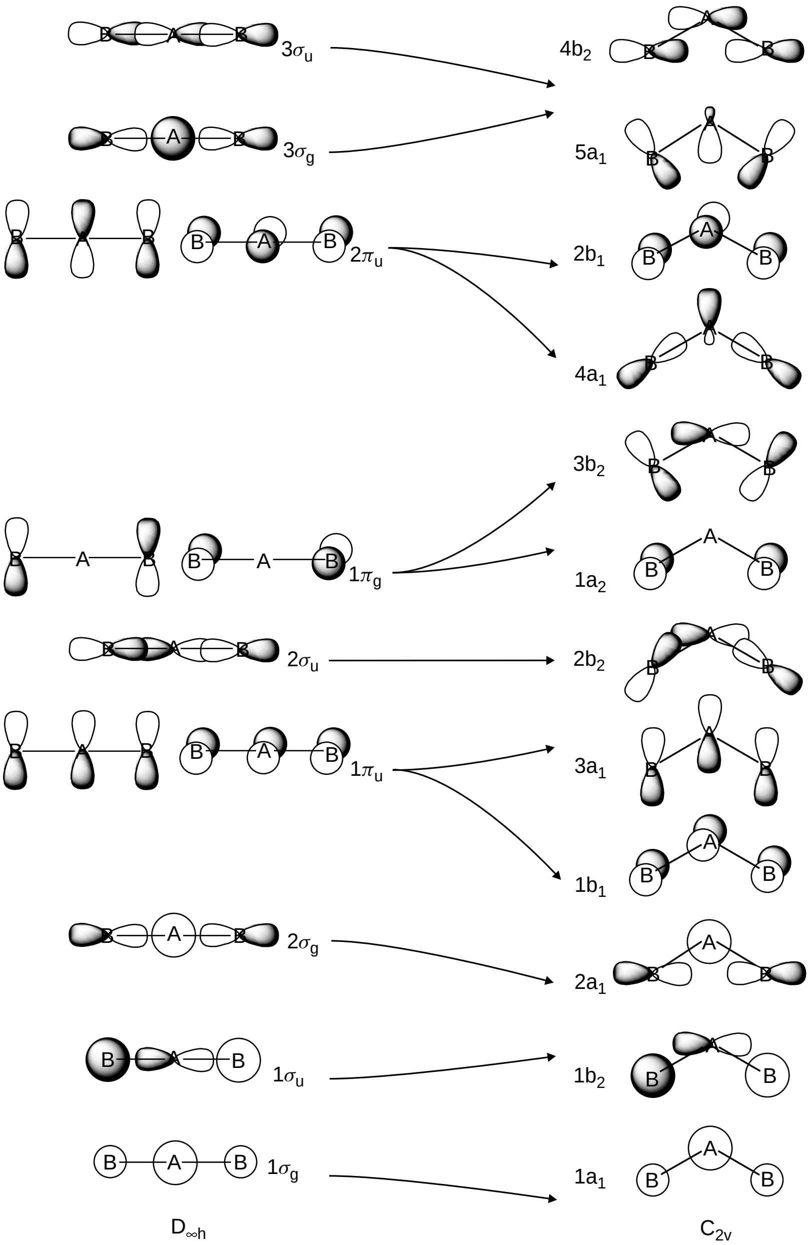

Figure 5 Qualitative MO correlation diagram for linear and bent AB_2 molecules. (Ref. 26. Reproduced by permission of Elsevier)

bent geometry is the participation of the outermost $(n-1)$d orbitals in the HOMO of the EX_2 molecules (Figure 6(b)). Note that this d orbital participation is different from the spd-hybridization model for hypervalent compounds. The d orbital participation shown in Figure 6(b) is small but relevant for the bending of EX_2. Theoretical studies showed that both core polarization and d orbital participation act simultaneously to favor bent structures in these systems. However, the two factors cannot be strictly separated from each other.[28]

A third factor that has a significant influence on the geometry of EX_2 molecule is the π interaction between the lone-pair orbitals of X and the empty orbitals of E. The NBO analysis showed that the empty nd(π) AOs of the heavy atoms Sr and Ba are important for the degenerate π bonding in linear EX_2 (Figure 6(c)).[26] Upon bending, the degenerate π bonding splits into in-plane and out-of-plane components of the E–X_2 interactions, which are further enhanced by π interactions using the nd AOs of E, which are not possible in the linear structure because of its higher symmetry. The bottom line of the analysis of the nontrivial orbital interactions in bent EX_2 is that, π bonding favors a linear structure but the π interactions are important for the actual geometry. This becomes obvious when the optimized geometries of $Ba(NH_2)_2$ with planar and perpendicular amino groups are compared with

Table 12 Calculated equilibrium structures of alkaline earth dihalides EX_2[28b][a]

E	F	Cl	Br	I
Be	linear	linear	linear	linear
Mg	linear	linear	linear	linear
Ca	quasilinear	quasilinear	quasilinear	quasilinear
Sr	bent ($\Delta E_{lin} = 1.6$)	quasilinear	quasilinear	quasilinear
Ba	bent ($\Delta E_{lin} = 5.0$)	bent ($\Delta E_{lin} = 1.6$)	bent ($\Delta E_{lin} = 1.1$)	quasilinear

[a] The numbers in parentheses gives the energy differences [kcal mol^{-1}] between the linear and the bent equilibrium structures.

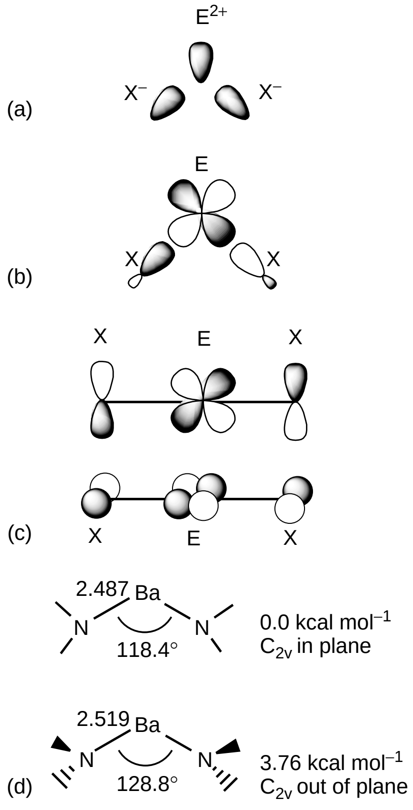

Figure 6 Factors that influence the bending of earth alkaline compounds EX_2. (a) Core polarization of the positively charged metal cation by the negatively charged X^- atoms. (b) Participation of the outermost ($n-1$)d orbitals of E in σ bonding. (c) Degenerate π bond in linear EX_2, which become the in-plane π_{ip} (b_2) and out-of-plane π_{op} (a_2) components in bent (C_{2v}) EX_2. (d) Calculated structures of the planar and perpendicular forms of $Ba(NH_2)_2$. (Ref. 28c. Reproduced by permission of Wiley-VCH)

each other (Figure 6(d)). The strongly bent planar structure **1** is the global energy minimum. It is 3.8 kcal mol^{-1} lower in energy than structure **2**, which has longer Ba–N bonds and a less acute bending angle than **1**. The difference can be explained with the influence of the out-of-plane π (a_2) and in-plane π (b_2) interaction on the electronic structure of $Ba(NH_2)_2$. The b_2 component is more angle dependent than the a_2 component because the π overlap of the former decreases more when the bending angle becomes more acute. A fourth factor that needs to be considered at small bending angles of EX_2 molecules is the Pauli repulsion between the atoms or groups X.

4.2 MO models for E_2H_4 and E_2X_4

Ethylene and acetylene are model compounds for the description of double and triple bonds in terms of σ and π bonding. The MO correlation diagram for the carbon–carbon bonding in C_2H_4 uses the CH_2 fragments in the $^3B_1$ triplet ground state for the construction of the molecular orbitals (Figure 7, E = C). The HOMO of ethylene is the well-known out-of-plane π orbital, which explains why the molecule has a D_{2h} equilibrium geometry. Rotation about the C–C axis would break the π bond, which, according to the EDA results (Table 7), contributes 79.2 kcal mol^{-1} of the total orbital

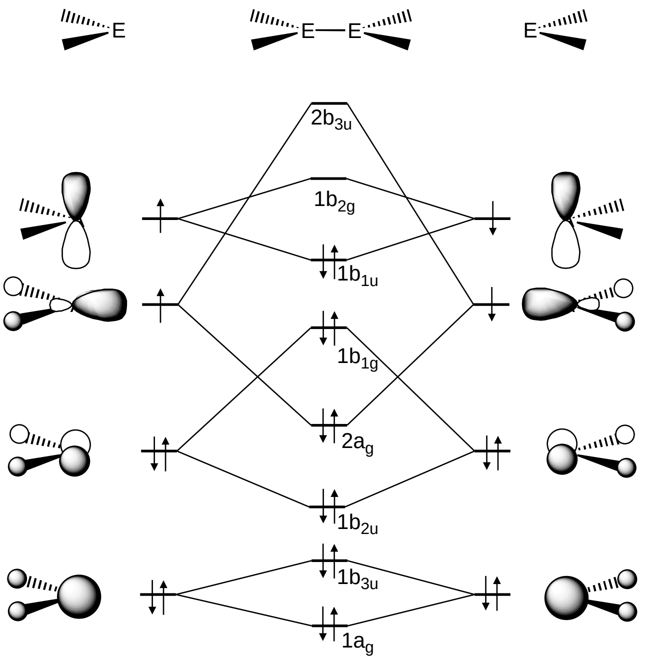

Figure 7 Qualitative MO correlation diagram for the orbital interactions between two EH_2 molecules with 6 valence electrons in the $^3B_1$ state yielding closed-shell E_2H_4

interactions. The latter value must not be confused with the rotational barrier of ethylene. The value of 79.2 kcal mol^{-1} for the out-of-plane π orbital interactions is calculated in the framework of the electronic structure of ethylene in D_{2h} symmetry. Rotating ethylene about the C–C bond changes the electronic structure significantly.

If the out-of-plane π orbital in E_2H_4 is empty like in B_2H_4 and in $C_2H_4^{2+}$, the molecule adopts a D_{2d} equilibrium geometry where the EH_2 fragments are rotated by 90°. Figure 8 shows the Walsh diagram for the $D_{2h} \rightarrow D_{2d}$ interconversion of E_2H_4. The rotation affects mainly the in-plane and out-of-plane π orbitals while the σ orbitals change little. It becomes obvious that molecules with 12 valence electrons should prefer a planar (D_{2h}) structure while species with 10 valence electrons should prefer a perpendicular (D_{2d}) geometry because of the energetically high-lying 2e HOMO (Figure 8). This is in agreement with quantum chemical calculations, which show that the D_{2d} structure of B_2H_4 is 17.7 kcal mol^{-1} lower in energy than the D_{2h} form.**[29]** The perpendicular structure of $C_2H_4^{2+}$ is even 31.0 kcal mol^{-1} more stable than the planar form.**[30]**

The MO models are also very helpful for explaining the effect of substituting hydrogen by halogen atoms yielding C_2X_4 species. Dihalocarbenes have a $^1A_1$ singlet ground state. It is not possible to build E_2X_4 with a planar geometry in the electronic ground state using EX_2 fragments in the ($^1A_1$) singlet state where the HOMO is the $2a_1$ lone-pair MO (Figure 7). The latter species must be excited to the $^3B_1$ state, which is the first excited state of CX_2. The excitation energy for the process ($^1A_1$) $\rightarrow$ ($^3B_1$) of the two CX_2 species (Table 13) is the price that has to be paid for the formation of the $X_2C{=}CX_2$ double bond. This explains why the bond dissociation energies of C_2X_4 are significantly smaller than the BDE of C_2H_4 (Table 14). The very low BDE of C_2F_4 (74.1 kcal mol^{-1}), which is less than one half of the value of C_2H_4 (178.9 kcal mol^{-1}) is caused by the big excitation energy of CF_2 (52.4 kcal mol$^{-1)}$.**[31]**

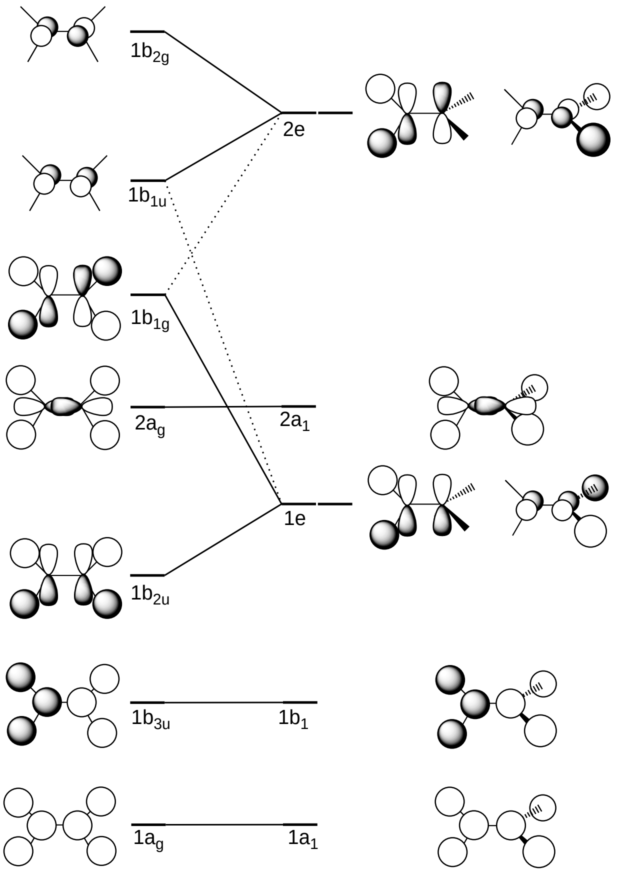

Figure 8 Qualitative MO correlation diagram for planar and staggered E_2H_4

The orbital interaction diagram shown in Figure 7 for C_2H_4 may not be used for the heavier analogs E_2H_4 (E = Si–Pb) because the latter species adopt a trans-bent (C_{2h}) geometry.**[32]** The bending angle increases from E = Si (20.4°) to E = Pb (37.6°) (Table 15). Trans-bent structures with rather larger bending angles are also calculated as equilibrium geometries for the halogen substituted heavier homologs E_2X_4. The preference for a trans-bent geometry rather than a planar form can be straightforwardly explained with the MO model given above. The heavier diylenes EX_2 (X = H, F–I) have singlet ground states. Table 13 shows that the ($^1A_1$) $\rightarrow$ ($^3B_1$) excitation energies are quite large, particularly for the dihalogen species where the calculated values are between 39.1 and 91.5 kcal mol^{-1}. This means that it may not be energetically favorable for two EX_2 molecules to bind through the excited $^3B_1$ state yielding a σ and a π bond in planar E_2X_4 but rather engage in two donor–acceptor type bonds between EX_2 in the $^1A_1$ state. This is shown in Figure 9. Table 14 shows that the planar tetrahalogen substituted molecules E_2X_4 with E = Si, Ge, and Sn are energetically higher lying than, or in case of Si_2I_4, are nearly degenerate with two EX_2 species. Calculation of the vibrational frequencies shows that the planar species are no minima on the PES. If the symmetry is relaxed toward C_{2h}, the molecules adopt trans-bent structures, which are slightly lower in energy than the sum of the EX_2 fragments. In the case of Sn_2X_4 (X = F, Cl, Br), the molecule rearranges towards a halogen-bridged geometry. Neither a planar nor a trans-bent structure of the tetrahalogen lead molecules Pb_2X_4 could be

Table 13 Calculated excitation energies at B3LYP/6−311G(2d,p) for the process ($^1A_1$) $\rightarrow$ ($^3B_1$) of EX_2 (E = C–Pb, X = H, F–I). Values in kcal mol^{-1}

E	H	F	Cl	Br	I
C	−12.6^a	52.4	17.0	13.6	7.2
Si	20.0	75.0	52.7	47.4	39.1
Ge	26.5	84.0	63.7	56.8	47.8
Sn	30.1	82.6	66.4	59.8	50.7
Pb	38.2	91.5	74.4	66.5	56.3

^{a}CH_2 has a $^3B_1$ ground state.

Table 14 Calculated bond dissociation energies D_e (kcal mol^{-1}) at B3LYP/6−311G(2d,p)[a] of planar (D_{2h}) and trans-bent (C_{2h}) molecules $E_2X_4 \rightarrow 2EX_2$[b] (E = C–Pb, X = H, F–I). The planar forms of the heavier compounds with E = Si–Pb, there are no minima on the potential energy surface

E	Symmetry	H	F	Cl	Br	I
C	D_{2h}	178.9	74.1	114.1	112.7	116.6
Si	D_{2h}	60.0	−36.9	−11.3	−7.5	1.0
	C_{2h}	60.8	5.1	9.6	11.3	15.4
Ge	D_{2h}	39.7	−76.5	−50.6	−43.3	−31.4
	C_{2h}	44.1	0.1	0.7	2.1	4.9
Sn	D_{2h}	13.2	−98.8	−75.4	−66.9	−54.2
	C_{2h}	25.5	–[c]	–[c]	–[c]	0.3
Pb	D_{2h}	−18.6	–[d]	–[d]	–[d]	–[d]
	C_{2h}	12.0	–[c]	–[c]	–[c]	–[c]

[a] Relativistic effective small-core core potentials with triple-zeta valence orbitals augmented by two sets of polarization functions were used for Sn and Pb. [b] Calculated with respect to the ($^1A_1$) singlet ground state of EX_2 except for CH_2, which has a ($^3B_1$) triplet ground state. [c] The trans-bent form (C_{2v}) is not a minimum on the PES (Potential Energy Surface). The structure rearranges during geometry optimization toward a halogen-bridged geometry. [d] The planar structure dissociates during geometry optimization into 2 EX_2 fragments.

located as stationary point on the PES. Halogens prevent the formation of planar E_2X_4 (E = Si–Pb) molecules because they yield very large ($^1A_1$) → ($^3B_1$) excitation energies in EX_2 and they weaken the donor–acceptor bonds between two EX_2 species in the singlet ground state because the electronegative halogens render the diyls to become poor donors. Halogen-bridged structures are the global minima on the PES of all tetrahalogen compounds E_2X_4.

The MO model given in Figure 9 explains nicely why the bending angle of E_2X_4 becomes in most cases larger for heavier atoms E. There is a correlation between the ($^1A_1$) → ($^3B_1$) excitation energy and the calculated bending angle. Note that, according to the MO model, there are two E–E bonds in the trans-bent structures. Unlike the classical σ/π bonds such as in ethylene, the two bonds in the former species are donor–acceptor bonds.

Table 15 Calculated bending Angle τ (degree) of the equilibrium structures E_2X_4 (E = C–Pb, X = H, F–I) at B3LYP/6−311G(2d,p)[a]

E	H	F	Cl	Br	I
C	0.0	0.0	0.0	0.0	0.0
Si	20.4	41.5	39.2	38.8	39.2
Ge	27.7	42.8	42.0	31.7	40.9
Sn	34.7	–[b]	–[b]	–[b]	42.2
Pb	37.6	–[b]	–[b]	–[b]	–[b]

[a] Relativistic effective small-core core potentials with triple-zeta valence orbitals augmented by two sets of polarization functions were used for Sn and Pb. [b] The trans-bent form rearranges during geometry optimization toward a halogen-bridged geometry.

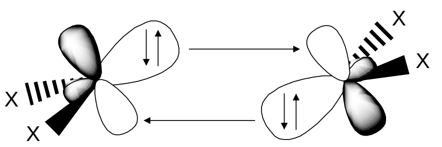

Figure 9 Qualitative orbital model showing the donor–acceptor interactions between two singlet ($^1A_2$) EX_2 fragments in trans-bent E_2X_4

The MO model also explains the effect of halogen atoms on the structure of $C_2X_4{}^{2+}$ and B_2X_4. The halogen atoms have p(π) lone-pair orbitals, which can donate electronic charge into the empty p(π) AO of C^+ and B (Figure 10), which means that the out-of-plane p(π) orbital of the planar form becomes partially occupied. The partial occupation in $C_2F_4{}^{2+}$ is large enough that the D_{2h} form becomes now 3 kcal mol^{-1} lower in energy than the D_{2d} form.**30** The energetic effect of fluorine in B_2F_4 is less dramatic but still significant. The D_{2d} form of B_2F_4 is still lower in energy than the D_{2h} form but the latter is only <1 kcal mol^{-1} less stable than the former.

The strength of the π bonding interactions in planar and perpendicular B_2X_4 can be estimated using the EDA method.

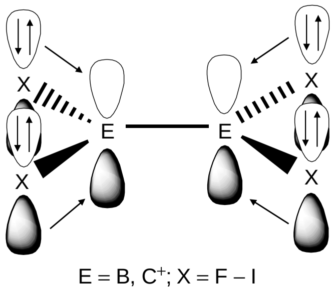

Figure 10 Qualitative orbital model for E_2X_4 (E = B, C^+; X = F–I) showing the π donation from the lone-pair p(π) orbitals of X into the empty p(π) orbitals of E

Table 16 Energy decomposition analysis of the B–B bond of the planar (D_{2h}) and perpendicular (D_{2d}) structures of B_2X_4 at BP86/TZ2P. Energy values in kcal mol^{-1}

Symm.	Term	X = H	X = F	X = Cl	X = Br	X = I
D_{2h}	ΔE_{int}	−96.8	−102.3	−96.7	−96.0	−94.4
	ΔE_{Pauli}	125.0	119.6	159.8	168.4	192.4
	$\Delta E_{elstat}{}^{a}$	−110.7 (49.9%)	−114.2 (51.5%)	−131.9 (51.4%)	−127.7 (48.3%)	−141.9 (49.5%)
	$\Delta E_{orb}{}^{a}$	−111.1 (50.1%)	−107.7 (48.5%)	−124.6 (48.6%)	−136.7 (51.7%)	−144.9 (50.5%)
	A_1	−108.3	−103.6	−117.2	−126.8	−131.6
	A_2	0.0	−0.1	−0.2	−0.2	−0.2
	B_1 ($\pi_\perp$)	0.0	−1.9	−4.2	−5.5	−8.0
	B_2 ($\pi_{\|\|}$)	−2.8	−2.1	−3.0	−4.2	−5.1
	$\Delta E_{\sigma}{}^{b}$	−108.3 (97.5%)	−103.7 (96.3%)	−117.4 (94.2%)	−127.0 (92.9%)	−131.8 (91.0%)
	$\Delta E_{\pi}{}^{b}$	−2.8 (2.5%)	−4.0 (3.7%)	−7.2 (5.8%)	−9.7 (7.1%)	−13.1 (9.0%)
D_{2d}	ΔE_{int}	−114.5	−102.6	−98.5	−98.7	−98.4
	ΔE_{Pauli}	161.7	123.8	175.8	187.2	223.6
	$\Delta E_{elstat}{}^{a}$	−140.5 (50.9%)	−116.5 (51.5%)	−141.6 (51.6%)	−139.5 (48.7%)	−162.6 (50.5%)
	$\Delta E_{orb}{}^{a}$	−135.7 (49.1%)	−109.9 (48.5%)	−132.7 (48.4%)	−146.6 (51.3%)	−159.4 (49.5%)
	A_1	−119.7	−105.1	−123.1	−133.9	−141.2
	A_2	0.0	−0.2	−0.2	−0.3	−0.2
	B_1	−8.0	−2.3	−4.7	−6.2	−9.0
	B_2	−8.0	−2.3	−4.7	−6.2	−9.0
	$\Delta E_{\sigma}{}^{b}$	−119.7 (88.2%)	−105.3 (95.8%)	−123.3 (92.9%)	−134.2 (91.5%)	−141.4 (88.7%)
	$\Delta E_{\pi}{}^{b}$	−16.0 (11.8%)	−4.6 (4.2%)	−9.4 (7.1%)	−12.4 (8.5%)	−18.0 (11.3%)
	$E_{rel}{}^{c}$	−17.7	−0.3	−1.8	−2.7	−4.0

[a]The value in parentheses gives the percentage contribution to the total attractive interactions. [b]The value in parentheses gives the percentage contribution to the total orbital interactions. [c]Energy difference between the planar and perpendicular form.

Table 16 gives the calculated data, which may be compared with the orbital correlation diagram shown in Figure 8. Note that the orbital contributions can only be given for MOs having different symmetry within C_{2v} constraint because the interacting BX_2 fragments have C_{2v} symmetry. The calculated data indicate that the strength of the out-of-plane π interactions increases from X = F (1.9 kcal mol^{-1}) to X = I (8.0 kcal mol^{-1}), that is, the π-donor strength increases with F < Cl < Br < I. The strength of the total π interactions in planar B_2X_4 increases in the order H < F < Cl < Br < I. The order changes in the perpendicular structures where the π bond strength (which is also called hyperconjugation) in the parent compound B_2H_4 becomes rather large (16.0 kcal mol^{-1}). Only B_2I_4 has a stronger hyperconjugation (18.0 kcal mol^{-1}). Note that the rotational barrier cannot be used to estimate the strength of hyperconjugation in B_2X_4 because the planar form of the halodiborenes(4) are significantly stabilized by π interactions.

4.3 MO Model for E_2H_2 (E = C–Pb)

Heavy-atom homologs of acetylene show very peculiar structures, which are at first sight difficult to explain with orthodox bonding models (Figure 11). The linear structure E, which is the global energy minimum on the C_2H_2 potential energy surface, is not even an energy minimum but a second-order saddle point for the heavier species E_2H_2 (E = Si–Pb). The most stable form of the latter species is the doubly-bridged butterfly structure **A**. The energetically next low-lying isomer

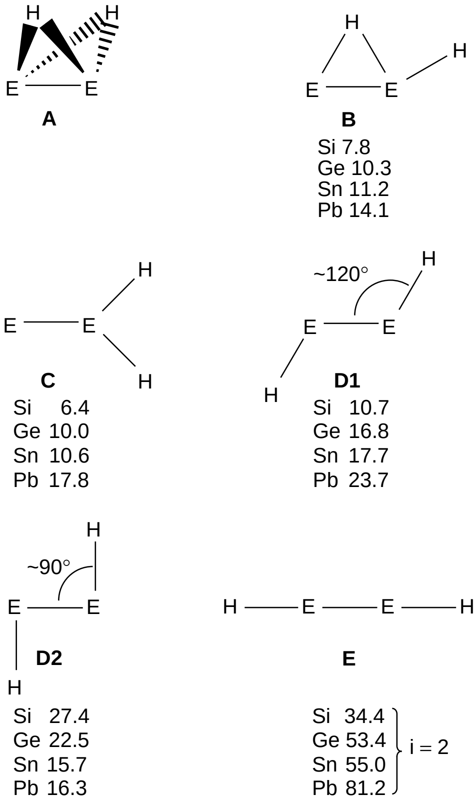

Figure 11 Stationary points and relative energies [kcal mol^{-1}] of E_2H_2 (E = Si, Ge, Sn, Pb) isomers calculated at CCSD(T)/TZ2P//B3LYP/6−31G(d)

is the singly bridged planar structure **B**. Both structures **A** and **B** are not known for C_2H_2. Isomer **C** is energetically nearly degenerate with structure **B** (Figure 11). The former structure resembles vinylidene CCH_2, which is a shallow minimum on the C_2H_2 potential energy surface being ~55 kcal mol^{-1} higher in energy than acetylene.

There are two trans-bent forms of E_2H_2 **D1** and **D2**, which are the only species for which substituted analogs E_2R_2 could be characterized by X-ray structure analysis. The difference between the electronic structures of the two trans-bent forms is that **D1** has an occupied π orbital, which is the out-of-plane component of the degenerate π orbital of planar HE≡EH. The out-of-plane p(π) AOs of E in **D2** are empty while each atom E has an occupied in-plane lone-pair orbital. The latter electronic structure corresponds to an excited state of linear HEEH where one component of the degenerate π orbital is empty, while for the other component both π and π^* orbitals are occupied, that is, the molecule has only a E–E single bond. E_2R_2 compounds with very bulky substituents having structure **D1** have been characterized with X-ray structure analysis for E = Ge, Sn while the isolated compound Pb_2R_2 has the structure **D2**.[33] The parent compounds E_2H_2 have been synthesized in low-temperature matrices. The comparison of the experimental vibrational spectra with high-level quantum chemical calculations shows clearly that structure **A** is the most stable form followed by **B**, which is in agreement with predictions that had previously been made using quantum chemical calculations.[34]

The puzzling results of theoretical and experimental research about the unusual structures of E_2H_2 can be explained using the MO model, which was introduced in the previous section.[49] The starting point of the MO approach is the electronic configuration of the interacting species EH, which are considered as the building block for the E_2H_2 isomers **A**, **B**, **D**, and **E**, while **C** would better be discussed in terms of interactions between E and EH_2. Figure 12 shows qualitatively the electronic structure of EH in the $^2\Pi$ ground state and in the $^4\Sigma^-$ first excited state.

It becomes obvious that the $^2\Pi$ ground state of EH is not the electronic reference state for the acetylene-type structure **E**, which has a triple bond HE≡EH. The latter form can only be built from the interactions between two EH molecules in the $^4\Sigma^-$ first excited state. Figure 12 shows also the experimental and calculated $(^2\Pi) \rightarrow (^4\Sigma^-)$ excitation energies. The excitation energies of the heavier diatomics are significantly larger than for CH. Table 17 compares the calculated bond dissociation energies of the linear species HE≡EH (**E**) with the energies that are necessary to promote two fragments EH from $^2\Pi$ to $^4\Sigma^-$. The calculated data show that the promotion energy for two CH molecules (40.8 kcal mol^{-1}) is much smaller than the BDE of HC≡CH ($D_e = 271.3$ kcal mol^{-1}).

The situation for the heavier homologs EH is quite different from the carbon system. The excitation energy of two SiH molecules (85.6 kcal mol^{-1}) is not much less than the BDE of the hypothetical HSi≡SiH species (121.0 kcal mol^{-1}). The difference is only 35.4 kcal mol^{-1}. If the binding interactions between two SiH fragments in the $^2\Pi$ ground state exceed this value it is energetically not favorable that the binding occurs through the $^4\Sigma^-$ excited state. The $^2\Pi$ ground state has one singly occupied orbital (Figure 12). Coupling the unpaired electrons yields a Si–Si single bond, which is typically stronger than 35.4 kcal mol^{-1}. Thus, two SiH molecules will prefer to bind through its $^2\Pi$ ground state, which does not yield an acetylene-type structure **E**. The situation is even more simple for the heavier species where E = Ge − Pb. Table 17 shows that the BDE of the linear form **E** is less than the $(^2\Pi) \rightarrow (^4\Sigma^-)$ excitation energy of the EH fragments. This means that two separated fragments EH are lower in energy than HE≡EH. The conclusion is that it is energetically favorable for the heavy-atom homologs E_2H_2 with E = Si–Pb to bind through interactions between EH in the $^2\Pi$ ground state.

The structures **A**, **B**, **D1**, and **D2** can be easily constructed using the electronic configuration of the $^2\Pi$ ground state in conjunction with simple MO models. Figure 13 shows three possible arrangements of two EH fragments where the unpaired electrons yield a E–E σ bond. Figure 13(a) shows the least favorable combination because the E–H bonds and the lone-pair electrons are in an eclipsing conformation. Rotation

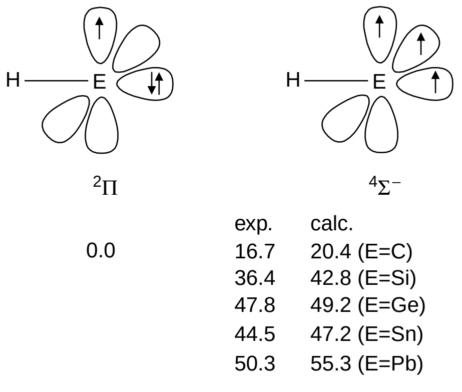

Figure 12 Experimental and calculated energy differences between the $^2\Pi$ ground state and the $^4\Sigma^-$ first excited state of EH (E = C–Pb)

Table 17 Calculated bond dissociation energies D_e of linear HE≡EH → 2 EH $(^4\Sigma^-)$ and excitation energies ΔE_{exc} $(^2\Pi) \rightarrow (^4\Sigma^-)$ of EH at B3LYP/6−311G(2d,p).[a] All values in kcal mol^{-1}

E	D_e	ΔE_{exc}	$D_e - 2 \times \Delta E_{exc}$
C	271.3	20.4	230.5
Si	121.0	42.8	35.4
Ge	97.1	49.2	−1.3
Sn	78.9	47.2	−17.5
Pb	69.2	55.3	−41.4

[a] Relativistic effective small-core core potentials with triple-zeta valence orbitals augmented by two sets of polarization functions were used for Sn and Pb.

about the E–E bond by 90° (Figure 13(b)) leads to a much more favorable conformation because the E–H bonds are facing the empty p(π) AO of the other EH fragments yielding two donor–acceptor bonds (hyperconjugation) in addition to the σ bond. The E–H bonds tilt toward the empty orbitals of the other fragment and vice versa, which leads to the doubly-bridged butterfly structure **A**. The MO model explains nicely why the bridging hydrogens are not trans to each other. Figure 13(c) shows that a conformation where the E–H bonds are in a trans position does not allow any other attractive interactions between the EH fragments. However, such a conformation may become favorable when hydrogen is substituted by a very bulky group R. Figure 13(c) shows that the electronic configuration that comes from the shown interactions gives structure **D2**, which was reported for the molecule RPbPbR where R is a substituted mesityl group.[33a] Note that atom E in **D1** has only an electron sextet in the valence shell.

The unpaired electron in the $^2\Pi$ ground state of EH may also be used to form a π bond between two EH molecules. Figure 14 shows that again three different conformations may be envisaged. The conformation shown in Figure 14(a) leads directly to the singly bridged structure **B**. Besides the π bond there is a donor–acceptor bond between the lone-electron pair of one fragment and the empty orbital of the other. A third bonding component comes from donor–acceptor interaction (hyperconjugation) between a E–H bond from the fragment that serves as acceptor for the lone-electron pair and the empty orbital of the other EH fragment. The donor and acceptor orbitals of the latter interactions are tilted to each other in order to maximize the attractive interactions. The tilting of the empty orbital leads to a bending of the terminal E–H bond towards the bridging E–H bond. Thus, the MO model shown in Figure 14(a) explains nicely why the bridging and the terminal hydrogen atoms of **B** are on the same side of the E–E axis and why the molecule is planar. Note that the MO model suggests that there are three binding components in **B**: One π bond, one lone-pair donor–acceptor bond, and one E–H donor–acceptor bond (hyperconjugation).

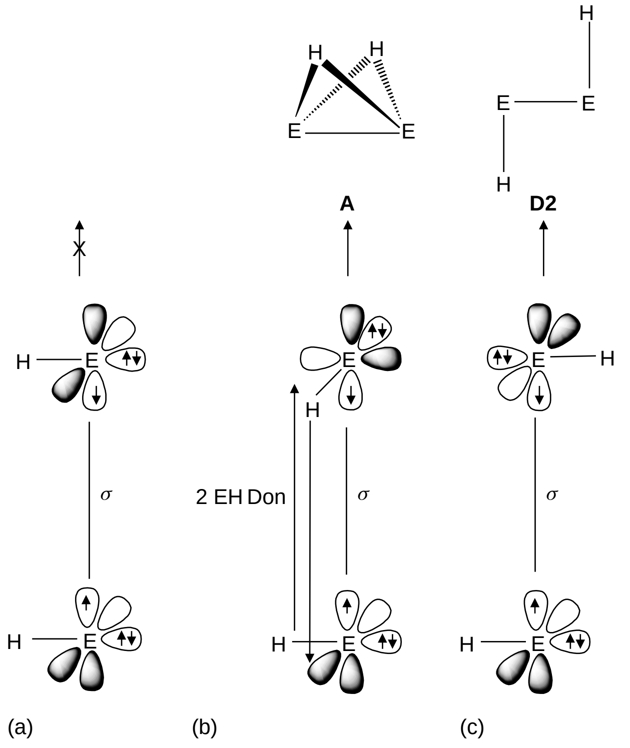

Figure 13 Qualitative orbital model for the bonding between two EH fragments (E = C–Pb) in the $^2\Pi$ ground state via σ coupling of the unpaired electrons showing three different conformations, which lead to different isomeric forms of E_2H_2. (a) Syn-conformation of the E–H bonds which does not yield an energy minimum structure. (b) Perpendicular orientation of the E–H bonds yielding structure **A** with two additional E–H donor–acceptor bonds. (c) Anticonformation of the E–H bonds yielding structure **D2**

The conformation shown in Figure 14(b) is unfavorable because there are no further binding interactions besides the π bond. The bonding interactions are enhanced by two donor–acceptor bonds between the lone-pair electrons and the empty orbitals of EH in addition to the π bond by tilting of the E–H bonds. The lone-pair orbitals are tilted towards the empty acceptor orbitals of the other EH fragment. The E–H bonds follow the tilting in the other directions towards a planar antiarrangement. This leads straightforwardly to structure **D1**. Note that the latter structure has also three bonding components: One π bond and two donor–acceptor bonds. The question if the trans-bent structure **D1** has a triple bond or not can be answered by referring to three bonding components that, however, are not the same and not as strong as one σ bond and a degenerate π bond.

5 THE VALENCE SHELL ELECTRON-PAIR REPULSION MODEL AND THE LIGAND CLOSE-PACKING MODEL

The VSEPR model for predicting the geometries of molecules is a simple and popular approach that has been developed by Sidgwick, Powell, Nyholm, and Gillespie.[3] The starting point of the VSEPR model is the assumption that the electron pairs in the valence shell of an atom E in a molecule EX_n adopt arrangements that keep them as far apart as possible. This approach is very different from the valence bond model, which suggests that the geometry of a covalently bonded molecule is determined by the angles between the sp^n hybridized bond orbitals (180° for sp, 120° for sp^2, 109.8° for sp^3). According to the VSEPR model, the driving force for the geometry of EX_n does not come from the attractive interactions between E and X but rather from the Pauli repulsion between the electron pairs of the E–X bonds. A nonbonding electron pair is treated like a E–X bonding pair but the former occupies

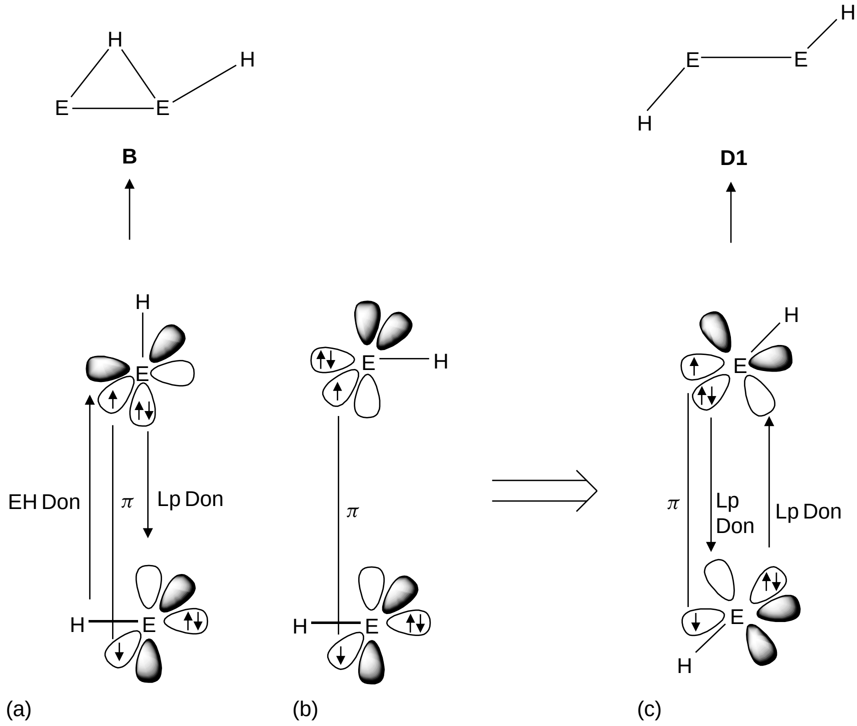

Figure 14 Qualitative orbital model for the bonding between two EH fragments (E = C–Pb) in the $^2\Pi$ ground state via π coupling of the unpaired electrons showing three arrangements, which lead to different isomeric forms of E_2H_2. (a) Top-to-side arrangement yielding structure **B** with additionally one lone-pair and one E–H donor–acceptor bond. (b) Antiarrangement of the E–H bonds which does not yield an energy minimum structure. Tilting of the E–H bonds gives the arrangement (c) with two lone-pair donor–acceptor bonds yielding structure **D1**

more space than the latter. Furthermore, the two-electron pairs of a double bond or the three electron pairs of a triple bond occupy more space than the electron pair of a single bond.

Figure 15 shows the molecular shapes that are predicted for molecules with up to six ligands in EX_nLp_m (Lp = electron lone pair). For each principal shape, there is one example shown in Figure 15. The VSEPR model explains nicely why compounds like SF_4 have a sawhorse geometry. The molecule has the formal structure SF_4Lp where the electron lone-pair occupies an equatorial position because it is considered being larger than the S–F bonding pair. The T-shaped structure of ClF_3, the square pyramidal geometry of IF_5 and the planar structure of XeF_4 are also in agreement with the predictions made by the VSEPR model. Problematic cases are molecules like XeF_6. There are six Xe–F bonding pairs and one-electron lone pair at Xe, which gives seven ligands. The VSEPR model would predict that the equilibrium geometry of XeF_6 should be distorted from O_h symmetry, which is correct. XeF_6 has a trigonally distorted octahedral structure.[22] However, there are various ions valence-isoelectronic with XeF_6 like ClF_6^-, BrF_6^-, and $BiCl_6^-$, which have a regular octahedral structure. This means that the electron lone pair is stereochemically active in some EX_6Lp molecules while it is inactive in others. The a posteriori rationalization of the distorted structures in terms of a stereochemically active electron pair as it is suggested by the VSEPR model has more a character of a tautology than a true explanation because the model does not say in the beginning if an electron lone pair is active or not. The conformation of N_2H_4 is another molecule where the VSEPR model fails, because the most stable form of hydrazine is not the anti but the gauche conformation where the lone-electron pairs are close to each other. It is obvious that the sole consideration of repulsive inter-ligand electron-pair interactions neglects other factors, which may be important for the geometry of a molecule.

The VSEPR model makes also predictions about the changes of the bond angles in molecules EX_n when E or X is substituted by other atoms or groups. It is predicted that bond angles decrease with increasing electronegativity of the ligand or decreasing electronegativity of the central atom E. Table 18 gives a list of bond angles in some trigonal pyramidal EX_3Lp molecules. The trend of the bond angles agrees in many cases with the VSEPR model but there are several exceptions. For example, the bond angle in NF_3 (102.2°) is smaller than in NH_3 (107.3°) but the bond angles in the phosphorus analogs PF_3 (97.8°) and PH_3 (93.8°) do not agree with the VSEPR approach. The prediction also fails for the series EMe_3 and ECl_3 (E = P, As, Sb) because the latter compounds have larger bond angles than the former. The VSEPR model is very useful for qualitatively predicting the geometry of

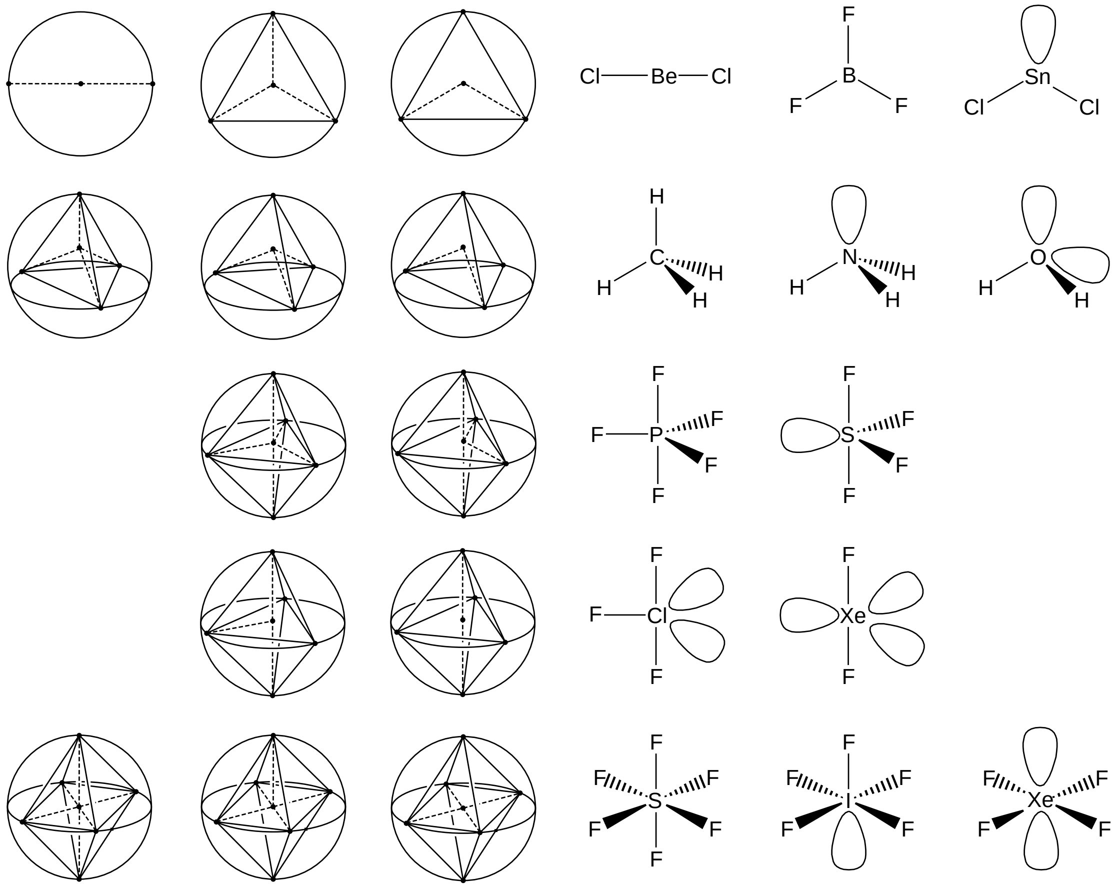

Figure 15 Molecular shapes based on the arrangement of 2–6 valence electron pairs

molecules that have a normal bonding situation. It is not useful for explaining molecular structures at a quantitative level because of its crude approximation.

A model that was introduced as an extension and a refinement of the VSEPR approach is the Ligand Close-packing (LCP) model.[35] The LCP model considers the ligand–ligand repulsion in molecules rather than bond pair-bond pair repulsion. The starting point of the LCP model was the observation that the inter-ligand distances of atoms X, which are bonded to a common central atom E, exhibit very nearly constant values X···X in related molecules EX_nL_m where L is another ligand group or atom. Examples for X = F are shown in Table 19.

Table 18 Bond angles (degrees) in some trigonal pyramidal AX_3Lp molecules[a]

Molecule	Bond angle	Molecule	Bond angle
NH_3	107.3	PBr_3	101.1
PH_3	93.8	$AsBr_3$	99.8
AsH_3	91.8	$SbBr_3$	98.2
SbH_3	91.7	PI_3	102
NF_3	102.2	AsI_3	100.2
PF_3	97.8	SbI_3	99.3
AsF_3	96.1	NMe_3	110.9
SbF_3	87.3	PMe_3	98.6
NCl_3	107.1	$AsMe_3$	96.0
PCl_3	100.3	$SbMe_3$	94.2
$AsCl_3$	98.6	SF_3^+	97.5
$SbCl_3$	97.2	SeF_3^+	94.5

[a] Reference 35.

The F···F distances of the beryllium, boron, and carbon compounds of fluorine are remarkably close to the mean values of 2.56, 2.26 and 2.16 Å, independent of the coordination number and the E–F bond length. The LCP model suggests that the fluorine atoms in the molecules EF_nL_m listed in Table 19 are squeezed together to their limit of compressibility. Each ligand is considered to be touching its neighbors, which makes it possible to assign the value of a nonbonded radius, which is called ligand radius. The value of the ligand radius of an atom depends on the nature of the atom to which it is bonded. Table 20 gives a list of ligand radii that have been suggested for the LCP model.[35]

The LCP model like the VSEPR approach thus suggests that the geometry of a molecule EX_n is primarily determined by the Pauli repulsion between nonbonded ligands X

Table 19 Bond lengths, bond angles, and F···F distances in some molecules containing BeF_n, BF_n, and CF_n groups[a]

Molecule	Coord. No.	E–F [Å]	F–E–F [°]	F···F [Å]
BeF_3^-	3	1.49	120	2.58
BeF_4^{2-}	4	1.554	109.5	2.54
				Mean 2.56
F_3B	3	1.307	120.0	2.26
F_2B–OH	3	1.323	118.0	2.27
F_2B–NH_2	3	1.325	117.9	2.27
F_2B–Cl	3	1.315	118.1	2.26
F_2B–H	3	1.311	118.3	2.25
F_4B^-	4	1.382	109.5	2.26
F_3B–CH_3^-	4	1.424	105.4	2.27
F_3B–CF_3^-	4	1.391	109.9	2.28
F_3B–PH_3	4	1.372	112.1	2.28
				Mean 2.26
CF_3^+	3	1.244	120	2.16
$F_2C{=}CF_2$	3	1.319	112.4	2.19
$F_2C{=}CCl_2$	3	1.315	112.1	2.18
$F_2C{=}CH_2$	3	1.324	109.4	2.16
$F_2C{=}CHF$	3	1.336	109.2	2.18
F_4C	4	1.319	109.5	2.15
F_3C–CF_3	4	1.326	109.8	2.17
F_3C–OF	4	1.319	109.4	2.15
F_3CO^-	4	1.392	101.3	2.15
				Mean 2.16

[a] Reference 35.

Table 20 Ligand radii in molecules EX_n (Å) suggested by the LCP model[a]

	Central Atom E			
Ligand X	Be	B	C	N
H	–	1.10	0.90	0.82
C	–	1.37	1.25	1.20
N	1.44	1.24	1.19	–
O	1.33	1.19	1.14	–
F	1.28	1.13	1.08	1.08
Cl	1.68	1.51	1.44	1.42

[a] Reference 35.

rather than by the attractive interactions between E and X. Some predictions are made based on the LCP model. One prediction suggests that bond lengths in EX_n molecules increase with increasing coordination number n. For heavier elements E of periods 3–6 it is necessary to consider the coordination number for the assignment of the ligand radii in molecules EX_n, because higher-coordinated compounds have frequently shorter bond length E–X than lower-coordinated species. For example, the S–F distance in SF_6 (1.561 Å) is shorter than in SF_2 (1.589 Å). Another point that needs to be considered is the atomic charge of the central atom E. A large positive charge means that the radius of E shrinks. The LCP model has been used for a posteriori explanations of the geometries of main-group compounds.**[35]** It needs to be seen how the LCP model accounts for the structures like those of heavy-atom E_2H_2 homologs (see above).

6 TOPOLOGICAL ANALYSIS OF THE ELECTRON DENSITY DISTRIBUTION

The topological analysis of the electron density distribution has been developed by Bader into a powerful method that gives important information about the electronic structure of molecules.**[36]** The name of the method has lately changed to Atoms In Molecules (AIM) and more recently to Quantum Theory of Atoms in Molecules (QTAIM) emphasizing the fact that atomic domains in a molecule can be defined such that they agree with fundamental theorems of physics like the virial theorem and the Hellman-Feynman theorem. The strength and the very nature of the QTAIM is that many concepts and models that are important and interesting in chemistry are derived using only the electron density distribution $\rho(\mathbf{r})$ as starting point, which is an experimentally observable quantity. There is no direct reference to the wave function or to orbitals in the QTAIM. Much insight into the electronic structure is obtained from the first and second derivatives of $\rho(\mathbf{r})$ with respect to the spatial coordinates, that is, the gradient vector field $\nabla\rho(\mathbf{r})$ and the Laplacian distribution $\nabla^2\rho(\mathbf{r})$.

The most important aspects of the QTAIM that are relevant for questions of chemical bonding shall be discussed using the first neutral argon compound HArF as an example,**[37]** which was recently synthesized.**[38]**

Figure 16 shows contour line diagrams of the Laplacian distribution $\nabla^2\rho(\mathbf{r})$ of ArF, Har, and HArF at the equilibrium distance. Solid lines show areas of electron concentration where the values of $\nabla^2\rho(\mathbf{r}) < 0$ while dashed lines show areas of electron depletion where $\nabla^2\rho(\mathbf{r}) > 0$. Figure 16(a) shows that the electronic structures of the atoms Ar and F are nearly undisturbed by the presence of the other atom. This is reasonable because ArF is a weakly bonded van der Waals complex. The spherical shape of $\nabla^2\rho(\mathbf{r})$ of argon shows nicely the shell structure of the atom where regions of electron concentration and electron depletion are surrounding the nucleus. The shape of $\nabla^2\rho(\mathbf{r})$ of fluorine indicates that the density of the valence electron in the direction that is perpendicular to the Ar–F internuclear axis is higher than along the bonding line. This is because the 2p-shell of F, which has the electronic configuration $(p_x)^2(p_y)^2(p_z)^1$, is aligned in such a way that the doubly occupied orbitals $(p_x)^2(p_y)^2$ become the p(π) orbitals while the singly occupied $(p_z)^1$ AO is the p(σ) AO.

The solid line in Figure 16(a), which connects the atomic nuclei, is the bond path. The definition of the bond path comes from the topological analysis of $\rho(\mathbf{r})$. Between the atoms Ar and F there is a point in space called the bond critical point $\mathbf{r}_b$ where the first derivative $\nabla\rho(\mathbf{r}) = 0$ and the value of the second derivative along the internuclear axis is positive. It

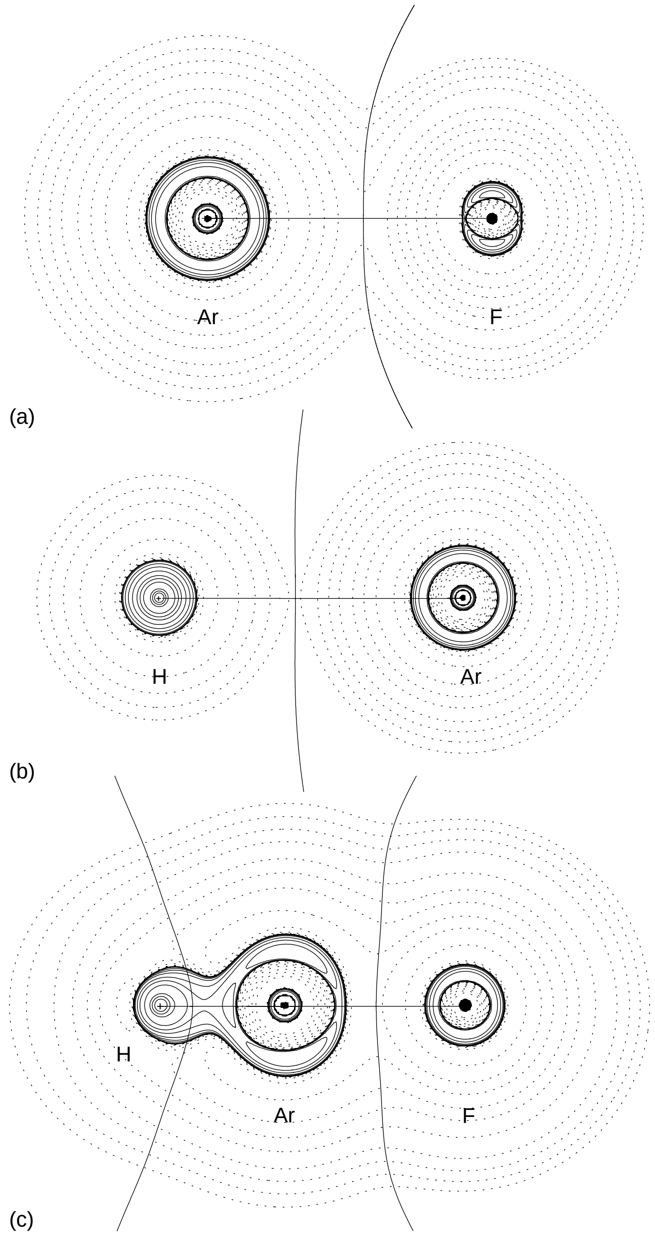

Figure 16 Contour line diagrams of the Laplacian distribution $\nabla^2\rho(\mathbf{r})$ of (a) ArF; (b) ArH; (c) HArF. Solid lines give areas of charge concentration ($\nabla^2\rho(\mathbf{r}) < 0$), while dashed lines give areas of charge depletion ($\nabla^2\rho(\mathbf{r}) > 0$). The solid line connecting the atomic nuclei is the bond path. The solid lines that cross the bond path at the bond critical point show the zero-flux surface crossing the shown plane. (Ref. 37. Reproduced by permission of Springer Verlag)

means that ρ is a minimum at $\mathbf{r}_b$, while the values of the other two second derivatives in the plane that is perpendicular to the internuclear axis are negative, that is, ρ is a maximum. Other critical points where $\nabla\rho(\mathbf{r}) = 0$ that are defined in a similar way are ring critical points (two positive and one negative eigenvalue), cage critical point (three positive eigenvalues), and atomic nuclei position (three negative eigenvalues). The bond path is defined as the line of maximum charge density linking the bond critical point $\mathbf{r}_b$ and the atomic nuclei. Thus, the QTAIM defines chemical bonds in molecules without ad hoc assumptions about the interatomic interactions. However, Figure 16(a) shows that the existence of a bond path does not mean that there is a true chemical bond, because ArF is only a weakly bonded van der Waals complex that is held together by dispersion forces but not by a genuine chemical bond. Additional criteria have to be fulfilled in order to distinguish a chemical bond from weak interatomic interactions. Various properties such as the electron density, the energy density and the value of the Laplacian at the bond critical point can be used for the characterization of a chemical bond.

There is another solid line that crosses the bond path at the bond critical point. This line shows where the zero-flux surface, which separates the atomic basins of Ar and F, is cutting the plane shown in Figure 16(a). Every atom in a molecule is bounded by a zero-flux surface, which is defined by the gradient vector field $\nabla\rho(\mathbf{r})$. The zero-flux surface is spanned by those trajectories $\nabla\rho(\mathbf{r})$ that vanish at the bond critical point $\mathbf{r}_b$. All other trajectories vanish at the atomic nuclei of either Ar or F. There is no gradient vector that crosses the zero-flux surface, which is the reason for its name. The advantage of the definition of an atomic basin using the zero-flux surfaces is that it comes directly from the topological analysis of the electron density distribution, which may be obtained from calculations or from experiment. The definition of an atom by the QTAIM is the physically most meaningful way to divide a molecule into atoms.

Figure 16(b) shows the contour line diagram for ArH, which is very similar to the diagram for ArF shown in Figure 16(a). Both molecules are weakly bonded van der Waals complexes. The strength of the QTAIM method for giving insight into the bonding situation in molecules becomes obvious when the shape of the Laplacian distribution of HArF (Figure 16(c)) is compared with Figures 16(a) and 16(b). The largest difference is found between the H–Ar bonds of HAr and HArF. There is a continuous area of charge concentration ($\nabla^2\rho(\mathbf{r}) < 0$, solid lines) between hydrogen and argon in the latter molecule, which indicates that the valence electron density of the two atoms is strongly distorted by the interatomic interactions. The bond critical point of the H–Ar bond is located in the region where $\nabla^2\rho(\mathbf{r}) < 0$. Table 21 shows that the values of the charge density $\rho(\mathbf{r}_b)$, the Laplacian $\nabla^2\rho(\mathbf{r}_b)$, and the energy density $H(\mathbf{r}_b)$ for the H–Ar bond in HArF are very different from the values in free ArH. In the former compound, the charge density at the bond critical point is much higher and the Laplacian even has an opposite sign than in the latter species. Also the energy density at the bond critical point $H(\mathbf{r}_b)$ for the H–ArF bond is more than three orders of magnitude larger than for Ar–H. The calculated values are typical for covalent bonds, which are called electron-sharing bonds in the QTAIM.[36] The values for the HAr–F and Ar–F bonds are less different because both arise from closed-shell interactions.

Table 21 Calculated electron density $\rho(r_b)$ [e/Bohr^3], Laplacian $\nabla^2\rho(r_b)$ [e/Bohr^5] and energy density $H(r_b)$ [Hartree/Bohr^3] at the bond critical points of the compounds ArH, ArF, and HArF

	Ar–H	Ar–F	H–ArF	HAr–F
$\rho(r_b)$	$2.768\cdot10^{-4}$	$1.614\cdot10^{-3}$	$2.053\cdot10^{-1}$	$8.520\cdot10^{-2}$
$\nabla^2\rho(r_b)$	$9.502\cdot10^{-4}$	$9.173\cdot10^{-3}$	$-5.539\cdot10^{-1}$	$3.608\cdot10^{-1}$
$H(r_b)$	$-7.242\cdot10^{-5}$	$-5.645\cdot10^{-4}$	$-1.769\cdot10^{-1}$	$-2.096\cdot10^{-3}$

The Laplacian distribution in the bonding region of the Ar–F bond of HArF appears not very different from ArF at first sight (Figures 16(b), (c)). Note, however, that the valence shell of the fluorine atom in HArF is spherically symmetric while it shows local areas of charge concentration in the π region in ArF. This is a visual hint that the p orbitals of fluorine are completely filled in HArF, which means that there is a F^- anion in the latter molecule while the fluorine atom in ArF is neutral. Integration of $\rho(\mathbf{r})$ over the atomic basins gives according to the QTAIM the partial charges in the molecule. The calculation for HArF confirms the visual impression of the bonding situation. The fluorine atom has a negative charge of -0.800 electrons while HAr carries a positive charge of $+0.800$ e, which is rather equally distributed over Ar ($+0.445$ e) and H ($+0.355$ e). Thus, the QTAIM suggests that the H–ArF bond has a covalent character while the HAr–F bond is ionic. Table 21 shows that the values of $\rho(\mathbf{r}_b)$, $\nabla^2\rho(\mathbf{r}_b)$, and $H(\mathbf{r}_b)$ for the HAr–F bond are close to the values of free Ar–F. The latter values are typical for closed-shell interactions like in weakly bonded van der Waals complexes but also in strongly ionic compounds. In order to distinguish between the two types of interactions, one has to consider the partial charges and the interatomic distance.

Another example that demonstrates the value of the topological analysis of the electron density distribution is the electronic structure of the donor–acceptor complex Cl_3B–CO. The molecule was already discussed in paragraph 2 in the context of the NBO analysis. The donor and acceptor atoms carbon and boron both carry a positive partial charge (Table 2). The donor atom C is even more positively charged ($+0.43$) than the acceptor atoms B($+0.29$). The atomic partial charges may not be used to estimate the interatomic electrostatic interactions. The atom that carries the largest positive charge (carbon) is actually the center of the negative charge concentration, which yields strong electrostatic attraction with the boron atom. Figure 17 shows the Laplacian distribution of Cl_3B–CO and the donor and acceptor moieties in the frozen geometry of the complex. It becomes obvious that the carbon atom of CO has an area of charge concentration along the bonding axis pointing away from oxygen, which comes mainly from the HOMO, which is a σ lone-pair orbital (Figure 17(b)). The σ charge concentration at carbon becomes deformed by the donor–acceptor interactions. Figure 17(a) shows that the σ charge concentration in Cl_3B–CO points towards the area of charge depletion at the boron atom. The electrostatic attraction (see the results of the EDA analysis below) comes from the interactions between the *local area of negative charge concentration of an overall positively charged atom with another positively charged atom.*

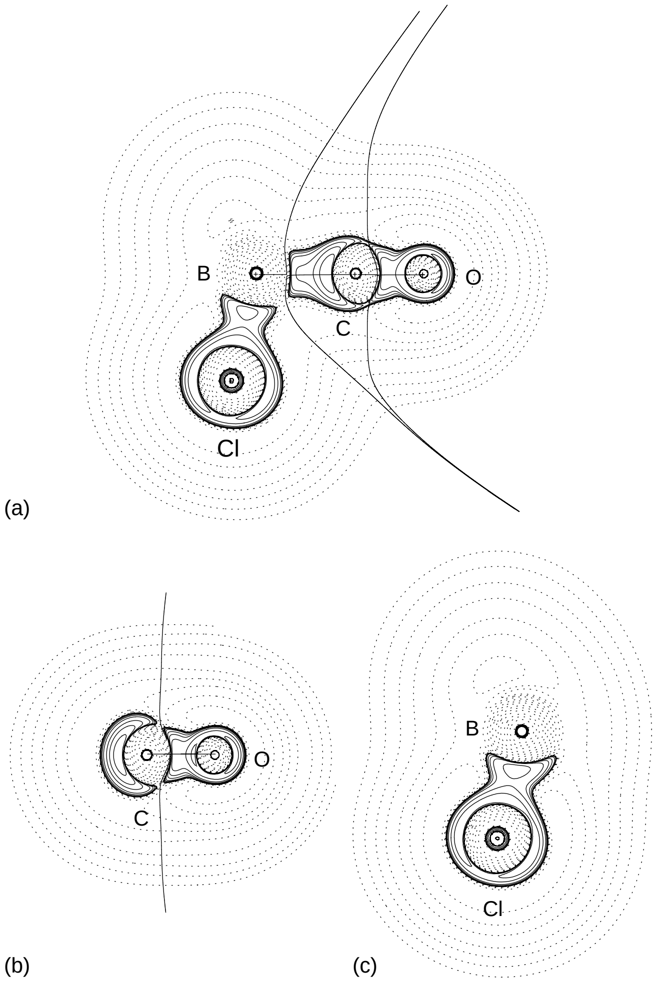

Figure 17 Contour line diagrams of the Laplacian distribution $\nabla^2\rho(\mathbf{r})$ of (a) Cl_3B–CO; (b) CO; (c) Cl_3B. CO and Cl_3B have been calculated in the frozen geometry of Cl_3B–CO. Solid lines give areas of charge concentration ($\nabla^2\rho(\mathbf{r}) < 0$), while dashed lines give areas of charge depletion ($\nabla^2\rho(\mathbf{r}) > 0$). The solid line connecting the atomic nuclei is the bond path. The solid lines that cross the bond path at the bond critical point show the zero-flux surface crossing the shown plane. The bond path and zero-flax surface of the BCl_3 moeity are not shown

7 CHEMICAL BONDING IN DONOR–ACCEPTOR COMPLEXES

A covalent two-electron bond A–B between two atoms or fragments A and B arises in most cases through the coupling of unpaired electrons at A and B. This type of bonding is also called a shared-electron interaction. A covalent bond A–B may also be formed through donation of the electron pair of a donor B to an acceptor A. This is called a donor–acceptor bond where the bond is sometimes written with an arrow A ← B. The latter bonding type has been the subject of pioneering studies by G. Lewis.[1] The bonding partners of a donor–acceptor complex are therefore called Lewis acids and bases. Donor–acceptor bonds are usually weaker than strong electron-sharing bonds. The strongest bonded main-group complexes have bond energies of $\sim 50\,\mathrm{kcal\,mol^{-1}}$.[39] The strength of the Lewis acids and Lewis bases for binding each other has been described by several chemical models in the past.

The donor–acceptor bond is usually explained in terms of two types of interactions. One type considers HOMO–LUMO interactions between the donor and acceptor moiety yielding a covalent bond and the other type considers electrostatic attraction between the negative charge of the donor electron pair and the nucleus of the acceptor atom. The dichotomy of bonding models is related to the concept of hard and soft acids and bases (HSAB) proposed by Pearson.[40] The central quantity of the HSAB model is the absolute hardness η. The hardness η was originally derived from the ionization energy I and the electron affinity A as $\eta = (\mathrm{I}-\mathrm{A})/2$. Since according to Koopman's theorem the ionization energy and the electron affinity are approximated by the energy levels of HOMO and LUMO, it follows that a larger HOMO–LUMO gap correlates with greater hardness. The HSAB model suggests that a hard base prefers to bind to a hard acid through electrostatic attraction while a soft base prefers to bind to a soft acid with a covalent bond. The predictions of the HSAB model are in qualitative agreement with experimental observations.[40]

Donor–acceptor complexes have already been discussed in Section 2 and in the previous paragraph, where it was shown that charge partitioning methods give insight into the electronic structure and bonding situation of the molecules. The energy decomposition analysis that was introduced in Section 3 can also be used for analyzing the nature of donor–acceptor interactions in complexes of main-group elements and transition metals.[10] Table 22 shows the EDA results for complexes of the Lewis acids BH_3, BF_3, BCl_3, AlH_3, $AlCl_3$ with the Lewis bases NH_3, NMe_3, PMe_3. The donor–acceptor bond in $H_3B\text{-}NH_3$ may be compared with the electron-sharing bond in isoelectronic H_3C-CH_3 (Table 8). The latter bond is much stronger, but the relative contributions of ΔE_{elstat} and ΔE_{orb} do not exhibit dramatic differences. The covalent contributions in ethane are somewhat larger (58.6%) than in $H_3B–NH_3$ (49.6%). The interaction energy and the BDE in $H_3B–NMe_3$ and particularly $H_3B–PMe_3$ are higher than in $H_3B–NH_3$. The bonding in $H_3B–PMe_3$ is also more covalent (57.3%) than in $H_3B–NH_3$. This is in agreement with the HSAB model, because BH_3 and PMe_3 are considered as soft molecules while NH_3 and NMe_3 are hard.

The HSAB model is also supported by the EDA results for the complexes of the hard Lewis acid BF_3 with NH_3, NMe_3, and PMe_3, which indicate a higher degree of electrostatic attraction than in the respective BH_3 complexes (Table 22). The calculated data show that the bond dissociation energy may not be a reliable probe for the strength of the donor–acceptor interaction. The D_e values of the complexes with BF_3 are significantly smaller than for the BH_3 complexes but the ΔE_{int} data are very similar. This is because the preparation energies of the BF_3 complexes are clearly higher than the preparation energies of the BH_3 complexes. The deformation of the planar structure of BF_3 towards the pyramidal form in the complexes is energetically more demanding than for BH_3. The EDA results for the BCl_3 complexes are very similar to the values that are calculated for the BF_3 complexes. The ΔE_{int} values and the bond dissociation energies of the former compounds are slightly larger than for the latter. The stronger Lewis acidity of BCl_3 compared with BF_3 comes from the larger contribution of the $\Delta\ E_{orb}$ term, which can be explained with the finding that BCl_3 has an energetically lower-lying LUMO than BF_3.[41] BCl_3 and BF_3 are hard acids but BCl_3 is not as hard as BF_3.[40] The data in Table 22 shows also that the HSAB model is not always correct. The hard acids BF_3 and BCl_3 should bind stronger to the hard bases NH_3 and NMe_3 than to the soft base PMe_3. The calculations predict stronger bonding in the phosphane complexes than in the amine complexes.

The calculated interaction energies for the aluminum complexes with AlH_3 and $AlCl_3$ are lower than for the respective BH_3 and BCl_3 complexes (Table 22). However, the bond dissociation energies of the $AlCl_3$ complexes are higher than the D_e values of the BCl_3 adducts because the preparation energies of the former species are much smaller than for the latter. $AlCl_3$ is considered to be a stronger Lewis acid than BCl_3.[39] Table 22 shows that the intrinsic Lewis acidity of BCl_3 is higher than that of $AlCl_3$. The donor–acceptor bonding in the aluminum complexes is clearly more electrostatic than in the boron complexes. Note that the D_e values at BP86/TZ2P, which are given in Table 22, are a bit smaller than the MP2/6–31G(d) data shown in Table 2 but the trends are always the same. This is because DFT underestimates the strength of donor–acceptor interactions.

8 CHEMICAL BONDING OF THE HEAVIER MAIN-GROUP ELEMENTS

Molecules of heavier main-group elements show significant differences to compounds of elements from the first-octal row of the periodic system. The coordination number of the lighter elements is rarely larger than 4 while many stable molecules of the heavier elements with coordination number 5 and 6 are known. Another difference concerns the stability of molecules with multiple bonds. Many stable molecules with double or triple bonds between the lighter elements are well known, particularly compounds that have C=C, C=N, C=O,

Table 22 Energy decomposition analysis of the donor–acceptor complexes of the Lewis acids BH_3, BF_3, BCl_3, AlH_3, $AlCl_3$ with Lewis bases NH_3, NMe_3, PMe_3 at BP86/TZ2P. Energy values in kcal mol^{-1}

	$H_3B–NH_3$	$H_3B–NMe_3$	$H_3B–PMe_3$
ΔE_{int}	−44.6	−51.4	−55.3
ΔE_{Pauli}	108.8	119.8	130.7
ΔE_{elstat}[a]	−77.3 (50.4%)	−89.4 (52.2%)	−79.4 (42.7%)
ΔE_{orb}[a]	−76.0 (49.6%)	−81.8 (47.8%)	−106.6 (57.3%)
ΔE_{σ}[b]	−68.4 (89.9%)	−71.1 (86.9%)	−92.7 (87.0%)
ΔE_{π}[b]	−7.7 (10.1%)	−10.7 (13.1%)	−13.9 (13.0%)
ΔE_{prep}	12.7	15.2	15.5
$\Delta E (= -D_e)$	−31.8	−36.2	−39.8
	$F_3B–NH_3$	$F_3B–NMe_3$	$F_3B–PMe_3$
ΔE_{int}	−40.2	−50.9	−42.6
ΔE_{Pauli}	126.0	136.4	116.0
ΔE_{elstat}[a]	−91.4 (55.0%)	−101.9 (54.4%)	−80.6 (50.8%)
ΔE_{orb}[a]	−74.8 (45.0%)	−85.4 (45.6%)	−78.0 (49.2%)
ΔE_{σ}[b]	−66.5 (88.8%)[b]	−72.4 (84.7%)	−70.4 (90.2%)
ΔE_{π}[b]	−8.2 (11.0%)[b]	−12.5 (14.7%)	−7.5 (9.6%)
ΔE_{prep}	21.8	28.3	31.1
$\Delta E (= -D_e)$	−18.4	−22.6	−12.5
	$Cl_3B–NH_3$	$Cl_3B–NMe_3$	$Cl_3B–PMe_3$
ΔE_{int}	−41.3	−52.2	−52.7
ΔE_{Pauli}	192.8	187.4	201.2
ΔE_{elstat}[a]	−120.5 (51.5%)	−123.7 (51.6%)	−121.8 (48.0%)
ΔE_{orb}[a]	−113.6 (48.5%)	−115.9 (48.4%)	−132.1 (52.0%)
ΔE_{σ}[b]	−102.2 (89.9%)	−99.3 (85.7%)	−119.0 (90.1%)
ΔE_{π}[b]	−11.3 (9.9%)	−15.8 (13.7%)	−12.8 (9.7%)
ΔE_{prep}	21.5	31.2	31.4
$\Delta E (= -D_e)$	−19.8	−21.0	−21.3
	$H_3Al–NH_3$	$H_3Al–NMe_3$	$H_3Al–PMe_3$
ΔE_{int}	−29.7	−33.6	−29.9
ΔE_{Pauli}	55.7	65.1	56.6
ΔE_{elstat}[a]	−56.7 (66.4%)	−65.3 (66.2%)	−50.2 (58.0%)
ΔE_{orb}[a]	−28.7 (33.6%)	−33.4 (33.8%)	−36.3 (42.0%)
ΔE_{σ}[b]	−24.4 (85.3%)	−26.3 (78.7%)	−31.0 (85.3%)
ΔE_{π}[b]	−4.2 (14.7%)	−7.1 (21.3%)	−5.3 (14.7%)
ΔE_{prep}	3.4	5.2	5.9
$\Delta E (= -D_e)$	−26.3	−28.4	−24.0
	$Cl_3Al–NH_3$	$Cl_3Al–NMe_3$	$Cl_3Al–PMe_3$
ΔE_{int}	−39.5	−46.1	−42.6
ΔE_{Pauli}	76.8	87.1	76.8
ΔE_{elstat}[a]	−75.9 (65.3%)	−84.8 (63.7%)	−69.3 (58.1%)
ΔE_{orb}[a]	−40.3 (34.7%)	−48.4 (36.3%)	−50.0 (41.9%)
ΔE_{σ}[b]	−33.5 (83.2%)	−36.5 (75.4%)	−43.0 (86.0%)
ΔE_{π}[b]	−6.8 (16.8%)	−11.4 (23.6%)	−6.9 (13.7%)
ΔE_{prep}	6.3	11.3	12.6
$\Delta E (= -D_e)$	−33.2	−34.8	−30.0

[a]Percentage of the total attractive interactions $\Delta E_{elstat} + \Delta E_{orb}$. [b]Percentage of the total orbital interactions ΔE_{orb}. Small contributions (<1 kcal mol^{-1}) by orbitals with a_2 symmetry have been neglected.

N=O, C≡C, and C≡N bonds. Molecules with multiple bonds between heavier elements are much less stable and they can only become isolated when the multiple bonds are stabilized by protective substituents.[42] The geometries of the latter molecules are frequently very different from homologs of the lighter elements. Molecules with double bonds $R_2E{=}ER_2$ are not planar like $R_2C{=}CR_2$ and molecules RE≡ER are not linear like RC≡CR (E = Si–Pb). The electronic structure and bonding situation in $R_2E{=}ER_2$ and $RE{\equiv}ER$ has been discussed in paragraphs 4.2 and 4.3.

What is the reason for the different structures and reactivities of molecules of the elements Li–F compared with the heavier main-group analogs? For a long time it was assumed that the larger coordination numbers 5 and 6 of the heavier elements come from the nd ($n \geq 3$) AOs, which are available as valence orbitals for the heavier elements. It was thought that the octet rule holds only for the first-octal row elements because they have only 2s and 2p valence AOs while the heavier elements may also use the nd orbitals in compounds that were considered to be hypervalent. Chemical bonding in the latter compounds was then discussed in terms of sp^{n}d^m orbitals. The heuristic bonding model seems plausible because d orbitals are available only for elements of rows ≥ 3. It is also attractive because it is easy to write a 'hypervalent' compound such as SF_6 with a Lewis structure that has six S–F bonding pairs. Several quantum chemical studies using different partitioning methods have been carried out in the past. All agree that the valence space of the heavy main-group elements in 'hypervalent' compounds rarely exceeds the number eight, that is, the octet role is fulfilled even for compounds like SF_6 and $HClO_4$.[43] A Lewis structure that correctly describes the bonding situation in such molecules is given in Figure 18. Heavy-atom molecules of main-group elements, which bind more than four ligands, are stable because they are larger than elements of the first-octal row. There are no stable hypervalent compounds of the lighter elements because the ligands would repel each other when there were more than four atoms bonded to the central atom, not because it does not have d valence orbitals.

The chemical instability of heavy-atom molecules, which have a multiple bond, has previously been explained with the suspected weakness of the π bond. It was thought that the overlap of the p(π) AOs of heavier elements is smaller compared with the atoms of the first-octal row because of the longer bonds of the former atoms. This is not true. The longer interatomic distance is compensated by the more diffuse orbitals of the heavier atoms, which yield similar overlaps to those of the lighter elements. Table 5 shows that the ratio of σ and π bond strength in the diatomic molecules E_2 (E = N–Sb) does not vary a lot.

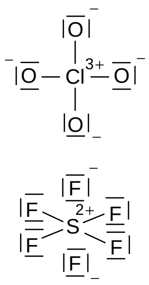

Figure 18 Lewis structures for ClO_4^- and SF_6 that obey the octet rule. Only one of several equivalent resonance forms is shown. The shown Lewis structures are suggested by quantum chemical calculations to be the best resonance forms for the molecules

The difference in the bonding situation between elements of the first octal row and heavier atoms has been analyzed by Kutzelnigg.[44] There is a significant difference between the ns and np valence orbitals of the first-octal row ($n = 2$) and the heavier atoms ($n \geq 3$). The difference does not come from the *energies* of the valence orbitals. The energy differences between ns and np orbitals for when $n \geq 3$ is smaller than for $n = 2$. Hybridization should therefore take place more easily for the heavier elements, which is not the case because of the *size* of the valence orbitals. Figure 19 shows the calculated values for the mean radius of the ns and np orbitals $\langle r_s \rangle$ and $\langle r_p \rangle$ of main-group elements with $n = 2 - 6$. It becomes obvious that the $\langle r_s \rangle$ and $\langle r_p \rangle$ values for B–F are very similar, that is, $\langle r_p \rangle$ values are only $\sim$10% larger than the $\langle r_s \rangle$ values. This means that the s and p valence orbitals of the second row elements are in the same region of space. The radii $\langle r_p \rangle$ of the heavier elements are significantly larger than the $\langle r_s \rangle$ radii, which means that the valence p orbitals of the latter atoms are clearly more diffuse than the valence s orbitals. The difference is particularly large for elements of the sixth row of the periodic system. Electrons in the valence ns orbitals of the heavier elements tend to behave more like core electrons when n becomes larger. It is known that compounds of elements of the sixth row may be stable when the heavy atom has only six electrons in the valence shell. An example has been presented in Section 4.3 above where the bonding situation of E_2H_2 is discussed. The trans-bent form of Pb_2H_2, which has a Pb–Pb single bond and σ electron lone pairs at Pb, is lower in energy than the trans-bent form that has a Pb=Pb double bond, although the lead atoms in the former species have only an electron sextet while there is an octet in the latter isomer. The octet rule is violated in many compounds of sixth row elements for which numerous stable molecules are known with only six electrons in the valence shell of the heavy atom. This is sometimes termed the 'lone-pair effect'. The important point is that the lower tendency of the heavier atoms toward formation of sp^n hybrid orbitals comes from the size of the ns and np valence orbitals but not from their energies.[44]

A second factor, which becomes important for the heavier elements, is relativistic effects. Many theoretical studies have been devoted to studying the influence of relativity on the structures and chemical properties of molecules in the last 10 years.[46] There are two major relativistic effects concerning the electronic structure of atoms that are important for chemistry. (i) The s and p orbitals are contracted by the influence of relativity while d and f orbitals are expanded. (ii) Coupling of spin and orbit movement of the electrons. The latter effect becomes obvious in Figure 19. The energy level of the p orbitals split into the components $p_{1/2}$ and $p_{3/2}$ because of spin-orbit coupling. The energy differences are very small and negligible for most chemical properties for elements of rows 2 and 3. They become larger in rows 4 and 5 and they are very important for elements of the rows 6 and above.

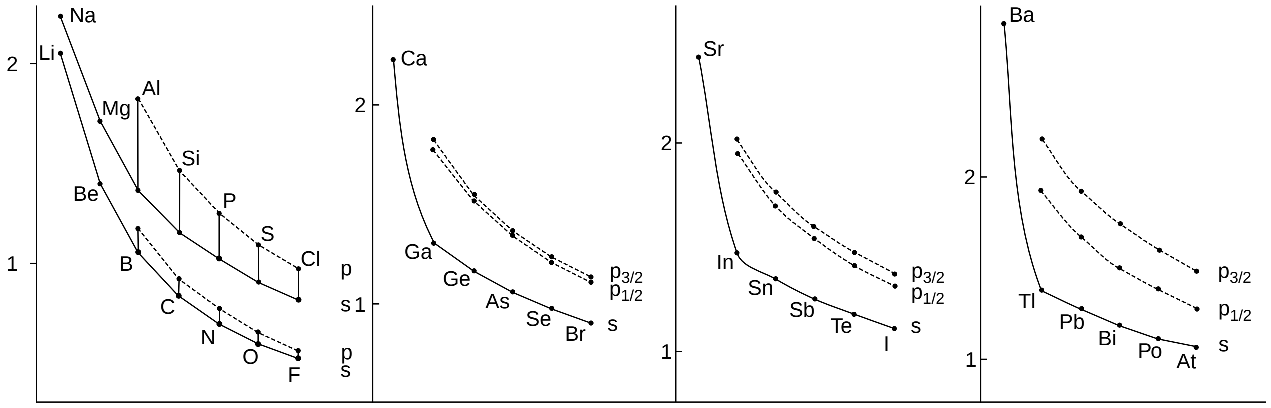

Figure 19 Calculated radii (expectation value) $\langle r_s \rangle$ and $\langle r_p \rangle$ for the s and p valence orbitals of main-group atoms. The indices $p_{1/2}$ and $p_{3/2}$ give the components of the p orbitals, which come from spin-orbit interactions. The calculated values have been taken from relativistic calculations of Desclaux.[45] (Ref. 15. Reproduced by permission of Wiley-VCH)

The difference between the structures and properties of the elements Li–F and the heavier homologs is not, however, caused by relativistic effects. The reason for the similar size of the 2s and 2p orbitals comes from the fact that there are no lower-lying filled p orbitals at the first-octal row elements. If the energy level l of an atomic shell n_l (l = s, p, d, etc.) is filled for the first time, the electrons can penetrate rather deeply into the core because there is no l–l repulsion with core electrons possessing the same l. This is the reason that the radii of the 2p orbitals are comparatively small having similar values as the 2s orbitals (Figure 19). This yields effective hybridization of the 2s and 2p orbitals in chemical bonds while the ns and np orbitals with $n \geq 3$ do not hybridize as well. It is important to learn that a correlation between hybridization and bond angle is valid only for elements of the first-octal row. For example, the localized bond orbitals in SiH_4 at silicon are $\sim sp^2$ hybridized and not sp^3 like the carbon atoms in methane although the molecule has tetrahedral (T_d) symmetry. The bond orbitals at P in PH_3 are $sp^{3.8}$ hybridized although the H–P–H bond angle is 95°, which would suggest nearly pure p AOs at phosphorus.[44]

The increasing reluctance of the heavier main-group elements to have more than six electrons in the valence shell and the corresponding stability of low-valent compounds shall be demonstrated using lead compounds in the oxidation state Pb(II) and Pb(IV) as examples.[47] The two systems show also the influence of relativity on the stability of the molecules. Most inorganic lead compounds such as halides and oxides are derived from Pb(II) while inorganic Pb(IV) compounds are either unknown or highly reactive. In contrast to this, organic Pb(IV) compounds are relatively stable while most lead organic species PbR_2 are unstable molecules. The calculated reaction energies of reactions 3–5 show typical differences:[47]

$$\begin{aligned} PbH_4 + 2PbF_2 &\longrightarrow PbF_4 + 2PbH_2 + 104.0\,\text{kcal mol}^{-1}\text{(rel)} \\ &\quad + 57.6\,\text{kcal mol}^{-1}\text{(nonrel)} \end{aligned} \tag{3}$$

$$PbH_4 + 2PbCl_2 \longrightarrow PbCl_4 + 2PbH_2 + 89.5\,\text{kcal mol}^{-1}\text{(rel)} \tag{4}$$

$$PbMe_4 + 2PbF_2 \longrightarrow PbF_4 + 2PbMe_2 + 103.2\,\text{kcal mol}^{-1}\text{(rel)} \tag{5}$$

The calculated values for reactions 3 and 4 show that Pb(II) compounds become stabilized relative to Pb(IV) by electronegative substituents. Reaction 3 was calculated with and without relativistic effects. Electronegative substituents attract electronic charge from Pb, which becomes more positively charged. The valence s orbitals contract more than the p orbitals when the central atom becomes more positive. Thus, the size difference increases owing to the electron-withdrawing effect of electronegative substituents. This effect is enhanced by relativity. The calculated values for reaction 1 show that the endothermicity increases from +57.6 kcal mol^{-1} to +104.0 kcal mol^{-1} when relativistic effects are included in the calculation. Chlorine stabilizes Pb(II) slightly less than fluorine while hydrogen and methyl exhibit similar behavior.

9 REFERENCES

1. (a) G. N. Lewis, *J. Am. Chem. Soc.*, 1916, **38**, 762; (b) G. N. Lewis, 'Valence and the Structure of Atoms and Molecules', Dover Publications, New York, 1923.
2. L. Pauling, 'The Nature of the Chemical Bond', 3rd edn., Cornell University Press, Ithaca, NY, 1960.
3. R. J. Gillespie and I. Hargittai, 'The VSEPR Model of Molecular Geometry', Allyn & Bacon, Boston, MA, 1991.
4. A. E. Reed, L. A. Curtiss, and F. Weinhold, *Chem. Rev.*, 1988, **88**, 899.
5. H. A. Bent, *Chem. Rev.*, 1961, **61**, 275.
6. A. Beste, O. Krämer, A. Gerhard, and G. Frenking, *Eur. J. Inorg. Chem.*, 1999, 2037.
7. K. Morokuma, *J. Chem. Phys.*, 1971, **55**, 1236.
8. T. Ziegler and A. Rauk, *Theor. Chim. Acta*, 1977, **46**, 1.

9. F. M. Bickelhaupt and E. J. Baerends, in ‘Reviews in Computational Chemistry’, eds. K. B. Lipkowitz and D. B. Boyd, Wiley-VCH, New York, 2000, Vol. 15, p. 1.
10. G. Frenking, K. Wichmann, N. Fröhlich, C. Loschen, M. Lein, J. Frunzke, and V. M. Rayón, *Coord. Chem. Rev.*, 2003, **55**, 238.
11. C. Esterhuysen and G. Frenking, *Theor. Chem. Acc.*, 2004, **111**, 381.
12. (a) K. P. Huber and G. Herzberg, ‘Molecular Spectra and Molecular Structure IV. Constants of Diatomic Molecules’, Van Nostrand-Reinhold, New York, 1990; (b) D. R. Lide ed., ‘CRC Handbook of Chemistry and Physics’, 81st edn., CRC Press, Boca Raton, FL, 2000.
13. F. L. Hirshfeld and S. Rzotkiewicz, *Mol. Phys.*, 1974, **27**, 1319.
14. M. A. Spackman and E. N. Maslen, *J. Phys. Chem.*, 1986, **90**, 2020.
15. W. Kutzelnigg, *Angew. Chem.*, 1984, **96**, 262; *Angew. Chem., Int. Ed. Engl.*, 1984, **23**, 272.
16. J. W. Ochterski, G. A. Petersson, and K. B. Wiberg, *J. Am. Chem. Soc.*, 1995, **117**, 11299.
17. B. Ruscic and J. Berkowitz, *J. Chem. Phys.*, 1991, **95**, 4378.
18. A. Ricca and C. W. Bauschlicher Jr, *J. Phys. Chem. A*, 1999, **103**, 11121.
19. N. Bartlett, *Proc. Chem. Soc.*, 1962, 218.
20. R. E. Rundle, *J. Am. Chem. Soc.*, 1963, **85**, 112.
21. M. Kaupp, C. van Wüllen, R. Franke, F. Schmitz, and W. Kutzelnigg, *J. Am. Chem. Soc.*, 1996, **118**, 11939.
22. K. O. Christe, W. W. Wilson, R. V. Chirakal, J. C. P. Sanders, and G. J. Schrobilgen, *Inorg. Chem.*, 1990, **29**, 350.
23. T. A. Albright, J. K. Burdett, and M. H. Whangbo, ‘Orbital Interactions in Chemistry’, Wiley, New York, 1985.
24. K. Fukui, ‘Theory of Orientation and Stereoselection’, Springer Verlag, Berlin, 1975.
25. A. D. Walsh, *J. Chem. Soc.*, 1953, 2260, 2266, 2288, 2296, 2301, 2306.
26. B. M. Gimarc, ‘Molecular Structure and Bonding – The Qualitative Molecular Orbital Approach’, Academic Press, New York, 1979.
27. J. P. Kenny, W. D. Allen, and H. F. Schaefer III, *J. Chem. Phys.*, 2003, **118**, 7353.
28. (a) M. Kaupp, P. v. R. Schleyer, H. Stoll, and H. Preuss, *J. Am. Chem. Soc.*, 1991, **113**, 6012; (b) M. Kaupp and Pv. R. Schleyer, *J. Am. Chem. Soc.*, 1992, **114**, 491; (c) M. Kaupp, *Angew. Chem.*, 2001, **113**, 3642; *Angew. Chem., Int. Ed. Engl.*, 2001, **40**, 3534.
29. M. Lein, A. Szabó, A. Kovács, and G. Frenking, *Faraday Discuss.*, 2003, **124**, 365.
30. (a) G. Frenking, *J. Am. Chem. Soc.*, 1991, **113**, 2476; (b) G. Frenking, W. Koch, and H. Schwarz, *J. Comput. Chem.*, 1986, **7**, 406.
31. E. A. Cater and W. A. Goddard III, *J. Phys. Chem.*, 1986, **90**, 998.
32. H. Jacobsen and T. Ziegler, *J. Am. Chem. Soc.*, 1994, **116**, 3667.
33. (a) L. Pu, B. Twamley, and P. P. Power, *J. Am. Chem. Soc.*, 2000, **122**, 3524; (b) A. D. Phillips, R. J. Wright, M. M. Olmstead, and P. P. Power, *J. Am. Chem. Soc.*, 2002, **124**, 5930; (c) M. Stendere, A. D. Phillips, R. J. Wright, and P. P. Power, *Angew. Chem.*, 2002, **114**, 1863; *Angew. Chem., Int. Ed. Engl.*, 2002, **41**, 1785.
34. (a) M. Cordonnier, M. Bogey, C. Demuynck, and J. L. Destombes, *J. Chem. Phys.*, 1992, **97**, 7984; (b) G. Maier, H. P. Reisenauer, A. Meudt, and H. Egenolf, *Chem. Ber.*, 1997, **130**, 1043; (c) X. Wang, L. Andrews, and G. P. Kushto, *J. Phys. Chem. A*, 2002, **106**, 5809; (d) X. Wang, L. Andrews, G. V. Chertihin, and P. F. Souter, *J. Phys. Chem. A*, 2002, **106**, 6302; (e) X. Wang and L. Andrews, *J. Am. Chem. Soc.*, 2003, **125**, 6581.
35. R. J. Gillespie and P. L. A. Popelier, ‘Chemical Bonding and Molecular Geometry’, Oxford University Press, New York, 2001.
36. R. F. W. Bader, ‘Atoms in Molecules: A Quantum Theory’, Oxford University Press, Oxford, 1990.
37. M. Lein, J. Frunzke, and G. Frenking, in ‘Structure and Bonding’, ed. T. Schönherr, Springer Verlag, Berlin, 2004, Vol. 106, p. 181.
38. L. Khriachtchev, M. Pettersson, N. Runeberg, J. Lundell, and M. Räsanen, *Nature*, 2000, **40**, 874.
39. A. Haaland, *Angew. Chem.*, 1989, **101**, 1017; *Angew. Chem., Int. Ed. Engl.*, 1989, **28**, 992.
40. R. Pearson ed., ‘Hard and Soft Acids and Bases’, Dowden, Hutchison and Ross, Stroudsburg, PA, 1973.
41. F. Bessac and G. Frenking, *Inorg. Chem.*, 2003, **42**, 7990.
42. (a) P. P. Power, *Chem. Rev.*, 1999, **99**, 63; (b) M. Weidenbruch, *J. Organomet. Chem.*, 2002, **646**, 39.
43. (a) A. E. Reed and P. v. R. Schleyer, *Am. Chem. Soc.*, 1990, **112**, 1434; (b) E. J. Magnusson, *Am. Chem. Soc.*, 1990, **112**, 7940; (c) J. Cioslowski and S. T. Mixon, *Inorg. Chem.*, 1993, **32**, 3209; (d) D. L. Cooper, T. P. Cunningham, J. Gerrat, P. B. Karadakov, and M. Raimondi, *J. Am. Chem. Soc.*, 1994, **116**, 4414; (e) M. Häser, *J. Am. Chem. Soc.*, 1996, **118**, 7311; (f) J. A. Dobado, H. Martinez-Garcia, J. M. Molina, and M. R. Sundberg, *J. Am. Chem. Soc.*, 1998, **120**, 8461.
44. W. Kutzelnigg, *Angew. Chem.*, 1984, **96**, 262; *Angew. Chem., Int. Ed. Engl.*, 1984, **23**, 272.
45. J. P. Desclaux, *At. Data Nucl. Data Tables*, 1973, **12**, 311.
46. P. Schwerdtfeger ed., ‘Relativistic Electronic Structure Theory’, Elsevier, Amsterdam, 2002, 2004, Vol. 1 (Fundamentals) and Vol. 2 (Application).
47. M. Kaupp and Pv. R. Schleyer, *J. Am. Chem. Soc.*, 1993, **115**, 1061.
48. A. Kovács, C. Esterhuysen and G. Frenking, *Chem. Eur. J.*, 2005, online.
49. M. Lein, A. Krapp and G. Frenking, *J. Am. Chem. Soc.*, 2005, in print.
50. M. Lein and G. Frenking, *Austr. J. Chem.*, 2004, **57**, 1191.

Electronic Structure of Organometallic Compounds

Thomas A. Albright
University of Houston, Houston, TX, USA

1	Introduction	1
2	The Elements of Orbital Interaction	1
3	Basic Splitting Patterns	5
4	Overlaying π Effects	13
5	Fragment Orbitals	17
6	The Isolobal Analogy	21
7	Related Articles	25
8	References	25

Glossary

Hybridization: the mixing of two atomic orbitals of differing angular quantum number at one atom
ML$_n$: a generic transition metal bonding to n ligands (L) where the ligand is considered to be a two-electron donor
Orthogonal: when the overlap between two wavefunctions is zero

Abbreviations

$e_i =$ The orbital energy associated with ϕ_i; SALC $=$ Symmetry adapted linear combination; $S_{ij} =$ The overlap between the wavefunctions ϕ_i and ϕ_j.

1 INTRODUCTION

There is a bewildering array of geometrical patterns offered to organometallic compounds. Consider that the transition metal can commonly be from two to nine coordinate and that there is a vast catalog of ligands that can be coordinated to the metal (*see* ***Coordination Numbers & Geometries***). The synthetic chemist can easily be overwhelmed when trying to determine the electronic structure for a specific molecule or comparing it to others. It is, of course, this diversity in the geometry of organometallic molecules that leads to a very rich set of bonding schemes. However, there are many simplification devices. These in turn can be exploited to see the threads that link the electronic structure of one structural type to another. Perhaps the earliest bonding concept was the 18-electron or EAN rule proposed by Sidgwick in 1927 (*see Effective Atomic Number Rule*). The hypothesis that most catalytic cycles involve alternating 16- and 18-electron intermediates is another concept directed towards the reactivity of organometallic molecules (*see* ***Mechanisms of Reaction of Organometallic Complexes***). Certainly another very important advance was the *Dewar–Chatt–Duncanson Bonding Model* of metal–alkene complexes. We shall see in this article the evolution of the Dewar–Chatt–Duncanson model to many other bonding situations.

This article will not cover the bonding in clusters (*see* ***Electronic Structure of Clusters***), in extended solids (*see* ***Electronic Structure of Solids***), or in main group compounds (*see* ***Electronic Structure of Main-group Compounds***). It will be confined to discrete transition metal compounds from Groups 4–11 in the *Periodic Table*. Detailed coverage of the bonding in organolanthanide/actinide molecules**[1]** and the electronic requirements of reaction mechanisms**[2–4]** have been provided elsewhere. With the advent of density functional methods, organometallic structures and reactions can be investigated on a more or less routine level with some confidence that the quantitative details will match experiment. But the insight into where these numbers come from and what they mean does not come from these computer programs. This is the focus of this article. The material discussed here is qualitative in nature and is applicable to evaluating the results from semiempirical, local density, or ab initio molecular orbital calculations (*see* ***Molecular Orbital Theory*** for a description and uses of these techniques in inorganic chemistry). It starts from an LCAO expansion of the wavefunction (*see LCAO Approximation*) and utilizes only symmetry properties and the qualitative application of perturbation theory. The principal rules that govern how orbitals interact with each other within the context of perturbation theory are given in the next section.

2 THE ELEMENTS OF ORBITAL INTERACTION

The construction of the electronic structure of an organometallic compound can be envisioned as a building block process, wherein the important valence orbitals of the ligands (a subset of the *Valence Orbitals* for the ligand set) interact with the valence AOs of the transition metal. Alternatively, the important valence orbitals of an ML$_n$ fragment can interact with the important valence orbitals of a ligand. In the former approach, the bonding between the metal and all surrounding ligands is highlighted. A practical consequence is that all of the ligands should be electronically similar (but not necessarily identical), although there are techniques to build in π bonding on one or more ligands as a second step in the building block process as outlined in Section 4. The latter method concentrates on the bonding between the metal (as influenced by auxiliary ligands) and a specific ligand. Both techniques utilize a qualitative application of perturbation theory[5] to estimate the magnitude of orbital interaction and the form of the resulting MOs. Certainly other qualitative or semiquantitative techniques exist (*see* ***Ligand Field Theory & Spectra***). The simplicity here is that any orbital interaction pattern can be constructed from two cases.

2.1 The Two Orbital Problem

Let us consider the formation of an M–L *σ-Bond* as a generic model. In most instances a lone pair on the ligand lies lower in energy than the metal d set of AOs prior to orbital interaction. This is reflected in (**1**) by the relative positioning of ϕ_i, a ligand centered orbital at an energy e_i, and ϕ_j, a metal d orbital at an energy e_j. The vertical scale, explicitly drawn for this case on the left side of (**1**), in this orbital interaction diagram then denotes potential energy with $e_i < e_j$. There are phases (the amplitude of the *Wavefunction*) associated with every AO and MO. The convention followed here is to denote positive phase by shading and negative phase by no shading in the two-dimensional representations of the wavefunctions.

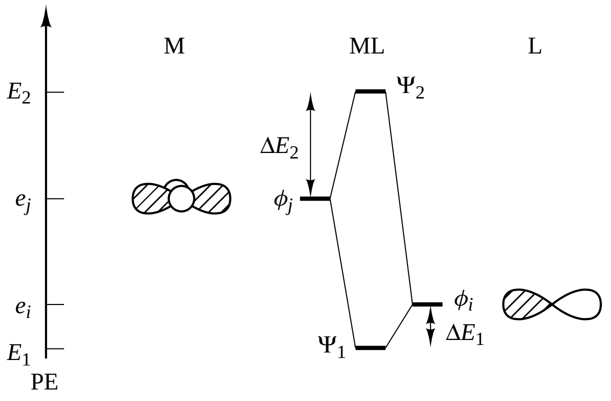

(**1**)

Notice in (**1**) that the relative phases of the starting, unperturbed wavefunctions, ϕ_i and ϕ_j, have been adjusted so that the *Overlap Integral*, S_{ij}, between them is positive. That is, upon going from atoms M to L along the bond vector there is no phase inversion in ϕ_i and ϕ_j. When ϕ_i and ϕ_j interact with each other, two molecular orbitals, Ψ_1 and Ψ_2, are produced. The mixing of ϕ_j into ϕ_i is given by a mixing coefficient, $t_{ji}^{(1)}$, that can be qualitatively assessed by equation (1). The resultant molecular orbital is approximately given by equation (2).

$$t_{ji}^{(1)} \propto \frac{-S_{ij}}{e_i - e_j} \tag{1}$$

$$\Psi_1 \approx \phi_i + t_{ji}^{(1)}\phi_j \tag{2}$$

Since $e_i < e_j$ and S_{ij} we have taken to be positive in drawing the relative phases in (**1**), then $t_{ji}^{(1)}$ is a positive number. That is, ϕ_j will mix into ϕ_i with the phase present in (**1**). The construction of Ψ_1 is diagrammatically indicated in (**2**). This is a bonding MO; there is no phase inversion on going from M to L. The value of $t_{ji}^{(1)}$ will be less than 1; however, Ψ_1 will be primarily associated with the ligand lone pair, ϕ_i. The magnitudes (or weights) of the orbitals that mix are pictorially represented in a qualitative fashion by the size of the orbitals. For Ψ_2, the mixing of ϕ_i into ϕ_j, $t_{ij}^{(1)}$ is given by equation (3) and the resultant MO, Ψ_2, by equation (4). Here $t_{ij}^{(1)}$ becomes negative, that is, ϕ_i mixes into ϕ_j with the opposite phase given in (**1**).

$$t_{ij}^{(1)} \propto \frac{-S_{ij}}{e_j - e_i} \tag{3}$$

$$\Psi_2 \approx \phi_j + t_{ji}^{(1)}\phi_i \tag{4}$$

Consequently, as shown by (**3**), Ψ_2 is primarily associated with the transition metal d AO (the absolute magnitude of $t_{ij}^{(1)}$ is also less than 1) and there is antibonding associated with this MO, that is, there is a phase inversion on going from M to L in Ψ_2.

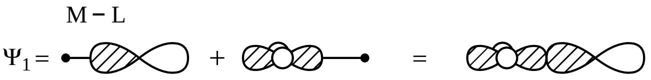

(**2**)

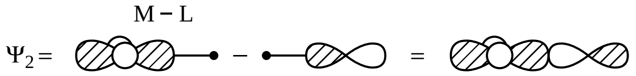

(**3**)

The bonding between ϕ_i and ϕ_j in Ψ_1 causes e_i to be lowered in energy by an amount ΔE_1 as provided by equation (5).

$$\Delta E_1 \propto \frac{S_{ij}^2}{e_i - e_j} \tag{5}$$

Notice that, since $e_i < e_j$, ΔE_1 is negative, that is, Ψ_1 is stabilized. The antibonding orbital Ψ_2 is destabilized by an amount ΔE_2. This is set by an equation analogous to equation (5) except that the ordering of e_i and e_j in the denominator is reversed. An important feature of perturbation theory, and indeed when one does a molecular orbital calculation at any level which that includes overlap, is that the antibonding combination (Ψ_2) is destabilized more than the bonding combination (Ψ_1) is stabilized, that is, $|\Delta E_2| > |\Delta E_1|$. Therefore the addition of two electrons to Ψ_1 in (**1**) is associated with stabilizing the formation of an M–L bond. However, adding two more electrons fills Ψ_2, and this will then represent a net destabilizing interaction.

2.2 The Three-orbital Problem

The three-orbital pattern results when two orbitals on one fragment (or atom) strongly interact with an orbital on another fragment. One possible, again generic, situation is illustrated in (**4**). In this instance, both a metal d, ϕ_j, and a metal p, ϕ_k, AO interact with a single p AO, ϕ_i, on a ligand.

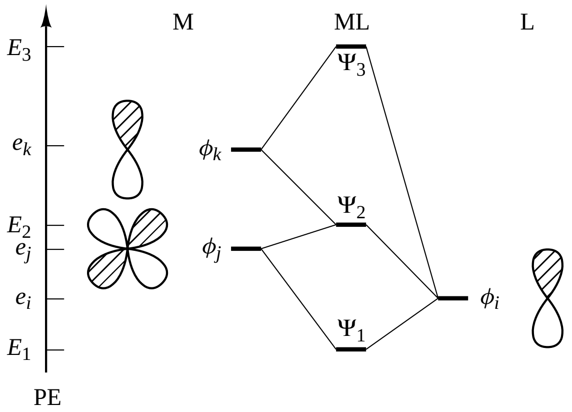

(**4**)

Notice that, again, the phases of the starting orbitals have been adjusted so that the overlap between ϕ_i and ϕ_j along with that between ϕ_i and ϕ_k are positive. Since ϕ_j and ϕ_k are on the same center, they are orthogonal (have no overlap between each other). The form of Ψ_1 is particularly simple. It represents just the sum of mixing ϕ_j into ϕ_i and ϕ_k into ϕ_i. There are then two terms analogous to equation (1). Since $e_i < e_j$ and e_k, both mixing terms are positive, that is, both ϕ_j and ϕ_k mix into ϕ_i in a bonding fashion as indicated by (**5**).

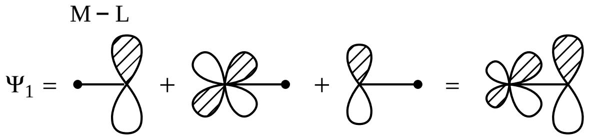

(**5**)

The metal orbital is hybridized in this MO to provide maximal bonding to the ligand. Ψ_2 will be primarily localized on ϕ_j; furthermore, ϕ_i will mix into ϕ_j with a negative mixing coefficient (in an antibonding fashion since ϕ_i lies lower in energy). However, ϕ_k can also mix into ϕ_2 with a mixing coefficient given by equation (6). The relative sign of $t_{kj}^{(2)}$ is negative; thus Ψ_2 is constructed as shown in (**6**).

$$t_{kj}^{(2)} \propto \frac{S_{ki}S_{ji}}{(e_j - e_k)(e_j - e_i)} \tag{6}$$

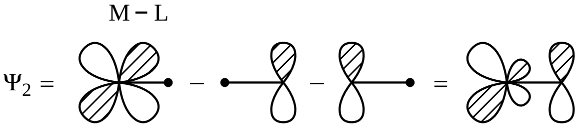

(**6**)

Notice the hybridization again at the metal; in this case it is in a direction away from the ligand. It is clear from the construction in (**6**) that Ψ_2 is a nonbonding MO. The form of Ψ_3 is determined in an analogous fashion in that it is primarily ϕ_k with ϕ_i mixed in an antibonding way. There is also the mixing of ϕ_j into ϕ_k which is given by equation (7).

$$t_{jk}^{(2)} \propto \frac{S_{ki}S_{ji}}{(e_k - e_j)(e_k - e_i)} \tag{7}$$

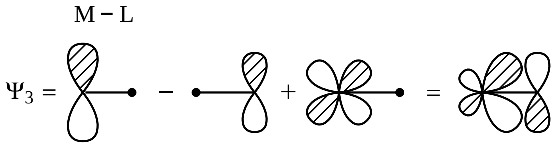

(**7**)

The construction of Ψ_3 is then given in (**7**). As in Ψ_1, it is hybridized towards the ligand now to produce a maximally antibonding MO. The bonding present in Ψ_1 causes e_i to be stabilized and the corresponding antibonding in Ψ_3 translates into a destabilization. We have indicated in (**4**) that Ψ_2 is destabilized. This is a reflection that the bonding between ϕ_k and ϕ_i is less than the amount of antibonding between ϕ_j and ϕ_i. However, Ψ_2 is *not* destabilized as much as Ψ_1 is stabilized (provided that the overlap between ϕ_i and ϕ_k is of reasonable magnitude). Therefore, the addition of four electrons, filling both Ψ_1 and Ψ_2, can lead to a net stabilizing situation.

Besides (**4**) there are two other three-orbital patterns that can be constructed as indicated by (**8**). One can easily work through the orbital mixings that evolve. In each instance, the pattern found in (**4**) is present. Namely, Ψ_1 and Ψ_3 are maximally bonding and antibonding between M and L, respectively, while Ψ_2 is nonbonding. The relative weight of each MO does change on going from (**4**) to (**8**). For example, Ψ_2 in (**4**) is primarily ϕ_j, whereas it is primarily ϕ_i in (**8a**) and ϕ_k in (**8b**). The important point is that the functional form of Ψ_2 always remains the same, that is, nonbonding.

2.3 Generalizations

The orbital interaction patterns that were presented in the previous two sections have a number of features in common. Any MO most strongly resembles the starting, unperturbed orbital closest to it in energy. A higher lying orbital will always mix into a lower lying one in a bonding fashion and a lower lying orbital mixes into a higher lying one in an antibonding

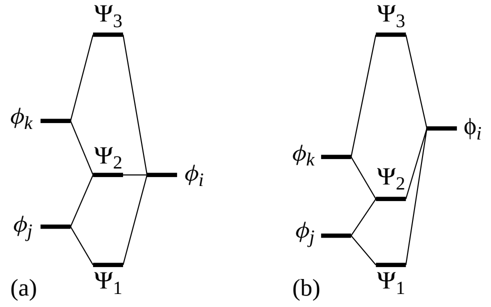

(**8**)

fashion. Notice that this occurs as well in the $t^{(2)}$ mixing terms for the three-orbital problem. In (**6**) the high-lying ϕ_k mixes with ϕ_j in a bonding way with respect to ϕ_i and in (**7**) the lower lying ϕ_j mixes into ϕ_k in a way which is antibonding to ϕ_i. The amount of stabilization or destabilization is dependent upon two factors: it directly depends upon the magnitude of the overlap between the two starting orbitals and inversely upon the energy difference. The overlap which exists between orbitals is sensitive to a number of factors. Firstly, it depends upon the type of overlap. The situation illustrated in (**1**) is that of σ overlap; there are no *nodes* along the internuclear axis (M–L), whereas that in (**4**) is of the π type where one node lies along the internuclear axis for each combination. A final type, shown in (**9**), represents δ overlap. Here two nodes lie along the internuclear axis. Since the amount of overlap in a nodal plane is necessarily zero, it then follows as a general rule that overlap varies in the manner of $\sigma > \pi > \delta$.

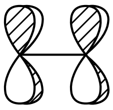

(**9**)

The geometry present in the molecule also has a decisive impact on the magnitude of the overlap. Figure 1 shows the angular dependence of the overlap between two d orbitals and an s orbital. The σ overlap in each instance is maximal at very different angles of θ. Furthermore, as shown above each curve, the functional form of the d AO creates a specific angular dependence on S_{ij}. This feature forms the basis for the *Angular Overlap Model*. The positions of the atoms in the periodic table is another variable to be considered. For valence orbitals, a general rule of thumb is that the more diffuse the orbital is, the less it overlaps with another orbital. A valence orbital becomes more diffuse when one goes down a column or proceeds from right to left along a row in the periodic table. Hence the overlap of the 2s/2p AOs on oxygen will create a larger overlap with a metal set of d AOs than for the 3s/3p AOs on sulfur, for example. There is, however, one important exception. The 3d AOs for the first transition metal row are too contracted. There is no inner core of d electrons. Consequently, they overlap less with ligand orbitals than do the 4d or 5d AOs of the second or third row analogs, respectively.**[6]**

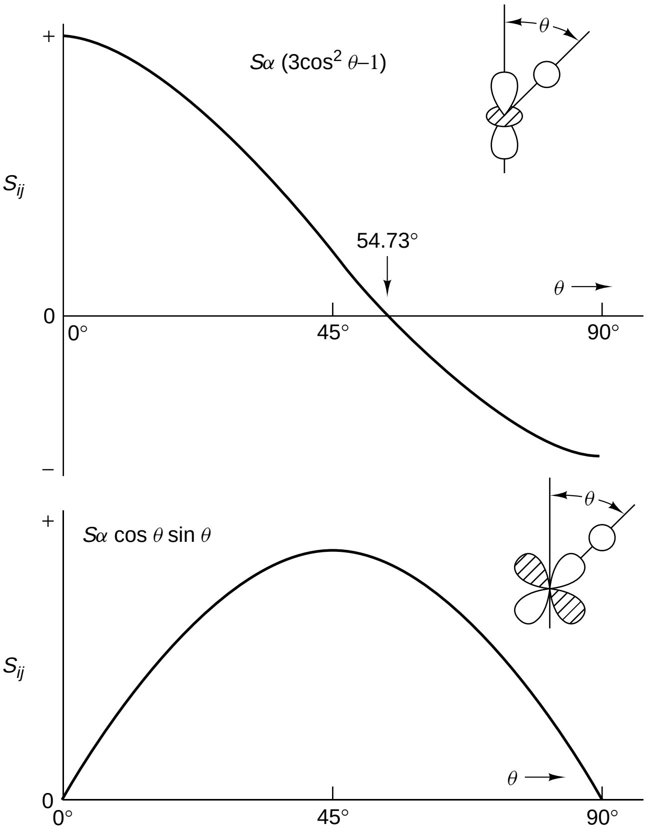

Figure 1 The angular dependence of the overlap, S_{ij}, between a metal d and a ligand s orbital for two different d AOs

The final variable in determining overlap lies in symmetry. A discussion of group theory and the formation of *Symmetry Adapted Linear Combinations* (SALC) lies beyond the scope of this entry.**[7]** For our purposes it is sufficient to state that when a collection of orbitals exists which can be interrelated by symmetry elements, then combinations of these orbitals can be constructed. Each SALC is orthogonal to all others and reflects the full symmetry properties present in the molecule. A short-hand way to designate these symmetry properties is by the Mullikan notation**[7]** for the irreducible representations of the group which are used throughout this contribution. Since irreducible representations are orthogonal to each other, then any orbitals and/or collections of orbitals with different Mullikan symbols have zero overlap with each other. An alternative, very powerful way of stating this is that only orbitals of the same symmetry can interact with each other.

The energy gap between two interacting orbitals also plays a critical role in determining the magnitude of the interaction. As indicated previously the amount of stabilization in the bonding combination is inversely proportional to the energy gap between the two interacting orbitals. The electronegativity of the atom(s) obviously is directly related to orbital energies. For example, the lone pair of a phosphine lies at a higher energy than that of an amine (*see* ***Photoelectron Spectroscopy of Transition Metal Systems***) and consequently will form a stronger bond to a transition metal. The presence of a charge or inductive effects of substituents will also scale the energies of orbitals. Electron-donating groups or the presence of a negative charge will raise orbital energies while a positive charge will lower orbital energies.

3 BASIC SPLITTING PATTERNS

In this section, we shall cover the electronic structure of the basic coordination types in organometallic compounds. Since σ interactions are stronger than π because of overlap, the strategy is to first build the MO's that are σ bonding. Any π type interactions can be added on in a second, separate step. The details of this are reserved for Section 4. All of the ligands in (**10**) present a high-lying filled orbital to the metal which can be used for σ interaction. In other words, a cylindrical field of electron density is donated to the metal. Of course, they will not all lie at the same energy; that can be treated as a subsequent minor perturbation. We shall then use a stylized representation for that orbital on L, a teardrop shape, and regard L as a neutral, two-electron σ donor ligand. It is recognized that when several specific ligand types coordinate to the transition metal, then the symmetry of the molecule is considerably lower than that of the parent ML_n complex. However, there is an effective pseudosymmetry that the transition metal experiences in the σ system that is the same as that in the ML_n example.

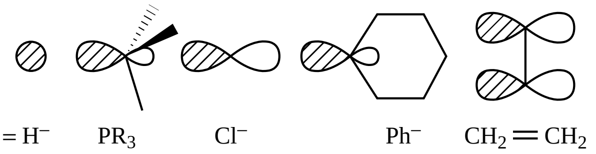

(**10**)

3.1 The Octahedron

Figure 2 presents an orbital interaction diagram for building the valence orbitals of an octahedral ML_6 complex. On the left side are the nine valence AOs of a transition metal. The six SALCs for the L_6 set of lone pairs are drawn on the right side. They have $a_{1g} + t_{1u} + e_g$ symmetry. The relative energies have been set so that the lone pairs lie slightly lower than the metal d set. This will be generally true; however, one can point to exceptional instances where combinations of very electronegative metals and electropositive ligands reverse this ordering. It is clear that metal s interacts only with the a_{1g} SALC and metal p with the t_{1u} set. Two metal d orbitals, $x^2 - y^2$ and z^2, interact with the e_g combination. Six ligand centered bonding MOs, $1a_{1g} + 1t_{1u} + 1e_g$, are produced. This is the delocalized equivalent of six 2-center−2-electron M–L σ bonds where one forms six equivalent sp^3d^2 hybrid orbitals at the metal and interacts each with one ligand σ orbital. The $2e_g + 2a_{1g} + 2t_{1u}$ MOs are the antibonding counterparts and are concentrated more at the metal. Left behind in this interaction are three d AOs; using the coordinate system at the top of Figure 2 they are *xz*, *xy*, and *yz*. Provided that the ligands have only σ donor capabilities (or at this stage of the electronic structure analysis recall that we are only concerned with σ effects), then these three orbitals, the t_{2g} set, are rigorously nonbonding.

A family of molecules exists with 12 valence electrons (e.g. WF_6, $W(NMe_2)_6$, $TiCl_6^{2-}$) and the $1a_{1g}$ through $1e_g$ molecular orbitals are filled. In cases where the ligands are strong σ donors (i.e. the metal d−ligand lone pair overlap is large and the ligand orbitals are close to or even above the metal d orbitals), then the $1e_g$ MOs may lie lower in energy than the $1t_{1u}$ set. The order of the MOs that is displayed in Figure 2 simply reflects the relative ordering of the starting orbitals. For a molecule to be stable at the octahedral geometry the *HOMO−LUMO Gap* between t_{2g} and $1t_{1u}$ or $1e_g$ must be large. In the 12-electron WMe_6 molecule, the $t_{2g}-1t_{1u}$ energy gap at the octahedral geometry is small (this is one instance where $1t_{1u}$ lies higher in energy than $1e_g$). Consequently, the molecule adopts a very unusual and sterically unfavorable distorted trigonal prismatic geometry.**[8,9]** This is also the case for a number of other d^0 ML_6 molecules.**[10]**

A more common bonding situation exists when the nonbonding t_{2g} set is filled with six electrons and, of course, there are 12 electrons in the M–L σ bonding orbitals, which yields a total of 18 electrons. The heavy box in Figure 2 highlights those orbitals that are metal d-centered. The HOMO-LUMO energy gap, now between t_{2g} and $2e_g$, is critical and controls the chemistry of these molecules. Recall that $2e_g$ is the antibonding combination of metal $x^2 - y^2$ and z^2 to the ligand σ set. It is explicitly drawn in (**11**).

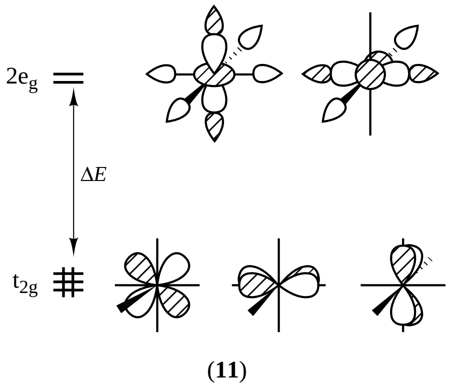

(**11**)

The magnitude of the $t_{2g} - 2e_g$ energy gap is primarily determined by how much $2e_g$ is destabilized by the ligand σ donor set. When the ligands are strong σ donors (e.g. PR_3, CO, alkyl, alkoxide, alkene), then $2e_g$ lies at a very high energy and

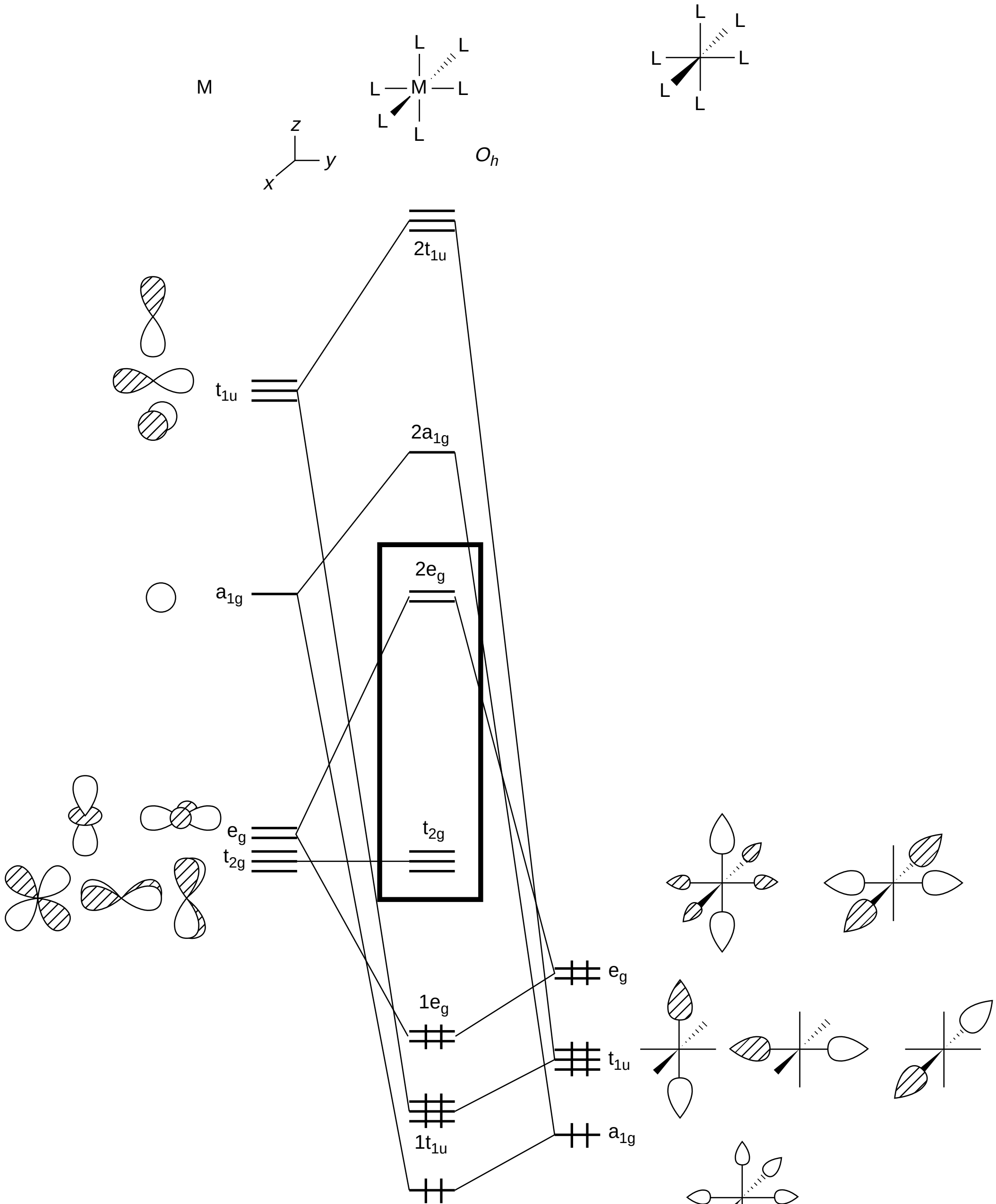

Figure 2 Building the valence orbitals for an octahedral ML_6 complex

population of it is energetically costly. Thus, addition of an electron to $Cr(CO)_6$ does not give the 19-electron $Cr(CO)_6{}^-$ molecule; instead, CO is lost to yield $Cr(CO)_5{}^-$.[11] In general 19- or 20-electron organometallic compounds are quite rare unless there is some symmetry based reason which prohibits one or more symmetry combination of ligand orbitals from overlapping with the metal orbitals. We shall cover a few of these cases in Section 4.3. On the other hand, the classic coordination complexes (*see* ***Coordination & Organometallic Chemistry: Principles***) possess weak σ donor ligands (e.g. NH_3, H_2O) and they are very electronegative. Consequently, the lone pairs lie at a low energy and the overlap between them and the metal d AOs is small. Much of the attractive interaction between the metal and ligand is electrostatic rather than covalent. The $2e_g$ orbitals are destabilized to a lesser extent and the $t_{2g} - 2e_g$ energy gap is small. Consider a hypothetical example where there are two electrons and two orbitals to place them in. When the energy difference between the two orbitals is smaller than the Coulomb repulsion integral generated by putting an electron in each orbital, it is then energetically favorable to unpair the electrons and put one in each orbital.[5] In the present case for coordination compounds, there is a delicate balance between high-spin (a maximum of unpaired spins in the d orbital splitting block) and low-spin electronic states. An 18-electron example such as $Fe(H_2O)_6{}^{2+}$ is high spin with the electron occupancy in (**12**), whereas $Cr(CO)_6$ and the vast majority of 18-electron organometallic complexes are low-spin with the electronic configuration shown in (**13**).

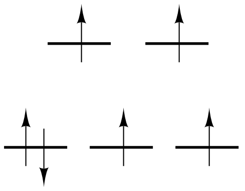

High spin

(**12**)

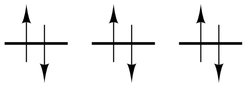

Low spin

(**13**)

3.2 The Square Plane

On the left side of Figure 3 are the metal s, p, and d orbitals. On the right side are the four ligand SALCs. The e_u set matches two metal p orbitals and b_{1g} combines with metal $x^2 - y^2$ (the coordinate system is shown at the top of Figure 3). Three bonding and antibonding MOs are formed. Just as in the octahedron, three metal d AOs, xz, yz (of e_g

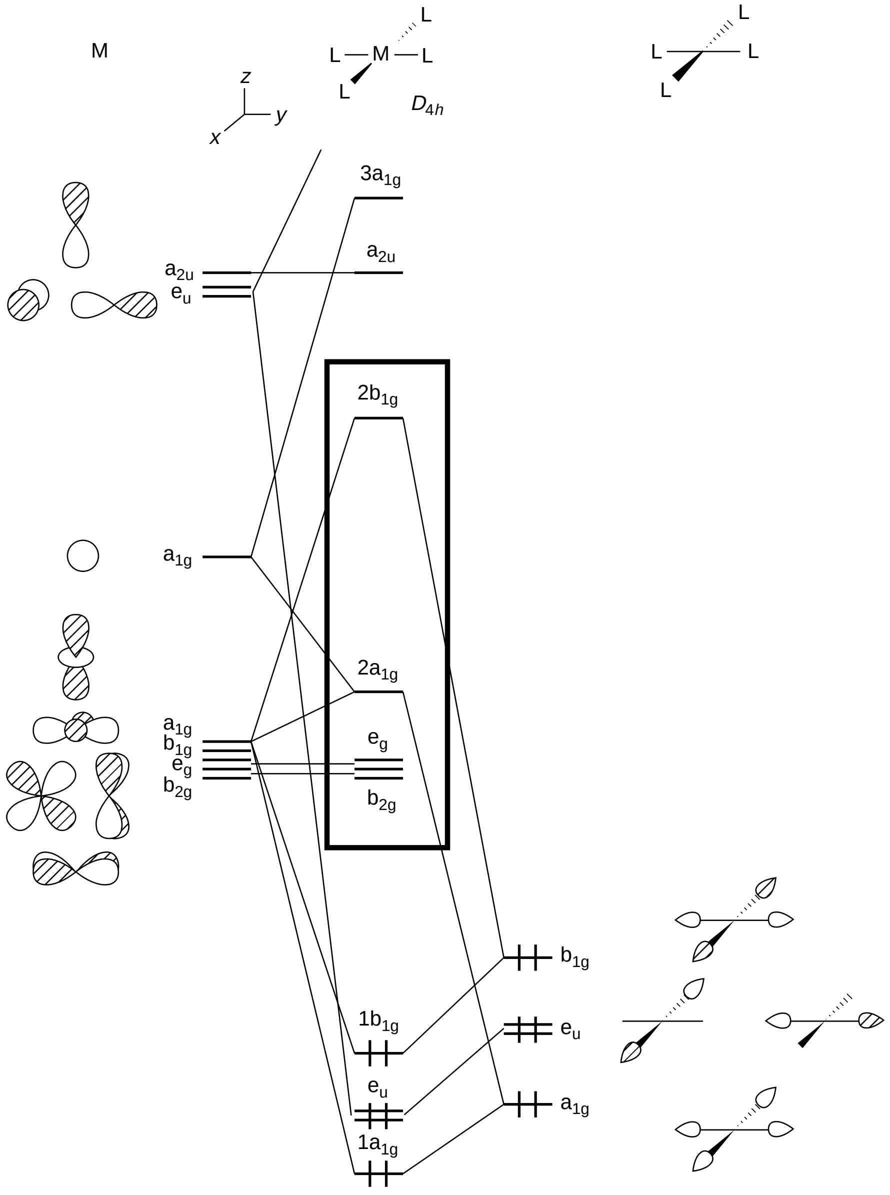

Figure 3 Construction of the valence orbitals of a square-planar ML_4 complex

symmetry), and *xy* (b_{2g}) are left nonbonding. The ligand a_{1g}, metal z^2, and metal s all have the same symmetry. Thus, we have a three-orbital pattern, precisely analogous to (**4**) which evolves. The lowest MO, $1a_{1g}$, is primarily ligand based with metal z^2 and s mixing into it in a bonding fashion. The fully antibonding analog is $3a_{1g}$. Here the MO is primarily metal s and the ligand SALC mixes in an antibonding fashion to metal s and z^2. The nonbonding MO, $2a_{1g}$, remains at about the same energy as the starting metal d AOs. Its constitution is given in (**14**). It is primarily metal z^2 antibonding to ligand a_{1g}. Metal s mixes into this orbital also in a bonding way to the lone pairs. The valence metal d region is highlighted with a box in Figure 3. One might think that a molecule with 8 valence electrons ($1a_{1g} + e_u + 1b_{1g}$ filled) might be stable. In fact, this is not the case. As we shall see in the next section, a tetrahedral geometry is preferred. In this context, when L is a strong σ donor, then the $1b_{1g}$ MO may lie lower in energy than the e_u set. We shall also see in Section 4.3 that π donors interact with and destabilize *xz*, *yz*, and *xy*. In $W(OR)_4$ with 10 valence electrons, this does, in fact, occur and the molecule is more stable at the square-planar geometry with the HOMO being $2a_{1g}$ (e_g and b_{2g} are destabilized by the alkoxide lone pairs). Filling all metal d nonbonding orbitals (e_g, b_{2g}, and $2a_{1g}$) leads to a 16 electron complex. This is a very common electron count for organometallic molecules.

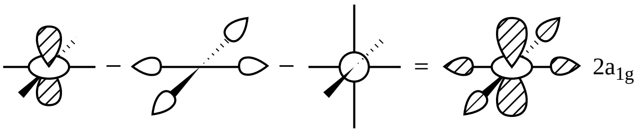

(**14**)

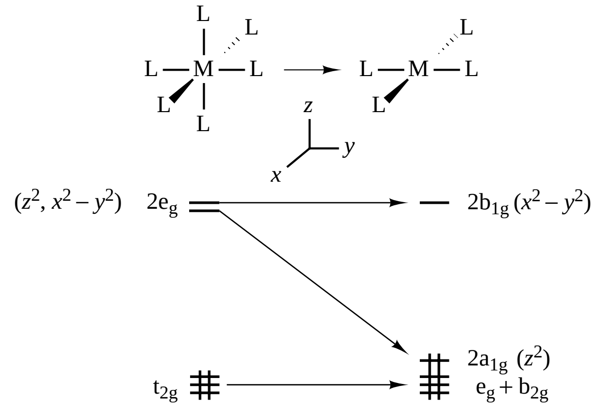

(**15**)

Notice in Figure 3 that the metal *z* AO, a_{2u}, also remains at high energy. It is clear that the addition of two electrons to yield an 18-electron complex will be energetically prohibitive. Yet, there is a strong electronic correlation between an 18-electron octahedral ML_6 complex and a 16-electron square-planar ML_4 one. This correspondence is illustrated in (**15**). When two trans ligands in an octahedral complex are removed, the z^2 component of $2e_g$ is considerably stabilized and joins the block of the other three nonbonding d AOs. The remaining four d-based MOs are identical. Thus, as shown, a d^6 ML_6 complex is electronically analogous to a d^8 square-planar ML_4 one.

3.3 The Tetrahedron

Figure 4 presents the MOs for a tetrahedral ML_4 complex. The a_1 ligand combination interacts with metal s to form the bonding, $1a_1$, and antibonding, $2a_1$, MOs. Using the coordinate system at the top of the figure, metal z^2 and *xy* are rigorously nonbonding and form an e set. The metal $x^2 - y^2$, *xz*, and *yz* along with the p AOs combine with the ligand t_2 set to form a three-orbital pattern. The $1t_2$ and $3t_2$ MOs are the bonding and antibonding components. The middle, nonbonding (or in this case slightly antibonding) member is the $2t_2$ set. The construction of it follows the pattern developed in the previous examples and is explicitly shown for the *yz* member in (**16**). Notice that the orbital is hybridized away from the ligand σ donor functions. Molecules with 8 valence electrons, for example, $ZrMe_4$ and $TiMe_4$, are more stable at this geometry with $1a_1$ and $1t_2$ filled than at the square-planar geometry. The reason behind this rests in the fact that $1t_2$ in Figure 4 lies lower in energy than e_u in Figure 3.

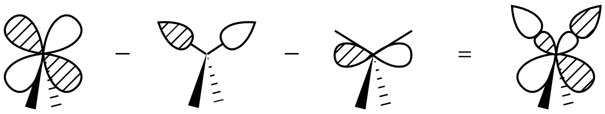

(**16**)

$Ru(Mes)_4$ and $Ir(Mes)_4{}^+$ have been isolated and found to possess a tetrahedral geometry.**12** These are rare examples of 12-electron count molecules. From Figure 4 the e set should be completely filled. Indeed, the molecules are diamagnetic. However, by far the most common tetrahedral organometallic molecules have an 18-electron count where $2t_2$ is the HOMO. There is a very specific dependence of the electron count on the geometry; recall that 16-electron ML_4 complexes were square planar. The variation of the valence MOs associated with the metal d-block going from the square planar to tetrahedral geometry is given in Figure 5. It is easy to see why d^{10} (18 electron) complexes prefer the tetrahedral geometry over the square-planar one; $2t_2$ lies lower in energy than $2b_{1g}$. For a d^8 (16 electron) complex, $2a_{1g}$ on the square-planar side lies much lower than $2t_2$. What is not so apparent is why $Ru(Mes)_4$ and $Ir(Mes)_4$ are tetrahedral. A high-spin square-planar geometry should lie at about the same or lower energy. The reason partially lies in the steric bulk of the Mes ligands, which is minimized in the tetrahedral structure. In fact, the isoelectronic $MnMe_4{}^-$ molecule is paramagnetic and square planar.**13** The d^2 system presents an analogous situation:

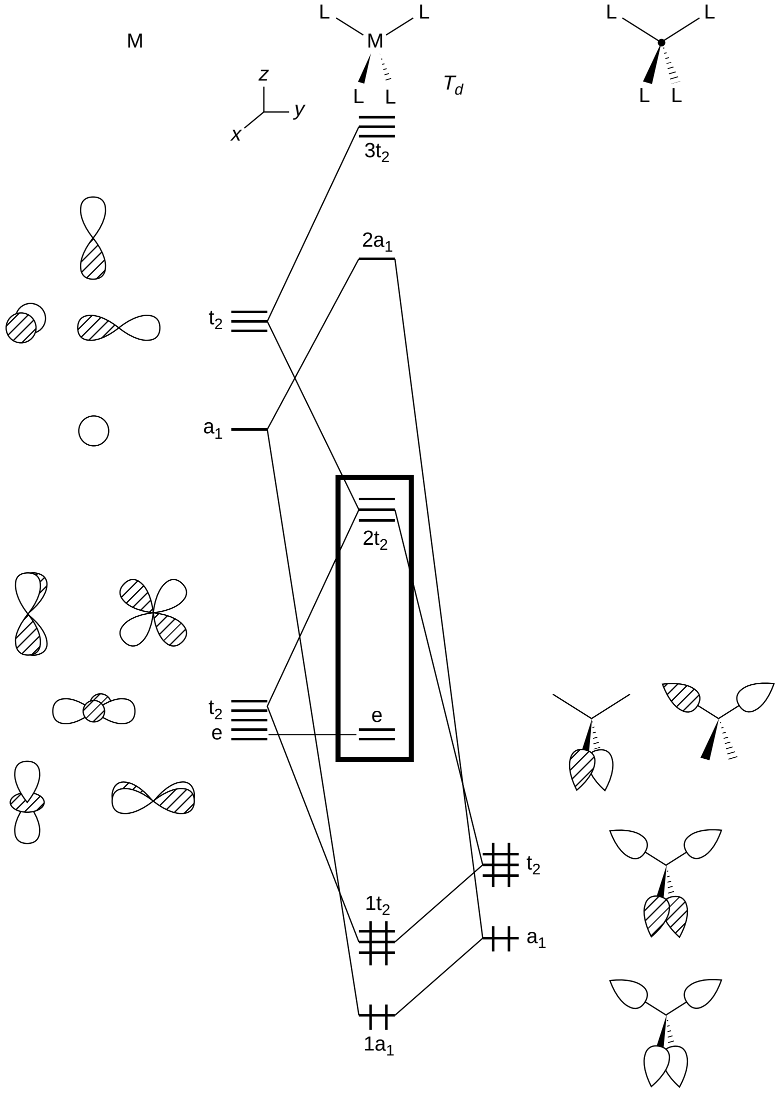

Figure 4 An orbital interaction diagram for the valence orbitals of a tetrahedral ML_4 complex

$Cr(C_6H_{11})_4$ is tetrahedral and a triplet;[14] however, square-planar d^2 systems are also known where π effects provide the discriminating factor. Another factor at work in these molecules is the spin pairing energies. As indicated previously, 3d valence orbitals are considerably more contracted that 4d and 5d; thus the Coulomb repulsion integrals are much larger for first-row transition metal complexes and high-spin states are more favored than is the case for second and third row complexes.

3.4 The Trigonal Bipyramid and Trigonal Plane

The orbital interaction diagram for a trigonal bipyramid is illustrated in Figure 6. Notice that there are two ligand SALCs of a_1' symmetry. The metal z^2 and s AOs also have a_1' symmetry so one might think that all four orbitals will interact with each other. However, this is not the case. The lower ligand SALC possesses no nodal planes; this is also the case for metal s. Therefore those two orbitals combine to produce the $1a_1'$ bonding and $4a_1'$ antibonding MOs. The higher ligand SALC has two nodal planes that match the pattern in z^2. Thus, $2a_1'$ and $3a_1'$ represent their bonding and antibonding interactions, respectively. The a_2'' ligand SALC interacts with metal z also in a two orbital pattern. The metal xz/yz (e$''$) set are left totally nonbonding. There is one three-orbital combination which arises from the ligand e$'$ SALC with the $xy/x^2 - y^2$ and x/y sets at the metal. The middle d-centered MOs (2e$'$) are determined in the standard fashion and are shown in (**17**). For an 18-electron complex, that is, $Fe(CO)_5$, 2e$'$ is the HOMO. Populating $3a_1'$ will create an unstable situation. One ligand will be lost to generate an 18-electron, tetrahedral ML_4 complex.

The situation for electron counts less than 18 is slightly more complicated since another ML_5 geometry, that of the square pyramid, must be considered. The evolution of orbital

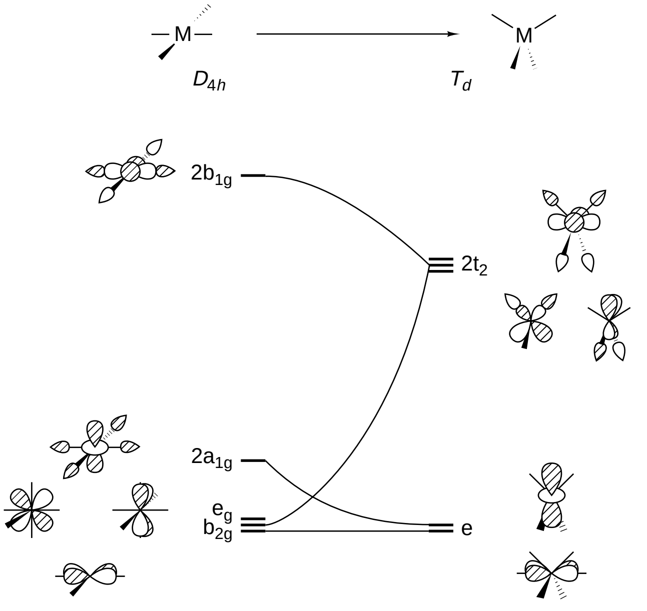

Figure 5 Variation of the orbital energies on going from the square planar to tetrahedral geometry

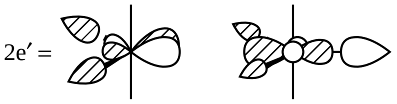

(**17**)

energies on going from a trigonal bipyramid to the square pyramid and the resulting shapes is given for the d-block orbitals in Figure 7. Any variation of energy is simply a reflection of changes in overlap between the metal and ligand orbitals and will not be discussed here.[5] For the d^8 (18 electron) system, there is actually a very small energy difference between the two structures. In fact, there exists a collection of solid-state structures for molecules at this electron count which lie along the *Berry Pseudorotation* path for converting a trigonal bipyramid into a square pyramid.[15] A d^6 system, like Cr(CO)$_5$, strongly prefers the square pyramid for a low-spin complex.[16] At the trigonal bipyramidal geometry the 2e′ set is half-filled and, therefore, a less stable triplet state is found at this geometry. For two electrons less, a d^4 complex, the trigonal bipyramid becomes more stable. The ground state for RePh$_3$(PEt$_2$Ph)$_2$ is a low-spin complex[17] with e″ filled; however, analogous manganese complexes are high-spin[18] with e″ and 2e′ occupied.

The valence orbitals of a trigonal planar complex can be easily constructed as we have done for the preceding examples. An alternative way to view the construction of the d-block manifold is shown in (**18**). Just as in the octahedral ML$_6$ to square-planar ML$_4$ transformation shown in (**15**), only one metal d-based MO is affected. The majority of the M–L σ antibonding is lost in z^2; furthermore, metal s mixes into this MO in a bonding way to the remaining ligands. Thus, the a$'_1$ orbital is stabilized considerably on going from ML$_5$ to ML$_3$. An 18-electron, d^8 ML$_5$ complex is, therefore, electronically analogous to a 16-electron, d^{10} ML$_3$ species. Just as a d^6 trigonal bipyramidal ML$_5$ complex distorts to a square pyramid, a d^8 trigonal planar ML$_3$ complex undergoes an analogous transformation to a T-shaped geometry.[8]

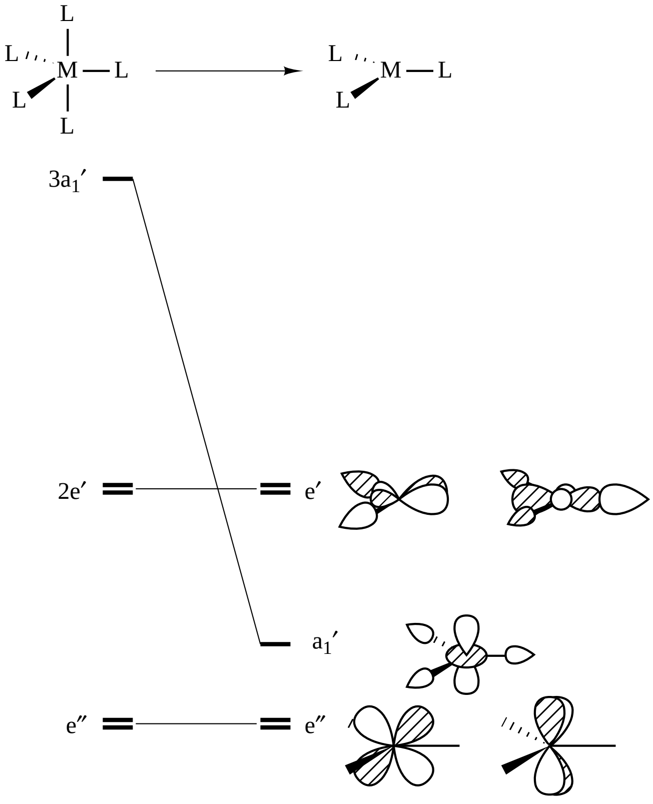

(**18**)

3.5 Electron Counting

The orbital interaction patterns that we have derived in the previous sections, along with those for seven- and eight-coordinate molecules,[19,20] can be generalized as indicated in Figure 8. If there are n ligands surrounding the transition metal, then n SALCs of ligand σ donor functions exist. All will be stabilized by metal d, s, and p AOs. Thus, n M–L bonding orbitals, centered on the ligands, are formed. There are of course n M–L σ antibonding orbitals also created. These MOs are pushed to high energies and are more concentrated at the metal. Left behind are $9 - n$ nonbonding orbitals provided that the metal and all of the ligands do not lie in a common plane. These nonbonding MOs are primarily d in character since d AOs have more nodes than the s and p AOs. Filling all bonding and nonbonding orbitals with two electrons then provides a total of $2(n + 9 - n) = 18$ electrons. Figure 8 provides an MO rationalization of the 18-electron rule. Notice that we are

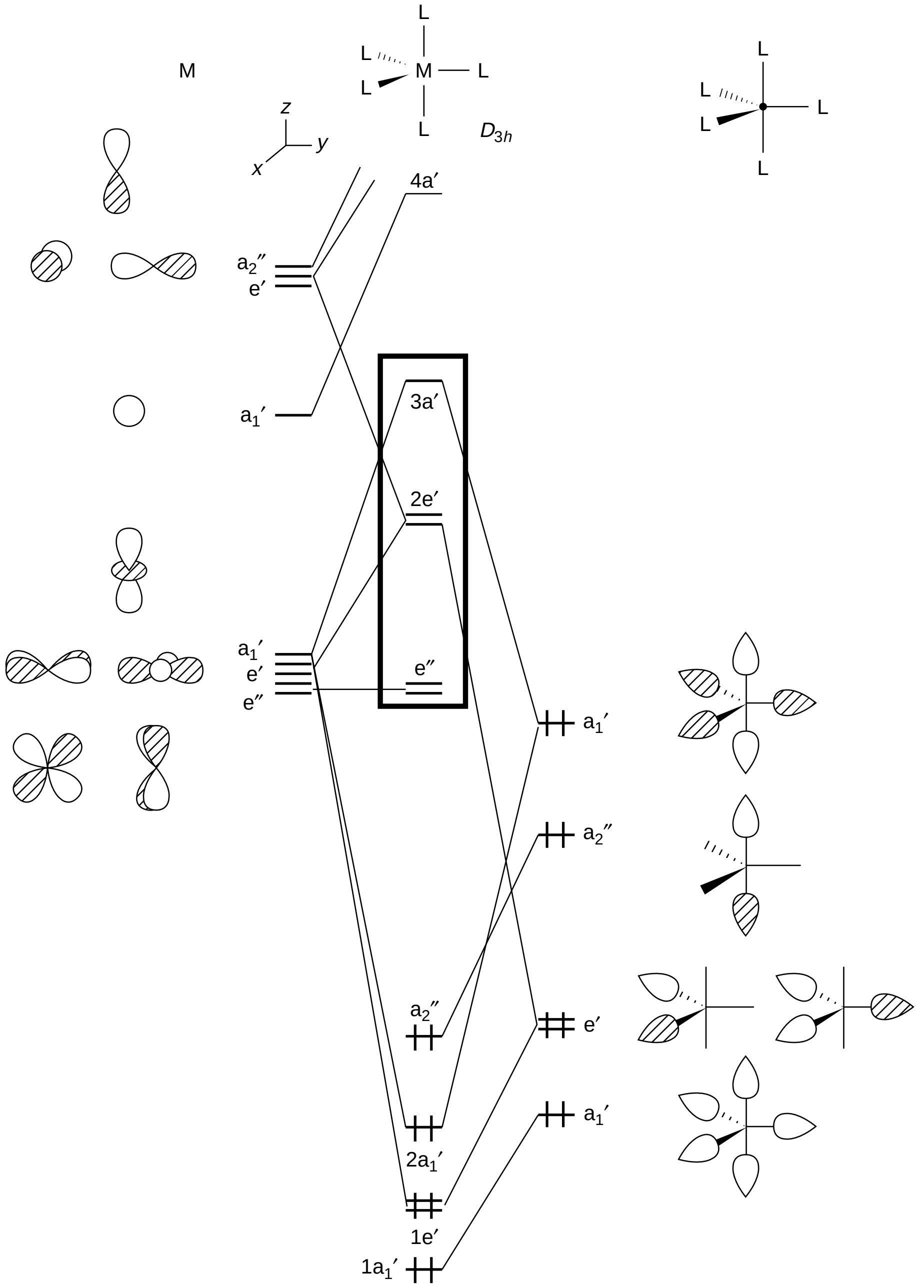

Figure 6 An orbital interaction diagram for the valence orbitals of a trigonal bipyramid

counting the number of electrons engaged in M–L bonding, as well as those localized at the transition metal. Figure 8 can easily be modified to include the two common instances where 16 electrons are preferred, namely, the square plane and trigonal plane. Since in these cases the metal and surrounding ligands lie in a plane, there can be no interaction between the ligand σ donor set and one of the p AOs at the metal. The metal p AO lies at a high energy and it is not energetically advantageous to fill it.

The assignment of formal charge at the metal can be problematic since it depends on a person's bias of how to view the ligands. As long as this is done in a consistent manner, one will always obtain the same total valence electron count. The particular convention described here has the virtue that it will immediately pinpoint how many d electrons are present, that is, the occupation of the metal d-centered MOs that have been described in the previous sections. We shall treat all ligands as Lewis bases. Listed in (**19**) are some ligands. In each case we will treat the ligand as a two-electron σ donor group. The total number of d electrons can be obtained by adding the formal charges assigned to the ligands in (**19**) and subtracting the sum from the charge on the molecule. This will yield the formal

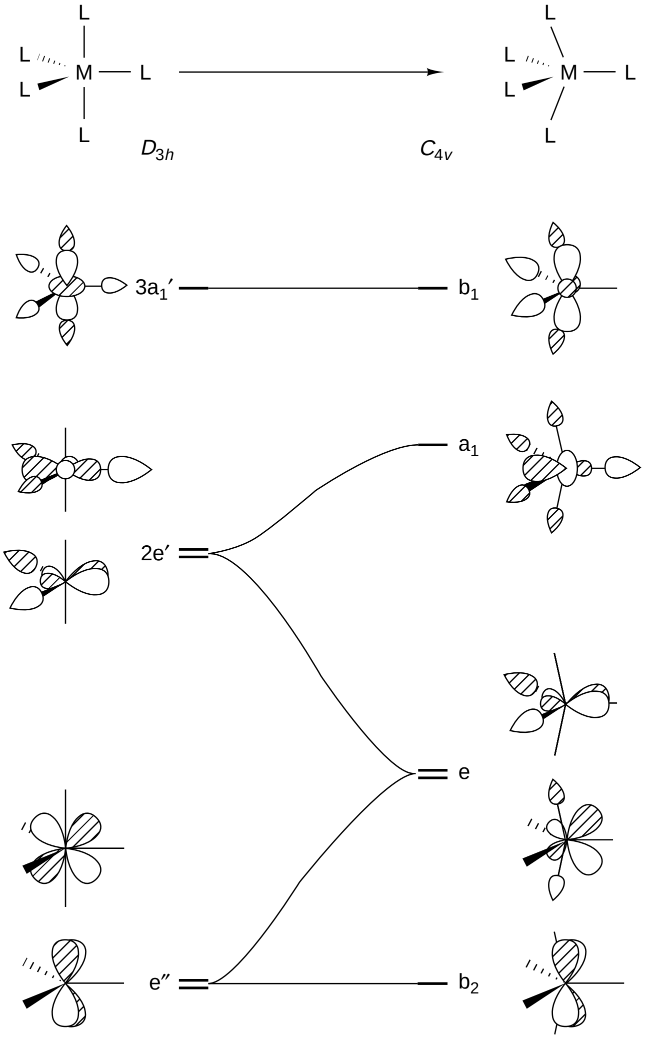

Figure 7 Variation of the orbital energies on going from the trigonal bipyramid to square pyramid

charge (oxidation state) at the metal and subtracting it from the number of d electrons for the metal in the zero oxidation state gives the number of d electrons formally assigned to the metal d orbitals (those orbitals within the boxes in the previous sections). Summing the number of electrons donated by the ligand set and the number of d electrons then equals the total number of valence electrons. Notice that we have only counted the number of electrons which are M–L σ bonding along with the d electrons localized at the metal. No M–L π interactions have been counted.

NR_3, PR_3, SR_2, CH_3^-, SiR_3^-, H^-	(σ donors)
CO, NO^+, CNR, SO_2, CR_2, CR^+	(π acceptors)
NR_2^-, Cl^-, OR^-, NR^{2-}, O^{2-}, P^{3-}	(π donors)

(**19**)

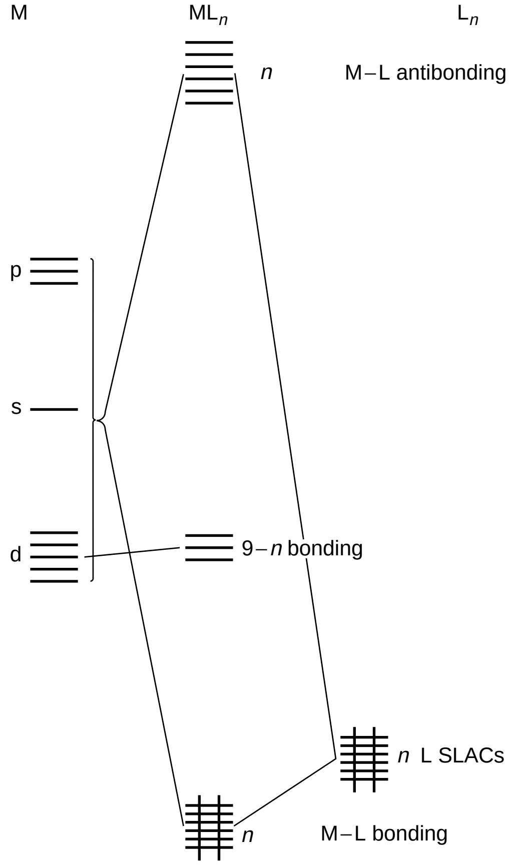

Figure 8 A generalized orbital interaction diagram for a ML_n transition metal complex

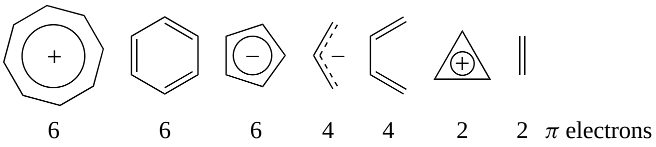

(**20**)

Polyenes are counted so that all bonding and nonbonding π orbitals associated with the polyene are occupied. The most commonly encountered examples are illustrated in (**20**). Below each structure is the number of π electrons (which interact with the metal in a σ fashion) used for polyene–M σ bonding provided that the metal is bonded to all carbon atoms in the polyene. Thus Cp donates six electrons only if it is an η^5 ligand. For an η^3-Cp situation, it donates four electrons analogous to a π-allyl ligand, etc.

There are two points that should be remembered. Firstly, the splitting patterns developed previously are not especially sensitive to the exact ligand set. This is especially true for the d-block. For example, in (**21**) there are six different ligands coordinated to the metal. There are three metal d MOs which are filled in this d^6 complex and lie very close together in energy. They correspond in shape to the t_{2g} set in Figure 2.

Two MOs lie at much higher energy and are metal–ligand antibonding, the $2e_g$ set. Secondly, the ligand σ donor set in (**21**) certainly is not contained within a narrow energy region. One might consider that the s orbital for H lies above the Ir d AOs; thus, it should be regarded as an H^+ (rather than H^-) ligand. Indeed, many metal hydrides are acidic (*see* ***Hydride Complexes of the Transition Metals***). One could then view (**21**) as a d^8 complex. The problem with this approach is that an Ir–H σ bond will be formed and lie lower than the t_{2g}-like set. It will be hybridized more at the metal (rather than the hydrogen). However, the t_{2g} set still contains six electrons. Little is gained by regarding (**21**) as a d^8 species.

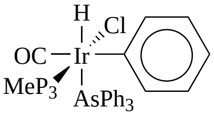

(**21**)

4 OVERLAYING π EFFECTS

The three t_{2g}-like orbitals in (**21**) do not all lie at the same energies. There will be some variation in energy because of the presence of the CO and Cl ligands which possess π-acceptor and π-donor functions, respectively. The t_{2g} set interact in a π-type fashion with the surrounding ligands. For the other splitting patterns this will occur always for the d-block nonbonding orbitals. Since π bonding is intrinsically weaker than σ, the latter can be viewed as a perturbation of the basic electronic structure set by the σ interactions.

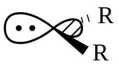

(**22**)

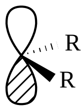

(**23**)

4.1 Typical π-Acceptor Patterns

A very simple π-acceptor ligand is the carbene. A carbene contains one hybrid orbital (**22**), which is used for σ bonding, and an orthogonal p AO (**23**), which can participate in π interactions with the metal.[21] Using the electron counting formalism in (**19**), (**22**) is regarded as being occupied with two electrons and (**23**) is empty. This is the signature of a π-acceptor ligand; a low-lying empty orbital must be present on the ligand. Figure 9 presents two cases for the π-type interaction between the carbene and metal in an octahedrally based system. In Figure 9(a), the carbene p AO lies well above the octahedral t_{2g} in energy. It mixes into, and stabilizes, one component of the metal t_{2g} set. As shown, the bonding combination is still largely localized on the metal. Electron density which in (**22**) is localized on the carbene is shared in the metal complex. The back donation of electron density from metal t_{2g} to the carbene for the π bond in Figure 9(a) does not entirely compensate that forward donation from the carbene to the metal in the σ system. Therefore, the carbene is electron deficient and the molecule behaves as an electrophile in terms of its reactivity. On the other hand, in Figure 9(b) the carbene p AO lies at the same energy (or perhaps even lower) as the metal t_{2g} set. The bonding combination, as shown, contains much more electron density on the carbene. Therefore, the molecule now reacts as a nucleophile. Of course, the situation also depends upon the metal and auxiliary ligands. The addition of other π acceptor ligands, for example, CO, and high oxidation states at the metal will cause t_{2g} to lie at a low energy and favor the situation in Figure 9(a). These are called Fisher-type carbene complexes. The addition of strong σ and/or π donating ligands, for example, Cp and amido, will favor Figure 9(b) and these complexes are called Schrock-type carbenes.

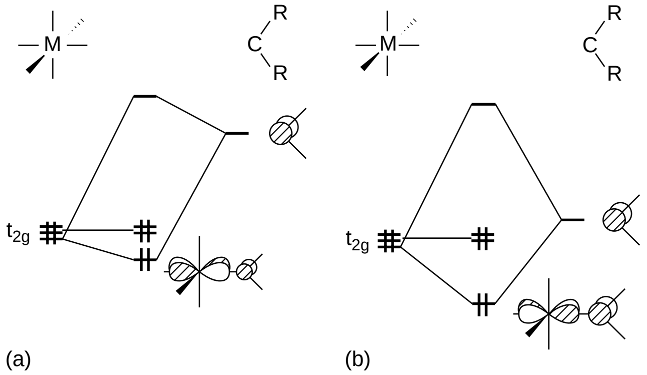

Figure 9 The π interaction between a carbene and metal for an octahedral system. Case (a) refers to a Fisher-type carbene and (b) to a Schrock-type carbene

A slightly more complicated pattern is presented by the carbonyl ligand. On the right side of Figure 10 are the π and π^* orbitals of a carbonyl ligand. The electronegativity difference between C and O serves to localize more electron density on the O atom for the π set, whereas π^* is more concentrated on the C atom. Consequently the overlap between metal t_{2g} and π^* is greater than that between t_{2g} and π (the carbonyl is, of course, bonded to the metal via the carbon end). A three-orbital interaction pattern is formed. Two components of the metal t_{2g} set interact with the π and π^* orbitals. The lowest MO, 1e, is primarily carbonyl π with some metal d mixed in a bonding fashion. This is shown for one component in Figure 10. The highest MO, 3e, is shown to be primarily π^* antibonding to metal d. The middle level, 2e, is derived in (**24**). It is metal d mixed in a bonding fashion to the higher energy π^* and in an antibonding way to the lower π orbital. There is an approximate cancellation of electron density at the carbon atom in 2e. Notice in Figure 10 that one member of t_{2g}

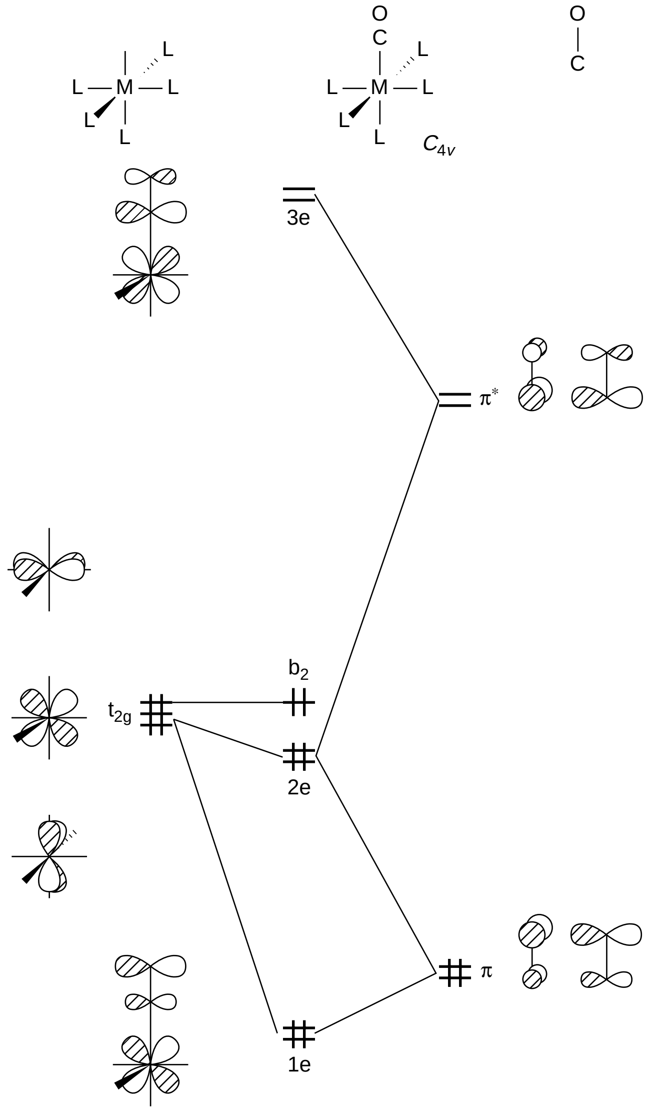

Figure 10 The π interactions for an octahedral complex with one carbonyl ligand

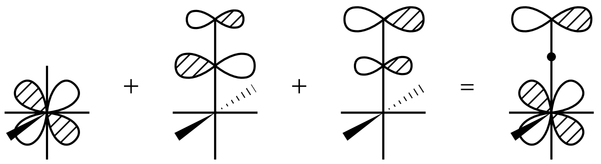

(**24**)

is unperturbed (b_2). How much the 2e MOs will be stabilized relative to b_2 will depend upon the metal and auxiliary ligands in an obvious manner. When the $t_{2g} - \pi^*$ energy gap increases, there is less stabilization associated with 2e. There is less π^* character in the 2e MOs. Since π^* is strongly C–O antibonding, the C–O stretching frequency increases. An example is provided by the isoelectronic $V(CO)_6{}^-$, $Cr(CO)_6$, and $Mn(CO)_6{}^+$ molecules where the C–O stretching frequencies are 1843, 1984, and 2094 cm^{-1}, respectively (*see **Transition Metal Carbonyls: Infrared Spectra***). The energy of the metal d AOs will decrease in that order since the electronegativity of the metal increases. Furthermore, there is a charging effect at work. The negative charge in $V(CO)_6{}^-$ causes the metal d AOs to rise in energy while the positive charge in $Mn(CO)_6{}^+$ has the opposite effect. These effects are nicely supported by density functional calculations on the isoelectronic series $Hf(CO)_6{}^{2-}$ to $Ir(CO)_6{}^{3+}$.**[22]** But just how much 'forward donation' from the lone pair of the CO ligand to empty $2e_g$ on the metal versus 'back donation' from the filled metal t_{2g} to the empty π^* on CO is there? Table 1 lists some calculated**[23]** values for a few representative $L{-}W(CO)_5$ complexes, where L is a π-acceptor ligand. Here 'forward' represents the electron density (in electrons) from the filled ligand σ orbital transferred to the metal and 'back' is the electron density transferred to the empty π-acceptor orbital on L. CO is a strong σ-donor and π-acceptor. On going to NO^+ one expects, on the grounds of electronegativity, that the σ and π levels will be lowered and so it should be a weaker σ-donor and a stronger π-acceptor than CO. The computations bear this out. Conversely, also for electronegativity reasons, CN^- is a very strong σ-donor and a weak π-acceptor and N_2 is neither a good σ-donor nor π-acceptor. The numbers here do not directly reflect the magnitude of the L–W bond energy. Other factors such as electrostatic and Pauli repulsion play and important role; however, it is easy to see why the N_2–W bond is extraordinarily weak. The CH_2 ligand, as indicated by Figure 9, is similar to CO. The last two entries in Table 1 will be discussed later.

4.2 π-Donor Effects

A π-donor ligand possesses a high-lying filled orbital that can serve to interact with and destabilize a member of the nonbonding metal d set. As an illustrative example we present the trans and cis dioxo problem. Figure 11(a) constructs the π orbitals for a trans dioxo–ML_4 complex. Two of the three members of the t_{2g} set can interact with two of the four SALCs of oxygen p AOs. Thus, one metal d and two oxo orbitals are left nonbonding. The orientation

Table 1 Charge decomposition for 'forward' and 'back' donation (in electrons) for a series of $L{-}W(CO)_5$ complexes**[23]**

L	Forward	Back (electrons)
CO	0.315	0.233
NO^+	0.119	0.378
CN^-	0.488	0.024
N_2	0.027	0.107
CH_2	0.314	0.282
C_2H_4	0.500	0.175
H_2	0.349	0.129

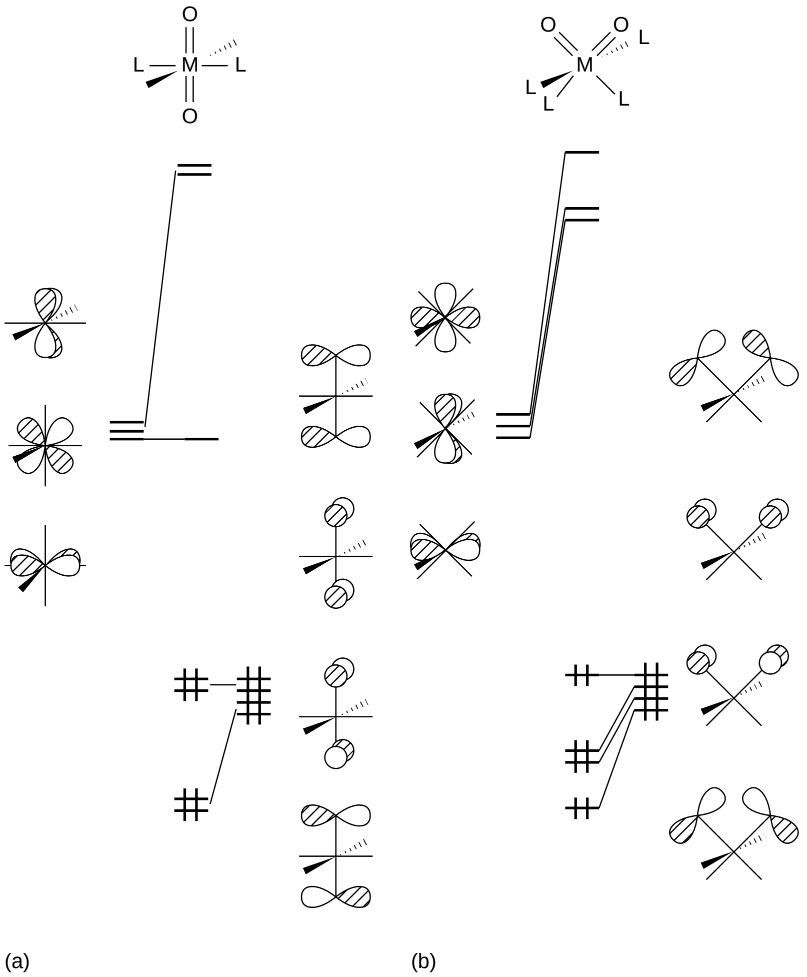

Figure 11 Building the π orbitals in a (a) *trans* and (b) *cis* dioxo–ML_4 complex

of the octahedron has been redrawn in Figure 11(b) for the cis dioxo–ML_4 case to facilitate comparison. Now all three members of t_{2g} are utilized for π bonding. One SALC of the dioxo set remains nonbonding. It is then clear that a d^0 complex prefers the cis geometry since maximal π bonding occurs at this geometry. But a d^2 complex prefers the trans structure since in it the HOMO is metal nonbonding. A cis d^2 complex has two electrons in a strongly M–O antibonding orbital. This is a general solution that can be applied to many different situations.**5** Given two geometries or conformations associated with a molecule, the most stable one maximizes all two electron–two orbital bonding patterns and minimize the four electron–two orbital ones. Thus, for a d^0 cis dioxo–ML_4 complex there are three two electron–two orbital interactions as opposed to the two in the trans dioxo–ML_4 case. In the d^2 system, there are no four electron–two orbital combinations for the trans geometry; however, there is one in the cis structure. Also notice that the oxo ligand has two perpendicular filled p AOs which can be used to form π bonds to the metal. Thus, in a dioxo complex one might naively be lead to the belief that there ought to be four π M–O bonds. Figure 11(a) and 11(b) demonstrate that this can never be the case. The trans complex (Figure 11(a)) can form two, and only two, π bonds for the d^0 and d^2 cases when symmetry has been properly taken into account. The cis structure can possess a maximum of three π bonds in a d^0 complex. A symmetry based approach in this instance lends itself to a clear and particularly simple solution. Some further effects of symmetry on the electronic structure of organometallic compounds are contained within the next section of material.

4.3 Extraordinary Symmetry Effects

Acetylenes are adaptable ligands in that there are two orthogonal π orbitals which can be used for bonding to the metal. These are indicated by (**25**) as radial and tangential π orbitals. The radial orbital has a σ type overlap with the metal; however, that for the tangential one is of the π sort. Thus the acetylene ligand can be viewed as a two or four electron donor. Consider then the case of tris(acetylene)W(CO), shown

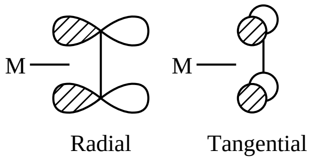
M
M
Radial
Tangential

(**25**)

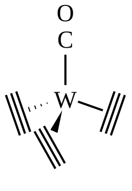

(**26**)

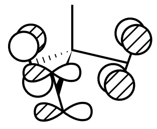

(**27**)

in (**26**). Counting the acetylene ligands as four electron donors yields a 20-electron complex. Given the discussion in Section 3, this would certainly seem to be unprecedented. When one forms the SALCs for the two types of acetylene π orbitals, then one radial combination, illustrated in (**27**), has unique symmetry features. This SALC cannot overlap with a d, s, or p AO on tungsten; it is left nonbonding and does not contribute to the electron count. Thus (**26**) is an 18-electron complex.

An even more spectacular example of the tricks that symmetry can play is provided by Ni(P-*t*-Bu)$_6$. Here the

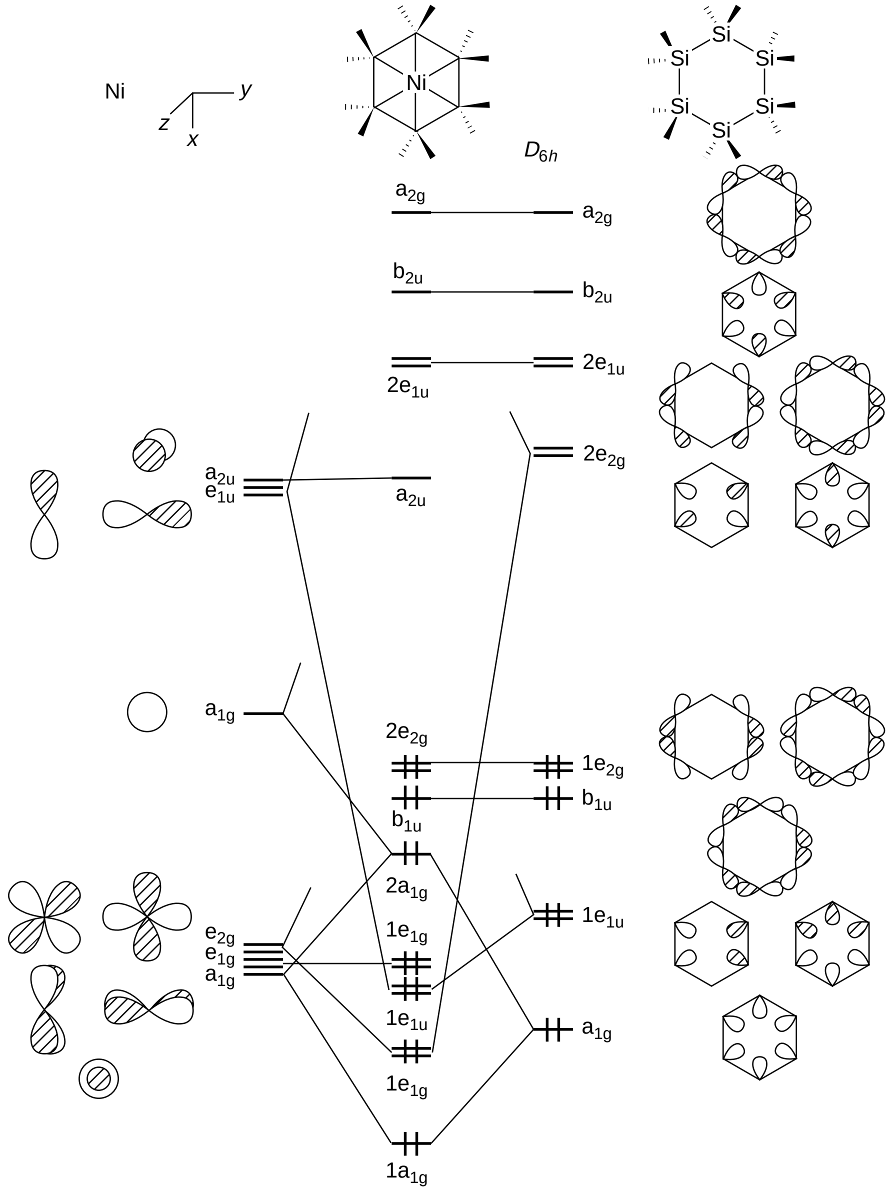
Ni
y
z
x
Ni
Si
D_{6h}
a_{2g}
a_{2g}
b_{2u}
b_{2u}
$2e_{1u}$
$2e_{1u}$
a_{2u}
e_{1u}
a_{2u}
$2e_{2g}$
a_{1g}
$2e_{2g}$
$1e_{2g}$
b_{1u}
b_{1u}
$2a_{1g}$
$1e_{1g}$
$1e_{1u}$
e_{2g}
e_{1g}
a_{1g}
$1e_{1u}$
$1e_{1g}$
a_{1g}
$1a_{1g}$

Figure 12 An orbital interaction diagram for Ni(SiR$_2$)$_6$

Ni and six phosphorus atoms lie in a common plane.[24] But rather than developing the electronic structure in this molecule, an isoelectronic example will be used to highlight the symmetry features more clearly. A SiR_2 ligand is electronically analogous to PR since in this instance the extra lone pair on PR is not involved in bonding to the metal. Of course, SiR_2 is isoelectronic with a carbene. Thus $Ni(SiR_2)_6$ along with $Ni(PR)_6$ might be considered to be a d^{10}, 22-electron complex! The Si atoms lie in a common plane so that, given a Ni−Si distance of 2.41 Å, the Si–Si distance between adjacent ligands is also 2.41 Å. This is somewhat longer than the Si–Si distances in silanes (≈ 2.35 Å; *see* ***Silicon: Inorganic Chemistry***). The same feature is present in Ni(P-*t*-Bu)$_6$. One might then consider $Ni(SiR_2)_6$ to be a Ni complex of cyclohexasilane. The important point is that there will also be Si–Si interactions present in the compound. There will be six SALCs derived from the radial orbitals on SiR_2 groups that are directly pointed at the Ni atom and analogous to (**22**). As indicated on the right side of Figure 12, three SALCs, $a_{1g} + 1e_{1u}$, are Si–Si bonding and stay at low energy while three, $2e_{2g} + b_{2u}$, are strongly Si–Si antibonding and are at a much higher energy for the radial set. The six SALCs of tangential Si p AOs analogous to (**23**) form the same pattern. Three, $b_{1u} + 1e_{2g}$, are Si–Si bonding and the other three, $2e_{1u} + a_{2g}$, are Si–Si antibonding. The formal electron count associated with the Si_6R_{12} fragment is put at 12 electrons, identical to that in a cyclohexasilane. The Ni x and y AOs interact with and stabilize the $1e_{1u}$ SALC. The $2e_{2g}$ SALC stabilizes Ni $x^2 - y^2$ and xy. The Ni z^2 and s AOs along with the a_{1g} SALC combine to form a three-orbital pattern where the bonding and nonbonding MOs are occupied. The Ni xz and yz d AOs remain rigorously nonbonding. A key feature in this analysis is that the $1e_{2g}$ SALC does not have an appreciable overlap with $x^2 - y^2$ and xy. Since $1e_{2g}$ is composed of tangential combinations, most of the electron density lies around and to the outside of the periphery of the Si ring. The b_{1u} SALC does not have a symmetry match with the metal set of AOs. Therefore three MOs, $b_{1u} + 2e_{2g}$, with six electrons remain Si–Si bonding in the molecule. There are eight MOs, $1a_{1g} + 1e_{2g} + 1e_{1u} + 2e_{1g} + 2a_{1g}$, with 16 electrons that are either metal centered or metal−ligand bonding, that is, this is a 16-electron, not 22-electron, complex. Electron density from the filled $1e_{1u}$ Si–Si bonding orbital is transferred to the Ni x and y AOs. There is also back donation from the filled $x^2 - y^2$, xy set to the empty Si–Si antibonding $2e_{2g}$ orbital. Thus the Si–Si bonding present in the cyclohexasilane is reduced upon forming the complex. Exactly the same electronic structure is present in $Ni(PR)_6$. Theoretical work[25] in this laboratory on $Ni(SiH_2)_6$ shows that it is a minimum at the geometry shown in Figure 12. Furthermore, the binding energy for it, calculated relative to ground-state Ni (d^8s^2) and the optimized geometry for Si_6H_{12} in the chair geometry, is over 280 kJ mol^{-1} at a highly correlated level.[25] This is similar to what has been found by theory for $Ni(PMe)_6$.[24]

5 FRAGMENT ORBITALS

The methods used in the two previous sections can be easily applied to any mononuclear transition metal complex where the ligand presents one σ donor function to the metal. For a polyene−ML_n complex or a transition metal dimer, it is frequently more useful to construct the electronic details by dividing the molecule into two fragments and then allowing the fragment orbitals to interact with each other. The virtue of this method is that one can concentrate exclusively on the bonding in one region of a molecule. The effects of the auxiliary ligands are present in that they will tailor the shapes and determine the relative energies of the fragment orbitals. Rather than assembling the orbitals of an ML_n fragment by interacting the n SALCs with the AOs of the metal, we shall take a reductive approach. Using the splitting patterns already established in Section 3, we will consider what occurs when one or more ligands are removed from the transition metal complex. The ligand L will again be viewed as a generic two-electron σ donor. Our starting point will be the octahedron and square plane in each instance.

5.1 The ML_5 and ML_3 Fragments

The metal d-centered orbitals for an octahedral ML_6 complex are shown on the left side of Figure 13. These are just the MOs developed in Section 3.1. When one ligand is removed, only one perturbation occurs. The z^2 component of $2e_g$ loses much of its antibonding. Therefore, that orbital, a_1 on the right side of Figure 13, is stabilized considerably. It also becomes hybridized by mixing metal s and p so that it has radial extent in the direction of the missing ligand. The other orbitals are unperturbed; there are three metal nonbonding orbitals, $e + b_2$, and one strongly M–L antibonding orbital, b_1. The five orbitals here are identical to those for a square pyramid on the right side of Figure 7 except for one minor detail. In Figure 7, the basal−M−apical angle is greater than 90°; therefore the e set is destabilized by the basal ligand σ donors relative to the b_2 orbital. In Figure 13 the basal−metal−apical angle is 90°; and e is at the same energy as b_2.

Figure 14 shows the evolution of the metal d oribtals in a square-planar complex when one ligand is removed to form an ML_3 fragment. Here again there is only one significant perturbation. One-fourth of the antibonding to metal $x^2 - y^2$ is removed and so the $2a_1$ fragment orbital of ML_3 is stabilized. It is also hybridized towards the missing ligand. The other four orbitals remain nonbonding. It was demonstrated in (**15**) that there is an electronic relationship between the metal d-centered orbitals for an octahedron and square plane. This extends to the fragment orbitals derived from them, as well. Each has a set of nonbonding orbitals (three for a ML_5 fragment and four for ML_3) and one hybridized orbital at moderate energy. Thus, a d^n ML_5 fragment is electronically analogous to a d^{n+2} ML_3 one. We shall defer an illustration of the use of these fragment orbitals to Section 5.3.

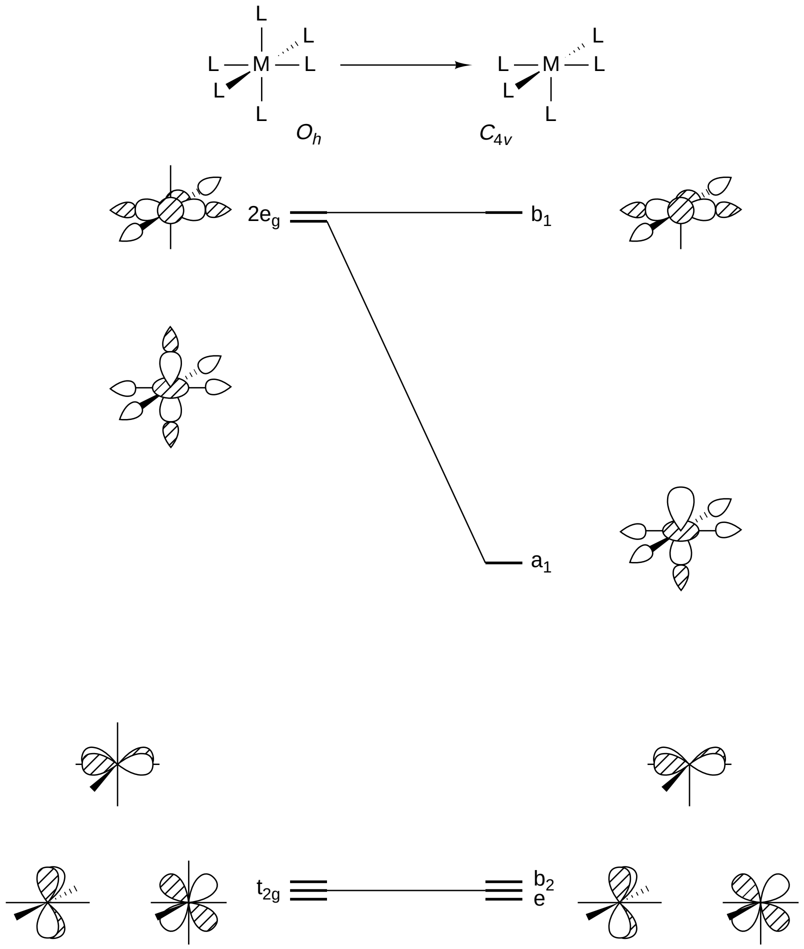

Figure 13 Construction of the important valence orbitals for a ML_5 fragment

5.2 The ML_4, ML_3, and ML_2 Fragments

The orbitals of an ML_4 and ML_2 fragment are constructed by removing two cis ligands. The resultant fragment orbitals are displayed in Figure 15 and 16. In each case, two M–L antibonding orbitals are stabilized. One is descended from a metal d and the other from a metal s-based orbital. For both orbitals in each example, metal p character also mixes in such a way to hybridize them towards the missing ligands. There is again a correspondence between the electronic structure of a d^n ML_4 and d^{n+2} ML_2 fragment.

The orbitals of a pyramidal ML_3 fragment can be obtained by removing three fac ligands from an octahedron. This is done in Figure 17. The orbitals of an octahedron on the left side have been modified in form to correspond to the removal of the three fac ligands. The t_{2g} set is still rigorously M–L nonbonding and e_g is M–L antibonding. Removing the three fac ligands stabilizes three antibonding orbitals. In each case, metal p mixes to hybridize the orbitals towards the missing ligands. The other three fragment orbitals do not change in their composition or energy.

The common theme which runs through this and the previous section is that when one removes one, two, or three ligands from an octahedron then one, two, or three fragment orbitals are formed at moderate energies. These orbitals originate from metal d or s orbitals which are antibonding to the surrounding ligands and are hybridized towards the missing ligand sites by mixing metal p character into them. All other orbitals in the metal d-block are essentially unaffected and remain at the same relative energies as their octahedral or square-planar counterparts.

5.3 The Electronic Structure of Polyene–ML_nComplexes

The utility of fragment orbitals can be documented in many different situations.**[8]** Here only two examples, alkene–ML_n and $CpML_3$ complexes, are covered. We start with Zeise's salt, ethylene–$PtCl_3^-$. A $PtCl_3^-$ fragment is d^8; the electron occupancy for the five fragment orbitals is shown on the left side of Figure 18(a). The empty $2a_1$ $PtCl_3^-$ hybrid interacts with and stabilizes the π orbital of the ethylene ligand while filled b_2 is stabilized by ethylene π^*. The same basic pattern

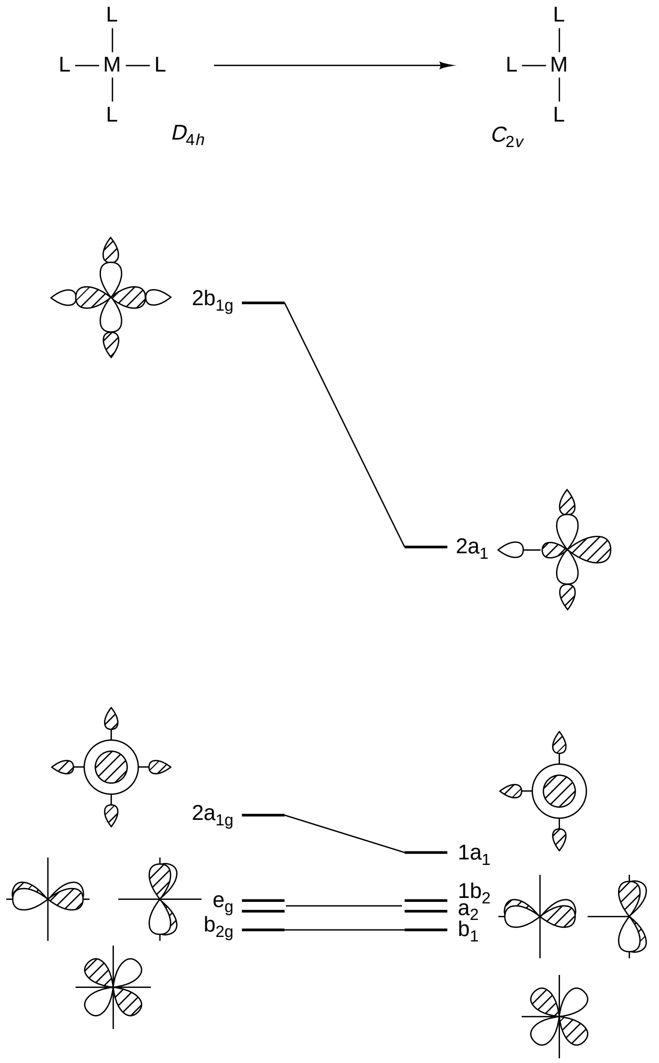

Figure 14 Correlation of the metal d orbitals from a square-planar complex to a ML_3 fragment

unfolds for ethylene–Fe(CO)$_4$ in Figure 18(b). One slight complication exists in that there are now two fragment orbitals, $1a_1$ and $2a_1$, on the Fe(CO)$_4$ fragment which interact with ethylene π. The bonding and nonbonding combination in this three-orbital interaction are filled. Notice that the splitting pattern for a trigonal bipyramid has been reestablished. The nonbonding a_1 combination along with the b_2–π^* MO are analogous to the $2e'$ set in the trigonal bipyramid (see (**17**) and Figure 7). The lower two MOs, b_1 and a_2, correspond to the e'' set. It is also clear in Figure 18(a) that the square-planar splitting pattern has been recreated.

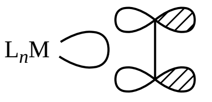

(**28**)

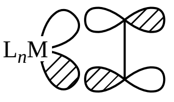

(**29**)

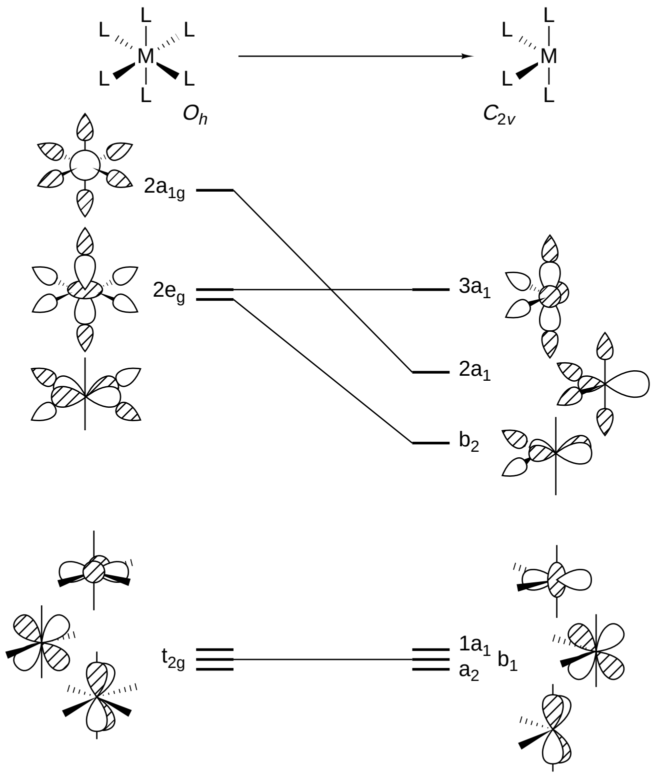

Figure 15 Derivation of the important valence orbitals in a ML_4 fragment

One can easily work through other examples of alkene–transition metal complexes. In each instance an empty orbital on the ML_n fragment will stabilize ethylene π as shown in (**28**). Electron density flows from the ethylene to the ML_n unit and is called forward donation. There will also always be one filled metal d orbital that will be stabilized by ethylene π^* (**29**), which is back donation. Electron density then is transmitted from the metal to the alkene. This is the essence of the Dewar–Chatt–Duncanson model. Referring back to Figure 13, a d^6 ML_5 fragment, for example, W(CO)$_5$, will use the a_1 orbital to interact with ethylene π and one member of the e set to participate in backbonding with ethylene π^*. Table 1 shows that for (C_2H_4) W(CO)$_5$ forward donation is more important than back donation. But there certainly is a spectrum of examples where the relative importance of each interaction varies and this, in turn, depends upon energy gap and overlap factors. The essence of the Dewar–Chatt–Duncanson bonding model is also present in the metal-carbene and metal-carbonyl bonding models that were presented in Section 4.1. A very related situation occurs in metal-dihydrogen complexes (**30**). Stylized representations of forward and back donation are given in (**31**). Table 1 shows that the relative magnitude of these interactions in $H_2W(CO)_5$ is similar to the ethylene example. A unique feature, however, in $H_2W(CO)_5$ is that forward donation of electron density from H_2 σ to the metal weakens the H–H bond. Likewise back donation from the

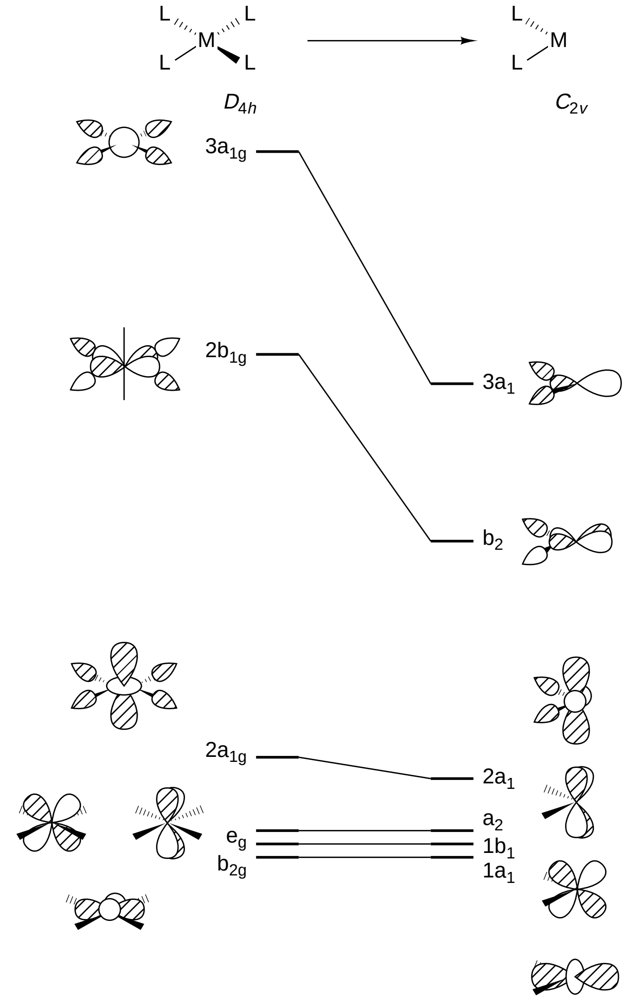

Figure 16 The orbitals for a ML$_2$ fragment

metal to H_2 σ^* also weakens the H–H bond. If the two interactions in (**31**) become strong enough, then the H–H bond will elongate to the extent that it becomes broken – oxidative addition occurs.

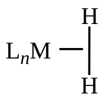

(**30**)

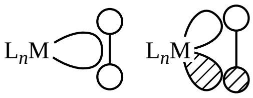

(**31**)

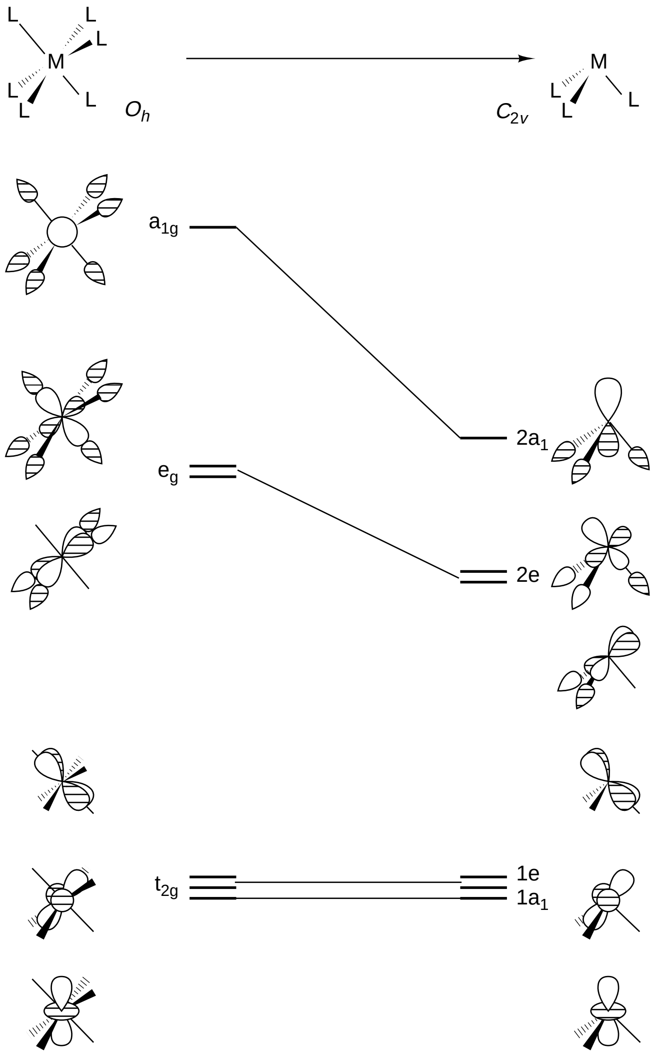

Figure 17 The orbitals of a pyramidal ML$_3$ fragment

The cyclopentadienyl ligand is pervasive in organometallic chemistry. An orbital interaction diagram for CpMn(CO)$_3$ is presented in Figure 19. The lowest Cp π orbital, a_2'', interacts primarily with $2a_1$ to form a filled bonding and empty antibonding combination. The overlap between a_2'' and $1a_1$ is quite small. The p AOs in a_2'' lie approximately in the nodal cone of the z^2 orbital (see the top of Figure 1). The 2e orbitals on Mn(CO)$_3{}^+$ interact with e_1'' on Cp to form a filled bonding and empty antibonding MO. The 1e set on Mn(CO)$_3{}^+$ do not overlap much with the π^* Cp orbitals (e_2'') and there is a large energy gap between these fragment orbitals. Therefore 1e is stabilized only a small amount and these orbitals are more localized on the metal. The situation which unfolds in Figure 19 should look familiar. Three Cp based orbitals bonding to the metal are at low energy. Another three CO σ donor orbitals will also lie in this energy region and are not shown. There are three predominantly nonbonding metal d orbitals grouped together in a narrow energy range which are also filled and lie at a moderate energy. Finally, there are two primarily metal d orbitals which are strongly Cp–Mn antibonding. They are at high energy and empty. We have restored the octahedral splitting pattern. Another way of putting this is that a Cp$^-$ ligand is electronically equivalent to a fac L_3 set of σ donors. The $a_2'' + e_1''$ set of π orbitals in Cp$^-$ are topologically analogous to the SALCs in L_3. This is also true for the three occupied π levels in benzene. Thus the

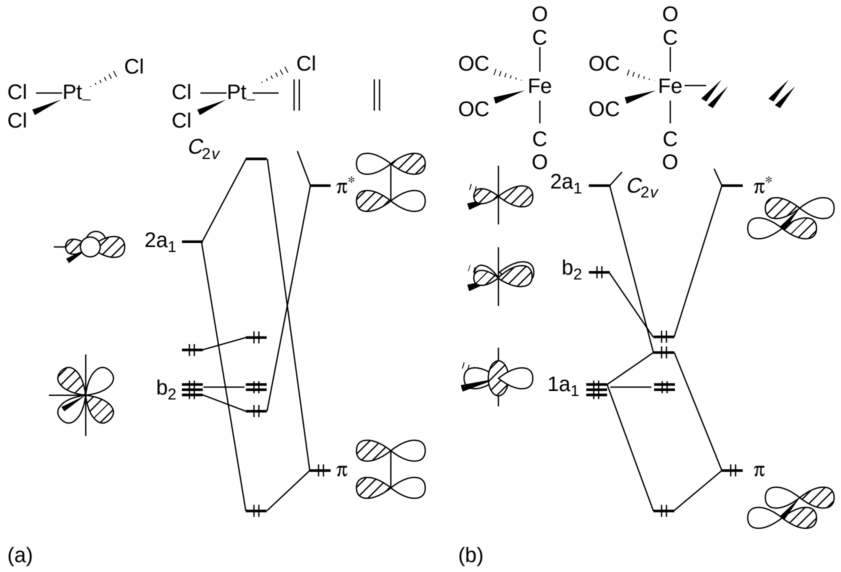

Figure 18 Orbital interaction diagrams for (a) Zeise's salt and (b) ethylene–Fe(CO)$_4$

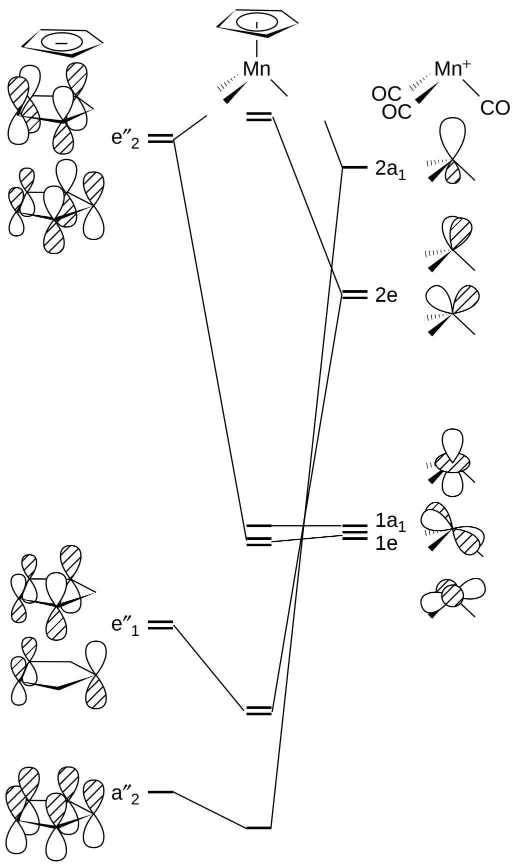

Figure 19 An orbital interaction diagram for CpMn(CO)$_3$

orbital interaction diagram for benzene–Cr(CO)$_3$, ferrocene, or bis(benzene)Cr all strongly resemble an octahedron.

6 THE ISOLOBAL ANALOGY

In the preceding sections, relationships between the electronic structure of different molecules and fragments have been stressed. We shall now formalize this relationship and extend it greatly via the isolobal analogy.**[5,26]** Two molecules or fragments are determined to be isolobal if their frontier orbitals:

- are equal in number
- are identical in symmetry properties
- have the same number of electrons
- have approximately the same relative energies in comparison to the other orbitals
- have approximately the same radial extent

The first three criteria are absolute; however, the last two standards are only approximated. Thus the isolobal analogy is relatively crude, but it is very useful since it relates the important orbitals in organic, organometallic, main group, and inorganic molecules to each other in a particularly simple fashion. The isolobal analogy can then be used as a short-cut to understand the basic electronic structure in a molecule. It can also be used to classify molecules that would appear to be quite different upon quick inspection and provide a mechanism for predicting the existence of unknown molecules. Finally, it offers clues about reactivity and possibly about reaction mechanisms.

6.1 Building Isolobal Fragments

Scheme 1 illustrates how isolobal fragments can be generated and specifies what the frontier orbitals are that were

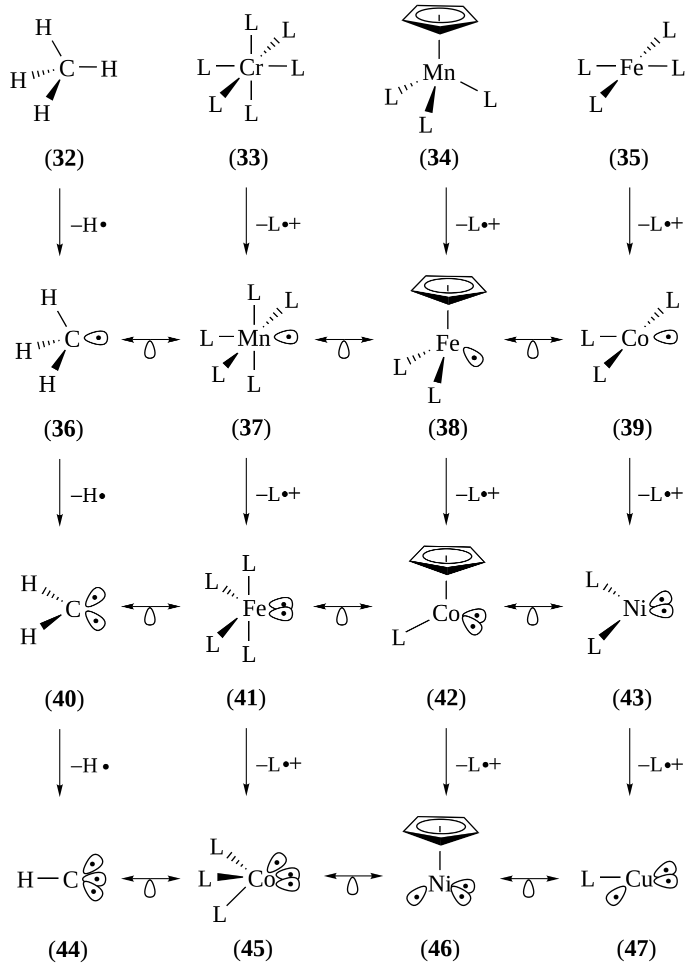

Scheme 1

discussed in the previous paragraph. Methane (**32**) is taken as the archetypical example of an 8-electron molecule. CrL_6 (**33**) and $CpMnL_3$ (**34**) are two particular starting points in the inorganic/organometallic world. In both cases, L is taken to be a neutral, two-electron donor ligand. So in (**33**) and (**34**) the metal has an 18-electron count associated with it. The square-planar FeL_4 complex (**35**) represents a 16-electron starting point. Molecules (**32**)–(**35**) then all represent electronically saturated molecules. All bonding and nonbonding orbitals are occupied and all antibonding MOs are empty. When a C–H bond in methane is broken in a homolytic fashion, one orbital (to use loose terms, an sp^3 hybrid) at moderate energy is formed and there is one electron associated with it. This is what shall be termed a frontier orbital; it is hybridized so that it points towards the missing ligand as in (**36**). Breaking one Cr–L bond in a homolytic fashion in CrL_6 generates a CrL_5^- fragment that is isoelectronic with MnL_5 (**37**). This fragment has also one frontier orbital at moderate energy with one electron in it. The specific orbital that we are referring to is a_1 in Figure 13. It too is hybridized out towards the missing ligand. Therefore (**36**) and (**37**) are said to be isolobal. This relationship is symbolized by the double-headed arrow with the teardrop shape below it as shown in Scheme 1.

Removing one ligand in a homolytic manner from $CpMnL_3$ and FeL_4 generate the $CpFeL_2$ (**38**) and CoL_3 (**39**) fragments, respectively. The frontier orbital for (**39**) is $2a_1$ in Figure 14. Recall that, in Section 5.1, it was shown that a d^n ML_5 fragment is electronically analogous to a d^{n+2} ML_3 one. Here we extend this to show that (**36**)–(**39**) are all isolobal to each other. Removing two hydrogen atoms in methane generates the methylene fragment (**40**). There are now two frontier orbitals with two electrons partitioned in them. Removing two cis ligands in CrL_6 forms the FeL_4 fragment (**41**), which is isolobal to CH_2. The frontier orbitals in (**40**) and (**41**) are localized constructions. Their delocalized, symmetry correct counterparts are shown in (**22**) and (**23**) for CH_2 and the $2a_1$ along with b_2 orbitals in Figure 15 for FeL_4. Both (**22**) and $2a_1$ are cylindrically symmetrical, whereas both (**23**) and b_2 contain one nodal plane. One can also generate the CpCoL (**42**) and NiL_2 (**43**) fragments by removing two ligands from the parent molecules and they are isolobal to CH_2 and FeL_4. Finally, breaking three C–H and M–L bonds in a homolytic manner generates the isolobal series (**44**)–(**47**). In each case there are three frontier orbitals with symmetry properties analogous to $2a_1$ and 2e in Figure 17 and three electrons are housed in them. The fragments shown in Scheme 1 are but a small subset. One can, of course, use isoelectronic replacements so that SiH_2, OsL_4, and $CpOsL^+$ are isolobal to the (**40**)–(**43**) series. There is almost a limitless diversity in the ligands that can be used for the transition metal complexes and the organic partners can have substituents other than hydrogen. Thus $Fe(CO)_4$, $Ni(PPh_3)_2$, CpPdCl, and Ph_2Pb are all isolobal and identical to the (**40**)–(**43**) generic examples. One can adjust the electron count in the frontier orbitals; an isolobal series where there is one frontier orbital and no electrons in it is CH_3^+, $Cr(CO)_5$, and $CpRu(CH_3)(PMe_3)$. Likewise, BH, $Fe(CO)_3$, and CpCo represent an isolobal set where there are three frontier orbitals with two electrons in them. Finally, one can also use many other starting points other than those listed in Scheme 1. For example, the 18-electron trigonal bipyramidal FeL_5, benzene–CrL_3, and tetrahedral NiL_4 could be used to generate fragments. For 16-electron species, trigonal planar NiL_3 or Cp_2ZrMe_2 are equally valid starting points. In this respect, it is important to establish the coordination geometry in the molecule that is formed. In other words, a $Ni(CO)_2$ fragment may have been derived from a 16-electron trigonal plane, a 16-electron square plane, an 18-electron trigonal bipyramid, an 18-electron tetrahedron, or even an 18-electron octahedron! All have different numbers of frontier orbitals and/or different numbers of electrons in them.

The species generated in Scheme 1 can be viewed as molecules in their own right. Thus, for example, CH_3, $Mn(CO)_5$, and $CpFe(CO)_2$ all are very reactive molecules that according to (**36**)–(**38**) have one electron in an orbital at moderate energy, so all undergo similar free radical abstraction reactions. The series of CH_2, $Fe(CO)_4$, and $CpIr(PMe_3)$ each have two electrons in two orbitals (see **40**–**42**); therefore each will have singlet and triplet electronic states associated with them. Singlet CH_2 undergoes a C–H insertion reaction with alkanes, as does $CpIr(PMe_3)$. The major use for the species in Scheme 1, however, is to use them as interchangeable fragments, thus generating alternative molecules. Some typical examples are demonstrated in the next section.

6.2 Uses of the Isolobal Analogy

Consider the first row of fragments given by (**36**)–(**39**) in Scheme 1. The methyl fragment is then isolobal to $Mn(CO)_5$, $CpFe(CO)_2$, and $Pt(PPh_3)_2Cl$ in terms of specific examples. Thus one methyl group in ethane can be replaced by an isolobal partner to generate $CH_3Mn(CO)_5$, $CpFe(CO)_2(CH_3)$, and $CH_3Pt(PPh_3)_2Cl$. All are known molecules. Replacing two methyl groups will generate $Mn_2(CO)_{10}$ (**48**) and $Cp_2Fe_2(CO)_4$ (**49**). However, $Cp_2Fe_2(CO)_4$ does not have this structure. Instead, two carbonyl groups migrate from terminal to bridging positions, as shown in (**50**). What occurs here is a common, low-energy phenomenon in metal-carbonyl chemistry (*see* ***Carbonyl Complexes of the Transition Metals***). What is perturbed most in the terminal to bridging structural distortion is the interaction between carbonyl π^* orbitals with the members of the nonbonding, t_{2g}-like orbitals. The frontier orbitals used by the isolobal analogy are not greatly affected. Thus (**49**) is regarded as being electronically analogous to (**50**).

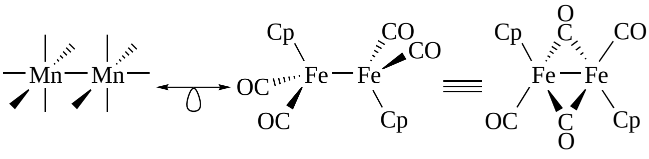

(**48**) (**49**) (**50**)

Using the second row of isolobal fragments (**40**)–(**43**), one can replace one, two, or all three CH_2 units in cyclopropane (**51**) by isolobal partners to form the molecules listed in (**52**). Notice that the top row of structures have been drawn as metallacyclopropanes and that these are equivalent (see Section 5.3) to metal–alkene complexes. The essential details of the bonding and their conformational preferences[5] are identical in each molecule.

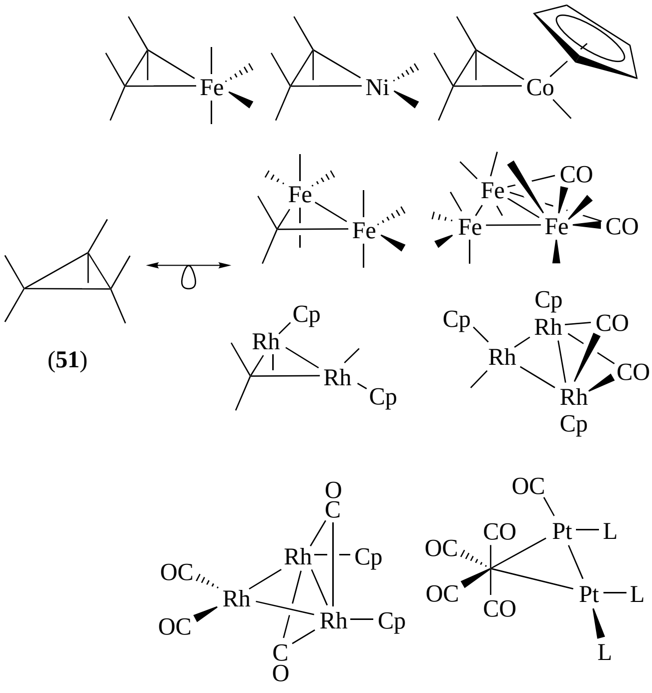

(**51**)

(**52**)

An interesting series is provided by (**53**)–(**55**). In (**53**), replacement of the $Os(CO)_4$ fragments with isolobal CH_2 and Sn with isoelectronic carbon yields spiropentane (**54**). Replacement of two CH_2 units in spiropentane with isolobal

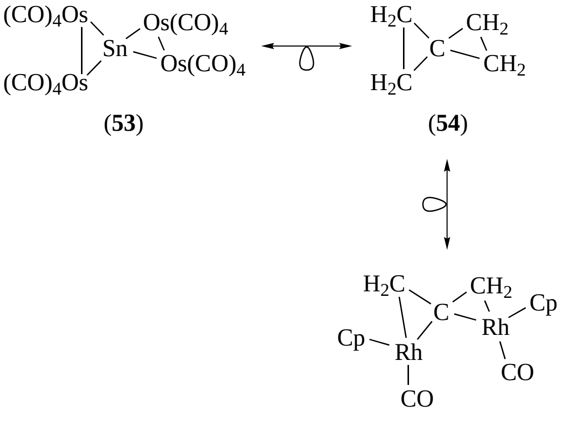
(**53**) (**54**) (**55**)

CpRh(CO) gives the allene complex (**55**). All three molecules, with very different architectures, are isolobal!

A special kind of sigmatropic rearrangement is shown in (**56**). The isolobal analog is shown in (**57**) where CH_2 has been replaced by $Pt(PR_3)_2$. What is interesting here is that there is a very specific stereochemistry predicted for the rearrangement in each case which is determined by orbital symmetry. However, an alternative route has been shown to occur for both molecules.[27] Thus the reaction mechanisms for (**56**) and (**57**) are thought to be identical. The stereochemical details have been experimentally determined for (**56**) but, thus far, only computationally for (**57**).[27] The reader should again note that the isolobal analogy has been constructed on a very elementary level. Of course, the activation energies for (**56**) and (**57**) are quite different.

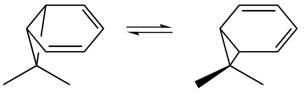
(**56**)

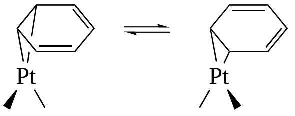
(**57**)

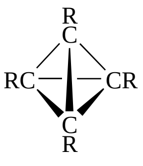
(**58**)

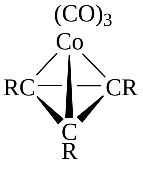
(**59**)

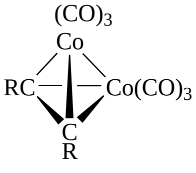
(**60**)

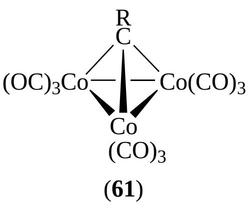
(**61**)

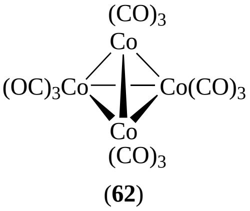
(**62**)

As a final example of the isolobal analogy consider the bottom row of isolobal fragments in Scheme 1. In particular, a CR and $Co(CO)_3$ fragment each have three frontier orbitals with three electrons partitioned in some fashion among them. All of the molecules given by (**58**)–(**62**) have been isolated. In the order that the compounds have been presented, one CR unit has been sequentially replaced by an isolobal $Co(CO)_3$ fragment. Molecule (**59**) is commonly represented as a cyclopropenium–$Co(CO)_3$ polyene type of complex and (**60**) as an acetylene π complex of $Co_2(CO)_6$. However, this is really more of a question of artistic taste than scientific merit. It is analogous to the metal–alkene versus metallacyclopropane controversy which was commented on in Section 5.3. The important point, and nicely illustrated by the frontier orbitals of (**44**) and (**45**), is that there will be three filled C–C σ bonds in (**59**). One frontier orbital with one electron then remains on each C–R unit. These will then form an additional three filled Co–C σ bonds with the $Co(CO)_3$ fragment. From a cyclopropenium–$Co(CO)_3$ perspective, the cyclopropenium cation ligand has three π orbitals (see **20**). The lowest, totally symmetrical π orbital is filled and the other two are empty. A $Co(CO)_3^-$ fragment is d^{10} and, therefore, there are four electrons in the 2e set in Figure 17 and $2a_1$ is empty. The $2a_1$ and 2e fragment orbitals combine with the three π orbitals of cyclopropenium to form three two orbital–two electron interactions. This is identical to what the isolobal analogy presents to us.

There is also an important caveat that the (**58**)–(**62**) series highlights. Tetrakis-*t*-butyltetrahedrane (**58**) has only recently been prepared. The parent ($R = H$) molecule certainly is predicted to be extremely reactive because of the ring strain present in (**58**). Ring strain, if at all present, is much less in (**61**) and (**62**). A comparison of the frontier orbitals for $Co(CO)_3$ and CH is given in (**63**) and (**64**), respectively. The e and a_1 set in (**63**) are stylized representations of 2e and $2a_1$ for an ML_3 fragment in Figure 17. The a_1 frontier orbital contains Co s and p character. Its form *and* radial extension precisely match the a_1 frontier orbital for the CH fragment in (**64**). The e set of $Co(CO)_3$ is primarily metal d with some p character, whereas that for the CH unit is exclusively comprised of carbon p AOs. Consequently, the angle formed between the lobes in the e set of $Co(CO)_3$, as shown in (**63**), is $\approx 90°$; whereas the lobes for the e set in CH are positioned 180° with respect to each other. The form (symmetry) of the e set in each isolobal fragment is identical. However, the radial extent is only similar; in both instances the e set is directed away from the carbonyls and hydrogen atom. In constructing the MOs of tetrahedrane the a_1 hybrids form one bonding and three antibonding MOs. The e sets produce five bonding/nonbonding and three antibonding MOs. Precisely the same combinations occur in (**59**)–(**62**). An important difference lies in the fact that the overlap of the e sets in the bonding MOs of tetrahedrane does occur in a σ-type fashion; however, the electron density does not reside along the C–C vectors. Because p AOs are used, the electron density maxima will occur on the outside of the tetrahedrane skeleton and this is the electronic origin of ring strain. Using d functions in the $Co(CO)_3$ e set for $Co_4(CO)_{12}$ creates σ

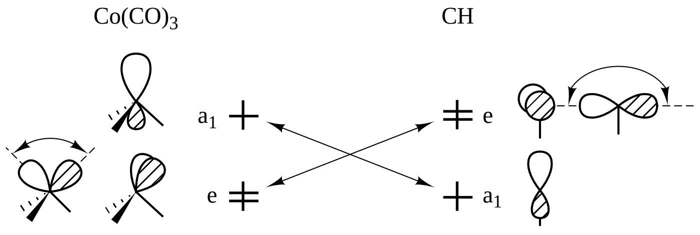

(**63**) (**64**)

overlap in a direction much closer to the Co–Co vectors. Notice that there is also an inversion of the level ordering for the a$_1$ and e frontier orbitals on going from Co(CO)$_3$ to CH. This is simply a reflection of the fact that a metal s AO in (**63**) lies higher in energy than the metal d AOs. On the other hand, in (**64**) the s AO for carbon or another main group atom lies lower in energy than the p AOs. This is a minor difference, since what is important is the number of MOs that are filled upon interacting the frontier orbitals in the molecule. That is identical in both number and form for the series given by (**58**)−(**62**). A molecule whose existence is predicted on the basis of the isolobal analogy may be too reactive to isolate. However, its utility allows one to cross many boundaries in chemistry and offers a very different vantage point for viewing the electronic structure in molecules.

7 RELATED ARTICLES

Bonding Energetics of Organometallic Compounds; Electronic Structure of Main-group Compounds; Electronic Structure of Solids; Electronic Structure of Clusters; Ligand Field Theory & Spectra; Molecular Orbital Theory; Photoelectron Spectroscopy of Transition Metal Systems.

8 REFERENCES

1. M. Pepper and B. E. Bursten, *Chem. Rev.*, 1991, **91**, 719.
2. A. Dedieu, in ‘Topics in Physical Organometallic Chemistry’, ed. M. F. Gielen, Freund, London, 1985, Vol. 1, p. 1.
3. M. Torrent, M. Solà, and G. Frenking, *Chem. Rev.*, 2000, **100**, 439.
4. S. Niu and M. B. Hall, *Chem. Rev.*, 2000, **100**, 353.
5. T. A. Albright, J. K. Burdett, and M.-H. Whangbo, ‘Orbital Interactions in Chemistry’, Wiley, New York, 1985.
6. G. Ohanessian and W. A. Goddard III, *Acc. Chem. Res.*, 1990, **23**, 386.
7. F. A. Cotton, ‘Chemical Applications of Group Theory’, 3rd edn., Wiley, New York, 1990.
8. V. Pfennig and K. Seppelt, *Science*, 1996, **271**, 626.
9. S. K. Kang, H. Tang, and T. A. Albright, *J. Am. Chem. Soc.*, 1993, **115**, 1971.
10. M. Kaupp, *Angew. Chem., Int. Ed. Engl.*, 2001, **40**, 3534.
11. P. A. Breeze, J. K. Burdett, and J. J. Turner, *Inorg. Chem.*, 1981, **20**, 3369.
12. R. S. Hay-Motherwell, G. Wilkinson, B. Hussain-Bates, and M. B. Hursthouse, *J. Chem. Soc., Dalton Trans.*, 1992, 3477.
13. R. J. Morris and G. S. Girolami, *Organometallics*, 1991, **10**, 792.
14. P. Stauropoulos, P. D. Savage, R. P. Tooze, G. Wilkinson, B. Hussain, M. Motevalli, and M. B. Hursthouse, *J. Chem. Soc., Dalton Trans.*, 1987, 557.
15. S. Alvarez and M. Llunell, *J. Chem. Soc., Dalton Trans.*, 2000, 3288.
16. M. J. Paterson, P. A. Hunt, M. A. Robb, and O. Takahashi, *J. Phys. Chem. A*, 2002, **106**, 10494.
17. J. Chatt, J. D. Garforth, and G. A. Rowe, *J. Chem. Soc. A*, 1966, 1834.
18. R. J. Morris and G. S. Girolami, *Organometallics*, 1991, **10**, 799.
19. R. Hoffmann, B. F. Beier, E. L. Muetterties, and A. R. Rossi, *Inorg. Chem.*, 1977, **16**, 511.
20. J. K. Burdett, R. Hoffmann, and R. C. Fay, *Inorg. Chem.*, 1978, **17**, 2553.
21. T. E. Taylor and M. B. Hall, *J. Am. Chem. Soc.*, 1984, **106**, 1576.
22. A. Diefenbach, F. M. Bickelhaupt, and G. Frenking, *J. Am. Chem. Soc.*, 2000, **122**, 6449.
23. A. W. Ehlers, S. Dapprich, S. F. Vyboishchikov, and G. Frenking, *Organometallics*, 1996, **15**, 105.
24. R. Ahlrichs, D. Fenske, H. Oesen, and U. Schneider, *Angew. Chem., Int. Ed. Engl.*, 1992, **31**, 323.
25. H. Tang, D. M. Hoffman, T. A. Albright, H. Deng, and R. Hoffmann, *Angew. Chem., Int. Ed. Engl.*, 1993, **32**, 1616.
26. R. Hoffmann, *Angew. Chem., Int. Ed. Engl.*, 1982, **21**, 711.
27. J. Silvestre and T. A. Albright, *Nouv. J. Chim.*, 1985, **9**, 659.

Acknowledgments

I want to thank the Robert A. Welch Foundation for generous support of our work that has been documented here.

Electronic Structure of Solids

Enric Canadell
Institut de Ciència de Materials de Barcelona (CSIC), Bellaterra, Spain

1 Introduction 1
2 Crystal Orbitals and Band Structure 1
3 Crystal Orbitals and Symmetry 7
4 Crystal Orbitals and Orbital Interactions; Peierls Distortions 9
5 Density of States 15
6 Fermi Surface 17
7 Electronic States Derived from a Metallic State 19
8 Computational Approaches 23
9 Concluding Remarks 25
10 Related Articles 25
11 References 25

Abbreviations

DOS = Density of states; BO = Bloch orbital; IBZ = Irreducible Brillouin zone; BZ = Brillouin zone; PZ = Primitive zone; COOP = Crystal orbital overlap population; CDW = Charge density wave; MO = Molecular orbital; DFT = Density functional theory; HF = Hartree-Fock; LAPW = Linear augmented plane wave; LMTO = Linear muffin tin orbital; LCAO = Linear combination of atomic orbitals.

1 INTRODUCTION

Solids are just infinite molecules. Thus, at least in principle, there is no reason why their electronic structures could not be studied using the same techniques and concepts currently used for molecules. However, there is an obvious technical problem because the size of the matrices to be handled is, in fact, infinite. In the case of periodic solids this problem can be easily circumvented by fully exploiting their translational symmetry. Once this is done, the size of the matrices is reduced to that of the unit cell and the problem disappears. A specially simple and useful technique developed by solid-state physicists is the so-called tight-binding method (*see Tight-binding Approximation*), in which the wavefunctions describing the motion of an electron in the solid (i.e. the *Crystal Orbitals*) (CO) are expressed as a linear combination of atomic orbitals (LCAO) or similar local functions. There is an obvious parallelism with the traditional Molecular Orbital Theory (*see* ***Molecular Orbital Theory***) developed by chemists, in which the wavefunctions describing the motion of an electron in the molecule (i.e. the *Molecular Orbitals*) (MO) are also expressed as a LCAOs. As a matter of fact, the first orbital describing the motion of an electron in a polyatomic system was written by Bloch in 1928 and it was a CO. Hence, MO theory finds its roots in solid-state physics.

Being able to calculate (remarkable advances in that direction have been accomplished during the last decade) does not mean being able to understand. Despite the common roots of the MO and tight-binding ideas, physicists and chemists have developed very different ways to rationalize the results of their calculations. A specially fruitful approach used by chemists in order to understand molecular structure and reactivity problems is that of the orbital interaction analysis[1] of the wavefunction. This method provides a simple yet very powerful way to relate the electronic and geometric structures of molecules. It was then a natural choice for chemists trying to understand why a certain solid has the physical properties or the crystal structure it has, to use the conceptual framework provided by the orbital interaction analysis. This approach has been indeed extremely fruitful in providing a real understanding of the chemistry and physics of solid-state materials.[2–5]

In the present contribution, we will examine the fundamentals of such an approach. We first describe some basic notions of the tight-binding method to build the COs of an infinite periodic solid. Then we consider how to analyze the nature of these COs from the viewpoint of orbital interaction by using some one-dimensional (1D) examples. We then introduce the notion of density of states (DOS) and its chemical analysis, which is especially valuable in understanding the structure of complex 3D solids or in studying surface related phenomena. Later, we introduce the concept of Fermi surface needed to examine the transport properties of metallic systems and consider the different electronic instabilities of metals. Finally, a brief consideration of the more frequently used computational approaches to the electronic structure of solids is presented.

2 CRYSTAL ORBITALS AND BAND STRUCTURE[6]

Let us consider the 1D lattice (**1**) with repeat distance a, where each unit cell contains just one atomic orbital (AO) χ. The simplest way to describe the energy levels of this system is to impose Born–von Karman boundary conditions. Essentially, this means that we are bending our system as shown in (**2**), that is, we are transforming the chain into a loop. However, since the number (N) of sites is very large, this bending of the chain is imperceptible as far as the atoms of the chain are concerned. The different orbitals of the system can now be easily found by using the symmetry properties of cyclic groups and they are given by equation (1)

$$\phi(k) = N^{-1/2} \sum_n \exp(ikna)\chi(r - na) \tag{1}$$

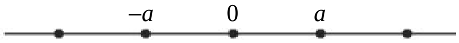

(**1**)

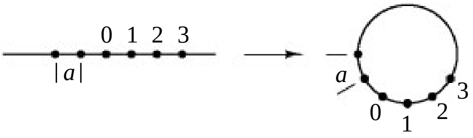

(**2**)

where N is the number of unit cells in (**1**), $\chi(r - na)$ is the AO χ located at the nth unit cell and $k = 2\pi j/Na$, with $j = 0, \pm 1, \pm 2, \ldots, \pm N/2$. The symmetry adapted orbitals $\phi(k)$ are the Bloch orbitals (BO) associated with the χ AO and are dependent on the wave vector k. The coefficient $\exp(ikna)$ is a periodic function of k so only the values of k

$$-\frac{\pi}{a} \le k \le \frac{\pi}{a} \tag{2}$$

may be used in constructing the BOs of χ. Every one of the N different $\phi(k)$ BOs belong to a different irreducible representation of the C_N cyclic group. The set of k values of equation (2) are known as the first *Brillouin Zone* (BZ) of the system. Because the infinite cyclic group C_N and the infinite translation group T_N are isomorphous, the $\phi(k)$ BOs are also the symmetry adapted solutions appropriate for the infinite translation group and every one of the BOs belongs to a different irreducible representation of the T_N group.

It is now possible to calculate the energy values associated with the $\phi(k)$ BOs according to equation (3)

$$e(k) = \frac{H(k)}{S(k)} = \frac{\alpha + 2\beta \cos ka + \cdots}{1 + 2S \cos ka + \cdots} \tag{3}$$

where α is the Coulomb integral, $\alpha = \langle \chi(r) | H^{\text{eff}} | \chi(r) \rangle$, β is the nearest-neighbor resonance integral, $\beta = \langle \chi(r) | H^{\text{eff}} | \chi(r - a) \rangle$, and S is the nearest-neighbor overlap integral, $S = \langle \chi(r) | \chi(r - a) \rangle$. When the overlap integrals are neglected within the first nearest-neighbor approximation, equation (3) is simplified as

$$e(k) = \alpha + 2\beta \cos ka \tag{4}$$

Since N is very large, the difference between two successive energy values is very small and thus the different energy values given by equation (4) lead to a continuous set of energy levels called a band, as schematically shown in (**3**). Within the approximations introduced above, the bandwidth W is given by $W = 4|\beta|$ (*see Band Theory*). In other words, the energy level of the AO χ (i.e. α) is spread into a band of width $4|\beta|$, as depicted in (**4**). An important property of the BOs is that $e(k) = e(-k)$, which is the reason why only half of the band energy levels are represented in (**3**).

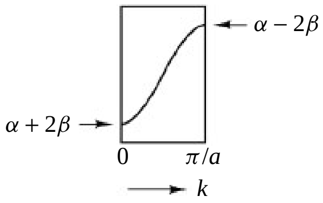

(**3**)

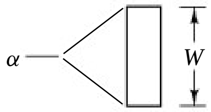

(**4**)

It is interesting to examine the nature of the BOs for some specific values of k. For instance, for $k = 0$ the coefficients $\exp(ikna)$ are $(1)^n$ and for $k = \pi/a$ they are $(-1)^n$. In other words, the BO at Γ $(k = 0)$ is obtained by repeating the AO χ with the same sign whereas the BO at X $(k = \pi/a)$ is obtained by repeating the AO χ with alternating signs. If χ is an s orbital, the two COs are as shown in (**5**). The CO at Γ represents the more bonding combination whereas the CO at X represents the more antibonding combination. The band dispersion should then be as shown in (**3**). However, this is only the case when $\beta < 0$. If $\beta > 0$, as is the case for a 1D chain of p orbitals making σ-type interactions, the CO at Γ is the more antibonding combination whereas that at X is the more bonding combination (see **6**). The band dispersion should then be as in (**7**). However, for a 1D chain of p orbitals making π-type interactions, $\beta < 0$ and, as shown in (**8**), the situation is similar to the 1D chain of s orbitals. Thus, careful examination of the shape and dispersion of a band can give important insight concerning the topology and strength of the interactions along the chain.

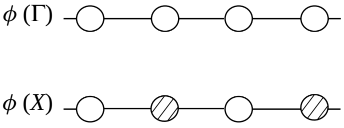

(**5**)

Extension to the case where there are many AOs χ_μ $(\mu = 1, 2, \ldots, M)$ per unit cell is straightforward. First, the

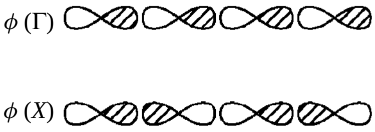

(6)

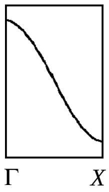

(7)

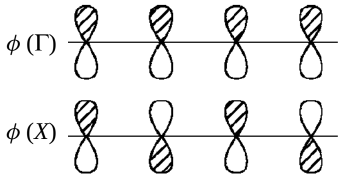

(8)

symmetry adapted BOs $\phi_\mu(k)$ associated with every AO χ_μ

$$\phi_\mu(k) = N^{-1/2} \sum_n \exp(ikna)\chi_\mu(r - na) \tag{5}$$

are built. Then, the COs ψ_i $(i = 1, 2, \ldots, M)$ describing the motion of electrons in (**1**) are built as a linear combination of these BOs. Since BOs associated with different k values belong to different irreducible representations of the infinite translational group, only those BOs with the same k can be linearly combined

$$\psi_i(k) = \sum_{\mu=1}^{M} C_{\mu i}(k)\phi_\mu(k) \tag{6}$$

The energies $e_i(k)$ of the COs $\psi_i(k)$ are the eigenvalues of the effective Hamiltonian H^{eff}

$$H^{\text{eff}}\psi_i(k) = e_i(k)\psi_i(k) \tag{7}$$

and the requirement that $\partial e_i(k)/\partial C_{\mu i}(k) = 0$ for $\mu = 1, 2, \ldots, M$ leads to the $M \times M$ secular determinant

$$|H_{\mu\nu}(k) - e_i(k)S_{\mu\nu}(k)| = 0 \tag{8}$$

where the matrix elements $H_{\mu\nu}(k)$ and $S_{\mu\nu}(k)$ are defined as

$$H_{\mu\nu}(k) = \langle\phi_\mu(k)|H^{\text{eff}}|\phi_\nu(k)\rangle \tag{9}$$

and

$$S_{\mu\nu}(k) = \langle\phi_\mu(k)|\phi_\nu(k)\rangle \tag{10}$$

Using equation (6) this matrix elements can be expressed as

$$\begin{aligned} H_{\mu\nu}(k) &= \langle\chi_\mu(r)|H^{\text{eff}}|\chi_\nu(r)\rangle \\ &\quad + \sum_{n=1}^{\infty}[\exp(ikna)\langle\chi_\mu(r)|H^{\text{eff}}|\chi_\nu(r - na)\rangle \\ &\quad + \exp(-ikna)\langle\chi_\mu(r - na)|H^{\text{eff}}|\chi_\nu(r)\rangle] \end{aligned} \tag{11}$$

and

$$\begin{aligned} S_{\mu\nu}(k) &= \langle\chi_\mu(r)|\chi_\nu(r)\rangle + \sum_{n=1}^{\infty}[\exp(ikna)\langle\chi_\mu(r)|\chi_\nu(r - na)\rangle \\ &\quad + \exp(-ikna)\langle\chi_\mu(r - na)|\chi_\nu(r)\rangle] \end{aligned} \tag{12}$$

In practice, the summations over n in these expressions are truncated to a reasonable value for which the integrals $\langle\chi_\mu(r)|H^{\text{eff}}|\chi_\nu(r - na)\rangle$ and $\langle\chi_\mu(r)|\chi_\nu(r - na)\rangle$ are negligible. This is the so-called nth nearest-neighbor approximation.

As is obvious from the preceding discussion, calculation of the electronic energy levels for a periodic solid is no more complex than calculation of the electronic energy levels of a molecule. The only difference is that in the case of a periodic solid the calculations have to be carried out for a large number of k values, sampling the first BZ of the solid, that is, from $-\pi/a$ to π/a for a 1D system. However, in this case, because of the general relationship $e_i(k) = e_i(-k)$, calculations can be restricted to the k values $0 \leq k \leq \pi/a$. This region of the BZ is called the irreducible Brillouin zone (IBZ) of the system.

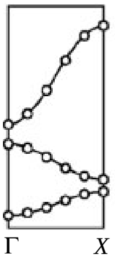

(9)

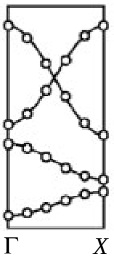

(10)

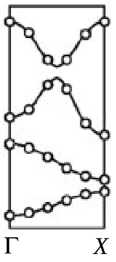

(11)

In general, the study of the electronic structure of a periodic solid requires the solution of the secular determinant (8) for a set of k values covering the IBZ of the system. This leads to a series of $e_i(k)$ values for the different k points chosen (see **9**, where the empty circles refer to the calculated energies). The band structure of the system is then obtained by connecting those calculated energy values. This is straightforward if the different bands do not overlap (see **9**). If two bands overlap in energy as shown in (**10**), the situation is a little bit more complex. If the symmetries of the two band levels are different for all k points along the Γ → X line, the two bands can cross as indicated in (**10**). However, if the two band levels have the same symmetry along this line, crossing of the two bands is not possible and narrower bands result, as shown in (**11**). To determine if the crossing is real or avoided, one has to consider carefully the symmetry properties of the COs (see Section 3), or alternatively one may calculate the $e_i(k)$ values for a fine mesh of k points in the vicinity of the crossing (or avoided crossing) point.

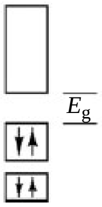

(**12**)

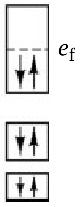

(**13**)

Since a band contains N different energy levels, there is room for $2N$ electrons. Usually the occupancy of the energy levels of a band is discussed in terms of the number of electrons per unit cell. Thus, a band is full when there are two electrons per unit cell to fill this band. For instance, if there are four electrons per unit cell to fill the energy levels of (**9**), the two lower bands will be completely filled. This situation can be represented as in (**12**). There is a *Band Gap* (E_g) between the highest occupied level (top of the second band) and the lowest unoccupied level (bottom of the third band from bottom). Such a system having only completely filled or completely empty bands is a semiconductor (*see* ***Semiconductors***) or an *Insulator*, depending on the magnitude of the band gap E_g. If there are five electrons per unit cell, there is only one electron left to fill the top band which is thus half filled and the situation can be represented as in (**13**). In one-electron band theory, where electron–electron repulsions are neglected, a system with one or more partially filled bands such as that represented in (**13**) is a metal (how the electron–electron repulsions can change this situation is discussed in Section 7.2). In a metallic system, there is no band gap between the highest occupied and lowest unoccupied energy levels and the highest occupied energy level is known as the *Fermi Level* (e_f). The corresponding k wave vector is the Fermi wave vector (k_f). For a 1D system it is very easy to know the value of k_f for a partially filled band. The N different k points of the first BZ (equation 2) is a mesh of equally spaced sets of k points. For a given band, when all the energy levels of the first BZ (i.e. $2\pi/a$) are filled, the band is full. When this band is $(1/n)$th filled, only a $(1/n)$th fraction of the $2\pi/a$ levels of the first BZ (i.e. $2\pi/na$) will correspond to occupied states. Consequently, k_f will be given by $1/2(2\pi/na) = \pi/na$ if the bottom of the band is at Γ (**3**), and at $\pi/a - 1/2(2\pi/na) = \pi/a(1-1/n)$ if the bottom of the band is at X (**7**). A similar reasoning can be used for more complex situations. For instance, when the Fermi level cuts two bands, as would be the case when there are six electrons per unit cell to be placed in the bands of (**10**), it is easy to see that the Fermi level would lie exactly at the crossing point of the two bands. As will be shown later, the magnitude of k_f plays a crucial role in understanding the structure and physical properties of many 1D systems.

The basic concepts of the electronic band structure theory introduced so far can be easily extended to 2D and 3D systems. As an example of a 2D system, let us consider the rectangular lattice (**14**) with one AO χ per site. The BOs associated with this AO are given by equation (13)

$$\phi(k_a, k_b) = \frac{1}{\sqrt{N}} \sum_m \sum_n \exp(ik_a ma)\exp(ik_b nb)\chi(r - ma - nb) \qquad (13)$$

where $\chi(r - ma - nb)$ denotes the AO χ located at the (ma, nb) site of the lattice. In this case, two independent wave vectors, k_a and k_b, are needed to allow all possible phase relationships between the AOs χ along the a- and b-directions, respectively. The coefficients $\exp(ik_a ma)$ and $\exp(ik_b nb)$ are periodic functions of k_a and k_b, respectively, so that only the wave vectors (k_a, k_b) falling in the following region

$$\begin{aligned} -\frac{\pi}{a} \le k_a \le \frac{\pi}{a} \\ -\frac{\pi}{b} \le k_b \le \frac{\pi}{b} \end{aligned} \qquad (14)$$

may be used in constructing the BOs. These wave vectors define the first BZ of the lattice (**15**). In (**15**), $\Gamma = (0, 0)$, $X = (\pi/a, 0)$, $Y = (0, \pi/b)$, and $M = (\pi/a, \pi/b)$. Within the first nearest-neighbor approximation and under neglect of overlap, the energy associated with the BO $\phi(k_a, k_b)$ is given by

$$\begin{aligned} e(k_a, k_b) &= \langle \phi(k_a, k_b)|H^{\text{eff}}|\phi(k_a, k_b)\rangle \\ &= \alpha + 2\beta_a \cos k_a a + 2\beta_b \cos k_b b \end{aligned} \qquad (15)$$

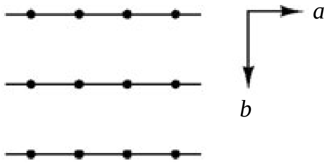

(**14**)

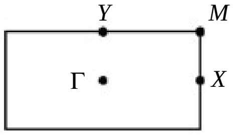

(**15**)

where β_a and β_b are the nearest-neighbor resonance integrals along the a- and b-directions, respectively: $\beta_a = \langle\chi(\mathbf{r})|H^{\text{eff}}|\chi(\mathbf{r}-\mathbf{a})\rangle$ and $\beta_b = \langle\chi(\mathbf{r})|H^{\text{eff}}|\chi(\mathbf{r}-\mathbf{b})\rangle$. Since the BZ is 2D, some representative lines are usually chosen in order to show the band structure of the system. For instance, the band structure along the $\Gamma \to X \to M \to Y \to \Gamma$ lines (see **15**) assuming that $\beta_a < \beta_b < 0$ is shown in (**16**). The main features of this band structure can be easily understood by looking at the COs of the endpoints of the lines. The values of the coefficients $\exp(ik_a ma)\exp(ik_b nb)$ at Γ, X, Y and M are $(1)^m(1)^n$, $(-1)^m(1)^n$, $(1)^m(-1)^n$ and $(-1)^m(-1)^n$,

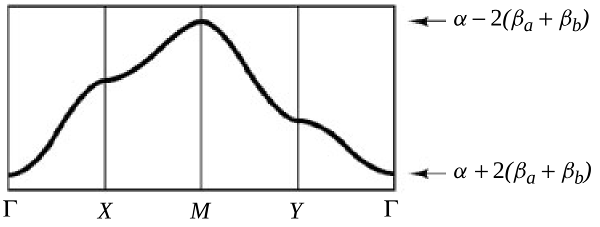

(**16**)

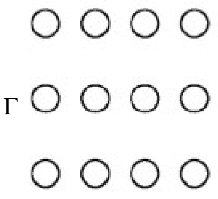

(**17**)

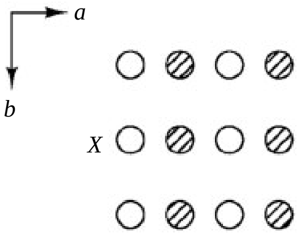

(**18**)

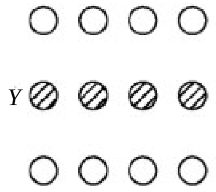

(**19**)

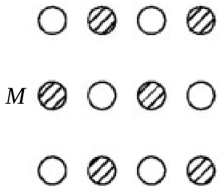

(**20**)

respectively. If χ is an s orbital, the phase relationships between the AOs at those k points are illustrated in (**17**–**20**). At Γ, the AOs repeat with the same sign along the a- and b-directions (**17**). At X, the AOs repeat with alternating signs along the a-direction but with the same sign along the b-direction (**18**). At Y, the AOs repeat with the same sign along the a-direction but with alternating signs along the b-direction (**19**). At M, the AOs repeat with alternating signs along the a- and b-directions (**20**). It is easy to explain the band dispersion relations of (**16**) on the basis of (**17**–**20**). For example, the energy is lowest at Γ because this point allows bonding arrangements of the AOs for every nearest-neighbor along the a- and b-directions. Along $\Gamma \rightarrow X$, the energy increases because the nearest-neighbor interaction along the a-direction changes gradually from bonding to antibonding.

The IBZ of (**15**) is the rectangle defined by the points Γ, X, M, and Y. Thus, the area of the IBZ is one-fourth that of the BZ. As mentioned before, the mesh of k points to be considered in actual computational work can be reduced to a mesh covering the IBZ. Thus, it is important to understand how the IBZ for 2D and 3D lattices can be determined. The shape of the IBZ is related to the symmetry properties of the system. For instance, in the rectangular lattice (**14**) there are symmetry planes perpendicular to the a (σ_a) and b (σ_b) directions. Let us see how a general point (k_a, k_b) of the BZ is changed under the effect of these symmetry operations. The BO $\phi(k_a, k_b)$ is given by equation (13) and can be graphically represented as in (**21**), where on top of each lattice point the $\exp(ik_a ma)\exp(ik_b nb)$ coefficient of the χ AO at this site is shown. A symmetry plane perpendicular to a will move the (k_a, k_b) point into $(-k_a, k_b)$. The BO $\phi\ (-k_a, k_b)$ is represented in (**22**). The BOs (**21**) and (**22**) are different but completely equivalent. In fact, (**22**) can be obtained from (**21**) after application of the σ_a symmetry operation. In a similar way it can be seen that the BOs corresponding to the $(k_a, -k_b)$ and $(-k_a, -k_b)$ points, that is, those points of the BZ obtained from the previous ones by the effect of a symmetry plane perpendicular to b, can be obtained from (**21**) and (**22**) by application of the σ_b symmetry operation. The BOs $\phi(k_a, -k_b)$ and $\phi(-k_a, -k_b)$ are different but completely equivalent to $\phi(k_a, k_b)$ (**21**) and $\phi(-k_a, k_b)$ (**22**). In general, when a set of points of the BZ can be generated from each other by application of the symmetry operations of the lattice, the BOs for all these points can be obtained from just one of them by using the appropriate symmetry operations. Thus, the BOs for these points are equivalent and, of course, degenerate in energy. Consequently, to determine the IBZ of a lattice (i.e. the minimum number of points needed to generate the BOs and energies for all the points of the BZ), one just needs to consider how a general point of the BZ is transformed under all the symmetry operations of this lattice. In addition, because of the relation $e_i(k) = e_i(-k)$, which by construction is a general property of BOs, the inversion symmetry should always be used even if it is not present in the lattice under consideration. In the case of the lattice (**14**), application of all the symmetry operations to a general (k_a, k_b) point leads to a set of four equivalent points and, consequently, the area of the IBZ is one-fourth the area of the BZ (see **15**). It should be remarked that in general the unit cell of a lattice contains several atoms. Hence the symmetry properties of the actual system can be lower than the symmetry of the general lattice.

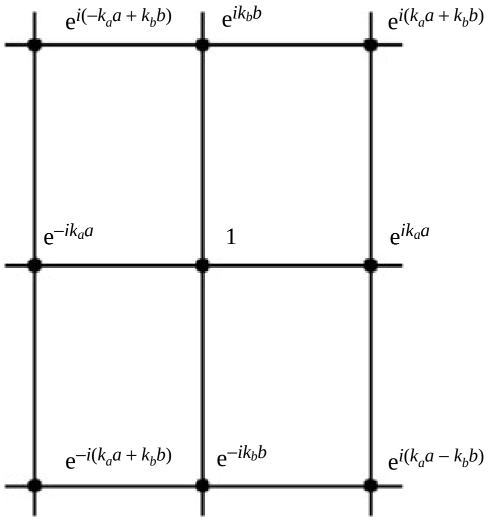

(**21**)

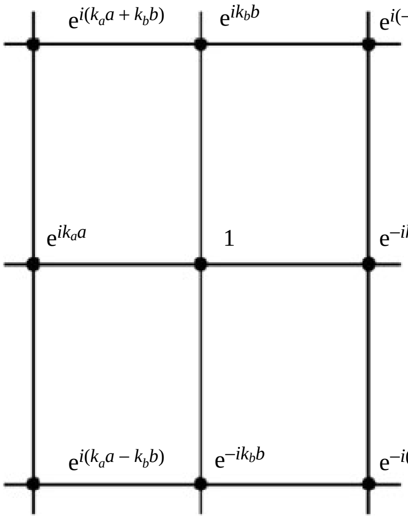

(22)

Extension to a 3D system is straightforward. As an example, consider the 3D orthorhombic lattice (**23**). Now an AO χ located at a lattice site (ma, nb, pc) ($m, n, p =$ integers) is given by $\chi(\mathbf{r} - m\mathbf{a} - n\mathbf{b} - p\mathbf{c})$, and the corresponding BO by

$$\phi(k_a, k_b, k_c) = \frac{1}{\sqrt{N}} \sum_m \sum_n \sum_p [\exp(ik_a ma)\exp(ik_b nb) \times \exp(ik_c pc)\chi(\mathbf{r} - m\mathbf{a} - n\mathbf{b} - p\mathbf{c})] \quad (16)$$

where the three independent wave vectors k_a, k_b, and k_c are needed to describe all possible phase relationships between the AOs along the a-, b-, and c-directions, respectively. Owing to the periodic nature of the coefficients $\exp(ik_a ma)$, $\exp(ik_b nb)$, and $\exp(ik_c pc)$, only the wave vectors (k_a, k_b, k_c) in the following region

$$\begin{aligned} -\frac{\pi}{a} &\le k_a \le \frac{\pi}{a} \\ -\frac{\pi}{b} &\le k_b \le \frac{\pi}{b} \\ -\frac{\pi}{c} &\le k_c \le \frac{\pi}{c} \end{aligned} \quad (17)$$

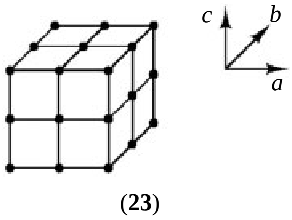

(23)

may be used in constructing the BOs. These wave vectors define the first BZ (**24**) of the 3D lattice (**23**). In (**24**), $\Gamma = (0, 0, 0)$, $X = (\pi/a, 0, 0)$, $Y = (0, \pi/b, 0)$ and $Z = (0, 0, \pi/c)$.

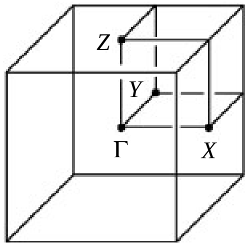

(24)

When the overlap integrals are neglected within the first nearest-neighbor approximation, the energy $e(k_a, k_b, k_c)$ of the BO $\phi(k_a, k_b, k_c)$ is given by

$$\begin{aligned} e(k_a, k_b, k_c) &= \langle \phi(k_a, k_b, k_c)|H^{\text{eff}}|\phi(k_a, k_b, k_c)\rangle \\ &= \alpha + 2\beta_a \cos k_a a + 2\beta_b \cos k_b b + 2\beta_c \cos k_c c \end{aligned} \quad (18)$$

where β_c is the nearest-neighbor resonance integral along the c-direction: $\beta_c = \langle \chi(\mathbf{r})|H^{\text{eff}}|\chi(\mathbf{r} - \mathbf{c})\rangle$. The width of the band given by equation (18) is $4(|\beta_a| + |\beta_b| + |\beta_c|)$. As in the cases of 1D and 2D systems, dispersion relations for 3D systems can be easily explained by knowing the coefficients $\exp(ik_a ma)$, $\exp(ik_b nb)$, and $\exp(ik_c pc)$ at a limited number of specific k points such as Γ, X, Y, and Z.

In order to extend the description of electronic band structures to general 2D and 3D systems, it is convenient to introduce the concepts of the direct and reciprocal lattices.[7] For a general 3D lattice with repeat vectors $\boldsymbol{a}$, $\boldsymbol{b}$, and $\boldsymbol{c}$, the positions of lattice sites (ma, nb, pc) can be represented as vectors $\boldsymbol{R}$

$$\boldsymbol{R} = m\boldsymbol{a} + n\boldsymbol{b} + p\boldsymbol{c} \quad (19)$$

A set of these vectors is usually called the direct lattice. For a given lattice, its reciprocal lattice is defined as a set of vectors $\boldsymbol{K}$ satisfying the relationship

$$\exp(\boldsymbol{K} \cdot \boldsymbol{R}) = 1 \quad (20)$$

Then, any vector $\boldsymbol{K}$ of the reciprocal lattice can be expressed as

$$\boldsymbol{K} = m\boldsymbol{a}^* + n\boldsymbol{b}^* + p\boldsymbol{c}^* \quad (21)$$

where $\boldsymbol{a}^*$, $\boldsymbol{b}^*$, and $\boldsymbol{c}^*$ are the reciprocal vectors. For the orthorhombic lattice (**23**) the lengths of $\boldsymbol{a}^*$, $\boldsymbol{b}^*$, and $\boldsymbol{c}^*$ are given by $2\pi/a$, $2\pi/b$, and $2\pi/c$, respectively, and their directions are along $\boldsymbol{a}$, $\boldsymbol{b}$, and $\boldsymbol{c}$, respectively.

Let us consider a direct lattice generated by three repeat vectors $\boldsymbol{a}$, $\boldsymbol{b}$, and $\boldsymbol{c}$ which are not necessarily orthogonal to each other, as shown in (**25**), where the volume V of the parallelepiped defined by the three vectors $\boldsymbol{a}$, $\boldsymbol{b}$, and $\boldsymbol{c}$ is given

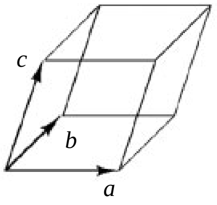

(25)

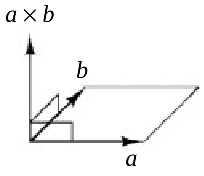

(26)

by $V = \boldsymbol{a} \cdot \boldsymbol{b} \times \boldsymbol{c}$. Then the reciprocal lattice vectors $\boldsymbol{a}^*$, $\boldsymbol{b}^*$, and $\boldsymbol{c}^*$ are given by

$$\begin{aligned} \boldsymbol{a}^* &= \left(\frac{2\pi}{V}\right)\boldsymbol{b} \times \boldsymbol{c} \\ \boldsymbol{b}^* &= \left(\frac{2\pi}{V}\right)\boldsymbol{c} \times \boldsymbol{a} \\ \boldsymbol{c}^* &= \left(\frac{2\pi}{V}\right)\boldsymbol{a} \times \boldsymbol{b} \end{aligned} \tag{22}$$

The lengths and directions of the vectors $\boldsymbol{b} \times \boldsymbol{c}$, $\boldsymbol{c} \times \boldsymbol{a}$, and $\boldsymbol{a} \times \boldsymbol{b}$ of equation (22) are easily determined. For example, the vector $\boldsymbol{a} \times \boldsymbol{b}$ has the length equal to the area of the parallelogram defined by the vectors $\boldsymbol{a}$ and $\boldsymbol{b}$, and has the direction perpendicular to both $\boldsymbol{a}$ and $\boldsymbol{b}$, as shown in (**26**). The positive direction of $\boldsymbol{a} \times \boldsymbol{b}$ is obtained according to the right-handed screw convention: rotate $\boldsymbol{a}$ around the axis of $\boldsymbol{a} \times \boldsymbol{b}$ toward $\boldsymbol{b}$ as if to advance a right-handed screw. Then the screw-advancing direction is the positive direction of $\boldsymbol{a} \times \boldsymbol{b}$.

It is convenient to express a general position, $\boldsymbol{k}$, of the reciprocal space in units of the reciprocal vectors

$$\boldsymbol{k} = x\boldsymbol{a}^* + y\boldsymbol{b}^* + z\boldsymbol{c}^* \tag{23}$$

where x, y, and z are dimensionless numbers. Then, for any general 3D lattice, the term $\exp(i\boldsymbol{k} \cdot \boldsymbol{R})$ can be written as

$$\exp(i\boldsymbol{k} \cdot \boldsymbol{R}) = \exp(ik_a ma)\exp(ik_b nb)\exp(ik_c pc) \tag{24}$$

where $k_a = x(2\pi/a)$, $k_b = y(2\pi/b)$, and $k_c = z(2\pi/c)$. Therefore, the 3D wave vectors (k_a, k_b, k_c) introduced to construct the BOs of a 3D orthorhombic lattice are also valid for any other nonorthorhombic lattice. The wave vector $\boldsymbol{k}$ is often represented by (x, y, z). Thus for the first BZ (**24**), $\Gamma = (0, 0, 0)$, $X = (1/2, 0, 0)$, $Y = (0, 1/2, 0)$, and $Z = (0, 0, 1/2)$. The primitive unit cell of reciprocal space defined by

$$\begin{aligned} -\tfrac{1}{2} &\le x \le \tfrac{1}{2} \\ -\tfrac{1}{2} &\le y \le \tfrac{1}{2} \\ -\tfrac{1}{2} &\le z \le \tfrac{1}{2} \end{aligned} \tag{25}$$

contains all wave vectors needed for constructing the BOs. This primitive cell of the reciprocal space may now be referred to as the first primitive zone (PZ). For orthorhombic lattices, the first PZ is identical with the first BZ. This is not the case for other lattices.

The notations for BOs and their related expressions are considerably simplified by the use of $\boldsymbol{k}$ and $\boldsymbol{R}$. An AO χ_μ located at $\boldsymbol{R}$ is given by $\chi_\mu(\mathbf{r} - \mathbf{R})$. Therefore, the BO ϕ_μ is written as

$$\phi_\mu(k) = \frac{1}{\sqrt{N}}\sum_{\boldsymbol{R}} \exp(i\boldsymbol{k} \cdot \boldsymbol{R})\chi_\mu(\boldsymbol{r} - \boldsymbol{R}) \tag{26}$$

and the COs ψ_i are given as linear combinations of the BOs ϕ_μ

$$\psi_i(\boldsymbol{k}) = \sum_\mu C_{\mu i}(\boldsymbol{k})\phi_\mu(\boldsymbol{k}) \tag{27}$$

The energies $e_i(\boldsymbol{k})$ of the COs $\psi_i(\boldsymbol{k})$ are eigenvalues associated with H^{eff}

$$H^{\text{eff}}\psi_i(\boldsymbol{k}) = e_i(\boldsymbol{k})\psi_i(\boldsymbol{k}) \tag{28}$$

which leads to the secular determinant

$$|H_{\mu\nu}(\boldsymbol{k}) - e_i(\boldsymbol{k})S_{\mu\nu}(\boldsymbol{k})| = 0 \tag{29}$$

The matrix elements $H_{\mu\nu}$ $(\boldsymbol{k})$ and $S_{\mu\nu}$ $(\boldsymbol{k})$ are then expressed as

$$\begin{aligned} H_{\mu\nu}(\boldsymbol{k}) &= \langle\phi_\mu(\boldsymbol{k})|H^{\text{eff}}|\phi_\nu(\boldsymbol{k})\rangle = \langle\chi_\mu(\boldsymbol{r})|H^{\text{eff}}|\chi_\nu(\boldsymbol{r})\rangle \\ &\quad + \sum_{\boldsymbol{R}}[\exp(-i\boldsymbol{k} \cdot \boldsymbol{R})\langle\chi_\mu(\boldsymbol{r} - \boldsymbol{R})|H^{\text{eff}}|\chi_\nu(\boldsymbol{r})\rangle \\ &\quad + \exp(i\boldsymbol{k} \cdot \boldsymbol{R})\langle\chi_\mu(\boldsymbol{r})|H^{\text{eff}}|\chi_\nu(\boldsymbol{r} - \boldsymbol{R})\rangle] \end{aligned} \tag{30}$$

and

$$\begin{aligned} S_{\mu\nu}(\boldsymbol{k}) &= \langle\phi_\mu(\boldsymbol{k})|\phi_\nu(\boldsymbol{k})\rangle \\ &= \langle\chi_\mu(\boldsymbol{r})|\chi_\nu(\boldsymbol{r})\rangle + \sum_{\boldsymbol{R}}[\exp(-i\boldsymbol{k} \cdot \boldsymbol{R})\langle\chi_\mu(\boldsymbol{r} - \boldsymbol{R})|\chi_\nu(\boldsymbol{r})\rangle \\ &\quad + \exp(i\boldsymbol{k} \cdot \boldsymbol{R})\langle\chi_\mu(\boldsymbol{r})|\chi_\nu(\boldsymbol{r} - \boldsymbol{R})\rangle] \end{aligned} \tag{31}$$

3 CRYSTAL ORBITALS AND SYMMETRY[8]

As mentioned before, when two bands overlap in energy they can show a real or an avoided crossing depending on the symmetry of the band levels. These real or avoided crossings have a special importance when they occur at the Fermi level. The existence or absence of an energy gap at the Fermi level dictates if the system is a semiconductor (or insulator) or a

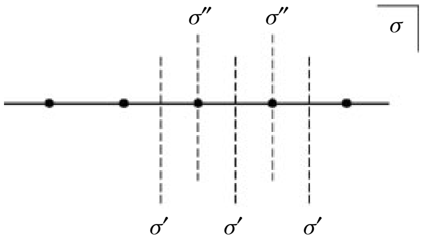

(**27**)

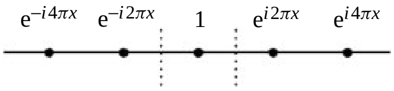

(**28**)

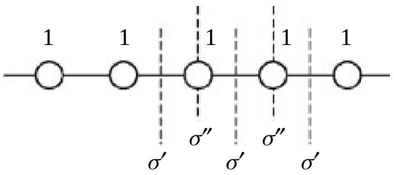

(**29**)

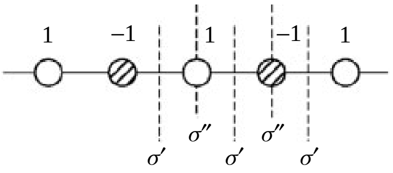

(**30**)

metal. Thus it is very important to know how the symmetry properties of the lattice determine the nature of the COs.

Let us first consider the 1D lattice (**1**) with one s orbital per site. Shown in (**27**) are three different types of symmetry planes. According to equations (23) and (26), a general $\phi_s(\boldsymbol{k})$ BO can be represented as in (**28**), where on top of each lattice point the $\exp(i\boldsymbol{k}\cdot\boldsymbol{R})$ coefficient is given and the dotted lines denote the reference cell. When $k = 0$, that is, $x = 0$, all coefficients are one (**29**) and the BO is symmetric with respect to the symmetry planes σ', σ'', and σ. When $k = \pi/a$, that is, $x = 1/2$, the coefficients are alternately one and minus one (**30**), so that the BO is symmetric with respect to the σ and σ'' planes but antisymmetric with respect to the σ' plane. Thus the BOs $\phi_s(0)$ and $\phi_s(\pi/a)$ are either symmetric or antisymmetric with respect to the σ, σ', and σ'' planes. This is not the case for an arbitrary value of the wave vector, as shown in (**31**) for $k = \pi/5a$, that is, $x = 1/10$. This BO is symmetric with respect to σ but is neither symmetric nor antisymmetric with respect to the σ' and σ'' planes. The reason for this observation is very simple. A BO is an eigenfunction of a symmetry operator if under application of this operator the same BO multiplied by a constant is generated. Because of the presence of the k wave vector in the exponential term, a BO can only be an eigenfunction of symmetry operators leaving the k wave vector unaltered or transforming it into a translationally equivalent one. The σ plane leaves the k vector unaltered whatever the value of k. However, the σ' and σ'' planes transform k into $-k$, so that only for the values 0 and π/a of the wave vector will the BO be an eigenfunction of the corresponding symmetry operators.

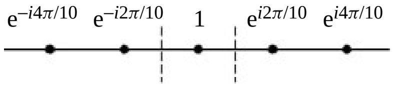

(**31**)

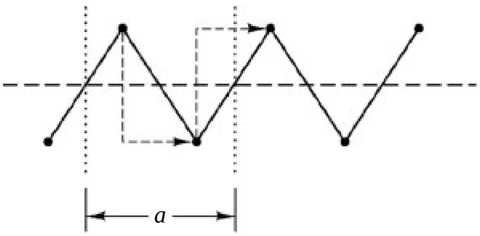

(**32**)

Some care is needed when among the symmetry operations of the lattice there are glide reflections or screw rotations. A glide reflection is a reflection followed by a fractional translation parallel to the reflection plane. A screw rotation is a rotation followed by a fractional translation parallel to the rotation axis. The lattice (**32**) with one s orbital per site is an example of a 1D system having both a glide reflection and a screw rotation along the propagation direction. The effect of the glide reflection is indicated in (**32**), where the dotted lines indicate the reference cell. Of course, application of the glide reflection operation twice is the equivalent of a translation by a. If $\boldsymbol{G}$ and $\boldsymbol{T}$ are the symmetry operators for the glide reflection and translation by a, respectively, equation (32) will hold for any ϕ_μ ($\boldsymbol{k}$) BO being an eigenfunction of $\boldsymbol{G}$, where λ is one of the eigenvalues.

$$\boldsymbol{G}\boldsymbol{G}\phi_u(\boldsymbol{k}) = \lambda^2\phi_\mu(\boldsymbol{k}) = \boldsymbol{T}\phi_\mu(\boldsymbol{k}) = \exp(ik_a)\phi_\mu(\boldsymbol{k}) \qquad (32)$$

It follows that

$$\lambda^2 = \exp(ik_a) = \exp(i2\pi x) \qquad (33)$$

and consequently, the possible values of λ are

$$\lambda = \exp[i(\pi x + 0)] \qquad (34)$$

$$\lambda = \exp[i(\pi x + \pi)] \qquad (35)$$

In general, when there are screw rotations or glide planes parallel to a certain direction, the BO for wave vectors along the same direction are eigenvectors of the corresponding symmetry operators. Since the glide reflection and the screw rotation in (**32**) are along the propagation axis, the BO for any value of k will be an eigenvector of these symmetry operators. Consequently the BO $\phi_s(\boldsymbol{k})$ for any value of the wave vector will be such that the ratio between the coefficients of two successive s AOs will be given by equation (34) or equation (35). The two types of BOs can be represented as in (**33**) or (**34**). An obvious consequence is that the two types of BOs for the wave vector $k = \pi/a$ are completely equivalent and, thus, degenerate. Since only BOs of the same symmetry can mix to generate COs (equation 27) the analysis developed in this section applies also to CO. Of course the same considerations can be used for 2D or 3D systems although some care is needed when the repeat vectors of the direct lattice are not orthogonal.

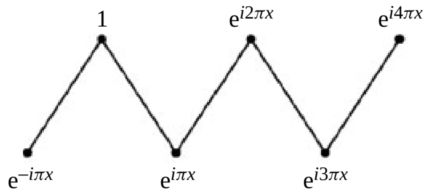

(**33**)

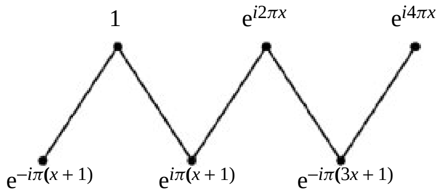

(**34**)

4 CRYSTAL ORBITALS AND ORBITAL INTERACTIONS;[2–6] PEIERLS DISTORTIONS[9]

In order to illustrate the workings of the orbital interaction analysis of the COs let us now consider the π-system of ideal polyacetylene (**35**). In (**35**) all the carbon–carbon distances are identical and the repeat unit contains two CH groups. If we are only interested in the π-system, the AO basis contains just two AOs which will be denoted as χ_1 and χ_2. The first step in the calculation of the COs of the system is the building up of the BOs for these two AOs according to equation (5). The BOs corresponding to $k = 0$ and $k = \pi/a$ are shown in (**36**) and (**37**), respectively. Now, the two BOs for a given k value should be linearly combined to generate the corresponding COs. Solving equation (29) for different values of k will lead to the band structure of the system, which is schematically shown in (**38**). For instance, the COs for $k = 0$ and $k = \pi/a$ are those shown in (**39**) and (**40**) respectively.

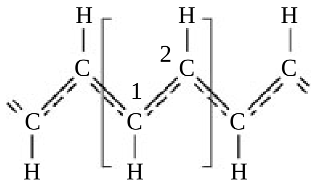

(**35**)

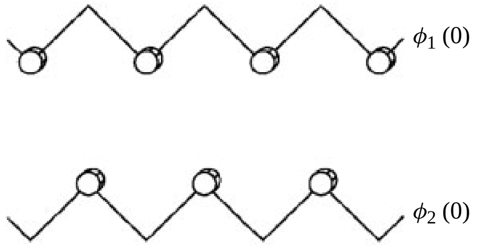

(**36**)

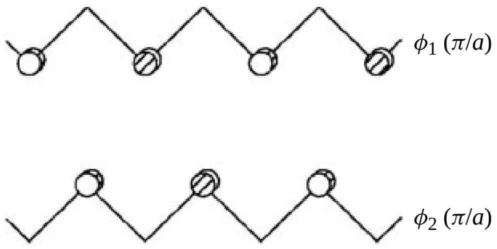

(**37**)

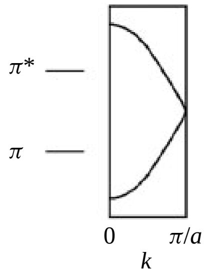

(**38**)

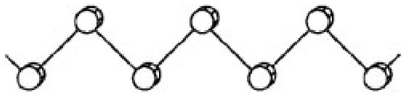

(**39a**)

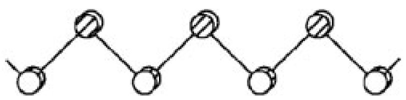

(**39b**)

The previous operations can be done automatically using a computer program. The object of this section is, however,

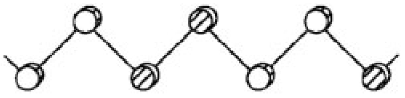

(**40a**)

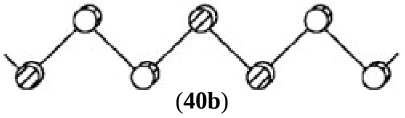

(**40b**)

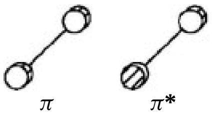

(**41**)

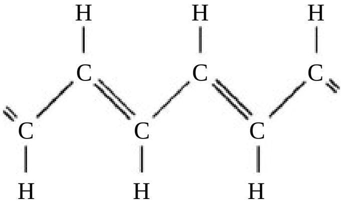

(**42**)

to try to understand the results of these calculations. It should be remarked that the BOs (**39a**) and (**39b**) are just the combinations always in phase of the π and π^* orbitals of the repeat unit (**41**), respectively. In addition, the BOs (**40a**) and (**40b**) are the combinations always out of phase of the same orbitals. In general, the easiest way to analyze or predict the band structure of a certain material is to build first the fragment orbitals of the repeat unit (or chemically significant fragments of the repeat unit in more complex cases), and later the corresponding BOs for selected points of the BZ. Once this is done the major aspects of the band structure can be discussed. In the present case, the two fragment orbitals would be the π and π^* orbitals of the repeat unit. Applying the known rules to build the COs for $k = 0$ and $k = \pi/a$, the BOs (**39**) and (**40**) would be generated. The main aspects of the band structure (**38**) can now be understood. The COs (**39a**) and (**39b**) are the more bonding and antibonding combinations of the system. When overlap integrals are neglected, and within the first nearest-neighbor approximation, the energies for (**39a**) and (**39b**) would be $\alpha + 2\beta$ and $\alpha - 2\beta$, respectively. It is easy to see that the two COs at $k = \pi/a$, (**40a**) and (**40b**), are completely equivalent and consequently, degenerate. These COs are essentially nonbonding because, as shown in (**40**), half of the carbon–carbon interactions are bonding and half are antibonding. Of course, when overlap integrals are neglected, and within the first nearest-neighbor approximation, the energy of these COs is α. The degeneracy of these two COs is a direct consequence of the existence of a screw rotation axis along the chain, as discussed at the end of Section 3. Essentially, the π and π^* levels of the repeat unit have been broadened into two bands which meet at the border of the BZ (see **38**). Consequently, polyacetylene with this structure would be metallic.

Since we know the origin of the degeneracy at the border of the BZ, we can try to design some way to create a band gap. The two COs (**40**) are alternatively bonding and antibonding in such a way that when one of them is bonding the other is antibonding. Consequently, a distortion towards a structure like (**42**), with alternating single and double bonds, will stabilize one of the orbitals but destabilize the other, creating a band gap. For a half-filled band, this distortion will lower the electronic energy and the distorted system will be a semiconductor (or insulator). Let us note that the distortion from (**35**) to (**42**) lowers the symmetry of the lattice. Essentially, this type of distortion is the solid state equivalent of the first-order Jahn–Teller distortion (*see Jahn–Teller Effect*) for molecules and is known as a *Peierls Distortion*.**[9]** Since the two COs (**40**) are degenerate, they can be linearly combined so that the COs (**37**) are an equally valid representation. The COs (**37**) suggest a different way to open a band gap in ideal polyacetylene by creating a difference in the electronegativity of the two centers of the repeat unit. For instance, this could be done by using substituents of different electronegativity for the two carbon atoms.

The Peierls distortion is not a peculiarity of metallic half-filled systems. In general, any partially filled 1D system will be susceptible towards a distortion that opens a band gap at the Fermi level, destroying its metallic properties. In order to show this, let us consider the 1D chain (**43**) in which the unit cell contains two atoms with an AO each. Given the Coulomb integrals of the AOs χ_1 and χ_2 as α_1 and α_2, respectively, and the first nearest-neighbors resonance integrals as defined in (**43**), solution of equation (8) leads to the following expression for the CO energy

$$e_i(k) = \frac{(\alpha_1 + \alpha_2)}{2 \pm [(\alpha_1 - \alpha_2)^2/4 + ({\beta_1}^2 + {\beta_2}^2 + 2\beta_1\beta_2 \cos ka)]^{1/2}} \tag{36}$$

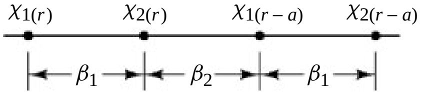

(**43**)

If $\alpha_1 = \alpha_2 = \alpha$ and $\beta_1 = \beta_2 = \beta$, equation (36) reduces to

$$e_i(k) = \alpha \pm 2\beta \cos\left(\frac{ka}{2}\right) \tag{37}$$

This expression leads to the band structure (**44**), which can be obtained by folding the band structure (**3**) at the midpoint along the $k = 0$ to $k = \pi/a$ line. This is not surprising because (**43**) with $\alpha_1 = \alpha_2 = \alpha$ and $\beta_1 = \beta_2 = \beta$ (case I) is identical to (**1**) except that the repeat distance has been doubled.

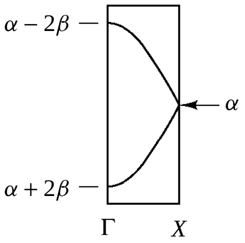

(**44**)

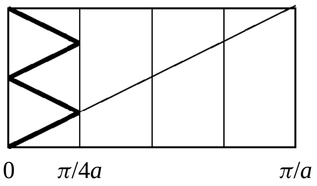

(**45**)

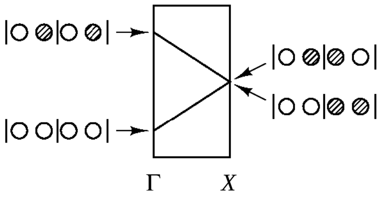

(**46**)

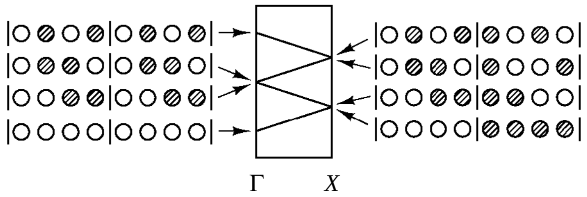

(**47**)

Consequently, the BZ associated with (**43**) must be one-half that appropriate for (**1**). Since the two systems are identical, the information contained in the larger BZ must be translated into the smaller BZ. In practice, for 1D systems this comes back to folding the band structure of the smaller unit cell system at the midpoint along the $k = 0$ to $k = \pi/a$ line. This is why the band structure (**44**) is just a folded version of the band structure (**3**). In general, when a unit cell size increases n times without lowering the symmetry of the system, the resulting band dispersion is folded n times. This is illustrated in (**45**) for $n = 4$. The nature of the degeneracies in (**44**) or (**45**) can be easily explained by building the COs from the dimeric or tetrameric levels of the unit cell as shown schematically in (**46**) and (**47**), respectively.

It should be noted that the two previous strategies to open a band gap for a half-filled band can be obtained from equation (36) when $\beta_1 < \beta < \beta_2 < 0$ and $\alpha_1 = \alpha_2 = \alpha < 0$ (case II, bond length alternation) or $\alpha_1 < \alpha < \alpha_2 < 0$ and $\beta_1 = \beta_2 = \beta < 0$ (case III, electronegativity perturbation). Either case II or case III results from case I by an appropriate perturbation. The essential outcome of such a perturbation, which lowers the symmetry of the lattice, is to open an energy gap in the middle of the band as depicted in (**48**). This band splitting becomes important when the band is half filled, because the band gap opening at the Fermi level lowers the electronic energy of the half-filled system. In general, when a unit cell size is increased n times by a distortion or an external potential (which introduces nonequivalent lattice sites), the band is split into n subbands. This is illustrated for $n = 4$ in (**49**), which can be easily explained on the basis of the folded band dispersion shown in (**47**), because symmetry lowering (as illustrated in (**50a**) and (**50b**)) will split the degeneracies at Γ ($k = 0$) and X ($k = \pi/4a$), thereby introducing band gaps. Consequently, a 1D system having a partially filled band of occupancy $1/n$ or $(n - 1)/n$ is likely to undergo a distortion which increases the unit cell size n times (see (**51a**) and (**51b**)). This general phenomenon is known as a Peierls distortion or a $2k_\mathrm{f}$ distortion (see Section 7.1).

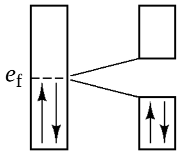

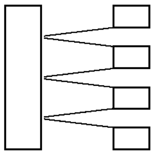

(**48**) (**49**)

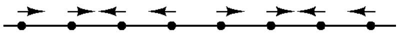

(**50a**)

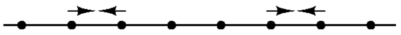

(**50b**)

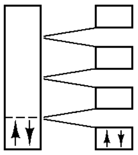

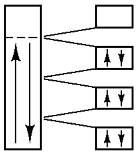

(**51a**) (**51b**)

As a second example of orbital interaction analysis of the COs, let us now consider the tetracyanoplatinate $Pt(CN)_4^{2-}$ chains.[10] Although $K_2[Pt(CN)_4]$ is an insulator, the salt can be cocrystallized with elemental bromine to produce partially oxidized salts, $K_2[Pt(CN)_4]Br_\delta \cdot 3H_2O$. These salts are metallic and have attracted a great deal of attention. The crystal structures of these partially oxidized salts exhibit linear chains with a staggered arrangement of $Pt(CN)_4^{2-}$ units as shown in (**52**). All Pt atoms are equivalent and the Pt–Pt distance becomes shorter when the partial oxidation of Pt increases.

In order to study the band structure of (**52**),[11] it is easiest to consider the eclipsed chain (**53**) first. The band structure

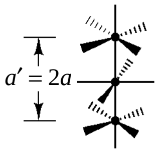

(52)

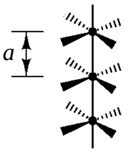

(53)

of (**52**) can be obtained from that of (**53**) by folding the bands. Every Pt(CN)$_4{}^{2-}$ unit contains a d^8 Pt. The orbitals of this group are as described schematically in (**54**), where the contributions of the ligands have been omitted for clarity. Using these orbitals and bearing in mind the relative strength of the σ-, π-, or δ-type interactions between the metal orbitals along the chain, the approximate block band diagram shown in (**55**) can be generated. On the basis of this qualitative band diagram it would be predicted that the nonoxidized system should be a semiconductor or insulator. In principle, partial oxidation empties the top of the z^2 band. Since this region contains antibonding Pt–Pt interactions, the Pt–Pt distance in the partially oxidized salts will be considerably shortened. This shortening will lead to a broadening of all the bands but especially those resulting from σ-type interactions. Hence, when trying to derive the band structure of the partially oxidized (**52**) chains one needs to consider the possibility of an overlap of the z^2 and z bands.

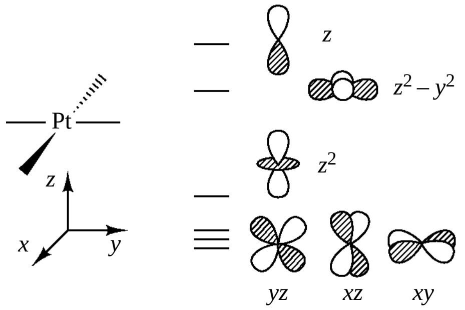

(54)

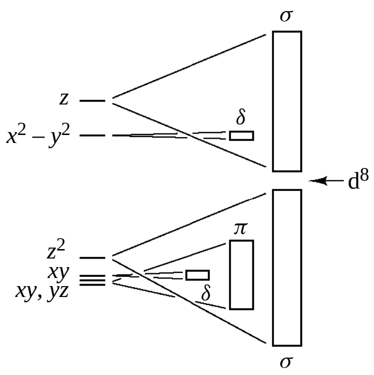

(55)

(**56**) is the schematic band structure for (**53**) where only the σ-type bands have been shown. The corresponding band

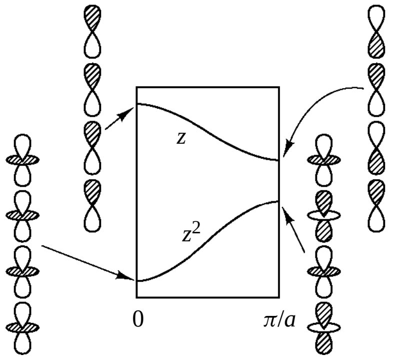

(56)

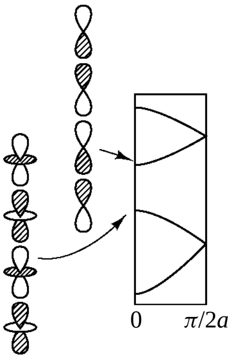

(57)

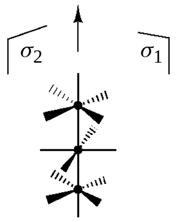

(58a)

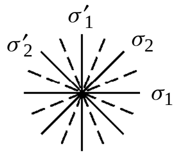

(58b)

structure for (**52**) is obtained by folding (**56**) around the $\pi/2a$ point as shown in (**57**). To understand if the z^2 and z bands can overlap we should consider carefully the symmetry of the chains (**52**). Applying the ideas discussed in Section 3, it is easy to see that the symmetry elements which can be used to classify the band levels for a general value of the wave vector k are the four symmetry planes σ_1, σ_1', σ_2, and σ_2' shown in (**58a**) and the projection view (**58b**), the rotation and screw rotation axes along the chain and the four glide reflection planes shown with dotted lines in (**58b**). As can be seen from the COs at $k = 0$ shown in (**57**), the two bands are of the same symmetry with respect to all the above-mentioned symmetry elements. Thus the z and z^2 bands cannot cross. Consequently, the evolution of the band structure as the Pt–Pt distance shortens will be such that there will always be a band gap between the two bands (see (**59**)) even if the orbital character of the two bands at Γ can be interchanged. A practical consequence of this analysis is that the only way to have metallic-type conductivity in the $Pt(CN)_4^{2-}$ chains is by partial oxidation. Even if very short Pt–Pt distances could be created by other means, like applying pressure, for instance, a semimetallic overlap of the z^2 and z bands would not be produced.

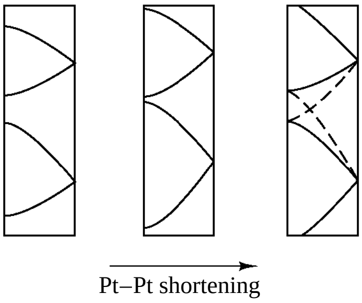

(**59**)

The main result of the previous analysis is that, as long as the oxidation is not too strong, the partially oxidized $Pt(CN)_4^{2-}$ chains have a partially filled single band. Hence, these chains should exhibit metallic properties. However, as any 1D metallic system, they should also be susceptible to a Peierls type distortion which would destroy these metallic properties and increase the periodicity of the lattice. These predictions are in agreement with the experimental results on the $K_2[Pt(CN)_4]Br_\delta \cdot 3H_2O$ salts. Usually, they are metallic at room temperature but the conductivity declines sharply at lower temperatures, becoming semiconducting. It has been shown that the change in the conductivity regime is associated with a periodic lattice distortion (i.e. a Peierls distortion).**[10,12]**

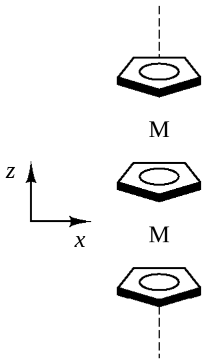

(**60**)

As a final example, let us consider the band structure for the infinite chain $[M(C_5H_5)]$ (**60**).**[13]** The important orbital interactions to consider are those between the d orbitals of the metal atom and the π-type orbitals of C_5H_5 (**61a**). For simplicity, the shorthand notation (**61b**) will be used for these π-type orbitals. The symmetry labels in (**61**) are those of the C_{5v} group which is the appropriate one for a general k wave vector inside the BZ, although at Γ and X the symmetry is higher (D_{5h}). The BOs for one of the e_1 metal orbitals (xz, yz) at Γ and X are shown in (**62**) and (**63**) respectively. The BOs at Γ and X for one of the $\pi(e_1)$ orbitals of C_5H_5 are shown in (**64**) and (**65**), respectively. By symmetry these BOs can mix at Γ but not at X. Thus (**62**) will be destabilized by mixing (**64**) in an antibonding way and vice versa. Therefore the metal

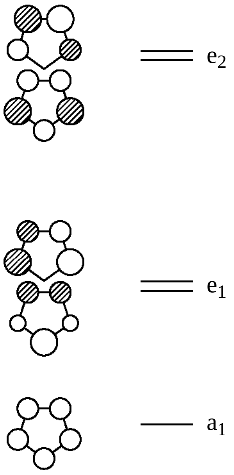

(**61a**)

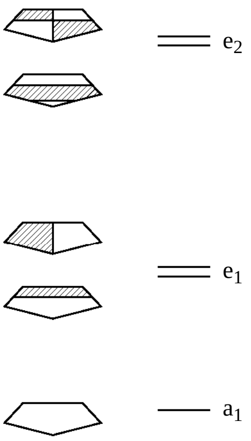

(**61b**)

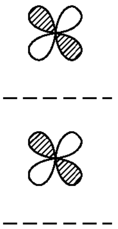

(**62**)

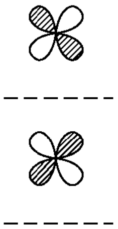

(**63**)

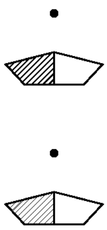

(**64**)

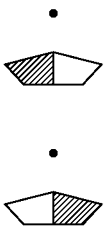

(**65**)

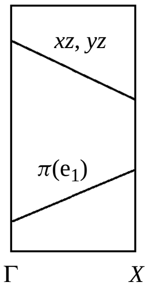

(**66**)

$e_1(xz, yz)$ and $\pi(e_1)$ bands will run as schematically shown in (**66**). The z^2 BOs at Γ and X are shown in (**67**) and (**68**), respectively. Because of its conical nodal surface the z^2 orbital practically does not interact with the $\pi(a_1)$ orbital of C_5H_5. In addition, the metal atoms are too far apart to have any sizeable direct interaction. Consequently, the z^2 band will be quite flat (**69**). The BOs for one of the e_2 metal orbitals (xy, $x^2 - y^2$) at Γ and X are those shown in (**70**) and (**71**), respectively. The BOs at Γ and X for one of the $\pi(e_2)$ orbitals of C_5H_5 are shown in (**72**) and (**73**), respectively. By symmetry these BOs can mix at X but not at Γ. Thus (**71**) will be stabilized by mixing (**73**) in an bonding way and vice versa. However, the e_2 metal orbitals are not well directed towards the $\pi(e_2)$ orbitals and the interaction will be weaker than it was for the e_1 orbitals. The metal $e_2(xy, x^2 - y^2)$ and $\pi(e_2)$ bands will run as schematically shown in (**74**). Finally, as show in (**75–78**), the $\pi(a_1)$ orbital can mix with the metal s orbital at X but not at Γ. The opposite is true for the mixing with the metal z orbital, but this mixing is weaker because of the larger energy difference. The $\pi(a_1)$ band will run as schematically shown in (**79**). Thus the schematic band structure for the $[M(C_5H_5)]$ chain (**60**) will be as shown in (**80**), which compares very well with the calculated one shown in (**81**).[13]

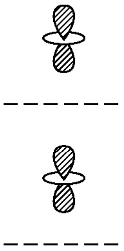
(67)

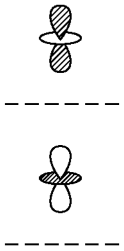
(68)

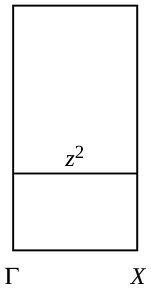

(69)

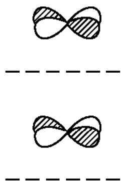
(70)

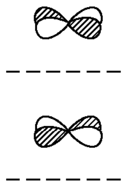
(71)

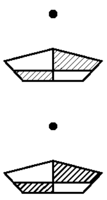
(72)

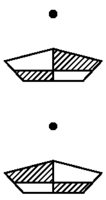
(73)

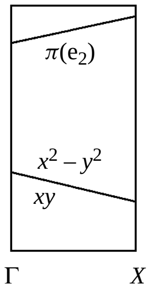

(74)

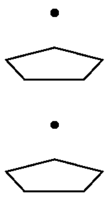
(75)

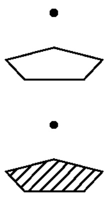
(76)

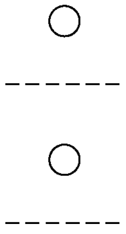
(77)

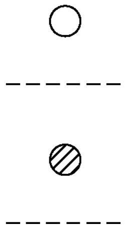
(78)

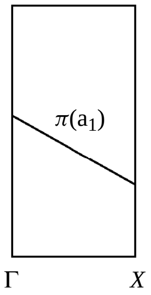

(79)

The examples discussed in this section are quite simple and have been chosen in order to illustrate some basic aspects of the orbital interaction analysis of the structure of solids. This type

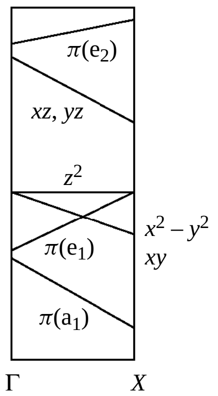

(80)

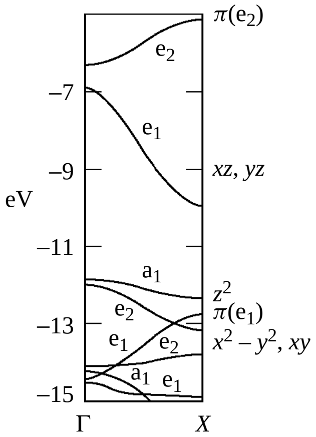

(81)

of approach is very useful in establishing structure–property correlations for solid-state materials, and has been used to understand the calculated band structures for structurally very complex systems.[5]

5 DENSITY OF STATES

Real solid-state materials are often structurally complex and there can be a large number of bands to be considered. In addition, for 2D or 3D materials it is practically impossible to examine $e_i(k)$ for all the regions of the BZ. Furthermore, inside the BZ the symmetry is usually quite low and there can be many avoided crossings between bands. Hence, although in principle one can always perform an orbital interaction analysis of several COs, a particular orbital of the repeat unit can be spread out between several bands. Under such conditions, it can be very difficult to single out an orbital or group of orbitals responsible for the structure or properties of the solid. However, since after all, solids are very big molecules, we should be able to develop qualitative arguments similar to those successfully used in molecular chemistry to explain the structure, properties, or reactivity of solids.

As the problem is that in general there are too many levels (or states) to consider, the more obvious way to circumvent it is to work with a DOS instead of the states themselves. The DOS, $n(e)$, of a solid is defined as the number of states in an energy interval between e and $e + \mathrm{d}e$.[7] Thus $n(e)$ is nonzero within the allowed energy region of a band and vanishes in the forbidden energy region. The $n_i(e)$ values of a given band i satisfy the normalization condition

$$\int_{-\infty}^{\infty} n_i(e)\,\mathrm{d}e = 1 \tag{38}$$

so that, since a band can accommodate two electrons per unit cell, integration of twice the DOS up to the Fermi level gives the total number of electrons of the system. The electronic structure of solids may be discussed solely on the basis of their DOS values. In such an approach the band orbital information is completely absent. Typical patterns of the DOS for 1D or 2D lattices are shown in (**82**) and (**83**), respectively. As shown in (**82**), the DOS values of a 1D band peak at the bottom and the top of the band. For a 2D square lattice with equal magnitudes of interaction along the a- and b-directions the DOS values peak in the middle of the band, as shown in (**83**). The DOS shape for a 3D lattice depends upon the nature of the lattice, but high DOS values generally occur in the middle of the band. An important DOS value in describing the physical properties of metals is the DOS value at the Fermi level, that is, $n(e_\mathrm{f})$.

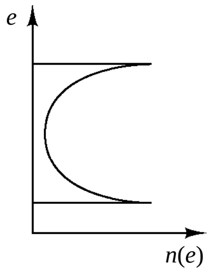

(82)

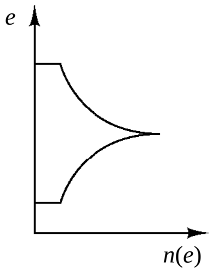

(83)

Since the COs have been written as a linear combination of BOs associated with the different AOs of the unit cell, the DOS curves can be analyzed in terms of contributions per AO of the unit cell. In other words, once the DOS plot has been calculated, we can project the contribution of certain AOs or fragment orbitals of interest for the analysis.[14] In order to illustrate the process let us consider the two-center MO

$$\Psi = c_1\chi_1 + c_2\chi_2 \tag{39}$$

The electron distribution in this MO is given by the normalization condition

$$1 = {c_1}^2 + {c_2}^2 + 2c_1c_2S_{12} \tag{40}$$

where S_{12} is the overlap integral between χ_1 and χ_2. Although it is clear that c_1^2 and c_2^2 should be assigned to χ_1 and χ_2, it is not clear how to assign the term $2c_1c_2S_{12}$ which is an overlap density. The simplest solution was suggested by Mulliken. In the Mulliken population analysis,[15] this term is equally shared between centers 1 and 2. Thus the center 1 is assigned a total of $c_1^2 + c_1c_2S_{12}$ and center 2 a total of $c_2^2 + c_1c_2S_{12}$. These contributions should now be multiplied by the occupation number of this MO. This type of analysis can be performed for the different states of a solid and, consequently, a local DOS can be projected out from the total DOS. These local DOS can be those of an AO, a fragment orbital,[14,16] an atom or group of atoms.

As an example of this type of analysis let us discuss the DOS of the [M(C_5H_5)] chain (**60**).[13] As mentioned in

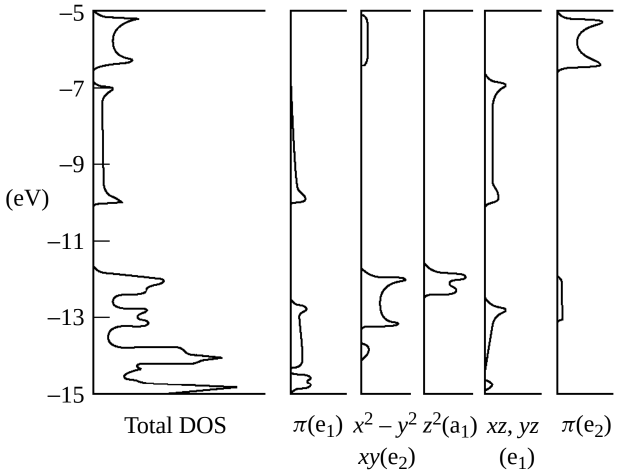

(**84**)

Section 4, the more important interactions in the polymer are those of the xz and yz (e_1) orbitals with the ligand π-type orbitals of the same symmetry. The total DOS for the infinite chain [$M(C_5H_5)$] as well as the projected densities of states for the orbitals $\pi(e_1)$, ($x^2 - y^2, xy$), z^2, (xz, yz), and $\pi(e_2)$ are shown in (**84**). Notice how the contributions of the interacting e_1 orbitals, π and (xz, yz), are split into two regions. The lower energy orbitals, $\pi(e_1)$, are most heavily weighted in the lower energy contribution and the higher energy orbital (xz, yz) most heavily represented in the upper energy contribution. This is the equivalent of our understanding of the interaction of two nondegenerate orbitals in molecules. The contribution of these interacting orbitals extends over a considerable energy range because the two types of orbitals are well oriented to interact, leading to dispersive energy bands. As mentioned, the z^2 orbital does not interact well with the $\pi(a_1)$ ligand orbital. Consequently, the projected contribution of this orbital appears as a very localized contribution. The $x^2 - y^2$ and xy orbitals can interact with the ligand $\pi(e_2)$ ones, which are higher lying in energy, and both types of orbital appear split into two contributions. However, the interactions are less effective than those of the xz and yz orbitals, because the $x^2 - y^2$ and xy orbitals are not directed towards the π orbitals of the ligand. As shown in (**84**), the mixing is weaker and the dispersion of the corresponding bands is smaller for the ($x^2 - y^2, xy$) and $\pi(e_2)$ orbitals than it was for the (xz, yz) and $\pi(e_1)$ orbitals. The main conclusions of this analysis parallel those of Section 4 as well as those reached when the orbital interactions in the molecular $(C_5H_5)_2M$ are considered.[1] Thus the use of projected or local DOS can be a very powerful tool to analyze the electronic structure of complex solids and to help establishing a link between our understanding of the electronic structure of molecules and solids.[17]

Some solids with interesting physical properties possess large and complex unit cells. In understanding the physical properties of such systems, it is important to have some guidelines by which to single out the parts of their crystal structure essential for the description of these properties. For instance, the purple bronze KMo_6O_{17} is a 2D metal and exhibits a resistivity anomaly at 120 K.[18] KMo_6O_{17} has separated metal–oxygen layers of composition Mo_6O_{17}, which are made up of both MoO_6 octahedra and MoO_4 tetrahedra (**85**). The K^+ cations reside in between these layers. As shown in (**85**), there are three different types of Mo atoms in KMo_6O_{17}: the Mo atoms of the MoO_4 tetrahedra (Mo_I in **85**), those of the MoO_6 octahedra in the outer two octahedral sublayers (Mo_{II} in **85**), and those of the MoO_6 octahedra in the inner two octahedral sublayers (Mo_{III} in **85**). According to the usual oxidation formalism of K^+ and O^{2-}, there are three electrons to fill the lower d-block levels of the Mo_6O_{17} layers. Thus it is interesting to enquire if the electrons responsible for the metallic properties (i.e. those near the Fermi level) are delocalized all over the layer or if they are confined into one of the sublayers. Shown in (**86**) is the projection of the Mo contribution to the DOS as well as the individual contributions of Mo_I, Mo_{II}, and Mo_{III}. It is clear from these results that the conducting electrons are those associated with the two inner sublayers of $Mo_{III}O_6$ octahedra. Consequently, the conducting electrons are quite well screened from the random potentials generated by possible alkali nonstoichiometry in these and related molybdenum bronzes.

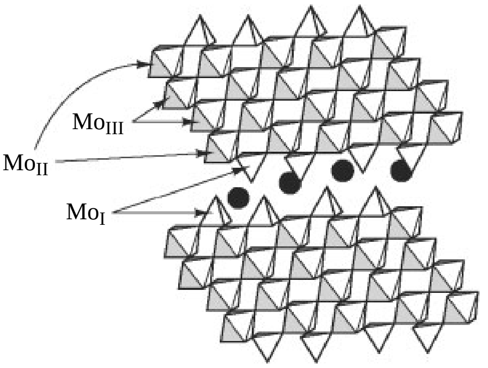

(**85**)

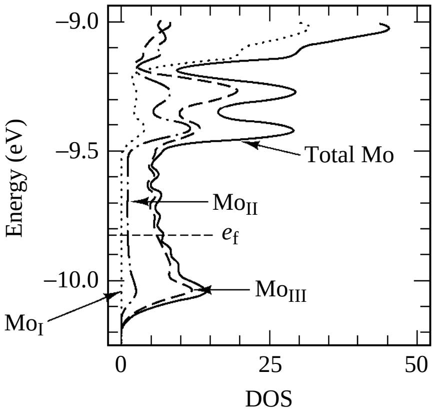

(**86**)

Useful as they are, local DOS do not allow us to know whether the levels in a certain energy range contribute to the bonding between a given pair of atoms. In molecular chemistry, this is often discussed on the basis of the so-called Mulliken overlap population.[15] This concept is related to the contribution $2c_1c_2S_{12}$ of equation (40). This term, an overlap population, is a characteristic of the bonding between the two centers 1 and 2. If the overlap integral is taken as positive, then this quantity is positive when the combination between the two orbitals is bonding and negative when the combination is antibonding. The Mulliken overlap population is the addition over all the orbitals on the two atoms over all occupied MOs of $2c_ic_jS_{ij}$. Exactly as was done for the local DOS, the quantities $2c_ic_jS_{ij}$ of interest can be evaluated for the different energy levels of a solid and projected from the total DOS. These overlap-population-weighted DOS curves are usually known as COOP curves (*Crystal Orbital Overlap Population*).[19]

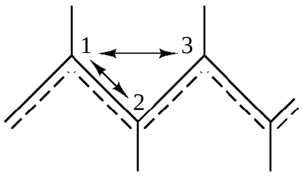

(**87**)

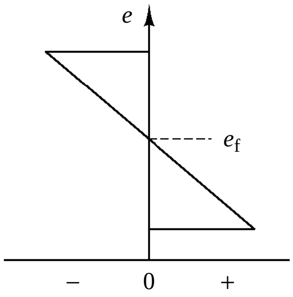

(**88**)

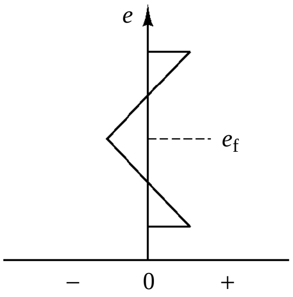

(**89**)

A very simple example of COOP curves are those corresponding to the 1,2 and 1,3 interactions in ideal polyacetylene (**87**). As discussed in Section 4, all the 1,2 interactions are bonding at the bottom of the lower band (**39a**) but antibonding at the top of the upper band (**39b**). The levels at the top of the lower band and bottom of the upper band are essentially nonbonding (**40**). Thus the COOP curve for the 1,2 interactions will be as schematically shown in (**88**). The 1,3 interactions are bonding both at the top of the upper band (**39b**) and the bottom of the lower band (**39a**). However, they are antibonding at the top of the lower band and the bottom of the upper band (**40**). Since these interactions are weaker than the 1,2 ones, the corresponding COOP curve should be as schematically shown in (**89**). COOP curves have been very useful in understanding the structure of complex solids as well as in chemisorption studies.[20]

6 FERMI SURFACE[21]

In order to examine the concept of Fermi surface, let us consider the case of the 2D lattice (**14**) for which the band dispersion relationships are given by equation (15). Diagrams (**90a–c**) show the band dispersion relations along $\Gamma \rightarrow X \rightarrow M \rightarrow Y \rightarrow \Gamma$ for cases (a) $\beta_a < \beta_b = 0$, (b) $\beta_a < \beta_b < 0$, and (c) $\beta_a = \beta_b < 0$, respectively. There is no interaction along the b-direction in case (a), so that the band is dispersionless along $\Gamma \rightarrow Y$ and $X \rightarrow M$. In case (b) the interaction along the b-direction is weaker in magnitude than that along the a-direction. In case (c) the interactions along the a- and b-directions are equally strong. The dashed lines of (**90a–c**) refer to the Fermi level when the band is half filled. For a partially filled band, wave vectors in a certain region of the BZ lead to occupied band levels (i.e. levels below the Fermi level), and wave vectors in the remaining region of the BZ lead to unoccupied band levels (i.e. levels above the Fermi level). The region of the occupied and unoccupied band levels for (**90a–c**) is shown in (**91a–c**), respectively, where shading corresponds to the wave vectors of the occupied levels. Since all k points of the BZ are equally allowed, the occupied region in each of (**91a–c**) is one-half the area of the BZ. For a completely filled band, all the wave vectors of the BZ are occupied. Diagrams (**91d**) and (**91e**) show the region of the occupied and unoccupied band levels of case (**c**) when the band is less-than-half and more-than-half filled, respectively.

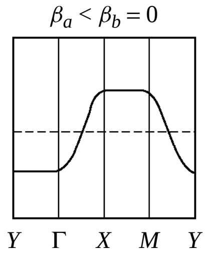

(**90a**)

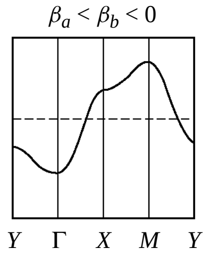

(**90b**)

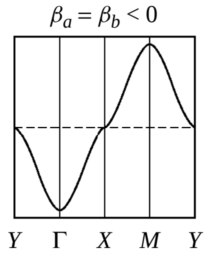

(**90c**)

The boundary surfaces dividing the region of the occupied and unoccupied wave vectors are known as Fermi surfaces. Thus a Fermi surface occurs as a surface in a 3D band description, a line in a 2D band description, and a pair of points in a 1D band description. The wave vectors lying on the Fermi surface are called the Fermi vectors, which

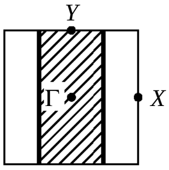

(**91a**)

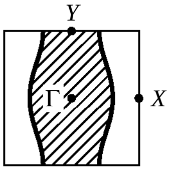

(**91b**)

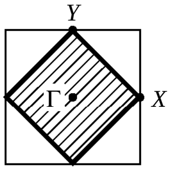

(**91c**)

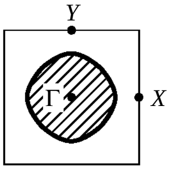

(**91d**)

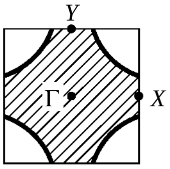

(**91e**)

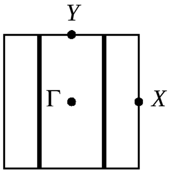

(**92a**)

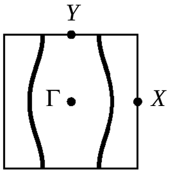

(**92b**)

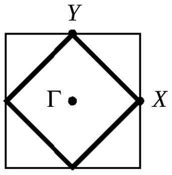

(**92c**)

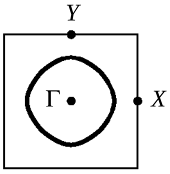

(**92d**)

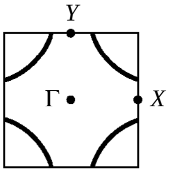

(**92e**)

are denoted by $\boldsymbol{k}_\mathrm{f}$. Thus the Fermi surfaces of (**91a–e**) are given by (**92a–e**), respectively. The Fermi surfaces of (**92a**) and (**92b**) consist of isolated lines, and hence are 1D Fermi surfaces. The Fermi surfaces of (**92c–e**) are closed loops, and therefore are 2D Fermi surfaces. (For (**92e**) the Fermi surface pattern needs to be repeated in reciprocal space to recognize the closed loops.) Carriers of metals are those electrons at the Fermi level. When a certain wave vector direction does not cross a Fermi surface (e.g. $\Gamma \rightarrow Y$ in (**92a**)), there are no electrons at the Fermi level having momentum along that direction and the system is not metallic along that direction. Therefore the Fermi surfaces of (**92a**) and (**92b**) correspond to 1D metals with metallic properties along the a-direction, while those of (**92c–e**) represent 2D metals. Fermi surfaces resulting from less-than-half and more-than-half filled bands are often referred to as electron and hole Fermi surfaces, respectively. For example, the Fermi surfaces of (**92d**) and (**92e**) (see also (**91d**) and (**91e**)) are electron and hole Fermi surfaces, respectively.

Let us now generalize our discussion of the Fermi surface. Within a 1D representation, the Fermi surface of a half-filled band is given by two k points ($\pm 0.25\ \boldsymbol{a}^*$ or, equivalently, $\pm\mathbf{k}_\mathrm{f}$) (**93**). Within a 2D representation, the Fermi surface of the half-filled 1D metal for $\beta_a < \beta_b = 0$ is given by two lines perpendicular to $\Gamma \rightarrow X$, as already seen from (**92a**). Within a 3D representation, the Fermi surface of the half-filled 1D band for $\beta_a < \beta_b = \beta_c = 0$ is given by two parallel planes, that is, $(\pm 0.25, y, z)$, perpendicular to $\Gamma \rightarrow X$ (see (**94**)). Likewise, the 2D Fermi surface of (**92d**) will be given by a cylinder in a 3D representation ($\beta_a = \beta_b < \beta_c = 0$) as shown in (**95**).

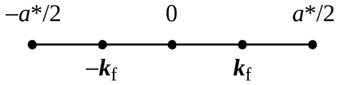

(**93**)

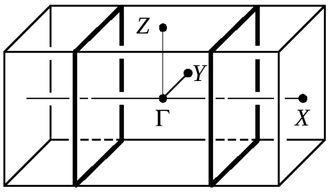

(**94**)

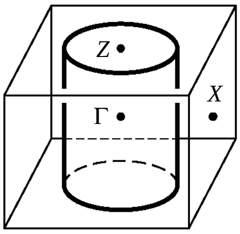

(**95**)

The concept of Fermi surface does not only play a key role in understanding the dimensionality of the transport properties of metals but also in explaining the electronic instabilities of partially filled band systems. When a piece of a Fermi surface can be translated by a vector $\boldsymbol{q}$ and superimposed on another piece of the Fermi surface, this Fermi surface is said to be nested by the vector $\boldsymbol{q}$. Since the Fermi surface of (**92a**) consists of two parallel lines, it is nested by an infinite number of wave vectors, two examples of which are shown in (**96**). In discussing Fermi surface nesting, it is important to consider Fermi surfaces in the entire reciprocal space, which is achieved by repeating the Fermi surface pattern of the first

BZ in reciprocal space. For example, the Fermi surface of (**92b**) is repeated along Γ → Y to generate (**97**). Then it is evident that the Fermi surface of (**97**) is nested by the vector $\boldsymbol{q}$ shown.

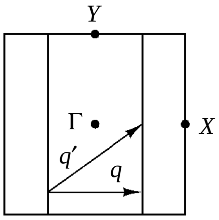

(**96**)

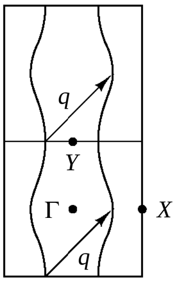

(**97**)

As a slightly more complicated example of Fermi surface nesting, consider the two partially filled 1D bands shown in (**98**). These two bands have an identical slope along Γ → X but opposite slopes along Γ → Y. Then the Fermi surface resulting from the two bands of (**98**) is found to have four separate pieces as shown in (**99**). In (**99**) the inner two pieces of the Fermi surface result from the upper band whereas the outer two pieces result from the lower band, and there are two pairs of nested pieces with an identical nesting vector. The importance of Fermi surface nesting lies with the fact that a metallic system with a nested Fermi surface possesses electronic instability and therefore is likely to undergo a metal-to-insulator phase transition. As will be discussed in the next section, the latter opens a band gap at the Fermi level, thereby destroying the Fermi surface.

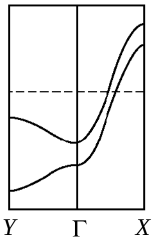

(**98**)

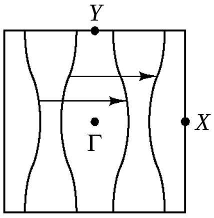

(**99**)

7 ELECTRONIC STATES DERIVED FROM A METALLIC STATE[5,22]

In discussing metal-to-insulator and metal-to-superconductor transitions, it is convenient to describe the insulating and the superconducting states as a consequence of a perturbation on the metallic state. In the following, we first examine why Fermi surface nesting is likely to induce a metal-to-insulator transition from the viewpoint of band orbital mixing. Then we discuss how the phenomenon of electron localization may be understood and also how a superconducting state can be described in terms of band orbital mixing.

7.1 Charge Density Wave and Spin Density Wave States

A metallic state predicted by one-electron band theory is not stable when its Fermi surface is nested, and becomes susceptible to a metal-to-insulator transition under a suitable perturbation. We now examine the nature of the nonmetallic states that are derived from a normal metallic state upon mixing its occupied and unoccupied band levels. For simplicity, consider the 2D representation of the nested Fermi surface shown in (**100**), where the vector $\boldsymbol{q}$ is one of many possible nesting vectors. The occupied and unoccupied wave vectors are denoted by $\boldsymbol{k}$ and $\boldsymbol{k}'$, respectively. Each unit cell will be assumed to contain one AO χ. Suppose we choose the $\boldsymbol{k}$ and $\boldsymbol{k}'$ values to satisfy the relationship

$$\boldsymbol{q} = \boldsymbol{k} - \boldsymbol{k}' \tag{41}$$

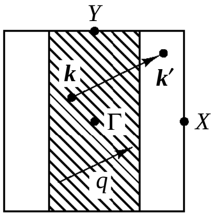

(**100**)

The orbitals $\phi(\boldsymbol{k})$ and $\phi(\boldsymbol{k}')$ are eigenfunctions of the unperturbed Hamiltonian H°. If a certain perturbation H' is introduced and the interaction matrix elements $\langle\phi(\boldsymbol{k})|H'|\phi(\boldsymbol{k}')\rangle$ are nonzero, these orbitals will not be eigenfunctions of $H^\circ + H'$ anymore. They will interact to give modified orbitals $\psi(\boldsymbol{k})$ and $\psi(\boldsymbol{k}')$

$$\begin{aligned} \psi(\boldsymbol{k}) &\propto \phi(\boldsymbol{k}) + \gamma\phi(\boldsymbol{k}') \\ \psi(\boldsymbol{k}') &\propto -\gamma\phi(\boldsymbol{k}) + \phi(\boldsymbol{k}') \end{aligned} \tag{42}$$

where γ is a mixing coefficient.

The electron density distributions of the modified orbitals, $\psi(\boldsymbol{k})$ and $\psi(\boldsymbol{k}')$, differ from those of the unmodified ones, $\phi(\boldsymbol{k})$ and $\phi(\boldsymbol{k}')$. As shown by Whangbo,[23] $\psi(\boldsymbol{k})$ and $\psi(\boldsymbol{k}')$ each have density wave character with respect to $\phi(\boldsymbol{k})$ or $\phi(\boldsymbol{k}')$, with periodicity in real space given by the term $\cos(\boldsymbol{q}\cdot\boldsymbol{R})$. $\psi(\boldsymbol{k})$ leads to density accumulation where $\psi(\boldsymbol{k}')$ has density depletion, and vice versa. If the density distribution arising from $\phi(\boldsymbol{k})$ or $\phi(\boldsymbol{k}')$ is represented by a straight line, then the density accumulation and depletion associated with $\psi(\boldsymbol{k})$ and $\psi(\boldsymbol{k}')$ occur in a waveform as shown in (**101**), where shaded

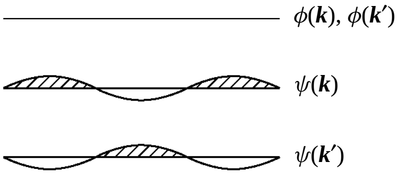

(**101**)

and unshaded half waves represent density accumulation and depletion, respectively.

Suppose that the orbital mixings defined in equation (42) are carried out for all occupied $\boldsymbol{k}$ under the condition $\boldsymbol{q} = \boldsymbol{k} - \boldsymbol{k}'$ to obtain sets of modified orbitals $\{\psi(\boldsymbol{k})\}$ and $\{\psi(\boldsymbol{k}')\}$ from sets of unmodified orbitals $\{\phi(\boldsymbol{k})\}$ and $\{\phi(\boldsymbol{k}')\}$. The normal metallic state is one in which all the $\phi(\boldsymbol{k})$ orbitals are doubly occupied (**102**). Then, as illustrated in (**103**) for a 1D chain, each site has no magnetic moment and has an identical amount of charge. A charge density wave (CDW) state occurs when the $\psi(\boldsymbol{k})$ orbitals are doubly occupied (**104**). As illustrated in (**105**) for a 1D chain, a CDW state has no local magnetic moment but charge densities on atomic sites which vary in a wave manner. When $\psi(\boldsymbol{k})$ and $\psi(\boldsymbol{k}')$ are each singly occupied by up-spin and down-spin electrons (**106**), respectively, a SDW state results. As shown in (**107**) for a 1D chain, the SDW state has a local magnetic moment at atomic sites but the total charge density on each atomic site is identical. The driving force leading to a CDW or an SDW state is the energy gain that results from the interactions of occupied levels $\phi(\boldsymbol{k})$ with unoccupied levels $\phi(\boldsymbol{k}')$, that is, $\langle\phi(\boldsymbol{k})|H'|\phi(\boldsymbol{k}')\rangle$, where the perturbation H' is the lattice vibration and electron–electron repulsion for CDW and SDW, respectively.

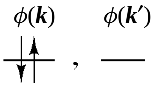

(**102**)

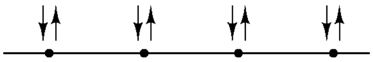

(**103**)

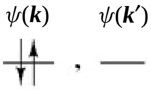

(**104**)

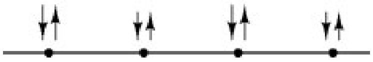

(**105**)

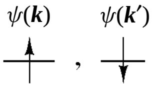

(**106**)

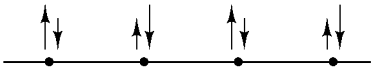

(**107**)

The orbital mixing between $\phi(\boldsymbol{k})$ and $\phi(\boldsymbol{k}')$ becomes more favorable as the energy difference between them decreases, that is, when the $\boldsymbol{k}$ value approaches the Fermi surface. The orbital mixing lifts the degeneracy between $\phi(\boldsymbol{k})$ and $\phi(\boldsymbol{k}')$ when $\boldsymbol{k}$ is on the Fermi surface, and increases the energy difference between $\phi(\boldsymbol{k})$ and $\phi(\boldsymbol{k}')$ when $\boldsymbol{k}$ does not lie on the Fermi surface. As illustrated in (**108**) for a partially filled 1D band system, the orbital mixing between $\phi(\boldsymbol{k})$ and $\phi(\boldsymbol{k}')$ changes their energies in the vicinity of the Fermi level most significantly and opens a band gap at the Fermi level. In (**108**) the band gap is given by 2Δ, where $\Delta = \langle\phi(\boldsymbol{k})|H'|\phi(\boldsymbol{k}')\rangle$ evaluated for $\boldsymbol{k} = \boldsymbol{k}_\mathrm{f}$. When there exists a Fermi surface nesting, the favorable orbital mixing can be achieved for a large region of $\boldsymbol{k}$ values in the vicinity of the Fermi surface. This explains why a metal with a nested Fermi surface is susceptible toward a phase transition that leads to orbital mixing between the levels around the Fermi level, thereby creating a band gap.

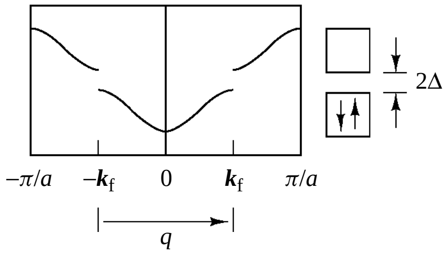

(**108**)

Metals and semiconductors have positive and negative slopes in their electrical resistivity (ρ) vs. temperature (T) curves as schematically shown in (**109**) and (**110**), respectively. By definition, the Fermi surface disappears when a band gap opens at the Fermi level. If the Fermi surface nesting is complete, all the Fermi surface is removed by the appropriate orbital mixing. However, if the Fermi surface nesting is incomplete, only the nested portion of the surface is removed by orbital mixing. The unnested portion is left as small Fermi surface pockets. The system will thus retain its metallic properties although the number of carriers (i.e. those electrons at the Fermi level) will be

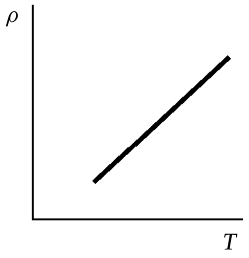

(**109**)

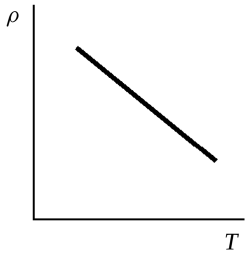

(**110**)

smaller. If a phase transition induced by temperature lowering gives rise to such Fermi surface change, the resistivity vs. temperature plot for the system will be as shown in (**111**) (i.e. a metal-to-metal transition). However, if the Fermi surface nesting is complete, (**112**) will be observed (i.e. a metal-to-semiconductor or metal-to-insulator transition). The CDW instabilities of NbSe$_3$,[24] Mo$_4$O$_{11}$,[25a–c] and KMo$_6$O$_{17}$[18,25a,b] are associated with metal-to-metal transitions, while those of TaS$_3$,[24] K$_{0.3}$MoO$_3$,[26] and K$_2$Pt(CN)$_4$Br$_{0.3}$·3H$_2$O,[10] with metal-to-semiconductor transitions. The charge transfer molecular conductor (TMTSF)$_2$PF$_6$ undergoes a metal-to-insulator transition near 12 K at ambient pressure as a result of an SDW instability.[27a]

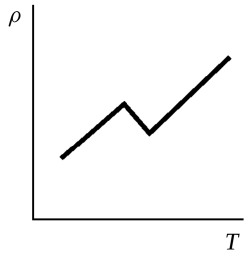

(**111**)

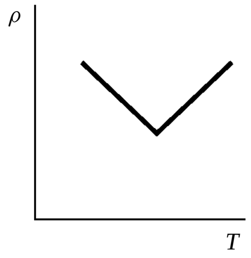

(**112**)

7.2 Electron Localization[28]

In order to examine the role of the on-site electron–electron repulsion U, let us first discuss the relative energies of the low- and high-spin states of a dimer. Consider a dimer with one orbital and one electron on each atomic site (**113**), the MOs of which are expressed as

$$\Psi_1 = \frac{(\chi_1 + \chi_2)}{\sqrt{2}}$$

$$\Psi_2 = \frac{(\chi_1 - \chi_2)}{\sqrt{2}} \tag{43}$$

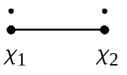

(**113**)

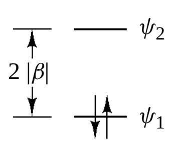

(**114**)

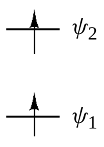

(**115**)

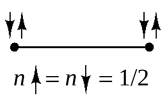

(**116**)

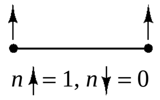

(**117**)

provided that the overlap integral $\langle \chi_1 | \chi_2 \rangle$ is neglected. Then, the energies of these orbitals are given by $e_1 = \alpha + \beta$ and $e_2 = \alpha - \beta$, where β is the resonance integral $\langle \chi_1 | H^{\mathrm{eff}} | \chi_2 \rangle$. With two electrons, one may construct the low-spin state (**114**) or the high-spin state (**115**). In a one-electron picture, in which electron–electron repulsion is neglected, the low-spin state is always more stable than the high-spin state. However, this is not necessarily the case when electron–electron repulsion is taken into consideration. To simplify our discussion, we neglect all repulsion integrals except the on-site repulsion $U = \langle \chi_1 \chi_1 | \chi_1 \chi_1 \rangle = \langle \chi_2 \chi_2 | \chi_2 \chi_2 \rangle$. Then, in any electronic state, an atomic site with the up- and down-spin electron densities $n\uparrow$ and $n\downarrow$, respectively, contributes the amount of repulsion given by $n\uparrow n\downarrow U$. The on-site charge densities associated with the low-spin (**114**) and high-spin (**115**) states are depicted in (**116**) and (**117**), respectively. In terms of the on-site repulsion, the low-spin state is less stable than the high-spin by $U/2$. In terms of the orbital energies, however, the low-spin state is more stable than the high-spin state by $2|\beta|$, which is equal to $W/2$, where W is the bandwidth (see **4**) of the corresponding 1D chain (**1**). Therefore, when electron–electron repulsion is taken into consideration, the high-spin state becomes more stable if $U > W$. A similar reasoning for chain (**1**), assuming the cosine like e(k) vs. k relationship of equation (4), leads to the analogous localization condition, $U > (4/\pi)W$. In general, for a solid in which $U > W$, the total energy can be lowered by introducing spin polarization on each lattice site (i.e. $n\uparrow \neq n\downarrow$) because it reduces the contribution of on-site repulsion to the total energy. This situation is realized in an SDW state as discussed in the previous section.

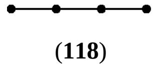

(**118**)

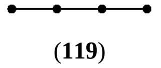

(**119**)

So far our discussion has been limited to those electronic states that originate from a normal metallic state, and is therefore appropriate when the on-site repulsion is small compared with the bandwidth (i.e. $W > U$). When $U \gg W$, electrons are localized on lattice sites. Consider the 1D lattice (**118**) that has one orbital and one electron per site, a typical half-filled band system. When $U \gg W$, favorable electronic states are those in which each site has one electron with either up or down spin. All these states are insulating in nature, because electron hopping from one site to another leads to a situation in which two electrons reside on a single site, thereby causing on-site repulsion (see **119**). Such insulating states resulting from partially filled bands are referred to as Mott–Hubbard localized states (*see Mott–Hubbard Transition*). Diagrams (**120**) and (**121**) represent ferromagnetic (*see Ferromagnetism*) and antiferromagnetic (*see Antiferromagnetism*) arrangements of spins, respectively. These two states have a long-range order. The spin arrangement of (**122**) is an example with no long-range order. Within the one-electron band picture, the ferromagnetic state (**120**) is represented by the electronic structure that results when all the band levels are singly occupied with an identical spin, as depicted in (**123**), which is a solid-state analog of the dimer high-spin state (**115**). If one neglects electron–electron repulsion terms except for the on-site and the nearest-neighbor intersite Coulomb repulsions, the electronic energies of the three states (**120**–**122**) are identical. Consequently, the high-spin band filling scheme (**123**) may be used to represent any localized electronic state arising from a half-filled band. This high-spin band filling scheme is useful. For instance, if a 1/4-filled band system adopts a low-spin band filling (i.e. each band level is occupied by up- and down-spin electrons) as shown in (**51a**), it is susceptible to a tetramerization. However, when this system adopts a high-spin band filling, it would undergo a dimerization instead of tetramerization because band gap opening at the Fermi level can be achieved only by a dimerization (see (**124**)). In 1D systems, the distortion (e.g. (**51a**)) arising from a low-spin band filling ($U < W$) is called a $2k_\mathrm{f}$ distortion, since the nesting vector is given by $\boldsymbol{q} = k_\mathrm{f} - (-k_\mathrm{f}) = 2k_\mathrm{f}$. The distortion arising from a high-spin band filling ($U > W$) (e.g. (**124**)) is referred to as a $4k_\mathrm{f}$ distortion.[29] An example of $4k_\mathrm{f}$ distortion is provided by the organic charge transfer salt MEM$^+$ (TCNQ)$_2{}^-$.[12,30]

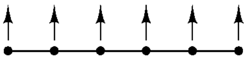

(**120**)

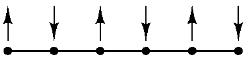

(**121**)

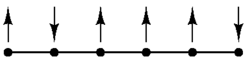

(**122**)

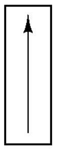

(**123**)

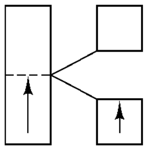

(**124**)

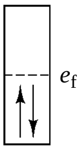

(**125**)

For a half-filled system, the low-spin metallic band filling (**125**) is appropriate when $U < W$. The energies for the low-lying excited states of the metallic state (**125**) are well described by the band orbital energy differences in the vicinity of the Fermi level. In contrast, it is difficult to describe the energies for the low-lying excited states of a Mott–Hubbard localized state (e.g. the energy differences between the states (**120**) and (**121**)) within a band electronic structure theory, because this theory is based upon the assumption that electrons are delocalized throughout the lattice. Localized electronic systems are typically examined in terms of model Hamiltonians (e.g. spin and Hubbard Hamiltonians) designed to study their low-lying excited states.[28b]

In addition to Mott–Hubbard localization, there is another common source of electron localization, which arises when a lattice is under a random potential (e.g. a random distribution of alkali metal ions in alkali metal containing transition metal oxides). For a metal, a practical consequence of a random potential is to open a band gap at the Fermi level. Insulating states induced by random potentials are referred to as Anderson localized states (*see Anderson Localization*).[31]

7.3 Superconducting State[32,33]

Upon lowering the temperature, a metal may become susceptible to another type of electronic instability, that is, formation of a superconducting state (*see* **126**; also ***Superconductivity***). Charge carriers of a superconducting state are not individual electrons as in a normal metallic state, but pairs of electrons (called Cooper pairs; *see Cooper Pair*) having opposite momenta (i.e. opposite wave vectors). Thus Cooper pairs are described by-product functions $\phi(\boldsymbol{k})\phi(-\boldsymbol{k})$ and $\phi(\boldsymbol{k}')\phi(-\boldsymbol{k}')$, where $\boldsymbol{k}$ and $\boldsymbol{k}'$ refer to occupied and unoccupied wave vectors of a normal metallic state, respectively. The energy lowering that brings about superconductivity is induced by the interaction of an occupied pair function $\phi(\boldsymbol{k})\phi(-\boldsymbol{k})$ with an unoccupied pair function $\phi(\boldsymbol{k}')\phi(-\boldsymbol{k}')$, that is, $\langle\phi(\boldsymbol{k})\phi(-\boldsymbol{k})|H'|\phi(\boldsymbol{k}')\phi(-\boldsymbol{k}')\rangle$, where the perturbation H' causing this mixing is electron–phonon interaction in traditional superconductors described by the BCS theory.[33] As a consequence of the interaction between the pair functions, the character of the unoccupied pair function is mixed into that of the occupied pair function. In this indirect way, a superconducting state incorporates unoccupied orbital character into the occupied orbital character.[22] Interactions between the pair functions $\phi(\boldsymbol{k})\phi(-\boldsymbol{k})$ and $\phi(\boldsymbol{k}')\phi(-\boldsymbol{k}')$ introduce an energy gap at the Fermi level, as do the

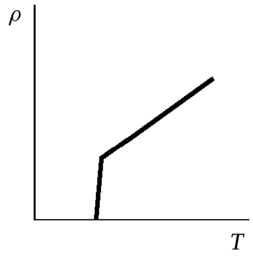

(**126**)

interactions between $\phi(\boldsymbol{k})$ and $\phi(\boldsymbol{k}')$ in forming CDW and SDW states. It should be recalled that charge carriers of a superconducting state are Cooper pairs. A superconducting energy gap prevents Cooper pairs from breaking up when there is no excitation energy greater than the gap. The latter is a few multiples of $k_B T_c$ at absolute zero temperature, where T_c is the superconducting transition temperature, and gradually decreases to zero at T_c.

For traditional superconductors, Cooper pair formation is induced by the electron–phonon interaction.**[33]** Simply speaking, a moving electron causes a slight, momentary lattice deformation around itself. The deformation affects the motion of a second electron (moving in the opposite direction) in the wake of the first in such a way that, effectively, the two electrons move as an entity as if bound together by an attractive force. Among the factors affecting the magnitude of the superconducting transition temperature T_c, the most important one is the electron–phonon coupling, the extent of which is measured by the electron–phonon coupling constant λ. In general, T_c increases with increasing λ. In addition, a large λ results when the lattice has a low-frequency phonon spectrum (i.e. soft phonons arising from vibrations with shallow potential wells). Therefore, when the lattice is soft toward the low-frequency phonons crucial for superconductivity, the electron–phonon coupling constant λ is large, thereby raising the T_c.

In order to become superconducting, a metal should avoid the electronic instability toward a metal-to-insulator transition leading to a CDW or an SDW state. The Fermi surface of a 1D metal is generally well nested so that a 1D metal rarely becomes superconducting. However, the preference for the CDW, SDW, or superconducting states sometimes can be delicately balanced by changes in pressure, temperature, or electron filling. For instance, the 12 K metal-to-insulator transition associated with the SDW instability of $(TMTSF)_2PF_6$ can be suppressed under an applied pressure of 9 kbar and the system becomes superconducting at 0.9 K.**[27b]** An interesting situation occurs for the $x^2 - y^2$ band of the CuO_2 layers in high T_c copper oxide superconductors. When this band is half filled, its 2D Fermi surface (see **91c**) is well nested and the CuO_2 layers are not metallic but antiferromagnetic, which is a particular case of a SDW state. This situation applies for stoichiometric La_2CuO_4. When some electrons are removed or added as in $La_{2-x}Sr_xCuO_4$ and $Nd_{2-x}Ce_xCuO_4$ respectively, the Fermi surfaces are no longer nested (see **91d** and **91e**) and the CuO_2 layers are metallic and eventually become superconducting.**[34]**

8 COMPUTATIONAL APPROACHES

The combination of impressive developments both at the computational level and in quantum mechanical methods during the last decade has made very precise descriptions of the electronic structure of solids with quite large unit cells possible. The solid-state chemist who needs to put on a firm, more quantitative basis the concepts developed in this article for the materials in which he or she is interested is frequently faced with a large series of approaches and computing codes. In this section, we will give a succinct description of some of the more often used approaches in the chemical literature. The interested reader will find detailed information about their basis and computational implementations in the web page addresses we provide.

Among semiempirical methods, the more frequently used has been the Extended Hückel method.**[11,35]** This approach has deep roots in the way chemists think about the electronic structure of molecules and has been successfully adapted to the peculiarities of infinite systems. This is an LCAO and non self-consistent approach in which overlap is retained. The diagonal elements of the Hamiltonian are considered to be the corresponding ionization potentials and the nondiagonal elements are evaluated on the basis of a Wolfsberg-Helmholz type approximation. The simplicity and transparency of the method has made it very popular and extremely useful in understanding the electronic structure of a wide variety of materials. The information that can be obtained is mostly qualitative and thus it is specially useful in looking at trends (for instance, it is an approach which cannot be used for structural optimizations). However, in some fields (for instance, in low-dimensional materials) the method has provided almost quantitative, and in some cases even provides predictive, information. There is no doubt that even if more sophisticated approaches are by now routinely used, the ideas originating from this approach will continue to provide a simple yet powerful way to discuss the electronic structure of solids.

Density Functional Theory (DFT) has become the method of choice for the study of the electronic structure of solids. Advances in computer technology have made possible the development of DFT-based codes providing a detailed ab initio description of the electronic structure of complex materials. Following the two celebrated papers by Hohenberg and Kohn**[36a]** and Kohn and Sham,**[36b]** a wide variety of approaches have been developed and turned into very efficient computational tools. These approaches differ in the way they represent the density, potential, and Kohn-Sham orbitals. Essentially DFT approaches can be classified in two main groups: all electron methods and pseudopotential methods.

The use of a pseudopotential is one of the ways to remedy for the more notorious deficiency of plane waves basis sets: the impossibility of describing correctly the rapid oscillation of the valence wave functions in the region around the ion cores. However plane waves offer several advantages (unbiased representation, arbitrarily good convergence accuracy, easiness of mathematical and computational implementation) which lie at the heart of their widespread use. In the pseudopotential approximation, the nucleus and core electrons are considered as a frozen core and the interaction of the valence electrons with this core is described by a pseudopotential which reproduces the eigenvalues and wave functions outside the core. Of course, this approach assumes that the exchange-correlation potential is separable into a core and a valence part. This assumption is never exact and although it works effectively in many cases, it can be problematic for transition metal atoms for instance. The partial nonlinear core correction scheme can be used in these cases. The use of pseudopotentials is not limited to plane wave approaches; although in this case it is not really needed, it can also be used when localized AOs-like basis sets are used. In that way, only the valence electrons are treated explicitly.

A number of efficient computer codes using the pseudopotential approach are presently available. Some of the more widely used include ABINIT,[37] VASP,[38] SIESTA,[39] CASTEP,[40] Spinor[41] and FH98md.[42] Every one of them has its own peculiarities, for instance, VASP is one of the fastest because of its use of ultrasoft pseudopotentials, Spinor includes spin-orbit coupling and generalized noncollinear magnetism, and ABINIT allows both DFT and density functional perturbation theory calculations. All of these codes use plane wave type basis sets. SIESTA differs from them in that it uses a numerical LCAOs basis set. Because of the localized nature of the basis, the computer time and memory scale linearly with the number of atoms allowing the study of very large systems. The code is very flexible, allowing both very fast simulations using minimal basis sets and very accurate calculations using multi-ζ and polarized bases depending on the required accuracy and available computational power. A nonnegligible advantage of the code, like all methods using local basis sets, is that it greatly facilitates the analysis of the results in familiar chemical terms.

All electron approaches in which no approximation concerning the shape of the potential is made are known as full potential schemes. The more widely used all-electron approach is the LAPW (linear augmented plane wave) method.[43] Its basis lies on the observation that near the nucleus the wave function and potential are close to those in the atom in that they are strongly varying and nearly symmetrical. However, between the atoms the wave function and potential are smoother. Thus, in the LAPW approach the unit cell of the system is divided into a series of nonoverlapping atomic spheres centered on the atoms and an interstitial region. In order to build the basis functions (not the potential), it is assumed that the potential is spherically symmetric inside the atomic spheres but constant outside (i.e. the so-called muffin tin approximation). As a result each plane wave is augmented by an atomic type function inside every atomic sphere. There are different schemes of varying accuracy in order to perform such augmentation. The more widely used code implementing these ideas is WIEN2k.[44]

Other full potential all-electron approaches have been developed. For instance, the FPLO (full potential local orbital) code[45] uses numerical orbitals constrained to be relatively short range. The use of linear muffin tin orbitals (LMTO)[46] has led to the development of a series of approaches of different degrees of complexity and accuracy from LMTO-ASA (linear muffin tin orbital-atomic spheres approximation) to full potential LMTO.[47]

The choice of one or the other of these approaches depends not only on the computing resources but more specially on the nature of the problem. It is obvious that properties relying on the density near the nucleus, hyperfine fields for instance, require the use of an all-electron method. In contrast, efficient structural optimizations when the unit cell changes are much more easily performed in pseudopotential approaches.

The very important work by Car and Parrinello[48] made feasible ab initio molecular dynamics studies for systems of practical interest. More importantly, the success of the method launched an enormous interest in the field and led to the development of several schemes that have made ab initio molecular dynamics practically a standard tool in materials science.[49] Besides the Car-Parrinello molecular dynamics code CPMD,[50] several of the above-mentioned codes like VASP, CASTEP, FH98md or SIESTA also allow molecular dynamics calculations for large systems. Judging from the fast growing number of studies using ab initio molecular dynamics to perform realistic simulations on materials of increasing complexity, there is no doubt that the technique will have a strong impact on our understanding of the structural and physical properties of materials.

Although the Hartree-Fock (HF) approach has been the more widely used and successful for ab initio studies of the electronic structure of molecules, this is not the case for solids. Here, as mentioned, DFT dominates the scene and most likely will continue to do it in the future. Nevertheless all electron ab initio LCAO periodic HF calculations for a variety of different materials have been reported. The best developed computer code implementing the all-electron ab initio LCAO periodic HF approach is CRYSTAL03.[51] The main drawbacks of the approach are the neglect of correlation energy, limitations in the choice of the basis set, and inaccuracies arising from the numerical approximations introduced in the implementation of the self-consistent field equations. The code is quite versatile and can perform both HF and DFT type calculations. All electron and valence-only basis sets with effective core pseudopotentials can be used. Despite the above-mentioned limitations, as well as quite severe computing time and memory requirements, the code has been successfully used for a variety of purposes like structural, elastic, vibrational and magnetic properties, chemisorption studies, and so on.

9 CONCLUDING REMARKS

The objective of this contribution is to convince chemists that the jargon of solid-state physics is not as impenetrable as at first sight it might seem. As a matter of fact, many of the main ideas of band theory have their equivalent in MO theory. In particular, the concept of orbital interaction can be used very easily to construct the band structure of many chemically interesting systems. Although there are some technical details that need to be considered carefully, the effort of building step-by-step the band structure of a solid from the orbitals of chemically significant fragments of the structure is worth doing. A clean, qualitative understanding of the relationship between the crystal and electronic structure emerges. Sometimes, when the complexity of the system increases, it can be better to focus on the analysis of the DOS instead of the band structure. Even there the orbital interaction language can be used to understand the problem. The importance of the use of the orbital interaction analysis is that it helps in looking for analogies and contrasts between the electronic structure of molecules and solids. Alternative approaches, like those based on the moments method,[52] for instance, can also be very useful in rationalizing structural choices. The impressive development during the last decade of very efficient ab initio approaches and codes applicable to very large solids provides an invaluable tool for the solid-state scientist who wants to approach the search for new materials in a more rational way. However, these advances should not make us forget the need for the development of new simple theoretical tools that are well adapted to the unravelling of the challenging problems that solid-state materials continuously bring to the fore.

10 RELATED ARTICLES

Electronic Structure of Main-group Compounds; Electronic Structure of Organometallic Compounds; Magnetism of Extended Arrays in Inorganic Solids; Molecular Orbital Theory; Solids: Computer Modeling; Structure & Property Maps for Inorganic Solids; Superconductivity.

11 REFERENCES

1. T. A. Albright, J. K. Burdett, and M.-H. Whangbo, ‘Orbital Interactions in Chemistry’, Wiley, New York, 1985.
2. J. K. Burdett, *Prog. Solid State Chem.*, 1984, **15**, 173; J. K. Burdett, ‘Chemical Bonding in Solids’, Oxford University Press, New York, 1995.
3. M.-H. Whangbo, in ‘Crystal Chemistry and Properties of Materials with Quasi-One-Dimensional Structures’, ed. J. Rouxel, Reidel, Dordrecht, 1986, p. 27.
4. R. Hoffmann, ‘Solids and Surfaces: A Chemist’s View of Bonding in Extended Structures’, VCH, New York, 1988.
5. E. Canadell and M.-H. Whangbo, *Chem. Rev.*, 1991, **91**, 965.
6. R. Altmann, ‘Band Theory of Solids: An Introduction from the Point of View of Symmetry’, Oxford University Press, Oxford, 1991; C. Iung and E. Canadell, ‘Description Orbitalaire de la Structure Électronique des Solides’, Ediscience International, Paris, 1997.
7. N. W. Ashcroft and N. D. Mermin, ‘Solid State Physics’, Holt, Rinehart, and Winston, Philadelphia, PA, 1985.
8. M. Lax, ‘Symmetry Principles in Solid State and Molecular Physics’, Wiley, New York, 1974.
9. R. E. Peierls, ‘Quantum Theory of Solids’, Oxford University Press, Oxford, 1955.
10. J. M. Williams, A. J. Schultz, A. E. Underhill, and K. Carneiro, in ‘Extended Linear Chain Compounds’, ed. J. S. Miller, Plenum Press, New York, 1982, Vol. 1, Chap. 3, p. 73.
11. R. Hoffmann and M.-H. Whangbo, *J. Am. Chem. Soc.*, 1978, **100**, 6093.
12. (a) R. Comes, M. Lambert, H. Launois, and H. R. Zeller, *Phys. Rev. B*, 1973, **8**, 571; (b) S. Kagoshima, in ‘Extended Linear Chain Compounds’, ed. J. S. Miller, Plenum Press, New York, 1982, Vol. 2, Chap. 7, p. 303; (c) H. Kobayashi and A. Kobayashi, in ‘Extended Linear Chain Compounds’, ed. J. S. Miller, Plenum Press, New York, 1982, Vol. 2, Chap. 6, p. 259.
13. J. K. Burdett and E. Canadell, *Organometallics*, 1985, **4**, 805.
14. R. Hoffmann, *Angew. Chem., Int. Ed. Engl.*, 1987, **26**, 846.
15. R. S. Mulliken, *J. Chem. Phys.*, 1955, **23**, 1833.
16. T. Hughbanks and R. Hoffmann, *J. Am. Chem. Soc.*, 1983, **105**, 1150.
17. (a) S. D. Wijeyesekera and R. Hoffmann, *Inorg. Chem.*, 1983, **22**, 3287; (b) J.-Y. Saillard and R. Hoffmann, *J. Am. Chem. Soc.*, 1984, **106**, 2006; (c) R. Hoffmann and C. Zheng, *J. Phys. Chem.*, 1985, **89**, 4175; (d) J. K. Burdett and T. Hughbanks, *J. Am. Chem. Soc.*, 1984, **106**, 3101; (e) M.-H. Whangbo, R. Brec, G. Ouvrard, and J. Rouxel, *Inorg. Chem.*, 1985, **24**, 2459; (f) R. L. Abdon and T. Hughbanks, *J. Am. Chem. Soc.*, 1995, **117**, 10035; (g) A. Rodríguez-Fortea and E. Canadell, *Inorg. Chem.*, 2003, **42**, 2759.
18. (a) C. Schlenker, J. Dumas, C. Escribe-Filippini, H. Guyot, J. Marcus, and G. Fourcadot, *Philos. Mag. B*, 1985, **52**, 643; (b) M.-H. Whangbo, E. Canadell, and C. Schlenker, *J. Am. Chem. Soc.*, 1987, **109**, 6308; (c) M.-H. Whangbo, E. Canadell, P. Foury, and J. P. Pouget, *Science*, 1991, **252**, 96.
19. T. Hughbanks and R. Hoffmann, *J. Am. Chem. Soc.*, 1983, **105**, 3528; R. Dronskowski and P. E. Blöchl, *J. Phys. Chem.*, 1993, **97**, 8617; W. V. Glassey and R. Hoffmann, *J. Chem. Phys.*, 2000, **113**, 1698.
20. (a) S. D. Wijeyesekera and R. Hoffmann, *Organometallics*, 1984, **3**, 949; (b) M. Kertesz and R. Hoffmann, *J. Am. Chem. Soc.*, 1984, **106**, 3453; (c) C. Zheng, Y. Apeloig,

and R. Hoffmann, *J. Am. Chem. Soc.*, 1988, **110**, 749; (d) J. K. Burdett, E. Canadell, and G. J. Miller, *J. Am. Chem. Soc.*, 1986, **108**, 6561; (e) G. J. Miller, in ‘Chemistry, Structure and Bonding of Zintl Phases and Ions’, ed. S. Kauzlarich, VCH Publishers, New York, 1996, p. 1; (f) M. T. Klem, J. T. Vaughey, J. G. Harp, and J. D. Corbett, *Inorg. Chem.*, 2001, **40**, 7020; (g) G. A. Laudrum and R. Dronskowski, *Angew. Chem,. Int. Ed.*, 2000, **39**, 1560.

21. (a) A. P. Cracknell and K. C. Wong, ‘The Fermi Surface’, Oxford University Press, Oxford, 1973; (b) H. Jones, ‘The Theory of Brillouin Zones and Electronic States in Crystals’, 2nd edn., North Holland, Amsterdam, 1975.
22. M.-H. Whangbo, in ‘Electron Transfer in Biology and the Solid State: Inorganic Compounds with Unusual Properties’, eds. M. K. Johnson, R. B. King, D. M. Kurtz, C. Kutal, M. L. Norton, and R. A. Scott, American Chemical Society, Washington, WA, 1990, p. 269.
23. (a) M.-H. Whangbo, *J. Chem. Phys.*, 1981, **75**, 4983; (b) M.-H. Whangbo, *J. Chem. Phys.*, 1980, **73**, 3854; (c) M.-H. Whangbo, *Acc. Chem. Res.*, 1983, **16**, 95.
24. (a) A. Meerschaut and J. Rouxel, in ‘Crystal Chemistry and Properties of Materials with Quasi-One-Dimensional Structures’, ed. J. Rouxel, Reidel, Dordrecht, 1986, p. 205; (b) E. Canadell, I. E.-I. Rachidi, J. P. Pouget, P. Gressier, A. Meerschaut, J. Rouxel, D. Jung, M. Evain, and M.-H. Whangbo, *Inorg. Chem.*, 1990, **29**, 1401.
25. (a) C. Schlenker, J. Dumas, C. Escribe-Filippini, and H. Guyot, in ‘Low-Dimensional Electronic Properties of Molybdenum Bronzes and Oxides’, ed. C. Schlenker, Kluwer, Dordrecht, 1989, p. 159; (b) M. Greenblatt, *Chem. Rev.*, 1988, **88**, 31; (c) E. Canadell, M.-H. Whangbo, C. Schlenker, and C. Escribe-Filippini, *Inorg. Chem.*, 1989, **28**, 1466.
26. (a) C. Schlenker and J. Dumas, in ‘Crystal Chemistry and Properties of Materials with Quasi-One-Dimensional Structures’, ed. J. Rouxel, Reidel, Dordrecht, 1986, p. 135; (b) M.-H. Whangbo and L. F. Schneemeyer, *Inorg. Chem.*, 1986, **25**, 2424.
27. (a) D. Jérome, F. Creuzet, and C. Bourbonnais, *Phys. Scr.*, 1989, **T27**, 130; (b) D. Jérome, A. Mazaud, M. Ribault, and K. Bechgaard, *J. Phys. Lett. (Paris)*, 1980, **41**, L-95.
28. (a) N. F. Mott, ‘Metal–Insulator Transitions’, Barnes and Noble, New York, 1977; (b) B. H. Brandow, *Adv. Phys.*, 1977, **26**, 651; (c) M.-H. Whangbo, *J. Chem. Phys.*, 1979, **70**, 4963.
29. S. Kagoshima, H. Nagasawa, and T. Sambongi, ‘One-Dimensional Conductors’, Springer-Verlag, Heidelberg, 1988.
30. S. Huizinga, J. Kommandeur, G. A. Sawatzky, B. T. Thole, K. Kopinga, W. J. M. deJonge, and J. Roos, *Phys. Rev. B*, 1979, **19**, 4723.
31. (a) P. W. Anderson, *Phys. Rev.*, 1958, **109**, 1492; (b) A. M. Stoneham, ‘Defects and Defect Processes in Nonmetallic Solids’, Wiley, New York, 1985, Chap. 8.
32. L. Solymar and D. Walsh, ‘Lectures on the Electrical Properties of Materials’, 4th edn., Oxford University Press, Oxford, 1988, Chap. 14; (b) A. D. C. Grassie, ‘The Superconducting State’, Sussex University Press, London, 1975, Chap. 2.
33. (a) J. Bardeen, L. N. Cooper, and J. R. Schrieffer, *Phys. Rev.*, 1957, **108**, 1175; (b) W. L. McMillan, *Phys. Rev.*, 1968, **167**, 331.
34. G. Burns, ‘High-Temperature Superconductivity. An Introduction’, Academic Press, San Diego, CA, 1992, Chap. 4.
35. (a) http://chvamw.chem.ncsu.edu;
    (b) http://yaehmop.sourceforge.net/.
36. (a) H. Hohenberg and W. Kohn, *Phys. Rev.*, 1964, **136**, 864; (b) W. Kohn and L. J. Sham, *Phys. Rev.*, 1965, **140**, 1133.
37. http://www.abinit.org/.
38. http://cms.mpi.univie.ac.at/vasp/vasp.html/.
39. http://www.uam.es/siesta/.
40. http://www.accelrys.com/cerius2/castep.html/.
41. http://spinor.sourceforge.net/.
42. http://www.fhi-berlin.mpg.de/th/fhimd/.
43. D. J. Singh, ‘Planewaves, Pseudopotentials and the LAPW Method’, Kluwer Academic Publishers, Boston, MA, Dordrecht, London, 1994.
44. http://www.wien2k.at.
45. http://www.ifw-dresden.de/agtheo/FPLO/.
46. O. K. Andersen, *Phys. Rev. B*, 1975, **12**, 3060.
47. http://www.mpi-stuttgart.mpg.de/andersen/.
48. R. Car and M. Parrinello, *Phys. Rev. Lett.*, 1985, **55**, 2471.
49. D. Marx and J. Hütter, in ‘Modern Methods and Algorithms of Quantum Chemistry’, NIC Series Vol.1, ed. J. Grotendorst, John von Neuman Institute for Computing, Jülich, 2000, p. 301.
50. http://www.cpmd.org/.
51. http://www.crystal.unito.it/.
52. (a) D. G. Pettifor, ‘Bonding and Structure of Molecules and Solids’, Clarendon Press, Oxford, 1995; (b) J. K. Burdett and S. Lee, *J. Am. Chem. Soc.*, 1985, **107**, 3050,; (c) S. Lee, *Acc. Chem. Res.*, 1991, **24**, 249; (d) S. Lee, R. Rousseau, and C. Wells, *Phys. Rev. B*, 1992, **46**, 12121.

Fluorides: Solid-state Chemistry

Werner Massa
Philipps-Universität Marburg, Marburg, Germany

1	Introduction	1
2	Synthesis	1
3	Structural Chemistry	3
4	Physical Properties	21
5	Related Articles	22
6	References	22

Abbreviations

CN = coordination number; fcc = face-centered cubic; hcp = hexagonal close packing; HTB = hexagonal tungsten bronze; r.t. = room temperature; s.g. = space group, TTB = tetragonal tungsten bronze.

1 INTRODUCTION

The solid-state chemistry of fluorides is a unique chapter owing to the extreme position of fluorine in the periodic system. The most electronegative element fluorine, reacting with nearly all other elements, forms the most ionic bonds. The fluoride ion is the smallest (ionic radius for coordination number (CN) 2 1.28 Å[1]) and most rigid ion. Its *Polarizability* is, for example, four times lower than that of oxygen. Fluorides belonged to the first subjects of investigation at the beginning of scientific chemistry. Synthetic cryolite Na_3AlF_6 or $MnF_3(H_2O)_3$, for instance, was described by Berzelius already in 1824.[2] Many 'famous' compounds, like the first rare-gas compounds, are fluorides. Spectacular high oxidation states like Ag^{IV} or Au^{V} have been stabilized in fluorides.

The structural chemistry of inorganic fluorine compounds is dominated by simple electrostatic and geometrical principles such as sphere packing and Pauling's rules. The ionic radii of nearly all transition metals in oxidation states +2, +3, and +4 are in the range where with fluoride ions CN 6 is favored as octahedral coordination. Thus, fluorometalate anions $[M^{n+}F_6]^{6-n}$ are formed, the charge of which is compensated by ligand sharing or counter cations or a combination of both. In binary compounds, only ligand sharing is possible and, for example, in AlF_3 all F atoms of $[AlF_{6/2}]$ octahedra are shared with neighbors. In some ternary compounds, for example, in the cryolite structure of Na_3AlF_6,[3] quasi-isolated $[AlF_6]^{3-}$ anions may form, whereas in others, poorer in F, for example, Tl_2AlF_5, fewer counter cations are needed to compensate for the charge of the octahedra, as these are linked to chains $[AlF_4F_{2/2}]^{2-}$. On the basis of these simple structural principles, a limited number of very large families of isostructural compounds are observed if the ratio of ionic radii is in a comparable range. The structural chemistry of fluorides is rather different from that of the compounds of the higher group VII elements because Cl, Br, and I are much larger in size, more covalent in bonding, and are easier to oxidize. There are some analogies between the structures of fluorides and oxides. However, isostructural compounds like the perovskites $K^{1+}Ni^{2+}F_3{}^{1-}$ and $Ba^{2+}Mn^{4+}O_3{}^{2-}$ present very different electronic situations and different physical properties owing to the different formal charges. Closer relationships are found to the structures of hydrides (*see* ***Hydrides: Solid State Transition Metal Complexes***) and in part even cyanides (*see* ***Cyanide Complexes of the Transition Metals***).

A certain orbital overlap of metal d and fluorine p orbitals occurs leading to magnetic superexchange interactions in M – F – M bridged transition metal compounds, although the bonding in metal fluoro compounds is mainly ionic, along with the short bond lengths. Fluorides have therefore been used as suitable model compounds for studies of magnetic properties. Along with the normally strong localization of electrons in fluorides, special optical properties are found, giving rise to technical applications, for example, for laser optics. For the same reason, fluorides are normally good insulators. However, some examples of fluorine compounds are mentioned in the final section of this article where ionic and even metallic and superconductivity is observed.

2 SYNTHESIS

While the preparation of oxides, sulfides, higher halogenides, and so on is routine in many laboratories, the number of groups dealing with preparative fluorine chemistry is rather limited because in many cases it is necessary to work with hazardous HF or even F_2 (*see* ***Fluorine: Inorganic Chemistry***). Owing to easy hydrolysis of most fluorides through mechanisms such as (1):

$$\begin{aligned} MF_3 + H_2O &\longrightarrow MF_2(OH) + HF \\ (\text{–}O)_3Si\text{–}OH + HF &\longrightarrow (\text{–}O)_3Si\text{–}F + H_2O \end{aligned} \qquad (1)$$

contact of fluorides with moisture and with glass or quartz surfaces has to be avoided, at least at higher temperatures. Solid-state reactions have to be performed in Pt or Au tubes using dry starting materials. Excellent comprehensive surveys on preparative methods in fluorine chemistry have been given by Grannec and Lozano**4** as well as Lutar, Borrmann, and Leblanc.**5** The most important techniques and some recent developments are presented in the following sections.

2.1 Gas Flow Fluorination

The most common methods of preparing anhydrous binary metal fluorides in the laboratory are based on reactions of gaseous HF or F_2 with suitable solid substrates. With HF, the oxidation state of the starting material is preserved, whereas with F_2, the fluoride with the highest stable oxidation state is obtained. The reactions are mostly carried out in tubes of Monel (a Cu/Ni alloy) at temperatures up to about 400–600 °C. As starting materials, hydrated fluorides (obtained from aqueous HF solutions), chlorides, carbonates, or easy decomposable ternary compounds like NH_4MnF_3 may be used, as shown by the following examples (2–4):

$$CrCl_3 + 3HF \xrightarrow{550\,^\circ C} CrF_3 + 3HCl \quad (2)$$

$$FeCl_3 + 6F_2 \xrightarrow{400\,^\circ C} FeF_3 + 3ClF_3 \quad (3)$$

$$NH_4MnF_3 \xrightarrow{F_2/450\,^\circ C} MnF_3 + \cdots \quad (4)$$

Worldwide significance of such fluorination reactions was attained in the course of the Manhattan project to produce UF_6 for isotope separation (5).**6**

$$\begin{aligned} UO_2 + 4HF &\longrightarrow UF_4 + 2H_2O \\ UF_4 + F_2 &\longrightarrow UF_6 \end{aligned} \quad (5)$$

The purity and dryness of binary fluorides is crucial if they are used for solid-state reactions. First, the reliability of composition of the desired compound is limited by the purity of the components used; second, moisture brought in by traces of water in the starting materials may lead to partial hydrolysis of the product and even bursting of the ampoule. Often commercially obtainable binary fluorides do not fulfill these crucial requirements.

Other possible gaseous fluorination agents are ClF_3 (oxidizing) or SF_4 (nonoxidizing).

2.2 Solid-state Reactions

The classical way to synthesize polynary anhydrous fluorides is by heating a stoichiometric and well pulverized mixture of the binary components in sealed platinum or gold tubes, for example, along equation (6).**7**

$$NaF + VF_3 \xrightarrow{800\,^\circ C} NaVF_4 \quad (6)$$

A special case of symproportionation in a solid-state reaction is shown in equation (7):**8**

$$Cs_2Mn^{IV}F_6 + Mn^{II}F_2 \xrightarrow{800\,^\circ C} 2CsMn^{III}F_4 \quad (7)$$

It has the advantage with respect to the alternative reaction of hygroscopic CsF and air-sensitive MnF_3 that both starting compounds are air-stable and obtainable without use of elemental F_2. The reaction demonstrates that some common rules for aqueous chemistry like that expecting the disproportionation of Mn(III) to Mn(II) and Mn(IV), are no longer valid for fluorides in the solid state.

The necessary alkali and alkaline earth fluorides for such reactions are accessible by dissolving the respective carbonates in aqueous HF. After reducing to a small volume, the precipitated bifluorides or fluorides are heated up to about 500 °C to obtain the anhydrous fluorides, which are highly hygroscopic for the larger alkali ions K^+, Rb^+, Cs^+.

High-pressure methods using *belt* type apparatus (*see* ***High Pressure Synthesis of Solids***) have been applied for synthesizing metastable high-pressure modifications of fluoro compounds. The structure of PdF_2, for example, transforms from rutile type to a variant of the fluorite type at 5 GPa and 400 °C.**9** As sample containers, gold cylinders were used mostly because they keep tight during the deformation and are not attacked at pressures up to 10 GPa and temperatures up to about 800 °C.

Decomposition Reactions. In some cases anhydrous fluorides can be obtained by decomposition of hydrated compounds like in equation (8)**10,11**

$$\begin{aligned} (NH_4)_2FeF_5(H_2O) &\xrightarrow{98\,^\circ C} \alpha\text{-}(NH_4)_2FeF_5 + H_2O \\ &\xrightarrow{109\,^\circ C} \beta\text{-}(NH_4)_2FeF_5 + H_2O \end{aligned} \quad (8)$$

In this way, low-temperature forms can be obtained, but, of course, as polycrystalline powders only.

2.3 Flux Methods

A series of binary, ternary, and even quaternary fluorides have been crystallized from melts. In most cases, chlorides or mixtures of chlorides are used because of their lower melting points and greater solubilities with respect to corresponding fluorides. It is advantageous to add an excess of the alkali chloride when an alkali fluorometalate is synthesized, as shown in the typical example of equation (9).**12**

$$LiF + 4ThF_4 \xrightarrow{LiCl/ZnCl_2} LiTh_4F_{17} \quad (9)$$

Using a flux, the reaction temperature can be chosen much lower than in a solid-state reaction, for example, 600 °C in the above reaction (9). Other suitable dichlorides are $PbCl_2$, $CoCl_2$, $NiCl_2$, or $MnCl_2$.

A flux serving at the same time as a reaction partner was used, for instance, for the preparation of crystalline K_3MnF_6[13] (equation 10).

$$Mn_2O_3 + 6KHF_2 \xrightarrow{n\mathrm{KHF_2}} 2K_3MnF_6 + 3H_2O \qquad (10)$$

2.4 Syntheses in Solution

Precipitation from aqueous solution, normally containing HF, is the oldest and the most used method of preparing fluorides. Berzelius, for example, reported the synthesis of fluorides from aqueous HF as long ago as 1824.[2] Sophisticated variants of this simple method are increasingly replacing the classical solid-state syntheses and gas flow techniques.[14]

In addition to simple precipitation reactions after mixing solutions of binary compounds in aqueous HF, simultaneous redox reactions may take place. By variation and optimization of concentrations and the pH of the solution and combination with diffusion techniques, the synthesis of different pure phases from the same system is possible, often as good crystals. In contrast to the high-temperature reactions, metastable phases can be obtained that are not otherwise accessible or that can be crystallized under avoidance of an intermediate phase transition. A good example is the system 4,4′-bipyridine/Mn(III)/HF/H_2O: Under slightly different conditions, either a salt 4,4′-bipy$H_2[MnF_4(H_2O)_2]_2 \cdot 2H_2O$[15] or the neutral 2D-coordination polymer 4,4′-bipyMnF_3 can be obtained.[16]

If the solution has high fluoride concentration and low pH values, anhydrous fluorides can be crystallized. The risk of substituting fluoride ligands by OH^- ions increases when the pH approaches the neutral regime; the formation of mixed aqua-fluoro complexes is favored at lower fluoride concentrations and low temperature.

During the last few years, many attempts have been made to design specific syntheses of fluorine compounds with, for instance, oligomeric anions, linear chain anions, layer structures, or framework structures using organic amines as templates, which serve mostly, after protonation, at the same time as counter cations (see Refs. 5, 17, 18, or for oxyfluorides with open framework structures Ref. 19).

Organic Solvents. Owing to the low solubility of most binary fluorides in organic solvents, few reactions are known that were carried out in such solutions, like reaction (11) in methanol.[20]

$$6NH_4F + AlBr_3 \xrightarrow{\mathrm{CH_3OH}} (NH_4)_3AlF_6 + 3NH_4Br \qquad (11)$$

However, it has been found to be a good way to obtain crystals, after performing a reaction in aqueous HF solution, to diffuse a mixable organic solvent like methanol, ethanol, or even acetone into the reaction vessel.

In contrast, like in oxide systems, amorphous high-surface fluoride materials for catalytic purposes can be synthesized from organic solvents and anhydrous HF, as shown recently for ‘HS-AlF_3’[21] (HS = high surface).

Crystalline ‘pyr-FeF_3’, a metastable cubic form of FeF_3 with pyrochlore-related structure, was obtained in a topotactical oxidation reaction of $NH_4Fe_2F_6$ with Br_2 in acetonitrile. At this example, the designation ‘*chimie douce (soft chemistry)*’ for this type of solid-state reaction under low-temperature conditions was propagated in the 1980s.[22]

Hydrothermal Reactions. In the attempts mentioned to build framework structures, often including other bridging ligands as phosphate, carbonate, oxalate and so on, working under hydrothermal conditions in aqueous HF has been found to be very useful. Such reactions are performed in Teflon containers or sealed platinum or gold tubes surrounded by steel autoclaves at pressures up to 1 GPa. Recently, microwave heating has been used for the hydrothermal synthesis of ‘hybrid’ compounds $[NH_3\text{-}(CH_2)_n\text{-}NH_3][AlF_5]$.[23] A big advantage is the favored formation of good crystals under these conditions. The higher the pressure and temperature, the higher is the probability of obtaining anhydrous fluorides. In a few laboratories, hydrothermal reactions are performed in anhydrous HF or other fluorinating solvents like BrF_3, BrF_5, IF_5, SeF_4 or SbF_5, especially for the synthesis of fluorides in high oxidation states like NiF_3[24] or AgF_3.[25] The most drastic fluorinating conditions are achieved by using elemental fluorine under high pressure.[4,26] In Monel or Ni reactors, F_2 is condensed – possibly together with HF, O_2, Ar – under cooling with liquid nitrogen. After closing, the vessel is heated up to 300–500 °C, generating pressures up to about 500 MPa. Under these conditions, compounds like A_2CoF_6 (A = K, Rb, Cs),[27] $O_2Pt_2F_{11}$,[28] or CrF_4[29] could be prepared in the form of single crystals, which were otherwise not accessible owing to easy thermal decomposition. Single crystals of metastable high-pressure phases could be obtained in HF solution under hydrothermal conditions in a *belt* apparatus at pressures of 3 GPa and 250 °C.[30]

3 STRUCTURAL CHEMISTRY

At least in compounds with metals of lower oxidation states up to three or four, the metal–fluorine bond is almost purely ionic and the small, least polarizable fluoride ion behaves as a small hard sphere with an ionic radius which varies, depending on the coordination number, between 1.285 (CN 2) and 1.320 Å (CN 6).[1] The structures of fluorides are therefore determined mainly by simple geometrical and electrostatic principles, such as *sphere packing*, the *rigid sphere concept*, which allows derivation of the coordination number around a central cation from the ratio of ionic radii, and *Pauling's rules*,**[31]** which postulate optimum local charge balance.

The structural chemistry of fluoro compounds is relatively simple, therefore. Many of them can be grouped into a few large structure families. Applying the above criteria, it is often possible to predict the structural type or even geometrical details for a given stoichiometric composition. On the other hand, it is possible to attribute individual deviations in the bonding geometry of transition metal fluorides to their specific electronic situation. That is why fluoro compounds are preferably used as model systems for studies of correlations between structure and electronic configuration, magnetic properties, and so on.

The main body of structural material in the solid-state chemistry of fluorides has been elaborated in the 1960s to the 1980s and is collected and discussed in several reviews.**[32–34]** A good collection of data is tabulated in Ref. 35. A recent survey from the point of view of materials science is given in Ref. 36. Here, a short survey will be given on the most important basic structural features and relations in binary and ternary (and higher) compounds, combined with an attempt to account for modern developments.

3.1 Binary Fluorides

AF Compounds. The structures of the a*lkali fluorides* are all of the NaCl type; however, the sensitivity to moisture for the K, Rb, and Cs compounds and their high-pressure phase transitions to the CsCl type show an increasing tendency to adopt the higher coordination number 8 with increasing ionic radius. In ternary compounds, it is mostly easier to adopt a more suitable coordination sphere of fluoride ligands: Li^+ may have tetrahedral coordination such as in scheelites $LiMF_4$ and a few other compounds**[33]** (see Section 3.2.13) but has normally CN 6. Na^+ shows CN 6–8 with a certain favoring of CN 7. K^+ clearly prefers CN 8, and Rb^+ and Cs^+ CN 10 to 12, in some cases up to 18.

MF_2 Compounds. The *alkaline earth fluorides* show quartz type structures for BeF_2 (CN 4), rutile-type (CN 6) for MgF_2 (Figure 1(a)), and the fluorite type (CN 8, Figure 1(b)) for CaF_2, SrF_2, and BaF_2. Fluorite, CaF_2, is not only of unique industrial importance as a starting material to produce HF, but also owing to the low optical absorption in the UV range, the production of large single crystals became important for laser optics used in the semiconductor industry.

Difluorides of the first transition metal row have the rutile structure (M = V, Cr, Mn, Fe, Co, Ni, Cu, Zn; Figure 1(a)). The electronic properties of the $3d^4$ and $3d^9$ configurations are manifested in strong Jahn–Teller distortions for the Cr^{2+} and Cu^{2+} case. The difluorides of the higher group 14 elements show characteristic influence of the lone pair: GeF_2 has a zig-zag chain structure with vertex-connected $[GeF_3]$ pyramids further connected by weak Ge···F contacts to a 3D net (Figure 2). For SnF_2, three polymorphs are known with the CN at Sn between 4 and 5. The monoclinic α-form is built from 4-membered rings (CN 3 + 2); the orthorhombic β-form has a 3D structure with meshes of three and of four $[SnF_5]$ Ψ-octahedra. In the tetragonal γ-form, a 3D network is formed by 6-membered rings of Ψ-octahedral $[SnF_4]$ units. PbF_2 also exists in two polymorphs: The α-form has the widespread $PbCl_2$ structure with 7 + 2 coordination (distorted tricapped trigonal prism), the β-form shows the fluorite-type structure (CN 8) and is – owing to disorder in the anion lattice – an F^- ion conductor. CdF_2, EuF_2, and SmF_2 also belong to the CaF_2 type but deviation from the stoichiometry is observed for the latter. AgF_2 has a buckled layer structure of corner-sharing planar AgF_4 units (Ag-F 2.085 Å).**[37]** The planes are staggered in a way that additional weak contacts (Ag···F 2.592 Å) complete the Ag coordination to an elongated octahedron (dashed bonds in Figure 3) as expected for this Jahn–Teller system.

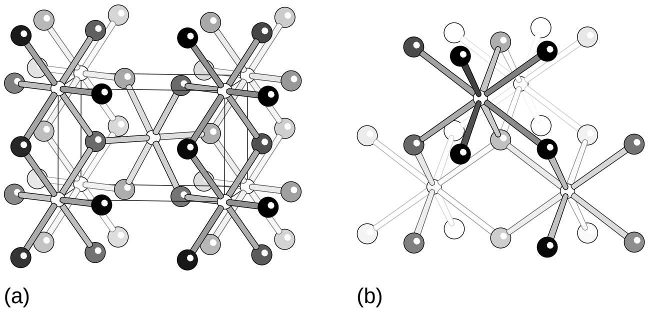

Figure 1 (a) Rutile; (b) CaF_2

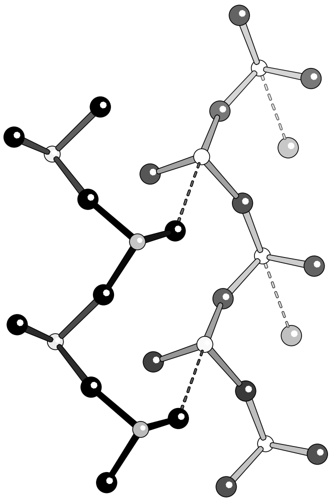

Figure 2 GeF_2

Another interesting case is PdF_2: Besides a rutile-type phase**[38]** it forms a metastable high-pressure modification with a new cubic AF_2 structure type**[39,40]** (Figure 4) where the $[PdF_6]$ octahedra show vertex-sharing only but with 12 surrounding octahedra. The HP phase is 9% higher in density although

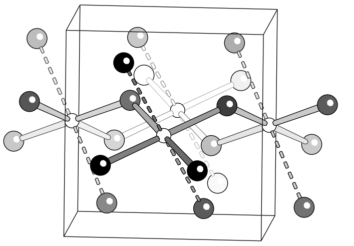

Figure 3 AgF_2

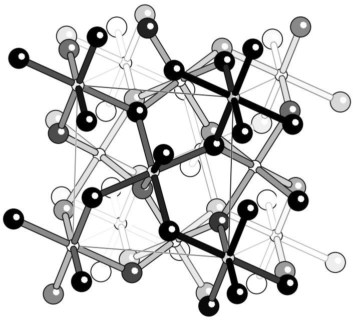

Figure 4 HP-PdF_2

the coordination of Pd^{2+} and F^{-} (CN 3) is the same in both phases, and even edge-sharing of octahedra takes place in the rutile structure. This is probably due to an angular distortion of the octahedra allowing for two additional weak Pd···F contacts (3.167 Å), and therefore relations to the CaF_2 and the FeS_2 type are discussed. Disordered variants of the HP-PdF_2 type are found in $CdPdF_4$ and $HgPdF_4$.

MF_3-Compounds. With the exception of the large rare-earth elements, the structures of the thermodynamically stable phases of MF_3 compounds derive from the cubic *ReO_3 structure type*. The cubic aristotype with an M–F–M bridge angle of 180° is realized only in NbF_3; in many other compounds it was found as a high-temperature form while at room temperature (r.t.), distorted variants, mainly of the *VF_3 type* (see Figure 5, Table 1), are realized. The ReO_3 structure can be described as face-centered cubic (fcc) packing of anions with 1/4 ordered vacancies where all octahedral sites having no neighboring vacancy (1/4 of all) are occupied. As the resulting 3D net of corner-connected octahedra has large cavities (which in the perovskite-type AMX_3 are occupied by the large A ions), the MF_3 structures tend to reduce these cavity volumes by rotation of the octahedra around a 3-fold axis and thus the bridge angle becomes bent from 180° in NbF_3 down to 132° in IrF_3. The symmetry is lowered to rhombohedral (space group $R\bar{3}c$) in that way. Depending on the size of the M^{III} ion, there is a continuous transition from cubic geometry (rhombohedral angle $\alpha = 60°$) down to $\alpha = 54.13°$ (IrF_3). At this angle, the rotation of anion layers of the former fcc packing achieves the hexagonal close packing (hcp) position where the vacancy completely disappears.**[41]** In between both extremes are the stable phases of the trifluorides of Al, Ga, In, Ti, V, Cr, Fe, Co, Mo, Ru, Rh. The rhombohedral symmetry is lowered to the monoclinic subgroup C2/c in MnF_3**[42]** owing to strong Jahn–Teller distortion of the d^4 configuration. During the last decade, an interesting variety of additional metastable MF_3 phases has been synthesized, using various thermal decomposition methods, mainly for AlF_3, shown here as an example. In addition to the thermodynamically stable VF_3-type α-AlF_3 (Figure 5), six further AlF_3 modifications have been reported here, the characteristics of which are collected in Table 1. Especially the amorphous forms and β-AlF_3 (Figure 6) are used nowadays as catalysts for Cl/F exchange and fluorination of chlorofluoro- carbons.**[43–45]** The higher the specific surface (e.g. up to $206\,m^2g^{-1}$ for 'high-surface' HS-AlF_3), the better the activity.

In the rhombohedral structure of NiF_3,**[24]** the symmetry of the VF_3 type is lowered from $R\bar{3}c$ to $R\bar{3}$ because it has to be formulated as $Ni^{II}Ni^{IV}F_6$ with ordering of larger (Ni^{II}-F 1.951 Å) and smaller [NiF_6] octahedra (Ni^{IV}-F 1.824 Å). The very strong oxidant NiF_3 as well as MnF_3 and CoF_3 may serve as catalysts for perfluorination of organic compounds. A unique 6_1 helical chain of [MF_4] squares is formed by AgF_3 and AuF_3**[51]** (Figure 10). The coordination of the d^9 ions is extended to elongated octahedra by two weak contacts to F ligands of neighboring chains.

Higher coordination numbers of 8 + 1 are adopted in the LT-YF_3 type by the trifluorides of the larger ions Tl^{3+}, Bi^{3+} and the smaller rare-earth ions Sm to Lu. The tysonite or LaF_3 type with CN 9 + 3 is found for the trifluorides of the larger 4f and the 5f elements**[52]** (*see* ***Scandium, Yttrium & the Lanthanides: Inorganic & Coordination Chemistry***).

MF_4 Compounds. Formation of an octahedral coordination for a composition MF_4 requires bridging of four fluoride ligands according to a formulation [$MF_{4/2}F_2$]. One possibility is realized in the structure of the SnF_4 type (space group (s.g.) P4/nmm, Figure 11) with perovskite like layers and two trans-terminal F ligands. This structure is found for the Sn, Pb, Nb, and Ru compounds and, in a distorted variant, in VF_4. A 3D network with meshes of six octahedra is formed in the PdF_4 structure where the nonconnected ligands are *cis*-terminal (Figure 12). This structure (adopted also by the tetrafluorides of Rh, Re, Os, Ir, Pt) can be described as rutile structure with 1:1 ordered vacancies along the edge-connected octahedral chains.

The tetrafluorides of the larger ions Ce, Pr, Tb, Hf, Th – Bk crystallize in the β-ZrF_4 type, a highly connected 3D structure in which the metal has (square antiprismatic) CN 8 and fluoride CN 2.**[53,54]**

Interestingly, very different structures have been found for the tetrafluorides of the 1st transition metal series. These provide good textbook examples to demonstrate the

Table 1 Polymorphs of AlF_3

Modification	α-AlF_3[a 46,47]	β-AlF_3[48]	γ-AlF_3[45]	η-AlF_3[b49]	θ (t)-AlF_3[49,50]	κ-AlF_3[49]	HS-AlF_3[21]
Crystal system	Rhombohedral	Orthorhombic	Tetragonal	Cubic	Tetragonal	Tetragonal	Amorphous
Space group	R $\bar{3}$c	Cmcm		Fd $\bar{3}$m	P4/nmm	P4/mbm	
Structure type	VF_3	HTB (empty)	α-NH_4AlF_4 ?	Pyrochlore	Own type	TTB (empty)	
Density (g cm$-^3$)	3.20	2.82			3.00	3.03	
Precursor		$AlF_3 \cdot 3H_2O$	α-NH_4AlF_4	pyH·AlF_4	$(CH_3)_4NAlF_4$	β-NH_4AlF_4	Al(O*i*pr$_3$)$_3$
Structural diagram	Figure 5	Figure 6		Figure 7	Figure 8	Figure 9	

[a] An amorphous sample was called α-AlF_3, too.[45] [b] Analogous phases containing OH groups are known.

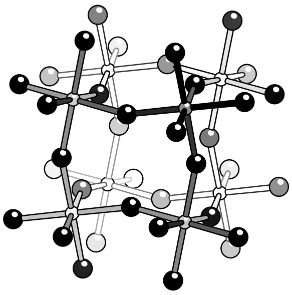

Figure 5 α-AlF_3 VF_3 – type

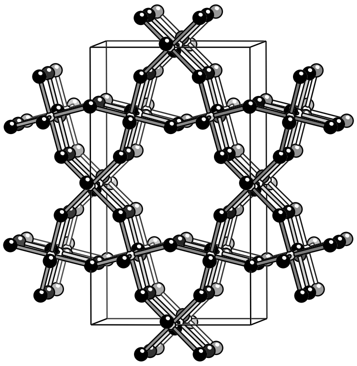

Figure 6 β-AlF_3 HTB-type

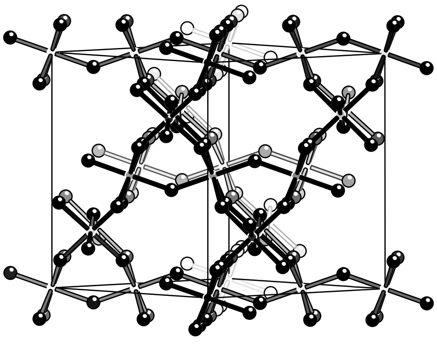

Figure 7 η-AlF_3 pyrochlore type

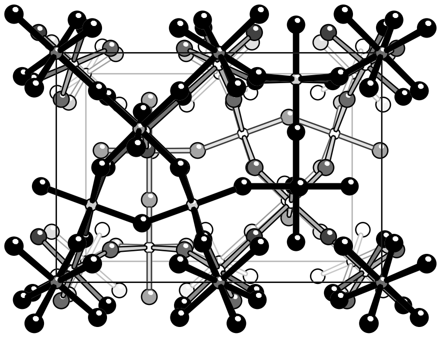

Figure 8 θ(t)-AlF_3 TTB-type

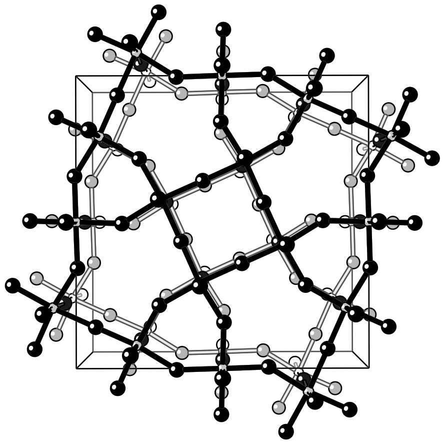

Figure 9 κ-AlF_3

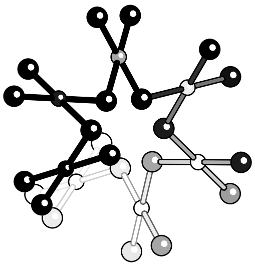

Figure 10 6_1 helix of AgF_3

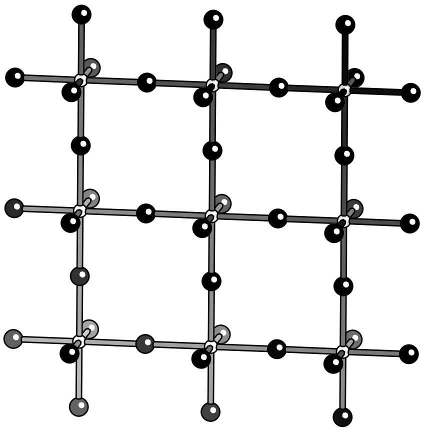

Figure 11 $\mathrm{SnF_4}$ layer section

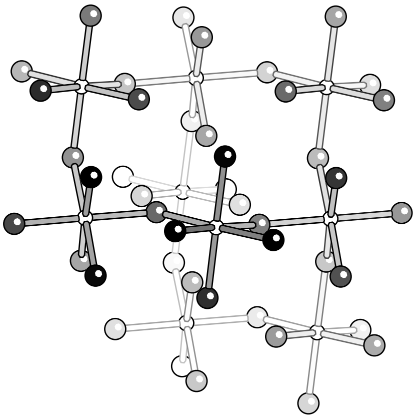

Figure 12 Section of the $\mathrm{PdF_4}$ structure

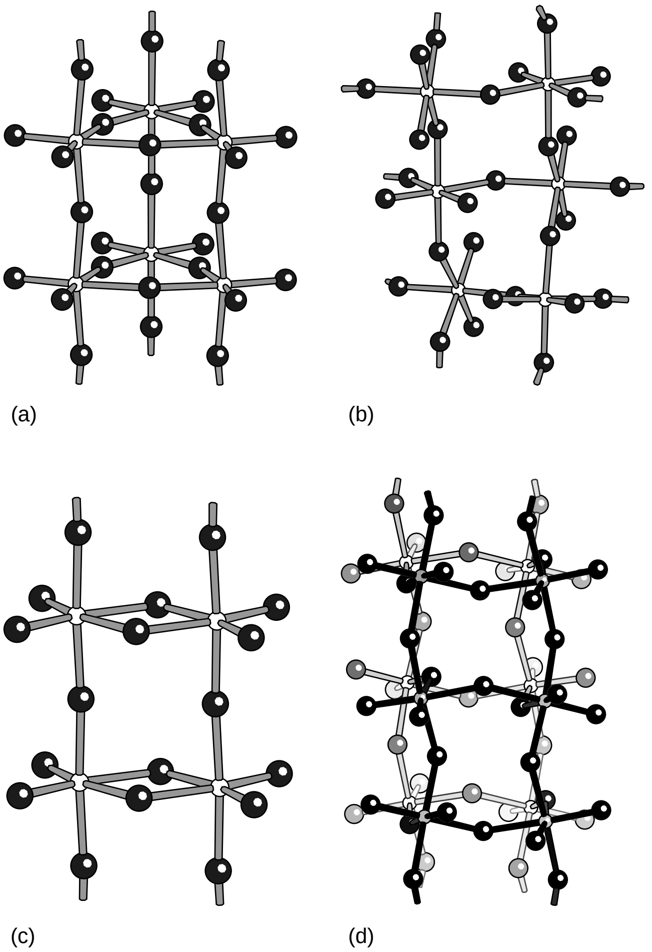

(a) (b) (c) (d)

Figure 13 (a) $\mathrm{TiF_4}$ triple-chain; (b) α-$\mathrm{MnF_4}$, section of 3D structure; (c) α-$\mathrm{CrF_4}$ double-chain; (d) β-$\mathrm{CrF_4}$ quadruple-chain

various possibilities to afford the $[\mathrm{MX_4}]$ stoichiometry by connecting $[\mathrm{MX_6}]$ octahedra leaving two cis-terminal F ligands: In $\mathrm{TiF_4}$,[55] a triple chain of vertex-connected $[\mathrm{TiF_6}]$ octahedra is observed as found in the $[\mathrm{MF_4}]^-$ anions of $\mathrm{CsAlF_4}$, $\mathrm{KCrF_4}$, and $\mathrm{CsCrF_4}$. The α-form of $\mathrm{CrF_4}$ obtained by fluorination of Cr under pressure of $\mathrm{F_2}$, HF, and Ar at 300 °C exhibits a double-chain of edge-connected octahedra[29] (Figure 13(c)), similar to that in several oxide-halides like $\mathrm{NbOCl_3}$. Recently, a β-form was reported, formed by thermal decomposition of $\mathrm{CrF_5}$, which shows unique quadruple-chains formed by trans-linking of tetrameric rings[56] (Figure 13(d)). α-$\mathrm{MnF_4}$[57] is built from strands of corner-connected $[\mathrm{MnF_6}]$ octahedra, all with *cis*-terminal F ligands as well, which are further linked to a 3D network (Figure 13(b)). The β-form[57] seems to be a variant of the $\mathrm{VF_3}$ type with vacancies. Thermodynamically unstable $\mathrm{MnF_4}$ evolves elemental $\mathrm{F_2}$ on thermal decomposition. This is the crucial step in the famous ‘chemical synthesis of fluorine’[58] (equation 12), which broke a dogma like that of the nonexistence of noble gas compounds.

$$\mathrm{K_2MnF_6} + 2\mathrm{SbF_5} \longrightarrow 2\mathrm{KSbF_6} + [\mathrm{MnF_4}]$$

$$[\mathrm{MnF_4}] \longrightarrow \mathrm{MnF_3} + \tfrac{1}{2}\mathrm{F_2} \qquad (12)$$

The starting materials can easily be prepared from aqueous HF.

$\mathrm{VF_4}$ has a layer structure with trans-terminal ligands, as mentioned above. The transition to molecular crystal structures (isolated molecules with Ψ -octahedral structures) is achieved in the group 16 tetrafluorides $\mathrm{SeF_4}$ and $\mathrm{TeF_4}$.

$\mathrm{MF_5}$ Compounds. For this stoichiometry, two bridging fluorine ligands only are needed for each octahedral $[\mathrm{MF_6}]$ unit. This can be realized by forming *cis*-chains as in $\mathrm{VF_5}$ (Figure 14(a)), trans-chains like α-$\mathrm{UF_5}$[59] (Figure 14(b)), four-membered rings in a more regular manner as in $\mathrm{NbF_5}$[60] or $\mathrm{MoF_5}$ (s.g. C2/m, Figure 14(c)), or distorted as in $\mathrm{RuF_5}$[61] (s.g. $P2_1/c$, Figure 14(d)), $\mathrm{OsF_5}$, or $\mathrm{PtF_5}$. A molecular dimer is found in $\mathrm{AuF_5}$[62] (Figure 14(e)), and a 3D structure is formed

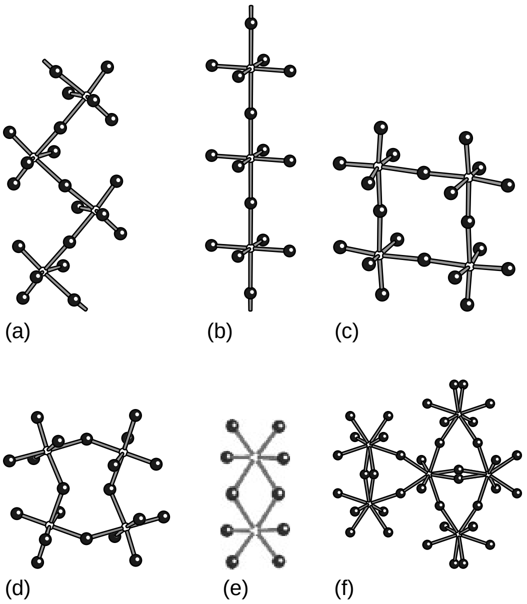

Figure 14 Structures of MF_5 compounds: (a) VF_5; (b) α-UF_5; (c) NbF_5; (d) RuF_5; (e) AuF_5; (f) Section of β-UF_5

in the β-form of UF_5**[63]** with edge- and corner-connection between square antiprismatic $[UF_8]$ polyhedra (Figure 14(f)).

MF_6 and MF_7 compounds have typical molecular structures and thus are outside the scope of this chapter.

3.2 Ternary and Quaternary Fluorides

The structures of ternary compounds can be understood often by comparing the anionic substructure $[M^{x-n}F_x]^{n-}$ with that of the corresponding binary fluoride MF_x. Owing to strong contributions to the lattice energy when building structures from anions with saturated coordination spheres as bricks and countercations as mortar, ternary compounds are mostly more stable and easier to synthesize than their binary constituents; the higher the oxidation state of the metal the more important is this effect. By the choice of suitable electronically or magnetically 'inert' counter cations, compounds can be tailored with certain desired structural properties in the anionic substructure. The ternary and higher compounds are compiled in classes with structures deriving from a common simple parent structure type, in the following discussion.

3.2.1 Rutile Related Structures

A formal ordered 1:1 substitution of the divalent metal in the rutile $M^{II}F_2$ (Figure 1) by a univalent and a tervalent metal may explain the topology of the structures of compounds $LiM^{III}F_4$ ($M = Mn$,**[64]** Co**[65]**) and $NaMnF_4$**[66]** (Figure 15(a)). Looking at the $[M^{III}F_6]$ octahedra only, the compounds are layer structures built from quadratic meshes of corner-sharing octahedra comparable with that of the $TlAlF_4$ type. Another order variant of rutile is the 'trirutile' structure formed by several $Li_2M^{IV}F_6$ and $LiM^{II}M^{III}F_6$ compounds, and well known in oxide systems. According to an isomorphous group-subgroup transition, M^{IV} and Li^{I} (Figure 15(b)) or Li^{I} and disordered M^{II} and M^{III} atoms occupy the octahedral sites in a 1:2 ratio leading to a unit cell with triple c-axis.

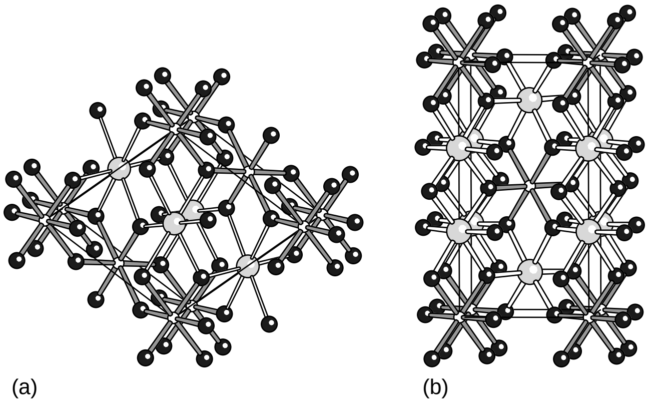

Figure 15 (a) $LiMnF_4$ structure (large grey spheres: Li); (b) trirutile Li_2MoF_6

The trirutile structure can also be described as deriving from a hcp-packing of anions and ordered occupation of half of the octahedral sites. Two alternative order variants based on the same hcp anionic substructure have been found for such Li and Na compounds: the Na_2SiF_6-type and the Li_2ZrF_6-type structures. Like the trirutile structure, the Na_2SiF_6-type is realized also by some $LiM^{II}M^{III}F_6$ compounds. For the Li_2ZrF_6-type, corresponding $LiM^{II}M^{III}F_6$ relatives are ascribed to the $LiCaAlF_6$-type. A detailed survey on compounds and structural relations in this structure family can be found in Ref. 33.

3.2.2 Structures Derived from the CaF_2-type

Substitution Variants. The fluorite-type structure is maintained in principle when alkaline earth elements are replaced partially by rare-earth elements. Charge compensation is achieved by occupation of additional interstitial anionic sites.**[67]** The coordination of the metal atoms may increase from 8 to 9 or even 10 by this. Another way of charge balance is the partial replacement of fluorine by oxygen to form oxyfluorides.**[68]** Since the possible interstitial positions provide pathways for anion disorder and movement, this class of materials shows fluoride ionic conductivity.

Subtraction Variants of the CaF_2-Type. There is a large and interesting group of structure types, which can formally be derived from the fluorite structure by subtraction of anion and/or cation positions and, of course, by substitutions within

Table 2 Subtraction variants of the fluorite type (□ = vacancy)

Fluorite	$[\mathrm{Ca}_4^{[8]}]$	$[\mathrm{Ca}_4^{[8]}]$	F_{16}	CaF_2
Weberite	$[\mathrm{Na}^{[8]}\mathrm{M}_3^{[6]}]$	$[\mathrm{Na}_3^{[8]}\mathrm{M}^{[6]}]$	$F_{14}\square_2$	Na_2 $MM'F_7$
Pyrochlore	$[\mathrm{A}^{[8]}\mathrm{M}_3^{[6]}]$	$[\mathrm{A}_3^{[8]}\mathrm{M}^{[6]}]$	$F_{14}\square_2$	$A_2{}^{a}M_2F_7{}^{b}$
$RbNiCrF_6$	$[\square\ \mathrm{M}_3^{[6]}]$	$[\square_3\ \mathrm{M}^{[6]}]$	$F_{12}Rb_2\square_2$	$A^{I}M^{II}M^{III}F_6$
Pyr-FeF_3	$[\square\ \mathrm{M}_3^{[6]}]$	$[\square_3\ \mathrm{M}^{[6]}]$	$F_{12}\square_2\square_2$	FeF_3, η-AlF_3
$Cs_2NaAl_3F_{12}$	$[\square\ \mathrm{M}_3^{[6]}]$	$[\square_3\ \mathrm{Na}^{[6]}]$	$F_{12}Cs_2\square_2$	$A_2^{I}NaM_3^{III}F_{12}$

[a] A_2 = Na,Ca, or Na,Cd. [b] The 7th F atom is not part of the octahedral net and may be replaced by O or S in compounds like $Cd_2M_2^{II}F_6O$, cf. also the mineral $(CaNa)Nb_2O_6(OH,F)$.

the resulting structure type.[69,70] In this way, the typical CN 8 of the CaF_2 structure is gradually reduced toward octahedral. Thus, these structures can also be classified using concepts of octahedral nets. They are discussed in detail later on from this point of view. A survey on this structure family and its relations to the CaF_2 structure (set up with doubled axes) are given in Table 2, where the coordination numbers are given as superscripts in brackets.

3.2.3 *ReO_3 and VF_3 Related Compounds*

A very large structure family derives from the basic motif of a cube of 3D corner-connected octahedra realized in the ReO_3 structure or from its distorted variants, the VF_3 and IrF_3 type, mentioned in the previous chapter (Table 1, Figure 5). The main derivatives are generated by ordered occupation of the octahedral sites and/or by filling the central cavity with a large cation, which becomes part of the fcc packing of the anions. Less frequently, the order of vacancies on the octahedral sites is observed.

Order Variants $M_{0.5}M'_{0.5}F_3 = MM'F_6$. M^{II}/M^{IV} and M^{I}/M^{V} compounds are known in many combinations (surveys in Refs. 33, 71). Their structures can be derived from the parent MF_3 structures (Section 3.1): Some of them crystallize in the cubic ReO_3 type, either with disorder on the metal site (s.g. $Pm\bar{3}m$) as in the recently discovered titanium(II) compound $Ti^{II}Hf^{IV}F_6$ or ordered with double lattice constants ($NaSbF_6$ type, s.g. $Fm\bar{3}m$) as in the vanadium(II) compounds $V^{II}Zr^{IV}F_6$ and $V^{II}Hf^{IV}F_6$.[72] The largest family is that derived from the VF_3 type structure (Figure 5). A few members show cationic disorder (VF_3-type, s.g. $R\bar{3}c$) such as $Pd^{II}Mn^{IV}F_6$, but most belong to the ordered $LiSbF_6$ type (s.g. $R\bar{3}$). A special case of this structure type is the already mentioned mixed-valence $NiF_3 = Ni^{II}Ni^{IV}F_6$.[24] Low-symmetry variants related to the MnF_3 structure have been found in $M^{II}M^{IV}F_6$ compounds with M^{II} = Cr, Cu, Ag. In recent structure determinations, triclinic $LiSbF_6$ variants were confirmed for Ag^{II} compounds.[73] For very large M^{IV} metal ions ($r > 0.8$ Å), $M^{II}M^{IV}F_6$ compounds are found to crystallize in the LaF_3 type structure.

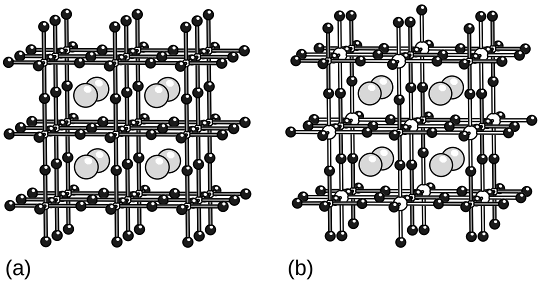

Figure 16 (a) Perovskite type (8 unit cells); (b) Elpasolite-type

Perovskites, Elpasolites, and Cryolites. If the cuboctahedral cavity in the cubic ReO_3-type structure is occupied by a cation A, the perovskite-type structure AMX_3 (s.g. $Pm\bar{3}m$, Figure 16(a)) results where the A ion becomes part of the fcc anionic packing (CN 12). In fluorides, this structure is found for many compounds $A^{I}M^{II}F_3$ with A = Na, K, Rb, Cs, NH_4, Tl, Ag and M = Mg, Ca, V, Mn, Fe, Co, Ni, Zn, Cd, Hg. If the octahedral M^{II} site is occupied in an ordered way by a small alkali ion A′ and an M^{III} ion, one arrives at the elpasolite-type structure (K_2NaAlF_6-type, s.g. $Fm\bar{3}m$, Figure 16(b)), a superstructure variant of perovskite. Cubic structures $A^{I}M^{II}F_3$ or $A_2^{I}A^{I\prime}M^{III}F_6$ are found if the tolerance factor $t = (r_A + r_F)/\sqrt{2}(r_M + r_F)$ is in the range 0.88–1.00 (for elpasolites $r_M = (r_{A'} + r_M)/2$). Surveys on the geometrical and structure-systematical rules valid in the structure family of perovskites and elpasolites and a large collection of compounds can be found in Refs. 33, 34. Recently, an investigation of phase transitions in elpasolites appeared.[74] For lower values of t (0.76–0.88), a distorted orthorhombic variant, the $GdFeO_3$-type (space group Pbnm (Pnma)) is realized in AMF_3 compounds (Figure 17(a)) while for $t > 1$, new hexagonal structures are found (see next section). Low t-values are obtained if the A cation (CN 12 in cubic perovskite) becomes too small for this high coordination, for example, in $NaNiF_3$. Thus, by tilting the octahedral network, the CN of the A ion is reduced to eight in the $GdFeO_3$-type structure.

A special case occurs if in elpasolite-type compounds $A_2A'MF_6$ (A: CN 12, A′: CN 6) the same alkali ion A is available for both positions. Thus, in compounds $Na_3M^{III}F_6$ a similar tilting variant of the elpasolite-type structure is observed as the $GdFeO_3$ variant is of the perovskite type. This is the cryolite structure (Figure 17(b)) named after the mineral Na_3AlF_6[3] (monoclinic, s.g. $P2_1/n$). This compound is of great technical significance for aluminium production and is now synthesized in large amounts since the naturally occurring mineral is exhausted. Cryolites are known for many tervalent metals, and the tilting angle of the octahedra can be predicted based on the ionic radii.[75] Based on powder data, a cryolite-like structure has been reported also for Na_2LiMF_6,[76] as suggested for the analogous Ni^{III} and Cu^{III} compounds before. For many compounds A_3MF_6, phase

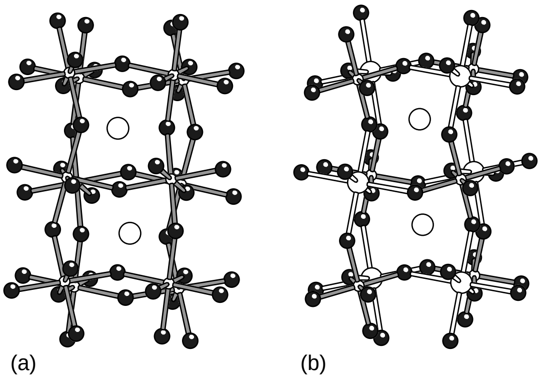

Figure 17 (a) $NaNiF_3$ structure ($GdFeO_3$-type); (b) Na_3AlF_6 (cryolite) structure. Na–F bonds drawn for Na on former perovskite M sites only. Both structures in perspectives to recognize two parent perovskite subcells. Na atoms as large spheres

transitions of ferroelastic type have been found leading to HT forms with the ideal elpasolite space group $Fm\bar{3}m$. A postulated orthorhombic high-temperature form 'β-Na_3AlF_6' (space group Immm,[77] 890 K, $R = 0.074$) can be described in the elpasolite s.g. $Fm\,\bar{3}m$ as well within the error limits (max. deviation from cubic in lattice constants 0.003 Å, of an atomic position (F2) 0.069 Å at r.m.s. displacements of 0.23–0.47 Å).

For A_3MF_6 compounds with larger alkali cations, only a few single-crystal investigations are known. It seems to be clear that K_3MoF_6 and K_3WF_6[78] crystallize in the cubic elpasolite-type structure, as well as most of the $(NH_4)_3M^{III}F_6$ compounds at room temperature. For $(NH_4)_3ScF_6$, a monoclinic structure variant has been reported recently.[79] Very complicated superstructures with five-fold axes have been found in different laboratories for some K and Rb compounds (see citation in Ref. 33). However, no structure determinations are known to date.

While all these structures derive from the elpasolite aristotype, the $Li_3M^{III}F_6$ compounds ($M = Al$, Ga, Ti, V, Cr, Fe) exist at room temperature in two modifications. The α-form (e.g. α-Li_3AlF_6[80]) is still a strongly distorted variant of the elpasolite/cryolite family in which the coordination of all lithium ions is reduced to six. The β-form, determined at β-Li_3VF_6[81] and confirmed by recent single-crystal work on the Al, Ga, Ti, and Cr compounds (Ref. 82 and literature cited herein), has a new structure type with part of the lithium ions in tetrahedral coordination.

Perovskite Relatives with Vacancies on Octahedral Sites. A special derivative of the elpasolite-type structure $A^{I}_2A^{I\prime}M^{III}F_6$ with half-occupation of the A′ site has only been found in compounds of Jahn–Teller ions Mn^{3+} and Cu^{2+}. $K_2(\square_{0.5}Mn^{II}_{0.5})Mn^{III}F_6 = K_4Mn_3F_{12}$, $CsBa(\square_{0.5}Cu^{II}_{0.5})Cu^{II}F_6 = Cs_2Ba_2Cu_3F_{12}$,[83] and recently $Cs_2(\square_{0.5}Pd^{II}_{0.5})Mn^{III}F_6$[84] show the vacancies on the octahedral sites ordered in layers like in the chiolite structure (see Section 3.2.5) and stacked and connected according to a 4_1 screw axis (s.g. $I4_1/amd$, Figure 18(a)) to form a 3D network.

Every second octahedral site of the elpasolite-type structure is unoccupied in compounds $A_2M^{IV}F_6$ of the K_2SiF_6 type, known also as the K_2PtCl_6-type (s.g. $Fm\bar{3}m$, Figure 18(b)). This structure can also be seen as an antifluorite structure if the whole complex $[MF_6]$ anion is compared with Ca. It can be observed for nearly all alkali hexafluorometallates(IV) of the first transition metal series as well as some noble metals like β-Cs_2PtF_6.[85] However, for many such compounds other polymorphs are known, too, and the cubic form is the HT-phase only. These alternative structures are mentioned in the next section. A survey on all of the main structure types mentioned up to now derived from the ReO_3/VF_3 type structure is given in Table 3.

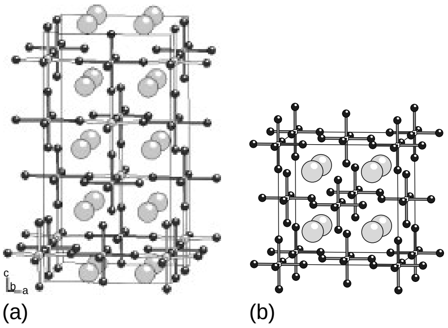

Figure 18 (a) Structure of $K_4Mn^{II}Mn^{III}_2F_{12}$. K large grey spheres, Mn^{II} medium grey open bonds; Mn^{III} small white, dark bonds; a chiolite-like layer is shown at z=1/8. (b) K_2SiF_6-type structure (Cs_2MnF_6)

Table 3 Main fluoride structure types (*italics*) derived from ReO_3-type (left) and its distortion variant VF_3-type (right) with site occupation schemes, space groups in parentheses

$\square_2(M\,M)F_6$	NbF_3 (*ReO_3*-type, $Pm\bar{3}m$)	$\square_2(M\,M)F_6$	*VF_3* ($R\bar{3}c$)
$\square_2(M\,M')F_6$	*$NaSbF_6$* ($Fm\bar{3}m$)	$\square_2(M\,M')F_6$	*$LiSbF_6$* ($R\bar{3}$)
$A_2(M\,M)F_6$	$KNiF_3$ ($Pm\bar{3}m$) *$CaTiO_3$ perovskite*	$A_2(M\,M)\,F_6$	$NaNiF_3$ (Pbnm) *$GdFeO_3$*
$A_2(A'\,M)F_6$	*K_2NaAlF_6* ($Fm\bar{3}m$) *elpasolite*	$A_2(A\,M)F_6$	*Na_3AlF_6* ($P2_1/n$) *cryolite*
$A_2(\{\square_{0.5}M_{0.5}\}M)F_6$	*$K_4Mn^{II}Mn^{III}_2F_{12}$* ($I4_1/amd$)		*α-Li_3AlF_6* ($Pna2_1$)
$A_2(\square\,M)F_6$	*K_2SiF_6/K_2PtCl_6* ($Fm\bar{3}m$)		

3.2.4 *Hexagonal ‘Perovskites’ and Derivatives*

If in compounds with perovskite (AMX_3) or elpasolite ($A_2A'MF_6$) composition, the tolerance factor t adopts values larger than 1, that is, the A cation becomes too large for the ReO_3 cage, new trigonal or hexagonal structures are formed with face-sharing $[MF_6]$ octahedra as new structural elements. Though the term ‘perovskite’ appears somewhat misleading because the typical feature of only corner-connected octahedra is broken, some justification arises since all structures are based on close-packed $AF_3{}^{2-}$ layers. In the classical cubic perovskites, the stacking is of fcc type **ABC**. As can be seen in the examples of Figure 19, the trigonal and hexagonal ‘perovskites’ can be described as stacking variants in which the occupation by M^{II} atoms of neighboring octahedral sites in hcp stacking units **ABA** generates face-sharing of octahedra. There are several polytypes with mixed stacking sequences, most structures of which are known from oxides as well. They are named, according to the layers’ periodicity, 2L, 3L, 6L structures, and so on. If ordered substitution of the octahedral sites by alkali ions or vacancies is considered, as done above for the derivatives of cubic perovskite, ‘trigonal or hexagonal elpasolites’ and trigonal or hexagonal $A_2M^{IV}F_6$ structure types, respectively, are the result (Table 4, see also survey in Refs. 32, 33 and recent papers[86,87]). In the case of pure hcp stacking, occupation of all of the octahedral sites formed by fluoride ions only leads to a chain structure of face-connected octahedra (2L *$CsNiF_3$-type*, Figures 19 and 20(a)). This compound became the subject of many physical investigations as a model for a 1D ferromagnetic chain. Quasi-isolated octahedra result if every second octahedral site remains empty in $K(\square_{0.5}Ge_{0.5})F_3$ (Figure 20(c)) or the 4L K_2MnF_6-type, the hexagonal analog of the 3L case K_2SiF_6, known as the K_2PtCl_6-type structure. An intermediate situation is found in the 2L structure of compounds $Cs_3M^{III}_2F_9$ ($=Cs(\square_{0.33}M_{0.67})F_3$, M = Fe,[88] Ga[89]), $[(CH_3)_4N]Fe_2F_9$[90] and $[(CH_3CH_2)_4N]_3M_2F_9$ (M = Cr, V, Fe)[91] showing the rare case of dimeric $[M_2F_9]^{3-}$ anions with face-sharing of octahedra (Figure 20(b)). In a series of Cs compounds of Ni^{II} (and partly also Mg, Zn, Co), not only analogous $[M_2F_9]$ dimers ($Cs_7Ni_4F_{15}$[92]), but also trimeric ($Cs_4M_3F_{10}$[93]) and even pentameric units ($Cs_6Ni_5F_{16}$[94]) were found, further linked by sharing vertices to form special layer structures.

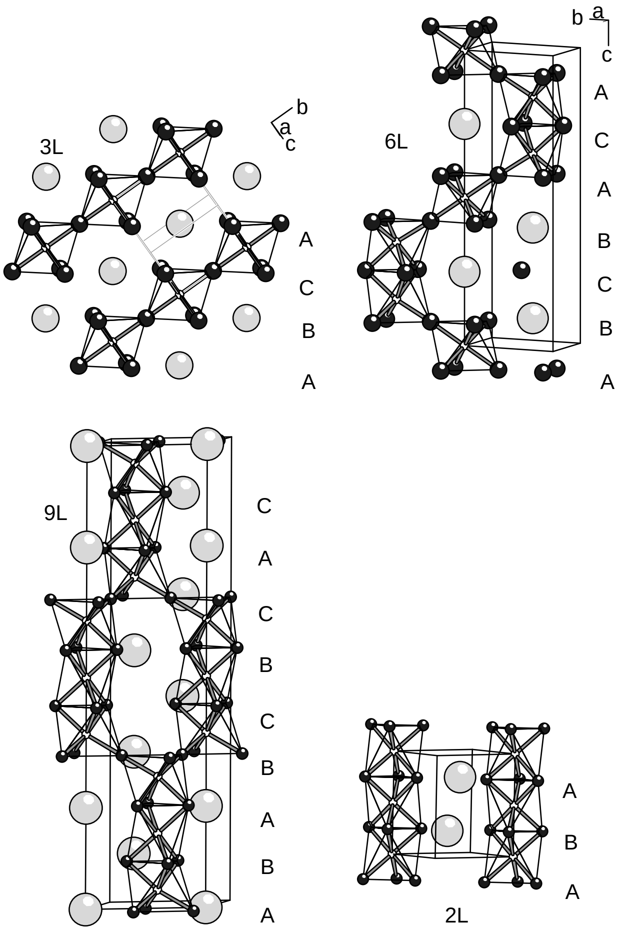

Figure 19 View of cubic (3L) and hexagonal perovskites along the close-packed AF_3 layers. 6L $RbZnF_3$, 9L $CsCoF_3$, 2L $CsNiF_3$

The higher the tolerance factor t the more face-connected octahedra are encountered in hexagonal perovskites. The sequence of structure types with rising t from <1.0 to 1.08 is cubic (3L) – 6L – 12L – 9L – 2L. Under high pressure, metastable AMF_3 or $A_2A'MF_6$ HP-polymorphs can be synthesized with structures corresponding to that of compounds with lower tolerance factors. Though octahedral coordination is maintained in both forms, they show longer M-F distances than in the normal-pressure form. This ‘pressure-distance

Table 4 Numbers and stacking schemes of close-packed $[AF_3]$ layers in trigonal and hexagonal fluoride ‘perovskites’, ‘elpasolites’, and derivatives and typical compounds (cubic perovskite included, structure types in *italics*, space groups in parentheses)

2L	AB	$CsNiF_3$ (*$BaNiO_3$*, $P6_3/mmc$)	$Cs_2(LiGa)F_6$ ($P\bar{3}m1$)	*$K_2(\square Ge)F_6$* ($P\bar{3}m1$)
3L	ABC	$KNiF_3$ (*perovskite,* $Pm\bar{3}m$)	2x3L $K_2(NaAl)F_6$ ($Fm\bar{3}m$)	*$K_2(\square Si)F_6$* ($Fm\bar{3}m$)
4L	ABAC			*$K_2(\square Mn)F_6$* ($P6_3mc$)
6L	ABCBAC	$CsMnF_3$ (*hex. $BaTiO_3$*, $P6_3/mmc$)	$Cs_2(NaTi)F_6$ ($P\bar{3}m1$)	
9L	ABABC BCAC	$CsCoF_3$ (*$BaRuO_3$*, $R\bar{3}m$)		
12L	ABABCA CABCBC		$Cs_2(NaCr)F_6$ ($R\bar{3}m$)	$Ba_2(Co_{0.5}\square_{0.5}Re)F_6 = Ba_4CoRe_2F_{12}$

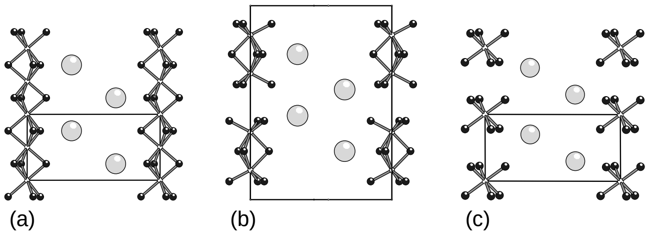

Figure 20 Structures deriving from hcp AF_3^{2-} layer stacking: (a) $CsNiF_3$; (b) $Cs_3Fe_2F_9$; (c) K_2GeF_6

paradox' can be understood when looking at the A-F distances, the decrease of which overcompensates the volume increase of the octahedra.[30,87]

3.2.5 Layer Structures Derived from Perovskite-type

K_2NiF_4-Type. If in a perovskite like $KNiF_3$ (Figure 16), the horizontal layers are separated by formally adding KF, a layer structure K_2NiF_4 results with square meshes of *trans*-corner-connected octahedra (Figure 21(a)). Neutral layers of this type are known from the SnF_4 structure (Figure 11). According to the space group I4/mmm, subsequent layers are shifted by $\frac{1}{2}, \frac{1}{2}, \frac{1}{2}$. This structure type is realized by many M^{II} fluoro compounds (M = Mg, Mn, Fe, Co, Ni, Zn, Cd, Ag) with the larger alkali ions K, Rb, Cs, and with NH_4 and Tl (survey in Ref. 33). The *K_2NiF_4* structure type is widespread in oxo compounds and became famous as the parent structure of the high-T_c superconductors deriving from La_2CuO_4.

$K_3Ni_2F_7$ or Ruddlesden–Popper-type. If in the perovskite structure AMF_3 the layer separation by addition of AF is performed every second layer only, the double-layer structure type *$K_3Ni_2F_7$* is obtained, known in oxides as $Sr_3Ti_2O_7$ or *Ruddlesden–Popper* structure (s.g. I4/mmm, Figure 21(b)).

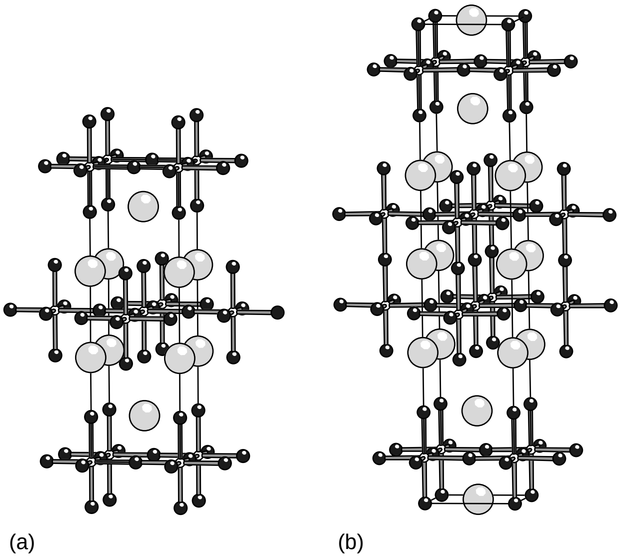

Figure 21 (a) K_2NiF_4-type layer structure; (b) $K_3Ni_2F_7$ or Ruddlesden–Popper type structure

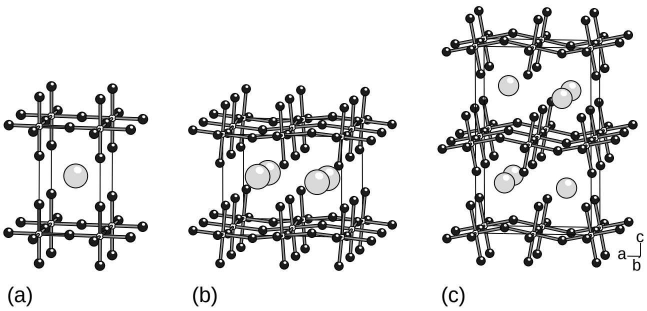

Figure 22 (a) HT-$TlAlF_4$ structure (s.g. P4/mmm); (b) γ-$CsFeF_4$ (s.g. P4/nmm); (c) HT-$KFeF_4$

Structures Derived from $TlAlF_4$-Type. Another way toward layers formally excised from the perovskite structure $A^IM^{II}F_3$ is to add an additional F atom and increase the oxidation state of M from two to three to obtain $A^IM^{III}F_4$ compounds. While in both structure types mentioned before the layers are planar (angles M–F–M 180°), most AMF_4 structures show puckered layers with M–F–M angles decreasing down to 132° with decreasing size of the alkali ion between the layers. Even for the name-giving structure $TlAlF_4$, the aristotype structure (s.g. P4/mmm) with planar layers has been shown to be realized at high temperatures only. Upon cooling, phase transitions occur at 514 K and at 435 K, leading to structures of lower symmetry containing tilted octahedra in space groups I4/mcm and s.g. I2/a, respectively.[95] Structural phase transitions have been reported for several other A^IAlF_4 (A = K, Rb, NH_4, Cs) and A^IFeF_4 compounds (A = K, Rb, Cs). Figure 22 shows as examples the aristotype HT-$TlAlF_4$, the derived γ-$CsFeF_4$ structure[96] with puckered layers, and $KFeF_4$ with layers alternately shifted by $b/2$ (see a recent paper[97] and references therein). In the corresponding Mn^{III} compounds, *antiferrodistortive* Jahn–Teller ordering of elongated octahedra is observed within the layers (alternating rotation by 90°).[98]

The strongest deformations of the $TlAlF_4$-type structure are encountered at $LiCoF_4$, $LiMnF_4$, and $NaMnF_4$, the structures of which were discussed already as relatives of the rutile structure (Section 3.2.1, Figure 15(a)). Rutile-type structure elements are also found in the related isostructural compounds α-$NaTiF_4$ and $NaCoF_4$ (see discussion in Ref. 65). For other $Na^IM^{III}F_4$ compounds, different structures have been found with partial *cis*-connection of $[MF_6]$ octahedra. They are mentioned below in Section 3.2.7.

Chiolites $A^I_5M^{III}_3F_{14}$. When in a $TlAlF_4$-type layer structure $A^IM^{III}F_4$ (or $A_4M_4F_{16}$), 1/2 of the octahedra (including their terminal F ligands) is removed and formally replaced by additional A atoms (Na or K), the composition

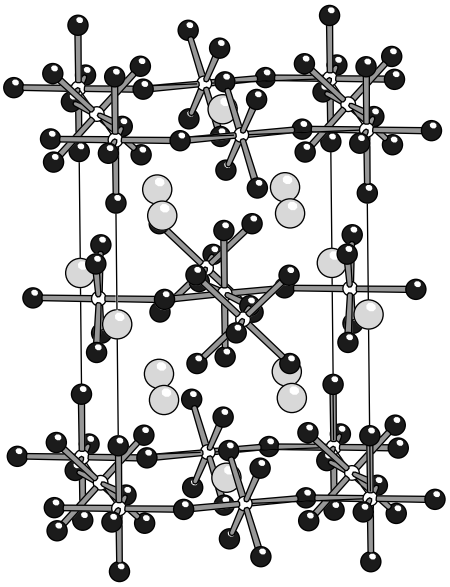

Figure 23 Chiolite structure $Na_5Al_3F_{14}$. Na atoms as grey spheres

$A_4(AM_3)F_{14}\square_2$ of the chiolite-type structure is obtained (Figure 23). Half of the remaining octahedra are rotated by 45° to achieve cube-like CN 8 for this intralayer alkali atom; the interlayer alkali atoms also have CN 8, but rather distorted. This structure is found in compounds $A_5M_3F_{14}$, mainly with $A = Na$, but some K analogs and an ammonium compound have also been reported. For most representatives, the tetragonal space group P4/mnc was found such as for the mineral $Na_5Al_3F_{14}$. However, low-symmetry variants and polymorphism have been reported (see Ref. 33), for instance, s.g. $P4_24_12$ for γ-$Na_5Fe_3F_{14}$ or s.g. Pnma for the Jahn–Teller system $Na_5Mn_3F_{14}$.[99,100]

Layer Structures $A^{II}_2M^{II}F_6$. Similar structures with square $[MF_4]$ layers such as in the K_2NiF_4-type are found if the alkali cations are replaced by Ba or Pb^{II} and the higher charge is compensated by additional 'free' fluoride ions, which are located only in the Ba/Pb layers (*Ba_2ZnF_6-type*). These compounds, found for M = Mg, Mn, Fe, Co, Ni, Cu, Ag, Zn, are thus better written $(BaF)_2MF_4$. The structures, in the early literature described in the space group I4/mmm with planar layers, show, at least in some cases, superstructures and puckering of the layers.[33] The Cu^{II} compounds display similar Jahn–Teller ordering as the $AMn^{III}F_4$ structures. Ba_2PdF_6[101] shows isolated $[PdF_4]$ squares ordered in a corresponding layer structure.

3.2.6 Chain Structures with Trans-connected Octahedra

Compounds $A^{II}M^{III}F_5$ and Relatives. Cutting up a perovskite like layer further leads to linear chains of trans-connected octahedra as realized in the structure of α-UF_5 (Section 3.1, Figure 14(b)). Similar trans-chains of composition $[MF_5]$ are found as anionic substructure in compounds $CaM^{III}F_5$ of $CaCrF_5$-type[102] structure (s.g. C2/c, M = Al(α), Ga(α), Ti, Cr, V, Mn, Co, and $CdMnF_5$) or the variant $CaFeF_5$-type[103] (M = Al(β), Ga(β), Fe), found also in $CdGaF_5$ and $CdCrF_5$. In addition, trans-chains are observed in the hydrates $BaFeF_5\cdot(H_2O)$[104] and, elongated by the Jahn–Teller effect, in $A^{II}MnF_5\cdot(H_2O)$ (A = Sr, Ba).[105] However, the anhydrous compounds of Mn^{III} show *cis*-chains (see below).

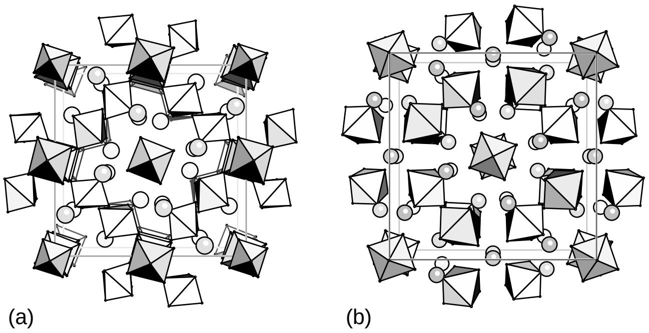

(a) (b)

Figure 24 Perspective view (a) of the $BaFeF_5$, (b) of the $Pb_5Cr_3F_{19}$ structure, from the chain direction *c* (Ba or Pb as spheres)

In the anhydrous Sr- and Ba compounds of other tervalent metals, a strange series of interrelated structures has been found, derived from the tetragonal structure of $BaFeF_5$.[106] In this structure (s.g. I4), 'branched' trans-chains were reported (Figure 24(a)) alternating with 'normal' trans-octahedral chains.

In a recent paper, an analogous structure has been described in s.g. I4/m for a mixed crystal $Ba_{0.43}Sr_{0.57}AlF_5$ while in pure $SrAlF_5$, a superstructure was refined in s.g. $I4_1/a$ (like for the related $Ba_5Cr_3F_{18}$[107] before) showing stacked edge-sharing $[Al_2F_{10}]$ dimers in place of the normal trans-chains.[108] The latter compound also crystallizes like $BaFeF_5$ in another polymorph with cis-connected octahedra discussed in the next section. Related structures with different compositions but similar tetragonal unit cells and s.g.s were found for compounds like $Sr_5M_3F_{19}$ (M = V, Cr, Fe)[109,110] where both types of chains are resolved to isolated dimers and isolated octahedra, respectively, or for phases $Pb_5M^{III}_3F_{19}$. In the Cr^{III} compound[111] of the latter type (Figure 24(b)), refined in the polar s.g. 14 cm, trans-chains (at the corners and in the center) alternate with isolated octahedra. Recently, 'structure-property correlations over five phases and four transitions' have been investigated for $Pb_5Al_3F_{19}$.[112]

Compounds $A^{I}_2M^{III}F_5$ and $A^{I}_2M^{III}F_5\cdot H_2O$. In alkali pentafluorometallates(III), the formation of trans-connected octahedral chain anions is mostly restricted to the Mn^{III} compounds where the strong Pseudo-Jahn–Teller effect stabilizes this type of bridging,[113] and induces additional lengthening of the bridging bonds. By choice of the counter cation, the geometry of the chain can be tuned in a wide range.

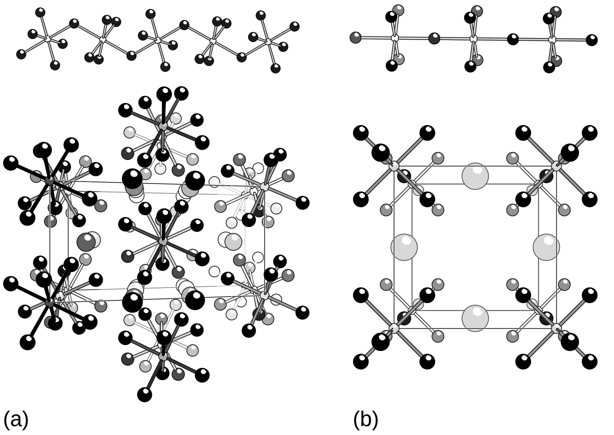

Figure 25 Chain sections and views along the chain axes for the structures of (a) Li_2MnF_5;[114] (b) Cs_2MnF_5[115]

In A_2MnF_5 compounds (A = Li, Na, K, NH_4, Rb, Cs) and the hydrated compounds $A_2MnF_5 \cdot H_2O$ (A = K, Rb, Tl, Cs), the bridge angle M–F–M varies between 121.5° (Li) and 180° (Cs) (Figure 25).

The Li, Na, and NH_4 compounds show pseudo-hexagonal and the other ones tetragonal chain packing (Figure 25). The close relations between hydrated and anhydrous compounds are documented in topotactical dehydrations found in experiments on single crystals of $Rb_2MnF_5(H_2O)$[116] and $Cs_2MnF_5(H_2O)$.[115] Similar chain structures were found also for some compounds with protonated organic amines as cations like enH_2^{2+} (en = ethylene diamine), $DAPH_2^{2+}$ (DAP = 1, 3-diaminopropane), $DABH_2^{2+}$ (DAB = 1, 4-diaminobutane), and $atriazH^+$ (atriaz = 3-amino-1,2,4-triazole). A survey on the structural chemistry of fluoromanganates(III) can be found in Ref. 113. The quasi-isolated anionic chain anions proved to be good model systems for studies of 1D magnetic properties like nonlinear excitations (solitons) (see Section 4.1).

With 'normal' M^{III} ions, only few trans-chain compounds $A_2MF_5 \cdot (H_2O)$ were found until now, for example, $A_2AlF_5 \cdot (H_2O)$(A = K,[117] Rb[118]), β-$(NH_4)_2FeF_5$,[10] or $(CH_3NH_3)_2FeF_5$.[119] The basic structure type for trans-chain compounds A_2MF_5 is known as 'Tl_2AlF_5-type' (s.g. $C222_1$[120]). However, it has been shown[121] that the investigated crystal probably was in fact $Tl_2AlF_5 \cdot (H_2O)$ and the s.g. Cmcm. The aristotype structure with highest possible symmetry (s.g. P4/mmm) is realized in Cs_2MnF_5 and, probably, the Rb compound also.

An intermediate between perovskite like layer and trans-chain structure is the unique double trans-chain structure of $K(H_5O_2)Al_2F_9$.[122] On the other side, as a link between trans-chain and isolated octahedra, vertex-sharing dimers have been found in $CsBa_2Cr_2F_{11}$[123] and in the aqua-fluoromanganate anion $[Mn_2F_9(H_2O)_2]^{3-}$ of $cyclamH_4[Mn_2F_9(H_2O)_2][MnF_4(H_2O)_2]$[18] (see also Section 3.2.12).

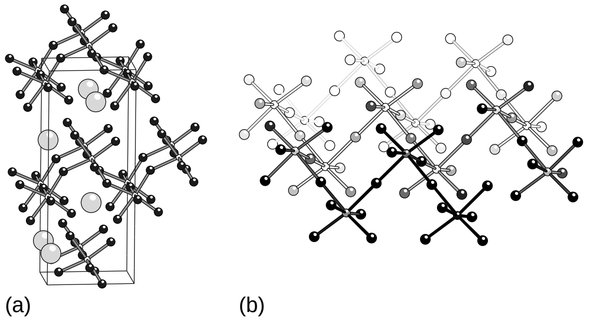

Figure 26 (a) *cis-trans*-linking of octahedra in $BaZnF_4$; (b) pure *cis*-connected layer structure of $Ba_2RbFe_2F_9$

3.2.7 *Structures with Cis-connected Octahedra*

An alternative way of linking octahedra to 1D, 2D, or 3D structures by sharing vertices is that of using *cis*-corners. The basic structural units may be visualized as formally cut from the ReO_3-type octahedral net as before for the trans-linked octahedral arrays.

Layer Structures. A combination of trans-linking as in the former Section 3.2.6 and of cis-linking leads to puckered layers of octahedra as realized in compounds $NaM^{III}F_4$ (*$NaNbO_2F_2$-type*, s.g. $P2_1/c$, M = V,Cr,Fe) and $A^{II}M^{II}F_4$ (*$BaZnF_4$-type*, s.g. $Cmc2_1$, A = Sr, Ba, M = Mg, Mn, Fe, Co, Ni, Cu, Zn) (see Ref. 33). As a consequence, the $[MF_6]$ octahedra have *cis*-terminal F ligands (Figure 26). According to the polar s.g. of the Ba compounds, ferro- and pyroelectrical properties are observed.

An interesting structure intermediate between pure trans–trans and cis–trans connected layers is realized in $KScF_4$,[124] where alternation of four trans-connections and one cis-connection gives 'staircase-like' layers.

A pure *cis*-connection is found in the honeycomb layer structure of *fac*-corner-sharing octahedra in compounds $Ba_2A^IM_2^{II}F_9$[125] (A = K, Rb, Cs; M = Fe, Co, Ni, Zn; Figure 26(b)).

Cis-Chain Structures. When a *cis-trans*-connected layer is cut parallel to the cis-chains, double chains or single chains of *cis*-connected octahedra are retained. Double chains are found in compounds Ba_2ZnAlF_9,[126] Ba_2CoFeF_9,[127] (Figure 27(a)) or $KPbCr_2F_9$.[128] Here similar simple zig-zag strands are formed while in the unique structure of $[O_2]Mn_2F_9$,[129] crenel-like double chains were found (Figure 27(b)).

Single *cis*-chains are found in two main types: a simple zig-zag chain in the $BaGaF_5$-type[130] structures (Figure 27(c)) found also for the analogous Al, Cr, Mn, Co compounds, and crenel-like flat helicoidal chains, for instance, in $SrFeF_5$[131] (Figure 27(d)), α'-$BaFeF_5$,[132] α'-$SrAlF_5$,[133] or $SrVF_5$.[134] Analogous chain structures are formed by $A_2^IM^{III}F_5$

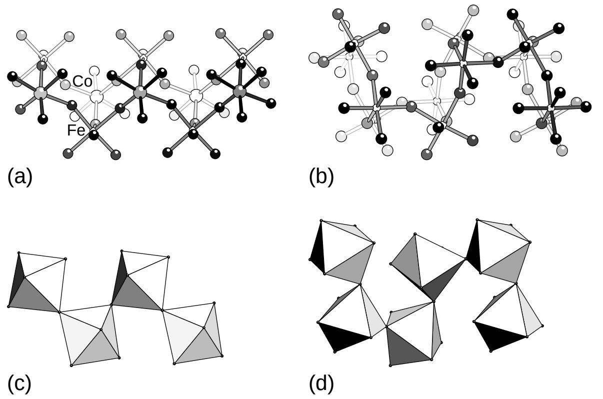

Figure 27 Double-*cis*-chain structures of (a) Ba_2CoFeF_9, (b) $[O_2]Mn_2F_9$, and single *cis*-chains of (c) $BaGaF_5$ and (d) $SrFeF_5$

compounds Rb_2CrF_5 and A_2FeF_5 ($A = K$ (two polymorphs), Rb, NH_4 (α-form), see Ref. 135 and literature given therein).

3.2.8 Structures Based on the (3,6)-Net (Kagomé or HTB Net)

All structures mentioned in Sections 3.2.3 to 3.2.5 are based on simple 2D or 3D nets with four-membered meshes of vertex-connected octahedra. In many structures, additional structural units formed by three vertex-sharing octahedra are encountered combined with the four-membered unit but also with higher aggregates of 5, 6, or more octahedra. 2D nets formed by regular combination of two or more such octahedral n-membered rings are named according to the participating units (n_1,n_2)-net, for instance. The most important mixed net is the (3,6)- or Kagomé net, named also the HTB net after the hexagonal tungsten bronze structure discussed below.

$Cs_2NaAl_3F_{12}$-Type Structure. A representative of this layer type, the $Cs_2NaAl_3F_{12}$-type structure (Figure 28(a)), has been mentioned already in the Section *Subtraction Variants of the CaF_2-Type* as a derivative of the CaF_2 or pyrochlore-type structure, respectively. Here, the large Cs ions are positioned between a six-membered ring of octahedra and a three-membered one of the shifted neighboring layer; the Na ions connect triple units only. This structure type is found in compounds $A^{I}_{2}A^{I\prime}M^{III}_{3}F_{12}$[136–139] with $M^{III} = $ Ti, V, Cr, Mn, Fe, Co, Sc, Ga and other combinations of alkali metals like Cs_2K, Cs_2Li, Rb_2Na, and K_2Na.[140] In compounds with Mn^{III},[141] the octahedra are strongly elongated and show a wind-wheel-like Jahn–Teller ordering pattern (Figure 28(b)).

Weberites. If the metal positions of the (6,3)-net above (Figure 28(a)) are occupied in an ordered way by M^{II} cations forming trans-chains and by linking M^{III} ions, the typical layer of weberites is achieved (Figure 29(a)). Additional replacement of Na atoms connecting in $Cs_2NaAl_3F_{12}$ subsequent shifted layers by M^{III} ions in the weberite structure leads to a 3D framework of two intersecting (6,3)-nets with common $[M^{II}F_6]$ chains (Figure 29(b)).

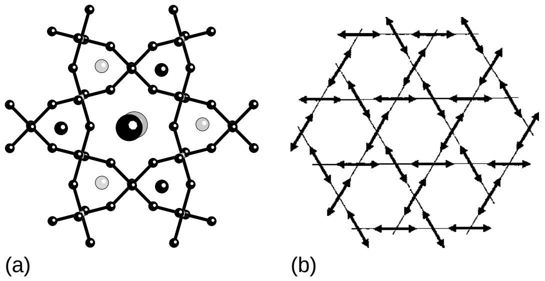

Figure 28 (a) $Cs_2NaAl_3F_{12}$ type. Large spheres Cs, small spheres Na; (b) Jahn–Teller ordering in $A_2A'Mn_3F_{12}$ compounds

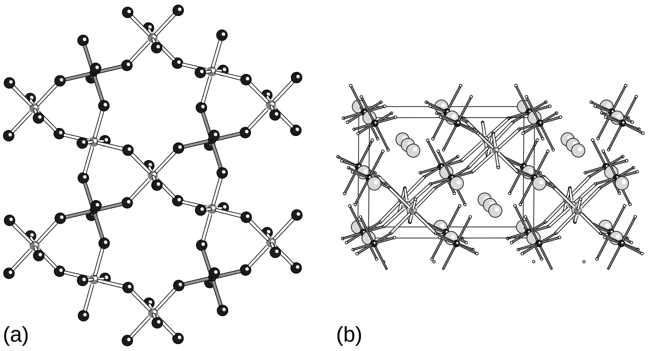

Figure 29 (a) Kagomé net formed by $[M^{II}F_6]$ (bright) and $[M^{III}F_6]$ (dark) octahedra; (b) O-I weberite structure of Na_2NiAlF_7. View along the M^{II} octahedral chains, Na grey spheres

An alternative interpretation of the weberite-type structure mentioned already in Section 3.2.3 emphasizes the relationship to the CaF_2-type structure. Formally, in the weberites $Na_2M^{II}M^{III}F_7$, one half of the Ca positions of CaF_2 are replaced by Na ions, retaining CN 8, and one half by M^{II} and M^{III} ions in an ordered way. In Figure 30, the cation distribution in the classical weberite (mineral Na_2MgAlF_7) of O-I type (s.g. Imma) is compared with that of fluorite. By generation of vacancies in the anion sublattice and shifts in some F positions, octahedral coordination is achieved for M^{II} and M^{III} atoms. For a survey of the hitherto found three orthorhombic (O-I, O-II, O-III), two monoclinic (M-I, M-II), and one trigonal variants (T) of weberites, see Ref. 69.

In the orthorhombic types O-I,II,III, the linking octahedra of M^{III} retain two trans-terminal F ligands. The M^{II} chains are therefore all parallel in subsequent layers, leading to the stacking sequence AAA. In the trigonal T-type weberite variant, all linking octahedra have *cis*-terminal ligands; three subsequent layers are rotated each by 120° leading to a stacking sequence ABCA. In the monoclinic M-I structure, only ABAB stacking is realized, and in the M-II type an

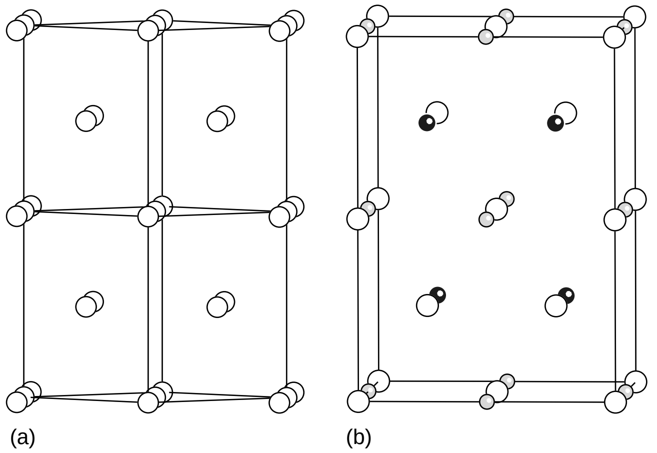

Figure 30 Cation distribution in (a) CaF_2 and (b) weberite O-I (white Na, grey M^{II}, black M^{III})

AABBAA variant is found. The Na ions keep the CN 8 of the parent CaF_2 type. However, depending on the stacking mode, the coordination changes partially from distorted cubic to hexagonal bipyramidal. From a magnetic point of view, weberites are interesting candidates for 1D magnetic behavior if the linking M^{3+} ions are diamagnetic elements. The structure of compounds $M^{II}Fe^{III}F_5\cdot 2H_2O$ (M^{II} = Mn, Fe, Zn)[142,143] where $[M^{III}F_6]$ octahedra form the trans-chains may be classified as inverse or antiweberite. $[M^{II}F_4(H_2O)_2]$ octahedra are in the linking positions with trans-aqua ligands oriented toward the empty Na positions of the orthorhombic weberite structure.

Pyrochlore- and $RbNiCrF_6$-Type Structures. Closely related to the weberite variants are pyrochlores $AA'M_2F_7$ (A = Na, A′ = Ca, Cd; M = Mg, Co, Ni, Cu, Zn). Here, all octahedra are equivalent and the cubic 3D network can be described as intersecting systems of Kagomé nets with planes parallel to the faces of a tetrahedron. Another approach is the description as cross-linked octahedral chains where at the crossing points typical tetrahedra of corner-connected octahedra are generated (Figure 31).

In the mineral pyrochlore $(NaCa)Nb_2O_6(OH,F)$, this framework is built by the $[Nb_2O_6]$ substructure. The seventh anion is in the center of the large pores and is tetrahedrally surrounded by the disordered Na^+ and Ca^{2+} ions, which keep cubic CN 8. In a fluoride pyrochlore like $NaCaNi_2F_7$, the complete [FNaCa] group can now be replaced by a single large alkali cation if at the same time the charge of the network is increased. The resulting cubic $RbNiCrF_6$ type is realized in a huge number of compounds $AM^{II}M^{III}F_6$.[33] Interestingly, even for a rather different size of M^{II} and M^{III} cations, normally statistical distribution over a single crystallographic site is observed. The alkali ion (K,Rb,Cs) adopts the unusually high CN 18. For smaller ions than Cs^+, off-center positions have been reported. The potassium compound may reversibly uptake water. Only if mixed-valence compounds like $NH_4Fe^{II}Fe^{III}F_6$ are prepared, charge ordering occurs, and an orthorhombic variant is formed with ordered M^{II} and M^{III} octahedral chains. Related ordered structures are found for special cations like Ag^{2+} and Pd^{2+}.

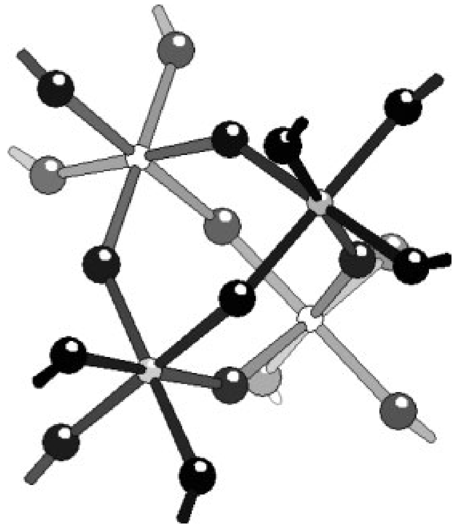

Figure 31 Tetrahedron of octahedra: basic unit of pyrochlore network

It is even possible to realize the neutral basic 3D pyrochlore framework $[M^{III}_2F_6]$ free of any further cations or anions in the cavities. As mentioned above, by special ‘soft chemistry’ preparative methods, metastable low-density forms of trifluorides with pyrochlore-related structures may be obtained: cubic pyr-FeF_3 and η-AlF_3 (see Table 1, Figure 7).

Fluorides with Hexagonal Tungsten Bronze-Type (HTB) Structure. This channel structure, well known from colored mixed-valent oxide phases A_xWO_3 and analogs, is found in fluorides as well. It can be seen as originating from condensation of (3,6)-nets (Figure 28(a)) over the terminal fluorine ligands. The resulting framework has the composition $[MF_3]$, as is also the case for pyrochlores and perovskites. The large hexagonal channels can be empty as in β-AlF_3[48] (Table 1, Figure 6) and its homologous Cr, V,[144] and Fe[145] compounds. Normally they are partially or completely filled by water as in $(H_2O)_{0.33}FeF_3$ or by alkali ions. In the latter case, the typical compositions $A_{0.25}$ MF_3 (or $A_{0.5}M_2F_6$) and A = K, NH_4, Rb, Cs, Tl; M = V, Cr, Fe, Nb (survey in Ref. 33) indicate mixed-valent compounds. The M positions can be occupied statistically by two different metals. In this way, unambiguous single-valence states are achieved like in $Cs_{0.4}Zn^{II}_{0.4}$ $Fe^{III}_{1.6}F_6$.[139] For this example, it could be shown by single-crystal X-ray investigation that in spite of hexagonal metrics the symmetry is in fact lower (here s.g. $P2_1$). The reason is that, like in the orthorhombic $(H_2O)_{0.33}FeF_3$ (s.g. Cmcm), the M–F–M bridges along the channel axis are strongly bent by 159° or even 150° in the latter. A derivative

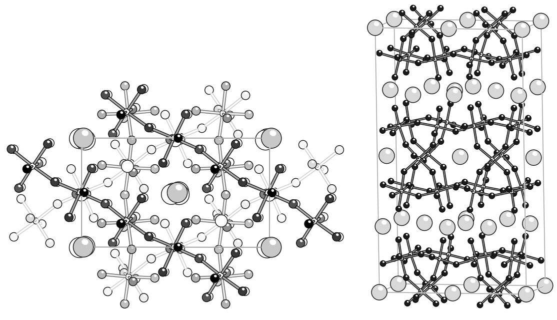
(a) (b)

Figure 32 (a) $KCaAl_2F_9$ structure projected along the pseudo-hexagonal channel axis. Ca medium white, K large grey spheres. (b) HTB slab structure of $Rb_2Cr_5F_{17}$

of this HTB-type structure was found in $KCaAl_2F_9$[146] and analogous phases (M = Cr, V, Fe). By ordered substitution of octahedral sites in the Kagomé net by Ca, trans-chains of $[AlF_6]$ octahedra are left similar to the $[M^{II}F_6]$ chains in weberites (Figure 29(a)). Such layers are stacked under rotations corresponding to a 6_1 axis to form a loose 3D framework (Figure 32).

An interesting layer structure has been found in $Rb_2Cr_5F_{17}$ (Figure 32(b)):[147] Here the 3D HTB structure has been formally cut into slabs *parallel* to the hexagonal channels not – as in $Cs_2NaAl_3F_{12}$ above – parallel to the Kagomé layers.

3.2.9 Structures Based on the (3,4,5)-Net (TTB Net)

Fluorides with Tetragonal Tungsten Bronze-Type (TTB) Structure. An alternative channel structure with the same composition $[MF_3]$ can be built based on a net of 3-, 4-, and 5-membered meshes of vertex-connected octahedra. This TTB-type structure is formed under similar conditions as the HTB-phases before. As two types of (smaller) channels can be occupied by alkali ions (mainly K) here, it is favored for higher alkali contents (e.g. TTB for $K_{1.2}Fe_2F_6$, but HTB for $K_{0.5}Fe_2F_6$). However, as has been shown in Table 1 (Figure 9) for κ-AlF_3, the structure can also be realized with empty channels. In addition, the structure has been found for some mixed-metal compounds $KM^{II}M^{III}F_6$. Interestingly, pyrochlore-related $KNiCrF_6$ has a high-pressure phase of this TTB structure (see Ref. 33).

TTB-Type Layer Structures. Like the (3,6)- or Kagomé-net in the $Cs_2NaAl_3F_{12}$-type, the (3,4,5)- or TTB net can be found quasi-isolated in the layer structure of β-$RbAlF_4$-type.[148] This structure (s.g. I4/mcm) is also adopted by β-NH_4AlF_4, the precursor for the κ-AlF_3 synthesis,[49] by $CsCoF_4$,[149] and by β-$CsAlF_4$.[150] In $Cs_4CoCr_4F_{18}$,[151] the vertices of the groups of three octahedra are capped by additional octahedra, alternatingly above and below the layer.

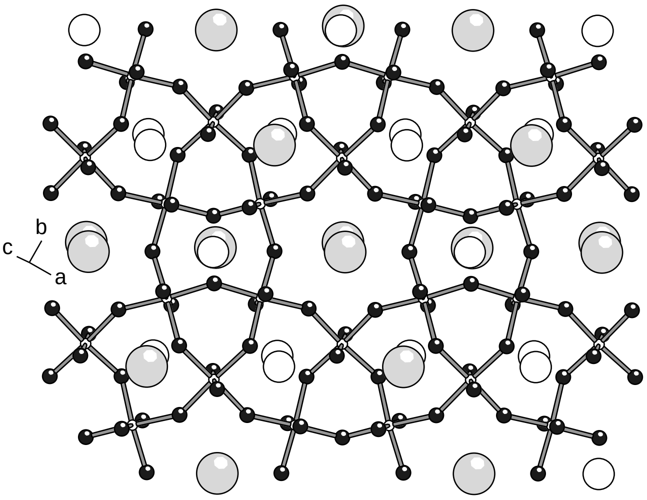

Figure 33 (3,4,6)-net of $CsBaCr_3F_{12}$ (Ba white, Cs grey spheres)

Layer Structure Based on a (3,4,6)-Net. An alternative way to form an $[MF_4]$ net of only vertex-sharing octahedra was found in $CsBaCr_3F_{12}$[152] (s.g. C2/c) (Figure 33).

3.2.10 Chain Structures with Triple-octahedral Units

Connection of triple-octahedral units to triple chains was encountered already in the structure of TiF_4 (Figure 13(a)). In ternary fluorides, corresponding anionic chains separated by the cations have been found in compounds $CsCrF_4$[153] and α-$CsAlF_4$,[154] as well as $KCrF_4$ in an angular variant.[155,156]

Another way of linking triple-octahedral units is realized in γ-$CsAlF_4$ (Figure 34), the structure of which can be deduced from the pyrochlore-type (Figure 31).

Complex bimetallic quinary compounds $Ba_2CaM^{II}M^{III}F_{14}$ and $Ba_7M^{II}M^{III}F_{34}$ with structures built from interconnected rings of four or eight octahedra, respectively, attracted interest because of their low-dimensional magnetic properties when appropriately substituted by transition metal ions (see recent survey in Refs. 157 and 158). The basic chain elements derived from the minerals usovite and jarlite are shown in Figure 35.

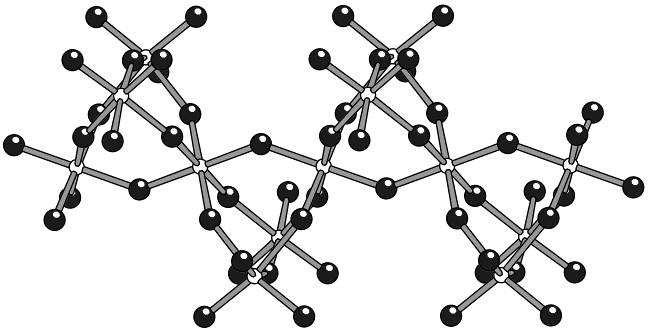

Figure 34 Chain of γ-$CsAlF_4$

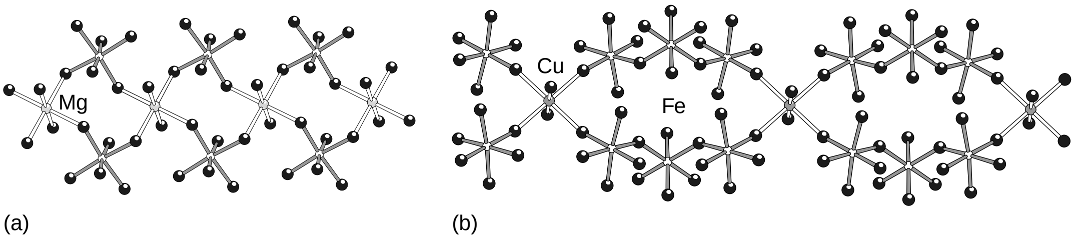

Figure 35 Chain sections of an usovite-type (a) and jarlite-type (b) structure

3.2.11 *Structures with [MF_6] Octahedra Sharing Common Edges*

The structure element of edge-sharing octahedra, encountered already in the rutile-type structure (Section 3.1, Figure 1(a)) and in AuF_5 (Figure 14(e)) is mainly found in some compounds $M^{II}M^{III}F_5$ and in a huge variety of Ba compounds. Structures $M^{II}M^{III}F_5$ have been mentioned already in Section 3.2.6 because the M^{III} cations are located in infinite *vertex-sharing* trans-chains. The M^{II} ions can also have octahedral coordination, and form infinite chains of *edge-sharing* octahedra alternatingly linked by common vertices to the M^{III} chains ($MnAlF_5$-type).

Quasi-isolated dimers [M_2F_{10}] of edge-sharing octahedra are aligned along the $c-$axis in the tetragonal compounds $BaTiF_5$,**159** $Sr_5Cr_3F_{19}$,**110** and an $SrAlF_5$ phase.**108** NH_4MnFeF_7**160** and $BaZnFeF_7$**161** are two different examples of 3D structures built from corner-sharing dimers (Figure 36).

In $BaMnFeF_7$, [Mn_2F_{10}] dimers are linked with [FeF_6] octahedra through vertices to form a dense 3D network. A typical structural unit is shown in Figure 37(a). A rich structural chemistry is reported for Ba-Cu^{II} and Ba-Zn^{II} compounds where the Ba:metal ratio can be varied in a large range. Here, edge-sharing octahedra are mostly condensed to linear trans-chains or kinked chains (or oligomeric chain sections) where alternatingly *trans*- and *skew*-edges are involved. An example for the latter mode is $Ba_2Cu_5F_{14}$ (Figure 37(b)) while pure quasi-isolated trans-chains are found in Na_2CuF_4 and Na_2CrF_4. Here, the Jahn−Teller effect leads to strongly asymmetrical bridges (Figure 37(c)).

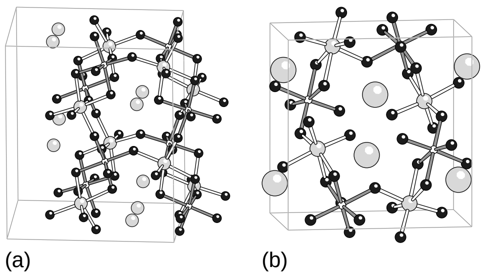

Figure 36 (a) Structure of NH_4MnFeF_6 (Mn white, Fe dark small, NH_4 large spheres); (b) Structure of $BaZnFeF_7$ (Zn white, Fe dark small, Ba large spheres)

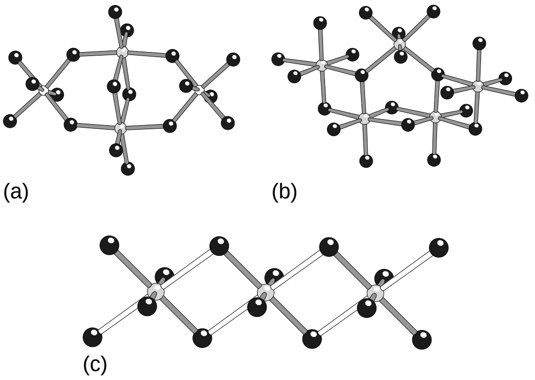

Figure 37 (a) Structural unit of Ba_2MnFeF_7 and (b) of $Ba_2Cu_5F_{14}$; (c) Distorted anionic chain of Na_2CuF_4 (elongated axes with open bonds)

3.2.12 *Structures with Oligonuclear Units*

Dimeric octahedral units sharing corners were reported for $CsBa_2Cr_2F_{11}$**123** and cyclamH_4[$Mn_2F_9(H_2O)_2$]-[$MnF_4(H_2O)_2$],**18** edge-sharing dimers for AuF_5,**62** $BaTiF_5$,**159** $SrAlF_5$,**108** and $Sr_5Cr_3F_{19}$,**110** as already mentioned. Four-membered rings of vertex-sharing octahedra are known from binary fluorides of NbF_5- or RuF_5-type (Section 3.1, Figure 14). In ternary compounds, corresponding units have been found in $Ba_3Al_2F_{12}$,**162** $Pb_3Al_2F_{12}$,**163** and $Pb_3Fe_2F_{12}$.**164** Tetrahedral 4-membered units [Al_4F_{18}] are formed with the dabcoH_2 cation (dabco = diaminobicyclooctane) in (dabcoH_2)$_2$(H_3O)[Al_4F_{18}] $\cdot 3H_2O$.**18** Even pentameric units of five vertex-sharing octahedra have been reported: a planar 'cross' in $Na_3Sr_4Al_5F_{26}$**165** (Figure 38(a)) and a tetrahedron-like unit in $Na_3Sr_4Cr_5F_{26}$**166** (Figure 38(b)). The central octahedron has in the first case the two terminal fluorine ligands in *trans*-, in the second in *cis*-positions: Using the voluminous guanidinium (guaH_2) dication, recently a heptameric anion was obtained**167** in which two tetrahedral four-octahedra units are

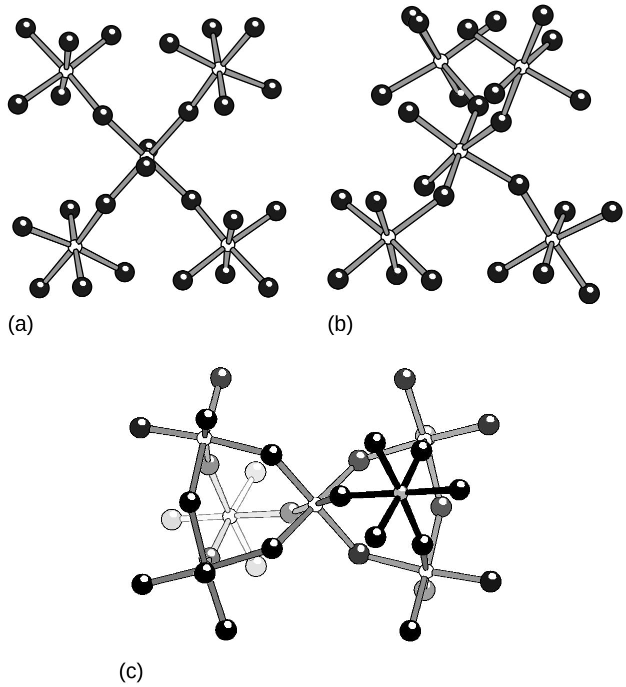

Figure 38 Pentameric units in (a) $Na_3Sr_4Al_5F_{26}$ and (b) $Na_3Sr_4Cr_5F_{26}$; (c) Heptameric anion in $[guaH_2][H_3O][Al_7F_{30}]$

condensed in the way of the pyrochlore-type structures (Figure 38(c)).

3.2.13 Structures with Unusual Coordination Numbers

Tetrahedral Coordination. Tetrahedral fluorine coordination is observed only for a few small cations, including some Li compounds as mentioned in Section 3.1 already: The only fluoride spinel Li_2NiF_4 has the inverse structure with half of the Li in octahedral and half in tetrahedral coordination.[168] In fluoride garnets $Li_3Na_3M_2F_{12}$ (M = Al, Ga, In, Sc, Ti, V, Cr, Mn, Fe, Co, Ni, Rh), Li has tetrahedral coordination, M octahedral, and Na CN 8 (see Ref. 33). In compounds $LiBaMF_6$[33] (M = Al, Ga, Ti, V, Cr, Fe, Co), $[LiF_4]$ tetrahedra are linked to a framework with $[MF_6]$ octahedra, and in β-$Li_3M^{III}F_6$[81,82] phases (see Section 3.2.3) the Li cations are located in edge-sharing double-tetrahedra. In compounds $LiMF_4$ with M = Tl, Bi or a rare-earth metal, the scheelite-type ($CaWO_4$) structure is observed with tetrahedral coordination for Li and CN 8 for M. However, there are also scheelites $CaZnF_4$ and $SrZnF_4$ with Zn in CN 4.[33]

There are many compounds with $BeF_4{}^{2-}$, $Be_2F_7{}^{3-}$, and $BF_4{}^{-}$ anions, the structural chemistry of which is less surprising. However, there are some analogies to more complex silicate structures in fluoroberyllates: In $CsBeF_3$[169] 'zweier single chains' (nomenclature after Liebau[170]) are observed, in the cyclotrifluoroberyllate $KZnBe_3F_9$[171] a benitoite-like 'dreier single ring', and in the phyllofluoroberyllate $RbBe_2F_5$[172] a layer structure built from 6-membered rings ('zweier single layer'). These examples illustrate how fluoroberyllates may be used successfully as (lower melting) models for silicate chemistry, as already proposed by Goldschmidt in the 1920s.

The occurrence of a tetrahedral $[AlF_4]^-$ anion in solid $[(CH_3)_4N]AlF_4$ was deduced early from infrared spectra.[173] However, it was confirmed by single-crystal X-ray analysis only in 1993 for this compound[174] and analogs with cations 1,8-bis(dimethylaminonaphthalene)H or collidineH[175] and, recently, $[(C_6H_5)_4P]^+$.[176] Interestingly, in $[(CH_3)_4N][(i\text{-}Bu)_2AlF_2]$ even a mixed organic/fluoride coordination was found[176] with remarkable elongation of the Al–F bond by 0.06 Å. The biological activity of 'tetrafluoroaluminates' and their significance for catalytic purposes have been reviewed recently.[177]

Square-planar and Fivefold Coordination. In most fluoro compounds of the d^9-ion Cu^{2+}, elongated octahedral coordination is observed. However, in a few cases, the coordination geometry is square planar or square pyramidal (*see also Square Pyramidal*). All three coordination types are realized in the structure of $CsCu_2F_5$.[178] Planar CN 4 is frequently found in fluorides of Pd^{II} (d^8) as mentioned, for example, in Section 3.1. Other examples are fluorides of Cr^{II}, Ag^{II}, Ag^{III}, and Au^{III}. Several compounds AMF_4, such as $CaCuF_4$ or $KAuF_4$, crystallize in the $KBrF_4$-type structure (see Ref. 33). The structural chemistry of fluorides of the noble metals, especially in higher oxidation states at which this coordination type is frequently found, is reviewed in Refs. 179–181.

7- and 8-Coordination. While all bi- and tervalent first-row transition metals have octahedral coordination, exceptional pentagonal bipyramidal CN is observed for Mn^{II} in $MnCrF_5$.[182] Partial 8-coordination for Mn^{II} is even found in $BaMnGaF_7$.[183] While in many compounds $A^{I}_{3}M^{IV}F_7$ and $A^{II}_{2}M^{III}F_7$, M has CN 6 and 'independent' fluoride ions are present bound only to the A ions, CN 7 is actually observed in some cases, for example, in K_2NbF_7.[33,184] Examples of edge-sharing chains of $[ZrF_7]$ and $[ZrF_8]$ polyhedra are reported for fluorozirconates with amino-guanidinium(1+)[185] and (2+)[186] cations, respectively. Coordination numbers of 7–9 are normal for some other fluorozirconates and – hafnates and for the numerous rare-earth fluoro compounds known at the present time.

3.2.14 Hybrid and Mixed-ligand Compounds

Though the term 'hybrid' is not sharply defined and is a matter of taste, it is used here to summarize compounds containing besides an inorganic part – here a fluoride species – an organic component. This may be an organic cation, a template molecule, or an organic ligand. As there is a large region of overlap between both classes of compounds, *mixed-ligand compounds* are mentioned here at the same time, even if no organic part is included.

Compounds with Organic Cations. As mentioned in Sections 3.2.12 and 3.2.13, unusual structural units like oligomeric anions could be obtained by using organic counter cations, normally protonated amines, which can vary widely in size and shape. The most frequently used cations are tma (tetramethylammonium), enH_2 (ethylenediammonium(2+)), and protonated higher diamines $H_3N\text{-}(CH_2)_n\text{-}NH_3$, pyH (pyridinium), $pipzH_2$ (piperazinium(2+)), $dabcoH_2$ (1,4-diazabicyclo[2.2.2]octane), $cyclamH_4$ (1,4,8,11-tetraaza cyclotetradecane), guaH (guanidinium), and derivatives of it. The preparation is performed in aqueous HF, often under hydrothermal conditions (cf. Section 2.4). The result is strongly dependent on the conditions, that is, concentrations, pH, temperature and pressure.

In systems containing no anion other than fluoride, mixed aqua-fluorometalates mainly with $[MF_5(H_2O)]^{2-}$ and $[MF_4(H_2O)_2]^-$ are frequently formed. Therefore the possibility of H-bond formation plays an important role (*see* ***Hydrogen Bonding & Dihydrogen Bonding***). The most investigated systems contain Al^{III}, Fe^{III}, Mn^{III} (surveys in Refs. 18, 113), and Zr^{IV}.[185,186] Aluminium compounds are of interest as possible precursors for the generation of catalytically active forms of AlF_3 (cf. Section 3.1) by thermal decomposition. Iron and manganese compounds are of interest because of their low-dimensional magnetic properties (see Section 4.1).

Mixed-Ligand Systems

Fluoride Phosphates (see ***Phosphates: Solid-state Chemistry****).* Simple metal fluoride phosphates like $M_2(PO_4)F$ (M = Mn, Fe, Cu) and alkali fluoride phosphates like $KFe(PO_4)F$ have been known since a long time. A modern development in the structural chemistry of fluoride phosphates (and phosphates) is the use of (mostly protonated) organic amines as templates to construct new structural architectures. As an example for the construction of microporous frameworks (*see* ***Porous Inorganic Materials***), the Ga compound $(C_6H_{14}N)_{1.5}(H_3O)_{0.5}[Ga_4F_2(PO_4)_4]\cdot 0.5H_2O$ ('ULM-16') is shown in Figure 39. The framework is built by Ga polyhedra of CN 6, 5, and 4 and orthophosphate anions. The large channels containing the cyclohexylammonium groups have a diameter of 10 × 10 Å. A survey on related fluoride phosphate microporous systems is given in Refs. 19, 187.

Several new fluoride phosphates with chain or layer structures have been reported for the Jahn–Teller ion Mn^{3+}.[113]

Other Mixed-Ligand Systems. From the smaller number of *sulfato-fluorometalates*, two recent examples are given. Compounds $A^I_2MnF_3(SO_4)$ have chain structures with antiferrodistortive Jahn–Teller ordering.[188] The mixed-valence iron compound $[HN(CH_2)_6\ NH][H_3O][Fe^{III}Fe^{II}_2F_6(SO_4)_2]$[189] exhibits a perfect $[FeF_3]$-Kagomé-net structure (similar to Figure 28) with 3-membered rings capped by sulfate units. With imidazole cations, *oxalato-fluoro* compounds of Mn^{III} and Fe^{III} could be prepared. While the manganese compound[113] has isolated $[MnF_2ox(H_2O)_2]^-$ anions, the iron compound $(imidH)_2[Fe_2oxF_6]$[190] has a ladder structure with low-dimensional magnetic properties (Section 4.1). *Fluoride carbonates* are generally built from alternating planar carbonate layers and fluoride containing layers (see structure-systematical survey in Ref. 191).

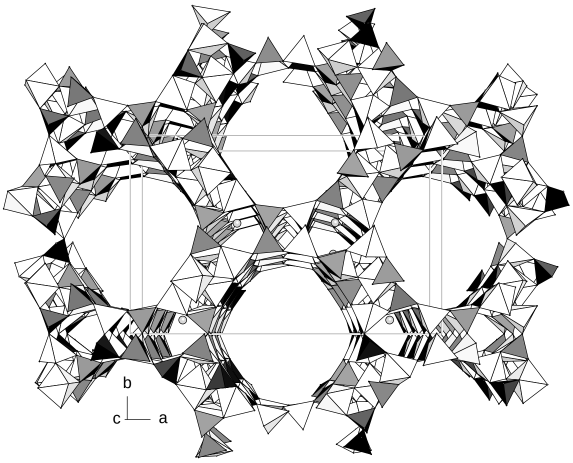

Figure 39 Open framework structure of the gallium fluoride phosphate ULM-16 (Ga polyhedra bright, PO_4 dark, amine molecules in the channels omitted)

In most fluorides with organic nitrogen bases, these are protonated and enter the structure as counter cations. However, the example of $4,4'\text{-}bipyMnF_3$ (bipy = bipyridine) shows that it is also possible to construct hybrid coordination polymers with the amine and fluoride as bridging ligands (Figure 40). The structure is modulated at low temperature and has 1D magnetic properties.[16]

Alternating pyridine and fluorine ligands are found in the chain structure $[\text{-}Cu(py)_4\text{-}F\text{-}TiF_4\text{-}F\text{-}]\cdot 3H_2O$[192] as

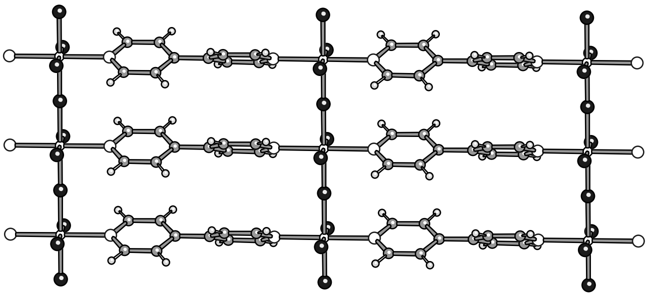

Figure 40 Section of the layer structure of $4,4'\text{-}bipyMnF_3$

well as in similar Zr, Nb, and Ta compounds. In mixed-ligand oligomers like the tetramer $[Zr_4F_{12}Cp^*{}_4]$[193] or finally the In/Mg cluster with mesityl and fluorine ligands $[(mes)InF_{10}MgF_2]\cdot 5toluene$,[194] the seamless transition from inorganic solids toward organometallics is completed (*see* ***Polynuclear Organometallic Cluster Complexes***).

4 PHYSICAL PROPERTIES

The physical properties of fluorides are determined mainly by the high ionicity of the metal–fluorine bond and the low polarizability of the fluoride ion (*see* ***Dielectric Polarizabilities of Oxides & Fluorides***). Therefore, magnetism based on superexchange interactions and high optical transparency in a wide spectral range are the most interesting properties. They define, together with the anionic conductivity in fluorite-like compounds, the main area of possible applications of fluorides in material science or industry.

4.1 Magnetic Properties

Exchange interactions between magnetic ions over bridging ligands (here over p orbitals of fluorine) are described by the superexchange mechanism following the rules of Anderson, Goodenough, and Kanamori[195] (*see* ***Magnetism of Extended Arrays in Inorganic Solids***; ***Magnetism of Transition Metal Ions***). In systems with localized electrons, the sign (positive for ferromagnetic, negative for antiferromagnetic coupling) and the strength of the exchange energy J depends on the state of the involved d orbitals at the metal centers (filled, half-filled, empty) and the bridge angle M–F–M (called β). In the common case of 'symmetrical' exchange (same metal, same orbital occupation), at $\beta = 180°$ *antiferromagnetic* properties are expected, at $\beta = 90°$ (in edge- or face-sharing octahedra) *ferromagnetic* coupling is expected.

1D Magnetic Systems. The experimental determination of exchange energies J can be done by fitting a theoretical model to the experimental data, namely, the temperature-dependent magnetic susceptibilities. The theoretical approach can be best applied to 1D systems. Fluorides with chain structures, where the chain geometry and the magnetic metal ion can be varied over a wide range, are textbook examples therefore for the confirmation of theoretical concepts. $CsNiF_3$ with a chain of face-sharing octahedra (Section 3.2.4) is a classical example for a 1D ferromagnet.[196] Antiferromagnetic fluoromanganates(III) A_2MnF_5 with trans-chain structures of varying bridge angles β (Section 3.2.6) provide the best experimental proof that the exchange energy J follows the orbital overlap:[114,197] Their values fit equation (13) very well.

$$\frac{J}{k} = 18\cos^2\beta[K] \qquad (k = \text{Boltzmann constant}) \qquad (13)$$

In addition, in these and related systems, nonlinear magnetic excitations (solitons) have been observed.[198,199]

Special 1D systems, chains made of rings, are fluorides with jarlite or usovite structures (Section 3.2.10). Homometallic or bimetallic chains with various combinations of spins (or nonmagnetic metals) allow the study of 1D antiferromagnets, 1D ferrimagnets, or linear trimers.[157,158]

2D Magnetic Systems. Fluorides with $TlAlF_4$-related layer structures (Section 3.2.5) normally have antiferromagnetic properties, when the exchange interactions along the M–F–M bridges are 'symmetrical', for example, $e_g^1–e_g^1$ in compounds $AFe^{III}F_4$. The only exception in homometallic compounds are Jahn–Teller systems like $A^I_2Cu^{II}F_4$, $A^I_2Ag^{II}F_4$, and $A^IMn^{III}F_4$ with antiferrodistortive ordering where 'asymmetrical' exchange $e_g^2–e_g^1$ or $e_g^1–e_g^0$, respectively, becomes possible. If the bridge angle β within the layers is higher than about 150°, *ferromagnetic* behavior is observed.[197,200,201]

3D Systems. Similar 'asymmetrical' ferromagnetic exchange conditions can be realized in ordered bimetallic systems, for example in compounds $M^{II}M^{IV}F_6$, by choosing appropriate cations. In most other cases, antiferromagnetic properties are observed or ferrimagnetism when two antiferromagnetically coupled sublattices do not compensate their moments. The sequence of strengths and sign of interaction can be understood when looking at the charge and the electron configurations of the involved magnetic ions and the dimensionality of the interaction.[202]

Systems with Triangular Units. In structures with layers of Kagomé- (HTB-) or TTB-type like pyrochlores or weberites (Sections 3.2.8–9) or chain structures with triple-octahedral units (Section 3.2.10), the magnetic exchange interactions within a triangular unit can be 'frustrated', that is, not all interactions can be satisfied at the same time in a 3D order (surveys in Refs. 203, 204). Different types of ordering of the magnetic moments can be encountered: a) a 'star' structure (120° angle between three moments or 109.5° angle in a tetrahedral spin array); b) orthogonal sublattices; c) colinear spin arrangement under breaking of one interaction; d) colinear array of 2/3 of the spins, one remaining disordered ('spin fou'); e) spin glass behavior.

4.2 Optical Properties

The main reasons for the interest in fluorides as optical materials are a) the high *transparency* especially in the infrared region, b) the *wide band gap* allowing for special luminescence properties (*see* ***Luminescence***), especially emission from high-energy levels, c) special *ligand-field properties* in rare-earth fluorides with high CN, and d) *low phonon energy* allowing for laser applications in the infrared.

Several fluoride systems have therefore found technical applications. Thus, large single crystals of CaF_2 are used, for instance, for optics in lithographic processes of the semiconductor industry. Crystals of $LiYF_4$ doped with rare earths like Nd, Dy, Er, Ho are used as laser sources or amplifiers. Tunable laser emissions were obtained in V^{2+} doped MgF_2 or $KMgF_3$.**[205]** For applications in glass fiber optics, fluoride glasses (*see* ***Noncrystalline Solids***) are used, mainly based on ZrF_4, BaF_2, InF_3, GaF_3, AlF_3, ZnF_2, and CdF_2.**[206]** Their refractive index n_D is between 1.5 and 1.65, and the transmission starts at about 250 nm in the UV and reaches up to 10 µm in the IR. They find applications as passive optical devices, as glass fibers, glass fiber lasers, glass channel waveguides, and so on.

Photostimulable phosphors based on Eu^{2+} doped BaBrF are used in area detector systems in X-ray crystallography and medicine.**[205]**

4.3 Electrical Conductivity

Electronic Conductivity. Fluorides usually are good insulators owing to the wide band gap of more than 6 eV in most compounds. In some cases it is possible, however, to obtain n-type semiconducting properties by doping, for example, in $CdF_2(Y)$.**[207]** Exceptional metallic conductivity is observed in the metal-rich compound Ag_2F,**[208]** even superconductivity in $Hg_{3-\delta}AsF_6$**[209]** – despite the presence of fluoride. Mixed-valence silver fluorides have been recently discussed as possible candidates for superconductivity.**[210]**

Ionic Conductivity (see ***Ionic Conductors****).* Fluoride anionic conductivity is observed mainly in derivatives of fluorite (CaF_2) and tysonite (LaF_3). If CaF_2 is doped by a tervalent rare-earth metal ion, the additional fluoride ions are positioned in interstitials where they become mobile by a hopping mechanism.

5 RELATED ARTICLES

Chalcogenides: Solid-state Chemistry; Chlorine, Bromine, Iodine, & Astatine: Inorganic Chemistry; Coordination Numbers & Geometries; Cyanide Complexes of the Transition Metals; Electronic Structure of Solids; Fluorine: Inorganic Chemistry; Halides: Solid-state Chemistry; Hydrides: Solid State Transition Metal Complexes; Hydrogen Bonding & Dihydrogen Bonding; Magnetism of Extended Arrays in Inorganic Solids; Noble Gases: Inorganic Chemistry; Oxides: Solid-state Chemistry; Structure & Property Maps for Inorganic Solids.

6 REFERENCES

1. R. D. Shannon, *Acta Crystallogr.*, 1976, **A32**, 751.
2. J. J. Berzelius, *Ann. Phys.*, 1824(St.5), **77**(St.1), 1.
3. S. V. Náray-Szabó and K. Sasvári, *Z. Kristallogr.*, 1938, **99**, 27.
4. J. Grannec and L. Lozano, in ‘Inorganic Solid Fluorides’, ed. P. Hagenmuller, Academic Press, Orlando, 1985, Chap. 2, p. 18.
5. K. Lutar, H. Borrmann, and M. Leblanc, in ‘Advanced Inorganic Fluorides’, eds. T. Nakajima, B. Žemva, and A. Tressaud, Elsevier, Lausanne, 2000, Chap. 2, p. 5.
6. H. Goldwhite, in ‘Fluorine, The First Hundred Years’, eds. R. E. Banks, D. W. A. Sharp, and J. C. Tatlow, Elsevier Sequoia, Lausanne, 1986, Chap. 5, p. 109.
7. B. Peschel and D. Babel, *Z. Anorg. Allg. Chem.*, 1997, **623**, 1614.
8. W. Massa, *Inorg. Nucl. Chem. Lett.*, 1977, **13**, 253.
9. A. Tressaud, F. Langlais, G. Demazeau, and P. Hagenmuller, *Mater. Res. Bull.*, 1982, **14**, 1147.
10. J. L. Fourquet, A. Le Bail, H. Duroy, and M. C. Moron, *Eur. J. Solid State Inorg. Chem.*, 1989, **26**, 435.
11. U. Bentrup and D.-H. Menz, *Z. Anorg. Allg. Chem.*, 1990, **591**, 230.
12. A. Cousson, M. Pages, J. C. Cousseins, and A. Vedrine, *J. Cryst. Growth*, 1977, **40**, 157.
13. R. D. Peacock, *J. Chem. Soc.*, 1957, 4684.
14. G. Corbel, G. Courbion, F. Le Berre, M. Leblanc, J. M. Le Meins, V. Maisonneuve, and N. Mercier, *J. Fluorine Chem.*, 2001, **107**, 193.
15. P. Nuñez, C. Elias, J. Fuentes, X. Solans, A. Tressaud, M. C. Marco de Lucas, and F. Rodriguez, *J. Chem. Soc. Dalton Trans.*, 1997, 4335.
16. J. Darriet, W. Massa, J. Pebler, and R. Stief, *Solid State Sci.*, 2002, **4**, 1499.
17. R. I. Walton, F. Millange, A. Le Bail, T. Loiseau, C. Serre, D. O’Hare, and G. Férey, *Chem. Commun.*, 2000, **3**, 203.
18. U. Bentrup, M. Feist, and E. Kemnitz, *Prog. Solid State Chem.*, 1999, **27**, 75.
19. G. Férey, T. Loiseau, and D. Riou, in ‘Advanced Inorganic Fluorides’, eds. T. Nakajima, B. Žemva, and A. Tressaud, Elsevier, Lausanne, 2000, Chap. 7, p. 209.
20. H. M. Haendler, F. A. Johnson, and D. S. Crocket, *J. Am. Chem. Soc.*, 1958, **80**, 2662.
21. E. Kemnitz, U. Groß, St. Rüdiger, and Ch. S. Shekar, *Angew. Chem., Int. Ed.*, 2003, **42**, 4251.
22. R. de Pape and G. Férey, *Mater. Res. Bull.*, 1986, **21**, 971.

23. S. P. Thanh, F. Gaslain, M. Leblanc, and V. Maisonneuve, *J. Fluorine Chem.*, 2000, **101**, 161.
24. C. Shen, L. C. Chacón, N. Rosov, S. H. Elder, J. C. Allman, and N. Bartlett, *C. R. Acad. Sci. Paris*, 1999, **2**, Serie II, 557.
25. G. M. Lucier, J. M. Whalen, and N. Bartlett, *J. Fluorine Chem.*, 1998, **89**, 101.
26. B. G. Müller, *Eur. J. Solid State Inorg. Chem.*, 1997, **34**, 627.
27. J. Grannec, P. Sorbe, and J. Portier, *C. R. Hebd. Séances Acad. Sci.*, 1976, **283**, 441.
28. O. Graudejus, O. Krämer, B. G. Müller, 11th European Symposium on Fluorine Chemistry, Bled 1995, Abstr., 179.
29. O. Krämer and B. G. Müller, *Z. Anorg. Allg. Chem.*, 1995, **621**, 1969.
30. E. Herdtweck, W. Massa, and D. Babel, *Z. Anorg. Allg. Chem.*, 1986, **539**, 87.
31. U. Müller, 'Inorganic Structural Chemistry', Wiley, Chichester, 1993, p. 44 ff.
32. D. Babel, *Struct. Bonding*, 1967, **3**, 1.
33. D. Babel and A. Tressaud, in 'Inorganic Solid Fluorides', ed. P. Hagenmuller, Academic Press, Orlando, 1985, Chap. 3, p. 78.
34. W. Massa and D. Babel, *Chem. Rev.*, 1988, **88**, 275.
35. W. Pies, and A. Weiss, eds, 'Landolt-Börnstein Tables, New Series', Springer-Verlag, Berlin, Heidelberg, New York, 1973, III, Vol. 7 a,g.
36. T. Nakajima, B. Žemva, A. Tressaud, 'Advanced Inorganic Fluorides', Elsevier, Lausanne 2000.
37. A. Jesih, K. Lutar, B. Žemva, B. Bachmann, S. Becker, B. G. Müller, and R. Hoppe, *Z. Anorg. Allg. Chem.*, 1990, **588**, 77.
38. B. Bachmann and B. G. Müller, *Z. Anorg. Allg. Chem.*, 1993, **619**, 387.
39. A. Tressaud, J. L. Soubeyroux, H. Touhara, G. Demazeau, and F. Langlais, *Mater. Res. Bull.*, 1981, **16**, 207.
40. B. G. Müller, *J. Fluorine Chem.*, 1982, **20**, 291.
41. U. Müller, 'Inorganic Structural Chemistry', Wiley, Chichester, 1993, p. 162.
42. F. Schrötter and B. G. Müller, *Z. Anorg. Allg. Chem.*, 1993, **619**, 1426.
43. E. Kemnitz and D. H. Menz, *Prog. Solid State Chem.*, 1998, **26**, 97.
44. E. Kemnitz and J. M. Winfield, in 'Advanced Inorganic Fluorides', eds. T. Nakajima, B. Žemva, and A. Tressaud, Elsevier, Lausanne, 2000, Chap. 12, p. 367.
45. C. Alonso, A. Morato, F. Medina, Y. Cesteros, P. Salagre, and J. E. Sueiras, *Appl. Catal. B: Environ.*, 2003, **40**, 259.
46. R. Hoppe and D. Kissel, *J. Fluorine Chem.*, 1984, **24**, 327.
47. P. Daniel, A. Bulou, M. Rousseau, J. Nouet, J. L. Fourquet, M. Leblanc, and R. Burriel, *J. Phys.: Condens. Matter*, 1990, **2**, 5663.
48. A. le Bail, C. Jacoboni, M. Leblanc, R. de Pape, H. Duroy, and J. L. Fourquet, *J. Solid State Chem.*, 1988, **77**, 96.
49. N. Herron, D. L. Thorn, R. L. Harlow, G. A. Jones, J. B. Parise, J. A. Fernandez-Baca, and T. Vogt, *Chem. Mater.*, 1995, **7**, 75.
50. A. le Bail, J. L. Fourquet, and U. Bentrup, *J. Solid State Chem.*, 1992, **100**, 151.
51. B. Žemva, K. Lutar, A. Jesih, W. J. Casteel Jr, A. P. Wilkinson, D. E. Cox, R. B. von Dreele, H. Borrmann, and N. Bartlett, *J. Am. Chem. Soc.*, 1991, **113**, 4192.
52. O. Greis and J. M. Haschke, *Rare Earth Fluorides, Handb. Phys. Chem. Rare Earths*, 1982, **5**, 387.
53. E. Benner and B. G. Müller, *Z. Anorg. Allg. Chem.*, 1990, **588**, 33.
54. R. Schmidt and B. G. Müller, *Z. Anorg. Allg. Chem.*, 1999, **625**, 605.
55. H. Bialowons, M. Müller, and B. G. Müller, *Z. Anorg. Allg. Chem.*, 1995, **621**, 1227.
56. P. Benkić, Z. Mazej, and B. Žemva, *Angew. Chem., Int. Ed.*, 2002, **41**, 1398.
57. B. G. Müller and M. Serafin, *Z. Naturforsch.*, 1987, **42b**, 1102.
58. K. O. Christe, *Inorg. Chem.*, 1986, **25**, 3721.
59. P. G. Eller, A. C. Larson, J. R. Peterson, D. D. Ensor, and J. P. Young, *Inorg. Chim. Acta*, 1979, **37**, 129.
60. A. J. Edwards, *J. Chem. Soc.*, 1964, 3714.
61. J. Darriet, J. L. Soubeyroux, H. Touhara, A. Tressaud, and P. Hagenmuller, *Mater. Res. Bull.*, 1982, **17**, 315.
62. I.-C. Hwang and K. Seppelt, *Angew. Chem., Int. Ed.*, 2001, **40**, 3690.
63. J. C. Taylor and A. B. Waugh, *J. Solid State Chem.*, 1980, **35**, 137.
64. K. H. Wandner and R. Hoppe, *Z. Anorg. Allg. Chem.*, 1987, **546**, 113.
65. P. Lacorre, J. Pannetier, R. Averdunk, R. Hoppe, and G. Férey, *J. Solid State Chem.*, 1989, **79**, 1.
66. M. Molinier, W. Massa, S. Khairoun, A. Tressaud, and J. L. Soubeyroux, *Z. Naturforsch.*, 1991, **46b**, 1669.
67. C. R. A. Catlow, 'Inorganic Solid Fluorides', ed P. Hagenmuller, Academic Press, Orlando 1985, Chap. 5, p. 259; J. M. Réau, J. Grannec, 'Inorganic Solid Fluorides', ed. P. P. Hagenmuller, Academic Press, Orlando 1985, Chap. 12, p. 423.
68. M. Takashima, in 'Advanced Inorganic Fluorides', eds. T. Nakajima, B. Žemva, and A. Tressaud, Elsevier, Lausanne, 2000, Chap. 6, p. 175.
69. O. Yakubovich, V. Urusov, G. Frenzen, W. Massa und, and D. Babel, *Z. Anorg. Allg. Chem.*, 1993, **619**, 1909.
70. P. Dahlke, B. Peschel, and D. Babel, *Z. Anorg. Allg. Chem.*, 1998, **624**, 1003.
71. D. Reinen and F. Steffens, *Z. Anorg. Allg. Chem.*, 1978, **441**, 63.

72. R. Schmidt, M. Kraus, and B. G. Müller, *Z. Anorg. Allg. Chem.*, 2001, **627**, 2344.
73. R. Fischer and B. G. Müller, *Z. Anorg. Allg. Chem.*, 2001, **627**, 445.
74. I. N. Flerov, M. V. Gorev, K. S. Alexandrov, A. Tressaud, J. Grannec, and M. Couzi, *Mater. Sci. Eng.*, 1998, **R24**, 81.
75. P. Dahlke and D. Babel, *Z. Anorg. Allg. Chem.*, 1994, **620**, 1686.
76. S. D. Kirik, J. N. Zaitseva, I. S. Yakimov, and N. N. Golovnev, *Acta Crystallogr.*, 2002, **C58**, i159.
77. H. X. Yang, S. Ghose, and D. M. Hatch, *Phys. Chem. Miner.*, 1993, **19**, 528.
78. S. E. Eklund, J. Q. Chambers, G. Mamantov, J. Diminnie, and C. E. Barnes, *Inorg. Chem.*, 2001, **40**, 715.
79. N. Böhmer and G. Meyer, *Z. Anorg. Allg. Chem.*, 2001, **627**, 1248.
80. J. H. Burns, A. C. Tennissen, and G. D. Brunton, *Acta Crystallogr.*, 1968, **B24**, 225.
81. W. Massa, *Z. Kristallogr.*, 1980, **153**, 201.
82. A. K. Tyagi and J. Koehler, *Mater. Res. Bull.*, 2000, **35**, 135.
83. G. Frenzen, S. Kummer, W. Massa und, and D. Babel, *Z. Anorg. Allg. Chem.*, 1987, **553**, 75.
84. R. Fischer and B. G. Müller, *Z. Anorg. Allg. Chem.*, 2002, **628**, 2592.
85. M. Bork and R. Hoppe, *Z. Anorg. Allg. Chem.*, 1996, **622**, 417.
86. R. E. Schmidt, M. Welsch, S. Kummer-Dörner, and D. Babel, *Z. Anorg. Allg. Chem.*, 1999, **625**, 637.
87. J. Graulich, St. Drüeke, and D. Babel, *Z. Anorg. Allg. Chem.*, 1998, **624**, 1460.
88. J. M. Dance, J. Mur, J. Darriet, P. Hagenmuller, W. Massa, S. Kummer, and D. Babel, *J. Solid State Chem.*, 1986, **63**, 446.
89. A. de Kozak, Y. Mary, P. Gredin, J. Renaudin, G. Férey, and D. Babel, *Eur. J. Solid State Inorg. Chem.*, 1994, **31**, 115.
90. L. Kiriazis and R. Mattes, *Z. Anorg. Allg. Chem.*, 1991, **593**, 90.
91. K. W. Krämer, R. Schenker, J. Hauser, H. Weihe, H. U. Güdel, and H.-B. Bürgi, *Z. Anorg. Allg. Chem.*, 2001, 2511.
92. R. E. Schmidt and D. Babel, *Z. Anorg. Allg. Chem.*, 1985, **529**, 118.
93. R. E. Schmidt, J. Pebler, and D. Babel, *Eur. J. Solid State Inorg. Chem.*, 1992, **29**, 679.
94. R. E. Schmidt and D. Babel, *Z. Anorg. Allg. Chem.*, 1984, **516**, 187.
95. A. Bulou and J. Nouet, *J. Phys. C*, 1987, **20**, 2885.
96. D. Babel, F. Wall, and G. Heger, *Z. Naturforsch.*, 1974, **29b**, 139.
97. A. Desert, A. Bulou, M. Leblanc, and J. Nouet, *J. Phys.: Condens. Matter*, 1998, **10**, 9067.
98. M. Molinier and W. Massa, *Z. Naturforsch.*, 1992, **47b**, 783.
99. K. H. Wandner and R. Hoppe, *Z. Anorg. Allg. Chem.*, 1987, **551**, 123.
100. S. Carlson and R. Norrestam, *Z. Kristallogr.*, 1995, **210**, 489.
101. C. de Nadai, A. Demourgues, P. Gravereau, and J. Grannec, *J. Solid State Chem.*, 1999, **148**, 242.
102. K. K. Wu and I. D. Brown, *Mater. Res. Bull.*, 1973, **8**, 593.
103. J. Graulich, W. Massa, and D. Babel, *Z. Anorg. Allg. Chem.*, 2003, **629**, 365.
104. J. L. Fourquet and H. Duroy, *Eur. J. Solid State Inorg. Chem.*, 1989, **26**, 413.
105. W. Massa and V. Burk, *Z. Anorg. Allg. Chem.*, 1984, **516**, 119.
106. R. von der Mühll, S. Anderson, and J. Galy, *Acta Crystallogr.*, 1971, **B27**, 2345.
107. M. Welsch, H. Holler, and D. Babel, *Z. Anorg. Allg. Chem.*, 1989, **575**, 171.
108. F. Kubel, *Z. Anorg. Allg. Chem.*, 1998, **624**, 1481.
109. J. Graulich and D. Babel, *Z. Anorg. Allg. Chem.*, 1991, **597**, 51.
110. P. Dahlke, J. Graulich, M. Welsch, J. Pebler, and D. Babel, *Z. Anorg. Allg. Chem.*, 2000, **626**, 1255.
111. S. C. Abrahams, J. Albertsson, C. Svensson, and J. Ravez, *Acta Crystallogr.*, 1990, **B46**, 497.
112. S. C. Abrahams, J. Ravez, H. Ritter, and J. Ihringer, *Acta Crystallogr.*, 2003, **B59**, 557.
113. W. Massa, *Rev. Inorg. Chem.*, 1999, **19**, 117.
114. J. Pebler, W. Massa und, H. Lass, and B. Ziegler, *J. Solid State Chem.*, 1987, **71**, 87.
115. F. Hahn and W. Massa, *Z. Naturforsch.*, 1990, **45b**, 1341.
116. J. R. Günter, J.-P. Matthieu, and H. R. Oswald, *Helv. Chim. Acta*, 1978, **61**, 328.
117. J. L. Fourquet, B. Boulard, and F. Plet, *J. Solid State Chem.*, 1989, **81**, 35.
118. J. L. Fourquet, F. Plet, and R. de Pape, *Rev. Chim. Miner.*, 1981, **18**, 19.
119. E. Herdtweck, J. Graulich, and D. Babel, *Z. Naturforsch.*, 1990, **45b**, 161.
120. C. Brosset, *Z. Anorg. Allg. Chem.*, 1937, **235**, 139.
121. M. Molinier and W. Massa und, *Acta Crystallogr.*, 1993, **C49**, 782.
122. A. Le Bail, H. Duroy, and J. L. Fourquet, *J. Solid State Chem.*, 1992, **98**, 151.
123. G. Férey, J. Renaudin, A. de Kozak, and Y. Mary, *Eur. J. Solid State Inorg. Chem.*, 1993, **26**, 427.
124. J. C. Champarnaud-Mesjard and B. Frit, *Eur. J. Solid State Inorg. Chem.*, 1992, **29**, 161.
125. E. Herdtweck, S. Kummer, and D. Babel, *Eur. J. Solid State Inorg. Chem.*, 1991, **28**, 959.
126. T. Fleischer, R. Hoppe, *Z. Anorg. Allg. Chem.*, 1982, **492**, 83; **493**, 59.

127. A. de Kozak, M. le Blanc, M. Samouel, G. Férey, and R. de Pape, *Rev. Chim. Miner.*, 1981, **18**, 659.

128. M. Vlasse, J. P. Chaminade, J. M. Dance, M. Saux, and P. Hagenmuller, *J. Solid State Chem.*, 1982, **41**, 272.

129. B. G. Müller, *J. Fluorine Chem.*, 1981, **17**, 409.

130. R. Domesle and R. Hoppe, *Rev. Chim. Miner.*, 1978, **15**, 439.

131. R. von der Muehll, F. Daut, and J. Ravez, *J. Solid State Chem.*, 1973, **8**, 206.

132. A. LeBail and A. M. Mercier, *Eur. J. Solid State Inorg. Chem.*, 1995, **32**, 15.

133. M. Weil, E. Zobetz, F. Werner, and F. Kubel, *Solid State Sci.*, 2001, **3**, 441.

134. J. Graulich and D. Babel, *Z. Anorg. Allg. Chem.*, 2003, **629**, 1223.

135. J. L. Fourquet and H. Duroy, *J. Solid State Chem.*, 1993, **103**, 353.

136. G. Courbion, C. Jacoboni, and R. de Pape, *C. R. Acad. Sci. Paris, Ser.C*, 1971, **273**, 809.

137. G. Courbion, C. Jacoboni, and R. de Pape, *Mater. Res. Bull.*, 1974, **9**, 425.

138. G. Courbion, C. Jacoboni, and R. de Pape, *Acta Crystallogr.*, 1976, **B32**, 3190.

139. A. Hartung, W. Verscharen, F. Binder, and D. Babel, *Z. Anorg. Allg. Chem.*, 1979, **456**, 106.

140. A. Le Bail, Y. Gao, J. L. Fourquet, and C. Jacoboni, *Mater. Res. Bull.*, 1990, **25**, 831.

141. U. Englich, Ch. Frommen, and W. Massa, *J. Alloys Compd.*, 1997, **246**, 155.

142. W. Hall, S. Kim, J. Zubieta, E. G. Walton, and D. B. Brown, *Inorg. Chem.*, 1977, **16**, 1884.

143. Y. Laligant, J. Pannetier, P. Labbé, and G. Férey, *J. Solid State Chem.*, 1986, **62**, 274.

144. R. de Pape, A. Le Bail, F. Lubin, and G. Férey, *Rev. Chim. Miner.*, 1987, **24**, 545.

145. M. Leblanc, J. Pannetier, R. de Pape, and G. Férey, *Solid State Commun.*, 1986, **58**, 171.

146. A. Hemon, A. Le Bail, and G. Courbion, *Eur. J. Solid State Inorg. Chem.*, 1993, **30**, 415.

147. Y. Laligant, A. LeBail, and G. Férey, *Eur. J. Solid State Inorg. Chem.*, 1989, **26**, 445.

148. J. L. Fourquet, F. Plet, and R. de Pape, *Acta Crystallogr.*, 1980, **B36**, 1997.

149. P. Lacorre, J. Pannetier, T. Fleischer, R. Hoppe, and G. Férey, *J. Solid State Chem.*, 1991, **93**, 37.

150. U. Bentrup, A. LeBail, H. Duroy, and J. L. Fourquet, *Eur. J. Solid State Inorg. Chem.*, 1992, **29**, 371.

151. G. Courbion, R. de Pape, G. Knoke, and D. Babel, *J. Solid State Chem.*, 1983, **49**, 353.

152. G. Férey, J. Renaudin, A. de Kozak, and Y. Mary, *Z. Kristallogr.*, 1989, **189**, 181.

153. D. Babel and G. Knoke, *Z. Anorg. Allg. Chem.*, 1978, **442**, 151.

154. R. Lösch and C. Hebecker, *Z. Naturforsch.*, 1979, **34b**, 1765.

155. J. C. Dewan, A. J. Edwards, and J. J. Guy, *J. Chem. Soc. Dalton Trans.*, 1986, 2623.

156. D. Kissel and R. Hoppe, *Z. Naturforsch.*, 1987, **42b**, 135.

157. J. Darriet, A. Le Lirzin, and R. Georges, in ‘Advanced Inorganic Fluorides’, eds. T. Nakajima, B. Žemva, and A. Tressaud, Elsevier, Lausanne, 2000, Chap. 9, p. 283.

158. V. Kaiser, A. Le Lirzin, J. Darriet, A. Tressaud, H. Holler, and D. Babel, *Z. Anorg. Allg. Chem.*, 2002, **628**, 2617.

159. S. M. Eicher and J. E. Greedan, *J. Solid State Chem.*, 1984, **52**, 12.

160. M. Leblanc, G. Férey, Y. Calage, R. de Pape, *J. Solid State Chem.*, 1983, **47**, 24; R. E. Marsh, *J. Solid State Chem.*, 1984, **51**, 405.

161. H. Holler and D. Babel, *Z. Anorg. Allg. Chem.*, 1982, **491**, 137.

162. R. Domesle and R. Hoppe, *Z. Anorg. Allg. Chem.*, 1982, **495**, 27.

163. G. Decap, R. Retoux, and Y. Calage, *Z. Anorg. Allg. Chem.*, 1994, **620**, 1449.

164. G. Decap, R. Retoux, and Y. Calage, *Z. Anorg. Allg. Chem.*, 1993, **619**, 1850.

165. A. Hémon, A. Le Bail, and G. Courbion, *J. Solid State Chem.*, 1989, **81**, 299.

166. A. Hémon and G. Courbion, *J. Solid State Chem.*, 1992, **98**, 358.

167. E. Goreshnik, M. Leblanc, and V. Maisonneuve, *Z. Anorg. Allg. Chem.*, 2002, **628**, 162.

168. J. L. Fourquet, H. Duroy, M. Leblanc, and G. Férey, *J. Solid State Chem.*, 1986, **78**, 184.

169. H. Steinfink and G. D. Brunton, *Acta Crystallogr.*, 1968, **B24**, 807.

170. F. Liebau, ‘Structural Chemistry of Silicates’, Springer-Verlag, Berlin, etc., 1985.

171. S. Aléonard and Y. le Fur, *Bull. Soc. Franc. Miner. Crist.*, 1966, **89**, 425.

172. V. V. Ilyukhin and N. V. Belov, *Kristallografiya*, 1961, **6**, 847.

173. P. Bucovec and J. Shiftar, *Monatsh. Chem.*, 1975, **106**, 483.

174. N. Herron, R. L. Harlow, and D. L. Thorn, *Inorg. Chem.*, 1993, **32**, 2985.

175. N. Herron, D. L. Thorn, R. L. Harlow, and F. Davidson, *J. Am. Chem. Soc.*, 1993, **115**, 3028.

176. M. Ferbinteanu, H. W. Roesky, F. Cimpoesu, M. Atanasov, S. Kopke, and R. Herbst-Irmer, *Inorg. Chem.*, 2001, **40**, 4947.

177. D. Couley and D. A. Atwood, *Struct. Bonding*, 2002, **104**, 181.

178. V. Kaiser and D. Babel, *Z. Anorg. Allg. Chem.*, 1991, **595**, 139.

179. R. Hoppe, in ‘Inorganic Solid Fluorides’, ed. P. Hagenmuller, Academic Press, Orlando, 1985, Chap. 6, p. 276.
180. B. G. Müller, *Angew. Chem., Int. Ed.*, 1987, **26**, 1081.
181. B. Žemva, in ‘Advanced Inorganic Fluorides’, eds. T. Nakajima, B. Žemva, and A. Tressaud, Elsevier, Lausanne, 2000, Chap. 4, p. 79.
182. G. Férey, R. de Pape, M. Poulain, D. Grandjean, and A. Hardy, *Acta Crystallogr.*, 1977, **B33**, 1409.
183. H. Holler, D. Babel, M. Samouel, and A. de Kozak, *Rev. Chim. Miner.*, 1984, **21**, 358.
184. R. Hoppe, *Angew. Chem., Int. Ed.*, 1981, **20**, 63.
185. B. V. Bukvetskii, A. V. Gerasimenko, and R. L. Davidovich, *Koord. Khim.*, 1992, **18**, 576.
186. B. V. Bukvetskii, A. V. Gerasimenko, and R. L. Davidovich, *Koord. Khim.*, 1990, **16**, 1479.
187. G. Férey, *J. Fluorine Chem.*, 1995, **72**, 187.
188. U. Klein and W. Massa, *Z. Anorg. Allg. Chem.*, 2002, **628**, 678.
189. G. Paul, A. Choudhury, E. V. Sampathkumaran, and C. N. R. Rao, *Angew. Chem., Int. Ed.*, 2002, **41**, 4473.
190. R. Leo, W. Massa, and J. Pebler, *J. Fluorine Chem.*, 2004, **126**, 923.
191. M. Mercier and M. Leblanc, *Eur. J. Solid State Inorg. Chem.*, 1997, **34**, 251.
192. A. J. Norquist, K. R. Heier, C. L. Stern, and K. R. Poeppelmeyer, *Inorg. Chem.*, 1998, **37**, 6495.
193. A. Herzog, F.-Q. Liu, H. W. Roesky, A. Demsar, K. Keller, M. Noltemeyer, and F. Pauer, *Organometallics*, 1994, **13**, 1251.
194. B. Neumüller and F. Gahlmann, *Z. Anorg. Allg. Chem.*, 1993, **619**, 718.
195. J. B. Goodenough, ‘Magnetism and the Chemical Bond’, Wiley, New York, 1963.
196. M. Steiner, W. Krüger, and D. Babel, *Solid State Commun.*, 1971, **9**, 227.
197. W. Massa, M. Molinier, and J. Pebler, *J. Fluorine Chem.*, 1995, **72**, 171.
198. R. van de Kamp, A. Krimmel, M. Mangold, and J. Pebler, *Phys. Rev. B*, 2000, **61**, 15221.
199. A. Krimmel, R. Stief, J. Pebler, L.-P. Regnault, and M. Ohl, *Phys. Rev. B*, 2003, **67**, 244051.
200. J. M. Dance and A. Tressaud, in ‘Inorganic Solid Fluorides’, ed. P. Hagenmuller, Academic Press, Orlando, 1985, Chap. 9, p. 371.
201. M. Molinier, Ch. Frommen, W. Massa, J. Pebler, and Th. Roisnel, *Z. Naturforsch.*, 1993, **48a**, 1054.
202. D. Babel, *Comments Inorg. Chem.*, 1986, **5**, 285.
203. G. Férey, M. Leblanc, R. de Pape, and J. Pannetier, in ‘Inorganic Solid Fluorides’, ed. P. Hagenmuller, Academic Press, Orlando, 1985, Chap. 10, p. 395.
204. P. Lacorre, J. Pannetier, J. Pebler, S. Nagel, D. Babel, A. de Kozak, M. Samuel, and G. Férey, *J. Solid State Chem.*, 1991, **101**, 298.
205. C. Fouassier, in ‘Advanced Inorganic Fluorides’, eds. T. Nakajima, B. Žemva, and A. Tressaud, Elsevier, Lausanne, 2000, Chap. 10, p. 315.
206. J. L. Adam, in ‘Advanced Inorganic Fluorides’, eds. T. Nakajima, B. Žemva, and A. Tressaud, Elsevier, Lausanne, 2000, Chap. 8, p. 235.
207. J. Wojciekowski and E. Kaminka, *J. Phys. D*, 1979, **12**, L157.
208. S. Ido, S. Uchida, K. Kitazawa, and S. Tanaka, *J. Phys. Soc. Jpn.*, 1988, **57**, 997.
209. R. Spal, C.-E. Chen, A. Denenstein, A. R. McGhie, A. J. Heeger, and A.-C. McDiarmid, *Solid State Commun.*, 1979, **32**, 641.
210. W. Grochala and R. Hoffmann, *Angew. Chem., Int. Ed.*, 2001, **40**, 2742.

Fluorine: Inorganic Chemistry

David A. Atwood
University of Kentucky, Lexington, KY, USA

Based in part on the article Fluorine: Inorganic Chemistry by Darryl D. DesMarteau, Charles W. Bauknight, Jr., & Todd E. Mlsna which appeared in the Encyclopedia of Inorganic Chemistry, First Edition.

1 Introduction 1
2 Methods for the Formation of Element–Fluorine Bonds 2
3 Bonding and Structure 5
4 Spectroscopy 6
5 Nonmetal Fluorides and Oxyfluorides 8
6 Related Articles 22
7 References 22

1 INTRODUCTION

Fluorine displays a unique reactivity among the elements in that it forms compounds with all naturally occurring elements except He and Ne. The first compound of argon, HArF, was only recently isolated in a solid argon matrix and characterized by infrared (IR).[1] Fluorspar and other fluorides were used for several hundred years as fluxes in metallurgy, but the elemental nature of fluorine was not recognized until the nineteenth century.[2,3] After Davy recognized the elementary nature of chlorine in 1810, Ampère proposed that the acid formed from fluorspar and sulfuric acid was like hydrochloric acid. For the next 70 years, numerous chemists attempted to isolate elemental fluorine. The high reactivity of fluorine thwarted all efforts at isolation until H. Moissan succeeded in 1886 to generate fluorine gas by the electrolysis of hydrogen fluoride and potassium fluoride.

Fluorine is widely distributed in Nature, representing about 0.065% of the earth's crust, making it the 13th most abundant element.[4,5] It is more abundant than chlorine and much more abundant than common metals such as zinc and copper. Fluorine occurs in many minerals in which fluoride ion replaces hydroxide. The conversion of hydroxyapatite to fluoroapatite strengthens tooth enamel.[6] However, this would result in an increased brittleness in bones. An untested theory is that the widespread use of fluoride in drinking water, which had remarkable benefits in preventing dental caries in the 1960s, may be the cause of the rise in osteoporosis in the elderly population.

The three most important fluorine-containing minerals are fluorspar (CaF_2), cryolite (Na_3AlF_6), and fluorapatites containing variable amounts of fluorine. Fluorspar is the main source of hydrogen fluoride from which essentially all fluorine compounds are derived either directly or indirectly. Hydrogen fluoride is the primary industrial source of fluorochemicals as well as the source of elemental fluorine, which gives it a position of great importance in the chemistry of fluorine-containing compounds.

The exceptional stability of fluorinated compounds, however, can have deleterious environmental impacts. Recently, for example, it has become apparent that fluorinated compounds such as perfluorooctanesulfonate are widespread in nature[7] and in living systems.[8]

1.1 Hydrogen Fluoride

Hydrogen fluoride is produced worldwide in $\approx 10^6\,\mathrm{t\,a^{-1}}$ by reaction of fluorspar with sulfuric acid (equation 1). The reaction is endothermic ($\Delta H_{298} = 59\,\mathrm{kJ\,mol^{-1}}$) and is carried out in rotary furnaces that produce up to $45\,\mathrm{t\,d^{-1}}$. The crude HF is scrubbed by H_2SO_4 and purified further by distillation as required. Silicon tetrafluoride is a by-product from silicate impurities (equation 2) and is recovered as H_2SiF_6 (equation 3). Another by-product, $CaSO_4$, is used in cement production and other applications.[5]

$$CaF_2 + H_2SO_4 \xrightarrow{200-350\,^\circ C} 2HF(g) + CaSO_4 \qquad (1)$$

$$CaF_2 + SiO_2 + 2H_2SO_4 \longrightarrow SiF_4 + 2CaSO_4 + 2H_2O \qquad (2)$$

$$SiF_4 + 2HF \xrightarrow{H_2O} H_2SiF_6 \qquad (3)$$

Hydrogen fluoride is an excellent solvent for many organic and inorganic compounds and has a wide liquid range.[9] Its properties are summarized in Table 1.

Commercial HF cylinders will contain H_2 owing to the slow reaction of HF with iron and varying amounts of H_2O. Very dry HF can be obtained in the laboratory by adding SbF_5 to HF and removing the HF from the mixture at −40 °C in a suitable vacuum system (equation 4).[10]

$$HF + SbF_5 + H_2O \longrightarrow H_3O^+ + SbF_6^- \qquad (4)$$

Hydrogen fluoride is very corrosive to many metals, glass, and other materials. Many plastics are resistant to HF and fluorinated polymers such as Kel-F, Teflon, Teflon-PFA, and others are inert to HF. A variety of useful equipment for handling and studying HF can be easily prepared from commercially available fluoropolymers and fluoropolymer components. Copper, Monel, and nickel are excellent metals for handling HF at higher temperatures. Stainless steels are satisfactory at lower temperatures.

Hydrogen fluoride causes severe burns to the skin and mucus membranes. Handling of HF should only be attempted

Table 1 Physical properties of hydrogen fluoride

Freezing point	$-83.55\,°\mathrm{C}$
Cryoscopic constant	$1.55 \pm 0.05\,°\mathrm{C\,mol^{-1}}$
Boiling point	$19.51\,°\mathrm{C}$
Vapor pressure (25 °C)	921.4 mmHg
Density (0 °C)	$1.002\,\mathrm{g\,L^{-1}}$
(25 °C)	$0.995\,\mathrm{g\,L^{-1}}$
Dielectric constant (0 °C)	83.6
Specific conductance (0 °C)	$1 \times 10^{6}\,\Omega^{-1}\,\mathrm{cm^{-1}}$

with proper protection and after consulting appropriate safety information.[11]

1.2 Fluorine

Elemental fluorine is produced commercially by the electrolysis of KF·2HF (mp 72 °C) using carbon anodes and steel cathodes.[5,9,12] The voltage of the cells is 8–12 V (standard electrode potential for $F_2 = 2.85$ V) and current is as high as 15 kA, depending on cell size. The cathode and anode are separated by skirts to prevent mixing of F_2 with H_2 formed at the cathode. The western world production of fluorine is ca. $2–3 \times 10^3\,\mathrm{t\,a^{-1}}$, of which about 55% is used for production of UF_6 and 40% is for SF_6. Other uses include production of CF_4, NF_3, and fluorinated graphite for batteries.

The physical properties of F_2 are given in Table 2. Fluorine is an orange-yellow liquid at −196 °C, and the gas at 1 atm in a 2 L glass bulb has a pale yellow-green color. Fluorine has an almost pleasant, sweet smell, and is easily detected by humans at the 1 ppm level in the air. It is highly toxic and can be very dangerous to handle in high concentrations unless proper precautions and equipment are employed.[13] Fluorine reacts exothermically with all elements at high concentrations except O_2, N_2, He, Ne, Ar, and Kr. Many metals form a protective fluoride coating on contact with fluorine at low concentrations and can be passivated towards further reaction at higher concentrations. Many fluoropolymers such as Teflon and Teflon-PFA are resistant to fluorine near room temperature but will burn at higher temperatures and high concentrations of fluorine. Fluorine can be handled under various conditions in properly cleaned and passivated metal apparatus of copper, brass, steel, stainless steel, Monel, and nickel. At high temperatures, Monel and nickel must be employed.

Table 2 Physical properties of fluorine

Melting point	53.54 K
Boiling point	85.02 K
Vapor pressure (77.17 K)	280.4 mmHg
(89.40 K)	1219.9 mmHg
Critical temperature and pressure	144 K and 55 atm
Density (liquid) (77.22 K)	$1.562\,\mathrm{g\,cm^{-3}}$

2 METHODS FOR THE FORMATION OF ELEMENT–FLUORINE BONDS

Fluorine forms bonds to all elements except He, Ne, and Ar and the bond strengths are generally high except with other very electronegative elements. The methods used for forming bonds with fluorine in main group compounds are diverse but can be broadly grouped into four classes based on hydrogen fluoride, elemental fluorine, metal fluorides, and nonmetal fluorides. Laboratory preparations favor the use of metal fluorides and nonmetal fluorides, which avoid the use of the more experimentally difficult reagents HF and F_2. Regardless of the method, the origin of the fluorine in every reagent can be traced back to HF. Naturally occurring CaF_2 (fluorspar) is perhaps the only exception, but CaF_2 is rarely used directly as a fluorinating reagent.

2.1 Hydrogen Fluoride

Hydrogen fluoride is most often employed to prepare metal fluorides by reaction of oxides, hydroxides, carbonates, and chlorides with either pure HF or concentrated aqueous solutions. Obviously water-sensitive fluorides require pure HF and conditions that will not result in a mixture of fluorides and oxides. Hydrogen fluoride reacts with all metals below hydrogen in the electromotive series and numerous metal fluorides can be prepared at high temperatures by reaction of the powdered metal with HF(g). Authoritative reviews on metal fluorides can be consulted for details.[2,9,14]

Many nonmetal fluorides can be prepared by reaction of readily available chlorides and bromides with HF, particularly groups 14, 15, and 16, excluding nitrogen and oxygen.[15,16] For example both SbF_3 and SbF_5 can be prepared from the respective chlorides (equations 5 and 6). In many reactions, much more rapid conversion of halides to the fluorides in HF is achieved by adding a Lewis acid catalyst such as SbF_5 or SbF_3/Cl_2 (SbF_3Cl_2). The pentahalide becomes the fluorination reagent and the resulting Sb–Cl bonds are converted to Sb–F bonds by the HF.

$$SbCl_3 + 3HF \longrightarrow SbF_3 + 3HCl \tag{5}$$

$$SbCl_5 + 5HF \longrightarrow SbF_5 + 5HCl \tag{6}$$

The reaction of HF with chlorocarbons in the presence of Lewis acid catalysts is the basis of much of the commercial production of aliphatic organofluorine compounds.[17,18] The important chlorofluorocarbons (CFCs) are produced on a large scale by this method as well as environmentally more friendly hydrofluorocarbons (HFCs) and hydrochlorofluorocarbons (HCFCs), which are replacing CFCs such as CF_2Cl_2, $CFCl_3$, and $CF_2ClCFCl_2$. As an indication of the importance of this method industrially, two important perfluoroalkene intermediates can be illustrated (equations 7 and 8). Both C_2F_4 and C_3F_6 are important monomers for a variety of fluoropolymers and other fluorochemicals having a broad spectrum of utility in modern technology. Recently, carbon–hydrogen bond hydrogenolysis involving the heterolytic activation of H_2 has been employed to prepare HFC-134a.[19]

$$\mathrm{CHCl_3 + 2HF \xrightarrow{catalyst} CHF_2Cl + 2HCl} \tag{7}$$

$$\mathrm{CHF_2Cl \xrightarrow{heat} CF_2{=}CF_2 + CF_3CF{=}CF_2 + HCl + Others} \tag{8}$$

Another aspect of HF fluorinations involves the process of electrochemical fluorination (ECF) (Simons process) carried out in anhydrous HF.[20] The Simons process is applied mainly to the synthesis of organofluorine compounds, but more inorganic compounds (e.g. CF_3SF_5 from CS_2 and CF_3SO_2F from $MeSO_2F$, Cl) are prepared in very high yield by this method. In ECF the fluorination takes place at a nickel or Cu/Ni anode in HF using a voltage below that required to produce elemental fluorine (5–6 V) and a current of a few to several hundred amps depending on cell size and electrode details. Fluorination is believed to take place via high-valent nickel fluorides formed on the surface of the anode, but after more than 50 years of use the process is still not well understood. Hydrogen gas is produced at the cathode and the consumed HF is replenished continuously to maintain an appropriate volume in the ECF cell. Products are removed as gases or liquids and the entire process can be operated continuously. To be effective, the compound to be fluorinated must be soluble in HF. Compounds containing oxygen, sulfur, and nitrogen are particularly useful because the heteroatoms are protonated in the HF medium, providing solubility and conductivity. Yields decrease with molecular complexity owing to cleavage reactions, incomplete fluorination, and other complications. The utility of the Simons ECF process is illustrated by two commercial fluorocarbon derivatives prepared in this way, $C_8F_{17}SO_2F$ from $C_8H_{17}SO_2F$ and $(n\text{-}C_4F_9)_3N$ from $(n\text{-}C_4H_9)_3N$. More recently the first example of the direct ECF of a thiazole ring was reported.[21]

2.2 Elemental Fluorine

In principle, all binary fluorides of main group elements could be prepared by direct combination with fluorine. In practice this is impossible since fluorine is a powerful oxidizer and favors high oxidation states of the elements. Nevertheless, F_2 is essential in the preparation of many compounds in both low and high oxidation states, particularly compounds of nitrogen, oxygen, sulfur, higher halogens, krypton, and xenon.[15,16] Increasingly, fluorine is also used in the preparation of fluorocarbons, especially complex fluorocarbon ethers.[22] For many metals, high oxidation state fluorides and oxyfluorides can only be obtained via F_2 or fluorine atom sources such as KrF_2 and O_2F_2.

The use of elemental fluorine in the preparation of main group fluorides is carried out in batch and flow systems depending on the activation required and the exothermicity of the reaction. Clearly it can be exceedingly dangerous and foolhardy to combine substantial amounts of fluorine with an easily oxidized element or compound in a batch reaction. As an illustration, SF_6 is prepared commercially by passing pure fluorine gas over lump sulfur, resulting in ignition and complete consumption of the fluorine ($\Delta H = -262\,\mathrm{kcal\,g\,mol^{-1}}$). If pure fluorine were condensed on to sulfur at $-196\,°\mathrm{C}$ in a closed vessel without ignition and then warmed, an explosive reaction would ensue at the moment the temperature reached a point where the fluorine began to react with the sulfur. On the other hand, ClF is safely prepared on a 0.2 mol scale by cocondensing equimolar amounts of F_2 and Cl_2 into a 150 mL Monel reactor at $-196\,°\mathrm{C}$, warming to 22 °C and then heating at 250 °C. The latter reaction proceeds first to ClF_3 ($\Delta H = 26\,\mathrm{kcal\,mol^{-1}}$) and the ClF_3 reacts with Cl_2 at 250 °C to give ClF.

Many reactions of nitrogen and oxygen compounds involving elemental fluorine require catalysts. Two of the most useful catalysts are AgF_2 and CsF. The catalysts function in different ways, as illustrated by equations (9) and (10).[23] Without the catalyst there is no reaction between F_2 and COF_2 up to 200 °C. The catalytic intermediate with AgF_2 may be an Ag^{II} derivative and with CsF the CF_3O^- anion is strongly suspected.

$$\mathrm{COF_2 + F_2 \xrightarrow[180-200\,°C]{AgF_2} CF_3OF + CF_3OOCF_3} \tag{9}$$

$$\mathrm{COF_2 + F_2 \xrightarrow[-78\,°C]{CsF} CF_3OF\ (no\ peroxide)} \tag{10}$$

2.3 Metal Fluorides

Because of the ready availability of chlorides and bromides of the main group elements, simple metathesis reactions provide an excellent route to many fluorinated compounds. Many metal fluorides have been employed in fluorinations of main group halides including groups 1 and 2 metal fluorides, ZnF_2, AgF, AgF_2, HgF_2, PbF_2, CoF_3, SbF_3, SbF_5, and SbF_3Cl_2. The high oxidation state fluoride AgF_2 is used in oxidative fluorinations and often in conjunction with F_2, for example, equations (11) and (12).

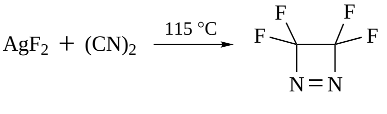

(11)

$$\mathrm{SO_3 + AgF_2 \xrightarrow[160\,°C]{F_2} (FSO_2O)_2} \tag{12}$$

Cobalt trifluoride is used almost exclusively to replace hydrogen on carbon and in oxidative fluorination of hydrocarbons,[24] for example, equations (13) and (14). Zinc fluoride, SbF_3, and PbF_2 are mild fluorinating reagents that can often be used to give partially fluorinated compounds depending on conditions and stoichiometry (equations 15–17).[15,16]

$$n\text{-}C_5H_{12} \xrightarrow[300\,°C]{CoF_3} n\text{-}C_5F_{12} \qquad (13)$$

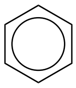

$$\xrightarrow[250\text{–}300\,°C]{CoF_3} \text{cyclo-}C_6F_{12} \qquad (14)$$

$$PCl_3 + SbF_3 \xrightarrow{40\,°C} SbClF_2 + PFCl_2 \qquad (15)$$

$$OPCl_3 + ZnF_2 \xrightarrow{40\,°C} OPClF_2 + ZnCl_2 \qquad (16)$$

$$OPCl_3 + SbF_3 \xrightarrow{150\,°C} OPF_3 + SbCl_3 \qquad (17)$$

Zinc fluoride can often be used in a polar solvent to effect fluorinations that are difficult with other reagents (equation 18). The addition of Cl_2 or $SbCl_5$ to SbF_3 as a catalyst greatly increases the utility of SbF_3 in fluorinations (equations 19–22).

$$CH_2(SO_2Cl)_2 \xrightarrow[Et_2O]{ZnF_2} CH_2(SO_2F)_2 \qquad (18)$$

$$SO_2Cl_2 \xrightarrow[300\,°C]{SbF_3/SbCl_5} SO_2ClF \qquad (19)$$

$$COCl_2 \xrightarrow[130\,°C]{SbF_3/Cl_2} COF_2 \qquad (20)$$

$$SO_2Cl_2 \xrightarrow[200\,°C]{SbF_3} \text{No reaction} \qquad (21)$$

$$COCl_2 \xrightarrow[300\,°C]{SbF_3} COF_2 + OCFCl \qquad (22)$$

The recognition that polar solvents such as MeCN, tetramethylene sulfone, benzonitrile, and others greatly increase the activity of the alkali metal fluorides NaF and KF has led to their widespread use in metathesis reactions.[25] Potassium fluoride is more active than NaF but the latter is easily dried and does not readily absorb H_2O. Many fluorinations are readily accomplished by refluxing the halide with excess NaF in the solvent in standard glass apparatus or by heating under autogenous pressure in an autoclave. Some examples of useful fluorinations are shown in equations (23–28). It was recently found that the reactivity of KF is enhanced when used in ionic liquids.[26]

$$SO_2Cl_2 \xrightarrow[MeCN]{NaF,\ 80\,°C} SO_2FCl \qquad (23)$$

$$SO_2Cl_2 \xrightarrow[sulfolane]{NaF,\ 150\,°C} SO_2F_2 \qquad (24)$$

$$SPCl_3 \xrightarrow[140\text{–}170\,°C]{NaF,\ sulfolane} SPF_3 \qquad (25)$$

$$COCl_2 \xrightarrow[MeCN]{NaF,\ 40\,°C} COF_2 \qquad (26)$$

$$(CNCl)_3 \xrightarrow[reflux]{NaF,\ sulfolane} (CNF)_3 \qquad (27)$$

$$C_4F_9SO_2Cl \xrightarrow[sulfolane]{KF,\ 35\,°C} C_4F_9SO_2F \qquad (28)$$

2.4 Nonmetal Fluorides

Many nonmetal fluorides have been employed for the preparation of other main group fluorides. These fluorination reagents fall into two general classes: strong oxidative fluorination reagents such as ClF, ClF_3, BrF_3, and IF_5, and weak oxidizing reagents such as SF_4, SeF_4, and AsF_3. The major utilization of these reagents has been in fluorocarbon derivatives and as selective fluorination reagents in organic chemistry, for which numerous authoritative reviews are available.[27–29] Sulfur tetrafluoride and halogen fluorides have been used extensively in the preparation of metal fluorides.[9,14]

The halogen fluorides react very vigorously with oxidizable substrates with the reactivity decreasing from chlorine to iodine. Often, halofluorination is a desired outcome of these reactions. While the number of reactions that have been examined with main group compounds is large, the number of useful preparative reactions is limited. Some examples of useful reactions involving the formation of element–fluorine bonds are given in equations (29–35).[16,30]

$$PF_3 + ClF \xrightarrow{-196\text{ to }22\,°C} F_4PCl \qquad (29)$$

$$4SOCl_2 + IF_5 \xrightarrow{22\,°C} 3SOClF + SOF_2 + ICl_3 + Cl_2 \qquad (30)$$

$$SO_2 + BrF(BrF_3/Br_2) \xrightarrow{22\,°C} SO_2BrF \qquad (31)$$

$$ClF + SO_3 \xrightarrow{22\,°C} FSO_2OCl \qquad (32)$$

$$6ClF + BrCN \xrightarrow{-196\text{ to }22\,°C} CF_3NCl_2 + BrF_3 + 2Cl_2 \qquad (33)$$

$$N{\equiv}SF_3 + 2ClF \xrightarrow{-196\text{ to }22\,°C} SF_5NCl_2 \qquad (34)$$

$$KBrO_3 + BrF_5 \xrightarrow{22\,°C} KBrO_2F_2 + BrO_2F \qquad (35)$$

Weak oxidizing fluorides such as SF_4 and SeF_4 are useful as fluorination reagents in selected cases to replace oxygen or hydroxide by fluorine and as mild oxidative fluorination reagents. Some useful examples are shown in equations (36–39).

$$SeO_2 + 2SF_4 \xrightarrow{200\,°C} SeF_4 + 2SOF_2 \qquad (36)$$

$$2Ph_3P + SF_4 \xrightarrow{150\,°C} 2Ph_3PF_2 + S \qquad (37)$$

$$2PhAsO_3H_2 + 3SF_4 \xrightarrow{70\,°C} 2PhAsF_4 + 3SOF_2 + 2HF \qquad (38)$$

$$4Me_3SiCl + SF_4 \xrightarrow{20\,°C} 4Me_3SiF + SCl_2 + Cl_2 \qquad (39)$$

Arsenic trifluoride is a particularly useful reagent for the fluorination of chlorides. Its physical properties (bp 63 °C) often make it more useful than SbF_3. Examples of useful fluorinations with AsF_3 include those in equations (40) and (41).

$$3PCl_5 + 5AsF_3 \xrightarrow{22\,^{\circ}C} 3PF_5 + 5AsCl_3 \qquad (40)$$

$$3HN(SO_2Cl)_2 + 2AsF_3 \xrightarrow{\text{reflux}} 3HN(SO_2F)_2 + 2AsCl_3 \qquad (41)$$

3 BONDING AND STRUCTURE

3.1 Bond Energies

Fluorine is unique in forming the largest number of examples of element–element bonds. It is also unique in forming chemical bonds ranging from one of the strongest single bonds known (BF_3) to some of the weakest bonds in compounds isolable under ordinary laboratory conditions (KrF_2). Table 3 lists the mean thermochemical bond energies for some main group fluorides.[9,31]

Two regular trends are evident in the decrease in bond energies across a row from left to right and a decrease in bond energies with increasing oxidation state. Clearly the often stated generalization that bond energies decrease in going down a group does not apply in general to nonmetal fluorides.

The very low dissociation energy of fluorine ($155\,\mathrm{kJ\,mol^{-1}}$), its small atomic size ($r = 0.5741\,Å$), high electronegativity (3.98, Pauling), and high electron affinity ($338.9\,\mathrm{kJ\,mol^{-1}}$) all contribute to the ability of fluorine to form a wide variety of stable fluorides and oxyfluorides of nonmetals. It has been pointed out, however, that many fluorides are not as stable as might be expected, based on comparisons with other halogens. This has been attributed to the fact that addition of an electron into the outer shell of the fluorine atom, as in the formation of a covalent bond, is energetically less favorable by a ca. $109\,\mathrm{kJ\,mol^{-1}}$ than would be expected by extrapolation from the other halogens. This anomaly is primarily due to the small size of the fluorine atom and is suggested as an explanation for the unusually small dissociation energy of difluorine. Based on the other halogens, an extrapolation of $1/R_e$ versus D_e would give $D_e \sim 381\,\mathrm{kJ\,mol^{-1}}$ for F_2, which is $2 \times 109\,\mathrm{kJ\,mol^{-1}}$ larger than the observed value. Similarly, based on an extrapolation of the ionization potential of the halogens versus electron affinity, fluorine would be expected to have an atomic electron affinity of $443\,\mathrm{kJ\,mol^{-1}}$, which is approximately $109\,\mathrm{kJ\,mol^{-1}}$ greater than the observed value.

Fluorine is generally able to produce the highest oxidation states in nonmetals, but in many cases this state can only be observed in an oxyfluoride of the nonmetal. These exceptions occur with nitrogen, chlorine, bromine, and xenon. Thus NF_5, ClF_7, BrF_7, and XeF_8 are unknown but NOF_3, ClO_2F_3, BrO_3F, ClO_3F, and XeO_3F_2 are well known.[30] However, for all the aforementioned elements except xenon, the maximum oxidation state for each has been achieved with fluorine in cationic derivatives of the unknown parent fluoride in $NF_4{}^+$, $ClF_6{}^+$, and $BrF_6{}^+$ salts. The X-ray structures of $[XF_6][Sb_2F_{11}]$ ($X = Cl$, Br, I) have recently been reported.[32] Numerous related examples of the inability of fluorine alone to form the highest oxidation state of an element are also observed among several transition metals.[33]

3.2 Molecular Structures

The structures of nonmetal fluorides and oxyfluorides are remarkably well predicted on the basis of VSEPR considerations (*see Valence Shell Electron Pair Repulsion Model*). In fact, nonmetal fluoride and oxyfluoride structures are the most often used examples of the success of VSEPR predictions of molecular shape. The small size of fluorine and its high electronegativity give rise to smaller bond angles in an analogous series of halogen compounds in cases where nonbonding electron pairs are present in the valence shell. In PX_3 the XPX bond angle increases from 96° in PF_3 to 102° in PI_3. Other examples include OF_2 (103°), OCl_2 (111°), and OSF_2 (93°), $OSCl_2$ (96°), and $OSBr_2$ (97°).

Table 3 Mean thermochemical bond energies of some main group fluorides[a]

13		14		15		16		17		18	
BF_3	644	CF_4	490	NF_3	276	OF_2	213				
		CF_2	527								
		SiF_4	598	PF_5	460	SF_6	330	ClF_5	146		
		SiF_2	598	PF_3	502	SF_4	330	ClF_3	176		
								ClF	255		
		GeF_4	469	AsF_5	385	SeF_6	301	BrF_5	188	KrF_2	50
		GeF_2	473	AsF_3	485	SeF_4	318	BrF_3	201		
								BrF	251		
				SbF_5	385	TeF_6	347	IF_7	230	XeF_6	134
				SbF_3	439	TeF_4	368	IF_5	264	XeF_4	134
								IF	280	XeF_2	134

[a] All in $\mathrm{kJ\,mol^{-1}}$.

Table 4 Some element–fluorine bond distances[a]

S_2F_2	164	ClF	163	GeF_2	173
SF_2	159	ClF_3	160 (eq), 160 (ax)	AsF_3	171
SF_4	154 (eq), 165 (ax)	ClF_5	162 (eq), 172 (ax)	SeF_4	168 (eq), 177 (ax)
SOF_4	155 (eq), 158 (ax)	$FClO_2$	170	BrF_3	172 (eq), 181 (ax)
SF_6	156	$FClO_3$	162	KrF_2	188

[a] All in pm.

Element–fluorine bond distances in neutral binary fluorides vary over a considerable range from BF_3 (1.31 pm) to XeF_2 (1.98 pm)[34] Table 4 shows the small variation in bond distances as a function of increasing oxidation state for a related series of compounds and the relatively small variation in bond distances across a given row in the periodic table, in spite of a more than fivefold decrease in the average thermochemical bond energies from KrF_2 to GeF_2.

4 SPECTROSCOPY

Nonmetal fluorides and oxyfluorides have been studied by nearly every available modern spectroscopic and diffraction technique. This is due in part to the strong practical and theoretical interest in the structure and reactivity of simple molecules of this type, the diversity of compounds that can be obtained, and their amenability to study by many different techniques. Many structures of simple fluorides and oxyfluorides have been determined by electron diffraction, microwave spectroscopy, X-ray diffraction, and vibrational analysis. For many chemists interested in the synthesis and reactivity of main group fluorides and derivatives, ^{19}F NMR, IR, and Raman spectroscopy, and mass spectrometry are the indispensable routine tools of analysis.

4.1 Fluorine NMR

Fluorine has 100% natural abundance of ^{19}F ($I = 1/2$) and ^{19}F NMR is arguably one of the most useful techniques for structural information, rivaling that provided by ^1H and ^{13}C NMR.[35,36] The relative sensitivity of ^{19}F is 0.83 compared to ^1H and the range of observed fluorine chemical shifts in diamagnetic compounds covers more than 1000 ppm. The accepted standard for ^{19}F NMR chemical shifts is $CFCl_3$ and since the late 1960s this reference has been used almost exclusively. Earlier chemical shifts are often reported relative to other standards and some care must be exercised in using earlier literature values if the reference standard is not given. Also, up to the early 1980s the sign convention for chemical shifts was not always uniform. At present, chemical shift values at lower frequency than $CFCl_3$ are assigned a negative value and vice versa. Again, care must be exercised in using literature values prior to the early 1980s in that the sign convention used was usually opposite to the presently accepted convention.

The range of ^{19}F chemical shifts for fluorine bonded to a given element can be very large, for example, +479 (FNO) versus −127 ($CF_3NH\underline{F}$) and −448 (ClF) versus 247 ($FClO_3$). In spite of the large dispersion observed in ^{19}F chemical shifts, chemical shift values can be used effectively as a diagnostic tool. With modern high-field NMR spectrometers, spectra of complex molecules are often easily interpreted. Line broadening for fluorine attached to quadrupolar nuclei is typically of the same magnitude as that observed with hydrogen bonded to the same nucleus. The effects of solvent on chemical shift values varies but, at the low concentrations needed for FT-NMR spectrometers, different noncomplexing solvents do not give large variations in chemical shifts. The difference in solvents such as $CDCl_3$ and CD_3CN is usually less than 0.1–0.2 ppm. Some representative ^{19}F NMR chemical shift values for a variety of nonmetal fluorides and oxyfluorides are given in Table 5.[35–38]

Fluorine undergoes strong spin–spin coupling with many other nuclei and with other magnetically nonequivalent fluorines, providing further structural information in many compounds. The magnitude of these J couplings is difficult to predict and long-range fluorine–fluorine couplings are dominated by through space interactions.[39] Long-range multiband $^nJ_{FF}$ couplings are often observed in fluorine compounds if the magnetically nonequivalent fluorine atoms are close through space owing to the molecular structure or conformation. The latter is most often of consequence in organofluorine compounds such as in 4,5-difluorophenanthrene ($^5J_{FF} = 174$ Hz), but it is clearly evident in many nonmetal fluorine derivatives. For example, in $SF_4{=}NF$ the two axial sulfur–fluorine bonds and S=N–F lie in a plane. The $^3J_{FF}$ *cis*-NF–SF_{ax} is 227 Hz compared to only 93 Hz for the *trans*-NF–SF_{ax}.[40]

Table 6 gives some possible values for spin–spin coupling constants as a function of the number of intervening bonds. Long-range ^nJ values can be observed in many cases, especially for F–F couplings. Values of ^2J and ^3J strongly depend on the element to which the fluorine is bonded (e.g. $^2J_{FF} = 422$ Hz in ClF_3, whereas $^2J_{FF} = 128$ in $ClCF_2NClF$) and ^3J values are strongly dependent on structure type ($^3J_{FF}$ CF_3OF, 34 Hz; FC(O)OF, 141 Hz).

In recent years, solid-state magic angle spinning NMR has become a direct and sensitive method for distinguishing different fluorine species in various solid-state materials. For

Table 5 Representative ^{19}F chemical shift values for nonmetal fluorides and oxyfluorides[a]

BF_3	−127	OPF_3	−92	SeF_6	52
BF_2H	−68.5	$P_2O_3F_4$	−86	$OSeF_2$	39
BF_2Cl	−79.8	PF_3Cl_2	67 (ax), −41 (eq)	O_2SeF_2	50
CF_4	−63.3	AsF_3	−40	$Se_2O_2F_8$	55.5, 93.3 (eq and ax)
CF_3I	−4.8	AsF_5	−65	SeF_5Cl	71.3 (ax), 32 (eq)
CF_3OF	−71	AsF_2Cl	−49	TeF_4	−25
COF_2	−20	AsF_6	−69	TeF_6	−56
SiF_4	−163	$Sb_2F_{11}^-$	−170(ax), −148 (eq), −121 (bridge)	TeF_5Cl	−43(ax), −4.0 (eq)
SiF_3H	−110	OF_2	249	ClF	−448
SiF_3OSiF_3	−157	O_2F_2	≈865	ClF_3	116 (ax), −4 (eq)
GeF_4	−176	CF_3OF	147	ClF_5	247 (ax), 412 (eq)
GeF_3Cl	−142	CF_3OOF	292	$FClO_3$	287
NF_3	147	SF_2	−122.5	BrF_3	−23
cis-N_2F_2	134	SF_4	71 (ax), 118 (eq)	BrF_5	270 (ax), 132 (eq)
FNO	479	SF_6	57	$FBrO_2$	210
F_3NO	365	SO_2F_2	32	F_3BrO	−152
DF_4=N					
PF_3	−34	SF_5Cl	62 (ax), 125 (eq)	IF_7	173
PF_2Cl	−37	SeF_4	12.1 (ax), 37.7 (eq),	OIF_5	109 (ax), 73 (eq)

[a] In ppm relative to $CFCl_3$.

Table 6 Some typical $J_{F\text{–}X}$ coupling constants[a]

^1J		^2J		^3J	
^{11}B–F	45–105	^{1}H–F	40–80	^{1}H–F	0–50
^{13}C–F	200–300	^{13}C–F	15–60	F–F	0–200
^{15}N–F	180–210	^{15}N–F	10–80	^{31}P–F	0–80
^{29}Si–F	110–480	F–F	25–600		
^{31}P–F	100–1440	^{31}P–F	10–300		
^{77}Se–F	302–1584	^{77}Se–F	5–50		
^{125}Te–F	3000–4000				
^{129}Xe–F	890–6299				

[a] In Hz.

example this technique can be used to demonstrate that at low fluoride loadings the basic hydroxyl groups on γ-alumina are replaced by fluoride.[41]

4.2 Vibrational Spectroscopy

As for other inorganic compounds, vibrational spectroscopy provides useful information on the identity and structure of main group fluorides and oxyfluorides.[42,43] Characteristic M–F stretching frequencies can be identified for all nonmetal fluorides and simple molecules have very characteristic fingerprints in the IR.[44] Sampling problems for highly oxidizing fluorides are challenging and Raman spectra are often more easily obtained. Many common IR window materials are attacked by reactive fluorides and silver chloride is one of the most useful window materials in this respect for liquid, solid, and gas-phase spectra. On the other hand, Raman spectra of liquids and solids can be obtained in glass or transparent fluoropolymer containers and low-temperature spectra are more easily obtained on highly reactive or unstable compounds. Gas-phase Raman spectra are generally difficult to obtain because of the high pressures required and spectra of compounds having boiling points well below 22 °C are generally obtained on condensed liquids or solids at low temperatures. Numerous excellent reviews and books can be consulted for details of instrumentation, sampling, and summaries of vibrational spectra of fluorides and oxyfluorides.[42,43] Some typical group frequencies for M–F stretching are shown in Table 7.

4.3 Mass Spectrometry

Modern mass spectrometers provide a powerful tool for the indentification and study of nonmetal fluorides and their derivatives.[45] Many compounds are sufficiently volatile to make sampling relatively easy. In highly fluorinated compounds, the 100% natural abundance of ^{19}F simplifies interpretation of many spectra and high-resolution spectra are often not required for unambiguous interpretation of mass spectra. Numerous nonmetal fluorides and derivatives were first identified by mass spectrometry and subsequently obtained in sufficient amounts to characterize by other methods. Modern quadropole mass spectrometers are particularly useful in the analysis of fluorine compounds and their open architecture facilitates the analysis of highly reactive fluorine compounds and compounds of low thermal stability.

Both positive and negative ion mass spectrometry are useful for fluorine compounds and often are complimentary. Fluorocarbons rarely show an M^+ peak in positive ion EI spectra but often exhibit intense M^- in negative ion spectra. Chemical ionization techniques routinely offered in inexpensive mass spectrometer systems greatly enhance the ability to observe molecular ions in both positive and negative ion spectra. Most mass spectral data on simple main group

Table 7 Main group element–fluorine stretching frequencies

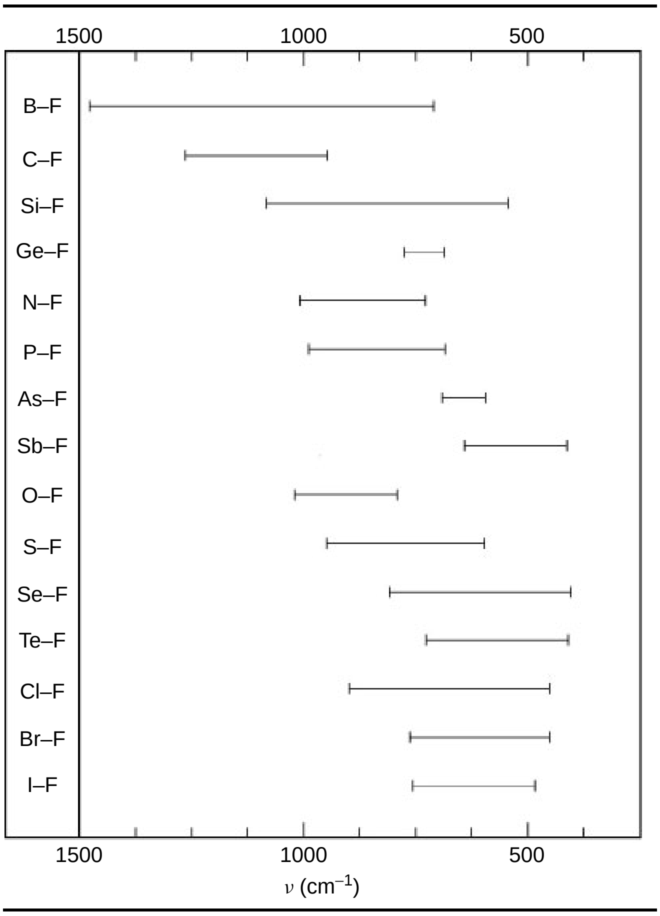

fluorides and oxyfluorides were obtained before the routine availability of CI.

Highly fluorinated nonmetal compounds in both positive and negative EI readily lose fluorine atoms on ionization. For example, the 70 eV EI spectrum of NF_3 gives M^+ (26%), M–F^+ (100%), and M–$2F^+$ (26%), and ONF_3 gives M^+ (0.2%), M–F^+ (78%), M–$2F^+$ (1.6%), and NO^+ (100%), as well as weak $NF_2{}^+$ and NF^+ ions. For SeF_6, the 70 eV EI spectra consist of $SeF_5{}^+$ and $SeF_4{}^+$ but no M^+. At 20 eV the negative ion spectra consist of $SeF_5{}^-$ (50%), $SeF_4{}^-$ (7%), $SeF_3{}^-$ (5%), Se^- (1%), and F^- (100%). Using SF_6 as a CI gas and below 10 eV, $SeF_6{}^-$ can be observed in appreciable amounts.

For very sensitive molecules like $\overline{O–CF_2–O}$, obtaining a molecular ion in the mass spectrum is difficult. However, by selective ion monitoring, M^+ at $m/z = 82$ was easily observed at 20 eV in EI.

Often soft ionization techniques such as fast-atom bombardment (FAB)[46] and matrix-assisted laser desorption (MALDI)[47] greatly increase the utility of mass spectrometry in the analysis of fluorinated compounds. Using a commercial matrix-assisted laser desorption time-of-flight mass spectrometer, molecular ions of a polyelectrolyte, $[–SO_2NNaSO_2(CF_2)_4SO_2–]_n$ could be observed. Future applications of these techniques are very promising.

5 NONMETAL FLUORIDES AND OXYFLUORIDES

The number of inorganic fluorine-containing compounds of metals and nonmetals is very large and many organofluorine compounds are borderline between the traditional boundaries of organic and inorganic chemistry. The following sections focus on the binary fluorides and tertiary oxyfluorides of main group nonmetals as representative examples of the extensive and interesting chemistry of fluorine-containing inorganic compounds. The cited literature and cross references provide easy access to compounds not covered.

5.1 Boron Fluorides

Boron forms strong bonds to fluorine (644 kJ mol^{-1}), usually combining with three or four fluorides in its compounds or salts. Several binary fluorides of boron are known including boron trifluoride, BF_3, a stable gas of great industrial importance as a Lewis acid. Boron trifluoride is synthesized industrially by reaction of hydrofluoric acid with borates or boric oxides (equation 42).[48]

$$Na_2B_4O_7 + 12HF \xrightarrow{-6H_2O} [Na_2O(BF_3)_4] \xrightarrow{2H_2SO_4} 4BF_3(g) + H_2O + 2NaHSO_4 \quad (42)$$

Boron trifluoride forms addition compounds that incorporate an sp^3 hybridized boron into a tetravalent structure.[49] Salts of $BF_4{}^-$ are readily formed with BF_3 and a suitable fluoride donor. Halogen fluorides such as chlorine trifluoride react with BF_3 to generate interhalogen cations such as $[ClF_2]^+[BF_4]^-$.[50] Some further examples are shown in equations (43) and (44). In an organic application, the Schiemann reaction provides an entry into fluorinated aromatics by thermal decomposition of a diazonium tetrafluoroborate (equation 45).

$$NO_2 + BF_3 + \tfrac{1}{2}F_2 \longrightarrow [NO_2]^+[BF_4]^- \quad (43)$$

$$[ClF_6]^+[AsF_6]^- + CsBF_4 \longrightarrow [ClF_6]^+[BF_4]^- + CsAsF_6 \quad (44)$$

$$PhNH_2 \xrightarrow[2.\ HBF_4]{1.\ NaNO_2,\ H^+} [PhN_2]^+[BF_4]^- \xrightarrow{heat} PhF \quad (45)$$

Reaction of BF_3 with B at 1850 °C generates the reactive intermediate species boron monofluoride, BF, which cannot be isolated. Cocondensation of BF with BF_3 yields B_2F_4, a metastable lower fluoride of boron, and BF_2–B(F)–BF_2, which is unstable and disproportionates according to equation (46).[51] Mixtures of boron trihalides undergo exchange reactions, presumably via a four-centered transition state, to yield the two boron chloride fluorides, for example, as shown in equation (47).

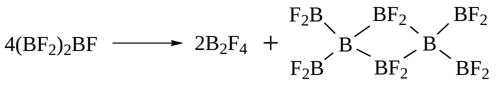

(46)

$$BCl_3 + BF_3 \rightleftharpoons BFCl_2 + BF_2Cl \qquad (47)$$

Heavier halogens such as chlorine and bromine provide their boron trihalides with better complexing ability than BF_3, but their facile hydrolysis makes BF_3 the more effective Lewis acid choice.

5.2 Carbon, Silicon, and Germanium Fluorides and Oxyfluorides

5.2.1 Carbon Fluorides and Oxyfluorides

As a result of the differences in polarity between the carbon–fluorine and the carbon–hydrogen bond, fluorocarbon chemistry is wrought with more differences than similarities to hydrocarbon chemistry despite their similarities in van der Waal's radii (1.20 vs. 1.35 Å). A great body of chemistry for the functionalized fluorocarbons has been developed in the areas of perfluoroalkenes, halofluoroalkanes, ethers, epoxides, peroxides, ketones, acids, and esters.

Fluorocarbons. Fluorocarbons represent a large class of compounds, which could in principle encompass the known variety of hydrocarbon derivatives. For the extensive literature in this area a number of comprehensive works can be consulted.[52–55] The focus of much fluorocarbon chemistry is technically organic chemistry and will not be covered here. The more inorganic aspects of carbon–fluorine chemistry such as the chemistry of simple fluorocarbons, oxyfluorides, and their derivatives will be covered. Trends in reactivity can often be generalized from small molecules to compounds with longer fluoroalkyl chains.

The simplest fluorocarbon, carbon tetrafluoride, CF_4, is an inert gas, bp −128 °C, which is made commercially by direct fluorination of carbon. Carbon tetrafluoride is used in the electronics industry for the purpose of dry etching of silicon.[56]

Among the simple transient species of carbon and fluorine are included: trifluoromethyl cation, CF_3^+, which has a very transient existence; trifluoromethyl anion, CF_3^-, which is stable at low temperature and can be generated from CF_3TMS (trimethylsilyltrifluoromethane); $CF_3\cdot$, a free radical available from irradiation of CF_3I; and difluorocarbene, CF_2:, which exists as a ground-state singlet.

Difluorocarbene can be generated by high-temperature reaction of chlorodifluoromethane in the production of tetrafluoroethylene (TFE) (equation 48). Another method of in situ generation of the carbene is thermal decomposition of hexafluoropropylene oxide (HFPO) (equation 49).

$$CHClF_2 \xrightarrow[0.5\,\text{atm}]{650\,°\text{C}} [CF_2] \longrightarrow CF_2{=}CF_2 \qquad (48)$$

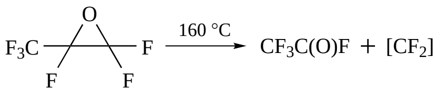

(49)

Finally, the trifluoromethyl anion decomposes on warming to give fluoride ion and difluorocarbene if it is not captured by a suitable electrophile.

Perfluorination techniques have been developed for the conversion of many hydrocarbons to their perfluorinated counterparts.[57,58] Fluorocarbons are chemically inert because of their kinetically unreactive carbon skeletons and have been considered as blood substitutes because of their high oxygen solubility. The thermal stability and low secondary bond forces of fluorocarbons have contributed to their use as greases, lubricants, and vapor-phase heat transfer reagents.

Perfluoroalkenes are significant industrial starting materials, of which the simplest and most important is TFE. This reactive alkene can be reacted, mainly under free radical or anionic conditions, to yield a variety of saturated addition products (Scheme 1). TFE displays versatile polymerization and copolymerization applications.[59]

Polytetrafluoroethylene (PTFE), better known as Teflon, is the preeminent member of the class of saturated fluoropolymers. Commercial uses span from nonstick cooking appliances to inert surfaces for high-energy oxidizing reactions and compressible, durable vacuum-tight gaskets and fittings. Teflon exhibits high stability and inertness and remains the material of choice for many industrial processes despite somewhat high costs.[60]

Despite the great strength of the C–F bonds, methods have been found for their cleavage. For example, a C–F bond may be protonated and cleaved with iridium compounds[61,62] and vinylic and allylic C–F bonds may be activated by $Cp^*{}_2ZrH_2$.[63]

Graphite Fluorides. Graphite fluorides, made by direct fluorination of graphite at different temperatures, have been characterized for the stoichiometries, $(CF)_n$ and $(C_2F)_n$. For the $(CF)_n$ variety (gray-white) temperatures from 300 to 600 °C are required while the $(C_2F)_n$ variety (black)

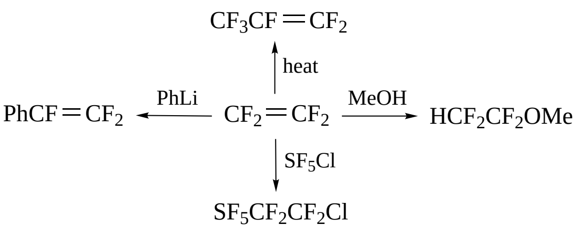

Scheme 1 Some reactions of tetrafluoroethylene

requires 350–400 °C. The bonds in these compounds are covalent, making them electrical insulators. The high density of repulsive fluorine lone pairs provides for good lubricating properties. Graphite fluoride and highly reducing lithium are coupled in Li/$(CF)_n$ batteries, where the $(CF)_n$ serves as the cathode in the electrochemical cell.

In a like manner fluorinated carbon nanotubes and fibers can be formed.[64,65] These materials are the subject of a great deal of interest, owing in part to their variable electronic properties.[66]

Fluorohalocarbons. Volatile CFCs like trichlorofluoromethane, $CFCl_3$, and dichlorodifluoromethane, CF_2Cl_2, developed as refrigerants, solvents, and blowing agents, are now being phased out because of deleterious effects to the ozone layer. The problem of ozone depletion has restricted the production of CFCs and turned attention to chlorine-free fluorinated hydrocarbons and ethers as alternative refrigerants. Some halofluorocarbons such as halothane, $CF_3CHClBr$, have found usage as anesthetics. Other halofluorocarbons are manufactured industrially as flame retardants (CF_2ClBr, CF_2BrCF_2Br).

Trifluoroiodomethane (CF_3I) is a critical starting point for synthetic fluorine chemistry. Many trifluoromethyl–element bonds can be achieved from the relatively reactive carbon–iodine bond. Scheme 2 shows some of the range of CF_3I chemistry. The industrial synthesis of CF_3I is based on the Hunsdiecker reaction of the silver salt of trifluoroacetic acid with iodine. Homologous perfluoroalkyl iodides, sources of longer chain perfluoroacid derivatives, can be made by free radical reaction of CF_3I with TFE.

Oxyfluorides of Carbon. The literature on compounds containing only carbon, oxygen, and fluorine is extensive, numerous reviews are available, and many compounds are of industrial importance.[67] Functional groups included under this classification are ketones, acid fluorides, ethers, epoxides, peroxides, and hypofluorites. Only very simple molecules are mentioned here as representatives of this large class of compounds.

The smallest carbon oxyfluoride, carbonyl difluoride, COF_2, can be synthesized from phosgene by metathesis with sodium fluoride or by the direct reaction of carbon monoxide and fluorine in the gas phase. Carbonyl difluoride boils at −83 °C. It reacts readily with nucleophiles with loss of one or two units of fluoride to yield acid fluorides, amides, and esters. A typical fluorinated nucleophile, $(CF_3)_2N^-$, is implicated as an intermediate in the reaction of the perfluoroimine depicted in equation (50).

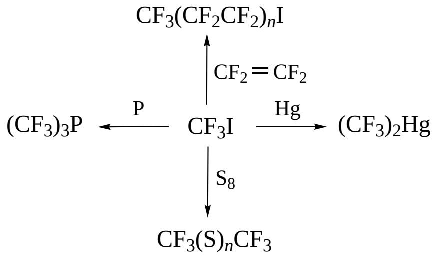

Scheme 2 Some reactions of trifluoromethyl iodide

$$CF_3N{=}CF_2 + COF_2 \xrightarrow{KF} (CF_3)_2N\text{–}C(O)F \qquad (50)$$

The electrophilic nature of COF_2 is beneficial in the reaction of carbonyl difluoride with CsF, which produces trifluoromethyl hypofluorite (CF_3OF) with fluorine and trifluoromethyl hypochlorite (CF_3OCl) with chlorine monofluoride. Both reactions imply the presence of the trifluoromethoxide anion as an intermediate.

A crystal structure of a stable salt of the trifluoromethoxide anion has been made.[68] The preparation involved the use of the stabilizing tris(dimethylamino)sulfonium cation, TAS, as the counterion for CF_3O^-. The reaction is shown in equation (51).

$$COF_2 + [(Me_2N)_3S]^+[SiMe_3F_2]^- \longrightarrow [(Me_2N)_3S]^+[CF_3O]^- + Me_3SiF \qquad (51)$$

Perfluoroalkoxide ions are postulated as intermediates in the mechanism leading to the hypohalites from acid fluorides. Generally, organic hypofluorites can be prepared from acid fluorides by the action of metal fluorides and elemental fluorine (equation 52).[69]

$$R_fCOF + MF \xrightarrow{F_2} R_fCF_2OF \qquad (52)$$
$$M = Cs, K$$

Trifluoromethyl hypofluorite, CF_3OF, the first organic hypofluorite, reacts as if the O–F bond is homolyzed to the trifluoromethoxy radical and a fluorine radical in many reactions, but it has been used effectively as a selective electrophilic fluorination reagent in organic chemistry.[70] It has limited selectivity as a fluorination reagent in inorganic chemistry but it can be oxidatively added to numerous compounds.

Trifluoromethyl hypofluorite can be reacted with carbonyl difluoride to yield bis(trifluoromethyl) peroxide, CF_3OOCF_3, a colorless gas, bp −37 °C, which is quite stable up to 220 °C and chemically relatively inert (equation 53). At high temperatures the peroxide appears to be in equilibrium with COF_2 and CF_3OF. The peroxide is best prepared by reaction of CO and F_2 over AgF_2 at ≈220 °C (equation 54).

$$COF_2 + CF_3OF \xrightleftharpoons{>220\,^\circ C} CF_3OOCF_3 \qquad (53)$$

$$2CO + 3F_2 \xrightarrow[220\,^\circ C]{AgF_2} CF_3OOCF_3 \qquad (54)$$

The reaction of CsF and fluorine with carbon dioxide generates the stable bis-hypofluorite $CF_2(OF)_2$. This remarkable, energetic compound is presumably formed via the intermediacy of the smallest acyl hypofluorite, FC(O)OF, which can itself be prepared by the photochemical fluorination of difluoroformyl peroxide, FC(O)OOC(O)F.

Bis(fluoroxy)difluoromethane reacts with carbonyl difluoride over CsF to yield a bis(trifluoromethyl) trioxide, CF_3OOOCF_3, bp −19 °C, or the peroxy acyl fluoride, $CF_3OOC(O)F$, depending on conditions (equation 55). At low temperature, the trioxide is favored.

$$F_2C(OF)_2 + 2COF_2 \xrightarrow{CsF} CF_3OOOCF_3 + CF_3OOC(O)F + CF_3OF \qquad (55)$$

Fluorine and trifluoromethyl groups appear to stabilize oxygen catenation. The trioxide can be approached alternatively by the reaction of oxygen difluoride and carbonyl difluoride over a metal fluoride catalyst.[71] Depending on conditions, the trioxide will be the major product (equations 56 and 57).

$$OF_2 + COF_2 \xrightarrow{CsF} CF_3OOF \qquad (56)$$

$$CF_3OOF + COF_2 \xrightarrow{CsF} CF_3OOOCF_3 \qquad (57)$$

The trioxide is thermally stable to 70 °C, where it slowly decomposes to CF_3OOCF_3 and oxygen. Many interesting reactions are known for the trioxide involving oxidative additions of both CF_3O and CF_3OO moieties to various substrates.[72]

Bis(fluoroformyl)peroxide, a diacyl peroxide, is a sublimable solid. It can be made in good yields in a flow system from carbon monoxide, fluorine, and oxygen at room temperature (equation 58).

$$F_2 + 2CO + O_2 \longrightarrow F(O)COOC(O)F \qquad (58)$$

The diacyl peroxide has been used as a source of $FCO_2\cdot$ radicals.[73] Fluorination of the peroxide by photolysis with F_2 gives access to the acyl hypofluorite, FC(O)OF, bp ca. −55 °C, in reasonable yields. The acyl hypofluorite is a precursor to a cyclic isomer, the simplest perfluorodioxirane, CF_2O_2, made by the method shown in equation (59).[74]

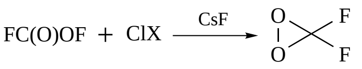

(59)

X = Cl, F

This reaction may involve the intermediacy of the radical $\cdot OCF_2OF$, which cyclizes to generate the dioxirane. The dioxirane is a potent oxygenating agent that generates COF_2 as a by-product. It is thermally stable at 20 °C at modest pressures.

A wide variety of other C–O–F compounds having interesting properties, structures, and reactivity are known, and the literature should be consulted for further information. Unlike traditional C–O–H chemistry, some functional groups have unusual stability and/or reactivity while other traditional groups are unstable and cannot be manipulated under normal conditions. For example, the simplest member of the perfluorinated alcohol family, CF_3OH, is unstable to the loss of HF, as are its higher homologs, R_fOH. It has been synthesized by the reaction of CF_3OCl and HCl at low temperature. The alcohol is collected along with chlorine gas as a by-product.[75]

The simplest perfluorinated ether is CF_3OCF_3, bp −59 °C, which can be prepared by fluorination of CCl_3OCCl_3 with HF and catalytic SbF_xCl_{5-x} or by the ECF of methyl ether using porous carbon electrodes. This fluorinated ether is highly inert chemically. Many ethers can be prepared in high yields by direct fluorination of their hydrocarbon counterparts. A good illustration is the preparation of perfluorinated crown ethers. The effects of fluorocarbon sections are observed in the negligible basicity of the oxygens and the failure of these crown ethers to complex metal cations.[76]

Fluorinated epoxides are very important synthetically. Perfluoroalkenes can be oxidized by numerous means to the corresponding epoxides. The most commonly encountered epoxide is hexafluoropropene oxide (HFPO), which is made from hexafluoropropene and is used in the synthesis of oligomers and as a source of difluorocarbene. HFPO is a colorless, nonflammable gas, boiling at −27.4 °C; it can be ring-opened easily by nucleophiles or electrophiles under a variety of conditions.[77] HFPO can be rearranged by fluoride ion to perfluoropropionyl fluoride and by Lewis acids such as TiO_2 to hexafluoroacetone (HFA). Nucleophiles typically attack the most substituted carbon of the epoxide, freeing the oxyanion to lose fluoride or act as a nucleophile itself. Some examples of HFPO reactivity are shown in Scheme 3.

Fluorinated ketones are important because of their versatile reactivity. HFA, the simplest perfluorinated ketone, reacts readily with nucleophiles as a result of the electron-withdrawing effect of the trifluoromethyl groups. A wide range of both linear and cyclic heteroatom adducts are accessible, as shown in Scheme 4.[78]

5.2.2 *Silicon Fluorides*

Of the simple binary silicon fluorides, SiF_2 and SiF_4, only the tetrafluoride is stable. It is available commercially or can be prepared on a laboratory scale from the elements or from SiO_2, CaF_2, and concentrated H_2SO_4.[79]

Silicon tetrafluoride reacts with pure silicon at low pressure in a flow system at 1200 °C to yield a transient species, SiF_2, which can be condensed to yield a fluorosilane polymer, $(SiF_2)_n$. Silicon difluoride has a half-life of about 150 s in glass at low pressure in the gas phase. The chemistry of SiF_2 shows many different reactions and has been reviewed.[80] When condensed at −196 °C, a red-yellow deposit is formed,

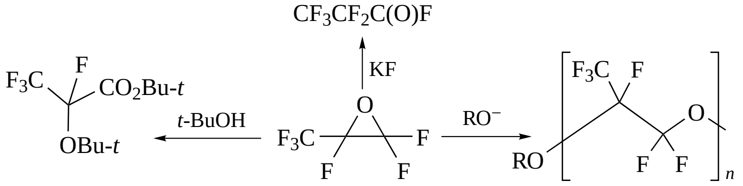

Scheme 3 Some reactions of hexafluoropropene oxide

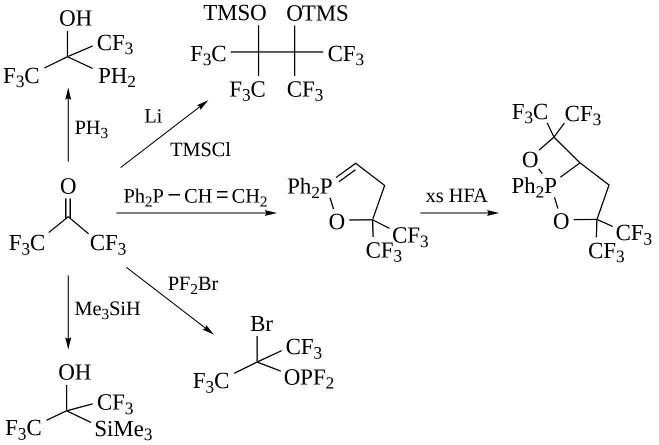

Scheme 4 Some reactions of hexafluoroacetone

which turns white at room temperature. The deposit has the overall stoichiometry of $(SiF_2)_x$ and with respect to its plastic properties and composition it is similar to Teflon. Unfortunately, it burns spontaneously in air. A series of fluoropolysilanes (Si_nF_{2n+2}) can be generated by heating the $(SiF_2)_x$ polymer to 200 °C.

Other types of insertions observed for SiF_2 include reactions with boron trifluoride to yield two different fluoroborosilanes, $F_2B(SiF_2)_nF$ ($n = 2, 3$), and the reaction with hexafluorobenzene to yield $C_6F_5SiF_3$. Silicon tetrafluoride can be hydrolyzed in the vapor phase to yield silicon dioxide and hydrogen fluoride or partially to give $F_3SiOSiF_3$, a colorless gas.[28] With liquid water, hexafluorosilicates are generated (equation 60).

$$3SiF_4 + 6H_2O \longrightarrow 2(H_3O)_2SiF_6 + SiO_2 \tag{60}$$

Many hexafluorosilicate salts from SiF_4 are known. The stable pentafluorosilicon anion $(Ph_4As)(SiF_5)$ can also be generated from silicon tetrafluoride.

The simplest oxide fluoride of silicon, $SiOF_2$, is known; it is prepared by the high-temperature reaction of silica with CaF_2 in an argon atmosphere. The other known oxide fluorides of silicon are a series of fluorosiloxanes, $SiF_3O(SiF_2O)_nSiF_3$, of which Si_2OF_6 is the best known.

5.2.3 *Germanium Fluorides*

There are two binary germanium fluorides known, GeF_2 and GeF_4. Germanium tetrafluoride can be prepared in high yields by pyrolyzing barium hexafluorgermanate, $BaGeF_6$.[81] By analogy to silicon–fluorine chemistry, germanium difluoride, GeF_2, can be made by combination of germanium and germanium tetrafluoride at 150–300 °C.[47]

Salts of trifluorogermanate, GeF_3^-, can be made from germanium difluoride in the presence of metal fluorides. Other species such as GeF_5^- and $Ge_3F_{10}^{2-}$ are also known.

The only known germanium oxyfluoride is Ge_2OF_2.[28] It was detected by mass spectrometry from a mixture of GeO_2, Ge, and NaF.

5.3 Pnicogen Fluorides and Oxyfluorides

5.3.1 *Nitrogen Fluorides*

Nitrogen–fluorine bonds (272 kJ mol^{-1}) are weaker than carbon–fluorine bonds (485 kJ mol^{-1}) but considerably stronger than oxygen–fluorine bonds (190 kJ mol^{-1}). A number of stable binary fluorides as well as nitrogen oxyfluorides have been synthesized and characterized.

Nitrogen trifluoride, the simplest perfluorinated amine, can be made by elemental fluorination of ammonia. Although unreactive like CF_4 at low temperatures, NF_3 acts as a fluorinating agent at higher temperatures, oxidizing copper and generating N_2F_4, a reactive high-energy oxidizer (equation 61).

$$2NF_3 + 2Cu \xrightarrow{\Delta} N_2F_4 + 2CuF \tag{61}$$

N_2F_4 is in equilibrium with $NF_2\cdot$ radicals and behaves as a reactive pseudohalogen. Nitrogen trifluoride has also been considered as the oxidizer in rocket fuels.[82]

Nitrogen trifluoride can be combined with fluorine and fluorinated Lewis acids to generate NF_4^+ salts like the hexafluoroantimonate shown below in equation (62).[83]

$$NF_3 + F_2 + SbF_5 \xrightarrow{200\,°C} [NF_4]^+[SbF_6]^- \tag{62}$$

NF_4^+ salts are usually colorless, crystalline solids. The highly sought ionic fluoride $NF_4^+F^-$ has been predicted to have greater stability than that of the theoretical covalent compound, NF_5. Recent unsuccessful synthetic attempts to generate either $NF_4{}^+F^-$ or the pentavalent NF_5 have been reported.[84]

Fluorine azide, FN_3, a very explosive gas, can be prepared by fluorination of hydrazoic acid (equation 63).[85] The difluorodiazine, N_2F_2, is a thermal decomposition product of FN_3 and exists as cis and trans isomers (equation 64).

$$2F_2 + 4HN_3 \longrightarrow 3FN_3 + N_2 + NH_4F \qquad (63)$$

$$2FN_3 \longrightarrow F\text{–}N{=}N\text{–}F(\textit{cis} \text{ and } \textit{trans}) + 2N_2 \qquad (64)$$

The FN nitrene has been proposed as an intermediate in the reactions of FN_3. The cis isomer of N_2F_2, bp $-105.7\,°C$, exhibits a noticeable difference from the trans form, bp $-111.4\,°C$, in the reaction with AsF_5 to form a hexafluoroarsinate salt, $[N_2F^+][AsF_6{}^-]$.[86]

Difluoroamine, HNF_2, can be made from hydrogen abstraction by N_2F_4 from benzenethiol or acetaldehyde.[87,88] A more direct preparation from elemental fluorine can also be employed (equation 65).[89]

$$H_2NC(O)NH_2 \xrightarrow[H_2O]{F_2/N_2} F_2NC(O)NH_2 \xrightarrow{H_2SO_4} HNF_2 \qquad (65)$$

Difluoroamine can be used as a source of NF_2 group in numerous reactions, but it is dangerously explosive.

Mixed halofluoroamines can be synthesized and isolated. Chlorodifluoroamine, $ClNF_2$, can be made in quantitative yield from the reaction of HNF_2 with NaClO in the presence of HgO.[90] Bromodifluoroamine, $BrNF_2$, is prepared in an analogous way by the reaction of Br_2 with HNF_2 over HgO, but is much less stable than NF_2Cl, decomposing at 22 °C into Br_2 and N_2F_4.[82] Chlorodifluoroamine can also be prepared from N_2F_4 and Cl_2. It has been extensively studied as a source of NF_2 derivatives. Dichlorofluoroamine, Cl_2NF, is explosive in the liquid or solid phase. It is formed by the reaction of ClF with NaN_3 at $-10\,°C$ or by the reaction of $FC(O)NCl_2$ with F_2.[91]

5.3.2 *Nitrogen Oxyfluorides*

There exist a number of important small oxyfluorides of nitrogen including nitrosyl fluoride, FNO, and nitryl fluoride, FNO_2, which can be made by fluoride attack or elemental fluorination.[92,93] Nitrosyl fluoride, FNO, was first synthesized from nitrosyl chloride and silver(I) fluoride, but it is more easily prepared by reaction of N_2O_4 with metal fluorides.[94] This compound is unstable in glass, attacks many metals, and behaves as a strong oxidizer and fluorinating agent. A principal mode of reactivity involves loss of fluoride and release of NO. One application is the fluorination of chloromethanes. Another mode of reactivity involves combination with Lewis acid fluorides to yield $[NO^+][EF_n{}^-]$ salts (E = Sb, As, P).

Nitryl fluoride, NO_2F, can be made by fluorination of NO_2 or by reaction of N_2O_5 with metal fluorides. The chemistry of NO_2F is similar to that of NOF although NO_2F is more stable and less oxidizing. Salt formation from NO_2F is possible with Lewis acids, giving, for example, $[NO_2{}^+][PF_6{}^-]$.

Trifluoroamine oxide, ONF_3, bp $-87.6\,°C$, can be made by fluorination of nitrosyl fluoride with IrF_6 or reaction of NO with F_2.[95] F_3NO is stable in glass at 22 °C and is kinetically much less reactive than FNO and FNO_2. Most reactions involve reaction of F_3NO with strong Lewis acids to form $ONF_2{}^+$ salts.

5.3.3 *Phosphorus Fluorides and Oxyfluorides*

Phosphorus–fluorine compounds have been known since before the isolation of elemental fluorine.[96] Owing to the strong interest in the biological activity and structural properties of fluorine-containing phosphorus compounds, a large number of compounds have been prepared and characterized.

Phosphorus Fluorides. The lowest oxidation state for a binary fluoride of phosphorus is found in P_2F_4 (bp $-6.2\,°C$). After the synthesis of N_2F_4, many unsuccessful attempts were made to prepare P_2F_4 and it was finally obtained from PF_2I after a good synthesis for the latter was developed (equation 66).[97]

$$2PF_2I + 2Hg \longrightarrow 2P_2F_4 + Hg_2I_2 \qquad (66)$$

The structure of P_2F_4 is trans with angles $FPF = 99.1°$ and $PPF = 95.4°$.[34] It hydrolyzes readily to F_2POPF_2, and O_2 reacts with it to give the same product. Unlike N_2F_4, it is not a ready source of the PF_2 radical.

Phosphorus trifluoride (bp $-101.8\,°C$) is readily obtained from PCl_3 or PBr_3 by direct reaction with metal fluorides such as ZnF_2, PbF_2, or CaF_2, or with NaF in a polar solvent, or by many other reactions. It is pyramidal (angle $FPF = 96.3°$) and is comparable to CO in donor properties, for example, $Ni(CO)_n(PF_3)_{4-n}$ ($n = 0$–4).[96] PF_3 is easily oxidized to P^V derivatives and numerous oxygenating reagents give OPF_3; Cl_2 and Br_2 add to give PF_3X_2 and ClF adds at very low temperature to give PF_4Cl.

Phosphorus trifluoride slowly hydrolyzes to H_3PO_3 and HF and in dilute alkaline solutions the intermediate monofluorophosphorus acid is observed. It can be used to prepare a variety of substituted organophosphorus fluorides but PCl_3 is far more important in this respect. Nearly all possible mixed $PF_{3-x}X_x$ (X = Cl, Br, I) have been prepared.

Phosphorus pentafluoride (bp $-84.5\,°C$) is most easily prepared by reaction of PCl_5 with AsF_3 or HF, but many other methods have been used. The molecule has a trigonal bipyramidal structure in the gas phase with longer axial bonds (158 pm compared to 153 pm for the equatorial fluorines). Pseudorotation in molecules was first recognized in PF_5 to explain the presence of only a single fluorine resonance in the ^{19}F NMR. Phosphorus pentafluoride is a strong Lewis acid and forms both neutral and ionic adducts with many donors such as THF and metal fluorides. The PF_6^- anion is a useful counterion for many complex inorganic cations. Phosphorus pentafluoride reacts with the strong Lewis acid SbF_5 to give the tetrahedral PF_4^+ cation.**[98]**

Mixed pentahalides, $PF_{5-n}X_n$ (X = Cl, Br, I), are known but only the chlorides PF_4Cl, PF_3Cl_2, PF_2Cl_3, and PF_3Br_2 are well characterized as molecular species. Many of the other mixed halides are complex salts or mixtures of complex salts of the type $PX_4^+X^-$ and $PX_4^+\ PX_6^-$.

Phosphorus Oxyfluorides. Numerous phosphorus(III and V) oxyfluorides and oxyfluoride anions are known. Two oxyfluorides containing P^{III} are PF_2OPF_2 (bp −183 °C) from reaction of P_2F_4 with H_2O or O_2, or PF_2I with Cu_2O (equation 67), and the mixed P^V–P^{III} oxide $PF_2OP(O)F_2$ (bp 48 °C) from OPF_2Br (equation 68).**[28]** Very little chemistry has been determined for either compound.

$$PF_2I + Cu_2O \longrightarrow PF_2OPF_2 + CuI \qquad (67)$$

$$OPF_2Br \xrightarrow[Hg]{h\nu} PF_2OP(O)F_2 \qquad (68)$$

The simplest oxyfluoride is POF_3 (bp −39.7 °C). It is obtained by many methods but most readily by fluorination of $OPCl_3$ with metal fluorides or HF. The structure (C_{3v}) has angle FPF = 101.3°. Phosphoryl fluoride hydrolyzes slowly to phosphoric acid via the intermediate difluoro- and monofluorophosphoric acids, $HOP(O)F_2$ and $(HO)_2P(O)F$. The latter are best prepared by reaction of P_4O_{10} with HF. Phosphoryl fluoride has little useful reaction chemistry and the large number of $RP(O)F_2$ and $R_2P(O)F$ derivatives that are known is due to the interest in the biological activity of compounds of this type (nerve gases); they have mostly been obtained starting with chlorides.**[96]**

The series $OPF_{3-n}X_n$ (X = Cl and Br) are well known and excellent methods are available for the preparation of OPF_2X.

Diphosphoryl tetrafluoride, $P_2O_3F_4$ (bp 71 °C), is the anhydride of difluorophosphoric acid and can be obtained by dehydration of $HOP(O)F_2$ with P_4O_{10}, or by photolysis of OPF_2Br with O_2 for an easily purified product (equations 69 and 70).**[99]**

$$HOP(O)F_2 + PBr_5 \xrightarrow{100\,^{\circ}C} HBr + OPBr_3 + POF_2Br \qquad (69)$$

$$POF_2Br \xrightarrow[O_2]{h\nu} F_2P(O)OP(O)F_2 \qquad (70)$$

The anhydride reacts with a variety of nucleophiles to cleave an O–P bond; Lewis acids react similarly. Thus CsF gives POF_3 and $CsPO_2F_2$, and $AlCl_3$ gives OPF_2Cl in high yield.

Other polyphosphoryl fluorides have been reported but are not well characterized.

5.3.4 Arsenic Fluorides and Antimony Fluorides

Arsenic trifluoride, AsF_3, a molecular species, is synthesized from As_2O_3 and anhydrous HF. Antimony trifluoride, SbF_3, can be made by the action of aqueous HF on Sb_2O_3. Both fluorides are important agents for fluorination of chlorinated substrates.

The pentafluorides, AsF_5 and SbF_5, are prepared by direct fluorination of the elements or their oxides. Both AsF_5 and SbF_5 are used as Lewis acid fluoride acceptors in the preparation of many MF_6^- salts. Anhydrous HF has greatly increased acidity in the presence of SbF_5 because of the creation of the H_2F^+ cation by removal of fluoride. The hexafluoroantimonate anion stabilizes many energetic cationic species, for example, $[NF_4^+][SbF_6^-]$.

5.4 Chalcogen Fluorine Compounds

The synthesis and chemistry of the chalcogen fluorides began with Henri Moissan over 100 years ago. In the last 40 years, these fluorides and their derivatives have been the subject of intense study, which has led to a large number of interesting compounds with a wide range of properties and reactivity. Some of these compounds have important industrial applications, most notably SF_6 and SO_2F_2.

5.4.1 Oxygen Fluorides

There have been many oxygen fluorides discussed in the literature, including OF_2, O_2F_2, F_2O_4, HOF, F_2O_3, F_2O_5, and F_2O_6. Of these, only OF_2 is stable and only the first four have been conclusively proven to exist (Table 8).**[100]** During the early development of the space program, oxygen fluorides attracted much attention. These fluorides are endothermic and powerful oxidizing agents. For these reasons, they were considered for potential use in high-energy propellant and explosive systems. The hazards involved with handling the compounds and by-products, that is, HF, caused the search for propellants to move elsewhere. Still, this initial interest has contributed greatly to the development of this area.

Oxygen difluoride is a colorless, poisonous gas that condenses to a pale yellow liquid. It can be most efficiently prepared by the electrolysis of aqueous HF (equation 71).**[101]**

$$2HF + 6H_2O \xrightarrow{e^-} OF_2 + O_3 + 7H_2 \qquad (71)$$

An alternative procedure involves reacting F_2 gas with a 2% aqueous NaOH solution (equation 72).**[102]**

$$2F_2 + 2NaOH \longrightarrow OF_2 + 2NaF + H_2O \qquad (72)$$

Table 8 Oxygen fluorides

Formula	Bp (°C)	Mp (°C)	Structural data
OF_2	−145.3	−223.8	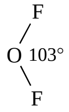
O_2F_2	−57	−153.3	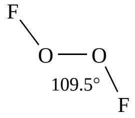
O_4F_2	-79^b	−191	–
HOF	<rt	−117	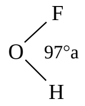

[a] Smallest known bond angle for two-coordinate oxygen in an open chain. [b] Extrapolated; decomposes at −183 °C.

OF_2 is a powerful fluorination agent that has proven effective as a source of the fluorides and oxyfluorides of many elements. Both xenon and krypton react with OF_2 in sunlight at 25 °C to give the corresponding difluorides. Reaction with nitrogen under an electric discharge at low temperature gives nitryl fluoride and fluorine nitrate, among other products (equation 73).[103]

$$OF_2 + N_2 \xrightarrow[\text{discharge}]{-180\,^\circ\text{C}} O_2 + N_2O + FNO_2 + FNO_3 \qquad (73)$$

Reactions of OF_2 can give rise to high-yield syntheses of peroxides and trioxides (equations 74 and 75).

$$OF_2 + COF_2/CsF \longrightarrow CF_3OOOCF_3 + CF_3OOF \qquad (74)$$

$$OF_2 + SO_3 \xrightarrow{h\nu} FSO_2OOF \qquad (75)$$

Dioxygen difluoride, O_2F_2, is a pale yellow liquid that can be prepared by exposing the liquid mixture of the elements to UV light. It is much less stable than OF_2 and decomposes above 195 K to give O_2 and F_2. The mechanism of its reactions can be explained generally as cleavage of the O–F bond, leading to the formation of F atoms and OOF radicals. The very weak O–F bonds in both O_2F_2 and O_2F are reasonably explained by molecular orbital theory involving multicenter four-electron bonds.[104]

Recently, O_2F_2 has shown promise as a controllable low-temperature fluorinating agent. PuF_6 and UF_6 are produced by the action of O_2F_2 on PuO_2 and U_3O_8 at room temperature. This has technological significance because typically direct fluorination of the actinides are achieved only at high temperatures. This has led to consideration of O_2F/F_2O_2 in nuclear waste recovery.

Electric discharge through mixtures of oxygen and fluorine also provides a route to O_4F_2. Tetraoxygen difluoride, a red–brown solid, is less stable than O_2F_2 and decomposes at −183 °C, but can be stored for weeks at −196 °C. Few studies of its reaction chemistry have been reported.

Manipulation of ratios of fluorine and oxygen in glow discharge have been reported to provide entry into the homologous O_3F_2, O_5F_2, and O_6F_2.[105] Though some evidence exists for these compounds, it is not conclusive and their existence remains the subject of some debate.

Hypofluorous Acid. Hypofluorous acid (HOF) may be prepared by passing fluorine over water in a Kel-F reactor at 0 °C (equation 76).[106]

$$F_2 + H_2O \xrightarrow[\text{Kel-F}]{0\,^\circ\text{C}} HOF + HF \qquad (76)$$

Warming HOF to room temperature releases HF and O_2. Hypofluorous acid is a strong oxidizer that oxidizes water to hydrogen peroxide in acidic solution. It is thought to be the reactive species when F_2 reacts in aqueous media. In general, HOF acts as an oxygen donor, or a donor of its conjugate acid OH^+, because of the great affinity between the protons and the neighboring fluorine atoms. Formally, HOF could be a source of the OF^- anion by reaction with an appropriate base but no indication of this has appeared. However, there is reasonable evidence for the generation of the anion by reaction of $FOSO_2F$ with CsF.[107]

A wide variety of oxyfluorides containing O–F bonds have been prepared and are discussed under the respective element oxyfluorides.

5.4.2 *Sulfur Fluorides*

The area of sulfur–fluorine chemistry is a particularly rich and diverse field. The seven known binary sulfur fluorides, FSSF, $S{=}SF_2$, SF_2, $FSSF_3$, SF_4, SF_6, and S_2F_{10}, have a range of formal oxidation states from 1 to 6 and a wide range of chemical properties (Table 9). The lower fluorides are extremely unstable while SF_6 is almost totally inert. Sulfur tetrafluoride is stable but highly reactive, and is used extensively for fluorinations in both organic and inorganic chemistry. The synthesis and chemistry of these compounds have been well developed and continue to be very active areas of research. Numerous general reviews can be found.[108–110] All of the fluorides of sulfur are colorless gases and liquids. SF_6 has the highest density of any substance that boils below room temperature (5.107 times as dense as air).

Considering the high stability of H_2S and SCl_2, SF_2 is surprisingly unstable.[111,112] It is only observed in very dilute mixtures or when trapped in an argon matrix. It is synthesized by fluorinating SCl_2 with activated KF or HgF_2 at 150 °C. This synthesis produces many sulfur fluorides, and sulfur difluoride is only a minor product. Separation of SF_2 from these other sulfur fluorides is difficult. Other difficulties arise

Table 9 Sulfur fluorides

Formula	Structure	Point group	Ox. State	Bp (°C)	Mp (°C)
FSSF	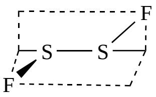	C_2	S^{I}	15	−133
SSF_2	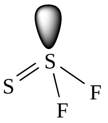	C_s	S^{II} and S^{IV}	−10.6	−164.6
SF_2	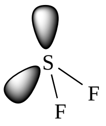	C_{2v}	S^{II}	–	–
$FSSF_3$	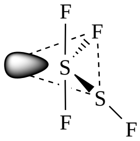	C_1	S^{I} and S^{III}	–	–
SF_4	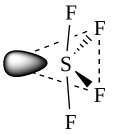	C_{2v}	S^{IV}	−40.4	−121
F_5SSF_5	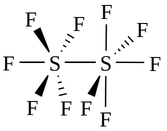	D_{4d}	S^{V}	30	−52.7
SF_6	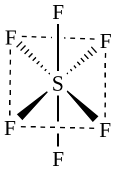	O_h	S^{VI}	−63.8	−50.5 (subl)

with characterization and storage of the compound because it rapidly dimerizes to form F_3SSF.

The reaction of sulfur vapor with AgF at 125 °C gives FSSF.[113] This in turn can be converted to the more stable isomer $S{=}SF_2$ in the presence of alkali metal fluorides or BF_3. Both isomers rapidly hydrolyze to give S_8, HF, and a mixture of polythionic acids, $H_2S_nO_6$ ($n = 4$–6).

Sulfur tetrafluoride is very stable when compared to the lower sulfur fluorides. It can be stored at room temperature for an indefinite period of time. It is very reactive and is valued as a selective fluorinating agent for both organic and inorganic compounds. Its remarkable fluorinating ability has been the subject of recent reviews.[114,115]

Sulfur tetrafluoride is best prepared by the reaction of S_8, Cl_2, and NaF in acetonitrile at 75 °C. It must be handled under anhydrous conditions because it will quickly hydrolyze to form HF and SOF_2 or SO_2. Sulfur tetrafluoride is amphoteric, and forms numerous stable adducts with both Lewis acids and Lewis bases. A number of nonmetal fluorides react with SF_4 to give salts containing the $SF_3{}^+$ cation (equation 77).

$$SF_4 + EF \longrightarrow [SF_3]^+[EF_2]^- \qquad (77)$$
$$EF = BF_3,\ PF_5,\ AsF_5,\ SbF_5,\ HF$$

SF_4 can also behave as a Lewis acid and reacts with pyridine and active fluoride sources to form stable adducts. With fluorides the $SF_5{}^-$ anion is formed (equation 78).[116]

$$SF_4 + EF \longrightarrow [SF_5]^-[E]^+ \qquad (78)$$
$$EF = CsF,\ (CF_3)_4NF,\ Me_4NF$$

Sulfur tetrafluoride has been successfully used as a selective fluorinating agent in a wide variety of organic and inorganic systems. It is particularly useful for converting element–oxygen bonds to the respective fluorides (Scheme 5).

While SF_4 continues to be used as a fluorinating agent, its low boiling point presents some difficulties and a series of liquid fluorosulfuranes have been developed that react similarly under milder conditions. Commercially available dialkylaminotrifluorosulfuranes (DAST) are made by the reaction of dialkylaminotrimethylsilanes with SF_4 in a solvent at low temperatures. These sulfuranes, like SF_4, are easily hydrolyzed, but are stable for long periods if protected from water.[117]

Sulfur tetrafluoride will undergo numerous oxidative addition reactions to give S^{VI} derivatives. Reactions of SF_4 with F_2, ClF, F_5SOOSF_5, and N_2F_4 give SF_6, SF_5Cl, *cis*-$SF_4(OSF_5)_2$, and SF_5NF_2, respectively.

Photolytically, reduction of SF_5Cl with H_2 gives the largest known binary sulfur fluoride, disulfur decafluoride. It is also a trace by-product of the industrial preparation of SF_6, but it is not isolated and is destroyed by heating to 400 °C. Disulfur decafluoride is a liquid at room temperature that will completely decompose at 200 °C to SF_4 and SF_6. It is intermediate in properties when compared to SF_4 and SF_6. It is not hydrolyzed by water alone, but it is slowly attacked by aqueous NaOH. Disulfur decafluoride can be stored at room temperature as a liquid for years. Like SF_4, it is extremely

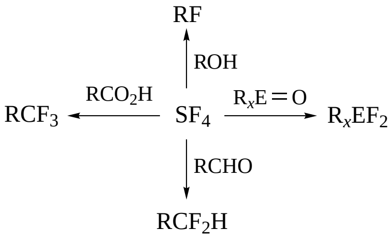

E = C, As, Ge, Sb, I

Scheme 5 Some reactions of SF_4

toxic and should be handled with care. Disulfur decafluoride reacts readily with Cl_2 and Br_2 to give SF_5Cl and SF_5Br and can serve as a source of SF_5 radicals in a variety of reactions.

SF_6 was first made by Henri Moissan in 1891 when he burned sulfur in a fluorine atmosphere. This is the heart of the commercial synthesis used today, which combines heating sulfur to 400 °C with fluorine gas, followed by scrubbing with NaOH to destroy traces of S_2F_{10}. The gas is then thoroughly dried. Sulfur hexafluoride is colorless, odorless, tasteless, and nontoxic. It is stable at 500 °C and does not react with distilling phosphorus. The compound shows some instability with certain metals at lower temperatures (200 °C), depending on the presence of water. Because of its remarkable kinetic stability, sulfur hexafluoride does not have much important reaction chemistry. It is, however, greatly valued in numerous industrial applications.**[118]** It has excellent insulating properties for high voltage apparati because of it high dielectric strength. Today it is used extensively in the electric power industry to protect circuit breakers, high voltage coaxial cables, power substations, and transformers. It is even used in space satellites to protect their electronic equipment. Since it is inert and has a high density, SF_6 is also used to inflate tires and tennis balls.

5.4.3 *Sulfur Oxyfluorides*

Three simple oxide fluorides of sulfur, thionyl fluoride (SOF_2), sulfuryl fluoride (SO_2F_2), and sulfur oxide tetrafluoride (SOF_4), have been known for years (Table 10). There also exists a large series of complex oxide fluorides that can be divided into two main groups. One has the $–SO_2F$ structural group and the other an $–SF_5$ group. These complexes generally involve $–O_n–$bridging between sulfur atoms. There have been several good reviews on sulfur oxide fluorides.**[119–123]**

Thionyl fluoride is a colorless gas that was first prepared by reacting $OSCl_2$ with ZnF_2; however, a better method is fluorination with NaF (equation 79).**[124]**

$$SOCl_2 + NaF \xrightarrow{MeCN} SOF_2 \tag{79}$$

Thionyl fluoride behaves as a weak Lewis base using the lone pair on oxygen for donation. It will react with SiF_2 to form a series of fluorosiloxanes and also with various fluorinating agents to give SOF_4.

Sulfuryl fluoride**[125]** is a colorless gas that was first prepared by direct fluorination of SO_2. Since then, numerous methods have been developed to prepare SO_2F_2, but the best three appear to be the reaction of SO_2Cl_2 with SbF_3, the thermal decomposition of barium fluorosulfate at 500 °C, and the reaction of KSO_2F with chlorine.**[126]**

Sulfuryl fluoride is generally a chemically inert gas and its hydrolysis in basic solution is slow. It will, however, react readily with nucleophiles to give substituted products (Scheme 6). Its major use is as a fumigant in the eradication of termites and other pests.

Fluorosulfuric acid, $HOSO_2F$, can be prepared by the replacement of chlorine in chlorosulfonic acid with fluoride, but is best prepared from HF and SO_3. It is a colorless fuming liquid, and is one of the strongest simple acids known. It has been the subject of a number of reviews.**[127]** This acid has many remarkable properties and industrial applications. It has the unique ability to solvate electrolytes and stabilize cationic species that are not stable in less acidic media. It has been successfully used as a fluorinating agent in both organic and inorganic chemistry. It can also be used as a catalyst in many organic reactions. As a fluorination reagent it is particularly effective in replacement of OH by F in nonmetal compounds, as in the synthesis of TeF_5OH from BaH_4TeO_6. Fluorosulfuric acid can be used to prepare a variety of metal fluorosulfate salts.

As stated earlier, SOF_4 can be prepared by elemental fluorination of SOF_2 (equation 80). Sulfur oxide tetrafluoride has been observed to behave as a fluoride ion acceptor and donor, forming $Cs^+[OSF_5\ ]^-$ and $[SOF_3]^+[SbF_6]^-$. It also provides, with F_2 gas over a CsF catalyst, an excellent route to SF_5OF.**[128]**

$$SOF_2 + F_2 \longrightarrow SOF_4 \tag{80}$$

Complex oxyfluorides of sulfur containing the $–SF_5$**[129]** group are SF_5OF and $SF_5O_nSF_5$ ($n = 1–3$), as well as other

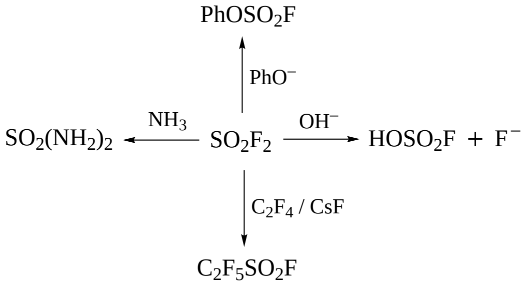

Scheme 6 Some reactions of SO_2F_2

Table 10 Sulfur oxyfluorides

	SOF_2	SO_2F_2	SOF_4	HSO_3F	SF_5OF	$(SF_5)_2O$	$(SF_5O)_2$	$S_2O_6F_2$
Bp (°C)	−43.8	−55.4	−49.0	163	−35.1	31	49.4	67.1
Mp (°C)	−129.5	−135.8	−99.6	89.0	−86	−55.4	−95.4	−55.4
Density ($g\,mL^{-1}$)	–	2.577	2.70	1.73	2.79	–	1.97	2.40

more complex compounds. Bis(pentafluorosulfur) peroxide, SF_5OOSF_5, was first prepared serendipitously when oxygen impurities in the fluorine used to fluorinate sulfur resulted in its low-yield synthesis. Recently, the peroxide has been made in excellent yield by the thermal reaction of SOF_4 and SF_5OF under high pressure in a copper reactor.[130] Bis(pentafluorosulfur) oxide, SF_5OSF_5, is produced in high yields from the photochemical reaction of SF_5OCl with SF_5Cl.

In recent years, the field of complex oxide fluorides has been dominated by the rich chemistry of peroxodisulfuryl difluoride, $S_2O_6F_2$.[131] It is a colorless liquid, best made on a large scale by the reaction of SO_3 with F_2 over an AgF_2 catalyst.

Peroxodisulfuryl difluoride reversibly dissociates into yellow fluorosulfate radicals at elevated temperatures. In a 1-l glass vessel, 100 Torr of $S_2O_6F_2$ gives a bright yellow color when heated to 150 °C. The $FSO_3\cdot$ radical is a powerful one-electron oxidant, forming the very stable fluorosulfate anion or covalent bonds with many metals and nonmetals (Scheme 7).

5.4.4 Selenium and Tellurium Fluorides

The range of known selenium and tellurium fluorides includes many examples similar to sulfur but important differences are found, with Se and Te often adopting higher coordination numbers (Table 11). No lower fluorides are known except the unstable species FSeSeF, $Se{=}SeF_2$, and SeF_2.

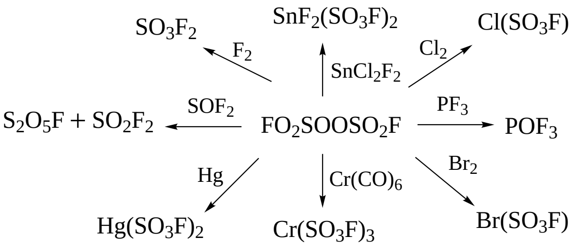

Scheme 7 Some reactions of FO_2SOOSO_2F

Table 11 Selenium and tellurium fluorides

	SeF_6	TeF_6	SeF_4	TeF_4	Te_2F_{10}
Bp (°C)	−47 subl.	−39 subl.	101	–	59
Mp (°C)	−35	−38	−9.5	129	−34

Both tetrafluorides can be synthesized from the action of SF_4 on the dioxides. Selenium tetrafluoride is a white solid that melts to a colorless liquid. It can be handled in rigorously dried Pyrex, reacting slowly with glass but violently with H_2O. Selenium tetrafluoride can solvate many fluorides. Selenium tetrafluoride and other organic Se^{IV} fluorides have been utilized as fluorinating agents for alcohols and carbonyl compounds.

Tellurium tetrafluoride forms colorless sublimable crystals that exist as chains of *cis*-linked square-pyramidal TeF_5 groups (**1**). Its chemistry is similar to SeF_4, but is less useful for fluorination.

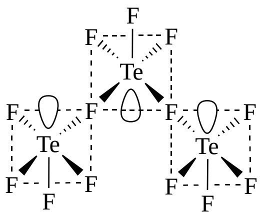

(**1**)

Both SeF_6 and TeF_6 may be prepared by the direct fluorination of the elements or by the reaction of BrF_3 with the dioxides. Both are toxic, colorless gases with offensive smells. The Se^{VI} and Te^{VI} fluorides are not as chemically inert as SF_6. Te_2F_{10} is a volatile liquid that can be synthesized from a mixture of F_2/O_2 and a mixture of Te/TeO_2 at 50–60 °C.

5.4.5 Selenium[132] and Tellurium[133] Oxyfluorides

Many compounds containing fluorine and oxygen are known for selenium and tellurium (Table 12). $SeOF_2$ is prepared by reaction of SeO_2 with SeF_4. SeO_2F_2 can be prepared from SeO_3 and SeF_4 in an analogous reaction or by reacting $SeOF_2$ with F_2. Reaction of SeO_2 with an F_2/N_2 mixture generates the hypofluorite SeF_5OF and the peroxide $F_5SeOOSeF_5$, depending on reaction conditions.

The two most important compounds for the synthesis of EF_5O derivatives (E = Se, Te) are the strong acids EF_5OH. TeF_5OH (bp 59.7 °C) is prepared in good yield by heating BaH_4TeO_6 with excess $HOSO_2F$. SeF_5OH (bp 47 °C) is prepared by reaction of SeO_2F_2 with a small excess of HF at 22 °C. These acids are used to prepare a variety of derivatives, including the important transfer agents $Hg(OEF_5)_2$ and $B(OTeF_5)_3$.

Both of the bispentafluoro peroxides can be prepared from $Xe(OMF_5)_2$ by UV irradiation of the melted xenon compound

Table 12 Selenium and tellurium oxyfluorides

	$SeOF_2$	SeO_2F_2	$(SeF_5O)_2$	$(SeF_5)_2O$	$(SeF_4O)_2$	$(TeF_5O)_2$	$(TeF_5)_2O$	$(TeF_4O)_2$
Bp (°C)	126	−9.5	−61.5	53	65	81.5	59.8	77.5
Mp (°C)	15	−99.5	−62.8	−85	−12	−39	−36.6	28

(equation 81).

$$Xe(OMF_5)_2 \xrightarrow{h\nu} Xe + F_5MOOMF_5 \qquad (81)$$

Thermolysis of $B(OSeF_5)_3$ and $B(OTeF_5)_3$ yields the compounds $Se_2O_2F_8$ and $Te_2O_2F_8$, which are dimers of the simple OMF_4 structure containing bridging oxygens (**2**).

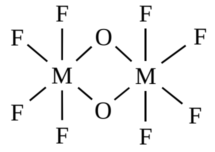

(**2**)

Some exotic structures have been made containing tellurium both as a central atom and as a fluorinated ligand. For example, the series of Te^{VI} octahedral compounds $F_4Te(OTeF_5)_2$ (cis and trans), $F_2Te(OTeF_5)_4$ (cis and trans), $FTe(OTeF_5)_5$, and $Te(OTeF_5)_6$ have been made via ligand exchange with $B(OTeF_5)_3$.

The $–OTeF_5$ group has been shown to provide a large nonbridging ligand with an electronegativity approaching that of fluorine. The ether $F_5Te–O–TeF_5$ was prepared by direct fluorination of TeO_2 with F_2/N_2.

5.5 Halogen Fluorides and Oxyfluorides

5.5.1 Halogen Fluorides[134,135]

Each of the halogens reacts exothermically with fluorine and, depending on stoichiometry and reaction conditions, generates compounds with four possible oxidation states. Stoichiometries of XF, XF_3, and XF_5 are known for Cl, Br, and I; IF_7 is also known (Table 13). All halogen fluorides are diamagnetic and have an even number of atoms. Their reaction chemistry is similar to that of fluorine, and they are extremely reactive fluorinating agents. They comprise one of the most reactive classes of compounds known. For a given stoichiometry XF_n, the following order of reactivity holds: $ClF_n > BrF_n > IF_n$. For a given halogen fluoride the reactivity generally decreases with the number of fluorine atoms. The sequence of reactivity for all the binary halogen fluorides usually quoted is as follows: $ClF_3 > ClF_5 > BrF_5 > IF_7 > ClF > BrF_3 > IF_5 > BrF > IF_3 > IF$. Under proper conditions, reactions with all organic materials, metals and nonmetals are known.

Table 13 Halogen fluorides[33]

XF (bp/mp °C)	XF_3	XF_5	XF_7
ClF (−100.1/ −155.6)	ClF_3 (11.8/ −76.3)	ClF_5 (−13.1/ −103)	[d]
BrF (≈20[a]/ ≈−33[a])	BrF_3 (125.8/ 8.8)	BrF_5 (41.3/ −60.5)	[d]
IF[a]	IF_3 (−28[a])	IF_5 (104.5/9.4)	IF_7 (4.8[c]/6.5[b])

[a]Decomposes. [b]Triple point. [c]Sublimation. [d]Compound unknown.

Diatomic Halogen Fluorides. All three diatomic halogen fluorides (XF) exist, but only ClF is stable. BrF exists only in equilibrium with Br_2 and BrF_5, so it is impossible to isolate. Both IF and BrF disproportionate rapidly and irreversibly to higher fluorides and Br_2 or I_2.

Chlorine monofluoride is a colorless gas that condenses to a very pale yellow liquid. It is prepared by the interaction of chlorine trifluoride and chlorine or by heating chlorine and fluorine together in a 1:1 ratio. It can be used to saturate multiply bonded systems or oxidize coordinatively unsaturated central atoms. Scheme 8 illustrates some types of ClF reactivity.[136]

Halogen Trifluorides. All the trifluorides (XF_3) of the halogens can be synthesized by direct combination of the proper proportions of the halogens with fluorine. IF_3, which is unstable above −28 °C, can also be made by the action of XeF_2 on I_2. ClF_3 and BrF_3 have a T-shaped structure with a C_{2v} symmetry (**3**).

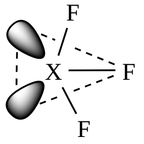

X = Cl, Br
(**3**)

Chlorine trifluoride, ClF_3, is violently reactive with many oxidizable substrates. It is available commercially and has been utilized to fluorinate uranium to UF_6 in the nuclear power industry. This is an important step in uranium enrichment because volatile UF_6 can be readily separated from the nonvolatile fluoride impurities.

Chlorine trifluoride may serve as a fluoride donor or fluoride acceptor to give cations and anions, depending on the substrate employed (Scheme 9).

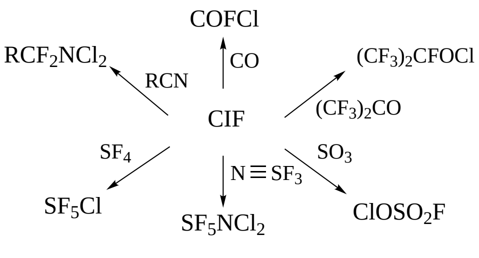

Scheme 8 Some reactions of ClF

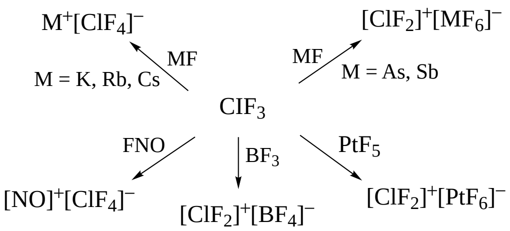

Scheme 9 Some reactions of chlorine trifluoride

Bromine trifluoride, BrF_3, is also commercially available and is used as a nonaqueous ionizing solvent. Its electrical conductivity is derived from a dissociative equilibrium (equation 82). It fluorinates most substrates that dissolve in it and typically gives fluorides in their highest valency state.

$$2BrF_3 \rightleftharpoons [BrF_2]^+ + [BrF_4]^- \qquad (82)$$

5.5.2 *Halogen Pentafluorides*

The three pentafluorides (XF_5)[137] are conveniently made by direct fluorination of the halogens or a lower halogen fluoride. All can be used as fluorinating agents. Chlorine pentafluoride, ClF_5, and BrF_5 are considerably more vigorous than IF_5. All three pentafluorides react vigorously with H_2O. Bromine pentafluoride and iodine pentafluoride react in a 1:3 ratio with H_2O to yield a mixture of hydrofluoric acid and either bromic or iodic acid. The chlorine analog gives $FClO_2$ and HF upon reacting in a 1:2 ratio with H_2O. All the pentafluorides are colorless gases and condense to volatile colorless liquids. The molecular structure of XF_5 is square pyramidal (C_{4v}) with the central X atom slightly below the plane of the four base fluorine atoms (**4**).

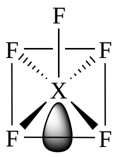

(**4**)

All three pentafluorides form adducts with AsF_5 and SbF_5. ClF_5 and IF_5 form 1:1 adducts while the adduct with BrF_5 is 1:2, $[BrF_4]^+[Sb_2F_{11}]^-$. Conversely, these pentafluorides can behave as fluoride ion acceptors: both $CsBrF_6$ and KIF_6 can be isolated. Several hundred tons of IF_5 are manufactured in the United States each year because of its important reactions with perfluoroalkenes. In the presence of SbF_5 the reaction of IF_5 with alkenes gives the telomer in high yields. BrF_5 thermally decomposes above 559 °C to give BrF_3 and F_2. BrF_5 fluorinates Mg_2N_3 at room temperature to give N_2F_2.[138]

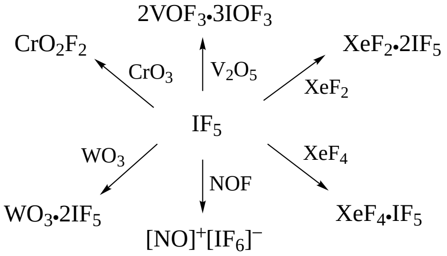

Scheme 10 Some reactions of iodine pentafluoride

The cations $ClF_6{}^+$ and $BrF_6{}^+$ have been made by oxidation of the pentafluorides with extremely strong oxidizers such as PtF_6 or KrF^+ (equation 83).

$$ClF_5 + PtF_6 \longrightarrow [ClF_6]^+[PtF_6]^- + [ClF_4]^+[PtF_6]^- \qquad (83)$$

Decomposition of the strongly oxidizing krypton fluorides in a solution of BrF_5 at ambient temperatures yields $BrF_6{}^+$ in small yields. The salt $[BrF_6{}^+][AsF_6{}^-]$ results when $Kr_2F_3AsF_6$ or $KrFAsF_6$ is decomposed in BrF_5.[139] The $[BrF_6{}^+][Sb_2F_{11}]$ salt is also known from the decomposition of $Kr_2F_3SbF_6$.

The chemistry of IF_5 has been extensively studied. It is easily handled in glass and less reactive than the other pentafluorides. Reaction of the pentafluoride frequently leads to partially fluorinated products (Scheme 10).

Iodine Heptafluoride. Iodine heptafluoride (IF_7) is the only known heptafluoride. Its structure is pentagonal bipyramidal (**5**). It is a stronger fluorinating agent than IF_5 and reacts with H_2O to give the oxyfluoride IOF_5 and HF. The oxyfluorides will be discussed in the following section as a separate class of compounds.

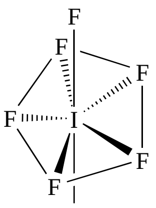

(**5**)

5.5.3 *Halogen Oxyfluorides*[140]

Five oxyfluorides of both chlorine[141,142] and iodine and three of bromine[143] have been characterized. They resemble the related halogen fluorides both structurally and chemically. They tend to be strong fluorinating and oxidizing agents. Many behave as both Lewis acids and bases, being able to donate

Table 14 Halogen oxyfluorides

	XO_2F (bp/mp °C)	XOF_3	XO_3F	XO_2F_3	XOF_5	XOF
Cl	$-6/-115$	$29/-43$	$-47/-148$	$-22/-81$	–	$^{d}/-70$
Br	$-9/-23^{a}$	$^{d}/-4$	$2.4/-110$	^{c}	^{c}	^{c}
I	$>200^{b}$	110^{b}	100^{b}	$^{d}/41$	$^{d}/4.5$	^{c}

[a] Sublimes. [b] Decomposes without melting.[87] [c] Compound not known. [d] Decomposes before boiling point.

and accept fluoride ions. Table 14 gives the known halogen oxyfluorides.

Chlorine Oxide Fluoride. The only member of the halogen oxide fluoride class is chlorine oxide fluoride (**6**). It forms a solid that melts to a red liquid at −70 °C. In the gaseous state, it is thermally unstable and decomposes to give $FClO_2$ and ClF. It can be made by the hydrolysis of ClF_3 with substoichiometric amounts of H_2O in a flow reactor. It is also produced by photolysis of a mixture of ClF and O_3 in Ar at 4–15 K.

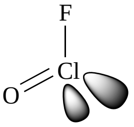

(**6**)

Halogenyl Fluorides. All three halogenyl fluorides (XO_2F) are known though bromyl fluoride is unstable above its melting point. Both ClO_2F and BrO_2F are pyramidal and monomeric in the gas phase (**7**), whereas IO_2F is polymeric. All three can behave as Lewis acids and bases through donating or accepting a fluoride ion.

Chloryl fluoride can be prepared in high yield by the action of ClF_3 on $NaClO_3$. It is a colorless gas and a powerful oxidizing and fluorinating agent.[144] It is the most common chlorine oxyfluoride and is typically encountered in reactions between ClF_x and oxides or hydroxides.

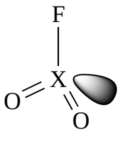

X = Cl, Br

(**7**)

Bromyl fluoride can be made almost quantitatively by the hydrolysis of BrF_5 in a 5:1 molar ratio with H_2O. Solid BrO_2F may be stored indefinitely in quartz ampules. Liquid BrO_2F is stable at ambient temperatures when stored in Kel-F. Gaseous BrO_2F has a half-life near 30 min at 15 °C.

Iodyl fluoride can be prepared by fluorination of I_2O_5 at 20 °C in anhydrous HF. Lewis acids form complexes with $[IO_2]^+$ and Lewis bases form complexes involving $[IO_2F_2]^-$.

Perhalogenyl Fluorides (XO_3F)[145]. Perchloryl fluoride can be prepared by the action of F_2 on $KClO_3$ or by HSO_3F-SbF_5 on $KClO_4$. It is a colorless gas that is thermally stable to about 400 °C and reacts slowly with H_2O at 300 °C. Compared to other members of this class, $FClO_3$ is remarkably inert and shows no tendencies to form adducts with Lewis acids or bases. It has been widely used as an oxidant for rocket fuels because of its low reactivity and high specific impulse. It is a mild fluorinating agent that has shown some use in selective fluorination of steroids and acidic methylenes. Because of its extraordinary kinetic stability and excellent dielectric properties, perchloryl fluoride offers a higher resistance to dielectric breakdown than any other gas.

Perbromyl fluoride can be prepared in high yield by fluorination of $KBrO_4$ with SbF_5 in HF. It decomposes slowly at room temperature and is much more reactive than $FClO_3$, reacting rapidly with glass.

Periodyl fluoride is a white crystalline solid that can be prepared by direct fluorination of HIO_4 in HF. Unlike $FClO_3$, it forms adducts with BF_3 and AsF_5. It is stable in glass but decomposes to FIO_2 upon heating to 100 °C.

Halogen Oxide Trifluorides (XOF_3). Chlorine oxide trifluoride (**8**) can be synthesized by the reaction of ClF_3 with OF_2 in UV radiation. The best large-scale preparation is fluorination of $ClONO_2$ at −35 °C. It is a powerful fluorinating and oxidizing agent and has been used as an oxidant for rocket fuels. It can behave as Lewis acid and base. It sublimes at room temperature and can be handled in metal, Teflon, or Kel-F.

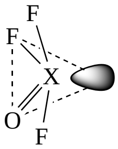

X = Cl, Br, I

(**8**)

Bromine oxide trifluoride can be prepared by the reaction of $KBrOF_4$ with HF. It decomposes slowly at room temperature to give O_2 and BrF_3.

Iodine oxide trifluoride, a colorless crystalline solid, is prepared by dissolving I_2O_5 in boiling IF_5 followed by cooling. Above 110 °C it thermally dismutates into FIO_2 and IF_5.

Halogen Dioxide Trifluorides (XO_2F_3). Both ClO_2F_3 and IO_2F_3 (**9**) are well known but attempts to make and isolate the

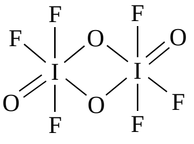

$(IO_2F_3)_2$, C_{2h}

(**9**)

bromine analog have been fruitless. ClO_2F_3 is a stable volatile gas prepared according to equation (84).

It can be purified by fractional distillation followed by complexing with BF_3. It is a strong oxidizing and fluorinating agent that forms stable adducts to some Lewis acids.

$$2FClO_2 + 2PtF_6 \longrightarrow [F_2ClO_2]^+[PtF_6]^- + [ClO_2]^+[PtF_6]^- \xrightarrow{2FNO_2} F_3ClO_2 + FClO_2 + 2[NO_2]^+[PtF_6]^- \quad (84)$$

Iodine dioxide trifluoride can be prepared by partial fluorination of $Ba_3H_4(IO_6)_2$ with HSO_3F. It decomposes upon heating (97 °C) to yield IOF_3 and O_2. It is highly associated under all conditions. It reacts with AsF_5, SbF_5, NbF_5, and TaF_5 to form oxygen-bridged polymers.

Halogen Oxide Pentafluorides (XOF_5). Only the iodine oxide pentafluoride is known (**10**). IOF_5 is a colorless liquid that can be made from the action of IF_7 and H_2O. IOF_5 is not easily hydrolyzed, and microwave spectroscopy yields a dipole moment of 1.08 D.

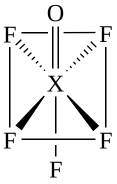

(**10**)

6 RELATED ARTICLES

Chlorine, Bromine, Iodine, & Astatine: Inorganic Chemistry; Noble Gases: Inorganic Chemistry.

7 REFERENCES

1. L. K. Khriachtchev, N. Runeberg, J. Lundell, and M. Rasanen, *Nature*, 2000, **406**, 874.
2. H. J. Emeleus, in ‘Fluorine Chemistry’, ed. J. H. Simmons, Academic Press, New York, 1950, Chap. 1.
3. R. E. Banks, *J. Fluorine Chem.*, 1986, **33**, 3.
4. L. Pelham, *J. Fluorine Chem.*, 1985, **30**, 1.
5. W. Büchner, R. Schliebs, G. Winter, and K. H. Büchel, ‘Industrial Inorganic Chemistry’, VCH, New York, 1989, p. 133.
6. N. H. de Leeuw, *J. Phys. Chem. B*, 2004, **108**, 1809.
7. K. Kurunthachalam, S. Corsolini, J. Falandysz, G. Oehme, S. Focardi, and J. P. Giesy, *Environ. Sci. Technol.*, 2002, **36**, 3210.
8. K. Kurunthachalam, J. Newsted, R. S. Halbrook, and J. P. Giesy, *Environ. Sci. Technol.*, 2002, **36**, 2566.
9. T. A. O’Donnell, in ‘Comprehensive Inorganic Chemistry’, ed. A. F. Trotman-Dickenson, Pergamon Press, New York, 1973, Chap. 25.
10. G. Mitra, *J. Am. Chem. Soc.*, 1958, **80**, 5639.
11. A. J. Finkel, *Adv. Fluorine Chem.*, 1973, **7**, 199.
12. A. J. Rudge, ‘The Manufacture and Use of Fluorine and Its Compounds’, Oxford University Press, New York, 1962.
13. W. Braker and A. L. Mossman, ‘Matheson Gas Data Book’, Matheson, Lyndhurst, NJ, 1980, p. 330.
14. J. Grannec and L. Lozano, in ‘Inorganic Solid Fluorides: Chemistry and Physics’, ed. P. Hagenmuller, Academic Press, New York, 1985, Chap. 2.
15. R. D. W. Kemmitt and D. W. A. Sharp, *Adv. Fluorine Chem.*, 1965, **4**, 142.
16. W. Kwasnik, in ‘Handbuch der Prepärativen Anorganischen Chemie’, ed. G. Brauer, Enke, Stuttgart, 1975, Chap. 3.
17. A. K. Barbour, in ‘Organofluorine Chemicals and Their Industrial Applications’, ed. R. E. Banks, Ellis Horwood, New York, 1979, Chap. 2.
18. For a recent example see: F. Lemaitre, D. Lucas, Y. Mugnier, and P. D. Harvey, *J. Org. Chem.*, 2002, **67**, 7537.
19. R. P. Hughes, S. Willemsen, A. Williamson, and D. Zhang, *Organometallics*, 2002, **21**, 3085.
20. T. Abe and S. Nagase, ‘Preparation, Properties and Industrial Applications of Organofluorine Compounds’, Ellis Horwood, New York, 1982, Chap. 1.
21. S. M. Riyadh and T. Fuchigami, *J. Org. Chem.*, 2002, **67**, 9379.
22. J. L. Margrave and R. J. Lagow, *Prog. Inorg. Chem.*, 1979, **26**, 161.
23. J. M. Shreeve, *Adv. Inorg. Chem. Radiochem.*, 1982, **26**, 119.
24. R. E. Banks and J. C. Tatlow, *J. Fluorine Chem.*, 1986, **33**, 227.
25. J. Wilkinson, *Chem. Rev.*, 1992, **92**, 505.
26. D. W. Kim, C. E. Song, and D. Y. Chi, *J. Am. Chem. Soc.*, 2002, **124**, 10278.
27. L. German and S. Zemskov eds, ‘New Fluorinating Agents in Organic Synthesis’, Springer, New York, 1989.
28. A. Haas and M. R. C. Gerstenberger, *Angew. Chem., Int. Ed. Engl.*, 1981, **20**, 647.

29. G. A. Boswell Jr, W. C. Ripka, R. M. Scribner, and C. W. Tullock, *Org. React.*, 1984, **21**, 1.
30. J. H. Holloway and D. Laycock, *Adv. Inorg. Chem. Radiochem.*, 1983, **27**, 157.
31. A. A. Woolf, *Adv. Inorg. Chem. Radiochem.*, 1981, **24**, 1.
32. J. F. Lehmann, G. J. Schrobilgen, K. O. Christie, A. Kornath, and R. J. Suontamo, *Inorg. Chem.*, 2004, **43**, 6905.
33. J. H. Holloway and D. Laycock, *Adv. Inorg. Chem. Radiochem.*, 1984, **28**, 73.
34. J. H. Callomon, E. Hirota, K. Kuchitsu, W. J. Laferty, A. G. Maki, and C. S. Pote, in 'Structure and Data of Free Polyatomic Molecules (Landolt-Börnstein)', eds. K. H. Hellwege and A. M. Hellwege, Springer, New York, 1976, p. 7.
35. J. W. Emsley and L. Phillips, *Prog. Nucl. Magn. Reson. Spectrosc.*, 1971, **7**, 1.
36. L. Covalli, *Annu. Rep. NMR Spectrosc.*, 1976, **6B**, 43.
37. V. Wray, *Annu. Rep. NMR Spectrosc.*, 1980, **10B**, 1; 1982, **14**, 1.
38. C. H. Dungan and J. R. Van Wazer, 'Compilation of Reported ^{19}F NMR Chemical Shifts', Wiley, New York, 1970.
39. J. W. Emsley, L. Phillips, and V. Wray, *Prog. Nucl. Magn. Reson. Spectrosc.*, 1976, **10**, 85.
40. D. D. DesMarteau and K. Seppelt, *Angew. Chem., Int. Ed. Engl.*, 1980, **19**, 643.
41. W. Zhang, M. Sun, and R. Prins, *J. Phys. Chem. B*, 2002, **106**, 11805.
42. N. R. Smyrl and G. Mamantov, *Adv. Inorg. Chem. Radiochem.*, 1978, **21**, 231.
43. D. J. Reynolds, *Adv. Fluorine Chem.*, 1973, **7**, 1.
44. K. Nakamoto, 'Infrared and Raman Spectra of Inorganic and Coordination Compounds', 4th edn., Wiley, New York, 1986.
45. J. M. Miller and G. L. Wilson, *Adv. Inorg. Chem. Radiochem.*, 1976, **18**, 229.
46. J. M. Miller, *Adv. Inorg. Chem. Radiochem.*, 1984, **28**, 1.
47. R. J. Cotter, *Anal. Chem.*, 1992, **64**, 1027A.
48. N. N. Greenwood and A. Earnshaw, 'Chemistry of the Elements', Pergamon, Oxford, 1984, p. 221.
49. J. J. Hartman and J. M. Miller, *Adv. Inorg. Chem. Radiochem.*, 1978, **21**, 147.
50. B. Rainer, 'Gmelin Handbook of Inorganic Chemistry: Boron', 8th edn., Springer, Berlin, 1988, 3rd Suppl., Vol. 3, p. 301.
51. P. L. Timms, *Acc. Chem. Res.*, 1973, **6**, 118.
52. R. D. Chambers, 'Fluorine in Organic Chemistry', Wiley, New York, 1973.
53. R. E. Banks ed., 'Organofluorine Compounds and their Industrial Applications', Ellis Horwood, Chichester, 1979.
54. J. Mann, *Chem. Soc. Rev.*, 1987, **16**, 381.
55. R. E. Banks, D. W. A. Sharp, and J. C. Tatlow eds, 'Fluorine: the First Hundred Years'', Elsevier, New York, 1986.
56. A. J. Woytek, *J. Fluorine Chem.*, 1986, **33**, 331.
57. R. J. Lagow, *J. Fluorine Chem.*, 1986, **33**, 321.
58. J. L. Adcock, *J. Fluorine Chem.*, 1986, **33**, 327.
59. R. D. Chambers, 'Fluorine in Organic Chemistry', Wiley, New York, 1973, p. 151.
60. R. E. Banks and J. C. Tatlow, *J. Fluorine Chem.*, 1986, **33**, 275.
61. R. P. Hughes, D. Zhang, L. N. Zakharov, and A. L. Rheingold, *Organometallics*, 2002, **21**, 4902.
62. P. J. Albietz Jr, J. F. Houlis, and R. Eisenberg, *Inorg. Chem.*, 2002, **41**, 2001.
63. B. M. Kraft and W. D. Jones, *J. Am. Chem. Soc.*, 2002, **124**, 8681.
64. T. Hayashi, M. Terrones, C. Scheu, Y. A. Kim, M. Ruhle, T. Nakajima, and M. Endo, *Nano Lett.*, 2002, **2**, 491.
65. M. J. Root, *Nano Lett.*, 2002, **2**, 541.
66. V. N. Khabashesku, W. E. Billups, and J. L. Margrave, *Acc. Chem. Res.*, 2002, **35**, 1087.
67. F. M. Mukhametshin, in 'New Fluorinating Agents in Organic Synthesis', eds. L. German and S. Zemskov, Springer, New York, 1989, Chap. 3.
68. W. Farnham, B. E. Smart, W. J. Middleton, J. C. Calabrese, and D. A. Dixon, *J. Am. Chem. Soc.*, 1985, **107**, 4565.
69. M. Lustig and J. M. Shreeve, *Adv. Inorg. Chem. Radiochem.*, 1983, **26**, 119.
70. F. M. Mukhametshin, *Russ. Chem. Rev.*, 1980, **7**, 49.
71. L. R. Anderson, D. E. Gould, and W. B. Fox, *Inorg. Synth.*, 1970, **12**, 312.
72. P. G. Thompson, *J. Am. Chem. Soc.*, 1967, **89**, 4316.
73. D. Pilipovich, C. J. Schack, and R. D. Wilson, *Inorg. Chem.*, 1972, **11**, 2531.
74. A. Russo and D. DesMarteau, *Angew. Chem., Int. Ed. Engl.*, 1993, **32**, 905.
75. K. Seppelt, *Angew. Chem., Int. Ed. Engl.*, 1977, **16**, 322.
76. R. J. Lagow, T. R. Bierschenk, T. J. Juhlke, and H. Kawa, in 'Synthetic Fluorine Chemistry', eds. G. A. Olah, R. D. Chambers, and G. K. S. Prakash, Wiley, New York, 1992, Chap. 5.
77. H. Millauer, W. Schwertfeger, and G. Siegemund, *Angew. Chem., Int. Ed. Engl.*, 1985, **24**, 161.
78. M. Witt, K. S. Dhathathreyan, and H. W. Roesky, *Adv. Inorg. Chem.*, 1986, **30**, 220.
79. J. C. Lockhart, 'Redistribution Reactions', Academic Press, London, 1970, p. 107.
80. J. L. Margrave and P. W. Wilson, *Acc. Chem. Res.*, 1971, **4**, 1454.
81. F. Glockling, 'The Chemistry of Germanium', Spottiswoode, London, 1969.
82. E. W. Lawless and I. C. Smith, 'Inorganic High Energy Oxidizers', Dekker, New York, 1968.
83. W. W. Wilson and K. O. Christe, *J. Fluorine Chem.*, 1980, **15**, 83.

84. K. O. Christe and W. W. Wilson, *J. Am. Chem. Soc.*, 1992, **114**, 9934.
85. K. Dehnicke, *Angew. Chem., Int. Ed. Engl.*, 1967, **6**, 240.
86. D. Moy and A. R. Young, *J. Am. Chem. Soc.*, 1965, **87**, 1889.
87. J. P. Freeman, A. Kennedy, and C. B. Colburn, *J. Am. Chem. Soc.*, 1960, **82**, 5304.
88. R. C. Petry and J. P. Freeman, *J. Am. Chem. Soc.*, 1961, **83**, 3912.
89. C. O. Parker and J. P. Freeman, *Inorg. Synth.*, 1970, **12**, 307.
90. H. J. Emeleus, J. M. Shreeve, and R. D. Verma, *Adv. Inorg. Chem.*, 1989, **33**, 139.
91. J. S. Thrasher and D. D. DesMarteau, *J. Fluorine Chem.*, 1991, **52**, 51.
92. C. Woolf, *Adv. Fluorine Chem.*, 1965, **5**, 1.
93. R. Schmutzler, *Angew. Chem., Int. Ed. Engl.*, 1968, **7**, 440.
94. J. H. Canterford, R. Colton, and T. A. O'Donnell, *Rev. Pure Appl. Chem.*, 1967, **17**, 123.
95. E. Fluck ed., 'Gmelin Handbook of Inorganic Chemistry: Fluorine', 8th edn., Springer, New York, 1987, Suppl. Vol. 5.
96. R. Schmutzler, *Adv. Fluorine Chem.*, 1965, **5**, 31.
97. R. W. Rudolph, R. S. Taylor, and R. W. Parry, *J. Am. Chem. Soc.*, 1966, **88**, 3729.
98. G. S. H. Chen and J. Passmore, *J. Chem. Soc., Chem. Commun.*, 1973, 559.
99. P. A. Bernstein, F. A. Hohorst, M. Eisenberg, and D. D. DesMarteau, *Inorg. Chem.*, 1971, **10**, 1549.
100. P. Merlet, 'Gmelin Handbook of Inorganic Chemistry: Fluorine', ed. Springer, New York, 1986, Suppl. Vol. 4.
101. D. Hass and P. Wolter, *Z. Anorg. Allg. Chem.*, 1980, **463**, 91.
102. A. G. Streng, *Chem. Rev.*, 1963, **63**, 607.
103. E. W. Lawless and C. S. Ivan, 'Inorganic High Energy Oxidizers', Dekker, New York, 1968, p. 213.
104. J. J. Turner, *Endeavour*, 1968, **27**, 42.
105. A. V. Grosse, A. G. Streng, and A. D. Kirshenbaum, *J. Am. Chem. Soc.*, 1961, **84**, 1004.
106. E. T. Appelman, *Acc. Chem. Res.*, 1973, **6**, 113.
107. J. K. Ruff and M. Lustig, *Inorg. Chem.*, 1964, **3**, 1422.
108. J. M. Shreeve, in 'Sulfur in Organic and Inorganic Chemistry', ed. A. Senning, Dekker, New York, 1983, Vol. 4, p. 131.
109. M. Schmidt and W. Siebert, *Environ. Sci. Technol.*, 2002, **2**, 843.
110. N. N. Greenwood and A. Earnshaw, 'Chemistry of the Elements', Pergamon, Oxford, 1984, p. 808.
111. F. Seel, 'Sulfur in Organic and Inorganic Chemistry', Dekker, New York, 1972, Vol. 2, p. 201.
112. H. Bitterer ed., 'Gmelin Handbuch der Anorganischen Chemie: Schwefel', 8th edn., Springer, New York, 1978, Suppl. Vol. B2.
113. F. Seel, *Adv. Inorg. Chem. Radiochem.*, 1974, **16**, 297.
114. A. I. Burmakov, B. V. Kunshenko, L. A. Alekseeva, and L. M. Yagupolskii, in 'New Fluorinating Agents in Organic Synthesis', eds. L. German and S. Zemskov, Springer, New York, 1989, p. 197.
115. S. Rozen, in 'Selective Fluorination in Organic and Bioorganic Chemistry', ACS Symposium Series 456, ed. J. T. Welch, American Chemical Society, Washington, DC, 1981, p. 56.
116. J. Bittner, J. Fuchs, and K. Seppelt, *Z. Anorg. Allg. Chem.*, 1988, **557**, 182.
117. L. N. Markovskii and V. E. Pashinnik, in 'New Fluorinating Agents in Organic Synthesis', eds. L. German and S. Zemskov, Springer, New York, 1989, p. 254.
118. D. T. Meshri, *J. Fluorine Chem.*, 1986, **33**, 195.
119. S. M. Williamson, *Prog. Inorg. Chem.*, 1966, **7**, 39.
120. J. M. Shreeve, *Inorg. Synth.*, 1986, **24**, 243.
121. D. Macaluso, 'Kirk-Othmer Encyclopedia of Chemical Technology', Wiley, New York, 1969, Vol. 19, p. 371.
122. G. H. Cady, *Adv. Inorg. Chem. Radiochem.*, 1960, **2**, 105.
123. G. H. Cady, *Intra-Sci. Chem. Rep.*, 1971, **5**, 1.
124. M. Davis, H. Szkuta, and A. J. Krubsack, *Mech. React. Sulphur Compd.*, 1970, **5**, 1.
125. F. Feher, 'Handbook of Preparative Inorganic Chemistry', Academic Press, New York, 1963, Vol. 1, p. 341.
126. J. H. Holloway and D. Laycock, *Adv. Inorg. Chem. Radiochem.*, 1983, **27**, 167.
127. A. W. Jacke, *Adv. Inorg. Chem. Radiochem.*, 1974, **16**, 177.
128. J. K. Ruff, *Inorg. Synth.*, 1968, **11**, 131.
129. R. A. DeMarco and J. M. Shreeve, *Adv. Inorg. Chem. Radiochem.*, 1974, **16**, 110.
130. S. H. Hwang, K. Naik, and D. D. DesMarteau, *Inorg. Chem.*, 1993, **32**, 2791.
131. F. Aubke and D. D. DesMarteau, *Fluorine Chem. Rev.*, 1977, **8**, 73.
132. B. von Tschirschnitz-Geibler ed., 'Gmelin Handbook of Inorganic Chemistry: Selenium', 8th edn., Springer, New York, 1984, Suppl., B2.
133. G. Hantke ed., 'Gmelin Handbuch der Anorganischen Chemie: Tellur', 8th edn., Springer, New York, 1977, Teil B2.
134. H. S. Booth and J. T. Pinkston, *Chem. Rev.*, 1947, **41**, 421.
135. H. C. Clark, *Chem. Rev.*, 1958, **58**, 869.
136. N. N. Greenwood and A. Earnshaw, 'Chemistry of the Elements', Pergamon, Oxford, 1984, p. 966.
137. W. K. R. Musgrave, *Adv. Fluorine Chem.*, 1960, **1**, 1.
138. P. Merlet ed., 'Gmelin Handbook of Inorganic and Organometallic Chemistry: Bromine', 8th edn., Springer, New York, 1991.
139. R. J. Gillespie and G. J. Schrobilgen, *J. Chem. Soc., Chem. Commun.*, 1974, 90.
140. J. H. Holloway and D. Laycock, *Adv. Inorg. Chem. Radiochem.*, 1983, **27**, 175.

141. K. O. Christe and C. J. Schack, *Adv. Inorg. Chem. Radiochem.*, 1976, **18**, 319.

142. L. Gmelin, ‘Gmelin Handbuch der Anorganischen Chemie: Chlor’, 8th edn., Springer, New York, 1969, Teil B2.

143. R. J. Gillespie and P. Spekkens, *Isr. J. Chem.*, 1978, **11**, 17.

144. K. O. Christe, R. D. Wilson, and C. J. Schack, *Inorg. Synth.*, 1986, **24**, 3.

145. U. M. Khutoretskii, L. V. Okhlobyrtina, and A. A. Fainzil’-berg, *Usp. Khim.*, 1967, **36**, 377.

Gallium: Inorganic Chemistry

Kulbinder Kumar Banger[1] **& Aloysius F. Hepp**[2]
[1] *Ohio Aerospace Institute & NASA Glenn Research Center, Cleveland, OH, USA*
[2] *NASA Glenn Research Center, Cleveland, OH, USA*

Based in part on the article Gallium: Inorganic Chemistry by Andrew R. Barron & Andrew N. MacInnes which appeared in the Encyclopedia of Inorganic Chemistry, First Edition.

1 Introduction 1
2 The Element 1
3 Spectroscopy 2
4 Binary Compounds 3
5 I-III-VI_2 Ternary Compounds 11
6 Gallium Nanocrystallites 13
7 Hydrides and Hydride Complexes 14
8 Group 14, 15, And 16 Donor Ligands 16
9 Halides 24
10 Polydentate Ligands 26
11 Ga(III): A Diamagnetic Mimic of Iron(III) 29
12 Related Articles 29
13 Further Reading 29
14 References 29

1 INTRODUCTION

The element gallium was predicted, as eka-aluminum, by Mendeleev in 1870, and subsequently discovered by Lecoq de Boisbaudran in 1875. The new element was named in honor of France (Latin *Gallia*). The chemistry of gallium was reviewed by Gmelin in 1936,[1] and in the following year by Einecke.[2] Several general but informative chemistry publications/books have appeared that deal with certain aspects of the history, occurrence, extraction, purification, analysis, physical, and chemical properties, toxicology, or uses of the element,[3–5] while the industrial application[6–8] and coordination chemistry[9,10] of gallium has been extensively reviewed. In addition, the area has generally been reviewed and published in annual reviews.[11–21]

2 THE ELEMENT

2.1 Abundance

Gallium is very much less abundant than aluminum and tends to occur at low concentrations in sulfide minerals rather than as oxides, although gallium is also found associated with aluminum in bauxite. At 19 ppm, gallium is about as abundant as nitrogen, lithium, and lead; it is twice as abundant as boron (9 ppm), but is more difficult to extract owing to the lack of any major gallium-containing ore. Gallium always occurs in association either with zinc or germanium, its neighbors in the periodic table, or with aluminum in the same group. Thus, the highest concentrations (0.1–1%) are in the rare mineral germanite (a complex sulfide of Zn, Cu, Ge, and As); concentrations in sphalerite (ZnS), bauxite, or coal are a hundredfold less.

2.2 Preparation and Use

Gallium was originally recovered from flue dusts emitted during sulfide roasting or coal burning (up to 1.5% Ga), but is now obtained as a by-product of the aluminum industry. The Bayer process for obtaining alumina from bauxite gradually enriches the alkaline solutions from an initial weight ratio Ga:Al of about 1:5000 to about 1:300; electrolysis of these extracts with an Hg electrode gives further concentration, and the solution of sodium gallate is then electrolyzed with a stainless steel cathode to give gallium metal. Ultra high-purity gallium for semiconductor growth is obtained by further chemical treatment with acids and oxygen at high temperatures followed by crystallization and zone refining. Since bauxite (Al_2O_3) contain 0.003–0.01% gallium, complete recovery would yield some 500–1000 tons per year; however, present consumption, though growing rapidly, is only a small fraction of this being of the order of 10 tons per annum. This can be compared with the estimate of 5 tons for the total of Ga metal in the 90 years following its discovery (1875–1965).

Gallium's main use is in semiconductor technology. For example, GaAs can convert electricity directly into coherent light (laser diodes) and convert sunlight into electricity (solar cells), is employed in electroluminescent light-emitting diodes (LEDs); it is also used for doping other semiconductors and in solid-state devices such as heterojunction bipolar transistors (HBTs). The compound $MgGa_2O_4$ is used in ultraviolet-activated powders as a brilliant green phosphor used in copying machines. Another very important application is to improve the sensitivity of various bands used in the spectroscopic analysis of uranium. Minor uses are as high-temperature liquid seals, manometric fluids, and heat-transfer media, and for low-temperature solders.

2.3 Properties

Gallium has a beautiful silvery-blue appearance; it wets glass, porcelain, and most other surfaces (except quartz, graphite, and Teflon) and forms a brilliant mirror when painted onto glass. Selected physical constants of gallium are summarized in Table 1. The atomic radius and first ionization potential of gallium are almost identical with those of aluminum and the two elements frequently resemble each

Table 1 Physical properties of gallium metal

Atomic number	31	Melting point (°C)	29.75
Atomic weight	69.72	Boiling point (°C)	2227
Atomic radius (Å)	1.245	d_4^{20} (solid) (g mL^{-1})	5.907
Ionic radius (Å)	0.62	$d_4^{29.8}$ (liquid) (g mL^{-1})	6.0948
Ionization potential (eV)	6.00	Atomic volume (29 °C) (mL)	11.81
Standard electrode potential (volts)	0.52	Atomic volume (30 °C) (mL)	11.44

other in chemical properties. Both are amphoteric, but gallium is less electropositive as indicated by its lower electrode potential. Differences in the chemistry of the two elements can be related to the presence of a filled set of 3d orbitals in gallium.

The unusual physical properties of metallic gallium arise from its unique crystal structure which consists of Ga_2 units arranged in deformed sets of hexagonal rings, Figure 1.**[6]** The orthorhombic unit cell has four Ga_2 units lying symmetrically in the *ac* plane at angles of 17° to the *c*-axis, the spacing of these molecular planes being *b*/2. Each gallium atom has seven Ga$\cdots$Ga interactions, one nearest neighbor at 2.44 Å, and three sets of two each at 2.71, 2.74, and 2.80 Å. This rather open structure collapses to a more nearly close-packed arrangement in the liquid state, and melting is accompanied by a contraction of 3.1% in atomic volume and by a considerable increase in electrical conductivity. Here gallium resembles its neighbor germanium, as well as antimony and bismuth. The structure of a denser form of gallium (orthorhombic) has been obtained by supercooling the liquid to −16.3 °C.**[22]** In this arrangement, the gallium atoms form zigzag chains along the *c*-axis. In a chain, the Ga–Ga distance is 2.68 Å, and the Ga–Ga–Ga angle is 72.3°. Between the chains, the gallium atoms have four additional neighbors at 2.87 Å, and two at 2.90 Å, making a total of eight Ga$\cdots$Ga interactions.

Elemental gallium has a very low-melting point, and an extraordinary low vapor pressure (less than 1 mmHg at 1300 °C). These factors combine to give gallium the longest liquid range of any known substance and form the basis of its (very limited) use in high-temperature thermometers.

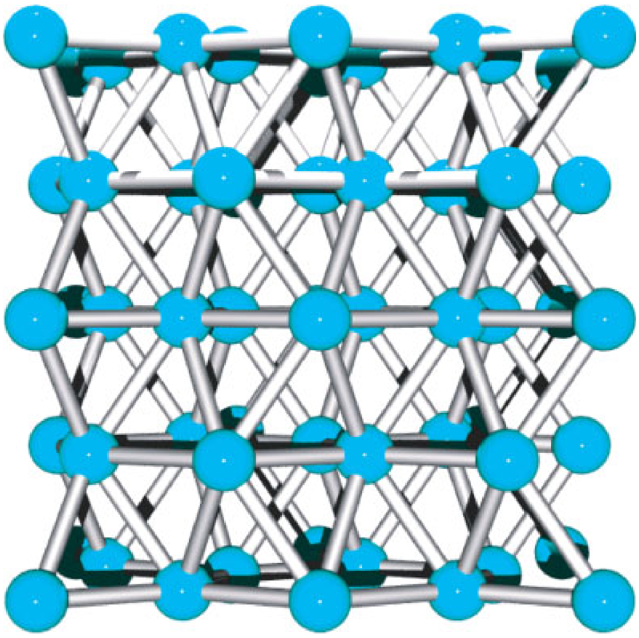

Figure 1 Unit cell of α-gallium metal

3 SPECTROSCOPY

3.1 Gallium NMR

Gallium has two NMR-active isotopes (spin $I = 3/2$), ^{69}Ga and ^{71}Ga, with the latter possessing a higher receptivity in addition to narrower relative line width; however, NMR studies for both isotopes are equally reported and studied. Chemical shifts are generally reported with respect to either $Ga(NO_3)_3$ or $[Ga(H_2O)_6]^{3+}$ with the chemical shift window being approximately 1400 ppm (this follows suit with the corresponding Al compounds) (Table 2).

Ga NMR studies have received increased impetus as a viable probing tool for some key areas. ^{69}Ga NMR studies have been used to support and follow Ga antitumor agents and their mode of action and uptake into tumor cells. ^{71}Ga NMR has thus been used to study how various ligands may form complexes with the cation. In another area, the use of ^{69,71}Ga NMR has been used to examine defects in semiconductors, which can have a crucial influence on the semiconductors' electronic and optical properties.**[23–25]** In addition, a number of very useful web sites detailing Ga NMR related studies are available.**[26–28]**

3.2 Mass Spectroscopy

The two naturally occurring isotopes of Gallium Table 2 can be used as an aid in mass spectroscopic studies. Isotopic distribution patterns have been used to model the masses and abundances of the isotopes for a given formula, and as a 'fingerprinting' tool when used in a comparative analysis with the experimental data. This technique has recently been used for identifying the formation, mechanism, and the fragmentation pattern of Ga_n clusters (Figure 2),**[29]** and more recently to confirm the formation of the first Ga=As containing species.**[30]**

Table 2 Summary of properties for magnetically active quadruploar ga nuclei

Isotope	Spin	Natural abundance (%)	Quadrupole moment (10^{-28} m^2)	Relative sensitivity	Width Factor	Relative Intensity	Absolute sensitivity	NMR frequency (MHz)
^{69}Ga	3/2	60.4	0.178	6.91E-2	5.93	0.007	4.17E-2	24.003
^{71}Ga	3/2	39.6	0.112	0.14	2.34	0.024	5.62E-2	30.495

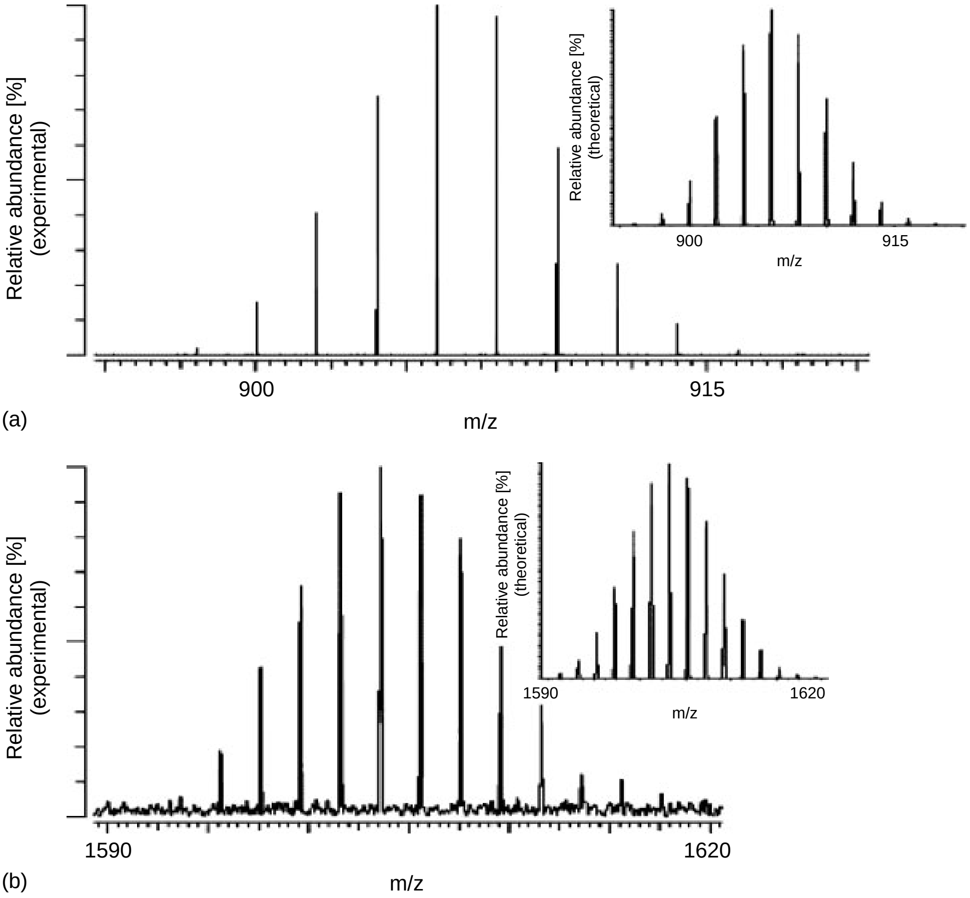

Figure 2 Mass spectra of the Ga_{13}^- cluster (a) and the Ga_{23}^- cluster (b) and the corresponding calculated spectra. (Reprinted from Ref. 29. © 2002, with permission from Elsevier)

4 BINARY COMPOUNDS

4.1 Gallium Pnictogens, (III-V)

Undoubtedly the binary compounds of gallium with the most industrial interest are those of the group 15 elements, GaE (E = N, P, As, Sb). The group 15 gallium alloys with nitrogen, phosphorus, arsenic, and antimony are isoelectronic with the group 14 elements. There has been considerable interest, particularly in the physical properties of these compounds, since 1952 when Welker first showed that they had semiconducting properties analogous to those of silicon and germanium.

4.1.1 Synthesis, Structure, and Physical Properties of Bulk Material

Gallium nitride is the only member of the group which cannot be prepared by direct reaction of the elements. It was first made by the reaction of gallium with ammonia at 1000 °C, but has also been prepared by the decomposition of either $[NH_4]_3[GaF_6]$ or the halide Lewis acid–base adduct $GaCl_3(NH_3)$. Gladfelter has shown that cubic GaN may be prepared by the low-temperature pyrolysis of the trimeric gallane compound $[H_2Ga(NH_2)]_3$ (equation 1).[31]

$$[H_2Ga(NH_2)]_3 \xrightarrow{\Delta} 3GaN + 6H_2 \qquad (1)$$

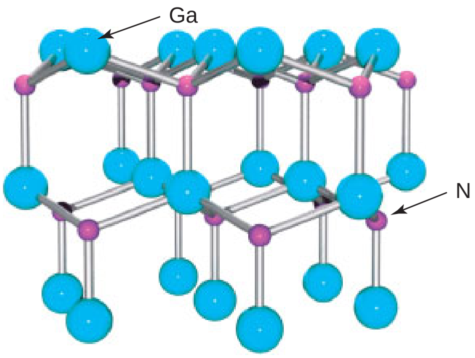

Figure 3 Lattice packing of würtzite GaN

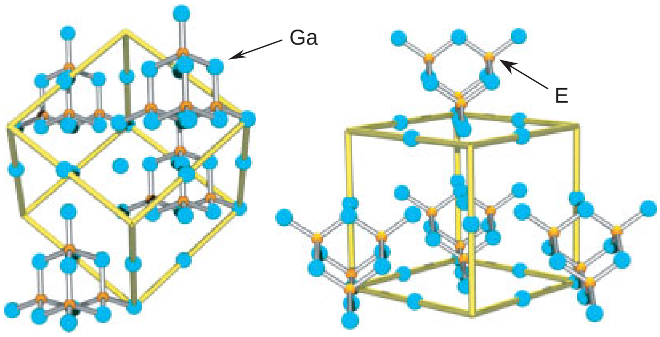

Figure 4 Unit cell structure of GaE (E = P, As, Sb); gallium atoms are cyan

Gallium nitride is commonly gray or yellow, diamagnetic, and crystallizes in the würtzite (ZnS) structure (Figure 3). Gallium nitride is not hydrolyzed by hot water or by acids such as dilute or concentrated hydrofluoric, hydrochloric, or nitric, or aqua regia. However, the compound dissolves slowly in hot concentrated sulfuric acid. With hot concentrated aqueous alkali, ammonia is evolved. There is no reaction with hydrogen at 800 °C but oxygen slowly reacts with gallium nitride at 900 °C over a period of days to give nitrogen and Ga_2O_3. The properties of GaN are summarized in Table 3.

Gallium phosphide, arsenide, and antimonide can all be prepared by direct reaction of the elements; this is normally done in sealed silica tubes or in a graphite crucible under hydrogen. Phase diagram data are hard to obtain in the gallium–phosphorus system because of loss of phosphorus from the bulk material at elevated temperatures. Thus, GaP has a vapor pressure of more than 13.5 atm at its melting point, compared to 0.89 atm for GaAs. The physical properties of these three compounds are compared with those of the nitride in Table 3. All three adopt the zinc blende crystal structure (Figure 4), and are more highly conducting than gallium nitride.

When considering the synthesis of group 13–15 compounds for electronic applications, the very nature of semiconductor behavior demands the use of high-purity single-crystal materials. The polycrystalline materials synthesized above are, therefore, of little use for 13–15 semiconductors but may, however, serve as the starting material for melt-grown single crystals. For gallium arsenide, undoubtedly the most important 13–15 semiconductor, melt-grown single crystals are achieved by one of two techniques: the Bridgman technique, and the Czochralski technique.

The Bridgman technique requires a two-zone furnace, of the type shown in Figure 5. The left-hand zone is maintained at a temperature of ca. 610 °C, allowing sufficient overpressure of arsenic within the sealed system to prevent arsenic loss from the gallium arsenide. The right-hand side of the furnace contains the polycrystalline GaAs raw material held at a temperature just above its melting point (ca. 1240 °C). As the furnace moves from left to right, the melt cools and solidifies. If a seed crystal is placed at the left-hand side of the melt (at a point where the temperature gradient is such that only the end melts), a specific orientation of the single crystal may be propagated at the liquid–solid interface eventually to produce a single crystal.

The Czochralski technique shown in Figure 6 relies on the controlled withdrawal of a seed crystal from a liquid melt. As the seed is lowered into the melt, partial melting of the tip occurs, creating the liquid–solid interface required for crystal growth. As the seed is withdrawn, solidification occurs and the seed orientation is propagated into the grown material. The

Table 3 Physical properties of group 13–15 compound semiconductors

Property	GaN	GaP	GaAs	GaSb
Melting point (°C)	>1250 (dec)	1350	1240	712
Density ($g\,cm^{-3}$)	–	4.138	5.3176	5.6137
Crystal structure	Würtzite	Zinc blende	Zinc blende	Zinc blende
Cell dimen. (Å)[a]	$a = 3.187$ $c = 5.186$	$a = 5.4505$	$a = 5.6532$	$a = 6.0959$
Refractive index[b]	2.35	3.178	3.666	4.388
κ ($ohm^{-1}\,cm^{-1}$)	10^{-9}–10^{-7}	10^{-2}–10^{2}	10^{-6}–10^{3}	6–13
Band gap (eV)[c]	3.44	2.24	1.424	0.71

[a] Values given for 300 K. [b] Dependent on photon energy; values given for 1.5 eV incident photons. [c] Dependent on temperature; values given for 300 K.

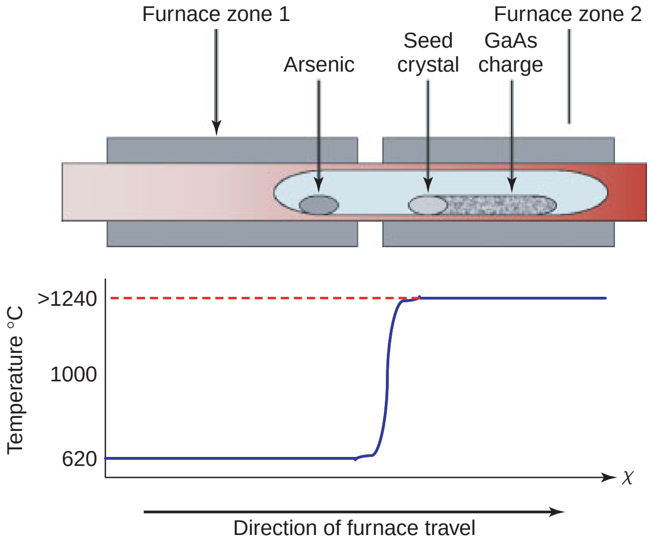

Figure 5 Schematic diagram of a Bridgman two-zone furnace used for melt growths of single-crystal GaAs

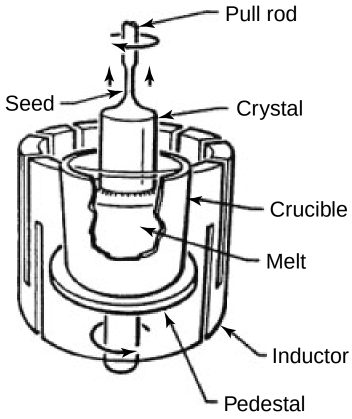

Figure 6 Schematic diagram of the Czochralski technique as used for the growth of single-crystal GaAs

variable parameters of rate of withdrawal and rotation rate can control crystal diameter and purity. The gallium arsenide melt is capped by boron trioxide (B_2O_3). The capping layer, which is inert to gallium arsenide, prevents arsenic loss when the pressure on the surface is above atmospheric pressure. The growth of gallium arsenide by this technique is thus termed liquid encapsulated Czochralski (LEC) growth.

While the Bridgman technique is largely favored for GaAs growth, larger diameter wafers can be obtained by the Czochralski method. Both of these melt techniques produce materials heavily contaminated by the crucible, making them suitable almost exclusively as substrate material. The methods by which higher purity single crystal of epitaxial GaAs can be obtained are therefore discussed below.

Table 4 Comparison of physical and semiconductor properties of GaAs and Si

Properties	GaAs	Si
Physical		
Formula weight	144.63	28.09
Crystal structure	Zinc blende	Diamond
Lattice constant	5.6532	5.43095
Melting point (°C)	1238	1415
Density (g cm^{-3})	5.32	2.328
Thermal conductivity (W cm^{-1} K^{-1})	0.46	1.5
Electronic		
Band gap (eV) at 300 K	1.424	1.12
Intrinsic carrier conc. (cm^{-3})	1.79×10^6	1.45×10^{10}
Intrinsic resistivity (Ω cm)	10^8	2.3×10^5
Breakdown field (V cm^{-1})	4×10^5	3×10^5
Minority carrier lifetime (s)	10^{-8}	2.5×10^{-3}
Mobility (cm^2 V^{-1} s^{-1})	8500	1500

4.1.2 Electronic Applications of GaAs

Gallium arsenide is a compound semiconductor with a combination of physical properties that has made it an attractive candidate for many electronic applications. From a comparison of various physical and electronic properties of GaAs with those of Si (Table 4), the advantages of GaAs over Si can be readily ascertained.

1. The band gap of GaAs is 1.42 eV, resulting in photon emission in the infrared range. Alloying GaAs with Al to give $Al_xGa_{1-x}As$ can extend the band gap into the visible red range. Unlike Si, the band gap of GaAs is direct, that is, the transition between the valence band maximum and conduction band minimum involves no momentum change and hence does not require a collaborative particle interaction to occur. Photon generation by interband radiative recombination is therefore possible in GaAs, whereas for Si, with an indirect band gap, this process is too inefficient to be of use. The ability to convert electrical energy into light forms the basis of the use of GaAs, and its alloys, in optoelectronics, for example, in LEDs (Figure 7), solid-state LASERs (light amplification by the stimulated emission of radiation), and solar cells.
   A significant drawback of small band-gap semiconductors, such as Si, is that electrons may be thermally promoted from the valence band to the conduction band. Thus, with increasing temperature the thermal generation of carriers eventually becomes dominant over the intentionally doped level of carriers. The wider band gap of GaAs gives it the ability to remain 'intentionally' semiconducting at higher temperatures; GaAs devices are generally more stable to high temperatures than are similar Si devices.
2. The low intrinsic carrier density of GaAs in a pure (undoped) form indicates that GaAs is intrinsically a very poor conductor and is commonly referred to as being semi-insulating. This property allows many active

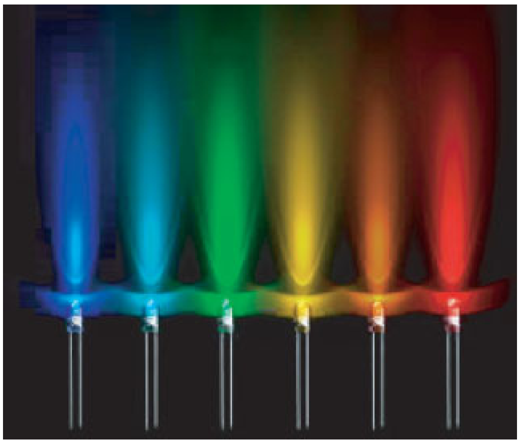

Figure 7 III-V based light-emitting diodes

devices to be grown on a single substrate, where the semi-insulating GaAs provides the electrical isolation of each device; this is an important feature in the miniaturization of electronic circuitry, that is, VLSI (very large-scale integration) involving over 100 000 components per chip (one chip is typically between 1 and 10 mm^2).

3. The higher electron mobility in GaAs than in Si potentially means that in devices where electron transit time is the critical performance parameter, GaAs devices will operate with higher response times than equivalent Si devices. However, the fact that hole mobility is similar for both GaAs and Si means that devices relying on cooperative electron and hole movement, or hole movement alone, show no improvement in response time when GaAs based.

The many desirable properties of gallium arsenide are offset to a great extent by a number of undesirable properties, which have limited the applications of GaAs-based devices to date.

1. The bulk crystal growth of GaAs (see Section 4.1.1) presents a problem of stoichiometric control owing to the loss, by evaporation, of arsenic both in the melt and the growing crystal (>ca. 600 °C). Melt-growth techniques are, therefore, designed to enable an overpressure of arsenic above the melt to be maintained, thus preventing evaporative losses. The loss of arsenic also negates diffusion techniques commonly used for wafer doping in Si technology, since the diffusion temperatures required exceed that of arsenic loss.
2. The thermal gradient and, hence, stress generated in melt-grown crystals have limited the maximum diameter of GaAs wafers (currently 3–4 inch diameter compared to over 12 inch for Si), because with increased wafer diameters the thermal stress-generated dislocation (crystal imperfection) densities eventually becomes unacceptable for device applications.
3. Gallium arsenide single crystals are very brittle, requiring considerably thicker substrates than those employed for Si devices.
4. Gallium arsenide's native oxide is found to be a mixture of nonstoichiometric gallium and arsenic oxides and elemental arsenic. Thus, the electronic band structure is found to be severely disrupted, causing a breakdown in 'normal' semiconductor behavior on the GaAs surface. As a consequence, the GaAs MISFET (metal–insulator semiconductor field-effect transistor) equivalent to the technologically important Si-based MOSFET (metal–oxide semiconductor field-effect transistor) is, therefore, presently unavailable.

4.1.3 Gallium Arsenide-Based Devices

The considerable difficulty of growing GaAs single crystals, added to the higher cost of the raw materials gallium and arsenic compared to silicon, has resulted in GaAs technology only being used where Si-based technology is impractical, that is, application areas utilize either the high-speed or light-emitting properties of GaAs. Two areas where GaAs-based devices display properties unobtainable in Si-based devices are in microwave and photonic devices. To illustrate the basic operating principles and complex structures involved in such devices, we can consider two currently operational devices.

1. The MESFET (metal–semiconductor field-effect transistor) is a GaAs device capable of operating at microwave frequencies (1–100 GHz) and in its simplest form is shown schematically (Figure 8). A lightly doped n-type (electrons as majority carriers) GaAs layer is grown on a semi-insulating (i.e. high purity) GaAs substrate. Source and drain contacts (Au/Ge alloy) are termed ohmic, that is, there is negligible contact resistance between metallization and semiconductor. The gate contact (Al) is rectifying and creates what is termed a Schottky diode with the n-type GaAs. Under appropriate applied voltage or biasing conditions, the gate contact can reduce or maintain conductance in the underlying layer between source and drain and can thus modulate current flow through the

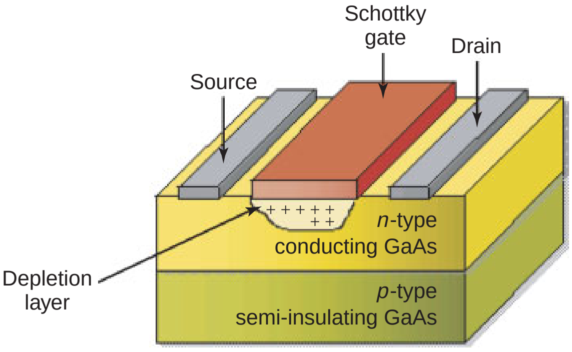

Figure 8 Schematic diagram of a GaAs-based MESFET device

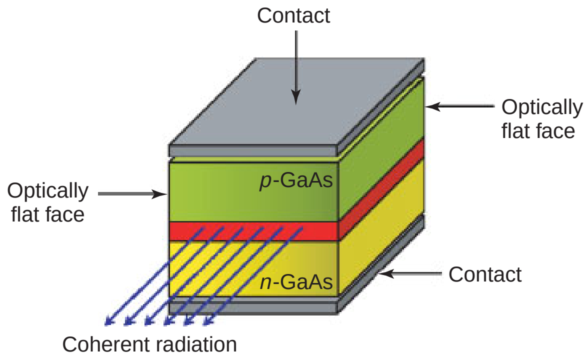

Figure 9 Schematic diagram of a GaAs-based solid-state laser

semiconducting layer. It is this high-speed switching that is utilized in microwave devices.

2. A schematic of a GaAs-based semiconductor laser structure is shown in Figure 9. The basic operating principle of this device is that a forward-biased p–n junction injects charged pairs (holes and electrons) into the 'active' region of the laser. Within this region, carrier recombination occurs, generating light. The injected charge carriers and generated light are confined within this active layer by the surrounding layer possessing both energy band discontinuities and high refractive indices. By this optical and carrier confinement method, stimulated emission of radiation can occur, that is, a generated photon can stimulate electron–hole recombination to produce a further photon in phase with the original. The laser structure thus generates a flux of coherent light. The absence of a direct band gap makes such a device impractical for silicon.

4.1.4 *Epitaxial Growth of GaAs*

The continuing drive for the scaling down of electronic device dimensions has necessitated the introduction of a new class of growth techniques where high-purity thin single-crystal layers are grown on a single-crystal substrate. The techniques of epitaxial growth (from the Greek *epi taxis* meaning *arrangement on*) are classified as either homo- or heteroepitaxy, depending on whether the base substrate is the same as or different from the growing film. The advantages of using epitaxial growth techniques include control of layer thicknesses, interfacial structure, material composition, and impurity concentration. Homoepitaxy, that is, GaAs on GaAs, is generally employed to provide either doping junctions, for example, *p*-type on *n*-type GaAs, or to allow low-impurity GaAs to be grown on considerably less pure substrates, whereby only the thin (high purity) epitaxial layer is electrically active in the device. Heteroepitaxy, that is, AlGaAs on GaAs, provides junctions with band discontinuities (conduction or valence) that can present either a barrier or enhancement to electron and hole mobility (and therefore current flow) depending on the appropriate doping and electronic biasing conditions. The techniques of epitaxy are discussed below.

4.1.5 *Liquid Phase Epitaxy (LPE)*

Liquid phase epitaxy (LPE) involves the growth of thin epitaxial layers on a crystalline substrate by direct precipitation from the liquid phase. The requirement for this process is that a suitable solvent for the film material can be obtained that provides a saturated melt solution at a temperature well below the melting point of the substrate. Gallium metal is used as the solvent for LPE of GaAs. A saturated solution of GaAs in gallium metal is introduced on to a substrate of GaAs and allowed to cool below the equilibrium saturation temperature. The melt solution becomes supersaturated, causing precipitation of GaAs on the GaAs substrate. As the melt temperature decreases, the precipitation reaction continues. Impurity additions can similarly be added to the melt to provide *n*- or *p*-type doping by segregation from the melt into the growing film.

4.1.6 *Metal-Organic Vapor-phase Epitaxy (MOVPE)*

Metal-organic Vapor-phase epitaxy (MOVPE) and what is commonly termed MOCVD (*metal–organic chemical vapor deposition*) are essentially the same technique whereby organometallic compounds, in the form of volatile liquids or sublimable solids, are transported via the vapor phase on to a heated substrate and decomposed alone or in combination with other vapors or gases to give the desired film (Figure 10). The vapor-phase techniques offer the advantages of low growth temperatures substantially below the melting point of the grown film, the ability to grow irregular shaped substrates with conformal, uniform growth, and in some instances the ability to selectively deposit only on desired areas of a substrate surface.

For the growth of group 13–15 compounds, the general embodiment of the vapor-phase process is that liquid

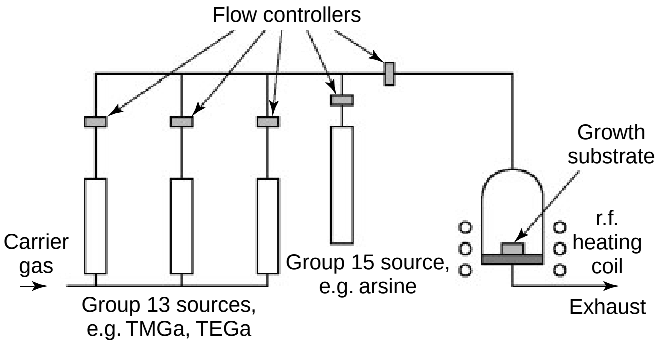

Figure 10 Schematic diagram of a typical MOVPE chamber

organometallic group 13 compounds react with group 15 hydrides at elevated temperatures (equation 2).

$$Me_3Ga + AsH_2 \xrightarrow{H_2} GaAs + 3MeH \qquad (2)$$

There are a number of properties required for compounds to be suitable as precursors for MOVPE; these include sufficient vapor pressure to allow suitable growth rates, ability to be highly purified, controllable deposition behavior, stability in storage, and stability with other species during vapor-phase transport.

Trimethylgallium is the most commonly used precursor owing to its relatively high vapor pressure (182 Torr at 20 °C) at both atmospheric and low pressure. Conversely, Et_3Ga, with both a lower vapor pressure (5.1 Torr at 20 °C) and lower thermal stability is used when higher purity films of GaAs are required. The increased purity of films grown from Et_3Ga, when compared to those grown from Me_3Ga, is a result of lower carbon incorporation (carbon is a *p*-dopant) in the growing film. Mechanistic studies reveal the differing carbon incorporation levels being due to

1. a decrease in Ga–C bond strength for Et_3Ga (52 kcal mol^{-1}) when compared to Me_3Ga (58 kcal mol^{-1}) allows for a lower temperature being required for the homolytic fission of the Ga–C bond in Et_3Ga
2. the ability of Et_3Ga to undergo a *β-Hydride Elimination* step involving the ‘clean’ elimination of an alkene also contributes to lower carbon incorporation (*see* ***Gallium: Organometallic Chemistry***).

The incorporation of a β-hydride elimination step into precursor pyrolysis has focused attention on alternative organometallic precursors for gallium. However, only limited success has been achieved. Other routes to ‘clean’ precursor decomposition include the pyrolysis of gallane adducts, that is, the gallane–trimethylamine adduct $H_3Ga(NMe_3)$; however, this and other related gallane compounds are thermally unstable and decompose at room temperature. Storage at low temperatures (−15 °C) and the difficulty of large-scale purification are some of the factors that limit the utility of such adducts. Several studies reported the presence of polymeric contaminant in MOVPE chambers in which the source vapors were allowed to react prior to the deposition zone. While this has now been circumvented by changes in reactor design, precursor compounds of the form $R_3Ga(AsR'_3)$ were found to provide a source of gallium alkyl without the unwanted prereaction with AsH_3. However, AsH_3 was still required as the arsenic source. Recently, many workers have focused on GaAs single-source precursors, with the general formula $[R_2Ga(\mu\text{-}AsR'_2)]_n$; however, the quality of films grown from these compounds still needs to be further improved for microelectronic applications.**[9,10]**

4.1.7 Molecular Beam Epitaxy

Molecular Beam Epitaxy (MBE) is essentially a modified and highly controllable form of vacuum evaporation, whereby elemental gallium and arsenic sources are held in effusion cells and heated in ultra-high vacuum (UHV) conditions to produce molecular fluxes. Under the UHV conditions, the molecular beams impinge on a heated rotating growth surface with no prior gas-phase collisions to produce precise epitaxial films. The advantages of MBE over vapor-phase techniques include the highly controlled growth that can be obtained, enabling structures of a few atomic layers to be grown, and with that multilayers and quantum-well structure where the layer thickness is less than the mean free path of an electron’s travel. The UHV conditions (ca. 10^{-10} Torr) allow both films of the highest purity to be grown and also enable diagnostic and growth monitoring techniques to be employed in situ, that is, reflection high energy electron diffraction (RHEED), low-energy electron diffraction (LEED), and others.

A variation of MBE utilizes organometallic rather than elemental sources for the molecular beams and is termed metal–organic molecular beam epitaxy (MOMBE) or chemical beam epitaxy (CBE). The molecular sources are commonly those used in vapor-phase epitaxy, that is, R_3Ga and AsH_3, and are generally gaseous under UHV conditions. The MOMBE technique offers several advantages over conventional MBE, including lower growth temperatures with concomitant control of layer and doping profiles by lowering interdiffusion processes. The gaseous sources (in UHV) also mean that precursor reservoirs can be externally connected to the UHV chamber, providing ‘constant’ operational capability. The use of organometallics, however, inevitably introduces impurities (mainly carbon) into the growth system.

4.1.8 Passivation of GaAs

As discussed earlier, GaAs has the potential to be widely used in high-speed electronics and optoelectronics, but its implementation is somewhat hampered by difficulties in reproducibility controlling surface composition and electrical properties. From the earliest days of solid-state electronics, it has been recognized that the presence or absence of surface states plays a decisive role in the usefulness of any semiconductor material. It is desirable to covalently satisfy all surface bonds, thereby shifting the surface states out of the band gap and into the valence and conduction bands. Owing to the high surface-state density of GaAs, and its inability to form a stable native oxide overlayer (see above), there has been much work investigating the chemical passivation of the surface.

Oxide layers on GaAs have been grown by exposure of the GaAs surface to water,**[9]** or hydrogen peroxide,**[32]** aniodic oxidation,**[33]** and oxidation by high kinetic energy atomic oxygen beams.**[34]** The first effective passivation layer was reported in 1987 by Sandroff and coworkers.**[35]** They discovered that a class of inorganic sulfides (Li_2S, $(NH_4)_2S$, $Na_2S{\cdot}9H_2O$, etc.) imparts excellent properties to GaAs surfaces. The surface recombination velocity (SRV) at the interface between $Na_2S{\cdot}9H_2O$ and GaAs begins to approach that of the nearly ideal AlGaAs/GaAs interface. These workers proposed, and this was confirmed by many subsequent studies, that a sulfide layer was covalently bonded to the GaAs surface. While these sulfide films result in a marked decrease in the SRV of GaAs, the effects are only temporary; after 18 h the SRV have returned to their pretreatment values. It is this lack of permanency that has prompted several groups to propose that MOCVD-grown films would make ideal passivation coatings.

The recently reported MOCVD-grown metastable cubic phase of gallium sulfide (GaS),[36] which forms a nearly lattice-matched layer on GaAs, shows promise as a stable commercially viable passivation layer for GaAs-based devices.[37,38] In addition, electrical characterization of the cubic GaS/GaAs interface shows that the Fermi level in both n- and p-type GaAs is completely unpinned, with the capacitance versus voltage curves showing well-defined accumulation and depletion regions.

4.2 Gallium Chalcogenides

4.2.1 Oxides and Hydroxides

The gallium oxide system is somewhat similar to that of aluminum, affording a high-temperature (α) and a low-temperature γ-Ga_2O_3, each having the same structure as their aluminum counterparts. β-Ga_2O_3 is the most stable crystalline modification (mp 1740 °C); it has a unique crystal structure with the oxide ions in distorted ccp and Ga^{III} in distorted tetrahedral and octahedral sites, with Ga-O distances of 1.83 and 2.00 Å, respectively (Figure 11).[39]

The structure appears to owe its stability to these distortions and, because of the lower coordination of half the Ga^{III}, the density is ca. 10% less than for the α (corundum-type) form. This preference of Ga^{III} for fourfold coordination, despite the fact that it is larger than Al^{III}, may indicate the polarizing influence of the d^{10} core; a similar tetrahedral site preference is observed for Fe^{III}. The trioxide is formed by heating the nitrate, the sulfate, or the hydrous oxides that are precipitated from Ga^{III} solutions by the action of ammonia. A summary of the transformations in the gallium oxide (and hydroxide) system is given in Scheme 1.

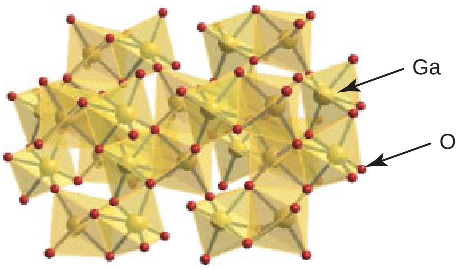

Figure 11 Structure of β-Ga_2O_3; oxygen atoms are shown red. (Ref. 27. Reproduced by permission from Dr Mark J Winter/WebElements. Source: WebElements [http://www.webelements.com/]; http://www.webelements.com/webelements/compounds/text/Ga/Ga2O3-12024214.html)

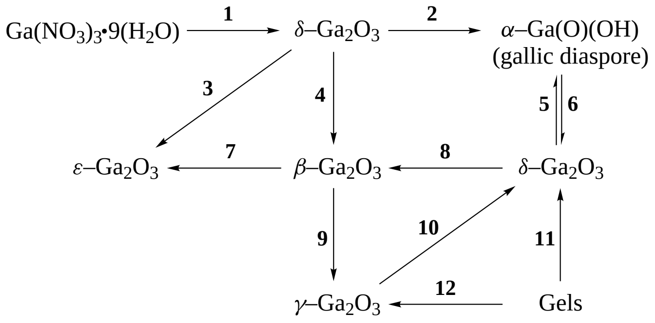

Scheme 1 Transformation relationships among the forms of gallium oxide and its hydrate. (1), 200 °C overnight; (2), <300 °C; (3), dry >500 °C, dry; (4), 300 °C wet; (5), 12 h, 500 °C, wet; (6), <300 °C, wet; (7), 870 °C, dry; (8), 300 °C wet, 600 °C, dry; (9), 650 °C, dry, 300 °C, wet; (10), 500 °C, few h; (11), 500 °C, 12 h, 400–500 °C, very rapid

β-Ga_2O_3 is classified as a transparent conducting oxide (TCO), that is, materials that, though having a wide band gap, are electrically conductive, and exhibits the largest band gap among TCOs with $E_g = 4.8\,eV$.[40] Consequently, it has a unique transparency from the visible into the UV wavelength region and is a viable candidate for the next generation of optoelectronic devices operating at shorter wavelengths. Large-size single crystals of high quality β-Ga_2O_3 (>2 cm diam.) have been grown by the floating zone technique.[41] Processed, cut, and polished wafers were found to be highly transparent in the visible and near UV, as well as electrically conductive, hence supporting its potential as a substrate for optoelectronic devices operating in the visible/near UV and with vertical current flow. Additionally, investigation into the formation of β-Ga_2O_3 nanocrystals has also been pursued.

A departure from the similarity of gallium oxides with those of aluminum is the stability of the gallium(I) oxide, which is made by high-temperature reactions (e.g. equations 3–5).

$$Ga_2O_3 + 4Ga \xrightarrow{700\,^\circ C} 3Ga_2O \tag{3}$$

$$2Ga + CO_2 \rightleftharpoons Ga_2O + CO \tag{4}$$

$$4Ga + SiO_2 \rightleftharpoons Si/Ga + 2Ga_2O \tag{5}$$

The dark brown, diamagnetic powder is stable in dry air and may be purified by vacuum sublimation at 500 °C, but undergoes surface oxidation at higher temperatures. Above 800 °C it disproportionates according to the reverse of equation (3). The hydrous oxides Ga(O)OH and $Ga(OH)_3$ are similar to their aluminum analogs. Thus gallium hydroxide is amphoteric, but a much stronger acid than aluminum hydroxide; for $Ga(OH)_3$ the first acid dissociation constant is 1.4×10^{-7}, while for $Al(OH)_3$ the value is 2×10^{-11}.

On heating with other metal oxides, gallium oxide forms gallates $M^{I}GaO_2$, $M^{II}Ga_2O_4$ (spinels), and $M^{III}GaO_3$. The latter include the solid solutions $M^{III}_{2-x}Ga_xO_3$ (M = Al, In). Mixed oxide stoichiometries other than 1:1 (O^{2-}; Ga_2O_3) are quite common. With sodium, there are complex gallates: $NaGaO_2$, Na_3GaO_3, $Na_8Ga_2O_7$, and Na_5GaO_4. The structures of these last two are built up from effectively isolated $[Ga_2O_7]^{8-}$ and $[GaO_4]^{5-}$ units. Some hydrated forms have also been studied, for example, $LiGaO_2{\cdot}6H_2O$, effectively $[Li(OH_2)_4][GaO_2(OH_2)_2]$. The compound $NaGa_{11}O_{16}(OH)_2$ has a complicated structure in which both GaO_4 tetrahedra and GaO_6 octahedra are present. Structures based on GaO_4 tetrahedra prevail among gallates of the divalent metals, for example, $SrGa_2O_4$, $CaGa_2O_4$, $Ca_3Ga_4O_9$, and $Pb_9Ga_8O_{21}$.

4.2.2 Sulfides and Selenides

Although not as extensively studied as the group 13–15 compound semiconductors, there has been increasing interest in the heavier gallium chalcogenides because of their possible application as semiconductors,[39] semimetals, photoconductors, and light emitters.[42,43] The gallium sulfides, GaS and Ga_2S_3, are wide band-gap semiconductors (3.05 and 2.85 eV respectively), and are, therefore, considered to hold promise as optoelectronic and photovoltaic materials. Additional work on gallium sulfide has been prompted by its application as passivation layers on GaAs. The chalcogenides of Ga are much more numerous than that of aluminum,[44] and are listed in Table 5.

The hexagonal α- and β-forms of Ga_2S_3 are isostructural with the aluminum analog, having a würtzite structure, while γ-Ga_2S_3 adopts the defect sphalerite structure derived from cubic ZnS (zinc blende). This latter structure is the only type found for Ga_2Se_3 and Ga_2Te_3. It is the isomorphism of γ-Ga_2S_3 with ZnS that is believed to account for the specific enrichment of gallium in sphalerite minerals. All three chalcogenides, Ga_2E_3, are readily prepared from the direct reaction of the elements at high temperature. In addition, Ga_2S_3 can be prepared by the solid-state reaction of $GaCl_3$ and sodium sulfide (equation 6).[45,46] Ga_2S_3 disproportionates at high temperatures to give a nonstoichiometric sulfide, $Ga_4S_{4.8-5.2}$ (equation 7).

Table 5 Stoichiometries and structures of the crystalline chalcogenides of gallium

Sulfide	Selenide	Telluride
Ga_2S green prisms	Ga_2Se	
GaS hexagonal layered structure, Ga–Ga bonds	GaSe like GaS	GaTe like GaS
GaS cubic (ZnS)		
Ga_4S_5		Ga_3Te_2
α-Ga_2S_3 würtzite (ZnS)		
β-Ga_2S_3 defect würtzite		
γ-Ga_2S_3 defect sphalerite	Ga_2Se_3 defect sphalerite	Ga_2Te_3 defect sphalerite Ga_2Te_5 chains of $GaTe_4$ plus Te atoms

$$2GaCl_3 + 3Na_2S \longrightarrow Ga_2S_3 + 6NaCl \qquad (6)$$

$$2Ga_2S_3 \rightleftharpoons Ga_4S_5 + \tfrac{1}{2}S_2 \qquad (7)$$

Unlike the chalcogenides of aluminum, those of gallium form subvalent compounds (i.e. those in which the metal is formally of an oxidation state less than +3). Of these subchalcogenides, the (formally) divalent compounds are of the most interest. The thermodynamic phase of GaS has a hexagonal layer structure (Figure 12) with Ga-Ga bonds (2.48 Å).[47] Each Ga is coordinated by 3 S and 1 Ga, and the sequence of layers along the z-axis is $\cdots$SGaGaS, SGaGaS$\cdots$. The compound can therefore be considered as an example of Ga^{II}, while the presence of Ga-Ga bonding accounts for the diamagnetism of the compound.

Two other phases of GaS are known. The first is a rhombohedral phase,[48] similar in structure to the hexagonal phase, found as an impurity in Ga_2S_3. The second is a metastable fcc phase prepared by MOCVD from the cubane precursor $[(t\text{-Bu})GaS]_4$.[36] The latter phase does not contain any Ga–Ga interactions and is therefore most probably a mixed valence Ga^{I}/Ga^{III} compound. However, while the electronic structure of the cubic phase is not fully understood, it does have significant applications as a passivation layer on GaAs and other group 13–15 materials. The structures of GaSe and GaTe are similar to the hexagonal phase of the sulfide.

Gallium(I) sulfide cannot be prepared directly from the elements, but is obtained from the thermal decomposition of the higher sulfides. Thus when gallium(II) sulfide is heated at 1100 °C for several hours in a stream of nitrogen, Ga_2S sublimes quantitatively as green hexagonal prisms or yellow–green plates. The compound is in fact a phase of variable composition, $Ga_2S_{0.8-1.1}$, and has a hexagonal lattice similar to that of gallium(II) sulfide (see above). Above

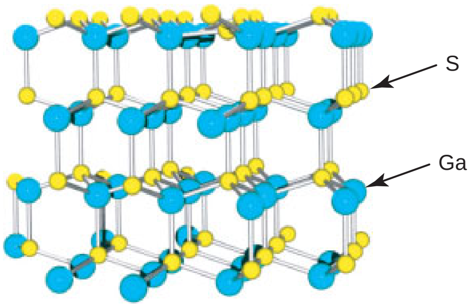

Figure 12 Lattice structure for hexagonal GaS

950 °C, pure Ga_2S decomposes to a liquid mixture of GaS and metallic gallium which becomes homogeneous above 1150 °C (equation 8).

$$Ga_2S(s) \longrightarrow GaS(l) + Ga(l) \rightleftharpoons Ga_2S(g) \qquad (8)$$

Gallium(I) selenide and gallium(I) telluride can be made by melting the elements together in evacuated quartz tubes for prolonged periods; their X-ray powder diffraction patterns have been recorded and indexed.

4.2.3 Chalcogenide Salts

Gallium forms a variety of ternary sulfides and selenides. Common types are $M^{I}GaS_2$, $M^{II}Ga_2S_4$, and $M^{III}GaS_3$; examples of each are $CuGaS_2$, $CdGa_2S_4$, and $LaGaS_3$, respectively. Owing to the unusual electrical properties of these and the corresponding indium compounds, there is an extensive literature concerned with their preparation, physical properties, growth as single crystals, and X-ray studies. Compounds of other stoichiometries occur in mixed sulfide systems involving gallium, for example, $Pb_2Ga_2S_4$ (or $2PbS{\cdot}Ga_2S_3$). All of these compounds have the common structural feature of extended lattices composed of linked GaS_4 tetrahedra, with Ga–S bond distances in the range 2.18–2.36 Å. The tetragallium anion $[Ga_4S_{10}]^{8-}$ has been isolated from the reaction of Ga_2S_3 with aqueous metal sulfides (e.g. equation 9).

$$2Ga_2S_3 + 4K_2S \longrightarrow K_8GaS_{10} \qquad (9)$$

The structure of the hydrated salt, $K_8Ga_4S_{10}{\cdot}14H_2O$, has been determined by X-ray crystallography (Figure 13).**[49]** The analogous seleno compound has been synthesized, as have the indium species, and all the structures have high thermal and solvolytic stability. Layers of isostructural Ga_4Se_{10} groups, linked through corners, comprise the structure of the ternary selenide $TlGaSe_2$.

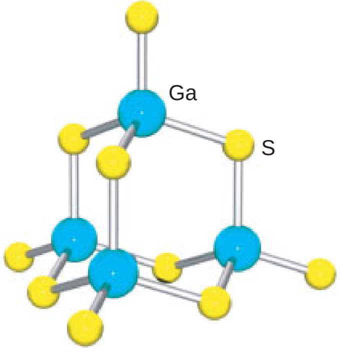

Figure 13 $[Ga_4S_{10}]^{8-}$ anion; Ga–S distances are 2.28 Å (bridging) and 2.25 Å (terminal)

Other gallium–chalcogenide anions are observed in the solid state, that is, discrete $[Ga_6Se_{10}]^{8-}$ anions occur in $Cs_5Ga_3Se_7$, while $Cs_6Ga_2Se_6$, obtained as moisture-sensitive crystals by the reaction of Cs_2Se with Ga_2Se_3, contains the $[Ga_2Se_6]^{6-}$ anion.

5 I-III-VI$_2$ TERNARY COMPOUNDS

The crystal structure of I-III-VI$_2$ ternary materials is common to the cubic zinc blende structure of II-VI material's (i.e. ZnS), but differs by group I and III atoms occupying the Zn sites alternatively. Consequently, each group I or III atom has a connectivity of four bonds to the group VI atom, hence each VI atom has two VI-I and two VI-III bonds (Figure 14). Owing to the different bond lengths of I & III with the group VI, atom lattice distortion is evident.

The most prevalent ternary chalcopyrite materials are *p*-type Cu(In:Ga)(S:Se)$_2$ (CIGS), which crystallize in the tetragonal chalcopyrite structure and are used in the photovoltaic modules. The complexity of the phase diagrams for Cu-III-VI materials results in a large number of intrinsic

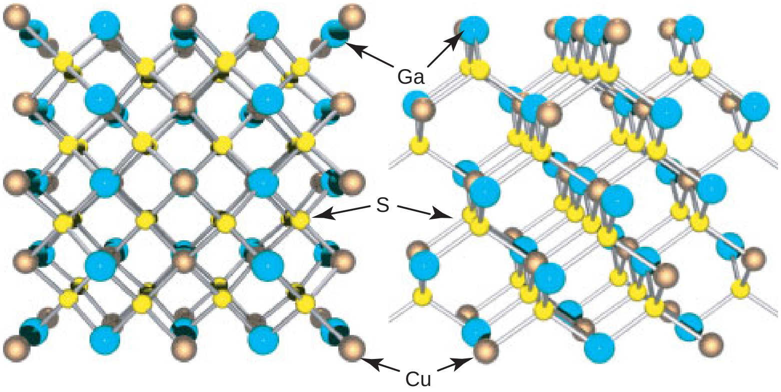

Figure 14 Structural representation of lattice packing for I-III-VI$_2$ materials

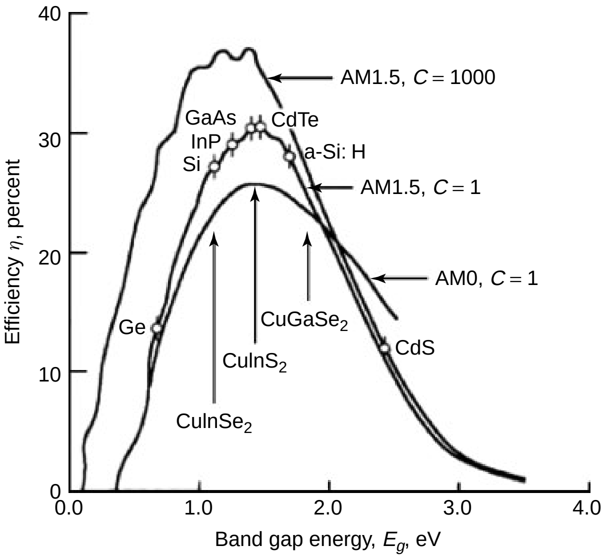

Figure 15 Predicted efficiency versus band gap for thin-film photovoltaic materials for solar spectra in space (AM0) and on the surface of the Earth (AM1.5) at 300 K compared with bandgaps of other PV materials with unconcentrated (C = 1) and high concentration (C = 1000) sunlight

defects in the semiconductor, which can influence the doping of the alloy and has been recently studied by Burgelman and Zhang.[50–53] The conductivity of the *p*-type CIGS is mainly due to copper atoms residing on indium vacant sites, whilst a deficiency in group VI atoms is considered to contribute to *n*-type doping. The use of a chalcopyrite semiconducting material is highly appealing since the band gap correlate well to the maximum photon power density in the solar spectrum for both terrestrial (AM 1.5), and space applications (AM0) (Figure 15), while displaying long-term stability and excellent radiation tolerance.[54] Furthermore, the band gap can be tuned from 1.0 eV to 2.4 eV, by adjusting the percent atomic composition of either Ga for In and S for Se.[55] The schematic of typical CIGS solar cell is shown in Figure 16.

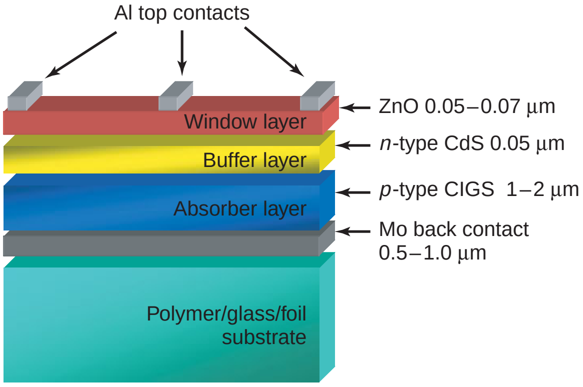

Figure 16 Schematic representation of a typical CIGS solar cell

Current methods for depositing ternary crystallite compounds include coevaporation of elements,[56] or alloys,[57] electrodeposition,[58] reactive-sintering,[59] and flash evaporation,[60] which are often followed by sulphurization/selenization steps, at elevated temperatures. The current world record cell has been reported by NREL with an efficiency of 19.2% based on their patented three-stage process.[55]

A more chemistry-based route to I-III-VI alloys is one that encompasses the design of molecular 'single-source precursors'. Two such routes are those involving the codeposition of two binary single-source precursors, namely, metal dithiocarbamates, and more recently the use of ternary single-source precursors. The first example of a ternary $CuGaS_2$ single-source precursor was recently reported, and although the exact molecular structure of the ternary precursor could not determined, well adhering stoichiometric thin films of $CuGaS_2$ were successfully deposited in an Aerosol Assisted CVD process.[61] Additionally, codeposition of Ga and In ternary single-source precursor to CIGS was also realized. Ternary single-source precursors of the form $[M^{(I)}(ER)_2Ga^{(III)}(ER)_2]$ ($M^{(I)}$ = Cu, Ag), to afford the semiconductor $CuGaS_2$ $AgGaS_2$ have also been designed, and their molecular structure have been elucidated[62] (Figure 17).

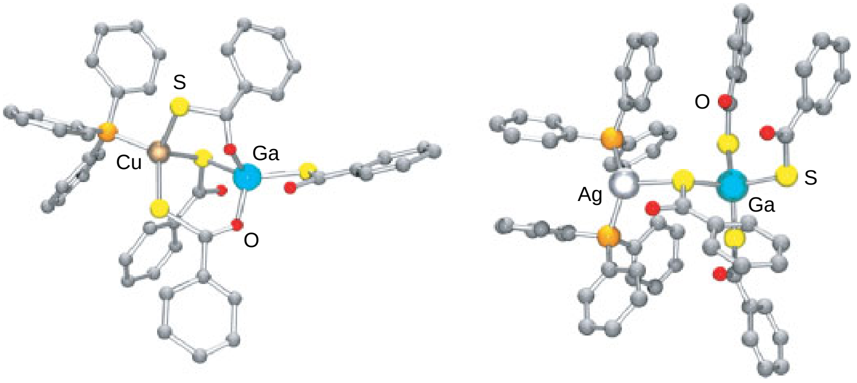

Figure 17 Molecular structure of $[\{PPh_3\}Cu(\mu\text{-}SC\{O\}Ph)_4Ga(SC\{O\}Ph)_2]$, $[\{PPh_3\}_2Ag(\mu\text{-}SC\{O\}Ph)_4Ga(SC\{O\}Ph)_2]$

Thermogravimetry and pyrolysis studies at 300 °C, (0.5 mmHg) for 30 min revealed that these compounds decompose to give the corresponding ternary metal sulfide materials, but thin-film deposition studies for the Ga derivatives are yet to be studied.

A series of trialkylammonium salts of indium and gallium thiocarboxylates, $[Et_3NH][M(SC\{O\}Ph)_4]\cdot H_2O$ (M = In, Ga) were synthesized and characterized for their use as precursors to metal chalcopyrite structures.[63] Thermogravimetric and pyrolysis experiments of these compounds showed the formation of tetragonal β-In_2S_3 and poorly crystalline monoclinic Ga_2S_3, respectively. In similar MOCVD studies, deposition on a nickel substrate gave thin films of cubic γ-Ga_2S_3 and hexagonal $Ni_{0.96}S$. Whereas deposition onto a Cu coated Si substrate afforded thin films of tetragonal $CuInS_2$, the gallium derivative furnished a mixture of tetragonal $Cu_{1.96}S$ and $CuGaS_2$. The composition of the thin films was found to be temperature-dependent during the growth process and the formation of $Cu_{1.96}S$ and $CuGaS_2$ results by the reaction of the group III compounds with the copper substrate to form the metal sulfide thin films.

6 GALLIUM NANOCRYSTALLITES

6.1 Introduction

Over the decade, there has been an immense drive to develop synthetic processes, and characterize binary nanocrystalline semiconducting material. The size dependent luminescence of these materials is a result of quantum confinement within the nanosized particulate resulting in an engineered band gap (eV) through the formation of discreet bonding/antibonding orbitals. As discussed earlier, many of the III-V materials are direct band-gap semiconductors, which have led to their increased use in optoelectronics and telecommunications. Consequently, it is the most frequently studied group of Ga nanocrystallites, but still falls well short of the number of studies for its Indium analogs. A few detailed reviews[9,64,65] and book chapters[66,67] have recently covered this area in depth.

6.2 III-V

Unlike the synthetic procedure established for fabricating II-VI semiconducting nanocrystallites, the use of a similar synthetic procedure cannot be directly translated for the synthesis of gallium pnictogens nanocrystallites, but requires modification. This is attributed to the reactivity of the gallium reagents, the greater covalent bonding nature of III-V material and the higher energetic barriers in the formation of the semiconductor from suitable precursors. The current reported methods that have been used are shown in equations (10–13).

$$GaCl_3 + As(SiMe_3)_3 \longrightarrow GaAs + 3ClSiMe_3 \qquad (10)$$

$$Ga(CH_3(CO)CH(CO)CH_3)_3 + As(SiMe_3)_3 \xrightarrow{\text{triglyme}} GaAs \qquad (11)$$

$$GaCl_3 + M_3E \xrightarrow[\substack{\text{M=K, Na}\\ \text{E=P, As}}]{\text{glymes}} GaE + 3ClSiMe_3 \qquad (12)$$

$$2GaCl_3 + 2InCl_3 + P(SiMe_3)_3 \xrightarrow{\text{TOPO}} GaInP_2 + 3ClSiMe_3 \qquad (13)$$

GaAs nanocrystals have been prepared by dehalosilyation reaction (equation 10), with the driving force being the high propensity for the formation of the Si–Cl bond.[68–70] In order to limit nucleation and particle growth via Ostwald ripening, coordinating ligands are used, which are commonly referred to a capping or passivating group/ligand. Initial studies using the dehalosilyation route where quinoline was used as both the solvent and capping ligand afforded 3–4 nm sized nanocrystals. However, optical interference from by-products during the synthesis was prevalent. Alternatively, the use of coordinating compounds such $Ga(acac)_3$ (acac = $CH_3(CO)CH(CO)CH_3$) has been studied (equation 11). However, size distribution control of the GaAs nanocrystals was not achievable owing to the large number of nucleation centers formed.[71] In the presence of a trioctylphosphine oxide (TOPO), which serves to passivate dangling surface bonds, nanocrystals of GaP and $GaInP_2$ were realized with good size distribution and optical properties.[64,72] In the continued pursuit of greater size distribution control and crystal quality, a polymeric Ga imide precursor $[Ga(NH_3)_{3/2}]_n$ heated in trioctylamine at 360 °C for one day was investigated.[73] The purified GaN particles, when partially dispersed in a nonpolar solvent, yielded transparent colloidal solution that consisted of individual spherical GaN particles (3 nm). The photoluminescence spectrum at 10 K (excited at 310 nm) showed a band edge emission with several emission peaks at 3.2–3.8 eV, while the photoluminescence excitation spectrum studies showed two excited-state transitions at higher energies.

A thermal reaction preparative route reacting Li_3N and $GaCl_3$ in benzene under pressure was successfully demonstrated to afford GaN 30 nm particles at low temperatures (280 °C) in high bulk yields of approximately 80%. Structural characterization revealed the sample was mainly hexagonal-phase GaN with a small fraction of rocksalt-phase GaN, which has a lattice constant of 4.100 Å. This rocksalt structure has been observed previously only under high pressure (>37 gigapascals).[74]

An interesting variation to this benzene thermal route is the preparation of GaN nanoparticles from the conversion of Ga_2S_3, as shown in equation (14). At 180 °C, a size distribution of 10–15 nm is achieved, whereas at 230 °C, a size distribution of 15–25 is achieved; however, crystal quality is poor at best or amorphous at the lower temperatures.[75]

$$Ga_2S_3 + 2Na_3N \xrightarrow{\text{benzene}} 2GaN + 3Na_2S \qquad (14)$$

A novel method receiving great interest is the use of binary III-V single-source precursors, for example, the controlled pyrolysis of the inorganic polymer $[(Cl_3Ga_2P)]_n$ or $[X_2GaP(SiMe_3)_2]_2$ at reduced temperatures and pressures affords GaP nanocrystallites.[65] Additionally, the hydride analog $[H_2GaE(SiMe_3)_2]_2$ ($E = As, P$) was also successfully decomposed in xylenes (450 °C) to form III-V particles (5 nm).[76] Thermolysis of $M(PBu^t_2)_3$ ($M = Ga$, In) in hot 4-ethylpyridine afforded InP and GaP nanocrystals.[65] Investigations into the thermal decomposition mechanisms have suggested three major processes, two of which are temperature dependent; reductive elimination and β-hydrogen elimination, and the third a minor pathway involving free-radical formation. Attempts to prepare III-V nanocrystallites from either $Ga(PBu^t_2)_3$ and $In(PBu^t_2)_3$ in TOPO failed to yield the desired product. The fabrication of nanoparticles using this method has been recently been published.[77]

A non-chemical solution route for nanocrystallites formation is via Stranski-Krastinow Epitaxial Growth.[78] The nanocrystallites are formed by epitaxial growth by either MBE or MOCVD. The principle behind the formation of nanocrystallites is the controlled deposition onto a semiconducting substrate with a differing lattice constant, then the III-V material being deposited. When the lattice mismatch is sufficiently high, after the deposition of the first few monolayers, small islands of nanocrystallites are formed. This technique has focused primarily on Ga_xInAs_{1-x} grown on GaAs. A number of reports have focused on the preparation of β-Ga_2O_3 nano derivatives. A patented high-temperature method involves heating (1600 °C), a mixture of boron powder and bulk Ga_2O_3 in a 2:1 ratio in an inert atmosphere to yield Ga_2O_3 nanowires with a diameter of 15–100 nm, coated with 3–5 nm of BN layer.[79] In a similar process, substituting activated carbon for boron affords β-Ga_2O_3 nanowhiskers (≤50-mm length, diameter 10–100 nm).[80]

Nanocrystal shape engineering has been demonstrated via a novel technique for the preparation of α-Ga_2O_3 nanoparticles, nano-hollow-particles, or nanorods and nanotubes via oxidation of nanocrystalline GaP at 400 °C for 30 min in dry O_2.[81] Additionally, a chemical vapor deposition process has been used to fabricate β-Ga_2O_3 from a gallium/gallium oxide mixture and oxygen. The diameter of the single-crystalline monoclinic nanowires were 30–80 nm with an average value of 50 nm. Nanowires grown without catalyst exhibited a significant planar defect, whereas the nanowires grown with nickel catalytic nanoparticles were reported to be almost defect-free.[82]

6.3 III-VI & I-III-VI$_2$

Binary III-VI alloys crystallize in a variety of forms such as defect wurtzite (Ga_2E_3), layered structures GaE, and a novel cubic form, whereas α, β, and $\gamma - Ga_2S_3$ are reported to have a wurtzite, hexagonal, and monoclinic phase respectively.[83] The two predominant binary stoichiometries are AB and A_2B_3, and these are categorized as mentioned earlier as mid to wide band-gap semiconductors. In comparison with II-VI and III-V nanocrystallites, there is a paucity of reports on preparation of III-VI and I-III-VI$_2$ nano derivatives, and of those they mostly focus on Indium derivatives (*see* ***Indium: Inorganic Chemistry***). The most widely used methods are pyrolysis of single-source precursors such as carbamate coordination compounds, selenolate thiolate complexes, and solvothermal high-temperature procedures of metal salts.

Although there are a limited number of reports for the preparation of InS and InSe nanoparticles via the use of single-source precursors such as $[In(S_2CNEt_2)_3]$ and $[In(Se_2CNEt_2)_3]$ respectively, there are no reported studies for their Gallium counterparts. However, decomposition of $[Bu^tGaSe]_4$ clusters under CVD condition has been shown to afford GaSe pseudo-spherical nanoparticles with a mean diameter of 42 ± 13 nm.[84] In addition, the use of ternary single-source precursors such as $[(PPh_3)_2CuIn(SEt)_4]$ and $[(PPh_3)_2CuIn(SePh)_4]$ have been successfully shown to yield I-III-VI$_2$ nanoparticles via pyrolysis in dioctyl phthalate at 200–300 °C (forming aggregated cluster with nanoparticles of size from 3 to 30 nm);[85,86] however, similar gallium derivatives remain to be studied for their potential use for the formation of Ga based I-III-IV$_2$ nanoparticles via this route.

Solvothermal routes have been used to realize the formation of I-III-VI$_2$ nanoparticles.[87–89] Aqueous and nonaqueous colloids, $CuInS_2$, $CuInSe_2$, $CuGaS_2$, $CuFeS_2$, $AgInS_2$, were prepared by the reaction of the respective metal salts in either water or $CNMe_3$ that has been saturated with H_2E, ($E = S$, Se) and stabilized with polyvinylalcohol (1%). For the formation of nanoparticle $CuGaS_2$ clusters, these were synthesized exclusively from a CuI solution in acetonitrile (0.01 mol/l and below) and gallium nitrate. Spherical $CuGaS_2$ particles (35-nm diameter) have been synthesized by adapting a low-temperature autoclave method used for preparing III-V nanoparticles. The reaction of CuCl with elemental Ga with excess sulfur at 200 °C for 12 h affords the crude product. Treatment of the precipitate, by washing with dilute acid, distilled water, and absolute ethanol, respectively, and drying under vacuum at 50 °C for 4 h gave the final nanocrystalline semiconductor. The synthesis of a number of analogous Ga-containing clusters has been reported, with the potential to afford ternary semiconducting alloys.[90]

7 HYDRIDES AND HYDRIDE COMPLEXES

The chemistry of the group 13 hydrides originated in 1912 with Alfred Stock's classic investigations into the synthesis and characterization of numerous boron hydrides (boranes) including the parent diborane, B_2H_6 (*see* ***Boron Hydrides***). Unlike boron, aluminum does not form a low-molecular weight hydride analogous to diborane, but a polymeric species $[AlH_3]_x$, in which each aluminum is surrounded octahedrally by six hydrogens. As early as 1941, the isolation of both $[GaH_3]_x$[91] and Ga_2H_6[92] was claimed, but failure to repeat this work and the anomalously high thermal stability of the compounds caused researchers to question the existence of these compounds. However, a recent series of definitive studies not only showed that gallane does indeed exist in both oligomeric, $[GaH_3]_x$, and dimeric, Ga_2H_6, forms, but also confirms that the previous synthetic claims were incorrect. The low thermal stability ($< -20\,°C$) of gallane is consistent, however, with the periodic decrease in the M–H bond strength.

The presence of a stable diborane-like molecule $[H_2Ga(\mu\text{-}H)]_2$ in both solution and the vapor phase suggests that the chemistry of gallane has a marked similarity to that of diborane, that is, (**1**). The analogy between the gallium and boron hydrides is extended by the synthesis and structural characterization of the mixed gallaborane, $GaBH_6$ (**1**).

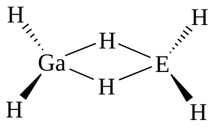

(**1**) E = B, Ga

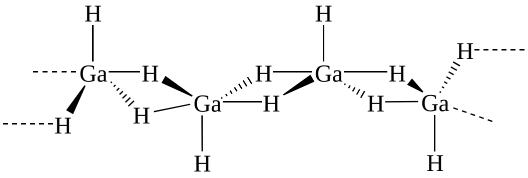

(**2**)

Although no structural details have been reported for the oligomeric form of gallane, $[GaH_3]_x$, IR spectroscopic evidence suggests the retention of terminal Ga–H bonds. This is unlike the all-bridging hydride six-coordinate structure of $[AlH_3]_x$, suggesting the gallium in $[GaH_3]_x$ is perhaps five-coordinate with a single terminal Ga–H bond along with doubly hydride-bridged $Ga(\mu\text{-}H)_2Ga$ units (**2**), similar to that observed in the structure of $HGa(BH_4)_2$.[93]

The adduct $[GaH_3(NMe_3)]$ is a colorless, crystalline compound (mp 70.5 °C), which is formed quantitatively by the reaction of ethereal solutions of $Li[GaH_4]$ and $[NHMe_3]Cl$; like the aluminum analog, it takes up a further mole of ligand to give the trigonal bipyramidal $[GaH_3(NMe_3)_2]$. Numerous complexes with other Lewis base ligands may be prepared from $[GaH_3(NMe_3)]$, and the structures of some of these have been determined by X-ray crystallography, for example, (**3**) and (**4**).[94] The stabilities of the 1:1 adducts have been determined to decrease in the sequences: $NHMe_2 > NMe_3 >$ pyridine $> NEt_3 > NMe_2Ph > NPh_3$; $NMe_3 \sim PMe_3 > PHMe_2$; $PPh_3 > NPh_3 > AsPh_3$; NR_3 or $PR_3 > OR_2$ or SR_2.

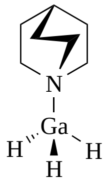

(**3**)

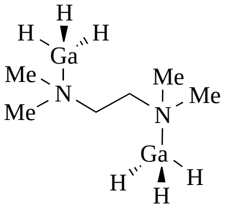

(**4**)

Gallane and its Lewis base complexes react readily with protic acids to eliminate hydrogen. Thus complexes of the type $GaH_2X(NMe_3)$ and $GaHX_2(NMe_3)$ (X = Cl, Br) are readily prepared by reaction of HX on the gallane complex at low temperatures. The reactions shown in Scheme 2[94] are examples of an elimination–condensation reaction with a secondary amine and the reduction of an imine; both reaction types have been observed for aluminum hydrides.

Gallium hydride complexes have also been studied for their use in fabricating binary thin films. $[H_3Ga(HNMe_2)]$ has been used in the growth of GaAs and AlGaAs film in low-pressure CVD type processes, which demonstrates reduced carbon contamination in the III-V films.[95] Unfortunately, as like most amine adducts of gallane they are very labile and require storage at low temperatures, therefore these GaAs films grown from $[H_3Ga(HNMe_2)]$ with AsH_3 or H_2AsBu^t have *p*-type behavior.[95]

Dichlorogallane $(HGaCl_2)_2$ was recently readily prepared from $GaCl_3$ and triethylsilane in high yields. Single-crystal X-ray diffraction revealed the Cl-bridged dimers as having C_{2h} symmetry, with the terminal H atoms in trans geometry. In the reaction of dichlorogallane with 2 equivalents of triethylphosphine, mononuclear $[(Et_3P)GaHCl_2]$ is formed.[96]

The reactions of trichlorogermane $HGeCl_3$ and dichlorogallane $HGaCl_2$ with pyridine donors has been recently studied. Pyridine was found to deprotonate $HGeCl_3$ to afford pyridinium trichlorogermanate(II), $PyH^+[GeCl_3]^-$.

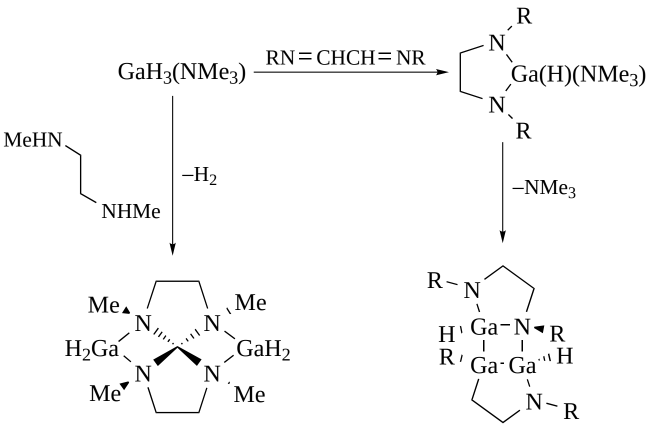

Scheme 2

This course of the reaction was examined and supports the assignment of an inverse polarization (−)Ge-H(+) of the bond in $HGeCl_3$ as compared to the (+)Si-H(−) bond in trichlorosilane $HSiCl_3$, which is known to form a 1:2 adduct with pyridine instead. Dichlorogallane was found to form 1:1 coordination compounds ($HGaCl_2L$), where L = pyridine, 4-dimethylaminopyridine, 4-cyanopyridine, and 3,5-dimethylpyridine.[97]

Dialkylgallium hydrides $[R_2GaH]_n$ (R = Me, Et, $CHMe_2$, CH_2CHMe_2, CH_2CMe_3) have been readily prepared by two different synthetic routes. The methyl and ethyl derivatives were formed by the reaction of LiH with the corresponding dialkylgallium chlorides via lithium dialkyldihydrogallate intermediates; however, they were not isolated in a pure form. In the second route, the trialkylgallium compound was treated with $[H_3Ga(NMe_2Et)]$ to yield the dialkylgallium hydrides by a substituent exchange reaction. The trimeric structure with inner Ga_3H_3-heterocycle was verified for R = $CHMe_2$ by a single-crystal structure determination, whereas for R = CH_2CMe_3, a dimeric structure both in solution and solid state is noted.[98]

The synthesis and structural characterization of a thermally stable group 13 hydride complexes derived from a gallium(I) carbene analog was achieved.[99] The reactivity of $[Ga\{NC(R)C(H)\}_2]^-$ (R = $C_6H_3(Pr^i)_2$) with $[AlH_3(NMe_3)]$ in an ethereal solution yielded $[Ga\{[NC(R)C(H)]_2\}_2][K(DME)_4]$. In addition, the reaction with tertiary amine adducts of GaH_3 and InH_3 in a 2:1 stoichiometry were found to give the respective salt complexes.

The first gallane-coordinated metal complex, $[(OC)5W(\eta^1\text{-}GaH_3\cdot\text{quinuclidine})]$, was synthesized by photolysis of a near 1:1 mixture of $W(CO)_6$ and $H_3Ga\cdot$(quinuclidine), in toluene and THF.[100] X-ray crystal-structure analysis revealed that product is bound to the W fragment via a W–H–Ga three-center-two-electron bond. Controlled test reactions indicated that the gallane ligand complex is inert toward direct substitution reactions and decomposes without releasing free $H_3Ga\cdot$(quinuclidine). The synthesis of Lewis acid/base-stabilized phosphanylgallanes $[(CO)_5WPH_2MH_2(NMe_3)]$ (M = Al, Ga) has been obtained via H_2 elimination reactions between $[(CO)_5WPH_3]$ and H_3MNMe_3. Crystal structures were determined for both complexes and comprehensive density functional theory (DFT) calculations on the aluminum systems were used to verify the high stability of the complexes.[101] In addition, a complete series of intermetallic gallane hydrides has been synthesized and studied with their potential aspect for depositing mixed metal gallium films.[102]

The preparation of $[Bu^t(H)Ga(\mu\text{-}NEt_2)]_2$ was accomplished by the metathesis reaction between Bu^tLi with $[Cl_2Ga(\mu\text{-}NEt_2)]_2$. Evidence suggests that two Bu^t groups are lost as isobutylene and result in Ga–H bond formation. The gallium hydride demonstrates high stability toward ambient air, oxygen, photolysis, and moderate heating; however, in $CHCl_3$ the hydride is replaced by chloride, producing $[Bu^t(Cl)Ga(\mu\text{-}NEt_2)]_2$. $[Bu^t(H)Ga(\mu\text{-}NEt_2)]_2$ was also synthesized by sequential additions of Bu^tLi to $[Cl_2Ga(\mu\text{-}NEt_2)]_2$. A singly substituted *tert*-Bu dimer, $[Bu^t(Cl)Ga(\mu\text{-}NEt_2)_2GaCl_2]$, was also isolated, and interconversions between three gallium hydrides were reported as was its utility in fabricating GaN. However, it was found to yield nitrogen deficient films as a consequence of facile Et_2NH elimination.[103]

8 GROUP 14, 15, AND 16 DONOR LIGANDS

8.1 Introduction

The majority of compounds reported in the literature containing ligands with either a group 15 or 16 donor atom are derived from a gallium alkyl, and as such they are covered in (*see* ***Gallium: Organometallic Chemistry***). However, a number of purely inorganic compounds and complexes are relevant to the present discussion. Where compounds contain both a group 15 or 16 donor ligand and either a hydride or halide ligand, they (and any relevant references) are included in the appropriate section depending on the ligand type of primary importance.

8.2 Silyl Gallium Compounds

Clearly, alkyl (and aryl) groups make up the largest contingent of group 14 ligands; however, surprisingly little work has been reported on compounds of gallium with silicon containing ligands, and no nonalkyl-based compounds with germanium or tin ligands are known. Tris(trimethylsilyl)gallium is produced by treating $GaCl_3$ and three equivalents of Me_3SiCl in the presence of lithium metal in THF. The initial solvated adduct, $Ga(SiMe_3)_3\cdot THF$, is converted to $Ga(SiMe_3)_3$ by vacuum sublimation. $Ga(SiMe_3)_3$ is monomeric, with a planar $GaSi_3$ framework, characterized by vibrational bands $\nu(\text{Ga–Si})_{\text{sym}} = 312\,\text{cm}^{-1}$ (Raman) and $\nu(\text{Ga–Si})_{\text{deg}} = 349\,\text{cm}^{-1}$. The area of Si gallium chemistry that has been explored thoroughly is the use of bulky silane groups to encourage cluster formation, and as such is reported in detail in ***Electronic Structure of Clusters***; ***Silicon: Inorganic Chemistry***; ***Silicon: Organosilicon Chemistry***.

Recently the first compounds containing Si=Ga or Si=In double bonds, 1,3-disila-2-gallata- and -indataallenic anions respectively, were obtained in the form of lithium salts as dark red crystals by the reaction of *bis*(di-*tert*-butylmethylsilyl)dilithiosilane, with the respective M(III) halide (Figure 18).[104] X-ray crystallographic analysis of gallium and indium salt derivatives showed that the >SiMSi< frameworks (M = Ga, In) are not linear and the two Si=M

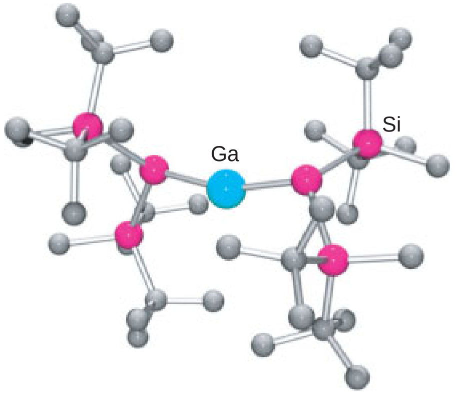

Figure 18 Li[(Bu$^t_2$MeSi)$_2$SiGaSi(Bu$^t_2$MeSi)$_2$]: hydrogen atoms and the cationic fragment [Li(thf)$_4$]$^+$ are omitted for clarity: Si-Ga-Si = 161.61(3) deg

bond lengths are about 9% shorter than typical Si–M single bonds (Figure 18). The ^{29}Si NMR spectra show the signals of the terminal Si atoms in both compounds are greatly shifted upfield (Ga: −79.9; In: −77.6 ppm). In addition, the gallium salt was found to react with MeI to give the corresponding iodogallane in nearly quantitative yield, thus confirming that the allenic [>SiMSi<]$^-$ fragments are highly polarized.

8.3 Nitrogen Derivatives

8.3.1 Amine and Amido Ligands

As discussed earlier, gallane and the trihalides all form Lewis acid−base complexes with amines and N-heterocyclic ligands. While the majority of these compounds are neutral and have a general formula of $GaX_3(L)_n$ ($n = 1, 2$), complexes formed with bidentate ligands such as 1,10-phenanthroline and 2,2′-bipyridyl are typically ionic. A common feature of these complexes is the presence of a gallium cation, for example, $[Ga(bipy)_3]^{3+}$ or $[GaCl_2(bipy)_2]^+$. Thus the crystal structure of '$GaCl_3$(bipy)' shows it to be *cis*-$[GaCl_2(bipy)_2]^+[GaCl_4]^-$.**4**

Potassium amidogallate, $K[Ga(NH_2)_4]$, is prepared by dissolving gallium in a solution of KOH in liquid ammonia. Heating this compound to 300 °C under vacuum removes two moles of ammonia, forming the imido complex $K[Ga(NH)_2]$, while partial neutralization of the ammonia solution of $K[Ga(NH_2)_4]$ with NH_4Cl yields $Ga(NH_2)_3$. The anion $[Ga(NH_2)_4]^-$ has tetrahedral symmetry, according to the single-crystal Raman spectrum in which ν(Ga–N) appears near 550 cm^{-1}. $NaGa(NH_2)_4$ crystallizes isotypic in space group P21/c was obtained by the reaction of the metals with NH_3 in autoclaves at 100 °C and $P(NH_3) = 60$ bar within 7 days.**105** A more highly coordinated complex, $Na_2[Ga(NH_2)_5]$, has also been prepared. From evidence of IR spectra, this contains six-coordinate gallium, with a structure based on linked $Ga(NH_2)_6$ octahedra with both bridging and nonbridging NH_2 groups.**4**

Dialkylamido compounds, $GaX_2(NR_2)$, $GaX(NR_2)_2$ (X = halide), and $Ga(NR_2)_3$, are obtained from the reaction of GaX_3 with the appropriate equivalents of $LiNR_2$; unless precluded owing to steric hindrance, an excess yields $Li[Ga(NR_2)_4]$. Hydrido-substituted amido compounds, $[H_2Ga(NXR)]_n$ (X = H or R, $n = 2$ or 3), may be prepared from the reaction of primary or secondary amines with $GaH_3(NMe_3)$. In the absence of steric hindrance, gallium amido compounds oligomerize as a result of the amido ligands bridging ability.**4** Thus for $Ga(NR_2)_3$ when R = Me, a dimerization through bridging dimethylamido ligands occurs, while in the case of R = $SiMe_3$ a monomeric structure is observed.

Gallane complexes with amido-amine ligands $-N(R)CH_2CMe_2CH_2NMe_2$ [R = H or $SiMe_3$ (TMS)], (**5**) $\{H_2Ga[N(H)CH_2CMe_2CH_2NMe_2]\}_2$, (**6**) $H_2Ga[N(TMS)CH_2CMe_2CH_2NMe_2]$, (**7**) $\{H(Cl)Ga[N(H)CH_2CMe_2CH_2NMe_2]\}_2$, (**8**) $\{[(TMS)_2N](H)Ga[N(H)CH_2CMe_2CH_2NMe_2]\}_2$, (**9**) and $HGa[N(TMS)CH_2CMe_2CH_2NMe_2]_2$, (**10**) were synthesized from the reactions of the quinuclidine adducts of mono- and dichlorogallane with the corresponding lithium amides. Structural determinations of compounds (**5**), (**7**), (**8**) showed they were dimeric with bridging amido groups. The tertiary amine groups in (**5**) and (**8**) were hydrogen-bonded to the amido N–H rather than being bonded directly to gallium center. In the structure of compound (**7**), the amine group was found to occupy an axial position in the trigonal bipyramidal geometry of the five-coordinate gallium. These results were rationalized in terms of the steric and electronic properties of respective gallium ligands.**106**

Base-free tris(primary amido) compounds of the type $M[N(H)Mes^*]_3$ (M = Al, Ga, In; Mes* = 2,4,6-tri-*tert*-butylphenyl) have been synthesized via the salt elimination reaction of Mes*N(H)Li with the respective MCl_3. Whereas the singly base-stabilized *tris*(primary amido) derivatives, $[M\{N(H)Dipp\}_3(py)]$ (Dipp = 2,6-diisopropylphenyl), have been prepared via an amine elimination reaction of H_2NDipp with $[E(NMe_2)_3]_2$. These derivatives were also to be examined for their potential as III-V precursors.**107**

In compounds where oligomerization occurs, the formation of dimeric versus trimeric species, as well as *cis* (**11**) and *trans* (**12**) isomers for compounds derived from primary (or asymmetric secondary) amines, is governed by the steric hindrance at both nitrogen and gallium.

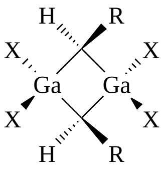

(**11**)

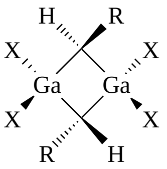

(**12**)

For example, an equilibrium mixture of the *trans* trimer, and the *cis* and *trans* dimers of $GaCl_2[NH(SiMe_3)]$, has been observed in toluene solution. When a methyl group is substituted for the hydrogen atom on the nitrogen, only the *cis* and *trans* dimers of $GaCl_2[NMe(SiMe_3)]$ were found in solution.**[108]** Substituted aminogallanes exhibit a similar trend. $GaH_2(NHMe)$ is trimeric in solution while $GaH_2(NMe_2)$ exists as a dimer. Apparently the introduction of a second substituent on the nitrogen atom creates sufficient steric strain to prohibit the formation of the trimer. The effect of the substituents bonded to the nitrogen on the degree of association and the conformational properties of aminogallanes has been examined extensively; however, the manner in which the substituents on the gallium atom influence the trimer–dimer equilibrium and the isomerization of the dimer has only been recently explored. One such study showed that the trimer–dimer equilibrium present for $GaCl_2[NH(SiMe_3)]$ is absent for $GaBr_2[NH(SiMe_3)]$, *cis* and *trans* isomers of the dimer being the only species observed.**[109]** Although the van der Waals radii of the chlorine and bromine atoms (1.70–1.90 and 1.80–2.00 Å) differ only slightly, the increase in the steric requirements of the bromide atoms compared with the chloride atoms is clearly sufficient to prohibit the formation of the trimer, leading to the exclusive formation of $[Br_3Ga(NHSiMe_3)]_2$.

8.3.2 Miscellaneous

While the transition metal chemistry of the pyrazolylborate ligands, $[H_xB(pz)_{4-x}]^-$ ($x = 0-2$, pz = pyrazolyl) has been extensively studied, it is only recently that the first gallium compounds have been reported. Reaction of $GaCl_3$ with the bis(pyrazolyl)borato ligands (equation 15) yields a five-coordinate complex (Figure 19).**[110]**

$$2K[H_2B(pz)_2] + GaCl_3 \longrightarrow [H_2B(pz)_2]_2GaCl + 2KCl \qquad (15)$$

In contrast, the substituted tris(pyrazolyl)borate ligand allows for the formation of the six-coordinate complex cation (**13**) (equation 16).**[111]** The 3,5-dimethylpyrazolate analog has also been reported.

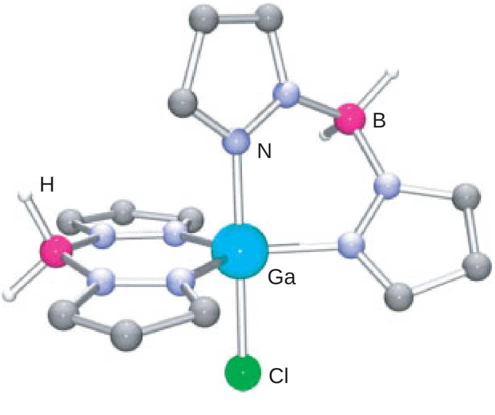

Figure 19 Molecular structure of $[H_2B(pz)_2]_2GaCl$

$$2K[HB(pz)_3] + 2GaCl_3 \longrightarrow [GaH\{(pz)_3BH\}_2]^+ + [GaCl_4]^- + 2KCl \qquad (16)$$

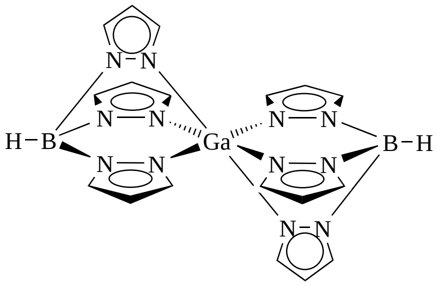

(**13**)

$[GaCl_2(pyrazole)_4]Cl$ and $[GaCl_2(pyrazole)_4]GaCl_4$ are formed in the reaction of pyrazole and anhydrous $GaCl_3$ in toluene/Et_2O solution. The crystal structure of the chloride salt shows the cations in a trans-configuration which are associated with the chloride counterions through N-H–Cl H bonds.

The triazenide anion, $RN{=}N{-}NR^-$, is formally isolobal with the carboxylate anion. However, while there are no well-characterized examples of gallium tris-carboxylates (see Section 8.7), the *tris*(1,3-diphenyltriazenide) complex $Ga(dpt)_3$ (**14**) has been isolated and fully characterized.**[112]**

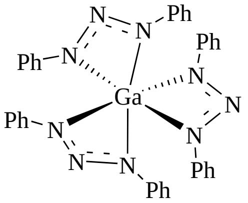

(**14**)

A number of simple N-donor ligand complexes are known; for example, azide, $[Ga(N_3)]$, thiocyanate, $[Ga(NCS)_4]^-$, and selenocyanate, $[Ga(NCSe)_4]^-$. However, spectroscopic evidence suggests that the cyanate anions coordinate via the oxygen.**[5]** The gallium secondary amines adducts $TMPH{\cdot}GaCl_3$ and $Pr^i_2NH{\cdot}GaCl_3$ (TMPH = tetramethylpiperidine) were achieved through synthesis from the respective reagents in toluene at −78 °C in very high yields of 80%. Characterization via single-crystal determinations revealed $TMPH{\cdot}GaCl_3$ having short $Ga\cdots H{-}N$ distances (2.28(9) Å).**[113]**

A series of group 13 metal complexes featuring the β-diketiminate ligand $[\{(C_6H_3\text{-}2,6\text{-}Pr^i_2)NC(Me)\}_2CH]^-$ (i.e. $[Dipp_2nacnac]^-$, Dipp = $C_6H_3\text{-}2,6\text{-}i\text{-}Pr^i_2$) have been prepared and fully characterized. The chloride derivative $Dipp_2nacnacGaCl_2$ was isolated by the reaction of 1 equivalent of $Dipp_2nacnacLi{\cdot}Et_2O$ and the respective metal halides. The iodide derivatives $Dipp_2nacnacGaI_2$, which are useful for reduction to afford M(I) species, were made by a variety of routes. Their X-ray crystal structures feature nearly planar C_3N_2 arrays in the $Dipp_2$nacnac ligand backbone with short C–C and C–N distances that are consistent with a delocalized structure. However, there are large dihedral angles between the C_3N_2 plane and the N_2Ga metal coordination plane, which have been attributed mainly to steric effects. The relatively short Ga–N distances are consistent with the coordination numbers of the metals and the normal/dative character of the nitrogen ligands.[114]

8.4 Phosphines and Arsines

While there are a large number of phosphines and arsine adducts of GaX_3, the number of nonorganometallic phosphide and arsenide compounds are few, and of those the steric bulk of the group 15 substitutes is of critical importance in controlling their isolation. Reaction of $GaCl_3$ with three equivalents of lithium dimesitylarsenide yields the monomeric triarsenide compound $Ga[As(Mes_2)]_3$,[115] whose structure has been shown by X-ray crystallography (Figure 20) to consist of a gallium atom bonded to three arsenic atoms in a trigonal-planar configuration. The Ga–As distances [2.470(1)–2.508(1) Å] are significantly shorter than those observed for four-coordinate gallium (below). A monomeric gallium phosphide, $Ga[P(t\text{-Bu})_2]_3$, has also been reported but no structural elucidation presented.

Reaction of four equivalents of $LiEPh_2$ (E = P, As) with $GaCl_3$ in THF yields the anionic perphosphido and perarsenido complexes $[Li(THF)_4][Ga(EPPh_2)_4]$. While the gallium atoms are in a tetrahedral GaE_4 coordination environment, analogous to those in the binary compounds GaP and GaAs, the bond lengths are slightly longer in the anions than the binary compounds (e.g. Ga–As, 2.497(4) vs. 2.448 Å). However, these small differences are presumably due to the steric repulsion between the phenyl rings in the anions as opposed to any significant electronic interactions.

The coordination of pnictogen ligands to gallium alkyl compounds has also been used in purification techniques similar to those implemented for its indium analogs (*see* ***Indium: Organometallic Chemistry***). For example, $[R_yGa_xL]$ where $L = PPh_3$, dppe, triphos ($Ph_2P(CH_2)_2P(Ph)(CH_2)_2PPh_2$), tetraphos ($Ph_2P(CH_2)_2P(Ph)(CH_2)_2P(Ph)(CH_2)_2PPh_2$), and MBDA 4,4′-methylene-bis(*N*,*N*′-dimethylaniline).[9] Subsequent controlled heating liberates the highly pure metal derivative, which is used for fabricating high quality Ga alloy thin films. It is commonplace to also use gallium pnictogen coordination complexes for III-V film growth. The adduct $[ClEt_2Ga(AsEt_3)]$ has been used in conjunction with $HPEt_2$, for epitaxial growth of $GaAs_{1-x}P_x$ at 500–650 °C, whereas GaAs thin films have been grown from the halide derivatives, $[(C_6F_5)Me_2Ga(AsEt_3)]$ and $[\{ClEt_2Ga(AsEt_2)\}_2CH_2]$ at 600–700 °C and 500–625 °C, respectively.[9]

The metathesis reaction of potassium (tris(*tert*-butyl)silyl) phosphanide with $GaCl_3$ in a 1:1 affords $[Cl_2GaP(H)SiBu^t_3]_2$ as a mixture of *cis* and *trans*. The molecular structure reveals a Ga_2P_2 moiety cycle with nearly planar coordinated phosphorus atoms neglecting hydrogen atoms and Ga–P distances of 2.39 Å. The reaction of $GaCl_3$ with 3 equivilents of potassium (tris(*tert*-butyl)silyl)phosphanide as well as the reaction of 1 with 2 equiv of $KP(H)SiBu^t_3$ yields $[Bu^t_3SiP(H)Ga(\text{-}PSiBu^t_3)]_2$. The central moiety comprises a four-membered Ga_2P_2 cycle with one planar P atom and extremely short Ga–P bonds of approximately 2.26 Å. The structure of $[Bu^t_3SiP(H)Ga(\text{-}PSiBu^t_3)]_2$ is described as a GaPGa heteroallyl system which is bonded to a phosphanidyl substituent.[116]

The gallium chloro complex $[GaCl\{Fe(CO)_2Cp\}_2]$ ($Cp = \eta^5\text{-}C_5H_5$) was reacted with $MP(SiMe_3)_2$, (M = K, Li) under special conditions to yield the complexes $[\{CpFe(CO)\}_2\{\text{-}(CO)\}[\text{-}Ga\{CpFe(CO)_2\}]]$ and $[\{CpFe(CO)_2\}GaP(SiMe_3)]_4$, whereas $[[\{CpFe(CO)_2\}ClGa](\text{-}PPh_2)_2FeCp\,CO]$ was obtained by the reaction of $[GaCl\{Fe(CO)_2Cp\}_2]$ with $LiPPh_2$. Complex $[\{CpFe(CO)_2\}GaP(SiMe_3)]_4$ represents an ideal Ga_4P_4-heterocubane, the first Ga-containing example of this structural type with organometallic substituted group 13 elements. In addition, in the solid state, $[[\{CpFe(CO)_2\}ClGa](\text{-}PPh_2)_2FeCpCO]$ possesses a near planar GaPFeP four-membered ring, which is a novel structural motif in mixed group 13/15 chemistry (Scheme 3).[117]

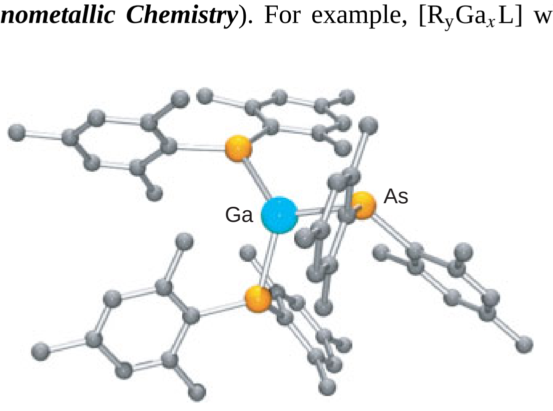

Figure 20 Molecular structure of $Ga[As(Mes_2)]_3$

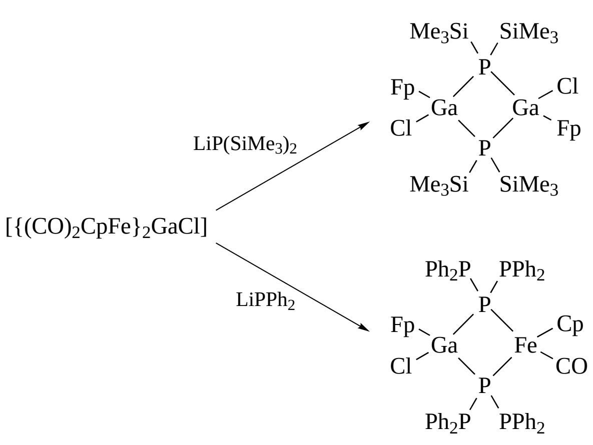

Scheme 3 Formation of mixed group 13/15 Fe derivatives

Examples of Ga derivatives with double bond character to group 15 centers have attracted much attention and review.[118–124] Power and coworkers recently published compounds with gallium–nitrogen multiple bonds,[125] and the first example of a Ga=As derivative, $[\{Li(THF)_3\}_2Ga_2\{As(SiPr^i_3)\}_4]$, has recently been synthesized and contains two As=Ga double bonds from the reaction of $GaCl_3$ with $Li_2AsSiPr^i_3$.[126]

8.5 Aqua ions and related

In acidic solutions, gallium exists as the hexaaqua cation $[Ga(H_2O)_6]^{3+}$ which, based on ^{17}O NMR studies, occurs in the hydrated crystals of oxyanion salts, for example, $Ga(X)_3{\cdot}xH_2O$ ($X = NO_3$, $x = 9$; $X = SO_4$, $x = 18$; $X = ClO_4$; $x = 6$).[5] Ligand exchange at 25 °C ($k_1 = 0.17\,s^{-1}$) is much faster in $[Ga(H_2O)_6]^{3+}$ than the associated exchange in $[Al(H_2O)_6]^{3+}$ ($k_1 = 1.8 \times 10^3\,s^{-1}$), thus reflecting the lesser affinity for oxygen donor ligands of Ga^{3+} versus Al^{3+}. A S_N2 type of mechanism, involving $[Ga(H_2O)_n]^{3+}$, has been suggested for ligand exchange. The gallium cation $[Ga(H_2O)_6]^{3+}$, with K_a of 2.5×10^{-3}, is a stronger acid than $[Al(H_2O)_6]^{3+}$ ($K_a = 1.1 \times 10^{-5}$).[5]

8.6 Alkoxides

Gallium alkoxides can be prepared by the methods employed for aluminum (*see* ***Aluminum: Inorganic Chemistry***). $Ga(OMe)_3$, a polymeric material, decomposes without melting but can be sublimed under vacuum. $Ga(OEt)_3$, $Ga(O\text{-}n\text{-}Pr)_3$, and $Ga(O\text{-}n\text{-}Bu)_3$ are more volatile than $Ga(OMe)_3$ and are tetrameric in solution. According to NMR studies, $Ga(O\text{-}i\text{-}Pr)_3$ and $Ga(O\text{-}t\text{-}Bu)_3$ have dimeric structures bridged by alkoxide ligands. The bulky trimethylsilyl ligand results in $Ga(OSiMe_3)_3$ being monomeric, but does not prevent the formation of a complex anion, $[Ga(OSiMe_3)_4]^-$. Aryloxides, for example, $Ga(OPh)_3$, are obtained by prolonged heating of Ga metal with the phenol at 180–220 °C. Like group 13 alkoxides generally, these compounds are Lewis acids and form 1:1 adducts with ammonia, pyridine, and other bases.

$$Ga_2X_4 + 3EtOH \xrightarrow{0\,^\circ C} [GaX(OEt)_2] + [GaX_3(HOEt)] + H_2 \quad (17)$$

Reaction of gallium trihalides, GaX_3 ($X = Cl$ or Br), with less than three moles of alcohol initially gives the Lewis acid–base adducts $GaX_3(HOR)$. However, these are readily converted into oligomeric halide–alkoxide compounds, $GaX_n(OR)_{3-n}$ ($n = 1$ or 2), in which the alkoxide ligands are bridging. Alcoholysis of the mixed valent dihalides, Ga_2X_4, involves oxidation of the Ga^+ by the alcohol (equations 17 and 18).

$$Ga_2X_4 + 2EtOH \xrightarrow{25\,^\circ C} 2[GaX_2(OEt)] + H_2 \quad (18)$$

Like their aluminum counterparts, gallium alkoxides are susceptible to hydrolysis, giving ill-defined products. Methanolysis of hydrated Ga^{3+} ions produces $Ga(OMe)^{2+}$ and $Ga(OMe)_2{}^+$ in solvated forms, as well as polymeric complexes. $Ga(OPh)_3$ reacts with boiling MeOH or EtOH to form the corresponding alkoxide. Reaction of the trialkoxide compounds with other metal alkoxides, for example, LiOR, results in the formation of four-coordinate complex anions of the type $[Ga(OR)_4]^-$.[5] A recent review of sesquihalides/oxides of group 13 derivatives has been published. The review covers the major synthetic routes and the structures of the corresponding products, and also reactions with compounds having sesquialkoxides as educts.[127]

Owing to the importance of Ga_2O_3 thin films, Ga alkoxides have also been examined as viable compounds to Ga_2O_3 materials. A general synthetic route to Ga alkoxide complexes involving reactions between Ga *tris*(dimethylamide) with alcohols has been developed. Their utility in a CVD process to deposit Ga oxide films was demonstrated.[128] $[Ga(NMe_2)_3]_2$ reacted with i-BuOH and i-PrOH to yield the tetramers $Ga[(\mu\text{-}OR)_2Ga(OR)_2]_3$ ($R = i$-Bu, i-Pr). In contrast to the results obtained using i-BuOH and i-PrOH, the bulkier alcohols t-BuOH and $EtMe_2COH$ reacted with $[Ga(NMe_2)_3]_2$ at room temperature to yield mixtures of the dimer $[Ga(\mu\text{-}OR)(OR)_2]_2$ and the amine adduct $[Ga(OR)_3(HNMe_2)]$, while $i\text{-}PrMe_2COH$ and Et_2MeCOH gave $[Ga(OR)_3(HNMe_2)]$ derivatives exclusively. The amine could be removed from the $[Ga(OR)_3(HNMe_2)]$ compound to yield the corresponding homoleptic alkoxide dimers. Low-pressure CVD using $[Ga(\text{-}OBu^t)(OBu^t)]$ and O precursors gave GaO films at substrate temperature between 300–700 °C, which were carbon-free, amorphous, and highly transparent in the 350–800-nm region.[129,130]

8.7 Carboxylates

A number of patents and publications have addressed the synthesis, properties, and application of gallium carboxylates.[10,131,132] Gallium carboxylates, $Ga(O_2CR)_3$, may be prepared by a variety of synthetic methods, including the reaction of the carboxylic acid with Ga_2O_3 (equation 19), $GaCl_3$ (equation 20), or directly with the metal (equation 21).[5] Basic carboxylates result if aqueous acids are employed (see below).

$$Ga_2O_3 + 3HO_2CR \longrightarrow [Ga(O_2CR)_3] + 3H_2O \quad (19)$$

$$GaCl_3 + 3HO_2CR \longrightarrow [Ga(O_2CR)_3] + 3HCl \quad (20)$$

$$Ga + 3HO_2CR \longrightarrow [Ga(O_2CR)_3] + 1.5H_2 \quad (21)$$

However, the gallium oxalate system has also been examined. $Ga(C_2O_4)_3{\cdot}4H_2O$ crystallizes from hot aqueous $Ga(NO_3)_3$ solution containing oxalic acid. On heating (>140 °C), a dihydrate and then anhydrous $Ga_2(C_2O_4)_3$

are produced. The latter decomposes to Ga_2O_3 at 200 °C. Complex salts containing $[Ga(C_2O_4)_2]^-$ and $[Ga(C_2O_4)_3]^{3-}$ anions have been prepared and the formation of these and the cation $[Ga(C_2O_4)]^+$, presumably hydrated, have been studied to obtain stability constants. It is thought that basic complexes are probably present in these aqueous solutions (see below). Raman spectra of gallium oxalate solutions confirm the presence of $[Ga(C_2O_4)_3]^{3-}$: $\nu(\text{M–O})_{\text{sym}} = 573\,\text{cm}^{-1}$ compared to $585\,\text{cm}^{-1}$ in $[Al(C_2O_4)_3]^{3-}$.[5]

While no crystallographic data have been obtained for a gallium tricarboxylate, Hepp, Duraj and co-workers have reported the synthesis and structural characterization of an oxo-centered trinuclear carboxylate, of the well-established class of complexes commonly referred to as 'basic carboxylates', $[M_3(O)(O_2CR)_6(L)_3]^+$.[133] The reaction of Ga_2Cl_4 with sodium benzoate in the presence of 4-methylpyridine (4-Mepy) allows the isolation of $[Ga_3(O)(O_2CPh)_6(\text{4-Mepy})_3][GaCl_4]$ in high yield. The solid-state structure of the cation, $[Ga_3(O)(O_2CPh)_6(\text{4-Mepy})_3]$ consists of a planar oxo-centered Ga_3O core; each edge is bridged by two benzoate ligands, and the sixth coordination site of each gallium is occupied by a terminal pyridine ligand.

There are many reports of complexes between gallium and hydroxy acids (including those derived from carboxylic acids) and other related organic chelating agents. The lactate, tartrate, and citrate have all been used in physiological studies involving gallium radioisotopes. According to NMR studies (^{1}H, ^{13}C, and ^{71}Ga), the 1:1 Ga/citrate complex predominates at low pH (<2), while oligomeric species exist in the range pH 2–6, unlike the aluminum citrate system.[134] The structural characterization for the gallium citrate complex has recently been realized; the gallium citrate complex $(NH_4)_3[Ga(C_6H_5O_7)_2]\cdot 4H_2O$ hydrate has been prepared from the reaction of gallium nitrate with citric acid. The X-ray crystal structure of the complex revealed it to exist as discrete ions, with the 6-coordinate gallium center bonded to two deprotonated carboxylate groups and one alcoholate group from each citrate ligand leaving one protonated pendent carboxy group.[135]

A range of other systems of Ga^{3+} with chelating organic acids has been studied and solution equilibria data have been obtained.[5] Based on these investigations it is clear that in all cases basic complexes (i.e. those containing oxo or hydroxo ligands) are involved, and the hydrated hydroxide cation $[Ga(OH)]^{2+}$ shows greater reactivity compared with the hydrated ion of Ga^{3+}.

8.8 β-Diketonates

Gallium tris-β-diketonate complexes are formed by the addition of acetylacetonate ions to aqueous solutions of Ga^{3+} (e.g. equation 22). However, at β-diketonate to gallium ratios less than three, basic hydroxo complexes are also formed.

$$Ga_2(SO_4)_3 + 3\text{Hacac} \xrightarrow{[NH_4][OH]\text{aq.}} [Ga(acac)_3] + 3[NH_4]_2[SO_4] \qquad (22)$$

Rates of ligand exchange have been measured for some β-diketonate complexes.[136] Exchange between $Ga(acac)_3$ and ^{14}C-labeled Hacac in THF solution is much faster than in the case of $Al(acac)_3$. A dissociative mechanism proceeds via a five-coordinate transition state in which one ligand is unidentate (Scheme 4). In addition, activation energies for cis–trans ligand rearrangements have been determined from NMR measurements. As expected, these studies place gallium between aluminum and indium in the order of decreasing bond strength, that is, Al–O > Ga–O > In–O. This result is consistent with Raman studies of $M(acac)_3$.[5] When $Ga(acac)_3$ is added to a solution of $Ga(ClO_4)_3$ in DMF, the NMR spectrum shows new signals attributable to $[Ga(acac)(DMF)_4]^{2+}$ and $[Ga(acac)_2(DMF)_2]^+$.

Tris(acetylacetonato)gallium(III) exists in two crystallographic modifications, differing slightly in density. The X-ray crystal-structure determination shows the central GaO_6 core to be close to octahedral, with an average Ga–O distance of 1.95 Å.

The dichlorogallium(III) β-diketonato derivatives of the type $GaCl_2L$ [L = acac (2,4-pentanedionato) and tmhd

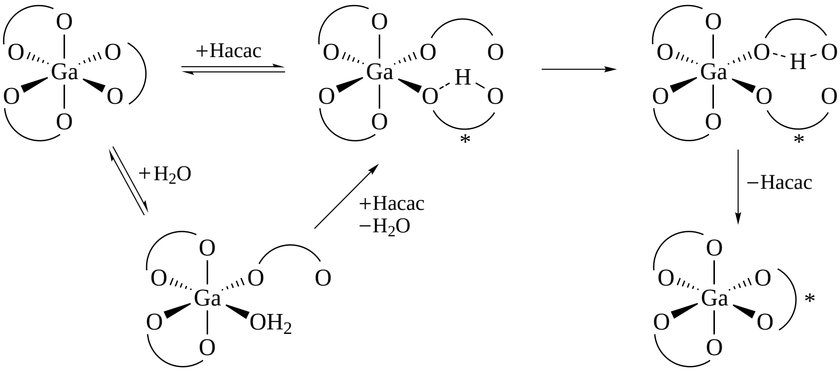

Scheme 4 Proposed mechanism for the ligand exchange of [Ga{acac}$_3$] with excess acac ligand, in THF solution, (*14-C labeled)

(2,2,6,6-tetramethylheptanedionato)] were prepared and characterized by a variety of spectroscopic techniques. The four-coordinate Ga compounds were found to react with THF to form $GaCl_2L{\cdot}THF$ derivatives. Single-crystal X-ray diffraction study identified $[GaCl_2(acac){\cdot}THF]$ to be the ion-pair [*trans*-$Ga(acac)_2(THF)_2]^+$ $[GaCl_4]^-$. The Ga atom in the cation is six-coordinate, whereas in the anion it is four-coordinate. Variable-temperature ^1H NMR spectral studies suggest that multiple processes including (i) a stereochemical rearrangement, (ii) THF exchange, and (iii) equilibria between $[GaL_2(THF)_2]^+[GaCl_4]^-$, $[GaCl_2L]$, and other species such as $[GaL_2(THF)]^+[GaCl_4]^-$ occur in solution. In contrast, the fluorinated derivatives $GaX_2(hfac)$ (X = Cl, Br; hfac = 1,1,1,5,5,5-hexafluoro-2,4-pentanedionato) cannot be isolated since they undergo ligand redistribution reactions to form $[Ga(hfac)_3]$.[137]

The gallium(II) derivatives $[GaCl(acac)]_2$, and $[GaCl(tmhd)]_2$ were prepared and characterized by X-ray structural studies.[138] Both compounds have direct gallium–gallium bonds between two tetracoordinated gallium atoms with each in the +2 oxidation state and each gallium bonded to a chloride and chelated to a β-diketonate ligand. Metal–metal bond lengths are Ga(1)-Ga(1a) = 2.396(3) Å. for the acac derivative, which has crystallographic imposed C2 symmetry and Ga(1)-Ga(2) = 2.391(2) Å. for the tmhd derivative.[138]

8.9 Pyridinones

The discovery that ^{67}Ga administered as the citrate localized in soft tumor tissue[139] initiated considerable clinical interest in gallium coordination chemistry. In fact the citrate complex is now widely used in oncological nuclear medicine for tumor detection; however, the mechanism of uptake is still to be determined. Despite this early success and the ready availability of both ^{67}Ga and ^{68}Ga, the application of gallium in medicine has been limited. One of the reasons for this is the complex hydrolysis chemistry of gallium compounds, and the majority of studies have been performed under acidic conditions. Clearly if the coordination chemistry of gallium is to be understood *in vivo*, then complexes stable at pH 7.4 are of great interest. While some researchers have concentrated on polydentate ligands, such as cryptands, others have investigated bidentate chelating ligands of biological relevance. The most successful work in this area is by Orvig and coworkers on complexes of gallium with hydroxypyrones and hydroxypyridinones.[140–142]

A series of tris(3-hydroxy-4-pyranato)gallium(III) complexes has been prepared by the neutralization of solutions of $GaCl_3$ and substituted pyrones (**15a–d**). The complexes of larixinic acid (**15b**) and kojic acid (**15c**) are water soluble but retain their neutral charge.

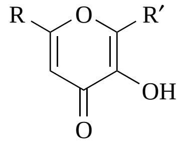

(**15a**) R = R′ = H; pyromeconic acid
(**15b**) R = H, R′ = Me; maltol (larixinic acid)
(**15c**) R = CH_2OH, R′ = H; kojic acid
(**15d**) R = CH_2Cl, R′ = H; chlorokojic acid

The known sequestering ability of various hydroxypyridinones for iron(III) prompted investigation of the gallium complexes. The tris complexes have been prepared with a wide range of substituted hydroxypyridinones (**16**).[140] The molecular structure of one such compound is shown in Figure 21. All the complexes form a rigid *fac* geometry, are water soluble, and have a wide window of stability to hydrolysis. Their lipophilicity is increased by the substitution of an aryl group at the nitrogen (see **17**).[141]

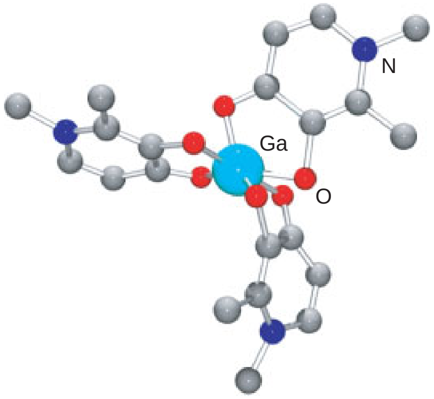

Figure 21 Molecular structure of $Ga(dpp)_3$; Hdpp = 3-hydroxy-1, 2-dimethyl-4-pyridinonate

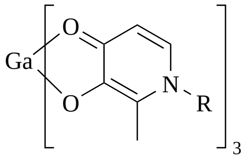

(**16**) R = H, Me, *n*-C_6H_{13}

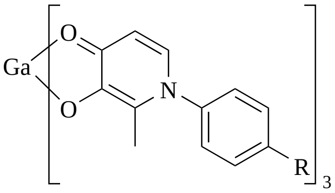

(**17**) R = H, Me, OMe, NO_2

Aqueous solution stability constants for the aryl substituted complexes have been determined. The ML_3 complexes are highly stable; at 25 °C the overall stability constant (β_3) for the parent complex (**17**); R = H is $10^{36.3}$. At ligand to metal ratios ≥ 1, the ligands prevent gallium hydrolysis even at millimolar concentrations and under slightly basic conditions; the effective formation constant ($\beta_{3\mathrm{eff}}$) for ML_3 at physiological pH is $10^{30.3}$. As a practical application of these data, comparative metal binding in a simple blood plasma model has been simulated, which in turn allowed for the design of biodistribution experiments in mice. The concentration of ligand required to inhibit removal of gallium from the GaL_3 complexes and the excretion pathway have been determined.[142]

8.10 Chalcogen Donor Ligands

While the donor chemistry for the heavier chalcogens with group 13 elements is generally poorly developed in comparison to the lighter chalcogen oxygen donor ligand chemistry, in the case of gallium there has been significant interest in non-oxide chalcogen-containing compounds with chalcogenide, and in particular sulfur, donor ligands for III-VI binary alloy formation. This anomaly for gallium is as a function of the similarities in its coordination chemistry to that of high-spin iron(III), and the biological importance of iron–sulfur proteins (*see* ***Iron: Heme Proteins & Dioxygen Transport & Storage***; ***Iron: Heme Proteins & Electron Transport***; ***Iron: Heme Proteins, Mono- & Dioxygenases***; ***Iron: Heme Proteins, Peroxidases, Catalases & Catalase-peroxidases***). The anionic gallium tetrathiolate complexes, $[Ga(SR)_4]^-$, may be prepared by the reaction of either $GaCl_3$ or $[GaCl_4]^-$ with five equivalents of LiSR, where R = Me, Et, *i*-Pr, Ph, 2,3,5,6-Me_4C_6H, or 2,4,6-i-$Pr_3C_6H_2$.[143] Because of the inaccessibility of the +2 oxidation state of gallium, the tetrathiolate complexes do not undergo the redox reaction (equation 23) that is responsible for the instability of many of the iron analogs.

$$2M^{3+} + 2RS^- \longrightarrow 2M^{2+} + RSSR \tag{23}$$

The structure of $[(n\text{-}Pr)_4N][Ga(SEt)_4]$ has been determined by X-ray crystallography to be isomorphous to the iron analog; however, although isostructural, $[Et_4N][Ga(SPh)_4]$ is not isomorphous with its iron analog. This difference has been rationalized with regard to the presence of steric interactions between the *ortho* hydrogens of two of the phenyl rings and the GaS_4 core. Although no examples of neutral three-coordinate gallium alkoxides have been reported, thiolate and selenolate derivatives, $Ga[E(2,4,6\text{-}t\text{-}Bu_3C_6H_2)]_3$ (E = S, Se), have been crystallographically characterized,[144] and the thiolate compound is shown in Figure 22. Structural data show that the gallium centers are three coordinate and almost planar. The slight distortion from idealized trigonal-planar coordination has been explained on the basis of ionic M–S bonding character and some agostic Ga···H interactions involving the *ortho* *t*-butyl groups of the ligand.

In addition to a variety of organometallic gallium thiolates (*see* ***Gallium: Organometallic Chemistry***), there are a number of mixed thiolate compounds, for example, the halide–thiolate dimers $[I_2Ga(SMe)]_2$ and $[I_2Ga(S\text{-}i\text{-}Pr)]_2$. The latter compound has the unusual feature of having a butterfly Ga_2S_2 core.[145] The first gallium thiolato compound to be structurally characterized was the adamantane cluster $Ga_4I_4(SMe)_4S_2$ (Figure 23), prepared from the reaction of Me_2S_2 with Ga_2I_4.[146] The Ga–S distances fall into two groups, those to the sulfide (average = 2.20 Å) and those to the methylthiolate ligands (average = 2.33 Å). The $[Ga_2S_2(SPh)_4]^{2-}$ anion has been prepared and structurally characterized (Figure 24). The structure is that of a centrosymmetric dimer consisting of two edge-sharing tetrahedra.

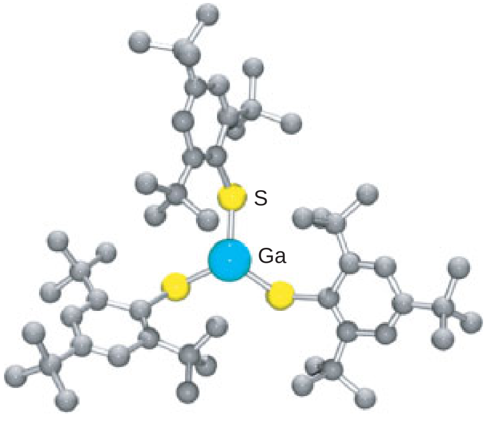

Figure 22 Molecular structure of $Ga[S(2,4,6\text{-}t\text{-}Bu_3C_6H_2)]_3$

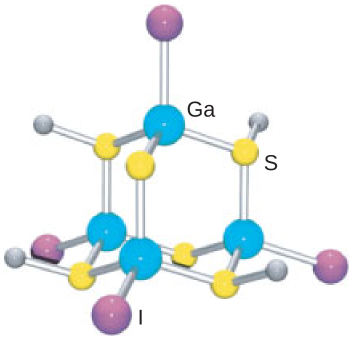

Figure 23 Molecular structure of $Ga_4I_4(SMe)_4(S)_2$

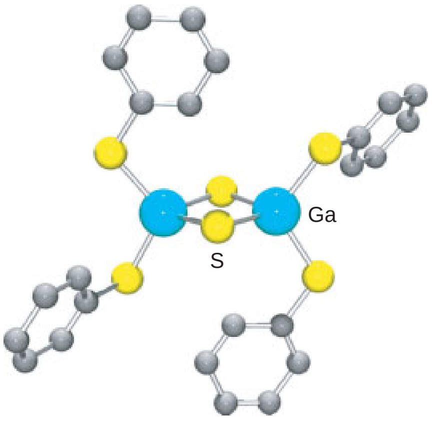

Figure 24 Structure of the $[Ga_2S_2(SPh)_4]^{2-}$anion

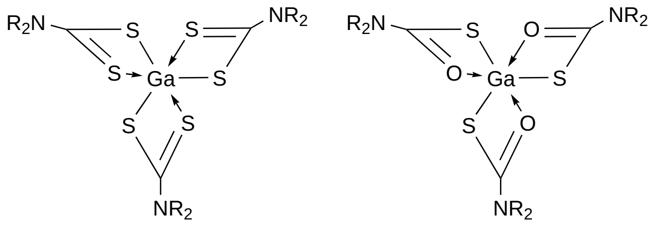

Figure 25 Schematic of $[Ga(S_2CNR_2)_3]$ & $[Ga(SOCNR_2)_3]$ derivatives

A number of gallium dithiocarbamate coordination complexes have been investigated for their potential suitability as single-source III-VI precursors. These type of compounds are often referred to as Mitsubishi™ compounds owing to their structural resemblance to the respective company logo (Figure 25). Additionally this area has recently been reviewed.[145]

The gallium *tris*-dialkyldithiocarbamates are monomeric solids that possess relatively low volatility. Improved volatility is achieved with asymmetric secondary amines derivatives; for example, the use of $[Ga\{S_2CN(Me)Hex\}_3]$ in a LP-MOCVD affords α-Ga_2S_3 thin films at 500 °C on GaAs(111).[147] Whereas the monothiocarbamato coordination complex $[Ga(SOCNEt_2)_3]$ affords thin films of GaS at 450 °C.[148] Again a more comprehensive array of the analogous indium derivatives has been synthesized and studied in comparison to gallium. The ^{71}Ga NMR studies have been preformed on a number of Mitsubishi™ complexes of the type $[Ga\{S_2CNR\}_3]$, $[Ga\{S_2CNR\}\{(SCH_2CH_2)_2O\}]$, where $R{=}CH_2CH_2OCH_2CH_2$, $CH_2CH_2N(Me)CH_2CH_2$, and $[GaCl_2\{S_2CN(CH_2CH_2)_2O\}]$, $[GaCl\{S_2CN(CH_2CH_2)_2O\}_2]$, and $[Ga\{S_2CN(CH_2CH_2)_2O\}\{S_2P(OR)_2\}_2]$ where R = Et, Pr^i have been investigated. The ^{71}Ga NMR chemical shifts and half line widths were found to be influenced by the coordination number of gallium and the substituents on the ligand moiety; additionally, an in-depth study of their spectroscopic properties has been reported.[149]

Dithiophosphinato complexes have found application as solvent extraction reagents for metals, insecticides, and pesticides, flotation agents for mineral ores, and additives to lubricant oils and can be used as precursors in metal-organic chemical vapor deposition (MOCVD).[150] The related indium compounds $[In(S_2PR)_3]$ (R = Me, Et, OEt, Ph) are monomeric in the solid state in contrast to the dinuclear species seen for the related group 12 zinc and cadmium species. The analogous group 13 derivatives $[In(S_2PBu^i_2)_3]$ and $[Ga(S_2PBu^i_2)_3]$ were prepared and characterized. Whereas the In metal center was found to be six-coordinate, the Ga metal center is four-coordinate, being bound to only one chelating and two pendant diisobutyldithiophosphinate ligands in a distorted tetrahedral geometry.

The sterically encumbering β-diketiminate ligand $[\{HC(MeCDippN)_2Ga\}]$ (Dipp = C_6H_3-2,6-Pr$^i_2$) has been used to stabilize the first dimeric galloxane derivative $[\{HC(MeCDippN)_2\}GaO]_2$, as well as its S analog $[\{HC(MeCDippN)_2\}GaS]_2$. Treatment of $\{HC(MeCDippN)_2\}Ga$ with N_2O or S_8 in a toluene solution at room temperature produced the respective compounds as colorless crystals. The Ga_2S_2 core is planar and has an average Ga–S bond length of 2.26(1) Å, which is just within the currently known range (2.20–2.27 Å) for low-coordinate Ga-S species.[151]

The reactions of $Ga(CH_2CH_3)_3$ with variable amounts of elemental sulfur, S_8, in toluene or benzene at different temperatures results in the insertion of sulfur into the Ga–C bonds to form the $Ga[(S\text{-}S)CH_2CH_3]_3$ and $Ga[(S\text{-}S\text{-}S)CH_2CH_3]_3$. Even when the reactions were carried out with more than 9.0 equiv of sulfur, the maximum extent of sulfur insertion was found to be three S units. However, the reactions of $Ga(CH_3)_3$ with various molar ratios of S in toluene or benzene only gave $Ga[(S\text{-}S)CH_3]_3$. In pyridine at −30 °C, deinsertion of the sulfur atoms from Ga-S-S-C bonds was noted for the first time from $Ga[(S\text{-}S)CH_2CH_3]_3$ and $Ga[(S\text{-}S\text{-}S)CH_2CH_3]_3$, resulting in formation of the six-membered Ga–S ring compounds $[PyEtGaS]_3$ and $[PyMeGaS]_3$ respectively.[152]

9 HALIDES

9.1 Ga(III) Halides

9.1.1 *Synthesis and Structure*

The halides (especially the chloride) are the most commonly employed synthons in the chemistry of gallium. This is undoubtedly due to their ease of synthesis and high reactivity. While the trihalides have been traditionally the most extensively studied, the mono- and dihalides have come under recent scrutiny.

Gallium fluoride differs markedly from the other halides of gallium and in this it resembles the fluorides of aluminum and indium. For example, the melting points of the fluorides are several hundred degrees above those of the chlorides, though this difference decreases from 1097 °C for aluminum, to 872 °C for gallium, to 584 °C for indium. The compound GaF_3 is produced by the thermal decomposition of either $[NH_4]_3[GaF]_6$ or $GaF_3(NH_3)_3$ in the absence of moisture; the latter brings about the formation of $(NH_4)_2GaF_3(OH)_2$. The GaF_3 molecule is planar with a Ga–F distance of 1.88 Å. This species and the dimer Ga_2F_6 have been examined in the vapor phase by mass spectrometry.[5]

The trihalides $GaCl_3$ and $GaBr_3$ are usually prepared directly from the elements, by burning the metal in a stream of Cl_2 (or Br_2) in an apparatus that uses all-glass, or greaseless, connections. GaI_3 can be obtained by dissolving

Table 6 Physical properties of gallium trihalides

Property	$GaCl_3$	$GaBr_3$	GaI_3
Mp (°C)	77.75 ± 0.05	122.3 ± 0.05	211.5 ± 0.1
Bp (°C)	201.2	279	346
Vapor pressure (mm Hg)	10.4 (at 78 °C)	4.7 (at 125 °C)	19.2 (at 215 °C)
Density ($g\,cm^{-3}$)	2.47	3.69	4.15
$\Delta H°_f$ ($kJ\,mol^{-1}$)	523	386	255
ΔH_{dimer} ($kJ\,mol^{-1}$)	87 (per Ga_2Cl_6)	77 (per Ga_2Br_6)	46 (per Ga_2I_6)

Ga in a refluxing solution of I_2 in CS_2. The trichloride and tribromide of gallium have some advantages over $AlCl_3$ as Friedel–Crafts catalysts, in particular, their high solubility in organic solvents.[4] All three halides are colorless, deliquescent, low-melting solids, whose physical properties are shown in Table 6. In solid and liquid states, and in noncoordinating solvents, the GaX_3 (X = Cl, Br, I) molecules are dimeric with bridging ligands spanning four-coordinate gallium atoms. In the vapor, there is increasing dissociation of Ga_2X_6 to GaX_3 for X = Cl (0.4%), Br (14%), or I (96%), in accord with the decreased ΔH of dimer formation (see Table 6). Molecular dimensions are known for the monomers $GaBr_3$ and GaI_3, and the dimers Ga_2Cl_6 and Ga_2I_6, but precise values are lacking for $GaCl_3$ and Ga_2Br_6. Vibrational assignments are available for the GaX_3 monomers (from gas-phase and matrix-isolation studies) and the Ga_2X_6 dimers.[4]

9.1.2 Complexes

The trihalides (except the fluorides) all function as Lewis acids, forming 1:1 adducts with a great variety of Lewis bases. This is one of the most important aspects of the chemistry of the gallium halides. The Lewis acidity of the GaX_3 groups has been extensively studied thermodynamically, and basicity sequences for a variety of donors have been established.

Neutral Adducts. Being powerful acceptors, the gallium trihalides react with donor molecules L to form the adducts $GaX_3(L)$, and in some instances $GaX_3(L)_2$. In the trigonal bipyramidal 2:1 complexes, the halogen atoms are usually equatorial. The 1:1 complexes of trimethylamine with gallium trichloride and tribromide are solids, stable above 200 °C, while the complexes with two moles of trimethylamine decompose above −48 °C to give the 1:1 complex. Pyridine and piperidine form 1:1 and 2:1 adducts with $GaCl_3$, but only the 1:1 complex with $GaBr_3$.[4,5] Ethers form stable complexes with GaX_3, and there seems to be less tendency than with the aluminum analogs for thermal elimination of alkyl halides. However, caution should be observed when dissolving $GaCl_3$ in coordinating ether solvents, for example, Et_2O or THF, since the formation of the $GaCl_3(L)$ complex is sufficiently exothermic to boil the solvent. While the donor atom is generally from group 15 or 16, several examples of neutral complexes between $GaCl_3$ and alkyl halides have been reported.[4]

Anionic Complexes. Gallium, like aluminum, forms tetrahedral tetrahalide ions, $[GaX_4]^-$. Crystalline salts can be obtained, for example, by the action of alkali metal halides or ammonium halides on Ga_2Cl_6. However, oxonium salts, for example, $[(Et_2O)_nH][GaCl_4]$, isolated from the reaction of $GaCl_3$ with HCl in ether, are viscous oils.[4] That the tetrahalogallates can be regarded as typical Lewis acid–base complexes is seen by the ease with which the halide is replaced by neutral donor ligands (e.g. equation 24).

$$M[GaCl_4] + L \xrightarrow[M = Li,\ NH_4;\ L = NR_3,\ py]{} GaCl_3(L) + MCl \qquad (24)$$

While the tetrahaloaluminates are unstable under acid conditions, the gallium analogs are readily extracted from aqueous solutions of gallium salts, into ethers, by 8 M HCl; the resulting ether phase contains $[GaCl_4]^-$ ions. This suggests the presence of a series of equilibria (equation 25):

$$[Ga(H_2O)_6]^{3+} \xrightarrow{+n\mathrm{HCl}} [GaCl_n(H_2O)_m]^{3-n} \xrightarrow{+m\mathrm{HCl}} [GaCl_4]^- \qquad (25)$$

In addition to crystallographic data for solids containing the $[GaX_4]^-$ ion, characteristic absorption spectra, vibrational frequencies, NMR chemical shifts, and NQR parameters are well established. These properties can be used to study effects such as ligand exchange processes of $[GaX_4]^-$ with Cl^-, ion pairing in nonaqueous solutions of alkylammonium chlorogallates, polymorphism of $K[GaCl_4]$, and solid-state interactions in the crystalline solids $[NO][GaCl_4]$ and $[Ga][GaCl_4]$. Bond dissociation energies $\Delta(X_3Ga–X)$ are 364 and 314 $kJ\,mol^{-1}$ for X = Cl and Br, respectively.

[GaSBr] and [GaSeBr] have been synthesized from $Ga[GaBr_4]$ and elemental S/Se in toluene or THF, respectively, with the formation of the by-product $GaBr_3(THF)_2$. The two ternary Ga bromides are insoluble in most common organic solvents, but are readily dissolved in pyridine and substituted pyridines (L) to give trinuclear $[GaSBr(L)]_3$

with L = 3,5-dimethylpyridine, 4-*tert*-butylpyridine, and 4-dimethylaminopyridine, and $[GaSeBr(L)]_3$ with L = 3,5-dimethylpyridine, respectively. The core units are six-membered rings with different substitution patterns and were found to depend largely on the steric requirements of the ligands L, and on the mode of crystallization undertaken. Similar studies have been preformed for the chloride analog.[153]

Cationic Complexes. Apart from the aqua ions and partially substituted species such as $[GaCl(H_2O)_5]^{2+}$, cationic complexes of gallium halides with pyridine, bipyridine, or phenanthroline are known, for example, $[GaCl_2(phen)_2]^+$ and $[Ga(phen)_3]^+$. Furthermore, given the steric hindrance about the gallium center in complexes formulated as $GaX_3(NH_3)_n$ (X = Cl, $n = 1, 3, 5, 6, 7, 14$; X = Br, $n = 1, 5, 7, 9, 14$; X = I, $n = 1, 5, 6, 7, 9, 13, 20$), it is likely that where n is greater than 3 these are also cationic solvates.[154]

9.2 Lower Oxidation State (I) & (II) halides

All four halides GaX (X = F, Cl, Br or I) are known as vapor-phase species, but tend to disproportionate when condensed, producing elementary gallium. The solid once thought to be GaI has been shown to be Ga_2I_3. Gallium forms a number of mixed valence halides containing gallium(I) cations. In these compounds, the Ga^+ cation is stabilized by the presence of the anion formed when the strong Lewis acid GaX_3 combines with halide ligands. Examples are the so-called 'dihalides' $[Ga][GaX_4]$ and the compounds Ga_3X_7, that is, $[Ga][Ga_2X_7]$ (X = Cl, Br, I). In the subhalides, Ga_2X_3, the stabilizing anion is $[Ga_2X_6]^{2-}$, the constitution being $[Ga]_2[Ga_2X_6]$ (X = Cl, Br, I).

The crystal structure of Ga_2Cl_4 shows each of the Ga^+ cations surrounded by eight chlorides of the $[GaCl_4]^-$ counterions. The gallium(I) chloride distance is more than 3.00 Å, to be compared with the Ga–Cl bond length of 2.19 Å in $[GaCl_4]^-$, and implies that the Ga^+ cation is not coordinated but 'solvated'. However, when Ga_2Cl_4 is vaporized, the vapor consists solely of GaCl and $GaCl_3$ molecules. Recent structural analyses of Ga_2I_4 and Ga_2I_3 have directed attention to the influence on these structures of the $4s^2$ electron pair of the Ga^+ ion, and confirm that in the case of the iodide no coordination is observed to the lower oxidation state center.

The halides Ga_2X_4 combine with various donor ligands to give products since shown to be molecular adducts of the metal–metal bonded Ga^{II} state. For example, the treatment of Ga_2Cl_4 with dioxane gives a crystalline solvate (**18**), in which each Ga atom has a distorted tetrahedral configuration and the Ga–Ga distance is 2.406(1) Å.

There are reports of reactions of the halides Ga_2X_4 with alcohols, water, aqueous NaOH, HCl or HF, and H_2S gas. Oxidative addition usually occurs, although there is evidence of the initial precipitation of Ga^I containing solids in the reactions of Ga_2Cl_4 in benzene solution with H_2O or H_2S.

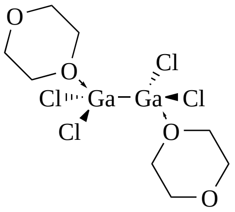

(**18**)

The crystalline solid Ga_2Cl_4 is soluble in benzene. Under regulated conditions this solution yields crystals that prove to contain the complex $[Ga(C_6H_6)_2][GaCl_4]$, and X-ray studies show the cation to be the η^6-bis(benzene) complex of Ga^I (*see* ***Gallium: Organometallic Chemistry***). The $[GaCl_4]^-$ ions interact weakly with Ga^+ to provide bridging chlorine atoms between the Ga^I centers. The anodic dissolution of gallium in 6 M HCl or HBr at 0 °C followed by addition of $[Me_4N]X$ precipitates white crystalline salts of the ion $[Ga_2X_6]^{2-}$ that are stable and diamagnetic owing to the presence of a Ga–Ga bond (2.39 Å for X = Cl and 2.41 Å when X = Br).[155]

Mixed metal derivatives of gallium have become novel target compounds for investigation. [Tetra(n-ethyl)-1,1′-diphosphaferrocene $GaCl_2]^+$ $[GaCl_4]^-$ was prepared by the reaction of the ferrocene derivative and $GaCl_3$ at room temperature. The synthesis of the corresponding complex incorporating octa(n-propyl)-1,1′-diphosphaferrocene was carried out to try an ascertain the bonding structure in these molecules the [octa(n-propyl)-1,1′-diphosphaferrocene-$GaCl_2]^+$ $[GaCl_4]^-$ complex, which was successfully characterized by X-ray crystallography. In octa derivative, the diphosphaferrocene ligand acts as a chelate and the overall geometry around the gallium is tetrahedral. Theoretical calculations indicated that the bonding of the diphosphaferrocene ligand to the $[GaCl_2]^+$ fragment involves the lone pairs on the phosphorus atoms and a contribution of the P–Fe bond.[156]

$[[(\eta5\text{-}Cp^*)Fe(CO)_2]_2GaCl]$ is a useful reagent that is readily prepared by a metathesis reaction with 2 equivalents of $Na[(\eta5\text{-}Cp^*)Fe(CO)_2]$ with $GaCl_3$ at room temperature. Treatment of the aforementioned with a boron anion allows for the formation of the unique cationic Fe complex $[[(\eta5\text{-}Cp^*)Fe(CO)_2]_2Ga]^+$ $[BAr^f_4]^-$ ($Ar^f = C_6H_3(CF_3)_2$-3,5) (Scheme 5), which contains a symmetrically bridging two-coordinate Ga atom and a delocalized Fe-Ga-Fe π system having partial Fe–Ga multiple bond character. DFT (BLYP/TZP) computational analysis showed that the fully optimized geometry is consistent with that for the crystallographically solved structure.[157]

10 POLYDENTATE LIGANDS

Kinetically stable complexes of gallium are being examined for use as imaging agents in diagnostic nuclear medicine

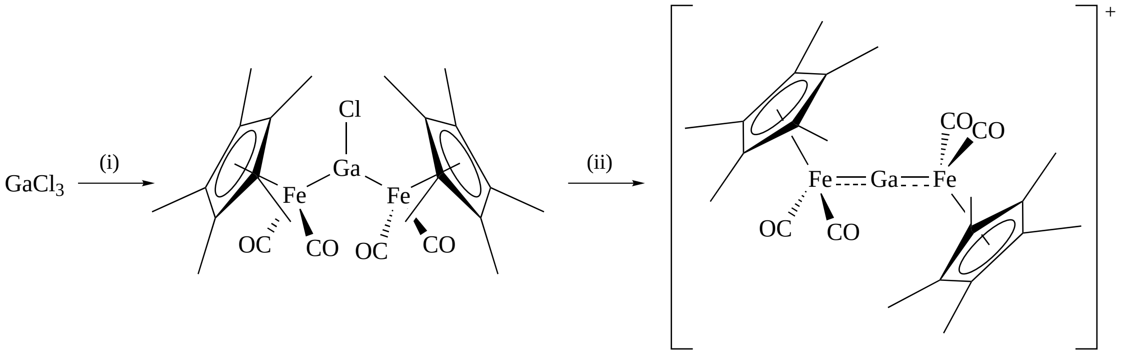

Scheme 5 Syntheses of $[[(\eta5\text{-}Cp^*)Fe(CO)_2]_2GaCl]$ and $[[(\eta5\text{-}Cp^*)Fe(CO)_2]_2Ga]^+$ $[BAr^f{}_4]^-$. Reagents and conditions: (i) $Na[(\eta5\text{-}Cp^*)Fe(CO)_2]$ 2 equiv., toluene, 20 °C, 12 h; (ii) $Na[BAr^f{}_4]$ 1 equiv., dichloromethane, 278 °C to 20 °C, 30 min

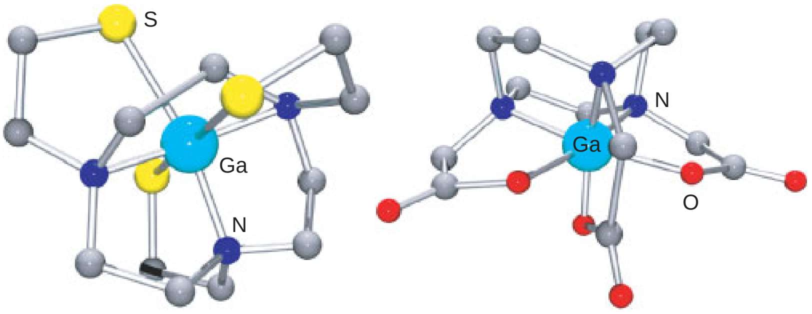

Figure 26 Molecular structure of Ga(TS-TACN); H_3TS-TACN = 1,4,7-tris(2-mercaptoethyl)-1,4,7-triazacyclononane and Ga(NOTA) (NOTAH_3 = 1,4,7-triazacyclononante-1,4,7-trisacetic acid)

(^{67}Ga, γ, $t_{1/2} = 3.25$ days; ^{68}Ga, β^+, $t_{1/2} = 68$ min). In order for these complexes to be used in vivo, they should resist acid (or cation) mediated decomplexation in the pH range 2–8. The synthesis of oxygen, nitrogen, and recently sulfur functionalized polydentate ligands, especially those that may be attached to tumor-localizing antibodies, has been investigated.

10.1 Cryptand Ligands

The development of new metal-chelating agents for medical applications is an actively growing area of research in gallium coordination chemistry. While much effort has been put into the synthesis and determination of stability constants of ethylenediamine derivatives, these ligands yield a potential coordination sphere consisting of an $[N_2O_4]^{4-}$ core, which produces an anionic complex when bound to gallium(III).[158,159] Accordingly, these complexes are not very lipophilic. Hydrophilicity may be the principal reason that some radio-labeled complexes of Ga^{3+} are unable to cross the blood–brain barrier. Research has therefore been directed toward the development of cryptand ligands that possess a potential coordination sphere consisting of an $[N_3O_3]^{3-}$ core, thereby producing neutral, highly lipophilic complexes of Ga^{3+}. Several groups have reported a variety of triprotic ligands with $[O_6]^{3-}$, $[N_3O_3]^{3-}$, and $[N_3S_3]^{3-}$ cores,[160–162] examples are shown in Figure 26.

10.2 Porphyrin and Related Ligands

Chlorogallium(III) porphyrins, Ga(Por)Cl, are obtained in good yield by treating the corresponding free bases with gallium trichloride. The action of the hydrogen halides HX (X = F or I) on the chloro derivatives Ga(Por)Cl led to the corresponding halogeno complexes Ga(Por)X. The crystal structure of the tetraphenylporphyrin derivative has been determined by X-ray diffraction methods and shows a square pyramidal coordination for the gallium.[163] The reactions of the Lewis bases (L) *N*-methylimidazole and pyridine with Ga(Por)X [H_2Por = octaethylporphyrin (OEP, (**19b**)), tetraphenylporphyrin (TPP, (**19a**)); X = Cl^-, OAc^-, OH^-, F^-] have been investigated, and demonstrated the stepwise formation of hexacoordinate gallium porphyrin species of the type [Ga(Por)(X)(L)] and $[Ga(Por)(L)_2]^+$ (Scheme 6).[164] These compounds represent the first monomeric, hexacoordinated gallium(III) porphyrins to be reported. Equilibrium constants for ligand binding by Ga(Por)X and Ga(Por)(X)(L) were calculated from the electronic absorption spectra.

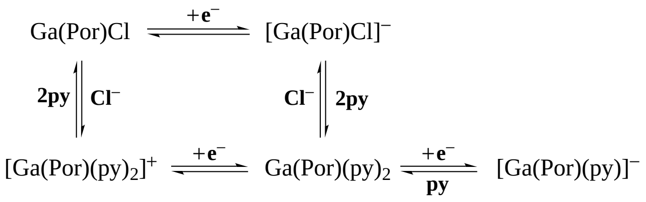

Scheme 6 Electrochemical reactions of gallium porphyrin complexes

The synthesis, spectroscopic, and structural characterization of the stable Ga hydride porphyrin [Ga(TPP)H] (TPP = 5,10,15,20-tetraphenylporphyrinato) was synthesized in high yield (85%) by reducing [Ga(TPP)Cl] with $NaBH_4$ in DMF. Infrared (IR) studies determined the Ga–H stretch at 1864 cm^{-1}, and the hydride ^1H NMR resonance located at −6.47 ppm. The Ga–H distance is 1.48(4) Å, whereas the Ga atom lies 0.46(1) Å from the perfect porphyrin plane.[165]

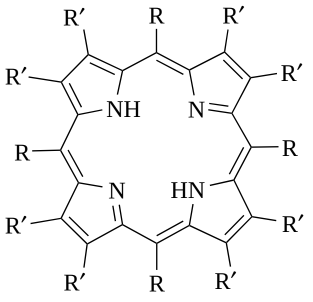

(**19a**) TPP; R = Ph, R′ = H
(**19b**) OEP; R = H, R′ = Et

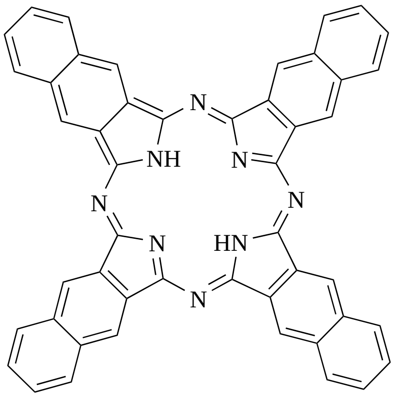

(**20**) H_2Nc

Gallium complexes of naphalocyanine (H_2Nc, (**20**)) have been investigated with respect to their application in photodynamic therapy agents for neoplastic disease. Compounds of the general formula Ga(Nc)X were prepared for X = F, Cl, OH, or $OSi(n\text{-}C_6H_{13})_3$.

Corroles are tetrapyrrole macrocycles that are closely related to porphyrins, with one carbon atom less in the outer periphery and one NH proton more in their inner core. They may also be considered as the aromatic version (identical skeleton) of the only partially conjugated corrin, the cobalt-coordinating ligand in Vitamin B_{12}. Two potential application of corroles are in tumor detection and their use in photovoltaic devices. Selective substitution of corroles via nitration, hydroformylation, and chlorosulfonation for the gallium were studied in detail and the respective mechanistic pathways and spectroscopic data were reported, (an example is shown in Figure 27). Overall, over 139 various corroles were synthesized and the effect of various metal complexation pertaining to their selective reactivity examined.[166,167]

The first highly characterized Ga and In halide complexes of tetraazamacrocycles have been reported. Gallium(III) and indium(III) complexes of cross-bridged cyclam and cyclen tetraaza macrocyclic ligands have been prepared and structurally characterized. In the crystalline state, both the $GaCl_3$ (cross-bridged cyclam) (**21**) and $InBr_3$ (cross-bridged cyclen) (**22**) complexes feature hexacoordinate cations in cis-folded tetradentate ligand clefts with ancillary cis-dihalides.[168]

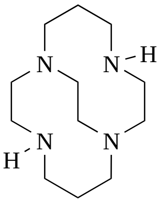

(**21**)

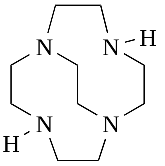

(**22**)

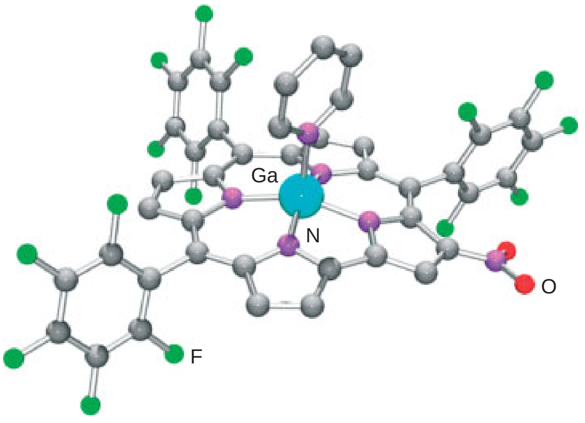

Figure 27 $C_{42}H_{12}F_{15}GaN_6O_2{\cdot}(C_6H_6)$, $M = 1065.4$, orthorhombic, space group $P2_12_12_1$, $a = 12.0410(2)$, $b = 18.2040(3)$, $c = 18.5900(3)$ Å, $V = 4074.8(1)$ Å^3, $D_c = 1.737$ g cm^{-3}, μ(Mo Kα) = 0.80 mm^{-1}. The observed Ga–N coordination distances to the four pyrrole and the pyridyl nitrogens are 1.972, 1.926, 1.942, 1.938, and 2.039(4) Å, respectively

Three hexadentate, asymmetric pendent arm macrocycles containing a 1,4,7-triazacyclononane-1,4-diacetate backbone and a third, *N*-bound phenolate or thiophenolate arm have been synthesized. In $[L^1]^{3-}$ the third arm is 3,5-di-*tert*-butyl-2-hydroxybenzyl, in $[L^2]^{3-}$ it is 2-mercaptobenzyl, and in $[L^3]^{3-}$ it is 3,5-di-*tert*-butyl-2-mercaptobenzyl. With trivalent metal ions these ligands form very stable neutral mononuclear complexes $[Ga^{III}L^{1to3}]$ where the gallium complexes possess an $S = 0$ ground state. Cyclic voltammetry studies revealed that all three $[Ga^{III}L^1]$ complexes undergo a reversible, ligand-based, one-electron oxidation generating the monocations $[GaL^1]^+$, which contain a coordinated phenoxyl radical as was unambiguously established by their electronic absorption, EPR, and Mössbauer spectra. In contrast, $[Ga^{III}L^2]$ complexes in CH_3CN solution undergo an irreversible one-electron oxidation where the putative thiyl radical monocationic intermediates dimerize with S–S bond formation yielding dinuclear disulfide species $[Ga^{III}L^2\text{-}L^2Ga^{III}]^{2+}$. $[GaL^3]$ behaves similarly despite the steric bulk of two tertiary butyl groups at the 3,5-positions of the thiophenolate.**169** Similar work has been performed on various gallium triazacyclononane with modified pendent arms and their crystal structures have been elucidated.**170**

11 Ga(III): A DIAMAGNETIC MIMIC OF IRON(III)

The hydrolytic behavior and aqueous chemistry of the Ga^{3+} ion is similar to that of the Fe^{3+} ion. In fact, useful extrapolations of properties have been made between the two. For instance, diamagnetic gallium analogs of the microbial iron chelates (siderophores) have been useful in NMR studies,**171** since the native Fe^{3+} ion complexes are paramagnetic. In reverse, the knowledge gained from studies of Fe^{3+} ion transport has been applied to the development of ^{67}Ga radiopharmaceuticals.**172** The basis for this replacement of Fe^{3+} by Ga^{3+} lies in the physical and chemical similarities of the two ions. Both have the same charge and similar ionic radii in six-coordinate complexes (0.620 Å for Ga^{3+} compared to 0.645 Å for Fe^{3+}). Neither ion is perturbed by crystal field effects. The Fe^{3+} ion configuration is high-spin d^5 while the gallium is diamagnetic d^{10}. Moreover, since neither have any crystal field stabilization and both have similar ionic radii, they are similar in many of their ligand exchange rates. However, there are some significant differences in the stabilities of Ga^{3+} and Fe^{3+} complexes. The formation constants of a series of catecholate complexes have been determined and the gallium complexes are found to be consistently less stable than the analogous iron complexes. The stabilities of the benzohydroxamate complexes show a similar disparity.

One notable difference in the properties of Ga^{3+} and Fe^{3+} is that while the Fe^{3+}/Fe^{2+} redox system is very important in biological systems, the absence of a stable divalent state for gallium removes from consideration any processes that involve one-electron reduction of Ga^{3+}.

12 RELATED ARTICLES

Aluminum: Inorganic Chemistry; Aluminum: Organometallic Chemistry; Boron Hydrides; Boron: Inorganic Chemistry; Gallium: Organometallic Chemistry; Indium: Inorganic Chemistry; Indium: Organometallic Chemistry; Iron: Heme Proteins & Dioxygen Transport & Storage; Iron: Heme Proteins, Peroxidases, Catalases & Catalase-peroxidases; Main Group: Multiple Bonding.

13 FURTHER READING

S. M. Bradley, R. A. Kydd, and R. Yamdagni, *J. Chem. Soc., Dalton Trans.*, 1990, 413.

Z. Liliental-Weber, C. W. Wilmsen, K. M. Geib, P. D. Kirchner, J. M. Baker, and J. M. Woodall, *J. Appl. Phys.*, 1990, **67**, 1863.

S. Nogai, A. Schier, and H. Schmidbaur, *Z. Naturforsch., B: Chem. Sci.*, 2002, **57**(2), 183.

K.-N. Tu, J. W. Mayer, L. C. Feldman, 'Electronic Thin Film Science for Electrical Engineers & Material Scientists', Prentice Hall College Div: 1st edition (December 2), 1996, p. 127.

K.-N. Tu, J. W. Mayer, L. C. Feldman, 'Electronic Thin Film Science for Electrical Engineers & Material Scientists', Prentice Hall College Div: 1st edition (December 2), 1996, p. 157.

K.-N. Tu, J. W. Mayer, L. C. Feldman, 'Electronic Thin Film Science for Electrical Engineers & Material Scientists', Prentice Hall College Div: 1st edition (December 2), 1996, , p. 194.

14 REFERENCES

1. Gmelin, 'Handbuch der Anorganischen Chemie', Syst. No. 36, Gallium, Springer, Berlin, 1936.
2. E. Einecke, 'Das Gallium', Voss, Leipzig, 1937.
3. N. Saunders, 'Aluminum and the elements of group 13', Heinemann Library, Chicago, IL, 2004, ISBN 1403416613.
4. N. N. Greenwood and A. Earnshaw, 'Chemistry of the Elements', Butterworth-Heinemann, 1997, ISBN 0750633654.
5. F. A. Cotton, G. Wilkinson, C. A. Murillo, and M. Bochmann, 'Advanced Inorganic Chemistry', John Wiley & Sons, New York, 1999, ISBN 0471199575.
6. D. A. Atwood, in 'Group 13 chemistry III: Industrial Applications', eds. H. W. Roesky and D. A. Atwood, Springer, Berlin, 2003, ISBN 3540441050.

7. H. Schnockel and C. Klemp, in ‘Inorganic Chemistry Highlights’, eds. G. Meyer, D. Naumann, and L. Wesemann, Wiley-VCH, Cambridge, 2002, p. 245, ISBN 3527302654.
8. P. J. Shapiro, and D. A. Atwood eds. ‘group 13 Chemistry: From Fundamentals to Applications’, ACS Symposium series; 822, Oxford University Press, Washington, DC, 2002, ISBN 0841237859.
9. P. O’Brien and N. L. Pickett, Coordination Complexes as Precursors for Semiconductor Films and Nanoparticles, in ‘Comprehensive Coordination Chemistry II: from Biology to Nanotechnology’, eds. J. A. McCleverty, and T. J. Meyer, Elsevier Science, 2004, p. 1005, ISBN 0080437486.
10. G. H. Robinson, Aluminum and Gallium, in ‘Comprehensive Coordination Chemistry II: From Biology to Nanotechnology’, eds. J. A. McCleverty and T. J. Meyer, Elsevier Science, 2004, p. 347, ISBN 0080437486.
11. J. P. Maher, *Annu. Rep. Prog. Chem., Sec. A: Inorg. Chem.*, 2003, **99**, 43.
12. J. P. Maher, *Annu. Rep. Prog. Chem., Sec. A: Inorg. Chem.*, 2002, **98**, 45.
13. J. P. Maher, *Annu. Rep. Prog. Chem., Sec. A: Inorg. Chem.*, 2001, **97**, 49.
14. J. P. Maher, *Annu. Rep. Prog. Chem., Sec. A: Inorg. Chem.*, 2000, **96**, 45.
15. J. P. Maher, *Annu. Rep. Prog. Chem., Sec. A: Inorg. Chem.*, 1999, **95**, 45.
16. J. P. Maher, *Annu. Rep. Prog. Chem., Sec. A: Inorg. Chem.*, 1998, **94**, 43.
17. J. P. Maher, *Annu. Rep. Prog. Chem., Sec. A: Inorg. Chem.*, 1997, **93**, 45.
18. J. P. Maher, *Annu. Rep. Prog. Chem., Sec. A: Inorg. Chem.*, 1996, **92**, 41.
19. J. P. Maher, *Annu. Rep. Prog. Chem., Sec. A: Inorg. Chem.*, 1995, **91**, 41.
20. J. P. Maher, *Annu. Rep. Prog. Chem., Sec. A: Inorg. Chem.*, 1994, **90**, 25.
21. P. P. Power, *Chem. Rev.*, 1999, **99**(12), 3463.
22. H. Curien, A. Rimsky, and A. Defrain, *Bull. Soc. Fr. Mineral. Crystallogr.*, 1961, **84**, 260.
23. J. P. Yesinowski and A. P. Purdy, *J. Am. Chem. Soc.*, 2004, **126**, 9166.
24. M.-C. Hsien, H.-M. Kao, and K.-H. Lii, *Chem. Mater.*, 2001, **13**, 2584.
25. A. Breuer and D. Siebert, *Berichte der Bunsen-Gesellschaft*, 1996, **100**, 1736.
26. P. P. Man, 2004, http://www.pascal-man.com/periodic-table/gallium.html.
27. M. Winter, 2004, http://www.webelements.com.
28. 2004, http://arrhenius.rider.edu/nmr/NMR_tutor/periodic_table/nmr_pt_frameset.html.
29. K. Weiß, R. Köppe, and H. Schnöckel, *Int. J. Mass Spectrom.*, 2002, **214**(3), 383.
30. Cv. Hanisch and O. Hampe, *Angew. Chem., Int. Ed.*, 2002, **41**(12), 2095.
31. J.-W. Hwang, S. A. Hanson, D. Britton, J. F. Evans, K. F. Jensen, and W. L. Gladfelter, *Chem. Mater.*, 1990, **2**, 342.
32. R. A. Logan, B. Schwartz, and W. J. Sundburg, *J. Electrochem. Soc.*, 1973, **120**, 1385.
33. H. Hasegawa, K. E. Forward, and H. L. Hartnagel, *Appl. Phys. Lett.*, 1975, **26**, 567.
34. M. A. Hoffbauer, J. B. Cross, and U. M. Bermudez, *Appl. Phys. Lett.*, 1990, **57**, 2193.
35. E. Yablonovitch, C. J. Sandroff, R. Bhat, and T. Gmitter, *Appl. Phys. Lett.*, 1987, **51**, 439.
36. A. N. MacInnes, M. B. Power, and A. R. Barron, *Chem. Mater.*, 1992, **4**, 11.
37. A. N. MacInnes, M. B. Power, A. R. Barron, P. P. Jenkins, and A. F. Hepp, *Appl. Phys. Lett.*, 1993, **62**, 711.
38. M. Tabib-Azar, A. N. MacInnes, M. B. Power, A. R. Barron, P. P. Jenkins, and A. Hepp, *Appl. Phys. Lett.*, 1993, **63**(5), 625.
39. M. Passlack, E. F. Schubert, W. S. Hobson, M. Hong, N. Moriya, S. N. G. Chu, K. Konstadinidis, J. P. Mannaerts, M. L. Schnoes, and G. J. Zydzik, *J. Appl. Phys.*, 1995, **77**(2), 686.
40. L. I. Berger, ‘Semiconductor Materials’, CRC Press, New York, 1997, ISBN 0-849389127.
41. E. Villora, K. Shimamura, Y. Yoshikawa, K. Aoki, and N. Ichinose, *J. Cryst. Growth*, 2004, **270**(3–4), 420.
42. S. Schulz, E. G. Gillan, J. L. Ross, L. M. Rogers, R. D. Rogers, and A. R. Barron, *Organometallics*, 1996, **15**(22), 4880.
43. S. Shigetomi and T. Ikari, *J. Appl. Phys.*, 2004, **95**(11), 6480.
44. L. I. Man, R. M. Imanov, and S. A. Semiletov, *Sov. Phys. Crystallogr.*, 1976, **21**, 255.
45. C. C. Landry, A. Hynes, A. R. Barron, I. Haiduc, and C. Silvestru, *Polyhedron*, 1996, **15**(3), 391.
46. C. C. Landry and A. R. Barron, 1992, unpublished results.
47. A. Kuhn and A. Chevy, *Acta Crystallogr.*, 1976, **B32**, 983.
48. M. P. Pardo and J. Flauhaut, *Mater. Res. Bull.*, 1987, **22**, 323.
49. A. R. Barron, *Comments Inorg. Chem.*, 1993, **14**, 123.
50. M. Burgelman, F. Engelhardt, J. F. Guillemoles, R. Herberholz, M. Igalson, R. Klenk, M. Lampert, T. Meyer, V. Nadenau, A. Niemegeers, J. Parisi, U. Rau, H. W. Schock, M. Schmitt, O. Seifert, T. Walter, and S. Zott, *Prog. Photovolt. Res. Appl.*, 1997, **5**(2), 121.
51. A. Niemegeers, M. Burgelman, R. Herberholz, U. Rau, D. Hariskos, and H.-W. Schock, *Prog. Photovolt. Res. Appl.*, 1998, **6**(6), 407.
52. S. B. Zhang, S.-H. Wei, A. Zunger, and Y. H. Katayama, *Phys. Rev. B*, 1998, **57**(16), 9642.
53. S.-H. Wei, S. B. Zhang, and A. Zunger, *Appl. Phys. Lett.*, 1998, **72**(24), 3199.

54. S. G. Bailey and D. J. Flood, *Prog. Photovolt. Res. Appl.*, 1998, **6**, 1.
55. K. Ramanathan, M. Contreras, C. L. Perkins, S. Asher, F. S. Hasoon, J. Keane, D. Young, M. Romero, W. Metzger, R. Noufi, J. Ward, and A. Duda, *Prog. Photovolt. Res. Appl.*, 2003, **11**(4), 225.
56. B. M. Basol, V. K. Kapur, A. Halani, C. R. Leidholm, J. Sharp, J. R. Sites, A. Swartzlander, R. Matson, and H. Ullal, *J. Vac. Sci. Technol. A*, 1996, **14**, 2251.
57. S. C. Park, D. Y. Lee, B. T. Ahn, K. H. Yoon, and J. Song, *J. Sol. Energy Mater. Sol. Cells*, 2001, **69**, 99.
58. C. Guillen and J. Herrero, *Thin Solid Films*, 2001, **387**, 57.
59. C. Eberspacher, K. Fredic, K. Paula, and J. Serra, *Thin Solid Films*, 2001, **387**, 18.
60. M. Klenk, O. Schenker, V. Alberts, and E. Bucher, *Thin Solid Films*, 2001, **387**, 47.
61. J. A. Hollingsworth, Chemical Routes to Nanocrystalline and Thin Film III-VI and I-III-VI Semiconductors, PhD Thesis, Washington University, 1999, Chap. 2–3.
62. T. C. Deivaraj, J. H. Park, M. Afzaal, P. O'Brien, and J. J. Vittal, *Chem. Mater.*, 2003, **15**(12), 2383.
63. T. C. Deivaraj, M. Lin, K. P. Loh, M. Yeadon, and J. J. Vittal, *J. Mater. Chem.*, 2003, **13**(5), 1149.
64. A. J. Nozik, *Annu. Rev. Phys. Chem.*, 2001, **52**, 193.
65. M. Green and P. O'Brien, *J. Mater. Chem.*, 2004, **14**, 629.
66. U. Brin, Synthesis and Characterisation of III-V Semiconductor Nanoparticles, in 'Nanoparticles: From Theory to Application', ed. G. Schmid, John Wiley & Sons, New York, 2004, p. 79, ISBN 3527305076.
67. U. Brin and O. Millo, Optical and Electronic Properties of III-V and II-VI Nanoparticles, in 'Nanoparticles: From Theory to Application', ed. G. Schmid, John Wiley & Sons, New York, 2004, p. 305, ISBN 3527305076.
68. R. L. Wells, C. G. Pitt, A. T. McPhail, A. P. Purdy, S. Shafieezad, and R. B. Hallock, *Chem. Mater.*, 1989, **1**, 4.
69. M. D. Healy, P. E. Laibinis, P. D. Stupik, and A. R. Barron, *J. Chem. Soc., Chem. Commun.*, 1989, 359.
70. M. A. Olshavsky, A. N. Goldstein, and A. P. Alivisatos, *J. Am. Chem. Soc.*, 1990, **112**, 9438.
71. H. Uchida, C. J. Curtis, P. V. Kamat, K. M. Jones, and A. J. Nozik, *J. Phys. Chem.*, 1992, **96**, 1156.
72. A. A. Guzelian, J. E. B. Katari, A. V. Kadavanich, U. Banin, K. Hamad, E. Juban, A. P. Alivisatos, R. H. Wolters and C. C. Heath, 1996, **100**, 7212.
73. O. I. Micic, S. P. Ahrenkiel, D. Bertram, and A. J. Nozik, *J. Appl. Phys. Lett.*, 1999, **75**, 478.
74. Y. Xie, Y. T. Qian, W. Z. Wang, S. Y. Zhang, and Y. H. Zhang, *Science*, 1996, **272**, 1926. Y. H.
75. J. Xiao, Y. Xie, R. Tang, and W. Luo, *Inorg. Chem.*, 2003, **42**(1), 107.
76. J. F. Janik, R. L. Wells, V. G. Young, A. L. Rheingold, and I. A. Guzei, *J. Am. Chem. Soc.*, 1998, **120**, 532.
77. M. Green, *Curr. Opin. Solid State Mater. Sci.*, 2002, **6**, 355.
78. M. C. Hanna, Z. H. Lu, A. F. Cahill, M. J. Heben, and A. J. Nozik, *J. Cryst. Growth*, 1997, **174**, 605.
79. Y. Banto and R. Ma, JP 2004182547, 2004.
80. Y. Banto and Y. Gao, JP 2004182546, 2004.
81. S. Gao, Y. Xie, L. Zhu, and X. Tian, *Inorg. Chem.*, 2003, **42**(17), 5442.
82. J. H. Chun, Y. S. Choi, S. Y. Bae, H. W. Seo, J. S. Hong, J. Park, and H. Yang, *J. Phys. Chem. B*, 2003, **107**, 9042.
83. M. Lazell, P. O'Brien, D. J. Otway, and J.-H. Park, *J. Chem. Soc., Dalton Trans.*, 2000, 4479.
84. S. L. Stoll, E. G. Gillan, and A. R. Barron, *Chem. Vap. Dep.*, 1996, **2**, 182.
85. S. L. Castro, S. G. Bailey, R. P. Raffaelle, K. K. Banger, and A. F. Hepp, *J. Phys. Chem. B*, 2004, **108**(33), 12429.
86. S. L. Castro, S. G. Bailey, R. P. Raffaelle, K. K. Banger, and A. F. Hepp, *Chem. Mater.*, 2003, **15**(16), 3142.
87. Q. Lu, J. Hu, K. Tang, Y. Qian, G. Zhou, and X. Liu, *Inorg. Chem.*, 2000, **39**, 1606.
88. Y. Cui, J. Ren, G. Chen, Y. Qian, and Y. Xie, *Chem. Lett.*, 2001, 236.
89. Y. Jiang, Y. Wu, S. Yuan, B. Xie, S. Zhang, and Y. Qian, *J. Mater. Res.*, 2001, **16**, 2805.
90. J. Olkowska-Oetzel, D. Fenske, P. Scheer, and A. Eichhoefer, *Z. Anorg. Allg. Chem.*, 2003, **629**(3), 415.
91. E. Wiberg and M. Schmidt, *Zeitschrift fuer Naturforschung*, 1951, **6**(b), 172.
92. E. Wiberg and T. Johannsen, *Naturwissenchaften*, 1941, **29**, 320.
93. M. T. Barlow, C. J. Dain, A. J. Downs, G. S. Laurenson, and D. W. H. Rankin, *J. Chem. Soc., Dalton Trans.*, 1982, 597.
94. J. L. Atwood, S. G. Bott, C. Jones, and C. L. Raston, *Inorg. Chem.*, 1991, **30**, 4868, and references therein.
95. H. Protzmann, T. Marschner, O. Zsebok, W. Stolz, E. O. Gobel, R. Dorn, and J. Lorberth, *J. Cryst. Growth*, 1991, **115**, 248.
96. S. Nogai and H. Schmidbaur, *Inorg. Chem.*, 2002, **41**(18), 4770.
97. S. Nogai, A. Schriewer, and H. Schmidbaur, *Dalton Trans.*, 2003, 3165.
98. W. Uhl, L. Cuypers, G. Geisler, K. Harms, and W. Massa, *Z. Anorg. Allg. Chem.*, 2002, **628**(5), 1001.
99. R. J. Baker, C. Jones, M. Kloth, and J. A. Platts, *Angew. Chem., Int. Ed.*, 2003, **42**(23), 2660.
100. K. Ueno, T. Yamaguchi, K. Uchiyama, and H. Ogino, *Organometallics*, 2002, **21**(12), 2347.
101. U. Vogel, A. Y. Timoshkin, and M. Scheer, *Angew. Chem., Int. Ed.*, 2001, **40**(23), 4409.
102. R. A. Fischer, A. Miehr, and T. Priermeier, *Chem. Ber.*, 1995, **128**(8), 831.

103. L. Grocholl, S. A. Cullison, J. Wang, D. C. Swenson, and E. G. Gillan, *Inorg. Chem.*, 2002, **41**(11), 2920.

104. N. Nakata, R. Izumi, V. Y. Lee, M. Ichinohe, and A. Sekiguchi, *J. Am. Chem. Soc.*, 2004, **126**(16), 5058.

105. H. Jacobs and B. Noecker, *Z. Anorg. Allg. Chem.*, 1993, **619**(2), 381.

106. B. Luo, M. Pink, and G. W. Gladfelter, *Inorg. Chem.*, 2001, **40**(2), 307.

107. J. S. Silverman, C. J. Carmalt, A. H. Cowley, R. D. Culp, R. A. Jones, and B. G. McBurnett, *Inorg. Chem.*, 1999, **38**(2), 296.

108. W. R. Nutt, J. A. Anderson, J. D. Odom, M. M. Williamson, and B. H. Rubin, *Inorg. Chem.*, 1985, **24**, 159.

109. W. R. Nutt, J. S. Blanton, F. O. Kroh, and J. D. Odom, *Inorg. Chem.*, 1989, **28**, 2224.

110. D. L. Reger, S. J. Knox, and L. Lebioda, *Inorg. Chem.*, 1989, **28**, 3092.

111. D. L. Reger, *Coord. Chem. Rev.*, 1996, **147**, 571.

112. J. T. Leman, A. R. Barron, J. W. Ziller, and R. M. Kren, *Polyhedron*, 1989, **8**, 1909.

113. D. A. Atwood, V. O. Atwood, D. F. Carriker, A. H. Cowley, F. P. Gabbai, R. A. Jones, M. R. Bond, and C. J. Carrano, *J. Organomet. Chem.*, 1993, **463**(1–2), 29.

114. M. Stender, B. E. Eichler, N. J. Hardman, P. P. Power, J. Prust, M. Noltemeyer, and H. W. Roesky, *Inorg. Chem.*, 2001, **40**(12), 2794.

115. C. G. Pitt, K. T. Higa, A. T. McPhail, and R. L. Wells, *Inorg. Chem.*, 1986, **25**, 2484.

116. S. Weinrich, H. Piotrowski, M. Vogt, A. Schulz, and M. Westerhausen, *Inorg. Chem.*, 2004, **43**(12), 3756.

117. E. Leiner and M. Scheer, *Organometallics*, 2002, **21**(21), 4448.

118. G. Trinquier, *J. Am. Chem. Soc.*, 1990, **112**, 2130.

119. M. Driess and H. Gratzmacher, *Angew. Chem., Int. Ed.*, 1996, **35**, 828.

120. J. Su, X.-W. Li, and R. C. Robinson, *J. Am. Chem. Soc.*, 1997, **119**, 5471.

121. R. J. Wehmschulte and P. P. Power, *Angew. Chem., Int. Ed.*, 1998, **37**, 3152.

122. S. Loss, C. Widauer, and H. Gratzmacher, *Angew. Chem., Int. Ed.*, 1999, **38**, 3329.

123. B. Twamley and P. P. Power, *Angew. Chem., Int. Ed.*, 2000, **39**, 3500.

124. P. P. Power, *Chem. Rev.*, 1999, **99**, 3463.

125. N. J. Hardman, C. Cui, H. W. Roesky, W. H. Fink, and P. P. Power, *Angew. Chem., Int. Ed.*, 2001, **40**, 2172.

126. C. Von Hanisch and O. Hampe, *Angew. Chem., Int. Ed.*, 2002, **41**(12), 2095.

127. B. Neumueller, *Chem. Soc. Rev.*, 2003, **32**(1), 50.

128. J. P. Oliver, R. Kumar, and M. Taghiof, The chemistry of Alkoxides, Thiolates, and the Heavier group 16 Derivatives of Aluminum and Gallium, in ‘Coordination Chemistry of Aluminum’, eds. R. Gregory Heagward, VCH, New York, 1993, p. 167.

129. M. Valet and D. M. Hoffman, *Chem. Mater.*, 2001, **13**(6), 2135.

130. J. W. Huang, D. F. Gaines, T. F. Kuech, R. M. Potemski, and F. Cardone, *J. Electron. Mater.*, 1994, **23**(7), 659.

131. H. W. Heuer and R. Wehrmann, Five-Coordinate of Gallium(III) Carboxylate Complexes With Blue/Blue–Green Photo- and Electroluminescence, Procedures for their Production as Well as their Use, DE 10225826, 2003.

132. L. V. Budaragin, V. Leonid, Cost-Effective Method for Coating Substrate with Metal Oxide Coating., US 20020041928, 2002.

133. M. T. Andras, S. A. Duraj, A. F. Hepp, P. E. Fanwick, and M. M. Bodnar, *J. Am. Chem. Soc.*, 1992, **114**, 786.

134. T. L. Feng, P. L. Gurian, M. D. Healy, and A. R. Barron, *Inorg. Chem.*, 1990, **29**, 408.

135. P. O’Brien, H. Salacinski, and M. Motevalli, *J. Am. Chem. Soc.*, 1997, **119**(51), 12695.

136. K. Saito and A. Nagasawa, *Polyhedron*, 1990, **9**, 215.

137. O. T. Beachley, J. R. Gardinier, and M. R. Churchill, *Organometallics*, 2003, **22**(5), 1145.

138. O. T. Beachley, J. R. Gardinier, and M. R. Churchill, *Organometallics*, 2000, **19**(22), 4544.

139. C. L. Edwards and R. L. Hayes, *J. Nucl. Med.*, 1969, **10**, 103.

140. W. O. Nelson, T. B. Karpishin, S. J. Rettig, and C. Orvig, *Inorg. Chem.*, 1988, **27**, 1045.

141. Z. Zhang, S. J. Rettig, and C. Orvig, *Inorg. Chem.*, 1991, **30**, 509.

142. D. J. Clevette, D. M. Lyster, W. O. Nelson, T. Rihela, G. A. Webb, and C. Orvig, *Inorg. Chem.*, 1990, **29**, 667.

143. L. E. Maelia and S. A. Koch, *Inorg. Chem.*, 1986, **25**, 1896.

144. K. Ruhlandt-Senge and P. P. Power, *Inorg. Chem.*, 1991, **30**, 2633, 3683.

145. M.-A. Munoz-Hernandez, P. Wei, S. Liu, and D. A. Atwood, *Coord. Chem. Rev.*, 2000, **210**, 1.

146. G. G. Hoffmann and C. Burschka, *Angew. Chem.*, 1985, **97**, 965; *Angew. Chem., Int. Ed. Engl.*, 1985, **24**, 970.

147. M. R. Lazell, P. O’Brien, D. J. Otway, and J.-H. Park, *Chem. Mater.*, 1999, **11**, 3430.

148. A. Horley, M. R. Lazell, and P. O’Brien, *Adv. Mater., Chem. Vap. Dep.*, 1999, **5**, 203.

149. D. P. Dutta, V. K. Jain, A. Knoedler, and W. Kaim, *Polyhedron*, 2002, **21**(2), 239.

150. J.-H. Park, P. O’Brien, A. J. P. White, and D. J. Williams, *Inorg. Chem.*, 2001, **40**(14), 3629.

151. N. J. Hardman and P. P. Power, *Inorg. Chem.*, 2001, **40**(11), 2474.

152. G. Shang, M. J. Hampden-Smith, and E. N. Duesler, *Inorg. Chem.*, 1996, **35**(9), 2611.

153. S. D. Nogai and H. Schmidbaur, *Dalton Trans.*, 2003, 2488.
154. W. Klemm, W. Tilk, and H. Jacobi, *Z. Anorg. Chem.*, 1932, **207**, 187.
155. R. J. Baker, H. Bettentrup, and C. Jones, *Eur. J. Inorg. Chem.*, 2003, **13**, 2446.
156. X. Sava, M. Melaimi, N. Mezailles, L. Ricard, and F. Mathey, *New J. Chem.*, 2002, **26**(10), 1378.
157. N. R. Bunn, S. Aldridge, D. L. Coombs, A. Rossin, D. J. Willock, C. Jones, and L. Ooi, *Chem. Commun.*, 2004, 1732.
158. D. J. Clevette and C. Orvig, *Polyhedron*, 1990, **9**, 151.
159. R. J. Motekaitis, Y. Sun, A. E. Martell, and M. J. Welch, *Inorg. Chem.*, 1991, **30**(13), 2737, and references therein.
160. D. A. Moore, P. E. Fanwick, and M. J. Welch, *Inorg. Chem.*, 1990, **29**, 672.
161. R. C. Matthews, D. Parker, G. Ferguson, B. Kaitner, A. Harrison, and L. Royle, *Polyhedron*, 1991, **10**, 1951.
162. R. J. Motekaitis, Y. Sun, and A. E. Martell, *Inorg. Chem.*, 1991, **30**, 1554.
163. A. Coutsolelos, R. Guilard, D. Bayeul, and C. Lecomte, *Polyhedron*, 1986, **5**, 1157.
164. K. M. Kadish, J.-L. Cornillon, A. Coutsolelos, and R. Guilard, *Inorg. Chem.*, 1987, **26**, 4167.
165. Y. Feng, S.-L. Ong, J. Hu, and W.-J. Ng, *Inorg. Chem. Commun.*, 2003, **6**(5), 466.
166. Z. Gross, A. Mahammed, and I. Saltsman, PCT Int. Appl. (2003), 47 pp. WO 2003004021.
167. I. Saltsman, A. Mahammed, I. Goldberg, E. Tkachenko, M. G. Botoshansky, and Z. Gross, *J. Am. Chem. Soc.*, 2002, **124**(25), 7411.
168. W. Niu, E. H. Wong, G. R. Weisman, R. D. Sommer, and A. L. Rheingold, *Inorg. Chem. Commun.*, 2002, **5**(1), 1.
169. S. Kimura, E. Bill, E. Bothe, T. Weyhermueller, and K. Wieghardt, *J. Am. Chem. Soc.*, 2001, **123**(25), 6025.
170. S. Y. Bylikin, D. A. Robson, N. A. Male, L. H. Rees, P. Mountford, and M. Schroder, *J. Chem. Soc., Dalton Trans.*, 2001, 170.
171. M. Linas, D. M. Wilson, and J. B. Neilands, *Biochemistry*, 1973, **112**, 3836.
172. S. M. Moerlien, M. L. Welch, K. N. Raymond, and F. L. Weitl, *J. Nucl. Med.*, 1982, **22**, 720.

Gallium: Organometallic Chemistry

Gregory H. Robinson
The University of Georgia, Athens, GA, USA

Based in part on the article Gallium: Organometallic Chemistry by Andrew R. Barron which appeared in the Encyclopedia of Inorganic Chemistry, First Edition.

1 Introduction 1
2 Simple Trialkyl and Triaryl Organogallium Compounds 1
3 Sterically Demanding Organogallium Compounds 3
4 Organometallic Compounds Containing Gallium–Gallium Bonds 5
5 Related Articles 7
6 References 7

1 INTRODUCTION

The organometallic chemistry of gallium has experienced substantial growth in the intervening decade since publication of the first edition of the *Encyclopedia of Inorganic Chemistry*. One could legitimately argue that the organometallic chemistry of gallium has only just begun to be studied with a critical hand and vigilant eye in the last two decades. It seems that much of the activity in the organometallic chemistry of gallium during this period was driven by the quest for single-source molecular precursors to advanced materials (e.g. semiconductors) and the utilization of organogallium compounds in *Metal-Organic Chemical Vapor Deposition* (MOCVD) procedures.[1] Although it is evident that the breadth of the organometallic chemistry of gallium is as wide as it is varied, fundamental issues relating to structure and bonding have been a substantial driving force in this field much of the past decade. Perhaps more than could ever have been imagined when Paul-E'mile Lecoq de Boisbaudran discovered this rare and oddly mercurial element in 1875, the organometallic chemistry of gallium has been proven to be engaging and exciting. This contribution does not seek to cover the same fundamental material so eloquently presented in the original chapter, *Gallium: Organometallic Chemistry*, authored by A.R. Barron. Rather, this contribution seeks to utilize the original chapter as a template and bring sharper focus to some of the more noteworthy advances in the organometallic chemistry of gallium of the past decade. Specifically, this contribution seeks to highlight two prominent areas: (1) Organogallium compounds utilizing sterically demanding ligands; and (2) Organogallium cluster compounds. However, for historical perspective it is important to first contrast the synthesis of sterically demanding organogallium compounds with that of simple trialkyl and triaryl organogallium compounds.

2 SIMPLE TRIALKYL AND TRIARYL ORGANOGALLIUM COMPOUNDS

2.1 Syntheses

Triethylgallium monoetherate, $Et_3Ga\cdot(Et_2O)$, the first reported organometallic compound of gallium, was isolated from reaction of ethylmagnesium bromide with gallium bromide in 1932 (equation 1).[2]

$$3EtMgBr + GaBr_3 \xrightarrow[Et_2O]{} Et_3Ga\cdot(Et_2O) \qquad (1)$$

Triethylgallium monoetherate was isolated as a colorless, moderately viscous, pyrophoric liquid. The workers also reported that ether-free triethylgallium, Et_3Ga, could be prepared from reaction of gallium metal with diethylmercury. These two synthetic methods – reaction of a gallium halide with a Grignard Reagent and reaction of metallic gallium with a dialkylmercury reagent – are indicative of the often straightforward manner in which simple gallium alkyls and aryls may be prepared. Generally, simple gallium alkyls and gallium aryls may be approached synthetically by variations of these methods. However, some methods are significantly more effective than others.

2.1.1 Grignard Reagents

The utilization of Grignard Reagents, RMgX, with gallium halides, GaX_3, is perhaps the most versatile synthetic method to approach simple gallium alkyls and aryls. Indeed, not only was this the preparative method of choice for triethylgallium[2] in 1932, but it was also used to prepare trimesitylgallium, Mes_3Ga (Mesityl = 1,3,5-trimethylphenyl) – arguably the first sterically demanding organogallium compound – more than five decades later (equation 2).[3]

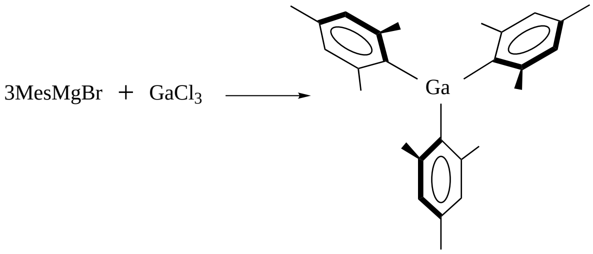

(2)

Mesitylmagnesium bromide was also utilized to prepare dichloromesitylgallium derivatives, which were reported as an inorganic polymer.[4] The following sterically demanding organogallium compounds, R_3Ga, have been prepared (where R =: -neopentyl[5] and $–CH_2CMe_2Ph$).[6] One of the more recent sterically demanding organogallium species to be prepared by this route is the bis(adamantyl)-based gallate anions, $[Ada_2GaMe_2]^-$ and $[Ada_2GaBr_2]^-$ (Ada = adamantyl).[7] As is widely known, diethyl ether is often present in the organogallium products of such reaction products. However, it is often possible to obtain the ether-free moiety after prolonged exposure to vacuum. In addition, if the ligand is sufficiently sterically demanding, such as (Me_5C_6) Ga, ether complexation with the metal center is often prevented.

2.1.2 *Lithium Reagents*

The utilization of organolithium reagents, RLi (R = alkyl or aryl), with gallium halides is also a fruitful route to organogallium compounds. The overall reaction is quite similar to that of the Grignard Reagents: for example, reaction of phenyllithium with gallium chloride readily yields triphenylgallium, Ph_3Ga (equation 3).

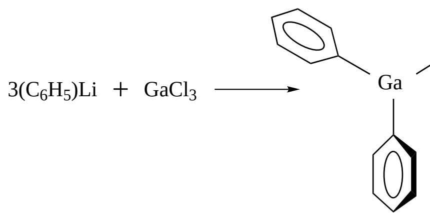

(3)

This method bears some similarities to the Grignard Reagent method in that product formation is often accomplished with solvent association. In particular, this method has been useful in preparing sterically demanding organogallium compounds, $(Aryl)_3Ga$ (vide infra).

2.1.3 *Organomercury Reagents*

Although organomercury reagents such as dimethylmercury, Me_2Hg, present significant toxicity concerns, these compounds offer a straightforward route to simple organogallium compounds. As demonstrated by the reaction of dimethylmercury with gallium metal, these reactions may be regarded as organometallic redox systems: the gallium metal is oxidized to R_3Ga while the mercury in Me_2Hg is reduced to elemental mercury (equation 4).

$$3Me_2Hg + 2Ga \longrightarrow 2Me_3Ga + 3Hg \qquad (4)$$

This method can also be utilized to prepare trimethylindium. It should be noted, however, that this preparative method is quite limited, being restricted to the simplest of alkyls.

2.1.4 *Ligand Redistribution*

Preparation of organogallium compounds by ligand redistribution between gallium halides and alkyls of metals such as zinc and mercury is severely limited. A noteworthy example is the preparation of $(CF_3)_3Ga$, isolated from reaction of $GaCl_3$ with $(CF_3)_2Cd$.[8,9] It should be noted that a potentially important class of organogallium compounds is the mixed trialkyls, $R_2R'Ga$. For example, ligand redistribution reactions involving Cp_3Ga and Me_3Ga, to give Me_2GaCp and $MeGaCp_2$, have been examined.[10]

2.2 Structural Characterization

In one sense, the coordination chemistry of simple gallium alkyls and aryls is rather restricted to three-coordinate trigonal planar. Although single-crystal X-ray diffraction remains the most important structural technique in the organometallic chemistry realm, gas-phase electron diffraction data of Me_3Ga unambiguously confirms a monomeric species with the gallium center residing in a trigonal planar environment.[11] While single-crystal X-ray diffraction data confirms the coordination of the gallium center in triphenylgallium, Ph_3Ga, as trigonal planar (Figure 1),[12] it is interesting to note one phenyl ring is observed to be coplanar with the GaC_3 plane while a second phenyl ring resides slightly out of the GaC_3 plane at 13°. In contrast, the third phenyl ring is found to reside considerably out of plane at 31°. Indeed, a more expansive view of the unit cell reveals significant secondary interactions of each gallium center with meta carbon atoms of other Ph_3Ga units (3.42 Å). This effectively results in the coordination approaching five-coordinate trigonal bipyramidal.

A similar intermolecular stabilization has also been observed in $(t\text{-Bu})_2Ga(OCPh_3)$[13] wherein the carbon atom of one of the phenyl rings approaches the gallium center offering

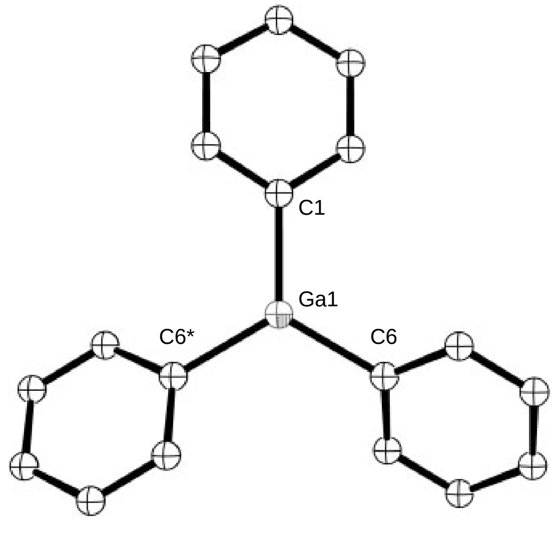

Figure 1 Solid-state structure of Ph_3Ga

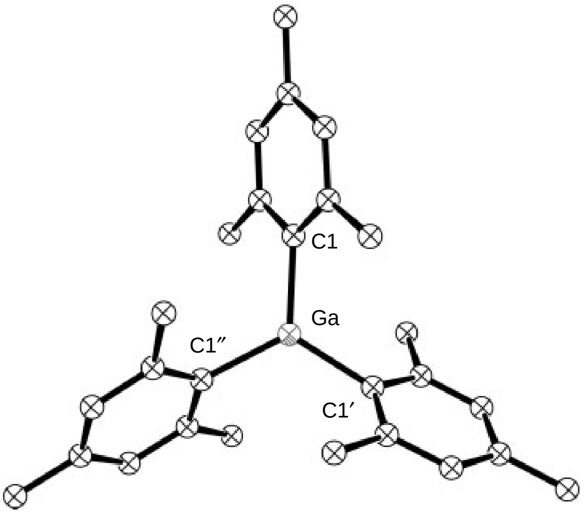

Figure 2 Solid-state structure of Mes_3Ga

additional electron density. Effectively, the coordination of the gallium center may be described as 'trigonal pyramidal': the gallium atom resides in a normal trigonal planar environment with further stabilization from one of the carbon atoms of a phenyl ring.

The solid-state structure of Mes_3Ga stands as a benchmark in organogallium chemistry.**[3]** The structure reveals the gallium atom in an almost idealized trigonal planar environment (C–Ga–C bond angle: 120°) (Figure 2). While the Ga–C bond distances are unremarkable (Ga–C: 1.968 Å), the mesityl rings of Mes_3Ga reside in a propeller arrangement at angles of 55.9° relative to the GaC_3 basal plane. Unlike Ph_3Ga, the steric bulk of the mesityl groups in Mes_3Ga preclude any significant secondary interaction from neighboring molecules in the unit cell or solvent donor interactions.

In notable contrast to Mes_3Ga, the solid-state structure of mesitylgallium dichloride, $MesGaCl_2$, reveals a one-dimensional polymer.**[14]**

3 STERICALLY DEMANDING ORGANOGALLIUM COMPOUNDS

3.1 Syntheses

Considerable activity in the synthesis of sterically demanding organogallium compounds has taken place in the past decade. In particular, there has been significant activity concerning sterically demanding *m*-terphenyl ligands. The synthesis of such organogallium compounds has predominantly been accomplished *via* the lithium reagent route. In particular, the lithium reagent method is often preferred to the Grignard reagent route by workers as it frequently provides uncomplicated reaction products. For example, the Grignard reagent method often yields ionic salts accompanied by $[Mg(Et_2O)_x]^+$ cations. Nonetheless, both Grignard reagents and lithium reagents have greatly contributed to the synthesis of sterically demanding organogallium compounds.

3.1.1 Grignard Reagents and Lithium Reagents

It is interesting that, arguably, the ligand most similar to mesityl, pentamethylphenyl, has only recently been utilized in organogallium chemistry. The synthesis of tris(pentamethylphenyl)gallium, $(C_6Me_5)_3Ga$, is cleanly achieved by reaction of the pentamethylphenylmagnesium bromide Grignard reagent with $GaCl_3$ in diethyl ether (equation 5).**[15]** Tris(pentamethylphenyl)gallium was isolated as colorless, needle crystals in modest yield.

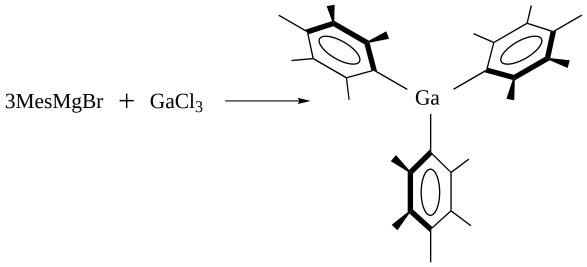

(5)

A particularly intriguing aryllithium reagent is the bis(etherate) of 2,6-diphenylphenyllithium, $(2,6\text{-}Ph_2C_6H_3)Li(Et_2O)_2$. This reagent, readily prepared by reaction of (2,6-diphenyl)-1-iodobenzene with *n*-butyllithium, is isolated as a white crystalline solid (equation 6).**[16]**

$$(2,6\text{-}Ph_2C_6H_3)I + n\text{-}BuLi \xrightarrow[Et_2O]{} (2,6\text{-}Ph_2C_6H_3)Li(Et_2O)_2 \quad (6)$$

The solid-state structure of $(2,6\text{-}Ph_2C_6H_3)Li(Et_2O)_2$ reveals the lithium atom in a trigonal planar environment with the Li–C bond (2.106(9) Å) being complemented by two Li–O interactions (1.943(5) Å). Reaction of $(2,6\text{-}Ph_2C_6H_3)Li$ with GaI_3 gives the neutral trigonal planar complex bis(2,6-diphenylphenyl)gallium iodide, $(2,6\text{-}Ph_2C_6H_3)_2GaI$ (equation 7).**[16]**

$$2(2,6\text{-}Ph_2C_6H_3)Li(Et_2O)_2 + GaI_3 \longrightarrow (2,6\text{-}Ph_2C_6H_3)_2GaI \quad (7)$$

It is noteworthy that when gallium(III) chloride, $GaCl_3$, instead of GaI_3, is allowed to react with $(2,6\text{-}Ph_2C_6H_3)Li(Et_2O)_2$, the ionic complex $[Li(Et_2O)_2][(2,6\text{-}Ph_2C_6H_3)GaCl_3]$ is obtained (instead of the neutral chloride analog of $(2,6\text{-}Ph_2C_6H_3)_2GaI$).**[16]** Indeed, the analogous ionic compound, $[Li(Et_2O)_2][(1,3,5\text{-}Ph_3C_6H_3)GaCl_3]$, is also isolated from reaction of the related lithium aryl 1,3,5-triphenylphenyllithium, $(1,3,5\text{-}Ph_3C_6H_2)Li$, with $GaCl_3$.**[16]** Thus, it appears that the propensity to obtain the neutral trigonal planar diarylgallium halide is enhanced when iodide is used instead of chloride.

Arguably, the most prominent aryllithium reagent in organogallium chemistry of the past decade is 2,6-dimesitylphenyllithium, (2,6-$Mes_2C_6H_3$)Li. The previous statement is justifiable owing to the significant organogallium compounds prepared using this sterically demanding *m*-terphenyl ligand. This reagent is conveniently prepared in a straightforward fashion from reaction of 2,6-dimesityl-1-iodobenzene**[17]** with *n*-butyllithium.**[18]** Reaction of 2,6-dimesitylphenyllithium with gallium chloride readily affords bis(2,6-dimesitylphenyl)gallium chloride, (2,6-$Mes_2C_6H_3)_2$GaCl, (equation 8) in high yield.**[19]**

$$2(2,6\text{-}Mes_2C_6H_3)Li + GaCl_3 \longrightarrow (2,6\text{-}Mes_2C_6H_3)_2GaCl \qquad (8)$$

This compound was noteworthy for two reasons: (1) The isolation of (2,6-$Mes_2C_6H_3)_2$GaCl demonstrated that it was possible to affix two of these large *m*-terphenyl ligands about a gallium center; and (2) The T-shaped coordination geometry about the gallium center in (2,6-$Mes_2C_6H_3)_2$GaCl was the first reported for a gallium center. Notably, both the corresponding bis(2,6-dimesitylphenyl)gallium bromide, (2,6-$Mes_2C_6H_3)_2$GaBr, and the dimeric (2,6-dimesitylphenyl)gallium dichloride complex, [(2,6-$MesC_6H_3)GaCl_2]_2$, have also been prepared and their solid-state structures determined.**[20]**

A variation on this method produces perhaps the most sterically protected gallium center reported in dimesityl-(2,6-dimesitylphenyl)gallium, $(Mes)_2$(2,6-$Mes_2C_6H_3$) Ga.**[20]** This compound was prepared by reaction of (2,6-$Mes_2C_6H_3$)Li with $GaCl_3$ followed by the in situ reaction with mesityllithium.

3.2 Structural Characterization

The structural characterization of sterically demanding organogallium compounds is arguably the most significant development in this area of the past decade. The fact that gallium atoms have been observed in a variety of coordination environments over the past decade underscores the fact that the organometallic chemistry of gallium is as varied as it is exciting.

It is perhaps expected that the pentamethylphenyl ligand has received considerably less attention than the closely related mesityl ligand. Indeed, the addition of two additional methyl groups in the two meta positions of a mesityl moiety would hardly be expected to result in any significant structural changes. The facts, however, bespeak as to why experiments are necessary. The coordination of the gallium center in $(C_6Me_5)_3$Ga is almost idealized trigonal planar with a C–Ga–C bond angle of 120.1(2)°. The structure of $(C_6Me_5)_3$Ga (Figure 3) is most easily compared to that of Mes_3Ga. Both $(C_6Me_5)_3$Ga and Mes_3Ga approximate D_3 symmetry. It is surprising that the mean Ga–C bond distance of 1.981 Å in $(C_6Me_5)_3$Ga is considerably longer than the reported values for either Ph_3Ga (1.957 Å) or Mes_3Ga (1.968 Å). The mesityl rings of Mes_3Ga reside in a propeller arrangement at angles of 55.9°. However, the angles of the (C_6Me_5)-rings in $(C_6Me_5)_3$Ga are 67.3°, 62.3°, and 60.9°. Contributing factors to this may be a weak aromatic–aromatic interaction, at a distance of 4.1 Å, between parallel rings of two molecules in the unit cell.

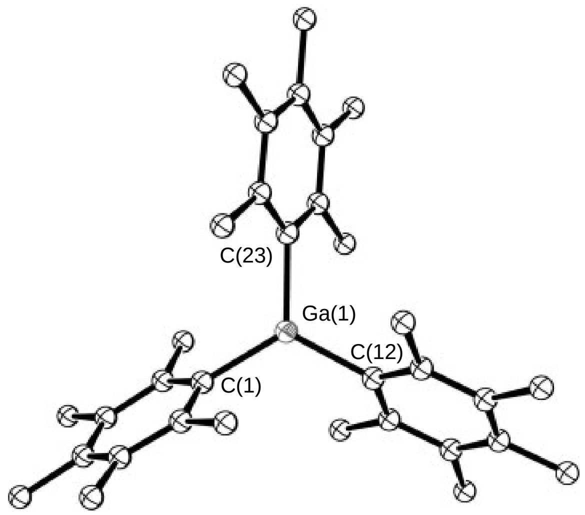

Figure 3 Solid-state structure of $(C_6Me_5)_3$Ga

The solid-state structure of bis(2,6-diphenylphenyl)gallium iodide, (2,6-$Ph_2C_6H_3)_2$GaI,**[16]** displays the gallium atom in a somewhat distorted trigonal planar environment (C–Ga–C: 134.3(3)°). The Ga–I bond distance of 2.550(1) Å is unremarkable (Figure 4).

Perhaps the most telling comparison of (2,6-$Ph_2C_6H_3$)- is with the closely related, but even more sterically demanding ligand system of 2,6-dimesitylphenyl, (2,6-$Mes_2C_6H_3$)-. The solid-state structures of both bis(2,6-dimesitylphenyl)gallium

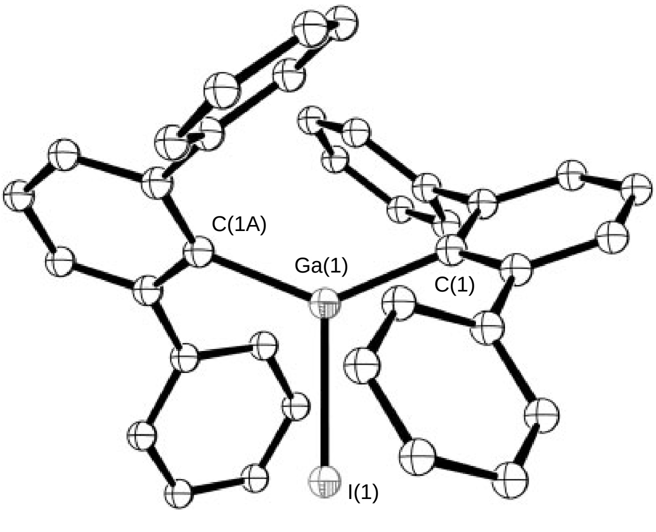

Figure 4 Solid-state structure of (2,6-$Ph_2C_6H_3)_2$GaI

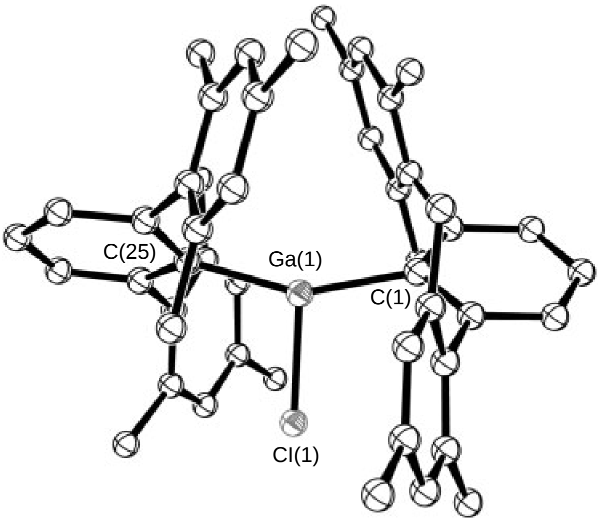

Figure 5 Solid-state structure of $(2,6\text{-}Mes_2C_6H_3)_2GaCl$

chloride, $(2,6\text{-}Mes_2C_6H_3)_2GaCl$ (Figure 5),[19] and bis(2,6-dimesitylphenyl)gallium bromide, $(2,6\text{-}Mes_2C_6H_3)_2GaBr$,[20] have been determined. They are isostructural. Although the Ga–X bond distances are rather long ($X = Cl$: 2.177(5) Å; $X = Br$: 2.3183(1) Å), the singular most striking feature of these compounds is the C–Ga–C bond angles of 153.5(5)°. The normal coordination for three-coordinate gallium is trigonal planar with bond angles about the metallic center approximating 120°. However, the C–Ga–C bond angles in these two compounds substantially exceed the 120° benchmark sufficiently to justify the T-shaped description. The T-shaped structure is almost exclusively reserved for interhalogen compounds such as ClF_3 and BrF_3 wherein the coordination is facilitated by the steric repulsion of the two lone pairs of electrons about the central halide ion. Thus, $(2,6\text{-}Mes_2C_6H_3)_2GaCl$ and $(2,6\text{-}Mes_2C_6H_3)_2GaBr$ are significant in that they represent rare examples of three-coordinate gallium atoms assuming the uncommon T-shaped coordination environment through sheer ligand steric repulsion (*without* the aid of lone pair–lone pair repulsion).

4 ORGANOMETALLIC COMPOUNDS CONTAINING GALLIUM–GALLIUM BONDS

The stabilization of the Ga–Ga bond is, arguably, the most important development of the past decade in the organometallic chemistry of gallium. Perhaps the most significant factor in the stabilization of these compounds is the utilization of sterically demanding ligands. Such ligands are necessary as they provide kinetic stabilization. It is anticipated that this field will only continue to grow as workers realize the variety of compounds that may be isolated.

4.1 Synthesis

4.1.1 Gallium Dimers and Tetrahedra

A notable difference between gallium and aluminum lies in the 2+ oxidation state: while aluminum(II) halides are not known, those of gallium are stable and well known. Indeed, the solid-state structures of bis-dioxane adducts of both gallium(II) chloride[21] and gallium(II) bromide[22] have been shown to reside about Ga–Ga bonds. Gallium(II) bromide was utilized with bis(trimethylsilyl)methyllithium in the preparation of the first organometallic compound unambiguously shown to possess a Ga–Ga bond: tetrakis[bis(trimethylsilyl)methyl]digallane, $[(Me_3Si)_2HC]_2Ga\text{–}Ga[(CH(SiMe_3)_2)]_2$ (equation 9).[23]

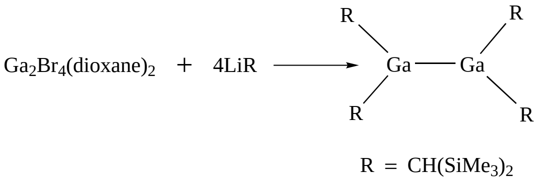

(9)

This novel compound was isolated as yellow crystals from pentane.

The first tetraaryldigallane, $[Pr_3C_6H_2]_2Ga\text{–}Ga[C_6H_2Pr_3]_2$, was prepared by reaction of $Ga_2Cl_4(dioxane)_2$ with the corresponding Grignard reagent.[24] Treatment of this digallane with an excess of lithium powder gave a dark solution. The addition of 12-crown-4 and workup produced a radical anion, $[Pr_3C_6H_2]_2Ga\text{–}Ga[C_6H_2Pr_3]_2{}^{\bullet -}$, that was held to possess a measure of multiple bond character in the Ga–Ga bond.

A particularly interesting synthesis concerns reaction of $Ga_2Br_4(dioxane)_2$ with ether-free $LiC(SiMe_3)_3$: this reaction gives the novel $[\{GaC(SiMe_3)_3\}_4]$ tetramer.[25] $[\{GaC(SiMe_3)_3\}_4]$, isolated as a dark red crystalline compound, is noteworthy as it represents the first example of gallium assuming the 1+ oxidation state in an organometallic compound. In addition, this remarkable compound demonstrated unusual thermal stability (only decomposing above 255 °C) and could be stored in air for months without decomposition.

Perhaps the organogallium compound most closely related to the tetrahedral metallic core of $[\{GaC(SiMe_3)_3\}_4]$ is $[\{(Me_3Si)_3C\}_6Ga]_8$.[26] The critical point in this synthesis is the utilization of gallium(I) bromide, GaBr. Reaction of trimethylsilyllithium (dissolved in toluene at −78 °C) with GaBr, after considerable workup, affords $[\{(Me_3Si)_3C\}_6Ga_8]$. This dark red/black crystalline compound contains a Ga_8 core: two Ga_4-tetrahedra linked by a single Ga–Ga bond.

4.1.2 Gallium Rings

Organometallic compounds containing gallium rings were first reported in 1995: sodium metal reduction of (2,6-$Mes_2C_6H_3$)$GaCl_2$[27] resulted in a deeply red colored solution from which a red (almost black) crystalline compound was isolated (equation 10). These crystals were determined to be $Na_2[(2,6\text{-}Mes_2C_6H_3)Ga]_3$.[28]

$$3(2,6\text{-}Mes_2C_6H_3)GaCl_2 + 8Na \xrightarrow[-6NaCl]{} Na_2[(2,6\text{-}Mes_2C_6H_3)_2Ga]_3 \tag{10}$$

Quite surprisingly, this compound was shown to contain an unprecedented gallium three-membered ring at its core. The potassium analog, $K_2[(2,6\text{-}Mes_2C_6H_3)Ga]_3$, was subsequently reported by the same laboratory.[29] Similar to the nomenclature used for organic ring compounds (i.e. cyclopropane), this class of organogallium compounds were referred to as *cyclogallanes*. Particularly significant, these compounds were shown to possess a new type of aromaticity – *metalloaromaticity*: traditional aromatic behavior derived from a metallic ring system (instead of carbon).[30–32] A noteworthy Ga_4-based cyclogallane, $K_2[(2,6\text{-}Mes_2C_6H_3)Ga]_4$,[33] and a ‘silagallane’,[34] an organometallic cluster with a III–IV skeleton of gallium and silicon atoms, have also been reported. In the silagallane, a trigonal arrangement of three gallium atoms is capped by two silicon atoms in the axial positions.

4.2 Structural Characterization

Certainly unambiguous single-crystal X-ray crystal structures are critical in this area of organogallium chemistry. The solid-state structure of tetrakis[bis(trimethylsilyl)methyl]digallane, $[(Me_3Si)_2HC]_2Ga{-}Ga[(CH(SiMe_3)_2)]_2$ (Figure 6),[23] with its Ga–Ga bond distance of 2.541(1) Å, remains a benchmark in organometallic chemistry. In addition, this gallane possesses a planar $C_2Ga{-}GaC_2$ core. Valence bond theory would hold that the gallium atoms are sp^2 hybridized with an empty p orbital orthogonal to the planar $C_2Ga{-}GaC_2$ core. It is also noteworthy that the planar $C_2Al{-}AlC_2$ core was reported for the corresponding $[(Me_3Si)_2HC]_2Al{-}Al[(CH(SiMe_3)_2)]_2$ alane.[35] This fact will become important as organometallic compounds containing multiple bond character in the Ga–Ga interaction are approached (vide infra). Perhaps expected, the Ga–Ga bond observed in $[(Me_3Si)_2HC]_2Ga{-}Ga[(CH(SiMe_3)_2)]_2$ (2.541(1) Å) was lengthened from that reported for the gallium(II) bromide bis(dioxane), $Br_2Ga{-}GaBr_2{\cdot}(dioxane)_2$, starting compound (2.395(6) Å).[22] Certainly, the important role of sterically demanding ligands and the manner in which they lend kinetic stabilization to such compounds was critically important in the development of the chemistry of the Ga–Ga bond.

Of all the polyhedra, the tetrahedra hold a unique place. The core of $[\{GaC(SiMe_3)_3\}_4]$[25] (Figure 7) bears a striking resemblance to that of white phosphorus, P_4: a nearly idealized tetrahedral core. The Ga–Ga bond distances in $[\{GaC(SiMe_3)_3\}_4]$, ranging from 2.678(4) to 2.702(4) Å, are slightly longer than those reported for the initial gallane of 2.541(1) Å.

The Ga_4 tetrahedral of $[\{GaC(SiMe_3)_3\}_4]$ readily compared with the striking double gallium tetrahedral, $[\{(Me_3Si)_3C\}_6Ga_8]$, reported by Schnöckel in 2001 (Figure 8).[26] The fact that two Ga_4 tetrahedra are connected by a single Ga–Ga bond is stunning and suggests that the Ga–Ga bond is sufficiently robust to possibly link larger polyhedra. All angles within the two tetrahedral approach 60°. The

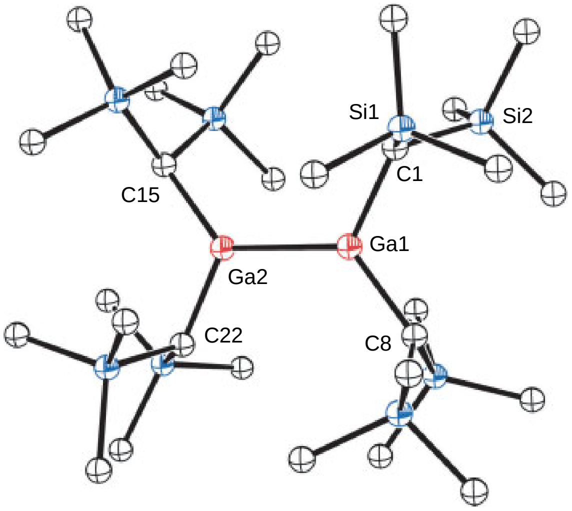

Figure 6 Solid-state structure of $[(Me_3Si)_2HC]_2Ga{-}Ga[(CH(SiMe_3)_2)]_2$

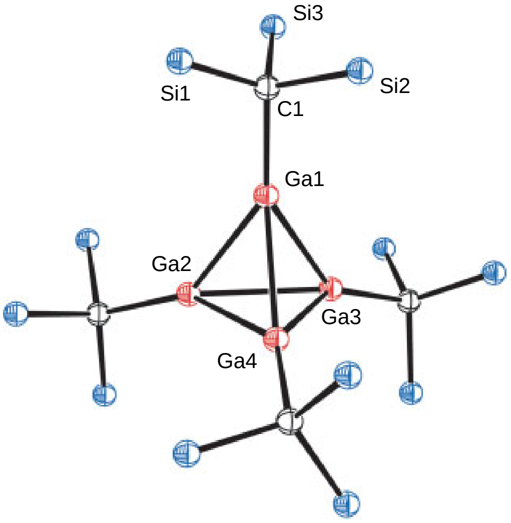

Figure 7 Solid-state structure of $[\{GaC(SiMe_3)_3\}_4]$

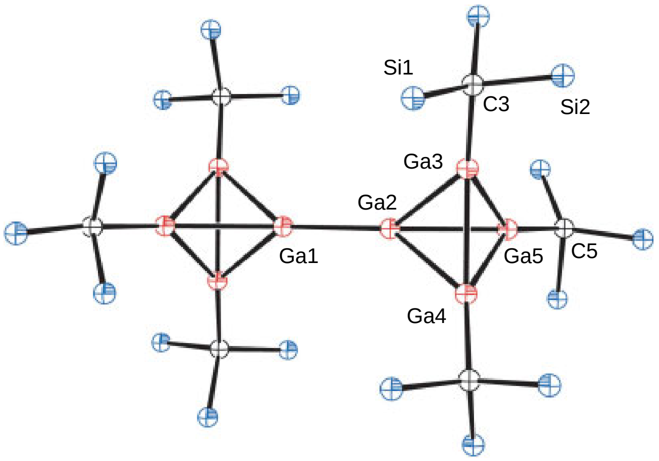

Figure 8 Solid-state structure of [$\{(Me_3Si)_3C\}_6Ga_8$]

Ga–Ga bond distances reside within the somewhat narrow range of 2.605 to 2.648 Å. As the authors stated, this was the first example of 'two tetrahedral R_3M units linked by a single metal–metal bond' in a homonuclear cluster.

The Ga–Ga bond distances in the first reported gallium ring system, $Na_2[(2,6\text{-}Mes_2C_6H_3)Ga]_3$ (Figure 9),**[28]** were determined to be 2.441(1) Å. The Ga–Ga–Ga bond angles within the metallic triangle were 60.01(1)°. While the sodium atoms do not appear to be engaged in any significant bonding interaction with the gallium atoms (Na···Ga approach: 3.1 Å), the sodium atoms appear to be assisted by subtle, yet significant, interactions with the π-electron cloud of the substituent rings of the m-terphenyl ligands.

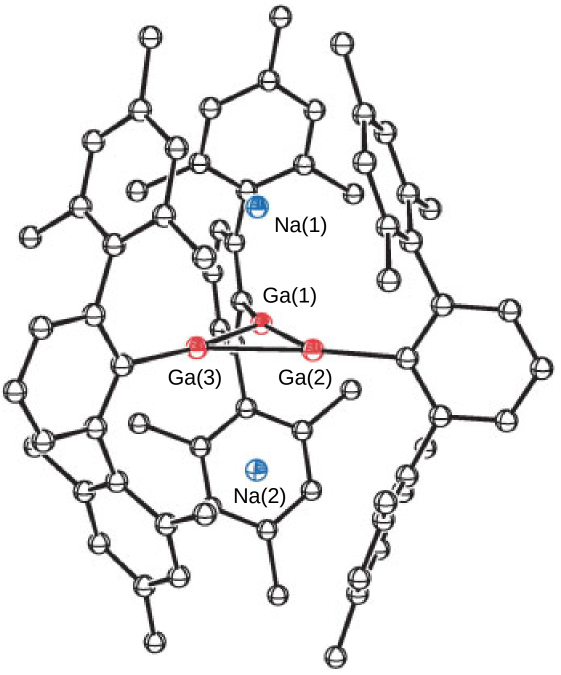

Figure 9 Solid-state structure of $Na_2[(2,6\text{-}Mes_2C_6H_3)Ga]_3$

The structural features of the potassium-based cyclogallane, $K_2[(2,6\text{-}Mes_2C_6H_3)Ga]_3$,**[29]** are very similar with Ga–Ga–Ga bond angles of 60.0° and Ga–Ga bond distances of 2.4260(5), 2.4317(5), and 2.4187(5) Å. These values are easily compared to $K_2[R_2Ga_4](R = 2,6\text{-}(2,4,6\text{-}i\text{-}Pr_3C_6H_2)_2C_6H_3)$,**[36]** which was described as having a 'planar, almost square Ga_4 core'. The Ga–Ga bond distances in this compound were shown to be slightly longer at 2.4624(4) and 2.4685(3) Å while the Ga–Ga–Ga bond angles were shown to be 87.222(11) and 92.778(11)°.

5 RELATED ARTICLES

Main Group: Multiple Bonding.

6 REFERENCES

1. A. C. Jones, *Chemtronics*, 1989, **4**, 15.
2. L. M. Dennis and W. Patnode, *J. Am. Chem. Soc.*, 1932, **54**, 182.
3. O. T. Beachley, M. R. Churchill, J. C. Pazik, and J. W. Ziller, *Organometallics*, 1986, **5**, 1814.
4. O. T. Beachley, M. R. Churchill, J. C. Pazik, and J. W. Ziller, *Organometallics*, 1987, **6**, 2088.
5. O. T. Beachley and J. C. Pazik, *Organometallics*, 1988, **7**, 1516.
6. O. T. Beachley, M. J. Noble, M. R. Churchill, J. C. Pazik, and J. W. Ziller, *Organometallics*, 1992, **11**, 1051.
7. J. K. Vohs, L. E. Downs, M. E. Barfield, K. Latibeaudiere, and G. H. Robinson, *J. Organomet. Chem.*, 2003, **666**, 7.
8. D. Neumann, W. Strauss, and W. Tyrra, *J. Organomet. Chem.*, 1991, **407**, 1.
9. M. A. Guerra, S. K. Mehrotra, D. W. Dyer, and R. J. Lagow, *J. Organomet. Chem.*, 1990, **390**, C37.
10. O. T. Beachley, T. L. Royster, and J. R. Arhar, *J. Organomet. Chem.*, 1992, **434**, 11.
11. B. Beagley, D. G. Schmidling, and I. A. Steer, *J. Mol. Struct.*, 1974, **21**, 437.
12. J. F. Malone and W. S. McDonald, *J. Chem. Soc. (A)*, 1970, 3362.
13. M. A. Petrie, M. M. Olmstead, and P. P. Power, *J. Am. Chem. Soc.*, 1991, **113**, 8704.
14. Z. Zhang, S. J. Rettig, and C. Orvig, *Inorg. Chem.*, 1991, **30**, 509.
15. J. K. Vohs, E. Downs, M. E. Barfield, S. D. Goodwin, and G. H. Robinson, *Polyhedron*, 2002, **21**, 531.

16. R. C. Crittendon, B. C. Beck, J. Su, X.-W. Li, and G. H. Robinson, *Organometallics*, 1999, **18**, 156.
17. C.-J. F. Du, H. Hart, and K.-K. Ng, *J. Org. Chem.*, 1986, **51**, 3162.
18. K. Ruhlandt-Senge, J. J. Ellison, R. J. Wehmschulte, F. Pauer, and P. P. Power, *J. Am. Chem. Soc.*, 1993, 11353.
19. X.-W. Li, W. T. Pennington, and G. H. Robinson, *Organometallics*, 1995, **14**, 2109.
20. R. C. Crittendon, X.-W. Li, J. Su, and G. H. Robinson, *Organometallics*, 1997, **16**, 2443.
21. J. C. Beamish, R. W. H. Small, and I. J. Worrall, *Inorg. Chem.*, 1979, **18**, 220.
22. R. W. H. Small and I. J. Worrall, *Acta Crystallogr., Sect. B*, 1982, **38**, 250.
23. W. Uhl, M. Layh, and T. Hildenbrand, *J. Organomet. Chem.*, 1989, **364**, 289.
24. X. He, R. A. Barlett, M. M. Olmstead, K. Ruhlandt-Senge, B. E. Sturgeon, and P. P. Power, *Angew. Chem., Int. Ed. Engl.*, 1993, **32**, 717.
25. W. Uhl, W. Hiller, M. Layh, and W. Schwarz, *Angew. Chem., Int. Ed. Engl.*, 1992, **31**, 1364.
26. A. Schnepf, R. Köppe, and H. Schnöckel, *Angew. Chem., Int. Ed. Engl.*, 2001, **40**, 1241.
27. J. Su, X.-W. Li, and G. H. Robinson, *Chem. Commun.*, 1998, 2015.
28. X.-W. Li, W. T. Pennington, and G. H. Robinson, *J. Am. Chem. Soc.*, 1995, **117**, 7578.
29. X.-W. Li, Y. Xie, P. R. Schreiner, K. D. Gripper, R. C. Crittendon, C. F. Campana, H. F. Schaefer, and G. H. Robinson, *Organometallics*, 1996, **15**, 3798.
30. Y. Xie, P. R. Schreiner, H. F. Schaefer, X.-W. Li, and G. H. Robinson, *J. Am. Chem. Soc.*, 1996, **118**, 10635.
31. Y. Xie, P. R. Schreiner, H. F. Schaefer, X.-W. Li, and G. H. Robinson, *Organometallics*, 1998, **17**, 114.
32. G. H. Robinson, *Acc. Chem. Res.*, 1999, **32**, 773.
33. B. Twamley and P. P. Power, *Angew. Chem., Int. Ed. Engl.*, 2000, **39**, 3500.
34. G. Linti, W. Köster, H. Piotrowski, and A. Rodig, *Angew. Chem., Int. Ed. Engl.*, 1998, **37**, 2209.
35. W. Uhl, *Z. Naturforsch.*, 1988, **43b**, 1113.
36. B. Twamley and P. P. Power, *Angew. Chem. Int. Ed. Engl.*, 2000, **39**, 3500.

Acknowledgment

The author wishes to thank a number of gifted coworkers and students for their contributions. In addition, gratitude is expressed to the National Science Foundation and to the Petroleum Research Fund, administered by the American Chemical Society, for financial support.

Germanium: Inorganic Chemistry

Chao Qin, Lei Gao & Enbo Wang
Northeast Normal University, Changchun, China

Based in part on the article Germanium: Inorganic Chemistry by Frank Glockling which appeared in the Encyclopedia of Inorganic Chemistry, First Edition.

1	Introduction	1
2	Analysis	1
3	The Element	1
4	Hydrides	3
5	Boron Derivatives	4
6	Nitrogen Compounds	4
7	Phosphorus and Arsenic Compounds	7
8	Oxygen-bonded Compounds	8
9	Sulfides, Selenides, and Tellurides	11
10	Halides	12
11	Metalloid and Metal-bonded Compounds	14
12	Polyoxometalates of Germanium	17
13	Related Articles	19
14	Further Reading	19
15	References	19

1 INTRODUCTION

Germanium (Ge), the 32nd element in the periodic table, lying between Si and Sn in group 14, was first predicted as the missing element of a triad between silicon and tin by J. A. R. Newlands in 1864. In 1871, D. I. Mendeleev specified the properties that ‘eka-silicon’ would have (eka = Sanskrit for ‘one’). By comparing Si and Sn, remarkably accurate predictions were made of the properties of a range of germanium compounds. When Winkler isolated the element from a new and rare mineral argyrodite, Ag_8GeS_6, in 1886,[1] the name ‘Germanium’, in honor of his homeland, Germany, came into use. Since then, Germanium has initiated special interest because of its intriguing inorganic and organic chemistry.

Germanium minerals are extremely rare but the element is widely distributed in trace amounts. Its abundance ratio is about 7×10^{-4}% and it is mainly associated with copper, zinc, lead, selenium, arsenic, silver, iron, and so on. There are twenty-one isotopes; ^{70}Ge, ^{72}Ge, ^{73}Ge, ^{74}Ge, ^{76}Ge are naturally occurring. Germanium is common in organisms, but it is not an indispensable trace element. In humans, it is nontoxic, but when it reaches 1000 ppm in animal’s food, the growth of animals will be inhibited and 50% of them will die. When drinking water contains 100 ppm GeO_2, a death rate of 50% will result in the fourth week. The hemolytic function of GeH_4 will detrimentally affect animals when its content exceeds 100 ppm.

Germanium’s general chemistry is closer to that of Si. It exhibits both +2 and +4 oxidation states when forming inorganic ionic and covalent compounds. It can form a wide range of binary compounds and eutectics with many metals and metalloid elements.[2] Its +2 oxidation state is like that of a singlet-state carbene, in which Ge is sp^2 hybridized with a lone pair of electrons and an empty p orbital. This electronic configuration results in a wide variety of structural types, determined largely by steric factors, and ranges from V-shaped monomeric molecules to polymers. The stability of the +2 state is greater than Si and less than Sn. In its +4 oxidation state, Ge compounds are four-, five-, or six-coordinate.

Structural differences resulting from the larger size of Ge relative to Si seem most apparent in some of the anionic oxides, where both tetrahedrally and octahedrally coordinated Ge atoms occur, as in the ion $[Ge_9O_{20}]^{4-}$.

Mainly used as semiconductor material, germanium also finds its extensive applications relating to optical devices and based on its infrared transmission properties (1 cm of Ge will transmit 25–46% of radiation in the 5000–600 cm^{-1} region).[3] Furthermore, germanium is also used in resistance thermometers and glass semiconductors ($Te_{21}Ge_{15}As_6$, $Te_{50}Ge_{20}As_{30}$). Current uses of germanium have been largely directed to its combination with other metals and metalloids. Table 1 lists selected properties of germanium. Table 2 gives typical bond lengths of germanium compounds. Standard enthalpies of the formation of selected germanium compounds are listed in Table 3.

2 ANALYSIS

Samples can be decomposed with sulfuric acid (sometimes nitric acid is added as an oxidant). When it is high in SiO_2, HF is then needed. Samples with chloride should be melted with alkali to avoid the volatility of $GeCl_4$. After decomposition, common ways such as extraction and distillation based on the volatility of $GeCl_4$ are then applied to separate the noise element. Ion exchange and coprecipitation processes are also used for the extraction of germanium. Classical methods of quantitative analysis involve precipitation of GeS_2 from acid solution, followed by ignition to GeO_2 and photometric measurements based on complexation with phenylfluorone.[3]

3 THE ELEMENT

Few minerals contain significant amounts of Ge, though it is widely distributed in the earth’s crust. The first process to

Table 1 Properties of germanium

Atomic number	32
Electronic structure	$[Ar]3d^{10}4s^24p^2$
Mean atomic weight	72.59
Terrestrial abundance	1.5 ppm
Stable isotopes	70 (20.5%), 72 (27.4%), 73 (7.8%), 74 (36.5%), 76 (7.7%)
Nuclear properties	^{73}Ge spin 9/2 Sensitivity rel to ^1H, 1.4×10^{-3} Receptivity 0.617
Radius	Nonbonded 158 pm Covalent Ge^{IV} 122.3 pm
Density at 25 °C	$5323\,kg\,m^{-3}$
Melting point	937.4 °C
Boiling point	2830 °C
Electronegativity (Pauling)/(Allred)	1.8/2.01
Enthalpy of fusion	$34.7\,kJ\,mol^{-1}$
Enthalpy of vaporization	$367.8\,kJ\,mol^{-1}$
Specific heat at 200 K	$22\,kJ\,mol^{-1}$
Hardness (Moh's scale)	6.0
Ips 1st, 2nd, 3rd, 4th	7.89, 15.86, 34.07, 45.5 eV
Electrical resistivity	$47\,\Omega\,cm^{-1}$ at 20 °C
Band gap	$64.2\,kJ\,mol^{-1}$
E° in volts[4]	
$H_2GeO_3 + 4H^+ + 4e^- \longrightarrow Ge + 3H_2O$	0.012
$HGeO_3{}^- + 5H^+ + 4e^- \longrightarrow Ge + 3H_2O$	0.141
$GeO_3{}^{2-} + 6H^+ + 4e^- \longrightarrow Ge + 3H_2O$	0.328
GeO_2 hexagonal $+ 4H^+ + 4e^- \longrightarrow Ge + 2H_2O$	−0.019
GeO_2 tetragonal $+ 4H^+ + 4e^- \longrightarrow Ge + 2H_2O$	−0.058

Table 2 Typical bond lengths of Ge compounds

Bond	Length (pm)
Ge–H ($GeHCl_3$)	152.9
Ge–F (GeH_3F)	170
Ge–Cl ($GeHCl_3$)	210
Ge–Br ($GeBr_4$)	230
Ge–I (GeH_3I)	255
Ge–N ($Ge(NSiMe_3)_2$)	189
Ge–O ($(H_3Ge)_2O$)	176.6
Ge–S ($(H_3Ge)_2S$)	220.9
Ge–C ($GePh_4$)	195.7
Ge–Ge (Ge_2H_6)	241
Ge–Ge (elemental)	245
Ge–Si (H_3GeSiH_3)	236
Ge–Mn ($H_3GeMn(CO)_5$)	248.7

Table 3 Standard enthalpies of formation

Compound	Enthalpy of formation ($kJ\,mol^{-1}$)
GeH_4 (g)	90.8
Ge_2H_6 (g)	162.3
Ge_3N_4 (s)	−61.9
GeO (g)	−37.7
GeO_2 (hexagonal)	−554.7
GeO_2 (tetragonal)	−580.2
GeO_2 (vitreous)	−539.0
GeS (s)	−75.3
GeS_2 (s)	−121.5
GeSe (s)	−92.0
GeF_2 (g)	−574.0
GeF_4 (g)	−1190.1
$GeCl_2$ (g)	−171.0
$GeCl_4$ (g)	−500.0
$GeBr_2$ (g)	−61.0
$GeBr_4$ (g)	−291.0
GeI_2 (g)	50.3
GeI_4 (g)	−64.0

obtain Ge is its enrichment from the ores. Recovery has been achieved from coal ash, but it is now normally recovered from the flue dusts of smelters processing Zn ores. Common ways to fabricate metal Ge from the enriched ores involve three processes: (1) preparation of $GeCl_4$, (2) hydrolysis of $GeCl_4$ into GeO_2, and (3) reduction of GeO_2 into Ge with H_2. For optical or semiconductor use, further purification is achieved by zone refining. Detailed means to obtain Ge can be found elsewhere.[5]

The element crystallizes in a diamond cubic lattice. It is brittle, and has a bright metallic luster. Ge can absorb H_2, O_2, CO_2, H_2O, alcohol, and other common substances containing hydrogen or oxygen.

Germanium is more reactive and electropositive than Si. It is stable in air and water. It dissolves slowly in hot concentrated H_2SO_4 and HNO_3, but does not react with dilute acids or alkalis unless an oxidizing agent such as H_2O_2 or NaOCl is present.

Fused alkalis react with incandescence to give germanates. When heating, it can be eroded by dry HCl. H_2O_2 in 3wt % can slowly dissolve Ge, and when the temperature is raised to 90–100 °C, the dissolution is accelerated. It also can be eroded by many gaseous alkyl- and vinyl-chlorides, and finally yields organic germanium chloride. Powdery Ge can conflagrate in Cl_2 and Br_2.

Germanium nanocrystals embedded in a silicon-oxide matrix display blue luminescence, a desirable property for the development of optoelectronic devices. This has made Ge an interesting subject in recent nano-material study.

In the following sections, the chemistry of neutral, anionic, and cationic germanium compounds are described for both oxidation states.

3.1 Anionic Germanium Clusters

Like Sn and Pb, anionic Germanium clusters are formed from the reaction of germanium and alkali metals.**[6]** The common way is to dissolve a binary compound of germanium and alkali metal in ethylenediamine or liquid ammonia, and, if the cation (Na^+, K^+) is suitably coordinated, a product containing the cluster can be crystallized by addition of cation-sequestering agents.**[7]** The anionic ${Ge_4}^{2-}$, ${Ge_9}^{2-}$, and ${Ge_9}^{4-}$ clusters have so far been characterized (equations 1 and 2 show the related reactions).**[8,9]** The tetranuclear ${Ge_4}^{2-}$ ion is diamagnetic and a crystal-structure determination on a disordered crystal reveals a disordered crystal slightly elongated to C_{3v} symmetry with Ge–Ge distances of 277 and 279 pm. In both the ${Ge_9}^{2-}$ and ${Ge_9}^{4-}$ anions, the shortest Ge–Ge distance is about 255 pm, considerably shorter than that in $[Ge_4]^{2-}$. The ${Ge_9}^{4-}$ ion, like $[Sn_9]^{4-}$, has a monocapped square antiprism (C_{4v}) geometry, whereas $[Ge_9]^{2-}$, with two less electrons, forms a distorted tricapped trigonal prismatic (D_{2h}) structure.

$$\text{NaGe} + \text{2,2,2-crypt in liq. NH}_3 \longrightarrow 2[\text{Na(crypt)}]^+[\text{Ge}_4]^{2-} \quad (1)$$

$$\text{KGe} + \text{2,2,2-crypt} + \text{en} \longrightarrow 6[\text{K(crypt)}]^+[\text{Ge}_9]^{2-}[\text{Ge}_9]^{4-}[\text{2.5en}] \quad (2)$$

The tight-binding (TB) approach to total-energy calculation is one of the simplest methods that explicitly treats the quantum-mechanical nature of electrons that form interatomic bonds. Some theoretical studies have given the TB models for germanium,**[10]** and the lowest energy geometries of small Ge_n ($n = 2-7$) clusters are summarized in Table 4.

Table 4 The lowest energy geometries of small Ge_n ($n = 2-7$) clusters

Ge_n	Sym.	Ge_n	Sym.
Ge_3	C_{2v}	Ge_4	D_{2h}
Ge_5	D_{3h}	Ge_6	O_h
Ge_7	D_{5h}		

Anion photoelectron spectra of small germanium clusters ($n = 2-15$) have been used to determine electronic properties and the most stable geometric configuration for Ge_n anions.**[11]**

4 HYDRIDES

Varieties of polymeric hydrides (GeH, GeH_2, and nonstoichiometric materials, $GeH_{0.9}$ to $GeH_{1.2}$) have been obtained by reactions such as the hydrolysis of Na_2Ge or CaGe. Monomeric Ge dihydride has not been described so far, even as a matrix isolated species. $(GeH_2)_n$ (equation 3) is a white solid, insoluble in liquid NH_3. It decomposes above – 33 °C to GeH_4 and a yellow polymer $(GeH)_n$. Although there is no structural information on these hydrides, it seems likely that they involve Ge–Ge as well as bridging and terminal Ge–H bonding.

$$\text{GeH}_3\text{Na} + \text{PhBr} \xrightarrow{\text{NH}_3} \text{GeH}_2 + \text{NaBr} + \text{C}_6\text{H}_6 \quad (3)$$

Ge^{IV} binary hydrides, with the general formula Ge_nH_{2n+2} (see Table 5), are colorless gases or volatile liquids for $n = 1-5$, and their preparation, physical properties, and chemical reactions are very similar to those of silanes. They were first obtained by the acid hydrolysis of Mg_2Ge, which yielded mono- to pentagermanes, including isomers of Ge_4H_{10} and Ge_5H_{12}.

Monogermane together with Ge_2H_6 and Ge_3H_8 can be made by heating GeO_2 and $LiAlH_4$, or by addition of $NaBH_4$ to GeO_2 in acid solution. Higher germanes are prepared by the action of a silent electric discharge on GeH_4. No cyclic or unsaturated hydrides have yet been prepared.

GeH_4 is a colorless gas, and it does not ignite in contact with air and is unaffected by aqueous acid or 30% aqueous NaOH. It acts as an acid in liquid NH_3 forming ${NH_4}^+$ and ${GeH_3}^-$ ions, and reacts with alkali metals in this solvent

Table 5 Selected properties of Ge_nH_{2n+2} ($n = 1-5$)

Property Ge_nH_{2n+2}	GeH_4	Ge_2H_6	Ge_3H_8	Ge_4H_{10}	Ge_5H_{12}
MP/ °C	−164.8	−109	−105.6	–	–
BP/ °C	−88.1	29	110.5	176.9	234
Density (T°C)/g cm^{-3}	1.52(−142 °C)	1.98(−199 °C)	2.20(−105 °C)	–	–

to give $MGeH_3$, which are white, crystalline compounds of considerable synthetic utility.

The higher hydrides become increasingly more reactive toward air or water, though less than Si analogs; even Ge_3H_8 is only slowly oxidized in air and is thermally stable to 190 °C. The higher germanes decompose thermally to H_2, GeH_4, and polymeric hydrides.

The reaction of GeH_4 with Na or K in liquid ammonia has been interpreted in terms of rapid formation of the solvated $[GeH_2]^{2-}$ ion, which is subsequently converted into $[GeH_3]^-$ (equations 4–6). The $[GeH_3]^-$ ion, extensively used in the synthesis of derivatives, may also be prepared in hexamethylphosphoric triamine (HMPT) solution or from GeH_4 and NaOH in monoglyme. Some structural information is available on these alkali metal derivatives: X-ray diffraction analysis shows that $KGeH_3$ and $RbGeH_3$ have the NaCl-type structure, implying free rotation of $GeH_3{}^-$. $CsGeH_3$ has the rare T1I structure. Similar reactions using Ge_2H_6 provide evidence for $[Ge_2H_4]^{2-}$.

$$GeH_4 + 2Na \longrightarrow Na_2GeH_2 + H_2 \qquad (4)$$

$$Na_2GeH_2 + GeH_4 \longrightarrow 2NaGeH_3 \qquad (5)$$

$$Na_2GeH_2 + NH_3 \longrightarrow NaGeH_3 + NaNH_2 \qquad (6)$$

4.1 Hydrido Halides

The germanium hydrohalides GeH_xX_{4-x} ($X = Cl, Br, I$; $x = 1, 2, 3$) are colorless, volatile, reactive liquids. Preparative routes include reactions of Ge, GeX_2, or GeH_4 with HX (equations 7–11). The compounds are valuable synthetic intermediates; they readily undergo halide exchange and provide a convenient route to a range of pseudohalide derivatives (CN, CNO, SCN), for example, GeH_3Br with $Pb(OAc)_2$ and $Pb(NCS)_2$ gives $GeH_3(OAc)$ and $GeH_3(SCN)$ respectively.

Oxidation of GeS by HCl gives $GeHCl_3$, which can slowly decompose to $GeCl_4$, $GeCl_2$, and H_2 in alcohol, and can be oxidized into the white $GeOCl_2$ in the air. GeH_3Br and GeH_2Br_2 are most readily prepared from GeH_4 and Br_2, whereas the thermally unstable $GeHBr_3$, mp – 24 °C, has been obtained from Ge and HBr. $GeHI_3$, formed from GeI_2 and HI, evidently exists only in HI solution.

$$GeH_4 + SnCl_4 \longrightarrow GeH_3Cl \qquad (7)$$

$$GeH_4 + HCl/AlCl_3 \longrightarrow GeH_2Cl_2 \qquad (8)$$

$$GeH_4 + I_2 \longrightarrow GeH_3I + GeH_2I_2 \qquad (9)$$

$$Ge + HCl \xrightarrow[500\,^\circ C]{N_2} GeHCl_3 \qquad (10)$$

$$GeCl_2 + HCl \longrightarrow GeHCl_3 \qquad (11)$$

Digermane likewise may be halogenated to yield unstable H_3GeGeH_2X compounds, and even Ge_3H_8 has been converted into an unstable monoiodide.

5 BORON DERIVATIVES

Germylpotassium and diborane form the Ge–B bonded anion $[H_3GeBH_3]K$. Several Ge^{II}–carborane complexes have been described for the +2 oxidation state of Ge (equations 12 and 13). In this compound (equation 12), Ge^{II} occupies a vertex of the icosahedron, being bonded to three B and two C atoms. It is a stable, colorless sublimable solid that reacts with MeOH to give the $[B_9C_2H_{12}]^-$ ion.**[12]**

$$[1,2\text{-}B_9C_2H_{11}]^{2-} + GeCl_2 \longrightarrow closo\text{-}Ge(BH)_9(CH)_2 \qquad (12)$$

Using a Me_3Si-substituted carborane anion with Ge^{II} (equation 13) or Ge^{IV} chlorides gives germacarboranes. In the Ge^{IV} derivative *closo*-$[(Me_3SiC)_2(BH)_4]_2Ge$, germanium is 10-coordinate.

$$Li[(Me_3SiC)_2B_4H_5] + GeCl_2 \longrightarrow closo\text{-}[(Me_3SiC)_2(BH)_4Ge] \qquad (13)$$

Anhydrous $GeCl_4$ reacting with the *closo*-stannacarboranes 1-Sn-2-($SiMe_3$)-3-(R)-2,3-$C_2B_4H_4$ (R = $SiMe_3$, Me, and H) in the absence of solvents gives the corresponding germacarboranes 1-Ge-2-($SiMe_3$)-3-(R)-5-($GeCl_3$)-2,3-$C_2B_4H_4$ (R = $SiMe_3$, Me, and H) respectively.**[13]**

6 NITROGEN COMPOUNDS

6.1 Nitrides

Ge_3N_2 is a brown/black solid, bp 650 °C; it decomposes to Ge and N_2 at 850 °C. Ge_3N_2 is prepared by heating the yellow imide $[GeNH]_n$ to 300 °C, which is formed from dissolving GeI_2 in liquid NH_3 (equation 14).

$$GeI_2 + \text{liq. } NH_3 \longrightarrow [GeNH]_n \longrightarrow Ge_3N_2 \qquad (14)$$

Ge^{IV} nitride, Ge_3N_4, is formed as a black solid from Ge and ammonia at 650 °C, or by heating the imide $[Ge(NH)_2]_n$ at 400 °C. It exists in two forms, both of which have a phenacite-type structure. It decomposes to the elements at 900 °C. Ge_3N_4 is stable to air and insoluble in HCl, HNO_3, H_2SO_4, and NaOH aqueous. At 700 °C, reaction of Ge_3N_4 with H_2 results in Ge and NH_3.

6.2 Amides and Azide of Ge^{II}

6.2.1 *Two-coordinate Compounds*

Two-coordinate Ge^{II} amides, $Ge(NR_2)_2$, have been obtained in cases where the ligand is very bulky. Many have sharp melting points and can be distilled or sublimed in vacuum; they remain monomeric both in solution and in the solid state. Typically, the N–Ge–N angle is 111° in the solid state and 101° as a gas. Examples include $Ge[(N(t\text{-}Bu)_2)]_2$, $Ge[N(SiMe_3)_2]_2$, $Ge[N(C_6H_2Me_3\text{-}2,4,6)_2]_2$, and $\overline{GeNC(Me)_2(CH_2)_3C(Me)_2N}$, formed from $GeCl_2$·dioxane and the lithio derivative of the amine.[14] More complex examples, also with two-coordinate Ge, are illustrated in structures (**1**) and (**2**).[16]

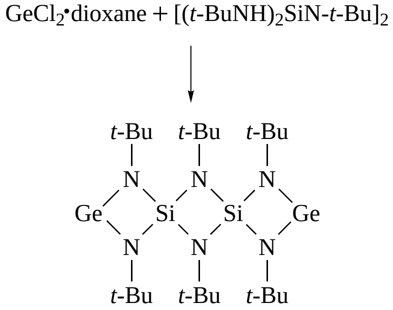

(**1**)

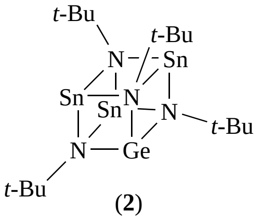

(**2**)

Reaction of $Ge[N(SiMe_3)_2]_2$ with bulky primary amines RNH_2 ($R = C_6H_3\text{-}i\text{-}Pr_2\text{-}2,6$) results in the formation of a cyclic trimer $[GeNR]_3$ with a planar Ge_3N_3 ring and a stereochemically active lone pair on each Ge. The Ge–N bond length of 186 pm is close to the value (189 pm) for $Ge[N(SiMe_3)_2]_2$. Using $GeCl_2$(dioxane) and RNH_2 ($R = C_6H_2\text{-}t\text{-}Bu_3\text{-}2,4,6$) has yielded $Ge(NHR)_2$, RNHGeN(R)GeNHR, and $(GeNR)_2$.[17]

Monomeric mixed O- and N-bonded Ge^{II} compounds with sterically hindered ligands have been obtained, for example, $t\text{-}BuOGeNR_2$ (R = 2,2,6,6-tetramethylpiperidino). Other types of Ge^{II}–N compounds include $Ge(NCO)_2$ and $Ge(NCS)_2$, readily formed from $GeCl_2$·dioxane and the cyanate or thiocyanate anions.

6.2.2 *Three-coordinate Compounds*

Ge^{II} amides containing Ge bonded to three nitrogen donors, such as $[CyNC(Me)NCy]_2Ge$,[18] $[CyNC(^tBu)NCy]_2Ge$, $[CyNC(Me)NCy]Ge[N(SiMe_3)_2]$,[18] $[CyNC(^tBu)NCy]_2Ge[N(SiMe_3)_2]$ (Cy = cyclohexyl),[18] $[Me_3SiNC(^tBu)NSiMe_3]Ge$ $[N(SiMe_3)_2]$,[19] and $[MeSi(N^tBu)_3]Ge_2[N(SiMe_3)_2]$[20] have been prepared by the reaction of $GeCl_2$·dioxane with the lithio derivative of the amine. These compounds possess similar geometries based on distorted tetrahedra in which one of the vertices is occupied by a stereochemically active lone pair of electrons. Ge^{II} azides, $(NRN)GeN_3$, have been isolated from (NRN)GeCl treated with NaN_3.[21,22] Monomeric mixed C- and N-bonded Ge^{II} compounds have been obtained, for example, $[Ge(2\text{-}\{(Me_3Si)_2C\}\text{-}C_5H_4N)\{CH(PPh_2)_2\}]$,[23] $[Ge(2\text{-}\{(Me_3Si)_2C\}\text{-}C_5H_4N)Cl]$,[23] and $py\cdot Ge(Cl)C_6H_3\text{-}2,6\text{-}Trip_2$ (py = pyridine, Trip = $C_6H_2\text{-}2,4,6\text{-}i\text{-}Pr_3$).[24]

The cubane-like Ge^{II} compound $[GeN\text{-}t\text{-}Bu]_4$ (**3**) has been obtained as a crystalline sublimable solid by the reaction shown in Scheme 1.[15,16,25] The related cage structure of $Ge_3(N\text{-}t\text{-}Bu)_2(HN\text{-}t\text{-}Bu)_2$ consists of a Ge–N cube with one corner vacant; this 'open' polycycle can be protonated by HCl to form $[Ge_3(N\text{-}t\text{-}Bu)(HN\text{-}t\text{-}Bu)_3]Cl$, in which Cl effectively occupies the vacant corner, interacting with the protons on three N atoms of the cube.

6.2.3 *Four-coordinate Compounds*

Ge^{II} compounds containing Ge in four coordination, such as $(CyNC(R)NCy)_2GeCh$ (R = Me, ^tBu; Ch = S, Se; Cy = cyclohexyl)[18] have been prepared by the reaction of $(CyNC(R)NCy)_2Ge$ with Se or styrene sulfide. Ge^{II} azide, $TpAGeN_3$ [TpA=hydrotris(3,5-dimethylpyrazol-1-yl)borato] (**4**),[26] synthesized from TpAGeCl and NaN_3, is a white, slightly air-sensitive solid, which is soluble in CH_2Cl_2, moderately soluble in THF, and insoluble in pentane. The mixed C- and N-bonded Ge^{II} compound, GeR_2 [$R = CPh(SiMe_3)(C_5H_4N\text{-}2)$],[27] has been synthesized by the reaction of two equivalents of the appropriate

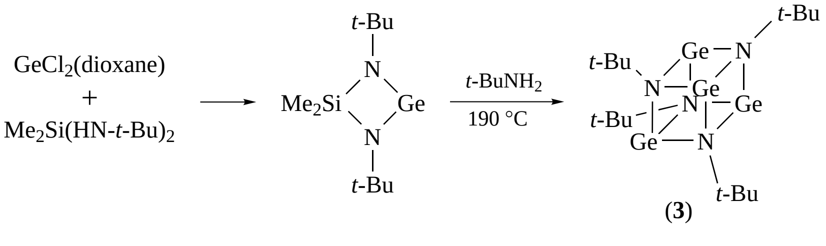

Scheme 1

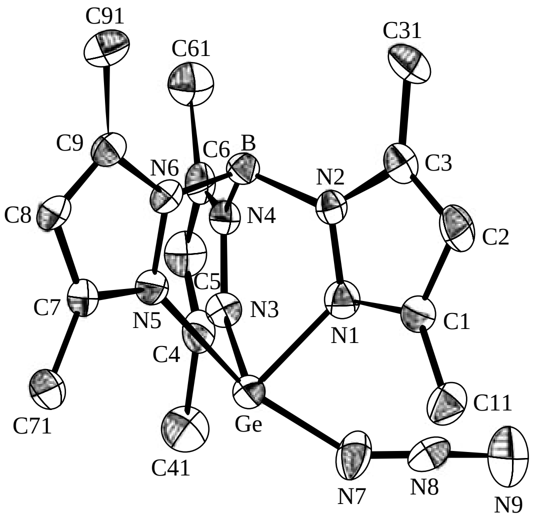

(**4**)

(Ref. 26. Reproduced by permission of The Royal Society of Chemistry)

lithium reagents LiR(tmen) (tmen = $Me_2NCH_2CH_2NMe_2$) with $GeCl_2$(dioxane) in diethyl ether solution. Crystal-structure analysis has shown that compound GeR_2 is monomeric with the N-functionalized alkyl ligands R bonded to the metal center in a C,N-chelate fashion, and the geometry around Ge is pyramidal, consistent with a stereoactive lone pair at the metal.

The reaction of two equivalents of [MeC(N*i*Pr)$_2$]Li·THF with $GeCl_2$·dioxane affords [MeC(N*i*Pr)$_2$]$_2$Ge.**[28]** In the monomeric molecule, the germanium atom is surrounded by four nitrogen atoms originating from two amidinate ligands, each spanning an axial and an equatorial site of a heavily distorted ψ-trigonal bipyramid, with the ‘lone pair’ of germanium(II) occupying the third equatorial position.

6.3 Amides and Imines of Ge^{IV}

Trigermylamine, $(H_3Ge)_3N$, prepared from H_3GeCl and NH_3, is extremely unstable. It has a planar (D_{3h}) structure in the vapor phase like the Si analog. The lowest IP in its photoelectron spectrum is due to the lone pair electrons of nitrogen, and the order of IPs in the series Me_3N, $(H_3Si)_3N$, $(H_3Ge)_3N$ is consistent with the idea that the lone pair electrons interact with empty d orbitals of Si or Ge.

Ge^{IV} amides, $Ge(NR_2)_4$, are obtained by standard procedures (equation 15); they are thermally stable and readily hydrolyzed. $GeCl_4$ and primary amines or ammonia yield white, involatile polymeric products. A polymeric imide, $Ge(NH)_2(NH_3)_n$, appears to be the final product of the reaction between $NaGeH_3$ and liquid ammonia.

$$\mathrm{GeCl_4 + R_2NH \longrightarrow Ge(NR_2)_4} \qquad (15)$$

The monomeric mixed O- and N-bonded Ge^{IV} compound, [GeCl(bipy)(Hcit)] (bipy = 2,2′-bipyridine, H_4cit = citric acid),**[29]** has been prepared by the reaction of [$GeCl_4$(bipy)] with H_4cit in acetonitrile solution. In this compound, the Ge center possesses an octahedral geometry coordinated with two nitrogen donors of a bipy group, three oxygen atoms of Hcit group, and one chlorine atom.

The dimeric mixed O- and N-bonded Ge^{IV} compound, 1,1′-oxybis(1-germa-5-aza- 2,8,9-trioxatribenzobicyclo[3.3.3]undeca-3,6,10-triene) (**5**)**[30]** has been synthesized by the reaction of tris(2-hydroxyphenyl)amine with $Ge(OEt)_4$. This reaction proceeds via 1-ethoxy-1-germa-5-aza-2,8,9-trioxatribenzobicyclo[3.3.3]undeca-3,6,10-triene (Scheme 2). In the oxo-bridged germatrane dimer, the Ge–O–Ge moiety is bent at an angle of 131.2(4)°, and Ge–O bridge distances are 175.0(7) and 174.3(6) pm. The other Ge–O distances, by comparison, average 178.5(7) pm. The germanium centers in the germatrane dimer are nearly trigonal bipyramidal by virtue of significant interaction with transannular nitrogen. The Ge–N distances are 223.5(8) and 224.7(7) pm.

Reaction of [MeC(N*i*Pr)$_2$]Li·THF with $GeCl_4$ results in the formation of [MeC(N*i*Pr)$_2$]$_2$$GeCl_2$.**[28]** Four nitrogen atoms originating from two amidinate ligands, each spanning an axial and an equatorial site of a distorted octahedron, with two chlorine atoms occupying other equatorial positions, surround the germanium center in the compound.

Monomeric germaimines have recently been prepared (equation 16), in which R is a bulky substituent such as C_6H_3-i-Pr_2-2, 6. The measured Ge=N bond length of 170.3 pm is

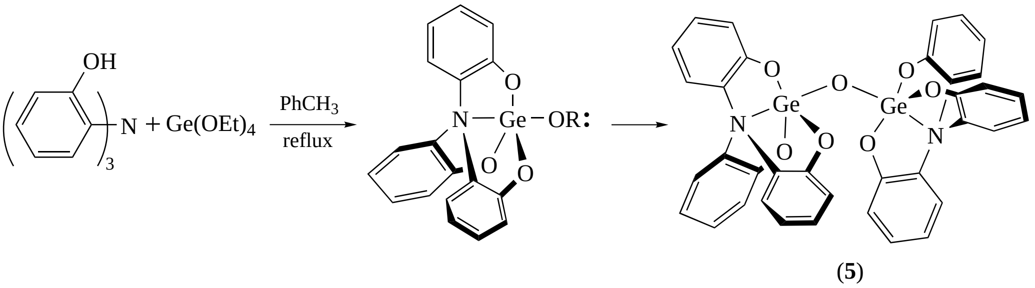

(**5**)

Scheme 2

close to the value predicted for the hypothetical compound $H_2Ge{=}NH$ of 169.5 pm.[31]

$$[R(Me_3Si)N]_2Ge + RN_3 \longrightarrow [R(Me_3Si)N]_2Ge{=}NR + N_2 \quad (16)$$

Similarly, the Ge^{II} complex (**6**) has been converted to the base-stabilized imine (**7**) that readily undergoes addition reactions, for example, with EtOH (Scheme 3).[32]

Porphyrin complexes, (porph)Ge and (porph)$GeCl_2$, are known for the +2 and +4 oxidation states. Reaction of phthalocyanine with $GeCl_4$ in quinoline gives the highly stable complex (phthalo)$GeCl_2$ in which the two Cl atoms are necessarily trans. It sublimes without decomposition at 450 °C. Recently, the crystal structure of bis(acetato)(*meso*-tetraphenylporphyrinato)germanium(IV), $Ge(tpp)(OAc)_2$[33] (**8**), has been reported. The acetate groups are unidentately coordinated to the germanium(IV) atom. Other Ge–N bonded derivatives include the azide, carbodiimide, isocyanate, and thiocyanate (equations 17–20). In H_3GeNCS, the Ge–N–C angle is 180° (C_{3v}), implying significant d–p π bonding, whereas H_3GeNCO and H_3GeN_3 are bent in the vapor phase.

$$H_3GeF + Me_3SiN_3 \longrightarrow H_3GeN_3 \quad (17)$$

$$H_3GeF + (Me_3SiN)_2C \longrightarrow H_3GeN{=}C{=}NGeH_3 \quad (18)$$

$$H_3GeBr + AgSCN \longrightarrow H_3GeNCS \quad (19)$$

$$GeCl_4 + AgCNO \longrightarrow Ge(NCO)_4 \quad (20)$$

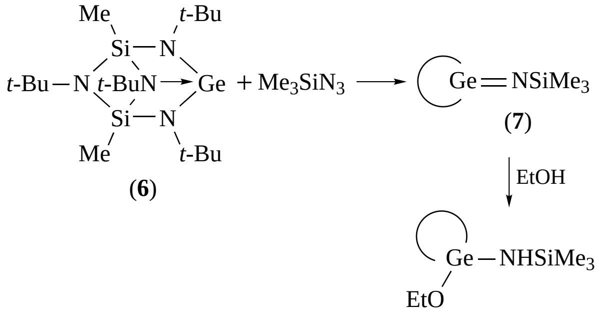
Me
t-Bu
Si
N
t-Bu
N
t-BuN
Ge
+ Me3SiN3
Si
N
Me
t-Bu
(6)
Ge
NSiMe3
(7)
EtOH
Ge
NHSiMe3
EtO

Scheme 3

7 PHOSPHORUS AND ARSENIC COMPOUNDS

Both GeP and GeAs are semiconductors, formed from the elements at 600–1200 °C and high pressure. They become superconductors at about 4K.

$CdGeP_2$, formed from the elements at 800 °C, has a strictly ordered tetragonal chalcopyrite structure having a symmetry that is almost tetragonal. A glassy disordered structure can be obtained through rapid quenching of the molten material.

Cy(H)$PGeCl_3$, produced by the 1:1 reaction of $CyPH_2$ and $GeCl_4$, is a white solid, which appears stable in solution under an inert atmosphere but immediately turns to an oil on exposure to air.[35]

The 1:1 reaction of $GeCl_4$ with PhPH yields a solid precipitate but this turns to oil on drying in a vacuum. Microanalyses of this oil confirm the formula $C_{12}H_{11}Cl_2PGe$.

Ge^{II}- and Ge^{IV}- phosphorus compounds exhibit a variety of structures. $GeCl_2{\cdot}$dioxane reacts with $[(Me_2P)_3C]^-$ to produce a stable crystalline four-coordinate Ge^{II} compound (**9**) with a distorted tbp structure in which the Ge lone

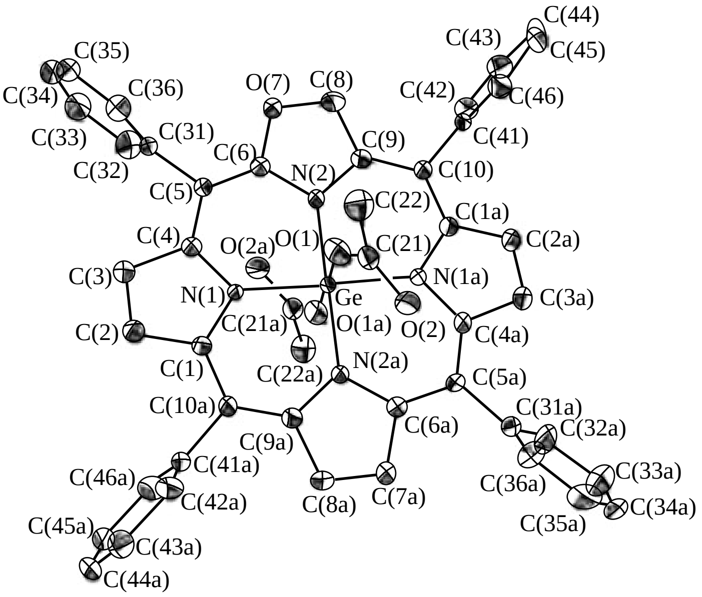
C(44)
C(43)
C(45)
C(35)
C(42)
C(46)
C(34)
C(36)
O(7)
C(8)
C(33)
C(31)
C(41)
C(9)
C(32)
C(6)
C(10)
N(2)
C(5)
C(22)
C(1a)
C(4)
O(2a)
O(1)
C(21)
C(2a)
C(3)
N(1a)
N(1)
Ge
C(3a)
C(21a)
O(1a)
O(2)
C(2)
C(4a)
C(1)
N(2a)
C(22a)
C(5a)
C(10a)
C(31a)
C(6a)
C(32a)
C(9a)
C(41a)
C(33a)
C(46a)
C(36a)
C(42a)
C(7a)
C(8a)
C(34a)
C(45a)
C(35a)
C(43a)
C(44a)

(**8**)

(Reprinted with permission from Ref. 33. © 1997 American Chemical Society) pair occupies an equatorial position. $GeCl_4$ reacts with $[(Me_2P)_2CSiMe_3]^-$ forming an octahedral derivative, *trans*-$GeCl_2[(PMe_2)_2CSiMe_3]_2$. If the reaction is carried out in the presence of Mg, the more complex Ge–Ge bonded product (**10**) is formed.

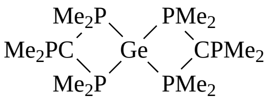

(**9**)

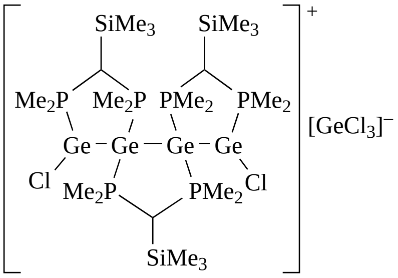

(**10**)

H_3GePH_2 redistributes to $H_2Ge(PH_2)_2$, $He(PH_2)_2$, and GeH_4 above – 30 °C. Mono- and trisgermylphosphines have been obtained through the reactions, such as equations (21) and (22).

$$LiAl(PH_2)_4 + H_2GeBr \longrightarrow H_3GePH_2 \qquad (21)$$

$$H_3GeX + (H_3Si)_3P \longrightarrow (H_3Ge)_3P \qquad (22)$$

The unusual layered compounds $K_8In_8Ge_5As_{17}$ and $K_5In_5Ge_5As_{14}$,[34] are formed from the elements at high temperature. Both contain In–Ge–As layers with interleaved potassium ions, Ge–Ge bonds, $InAs_4$ tetrahedra, As–As bonds, and rows of Ge_2As_6 dimers.

8 OXYGEN-BONDED COMPOUNDS

8.1 Oxides

Germanium(II) oxide was formed by reducing GeO_2 with H_3PO_2 in HCl solution. The immediate product, $Ge(OH)_2$, dehydrates on heating and GeO may be sublimed above 700 °C. In addition, reaction of Ge with CO_2 at 700 °C and heating Ge or GeO_2 at 800 °C also could gain GeO. In the gas phase or as a matrix in Ar, $\nu_o(^{74}Ge\text{–}O) = 977.4\,cm^{-1}$.

GeO is variously described as a yellow or dark brown solid. It may be sublimed or disproportionated to Ge and GeO_2 above 700 °C, and is stable to air and water at room temperature. It is unaffected by HCl, H_2SO_4, and $NaOH/H_2O$. Oxidation in air to GeO_2 is rapid at 550 °C; HCl at 175 °C gives $HGeCl_3$, and Cl_2 and Br_2 oxidize it to GeO_2 and GeX_4.

The germanium(IV) oxide was obtained by the hydrolysis of $GeCl_4$. It exists in hexagonal, tetragonal, and vitreous forms. Of these, the hexagonal form has a β-quartz structure with four-coordinate Ge, and it is commercially available. It dissolves in HF and is moderately soluble in hot water. It reacts with BrF_3, forming GeF_4. The tetragonal form is obtained through evaporating an aqueous solution of GeO_2 followed by heating at about 380 °C. It is slightly dissolved in water, unaffected by aqueous HCl or HF, but dissolves in 5M NaOH at 100 °C. The tetragonal form has a rutile-type structure (six-coordinate Ge). Vitreous GeO_2, which resembles fused silica, is formed when the fused dioxide solidifies. GeO_2 is less acidic than SiO_2.

8.2 Anionic Oxides

The known chemistry of germanates is much less extensive than that of silicates. Although there are many similarities, some differences exist because Ge more readily accepts higher coordination numbers. A wide range of anionic Ge^{IV} oxides are known. Examples include $[GeO_3]^{2-}$, $[GeO_4]^{4-}$, $[Ge_2O_7]^{6-}$, $[Ge_3O_{10}]^{8-}$, $[Ge_5O_{11}]^{2-}$, $[Ge_5O_{12}]^{4-}$, $[Ge_6O_{18}]^{12-}$, $[Ge_8O_{17}]^{2-}$, and $[Ge_9O_{20}]^{4-}$.[36–38]

Preparative methods include precipitation of the anion from aqueous solutions of GeO_2 at defined pH values and fusion techniques. For example, $Li_4Ge_5O_{12}$ is obtained from a melt of GeO_2 and Li_2O. When heating CsO, Li_2O, and GeO_2 at 600 °C, $Cs_2Li_2Ge_4O_{10}$ can be yielded. In aqueous solution, with pH ranging from 6.9–9.4, the dominant species is evidently $[Ge_5O_{11}]^{2-}$. Oxygermanate $K_2Ge_2O_3$ in addition to $K_6Ge_2O_7$ will form from the reaction of KGe and oxygen at 400 °C.

Varieties of germanium containing zeolite structures are known. Typical structures with framework compositions include feldspar, paracelsian, sodalite, analcime, natrolite, cancrinite, DAF-2(DFT), gismondine, and faujasite. $BaGaGe_2O_8$ and $NaAlGe_3O_8$ are well-established Ge analogs with feldspar structures. $SrGa_2Ge_2O_8$ and $BaGa_2Ge_2O_8$ own the paracelsian framework.[56] $AlGeO_4$, $BeGeO_4$, $GaGe_5O_{12}$, and $GaGe_2O_6$ are germanate sodalites with framework compositions.

GeO_4 tetrahedra, GeO_6 octahedra, and GeO_5 trigonal bipyramids are the common coordination forms that Ge atoms adopt in these oxyanions. In $K_6Ge_2O_7$, the Ge atoms are tetrahedrally coordinated with a common apex, the Ge–O–Ge angle being 157°, whereas in $[Ge_9O_{20}]^{4-}$ and $[Ge_5O_{12}]^{4-}$, four and three of the Ge atoms are octahedrally coordinated respectively. The metagermanate $BaTiGe_3O_9$ has cyclic Ge_3O_9 units and infinite GeO_3 chains, whereas in $Pb_4Ge_4O_9$, both tetrahedrally and octahedrally coordinated Ge atoms exist. In $K_2Ba[Ge_4O_9]$, the anions consist of rings built up from GeO_4 tetrahedra linked to GeO_6 octahedra in a three-dimensional network. Two forms of $BaGeO_3$ have been characterized: an α-form with a pseudo-wollastonite hexagonal ring structure and a β-form consisting of infinite chains of GeO_4 tetrahedra. In the mixed oxide, $Na[AlGeO_4]$, Al and Ge are randomly distributed on octahedral sites. In $K_2Ge_8O_{17}$, six of the Ge atoms are in GeO_4 tetrahedra but two are five-coordinate, as silicon seldom is under normal conditions.

Reaction of GeO_2 with $[Me_4N][OH]$ in H_2O at 180 °C yields a microporous germanate. The asymmetric unit contains $[Ge_6O_{12},Me_4NOH]$ and the three-dimensional framework is composed of GeO_4 tetrahedra and GeO_5 tbp's that form four-, six-, and eight-membered ring channels along the c-axis with the cation located in the six-membered ring channel.**[39]**

These kinds of microporous materials have been consecutively synthesized, mainly under hydrothermal conditions. Table 6 gives some materials synthesized in the recent years. The basic framework units involving Ge are also exhibited.

8.3 Hydroxides

$Ge(OH)_2$ is a yellow solid. When GeO_2 is reduced by H_3PO_2 in HCl solution, the immediate product, $Ge(OH)_2$, is formed after raising the pH value by the addition of NH_3. It readily dehydrates and is oxidized in a strong alkaline solution. Its IR spectrum provides evidence for the species.**[55]**

Evidence for $Ge(OH)_4$ is scant: ^{73}Ge NMR resonance of GeO_2 in neutral D_2O solution has been assigned to the $Ge(OD)_4$ molecule, whereas in the presence of a base (Et_3N), the signal corresponds to $[Ge(OD)_6]^{2-}$. In dilute aqueous solution, the main germanate ions have been identified as $[GeO(OH)_3]^-$, $[GeO_2(OH)]^{2-}$, and $\{[Ge(OH)_4]_8(OH)_3\}^{3-}$. The crystalline mineral stoettite contains the anion $[Ge(OH)_6]^{2-}$.

$GeO(OH)_2$ is planar and electronically analogous to H_2CO_3. It is not possible to determine which species is obtained; coexistence of the both hydroxides must be considered (equations 23 and 24).**[55]**

$$GeO_2 + H_2O \longrightarrow GeO(OH)_2 \tag{23}$$

$$GeO(OH)_2 + H_2O \longrightarrow Ge(OH)_4 \tag{24}$$

(phthalocyanine)$Ge(OH)_2$, obtained by the hydrolysis of (phthalocyanine)$GeCl_2$, is very stable. When heated under vacuum at 440 °C, it forms a Ge–O bridged polymer.

8.4 Alkoxides and Esters

8.4.1 Compound of Ge (II)

Ge^{II} dialkoxides, $Ge(OR)_2$, are polymeric if the R groups are small. $Ge(O\text{-}t\text{-}Bu)_2$ is a cyclic dimmer. When R groups are even bulkier, monomeric compounds, which can usually be sublimed in vacuum, will result readily, examples include R = $C\text{-}t\text{-}Bu_3$ and $C_6H_2\text{-}t\text{-}Bu_3$-2,4,6. They are usually made from $GeCl_2\cdot$dioxane,**[14]** or by exchange reactions (equation 25).**[57]**

$$Ge[N(SiMe_3)_2] + t\text{-}Bu_3COH \longrightarrow Ge[OC\text{-}t\text{-}Bu_3]_2 \tag{25}$$

Table 6 Information about the materials with framework structure

Molecular formula	Structure feature	Reference
$GaGe_3O_8$	I-centered cubic	40
$GaGe_5O_{12}$	The first germanate with five rings	40
$Ga_2Ge_4O_{12}$	GeO_4	40
$NH_4GaGe_2O_6$	Analcime-like structure	40
$CsGaGe_2O_6$	Analcime-like structure	40
$(CH_3NH_3)2Ga_2Ge_3O_{10}$	The first germanate with ternary Ga rings	41
$(NH_4)_2Ge_7O_{15}$	GeO_4 and GeO_6	42
$(NH_4)^+ [M(NH_3)_2]^+ (Ge_9O_{19})^{2-}$ (M = Cu, Ag)	The first microporous germanates containing a transition metal complex in the channels	43
$(NH_4)(CH_3NH_3)(Ge_9O_{19})$	Eight GeO_4 and one GeO_6	44
$K_2ZrGe_2O_7$	GeO_4 and ZrO_6	45
$[Ge_9O_{18}(OH)_4]\cdot 2H_2ppz\cdot 0.5H_2O$	GeO_4 and GeO_6	46
$[Ge_9O_{18}(OH)_4]\cdot 2(NH_3CH_2CH_2CH_2NH_3)\cdot H_2O$	GeO_4 and GeO_6	47
$[Ge_9O_{17}(OH)_4][N(CH_2CH_2NH_3)_3]_{2/3}[HCON(CH_3)_2]_{1/6}(H_2O)_{11/3}$	GeO_5	48
$Ge_8O_{16}[(OH)^- (MeNH_3)^+ (MeNH_2)]$	GeO_4	49
$Ge_{10}O_{21}(OH)\cdot N_4C_6H_{21}$	GeO_4, $GeO_3(OH)$, GeO_5, and GeO_6	50
$Cu_2Fe_2Ge_4O_{13}$	GeO_4	51
$ZrGe_3O_8(OH)F\cdot H_2BAPP\cdot H_2O$	GeO_4	52
$Zr_3Ge_6O_{18}(OH_2F)_4F_2\cdot[H_2DAH]\cdot[HDAH]_2H_2O$	GeO_4	52
$ZrGe_3O_9\cdot H_2DAP$	GeO_4	52
$ZrGe_3O_9\cdot H_2DAE$	GeO_4	52
$K_2ZrGe_3O_9\cdot H_2O$	GeO_4	52
$(C_2H_{10}N_2)H_2O[ZrGe_3O_9]$	GeO_4	53
$In_2Ge_6O_{15}(en)_2$	GeO_4	54

Stable monomeric complexes can also be obtained without the presence of bulky ligands. Intramolecular donation of electrons into the empty valency orbital of Ge^{II} from nitrogen renders them stability,[58] as seen in (**11**), which is stable to dry oxygen, but readily hydrolyzes. The same phenomenon occurs in the acetylacetonato complex of Ge(II) and Ge(acac)I, in which germanium is three-coordinate with a stereochemically active lone pair.

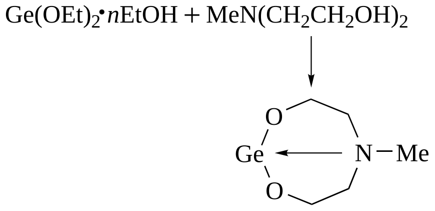

(**11**)

In these monomeric compounds, the O–Ge–O angle is close to 90°, compared to 110° in the analogous N–Ge–N compounds.

8.4.2 *Compounds of Ge (IV)*

Germanium alkoxides are widely used in sol-gel processes for the preparation of Ge-containing glasses[59] and important materials such as GeS_2,[60] and in vapor chemical processes for deposition of GeO_2 and organogermanium films.[61] The search for synthetic pathways of germanates that can be used as frameworks of new porous materials[62] also provides a timely motivation for exploring the reactivity of germanium alkoxides.

Ge^{IV} tetraalkoxides and alkoxyhalides are colorless liquids that are thermally stable but readily hydrolyzed. Partial hydrolysis has yielded alkoxygermoxanes (equation 26). The simplest Ge^{IV} tetraalkoxide, methoxygermane, is unstable even at – 23 °C.

$$\mathrm{Ge(O\text{-}\mathit{i}\text{-}Pr)_4 + H_2O \longrightarrow [(\mathit{i}\text{-}PrO)_3Ge]_2O + [Ge_2O_3(O\text{-}\mathit{i}\text{-}Pr)_2]_{\mathit{n}}} \quad (26)$$

Ge^{IV} tetraalkoxides can be produced through the complete alcoholysis of Ge halides in the presence of a base. Partial substitution yields many Ge^{IV} alkoxy derivatives (alkyl orthogermanates) (equations 27 and 28).

$$\mathrm{H_3GeCl + NaOMe \longrightarrow H_3GeOMe} \quad (27)$$

$$\mathrm{GeCl_4 + nROH[NaOR\ or\ pyridine] \longrightarrow (RO)_{\mathit{n}}GeCl_{4-\mathit{n}}} \quad (28)$$

The exchange between different Ge^{IV} tetraalkoxides can be easily obtained through alkoxide exchange. $AlCl_3$-catalyzed reactions and cleavage of cyclic ethers can also produce alkoxyhalegermanes (equations 29 and 30).

$$\mathrm{GeCl_4 + \mathit{n}ROH \xrightarrow{AlCl_3} (RO)_3GeCl + (RO)_2GeCl_2 + ROGeCl_3} \quad (29)$$

$$\mathrm{GeCl_4 + Me\overline{CHCH_2O} \longrightarrow (MeCHCl_2H_2O)_{\mathit{n}}GeCl_{4-\mathit{n}}} \quad (30)$$

A digermoxane compound, $(GeH_3)_2O$ with the Ge–O–Ge angle of 126.5°, can be prepared by hydrolysis of GeH_3Cl or from the reaction of $(H_3Ge)_2S$ with HgO. Compared to the predicted value of 182.7 pm, the shorter distance of Ge–O, 176.6 pm, is attributed to some degree of p–d π bonding.

Reaction of GeH_3Cl with $Pb(OAc)_2$ yields H_3GeOAc. $Ge(OCOCF_3)_4$ is prepared from $GeCl_4$ and $Hg(OCOCF_3)_2$. $Ge(OAc)_4$, with the unidentate acetato group, is formed from $GeCl_4$ and TlOAc or Ac_2O.

Esters of various oxyacids have been isolated: the anhydrous sulfate (equation 31), formed at 160 °C, is unstable.

$$\mathrm{GeCl_4 + 6SO_3 \longrightarrow Ge(SO_4)_2 + 2S_2O_5Cl_2} \quad (31)$$

White crystalline phosphite, GeOP(O)OH, is formed from the reduction of GeO_2 with hypophosphorous acid.

Reaction of $GeCl_4$ with Cl_2O_6 produces four-coordinate complexes such as $Cl_3GeOClO_3$ and $Cl_2Ge(OClO_3)_2$. With excess Cl_2O_6, the octahedral complex $2[ClO_2]^+[Ge(OClO_3)_6]^{2-}$ is formed.[63]

8.5 Chelate Complexes of Ge^{IV}

Chelating ligands frequently yield five- or six-coordinate complexes. For example, the octahedral anion (**12**) is obtained through the reaction of GeO_2 with catechol in NaOMe/MeOH, whereas in the presence of pyridine, the neutral six-coordinate complex $[C_6H_4O_2]_2Ge(py)_2$ is formed. Square pyramidal anionic Ge^{IV} complexes, such as (**13**), have been characterized.

A F,O-bonded Ge^{IV} complex is obtained when GeF_2 is oxidized by reaction with quinines (equation 32).

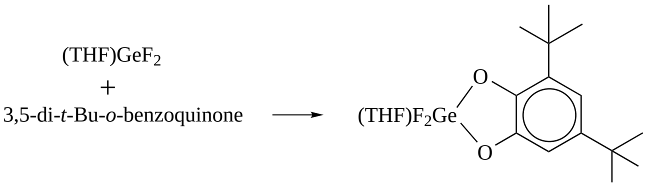

(32)

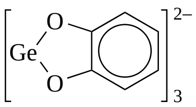

(**12**)

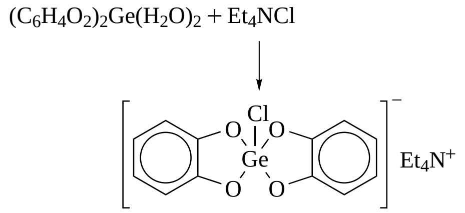

(**13**)

The reaction of GeO_2 with oxalic acid evidently gives $H_2[Ge(C_2O_4)_3]$. The enantiomers of the tris-oxalato complex $K_2Ge(C_2O_4)_3 \cdot H_2O$ have been separated. The *cis*-octahedral complex $(acac)_2GeCl_2$, with a dipole moment of 7.4 D, is formed from the combination of acetylacetone and $GeCl_4$. The absolute configuration of the corresponding cationic complex, $[Ge(acac)_3]^+ [ClO_4]^-$, has been determined. In the EDTA complex of Ge^{IV}, the ligand is pentadentate, with H_2O occupying the sixth coordination site.

Subvalent germanium complexes combined with a dianionic calixarene ligand have been found. The reaction of *p-tert*-butylcalix[4] arene with Me_3SiI in the presence of pyridine provides a useful synthetic route for $[Butcalix^{(TMS)2}]H_2$.

The divalent Ge complex $[Butcalix^{(TMS)2}]Ge$ (**14**) can be readily obtained by the reaction of $[Butcalix^{(TMS)2}]H_2$ with $M[Ge(SiMe_3)_2]_2$, as illustrated in Scheme 4.**[64]**

9 SULFIDES, SELENIDES, AND TELLURIDES

9.1 Preparation and Properties of Simple Compounds

GeS can be made through reduction of GeS_2 using H_2 or H_3PO_2. The GeS single crystal is orthorhombic with a = 429 pm, b = 1042 pm, c = 364 pm, and space group, Pnma-$D^{16}{}_{2h}$, in which each Ge atom is surrounded by six S atoms exhibiting octahedral configuration. It has a layer structure similar to the isoelectronic black phosphorus.**[65]** It is a red–brown solid and sublimes in vacuum at 600 °C. It is readily hydrolyzed, and is oxidized in air at 350 °C to GeO_2. HCl at 175 °C converts it into $HGeCl_3$ and H_2S.

GeS_2 is formed from GeO_2, H_2SO_4, and H_2S. GeO_2, is orthorhombic with a = 1166 pm, b = 2234 pm, c = 686 pm, and Z = 16. It has an unusual structure with Ge_3S_3 rings that transform into a crystobalite structure at high pressure.

GeSe can be prepared by two methods. One is the direct combination of the elements Ge and Se in CO_2 atmosphere at 500 °C, and the other is the reaction of H_2Se with $GeCl_2$. It is a brown solid and is readily oxidized in air, having the same structure with GeS.**[65]** The GeSe crystal is tetragonal with a = 883 pm, c = 976 pm, Z = 16. Its melting point is about 667 °C. It is unaffected by 5% HCl solution, alcohol, or ether, but dissolves in HCl solution containing bromine. It can be oxidized by nitric acid to GeO_2 and H_2SeO_3.

$GeSe_2$, formed from GeO_2/H_2SO_4 and H_2Se, is orthorhombic with a = 1296 pm, b = 693 pm, c = 2209 pm, Z = 24, $D^{25} = 4.56\ g\,cm^{-3}$, mp. = 707 °C. It is a white crystalline solid. It is unaffected by HCl and H_2SO_4 solution but is oxidized to Se by H_2O_2 in alkaline solution.

GeTe, mp. = 725 °C, can react with dense HCl solution, H_2SO_4 solution, and water when it is heated, while the mixture of royal water, H_2O_2, and HCl solution can erode it without heating.

In recent years, germanium sulfides have been prepared for glass films that are widely applied in many fields.

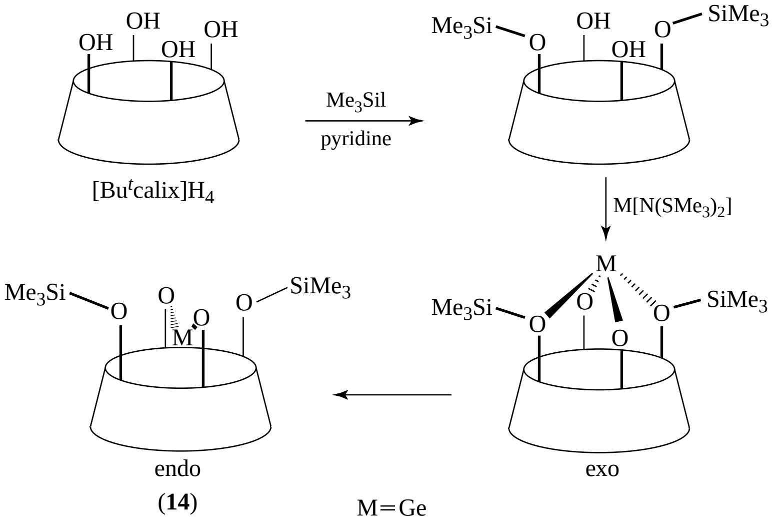

Scheme 4 (Ref. 64. Reproduced by permission of The Royal Society of Chemistry)

9.2 Structures of the Germanium Anions

Considerable structural variations have been found in germanium sulfide anions obtained, which is obviously indicated in the reaction of GeS_2 with Na_2S. In Na_2GeS_3, the $[GeS_3]^{2-}$ ions form infinite chains of tetrahedra, whereas in $Eu_3[Ge_3S_9]^{6-}$, the anion forms a $(Ge–S)_3$ six-membered ring having a chair conformation with two exo sulfur atoms bridging each Ge and Eu. By contrast, La_2GeS_5 has a two-dimensional sheet structure. The $[GeS_4]^{4-}$ ion is tetrahedral, whereas $[Ge_2S_6]^{4-}$ consists of edge-sharing tetrahedra and the $[Ge_2S_7]^{6-}$ ion has vertex-sharing tetrahedra. The selenides are structurally similar, but by contrast $[Ge_2Te_6]^{6-}$ has a Ge–Ge bond with a staggered conformation of tellurium atoms. $[Ge_4S_{10}]^{4-}$ together with the Se and Te analogs have adamantane-like structures, that is, four GeS_4 tetrahedra sharing two vertices with adjacent tetrahedra. The telluride $[Ge_4Te_{10}]^{8-}$ has a cyclic structure, $[Te(GeTe_2)_4Te]^{8-}$.

Alkylthiogermanes have been prepared by ligand exchange (equation 33). In $(H_3Ge)_2S$, the Ge–S bond length, 220.9 pm, and Ge–S–Ge angle of 98.9° indicate negligible d–p π interaction. Treating GeH_3Cl with AgSCN gives H_3GeSCN; similar reactions lead to H_3GeSMe.

$$GeCl_4 + RSH \longrightarrow (RS)_4Ge \longleftarrow (RO)_4Ge + RSH \qquad (33)$$

Reactions involving sulfides have produced some unexpected structures, such as (**15**), in which the $S_2P(OMe)_2$ ligands are unidentate.

The reaction between $GeBr_4$ and H_2S in CS_2 gives $Ge_4S_6Br_4$ with the adamantane-like structure (**16**),[66] similar to the isoelectronic P_4O_{10}.

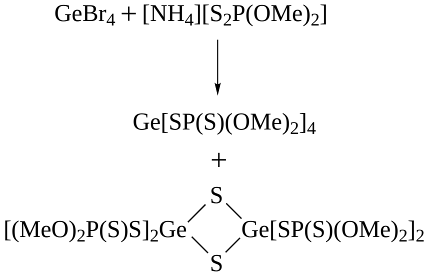

(**15**)

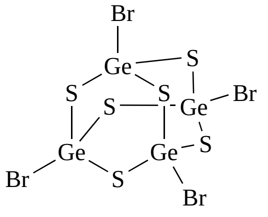

(**16**)

9.3 Terminal Multiple Bonds Between Chalcogen Elements and Ge

Recent developments in the preparation of complexes with terminal multiple bonds between chalcogen elements and Ge have yielded significant results,[18] as illustrated by the successful isolation and structural characterization of several terminal chalcogenido complexes $\{\eta^3\text{-}[(\mu\text{-}Bu^tN)_2(SiMeNBu^t)_2]\}GeS$ and (Tbt)(Tip)GeE (E = S, Se) (Tbt = 2,4,6-$[(Me_3Si)_2CH]_3C_6H_2$, Tip = 2,4,6-$Pr^i_3C_6H_2$).[67]

Isolation and structural characterization of species with Ge=S, Ge=Se, and Ge=Te moieties have been realized by virtue of kinetic stabilization provided by sterically protecting groups on the Ge center (e.g. $Tbt(CH(SiMe_3)_2)Ge{=}Te$). Complexes $[\eta^4\text{-}Me_8taa]Ge{=}E$ (E = S, Se, Te) (taa = tetraazaannulenes) are all structurally characterized. A series of compounds bis[(2-pyridyl)-bis(trimethylsilyl)methyl]Ge=E (E = S, Se, Te) have been reported, and meanwhile Se and Te derivatives have also been structurally characterized.[18]

Although compounds featuring a double bond between heavier main group C14–16 elements are considered to be unstable due to the weak pπ–pπ bonding, thioketone analogues comprised of group 14 and group 16 congeners such as germanethione (Ge=S) and germaneselone (Ge=Se), have been isolated in the past few years. These compounds are stabilized either by alkali or by using a sterically hindered protecting group, as in [Tip(Tbt)Ge=E] (E = S and Se).[68]

Ge amidinate complexes are susceptible to oxidation of elemental chalcogens. Many of these complexes are excellent catalysts for the cyclization of aryl isocyanates.[69]

10 HALIDES

All four Ge^{II} halides are known. GeF_2, $GeCl_2$, and $GeBr_2$, formed reversibly by heating Ge with GeX_4, are polymeric in the solid state but monomeric as a gas. Electron diffraction examination of $GeBr_2$ reveals the presence of the monomer with a Br–Ge–Br angle of 101.2° and a bromine-bridged dimer. GeF_2 and $GeCl_2$ have carbene-type structures in the vapor phase with bond angles of 97.2° and 100.3°, respectively. In the solid state, GeF_2 forms spiral chains involving bridging F atoms; each Ge has a pseudo tbp geometry with an equatorial lone pair. It undergoes a phase change from orthorhombic to monoclinic at 62°C. GeI_2 is an orange solid that is grown in a vapor reaction or is best prepared by reduction of GeI_4 with aqueous H_3PO_2 in the presence of HI to prevent hydrolysis.[70,71] It is structurally similar to CdI_2, with the Ge atoms octahedrally coordinated. It can be sublimed and is stable in air; when heated it disproportionates to Ge and GeI_4.

Apart from GeI_2, the other dihalides are rapidly hydrolyzed by water. All four are readily oxidized by O_2 at an elevated temperature and by halogens. $GeCl_2$ reacts easily with Cl_2 and

Br_2 to gain $GeCl_4$ and $GeBr_4$ respectively. The reaction between $GeCl_2$ and H_2S gives GeS and HCl at room temperature. $GeCl_2$ is a strong deoxidizer in aqueous HCl solution. $GeBr_2$, mp 122°C, dissolved slightly in $5\,\mathrm{mol\,L^{-1}}$ HBr, reacts with dry HBr gas to gain $GeHBr_3$ immediately. $GeBr_2$ is liable to decompose to $GeBr_4$ and Ge at 150°C.

The dihalide solids react with donors or with butadiene to complete their octets, for example, equations (34) and (35).

$$GeI_2 + R_3P \longrightarrow R_3PGeI_2 \qquad (34)$$

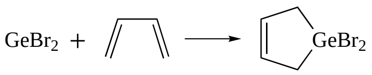
(35)

$GeCl_2$(dioxane) is a useful source of $GeCl_2$ and can fast and selectively react with various chloro and hydrido complexes of molybdenum and tungsten to afford trichlorogermyl and dichlorogermyl complexes respectively, $(\eta^5\text{-}C_5R_5)M(CO)_{3-n}L_n(GeCl_{3-m}H_m)$ (R = H, Me; M = Mo, W; $n = 0{-}2$; L = EtNC, PMe_3; $m = 0$, 1)[72–74] and $[(\eta^5\text{-}C_5R_5)M(CO)_3]_2GeX_2$ (R = H, Me; M = Mo, W; X = H, Cl).[75] During these reactions, the metal complex acts as a Lewis base and $GeCl_2$ as a Lewis acid.[76] These complexes contain two reactive sites (i.e. transition metal and the germanium center) that provide the possibility for further functionalization.

GeI_2 reacts with $Na[\{Cp'(CO)_2Mn\}_2H]$ to form an inidene type compound, $[\{Cp'(CO)_2Mn\text{-}GeI\text{-}Mn(CO)_2Cp'\}]^-$, with Ge in a trigonal planar coordination embedded between two $Cp'(CO)_2Mn$ groups and an iodo ligand.[77]

All of the tetrahalides, and most of the mixed halides (e.g. $GeClF_3$ and $GeCl_2F_2$), are known and are stable in dry air. GeF_4, bp −36.5 °C, is made by decomposing $BaGeF_6$ at 600 °C. It is thermally stable to about 1000 °C and hydrolyzes readily to GeO_2. $GeCl_4$, bp 83.1 °C, is best prepared from GeO_2 and conc. HCl, or by passing Cl_2 over Ge. It is very stable thermally but readily hydrolyzed; it is the starting material for many synthetic reactions. $GeBr_4$ has been made from Ge and Br_2, whereas the tetraiodide is most readily made from GeO_2 and aqueous HI; both are crystalline solids at room temperature. GeI_4 sublimes at 100°C.

All Ge tetrahalides are tetrahedral and monomeric. They are freely soluble in most organic solvents, and in aqueous acid solution hydrolysis is only partial, in contrast to silicon. Reaction of GeF_4 with various anhydrous chlorides at 200−600°C gives only $GeCl_4$, with no evidence for intermediate chlorofluoro compounds, but the Raman spectra of mixtures of GeX_4 compounds provide evidence for the presence of all combinations of mixed halides. GeX_4 compounds are sufficiently strong Lewis acids that can form a range of five- and six-coordinate complexes with, for example, amines. In py_2GeCl_4, the pyridines are *trans*-$GeCl_4$ and bidentate donors such as ethylenediamine and bipyridyl form 1:1 complexes. H_3P and Me_3P form 1:1 complexes with GeF_4, which evidently sublime with some dissociation at 25 °C. Oxygen donors, as in ketones, ethers, and amine oxides, form both 1:1 and 1:2 complexes with GeF_4, as do sulfides like H_2S and Me_2S. Whereas the 1:2 complexes are undoubtedly six-coordinate with the possibility of cis/trans isomers, the five-coordinate 1:1 complexes are associated so that the Ge becomes six-coordinate. ^{19}F NMR spectra of GeF_4 complexes give definitive evidence of stereochemistry and of temperature-dependent reversible dissociation of coordinated ligands. There are, however, examples of five-coordination complexes, for example, Me_3N, $GeCl_4$, and $AgClO_4$ that yield a salt $[(Me_3N)_2GeCl_3]ClO_4$ in which the cation has D_{3h} symmetry. Photochemical reaction of $W(CO)_6$ with bicyclo[2.2.1]hepta-2,5-diene and $GeCl_4$ forms a heterobimetallic complex $[W(\mu\text{-}Cl)(GeCl_3)(CO)_3(\eta^4\text{-}C_7H_8)]$. The germanium atom in the compound is five-coordinate, with one chlorine atom occupying a bridging position between the two metal atoms. This complex has been found to be an active catalyst for the ring-opening metathesis polymerization of norbornene and norbornadiene.[78] Reaction of equivalent $[MeC(N\textit{i}Pr)_2]Li\cdot THF$ and $GeCl_4$ affords $[MeC(N\textit{i}Pr)_2]_2GeCl_2$.[28]

Dropwise addition of an ice-cooled (0 °C) solution of $GeCl_4$ in toluene to a solution of 2,2′-bipyridyl in toluene gives a colorless diamond-shaped crystal $[GeCl_4(bipy)]$. $[GeCl_4(bipy)]$ further reacts with citric acid (H_4cit) in acetonitrile solution to give a colorless crystal $[GeCl(bipy)(Hcit)]$.[29]

$[GeCl_3(L^1)]_2{}^+\ [H_3O]^+\ Cl_3{}^-\cdot MeCN$ (L^1 = 1,4,7-trimethyl-1,4,7-triazacyclononane), which are light yellow needles, is made by $GeCl_4$ with L^1 in acetonitrile.[79] The structure of the $[GeCl_3(L^1)]^+$ cation of $[GeCl_3(L^1)]_2{}^+\ [H_3O]^+\ Cl_3{}^-\cdot MeCN$ is shown in Figure 1.

Catenated germanium halides are rare, in contrast to Si. The well-characterized polygermanium Ge_2Cl_6, a colorless solid, has been prepared.[80–83] An improved method involves passing $GeCl_4$ at low pressure through a microwave discharge.[81,82]

$Ge_5Cl_{12}\cdot GeCl_4$, a colorless cuboidal crystal, is moisture-sensitive. The structure consists of discrete Ge_5Cl_{12} and $GeCl_4$

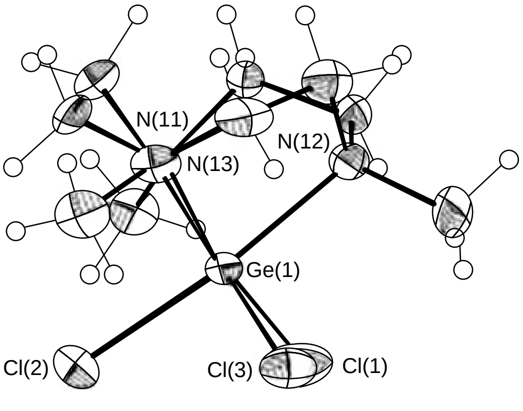

Figure 1 The structure of $[GeCl_3(L^1)]^+$ cation of $[GeCl_3(L^1)]^+{}_2[H_3O]^+\ Cl_3{}^-\cdot MeCN$. (Ref. 79. Reproduced by permission of The Royal Society of Chemistry)

molecules. The present Ge–Ge distance is 2.4131 Å; the Ge–Ge angle is 109.5°; the Cl–Ge–Ge–Ge torsion angle is 38.68°.[84]

A highly unusual mixed oxidation state compound, $(F_8Ge_4)GeF_4$, is formed from GeF_4 and Ge at 350 °C as a colorless crystalline solid. The overall structure is polymeric with fluorine bridges; the Ge^{IV} atom is octahedrally coordinated by fluorines and four Ge^{II} atoms fall into two groups, both with distorted square pyramidal coordination by F and active lone pairs.

10.1 Anionic Halides

$[GeX_3]^-$ ions are readily obtained by reactions such as equations (36) and (37), and can hydrolyze with $Ge(OH)_2$ precipitates. The pyramidal $GeCl_3{}^-$ ion occurs in $RbGeCl_3$. By contrast, $CsGeCl_3$ has a perovskite-type structure; it is a hexagonal crystal and is changed into a cubic crystal at 155 °C. The $[GeCl_3]^-$ ion forms a series of complexes with strong Lewis acids (equation 38). The semiconductor $RbGeI_3$ and conductor $CsGeI_3$ both belong to the orthorhombic crystal system. The weak base pyridine has been found to deprotonate trichlorogermane $HGeCl_3$ with a quantitative formation of pyridinium trichlorogermanate(II), $[Py\text{-}H]^+\ [GeCl_3]^-$, which is monoclinic and a $P2_1/c$ space group (equation 39).[85]

$$CsF + GeF_2 \longrightarrow CsGeF_3 \tag{36}$$

$$GeCl_4 + CsCl + H_3PO_2 \longrightarrow CsGeCl_3 \tag{37}$$

$$[Ph_4As]^+[GeCl_3]^- + BX_3 \longrightarrow [Ph_4As] + [X_3BGeCl_3]^- \tag{38}$$

$$HGeCl_3 + Py \longrightarrow [Py\text{-}H]^+[GeCl_3]^- \tag{39}$$

CsBr added to $GeBr_2$ solution can produce brick-red $CsGe_2Br_3$, but $RbGe_2Br_3$ cannot be obtained by using the same method.

In $[GeF_5]^-$ complexes, prepared from GeF_4 and a fluoride donor, Ge is six-coordinate (equations 40–42). The xenon complex consists of GeF_6 octahedra sharing trans vertices, whereas in the $[ClO_2]^+$ complex, GeF_5 units form an infinite chain of octahedra sharing cis vertices, the chain being an extended helix with all Ge atoms of a chain essentially coplanar. In the $[SF_3]^+$ complex, GeF_6 octahedra share cis vertices.[86]

$$GeF_4 + XeF_6 \longrightarrow [XeF_5]^+[GeF_5]^- \tag{40}$$

$$GeF_4 + ClO_2F \longrightarrow [ClO_2]^+[GeF_5]^- \tag{41}$$

$$GeF_4 + SF_3BF_4 \longrightarrow [SF_3]^+[GeF_5]^- + BF_3 \tag{42}$$

Octahedral $[GeF_6]^{2-}$ complexes have been obtained (equations 43–47). Thermolysis of K_2GeF_6 gives a complex mixture of products, including GeF_4 and K_3GeF_7. In $[SF_3]^+$ $[GeF_6]^{2-}$, each SF_3 makes close contact with one F from each of the three octahedral $GeF_6{}^{2-}$ ions, resulting in a distorted octahedron of fluorines about sulfur. $MnGeF_6$ can be prepared in HF (equations 48 and 49), however, the pure product can only be obtained by the reaction in equation (48). $Mn(GeF_5)_2$, formed from XeF_5GeF_5 and $Mn(AsF_6)_2$ (equation 50), decomposes to $MnGeF_6$ and GeF_4 due to its instability. So $MnGeF_6$ is dominant and only slight amounts of $Mn(GeF_5)_2$ are present in the final products.[87–89] The $[GeF_6]^{2-}$ ion is completely hydrolyzed in alkaline solution.

$$GeF_4 + 2KF/HF/H_2O \longrightarrow K_2GeF_6 \tag{43}$$

$$Ge + CuF_2 + 2RbF \longrightarrow Rb_2GeF_6 \tag{44}$$

$$GeF_4 + 2BrF_3 \longrightarrow 2[BrF_2]^+[GeF_6]^{2-} \tag{45}$$

$$GeF_4 + 2SF_3BF_4 \longrightarrow 2[SF_3]^+[GeF_6]^{2-} + 2BF_3 \tag{46}$$

$$CsGeF_3 + CsF + 2HF \longrightarrow Cs_2GeF_6 + H_2 \tag{47}$$

$$MnF_4 + nGeF_4 \xrightarrow[298\,K]{HF} MnGeF_6 + (n-1)GeF_4 \tag{48}$$

$$K_2GeF_6 + Mn(AsF_6)_2 \xrightarrow{298\,K} MnGeF_6 + 2KAsF_6 \tag{49}$$

$$2XeF_5GeF_5 + Mn(AsF_6)_2 \xrightarrow{298\,K} Mn(GeF_5)_2 + 2XeF_5AsF_5 \tag{50}$$

11 METALLOID AND METAL-BONDED COMPOUNDS

Germanium forms a wide range of compounds with hydrogen, silicon, the heavier group 14 elements, some main group metals, and transition metals. Catenated hydrides, Ge_nH_{2n+2}, have already been discussed. The majority have carbon bonded to Ge and are included in the next article (*see* ***Germanium: Organometallic Chemistry***).

11.1 Ge–M Compounds (M = Al, Ba, Te)

The cubane-type compound $[GeN\text{-}t\text{-}Bu]_4$, referred to earlier, forms a Lewis acid–base complex with $AlCl_3$ having the composition $[GeN\text{-}t\text{-}Bu]_4\cdot 2AlCl_3$ with Ge–Al bonding.[25]

In polycrystalline Ba_6Ge_{25}, the Ba atoms interact strongly with the Ge host.[90]

Ge–Te double bond compounds and germanetellones are successfully synthesized through the reaction illustrated in equation (51).[91–93]

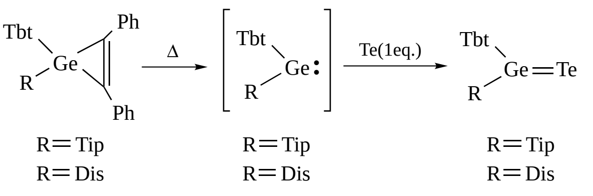

(51)

11.2 Ge–M Compounds (M = Si, Ge, Sn)

Germylsilane,[94] a gas stable at room temperature, can be obtained by equation (52).

$$\mathrm{Si_2H_6 + KH \longrightarrow H_3SiK + SiH_4}$$
$$\mathrm{H_3SiK + H_3GeCl \longrightarrow H_3SiGeH_3} \qquad (52)$$

H_3GeSiH_3, n-$SiGe_4H_{12}$, and *iso*-$Si_2Ge_4H_{14}$ can be obtained by passing a mixture of GeH_4 and SiH_4 (or Si_2H_6) through a silent electric discharge. Ge–Si bonds are formed by equation (53). In this reaction, a Ge–Ge single bond is also formed.

$$\mathrm{GeCl_4 + Me_3SiCl + Li/THF \longrightarrow}$$
$$\mathrm{(Me_3Si)_4Ge\ or (Me_3Si)_3Ge\text{-}Ge(SiMe_3)_3} \qquad (53)$$

The following is a further example of bulky substituents influencing the course of a reaction, in which a likely intermediate $(Me_3Si)_3SiGeCl_2Li$ is formed by halogen–metal exchange (equation 54).[95]

$$\mathrm{GeCl_4 + (Me_3Si)_3SiLi(THF)_3 \longrightarrow}$$
$$\mathrm{(Me_3Si)_3SiGe(Cl)_2Ge(Cl)_2Si(SiMe_3)_3} \qquad (54)$$

Some compounds with a Ge=Ge double bond have been synthesized.[96–99] (examples are in equations 55–57)

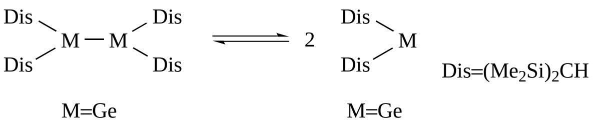

(55)

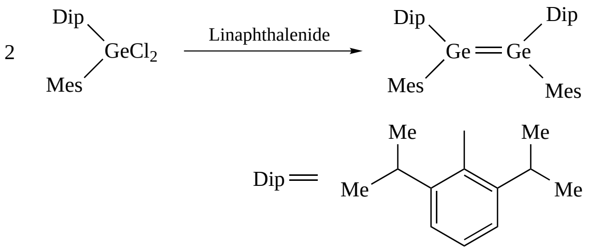

(56)

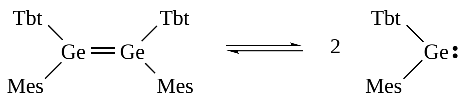

(57)

Scheme 5 gives some reactants involving the formation of the Ge–Sn bond.

$$\begin{tikzcd}
\mathrm{Ph_3GeSn(OAc)_3 + AcOH} \arrow[r] & \mathrm{(AcO)_3GeSn(OAc)_3} \arrow[d, "\mathrm{HCl}"] \\
\mathrm{H_3GeSnH_3} & \mathrm{Cl_3GeSnCl_3} \arrow[l, "\mathrm{LiAlH_4}"']
\end{tikzcd}$$

Scheme 5

11.3 Inorganic Ge–Transition Metal Compounds

The chemistry of Ge-transition metal compounds is a field experiencing relatively fewer studies. However, varieties of such compounds have been prepared and characterized. In reactions with transition metal complexes, Ge^{II} behaves as a donor–acceptor ligand like CO or an alkene; crystallographic studies indicate that the Ge–M bonds have a significant double bond character.

The following are the common ways used to establish Ge-transition metal bonds.

11.3.1 *Ge^II-Transition Metal Compounds*

Such compounds are usually obtained through addition of neutral or anionic Ge^{II} compounds to transition metal complexes (equations 58–68).

$$\mathrm{X_2GeH{\cdot}dioxane + M(CO)_6 + THF \longrightarrow X_2GeM(CO)_5THF + CO}$$
$$\mathrm{X = F, Cl;\ M = Cr, W} \qquad (58)$$

$$\mathrm{GeI_2 + 2[R_2N]^-[Cr_2(CO)_{10}]^{2+} \longrightarrow [(CO)_5CrGe(I)_2Cr(CO)_5]^{2+}} \qquad (59)$$

$$\mathrm{[Ph_4As]^+[GeCl_3]^- + M(CO)_6 \longrightarrow}$$
$$\mathrm{[Cl_3GeM(CO)_5]^- + [(Cl_3Ge)_2M(CO)_4]^{2-}} \qquad (60)$$
$$\mathrm{M = Mo, W}$$

$$\mathrm{[Et_4N]GeCl_3 + Cr(C_6H_6)_2 \longrightarrow [Cr(GeCl_3)_6]^{6-}} \qquad (61)$$

$$\mathrm{[Et_4N]GeCl_3 + Mo(mesitylene)(CO)_3 \longrightarrow [(Cl_3Ge)_3Mo(CO)_3]^{3-}} \qquad (62)$$

$$\mathrm{(OEP)GeCl_2 + Na_2Fe(CO)_4 \longrightarrow (OEP)GeFe(CO)_4} \qquad (63)$$
$$\mathrm{(OEP = octaethylporphyrin)}$$

$$\mathrm{GeI_2 + Co_2(CO)_8 \longrightarrow I_2Ge[Co(CO)_4]_2} \qquad (64)$$

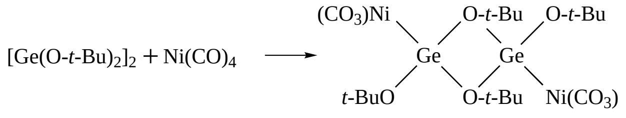

(65)

$$\mathrm{[Et_4N]GeCl_3 + Ni(CO)_4 \longrightarrow [Cl_3GeNi(CO)_3]^-}$$
$$\mathrm{+\ [(Cl_3Ge)_2Ni(CO)_2]^{2-}} \qquad (66)$$

$$\mathrm{Ge[N(SiMe_3)_2]_2 + Pd(cod)_2 \longrightarrow Pd\{Ge[N(SiMe_3)_2]_2\}_3} \qquad (67)$$

$$\mathrm{CsGeCl_3 + Rh(PPh_3)_2(CO)Cl \longrightarrow Cl_3GeRh(PPh_3)_2(CO)} \qquad (68)$$

A trichlorogermyl–Mn complex has been made by the chlorinative cleavage of phenyl groups from $Ph_3GeMn(CO)_5$, reflecting the stability of the Ge–Mn bond.

11.3.2 Ge^{IV}-Transition Metal Compounds

1. Reactions between GeH_4, GeX_4, or GeH_nX_{3-n}, and transition metal complexes (equations 69–74).

$$GeH_4 + HMn(CO)_5 \longrightarrow (CO)_5MnGe(H)_2Mn(CO)_5 \quad (69)$$

$$HGeX_3 + ClMn(CO)_5 \longrightarrow X_3GeMn(CO)_5 \quad (70)$$

$$X = Cl, Br$$

$$H_3GeBr + NaMn(CO)_5 \longrightarrow H_3GeMn(CO)_5 \quad (71)$$

$$GeCl_4 + (bipy)(CO)_4Mo \longrightarrow Cl_3GeMo(CO)_3(bipy) \quad (72)$$

$$H_3GeBr + Na_2Fe(CO)_4 \longrightarrow \textit{trans}\text{-}(H_3Ge)_2Fe(CO)_4 \quad (73)$$

$$GeF_4 + Me_3SiCo(CO)_4 \longrightarrow F_3GeCo(CO)_4 \quad (74)$$

Some of the isolated products can be explained in terms of a series of oxidative addition/reductive elimination intermediates. The orange linear complex $Me_5C_5(CO)_2Mn{=}Ge{=}Mn(CO)_2C_5Me_5$ is formed from the reaction of GeH_4 with $Me_5C_5(CO)_2THF$. The Ge–Mn bond length is 218 pm, indicating a considerable double bond character. When GeH_4 reacts with the less sterically hindered complex $CpMn(CO)_3$, the product is μ_3-$Ge[CpMn(CO)_2]_3$.

Trigonal planar complex (**17**), presumably formed via $(CO)_5WGeCl_2$, is prepared through the reaction of $GeCl_4$ with $Na_2W_2(CO)_{10}$.

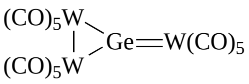
(CO)5W
Ge=W(CO)5
(CO)5W

(**17**)

Schemes 6 and 7 show the types of Ge–Fe compounds and their chemistry.[100]

2. Oxidative addition of Ge–H or Ge–X to a transition metal complex (equations 75 and 76).

$$2GeCl_4 + 2Fe(CO)_5 \longrightarrow \textit{cis-}\text{ and }\textit{trans-}(GeCl_3)_2Fe(CO)_4 + FeCl_2 + 6CO \quad (75)$$

$$GeCl_4 + Cp(CO)_2Co \longrightarrow Cl_3GeCo(CO)(Cl)Cp + (Cl_3Ge)_2Co(CO)Cp \quad (76)$$

Under vigorous conditions, the four-membered ring is produced (**18**).

Adding $HGeCl_3$ to rhodium (I) complexes produces Rh^{III} products that may react further under proper experimental conditions (Scheme 8).

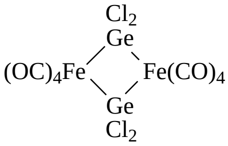
Cl2
Ge
(OC)4Fe
Fe(CO)4
Ge
Cl2

(**18**)

A series of oxidative addition/reductive elimination stages follow the oxidative addition of $HGeCl_3$ to $[PtCl_4]^{2-}$, yielding five- and six-coordinate products: $[Pt(GeCl_3)_5]^{3-}$, with a tbp structure, and the octahedral complexes $[PtH(GeCl_3)_5]^{2-}$ and $[PtCl_4(GeCl_3)_2]^{2-}$. In other cases, the primary oxidative addition product (**19**) can be isolated.

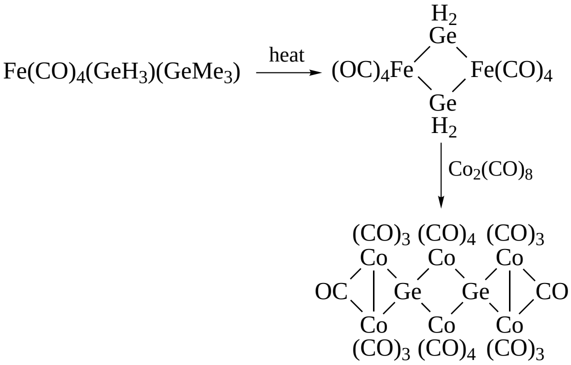
Fe(CO)4(GeH3)(GeMe3)
heat
H2
Ge
(OC)4Fe
Fe(CO)4
Ge
H2
Co2(CO)8
(CO)3 (CO)4 (CO)3
Co Co Co
OC
Ge
Ge
CO
Co Co Co
(CO)3 (CO)4 (CO)3

Scheme 7

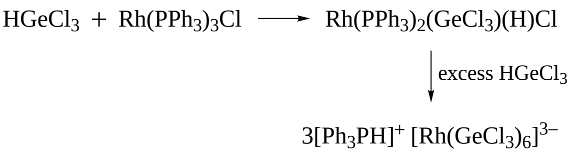
HGeCl3 + Rh(PPh3)3Cl
Rh(PPh3)2(GeCl3)(H)Cl
excess HGeCl3
3[Ph3PH]+ [Rh(GeCl3)6]3–

Scheme 8

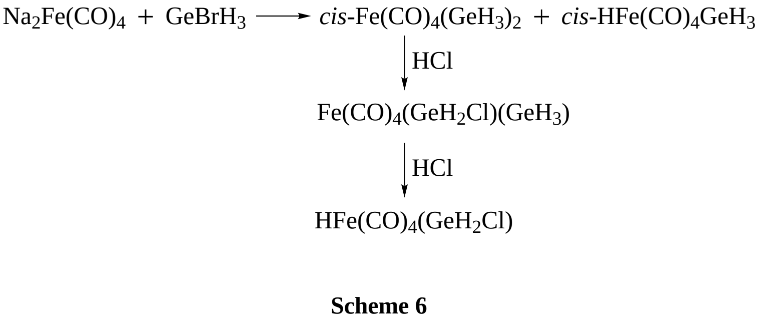
Na2Fe(CO)4 + GeBrH3
cis-Fe(CO)4(GeH3)2 + cis-HFe(CO)4GeH3
HCl
Fe(CO)4(GeH2Cl)(GeH3)
HCl
HFe(CO)4(GeH2Cl)

Scheme 6

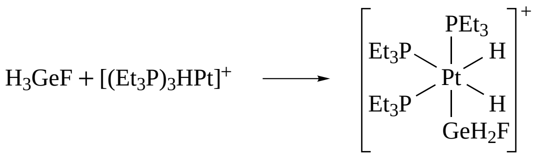

(**19**)

12 POLYOXOMETALATES OF GERMANIUM

The early transition metals (V, Nb, Ta, Mo, W) in their highest oxidation states are able to form metal–oxygen cluster anions, commonly referred to as polyoxoanions**[101]** or polyoxometalates.**[102]** In the gigantic family, the Keggin polyoxoanion is an important and classic subclass. Its general formula is $[XM_{12}O_{40}]^{n-}$ ($X_{\text{heteroatom}} = P^{V}$, Si^{IV}, Ge^{IV}, As^{V}, $M_{\text{coordinated atom}} = Mo^{VI}$, W^{VI}). Ge, as one of heteroatoms, forms two classic Keggin heteropolyoxometalates, $[GeW_{12}O_{40}]^{4-}$ and $[GeMo_{12}O_{40}]^{4-}$, in which heteroatom Ge exhibits $\{GeO_4\}$ tetrahedral geometry and coordinated atoms W or Mo exhibit $\{MO_6\}$ octahedral configuration. Each three edge-sharing $\{MO_6\}$ octahedra constitute a $\{M_3O_{13}\}$ cluster; four such corner-sharing trimetal clusters are arrayed around the center $\{GeO_4\}$ tetrahedron forming a beautiful 'basket' structure (see Figure 2). The forty oxygen atoms in the Keggin anion can be divided into four groups, that is, four O_a, twelve O_b, twelve O_c, and twelve O_t. O_a represents oxygen atoms of a $\{GeO_4\}$ tetrahedron; both O_b and O_c are bridging oxygen atoms, O_b are the common oxygen atoms of different trimetal clusters, while O_c are the common oxygen atoms of a trimetal cluster; O_d are terminal oxygen atoms, that is, noncommon oxygen atoms of each $\{MO_6\}$ octahedron. In the four kinds of oxygen atoms, terminal oxygen atoms (O_d) are the most active, and many new compounds are formed through the further linkages of them. Since the $[GeW_{12}O_{40}]^{4-}$ anion was first found in 1930, extensive research for the potential applications of heteropolyoxogermanates has been carried out. To date, plenty of research work mainly focuses on medicine. In vitro antiviral activities of many polyoxogermanates derivatives have been studied.**[103]** Furthermore, the specific resistance of the compression molded $H_4GeW_{12}O_{40}\cdot 30H_2O$ plate has been studied, which indicates that it may function effectively as partition walls between the anode and cathode chambers of H_2 (catalyst Pt or Pd)/O_2 fuel cells.**[104]** These excellent properties increasingly prompt the development of polyoxogermanate chemistry.

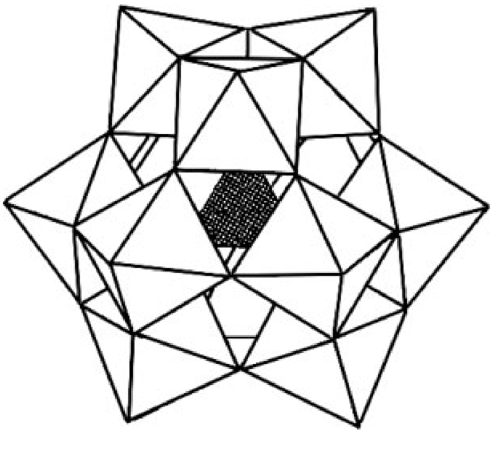

Figure 2 The structure of the Keggin polyoxoanion $[GeM_{12}O_{40}]^{4-}$ (M = Mo or W)

12.1 Preparation and Properties of Classic Keggin Polyoxogermanates

An alkaline germanate solution is added to a solution of molybdate or tungstate, and the mixture is acidified with nitric acid. After a classical Et_2O extraction process, water is added to the separated Et_2O layer. Then the mixture of Et_2O and H_2O is put in a vacuum desiccator with concentrated H_2SO_4, and it is left without disturbance. Finally, yellow or colorless aim crystals with $[GeMo_{12}O_{40}]^{4-}$ or $[GeW_{12}O_{40}]^{4-}$ anions are obtained. Detailed synthetic steps can be seen in Reference 105.

$[GeW_{12}O_{40}]^{4-}$ and $[GeMo_{12}O_{40}]^{4-}$ anions are stable in acid solution, however, when the pH value reaches 5.3 or 7.3, they decompose to GeO_2 and polyoxomolybdate or polyoxotungsten.

12.2 Derivatives of Polyoxogermanates

Polyoxometalates have been found to be extremely versatile inorganic building blocks due to their ability to accept electrons. Being members of them, polyoxogermanates make no exceptions. The oxygen atoms on the surface of polyoxogermanates are rather reactive and are easily combined with the highly oxophilic rare earth ions to form precipitation. However, if suitable organic-ligands-coordinated rare earth ions are introduced, a crystallized product can be obtained. Three lanthanide-containing compounds, $[Ce(NMP)_4(H_2O)_4][GeMo_{12}O_{40}]\cdot 2NMP\cdot 3H_2O$, $[Pr(NMP)_4(H_2O)_4][GeMo_{12}O_{40}]\cdot 2NMP\cdot 3H_2O$, and $[Nd(NMP)_4(H_2O)_4][HGeMo_{12}O_{40}]\cdot 2NMP\cdot 3H_2O$**[106]** have been prepared. In these compounds, the building blocks of $[GeMo_{12}O_{40}]^{4-}$ anions and $[Ln(NMP)_4(H_2O)_4]^{3+/4+}$ cations are connected via hydrogen-bonding interactions, and the whole crystal structure of these compounds displays a two-dimensional supramolecular network with porous structures. By contrast, the two-dimensional network $[\{Ba(DMSO)_3(H_2O)_3\}\{Ba(DMSO)_5(H_2O)\}(GeMo_{12}O_{40})]$**[107]** is formed by covalent linkages of terminal oxygen atoms of $[GeMo_{12}O_{40}]^{4-}$ with Ba^{2+} ions.

With the wide use of hydrothermal and solvothermal synthesis, many polyoxogermanates with unique structures have been prepared. Polyoxoalkoxovanadium germanate, $(NH_4)_2[H_2V_9Ge_8O_{26}(L)_6]\cdot 0.65H_2O$ ($H_2L = HOCH_2CH_2$-

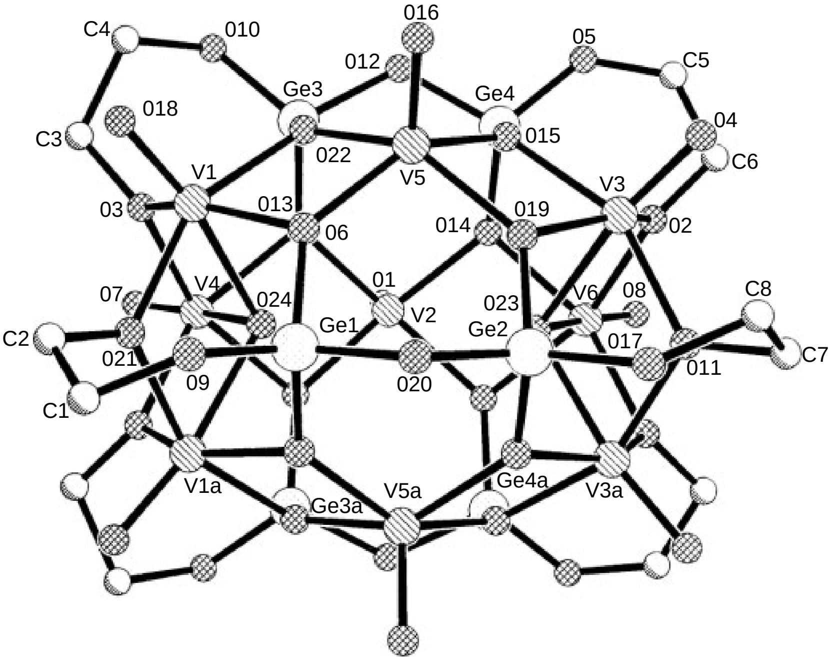
016
C4
010
05
012
C5
Ge3
Ge4
018
04
C3
022
015
C6
V5
V3
V1
013
019
03
014
02
06
01
C8
07
V4
023
V6
08
024
V2
Ge1
Ge2
C2
017
C7
021
011
09
020
C1
V1a
V5a
Ge4a
V3a
Ge3a

Figure 3 The structure of the $[H_2V_9Ge_8O_{26}(L)_6]^{2-}$ polyanion. (Ref. 108. Reproduced by permission of The Royal Society of Chemistry)

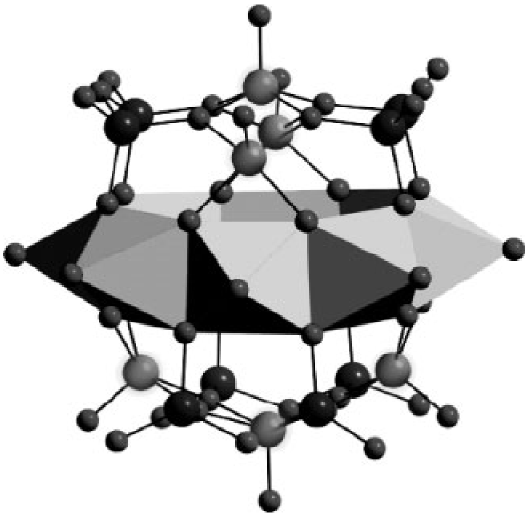

Figure 4 The structure of $[V_{14}O_{44}(GeOH)_8]^{8-}$. Gray polyhedra and large balls represent V, the large black balls represent Ge atoms, and the smallest black balls are oxygen atoms. (Reprinted in part with permission from Ref. 109, © 2003 American Chemical Society)

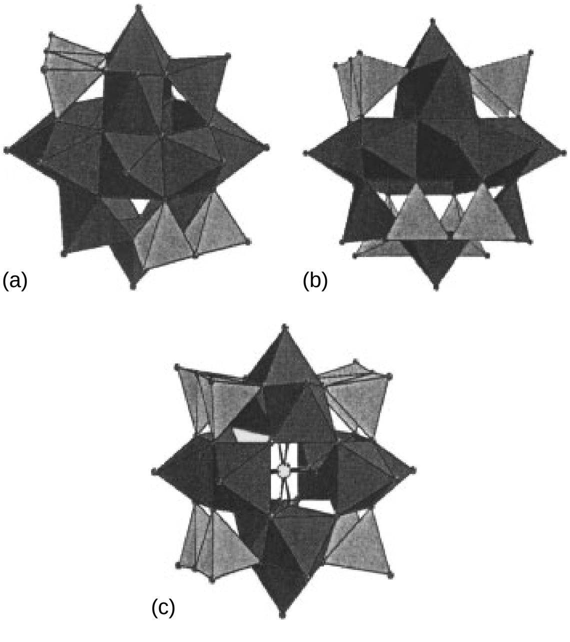

Figure 5 Polyhedral representations of the cluster ions. VO_5 polyhedra are black and GeO_4 polyhedra are gray. (Reprinted in part with permission from Ref. 110, © 2003 American Chemical Society)

OH),[108] is synthesized solvothermally by a mixture of NH_4VO_3, GeO_2, H_2O, and ethylene glycol at 170 °C for 3 d. Its polyanion is made up of six VO_6 octahedra, three VO_5 square pyramids, and six GeO_4 tetrahedra with six bridging ethylene glycol ligands projecting outwards from the central core (Figure 3). $(H_2DAB)_4[V_{14}O_{44}(GeOH)_8]\cdot 6H_2O$ (DAB = 1,4-diaminobutane)[109] is synthesized by a hydrothermal method with the mixture of GeO_2, V_2O_5, DAB, and water at 170°C for 5 d. The structure of the nearly spherical cage includes fourteen tetravalent VO_5 square pyramids sharing edges via basal oxygen atoms and four Ge_2O_7 dimers, as shown in Figure 4. $Cs_8[Ge_4V_{16}O_{42}(OH)_4]\cdot 4.7H_2O$

(a), $(pipH_2)_4(pipH)_4[Ge_8V_{14}O_{50}\cdot(H_2O)]$ (pip $= C_4N_2H_{10}$) (b), and $K_5H_8Ge_8V_{12}SO_{52}\cdot H_2O$ (c),[110] deriving from the cluster anion shell $\{V_{18}O_{42}\}$, although isolated, are the first examples that contain Ge_2O_7 anions incorporated into vanadate polyhedra based on the Keggin cluster anion (Figure 5).

13 RELATED ARTICLES

Germanium: Organometallic Chemistry; Lead: Inorganic Chemistry; Silicon: Inorganic Chemistry; Tin: Inorganic Chemistry.

14 FURTHER READING

M. Zacharias and P. M. Fauchet, *Appl. Phys. Lett.*, 1997, **71**, 380.

15 REFERENCES

1. C. Winkler, *J. Prakt. Chem.*, 1886, **34**, 188.
2. E. G. Rochow, in 'Comprehensive Inorganic Chemistry', eds. J. C. Bailar, H. J. Emeleus, R. Nyholm, and A. F. Trotman-Dickenson, Pergamon Press, Oxford, 1973, Vol. 2, p. 1.
3. Kirk-Othmer, 'Encyclopedia of Chemical Technology', 3rd edn., Wiley, New York, 1980, Vol. 11, p. 791.
4. A. J. Bard, R. Parsons, and J. Jordon, in 'Standard Potentials in Aqueous Solution', Dekker, New York, 1985, p. 207.
5. N. N. Greenwood, A. Earnshaw Greenwood, and N. N. Norman Neill, 'Chemistry of the elements', 2nd edn., reprinted with corrections, Butterworth-Heinemann, Oxford, 1998, p. 429.
6. L. L. Lohr, *Inorg. Chem.*, 1981, **20**, 4229.
7. J. D. Corbett, *Chem. Rev.*, 1985, **85**, 383.
8. S. C. Critchlow and J. D. Corbett, *J. Chem. Soc., Chem. Commun.*, 1981, 236.
9. C. H. E. Belin, J. D. Corbett, and A. Cisar, *J. Am. Chem. Soc.*, 1977, **99**, 7163.
10. N. Bernstein, M. J. Mehl, and D. A. Papaconstantopoulos, *Phys. Rev. B.*, 2002, **66**, 075212.
11. G. R. Burton, C. Xu, C. C. Arnold, and D. M. Neumark, *J. Chem. Phys.*, 1996, **104**, 2757.
12. R. W. Rudolph, R. L. Voorhees, and R. E. Cochoy, *J. Am. Chem. Soc.*, 1970, **92**, 3351.
13. U. Siriwardane, M. S. Islam, J. A. Maguire, and N. S. Hosmane, *Organometallics*, 1988, **7**, 1893.
14. A. Mellor and C.-P. Graebe, *Chem. Ber.*, 1985, **118**, 2020.
15. M. Veith, *Chem. Rev.*, 1990, **90**, 3.
16. M. Veith and M. Grosser, *Z. Naturforsch., Teil B.*, 1982, **37B**, 1375.
17. P. B. Hitchcock, M. F. Lappert, and A. J. Thorne, *J. Chem. Soc., Chem. Commun.*, 1990, 1587.
18. S. R. Foley, C. Bensimon, and D. S. Richeson, *J. Am. Chem. Soc.*, 1997, **119**, 10359.
19. S. R. Foley, Y. L. Zhou, G. P. A. Yap, and D. S. Richeson, *Inorg. Chem.*, 2000, **39**, 924.
20. M. Veith and M. Zimmer, *Z. Anorg. Allg. Chem.*, 1996, **622**, 1471.
21. A. E. Ayers, T. M. Klapötke, and H. V. R. Dias, *Inorg. Chem.*, 2001, **40**, 1000.
22. A. E. Ayers, D. S. Marynick, and H. V. R. Dias, *Inorg. Chem.*, 2000, **39**, 4147.
23. S. Benet, C. J. Cardin, D. J. Cardin, S. P. Constantine, P. Heath, H. Rashid, S. Teixeira, J. H. Thorpe, and A. K. Todd, *Organometallics*, 1999, **18**, 389.
24. M. Stender, L. H. Pu, and P. P. Power, *Organometallics*, 2001, **20**, 1820.
25. M. Veith and W. Frank, *Angew. Chem., Int. Ed. Engl.*, 1985, **24**, 223.
26. A. C. Filippou, P. Portius, and G. Kociok-Köhn, *J. Chem. Soc., Chem. Commun.*, 1998, 2327.
27. W. P. Leung, W. H. Kwok, L. H. Weng, L. T. C. Law, Z. Y. Zhou, and T. C. W. Mak, *J. Chem. Soc., Dalton Trans.*, 1997, 4301.
28. H. H. Karsch, P. A. Schlüter, and M. Reisky, *Eur. J. Inorg. Chem.*, 1998, 433.
29. G. R. Willey, U. Somasundaram, D. R. Aris, and W. Errington, *Inorg. Chim. Acta.*, 2001, **315**, 191.
30. P. Livant, J. Northcott, and T. R. Webb, *J. Organomet. Chem.*, 2001, **620**, 133.
31. A. Meller, G. Ossig, W. Maringgele, D. Stalke, R. Herbst-Irmer, S. Freilag, and G. M. Sheldrick, *J. Chem. Soc., Chem. Commun.*, 1991, 1123.
32. M. Veith, A. Detemple, and V. Huch, *Chem. Ber.*, 1991, **124**, 1135.
33. S. J. Lin, T. N. Hong, J. Y. Tung, and J. H. Chen, *Inorg. Chem.*, 1997, **36**, 3886.
34. J. L. Schreeve-Keyer, R. C. Haushalter, Y.-S. Lee, S. Li, C. J. O'Connor, D.-K. Seo, and M.-H. Whangbo, *J. Solid State Chem.*, 1997, **130**, 234.
35. L. Apostolico, M. F. Mahon, K. C. Molloy, R. Binions, C. S. Blackman, C. J. Carmalt, and I. P. Parkin, *J. Chem. Soc. Dalton Trans.*, 2004, **3**, 470.
36. 'Dictionary of Inorganic Compounds', Chapman and Hall, London, 1992.
37. C. Linke and M. Jansen, *Z. Naturforsch.*, 1996, **51b**, 1591.
38. H.-J. Brandt and H. H. Otto, *Z. Kristallogr.*, 1997, **212**, 34.
39. J. Cheng, R. Xu, and G. Yang, *J. Chem. Soc., Dalton Trans.*, 1991, 1537.

40. X. Bu, P. Feng, T. E. Gier, D. Zhao, and G. D. Stucky, *J. Am. Chem. Soc.*, 1998, **120**, 13389.
41. X. Bu, P. Feng, and G. D. Stucky, *J. Am. Chem. Soc.*, 1998, **120**, 11204.
42. C. Cascales, E. Gutiérrez-Puebla, M. Iglesias, M. A. Monge, and C. Ruíz-Valero, *Angew. Chem. Int. Ed.*, 1998, **37**, 129.
43. C. Cascales, E. Gutiérrez-Puebla, M. Iglesias, M. A. Monge, and C. Ruíz-Valero, *Angew. Chem. Int. Ed.*, 1999, **38**, 2736.
44. P. Feng, X. Bu, and G. D. Stucky, *Chem. Mater.*, 1999, **11**, 3025.
45. P. Pertierra, M. A. Salvado, S. Garcia-Granada, C. Trabajo, and J. R. Garcia, *J. Solid State Chem.*, 1999, **148**, 41.
46. H. Li, M. Eddaoudi, and O. M. Yaghi, *Angew. Chem. Int. Ed.*, 1999, **38**, 653.
47. X. Bu, P. Feng, and G. D. Stucky, *Chem. Mater.*, 2000, **12**, 1505.
48. Y. Zhou, H. Zhu, Z. Chen, M. Chen, Y. Xu, H. Zhang, and D. Zhao, *Angew. Chem. Int. Ed.*, 2001, **40**, 2166.
49. C. Cascales, E. Gutiérrez-Puebla, M. Iglesias, M. A. Monge, C. Ruíz-Valero, and N. Snejko, *J. Chem. Soc., Chem Commun.*, 2000, **21**, 2145.
50. L. Beitone, T. Loiseau, and G. Férey, *Inorg. Chem.*, 2002, **41**, 3962.
51. T. Masuda, B. C. Chakoumakos, C. L. Nygren, S. Imai, and K. Uchinokura, *J. Solid State Chem.*, 2003, **176**, 175.
52. J. Plévert, R. Sanchez-Smith, T. M. Gentz, H. Li, T. L. Groy, O. M. Yaghi, and M. O'Keeffe, *Inorg. Chem.*, 2003, **42**, 5954.
53. Z. Liu, L. Weng., Z. Chen, and D. Zhao, *Inorg. Chem.*, 2003, **42**, 5960.
54. D. Pitzschke and W. Bensch, *Angew. Chem. Int. Ed.*, 2003, **42**, 4389.
55. J. R. Tobias Johnson and I. Panas, *Chem. Phys.*, 1999, **249**, 273.
56. M. O'Keeffe and O. M. Yaghi, *Chem. Eur. J.*, 1999, **5**, 2796.
57. T. Fjeldberg, P. B. Hitchcock, M. F. Lappert, S. J. Smith, and A. J. Thorne, *J. Chem. Soc., Chem. Commun.*, 1985, 939.
58. L. D. Silverman and M. Zeldin, *Inorg. Chem.*, 1980, **19**, 272.
59. K. Kamiya, M. Tatsumi, J. Matsuoka, and H. Nasu, *Phys. Chem. Glasses*, 1998, **39**, 9.
60. V. Stanic, T. H. Etsell, A. C. Pierce, and R. J. Mikula, *J. Mater. Chem.*, 1997, **7**, 105.
61. J. Pola, R. Fajgar, Z. Bastl, and L. Diaz, *J. Mater. Chem.*, 1992, **2**, 961.
62. H. Li, M. Eddaoudi, D. A. Richardson, and O. M. Yaghi, *J. Am. Chem. Soc.*, 1998, **120**, 8567.
63. M. Fourati, *Can. J. Chem.*, 1989, **67**, 1693.
64. T. Hascall, A. L. Rheingold, I. Guzei, and G. Parkin, *Chem. Commun.*, 1998, 101.
65. H. Wiedemeier and H. G. von Schnering, *Z. Kristallogr.*, 1978, **148**, 295.
66. S. Pohl and U. Seyer, *Z. Naturforsch., Teil B*, 1981, **36B**, 1432.
67. M. C. Kuchta and G. Parkin, *J. Chem. Soc., Chem. Commun.*, 1996, 1669.
68. S. R. Foley, G. P. A. Yap, and D. S. Richeson, *J. Chem. Soc., Dalton. Trans.*, 2000, 1663.
69. W. P. Leung, W. H. Kwok, Z. Y. Zhou, and T. C. W. Mak, *Organometallics*, 2000, **19**, 296.
70. H. M. Powell and F. M. Brewer, *J. Chem. Soc.*, 1938, 197.
71. E. Urgiles, P. Melo, and C. C. Coleman, *J. Crystal Growth*, 1996, **165**, 245.
72. A. C. Filippou, J. G. Winter, G. Kociok-Köhn, and I. Hinz, *J. Organomet. Chem.*, 1997, **542**, 35.
73. A. C. Filippou, J. G. Winter, G. Kociok-Köhn, and I. Hinz, *J. Organomet. Chem.*, 1997, **544**, 225.
74. A. C. Filippou, J. G. Winter, G. Kociok-Köhn, C. Troll, and I. Hinz, *Organometallics*, 1999, **18**, 2649.
75. A. C. Filippou, J. G. Winter, G. Kociok-Köhn, and I. Hinz, *J. Chem. Soc. Dalton Trans.*, 1998, 2029.
76. A. C. Filippou, P. Portius, J. G. Winter, and G. Kociok-Köhnœ, *J. Organomet. Chem.*, 2001, **628**, 11.
77. B. Schiemenz and G. Huttner, *Chem. Ber.*, 1994, **127**, 2129.
78. T. Szymánska-Buzar, T. Głowiak, I. Czeluoniak, and M. Górski, *Inorg. Chem. Comm.*, 2002, **5**, 682.
79. G. R. Willey, T. J. Woodman, U. Somasundaram, D. R. Aris, and W. Errington, *J. Chem. Soc., Dalton Trans.*, 1998, 2573.
80. R. Schwarz and E. Z. Baronetzky, *Anorg. Allg. Chem.*, 1954, **275**, 1.
81. D. Shriver and W. L. Jolly, *J. Am. Chem. Soc.*, 1958, **80**, 6692.
82. W. L. Jolly, C. B. Lindahl, and R. W. Kopp, *Inorg. Chem.*, 1962, **1**, 958.
83. K. Mochida, Y. Nakai, and S. Shiota, *Bull. Chem. Soc. Jpn.*, 1988, **61**, 3002.
84. I. R. Beattie, P. J. Jones, G. Reid, and M. Webste, *Inorg. Chem.*, 1998, **37**, 6032.
85. S. Nogai, A. Schriewer, and H. Schmidbaur, *J. Chem. Soc. Dalton Trans.*, 2003, 3165.
86. T. E. Mallouk, B. Desbat, and N. Bartlett, *Inorg. Chem.*, 1984, **23**, 3160.
87. J. E. Griffiths and D. E. Irish, *Inorg. Chem.*, 1964, **3**, 1134.
88. G. M. Begun and A. C. Rutenberg, *Inorg. Chem.*, 1967, **6**, 2212.
89. P. Benkiš and Z. Mazej, *Z. Anorg. Allg. Chem.*, 2001, **627**, 1952.
90. M. Schmidt, P. G. Radaelli, M. J. Gutmann, S. J. L. Billinge, N. Hur, and S. W. Cheong, *Condensed Matter*, 0303247.
91. T. Matsumoto, N. Tokitoh, and R. Okazaki, *J. Am. Chem. Soc.*, 1999, **121**, 8811.
92. N. Tokitoh, K. Kishikawa, T. Matsumoto, and R. Okazaki, *Chem. Lett.*, 1995, 827.
93. N. Tokitoh, T. Matsumoto, and R. Okazaki, *J. Am. Chem. Soc.*, 1997, **119**, 2337.

94. T. Lobreyer, J. Oeler, and W. Sundermeyer, *Chem. Ber.*, 1991, **124**, 2405.
95. S. P. Mallela and R. A. Geanangel, *Inorg. Chem.*, 1991, **30**, 1480.
96. P. J. Davidson, D. H. Harris, and M. F. Lappert, *J. Chem. Soc., Dalton Trans.*, 1976, 2268.
97. D. E. Goldberg, P. B. Hitchcock, and M. F. Lappert, *J. Chem. Soc., Dalton Trans.*, 1986, 2387.
98. S. A. Batcheller, T. Tsumuraya, O. Tempkin, W. M. Davis, and S. Masamune, *J. Am. Chem. Soc.*, 1990, **112**, 9394.
99. K. Kishikawa, N. Tokitoh, and R. Okazaki, *Chem. Lett.*, 1998, 239.
100. S. G. Anema, J. A. Audett, K. M. Mackay, and B. K. Nicholson, *J. Chem. Soc., Dalton Trans.*, 1988, 2629.
101. P. Souchay, ‘Polyanions et Polycations’, Gauthier-Villars, Paris, 1963.
102. M. P. Pope, ‘Heteropoly and Isopoly Oxometalates’, Springer Verlag, New York, 1983.
103. J. T. Rhule, C. L. Hill, and D. A. Judd, *Chem. Rev.*, 1998, **98**, 327.
104. D. E. Katsoulis, *Chem. Rev.*, 1998, **98**, 359.
105. C. R. Deltcheff, M. Fournier, R. Franck, and R. Thouvenot, *Inorg. Chem.*, 1983, **22**, 207.
106. H. Zhang, L. Y. Duan, Y. Lan, E. B. Wang, and C. W. Hu, *Inorg. Chem.*, 2003, **42**, 8053.
107. J. Y. Niu, Q. Wu, and J. P. Wang, *J. Chem. Soc., Dalton Trans.*, 2002, 2512.
108. Y. M. Chen, E. B. Wang, B. Z. Lin, and S. T. Wang, *J. Chem. Soc., Dalton Trans.*, 2003, 519.
109. A. Tripathi, T. Hughbands, and A. Clearfield, *J. Am. Chem. Soc.*, 2003, **125**, 10528.
110. T. Whitfield, X. Wang, and A. J. Jacobson, *Inorg. Chem.*, 2003, **42**, 3728.

Acknowledgment

We are greatly thankful to Dr. Dongrong Xiao, Jian Lü, Yaqin Guo, Yanfei Qi, Xinxin Xu, Chao Zhang, Chunlei Wang, Zhongliang Wang, Linlin Fan for the collection of material; Xinlong Wang and Suoyuan Lian for their preparation of the figures and equations.

Germanium: Organometallic Chemistry

Mark Banaszak Holl & David R. Peck
University of Michigan, Ann Arbor, MI, USA

1 Introduction 1
2 Advances in Physical Chemical Understanding of Organogermanium Compounds 1
3 Methods for Formation and Cleavage of Germanium–Carbon Bonds 2
4 Organogermanium Heterocycles 6
5 Organic Derivatives of Three-Coordinate Germanium 7
6 Organic Derivatives of Two-Coordinate Germanium 9
7 Organic Derivatives of Hypercoordinate Germanium 12
8 Polygermanes 13
9 Biological Activity of Organogermanium Compounds 14
10 Conclusions and Future Prospects of Organogermanium Chemistry 14
11 References 15

1 INTRODUCTION

1.1 Scope

The field of organogermanium chemistry describes those compounds containing at least one germanium–carbon bond. This review describes the major advances made in the field since 1993. For work prior to that time, the reader is referred to the article ‘Germanium: Organometallic Chemistry’ in the first edition of the Encyclopedia of Inorganic Chemistry written by Mikhail P. Egorov and Peter P. Gaspar. The brief history of germanium chemistry included in the first edition, and the sections on the ‘Comparison of Organogermanium Compounds with Other Elements’, and on the ‘Coordination State of Germanium in Organogermanium Compounds’ discuss material that is largely unchanged. It is not repeated here. A new section entitled ‘Advances in Physical Chemical Understanding of Organogermanium Compounds’ has been included, reflecting the advances in both computational chemistry and experimental measurements of the electronic structure of organogermanium compounds.

1.2 Evolution of Interest

In the conclusions of the chapter on organogermanium chemistry for the first edition, Egorov and Gaspar presciently stated that emphasis in the field was ‘... shifting from the accumulation of knowledge about the synthesis and properties of organogermanium compounds to the study of reaction mechanisms and reactive intermediates’. The past decade has seen a major focus on the development of new reactions and the development of novel germanium-based chemistries. This experimental work has been accompanied by major advances in theoretical understanding. There has been a large number of review articles published in the last decade. These can be roughly classified by area: general reviews and discussions of molecular compounds;[1–62] surfaces and materials;[63–69] polymers;[70–75] photochemistry;[76–78] structure;[79,80] biological applications;[47,81–88] spectroscopy and calculations;[89–100] reactivity and reagents.[101–111]

Organogermanium species are still not employed in large-scale synthetic processes, possibly because of the high price as compared to silicon and tin chemistries, and certainly because no chemistry yet discovered was unique enough to warrant the use of the more expensive germanium reagent.

2 ADVANCES IN PHYSICAL CHEMICAL UNDERSTANDING OF ORGANOGERMANIUM COMPOUNDS

The rapid developments in theoretical methods and substantial enhancement of computing power over the past decade have had a dramatic impact on all areas of chemistry including organogermanium chemistry. Advances in computational methods applied to germanium chemistry as well as complementary experiments exploring the electronic structure will be discussed.

2.1 Electronic Structure Calculations Applied to Organogermanium Compounds

The past decade has seen considerable application of density functional calculations to germanium systems. All-electron B3LYP calculations have been applied to germylenes, germynes, germenes, digermenes, and germanones.[112–119] In general, these calculations appear to describe the geometric and electronic structure of germanium systems quite well. For example, B3LYP/6-311G(d, p) structures of CH_3GeH and $(CH_3)_2Ge{=}CH_2$ are nearly identical to those obtained using MP2/DZ + d.[120] Insertion reactions of germylenes have been extensively studied[114,121–124] as well as addition reactions[125] and oxygen atom transfer reactions.[126] Estimation of the standard reduction potential for a stable germylene (a diazagermol-2-ylidene) has been performed using B3LYP/6-31 + G* (-2.88 V vs. SCE) and compared to experimental values for germylenes of this type which showed a reduction wave at ~ -2.8 V.[127]

2.2 Recent Experimental Advances in the Physical Chemistry of Organogermanium Compounds

Photoelectron spectra have been experimentally measured and calculated for (1,3-di-*tert*-butyl-1,3,2-diazagermol-2-ylidene).[128] For this germylene, the HOMO is a π-symmetry orbital containing substantial Ge, N, and C=C π-character. The Ge-based lone pair is actually found to be $\sim$2 eV lower in energy. The He II gas-phase photoemission spectrum is shown in Figure 1.

Gas-phase photoelectron spectra have also been obtained for germaimines, germaisonitriles, and additional germylenes.[129–131]

The electron affinity (31.9 ± 0.7 kcal mol^{-1}) and gas-phase acidity (361.5 ± 2.8 kcal mol^{-1}) for Me_3GeH have been determined using photodetachment spectroscopy.[132] The bond dissociation energy (Ge–H) derived from these values was determined to be 79.8 ± 3.5 kcal mol^{-1}, in excellent agreement with other determinations.[133,134]

Ion/molecule reactions of F^- or MeO^- with $Ge(OMe)_4$ can be used to generate germyl anions such as $Ge(OMe)_3{}^-$ and $GeF(OMe_2)^-$.[135,136] The electron affinities of the corresponding neutral three-coordinate compounds have been calculated and follow the expected trend of increasing electron affinity with an increasing number of electronegative ligands bound to germanium.[133]

Significant progress has also been made in the area of ^{73}Ge NMR spectroscopy.[137,138] The ^{73}Ge nucleus has low natural abundance (7.61%), poor sensitivity (0.00140 at constant field as compared to ^{1}H), and a high spin ($s = 9/2$). These factors combined with a high quadrupole moment have typically resulted in extensive line broadening and efficient quenching of spin–spin coupling with neighboring nuclei. The key exceptions to these problems have been spectra of compounds with high symmetry (T_d or C_{3v}) securing a zero field gradient at the germanium nucleus.[139] Recently, ^{73}Ge NMR spectra have been obtained for a family of aryl germanes $HGePh_3$, H_2GePh_2, and H_3GePh_3 where the Ge–H coupling contants were well-resolved and had values of 98, 94, and 98 Hz respectively.[139] A number of other compounds with substituted aryl groups were reported as well. However, similar germanes with thiophene substitutents showed substantial peak broadening and no ^{1}H-^{73}Ge coupling could be resolved.[140] It has also been noted that hypervalent organogermanes compounds show a much larger ^{73}Ge peak half-width (100–600 Hz) as compared to similar nonhypervalent germanes (25–100 Hz).[141,142] ^{73}Ge NMR have been obtained for organogermanes in the solid state and spin-lattice relaxation times (T1) obtained.[143,144] The ^{73}Ge NMR spectra of a variety of other organogermanes have also been reported.[145–148]

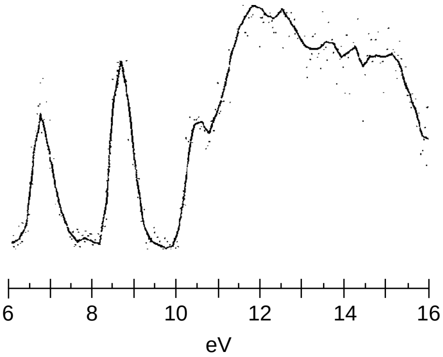

Figure 1 He II gas-phase photoemission spectrum of 1,3-di-*tert*-butyl-1,3,2-diazagermol-2-ylidene

3 METHODS FOR FORMATION AND CLEAVAGE OF GERMANIUM–CARBON BONDS

3.1 Formation of Germanium–Carbon Bonds

An excellent discussion of the primary methods used for germanium–carbon bond formation (direct synthesis, salt elimination, redistribution, and hydrogermylation) was provided in the first edition. The techniques all typically employ Ge(IV) starting materials. Key updates are provided below for these areas as needed. In the past decade, the application of Ge(II) starting materials has allowed observation of the following new germanium–carbon bond forming reactions: C–X insertions, CH-insertions, CH-activations, and formal 4 + 2 cycloadditions.

3.1.1 *Direct Synthesis*

Major advances in the application of the direct synthesis method, reaction of metallic germanium with an alkyl halide, have been realized. Solvochemical activation of germanium via the $Li[Et_3BH]$ reduction of $GeCl_2$•dioxane yields amorphous, orange-colored ‘activated’ germanium.[149] Upon reaction of this material with methyl ester, cyano, and chloro functionalized alkyl bromides at 130–150 °C, germanes of general stoichiometry R_2GeBr_2 can be formed in 80–95% yield. In contrast to industrial direct synthesis, the whole family of organobromogermanes $R_{4-n}GeBr_n$ are not formed. Recent studies on the use of metal chloride catalysts for the direct reaction to make phenylchlorogermanes from metallic germanium and chlorobenzene have also been reported.[150] Additionally, a noncatalyzed method to selectively make phenyltrichlorogermane from a mixture of germanium metal, germanium tetrachloride, and chlorobenzene takes advantage of the in situ generation of divalent germanium, $GeCl_2$, as an intermediate.[151]

In 2002, the formation of a germanium–carbon bond directly from GeO_2 was reported.[152] The synthesis of $MeGe(OMe)_3$ was accomplished by heating a mixture of GeO_2 and 5% KOH to 350 °C in a fixed bed reactor while flowing dimethyl carbonate over the mixture (equation 1).

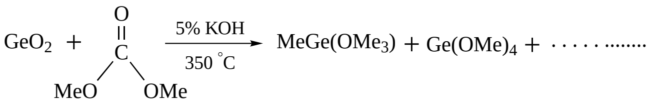

$$GeO_2 + (MeO)_2C{=}O \xrightarrow[350\,^{\circ}\mathrm{C}]{5\%\ \mathrm{KOH}} MeGe(OMe_3) + Ge(OMe)_4 + \cdots\cdots\cdots \tag{1}$$

3.1.2 Hydrogermylation

Chiral organogermanes have been directly synthesized by utilizing C_2-symmetric dithiol complexes[153,154] (equation 2).

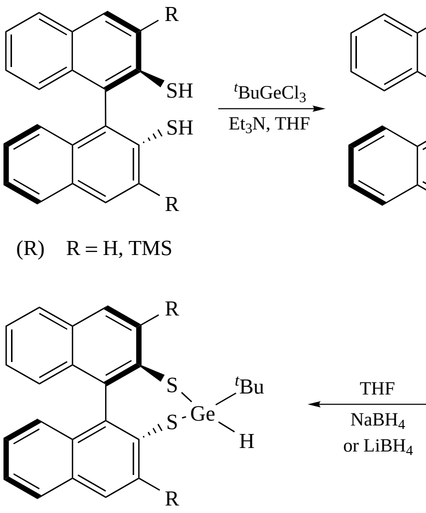

(2)

Dendrimeric macromolecules containing germanium have also been made via hydrogermylation.[155] The cyclization/hydrogermylation of functionalized 1,6-dienes catalyzed by cationic palladium complexes has also been carried out.[156] Hydrogermylation is also an effective synthetic method for the synthesis of germatranes.[157]

Hydrogermylation chemistry has been employed to make germanium–carbon bonds at surfaces via the reaction of alkynes and alkenes with the Ge–H bonds of HF-treated surfaces.[158] Recently, this method has also been employed to functionalize the surface of germanium quantum dots[159] (Figure 2).

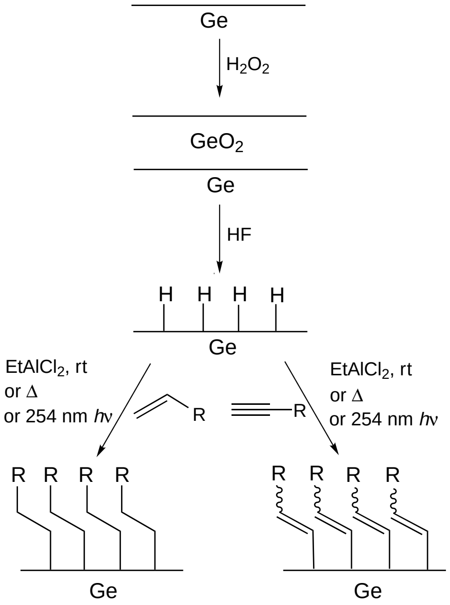

Figure 2 Preparation of hydrogen-terminated Ge followed by hydrogermylation

3.1.3 Salt Elimination

Salt elimination reactions can also be used to form germanium–carbon bonds at surfaces. This has recently been studied for the case of Ge(111)-Cl reacting with Grignard reagents to form self-assembled alkyl monolayers on germanium.[160] The formation of (diarylgermyl) lithium reagents (R_2HGeLi) has allowed the salt elimination reaction to be employed with a greatly enhanced degree of specificity[161] (equation 3).

$$RR'GeH_2 \xrightarrow{{}^{t-}\mathrm{BuLi/THF}} RR'GeHLi \xrightarrow[\mathrm{LiI}]{\mathrm{MeI}} RR'GeHMe \tag{3}$$

3.1.4 C–X Insertion Reactions

Chiral adamantyl cages containing C–Br bonds at the bridgehead carbons will undergo oxidative-addition reactions with $GeCl_2$•dioxane to yield chiral germanes.[162]

3.1.5 C–H Insertion Reactions

The first report of germylene insertion into a CH-bond occurred in 1987.[163] Subsequently, it was demonstrated that this reactivity was Lewis acid dependant.[164] Intramolecular CH-insertion has also been observed as part of the reaction of silylene insertion into $Ge[N(SiMe_3)_2]_2$ and occurs spontaneously for a remarkable germylene containing a Fe–Ge bond.[165,166] In addition to these solution-phase reactions, Me-Ge-$SiMe_3$ can be thermally generated by the reductive elimination of $HSiMe_3$ from $MeHGe(SiMe_3)_2$. This germylene subsequently undergoes an intramolecular C–H insertion reaction to generate 1,1,2-trimethyl-silagermirane[167] (Figure 3). In this case, Lewis acids do not appear to play a role.

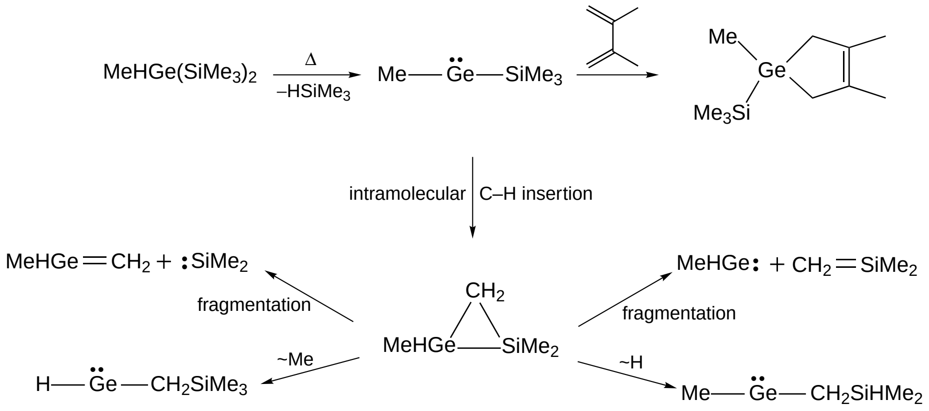
MeHGe(SiMe3)2
Δ
–HSiMe3
Me—Ge—SiMe3
Me
Ge
Me3Si
intramolecular C–H insertion
MeHGe=CH2 + :SiMe2
fragmentation
CH2
MeHGe—SiMe2
MeHGe: + CH2=SiMe2
fragmentation
~Me
H—Ge—CH2SiMe3
~H
Me—Ge—CH2SiHMe2

Figure 3 Thermal generation of a germylene followed by intramolecular C–H bond insertion

Intermolecular CH-insertion chemistry has been achieved for the cases of nitriles[168] and acetyl groups[169] by employing $Ge[CH(SiMe_3)_2]_2$ accompanied by a salt promoter (equation 4).

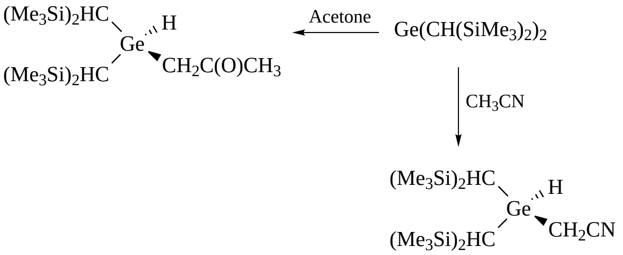
(Me3Si)2HC
H
Ge
(Me3Si)2HC
CH2C(O)CH3
Acetone
Ge(CH(SiMe3)2)2
CH3CN
(Me3Si)2HC
H
Ge
(Me3Si)2HC
CH2CN

(4)

For the case of nitriles, LiX (X = Cl, Br, I) or $MgCl_2$ were shown to be effective. For the case of acetyl groups, only $MgCl_2$ effectively promoted the reaction.

This reaction has attracted recent theoretical attention in the form of Density Functional calculations.[114,121] These studies indicate that CH-insertion chemistry should be favored for germylenes containing bulky, electropositive substituents and disfavored for germylenes containing electronegative or π-donating substituents. Provocatively, it is suggested that unactivated C–H bonds such as methane should be amenable to germylene-based CH-insertion chemistry.

3.1.6 *CH-activation Reactions*

An initial report of CH-activation for the formation of germanium–carbon bonds appeared in 2003[170] (Figure 4).

A mixed reagent formed from $Ge[CH(SiMe_3)_2]_2$ or $Ge[N(SiMe_3)_2]_2$ and PhX (X = Cl, Br, I) was shown to reaction directly with alkanes (cyclohexane, cyclopentane, butane, methylcyclopentane), aromatics (toluene, ethyl

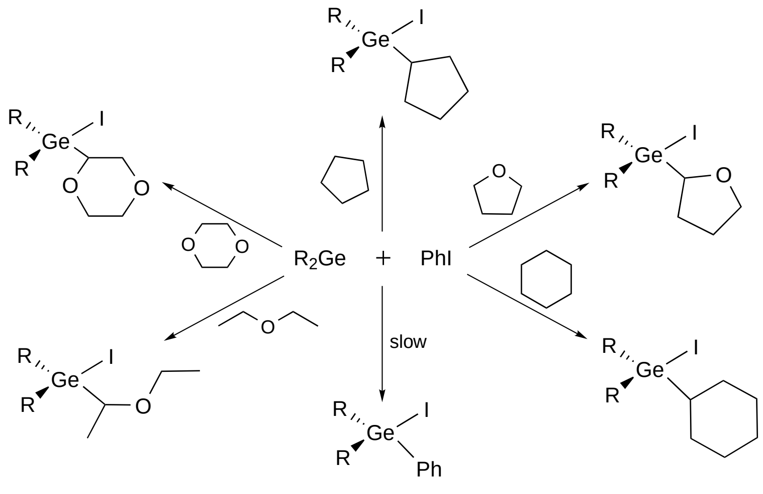
R
Ge
I
R
O
R2Ge + PhI
slow
Ph

R = CH(SiMe3)2, N(SiMe3)2

Figure 4 Intermolecular CH-activation reactions reported for GeR_2/PhI reagent

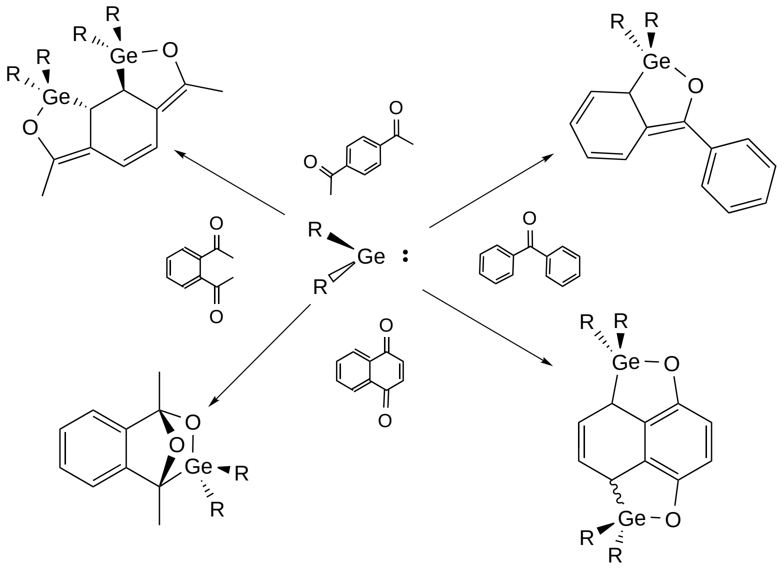

Figure 5 Reactions of GeR_2 with phenone and quinones

benzene, cumene), and ethers (tetrahydrofuran, diethyl ether, 1,4-dioxane) to yield products of the general form L_2GeRX. The regioselectivity of the reaction was observed to be radical-like: tertiary > secondary > primary.

3.1.7 *Formal 4 + 2 Cycloadditions*

Germanium–carbon bond formation can also be achieved with Ge(II) by taking advantage of formal 4 + 2 cycloaddition reactions. For example, it was shown in the 1970s that $GeCl_2$ will reaction directly with butadiene to form 1,1-dichlorogermacyclopent-3-ene, albeit in a low 15% yield.[171] This general reaction was extended to include phenones and quinines[172,173] (Figure 5).

The germylene forms new bonds with the ketone oxygen and the ortho carbon of the adjacent phenyl group to form a five-membered ring.

Cycloadditions have also been used to form germanium–carbon bonds at germanium surfaces. For example, 1,3-butadiene and 2,3-dimethyl-1,3-butadiene react with the dimers present on Ge(100)-2x1 to form a six-membered ring and two new Ge–C bonds.[174,175] Reactions with other unsaturated species such as ethylene, ketones, and nitriles have also been explored.[176–179]

3.2 Reactions of Germanium–Carbon Bonds

Although several methods for the formation of germanium–carbon bonds now exist, the chemistry of germanium–carbon bond reactions remains woefully underdeveloped by comparison to silicon and tin. The importance and utility of many of the formation reactions will likely remain low until a set of reactivity can be developed that mirrors the important chemistry of the Sn–C (Stille-Migata-Kosugi reaction) and Si–C bonds (Hiyama reaction). The general reactivity towards oxygen and sulfur, halogens, acids, and nucleophiles was previously reviewed in the first edition. This section will focus on new developments of the past decade.

3.2.1 *Reductive Cleavage*

Reduction of R_2GeX_2 compounds to transiently yield R_2Ge species followed by trapping with alkynes is a well-established method for making Ge–C bonds in the form of germacyclopropenes.[180–182] Recently, it has been discovered that lithium reduction of the germacyclopropene generates the corresponding dilithiogermane and an equivalent of the original alkyne[183] (equation 5).

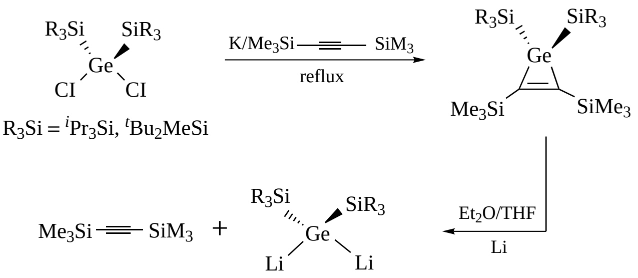

(5)

3.2.2 *Cross-coupling Reactions*

Palladium-catalyzed cross-coupling of a variety of alkyl groups with germatranes and carbogermatranes with aryl halides has recently been demonstrated.[184,185]

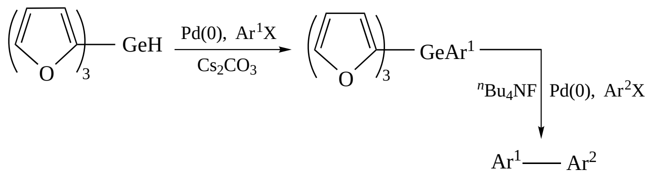

(6)

The internal coordination of the nitrogen to germanium is thought to be the source of the increased reactivity of these species as compared to tris(alkoxy) germanes. Significant improvements in cross-coupling have also been realized by employing tris(2-furyl)germane[186] (equation 6).

4 ORGANOGERMANIUM HETEROCYCLES

4.1 Heterocycles Containing Germanium in an Aromatic Ring

An important milestone in the field of organogermanium heterocycles was achieved over the past decade with the syntheses and full characterization of germabenzene and 2-germanaphthalene.[187–190] In both cases, kinetically stabilized compounds were obtained by employing 2,4,6-tris[bis(trimethylsilyl)methyl]phenyl (Tbt) ligated to germanium. On the basis on NMR, UV-Vis, and Raman spectra it was concluded that a significant amount of aromatic character existed for both the germabenzene and the 2-germanaphthalene. The amount of electronic stabilization is not sufficient to prevent the Ge–C bond from reacting like a typical germanium–carbon double bond. For example, the Ge–C bond of germabenzene reacts in a $4 + 2$ sense with styrene and phenylacetylene and in a $2 + 4$ sense with dimethylbutadience and mesitonitrile (Figure 6).

In addition, both water and methanol are observed to add across the Ge–C bond. Similar results were obtained for the 2-germanaphthalene. Sulfur and selenium have also been observed to add across the Ge–C bond.[191,192] Although these compounds show spectroscopic and structural data consistent with aromatic behavior, their reaction chemistry is generally more like a germanium–carbon double bond and does not exhibit significant signs of deactivation as noted for the all organic parent compounds benzene and naphthalene. Germabenzene has been successfully employed to make η^6-π-complexes of both Cr and Mo.[193]

4.2 Nonaromatic Organogermanium Heterocycles

A wide variety of other organogermanium heterocycles have been synthesized, characterized, and applied to a variety of synthetic transformations. Selected examples are discussed below.

4.2.1 Three-membered Rings

A particularly interesting three-membered ring, an alkylidenetelluragermirane, provides a convenient route to a 1-germaallene via abstraction of tellurium with hexamethylphosphorus triamide.[194,195] Analogous rings can also be synthesized containing Se or S. Another novel three-membered ring recently synthesized is a germacyclopropylbenzene.[196] Heterocyclic three-membered rings can also be made via atom transfer to M–Ge bonds.[197]

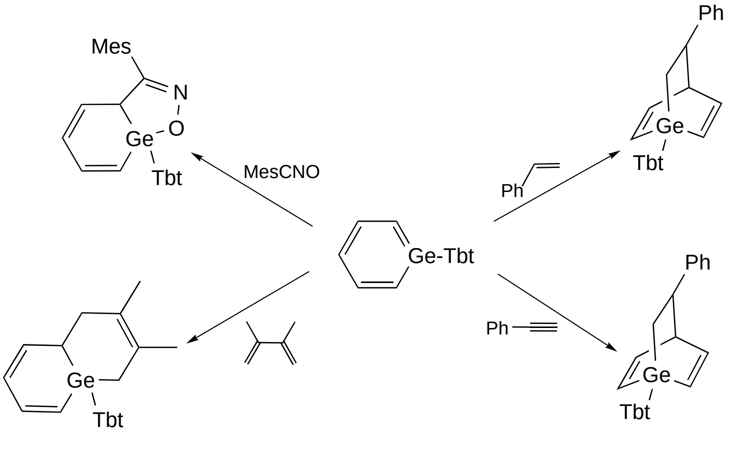

Figure 6 Cycloaddition reactions of germabenzene

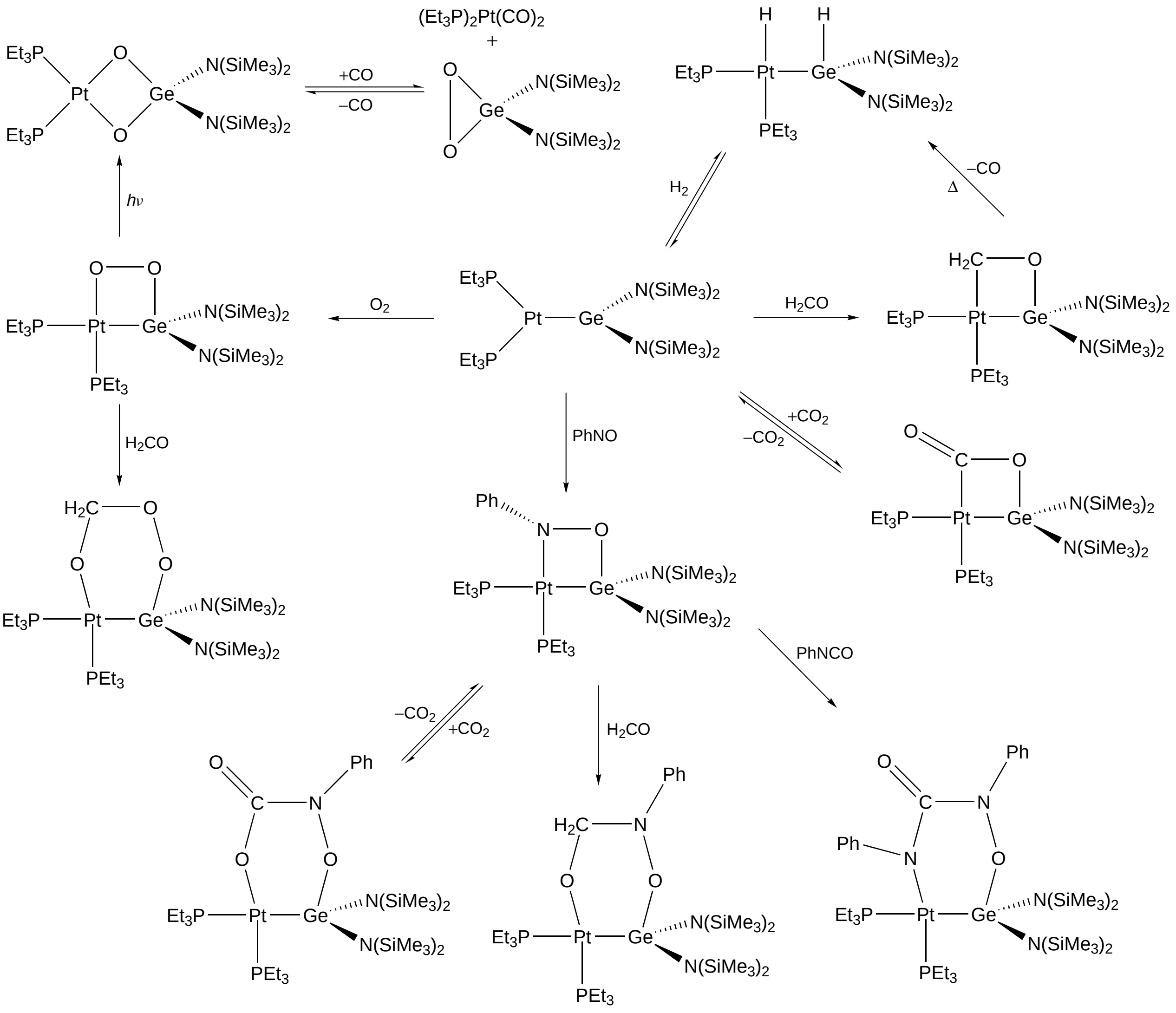

Figure 7 Examples of heterocycle formation and reactions using $(Et_3P)_2PtGe[N(SiMe_3)_2]_2$

4.2.2 *Four- to Six-membered Rings*

Cycloaddition reactions are common routes to the formation of four- to six-membered ring heterocycles. Germylenes,[198,199] germenes,[200–203] and metal germylene complexes[204–209] have been utilized extensively for these reactions (Figure 7).

Absolute rate constants for the head-to-tail [2 + 2]-dimerization of 1,1-diphenylgermane have been measured.[200] Heterocyclic rings can also be made by metathesis reactions using germanium halides.[210,211] Five-membered ring heterocycles can make effective cyclopentadienyl (Cp) analogs as exemplified by the η^5-germolyl complexes that have been made for Zr and Hf.[212,213] The germanium in the ring can be used to bond to another metal and heterobimetallic Hf–Ir and Hf–Rh complexes have been synthesized.[214]

The detailed structure of germacyclobutane has been studied using gas-phase electron diffraction.[215]

5 ORGANIC DERIVATIVES OF THREE-COORDINATE GERMANIUM

Three-coordinate organogermanium complexes will be discussed in terms of seven primary classes: (1) germanium-centered radicals, (2) germenes, (3) germanium with a double bond to an element other than carbon, (4) aromatic germanium rings, (5) cationic compounds, (6) three-coordinate germylenes, and (7) germylenes acting as donors in transition metal complexes.

5.1 Germanium-centered Radicals

Persistent and stable organogermanium radicals were recently reviewed as part of a comprehensive article on 3rd row and heavier main group radical species.[216] In 2002, the first example of a stable, three-coordinate R_3Ge germanium radical was reported (equation 7).[217]

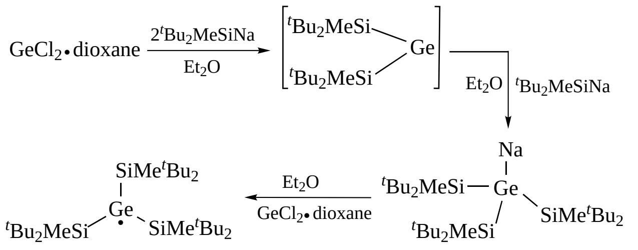

(7)

This remarkable compound, Ge[SiMe^{t}Bu$_2$]$_3$, was characterized by mass spectrometry, UV/vis spectroscopy, electron paramagnetic resonance (EPR), and X-ray crystallography. Two stable germanium radicals containing germanium triangles have been isolated. Both [2,6-Mes$_2$C$_6$H$_3$Ge]$_3$ and 1,6,7-trigermabicyclo[4.1.0]hept-3-en-7-yl have also been characterized by EPR and X-ray crystallography (Figure 8).[218,219]

Calculations on organometallic radicals such as GeCH$_3$ and GeC$_2$H$_5$ have been performed because of relevance of these species to chemical vapor deposition.[220]

5.2 Germenes

Many reviews have been written recently on the subject of germenes[4,45,96,221,222] and they have been the subject of numerous computational studies.[112,223–227] In the absence of sterically bulky ligands, germenes rapidly dimerize or react with available substrates. For this reason, germenes are frequently studied as transient, reactive intermediates[77,200,228,229] isolated in a matrix,[230,231] or inferred from trapping reactions.[232,233]

Sterically bulky ligands allow the isolation of stable germenes. A recent example was made via the reaction of 2 equivalents of a sterically bulky germylene with CS$_2$ to yield a germaketenethioacetal.[234] Germenes have been applied to a variety of reactions with organic molecules.[201,235]

The synthesis of stable germaallenes and 1,3-germaphosphaallenes has occurred in the past decade.[195,236–238] These species are reactive towards atom transfer reactions (S, Se, Te), additions of O–H bonds, and cycloaddition chemistry at the Ge=C bond.[203,239,240]

5.3 Compounds with Ge Double Bonds to Elements Other Than Carbon

5.3.1 *Heavy Ketone Analogs of Germanium (O, S, Se, Te)*

Substantial progress has been made synthesizing stable 'heavy ketone' analogs of germanium R$_2$Ge=E (E = O, S, Se, Te).[20,26,30,241–247] A number of computational studies have been reported.[248–251] The germanone can only be generated solution, it has not yet been isolated as a stable species. The reaction products of germanone decomposition have been studied.[252,253] Germanones are frequently invoked as transient species present in reactions.[199,254,255]

5.3.2 *Organogermanium Imines*

A number of reports of stable R$_2$Ge=NR species have appeared.[256–259] The stable germaphosphene Mes$_2$Ge=PAr has been shown to react in a 4 + 2 sense with *o*-quinones and α-diketones.[260]

5.3.3 *Organogermanium Compounds Containing Ge=Si, Ge=Ge, and Ge=Sn Bonds*

The synthesis and reactivity of germanium compounds containing double bonds to Si, Ge, and Sn has been a very active area of research over the past decade and has been extensively and recently reviewed.[1,40,261,262] Particularly striking

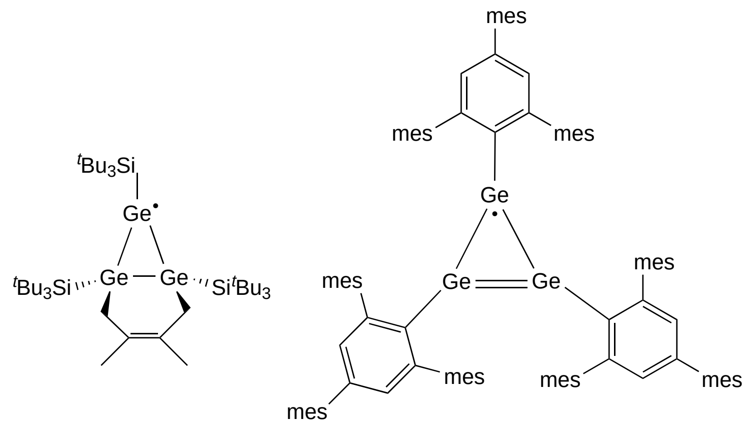

Figure 8 Stable germanium radicals based upon a germanium triangle

new examples of molecules include a hexaaryltetragermabuta-1,3-diene containing conjugated Ge–Ge double bonds,[263] a four-membered ring composed of 2 Si atoms, 2 Ge atoms, and a Ge=Ge,[264] and the synthesis of the first Ge=Sn.[265] In addition, general methods for making digermenes with mixed aryl and alkyl substituents was demonstrated.[266] Digermenes that are analogs of cyclopropenes have also been synthesized.[1,267,268]

A series of detailed mechanistic studies have been published delineating the addition reaction of carbonyl compounds, alkenes, Grignard reagents, and halocarbons to digermenes, germasilenes, and disilenes.[269–282] The preference of biradical intermediates (for disilenes) and zwitterionic intermediates (for germasilenes and digermenes) provides insight into the different reactions observed for germanium and silicon organometallics. Detailed laser pulse photolysis and ^{1}H Chemically Induced Dynamic Nuclear Polarization (CIDNP) studies of the photolysis of 7,8-digermabicyclo[2.2.2]octadiene have provided insight into the reverse reaction to form alkene and digermene.[283,284]

5.4 Aromatic Germanium Rings

The germanium-ring cyclopropene analogs can be oxidized to yield 2π-electron aromatic rings.[1,285–287] These compounds, $[^t\text{Bu}_3\text{EGe}]_3^+[\text{BF}_4]^-$ (E = Si, Ge), are not technically organometallic compounds, as no Ge–C bonds are present; however, this remarkable discovery is included here because of the significance of this chemistry and its close relationship to the chemistry discussed in Section 5.3. These compounds can be further converted to a cationic trishomoaromatic cluster with a Ge_{10} core.[288,289]

5.5 R_3Ge Cations

Simple three-coordinate organogermanium cations, R_3Ge^+, have not yet been isolated and characterized crystallographically. There are two reports of the cations being generated in solution, $[\text{Mes}_3\text{Ge}]^+$ and $\{[(\text{Me}_3\text{Si})_2\text{CH}]\text{Me}_2\text{Si}\}\{[4\text{-}tert\text{-Bu-C}_6\text{H}_4]_3\text{C}\}\{\text{Me}_2\text{Si}\}\text{HCMe}_2\text{Ge}^+$, and characterized by ^{1}H and ^{13}C NMR.[290,291] Both compounds were obtained using the $[\text{B}(\text{C}_6\text{F}_5)_4]^-$ anion. In addition to these compounds, the protonated digermyl ether, bis(trimethylgermyl)oxonium, has been studied by X-ray crystallography. The existence of a long Ge–O bond and a flattening of the pyramidal geometry around Ge are both consistent with the development of a substantial positive charge on Ge.[292] Norbornyl cations have also been generated, although these species are more realistically considered five-coordinate species.[293] Lastly, an isolable free germylium cation, $[^t\text{Bu}_2\text{MeSi}]_3\text{Ge}^+$, has been fully characterized including by X-ray crystallography.[294] Note that like the cation three-membered rings described in Section 5.4, this compound does not contain a Ge–C bond.

5.6 Three-coordinate Germylenes

The use of the bidentate, anionic amidinate ligands has allowed the synthesis of three-coordinate germylene compounds.[247] Carbenes have been used as the ligand in the third site although this results in a very long Ge–C bond and may be best considered as an acid-based adduct.[295] In general, base-adducts of germylenes are a very well explored area of chemistry and are not being considered in this class of three-coordinate germylene complexes. The first example of a germanium(II) hydroxide was recently reported as a three-coordinate germylene.[296]

5.7 Germylenes Acting as Donors to Transition Metals

Over the past decade, several more transition metal germylene complexes with μ_1 coordination have been synthesized and characterized by X-ray crystallography for Mo,[297] W,[298,299] Rh,[300] Ir,[301] Ni,[302,303] Pd,[304] and Pt.[305] Germylenes bound in an μ_2 sense have been synthesized and characterized by X-ray crystallography for Cr,[306] Mo,[307] W,[307] Mn,[308] Fe,[309–311] Ru,[312–314] Os,[315,316] Co,[317] Rh,[318] and Pt.[314]

6 ORGANIC DERIVATIVES OF TWO-COORDINATE GERMANIUM

6.1 Organogermylenes

Substantial progress in both the synthesis and reactivity of germylenes has been made in the past decade. The development of a high-yield, convenient synthesis of $\text{GeCl}_2\cdot$dioxane has greatly helped the field.[319] Numerous reviews have been published.[3,21,22,30,37,56,109,320]

6.1.1 Preparation of Organogermylenes

Germylenes can be made via a number of synthetic pathways including thermal or photochemical elimination reactions and redistribution reactions (see 1st edition). These methods are particularly convenient for generating germylenes that are not stable as monomers. The most flexible method for making sterically bulky, monomeric germylene is salt elimination. The reagent of choice has typically been $\text{GeCl}_2\cdot$dioxane which is best prepared by organosilane-based reduction of $GeCl_4$.[319] Other important synthetic methods have included alcoholysis and metathesis reactions employing $Ge[N(SiMe_3)_2]_2$ and direct reduction of R_2GeCl_2. New examples of germylenes synthesized are found for the classes of alkyl,[321] aryl,[322–324] carbodiimide,[325,326] and 1,8-di(isopropylamino)naphthalene ligands.[302]

Considerable progress has been in the area of heteroleptic germylenes. Cyclopentadienyl derivatives include $(Me_2NCH_2CH_2)Me_4C_5GeCl$,[327] Cp*GeCl, $[Cp^*GeBr]_2$ and $[Cp^*Ge][BF_4]$.[328] The use of the supermesityl ligand, $(^tBu_3C_6H_2)$, has allowed the isolation of $^tBu_3C_6H_2GeCl$, $^tBu_3C_6H_2Ge[Fe(CO)_2Cp]$, and $^tBu_3C_6H_2Ge\mu_2\text{-}Cp^*$.[166] A transiently stable heteroleptic germylene was obtained by the reduction of $(Me_3Si)_3CGeBr_3$ with magnesium to yield $(Me_3Si)_3CGeBr$.[329] The germylene fragment has also been incorporated into a variety of heterocyclic frameworks containing both Ge–O and Ge–S bonds.[330] Application of the bis(2-pyridyl)bis(trimethylsilyl)methyl ligand (2-$\{(Me_3Si)_2\}$-C_5H_4N) has allowed the isolation of [Ge(2-$\{(Me_3Si)_2\}$-C_5H_4N)X] compounds (X = Cl, $CH(PPh_3)_2$).[331]

This last example fits in the general class of base-stabilized germylenes and the ligand has also been employed to make homoleptic examples.[246] Nitrogen base stabilization has been used for several other examples even allowing the rather shocking isolation of a heteroleptic germylene containing a hydroxyl as one of the ligands.[332–335] Aryl ligands containing ether functionality in the ortho position have also been developed.[334,336]

Photochemical methods have been particularly popular for generating transiently stable germylenes. Example precursors include cyclotrigermanes,[337] disiladigermacyclobutane,[338] siladigermiranes,[339] and 1,2-digermacyclobutane.[340] The electronic structure of nitrogen stabilized germylenes has been pursued experimentally using photoelectron spectroscopy as well as theoretically.[118,128]

Evidence for the formation of a surface stabilized organogermylene has also been presented.[341] Lastly, both experimental and theoretical papers have appeared describing the formation of germylene radical anions.[127,342,343]

6.1.2 *Reaction of Germylenes*

Germylenes have long been known to react with multiple bonds such as C=C, C≡C, and C=O. In addition, insertion reactions into carbon halogen, O–H, and N–H bonds, are well precedented. In the last 10 years, substantial progress has been made in the reaction with C–H bonds.

Insertion of Germylenes into σ-bonds. The discussion of germylene insertion into C–X and C–H σ-bonds was presented in Sections 3.1.4 and 3.1.5. Germylene insertion into a variety of other σ-bonds is a common reaction that is been observed for E–H (Si, Ge), and M–X bonds. Selected recent examples include insertion into W–Cl[328] and Si-bonds.[337]

CH-bond Activation Using Germylenes. The discussion of CH-activation using germylenes was presented in Section 3.1.6.

Addition of Germylenes to Multiple Bonds. Addition reactions of germylenes to the C=O of para quinones typically yield alternating 2:1 polymers. An exception was noted for $Ge[N(SiMe_3)_2]_2$ which gave a 1:1 polymer upon reaction with 1,4-quinones.[344–347] Cyclic α, β-unsaturated ketones and ethylene and propylene sulfide have also been found to be excellent monomers for the formation of alternating copolymers.[348–350] Recall that related reactions with quinones and phenones noted in the Ge–C bond formation Section (3.1.7) lead to the dearomatization of the ring and the isolation of molecular products.[173] For 1,4-napthoquinone, both molecular and polymeric products have been observed (equation 8).

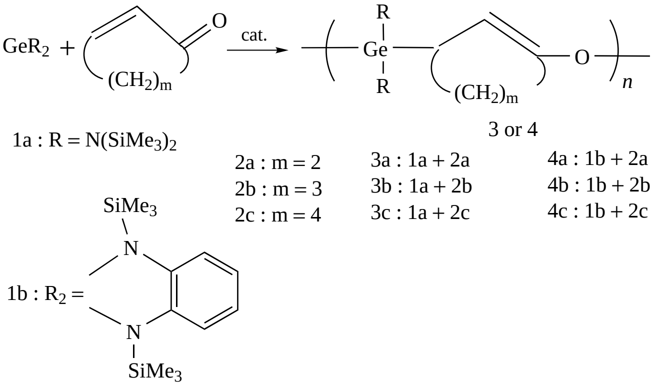

(8)

Reduction of Germylenes. Reduction of $Ge[CH(SiMe_3)_2]_2$ in tetrahydrofuran using a sodium mirror results in the formation the radical anion.[342] The solution changes from the yellow−orange color associated with the germylene ($\lambda_{max} = 410$ nm) to green ($\lambda_{max} = 666$ nm) and a strong 1:2:1 triplet with a hyperfine splitting $a = 2.6$ G appears in the EPR spectrum. Four weak satellites ($a = 12.5$ G) are also apparent arising from the I = 9/2 ^{73}Ge nucleus (7.61% abundance).

Reaction of Germylenes with Chalcogens. Germylenes react with elemental chalcogens or chalcogen transfer reagents to give compounds of general formula R_2GeY (Y = S, Se, Te).[351]

Reactions of Germylenes with Stabilized Radicals. The stable germylene $Ge[C_4H_4(SiMe_3)_4]$ reacts with 2 equivalents 2,2,6,6-tetramethylpiperidine N-oxide (TEMPO, -ONR$'_2$) to yield the addition product $(R'_2NO)_2Ge[C_4H_4(SiMe_3)_4]$.[352,353] Heating this product extrudes TEMPO, 2,2,6,6-tetramethylpiperidine, and a 1,3-digermadioxetane.

6.2 Multiple-bonded Species

6.2.1 Compounds Containing a Ge Triple Bond

The digermenium analog of an alkyne, Ar*GeGeAr* was synthesized and characterized (Ar* = C_6H_3-2,6Trip$_2$; Trip = C_6H_2-2,4,6-$Pr^i{}_3$) (Figure 9). The compound exhibits a trans-bent structure (Ge–Ge–C = 128.67(8)°; Ge–Ge bond 2.2850(6) Å) similar to that reported for both the Si and Sn analogs and as anticipated by calculations.[354] Cyclic voltammetry in THF displayed a reduction wave at −1.38 V and an oxidation wave at +0.7 eV. Reduction of Ar*GeCl or Ar′GeCl (Ar′ = C_6H_3-2,6-Dipp$_2$, Dipp = C_6H_3-2,6-$Pr^i{}_2$) yielded the neutral alkyne analogs as well as the singly reduced species (NaAr*GeGeAr* and KAr′GeGeAr′) and the doubly reduced species (Li_2Ar′GeGeAr′, Na_2Ar*GeGeAr*, and K_2Ar*GeGeAr*).[355–358] Similar compounds have also been synthesized for Sn.

Reaction with one equivalent of a diphenyl acetylene yields a stable digermacyclobutadiene. Two equivalents of the less sterically hindered alkyne $HCCSiMe_3$ react to give a unique bicyclic compound[359] (equation 9).

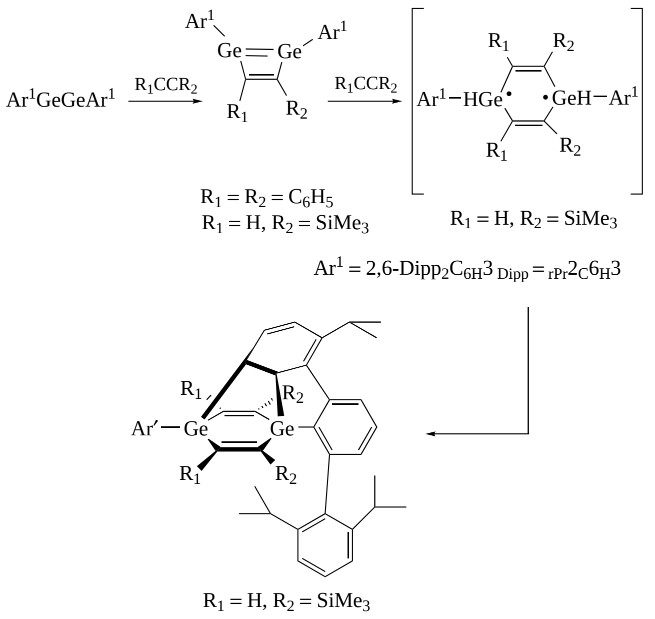

(9)

The Metal–germanium Triple Bond. Metal–germanium complexes with the connectivity RGe–M can be considered as germylenes containing one transition metal ligand, for example, (supermesityl)ferriogermylene, or as germylynes containing a germanium–metal triple bond (Figure 10).

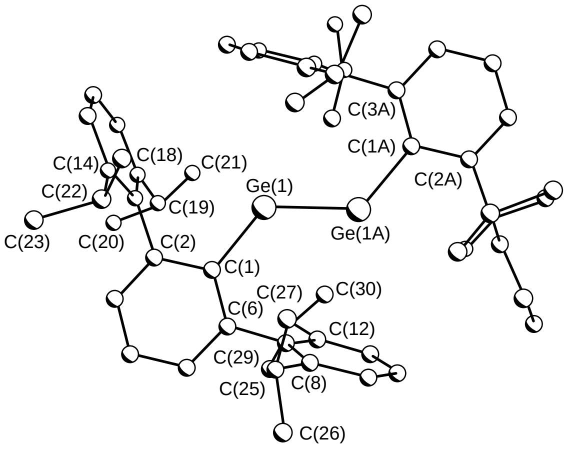

Figure 9 X-ray crystal structure of Ar*GeGeAr*

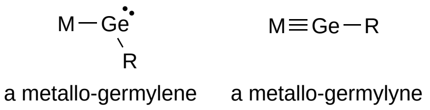

Figure 10 Lewis structures of metallo-germylene and metallo-germylyne

A series of complexes have been reported that allow a direct comparison between these two cases.[360] The metallo-germylene complexes of Cr and W were prepared by the metathesis reaction of the requisite organometallic anion with $Ge(Cl)\{C_6H_3\text{-}2,6\text{-}Trip_2\}$ (equation 10).

$$\mathrm{Na[M(}n^5\mathrm{\text{-}C_5H_5)(CO)_3]\cdot 2DME + Ge(Cl)\{C_6H_3\text{-}2,6\text{-}Trip_2\}} \xrightarrow[\substack{\mathrm{M = Cr}\\ \mathrm{M = W}}]{\text{PhMe, }-78\text{ to }25\,^\circ\text{C}} (n^5\mathrm{\text{-}C_5H_5)(CO)_3M\text{-}\ddot{G}e\text{-}C_6H_3\text{-}2,6\text{-}Trip_2 + NaCl} \tag{10}$$

Subsequent thermal or photolytic loss of CO results in conversion of the metallo-germylyne complex (equation 11).

$$(n^5\mathrm{\text{-}C_5H_5)(CO)_3M\text{-}\ddot{G}e\text{-}C_6H_3\text{-}2,6\text{-}Trip_2} \xrightarrow[\substack{-\mathrm{CO}\\ \mathrm{M = Cr}\\ \mathrm{M = W}}]{\text{reflux PhMe or }h\nu} (n^5\mathrm{\text{-}C_5H_5)(CO)_2M{\equiv}Ge\text{-}C_6H_3\text{-}2,6\text{-}Trip_2} \tag{11}$$

The metallo-germylenes exhibit C–Ge–M bond angles of 117.9(3)° and 114.7(6)° for Cr and W, respectively, consistent with the presence of a stereoactive lone pair on germanium. By way of contrast, the metallo-germylynes exhibit C–Ge–M bond angles of 175.99(6)° and 170.9(3)° for Cr and W, respectively, consistent with the linearity anticipated for a metal–germanium triple bond. The germanium–metal bond distances, 2.590(2) and 2.2767(14) Å for Cr and W respectively, are not notably different from the distance anticipated, or obtained experimentally, for comparative M–Ge single bonds. Several additional Mo and W germylyne complexes have also been synthesized and structurally characterized.[360–363] The results from density functional calculations (BP86 and B3LYP) are in good structural agreement with both the metallo-germylenes and metallo-germylynes.[364,365]

7 ORGANIC DERIVATIVES OF HYPERCOORDINATE GERMANIUM

The past decade has witnessed a substantial development of hypercoordinate germanium chemistry. The largest single class of these molecules are the pentacoordinate germatranes, $RGe(OCH_2CH_2)_3N$. Work has also progressed in making compounds in which the ligands have no geometrical constraints that help to drive the structure to a hypercoordinate state. Germanium compounds containing the Cp ligand are formally five-coordinate to each ligand when symmetrically bonded and so are included in this section. Substantial progress has been made in this area in terms of both synthesis and theory. Lastly, new germanium-containing clusters have been synthesized stabilized by bulky organic ligands.

7.1 Germatranes

Germatrane synthesis and control of the desired R′-group has most commonly been accomplished by the addition of triethanolamine to $R'GeX_3$ (X = halogen, OR, NR_2).[366–384] The use of boratrane, $B(OCH_2CH_2)_3N$, as an aprotic source of the triethanol amine ligand, has been found to be a valuable synthetic strategy.[380] Another successful strategy for variation of the R′-group has been the use of metal-catalyzed hydrogermylation reactions employing the parent germatrane, $HGe(OCH_2CH_2)_3N$.[157,385] The Ge–N transannular bond distances are typically 0.05 to 0.1 Å longer the distances obtained for the same compounds containing silicon. This is consistent with the difference in the covalent radii of the elements for these compounds.[386]

7.2 Organogermanium Complexes Containing Cyclopentadienyl and Other Five- and Six-membered Ring Aromatic Heterocyclic Ligands

Trends in the bonding preferences for Cp ligands with main group metals, including germanium, were recently reviewed.[387–389] Germanium adopts a number of different bonding modes with Cp ligands including η^2, η^3, and η^5. Compounds adopting an η^5 bonding configuration include linked di-germanocenes,[390,391] Cp^s ($Cp^s = C_5Me_4(SiMe_2Bu^t)$),[392] Cp* ($Cp^* = C_5Me_5$),[328] and the ligands 1-methylboratabenzene, 1-dimethylaminoboratabenzene, and 2,5-di(tert-butyl)phosphoyl.[393–395] These Ge(II) compounds range from five-coordinate, for example, $[Cp^*Ge][BF_4]$,[328] to 10-coordinate, for example, $Cp^s{}_2Ge$.[392] Other recent Ge(II) compounds have exhibited substantial asymmetry in the Ge-ring bonding and are described as η^2 or η^3 structures.[328,396] For example, Cp*GeCl contains two shorter Ge–C interactions of ∼2.22 Å and three longer interactions of 2.487(3), 2.599(3) and 2.437(3) Å.

7.3 Germane σ Complexes to Transition Metals

Four-coordinate germanes can be considered hypercoordinate at germanium upon the formation of an η^2-Ge-H σ-bond to a transition metal. Such complexes have been characterized by NMR, IR for the interaction of GeH_4 and $PhGeH_3$ with $Mo(CO)(dppe)_2$ and by NMR, IR, and X-ray crystallography for the interaction of Ph_2GeH_2 with $Mo(CO)(depe)_2$ (dppe = $Ph_2PC_2H_4PPh_2$; depe = $Et_2PC_2H_4PEt_2$).[397]

7.4 Other Hypercoordinate Organogermanium Complexes

The reaction of mercaptoacetic acid with $^tBuGeCl_3$ forms pentacoordinate 2-(2-*tert*-butyl-5-oxo-1,3,2-oxathiagermolan-2-ylthio)acetic acid.[398] In this molecule, the covalent Ge–O (2.045(1) Å) and the dative Ge–O bond (2.043(1) Å) are identical within error and both only 0.16 Å longer than the sum of the covalent radii (Figure 11). The phenyl derivative can also be synthesized and both compounds can be deprotonated to yield cationic products that maintain the pentacoordinate geometry.[399] Direct metathesis reactions using Li[naccac] and $GeCl_4$ also yield pentacoordinate germanium.[400]

It has been noted that the chemical shift of ^{73}Ge NMR signals is rather insensitive to hypercoordination; however, the width of the NMR peak changes dramatically. On the basis of the width of the NMR signal, a number of germanes containing Ge–Y (Y = N, O, S) contacts that are a*ll* < 15% shorter than sum of the van der Waals radii are also assigned as hypercoordinate compounds.[141,142]

Fluorine–germanium contacts have also been noted to yield hypervalent germylene and germane species. Four such contacts are observed in $Ge[2,4,6\text{-}(CF_3)_3C_6H_2]_2$ at distances of 2.5–2.8 Å, considerably shorter than the sum of the van

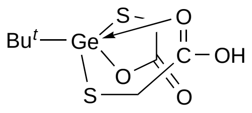

Figure 11 2-(2-*tert*-butyl-5-oxo-1,3,2-oxathiagermolan-2-ylthio) acetic acid

der Waals radii (3.66 Å) and rather longer than the sum of the covalent radii (1.86 Å).[322] Short Ge–F contacts have also been noted for organogermanes.[401]

Hypervalent germanium has also been observed in the clusters $Ge_6Ar'_2$ and $Sn_4(GeAr')_2$ ($Ar' = 2,6\text{-}Dipp_2$; Dipp $=$ C_6H_3-2,6-^{i}Pr_2).[402] The Ge_6 cluster consists of an octahedron of germanium atoms with opposite vertices capped by Ar′. The capped germanium atom is bound to the phenyl carbon and to the four equatorial Ge atoms of the octahedron. The Sn_4Ge_2 cluster is also an octahedron with opposing vertices consisting of GeAr′. In this instance, the germanium is bound to the phenyl carbon and four Sn atoms.

8 POLYGERMANES

The past decade has seen considerable effort focused on developing new methods for controlling germanium catenation, probing the mechanisms of polygermane degradation, and gaining a deeper understanding of electronic properties. Ten years ago the synthetic methods known for polygermanes were Wurtz coupling (typically sodium reduction of R_2GeCl_2) and electrochemical reduction at a Mg electrode. A much wider array of synthetic approaches is now available.

8.1 Synthesis of Polygermanes

8.1.1 Kipping Method

Wurtz-coupling conditions (Kipping method) for polygermane formation was explored for R_2GeCl_2 with an emphasis on R group (R = Et, Pr, Bu, ^{i}Bu, Hex, PhMe, PhHex), salt-binding additives (hexamethylphosphoric triamide (HMPA) and 18-crown-6), order of addition, and temperature dependence.[403] Weight and number average molecular weight data, yields, and λ_{max} values are reported.

8.1.2 In Situ Generation of Germylenes

In situ generation of germylenes utilizing the reaction of GeI_2 or $GeCl_2$·dioxane with RMgX or RLi has also been employed to synthesize polygermanes.[74,403] This approach often gives improved yields, however, molecular weights (MW) are also typically lower, leading to λ_{max} values of ~300 nm. Typical molecular weights were greater for Wurtz-coupling leading to λ_{max} values of ~320 nm.

8.1.3 Copolymerization of Germanes

Copolymerization of germanes with differing R groups, or with silanes and stannanes, has been achieved using electrochemical methods.[404–406] The 1:1 copolymers of Ge and Si give comparable MW values ($M_n \sim 3000$, $M_w/M_n = 2.0$) and intermediate λ_{max} values of 350 nm (as compared to ~480 nm for a comparable polysilane).[405] The λ_{max} values for mixed Ge and Sn polymers were reported to be ~320 nm, comparable to pure polygermanes.[406]

8.1.4 Metal-catalyzed Catenation Methods

Metal-catalyzed catenation methods have also been reported. The use of the ruthenium-based catalyst $Ru(PMe_3)_2(GeMe_3)_2$, or the precatalyst $Ru(PMe_3)_4Me_2$, catalytically demethanatively polymerizes $HGeMe_3$ or Me_2GeArH at 25 °C.[407,408] M_w values range from 3000–7000 (gel permeation chromatography (GPC), polystyrene calibration) or 6000–10 100 (light scattering). Demethanative polymerization of meta or para (S)-2-methylbutylphenyldimethygermane yield optically active polygermanes exhibiting a preferential screw sense helicity.[409] Dehydrogenative methods have also been pursued. Treatment of Cp_2ZrCl_2 or $CpCp^*ZrCl_2$ with two equivalents of BuLi followed by the addition of $PhGeH_3$ provides polyphenylgermanes.[410] SmI_2 has been employed to polymerize Et_2GeCl_2 giving low-molecular weight, $M_w =$ 1500–2400, and a corresponding higher energy λ_{max} value of ~290 nm.[411] Initial species in a Pt-based dehydrogenative coupling were reported for the reaction of $(Et_3P)_2PtGe[N(SiMe_3)_2]_2$ with H_2GePh_2.[412]

8.1.5 Characterization of Polygermanes and Related Species

Variable-temperature Raman spectroscopy has been used to explore the structure of polygermanes.[413] Ultraviolet photoelectron spectroscopy has been employed to characterize the Ge–Ge backbone bonding.[414] Additional, ^{73}Ge NMR spectra have been taken of key precursors for dehydrogenative polymerization, $ArGeH_3$, Ar_2GeH_2, and Ar_3GeH.[415]

8.2 Degradation of Polygermanes

Polygermanes are photosensitive, particularly in the presence of oxygen.[407,416] Ge–Ge bond cleavage to yield digermoxanes, polygermyl radicals, and germylenes has been reported.[416–418] Theoretical calculations suggest that homoleptic (1,2)-translocations of germyl groups is an unlikely mechanistic step in these degradation processes.[419]

8.3 Electronic and Optical Properties and Applications of Polygermanes

Electronic charge transport has been measured for $(PhMeGe)_n$ with M_w values of 2000 and 5700, M_w/M_n

values of 1.3 and 1.4 respectively, and λ_{max} values of 324 and 325 respectively. These materials have a mobility of about 10^{-5} cm^2/Vs.[420] Calculations of electron density for small oligomers of radical anions ($n = 3-7$) of polygermanes suggest the electrons are primarily located in orbitals associated with germanium atoms.[421]

Optical tuning of polygermanes and mixed polysilane/polygermane systems have been discussed.[422] Nonlinear optical effects are of particular interest. Third-order nonlinear susceptibilities (χ^3) for thin films of oligo- and polygermanes have been measured.[423] A χ^3 value of 86×10^{-12} esu was obtained for copoly(methylphenylsilylene/methylphenylgermylene)[424]

Optically-induced degradation has been employed to write GeO_2 and GeC lines starting from polygermane thin films.[425] Photoinduced electron transfer from $(MePhGe)_n$ to C60 has also been explored.[426]

9 BIOLOGICAL ACTIVITY OF ORGANOGERMANIUM COMPOUNDS

A number of reviews have appeared in the past decade regarding the biological activity of organogermanium compounds.[47,84,85,88,427,428] Although organogermanium compounds exhibit many types of biological activity, including analgesic, antimalarial, antitumor, antiviral, bactericidal, fungistatic, hypotensive, immunomodulating, interferon-inducing, radioprotective modalities, no natural role for germanium is known in human biology.

Over the past decade there has been increasing interest in nutritional supplements including those containing germanium. In fact, the leading supplement sold contains 2-carboxyethylgermasesquioxane and is typically solid as Ge-132, propagermanium, or SK-818. In light of this interest in germanium supplements, the United States Food and Drug Administration issued a report in 1997, which summarizes both human and animal studies.[429] Quoting from the report: ‘evidence of Ge-132 toxicity is incomplete; nephrotoxicity was shown in some studies and not in others. However, Ge-132 has also been shown to accumulate, although to a lesser degree than the dioxide, in kidneys, liver, spleen, and other tissues’. By way of comparison, animal studies clearly show that GeO_2 is nephrotoxic and numerous cases of renal failure have been reported related to taking germanium supplements containing GeO_2. The synthesis of Ge-132 starts from GeO_2 and the oxide is a typical impurity. For these reasons, the report concludes that ‘germanium products present a potential human health hazard’.

9.1 Germanium-containing α-amino Acids and Peptides

The (R)- and (S)-enantiomers of β-(trimethyl)germyl)alanine were treated with (fluoren-9-yl)methyl chloroformate to give N-Fmoc-protected amino acids to be used as building blocks in solid-phase peptide synthesis.[430–432] The decapeptides Ac-D-Nal^1-4-Cl-D-Phe^2-D-Pal^3-Ser^4-Me$_3$El-Ala^5-D-Cit^6-Leu^7-Arg^8-Pro^9-D-Ala^{10}-NH$_2$ (El = C, Si, Ge) were prepared and studied for in vivo and in vitro efficacy as GnRH antagonists. Both the Si and Ge derivatives exhibited enhanced testosterone and luteinizing hormone (LH) suppression as compared to the carbon analog.

9.2 Applications to Cancer and Other Human Diseases

A number of organogermanium derivatives have been prepared and tested for anticancer activity.[433–436] Studies to test efficacy against a number of other diseases have also been explored.[372,430–432,437–439] In particular, the dramatic claim has been made that 2-carboxyethylgermasesquioxane (Ge-132) inhibits the Maillard reaction which is responsible for the glycation of proteins in vivo.[440] Protein glycation by this reaction may be related to diseases such as diabetes and Alzheimer’s disease.

9.3 Applications as Insecticides and Antibacterial Agents

Organogermanium species have also been explored for biological activity as insecticide and antibacterials agents.[441] Typically, the hope is that they will maintain activity and be less toxic than existing tin-based reagents.

10 CONCLUSIONS AND FUTURE PROSPECTS OF ORGANOGERMANIUM CHEMISTRY

The first edition concluded with the statement that ‘smaller scale applications in organic synthesis may be envisioned...’. Progress in this direction over the last decade has been substantial in terms of the development of CH-insertion and activation reactions involving germanium and the substantial progress made in terms of Pd/Ge-mediated C–C coupling chemistry. Methods developed for the facile incorporation of germanium into polymers may also prove of substantial importance. Continued progress in these areas can be anticipated.

Substantial progress has also been made in the area of transition metal complexes containing germanium ligands. The metal–germanium bond nexus has been shown to be active to a variety of small molecule activations and to undergo facile reaction in the formal $2 + 2$ sense.

The community has increasingly recognized the importance of radicals in organogermanium chemistry over the past decade. Both the synthesis and characterization of stable radicals and the recognition of the importance of radical mechanisms have dramatically altered the way the chemistry of organogermanium compounds is viewed. Continued efforts in understanding the role of radicals will be critical to uncovering the mechanistic aspects of organogermanium reactions.

11 REFERENCES

1. A. Sekiguchi and V. Y. Lee, *Chem. Rev.*, 2003, **103**, 1429.
2. A. C. Spivey and C. M. Diaper, *Sci. Synth.*, 2003, **5**, 127.
3. N. Takeda, N. Tokitoh, and R. Okazaki, *Sci. Synth.*, 2003, **5**, 51.
4. N. Takeda, N. Tokitoh, and R. Okazaki, *Sci. Synth.*, 2003, **5**, 47.
5. N. Takeda, N. Tokitoh, and R. Okazaki, *Sci. Synth.*, 2003, **5**, 43.
6. N. Takeda, N. Tokitoh, and R. Okazaki, *Sci. Synth.*, 2003, **5**, 39.
7. N. Takeda, N. Tokitoh, and R. Okazaki, *Sci. Synth.*, 2003, **5**, 33.
8. P. Thornton, *Sci. Synth.*, 2003, **5**, 101.
9. P. Thornton, *Sci. Synth.*, 2003, **5**, 97.
10. P. Thornton, *Sci. Synth.*, 2003, **5**, 93.
11. P. Thornton, *Sci. Synth.*, 2003, **5**, 89.
12. P. Thornton, *Sci. Synth.*, 2003, **5**, 85.
13. P. Thornton, *Sci. Synth.*, 2003, **5**, 75.
14. P. Thornton, *Sci. Synth.*, 2003, **5**, 55.
15. C. Bibal, S. Mazieres, H. Gornitzka, and C. Couret, *Polyhedron*, 2002, **21**, 2827.
16. I. V. Borisova, M. S. Nechaev, V. N. Khrustalev, N. N. Zemlyanskii, and Y. A. Ustynyuk, *Russ. Chem. Bull.*, 2002, **51**, 721.
17. E. Fouquet, *Chem. Org. Germanium, Tin, Lead Comp.*, 2002, **2**, 1333.
18. T. Murafuji, K. Kurotobi, N. Nakamura, and Y. Sugihara, *Curr. Org. Chem.*, 2002, **6**, 1469.
19. M. Weidenbruch, *J. Organomet. Chem.*, 2002, **646**, 39.
20. R. Okazaki and N. Tokitoh, *Acc. Chem. Res.*, 2000, **33**, 625.
21. J. Satge, *Chem. Heterocycl. Compd. (New York)(Translation of Khimiya Geterotsiklicheskikh Soedinenii)*, 2000, **35**, 1013.
22. N. Tokitoh and R. Okazaki, *Coord. Chem. Rev.*, 2000, **210**, 251.
23. J. Escudie, and H. Ranaivonjatovo, *Adv. Organomet. Chem.*, 1999, **44**, 113.
24. B. R. Jagirdar, E. F. Murphy, and H. W. Roesky, *Prog. Inorg. Chem.*, 1999, **48**, 351.
25. J. Satge, *Khim. Geterotsiklicheskikh Soedinenii*, 1999, **9**, 1155.
26. N. Tokitoh, T. Matsumoto, and R. Okazaki, *Bull. Chem. Soc. Jpn.*, 1999, **72**, 1665.
27. M. Veith, *Metal Clusters Chem.*, 1999, **1**, 73.
28. M. Veith, A. Rammo, S. Faber, and B. Schillo, *Pure Appl. Chem.*, 1999, **71**, 401.
29. Q. Wang, X. Zeng, Z. Chen, and Q. Zeng, *Huaxue Tongbao*, 1999, **8**, 13.
30. J. Barrau and G. Rima, *Coord. Chem. Rev.*, 1998, **180**, 593.
31. C. Boehme and G. Frenking, *Organometallics*, 1998, **17**, 5801.
32. E. A. Chernyshev, N. G. Komalenkova, and V. G. Bykovchenko, *Russ. Chem. Bull.*, 1998, **47**, 1029.
33. H. V. R. Dias, Z. Y. Wang, and W. C. Jin, *Coord. Chem. Rev.*, 1998, **176**, 67.
34. J. Escudie, C. Couret, and H. Ranaivonjatovo, *Coord. Chem. Rev.*, 1998, **180**, 565.
35. M. Kako and Y. Nakadaira, *Coord. Chem. Rev.*, 1998, **176**, 87.
36. M. C. Kuchta and G. Parkin, *Coord. Chem. Rev.*, 1998, **176**, 323.
37. H. Ogino and H. Tobita, *Adv. Organomet. Chem.*, 1998, **42**, 223.
38. H. Ogino, *Kikan Kagaku Sosetsu*, 1998, **34**, 235.
39. H. Ogino and H. Tobita, *Adv. Organomet. Chem.*, 1998, **42**, 223.
40. P. P. Power, *J. Chem. Soc.,-Dalton Trans.*, 1998, 2939.
41. V. O. Gel'mbol'dt, *Russ. J. Coord. Chem.*, 1997, **23**, 299.
42. V. V. Negrebetsky and Y. I. Baukov, *Russ. Chem. Bull.*, 1997, **46**, 1807.
43. D. A. Armitage, *Annu. Rep. Prog. Chem., Sec. A: Inorg. Chem.*, 1996, **92**, 53.
44. N. Auner, *Synth. Methods Organomet. Inorg. Chem.*, 1996, **2**, 142.
45. M. A. Chaubon, H. Ranaivonjatovo, J. Escudie, and J. Satge, *Main Group Met. Chem.*, 1996, **19**, 145.
46. G. Manuel, W. P. Weber, and R. Boukherroub, *Main Group Met. Chem.*, 1996, **19**, 263.
47. V. S. Petrosyan, N. S. Yashina, S. V. Ponomarev, A. S. Zolotareva, S. N. Nikolaeva, and T. V. Drovetskaia, *Main Group Met. Chem.*, 1996, **19**, 397.
48. D. A. Armitage, *Organomet. Chem.*, 1995, **24**, 83.
49. K. M. Baines and W. G. Stibbs, *Coord. Chem. Rev.*, 1995, **145**, 157.
50. B. P. Clark, *Comp. Org. Funct. Group Trans.*, 1995, **5**, 923 & 1161.
51. H. Tobita and H. Ogino, *Yuki Gosei Kagaku Kyokaishi*, 1995, **53**, 530.
52. B. Wrackmeyer, *Coord. Chem. Rev.*, 1995, **145**, 125.
53. T. Ye and M. A. McKervey *Comp. Org. Funct. Group Trans.*, 1995, **3**, 501 & 733.

54. M. Akiba and N. Kakimoto, *Nippon Kagaku Kaishi*, 1994, **3**, 286.
55. Y. I. Baukov, A. G. Shipov, Y. E. Ovchinnikov, and Y. T. Struchkov, *Izv. Akad. Nauk., Ser. Khim.*, 1994, 982.
56. J. Escudie, C. Couret, H. Ranaivonjatovo, and J. Satge, *Coord. Chem. Rev.*, 1994, **130**, 427.
57. Y. Feng and L. Zhang, *Huaxue Gongye Yu Gongcheng (Tianjin)*, 1994, **11**, 10.
58. M. Kira and H. Sakurai, *Kagaku (Kyoto, Japan)*, 1994, **49**, 876.
59. Y. Sato and S. Ando-Inoue, *Nippon Kagaku Kaishi*, 1994, **3**, 274.
60. N. Tokitoh, *J. Synth. Org. Chem. Jpn.*, 1994, **52**, 136.
61. C. Y. Wong and J. D. Woollins, *Coord. Chem. Rev.*, 1994, **130**, 175.
62. K. M. Baines and W. G. Stibbs, *Adv. Organomet. Chem.*, 1996, **39**, 275.
63. S. F. Bent, *Surf. Sci.*, 2002, **500**, 879.
64. J. M. Buriak, *Chem. Rev.*, 2002, **102**, 1271.
65. F. Lefebvre and J.-M. Basset, *Main Group Met. Chem.*, 2002, **25**, 15.
66. R. J. Hamers, S. K. Coulter, M. D. Ellison, J. S. Hovis, D. F. Padowitz, M. P. Schwartz, C. M. Greenlief, and J. N. Russell, *Acc. Chem. Res.*, 2000, **33**, 617.
67. M. Gazicki, *Chaos Solitons Fractals*, 1999, **10**, 1983.
68. J. P. Carpenter, C. M. Lukehart, S. B. Milne, S. R. Stock, J. E. Wittig, B. D. Jones, R. Glosser, and J. G. Zhu, *J. Organomet. Chem.*, 1998, **557**, 121.
69. J. Kouvetakis, D. Nesting, and D. J. Smith, *Chem. Mater.*, 1998, **10**, 2935.
70. F. J. Gomez and K. B. Wagener, *NATO Sci. Ser., II: Math. Phys. Chem.*, 2002, **56**, 285.
71. K. Jurkschat, and M. Mehring, *Chem. Org. Germanium, Tin, Lead Comp.*, 2002, **2**, 1543.
72. S. Kobayashi, S.-I. Shoda, and S. Iwata, *Desk Ref. Funct. Polymers*, 1997, 169.
73. S. Kobayashi, S.-i. Shoda, S. Iwata, M. Hiraishi, and S. Cao, *Macromol. Symp.*, 1995, **98**, 91.
74. S. Kobayashi, S.-I. Shoda, S. Cao, S. Iwata, M. Abe, K. Yajima, K. Yagi, and M. Hiraishi, *J. Macromol. Sci., Pure Appl. Chem.*, 1994, **A31**, 1835.
75. J.-P. Majoral and A.-M. Caminade, *Chem. Rev. (Washington, D. C.)*, 1999, **99**, 845.
76. C. Long, and M. T. Pryce, *Chem. Org. Germanium, Tin, Lead Comp.*, 2002, **2**, 1521.
77. W. J. Leigh, *Pure Appl. Chem.*, 1999, **71**, 453.
78. K. Mochida, *Main Group Met. Chem.*, 1994, **17**, 25.
79. C. E. Holloway and M. Melnik, *Main Group Met. Chem.*, 2002, **25**, 185.
80. K. W. Klinkhammer, *Chem. Org. Germanium, Tin, Lead Comp.*, 2002, **2**, 283.
81. E. Lukevics and L. Ignatovich, *Chem. Org. Germanium, Tin, Lead Comp.*, 2002, **2**, 1653.
82. H. Li, *Guangdong Weiliang Yuansu Kexue*, 2001, **8**, 9.
83. K. Yang, D. Wang, and X. Li, *Guangdong Weiliang Yuansu Kexue*, 2000, **7**, 7.
84. G. Rima, J. Satge, R. Dagiral, C. Lion, H. Sentenac-Roumanou, M. Fatome, V. Roman, and J.-D. Laval, *Metal-Based Drugs*, 1999, **6**, 49.
85. V. S. Petrosyan, N. S. Yashina, and S. V. Ponomarev, *Metal-Based Drugs*, 1998, **5**, 237.
86. Q. Zeng, X. Zeng, Q. Wang, T. Cui, and F. Xu, *Guangdong Weiliang Yuansu Kexue*, 1998, **5**, 5.
87. Y. L. Wang, *Chung-Hua Yu Fang I Hsueh Tsa Chih [Chinese J. Prev. Med.]*, 1994, **28**, 372.
88. J. Feldmann, 'Organometallic Compounds in the Environment', 2nd edn., 2003, p. 353.
89. S. E. Boganov, M. P. Egorov, V. I. Faustov, and O. M. Nefedov, *Chem. Org. Germanium, Tin, Lead Comp.*, 2002, **2**, 749.
90. I. Ganzer, M. Hartmann, and G. Frenking, *Chem. Org. Germanium, Tin, Lead Comp.*, 2002, **2**, 169.
91. H. C. Marsmann, and F. Uhlig, *Chem. Org. Germanium, Tin, Lead Comp.*, 2002, **2**, 399.
92. L. A. Leites and S. S. Bukalov, *J. Raman Spectrosc.*, 2001, **32**, 413.
93. T. V. Leshina, O. S. Volkova, and M. B. Taraban, *Russ. Chem. Bull.*, 2001, **50**, 1916.
94. S. Sakaki, B. Biswas, Y. Musashi, and M. Sugimoto, *J. Organomet. Chem.*, 2000, **611**, 288.
95. K. H. Chen and N. L. Allinger, *J. Phys. Org. Chem.*, 1999, **12**, 528.
96. V. N. Khabashesku, S. E. Boganov, K. N. Kudin, J. L. Margrave, J. Michl, and O. M. Nefedov, *Russ. Chem. Bull.*, 1999, **48**, 2003.
97. K. Mayumi, *J. Mass Spectrom. Soc. Jpn.*, 1998, **46**, 151.
98. Q. Zeng, Q. Wang, Z. Zhang, and F. Xu, *Bopuxue Zazhi*, 1998, **15**, 95.
99. Q. Zeng, Q. Wang, F. Xu, and X. Zeng, *Bopuxue Zazhi*, 1997, **14**, 267.
100. I. Zicmane and E. Lukevics, *Appl. Organomet. Chem.*, 1994, **8**, 287.
101. T. Hiyama and E. Shirakawa, in 'Handbook of Organopalladium Chemistry for Organic Synthesis', Wiley-Interscience, New York, 2002, Vol. 2, p. 285.
102. C. M. Rienaecker and T. M. Klapoetke, *Chem. Org. Germanium, Tin, Lead Comp.*, 2002, **2**, 461.
103. J. M. Riveros, *Int. J. Mass Spectrom.*, 2002, **221**, 177.
104. M. B. Taraban, O. S. Volkova, A. I. Kruppa, and T. V. Leshina *Chem. Org. Germanium, Tin, Lead Comp.*, 2002, **2**, 579.
105. J. A. Reichl, and D. H. Berry, *Adv. Organomet. Chem.*, 1999, **43**, 197.

106. M. P. Egorov and O. M. Nefedov, *Main Group Met. Chem.*, 1996, **19**, 367.
107. N. Sasaki and Y. Yamamoto, *Kagaku Kogyo*, 1996, **47**, 859.
108. W. Ando, *Pure Appl. Chem.*, 1995, **67**, 805.
109. W. P. Neumann, M. P. Weisbeck, and S. Wienken, *Main Group Met. Chem.*, 1994, **17**, 151.
110. P. Riviere, M. Riviere-Baudet, and A. Castel, *Main Group Met. Chem.*, 1994, **17**, 679.
111. M. Riviere-Baudet, *Main Group Met. Chem.*, 1995, **18**, 353.
112. K. N. Kudin, J. L. Margrave, and V. N. Khabashesku, *J. Phys. Chem. A*, 1998, **102**, 744.
113. F. A. Cotton, A. H. Cowley, and X. J. Feng, *J. Am. Chem. Soc.*, 1998, **120**, 1795.
114. M. D. Su and S. Y. Chu, *J. Am. Chem. Soc.*, 1999, **121**, 4229.
115. S. M. Stogner and R. S. Grev, *J. Chem. Phys.*, 1998, **108**, 5458.
116. J. J. BelBruno, *Heteroat. Chem.*, 1998, **9**, 195.
117. J. Karolczak, W. W. Harper, R. S. Grev, and D. J. Clouthier, *J. Chem. Phys.*, 1995, **103**, 2839.
118. C. Boehme and G. Frenking, *J. Am. Chem. Soc.*, 1996, **118**, 2039.
119. C. Heinemann, W. A. Herrmann, and W. Thiel, *J. Organomet. Chem.*, 1994, **475**, 73.
120. V. N. Khabashesku, K. N. Kudin, J. Tamas, S. E. Boganov, J. L. Margrave, and O. M. Nefedov, *J. Am. Chem. Soc.*, 1998, **120**, 5005.
121. M. D. Su and S. Y. Chu, *J. Phys. Chem. A*, 1999, **103**, 11011.
122. M. D. Su and S. Y. Chu, *Inorg. Chem.*, 1999, **38**, 4819.
123. M. D. Su and S. Y. Chu, *Tetrahedron Lett.*, 1999, **40**, 4371.
124. M. D. Su and S. Y. Chu, *J. Chin. Chem. Soc.*, 2000, **47**, 135.
125. M. D. Su and S. Y. Chu, *J. Am. Chem. Soc.*, 1999, **121**, 11478.
126. M. D. Su, *J. Phys. Chem. A*, 2002, **106**, 9563.
127. L. Pause, M. Robert, J. Heinicke, and O. Kuhl, *J. Chem. Soc.,-Perkin Trans. 2*, 2001, 1383.
128. A. J. Arduengo, H. Bock, H. Chen, M. Denk, D. A. Dixon, J. C. Green, W. A. Herrmann, N. L. Jones, M. Wagner, and R. West, *J. Am. Chem. Soc.*, 1994, **116**, 6641.
129. A. Laporte-Chrostowska, S. Foucat, T. Pigot, V. Lemierre, and G. Pfister-Guillouzo, *Main Group Met. Chem.*, 2002, **25**, 55.
130. S. Foucat, T. Pigot, G. Pfister-Guillouzo, H. Lavayssiere, and S. Mazieres, *Organometallics*, 1999, **18**, 5322.
131. S. Foucat, T. Pigot, G. Pfister-Guillouzo, S. Mazieres, and H. Lavayssiere, *Eur. J. Inorg. Chem.*, 1999, 1151.
132. E. A. Brinkman, K. Salomon, W. Tumas, and J. I. Brauman, *J. Am. Chem. Soc.*, 1995, **117**, 4905.
133. N. H. Morgon and J. M. Riveros, *Int. J. Mass Spectrom.*, 2001, **210**, 173.
134. P. M. Mayer, J. F. Gal, and L. Radom, *Int. J. Mass Spectrom.*, 1997, **167**, 689.
135. N. H. Morgon, L. A. Xavier, and J. M. Riveros, *Int. J. Mass Spectrom.*, 2000, **196**, 363.
136. L. A. Xavier, N. H. Morgon, J. J. Menegon, and J. M. Riveros, *Int. J. Mass Spectrom.*, 2002, **219**, 485.
137. H. C. Marsmann and F. Uhlig, *Chem. Org. Germanium Tin Lead Compd.*, 2002, **2**, 399.
138. R. A. Thomson, A. L. Wilkins, and K. M. Mackay, *Phosphorus Sulfur Silicon Rel. Elem.*, 1999, **150–151**, 319.
139. F. Riedmiller, G. L. Wegner, A. Jockisch, and H. Schmidbaur, *Organometallics*, 1999, **18**, 4317.
140. F. Riedmiller and H. Schmidbaur, *J. Chem. Soc.,-Dalton Trans.*, 2000, 4117.
141. Y. Takeuchi, K. Tanaka, S. Aoyagi, and H. Yamamoto, *Magn. Reson. Chem.*, 2002, **40**, 241.
142. Y. Takeuchi, H. Yamamoto, K. Tanaka, K. Ogawa, J. Harada, T. Iwamoto, and H. Yuge, *Tetrahedron*, 1998, **54**, 9811.
143. Y. Takeuchi, M. Nishikawa, K. Tanaka, and T. Takayama, *Chem. Lett.*, 2001, 572.
144. Y. Takeuchi, M. Nishikawa, K. Tanaka, T. Takayama, M. Imanari, K. Deguchi, T. Fujito, and Y. Sugisaka, *Chem. Commun.*, 2000, 687.
145. N. W. Mitzel, U. Losehand, and A. D. Richardson, *Inorg. Chem.*, 1999, **38**, 5323.
146. M. Charisse, A. Zickgraf, H. Stenger, E. Brau, C. Desmarquet, M. Drager, S. Gerstmann, D. Dakternieks, and J. Hook, *Polyhedron*, 1998, **17**, 4497.
147. Y. Takeuchi, J. Popelis, G. Manuel, and R. Boukherroub, *Main Group Met. Chem.*, 1995, **18**, 191.
148. Y. Takeuchi, K. Ogawa, G. Manuel, R. Boukherroub, and I. Zicmane, *Main Group Met. Chem.*, 1994, **17**, 121.
149. S. Schlecht, *Angew. Chem.,-Int. Ed.*, 2002, **41**, 1178.
150. M. Okamoto, T. Asano, and E. Suzuki, *Catal. Lett.*, 2002, **78**, 33.
151. M. Okamoto, T. Asano, and E. Suzuki, *Organometallics*, 2001, **20**, 5583.
152. L. N. Lewis, K. E. Litz, and J. M. Anostario, *J. Am. Chem. Soc.*, 2002, **124**, 11718.
153. D. P. Curran and G. Gualtieri, *Synlett*, 2001, 1038.
154. G. Gualtieri, S. J. Geib, and D. P. Curran, *J. Org. Chem.*, 2003, **68**, 5013.
155. V. Huc, P. Boussaguet, and P. Mazerolles, *J. Organomet. Chem.*, 1996, **521**, 253.
156. R. A. Widenhoefer, A. Vadehra, and P. K. Cheruvu, *Organometallics*, 1999, **18**, 4614.
157. J. W. Faller, R. G. Kultyshev, and J. Parr, *J. Organomet. Chem.*, 2004, **689**, 2565.
158. K. Choi and J. M. Buriak, *Langmuir*, 2000, **16**, 7737.
159. E. Fok, M. L. Shih, A. Meldrum, and J. G. C. Veinot, *Chem. Commun.*, 2004, 386.

160. J. L. He, Z. H. Lu, S. A. Mitchell, and D. D. M. Wayner, *J. Am. Chem. Soc.*, 1998, **120**, 2660.
161. A. Castel, P. Riviere, F. Cosledan, J. Satge, M. Onyszchuk, and A. M. Lebuis, *Organometallics*, 1996, **15**, 4488.
162. M. Taoufik, C. C. Santini, and J. M. Basset, *J. Organomet. Chem.*, 1999, **580**, 128.
163. L. Lange, B. Meyer, and W.-W. d. Mont, *J. Organomet. Chem.*, 1987, **329**, C17.
164. P. Jutzi, H. Schmidt, B. Neumann, and H.-G. Stammler, *Organometallics*, 1996, **15**, 741.
165. B. Gehrhus, P. Hitchcock, and M. Lappert, *Angew. Chem. Int. Ed. Engl.*, 1997, **36**, 2514.
166. P. Jutzi and C. Leue, *Organometallics*, 1994, **13**, 2898.
167. D. Lei, M. E. Lee, and P. P. Gaspar, *Tetrahedron*, 1997, **53**, 10179.
168. K. A. Miller, T. W. Watson, J. E. Bender, M. M. Banaszak Holl, and J. W. Kampf, *J. Am. Chem. Soc.*, 2001, **123**, 982.
169. R. D. Sweeder, K. A. Miller, F. A. Edwards, J. Wang, M. M. B. Holl, and J. W. Kampf, *Organometallics*, 2003, **22**, 5054.
170. K. A. Miller, J. M. Bartolin, R. M. O’Neill, R. D. Sweeder, T. M. Owens, J. W. Kampf, M. M. Banaszak Holl, and N. J. Wells, *J. Am. Chem. Soc.*, 2003, **125**, 8986.
171. E. M. Berliner, T. K. Gar, and V. F. Mironov, *J. Gen. Chem. USSR*, 1972, **42**, 1165.
172. R. D. Sweeder, F. A. Edwards, K. A. Miller, M. M. Banaszak Holl, and J. W. Kampf, *Organometallics*, 2002, **21**, 457.
173. R. D. Sweeder, R. L. Gdula, B. J. Ludwig, M. M. Banaszak Holl, and J. W. Kampf, *Organometallics*, 2003, **22**, 3222.
174. A. V. Teplyakov, P. Lal, Y. A. Noah, and S. F. Bent, *J. Am. Chem. Soc.*, 1998, **120**, 7377.
175. C. Mui, S. F. Bent, and C. B. Musgrave, *J. Phys. Chem. A*, 2000, **104**, 2457.
176. P. Lal, A. V. Teplyakov, Y. Noah, M. J. Kong, G. T. Wang, and S. F. Bent, *J. Chem. Phys.*, 1999, **110**, 10545.
177. M. A. Filler, C. Mui, C. B. Musgrave, and S. F. Bent, *J. Am. Chem. Soc.*, 2003, **125**, 4928.
178. G. T. Wang, C. Mui, C. B. Musgrave, and S. F. Bent, *J. Am. Chem. Soc.*, 2002, **124**, 8990.
179. G. T. Wang, C. Mui, C. B. Musgrave, and S. F. Bent, *J. Phys. Chem. B*, 2001, **105**, 12559.
180. N. Tokitoh, K. Kishikawa, T. Matsumoto, and R. Okazaki, *Chem. Lett.*, 1995, 827.
181. W. Ando, H. Ohgaki, and Y. Kabe, *Angew. Chem.,-Int. Ed. Engl.*, 1994, **33**, 659.
182. N. Fukaya, M. Ichinohe, Y. Kabe, and A. Sekiguchi, *Organometallics*, 2001, **20**, 3364.
183. A. Sekiguchi, R. Izumi, S. Ihara, M. Ichinohe, and V. Y. Lee, *Angew. Chem., Int. Ed.*, 2002, **41**, 1598.
184. J. W. Faller and R. G. Kultyshev, *Organometallics*, 2002, **21**, 5911.
185. M. Kosugi, T. Tanji, Y. Tanaka, A. Yoshida, K. Fugami, K. Kameyama, and T. Migita, *J. Organomet. Chem.*, 1996, **508**, 255.
186. T. Nakamura, H. Kinoshita, H. Shinokubo, and K. Oshima, *Org. Lett.*, 2002, **4**, 3165.
187. N. Tokitoh, *Acc. Chem. Res.*, 2004, **37**, 86.
188. N. Nakata, N. Takeda, and N. Tokitoh, *Organometallics*, 2003, **22**, 481.
189. N. Nakata, N. Takeda, and N. Tokitoh, *J. Am. Chem. Soc.*, 2002, **124**, 6914.
190. N. Nakata, N. Takeda, and N. Tokitoh, *Organometallics*, 2001, **20**, 5507.
191. N. Nakata, N. Takeda, and N. Tokitoh, *J. Organomet. Chem.*, 2003, **672**, 66.
192. N. Nakata, N. Takeda, and N. Tokitoh, *Chem. Lett.*, 2002, 818.
193. N. Nakata, N. Takeda, and N. Tokitoh, *Angew. Chem.,-Int. Ed.*, 2003, **42**, 115.
194. K. Kishikawa, N. Tokitoh, and R. Okazaki, *Organometallics*, 1997, **16**, 5127.
195. N. Tokitoh, K. Kishikawa, and R. Okazaki, *Chem. Lett.*, 1998, 811.
196. N. Tokitoh, K. Hatano, T. Sasaki, T. Sasamori, N. Takeda, N. Takagi, and S. Nagase, *Organometallics*, 2002, **21**, 4309.
197. Z. T. Cygan, J. W. Kampf, and M. M. Banaszak Holl, *Inorg. Chem.*, 2003, **42**, 7219.
198. Y. Murata, A. Han, and K. Komatsu, *Tetrahedron Lett.*, 2003, **44**, 8199.
199. T. Matsumoto, N. Tokitoh, and R. Okazaki, *Chem. Commun. (Cambridge)*, 1997, 1553.
200. N. P. Toltl, M. Stradiotto, T. L. Morkin, and W. J. Leigh, *Organometallics*, 1999, **18**, 5643.
201. S. E.-C. El Kettani, M. Lazraq, H. Ranaivonjatovo, J. Escudie, C. Couret, H. Gornitzka, and N. Merceron, *Organometallics*, 2004, **23**, 5062.
202. F. Meiners, D. Haase, R. Koch, W. Saak, and M. Weidenbruch, *Organometallics*, 2002, **21**, 3990.
203. B. E. Eichler, D. R. Powell, and R. West, *Organometallics*, 1999, **18**, 540.
204. K. E. Litz, K. Henderson, R. W. Gourley, and M. M. Banaszak Holl, *Orgnaometallics*, 1995, **14**, 5008.
205. K. E. Litz, M. M. Banaszak Holl, and J. W. Kampf, *Inorg. Chem.*, 1998, **37**, 6461.
206. K. E. Litz, J. W. Kampf, and M. M. Banaszak Holl, *J. Am. Chem. Soc*, 1998, **120**, 7484.
207. K. E. Litz, J. E. Bender, R. D. Sweeder, and M. M. Banaszak Holl, *Organometallics*, 2000, **19**, 186.
208. Z. T. Cygan, J. W. Kampf, and M. M. Banaszak Holl, *Organometallics*, 2004, **23**, 2370.
209. Z. T. Cygan, J. W. Kampf, and M. M. B. Holl, *Inorg. Chem.*, 2004, **43**, 2057.

210. S. Faure, B. Valentin, J. Rouzaud, H. Gornitzka, A. Castel, and P. Riviere, *Inorg. Chim. Acta*, 2000, **305**, 46.
211. Y. Liu, D. Ballweg, T. Mueller, I. A. Guzei, R. W. Clark, and R. West, *J. Am. Chem. Soc.*, 2002, **124**, 12174.
212. J. M. Dysard and T. D. Tilley, *J. Am. Chem. Soc.*, 2000, **122**, 3097.
213. J. M. Dysard and T. D. Tilley, *J. Am. Chem. Soc.*, 1998, **120**, 8245.
214. J. M. Dysard and T. D. Tilley, *Organometallics*, 2000, **19**, 2671.
215. A. Haaland, S. Samdal, T. G. Strand, M. A. Tafipolsky, H. V. Volden, B. J. J. van de Heisteeg, O. S. Akkerman, and F. Bickelhaupt, *J. Organomet. Chem.*, 1997, **536/537**, 217.
216. P. P. Power, *Chem. Rev.*, 2003, **103**, 789.
217. A. Sekiguchi, T. Fukawa, M. Nakamoto, V. Y. Lee, and M. Ichinohe, *J. Am. Chem. Soc.*, 2002, **124**, 9865.
218. Y. Ishida, A. Sekiguchi, K. Kobayashi, and S. Nagase, *Organometallics*, 2004, **23**, 4891.
219. M. M. Olmstead, L. H. Pu, R. S. Simons, and P. P. Power, *Chem. Commun.*, 1997, 1595.
220. J. J. BelBruno, *J. Chem. Soc., Faraday Trans.*, 1998, **94**, 1555.
221. J. Escudie, C. Couret, and H. Ranaivonjatovo, *Coord. Chem. Rev.*, 1998, **178–180**, 565.
222. T. Ye, and M. A. McKervey, *Compr. Org. Func. Group Transformations*, 1995, **3**, 501, 733.
223. V. G. Avakyan, S. L. Guselnikov, and L. E. Gusel'nikov, *J. Organomet. Chem.*, 2003, **686**, 257.
224. V. N. Khabashesku, K. N. Kudin, and J. L. Margrave, *Russ. Chem. Bull. (Translation of Izv. Akad. Nauk, Ser. Khim.)*, 2001, **50**, 20.
225. H. Jacobsen and T. Ziegler, *J. Am. Chem. Soc.*, 1994, **116**, 3667.
226. C. Jouany and G. Trinquier, *Organometallics*, 1997, **16**, 3148.
227. C. Jouany, S. Mathieu, M. A. Chaubonderedempt, and G. Trinquier, *J. Am. Chem. Soc.*, 1994, **116**, 3973.
228. W. J. Leigh, N. P. Toltl, P. Apodaca, M. Castruita, and K. H. Pannell, *Organometallics*, 2000, **19**, 3232.
229. N. P. Toltl and W. J. Leigh, *J. Am. Chem. Soc.*, 1998, **120**, 1172.
230. V. N. Khabashesku, K. N. Kudin, C. J. Tamas, S. E. Boganov, J. L. Margrave, and O. M. Nefedov, *J. Am. Chem. Soc.*, 1998, **120**, 5005.
231. V. N. Khabashesku, S. E. Boganov, D. Antic, O. M. Nefedov, and J. Michl, *Organometallics*, 1996, **15**, 4714.
232. M.-A. Chaubon, J. Escudie, H. Ranaivonjatovo, and J. Satge, *J. Chem. Soc., Dalton Trans.: Inorg. Chem.*, 1996, 893.
233. D. Bravo-Zhivotovskii, I. Zharov, M. Kapon, and Y. Apeloig, *J. Chem. Soc., Chem. Commun.*, 1995, 1625.
234. N. Tokitoh, K. Kishikawa, and R. Okazaki, *J. Chem. Soc.,-Chem. Commun.*, 1995, 1425.
235. S. E.-C. El Kettani, J. Escudie, C. Couret, H. Ranaivonjatovo, M. Lazraq, M. Soufiaoui, H. Gornitzka, and G. C. Nemes, *Chem. Commun.*, 2003, 1662.
236. J. Escudie, H. Ranaivonjatovo, and L. Rigon, *Chem. Rev.*, 2000, **100**, 3639.
237. H. Ramdane, H. Ranaivonjatovo, J. Escudie, S. Mathieu, and N. Knouzi, *Organometallics*, 1996, **15**, 3070.
238. B. E. Eichler, D. R. Powell, and R. West, *Organometallics*, 1998, **17**, 2147.
239. N. Tokitoh, K. Kishikawa, and R. Okazaki, *Phosphorus Sulfur Silicon Rel. Elem.*, 1999, **151**, 137.
240. K. Kishikawa, N. Tokitoh, and R. Okazaki, *Phosphorus Sulfur Silicon Rel. Elem.*, 1998, **136**, 505.
241. T. Matsumoto, N. Tokitoh, and R. Okazaki, *Angew. Chem.,-Int. Ed. Engl.*, 1994, **33**, 2316.
242. N. Tokitoh and R. Okazaki, *Adv. Organomet. Chem.*, 2001, **47**, 121.
243. T. Matsumoto, N. Tokitoh, and R. Okazaki, *J. Am. Chem. Soc.*, 1999, **121**, 8811.
244. N. Tokitoh, T. Matsumoto, and R. Okazaki, *J. Am. Chem. Soc.*, 1997, **119**, 2337.
245. S. R. Foley, C. Bensimon, and D. S. Richeson, *J. Am. Chem. Soc.*, 1997, **119**, 10359.
246. G. Ossig, A. Meller, C. Bronneke, O. Muller, M. Schafer, and R. HerbstIrmer, *Organometallics*, 1997, **16**, 2116.
247. S. R. Foley, Y. L. Zhou, G. P. A. Yap, and D. S. Richeson, *Inorg. Chem.*, 2000, **39**, 924.
248. C. L. Lin, M. D. Su, and S. Y. Chu, *Chem. Phys. Lett.*, 2001, **339**, 147.
249. C. L. Lin, M. D. Su, and S. Y. Chu, *Chem. Commun.*, 2000, 1447.
250. C. L. Lin, M. D. Su, and S. Y. Chu, *Chem. Commun.*, 2000, 723.
251. J. Kapp, M. Remko, and P. V. Schleyer, *J. Am. Chem. Soc.*, 1996, **118**, 5745.
252. L. H. Pu, N. J. Hardman, and P. P. Power, *Organometallics*, 2001, **20**, 5105.
253. P. Jutzi, H. Schmidt, B. Neumann, and H. G. Stammler, *Organometallics*, 1996, **15**, 741.
254. N. Tokitoh, K. Kishikawa, R. Okazaki, T. Sasamori, N. Nakata, and N. Takeda, *Polyhedron*, 2002, **21**, 563.
255. V. N. Khabashesku, S. E. Boganov, K. N. Kudin, J. L. Margrave, and O. M. Nefedov, *Organometallics*, 1998, **17**, 5041.
256. F. El Baz, M. Riviere-Baudet, C. Chazalette, and H. Gornitzka, *Phosphorus Sulfur Silicon Rel. Elem.*, 2000, **163**, 121.
257. D. Agustin, G. Rima, H. Gornitzka, and J. Barrau, *Main Group Met. Chem.*, 1999, **22**, 703.
258. F. El Baz, M. Riviere-Baudet, and M. Ahra, *J. Organomet. Chem.*, 1997, **548**, 123.

259. M. Rivierebaudet, J. Satge, and F. Elbaz, *J. Chem. Soc.,-Chem. Commun.*, 1995, 1687.

260. A. Kandri-Rodi, J. P. Declercq, A. Dubourg, H. Ranaivonjatovo, and J. Escudie, *Organometallics*, 1995, **14**, 1954.

261. V. Y. Lee and A. Sekiguchi, *Organometallics*, 2004, **23**, 2822.

262. P. P. Power, *Chem. Rev.*, 1999, **99**, 3463.

263. H. Schafer, W. Saak, and M. Weidenbruch, *Angew. Chem.,-Int. Ed.*, 2000, **39**, 3703.

264. V. Y. Lee, K. Takanashi, M. Ichinohe, and A. Sekiguchi, *J. Am. Chem. Soc.*, 2003, **125**, 6012.

265. A. Schafer, W. Saak, and M. Weidenbruch, *Organometallics*, 2003, **22**, 215.

266. M. Stender, L. H. Pu, and P. P. Power, *Organometallics*, 2001, **20**, 1820.

267. A. Sekiguchi, Y. Ishida, N. Fukaya, M. Ichinohe, N. Takagi, and S. Nagase, *J. Am. Chem. Soc.*, 2002, **124**, 1158.

268. A. Sekiguchi, N. Fukaya, M. Ichinohe, N. Takagi, and S. Nagase, *J. Am. Chem. Soc.*, 1999, **121**, 11587.

269. M. S. Samuel and K. M. Baines, *J. Am. Chem. Soc.*, 2003, **125**, 12702.

270. M. S. Samuel, H. A. Jenkins, D. W. Hughes, and K. M. Baines, *Organometallics*, 2003, **22**, 1603.

271. K. L. Fujdala, D. W. K. Gracey, E. F. Wong, and K. M. Baines, *Can. J. Chem.,-Rev. Can. De Chim.*, 2002, **80**, 1387.

272. N. J. Mosey, K. M. Baines, and T. K. Woo, *J. Am. Chem. Soc.*, 2002, **124**, 13306.

273. M. S. Samuel, M. C. Jennings, and K. M. Baines, *J. Organomet. Chem.*, 2001, **636**, 130.

274. M. S. Samuel, M. C. Jennings, and K. M. Baines, *Organometallics*, 2001, **20**, 590.

275. K. M. Baines, C. E. Dixon, and M. S. Samuel, *Phosphorus Sulfur Silicon Rel. Elem.*, 1999, **151**, 393.

276. K. M. Baines, C. E. Dixon, J. M. Langridge, H. W. Liu, and F. Zhang, *Organometallics*, 1999, **18**, 2206.

277. C. E. Dixon, D. W. Hughes, and K. M. Baines, *J. Am. Chem. Soc.*, 1998, **120**, 11049.

278. C. E. Dixon, M. R. Netherton, and K. M. Baines, *J. Am. Chem. Soc.*, 1998, **120**, 10365.

279. C. E. Dixon and K. M. Baines, *Phosphorus Sulfur Silicon Rel. Elem.*, 1997, **125**, 123.

280. C. E. Dixon, J. A. Cooke, and K. M. Baines, *Organometallics*, 1997, **16**, 5437.

281. C. E. Dixon, H. W. Liu, C. M. VanderKant, and K. M. Baines, *Organometallics*, 1996, **15**, 5701.

282. K. M. Baines, J. A. Cooke, and J. J. Vittal, *Heteroat. Chem.*, 1994, **5**, 293.

283. K. Mochida, T. Kayamori, M. Wakasa, H. Hayashi, and M. P. Egorov, *Organometallics*, 2000, **19**, 3379.

284. M. B. Taraban, O. S. Volkova, V. F. Plyusnin, Y. V. Ivanov, T. V. Leshina, M. P. Egorov, O. M. Nefedov, T. Kayamori, and K. Mochida, *J. Organomet. Chem.*, 2000, **601**, 324.

285. A. Sekiguchi, M. Tsukamoto, and M. Ichinohe, *Science*, 1997, **275**, 60.

286. V. Y. Lee, A. Sekiguchi, M. Ichinohe, and N. Fukaya, *J. Organomet. Chem.*, 2000, **611**, 228.

287. M. Ichinohe, N. Fukaya, and A. Sekiguchi, *Chem. Lett.*, 1998, 1045.

288. Z. F. Chen, A. Hirsch, S. Nagase, W. Thiel, and P. V. R. Schleyer, *J. Am. Chem. Soc.*, 2003, **125**, 15507.

289. A. Sekiguchi, Y. Ishida, Y. Kabe, and M. Ichinohe, *J. Am. Chem. Soc.*, 2002, **124**, 8776.

290. J. B. Lambert, Y. Zhao, H. Wu, W. C. Tse, and B. Kuhlmann, *J. Am. Chem. Soc.*, 1999, **121**, 5001.

291. M. Ichinohe, Y. Hayata, and A. Sekiguchi, *Chem. Lett.*, 2002, 1054.

292. C. S. Lambert JB, and C. L. Stern, *J. Organomet. Chem.*, 1995, **499**, 49.

293. T. Muller, C. Bauch, M. Ostermeier, M. Bolte, and N. Auner, *J. Am. Chem. Soc.*, 2003, **125**, 2158.

294. A. Sekiguchi, T. Fukawa, V. Y. Lee, M. Nakamoto, and M. Ichinohe, *Angew. Chem.,-Int. Ed.*, 2003, **42**, 1143.

295. B. Gehrhus, P. B. Hitchcock, and M. F. Lappert, *J. Chem. Soc.,-Dalton Trans.*, 2000, 3094.

296. L. W. Pineda, V. Jancik, H. W. Roesky, D. Necuali, and A. M. Neculai, *Angew. Chem.,-Int. Ed.*, 2004, **43**, 1419.

297. O. Kuhl, P. Lonnecke, and J. Heinicke, *Inorg. Chem.*, 2003, **42**, 2836.

298. N. Tokitoh, K. Manmaru, and R. Okazaki, *Organometallics*, 1994, **13**, 167.

299. K. Ueno, K. Yamaguchi, and H. Ogino, *Organometallics*, 1999, **18**, 4468.

300. M. Veith, A. Muller, L. Stahl, M. Notzel, M. Jarczyk, and V. Huch, *Inorg. Chem.*, 1996, **35**, 3848.

301. J. D. Feldman, J. C. Peters, and T. D. Tilley, *Organometallics*, 2002, **21**, 4065.

302. P. Bazinet, G. P. A. Yap, and D. S. Richeson, *J. Am. Chem. Soc.*, 2001, **123**, 11162.

303. K. E. Litz, J. E. Bender, J. W. Kampf, and M. M. B. Holl, *Angew. Chem.,-Int. Ed. Engl.*, 1997, **36**, 496.

304. Z. T. Cygan, J. E. Bender, K. E. Litz, J. W. Kampf, and M. M. B. Holl, *Organometallics*, 2002, **21**, 5373.

305. K. E. Litz, K. Henderson, R. W. Gourley, and M. M. B. Holl, *Organometallics*, 1995, **14**, 5008.

306. P. Kircher, G. Huttner, K. Heinze, B. Schiemenz, L. Zsolnai, M. Buchner, and A. Driess, *Eur. J. Inorg. Chem.*, 1998, 703.

307. A. C. Filippou, J. G. Winter, G. Kociok-Kohn, and I. Hinz, *J. Chem. Soc.,-Dalton Trans.*, 1998, 2029.

308. F. Ettel, M. Schollenberger, B. Schiemenz, G. Huttner, and L. Zsolnai, *J. Organomet. Chem.*, 1994, **476**, 153.

309. S. G. Anema, K. M. Mackay, and B. K. Nicholson, *J. Chem. Soc. Dalton. Trans.*, 1996, **19**, 3853.
310. Y. Kawano, K. Sugawara, H. Tobita, and H. Ogino, *Chem. Lett.*, 1994, **23**, 293.
311. J. Fujita, Y. Kawano, H. Tobita, and H. Ogino, *Chem. Lett.*, 1994, **23**, 1353.
312. R. D. Adams, B. Captain, and W. Fu, *Inorg. Chem.*, 2003, **42**, 1328.
313. Y. Q. Zhang, B. Q. Wang, S. S. Xu, and X. Z. Zhou, *Organometallics*, 2001, **20**, 3829.
314. R. D. Adams, B. Captain, and W. Fu, *J. Organomet. Chem.*, 2003, **671**, 158.
315. W. K. Leong, F. W. B. Einstein, and R. K. Pomeroy, *Organometallics*, 1996, **15**, 1589.
316. W. K. Leong, F. W. B. Einstein, and R. K. Pomeroy, *Acta Crystallogr.*, 1997, **C53**, 22.
317. J. S. McIndoe and B. K. Nicholson, *J. Organomet. Chem.*, 1999, **577**, 181.
318. J. M. Dysard and T. D. Tilley, *Organometallics*, 2000, **19**, 2671.
319. V. V. Shcherbinin, I. P. Shvedov, K. V. Pavlov, N. G. Komalenkova, and E. A. Chernyshev, *Russ. J. Gen. Chem.*, 1998, **68**, 1013.
320. S. E. Boganov, M. P. Egorov, V. I. Faustov, and O. M. Nefedov, *Chem. Org. Germanium Tin Lead Compd.*, 2002, **2**, 749.
321. W. Setaka, K. Sakamoto, M. Kira, and P. P. Power, *Organometallics*, 2001, **20**, 4460.
322. J. E. Bender, M. M. B. Holl, and J. W. Kampf, *Organometallics*, 1997, **16**, 2743.
323. R. S. Simons, L. H. Pu, M. M. Olmstead, and P. P. Power, *Organometallics*, 1997, **16**, 1920.
324. G. L. Wegner, R. J. F. Berger, A. Schier, and H. Schmidbaur, *Organometallics*, 2001, **20**, 418.
325. M. Riviere-Baudet, M. Dahrouch, P. Riviere, K. Hussein, and J. C. Barthelat, *J. Organomet. Chem.*, 2000, **612**, 69.
326. M. Riviere-Baudet, M. Dahrouch, and H. Gornitzka, *J. Organomet. Chem.*, 2000, **595**, 153.
327. P. Jutzi, H. Schmidt, B. Neumann, and H. G. Stammler, *J. Organomet. Chem.*, 1995, **499**, 7.
328. J. G. Winter, P. Portius, G. Kociok-Kohn, R. Steck, and A. C. Filippou, *Organometallics*, 1998, **17**, 4176.
329. H. Ohgaki, N. Fukaya, and W. Ando, *Organometallics*, 1997, **16**, 4956.
330. S. Mazieres, H. Lavayssiere, G. Dousse, and J. Satge, *Inorg. Chim. Acta*, 1996, **252**, 25.
331. S. Benet, C. J. Cardin, D. J. Cardin, S. P. Constantine, P. Heath, H. Rashid, S. Teixeira, J. H. Thorpe, and A. K. Todd, *Organometallics*, 1999, **18**, 389.
332. N. N. Zemlyansky, I. V. Borisova, M. G. Kuznetsova, V. N. Khrustalev, Y. A. Ustynyuk, M. S. Nechaev, V. V. Lunin, J. Barrau, and G. Rima, *Organometallics*, 2003, **22**, 1675.
333. C. Bibal, S. Mazieres, H. Gornitzka, and C. Couret, *Organometallics*, 2002, **21**, 2940.
334. J. Barrau, G. Rima, and T. El Amraoui, *Organometallics*, 1998, **17**, 607.
335. N. N. Zemlyansky, I. V. Borisova, V. N. Khrustalev, M. Y. Antipin, Y. A. Ustynyuk, M. S. Nechaev, and V. V. Lunin, *Organometallics*, 2003, **22**, 5441.
336. P. Jutzi, S. Keitemeyer, B. Neumann, A. Stammler, and H. G. Stammler, *Organometallics*, 2001, **20**, 42.
337. N. Fukaya, H. Sekiyama, M. Ichinohe, and A. Sekiguchi, *Chem. Lett.*, 2002, 802.
338. H. Hashimoto, Y. Yagihashi, L. Ignatovich, and M. Kira, *Heteroat. Chem.*, 2001, **12**, 398.
339. N. P. Toltl, W. J. Leigh, G. M. Kollegger, W. G. Stibbs, and K. M. Baines, *Organometallics*, 1996, **15**, 3732.
340. Y. Apeloig, D. Bravo-Zhivotovskii, I. Zharov, V. Panov, W. J. Leigh, and G. W. Sluggett, *J. Am. Chem. Soc.*, 1998, **120**, 1398.
341. M. Taoufik, C. C. Santini, J. P. Candy, A. deMallmann, and J. M. Basset, *J. Am. Chem. Soc.*, 1996, **118**, 4167.
342. M. P. Egorov, O. M. Nefedov, T. S. Lin, and P. P. Gaspar, *Organometallics*, 1995, **14**, 1539.
343. M. P. Egorov, O. M. Nefedov, T. S. Lin, and P. P. Gaspar, *Organometallics*, 1996, **15**, 894.
344. S. Kobayashi, S. Iwata, M. Abe, and S. Shoda, *J. Am. Chem. Soc.*, 1995, **117**, 2187.
345. S. Kobayashi, S. Iwata, and M. Hiraishi, *J. Am. Chem. Soc.*, 1994, **116**, 6047.
346. S. Kobayashi, S. I. Shoda, S. Cao, S. Iwata, M. Abe, K. Yajima, K. Yagi, and M. Hiraishi, *J. Macromol. Sci.,-Pure Appl. Chem.*, 1994, **A31**, 1835.
347. E. Broclawik and A. Bocho-Janiszewska, *J. Molecul. Structure-Theochem*, 2000, **531**, 241.
348. S. Kobayashi, S. Iwata, H. J. Kim, and S. Shoda, *Macromolecules*, 1996, **29**, 486.
349. S. I. Shoda, S. Iwata, H. J. Kim, M. Hiraishi, and S. Kobayashi, *Macromol. Chem. Phys.*, 1996, **197**, 2437.
350. S. Shoda, S. Iwata, K. Yajima, K. Yagi, Y. Ohnishi, and S. Kobayashi, *Tetrahedron*, 1997, **53**, 15281.
351. G. Ossig, A. Meller, C. Bronneke, O. Muller, M. Schafer, and R. Herbst-Irmer, *Organometallics*, 1997, **16**, 2116.
352. T. Iwamoto, H. Masuda, S. Ishida, C. Kabuto, and M. Kira, *J. Organomet. Chem.*, 2004, **689**, 1337.
353. T. Iwamoto, H. Masuda, S. Ishida, C. Kabuto, and M. Kira, *J. Am. Chem. Soc.*, 2003, **125**, 9300.
354. N. Takagi and S. Nagase, *Organometallics*, 2001, **20**, 5498.
355. L. H. Pu, A. D. Phillips, A. F. Richards, M. Stender, R. S. Simons, M. M. Olmstead, and P. P. Power, *J. Am. Chem. Soc.*, 2003, **125**, 11626.
356. P. P. Power, *Chem. Commun.*, 2003, 2091.
357. M. Stender, A. D. Phillips, and P. P. Power, *Chem. Commun.*, 2002, 1312.

358. M. Stender, A. D. Phillips, R. J. Wright, and P. P. Power, *Angew. Chem.,-Int. Ed.*, 2002, **41**, 1785.
359. C. M. Cui, M. M. Olmstead, and P. P. Power, *J. Am. Chem. Soc.*, 2004, **126**, 5062.
360. L. H. Pu, B. Twamley, S. T. Haubrich, M. M. Olmstead, B. V. Mork, R. S. Simons, and P. P. Power, *J. Am. Chem. Soc.*, 2000, **122**, 650.
361. R. S. Simons and P. P. Power, *J. Am. Chem. Soc.*, 1996, **118**, 11966.
362. A. C. Filippou, A. I. Philippopoulos, P. Portius, and G. Schnakenburg, *Organometallics*, 2004, **23**, 4503.
363. A. C. Filippou, P. Portius, and A. I. Philippopoulos, *Organometallics*, 2002, **21**, 653.
364. A. C. Filippou, A. I. Philippopoulos, P. Portius, and D. U. Neumann, *Angew. Chem.,-Int. Ed.*, 2000, **39**, 2778.
365. K. K. Pandey, M. Lein, and G. Frenking, *J. Am. Chem. Soc.*, 2003, **125**, 1660.
366. E. Lukevics, L. Ignatovich, and S. Belyakov, *Appl. Organomet. Chem.*, 2004, **18**, 203.
367. E. Lukevics, P. Arsenyan, S. Belyakov, and O. Pudova, *Eur. J. Inorg. Chem.*, 2003, 3139.
368. A. A. Selina, S. S. Karlov, K. Harms, D. A. Tyurin, Y. F. Oprunenko, J. Lorberth, and G. S. Zaitseva, *Z. Naturforsch. Sec., B-a J. Chem. Sci.*, 2003, **58**, 613.
369. E. Lukevics, L. Ignatovich, T. Shul'ga, and S. Belyakov, *Appl. Organomet. Chem.*, 2003, **17**, 745.
370. A. A. Korlyukov, K. A. Lyssenko, M. Y. Antipin, N. V. Alekseev, S. P. Kniazev, and E. A. Chernyshev, *J. Molecul. Struct.*, 2003, **655**, 215.
371. S. S. Karlov, D. A. Sorokin, Y. F. Oprunenko, J. Lorberth, and G. S. Zaitseva, *Z. Naturforsch. Sec., B-a J. Chem. Sci.*, 2002, **57**, 993.
372. E. Lukevics, L. Ignatovich, T. Shul'ga, O. Mitchenko, and S. Belyakov, *J. Organomet. Chem.*, 2002, **659**, 165.
373. A. V. Churakov, L. G. Kuz'mina, P. L. Shutov, S. S. Karlov, A. A. Selina, and G. S. Zaitseva, *Russ. J. Inorg. Chem.*, 2002, **47**, 983.
374. A. A. Korlyukov, N. V. Alekseev, S. P. Knyazev, E. A. Chernyshev, O. V. Krivolapova, K. V. Pavlov, and V. V. Shcherbinin, *Dokl. Chem.*, 2001, **379**, 222.
375. S. S. Karlov, P. L. Shutov, A. V. Churakov, J. Lorberth, and G. S. Zaitseva, *J. Organomet. Chem.*, 2001, **627**, 1.
376. R. Eujen, A. Roth, and D. J. Brauer, *Monatsh. Chem.*, 1999, **130**, 1341.
377. E. Lukevics, L. Ignatovich, and S. Belyakov, *J. Organomet. Chem.*, 1999, **588**, 222.
378. G. S. Zaitseva, S. S. Karlov, G. V. Pen'kovoy, A. V. Churakov, J. A. K. Howard, B. A. Siggelkow, E. V. Avtomonov, and J. Lorberth, *Z. Anorg. Allg. Chem.*, 1999, **625**, 655.
379. G. S. Zaitseva, S. S. Karlov, B. A. Siggelkow, E. V. Avtomonov, A. V. Churakov, J. A. K. Howard, and J. Lorberth, *Z. Naturforsch. Sec., B-a J. Chem. Sci.*, 1998, **53**, 1247.
380. V. Gevorgyan, L. Borisova, A. Vyater, V. Ryabova, and E. Lukevics, *J. Organomet. Chem.*, 1997, **548**, 149.
381. V. V. Shcherbinin, K. V. Pavlov, I. P. Shvedov, O. S. Korneva, L. G. Menchikov, and O. M. Nefedov, *Russ. Chem. Bull.*, 1997, **46**, 1632.
382. G. S. Zaitseva, S. S. Karlov, A. V. Churakov, J. A. K. Howard, E. V. Avtomonov, and J. Lorberth, *Z. Anorg. Allg. Chem.*, 1997, **623**, 1144.
383. Q. Wang and R. Huang, *Tetrahedron Lett.*, 2000, **41**, 3153.
384. R. G. Kultyshev, G. K. S. Prakash, G. A. Olah, J. W. Faller, and J. Parr, *Organometallics*, 2004, **23**, 3184.
385. J. W. Faller and R. G. Kultyshev, *Organometallics*, 2003, **22**, 199.
386. S. Belyakov, L. Ignatovich, and E. Lukevics, *J. Organomet. Chem.*, 1999, **577**, 205.
387. P. H. M. Budzelaar, J. J. Engelberts, and J. H. van Lenthe, *Organometallics*, 2003, **22**, 1562.
388. V. M. Rayon and G. Frenking, *Chem. Eur. J.*, 2002, **8**, 4693.
389. J. D. Smith and T. P. Hanusa, *Organometallics*, 2002, **21**, 1518.
390. J. Rouzaud, A. Castel, P. Riviere, H. Gornitzka, and J. M. Manriquez, *Organometallics*, 2000, **19**, 4678.
391. J. Rouzaud, M. Joudat, A. Castel, F. Delpech, P. Riviere, H. Gornitzka, J. M. Manriquez, and I. Chavez, *J. Organomet. Chem.*, 2002, **651**, 44.
392. S. P. Constantine, H. Cox, P. B. Hitchcock, and G. A. Lawless, *Organometallics*, 2000, **19**, 317.
393. G. E. Herberich, X. L. Zheng, J. Rosenplanter, and U. Englert, *Organometallics*, 1999, **18**, 4747.
394. K. Forissier, L. Ricard, D. Carmichael, and F. Mathey, *Chem. Commun.*, 1999, 1273.
395. X. Zheng and G. E. Herberich, *Eur. J. Inorg. Chem.*, 2001, 3013.
396. M. Joudat, A. Castel, F. Delpech, P. Riviere, A. McHeik, H. Gornitzka, S. Massou, and A. Sournia-Saquet, *Organometallics*, 2004, **23**, 3147.
397. J. L. Vincent, S. Luo, B. L. Scott, R. Butcher, C. J. Unkefer, C. J. Burns, G. J. Kubas, A. Lledos, F. Maseras, and J. Tomas, *Organometallics*, 2003, **22**, 5307.
398. Y. Takeuchi, K. Tanaka, M. Ohnishi-Kameyama, A. Kalman, and L. Parkanyi, *Chem. Commun.*, 1998, 2289.
399. Y. Takeuchi, L. Parkanyi, A. Kalman, M. Nishikawa, K. Tanaka, W. Mori, and M. Kinoshita, *J. Organomet. Chem.*, 2003, **687**, 33.
400. B. Rake, F. Zulch, Y. Ding, J. Prust, H. W. Roesky, M. Noltemeyer, and H. G. Schmidt, *Z. Anorg. Allg. Chem.*, 2001, **627**, 836.
401. J. E. Bender, M. M. B. Holl, A. Mitchell, N. J. Wells, and J. W. Kampf, *Organometallics*, 1998, **17**, 5166.

402. A. F. Richards, H. Hope, and P. P. Power, *Angew. Chem. Int. Ed. Engl.*, 2003, **42**, 4071.

403. K. Mochida and H. Chiba, *J. Organomet. Chem.*, 1994, **473**, 45.

404. M. Ishifune, S. Kashimura, Y. Kogai, Y. Fukuhara, T. Kato, H.-B. Bu, N. Yamashita, Y. Murai, H. Murase, and R. Nishida, *J. Organomet. Chem.*, 2000, **611**, 26.

405. K. Huang and L. A. Vermeulen, *Chem. Commun. (Cambridge)*, 1998, 247.

406. M. Okano and K. Watanabe, *Electrochem. Commun.*, 2000, **2**, 471.

407. S. M. Katz, J. A. Reichl, and D. H. Berry, *J. Am. Chem. Soc.*, 1998, **120**, 9844.

408. J. A. Reichl, C. M. Popoff, L. A. Gallagher, E. E. Remsen, and D. H. Berry, *J. Am. Chem. Soc.*, 1996, **118**, 9430.

409. M. Motonaga, H. Nakashima, S. Katz, D. H. Berry, T. Imase, S. Kawauchi, J. Watanabe, M. Fujiki, and J. R. Koe, *J. Organomet. Chem.*, 2003, **685**, 44.

410. N. Choi and M. Tanaka, *J. Organomet. Chem.*, 1998, **564**, 81.

411. Y. Yokoyama, M. Hayakawa, T. Azemi, and K. Mochida, *J. Chem. Soc., Chem. Commun.*, 1995, 2275.

412. J. E. Bender IV, K. E. Litz, D. Giarikos, N. J. Wells, M. M. Banaszak Holl, and J. W. Kampf, *Chem. Eur. J.*, 1997, **3**, 1793.

413. S. S. Bukalov and L. A. Leites, *Proc. SPIE- Int. Soc. Opt. Eng.*, 2000, **4069**, 2.

414. K. Mochida, R. Hata, M. Shimoda, F. Matsumoto, H. Kurosu, A. Kojima, M. Yoshikawa, S. Masuda, and Y. Harada, *Polyhedron*, 1996, **15**, 3027.

415. F. Riedmiller, G. L. Wegner, A. Jockisch, and H. Schmidbaur, *Organometallics*, 1999, **18**, 4317.

416. K. Mochida, S.-S. Nagano, H. Kawata, M. Wakasa, and H. Hayashi, *J. Organomet. Chem.*, 1997, **542**, 75.

417. K. Mochida, K. Kimijima, H. Chiba, M. Wakasa, and H. Hayashi, *Organometallics*, 1994, **13**, 404.

418. I. Borthwick, L. C. Baldwin, M. Sulkes, and M. J. Fink, *Organometallics*, 2000, **19**, 139.

419. S. M. Horvat and C. H. Schiesser, *J. Chem. Soc., Perkin Trans. 2*, 2001, 939.

420. K. Mochida and S. Nagano, *Inorg. Chem. Commun.*, 1998, **1**, 289.

421. H. Tachikawa, *J. Organomet. Chem.*, 1997, **547**, 337.

422. H. Tachibana and Y. Tokura, *Synth. Met.*, 1995, **71**, 2005.

423. T. Kodaira, A. Watanabe, O. Ito, M. Matsuda, S. Tokura, M. Kira, S. S. Nagano, and K. Mochida, *Adv. Mater. (Weinheim, Germany)*, 1995, **7**, 917.

424. K. Mochida, S.-S. Nagano, S. Maeyama, T. Kodaira, A. Watanabe, O. Ito, and M. Matsuda, *Bull. Chem. Soc. Jpn.*, 1997, **70**, 713.

425. K. Mochida, S.-S. Nagano, H. Kawata, M. Wakasa, and H. Hayashi, *Appl. Organomet. Chem.*, 1997, **11**, 949.

426. A. Watanabe, O. Ito, and K. Mochida, *Organometallics*, 1995, **14**, 4281.

427. G. Gerber and A. Leonard, *Mutat. Res.*, 1997, **387**, 141.

428. P. Kopf-Maier, *Eur. J. Clin. Pharmacol.*, 1994, **47**, 1.

429. S.-H. Tao and P. M. Bolger, *Regul. Toxicol. Pharmacol.*, 1997, **25**, 211.

430. R. Tacke, M. Merget, R. Bertermann, M. Bernd, T. Beckers, and T. Reissmann, *Organometallics*, 2000, **19**, 3486.

431. M. Merget, K. Gunther, M. Bernd, E. Gunther, and R. Tacke, *J. Organomet. Chem.*, 2001, **628**, 183.

432. R. Tacke, T. Heinrich, T. Kornek, M. Merget, S. A. Wagner, J. Gross, C. Keim, G. Lambrecht, E. Mutschler, T. Beckers, M. Bernd, and T. Reissmann, *Phosphorus Sulfur Silicon Rel. Elem.*, 1999, **151**, 69.

433. G.-y. Hao, S. Liu, and T.-h. Li, *He Huaxue Yu Fangshe Huaxue*, 2002, **24**, 240.

434. B. Celaries, M. Gielen, D. de Vos, and G. Rima, *Appl. Organomet. Chem.*, 2003, **17**, 191.

435. E. Lukevics, L. Ignatovich, and I. Shestakova, *Appl. Organomet. Chem.*, 2003, **17**, 898.

436. O. Schimmer, H. Eschelbach, D. K. Breitinger, T. Gruetzner, and H. Wick, *Arzneimittelforschung*, 1997, **47**, 1398.

437. H. Shimokawa, Y. Ishiwatari, S. Yokoji, and H. Hashimoto, in ‘Jpn. Kokai Tokkyo Koho’, Sanwa Kagaku Kenkyusho Co., Japan, 2000.

438. Y. Ishiwatari, S. Yokoji, H. Hashimoto, and H. Awatani, in ‘Jpn. Kokai Tokkyo Koho’, Sanwa Kagaku Kenkyusho Co., Japan, 2000.

439. E. V. Soloviev, V. V. Shcherbinin, E. A. Chernyshev, M. V. Kotrelev, K. V. Pavlov, N. Y. Khromova, and N. G. Komalenkova, *PCT Int. Appl.; (Fr.).*, 2000, 52.

440. T. Osawa, S. Kawakishi, M. Akiba, and N. Kakimoto, *Main Group Met. Chem.*, 1994, **17**, 251.

441. Q.-M. Wang and R.-Q. Huang, *Appl. Organomet. Chem.*, 2002, **16**, 593.

Gold: Inorganic & Coordination Chemistry

Jagadese J. Vittal[1] **& Richard J. Puddephatt**[2]
[1] *National University of Singapore, Singapore*
[2] *The University of Western Ontario, ON, Canada*

1 Introduction 1
2 Bonding in Gold(I) and Gold(III) Complexes 1
3 Relativistic Effects 1
4 Aurophilicity 2
5 Isolobal Analogy 2
6 Gold in Oxidation State −I 2
7 Gold in Zero Oxidation State 2
8 Gold(I) Complexes 2
9 Gold(II) Complexes 5
10 Gold(III) Complexes 6
11 Gold(IV) Complexes 7
12 Gold(V) Complexes 7
13 Homonuclear Gold Clusters 7
14 Heteronuclear Gold−Metal Clusters 9
15 Complexes of Gold(I) with Au···Au Interactions 11
16 Gold-containing Polymers, Rings, And Dendrimers 13
17 Gold Compounds with Rare Gases 13
18 Related Articles 13
19 Further Reading 13
20 References 13

Abbreviations

Et = ethyl; dcpe = 1,2-Bis(dicyclohexylphosphino)ethane; diars 1,2-Bis(dimethylarsino)benzene; diphos 1,2-Bis (dimethylphosphino)benzene; dppm = Bis(diphenylphosphino)methane; dppp = 1,3-bis(diphenylphosphino)propane; PCy_3 = tricyclohexylphosphine; Ph = phenyl; $Ptol_3$ = tris(4-methylphenyl)phosphine; bdt = benzenedithiolate.

1 INTRODUCTION

Gold is one of the most noble of the metals (the electrochemical potential is the lowest for any metal) and has a unique position among elements in the periodic table. Further, gold is the most electronegative of all the metals (on Pauling scale) and can easily be reduced to Au^-. Similarly, the inorganic and coordination compounds of gold are unique and have displayed exceptional properties like the ability to form Au–Au and metal−gold bonds in clusters, and to form complexes in oxidation states from (−I) to (+V), often with unusual stereochemistry. The linear two-coordinate gold(I) compounds and the square-planar four-coordinate gold(III) complexes are ubiquitous in gold chemistry.[1–5]

2 BONDING IN GOLD(I) AND GOLD(III) COMPLEXES

Molecular orbital (MO) calculations suggest that the bonding in linear gold(I) complexes involves mostly the $5d_{z^2}$ and 6s orbitals. However, sp hybridization, without the involvement of 5d orbitals, is commonly used to interpret ^{197}Au Mössbauer and magnetic circular dichroism (MCD) spectra of gold(I) complexes. In square-planar gold(III) compounds, the $5d_{x^2-y^2}$,6s,6p_x,6p_y orbitals are used. The gold(I) and gold(III) complexes in their most common stereochemistry, therefore, have 14 and 16 valence electrons, respectively. Most gold complexes are coordinatively unsaturated (*see Coordinative Saturation & Unsaturation*).

3 RELATIVISTIC EFFECTS

The position of gold in the periodic table is such that the *Relativistic Effects* are at a maximum.[6] Many of the anomalous properties of Au, as compared to Ag and Cu, are ascribed to such effects.[7,8] The relativistic effect strongly stabilizes the 6s orbitals, stabilizes the 6p levels to a lesser extent, and destabilizes the 5d levels. The initial resistance of gold to oxidation, its greater extent of oxidation once oxidized, higher melting point, yellow color of gold, and smaller metallic and ionic radii as compared to silver may be attributed largely to the relativistic effect.[9,10] The common occurrence of Au–Au bonds in complexes, the shorter and stronger bonds formed by Au compared to Ag, and the higher ionization energy and electron affinity (EA) of gold can as well be explained in terms of the relativistic contraction of the 6s orbital of Au.

The tendency of gold(I) to form linear two-coordinate complexes can be explained by the large 6s → 6p energy separation caused by relativistic effects of gold. The low 5d → 6s separation of gold, which is also caused by relativistic effects, is responsible for the stabilization of the higher oxidation states +III and +V for gold with respect to Ag and Cu. Gold(0) has the electronic configuration $[Xe]4f^{14}5d^{10}6s^1$; for Au^+, it is $[Xe]4f^{14}5d^{10}6s^0$, and for Au^-, $[Xe]4f^{14}5d^{10}6s^2$. From these electronic configurations, the predominance of the metallic form of gold, Au^0, is not obvious, but it can be explained through consideration of the relativistic effects.

Although relativistic effects contribute to the instability of AuF with respect to AuF_3 and Au, its stability has been predicted and AuF has been shown to exist.[11] The gold(III) halides follow the stability order AuF_4^- >

$AuCl_4^- > AuBr_4^- > AuI_4^-$. The relativistic enhancement of the dissociation energy decreases from AuF_4^- to AuI_4^-.[8]

4 AUROPHILICITY

Many molecular gold complexes pack in their crystal lattice in such a way that there are short intermolecular Au···Au contacts.[12] The intermolecular attractive forces between gold atoms are weak but important in determining structures in the solid state. The phenomenon is most marked for gold and is especially significant for two-coordinate gold(I) centers, and the interactions invariably occur perpendicularly to the molecular axis.[13–15] The effect is called *aurophilicity*. The aggregation occurs with $Au^I \cdots Au^I$ distances between 2.7 and 3.3 Å (the estimated van der Waals distance being 3.60 Å). The estimated bond energy for the $Au^I \cdots Au^I$ interaction is 7–12 $kcal\,mol^{-1}$, which is of the same order of magnitude as the hydrogen-bond energy.[16–18] Examples will be found throughout this article.

5 ISOLOBAL ANALOGY

The structures of some heteronuclear transition metal–gold compounds containing $[Au–PR_3]^+$ fragments are very similar to those of the related hydrido complexes. Further, the $[Au–PR_3]$ positions in the compounds have been proposed as evidence for the location of hydrido-ligand positions in hydride analogs. The $[Au–PR_3]^+$ cation is isolobal with H^+.[19] The hydrogen atom uses its 1s orbital, and the $[Au–PR_3]^+$ group mostly uses the 6s orbital of gold in bonding. This isolobal analogy between H^+ and $[AuPR_3]^+$ has been found to be very useful in rationalizing the synthesis and structures of many of these compounds.[20] Some well-known isolobal pairs of complexes are $[Co(CO)_4(AuPPh_3)]$ and $[Co(CO)_4H]$, $[Mn(CO)_5(AuPPh_3)]$ and $[Mn(CO)_5H]$, and $[Fe(CO)_4(AuPPh_3)_2]$ and $[Fe(CO)_4H_2]$. However, a strict relationship fails in some cases where two or more $[AuPPh_3]^+$ groups are present, there being a marked tendency to form Au–Au bonds in such compounds. The $Au_2(PPh_3)_2$ species present in clusters are sometimes considered as isolobal models of dihydrogen complexes. This analogy is further extended[21] between H_3^+ and $[Au_3(PR_3)_3]^+$.

6 GOLD IN OXIDATION STATE −I

The relatively high electron affinity of Au (EA = 2.3 eV) suggests that Au could behave as a pseudohalogen in forming negatively charged ions. In addition, Au^- (electronic configuration [Xe] $4f^{14}5d^{10}6s^2$) is isoelectronic with Hg^0. A few alkali metal aurides M^+Au^- are known (M = Na, K, Rb & Cs). Gold in Cs^+Au^- is present as the Au^- ion.[4] The ionic salt Cs^+ Au^- has the CsCl lattice structure. Metallic gold dissolves in anhydrous liquid NH_3 containing Cs, Rb, or K ro form Au^- in solution. $BaAu_2$ is a semiconductor and has AlB_2-type crystal structure with Au–Au distance of 2.77 Å.[22] The tetramethylammonium auride is found to be isostructural with $(Me_4N)Br$.[23] The auride ion is also found in M_3AuO (M = K, Rb, Cs), aurideaurates $Cs_7Au_5O_2$, which is, in fact, $(CsAu)_4(Cs_3AuO_2)$, and $Rb_5Au_3O_2$, which is $(RbAu)_2(Rb_3AuO_2)$ containing Au^{-1} and Au^I ions.

7 GOLD IN ZERO OXIDATION STATE

In the gas phase, gold exists largely as Au_2 molecules with $d(Au–Au) = 2.50$ Å and $D_o(Au–Au) = 221\,kJ\,mol^{-1}$. The simplest gold(0) complex is $[Ph_3PAuAuPPh_3]$.

8 GOLD(I) COMPLEXES

The most common oxidation states for gold are I and III. In general, Au^{III} is favored with hard ligands and Au^I with soft ligands. Au^I complexes are diamagnetic. The majority of Au^I compounds have a coordination number of two with linear geometry. However, compounds with trigonal planar and tetrahedral structures are also known. The compounds of the type $[X(Au\{PR_3\})_n]$, where X = O, S, Se, Cl, Br, I, N, P, As, C, and so on, with $n > 1$ will be discussed in Section 15.

Simple neutral Au^I halides, AuX (X = Cl, Br, I), are all polymers with bridging halide ligands. The complex ions $[AuX_2]^-$, disproportionate in aqueous solution according to equation (1), where X = Cl, Br, or SCN, are stable when X = CN. The ions $[AuX_2]^-$ can be stabilized in the presence of excess of halide or pseudohalide ions.

$$[Au^IX_2]^- \longleftrightarrow [Au^{III}X_4]^- + 2Au + 2X^- \qquad (1)$$

Chloro(carbonyl)gold(I), [AuCl(CO)], is prepared in quantitative yield by the reaction of anhydrous Au_2Cl_6 with CO at atmosphere pressure (equation 2).[24] With insufficient carbon monoxide, Au_4Cl_8 is the product (equation 3). Anhydrous Au_2Cl_6 is itself prepared *in situ* by dehydration of $H[AuCl_4]\cdot 3H_2O$ with thionyl chloride as solvent (equation 4).

$$[Au_2Cl_6] + 2CO \longrightarrow 2COCl_2 + 2[AuCl(CO)] \qquad (2)$$

$$2[Au_2Cl_6] + 2CO \longrightarrow 2COCl_2 + [Au_4Cl_8] \qquad (3)$$

$$H_3O^+ + [AuCl_4]^- + SOCl_2 \longrightarrow 3HCl + SO_2 + \tfrac{1}{2}[Au_2Cl_6] \qquad (4)$$

An interesting gold polysulfide anion $[Au_{12}S_8]^{4-}$ has been prepared[25] by dissolving Au_2S, Au_2S_3, or $[AuCl_4]^-$ in aqueous Na_2S and has been isolated as the Ph_4As^+ salt. The cubane-like anion (**1**) has sulfur atoms at the corners of a cube and Au^I atoms at the center of each edge. In a similar selenium analog (**2**), a sodium ion is encapsulated at the center of the cube and Na^+ is bonded to all gold atoms ($Na \cdots Au = 3.327(3)-3.467(3)$ Å). The volume of the sulfur cluster is 12% smaller than the selenium analog (98 vs 111 $Å^3$), and, hence, the sodium anion cannot be included inside the cage.[26] This inorganic cryptand complex anion $[NaAu_{12}Se_8]^{3-}$, (**2**), is prepared from a mixture of AuCN, Na_2Se, and Et_4NCl.

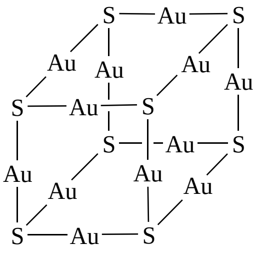

(**1**)

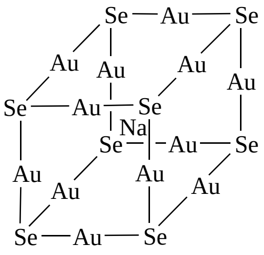

(**2**)

The thioether complexes of the type $[AuCl(SR_2)]$ are useful synthetic intermediates and prepared by the reaction of $[AuCl_4]^-$ with the corresponding dialkylsulfide according to equation (5).

$$[AuCl_4]^- + 2R_2S + H_2O \longrightarrow [AuCl(SR_2)] + R_2SO + 2H^+ + 3Cl^- \qquad (5)$$

The water-soluble gold–thiourea complex cation $[Au\{S{=}C(NH_2)_2\}_2]^+$ is useful in the extraction of gold from its ore.

Thiolate compounds of gold(I) have been studied extensively due to their applications in crysotherapy (the treatment of rheumatoid arthritis by gold drugs)[27–30] and in gold coating processes. Gold(I) sodium thiomalate (Myochrysin) (**3**) and gold(I) thioglucose (Solganol) (**4**) have been used for many years, but 2,3,4,6-tetra-O-acetyl-1-β-1-thio-β-D-pyranosato-S-(triethylphosphine)gold(I) (Auranofin or Ridaura) (**5**) has been found to be more effective since it can be given orally. The X-ray structure of the Auranofin (**5**) shows[2] that Au^I has linear two-coordinate geometry with S–Au–P = 173.6°. The structures[27–31] of Myochrisin and Solganol are polymeric with thiolate bridging as shown in (**3**), with R = malate, or (**4**) with R = glucose.

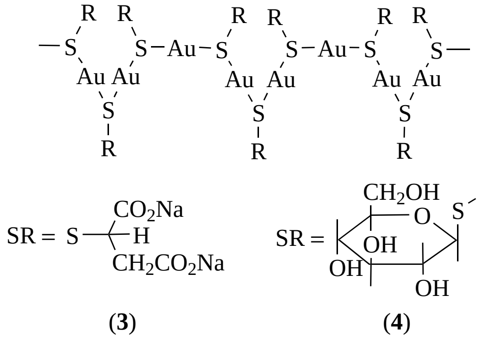

(**3**) (**4**)

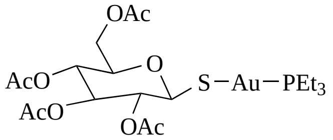

(**5**)

Gold(I) forms dinuclear complexes with N,N-dialkyl dithiocarbamates, O,O'-diisopropyl dithiophosphate, and dithio-phosphinates. In the solid state, the dinuclear units are further associated by intermolecular Au–Au interactions to form chains. The intramolecular and intermolecular Au–Au distances in these complexes range from 2.76–3.10 Å and 3.05–3.40 Å respectively, compared to the Au–Au distances of 2.768 Å in metallic gold. A typical structure of a dithiocarbamate is shown as (**6**).

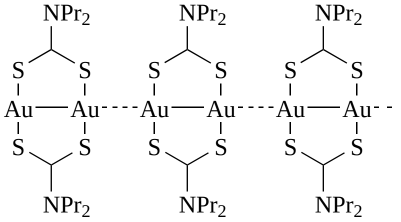

(**6**)

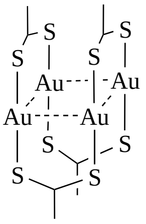

(**7**)

The reaction between $AuCl_4{}^-$ and dithioacetic acid gives the tetramer $[Au(S_2CMe)]_4$. The molecular structure consists of a square of gold atoms with the dithioacetato ligands bridging above and below the Au_4 plane as shown in (**7**).

The compound $[Me_3P\text{–}Au\text{–}OSiMe_3]$ is volatile and sublimes in vacuo. At 190 °C, it decomposes to form a gold mirror and $(Me_3Si)_2O$, Me_3PO, and Me_3P. Another volatile gold compound, $[Me_3P\text{–}Au\text{–}N(SiMe_3)_2]$, melts at 35–37 °C, and the liquid can be distilled under vacuum without decomposition.[32] Some gold complexes with ligands containing additional N-donor sites, such as benzylimidazolates (**8**), pyrazolates (**9**), and carbeniates (**10**), are trimers in the solid state and stacked with short Au^I–Au^I contacts. Irradiation with ultraviolet (UV) light causes the crystals of (**8**) to emit red light. A yellow burst of light was observed when a drop of dichloromethane solvent was placed upon the irradiated crystals of (**8**) ('solvoluminescence').[33]

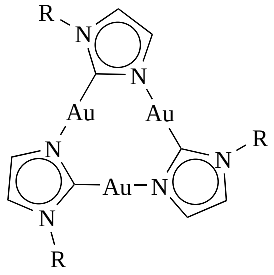

(**8**)

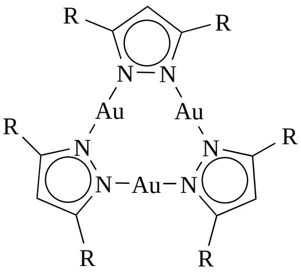

(**9**)

A great number of Au^I complexes with monodentate phosphine, arsine, and stibine ligands of the type $[R_3Y\text{–}Au\text{–}Cl]$

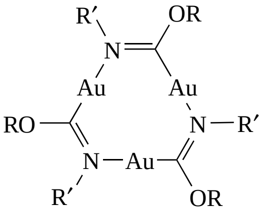

(**10**)

are known. They are easily prepared from the reaction of $[AuCl_4]^-$ with the appropriate tertiary phosphine, arsine, or stibine, R_3Y (equation (6)).

$$[AuCl_4]^- + 2R_3Y \longrightarrow [R_3Y\text{–}Au\text{–}Cl] + R_3YCl_2 + Cl^- \qquad (6)$$

With excess phosphine, Au^I forms complexes of the type $[Au(PR_3)_n]^+$ ($n = 2$, 3, or 4). The maximum coordination number is dependent on the bulk of the phosphine. For example, when $L = P(C_6H_{11})_3$, only $[AuL_2]^+$ is observed in solution. For $L = PBu_3$ or $P(tol)_3$, $[AuL_2]^+$ and $[AuL_3]^+$ are found, and, when $L = PEt_3$ or $P(OEt)_3$, $[AuL_2]^+$, $[AuL_3]^+$, and $[AuL_4]^+$ are detected in solution.

$[AuCl(PPh_3)]$ reacts with excess of phosphine to form $[AuCl(PPh_3)_2]$ and $[AuCl(PPh_3)_3]$. The structures are distorted trigonal planar and tetrahedral, respectively, with coordinated chloride ion. For the same stoichiometry, Au^I in $[Au(PCy_3)_2](SCN)$ has two-coordinate linear geometry, and in $[Au(PPh_3)_2(SCN)]$ has trigonal planar structure, the difference clearly being due to different steric effects of the phosphine ligands. Distorted tetrahedral structures have been reported for $[Au(PPh_3)_3X]$ ($X = Cl$ or SCN), with the Au–X bonds much longer than Au–P, whereas a regular tetrahedral geometry is found for Au^I in $[Au(PPh_2Me)_4]^+$.

In the dinuclear complex $[Au\{P(CH_2CH_2PPh_2)_3\}]_2Cl_2$, (**11**), each gold atom is tetrahedral, and the Au–Au distance of 6.199 Å is clearly nonbonding.**34**

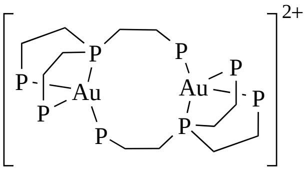

(11)

Bidentate phosphines such as $Ph_2PCH_2PPh_2$ or $Ph_2PNHPPh_2$ form cyclic dinuclear complexes with gold(I). These complexes can be deprotonated**35** with strong bases to give the corresponding methanide or amide complex as shown in equation (7).

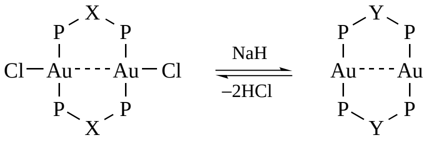

(7)

$X = CH_2$ or NH; $Y = CH$ or N

Several dinuclear or oligomeric gold(I) complexes as well as gold–metal (M = Ir, etc.) heterobimetallic gold(I) complexes are luminescent with λ_{max} ranging from 465 to 593 nm and excited state lifetimes ranging from 1 to 24 µs in the solid state as well as in solution.**36–38** This photoemission property has been attributed to the Au–Au or Au–M interactions. Molecular orbital calculations carried out on the compound $[Au_2(\mu\text{-}H_2PCH_2PCH_2)_2]^{2+}$ showed the Au–Au σ^* highest occupied molecular orbital (HOMO) has 78% Au character; of this 41% is from the 6s orbital and 41% is from the $5d_{z}{}^2$ orbital.**39** Gold–heterometal clusters have attracted as candidates for optoelectronic materials as they show interesting optical properties, including phosphorescence.**40**

A few mononuclear Au^I compounds have been found to photoluminesce in the solid state but not in solution. The lowest energy band in the absorption spectrum of $[Au_2(\mu\text{-}dmpm)_2]^{2+}$, which is reported to be luminescent in the solid state, has been assigned by using circular dichroism (CD) spectra to the transition $\sigma(p_z) \leftarrow \sigma^*(d_z{}^2)$.**41** However, the compound $[Au_2(\mu\text{-}dcpe)_3](PF_6)_2$, which has no Au–Au contact, emits in the solid state as well as in acetonitrile solution ($\lambda_{max} = 508$ nm, $\tau = 21.5(5)$ µs), indicating that Au–L bonding is also a factor to be considered in Au^I photophysics.**42**

A series of dinuclear gold(I) thiolate complexes with crown ether pendants has been successfully employed to switch on and off the Au–Au interactions (shown in equation (8)), and, hence, the photoemission induced by ion-binding, which provides a new strategy for the design of chemosensors and luminescence signaling.**43,44**

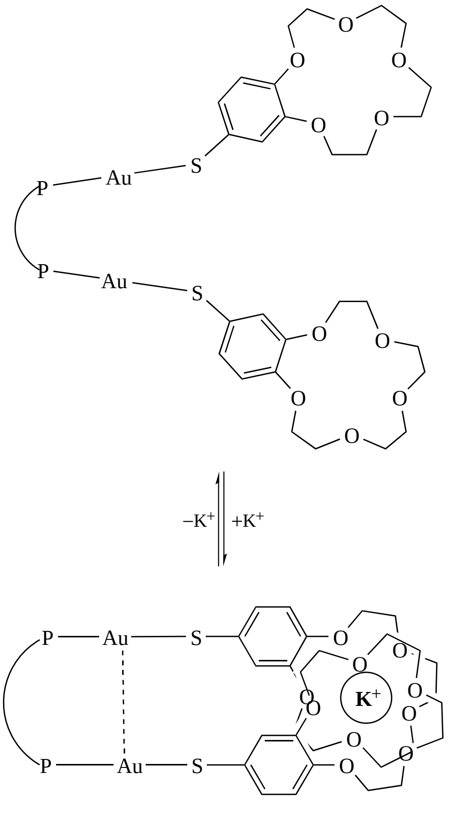

(8)

Perhaps the most stable complex formed by gold(I) is the linear $[Au(CN)_2]^-$.[1] In aqueous solution, the stability constant, K, has been estimated to be $\sim 10^{39}$ for the reaction of equation (9).

$$Au^+ + 2CN^- \longrightarrow [Au(CN)_2]^- \qquad (9)$$

This cyanide complex is used in the extraction of gold from its ore. Gold present in the ore dissolves in alkali cyanide in the presence of compressed air according to equation (10).

$$4Au + 8CN^- + O_2 + 2H_2O \longrightarrow 4[Au(CN)_2]^- + 4OH^- \qquad (10)$$

The cyanide solution is further filtered and purified, and gold can then be precipitated with zinc (equation (11)).

$$[Au(CN)_2]^- + Zn \longrightarrow [Zn(CN)_4]^{2-} + 2Au \qquad (11)$$

9 GOLD(II) COMPLEXES

Many complexes that appeared to be Au^{II} based on their empirical formulae are really mixed oxidation state Au^I-Au^{III} complexes. A number of well-characterized examples are given in Table 1. Electron spectroscopy for chemical analysis (ESCA), ^{197}Au Mossbauer spectroscopy, and single-crystal X-ray structure analyses have been used to distinguish these mixed oxidation state complexes from true Au^{II} complexes. The compound '$AuCl_2$' was shown to be a mixed Au^I-Au^{III} tetrameric cyclic complex $[Au_4Cl_8]$ (**12**) by X-ray structure analysis.

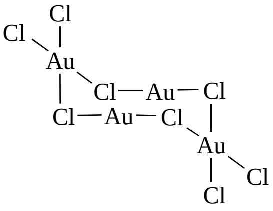

(**12**)

The electronic configuration of Au^{II} is $[Xe]4f^{14}5d^9$, and, hence, the mononuclear gold(II) complexes are paramagnetic and have deep color similar to Cu(II) compounds. They have a strong tendency to disproportionate to give Au^I and Au^{III} or to form a dinuclear complex containing a Au–Au bond. Hence, mononuclear Au^{II} compounds are rare. The first evidence for mononuclear Au^{II} complexes was obtained from electron spin resonance (ESR) studies[4] of the reaction mixture in Scheme (1), in which oxidation of $[Au_2(\mu\text{-}S_2CNR_2)_2]$ by $(R_2NCS_2)_2$ to give $[Au(S_2CNR_2)_3]$ was shown to proceed by way of the paramagnetic gold(II) complex $[Au(S_2CNR_2)_2]$. Gold(II) intermediates have been proposed for many redox reactions involving Au^I-Au^{III} interconversions, but they cannot usually be detected by ESR.

Table 1 Some apparent gold(II) complexes

Formula	Correct formulation
AuO	$Au^IAu^{III}O_2$
AuS	$Au^IAu^{III}S_2$
$AuSe$	$Au^IAu^{III}Se_2$
$AuSO_4$	$Au^IAu^{III}(SO_4)_2$
$CsAuBr_3$	$Cs_2[Au^IBr_2][Au^{III}Br_4]$
Au(maleonitriledithiolate)PPh_3	$[Au^I(PPh_3)_2]^+$ $[Au^{III}$(maleonitriledithiolate)$_2]^-$
$(n\text{-}Bu_2NCS_2)AuCl$	$[(n\text{-}Bu_2NCS_2)_2Au^{III}]^+$ $[Au^ICl_2]^-$

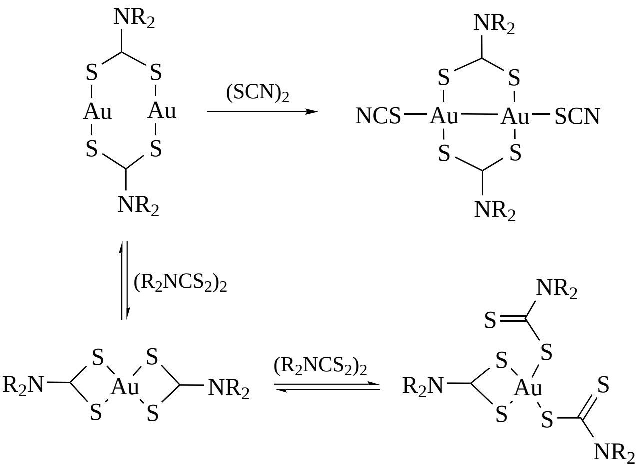

Scheme 1

The crystallographically characterized, neutral, and air-sensitive complex of gold(II), $[Au\{S_2C_2(CN)_2\}_2]$ (**13**), which contains the maleonitriledithiolate ligand, has square-planar geometry. An air-stable octahedral Au^{II} complex $[AuL_2](BF_4)_2$ (L = 1, 4, 7-trithiacyclononane) (**14**) is obtained from the reaction of $K[AuCl_4]$ with L.[34]

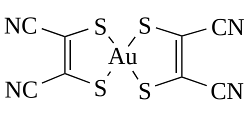

(**13**)

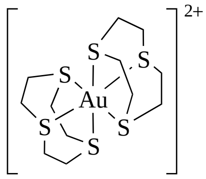

(**14**)

The gold(II) compounds without Au–Au bonds are in general prepared by reduction of Au^{III}.[45] There are several dinuclear gold(II) complexes with Au–Au bonds. They are obtained from the corresponding gold(I) complexes by oxidative addition reactions as shown in Scheme (2). In a special case, both the $Au^{II}-Au^{II}$ and $Au^I\cdots Au^{III}$ isomeric products were isolated.[46]

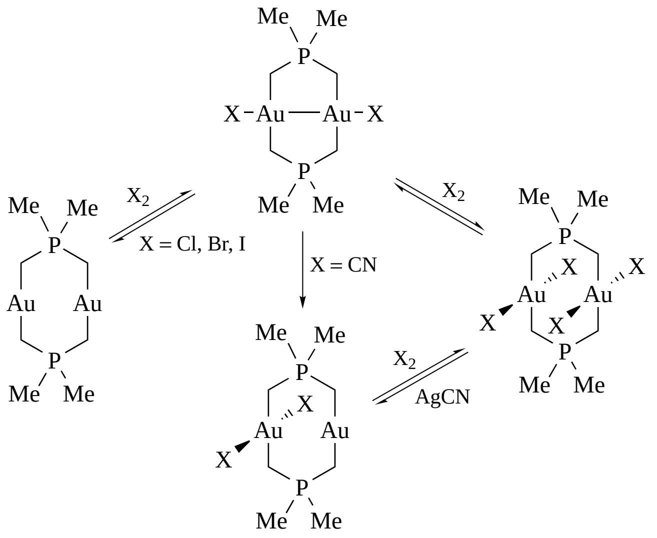

Scheme 2

Several dinuclear units have been assembled to form linear Au_5^{9+} and Au_6^{10+} complexes. However, they were shown to be Au^I-Au^{III} mixed-valent compounds.[45] The normal $Au^{II}-Au^{II}$ distances are in the range 2.5–2.7 Å. The only binuclear gold(II) complex (**15**) with unsupported $Au^{II}-Au^{II}$ bond has been shown to possess interesting photophysical and thermal redox properties.[47]

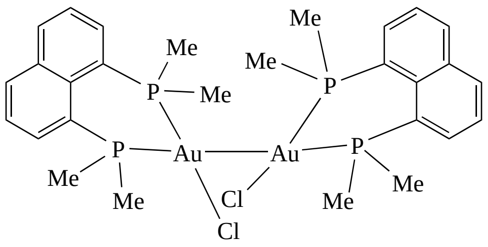

(**15**)

10 GOLD(III) COMPLEXES

All known Au^{III} compounds are diamagnetic ($[Xe]4f^{14}5d^8$ low-spin configuration), and the large majority have square-planar geometry. However, Au^{III} complexes with coordination number five or six are also known.

Gold reacts directly with all the halogens. With chlorine, gold forms AuCl or Au_2Cl_6 depending on the reaction conditions. Liquid bromine reacts with gold powder to form dark red-brown Au_2Br_6. Bright golden yellow AuF_3 can be conveniently produced by reacting either gold(III) chloride or gold powder with fluorine at high temperature. Gold(III) bromide and chloride are both dimeric in the solid state as shown in (**16**), whereas the fluoride is polymeric with a helical structure.

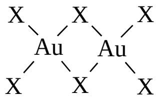

(16)

Gold metal dissolves in aqua regia or in a mixture of HBr and HNO_3 to give tetrachloroauric(III) acid, $H[AuCl_4]$, or tetrabromoauric(III) acid, $H[AuBr_4]$, respectively. These strong acids give salts with bases. The $[AuCl_4]^-$ and $[AuBr_4]^-$ ions have regular square-planar geometry both in the solid state and in solution. The halide ligands in these complex anions are easily substituted by other ligands such as NO_2^-, N_3^-, I^-, or SCN^-. The reactions proceed by way of five-coordinate intermediates.

The tetraethylammonium salt of the $[AuI_4]^-$ anion has been prepared by reaction of $(Et_4N)[AuCl_4]$ with anhydrous liquid HI. However, $[AuI_4]^-$ is unstable and easily reduced to $[AuI_2]^-$. Au(CO)X (X = Cl, Br) may be obtained by the reaction of AuX_3 with CO as shown in equation (12).

$$AuX_3 + 2CO \longrightarrow Au(CO)X + COX_2 \tag{12}$$

On oxidation with halogens, the $[Au(CN)_2]^-$ ion forms *trans*-$[Au(CN)_2X_2]^-$ (X = Cl, Br, I). The cyanide complex anion, $[Au(CN)_4]^-$, is prepared by the exchange reaction between $[AuCl_4]^-$ and CN^- ions. The square-planar $[Au(CN)_4]^-$ anion further reacts with cyanide ions in aqueous solution to form $[Au(CN)_5]^{2-}$ and $[Au(CN)_6]^{3-}$ ions.

The nitrogen-donor complexes of gold(III) are usually formed by the displacement of chloride in $H[AuCl_4]$ by nitrogen-donor ligands. The complex $[Au(NH_3)_4](NO_3)_3$, for example, is obtained by bubbling gaseous ammonia into an aqueous solution of $H[AuCl_4]$ and ammonium nitrate.

The amine complexes of Au^{III} are acidic (pKa 2.2 to 7.5) in nature. The acidity increases with the degree of substitution at nitrogen. The weakening of N–H bonds in amine complexes of gold(III) has been attributed to the high polarizing power of Au^{III}. The ethylenediamine complex $[Au(en)_2]^{3+}$ reacts with chloride ions to form the complex cation $[AuCl_2(en)_2]^+$, which has a distorted octahedral geometry in the solid state.

Au^{III} forms distorted square-pyramidal complexes with 2,2′-biquinolyl and 2,9-dimethyl-1,10-phenanthroline ligands.

The complexes of the type $[AuX_3(PR_3)]$ are synthesized by oxidation of $[R_3PAuX]$ with halogen. The complexes $[AuX_nX'_{3-n}(PR_3)]$, in which X and X' are different halogens, formed in this way exist as mixtures containing all possible values of n and all possible isomers.

Four-, five-, and six-coordinate Au^{III} compounds $[AuL_2]^{3+}$, $[AuClL_2]^{2+}$, and $[AuCl_2L_2]^+$ have been isolated for the ligand L = diphos. The distorted octahedral complex $[AuI_2(diars)_2]^+$ is isolated from redox reactions between I_2 and $[Au(diars)_2]^+$.

A dinuclear selenide complex anion $[Au_2(\mu\text{-}Se)_2(Se_4)_2]^{2-}$ is the product of the reaction[48] between $[AuCN]_n$ and Na_2Se_5. Square-planar gold(III) complexes are readily formed by a variety of bidentate sulfur-donor ligands such as toluene-1,2-dithiolate, maleonitriledithiolate, and dithiocarbamate. On oxidation with Cl_2 or Br_2, $[\{Au(S_2CNR)_2\}_2]$ forms $Au^I{-}Au^{III}$ complexes, which may be oxidized further to an Au^{III} complex.

Gold(III) has been found to catalyze various organic reactions including Diels-Alder due to its Lewis acidic properties.[49,50]

11 GOLD(IV) COMPLEXES

Gold(IV) complexes are very rare. The only monomer $[Au(bdt)_2]$ characterized by X-ray analysis was found to be square planar. This Au^{IV} compound was prepared from the corresponding Au^{III} anion by one-electron oxidation in an electrochemical cell as shown in equation (13).

$$[(C_5H_9)_4N][Au(bdt)_2] \xrightarrow{-e^-} [Au(bdt)_2] \tag{13}$$

Another Au^{IV} compound, AuL_2 (where L is a dithiolate ligand, 5,6-dihydro-1,4-dithio-2,3-dithiolate), is a dimer in the solid state and has no ESR spectrum due to its dimeric nature, which is maintained in solution.

12 GOLD(V) COMPLEXES

Only fluoride compounds of Au^V are known, and they all have octahedral stereochemistry as expected for a d^6 metal ion. Reaction between AuF_3, fluorine, and XeF_2 yielded the first gold(V) complex $[XeF_{11}][AuF_6]$ (equation (14)).

$$2XeF_2 + AuF_3 + 5F_2 \longrightarrow [Xe_2F_{11}][AuF_6] \tag{14}$$

The anion $[AuF_6]^-$ has distorted octahedral structure with $d(\text{Au–F}) = 1.85$ to $1.90\,\text{Å}$. Oxidation of $M[AuF_4]$ (where M = K, Cs, or NO) by fluorine also produced $[AuF_6]^-$. Gold(V) fluoride is formed by the thermal decomposition of $[KrF][AuF_6]$ or $[O_2]^+[AuF_6]^-$. AuF_5 is a fluorine-bridged polymer in the solid state.

13 HOMONUCLEAR GOLD CLUSTERS

Gold clusters containing 2 to 13 gold atoms have been characterized by single-crystal X-ray crystallography, which is the only definitive technique for structural characterization of gold clusters.[2,11,51] Other techniques such as UV-Visible, Mossbauer and nuclear magnetic resonance (NMR) spectroscopies, conductivity, and fast atom bombardment mass spectrometry (FABMS) are also useful. In these clusters, the average oxidation state of gold is less than one. These compounds are usually synthesized by reduction of $[Au(PR_3)X]$ (X = halide, NO_3^-, etc.) by such reducing agents as $NaBH_4$, CO, H_2, B_2H_6, and $Ti(C_6H_5{-}CH_3)_2$. The nuclearity of the clusters appears to be dictated by the nature of the PR_3 used. Cluster degradation, aggregation, and substitution reactions are often employed to convert one cluster into another using phosphines, halides, and pseudohalides.

The simple dinuclear complex $[Au_2(PPh_3)_2]$ has the trans bent structure with $d(\text{Au–Au}) = 2.76$ Å and Au–Au–P angle of 129°. It was prepared from the reaction of $[AuI(PPh_3)]$ with sodium naphthalide. The trinuclear gold-cluster (**17**), P = PPh_2, is photoluminescent in solution.[52]

Two tetrahedral gold clusters have been reported. The cluster $[Au_4(PPh_3)_4I_2]$ (**18**) was prepared by the reaction of $[Au_9(PPh_3)_8]^{3+}$ with iodide ion, and has a tetrahedral Au_4 unit bridged on opposite edges by iodide. However, the compound $[Au_4(dppm)_3I_2]$ (**19**) contains a tetrahedron of gold atoms, in which a terminal iodide binds to one gold atom and the second iodide is bonded rather weakly to the other three Au atoms.

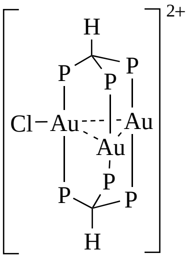

(**17**)

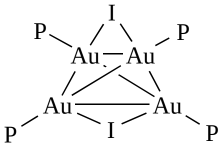

(**18**)

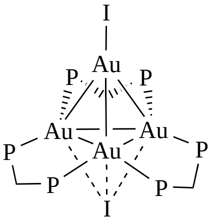

(**19**)

The structure of the pentanuclear gold-cluster $[Au_5(dppm)_3(dppm{-}H)]^{2+}$ is related to that of the Au_4 clusters, with the fifth gold atom appended (**20**). This Au_5 cluster can be synthesized by reduction of $[Au_2(dppm)](NO_3)_2$ with $NaBH_4$ by the evaporation of metallic gold into ethanolic solution of dppm and NH_4NO_3 or by reaction of $[Au_9(PPh_3)_8]^{3+}$ with dppm ligand.

Addition of $[\mathrm{Ag(CN)_2}]^-$ to $[\mathrm{Au_8(PPh_3)_8}](\mathrm{NO_3})_2$ has produced the cluster $[\mathrm{Au_6(PPh_3)_6}](\mathrm{NO_3})_2$, which has an edge-shared bitetrahedral structure (**21**). Another $\mathrm{Au_6}$ cluster, $[\mathrm{Au_6(dppp)_4}](\mathrm{NO_3})_2$, has a structure described as bis(edge-capped) tetrahedral as shown in (**22**).

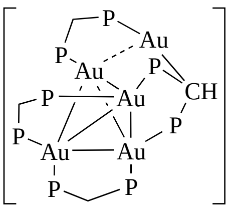

(**20**)

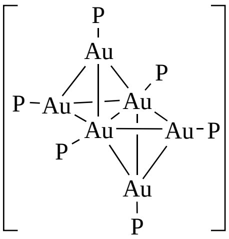

(**21**)

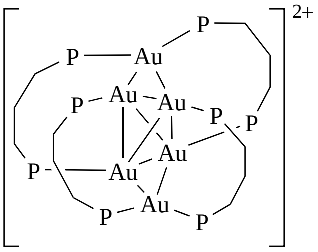

(**22**)

Low-temperature ^{31}P NMR studies showed that the energy difference between the edge-shared bitetrahedral and bis(edge-capped) tetrahedral structures is very small. The $\mathrm{Au_7}$ cluster having pentagonal bipyramidal geometry was synthesized from the gold vapor as shown in equation (15).

$$\mathrm{Au(vapor)} + \mathrm{PPh_3} \xrightarrow{\text{toluene}} [\mathrm{Au_7(PPh_3)_7}](\mathrm{OH}) \tag{15}$$

The cluster ion $[\mathrm{Au_8(PPh_3)_8}]^{2+}$ has been synthesized from $[\mathrm{Au_9(PPh_3)_8}]^{3+}$ and $\mathrm{PPh_3}$, and has the structure (**23**). The structure may be described in terms of a centered chair of gold atoms with an additional gold atom capping the chair by bonding to three alternate gold atoms in the chair. A phosphine ligand can be removed from this cluster by the addition of $[\mathrm{RhCl(C_8H_{14})}]$. The resultant cationic cluster $[\mathrm{Au_8(PPh_3)_7}]^{2+}$ has the structure (**24**), described as a centered chair of gold atoms with an additional gold atom attached to three adjacent Au atoms in the chair.

The structures of the large Au clusters with 8–13 gold atoms may be described to be derived from a centered icosahedral $\mathrm{Au_{13}}$ cluster by removal of peripheral gold atoms. The structure of $[\mathrm{Au_9(Ptol_3)_8}]^{3+}$ can be derived from a centered icosahedron, but it is more simply pictured as a bicapped centered chair as shown in (**25**). The cluster $[\mathrm{Au_9(Ptol_3)_9}](\mathrm{NO_3})_3$ has been prepared by $\mathrm{NaBH_4}$ reduction of $[\mathrm{Au(Ptol)_3(NO_3)}]$. The structure of the related ion, $[\mathrm{Au_9(P(4\text{-}MeOC_6H_4)_3)_8}]^{3+}$, has a centered crown structure (**26**). The two compounds have similar electronic spectra and ^{31}P NMR spectra even at low temperature, indicating that these compounds undergo facile intramolecular skeletal rearrangement in solution.

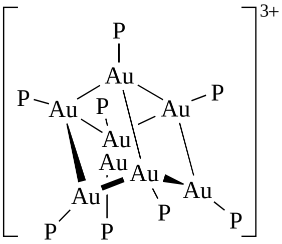

(**23**)

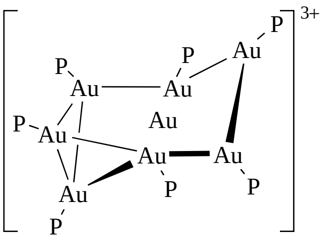

(**24**)

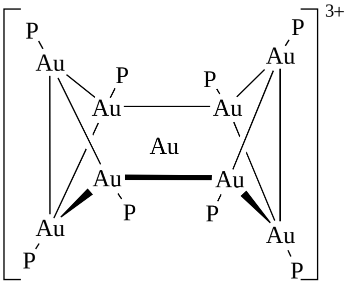

(**25**)

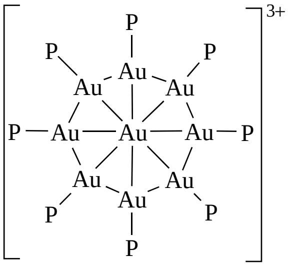

(**26**)

Another $\mathrm{Au_9}$ cluster, $[\mathrm{Au_9(PCy_3)_5(SCN)_3}]$, was prepared by $\mathrm{NaBH_4}$ reduction of $[\mathrm{Au(PCy_3)SCN}]$, and this structure can also be described in terms of a centered icosahedron with different gold atoms missing or as bicapped centered chair as shown in (**27**). The reduction of $[\mathrm{Au_9(PPh_3)_8}]^{3+}$ gives $[\mathrm{Au_9(PPh_3)_8}]^{+}$ with a distorted centered cubane structure (**28**). On the other hand, the structure of $\mathrm{Au_{10}}$ cluster can be described as three trigonal bipyramidal $\mathrm{Au_5}$ cluster sharing a common central gold atom and edge sharing.**[5]**

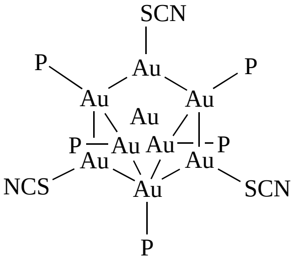

(**27**)

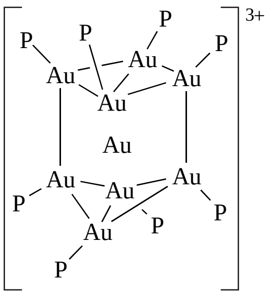

(**28**)

The gold clusters $[\mathrm{Au_{11}X_3L_7}]$ (X = SCN, CN or I, L = $\mathrm{P(C_6H_4\text{–}X)_3}$ (X = Cl, H, F), $\mathrm{PCy_3}$) were the first gold clusters to be characterized. They are obtained by reduction of

[AuXL] by $NaBH_4$ or $[Ti(PhMe)_2]$, or by gold atom reactions with [AuXL]. The structures of these compounds are based on a centered icosahedron of gold atoms, in which a triangle of gold atoms is replaced by a single atom, and each peripheral gold is bound to either a phosphine or a halide or thiocyanate ligand (**29**). The cluster $[Au_{11}(dppp)_5](SCN)_3$ is obtained by the addition of dppp to $[Au_{11}(SCN)_3L_7]$. The skeletal structure is very similar to that of $[Au_{11}X_3L_7]$.

Several clusters are known with the general formula $[Au_{13}X_n(PR_3)_{12-n}]^{(5-n)+}$ (X = halide, $n = 2$ to 4). However, larger gold clusters that have been established by X-ray crystallography[53] are $[Au_{13}(PMe_2Ph)_{10}Cl_2]^{3+}$ and $[Au_{13}(dppm)_6]^{4+}$. The $[Au_{13}Cl_2(PMe_2Ph)_{10}](PF_6)_3$ was prepared by addition of chloride ions to $[Au_{11}(PMe_2Ph)_{10}]^{3+}$, and the $[Au_{13}(dppm)_6](NO_3)_4$ was obtained from $NaBH_4$ reduction of $[Au_2(dppm)](NO_3)_2$. The structures of these clusters are based on a centered icosahedron of gold atoms, as illustrated for $[Au_{13}Cl_2(PMe_2Ph)_{10}]^{3+}$ in (**30**), where o = $AuPMe_2Ph$. This structure is considered to be the parent of structures found for many Au_8–Au_{11} clusters that have different numbers of gold atoms missing from the periphery.

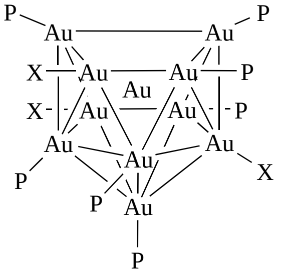

(**29**)

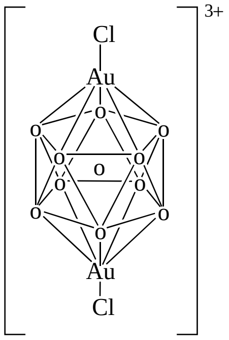

(**30**)

The largest gold cluster claimed is $[Au_{55}Cl_6(PPh_3)_{12}]$, for which the proposed stoichiometry is based on electron microscopy, ^{31}P NMR spectroscopy, analytical, and molecular weight data.[54] The cluster was isolated from the reduction of $[AuCl(PPh_3)]$ with diborane. A two-shell cuboctahedral structure involving an icosahedral Au_{13} unit embedded in an outer layer of 42 Au atoms in a cuboctahedron was proposed. However, the exact nuclearity of the structure is controversial. In the absence of suitable single crystals for X-ray diffraction study, all the experimental data currently available support a cuboctahedral 55-atom gold cluster.[55] However, the largest gold cluster that has been unequivocally characterized in the solid state is $[Au_{39}(PPh_3)_{14}Cl_6]^{2+}$ formed by the reaction of $HAuCl_4$ with PPh_3.[56] Recently, a fourth-generation dendrimer with 96 SH groups has been reacted with $Au_{55}(PPh_3)_{12}Cl_6$ in 3:1 molar ratio to prepare 'naked Au_{55}' clusters.[57]

Of the higher nuclearity gold clusters described above, two classes have been identified. The clusters of the type $[Au\{Au(PPh_3)\}_n]^{x+}$, where the peripheral atoms lie on the surface of a sphere, are characterized by a total of $12n + 18$ valence electrons. The structures $[Au_{13}Cl_2\{P(Me_2Ph)_3\}_{10}]^{3+}$ (162 valence electrons), $[Au_{11}I_3(PPh_3)_7]$ (138 valence electrons), $[Au_9\{P(4\text{-}MeC_6H_4)_3\}_8]^+$ (114 valence electrons), and $[Au_8(PPh_3)_8]^{2+}$ (102 valence electrons) are examples of spheroidal structures. The low nuclearity clusters of the type $[Au\{Au(PR_3)\}_n]^{x+}$, where the peripheral atoms have a ring or torus structure, are characterized by a total of $12n + 16$ valence electrons. Examples for the toroidal structures are $[Au\{Au(PPh_3)\}_8]^{3+}$ (112 valence electrons) and $[Au\{Au(PPh_3)\}_7]^{2+}$ (100 valence electrons).

Both electronic and steric factors influence the geometries and stoichiometries of gold-cluster compounds. The clusters of the type $[Au_{13}L_{12}]^{5+}$, for example, could be formed only for small ligands L. The steric restrictions are further set by the number of ligands L. Calculations of the Kitaigorodski packing coefficients or of cluster cone angles (*see Cone Angle*) are used to understand the steric effects quantitatively. For example, the calculation of Kitaigorodski coefficient would predict that not more than eight PPh_3 can be packed around the metal frame in icosahedral symmetry.[58] As well, it can be shown[59] that an icosahedral gold-cluster $[Au(AuL)_{12}]^{n+}$ could be synthesized with the ligands L having a mean cone angle lying between 70 and 83°.

The gold clusters appear to be ideal models for bulk metals, metal surfaces, and colloidal particles. The gold clusters are used for labelling in electron microscopy studies of biological materials.

14 HETERONUCLEAR GOLD–METAL CLUSTERS[60]

The reagents R_3P–Au–X or $[(R_3P\text{–}Au)_3O]^+$ are commonly used to introduce gold into metal clusters. These gold–metal clusters may contain from one to four gold atoms bound to one or more transition metals. A large number of such clusters have been studied.[61–63] Table 2 gives selected examples of such heteronuclear gold–metal clusters. The structures of the clusters having formula $M(AuPR_3)_x$ (M = a transition metal fragment and $x = 4$–8) can be expressed in terms of a metal-centered icosahedron,[64–66] in which the gold atoms occupy some of the corners as shown in Table 3. Most of these clusters are synthesized by photolysis of Ph_3PAuN_3 with metal carbonyls.

The cluster $[Pt(AuPPh_3)_8]^{2+}$ has a centered crown-like toroidal structure like that of $[Au\{AuP(C_6H_4\text{-}OMe)_3)_8]^{3+}$ (**26**). On treatment with CO or CNR, this cluster cation is converted to $[L\text{-}Pt(AuPPh_3)_8]^{2+}$ (**31**) with a hemispherical geometry.[67]

The reaction of HgX_2 (X = NO_3, Cl, or Br) with the cluster cation $[Pt(AuPPh_3)_8]^{2+}$ yields $[Pt(AuPPh_3)_8(Hg)_2]^{4+}$ (**32**), in which the Pt atom at the center of the cluster is bonded to all Au and Hg atoms.

When a mixture of $R_3P–Au–X$ and $(R_3P–Ag–X)_n$ undergoes reduction by $NaBH_4$, clusters containing 25 atoms ($Au_{13}Ag_{12}$), 37 atoms ($Au_{18}Ag_{19}$), and 38 atoms ($Au_{18}Au_{20}$)

Table 2 Some heteronuclear gold–metal clusters

Cluster type	Skeletal structure	Selected examples
MAu	M-Au-L	$[Co(CO)_4(AuPPh_3)]$ $[Mn(CO)_5(AuPPh_3)]$ $[V(CO)_6(AuPPh_3)]$ $[M(PF_3)_4(AuPPh_3)]$ (M = Rh, Ir)
M_2Au	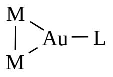	$[Pt_2(dppm)2(C{\equiv}C\text{-}t\text{-}Bu)_2(AuI)]$ $[Re_2(PPh_3)_4(H)_4(\mu\text{-}H)_3(AuPPh_3)]$ $[\{(C_5Me_5)Rh(\mu\text{-}CO)\}_2(AuCl)]$
M_3Au	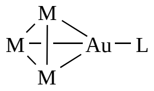	$[Pt_3(CO)_3(Pcy_3)_3(AuPCy_3)]^+$ $[CoRu_3(CO)_{13}(AuPPh_3)]$ $[MCo_3(CO)_{12}(AuPPh_3)]$ (M = Fe, Ru)
MAu_2	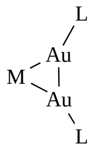	$[M(CO)_4(AuPPh_3)_2]$ (M = Fe, Ru, Os) $[Pt(PEt_3)_2Cl(AuPPh_3)_2]^+$
M_2Au_2	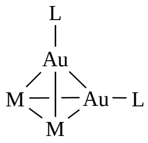	$[Os_4(\mu\text{-}H)_2(CO)_{12}(AuPPh_3)_2]$
	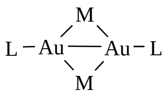	$[Pt_2(PPh_3)_4(CNR)_4(AuPPh_3)_2]^{2+}$ (R = 2, 6-dimethylphenyl)
M_3Au_2	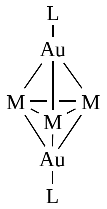	$[Pt_3(\mu\text{-}SO_2)(\mu\text{-}Cl)(Pcy_3)_3\{AuP(p\text{-}C_6H_4F)_3\}_2]^+$ $[Pt_3(\mu\text{-}dppm)_3(AuPMe_3)_2]^{2+}$
	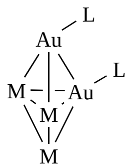	$[CoRu_3(H)(CO)_{12}(AuPPh_3)_2]$
MAu_3	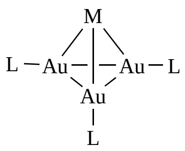	$[(OC)_5V(AuPPh_3)_3]$ $[(OC)_4M(AuPPh_3)_3]$ (M = Mn, Re)
	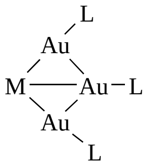	$[Ir(PPh_3)_2(NO_3)(AuPPh_3)_3]^+$
MAu_4	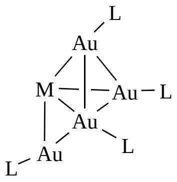	$[ReH_4(Ptol_3)_2(AuPPh_3)_4]^+$
MAu_4	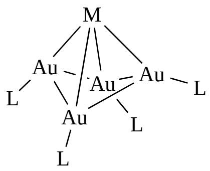	$[Ir(\mu\text{-}H)_2(PPh_3)_2(AuPPh_3)_4]^+$
MAu_5	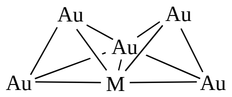	$[Re(H)_4(PPh_3)(AuPPh_3)_5]^{2+}$
MAu_6	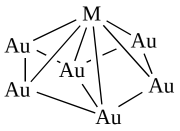	$[Pt(C{\equiv}C\text{-}t\text{-}Bu)(PPh_3)(AuPPh_3)_6]^+$

Table 3 Some polyhedral clusters of gold[a]

1. MAu_4 clusters	2. MAu_5 clusters
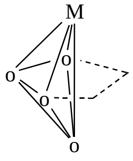	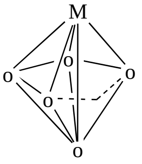
$[(LAu)_4Mn(CO)_4]^+$ $[(LAu)_4CO(CO)_3]^+$	$[(LAu)_5Fe(CO)_3]^+$ $[(LAu)_5Mo(CO)_4]^+$
3. MAu_6 clusters	
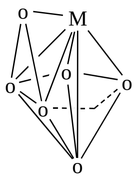	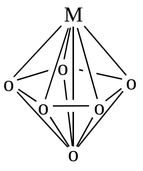
(a) $[(LAu)_6V(CO)_4]$	(b) $[(LAu)_6Mn(CO)_3]^+$
4. MAu_7 clusters	
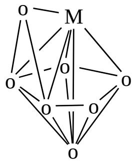	
$[(LAu)_7Mo(CO)_3]^+$	

[a] o = LAu, L = phosphine ligand.

have been isolated depending upon the Ag:Au ratio and the nature of R and X.[68,69] Their structures, which have been determined crystallographically, are based on a gold-centered Au_7Ag_6 icosahedron. For example, the metal core in the $[(Ph_3P)_{10}Au_{13}Ag_{12}Br_8]^+$ cluster ion has two Au_7Ag_6 icosahedra sharing one vertex. For this reason, these clusters are termed ‘clusters of clusters’. They are among the largest metal clusters to be fully characterized. The basic building block for these ‘clusters of clusters’, namely, the icosahedral Au–Ag cluster ion, has been isolated[70] from the reaction of equation (16).

$$[Au_{11}(PPh_2Me)_{10}]^{3+} + 4[Ag(PPh_2Me)Cl] \longrightarrow [Au_9Ag_4Cl_4(PPh_2Me)_8]^+ + 2[Au(PPh_2Me)_3]^+ \qquad (16)$$

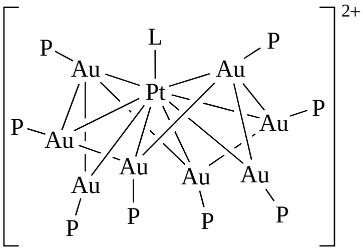

(31)

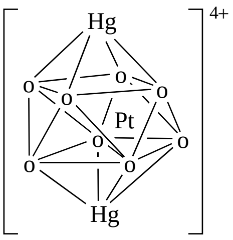

o = Ph_3PAu

(32)

The structure of the cluster cation $[Au_9Ag_4Cl_4(PPh_2Me)_8]^+$ is shown in (**33**). The largest heteronuclear cluster so far is $[Au_{22}Ag_{24}(PPh_3)_{12}Cl_{10}]$.[71]

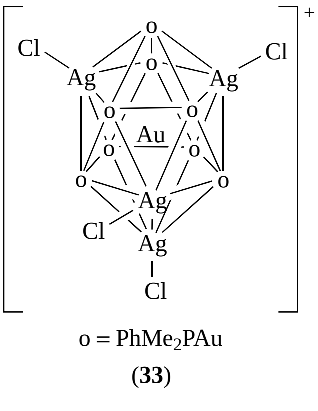

o = $PhMe_2PAu$

(33)

15 COMPLEXES OF GOLD(I) WITH Au· · ·Au INTERACTIONS

There are many unusual gold(I) complexes, in which the structures are greatly affected by secondary gold· · ·gold bonding. For example, the gold fragment $[AuPPh_3]^+$ has been used to synthesize several cluster compounds[72,73] of the type $[M(AuPR_3)_x]^{y+}$, where $2 < x < 12$; and M = Cl, Br, I, S ($x = 2$); O, S, or Se ($x = 3$), N ($x = 4, 5$), P ($x = 4, 5, 6$), C ($x = 4, 5, 6$). In all these compounds, there are Au–Au interactions that govern the geometry.

The synthetic routes for these compounds are given in equations (17–26), and the structures are shown schematically as (**34**)–(**39**), in which P = PPh_3. The oxonium salt, $[(Ph_3PAu)_3O]^+$, is a versatile aerating agent that is often used to introduce $AuPPh_3$ units into organometallic and cluster compounds. It is also a useful reagent in organic syntheses.

$$2Ph_3PAuX + AgBF_4 \longrightarrow [(Ph_3PAu)_2X]^+(BF_4)^- + AgX \qquad (17)$$

$$X = Cl, Br, I, SCN$$

$$2Ph_3PAuCl + Na_2S \longrightarrow [(Ph_3PAu)_2S] + 2NaCl \qquad (18)$$

$$3Ph_3PAuCl \xrightarrow{Ag_2O/NaBF_4} [(PPh_3Au)_3O]^+(BF_4)^- + 2AgCl + NaCl \qquad (19)$$

$$3Ph_3PAuCl + Se(SiMe_3)_2 \longrightarrow [(Ph_3PAu)_3Se]^+\,Cl^- + 2Me_3SiCl \qquad (20)$$

$$4Ph_3PAuCl + N(SiMe_3)_3 + CsF \longrightarrow [(Ph_3PAu)_4N]^+F^- + CsCl + 3Me_3SiCl \qquad (21)$$

$$4Ph_3PAuCl + As(SiMe_3)_3 \longrightarrow [(Ph_3PAu)_4As]^+Cl^- + 3Me_3SiCl \qquad (22)$$

$$[(Ph_3PAu)_4N]^+BF_4^- + Ph_3PAu^+BF_4^- \longrightarrow [(Ph_3PAu)_5N]^{2+}(BF_4^-)_2 \qquad (23)$$

$$5Ph_3PAuCl + 5CsF + CH_2[B(OMe)_2]_2 \xrightarrow{HMPA} [(Ph_3PAu)_5C]^+(BF_4)^- + 5CsCl + BF(OMe)_2 + 2MeOH \qquad (24)$$

$$6Ph_3PAuCl + 6CsF + C[B(OMe)_2]_4 \xrightarrow{HMPA} [(Ph_3PAu)_6C]^{2+}(MeOBF_3^-)_2 + 6CsCl + 2B(OMe)_3 \qquad (25)$$

$$4Ph_3PAuCl + 3CsF + 2Me_3P{=}C(H)SiMe_3 \longrightarrow [Me_3PC(AuPPh_3)_3]^+Cl^- + 2Me_3SiF + 3CsCl + [Me_3PCH_2AuPPh_3]F \qquad (26)$$

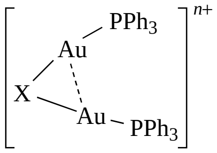

X = Cl, n = 1; X = S, n = 0

(34)

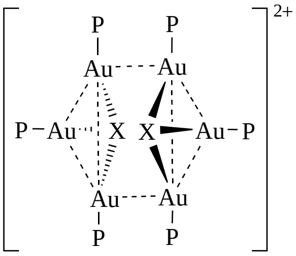

X = O, S, Se

(35)

In some of these mixed gold-main group compounds, the coordination numbers and stereochemistry associated with main group atoms such as carbon and nitrogen are very

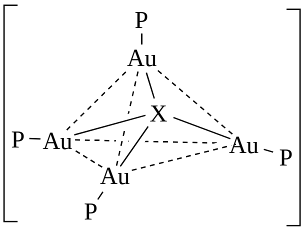

X = C, $n = 0$; X = N, $n = 1$

(**36**)

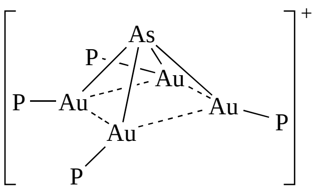

(**37**)

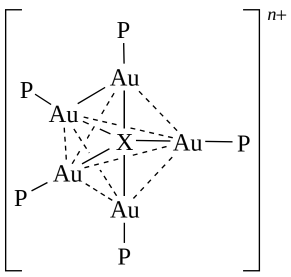

X = C, $n = 1$; X = N, $n = 2$

(**38**)

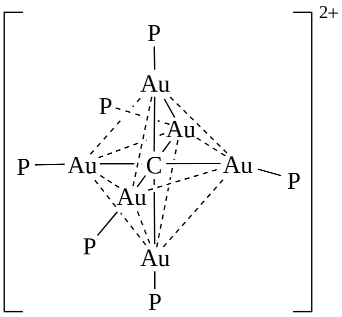

(**39**)

unusual. For example, in the cations $[C\{Au(PPh_3)\}_5]^+$ and $[C\{Au(PPh_3)\}_6]^{2+}$, the central carbon atoms have trigonal bipyramidal and octahedral geometry, respectively, as shown in (**38**) and (**39**).[74,75] These nonclassical hypercoordinated carbon compounds are stabilized by the strong intermetallic Au–Au interactions.

On the basis of bonding theory, one would expect a tetrahedral configuration (sp^3 hybridization) for the cation $[As\{Au(PPh_3)\}_4]^+$ similar to the nitrogen analog, $[N\{Au(PPh_3)\}_4]^+$, (**34**). However, it was found that the cation preferred the square-pyramidal geometry (**35**), with arsenic atoms capping a square of gold atoms over the classical tetrahedral structure.[76] For a tetrahedral structure, the radius of the central atom arsenic is too large to allow for Au–Au interactions, so the alternative structure is adopted instead. An interesting tetrahedral AuL (L = tri-(2-methylphenyl)phosphine) core incorporating an oxygen atom, namely, $[(\mu\text{-}O)(AuL)_4](BF_4)_2$, has been reported by Schimidbaur as the formal analog of H_4O^{2+}.[77] The corresponding sulphur derivative, $[S(AuPPh_3)_4](ClO_4)_2$, as expected, has square-pyramidal structure stabilized by Au–Au interactions.[78]

No Au–Au interactions occur in the monocation $[RP(AuPPh_3)_3]^+$ (R = *o*-tolyl group) in which the central P atom has an ideal tetrahedral geometry. However, by treatment of this compound with $[Ph_3Au]^+(BF_4)^-$ (Scheme (3)), the dication $[RP(AuPPh_3)_4]^{2+}$, which has square-pyramidal geometry with the phosphorus atom at the apex, is formed. The Au–Au interactions are responsible for this unexpected stereochemistry.[79]

This aurophilic property has been used to prepare trimeric and tetrameric gold clusters[80] with 8-aminoquinoline ligands, as shown in Scheme (4).

Finally, octahedral complexes $[P(AuL)_6]^{3+}$ have been prepared by reaction of LAu^+ with $P(SiMe_3)_3$ according to equation (27).[81]

$$6LAu^+BF_4^- + (Me_3Si)_3P + 3KF \longrightarrow 3KBF_4 + 3Me_3SiF + [(LAu)_6P]^{3+}(BF_4^-)_3 \qquad (27)$$

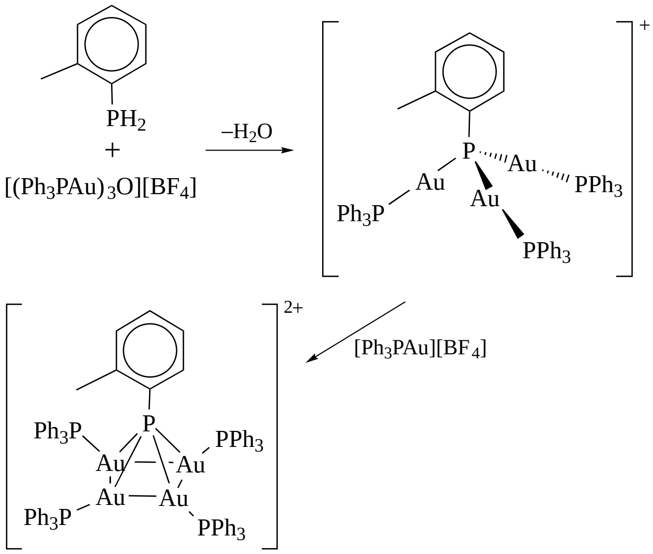

Scheme 3

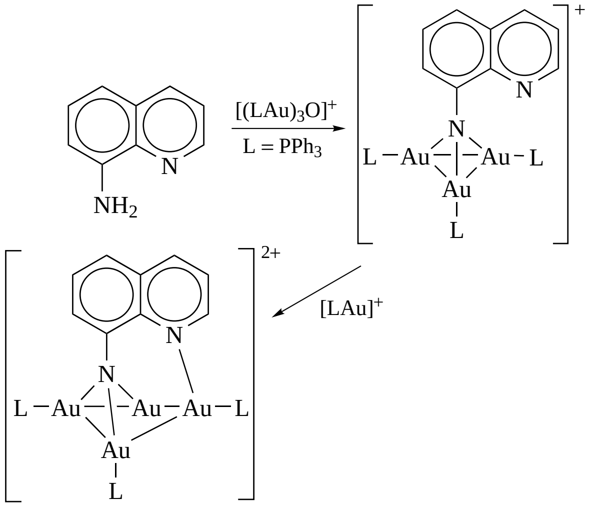

Scheme 4

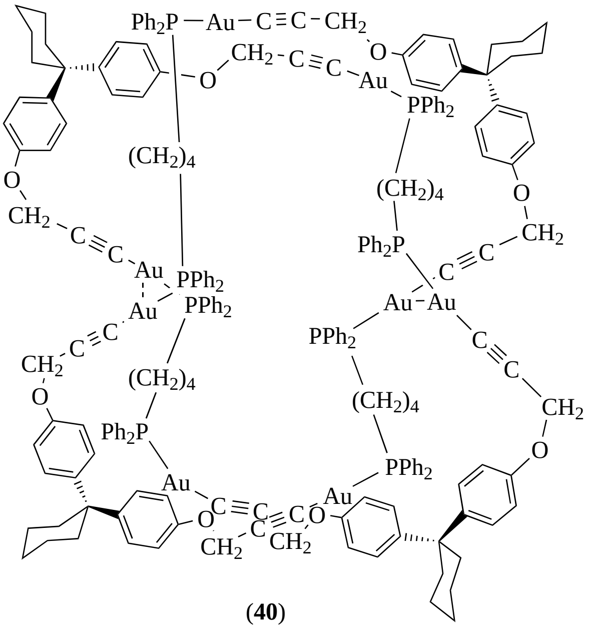

(**40**)

16 GOLD-CONTAINING POLYMERS, RINGS, AND DENDRIMERS

Gold(I) compounds are attractive candidates for synthesizing various types of supramolecular systems including polymers,[82–84] rings,[84,85] dendrimers,[86] and so on, with unusual optical or electrical properties making use of the linear coordination geometry and Au^I-Au^I interactions. An interesting doubly braided[2]catenane containing two 50-membered ring has been found to exhibit fast 'rocking' motion in solution (**40**).[84]

Nanoscale super clusters containing $[Au_2Ru_6C(CO)_{16}]$ has been assembled on the surface of a third-generation dendrite.[87]

17 GOLD COMPOUNDS WITH RARE GASES

Many gold compounds containing rare gases such as Ar–Au–Cl, Kr–Au–Cl, and Xe–Au–Cl have been detected by microwave and mass spectroscopes.[88] The first stable gold–xenon compound, $[AuXe_4]^{2+}$ $(Sb_2F_{11}{}^-)_2$, has been isolated and characterized in the solid state by the reaction of AuF_3 and Xe in the presence of HF/SbF_5 medium.[89] In the dark red crystals, the Au^{2+} has square-planar geometry with four terminal Xe atoms. Further, *cis*-$[AuXe_2(Sb_2F_{11})_2]$ has been synthesized by changing the HF/SbF_5 ratio, while the trans isomer was obtained oxidizing finely divided gold in HF/SbF_5 with XeF_2 under pressure of Xe.[90] After Pyykkö, who predicted that $[AuXe_2]^+$ ion could exist,[91] the first Au^I–Xe compound $[(F_3As)–Au–Xe](Sb_2F_{11})$ was reported recently.[92] The Au^I–Xe distance, 2.607 Å, has been found to be shorter than the Au^{II}–Xe bonds, which is ~2.74 Å.

18 RELATED ARTICLES

Cluster Compounds: Inorganometallic Compounds Containing Transition Metal & Main Group Elements; Copper: Inorganic & Coordination Chemistry; Dinuclear Organometallic Cluster Complexes; Polynuclear Organometallic Cluster Complexes; Silver: Inorganic & Coordination Chemistry.

19 FURTHER READING

H. Schmidbaur and K. C. Dash, *Adv. Inorg. Chem. Radiochem.*, 1982, **25**, 239.

P. Schwerdtfeger, P. D. W. Boyd, S. Brienne, and A. K. Burrell, *Inorg. Chem.*, 1992, **31**, 3411.

20 REFERENCES

1. R. J. Puddephatt, 'The Chemistry of Gold', Elsevier, Amsterdam, NY, 1978.
2. R. J. Puddephatt, in 'Comprehensive Coordination Chemistry', eds. G. Wilkinson, R. D. Gillard, and J. A. McCleverty, Pergamon, Oxford, 1987, Vol. 5, p. 861.
3. B. F. G. Johnson and R. Davis, in 'Comprehensive Inorganic Chemistry', eds. J. C. Bailar, H. J. Emeleus, R. Nyholm, and A. F. Trotman-Dickenson, Pergamon, Oxford, 1973.
4. H. Schmidbaur and K. C. Dash, *Adv. Inorg. Chem. Radiochem.*, 1982, **25**, 239.

5. H. Schmidbaur ed., ‘Gold: Progress in Chemistry, Biochemistry and Technology’, John Wiley & Sons, Chichester, 1999.
6. P. Pyykkö and J. P. Desclaux, *Acc. Chem. Res.*, 1979, **12**, 276.
7. K. S. Pitzer, *Acc. Chem. Res.*, 1979, **12**, 271.
8. P. Pyykkö, *Acc. Chem. Res.*, 1988, **88**, 563.
9. N. Bartlett, *Gold Bull.*, 1998, **31**, 22.
10. P. Pyykkö, *Chem. Rev.*, 1997, **97**, 597.
11. D. Schröder, J. Hrusak, I. C. Tornieporth-Oetting, T. M. Klapötke, and H. Schwarz, *Angew. Chem., Int. Ed. Engl.*, 1994, **33**, 212.
12. P. G. Jones, *Gold Bull.*, 1981, **14**, 102; 1981, **14**, 159; 1983, **16**, 114.
13. H. Schmidbaur, *Gold Bull.*, 1990, **23**, 11.
14. M. Bardaji and A. Laguna, *J. Chem. Educ.*, 1999, **76**, 201.
15. H. Schmidbaur, *Gold Bull.*, 2000, **33**, 3.
16. H. Schmidbaur, A. Kolb, and P. Bissinger, *Inorg. Chem.*, 1992, **31**, 4370.
17. J. Zank, A. Schier, and H. Schmidbaur, *J. Chem. Soc., Dalton Trans.*, 1998, 323.
18. H. Schmidbaur, *Chem. Soc. Rev.*, 1995, 391.
19. K. P. Hall and D. M. P. Mingos, *Prog. Inorg. Chem.*, 1984, **32**, 237.
20. J. W. Lauher and K. Wald, *J. Am. Chem. Soc.*, 1981, **103**, 7648.
21. M. I. Bruce, P. E. Corbin, P. A. Humphrey, G. A. Koutsantonis, M. J. Liddell, and E. R. T. Tiekink, *J. Chem. Soc., Chem. Commun.*, 1990, 674.
22. P. Pyykkö, *Angew. Chem., Int. Ed. Engl.*, 2002, **41**, 3573.
23. P. D. C. Dietzel and M. Jansen, *Chem. Commun.*, 2001, 2208.
24. F. Calderazzo, *J. Organomet. Chem.*, 1990, **400**, 303.
25. G. Marbach and J. Strahle, *Angew. Chem., Int. Ed. Engl.*, 1984, **23**, 715.
26. S.-P. Huang and M. Kanatzidis, *Angew. Chem., Int. Ed. Engl.*, 1992, **31**, 787.
27. R. V. Parish, *Interdiscip. Sci. Rev.*, 1992, **12**, 221.
28. E. R. T. Tiekink, *Critical Revs. Oncology/Hematology*, 2002, **42**, 225.
29. E. R. T. Tiekink, *Bioinorg. Appl.*, 2003, **1**, 53.
30. A. A. Mohamed, H. E. Abdou, J. Chen, A. E. Bruce, and M. R. M. Bruce, *Comments Inorg. Chem.*, 2002, **23**, 321.
31. P. J. Sadler, *Adv. Inorg. Chem.*, 1991, **36**, 1.
32. A. Shiotani and H. Schmidbaur, *J. Am. Chem. Soc.*, 1970, **92**, 7003.
33. J. C. Vickery and A. L. Balch, *Inorg. Chem.*, 1997, **36**, 5978.
34. C. H. Housecroft, *Coord. Chem. Rev.*, 1992, **115**, 117.
35. A. Laguna and M. Laguna, *J. Organomet. Chem.*, 1990, **343**, 743.
36. C. King, M. N. I. Khan, R. J. Staples, and J. P. Fackler, Jr, *Inorg. Chem.*, 1992, **31**, 3236.
37. J. M. Forward, J. P. Fackler, Jr, and Z. Assefa in ‘Optoelectronic Properties of Inorganic Compounds’, eds. D. M. Roundhill and J. P. Fackler, Jr, Plenum Press, New York, 1999, p. 195.
38. D. M. Roundhill, ‘Photochemistry and Photophysics of Metal Complexes’, Plenum Press, New York, 1994.
39. C. King, J.-C. Wong, M. N. I. Khan, and J. P. Fackler, Jr *Inorg. Chem.*, 1989, **28**, 2145.
40. E. J. Fernândez, A. Laguna, and J. M. López-de-Luzuriaga, *Gold Bull.*, 2001, **34**, 14.
41. H.-R. Jaw, M. M. Savas, R. D. Rogers, and W. R. Mason, *Inorg. Chem.*, 1989, **28**, 1028.
42. T. M. CcCleskey and H. B. Gray, *Inorg. Chem.*, 1992, **31**, 1733.
43. V. W.-W. Yam and K. K.-W. Lo, *Chem. Soc. Rev.*, 1999, **28**, 323.
44. V. W.-W. Yam and E. C.-C. Cheng, *Gold Bull.*, 2001, **34**, 20.
45. A. Laguna and M. Laguna, *Coord. Chem. Rev.*, 1999, **193–195**, 837.
46. J. P. Fackler, Jr, *Polyhdron*, 1997, **16**, 1.
47. V. W.-W. Yam, S. W.-K. Choi, and K.-K. Cheung, *Chem. Commun.*, 1996, 1173.
48. S.-P. Huang and M. Kanatzidis, *Inorg. Chem.*, 1991, **30**, 3573.
49. N. Asao, K. Takahashi, S. Lee, T. Kasahara, and Y. Yamamoto, *J. Am. Chem. Soc.*, 2002, **124**, 12650.
50. G. Dyker, D. Hildebrandt, J. Liu, and K. Merz, *Angew. Chem., Int. Ed. Engl.*, 2003, **42**, 4399.
51. D. M. P. Mingos, *Gold Bull.*, 1984, **17**, 5.
52. C.-M. Che, H.-K. Yip, V. W.-W. Yam, P.-Y. Cheung, T.-F. Lai, S.-J. Shieh, and S.-M. Peng, *J. Chem. Soc., Dalton Trans.*, 1992, 427.
53. C. E. Briant, B. R. C. Theobald, J. W. White, L. K. Bell, and D. M. P. Mingos, *J. Chem. Soc., Chem. Commun.*, 1981, 201.
54. G. Schmid, *Structure and Bonding*, 1985, **62**, 51.
55. R. C. Thiel, R. E. Benfield, R. Zanoni, H. H. A. Smit, and M. W. Dirken, *Structure and Bonding*, 1993, **81**, 1.
56. B. K. Teo, X. Shi, and H. Zhang, *J. Am. Chem. Soc.*, 1992, **114**, 2743.
57. G. Schmid, W. Meyer-Zaika, R. Pugin, T. Sawitowski, J.-P. Majoral, A.-M. Caminade, and C.-O. Turrin, *Chem. – Eur. J.*, 2000, **6**, 1693.
58. J. J. Steggerda, *Recl. Trav. Chim. Pays-Bas.*, 1982, **101**, 164.
59. D. M. P. Mingos, *Inorg. Chem.*, 1982, **21**, 464.
60. L. H. Pignolet and D. A. Krogstad, ‘The Chemistry of Gold’, Elsevier, Amsterdam, NY, 1978, Chap. 13, p. 429.
61. P. Braunstein and J. Rose, *Gold Bull.*, 1985, **18**, 17.
62. A. M. Mueting, W. Bos, B. D. Alexander, P. D. Boyle, J. A. Casalnuovo, S. Balaban, L. N. Ito, S. M. Johnson, and L. H. Pignolet, *New J. Chem.*, 1988, **12**, 505.
63. D. M. P. Mingos and M. J. Watson, *Transition Met. Chem.*, 1991, **16**, 285.

64. K. Wurst, J. Strahle, G. Beuter, D. B. Dell'Amico, and F. Calderazzo, *Acta Chem. Scand.*, 1991, **45**, 844.

65. J. Mielcke and J. Strahle, *Angew. Chem., Int. Ed. Engl.*, 1992, **31**, 464.

66. T. G. M. M. Kappen, A. C. M. van den Broek, P. P. J. Schlebos, J. J. Bour, W. P. Bosman, J. M. M. Smits, P. T. Beurskens, and J. J. Steggerda, *Inorg. Chem.*, 1992, **31**, 4075.

67. J. J. Steggerda, *Comments Inorg. Chem.*, 1990, **11**, 113.

68. B. K. Teo, X. Shi, and H. Zhang, *J. Am. Chem. Soc.*, 1991, **113**, 4329.

69. B. K. Teo, H. Zhang, and X. Shi, *J. Am. Chem. Soc.*, 1990, **112**, 8552.

70. R. C. B. Copley and D. M. P. Mingos, *J. Chem. Soc. Dalton Trans.*, 1992, 1755.

71. B. K. Teo and H. Zhang, *Coord. Chem. Rev.*, 1995, **143**, 611.

72. H. Schmidbaur, *Interdiscip. Sci. Rev.*, 1992, **17**, 213.

73. H. Schmidbaur, B. Brachthauser, O. Steigelmann, and H. Beruda, *Chem. Ber.*, 1992, **125**, 2705.

74. F. Scherbaum, A. Grohmann, G. Muller, and H. Schmidbaur, *Angew Chem., Int. Ed. Engl.*, 1989, **28**, 463.

75. F. Scherbaum, A. Grohmann, B. Huber, C. Kruger, and H. Schmidbaur, *Angew. Chem., Int. Ed. Engl.*, 1988, **27**, 1544.

76. E. Zeller, H. Beruda, A. Kolb, P. Bissinger, J. Riede, and H. Schmidbaur, *Nature (London)*, 1991, **352**, 141.

77. H. Schmidbaur, S. Hofreiter, and M. Paul, *Nature (London)*, 1995, **377**, 503.

78. F. Canales, M. C. Gimeno, P. G. Jones, and A. Laguna, *Angew. Chem., Int. Ed. Engl.*, 1994, **33**, 769.

79. H. Schmidbaur, E. Zeller, G. Weidenhiller, O. Steigelmann, and H. Beruda, *Inorg. Chem.*, 1992, **31**, 2370.

80. H. Schmidbaur, A. Kolb, and P. Bissinger, *Inorg. Chem.*, 1992, **31**, 4370.

81. E. Zeller and H. Schmidbaur, *J. Chem. Soc., Chem. Commun.*, 1993, 69.

82. R. J. Puddephatt, *Chem. Commun.*, 1998, 1055.

83. R. J. Puddephatt, *Coord. Chem. Revs.*, 2001, **216–217**, 313.

84. C. P. McArdle, J. J. Vittal, and R. J. Puddephatt, *Angew. Chem., Int. Ed. Engl.*, 2000, **39**, 3819.

85. C. P. McArdle, M. J. Irwin, M. C. Jennings, J. J. Vittal, and R. J. Puddephatt, *Chem. – Eur. J.*, 2002, **8**, 723.

86. O. Rossell, M. Seco, A.-M. Caminade, and J.-P. Majoral, *Gold Bull.*, 2001, **34**, 88.

87. N. Feeder, J. Geng, P. G. Goh, B. F. G. Johnson, C. M. Martin, D. S. Shephard, and W. Zhou, *Angew. Chem., Int. Ed. Engl.*, 2000, **39**, 1661.

88. D. Schröder, H. Schwarz, J. Hrušák, and P. Pyykkö, *Inorg. Chem.*, 1998, **37**, 624.

89. S. Seidel and K. Seppelt, *Science*, 2000, **290**, 117.

90. T. Drews, S. Seidel, and K. Seppelt, *Angew. Chem., Int. Ed. Engl.*, 2002, **31**, 454.

91. P. Pyykkö, *J. Am. Chem. Soc.*, 1995, **117**, 2067.

92. I.-C. Hwang, S. Seidel, and K. Seppelt, *Angew. Chem., Int. Ed. Engl.*, 2003, **42**, 4392.

Gold: Organometallic Chemistry

Annette Schier & Hubert Schmidbaur
Technische Universität München, Garching, Germany

1 Definition, Introduction, and History 1
2 General Synthetic Pathways 2
3 Conversion of Organogold Compounds 4
4 Analysis and Spectral Characteristics 5
5 Structure and Bonding 6
6 Selected Individual Compounds 7
7 Usage of Organogold Compounds 8
8 Related Articles 9
9 References 9

1 DEFINITION, INTRODUCTION, AND HISTORY

Organogold chemistry is defined as the chemistry of compounds containing at least one direct gold-to-carbon bond, regardless of the oxidation state and coordination number of the metal atoms, which may be single in mononuclear complexes or part of aggregates as in polynuclear complexes (*see* ***Polynuclear Organometallic Cluster Complexes***) or in clusters. The only class of compounds with a Au–C bond excluded for systematic reasons is the family of cyanides (*see Cyanides*), which are considered under a separate entry (*see* ***Cyanide Complexes of the Transition Metals***). Although there is also a separate entry on carbonyl compounds (*see* ***Carbonyl Complexes of the Transition Metals***), the few carbon monoxide complexes of gold have been included in this article owing to their very small number, their unusual properties compared to standard transition metal carbonyls, and their use in synthesis. All other types of Au–C species have been reviewed and included where it was found appropriate for a concise treatment of the subject.

Gold forms chemical compounds in the oxidation states -1, 0, $+1$, $+2$, $+3$, and $+5$. As expected from the position of the element in the periodic table, the oxidation states $+1$ and $+3$ are the most common and stable, and this is also borne out in the organometallic chemistry of gold. As is easily derived from the electronic configuration of these two oxidation states, the standard coordination numbers and geometries are linear two-coordinate for $\mathrm{Au^I}$ and square planar and four coordinate for $\mathrm{Au^{III}}$. Virtually all organogold compounds obey these simple rules. While there are no well-defined organogold derivatives for $\mathrm{Au^{-I}}$, $\mathrm{Au^0}$, or $\mathrm{Au^V}$, there is some interesting organometallic chemistry for $\mathrm{Au^{II}}$, mainly based on metal–metal bonded dinuclear units $[\mathrm{Au_2}]^{4+}$ (*see* ***Dinuclear Organometallic Cluster Complexes***).

Organogold chemistry is a chemistry of metastable compounds: none of the organogold compounds is thermodynamically stable relative to gold metal and any organic component meeting the stoichiometry of the system, like a hydrocarbon, a haloalkane, or an organic oxygen, sulfur, or nitrogen compound. As expected from the 'noble character' of gold metal, none of the organogold compounds can be prepared directly from gold metal, and all synthetic pathways for gold organyls have their origin from gold halides or their complexes, which along with a few selenides and tellurides are the only thermodynamically stable binary compounds of gold. Though this situation is not unlike that encountered with elements such as platinum, gold is an extreme case owing to its extreme electrochemical potential. Working in organogold chemistry therefore requires careful control of experimental conditions to avoid the thermal decomposition of the compounds favored by thermodynamics. More often than not, experiments in organogold chemistry are terminated by the appearance of a gold mirror on the walls of the reaction vessel, with nothing but the organic decomposition products remaining in the solution or gas phase.

Historically, organogold chemistry started with the first preparation of dialkylgold(III) halides of the type $\mathrm{R_2AuX}$ from tetrahaloauric acids $\mathrm{HAuX_4}$ or gold trihalides $\mathrm{AuX_3}$ ($\mathrm{X = Cl, Br}$) by treatment with an excess of a Grignard reagent RMgX (*see Grignard Reagents*) by Pope and Gibson[1] in 1907. These experiments were the obvious approach to organogold compounds shortly after the turn of the century, because tetrachlorauric acid and gold trichloride are obtained as the primary products in the treatment of gold with *aqua regia* (a mixture of conc. HCl and $\mathrm{HNO_3}$), and because the first decade of the twentieth century saw the discovery of the Grignard reagents as a major breakthrough for organometallic synthesis in general. Through the following three decades, the dialkylgold halides remained the key intermediates for all further developments in the field, largely by Gibson,[2] and, after World War II, by Tobias.[3] By contrast, alkylgold(I) and trialkylgold(III) chemistry could only be developed much later after the discovery of organolithium reagents and the introduction of tertiary phosphines as almost indispensable stabilizing ligands in the 1950s by Gilman[4] and by Coates.[5]

Arylgold(I) and arylgold(III) chemistry had a late start in the 1960s, but then grew rapidly through the work by Uson[6] and Nesmeyanov,[7] complemented by work on cyclopentadienyl- (*see Cyclopentadienyl*), ferrocenyl- (*see Ferrocene*), and cymantrenyl- (*see Cymantrene*) gold compounds.

Explosive gold acetylide has been known since the mid-nineteenth century, but systematic studies of this type of compounds were initiated by Coates[8] in 1959. The early work on gold carbonyls dates back to 1925, when Manchot[9] discovered (OC)AuCl, while the related isocyanide complexes were prepared only in 1956 by Sacco.[10] Gold–carbene complexes have been known since 1970, on the basis of the work of Bonati[11] and Raubenheimer.[12]

Alkene complexes of platinum have been well established since the middle of the nineteenth century (*see Zeise's Salt*), but π-complexes of gold were only discovered by Hüttel[13] in 1965, with alkyne complexes following in 1972. All of these complexes have very limited stability, and therefore their chemistry is still poorly developed, even today.

While other gold compounds are recently finding widespread application in modern technology,[14] organogold compounds are not among the prominent classes of compounds in industry. Only for depositing thin gold films on surfaces some of the more volatile organogold derivatives hold a certain potential, which is being exploited for the production of electrical and semiconductor devices or for obtaining specific optical and wear- or chemical-resisting properties. The state of the art is similar for electrolytic or electroless gold plating from solution. In chemotherapy and pharmacology, organogold compounds have shown no major advantages over established gold drugs, which have no organic groups directly attached to the gold center.

In basic research, the chemistry of gold and organogold compounds merits special interest because of the unique position of gold in the periodic table, which is characterized by the highest electron affinity, electronegativity, and redox potential of all metals. These properties have their origin in a pronounced maximum in the relativistic contraction of the valence electron orbitals and associated effects.[15] Several reviews on organogold chemistry have been published.[16–25]

2 GENERAL SYNTHETIC PATHWAYS

Conventional organic groups (alkyl, alkenyl, alkynyl, aryl, cyclopentadienyl, ferrocenyl, and others) are introduced at a given gold(I) or gold(III) center by treatment of the corresponding halide complexes with an organometallic reagent. As a historical example, $AuBr_3$ is reacted with the Grignard compound EtMgBr in diethyl ether (or pyridine) as a solvent to give diethylgold bromide and $MgBr_2$.[1] An excess of the RMgX reagent does not lead to full alkylation, but by employing the more powerful alkyllithium compounds, the trialkylgold species can finally be generated.[4] This product needs a donor ligand L (such as a tertiary phosphine) as a stabilizing ligand. With three equivalents of the LiR reagent, $AuBr_3$ can be converted directly into the trialkylgold complex (equations 1–3).

$$AuBr_3 + 2EtMgBr \longrightarrow 2MgBr_2 + Et_2AuBr \quad (1)$$

$$Et_2AuBr + EtLi + L \longrightarrow LiBr + Et_3Au\cdot L \quad (2)$$

$$AuBr_3 + 3EtLi + L \longrightarrow 3LiBr + Et_3Au\cdot L \quad (3)$$

Dialkylmercury compounds cannot be used for alkylating gold halides (as already noted by Frankland in 1864), while both alkylzinc and alkylcadmium species can be employed, but offer advantages only for perfluoroalkyl species.[26] The alkylation of AuX_3 or $HAuX_4$ with organotin reagents SnR_4 leads to R_2AuX compounds, but the process is difficult to control, because the separation of the product from the R_nSnX_{4-n} by-products proved to be difficult.[27]

Like trialkylgold compounds (R_3Au), monoalkylgold compounds (RAu) are unstable in the absence of a donor ligand L. Their preparation is therefore carried out by treatment of a suitable complex of a gold(I) halide (L·AuX) with the organolithium reagent.[5] Arylation follows the same pathway (equations 4 and 5).

$$L\cdot AuCl + MeLi \longrightarrow LiCl + L\cdot AuMe \quad (4)$$

$$L\cdot AuBr + PhLi \longrightarrow LiBr + L\cdot AuPh \quad (5)$$

A useful method for the formation of Au–C bonds is the insertion of diazoalkanes into the Au–halogen bond (equation 6).[7]

$$Ph_3P\cdot AuCl + CH_2N_2 \longrightarrow Ph_3P\cdot AuCH_2Cl + N_2 \quad (6)$$

Arylation of gold(III) compounds is not limited to the organometallic route, but can be accomplished in direct 'aromatic auration' of the hydrocarbon by anhydrous $AuCl_3$ with evolution of HCl (equations 7 and 8).[28–30] In special cases, arylation is accomplished by arylthallium reagents (equation 9), or by using arenediazonium salts.

$$(AuCl_3)_2 + 2C_6H_6 \longrightarrow 2HCl + (PhAuCl_2)_2 \quad (7)$$

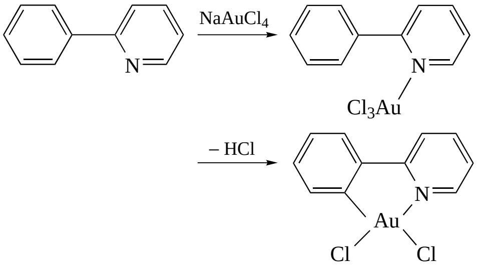

(8)

$$Ph_3P\cdot AuCl + (HC_6Cl_4)_3Tl \longrightarrow (HC_6Cl_4)_2TlCl + Ph_3P\cdot AuC_6Cl_4H \quad (9)$$

Alkenylgold compounds, including the cyclopentadienyl and ferrocenyl or cymantrenyl species with σ-bonded alkene ligands, are also generated through treatment of alkenyl-Grignard or alkenyllithium precursors with the corresponding gold–halide complexes. Fluoroalkyl derivatives are obtained through the insertion of fluoroalkenes into the Au–C bond of organogold compounds. A similar insertion has been observed with alkynes and gold(III) halides.[31]

Alkynylgold compounds are readily available from reactions of the parent alkyne and gold(I) halides in the presence of even a very weak base, owing to the enhanced CH acidic properties of alkynes. The donor-free products are oligomeric, probably through a combination of σ- and

π-coordination. In the presence of donors, L, linear 1:1 complexes are generated (equations 10 and 11). Dinuclear complexes LAuC≡CAuL are also readily accessible[32] (equation 12), and are found to be associated into aggregates through aurophilic bonding (Au$\cdots$Au).[33]

$$n\ \mathrm{RC{\equiv}CH} + n\ \mathrm{base} + n\ \mathrm{AuX} \longrightarrow (\mathrm{RC{\equiv}CAu})_n + n\ [(\mathrm{base})\mathrm{H}]\mathrm{X} \quad (10)$$

$$(\mathrm{RC{\equiv}CAu})_n + n\ \mathrm{L} \longrightarrow n\ \mathrm{L{\cdot}AuC{\equiv}CR} \quad (11)$$

$$\mathrm{HC{\equiv}CH} + 2\ \mathrm{base} + 2\mathrm{L{\cdot}AuX} \longrightarrow \mathrm{L{\cdot}AuC{\equiv}CAu{\cdot}L} + 2\ [(\mathrm{base})\mathrm{H}]\mathrm{X} \quad (12)$$

Alkene and alkyne π-complexes (*see Alkene Complexes* and *Alkyne Complexes*) are known both for $\mathrm{Au^{I}}$ and $\mathrm{Au^{III}}$. They are prepared at low temperature from AuCl or $\mathrm{AuCl_3}$ with an excess of the alkene or alkyne in the absence of any other potential donor molecules. The products, for example, of the types $(\mathrm{MeCH{=}CHMe})\mathrm{AuCl}$ and $\mathrm{MeC{\equiv}CMe{\cdot}(AuCl_3)_2}$, are generally of low stability, and the complexation is reversible in a vacuum or on heating. Representative examples have recently been structurally characterized.[34,35] Strained cyclic alkenes and alkynes give the most stable products. Multiple coordination of monoalkenes or of dialkenes (like butadiene) is known, but information about the products is limited. Alkene coordination to neutral gold atoms has been studied by matrix-isolation techniques at very low temperature.[36] The adduct $(\mathrm{C_2H_4})\mathrm{Au}$ appears to be stable only below 40 K.

Carbene complexes of gold are available through the addition of alcohols or amines to isocyanide complexes. The latter are readily prepared from the free isocyanides (*see Isocyanide Ligands*) and other gold–halide complexes containing a weaker ligand such as dimethyl sulphide or carbon monoxide (equations 13–15). Carbeniate derivatives are generated through deprotonation of a suitable carbene precursor by base (equations 16 and 17).

$$\mathrm{Me_2S{\cdot}AuCl} + \mathrm{RN{\equiv}C} \longrightarrow \mathrm{Me_2S} + \mathrm{RN{\equiv}C{\cdot}AuCl} \quad (13)$$

$$\mathrm{RN{\equiv}C{\cdot}AuCl} + \mathrm{R'OH} \longrightarrow \mathrm{(R'O)(RHN)C{\cdot}AuCl} \quad (14)$$

$$\mathrm{RN{\equiv}C{\cdot}AuCl} + \mathrm{R_2'NH} \longrightarrow \mathrm{(R_2'N)(RHN)C{\cdot}AuCl} \quad (15)$$

$$\mathrm{(R'O)(RNH)C{\cdot}AuCl} + \mathrm{KOH} + \mathrm{L} \longrightarrow \mathrm{H_2O} + \mathrm{KCl} + \mathrm{L{\cdot}AuC({=}NR)(OR')} \quad (16)$$

$$3\ \mathrm{(R'O)(RNH)C{\cdot}AuCl} + 3\mathrm{KOH} \longrightarrow 3\mathrm{H_2O} + 3\mathrm{KCl} + [\mathrm{(R'O)(RN)CAu}]_3 \quad (17)$$

Up to two carbene units have been introduced at $\mathrm{Au^{I}}$ and up to four at $\mathrm{Au^{III}}$ centers.[37] Donor-free $\mathrm{Au^{I}}$ carbene complexes are oligomeric and form planar trimeric structures, $[\mathrm{AuC(OR')(NR)}]_3$ or $[\mathrm{AuC(NHR')(NR)}]_3$.

Carbonyl complexes of gold are only known for $\mathrm{Au^{I}}$. The classical example, (CO)AuCl, is obtained from $(\mathrm{AuCl_3})_2$ and CO at ca. 100 °C, or from AuCl and CO.[9] A more recent preparation from commercial $\mathrm{HAuCl_4}$, $\mathrm{SOCl_2}$, and CO is more convenient and gives quantitative yields of this important reagent (equation 18).[38]

$$\mathrm{HAuCl_4{\cdot}H_2O} + \mathrm{SOCl_2} + 2\mathrm{CO} \longrightarrow 3\mathrm{HCl} + \mathrm{COCl_2} + \mathrm{SO_2} + \mathrm{(CO)AuCl} \quad (18)$$

The corresponding complexes of AuF, AuBr, and AuI are much less stable and not fully characterized. Gold atoms form CO adducts under matrix-isolation conditions (*see Matrix Isolation*) (below 20 K), but ligand dissociation occurs at a slightly elevated temperature.

Formation of gold–carbon σ-bonds is perhaps most easily accomplished by treatment of gold(I) and gold(III) compounds with phosphorus ylides (phosphonium alkylides, *see Ylide*). Through their strongly nucleophilic carbanionic center, these reagents are able to displace virtually every other ligand attached to gold, even under mild conditions.[39] Phosphonium bis(methylide) reagents, obtained by treatment of an ylide with an organolithium base or through transylidation, lead to multinuclear organogold compounds with open-chain or cyclic structures (equations 19–23).

$$\mathrm{L{\cdot}AuCl} + \mathrm{R_3PCH_2} \longrightarrow [\mathrm{L{\cdot}AuCH_2PR_3}]\mathrm{Cl} \quad (19)$$

$$\mathrm{L{\cdot}AuCl} + 2\mathrm{R_3PCH_2} \longrightarrow \mathrm{L} + [\mathrm{Au(CH_2PR_3)_2}]\mathrm{Cl} \quad (20)$$

$$\mathrm{L{\cdot}AuR'} + \mathrm{R_3PCH_2} \longrightarrow \mathrm{L} + \mathrm{R_3PCH_2AuR'} \quad (21)$$

$$2\mathrm{L{\cdot}AuCl} + 4\mathrm{R_2(Me)PCH_2} \longrightarrow 2\ [\mathrm{R_2PMe_2}]\mathrm{Cl} + [\mathrm{R_2P(CH_2)_2Au}]_2 \quad (22)$$

$$\mathrm{L{\cdot}AuR_3'} + \mathrm{R_3PCH_2} \longrightarrow \mathrm{L} + \mathrm{R_3'AuCH_2PR_3} \quad (23)$$

From carbodiphosphoranes $\mathrm{R_3P{=}C{=}PR_3}$ and dialkylgold(III) halides, cyclic ylide complexes containing four Au–C σ-bonds are obtained in a multiple transylidation reaction (equation 24). Related thiophosphorus ylides and sulfonium and sulfoxonium ylides are equally effective in the formation of Au–C σ-bonds, and a series of analogous gold–thiophosphonium and sulfoxonium–methylide complexes is available (equations 25–27).[40]

$$(\mathrm{R_2AuBr})_2 + 4\mathrm{MeR_2'PCPR_2'Me} \longrightarrow 2\ [\mathrm{MeR_2PCH_2PR_2Me}]\mathrm{Br} + 2\mathrm{R_2Au(CH_2PR')_2CH} \quad (24)$$

$$2\mathrm{L{\cdot}AuCl} + 2\mathrm{R_2P(S)CH_2^-} \longrightarrow 2\mathrm{L} + 2\mathrm{Cl^-} + [\mathrm{R_2P(S)CH_2Au}]_2 \quad (25)$$

$$\mathrm{R_3Au{\cdot}L} + \mathrm{R_2'S(O)CH_2} \longrightarrow \mathrm{L} + \mathrm{R_3AuCH_2S(O)R_2'} \quad (26)$$

$$\mathrm{R_3Au{\cdot}L} + \mathrm{R_2'SCH_2} \longrightarrow \mathrm{L} + \mathrm{R_3AuCH_2SR_2'} \quad (27)$$

The cyclic gold(I) phosphonium methylide heterocycles are the precursors for the few organogold(II) species reported. Oxidative addition (*see Oxidative Addition*) of halogen and alkyl halides leads to bicyclic compounds containing a transannular Au–Au bond (equations 28 and 29). These reactions are surprisingly facile and are now known to be reversible and to lead to different regio- and stereoisomers.[39,40]

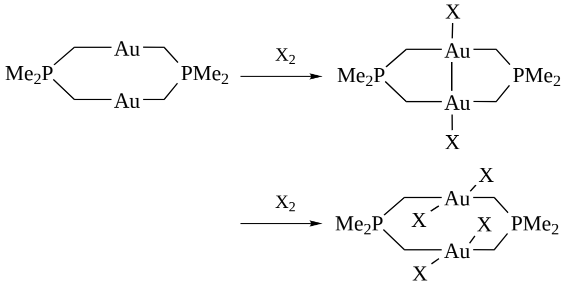

(28)

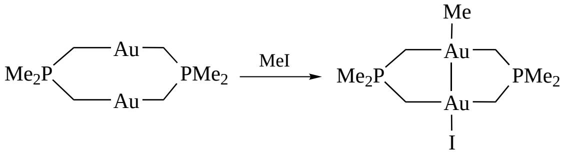

(29)

Introduction of more than one gold atom at a given carbon center proved to be very difficult in many early experiments, but later studies have shown that multiauration of a carbon atom is possible and leads to a large, and highly interesting, family of organogold compounds. The syntheses are more facile with increasing C–H acidity of the precursor. Thus, phosphorus ylides can be doubly and triply aurated, and C–H acids, like malodinitrile, malonic acid diesters, and methyloxazoline, are easily aurated. Reactions of metalated or silylated precursors with gold–halide complexes, or treatment of the organic compound with strongly nucleophilic agents such as $[R_3PAu]BF_4$ or $[(R_3PAu)_3O]BF_4$, give high yields of the polygold products (equations 30–32).

$$R_3PCPR_3 + 2L\cdot AuMe \longrightarrow 2L + (R_3P)_2C(AuMe)_2 \quad (30)$$

$$R_3PC(SiR_3')_2 + 3L\cdot AuX \longrightarrow 2R_3'SiX + [R_3PC(AuL)_3]X \quad (31)$$

$$(NC)_2CH_2 + 2R_3P\cdot AuX + \text{base} \longrightarrow 2\,[(\text{base})H]X + (NC)_2C(AuPR_3)_2 \quad (32)$$

The auration of acetylacetone and other β-diketo compounds affords complexes of the type $[RC(O)]_2CHAuL$ and $[RC(O)]_2C(AuL)_2$, with the gold atoms exclusively C-bonded.[41] The former are useful aurating reagents.[42]

Unexpected reactions are observed in the auration of arylgold(I) complexes. Thus, treatment of (triphenylphosphine)-p-tolylgold with HBF_4 gives one equivalent of toluene and a novel dinuclear compound (equation 33).[7] Similar reactions were found with ferrocenylgold(I) complexes, which give analogous products with one ring carbon atom bonded to two gold atoms (equation 34)

$$2[4\text{-}MeC_6H_4Au\cdot PPh_3] + HBF_4 \longrightarrow PhMe + [4\text{-}MeC_6H_4(Au\cdot PPh_3)_2]BF_4 \quad (33)$$

$$CpFe(C_5H_4Au\cdot PR_3) + [Au\cdot PR_3]X \longrightarrow \{CpFe[C_5H_4(Au\cdot PR_3)_2]\}X \quad (34)$$

Tetragoldmethane complexes are obtained from tetra(boryl)methane compounds upon reaction with gold–halide complexes in the presence of an ionic fluoride (equation 35).[43] Tetragoldmethane species, such as (**1**), can only be isolated with bulky tertiary phosphines, L, which shield the molecule from further attack by $[LAu]^+$ nucleophiles. With smaller ligands L, penta- and hexaauration occurs, leading to hypercoordinate carbon compounds.[33,44,45]

$$[(RO)_2B]_4C + 4L\cdot AuX/F \longrightarrow 4(RO)_2BX/F + (L\cdot Au)_4C \quad (35)$$

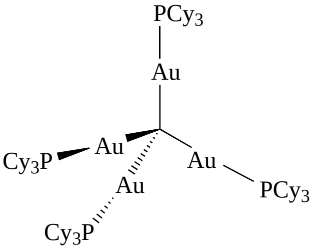

(**1**)

Lithiated dicarbaborane clusters yield (organo)gold-substituted clusters on reaction with $L\cdot AuX$ or R_2AuX compounds, also with hypercoordinate carbon atoms (equations 36–38).[46,47]

In all of these clusters, the interaction of the gold atoms is stronger with the boron atoms than that with the carbon atoms of the carborane units.

$$L\cdot AuX + NaC_2B_4H_7 \longrightarrow NaX + L\cdot Au(C_2B_4H_7) \quad (36)$$

$$L\cdot AuX + Li[RC_2B_{10}H_{10}] \longrightarrow LiX + L\cdot Au(RC_2B_{10}H_{10}) \quad (37)$$

$$AuCl_3 + 2Li_2[C_2B_9H_{11}] \longrightarrow 3LiCl + Li[Au(C_2B_9H_{11})]_2 \quad (38)$$

3 CONVERSION OF ORGANOGOLD COMPOUNDS

In Section 2, the principles of formation of gold-to-carbon bonds have been introduced. The primary products can be transformed into other organogold species with the creation of more Au–C bonds than initially present. Au–C bonds are generally retained and only the other substituents or ligands are replaced.

The most common organogold(I) compounds of the type $L\cdot AuR$ can undergo ligand exchange of L, which is known to follow an associative mechanism (equation 39) (*see* ***Mechanisms of Reaction of Organometallic Complexes***).

$$L\cdot AuR + L' \longrightarrow RAu\cdot L(L') \longrightarrow L + L'\cdot AuR \quad (39)$$

Ligands may be classified as forming more or less stable complexes with RAu, with trialkylphosphines being generally the most stable, followed by triarylphosphines, dialkyl sulfides, or diaryl sulfides, in good agreement with the usual sequence for ‘soft’ donor ligands. With carbanions as incoming ligands, anionic dialkylaurates(I) are formed (equation 40).**[48]**

$$L{\cdot}AuR + LiR \longrightarrow L + Li[RAuR] \qquad (40)$$

A second important reaction of L·AuR species is the oxidative addition (*see Oxidative Addition*) of halogen or alkyl halides, which leads, at least in a first step, to organo(dihalo)gold(III) or diorgano(halo)gold(III) products. The structures are transformed from linear to square planar, and therefore cis and trans isomers are possible. The products may undergo secondary reactions and/or become subject to a reductive elimination (*see Reductive Elimination*) of other substituent combinations (equations 41 and 42).**[49,50]**

$$L{\cdot}AuR + X_2 \longrightarrow L{\cdot}AuX_2R \qquad (41)$$

$$L{\cdot}AuR + R'X \longrightarrow L{\cdot}AuR(R')X \qquad (42)$$

The oxidative addition of stoichiometric quantities of X_2 or RX to cyclic dinuclear gold(I) compounds to give cyclic Au^{II} compounds has already been mentioned.

Treatment of L·AuR species with strong acid or base leads to the cleavage of the Au–R bond, but otherwise these bonds are remarkably robust. Au–R bonds are not readily hydrolized, and they are stable to air at ambient temperature, mainly owing to the low polarity of the Au–C units. In this respect, they resemble organomercurials.

Thermal decomposition of L·AuR species has been carefully studied, and there is agreement that the reaction pathway follows a radical mechanism. Mixtures of alkanes and alkenes (diaryls for R = aryl) are formed, together with free ligand L and elemental gold.

In organogold(III) compounds, L·AuR_3, the ligand L can also be exchanged, but the reactions are generally much slower than for L·AuR. Addition of LiR yields the square-planar tetraalkylaurate(III) (equation 43).

$$L{\cdot}AuR_3 + LiR \longrightarrow L + Li[AuR_4] \qquad (43)$$

Cleavage of R–Au bonds in L·AuR_3 with HX or X_2 gives (dimeric) R_2AuX and finally (dimeric) $RAuX_2$ compounds that form complexes of the types $R_2AuX{\cdot}L$ and $RAuX_2{\cdot}L$. In the latter, both X and L can be replaced by nucleophiles, following the usual mechanistic pattern of substitution at square-planar complexes. Cis/trans isomerism is common, leading to interesting differences in reactivity according to changes in the trans effect (*see Trans Effect*). ‘Soft’ ligands X and L are preferred, and a large variety of thiocyanates, thiolates, thiocarbamates, selenolates, phosphides, or arsenides have been prepared, while ‘hard’ ligands are less common. Tetrameric dimethylgold hydroxide and cyanide, and dimeric dimethylgold trimethylsilyloxide and azide have been prepared, however, and have been fully characterized.

Thermal decomposition of L·AuR_3 compounds proceeds mainly with reductive elimination of R_2 by radical cleavage, as outlined for L·AuR.

4 ANALYSIS AND SPECTRAL CHARACTERISTICS

Organogold compounds have been carefully analyzed by use of the full range of analytical, spectroscopic, and diffraction techniques.

Elemental analysis generally poses no problems because of the limited stability of the compounds and the formation of elemental gold in decomposition and combustion, which does not form carbides, nitrides, or other interstitial phases. Atomic absorption and inductively coupled plasma spectroscopy are presently the methods of choice for Au estimation. Many organogold compounds are sufficiently volatile to allow registration of good mass spectra by gas-phase electron impact. Field desorption, fast-atom bombardment, and chemical ionization mass spectrometry have also been successfully applied.

Gold is not amenable to common magnetic resonance techniques,**[51]** and to date no ^{197}Au NMR or NQR spectra have been obtained owing to the adverse properties of this nucleus. ^{197}Au is an excellent Mössbauer nucleus, however, and recoil-free γ-resonance spectra have been obtained for a large variety of organogold compounds. Determination of isomeric shifts and quadrupole coupling constants can be used to obtain information on the oxidation state, coordination number, coordination geometry, and environment of the gold atom in solids.**[51]**

Electron spectroscopy for chemical analysis (ESCA) has also been applied successfully for elucidating oxidation states and coordination numbers of gold compounds, but the number of studies is still very limited.

Proton, carbon, and other standard nuclei in organogold compounds can routinely be studied by NMR spectroscopy. Since virtually all organogold compounds are diamagnetic, the results are generally of high quality, both in solution and solid-state (magic-angle spinning/cross-polarization (MAS/CP)) investigations. Chemical shifts and coupling constants are not unusual and follow general trends in organometallics of heavy late-transition elements. Solution kinetics has been followed by temperature-dependent measurements.

In vibrational studies (IR/Raman, *see Infrared Spectroscopy* and *Raman Spectroscopy*), characteristic frequencies for Au–C bonds have been compiled, which are useful for suggestions regarding molecular symmetries and structures and to calculate force constants for the Au–C bonds. The values have been tabulated in handbooks, and they show consistent results for the individual groups of compounds. Moreover, there are the expected parallels with data for organometallic compounds of neighboring elements (Hg, Pt).

Only very few organogold compounds are colored. Spectroscopy in the visible region is therefore rarely used. Only a few groups of Au^{III} compounds and the ferrocenylgold(I) complexes have been investigated, and the results have not yet been evaluated in detail. UV absorption studies are also quite limited, except for some more recent luminescence and fluorescence (*see Fluorescence*) work on multinuclear complexes or clusters.

Single-crystal X-ray diffraction (*see X-ray Diffraction*) studies have been carried out on a large number of organogold compounds. Since only very few compounds are sensitive to X-rays, structure determination rarely presents problems, if appropriate corrections are applied, including those for absorption, which are mandatory for the data sets used for calculations.

5 STRUCTURE AND BONDING

As in many gold(I) compounds, the metal atom in organogold(I) species is strictly two-coordinate with a linear array of the two ligands. For example, in crystals of methyl(triphenylphosphine)gold(I), the C–Au–P axis has an angle of 179.1°. The Au–C bond is 2.124 Å long and absorbs in the IR region at $531\,\text{cm}^{-1}$ (the Au–P bond is 2.279 Å long). The UV absorption maximum is found at 275 nm, meaning that the compound is colorless. These data are interpreted in terms of covalent Au–C σ-bonding of low polarity. Employing two Au(sp) hybrid orbitals, together with a $C(sp^3)$ and a $P(sp^3)$ hybrid orbital, two localized two-center/two-electron bonds can be constructed with Au^+, $CH_3{}^-$, and PMe_3 as the components.

In alkenyl- and arylgold compounds, or in carbene complexes, the ligating carbon atoms are to be taken as sp^2 hybridized, but no other assumptions have to be made. The same scheme is valid for the linear complexes (CO)AuCl, $Me_3CC{\equiv}CAuPMe_3$, or MeNCAuCN, where CO, PMe_3, or MeNC are neutral donors, and Cl^-, $Me_3CC{\equiv}C^-$, and CN^- are the anionic ligands, respectively, the latter with C(sp) hybrids.

Gold(I) appears to be a very weak π-acceptor (*see π-Acid Ligand*), and back bonding (*see Back Bonding*) from filled π-orbitals of the ligands into empty orbitals of the metal is not likely to contribute significantly to the C–Au interactions. Au–C bonds are therefore taken as σ-bonds of unit bond order. The closed-shell $5d^{10}$ configuration of Au^I leaves only the 6p states available for π-interactions. The low stability of the few π-complexes of Au^0 and Au^I reported in the literature also reflects this low-acceptor character of gold(0) and gold(I).

For the same reason, cyclopentadienylgold(I) compounds are exclusively monohapto or σ-bonded (*see Hapticity*). In solution, there is rapid site exchange of the metal at the ring carbon atoms, but at low temperature, a monohapto structure is readily detected by NMR spectroscopy.

Organogold(II) compounds are only well established for dinuclear cases with direct metal–metal bonding. The metal atoms in these species are square-planar tetracoordinate, and the description of their bonding follows the models for gold(III) complexes with the same coordination geometry (below). The Au–Au distances observed fall in the range 2.60–2.80 Å and are unique cases of localized Au–Au single bonding. The dimeric ylide complex $[(Me_2PCH_2)AuI]_2$ is a representative example for this class of compounds.

Organogold(III) compounds with one to four organic groups attached to Au^{III} are square planar and four coordinate. Complexes having a lower coordination number appear to be inherently unstable. In the absence of independent donor ligands, the organogold fragments associate with the formation of ligand bridges between metal atoms. Organic groups appear to be unsuitable for metal bridging, however, and structures like those of dimeric trialkylaluminium compounds have not been found in organogold chemistry (*see* ***Aluminum: Organometallic Chemistry***).

Thus, ‘naked’ R_3Au compounds are unknown (as are ‘naked’ RAu), but $R_3Au{\cdot}L$ compounds are stable. For R_2AuX systems, oligomerization occurs if X has donor capabilities, to give X-bridged aggregates, while the addition of donor ligands leads to mononuclear complexes $R_2AuX{\cdot}L$. $RAuX_2$ species appear as unsymmetrical dimers. In a redistribution of the ligands R and X, compounds of the type $R_2AuX{\cdot}AuX_3$ are formed.

In $Me_3Au{\cdot}PPh_3$, the two cis Au–C bonds are longer than the trans Au–C bond owing to the trans influence (*see Trans Effect*) of the tertiary phosphine: Au–C (cis) = 2.100 and 2.168 Å; Au–C (trans) = 1.923 Å (Au–P = 2.350 Å). All angles at Au are close to 90°. The structure of the complex is configurationally stable, and two different methyl groups can be distinguished in the proton or carbon NMR spectra of solutions (intensity ratio 2:1). IR absorption bands at 512 and $530\,\text{cm}^{-1}$ can be ascribed to the Au–C stretching vibrations of the complex.

For a description of the chemical bonding, Au^{III} can be introduced as dsp^2 hybridized, and a set of localized σ-bonds can be constructed with the σ-orbitals of the three carbon atoms and the phosphorus atom. In the more symmetrical case of $[AuMe_4]^-$, four equivalent Au–C bonds arise from this model. In a different approach, crystal or ligand field theory may also be successfully employed for a description of bonding in this anion. With $CH_3{}^-$ anions as extremely strong ligands, a low-spin d^8 state is obtained, which accounts very well for the diamagnetism observed with all organogold(III) compounds. Like gold(I), gold(III) is also a weak π-acceptor, and R–Au^{III} bonds are probably of pure σ-character. π-Complexes of Au^{III}, for example with alkenes, are unstable in most situations, that is, in nonforcing structures.

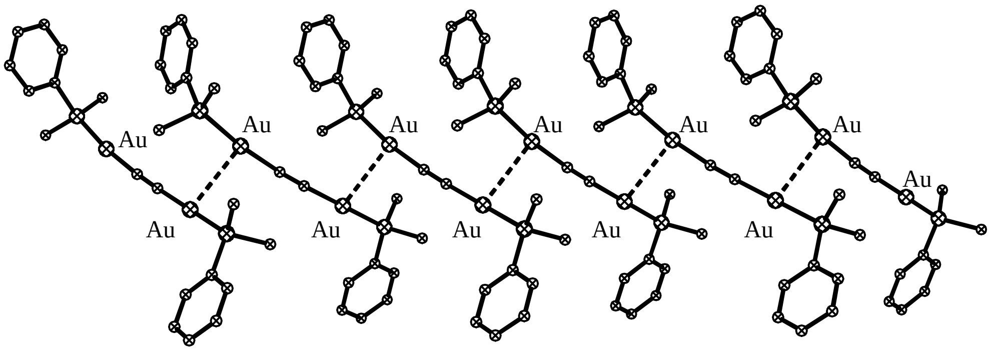

(**2**) [PhMe$_2$P·AuC≡CAu·PMe$_2$Ph]$_n$

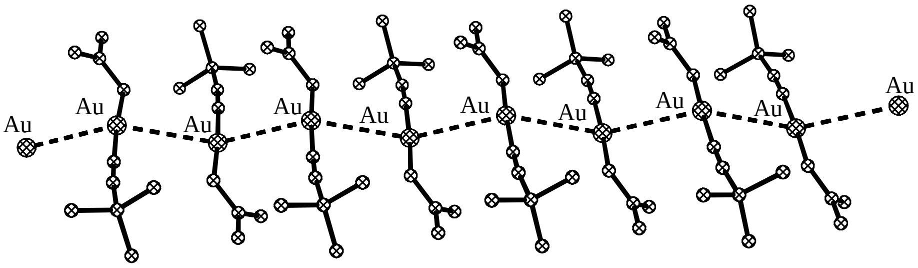

(**3**) [(NO$_3$)AuC≡N^{t}Bu]$_n$

For multinuclear structures, and for details of energy levels as related to optical properties, the theoretical treatment of organogold compounds has to be modified to include relativistic effects (*see Relativistic Effects*), which are particularly strong for gold.**15** With two, three, or more gold atoms attached to a given carbon atom, significant metal–metal bonding arises, which leads to unusually small Au–C–Au angles (<109°; for aliphatic carbon) and short Au···Au contacts (ca. 2.80 Å). These structural effects can be accounted for by calculations with relativistic Au(6s) contraction and Au(5d) expansion, which lead to a mixing of states. Hypercoordinate (*see Hypercoordination*) carbon, as in $[C(AuL)_5]^+$ and $[C(AuL)_6]^{2+}$, adopts a trigonal bipyramidal and octahedral structure, respectively, with similar geometrical characteristics and with both radial and peripheral (Au···Au) bonding. Pertinent examples are given below.**33**

The same phenomenon is responsible for the aggregation of independent RAu·L species via Au···Au contacts in the solid state, or of RAu·L units in polynuclear compounds, which leads to unusual conformations. Illustrative examples are the oligomeric gold(I) acetylide and isonitrile (isocyanide) complexes (**2**) and (**3**), where the slim ligands give unlimited access to the gold atoms.**32,52,53** Generally, however, this effect is weaker for organogold compounds than for other gold(I) complexes, probably due to the strong electron-donating capabilities of the organic substituents. Au···Au interactions are also less common for Au^{III} pairs than for Au^{I} pairs or Au^{I}Au^{III} mixed-valence systems, although examples are known for these combinations as well.

6 SELECTED INDIVIDUAL COMPOUNDS

Very much like the RCu and RAg analogs, simple organogold(I) compounds of the type RAu are generally unstable. 2,4,6-Trimethylphenylgold(I) was shown to form pentamers with mesityl-bridging of the gold atoms.**54** If R contains a donor center E, as in α-pyridyl, the RAu compounds also oligomerize with the formation of linear R–Au–E units (see **4** and **5**). The α-pyridylgold trimer is an example in case, and also the numerous carbene–gold compounds. In most of these oligomers, the Au···Au contacts are short enough to allow transannular bonding interactions.

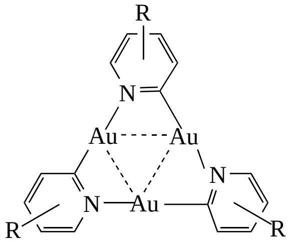

(**4**)

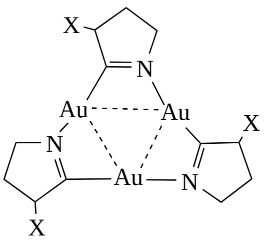

(**5**)

R$_2$AuX compounds are dimeric for X = Cl, Br, I, SCN, RCO$_2$, OSiR$_3$, SR, SeR, NR$_2$, PR$_2$, or AsR$_2$ (see **6**), and tetrameric for X = OH or CN (see **7**). Fluorides R$_2$AuF have not been reported, but are likely to have a larger ring or chain structure, like AuF$_3$. Sulfates and phosphates are also associated but most of their structures are unknown.

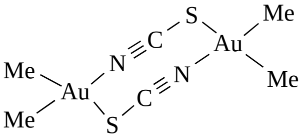

(6)

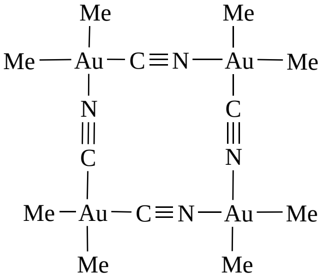

(7)

The chemistry of carbene complexes is well advanced, and numerous examples have been synthesized and structurally characterized. Prototypes are represented by structures (**8**–**10**).

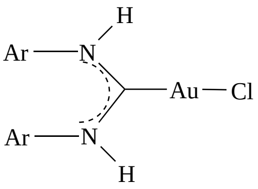

(8)

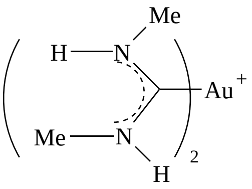

(9)

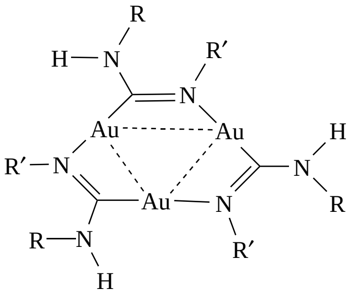

(10)

Gold compounds with hypercoordinate (*see Hypercoordination*) carbon atoms are a rapidly growing class of multinuclear organogold compounds with very special features of structure and bonding. It is important to note in this context that gold does not form any ligand-free carbide phases Au_mC_n. Clustering of gold around carbon is thus unique to this chemistry developed out of the addition of LAu^+ acceptors to organogold precursors. Neighboring elements in an isoelectronic state, such as Hg^{II} or Pt^0, do not form similar clusters.

Early examples for this phenomenon are the addition reactions of Ph_3PAu^+ to *p*-toly(triphenylphosphine)gold(I) (**11**) and to ferrocenyl(triphenylphosphine)gold(I) (**12**) to give cationic species with *p*-tolyl and cyclopentadienyl ring carbon atoms engaged in bonding to a pair of gold atoms. This reaction pattern was confirmed for heteroarenes such as furan and thiophene (**13**).[55]

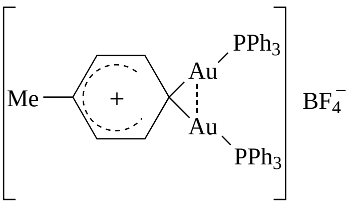

(11)

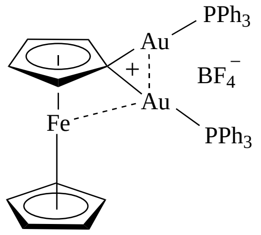

(12)

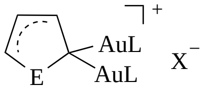

(13)

R-C(AuL)$_3$ moieties are present in onium cations $[P_3P–C(AuL)_3]^+$, obtained from silylated ylides $R_3P{=}C(SiR_3)_2$ on treatment with L·AuCl and CsF. Polyborylmethanes or -ethanes are the precursors not only for tetragoldmethane complexes[56,57] but also for penta- and hexagoldmethanium cations and of 1,1,1,1-tetragoldethanium cations, (**14**)–(**16**).[33] Another route uses the silyldiazomethane Me_3SiCHN_2 as a source for the interstitial carbon atom of the clusters (equation 44).[58] Owing to the high stability of the salts containing these novel cations, the compounds are readily identified by elemental analyses, field desorption mass spectrometry, NMR spectroscopy, and X-ray diffraction of single crystals, and rationalized by theoretical calculations.[59] The presence of the interstitial carbon atom has been confirmed by ^{13}C NMR using material enriched in ^{13}C. Up to four gold atoms could also be attached to the carbon atom of sulfur ylides (**17**).[60,61]

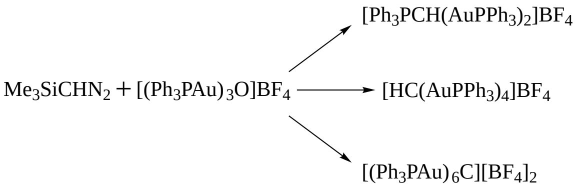

$$Me_3SiCHN_2 + [(Ph_3PAu)_3O]BF_4 \longrightarrow \begin{cases} [Ph_3PCH(AuPPh_3)_2]BF_4 \\ [HC(AuPPh_3)_4]BF_4 \\ [(Ph_3PAu)_6C][BF_4]_2 \end{cases} \qquad (44)$$

7 USAGE OF ORGANOGOLD COMPOUNDS

For several decades, many organogold compounds have been tested as potential drugs for the treatment of rheumatoid arthritis and related diseases, for venereal diseases, and, more recently, for cancer therapy. None of these investigations has led to a medical breakthrough, and such efforts have largely been discontinued. Current research is oriented toward an improvement of existing drugs (none of which is an organogold chemical), regarding side effects and administrational aspects.

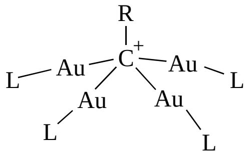

(**14**)

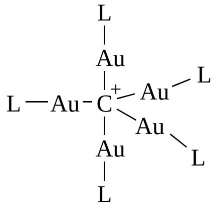

(**15**)

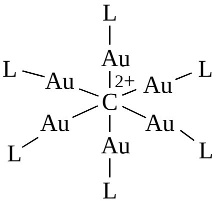

(**16**)

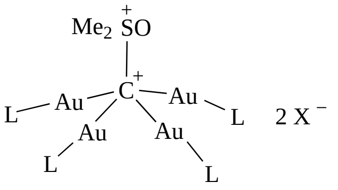

(**17**)

L = PR_3; R = alkyl, aryl, $S(O)R_2^+$

Volatile organogold compounds are candidates for new ways of depositing gold films on surfaces (*see* ***Metallic Materials Deposition: Metal-organic Precursors***). The most promising materials are dimethyl(acetylacetonato)gold(III) and its hexa- (**18**) or trifluoro derivatives, dimethyl(trimethylsilyloxy) gold(III) (**19**), methyl(trimethylphosphine)gold(I) (**20**), and methyl(methyl isocyanide)gold(I) (**21**). Thermal as well as plasma and photodecomposition experiments have been very successful for all of these compounds. The major disadvantage of the dimethylgold(III) compounds is the high cost of their production, caused by low yields in the preparation of any Me_2AuX precursor (<35%). The volatility of the compounds, and of the fluorinated acac compounds in particular, is quite satisfactory as already demonstrated in earlier analytical studies using gas/liquid chromatography. With the isocyanide complex, incorporation of carbon into the gold films has been reported, and with the phosphine complex, some environmental concern is becoming apparent. Therefore, usage of organogold compounds is still rather limited, even on the small scale required for the microelectronics industry.

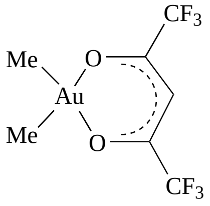

(**18**)

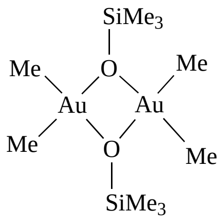

(**19**)

$Me{-}Au{-}PMe_3$

(**20**)

$Me{-}Au{-}C{\equiv}N{-}Me$

(**21**)

A rather new field emerging in organogold research is the study of luminescence and phosphorescence phenomena, associated in most cases with Au···Au secondary bonding. The optical properties and the mechanism of the excitation and emission are still poorly understood, but may provide a new basis for applications[62–64] (*see* ***Photochemistry of Transition Metal Complexes***).

Gold(I) complexes of alkenes and alkynes appear to play an important role as intermediates of the gold(I)-catalyzed addition of water, alcohols, carboxylic acids, or amines to these substrates. The effect of this π-complexation (**22**) is superior to the performance of mercury(II) in this type of reactions.[65–67] In a similar way, gold(III) salts have found applications in homogeneous catalysis.[68]

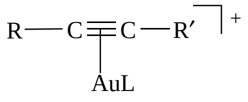

$\left[R{-}\underset{\displaystyle AuL}{C{\equiv}C}{-}R'\right]^+$

(**22**)

8 RELATED ARTICLES

Carbonyl Complexes of the Transition Metals; Cluster Compounds: Inorganometallic Compounds Containing Transition Metal & Main Group Elements; Cyanide Complexes of the Transition Metals; Dinuclear Organometallic Cluster Complexes; Gold: Inorganic & Coordination Chemistry.

9 REFERENCES

1. W. J. Pope and C. S. Gibson, *J. Chem. Soc.*, 1907, 2061.
2. C. S. Gibson and W. M. Colles, *J. Chem. Soc.*, 1931, 2407.
3. M. G. Miles, G. E. Glass, and R. S. Tobias, *J. Am. Chem. Soc.*, 1966, **88**, 5738.
4. H. Gilman and L. A. Woods, *J. Am. Chem. Soc.*, 1948, **70**, 550.
5. G. E. Coates and C. Parkin, *J. Chem. Soc.*, 1963, 421.
6. R. Uson, A. Laguna, and J. Vicente, *Synth. React. Inorg. Met.-Org. Chem.*, 1977, **7**, 463.
7. A. N. Nesmeyanov, E. G. Perevalova, K. I. Grandberg, D. A. Lemenovskii, T. V. Baukova, and O. B. Afanosova, *J. Organomet. Chem.*, 1974, **65**, 131.
8. G. E. Coates and C. Parkin, *J. Chem. Soc.*, 1962, 3220.
9. W. Manchot and H. Gall, *Ber. Dtsch. Chem. Ges.*, 1925, **58**, 2175.
10. A. Sacco and M. Freni, *Gazz. Chim. Ital.*, 1956, **86**, 195.
11. F. Bonati and G. Minghetti, *Gazz. Chim. Ital.*, 1972, **102**, 205.

12. H. G. Raubenheimer and S. Cronje, in 'Gold – Progress in Chemistry, Biochemistry and Technology', ed. H. Schmidbaur, John Wiley & Sons, Chichester, 1999, p. 604.
13. R. Hüttel and H. Dietl, *Angew. Chem.*, 1965, **77**, 456; *Angew. Chem., Int. Ed. Engl.*, 1965, **4**, 438.
14. H. Schmidbaur ed., 'Gold – Progress in Chemistry, Biochemistry and Technology', John Wiley & Sons, Chichester, 1999.
15. P. Pyykkö, *Chem. Rev.*, 1997, **97**, 597.
16. H. Schmidbaur, Gold: Organic compounds, in 'Gmelin Handbook of Inorganic Chemistry', ed. A. Slawisch, Springer-Verlag, Berlin, 1980.
17. R. J. Puddephatt, 'The Chemistry of Gold', Elsevier, Amsterdam, 1978.
18. W. S. Rapson and T. Groenewald, 'Gold Usage', Academic Press, London, 1978.
19. R. J. Puddephatt, in 'Comprehensive Organometallic Chemistry', eds. G. Wilkinson, F. G. A. Stone, and E. W. Abel, Pergamon Press, Oxford, 1982, Vol. 2.
20. B. Armer and H. Schmidbaur, *Angew. Chem.*, 1970, **82**, 120; *Angew. Chem., Int. Ed. Engl.*, 1970, **9**, 101.
21. K. C. Dash and H. Schmidbaur, in 'Metal Ions in Biological Systems', ed. H. Sigel, Dekker, New York, 1982, Vol. 14, p. 197.
22. H. Schmidbaur, *Gold Bull.*, 1990, **23**, 11.
23. H. Schmidbaur, *Interdiscipl. Sci. Rev.*, 1992, **17**, 213.
24. H. Schmidbaur, A. Grohmann, M. E. Olmos, and A. Schier, in 'The Chemistry of Organic Derivatives of Gold and Silver', eds. S. Patai and Z. Rappoport, John Wiley & Sons, Chichester, 1999, p. 227.
25. H. Schmidbaur, A. Grohmann, and M. E. Olmos, in 'Gold – Progress in Chemistry, Biochemistry and Technology', ed. H. Schmidbaur, John Wiley & Sons, Chichester, 1999, p. 648.
26. R. D. Sanner, J. H. Satcher Jr, and M. W. Droege, *Organometallics*, 1989, **8**, 1498.
27. M. Paul and H. Schmidbaur, *Z. Naturforsch., Teil B*, 1994, **49**, 647.
28. M. S. Kharasch and H. S. Isbell, *J. Am. Chem. Soc.*, 1931, **53**, 3053.
29. P. W. J. De Graaf, J. Boersma, and G. J. M. van der Kerk, *J. Organomet. Chem.*, 1976, **195**, 399.
30. M. A. Cinellu, A. Zucca, S. Stoccoro, G. Minghetti, M. Manassero, and M. Sansoni, *J. Chem. Soc., Dalton Trans.*, 1995, 2865.
31. A. Johnson and R. J. Puddephatt, *J. Chem. Soc., Dalton Trans.*, 1977, 1384.
32. R.-Y. Liau, A. Schier, and H. Schmidbaur, *Organometallics*, 2003, **22**, 3199.
33. H. Schmidbaur, *Chem. Soc. Rev.*, 1995, **24**, 391.
34. R. M. Davila, R. J. Staples, and J. P. Fackler Jr, *Organometallics*, 1994, **13**, 418.
35. D. Belli Dell'Amico, F. Calderazzo, R. Dantona, J. Strähle, and H. Weiss, *Organometallics*, 1987, **6**, 1207.
36. D. McIntosh and G. A. Ozin, *Inorg. Chem.*, 1977, **16**, 51; *Acc. Chem. Res.*, 1977, **10**, 21.
37. W. Beck, K. Burger, and W. Fehlhammer, *Chem. Ber.*, 1972, **104**, 1816.
38. D. Belli Dell'Amico and F. Calderazzo, *Gazz. Chim. Ital.*, 1973, **103**, 1099.
39. H. Schmidbaur, *Acc. Chem. Res.*, 1975, **8**, 62.
40. L. C. Porter and J. P. Fackler Jr, *Acta Crystallogr., Sect. C*, 1987, **C43**, 587.
41. B. Djordjevic, K. A. Porter, S. Nogai, A. Schier, and H. Schmidbaur, *Organometallics*, 2003, **22**, 5336.
42. J. Vicente and M. T. Chicote, *Coord. Chem. Rev.*, 1999, **193–195**, 1143.
43. H. Schmidbaur and O. Steigelmann, *Z. Naturforsch., Teil B*, 1092, **47**, 1721.
44. F. Scherbaum, A. Grohmann, B. Huber, C. Krüger, and H. Schmidbaur, *Angew. Chem.*, 1988, **100**, 1602; *Angew. Chem., Int. Ed. Engl.*, 1988, **27**, 1544.
45. F. Scherbaum, A. Grohmann, G. Müller, and H. Schmidbaur, *Angew. Chem.*, 1989, **101**, 464; *Angew. Chem., Int. Ed. Engl.*, 1989, **28**, 463.
46. L. F. Warren and M. F. Hawthorne, *J. Am. Chem. Soc.*, 1968, **90**, 4823.
47. H. M. Colquhoun, T. J. Greenhough, and M. G. H. Wallbridge, *J. Chem. Soc., Dalton Trans.*, 1978, 303.
48. G. W. Rice and R. S. Tobias, *Inorg. Chem.*, 1975, **14**, 2402.
49. A. Shiotani and H. Schmidbaur, *J. Organomet. Chem.*, 1972, **37**, C24.
50. A. Tamaki and J. K. Kochi, *J. Organomet. Chem.*, 1974, **64**, 411.
51. G. A. Bowmaker, in 'Gold – Progress in Chemistry, Biochemistry and Technology', ed. H. Schmidbaur, John Wiley & Sons, Chichester, 1999, p. 841.
52. T. Mathieson, A. Schier, and H. Schmidbaur, *J. Chem. Soc., Dalton Trans.*, 2001, 1196.
53. W. Schneider, A. Sladek, A. Bauer, K. Angermaier, and H. Schmidbaur, *Z. Naturforsch., Teil B*, 1997, **52**, 53.
54. S. Gambarotta, C. Floriani, A. Chiesi-Villa, and C. Guastino, *J. Chem. Soc., Chem. Commun.*, 1983, 1087.
55. K. A. Porter, A. Schier, and H. Schmidbaur, *Organometallics*, 2003, **22**, 4922.
56. H. Schmidbaur, F. Scherbaum, B. Huber, and G. Müller, *Angew. Chem.*, 1988, **100**, 441; *Angew. Chem., Int. Ed. Engl.*, 1988, **27**, 419.
57. O. Steigelmann, P. Bissinger, and H. Schmidbaur, *Z. Naturforsch., Teil B*, 1993, **48**, 72.
58. H. Schmidbaur, F. P. Gabbai, A. Schier, and J. Riede, *Organometallics*, 1995, **14**, 4969.

59. A. Görling, N. Rösch, D. E. Ellis, and H. Schmidbaur, *Inorg. Chem.*, 1991, **30**, 3986.
60. J. Vicente, M. T. Chicote, R. Guerriero, and P. G. Jones, *J. Am. Chem. Soc.*, 1996, **118**, 699.
61. I. J. B. Lin, C. W. Liu, L.-K. Liu, and Y.-Sh. Wen, *Organometallics*, 1992, **11**, 1447.
62. C. King, J.-C. Wang, M. N. I. Khan, and J. P. Fackler Jr, *Inorg. Chem.*, 1989, **28**, 2145.
63. V. V. W. Yam, T.-F. Lai, and C.-M. Che, *J. Chem. Soc., Dalton Trans.*, 1990, 3747.
64. J. C. Vickery, M. M. Olmstead, E. Y. Fung, and A. L. Balch, *Angew. Chem., Int. Ed. Engl.*, 1997, **36**, 1179.
65. J. H. Teles, S. Bode, and M. Chabanas, *Angew. Chem., Int. Ed. Engl.*, 1998, **37**, 1415.
66. E. Mizushima, K. Sato, T. Hayashi, and M. Tanaka, *Angew. Chem., Int. Ed. Engl.*, 2002, **41**, 4563.
67. P. Roembke, H. Schmidbaur, S. Cronje, and H. G. Raubenheimer, *J. Mol. Catal.*, 2003, **212**, 35.
68. A. S. K. Hashmi, *Gold Bull.*, 2003, **36**, 3.

Halides: Solid-state Chemistry

J. Köhler
Max-Planck-Institut FKF, Stuttgart, Germany

Based in part on the article Halides: Solid State Chemistry by Gordon J. Miller which appeared in the Encyclopedia of Inorganic Chemistry, First Edition.

1 Introduction 1
2 Thermodynamic Aspects of Halide Formation 1
3 Composition, Coordination Number, and Polyhedra Connectivity 2
4 Main Group Halides 3
5 Transition Metal Halides 9
6 Rare Earth Halides 15
7 Summary 17
8 Related Articles 17
9 References 17

1 INTRODUCTION

Halides have been known since earliest times and archeological evidence for the use of rocksalt, the most generally known halide, dates back thousands of years. The trade with this salt was the origin of wealth and prosperity in many regions around the globe, but other halides also have had a tremendous impact on all aspects of our world's history. In particular, during the past 200 years, the halogens and their compounds have significantly contributed to the development of both experimental and theoretical chemistry.

The immense number of chemical compounds formed by the halogens provides chemists with an extraordinary database from which numerous chemical and physical phenomena can be correlated with respect to various periodic trends.[1,2] From databases like *Inorganic Crystal Structure Data* (ICSD, 'http://www.fiz-karlsruhe.de') and *International Centre for Diffraction Data* (ICDD, http://www.icdd.com) with ∼67 000 and ∼25 000 entries, respectively, one can easily make out that halides are one of the dominant classes of compounds besides oxides. Even within the subset of inorganic solids, there is tremendous diversity of composition, structure, and properties and to summarize this would create its own encyclopedia. Therefore, the discussion in this article is limited primarily to binary halides, their structures, and some of their properties, except halides of elements which are nonmetals. Binary actinide halides are discussed elsewhere (*see* ***Actinides: Inorganic & Coordination Chemistry***). Complex halides (solid phases containing two or more kinds of metal ions),[3] mixed halides, halides containing other anions (H^-, O^{2-}, S^{2-}, $N^{3-}C^{4-}$, B^{n-}, etc.), and polyhalides[4] will also not be addressed.

2 THERMODYNAMIC ASPECTS OF HALIDE FORMATION

2.1 Halide Formation from Elements

A dominant feature of the chemistry of the halogens is the facility with which their atoms acquire an electron from a metal to form the uninegative ion X^-. The main reason for that lies in the electronic structure of the free atoms, $[A]ns^2np^5$ ($A =$ previous noble gas), which accounts for the strong affinity for electrons and reducing capabilities in order to achieve the electronically stable closed-shell (octet) configuration. As the oxidation potentials of Table 1 and other data suggest, however, this uninegative oxidation state becomes progressively less stable with respect to the free element of atomic number ($I < Br < Cl < F$), and fluorine is indeed the most reactive of all elements.

Thermodynamic stability of a general metal–halide MX_n with respect to its elements under ambient conditions is assessed according to $\Delta G^\circ{}_f(MX_n)$, which necessarily has a large entropic contribution for solid fluorides and chlorides. Basic knowledge for the understanding of the existence and stability of halides is wonderfully described by D.A. Johnson.[5] One can break down a chemical reaction, such as $M(s) + (n/2)X_2 \longrightarrow M^{n+}(g) + nX^-(g) \longrightarrow MX_n(s)$, into a series of hypothetical steps known as a Born-Haber cycle (equation 1).[5] The enthalpy change for the first process is given by $\Delta H^\circ{}_f(M^{n+}, g) + n\Delta H^\circ{}_f(X^-, g)$. Table 1 contains values of $\Delta H^\circ{}_f$ (X^-, g) for the halogens. $\Delta H^\circ{}_f(M^{n+}, g)$ will have large positive values due to both sublimation and subsequent atomic ionization energies for each metal, so the first process is endothermic.

The energetics of the second step has received a tremendous amount of theoretical attention.[6,7] The enthalpy change is defined as the negative of the lattice energy for the solid MX_n, which itself is defined as the energy needed to separate a solid into its constituent gaseous ions. Since the forces holding atoms together in molecules and solids are largely electrostatic, and the thermodynamic values in Table 1 suggest that a large degree of charge transfer takes place in metal halides, the lattice energies for these compounds are generally large, positive, and usually outweigh the enthalpy term for the first reaction. Therefore, $\Delta H^\circ{}_f(M^{n+}; s)$ for most metal halides adopts large negative values. Moreover, $\Delta G^\circ{}_f(MX_n, s)$ will also be negative, except at very high temperatures, at which point entropic effects are influential.

Table 1 Contributions to the standard enthalpies of formation of gaseous halide ions at 298.15 K

Property	F	Cl	Br	I
Ionic radius, X^-/pm	133	165	181	199
van der Waals radius/pm	135	180	195	215
$1/2\Delta H_f^{\ominus}(X^-, g)$/kJ mol^{-1}	0	0	15.5	31.2
$1/2D(X_2)$/kJ mol^{-1}	79.0	121.7	96.4	75.6
$-Ea(X)$/kJ mol^{-1}	−343.5	−361.5	−339.6	−297.2
$5/2RT$/kJ mol^{-1}	−6.2	−6.2	−6.2	−6.2
$\Delta H^\circ{}_f(X^-, g)/(\text{kJ mol}^{-1})^a$	−270.7	−246.0	−233.9	−196.6

$^a\Delta H^\circ{}_f(X^-, g) = \Delta H^\circ{}_f(X_2, g) + 1/2D(X_2) - E_a(X) - 5/2RT$.

2.2 Stability of Halides Containing High and Low Metal Oxidation States

Many elements exhibit several different oxidation states, and the relative stabilities of MX_n and MX_m are often more difficult to assess. Assuming the lattice energy to be inversely proportional to the shortest M–X distance in the structure, then, since halide ion radii increase from F^- to I^-(Table 1), fluorides generally have the largest values and iodides the smallest values for lattice energies. However, one has to consider the stabilities of fluorides or iodides with respect to each other, for example, a solid salt MX_{n+1} decomposing into another, MX_n, and $1/2X_2$. From the Born-Haber cycle (with some approximations) one obtains for such a reaction

$$\Delta H_m^{\ominus} = L(MX_{n+1}) - L(MX_n) - I_{n+1} - \Delta H_f^{\ominus}(X^-, g) \qquad (1)$$

where I_{n+1} is the $(n+1)$th ionization potential and $L(MX_{n+1})$ and $L(MX_n)$ are the lattice energies of the salts MX_{n+1} estimated by the Kapustinskii equation**8** with

$$L_0 = \frac{W\nu}{r_+ + r_-} \quad (W = 1.079 \times 10^5 \text{kJ} \times \text{mol}^{-1}\ \text{pm},$$
$$r_+ = \text{cation and } r_- = \text{anion radius}) \qquad (2)$$

$$\Delta H_m^{\ominus} = \left[\frac{W(n+1)(n+2)}{r(M^{(n+1)+}) + r(X^-)} - \frac{Wn(n+1)}{r(M^{n+}) + r(X^-)}\right] - I_{n+1} - \Delta H_f^{\ominus}(X^-, g) \qquad (3)$$

If the term in the bracket is put equal to x, while n and the cation radii are kept constant, one obtains for the change of x with the size of the anion as

$$\frac{\partial x}{\partial r(X^-)} = -W(n+1)\left[\frac{(n+2)}{[r(M^{(n+1)+}) + r(X^-)]^2} - \frac{n}{[r(M^{n+}) + r(X^-)]^2}\right] \qquad (4)$$

In most of the cases, $r(M^{(n+1)+})$ will be less than $r(M^{n+})$, although it is not necessarily crucial. Consequently, as n is positive $\partial x/\partial r(X^-)$ will be less than zero, and x will become more negative as the size of the anion is increased. Now the changes in $T\Delta S$ from halogen to halogen are small compared to $\Delta H^\circ{}_f$. Thus the variations in both $\Delta H^\circ{}_f$ (X^-, g) and the difference in lattice energies place the capacities to stabilize the higher oxidation states in the order F > Cl > Br > I. The stabilities of lower or medium oxidation states can be derived in a similar manner for the large anions. For example, the fluorides are the only halides of dipositive silver, trivalent cobalt or tetravalent manganese, cerium, praseodymium and terbium or pentavalent gold which have been prepared. On the other hand, the fluorides are the only unknown halides of gold(I) and copper(I), presumably because they are unstable with respect to the formation of Au and AuF_3 and Cu and CuF_2, respectively. That the iodides of copper(II) and iron(III) have not been obtained pure, because they are unstable at room temperature, decomposing into CuI and FeI_2 can also be understood by such an approach. To summarize, within the series iodides, bromides, chlorides, and fluorides the difference in the stabilities of the halide with metal atoms in high oxidation states and the corresponding reduced halide increases and therefore the tendency for disproportionation reactions is maximal among fluorides.

3 COMPOSITION, COORDINATION NUMBER, AND POLYHEDRA CONNECTIVITY

The compositions of metal halides are dominated largely by the stable oxidation states for the metal component. It is important at this point to realize that thermodynamics, when applied to solid-state systems, treats compounds as solid solutions. Thus, most of the compounds to be discussed in this article are considered as ‘line’ compounds, which have extremely narrow (but nonzero) ranges of homogeneity because extremely large variations of chemical potential accompany negligible changes in chemical composition.**9** Nevertheless, significant crystal chemical information can be derived from a simple empirical formula for an inorganic solid. In fact, the empirical formula provides information on the possible topologies (connectivities) of structural networks available for a given composition. Like for any compound the number and kind of possible crystal structures of halides can be easily derived from a given formula, especially when using graph theoretical tools.[10] In particular, if the average coordination number (C.N.) of M by X in the halide MX_n is C.N. (M: MX_n), then the coordination number of X by M is C.N.(X; MX_n) $= 1/n$ C.N. (M: MX_n). Therefore, for large n, the topology of metal halides is generally low dimensional for small cations, higher dimensional for larger cations. As a simple example, Al^{3+} is large enough to coordinate 6 F atoms and the crystal structure of AlF_3 consists of a 3D framework of connected AlF_6 octahedra. The neighboring tetravalent elements Si and Ge are smaller, their coordination number in the tetrafluorides MF_4 is 4, equal to the anion/cation ratio, and a molecular structure (0D) with isolated MF_4 tetrahedra is found. As a consequence AlF_3 melts at 1254 °C whereas SiF_4 and GeF_4 are gaseous at room temperature. The larger Sn has a C.N. of 6 in SnF_4, which on the other hand is a solid at room temperature containing a condensed network of SnF_6 octahedra.

Another aspect that will become clear in the following chapters is the fact that condensation via corners is favored in fluorides whereas condensation via edges or faces is more common among the higher homologues. Short M–F distances in fluorides lead to short M–M distances and electrostatic repulsion of the higher charged metal atoms makes corner sharing much more favorable. This changes gradually from chlorides via bromides to iodides, besides direct metal–metal bonding as stabilizing factor for edge sharing or face sharing. For example, face-sharing polyhedra are not found among fluorides and one finds condensation of polyhedra via corners, edges, or faces correlated with the size of the halide.

4 MAIN GROUP HALIDES

Information about the binary main group metal halides abounds in numerous texts and tabulations.[1,3,4,11,12] Table 2 gives a qualitative listing of many of the halide stoichiometries adopted by the main group metals. All solid-state compounds tend to behave as salts with very low electrical conductivity. Many of the pure compounds with metals in their higher

Table 2 Representative binary halides of the main group metals[a]

Group	Fluorides	Chlorides	Bromides	Iodides
	LiF	LiCl	LiF	LiF
	NaF	NaCl	NaF	NaF
	KF	KCl	KF	KF
1	RbF	RbCl	RbF	RbF
	CsF	CsCl	CsF	CsF
	BeF_2	$BeCl_2$	$BeBr_2$	BeI_2
	MgF_2	$MgCl_2$	$MgBr_2$	MgI_2
	CaF_2	$CaCl_2$	$CaBr_2$	CaI_2
2	SrF_2	$SrCl_2$	$SrBr_2$	SrI_2
	BaF_2	$BaCl_2$	$BaBr_2$	BaI_2
	AlF_3	$AlCl_3$	$AlBr_3$	AlI_3
	GaF_3	$GaCl_3$, GaCl, $GaCl_2$, Ga_3Cl_7	$GaBr_3$, GaBr, $GaBr_2$, Ga_2Br_3, Ga_3Br_7	GaI_3, GaI, GaI_2, Ga_2I_3
13	InF_3	$InCl_3$, InCl, $InCl_2$, In_3Cl_5, In_4Cl_6, In_3Cl_7	$InBr_3$, InBr, In_5Br_7,	InI_3, InI
	TlF_3, TlF, TlF_2, Tl_3F_5, Tl_4F_6, Tl_3F_7	$TlCl_3$, TlCl, Tl_3Cl_4, Tl_2Cl_3,	$TlBr_3$, TlBr, Tl_3Br_4, Tl_2Br_3,	TlI_3, TlI, Tl_3I_4, Tl_2I_3,
	GeF_4, GeF_2, Ge_5F_{12}, Ge_7F_{16}	$GeCl_4$, $GeCl_2$, Ge_2Cl_6, Ge_6Cl_{16}	$GeBr_4$, $GeBr_2$	GeI_4, GeI_2
	SnF_4, SnF_2, Sn_3F_8, Sn_7F_{16}, $Sn_{10}F_{34}$	$SnCl_4$, $SnCl_2$, Sn_2Cl_6, Sn_6Cl_{16}	$SnBr_4$, $SnBr_2$	SnI_4, SnI_2
14	PbF_4, PbF_2, Pb_2F_6	$PbCl_4$, $PbCl_2$, Pb_2Cl_6, Pb_6Cl_{16}	$PbBr_2$	PbI_2
	SbF_5, SbF_3, Sb_2F_8, Sb_3F_8, Sb_3F_{11}, Sb_2F_7, Sb_7F_{29}, Sb_8F_{30}, $Sb_{11}F_{43}$	$SbCl_5$, $SbCl_3$, Sb_6Cl_{16}	$SbBr_3$	SbI_3, Sb_2I_4
15	BiF_5, BiF_3	$BiCl_3$, Bi_6Cl_7	$BiBr_3$, BiBr Bi_6Br_7,	BiI_3, BiI, Bi_7I_2, Bi_9I_2

[a] Structures are discussed in the text.

possible oxidation states are colorless, while lower oxidation states develop yellowish, orange, or red colored crystals. Iodides and some bromides often show red/lustrous dark brown colors. There are also relatively few examples of metal–metal bonding in any of the reduced binary halides.

Vertical trends are affected by both the metal and the halide. As one goes down a column, larger cation radii lead, in general, to larger coordination numbers. On the other hand, increasing anion radii from fluoride to iodide (Table 1) generates increased anion–anion repulsions and smaller coordination numbers. Furthermore, oxidation states two less than their maximum allowed values (the 'inert-pair effect') are prevalent for the heavier atoms in a group, and are manifested in the relative stabilities of, for example, TlCl and $TlCl_3$.

Recent efforts involving these systems include: (i) high-pressure studies and structural phase transformation; stabilization of mixed valence main group metal halides; (iii) synthesis of low oxidation state halides; and (iv) characterization of mixed metal halides.

4.1 Alkali Metal Halides

At ambient conditions, the crystalline alkali halides CsCl, CsBr, and CsI have the CsI structures whereas all others adopt the rocksalt structure (*see* ***Alkali Metals: Organometallic Chemistry***); see Figure 1.

Radius ratio rules would ascribe the differences to the increased size of the cations, since Cs^+ is eight-coordinate cubic in CsCl, whereas Na^+ is six-coordinate octahedral in NaCl. However, these 'rules' are not successful for some of the alkali metal halides. For example, LiCl should adopt the zinc blende structure with four-coordinate tetrahedral Li^+ ions rather than the observed NaCl type. It is, therefore, not so surprising that mixed metal halides like $RbLiBr_2$ show significant differences from the parent rock salt structure.[13] Nevertheless, these halides nearly fit the classical conception of ionic bonding. Their heats of formation are reproduced using Born-Haber cycles with the lattice energy evaluated from Madelung terms, short-range repulsions, and van der Waals attractions.[7] However, precise electron density plots obtained from careful diffraction experiments on LiF, NaCl, and KCl indicate some electron density between cation and anion (the ions are not hard spheres) and, for example, the Li centers in LiF are not spherically symmetric.[14] Ionic radii obtained from these plots give larger cation and smaller anion values than those found in standard tables. Therefore, the M^+X^- formulation is an extreme description of the bonding in these traditional ionic materials, and even in the simple rocksalt structure type there must be an intricate balance between nearest neighbor (cation–anion) and next nearest neighbor interactions (anion–anion, cation–cation), which cannot simultanously be satisfied in a given structure. Therefore, if the cation is small and the anion is large or vice versa, unusual properties are observed, for example, the solubility of LiI in organic solvents or the strong hydrophilic properties of RbF or CsF compared to their lighter homologues NaF and KF. CsF also reacts with bromine under the formation of $CsFBr_2$,[15,16] which exhibits a distorted CsF structural framework with embedded neutral molecular Br_2 units. This situation is completely different from $CsBr_3$, which is a polybromide with $[Br_3]^-$ units or CsI_3or RbI_3 with linear $[I_3]^-$ anions.[4]

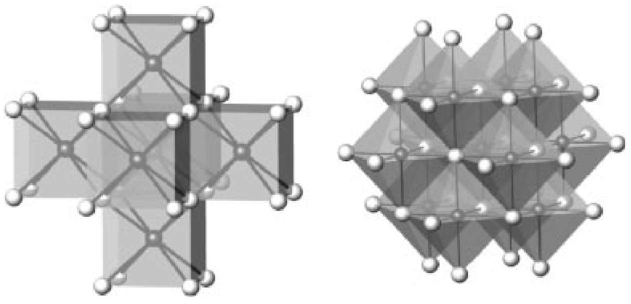
(a) (b)

Figure 1 Polyhedral representation of the structures of (a) CsI and (b) NaCl

Under elevated pressures, the rocksalt structure transforms into the CsCl structure.[3] Changes in lattice constants and measurements of other physical properties have provided much quantitative information for empirical fits to equations of state. Modern theoretical tools are used for obtaining a deeper understanding of charge being transferred back from the anion towards the cation in the alkali halides. However, as can be seen from calculations of their cohesive properties,[17] even nowadays there are problems to be solved for such simple structures. The data for the halide ions, in particular, are quite useful and may be transferred to other halide systems, and give good predictive values for more complex systems.

4.2 Alkaline Earth Metal Halides

All of the alkaline earth metals form saltlike MX_2 dihalides (*see* ***Alkaline Earth Metals: Inorganic Chemistry***). Within this group, we observe structural effects owing to both cation sizes and properties of the halide ions. From Be to Ba, coordination numbers monotonically increase from four (tetrahedral) in Be dihalides to eight (cubic) or nine (tricapped trigonal prismatic) in the Ba systems.

BeF_2, which is best made by thermal decomposition of $(NH_4)_2BeF_4$, is a glassy compound that crystallizes with difficulty. Like SiO_2, BeF_2 shows various frameworks of corner-sharing tetrahedra, both crystalline and amorphous. With the larger chlorine there is an α-modification of $BeCl_2$ which adopts an unusual tetrahedral framework,[18] whereas the β-modification of $BeCl_2$,[19] is isotypic to SiS_2, like $BeBr_2$ containing chains of edge-sharing tetrahedra ${}^1_\infty[BeX_{4/2}]$ (this notation indicates the dimensionality (1) of a quasi-infinite extended network; Figure 2). The X–Be–X angle within each

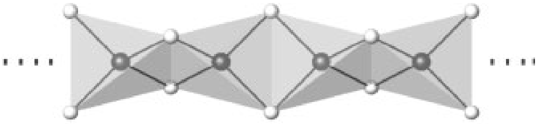

Figure 2 Chain structure of $BeCl_2$. In every figure, open circles represent halides, filled circles represent metal atoms

X–Be–X–Be rhombus is substantially smaller than 109.5°, suggesting that the local coordination at Be tries to diminish the repulsions between Be^{2+} ions. The highly moisture sensitive BeI_2 has been known for more than a century, but its structure is still unknown and the question arises whether the coordination number of Be by I is still four and not three as one might expect.[20]

The MgX_2 have Mg^{2+} ions in octahedral coordination, and their structures reflect the properties of each halide ion, especially with respect to polarizability. MgF_2 adopts the rutile structure, whereas layered morphologies occur for the heavier halides: $CdCl_2$ and CdI_2. A fundamental difference between these structures is that in rutile each F^- is nearly trigonal planar coordinated by Mg^{2+} (but planar), and in CdI_2 the I^- ions have trigonal pyramidal environment. The heavier metal dihalides of Ca, Sr, and Ba reveal an interesting effect of optimizing cation coordination number and anion–anion repulsion.[21] Moreover, these two forces need to be coupled with the covalent character and polarizability of the anion. Thus, the MF_2 compounds adopt fluorite structures, whereas other geometries are found for chlorides, bromides, and iodides.

The $CaCl_2$ structure for $CaCl_2$, $CaBr_2$, and $SrCl_2$ is slightly distorted from rutile, but the anion coordination is pyramidal rather than planar. In fact, whereas the anion packing in rutile is a distortion of hexagonally close-packed anions (hcp), the anion arrangement in $CaCl_2$ is nearly ideal hcp. Compounds of the type BaX_2 ($X = Cl, Br, I$) all show the complex $PbCl_2$ structure (Figure 3) with nine-coordinate Ba^{2+}. There are two symmetry inequivalent anions whose coordinations are nearly tetrahedral for one and nearly square pyramidal for the other. The forces we mentioned earlier lead to an interesting trend in the SrX_2 series: maximum coordination around Sr^{2+} occurs in $SrBr_2$, approximately nine ($PbCl_2$-type). SrI_2, on the other hand, adopts a unique structure in which each Sr^{2+} is seven coordinate: the polyhedral arrangement is a hybrid between a cube and a trigonal antiprism.[22] A metastable form of SrI_2 was recently isolated with seven-coordinate Sr as well.[23] n

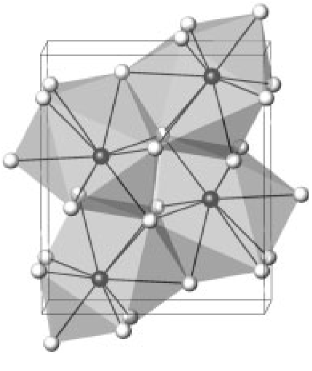

Figure 3 Structure of $PbCl_2$

Recent high-pressure experiments on alkaline earth metal dihalides indicate that most of the observed transitions can be interpreted in purely geometric terms by considering ion compression, radius ratios, and increase in coordination and packing efficiency.[24] The Sr and divalent rare earth halides undergo transitions to the $PbCl_2$-type. Crystal chemical analysis of compounds adopting the orthorhombic $PbCl_2$-type structure show that there are two adjustable parameters, that is, the a/b and c/b ratios, that separate these compounds into 'ionic' and 'non-ionic' regions.[25] SrI_2, SmI_2, and EuI_2 fall in a region which indicates a low ionicity, unlike the saltlike BaX_2 phases at normal pressure.

On the other hand, the high-pressure phase BaI_2-II, which can be quenched and retained at ambient conditions, forms the *anti*-Fe_2P structure (Figure 4a). This modification is structurally related to the $PbCl_2$-type formed at normal pressures (Figure 4b) but slightly more dense.[26] Surprisingly, neither $BaCl_2$ nor $BaBr_2$ will undergo a similar transformation under pressures up to 3.0 GPa in a belt apparatus. However, solvolytic decomposition of mixed halide precursors have led to the *anti*-Fe_2P type for these two systems.[27]

At one point, Ca, Sr, and Ba were believed to adopt monohalides as well.[28] Their geometries, based upon X-ray powder diffraction, suggested a distortion of the rocksalt structure, but without significant metal–metal bonding. With nine valence electrons per formula unit, simple models

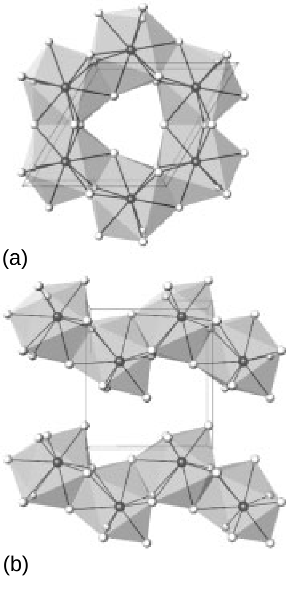

Figure 4 Projection of layers of condensed MX_9 polyhedra together with the unit cells in the structures of (a) BaI_2-II and (b) $PbCl_2$

predicted metallic character, yet 'these compounds' are colorless insulators. The monohalides are, in fact, hydride halides MXH.**[29]** Treating each hydrogen atom as H^- provides a rationale for their insulating behavior.

4.3 Group 13 Metal Halides

The lightest element of the group 13, boron, exhibits aspects of covalent metal–halide interactions. It is the first element to form reduced halides in which the access valence electrons are localized in boron–boron bonds. As a consequence the chemistry of reduced boron halides chemistry is very rich, consisting of numerous phases containing polymeric boron units embedded in a halide matrix (*see* ***Boron: Inorganic Chemistry***). The group 13 metals are the first main group elements to show multiple stoichiometries in their halides (*see* ***Aluminum: Inorganic Chemistry***; ***Gallium: Inorganic Chemistry***; ***Indium: Inorganic Chemistry***; ***Thallium: Inorganic Chemistry***). Most of the structures show evidence for both $M^I$and M^{III}, both of which are closed-shell configurations and adopt typical lone pair structures. However, few of them indicate strong metal–metal bonding.

The variation in cation size from Al^{3+} to Tl^{3+} in MX_3 leads to structures that range from three-dimensional (3D) frameworks to packings of molecular species. Most of the trihalides are made by direct combination of the elements. The trifluorides, on the other hand, are obtained from thermal decomposition of NH_4MF_6 or $(R_4N)AlF_6 \cdot H_2O$. Also, HF reacts at 970 K with Al_2O_3 to give AlF_3.

The fluorides, AlF_3, GaF_3, and InF_3, adopt structures related to ReO_3. In ReO_3, each metal ion is octahedrally coordinated and each anion is linearly coordinated. In these MF_3 systems, however, the M–F–M angles are around 150°, which suggests some polar covalent character to the metal–fluoride interaction, although these observations are not well understood. A recent investigation reports a new corner-sharing octahedral 3D network for τ-AlF_3.**[30]** With the heavier halides, these three metals form either the layered $AlCl_3$-type (Figure 5) with six-coordinate metals or the molecular Ga_2Cl_6-type (Figure 6) with tetrahedrally surrounded cations. In $AlCl_3$, the anions are cubic closest packed (ccp) with metals in 1/3 of the octahedral holes. Each MX_6 octahedron shares three edges with neighboring octahedra according to ${}^2_\infty[(\square X_{6/3})(MX_{6/3})_2]$. Near the melting point of $AlCl_3$ (465 K), the Al^{3+} ions must diffuse in the chloride matrix from the octahedral to tetrahedral interstices because Al_2Cl_6 molecules are formed in both the liquid and gaseous states. In addition, the conductivity of $AlCl_3$ drops dramatically near the melting point, unlike most other ionic salts.**[31]** The dimers consist of two edge-sharing MX_4 tetrahedra to give $MX_2X_{2/2}$ and distort in a similar fashion as $BeCl_2$ to minimize cation–cation repulsions.

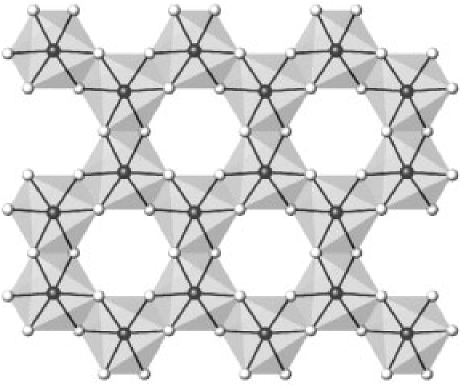

Figure 5 Part of a layer from the structure of $AlCl_3$

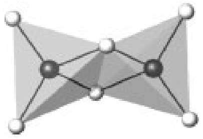

Figure 6 Edge-sharing tetrahedral molecules in Ga_2Cl_6

The halides TlX_3 (X = I, Br, Cl, I) provide an interesting series which couples both anion packing forces and the electronic stability of Tl^I against Tl^{III}. TlF_3 adopts the YF_3 structure: a 3D framework with Tl^{III} in a distorted tricapped trigonal prism of F^- ions.**[32]** $TlCl_3$ is isomorphous with YCl_3 and can be described as an ordered defect rocksalt structure. It is hygroscopic and easily forms hydrates. $TlBr_3$ presumably contains Tl_2Br_5 dimers. TlI_3, however, contains I_3^- ions, another indication of larger anions stabilizing low oxidation states of metals. In fact, $TlCl_3$ and $TlBr_3$ lose X_2 (X = Cl, Br) at around 320 K to give TlCl and TlBr.

The heavier group 13 metals In and Tl form stable monohalides, owing to the inert-pair effect, which can be attributed to relativistic effects on the electronic motion in atoms and ions. These can be obtained in different ways: (1) by heating the elements directly; (2) by heating stoichiometric mixtures of M(s) and MX_3(s); or (3) by halogenation of the metal using HgX_2 or Hg_2X_2. InCl at temperatures below 390 K (α-InCl) adopts a yellow modification that is a distorted rocksalt structure.**[33]** With an electronic configuration $[Cd]5s^2$, In^I ions show stereochemically active lone pairs within the ccp Cl matrix. In α-InCl, distortions of the $InCl_6$ octahedra suggest these lone pairs to be directed towards either an edge or a face. Although concurrent shifts in In^+ positions create a range of In–In distances, there is neither direct experimental evidence nor theoretical conclusions supporting In–In bonding. Red InCl ($T > 390$ K), InBr, InI, and TlI have the layered TlI structure (Figure 7),**[3]** which is related to the NaCl structure by displacing two adjacent (001) planes in NaCl by 1/2 [110] relative to the next two planes. This transformation creates five-coordinate square pyramidal Tl and the formation of zig-zag chains of weakly interacting Tl ions. At 4.7 kbar, TlI converts to a red modification (cubic CsCl

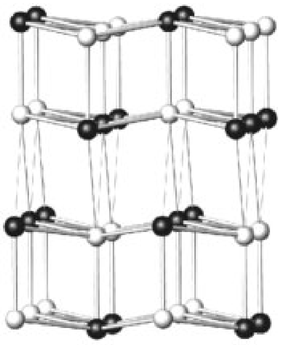

Figure 7 Structure of TlI

structure type), as found under normal conditions for TlCl and TlBr. All three compounds become metallic conductors at even higher pressures.

TlF adopts a distorted rocksalt structure, which transforms at 81 °C to a tetragonal distorted variant, slightly more dense than the room temperature form. A high-pressure phase appears at 12.6 kbar.[34]

Although there is no example of a purely binary M^{II} halide among the group 13 metals, Ga, In, and Tl do form dihalides, which can be prepared using the same techniques as for the monohalides. These compounds contain M^+ besides MX_4^- ions. $TlCl_2$, for example, is isostructural with scheelite ($CaWO_4$), which can be derived from fluorite by distorting the anion array.[35] The topology of $GaCl_2$ and $TlBr_2$ is different. It has been extremely difficult to rationalize the absence of metal–metal bonds for these stoichiometries, but one again finds large anions stabilizing low oxidation state cations. A wonderful example of this occurs in Ga_3Cl_7,[36] which contains Ga^+ besides $[Ga_2Cl_7]^-$ vertex-sharing tetrahedra (like $Si_2O_7^{6-}$, $P_2O_7^{4-}$or $S_2O_7^{2-}$). The larger In^{3+} and Tl^{3+} ions can also accommodate octahedral coordination, and the complex ions, like $[InCl_6]^{3-}$ or $[TlBr_6]^{3-}$, can form numerous intermediate halides. Thus, compounds like In_2Cl_3 are formulated as $(In^+)_3[InCl_6]^{3-}$ and In_7Br_9 as $(In^+)_6[In_2Br_6]^{3-}$ $(Br^-)_3$.

Dimers of M^{II} centers occur in the mixed valent compounds Ga_2X_3 $(X = Br, I) = (Ga^+)_2$ $[Ga_2X_6]^{2-}$ which contain ethane-type $[Ga_2X_6]^{2-}$ units with Ga–Ga single bonds.[37] As in the dihalides, mixtures of complex and simple ions combine also in $In_5X_7 = (In^+)_3[In_2Br_6]Br$, which contains the ethane-like units with M–M single bonds as well.[38–40]

4.4 Group 14 Metal Halides

Moving across a row of the periodic table to the right electronegativities increase. The lighter homologues of group 14 elements C, Si, and partly Ge are nonmetals and begin to exhibit aspects of covalent metal–halide interactions and homonuclear bonds, as observed for the reduced B halides (*see* ***Boron: Inorganic Chemistry***). Classical ionic forces, which were incorporated to evaluate and analyze the energetics of alkali and alkaline earth metal halides, become interwoven with covalent orbital interactions. Thus, the global structures of these inorganic solids minimize ionic contributions, in general, while local coordination geometries are well described using the valence shell electron pair repulsion (VSEPR) model.[41] The fullerene halides and the graphite halides are excluded from this discussion of main group metal halides, although graphite is poorly metallic. Silicon forms volatile tetrahalides and with fluorine and chlorine numerous halopolysilanes (*see* ***Silicon: Inorganic Chemistry***) which will also not be addressed.

Germanium, tin, and lead form numerous complex ternary halides that involve interesting anionic fragments. Within the set of purely binary compounds, MX_2 and MX_4 compounds predominate, and there is tremendous structural diversity. In terms of thermodynamic stabilities, dihalides PbX_2 are preferred over tetrahalides PbX_4, whereas the reverse is true for Ge, especially for the higher homologues of the halogens. The number of reported intermediate compositions is limited, and those, which have been characterized, are mixed valent compounds (*see* ***Germanium: Inorganic Chemistry***; ***Tin: Inorganic Chemistry***; ***Lead: Inorganic Chemistry***).

The tetrahalides of Ge and Sn are all known, but only the iodides and SnF_4 are crystalline solids at room temperature. The iodides consist of ccp iodine with Ge^{4+} or Sn^{4+} in one-eighth of the tetrahedral holes. When $SnCl_4$ condenses,[42] the chlorine atoms adopt hcp. In other words, these solids are packings of $SnCl_4$ tetrahedral molecules, like GeF_4.[43] On the other hand, SnF_4 and PbF_4 are both tetragonal with MF_6 octahedra sharing four vertices to give a flat two-dimensional analog to the ReO_3 structure (see Figure 8). The checkerboard-like $MX_{4/2}X_{2/1}$ sheets with four shared equatorial and two terminal anions which are connected via van der Waals interactions are also found in many complex fluorides and oxides, for example, K_2NiF_4 or the cuprate network in the

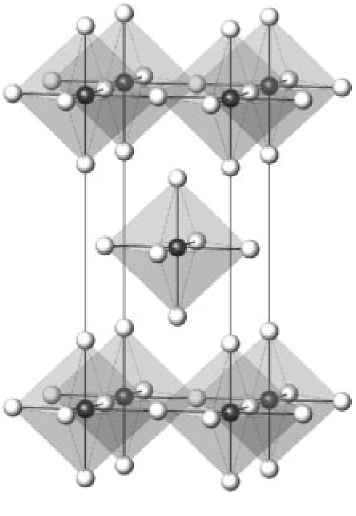

Figure 8 Structure of SnF_4

high-temperature superconductors $La_{2-x}Sr_xCuO_{4-y}$.[35] $PbCl_4$ is a yellow liquid at room temperature, decomposes at 50 °C into $PbCl_2$ and Cl_2 and solidifies at −15 °C. Its structure is still unknown. $PbBr_4$ and PbI_4 do not seem to be stable at all, which can be considered in terms of the oxidizing power of Pb^{4+} which is reduced to Pb^{2+} by Br^- and I^-, respectively.

Various synthetic methods produce the dihalides, the simplest of which involves heating stoichiometric mixtures of M(s) and MX_4. SnI_2, however, forms by heating Sn with I_2 in 2M HCl. Its structure shows two types of Sn sites: two-thirds of them occupy sites similar to those in $SnCl_2$ ($PbCl_2$-type) and the remaining are in rutile-type chains.[44] As in the reduced group 13 halides, there is no evidence for Sn–Sn bonding, but the regular geometry around one set of Sn atoms in SnI_2 suggests a degree of electron delocalization of the lone pair into a low lying crystal band (orbital).[45]

More generally, for the element halides $:MX_n$ the stereochemical activity of a free electron pair (:) decreases with increasing period number of M within an element group and in the series $:MF_n > :MCl_n > :MBr_n > :MI_n$ due to the space required by the anion near the lone pair atom. Thus SiF_2 should show this activity most effectively, however, it polymerizes after milliseconds to a Teflon analogue. GeF_2 crystallizes with a typical lone pair structure[46] in which channels provide space for the lone pairs (see Figure 9). A comparable structure can also be expected for $GeCl_2$, although it is not yet determined. SnF_2, which exists in three polymorphs[47] and $SnCl_2$, also demonstrate a stereochemically active lone pair at Sn. At low temperatures, α-SnF_2 contains two kinds of Sn atoms: three-coordinate $[SnF_3E]$ (E = lone pair) pyramids and 3 + 2 coordinate $[SnF_5E]$ tetragonal pyramidal units, which are linked together to form tetrameric molecules. Between 150 and 190 °C the α form transforms into γ-SnF_2, which contains $[SnF_4E]$ trigonal bipyramids. Upon subsequent cooling, the second order displacive transformation to β-SnF_2 ensues giving $[SnF_4F'E]$ coordination that is intermediate between trigonal bipyramidal and octahedral as found for the isotypic GeF_2. The fluorides with intermediate compositions, Ge_5F_{12},[48] Ge_7F_{16},[49] and Sn_3F_8,[50] are mixed valence compounds and their structures show features of both MF_2 (stereochemically active lone pairs) and MF_4 with octahedral coordination for the M^{IV}. $Ge_5F_{12}$and Ge_7F_{16} are less hygroscopic than either GeF_2 or GeF_4, and both thermally decompose into these two phases. Another mixed valency example is $SnF_3 = Sn[SnF_6]$ and in this case the high-temperature modification has an ordered ReO_3 type structure with octahedral coordination of both Sn atoms by F (Sn^{II}–F = 2.29 Å and Sn^{IV} = 1.86 Å)[51] indicating the absence of a stereochemical effectiveness of the free electron pair at Sn^{II}.

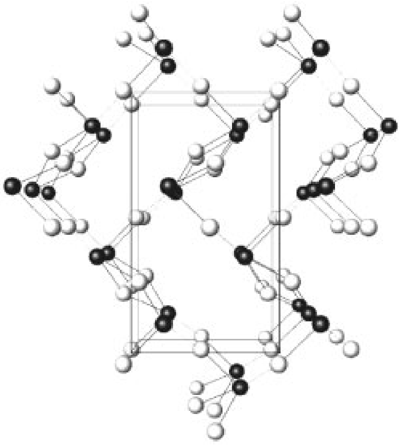

Figure 9 Structure of GeF_2

The dihalides PbX_2 (except PbI_2) occur in the orthorhombic $PbCl_2$ structure type[3] (see Figure 3), and their structural parameters are consistent with an ionic formulation. In particular, with Pb the relativistic effect plays an additional role and therefore the s-character of the free electron pair is in addition favorized over the p-character, that is, the stereochemical effectivity is less pronounced. This is reflected by PbF_2 which undergoes an irreversible transition to the cubic fluorite structure at 648 K. At temperatures near 973 K, well below the melting point of PbF_2 (ca. 1200 K), it becomes a good F^- ion conductor.[52] PbI_2 is isotypic with CdI_2, showing several polymorphs and no stereochemical activity of its lone pair, which parallels observations in SnI_2 and other complex Sn^{II} and Pb^{II} halides.[45] The intermediate stoichiometry, PbF_3, is mentioned but not well characterized.[53]

4.5 Group 15 Metal Halides

Many halides of the group 15 elements, which are molecular species,[3,4] have received a great deal of attention (*see* ***Arsenic: Inorganic Chemistry***; ***Antimony: Inorganic Chemistry***; ***Bismuth: Inorganic Chemistry***). Only the halides with antimony and bismuth, which form binary compounds of the type MX_3, subhalides with the larger anions, and compounds of the type MX_5 with smaller anions, will be discussed here. With Sb, the two pentahalides SbF_5 and $SbCl_5$ are known; however, among the Bi trihalides, only BiF_3 can be oxidized by F_2 (∼500 °C) to BiF_5, which is an extremely strong fluorinating agent. In $SbCl_5$, the coordination number of Sb is five and the $SbCl_5$ trigonal bypyramids are packed in a molecular structure,[54] which is isotypic to AsF_5.[55] With the smaller F, the coordination numbers of Sb and Bi are six and the structure of SbF_5 contains tetrameric rings of cis corner-sharing SbF_6 octahedra,[56] whereas BiF_5 crystallizes with chains of trans corner-sharing BiF_6 octahedra[57] (see Figure 10). The pentahalides $BiCl_5$, $BiBr_5$, and BiI_5 are not known and obviously the equilibrium is on the BiX_3 and X_2 (X = Cl, Br, I) side.

Discrete pyramidal molecules of SbX_3 and BiX_3, except BiF_3 and BiI_3, can be detected in the solid phase. β-bismuth

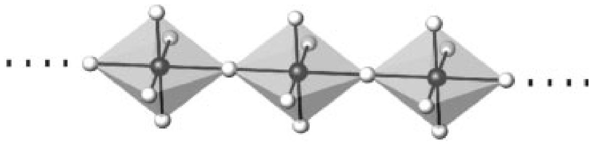

Figure 10 Chains of corner-sharing octahedra in the structure of BiF_5

trifluoride has a distorted uranium trichloride structure, in which the Bi^{3+} cations are surrounded by nine F^- ions in a triply capped trigonal prismatic structure. One fluorine cap is somewhat farther away from the bismuth, giving Bi the coordination number $8 + 1$. This may be a result of the steric effect of the free electron pair on the bismuth. The trichlorides and tribromides of antimony and bismuth have analogous structures and differences are based on the size effect.**[58]** Of particular crystal chemical interest are SbI_3 and BiI_3, which occur in the layered BiI_3 structure with hcp iodide ions and M^{III} in the octahedral holes. Each of the layers, which are stacked via van der Waals interactions, is topologically equivalent to the sheets in $AlCl_3$ (Figure 5). Although crystallographic symmetry does not demand that the cations lie exactly on the center of the octahedral interstices, Bi nearly centers this site whereas Sb is shifted away from the center resulting in $3 + 3$ coordination.

Similar to the mixed valent Ge fluorides there is also a large chemistry of Sb halides with intermediate compositions, see Table 2. These compounds are adducts according to $n\text{SbX}_3{\cdot}m\text{SbX}_5$ ($n, /m = 1, 2, 3\ldots$) and their structures are built from anionic units $SbX_6{}^-{\cdot}(n-1)SbX_5$ and cationic building units $SbX_2{}^+ \cdot (m-1)SbX_3$.

With Sb only one subhalide, Sb_2I_4, is known so far, which is formed by the reaction of elemental Sb in molten SbI_3 below 230 °C. Besides the BiX_3 phases, several subhalides with the larger halides are known, for example, BiBr, BiI,**[59]** Bi_7I_2 and Bi_9I_2, which contain Bi clusters with strong metal–metal bonding. A subchloride of bismuth has also been isolated from $Bi/BiCl_3$ mixtures and was determined to be Bi_6Cl_7: $[(Bi_9{}^{5+})_2(BiCl_5{}^{2-})_4(Bi_2Cl_8{}^{2-})]$,**[60]** a compound built from Zintl cations and units known from complex salts like $KBiCl_4$. The $Bi_9{}^{5+}$ polycation is a tricapped trigonal prism, and corresponds to a closo system in Wade's scheme of counting valence electrons in clusters, whereas the other complex ions do not show close Bi–Bi contacts.**[61]**

4.6 Group 16 Metal Halides

The prevalent solid-state examples contain tellurium and polonium (*see* ***Tellurium: Inorganic Chemistry***; ***Polonium: Inorganic Chemistry***). The lower halides of Te are polymeric. A recent review covering the chalcogen halides, which includes aspects of their solid-state chemistry, provides an excellent overview of these materials.**[62]**

5 TRANSITION METAL HALIDES

Few classes of inorganic solids can surpass the diverse chemical and physical properties of the transition metal halides.**[63–65]** Through countless studies in the literature, each transition metal provides a fascinating individual collection of structures and properties, although, as chemists, we are always trying to ascertain periodic trends and relationships from one metal to the next. Much of the current research efforts involve stabilizing reduced metal halides in order to probe their potentially interesting electronic and magnetic properties.

From a theoretical perspective, these compounds have provided a basis for testing various crystal field and ligand field theories due to the large electronegativity and size of the halide anions with respect to the transition metal cations.**[66,67]** The increased size factor of the second and third row metals provides additional forces that compete with the omnipresent attractive cation–anion and repulsive anion–anion interactions, and present special challenges for an understanding of their structures. Chemical bonding in these systems can also be characterized from magnetic susceptibility measurements due to the open shell configurations of these metals, in contrast to the main group elements.

Most of the commonly observed compositions are listed in Table 3. As mentioned above (see Section 3) fluorides, in general, occur for the higher oxidation states, chlorides through iodides for the lower ones. However, the relative stability of higher oxidation states increases down a particular group, and thus we find WF_6, WCl_6, and WBr_6, MoF_6 and $MoCl_6$, and just CrF_6, which forms only above 200 atm at temperatures of 400 °C. For the largest part, beyond group 3, the transition metals are coordinated by an octahedron of halide ions. Exceptions occur usually when metal–metal bonding takes place, as in $ReCl_3$ or Nb_6F_{15}, or when the metal's electronic configuration prefers another geometry, as in d^8 square-planar $PdCl_2$.

Synthetic approaches are numerous, but many of the halides can be obtained by allowing the halogen to react directly with the pure metal under mild conditions. In general, fluorides require special handling and procedures, and we refer the reader to other articles in this volume (in particular ***Fluorides: Solid-state Chemistry***). Heavier halides can be obtained from the lighter halides by exchange reactions with the heavier anhydrous hydrogen halide, for example, TaI_6 results from treating $TaCl_6$with dry HI.**[68–70]** A very successful preparative route to numerous transition metal halides, in particular reduced metal halides, involves chemical transport.**[71]** In order to control reactions to obtain desired products, an enormous amount of thermodynamic data for these heterogeneous systems are required.

In the set of main group metal halides, we could readily systematize the solid-state examples according to group number. Since, in general, several oxidation states are observable for each transition metal, it is more convenient to discuss these halides according to their empirical formulas,

Table 3 Binary halides of the transition metals[a]

Group	Fluorides	Chlorides	Bromides	Iodides
4	TiF_4, TiF_3, TiF_2	$TiCl_4$, $TiCl_3$, $TiCl_2$, Ti_7Cl_{16}	$TiBr_4$, $TiBr_3$, $TiBr_2$, Ti_7Br_{16}	TiI_4, TiI_3, TiI_2
	ZrF_4, ZrF_3, ZrF_2	$ZrCl_4$, $ZrCl_3$, $ZrCl_2$, ZrCl	$ZrBr_4$, $ZrBr_3$, $ZrBr_2$, ZrBr	ZrI_4, ZrI_3, ZrI_2ZrI
	HfF_4	$HfCl_4$, $HfCl_3$, $HfCl_2$, HfCl	$HfBr_4$, $HfBr_3$, $HfBr_2$, HfBr	HfI_4, HfI_3
5	VF_5, VF_4, VF_3, VF_2	VCl_4, VCl_3, VCl_2	VBr_4, VBr_3, VBr_2	VI_3, VI_2
	NbF_5, NbF_4, NbF_3^*, Nb_6F_{15}	$NbCl_5$, $NbCl_4$, Nb_6Cl_{14}, Nb_3Cl_8	$NbBr_5$, $NbBr_4$, Nb_6Br_{14}, Nb_3Br_8	NbI_5, NbI_4, Nb_6I_8
	TaF_5, TaF_3^*	$TaCl_5$, $TaCl_4$, Ta_6Cl_{15}	$TaBr_5$, Ta_6Br_{15}	TaI_5, TaI_4, Ta_6I_{14}
6	CrF_5, CrF_4, CrF_3, CrF_2,	$CrCl_4$, $CrCl_3$, $CrCl_2$	$CrBr_3$, $CrBr_2$	CrI_3, CrI_2
	MoF_6, MoF_5, MoF_4, MoF_3	$MoCl_6$, $MoCl_5$, $MoCl_4$, $MoCl_3$, $MoCl_2$	$MoBr_5$, $MoBr_4$, $MoBr_3$, $MoBr_2$	MoI_4, MoI_3, MoI_2
	WF_6, WF_5, WF_4, WF_3	WCl_6, WCl_5, WCl_4, WCl_3, WCl_2	WBr_6, WBr_5, WBr_4, WBr_3, WBr_2	WI_4, WI_3, WI_2
7	MnF_4, MnF_3, MnF_2	$MnCl_3$, $MnCl_2$	$MnBr_2$	MnI_2
	TcF_6, TcF_5	$TcCl_5$, $TcCl_4$	$TcBr_4$	
	ReF_7, ReF_6, ReF_5, ReF_4	$ReCl_4$, $ReCl_2$, Re_2Cl_6, Re_6Cl_{16}	$ReBr_4$, $ReBr_2$	ReI_4, ReI_2,
8	FeF_2, FeF_3	$FeCl_2$, $FeCl_3$	$FeBr_2$, $FeBr_3$	FeI_2, FeI_3
	RuF_6, RuF_5, RuF_4, RuF_3	$RuCl_4$, $RuCl_3$	$RuBr_3$	RuI_3
	OsF_7, OsF_5, OsF_4	$OsCl_5$, $OsCl_4$, $OsCl_3$	$OsBr_4$, $OsBr_3$	OsI_3
9	CoF_2, CoF_3	$CoCl_2$	$CoBr_2$	CoI_2
	RhF_6, RhF_5, RhF_4, RhF_3	$RhCl_3$	$RhBr_3$	RhI_3
	IrF_6, IrF_5, IrF_4, IrF_3	$IrCl_3$	$IrBr_3$	IrI_3
10	NiF_2, NiF_3	$NiCl_2$	$NiBr_2$	NiI_2
	PdF_4, PdF_3, PdF_2	$PdCl_4$, $PdCl_3$, $PdCl_2$	$PdBr_4$, $PdBr_3$, $PdBr_2$	PdI_4, PdI_3, PdI_2
	PtF_6, PtF_5, PtF_4	$PtCl_4$, $PtCl_2$	$PtBr_4$, $PtBr_3$, $PtBr_2$	PtI_4, PtI_3, PtI_2
11	CuF_2	CuCl, $CuCl_2$	CuBr, $CuBr_2$	CuI
	AgF, AgF_2, AgF_3, Ag_3F_8, Ag_2F	AgCl	AgBr	AgI
	AuF_3, AuF_5	AuCl, $AuCl_3$	AuBr, $AuBr_3$	AuI
12	ZnF_2	$ZnCl_2$	$ZnBr_2$	ZnI_2
	CdF_2	$CdCl_2$	$CdBr_2$	CdI_2
	HgF_2, Hg_2F_2	$HgCl_2$, Hg_2Cl_2	$HgBr_2$, Hg_2Br_2	HgI_2, Hg_2I_2

[a] Structures are discussed in the text.

which also allows us to correlate structure (topology) and properties with d electron concentration at the metal atoms.

5.1 MX_6 and Higher Halides

The MX_6 series represents a set of molecular solids and liquids at ambient conditions, owing to the octahedral coordination of the transition metals. Many of the other second and third row metal hexafluorides show the same phenomenon.**[72]** $MoCl_6$ and WCl_6 have Cl^- ions in hcp with 1/6 of the octahedral holes occupied. The fluorides are volatile solids with low melting and boiling points, while WCl_6 and WBr_6 melt around 570 K.

ReF_7 is the only thermally stable binary heptahalide, and crystallographic studies indicate a high-temperature, body-centered cubic (bcc) lattice which transforms to a lattice with lower symmetry at lower temperatures.**[72]** Spectroscopic evidence suggests pentagonal bipyramidal geometry. Only within ternary systems, hepta-anions are more often found, for example, in K_3ZrF_7 or K_2TaF_7.**[3]** The $[TaF_7]^{2-}$ ion is a monocapped trigonal prism rather than a pentagonal bipyramid. There are speculations about the existence of OsF_8, however, there is simply not enough space for eight ligands of the size of F^- and with Os^{VIII} only the oxyfluorides OsO_2F_4 and OsO_3F_2 could so far be prepared.**[73]**

5.2 MX_5 Halides

The relatively high +5 oxidation state for these compounds parallels the frequency of fluorides relative to the heavier halides. In contrast to the structure of BiF_5 (see Figure 10), all of the reported transition metal pentafluorides occur as tetramers composed of four MF_6 units sharing two cis ligands (see Figure 11). The ring formation via common corners (any ring size) is another way of realizing the composition $MX_4X_{2/2}$. An interesting trend is observed for the M–F–M bridging angle as the metal d count changes: for d° and d^1 systems, this angle is 180°; for d^2, ca. 150°; and for

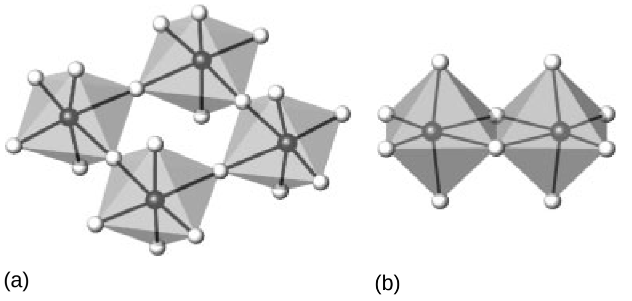

Figure 11 Connection of MX_6 octahedra in MX_5 type halides of the transition metals (a) for X = F and (b) for X = Cl, Br, I

d^3–d^5; nearly 132°, which equals the M–X–M angle when metal atoms occupy adjacent octahedral holes in a hcp anion array.[3] This bending can be assigned to the occupation of M–F π^* orbitals,[66] but trends in bond distances are not that conclusive.[74]

The heavier halides form molecular solids by sharing edges of the MX_6 octahedra, and thus dimers (Figure 11b). The corresponding angles at the bridging halides are close to 90°, indicating the greater polarizability of these halides relative to F^-. Although electron counts vary from d^0 to d^6, their structures and properties negate strong metal–metal interactions. Each metal atom shifts away from the center of the octahedron and increases the metal–metal separation and, as expected, bridging ligands lie farther from the metals than the terminal ligands. An exception among the heavier halides is NbI_5 which crystallizes with a close packing arrangement of the anions and a polymeric structure based upon NbI_6 octahedra sharing cis vertices to form a complex skew chain $[NbI_4I_{2/2}]$ is found.[31]

The magnetic susceptibility measurements of halides containing non-d^0 metal atoms are a useful indicator for the presence or absence of metal–metal interactions. They show Curie-Weiss behavior and effective magnetic moments are in reasonable agreement with spin-only values: $MoCl_5$ ($1.67\mu_{eff}$), WCl_5 ($1.00\mu_{eff}$), $ReCl_5$ ($2.21\mu_{eff}$), $OsCl_5$ ($3.39\mu_{eff}$). Only when spin-orbit coupling is considered, these values are somewhat high. $OsCl_5$, for example, also has a Weiss constant that suggests antiferromagnetic coupling between Os atoms,[75] but strong metal–metal bonding can be excluded. This is also valid for the red-colored AuF_5, whose diamagnetism results from the low-spin ground state.

5.3 MX_4 Halides

At this stoichiometry, the numbers of two- and one-coordinate halides are equal, and their solid-state structures begin to exhibit 1D, 2D, and 3D characteristics. Furthermore, as the oxidation states now become lower, effects due to metal–metal bonding become observable, especially for the 4d and 5d transition metals. Moreover correlations in M–X–M angles continue to differentiate fluorides from the rest of the halides.

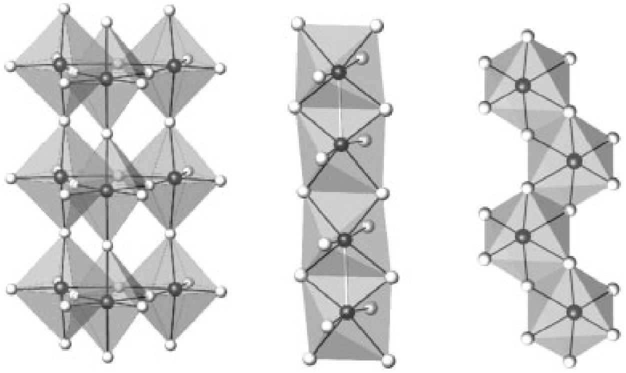

Figure 12 (a) Chains of MX_6 octahedra in MX_4 type halides of the transition metals, for example, (a) TiF_4, (b) NbI_4, and (c) $TcCl_4$

The tetrafluorides all have six-coordinate metals and adopt either 1D, 2D, or 3D structures, all of which involve sharing four vertices among adjacent metal centers. TiF_4[76] adopts a unique 1D structure with triple chains of TiF_6 corner-sharing octahedra with two shared ligands in cis position (see Figure 12a). In VF_4,[77] NbF_4,[78] and RuF_4,[74] the unshared ligands are trans to each other. NbF_4 is isotypic to SnF_4 (2D) with linear Nb–F–Nb bridging angles (see Figure 8), whereas VF_4 and RuF_4 crystallize as distorted variants of this structure type with V–F–V[79] and Ru–F–Ru angles[75] of approximately 151° and 135°, respectively. The structures of MoF_4 and WF_4 have not yet been elucidated, to our knowledge. In α-MnF_4[79] and the remaining systems MF_4 (M = Os, Rh, Ir, Pd Pt)[80–83] cis vertices remain unshared. Their structures are 3D and closely related to rutile, from which alternate metal atoms along each of the edge-sharing octahedral chains are removed. Again, the M–F–M angles approach 132°, in accordance with the occupation of M–F π^* orbitals.

The dimers found in MX_5 systems now develop into chains for the heavier tetrahalides.[3] However, close metal–metal contacts, as well as low values for magnetic susceptibilities, provide the rationale for metal–metal bonding. The tetrahalides Nb (α-forms), Ta, Mo (α-forms), W, Re (α-forms), and $OsCl_4$ adopt trans edge-sharing octahedral chains (Figure 12b).[84] In general, the metal atoms shift to form distinct pairs along the chain, that is, metal–metal distances alternate between short and long. $TcCl_4$, $ZrCl_4$, $OsBr_4$, and PtX_4 form zig-zag metal chains without bond distance alternation (Figure 12c).[85] In general, there is an indefinite number of ways that these types of chains can grow.[86] ZrI_4 and HfI_4 show two of these more complex configurations. Lastly, such chains can also close upon themselves in the way that benzene is related to polyacetylene. $MoCl_4$ shows a hexameric ring,[87] as well as a random arrangement of metal vacancies in the layered $MoCl_4$ structure.[88] β-$ReCl_4$ with d^3 Re^{4+} adopts another modification involving two face-sharing

$ReCl_6$ octahedra which form a quasi-infinite chain by sharing one vertex at each metal center.[3] Such dimeric units are observed in the complex salts $A_3M_2X_9$ with trivalent atoms ($M = Tl$, V, Nb, Cr, Mo, W).[4]

5.4 MX_3 Halides

The transition metal trihalides have mostly structures based upon close packings of halide atoms with the metal ions in octahedral holes. Exceptions include those of W and Re with the metal atoms in a five-coordinate square pyramidal environment,[89] and the series AuX_3 with square-planar coordinated Au atoms.[31] The stoichiometric ratio in the transition metal trihalides provides structures that can range from 1D to 3D arrangements. The most common general structure types are: VF_3, BiI_3, $AlCl_3$, and TiI_3. The differences occur in either the three-dimensional anion packing modes or the distribution of occupied metal sites.

All known trifluorides are related to the VF_3 structure, which represents an intermediate geometry between the cubic ReO_3-type and the rhombohedral RhF_3-type.[90] RhF_3 contains a hcp arrangement of fluoride ions. These materials consist of an array of rigid octahedra that have been rotated around their trigonal axes.[91,92] The MF_6 octahedral units remain virtually regular throughout the series, while the M–F–M angle varies from 180° in NbF_3 to 132° in RhF_3. Figure 13 illustrates the geometrical relationships between the three varieties of MF_3 structures, which is reminiscent of cubic perovskites $A[BO_{6/2}]$ and distorted variants, such as $GdFeO_3$, where the size of the A cation determines the skewing of the octahedral framework. The structures of PdF_3 and PtF_3 contain two differently sized $[MF_6]$ octahedra comparable to what has been found for the high-temperature modification $SnCl_3$ (see above) indicating mixed valency according to $M^{2+}M^{4+}F_6$, in which both M atoms remain octahedrally surrounded by F atoms.[90] For the M^{2+}, this is quite unusual as Pd^{2+} and Pt^{2+} with d^8 configuration normally prefer a square-planar coordination.

The trifluorides occur as three-dimensional networks, whereas the heavier trihalides crystallize as either layer or chain structures.[31] The commonly observed layer structures are BiI_3 and $AlCl_3$, which correspond to ordered defect derivatives of the CdI_2 and $CdCl_2$ types, respectively. Both consist of $^2_\infty[(\square X_{6/3})(MX_{6/3})_2]$ sheets ($\approx M_2X_6$; see Figure 6), in which the metal atoms form a honeycomb network. The complete structures of BiI_3 and $AlCl_3$ form by stacking this two-dimensional motif in two different ways: for rhombohedral BiI_3, the halide ions are hcp and, moreover, the vacancies in the metal layers spiral trigonally along the stacking direction; in the monoclinic $AlCl_3$ structure, the anions are ccp and the metal vacancies are ordered along the monoclinic a axis. In each case, the planes of possible metal atom sites alternate with 66% and 0% occupancy along the stacking direction. The structure of TiI_3, unlike $AlCl_3{}^-$, and BiI_3 is quasi one-dimensional.[93,94] The anions in TiI_3 form a hcp arrangement, but the metal atoms occupy 1/3 of each plane to form quasi-infinite one-dimensional chains, $[MX_{6/2}]$, of face-sharing MX_6 octahedra (see below).

Besides vertical trends exhibited by the transition metal trihalides, they also vary systematically with the number of d electrons. We begin our summary with the trifluorides.[90] The d° compounds generally do not adopt structures based upon octahedral coordination of the metal. No d^1 (except TiF_3) or d^4 systems have been noted. For $d^2$and d^3 compounds, older literature reports the cubic ReO_3-type with a M-F-M angle of 180°; these were in fact oxyfluorides, $MO_{3x}F_{3-3x}$.[95] The highest purity of NbF_3 has been obtained by high-pressure synthesis (High-Pressure Synthesis of Solids), and retains the cubic structure.[96] Careful neutron diffraction investigation on MoF_3 shows the VF_3-type and antiferromagnetic ordering of three unpaired spins per Mo atom.[97] In the d^4 fluoride MnF_3[98] with ccp of the anions and in the d^5 and d^6 systems with hcp-based RhF_3 structure type the M–F–M angle bends significantly away from linearity. We have already referred to the interesting case of PdF_3, which, in addition, shows ferromagnetic ordering with T_C of 10 K.[99]

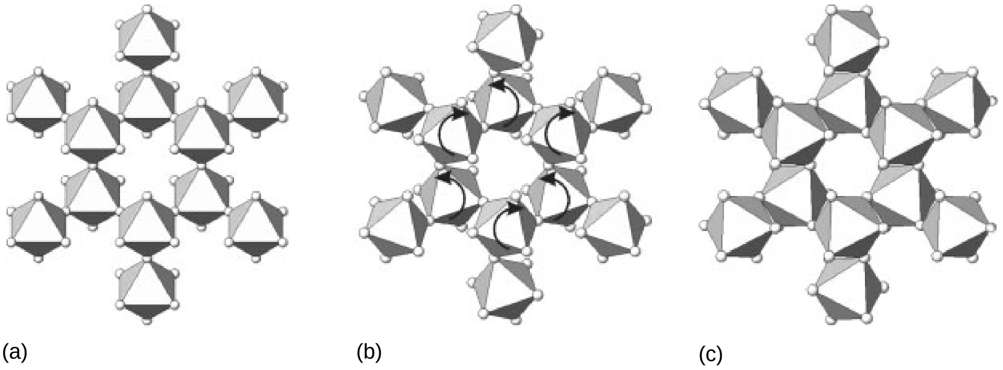

Figure 13 Projections of the structures of (a) NbF_3, (b) RhF_3, and (c) VF_3. The arrows in (b) indicate the skewing of the framework of MF_6 octahedra for the hypothetical transition from (a) via (b) to (c)

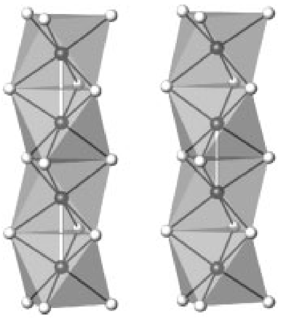

Figure 14 Chains of face-sharing octahedra in TiI_3. Alternating metal–metal bonding within chains is indicated

The heavier trihalides show their own intrinsic structural systematics. For the group 4(d^1) metals, distorted TiI_3 structures are found.**100–102** Most compounds assigned to this structure class actually crystallize in an orthorhombic space group in which the metal atoms move away from their regular octahedral sites to form one-dimensional chains with alternating short and long metal–metal distances (Figure 14). In addition, the anions shift to form two different isosceles triangles bridging pairs of metal atoms. In group 5 (d^2), NbI_3 is the only reported compound. A recent X-ray diffraction study indicates that it also adopts the distorted TiI_3 structure with an extremely short Nb–Nb bond distance. All of the other trihalides of this transition metal group, that is, Nb and Ta, are thermodynamically not stable, but rather homogeneous mixtures of M_3X_8 and MX_4.**103,104**

The group 6 trihalides form three different kinds of structures. α-$MoCl_3$ crystallizes in a distorted $AlCl_3$ structure with Mo–Mo dimers.**105** β-$MoCl_3$, which also contains Mo–Mo pairs, is related to the BiI_3 phase.**88** Figure 15 illustrates the distortion of the metal arrangement in β-$MoCl_3$ from a regular honeycomb (6^3) net. The heavier halides, $MoBr_3$ and MoI_3, however, crystallize in the distorted TiI_3 structure with pairing of Mo atoms along the c axis.**102,105** WCl_3 and WBr_3 are exceptional cases which also show metal–metal bonding.**106,107** (see Section 5.5). Metal clusters continue into the higher homologues of group 7 (d^4) compounds as well. Although nothing is yet reported for the Tc system, all of the rhenium trihalides ReX_3 contain triangular rhenium clusters, Re_3X_{12} (see Figure 16a), which are connected to three other neighboring clusters through bridging halogen atoms to form a buckled two-dimensional layer.**108–110** In lower transition metal halides with fewer d electrons, such as Nb_3Cl_8 (see Section 4.5), metal–metal bonded triangular M_3 units with a higher coordination by the ligands are found (see Figure 16b).

The group 8 (d^5) metal trihalides in some cases are very similar to the d^1 systems. Distorted face-sharing octahedral chains, ${}^1_\infty[MX_{6/2}]$ have been found for all Ru trihalides.**111,112** In addition, another modification of ruthenium trichloride, α-$RuCl_3$, is believed to belong to the $AlCl_3$ type by an X-ray powder diffraction study. It exhibits ferromagnetic coupling of Ru^{III} atoms within a layer, and antiferromagnetic coupling between layers. A recent structural investigation on α-$RuCl_3$ by means of scanning tunneling microscopy showed distortions of $RuCl_6$ octahedra on the surface of the crystal.**113** The images have been interpreted as a shift in surface chloride positions owing to the formation of Ru–Ru pairs. Although the structural arrangement in the crystalline bulk is still not clear, the distortion found on the surface of the crystal may indicate a similar distortion within the crystal. For the group 9 metals (d^6), we again find the regular $AlCl_3$ structure for all of the trihalides,**114** with numerous examples of stacking disorder. Pd does not form stable trihalides beyond the fluoride, but both $PtCl_3$ and $PtBr_3$ have been reported.**115,116** As in PdF_3, these compounds apparently contain Pt in two different oxidation states: 50% as Pt^{2+} square planar surrounded and 50% as Pt^{4+} in $[PtX_2X_{4/2}]$ cis edge-sharing octahedral chains.

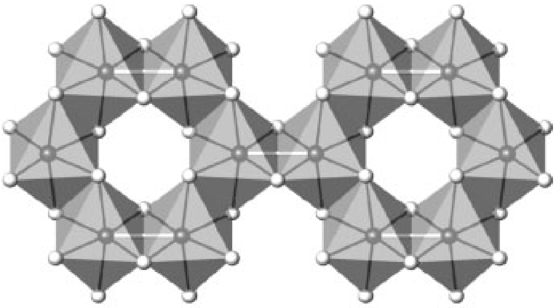

Figure 15 Honeycomb-like (6^3) network of edge-sharing octahedra in β-$MoCl_3$. Alternating metal–metal bonding is indicated

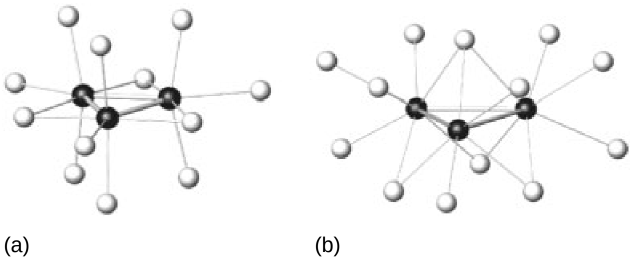

Figure 16 (a) Re_3X_{12} cluster as found in ReX_3 and (b) M_3X_{13} cluster in Nb_3X_8 (X = Cl, Br, I)

Finally trifluorides are found among the group 11 elements. AgF_3 contains highly elongated AgF_6 octahedra which are connected to a 3D framework.**117** It is one of the few metallic fluorides known so far. Au forms a stable molecular trihalides with each of the halides, Au_2X_6, with square-planar coordinated Au atoms.**31**

The structural preference within the series of trifluorides is dominated by the nature of the M–F covalent interaction. As we move to the heavier halides, that is, as the anion polarizability increases, lower dimensional structures become prevalent. For these materials, three major interatomic interactions influence the observed geometries: (1) the ligand field effects of halide ions on the d orbitals of the transition metal; (2) direct (through-space) metal–metal interactions; and (3) the matrix effect of halide ions.[118] Furthermore, the later transition elements tend to form mixed valence compounds, like groups 13 and 14 metals, rather than metal–metal bonded units.

5.5 MX_n Halides ($n < 3.0$)

These types of halides comprise the MX_2 type compounds of the 3d metals, halides of the 4d and 5d metals with strong metal–metal bonding, and the Cu and Zn families. TiF_2 can only be prepared under high pressure and crystallizes in the fluorite-type structure.[119] The other 3d difluorides are isotypic to rutile, except CrF_2 and CuF_2 which show distortions arising from a first-order Jahn-Teller instability of the high-spin d^4 and d^9 configurations in an octahedral field.[3] The chlorides, bromides, and iodides, when they exist, adopt either CdI_2- or $CdCl_2$-type structures. First principle calculations show that interactions of occupied t_{2g} levels of transition metal atoms with the ligand orbitals often play an essential role for the stability of the CdI_2 type over the rutile type.[120]

Other than 3d element dihalides are found with Ru which are thought to occur as intermediates in the reduction of RuX_3 with H_3PO_2. α-PdX_2 show chains of edge-sharing square-planar PdX_4 units, while the β-form contains octahedral clusters, which are cuboctahedrally surrounded by 12 X (see Figure 17(a)).[4] However, metal–metal distances preclude any strong bonding between the metal centers, like in the isostructural β-$PtCl_2$ which is built from Pt_6Cl_{12} molecules. The Pt atoms are slightly shifted outside the Cl_{12} cuboctahedron indicating Pt–Pt repulsive interactions.[121] With silver, there exists only one dihalide, the fluoride AgF_2, which contains highly distorted AgF_6 octahedra and Ag_3F_8 which according to $Ag^{2+}(AgF_4)_2^-$ is a mixed valent Ag(II)Ag(III)fluoride.[122]

Much recent research has centered on the chemistry of reduced 4d and 5d metal halides (Zr, Nb, Mo, Hf, Ta, W, and Re), and has contributed a great deal to our knowledge of metal–metal interactions as well as the relationship between geometrical and electronic structure.[123–127] These phases are generally prepared using synproportionation reactions involving a high oxidation state halide and either the metal or a lower halide, when appropriate,[126] and most of them have noninteger anion/cation ratios (see Table 3).

Transition elements that form triangular metal clusters in reduced halides are Ti, Nb, Mo, W, and Re. In contrast to the clusters in halides ReX_3, in many other cases the M_3 triangles are surrounded by 13 X atoms to form M_3X_{13} clusters (see Figure 16b). These units contain 6–9 valence electrons. The structures of the halides Ti_7X_{16} ($X = Cl$, Br) are built from $TiCl_6$ octahedra and Ti_3Cl_{13} clusters. However, among the 3d elements such halides are exceptions, as metal–metal bonded M_3X_{13} units are more frequently found with the 4d and 5d transition elements. They have first been observed in the Nb_3X_8 ($X = Cl$, Br, I) type compounds, in which the metal–metal bonding within the Nb_3 clusters containing seven valence electrons is indicated by an effective magnetic moment corresponding to one unpaired electron per formula unit.[103]

However, most of the halides with metal–metal bonding are based on one of two types of octahedral metal cluster: (i) M_6X_{12} and (ii) M_6X_8 (Figure 17). In (i), the 12 edges of the cluster are bridged by ligands and the M–X distances are approximately $1/2\cdot\sqrt{2}$ times shorter than the M–M distances, whereas in (ii), the ligands cap the eight faces and the M–X distances are nearly the same as the M–M distances. Therefore, one finds M_6X_{12} clusters preferably among fluorides and chlorides, whereas for iodides only the M_6X_8 cluster is observed. Bromides lie somewhere in between and depending on the kind of transition element both types can be found. However, besides geometrical aspects there are certain valence electron counts for the metal cluster that maximize stability, as could be shown by numerous molecular orbital calculations.[123–125] For the M_6X_8 cluster, 20–24 valence electrons are optimal, whereas for the M_6X_{12} cluster, 14–16 valence electrons are found. These valence electrons occupy orbitals that are concentrated largely on the metal atoms of the cluster. Thus, these counts represent the

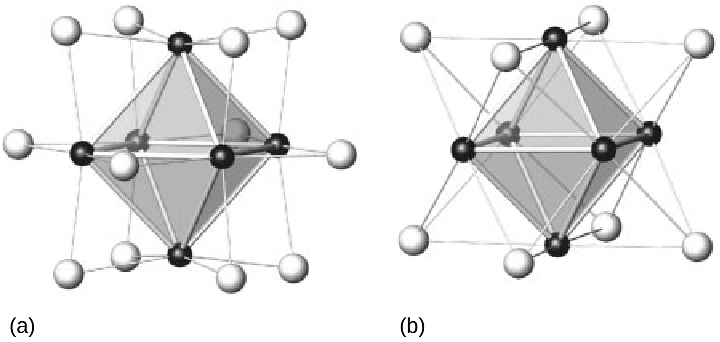
(a) (b)

Figure 17 (a) M_6X_{12} and (b) M_6X_8 cluster number of valence electrons in excess of the number required for each halide ligand to achieve a closed-shell configuration. In addition, McCarley and coworkers have demonstrated that $TaBr_3$ is a metastable phase ($TaBr_{2.80}$) that probably contains $[Ta_6Br_8]$ cluster units.

MoX_2 and WX_2 (X = Cl, Br, I) are all isomorphous.[87] Their structural formulas are $[M_6X^i_8]\ X^a_2X^{a-a}_{4/2}$, using a special notation,[128] where X^i are ligands belonging to either the M_6X_8 or M_6X_{12} cluster (i = innen = inner), and X^a are ligands coordinated radially (axially) to a metal atom (a = ausser = outer). X^{a-a}, therefore, indicates that this ligand is shared between two clusters and adopts ausser positions with respect to both clusters. These axial ligands are important components to the complete structures of these cluster compounds, and are responsible for the diversity of observed arrangements. The $[Mo_6Cl_{12}]^{4+}$ cluster unit has 24 valence electrons in agreement with its diamagnetic behavior and stability. In these dihalides, four axial ligands bridge two clusters to give a 2D system. These clusters can be formally oxidized, as seen in the series W_6Br_{14}, W_6Br_{16}, and W_6Br_{18}, all of which contain M_6X_8 clusters.[11] All of these clusters, however, have formally 22 electrons because some of the axial ligands involve the polybromide ion $Br_4{}^{2-}$. Thus, for example, $W_6Br_{16} = [W_6Br_8]Br_4(Br_4)_{2/2}$. Although a M_6X_8 cluster occurs in Nb_6I_{11},[124] with one less valence electron in the group 5 atoms, M_6X_{12} clusters are more common. Therefore, compounds like Nb_6Cl_{14} and Ta_6Br_{15}, with 16 and 15 valence electrons, respectively, are optimal for the M_6X_{12} system. The observed M_6X_{15} systems have magnetic moments corresponding to one unpaired electron per cluster.

Cluster systems have also been observed with group 4 metals, but they adopt low valence electron concentrations. Upon careful synthetic and crystallographic investigations, Zr dihalides were found to be exceptionally stabilized by interstitial species like H, C, B, and Be, and this has opened a rich chemistry in this field.[129,130] $ZrCl_2$, when synthesized by allowing $ZrCl_4$ and ZrCl to react, leads to MoS_2-type phases, with Zr in trigonal prismatic coordination.[131] Like the d^1 dichalcogenides (and unlike d^2 systems), there are also phases which are nonstoichiometric according to the description $Zr_{1+x}Cl_2$ with excess Zr atoms in the van der Waals gaps. ZrI_2 also forms a distorted variant of the CdI_2 structure with zig-zag chains of Zr atoms within each planar sheet of metals.[31]

The monohalides ZrCl, ZrBr, HfCl, and HfBr (Figure 16) are formed by high-temperature reduction of ZrX_4 with the metal.[126] These are layered compounds constructed of two adjacent close-packed sheets of metal atoms surrounded by similar arrangements of halide ions (see Figure 18). These four-atom slabs then stack differently to give the 3D structures. The corresponding iodides are unknown and probably the iodide ion is too large to allow such a topology. As expected, there is strong metal–metal bonding within the slabs and the monohalides of Zr and Hf show 2D electrical conductivity. The systematic studies of these reduced Zr and Hf halides have stressed the relationships between such layer structures and the M_6X_{12} clusters via cluster condensation.[123–130]

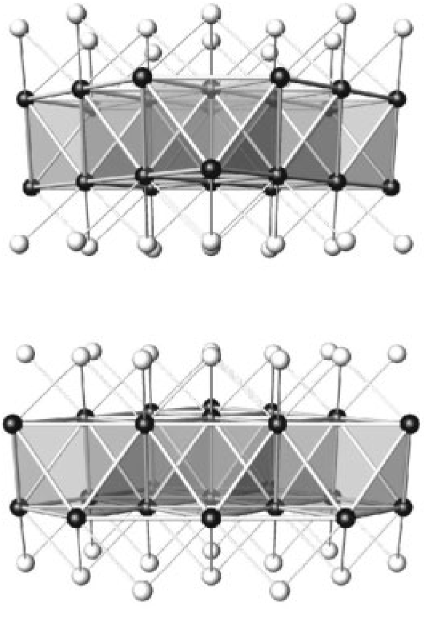

Figure 18 Structure of ZrCl

Moving to the right across the rows of the periodic table, we again find monohalides. All of the group 11 element monohalides, except CuF, CuI_2, and AuF, are known. The monofluorides CuF and AuF are unstable with respect to disproportionation into the metals and CuF_2 and AuF_3 respectively, whereas CuI_2 is unstable because iodide ions reduce Cu^{2+}. The silver monohalides crystallize all, except AgI, in the rocksalt type structure, whereas AuCl, AuBr, and AuI are chain polymers which feature two-coordinate Au. Finally, we should mention the metallic, bronze colored silver subfluoride, Ag_2F, which is formed in the reaction between finely divided Ag powder and AgF in hydrogen fluoride or by electrochemical reduction of AgF. It has an *anti*-CdI_2 structure in which double layers of Ag alternate with layers of F. The compound is rather unstable and decomposes at temperatures above 100 °C into AgF and Ag. Strong metal–metal bonding is found in the mercury monohalides Hg_2X_2 (X = F, Cl, Br, I) which are formed by the reduction of the dihalides with elemental Hg. They contain single bonded Hg–Hg dumbbells ($d^{10}s^1$ configuration) with distances ranging from 2.51 Å (X = F) to 2.69 Å (X = I). With the lighter homologues Zn and Cd only the dihalides could be obtained so far.

6 RARE EARTH HALIDES

Rare earth metal halides have received a great deal of attention during the past 50 years.[132–135] The lanthanide trihalides are colored, magnetic salts, which have provided a stockpile of structural parameters and spectroscopic transitions. These data helped to develop both crystal field theory and the angular overlap method. In recent years, their optical and magnetic characteristics due to the $4f^n$ configurations of these ions have contributed to widespread applications (*see* ***Scandium, Yttrium & the Lanthanides: Inorganic & Coordination Chemistry***). Rare earth halide salts have compositions MX_3 and MX_2, besides a few more reduced ones, some with intermediate compositions and very few with rare earth elements in oxidation states higher than +3.

The trihalides MX_3 are well known and well characterized for all rare earth elements with the exception of EuI_3. Most of them are colored as a result of $f \rightarrow f$ and/or $f \rightarrow d$ transitions. The lanthanide contraction as well as anion–anion repulsions contribute to the observed trends in the structures of the trihalides at ambient conditions (see Figure 19). The trifluorides with the larger rare earth ions adopt the tysonite type structure (LaF_3) with 11-fold coordination of the metal ion, the highest one known in a binary ionic solid (see Figure 20). The coordination polyhedra can be described as a trigonal prism squeezed along the threefold axis and capped on the two triangular and the three rectangular faces.

For the smaller rare earth ions the YF_3 structure type with nine-coordinated metal atoms occurs. This first coordination sphere is similar to the $PbCl_9$ polyhedra in $PbCl_2$, however, its connection leads to a much more complicated arrangement. For ScF_3 with the smallest rare earth element, the ReO_3 type structure with octahedral metal coordination is found. Four major structure types occur for the heavier halides: UCl_3, with nine-coordinated metals (tricapped trigonal prisms as in the $PbCl_2$ and BaI_2–II type structures, however, less condensed; see Figure 21), $PuBr_3$, with 8 + 1 coordinate metals, $AlCl_3$ (YCl_3) with six-coordinate metal atoms (defect rocksalt) and BiI_3 ($FeCl_3$), also with six-coordinate metal atoms.

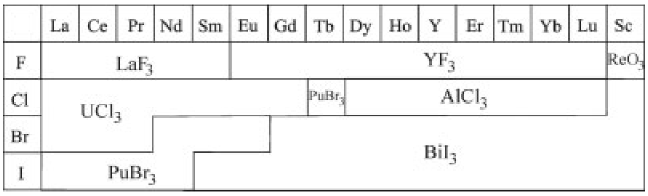

	La	Ce	Pr	Nd	Sm	Eu	Gd	Tb	Dy	Ho	Y	Er	Tm	Yb	Lu	Sc
F	LaF_3					YF_3										ReO_3
Cl	UCl_3							$PuBr_3$	$AlCl_3$							BiI_3
Br	UCl_3			$PuBr_3$			BiI_3									
I	$PuBr_3$				BiI_3											

Figure 19 Structures of the rare earth trihalides at ambient conditions

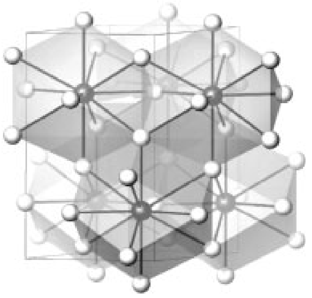

Figure 20 Structure of LaF_3

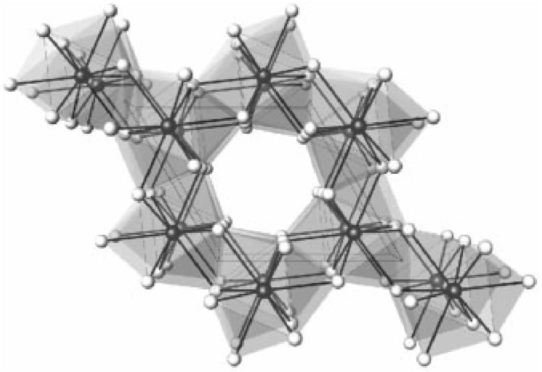

Figure 21 Structure of UCl_3

Rare earth dihalides REX_2 are all known for RE = Sm, Eu, Yb, with RE = La, Ce, Pr, Nd, Gd, Tm, and Sc only chlorides, bromides, or just the iodides have been obtained, whereas it seems that with Ho, Er, Lu, and Y, the dihalides do not to exist. Most of them can be synthesized by the reduction of the trihalides with the corresponding metals in Ta ampoules or other preparative routes. However, care should be taken as hydrogen is easily incorporated and indeed some of the dihalides reported in literature are in fact halide hydrides.**[136]** The binary dihalides are either saltlike compounds according to $RE^{2+}(X^-)_2$ or metallic with one delocalized electron per formula unit according to $RE^{3+}(X^-)_2{\cdot}(e^-)$. Their structures follow mainly the crystal chemical principles outlined for the alkaline earth dihalides**[3]** and reflect effects of size relations between cations and anions and covalent interactions. The ionic difluorides SmF_2, EuF_2, and YbF_2 crystallize in the fluorite structure. Their stability with respect to disproportionation into the trivalent oxidation state and metal can be attributed to the stabilities of the f^6 configuration (thermal excitations of low lying states),**[137]** the half-filled f^7 shell, and the filled f^{14} shell. Chlorides and bromides crystallize in the $PbCl_2$, MoS_2, $SrBr_2$, and iodides mainly in the $MoSi_2$, $CdCl_2$, and CdI_2 type structures.**[135]** NdI_2 undergoes a pressure induced phase transformation from the $SrBr_2$ type to the $MoSi_2$ type which is accompanied by an insulator → metal transition ($Nd^{2+} \rightarrow Nd^{3+}{\cdot}(e^-)$). Examples, where owing to the nonclosed-shell configurations of the rare earth atoms unusual properties are found, are numerous. Already in 1961 the use of rare earth lasers began with Sm^{2+} in CaF_2,**[138]** shortly after the ruby laser was discovered. SmI_2, a dark blue salt with remarkably good solubility in tetrahydrofuran (THF), is widely used as reducing agent in organic chemistry.**[139]** Structures based on the MoS_2 phase are particularly susceptors for the incorporation of hydrogen, as in CeI_2 109 or LaI_2.**[140]** Magnetic ordering has been found for GdI_2**[141]** below 313 K which is accompanied by a large change of the electrical resistivity, that is, GdI_2 shows a giant magneto resistance effect near room temperature.[142]

The chemistry of phases with intermediate compositions REX_n ($2.0 < n < 3.0$), which are complex mixed valent RE(II)/RE(III) halides, reminds on the AX_2/REX_3 systems (A = Ca, Sr, Ba). In fluorides REF_n ($n \approx 2.0-2.2$) divalent ions and trivalent ions occupy the sites within a fluorite-type variant, in which, for charge compensation, interstitiell halides are incorporated into the primitive anion sublattice and solid solutions REX_2/REX_3 are observed. For higher n, the anions form clusters and line phases are formed which crystallize as so-called anion ordered excess fluorite-type variants or in other complicated structure types.

Highly reduced binary rare earth halides (more than one electron per metal atom) are relatively rare.[143] Similar to the early transition metal systems, their structures are derived from M_6X_8 or M_6X_{12} clusters, which can be either isolated in a halide matrix, or condensed to form metal frameworks with 1D, 2D, and 3D characteristics. Since these clusters are even more electron deficient than the corresponding Zr systems, interstitial species, which include H, small main group atoms and fragments (C_2^{n-}), and even transition metals,[130] are often critical for their formation.[123–125] Therefore, only few binary halides are found which belong to this class of compounds, such as the sesquihalides RE_2X_3 for RE = Y, Gd, Tb and X = Cl, Br. They are isostructural and contain chains of trans vertex-sharing octahedral clusters (see Figure 22). Using simple chemical ideas to predict properties, the metal networks, coupled with the formal oxidation state of +1.5, would suggest metallic behavior for the RE_2X_3 type compounds. However, Gd_2Cl_3 and Gd_2Br_3 are semiconductors. Determinations of the band structures for these materials agree with experiments and predict a band gap. A neutron diffraction study for Tb_2Cl_3 shows that there is strong antiferromagnetic ordering between the basal Tb atoms which is accompanied by a high degree of frustration of the apical Tb atoms.[144] Further examples of highly reduced rare earth halides are Sc_7Cl_{12} and RE_7I_{12} (RE = La, Pr, Tb) which contain discrete M_6X_{12} clusters. Characteristic building units in Sc_5Cl_8 are single chains of edge-sharing metal octahedra along with parallel chains of edge-sharing $ScCl_6$ octahedra and in Sc_7Cl_{10} double chains of edge-sharing metal octahedra. There is also a recent report on a most metal-rich rare earth halide, LaI;[145] however, this compound could be synthesized only in the presence of other metals (Cr, Mn) so that its existence remains at least doubtful.

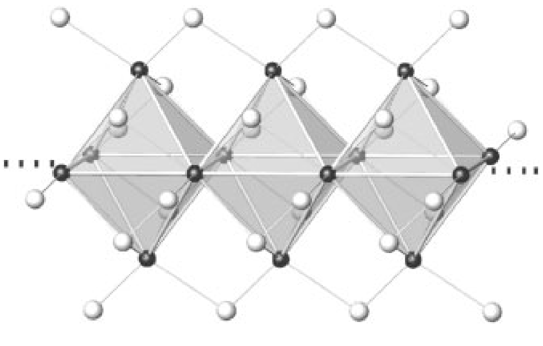

Figure 22 Structure of a condensed cluster chain in Gd_2Cl_3

Higher oxidation states of the rare earth element halides are only found among the fluorides.[146] Three binary examples are known, CeF_4,[147] PrF_4,[148] and TbF_4,[149] which all crystallize in the ZrF_4 type structure. They decompose thermally into fluorine and the corresponding trifluorides. All attempts to prepare other rare earth tetrafluorides, for example, NdF_4 and DyF_4, have proved unsuccessful and only the deep-orange complexes, Cs_3NdF_7 and Cs_3DyF_7 could so far be prepared.

7 SUMMARY

Binary metal halides are crystalline solids that demonstrate an enormous richness of structural topologies as well as compositions.

8 RELATED ARTICLES

Chlorine, Bromine, Iodine, & Astatine: Inorganic Chemistry; Fluorides: Solid-state Chemistry; Fluorine: Inorganic Chemistry.

9 REFERENCES

1. Landolt-Börnstein, ‘Group III/7a, Crystal Structure Data of Inorganic Compounds, Key Elements F, Cl, Br, I, Halides and Complex Halides’, eds. K.-H. Hellwege and A. M. Hellwege, Springer-Verlag, Berlin, 1973.
2. V. I. Posypaiko, E. A. Alekseeva, and H. B. Bell, ‘Phase Equilibria in Binary Halides’, IFI/Plenum Press, New York, 1987.
3. A. F. Wells, ‘Structural Inorganic Chemistry’, 5th edn., Oxford University Press, Oxford, 1984.
4. N. N. Greenwood and A. Earnshaw, ‘Chemistry of the Elements’, 2nd edn., Pergamon Press, Oxford, 1998.
5. D. A. Johnson, ‘Some Thermodynamic Aspects of Inorganic Chemistry’, 2nd edn., Cambridge University Press, Cambridge, 1982.
6. M. P. Tosi, *Solid State Phys.*, 1964, **16**, 1.
7. T. C. Waddington, *Adv. Inorg. Chem. Radiochem.*, 1959, **1**, 157.
8. A. F. Kapustinskii, *Q. Rev. Chem. Soc.*, 1956, **20**, 203.

9. H. F. Franzen, ‘Physical Chemistry of Inorganic Crystalline Solids’, Springer-Verlag, Berlin, 1986.
10. R. Hoppe and J. Köhler, *Z. Kristallogr.*, 1988, **183**, 77.
11. F. A. Cotton and G. Wilkinson, ‘Advanced Inorganic Chemistry’, 5th edn., Wiley, New York, 1988.
12. A. F. Trotman-Dickinson, ‘Comprehensive Inorganic Chemistry’, Pergamon Press, Oxford, 1973, Vol. 1 and 2.
13. H.-C. Gaebell and G. Meyer., *Z. Anorg. Allg. Chem.*, 1984, **513**, 15.
14. H. Witte and E. Wölfel, *Rev. Mod. Phys.*, 1958, **30**, 51.
15. D. D. DesMarteau, T. Grelbig, S.-H. Hwang, and K. Seppelt, *Angew. Chem.*, 1990, **102**, 1519.
16. T. Drews, R. Marx, and K. Seppelt, *Chem. Eur. J.*, 1996, **2**, 1303.
17. K. Doll and H. Stoll, *Phys. Rev. B*, 1997, **56**, 10121.
18. E. Spundflasche, H. Fink, and H. J. Seifert, *Z. Anorg. Allg. Chem.*, 1995, **621**, 1723.
19. R. E. Rundle and P. H. Lewis, *J. Chem. Phys.*, 1952, **20**, 132.
20. N. A. Bell, *Adv. Inorg. Chem. Radiochem.*, 1972, **14**, 255.
21. W. Döll and W. Klemm, *Z. Anorg. Allg. Chem.*, 1939, **241**, 239.
22. E. T. Rietschel and H. Bärnighausen, *Z. Anorg. Allg. Chem.*, 1969, **368**, 62.
23. G. Liu and H. Eick, *J. Less-Common Met.*, 1989, **156**, 237.
24. H. P. Beck, *Z. Anorg. Allg. Chem.*, 1979, **459**, 72.
25. B. G. Hyde, M. o’Keeffe, W. M. Lyttle, and N. E. Brese, *Acta Chem. Scand.*, 1992, **46**, 216.
26. H. P. Beck, *J. Solid State Chem.*, 1983, **47**, 328.
27. G. Liu and H. Eick, *J. Solid State Chem.*, 1991, **95**, 99.
28. R. W. K. Wyckoff, ‘CrystaI Structures’, 2nd edn., Wiley, New York, 1960, Vol. 1, p. 155.
29. R. W. K. Wyckoff, ‘Crystal Structures’, 2nd edn., Wiley, New York, 1960, Vol. 1, p. 294.
30. A. Le Bail, J. L. Fourquet, and U. Bentrup, *J. Solid State Chem.*, 1992, **100**, 151.
31. F. Hulliger, ‘Structural Chemistry of Layer-Type Phases’, Reidel, 1976.
32. C. Hebecker and R. Hoppe, *Naturwissenschaften*, 1966, **53**, 104.
33. C. P. J. M. Van der Vorst and W. J. A. Maaskant, *J. Solid State*, 1980, **34**, 301.
34. C. W. F. T. Pistorius and J. B. Clark, *Phys. Rev. C*, 1968, **173**, 692.
35. B. G. Hyde and S. Andersson, ‘Inorganic Crystal Structures’, Wiley, New York, 1989.
36. W. Frank, W. Hönle, and A. Simon, *Z. Naturforsch., Teil B*, 1990, **15B**, 1.
37. G. Gerlach, W. Hönle, and A. Simon, *Z. Anorg. Allg. Chem.*, 1982, **486**, 7.
38. T. Staffel and G. Meyer, *Z. Anorg. Allg. Chem.*, 1988, **563**, 27.
39. R. E. Marsh and G. Meyer, *Z. Anorg. Allg. Chem.*, 1990, **582**, 128.
40. M. Ruck and H. Bärnighausen, *Z. Anorg. Allg. Chem.*, 1999, **625**, 577.
41. R. J. Gillespie, ‘Molecular Geometry’, Van Nostrand-Reinhold, London, 1972.
42. H. Reuter and R. Pawlak, *Z. Anorg. Allg. Chem.*, 2000, **626**, 925.
43. J. Köhler, A. Simon, and R. Hoppe, *J. Less-Common Met.*, 1988, **137**, 333.
44. R. A. Howie, W. Moser, and I. C. Trevina, *Acta Crystallogr. B*, 1972, **28**, 2965.
45. I. J. D. Donaldson, J. Silver, S. Hdjiminolis, and S. D. Ross, *J. Chem. Soc., Dalton Trans.*, 1975, 1500.
46. J. Trotter, M. Akhtar, and N. Bartlett, *J. Chem. Soc. A*, 1966, 30.
47. G. Denes, *J. Solid State Chem.*, 1989, **78**, 52.
48. J. C. Taylor and P. W. Wilson, *J. Am. Chem. Soc.*, 1973, **95**, 1834.
49. J. Köhler and J.-H. Chang, *Z. Anorg. Allg. Chem.*, 1997, **623**, 596.
50. M. F. A. Dove, R. King, and T. J. King, *J. Chem. Soc. Chem. Commun.*, 1973, 944.
51. M. Ruchaud, C. Mirambert, L. Fournes, J. Grannec, and J. L. Soubeyroux, *Z. Anorg. Allg. Chem.*, 1990, **590**, 173.
52. Y. Ito, K. Koto, S. Yoshikado, T. Ohachi, F. Kanamaru, and T. Mukoyama, *J. Solid State Chem.*, 1991, **95**, 94.
53. P. Charpin, H. Marquet-Ellis, N. Nghi, and P. Plurien, *C. R. Hebd. Sceances Acad. Sci., Ser. C*, 1972, **275**, 1503.
54. S. M. Ohlberg, *J. Am. Chem. Soc.*, 1959, **81**, 811.
55. J. Köhler, A. Simon, and R. Hoppe, *Z. Anorg. Allg. Chem.*, 1989, **575**, 55.
56. A. J. Edwards and P. J. Taylor, *J. Chem. Soc. D, Chem. Commun.*, 1971, 1376.
57. C. Hebecker, *Z. Anorg. Allg. Chem.*, 1971, **384**, 111.
58. H. v. Benda and A. Simon, *Acta Crystallogr., Sect. A*, 1978, **34**, 172.
59. H. G. v. Schnering, H. v. Benda, and C. Kalveram, *Z. Anorg. Allg. Chem.*, 1978, **438**, 37.
60. A. Hershaft and J. D. Corbett, *Inorg. Chem.*, 1963, **2**, 979.
61. C. Wade, *Adv. Inorg. Chem. Radiochem.*, 1976, **18**, 1.
62. B. Krebs and F.-P. Ahlers, *Adv. Inorg. Chem. Radiochem.*, 1990, **35**, 235.
63. R. Colton and J. H. Canterford, ‘Halides of the First Row Transition Metals’, Wiley, New York, 1968.
64. J. H. Canterford and R. Colton, ‘Halides of the Second and Third Row Transition Metals’, Wiley, New York, 1969.
65. A. F. Trotman-Dickinson, ‘Comprehensive Inorganic Chemistry’, Pergamon Press, Oxford, 1973, Vol. 3.
66. C. J. Ballhausen, ‘Introduction to Ligand Field Theory’, McGraw-Hill, New York, 1962.

67. T. M. Dunn, D. S. McClure, and R. G. Pearson, ‘Some Aspects of Crystal Field Theory’, Harper and Row, New York, 1965.
68. P. Biagini, F. Calderazzo, G. Pampaloni, and P. F. Zanuzzi, *Gazz. Chim. Ital.*, 1987, **117**, 27.
69. F. Calderazzo, P. Pallavicini, G. Pampaloni, and P. F. Zanuzzi, *J. Chem. Soc., Dalton Trans.*, 1990, 2743.
70. F. Calderazzo, P. Pallavicini, and G. Pampaloni, *J. Chem. Soc., Dalton Trans.*, 1990, 1813.
71. H. Schäfer, ‘Chemical Transport Reactions’, Academic Press, New York, 1964.
72. S. Siegel and D. A. Northrup, *Inorg. Chem.*, 1966, **5**, 2187.
73. R. Bougon, B. Buu, and K. Seppelt, *Chem. Ber.*, 1993, **126**, 1331.
74. W. J. Castell Jr, A. P. Wilkinson, H. Borrmann, R. E. Serfass, and N. Bartlett, *Inorg. Chem.*, 1992, **31**, 3124.
75. R. C. Burns and T. A. O’Donnell, *Inorg. Chem.*, 1979, **18**, 3081.
76. H. Bialowons, M. Müller, and B. G. Müller, *Z. Anorg. Allg. Chem.*, 1995, **621**, 1227.
77. S. Becker and B. G. Müller, *Angew. Chem., Int. Ed. Engl.*, 1990, **29**, 406.
78. R. Hoppe and W. Dähne, *Naturwissenschaften*, 1962, **49**, 254.
79. B. G. Müller and M. Serafin, *Z. Naturforsch., Teil B*, 1987, **42**, 1102.
80. B. Zemva, K. Lutar, A. Jesih, W. J. Castell Jr, and N. Bartlett, *J. Chem. Soc., Chem. Commun.*, 1989, 346.
81. N. Bartlett and A. Tressaud, *C. R. Hebd. Sceances Acad. Sci., Ser. C*, 1974, **278**, 1501.
82. A. F. Wright, B. E. F. Fender, and N. Bartlett, *Inorg. Chem.*, 1978, **17**, 748.
83. P. R. Rao, A. Tressaud, and N. Bartlett, *J. Inorg. Nucl. Chem. Suppl.*, 1976, 23.
84. E. A. Pisarev, D. V. Drobot, and I. V. Makarchuk, *Russ. J. Inorg. Chem., (Engl. Transl.)*, 1982, **27**, 10.
85. G. Thiele, H. Wochner, and H. Wagner, *Z. Anorg. Allg. Chem.*, 1985, **530**, 178.
86. U. Müller, *Acta Crystallogr., Sect. B*,1981, **37**, 532.
87. U. Müller, *Angew. Chem. Int. Ed. Engl.*, 1981, **20**, 692.
88. H. Schäfer, H. G. von Schnering, J. Tillack, F. Kuhnen, H. Wöhrle, and H. Baumann, *Z. Anorg. Allg. Chem.*, 1967, **353**, 281.
89. D. L. Kepert, ‘The Early Transition Metals’, Academic Press, London, 1972.
90. D. Babel and A. Tressaud, in ‘Inorganic Solid Fluorides’, ed. P. Hagenmüller, Academic Press, New York, 1985, p. 77.
91. C. Michel, J. M. Moreau, and W. J. James, *Acta Crystallogr., Sect. B*, 1971, **B27**, 501.
92. M. A. Hepworth, K. H. Jack, R. D. Peacock, and G. J. Westland, *Acta Crystallogr.*, 1957, **10**, 63.
93. G. Natta, P. Corrandini, I. E. Bassi, and L. Porri, *Atti. Accad. Naz. Lincei, Cl. Sci. Fis., Mat. Nat. Rend.*, 1958, **24**, 121.
94. D. M. Adams, ‘Inorganic Solids’, Wiley, London, 1974.
95. B. L. Chamberland, in ‘Inorganic Solid Fluorides’, ed. P. Hagenmüller, Academic Press, New York, 1985, p. 205.
96. M. Pouchard, M. R. Torki, G. Demazeau, and P. Hagenmüller, *C. R. Hebd. Sceances Acad. Sci.*, 1971, **273**, 1093.
97. M. K. Wilkinson, E. O. Wollan, H. R. Child, and J. W. Cable, *Phys. Rev.*, 1961, **121**, 74.
98. F. Schrötter and B. G. Müller, *Z. Anorg. Allg. Chem.*, 1993, **619**, 1426.
99. J.-M. Dance and A. Tressaud, in ‘Inorganic Solid Fluorides’, ed. P. Hagenmüller, Academic Press, New York, 1985, p. 379.
100. A. Lachgar, D. S. Dudis, and J. D. Corbett, *Inorg. Chem.*, 1990, **29**, 2242.
101. A. Lachgar, D. S. Dudis, P. K. Dorhout, and J. D. Corbett, *Inorg. Chem.*, 1991, **30**, 3321.
102. K. Dorhout and J. D. Corbett, *Inorg. Chem.*, 1991, **30**, 3326.
103. A. Simon and H. G. von Schnering, *J. Less-Common Met.*, 1966, **11**, 31.
104. J. G. Converse, J. B. Hamilton, and R. E. McCarley, *Inorg Chem.*, 1970, **9**, 1366.
105. D. Babel, *J. Solid State Chem.*, 1972, **4**, 410.
106. R. Siepmann and H. G. von Schnering, *Z. Anorg. Allg. Chem.*, 1968, **357**, 289.
107. U. Lange and H. Schäfer, *J. Less-Common Met.*, 1971, **21**, 472.
108. F. A. Cotton and J. T. Mague, *Inorg. Chem.*, 1964, **3**, 1402.
109. M. J. Bennett, F. A. Cotton, and B. M. Foxman, *Inorg. Chem.*, 1968, **7**, 1563.
110. J. Gelinek and W. Rüdorff, *Naturwissenschaften*, 1964, **51**, 85.
111. J. M. Fletcher, W. E. Gardner, A. C. Fox, and G. Topping, *J. Chem. Soc. A*, 1967, 1038.
112. K. Brodersen, H.-K. Breitbach, and G. Thiele, *Z. Anorg. Allg. Chem.*, 1968, **357**, 162.
113. H.-J. Cantow, H. Hillebrecht, S. N. Magonov, H. W. Rolter, M. Drechsler, and G. Thiele, *Angew. Chem., Int. Ed. Engl.*, 1990, **29**, 537.
114. D. Babel and P. Deigner, *Z. Anorg. Allg. Chem.*, 1965, **139**, 57.
115. G. Thiele and P. Woditsch, *Angew. Chem., Int. Ed. Engl.*, 1969, **8**, 672.
116. U. Wiese, H. Schäfer, H. G. von Schnering, C. Brendel, and K. Rinke, *Angew. Chem., Int. Ed. Engl.*, 1970, **9**, 158.
117. B. Zemva, K. Lutar, A. Jesih, W. J. Casteel, A. P. Wilkinson, D. E. Cox, R. B. v. Dreele, H. Borrmann, and N. Bartlett, *J. Am. Chem. Soc.*, 1991, **113**, 4192.
118. J. Lin and G. J. Miller, *Inorg. Chem.*, 1993, **32**, 1476.
119. N. Morita, T. Endo, T. Sato, and M. Shimada, *J. Mat. Sci. Lett.*, 1987, **6**, 859.

120. C. Soulard, X. Rocquefelte, S. Jobic, D. Dai, H.-J. Koo, and M.-H. Whangbo, *J. Solid State Chem.*, 2003, **175**, 355.

121. H. G. v. Schnering, J. H. Chang, K. Peters, E. M. Peters, F. R. Wagner, Y. Grin, and G. Thiele, *Z. Anorg. Allg. Chem.*, 2003, **629**, 516.

122. O. Graudejus, A. P. Wilkinson, and N. Bartlett, *Inorg. Chem.*, 2000, **39**, 1545.

123. A. Simon, *Angew. Chem., Int. Ed. Engl.*, 1981, **20**, 1.

124. A. Simon, *J. Solid State Chem.*, 1985, **57**, 2.

125. A. Simon, *Angew. Chem., Int. Ed. Engl.*, 1988, **27**, 160.

126. J. D. Corbett, *Acc. Chem. Res.*, 1981, **14**, 239.

127. J. D. Corbett and R. E. McCarley, 'Crystal Chemistry and Properties of Materials with Quasi-One-Dimensional Structures', Reidel, Dordrecht, 1986, p. 179.

128. H. Schäfer and H. G. Schnering, *Angew. Chem.*, 1964, **76**, 833.

129. R. P. Ziebarth and J. D. Corbett, *Acc. Chem. Res.*, 1989, **22**, 2.

130. J. D. Corbett, in 'Modern Perspectives in Inorganic Chemistry', ed. E. Parthe, Kluwer, Dordrecht, 1992, p. 27.

131. A. Cisar, J. D. Corbett, and R. L. Daake, *Inorg. Chem.*, 1979, **18**, 836.

132. D. Brown, 'Halides of the Lanthanides and Actinides', Wiley, New York, 1968.

133. O. Greis and J. M. Haschke, in 'Handbook on the Physics and Chemistry of Rare Earths', eds. K. A. Gschneidner Jr and L. Eyring, North-Holland, Amsterdam, NY, 1982, Vol. 5, p. 387.

134. A. F. Trotman-Dickinson, 'Comprehensive Inorganic Chemistry', Pergamon Press, Oxford, 1973, Vols. 4 and 5.

135. G. Meyer, M. S. Wickleder, in 'Handbook on the Physics and Chemistry of Rare Earths', eds. K. A. Gschneidner Jr and L. Eyring, North-Holland, Amsterdam, 2000, Vol. 28, p. 53.

136. C. Michaelis, W. Bauhofer, H. Buchkremer-Hermanns, R. K. Kremer, G. J. Miller, and A. Simon, *Z. Anorg. Allg. Chem.*, 1992, **618**, 98.

137. G. S. Offelt, *J. Chem. Phys.*, 1963, **38**, 2171.

138. P. P. Sorokin and M. J. Stevenson, *IBM J. Res. Dev*, 1961, **5**, 56.

139. T. Imamoto, 'Lanthanides in Organic Synthesis', Academic Press, San Diego, CA, 1994, p. 40.

140. J. H. Burrow, C. H. Maule, P. Strange, J. N. Tothill, and J. A. Wilson, *J. Phys. C*, 1987, **20**, 4115.

141. A. Kasten, P. H. Müller, and M. Schienle, *Solid State Commun.*, 1984, **51**, 919.

142. K. Ahn, C. Felser, R. Seshadri, R. K. Kremer, and A. Simon, *J. Alloys Compd.*, 2000, **303**, 252.

143. G. Meyer, *Chem. Rev.*, 1988, **88**, 93.

144. R. K. Kremer, U. Beck, P. Fischer, and A. Simon, *J. Magn. Magn. Mater.*, 1995, **140**, 1679.

145. J. D. Martin and J. D. Corbett, *Angew. Chem.* 1995, **107**, 234; *Angew. Chem., Int. Ed. Engl.*, 1995, **34**, 233.

146. R. Hoppe, in 'Inorganic Solid Fluorides', ed. P. Hagenmüller, Academic Press, New York, 1985, p. 275.

147. W. Klemm and P. Henkel, *Z. Anorg. Allg. Chem.*, 1934, **220**, 180.

148. L. B. Asprey, J. S. Coleman, and M. J. Reisfeld, *Adv. Chem. Ser.*, 1967, **71**, 122.

149. B. B. Cunningham, D. C. Feay, and M. A. Rollier, *J. Am. Chem. Soc.*, 1954, **76**, 3361.

Heterogeneous Catalysis by Metals

Zhen Ma & Francisco Zaera
University of California, Riverside, CA, USA

1 Introduction 1
2 Fundamentals of Heterogeneous Metal Catalysis 1
3 Applications of Heterogeneous Metal Catalysis 5
4 Promising New Directions in Heterogeneous Metal Catalysis 12
5 References 16

1 INTRODUCTION

Catalysis refers to the phenomenon by which the rate of a chemical reaction is accelerated by a substance (the catalyst) not appreciably consumed in the process. The term 'catalysis' was coined by Berzelius in 1835 and scientifically defined by Ostwald in 1895, but applications based on catalysis can be traced back to thousands of years ago with the discovery of fermentation to produce wine and beer.[1] Nowadays, catalysts are used in 80% of all chemical industrial processes, and create annual global sales of about 1500 billion dollars and contribute directly or indirectly to approximately 35% of the world's GDP.[2] Catalysis is central to a myriad of applications, including the manufacture of commodity, fine, specialty, petro-, and agro- chemicals as well as the production of pharmaceuticals, cosmetics, foods, and polymers. Catalysis is also an important component in new processes for the generation of clean energy, and in the protection of the environment both by abating environmental pollutants and by providing alternative cleaner chemical synthetic procedures.

Most catalytic processes are heterogeneous in nature, typically involving a solid catalyst and gas or liquid phase reactants. When compared with homogeneous catalysts, heterogeneous catalysts offer inherent advantages because of their ease of preparation, handling, separation from the reaction mixture, recovery, and reuse, and also in terms of their stability, low cost, and low toxicity. Heterogeneous catalysts are most commonly made out of metals and metal oxides, although metal sulfides, nitrides, carbides, phosphates and phosphides, ion-exchange resins, and clays are also employed in selected applications. Metal catalysts, especially those containing transition metals, have proven particularly useful in industrial catalysis, because they have the ability to easily activate key molecules such as H_2, O_2, N_2, and CO as well as polyatomic organic molecules with C–H, C–O, C–N, and C–Cl bonds.[3] Table 1 summarizes some of the most important metal-based catalytic processes developed since the 1870s.[1,4]

In the following sections, the basic chemical concepts behind heterogeneous metal catalysis will be introduced. Then, typical examples of practical catalytic systems related to the generation of energy, the production of chemicals, the preparation of materials, and the cleaning of the environment will be provided. Finally, several promising directions related to heterogeneous metal catalysis will be highlighted.

2 FUNDAMENTALS OF HETEROGENEOUS METAL CATALYSIS

2.1 Kinetics Versus Thermodynamics, Active Centers, Catalytic Cycles

Catalysis relies on changes in the kinetics of chemical reactions. Thermodynamics acts as an arrow to show the way to the most stable products, but kinetics defines the relative rates of the many competitive pathways available for the reactants, and can therefore be used to make metastable products from catalytic processes in a fast and selective way. Indeed, catalysts work by opening alternative mechanistic routes with lower activation energy barriers than those of the noncatalyzed reactions.[5] As an example, Figure 1 illustrates how the use of metal catalysts facilitates the dissociation of molecular oxygen, and with that the oxidation of carbon monoxide. Thanks to the availability of new pathways, catalyzed reactions can be carried out at much faster rates and at lower temperatures than noncatalyzed reactions. Note, however, that a catalyst can shorten the time needed to achieve thermodynamic equilibrium, but cannot shift the position of that equilibrium, and therefore cannot catalyze a thermodynamically unfavorable reaction.[6]

The new mechanistic routes opened by the introduction of a catalyst to the reaction mixture typically start with the adsorption of the reactants. Because of the heterogeneous nature of the surface of the catalyst, both the adsorption and the subsequent conversion reactions may take place preferentially at particular ensembles of surface sites, often called active sites or active centers.[7,8] An atomic ensemble may become active because of a specific structural arrangement of those atoms. Alternatively, the electronic properties of metal atoms may also influence the adsorption and activation of reactants. Typically, the performance of catalytic active sites depends on both structural and electronic effects.

After diffusion towards and adsorption on the surface-active sites, the reactants are converted to products. Those products then desorb and diffuse out of the catalyst, leaving the active centers available for new incoming reactants.[7] That way, the catalytic cycle can be repeated many times on each active site. For this to work, however, the bond strength between the adsorbed surface species and the active sites

Table 1 Important industrial heterogeneous catalytic processes promoted by metals[1,4]

Process	Year	Main uses	Key reaction scheme	Typical catalyst
SO_2 oxidation to sulfuric acid	1875	Chemicals, Metallurgic processing	$SO_2 + 1/2O_2 \rightarrow SO_3$	Pt on asbestos, $MgSO_4$, or SiO_2 (replaced by $V_2O_5 - K_2SO_4/SiO_2$ since the 1920s)
Methanol to formaldehyde	1890	Resins for adhesives	$CH_3OH + 1/2O_2 \rightarrow HCHO + H_2O$	Ag wire gauze or Ag crystals
Olefin hydrogenation	1902	Oil refining	$C_2H_4 + H_2 \rightarrow C_2H_6$	Ni, Pt
Hydrogenation of edible fats and oils	1900s	Food production	unsaturated fatty acids → partially saturated acids	Ni on a support
Methanation	1900s	Fuels	$CO + 3H_2 \rightarrow CH_4 + H_2O$	Ni on Al_2O_3 or other oxide supports
Ammonia synthesis (Haber)	1913	Fertilizers	$N_2 + 3H_2 \rightarrow 2\,NH_3$	Fe promoted with Al_2O_3, K_2O, CaO, and MgO
Ammonia oxidation (Ostwald)	1906	Nitric acid production	$4NH_3 + 5O_2 \rightarrow 4NO + 6H_2O$	90%Pt-10% Rh wire gauze
Fisher–Tropsch synthesis	1938	Fuels	$CO + H_2 \rightarrow$ paraffins	Fe or Co with promoters on support
Steam reforming	1926	Synthesis gas	$C_nH_m + nH_2O \rightarrow nCO + [n + (m/2)]H_2$	Ni on support promoted by K_2O
Ethylene to ethylene oxide	1937	Antifreeze	$C_2H_4 + 1/2O_2 \rightarrow (CH_2)_2O$	Ag on α-Al_2O_3, promoted by Cl and Cs
Hydrogen cyanide synthesis	1930s	Chemicals	$CH_4 + NH_3 + 3/2O_2 \rightarrow HCN + 3H_2O$	90%Pt-10% Rh wire gauze
Catalytic reforming	1940s	Fuels	e.g., n-$C_6H_{14} \rightarrow i$-C_6H_{14}	Pt, Pt–Re or Pt–Sn on acidified Al_2O_3 or zeolite
Benzene to cyclohexane	1940s	Nylon	$C_6H_6 + 3H_2 \rightarrow C_6H_{12}$	Ni, Pt, or Pd catalysts
Vinyl acetate synthesis	1968	Polymers	$C_2H_4 + CH_3COOH + 1/2O_2 \rightarrow CH_3COOCH{=}CH_2 + H_2O$	Pd on SiO_2 or α-Al_2O_3
Automobile three-way catalysis	1970s	Pollution control	$CO + H.C. + NO_x + O_2 \rightarrow CO_2 + H_2O + N_2$	Pt, Pd, Rh on monolith support

needs to be neither too weak nor too strong: too weak and the reactants cannot be readily activated; too strong and either the reactants are completely decomposed on the surface or the products cannot desorb.[6] This relationship between adsorption energy and catalytic performance is epitomized by volcano plots such as those in Figure 2.[9–12] In many instances, the adsorption energy can also be correlated to specific properties of the metals such as their d-band occupancy (%d) character (Figure 2b).[12]

2.2 Activity, Selectivity, Stability

Three key parameters, activity, selectivity, and stability, can be used to evaluate catalyst performance. Achieving good and sustainable activity and selectivity at low cost is an everlasting goal in catalyst design and development. Activity refers to the rate at which a given reaction proceeds. In practice, activity can be expressed in absolute terms, but is often reported using relative units such as specific rate (rate divided by catalyst weight), areal rate (rate divided by surface area), turnover frequency (molecules converted per active center per unit time), conversion after specified time (fraction of reactants converted per fixed time), or required temperature for a given conversion under specific conditions.[13] In industry, activity is often expressed by space-time yield, the amount of product formed per unit time per unit volume of reactor. Regardless of the parameters adopted to express activity, however, it needs to be appreciated that such activity depends on the catalyst load in the reactor, the concentration of the reactants, and the temperature, pressure, and flow during operation.

In addition to activity, the design of catalytic processes needs to consider their selectivity towards the desirable products.[14] In fact, selectivity is arguably the most important criterion to take into account to decide on a particular catalytic process. Selective reactions consume less reactant, avoid the need of costly separations, and do not produce potentially polluting by-products. Unfortunately, it is not easy to design selective catalytic processes from first principles. For one, a catalyst active for a given reaction may be inactive for a closely related one. In addition, given a set of reactants, the use of different catalysts may lead to different products. For example, ethanol is dehydrogenated to acetaldehyde on Cu

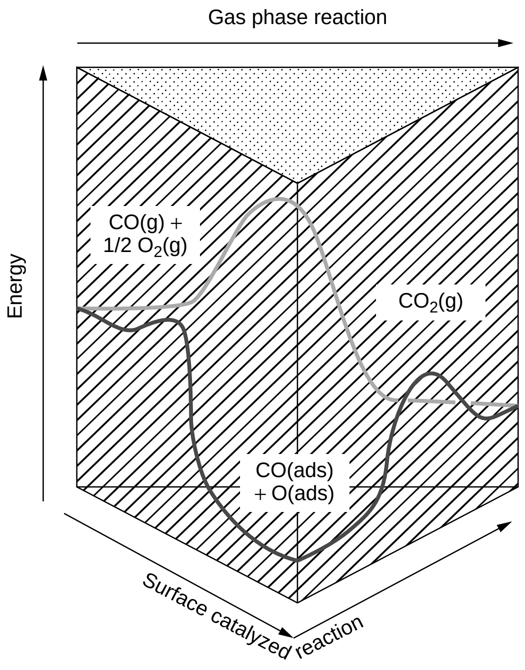

Figure 1 Energy diagram illustrating how solid catalysts facilitate reactions by opening new mechanistic routes. This example corresponds to the oxidation of carbon monoxide, a conversion that can be accelerated by previous dissociation of the molecular oxygen on many transition metal surfaces

but dehydrated to ethylene or ethyl ether on γ-Al_2O_3.[4] Many competing reactions may also be promoted by one particular catalyst, in which case the distribution of the resulting products may depend on experimental conditions such as reaction temperature, pressure, and contact time.

Finally, there is the issue of stability. Ideally, catalysts are expected not to be consumed and to maintain a constant level of performance during the course of the reaction. In reality, however, both catalytic activity and catalytic selectivity may deteriorate during operation. The lifetime of most industrial catalysts is finite, ranging from months to years. The most common reasons for this catalyst deactivation include the evaporation, washout, reduction, corrosion or other transformation of the active catalytic species during reaction, the formation of carbonaceous deposits (coking), the poisoning due to strong adsorption of impurities such as sulfur or carbon monoxide on the surface of the catalyst, and/or the coalescence of metal particles (sintering).[4,13] Some of these processes are reversible, in which case the catalysts can be regenerated by special treatments in situ in the reactor such as burning off of the coke deposits or other in situ chemical treatments, but many are irreversible and require the replacement of the catalyst. Fluctuations in processing conditions may influence the stability of catalysts as well, so engineering optimization is also crucial in the design of catalytic processes.

2.3 Supports, Promoters

As mentioned above, heterogeneous catalysis is centered around the chemistry of adsorbed species on solid surfaces. Consequently, it is important to maximize the surface-to-volume ratio of the active phase to minimize cost and

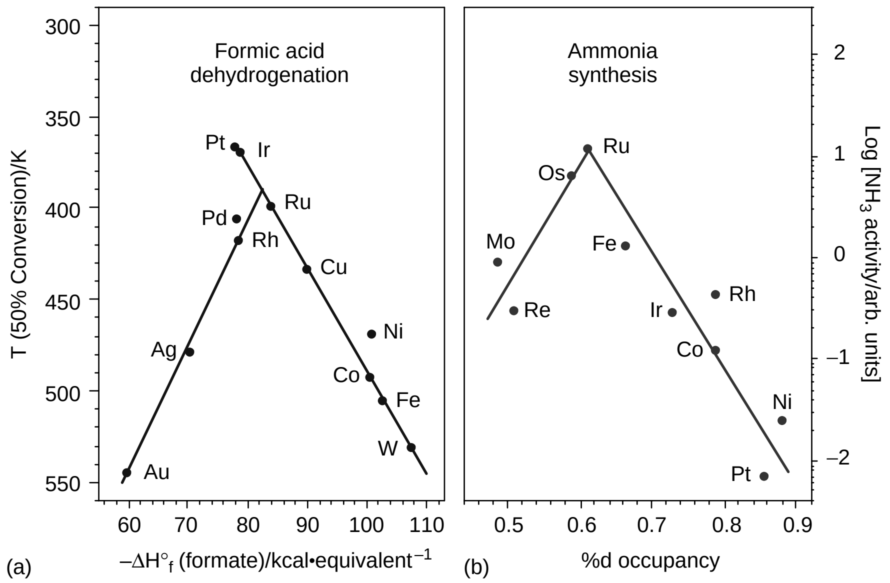

Figure 2 Volcano plots illustrating how catalytic activities depend on the nature of the metal used as catalyst. (a) Correlation between catalytic activity for formic acid dehydrogenation and enthalpy of formation of metal formates. (Ref. 10. Reproduced by permission of John Wiley & Sons, Inc.)[9,10] (b) Correlation between catalytic activity for ammonia synthesis and degree of d-band filling in the metal used as catalyst. (Ref. 12. Reproduced by permission of John Wiley & Sons, Inc.)[11]

improve performance. Because of this, the direct use of metal wires, gauzes, and foils in industrial catalysis is rare. The surface area of bulk metals is rather small, with only a few active sites exposed, and pure metals in high surface area forms are generally not thermally stable under catalytic conditions. Instead, metals are typically dispersed onto high surface area refractory supports such as alumina, silica, zeolites, activated carbon, titania, zirconia, or mixed oxides. Pillared clays, mesoporous materials, ceramics, silicon carbide, graphite, carbon nanofibers, magnesia, metal fluorides, calcium carbonate, and barium sulfate have also been used occasionally for this purpose. Figure 3 shows a transmission electron microscopy (TEM) picture of a typical catalyst; in this case silver particles approximately 10–20 nm in diameter are deposited on a porous alumina support.[15] The choice of support is primarily based on its surface area, but thermal and chemical stability, chemical properties, mechanical strength, and price also need to be considered.[13] Although most supports are used primarily to disperse a catalytic active phase, they often add to the overall chemistry of the catalytic process. In particular, supports with different acid-base or redox properties often exert marked influence on catalytic behavior. Zeolites (*see* ***Zeolites***) can also provide unique shape selectivity, since the uniformity of their pores can regulate the relative flows of the entering reactants, the leaving products, and the transition states of the reaction based on their sizes, thus determining the product distribution.[16] Last but not least, strong interactions between metal catalysts and supports such as titania (SMSI) can significantly modify the electronic and chemical properties of the former.[4]

To further optimize the performance of metal catalysts, promoters are often added. Textural promoters work by separating metal particles from one another to minimize sintering, whereas electronic and structural promoters change the electronic or crystal structure of the active metal. For instance, a small amount of potassium acetate is added to the Pd/SiO_2 or Pd/α-Al_2O_3 catalysts used in the synthesis of vinyl acetate to promote the adsorption of acetic acid and lower the barrier to vinyl acetate formation, thus increasing the overall activity and minimizing the yield of CO_2.[17] The addition of potassium compounds or other alkaline substances to nickel catalysts during steam reforming can facilitate both the adsorption of water and the removal of carbonaceous deposit.[4] In ammonia synthesis, Al_2O_3, CaO, and MgO are added to the iron catalyst as textural promoters to minimize the sintering of Fe, and K_2O as an electronic promoter to increase the activity for the dissociative adsorption of N_2.[4] Nowadays, almost all catalytic processes in industry involve the incorporation of promoters during catalyst preparation and/or the feed of additives with the reaction mixture.

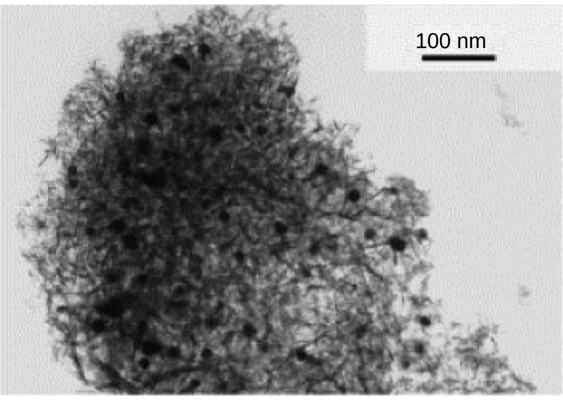

Figure 3 TEM picture of a typical supported metal catalyst, silver nanoparticles (dark spots) deposited on a high surface area alumina support. (Reprinted from Ref. 15. © 1998, with permission from Elsevier)

2.4 Preparation and Characterization of Metal Catalysts

Because of the complexity of solid catalysts, where the active phase is dispersed onto a high surface area solid and promoted with a number of additives, the preparation of catalysts is still somewhat of an art. Numerous methods have been developed over the years for the preparation of metal catalysts. For example, some iron-based catalysts for ammonia synthesis are manufactured by fusion of Fe_3O_4 with small amounts of K_2CO_3, Al_2O_3, and other ingredients.[4] The porous Raney nickel catalysts used for the selective hydrogenation of organic chemicals are prepared by alloying Ni with Al and then leaching away the Al in a boiling NaOH solution.[17] The silver catalyst used in the partial oxidation of methanol is made electrochemically using an $AgNO_3$ electrolyte.[17] However, the most common way to prepare supported metal catalysts is by impregnation, where a porous support is soaked into a solution containing a metal precursor such as $HAuCl_4$ or H_2PtCl_6.[18] Coprecipitation is another traditional method where a solution containing a soluble metal salt and a precursor for the support such as $Al(NO_3)_3$ or $ZrOCl_2$ are thoroughly mixed with an aqueous inorganic base to precipitate the cations as hydroxides or carbonates.[19] Sol-gel methods (*see* ***Sol–Gel Synthesis of Solids***) involving the hydrolysis of metal alkaloids such as $Si(OC_2H_5)_4$ and Al(i-$OC_3H_7)_3$ can also be used to form high surface area supports.[20] In all of these three cases, the resulting materials need to be calcined and reduced in order to expose the metallic phase. Decarbonylation of metal carbonyls adsorbed on appropriate supports, oxidative transformation of amorphous alloys into supported metal catalysts, and flame spray pyrolysis, are also viable routes to catalyst preparation.[17] Finally, for industrial applications, the powder catalysts obtained are further shaped into tablets, pellets, rings, extrudates, spheres, shells, or granules (Figure 4).

The processes used for the preparation of heterogeneous catalysts are not only versatile, but also complex; even subtle changes in preparation conditions often lead to clear differences in catalyst performance. Therefore, it is highly desirable to develop a microscopic understanding of the

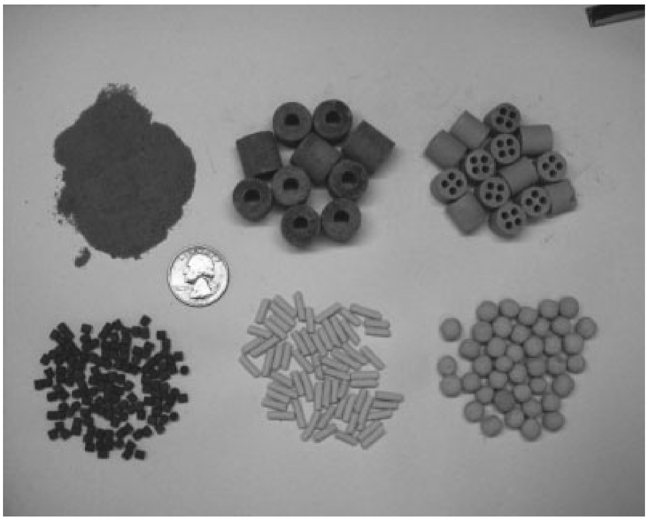

Figure 4 Examples of the final forms of the catalysts used in industrial processes. Shown are powders, rings, four-hole cylinders, tablets, pellets, and spheres of different supported metal catalysts

relation between structure and reactivity in catalysts. For now, however, the design of catalyst preparation from first principles is still not possible. Luckily, a number of analytical methods are available for the characterization of the final solids.[21] X-ray diffraction (XRD) provides information on the bulk structure, degree of crystallinity, and average crystal size of supported catalysts. Electron microscopy, in either transmission (TEM) or scanning (SEM) modes, aids in the determination of individual metal particle sizes and morphology, and of metal dispersion. Nitrogen adsorption isotherms are used to derive surface areas, pore size distributions, and pore volumes. X-ray photoelectron spectroscopy (XPS) facilitates the identification of surface species and their oxidation states. Infrared spectroscopy of probe adsorbates such as CO, NO, NH_3, C_2H_4, CH_3OH, and pyridine gives information on the nature of adsorption sites and reaction mechanism on catalyst surfaces.[22] Finally, chemical titration can be used to identify specific properties of active sites. For instance, temperature programmed desorption (TPD) of NH_3 or CO_2 can provide an indication of the acidic or basic nature of the solid catalysts. The use of these and other characterization methods such as nuclear magnetic resonance (NMR), X-ray absorption fine structure, and in situ Raman spectroscopy have already been well documented.[23–25]

3 APPLICATIONS OF HETEROGENEOUS METAL CATALYSIS

Metal catalysis is widely used in processes related to energy production, chemicals manufacture, materials synthesis, and environmental controls, among others. In this section, both traditional and recent examples highlighting the role of metal catalysts in each of these areas are provided.

3.1 Metal Catalysis Related to Energy Production

Metal catalysis plays a key role in the utilization of fossil fuels such as petroleum, coal, and natural gas. Petroleum technology has been identified as one of the 20 most world-shaping engineering achievements of the 20th century, supplying 40% of the global energy and 90% of the industrial organic chemicals.[26,27] However, crude oil consists of a vast mixture of hydrocarbons (together with small amounts of sulfur and nitrogen-containing organic compounds) and therefore cannot be used efficiently without extensive processing. Components with different boiling point ranges are first separated via fractional distillation, and the naphtha fractions are then treated with hydrodesulfurization (HDS) and hydrodenitrogenation (HDN) catalysts (*see* ***Hydrodesulfurization & Hydrodenitrogenation***) to remove impurities, the precursors of environmental pollutants such as SO_2 and NO_x, and with reforming, cracking, and hydrocracking catalysts to produce high quality fuels.

Metals, metal oxides, zeolites, and metal sulfide catalysts are at the heart of these oil conversion processes. HDS and HDN are commonly carried out on molybdenum sulfide catalysts. Catalytic cracking uses zeolites to breakdown large hydrocarbon molecules into branched or cyclic hydrocarbons and alkenes. More to the point of this review, catalytic reforming uses noble metals to promote isomerization and cyclization reactions without significantly changing the molecular weight of the naphtha fraction.[4,28] Reforming catalysts are almost exclusively based on a platinum metallic phase. Indeed, the most common processes used nowadays are the UOP Platforming, based on Pt/Al_2O_3-SiO_2, and the Chevron Rheniforming, which employs Re–Pt/Al_2O_3-SiO_2. Typical reforming processes are carried out at temperatures between 480 and 540 °C, and with hydrogen-rich reaction mixtures under several atmospheres of pressure. The reforming catalyst is believed to rely on its dual functionality, with hydrogenation-dehydrogenation steps taking place on the metallic phase and isomerization reactions on acid sites furnished by the support, although it has been shown that platinum alone can perform all reforming steps.[29] Platforming and Rheniforming processes are currently used in more than 170 plants worldwide.[27]

Coal and natural gas are also major sources of energy. Coal supplies 27% of the energy used worldwide, and natural gas, which is mainly composed of methane, provides another 23%.[27] At present, both coal and natural gas are primarily burned to produce energy. However, in order to fully exploit their energy and chemical potential, they are also increasingly being converted to synthesis gas, a mixture of CO and H_2, via gasification ($C + H_2O \rightarrow CO + H_2$), steam reforming ($CH_4 + H_2O \rightarrow CO + 3H_2$), or direct oxidation ($CH_4 + 1/2O_2 \rightarrow CO + 2H_2$), and further transformed into heavier hydrocarbons and into alcohols via Fischer–Tropsch (F-T) type processes.

Again, most of the conversions enumerated above require the use of heterogeneous catalysts. F-T synthesis, for instance, uses Fe-, Co-, or Ru-based catalysts dispersed onto high surface area Al_2O_3, SiO_2, or TiO_2 supports. This process was initially commercialized in Germany to produce transportation fuels during World War II, and later employed in South Africa to cover their domestic fuel demands during apartheid. More recently, new F-T plants have been built in New Zealand, Malaysia, South Africa, and the Netherlands.[30,31] The classical F-T process follows an overall reaction stoichiometry of $2n\mathrm{CO} + 2n\mathrm{H}_2 \rightarrow (-\mathrm{CH}_2-)_n + n\mathrm{CO}_2$, and typically yields a mixture of hydrocarbons with a range of hydrocarbon chain lengths. The most accepted mechanism for those reactions requires three main types of steps, namely, the initial formation of C_1 intermediates by CO dissociation and hydrogenation, the growth of hydrocarbon chains by successive insertion of C_1 building blocks into the growing hydrocarbon surface chains, and the termination and desorption of surface species.[30,32]

Small amounts of oxygenated products such as alcohols may also be made in F-T processes depending on the catalyst used, and various parameters, including catalyst composition and operation conditions, can be used to influence the distribution of the various paraffins, olefins, and oxygenates produced. For instance, iron-based catalysts, which can be operated at high temperatures and are relatively tolerant to impurities such as sulfur in the feedstock, tend to produce straight hydrocarbon chains. Cobalt-based catalysts are even more selective, producing a much higher ratio of paraffins to olefins and much less oxygenated products. Rhodium-containing catalysts, on the other hand, yield high fractions of alcohols, allegedly because of the slow dissociation of CO on that metal. Nowadays, F-T based gas-to-liquids (GTL) processes are used to produce diesel fuels for urban local transportation. It has been estimated that this process will supply 10% of the global diesel demand within the next 15 years.[31]

Metal catalysts are not only useful for producing gasoline, oil, diesel, and jet fuels, but also promise to contribute to the next generation of environmentally friendly energy production technology. For instance, the room temperature decomposition of liquid hydrazine (N_2H_4) to N_2, H_2, and NH_3 over a commercial Ir/γ-Al_2O_3 catalyst is already used as a propellant to control and adjust the orbit and attitude of satellites.[33] Perhaps more promising is the use of H_2-fuelled electrochemical energy converters (fuel cells) in cars, space shuttles, and other power systems. This application has already been demonstrated on a commercial scale, and is predicted to reach a market in excess of 23 billion dollars by 2010.[34] The reaction involved, $2H_2 + O_2 \rightarrow 2H_2O$, is quite simple and thermodynamically favorable, but kinetically nonviable for practical applications without the use of catalysts. Figure 5 shows a typical fuel cell setup indicating the Pt-coated anode used to catalyze the oxidation of H_2 ($2H_2 \rightarrow 4H^+ + 4e^-$) and the also Pt-based cathode that catalyzes the combination of the resulting protons with O_2 from air ($4H^+ + 4e^- + O_2 \rightarrow 2H_2O$).[35] The two electrodes are separated by an ion-conductive electrolyte to allow for the proton transfer. The overall combination of H_2 and O_2

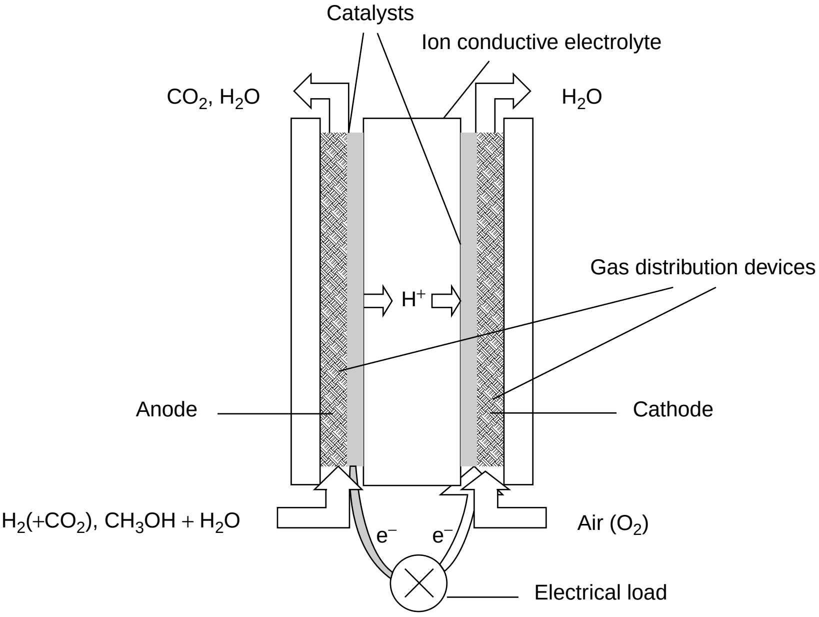

Figure 5 Schematics of a typical proton-exchange membrane fuel cell, indicating the platinum-based electrodes used for hydrogen oxidation and oxygen reduction, the interconnecting electrolyte, and the electrical circuit used to harvest the energy produced. (Reprinted from Ref. 35, © 1998, with permission from Elsevier)

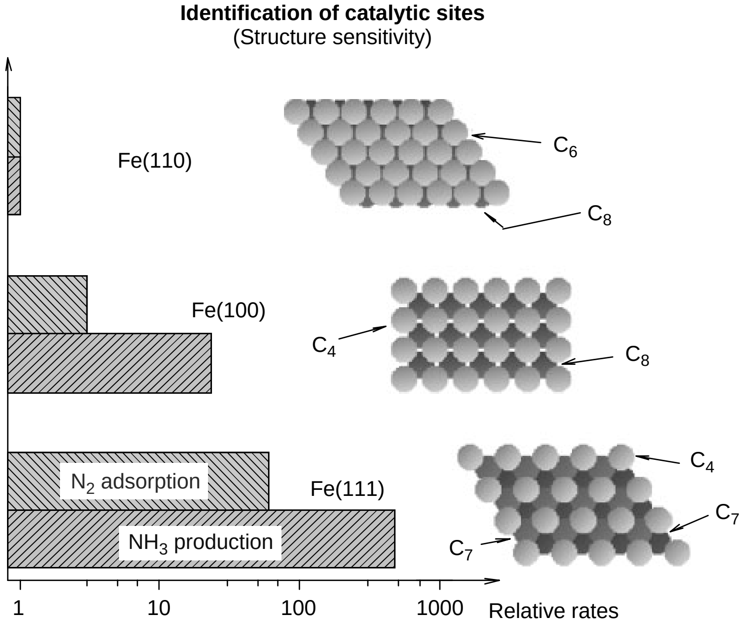

Figure 6 Correlation between both N_2 adsorption and NH_3 production rates and the structure of the catalytic surface, as determined by studies with various single crystals of iron.[38] These results explain the strong dependence of the performance of commercial ammonia synthesis catalysts on their method of preparation[39]

is fast, generating an electrochemical current and additional heat. Some technical problems related to surface poisoning by CO and to fuel storage have so far limited the widespread use of fuel cell technology, but solutions to these roadblocks are already underway.[36] It is clear that metal catalysts will continue to play a crucial role in most future energy generation technologies.

3.2 Metal Catalysis Related to the Manufacturing of Chemicals

Metal catalysts play a pivotal role in the production of most commodity, fine, and specialty chemicals. In fact, a large number of hydrogenation and oxidation processes would not be viable without the use of heterogeneous catalysis. Perhaps the most important and mature example of a catalytic process for the production of chemicals is the synthesis of ammonia from nitrogen and hydrogen, a process that was initially commercialized in 1913 and is nowadays responsible for the production of more than 100 million tons of synthetic ammonia and associated chemicals such as nitric acid, fertilizers, explosives, caprolactam, acrylonitrile, and hydrogen cyanide each year.[27,37] A typical ammonia synthesis catalyst is made by combining Fe_3O_4, Al_2O_3, K_2O, CaO, and MgO, and reducing this mixture in the reactor before operation to expose metallic iron sites. Surface science studies have indicated that this reaction is particularly sensitive to the structure of the active metal phase, with the dissociative adsorption of N_2, the rate-limiting step, being a couple of orders of magnitude faster on Fe(111) planes than on Fe(100) or Fe(110) surfaces (Figure 6).[38,39] The efficiency of the ammonia-producing process is limited by thermodynamic considerations, and reaches yields of only about 14% under the optimized reaction conditions of temperature (around 450 °C) and pressures (~100 atm). Recirculation of the reaction mixture, however, allows for ammonia yields of up to 98% under industrial settings. Supported ruthenium catalysts promoted by alkali metals have been introduced since the early 1970s to synthesize ammonia at lower temperature and pressures, and have resulted in the commercialization of the ruthenium-based Kellogg Advanced Ammonia process in Canada in 1992. Nevertheless, because of the high cost of Ru, most of the industrial ammonia plants still rely on iron catalysts.[11,17]

Successful examples of selective oxidation catalysis in industry include the conversions of ethylene to ethylene oxide and of methanol to formaldehyde, both on silver catalysts. Ethylene oxide, with an annual worldwide production capacity over 11 million tons, is an important intermediate for the production of glycols (antifreeze agents), ethoxylates (additives in washing powder), cosmetics, polyester fibers, and pharmaceuticals.[27] The partial oxidation of ethylene to ethylene oxide is carried out on silver metal particles supported on α-Al_2O_3 or SiC and promoted by alkaline earth or alkali metals. Trace amounts of ethylene dichloride are also fed continuously into the reactor to suppress deep oxidation. Selectivities of about 75–85% are typical nowadays for this process. Formaldehyde, with a production capacity of

30 million tons per year, is employed for the production of the resins used as adhesives in various boards and other miscellaneous products.[27] This chemical is commercially produced by oxidation of methanol on electrolytic silver while feeding water vapor, nitrogen, and/or trace amounts of additives to promote methanol adsorption and inhibit deep oxidation. In addition, silver catalysts supported on low surface area pumice, ceramics, sol-gel derived SiO_2, SiO_2-TiO_2, and SiO_2-Al_2O_3 have been used to inhibit sintering. At present the formaldehyde yield in industrial plants is 86–90%, the main by-products being carbon oxides, formic acid, and methyl formate.[27]

The key to the success of the oxidation examples cited above is the ability of the catalysts used to exert proper kinetic control on the possible side reactions. Without it, thermodynamically favorable but undesired products such as CO_2 and H_2O are made instead. Controlling oxidation kinetics to stop at the desired oxygenated products is quite difficult, and has yet to be solved for many other systems. For instance, although many attempts have been made to develop a commercial process for the oxidation of propylene to propylene oxide, both the activity and the selectivity of the systems proposed to date, mostly based on silver catalysts, are still too low to be of industrial interest;[40] propylene oxide is presently manufactured by processes based on chlorohydrin or hydrogen peroxide instead.[27] In spite of these difficulties, though, recent advances in selective liquid phase oxidation of fine chemicals on supported metal catalysts have shown some promise, offering high yields (close to 100%) under mild reaction conditions.[41]

Other commercial approaches to the production of chemicals use selective hydrogenation of unsaturated bonds, dehydrogenation, or coupling reactions promoted by various metal catalysts.[42] One old example related to food production is that of the manufacture of margarine by hydrogenation of unsaturated vegetable oils on nickel catalysts.[4,17] Table 2 provides a list of other key catalytic conversion processes of commercial value in the chemical industry.[42–46] These reactions are particularly useful for the production of 'building blocks' for the manufacturing of pharmaceuticals, agrochemicals, and other fine and specialty chemicals of high added value. For instance, aromatic haloamines, important intermediates in the synthesis of agrochemicals, drugs, dyestuffs, and pigments, can be manufactured via hydrogenation of aromatic halonitro compounds on supported Pt catalysts.[43] Ethyl (R)-2-hydroxy-4-phenylbutanoate, an intermediate for the production of benazepril, a drug used to treat high blood pressure, can be made by chiral hydrogenation of the corresponding α-ketoester on Pt/Al_2O_3 modified by chiral cinchona alkoloids.[44] Iminostilbene, a key intermediate in producing Carbamazepine, a medicine to treat psychiatric disorders, is made by dehydrogenation of iminodibenzyl on Pd/C catalysts.[43] Octyl p-methoxy cinnamate, the most common UV-B sunscreen in the market, can be produced via Heck coupling also using Pd/C catalysts.[45] Metal catalysts play a central role in these and many other processes, providing highly selective pathways toward the making of desired products by activating specific functional groups in the presence of other potentially reactive moieties.

3.3 Metal Catalysis Related to the Synthesis of Materials

Heterogeneous catalysis is also extensively used for the manufacture of materials such as polymers, plastics, fibers, and carbon filaments. For example, Ziegler-Natta catalysts, based on $TiCl_4$, $Al(C_2H_5)_3$ and $MgCl_2$, are commercially used to fabricate many polymers, including polyethylene, polypropylene, polybutadiene, and polystyrene.[13] Metallocene complexes have also been developed to control molecular weight and tacticity in polymerization processes. Most polymerization catalysts are homogeneous in nature (*see* ***Oligomerization & Polymerization by Homogeneous Catalysis***), but are sometimes anchored on solid supports to facilitate the catalytic process. A more direct example of the use of heterogeneous metal catalysts in this area is that of the commercial production of caprolactam, the precursor to nylon-6 and nylon-66. This is done by using the Allied-Signal process, which involves the liquid phase hydrogenation of phenol to cyclohexanone on a palladium catalyst. That product is then converted to cyclohexanone oxime, and further to caprolactam via Beckmann rearrangement.[27] An alternative route for this synthesis is the Snia Viscosa process, which involves the hydrogenation of benzoic acid to hexahydrobenzoic acid on a Pd/C catalyst followed by direct conversion to caprolactam via nitrosation with nitrosylsulfuric acid.[27] Another practical example of the synthesis of precursors for the manufacture of materials is the hydrosilylation process, in which silicon hydrides undergoes an addition reaction with an unsaturated reactant. This reaction is particularly useful for the catalytic production, curing, and functionalization of polysiloxanes and other organosilicon polymers. Although homogeneous metal complexes are often used for these hydrosilylation reactions, supported Pt catalysts are preferred in many applications.[46]

Carbonaceous deposits have been long regarded as unwanted side products during catalysis.[47] However, with the advent of nanotechnology, there has been a renewed interest in the use of metal catalysts for the production of filamentous carbon materials such as carbon nanotubes (*see* ***Carbon: Nanotubes***) and nanofibers because of their potential applications in electron emission devices, hydrogen-storage materials, fuel cell electrodes, and catalyst supports.[48] Physical synthetic methods such as arc-discharge and laser ablation are already available for the production of carbon filaments, but their yields are relative low. Metals such as Fe, Co, and Ni, on the other hand, can be used to convert CH_4, CO, synthesis gas, C_2H_2, C_2H_4, or C_2H_6 efficiently to carbon nanofilaments or composite materials in good quantities. Figure 7 provides

Table 2 Important hydrogenation, dehydrogenation, and coupling processes catalyzed by metals[42–46]

Process	Example reaction scheme		Metal catalyst
Hydrogenation of alkenes and alkynes	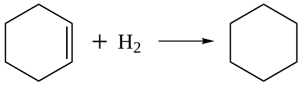	$—C{\equiv}C— + H_2 \longrightarrow —C{=}C—$	Pd, Rh, Pt
Hydrogenation of aromatic rings	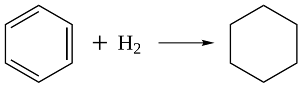	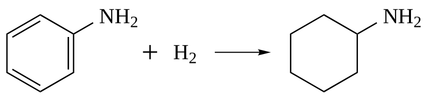	Rh, Ru, Pt
Hydrogenation of aldehydes, acetones, and carboxylic acids to alcohols	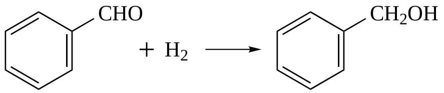 CHO $+ H_2$ CH_2OH	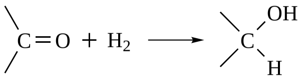	Pt, Ru, Pd, Ir
Hydrogenation of nitro and nitroso compounds to amines	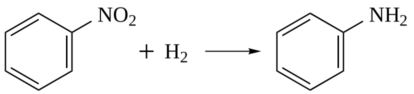	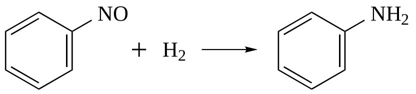	Pd, Pt
Hydrogenation of nitriles to amines	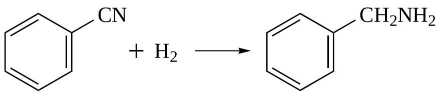 CN $+ H_2$ CH_2NH_2		Rh, Pt, Pd
Hydrogenation of oximes to amines, hydroxyamines or imines	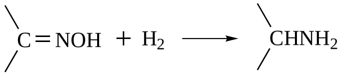 $C{=}NOH + H_2$ $CHNH_2$	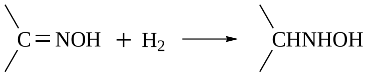 $C{=}NOH + H_2$ CHNHOH	Rh, Pt, Pd
Hydrogenation of imines to amines	$—CH{=}NNH_2 + H_2 \longrightarrow —CH_2NHNH_2$		Pt
Enantioselective hydrogenation of α- or β-ketoesters	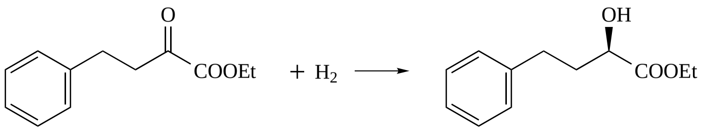 O COOEt $+ H_2$ OH COOEt		Cinchona-modified Pt, Pd, or tartaric acid-modified Ni

(cont'd overleaf)

Table 2 cont'd

Process		Example reaction scheme	Metal catalyst
Hydrodehalogenation	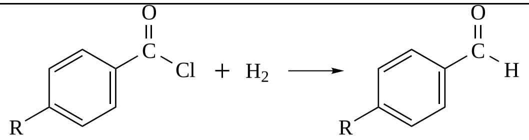	Rosenmund reduction	Pd
Dehydrogenation	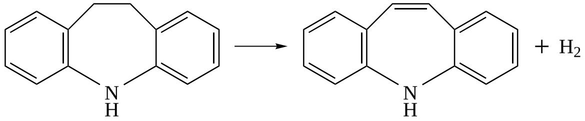	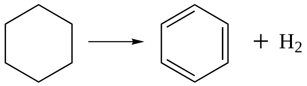	Pd, Pt, Rh
Hydrogenolysis of sulfides	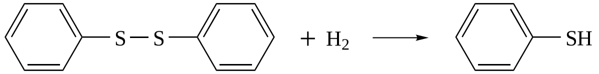		Re
Reductive alkylation	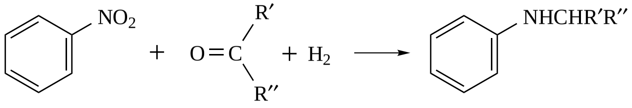		Pt, Pd
Arylation or vinylation of alkenes with aryl or vinyl halides (Heck coupling)	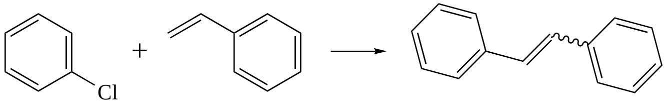		Pd
Suzuki coupling of aryboronic acids and aryl halides to biarys	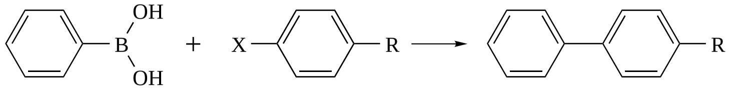		Pd
Hydrosilyation	$—CH{=}CH_2 + SiHR_3 \longrightarrow —CH_2CH_2SiR_3$		Pt

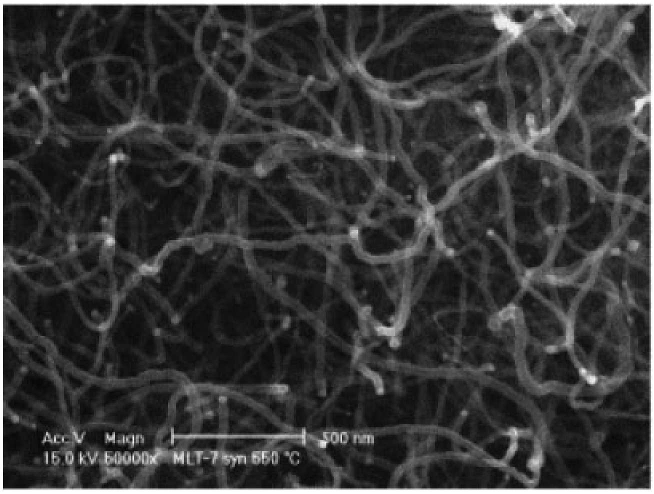

Figure 7 SEM image of carbon nanofibers fabricated using a Ni/SiO_2 catalyst. The nickel catalytic particles are seen here as capping light-colored spheres. Carbon nanotubes grow by decomposition of hydrocarbons on the surface of those metal particles followed by insertion into the carbon growing structures. (Reprinted from Ref. 49. © 2003, with permission from Elsevier)

an example of the nanofibers that can be grown this way.[49] It shows both the grown carbon fibers and the capping metal particles that catalyze the carbon deposition process. The rate-determining step in most of those catalytic reactions is thought to be the diffusion of carbon atoms through metal particles, and the properties of the resultant products are believed to depend on the composition and nature of the catalyst as well as on operational parameters such as temperature, reaction time, composition of reactant mixture, and gas flow rate.[4] Other carbon materials such as diamond can also be synthesized with the aid of metal alloy catalysts.[50] Unfortunately, full understanding of these processes is at present limited, and the production and practical use of well-defined carbon fibers and diamond materials by catalytic means are still in the future.

3.4 Metal Catalysis Related to Environmental Control

Metal catalysis is not only good for the production of chemicals, but has also been increasingly employed for the control of pollutant emissions and for the removal of contaminants. In fact, a third of the 9–10 billion dollars market for world catalyst consumption nowadays is related to environmental catalysis.[2,51] One of the most prominent uses of environmental catalysis is in the control of automobile exhausts. Stringent regulations on car gas emissions have now been imposed by numerous governments around the world to minimize the buildup of noxious CO, NO_x, and hydrocarbon gases in the troposphere. To meet these standards, modern internal combustion engines are fitted with commercial catalytic converters designed to transform those pollutants to less toxic N_2, H_2O, and CO_2. The typical so-called three-way catalyst used for this in most countries is composed of a combination of Pt, Rh, and Pd metal particles supported on a γ-Al_2O_3 washcoat stabilized with La_2O_3 or BaO and modified with CeO_2 or CeO_2/ZrO_2. These catalysts are set onto a ceramic honeycomb or monolith to obtain high thermal stability, high heat and mass transfer rates, low pressure drops, and long catalyst life (Figure 8).[52]

The conversion of automobile exhaust gases involves a number of complex oxidation and reduction reactions, which with today's catalysts requires careful control of the air/fuel ratio within a narrow window around the stoichiometric value of 14.6. Direct injection gasoline engines, however, operate best with a large excess of air, and that compromises the reduction efficiency for NO_x. In order to address this problem, alkaline metal oxides such as BaO are being incorporated into new catalytic designs to adsorb NO_x; periodic brief incursions into rich fuel-burn operation conditions are then induced to release and reduce the trapped NO_x on the metal catalyst.[53] Another technical problem in the present systems is their ineffectiveness during the so-called cold start, right after the engine is turned on; this is the time when most of the polluting hydrocarbon emissions takes place. The challenge here is to either develop ways to achieve fast heating of the catalyst to its light-off temperature or to design catalysts more active under lower operating temperatures.[53] New metal-based formulations have already been incorporated in the new generations of automobile catalytic converters.

Three-way catalysts are mainly used to treat gaseous pollutants from mobile engines. In stationary sources such as power generators and industrial plants for the production of nitric acid and other chemicals, the most important requirements in terms of environmental control are the removal of NO_x and volatile organic compounds (VOCs) from gas discharges. In general, NO_x is selectively reduced (SCR) on either V_2O_5-WO_3/TiO_2 or metal-exchanged zeolite catalysts with NH_3 or urea. However, the use of nitrogen-containing reducing agents can lead to the production of other pollutants, so recent attempts have been made to use metal catalysts such as Pd/TiO_2 together with methane as the reducing agent instead.[54] In terms of the treatment of VOCs, they are often burned over Pt/Al_2O_3-BaO or Pd/Al_2O_3 catalysts in order to lower the temperature of the process well below those used in conventional flame combustion (up to 2000 °C).[51]

Customized catalysts are also available for more specialized environmental uses. For instance, Pt/mordenite catalysts are used for the treatment of air pollutants in spray painting and coating workshops, and also to control emission in benzoic anhydride manufacturing industries. Pt–V_2O_5–$SO_4{}^{2-}$/mordenite is sometimes employed to purify flue gases containing sulfur compounds. Metal-based catalysts are ideal for such applications, because they work at low reactant concentrations (4–6 g/m^3), high space velocities

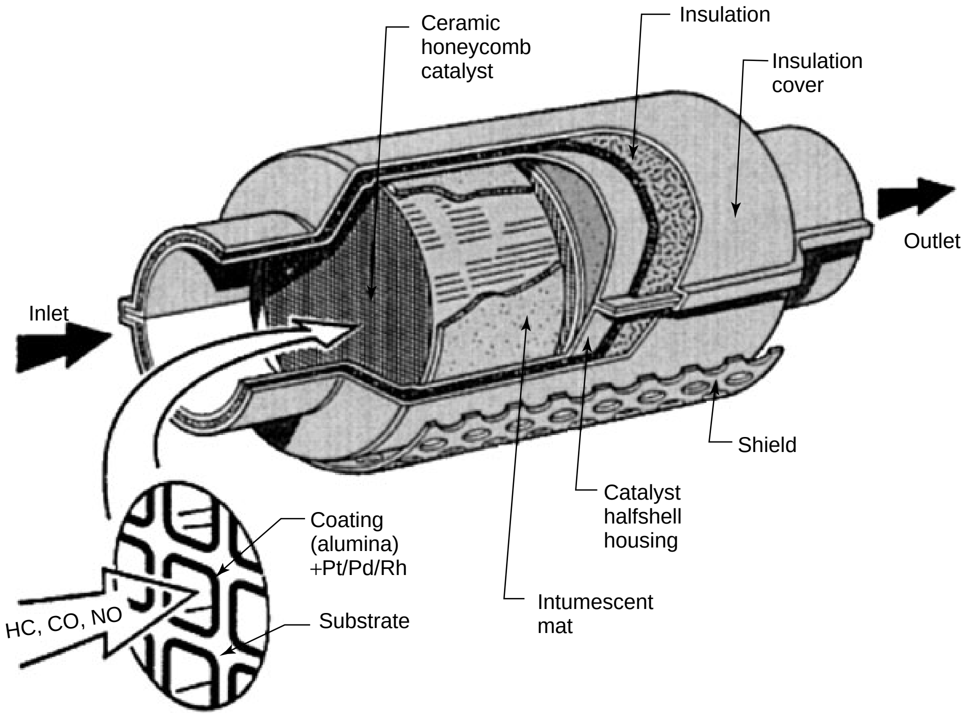
Ceramic honeycomb catalyst
Insulation
Insulation cover
Outlet
Inlet
Shield
Catalyst halfshell housing
Coating (alumina) +Pt/Pd/Rh
HC, CO, NO
Substrate
Intumescent mat

Figure 8 Typical design of a three-way catalyst for automobile exhaust control. Highlighted here are the honeycomb support and the mounting can used. So-called three-way catalysts, consisting of a combination of Pt, Rh, and Pd particles dispersed on high surface area alumina, are spread on the honeycomb structure to oxidize the carbon monoxide and unburned hydrocarbons and to reduce the nitrogen oxides released by the engine of the car. (Reprinted from Ref. 52, © 1998, with permission from Elsevier)

($4500-20\,000\,\text{h}^{-1}$), and low temperatures ($150-400\,°\text{C}$). Processes such as those mentioned above have been adopted in more than 1000 factories in China and Japan alone.[55]

Another use of environmental catalysis is in the hydrodechlorination of chlorine-containing pollutants such as chlorinated olefins, chlorobenzenes, chlorophenols, and chlorofluorocarbons. Thermal combustion of these chemicals has been demonstrated on a commercial scale, but the required high temperatures for incineration lead to the formation of toxic dioxins. Alternatively, supported Pd, Pt, Rh, Ni, Pd–Au and Pd–Re catalysts can be used to remove the chlorine atoms from those molecules via hydrogenation reactions.[56,57] Hydrodechlorination is also one of the purifying steps needed to improve the quality of drinking water and to clean waste water.[58] In another example, zero-valent iron has been used as an electrocatalyst for the removal of both organic chlorinates and inorganic salts such as arsenates from groundwater.[59] Wet air oxidation is used to remove dissolved organic pollutants, and hydrodenitrification is used to abate inorganic salts such as nitrates and nitrites in water.[58] Other applications of metal catalysis in this area include the indoor detection and room temperature oxidation of carbon monoxide, the elimination of odors in indoor environments, and the decomposition of aqueous ozone.[51]

4 PROMISING NEW DIRECTIONS IN HETEROGENEOUS METAL CATALYSIS

The field of catalysis is a mature one, with a history over 100 years old. Nevertheless, new opportunities keep on developing in this area. Below, some of the new directions that we believe will lead the near future of heterogeneous catalysis are advanced.

4.1 Novel Catalytic Materials

One of the main problems of traditional metal catalysts is that they are fairly ill-defined, in that the shapes of the metal particles on the supports are often irregular, that their particle size distributions are broad, and that no strict control can be exerted on interparticle distances. Recent developments in material technologies promise to provide new metallic materials, new supports, and new methodologies for the fabrication of better defined catalysts.

One family of new materials with potential use in metal catalysis is that of metal nanostructures such as metal nanoparticles (*see* ***Metal Nanoparticles, Synthesis of*** and ***Metal Nanoparticles, Organization & Applications of***), nanoshells, nanowires, nanorods, nanotubes, nanobelts, and nanoplates.[60–62] For instance, it has been recently shown that Ag nanowires and nanoparticles can be produced by

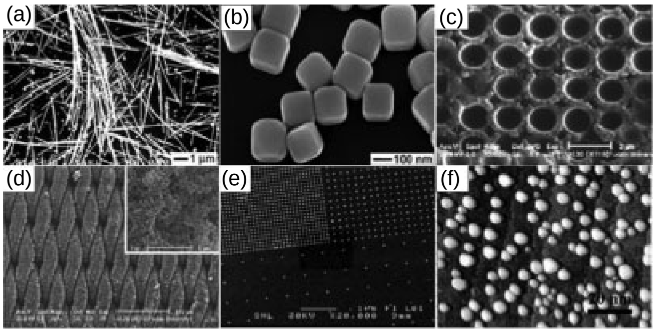

Figure 9 Examples of novel materials with potential catalytic applications. From left to right and top to bottom, these pictures represent: (a) Ag nanowires. (Reprinted with permission from Ref. 63. © 2002 American Chemical Society); (b) Ag nanoparticles. (Reprinted with permission from Y. Sun and Y. Xia, *Science*, 2002, **298**, 2176. © 2002 AAAS (www.sciencemag.org)); (c) zeolite monolith. (Ref. 67. Reproduced by permission of Kluwer Academic/Plenum Publishers); (d) zeolite coatings on stainless steel grids. (Ref. 68. Reproduced by permission of Wiley-VCH); (e) arrays of Pt nano lithography-made particles on SiO_2. (Ref. 70. Reproduced by permission of Kluwer Academic/Plenum Publishers); and (f) Ag nanoparticles vapor deposited on an Al_2O_3 thin film[71]

nucleation and growth on nanoseeds produced by first reducing $PtCl_2$ or $AgNO_3$ with ethylene glycol (Figures 9a and 9b).[63,64] Moreover, those Ag nanowires can be further used as templates to grow Au, Pt, or Pd nanotubes with hollow interiors.[62] The controlled growth of other metals with various nanostructures have been reported in the recent literature, but their uses in catalysis are still in the embryonic stages. One tantalizing result in this direction is that of the use of palladium nanoshells and nanotubes to catalyze the Suzuki coupling reaction with up to 100% yield.[61,62]

Because of their ordered pore structures and adjustable acid-base properties, zeolites have long been used as supports for many catalysts. However, the small size of the micropores in zeolites (diameter < 1 nm) limits their application when dealing with bulky molecules.[16,65] The recent development of mesoporous metal oxides (*see* ***Porous Inorganic Materials***) with ordered nano channels promises to allow for the engineering of ‘nano reactors’ for reactions involving fine chemicals and pharmaceuticals. Organometallic compounds, metal oxides, heteropolyacids, and enzymes have all been supported onto mesoporous silica, but the application of mesoporous supports in metal catalysis has only started.[65,66] Advanced zeolite-based architectures such as zeolite shells, fibers, tissues, monoliths, capsules, membranes, and coatings as well as mesoporous materials with sturdy zeolite walls have also been constructed by assembly of nanozeolite building blocks (Figures 9c and 9d).[67–69] These new materials with ordered secondary advanced structures are expected to allow for fast mass transfer during catalysis.

Physical methods such as those developed for the semiconductor industry have also started to make an inroad into metal catalysis.[38,70,71] Figures 9e and 9f show micrographs of metal particles supported on metal oxide thin films fabricated by electron beam lithography and by metal vapor deposition, respectively.[70,71] As exemplified by Figure 9e, the size, height, and spatial distribution of the metal particles may be easily adjusted with these techniques according to experimental needs. Although applications of these new materials technologies to the manufacturing of new commercial catalysts are still somewhere in the future, they already offer new opportunities for the study of reaction kinetics on supported metal particles with unique and uniform structures.

4.2 Surface Science of Catalysis

The development of new catalytic materials needs to be complemented with detailed studies of the surface chemistry of catalysis at the molecular level in order to better define the requirements for the catalytic active sites. The wide array of modern spectroscopies available to surface scientists today is ideally suited for this task (*see* ***Surfaces***). Surface science studies on catalysis typically probe reaction intermediates on model metal samples under well controlled conditions. This kind of study is traditionally carried out in ultrahigh vacuum (UHV) systems such as that shown in Figure 10. Single crystals or other well-defined metal surfaces are cleaned and characterized in situ by physical and chemical means, and then probed using a battery of surface sensitive techniques such as photoelectron (XPS and UPS), electron energy loss (ELS

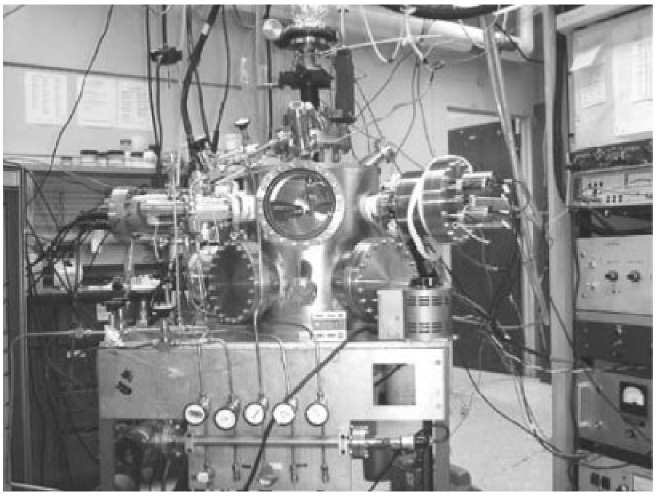

Figure 10 Typical ultrahigh vacuum system used for surface science studies of catalytic reactions on model systems.[74] The combined development of new preparation methods for realistic catalytic samples and in situ spectroscopies for the molecular level characterization of surface species during catalysis promises to advance the basic understanding of catalytic processes

and HREELS), secondary ion mass (SIMS), infrared (IR), and temperature programmed desorption (TPD) spectroscopies. By characterizing the catalytic surface before, during, and after chemical reactions using a combination of these surface science methods, a molecular picture of the reaction pathways of catalytic processes on solid surfaces can be extracted.[38,72–74]

Although traditional surface science studies have greatly helped advance our understanding of catalysis at a fundamental level, the differences between the pressure and materials employed in UHV studies and those encountered in applied catalysis have limited the extrapolation of the knowledge developed this way to real systems. Ex-situ characterization experiments can be carried out on catalytic surfaces before and after reactions, but those are also subject to limitations due to potential changes during the handling of the sample. This is why there has been a renewed interest in closing these so-called ‘materials’ and ‘pressure’ gaps between surface science and catalysis by using new spectroscopic and material preparation methods. To bridge the materials gap, novel model catalysts consisting of metal particles supported on planar metal oxide thin films have started to be developed and tested for a number of simple catalytic reactions such as ethylene hydrogenation, CO methanation, CO oxidation, ethane hydrogenolysis, NO reduction, and methanol decomposition.[38,75,76] To bridge the pressure gap, in situ spectroscopic methods such as sum frequency generation (SFG), Fourier transform infrared (FT-IR), and Raman spectroscopies as well as scanning (STM) and electron (SEM, TEM) microscopies adopted for *in situ* operation under nonvacuum conditions have been employed to study reactions on metal surfaces under realistic conditions.[77] These approaches promise to advance our fundamental chemical understanding of complex catalytic systems at the molecular level.

4.3 High Throughput Catalyst Testing

Because of the complexity of catalytic systems and the lack of understanding of their microscopic properties, the design of catalysts from first principles is still limited. Instead, the traditional way of developing successful catalysts in industry has been by trial and error. This approach is not only costly, but also time-consuming. Consequently, to expedite the development of new catalysts, intensive efforts have been recently placed on automating their production and characterization during the first stages of screening. With these high throughput (sometimes called combinatorial) techniques, small amounts of many catalysts with slightly different and systematically varied compositions are prepared in parallel, and simultaneously subjected to reaction testing by techniques such as scanning mass spectrometry, resonance-enhanced multiphoton ionization, fluorescence detection, and IR thermography. The data collected are subsequently analyzed with the aid of computers and sophisticated software to mine promising leads from the thousands of candidates. The best cases are then scaled up, optimized, and subjected to a more quantitative second screening to select even better leads for further scaling up and testing in conventional lab reactors.[78]

High throughput catalyst screening is especially useful for the development of metal catalysts with multiple components such as alloys. Figure 11 shows the results of a secondary screening of four-component catalysts for the

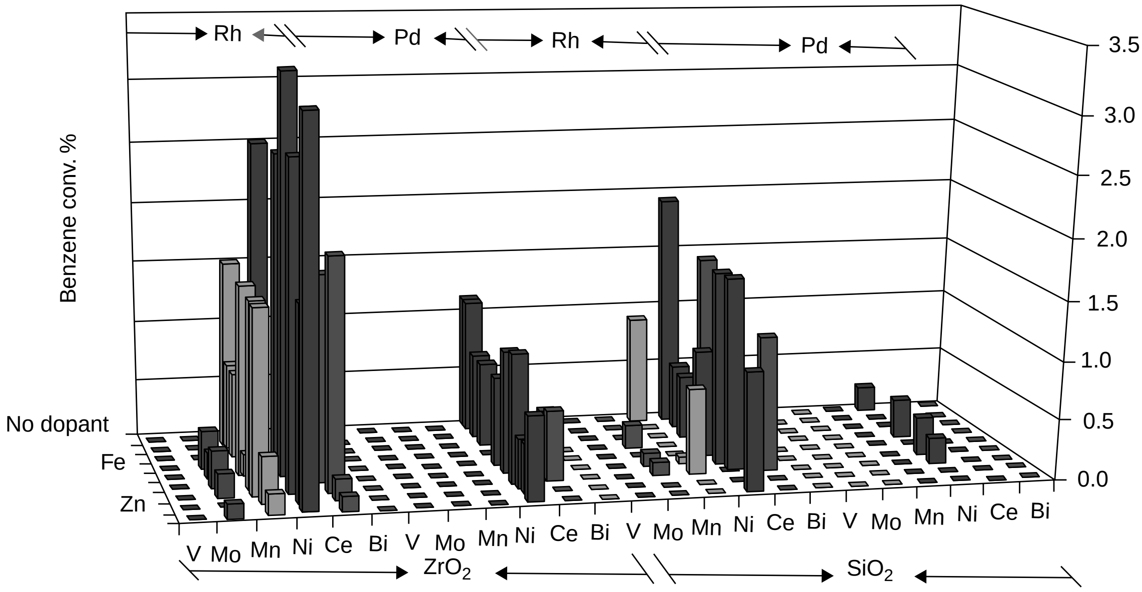

Figure 11 Results from high throughput studies on four-component catalysts for the direct ammination of benzene to aniline. A library with (Rh, Pd)–M_1–M_2–(ZrO_2, SiO_2) components was tested. New technology for the fast screening of complex materials offers an opportunity to test a wide variety of potential catalysts for specific catalytic applications. (Reprinted from Ref. 79, © 1998, with permission from Elsevier)

direct ammination of benzene to aniline. The library used there consists of combinations of an active metal (Rh or Pd), a support (ZrO_2 or SiO_2), an oxidant (V, Mo, Mn, Ni, Ce, or Bi), and a dopant (blank, V, Cr, Mn, Fe, Co, Ni, Cu, or Zn).[79] 216 samples generated by the combination of these four components were tested 24 samples at a time by using parallel high-pressure batch reactors. It became clear from these data that ZrO_2 is a better support than SiO_2, that Rh is a better metal than Pd, that NiO is the best oxidant, and that metal dopants can further modify the overall activity of the system.[79] The use of combinatorial methods for the development of a few other catalysts for processes such as the oxidation of CO by O_2 or NO with Rh–Pd–Pt alloys has been reported as well. Nevertheless, their usefulness for the design of commercial catalysts is still in question.[78,80]

4.4 Improved Selectivities, Green Chemistry

Historically, the emphasis in catalysis has been on increasing activity rather than selectivity. This is not surprising, since catalysts are generally regarded as substances that can speed up reactions. In addition, many early catalytic processes were based on relatively simple reactions with negligible sidesteps. As the field of catalysis expanded and covered more complex reactions, however, selectivity started to become crucial in designing industrial processes.[81] One example of this already mentioned above is that of the partial oxidation of alcohols to oxygenated hydrocarbons.[82]

A more subtle but important example of the need for good catalytic selectivity is that of the manufacture of chiral medicines. The market for single-enantiomer drugs has recently reached 160 billion dollars, accounting for close to half of the profits from sales of drugs worldwide.[83] If regular catalysts are used, only racemic mixtures of the products are obtained. This is at the very least quite wasteful, since those processes require at least twice the amount of reactants. Moreover, in many instances, one enantiomer may be biologically active but the other may be poisonous, so the desired product needs to be isolated by expensive separation techniques such as selective crystallization, chiral chromatography, membrane separation, or chemical methods. Clearly, the production of enantiomerically pure chemicals directly via heterogeneous catalysis would be much preferred. In this direction, tartaric acid-modified nickel and cinchona-modified platinum catalytic systems have proven successful for the enantioselective hydrogenation of β- and α-ketoesters, respectively, showing enantioselectivities of up to 98%.[44,84] The role of the chiral modifiers is still not fully understood, but in the latter case appears to involve the formation of a 1:1 complex with the reactant on the surface to force an adsorption geometry where the hydrogenation is only possible on one side of the molecule (Figure 12).[84] The use of heterogeneous catalysis in chiral manufacturing is still quite limited, but ongoing work to try to understand the details of this chemistry promises to lead to the development of new catalysts for these applications.[85]

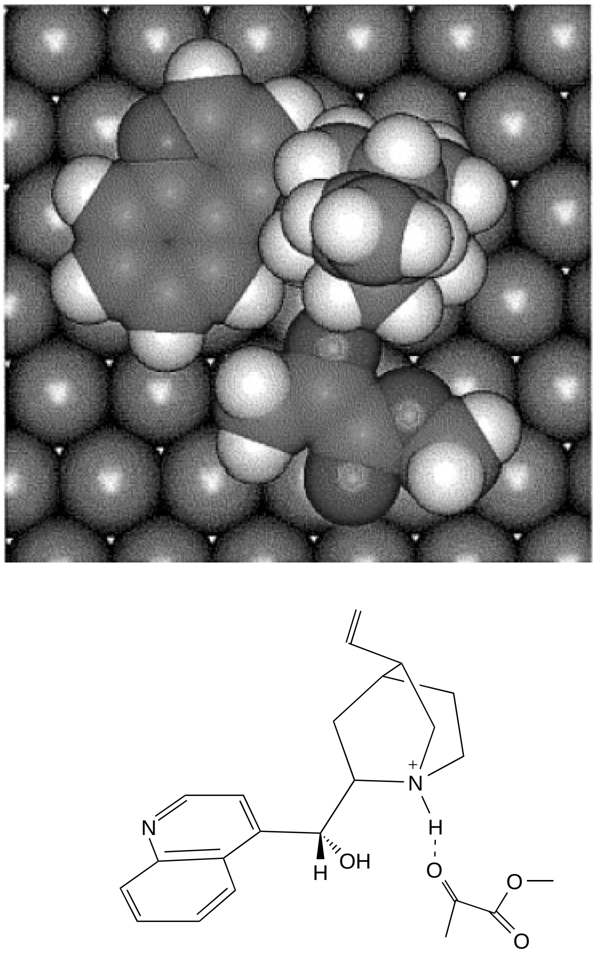

Figure 12 Schematic representation of the mechanism proposed for the enantioselective hydrogenation of α-ketoesters on cinchonidine-modified platinum catalyst. The development of general methods for imparting enantioselectivity to regular heterogeneous catalysts promises to revolutionize the pharmaceutical and agrochemical industries[84]

Many industrial catalytic processes in use nowadays are far from ideal in terms of cleanliness, economy, and simplicity. For one, multiple-steps processes often require the disposal of many side products, and display low compounded yields. With the introduction of the concept of green chemistry in the 1990s, whereby a new emphasis is placed on the design of chemical products and processes that reduce or eliminate the use and generation of hazardous substances, significant efforts are being placed to develop alternative more efficient routes to replace some existing processes in industry.[86,87] Heterogeneous metal catalysis is expected to play a crucial role in these new processes as well.

5 REFERENCES

1. R. A. van Santen, P. W. N. M. van Leeuwen, J. A. Moulijn, and B. A. Averill eds, 'Catalysis: An Integrated Approach', Elsevier, Amsterdam, 1999.
2. North American Catalysis Society, http://www.nacatsoc.org/edu_catalysis.asp, 2005.
3. G. C. Bond, 'Catalysis by Metals', Academic Press, London, 1962.
4. C. N. Satterfield, 'Heterogeneous Catalysis in Industrial Practice', Krieger Publishing, Malabar, 1996.
5. F. Zaera, *Acc. Chem. Res.*, 2002, **35**, 129.
6. G. C. Bond, 'Heterogeneous Catalysis: Principles and Applications', Clarendon Press, Oxford, 1974.
7. J. M. Thomas and W. J. Thomas, 'Introduction to the Principles of Heterogeneous Catalysis', Academic Press, London, 1967.
8. M. Boudart and G. Djéga-Mariadassou, 'Kinetics of Heterogeneous Catalytic Reactions', Princeton University Press, Princeton, NJ, 1984.
9. W. J. M. Rootsaert and W. M. H. Sachtler, *Z. Phys. Chem. N.F.*, 1960, **26**, 16.
10. B. C. Gates, 'Catalytic Chemistry', John Wiley & Sons, New York, 1992.
11. A. Ozaki and K. Aika, in 'Catalysis: Science and Technology', eds. J. R. Anderson and M. Boudart, Springer-Verlag, New York, 1981, Vol. 1, p. 87.
12. G. A. Somorjai, 'Introduction to Surface Chemistry and Catalysis', John Wiley & Sons, New York, 1994.
13. B. Cornils, W. A. Herrmann, R. Schlögl, and C. H. Wong eds, 'Catalysis from A to Z', Wiley-VCH, Weinheim, 2000.
14. F. Zaera, *J. Phys. Chem. B*, 2002, **106**, 4043.
15. E. A. Sales, B. Benhamida, V. Caizergues, J.-P. Lagier, F. Fiévet, and F. Bozon-Verduraz, *Appl. Catal. A*, 1998, **172**, 273.
16. M. E. Davis, *Ind. Eng. Chem. Res.*, 1991, **30**, 1675.
17. G. Ertl, H. Knözinger, and J. Weitkamp eds, 'Handbook of Heterogeneous Catalysis', VCH, Weinheim, 1997.
18. C. Perego and P. Villa, *Catal. Today*, 1997, **34**, 281.
19. F. Pinna, *Catal. Today*, 1998, **41**, 129.
20. R. D. Gonzalez, T. Lopez, and R. Gomez, *Catal. Today*, 1997, **35**, 293.
21. R. B. Anderson and P. T. Dawson eds, 'Experimental Methods in Catalytic Research', Academic Press, New York, 1976, Vol. 3.
22. G. Leofanti, G. Tozzola, M. Padovan, G. Petrini, S. Bordiga, and A. Zecchina, *Catal. Today*, 1997, **34**, 307.
23. J. W. Niemantsverdriet, 'Spectroscopy in Catalysis', Wiley-VCH, Weinheim, 2000.
24. J. F. Haw ed., 'In Situ Spectroscopy in Heterogeneous Catalysis', Wiley-VCH, Weinheim, 2002.
25. F. Zaera, in 'Encyclopedia of Chemical Physics and Physical Chemistry', eds. J. Moore and N. Spencer, Institute of Physics Publishing, Bristol, 2001, Vol. 2, p. 1563.
26. US National Academy of Engineering, http://www.greatachievements.org, 2000.
27. Kirk-Othmer ed., 'Kirk-Othmer Encyclopedia of Chemical Technology', 4th ed., Wiley-Interscience, New York, 1992–1998, Vols. 1–27.
28. J. H. Sinfelt, in 'Catalysis: Science and Technology', eds. J. R. Anderson and M. Boudart, Springer-Verlag, New York, 1981, Vol. 1, p. 257.
29. F. Zaera and G. A. Somorjai, in 'Hydrogen Effects in Catalysis: Fundamental and Practical Applications', eds. Z. Paál and P. G. Menon, Marcell Dekker, New York, 1988.
30. M. E. Dry, *Catal. Today*, 2002, **71**, 227.
31. A. H. Tullo, *Chem. Eng. News*, 2003, **81**(29), 18.
32. P. Biloen and W. M. H. Sachtler, *Adv. Catal.*, 1981, **30**, 165.
33. S. Balcon, S. Mary, C. Kappenstein, and E. Gengembre, *Appl. Catal. A*, 2000, **196**, 179.
34. M. Jacoby, *Chem. Eng. News*, 2003, **81**(3), 32.
35. P. M. Urban, A. Funke, J. T. Müller, M. Himmen, and A. Doctor, *Appl. Catal. A*, 2001, **221**, 459.
36. L. Carrette, K. A. Friedrich, and U. Stimming, *Chem. Phys. Chem.*, 2000, **1**, 162.
37. M. Grunze, in 'The Chemistry and Physics of Solid Surface and Heterogeneous Catalysis', eds. D. A. King and D. P. Woodruff, Elsevier, Amsterdam, 1982, Vol. 4, p. 143.
38. G. A. Somorjai, *J. Phys. Chem. B*, 2000, **104**, 2969.
39. F. Zaera, *Surf. Sci.*, 2002, **500**, 947.
40. J. R. Monnier, *Appl. Catal. A*, 2001, **221**, 73.
41. M. Besson and P. Gallezot, *Catal. Today*, 2000, **57**, 127.
42. R. L. Augustine, *Catal. Today*, 1997, **37**, 419.
43. Johnson Matthey Catalysts, http://www.chemicals.matthey.com/catalysts/introhet.asp, 2001.
44. H. U. Blaser, F. Spindler, and M. Studer, *Appl. Catal. A*, 2001, **221**, 119.
45. H. U. Blaser, A. Indolese, A. Schnyder, H. Steiner, and M. Studer, *J. Mol. Catal. A*, 2001, **173**, 3.
46. B. Marciniec, *Silicon Chem.*, 2002, **1**, 155.
47. S. M. Davis, F. Zaera, and G. A. Somorjai, *J. Catal.*, 1982, **77**, 439.
48. K. P. de Jong and J. W. Geus, *Catal. Rev.-Sci. Eng.*, 2000, **42**, 481.
49. M. L. Toebes, F. F. Prinsloo, J. H. Bitter, A. J. van Dillen, and K. P. de Jong, *J. Catal.*, 2003, **214**, 78.
50. Y. Li, Y. Qian, H. Liao, Y. Ding, L. Yang, C. Xu, F. Li, and G. Zhou, *Science*, 1998, **281**, 246.
51. G. Centi, P. Ciambelli, S. Perathoner, and P. Russo, *Catal. Today*, 2002, **75**, 3.
52. R. M. Heck and R. J. Farrauto, *Appl. Catal. A*, 2001, **221**, 443.

53. M. Shelef and R. W. McCabe, *Catal. Today*, 2000, **62**, 35.
54. M. D. Fokema and J. Y. Ying, *Catal. Rev.*, 2001, **43**, 1.
55. Z. Gao, *Stud. Surf. Sci. Catal.*, 1998, **121**, 143.
56. M. Makkee, A. Wiersma, E. J. A. X. van de Sandt, H. van Bekkum, and J. A. Moulijn, *Catal. Today*, 2000, **55**, 125.
57. G. Yuan and M. A. Keane, *Catal. Commun.*, 2003, **4**, 195.
58. Y. I. Matatov and M. Sheintuch, *Ind. Eng. Chem. Res.*, 1998, **37**, 309.
59. J. Farrell, J. Wang, P. O'Day, and M. Conklin, *Environ. Sci. Technol.*, 2001, **35**, 2026.
60. M. A. El-Sayed, *Acc. Chem. Res.*, 2001, **34**, 257.
61. S.-W. Kim, M. Kim, W. Y. Lee, and T. Hyeon, *J. Am. Chem. Soc.*, 2002, **124**, 7642.
62. Y. Sun, B. Mayers, and Y. Xia, *Adv. Mater.*, 2003, **15**, 641.
63. Y. Sun, Y. Yin, B. T. Mayers, T. Herricks, and Y. Xia, *Chem. Mater.*, 2002, **14**, 4736.
64. Y. Sun and Y. Xia, *Science*, 2002, **298**, 2176.
65. A. Corma, *Chem. Rev.*, 1997, **97**, 2373.
66. D. T. On, D. Desplantier-Giscard, C. Danumah, and S. Kaliaguine, *Appl. Catal. A*, 2003, **253**, 545.
67. Y. Wang, Y. Tang, X. Wang, W. Shan, C. Ke, Z. Gao, J. Hu, and W. Yang, *J. Mater. Sci. Lett.*, 2001, **20**, 2091.
68. A. Dong, Y. Wang, Y. Tang, Y. Zhang, N. Ren, and Z. Gao, *Adv. Mater.*, 2002, **14**, 1506.
69. Y. Liu and T. J. Pinnavaia, *J. Mater. Chem.*, 2002, **12**, 3179.
70. B. Kasemo, S. Johansson, H. Persson, P. Thormählen, and V. P. Zhadanov, *Top. Catal.*, 2000, **13**, 43.
71. X. Lai and D. W. Goodman, *J. Mol. Catal. A*, 2000, **162**, 33.
72. D. P. Woodruff and T. A. Delchar, 'Modern Techniques of Surface Science', Cambridge University Press, Cambridge, MA, 1988.
73. C. T. Campbell, *Adv. Catal.*, 1989, **361**, 1.
74. F. Zaera, *Prog. Surf. Sci.*, 2001, **69**, 1.
75. D. W. Goodman, *J. Catal.*, 2003, **216**, 213.
76. H.-J. Freund, M. Bäumer, J. Libuda, T. Risse, G. Rupprechter, and S. Shaikhudinov, *J. Catal.*, 2003, **216**, 223.
77. G. A. Somorjai, *CATTECH*, 1999, **3**, 84.
78. B. Jandeleit, D. J. Schaefer, T. S. Powers, H. W. Turner, and W. H. Weinberg, *Angew. Chem., Int. Ed. Engl.*, 1999, **38**, 2494.
79. A. Hagemeyer, R. Borade, P. Desrosiers, S. Guan, D. M. Lowe, D. M. Poojary, H. Turner, H. Weinberg, X. Zhou, R. Armbrust, G. Fengler, and U. Notheis, *Appl. Catal. A*, 2002, **227**, 43.
80. A. H. Tullo, *Chem. Eng. News*, 2003, **81**(29), 14.
81. F. Zaera, *Catal. Lett.*, 2003, **91**, 1.
82. F. Zaera, *Catal. Today*, 2003, **81**, 149.
83. A. M. Rouhi, *Chem. Eng. News*, 2003, **81**(18), 45.
84. A. Baiker, *J. Mol. Catal. A*, 2000, **163**, 205.
85. Z. Ma, I. Lee, J. Kubota, and F. Zaera, *J. Mol. Catal. A*, 2004, **216**, 199.
86. W. F. Höelderich, *Catal. Today*, 2000, **62**, 115.
87. P. T. Anastas, M. M. Kirchhoff, and T. C. Williamson, *Appl. Catal. A*, 2001, **221**, 3.

High Pressure Synthesis of Solids

Mikio Takano,[1] Yasuo Takeda[2] & Osamu Ohtaka[3]
[1]*Kyoto University, Kyoto, Japan*
[2]*Mie University, Mie, Japan*
[3]*Osaka University, Osaka, Japan*

1 Introduction 1
2 Hydrothermal Synthesis 1
3 High Oxygen Pressure 3
4 High Pressure above 1 GPA 6
5 Related Articles 15
6 References 15

1 INTRODUCTION

Chemical composition, temperature, and pressure may be considered as the independent axes of the three-dimensional space in which materials exist. At high pressures, materials assuming compact structures are formed. Artificially, high pressure is generated by focusing a relatively small, manageable mechanical force upon a small area, and it is transmitted to the material to be compressed through a medium of gas, liquid, or solid. The highest static pressure attained using specially designed diamond anvils reaches ∼400 GPa, which is comparable with the Earth's core pressure.

The Earth itself is a huge high pressure and high temperature vessel.[1] The interior is so dynamic and mysterious that geochemists and geophysicists have long been driven to develop high pressure technology as a means to look into the interior. Another attractive research subject is concerned with behavior of solidified hydrogen under pressures of the order of 100 GPa.[2] In 1935, Wigner and Huntington predicted a pressure-induced transition from the insulating molecular phase to a metallic monoatomic phase.[3] Interest in the metallic monoatomic phase has increased because of the possibility of high-temperature superconductivity[4] and also for its possible existence on a massive scale in Jupiter and Saturn.

Diamond, the hardest material known, is the most representative inorganic product of natural and artificial high pressure synthesis. As illustrated later, it can be obtained from graphite at 5.4 GPa and 1667 K, typically,[5] while it is not diamond but graphite that is thermodynamically stable at ambient conditions. Though solid hydrogen cannot be 'quenched' to ambient conditions, diamond can be and remains stable, in effect, to about 600 K. From practical viewpoints, high pressure synthesis is of value if the product has a particular important property and, at the same time, if it is stable after being decompressed.

Also included in some successful cases is the application of high pressure for the purpose of crystal growth: growth of huge rock crystals (∼1 kg each) by means of a hydrothermal technique utilizing hot compressed water (650 K and 150 MPa, typically)[6] has proved to be of great technological significance. In this case, high pressure is generated internally by heating volatile water confined in a vessel (autoclave), not by application of a mechanical force from the outside. The use of high oxygen pressures generated similarly, will also be included in this article.

From an academic viewpoint, factors such as metastability and crystal size are not so important. Phase identification, chemical reaction, and physical properties such as magnetism, conductivity, elasticity, and so on can be studied for a sample of 10 mg (or even much less depending upon the research subject) in a short time. These studies can even be done in situ, that is, under high pressure at various temperatures.

In this article, both classical and modern aspects of high pressure synthesis will be outlined, taking diamond, rock crystals (α-quartz), perovskites, and some other materials as examples.

2 HYDROTHERMAL SYNTHESIS[6–8]

2.1 Outline

Hydrothermal synthesis is carried out in the presence of water heated above 373 K in a pressure vessel. Geologists and mineralogists initiated this method in the nineteenth century, since they knew that many kinds of minerals, and beautiful crystals of them, formed from magma containing compressed hot water and steam.

The system enclosed in the vessel contains water as a volatile, low-melting point component which lowers the liquidus curve. The increase in the solubility of solids, even of those insoluble at ambient pressure up to the boiling point of water, such as $BaSO_4$, SiO_2, and metals, is quite remarkable, and this makes it possible to control their reactivity and also to control their precipitation or their reaction products, so that beautiful and pure crystals may grow. Water plays multiple roles as a solvent, as a catalyst accelerating the attainment of equilibrium between different crystalline solids, and as a mineralizer that accelerates crystal growth. It is known that the appropriate choice of pH and additive is also important. Water may or may not remain in the precipitates as an ingredient. A variety of crystals obtained with this method are listed, with the temperature and pressure conditions, in Table 1.

The advantages of this method are as follows. These essentially come from the use of a low temperature homogeneous reaction in a closed system.

Table 1 Hydrothermal crystal growth

		Temperature (K)		
Material	Solvent	Solution zone	Growth zone	Pressure (MPa) (Degree of fill (%)
α-Al_2O_3	2–3.4 M Na_2CO_3 or K_2CO_3	770–810	660–760	110–160 (75–82)
$AlPO_4$	6.1 M H_2PO_4 + 3.8 M $NH_4H_2PO_4$		Slow heating: 520 → 670	(80)
$BaPb_{0.75}Bi_{0.25}O_3$	3 M NaOH	700–750	670–720	100
$CaCO_3$	0.1–0.2 M NH_4NO_3	430–480	420–470	50–150
$CaWO_4$	4% wt NaOH	700	650	(60–70)
CdS	1 M HCl or HBr		770	130
ZnO	3–6 M KOH + 0.5–2 M LiOH	650–670	630–650	60–120
Fe_3O_4	1–5 M NaOH	650–680	625–655	(75–80)
$NiFe_2O_4$	0.5 M NH_4Cl		740–750	110–130 (70–75)
α-SiO_2	0.5–1 M NaOH or 0.25–0.5 M Na_2CO_3	630–640	600–610	80–150 (75–85)
$Y_3Al_5O_{12}$	2 M K_2CO_3	870	820	100
$YfeO_3$	20–25 M KOH	680	650	(70–90)
$Y_3Fe_5O_{12}$	20 M KOH	700	660	(87)

1. Crystals that decompose or lose volatile components at elevated temperatures can be prepared.
2. Low temperature polymorphs can be obtained (*see Polymorph*).
3. Pure and high-quality crystals can be grown. Concentrations of impurities, point defects, and dislocations are generally low (*see* ***Defects in Solids***).
4. The oxidation state of transition metals can be controlled by using appropriate oxidants or reductants (*see Formal Oxidation State* and *Oxidation Number*).

2.2 Apparatus

Laboratory experiments below 800 K and 100 MPa can be conducted with sealed autoclaves developed initially by Morey *et al.*[9] Figure 1(a) shows this type of vessel, which is to be wholly put into a furnace. The liner and the seal disk are made of an inactive metal such as silver or gold. Since the pressure cannot be measured directly, one should calculate it from the degree of fill and the pressure–volume–temperature (*PVT*) data of water.[10]

At higher temperatures and pressures to 1300 K and 300 MPa, test-tube type vessels, like the one illustrated in Figure 1(b), are most generally used (first developed by Tuttle).[11] The vessel is made of superalloy, a group of alloys containing Co and Ni and some additional elements such as Cr and Mo. A small silver or gold-welded capsule containing starting solid materials and an appropriate aqueous solution is placed in the bottom of the vessel. The degree of fill and temperature determine the pressure balance with the surrounding water in the tube.

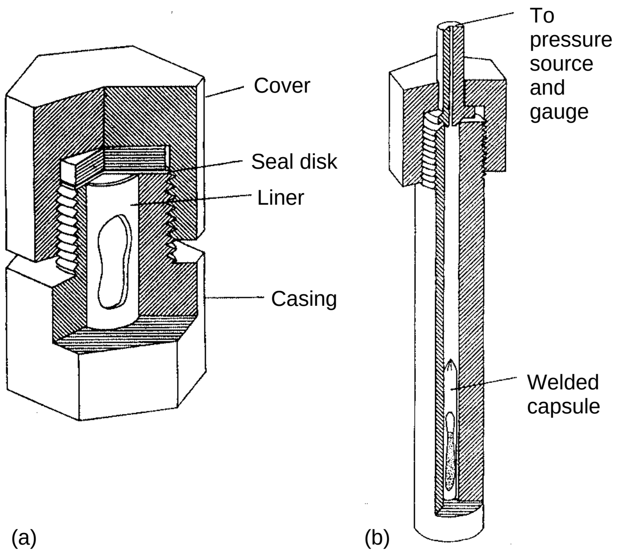

Figure 1 (a) Morey vessel and (b) test-tube type vessel

2.3 α-Quartz (Rock Crystal)[12]

α-Quartz, α-SiO_2, is an extremely important material for its piezoelectricity and also for its optical transparency over a wide range from ultraviolet to infrared. Because the piezoelectric property is anisotropic, depending upon the crystalline orientation, and because polycrystalline compacts are far less transparent, single crystals serve for commercial use. A suitable hydrothermal growth technique was basically established in the 1950s. 2.5 tons of crystals can be grown in one run in a huge autoclave of 5-m^3 capacity, working at 150 MPa.

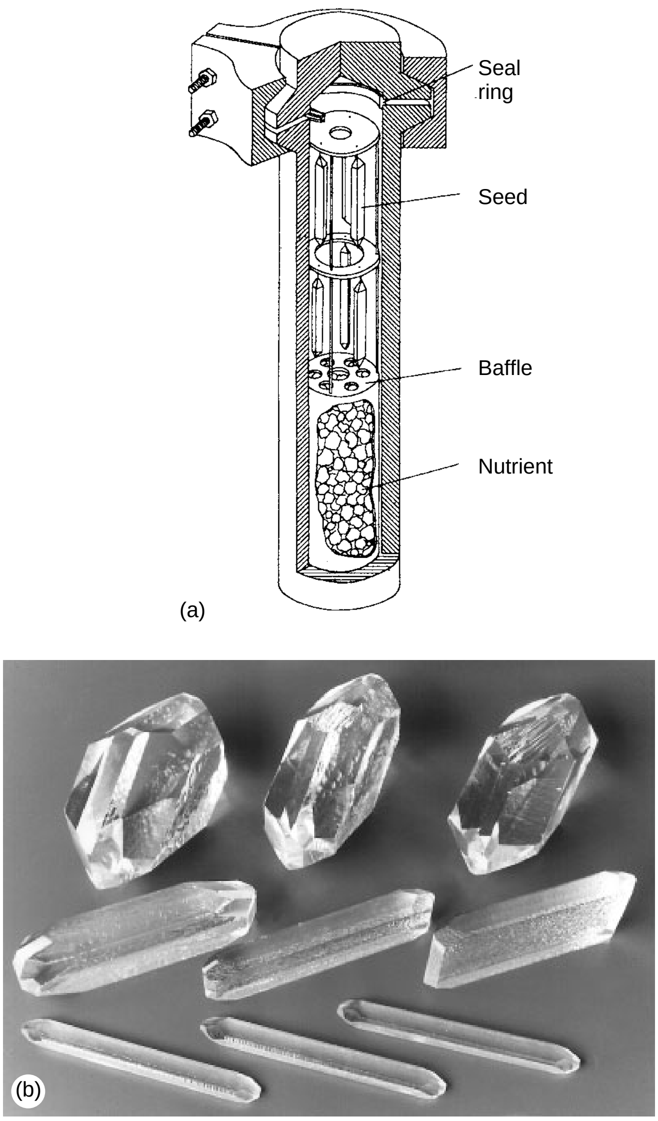

Figure 2 (a) Autoclave for the growth of rock crystals and (b) a photo of cultured crystals. (Courtesy Nihon Dempa Kogyo Co., Ltd)

In the autoclave illustrated in Figure 2(a), a baffle plate separates the reaction chamber into two parts, the upper cool zone and the lower hot zone. α-Quartz is dissolved in the lower zone and deposited on the seed crystals supported in the upper zone. This is because the solubility in water depends upon temperature at 150 MPa. The solution is made alkaline (0.5–1 M) with NaOH or Na_2CO_3 to raise the solubility by an order of magnitude.

To minimize the content of a specific impurity, the OH group, that seriously affects the piezoelectric properties, crystals are grown slowly, at a rate of 0.5–1.5 mm day^{-1}. The temperature of the hot and cool zones are kept at 630–640 K and 600–610 K, respectively, for 20–100 days. Some beautiful crystals thus obtained are shown in Figure 2(b). It should be noted that the crystal growth is carried out at such a low temperature. More common techniques allowing crystals to grow from their molten liquids cannot be applied to α-quartz, because a structural transition to the β-form occurs at 846 K.

Note finally that the solubility does not always vary monotonically with temperature and pressure. So the optimum experimental conditions need to be searched for very carefully. Mentioning an unusual example from Table 1, $AlPO_4$ dissolves at 520 K and grows at 670 K.

3 HIGH OXYGEN PRESSURE

3.1 Outline

Structural details and physical properties of transition metal oxides depend quite remarkably upon their oxygen content.[13] $SrFeO_3$ crystallizing in the cubic perovskite structure (see Figure 9(b)) retains metallic conductivity down to the lowest temperature, while $SrFeO_{2.95}$ is semiconductive at room temperature. A better known case is $YBa_2Cu_3O_{7-z}$.[14] It is a superconductor with a transition temperature (T_c) at 93 K for $z \leq 0.1$, while it is insulative at $z = 1$. On the other hand, $SrTiO_3$ is an insulator, while $SrTiO_{3-x}$ is a superconductor. Moreover, oxygen vacancies usually interact very strongly with each other, leading to a series of compounds with discrete vacancy contents and vacancy ordered superstructures. For example, a homologous series of oxygen-deficient phases $SrFeO_{3-1/n}$ with $n = \infty$, 8, 4, and 2 are known.[15] It is to be noticed that the formal oxidation state of transition metals changes with oxygen content as it varies from Fe^{IV} for the $n = \infty$ phase, $SrFeO_3$, to Fe^{III} for the $n = 2$ phase, $Sr_2Fe_2O_5$ (*see* ***Mixed Valence Compounds***; ***Oxides: Solid-state Chemistry***; ***Superconductivity***; *Metal–Insulator Transitions*; *Formal Oxidation State*; *Oxidation Number*).

Change in oxygen content also causes a change in color. TiO_2 is a colorless insulator, while reduction toward Ti_2O_3 makes it colored and conductive. Between these is a series of many phases formulated as Ti_nO_{2n-1} with $3 \leq n \leq 50$. Ti_2O_3 powder looks reddish black, while slightly oxidized Ti_3O_5 powder is bluish black. A mixed powder of these (1:1) looks completely black and is used as a harmless cosmetic pigment.[16]

Control of oxygen content is thus very important from various aspects. High oxygen pressure[17] can be used in two seemingly opposite ways, to increase oxygen content (as in equation 1) and to decrease it (as in equation 2). In either case, high pressure is used as a means to control oxygen fugacity. Representative experiments are listed in Table 2.

$$2SrFeO_{3-z} + zO_2 \longrightarrow 2SrFeO_3 \qquad (1)$$

$$2CrO_3 \longrightarrow 2CrO_2 + O_2 \qquad (2)$$

Table 2 Treatments at high oxygen pressure

Structure type	Product[a]	Starting material	Oxygen pressure (MPa)	Temperature (K)	Remarks (Special oxygen source)
Rutile	$Cr^{IV}O_2$	CrO_3	10	670	
	CrO_2	$Cr(OH)_3$	10	670	
	$Pt^{IV}O_2$	‘Hexagonal PtO_2’	300	970	
	$Rh^{IV}O_2$	‘Unidentified structure RhO_2’	300	970	
Pyrochlore	$R_2Pt_2^{IV}O_7$	$R_2O_3 + 2$ ‘PtO_2’	300	970	$R = Nd$ to Ho, Y
	$R_2Pd_2^{IV}O_7$	$R_2O_3 + 2PdO_2$	6000	1300	$R = Gd$, Dy, Y $(KClO_4)^b$
	$Y_2Cr_2^{IV}O_7$	$Y_2O_3 + Cr_2O_3$	7000	1250	$(KClO_4)^b$
Perovskite	$CaFe^{IV}O_3$	$Ca_2Fe_2O_5$	2000	1220	$(CrO_3, KClO_4)^b$
	$SrFe^{IV}O_3$	$SrFeO_{2.8}$	100	570	
	$La_2LiFe^{V}O_6$	$2La_2O_3 + Li_2O + Fe_2O_3$	6500	1270	$(KClO_3)^b$
	$SrCo^{IV}O_3$	$SrCoO_{3-z}$	100	570	
	$RNi^{III}O_3$	$R_2O_3 + NiO$	20–40	1270	$R = Pr$, Nd
	$LaCu^{III}O_3$	$La_2CuO_4 + CuO$	6500	1270	$(KClO_3)^b$
	$Tl^{I}Tl^{III}OF_2$	TlF_2	450	770	
Copper oxide superconductor	$Bi_2Sr_2CuO_{6+z}$	$Bi_2O_3 + 2SrO + CuO$	3	1110	
	$La_{1.8}Ca_{1.2}Cu_2O_{6+z}$	$La_{1.8}Ca_{1.2}Cu_2O_{6-z}$	40	1340	
	$Y_{0.9}Ca_{0.1}Ba_2Cu_4O_8$	Y_2O_3, CaO, BaO, CuO	20	1250	
	$La_2CuO_{4.08}$	La_2CuO_4	6000	1220	$(KClO_4)^b$

[a] Superscripts indicate the oxidation numbers of transition metals. [b] See Section 4.2.

3.2 Apparatus

Hydothermal vessels of the test-tube type can be used for the generation of high oxygen pressures below 800 MPa and 1100 K. A typical experimental system is illustrated in Figure 3(a), where oxygen is introduced from a reservoir to the reactor, by the aid of a compressor if necessary. The sample is contained in an open cell, not sealed. The degree of oxygen fill, temperature, and absorption, or release of oxygen by the sample determine the operational oxygen pressure. To avoid any explosive accident, special care should be taken. Any part of the system that the oxygen touches, the pipe line, valves, and so on should not be oiled or greased.

Illustrated in Figure 3(b) is an apparatus designed for hot isostatic pressing in an oxidizing atmosphere (O_2–HIP). The inside is filled with high pressure Ar–O_2 mixed gas. The maximum oxygen ratio is limited to 20% for safety and the maximum total gas pressure to 200 MPa. A large sample of $50\,cm^3$ can thus be treated at an oxygen partial pressure of 40 MPa and 1900 K. The heating element is a Pt–Rh alloy. Uniformity of oxygen pressure over the large sample volume, and the use of relatively high temperatures, accelerating reaction and crystallization, are the merits of this apparatus.

3.3 Materials

3.3.1 $SrFeO_3$

$SrFeO_3$ was the first phase found containing iron in its unusual high oxidation state of IV only.**[18]** By heating an appropriate mixture of $SrCO_3$ and α-Fe_2O_3 at 1300 K in air, one obtains $SrFeO_{3-z}$ with $z \approx 0.2$, not a single phase but a mixture of the $n = 8$ and 4 phases mentioned above.**[15]** For conversion to $SrFeO_3$ this mixture is treated at about 600 K at an oxygen pressure of 100 MPa.

3.3.2 CrO_2

CrO_2 is a metallic ferromagnet which can be used as a magnetic recording medium (*see* ***Magnetic Oxides*** and *Ferromagnetism*. Thermal decomposition of CrO_3 is the most common way to obtain this interesting material. The decomposition proceeds sequentially (as shown in equation 3), while at ambient atmosphere it is almost impossible to freeze the rapid process at CrO_2 before Cr_2O_3 forms. If CrO_3 is confined in a Morey’s vessel, it transforms with oxygen pressure and temperature as illustrated in Figure 4.**[19]** It is to be noted that the oxygen in the vessel originates from CrO_3 itself. By choosing the amount of CrO_3 and temperature one can thus obtain pure CrO_2 rather easily.

$$CrO_3 \longrightarrow Cr_3O_8 \longrightarrow Cr_2O_5 \longrightarrow CrO_2 \longrightarrow Cr_2O_3 \quad (3)$$

3.3.3 $YBa_2Cu_3O_7$, $Y_2Ba_4Cu_7O_{15}$, $YBa_2Cu_4O_8$

In 1986, Bednorz and Müller announced the high T_c superconductivity of $La_{2-x}Ba_xCuO_4$ ($x \approx 0.15$) (*see High-temperature Superconductivity*). Since then a few tens of superconducting copper oxides have been discovered, and the highest T_c reaches 135 K, far beyond liquid nitrogen temperature. Among these, $YBa_2Cu_3O_7$ is the celebrated

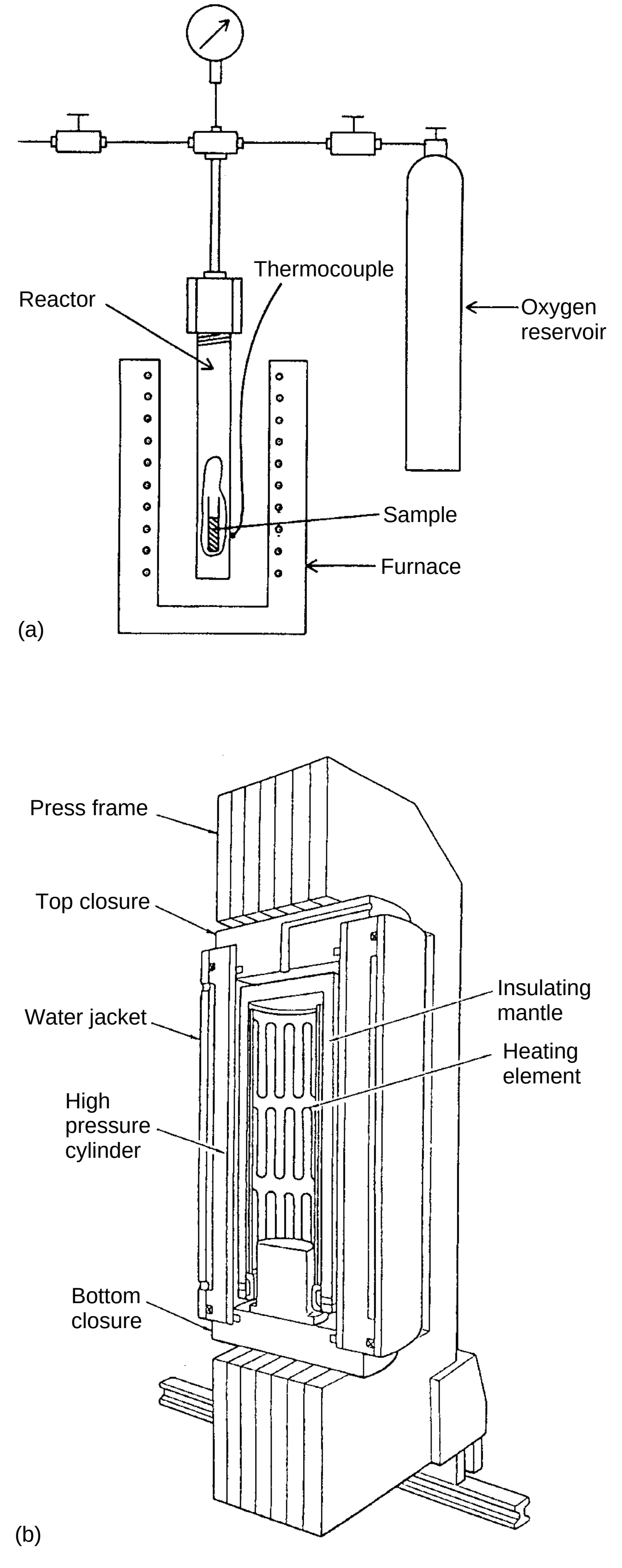

Figure 3 (a) Conventional high oxygen pressure system and (b) oxygen–hot isostatic pressing (O_2–HIP) apparatus. (Courtesy Kobe Steel, Ltd)

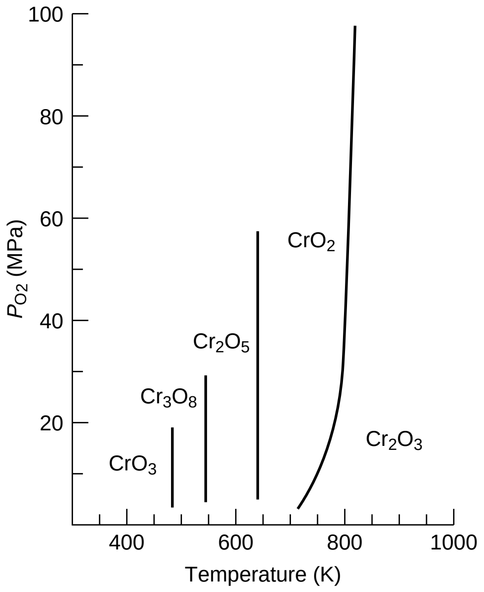

Figure 4 Formation of chromium oxides as a function of oxygen pressure and temperature. (Ref. 19. Reproduced by permission of Blackwell)

material whose T_c went beyond 77 K for the first time. In due course, two other superconductors were found in the Y–Ba–Cu–O system, $Y_2Ba_4Cu_7O_{15}$ and $YBa_2Cu_4O_8$. Their structures are compared in a schematical way in Figure 5(a). All these contain atomic sheets stacked sequentially as /BaO/CuO_2/Y/CuO_2/BaO/ in common, while those sandwiched between these are different. There are single CuO chains for $YBa_2Cu_3O_7$ and double CuO chains for $YBa_2Cu_4O_8$·$Y_2Ba_4Cu_7O_{15}$ contains both types of chains at a ratio of 1:1.

Karpinski *et al.*[20] studied the stability of these phases as a function of oxygen pressure and temperature, using a specially designed two-chamber autoclave.[21] The inner chamber contains the sample and oxygen gas, and it is placed in the outer chamber which is filled with argon. A relatively large amount of sample ($\sim$10 g) can be treated safely in oxygen pressures up to 300 MPa and 2000 K. The obtained phase relation is reproduced in Figure 5(b), where 123, 123.5, and 124 indicate the structure types in terms of the Y:Ba:Cu ratio. The 124 phase is stabilized over a wide oxygen pressure range, especially at high oxygen pressures. Discussion of the relative stability as a function of oxygen pressure and temperature is, however, difficult, because the 123 and 123.5 phases do not keep a constant oxygen content.

One important feature of $YBa_2Cu_4O_8$ is its thermal stability. $YBa_2Cu_3O_7$ begins to release oxygen at about 650 K, while $YBa_2Cu_4O_8$ loses little oxygen up to about 1050 K. Moreover, the T_c can be raised to 90 K by partially substituting Ca for Y, to give $Y_{0.9}Ca_{0.1}Ba_2Cu_4O_8$. These two points may be of importance for practical applications.

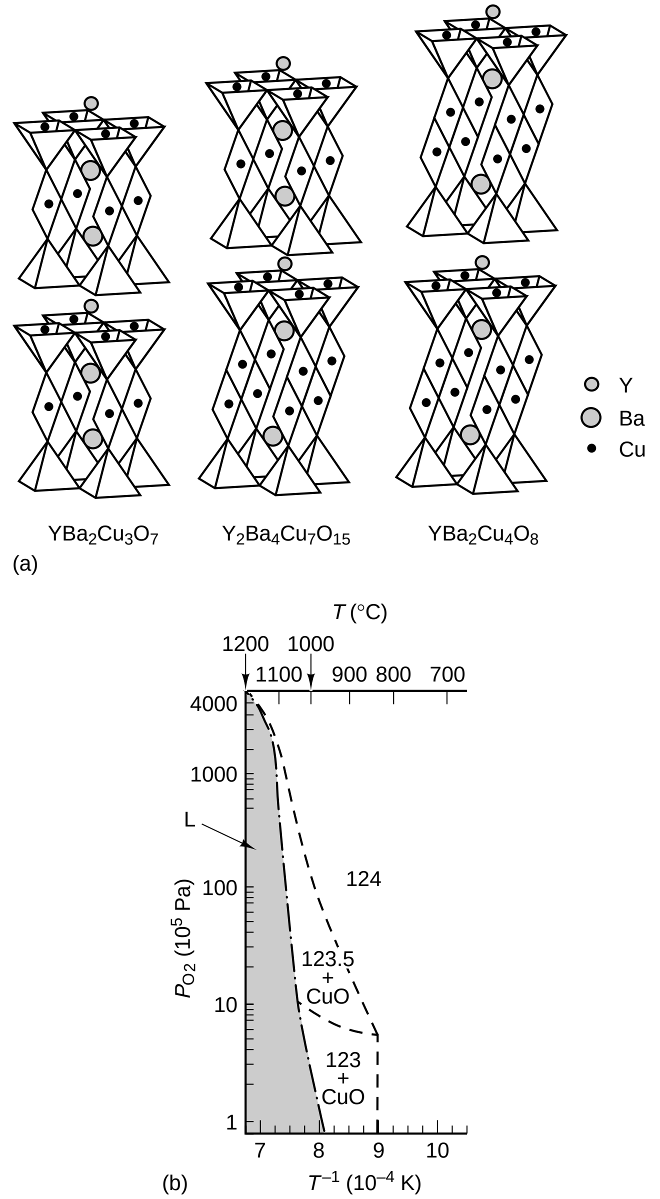

Figure 5 (a) Schematic structures of Y–Ba–Cu oxide superconductors and (b) the formation diagram as a function of oxygen pressure and temperature. (Reprinted from Ref. 20. © 1989, with permission from Elsevier)

4 HIGH PRESSURE ABOVE 1 GPA

4.1 Outline

A variety of solid materials, including metals, semiconductors, molecular solids, and ionic compounds, show a remarkable deviation from the simple Hooke's law in the pressure dependence of volume at 1–10 GPa. The deviation is quite often a prelude to a pressure-induced transition to a denser structure.[22–24] For example, Fe metal changes its structure from cubic (α-phase) to hexagonal (ε-phase) at 11 GPa at room temperature, when ferromagnetism is lost. Ge and Si show a very sharp decrease in resistance by orders of magnitude at 9.2 GPa and 12 GPa, respectively. Their high pressure metallic phases assuming the β-Sn structure show superconductivity below $T_c = 5.4\,\mathrm{K}$ and 6.7 K, respectively.[25] As is well-known, NaCl, KCl, and RbCl transform from the NaCl type to the CsCl type at 29.5, 1.9, and 0.53 GPa, respectively, when the coordination number increases from six to eight. After seeing these, it sounds quite reasonable to expect that pressure of the order of 10 GPa or even less would also strongly influence the phase formation: compounds stabilized at ambient pressures in a given composition system may be replaced by some others with new compositions and new structures.

As stated by Goodenough *et al.* in their review article,[26] high pressure effects from the viewpoint of inorganic synthesis can be divided into three groups.

1. High pressure transformations of compositions prepared at atmospheric pressure.
2. Composition formations requiring elevated pressures.
3. Syntheses greatly facilitated by pressure.

Some typical examples of the first two cases are listed in Tables 3 and 4, respectively. Since solid-state reactions and transformations are accelerated at elevated temperatures, high pressure synthesis almost automatically assumes treatments at elevated temperatures. Reaction times are usually short, 0.5–1 h. However, discrimination between these kinetic effects and thermodynamical stability should always be kept in mind.

The increase in density ranges widely in Table 3 from 1.3% for $CsMnCl_3$ (9L → 6L) to 46% for SiO_2 (coesite → rutile). The two successive transformations of SiO_2 provide an instructive comparison of the degrees of structural change. The density of coesite is higher than that of quartz by only 11%. In either phase, every Si atom is tetrahedrally coordinated by oxygen atoms and every O atom has two Si neighbors. The densification mainly results from a more compact packing of the oxygen arrays in coesite. On the other hand, in the rutile phase, SiO_6 octahedra form and every O atom is shared by three Si atoms. It is a general rule that transitions accompanied by relatively large increases in density involve changes in primary coordination. The coordination increase under high pressures has been thought to occur because large anions have higher compressibilities so that the radius ratio of cations and anions, r_c/r_a, increases (*see* ***Coordination Numbers & Geometries***).

Another remarkable tendency results from the electrostatic repulsion of cations of small sizes. Transition metal–anion octahedra are linked by face sharing in the 2L phases of $BaMnO_3$ and $CsNiF_3$, by corner sharing in the 3L (perovskite, see Section 4.3.2) phase of $CsMnCl_3$, and in a mixed way in $BaRuO_3$ (9L) and $CsMnCl_3$ (9L).[27,28] The sequential densification of 2L → 9L → 4L → 6L → 3L (perovskite)

Table 3 Transformations to denser structures

Low-pressure phase[a] (Structure type)	High-pressure phase[a] (Structure type)	Pressure (GPa)	Temperature (K)
${}^{\mathrm{III}}\mathrm{C}$ (graphite)	${}^{\mathrm{IV}}\mathrm{C}$ (diamond)	5.4	1667
${}^{\mathrm{III}}\mathrm{C}_{60}$	${}^{\mathrm{IV}}\mathrm{C}$ (diamond)	20[b]	300
${}^{\mathrm{III}}\mathrm{B}^{\mathrm{III}}\mathrm{N}$ (h-BN)	$c-{}^{\mathrm{IV}}\mathrm{B}^{\mathrm{IV}}\mathrm{N}$ (zinc blende)	6	1750
${}^{\mathrm{III}}\mathrm{B}_2\mathrm{O}_3$ (hexagonal)	${}^{\mathrm{IV}}\mathrm{B}_2\mathrm{O}_3$ (orthorhombic)	2	770
${}^{\mathrm{IV}}\mathrm{SiO}_2$ (quartz)	${}^{\mathrm{IV}}\mathrm{SiO}_2$ (coesite)	3	870
${}^{\mathrm{IV}}\mathrm{SiO}_2$ (coesite)	${}^{\mathrm{VI}}\mathrm{SiO}_2$ (rutile)	9	970
${}^{\mathrm{VI}}\mathrm{PbO}_2$ (rutile)	${}^{\mathrm{VI}}\mathrm{PbO}_2$ (orthorhombic)	2	870
${}^{\mathrm{VI}}\mathrm{PbO}_2$ (orthorhombic)	${}^{\mathrm{VIII}}\mathrm{PbO}_2$ (fluorite)	7.5	970
${}^{\mathrm{VI}}\mathrm{Mn}^{\mathrm{IV}}\mathrm{GeO}_3$ (pyroxene)	${}^{\mathrm{VI}}\mathrm{Mn}^{\mathrm{VI}}\mathrm{GeO}_3$ (ilmenite)	2.5	970
${}^{\mathrm{VI}}\mathrm{Mn}^{\mathrm{VI}}\mathrm{VO}_3$ (ilmenite)	${}^{\mathrm{VIII}}\mathrm{Mn}^{\mathrm{VI}}\mathrm{VO}_3$ (GdFeO_3)	4.5	1270
${}^{\mathrm{VIII}}\mathrm{Sr}^{\mathrm{IV}}\mathrm{CuO}_2$ (SrCuO_2)	${}^{\mathrm{VIII}}\mathrm{Sr}^{\mathrm{IV}}\mathrm{CuO}_2$ (infinite layer)	6	1220
${}^{\mathrm{VIII}}\mathrm{Y}^{\mathrm{V}}\mathrm{MnO}_3$ (hexagonal)	${}^{\mathrm{VIII}}\mathrm{Y}^{\mathrm{VI}}\mathrm{MnO}_3$ (GdFeO_3)	4.5	1070
${}^{\mathrm{VIII}}\mathrm{Zr}^{\mathrm{IV}}\mathrm{SiO}_4$ (zircon)	${}^{\mathrm{VIII}}\mathrm{Zr}^{\mathrm{IV}}\mathrm{SiO}_4$ (scheelite)	12	1170
${}^{\mathrm{VI}}\mathrm{Ca}_2^{\mathrm{IV}}\mathrm{GeO}_4$ (olivine)	${}^{\mathrm{IX}}\mathrm{Ca}_2^{\mathrm{VI}}\mathrm{GeO}_4$ ($\mathrm{K}_2\mathrm{NiF}_4$)	11	1370
${}^{\mathrm{VI}}\mathrm{Mg}_2^{\mathrm{IV}}\mathrm{SiO}_4$ (olivine)	${}^{\mathrm{VI}}\mathrm{Mg}_2^{\mathrm{IV}}\mathrm{SiO}_4$ (spinel)	130	870
${}^{\mathrm{IV}}\mathrm{Li}_2^{\mathrm{IV}}\mathrm{MoO}_4$ (phenacite)	${}^{\mathrm{VI}}\mathrm{Li}_2^{\mathrm{IV}}\mathrm{MoO}_4$ (spinel)	1	770
${}^{\mathrm{VI}}\mathrm{Mn}_2^{\mathrm{IV}}\mathrm{MnO}_4$ (spinel)	${}^{\mathrm{VI}}\mathrm{Mn}_2^{\mathrm{VIII}}\mathrm{MnO}_4$ ($\mathrm{CaMn}_2\mathrm{O}_4$)	10	1170
${}^{\mathrm{VI}}\mathrm{Sr}_2^{\mathrm{IV}}\mathrm{CrO}_4$ (β-$\mathrm{K}_2\mathrm{SO}_4$)	${}^{\mathrm{VIII}}\mathrm{Sr}_2^{\mathrm{VI}}\mathrm{CrO}_4$ ($\mathrm{K}_2\mathrm{NiF}_4$, distorted)	6.5	1270
${}^{\mathrm{XII}}\mathrm{Ba}^{\mathrm{VI}}\mathrm{MnO}_3$ (2L)	${}^{\mathrm{XII}}\mathrm{Ba}^{\mathrm{VI}}\mathrm{MnO}_3$ (9L)	3	1120
${}^{\mathrm{XII}}\mathrm{Ba}^{\mathrm{VI}}\mathrm{MnO}_3$ (9L)	${}^{\mathrm{XII}}\mathrm{Ba}^{\mathrm{VI}}\mathrm{MnO}_3$ (4L)	9	1470
${}^{\mathrm{XII}}\mathrm{Ba}^{\mathrm{VI}}\mathrm{RuO}_3$ (9L)	${}^{\mathrm{XII}}\mathrm{Ba}^{\mathrm{VI}}\mathrm{RuO}_3$ (4L)	1.5	1270
${}^{\mathrm{XII}}\mathrm{Ba}^{\mathrm{VI}}\mathrm{RuO}_3$ (4L)	${}^{\mathrm{XII}}\mathrm{Ba}^{\mathrm{VI}}\mathrm{RuO}_3$ (6L)	3	1270
${}^{\mathrm{XII}}\mathrm{Cs}^{\mathrm{VI}}\mathrm{NiF}_3$ (2L)	${}^{\mathrm{XII}}\mathrm{Cs}^{\mathrm{VI}}\mathrm{NiF}_3$ (9L)	0.5	1070
${}^{\mathrm{XII}}\mathrm{Cs}^{\mathrm{VI}}\mathrm{NiF}_3$ (9L)	${}^{\mathrm{XII}}\mathrm{Cs}^{\mathrm{VI}}\mathrm{NiF}_3$ (6L)	5	1070
${}^{\mathrm{XII}}\mathrm{Cs}^{\mathrm{VI}}\mathrm{MnCl}_3$ (9L)	${}^{\mathrm{XII}}\mathrm{Cs}^{\mathrm{VI}}\mathrm{MnCl}_3$ (6L)	0.8	970
${}^{\mathrm{XII}}\mathrm{Cs}^{\mathrm{VI}}\mathrm{MnCl}_3$ (6L)	${}^{\mathrm{XII}}\mathrm{Cs}^{\mathrm{VI}}\mathrm{MnCl}_3$ (3L, perovskite)	2.7	970

[a] Superscripts indicate the coordination numbers. [b] Nonhydrostatic pressure.

results from a successive increase in the proportion of corner sharing. Because the distance between cations in a pair of corner-sharing octahedra is greater than the distance between those in face-sharing octahedra, the above transitions have been thought to imply that small cations are redistributed under pressure in order to reduce the electrostatic repulsion. No doubt this tendency is enhanced if the cations have high oxidation numbers.

Roth and De Vries treated the 1:1 mixture of PbO and CrO_2 at various pressures and temperatures.[29] If the pressure is fixed at 5.5 GPa, the product varies as a function of temperature as $\mathrm{PbO} + \mathrm{Cr}^{\mathrm{IV}}\mathrm{O}_2$ (below about 1020 K), $\mathrm{PbCr}^{\mathrm{IV}}\mathrm{O}_3$ (between 1020 K and 1370 K), and $\mathrm{Pb}_2\mathrm{Cr}^{\mathrm{VI}}\mathrm{O}_5 + \mathrm{Cr}_2^{\mathrm{III}}\mathrm{O}_3 + \mathrm{PbO}$ (above 1370 K). The temperature range for PbCrO_3 (cubic perovskite) becomes narrower as pressure is lowered, and one cannot obtain this compound below about 5 GPa. It is not straightforward to explain this kind of change in phase formation as a function of pressure, temperature, and composition: Goodenough *et al.*[26] have mentioned the specificity of the electronic state of $\mathrm{Cr}^{\mathrm{IV}}$ ions in addition to the size effects in relation to the necessity of high pressure to stabilize these ions in the perovskite structure. Cr ions can assume a variety of oxidation states of I–VI, while octahedral site $\mathrm{Cr}^{\mathrm{III}}$ and tetrahedral $\mathrm{Cr}^{\mathrm{VI}}$ ions are by far the most common (*see* ***Chromium: Inorganic & Coordination Chemistry***). The $\mathrm{Cr}^{\mathrm{IV}}$ ($3\mathrm{d}^2$) state is special also in a sense that it is a transitional state between two normal states, the localized electron state and the itinerant electronic state (*see* ***Electronic Structure of Solids***). Application of high pressure at relatively low temperatures seems to be required to stabilize the relatively unstable $\mathrm{Cr}^{\mathrm{IV}}$ ions in oxygen octahedra.

The materials described below include diamond, cubic BN (the hardest material next to diamond), SrCuO_2 (from which two types of superconductors have been derived by compositional modification), MgSiO_3 (a geologically interesting perovskite), and GeO_2 (amorphized under pressure at room temperature).

4.2 Apparatus[30]

Static and shock wave compressions are the two remarkably different ways for generating pressures above 1 GPa. Here, only apparatus generating static pressures of more general use will be considered. These are classified into several types, piston-cylinder, Bridgman anvil, belt, multi-anvil, and cascaded multi-anvil types. The available pressure range depends on the type and also on the volume of the sample chamber used. It is 2–4 GPa with the piston-cylinder type, 5–8 GPa with the belt type, 10–20 GPa with

Table 4 Syntheses requiring high pressures

Product			Preparation		
Structure type	Composition[a]	Starting material	Pressure (GPa)	Temperature (K)	Remarks
Rock salt	$Fe_{0.980}O$	$10Fe_{0.952}O + Fe$	18	1270	
Corundum	$Ni^{III}Cr^{III}O_3$	$Ni^{II}Cr^{VI}O_4$	8	1270	
	Co_2O_3[b]	$2CoF_3 + 3Na_2O_2$	8	1270	
Ilmenite	$MnSnO_3$	$MnO + SnO_2$	6–7	1270	
	$CoVO_3$	$CoO + VO_2$	6.5	1270	
Rutile	TiOF	$Ti_2O_3 + TiF_3$	6.5	1470	
	VOF	$V_2O_3 + VF_3$	6.5	1270	
	$CrO_{2-x}F_x$	Cr_2O_3, CrF_3	6	1470	
$LiNbO_3$	$CuTaO_3$	$Cu_2O + Ta_2O_5$	6.5	1270	
Pyroxine	$FeSiO_3$	$Fe_2SiO_4 + SiO_2$	2	1270	
	$CoSiO_3$	$Co_2SiO_4 + SiO_2$	2.5	1270	
Perovskite	$CaCrO_3$	$CaO + CrO_2$	6.5	970	
	$SrCrO_3$	$Sr_2CrO_4 + CrO_2$	6.5	1070	
	$PbCrO_3$	$PbO + CrO_2$	5	1420	
	$BiCrO_3$	$Bi_2O_3 + Cr_2O_3$	3–5	1070	
	$BiMnO_3$	$Bi_2O_3 + Mn_2O_3$	3–5	970	
	$TlFeO_3$	$Tl_2O_3 + Fe_2O_3$	6.5	1120	
	$RGaO_3$	$R_2O_3 + Ga_2O_3$	4.5–7	1270	R = Sm to Lu, Y
	$PbSnO_3$	$PbO + SnO_2$	6–7	770	
	$InRhO_3$	$In_2O_3 + Rh_2O_3$	6.5	1620	
	$KTiO_2F$	$KF + TiO_2$	6–6.5	1270	
Nd_2CuO_4	R_2CuO_4	$R_2O_3 + R_2Cu_2O_5$	6	1220	R = Tb to Tm, Y
$Sr_3Ti_2O_7$	$Sr_3Cr_2O_7$	$3Sr_2CrO_4 + CrO_2$	6.5	1270	
Arseno pyrite	CoP_2	$Co + 2P + Ge$	6.5	1270	Ge:flux
Marcasite	$MnCoP_4$	$Mn + Co + 4.5P$	6.5	1470	
NbPS	NbPS	$Nb + 1.3P + 1.1S$	6.5	1470	

[a]Superscripts indicate the oxidation numbers. [b]$2CoF_3 + 3Na_2O_2 \rightarrow Co_2O_3 + 6NaF + 3/2\ O_2$.

the Bridgman anvil type, 5–10 GPa with the multi-anvil type, and 10–30 GPa with the cascaded multi-anvil type. Anvils are made of sintered tungsten carbide (WC) superhard alloys. Recent attempts to use sintered diamond instead of WC are expected to extend these pressure ranges. While a sample of tens of cm^3 can be treated at 2 GPa with a conventional piston-cylinder type apparatus, it is limited to several mm^3 for compression at 30 GPa with a cascaded multi-anvil type apparatus.

The pressure generated in a sample chamber is first calibrated against the supplied load in reference to the pressure fixed points listed in Table 5. This pressure calibration is carried out at room temperature by detecting changes in the electric resistance of these standard materials as they transform to their denser phases. For accuracy of temperature and pressure at elevated temperatures, an additional calibration is done utilizing melting of gold, silver, copper, and various solid-state transitions.

The practical pressure strongly depends on details of the sample chamber assembly and also on the change in sample volume during treatment. In addition, a pressure gradient and a sheer stress are, more or less, inevitable. This kind of pressure quality largely depends on the type of apparatus and often affects the results of high pressure synthesis. The piston-cylinder, Bridgman anvil, and belt types generate rather a uniaxial pressure, while more isostatic compression can be generated with the multi-anvil types.

Table 5 Pressure fixed points

Material (Transition)	Pressure (GPa)	Temperature (K)
Bi (1–2)	2.55	273
Tl (2–3)	3.77 ± 0.03	298
Cs (2–3)	4.25 ± 0.1	298
Cs (3–4)	4.30 ± 0.1	298
Ba (1–2)	5.5 ± 0.2	298
Bi (5–6)	7.7 ± 0.3	298
Fe ($\alpha - \varepsilon$)	11.0–11.3	298
Ba (2–3)	11.8–12.2	298
ZnS	15.0 ± 0.5	298
GaP	22.0 ± 1.0	298
NaCl[a]	29–30	298

[a]Change in resistivity is not remarkable.

Sample heating up to about 2300 K is performed by applying an electric current through a cylindrical or sheet heater around the sample. The heater may be made of graphite, platinum, or lanthanum chromite. Thermal quenching is possible by turning off the current. The sample temperature decreases below 600 K in a few seconds and to ambient temperature in a minute, since the anvils and blocks act as massive heat sinks. Whether the high-pressure phase can be recovered after decompression or not depends upon the kinetics. A flash heating technique has been introduced for further heating up to 10^4 K. In this case, however, the temperature is estimated indirectly from the electric power supply.

If the fugacity of a volatile component such as oxygen or water needs to be controlled, the sample is sealed with an appropriate buffer material in platinum, gold, molybdenum, or tantalum. If metal powder of Ti or Zr is used as the buffer material, it would work as a strong oxygen remover, while oxygen released at elevated temperatures from $KClO_4$ and CaO_2, and so on will fill the capsule. To prevent mixing and reaction of the sample with the buffer material, these are separated by a disk or layered powder of an appropriate inactive substance such as gold, platinum, ZrO_2, BN, and so on. $R_2Pd_2O_7$ and others prepared using 'special oxygen sources' listed in Table 2 were treated in this way.

The Bridgman anvil**[31]** is illustrated in Figure 6(a). Tapered anvils made of WC are supported by steel rings. The sample (or sample cell) is surrounded by a gasket made of pyrophyllite. By placing the assembly into a large conventional hydraulic press, pressures up to 20 GPa can be generated.

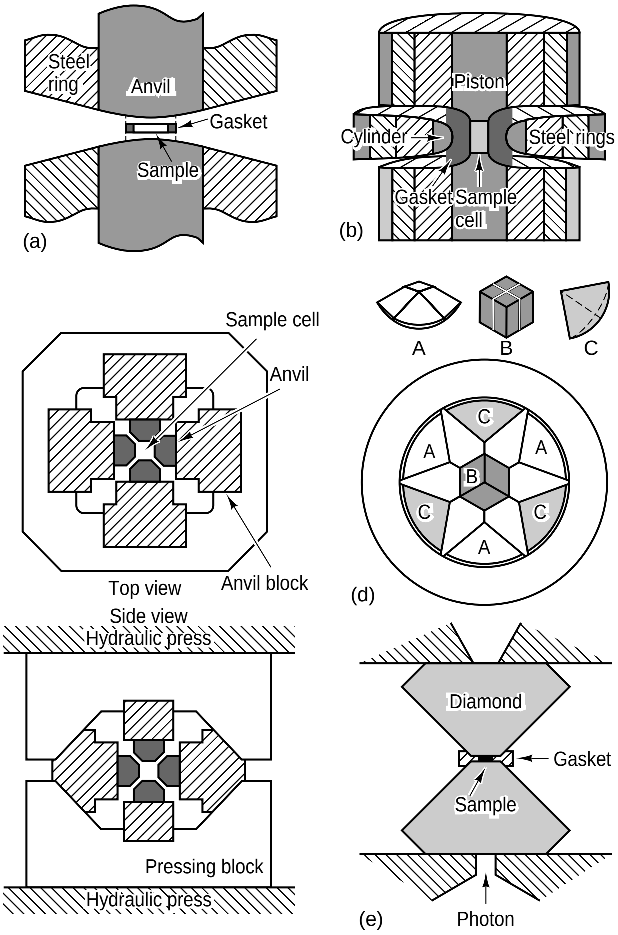

Figure 6 Essential parts of high pressure apparatus of (a) the Bridgman type, (b) the belt type, (c) the cubic anvil type, (d) the 6–8 split sphere anvil type, and (e) the diamond anvil type

Figure 6(b) shows the essential part of a belt apparatus schematically. It consists of two tapered pistons and a cylinder. By using strongly tapered pistons, a large piston motion becomes possible without thinning out the pyrophyllite gasket. The pistons and the cylinder are made of WC, and these are supported by special steel rings. The first synthetic diamond was produced with this type of apparatus. This type is most widely used in both laboratories and industry, since the preparation of the sample cell assembly and the compressing operation are relatively easy.

Diagrams illustrating the core of a cubic anvil type apparatus are shown in Figure 6(c). The apparatus consists of six anvils, four of which are fixed horizontally to the anvil blocks. These blocks contact with the upper and lower pressing blocks, at the centers of which the other two anvils are fixed vertically. When a hydraulic press works, the lower pressing block advances upwards. Through the contact at an angle of 45° the pressing blocks move the horizontal anvil blocks centripetally. In this way, the six anvils synchronously compress the sample three dimensionally.

The '6–8' split-sphere device**[32]** is one of the cascaded multi-anvil type apparatus, the essential parts of which are illustrated in Figure 6(d). Six equal wedge-shaped anvils, A, each having a square surface in front and one corner cut off into a fan shape, are placed together with faceted blocks, C, in two hemispherical cylinders, as illustrated. When these hemispheres are put together face to face, a cubic space remains open at the center of the sphere. The space is to be filled with eight, equal small cubes, B. If the inmost corner of each small cube is cut into a regular triangle, a small octahedral void forms. By placing a sample covered with a pressure medium in the void, compression along the four axes perpendicular to the triangular faces of the octahedron can be done. The more axes along which compression is carried out, the more isotropic is the generated pressure. MgO and pyrophyllite are the medium materials generally used. This sophisticated type of high pressure apparatus has mainly been used by scientists studying the Earth's interior.

To be referred to next is the most modern diamond anvil type, generating pressures of order of 10–100 GPa.**[33]** The cell illustrated in Figure 6(e) consists of two gem diamonds with optically flat surfaces, between which a sample confined in a drilled hole of a thin metal gasket is sandwiched. To attain isostatic compression an inert gas or an organic liquid, like a 4:1 volume mixture of methanol and ethanol, is contained with the sample. The generated pressure is measured directly from the pressure shift of the fluorescence line of ruby powder mixed with the sample. Temperatures to 5000 K can be obtained by laser heating. The quantity of sample confined in a typically 0.1-mm-wide hole is extremely small, just a few microcrystals. At present, research has focused on in situ observations using X-ray and other optical methods, rather than synthesis. Diamond acts not only as the anvils but also as an optical window.

4.3 Materials

4.3.1 Diamond[5]

Diamond, the hardest substance known to man, is the only material that is produced using high pressure on a commercial scale. The most probable pressure–temperature phase diagram of carbon is shown in Figure 7(a) (*see* ***Carbon: Inorganic Chemistry***).[34] Laborious studies over years by many investigators were required to establish the diagram, though some details still remain uncertain. Diamond is actually a high pressure form of carbon and exists metastably at ambient pressure. It is a considerable kinetic barrier that prevents the conversion of hard and sparkling gem diamonds to flaky and darkish graphite. On the other hand, because of this kinetic barrier, early investigators were unfortunately unable to synthesize diamond, even though they managed to achieve the pressure–temperature conditions for thermodynamic stabilization of diamond. A series of technological innovations were required before controlled diamond crystallization became possible.[35] It is also true that the demand for 'diamond made by men' accelerated the development of high pressure technology.

It is evident from the phase diagram that diamond may be obtained in a very wide pressure–temperature range, thus allowing several synthesizing methods to work in various regions. Those mainly applied are conversion of graphite to diamond by a flux method, direct conversion by shock wave compression, and direct conversion by static compression. Synthetic diamond is mostly produced by the flux method, which will be outlined below.

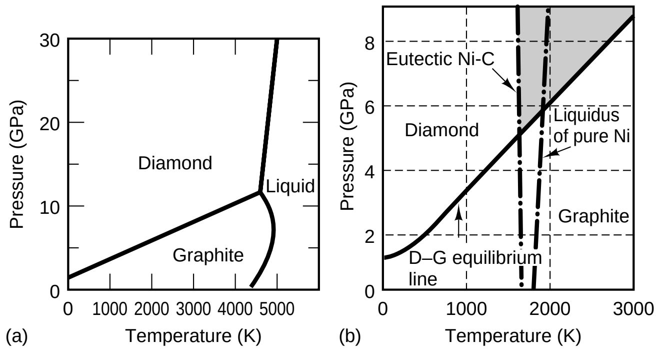

Figure 7 (a) Phase diagram of carbon. (Reproduced by permission of Elsevier from F.P. Bundy, *Physica*, 1989, **A156**, 169) (b) A portion of the phase diagram including the melting line of pure Ni, the Ni–graphite eutectic, and the diamond synthesis zone. (Reproduced by permission of Decker from F.P. Bundy.[5])

Flux Method. Certain kinds of metals and alloys, when molten in a high-pressure cell, dissolve graphite and precipitate diamond. This conversion process proceeds under much milder temperature–pressure conditions than required for the direct conversion. The group 8–10 metals Fe, Ni, and Co, and also Fe–Ni, Fe–Ni–Co, Ni–Mn, and some other alloys, have been used traditionally for this purpose. Figure 7(b) contains the melting line of pure Ni and the Ni–graphite eutectic superimposed on the phase diagram of carbon. In the shaded region, the Ni-mediated graphite–diamond conversion proceeds as a result of the difference in solubility between graphite and diamond in Ni. For example, at 9 GPa and 1800 K, molten nickel can dissolve about 4% wt of carbon from metastable graphite, while the solubility of carbon from diamond is limited to 3.6% wt. Thus carbon corresponding in amount to the solubility difference of 0.4% wt crystallizes out as diamond, because diamond is the stable form under the given conditions. Diamond thus formed contains a small amount of Ni impurity, of about 10^{-4} at%. The metals and alloys that mediate the transformation as above are often referred to as catalyst/solvent. Interestingly, elemental phosphorus and also certain inorganic compounds such as $CaCO_3$, $Ca(OH)_2$, $MgSO_4$, and so on have recently been found to catalyze the transformation, probably in their molten state.[36]

A typical arrangement of the reactants in a pyrophyllite cell is illustrated in Figure 8(a). The reaction zone consists of alternately stacked cylinders of graphite and nickel. After compression to 5.4 GPa, the temperature is raised to 1667 K to melt the nickel plates and to stabilize diamond coming out. Molten nickel dissolves graphite and precipitates diamond at the interface initially. In a few minutes, graphite wholly transforms to diamond as the molten nickel moves through the graphite disks from both ends toward the center. Crystals thus obtained measure from a few dozen µm to 0.5–1.0 mm. The crystal habit largely depends on temperature. At relatively low temperatures the (100) faces tend to develop preferentially, while the (111) faces develop at high temperatures.

For the growth of large and clear diamond crystals of desired morphologies, such as shown in Figure 8(b), it is necessary to control both the nucleation and the growth carefully.[37] A reaction chamber suitable for this is illustrated in Figure 8(c). A vertical temperature gradient of the order of $10\,\mathrm{K\,mm^{-1}}$ is given to the chamber to take advantage of the fact that the solubility of carbon in the flux increases with temperature. From the upper hot zone, carbon is transported through the molten flux metal toward the seed crystal fixed at the bottom of the lower cool zone. The carbon source in the hot zone may either be graphite or diamond. Large single crystals of about 1 cm in size can be grown. This process is essentially the same as the hydrothermal growth of α-SiO_2 crystals described in Section 2.3: molten flux here corresponds to hot water.

Sintered Diamond. A natural polycrystalline form of diamond called *carbonado* is known. It is much tougher

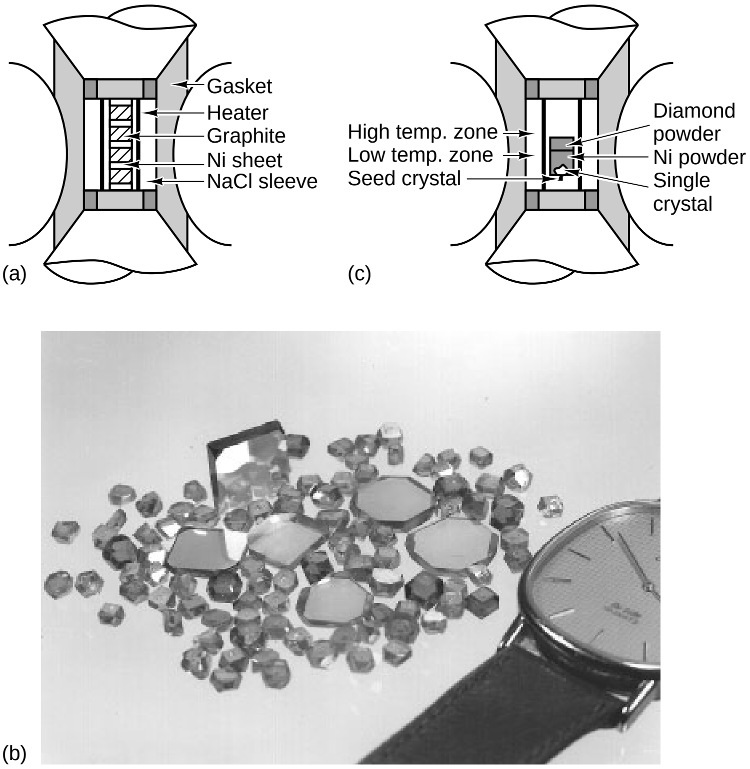

Figure 8 (a) Belt type apparatus containing a sample cell for graphite to diamond conversion. (b) Single crystals of diamond. (Courtesy of Sumitomo Electric Industry, Ltd). (c) A typical arrangement of reactants for the crystal growth

than single crystals. Small, randomly oriented microcrystals are tightly compacted, so that the cleavage brittleness of single crystals is overcome. However, carbonado that looks black is not pure diamond.

A close approach to carbonado is an as-grown compact of synthetic grains cemented with a solvent metal. To increase direct intergrain diamond–diamond bonding, fairly high pressures and temperatures and/or a special additive that promotes carbon diffusion and then remains as a binder are used. Although several kinds of thus sintered diamond have been produced on a commercial scale, their performance is not so high as that of natural carbonado. Demand for man-made superhard and highly tough materials like carbonado is keen.

4.3.2 Cubic Boron Nitride[38,39]

Boron nitride shows polymorphism which is parallel to that of carbon (*see* ***Boron–Nitrogen Compounds***). The hexagonal low-pressure phase, *h*-BN, crystallizes in a graphite-like structure where boron and nitrogen are arranged in an ordered way so that these are threefold coordinated with each other. Under high pressures and temperatures it transforms into the cubic phase assuming the zinc blende structure, *c*-BN, where boron and nitrogen are tetrahedrally coordinated with each other. This is the same type of structure as diamond. Both *h*- and *c*-BN are synthetic materials; graphite and diamond can be found in nature.

c-BN is the hardest material following diamond, and its thermal conductivity is very high, as it is for diamond. The merits of *c*-BN in comparison with diamond from the viewpoint of applications as a grinding medium and use in cutting tools are the low reactivity with the iron group metals and the strong thermal resistance in oxidizing atmosphere.

c-BN is prepared from *h*-BN mainly by a flux method, as diamond is from graphite. Direct conversion is also possible. A wide variety of materials can be used as the flux, including alkaline and alkaline-earth metals, their nitrides and fluoronitrides, ammonium borate, and so on. If reactive metals like Li and Mg are to be used, these are heat-treated beforehand with *h*-BN in a stream of dry nitrogen. Disks of the flux material and *h*-BN are stacked alternately, as illustrated in Figure 8(a) for the case of diamond, and the assemblage is treated at 6 GPa and 1750 K, typically. The presence of oxygen should be carefully avoided. The flux is removed chemically by using hydrochloric acid or other appropriate solvents. Transparent yellowish single crystals faceted mainly with the (111) planes can be grown up to about 2 mm.

4.3.3 $SrCuO_2$

All the copper oxide superconductors ever known contain a common structural unit: the two-dimensional CuO_2 sheet

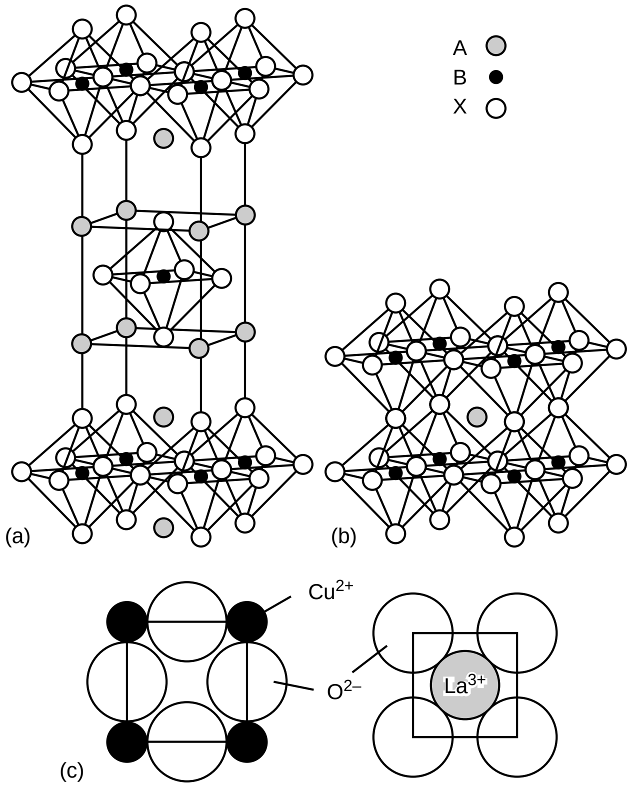

Figure 9 (a) K_2NiF_4 structure, (b) perovskite structure, and (c) comparison of the specific area of the free $(CuO_2)^{2-}$ and $(LaO)^+$ sheets

(see Figure 5(a)). $La_{2-x}Ba_xCuO_4$ ($x \approx 0.15$), the first high T_c superconductor, crystallizes in the K_2NiF_4 structure.[26–28] In the ideal tetragonal structure illustrated in Figure 9(a), regular NiF_6 octahedra share corners with each other along the *a* and *b* axes, a two-dimensional Ni–F–Ni bond network thus being formed. However, La_2CuO_4 and the Ba-substituted superconductor are subject to an orthorhombic distortion, making the CuO_2 sheet puckered. Moreover, the CuO_6 octahedra are considerably elongated along the *c* axis as a result of the Jahn–Teller effect of the Cu^{II} ions (*see* ***Structure & Property Maps for Inorganic Solids*** and *Jahn–Teller Effect*).

A regular three-dimensional cation–anion–cation network is developed in the ideal perovskite structure (illustrated in Figure 9(b)).[26–28] Perovskite compounds are often formulated as ABX_3, where A stands for a relatively large cation like Sr^{2+}, B a small cation like Ti^{4+}, and X an anion like O^{2-}. $SrTiO_3$ is the representative perovskite oxide. Along this line, K_2NiF_4 type compounds may be formulated as A_2BX_4. These two structures can be easily interconverted. To derive the latter structure from the former requires the replacement of the single AX sheets by the double $(AX)_2$ sheets and a shift of the alternate BX_2 sheets along the direction.

In Figure 9(c) the ideal specific areas for flat LaO and CuO_2 sheets, calculated from Shannon's ionic radii, are compared.[40] If the regular K_2NiF_4 structure is to be assumed for La_2CuO_4, these sheets should be stacked along the *c* axis without any distortion. In reality, however, these sheets match each other very poorly. The puckering of the CuO_2 sheet may thus be considered to be a strategy to improve the matching by making the Cu–Cu distance shorter. Generally speaking, it is quite interesting to learn from complex compounds containing two or more different kinds of cations (or anions) how they manage to minimize the free energy by modifying bond angles, bond distances, and oxidation states from the ideal, unstrained ones.

For the perovskite and related structures, including K_2NiF_4, the 'tolerance factor', t, measures the degree of bond length mismatch. Denoting the radius of the ith ion as r_i, the tolerance factor is given by equation (4). If the matching is perfect, the value is equal to unity. For K_2NiF_4 and $SrTiO_3$, $t = 1.00$ and 1.05, respectively, and their structures are not distorted at room temperature. On the other hand, a small value of $t = 0.87$ for La_2CuO_4 leads to an orthorhombic distortion.

$$t = \frac{r_A + r_X}{2^{1/2}(r_B + r_X)} \tag{4}$$

One important thing to be kept in mind here is that the ionic radii are derived from the cation–anion bond distances measured experimentally at room temperature, not at the temperatures where the formation reactions take place. At present, there is no way to estimate exactly the tolerance factor at high (or low) temperatures. So, whether one can obtain a perovskite or related material from a given A–B–X combination or not depends mostly upon experimental tests.

Generally, cation–anion bonding is soft for large cations and anions. In other words, the coefficients of thermal expansion and compressibility are both larger for the A–X bond than for the B–X bond. Thus, not only temperature but also pressure should be considered to affect the bond length matching to be estimated in terms of tolerance factor.

$SrCuO_2$ compressed at 6 GPa and 1200 K crystallizes in an oxygen-deficient perovskite structure in which all the oxide ions on the vertical axes of the unit cell illustrated in Figure 9(b) are lost.[41] This is the simplest structure containing the two-dimensional CuO_2 sheet, the superconducting structural unit. $LaNiO_2$ was the first compound found to crystallize in this structure, and $Ca_{0.84}Sr_{0.16}CuO_2$ followed.[42] This structure is often called an 'infinite layer' structure. If the alkaline earth–copper–oxygen system is studied at atmospheric pressure, this structure is stabilized only for a narrow composition range of $Ca_{1-x}Sr_xCuO_2$ with $x \approx 0.1$ and only in a narrow temperature range near the melting point. However, at 6 GPa and 1200 K the composition range can be extended in the large alkaline-earth ion side up to $Sr_{2/3}Ba_{1/3}CuO_2$, passing $SrCuO_2$. It should be noted here that $SrCuO_2$ prepared at atmospheric pressure crystallizes in a quite different type of structure. The high-pressure phase is denser by 8%, as estimated from the lattice constants measured at room temperature.

As the average counter cation size increases, the unit cell volume increases as a matter of course. However, the expansion is quite anisotropic. The c axis length, which is equal to the inter-CuO_2 sheet distance, increases three times as fast as the a axis length, the Cu–O–Cu distance. The oxygen polyhedron trapping the counter cations should preferably be cubic, because alkaline-earth ions have spherical electronic configurations. However, in reality they become more and more stretched along the c axis. This is because the Cu–O bond is so stiff that its length is almost saturated for $SrCuO_2$.

One way to relax the stress caused by the substitution of large alkaline-earth ions is to inject excess electrons into the CuO_2 sheets. The Cu–O bond accepting the excess electron into its lowest incompletely filled antibonding orbital becomes weak and long. The injection can be done by substituting trivalent rare earth ions at the counter cation site so that $A_{1-x}R_xCuO_2$ (R = rare-earth elements, La to Gd) may form. Another way is to partially remove the too large counter cations so that $A_{1-x}CuO_2$ may form. In this case, the CuO_2 sheet is oxidized, in contrast to the reduction in $A_{1-x}R_xCuO_2$.

It is known that high T_c superconductivity occurs if the CuO_2 sheets are properly oxidized or reduced, as first recognized from $La_{2-x}Ba_xCuO_4$ ($x \approx 0.15$) and $Nd_{2-x}Ce_xCuO_4$ ($x \approx 0.15$), respectively. It is clear that the Ba^{II}-for-La^{III} substitution and the Ce^{IV}-for-Nd^{III} substitution work differently on the CuO_2 sheets, and from the sign of the carriers created in the CuO_2 sheets these superconductors are classified into p-type and n-type, respectively. $(Ca_{0.7}Sr_{0.3})_{1-x}CuO_2$ ($x \leq 0.1$) is a p-type superconductor with a T_c of 110 K,[43] while $Sr_{1-x}R_xCuO_2$ (R = La to Gd, $x \approx 0.1$) is an n-type superconductor with a T_c of 43 K.[44]

All the efforts to make $Ca_{0.84}Sr_{0.16}CuO_2$ superconducting have failed. Injection of carriers into the CuO_2 sheets seems to go well when these are subject to an instability caused by the counter part. Extension of the composition range of a given structure using high pressure sounds quite meaningful in this sense.

4.3.4 *(Mg,Fe)SiO₃ (Perovskite)*[1,45]

A silicate perovskite, $Mg_{1-x}Fe_xSiO_3$ ($x \geq 0.8$), is likely to be the most abundant single phase of the Earth. It is confined, however, to the lower mantle, extending from about 670 km to 2900 km in depth, where pressure and temperature both increase from 26 GPa and 2000 K to 140 GPa and 3000 K with increasing depth. Numerous phase equilibrium studies of the $MgO–FeO–SiO_2$ system and others have revealed that all the major minerals of the upper mantle transform to dense phase assemblages dominated by the silicate perovskite in the pressure–temperature range appropriate to the lower mantle.

From seismic evidence, the density and elastic properties of the Earth are known to change markedly at the boundary between the mid-mantle (the transition zone) and the lower mantle. The ‘670-km discontinuity’ has been attributed to a pressure-induced transformation of $(Mg,Fe)_2SiO_4$ to a fine mixture of the above silicate perovskite and magnesio-wüstite, (Mg,Fe)O (equation 5). Iron is likely to be preferentially condensed in the wüstite phase. It is not difficult to prepare magnesio-wüstite at atmospheric pressure. The above transformation includes coordination changes. The spinel structure of $(Mg,Fe)_2SiO_4$ provides Mg and Fe with sixfold octahedral coordination and Si with fourfold tetrahedral coordination, while after the transformation the coordinations are sixfold or more.

$$(Mg, Fe)_2SiO_4 \longrightarrow (Mg, Fe)SiO_3 + (Mg, Fe)O \qquad (5)$$

It is well-established that pure and iron-substituted $MgSiO_3$, quenched to ambient pressure and temperature, exhibit a distortion to the so-called $GdFeO_3$ type structure in which the Mg and Fe ions are only eightfold coordinated, not twelvefold coordinated as in the ideal perovskite structure. However, their structures under the lower-mantle conditions still remain uncertain, though some experimental evidence suggesting transitions toward the ideal structure at elevated pressures and temperatures has been reported.

The perovskite phase of $MgSiO_3$ does not form at atmospheric pressure, because both Mg^{II} and Si^{IV} ions are far too small to meet the qualifications for the perfect perovskite of $r_A{:}r_B{:}r_X = 1{:}0.41{:}1$. It is an accelerated contraction of the oxide ions that makes the Mg–Si–O combination tolerated under high pressures. The $GdFeO_3$ type structure is the most frequently encountered type of distortion for compositions having relatively small t values of about 0.9. This structure can be derived from the ideal one by rotating BX_6 octahedra around the three crystal axes appropriately.[46] Rotate one octahedron around the a, b, and c axes by angles $+\alpha$, $+\alpha$, $+\gamma$, respectively. Next, rotate its edge-sharing neighbor on the a axis by $-\alpha$, $-\alpha$, $-\gamma$, the neighbor on the b axis also by the same degree, $-\alpha$, $-\alpha$, $-\gamma$, and finally the third neighbor on the c axis by $-\alpha$, $-\alpha$, $+\gamma$. By repeating the same process, one eventually obtains the $GdFeO_3$ structure. The addition of slight atomic shifts is quite common. The lattice constants of the resulting orthorhombic structure (space group *Pbnm*) are related to the cubic lattice constant, a_c, as $a_0 \approx b_0 \approx 2^{1/2}a_c$ and $c_0 \approx 2a_c$. The degree of distortion depends on the t value. Generally, the BX_6 octahedra remain relatively regular, while the oxygen polyhedra around the A ions are remarkably distorted so that the coordination number is reduced to eight, as in $GdFeO_3$ and quenched $MgSiO_3$, and nine, as in $LaFeO_3$.

Exactly as for $MgSiO_3$, high pressure stabilizes a variety of compositions in the compact perovskite structure. Competition with other structures, such as ilmenite, defect pyrochlore, and various polytypes of perovskite, as a function of ionic radius, pressure, and temperature has been reviewed.[26,28]

4.3.5 *Pressure-Induced Amorphization: Amorphous GeO₂*

Glass obtained by quenching a molten liquid to room temperature is an amorphous metastable state, and the loose atomic packing leads to a low density (*see* ***Noncrystalline Solids***). Since we have learned that high pressure stabilizes high density forms of materials, pressure-induced amorphization might sound strange. GeO_2, SiO_2, $Ca(OH)_2$, Fe_2SiO_4, and some other materials have, in fact, been found to vitrify if they are compressed at low temperatures, low enough to kinetically suppress the formation of the crystalline phase that is thermodynamically stable under the pressure. Pressure-induced amorphization is a transition to a metastable, highly dense amorphous phase. If it were possible to quench it to ambient pressure, one would obtain another kind of glass.

Pressure-induced amorphization was reported for the first time in 1984 for hexagonal ice.[47] Since then, a number of fundamental questions have been raised and are still now under investigation. Here, typical experimental data for GeO_2 will be outlined in brief.[48]

At ambient pressure, GeO_2 is stabilized in the rutile form below about 1300 K, while at higher temperatures it transforms to the α-quartz type. It is to be noted that the coordination polyhedron is octahedral in the former and tetrahedral in the latter. The specific density at ambient pressure and temperature is very different, 6.27 g cm^{-3} for rutile but only 4.28 g cm^{-3} for α-quartz. Because conversion from α-quartz to rutile is kinetically very slow even at 1273 K, it is quite easy to quench α-quartz GeO_2 to room temperature.

Effects of pressure upon the α-quartz form are strongly temperature dependent. As can be seen in Figure 10, conversion to rutile is accelerated if both pressure and temperature are elevated slightly: the (110) peak from rutile appears even at 0.1 GPa at 358 K. In contrast, at 335 K it is absent up to 20 GPa. Amorphization occurs at 7 GPa, as confirmed by complementary methods including in situ

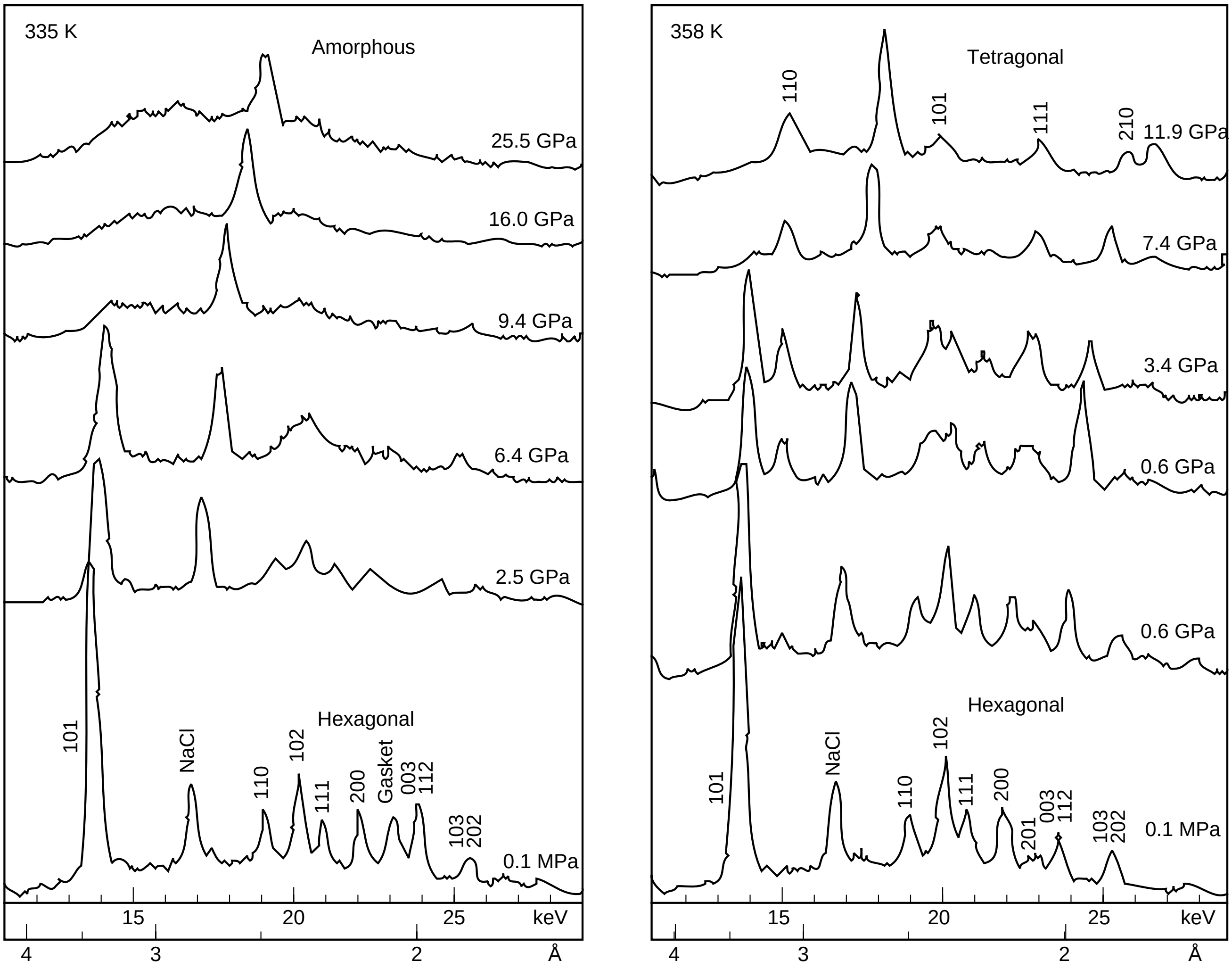

Figure 10 X-ray diffraction patterns of α-SiO_2 under pressure at (a) 335 K and (b) 358 K. (Ref. 48. Reproduced by permission of American Geophysical Union)

Raman scattering and high-resolution electron microscopy on a decompressed specimen.

The amorphization is preceded by some disruption of the α-quartz lattice at about 6 GPa. A gradual fourfold to sixfold coordination change occurs as the pressure increases, and in a specimen decompressed from 20 GPa nucleation of the rutile form was found in the amorphous matrix. An amorphous sample decompressed from 13 GPa has a specific density of $4.5\,\mathrm{g\,cm^{-3}}$, which is considerably higher than that of α-quartz mentioned above.

The pressure-induced amorphous phase should be discriminated from thermally vitrified glass by the difference in density and also by different behavior under pressure: compression of the glass up to 60 GPa does not yield rutile, and germanium completely reverts to tetrahedral coordination on decompression.

The physical and chemical properties of these new pressure-induced amorphous phases may be quite interesting.

5 RELATED ARTICLES

Diffraction Methods in Inorganic Chemistry; Electronic Structure of Solids; Mixed Valence Compounds; Oxides: Solid-state Chemistry; Solids: Computer Modeling.

6 REFERENCES

1. D. L. Anderson, ‘Theory of the Earth’, Blackwell, Boston, 1989.
2. I. F. Silvera, in ‘Frontiers of High Pressure Research’, eds. H. D. Hochheimer and R. D. Etters, Plenum Press, New York, 1991, p. 101.
3. E. Wigner and H. B. Huntington, *J. Chem. Phys.*, 1935, **3**, 764.
4. N. W. Ashcroft, *Phys. Rev. Lett.*, 1968, **21**, 1748.
5. F. P. Bundy, in ‘High Pressure Technology’, eds. I. L. Spain and J. Paauwe, Dekker, New York, 1977, Vol. II, Chap. 8.
6. R. A. Laudise, ‘The Growth of Single Crystals’, Prentice Hall, 1970, p. 275.
7. J. A. James and R. C. Kell, in ‘Crystal Growth from Aqueous Solutions’, ed. B. R. Pamplin, Pergamon Press, Oxford, 1975, Chap. 14.
8. W. D. Wilson, in ‘High Pressure Technology’, eds. I. L. Spain and J. Paauwe, Dekker, New York, 1977, Chap. 7.
9. G. W. Morey and P. Niggli, *J. Am. Chem. Soc.*, 1913, **35**, 1086.
10. G. C. Kennedy, *Am. J. Sci.*, 1950, **248**, 540.
11. O. F. Tuttle, *Am. J. Sci.*, 1948, **246**, 628.
12. S. Taki, *Prog. Cryst. Growth Charact.*, 1991, **23**, 313.
13. K. Kosuge, ‘Chemistry of Nonstoichiometric Compounds’, Oxford University Press, Oxford, 1993.
14. R. J. Cava, B. Batlogg, K. M. Rabe, E. A. Rietman, P. K. Gallagher, and L. W. Rupp Jr, *Physica*, 1988, **C156**, 523.
15. Y. Takeda, R. Kanno, T. Takada, O. Yamamoto, M. Takano, N. Nakayama, and Y. Bando, *J. Solid State Chem.*, 1986, **63**, 237.
16. F. Suzuki, S. Fukushima, T. Mitsui, and S. Ohta, *J. Soc. Cosmet. Chem.*, 1978, **29**, 59.
17. J. C. Joubert and J. Chenavas, in ‘Treatise on Solid State Chemistry’, ed. N. B. Hannay, Plenum Press, New York, 1975, Vol. 5, p. 463.
18. J. B. MacChesney, R. C. Sherwood, and J. F. Potter, *J. Chem. Phys.*, 1965, **43**, 1907.
19. B. Kubota, *J. Am. Ceram. Soc.*, 1961, **44**, 239.
20. J. Karpinski, S. Rusiecki, E. Kaldis, B. Bucher, and E. Jilek, *Physica*, 1989, **C160**, 449.
21. J. Karpinski and E. Kaldis, *J. Cryst. Growth*, 1986, **79**, 477.
22. C. W. F. T. Pistorius, *Prog. Solid State Chem.*, 1976, **11**, 1.
23. I. L. Spain, in ‘High Pressure Technology’, eds. I. L. Spain and J. Paauwe, Dekker, New York, 1977, Chap. 4.
24. E. Yu. Tonkov, ‘High Pressure Phase Transformation: A Handbook’, Gordon and Breach, London, 1992.
25. K. J. Chang, M. M. Dacorogna, M. L. Cohen, J. M. Mignot, G. Chouteau, and G. Martinez, *Phys. Rev. Lett.*, 1985, **54**, 2375.
26. J. B. Goodenough, J. A. Kafalas, and J. M. Longo, in ‘Preparative Methods in Solid State Chemistry’, ed. P. Hagenmuller, Academic Press, New York, 1972, p. 1.
27. J. B. Goodenough, W. Graper, F. Holtzberg, D. L. Huber, R. A. Lefever, J. M. Longo, T. R. McGuire, and S. Methfessel, ‘Landort-Börnstein’, New Series, Group III, Springer, Berlin, 1970, Vol. 4, Part a.
28. O. Muller and R. Roy, ‘The Major Ternary Structural Families’, Springer, Berlin, 1974.
29. W. L. Roth and R. C. De Vries, *J. Appl. Phys.*, 1967, **38**, 951.
30. I. L. Spain, in ‘High Pressure Technology’, eds. I. L. Spain and J. Paauwe, Dekker, New York, 1977, Vol. 1, Chap. 11.
31. P. W. Bridgman, *Proc. Am. Acad. Arts Sci.*, 1952, **81**, 165.
32. N. Kawai, M. Togaya, and A. Onodera, *Proc. Jpn. Acad.*, 1973, **49**, 628.
33. H. K. Mao, in ‘Simple Molecular Systems at Very High Densities’, eds. P. Loubeyre and A. Polian, Plenum Press, New York, 1988, p. 221.
34. F. P. Bundy, *Physica*, 1989, **A156**, 169.
35. F. P. Bundy, H. T. Hall, H. M. Strong, and R. H. Wentorf Jr, *Nature*, 1955, **176**, 51.
36. M. Akaishi, H. Kanda, and S. Yamaoka, *Science*, 1993, **259**, 1592, and references therein.

37. H. M. Strong and R. M. Chrenko, *J. Phys. Chem.*, 1971, **75**, 1838.
38. R. H. Wentorf Jr, *J. Chem. Phys.*, 1957, **26**, 956.
39. L. Vel, G. Demazeau, and J. Etourneau, *Mat. Sci. Eng.*, 1991, **B10**, 149.
40. R. D. Shannon, *Acta Crystallogr., Sect. A*, 1976, **A32**, 751.
41. M. Takano, in 'Chemistry of High Temperature Superconductors', ed. C. N. R. Rao, World Scientific, Singapore, 1991, p. 243.
42. T. Siegrist, S. Zahurac, D. W. Murphy, and R. S. Roth, *Nature*, 1988, **334**, 231.
43. M. Azuma, Z. Hiroi, M. Takano, Y. Bando, and Y. Takeda, *Nature*, 1992, **356**, 775.
44. M. Smith, A. Manthirum, J. Zhou, J. B. Goodenough, and J. T. Merkert, *Nature*, 1991, **351**, 549.
45. A. Navrotsky, D. J. Weidner, R. C. Liebermann, and C. T. Prewitt, *MRS Bull.*, 1992, and references therein.
46. A. M. Glazer, *Acta Crystallogr., Sect. B*, 1972, **B28**, 3384.
47. O. Mishima, L. D. Calvert, and E. Whalley, *Nature*, 1984, **310**, 393.
48. T. Yamanaka, T. Shibata, S. Kawasaki, and S. Kume, in 'High Pressure Research: Application to Earth and Planetary Sciences', eds. Y. Shono and M. H. Manghnani, Terra Scientific, Tokyo/American Geophysical Union, Washington, DC, 1992, p. 493.

Hydride Complexes of the Transition Metals

Robert H. Crabtree
Yale University, New Haven, CT, USA

1 Introduction 1
2 Structure and Bonding 1
3 Spectroscopy 2
4 Energetics 3
5 Synthesis 3
6 Reactions 4
7 Individual Hydrides of Interest 7
8 Related Articles 8
9 References 8

Glossary

Dihydrogen complex: complex of H_2 that retains the H–H bond

Abbreviations

tacn = 1,4,7-tetraazacyclononane.

1 INTRODUCTION

As the simplest ligand, H or hydride has a special place in coordination chemistry. In spite of its simplicity, it shows a remarkable variation in structure and reactivity. With $H_2Fe(CO)_4$[1] and $HCo(CO)_4$,[2] Hieber was the first to describe transition metal hydrides in the 1930s, but his formulations were not always regarded as correct; for example, his iron hydride was wrongly reformulated as $Fe(COH)_2(CO)_2$ by Sidgwick (1950). In the absence of further examples, they remained chemical curiosities for many decades. Only with the discovery of several series of hydride complexes in the mid-1950s did the existence of the M–H bond as a normal covalent bond become widely accepted. The neutron diffraction (*see* ***Diffraction Methods in Inorganic Chemistry***) study of $[ReH_9]^{2-}$ by Ginsberg[3] (1960), the first on a hydride complex, was very influential. By the mid-1960s, it had become clear that metal hydrides were key intermediates in important metal-catalyzed reactions, such as alkene hydrogenation (*see* ***Hydrogenation & Isomerization of Alkenes***).

In the first description of a dihydrogen complex (1984), $[W(H_2)(CO)_3(PCy_3)_2]$, Kubas[4] showed by neutron diffraction that H_2 is coordinated to the metal as an intact molecule. This opened a new phase in hydride chemistry, and hundreds of examples of this phenomenon are now recognized, including some pre-1984 examples that lay unrecognized in the literature (*see* ***Dihydrogen Complexes & Related Sigma Complexes***). The existence of [Ni,Fe] and [Fe] *Hydrogenase*,[5] in which H_2 is believed to bind Ni and Fe respectively, suggests that hydride chemistry also has biological relevance. Useful reviews have appeared on the chemistry of polyhydrides,[6] and dihydrogen complexes.[7,8] In addition, two recent monographs are largely devoted to the subject.[9] Some hydrides, such as MnH_2 and CoH, are only known in the gas phase; others, such as $FeTiH_2$, occur only in the solid phase. Solid-state hydrides are discussed elsewhere (*see* ***Hydrides: Solid State Transition Metal Complexes***).

2 STRUCTURE[6–9] AND BONDING

2.1 Terminal Hydrides

The terminal hydride (**1**) is the most common type. In these species, the M–H distance is close to the sum of the *Covalent Radii*. Neutron diffraction gives this distance reliably, but X-ray methods, because they detect electron density and not the nuclear positions, underestimate the M–H distance by about 0.1 Å. It is not uncommon for the H to escape detection entirely by X-ray methods as a result of the proximity of the metal, always a strong diffractor of X rays. Typical M–H distances are 1.45 to 1.6 Å for first-row elements, 1.6 to 1.7 Å for the second row, and 1.65 to 1.75 Å for the third row; actinides have M–H distances near 2 Å. Early transition metals have M–H distances about 0.1 Å longer than do late metals. Electron diffraction methods have been used for volatile carbonyl hydrides such as $HMn(CO)_5$, $HCo(CO)_4$, and $H_2Fe(CO)_4$; for the Mn compound, the e-diffraction and n-diffraction Mn–H bond lengths are in good agreement.

Because of the small size of the hydride ligand and its tendency to give weak attractive interactions with neighboring hydrides, it is often found in high coordination compounds such as $[ReH_9]^{2-}$, ReH_7L_2, $CpReH_5$, WH_6L_3, and MoH_4L_4 (L = tertiary phosphine), in which the typical coordination geometries (*see* ***Coordination Numbers & Geometries***) are nine coordinate, *Tricapped Trigonal Prism* (TTP); eight coordinate, *Dodecahedral*; seven coordinate, *Pentagonal Bipyramid*.

2.2 Bridging Hydrides

The bridging hydride (**2**) is also very common. Normally, the M–H distances are 0.15 to 0.2 Å longer in this situation,

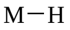

(1)

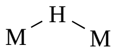

(2)

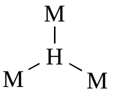

(3)

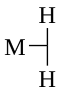

(5)

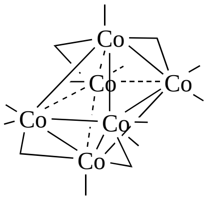

(4)

(M— = M—CO)

but the M–H–M system is usually bent, not linear. One, two, and three bridges are common, and there are a few examples of the M(μ^4-H)M system. Triple (**3**) and higher-order bridging hydrides are found in cluster compounds, the highest coordination number recorded to date being six in $[Co_6(\mu^6\text{-}H)(CO)_{15}]^-$ (**4**).

Dihydrogen complexes (**5**)**[10,11]** such as $[Cr(H_2)(CO)_5]$ are covered in a separate article. Dihydrogen bonding, the tendency of an MH bond to act as proton acceptor in an unconventional hydrogen bond with an OH or NH group, is also covered in a separate article. (*see Hydrogen Bonding*).**[6d]**

2.3 Stereochemical Activity

Hydrides can be more or less stereochemically active. For example, in $HPtCl(PR_3)_2$, the T-shaped geometry of the heavy ligands around Pt shows that the H is fully stereochemically active. On the other hand, in $HCo(CO)_4$, the CO groups are close to tetrahedral and the H occupies a face-capping position. The difference seems to be controlled by the charge on the H. For example, in the first case the hydride is truly hydride-like and the metal has the T-shaped geometry appropriate for a $[PtCl(PR_3)_2]^+$ group, while in $HCo(CO)_4$, the hydride is very protonic and the metal has the tetrahedral geometry appropriate to a $[Co(CO)_4]^-$ group.**[12]**

2.4 Ligand Field Strength

The hydride ligand is one of the highest-field ligands in terms of *Crystal Field Theory* and this, together with its small size, very often makes hydrides 18e and diamagnetic. Formulations that do not conform to the 18e rule (*see Effective Atomic Number Rule*) have frequently been proposed, but they often turn out to be erroneous. As a soft ligand (*see **Hard & Soft Acids and Bases***), H is often found with CO, Cp, or PR_3 as a co-ligand, but a few examples are known where such hard ligands as oxo, amine, and fluoride coexist with hydride in the same complex. Polyhydrides without Cp or PR_3 as co-ligands, such as $ReH_5\{HB(pz)_3\}$, are still very rare. Hydride chemistry provides something of a bridge between coordination and organometallic chemistry in that it is a noncarbon ligand that imparts properties to the complex similar to those found for organometallic species.

Hydride is also one of the highest *Trans Effect* and *Trans Influence* ligands. Structures of hydride complexes often show rather long M–L bond lengths trans to H. H_2 is a low trans effect ligand, however, and a trans H–M–(H_2) arrangement is found in many nonclassical hydrides.

3 SPECTROSCOPY

3.1 NMR

The NMR method is extremely useful for hydride complexes because the corresponding resonance usually appears from 0 to 40 ppm to high field of TMS, a region otherwise free of signals. Exceptions can be found, especially among d^0 and d^{10} species, such as $Cp_2ZrH(BH_4)$ at +4.3 ppm. Coupling to any phosphines present can help determine the stereochemistry, because $^2J(P,H)$ is ca. 15 to 30 Hz for a cis arrangement and 90 to 200 Hz for a trans arrangement. Integration of the signal to determine the number of hydrides may need special care because the T_1 for M–H and ligand signals is often quite different. $IrH_5(PPh_3)_2$ was originally assigned as $IrH_3(PPh_3)_2$ for this reason.

Even in cases where several different hydride ligands are present, a single proton NMR resonance is often observed at room temperature and even below. For example, ReH_7L_2 species have at least three distinct types of hydrogen, yet only a single hydride resonance is normally seen down to −100 °C. This is because hydrides have a high tendency to be fluxional (i.e. undergo rapid positional permutation, *see Fluxional Molecule*). Possible reasons are the small size of hydride ligands and their facility in forming H_2 complexes, which then undergo rotation about the M–(H_2) axis, leading to permutation of the H nuclei. Bridging hydrides resonate to high field of TMS, except in rare cases such as the μ^6-H of the cluster $[Co_6(\mu^6\text{-}H)(CO)_{15}]^-$, which resonates at +23.2 ppm. Coupling constants are lower for bridging hydrides than for terminal ones, in line with the reduction in M–H bond order implied by the presence of a 2e, *n*-center bond. Coupling to spin-1/2 metals, such as ^{187}Os (1.3% abundance), ^{195}Pt (33.7%), ^{103}Rh (100%), and ^{183}W (14.3%) can give information about the number of metals directly bonded.**[13]** If an (H_2) ligand is present in a complex, special techniques are available for NMR studies.**[7–9,14]**

Isotopic Perturbation of Resonance is a method for detecting X–H–M bridges (X = C, Si, ...) or $HM(H_2)$ species in highly fluxional systems and relies on temperature-dependent shifts in the averaged resonances between the different isotopomers in partially deuterated samples.**[15]** This is caused by zero-point energy differences, which make H prefer the weaker (usually bridging) bond over D. If the system is nonfluxional, deuteration is not needed and reduced Si–C or C–H coupling constants in the bridged X–H bonds is usually sufficient to diagnose the structure.

Tunneling effects are apparent in some polyhydrides, particularly trihydrides.[6] This leads to an apparent J(H,H′) that is highly temperature dependent and can be extremely large (up to 45 000 Hz). The best-known examples are Chaudret's $[\mathrm{Cp^*Ru(PR_3)H_3}]$ and Heinekey's $[\mathrm{CpIr(PR_3)H_3}]^+$. The $\mathrm{H \cdots H}$ distances are not short (1.6 Å), so these are not ground-state H_2 or H_3 complexes. These exchange couplings are a quantum tunneling effect, as shown by D and T substitution,[6b,6c] and are relatively rare – most trihydrides behave normally. There is still some discussion as to exactly how the tunneling occurs.[6a]

3.2 IR Spectroscopy

M–H bands often appear in the IR (*see Infrared Spectroscopy*) in the range 1500 to 2300 $\mathrm{cm^{-1}}$, although their intensity can be low or very low for late metal cations. Lower frequencies tend to be observed for the early transition metals. In certain systems, for example, $\mathrm{Ir^{III}}$, enough examples are known to be able to define the ranges of ν(M–H) that tend to be found depending on the nature of the trans ligand.[16] Bridging hydrides appear in the range 1200 to 1700 $\mathrm{cm^{-1}}$ (ν_{as}). M–H bending modes have been seen in the range 700 to 900 $\mathrm{cm^{-1}}$. An M–H stretching vibration can be identified by isotopic substitution, in which case the M–D band appears at ca. 1.414[ν(M–H)].

3.3 Other Spectroscopic Methods

Binary hydrides such as MH and $\mathrm{M'H^-}$ (M = Ti, Cr, Mn, Fe, Co, Ni, Pd, Pt, Cu; M′ = Ti, Cr, Mn, Co, Ni) exist in the gas phase and can be detected in ion beam *Mass Spectrometry* experiments. More generally useful is electrospray MS in which large complexes such as $\mathrm{Fe(dmpe)_2H_2}$ can be detected in solution.[17]

Few paramagnetic hydrides are known and even fewer have been studied by *Electron Paramagnetic Resonance*. For example, $[\mathrm{TiH_2Cp_2}]^-$ and $\mathrm{TaH_2(dmpe)_2Cl_2}$ have been examined in this way.

3.4 Matrix Studies

Matrix studies (*see Matrix Isolation*) of hydrides have been useful for determining the electronic and vibrational spectra of unstable hydride species, sometimes ones produced by photolysis.[18] For example, $\mathrm{HCo(CO)_3}$ has been detected from irradiation of the tetracarbonyl.

4 ENERGETICS

The M–H dissociation energies (*see Bond Dissociation Energy*) estimated from ion beam experiments are quite large (see Table 1). The strength of the bond has been correlated with the promotion energy from the ground-state electronic configuration of the atom or ion to the lowest-energy $ns(n-1)d^{n-1}$ spin-decoupled state: the lower the promotion energy, the stronger the bond. Eighteen-electron hydride complexes have been studied in solution and their M–H bond strengths estimated; some are given in Table 1.

Table 1 M–H dissociation energies[a] of some M–H cations, neutrals, and anions in the gas phase and of some hydride complexes in solution

M–H	Cation	Neutral	Anion
Fe–H	208 (6)	157 (8)	235 (17)
Co–H	195 (6)	194 (13)	195 (13)
Ni–H	166 (8)	252 (8)	187 (8)
$\mathrm{HMn(CO)_5}$	–	245 (15)	–
$\mathrm{H_2Fe(CO)_4}$	–	272 (4)[b]	–
$\mathrm{HCo(CO)_4}$	–	227 (18)	–

[a] In kJ $\mathrm{mol^{-1}}$; uncertainties in parentheses. [b] Average of the two Fe–H bonds.

5 SYNTHESIS

5.1 Hydride Reagents

The commonest route is treatment of a metal halo complex with a hydride donor such as $\mathrm{NaBH_4}$ (equation 1), $\mathrm{LiAlH_4}$, or $\mathrm{LiBHEt_3}$ (equation 2). The last reagent is useful in that it tends to be more selective and partial substitution can be achieved if desired; in addition, there is less risk of forming bridging borohydride or aluminohydride complexes of the type $\mathrm{L_nM(\eta^3\text{-}QH_4)_m}$ (Q = B or Al). Sometimes, these can revert to normal hydrides on hydrolysis.[19] $\mathrm{HCO_2H}$ and $\mathrm{HCO_2Na}$ are particularly mild hydride forming reagents.

$$\mathrm{FeCl_2(triphos)} + \mathrm{NaBH_4} \longrightarrow \mathrm{(triphos)Fe(\mu\text{-}H)_3Fe(triphos)} \tag{1}$$

$$\mathrm{WCl_6} + \mathrm{LiBHEt_3} + \mathrm{PR_3} \longrightarrow \mathrm{WH_6(PR_3)_3} \tag{2}$$

5.2 Oxidative Addition

A wide variety of hydrides are formed by *Oxidative Addition* of H_2 to metal complexes (equation 3). There has been some interest in the direction of H_2 addition to square-planar $\mathrm{Ir^I}$. Of the two possible outcomes, one is usually favored kinetically.[20]

$$\mathrm{Ir^ICl(CO)(PR_3)_2} + \mathrm{H_2} \longrightarrow \mathrm{Ir^{III}H_2Cl(CO)(PR_3)_2} \tag{3}$$

Hydrogenolysis of metal alkyls is another route involving H_2 (equation 4). This probably involves initial formation of an H_2 complex that leads to protonolysis of the W–Me bond.

For non-d^0 cases, oxidative addition/*Reductive Elimination* is also a possibility (equation 5).

$$WMe_6 + H_2 + PR_3 \longrightarrow WH_6(PR_3)_3 \qquad (4)$$

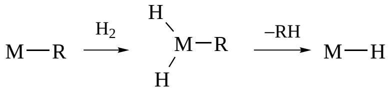
(5)

Oxidative addition of other X–H compounds other than H_2 can also lead to the formation of hydrides. For example, silanes H–SiR_3 give silyl hydrides, hydrohalic acids give halohydrides, and *Orthometalation* of aryl C–H gives an orthometalated aryl hydride (equations 6 and 7).

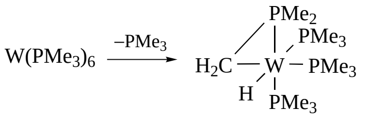
(6)

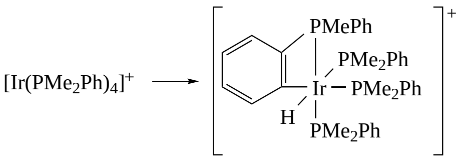
(7)

Dihydrogen complexes are sometimes formed by H_2 addition to N_2 complexes or to agostic species (equations 8 and 9) (*see Agostic Bonding*). Complexes that prefer oxidation by 1e rather than 2e can undergo a dinuclear oxidative addition of the type shown in equation (10). Catalytic processes involving hydride intermediates, often formed by oxidative addition, include isomerization, hydrogenation, hydroformylation, hydrocyanation, and hydrosilation of unsaturated species (*see* ***Hydrocyanation by Homogeneous Catalysis***; ***Hydrogenation & Isomerization of Alkenes***; ***Hydrosilation Catalysis***).

$$FeH_2(N_2)(PEt_2Ph)_3 + H_2 \xrightarrow{-N_2} FeH_2(H_2)(PEt_2Ph)_3 \qquad (8)$$

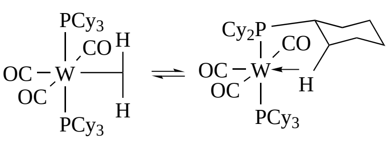
(9)

$$2[Co^{II}(CN)_5]^{3-} + H_2 \longrightarrow 2[HCo^{III}(CN)_5]^{3-} \qquad (10)$$

5.3 β-elimination

β-Elimination from any of a variety of alkyls or alkoxides is a source of hydrides, although when formed in this way, they are often intermediates in a larger reaction scheme rather than being simple preparative reactions. Some purely preparative examples have been reported, however (equation 11).

$$RuCl_2(PR_3)_4 + 2KOCHMe_2 \xrightarrow[-Me_2CO]{-KCl} RuH_2(PR_3)_4 \qquad (11)$$

5.4 Protonation

Addition of protons often occurs readily to a variety of neutral and anionic complexes and is a rich source of hydrides (equation 12). Protonation can also take place on a ligand in certain cases. Protonation of metal hydrides is a common source of H_2 complexes (equation 13).

$$[Co(CO)_4]^- + H^+ \longrightarrow HCo(CO)_4 \qquad (12)$$

$$IrH_5(PCy_3)_2 + H^+ \longrightarrow [Ir(H)_2(H_2)_2(PCy_3)_2]^+ \qquad (13)$$

5.5 Clusters and Bridging Hydrides

Compounds with M–H–M bridges can often be formed by oxidative addition to preformed *Cluster* compounds (equation 14). A general strategy for synthesizing hydride clusters from mononuclear precursors is to generate a coordinatively unsaturated (*see Coordinative Saturation & Unsaturation*) fragment L_nM in the presence of a metal hydride, say L_nM'–H. The metal hydride tends to bind to the second metal, as might any classical 2e ligand like PPh_3, to give the bridged system L_nM'–H–ML_n (equation 15).

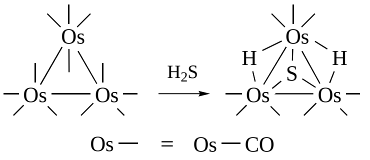
(14)

$$[IrH_2(solv)_2(PPh_3)_2]^+ + ReH_7(PPh_3)_2 \longrightarrow [H(PPh_3)_2Ir(\mu\text{-}H)_3ReH_3(PPh_3)_2]^+ \qquad (15)$$

6 REACTIONS

Even before any real understanding of hydride chemistry had been obtained, alkene *Hydroformylation* (also *see Oxo Process*), a catalytic reaction involving hydride intermediates, was being practiced on an industrial scale (Otto Roelen, Ruhrchemie, 1938) (equation 16).

$$RCH{=}CH_2 + 2H_2 + CO \xrightarrow{HCo(CO)_4} RCH_2CH_2CHO \qquad (16)$$

6.1 Stability of Hydrides

The first reactivity issue is stability, that is, the complex must be stable enough to isolate or at least to exist as a kinetically significant intermediate. A coordination inert metal (*see Coordinatively Inert & Labile Complexes* and ***Coordination & Organometallic Chemistry: Principles***) is useful, and third-row metals tend to bind H and other ligands more strongly. More hydrides are known for Ir and Re than for any other elements. Hydrides often decompose by loss of H_2, or by loss of HX, where X is a co-ligand such as a Me group. High-field co-ligands and a strongly backbonding metal site can minimize these reactions, but loss of CH_4 is so favorable that very few methyl or alkyl hydrides are known. Early metal hydrides can be hydridic and therefore unstable to water, and hydrides with strong donor ligands can be unstable to air. Finally, they can be light sensitive.

6.2 Reaction Types

In spite of the fact that the term 'hydride' is used for all M–H groups, their reactivity patterns suggest that most hydrides have little net charge on H. Hydrides $L_nM{-}H$ can act as H^-, $H^\bullet$, or H^+ donors according to the nature of the attacking group and the stability of L_nM^+, $L_nM^\bullet$, or L_nM^-, respectively. A di- or polyhydride can also lose H_2. The polarization of the M–H bond in the ground-state structure ($M^+{-}H^-$ or $M^-{-}H^+$) may not be the key factor; Sweany has IR evidence on $HM(CO)_n$ and $M(CO)_n$ that suggests that the charge on H in $HMn(CO)_5$, $H_2Fe(CO)_4$, and $HCo(CO)_4$ is always negative to about the same extent through the series,[21] yet these hydrides differ markedly in their propensity to donate hydride or protons: the cobalt compound is a strong acid in water, but the Mn compound tends to donate H^- or $H^\bullet$ in its reactions. This implies that the stability of the product, L_nM^+, $L_nM^\bullet$, or L_nM^-, may be more important, including such factors as solvation of these species.

6.3 Hydridic Reactivity

True hydride-like reactivity is often seen for the early metals, for anionic complexes, and for some polyhydrides. These metals are closer in behavior to the main group hydrides, which are often hydridic in character. One problem pointed out by Labinger[22] is that if L_nMH is an 18e compound, hydride loss will give a 16e L_nM^+ species that is rarely, if ever, stable. Coordinative unsaturation encourages the reduced substrate to bind to the metal (equation 17). This makes it difficult to define a scale of H^- donor power independent of the nature of the substrate. Another ambiguity is whether the reaction is a true H^- transfer or whether electron transfer is followed by H atom transfer (equation 18).

$$L_nMH + RCHO \longrightarrow L_nMOCH_2R \qquad (17)$$

$$L_nMH^- + S \longrightarrow L_nMH^\bullet + HS^{\bullet -} \longrightarrow L_nM + SH^- \qquad (18)$$

An early example of a hydride with pronounced H^- donor character is $[Cp_2ZrHCl]_n$, which attacks ketones, aldehydes, esters, epoxides, and even CO_2, as shown in Scheme 1. $Cp^*{}_2ScH$ is so active that it even attacks nitriles to give $Cp^*Sc(N{=}CHR)$; the resulting imine complexes react with H_2 to give amines, and the Sc complex is a nitrile hydrogenation catalyst.[23]

Berke and coworkers have shown how hydrides can be activated by a trans nitrosyl so that CO_2 inserts into the MoH bond of *mer*-$Mo(CO)H(NO)(PMe_3)_3$ to give a formato-complex.[24]

6.4 Homolytic Reactivity

A wide variety of hydrides act as H atom donors; for example, the key step in the hydrogenation of alkenes by $[HCo^{III}(CN)_5]^{3-}$ is known to go in this way (equation 19). A number of metal hydrides react with CCl_4 to give $CHCl_3$ and the metal halo complex. The mechanism may involve electron transfer, followed by H atom abstraction from the metal by $\bullet CCl_3$.

$$2[HCo^{III}(CN)_5]^{3-} + PhCH{=}CH_2 \longrightarrow 2[Co^{II}(CN)_5]^{3-} + PhCH_2CH_3 \qquad (19)$$

6.5 Proton Donor Reactions

Carbonyl hydrides tend to be acids because of the stabilization of the resulting anions by the strong π-acceptor power of the CO ligand (equation 20). H_2 complexes can also be relatively acidic, because they are only formed when

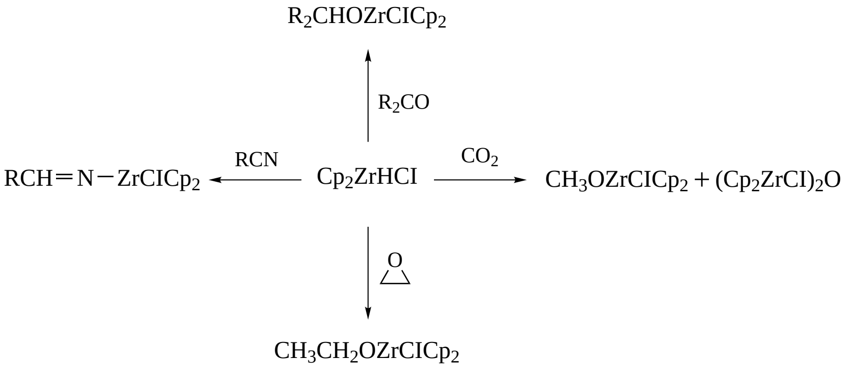

Scheme 1 Some reactions of Cp_2ZrHCl

back donation from the metal is weak, and hence, the H_2 tends to accumulate a net positive charge. pK_a values of -2 to 15 have been reported for H_2 complexes, which implies a high degree of acidification of H_2 [pK_a(H_2, free) $\sim$ 35] on binding. Proton loss is possible if the L_nM fragment that remains can stabilize the negative charge. This is particularly the case for carbonyl hydrides and for cationic dihydrogen complexes. For example, pK_a values have been determined for several hydrides (Table 2). The cation radicals derived from oxidizing typical 18e metal hydrides are about 20 pK_a units more acidic.**[25]**

$$\mathrm{HCo(CO)_4} \longrightarrow \mathrm{H^+} + \mathrm{[Co(CO)_4]^-} \qquad (20)$$

The rate of proton transfer has been measured for a number of metal hydride/organic amine combinations. The rates appear to follow Marcus behavior (*see Marcus Treatment*), in which the rate goes up with driving force (equation 21, where k_{AB} is the rate of proton transfer between AH and B^-, and K_{AB} is the equilibrium constant for the proton transfer). Proton transfer appears to be the slow step in the process, rather than slow electron transfer followed by fast H atom transfer, because the rates show an isotope effect. For example, in the self-exchange of $[CpM(H,D)(CO)_3]/[CpM(CO)_3]^-$, k_H/k_D is 3.6, 3.7, and 3.7 for Cr, Mo, and W. There seems to be a good relation between thermodynamic acidity and kinetic acidity for a variety of terminal hydrides, although bridging hydrides are often kinetically weaker acids than would be expected from their pK_a. For example, Table 3 shows rates of proton transfer for some hydride complexes. The fact that deprotonation from bridging hydride positions is slower than for terminal positions implies that a protonation that eventually gives a bridging hydride may well go via a terminal hydride intermediate. An excellent example is shown in equation (22), where the second step takes two weeks at 25 °C.

Table 2 Thermodynamic acidities[a] for some hydride complexes

Complex	Acidity
$VH(CO)_5(PPh_3)$	6.8 (H_2O)
$[MoH(CO)_3(tacn)]^+$	2.4 (H_2O)
$H_2Fe(CO)_4$	4.0, 12.7 (H_2O)
$[NiH\{P(Ome)_3\}_4]^+$	1.7 (MeOH), 13.4 (MeCN)
$HCo(CO)_4$	Strong (H_2O), ca. 1 (MeOH), 8.4 (MeCN)
$CpCrH(CO)_3$	13.3 (MeCN)
$[CpCrH(CO)_3]^{+\bullet}$	-9.5(MeCN)
$CpMoH(CO)_3$	13.9 (MeCN)
$[CpMoH(CO)_3]^{+\bullet}$	-6.0(MeCN)
$CpWH(CO)_3$	16.1 (MeCN)
$[CpWH(CO)_3]^{+\bullet}$	-3.0(MeCN)

[a]Water scale; solvent in brackets.

Table 3 Rates of proton transfer to aniline in acetonitrile[a]

Compound	Rate ($M^{-1}\ s^{-1}$)	pK_a
$HCo(CO)_4$	1.7×10^7	8.4
$H_2Fe(CO)_4$	5.4×10^4	11.4
$CpCrH(CO)_3$	1.7×10^4	13.3
$CpMoH(CO)_3$	3.9×10^3	17.1
$CpWH(CO)_3$	250	16.1
$HMn(CO)_5$	210	14.2
$CpFeH(CO)_2$	0.4	19.4
$CpWH(CO)_2(PMe_3)$	$<10^{-3}$	26.6

[a]At 25 °C.

$$k_{AB} = [k_{AA}k_{BB}K_{AB}]^{1/2} \qquad (21)$$

$$\begin{aligned}&\mathrm{Cp(CO)_2M(\mu\text{-}PPh_2)Pt(CO)PPh_3}(M\!-\!Pt) + \mathrm{HBF_4} \longrightarrow\\ &\quad \mathrm{[Cp(CO)_2HM(\mu\text{-}PPh_2)Pt(CO)PPh_3}(M\!-\!Pt)\mathrm{]BF_4} \longrightarrow\\ &\qquad \mathrm{[Cp(CO)_2M(\mu\text{-}PPh_2)(\mu\text{-}H)Pt(CO)PPh_3}(M\!-\!Pt)\mathrm{]BF_4}\end{aligned} \qquad (22)$$

In some cases, the second step is too slow to observe without a catalyst being present. For example, Cp(NO)Re(μ-PCy_2)Pt(PPh_3)$_2$(*Re–Pt*) protonates at Re to give a terminal hydride. Only on treatment with Cl^- does the rearrangement to Cp(NO)Re(μ-PCy_2)(μ-H)Pt(PPh_3)$_2$(*Re–Pt*) occur. This is not simply base catalysis because F^- is ineffective, and it has been proposed that Cl^- attacks the complex and breaks the M–M bond, allowing the H to reach the terminal position in the product.**[26]** The finding that the rate of a reaction for differing hydrides parallels the known rates for proton transfer, for the same hydrides, helps establish proton transfer as the slow step in that reaction.**[27]**

Protonation can take place on a ligand in preference to the metal; proton transfer to a hydride occurs in $CpFe(Ph_2CH_2CH_2PPh_2)H$ to give an H_2 complex as the kinetic product that only slowly rearranges to the final thermodynamic product, a cationic Fe(IV) dihydride.**[28]**

6.6 Insertion Reactions

Unsaturated ligands such as alkenes often undergo insertion into M–H bonds to give alkyls or vinyls (equation 23). This is an important step in catalytic alkene isomerization, hydrogenation, hydroformylation, hydrocyanation, and perhaps also hydrosilation, although in this last case, insertion into the M–Si bond may be preferred. This is simply the reverse of the β-elimination reaction discussed above.

$$\mathrm{Cl(PR_3)_2Pt{-}H} + \mathrm{C_2H_4} \longrightarrow \mathrm{Cl(PR_3)_2Pt{-}C_2H_5} \qquad (23)$$

Insertion of an M–H bond into a multiple bond of an unsaturated ligand is a very important reaction, because it is a key step in catalytic processes such as hydrogenation. Osborn has observed a rare reversible example (equation 24).**[29]**

$$\begin{aligned}&\mathrm{Mo(C_2H_4)_2(dppe)_2} \xrightarrow{\mathrm{H^+}} \mathrm{[HMo(C_2H_4)_2(dppe)_2]^+} \rightleftharpoons\\ &\qquad \mathrm{[C_2H_5Mo(C_2H_4)(dppe)_2]^+}\end{aligned} \qquad (24)$$

The selectivity of hydride insertion into an unsymmetrical unsaturated species plays a role in determining the selectivity of catalytic reactions; the outcome is a complex function of electronic and steric effects and cannot readily be predicted other than by analogy with similar systems. In hydrogenation, the direction of insertion is usually not an important issue because an H is added to each end of the multiple bond, but in hydroformylation and hydrocyanation, where HX ($X = CHO$ or CN) adds to the unsaturate, the direction of the initial insertion can be inferred. In hydrosilation, an Si–H bond is added, but there is some doubt as to whether the first insertion occurs into the M–H or M–Si bonds. Among non-H ligands, the M–Si bond is the closest analog to M–H in polarity and reactivity.

6.7 Photochemical Reactions

Hydride complexes have a rich photochemistry. Often, nonhydride ligands are lost, but a common reaction of polyhydrides is loss of H_2. Photoextrusion of H_2 from Cp_2WH_2 in benzene gives Cp_2W, which inserts into a C–H bond of the solvent (equation 25). $CpIrH_2(PMe_3)$ gives a species that even attacks alkanes (equation 26).[30] For linear and branched alkanes, preferential attack takes place at primary and relatively unhindered secondary C–H bonds, presumably for steric reasons. Time-resolved infrared experiments probing the initial femtosecond dynamics through the nano- and microsecond kinetics to the final stable products have been used to generate a detailed picture of the C–H activation reaction.[30a]

$$Cp_2WH_2 \xrightarrow{h\nu} Cp_2W \xrightarrow{PhH} Cp_2WH(Ph) \qquad (25)$$

$$CpIrH_2(PMe_3) \xrightarrow{h\nu} CpIr(PMe_3) \xrightarrow{CyH} CpIrH(Cy)(PMe_3) \qquad (26)$$

6.8 Other Reactions

Hydride complexes have been important precursors in the study of *Alkane Activation*. For example, alkanes can be catalytically dehydrogenated by $ReH_7(PR_3)_2$ or $[IrH_2(OH_2)_2(PR_3)_2]^+$ or $(PCP)IrH_2$ thermally or photochemically.[30c–30d] Cyclooctane is the best substrate, presumably because it has the least unfavorable heat of dehydrogenation of all common alkanes (equation 27).

$$C_8H_{16} + t\text{-BuCH=CH}_2 \xrightarrow{\text{catalyst}} C_8H_{14} + t\text{-BuCH}_2\text{CH}_3 \qquad (27)$$

7 INDIVIDUAL HYDRIDES OF INTEREST

7.1 $[ReH_9]^-$

This remarkable species is one of the very few homoleptic transition metal hydrides (*see Homoleptic Compound*). The neutron diffraction structure dating from 1964[3] put the M–H bond on a secure footing. The molecule has a TTP geometry. It was originally formulated as $K[Re(H_2O)_4]$, then $K[ReH_4]\cdot 2-4H_2O$ or $K_6[Re_2H_{14}]\cdot 6H_2O$, then $KReH_8$, illustrating the difficulty of characterizing the complex.

7.2 $ReH_7(PR_3)_2$

These species can be classical with a TTP geometry or nonclassical with a dodecahedral geometry. For example, the dppe compound is TTP but the P(*o*-tolyl)$_3$ complex is dodecahedral with one coordination site occupied by an H_2 ligand with a long (1.357 Å) H–H distance. These species more or less easily lose H_2, and the resulting 16e intermediate can react with a number of 2e ligands, such as pyridine, or with a silane $HSiR'_3$. In the latter case, an interesting silyl hydride $ReH_6(SiR'_3)(PR_3)_2$ is obtained.[31] In the case of the $SiHEt_2$ complex, a neutron diffraction study[32] has revealed several short Si···H distances, suggesting that attractive Si···H interactions replace the H···H interactions present in the original molecule. In such a high coordination compound, attractive interactions between ligands are probably important in stabilizing the structure.

7.3 $[(OC)_5Cr–H–Cr(CO)_5]^-$

Early work on this compound suggested the M–H–M bridge might be linear, but careful analysis[33] of the neutron diffraction data showed that the H is disordered over four positions so that although the averaged H position leads to an apparently linear M–H–M group each of the disordered structures has a bent M–H–M group. This implies that the system is trying to maximize the bonding between all three atoms, as appropriate for a 2e, three-center bond.

7.4 $[IrH_2(8\text{-methylbenzoquinoline})(PPh_3)_2]^+$

This complex is agostic and contains a short C–H···M interaction; comparison with related structures led to the definition of a reaction trajectory for the M + C–H reaction.[34]

7.5 $CpMn(CO)_2(H\cdots SiR_3)$

These interesting molecules were discovered and briefly studied by Graham,[35] but Schubert[36] put them on a firm basis with his systematic neutron diffraction studies. The H···Si distances can be short or long, bonding or nonbonding, depending on the nature of R. Replacing the CO groups by other ligands also affects the H···Si distance. This system shows a series of σ-bond complexes, which more closely resemble the full oxidative addition products than the silane precursor. Sabo-Etienne, Chaudret, and collaborators have produced some of the most remarkable such structures, including one, $(PR_3)_2H_2Ru(SiH_4)RuH_2(PR_3)_2$, with an SiH_4 ligand bridging between the two metals.[37]

8 RELATED ARTICLES

Dihydrogen Complexes & Related Sigma Complexes; Dinuclear Organometallic Cluster Complexes; Hydrogenation & Isomerization of Alkenes; Polynuclear Organometallic Cluster Complexes.

9 REFERENCES

1. W. Hieber and F. Leutert, *Naturwissenschaften*, 1931, **19**, 360.
2. W. Hieber and E. Fack, *Z. Anorg. Allg. Chem.*, 1938, **236**, 83.
3. K. Knox and A. P. Ginsberg, *Inorg. Chem.*, 1964, **3**, 555.
4. G. J. Kubas, R. R. Ryan, and D. A. Wrobleski, *J. Am. Chem. Soc.*, 1986, **108**, 1339.
5. M. Y. Darensbourg, E. J. Lyon, and J. J. Smee, *Coord. Chem. Rev.*, 2000, **206**, 533.
6. (a) F. Maseras, A. Lledos, E. Clot, and O. Eisenstein, *Chem. Rev.*, 2000, **100**, 601; (b) G. S. McGrady and G. Guilera, *Chem. Soc. Rev.*, 2003, **32**, 383; (c) S. Sabo-Etienne and B. Chaudret, *Chem. Rev.*, 1998, **98**, 2077; (d) L. Brammer, *J. Chem. Soc., Dalton Trans.*, 2003, 1.
7. G. J. Kubas, *J. Organomet. Chem.*, 2001, **635**, 37.
8. G. J. Kubas, *Acc. Chem. Res.*, 1988, **21**, 120; R. H. Crabtree, *Acc. Chem. Res.*, 1990, **23**, 95; *Angew. Chem., Int. Ed. Engl.*, 1993, **32**, 789.
9. G. J. Kubas ed., 'Metal Dihydrogen and σ-Bond Complexes', Kluwer/Plenum, New York, 2001; A. Dedieu ed., 'Transition Metal Hydrides', VCH, Weinheim, 1990.
10. L. Brammer, J. A. K. Howard, O. Johnson, T. F. Koetzle, J. L. Spencer, and A. M. Stringer, *J. Chem. Soc., Chem. Commun.*, 1991, 241.
11. (a) R. H. Morris, *Inorg. Chem.*, 1992, **31**, 1471; (b) S. Sabo-Etienne and B. Chaudret, *Coord. Chem. Rev.* 1998, **178**, 381.
12. S. A. Jackson, O. Eisenstein, J. D. Martin, A. C. Albeniz, and R. H. Crabtree, *Organometallics*, 1991, **10**, 3062.
13. E. C. Constable, B. F. G. Johnson, J. Lewis, G. N. Pain, and M. J. Taylor, *J. Chem. Soc., Chem. Commun.*, 1982, 754.
14. (a) K. A. Earl, G. Jia, P. A. Maltby, and R. H. Morris, *J. Am. Chem. Soc.*, 1991, **113**, 3027; (b) X.-L. Luo and R. H. Crabtree, *Inorg. Chem.*, 1990, **29**, 2788; X.-L. Luo, J. A. K. Howard, and R. H. Crabtree. *Magn. Reson. Chem.*, 1991, **29**, S89; (c) W. Yao, J. W. Faller, and R. H. Crabtree, *Inorg. Chim. Acta*, 1997, **259**, 71.
15. E. Gutierrez-Puebla, A. Monge, M. Paneque, M. L. Poveda, S. Taboada, M. Trujillo, and E. Carmona, *J. Am. Chem. Soc.*, 1999, **121**, 346 and references cited.
16. J. Chatt, R. S. Coffey, and B. L. Shaw, *J. Chem. Soc.*, 1965, 7391.
17. L. D. Field, W. J. Shaw, and P. Turner, *Organometallics*, 2001, **20**, 3491.
18. S. S. Kristjansdottir, J. R. Norton, A. Moroz, R. L. Sweany, and S. L. Whittenburg, *Organometallics*, 1991, **10**, 2357 and references cited.
19. B. D. James and M. G. Wallbridge, *Prog. Inorg. Chem.*, 1970, **11**, 99.
20. M. J. Burk, M. P. McGrath, and R. H. Crabtree, *J. Am. Chem. Soc.*, 1988, **110**, 5034.
21. R. L. Sweany and J. W. Owens, *J. Organomet. Chem.*, 1983, **255**, 327.
22. J. A. Labinger, in Ref. 6, Chap. 10.
23. J. E. Bercaw, D. L. Davies, and P. T. Wolczanski, *Organometallics*, 1986, **5**, 443.
24. F. P. Liang, H. Jacobsen, H. W. Schmalle, T. Fox, and H. Berke, *Organometallics*, 2000, **19**, 1950.
25. S. S. Kristjansdottir and J. R. Norton, in Ref. 6, Chap. 9.
26. J. Powell, J. F. Sawyer, and S. J. Smith, *J. Chem. Soc., Chem. Commun.*, 1985, 1312.
27. R. M. Bullock, *J. Am. Chem. Soc.*, 1987, **109**, 8087.
28. N. V. Belkova, P. O. Revin, L. M. Epstein, E. V. Vorontsov, V. I. Bakhmutov, E. S. Shubina, E. Collange, and R. Poli, *J. Am. Chem. Soc.*, 2003, **125**, 11106 references cited therein.
29. J. W. Byrne, H. U. Blaser, and J. A. Osborn, *J. Am. Chem. Soc.*, 1975, **97**, 3871.
30. (a) S. E. Bromberg, H. Yang, M. C. Asplund, T. Lian, B. K. McNamara, K. T. Kotz, J. S. Yeston, M. Wilkens, H. Frei, R. G. Bergman, and C. B. Harris, *Science*, 1997, **278**, 260; (b) A. H. Janowicz and R. G. Bergman, *J. Am. Chem. Soc.*, 1982, **104**, 352; (c) R. H. Crabtree *J. Chem. Soc., Dalton Trans.*, 2001, 2437; (d) K. B. Renkema, Y. V. Kissin, A. S. Goldman, *J. Am. Chem. Soc.*, 2003, **125**, 7770.
31. X. L. Luo, D. B. Baudry, P. Boydell, P. Charpin, M. Nierlich, M. Ephritikhine, and R. H. Crabtree, *Inorg. Chem.*, 1990, **29**, 1511.
32. A. D. Batsanov, J. A. K. Howard, J. B. Love, and J. L. Spencer, *Organometallics*, 1995, **14**, 5657 references cited.
33. R. Bau, R. G. Teller, S. W. Kirtley, and T. F. Koetzle, *Acc. Chem. Res.*, 1979, **12**, 176.
34. T. R. Cundari, *J. Am. Chem. Soc.* 1994, **116**, 340; R. H. Crabtree, E. M. Holt, M. E. Lavin, and S. M. Morehouse, *Inorg. Chem.*, 1985, **24**, 1986.
35. W. A. G. Graham and M. J. Bennett, *Chem. Eng. News*, 1970, **48**(25), 75.
36. U. Schubert, J. Muller, and H. G. Alt, *Organometallics*, 1987, **6**, 469.
37. I. Atheaux, F. Delpech, B. Donnadieu, S. Chaudret, B. Sabo-Etienne, K. Hussein, J. C. Barthelat, T. Braun, S. B. Duckett, R. N. Perutz, *Organometallics*, 2002, **21**, 5347; I. Atheaux, B. Donnadieu, V. Rodriguez, S. Sabo-Etienne, B. Chaudret, K. Hussein, J. C. Barthelat, *J. Am. Chem. Soc.*, 2000, **122**, 5664.

Hydrides: Solid State Transition Metal Complexes

Klaus Yvon & Guillaume Renaudin
University of Geneva, Geneva, Switzerland

1	Introduction	1
2	Experimental Details	2
3	Hydride Structure Types and Properties	4
4	Crystal Chemistry	23
5	Properties	28
6	Conclusions	29
7	Related Articles	30
8	References	30

Glossary

Complex metal hydride: solid-state compound containing homoleptic, anionic metal–hydrogen complexes
d^1, d^2, d^3 etc: electron configuration of transition element
ΔH: enthalpy of hydride formation as determined from pressure–composition isotherms during desorption by using van't Hoff's method
Homoleptic hydride complexes: complexes having hydrogen ligands only
Hydrido complexes: structural units formed by central metal atoms and terminal hydrogen ligands

Abbreviations

APW = Augmented plane wave; HT = High temperature; INS = Inelastic neutron scattering, IR = Infrared; lif = Limiting ionic formula; lin = Linear; LCAO-MO = Linear combination of atomic orbitals-molecular orbitals; LT = Low temperature; M = Alkali (Li, Na, K, Rb, Cs), alkaline earth (Mg, Ca, Sr, Ba), divalent (Yb, Eu) or trivalent (La, Nd) lanthanide; NMR = Nuclear magnetic resonance; μ_{eff} = Magnetic moment in units of Bohr magneton, μ_B; npd = Neutron powder diffraction; oct = Octahedral; pbp = Pentagonal bipyramidal; sad = Saddle-like; spl = Square planar; spy = Square pyramidal; SQUID = Superconducting quantum interference device; T-metal = Transition metal (Mn, Fe, Co, Ni, Cu, Zn, Tc, Ru, Rh, Pd, Cd, Re, Os, Ir, Pt); T_C = Curie temperature; dis = Disordered; tet = Tetrahedral; tri = Triangular; ts = T-shaped; ttp = Tricapped trigonal prismatic; Z = Number of formula units per crystallographic unit cell.

1 INTRODUCTION

This article is an update of a review written[1] some 10 years ago. It covers the currently known solid-state complex homoleptic transition (T) metal hydrido complexes and some of their properties of interest for science and technology. The complexes occur in a wide variety of solid-state compounds. Historically, the first fully characterized example is K_2ReH_9. Its structure was reported in 1964 by Abrahams, Ginsberg, and Knox,[2] and found to contain tricapped trigonal prismatic $[ReH_9]^{2-}$ complex anions. The second member is Sr_2RuH_6, which was reported in the 1970s by Moyer and collaborators,[3] was found to contain octahedral $[RuH_6]^{4-}$ complexes. Wider interest in this type of hydride started only in the 1980s after the discovery of ternary transition metal hydrides such as $LaNi_5H_6$ and $FeTiH_2$, which were suitable media for reversible hydrogen storage (for useful reviews see books and journal issues edited by Schlapbach).[4] The compounds showed metallic properties and had a large homogeneity range with respect to hydrogen. One of them, however, Mg_2NiH_4, was nonmetallic and had a fixed hydrogen content. Originally reported in 1968 by Reilly and Wiswall,[5] it was classified as a hydride containing a T-metal hydrido complex only 18 years later, after its structure was fully characterized by Zolliker *et al.*[6] and found to contain tetrahedral $[NiH_4]^{4-}$ units called 'complexes'. In the meantime, other homoleptic hydrido complexes were discovered, such as square-pyramidal $[CoH_5]^{4-}$, square-planar $[PtH_4]^{2-}$, and linear $[PdH_2]^{2-}$, and also hydrides that contained both complex bonded hydrogen and ionic hydrogen not bonded to the transition metal. In 1991, some 13 ternary hydride structure types were known. Some of them were reviewed and named 'complex transition metal hydrides' by Bronger,[7] a term now widely accepted. The first comprehensive review as written in 1993 by Yvon[1] covered 25 different transition metal hydride complexes in some 69 compounds, including quaternary hydrides. Over the years, the number of complex metal hydrides increased continuously and reviews appeared on various of their aspects such as synthetics,[8,9] diffraction methodology,[10,11] bonding,[12–14] crystal chemistry,[15,16] complex formation in hydrogenated intermetallic compounds,[17] and materials science.[18,19] The hydrides were also incorporated into a public online database.[20] At present, over 127 complex T-metal hydrides covering 47 structure types are known, that is, since the 1993 review their number has almost doubled. In this update, both mononuclear (terminal hydrogen ligands only) and polynuclear (terminal and bridging hydrogen ligands) complexes are covered. Only those hydrides are treated whose structures are fully characterized. Most contain well-defined T-metal hydride complexes and show nonmetallic behavior. Some, however, do not, and their classification as ‘complex’ hydrides is debatable. They are, nevertheless, included here because they illustrate the continuous transition that exists between complex and interstitial (metallic) hydrides. Among the aspects discussed are factors that govern the formation of complex hydrides, hydrogen contents, and thermal stability. These factors are not only of fundamental interest but also of practical relevance, because they determine the potential of metal hydrides for hydrogen storage applications.

2 EXPERIMENTAL DETAILS

2.1 Compositions and Structures

The presently known complex transition metal hydrides are based on late 3d, 4d, and 5d transition elements of groups 7–10, and on monovalent, divalent, and trivalent metals (M) belonging to the alkali, alkaline earth, and/or lanthanide series, respectively. For completeness, complexes based on closed-shell elements of group 11 (Cu, etc.) and 12 (Zn, etc.) are also included. Most hydrides are true ternary (or quaternary) compounds in the sense that they do not derive from stable intermetallic compounds, but form only in the presence of hydrogen. Some hydrides, however, do and show interesting physical phenomena. The metal ratios are usually situated in the range $M/T = 1-4$, and the hydrogen contents in the range $H/(M + T) = 1-4.5$. The compounds crystallize with 47 different, mostly new, structure types and represent over 127 hydrides. The first representative of each hydride structure type and the isostructural compounds known are listed in chronological order in Table 1 (year of publication in parentheses).

There exist two broad families of complex transition metal hydrides. The first contains hydrogen bonded to transition elements only and has the general composition

$$M_m{}^{\delta+}[TH_n]^{\delta-} \quad (m, n, \delta = 1, 2, 3\ldots) \tag{1}$$

where $[TH_n]^{\delta-}$ are complexes that are stabilized by charge transfer from the surrounding metal cations $M^{\delta+}$. The second family contains hydrogen bonded to T elements and hydride anions H^- bonded to metal cations $M^{\delta+}$ only, corresponding to the general composition

$$M_m{}^{\delta+}[TH_n]^{\delta-}M_o{}^{\delta+}H^-{}_p \quad (m, n, o, p, \delta = 1, 2, 3\ldots) \tag{2}$$

These ‘composite’ hydrides are of particular interest because they combine different types of metal–hydrogen bonding in the same structure.

Table 1 Complex transition metal hydride structure types and representatives

Structure types	Representatives	Complex transition metal hydrides
I	K_2ReH_9 (1964)	K_2TH_9 (T = Tc, Re)
II	Sr_2RuH_6 (1971)	M_2FeH_6 (M = Mg, Ca, Sr, Eu, Yb) M_2RuH_6 (M = Mg, Ca, Sr, Ba, Eu, Yb) M_2OsH_6 (M = Mg, Ca, Sr, Ba) M_2PtH_6 (M = Na, K, Rb, Cs)
III	Sr_2IrH_5 (1971)	Mg_2CoH_5 M_2RhH_{5+x} (M = Ca, Sr, Eu) M_2IrH_{5+x} (M = Mg, Ca, Sr, Eu)
IV	Na_2PtH_4 (1984)	M_2PdH_4 (M = Na, K) Na_2PtH_4
V	Mg_2NiH_4 (1986)	Mg_2NiH_4
VI	K_2PtH_4 (1986)	M_2PdH_4 (M = Rb, Cs) M_2PtH_4 (M = K, Rb, Cs)
VII	Na_2PdH_2 (1988)	M_2PdH_2 (M = Li, Na)
VIII	K_3PtH_5 (1988)	M_3TH_5 (M = K, Rb, Cs and T = Pd, Pt)
IX	K_3PdH_3 (1990)	M_3PdH_3 (M = K, Rb, Cs)
X	$CaPdH_2$ (1990)	$MPdH_{3-x}$ (M = Ca, Sr, Eu, Yb) $MNidH_{3-x}$ (M = Ca, Yb)
XI	Li_4RuH_6 (1991)	M_4RuH_6 (M = Li, Na) Li_4OsH_6
XII	Na_3RhH_6 (1991)	M_3TH_6 (M = Li, Na and T = Rh, Ir)
XIII	Li_3RhH_4 (1991)	Li_3RhH_4
XIV	$MgRhH_{1-x}$ (1992)	$MgRhH_{0.94}$
XV	Mg_3RuH_3 (1992)	Mg_3RuH_3
XVI	$SrMg_2FeH_8$ (1992)	MMg_2FeH_8 (M = Sr, Ba, Eu)
XVII	$Mg_6Co_2H_{11}$ (1992)	$Mg_6Co_2H_{11}$
XVIII	Mg_2RuH_4 (1992)	Mg_2RuH_4
XIX	$CaMgNiH_4$ (1992)	$MMgNiH_4$ (M = Ca, Sr, Eu, Yb)
XX	$Ca_4Mg_4Fe_3H_{22}$ (1992)	$M_4Mg_4Fe_3H_{22}$ (M = Ca, Yb)
XXI	Ba_2PtH_6 (1993)	M_2PtH_6 (M = Sr, Ba)
XXII	$LiSr_2PdH_5$ (1993)	$LiSr_2PdH_5$
XXIII	Mg_3ReH_7 (1993)	Mg_3TH_7 (T = Mn, Re)
XXIV	Mg_4IrH_5 (1993)	Mg_4IrH_5
XXV	Mg_3RuH_6 (1993)	Mg_3RuH_6
XXVI	$Sr_8Rh_5H_{23}$ (1994)	$M_8Rh_5H_{23}$ (M = Ca, Sr)
XXVII	$LiMg_2RuH_7$ (1994)	$LiMg_2TH_7$ (T = Ru, Os)
XXVIII	$BaReH_9$ (1994)	$BaReH_9$
XXIX	K_2ZnH_4 (1994)	M_2ZnH_4 (M = K, Rb, Cs) M_2PdH_4 (M = Sr, Ba, Eu)
XXX	K_3ZnH_5 (1994)	M_3TH_5 (M = K, Rb, Cs and T = Mn, Zn) Cs_3CdH_5
XXXI	$Ba_3Ir_2H_{12}$ (1994)	$Ba_3Ir_2H_{12}$
XXXII	$Ca_4Mg_4Co_3H_{19}$ (1995)	$M_4Mg_4Co_3H_{19}$ (M = Ca, Yb)
XXXIII	$KNaReH_9$ (1995)	$KNaReH_9$
XXXIV	$Li_5Pt_2H_9$ (1995)	$Li_5Pt_2H_9$
XXXV	$Ba_7Cu_3H_{17}$ (1996)	$Ba_7Cu_3H_{17}$
XXXVI	$LiMg_4Os_2H_{13}$ (1996)	$LiMg_4T_2H_{13}$ (T = Ru, Os)
XXXVII	Li_2PtH_2 (1996)	Li_2PtH_2
XXXVIII	$BaMg_2RuH_8$ (1997)	$BaMg_2TH_8$ (T = Ru, Os)
XXXIX	$NaBaPdH_3$ (1998)	$NaBaPdH_3$

Table 1 cont'd

Structure types	Representatives	Complex transition metal hydrides
XL	K_3ReH_6 (1998)	K_3ReH_6
XLI	$Ca_8Rh_6H_{24}$ (1998)	$Ca_8Rh_6H_{24}$
XLII	Rb_3ReH_{10} (1998)	M_3ReH_{10} (M = K, Rb, Cs)
XLIII	Na_3OsH_7 (2002)	Na_3TH_7 (T = Ru, Os)
XLIV	Cs_3OsH_9 (2002)	M_3OsH_9 (M = Rb, Cs)
XLV	$Mg_6Ir_2H_{11}$ (2002)	$Mg_6Ir_2H_{11}$
XLVI	$NdMgNi_4H_4$ (2003)	$MMgNi_4H_{\sim 4}$ (M = La, Nd)
XLVII	$LaMg_2NiH_7$ (2003)	$LaMg_2NiH_7$

2.2 Synthesis

The most common route of synthesis is by solid-state reaction, such as sintering powder mixtures of the elements, binary alloys, and/or binary metal hydrides at relatively high pressures (up to 160 bar) and moderate temperatures (<1000 K). Synthesis from binary metal compounds is rarely possible because such compounds either do not exist, such as in the Mg–Fe and Mg–Os systems, or form at metal ratios that differ significantly from those of the ternary (or quaternary) complex metal hydrides, such as Mg_2CoH_5 (MgCo, $MgCo_2$) or Mg_2RuH_6 (Mg_3Ru_2). Some hydrides derive from two-phase mixtures such as $Ba_7Cu_3H_{17}$ (Ba–Cu alloy with compositional ratio Ba/Cu$\sim$7/3) while others can be prepared by inexpensive ball milling (Mg_2FeH_6) and combustion synthesis (Mg_2NiH_4). Solution methods, such as those employed to synthesize K_2ReH_9 and related hydrides, are not yet fully explored. The only other soluble T-metal hydride complex known is $[FeH_6]^{4-}$.[21] The solid-state reaction products are mostly polycrystalline and often colored. They usually contain impurity phases (nonreacted T and/or binary M metal hydrides), but rarely contain single crystals of sufficient size and quality for diffraction measurements or measurements of physical properties. Those based on alkali and heavy alkaline earth metals are often sensitive to air and moisture.

A decisive parameter for hydride formation is pressure. The synthesis of hydrides based on light transition elements usually requires higher hydrogen pressures than those based on heavier congeners. Examples are the palladium compounds M_2PdH_4 and M_3PdH_5, which form at 20 and 70 bar, respectively, in contrast to their platinum congeners, that form already at 1 bar. For a given transition metal, an increase of hydrogen pressure usually allows the stabilization of higher formal oxidation states. Examples are found for palladium in $M_3Pd^0H_3$ and $M_2Pd^{II}H_4$, which form at 1 and 20 bar, respectively, for platinum in $K_2Pt^{II}H_4$ and $K_2Pt^{IV}H_6$, which form at 1 and 1800 bar respectively, and for ruthenium in $Mg_2Ru^0H_4$ and $Mg_2Ru^{II}H_6$, which form at 20 and 90 bar, respectively. However, the inverse situation prevails for manganese based $Mg_3Mn^IH_7$, which forms under a mechanical pressure of 20 kbar, while $K_3Mn^{II}H_5$ forms under a hydrogen gas pressure of only 3 kbar.

2.3 Structure Analysis

Owing to the low X-ray scattering power of hydrogen, neutron diffraction experiments on deuterides are necessary. Most atomic arrangements are determined on powders, and this may cause difficulties owing to poor crystallinity, the presence of impurity phases (often not detected by X rays), structural complexity ($Mg_6Ir_2D_{11}$, e.g., has 126 free positional parameters), heavy absorption (Eu, Cd), microtwinning owing to temperature induced phase transitions, and disorder in the hydrogen complex ligand spheres. High-resolution measurements (e.g. with synchrotron radiation) are rare. The data are usually analyzed by the Rietveld method. For better convergence, the number of refined parameters, in particular, those of the atomic displacement amplitudes, are reduced by constraints. For all these reasons, hydride structures are generally less well characterized than other solid-state structures.

2.4 Properties

Most compounds are nonmetallic. Only few other properties are known. The main reason for this is the lack of single crystals, the presence of impurity phases in the samples, and the sensitivity of many compounds to air and moisture. Data on magnetic, electric, and spectroscopic (NMR, Mössbauer, IR) properties are scarce. Enthalpies of hydride formation as measured from pressure–composition isotherms are known for hydrides based on 3d elements only. Theoretical band structure calculations are available only on relatively simple crystal structures. Structural dynamics are investigated by spectroscopic methods (INS, Raman, IR, NMR) and magnetic properties on SQUID magnetometers. Owing to the absence of single crystals of suitable size, reliable measurements of the electric conductivity are rare. Enthalpies of hydride formation, ΔH, are usually determined from pressure-composition isotherms as measured on Sievert's apparatus or on a thermobalance, by using the relation

$$\ln(p_{\mathrm{eq}}) = \frac{-\Delta H}{R.T} + \frac{\Delta S}{R} \quad \text{Van't Hoff equation} \qquad (3)$$

where p_{eq} is the hydrogen equilibrium pressure and T the absolute temperature. Given that the entropy term, ΔS, does not much change from one system to another ($\Delta S \sim 130\ \mathrm{J\,K^{-1}\,mol^{-1}}\ H_2$) the hydrogen decomposition temperatures at a given pressure scale roughly with enthalpy (293 K: $\Delta H \sim 30$ kJ/H_2 for $p_{\mathrm{eq}} = 1$ bar). Finally, the reaction products ought to be handled with care because many are air sensitive and some are extremely pyrophoric. For these reasons, quite a few complex metal hydrides are known to exist but have not yet been fully characterized.

3 HYDRIDE STRUCTURE TYPES AND PROPERTIES

Complex transition metal hydrides combine structural features typical for coordination compounds and ionic solids. They display covalently bonded hydrogen such as in molecular transition metal complexes[22] (*see* ***Hydride Complexes of the Transition Metals***), and hydride anions (H^-) bonded to electropositive metals (M^+, M^{2+}, M^{3+}) only, such as in saline hydrides. In metal-rich systems, hydrogen has interstitial character, as in typically metallic transition metal hydrides.[23] The structural and physical properties of the 47 known hydride structure types and of their representatives (stated in parentheses) are summarized below. Limiting ionic formulas (lif) and the corresponding formal oxidation states and electron configurations of the transition elements are indicated whenever possible. Such formulas do not provide an adequate description of the bonding but allow one to rationalize the H content (see below). For each structure, T–D bond distances and shortest M–D (complex D), M–D^- (anionic D^-) and D–D distances are stated. For all structure types, illustrations are given (see Figures 1–47; TH_n complexes are drawn by heavy lines, disordered ligands by double lines, M–M contacts surrounding TH_n complexes by single lines, M atoms as large circles, and H^- ions as small isolated circles).

3.1 K_2ReH_9 (K_2TcH_9)

From reaction of $KReO_4$ with K metal in ethylenediamine–water solution;[2] colorless crystals, unstable in moist air; NMR and IR data, optical absorption spectra and LCAO-MO calculations; ordered structure (Figure 1) from single-crystal neutron diffraction on hydride and later on deuteride:[24] $P\bar{6}2m$, $Z = 3$; two different Re sites, occurring at the ratio Re1:Re2 = 1:2, both forming ttp-$[ReH_9]^{2-}$ 18-electron complexes with T site symmetries $\bar{6}2m$ and $\bar{6}$, respectively; surrounded by two types of K cations; four H sites; lif: $2\,K^+{\cdot}[ReH_9]^{2-}$; Re^{VII}, d^0; no structure data on Tc compound.

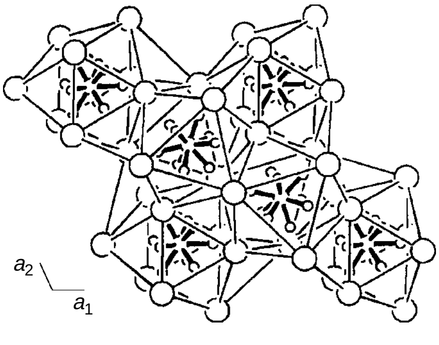

Figure 1 Structure of K_2ReH_9

Distances (Å):[24] Re–H (3×) = 1.68 (Re1); 1.67 (Re2); Re–H (6×) = 1.69 (Re1); 1.70 (Re2); K–H = 2.69; H–H = 1.90.

3.2 Sr_2RuH_6 (M_2FeH_6, M = Mg, Ca, Sr, Yb, Eu; M_2RuH_6, M = any; M_2OsH_6, M = Mg, Ca, Sr, Ba; M_2PtH_6, M = Na, K, Rb, Cs)

Sr_2RuH_6 and isostructural hydrides M_2TH_6 from elemental T (Fe, Ru, Os) and binary hydrides MH_2 or Mg by sintering at various temperatures and hydrogen pressures;[3,25–30] or by mechanical alloying followed by sintering (T = Fe);[31,32] powders either colored (Mg_2FeH_6, green; Eu_2RuH_6, red), or white-gray (Ca_2RuH_6, Mg_2OsH_6), or black (Yb_2RuH_6); moisture sensitive and partly pyrophoric (Mg_2OsH_6); M_2FeH_6 (M = Ca, Sr, Eu), M_2OsH_6 (M = Mg, Ca), Mg_2RuH_6 and various solid solutions;[29] M_2PtH_6 (M = Na, K, Rb, Cs)[33–35] by reaction of alkaline hydride with platinum sponge at 770 K under high hydrogen pressure (between 2 and 4 kbar); M_2PtH_6 are colorless and very sensitive to moisture and air; IR stretching frequencies of T–H (T = Fe, Ru, Os) bonds range between 1450 and 1850 cm^{-1}, and increase in the sequence Fe, Ru, Os, and decrease as the ionic size of M^{2+} increases;[28] Eu_2RuH_6 and solid solution series $(Ca,Eu)_2RuH_6$ and $(Sr,Eu)_2RuH_6$ are paramagnetic with $\mu_{eff} = 7.7\mu_B$, and magnetic order below $T_C = 29$ K;[25] low-temperature magnetic properties of Eu–Ru, (Ca,Eu)–Ru, and (Sr,Eu)–Ru hydrides[36] show ferromagnetic behavior; electric resistivities of Mg_2FeH_6, Ca_2RuH_6, Sr_2RuH_6, Yb_2RuH_6, and Eu_2RuH_6 indicate nonmetallic behavior; band structure calculations[37] predict band gaps that range from 1.3 eV (Sr_2FeH_6) to 4.0 eV (Mg_2OsH_6) and increase in the sequence Mg_2TH_6 (T = Fe, Ru, Os) and decrease in the sequence M_2FeH_6 (M = Mg, Ca, Sr); Mg_2FeH_6, Ca_2RuH_6, Sr_2RuH_6 are diamagnetic, or weakly paramagnetic; other properties of Mg_2FeH_6: Mössbauer spectra[26] consistent with low-spin Fe^{II}; hydrogen density 5.4 wt%; 9.0×10^{22} H atoms cm^{-3}; desorption enthalpy[26] $\Delta H = 98\,kJ\,mol^{-1}$ H_2; INS, infrared, and Raman spectroscopies;[38] has potential for thermochemical thermal energy storage;[39] IR of Ru based hydrides;[40] ordered structures (Figure 2) by npd on deuterides;[3,26–29] $Fm\bar{3}m$, $Z = 4$; K_2PtCl_6 type structure; octahedral $[TH_6]^{4-}$ 18-electron complexes having T site symmetry $m\bar{3}m$; surrounded by M in eightfold cubic configuration corresponding to a CaF_2 type metal substructure; lif: $2M^{2+}{\cdot}[TH_6]^{4-}$; T = Fe^{II}, Ru^{II}, Os^{II}; d^6. Interatomic distances are given in Table 2.

3.3 Sr_2IrH_5 (Mg_2CoH_5, Mg_2IrH_5, Ca_2IrH_5, $Ca_2RhH_{5.4}$, $Sr_2RhH_{5.3}$, Eu_2IrH_5)

Sr_2IrH_5 from Ir and SrH_2 powder at 1033 K under hydrogen;[41] Eu_2IrD_5 from ^{153}Eu isotope enriched intermetallic $EuIr_2$ at 673 K under deuterium,[42] or by reaction of binary europium hydride (natural isotope mixture) with iridium metal

Table 2 Interatomic distances (Å) in Sr_2RuD_6 and analogs

		T = Fe	T = Ru	T = Os			T = Pt
M = Mg	T–D	1.56	1.67	1.68	M = Na	T–D	1.62
	T–Mg	2.79	2.87	2.89		T–Na	3.18
	Mg–D	2.28	2.34	2.36		Na–D	2.60
	Mg–Mg	3.22	3.31	3.34		Na–Na	3.67
	D–D	2.20	2.32	2.34		D–D	2.28
M = Ca	T–D	1.62		1.73	M = K	T–D	1.64
	T–Ca	3.05		3.14		T–K	3.62
	Ca–D	2.49		2.57		K–D	2.90
	Ca–Ca	3.52		3.63		K–K	4.07
	D–D	2.29		2.45		D–D	2.32
M = Sr	T–D		1.69		M = Rb	T–D	1.63
	T–Sr		3.29			T–Rb	3.70
	Sr–D		2.69			Rb–D	3.06
	Sr–Sr		3.80			Rb–Rb	4.27
	D–D		2.40			D–D	2.30
M = Ba	T–D		1.72	1.78	M = Cs	T–D	1.64
	T–Ba		3.47	3.48		T–Cs	3.88
	Ba–D		2.85	2.85		Cs–D	3.23
	Ba–Ba		4.01	4.02		Cs–Cs	4.48
	D–D		2.44	2.51		D–D	2.32

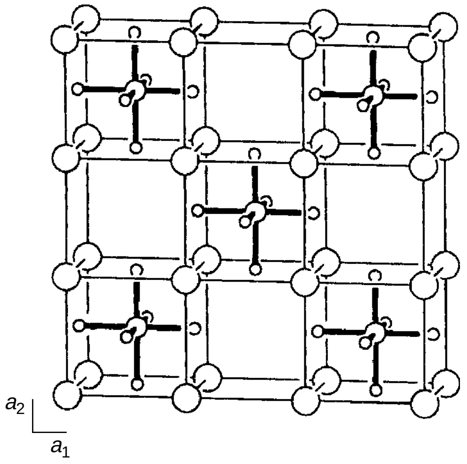

Figure 2 Structure of Sr_2RuD_6

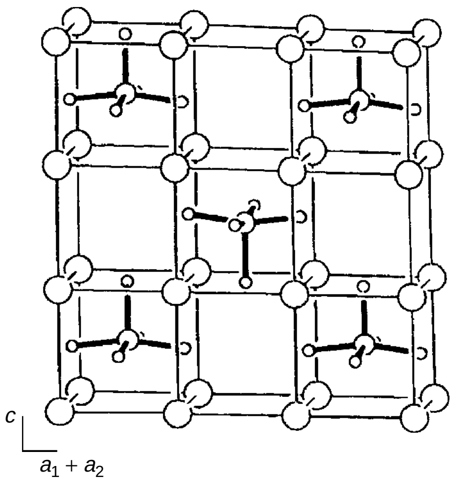

Figure 3 Structure of Mg_2CoD_5

at 970 K under deuterium pressure;[43] Mg_2CoH_5 by sintering metal powder mixtures at 620–770 K under 40–60 bar hydrogen pressure;[44] or by mechanical alloying followed by sintering;[31] properties of Mg_2CoH_5: black powder; electric resistivity consistent with nonmetallic behavior; band structure calculations[37] predict band gap of 1.9 eV, magnetization measurements indicate weak paramagnetism (possibly diamagnetism); ordered structure (Figure 3) from npd:[44] $P4/nmm$, $c/a = 1.477$; $Z = 1$; square-pyramidal $[CoH_5]^{4-}$ 18-electron complex with T site symmetry $4mm$; surrounded by two Mg sites in eightfold nearly cubic configuration; two D sites, both ordered; transforms at 488 K into disordered cubic HT (high temperature) modification similar to II; lif: $2Mg^{2+}\cdot[CoH_5]^{4-}$; Co^I; d^8; H distribution in presumably isostructural Mg_2IrH_5 not yet confirmed; hydrogen density: 4.5 wt%, 7.5×10^{22} H atoms cm^{-3}; desorption enthalpy $\Delta H = 86\,kJ\,mol^{-1}$ H_2; decomposes into δ-MgCo and MgH_2;[45] Sr_2IrD_5: partially disordered structure from npd[41] at 4.2 K: $I4/mmm$, $c/a = 1.465$, $Z = 2$; Ir surrounded by five D in a partially disordered average octahedral configuration having $4/mmm$ site symmetry; equatorial D sites fully and apical D sites half occupied; transforms between 140 and 200 K into disordered cubic HT modification similar to II; $Ca_2RhD_{5.4}$ and $Sr_2RhD_{5.3}$ with higher occupancy factor 0.89(2),[46,47] disordered cubic structure by npd: $Fm\bar{3}m$, $Z = 4$, no phase transition; Eu_2IrD_5,

Table 3 Interatomic distances (Å) in Sr_2IrD_5 and analogs

		Cubic HT-phases			Tetragonal LT-phases		
		T = Co	T = Rh	T = Ir	T = Co	T = Rh	T = Ir
M = Mg	T–D	1.53			(4×)1.51 (1×)1.59		
	T–Mg	2.79			2.75		
	Mg–D	2.28			2.23		
	Mg–Mg	3.23			3.16		
	D–D	2.16			2.12		
M = Ca	T–D		1.75	1.70			(4×) 1.68 (2×, dis.[a]) 1.81
	T–Ca		3.14	3.14			3.13
	Ca–D		2.57	2.56			2.52
	Ca–Ca		3.63	3.62			3.56
	D–D		2.48	2.41			2.38
M = Sr	T–D		1.73	1.71			(4×) 1.69 (2×, dis.) 1.82
	T–Sr		3.28	3.31			3.30
	Sr–D		2.69	2.71			2.66
	Sr–Sr		3.79	3.82			3.76
	D–D		2.45	2.42			2.39
M = Eu	T–D			1.69			(4×) 1.70 (2×, dis.) 1.75
	T–Eu			3.28			3.27
	Eu–D			2.68			2.64
	Eu–Eu			3.78			3.73
	D–D			2.39			2.40

[a] Disordered.

Ca_2IrD_5, and solid solutions $(Ca,Eu)_2IrD_5$, $(Sr,Eu)_2IrD_5$: disordered structure by npd at room temperature:[42] $Fm\bar{3}m$, $Z = 4$; Ir surrounded by five D atoms in a disordered average octahedral configuration similar to II; transition occurs between 200 and 275 K to partially ordered tetragonal modification $I4/mmm$ similar to Sr_2IrD_5;[43] paramagnetic with $\mu_{\text{eff}} = 7.3\mu_B$; ferromagnetic below $T_C = 20$ K; rhodium-based 'Mg_2RhH_5' analog not obtained, presumably because of the formation of competing hydride $Mg_2RhH_{1.1}$ (filled Ti_2Ni type structure) and binary Mg_2Rh (Ti_2Pd type structure).[48] Other Rh compounds known:[49] Eu_2RhH_5 and solid solutions $(Sr,Eu)_2RhH_5$. Interatomic distances are given in Table 3.

3.4 Na_2PtH_4 (K_2PdH_4, Na_2PdH_4)

Na_2PtH_4 by sintering NaH and Pt at about 573 K under hydrogen;[50] red-violet powder; diamagnetic from susceptibility measurements; K_2PdH_4 by heating KH with Pd at 610 K under 16 bar hydrogen pressure;[51] yellow-green powder, nonmetallic; band gap of 1.2 eV predicted from theoretical band structure calculations;[52] decomposes before melting; Na_2PdH_4 from NaH and Pd at up to 2500 bar and 770 K;[53] ordered structures (Figure 4) from npd on deuterides: $I4/mmm$, $Z = 2$; square-planar $[PtH_4]^{2-}$ (or $[PdH_4]^{2-}$) 16-electron complexes with T site symmetry $4/mmm$; surrounded by Na (K) in eightfold cubic configuration; one D site; Na_2PtH_4 transforms at about 573 K into disordered cubic HT modification similar to II; Na_2PdH_4 does not transform up to 600 K and decomposes into Na_2PdH_2;[53] lif: $2M^+ \cdot [TH_4]^{2-}$; T = Pd^{II}, Pt^{II}, d^8. Interatomic distances are given in Table 4.

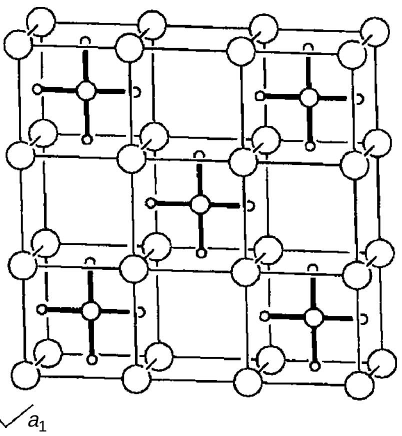

Figure 4 Structure of Na_2PtD_4

3.5 Mg_2NiH_4

From binary alloy Mg_2Ni by hydrogenation at temperatures above 623 K,[5] or by sintering powder mixtures of the elements at 723–773 K under 90 bar hydrogen pressure;[30] fine powder

Table 4 Interatomic distances (Å) in Na_2PtD_4 and analogs

		T = Pd	T = Pt
M = Na	T–D	1.61	1.64
	T–Na	3.14	3.12
	Na–D	2.52	2.52
	Na–Na	3.31	3.38
	D–D	2.27	2.32
M = K	T–D	1.62	
	T–K	3.49	
	K–D	2.85	
	K–K	3.84	
	D–D	2.30	

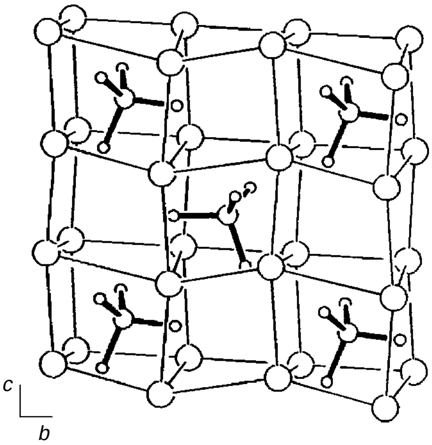

Figure 5 Structure of Mg_2NiD_4

of dark-red (fully hydrided) or brownish (partially hydrided) color; stable in air; diamagnetic, nonmetallic; theoretical band structure calculations[37] on disordered structure model predict band gap of 1.8 eV; vibrational spectroscopy;[54] bonding and stability investigated by ab initio density functional calculations;[14,55] H density: 3.6 wt%, 5.8×10^{22} H atoms cm^{-3}; desorption enthalpy $\Delta H = 64\,kJ\,mol^{-1}$ H_2; ordered structure (Figure 5) by high-resolution npd on deuteride:[6] $C2/c$, $Z = 8$; tetrahedral $[NiH_4]^{4-}$ 18-electron complex having symmetry 1; surrounded by three Mg sites in eightfold, strongly distorted cubic configuration; four D sites; X-ray and electron microscopy evidence for microtwinning[56] parallel to *bc* plane; transforms between 483 and 513 K into disordered cubic HT modification similar to II;[57] influenced by mechanical grinding;[58] lif: $2Mg^{2+}\cdot[NiH_4]^{4-}$; Ni^0, d^{10}.

Distances (Å) and angles: Ni–D = 1.52–1.57; D–Ni–D = 104–119°; Mg–Ni = 2.65; Ni–Ni = 4.30; Mg–Mg = 3.10; Mg–D = 1.97; D–D = 2.42.

3.6 K_2PtH_4 (Rb_2PtH_4, Cs_2PtH_4, Rb_2PdH_4, Cs_2PdH_4)

From binary hydrides and Pt(Pd) sponge at 593–693 K under 0.8 bar (Pd compounds 20 bar) hydrogen pressure;[59]

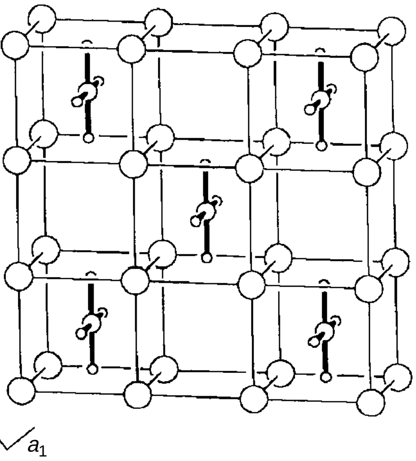

Figure 6 Structure of K_2PtD_4

pyrophoric, colorless powders; sensitive to moisture and air; K_2PtH_4: diamagnetic; NMR data at room temperature consistent with rotational disorder of PtH_4 groups; structures from npd on deuterides at 295 and 15 K (K_2PtD_4, Rb_2PdD_4, Cs_2PdD_4), 16 K (Rb_2PtD_4), and 12 K (Cs_2PtD_4); disordered room temperature structure: cubic, $Fm\bar{3}m$, $Z = 4$, CaF_2 type metal substructure similar to II; transforms at 250 K (Rb_2PdD_4), 225 K (Cs_2PdD_4), 195 K (K_2PtD_4), 170 K (Rb_2PtD_4), and 150 K (Cs_2PtD_4), into ordered tetragonal low-temperature (LT) structure (Figure 6): $P4_2/mnm$, $Z = 2$; planar $[PtH_4]^{2-}$ (or $[PdH_4]^{2-}$) 16-electron complexes with T site symmetry *m.mm*; unlike Na_2PtH_4, these complexes are oriented perpendicular to the tetragonal base; surrounded by M^+ in eightfold, nearly cubic configuration; two D sites; lif: $2M^+\cdot$ $[TH_4]^{2-}$; T = Pd^{II}, Pt^{II}, d^8. Interatomic distances are given in Table 5.

3.7 Na_2PdH_2 (Li_2PdH_2)

Na_2PdH_2 from NaH with Pd at 643 K under 50 bar hydrogen pressure;[60] brittle solid; single crystals show metallic luster; melts at 681 K without decomposing; metallic conductivity measured on single crystals and semiconducting behavior on powder; Li_2PdH_2[51] from LiH and Pd at 680 K; melts at 773 K; electronic band structure calculations[52,61] predict filled d bands and metallic properties in two dimensions (*ab* plane), originating from overlap between Pd d-block bands and alkali metal s- and p-block bands; Na_2PdH_2 found to be metallic;[61] ordered structure of Na_2PdH_2 (Figure 7) from X-ray single-crystal diffraction on hydride and npd on deuteride: $I4/mmm$, $Z = 2$; Na_2HgO_2 type structure; linear $[PdH_2]^{2-}$ 14-electron complexes centered on site having $4/mmm$ symmetry; surrounded by Na in 10-fold bicapped cubic configuration; one D site; lif: $2Na^+\cdot[PdH_2]^{2-}$; Pd^0, d^{10}; structure of Li_2PdH_2 from npd;[51] evidence for linear $[PtH_2]^{2-}$ complexes in quaternary Na_2PdH_2–Na_2PtH_4 system.[62]

Table 5 Interatomic distances (Å) in K_2PtD_4 and analogs

		Cubic HT-phases		Tetragonal LT-phases	
		T = Pd	T = Pt	T = Pd	T = Pt
M = K	T–D		1.62		(2×) 1.58
					(2×) 1.59
	T–K		3.47		3.45
	K–D		2.86		2.83
	K–K		4.01		3.95
	D–D		2.29		2.24
M = Rb	T–D	1.63	1.63	(2×) 1.67	(2×) 1.60
				(2×) 1.67	(2×) 1.69
	T–Rb	3.64	3.63	3.61	3.60
	Rb–D	3.01	3.00	2.95	2.95
	Rb–Rb	4.21	4.19	4.12	4.14
	D–D	2.31	2.31	2.36	2.33
M = Cs	T–D	1.60	1.61	(2×) 1.59	(2×) 1.58
				(2×) 1.64	(2×) 1.61
	T–Cs	3.84	3.80	3.80	3.75
	Cs–D	3.20	3.15	3.14	3.12
	Cs–Cs	4.44	4.38	4.36	4.32
	D–D	2.26	2.28	2.28	2.25

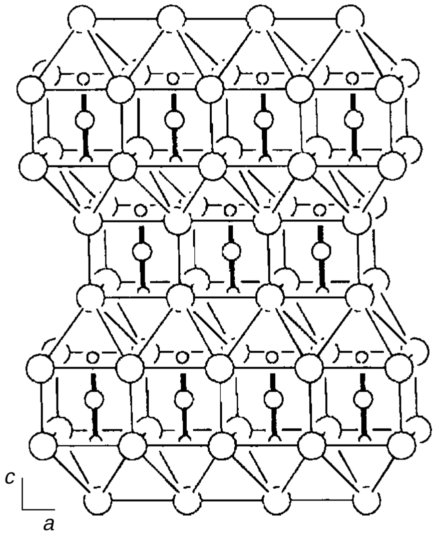

Figure 7 Structure of Na_2PdD_2

Distances (Å): Pd–D = (2×) 1.68 (Na), (2×) 1.67 (Li); Pd–Na(Li) = 3.13 (2.64); Pd–Pd = 3.60 (Na), 3.11 (Li); Na(Li)–D = 2.42 (2.03); D–D = 3.35 (Na), 2.85 (Li).

3.8 K_3PtH_5 (Rb_3PtH_5, Cs_3PtH_5, K_3PdH_5, Rb_3PdH_5, Cs_3PdH_5)

From binary alkali hydrides and platinum (palladium) sponge at 573–623 K under 0.8 bar (Pd compounds 70 bar) hydrogen;[63] colorless powders, sensitive to air and moisture; ordered structures (Figure 8) by npd on deuterides: $P4/mbm$, $Z = 2$; isostructural to Rb_3PdF_5; planar $[PtH_4]^{2-}$ (or $[PdH_4]^{2-}$) 16-electron complexes with T site symmetry $m.mm$; surrounded by two M sites in irregular ninefold configuration; two D sites, of which the twofold is octahedral surrounded by M^+ only; lif: $3M^+{\cdot}[TH_4]^{2-}{\cdot}H^-$; T = Pd^{II}, Pt^{II}, d^8; K_3PtH_5 decomposes at 673 K into K_2PtH_4 and KH; Rb_3PtH_5 and Cs_3PtH_5 transform reversibly above 615 and 465 K, respectively, into disordered cubic HT modifications with Cu_3Au type metal substructure ($Pm\bar{3}m$, $Z = 1$; H positions not refined); no evidence for such transitions in Pd compounds; ordered substitution on M sites leads to quaternary hydrides K_2RbPtH_5 and K_2CsPtH_5 (H positions not refined). Interatomic distances are given in Table 6.

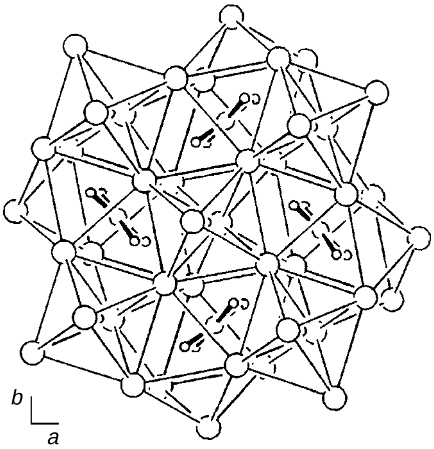

Figure 8 Structure of K_3PtD_5

3.9 K_3PdH_3 (Rb_3PdH_3, Cs_3PdH_3)

From KH and Pd sponge at 623 K under hydrogen; yellow powder at room temperature, orange-red at high temperature,[64] ordered structure (Figure 9) from npd on deuteride: $P4_2/mnm$, $Z = 8$; three Pd sites with ratios Pd1:Pd2:Pd3 = 1:1:2, each forming a linear $[PdH_2]^{2-}$ 14-electron complex having

Table 6 Interatomic distances (Å) in K_3PtD_5 and analogs

		M = K	M = Rb	M = Cs
T = Pd	Pd–D	1.63	1.61	1.64
	Pd–M	3.46	3.62	3.67
	M–D	2.84	2.99	3.04
	$M–D^-$	2.73	2.85	3.01
	M–M	3.74	4.03	4.20
	Pd–Pd	5.26	5.52	5.87
	D–D	2.20	2.17	2.30
T = Pt	Pt–D	1.63	1.58	1.64
	Pt–M	3.47	3.57	3.68
	M–D	2.74	2.98	3.03
	$M–D^-$	2.72	2.86	2.96
	M–M	3.85	4.05	4.25
	Pt–Pt	5.28	5.54	5.90
	D–D	2.23	2.14	2.25

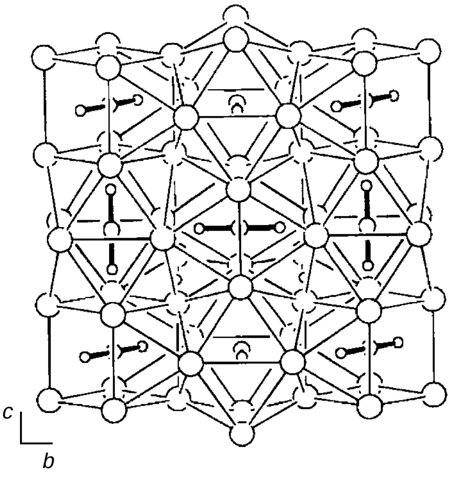

Figure 9 Structure of K_3PdD_3

respectively *m.mm*, *m.mm*, and 2/*m* environments; surrounded by three K sites in 12-fold configurations; four D sites, of which one eightfold is coordinated by K^+ in oct configuration; lif: $3K^+\cdot[PdH_2]^{2-}\cdot H^-$; Pd^0, d^{10}; X-ray evidence[59,63] for isostructural Cs_3PdH_3 and Rb_3PdH_3; K_3PdH_3 transforms at ~473 K into disordered HT modification ($Pm\bar{3}m$) with cubic Cu_3Au type metal substructure while Rb_3PdH_3 transforms into $Im\bar{3}$ HT modification.

Distances (Å): Pd–D = (2×) 1.68 (Pd1), (2×) 1.68 (Pd2), (2×) 1.69 (Pd3); Pd–K = 3.04; K–D = 2.64, K–D^- = 2.74, D–D = 3.37.

3.10 $CaPdH_2$ ($SrPdH_{2.7}$, $EuPdH_3$, $YbPdH_{2.7}$, $CaNiH_3$, $YbNiH_{2.7}$)

$CaPdH_2$ from CaH_2 and Pd sponge at 1123 K under hydrogen pressures up to 300 bar;[65] disordered structure (Figure 10) from npd on deuteride at 295 and 10 K: $Pm\bar{3}m$, $Z = 1$; Pd and Ca form CsCl-type metal substructure as in binary CaPd; disordered D site near anion positions of perovskite-type structure with 2/3 occupancy and large displacement amplitudes; structure model consistent with orientationally disordered linear $[PdH_2]^{2-}$ 14-electron complexes; no evidence for D ordering down to 10 K; lif: $Ca^{2+}\cdot[PdH_2]_{av}{}^{2-}$; Pd^0, d^{10}; X-ray evidence for rhombohedral distortion at room temperature;[66] copper-red $SrPdH_{2.7}$ by hydrogenation of Sr–Pd alloy;[67] structure of deuteride from npd: D site occupancy 0.91; black $EuPdH_3$ by hydrogenation of intermetallic EuPd (with CrB type structure) at 15 bar hydrogen pressure at 500 K;[68] structure of deuteride from npd: full D site occupancy; metallic conductor; orders ferromagnetic at 21 K; X-ray evidence for presumably isostructural $YbPdH_{2.7}$,[69] $YbNiH_{2.7}$[69] and $CaNiH_3$.[70] Electronic band structure calculations on stoichiometric $APdH_3$ (A = Sr, Eu, Yb) predict metallic properties.[71] Interatomic distances are given in Table 7.

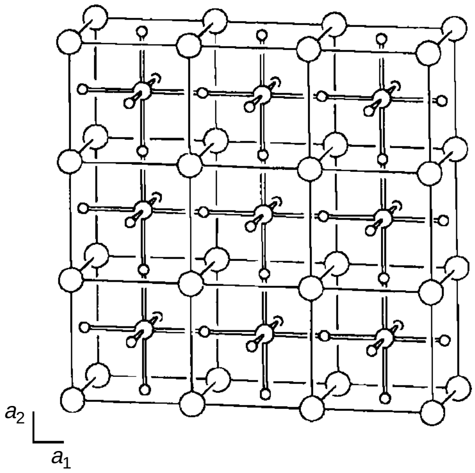

Figure 10 Structure of $CaPdD_2$

Table 7 Interatomic distances (Å) in $CaPdD_2$ and analogs

	M = Ca	M = Sr	M = Eu
Pd–D	1.84	1.92	1.90
Pd–M	3.19	3.33	3.29
M–D	2.61	2.72	2.69
M–M	3.69	3.84	3.80
D–D	2.61	2.72	2.69

3.11 Li_4RuH_6 (Na_4RuH_6, Li_4OsH_6)

From reactions of binary hydrides MH with T at 753 K and 10 bar hydrogen pressure;[72] no compound formation with KH and Fe up to 1073 K and 100 bar; Ru does not react with KH, and Os not with NaH and KH under experimental conditions; powders either white (Li) or green (Na); all air sensitive; ordered structures (Figure 11) from npd at room temperature on deuterides: $R\bar{3}c$, $Z = 6$ (hex setting), K_4CdCl_6 type structure; octahedral $[TH_6]^{4-}$ 18-electron complex with T site symmetry $\bar{3}$; surrounded by two M sites in nearly cubic configuration; one D site; lif: $4M^+\cdot[TH_6]^{4-}$; T = Ru^{II}, Os^{II}, d^6. Interatomic distances are given in Table 8.

3.12 Na_3RhH_6 (Li_3RhH_6, Na_3IrH_6, Li_3IrH_6)

From powder mixtures of binary MH and Ir(Rh) at 630–770 K under hydrogen;[73] colorless powders, sensitive to air and humidity; Li_3RhH_6 forms either during decomposition of Li_3RhH_4[74] in hydrogen atmosphere or by sintering powder mixtures of LiH and Rh under 80 bar hydrogen pressure at 823 K;[75] ordered structures (Figure 12) from npd on deuterides[73,75] at 295 K (Na–Rh, Na–Ir, Li–Rh, Li–Ir) and 11 K (Na–Rh, Na–Ir); *Pnma*, $Z = 4$; isolated octahedral $[TH_6]^{3-}$ 18-electron complex with T site symmetry *m*; surrounded by three M sites in irregular 11-fold coordination; four D sites; no evidence for structural phase transition in Na_3RhH_6 and

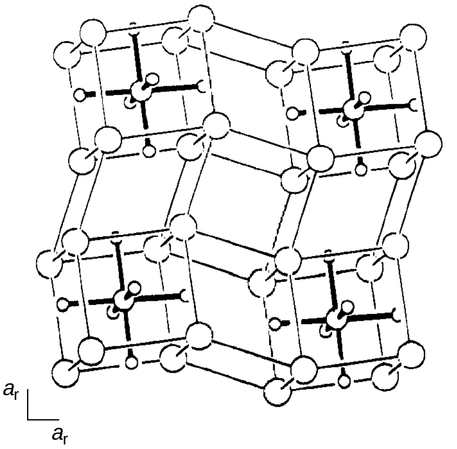

Figure 11 Structure of Li_4RuD_6

Table 8 Interatomic distances (Å) in Li_4RuD_6 and analogs

		T = Ru	T = Os
M = Li	T–D	1.71	1.71
	T–Li	2.49	2.52
	Li–D	2.05	2.13
	Li–Li	3.03	3.014
	D–D	2.41	2.27
M = Na	T–D	1.79	
	T–Na	2.84	
	Na–D	2.35	
	Na–Na	3.40	
	D–D	2.50	

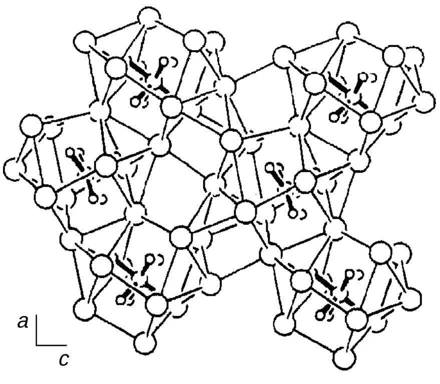

Figure 12 Structure of Na_3RhD_6

Na_3IrH_6 down to 11 K and up to 670 K; lif: $3M^+{\cdot}[TH_6]^{3-}$; T = Ir^{III}, Rh^{III}; d^6. Interatomic distances are given in Table 9.

Table 9 Interatomic distances (Å) in Na_3RhD_6 and analogs

		T = Rh	T = Ir
M = Li	T–D	1.56–1.64	1.61–1.70
	T–Li	2.66	2.72
	Li–D	1.81	1.88
	Li–Li	2.59	2.59
	D–D	2.07	2.21
M = Na	T–D	1.63–1.68	1.64–1.70
	T–Na	2.98	2.94
	Na–D	2.17	2.08
	Na–Na	3.22	3.18
	D–D	2.28	2.26

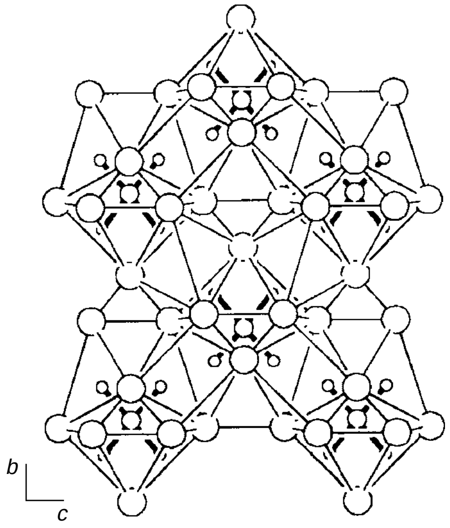

Figure 13 Structure of Li_3RhD_4

3.13 Li_3RhH_4

From LiH and Rh powder at 870 K under hydrogen;[74] powder of metallic appearance; oxygen and moisture sensitive; corresponds to previously reported 'Li_4RhH_5' as characterized by X-ray diffraction on single crystals;[76] decomposes at high temperature under 80 bar hydrogen pressure into Li_3RhH_6 (XII); ordered structure (Figure 13) by npd on deuteride: *Cmcm*; $Z = 4$; planar $[RhH_4]^{3-}$ 16-electron complexes with T site symmetry $m2m$; surrounded by two Li sites in irregular 11-fold coordination; two D sites; lif: $3Li^+{\cdot}[RhH_4]^{3-}$; Rh^I, d^8.

Distances (Å): Rh–D = 1.79(2×), 1.75(2×); Rh–Li = 2.31; Rh–Rh = 3.87(2×); Li–Li = 2.35; Li–D = 2.15; D–D = 2.21.

3.14 $MgRhH_{1-x}$

From binary alloy MgRh (CsCl-type structure) at 748 K and 130 bar hydrogen pressure;[77] powder of gray color and metallic appearance; partially disordered structure (Figure 14) by in situ npd at 39 bar, 2.5 bar and 10^{-2} mbar deuterium pressure: $P4/mmm$, $Z = 4$; one Rh and two Mg sites forming a tetragonal distorted CsCl-type structure with doubled a parameter ($2c/a = 1.012$ at 39 bar); one D site connecting

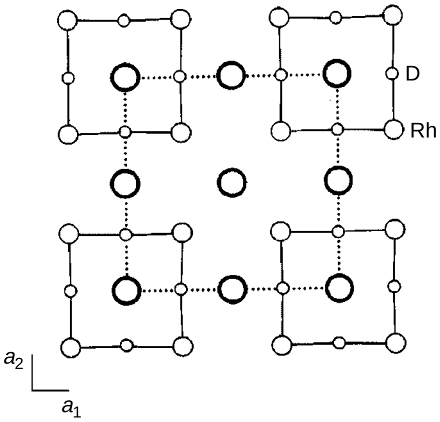

Figure 14 Structure of $MgRhD_{1-x}$

Rh into cyclic tetramer Rh_4D_4 having 4/*mmm* symmetry with nearly linear Rh–D–Rh and rectangular D–Rh–D bonds; occupancy of D site increasing as a function of D pressure (94% at 39 bar, 86% at 2.5 bar, 61% at 10^{-2} mbar), metal substructure resembles $CaPdH_2$ (X); likely phase limit near stoichiometric composition MgRhH; lif (border case) at that composition: $4Mg^{2+}\cdot[Rh_4H_4]^{8-}$; X-ray evidence for cubic $MgIrH_x$ phase ($a = 3.23$ Å) at high pressure with CsCl-type metal substructure.

Distances (Å) at 39 bar ($MgRhD_{0.94}$): Rh–D (2×) = 1.71; Mg–Rh = 2.66; Mg–D = 2.23; Rh–Rh = 2.98; Mg–Mg = 3.20; D–D = 2.36.

3.15 Mg_3RuH_3

From elements by sintering at 883 K under 9 bar hydrogen pressure;[78] dark gray powder, stable in air; partially disordered structure (Figure 15) by npd on deuteride: $P4_2/mnm$, $Z = 4$; Ru at center of orientationally disordered ts-RuH_3 units (*m*.2*m* site symmetry) containing two D sites, one ordered and the other disordered (split atom position with D–D = 0.87 Å); surrounded by two Mg sites forming an eightfold bicapped prismatic coordination; joined to dimers of *m*.*mm* site symmetry by possible Ru–Ru bond; lif: $3Mg^{2+}\cdot[RuH_3]^{6-}$ (monomer without Ru–Ru bond, 17 electrons/Ru); $6Mg^{2+}\cdot[Ru_2H_6]^{12-}$ (dimer with Ru–Ru bond, 18 electrons/Ru); Ru–Ru bond formation not supported by extended Hückel calculations.[12]

Distances (Å): Ru–D = 1.71 (split atom), 1.71 (2×); Mg–Ru = 2.73; Ru–Ru = 3.31; Mg–D = 2.01; Mg–Mg = 3.03; D–D = 0.87 (split atom), 2.52.

3.16 $SrMg_2FeH_8$ ($BaMg_2FeH_8$, $EuMg_2FeH_8$)

From binary alloys $SrMg_{2.2}$ ($BaMg_2$, $EuMg_2$) and Fe powder at 763–783 K under 140 bar hydrogen pressure;[66,79] green (Sr) or brownish (Ba) powder; sensitive to air; ordered structure (Figure 16) by npd on deuterides of Sr and Ba compounds: $P\bar{3}m1$, $Z = 1$; octahedral $[FeH_6]^{4-}$ 18-electron units having T site symmetry $\bar{3}m$, surrounded by eight M^{2+} in nearly cubic configuration; one Mg and one Sr(Ba) site; two D sites, of which the twofold is tetrahedrally coordinated by M^{2+} with one short Mg–D and three long Sr(Ba)–D bonds; lif: $M^{2+}\cdot 2Mg^{2+}\cdot[FeH_6]^{4-}\cdot 2H^-$; Fe^{II}, d^6. Ru analog $BaMg_2RuD_8$ (XXXVIII) crystallizes with tetragonal symmetry. Interatomic distances are given in Table 10.

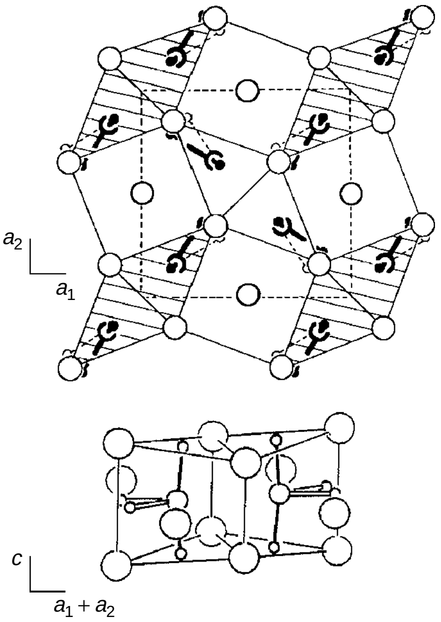

Figure 15 Structure of Mg_3RuD_3

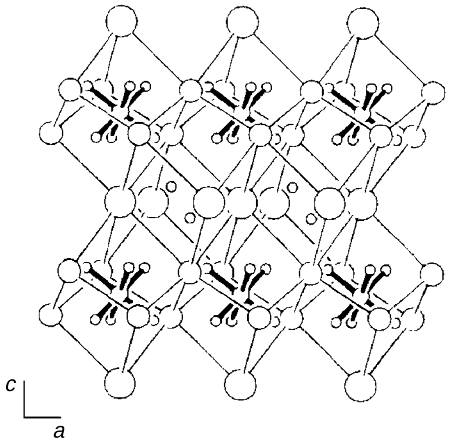

Figure 16 Structure of $SrMg_2FeD_8$

3.17 $Mg_6Co_2H_{11}$

From elements by sintering at 753–773 K under 40–50 bar hydrogen pressure;[80] black powder, stable in air; nonmetallic; pressure–composition isotherms show two plateaus of

Table 10 Interatomic distances (Å) in $SrMg_2FeD_8$ and barium analog

	M = Sr	M = Ba
Fe–D	1.58	1.58
Fe–Mg	2.72	2.75
Fe–M	3.28	3.46
Mg–D	2.20	2.22
$Mg–D^-$	1.92	1.92
M–D	2.65	2.81
$M–D^-$	2.66	2.74
Mg–Mg	3.06	3.08
Mg–M	3.60	3.75
D–D	2.19	2.18

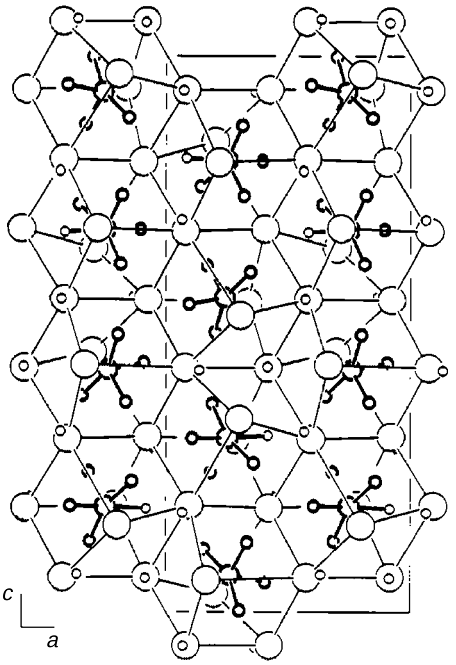

Figure 17 Structure of $Mg_6Co_2D_{11}$

which that at low pressure is attributed to decomposition of $Mg_6Co_2H_{11}$ ($\Delta H = 79\,kJ\,mol^{-1}$ H_2) and that at high pressure to decomposition of tetragonal Mg_2CoH_5 ($\Delta H = 79\,kJ\,mol^{-1}$ H_2);[81] partially disordered structure (Figure 17) from joint synchrotron X-ray and high-resolution npd:[80] *Pnma*, $Z = 8$, 63 positional parameters; two eightfold Co sites, one (Co1) forming an ordered sad-$[CoH_4]^{5-}$ 18-electron complex of symmetry 1, and the other (Co2) a partially disordered spy configuration with one half-occupied ligand; interpreted as a 1:1 mixture of spy-$[CoH_5]^{4-}$ and sad-$[CoH_4]^{5-}$ 18-electron complexes; surrounded by eight Mg sites in distorted cubic configurations; 14 D sites, of which five are surrounded by Mg in tri and sad configurations; metal substructure derives from trigonal $SrMg_2FeH_8$ (XVI) by orthorhombic distortion; short Mg–Mg bonds; lif: $2Mg_6Co_2H_{11} = 12Mg^{2+}\cdot[CoH_5]_{av}{}^{4-}\cdot 2[CoH_4]^{5-}\cdot[CoH_4]_{av}{}^{5-}\cdot 5H^-$; monoclinic distorted Ir analog $Mg_6Ir_2H_{11}$ (XLV) has different T–H complex ordering; other hydrides with similar metal substructure: Mg_3RuH_6 (XXV), Mg_3ReH_7 (XXIII), and $LiMg_2RuH_7$ (XXVII).

Distances (Å): Co1–D = 1.52–1.57, Co2–D = 1.51–1.62; Co–Co = 4.58; Co–Mg = 2.52; Mg–Mg = 2.78; Mg–D = 1.94; $Mg–D^-$ = 1.82; D–D = 2.09.

3.18 Mg_2RuH_4

From the elements, by sintering at 723 K under 20 bar, or at 1050 K under 160 bar hydrogen pressure;[82] powder of reddish-brown to dark-red color, sensitive to moisture and air; ordered structure (Figure 18) from npd on deuteride: *Cmcm*, $Z = 4$; sad-$[RuH_4]^{4-}$ 16-electron complex with T site symmetry $m2m$, derives from the oct-$[RuH_6]^{4-}$ complex in Mg_2RuH_6 by removal of two cis D ligands; two D sites; surrounded by Mg in eightfold distorted cubic configuration, neighboring cubes share faces; possible Ru–Ru interactions across these faces (Ru–Ru = 3.24 Å) could lead to polyanionic $[RuH_4]_n{}^{4n-}$ zig-zag chains running along *c*; magnetic measurements consistent with d^8 low-spin configuration; lif: $2Mg^{2+}\cdot[RuH_4]^{4-}$ (monomer); Ru^0, d^8; $2nMg^{2+}\cdot[Ru_nH_{4n}]^{4n-}$ (polymer); Ru–Ru bonds not supported by extended Hückel calculations.[12]

Distances (Å) and angles: Ru–D = 1.67(2×), 1.68 (2×); D–Ru–D = 84.2°, 93.6° (cis), 170.3° (trans); Ru–Mg = 2.69; Ru–Ru = 3.24(2×); Mg–D = 2.10; Mg–Mg = 2.93; D–D = 2.23.

3.19 $CaMgNiH_4$ ($SrMgNiH_4$, $YbMgNiH_4$, $EuMgNiH_4$)

From mixtures of arc-melted binary alloys ($CaNi_2$, $CaMg_2$, SrNi, YbNi, EuNi) or Mg sintered at 723–763 K under

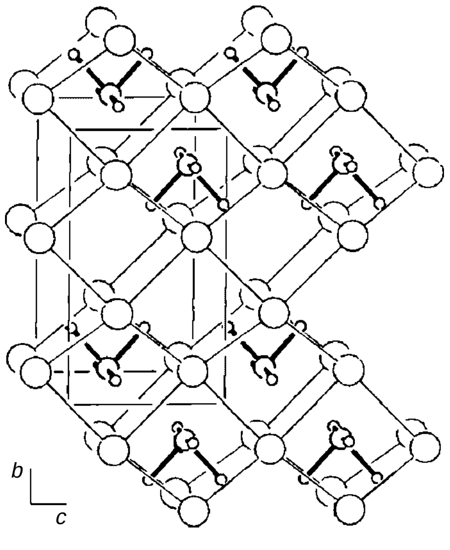

Figure 18 Structure of Mg_2RuD_4

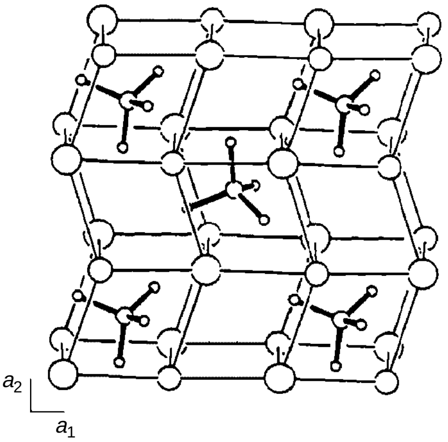

Figure 19 Structure of $CaMgNiD_4$

Table 11 Interatomic distances (Å) in $CaMgNiD_4$ and analogs

	M = Ca	M = Sr	M = Yb
Ni–D	1.59–1.61	1.54–1.64	1.57–1.62
Ni–Mg	2.54	2.55	2.53
Ni–M	3.03	3.21	3.03
Mg–D	2.08	2.15	2.09
M–D	2.45	2.53	2.43
Mg–Mg	4.18	4.24	4.15
Mg–M	3.48	3.54	3.50
D–D	2.59	2.54	2.60
D–Ni–D	108°, 111°	108°, 111°	109°, 110°

130–140 bar hydrogen pressure;[83] greenish (Ca, Sr) or black (Yb) powders; translucent single crystals of $CaMgNiH_4$ having yellow–brownish color obtained by sintering binary hydrides with LiH flux in Ni crucible at 737 K under 95 bar hydrogen pressure;[84] desorption enthalpy $\Delta H = 129(3)$ (Ca), 111(3) (Yb) $kJ\,mol^{-1}$ H_2; ordered structures (Figure 19) from npd on deuterides (Ca, Sr, and Yb[83]): $P2_13$, $Z = 4$; tetrahedral $[NiH_4]^{4-}$ 18-electron complex having T site symmetry 3, surrounded by one Ca (Sr, Yb) site, and one Mg site in ordered distorted cubic configuration; two D sites; derived from Mg_2NiD_4 (V) by partial substitution of Mg; lif: $M^{2+}{\cdot}Mg^{2+}{\cdot}[NiH_4]^{4-}$; Ni^0, d^{10}; X-ray evidence for isostructural $EuMgNiH_4$.[83] Interatomic distances are given in Table 11.

3.20 $Ca_4Mg_4Fe_3H_{22}$ ($Yb_4Mg_4Fe_3H_{22}$)

From mixtures of arc-melted binary alloys (CaMg, YbMg) and Fe powder, by adding LiH as a flux, at about 773–793 K under 100–150 bar hydrogen pressure;[85] $Ca_4Mg_4Fe_3H_{22}$: brownish powder containing brownish translucent single crystals; $Yb_4Mg_4Fe_3H_{22}$: black powder; both stable in air for several weeks; desorption enthalpies $\Delta H = 122(4)$ (Ca), 137(3) (Yb) $kJ\,mol^{-1}$ H_2; decomposition of Ca compound shows two plateaus: formation of Ca_2FeH_6, Mg, Fe, and H_2 (upper plateau), and of CaH_2, Fe, and H_2 (lower plateau); decomposition of Yb compound shows one plateau: formation of YbH_2, Mg, Fe, and H_2; ordered structures (Figure 20) from single-crystal X-ray ($Ca_4Mg_4Fe_3H_{22}$) and npd on deuterides; $P\bar{4}3m$, $Z = 1$; octahedral $[FeH_6]^{4-}$ 18-electron complexes with T site symmetry $\bar{4}2.m$, surrounded by one M and one Mg site in deformed cubic configuration; three D sites, of which the fourfold is tetrahedrally surrounded by one Mg^{2+} and three M^{2+}; derived from Mg_2FeH_6 (II) by partial substitution of Mg by Ca, and of every fourth $[FeH_6]^{4-}$ by $4H^-$; lif: $4M^{2+}{\cdot}4Mg^{2+}{\cdot}3[FeH_6]^{4-}{\cdot}4H^-$; Fe^{II}, d^6. Interatomic distances are given in Table 12.

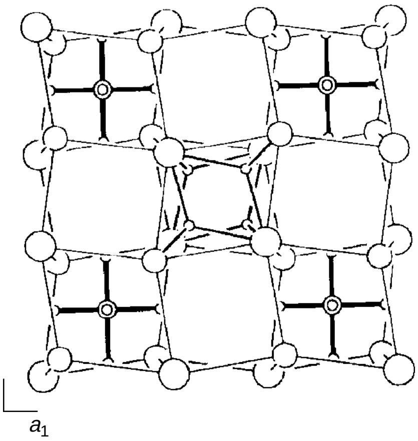

Figure 20 Structure of $Ca_4Mg_4Fe_3D_{22}$

Table 12 Interatomic distances (Å) in $Ca_4Mg_4Fe_3D_{22}$ and ytterbium analog

	M = Ca	M = Yb
Fe–D	1.56–1.58	1.55–1.59
Fe–Mg	2.79	2.78
Fe–M	3.09	3.06
Mg–D	2.07	2.02
Mg–D^-	1.81	1.91
M–D	2.43	2.41
M–D^-	2.39	2.41
Mg–Mg	4.08	3.98
Mg–M	3.39	3.40
D–D	2.22	2.22

3.21 Ba_2PtH_6 (Sr_2PtH_6)

From BaH_2 (SrH_2) and Pt powder in hydrogen;[86] ordered Ba_2CuF_6 type structure (Figure 21) from npd on deuteride: *Cmca*, $Z = 4$; planar $[PtD_4]^{2-}$ 16-electron complexes with T site symmetry $2/m$, surrounded by M in 10-fold bicapped cubic configuration; three D sites, of which one eightfold is tetrahedrally surrounded by M^{2+}; lif: $2M^{2+}{\cdot}[PtH_4]^{2-}{\cdot}2H^-$; Pt^{II}, d^8.

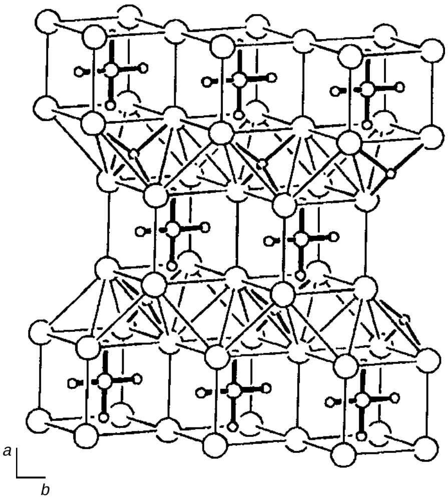

Figure 21 Structure of Ba_2PtD_6

Distances (Å): Pt–D = 1.66(2×) and 1.67 (2×); Pt–Ba = 3.63; Pt–Pt = 4.24; Ba–Ba = 4.09; Ba–D = 2.97; $Ba–D^-$ = 2.62; D–D = 2.36.

3.22 $LiSr_2PdH_5$

From reaction of arc-melted ternary alloy $Li_{1.5}Sr_2Pd$ at 793–803 K under 155 bar hydrogen pressure;[87] dark-green powder, sensitive to air; partially disordered structure (Figure 22) from npd on deuteride at 14 K: $P4/mmm$, $Z = 1$; metals form ordered superstructure of CsCl; contains ordered $SrLiD_3$ type slabs having inverse perovskite-type structure; Pd surrounded by three D, on average, in partially disordered octahedral configuration with four half occupied equatorial D sites forming linear Pd–D–Pd bridges similar to those in $CaPdH_2$ (X), and two fully occupied axial sites belonging to the $SrLiD_3$ type slabs; both have large displacement amplitudes; three D sites, of which a twofold is octahedral surrounded by four Sr and two Li; lif: $Li^+\cdot 2Sr^{2+}\cdot[PdH_3]_{av}{}^{3-}\cdot 2H^-$; Pd^0, d^{10} (average).

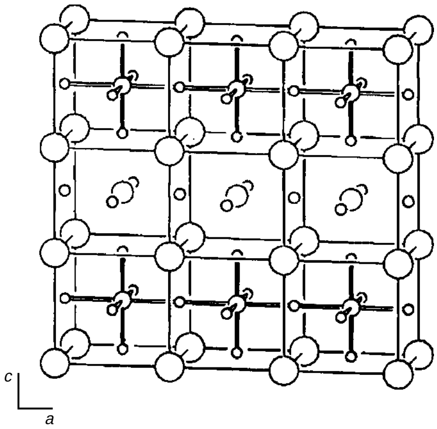

Figure 22 Structure of $LiSr_2PdD_5$

Distances (Å): Pd–D = 1.69(2×), 1.95 (4×, disordered); Pd–Sr = 3.34; Pd–Li = 3.70; Pd–Pd = 3.90; Li–D = 2.01; $Li–D^-$ = 1.95; Li–Sr = 3.30; Sr–D = 2.71; $Sr–D^-$ = 2.66; D–D = 2.58.

3.23 Mg_3ReH_7 (Mg_3MnH_7)

From elements by sintering powder mixtures at 783–793 K under 120 bar hydrogen pressure;[88] gray powder; sensitive to air; orange-red Mn analog Mg_3MnH_7 from powder mixtures of MgH_2 and Mn at 20 kbar pressure and 1073 K in multianvil device;[89] ordered structures (Figure 23) by npd on deuterides: $P6_3/mmc$, $Z = 2$; octahedral $[TH_6]^{5-}$ 18-electron complexes with T site symmetry $\bar{3}m$, surrounded by two Mg sites in eightfold distorted cubic configuration similar to that of $SrMg_2FeH_8$ (XVI); two D sites, of which the twofold is surrounded by Mg in trigonal bipyramidal configuration with two short collinear and three long triangular Mg–D bonds; lif: $3Mg^{2+}\cdot[TH_6]^{5-}\cdot H^-$; T^I, d^6; electronic band structure calculation on Mn compound.[90] Interatomic distances are given in Table 13.

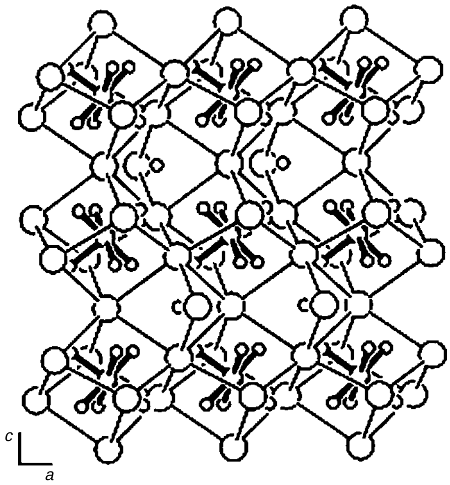

Figure 23 Structure of Mg_3ReD_7

Table 13 Interatomic distances (Å) in Mg_3ReD_7 and manganese analog

	T = Mn	T = Re
T–D	1.63	1.72
T–Mg	2.56	2.64
T–T	4.70	4.85
Mg–D	2.08	2.14
$Mg–D^-$	1.87	1.90
Mg–Mg	3.05	3.17
D–D	2.29	2.41

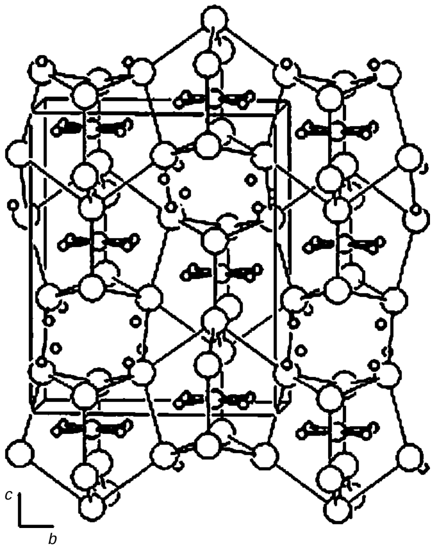

Figure 24 Structure of Mg_4IrD_5

3.24 Mg_4IrH_5

From elements by sintering powder mixtures at 783 K and 41 bar hydrogen pressure;[91] dark gray powder, stable in air; presumably metallic; partially disordered structure (Figure 24) from npd on deuteride at room temperature and 9 K: *Imma*, $Z = 4$; Ir surrounded by three D atoms, on the average, in disordered planar configuration with 75% occupancy (average T site symmetry *mm*2); surrounded by three Mg sites in irregular ninefold coordination; two D sites, of which the eightfold is coordinated by Mg in saddle-like configuration; short Mg–Mg bonds along backbone of $[Mg_9IrD_3]$ units; no apparent homogeneity range; lif (border case): $4Mg^{2+}{\cdot}[IrH_3]_{av}{}^{6-}{\cdot}2H^-$.

Distances (Å): Ir–D $= 1.70(4\times$, dis); Ir–Mg $= 2.75$; Ir–Ir $= 4.62$; Mg–Mg $= 2.76$; Mg–D $= 2.15$; Mg–D$^-$ $= 1.88$; D–D $= 2.34$.

3.25 Mg_3RuH_6

From elements by sintering powder mixtures at 1053 K under 90 bar hydrogen pressure;[92] powder of rusty-brown color, sensitive to moisture and air; partially disordered structure (Figure 25) from npd on deuteride at room temperature and 15 K: *Cmcm*, $Z = 4$; Ru surrounded by five D, on average, in disordered octahedral configuration (average T site symmetry $2/m$); equatorial sites have 75% and axial sites full occupancy; surrounded by two Mg sites in eightfold cubic configuration similar to Mg_3ReH_7 (XXIII); three D sites, of which the fourfold is coordinated by two Mg in linear configuration; no indication for D ordering down to 15 K; lif: $3Mg^{2+}{\cdot}[RuH_5]_{av}{}^{5-}{\cdot}H^-$; Ru^0, d^8 (average).

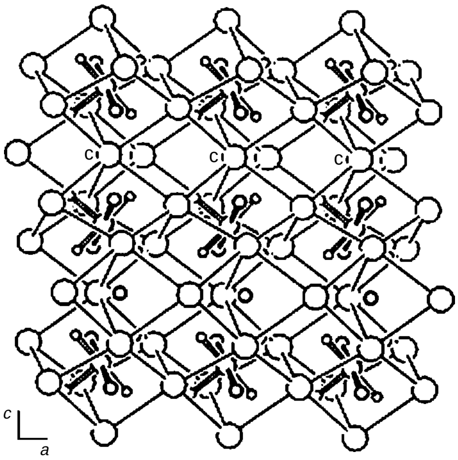

Figure 25 Structure of Mg_3RuD_6

Distances (Å): Ru–D $= 1.66$ ($4\times$, dis), 1.73 ($2\times$); Ru–Mg $= 2.67$; Ru–Ru $= 4.79$; Mg–Mg $= 3.04$; Mg–D $=$ 1.91; Mg–D$^-$ $= 1.87$; D–D $= 2.29$.

3.26 $Sr_8Rh_5H_{23}$ ($Ca_8Rh_5H_{23}$)

From alkaline earth hydrides and rhodium metal by sintering powder mixtures at 1073 K under 5 bar hydrogen pressure;[46,47,93] powder of black-red (Sr) and black (Ca) color, sensitive to moisture and air; partially disordered, structure intermediate to anion deficient K_2PtCl_6 type (II) and perovskite type (Figure 26); from npd on deuterides (Sr, Ca)[46,93] at room temperature and 10 K: $Pm\bar{3}m$, $Z = 1$; three D sites of which two are terminal to Rh with full occupancies and one sixfold is bridging two Rh with partial occupancy (5/6); 3 Rh sites surrounded in octahedral configurations (site symmetries $m\bar{3}m$ *and* $4/mm.m$) by six ordered terminal (Rh1), six disordered (5/6 occupancy) bridging (Rh3), and four ordered terminal plus two disordered bridging (Rh2) deuterium sites, the two latter forming a quasi-infinite polynuclear $[Rh_4H_{17}]_n{}^{13n-}$ complex; one Sr (Ca) site surrounds Rh in eightfold cubic configuration; no indication for D ordering down to 10 K; lif: $8nM^{2+}{\cdot}n[RhH_6]^{3-}{\cdot}[Rh_4H_{17}]_n{}^{13n-}$ mixed valence Rh^I (d^8) and Rh^{III} (d^6). Interatomic distances are given in Table 14.

3.27 $LiMg_2RuH_7$ ($LiMg_2OsH_7$)

From LiH, Mg, and Ru (Os) powders at up to 823 K under hydrogen pressure of up to 155 bar;[94,95] light yellow powder; sensitive to air; ordered derivative of Mg_3ReH_7 type (XXIII) structure (Figure 27) by npd on deuteride of Ru compound: $P6_3/mmc$, $Z = 2$; octahedral $[RuH_6]^{4-}$ 18-electron units having T site symmetry $\bar{3}m$, surrounded by six Mg^{2+} and two Li^+ in nearly cubic configuration; one Mg and one Li site; two D sites, of which the twofold is trigonal

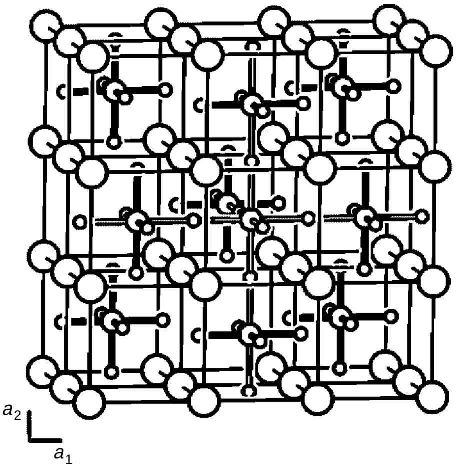

Figure 26 Structure of $Sr_8Rh_5D_{23}$

Table 14 Interatomic distances (Å) in $Sr_8Rh_5D_{23}$ and calcium analog

	M = Ca	M = Sr
Rh1–D	1.69(6×)	1.69(6×)
Rh2–D	1.70(4×)	1.70(4×)
	1.77(2×, dis)	1.89(2×, dis)
Rh3–D	1.87(6×, dis)	1.92(6×, dis)
Rh–M	3.14	3.29
Rh–Rh	3.64	3.81
M–D	2.56	2.69
M–M	3.62	3.80
D–D	2.39	2.38

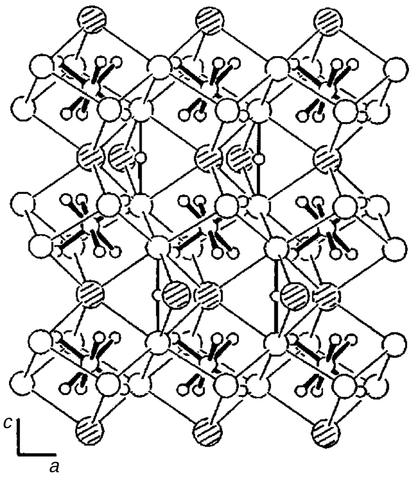

Figure 27 Structure of $LiMg_2RuD_7$

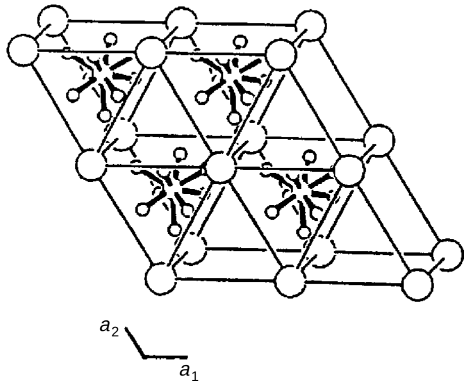

Figure 28 Structure of $BaReH_9$

bipyramidal coordinated with two short linear Mg–D and three long triangular Li–D bonds; lif: $Li^+ \cdot 2Mg^{2+} \cdot [RuH_6]^{4-} \cdot H^-$; Ru^{II}, d^6.

Distances (Å): Ru–D = 1.69(6×); Ru–Mg = 2.83; Ru–Li = 2.67; Ru–Ru = 4.70; Mg–Li = 3.29; Mg–Mg = 3.17; Li–D = 2.14; Li–D^- = 2.71; Mg–D = 2.27; Mg–D^- = 1.85; D–D = 2.34.

3.28 $BaReH_9$

From di-sodium salt Na_2ReH_9 (obtained from reaction of $KReO_4$ with K metal in ethylene diamine–water solution) converted to the di-potassium salt by way of the Ba salt;[96] white powder, transparent crystals, unstable in moist air; ordered structure (Figure 28) from single-crystal X-ray diffraction, and IR and NMR data on hydride:[97] $P6_3/mmc$, $Z = 2$; Re site forming ttp-$[ReH_9]^{2-}$ 18-electron complexes with site symmetry $\bar{6}m2$; surrounded by Ba cations in NiAs type configuration; two H sites (not refined); lif: $Ba^{2+} \cdot [ReH_9]^{2-}$; Re^{VII}, d^0; electronic band structure by APW calculations.[98]

Interatomic distances (Å): Re–H ∼ 1.69[a] (3× and 6×); Re–Ba = 3.84; Re–Re = 5.29; Ba–Ba = 4.66; Ba–H = 2.71[a], 2.86; H–H ∼ 1.97[a] (distances not refined).

3.29 K_2ZnH_4 (Rb_2ZnH_4, Cs_2ZnH_4, Sr_2PdH_4, Ba_2PdH_4, Eu_2PdH_4)

M_2ZnH_4 (M = K, Rb, Cs) from elements by sintering powder mixtures at 783–793 K under 120 bar hydrogen pressure;[99,100] M_2PdH_4 (M = Sr, Ba,[101] Eu[102]), from elements gray powder; sensitive to air; ordered structure (Figure 29) by npd on deuteride: $Pnma$, $Z = 2$; β-K_2SO_4 type structure, tetrahedral $[ZnH_4]^{2-}$ 18-electron complexes with T site symmetry m surrounded by two M sites in eightfold distorted square antiprismatic configuration; three D sites; evidence for nonconducting behavior of Sr_2PdH_4 and Ba_2PdH_4 (measurement on powdered hydrides);[101] electronic band structure on Eu_2PdH_4;[103] lif: $2K^+ \cdot [ZnH_4]^{2-}$; Zn^{II}, d^{10}; $2M^{2+} \cdot [TH_4]^{4-}$, Pd^0, d^{10}. Interatomic distances are given in Table 15.

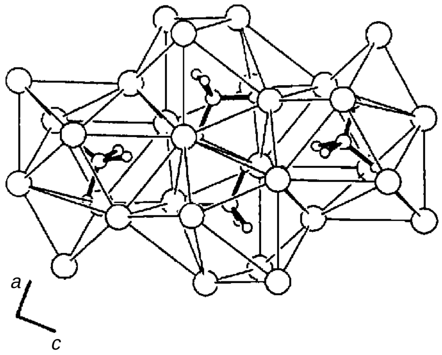

Figure 29 Structure of K_2ZnD_4

Table 15 Interatomic distances (Å) in K_2ZnD_4 and analogs

		M = K	M = Rb	M = Cs
T = Zn	Zn–D	1.63–1.66	1.66–1.68	1.67–1.69
	Zn–M	3.31	3.49	3.59
	M–D	2.72	2.89	2.97
	Zn–Zn	4.97	5.24	5.56
	M–M	3.86	3.94	4.12
	D–D	2.69	2.72	2.73
		M = Sr	M = Ba	M = Eu
T = Pd	Pd–D	1.76–1.81	1.78–1.81	1.67–1.83
	Pd–M	3.09	3.23	3.07
	M–D	2.49	2.72	2.54
	Pd–Pd	4.83	5.07	4.78
	M–M	3.65	3.78	3.57
	D–D	2.58	2.80	2.69

3.30 K_3ZnH_5 (Rb_3ZnH_5, Cs_3ZnH_5, Cs_3CdH_5, K_3MnH_5, Rb_3MnH_5, Cs_3MnH_5)

M_3ZnH_5 (M = K, Rb, Cs) from elements by sintering powder mixtures at 783–793 K under 120 bar hydrogen pressure;[104,105] M_3MnH_5 (M = Sr, Ba) from alkali metal hydrides and Mn powder at 875 K and 3 kbar H_2 gas pressure,[106,107] Cs_3CdH_5[108] from elements, gray (Zn, Cd) and rose colored (Mn) powders; sensitive to air; ordered structure (Figure 30) by npd on deuteride: *I4/mcm*, $Z = 4$; Cs_3CoCl_5 type structure, tetrahedral $[TH_4]^{2-}$ 18-electron complexes with T site symmetry $\bar{4}2m$ surrounded by two M sites in an eightfold configuration; two D sites, of which the fourfold is surrounded by M in octahedral configuration; arrangement of H^- and $[TH_4]^{2-}$ complexes similar to that in K_3PtH_5 (VIII); vibrational spectroscopy of Rb_3ZnH_5;[54] lif: $3M^+{\cdot}[TH_4]^{2-}.H^-$; Zn^{II}, d^{10}; Cd^{II}, d^{10}; Mn^{II}, d^5; Mn compounds order magnetically below 50 K.[9] Interatomic distances are given in Table 16.

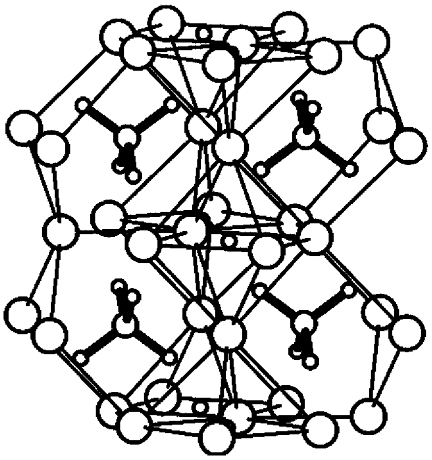

Figure 30 Structure of K_3ZnD_5

Table 16 Interatomic distances (Å) in K_3ZnD_5 and analogs

		M = K	M = Rb	M = Cs
T = Zn	Zn–D	1.66	1.66	1.68
	Zn–M	3.41	3.56	3.72
	M–D	2.75	2.94	3.15
	$M–D^-$	2.78	2.91	3.04
	Zn–Zn	5.36	5.61	5.87
	M–M	3.92	4.10	4.26
	D–D	2.66	2.69	2.72
T = Cd	Cd–D			1.82
	Cd–M			3.83
	M–D			3.11
	$M–D^-$			3.08
	Cd–Cd			5.96
	M–M			4.35
	D–D			2.93
T = Mn	Mn–D	1.75	1.76	1.79
	Mn–M	3.55	3.69	3.82
	M–D	2.73	2.88	3.11
	$M–D^-$	2.80	2.92	3.07
	Mn–Mn	5.43	5.66	5.94
	M–M	3.96	4.12	4.34
	D–D	2.78	2.85	2.87

3.31 $Ba_3Ir_2H_{12}$

From powder mixtures of BaH_2 and Ir at 837 K and 80 bar hydrogen pressure;[109] white powder, sensitive to air; ordered structure (Figure 31) from npd on deuteride at room temperature; $P\bar{3}m1$, $Z = 1$; octahedral $[IrH_6]^{3-}$ 18-electron complex with Ir site symmetry 3*m*; surrounded by two Ba sites in irregular sevenfold coordination; two D sites; lif: $3Ba^{2+}{\cdot}2[IrH_6]^{3-}$, Ir^{III}, d^6.

Distances (Å): Ir–D = 1.60(3×) and 1.76 (3×); Ir–Ba = 3.30; Ir–Ir = 5.43; Ba–D = 2.72; D–D = 2.25.

3.32 $Ca_4Mg_4Co_3H_{19}$ ($Yb_4Mg_4Co_3H_{19}$)

From mixtures of arc-melted binary alloys (CaMg, YbMg) and Co rods, by adding LiH as a flux, at up to 800 K and 155 bar hydrogen pressure;[110] black powders, Ca compound containing brownish translucent single crystals; partially

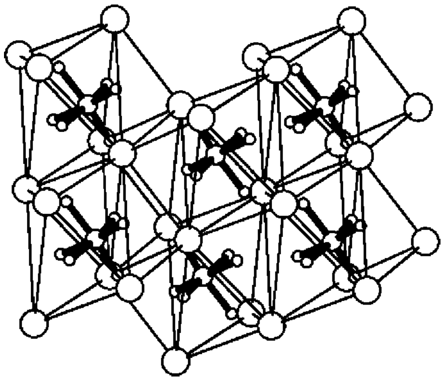

Figure 31 Structure of $Ba_3Ir_2D_{12}$

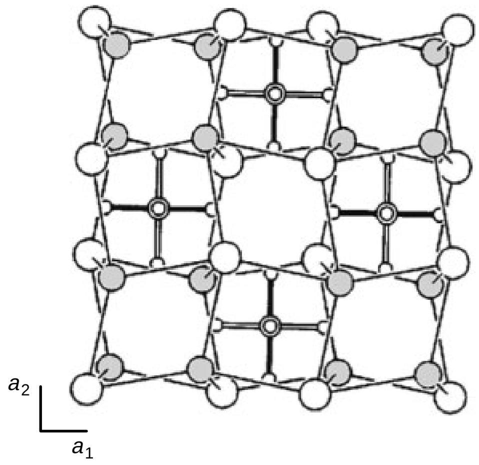

Figure 32 Structure of $Ca_4Mg_4Co_3D_{19}$

Table 17 Interatomic distances (Å) in $Ca_4Mg_4Co_3D_{19}$ and ytterbium analog

	M = Ca	M = Yb
Co–D	1.55–1.59	1.55–1.58
Co–Mg	2.75	2.74
Co–M	3.11	3.10
Mg–D	1.91	1.89
$Mg–D^-$	1.96	1.94
M–D	2.44	2.43
$M–D^-$	2.35	2.36
Co–Co	4.72	4.71
Mg–Mg	3.72	3.67
Mg–M	3.42	3.40
D–D	2.19	2.19

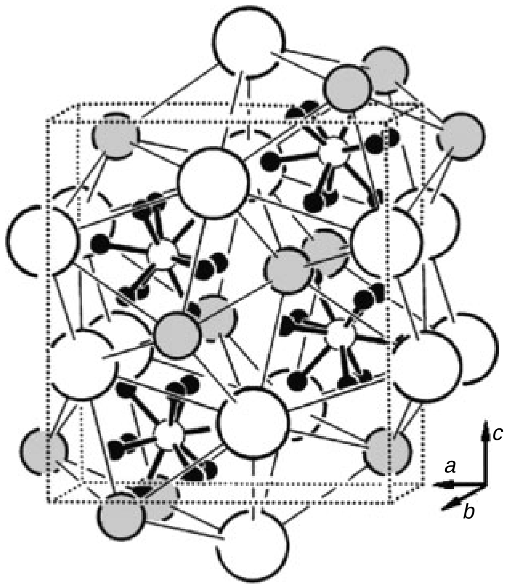

Figure 33 Structure of $KNaReH_9$

disordered structures (Figure 32) from npd on deuterides and single-crystal X ray on $Ca_4Mg_4Co_3H_{19}$; $P\bar{4}3m$, $Z = 1$; derives from Fe analog $Ca_4Mg_4Fe_3H_{22}$ (XX) by substitution of oct $[FeH_6]^{4-}$ by spy $[CoH_5]^{4-}$ 18-electron complexes; apical Co ligands disordered (half occupancy), Co site symmetry $\bar{4}2.m$, surrounded by Mg and Ca (Yb) sites in deformed cubic configuration; three D sites, of which one anionic D^- tetrahedral surrounded by one Mg^{2+} and three M^{2+}; derives from Mg_2CoH_5 (III) by partial substitution of Mg by Ca, and of every fourth $[CoH_5]^{4-}$ by $4\,H^-$; lif: $4M^{2+}\cdot 4Mg^{2+}\cdot 3[CoH_5]_{av}{}^{4-}\cdot 4H^-$; Co^I, d^8. Interatomic distances are given in Table 17.

3.33 KNaReH$_9$

Translucent crystals obtained from di-sodium salt Na_2ReH_9**[96]** by slow evaporation of a solution in KOH; unstable in moist air; ordered structure (Figure 33) from single-crystal X-ray diffraction at 193 K, and IR data:**[111]** *Pnma*, $Z = 4$; Re site forming ttp-$[ReH_9]^{2-}$ 18-electron complexes with site symmetry *m*; surrounded by K and Na cations in TiNiSi type metal configuration; six H sites (not refined); lif: $K^+.Na^+\cdot[ReH_9]^{2-}$; Re^{VII}, d^0.

Interatomic distances (Å): Re–H = $1.69–1.71^a$; Re–Na = 3.35; Re–K = 3.69; Re–Re = 5.33; Na–Na = 4.00; Na–K = 4.01; K–K = 4.49; Na–H = 2.33^a; K–H = 2.61^a; H–H = 1.73^a (not refined).

3.34 Li$_5$Pt$_2$H$_9$

From reaction of LiH and Pt at 1250 bar H_2 pressure and 820 K;**[112]** anthracite colored caked solid, sensitive to air and moisture; ordered structure (Figure 34) from npd on deuteride: $I4/mcm$, $Z = 4$; contains $[Pt_2H_9]^{5-}$ dimer with *m.mm* symmetry in which four D surround each Pt in spl configuration and one D bridges two Pt; 2 Li sites; diamagnetic; lif: $5M^+\cdot[T_2H_9]^{5-}$; Pt^{II}, d^8.

Distances (Å): Pt–D = 1.64(4×), 1.85; Pt - Li = 2.64; Pt–Pt = 3.71; Li–D = 2.13; D–D = 2.28.

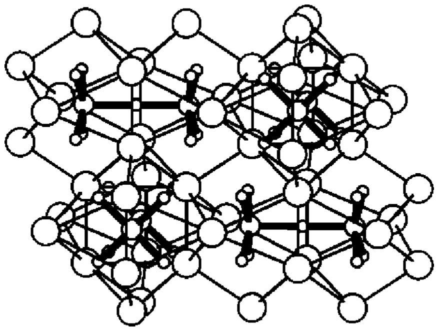

Figure 34 Structure of $Li_5Pt_2D_9$

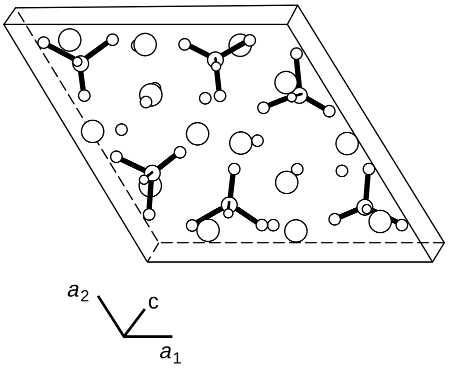

Figure 35 Structure of $Ba_7Cu_3D_{17}$

3.35 $Ba_7Cu_3H_{17}$

By hydrogenation of Ba–Cu alloys at 10 bar H_2 pressure and room temperature, followed by annealing at 643 K under 160 bar H_2 pressure;**113** dark brownish powder sensitive to air and moisture; ordered structure (Figure 35) from npd on deuteride: $P31c$, $Z = 2$; contains distorted 18-electron tet-$[CuD_4]^{3-}$ complexes (symmetry 1) surrounded by nine Ba (three sites) in ttp configuration; seven D sites, of which three anionic D^- tetrahedral surrounded by four M^{2+}; lif: $7Ba^{2+}\cdot 3[CuH_4]^{3-}.5H^-$; Cu^I, d^{10}.

Distances (Å): Cu–D = 1.64–1.75; Cu–Ba = 3.19; Cu–Cu = 5.07; Ba–D = 2.36; Ba–D^- = 2.59; D–D = 1.94.

3.36 $LiMg_4Os_2H_{13}$ ($LiMg_4Ru_2H_{13}$)

By sintering of mixtures of LiH, Mg, and Os (Ru) powders at up to 833 K under hydrogen pressure between 70 and 155 bar;**95** powders having light green (low pressure) and grey (high pressure) color; sensitive to air; Os sample pyrophoric; ordered structure (Figure 36) by npd on deuteride of Os compound: $P6_3/mmc$, $Z = 2$; octahedral $[OsH_6]^{4-}$ 18-electron units having T site symmetry $3m$ surrounded by six Mg^{2+} and two Li^+ in nearly cubic configuration; one Mg and one Li site; three D sites, of which an anionic D^- in trigonal bipyramidal coordination with two short linear Mg–D and three long triangular Li–D bonds; structure derives from Mg_2OsH_6 by intercalation of LiH sheets; intermediate between Mg_2OsH_6 (II) and $LiMg_2OsH_7$ (XXVII); lif: $Li^+\cdot 4Mg^{2+}\cdot 2[TH_6]^{4-}\cdot H^-$; Os^{II}, d^6.

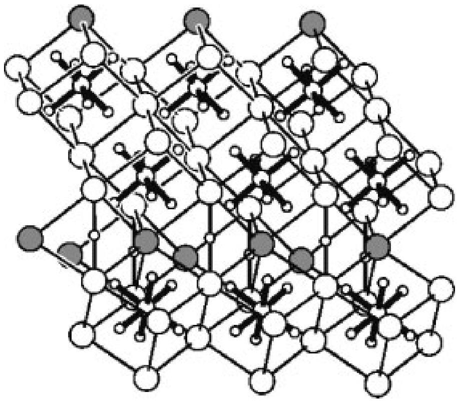

Figure 36 Structure of $LiMg_4Os_2D_{13}$

Distances (Å): Os–D = 1.69(3×) and 1.70 (3×); Os–Li = 2.69; Os–Mg = 2.85; Mg–Li = 3.31; Mg–Mg = 3.26; Li–D = 2.13; Li–D^- = 2.73; Mg–D = 2.24; Mg–D^- = 1.87; D–D = 2.31.

3.37 Li_2PtH_2

By thermal decomposition of $Li_5Pt_2H_9$ (XXXIV) at 493 K under argon;**114** ordered structure (Figure 37) from npd on deuteride: $Immm$, $Z = 2$; contains linear $[PtD_2]^{2-}$ 14-electron complexes with mmm symmetry; orthorhombic distortion of tetragonal Pd analog Li_2PdH_2 (VII); lif: $2Li^+\cdot[PtH_2]^{2-}$; Pt^0, d^{10}.

Distances (Å): Pt–D = 1.64(2×); Pt–Pt = 2.99; Pt–Li = 2.61; Li–Li = 2.75; Li–D = 2.01; D–D = 2.82.

3.38 $BaMg_2RuH_8$ ($BaMg_2OsH_8$)

By sintering powder mixtures of $BaMg_2$ alloy, BaH_2, and Ru with LiH flux at temperatures of up to 803 K and H_2 pressures of up to 150 bar;**115** greenish powder;

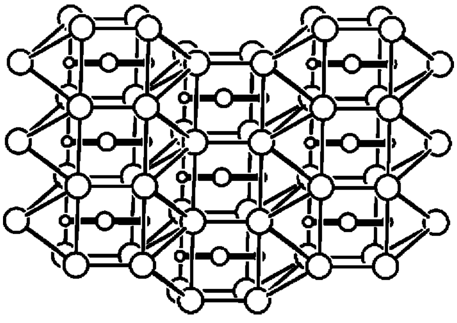

Figure 37 Structure of Li_2PtD_2

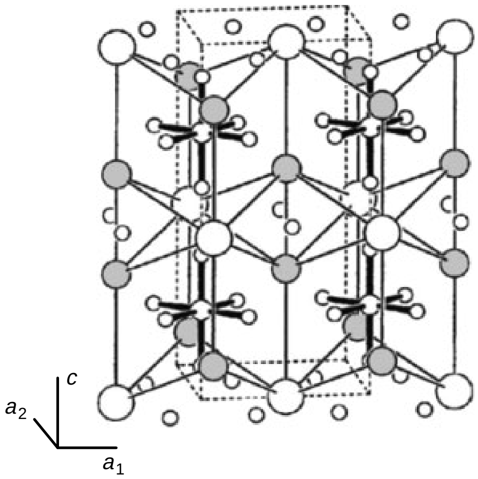

Figure 38 Structure of $BaMg_2RuD_8$

Table 18 Interatomic distances (Å) in $BaMg_2RuD_8$ and osmium analog

	T = Ru	T = Os
T–D	1.68–1.72	1.70–1.72
T–Mg	2.74	2.75
T–Ba	3.67	3.67
Mg–D	2.10	2.12
Mg–D^-	1.99	1.97
Ba–D	2.68	2.68
Ba–D^-	2.77	2.77
T–T	4.96	4.97
Mg–Mg	3.08	3.03
Mg–Ba	3.83	3.82
D–D	2.04	2.02

ordered structure (Figure 38) by npd on deuterides of Ru and Os compounds at room temperature: $P4_2/mmc$, $Z = 2$; octahedral $[TH_6]^{4-}$ 18-electron units having T site symmetry $\bar{4}m2$ surrounded by four Mg^{2+} and four Ba^{2+} forming two interpenetrating tetrahedral; similarity to iron analog $BaMg_2FeH_8$ (XVI); three D sites, of which one hydridic D^- is tetrahedral coordinated by two Ba and two Mg; lif: $Ba^{2+}\cdot 2Mg^{2+}\cdot[TH_6]^{4-}\cdot 2H^-$; T^{II}, d^6. Interatomic distances are given in Table 18.

3.39 $NaBaPdH_3$

By sintering of compacted powder mixtures of NaH, BaH_2, and Pd at temperatures of up to 783 K under H_2 pressures of 90 bar;[116] solid having metallic luster, sensitive to air and moisture, contains ruby-red single crystals; ordered structure (Figure 39) from single-crystal X-ray diffraction on hydride and npd on deuteride: $P6_3/mmc$, $Z = 2$; contains trigonal planar $[PdH_3]^{3-}$ 16-electron complexes with $\bar{6}m2$ symmetry; surrounded by five Ba in trigonal bipyramidal configuration; one Pd site, one Na site, one Ba site and one D site; lif: $Na^+\cdot Ba^{2+}\cdot[PdH_3]^{3-}$; Pd^0, d^{10} (supported by ac-magnetic susceptibility measurements).

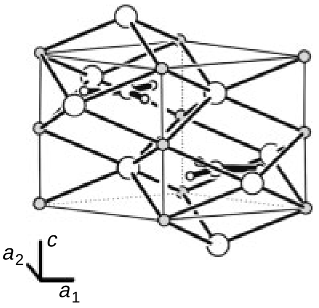

Figure 39 Structure of $NaBaPdD_3$

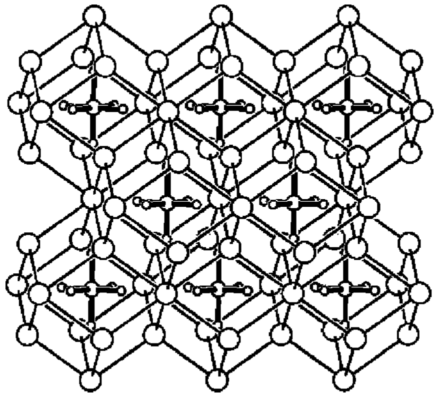

Figure 40 Structure of K_3ReD_6

Distances (Å): Pd–D = 1.72(3×); Pd–Ba = 3.04; Pd–Na = 3.81; Pd–Pd = 4.63; Ba–Na = 3.81; Na–Na = 3.04; Na–D = 2.33; Ba–D = 3.03; D–D = 2.98.

3.40 K_3ReH_6

By hydrogenation of powder mixtures of KH and Re at 850 K and H_2 pressures of up to 3500 bar.[117] Reaction product has olive green color, is unstable in air and moisture, and decomposes under vacuum; ordered structure (Figure 40) from npd on deuteride: cubic variant of cryolite type (K_2NaAlF_6), $Fm\bar{3}m$, $Z = 4$; Re site forming oct-$[ReH_6]^{3-}$ 16-electron complexes with site symmetry $m\bar{3}m$; surrounded by 14 K^+ forming a bicapped cuboctahedron (of which the closest K^+, site K1, in eightfold cubic configuration); lif: $3K^+\cdot[ReH_6]^{3-}$; Re^{III}, d^4 (consistent with experimentally measured weak temperature independent paramagnetism).

Distances (Å): Re–D = 1.71(6×); Re–D = 3.73; Re–Re = 6.10; K–D = 2.60; K–K = 3.73; D–D = 2.41.

3.41 $Ca_8Rh_6H_{24}$

From calcium hydride and rhodium metal by sintering powder mixtures at temperatures of up to 1133 K under

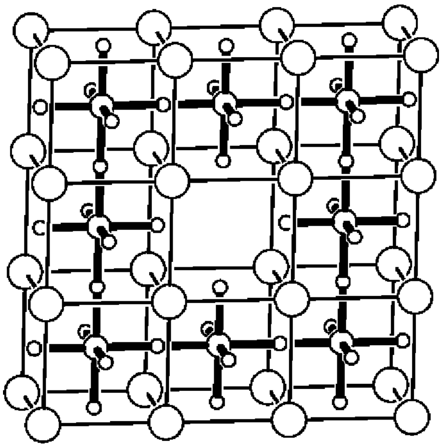

Figure 41 Structure of $Ca_8Rh_6D_{24}$

5 bar hydrogen pressure;[93] powder of metallic brass-like appearance, sensitive to moisture and air; ordered structure (Figure 41) closely related to partially disordered more Rh poor $Ca_8Rh_5H_{23}$ (XXVI), intermediate to anion deficient K_2PtCl_6 type (II) and perovskite type; from npd on deuteride: $Im\bar{3}m$, $Z = 1$; three-dimensional network of Rh centered, corner-sharing D octahedra (site symmetry 4/*mm.m*) consisting of four bridging (D2) and two terminal (D1); Ca surrounds octahedra in eightfold cubic configuration; lif: $4nCa^{2+}\cdot[Rh_3H_{12}]_n{}^{8n-}$, mixed valence $Rh^{\text{‘}1.33\text{’}}$

Distances (Å): Rh–D = 1.73(2×) and 1.82 (4×); Rh–Ca = 3.15; Rh–Rh = 3.64; Ca–D = 2.58; Ca–Ca = 3.64; D–D = 2.51.

3.42 Rb_3ReH_{10} (K_3ReH_{10}, Cs_3ReH_{10})

By hydrogenation of powder mixtures of alkali hydrides and Re up to 870 K and H_2 pressures of up to 3500 bar (K,[9,118] Rb,[118] Cs[119]); reaction products are light grey and unstable in air and moisture; disordered structure (Figure 42) from npd on Rb deuteride: cubic room temperature variant: $Pm\bar{3}m$, $Z = 1$; described as ReO_3 type framework containing strongly disordered $[ReH_9]^{2-}$ 18-electron complexes (average site symmetry $m\bar{3}m$) with two 24-fold disordered D sites (occupancies 0.187 and 0.194), and hydride anions H^- in octahedral M^+ environment; transforms below 110 K into presumably ordered ttp-$[ReH_9]^{2-}$ complexes (described as ‘monocapped square antiprisms’[9,118]) having rhombohedral symmetry; lif: $3M^+\cdot[ReH_9]^{2-}\cdot H^-$; Re^{VII}, d^0 (consistent with experimentally measured diamagnetism on Rb compound).

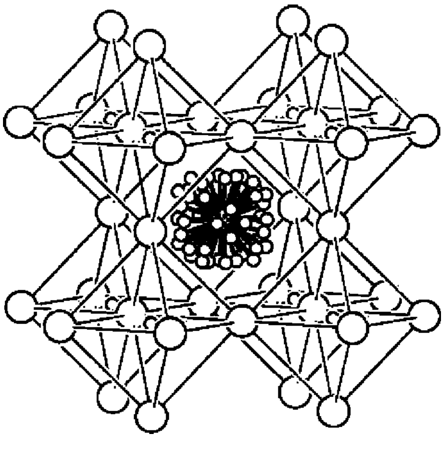

Figure 42 Structure of Rb_3ReD_{10}

Distances for disordered structure (Å): Re–D = 1.70 (24×, dis) and 1.71 (24×, disordered); Re–Rb = 4.18; Rb–Rb = 4.18; Re–Re = 6.10; Rb–D = 2.83; Rb–D^- = 2.96; D–D = 0.58 (dis).

3.43 Na_3OsH_7 (Na_3RuH_7)

By sintering powder mixtures of NaH and Os (Ru) at temperatures of up to 870 K and H_2 pressures of up to 1500 (Os) and 6000 (Ru) bar.[120] ordered structure (Figure 43) by npd on deuteride of Os compounds at room temperature: $P4_2/mnm$, $Z = 4$; contains isolated distorted pentagonal bipyramid $[OsH_7]^{3-}$ 18-electron units having Os site symmetry $m.2m$ surrounded by eight Na^+ (from two Na sites) forming a distorted cube; four D sites; transforms into a HT modification at 459 K; lif: $3Na^+\cdot[TH_7]^{3-}$, T^{IV}, d^4 (supported by experimentally measured weak temperature independent paramagnetism on Os compound). Diffraction evidence[120] for the existence of cubic phases $M_{3-\delta}$ $TH_{7-\delta}$ (M = K, Rb, Cs; T = Ru, Os; $\delta \sim 0.12$ for the K–Ru compound).

Distances (Å): Os–D = 1.62–1.70; Na–Os = 3.15; Os–Os = 5.35; Na–D = 2.21; Na–Na = 3.12; D–D = 1.84.

3.44 Cs_3OsH_9 (Rb_3OsH_9)

By sintering powder mixtures of alkali hydrides and Os under conditions similar to Na_3OsH_7 (XLIII).[120] Partially disordered structure (Figure 44) by npd on deuteride of Cs compound at room temperature: $Pm\bar{3}m$, $Z = 1$; contains

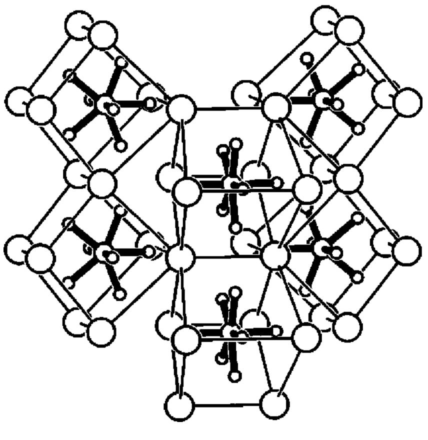

Figure 43 Structure of Na_3OsD_7

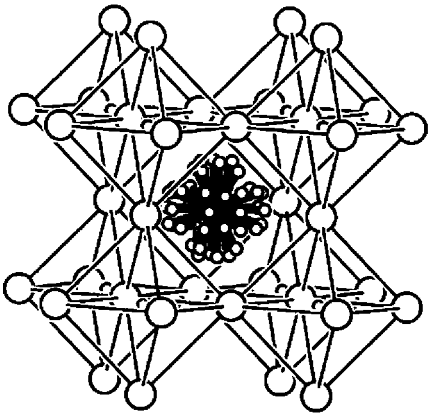

Figure 44 Structure of Cs_3OsD_9

isolated $[OsH_8]^{3-}$ 18-electron units having strongly disordered D ligands at room temperature as described by two partially occupied 24-fold D sites (occupancy $= 1/6$, not refined), and one D^- site in octahedral M^+ surrounding; Os (average site symmetry $m\bar{3}m$) surrounded by eight M^+ in cubic configuration; lif: $3M^+{\cdot}[OsH_8]_{av}{}^{2-}.H^-$; Os^{VI}, d^2.

Distances (Å): Os–D $= 1.59$ (24×, dis) -1.70 (24×, dis); Os–Cs $= 4.33$; Os–Os $= 6.13$; Cs–D $= 2.91$; Cs–D^- $= 3.06$; Cs–Cs $= 4.33$; D–D $= 0.70$ (dis).

3.45 $Mg_6Ir_2H_{11}$

From either hydrogenated binary Mg_3Ir alloy or by sintering powder mixtures of the elements at up to 773 K under a H_2 pressure of up to 150 bar.[121] Red colored hydride; partially disordered structure (Figure 45) from npd on deuteride,: $P2_1/c$, $Z = 8$; contains four symmetry independent Ir hydride complexes: a spy $[IrH_5]^{4-}$ and three sad $[IrH_4]^{5-}$ complexes of which two are disordered, and five hydride anions are exclusively bonded to Mg; all complexes are surrounded by Mg in distorted cubic configurations; metal substructure represents a monoclinic distortion of orthorhombic Co analog $Mg_6Co_2D_{11}$ (XVII); lif: $12Mg^{2+}{\cdot}[IrH_5]^{4-}{\cdot}[IrH_4]^{5-}{\cdot}2[IrH_4]_{av}{}^{5-}{\cdot}5H^-$; mixed valence Ir^I, d^8 and Ir^{-I}, d^{10}.

Distances (Å): Ir1–D $= 1.67$–2.07, Ir2–D $= 1.66$–1.74, Ir1a–D $= 1.67$–1.99, Ir2a–D $= 1.64$–1.90; Ir–Mg $= 2.65$; Ir–Ir $= 4.62$; Mg–Mg $= 2.79$; Mg–D $= 1.79$; Mg–D^- $=$ 1.74; D–D $= 2.11$.

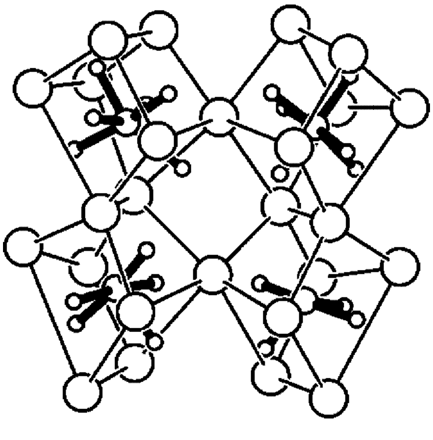

Figure 45 Structure of $Mg_6Ir_2D_{11}$

3.46 $NdMgNi_4H_{3.6}$ ($LaMgNi_4H_{\sim 3.6}$)

From hydrogenation of intermetallic compounds $NdMgNi_4$ and $LaMgNi_4$ at 323 K under H_2 pressure of up to 7–8 bar;[122] metallic powders decompose in air by catalytic water formation; nearly ordered structure of $NdMgNi_4H_{3.6}$ (Figure 46) from npd on deuteride; $Pnm2_1$, $Z = 4$; contains three Ni sites and three almost fully occupied D sites (occupancies 0.89–0.92) forming $[Ni_4H_{\sim 4}]^{5-}$ tetramers in which three edges and one face of the Ni tetrahedron is bridged by hydrogen; tetramers are surrounded by monocapped trigonal prisms formed by four Nd and three Mg; lif: $M^{3+}{\cdot}Mg^{2+}{\cdot}[Ni_4H_{\sim 4}]^{5-}$.

Distances (Å): Ni–D $= 1.64$–1.72; Ni–Ni $= 2.44$; Ni–Mg $= 2.83$; Ni–Nd $= 2.90$; Mg–Mg $= 4.92$; Mg–Nd $=$ 3.14; Mg–D $= 2.17$; Nd–Nd $= 4.98$; Nd–D $= 2.34$; D–D $=$ 2.47.

3.47 $LaMg_2NiH_7$

From hydrogenation of ternary metal compound $LaMg_2Ni$ below 473 K under H_2 pressure of up to 8 bar;[123] dark grey colored powder sable in air; ordered structure (Figure 47) from npd on deuteride: $P2_1/c$, $Z = 8$; contains two symmetry independent tet-$[NiH_4]^{4-}$ 18-electron complexes having eight terminal D atoms, and six hydride anions bonded to two Mg and two La only; Ni (site symmetry 1) surrounded by three La (two sites) and six Mg (four sites) in monocapped square antiprismatic configuration;

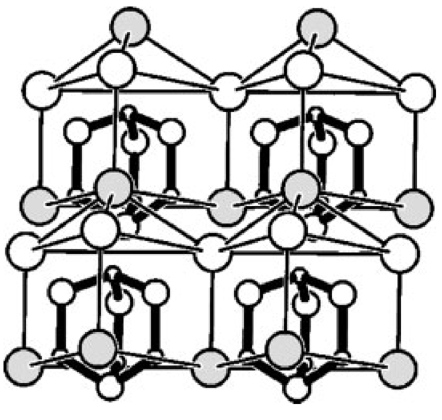

Figure 46 Structure of $NdMgNi_4D_{\sim 4}$

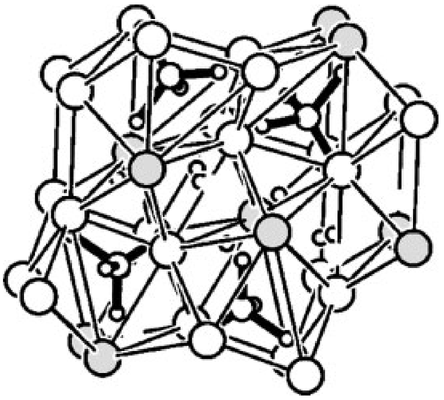

Figure 47 Structure of $LaMg_2NiD_7$

lif: $La^{3+}\cdot 2Mg^{2+}\cdot[NiH_4]^{4-}\cdot 3H^-$; Ni^0, d^{10}; hydride is nonmetallic; provides example for hydrogation induced metal ($LaMg_2Ni$) – to – nonmetal ($LaMg_2NiH_7$) transition.

Distances (Å): Ni1–D = 1.49–1.63, Ni2–D = 1.48–1.63; Ni–Mg = 2.59; Ni–La = 3.36; Ni–Ni = 4.14; Mg–Mg = 3.02; Mg–La = 3.42; La–La = 4.06; Mg–D = 1.94; $Mg–D^-$ = 1.82; La–D = 2.39; $La–D^-$ = 2.33; D–D = 2.12.

4 CRYSTAL CHEMISTRY

4.1 Hydride Complexes

Occurrence. At present, some 50 different homoleptic hydride complexes have been identified in over 127 compounds that cover 47 structure types. Their occurrence across the 3d, 4d, and 5d transition metal series is summarized in Table 19. The complexes form with transition elements from group seven (Mn), eight (Fe), nine (Co) and ten (Ni), to closed d-shell elements of group eleven (Cu) and twelve (Zn). Hydride complexes have not been characterized as yet for elements of group four (Ti), five (V) and six (Cr), and none for Ag, Au, and Hg. Interestingly, most complexes contain T-metals that do not form stable binary hydrides such as iron, cobalt, and congeners, or form relatively unstable hydrides such as nickel and congeners. While the great majority of complexes are centred by one T-metal atom (‘mononuclear’ complexes) and display terminal hydrogen ligands only, some are centred by two (Ru, Pt), four (Rh, Ni) or more (Ru, Rh) and display both terminal and bridging hydrogen ligands, and/or T–T metal–metal bonds (‘polynuclear’ complexes).

Mononuclear Complexes. They show at least 10 different geometries that are represented in Table 20. They range from tricapped trigonal prismatic (e.g. $[ReH_9]^{2-}$), pentagonal bipyramidal (e.g. $[OsH_7]^{3-}$), octahedral (e.g. $[FeH_6]^{4-}$, $[ReH_6]^{3-}$), square pyramidal (e.g. $[CoH_5]^{4-}$), planar (e.g. $[RhH_4]^{3-}$), tetrahedral (e.g. $[NiH_4]^{4-}$), saddle-like (e.g. $[IrH_4]^{5-}$), triangular (e.g. $[PdH_3]^{3-}$), T-shaped (e.g. $[RuH_3]^{6-}$) to linear (e.g. $[PdH_2]^{2-}$). Generally speaking, the ligand geometries resemble those of transition metals in ‘inorganic molecules[124]’and coordination compounds such as metal carbonyls and cyanides, and are consistent with conventional electron counts, that is, they are octahedral (usually 18 electrons and d^6), such as $Mo(CO)_6$; square planar (usually 16 electrons, d^8), such as $Ni(CN)_4{}^{2-}$; square pyramidal (18 electrons, d^8), such as $[Ni(CN)_5]^{3-}$; saddle-like, such as the binuclear nonbridged structure of $Co_2(CO)_8$ (formally 17 electrons, d^9) or the trinuclear structure of $Ru_3(CO)_{12}$ (formally 16 electrons, d^8); tetrahedral (usually 18 electrons, d^{10}), such as $Ni(CO)_4$; or linear (usually 14 electrons, d^{10}), such as the usual ligand geometry of Ag^I (d^{10}) and congeners. Complexes having less than 13 electrons or more than 18 electrons have not yet been reported. The tetrahedral 13-electron $[MnH_4]^{2-}$ complex in K_3MnH_5 (XXX) is remarkable because it displays a half-filled d shell and leads to a pink colored hydride that orders magnetically. Other interesting cases are the T-shaped formally 17-electron $[RuH_3]^{6-}$ complex in Mg_3RuH_3 (XV) and the saddle-like formally 16-electron $[RuH_4]^{4-}$ complex in Mg_2RuH_4 (XVIII), because they provides possible links to polynuclear complexes (see below). Some complex geometries represent only averages such as $[CoH_4]_{av}{}^{5-}$, $[RuH_5]_{av}{}^{5-}$, $[OsH_8]_{av}{}^{2-}$ (not included in Table 20), $[PdH_3]_{av}{}^{3-}$, and $[IrH_3]_{av}{}^{6-}$ (not included in Table 20), because of structural disorder. A five-coordinate trigonal bipyramidal hydrogen configuration similar to the ligand geometry in $Fe(CO)_5$ has not yet been reported. The presumably square antiprismatic configuration in Cs_3OsH_9 (XLIV) has not yet been ascertained.

Some T-metals adopt one type of ligand geometry only, such as Fe that forms exclusively oct-$[FeH_6]^{4-}$ complexes (occurring in three hydride structure types, see Table 19), while others adopt two geometries, such as Co that forms sad-$[CoH_4]^{5-}$ and spy-$[CoH_5]^{4-}$ complexes (either ordered or disordered), or three or more geometries, such as Ru that forms five: ts-$[RuH_3]^{6-}$, sad-$[RuH_4]^{4-}$, spy-$[RuH_5]_{av}{}^{4-}$, oct-$[RuH_6]^{4-}$, and pbp-$[RuH_7]^{3-}$. Each hydride structure usually contains one crystallographic T-metal site. Exceptions are K_2ReH_9 (I), $Mg_6Co_2H_{11}$ (XVII), and $LaMg_2NiH_7$ (XLVII) that contain two, K_3PdH_3 (IX), $Sr_8Rh_5H_{23}$ (XXVI), and $LaMgNi_4H_4$ (XLVI) that contain three, and $Mg_6Ir_2H_{11}$ (XLV) that contains four independent T-metal sites. Among these $Mg_6Co_2H_{11}$ (XVII) and $Mg_6Ir_2H_{11}$ (XLV) are remarkable because the T-metal sites display different complex geometries in the same structure: one sad-$[TH_4]^{5-}$ and three spy-$[TH_5]^{4-}$ of which two are disordered (T = Co, Ir). T-metal complexes having a given geometry usually occurs in different structure types such as oct-$[FeH_6]^{4-}$ in Mg_2FeH_6 (II), $SrMg_2FeH_6$ (XVI) and $Ca_4Mg_4Fe_3H_{22}$ (XX), and tet-$[NiH_4]^{4-}$ in Mg_2NiH_4 (V) $CaMgNiH_4$ (XIX) and $LaMg_2NiH_7$ (XLVII). Complexes centred by different T-metals in the

Table 19 Homonuclear and polynuclear complex anions as found in various hydride structure types

Mn		**Fe**		**Co**		**Ni**		**Cu**		**Zn**	
$[MnH_4]^{2-}$	XXX	$[FeH_6]^{4-}$	II, XVI, XX	$[CoH_4]^{5-}$, $[CoH_4]_{av}{}^{5-}$	XVII	$[NiH_4]^{4-}$	V, XIX, XLVII	$[CuH_4]^{3-}$	XXXV	$[ZnH_4]^{2-}$	XXIX, XXX
$[MnH_6]^{5-}$	XXIII			$[CoH_5]^{4-}$	III	$[Ni_4H_4]^{5-}$	XLVI				
				$[CoH_5]_{av}{}^{4-}$	XVII, XXXII	$[NiH_{3-x}]^{2n-}_{n,av}$	X				
Tc		**Ru**		**Rh**		**Pd**		**Ag**		**Cd**	
$[TcH_9]^{2-}$	I	$[Ru_2H_6]^{12-}$	XV	$[Rh_4H_4]^{8-}$	XIV	$[PdH_2]^{2-}$	VII, IX			$[CdH_4]^{2-}$	XXX
		$[RuH_4]_n{}^{4n-}$	XVIII	$[RhH_4]^{3-}$	XIII	$[PdH_{2+x}]^{2n-}_{n,av}$	X				
		$[RuH_5]_{av}{}^{5-}$	XXV	$[Rh_3H_{12}]_n{}^{8n-}$	XLI	$[PdH_3]^{3-}$	XXXIX				
		$[RuH_6]^{4-}$	II, XI, XXVII, XXXVI, XXXVIII	$[Rh_4H_{17}]_n{}^{13n-}$	XXVI	$[PdH_3]_{av}{}^{3-}$	XXII				
				$[RhH_5]_{av}{}^{4-}$	III	$[PdH_4]^{2-}$	IV, VI, VIII				
				$[RhH_6]^{3-}$	XII, XXVI	$[PdH_4]^{4-}$	XXIX				
		$[RuH_7]^{3-}$	XLIII								
Re		**Os**		**Ir**		**Pt**		**Au**		**Hg**	
$[ReH_6]^{3-}$	XL	$[OsH_6]^{4-}$	II, XI, XXVII, XXXVI, XXXVIII	$[IrH_3]_{av}{}^{6-}$	XXIV	$[PtH_2]^{2-}$	XXXVII				
$[ReH_6]^{5-}$	XXIII			$[IrH_4]^{5-}$	XLV	$[PtH_4]^{2-}$	IV, VI, VIII, XXI				
$[ReH_9]^{2-}$	I, XXVIII, XXXIII			$[IrH_4]_{av}{}^{5-}$	XLV						
		$[OsH_7]^{3-}$	XLIII	$[IrH_5]^{4-}$	XLV	$[Pt_2H_9]^{5-}$	XXXIV				
$[ReH_9]_{av}{}^{2-}$	XLII	$[OsH_8]_{av}{}^{2-}$	XLIV	$[IrH_5]_{av}{}^{4-}$	III	$[PtH_6]^{2-}$	II				
				$[IrH_6]^{3-}$	XII, XXXI						

same structure have not yet been reported. 'Composite' hydride structures made up by covalent bonded hydride complexes and ionic bonded hydrogen occur with $SrMg_2FeH_8$ (XVI), Ba_2PtH_6 (XXI), $LiSr_2PdH_5$ (XXII), Mg_3ReH_7 (XXIII), Mg_3RuH_6 (XXV), $LiMg_2RuH_7$ (XXVII), $LiMg_4Os_2H_{13}$ (XXXVI), $LaMg_2NiH_7$ (XLVII), and can be studied on Figures 16, 21, 22, 23, 25, 27, 36, and 47, respectively. Those belonging to the series $LiH{\cdot}nMg_2TH_4$ ($T = Ru$, Os; $n = 1, 2, \infty$, groups XXVII, XXXVI, and II, respectively) are made up by slabs of $[TH_6]^{4-}$ complexes and sheets of ionic Li^+H^-. Finally, only relatively few 3*d* analogs exist to the more numerous 4d and 5d hydrides, that is, four Mn *versus* eight Re compounds, five Co *versus* twelve Rh and ten Ir compounds, and ten Ni *versus* twenty-one Pd and seventeen Pt compounds. In particular, no iron analog exists for the ruthenium (osmium) series of composite structures, and no nickel analogs exist for any of the palladium and platinum compounds.

Polynuclear Complexes. Dinuclear complexes occur in nonmetallic $Li_5Pt_2H_9$ (XXXIV) and metallic Mg_3RuH_3 (XV). The former displays planar PtH_4 units that are connected *via* Pt–H–Pt bridges to $[Pt_2H_9]^{5-}$ complexes, and the latter display T-shaped RuH_3 units that are possibly connected *via* Ru–Ru bonds to $[Ru_2H_6]^{12-}$ dimers. Tetranuclear complexes occur in metallic $MgRhH_{0.94}$ (XIV) and $NdMgNi_4H_{\sim 4}$ (XLVI). The former displays cyclic tetramers $[Rh_4H_{\sim 4}]^{8-}$ having nearly linear T-H-T bridges, and the latter tetrahedron shaped $[Ni_4H_{\sim 4}]^{5-}$ units in which three edges and one face of the Ni tetrahedron are bridged by hydrogen. Quasi one-dimensional $[Ru_nH_{4n}]^{4n-}$ polymers displaying T–T bonds can be formulated in Mg_2RuH_4 (XVIII), and a two-dimensional disordered $[Rh_4H_{17}]_n{}^{13n-}$ network of corner-sharing RhH_6 octahedra occurs in $Ca_8Rh_5H_{23}$ (XXVI). Three-dimensional ordered networks of corner-sharing TH_6 octahedra occur in brass colored $Ca_8Rh_6H_{24}$ (XLI; $[Rh_3H_{12}]_n{}^{8n-}$ anion), and the perovskite structure of metallic $EuPdH_3$ (X; $[PdH_3]_n{}^{2n-}$ anion). Polynuclear complexes with mixed T-metals such as in metal carbonyls have not been reported as yet.

Complex Formation In Intermetallic ('Interstitial') Hydrides. The historically first example for a hydrogenation induced complex formation is Mg_2NiH_4 (V). The brownish colored hydride derives by hydrogenation of the intermetallic compound Mg_2Ni and was originally classified as an 'interstitial' hydride. It contains an ordered array of $[NiH_4]^{4-}$ complexes, is stoichiometric and nonmetallic, and shows a relatively important but reversible rearrangement of its metal atom substructure. Complex formation also occurs in other metal-rich metal framework structures such as the palladium compounds $CaPdH_2$ (X and analogs) and $LiSr_2PdH_5$ (XXII). The hydrides have CsCl-type metal substructures and can be described in terms of isolated, partially disordered $[PdH_2]_{av}{}^{2-}$ and $[PdH_3]_{av}{}^{3-}$ groups, respectively, but the data are also compatible with 3-dimensional networks of Pd–H–Pd bridges as in 'interstitial' hydrides.[23] More palladium rich hydrides based on close-packed metal atom arrangements are $NaPd_3H_2$[125] and $LiPdH_{0.7}$[126] (not included in this review). While the former shows an ordered array of well-defined linear H–Pd–H

Table 20 Homonuclear transition metal hydride complexes[a] and formal electron configurations

	CN Geometry	Complex	Structure types	T	# e-
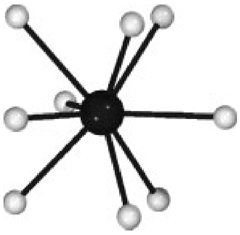	9 Tricapped trigonal prismatic	$[ReH_9]^{2-}$	I, XXVIII, XXXIII, XLII	d^0	18
		$[TcH_9]^{2-}$	I	d^0	18
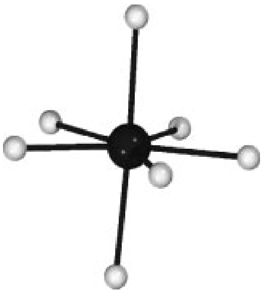	7 pentagonal bipyramidal	$[OsH_7]^{3-}$	XLIII	d^6	18
		$[RuH_7]^{3-}$	XLIII	d^6	18
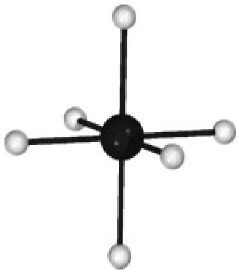	6 octahedral	$[MnH_6]^{5-}$	XXIII	d^6	18
		$[ReH_6]^{5-}$	XXIII	d^6	18
		$[ReH_6]^{3-}$	XL	d^4	16
		$[FeH_6]^{4-}$	II, XX, XVI	d^6	18
		$[RuH_6]^{4-}$	II, XI, XXVII, XXXVI XXXVIII	d^6	18
		$[OsH_6]^{4-}$	II, XI, XXVII, XXXVI XXXVIII	d^6	18
		$[RhH_6]^{3-}$	XII, XXVI	d^6	18
		$[IrH_6]^{3-}$	XII, XXXI	d^6	18
		$[PtH_6]^{2-}$	II	d^6	18
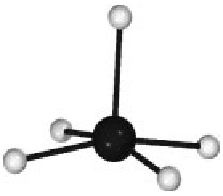	5 square pyramidal	$[RuH_5]_{av}{}^{5-}$	XXV	d^8 av	18
		$[CoH_5]^{4-}$	III	d^8	18
		$[CoH_5]_{av}{}^{4-}$	XVII, XXXII	d^8 av	18
		$[IrH_5]^{4-}$	XLV	d^8	18
		$[IrH_5]_{av}{}^{4-}$	III, XLV	d^8 av	18
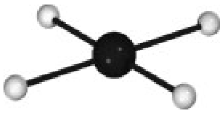	4 square planar	$[RhH_4]^{3-}$	XIII	d^8	16
		$[PdH_4]^{2-}$	IV, VII, VIII	d^8	16
		$[PtH_4]^{2-}$	VII, VIII, XXI	d^8	16
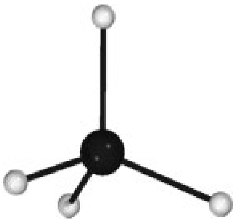	4 tetrahedral	$[MnH_4]^{2-}$	XXX	d^5	13
		$[NiH_4]^{4-}$	V, XIX, XLVI	d^{10}	18
		$[PdH_4]^{4-}$	XXIX	d^{10}	18
		$[CuH_4]^{3-}$	XXXV	d^{10}	18
		$[ZnH_4]^{2-}$	XXIX, XXX	d^{10}	18
		$[CdH_4]^{2-}$	XXX	d^{10}	18
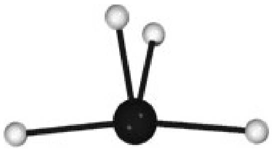	4 saddle-like	$[CoH_4]^{5-}$	XVII	d^{10}	18
		$[RuH_4]^{4-}$	XVIII	d^8	16
		$[IrH_4]^{5-}$	XLV	d^{10}	18

(cont'd overleaf)

Table 20 cont'd

	CN Geometry	Complex	Structure types	T	# e-
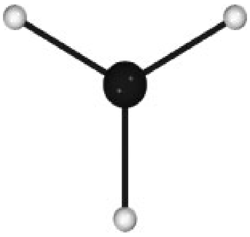	3 triangular	$[PdH_3]^{3-}$	XXXIX	d^{10}	16
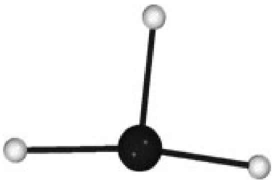	3 T-shaped	$[RuH_3]^{6-}$ $[PdH_3]_{av}{}^{3-}$	XV XXII	Dimer d^{10} av	17 16
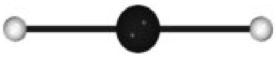	2 linear	$[PdH_2]^{2-}$ $[PdH_2]_{av}{}^{2-}$ $[PtH_2]^{2-}$	VI, IX X XXXVII	d^{10} d^{10} av d^{10}	14 14 14

[a] In decreasing coordination number, CN; only structurally characterized, essentially ordered monomers having terminal H ligands are included; av: average due to disorder.

groups, the latter is disordered and shows only a weak tendency for complex formation. As to the above mentioned metallic hydrides MgRhH$_{\sim 0.9}$ (XIV) and NdMgNi$_4$H$_{\sim 4}$ (XLVI), their hydrogen distributions can be described as 'interstitial', but the stereochemical activity of the tetramers $[Rh_4H_4]^{8-}$ and $[Ni_4H_4]^{5-}$, respectively, is evident. These findings suggest that hydride complex formation could be a general phenomenon in interstitial hydrides, at least on a local level. Some striking examples for hydrogenation induced complex formations and metal-insulator transitions have been recently reported in the systems Mg$_3$Ir–H$_2$**[121]** and LaMg$_2$Ni–H$_2$.**[123]** The former contains the intensely red colored hydride Mg$_6$Ir$_2$H$_{11}$ (XLV) the structure of which can be rationalized in terms of pyr-$[IrH_5]^{4-}$ and sad-$[IrH_4]^{5-}$ 18-electron complexes and hydride anions H$^-$, in agreement with the limiting ionic formula $4Mg_6Ir_2H_{11} = 5MgH_2 \cdot 19Mg^{2+} \cdot 2[IrH_5]^{4-} \cdot 6[IrH_4]^{5-}$. The latter contains the grey colored hydride LaMg$_2$NiH$_7$ (XLVII) that is nonmetallic. Its structure contains tetrahedral $[NiH_4]^{4-}$ complexes and hydride anions H$^-$ corresponding to the limiting ionic formula $LaH_3 \cdot 2Mg^{+2} \cdot [NiH_4]^4$. Thus both compounds can be considered as 'complex' hydrides for which the 'interstitial' concept fails.

Order–Disorder Transitions. The mobility of the hydrogen ligands (or of the entire complexes) at room temperature is generally high. Well-characterized order–disorder transitions within the complexes near room temperature occur in Mg$_2$CoH$_5$ (III), Mg$_2$NiH$_4$ (V), K$_3$PdH$_3$ (IX), Na$_2$PtH$_4$ (IV), M$_3$PtH$_5$ (M = Rb, Cs; VIII), and M$_2$PtH$_4$ (M = K, Rb, Cs; VI). Complexes that are partially disordered at room temperature and do not readily order at low temperature occur in CaPdH$_2$ (X), LiSr$_2$PdH$_5$ (XXII), Mg$_4$IrD$_5$ (XXIV), Mg$_3$RuH$_6$ (XXV), M$_2$TH$_5$ (T = Rh, Ir; M = Mg, Ca, Sr, Eu; III) and Mg$_6$T$_2$H$_{11}$ (T = Co; XVII, and Ir; XLV). In some structures, the hydride complexes undergo rigid motions, such as in K$_2$PtH$_4$ for which LT-NMR data suggest rotational jumps of the spl-PtH$_4$ units in the plane of the square.**[8]**

4.2 Cation Configurations

The cations M (alkali, alkaline earth, lanthanide) surrounding the complexes have various configurations, of which the eightfold cubic (or approximately cubic) is by far the most common. Depending on the metal ratios M/T the cubes are joined via corners, edges, or faces. Edge sharing occurs in Sr$_2$RuH$_6$ (II), Sr$_2$IrH$_5$ (III), Na$_2$PtH$_4$ (IV), Mg$_2$NiH$_4$ (V), K$_2$PtH$_4$ (VI), and K$_3$ReH$_6$ (XL) that adopt one arrangement, and Ca$_4$Mg$_4$Fe$_3$H$_{22}$ (XX) and Ca$_4$Mg$_4$Co$_3$H$_{19}$ (XXXII) that adopt another. Corner sharing occurs in Li$_4$RuH$_6$ (XI). Corner and edge sharing occurs in Mg$_3$ReH$_7$ (XXIII), Mg$_6$Co$_2$H$_{11}$ (XVII), Mg$_3$RuH$_6$ (XXV), LiMg$_2$RuH$_7$ (XXVII), and Mg$_6$Ir$_2$H$_{11}$ (XLV) that adopt one arrangement, and Sr$_2$MgFeH$_8$ (XVI), LiMg$_4$Os$_2$H$_{13}$ (XXXVI), and LiMg$_4$Os$_2$H$_{13}$ (XXXVI) that adopt another. Sheets of face-sharing cubes occur in Mg$_2$RuH$_4$ (XVIII) and Ba$_3$Ir$_2$H$_{12}$ (XXXI) for which the sheets are connected via edges, and in LiSr$_2$PdH$_5$ (XXII) for which the sheets are connected via additional M atoms, and in Na$_2$PdH$_2$ (VII), Ba$_2$PtH$_6$ (XXI), and Li$_2$PtH$_2$ (XXXVII) that have other arrangements. Three-dimensional arrays of face-sharing cubes occur in CaPdH$_2$ (X) and MgRhH$_{1-x}$ (XIV) where all faces are shared, in Sr$_8$Rh$_5$H$_{23}$ (XXVI) where edges, edges and faces, or faces are shared, and in Ca$_8$Rh$_6$H$_{24}$ (XLI) where edges and faces are shared. Face-sharing configurations are of particular interest because they favor interactions between neighboring hydride complexes.

The distortion of the M cube depends mainly on the symmetry and dynamics of the hydrido complex. This can be seen in Mg_2CoH_5 (III) and Mg_2NiH_4 (V), whose T-metal centered Mg cubes are regular in the disordered cubic HT structure (such as in Mg_2FeH_6; II), and strongly distorted in the tetragonal (Mg_2CoH_5) and monoclinic (Mg_2NiH_4) LT structures owing to ordering of the spy-CoH_5 and tet-NiH_4 units, respectively. Another example is Mg_2RuH_4 (XVIII) whose Mg cubes surrounding the sad-RuH_4 units are strongly distorted compared to the regular Mg cubes surrounding the oct-RuH_6 units in Mg_2RuH_6 (II). The influence of the complex geometry on the metal atom array is also apparent in $Mg_6Co_2H_{11}$ (XVII), $Mg_6Ir_2H_{11}$ (XLV), and Mg_3RuH_6 (XXV). They contain various nonoctahedral TH_4 and TH_5 units, and their metal substructure derives from that of trigonal Mg_3ReH_7 (XXIII) containing octahedral ReH_6 units by an orthorhombic (or monoclinic) distortion. Finally, the atomic size difference between alkaline earths also plays a role, as can be seen from the severe distortions of the partially substituted M cubes in the quaternary hydrides $Ca_4Mg_4Fe_3H_{22}$ (XX) and $CaMgNiH_4$ (XIX) that derive from Mg_2FeH_6 (II) and Mg_2NiH_4 (V), respectively.

4.3 Bond Distances

Metal–Hydrogen Bonds. The T–H bond distances of the complexes can be rationalized in terms of covalent radii and a fixed hydrogen radius of 0.28 Å. The distances range from 1.50–1.60 Å for 3d metals, to 1.70–1.80 Å for 4d and 5d metals, except for Pd (1.60–1.70 Å) and Pt (1.58–1.67 Å), the T–H bonds of which are shortened owing to low-coordination numbers. Apparent bond shortening may also occur as a result of partial hydrogen site occupancy in disordered HT structures. On the other hand, the relatively long Pd–D distances in disordered $CaPdD_2$ (X) (Pd–D = 1.84 Å) and $LiSr_2PdD_5$ (XXII) (Pd–D = 1.95 Å) are only averages, and are presumably shortened locally owing to the formation of linear PdD_2 groups. Owing to matrix effects,[127] the T–D bond lengths generally increase with the size of the M cations.

The M–H distances are consistent with tabulated ionic radii. Those involving hydride anions H^- surrounded by cations M only (occurring in some 25 compounds from 19 different structure types) are generally shorter than those involving hydrogen ligands of the complex. Exceptions are found in K_3PdH_3 (IX), K_3ZnH_5 and K_3MnH_5 (XXX), $Ba_7Cu_3H_{17}$ (XXXV), Rb_3ReH_{10} (XLII), and Cs_3OsH_9 (XLIV). Unlike the complex hydrogen ligands, the hydride anions are neither mobile nor disordered. Their metal configurations range from octahedral in $LiSr_2PdH_5$ (XXII), K_3PdD_3 (IX), K_3ZnH_5 (XXX), Rb_3ReH_{10} (XLII), Cs_3OsH_9 (XLIV), and $LaMg_2NiH_7$ (XLVII), to trigonal bipyramidal in $LiMg_2RuH_7$ (XXVII) and $LiMg_4Os_2H_{13}$ (XXXVI), tetrahedral in $SrMg_2FeH_8$ (XVI), $Ca_4Mg_4Fe_3H_{22}$ (XX), $Ca_4Mg_4Co_3H_{19}$ (XXXII), $Ba_7Cu_3H_{17}$ (XXXV), and $BaMg_2RuH_8$ (XXXVIII), triangular in $Mg_6Co_2H_{11}$ (XVII) and $LaMg_2NiH_7$ (XLVII), and linear in Mg_3ReH_7 (XXIII) and Mg_3RuH_6 (XXV). As expected, low-coordinate M–H bonds are significantly shorter, for example, Mg-H = 1.74 Å in $Mg_6Ir_2H_{11}$ (XLV) and K–H = 2.73 Å in K_3PdH_5 (VIII) compared to higher coordinate M–H bonds such as in binary MgH_2 (1.95 Å), BaH_2 (2.57 Å) and KH (2.85 Å). As in saline ternary hydrides, the Yb–D distances are close to Ca–D distances and the Eu–D distances close to Sr–D distances.[128]

Metal–Metal Bonds. The T- and M-metals are likely to interact in complex hydride structures because of their proximity. The shortest M–T distances are in the range 2.5–3.5 Å and give rise to metallic properties in metal-rich compounds, such as $MgRhD_{1-x}$ (XIV) (Mg–Rh = 2.66 Å) and Na_2PdH_2 (VII) (Na–Pd = 3.13 Å). The shortest M–M distances are in the range 2.5–4.5 Å and come close to the sum of covalent radii, such as Mg–Mg = 2.75 Å in Mg_4IrH_5 (XXIV), 2.78 Å in $Mg_6Co_2H_{11}$ (XVII) or 2.79 Å in $Mg_6Ir_2H_{11}$ (XLV). Clearly, these M–T and M–M interactions are not taken into account by a limiting ionic bond description and require more sophisticated electron counting schemes (see 4.4). Interactions between T-atoms are less common, because the T–T distances usually exceed 3.5 Å. However, T–T interactions do occur in metallic Li_2PdH_2 (VII) (Pd–Pd = 3.11 Å) and Na_2PdH_2 (VII) (Pd–Pd = 3.60 Å), and possibly also in Mg_2RuH_4 (XVIII) (Ru–Ru = 3.24 Å) and Mg_3RuH_3 (XV) (Ru–Ru = 3.31 Å) as suggested by their stereochemistry and the existence of carbonyls displaying such interactions across similar long distances.

Hydrogen–Hydrogen Contacts. The H–H contacts in ordered hydride structures usually exceed 2.1 Å, and thus indicate nonbonding (or repulsive) H–H interactions. In disordered structures, H sites closer than 2.1 Å are always half (or less) occupied. The shortest H–H contact occurs in K_2ReD_9 (I) for which the most recently reported value is D–D = 1.90 Å.[24] Thus, there is no evidence for hydrogen pairing in homoleptic solid-state T-metal hydrides, unlike in molecular T-metal hydride complexes for which dihydrogen groups with H–H distances as short as 0.82 Å do occur.[10,129]

4.4 Bonding

The compositions and ligand geometries of most mononuclear T-metal hydride complexes can be rationalized in terms of conventional electron counts based on full charge transfer from the surrounding cation matrix M, and s-p-d hybridization schemes that involve two-center-two-electron (2c–2e) bonds, such as $(d^0)d^5sp^3$ for 18-electron ttp-$[ReH_9]^{2-}$, $(d^6)d^2sp^3$ for octahedral 18-electron $[FeH_6]^{4-}$, $[MnH_6]^{5-}$, and $[ReH_6]^{5-}$, $(d^8)dsp^3$ for square-pyramidal 18-electron $[CoH_5]^{4-}$, $(d^{10})sp^3$ for 18-electron tetrahedral $[NiH_4]^{4-}$ and $[PdH_4]^{4-}$, $(d^8)dsp^2$ for planar 16-electron $[PdH_4]^{2-}$ and $[RhH_4]^{3-}$, $(d^{10})sp^2$ for triangular 16-electron $[PdH_3]^{3-}$, and $(d^{10})sp$ for linear 14-electron $[PdH_2]^{2-}$. However, for some hydrides, in particular those containing early T-metals and/or showing metal–metal interactions, more elaborate electron counting schemes evoking s-d hybridization only, three-center-four-electron (3c–4e) bonds, and partial charge transfer from the cation matrix M are also possible, as was shown by Firman and Landis.**[13]** Mg_2CoH_5 (III), for example, can be formulated in terms of univalent Mg^+ and sd^2 hybridized 16-electron $[CoH_3\ 2H^-]$ complexes having two 3c–4e bonds. The merits and limitations of this bonding model have been discussed by King.**[16]** For polynuclear hydride complexes, the bonding situation is more difficult to describe. Some can be rationalized by mixtures between two-center-two-electron and three-center-two-electron (3c–2e) bonds, such as dinuclear $[H_4Pt\text{–}H\text{–}PtH_4]^{5-}$ in $Li_5Pt_2H_9$ (XXXIV) for which eight 2c–2e bonds (terminal H's) and one 3c–2e bond (bridging H) can be formulated, while for others such as tetranuclear $[Ni_4H_{\sim 4}]^{5-}$ in $LaMgNi_4H_{\sim 4}$ (XLVI) a similar bond description is less apparent.

As expected from its small atomic size and high-field ligand character, hydrogen favors 18-electron complexes (about 40 representatives with groups 7, 8, 9, and 10 elements). Complexes with 16 electrons (some 11 representatives with Re, Ru, Rh, Pd, and Pt), or 14 electrons (4 representatives with Pd and Pt) are less numerous. The only octahedral 16 electron $(d^4)d^2sp^3$ bonded complex is $[ReH_6]^{3-}$ in K_3ReH_6 (XL), and the only tetrahedral 13-electron $(d^5)sp^3$ bonded complex is $[MnH_4]^{2-}$ in K_3MnH_5 (XXX) that displays a half-filled d shell. On the other hand, the relative softness of hydrogen as a ligand and its stability as an anion favors structural diversity. This is illustrated by 'composite' hydrides such as quaternary $Ca_4Mg_4Fe_3H_{22}$ (XX) that derives from ternary Mg_2FeH_6 (II) by partial substitution of a fourfold negative $[FeH_6]^{4-}$ by four H^-, and Mg_3ReH_7 (XXIII), $Mg_6Co_2H_{11}$ (XVII), and Mg_3RuH_6 (XXV) that have a common metal substructure and are capable of accommodating various complex geometries and H^- ions.

The formal oxidation numbers of the T-metal in most hydride structures range between –I (Co, Rh), zero (Ru, Ni, Pd), I (Mn, Re, Co, Ir, Rh, Cu), II (Fe, Ru, Os, Pd, Pt, Zn), III (Ir, Rh), IV (Ru, Os, Pt), VI (Os) and VII (Re). They are consistent with configurational differences as found, for example, in palladates that change from tetrahedral as in $[Pd^0H_4]^{4-}$ to planar as in $[Pd^{II}H_4]^{2-}$. As expected, high formal oxidation numbers occur mainly with heavier T elements such as Re^{VII} in $[ReH_9]^{2-}$, Os^{VI} in $[OsH_8]^{2-}$, and Pt^{IV} in $[PtH_6]^{2-}$, for which no 3d analogs exist. As the H/M ratios decrease, the systems tend to become metallic and electron counting becomes less obvious. Illustrative examples are Mg_3RuH_3 (XV) and Mg_4IrH_5 (XXIV) for which the neglect of Mg–Mg bonding leads to unreasonable electron configurations and formal oxidation numbers (–III for Ru and Ir). Clearly, limiting ionic formulas for such hydrides are misleading, at least from a bonding point of view, but they are still useful for rationalizing hydrogen contents, which is generally not possible with 'interstitial' (metallic) metal hydrides.

Finally, an important bonding feature of complex metal hydrides are the interactions between the complex hydrogen ligands and the surrounding cation matrix. As can be seen from the isoelectronic series $Mg_2FeH_6 - Mg_2CoH_5 - Mg_2NiH_4$, the cations adopt cubic – or nearly cubic – configurations that maximize the Mg–H interactions. Clearly such M–H interactions not only help stabilizing the complexes but also contribute to the thermal stability of the overall structure, as shown by the desorption enthalpies of substitution pairs such as $Mg_2NiH_4\text{–}CaMgNiH_4$ and $Mg_2FeH_6\text{–}Ca_4Mg_4Fe_3H_{22}$ (see Section 5). On the other hand, T–H interactions do not much contribute to thermal stability as suggested by the relatively weak force constants as measured in metal hydrides such as Mg_2FeH_6 (Fe–H stretching mode $\sim$1.9 mdyne $Å^{-1}$; Fe–H = 1.56 Å),**[38]** and the significant elongation of the T–H bonds in the thermally more stable analog Ca_2FeH_6 (Fe–H = 1.62 Å). Theoretical band structure calculations are available for some of these systems, for example, Mg_3MnH_7 (XXIII),**[90]** Na_2PdH_4 (IV), Na_2PdH_2 (VII), Li_2PdH_2 (VII), $NaBaPdH_3$ (XXXIX), and Ba_2PdH_4 (XXIX),**[14]** Mg_2NiH_4 (V), Mg_2CoH_5 (III), Mg_2TH_6 (II; T = Fe, Ru, Os), M_2FeH_6 (II; M = Mg, Ca, Sr),**[37]** $APdH_3$ (X; A = Sr, Eu, Yb),**[71]** $BaReH_9$ (XXVIII),**[98]** and Eu_2PdH_4 (XXIX),**[103]** but have not yet addressed the issue of thermal stability.

5 PROPERTIES

In contrast to their 'interstitial' counterparts, complex metal hydrides have no apparent homogeneity range and are usually nonmetallic. Many are colored (greenish: Mg_2FeH_6, Na_4RuH_6, $SrMg_2FeH_8$, $LiSr_2PdH_5$; reddish: Eu_2RuH_6, Mg_2RuH_4; red-violet: Na_2PtH_4; yellow: K_3PdH_3; yellow-green: K_2PdH_4; brownish: Mg_2RuH_6, Mg_2NiH_4, Mg_3RuH_6, $Ca_4Mg_4Fe_3H_{22}$, $BaMg_2FeH_8$), while some are colorless (K_2PtH_4, K_3PtH_5, Na_3RhH_6), or appear as white (Mg_2OsH_6, Li_4RuH_6) or gray powders (Ca_2RuH_6, Mg_3RuH_3, Mg_3ReH_7). Only few are black (Yb_2RuH_6, $Mg_6Co_2H_{11}$, Mg_2CoH_5, $YbMgNiH_4$, $Yb_4Mg_4Fe_3H_{22}$) or have metallic luster (Li_3RhH_4, Na_2PdH_2). Relatively well-characterized complex hydrides having metallic properties are Li_2PdH_2 and Na_2PdH_2 that are considered to be two-dimensional metals.

Among complex hydrides that derive from intermetallic compounds, some show hydrogenation induced metal to nonmetal transitions such as brownish-red Mg_2NiH_4 (Mg_2Ni), red $Mg_6Ir_2H_{11}$ (Mg_3Ir), and dark grey $LaMg_2NiH_7$ ($LaMg_2Ni$). Such transitions are of both fundamental and technological interest as shown for binary systems like Y–H_2 (switchable mirrors) and ternary systems like Mg_2Ni–H_2 (tuneable optic windows).[130]

Many hydrides are diamagnetic, as expected for closed-electron shells associated with low-spin d^6 (oct), d^8 (spl), and d^{10} (tet, lin) configurations. Others show weak temperature independent paramagnetism such as the d^4 systems K_3ReH_6 (XL) and Na_3OsH_7 (XLIII). Finally, systems containing magnetic ions tend to order magnetically at low temperature, such as rose colored K_3MnH_5 (Mn(II), $\mu_{eff} = 4.5\mu_B$, $T_N = 28\,K$) and faint violet colored Eu_2PdH_4 (Eu(II), $\mu_{eff} = 8\mu_B$, $T_C = 15\,K$).

Vibrational spectra as measured by INS on hydrides such as M_2TH_6 (II, M = Mg, Ca, Sr, Ba; T = Fe, Ru, Os),[28,38] Mg_2NiH_4 (V) and Rb_3ZnH_5 (XXX)[54] indicate T–H stretching and bending modes in the expected ranges of $1600–2000\,cm^{-1}$ and $800–1000\,cm^{-1}$, respectively. These modes correlate with bonding properties, such as the T–H stretching frequencies in the K_2PtCl_6 type series (II) that increase in the sequence T = Fe, Ru, Os, and decrease as the M–H bond lengths increase. Their theoretical band gaps show the opposite trend, that is, they increase in the sequence Mg_2TH_6 (T = Fe, Ru, Os) owing to the increasing atomic number of T, and that decrease in the sequence M_2FeH_6 (M = Mg, Ca, Sr) owing to the increased participation of M d orbitals.

Properties of relevance for hydrogen storage applications, such as desorption enthalpies and weight and volume efficiencies, are summarized in Table 21.

Clearly, some compounds have outstanding properties, such as Mg_2FeH_6, which shows the highest known volume efficiency for hydrogen storage of all materials known ($120\,g\ H_2\ L^{-1}$, that is, more than twice that of liquid hydrogen), and $BaReH_9$, which has an H/M ratio that surpasses the hydrogen-to-carbon ratio of methane (H/C = 4). The weight efficiencies are also remarkable as shown by Mg_2FeH_6 and Mg_3MnH_7, which can store up to 5 wt% hydrogen, that is, more than currently used interstitial hydrides such as $AB_5H_{\sim 6}$ (A = La, etc., B = Ni, etc.) and $AB_2H_{\sim 4}$ (A = Ti, etc., B = Mn, etc.), which store only up to ∼2 wt% hydrogen. Unfortunately, regarding thermal stability complex metal hydrides perform less well than their interstitial counterparts. Only few hydrides decompose near room temperature such as $BaReH_9$ and $Ba_7Cu_3H_{17}$ that are, however, relatively heavy and expensive and not completely reversible. Mg_2NiH_4, which is the only commercialized hydride of this class, decomposes only above 523 K, corresponding to a desorption enthalpy of $\Delta H = 64\,kJ\,mol^{-1}$ H_2. Most other complex metal hydrides are more stable (decomposition temperatures >573 K, $\Delta H > 80\,kJ/H_2$) and must be heated to yield hydrogen at useful pressures, which represents a penalty in energy. On the other hand, compounds such as Mg_2FeH_6 are of interest for high-temperature applications[39] because of their high thermal stability and ease of cycling.

Owing to the scarcity of thermodynamic data, empirical models such as that used to rationalize thermal stabilities of interstitial metal hydrides[131] do not exist for complex metal hydrides. Metal–hydrogen interactions obviously play a role, as can be seen from the substitution pairs Mg_2NiH_4–$CaMgNiH_4$ and Mg_2FeH_6–$Ca_4Mg_4Fe_3H_{22}$, whose stabilities increase strongly as one goes from the ternary Mg compounds to the quaternary Ca compounds (see Table 21). This trend correlates with the relatively strong interactions between hydrogen and calcium that forms a very stable binary hydride, compared to the relatively weak interactions of hydrogen with magnesium that forms a less stable binary hydride. This suggests that interactions between hydrogen and metal cations govern to a large extent the thermal stability of complex metal hydrides.

Table 21 Desorption enthalpies and hydrogen storage efficiencies

	ΔH $kJ\,mol^{-1}\,H_2$	Weight efficiency wt%	Volume efficiency gH_2L^{-1}
Complex hydrides			
Mg_2NiH_4	64	3.6	18
Mg_2CoH_5	86	4.5	126
Mg_2FeH_6	98	5.5	150
$CaMgNiH_4$	129	3.2	87
$Ca_4Mg_4Fe_3H_{22}$	122	5.0	121
Binary hydrides			
MgH_2	74	7.7	109
CaH_2	184[a]	4.8	92
Metallic hydride			
$LaNi_5H_6$	31	1.4	93

[a] Model prediction.[131]

6 CONCLUSIONS

Solid-state transition metal hydride complexes occur mainly with the late transition elements. The complexes are usually mononuclear (centred by one T-metal atom only) and contain between two and nine terminal hydrogen ligands, while some are polynuclear (centred by more than one T-metal atom) and display bridging hydrogen ligands. The ligands tend to be disordered at higher temperatures and ordered at lower temperatures. The structural and electronic configurations of the hydrido complexes are consistent with those usually found in coordination compounds. They are stabilized by charge transfer from the surrounding cation matrix, are often 18-electron, and less often 16- or 14-electron. Some hydride structures show evidence for metal–metal interactions, as in typically interstitial metal hydrides, while others contain additional hydride anions (H^-) bonded to electropositive metals only, such as in saline hydrides. In metal-rich systems, hydrogen has interstitial character, as in typically metallic transition metal hydrides. No H–H bond formation is observed. Most complex hydride systems are nonmetallic and many are colored. Some systems, however, show hydrogenation induced complex formation and metal-to-insulator transitions. They generally display very high volume efficiencies for hydrogen storage but are thermally too stable and/or too expensive for practical applications. Thermodynamic data suggest that their enthalpy of formation scales with the thermal stability of the binary hydrides of the electropositive metal constituents.

7 RELATED ARTICLES

Hydride Complexes of the Transition Metals.

8 REFERENCES

1. K. Yvon, Hydrides: Solid State Transition Metal Complexes, in 'Encyclopedia Inorganic Chemistry', ed. R. B. King, John Wiley, New York 1994, Vol. 3, p. 1401.
2. S. C. Abrahams, A. P. Ginsberg, and K. Knox, *Inorg. Chem.*, 1964, **3**, 558; see also K. Knox and A. P. Ginsberg, *Inorg. Chem.*, 1964, **3**, 555; for K_2TcH_9 see also A. P. Ginsberg, *Inorg. Chem.*, 1964, **3**, 567.
3. R. O. Moyer Jr, C. Stanitski, fnmJ. Tanaka, M. I. Kay, and R. Kleinberg, *J. Solid State Chem.*, 1971, **3**, 541; for a review of work by these authors see R. O. Moyer Jr, R. Linsay, and D. N. Marks, *Adv. Chem. Ser.*, 1978, **167**, 366.
4. L. Schlapbach, *Top. Appl. Phys.*, 1988, **63**, 1; 1992, **67**, 1; see also *MRS Bull.*, 2002, **27/9**, 675.
5. J. J. Reilly and R. H. Wiswall, *Inorg. Chem.*, 1968, **7**, 2254.
6. P. Zolliker, K. Yvon, J. D. Jorgensen, and F. J. Rotella, *Inorg. Chem.*, 1986, **25**, 3590; see also K. Yvon, J. Schefer, and F. Stucki, *Inorg. Chem.*, 1981, **20**, 2776.
7. W. Bronger, *Angew. Chem., Int. Ed. Engl.*, 1991, **30**, 759.
8. W. Bronger, *J. Alloys Comp.*, 1995, **229**, 1.
9. W. Bronger and G. Auffermann, *Chem. Mater.*, 1998, **10**, 2723.
10. R. Bau and M. H. Drabnis, *Inorg. Chim. Acta*, 1997, **259**, 27.
11. K. Yvon, *Z. Kristallogr.*, 2003, **218**, 108.
12. G. J. Miller, H. Deng, and R. Hoffmann, *Inorg. Chem.*, 1994, **33**, 1330.
13. T. K. Firman and C. R. Landis, *J. Am. Chem. Soc.*, 1998, **120**, 12650.
14. M. Olofsson-Martensson, U. Häussermann, J. Tomkinson, and D. Noréus, *J. Am. Chem. Soc.*, 2000, **122**, 6960.
15. K. Yvon, *Chimia*, 1998, **52**, 613.
16. R. B. King, *Coord. Chem. Rev.*, 2000, **200–202**, 813.
17. K. Yvon, *Swiss Neutron News*, 2002, **22**, 11.
18. K. Yvon, 'Encyclopedia of Materials: Science and Technology Updates', ed. K. H. J. Buschow, Elsevier Ltd., 2004, pp. 1–9.
19. W. Grochala and P. P. Edwards, *Chem. Rev.*, 2004, **104**, 1283.
20. G. Sandrock, and G. Thomas, 1997, Hydrogen Information Center, http://hydpark.ca.sandia.gov/, IEA/DOE/SNL Hydride Databases.
21. R. Bau, D. M. Ho, and S. G. Gibbins, *J. Am. Chem. Soc.*, 1981, **103**, 4960; see also D. E. Linn Jr, G. M. Skidd, and E. M. Tippmann, *Inorg. Chim. Acta*, 1999, **291**, 142.
22. R. G. Teller and R. Bau, *Struct. Bonding (Berlin)*, 1981, **44**, 1; see also R. Bau, M. Y. Chiang, D. M. Ho, S. G. Gibbins, T. J. Emge, and T. F. Koetzle, *Inorg. Chem.*, 1984, **23**, 2823.
23. K. Yvon and P. Fischer, *Top. Appl. Phys.*, 1988, **63**, 87 (Springer).
24. W. Bronger, L. à Brassard, P. Müller, B. Lebech, and Th. Schultz, *Z. Anorg. Allg. Chem.*, 1999, **625**, 1143.
25. R. Lindsay, R. O. Moyer, J. S. Thompson, and D. Kuhn, *Inorg. Chem.*, 1976, **15**, 3050; see also R. Lindsay and R. O. Moyer Jr, *Inorg. Chem.*, 1981, **80**, P37; see also R. O. Moyer Jr, R. Lindsay, and D. F. Storey, *Z. Phys. Chem. Neue Folge*, 1989, **165**, 83; see also R. Lindsay, R. O. Moyer, W. Strange, W. H. Klapp, D. F. Storey, and J. R. Knapp, *Z. Phys. Chem. Neue Folge*, 1993, **179**, 457; for Eu_2IrH_5 see R. O. Moyer Jr and R. Lindsay, *J. Less-Common Met.*, 1980, **70**, P57.
26. J.-J. Didisheim, P. Zolliker, K. Yvon, P. Fischer, J. Schefer, M. Gubelmann, and A. F. Williams, *Inorg. Chem.*, 1984, **23**, 1953.
27. M. Kritikos, D. Noréus, B. Bogdanovic, and U. Wilczok, *J. Less-Common Met.*, 1990, **161**, 337.
28. M. Kritikos and D. Noréus, *J. Solid State Chem.*, 1991, **93**, 256.
29. B. Huang, F. Bonhomme, P. Selvam, K. Yvon, and P. Fischer, *J. Less-Common Met.*, 1991, **171**, 301.
30. P. Selvam and K. Yvon, *Int. J. Hydrogen Energy*, 1991, **16**, 615.
31. J. Huot, H. Hayakawa, and E. Akiba, *J. Alloys Comp.*, 1997, **248**, 164; see also J. Huot, S. Boily, E. Akiba, and R. Schulz, *J. Alloys Comp.*, 1998, **280**, 306.

32. A. Hightower, B. Fultz, and R. C. Bowman Jr, *J. Alloys Comp.*, 1997, **252**, 238; see also S. S. Sai Raman, D. J. Davidson, J.-L. Bobet, and O. N. Srivastava, *J. Alloys Comp.*, 2002, **333**, 282; see also F. C. Gennari, F. J. Castro, and J. J. A. Gamboa, *J. Alloys Comp.*, 2002, **339**, 261.
33. W. Bronger and G. Auffermann, *Angew. Chem., Int. Ed. Engl.*, 1994, **33**, 1112.
34. W. Bronger and G. Auffermann, *J. Alloys Comp.*, 1995, **219**, 45.
35. W. Bronger and G. Auffermann, *Z. Anorg. Allg. Chem.*, 1995, **621**, 1318.
36. J. S. Thompson, R. O. Moyer, and R. Lindsay, *Inorg. Chem.*, 1975, **14**, 1866; see also R. Lindsay, R. O. Moyer Jr, W. Strange, and B. J. Burnim, *J. Alloys Comp.*, 1996, **243**, 90; for Yb_2RuH_6 see R. Lindsay, R. O. Moyer Jr, J. S. Thompson, and D. Kuhn, *Inorg. Chem.*, 1976, **15**, 3050.
37. E. Orgaz and M. Gupta, *Z. Phys. Chem.*, 1993, **181**, 1; see also M. Gupta and L. Schlapbach, *Top. Appl. Phys.*, 1988, **63**, 139; see also M. Gupta, *J. less-Common Met.*, 1984, **103**, 325.
38. S. F. Parker, K. P. J. Williams, M. Bortz, and K. Yvon, *Inorg. Chem.*, 1997, **36**, 5218.
39. B. Bogdanovic, A. Reiser, K. Schlichte, B. Spliethoff, and B. Tesche, *J. Alloys Comp.*, 2002, **345**, 77.
40. R. O. Moyer Jr, J. R. Wilkins, and P. Ryan, *J. Alloys Comp.*, 1999, **290**, 103.
41. J. Zhuang, J. M. Hastings, L. M. Corliss, R. Bau, C.-Y. Wei, and R. O. Moyer Jr, *J. Solid State Chem.*, 1981, **40**, 352.
42. J. Zhuang, W. Kunnmann, L. M. Corliss, J. M. Hastings, and R. O. Moyer Jr, *J. Solid State Chem.*, 1983, **48**, 117; for Ca_2IrD_5 see R. O. Moyer Jr and B. H. Toby, *J. Alloys Comp.*, 2004, **363**, 99.
43. H. Kohlmann, R. O. Moyer, T. Hansen, and K. Yvon, *J. Solid State Chem.*, 2003, **174**, 35.
44. P. Zolliker, K. Yvon, P. Fischer, and J. Schefer, *Inorg. Chem.*, 1985, **24**, 4177.
45. M. Yoshida, F. Bonhomme, K. Yvon, and P. Fischer, *J. Alloys Comp.*, 1993, **190**, L45.
46. W. Bronger, K. Jansen, and L. Breil, *Z. Anorg. Allg. Chem.*, 1998, **624**, 1477.
47. W. Bronger, R. Beissmann, and G. Ridder, *J. Alloys Comp.*, 1994, **203**, 91.
48. F. Bonhomme, P. Selvam, M. Yoshida, K. Yvon, and P. Fischer, *J. Alloys Comp.*, 1992, **178**, 167.
49. R. O. Moyer Jr, B. J. Burnim, and R. Lindsay, *J. Solid State Chem.*, 1996, **121**, 56.
50. W. Bronger, P. Müller, D. Schmitz, and H. Spittank, *Z. Anorg. Allg. Chem.*, 1984, **516**, 35.
51. K. Kadir, M. Kritikos, D. Noréus, and A. F. Andresen, *J. Less-Common Met.*, 1991, **172–174**, 36.
52. M. Gupta, *Z. Phys. Chem.*, 1993, **181**, 9.
53. W. Bronger and G. Auffermann, *J. Alloys Comp.*, 1995, **228**, 119.
54. S. F. Parker, K. P. J. Williams, T. Smith, M. Bortz, B. Bertheville, and K. Yvon, *Phys. Chem. Chem. Phys.*, 2002, **4**, 1732.
55. U. Häussermann, H. Blomqvist, and D. Noréus, *Inorg. Chem.*, 2002, **41**, 3684.
56. P. Zolliker, K. Yvon, and C. Baerlocher, *J. Less-Common Met.*, 1986, **115**, 65; see also D. Noréus and L. Kihlborg, *J. Less-Common Met.*, 1986, **123**, 233.
57. K. Yvon, J. Schefer, and F. Stucki, *Inorg. Chem.*, 1981, **20**, 2776.
58. E. Rönnebro, J. O. Jensen, D. Noréus, and N. J. Bjerrum, *J. Alloys Comp.*, 1999, **293–295**, 146.
59. W. Bronger, G. Auffermann, and P. Müller, *J. Less-Common Met.*, 1986, **116**, 9; see also W. Bronger, G. Auffermann, and P. Müller, *J. Less-Common Met.*, 1988, **142**, 243; see also W. Bronger, and G. Auffermann, *J. Alloys Comp.*, 1992, **187**, 87.
60. D. Noréus, K. W. Törnroos, A. Börje, T. Szabó, W. Bronger, H. Spittank, G. Auffermann, and P. Müller, *J. Less-Common Met.*, 1988, **139**, 233; see also K. Kadir and D. Noréus, *Z. Phys. Chem. NF.*, 1989, **163**, 231.
61. R. V. Kasowski, D. Noréus, L. Wang, and M.-H. Whangbo, *Inorg. Chem.*, 1992, **31**, 4737.
62. W. Bronger and G. Auffermann, *J. Less-Common Met.*, 1991, **169**, 173.
63. W. Bronger, G. A uffermann, and P. Müller, *Z. Anorg. Allg. Chem.*, 1988, **566**, 31; see also W. Bronger and G. Auffermann, *J. Alloys Comp.*, 1992, **187**, 81; W. Bronger and G. Auffermann, *J. Alloys Comp.*, 1992, **179**, 235.
64. W. Bronger and G. Auffermann, *J. Less-Common Met.*, 1990, **158**, 163.
65. W. Bronger, K. Jansen, and P. Müller, *J. Less-Common Met.*, 1990, **161**, 299.
66. B. Huang, Synthèse, Structure et Stabilité Thermique des Hydrures Ternaires et Quaternaires Complexes des Métaux de Transition, Thesis No 2765 (in English), University of Geneva, 1995.
67. W. Bronger and G. Ridder, *J. Alloys Comp.*, 1994, **210**, 53.
68. H. Kohlmann, H. E. Fischer, and K. Yvon, *Inorg. Chem.*, 2001, **40**, 2608; see also K. H. J. Buschow, R. L. Cohen, and K. W. West, *J. Appl. Phys.*, 1977, **48**, 5289.
69. K. Ensslen, E. Bucher, and H. Oesterreicher, *J. Less-Common Met.*, 1983, **92**, 343.
70. H. T. Takeshita, T. Oishi, and N. Kuriyama, *J. Alloys Comp.*, 2002, **333**, 266.
71. E. Orgaz, V. Mazel, and M. Gupta, *J. Alloys Comp.*, 1997, **253–254**, 330.

72. M. Kritikos, D. Noréus, A. F. Andresen, and P. Fischer, *J. Solid State Chem.*, 1991, **92**, 514.
73. W. Bronger, M. Gehlen, and G. Auffermann, *J. Alloys Comp.*, 1991, **176**, 255.
74. W. Bronger, P. Müller, J. Kowalczyk, and G. Auffermann, *J. Alloys Comp.*, 1991, **176**, 263.
75. W. Bronger, M. Gehlen, and G. Auffermann, *Z. Anorg. Allg. Chem.*, 1994, **620**, 1983.
76. L. B. Lundberg, D. T. Cromer, and C. B. Magee, *Inorg. Chem.*, 1972, **11**, 400.
77. F. Bonhomme, K. Yvon, and P. Fischer, *J. Alloys Comp.*, 1992, **186**, 209; erratum, F. Bonhomme, K. Yvon, and P. Fischer, *J. Alloys Comp.*, 1992, **190**, 141; see also F. Bonhomme, Synthèse et Caractérisation Structurale d'Hydrures Ternaires Contenant du Magnésium et un Métal de Transition du Groupe VIII, Thesis No 2720 (in French), University of Geneva, 1995.
78. F. Bonhomme, K. Yvon, and P. Fischer, *J. Alloys Comp.*, 1992, **186**, 309.
79. B. Huang, K. Yvon, and P. Fischer, *J. Alloys Comp.*, 1992, **187**, 227; see also Huang, K. Yvon, and P. Fischer, *J. Alloys Comp.*, 1995, **227**, 121.
80. R. Černý, F. Bonhomme, K. Yvon, P. Fischer, P. Zolliker, D. E. Cox, and A. Hewat, *J. Alloys Comp.*, 1992, **187**, 233.
81. E. J. Ivanov, I. Konstanchuk, A. Stepanov, Yan. Jie, M. Pezat, and B. Darriet, *Inorg. Chem.*, 1989, **28**, 613; see also I. G. Konstanchuk, E. Yu. Ivanov, A. A. Stepanov, and T. I. Samsonova, *Izv. Akad. Nauk SSSR, Ser. Khim. Nauk*, 1989, **3**, 93 (in Russian).
82. F. Bonhomme, K. Yvon, G. Triscone, K. Jansen, G. Auffermann, P. Müller, W. Bronger, and P. Fischer, *J. Alloys Comp.*, 1992, **178**, 161.
83. B. Huang, K. Yvon, and P. Fischer, *J. Alloys Comp.*, 1992, **178**, 173; see also B. Huang, K. Yvon, and P. Fischer, *J. Alloys Comp.*, 1994, **204**, L5.
84. F. Gingl and K. Yvon, *Z. Kristallogr.*, 1993, **207**, 247.
85. B. Huang, K. Yvon, and P. Fischer, *J. Alloys Comp.*, 1992, **190**, 65; see also B. Huang, K. Yvon, and P. Fischer, *J. Alloys Comp.*, 1993, **197**, 65.
86. K. Kadir and D. Noreus, *Z. Phys. Chem.*, 1993, **179**, 237.
87. M. Yoshida, K. Yvon, and P. Fischer, *J. Alloys Comp.*, 1993, **194**, L11.
88. B. Huang, K. Yvon, and P. Fischer, *J. Alloys Comp.*, 1993, **197**, 97.
89. M. Bortz, B. Bertheville, K. Yvon, E. A. Movlaev, V. N. Verbetzky, and F. Fauth, *J. Alloys Comp.*, 1998, **279**, L8.
90. E. Orgaz and M. Gupta, *J. Alloys Comp.*, 1999, **330–332**, 323.
91. F. Bonhomme, N. T. Stetson, K. Yvon, P. Fischer, and A. W. Hewat, *J. Alloys Comp.*, 1993, **200**, 65.
92. W. Bronger, K. Jansen, and G. Auffermann, *J. Alloys Comp.*, 1993, **199**, 47.
93. W. Bronger and L. Breil, *Z. Anorg. Allg. Chem.*, 1998, **624**, 1819.
94. B. Huang, K. Yvon, and P. Fischer, *J. Alloys Comp.*, 1994, **210**, 243.
95. B. Huang, P. Fischer, and K. Yvon, *J. Alloys Comp.*, 1996, **245**, L24.
96. A. P. Ginsberg and C. R. Sprinkle, *Inorg. Synth.*, 1972, **13**, 219, and references therein.
97. N. T. Stetson, K. Yvon, and P. Fischer, *Inorg. Chem.*, 1994, **33**, 4598.
98. E. Orgaz and M. Gupta, *J. Alloys Comp.*, 1999, **293–295**, 217.
99. M. Bortz, K. Yvon, and P. Fischer, *J. Alloys Comp.*, 1994, **216**, 39.
100. M. Bortz, A. Hewat, and K. Yvon, *J. Alloys Comp.*, 1997, **248**, L1.
101. M. Olofsson-Martensson, M. Kritikos, and D. Noréus, *J. Am. Chem. Soc.*, 1999, **121**, 10908.
102. H. Kohlmann, H. E. Fischer, and K. Yvon, *Inorg. Chem.*, 2001, **40**, 2608.
103. E. Orgaz, *J. Alloys Comp.*, 2003, **356–357**, 191.
104. M. Bortz, K. Yvon, and P. Fischer, *J. Alloys Comp.*, 1994, **216**, 43.
105. M. Bortz, A. Hewat, and K. Yvon, *J. Alloys Comp.*, 1997, **253–254**, 13.
106. W. Bronger, S. Hasenberg, and G. Auffermann, *Z. Anorg. Allg. Chem.*, 1996, **622**, 1145.
107. W. Bronger, S. Hasenberg, and G. Auffermann, *J. Alloys Comp.*, 1997, **257**, 75.
108. M. Bortz, M. Gutmann, and K. Yvon, *J. Alloys Comp.*, 1999, **285**, L19.
109. K. Kadir and D. Noréus, *J. Alloys Comp.*, 1994, **209**, 213.
110. B. Huang, K. Yvon, and P. Fischer, *J. Alloys Comp.*, 1995, **227**, 116.
111. N. T. Stetson and K. Yvon, *J. Alloys Comp.*, 1995, **223**, L4.
112. W. Bronger and L. à Brassard, *Angew. Chem., Int. Ed. Engl.*, 1995, **34**, 898.
113. B. Huang, F. Fauth, and K. Yvon, *J. Alloys Comp.*, 1996, **244**, L1.
114. W. Bronger and L. à Brassard, *Z. Anorg. Allg. Chem.*, 1996, **622**, 462.
115. B. Huang, F. Gingl, F. Fauth, A. Hewat, and K. Yvon, *J. Alloys Comp.*, 1997, **248**, 13.
116. M. Olofsson, M. Kritikos, and D. Noréus, *Inorg. Chem.*, 1998, **37**, 2900.
117. W. Bronger, G. Auffermann, and H. Schilder, *Z. Anorg. Allg. Chem.*, 1998, **624**, 497.

118. W. Bronger and G. Auffermann, *Z. Anorg. Allg. Chem.*, 1999, **625**, 1147.

119. G. Auffermann, W. Bronger, R. M. Ibberson, and S. Hull, ISIS Facility Annual Report 2001–2002 – Highlights of ISIS Science, 2002, 22.

120. W. Bronger, T. Sommer, G. Auffermann, and P. Müller, *J. Alloys Compd.*, 2002, **330–332**, 536.

121. R. Cerny, J. M. Joubert, H. Kohlmann, and K. Yvon, *J. Alloys Comp.*, 2002, **340**, 180; see also R. Cerny, J. M. Joubert, and K. Yvon, *Mater. Sci. Forum*, 1998, **278–281**, 121.

122. L. Guénée, V. Favre-Nicolin, and K. Yvon, *J. Alloys Compd.*, 2003, **348**, 129.

123. G. Renaudin, L. Guénée, and K. Yvon, *J. Alloys Comp.*, 2003, **350**, 145.

124. D. M. P. Mingos, and J. C. Hawes, *Struct. Bonding (Berlin)*, 1985, **63**, 1; see also R. Hoffmann, *Angew. Chem., Int. Ed. Engl.*, 1982, **21**, 711.

125. K. Kadir, and D. Noréus, *Z. Phys. Chem.*, 1993, **179**, 249; see also K. Kadir, P. Lundqvist, D. Noréus, and O. Rapp, *Solid State Commun.*, 1993, **85**, 891.

126. B. Nacken and W. Bronger, *Z. Anorg. Allg. Chem.*, 1978, **439**, 29.

127. J. D. Corbett, *J. Solid State Chem.*, 1981, **39**, 56.

128. K. Yvon, H. Kohlmann, and B. Bertheville, *Chimia*, 2001, **55**, 505.

129. R. H. Crabtree, *Acc. Chem. Res.*, 1990, **23**, 95.

130. R. Griessen, *Europhys. News*, 2001, **32**, 41.

131. R. Griessen and T. Riesterer, *Top. Appl. Phys.*, 1988, **63**, 219.

Acknowledgment

The work was supported by the Swiss National Science Foundation and the Swiss Federal Office of Energy.

Hydroboration Catalysis

Christopher M. Vogels & Stephen A. Westcott
Mount Allison University, Sackville, Canada

Based in part on the article Hydroboration Catalysis by Kevin Burgess & Wilfred A. van der Donk which appeared in the Encyclopedia of Inorganic Chemistry, First Edition.

1 Introduction 1
2 Mechanism 1
3 Rhodium Complexes 2
4 Iridium Complexes 3
5 Other Late Metal Complexes 4
6 Early Metal Complexes 4
7 Catalyzed Hydroborations in Organic Chemistry 4
8 Conclusions and Prospects 7
9 Related Articles 7
10 References 7

Abbreviations

HBcat (cat = 1,2-$O_2C_6H_4$); HBpin (pin = 1,2-$O_2C_2Me_4$); coe = *cis*-Cyclooctene; cod = *cis*-Cycloocta-1,5-diene; dppe = 1,2-Bis(diphenylphosphino)ethane; dppf = 1,1'-Bis (diphenylphosphino)ferrocene; dba = Dibenzylideneacetone; acac = Acetylacetonato; py = Pyridine; 9-H-BBN = Borabicyclo[3.3.1]nonane; Cp* = C_5Me_5.

1 INTRODUCTION

One of the most important synthetic methodologies to emerge from organic chemistry in the last century has been the discovery that boron–hydrogen bonds add to unsaturated organics to form a class of compounds known as organoboranes (*see* ***Boron: Organoboranes***). That transition metals (*see Transition Metals*) accelerate the addition of boron hydrides (*see* ***Boron Hydrides***) to unsaturated organic moieties was initially reported for catalyzed hydroborations (*see Hydroboration*) of alkenes and alkynes using polyhedral boranes (*see* ***Boron: Polyhedral Carboranes***).[1,2] Männig and Nöth then demonstrated that $RhCl(PPh_3)_3$ (*see Wilkinson's Catalyst*) could be used to catalyze the hydroboration of alkenes with catecholborane (HBcat) under mild conditions and with *chemoselectivity differing from that of the uncatalyzed reaction* (equation 1).[3] Indeed, in the catalyzed hydroboration of 5-hexen-2-one, addition of HBcat occurred preferentially at the C=C double bond, even in the presence of the more reactive ketone group.

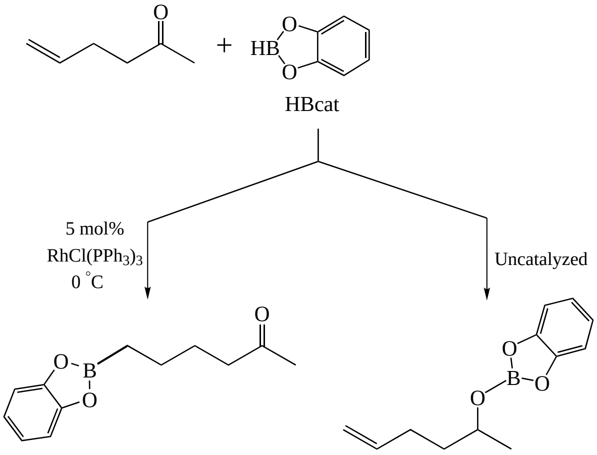

(1)

Since this seminal discovery, a considerable amount of research has focused on investigating the mechanism and scope of these catalyzed hydroboration reactions. Several reviews have already been published in this area.[4–8]

2 MECHANISM

Although other transition metals have been found to catalyze hydroborations with HBcat, early studies have shown that rhodium complexes are the most effective for reactions of simple alkenes. The catalytic cycle proposed resembles one suggested previously[2] for the rhodium-catalyzed addition of carborane B–H bonds to the C=C unit in acrylate esters. The reaction is believed to proceed via initial loss of phosphine and oxidative addition (*see Oxidative Addition*) of the B–H bond of HBcat to the coordinatively unsaturated (*see Coordinative Saturation & Unsaturation*) rhodium center.[9,10] Coordination of the alkene (*see Alkene Complexes*) and subsequent insertion (*see Insertion*) into the Rh–H bond and reductive elimination (*see Reductive Elimination*) of the B–C bond then generates the organoboronate ester product(s) (Scheme 1).

Mechanistic work by Evans and Fu[11] has shown that hydroboration of 1-decene with deuteriocatecholborane (DBcat) using Wilkinson's catalyst gave predominant formation of 1-decanol, upon oxidation with $NaOH/H_2O_2$, where the expected regiospecific incorporation of deuterium at the β-carbon of the alkene was not observed. Indeed, a significant amount of deuterium was observed at the hydroxyl-bearing carbon of the isolated alcohol (ca. 14%) and in the recovered alkene. These observations were rationalized in terms of both the alkene binding and migratory insertion steps being reversible. A number of theoretical studies[12–18] have examined the metal catalyzed hydroboration and Ziegler and coworkers[12] have suggested that the hydride and the boryl fragment (Bcat) are probably trans to one another in reactions

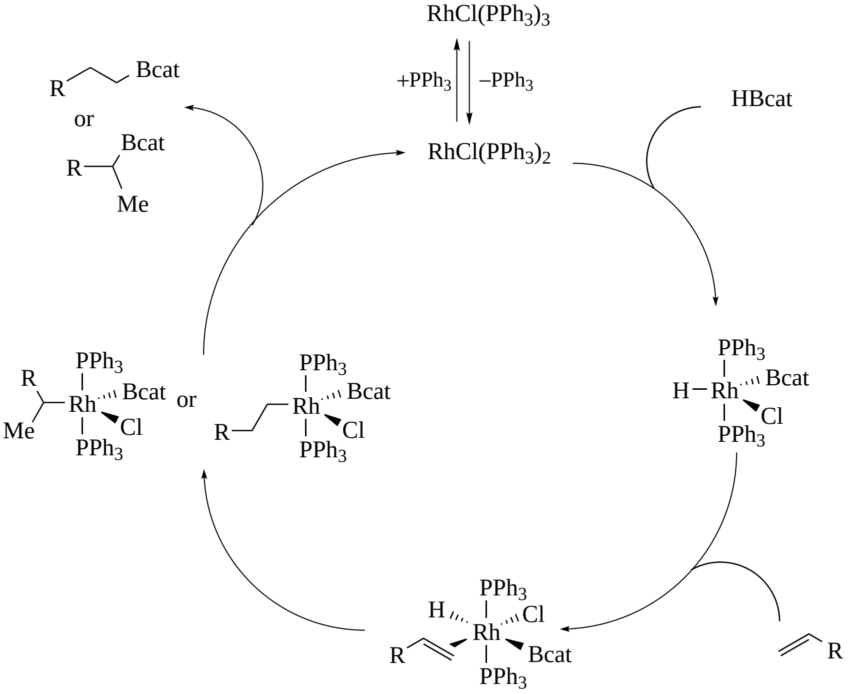

Scheme 1 A general proposed mechanism for the rhodium-catalyzed hydroboration of alkenes using HBcat

with Wilkinson's catalyst, leaving the coordinated alkene cis to both of these reactive moieties.

3 RHODIUM COMPLEXES

3.1 Neutral Complexes

As mentioned previously, early work has focused on the use of $RhCl(PPh_3)_3$ to catalyze hydroborations of alkenes using HBcat. However, competing reactions, such as hydrogenation (*see* ***Hydrogenation & Isomerization of Alkenes***), and degradation of the borane[19,20] have resulted in considerable research into the development of other rhodium complexes as possible catalyst precursors for this important reaction. For instance, while hydroborations of vinyl arenes ($ArCH = CH_2$) with HBcat catalyzed by most rhodium complexes give the unusual branched products ($ArCH(Bcat)CH_3$) selectively, use of $[RhCl(coe)_2]_2/2PPh_3$ gave exclusive formation of the linear isomer ($ArCH_2CH_2Bcat$).[21] The unexpected branched product is presumed to result from the rhodium's ability to stabilize a benzylic intermediate during the catalytic cycle.[22] Interestingly, reactions of vinyl arenes with pinacolborane (HBpin) catalyzed by phosphine-free $[RhCl(cod)]_2$ gave the corresponding (E)-2-arylethenylboronates ($ArCH = CHBpin$) in high yields (equation 2).[23] Similar chemistry has also been observed for reactions with HBcat, although hydrogenation and/or subsequent hydroboration of the resulting alkenylboronate ester is frequently observed.[20,24–27] These dehydrogenative borylation reactions are believed to proceed via initial oxidative addition of HBcat to the rhodium center, followed by coordination of the alkene and regioselective insertion into the Rh–B bond. A subsequent β-hydride elimination (*see β-Hydride Elimination*) would then generate the desired alkenyl boronate ester along with a rhodium dihydride intermediate, which can act as an active hydrogenation catalyst (Scheme 2).[20]

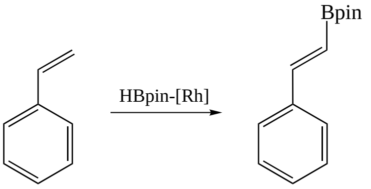

(2)

3.2 Cationic Complexes

Probably the most important developments in this field over the past 10 years, however, have been in the area of enantioselective (*see Enantioselectivity*) hydroborations using cationic rhodium complexes of the type $[Rh(diene)L^*]^+$ ($L^* =$ chiral ligand). An excellent review on this topic has recently been published.[5] New chiral (*see Chiral*) catalyst systems are typically tested in hydroborations of vinyl arenes. Although catalyzed hydroboration of vinyl arenes can be used as a mild and efficient route to preparing 1-arylethanol

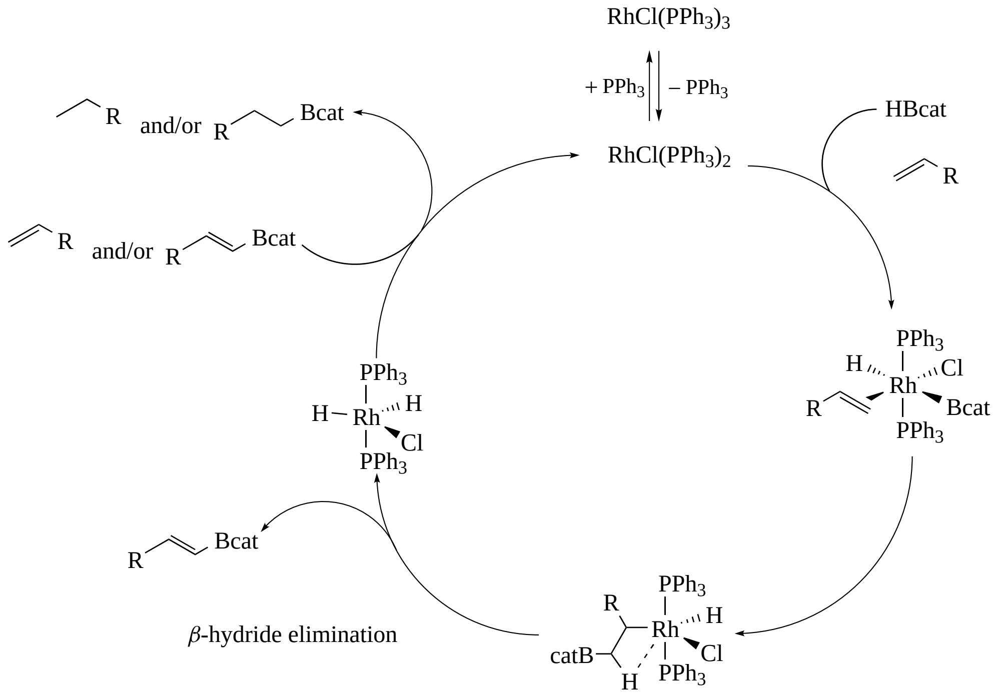

Scheme 2 A general proposed mechanism for the rhodium-catalyzed dehydrogenative borylation of alkenes using HBcat

derivatives, J. M. Brown has applied this methodology, in conjunction with a subsequent electrophilic amination, to generate primary and secondary amines. These reactions proceed with essentially complete retention of configuration and lead to a wide range of primary α-arylalkylamines in up to 98% enantiomeric excess (equation 3).[28,29] An elegant recent study by Crudden and coworkers has shown that hydroborations of vinyl arenes with HBpin using a chiral rhodium catalyst leads to products with enantioselectivities opposite to those obtained in analogous reactions using HBcat.[30]

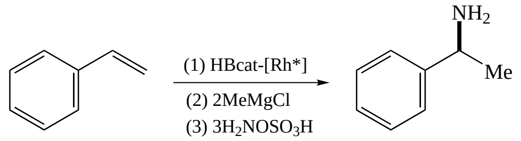

(3)

3.3 Zwitterionic Complexes

A unique zwitterionic (*see Zwitterion*) catalyst of the type Rh(η^6-catBcat)(dppe), derived from the addition of HBcat to Rh(acac)(dppe), has been found to selectively catalyze the hydroboration of a wide variety of substrates, including the first examples of a tetrasubstituted alkene (2,3-dimethylbut-2-ene).[21] The P_2Rh fragment is bound to the $[Bcat_2]^-$ anion in an η^6-fashion (*see Arene Complexes*) through one of the catecholato groups. Remarkably, the zwitterionic complexes $Rh(Bcat_2)(P_2)$ (P_2 = diphosphine) can also be prepared by the addition of B_2cat_3 (equation 4), a redistribution product arising from the nucleophilic degradation of HBcat, to $Rh(acac)(P_2)$.[31]

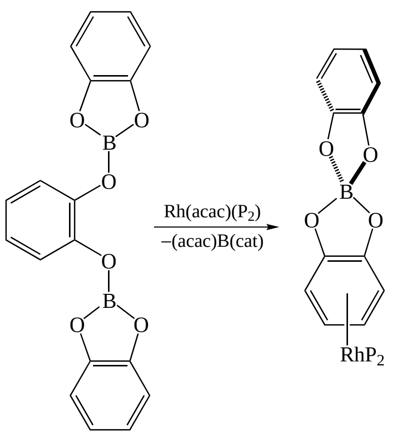

(4)

4 IRIDIUM COMPLEXES

Although early reports suggested that iridium complexes were ineffective catalysts for the hydroboration reaction, subsequent work has shown that Crabtree's catalyst (*see Crabtree's Catalyst*), $[Ir(cod)(py)(PCy_3)]PF_6$, can be used for ether or amide-directed hydroborations.[32,33] For instance, iridium catalyzed hydroborations of pyrrolidinyl amides with HBcat gave *syn* 1,3-hydroxyl amides with high levels of regio- and stereocontrol (equation 5). In contrast, reactions catalyzed by neutral and cationic rhodium complexes afforded a nearly statistical mixture of the four possible isomers. Likewise, both indenylrhodium[34] and iridium[35] complexes have been used in the ether-directed hydroboration reactions. In other studies, either $[IrCl_2(\eta^5\text{-}C_5Me_5)]_2$[36] or $[IrCl(coe)_2]_2/4PPh_3$[30,36] could be used to effectively catalyze the hydroboration of vinyl arenes to give the corresponding linear products and $[IrCl(cod)]_2/4P^i pr_3$ catalyzes the trans-hydroboration of alkynes with HBcat or HBpin.[37] Previous studies by Sneddon and Mirabelli have shown that $[IrCl_2(\eta^5\text{-}C_5Me_5)]_2$ can also be used to facilitate the addition of polyhedral boranes to alkynes.[38]

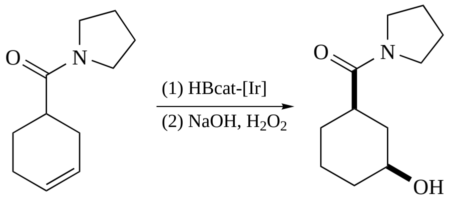

(5)

diastereoselection 95:5 (44%)

5 OTHER LATE METAL COMPLEXES

Conventional hydroboration of 1,3-dienes with dialkylboranes generally affords products derived from addition of the borane at the terminal C=C double bond. In contrast, catalytic 1,4-hydroboration of 1,3-dienes with HBcat using $Rh_4(CO)_{12}$ or $Pd(PPh_3)_4$ gave (Z)-allylic boronates with high isomeric purity.[39] The reaction is believed to go through a π-allyl intermediate that reductively eliminates to give the allylic boronate ester. Nickel (*see* ***Nickel: Organometallic Chemistry***) and cobalt (*see* ***Cobalt: Organometallic Chemistry***) complexes have also been used in the catalyzed hydroboration of conjugated dienes, where 1,2 addition products were observed.[40] Related hydroborations of conjugated enynes using $Pd(PPh_3)_4$ afforded allenic boronate esters and isomers derived from 1,2 addition of HBcat to the triple bond (equation 6).[41] Product distributions were a sensitive function of catalyst precursor employed. For instance, while reactions of 2-methyl-1-buten-3-yne with the palladium (*see* ***Palladium: Organometallic Chemistry***) catalyst generated in situ by addition of bis(phosphines) to $Pd_2(dba)_3{\cdot}CHCl_3$ gave exclusive formation of the (E)-dienyl boronate ester, hydroborations with one equivalent of PPh_3 per palladium gave the desired allenyl boronate ester in high yield (92%). Finally, $NiCl_2(dppe)$ and $NiCl_2(dppf)$ have been found to effectively catalyze the hydroboration of thioacetylenes with HBcat.[42]

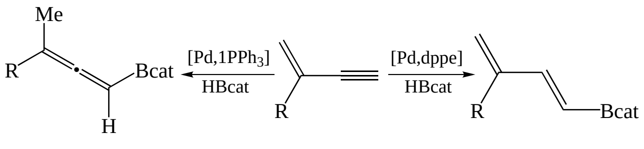

(6)

6 EARLY METAL COMPLEXES

While organoscandium,[43] lanthanide[44] (*see* ***Scandium, Yttrium & the Lanthanides: Inorganic & Coordination Chemistry***), niobium[45] (*see* ***Niobium & Tantalum: Organometallic Chemistry***), and titanium[46,47] (*see* ***Titanium: Organometallic Chemistry***) complexes have all been examined for their ability to catalyze hydroborations, their utility in organic synthesis has remained somewhat limited. Reactions with these catalysts are generally believed to proceed via insertion of the alkene into the M-H bond, followed by a four-centered metathesis (*see Metathesis*) reaction with HBcat to generate the linear product (Scheme 3). For example, complexes of the type $Cp^*{}_2LnR$ (Ln = La, Sm; R = H, $CH(SiMe_3)_2$) were found to be effective catalyst precursors for a wide range of substrates, including trisubstituted alkenes 1-methylcyclopentene and 1-methylcyclohexene.[44]

Interestingly, Schwartz's reagent, Cp_2ZrHCl (*see Schwartz's Reagent*), has found significant use for its ability to catalyze the hydroboration of alkynes selectively with HBpin.[48–50] For example, alkoxyalkynes have been hydroborated with HBpin using Cp_2ZrHCl to give the corresponding alkenylboronates, which were further subjected to the Matteson–Brown homologation (*see Homologation Reactions*) with $LiCH_2Cl$ to give (E)-γ-alkoxyallylboronates in good yield.[48] Liberation of the aldehyde with $LiBF_4$ in moist acetonitrile gave bicylic *bis*-tetrahydropyrans, arising from an intramolecular allylboration reaction (equation 7).

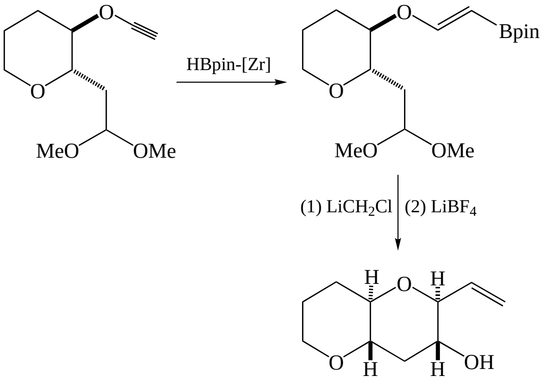

(7)

7 CATALYZED HYDROBORATIONS IN ORGANIC CHEMISTRY

The use of transition metal catalysts for the hydroboration of unsaturated substrates offers many advantages to the synthetic chemist, as products formed from this reaction can have regio-, chemo-, and/or stereoselectivities different to those obtained from the uncatalyzed variant. The selectivities can often be altered by using a different metal catalyst to affect these transformations. In this section, an overall account will be provided of the recent advances in the application of catalyzed hydroborations in organic syntheses.

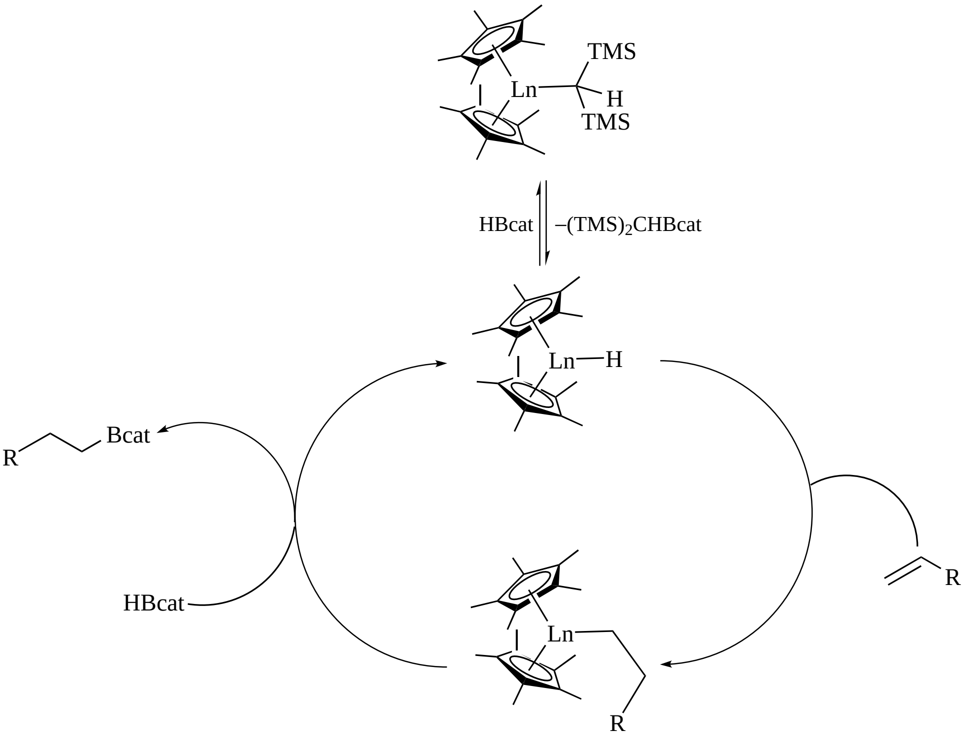

Scheme 3 A general proposed mechanism for the organolanthanide catalyzed hydroboration of alkenes using HBcat

7.1 Chemoselectivity

An important aspect of the metal catalyzed hydroboration reaction is its ability to selectively reduce certain functionalities within a molecule. For instance, a key step in the synthesis of a tripeptide derivative containing the Phe-Arg hydroxyethylene dipeptide iosostere is the selective rhodium-catalyzed hydroboration of a lactone.**51** The use of disiamylborane, 9-H-BBN, dicyclohexylborane, and (*S*)-alpineborane, however, gave only low to variable yields of the alcohol due to competitive reduction of the γ-lactone to the hemiacetal (equation 8). In another example, hydroboration of the diene illustrated in equation (9) with HBcat and $RhCl(PPh_3)_3$ gave exclusive formation of the terminal alcohol derived from reaction of the less substituted alkene. Interestingly, uncatalyzed reactions failed to hydroborate this substrate selectively.**33**

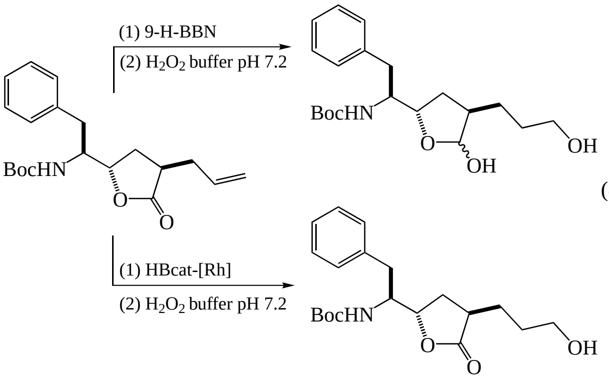

(8)

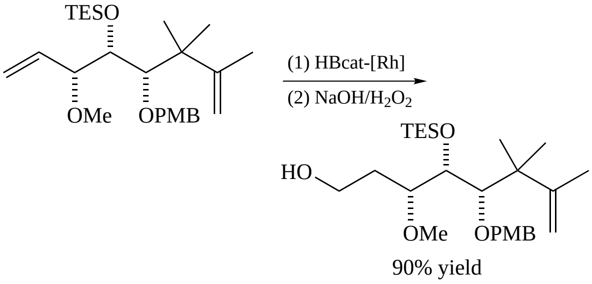

(9)

7.2 Regioselectivity

The ability to alter the regiocontrol of the hydroboration reaction by using a metal catalyst offers innumerable advantages to the synthetic chemist. In recent work, cationic rhodium complexes have been used in the hydroboration of perfluoroalkylethylenes ($R_FCH = CH_2$) with either HBcat or HBpin to give selective formation of the branched regioisomers (equation 10).**52,53** This reversal of regioselectivity has been attributed to the directing effect of the electronegative 2-substituted fluorine atoms. Conversely, reactions employing a neutral rhodium catalyst gave predominant formation of the expected linear product. In a similar study, the directing effect of the sulfone oxygen gave rise to the branched product exclusively in the rhodium-catalyzed hydroboration of vinyl sulfones using

HBcat (equation 11).[54]

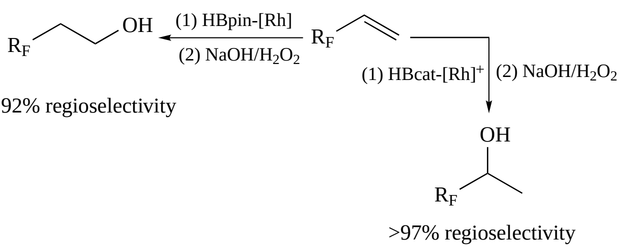
OH
R_F
(1) HBpin-[Rh]
(2) NaOH/H_2O_2
R_F
(1) HBcat-[Rh]$^+$
(2) NaOH/H_2O_2
>92% regioselectivity
OH
R_F
>97% regioselectivity

(10)

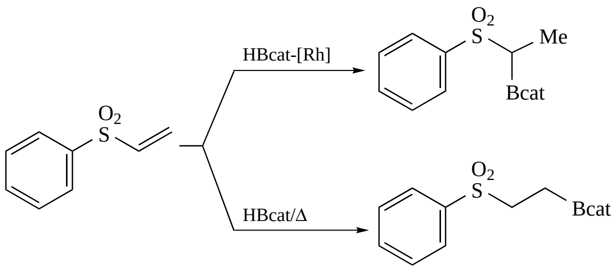
O_2
S
HBcat-[Rh]
O_2
S
Me
Bcat
HBcat/Δ
O_2
S
Bcat

(11)

Renaud and coworkers have also recently found that related TBDMS-protected *B*-alkylboronate esters are suitable radical (*see Radicals*) precursors for conjugate addition to activated olefins such as methyl acrylate (equation 12).[55] Catalyzed hydroborations gave the 1,3-addition products with regioselectivity opposite to those obtained in uncatalyzed reactions.

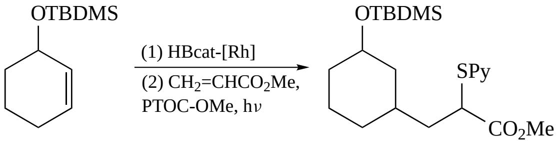
OTBDMS
(1) HBcat-[Rh]
(2) CH_2=$CHCO_2Me$,
PTOC-OMe, hν
OTBDMS
SPy
CO_2Me

(12)

7.3 Stereoselectivity

Without question, the most important developments in this field over the past 10 years have been in the area of enantioselective hydroborations.[5,56] New chiral catalyst systems are typically tested in hydroborations of vinyl arenes, as reactions using HBcat and a cationic rhodium catalyst are well known to give selective formation of the unusual branched isomer. In related studies, enantiopure 2,2-disubstituted cyclopropyl boronates were easily prepared via the catalytic asymmetric hydroboration of 3,3-disubstituted cyclopropenes using a number of chiral neutral rhodium complexes (equation 13).[57] Directing groups, such as esters and alkoxymethyl substituents, were necessary for achieving high degrees of enantioselectivity.

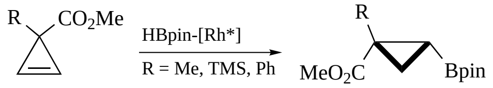
R
CO_2Me
HBpin-[Rh*]
R = Me, TMS, Ph
R
MeO_2C
Bpin

(13)

The catalytic asymmetric hydroboration reaction can also be applied to *meso*-bicyclic hydrazines. The resulting alcohols are of great synthetic interest and can lead to cyclopentanic diamino alcohols with good enantiomeric purity (equation 14). Interestingly, a reversal of enantioselectivity is observed between reactions employing rhodium and iridium catalysts.[58]

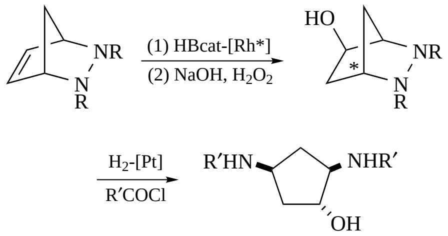
NR
N
R
(1) HBcat-[Rh*]
(2) NaOH, H_2O_2
HO
*
NR
N
R
H_2-[Pt]
R′COCl
R′HN
NHR′
OH

(14)

The first facially selective hydroboration of a 5-methylidene[2.2.1]bicyclic intermediate has also recently been reported.[59] The rhodium-catalyzed hydroboration of the methylidene group with HBcat proved superior to stoichiometric borane or dialkylborane reagents, in terms of higher diastereomeric excess and chemical yields (equation 15). For instance, while borane gave 89% of the desired 5-*endo* product along with 11% of the 5-*exo* product, the catalyzed variant with HBcat gave 95% for the desired 5-*endo* product when the reaction was run at room temperature. No improvement in diastereoselectivity was observed when reactions were run at lower temperatures.

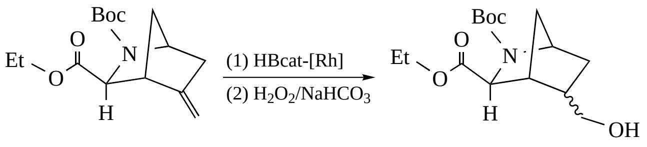
Boc
O
Et
O
N
H
(1) HBcat-[Rh]
(2) H_2O_2/$NaHCO_3$
Boc
O
Et
O
N
H
OH

(15)

7.4 Natural Products

Lonomycin A is a structurally complex polyether antibiotic whose array of sensitive functionalities poses a considerable synthetic challenge. A rhodium-catalyzed hydroboration of a 1,1-disubstituted alkene has been applied by Evans and Sheppard to the penultimate step in the construction of a lonomycin C_1–C_{11} synthon.[60] High diastereoselectivities were observed for the desired C_{11}

alcohol in reactions using HBcat and $RhCl(PPh_3)_3$, while uncatalyzed reactions with disiamylborane gave the other diastereomeric alcohol in high yields (equation 16). These results were somewhat surprising as catalyzed hydroborations of a closely related model compound proceeded with little stereocontrol.

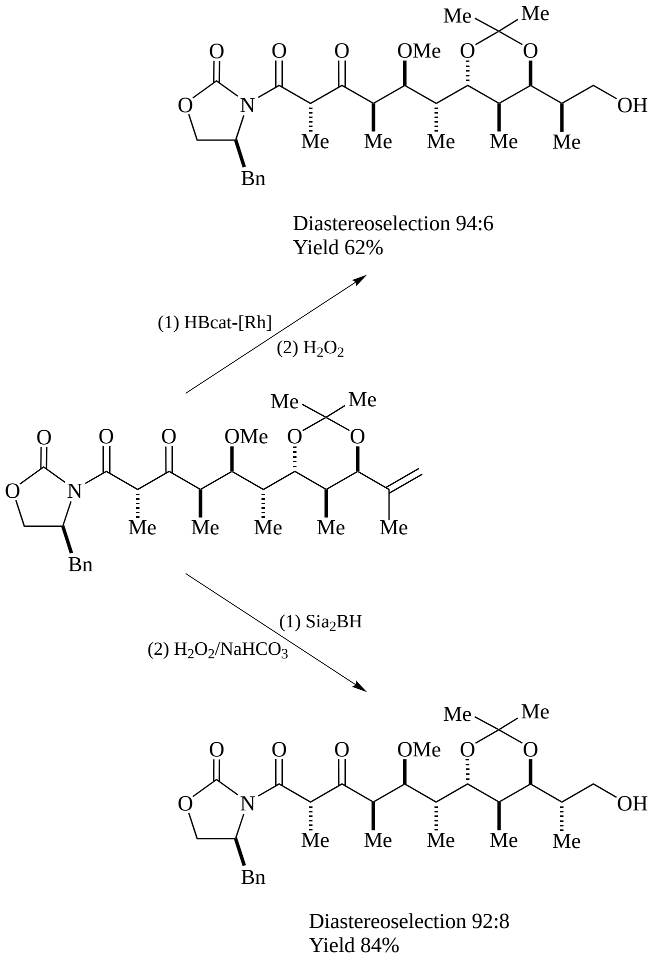

(16)

Pederin is a vesicant from the beetle *Paederus fuscipes* and is one of a small class of potent biologically active natural products whose complicated structure presents a substantial challenge as a target for synthesis. An account on the total synthesis of this insect toxin incorporated the use of a rhodium-catalyzed hydroboration reaction.**[61]** Stereoselective reduction of an *N*-acylimidate to the desired *N*-acyl aminal was achieved via a 1,4-hydroboration with HBcat carried out in the presence of a catalytic amount of $RhCl(PPh_3)_3$ (equation 17). Interestingly, a variety of reducing agents failed to generate the desired diastereomer selectively and catalyzed hydrogenations were equally ineffective. Other accounts using the metal catalyzed hydroboration in the total synthesis of natural products have also recently been published.**[62,63]**

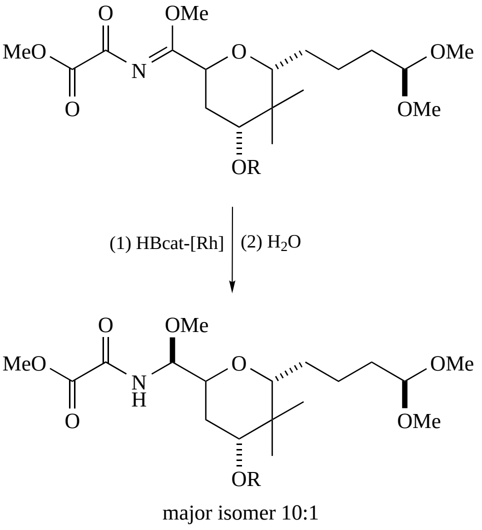

(17)

8 CONCLUSIONS AND PROSPECTS

In summary, the potential utility of the metal catalyzed hydroboration reaction is vast. Future work will focus on its applicability in the synthesis of biologically active compounds where conventional electrophilic additions have proven ineffective. Convenience and mild conditions required for these reactions provide the organic chemist with a valuable synthetic tool.

9 RELATED ARTICLES

Asymmetric Synthesis by Homogeneous Catalysis; Boron Hydrides; Boron: Organoboranes; Hydrosilation Catalysis; Rhodium: Organometallic Chemistry.

10 REFERENCES

1. R. Wilczynski and L. G. Sneddon, *J. Am. Chem. Soc.*, 1980, **102**, 2857.
2. J. D. Hewes, C. W. Kreimendahl, T. B. Marder, and M. F. Hawthorne, *J. Am. Chem. Soc.*, 1984, **106**, 5757.
3. D. Männig and H. Nöth, *Angew. Chem., Int. Ed. Engl.*, 1985, **24**, 878.
4. K. Burgess and M. J. Ohlmeyer, *Chem. Rev.*, 1991, **91**, 1179.
5. C. M. Crudden and D. Edwards, *Eur. J. Org. Chem.*, 2003, 4695.
6. C. M. Vogels and S. A. Westcott, *Curr. Org. Chem.*, 2004, in press.

7. I. Beletskaya and A. Pelter, *Tetrahedron*, 1997, **53**, 4957.
8. C. J. Ruffing, *Aldrichimica Acta*, 1989, **3**, 80.
9. H. Kono, K. Ito, and Y. Nagai, *Chem. Lett.*, 1975, 1095.
10. S. A. Westcott, N. J. Taylor, T. B. Marder, R. T. Baker, N. J. Jones, and J. C. Calabrese, *J. Chem. Soc., Chem. Commun.*, 1991, 304.
11. D. A. Evans and G. C. Fu, *J. Org. Chem.*, 1990, **55**, 2280.
12. C. Widauer, H. Grützmacher, and T. Ziegler, *Organometallics*, 2000, **19**, 2097.
13. D. G. Musaev, A. M. Mebel, and K. Morokuma, *J. Am. Chem. Soc.*, 1994, **116**, 10693.
14. M. Torrent, M. Solà, and G. Frenking, *Chem. Rev.*, 2000, **100**, 439.
15. A. E. Dorigo and P. von Ragué Schleyer, *Angew. Chem., Int. Ed. Engl.*, 1995, **34**, 115.
16. D. Liu, K.-C. Lam, and Z. Lin, *J. Organomet. Chem.*, 2003, **680**, 148.
17. S. A. Kulkarni and N. Koga, *J. Mol. Struct. (Theochem)*, 1999, **461–2**, 297.
18. D. Liu and Z. Lin, *Organometallics*, 2002, **21**, 4750.
19. S. A. Westcott, H. P. Blom, T. B. Marder, R. T. Baker, and J. C. Calabrese, *Inorg. Chem.*, 1993, **32**, 2175.
20. K. Burgess, W. A. van der Donk, S. A. Westcott, T. B. Marder, R. T. Baker, and J. C. Calabrese, *J. Am. Chem. Soc.*, 1992, **114**, 9350.
21. S. A. Westcott, H. P. Blom, T. B. Marder, and R. T. Baker, *J. Am. Chem. Soc.*, 1992, **114**, 8863.
22. T. Hayashi, Y. Matsumoto, and Y. Ito, *Tetrahedron: Asymmetry*, 1991, **2**, 601.
23. M. Murata, S. Watanabe, and Y. Masuda, *Tetrahedron Lett.*, 1999, **40**, 2585.
24. J. M. Brown and G. C. Lloyd-Jones, *J. Chem. Soc., Chem. Commun.*, 1992, 710.
25. J. M. Brown and G. C. Lloyd-Jones, *J. Am. Chem. Soc.*, 1994, **116**, 866.
26. R. T. Baker, J. C. Calabrese, S. A. Westcott, P. Nguyen, and T. B. Marder, *J. Am. Chem. Soc.*, 1993, **115**, 4367.
27. P. Nguyen, H. P. Blom, S. A. Westcott, N. T. Taylor, and T. B. Marder, *J. Am. Chem. Soc.*, 1993, **115**, 9329.
28. K. Maeda and J. M. Brown, *Chem. Commun.*, 2002, 310.
29. E. Fernàndez, K. Maeda, M. W. Hooper, and J. M. Brown, *Chem. – Eur. J.*, 2000, **6**, 1840.
30. C. M. Crudden, Y. B. Hleba, and A. C. Chen, *J. Am. Chem. Soc.*, 2004, **126**, 9200.
31. C. Dai, E. G. Robins, A. J. Scott, W. Clegg, D. S. Yufit, J. A. K. Howard, and T. B. Marder, *Chem. Commun.*, 1998, 1983.
32. D. A. Evans and G. C. Fu, *J. Am. Chem. Soc.*, 1991, **113**, 4042.
33. D. A. Evans, G. C. Fu, and A. H. Hoveyda, *J. Am. Chem. Soc.*, 1992, **114**, 6671.
34. C. E. Garrett and G. C. Fu, *J. Org. Chem.*, 1998, **63**, 1370.
35. J. A. Brinkman, T. T. Nguyen, and J. R. Sowa Jr, *Org. Lett.*, 2000, **2**, 981.
36. S. A. Westcott, T. B. Marder, R. T. Baker, and J. C. Calabrese, *Can. J. Chem.*, 1993, **71**, 930.
37. T. Ohmura, Y. Yamamoto, and N. Miyaura, *J. Am. Chem. Soc.*, 2000, **122**, 4990.
38. M. G. L. Mirabelli and L. G. Sneddon, *J. Am. Chem. Soc.*, 1988, **110**, 449.
39. M. Satoh, Y. Nomoto, N. Miyaura, and A. Suzuki, *Tetrahedron Lett.*, 1989, **30**, 3789.
40. M. Zaidlewicz and J. Meller, *Tetrahedron Lett.*, 1997, **38**, 7279.
41. Y. Matsumoto, M. Naito, and T. Hayashi, *Organometallics*, 1992, **11**, 2732.
42. I. D. Gridnev, N. Miyaura, and A. Suzuki, *J. Org. Chem.*, 1993, **58**, 5351.
43. D. A. Evans, A. R. Muci, and R. Stürmer, *J. Org. Chem.*, 1993, **58**, 5307.
44. K. N. Harrison and T. J. Marks, *J. Am. Chem. Soc.*, 1992, **114**, 9220.
45. K. Burgess and M. Jaspers, *Tetrahedron Lett.*, 1993, **34**, 6813.
46. K. Burgess and W. A. van der Donk, *Organometallics*, 1994, **13**, 3616.
47. X. He and J. F. Hartwig, *J. Am. Chem. Soc.*, 1996, **118**, 1696.
48. R. W. Hoffmann, J. Krüger, and D. Brückner, *New J. Chem.*, 2001, **25**, 102.
49. S. Pereira and M. Srebnik, *Tetrahedron Lett.*, 1996, **37**, 3283.
50. S. Pereira and M. Srebnik, *Organometallics*, 1995, **14**, 3127.
51. M. Brewer and D. H. Rich, *Org. Lett.*, 2001, **3**, 945.
52. P. V. Ramachandran, M. P. Jennings, and H. C. Brown, *Org. Lett.*, 1999, **1**, 1399.
53. A. M. Segarra, C. Claver, and E. Fernandez, *Chem. Commun.*, 2004, 464.
54. C. A. G. Carter, C. M. Vogels, D. J. Harrison, M. K. J. Gagnon, D. W. Norman, R. F. Langler, R. T. Baker, and S. A. Westcott, *Organometallics*, 2001, **20**, 2130.
55. P. Renaud, C. Ollivier, and V. Weber, *J. Org. Chem.*, 2003, **68**, 5769.
56. P. J. Guiry, M. McCarthy, P. M. Lacey, C. P. Saunders, S. Kelly, and D. J. Connolly, *Curr. Org. Chem.*, 2000, **4**, 821.
57. M. Rubin and V. Gevorgyan, *Synthesis*, 2004, 796.
58. A. Pérez Luna, M. Bonin, L. Micouin, and H.-P. Husson, *J. Am. Chem. Soc.*, 2002, **124**, 12098.
59. L. Bunch, T. Liljefors, J. R. Greenwood, K. Frydenvang, H. Bräuner-Osborne, P. Krogsgaard-Larsen, and U. Madsen, *J. Org. Chem.*, 2003, **68**, 1489.
60. D. A. Evans and G. S. Sheppard, *J. Org. Chem.*, 1990, **55**, 5192.
61. P. Kocienski, K. Jarowicki, and S. Marczak, *Synthesis*, 1991, 1191.
62. J. S. Panek, F. Xu, and A. C. Rondón, *J. Am. Chem. Soc.*, 1998, **120**, 4113.

63. B. M. Trost, W. Tang, and J. L. Schulte, *Org. Lett.*, 2000, **2**, 4013.

Acknowledgments

Thanks are gratefully extended to the Natural Sciences and Engineering Research Council of Canada, the American Chemical Society-Petroleum Research Fund (Grant #37824-B1), Mount Allison University, and the Canada Research Chair/Atlantic Innovation Fund programs.

Hydrocyanation by Homogeneous Catalysis

Albert L. Casalnuovo, Ronald J. McKinney & Chadwick A. Tolman
The DuPont Company, Wilmington, DE, USA

1 Introduction 1
2 The Hydrocyanation of Butadiene to Adiponitrile 2
3 Asymmetric Hydrocyanation 4
4 Related Articles 5
5 References 5

Glossary

Anti-Markovnikov addition: addition that puts the X of HX on the end carbon of a terminal alkene (cf. Markovnikov addition below)
ee (enantiomeric excess): the excess of (R) or (S) enantiomers given by the equations $(N_R - N_S)/(N_R + N_S)$ or $(N_S - N_R)/(N_R + N_S)$, where N_R and N_S are the amounts of R and S enantiomers, respectively
Enantioselectivity: the degree of preference for (R) or (S) enantiomeric products in a chemical reaction
Epoxidation: the addition of an oxygen atom across a C=C bond to give a three-membered ring
Markovnikov addition: addition of the elements of HX to a terminal alkene such that the H goes on the end carbon and the X on the carbon next to the end
Phosphinites: compounds of P^{III} with two P–C bonds and one P–O bond
(R)/(S): designations given to the right-handed and left-handed enantiomers in the traditional Cahn–Ingold–Prelog system
Regioselectivity: the degree of preference for reaction at different positions in a molecule when more than one structural isomeric product can be formed as a product (*see Regiochemistry*)

Abbreviations

A = a Lewis acid such as $AlCl_3$, $ZnCl_2$, or BR_3; ADN = Adiponitrile, $NC(CH_2)_4CN$; BD = 1,3-butadiene, $(CH_2{=}CH)_2$; *ee* = Enantiomeric excess; ESN = Ethylsuccinonitrile, $NCCH_2CH(CN)CH_2Me$; L = A P-donor ligand such as a phosphite or phosphine; 2M3BN = 2-methyl-3-butenenitrile, $NCCH(Me)CH{=}CH_2$; MGN = 2-methylglutaronitrile, $NC(CH_2)_2CH(CN)Me$; 2PN = 2-pentenenitrile, $MeCH_2CH{=}CHCN$; 3PN = 3-pentenenitrile, $MeCH{=}CHCH_2CN$; 4PN = 4-pentenenitrile, $CH_2{=}CHCH_2CH_2CN$.

1 INTRODUCTION

Organic compounds containing nitrile (–CN) groups are commercially important intermediates, because they can be converted into a variety of useful compounds, and because nitrile groups can be converted to other functional groups. Acrylonitrile ($CH_2{=}CHCN$), the largest volume organonitrile, is an important monomer for polymers (*see Polymer*) used for both plastics and synthetic fibers. Hydrogenation of dinitriles to diamines provides important intermediates both for polyurethanes ($–NH(CH_2)_mNHCO_2(CH_2)_nCO_2–$) and polyamides ($–NH(CH_2)_mNHCO(CH_2)_nCO–$); adiponitrile ($NC(CH_2)_4CN$), after hydrogenation to hexamethylenediamine and reaction with adipic acid (equation 1), gives 6,6-nylon, so named because there are six carbon atoms in both the diamine and diacid parts of the polyamide. More than 4 billion pounds of 6,6-nylon are produced this way annually.

$$H_2N(CH_2)_6NH_2 + HO_2C(CH_2)_4CO_2H \longrightarrow [–NH(CH_2)_6NHCO(CH_2)_4CO–]_n + H_2O \qquad (1)$$

Further examples of organonitriles include cyanohydrins, important intermediates in the production of acrylates (equation 2), and aminonitriles, intermediates in the synthesis of chelates such as EDTA (equation 3) and nitrilotriacetate (NTA) (equation 4). A host of smaller volume commercial processes use nitrile intermediates for the production of pharmaceuticals, agrichemicals, cosmetics, and other consumer products.

$$Me_2C(CN)(OH) + H_2SO_4 + H_2O \longrightarrow H_2C{=}C(Me)CO_2H + (NH_4)HSO_4 \qquad (2)$$

$$(NCCH_2)_2NCH_2CH_2N(CH_2CN)_2 + NaOH \longrightarrow \underset{\text{EDTA}}{(NaO_2CCH_2)_2NCH_2CH_2N(CH_2CO_2Na)_2} \qquad (3)$$

$$N(CH_2CN)_3 + H_2O \longrightarrow \underset{\text{NTA}}{N(CH_2CO_2H)_3} \qquad (4)$$

While hydrocyanation, the addition of HCN to an unsaturated substrate, is not the only method of producing an organonitrile, it is often the easiest and most economical. The addition of HCN to aldehydes and ketones is readily accomplished with simple base catalysis, as is its addition to activated alkenes (Michael addition). However, the addition of HCN to unactivated alkenes and dienes is best accomplished with a transition metal catalyst.[1] The hydrocyanation of alkenes and dienes is the most important way to prepare nitriles and is the focus of this article.

1.1 Safety Considerations in Using HCN

Great care must be used in handling HCN. The lack of reported incidents, coupled with the widespread commercial use of volatile and highly toxic HCN, points to the respect and care with which it is treated within industry. In a laboratory, HCN should be used only in small quantities in a well-ventilated fume hood. Vapors may be scrubbed or small samples (up to a few milliliters) may be disposed of by treatment with an equimolar mixture of caustic (NaOH) and hypochlorite bleach (NaOCl). Larger samples or vapor streams should be burned. The use of a 'buddy system' and first response training is essential when using HCN.[2]

2 THE HYDROCYANATION OF BUTADIENE TO ADIPONITRILE

The DuPont ADN process[3] involves hydrocyanation of butadiene (equations 5–8), catalyzed by air- and moisture-sensitive triarylphosphite–nickel(0) complexes $[Ni(P(OAr)_3)_4]$. The nickel is zero valent (*see Oxidation Number*) because it has its full complement of 10 electrons beyond the preceding inert gas (Ar) configuration, and the catalysts can actually be made directly from nickel metal and the phosphite ligands (*see* ***P-donor Ligands***).[4] The four phosphorus atoms each contribute an electron pair to give a total of 18 electrons, corresponding to the next inert gas (Kr), (*see Effective Atomic Number Rule* and ***Electronic Structure of Organometallic Compounds***).

The first HCN addition (equation 5) occurs at practical rates above 70 °C under sufficient pressure to keep butadiene condensed in solution and produces the 1,4- and 1,2-addition products (3PN and 2M3BN) in a 2:1 ratio. Fortunately, thermodynamics favors 3PN (about 9:1), and 2M3BN may be isomerized to 3PN (equation 6) in the presence of the nickel catalyst. (The relative lengths of the arrows in the forward and reverse directions are meant to indicate the relative interconversion rates at equilibrium.)

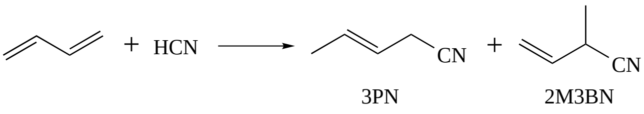

(5)

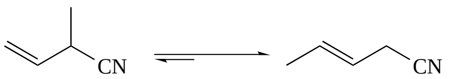

(6)

The selective addition of the second HCN to provide ADN requires the concurrent isomerization of 3PN to 4PN (equation 7), and anti-Markovnikov HCN addition to 4PN (equation 8). A Lewis acid promoter is added to improve the selectivity and increase the rates of these latter steps. Temperatures for the addition of the second HCN are significantly lower than for the first, and practical rates may be achieved above 20 °C at atmospheric pressure. MGN (**1**), ESN (**2**), and 2PN (**3**) are produced as byproducts of the process.

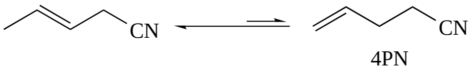

(7)

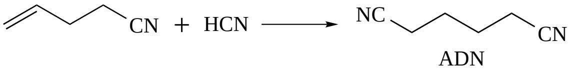

(8)

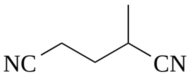

(**1**) MGN

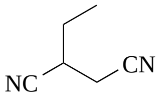

(**2**) ESN

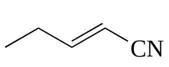

(**3**) 2PN

2.1 Chemical and Mechanistic Information

Though most chemical and mechanistic studies related to the 1971 DuPont ADN process[5] have been published only recently, many of the fundamental studies done as part of the development of the process have greatly advanced our understanding of the organometallic chemistry of nickel (*see* ***Nickel: Organometallic Chemistry***) and other transition metals (*see* ***Mechanisms of Reaction of Organometallic Complexes***) and of their roles in homogeneous catalysis. Some of the more well known concepts to arise from this work include the discovery and quantification of the importance of phosphorus ligand steric effects using ligand cone angles[6] (*see Cone Angle*), the proposal that most transition metal catalyzed processes occur through discreet 16- and 18-electron intermediates[7] (*see Counting Electrons*), and the pictorial use of catalytic cycles in describing the sequence of reactions in catalytic systems.[8]

Some of these features are illustrated in Figure 1, which shows the reactions involved in the addition of the first HCN to butadiene using an NiL_4 catalyst.

Ligand dissociation from the 18-electron NiL_4 complex (L is a phosphite ligand) in step 1 allows *Oxidative Addition* of HCN to the 16-electron NiL_3. (NiL_3 complexes can be isolated for very bulky ligands like $P(O\text{-}o\text{-tolyl})_3$,[9] but not for smaller ligands.) Step 2 gives hydrido–nickel–cyanide complexes ($HNiL_3CN$) (*see* ***Hydride Complexes of the Transition Metals*** and ***Cyanide Complexes of the Transition Metals***),[10,11] characterized by a strong CN stretching vibration in the IR spectrum and 1:3:3:1 quartet in the proton NMR spectrum. Ligand dissociation in step 3 gives a highly reactive 16-electron $HNiL_2CN$ complex which reacts rapidly with butadiene in step 4 to give a π-allyl (*see π-Bond*) nickel cyanide complex observable by NMR and IR spectroscopy at ambient temperature. The hydrogen which was formerly attached to nickel is now found in the terminal CH_3 group of the π-allyl, which is written with a curved line to show that the Ni is bound to all three carbons in the $CH_2CHCH–CH_3$

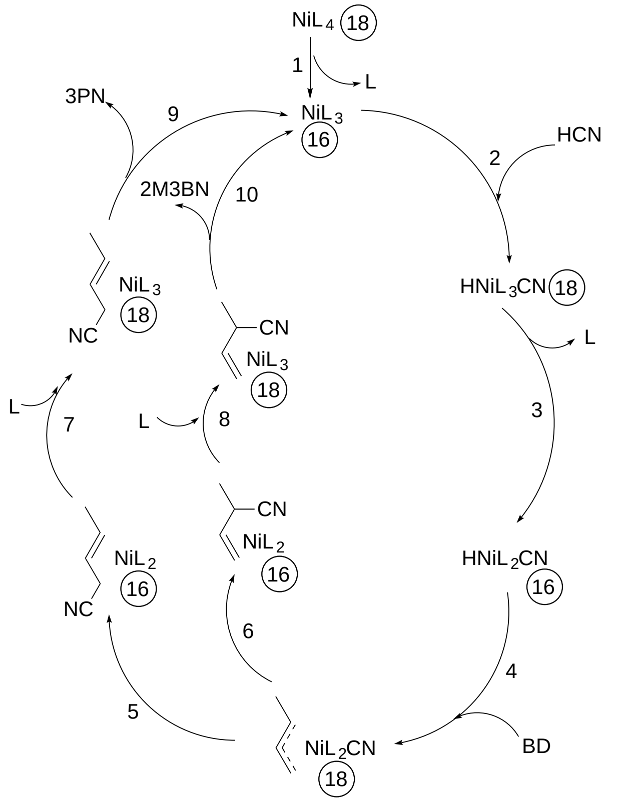

Figure 1 Proposed mechanism of butadiene hydrocyanation with Ni catalysts showing the pathway that introduces the first CN group

chain. Coupling of the CN carbon with carbons 1 or 3 of the chain by *Reductive Elimination* in steps 5 or 6 first gives alkene complexes of 3PN or 2M3BN, and eventually the free products. Steps 5–10 are reversible and provide a mechanism for the isomerization of 2M3BN to 3PN[12] that we saw earlier (equation 6).

This mechanism predicts that the hydrogen atom and cyanide group of HCN will be added across the same side of the carbon–carbon double bond and, consistent with this prediction, the addition of DCN (*see Isotopes & Isotope Labeling*) to cyclohexadiene (equation 9) has been shown to occur stereospecifically *cis* (*see Stereochemistry*).[13]

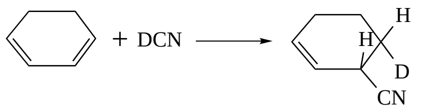

(9)

The isomerization of 3PN to 4PN (equation 7) is catalyzed by a cationic nickel–hydride complex generated by removal of cyanide by a Lewis acid promoter (equation 10).

$$\mathrm{HNi(CN{\cdot}A)L_3} \rightleftharpoons \mathrm{HNiL_3{}^{+}CN{\cdot}A^{-}} \qquad (10)$$

A remarkable feature of this isomerization is the kinetic control which allows 4PN to be made more than 70 times faster than the thermodynamically favored 2PN. The ability of the nitrile group to coordinate to the catalyst and direct the insertion (Scheme 1) is believed to be responsible.[14]

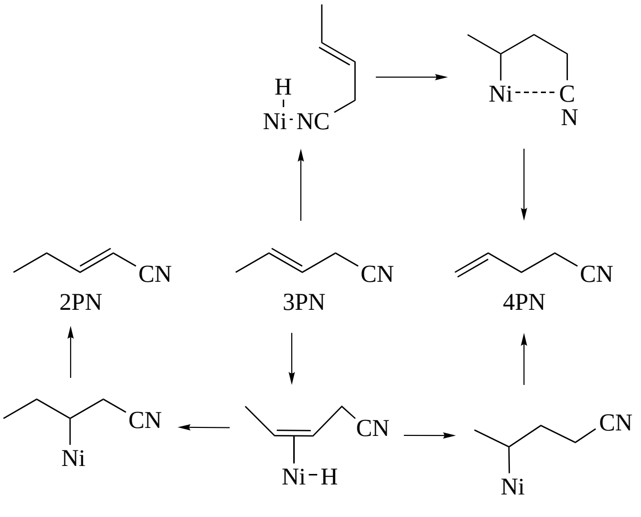

Scheme 1

Alkene bonding to nickel, the *Insertion* of an alkene into the nickel–hydride bond, and the reductive elimination of ADN (or MGN or ESN) from the resulting alkylnickel cyanide complex are the principal features of the second HCN addition in the ADN process. All of the ADN and most of the MGN produced in this process arise from hydrocyanation of 4-PN, even though MGN can be made from hydrocyanation of 3-PN and there is a much greater amount of 3-PN present in the reaction mixture. This result is most likely due to the preferred bonding of 4-PN with the nickel catalyst. One study of a nickel catalyst suggests that the catalyst prefers to bond with 4-PN over 3-PN by about a factor of 200.[15] Insertion of the 4-PN internal alkene carbon into the nickel–hydride bond gives a linear alkylnickel cyanide (**4**; Figure 2), whereas insertion of the terminal alkene carbon gives a branched alkylnickel cyanide (**5**). Reductive elimination from (**4**) yields ADN, while reductive elimination from (**5**) yields MGN. The role of the Lewis acid promoter A in this reaction remains under study, but it is clear that the Lewis acid prefers to bind to an electron pair of the nitrogen of a CN bound to nickel, and that the size of the Lewis acid has a direct bearing on the

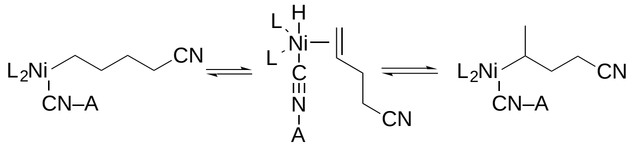

(**4**) A = Lewis acid (**5**)

Figure 2 Proposed mechanism of butadiene hydrocyanation with Ni catalysts showing the alternate insertion modes that prepare the way for introduction of the second CN group

selectivity of products, with bulkier Lewis acids favoring the production of linear nitriles.[16,17]

The exact nature of the complex from which the final reductive elimination occurs remains subject to speculation. The involvement of a five-coordinate nickel complex $RNiL_3CN\cdot A$ appears likely, based on the observation that reductive elimination of benzonitrile from $PhNi(Et_3P)_2(CN)$ is promoted by adding triethyl phosphite,[18] and that reductive elimination of propionitrile from $EtNi[P(O\text{-}o\text{-}tolyl)_3](C_2H_4)(CN)$ is first order in triaryl phosphite concentration.[19]

2.2 Hydrocyanation of Other Alkenes

The use of similar catalyst systems allows the selective HCN addition to many other unsaturated substrates; primary alkenes such as those obtained from the Shell Higher Olefin Process, represented by the formula $CH_2{=}CH(CH_2CH_2)_nCH_2Me$, are readily hydrocyanated under conditions similar to those described above for the second step of the ADN process, and can lead to primary amines (RNH_2), amides ($RCONH_2$), and acids (RCO_2H) containing odd numbers of carbons. Addition of HCN to styrene or other vinylarenes leads to high yields of 2-arylpropionitriles[20] (ArCH(Me)CN), the Markovnikov addition products, which are excellent intermediates for 2-arylpropionic acids ($ArCH(Me)CO_2H$), members of a class of nonsteroidal antiinflammatory drugs which includes ibuprofen and naproxen. The hydrocyanation of dienes, trienes,[21,22] and other polyenes leads to polyfunctionalized molecules which have many potential applications, including polymers and lubricants.

Some metal complexes of metals other than nickel are known to catalyze the hydrocyanation of alkenes, among the best being those of palladium and cobalt.[1]

3 ASYMMETRIC HYDROCYANATION

Asymmetric catalysis (*see* ***Asymmetric Synthesis by Homogeneous Catalysis***), the selective synthesis of left- or right-handed enantiomers using chiral catalysts, has become an important field of research that promises to greatly enhance our ability to make optically pure products for such diverse areas as pharmaceuticals, agrichemicals, and plastics. Impressive advances have been made in asymmetric hydrogenation, epoxidation, and dihydroxylation catalysis, while catalytic asymmetric carbon–carbon bond-forming reactions, such as asymmetric hydrocyanation, have proven more difficult. Until recently, the highest selectivity obtained for the asymmetric hydrocyanation reaction was 40% *ee* for a norbornene substrate. This result was achieved by using nickel or palladium complexes of chiral bidentate phosphines or phosphites as catalysts (equation 11).[23–25]

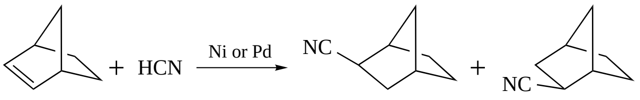

(11)

Recently, *ee*’s of 85–90% have been obtained for the asymmetric hydrocyanation of 6-methoxy-2-vinylnaphthalene using nickel complexes of chiral bidentate phosphinites derived from glucose (abbreviated PP, equation 12).[26] This reaction is of great interest to the pharmaceutical industry because the (*S*) enantiomer of the product nitrile is a useful precursor for the widely marketed antiinflammatory drug naproxen (equation 13). The same reaction can be applied to a number of other vinyl aromatic compounds, including the precursor for the antiinflammatory drug ibuprofen (**6**); however, the *ee* is not as high.

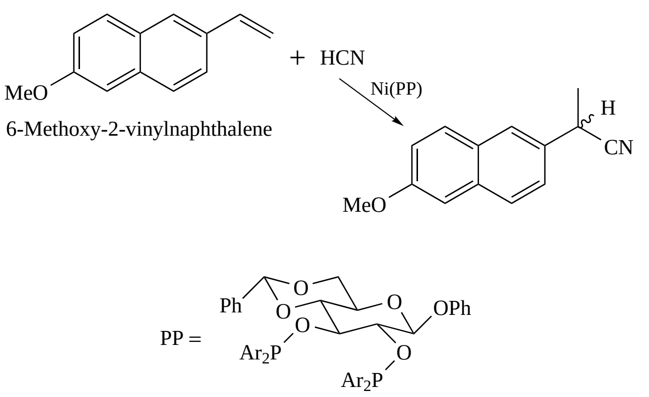

(12)

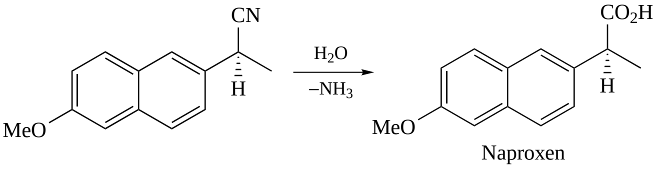

(13)

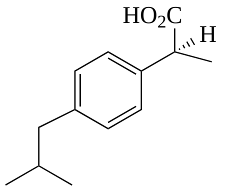

(**6**) (*S*)-Ibruprofen

HCN addition to 6-methoxy-2-vinylnaphthalene occurs readily at 25 °C in the presence of these optically active Ni complexes to give the branched nitrile exclusively and in high yield. The enantioselectivity (*R* versus *S*) of the reaction can be increased by lowering the temperature or decreasing the solvent polarity, but is most dramatically affected by the electronic properties of the aryl group Ar on phosphorus. Thus, the *ee* increases from 16 to 78% upon changing from the relatively electron-donating 3,5-dimethylphenyl group to the relatively electron-withdrawing 3,5-bis(trifluoromethyl)phenyl group (Table 1). A study of a number of other substituted styrene substrates confirms that this electronic effect is general.

The active nickel catalyst contains one bidentate phosphinite ligand and the overall mechanism of the reaction is believed to be similar to butadiene hydrocyanation except that the final reductive elimination step is irreversible under the conditions of the reaction. π-Allyl intermediates (**7**) are believed to play an important role in the exclusive formation of the branched nitrile product observed. Formation of the C–CN bond in the final reductive elimination from the π-allyl intermediate occurs at C(2) and not C(4), because the aromaticity of the naphthalene ring is preserved only when the bond forms with C(2). A σ-alkyl complex (*see σ-Bond*) with the Ni bound to C(1), which could give the linear (anti-Markovnikov) nitrile product, does not contribute because of the much greater stability of intermediate (**7**), accounting for the high regioselectivity observed.

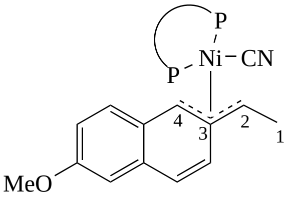

(**7**)

High enantioselectivity results when the reaction proceeds much faster through one of two competing reaction pathways in which Ni(PP) is bound to opposite sides of the plane defined by the atoms C(2)–C(3)–C(4). Although both sides of this plane appear equivalent, the Ni(PP) group distinguishes between the two sides because of the chirality of the PP ligand. While the mechanistic implications of the electronic effect are not clearly understood, deuterium-labeling studies suggest that insertion of the alkene into the nickel hydride bond is nearly irreversible for the electron-poor Ni phosphinite complexes and that this step controls the relative rates of the (R) and (S) pathways.

Table 1 Effect of ligand P–Ar group on enantioselectivity of methoxyvinylnaphthalene hydrocyanation

Ar	*ee* (%)	Solvent
3,5-$Me_2C_6H_3$	16	Benzene
C_6H_5	40	Benzene
3,5-$F_2C_6H_3$	77	Hexane
3,5-$(CF_3)_2C_6H_3$	78	Benzene
3,5-$(CF_3)_2C_6H_3$	85–90	Hexane

4 RELATED ARTICLES

Asymmetric Synthesis by Homogeneous Catalysis; Cyanide Complexes of the Transition Metals; Electronic Structure of Organometallic Compounds; Hydride Complexes of the Transition Metals; Mechanisms of Reaction of Organometallic Complexes; Nickel: Organometallic Chemistry; P-donor Ligands.

5 REFERENCES

1. E. S. Brown, ‘Organic Synthesis via Metal Carbonyls’, eds. I. Wender and P. Pino, Wiley, New York, 1977, Vol. 2, p. 655; *Aspects Homogeneous Catal.*, 1974, **2**, 57.
2. For additional details on using HCN safety, see ‘Prudent Practices for Handling Hazardous Chemicals in Laboratories’, National Academy Press, Washington, DC, 1981, p. 45. Safety literature is also delivered with commercial samples from Fumico, Inc.
3. C. A. Tolman, R. J. McKinney, W. C. Seidel, J. D. Druliner, and W. R. Stevens, *Adv. Catal.*, 1985, **33**, 1.
4. H. E. Shook Jr and J. B. Thompson, *U. S. Pat.*, 3 903 120, 1975.
5. *Chem. Eng. News*, 1971, **49**(17), 30.
6. C. A. Tolman, *Chem. Rev.*, 1977, **77**, 313.
7. C. A. Tolman, *Chem. Soc. Rev.*, 1972, **1**, 337.
8. C. A. Tolman, *J. Am. Chem. Soc.*, 1970, **92**, 6777.
9. L. W. Gosser and C. A. Tolman, *Inorg. Chem.*, 1970, **9**, 2350.
10. J. D. Druliner, A. D. English, J. P. Jesson, P. Meakin, and C. A. Tolman, *J. Am. Chem. Soc.*, 1976, **98**, 2156.
11. C. A. Tolman, W. C. Seidel, J. D. Druliner, and P. Domaille, *Organometallics*, 1984, **3**, 33.
12. J. D. Druliner, *Organometallics*, 1984, **3**, 205.
13. J.-E. Backvall and O. S. Andell, *Organometallics*, 1986, **5**, 2350.
14. R. J. McKinney, *Organometallics*, 1985, **4**, 1142.
15. C. A. Tolman, *J. Chem. Educ.*, 1986, **63**, 199.
16. B. W. Taylor and H. E. Swift, *J. Catal.*, 1972, **26**, 254.
17. R. J. McKinney and W. A. Nugent, *Organometallics*, 1989, **8**, 2871.
18. G. Favero, M. Gaddi, A. Morvillo, and A. Turco, *J. Organomet. Chem.*, 1978, **149**, 395.

19. R. J. McKinney and D. C. Roe, *J. Am. Chem. Soc.*, 1986, **108**, 5167.
20. W. A. Nugent and R. J. McKinney, *J. Org. Chem.*, 1985, **50**, 537.
21. W. Keim, A. Behr, H.-O. Luhr, and J. Weisser, *J. Catal.*, 1982, **78**, 209.
22. E. M. Campi, P. Elmes, W. R. Jackson, C. G. Lovel, and M. K. S. Probert, *Aust. J. Chem.*, 1987, **40**, 1053.
23. P. S. Elmes and W. R. Jackson, *Aust. J. Chem.*, 1982, **35**, 2041.
24. M. Hodgson, D. Parker, R. J. Taylor, and G. Ferguson, *Organometallics*, 1988, **7**, 1761.
25. M. J. Baker and P. G. Pringle, *J. Chem. Soc., Chem. Commun.*, 1991, 1292.
26. T. V. RajanBabu and A. L. Casalnuovo, *J. Am. Chem. Soc.*, 1992, **114**, 6265.

Hydrodesulfurization & Hydrodenitrogenation

Robert J. Angelici
Iowa State University, Ames, IA, USA

1 Introduction 1
2 Hydrodesulfurization 2
3 Hydrodenitrogenation 10
4 Related Articles 14
5 References 15

Abbreviations

$Cp^* = C_5Me_5$; cod = 1,5-cyclooctadiene; T = Thiophene; 2-MeT = 2-methylthiophene; 2,5-Me_2T = 2,5-dimethylthiophene; Me_4T = Tetramethylthiophene; THT = Tetrahydrothiophene; DBT = Dibenzothiophene; 4-MeDBT = 4-methyldibenzothiophene; 4,6-Me_2DBT = 4,6-dimethyldibenzothiophene; Q = Quinoline; THQ = 1,2,3,4-tetrahydroquinoline; py = Pyridine.

1 INTRODUCTION

Hydrodesulfurization (HDS) and hydrodenitrogenation (HDN) are the processes by which sulfur and nitrogen are removed from various petroleum feedstocks.**[1–4]** Both reactions occur during hydrotreating, which is practiced on an enormous scale, 38.3 million barrels per day worldwide in 2002.**[5]** The sulfur content of crude oils usually ranges from 0.2 to 4%,**[6–9]** while nitrogen is approximately 0.1–0.9%. Both elements are present as a plethora of organosulfur and organonitrogen compounds. Under typical conditions, the reactions (equations 1 and 2)

$$C_aH_bS + cH_2 \longrightarrow H_2S + C_aH_d \quad (1)$$

$$C_aH_bN + cH_2 \longrightarrow NH_3 + C_aH_d \quad (2)$$

are performed at 300–450 °C and H_2 pressures of up to 200 atm. The catalysts are often Al_2O_3-supported oxides of Mo and Co or Mo and Ni (*see Catalysis*). During the reactions the transition metals are converted to their sulfides; thus, MoS_2 is a major component of molybdenum-containing catalysts. Under HDS and HDN conditions, these catalysts also promote the hydrogenation of unsaturated hydrocarbons (*see* ***Hydrogenation & Isomerization of Alkenes***); this is often considered to be a disadvantage of the process because of the relatively high cost of H_2. Oxygen removal from organooxygen compounds also occurs, but oxygen is present in only small amounts initially and is not a pollutant; so hydrodeoxygenation (HDO) is not normally the goal of hydrotreating.

There are two major reasons for reducing sulfur and nitrogen levels in petroleum feedstocks: (1) to minimize the amounts of sulfur and nitrogen oxides introduced into the atmosphere by the combustion of petroleum-based fuels, and (2) to prevent poisoning of reforming and cracking catalysts that are used to upgrade feedstocks to product fuels. Since new drilling techniques allow the recovery of heavier crude oils that contain higher levels of sulfur and nitrogen, removal of these elements is becoming even more important. In general, sulfur removal is more important than nitrogen because sulfur levels are higher and governments have put limits on sulfur levels in transportation fuels. For example, sulfur in diesel fuel is currently limited by the U.S. Environmental Protection Agency to 500 ppm; however, in 2006, the limit will be only 15 ppm.**[10]** Since diesel is a higher boiling fraction than gasoline, it contains higher levels of dibenzothiophenes (DBTs), which are the most difficult organosulfur molecules to desulfurize under standard HDS conditions. It is the hindered or refractory DBTs, 4-MeDBT, and 4,6-Me_2DBT, which contain methyl groups near the sulfur, that are especially slow to undergo HDS.**[10,11]** Because it is necessary to desulfurize these refractory DBTs or remove the molecules from diesel fuels in order to achieve the 15 ppm limit, there is a great deal of interest in developing improved HDS processes or other methods for removing these compounds.

Lower sulfur and nitrogen levels are also necessary for both the catalytic hydrocarbon cracking and reforming processes. Basic nitrogen compounds, such as amines and pyridines, are severe poisons of the active acidic sites of zeolite cracking catalysts, which convert larger hydrocarbon molecules to those that can be used in gasoline. The reforming process isomerizes gasoline-range hydrocarbons to those with higher octane numbers. It is also the major process for the synthesis of benzene, toluene, and xylenes. With a worldwide capacity of 11.2 million barrels per day,**[5]** the reforming process requires large quantities of desulfurized feedstocks. It uses an Al_2O_3-supported Pt/Re catalyst that is poisoned by large amounts of sulfur; however, a low sulfur level is actually beneficial because it reduces hydrogenolysis of the hydrocarbons to smaller molecules.

It is the need for improvements in the HDS and HDN processes or the development of new methods for the removal of sulfur and nitrogen from fuels that has attracted the interest of inorganic and organometallic chemists. Their investigations have been directed toward understanding how organosulfur and organonitrogen compounds bind in transition metal complexes as models for their adsorption on active sites of catalyst surfaces; such studies have also provided

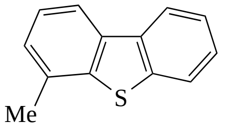

4-MeDBT

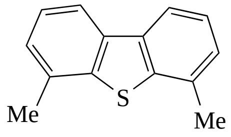

4,6-Me_2DBT

a basis for designing metal ion extractants that remove refractory DBTs from fuel feedstocks. In addition, studies directed at understanding how metal ion binding activates organosulfur and organonitrogen compounds to undergo reactions that lead to their desulfurization or denitrogenation have been pursued in an effort to understand details of the heterogeneously catalyzed HDS and HDN processes. All of these investigations have led to the introduction of new approaches to the desulfurization and denitrogenation of petroleum feedstocks.

2 HYDRODESULFURIZATION

The types of organosulfur compounds found in petroleum feedstocks are shown in Table 1.[12,13] Of them, the alkyl and aryl thiols (RSH), sulfides (RSR′), and disulfides (RSSR′) are the most rapidly desulfurized (equation 1). It is the broad class of thiophenes, stabilized by their aromatic character, that are most difficult to desulfurize and require relatively severe temperatures (≈400 °C) and H_2 pressures (≈100 atm). Thus, it is the HDS of thiophenes that has been of greatest interest to inorganic and organometallic chemists. There are fewer model studies of the HDS of thiols, sulfides, and disulfides.[14–16] Organometallic aspects of HDS and HDN have been summarized most comprehensively in a recent book by Sanchez-Delgado.[17] A briefer overview has also been published.[18] More specific reviews are cited in later sections of this chapter.

While commercial HDS catalysts are based on Mo, other transition metals are also active, some more active than Mo. In Figure 1 is a plot of the HDS activities of transition metal sulfides (*see* ***Chalcogenides: Solid-state Chemistry***) in the conversion of DBT to biphenyl at 400 °C.[19] A similar 'volcano plot' of catalyst activity versus various carbon-supported transition metals is observed in the HDS of thiophene.[20,21] In each study the most active catalysts are the second and third row metals Ru, Os, Rh, and Ir. While their high cost prevents them from being used commercially, their high activity makes them of interest to those who seek to understand the role of the metal as a catalyst. In fact, many of the model organometallic complex studies have been done with these metals.

Table 1 Types of organosulfur compounds in petroleum

RSH, thiols RSR′, sulfides RSSR′, disulfides	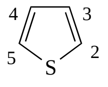 Thiophene (T)
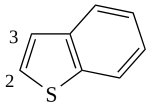 Benzo[*b*]thiophene (BT)	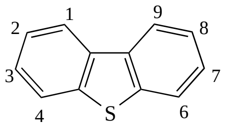 Dibenzothiophene (DBT)

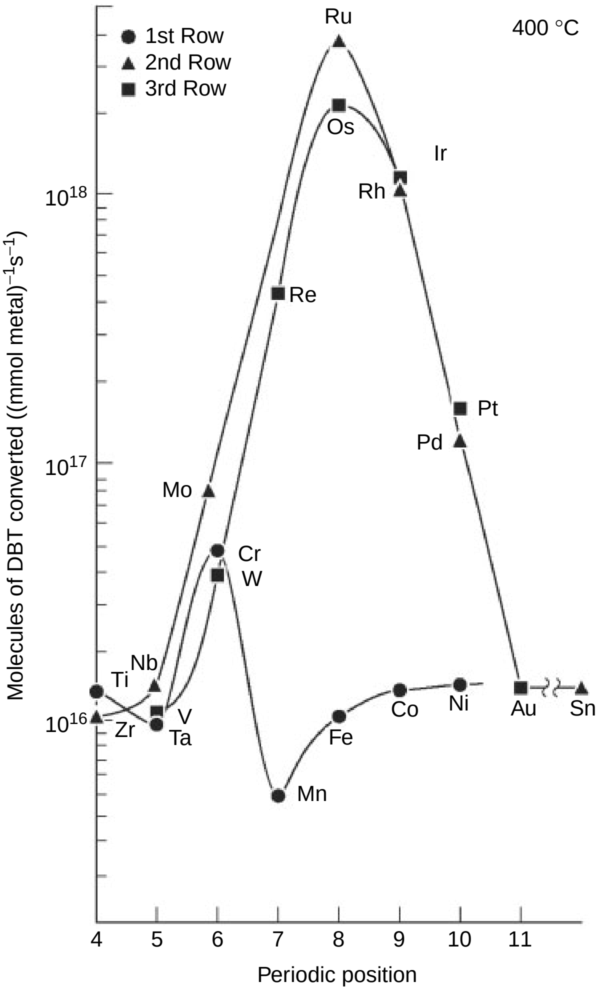

Figure 1 Plot of the rates of dibenzothiophene HDS as a function of the transition metal sulfide catalyst. (Reprinted from Ref. 19. © 1981, with permission from Elsevier)

Under HDS conditions, thiophene is converted to H_2S and C_4 products (equation 3).[22] Often 1,3-butadiene is not observed, but there is evidence to support the suggestion that it is the initial product of the desulfurization and is then hydrogenated to the observed more saturated C_4 products.[23] This is consistent with the fact that most HDS catalysts are also alkene hydrogenation catalysts under HDS conditions.

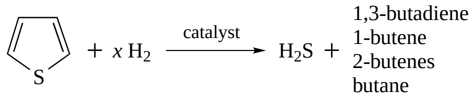

(3)

In order to understand details of the mechanism of thiophene HDS (equation 3), it is necessary to establish the mode of thiophene binding to a metal site on the catalyst surface and to understand how this adsorption activates the thiophene in a way that leads to the final products. Although there is some information on the modes of thiophene binding on clean metal surfaces,**[15]** there are few studies of thiophene adsorbed on MoS_2/Al_2O_3 catalysts themselves. However, a recent vibrational investigation**[24]** of thiophene adsorbed on MoS_2/Al_2O_3, in which infrared and Raman bands are compared with those of model transition metal complexes containing η^1(S)- and η^5-coordinated thiophene, indicates that the thiophene is coordinated through its sulfur η^1(S) to a Mo site. Theoretical treatments**[25]** of thiophene adsorption on cluster MoS_2 models of HDS catalysts show that both η^1(S) and η^5 adsorption modes are favorable. DFT calculations**[26]** of DBT adsorbed on a MoS_2 nanocluster show that the 4,6-methyl groups in 4,6-Me_2DBT do not interfere with adsorption when it is adsorbed parallel to the surface, but η^1(S) adsorption is considerably weaker for 4,6-Me_2DBT than for DBT.

2.1 Thiophene Binding at Metal Centers

Thiophene is known to coordinate in metal complexes in the four ways shown in Figure 2.**[17,27,28]** In the η^1(S) bonding mode, the sulfur acts as a two-electron donor; the metal does not lie in the plane of the thiophene as the ring is tilted. The angle between the M–S bond and the vector from the S to the midpoint of the C(3)−C(4) bond is 119.1° in Cp(CO)(PPh_3)Ru(2-MeT)$^+$ (**1**)**[29]** and 140.4° in Cp*$(CO)_2$Re(T) (**2**).**[30]** The thiophene ligand itself remains planar, but the C–S bond distances increase about 0.04 Å from 1.71 Å in free T to 1.75 Å in the η^1(S) complexes. The tilt at the S and the C–S bond lengthening suggest that the sulfur is approximately sp^3 hybridized (*see Hybridization*) and π-bonding of sulfur within the thiophene ring is reduced. The tilted η^1(S) coordination**[18,31,32]** is common to all thiophenes, benzothiophenes, and DBTs, and even thiophenes incorporated into a porphyrin ring.**[33]** This strong preference for a tilted structure in which the metal does not lie in the plane of the thiophene ligand suggests that η^1(S) thiophene adsorbed at a metal site on a catalyst surface would also be tilted.

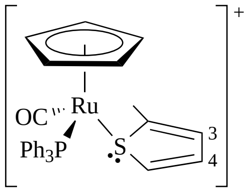

(**1**)

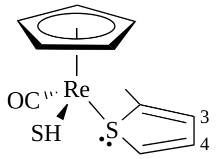

(**2**)

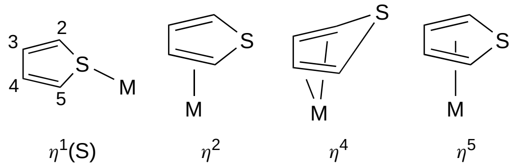

Figure 2 Known modes of thiophene coordination in transition metal complexes

The η^1(S) thiophene ligand is very weakly coordinated (equation 4).**[29]** Thiophene itself is bound less strongly than even MeI. Much more strongly coordinating are tetrahydrothiophene (THT) and acetonitrile. The binding ability of thiophene is generally increased by adding methyl groups to the ring; this makes the sulfur a stronger σ-donor ligand. Only when there are Me groups at both the 2- and 5-positions do steric repulsions reduce the $K_{\eta 1}$ values in Cp(CO)(PPh_3)Ru(η^1(S)-thiophene)$^+$, although not in $Cp(CO)_2Ru$(η^1(S)-thiophene)$^+$ complexes.**[34]**

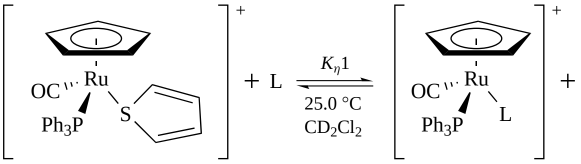

(4)

$K_{\eta 1}$ for the following L ligands: T (1.0) < MeI (2.0) < 2,5-Me_2T (2.76) < 2-MeT (4.11) < 3-MeT (6.30) < BT (29.9) < Me_4T (57.4) < DBT (74.1) << THT and MeCN (7.1 × 10^6)

The η^2 coordination mode (Figure 2) was first identified**[35–37]** in $(NH_3)_5Os(\eta^2\text{-T})^{2+}$. It is also known in Tp(CO)(L)Re(η^2-T), where Tp = hydrotrispyrazolylborate and L = PMe_3, py, or CN–Bu^t,**[38]** but in the less electron-rich complex, $Tp(CO)_2Re(\eta^1$(S)-T), T is η^1(S)-coordinated.**[39]** Selenophene (Sel) in Cp*$(CO)_2$Re(η^2-Sel) is η^2-coordinated;**[40]** however, in Cp*$(CO)_2$Re(η^1(Se)-2,5-Me_2Sel), the 2,5-Me_2Sel is coordinated through Se. Cp*$(CO)_2$Re(2-MeSel) is a tautomeric mixture of the η^2 and η^1(Se) isomers in rapid equilibrium (equation 5). The η^2 isomer is favored in Cp*$(CO)_2$Re(2-MeSel), but the η^1(Se) isomer dominates in the η^5-C_5H_5 analog $Cp(CO)_2$Re(2-MeSel). Cp* stabilizes η^2 coordination by promoting π *Back Bonding* from the Re to the alkene and by disfavoring Se → Re electron donation in the η^1(Se) isomer.

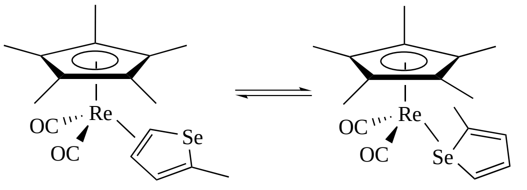

(5)

An η^1(S) $\rightleftharpoons$ η^2 equilibrium (equation 6) is observed in the benzo[*b*]thiophene (BT) complexes Cp′(CO)$_2$Re(BT), where Cp′ is Cp or Cp*.[41] As for selenophene, the Cp* ligand favors η^2-BT, while Cp favors the η^1(S) form; it should be noted that 2-MeBT and 3-MeBT form only the η^1(S) complexes. The formation of the η^2 form from the η^1(S) is important for understanding the first step in the HDS of BT, which gives dihydrobenzothiophene (equation 7). This alkene hydrogenation reaction is catalyzed by homogeneous catalysts[42] and may occur similarly on heterogeneous HDS catalysts. While there is no evidence that there is an η^2 $\rightleftharpoons$ η^1(S) equilibrium in thiophene complexes, both thiophene species *may* exist on a catalyst surface. Low metal oxidation states would favor η^2 coordination, which could lead to the initially observed alkene hydrogenation products.

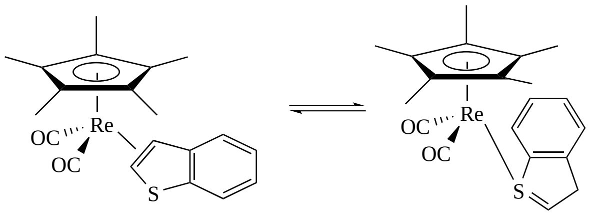

(6)

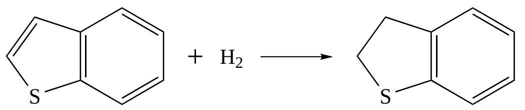

(7)

Complexes with η^4-thiophene ligands have been prepared by a two-electron reduction of η^5-thiophene complexes of Ir[43] and Rh[44] (equation 8) and Ru.[45] Reduction releases the coordinated sulfur in order to maintain the 18-electron configuration (*see Electron Configuration*); the η^4-thiophene ligand acts as a four-electron donor. A structural determination of Cp*Ir(η^4-2,5-Me$_2$T) shows the Ir–S distance (2.969(4) Å) to be substantially longer than a normal Ir–S single bond (2.35 Å). The C–S distances (1.76(2) and 1.79(2) Å) are significantly longer than those (1.71 Å) in thiophene itself; thus, η^4-bonding weakens the C–S bonds, which is partly responsible for the high reactivity of the thiophene ligand in these complexes (see Section 2.2).

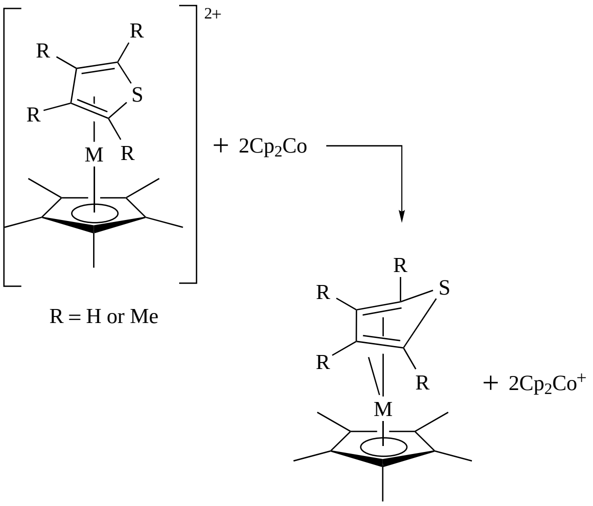

(8)

The most common mode of thiophene coordination in its complexes is η^5 (Figure 2),[28] in which it acts as a six-electron donor. In an equilibrium study[46] of the displacement of thiophene in CpRu(η^5-thiophene)$^+$ by various methyl-substituted thiophenes (equation 9), the K_{η^5} values show that thiophene binding increases with increasing methyl substitution of the thiophene. This is the same trend as that observed[47] for the equilibrium adsorption of thiophenes on a Co–Mo/Al$_2$O$_3$ HDS catalyst at 350 °C: T (1.0) <2-MeT (1.6) ~3-MeT (1.7) <2,5-Me$_2$T (2.5). While the similarity of these trends suggests that thiophene is η^5 adsorbed on the catalyst, it is not possible to exclude η^1(S) adsorption because thiophene binding in Cp(CO)$_2$Ru(η^1(S)-thiophene)$^+$ also increases (equation 4)[29,34] with the number of methyl groups in the thiophene.

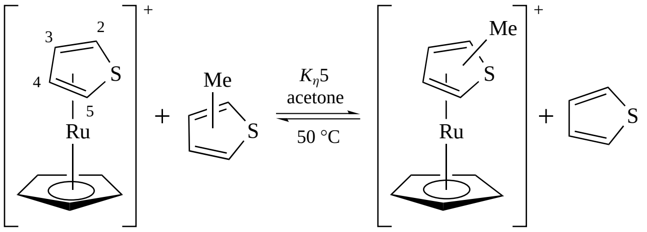

K_{η^5}: T (1) < 2-MeT (6) ≤ 3-MeT (7) < 2,5-Me$_2$T (35) < 2,3-Me$_2$T (50) < 2,3,4-Me$_3$T (200) < 2,3,5-Me$_3$T (300) < Me$_4$T (1300)

(9)

However, η^5 adsorption on catalysts is also supported by deuterium exchange studies of thiophene. When thiophene and D$_2$ are passed over Mo-based HDS catalysts at temperatures below which substantial HDS occurs, the thiophene protons exchange with deuterium. This exchange occurs much more rapidly at the 2- and 5-positions than at the 3- and 4-sites. When CpRu(η^5-T)$^+$ (equation 9) is dissolved in CD$_3$OD in the presence of OD$^-$ at 23 °C, the 2,5-hydrogens of thiophene undergo exchange with deuterium at a rate that is more than 1500 times faster than that of the 3,4-hydrogens.[48] The rate of exchange of the 3,4-hydrogens is first order each in the complex and base (OD^-) concentrations. Thus, η^5-thiophene coordination in $CpRu(\eta^5\text{-T})^+$ activates the thiophene to undergo base-promoted exchange preferentially at the 2,5-positions. This presumably occurs as a result of the metal withdrawing electron density from the thiophene ring, which makes the hydrogens susceptible to deprotonation by the base; the resulting deprotonated carbon is then rapidly deuterated by the CD_3OD solvent. A similar mechanism could account for the deuteration of thiophene on HDS catalysts. After initial η^5 adsorption, the thiophene would be deprotonated by a basic oxide or sulfide site; transfer of a deuterium from a surface OD or SD group to the deprotonated carbon would give the deuterated thiophene. Indeed, when $[CpRu(\eta^5\text{-T})]BF_4$ is adsorbed on Al_2O_3 that contains surface OD groups, partial exchange of the 2,5-hydrogens in the η^5-T ligand occurs.[49]

Considering the importance of removing DBTs from petroleum feedstocks, one might note that these molecules bind in metal complexes primarily through the sulfur η^1(S)[50–52] or η^6 [17,31] through an arene ring. There is no evidence for η^5 coordination through the thiophene ring although there are a few examples[53] of η^4-coordinated DBT (through four nonthiophenic benzocarbons). As described in equation (4), DBT binds in the η^1(S) mode to $Cp(CO)(PPh_3)Ru^+$ more strongly than T. However, equilibrium studies[54,55] of the reaction in equation (10) show that methyl substitution in the 4,6-positions substantially decreases the

$$\begin{gathered}Cp^*(CO)_2Ru(DBT)^+ + Me_xDBT \xrightleftharpoons{K_{DBT}} \\ Cp^*(CO)_2Ru(Me_xDBT)^+ + DBT \\ K_{DBT} \text{ for the following } Me_x \text{ DBT ligands: } 2,8\text{-}Me_2DBT(3.6) > \\ DBT(1.0) > 4\text{-}MeDBT(0.32) > 4,6\text{-}Me_2DBT(0.016) \qquad (10)\end{gathered}$$

coordinating ability of the DBT ligand, which is consistent with the conclusion[25] that 4,6-methyl groups decrease binding of DBTs on metal sites of HDS catalysts. It is interesting that methyl groups in the 2,8-positions, away from the sulfur coordination site, actually increase the binding ability of the DBT due to the electron-donating ability of the methyl groups.

2.2 Reactions of Coordinated Thiophenes

In order to understand the mechanism(s) of thiophene HDS, it is useful to know how thiophene can be activated to react by coordination to a metal; many of these reactions have been reviewed.[56] Of particular interest are reactions that lead to cleavage of the C–S bonds.

Although η^1(S) coordination of thiophene might be expected to make the C_4 portion of the ligand behave like a diene, only one example of this behavior is known (equation 11).[30] Other reactions of η^1(S)-thiophene are unknown, perhaps because the weak coordinating ability of thiophene (Section 2.1) results in its facile displacement.

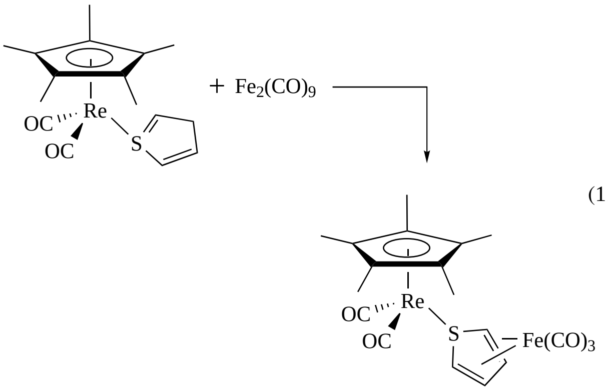

(11)

η^4-Thiophenes are substantially more reactive. The sulfur in $Cp^*Ir(\eta^4\text{-}2,5\text{-}Me_2T)$ (**3**) is a much stronger Lewis base than free thiophene or even Me_2S. Thus, (**3**) forms adducts with Lewis acids such as BH_3 and $Fe(CO)_4$ (equation 12).[57] The sulfur in other η^4-thiophene ligands form similar adducts.[58] Bases such as basic Al_2O_3 and Et_3N catalyze the isomerization (equation 13) of (**3**) to the ring-opened isomer $Cp^*Ir(C,S\text{-}2,5\text{-}Me_2T)$ (**4**).[43] Although the mechanism of this reaction is not known, it illustrates a remarkably facile cleavage of a thiophene C–S bond. Product (**4**) has a structure in which the six-membered ring is planar. This, together with other features of the structure and its ^1H NMR spectrum, suggests that the ring has a delocalized π-system.[59] This is supported by the observation that the six-membered ring in (**4**) forms η^6-complexes analogous to those of η^6-benzene.[59,60]

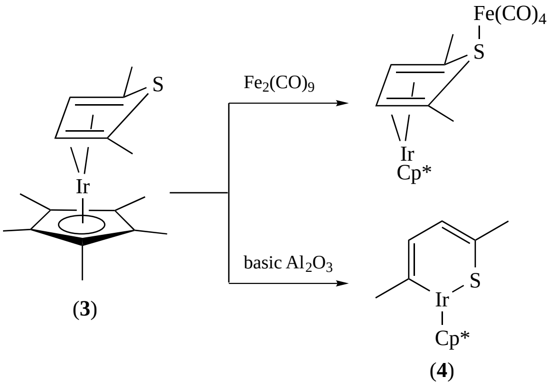

(12)

(13)

While the Rh analog of (**3**) has not been reported to undergo the ring-opening reaction in equation (13), related ring-opened products, including those of benzothiophenes and DBTs,[61] have been obtained by the reaction in equation (14).[62,63] The reaction proceeds by initial *Reductive Elimination* of benzene (PhH) to give an unsaturated $Cp^*Rh(PMe_3)$ intermediate that reacts with thiophene to give the ring-opened product.

The analogous Ir product is obtained from the reaction of $Cp^*Ir(C,S\text{-}2,5\text{-}Me_2T)$ (**4**) with PR_3.[59] Unlike the structure of (**4**), the phosphine adduct structures contain a six-membered ring which is no longer planar or delocalized. Thiophene ring-opening reactions with molybdenum,[52] iron and ruthenium carbonyls,[64,65] and $Cp^*Co(C_2H_4)_2$[61] have also been reported. Related selenophene and tellurophene ring-openings occur in reactions with osmium carbonyl complexes.[64]

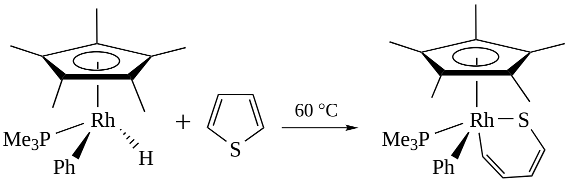

(14)

Besides the ring-opening reactions described above, there are many other examples of this type of reaction with low-valent, electron-rich metal complexes.[56] Among the more thoroughly studied systems is that involving $Pt(PEt_3)_3$, whose reaction with BT is illustrated in equation (15).[66,67] Thiophenes and DBTs also undergo analogous reactions. The

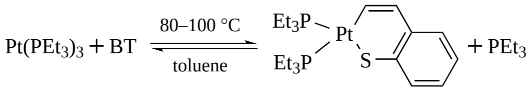

(15)

reversibility of the reactions means that one thiophene in the ring-opened complex can be replaced by another. Reaction of the ring-opened complex of DBT with H_2 results in desulfurization and the formation of biphenyl.[68]

Ring-opening reactions of the type in equation (15) require the very electron-rich $Pt(PEt_3)_3$. The less electron-rich and more sterically hindered $Pt(PPh_3)_3$ does not react. However, Sweigart and coworkers[69,70] showed that electron-withdrawing ML_n metal fragments η^6-coordinated through a benzo ring of BT or DBT activate a C–S bond to ring-open as shown in equation (16). Qualitatively, the rates of these reactions at room temperature decrease

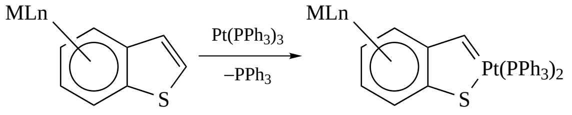

(16)

as the electron-withdrawing ability of the ML_n fragment decreases: $Ru(C_6Me_6)^{2+}$, $Mn(CO)_3{}^+ > FeCp^+$, $RuCp^+ \gg Cr(CO)_3$. If η^6-coordination of BT or DBT were to occur on an electropositive metal site of an HDS catalyst, this could facilitate ring-opening by reaction with a more electron-rich metal nearby as in equation (16). Such a ring-opening reaction would destroy the aromaticity of the thiophene ring and make the BT or DBT more susceptible to complete desulfurization.

Ring-opening of thiophene involves the cleavage of one C–S bond, but the presence of another metal can lead to the cleavage of the remaining C–S bond. On a catalyst surface, several adjacent metal atoms could be available for reaction. The reaction of the ring-opened $Cp^*Ir(C,S\text{-}2,5\text{-}Me_2T)$ (**4**) with the iron carbonyls $Fe(CO)_5$, $Fe_2(CO)_9$, and $Fe_3(CO)_{12}$,[57] while complicated, gives one product (**5**) of particular interest for HDS since it includes all of the elements of $2,5\text{-}Me_2T$, but both C–S bonds are cleaved (equation 17). Both C–S bond cleavage reactions (equations 13 and 17) are models for key steps in a proposed thiophene HDS mechanism (see Section 2.3).

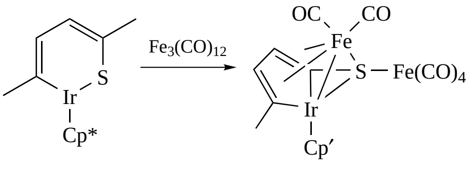

(17)

(**4**) (**5**)

A metal sulfide cluster $Cp'_2Mo_2Co_2(CO)_4S_3$ (**6**), potentially having some structural features of a sulfided Co–Mo/Al_2O_3 catalyst surface, reacts with thiophene at 150 °C under 15 atm of H_2 (equation 18) to give an essentially quantitative yield of the cubane cluster $Cp'_2Mo_2Co_2(CO)_2S_4$ (**7**).[71,72] The thiophene sulfur is incorporated into the cluster, and the hydrocarbon portion is converted to a mixture of C_{1-4} alkanes and alkenes. The mechanism of this reaction may involve initial S-coordination of thiophene to (**6**).

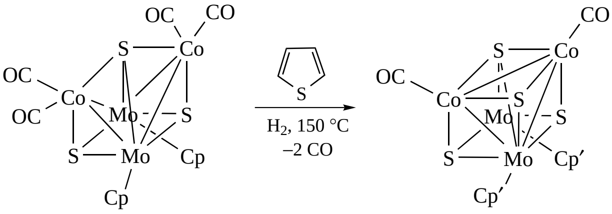

(18)

(**6**) (**7**)

η^5-Thiophene can undergo nucleophilic attack in its cationic complexes. As a model for a hydride on the catalyst surface, $HFe(CO)_4{}^-$ reacts with $(\eta^5\text{-}T)Mn(CO)_3{}^+$ (equation 19) to give the hydrothiophene product (**8**).[73] When $DFe(CO)_4{}^-$ was used, both exo and endo deutero products were formed. Pure endo transfer has been established in the reaction of $ReH_7(PPh_3)_2$ with thiophene (equation 20).[74] This reaction presumably proceeds by initial dehydrogenation of $ReH_7(PPh_3)_2$ to give $ReH_3(PPh_3)_2$, which reacts with thiophene to give the hydrothiophene product resulting from the transfer of H from Re to C(2). The reaction of $RuH_2(\eta^2\text{–}H_2)_2(PCy_3)_2$ with thiophene gives an analogous product;[75] in this case, $RuH_2(\eta^2\text{–}H_2)_2(PCy_3)_2$ also catalyzes the hydrogenation of T to THT.

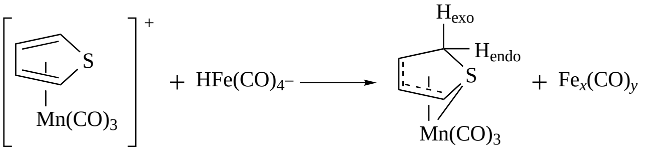

(**8**)

(19)

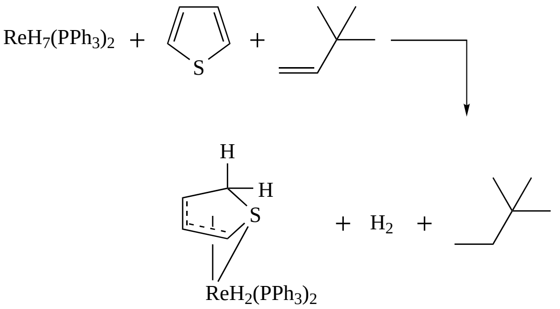

(20)

Hydride nucleophiles (*see Nucleophile*) ($H_2Al(OCH_2CH_2OMe)_2{}^-$, $AlH_4{}^-$, or $HBEt_3{}^-$) also add to the η^5-thiophene ligand in $CpRu(\eta^5\text{-}T)^+$ (equation 21).[73,76] Like the reaction in equation (19), H^- adds to C(2), but in this case the C–S bond is cleaved to give a butadienethiolate complex. An intramolecular version of H^- addition (in this case provided by a PMe_3 ligand) to thiophene to give a butadiene thiolate complex is observed in the reaction of $Mo(PMe_3)_6$ with thiophene (equation 22).[77] It is not clear why the C–S bond remains intact in the products of reactions 19 and 20 but is cleaved in the products of reactions 21 and 22.

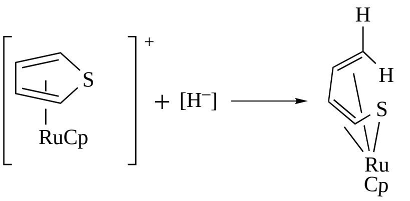

(21)

(**9**)

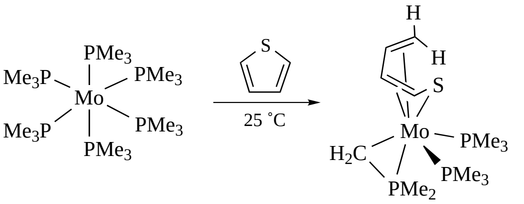

(22)

An intermediate case occurs in another Ru complex, which is formed (equation 23) by endo protonation of the η^4-Me_4T in the η^6-hexamethylbenzene complex (η^4-$Me_4T)Ru(\eta^6$-C_6Me_6).[45] The C(sp^3)–S distance (1.91(1) Å) in (**10**) is considerably longer than a normal C(sp^3)–S bond (1.83 Å), but this bond is not completely cleaved as in (**9**).

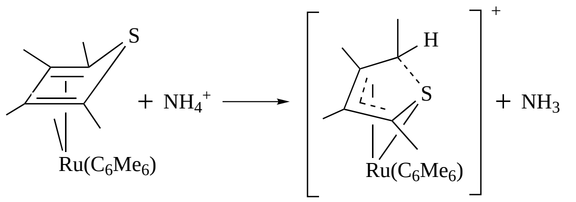

(23)

(**10**)

Simple protonation of (**8**) with a strong acid at 25 °C yields the 2,3-dihydrothiophene (2,3-DHT) complex (equation 24); –SH groups on MoS_2 have been proposed[17,73] to be strong acids and may therefore be relevant. The stepwise addition of H^- (equation 19) and H^+ (equation 24) to η^5-thiophene forms the basis of an important mechanism proposed for thiophene HDS (see Section 2.3).

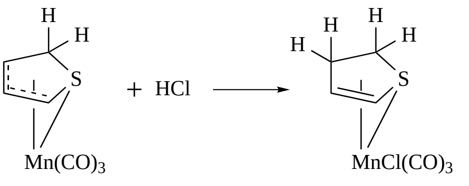

(**8**) (**11**)

(24)

2.3 Mechanisms of Thiophene Hydrodesulfurization

In recent years, mechanisms based on organometallic model studies have been proposed. Several reviews give further details of these studies and proposals.[17,73,78–83] Prior to organometallic model studies, there was little evidence to support the few mechanisms[2,3,17,73] that had been proposed. Two types of mechanisms for the HDS of thiophene based on model studies have been proposed. One (Figure 3) involves initial partial hydrogenation of the thiophene prior to desulfurization.[73,84] Thiophene adsorbs (Figure 3) as an η^5 ligand at a metal site; as in the reaction (equation 19) of $(\eta^5\text{-}T)Mn(CO)_3{}^+$ with $HFe(CO)_4{}^-$, the thiophene is thereby activated to attack (step a) by an adjacent metal hydride (M–H) to give a hydrothiophene intermediate. Protonation by an acidic –SH group (step b) leads to 2,3-dihydrothiophene (2,3-DHT); this is the same type of protonation that was observed (equation 24) in the manganese system. The 2,3-DHT may be coordinated through both the alkene and the sulfur as shown in Figure 3, or it may bind just through the sulfur as observed in its transition metal complexes.[85] Steps (a) and (b) are equivalent to adding two hydrogen atoms, and it is therefore possible that 2,3-DHT is formed by the standard mechanism for metal-catalyzed alkene hydrogenation. The intermediacy of 2,3-DHT in thiophene HDS is supported by the result[84] that 2,3-DHT undergoes HDS over 5% Mo/Al_2O_3 and 5% Re/Al_2O_3 much more rapidly than does thiophene, which accounts for the fact that 2,3-DHT is not observed

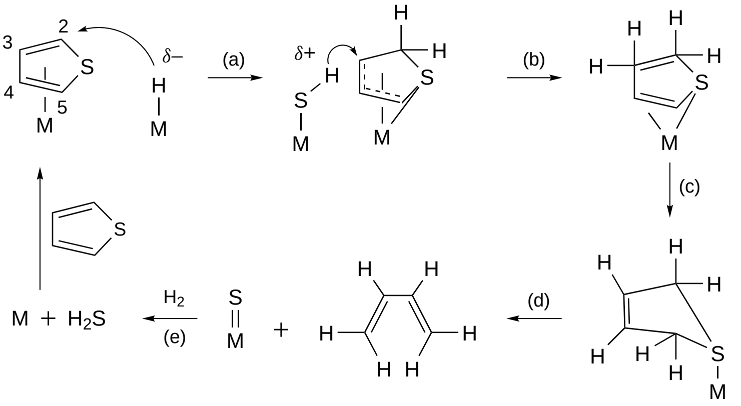

Figure 3 Hydrogenation mechanism proposed for thiophene HDS[73,84]

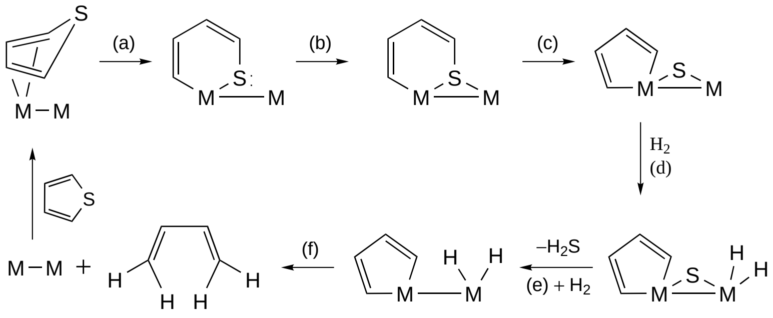

Figure 4 C–S cleavage mechanism proposed for thiophene HDS[57]

as a thiophene HDS product. In addition, the distribution of 1-butene, 2-butene, and butane products is the same for the HDS of both thiophene and 2,3-DHT over 5% Mo/Al_2O_3 at 400 °C.

In step (c) (Figure 3), 2,3-DHT isomerizes to the slightly more thermodynamically stable 2,5-DHT; this alkene isomerization has been observed on a Re/Al_2O_3 catalyst at 300 °C.[84] The desulfurization step (d) involves the elimination of butadiene from an S-coordinated 2,5-DHT; this step is modeled by the evolution of 1,3-butadiene from the S-coordinated 2,5-DHT complexes $Fe(CO)_4$(2,5-DHT), $W(CO)_5$(2,5-DHT), and $Re_2(CO)_9$(2,5-DHT), when they are heated at 110 °C.[85,86] Coordination to the metal is essential for this reaction since free 2,5-DHT does not eliminate 1,3-butadiene under these conditions. The 2,5-DHT also releases 1,3-butadiene when adsorbed on single crystal Mo(110) surfaces[15] and when passed over a 5% Re/Al_2O_3 catalyst at 300 °C under HDS conditions.[84] The more saturated C_4 products (equation 3) observed in thiophene HDS are presumably formed by hydrogenation of the 1,3-butadiene. In step (e), the active metal site is regenerated by removal of the sulfide ligand as H_2S upon reaction with H_2. The key steps (a–d) in this HDS mechanism (Figure 3) have all been observed either in reactions of thiophene complexes or on catalyst surfaces.

From a detailed study[87] of the deuterodesulfurization (DDS) of thiophene over a Chevrel-phase catalyst $PbMo_6S_8$, it was concluded that the mechanism in Figure 3 is consistent with all of the observed results. This study eliminated two other mechanisms that had been previously proposed. The mechanism described below (Figure 4) is also consistent with results of the DDS investigation.

The C–S cleavage mechanism (Figure 4)[57] involves the removal of sulfur from the thiophene ring prior to the transfer of hydrogen to the thiophene. This mechanism begins with η^4 adsorption of thiophene on a metal site. In metal complexes this binding mode is not as common as η^1(S) or η^5 coordination; it occurs when the metal requires the thiophene to act as a four-electron donor. Thus, η^4 adsorption may be demanded by the electronic state and/or the steric environment at the site. The first step (a) in this mechanism (Figure 4), which involves C–S cleavage, is based on the isomerization (equation 13) of Cp*Ir(η^4-2,5-Me_2T) (**3**) to the ring-opened product Cp*Ir(C,S-2,5-Me_2T) (**4**). This reaction may be base-catalyzed as reaction 13 is catalyzed by basic Al_2O_3. On an HDS catalyst surface, S^{2-} or O^{2-} ions may serve as the base. Rather than originating from an η^4-coordinated T, the ring-opened product of step (a) may occur by C–S bond cleavage at an electron-rich metal site, as in equations (14) and (15). Equation (17) shows that a second metal could promote cleavage of the second C–S bond to give a metallacyclopentadiene complex (**5**). An analogous reaction is proposed in step (c). The metallacyclopentadiene could bind to one metal through two M–C σ-bonds as shown in Figure 4 or the diene portion of the ring could also bind to another metal atom as observed in (**5**). Evidence for metallacyclopentadiene units on Pt(111) has been obtained in surface studies of thiophene.**[88,89]** Following formation of the metallacyclopentadiene intermediate, the sulfur is removed with H_2 as H_2S (steps d and e), and 1,3-butadiene is formed in step (f). While these latter reactions are proposed to involve surface hydrides, which may be present on MoS_2 during HDS,**[90]** there is evidence in organomolybdenum chemistry to suggest that –SH groups might serve as the source of hydrogen in these reactions.**[14,91]**

Although HDS using Mo/Al_2O_3-based heterogeneous catalysts is highly effective for many thiophenes, similar reactions catalyzed by homogeneous metal complexes are very limited.**[17,78–83]** Bianchini and coworkers have made especially important contributions in this area. The hydrogenation of thiophene to THT is catalyzed by $[Ir(H)_2(PPh_3)_2(\eta^1(S)\text{-}T)_2]PF_6$ at 1 atm H_2 and 80 °C, but it stops after the formation of 2 moles of THT which binds strongly in $[Ir(H)_2(PPh_3)_2(\eta^1(S)\text{-}THT)_2]PF_6$ and inactivates the Ir complex catalyst.**[92]** In general, a major problem for the development of homogeneous catalysts for HDS reactions is the strong coordinating properties of the hydrogenated organosulfur product (e.g. THT) or H_2S, which inactivates the metal complex catalyst. There is one report of the (triphos)Rh(H)/$KOBu^t$-catalyzed HDS of thiophene to butane, 1-butanethiol and H_2S at 160° and 30 atm H_2, although the turnover numbers are low;**[93]** the authors do not rule out the possibility that the reactions are catalyzed by Rh metal despite studies in the presence of excess mercury metal.**[79]**

The hydrogenation of benzothiophene (BT) to 2,3-dihydrobenzothiophene is catalyzed by several transition metal complexes, including $[Rh(PPh_3)_2(COD)]PF_6$, $Rh(PPh_3)_3Cl$, and $Ru(PPh_3)_3Cl_2$, at 170 °C and 110 atm pressure.**[82]** Using (triphos)Rh(H), where triphos = $MeC(CH_2PPh_2)_3$, as the catalyst at 160° and 30 atm H_2 pressure, the BT in the presence of an equivalent amount of $KOBu^t$ is converted to 2-ethylthiophenol (ETP) with a turnover frequency of 90 mol ETP mol $Rh^{-1}h^{-1}$.**[93]** Detailed mechanistic studies**[79]** show that the reaction proceeds by initial Rh insertion into a C–S bond of BT followed by the hydrogenation steps in Figure 5. This catalyst has been modified by incorporating a sulfonate group into the triphos ligand as $^{-}O_3S\text{–}C_6H_4\text{–}CH_2\text{–}C(CH_2PPh_2)_3$, sulphos. The resulting $(sulphos)Rh(H)^{-}$ complex, together with $KOBu^t$ in the MeOH phase of a two-phase MeOH/*n*-heptane system, catalyzes the hydrogenolysis of BT to ETP at essentially the same rate as the homogeneous reaction using (triphos)Rh(H)/$KOBu^t$. The triphos ligand has also been covalently attached to polystyrene and converted into $[(COD)Rh(polytriphos)]PF_6$, where COD = 1,5-cyclooctadiene.**[94]** This catalyst, which presumably is converted into (polytriphos)Rh(H) under the conditions of the reaction (160 °C, 30 atm H_2), has a slightly higher turnover frequency (124 mol ETP mol $Rh^{-1}h^{-1}$) than either the homogeneous or two-phase catalyst systems.

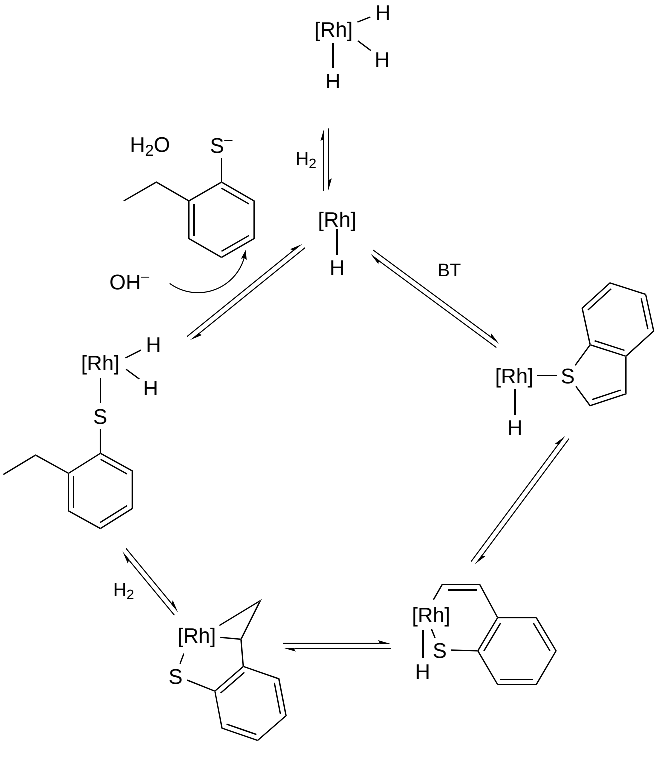

Figure 5 Mechanism for the hydrogenolysis of BT to ETP using (triphos)Rh(H) as the catalyst.**[79]**

The hydrogenolysis of DBT to 2-phenylthiophenol (PTP) is catalyzed by (triphos)Rh(H), generated in situ, at 160 °C and 30 atm H_2 pressure with a very low turnover frequency (2 mol TPT mol $Rh^{-1}h^{-1}$).**[93]** The DBT ring-opened Ir complex (triphos)Ir(H)(η^2-C,S–DBT) catalyzes the formation of PTP in only 8% yield at 170 °C under 30 atm H_2 pressure over a period of 24 h.**[95]** Some biphenyl (5%), the completely desulfurized form of DBT, is also formed in the reactions, but the authors do rule out the possibility that the formation of this product is due to catalysis by a heterogeneous form of Ir. Therefore, there appear to be no unequivocal examples of HDS catalyzed by a homogeneous metal complex that results in the complete removal of sulfur from T, BT, or DBT.

2.4 Extraction of Dibenzothiophenes Using Metal Ion Complexes

As described in the Introduction (Section 1), the new U.S. Environmental Protection Agency regulations for diesel fuel require the removal of DBTs that are not desulfurized under standard HDS conditions. Considering the ability of thiophenes to bind in a variety of transition metal complexes, one can imagine that their affinity for metal ions could be used to remove DBTs, especially the hindered 4,6-Me_2DBT, from diesel fuels. Previously described studies, equations (4) and (10), showed that $Cp(CO)(PPh_3)Ru^+$ and $Cp^*(CO)_2Ru^+$, coordinate DBT much more strongly than T (equation 4); however, 4,6-Me_2DBT binds much less strongly than DBT. To take advantage of this binding ability, the complex $Cp(CO)_2Ru(BF_4)$, generated by the reaction of $Cp(CO)_2RuCl$ with $AgBF_4$, was adsorbed on a mesoporous silica.[96] The resulting solid-phase extractant $CpRu(CO)_2(BF_4)/SiO_2$ was stirred with a simulated fuel consisting of 400 ppm of sulfur (in the form of DBT) in 45% toluene/55% hexanes. Analysis of the solution showed that the DBT had been reduced to only 3.5 ppm of sulfur, that is, a 99% reduction in sulfur. Under the same conditions using 4,6-Me_2DBT instead of DBT, only 72% of the 4,6-Me_2DBT was removed. The reduced effectiveness of $Cp(CO)_2Ru(BF_4)/SiO_2$ for 4,6-Me_2DBT probably reflects steric factors in 4,6-Me_2DBT that were also observed in the solution equilibrium binding studies (equation 10).

Another approach to the extraction of DBTs from a simulated petroleum fuel was the use of the water-soluble $(NH_3)_5Ru(H_2O)^{2+}$, which is known[97] to bind to thiophene (T) as $(NH_3)_5Ru(T)^{2+}$. Because DBT binds more strongly than T in other metal complexes, it was expected that DBT would form $(NH_3)_5Ru(\eta^1(S)\text{-DBT})^{2+}$. The complex is thermally stable but is very air-sensitive, requiring manipulations to be conducted with the careful exclusion of air. The $(NH_3)_5Ru(H_2O)^{2+}$ complex dissolved in a solution of 30% H_2O and 70% dimethyl formamide was able to extract 50% of the 400 ppm of sulfur (in the form of DBT) in a 45% toluene/55% hexanes phase. An analogous extraction of 4,6-Me_2DBT was able to remove only 15% of the 4,6-Me_2DBT.

Relatively simple metal salts adsorbed on silica are able to effectively remove DBTs from hydrocarbon solutions. The extraction of DBT (400 ppm sulfur) in decane with 10% $AgNO_3/SiO_2$ reduced the sulfur level by 72%.[98] An especially interesting result was that a similar extraction of 4,6-Me_2DBT also reduced the sulfur level by 72%.

Extensive studies by Yang and coworkers[99–104] of Ag(I), Cu(I), and Ni(II) forms of zeolites show that these materials are highly effective adsorbents for the removal of DBTs from a variety of transportation fuels. Song and coworkers[10,105] have also developed a range of supports incorporating various metal salts for the removal of DBTs and their hindered derivatives such as 4,6-Me_2DBT from transportation fuels. The details of some of these investigations have either not been published or are contained in patents.

3 HYDRODENITROGENATION

Some of the major types of organonitrogen compounds found in petroleum feedstocks are shown in Table 2.[1,17,106,107] The amines undergo HDN (equation 25) under relatively mild conditions. The unsaturated indoles, pyridines, quinolines, and related derivatives are less reactive, and they consume large quantities of H_2 because hydrogenation of the unsaturated rings occurs before the nitrogen is removed. This is illustrated for the reactions of indole, pyridine, and quinoline over Ni–Mo/Al_2O_3 or Co–Mo/Al_2O_3 catalysts by the networks[22] in equations (26–28). In the case of quinoline (equation 28), not only is the nitrogen-containing ring hydrogenated, but substantial hydrogenation of the benzene ring occurs in path a → d → e → f. Clearly, path a → b → c consumes less H_2, and it produces propylbenzene which has a higher octane rating than propylcyclohexane formed by the other pathway. To reduce H_2 consumption further, it would be desirable to remove nitrogen from these rings without first hydrogenating even the nitrogen-containing ring.

$$RNH_2 + H_2 \longrightarrow RH + NH_3 \qquad (25)$$

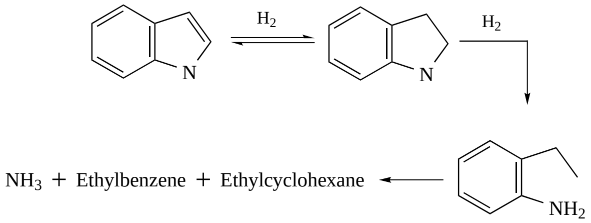

(26)

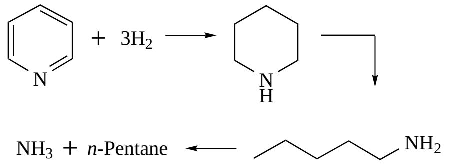

(27)

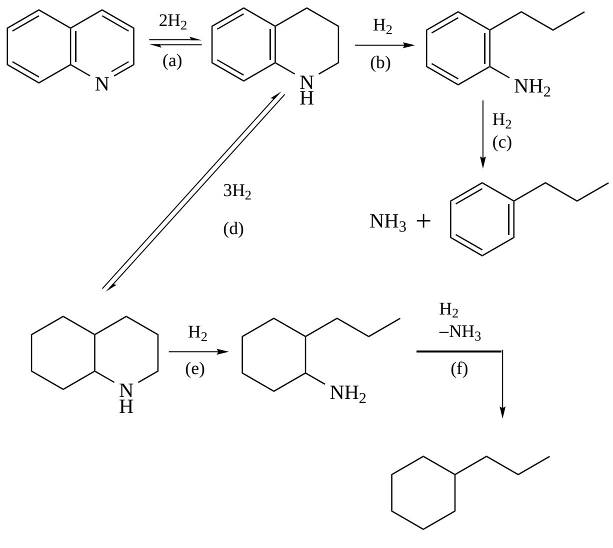

(28)

Table 2 Types of organonitrogen compounds in petroleum

RNH_2 R_2NH } amines R_3N	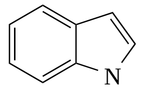 Indole
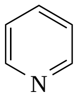 Pyridine	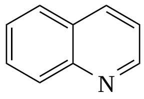 Quinoline

Since HDN occurs in the same process as HDS, H_2S is always present. In fact, H_2S is necessary to maximize the HDN activity of the Co–Mo/Al_2O_3 and Ni–Mo/Al_2O_3 catalysts. One role of the H_2S is to maintain the catalyst in the sulfided form, but there is evidence to suggest that it is also more directly involved in the HDN mechanism. Less is known about possible mechanisms for HDN than HDS based on organometallic models,[17,106–109] but recent studies of amine, pyrrole, pyridine, and quinoline binding and reactions at metal centers offer some possibilities.

3.1 Organonitrogen Compound Binding to Metal Centers

Amines (Table 2) are relatively strong Lewis bases and are known to coordinate to metals (*see **Ammonia & N-donor Ligands***) in a multitude of transition metal complexes.[110] On an HDN catalyst, they are also likely to coordinate through the nitrogen lone electron pair to a metal site; as discussed in Section 3.2, this mode of coordination can activate the hydrocarbon R group in R_3N amines in ways that lead to C–N bond cleavage.

Among the unsaturated heterocyclic nitrogen compounds (Table 2), the indoles are nonbasic because there are no lone electron pairs on the nitrogen. They are, however, known[17,107] to form η^6 complexes, for example, CpRu(η^6-indole)$^+$, in which the indole coordinates as a π ligand through its benzene ring, and an η^2 complex of Cu(I) in which C(2) and C(3) are π-coordinated to the Cu(I).[111] There are also many examples of complexes in which the deprotonated nitrogen of indole is coordinated to a metal.[17,107] There is no evidence that these modes of coordination activate the indole to react in a manner that leads to C–N bond cleavage.

Pyridines in their transition metal complexes coordinate as η^1(N), η^2(C,C), η^2(N,C), or η^6 ligands (Figure 6). By far the most common coordination mode[112] is η^1(N), in which the lone electron pair on the nitrogen donates to a Lewis acidic metal center (*see Lewis Acids & Bases*). The M–N bond lies in the plane of the pyridine ring (Figure 6). Few reactivity studies of η^1(N) pyridine ligands have been reported. One of potential interest for HDN is the base-catalyzed exchange of the pyridine protons for deuterium in the 2,2′-bipyridyl complex $Os(bipy)_3{}^{2+}$ (equation 29) in D_2O/dimethyl sulfoxide solution.[113] The rate of exchange of the 3,3′-hydrogens is first order in the osmium complex and first order in OD^-. A mechanism involving base-promoted deprotonation of the pyridine followed by rapid deuteration was proposed. Exchange of the 3,3′-protons is much faster than those of the others, which decrease in rate in the order: 5, 5′ > 6, 6′ > 4, 4′. When passed with D_2 over a Mo/Al_2O_3 catalyst at 200 °C, 4-methylpyridine undergoes preferential deuterium exchange at the 2 and 6 positions.[114] This exchange may occur by η^1(N) coordination of the pyridine to a metal on the surface, which makes the two and six protons susceptible to deprotonation by surface O^{2-} and subsequent deuteration.

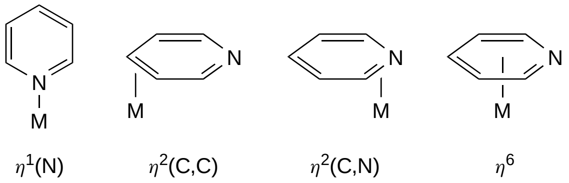

Figure 6 Known modes of pyridine coordination in transition metal complexes

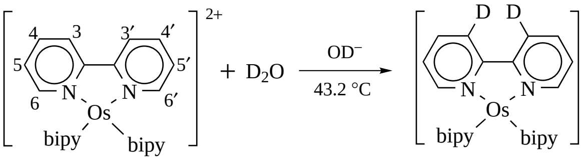

(29)

In a rare example[115] of a bridging pyridine (py) complex, $\{Mo(O)(S_2P\text{-}i\text{-}Pr_2)\}_2(\mu\text{-}O)(\mu\text{-}S)(\mu\text{-}py)$ (**12**), the pyridine ring is almost coplanar with the bridging O and S atoms and the Mo–N distances (2.95(2) and 2.93(2) Å) are very long compared with normal Mo–N bonds (2.23 Å).

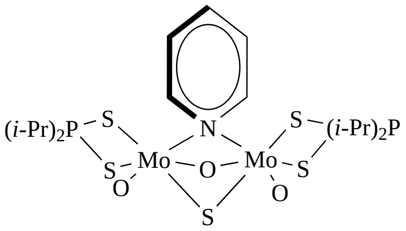

(**12**)

An η^2(C,C)-coordinated 2,6-dimethylpyridine (2,6-Me_2py) ligand has been observed[116] in the Os^{II} complex $Os(NH_3)_5[\eta^2(C,C)\text{-}2,6\text{-}Me_2py]^{2+}$ (equation 30). The $Os(NH_3)_5{}^{2+}$ fragment coordinates η^2(C,C) to a variety of other aromatic ligands;[35] this presumably reflects the strong π back bonding ability of the $Os(NH_3)_5{}^{2+}$ group. Oxidation of the Os^{II} complex to Os^{III} causes the 2,6-dimethylpyridine to rearrange to its common η^1(N) bonding mode (equation 30). This isomerization suggests that the mode of pyridine bonding to a metal site on a catalyst may depend on the oxidation state of the metal.

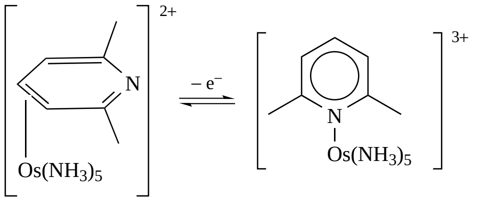

(30)

One of the few examples of an η^2(N,C)-pyridine (Figure 5) is the well-characterized (silox)$_3$Ta[η^2(N,C)-py], prepared according to equation (31).[108,117] A diene-like pattern of alternating short and long double bonds is seen in the uncoordinated segment of the ring. An MO study indicates that the η^2(N,C) structure is stabilized by strong Ta(dπ) $\rightarrow$ py(π^*) back bonding. Another py complex of tantalum, (2,6-diisopropylphenoxide)$_2$(Cl)Ta[η^2(N,C)-2,4,6-*t*-Bu$_3$py], has a distorted η^2(N,C)-py ligand.[118]

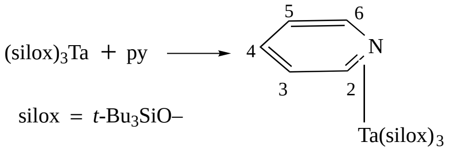

(31)

Most of the known η^6-pyridine complexes contain pyridines with alkyl groups at the 2,6-positions in order to inhibit η^1(N) binding: for example, (CO)$_3$Cr(η^6-2,6-*t*-Bu$_2$py)[119,120] and (CO)$_2$(PPh$_3$)Cr(η^6-2,6-Me$_2$py).[121] Unsubstituted η^6-pyridine complexes also exist, for example, (CO)$_3$Cr(η^6-py)[122] and (PMePh$_2$)$_3$Mo(η^6-py).[123] Factors that influence η^1(N) or η^6 coordination are illustrated in studies (equation 32) of methyl-substituted pyridines (py′) with CpRu(NCMe)$_3{}^+$.[124,125] The 2-methyl- and 2,4-dimethylpyridines initially form the η^1(N)-py′ complex but then more slowly rearrange with loss of MeCN to give the η^6-py′ complex (equation 32). Pyridine itself gives the η^1(N) complex CpRu(η^1(N)-py)$_3{}^+$. If Cp is replaced by the more electron-donating Cp*, even the pyridine complex Cp*Ru(η^1(N)-py)(NCMe)$_2{}^+$ rearranges to the η^6 form Cp*Ru(η^6-py)$^+$. Thus, a relatively high electron density on the metal promotes formation of the η^6 complex. For the less electron-rich system Cp*Rh(NCMe)$_3{}^{2+}$,[126] the tendency to give η^6-py′ complexes is less. Thus, 2-methyl- and 2,4-dimethylpyridines give only the η^1(N) complexes Cp*Rh(η^1(N)-py′)(NCMe)$_2{}^{2+}$; it is only the most sterically hindered 2,4,6-trimethylpyridine that gives the η^6 complex Cp*Rh(η^6-2,4,6-Me$_3$py)$^{2+}$.

$$\mathrm{CpRu(NCMe)_3{}^+ + py' \longrightarrow CpRu(\eta^1(N)\text{-}py')(NCMe)_2{}^+ \xrightarrow{-2NCMe} CpRu(\eta^6\text{-}py')^+} \qquad (32)$$

3.2 Mechanisms of Amine and Quinoline Hydrodenitrogenation

The HDN of aliphatic amines (equation 25) is relevant to the HDN of indoles (equation 26), pyridine (equation 27), and quinoline (equation 28) because these heterocycles are first hydrogenated to the aliphatic amines. A general mechanism[127] proposed for the HDN of aliphatic amines is based on metal cluster catalysis of the transalkylation reaction in equation (33) and on metal complex catalyzed exchange of deuterium for hydrogen in tertiary aliphatic amines (equation 34). There are other examples of amine activation in metal complexes.[128,129]

$$\mathrm{R_3N + R'_3N \xrightarrow[125\,^\circ C]{M_3(CO)_{12},\ M\,=\,Ru,\,Os} R_2NR' + R'_2NR} \qquad (33)$$

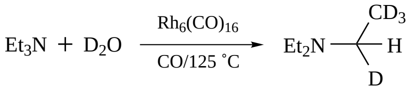

(34)

The HDN mechanism (equation 35)[127] for aliphatic amines, illustrated with piperidine, an intermediate in the HDN of pyridine (equation 27), is shown as involving only one metal atom, but more than one metal could easily be involved. The first step is an oxidative addition of a C–H bond adjacent to the nitrogen to give η^2-piperidinyl and hydride ligands. Cleavage of a C–N bond occurs by attack of a nucleophile (Nuc$^-$) at the coordinated carbon of the piperidinyl ligand to give an amido intermediate. On a MoS$_2$-based hydrotreating catalyst, Nuc$^-$ could be a surface species such as H$^-$, SH$^-$, or OH$^-$, a gas-phase species such as H$_2$S or NH$_3$, or piperidine itself. The known abilities of H$_2$S and H$_2$O to enhance the rate of HDN may be explained if it is assumed that they serve as the nucleophiles, or precursors to the nucleophiles, in the C–N cleavage step. While the mechanism in equation (35) is consistent with results from several catalytic studies,[127] variations of this mechanism cannot be ruled out. Nevertheless, it provides a useful starting point for probing the details of aliphatic amine HDN.

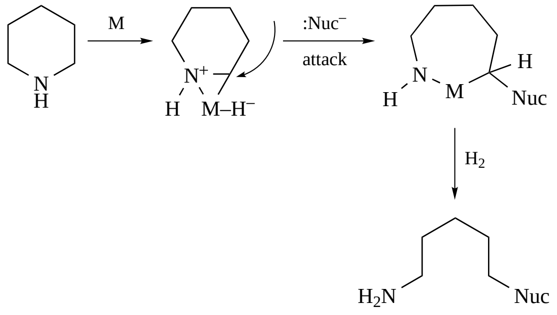

(35)

Other mechanisms for the HDN of aliphatic amines have been proposed on the basis of heterogeneous catalytic studies.[106,107] One of them (equation 36) involves a Hofmann-type elimination of NH_3 from the protonated amine using a basic site on the catalyst surface to remove a β hydrogen. The other (equation 37) again involves initial protonation of the amine which undergoes nucleophilic attack by a basic species to displace the NH_3. Both of these mechanisms are based primarily on the creation of acidic and basic sites under hydrotreating conditions.

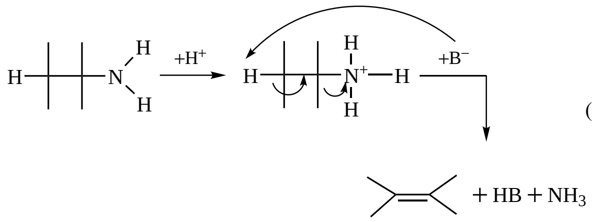

(36)

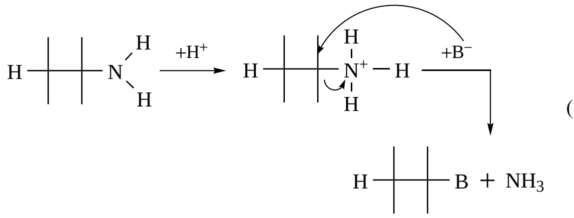

(37)

A mechanism has also been proposed for the first step (a in equation 28) in the HDN of quinoline: the hydrogenation of Q to 1,2,3,4-tetrahydroquinoline (THQ).[42] Not only is this hydrogenation observed on heterogeneous catalysts,[106,127] but it occurs homogeneously when catalyzed by $Fe(CO)_5$,[130] $RuCl_2(PPh_3)_3$, $Ru(H)(Cl)(CO)(PPh_3)_3$, $Os(H)(Cl)(CO)(PPh_3)_3$, $Rh(Cl)(PPh_3)_3$, $Rh(cod)(PPh_3)_2{}^+$, and $Ir(cod)(PPh_3)_2{}^+$.[42,131] The most detailed studies[42] of this hydrogenation were performed with $Cp^*Rh(NCMe)_3{}^{2+}$ at 40 °C in CH_2Cl_2 under 500 psi of H_2. Results of organometallic, NMR, and catalytic reactor studies were most consistent with the mechanism shown in Figure 7. The first step involves coordination of Q through the nitrogen in $Cp^*Rh(\eta^1(N)\text{-}Q)(NCMe)_2{}^{2+}$, a complex that has been isolated and identified by NMR under catalytic conditions. It is the η^1(N)-coordinated form of Q and the availability of two easily replaceable NCMe ligands in this complex that make it catalytically active. This complex is proposed to react with H_2 to form a complex (step a, Figure 7) with η^2(N,C)-coordinated Q and hydride ligands; this intermediate is probably in low concentration as no NMR hydride signals are observed during the reaction. Therefore, hydrogen transfer to the quinoline occurs rapidly. Steps (a) and (b) must be reversible since the Q recovered from reactions using D_2 contained deuterium at the 2-position. Formation of the η^2(C,C) complex in step (c) leads

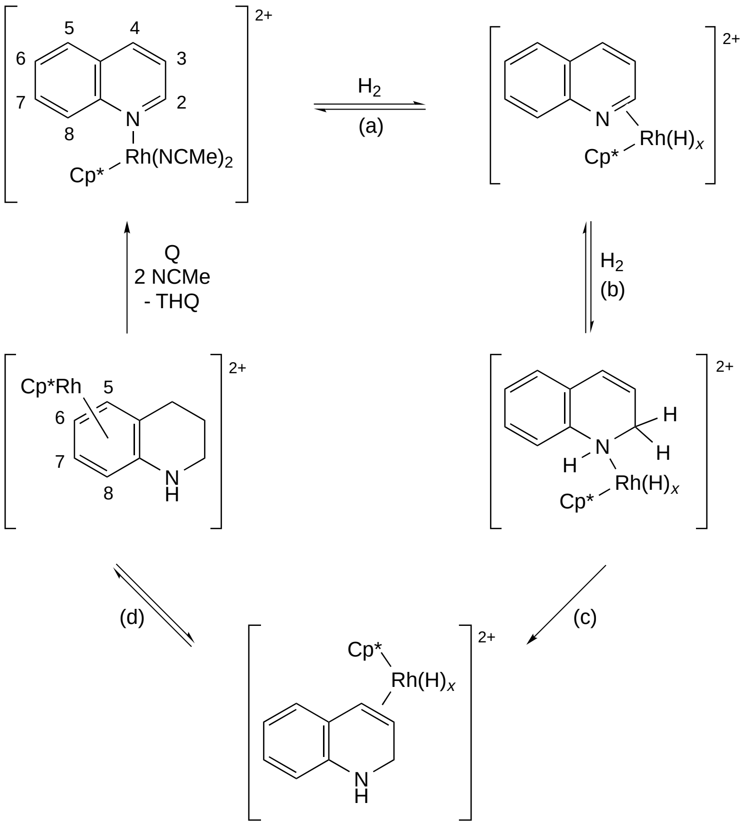

Figure 7 Mechanism for the hydrogenation of quinoline to 1,2,3,4-tetrahydroquinoline[42]

to hydrogenation of the 3,4-positions, and the THQ product remains coordinated as Cp*Rh(η^6-THQ)$^{2+}$, a complex that has been isolated and also identified in NMR spectra of the catalytic reaction mixtures. Displacement of the THQ ligand by Q and two acetonitrile molecules completes the catalytic cycle. The key steps involving hydrogenation of the C=N and C=C double bonds are essentially the same as in catalytic alkene hydrogenation. Complete HDN of Q requires denitrogenation of THQ; a mechanism for this process has not been proposed, but it may be similar to that suggested (equations 35–37) for the HDN of alkylamines.[106,127]

Homogeneous hydrogenation of Q to THQ is also catalyzed by $Os_3(CO)_{12}$ and its derivatives.[107,132] These studies, together with the synthesis of osmium cluster complexes of quinoline, have led to another mechanism for quinoline hydrogenation which involves more than one metal center. It is likely that reactions catalyzed by Cp*Rh(NCMe)$_3^{2+}$ and $Os_3(CO)_{12}$ proceed by different mechanisms. Whether either of these mechanisms is consistent with the heterogeneously catalyzed conversion of Q to THQ is unknown.

While there is no evidence that Mo-based HDN catalysts promote C–N bond cleavage prior to pyridine ring hydrogenation, such a cleavage (equation 38) has been observed[133] in the reaction of the hydride (H$^-$) donor Et_3BH^- with (2,6-diisopropylphenoxide)$_2$(Cl)Ta[η^2(N,C)-2,4,6-*t*-Bu$_3$py] (see Section 3.1). This reaction offers the possibility that nitrogen can be removed without consuming the large quantities of H_2 that are presently required to hydrogenate pyridine, quinoline, and indole rings in the currently practiced HDN process.

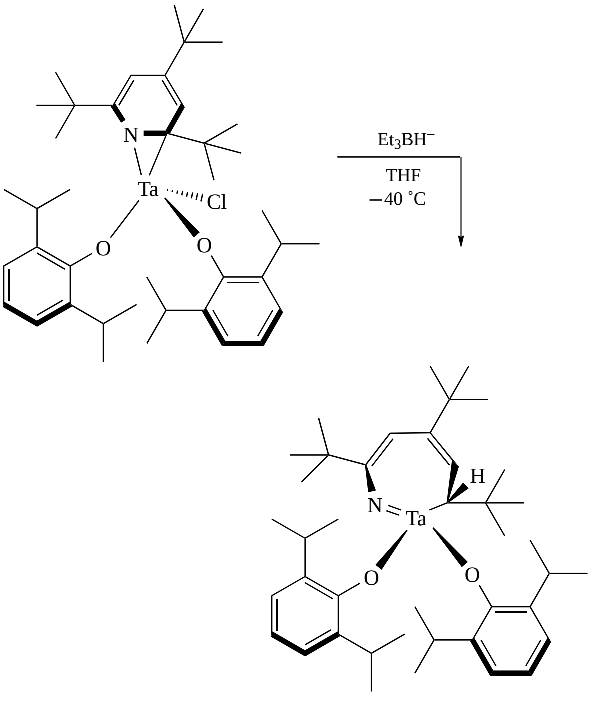

(38)

An even more remarkable pyridine C–N bond cleavage (equation 39) again begins with an η^2(N,C) complex.[134,135] Thermolysis of this complex gives the ring-opened product in which the cleaved C=N bond forms a Nb=C alkylidene complex with one Nb and a Nb=N imido complex with the other. Although the mechanism is not known, this reaction suggests new ways to think about C=N cleavage without first hydrogenating the pyridine ring.

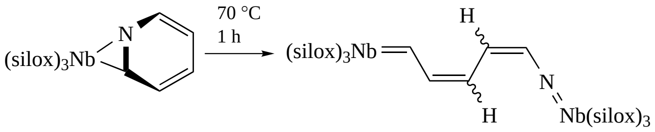

(39)

In reactions that lead to the cleavage of C–N or N–H single bonds, Wolczanski and coworkers[136] studied the reactions of (silox)$_3$Ta and anilines (equation 40). The C–N oxidative-addition product is favored by electron-withdrawing X groups, for example, CF_3, whereas electron-donating X groups (Me or OMe) give exclusively the N–H oxidative-addition product. This reaction is especially interesting because it demonstrates that it is possible to cleave C–N bonds even though the HDN of aniline requires hydrogenation of the arene ring before C–N cleavage occurs.[2,106,137]

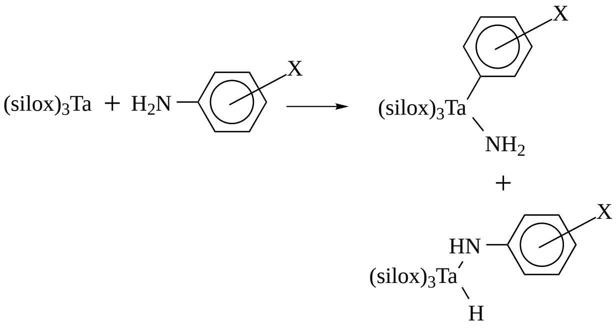

(40)

These C–N cleavage reactions suggest that it may be possible to develop HDN catalysts that will eliminate nitrogen from unsaturated organonitrogen compounds without first hydrogenating the hydrocarbon framework.

4 RELATED ARTICLES

Ammonia & N-donor Ligands; Chalcogenides: Solid-state Chemistry; Heterogeneous Catalysis by Metals; Hydrogenation & Isomerization of Alkenes; S-donor Ligands; Surfaces.

5 REFERENCES

1. C. N. Satterfield, ‘Heterogeneous Catalysis in Industrial Practice’, McGraw-Hill, New York, 1991, p. 378.
2. H. Topsøe, B. S. Clausen, and F. E. Massoth, ‘Hydrotreating Catalysis: Science and Technology’, Springer-Verlag, Berlin, 1996.
3. T. Kabe, A. Ishihara, and W. Qian, ‘Hydrodesulfurization and Hydrodenitrogenation: Chemistry and Engineering’, Kondasa-Wiley-VCH, Tokyo, 1999.
4. V. Vanrysselberghe and G. F. Froment, in ‘Encyclopedia of Catalysis’, ed. I. T. Horvath, Wiley-Interscience, New York, 2003, Vol. 3, p. 667.
5. R. P. Silvy, *Appl. Catal. A: General*, 2004, **261**, 247.
6. W. L. Orr and C. M. White eds, ‘Geochemistry of Sulfur in Fossil Fuels’, ACS Symposium Series 429, American Chemical Society, Washington, DC, 1990.
7. N. K. Lyapina, *Russ. Chem. Rev. (Engl. Transl.)*, 1982, **51**, 189.
8. V. A. Aksenov and V. F. Kamyanov, in ‘Organic Sulfur Chemistry’, eds. R. Kh. Freidina, and A. E. Skorova, Pergamon Press, New York, 1981, p. 201.
9. C. J. Thompson, in ‘Organic Sulfur Chemistry’, eds. R. Kh. Freidina and A. E. Skorova, Pergamon Press, New York, 1981, p. 9.
10. C. Song, *Catal. Today*, 2003, **86**, 211.
11. D. D. Whitehurst, T. Isoda, and I. Mochida, *Adv. Catal.*, 1998, **42**, 345.
12. B. C. Gates, J. R. Katzer, and G. C. A. Schuit, ‘Chemistry of Catalytic Processes’, McGraw-Hill, New York, 1979, Chap. 5.
13. J. G. Speight, ‘The Desulfurization of Heavy Oils and Residua’, Marcel Dekker, New York, 1981.
14. M. Rakowski Dubois, *Chem. Rev.*, 1989, **89**, 1.
15. B. C. Wiegand and C. M. Friend, *Chem. Rev.*, 1992, **92**, 491.
16. R. D. Adams, J. E. Cortopassi, and S. B. Falloon, *Organometallics*, 1992, **11**, 3794; P. M. Boorman, K. Gao, and M. Parvez, *J. Chem. Soc., Dalton Trans.*, 1992, 25.
17. R. A. Sánchez-Delgado, ‘Organometallic Modeling of the Hydrodesulfurization and Hydrodenitrogenation Reactions’, Kluwer Academic Publishers, Dordrecht, 2000.
18. R. A. Sánchez-Delgado, in ‘Encyclopedia of Catalysis’, ed. I. T. Horvath, Wiley-Interscience, New York, 2003, Vol. 3, p. 636.
19. T. A. Pecoraro and R. R. Chianelli, *J. Catal.*, 1981, **67**, 430; R. R. Chianelli, *Catal. Rev.*, 1984, **26**, 361.
20. M. J. Ledoux, O. Michaux, G. Agostini, and P. Panissod, *J. Catal.*, 1986, **102**, 275.
21. J. P. R. Vissers, C. K. Groot, E. M. van Oers, V. H. de Beer, and R. Prins, *Bull. Soc. Chim. Belg.*, 1984, **93**, 813.
22. M. J. Girgis and B. C. Gates, *Ind. Eng. Chem. Res.*, 1991, **30**, 2021.
23. K. F. McCarty and G. L. Schrader, *J. Catal.*, 1987, **103**, 261.
24. P. Mills, S. Korlann, M. E. Bussell, M. A. Reynolds, M. V. Ovchinnikov, R. J. Angelici, C. Stinner, T. Weber, and R. Prins, *J. Phys. Chem. A*, 2001, **105**, 4418.
25. H. Orita, K. Uchida, and N. Itoh, *J. Mol. Catal. A: Chem.*, 2003, **193**, 197.
26. H. Yang, C. Fairbridge, and Z. Ring, *Energy & Fuels*, 2003, **17**, 387.
27. R. J. Angelici, *Coord. Chem. Rev.*, 1990, **105**, 61.
28. T. B. Rauchfuss, *Prog. Inorg. Chem.*, 1991, **39**, 259.
29. J. W. Benson and R. J. Angelici, *Organometallics*, 1992, **11**, 922.
30. M.-G. Choi and R. J. Angelici, *Organometallics*, 1991, **10**, 2436.
31. R. J. Angelici, *Bull. Soc. Chim. Belg.*, 1995, **104**, 265.
32. S. Harris, *Polyhedron*, 1997, **16**, 3219.
33. C. H. Hung, C. K. Ou, G. H. Lee, and S. M. Peng, *Inorg. Chem.*, 2001, **40**, 6845.
34. J. W. Benson and R. J. Angelici, *Organometallics*, 1993, **12**, 680.
35. W. D. Harman, *Chem. Rev.*, 1997, **97**, 1953.
36. B. C. Brooks, T. B. Gunnoe, and W. D. Harman, *Coord. Chem. Rev.*, 2000, **206–207**, 3.
37. W. D. Harman, *Coord. Chem. Rev.*, 2004, **248**, 853.
38. S. H. Meiere, B. C. Brooks, T. B. Gunnoe, E. H. Carrig, M. Sabat, and W. D. Harman, *Organometallics*, 2001, **20**, 3661.
39. T. B. Gunnoe, M. Sabat, and W. D. Harman, *J. Am. Chem. Soc.*, 1998, **120**, 8747.
40. M.-G. Choi and R. J. Angelici, *J. Am. Chem. Soc.*, 1991, **113**, 5651.
41. M.-G. Choi and R. J. Angelici, *Organometallics*, 1992, **11**, 3328.
42. E. Baralt, S. J. Smith, J. Hurwitz, I. Horvath, and R. H. Fish, *J. Am. Chem. Soc.*, 1992, **114**, 5187.
43. J. Chen, L. M. Daniels, and R. J. Angelici, *J. Am. Chem. Soc.*, 1990, **112**, 199.
44. S. Luo, A. E. Ogilvy, T. B. Rauchfuss, A. L. Rheingold, and S. R. Wilson, *Organometallics*, 1991, **10**, 1002.
45. S. Luo, T. B. Rauchfuss, and S. R. Wilson, *J. Am. Chem. Soc.*, 1992, **114**, 8515.
46. J. W. Hachgenei and R. J. Angelici, *Organometallics*, 1989, **8**, 14.
47. M. Zdrazil, *Collect. Czech. Chem. Commun.*, 1977, **42**, 1484.
48. N. N. Sauer and R. J. Angelici, *Organometallics*, 1987, **9**, 1146.

49. G. H. Spies and R. J. Angelici, *J. Am. Chem. Soc.*, 1985, **107**, 5569.
50. M. A. Reynolds, I. A. Guzei, B. C. Logsdon, L. M. Thomas, R. A. Jacobson, and R. J. Angelici, *Organometallics*, 1999, **18**, 4075.
51. M. A. Reynolds, I. A. Guzei, and R. J. Angelici, *Organometallics*, 2001, **20**, 1071.
52. D. G. Churchill, B. M. Bridgewater, and G. Parkin, *J. Am. Chem. Soc.*, 2000, **122**, 178.
53. S. T. H. Willems, P. H. M. Budzelaar, N. N. P. Moonen, R. De Gelder, J. M. M. Smits, and A. W. Gal, *Chem. – Eur. J.*, 2002, **8**, 1310.
54. P. A. Vecchi, A. Ellern, and R. J. Angelici, *J. Am. Chem. Soc.*, 2003, **125**, 2064.
55. C. J. White, T. Wang, R. A. Jacobson, and R. J. Angelici, *Organometallics*, 1994, **13**, 4474.
56. R. J. Angelici, *Organometallics*, 2001, **20**, 1259.
57. J. Chen, L. M. Daniels, and R. J. Angelici, *J. Am. Chem. Soc.*, 1991, **113**, 2544.
58. S. Luo, T. B. Rauchfuss, and S. R. Wilson, *Organometallics*, 1992, **11**, 3497.
59. J. Chen and R. J. Angelici, *Coord. Chem. Rev.*, 2000, **206–207**, 63.
60. J. Chen, V. G. Young, and R. J. Angelici Jr, *Organometallics*, 2002, **21**, 5951.
61. W. D. Jones, D. A. Vicic, R. M. Chin, J. H. Roache, and A. W. Myers, *Polyhedron*, 1997, **16**, 3115.
62. W. D. Jones and L. Dong, *J. Am. Chem. Soc.*, 1991, **113**, 559.
63. L. Dong, S. B. Duckett, K. F. Ohman, and W. D. Jones, *J. Am. Chem. Soc.*, 1992, **114**, 151.
64. M. Brorson, J. D. King, K. Kiriakidou, F. Prestopino, and E. Nordlander, in ‘Metal Clusters in Chemistry’, eds. P. Braunstein, L. A. Oro, and P. R. Raithby, Wiley-VCH, New York, 1999, p. 741.
65. A. Chehata, A. Oviedo, A. Arevalo, S. Bernes, and J. J. Garcia, *Organometallics*, 2003, **22**, 1585.
66. J. J. Garcia, B. E. Mann, H. Adams, N. A. Bailey, and P. M. Maitlis, *J. Am. Chem. Soc.*, 1995, **117**, 2179.
67. M. Hernandez, G. Miralrio, A. A. Georgina, S. Bernes, J. J. Garcia, C. Lopez, P. M. Maitlis, and F. del Rio, *Organometallics*, 2001, **20**, 4061.
68. A. Iretskii, J. J. Garcia, G. Picazo, and P. M. Maitlis, *Catal. Lett.*, 1998, **51**, 129.
69. K. Yu, H. Li, E. J. Watson, K. L. Virkaitis, G. B. Carpenter, and D. A. Sweigart, *Organometallics*, 2001, **20**, 3550.
70. M. Oh, K. Yu, H. Li, E. J. Watson, G. B. Carpenter, and D. A. Sweigart, *Adv. Synth. Catal.*, 2003, **345**, 1053.
71. U. Riaz, O. Curnow, and M. D. Curtis, *J. Am. Chem. Soc.*, 1991, **113**, 1416.
72. M. D. Curtis, *Appl. Organometal. Chem.*, 1992, **6**, 429.
73. R. J. Angelici, *Acc. Chem. Res.*, 1988, **21**, 387.
74. G. P. Rosini and W. D. Jones, *J. Am. Chem. Soc.*, 1992, **114**, 10 767.
75. A. F. Borowski, S. Sabo-Etienne, B. Donnadieu, and B. Chaudret, *Organometallics*, 2003, **22**, 4803.
76. J. W. Hachgenei and R. J. Angelici, *J. Organometal. Chem.*, 1988, **355**, 359; G. H. Spies and R. J. Angelici, *Organometallics*, 1987, **6**, 1897.
77. K. E. Janak, J. M. Tanski, D. G. Churchill, and G. Parkin, *J. Am. Chem. Soc.*, 2002, **124**, 4182.
78. C. Bianchini and A. Meli, *J. Chem. Soc., Dalton Trans: Inorg. Chem.*, 1996, (6), 801.
79. C. Bianchini and A. Meli, *Acc. Chem. Res.*, 1998, **31**, 109.
80. C. Bianchini and A. Meli, in ‘Aqueous-Phase Organometallic Catalysis’, eds. B. Cornils, and W. A. Herrmann, Wiley-VCH, Weinheim, 1998, p. 477.
81. C. Bianchini and A. Meli, *NATO ASI Ser., Ser. 3: High Technol.*, 1998, **60**, 129.
82. C. Bianchini and A. Meli, in ‘Applied Homogeneous Catalysis with Organometallic Compounds’, eds. B. Cornils, and W. A. Herrmann, VCH, Weinheimm, 1996, Vol. 2, p. 969.
83. C. Bianchini, A. Meli, and F. Vizza, ‘Applied Homogeneous Catalysis with Organometallic Compounds’, 2nd edn., Wiley-VCH, Weinheim, 2002, Vol. 3, p. 1099.
84. E. J. Markel, G. L. Schrader, N. N. Sauer, and R. J. Angelici, *J. Catal.*, 1989, **116**, 11; N. N. Sauer, E. J. Markel, G. L. Schrader, and R. J. Angelici, *J. Catal.*, 1989, **117**, 295.
85. N. N. Sauer and R. J. Angelici, *Inorg. Chem.*, 1987, **26**, 2126; G. N. Glavee, L. M. Daniels, and R. J. Angelici, *Inorg. Chem.*, 1989, **28**, 1751.
86. M.-G. Choi, L. M. Daniels, and R. J. Angelici, *Inorg. Chem.*, 1991, **30**, 3647.
87. J. W. Benson, G. L. Schrader, and R. J. Angelici, *J. Mol. Catal. A: Chem.*, 1995, **96**, 283.
88. J. Stohr, J. Gland, E. B. Kollin, R. J. Koestner, A. L. Johnson, E. L. Muetterties, and F. Setten, *Phys. Rev. Lett.*, 1984, **53**, 2161; J. F. Lang and R. I. Masel, *Surf. Sci.*, 1987, **183**, 44.
89. C. H. Patterson, P. Y. Mundenar, A. J. Timbrell, A. J. Gellman, and R. M. Lambert, *Surf. Sci.*, 1989, **208**, 93.
90. L. S. Byskov, M. Bollinger, J. K. Nørskov, B. S. Clausen, and H. Topsøe, *J. Mol. Catal. A: Chem.*, 2000, **163**, 117.
91. L. L. Lopez, P. Bernatis, J. Birnbaum, R. C. Haltiwanger, and M. Rakowski DuBois, *Organometallics*, 1992, **11**, 2424.
92. C. Bianchini, A. Meli, M. Peruzzini, F. Vizza, V. Herrera, and R. A. Sánchez-Delgado, *Organometallics*, 1994, **13**, 721.
93. C. Bianchini, J. A. Casares, A. Meli, V. Sernau, F. Vizza, and R. A. Sánchez-Delgado, *Polyhedron*, 1997, **16**, 3099.
94. C. Bianchini, M. Frediani, and F. Vizza, *Chem. Commun.*, 2001, 479.
95. C. Bianchini, M. V. Jiménez, A. Meli, S. Moneti, F. Vizza, V. Herrera, and R. A. Sánchez-Delgado, *Organometallics*, 1995, **14**, 2342.

96. S. G. McKinley, P. A. Vecchi, A. Ellern, and R. J. Angelici, *Dalton Trans.*, 2004, 788.
97. C. G. Kuehn and H. Taube, *J. Am. Chem. Soc.*, 1976, **98**, 689.
98. S. G. McKinley and R. J. Angelici, *Chem. Commun.*, 2003, 2620.
99. F. H. Yang, A. J. Hernandez-Maldonado, and R. T. Yang, *Sep. Sci. Technol.*, 2004, **39**, 1717.
100. A. J. Hernandez-Maldonado and R. T. Yang, *AIChE J.*, 2004, **50**, 791.
101. A. J. Hernandez-Maldonado and R. T. Yang, *J. Am. Chem. Soc.*, 2004, **126**, 992.
102. A. J. Hernandez-Maldonado and R. T. Yang, *Ind. Eng. Chem. Res.*, 2004, **43**, 1081.
103. R. T. Yang, A. J. Hernandez-Maldonado, and F. H. Yang, *Science*, 2003, **301**, 79.
104. A. J. Hernandez-Maldonado and R. T. Yang, *Ind. Eng. Chem. Res.*, 2003, **42**, 123.
105. (a) C. Song and X. Ma, *Appl. Catal. B: Environ.*, 2003, **41**, 207; (b) S. Velu, X. Ma, and C. Song, *Ind. Eng. Chem. Res.*, 2003, **42**, 5293.
106. R. Prins, *Adv. Catal.*, 2002, **46**, 399.
107. C. Bianchini, A. Meli, and F. Vizza, *Eur. J. Inorg. Chem.*, 2001, 43.
108. K. J. Weller, P. A. Fox, S. D. Gray, and D. E. Wigley, *Polyhedron*, 1997, **16**, 3139.
109. R. J. Angelici, *Polyhedron*, 1997, **16**, 3073.
110. D. A. House, in 'Comprehensive Coordination Chemistry', ed. G. Wilkinson, Pergamon Press, Oxford, 1987, Vol. 2, p. 23.
111. Y. Shimazaki, H. Yokoyama, and O. Yamauchi, *Angew. Chem., Int. Ed. Engl.*, 1999, **38**, 2401.
112. J. Reedijk, in 'Comprehensive Coordination Chemistry', ed. G. Wilkinson, Pergamon Press, Oxford, 1987, Vol. 2, p. 73.
113. O. Wernberg, *J. Chem. Soc., Dalton Trans.*, 1986, 1993.
114. G. V. Smith, C. C. Hinckley, and F. Behbahany, *J. Catal.*, 1973, **30**, 218.
115. M. G. B. Drew, P. C. H. Mitchell, and A. R. Read, *J. Chem. Soc., Chem. Commun.*, 1982, 238.
116. R. Cordone and H. Taube, *J. Am. Chem. Soc.*, 1987, **109**, 8101.
117. K. J. Covert, D. R. Neithammer, M. C. Zonnevylle, R. E. LaPointe, C. P. Schaller, and P. T. Wolczanski, *Inorg. Chem.*, 1991, **30**, 2494.
118. D. P. Smith, J. R. Strickler, S. D. Gray, M. A. Bruck, R. S. Holmes, and D. E. Wigley, *Organometallics*, 1992, **11**, 1275.
119. R. E. Schmidt and W. Massa, *Z. Naturforsch., Teil B*, 1984, **39B**, 213.
120. K. Dimroth, R. Thamm, and H. Kaletsch, *Z. Naturforsch., Teil B*, 1984, **39B**, 207.
121. H. W. Choi and M. S. Sollberger, *J. Organomet. Chem.*, 1983, **243**, C39.
122. S. G. Davies and M. R. Shipton, *J. Chem. Soc., Perkin Trans. 1*, 1991, 501.
123. R. H. Morris and J. M. Ressner, *J. Chem. Soc., Chem. Commun.*, 1983, 909.
124. R. H. Fish, H.-S. Kim, and R. H. Fong, *Organometallics*, 1991, **10**, 770.
125. R. H. Fish, R. H. Fong, A. Tran, and E. Baralt, *Organometallics*, 1991, **10**, 1209.
126. R. H. Fish, E. Baralt, and H.-S. Kim, *Organometallics*, 1991, **10**, 1965.
127. R. M. Laine, *Catal. Rev.-Sci. Eng.*, 1983, **25**, 459.
128. R. D. Adams and J. T. Tanner, *Appl. Organomet. Chem.*, 1992, **6**, 449.
129. S. E. Kabir, M. Day, M. Irving, T. McPhillips, H. Minassian, E. Rosenberg, and K. I. Hardcastle, *Organometallics*, 1991, **10**, 3997.
130. T. J. Lynch, M. Banah, H. D. Kaesz, and C. R. Porter, *J. Org. Chem.*, 1984, **49**, 1266.
131. R. A. Sanchez-Delgado and E. Gonzalez, *Polyhedron*, 1989, **8**, 1431.
132. R. M. Laine, *Nouv. J. Chim.*, 1987, **11**, 543.
133. S. D. Gray, D. P. Smith, M. A. Bruck, and D. E. Wigley, *J. Am. Chem. Soc.*, 1992, **114**, 5462.
134. T. S. Kleckley, J. L. Bennett, P. T. Wolczanski, and E. B. Lobkovsky, *J. Am. Chem. Soc.*, 1997, **119**, 247.
135. J. B. Bonanno, A. S. Veige, P. T. Wolczanski, and E. B. Lobkovsky, *Inorg. Chim. Acta*, 2003, **345**, 173.
136. J. B. Bonnano, T. P. Henry, D. R. Neithamer, P. T. Wolczanski, and E. B. Lobkovsky, *J. Am. Chem. Soc.*, 1996, **118**, 5132.
137. P. Geneste, C. Moulinas, and J. L. Olivé, *J. Catal.*, 1987, **105**, 254.

Hydrogen: Inorganic Chemistry

Masahisa Kakiuchi
Gakushuin University, Tokyo, Japan

1 Introduction 1
2 Occurrence, Preparation, use, and Analysis of Hydrogen 2
3 Isotopes of Hydrogen 4
4 Isotope Effect of Hydrogen 10
5 Chemical Properties of Hydrogen 15
6 Physical Properties of Hydrogen 20
7 Related Articles 22
8 References 22

1 INTRODUCTION

Hydrogen is the first element in the periodic table and has the simplest atomic structure of all the elements; its nucleus consists of a single proton and it has one outer electron. There are three isotopes of hydrogen: ^{1}H (also called protium or H), the lightest and the most abundant isotope, ^{2}H (deuterium or D), and ^{3}H (tritium or T). Terrestrial hydrogen contains about 0.0156 atom % of deuterium and a very small amount (1 atom per 10^{18} atoms of hydrogen) of tritium.

The name hydrogen was derived from the Greek words 'hydro', meaning water, and 'gene', meaning form. In 1766, Cavendish discriminated hydrogen gas as an element, by measuring its density and the volume of gas evolved from a given amount of acid and metal. In 1932, deuterium was discovered in the spectrum of the final fraction left after the evaporation of a large sample of liquid hydrogen.[1] Tritium was generated by *Deuteron* bombardment of D_3PO_4 and $(ND_4)_2SO_4$ by Oliphant *et al.*[2] in 1934. The presence of tritium in the atmosphere and in natural waters was proved in 1950 by Harteck and Faltings,[3] and in 1951 by Grosse *et al.*[4] The tritium concentration in atmospheric hydrogen molecules and in natural waters was found to be about one atom in 10^{15} protium atoms and one atom in 10^{18} protium atoms, respectively.

Hydrogen abundance in the solar system (formerly known as cosmic abundance) account for 71% of the mass fraction or 91% of all the atoms.[5] Captured by the gravitational force of the Sun, hydrogen is converted into helium by nuclear fusion, a process that supplies the energy to the Sun. Current theories consider hydrogen as the primary constituent of the universe, which were condensed into stars by gravitational forces. This condensation led to fusion reactions, converting hydrogen into helium, with the release of energy.

Molecular hydrogen is a colorless, odorless gas, and is virtually insoluble in water. It is most easily prepared on a small scale by the reaction between a dilute acid and a metal, such as Zn and Fe, and by the electrolysis of water. A large-scale production of hydrogen is available mainly from the reactions of hydrocarbons and coke. A major share of manufactured hydrogen comes from hydrocarbons. The thermal cracking of hydrocarbons is an important part of petroleum refining and produces a large amount of hydrogen. Steam passed over coke heated to more than 1000 °C undergoes the well-known *Water Gas Reaction* (equation 1). Hydrogen production is used in manufacture of Ammonia Synthesis ($N_2 + 3H_2$) and methanol synthesis ($CO + 2H_2$) gas.

$$H_2O + C \longrightarrow CO + H_2 \qquad (1)$$

Although the abundance of molecular hydrogen on the Earth is trivial (e.g. the atmosphere contains about 0.5 ppm H_2), hydrogen in the form of compound is very abundant. In the combined state, hydrogen is most commonly found in compounds with oxygen, carbon, and nitrogen. Water is the most important hydrogen compound (*see* ***Water & O-donor Ligands***). Other compounds of significance are organic ones such as hydrocarbons, ammonia, and its derivatives (*see* ***Ammonia & N-donor Ligands***), and hydroxide. In addition, hydrogen combines with a variety of elements to form compounds with widely differing properties. The combined compounds are generally known as hydrides.

The hydrogen atom is the lightest and least complex atom, and forms the most basic diatomic molecules. Consequently, the physical and chemical properties of hydrogen have been studied very thoroughly in connection with fundamental studies on atomic and molecular structures. Ortho- and para-hydrogen were discovered spectroscopically and interpreted quantum mechanically by Heisenberg in 1927.[6] The technique of nuclear magnetic resonance (NMR) spectroscopy, which was first demonstrated in 1946 using the hydrogen nucleus (proton), has revolutionized the study of structural chemistry.[7]

Hydrogen was recognized as the essential element in acid by Davy after his work on hydrohalic acid. Theories of acid and base have played an important role ever since. The electrolytic dissociation theory of Arrhenius and Ostwald, the introduction of the pH scale for hydrogen-ion concentrations by Sorensen, the theory of acid-base titration and the use of indicators, and Bronsted's concept of acid and conjugate base as proton donors and acceptors are other landmarks in the recognition of hydrogen as an acid.

Studies on energy production from hydrogen are technologically important for developing an energy source for the future.

In this article, we mainly discuss the properties and behavior of hydrogen and its isotopes, and present the various applications of hydrogen. Excellent reviews on hydrogen are given in reference books of inorganic chemistry.[8]

2 OCCURRENCE, PREPARATION, USE, AND ANALYSIS OF HYDROGEN

2.1 Natural Occurrence

The atmosphere contains only about 0.5 ppm of free hydrogen molecules owing to the chemically active nature of hydrogen. Combined hydrogen comprises 11.2% of water, and is an essential constituent of all acid, hydrocarbons, and living organisms. It is present in the great majority of organic compounds. Hydrogen is sometimes liberated during the decomposition of organic matter, and may be present in the intestinal gases of animals.

Hydrogen gas has been found occluded in meteorites, and also is present in nebulae, fixed stars, and in the Sun. Anders and Grevesse[5] calculated mass fractions of H, He, and heavier elements (Li–U) in the solar system, and derived values of 70.683, 27.431, and 1.886%, respectively. The major planets (Jupiter, Neptune, Saturn, and Uranus) contain large amounts of hydrogen in their atmospheres, along with He, CH_4, and NH_3.

2.2 Molecular Hydrogen in Nature

2.2.1 Hydrogen Content in the Atmosphere

Our knowledge about the distribution of molecular hydrogen in the atmosphere is incomplete. The first reliable analyses were made in 1923 by Schuftan, who found 0.50 ± 0.10 ppmv (parts per million by volume) for hydrogen in air samples from different liquid air plants. This concentration has since been considered constant and representative for atmospheric air.

The measurements of H_2 mixing ratios in the atmosphere, the troposphere, and the lower stratosphere were carried out by Schmidt[9] in 1974. A constant mixing ratio of 0.548 ppmv was found in the southern troposphere and in the lower stratosphere of the northern hemisphere. Higher levels of 0.558 and 0.585 ppmv were obtained in the northern hemisphere in the upper troposphere and in surface air, respectively. The data do not indicate any change in the H_2 mixing ratio of the lower stratosphere up to 4 km above the tropopause. The almost constant H_2 mixing ratio in the tropopause region indicates that the flux of H_2 between the troposphere and the stratosphere is very small.

2.2.2 Hydrogen Content in Seawater

Schmidt[9] also measured the H_2 content of surface waters in the North and South Atlantic Oceans. The data varied from 0.8 to 5.0×10^{-5} mL/L(H_2O), corresponding to saturation factors of $F = 0.8–5.4$, where $F = 1$ represents equilibrium conditions between surface water and air, while $F < 1$ or $F > 1$ indicate undersaturation or supersaturation, respectively. The H_2 supersaturation in ocean water may be due to the production of hydrogen by microbiological activity. Several vertical profiles through the ocean showed H_2 contents to decrease with depth to equilibrium values compared with surface air. These profiles also showed distinct layers slightly enriched in H_2 in the oceans.

2.2.3 Hydrogen Release in Natural Processes

It has been suggested by various authors that the origin of tropospheric H_2 might be the photolysis of water vapor in the upper atmosphere. However, on the Earth's surface, H_2 is released from volcanic gases and bubbling gases in geothermal areas (e.g. the H_2 concentration of volcanic gas of Mt. Unzen in Japan in 1992 is above 7000 ppmv and that of bubbling gas in some geothermal areas has often amounted to several thousand ppmv). The hydrogen gas-water ratio, H_2/H_2O, in fumarolic gas summarizes the available information on gas chemistry related to volcanic systems. Giggenbach[10] showed that the H_2/H_2O ratio is governed by the buffer of the system $2H_2 + O_2 \rightleftharpoons 2H_2O$ at high temperatures, and by the buffer of the system $SO_2 + 3H_2 \rightleftharpoons H_2S + 2H_2O$ at low temperatures. In addition, H_2 is released from natural gas and coal deposits, and is also generated in soils by biological activity.

A significant amount of H_2 (amounting to more than 3 vol % in soil gas) was observed in 1980 along the Yamasaki Fault, one of the active faults in southwestern Japan.[11] In order to understand the mechanism of H_2 production caused by fault movement, Kita *et al.*[12] measured the amounts of H_2 gas generated by crushing granite and quartz in laboratory experiments, and found that the amount of H_2 generated increases with temperature.

2.2.4 Hydrogen Budgets

Junge[13] showed that H_2, CH_4, CO, and N_2O belong to a group of atmospheric constituents, which are strongly influenced, by microbiological sources. Conversely, there is some evidence indicating other sources of hydrogen release, as mentioned above. The quantities of H_2 released from some sources have not been quantitatively estimated.

Assuming a concentration of 0.5 ppmv and a residence time of 8 years, the Earth's total annual emission of H_2 into the atmosphere is 20×10^6 g.[14] The annual emissions of H_2 from nongasoline fossil fuels and that from gasoline were estimated to be approximately 1×10^6 g and 4×10^6 g, respectively. These estimates of H_2 anthropogenic emission may be much too low. Schmidt[9] based his residence time of 4–7 years on a 'budget' of hydrogen consisting of sources and sinks and estimated the annual anthropogenic emission of H_2 to be 1.3×10^6 g. Annual releases of H_2 have been also estimated for the oceans (4×10^6 g), methane oxidation ($5–9 \times 10^6$ g), and volcanoes (0.2×10^6 g).

Judging from the amount of H_2 generated on the Earth's surface and from the constant mixing ratio in the atmosphere, it is considered that the quantity of H_2 released into surface air has been constant and has been maintained at a steady state with a continual escape of H_2 from the Earth's gravitational field into space.

2.3 Preparation of Hydrogen

2.3.1 Conventional Laboratory Preparation

Hydrogen is prepared in a variety of ways, most commonly from water, acid, hydroxide bases, and hydrocarbons. The most frequently used laboratory preparations are as follows.

Electrolysis of Water. Electrolysis of acidified water at Pt electrodes is commonly used to demonstrate the composition of water, and is a small-scale production method for generating hydrogen and oxygen. Very pure hydrogen of more than 99.99% can be formed from the electrolysis of warm aqueous solutions of barium hydroxide between nickel electrodes, via the following reaction:

$$\begin{aligned}&\text{Anode:} && 4OH^- \longrightarrow 2H_2O + O_2 + 4e^-\\ &\text{Cathodes:} && 4H_2O + 4e^- \longrightarrow 2H_2 + 4OH^- \qquad (2)\end{aligned}$$

Reaction of Metals on Water or Dilute Acid. Electropositive metals, such as the alkali metals and alkaline earth metals, are so chemically reactive that they rapidly displace hydrogen from water or dilute acid at room temperature. Convenient laboratory methods employ sodium amalgam or calcium with water, or zinc with hydrochloric acid:

$$2Na + 2H_2O \longrightarrow 2Na^+ + 2OH^- + H_2 \qquad (3)$$

$$Ca + 2H_2O \longrightarrow Ca^{2+} + 2OH^- + H_2 \qquad (4)$$

$$Zn + 2H^+ \longrightarrow Zn^{2+} + H_2 \qquad (5)$$

Reaction of Water with Hydrides of Metals. For small-scale preparations, the hydrolysis of metal hydrides is convenient and generates twice the amount of hydrogen as contained in the hydride, for example,

$$CaH_2 + 2H_2O \longrightarrow Ca(OH)_2 + 2H_2 \qquad (6)$$

Reaction of Silicon on Solutions of Alkali Hydroxides. This method is based on the reaction of a concentrated solution of sodium hydroxide on powdered silicon or ferrosilicon, where hydrogen and a solution of sodium silicate are the products of the reaction:

$$Si + 2OH^- + H_2O \longrightarrow [SiO_3]^{2-} + 2H_2 \qquad (7)$$

Reaction of Metal on Solutions of Alkali Hydroxides. The reaction of aluminum or zinc with aqueous sodium hydroxide is the most commonly used methods:

$$Al + OH^- + H_2O \longrightarrow [AlO_2]^- + H_2 \qquad (8)$$

$$Zn + 2OH^- + 2H_2O \longrightarrow [Zn(OH)_4]^{2-} + H_2 \qquad (9)$$

Other amphoteric metals can be substituted (*see Amphoterism*).

2.3.2 Industrial Production

Hydrogen is produced on a large scale by a number of industrial processes, some of which classify the produced gas as a by-product. The main production methods are as follows.

Electrolytic Decomposition of Water. This industrial process is economically feasible in localities where low-cost electricity is available, where there is a demand for oxygen as well as for hydrogen, and where the hydrogen is required to be completely free from carbon compounds. Sodium and potassium hydroxides are the practicable electrolytes in this process.

Reaction of Steam on Hydrocarbons. The catalytic interaction of steam and hydrocarbons has been used commercially on a large scale. The thermal cracking of hydrocarbons is an important part of petroleum refining and produces a large amount of hydrogen. The reaction of steam on methane from natural gas at about 1100 °C is

$$CH_4 + H_2O \longrightarrow CO + 3H_2 \qquad (10)$$

Reaction of Steam on Coke. When passes over coke heated to over 1000 °C, steam undergoes the well-known water gas reaction:

$$C + H_2O \longrightarrow CO + H_2 \qquad (11)$$

Water gas, or the methane steam gases, may be subjected to CO conversion by passing the gases and steam over an iron or cobalt oxide catalyst at 400 °C:

$$CO + H_2O \longrightarrow CO_2 + H_2 \qquad (12)$$

This is known as the water gas shift reaction. Recently this reaction has been known to be affected by low-temperature homogeneous catalysts in aqueous acid solution.[15] The extent of subsequent purification of the hydrogen depends on its intended use.

2.4 Use of Hydrogen

The largest use of industrial hydrogen is in ammonia synthesis, in the catalytic hydrogenation of unsaturated liquid vegetable oils to solid, edible fats (margarine), and in the manufacture of bulk organic chemicals, particularly methanol, by the *Oxo Process* using a cobalt catalyst:

$$CO + 2H_2 \longrightarrow CH_3OH \qquad (13)$$

Direct reaction of hydrogen with chlorine is a major source of hydrogen chloride, used in the preparation of metal hydrides and complex metal hydrides.

In nuclear science, liquid hydrogen is used in bubble chamber detectors for high-energy particles and in the space program as a rocket fuel. Hydrogen gas is potentially a large-scale fuel in future for internal combustion engines and fuel cells.

2.5 Analysis of Hydrogen

2.5.1 Analysis of a Gas Mixture

The presence of hydrogen molecules in a gas mixture can be determined by converting the gas to water overheated copper oxide at 300 °C, although the presence of volatile hydrides must first be determined. In the absence of combustible gases, the determination of hydrogen is usually made by exploding a measured volume of the gas in the presence of a large excess of oxygen, using a high-tension discharge across Pt electrodes; the contraction in volume gives a measure of the hydrogen content of the gas according to the equation:

$$2H_2 + O_2 \longrightarrow 2H_2O \qquad (14)$$

Gas chromatography (GC) is used to measure hydrogen concentration, using helium gas as a carrier gas and molecular sieve columns. Combustion plus gas chromatographic determination of the water produced is commonly used in determining the hydrogen content of organic compounds.

The hydrogen composition of subsurface gases has been measured in geochemical studies. The H_2 gas component in the gas mixture must be separated chromatographically and detected using high sensitivity instruments. The concentration of H_2, He, Ne, Ar, N_2, and CH_4 in gas samples can be directly determined under optimum conditions: use of an 8 m column packed with a 60–80 mesh 5 Å molecular sieve activated at 360 °C for 12 h, and the use of oxygen gas as the carrier gas.[16] The determination limit for H_2 is 10^{-6} mL with a preamplifier.

2.5.2 Hydrogen Analysis in Rocks and Minerals

In rocks and minerals, hydrogen may be present in several different forms and is generally classified as essential and nonessential hydrogen. Essential hydrogen is present in regular arrangement in the molecular or crystal structure, whereas nonessential hydrogen is not necessary for characterization of the mineral, for example, hydrogen held by surface forces. The determination of total hydrogen in rocks and minerals is usually based on oxidation of the sample in a stream of oxygen at about 1150 °C in the presence of a lead chromate flux. A modified form of this procedure has been applied to the determination of hydrogen in coal. The evolved water is determined and used as a basis for calculating the hydrogen content of the sample. Several dehydrating agents, such as $CaCl_2$, P_2O_5, and $Mg(ClO_4)_2$, have been used for absorbing the water.

2.5.3 Hydrogen Analysis in Metals

In metals, hydrogen occurs in the occluded and combined states. Numerous methods have been used for the determination of hydrogen in metals. Some of them are as follows.

Gravimetric Method. A method in which the metal sample is heated in atmospheric oxygen and the water formed is absorbed in a dehydrating agent such as $Mg(ClO_4)_2$.

Vacuum Extraction. Vacuum extraction requires the sample to be heated in an evacuated system with determination of the evolved gas, either volumetrically or by differential pressure measurement. This method is recommended whenever possible because of the speed and precision, particularly where the amount of hydrogen is below 0.01%.

Extraction of the Gas by Vacuum Fusion. In this procedure, which is primarily intended for the determination of oxygen in metallurgical materials, the sample is melted in a graphite crucible in an evacuated system. Oxygen is converted to CO and hydrogen is quantitatively liberated and determined as in the Section *Vacuum Extraction*.

A Method Based on Ionic Bombardment. In this procedure, the specimen is placed in a discharge tube, made into a cathode, and is then bombarded with mercury ions. The ionized gas, drawn from the metal by the high potential between the electrodes, is collected and subsequently analyzed by conventional procedures.

A Method that Utilizes Electrochemical Sensors. Various electrochemical sensors have been developed to measure hydrogen, both in the molten and solid states.[17]

3 ISOTOPES OF HYDROGEN

3.1 General

Of all the elements, isotope effects (*see Isotope Effect*) are greatest for hydrogen, justifying the use of distinctive names for the hydrogen isotopes: protium, deuterium, and tritium. However, the chemical properties of H, D, and T are essentially identical, except in matters such as equilibrium constants. The isotopes of hydrogen are extensively used as tracers in deuterium- or tritium-labeled compounds.

The atomic properties of H, D, and T and the physical properties of H_2, D_2, and T_2 are compared in Tables 1

Table 1 Atomic properties of hydrogen, deuterium, and tritium

Properties	H	D	T
Relative atomic mass (a.m.u.)	1.007825	2.014102	3.016049
Nuclear spin quantum number	1/2	1	1/2
Nuclear magnetic moment (nuclear magnetons)[a]	2.79268	0.857386	2.9788
Nuclear quadrupole moment ($e \times 10^{-28}\,m^2$)	0	2.766×10^{-3}	0
Radioactive stability	Stable	Stable	β^-

[a] Nuclear magneton, $\mu_N = eh/4\pi m_p c = 5.0508 \times 10^{-27}\,J\,T^{-1}$.

Table 2 Physical properties of isotopic molecular hydrogen[a]

Properties	H_2[b]	D_2	T_2
Melting point (K)	13.957	18.73	20.62
Boiling point (K)	20.39	23.67	25.04
Heat of fusion ($kJ\,mol^{-1}$)	0.117	0.197	0.250
Heat of vaporization ($kJ\,mol^{-1}$)	0.904	1.226	1.393
Critical temperature (K)	33.19	38.35	40.6
Critical pressure (kPa)	1315.20	1664.77	1834
Heat of dissociation at 25 °C ($kJ\,mol^{-1}$)	435.88	443.35	446.9
Zero-point energy ($kJ\,mol^{-1}$)	25.9	18.5	15.1
Internuclear distance (pm)	74.14	74.14	(74.14)

[a] All data refer to the mixture of ortho and para forms that are in equilibrium at room temperature. [b] Data refer to H_2 of normal isotopic composition (i.e. containing 156 ppm of deuterium, predominantly as HD).

and 2, respectively. Protium and deuterium are stable isotopes. Tritium is radioactive, emitting low-energy β^- particles with a half-life of 12.4 years; $^3T \rightarrow {}^3He + e^-$.

Deuterium magnetic resonance spectroscopy has found wider applications since the advent of highly sensitive Fourier transform spectrometers. Deuterium is preferred choice in molecular and in ^1H NMR spectroscopy in order to provide additional information about proton vibrations and resonances; spectra measured before and after deuteration help to locate the exchanging hydrogen atoms.**18**

Deuterium is invariably prepared from heavy water, which itself is manufactured by the electrolytic enrichment of water, and is available for use as a moderator in nuclear reactors. D_2O is useful as a source of deuterium in deuterium-labeled compounds. Deuterium compounds such as heavy water have been extensively studied. In Table 3, a number of physical properties of normal water and heavy water are compared.

Tritium is made artificially in a nuclear reactor by the reaction of the light isotope of lithium with neutrons:

$$^6Li + {}^1n \longrightarrow {}^4He + {}^3T \qquad (15)$$

Table 3 Major physical properties of H_2O, D_2O, and T_2O

Properties	H_2O	D_2O	T_2O
Molecular weight	18.015	20.028	22.032
Freezing point (°C)	0.00	3.81	–
Boiling point (°C)	100.00	101.42	101.51
Triple point (°C)	0.01	3.82	4.49
Critical temperature (°C)	374.15	370.9	–
Critical pressure (atm)	218.3	215.7	–
Temperature of maximum density of liquid (°C)	3.984	11.185	13.403
Maximum density of liquid ($g\,cm^{-3}$)	0.999972	1.10600	1.21501
Dielectric constant of liquid at 20 °C	81.5	80.7	–
Refractive index of liquid at 20 °C (n_D = 589 nm)	1.33300	1.32830	–
Viscosity of liquid at 20 °C (mPa s)	1.002	1.248	–
Ion product of liquid at 25 °C ($mol\,dm^{-3}$)	1.0×10^{-14}	0.3×10^{-14}	–
Lattice constant of solid (pm)	*a*451.4	451.7	–
	*c*735.2	735.4	–

The tritium may be purified by diffusion through palladium or separated from helium by preferential adsorption on charcoal at 77 K. The most convenient way of storing tritium gas is by reacting it with finely divided uranium to produce UT_3. The tritium may be released when required by heating the UT_3, having first removed any decay product (helium) by pumping.

Based on the value of the tritium content in atmospheric hydrogen, tritium has been produced by nuclear fusion in the upper layers of the atmosphere, and does not take part in any atmospheric circulation, but instead remains as elementary hydrogen.**3**

Grosse *et al.***4** measured highly concentrated heavy water samples produced from surface waters that contained concentrations of natural tritium approximately one million times higher than the original water. Observations have shown that concentrated samples are indeed radioactive to a level corresponding to a natural abundance of tritium of about 10^{-18} by atomic ratio.

The radioactive emission from tritium is solely composed of low-energy β^- particles, with an average energy of 5.70 keV and a maximum energy of 18.6 keV. As this energy is of a low level, the penetrating range is very small, resulting in some difficulties in measuring the radioactivity. Thus the half-life value is slightly uncertain; the generally accepted value is 12.4 years.

By far the most important application of tritium is its use as a radioactive tracer in extensive labeling studies. The production of tritium-labeled organic compounds was greatly enhanced with the discovery that tritium could be introduced to a compound merely by storing that compound under tritium gas for a few days or weeks; the β^- radiation induces exchange reactions between the hydrogen atoms in the compound and the tritium gas. Another widely used application of general applicability is catalytic exchange in solution using either a tritiated solution or tritium gas. This is valuable in the routine production of tritium compounds for high radiochemical yield and at high specific activity. These tritium applications are partly displacing deuterium substitution in the biological and natural product research fields.

3.2 Measurements of Hydrogen Isotopes

A large variety of methods have been proposed for determining the deuterium content of hydrogen compounds. The important methods are those used for examining H_2, HD, and D_2 mixtures and those used for H_2O, HDO, and D_2O mixtures. Deuterium samples may be converted into water or hydrogen gas; however, the isotopic composition of samples should be kept intact in the conversion step.

The deuterium content of hydrogen gas is usually determined by thermal conductivity or *Mass Spectrometry*. In the thermal conductivity method, the resistance of a heated platinum wire in a binary mixture of hydrogen isotopic molecules varies linearly with deuterium content, while a ternary mixture gives a nonlinear relation. In the low deuterium content range, this method is applicable for deuterium contents above 0.1% and has an accuracy of 0.01% by calibrating with samples of known isotopic composition. The mass spectrometer usually measures the HD^+ /$H_2{}^+$ ratio of hydrogen gas.

High deuterium content of water can be measured by a variety of techniques, such as density determinations, refractive index changes, infrared (IR), and by velocity changes of ultrasound. Specific gravity or density determinations can be made using a pycnometer, or by finding the temperature or pressure at which a float neither falls nor rises in the sample. The refractive index of H_2O is 0.0047 higher for the sodium D-line ($\lambda_D = 589.3\,\mathrm{nm}$) than for that of D_2O at 20 °C. A linear relationship exists between the change in the refractive index of H_2O and the mole fraction of D_2O present. The low deuterium content of water is determined by measuring the ratio of $m/e = 18$ (H_2O^+) and 19 (HDO^+) peaks by the use of mass spectrometry.

The deuterium content of any hydrogen compound may be detected by observing the IR spectrum in which the M–H stretching frequency shifts to lower energy by approximately $1/\sqrt{2}$ when the H atom in the M–H bond is replaced by a D atom. The IR spectrum has been used for the semiquantitative determination of deuterium contents of water by comparing the intensities of the O–H stretching mode at $3620\,\mathrm{cm^{-1}}$, or the O–D mode at $2630\,\mathrm{cm^{-1}}$. By calibrating with samples of known isotopic composition, the deuterium content can be measured to about 0.01% at $2630\,\mathrm{cm^{-1}}$ on samples containing up to 5% D on mole fraction. Similar results for the protium content of deuterium-rich samples are obtained at $3620\,\mathrm{cm^{-1}}$.

Instruments that can accurately measure the velocity of ultrasound in relatively small samples of water are now available for measuring the isotopic analysis of H or D in water. The change in sound velocity from pure D_2O to pure H_2O is $97.7\,\mathrm{m\,s^{-1}}$ or some 7% of the value for pure D_2O.**[19]**

A useful method of measuring the deuterium content of water has been developed using a novel hydrophobic Pt catalyst consisting of dispersed platinum in a styrene/divinylbenzene copolymer. The sample water is injected into a column in which water vapor and a pure H_2 carrier gas are isotopically exchanged on the surface of the catalyst. The equilibrated hydrogen gas concentration is measured by a thermal conductivity detector (TCD) mentioned above.

GC has conventionally been used as the fundamental measurement method for isotopes of molecular hydrogen. Many experimental reports have described H_2, HD, and D_2, but only a few have provided an analytical study of hydrogen isotopes that include tritium. Gently and Schott**[20]** reported quantitative analysis of isotopic hydrogen molecules, H_2, D_2, T_2, HD, HT, and DT. In 1991, Uda *et al.***[21]** experimentally measured the hydrogen isotopes of mixed gases by GC and attempted to identify and obtain their measurement characteristics. A liquid nitrogen-cooling column was used for isotope separation, along with a TCD and a small-volume ionization chamber. The intensity ratio of the six hydrogen isotopic species, as measured by the TCD, is $H_2{:}HD{:}HT{:}D_2{:}DT{:}T_2 = 100{:}73{:}61{:}57{:}49{:}43$. When the sampling volume was $1\,\mathrm{cm^3}$, the estimated detection limit for H_2 and T_2 were 20 and 50 Pa partial pressure, and concentration of 200 and 500 ppm, respectively.

The content of tritium is usually determined by measuring its activity. Solid samples may be converted into liquid or gaseous compounds, and the tritium content measured by a liquid scintillation counter or a gas proportional counter, respectively.

A liquid scintillation counter for measuring tritium has been designed for 20 or 100 mL vials and minimized background fluctuations. In recent years, a popular method for measuring tritium utilizes the suspension of water in aromatic solvents using a nonionic surfactant (emulsion system). This suspension is capable of incorporating up to 40% water; thus this technique is widely used for low-level counting of tritium. Premixed aromatic solvent and surfactant-dissolving scintillation flours are available commercially.

A gas proportional counter with an anticoincidence shielding counter has also been utilized. Ethane gas is commonly used as a counting gas. A water sample is reduced to hydrogen gas using Mg or Zn powder in a furnace. Hydrogen gas thus produced is added to ‘dead’ ethylene or acetylene gas with a Pd catalyst to form ethane-counting gas.

Techniques for monitoring tritium in the atmosphere have been developed in order to prevent possible health hazards arising from tritium produced by fission and various other nuclear reactions.**[22]**

3.3 Deuterium in Nature

3.3.1 *Preparation Technique and Mass Spectrometer Measurements*

The deuterium content in Nature is usually expressed in D/H ratios in terms of δ values (the delta notation) defined as

$$\delta\mathrm{D}(‰) = \left[\frac{(\mathrm{D/H})}{(\mathrm{D/H})_{\mathrm{standard}}} - 1\right] \times 10^3 \tag{16}$$

where $(\mathrm{D/H})_{\mathrm{standard}}$ is the D/H ratio of V-SMOW (Vienna Standard Mean Ocean Water), 1.558×10^{-6}. The V-SMOW distributed by the International Atomic Energy Agency (IAEA) is a reference water sample for hydrogen and oxygen isotopes. The IAEA distributes a second water standard called SLAP (Standard Light Antarctic Precipitation), which has a δD value of −428‰.

The determination of D/H ratios of hydrogen compounds from natural sources is usually performed on hydrogen gas by a mass spectrometer. The D/H ratio of the hydrogen gas is measured as the HD^+ /$H_2{}^+$ ratio. The formation of $H_2{}^+$ and HD^+ in the ion source, together with $H_3{}^+$, are produced as by-products through the reaction

$$H_2{}^+ + H_2 \longrightarrow H_3{}^+ + H \tag{17}$$

Thus a $H_3{}^+$ correction needs to be made, utilizing the relationship that the quantity of $H_3{}^+$ produced is linear with respect to the hydrogen pressure squared.

Mass spectrometric measurements using hydrogen gas are prepared from the sample by fractionation free techniques. Water is converted into H_2 gas by being passed over uranium metal at 750 °C as a continuous method,[23] or by being reacted with heated zinc shot or melted in a Pyrex or quartz tube at approximately 450 °C as a batch method.[24]

In 1986, a new preparation method was developed, using a hydrophobic Pt catalyst, which served as the equilibration between H_2 gas and water vapor. The D/H ratio of the sample water is calculated from the measured D/H ratio in H_2 gas equilibrated with the sample water.[25] In combination with this method, the automatic CO_2-water equilibration set-up was designed for the simultaneous $^{18}O/^{16}O$ ratio measurement.[26]

Most of the hydrogen generated from hydroxyl-bearing minerals liberated in the form of water, although some is liberated as hydrogen gas. The resulting hydrogen gas is converted in many laboratories into water by the reaction with a Cu–CuO mixture. The water is then treated as described above.

The analytical errors of D/H ratio data based on the preparation method and mass spectrometer analysis varies usually from ±0.5 to 2‰.

In 1983, the first attempts to use the ion probe for D/H ratio measurements were made on meteoric samples and stratospheric dust.[27] In 1991, an analytical procedure was reported in situ measurement of D/H ratios by application of the ion probe to terrestrial hydrous minerals. This method is capable of measuring the δD values of individual minerals.[28] The δD values with a precision of ±10‰ have been measured by this method.

3.3.2 *The Natural Variation of Deuterium Content*

Most hydrogen on the Earth exists in the chemical forms H_2O, OH-bearing minerals, CH_4, and H_2. The δD values for terrestrial waters and OH minerals have been extensively measured and are generally in the range from −350 to +50‰. Ocean waters are typically 0‰ with a very narrow range of less than 10‰. The lowest values of −460 and −420‰ were reported for Antarctic ice[29] and pectolite[30] (a hydrous silicate), respectively. The δD values of OH-bearing minerals (muscovite, biotite, chlorite, and glaucophane) range from −104 to −28‰.[31] The δD values of biotites and hornblendes extracted from igneous rocks are in most cases in the range −90 to −50‰.[32] The mean δD value of atmospheric methane is −113‰,[33] and that of CH_4 from hydrothermal gases is −262‰.[34] The δD values of CH_4 from some volcanic areas in Japan fall within a range from −180 to −487‰.[35]

The δD values of molecular hydrogen are significantly different depending on its origin. The δD value of atmospheric H_2 is approximately $+70 \pm 30$‰, which has remained constant since 1957.[36] The δD values of H_2 in volcanic gases are reported to be in the range −158 to −144‰.[37] Those from some volcanic areas in Japan are in the range −515 to −220‰.[35] A value of about −660‰ was obtained for H_2 in fumarolic gases from the Yellowstone Park hydrothermal area in the United States.[34]

Molecular H_2 can be generated in soil by biological activity. Some marine bacteria have been known to produce H_2 highly depleted in deuterium in cultivating experiments. The δD value of the H_2 produced is about −800‰ (ca. 30 ppm).[38] The δD values of H_2 in soil gases obtained from sites along the active Yamasaki fault, in southwestern Japan, were in the range −770 to −470‰.[39] The source of molecular hydrogen in the atmosphere is not consistent with the δD values of the generated hydrogen gas.

During photosynthesis, plants remove hydrogen from water and transfer it into organic matter. The fixation of CO_2 and H_2 to organic compounds leads to deuterium depletion in the plants relative to environmental water.[40] After the formation of organic matter, the oxygen-bound hydrogen atoms are readily exchangeable,[41] while the carbon-bound hydrogen atoms appear to be nonexchangeable. There are systematic differences in the D/H ratios among classes of compounds in plants: lipids usually contain less deuterium than do the protein and carbohydrates of the extracted plants.

Figure 1 shows the natural variation ranges of δD values for some important reservoirs. Hydrogen has by far the largest relative mass difference between its two stable isotopes among all the elements. This difference results in the largest

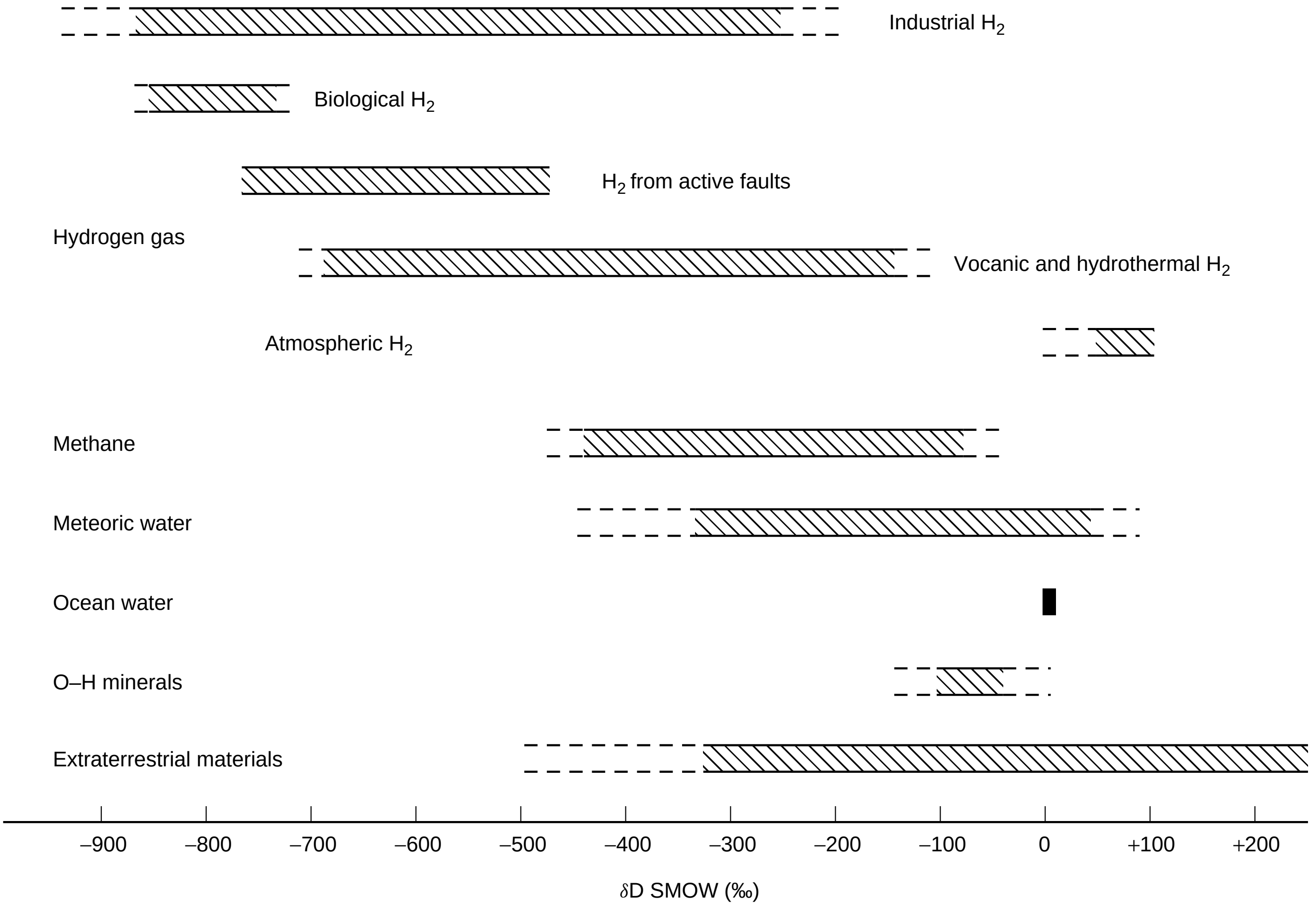

Figure 1 The ranges of D/H ratio in important hydrogen compounds (δD values relative to SMOW)

variations in stable isotope ratios of hydrogen; that is, from -900 to $+100$‰ on the Earth, and from -500 to $+4500$‰ in extraterrestrial and stratospheric materials. Geochemical reviews on stable isotopes including deuterium have been published elsewhere.[42]

3.3.3 The Deuterium Content of Meteoric Water

The term 'meteoric' applies to water that has recently been involved in atmospheric circulation. The natural water cycle has been compared to a multiple-stage distillation column with a reflux of the condensates to the reservoir. The oceans correspond to the reservoir, while the ice fields at the poles correspond to the highest stages of the column. The most efficient process for creating variations in the isotope ratios of water is caused by vapor pressure differences (isotope fractionations). In all processes concerning the evaporation and condensation of water, the hydrogen isotopes are fractionated in proportion to the oxygen isotopes, as a corresponding difference in vapor pressures or fractionation factors exists between H_2O and HDO in one case and $H_2{}^{16}O$ and $H_2{}^{18}O$ in the other case. Hence, the distribution of hydrogen and oxygen isotope can be correlated in meteoric waters. Craig[43] first gave the following relationship

$$\delta D = 8\delta^{18}O + 10 \tag{18}$$

The slope of 8 in this relationship corresponds approximately to the ratio of the D/H and $^{18}O/^{16}O$ fractionation factors between vapor and liquid water at 25 °C, and the intercept corresponds to the kinetic effect of evaporation from the ocean. Dansgaard[44] interpreted the variation of the hydrogen and oxygen isotopic composition in precipitation.

Isotopic data (D, ^{18}O, and T contents) of meteoric waters, such as precipitation, rivers and groundwater, are commonly combined with geological, hydrological, and hydrochemical evidence in order to determine fluid sources and flow patterns of groundwater.

3.4 Tritium in Nature

3.4.1 Preparation Technique and Measurements

The measurement of low levels of tritium has become important in the studies related to hydrology, meteorology, and monitoring programs of health physics for tritium released from nuclear power facilities.

Tritium is naturally produced to the extent of about 1 atom per 10^{18} hydrogen atoms as a result of nuclear reactions induced by cosmic rays in the upper atmosphere:

$$^{14}\mathrm{N} + {}^{1}\mathrm{n} \longrightarrow {}^{12}\mathrm{C} + {}^{3}\mathrm{T} \tag{19}$$

The natural inventory of tritium produced by this reaction is about 4×10^{18} Bq (11 kg), of which 90% is contained in the ocean as HTO. The tritium produced by man's activities (largely thermonuclear weapons testing) has increased to approximately 2×10^{20} Bq. Although most of this tritium has been transferred to the oceans, environmental tritium is still half an order of magnitude higher than was present before nuclear testing.

Tritiated-water standards have been distributed by the National Bureau of Standard (NBS), USA, and IAEA, meeting the demands from laboratories measuring the natural tritium.

The concentrations of tritium in natural waters are expressed by the atomic ratio of T to H: a ratio of $\mathrm{T/H} = 10^{-18}$ is defined as 1 tritium unit (1 TU or 1 TR). 1 TU in water corresponds to approximately $0.12\,\mathrm{Bq\,dm^{-3}}$ ($1\,\mathrm{Ci} = 3.7 \times 10^{10}$ Bq). In the early 1990s, the tritium content of water in Nature was at a low level (under 20 TU), so it becomes necessary to enrich the tritium in order to obtain precise measurements. Measurement of tritium in environmental waters by conventional techniques combines enrichment and counting, so that precision depends on reducing the errors of both techniques as much as possible.

For the detection of soft β-emitting radionuclides such as tritium or carbon-14, liquid scintillation counting or gas-filled counting has been used in many laboratories. The liquid scintillation counting process indicates a somewhat high background and lower efficiency, while the gas-filled counting method has a higher efficiency. Background reduction in gas proportional counting has been efficiently achieved through the use of coaxially enveloping counters surrounding the sample counter with anticoincidence circuits. Sample preparation for liquid scintillation counting takes only a few minutes, compared to many hours for the gas proportional counting method.

The enrichment of tritium is usually determined by the tritium separation (fractionation) factor during electrolysis, and by measuring the initial and final amounts of water. However, many workers have reported that the value of the separation factor of tritium depends on the electrode material, the type of electrolytic enrichment cell, the current density, the mode by which water is fed into the electrolytic cell, and the temperature of the electrolytic cell. In 1991, a reliable method was proposed for estimating tritium concentrations in water, based on a reliable correlation between the water electrolytic enrichment of deuterium and tritium.**[45]** The constancy of the ratio, k, during the electrolysis, $k = \alpha(\beta - 1)/\beta(\alpha - 1)$, was verified experimentally, where α and β are the separation factors of deuterium and tritium, respectively. The value of k is far more reproducible than the values of $\beta/\alpha(= 2.1)$**[46]** and $\log\beta/\log\alpha(= 1.337)$.**[47]** When the value of k was first measured experimentally, the initial tritium content of sample water, $(\mathrm{T/H})_0$, could be estimated by the formula

$$\left(\frac{\mathrm{T}}{\mathrm{H}}\right)_0 = \left(\frac{\mathrm{T}}{\mathrm{H}}\right)_\mathrm{f}\left[\frac{(\mathrm{D/H})_\mathrm{f}}{(\mathrm{D/H})_0}\right]^{-k} \tag{20}$$

where $(\mathrm{T/H})_\mathrm{f}$ and $(\mathrm{D/H})_\mathrm{f}$ are the tritium and deuterium contents after electrolysis, and $(\mathrm{D/H})_0$ is the deuterium content before the electrolysis.

A sample of hydrogen gas from the atmosphere can be obtained by passed the crude He–Ne fraction in the air liquefaction plant over hot CuO, and by freezing out the water. The water sample is carefully sealed prior to analysis in order to avoid contamination with atmospheric moisture.

In the 1970s, Clark *et al.*[48] developed a method for analysis of environmental tritium by means of mass spectrometric measurements of ^{3}He, which was allowed to accumulate for suitable periods in degassed samples of water sealed in containers. Oliver *et al.*[49] measured the half-life of tritium using the accumulation rate of ^{3}He. The results yielded a mean tritium half-life of 12.38 ± 0.03 year. This value is consistent with the value of 12.43 ± 0.05 year recently recommended by Unterweger *et al.*,[50] based on the gas counting measurements of NBS standards over a time span of 18 years. Recent advance in a mass spectrometric facility for low-level tritium determination, represented by the ^{3}He growth method, shows that the ^{3}He detection limit of the system is close to $10^{-16}\,\mathrm{cm^3}$ at STP ($0\,^\circ\mathrm{C}$, $1\,\mathrm{atm} = 1.01 \times 10^5$ Pa), corresponding to a tritium level of 0.003 TU for a 500 g water sample stored for six months.[51]

3.4.2 *The Natural Distribution of Tritium*

Large-scale release of anthropogenic tritium to the atmosphere began in 1953 with thermonuclear explosion testing. During the 1960s, high concentrations of tritium were originally deposited. The tritium concentration in precipitation rapidly increased several hundredfold until 1963, but has since declined as a result on the moratorium on testing. The worldwide deposition of HTO through precipitation has been summarized on the basis of the data published by the IAEA. The results indicate that HTO concentration decreased significantly over the oceans. In 1979, studies of behavior of tritium in the environment were compiled by the IAEA.[52]

The three major chemical forms of atmospheric tritium are HTO, HT, and $\mathrm{CH_3T}$. At present, approximately 99% of tritium atoms exist as HTO, and the remaining 1% is mostly HT with a significant fraction as $\mathrm{CH_3T}$. The HTO species follows the water cycle in the atmosphere, having a residence time from a few days in the troposphere, to years in the stratosphere. The HT, on the other hand, is found well mixed globally, holding a consistent concentration in areas away from nuclear industry, over the entire troposphere and in the lower stratosphere. Conversion from HT to HTO in the atmosphere occurs quite slowly.

A tritium content of approximately 2×10^4 TU in atmospheric methane was measured between 1960 and 1963.[33] The tritiated methane, CH_3T, in the atmosphere could be accounted for by a leakage equivalent to less than 1% of the maximum amount of tritium estimated to have been released anthropogenically.

Most of the interest in tritium has been focused on HTO. The tritium content of water has been extensively applied to meteorological and hydrological studies as a natural tracer. The natural distribution of HTO before thermonuclear tests was reported by Kaufman and Libby.[46] The measured values of tritium contents in precipitation, river and lake waters, and vintage wines were mostly under 10 TU. Tritium contents of vintage wines appear to agree with the time elapsed since the harvest, indicating that tritium abundances over the preceding 18 years were essentially at identical levels during that time. The stratospheric distribution of HTO is found to increase rapidly with height above the tropopause. An annual cycle is observed in which the lower stratosphere was depleted during the spring, and replenished during summer and fall by subsidence from higher levels of HTO, the so-called meteorological ‘spring leak’ from the stratosphere. Consequently, the tritium content of precipitation in spring and early summer is relatively higher than that of the annual average.

Cosmic radiation and H_2–H_2O exchange reactions in the upper atmosphere produce and maintain a small atmospheric HT inventory. However, at the present time the man-made one appears to be by far the largest part of the atmospheric HT. Since 1949, the tritium content of atmospheric hydrogen molecules has been measured after being extracted from the so-called ‘neon fraction’ obtained at liquid air plants. The values have increased from 10^4 TU in 1954[53] to 10^6 TU in the 1960s, in comparison with 10^3 TU in 1949.[36] Monitoring of HT in 1971 and 1972 showed that HT did not undergo seasonal fluctuations, observed in HTO, and variations were small around a mean of approximately 46 HT molecules per mg of air.[54]

Tritium in water vapor has also been utilized in the study of meteorology. Kigoshi and Yoneda[55] observed daily variations in the tritium content of atmospheric moisture (water vapor) collected in Tokyo. High tritium contents indicate the arrival of continental air masses from the north, and the low contents in tropical low-pressure air masses are nearly equal to that of surface ocean water.

Because of greatly contrasting low tritium levels before thermonuclear tests and because of the distinct peak tritium levels that occurred in the atmosphere during 1962–1965, tritium has been used as an environmental tracer in the studies on surface water budgets, groundwater age and flow velocities, groundwater recharge, and dispersion and diffusion in aquifers. A 1989 study detailed the distribution of tritium in a recharge area of a shallow unconfined sand aquifer near Sturgeon Falls, Ontario.[56] It concluded that tritium concentrations of more than 100 TU were measured in the groundwater recharged between 1957 and 1961, while concentrations of more than 200 TU occurred only in groundwater recharged between 1961 and 1967. Because tritium released into the atmosphere by thermonuclear tests has been mostly transferred into the ocean, and has decreased by radioactive decay, so the tritium content of precipitation has already declined. Consequently, the role of tritium as a natural tracer is about to cease.

4 ISOTOPE EFFECT OF HYDROGEN

4.1 General

Differences in chemical and physical properties arising from differences in the nuclear mass of an element are called isotope effects. The isotope effect is greatest for hydrogen among all the elements, principally owing to the largest differences in relative mass of the isotopes.

From the classical chemical aspect, isotopes of an element are expected to have same chemical properties. Therefore, it has been believed that the behaviors of isotopes of an element are essentially the same. However, a change in the mass of an atom in a molecule produces changes in vibrational, rotational, and translational motions of the molecule. In the diffusion of gases it has long been known that the velocity of molecules changes with the mass of the molecule, thus producing a physical isotope effect.

In quantum mechanics, vibrational and rotational states are quantized, resulting in the isotopic molecules having different discrete energy level. This difference in energy levels results in differences in the distribution of isotopic molecules between different states. The observed differences in the physical properties among H_2, D_2, and T_2, and among H_2O, D_2O, and T_2O, are examples of quantum mechanical effects and are shown in Tables 2 and 3.

Consider two molecular species in equilibrium, each of which has a different set of energy levels for each isotopic molecule. In the mixture of the isotopic molecules, each isotope distributes between the two molecular species according to the energy levels set for the isotope. This results in uneven distribution of hydrogen isotopes between the two phases. In practice, the contribution of the vibrational energy is dominant over rotational and translational energies in equilibrium isotope effects.

Isotope fractionation may occur either by equilibrium isotope exchange reactions or kinetic processes. Kinetic isotope effects are mainly dependent on the differences in reaction rates of isotopic molecules. The kinetic isotope effect for hydrogen compounds have reviewed by Westheimer.[57]

4.2 Isotopic Properties of Hydrogen and Water

Equilibrium isotope effects can be considered in terms of the effect of atomic mass on *Bond Energies*. The forces binding atoms are independent of changes in atomic mass owing to isotopic substitution. Therefore the potential energy curve remains unchanged. For a diatomic molecule in the harmonic oscillator approximation, the vibrational energy levels are given by

$$E = \left(n + \frac{1}{2}\right) h\nu \tag{21}$$

where n represents an integer number from zero, and h is Plank's constant. The lowest vibrational energy ($n = 0$), $(1/2)h\nu$, is well known as the vibrational *Zero Point Energy* that molecules possess even at a temperature of absolute zero. The vibrational frequency, ν, is given by

$$\nu = \frac{1}{2\pi}\left(\frac{k}{\mu}\right)^{1/2} \tag{22}$$

where k represents the force constant that is constant for isotope substitution, and μ is the reduced mass of the two nuclei. At lower temperatures, all of the molecules will be in their lowest vibrational levels, and thus isotopic substitution will affect all processes involving vibrational excitation.

When a lighter isotope is substituted by a heavier isotope, the value of μ becomes larger, and the vibrational frequency, ν, becomes smaller. Therefore the molecules substituted by deuterium and tritium have correspondingly smaller zero-point energies, as shown in Table 2. The schematic potential energy curve for hydrogen molecules is shown in Figure 2. The difference in zero-point energy between H_2 and HD is $3\,\mathrm{kJ\,mol^{-1}}$ and that between H_2 and D_2 is $8\,\mathrm{kJ\,mol^{-1}}$. This means that the binding of a lighter nucleus is weaker than that of a heavier nucleus. In general, during chemical reactions a molecule with a light isotope is more active than a molecule with a heavy isotope.

The 10% mass change in water by the replacement of protium by deuterium results in substantial changes in many commonly known properties of water. In Table 3, a number of physical properties of normal water, H_2O, and heavy water, D_2O, are compared. The viscosity of D_2O is 25% higher than that of H_2O at 25 °C, which is the most conspicuous difference between H_2O and D_2O.

The differences in many of the physical properties of liquid H_2O and D_2O can be qualitatively understood in terms of strength. The hydrogen bond between O and D is stronger than between O and H. In the IR spectra of H_2O and D_2O, peaks are observed at 700 and $500\,\mathrm{cm^{-1}}$, respectively, and are assigned to the librational motion of H_2O and D_2O molecules. Librational motion is a kind of rotational motion associated with the hydrogen bonds. The smaller wave number for D_2O indicates that the strength of the hydrogen bond is stronger in D_2O than in H_2O.

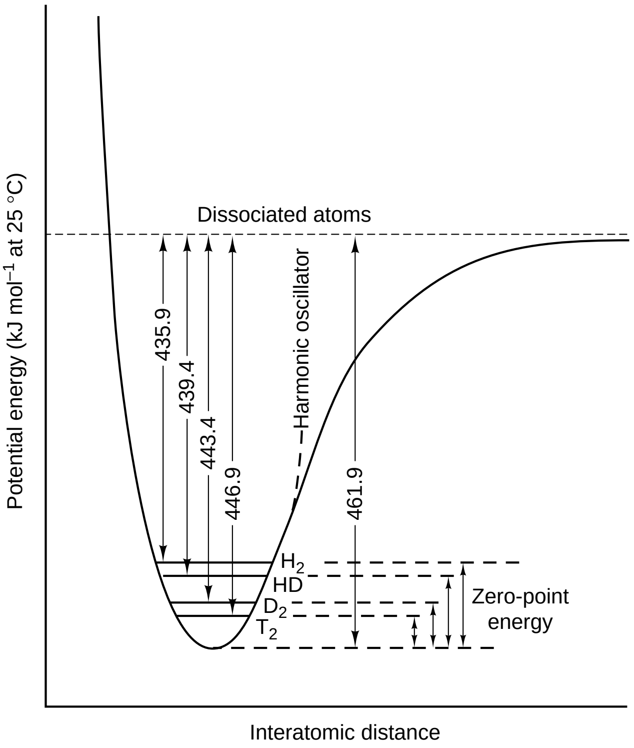

Figure 2 Schematic potential energy curve for the hydrogen molecules with scale at bottom of the curve exaggerated to show relation between $n = 0$ vibrational energy levels of the four isotopic forms of the molecules. Note that molecules containing a heavy isotope are more stable (have higher dissociation energies) than molecules with a light isotope. Isotope fractionations between molecules are explained by differences in their *zero-point energies*

In order to account for some of the differences in thermodynamic properties of H_2O and D_2O, theoretical studies have been applied. Swain and Bader**[58]** first calculated the differences in heat content, entropy, and free energy by treating the librational motion of each water molecule as a three-dimensional isotopic harmonic oscillator. Van Hook**[59]** demonstrated that the vapor pressure of H_2O and D_2O on liquid water and ice could be understood quantitatively within the framework of the theory of isotope effects in condensed systems. Nemethy and Scheraga**[60]** showed that in a model based on the 'flickering cluster' concept, the mean number of hydrogen bonds formed by each water molecule is about 5% larger in D_2O than in H_2O at 25 °C.

4.3 Relationship Between Fractionation Factor and Vapor Pressure

The fractionation factor α_{C-V} for the equilibration between a condensed phase and its saturated vapor is defined as

$$\alpha_{C-V} = \frac{(D/H)_C}{(D/H)_V} \tag{23}$$

where $(D/H)_C$ and $(D/H)_V$ are the D/H ratios of the condensed phase and vapor, respectively. The measurements of the D/H fractionation factor, α_{L-V}, between liquid water and vapor, have been performed by various workers.[61–63] In Figure 3, D/H fractionation factors are shown in the temperature range 10–40 °C. These results are obtained within the range of 0.5%. The results of Kakiuchi and Matsuo[61] are close to those of Majoube[62] at the high end of the temperature range, and are placed in the middle of those of Majoube[62] and Merlivat *et al.*[63] at the lower temperatures.

At temperatures higher than 100 °C, $\ln\alpha_{L-V}$ does not show a linear relationship with $1/T^2$ [63] however, the logarithm of the oxygen isotope fractionation factor, $\ln\alpha_{L-V}(^{18}O)$, does show a linear relationship with $1/T^2$, up to the critical temperature.

The D/H fractionation factors between ice and its vapor,α_{S-V}, were measured between −40 and 0 °C and expressed as the following relationship[64]

$$\log\alpha_{S-V} = -4.10\times 10^{-2} + \frac{7074}{T^2} \qquad (24)$$

In a system containing condensed and gases phases, Bigeleisen[65] derived the relationship between the reduced partition function ratio (RPFR), f, and the measured fractionation factor in the infinite dilution limit, α_{C-V}, which refers to single isotopic enrichment (on distillation):

$$\ln\alpha_{C-V} = \ln\left(\frac{f_C}{f_V}\right) - \frac{(V'-V)^2}{(2\kappa' V' RT)} \qquad (25)$$

where the primes (′) refer to the lighter isotopes, κ represents the isothermal compressibility, V represents the partial molar volume of the condensed phase, and R represents the gas constant. The second term is generally quite small and is often neglected. Thus, RPFRs are obtained directly from fractionation factors between gaseous and condensed phases in distillation experiments.

In experiments measuring the vapor pressure ratio of separated isotopes, P′/P, theoretical interest arises in the relationship between f and P′/P. Bigeleisen[66] introduced the following relationship:

$$\ln\left(\frac{f_C}{f_V}\right) = \ln\left(\frac{P'}{P}\right) - \left(\frac{1}{RT}\right)(P'V' - PV) + (B'P' - BP) \qquad (26)$$

where P represents the vapor pressure and B represents the second virial coefficient in the pressure expansion form of the equation of state.

A relationship connecting $\ln(P'/P)$ and $\ln\alpha_{C-V}$ can now be written from equations (25) and (26) as follows:

$$\ln\alpha_{C-V} = \ln\left(\frac{P'}{P}\right) - \left(\frac{1}{RT}\right)(P'V' - PV) + (B'P' - BP) - \frac{(V'-V)^2}{(2\kappa' V' R\,T)} \qquad (27)$$

We now turn our attention to the experimental results. The D/H fractionation factor between liquid and water vapor, α_{L-V}, and the vapor pressure ratio, (P_{H_2O}/P_{HDO}), are combined in equation (27). In order to compare the data, which were obtained by the measurement of the vapor pressure ratio, (P_{H_2O}/P_{D_2O}), between H_2O and D_2O, and by those of the D/H fractionation factor, the value of the HDO vapor pressure is estimated by the geometric mean. The $\ln(P_{H_2O}/P_{HDO})$ values calculated from the measured $\ln(P_{H_2O}/P_{D_2O})$ and $\ln\alpha_{L-V}$ values are shown in Figure 3. The values of $\ln\alpha_{L-V}$ are somewhat larger than those of $\ln(P_{H_2O}/P_{HDO})\{=(1/2)\ln(P_{H_2O}/P_{D_2O})\}$ in this temperature range.

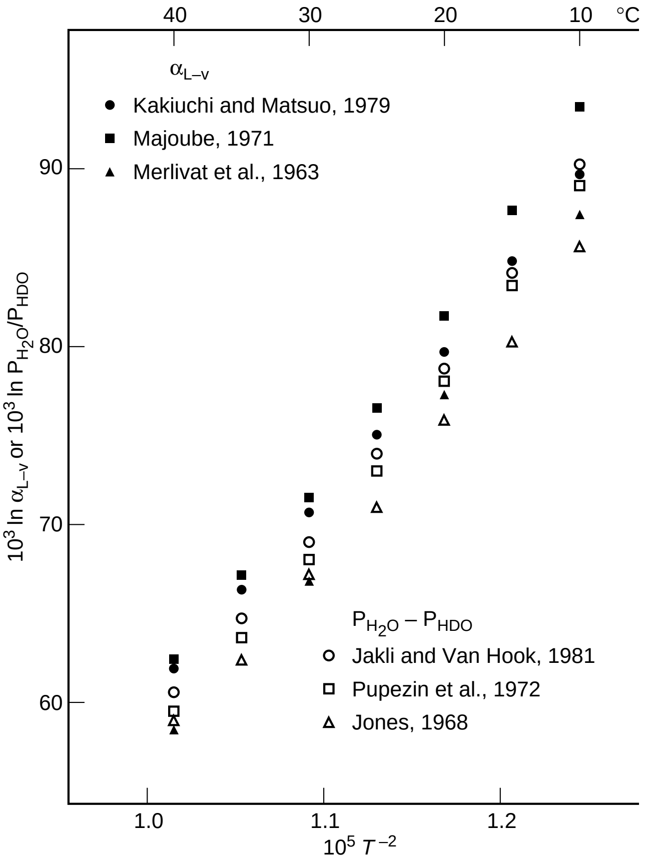

Figure 3 Comparison of the values of $\ln\alpha_{L-V}$ and $\ln(P_{H_2O}/P_{HDO})$ for pure water in the temperature range from 10 to 40 °C

4.4 Isotope Effect in Aqueous Solution

4.4.1 Solvent Isotope Effects in Hydration[67]

The term ‘solvent isotope effect’ is used in discussions of equilibrium processes in normal and heavy water for the isotope effect, which is attributed to isotopic substitution of the solvent. Solvent isotope effects may be due primary to differences in the structure constructed by the two isotopic water molecules.

The differences in the hydration of a solute in H_2O and D_2O have been extensively studied by measuring their thermodynamic properties, the change of free energy ($\Delta G^0{}_t$), enthalpy ($\Delta H^0{}_t$), and entropy ($\Delta S^0{}_t$) at the transfer of 1 mol of solute from a highly dilute solution in H_2O to the same concentration in D_2O under reversible conditions (mostly 25 °C and atmospheric pressure). Greyson[68] measured the electromotive force (emf) of electrochemical cells of several alkali halides containing heavy and normal water solutions. The cell potentials had been combined with available heat of solution data to determine the entropy of transfer of the salts between the isotopic solvents. The thermodynamic properties for the transfer from H_2O to D_2O and the solubilities of alkali halides at 25° in H_2O and D_2O are shown in Table 4.

The $\Delta G^0{}_t$ studies using electrochemical cells with dilute solutions or the solubility studies of alkali halide suggest that most salts have a higher standard free energy in D_2O than in H_2O between 0 and 100 °C; thus they are 'more soluble' in H_2O, as shown in Table 4. LiF is shown to have the highest driving force to go from H_2O to D_2O. The $\Delta H^0{}_t$ for alkali halides is correlated with the $\Delta S^0{}_t$. Alkali halide salts, except LiF, break more structure in D_2O than in H_2O, because there is more structure to break, thereby producing the positive $\Delta H^0{}_t$ and $\Delta S^0{}_t$. Judging from the values of thermodynamic properties of transfer, the orders of effects of alkali metal cations and halide anions on the structure of water were found to be $Cs^+ > K^+ > Na^+ > Li^+$, and $I^- > Br^- > Cl^- > F^-$, respectively.

4.4.2 *Solvent Vapor Pressure Isotope Effect*

The vapor pressure ratio measurements of separated isotopes are particularly useful because they directly measure the isotopic free energy ratios of the solvent. The solvent vapor pressure isotope effect between H_2O and D_2O is determined in terms of

$$\Delta \ln\left(\frac{P_{H_2O}}{P_{D_2O}}\right)^m = \ln\left(\frac{P_{H_2O}}{P_{D_2O}}\right)^0 - \ln\left(\frac{P_{H_2O}}{P_{D_2O}}\right)^m \qquad (28)$$

where the superscript 0 denotes pure water, while m represents the aquamolality, which corresponds to the molality of the solute in 55.51 mol of solvent. The values of $\Delta \ln(P_{H_2O}/P_{D_2O})^m$ for alkali chlorides and some salts were measured over a broad range in temperature and concentration by Pupezin *et al.*[69] and Jakli *et al.*[70] The measured values are positive except for the value obtained with 2 m LiCl, and become larger if salt is added to the both solvents. Changes in $\Delta \ln(P_{H_2O}/P_{D_2O})^m$ values with changing temperature for several concentrations of alkali chlorides mostly arise near 50 °C.

Jakli and Van Hook[71] also measured the values of $\Delta \ln(P_{H_2O}/P_{D_2O})^m$ in aqueous urea solutions. The values $\Delta \ln(P_{H_2O}/P_{D_2O})^m$ in urea solution are positive and increase with increasing molality of urea. There is little temperature dependence of $\Delta \ln(P_{H_2O}/P_{D_2O})^m$ in the temperature range 15–60 °C. The value of $\Delta \ln(P_{H_2O}/P_{D_2O})^m$ is significantly smaller than that for an alkali halide solution. Data of $\Delta \ln(P_{H_2O}/P_{D_2O})^m$ of some salts and urea at 25 °C are shown in Table 5.

4.4.3 *Fractionation Between Aqueous Solution and Water Vapor*

In order to explain the isotopic fractionation of hydrogen and oxygen isotopes between aqueous solution and water vapor or between aqueous solution and carbon dioxide,[72–77] the following model is proposed. In the aqueous solutions the presence of two different species of water molecules is assumed; one species represents the water molecules coordinated to the solute ions or molecules forming the hydration sphere, and another species represents the 'free' (or

Table 4 Free energy ($\Delta G^0{}_t$), enthalpy ($\Delta H^0{}_t$), and entropy ($\Delta S^0{}_t$) of transfer from H_2O to D_2O, and solubilities in H_2O and D_2O for alkali halides at 25 °C

				Solubilities[a]		$X_{D_2O}{}^b$
Salts	$\Delta G^0{}_t$ (cal mol^{-1})	$\Delta H^0{}_t$ (cal mol^{-1})	$\Delta S^0{}_t$ (cal mol^{-1} K^{-1})	H_2O	D_2O	X_{H_2O}
LiF	−58	−155	−0.33	–	–	1.15
LiCl	32	420	1.30	19.90	20.28	1.014
LiBr	67	560	1.65	–	–	–
LiI	100	720	2.08	–	–	–
NaF	−28	10	0.13	–	–	–
NaCl	110	510	1.34	6.145	5.76	0.943
NaBr	170	650	1.61	9.20	9.07	0.988
NaI	230	810	1.95	12.34	12.18	0.989
KF	−3	60	0.21	–	–	–
KCl	130	560	1.44	4.80	4.38	0.919
KBr	180	695	1.73	5.71	5.10	0.902
KI	240	865	2.09	8.90	8.07	0.919

[a] Solubilities are expressed as moles of salt per 55.5 moles of solvent. [b] Solubility ratios are expressed as molar fraction ratios.

Table 5 Values of $10^3\Delta\ln(P_{H_2O}/P_{D_2O})^m$ and $-10^3\ln\beta$ for some salts and urea at 25 °C

Solute	Aquamolality	$10^3\Delta\ln(P_{H_2O}/P_{D_2O})^{m\,a}$	Molality	$-10^3\ln\beta^b$
LiCl	2	−0.1	1.9	2.3
	4	0.1	3.1	3.5
			5.0	5.3
	6	0.8	6.0	5.3
			7.9	7.5
	10	5.9	10.6	9.8
			12.0	11.7
			13.7	16.5
	15	23.6	15.0	17.5
			16.3	18.0
			16.9	19.9
			19.0	25.4
NaCl	2	0.3	2.0	4.8
			2.14	4.7
	4	1.0	4.0	8.8
			4.27	9.3
	6	2.3	6.0	12.6
NaI			1.66	7.0
	2	0.3	2.0	8.0
			3.31	13.9
	4	1.6	4.0	15.9
	6	4.7	6.0	22.6
	8	10.1	8.0	27.6
	10	18.6		
Urea			2.1	−12.2
	4	0.3	5.0	−18.7
			5.2	−20.7
	8	2.1	10.0	−30.7
	12	4.3		
	16	4.8	15.0	−38.8
	18	3.6		
	20	5.3	20.1	−50.2

[a] $\Delta\ln(P_{H_2O}/P_{D_2O})^m$ values for LiCl and NaCl, by Pupezin *et al.*,[69] for NaI by Jakli *et al.*,[70] and for urea by Jakli and Van Hook.[71]
[b] $\ln\beta$ values for LiCl by Kakiuchi,[72] for NaCl and NaI by Stewart and Friedman,[73] and by Kakiuchi,[74] and for urea by Kakiuchi and Matsuo.[75]

'bulk') water molecules that are not involved in hydration, and is structurally similar to pure water. These two species of water molecules must be in energetically different states, resulting in D/H and $^{18}O/^{16}O$ fractionations between these two species. Addition of a solute to the aqueous phase changes the D/H and $^{18}O/^{16}O$ ratios in the 'free' water since newly formed hydration spheres selectively take hydrogen and oxygen isotopes. This in turn results in the change in the D/H and $^{18}O/^{16}O$ ratios in the water vapor or the $^{18}O/^{16}O$ ratio in the carbon dioxide in equilibrium with the 'free' water, which is considered to have an energy state similar to pure water.

The D/H fractionation factor, $\alpha_{\text{sol}-\text{V}}$, between an aqueous solution and vapor is defined by the relation

$$\alpha_{\text{sol}-\text{V}} = \frac{(\text{D/H})_{\text{sol}}}{(\text{D/H})_{\text{V}}} \tag{29}$$

where $(\text{D/H})_{\text{sol}}$ and $(\text{D/H})_{\text{V}}$ are the D/H ratios of solution and vapor, respectively.

In order to compare the aqueous solution with pure water, Kakiuchi and Matsuo[75] defined β as

$$\beta = \frac{\alpha_{\text{sol}-\text{V}}}{\alpha_{\text{pw}-\text{V}}} = \frac{[(\text{D/H})_{\text{sol}}/(\text{D/H})_{\text{V}}{}^{\text{sol}}]}{[(\text{D/H})_{\text{pw}}/(\text{D/H})_{\text{V}}{}^{\text{pw}}]} \tag{30}$$

where $\alpha_{\text{pw}-\text{V}}$ represents the fractionation factor between pure water and vapor, and $(\text{D/H})_{\text{V}}{}^{\text{sol}}$ and $(\text{D/H})_{\text{V}}{}^{\text{pw}}$ are the D/H ratios of water vapor over the solution and pure water, respectively. When isotopically identical water is used as pure water and in aqueous solution, then $(\text{D/H})_{\text{sol}}$ and $(\text{D/H})_{\text{pw}}$ in equation (30) becomes the same. β indicates the ratio between the D/H ratio of vapor equilibrated with pure water and that of vapor equilibrated with an aqueous solution as follows

$$\beta = \frac{(\text{D/H})_{\text{V}}{}^{\text{pw}}}{(\text{D/H})_{\text{V}}{}^{\text{sol}}} \tag{31}$$

The negative values of $\ln\beta$ indicate that the D/H ratio of water vapor equilibrated with aqueous solutions is higher than that of water vapor equilibrated with pure water.

Kakiuchi[72] measured the D/H ratio of hydrogen gas in equilibrium with aqueous solution by means of catalytic exchange using a hydrophobic Pt catalyst. The aqueous solution–hydrogen gas equilibrium, $\alpha_{\text{sol}-\text{g}}$, can be expressed as

$$\alpha_{\text{sol}-\text{g}} = \frac{(\text{D/H})_{\text{sol}}}{(\text{D/H})_{\text{g}}{}^{\text{sol}}} \tag{32}$$

where the subscript g indicates hydrogen gas. Similarly, with the solution-vapor equilibration method, β is also defined as

$$\beta = \frac{\alpha_{\text{sol}-\text{g}}}{\alpha_{\text{pw}-\text{g}}} = \frac{(\text{D/H})_{\text{g}}{}^{\text{pw}}}{(\text{D/H})_{\text{g}}{}^{\text{sol}}} \tag{33}$$

where, $\alpha_{\text{pw}-\text{g}}$ represents the fractionation factor between pure water and hydrogen gas, and $(\text{D/H})_{\text{g}}{}^{\text{sol}}$ and $(\text{D/H})_{\text{g}}{}^{\text{pw}}$ are the D/H ratios of hydrogen gas over the aqueous solution and pure water, respectively. Water vapor equilibrated with the aqueous solution is also equilibrated with the hydrogen gas on the catalyst at the same temperature. β is defined by equations (31) and (33), which are identical.

Table 5 presents the results of $\ln\beta$ determinations in relation to the concentration of some alkali halides[72–74] and urea[75] at 25 °C. Based on the assumption that the 'free' (or 'bulk') water in aqueous solutions is identical with pure water, the fractionation factor between the 'free' water molecules in solution and water vapor or between that and hydrogen gas, $\alpha_{\text{f}-\text{V}}$ or $\alpha_{\text{f}-\text{g}}$, should be equal to that between pure water and water vapor or between that and hydrogen gas, $\alpha_{\text{pw}-\text{V}}$ or $\alpha_{\text{pw}-\text{g}}$, respectively. Then the negative value of the $\ln\beta$ for alkali halide solutions indicates that the fractionation factor between hydrated water and the 'free' water in solution, $\alpha_{\text{h}-\text{f}}$, is smaller than unity. This means that HDO is depleted in the hydration sphere of alkali halides. The observed $\ln\beta$ values show a linear relationship with concentration up to 6 m in various alkali halide solutions. Conversely, the $\ln\beta$ values obtained for urea solution are positive and do not show a linear relationship.

The temperature dependence of $\ln\beta$in the aqueous sodium chloride solution in the temperature range from 10 to 95 °C using the solution–hydrogen gas equilibration method,**74** and from 50 to 100 °C using the solution-vapor method.**77** $\ln\beta$ values show a linear relationship with concentration at each temperature. Concentrations of 2, 4, and 6 molal change linearly with the reciprocal temperature squared.

The relationship between $\ln\beta$ and $\Delta\ln(P_{H_2O}/P_{D_2O})^m$ can be expressed as: $\ln\beta = -(1/2)\Delta\ln(P_{H_2O}/P_{D_2O})^m$, based on the assumptions that the mixing behavior of H_2O–HDO–D_2O is ideal, and that both equilibrium constants of the reaction, $H_2O + D_2O \rightleftharpoons 2HDO$, of the liquid and gas phases, are identical, even in aqueous solutions. Comparison of with natural D/H ratios, with $\Delta\ln(P_{H_2O}/P_{D_2O})^m$ values obtained by the vapor pressure measurements on separated isotopes at 25 °C (Table 5), shows the qualitative trends on concentration for alkali halide to be the same. However, the difference between the values of $-\ln\beta$ and those of $(1/2)\Delta\ln(P_{H_2O}/P_{D_2O})^m$ are remarkably large.

5 CHEMICAL PROPERTIES OF HYDROGEN

5.1 General

As the dissociation energy of a single H–H bond is high (436 kJ mol^{-1}), molecular hydrogen is stable and relatively inert at room temperature. It burns in air to form water and will react explosively with oxygen and halogens under certain conditions. At high temperature, hydrogen gas will reduce many oxides, either to lower oxides or to metal. In the presence of suitable catalysts, hydrogen reacts with N_2 to form NH_3. Hydrogen also forms hydrides with electropositive metals and nonmetals.

A number of reactions of hydrogen and organic molecules are catalyzed by transition metals. In the presence of suitable catalysts, usually groups 8–10 metals or their compounds, a great variety of both inorganic and organic substances can be reduced (*see* ***Heterogeneous Catalysis by Metals***). Heterogeneous *Hydrogenation* may be carried out in a gas phase or in solution, and a number of transition metal ions and complexes can react with hydrogen, transferring it to a substrate homogeneously in solution (*see* ***Hydrogenation & Isomerization of Alkenes***). Hydrogen recombination, which is one of the simplest chemical reactions, has generated wide interest, both theoretically and experimentally. Because of its electronic simplicity, hydrogen is a suitable subject for theoretical consideration of adsorbate-surface bonding. Hydrogen is important as a reactant in heterogeneously catalyzed process. In exchange reactions with organic molecules, hydrogen and deuterium have been extensively investigated in relation to catalysis.

Interesting issues in modern fundamental hydrogen chemistry include the possible appearance of unusual valence states of hydrogen under highly unusual thermobaric conditions. In particular, such unusual valence states may include the state of 'metallic' or 'metallized' hydrogen. The issue of metallic hydrogen as an individual phase was actively debated during the mid-1970 s. Data were obtained for the first time in 1989 by Mao *et al.***78** as evidence for band overlap metallization of hydrogen above 200 GPa at 77 K. Measurements of absorption and Raman spectra provide evidence that electronic excitation in the visible region begin at 200 GPa. Strongly compressed solid hydrogen is reported to have a much greater electrical conductivity than that of other solid elements. It would be interesting to measure the electrical conductivity in 'metallic' hydrogen if that measurement were possible.

5.2 Atomic Hydrogen

Although the hydrogen molecules is the simplest stable form of hydrogen under ordinary conditions, atomic hydrogen can be formed from this species if sufficient energy is supplied:

$$H_2 \longrightarrow 2H \qquad \Delta H = 436\,\mathrm{kJmol^{-1}} \tag{34}$$

Under experimental conditions when hydrogen gas is heated the decomposition of the molecules to atoms begins at approximately 2000 °C. Values for the equilibrium constant of the dissociation of hydrogen molecule, $H_2 \rightleftharpoons 2H$, are given in Table 6. In addition, atomic hydrogen can be produced by electrical discharge, by irradiation with a mercury arc, or by

Table 6 Equilibrium constants for dissociation of a hydrogen molecule, $H_2 = 2H$, $K_p = P_H{}^2/P_{H_2}$

T(K)	K_p(atm)
298	1.6×10^{-71}
400	3.8×10^{-52}
600	3.6×10^{-33}
800	1.2×10^{-23}
1000	7.0×10^{-18}
1200	5.05×10^{-14}
1400	2.96×10^{-11}
1600	3.59×10^{-9}
1800	1.52×10^{-7}
2000	3.10×10^{-6}
2200	3.66×10^{-5}
2400	2.89×10^{-4}
3000	2.78×10^{-2}
4000	2.768
5000	44.66

bombardment with electrons in the 10–20 eV energy range. A more convenient source of atomic hydrogen is available by passing a glow discharge through hydrogen gas at 100 Pa.

At pressures less than 1 Pa, hydrogen atoms are formed by heated wires of W, Pd, or Pt. Under such conditions, concentration hydrogen atoms up to 95% may be obtained using a discharge tube. The half-life of the H atom is about 1.0 s at 30 Pa, which allows it to be transported out of the discharge and its reactions examined. The presence of hydrogen atoms in such experiments is established by observation of the Balmer series of the H atom spectrum and the diminution in intensity of the H_2 molecules band spectrum. The very long half-life shows that only about 1 in 10^6 collisions between atoms leads to recombination.

The H atoms formed by the methods mentioned above are highly reactive and unite with many elements to give hydrides.**[79]** The reactions of H atoms in the gaseous phase and in solution have very extensively studied using kinetic methods because of the transient nature of this species.

As the recombination of H atoms is strongly catalyzed by many metals, recent work has used electrodeless discharges operating at microwave or radio frequencies. The high heat generated in the process of H atom recombination can be utilized as an atomic hydrogen torch, where hydrogen is dissociated in an arc and recombines on the surface of the metal to be melted. Temperatures of approximately 4000 °C are attained, capable of welding metals with very high melting points such as Ta or W.

If a metal such as Zn is dissolved in acid, hydrogen gas is produced, and thus the dissolving metal is a good reducing agent. Therefore hydrogen is being formed as a reduction product of the proton and it is not in itself the reducing agent. However, in practice, molecular hydrogen is a poor reducing agent, because of its kinetic stability. It is most likely that hydrogen atoms can be produced by proton reduction (i.e. by the process, $H^+ + e^- \longrightarrow H$). Hydrogen atoms will usually unite with each other to produce molecular hydrogen, but can attack other species. Thus, in the reduction of an arsenic-containing compound to AsH_3, or an alkyl halide to an alkane by a metal couple (Al–Zn–Cu) in aqueous acid, atomic hydrogen may participate in the reaction.

5.3 Ionized Forms of Hydrogen

In this section, we will consider the *Proton* H^+, the hydride ion H^-, the hydrogen molecule ion $H_2{}^+$, and the triatomic two-electron species $H_3{}^+$.

The first ionization energy of H atom (1311 kJ mol^{-1}) is very high in comparison with that of many other elements, such as alkali metals. Removal of the 1s electron leaves a bare proton, which, having a radius of only about 1.5×10^{-3} pm, never exists in the condensed phase. However, when bonded to other species it is well known in solutions and in solids (e.g. H_3O^+, $NH_4{}^+$, etc.). The proton affinity of water and the solvation energy of the H^+ ion in water have been estimated from the thermodynamic cycle at 25 °C:

$$H^+(g) + H_2O(g) \longrightarrow H_3O^+(g) \qquad -\Delta H = 690\,\text{kJmol}^{-1} \quad (35)$$

$$H^+(g) + xH_2O(aq) \longrightarrow H^+(aq) \qquad -\Delta H = 1090\,\text{kJmol}^{-1} \quad (36)$$

It follows that the heat of solution of the H_3O^+ ion in water is 400 kJ mol^{-1}.

Compounds that furnish solvated H^+ ions in suitable polar solvents, such as water, are protonic acids. The nature of the H^+ ions in water, which should more correctly be called the hydroxonium ion, H_3O^+, is customarily referred to as ‘the hydrogen ion’.

The hydrogen atom, like the alkali metals and halogens, has an affinity for the electron (*see Electron Affinity*). From the following reaction, heat is produced:

$$H(g) + e^- \longrightarrow H^-(g) \qquad -\Delta H = 72\,\text{kJmol}^{-1} \quad (37)$$

This value is larger than the corresponding value for Li (57 kJ mol^{-1}) but substantially smaller than the value for F (333 kJ mol^{-1}). The hydride ion H^- has the same electron configuration as He, but is much less stable because the single positive charge on the proton must control the two electrons. The hydride ion is thus readily deformable, a characteristic feature of its structural chemistry.

The species $H_2{}^+$ and $H_3{}^+$ are important as model systems for *Chemical Bonding* theory. The hydrogen molecule ion, $H_2{}^+$, comprises two protons and one electron, and is extremely unstable even in a low-pressure gas discharge system. The energy of dissociation of an $H_2{}^+$ ion is smaller than that of an H_2 molecule (436 kJ mol^{-1}) and the internuclear distance of an $H_2{}^+$ ion is larger than that of an H_2 molecule (74.1 pm).

The triatomic hydrogen molecule ion $H_3{}^+$, was first detected in gas discharges and later fully characterized by mass spectrometry; its relative atomic mass, 3.027, clearly distinguishes itself from tritium, 3.016. The ‘observed’ triangular three-center two-electron structure is more stable than the hypothetical linear structure.

5.4 Reactions of Molecular Hydrogen

5.4.1 General

Molecular hydrogen is not reactive at ordinary temperatures. However, at higher temperature, hydrogen gas combines with most elements, either directly or with the aid of a catalyst. Some of the more important reactions are shown in Figure 4. The resultant hydrides are described simply in Section 5.5.

Only a few compounds are reduced by H_2 at room temperature. An aqueous solution of palladium chloride is readily reduced:

$$PdCl_2(aq) + H_2 \longrightarrow Pd(s) + 2HCl(aq) \quad (38)$$

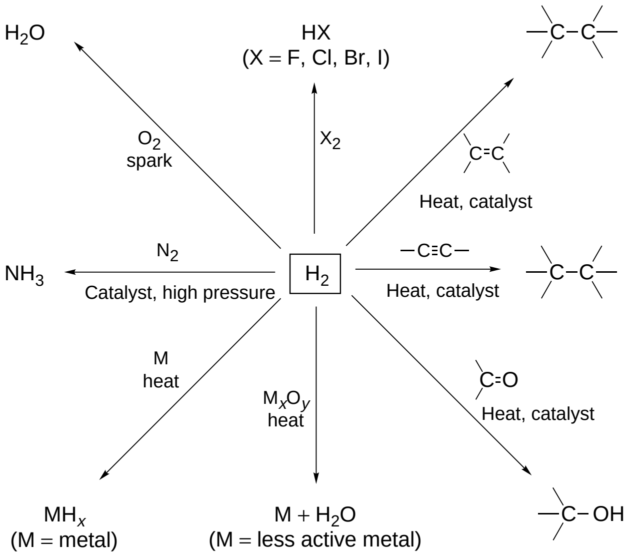

Figure 4 Major reactions of molecular hydrogen

This reaction, using a 1% solution of $PdCl_2$, acts as a sensitive test for the presence of hydrogen and may be used quantitatively.

Inorganic reactions and experimental method for hydrogen are thoroughly described in the literature.[80]

5.4.2 Reactions of Hydrogen with Halogens

Mixtures of hydrogen gas and halogens combine vigorously. The reactions are initiated by the dissociation of the halogen molecules in presence of heat, light, or other agents. All of the reactions are exothermic (*see **Chlorine, Bromine, Iodine, & Astatine: Inorganic Chemistry*** and ***Fluorine: Inorganic Chemistry***).

Even at the temperature of liquid nitrogen, 77 K, hydrogen react violently with fluorine:

$$H_2 + F_2 \longrightarrow 2HF \qquad (39)$$

The combination is highly efficient owing to the strength of the H–F bond. The stability of the H–F bond and its high heat of formation give the combination of H_2 and F_2 the highest specific impulse available to the science of rocket propulsion.

Hydrogen and chlorine combine to form HCl:

$$H_2 + Cl_2 \longrightarrow 2HCl \qquad (40)$$

Enclosed mixtures of H_2 and Cl_2 undergo rapid combination at 20 °C if exposed to light. The thermal combination of H_2 and Cl_2 is carried out in the absence of a catalyst, although charcoal is a catalyst.[81] Without a catalyst, the elements combine slowly at 100 °C and more rapidly at 200 °C. In the presence of a catalyst, rapid combination occurs at 20 °C or below.

Direct combination of H_2 and Br_2 is the most economical method for the preparation of pure HBr:

$$H_2 + Br_2 \longrightarrow 2HBr \qquad (41)$$

This reaction is more difficult to achieve than those involving F_2 or Cl_2 are. In the absence of a catalyst, the reaction occurs slowly at 250 °C, but rapidly at 500 °C. The reaction is most readily brought about in the presence of a carbon catalyst at a temperature above 150 °C. In contrast to Cl_2, there is no reaction at 20 °C indirect sunlight. At 200 °C, sunlight causes rapid combination, forming HBr.

The formation of HI from its elements is the least favorable, in terms of energy, of the hydrogen−halogen combination reactions (excluding At):

$$H_2 + I_2 \longrightarrow 2HI \qquad (42)$$

In the absence of a catalyst, the combination of H_2 and I_2 occurs only above 500 °C, although at these temperatures HI undergoes extensive thermal decomposition, producing an equilibrium mixture. This reaction, therefore, is always brought about by the presence of a catalyst.

5.4.3 Reactions of Hydrogen with Major Elements

Molecular hydrogen reacts with oxygen to form water (*see **Oxygen: Inorganic Chemistry***):

$$2H_2 + O_2 \longrightarrow 2H_2O \qquad (43)$$

This reaction is exothermic. The heat required to produce gaseous H_2O and liquid H_2O in this reaction at 25 °C and 1 atm is 242 and 286 kJ mol^{-1}, respectively. This reaction proceeds spontaneously at temperatures above 500 °C. At temperatures lower than 500 °C this reaction occurs in the presence of a suitable catalyst, such as Pt or Pd, or if activated by an electric spark or a flame. The combustion of hydrogen in oxygen produces flame temperatures as high as 2800 °C, a technique utilized in oxyhydrogen welding torches.

The direct reduction of sulfur by hydrogen to produce hydrogen sulfide does not take place readily at room temperature, but does take place at 250 °C:

$$H_2 + S \longrightarrow H_2S \qquad (44)$$

A catalyst is usually requires in the formation of H_2S. Metal sulfides are the most common catalysts used in the laboratory or in large-scale production of H_2S. The catalytic activity of metal sulfides is linked to the metal−sulfur bond strength.

Large quantities of ammonia are produced from the exothermic reaction of gases H_2 and N_2:

$$N_2 + 3H_2 \rightleftharpoons 2NH_3 \qquad -\Delta H = 92\,\text{kJmol}^{-1} \qquad (45)$$

The equilibrium favors NH_3 formation at low temperature and high pressure. In order to achieve acceptable reaction rates and conversion to NH_3, the reaction is carried out over an Fe or Fe_2O_3 catalyst at 500 °C and ca. 10^5 Pa.

Under ordinary conditions, carbon does not react with H_2 at an appreciable rate. At high temperatures and in the presence of catalysts, the following reaction occurs:

$$\text{C(graphite)} + 2H_2 \longrightarrow CH_4 \tag{46}$$

Powdered graphite impregnated with Ni, or C in the presence of Fe–Cr sponge, reacts at 500–1000 °C to form CH_4, along with small quantities of other hydrocarbons.[82]

5.4.4 *Reduction of Metal Compounds*

The reduction of metal oxides (M_xO_y) by hydrogen gas is metallurgically valuable. Water is produced in this reaction:

$$\left(\frac{1}{y}\right) M_xO_y + H_2 \rightleftharpoons \left(\frac{x}{y}\right) M + H_2O \tag{47}$$

The reduction of metal sulfates by H_2 also produces water; for example, $MgSO_4$ at approximately 750 °C and $CaSO_4$ at approximately 900 °C. But the reactions proceed in different ways because the thermodynamically stable products are MgO and CaS:

$$MgSO_4 + 4H_2 \longrightarrow MgO + H_2S + 3H_2O \tag{48}$$

$$CaSO_4 + 4H_2 \longrightarrow CaS + 4H_2O \tag{49}$$

5.4.5 *Miscellaneous Reactions*

The reduction of SO_2 by H_2, according to the equation

$$SO_2 + 3H_2 \longrightarrow 2H_2O + H_2S \tag{50}$$

is important in sulfur chemistry (*see* ***Sulfur: Inorganic Chemistry***). Inorganic nitrogen compounds react with H_2, yielding products containing N–H. Germanium nitride reacts with H_2 at 600 °C (*see* ***Nitrogen: Inorganic Chemistry***):

$$Ge_3N_2 + 3H_2 \longrightarrow 3Ge + 2NH_3 \tag{51}$$

Unsaturated organic compounds such as alkynes, alkenes, ketones, oximes, nitriles, and imines, are readily reduced by H_2 using a catalyst; for example:

$$C_2H_2 + 2H_2 \longrightarrow C_2H_6 \tag{52}$$

$$C_2H_4 + H_2 \longrightarrow C_2H_6 \tag{53}$$

$$C_6H_6 + 3H_2 \longrightarrow C_6H_{12} \tag{54}$$

$$(CH_3)_2CO + H_2 \longrightarrow (CH_3)_2CHOH \tag{55}$$

Hydrogenations using heterogeneous catalysts usually require thermal condition above room temperature and H_2 pressures higher than 10^3 Pa. Homogeneous catalysts are often more selective with individual reactions and make the reactions possible at lower temperatures and H_2 pressures.

5.5 Hydrides

Hydrogen combines a variety of elements to form hydrides, compounds with widely differing properties.[83] Figure 5

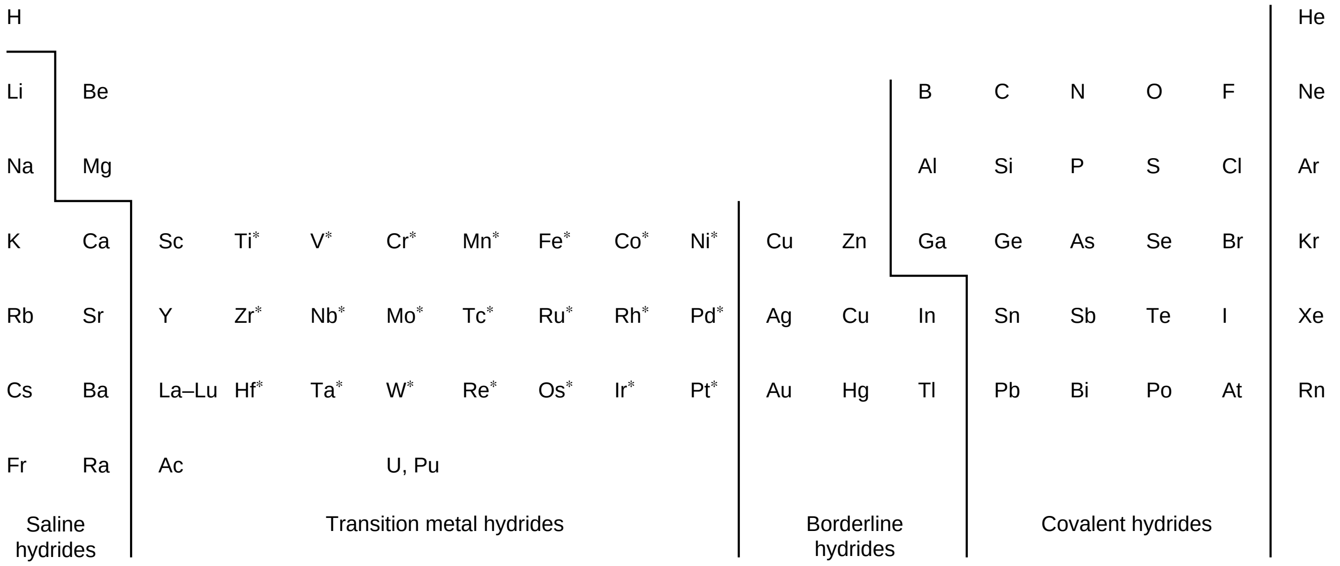

H																	He
Li	Be											B	C	N	O	F	Ne
Na	Mg											Al	Si	P	S	Cl	Ar
K	Ca	Sc	Ti*	V*	Cr*	Mn*	Fe*	Co*	Ni*	Cu	Zn	Ga	Ge	As	Se	Br	Kr
Rb	Sr	Y	Zr*	Nb*	Mo*	Tc*	Ru*	Rh*	Pd*	Ag	Cu	In	Sn	Sb	Te	I	Xe
Cs	Ba	La–Lu	Hf*	Ta*	W*	Re*	Os*	Ir*	Pt*	Au	Hg	Tl	Pb	Bi	Po	At	Rn
Fr	Ra	Ac			U, Pu												
Saline hydrides		Transition metal hydrides								Borderline hydrides			Covalent hydrides				

Figure 5 A classification of the hydrides. The starred elements are the transition elements for which complex molecules or ions containing M–H bonds are known. (Ref. 84. Reproduced by permission of Wiley Inc.)

represents an approximate classification of the various hydrides.[84]

Elements with very low electronegativeties of approximately 1.0 (*see Electronegativity*), form compounds in which the hydrogen appears as an anion, H^-. These compounds have many of the properties associated with ionic substances and are sometimes called ionic or saline hydrides. Ionic hydrides, formed with alkali (M^+H^-) and alkaline earth ($M'^{2+}{H_2}^{2-}$) metals, are colorless crystalline solids that either melt or decompose at temperatures above 600 °C. All of the hydrides can be formed by direct combination of the elements at elevated temperatures:

$$2M + H_2 \longrightarrow 2MH \qquad (56)$$

$$M' + H_2 \longrightarrow M'H_2 \qquad (57)$$

For lithium and sodium the hydrides can also be prepared by heating the corresponding nitride in a stream of hydrogen:

$$2M_3N + 3H_2 \longrightarrow 6MH + N_2 \qquad (58)$$

Elements with electronegativities of approximately 2.0 or greater form hydrogen compounds with covalent bonds. These substances are generally volatile and are often referred to as covalent hydrides. The covalent hydrides fall into two distinct classes. The first are the compounds of the carbon, nitrogen, oxygen, and fluorine groups, which have normal electron-pair bonds between the element and hydrogen. The second are compounds exemplified by the simplest boron hydride, B_2H_6, which do not have enough valance electrons to form electron-pair bonds to all of the hydrogen and therefore are termed ‘electron deficient’ (*see* ***Boron Hydrides***). Into this category fall the hydrides of Be, B, Al, and Ga.

The transition metal hydrides are formed by the elements with intermediate electronegativities (*see* ***Hydride Complexes of the Transition Metals***; ***Hydrides: Solid State Transition Metal Complexes***). The fundamental difference between the ionic hydrides and the transition metal hydrides is clearly illustrated by their differentially corresponding absorption of hydrogen.

5.6 Interaction of Hydrogen with Metals

5.6.1 Hydrogen Absorption

The metals, which form ionic hydrides, show extended temperature ranges in which hydrogen absorption does not occur until favorable conditions for the formation of the hydride are reached. At this point the expected stoichiometric amount of hydrogen is absorbed. In contrast, some of the metals that form transition metal hydrides are capable of absorbing a considerable amount of hydrogen.

The nature of the hydrogen atoms bound in the transition metal hydrides is not clearly understood. Some of these substances are good reducing agents, suggesting the presence of hydridic or atomic hydrogen. Rapid diffusion of hydrogen in metals such as Pd indicates that unbound hydrogen atoms may be present. The constitution of these systems may vary with composition. For example, up to a composition of $PdH_{0.5}$ the palladium–hydrogen system has properties associated with conduction, but at higher concentrations of hydrogen it becomes a semiconductor. In the same range of stoichiometries the paramagnetisum decreases from a value for a pure metal to a minimum value at a composition corresponding to $PdH_{0.6}$.

Formation of a binary hydride is an exothermic process, excluding some cases such as Ni and Cu where it is endothermic, and also Cr where it becomes endothermic at higher temperature. For other metals, which dissolve hydrogen without hydride formation, such as Fe, Co, Mo, Ag, and Pt, the process is endothermic; that is, hydrogen uptake increases with increasing temperature. This may complicate the interpretation of thermal desorption spectra, since some hydrogen may enter the bulk rather than appear in the gas phase. Very large quantities of hydrogen can be absorbed in Pd, Ti, Zr, V, Ta, and U hydrides. In the endothermic systems, however, the H to metal atom ratio is generally very small at elevated temperatures. Finally, with metals such as W, Re, Os, and Ir, no solubility is detectable by macroscopic techniques, although this does not exclude the possibility that significant amounts may be dissolved on the scale of surface process.

5.6.2 Hydrogen Adsorption

Single-crystal hydrogen adsorption results are available to data only for atomic hydrogen, that is, the H_2 molecule has to be split by external means, such as a gas discharge or by a hot wire as mentioned in Section 5.2. The large surface area of powders allows adsorption studies by means of volumetric measurements. In contrast, single crystals exhibit only a few square millimeters of surface, and adsorbed hydrogen has been detected to date only through changes of surface conductivity and work function. Studies show that adsorption processes and surface reactions of single crystals depend on the crystallographic orientation of the crystal surface. For powders, the orientation of the adsorbing face is not yet known (*see* ***Surfaces***).

Hydrogen adsorption has been extensively studied on metals and metal oxides. In particular, detailed explanations have been given for the interactions of hydrogen with metals Mo, W, Ni, Pd, and Pt,[85] and with the metal oxides ZnO and TiO_2.[86]

Knowledge of the adsorption of hydrogen on silicon and germanium surfaces is important in order to obtain information on interfacial phenomenon of semiconductors.[87] The adsorption of hydrogen on Si (111) surfaces is one of the best understood systems, although the exact nature of the clean surfaces is not well understood.

6 PHYSICAL PROPERTIES OF HYDROGEN

6.1 General

There has been a tremendous upsurge in research and development studies of hydrogen: determinations of its properties at temperatures ranging from 0 to 10^6 K, and at pressures ranging from 10 to 4×10^{10} Pa. In space programs, hydrogen is widely used as a rocket fuel and it is well known for generating energy by nuclear fusion.

Major physical properties of atomic hydrogen and molecular hydrogen of natural composition are listed in Tables 1 and 2. The basic physical properties of hydrogen have been measured with high precision. The hydrogen molecule, owing to its simple nature, has been used extensively as a model for detailed calculations, often accompanied by a wide range of measurements of suitable properties. For example, values for ortho- and para-hydrogen are discussed later in Section 6.3. Hydrogen is very sparingly soluble in water: at STP (0 °C, 1 atm $= 1.01 \times 10^5$ Pa) only 2.14 volumes of hydrogen dissolve in 100 volumes of water.[88] Its solubility in liquid hydrocarbons such as hexane, cyclohexane, and benzene is a linear function of pressure up to 1.5×10^7 Pa. The solubility of hydrogen in liquid ammonia increases with increasing temperature,[89] in contrast to the solubility of usual gases, which decrease with increasing temperature. The solubilities of hydrogen in water and liquid ammonia are shown in Table 7. The thermal conductivity of hydrogen is approximately seven times that of air; this property is useful when analyzing for the presence hydrogen in other gases.

Solid hydrogen has been studied extensively. Molecular hydrogen usually freezes in the hexagonal close-packed form, with $a_0 = 376.1$ pm and $c_0 = 610.5$ pm for H_2,[90] and $a_0 = 365$ pm and $c_0 = 583$ pm for D_2,[91] as determined by X-ray diffraction. It has been shown, however, that the formation of molecular hydrogen can be modified into a cubic close-packed geometry in the presence of gold foil with a cube texture at 4.2 K. D_2 and para-H_2 behave similarly.[91]

Table 7 Solubilities of hydrogen in water and liquid ammonia[a]

			Water		
t(°C)	1 atm	50 atm	100 atm	500 atm	1000 atm
0	0.0214	1.068	2.130	9.838	18.001
10	0.0193	0.9690	1.932	8.980	16.623
20	0.0178	0.8945	1.785	8.328	15.592
30	0.0163	0.8475	1.689	7.922	14.928
50	0.0141	0.8090	1.612	7.613	14.404
80	0.0085	0.8385	1.667	7.885	14.867
100	0.0000	0.9120	1.805	8.429	15.775
		Liquid ammonia			
t(°C)	50 atm	100 atm	400 atm	1000 atm	
0	3.28	6.70	24.33	49.77	
25	4.47	9.88	38.13	79.25	
50	5.10	13.49	58.33	124.9	
75	3.49	16.35	88.34	203.3	
100	–	15.67	140.6	388.2	

[a] cm^3 of H_2 (reduced to 0 °C and 1 atm) g^{-1} (H_2O or liq NH_3).

High-temperature hydrogen plasmas are used in experiments to produce energy by thermonuclear fusion of hydrogen to helium; this is the same reaction by which the energy of the Sun and other stars is generated.

6.2 Hydrogen Spectroscopy

The observation and interpretation of the spectrum of atomic hydrogen played a vital part in the development of quantum chemistry. Studies of the spectrum of the hydrogen atom are presented in the literature.[92] The laser technique has contributed to recent advances in the analysis of the spectrum.[93] The fine detail in the spectrum can only be distinguished by light that is highly monochromatic or confined to a narrow range of wavelengths. Lasers are a source of such light, used in the exploration of the hydrogen spectrum.

The spectroscopy and dynamics of superexcited molecules, including the hydrogen atom and molecule, are reviewed in the literature.[94] Synchrotron radiation has been used in the study of photodissociation of a highly excited H_2 molecules into two excited H atoms.[95]

6.3 Ortho- and Para-hydrogen

All diatomic molecules for which the constituent nuclei have spin exhibit the phenomenon of spin isomerism. The nuclear spins can be parallel (the ortho isomer) or opposed (the para isomer). For most diatomic molecules, which might be expected to exhibit, spin isomerism the energy separation of the rotational states is small compared to kT, even at low temperatures. However, in the case of hydrogen molecules, which have the smallest moment of inertia of any diatomic molecules, the energy difference between the rotational energy levels is relatively large and only the lowest states are populated at room temperature.

The ortho-para ratio is determined by the statistical calculation of the availability of states given by the partition function. Calculated ortho–para equilibria for H_2, D_2, and T_2 are shown in Figure 6 at the temperature range from 0 to 300 K.[96–98] When the two nuclear spins are parallel, the resultant nuclear spin quantum number is 1 (i.e. $1/2 + 1/2$) and the state is threefold degenerate. When the two spins are opposed, however, the resultant nuclear spin is zero and the state is nondegenerate. Therefore para-H_2 has the lower energy and this state is favored at lower temperatures. The equilibrium concentration of H_2 approaches three parts ortho to one part para at room temperature.[96] As the nuclear spin quantum number of the deuteron is 1 rather than 1/2 for the proton (see Table 1), the D_2 system is described by Bose-Einstein

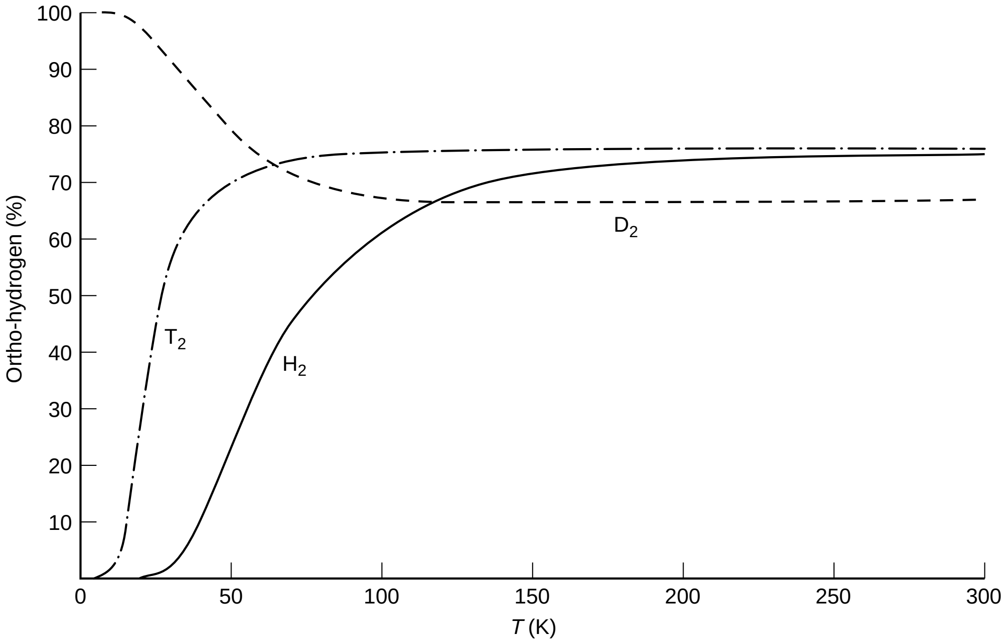

Figure 6 Ortho–para equiblia for H_2, D_2, and T_2 from 0 to 300 K

statistics rather than the more familiar Fermi-Dirac statistics. For this reason the stable low-temperature form is ortho-D_2 and at high temperatures the equilibrium concentration approaches two parts ortho to one part para, as shown in Figure 6.[97] Tritium molecules, T_2, of which the nuclear spin is 1/2, resemble H_2 molecules in their ortho–para relationship.[98]

As the ortho–para conversion involves the forbidden triplet-singlet transition in the nuclear spin state, spontaneous transformation is very slow. Thus, samples of hydrogen that have been cooled exhibit the proportion of the two forms corresponding to the equilibrium composition at room temperature. The conversion of the ortho molecules to para molecules and vice versa requires the simultaneous breaking of both the spin and orbital symmetries, and the equilibrium ratio is therefore established slowly.

The rate constant for the ortho–para conversion in the solid H_2 is 1.9%/h.[99] This value is expected to be different when confined to a restrict geometry owing to interactions with the walls, the changes in the phonon spectrum, and the reduced number of nearest neighbors. The orientational ordering of ortho-H_2 in zeolite as well as the supercooling of the liquid–solid transition has been studied using NMR techniques.[100] Two distinct conversion rates were observed over short and long timespans. An apparently bimolecular conversion rate of 0.43%/h (one-fourth of the bulk value) dominates during the first 500 h, after which the rate increases to 2.2%/h.

The conversion is catalyzed by a number of surface-active or paramagnetic species such as Pd, Pt, or active Fe_2O_3. The presence of both ortho- and para-hydrogen molecules is seen in experiments as an alternation in the intensities of successive rotational lines in the fine structure of the electronic band spectrum of hydrogen molecules. The dual presence also explains the temperature dependence of the heat capacity of hydrogen gas.

According to the quantum theories, it is predicted that molecular hydrogen has a nonstatistical ortho–para composition at low temperature. The calculated values of the ortho-para ratio are found to be sensitive towards the actual model and approximation being used. Therefore measurements of the ortho–para ratio could provide much needed information to improve our understanding of the recombination processes. Although the importance of measuring the ortho–para composition was recognized in the 1970s, with many experimental studies of hydrogen recombination having been reported,[101] a truly convincing measurement is yet to be reported. One of the obstacles towards measuring the composition is that the recombination produces molecules in vibrationally excited states and the analysis of the ortho-para composition is typically carried out after the molecules have relaxed back to the vibrational ground state. Nonstatistical ortho-para ratios in hydrogen recombinations at temperatures below 1 K have been observed, and no ortho-para conversion during the vibrational relaxation process was demonstrated.[102]

6.4 Hydrogen in Semiconductors

In semiconductor science (*see* ***Semiconductor Interfaces***), hydrogen has long been used as an inert gas for crystal growth, or as a component in gases for the various forms of chemical vapor deposition (SiH_4, AsH_3, $Ga(CH_3)_3$, etc.).

Despite its omnipresence and chemical reactivity, hydrogen as an impurity has until recently received limited attention.

Under certain conditions, hydrogen can have a large influence on the electronic properties of a semiconducting material. This was first realized in the research of amorphous silicon in the 1970s. At that time, evaporation of pure Si as the principal deposition method was replaced by plasma-enhanced chemical vapor deposition of silane. Because of the relatively low temperatures needed to obtain amorphous rather than polycrystalline silicon, several atomic per cent of hydrogen remained trapped in the amorphous silicon matrix, mostly in the form of Si–H. An immediate consequence of the presence of hydrogen in silicon is a pronounced reduction of structural defect via Si–H bond formation. This passivation of deep electronic defects is a prerequisite for almost all-technical applications of hydrogenated amorphous silicon (a-Si:H). There has been a significant amount of research dealing with hydrogen in amorphous silicon and its influence on electronic properties.

Experimental and theoretical studies on hydrogen in crystalline semiconductors have been compiled in the literature.[103]

6.5 Hydrogen Energy

In the space exploration program, large quantities of liquid hydrogen have been used both as a fuel for generating electric power in fuel cells, and as a rocket fuel with oxygen or fluorine as the oxidizer.

Active searches for alternative forms of energy have been prompted by the growing recognition that reserves of coal and oil are finite and that nuclear power cannot supply all our energy requirements. Hydrogen has been considered as a source of fusion energy and/or clean energy.

High-temperature hydrogen plasmas, in addition to being a key component in energy projects of the nuclear fusion reaction using deuterium and/or tritium, have also been studied as agents for chemical reactions.

Since the energy crisis in 1973, a number of laboratories have undertaken intensive research projects with the aim of developing methods for hydrogen production by utilizing solar energy. Because of its physical and chemical properties, hydrogen is accepted as a nearly ideal energy carrier for the future. It can be produced from water by various techniques and has advantages over electricity because it can be stored. On combustion, hydrogen reforms to water (closed cycle), so produces little pollution. The photoelectrochemical and photocatalytic methods for hydrogen production are of special benefit, because solar energy is free and practically inexhaustible. However, the supply of energy on the surface of the Earth is not so enormous in comparison with the amount of energy consumed by mankind. Progress in this field is featured in a review article.[104]

In 1989, the phenomenon of cold fusion was first reported during electrolysis of heavy water by Fleischmann *et al.*[105] These workers observed the generation of neutrons and tritium from electrochemically compressed D^+ in a Pd cathode. Their study has stimulated a variety of calorimetric and nuclear measurements. However, the occurrence of the phenomena is sporadic and appears unreproducible on a consistent basis. Therefore a pessimistic view of cold fusion must be taken with respect to the possibility of future energy production.

7 RELATED ARTICLES

Ammonia & N-donor Ligands; Boron Hydrides; Chlorine, Bromine, Iodine, & Astatine: Inorganic Chemistry; Fluorine: Inorganic Chemistry; Heterogeneous Catalysis by Metals; Hydride Complexes of the Transition Metals; Hydrides: Solid State Transition Metal Complexes; Hydrogenation & Isomerization of Alkenes; Nitrogen: Inorganic Chemistry; Semiconductors; Sulfur: Inorganic Chemistry; Surfaces; Water & O-donor Ligands.

8 REFERENCES

1. H. C. Urey, F. G. Brickwedde, and G. M. Murphy, *Phys. Rev.*, 1932, **39**, 164, 864; 1932, **40**, 1.
2. M. L. E. Oliphant, P. Harteck, and O. M. Rutherford, *Proc. R. Soc. London, Ser. A*, 1934, **144**, 692.
3. V. Faltings and P. Harteck, *Z. Naturforsch., Teil A*, 1950, **5a**, 438; *Nature*, 1950, **116**, 1109.
4. A. V. Grosse, W. M. Johnston, R. L. Wolfgang, and W. F. Libby, *Science*, 1951, **113**, 1.
5. E. Anders and N. Grevesse, *Geochim. Cosmochim. Acta*, 1989, **53**, 197.
6. W. Heisenberg, *Z. Physik*, 1927, **41**, 239.
7. F. Bloch, W. W. Hansen, and M. Packard, *Phys. Rev.*, 1946, **70**, 474.
8. K. M. Mackay, in 'Comprehensive Inorganic Chemistry', eds. J. C. Bailar, H. J. Emeleus, R. Nyholm, and A. F. Trotman-Dickenson, Pergamon Press, Oxford, 1973, Vol. 1, Chaps. 1–3; N. N. Greenwood and A. Earnshaw, 'Chemistry of the Elements', Pergamon Press, Oxford, 1984, Chap. 3, p. 38.
9. U. Schmidt, *Tellus*, 1974, **26**, 78.
10. W. F. Giggenbach, *Appl. Geochem.*, 1987, **2**, 143.
11. H. Wakita, Y. Nakamura, I. Kita, N. Fujii, and K. Notsu, *Science*, 1980, **210**, 188.
12. I. Kita, S. Matsuo, and H. Wakita, *J. Geophys. Res.*, 1982, **87**, 10789.
13. C. Junge, *Q. J. R. Meteorol. Soc.*, 1972, **98**, 711.
14. R. D. Cadle, *Rev. Geophys. Space Phys.*, 1980, **18**, 746.

15. C. H. Cheng and R. Eisenberg, *J. Am. Chem. Soc.*, 1978, **100**, 5968.
16. R. Sugisaki, H. Takeda, I. Kawabe, and H. Miyazaki, *Chem. Geol.*, 1982, **36**, 217.
17. D. R. Morris, R. V. Kumar, and D. J. Fray, *Ironmak. Steelmak.*, 1989, **16**, 429.
18. H. H. Mantsch, H. Saito, and I. C. P. Smith, *Prog. Nucl. Magn. Reson. Spectrosc.*, 1977, **11**, 211.
19. J. G. Mathieson and B. E. Conway, *Anal. Chem.*, 1972, **44**, 1517.
20. C. Genty and R. Schott, *Anal. Chem.*, 1970, **42**, 7.
21. T. Uda, K. Okuno, T. Suzuki, and Y. Naruse, *J. Chromatogr.*, 1991, **586**, 131.
22. B. Brigoli, F. Campi, A. Foglio Para, and S. Terrani, *Health Phys.*, 1991, **61**, 105.
23. J. Bigeleisen, M. L. Perlman, and H. C. Prosser, *Anal. Chem.*, 1952, **24**, 1356.
24. M. L. Coleman, T. J. Shepherd, J. J. Durham, J. E. Rouse, and G. R. Moore, *Anal. Chem.*, 1982, **54**, 993; N. Sudzuki, *Geochem. J.*, 1987, **21**, 29.
25. T. Ohsumi and H. Fujino, *Anal. Sci.*, 1986, **2**, 489.
26. J. Horita, A. Ueda, K. Mizukami, and I. Takatori, *Appl. Radiat. Isot.*, 1989, **40**, 801.
27. E. Zinner, K. D. McKeegan, and R. M. Walker, *Nature*, 1983, **305**, 119.
28. E. Deloule, C. France-Lanord, and F. Albarede, in 'Stable Isotope Geochemistry: A Tribute to Samuel Epstein', eds. H. P. Taylor, J. R. O'Neil, and I. R. Kaplan, The Geochemical Society, London, 1991, p. 53.
29. S. Epstein and R. P. Sharp, *J. Geophys. Res.*, 1965, **70**, 1809.
30. Y. Kuroda, T. Suzuoki, and S. Matsuo, *Nature*, 1979, **279**, 227.
31. J. D. Godfrey, *Geochim. Cosmochim. Acta*, 1962, **26**, 1215.
32. S. M. F. Sheppard and S. Epstein, *Earth Planet. Sci. Lett.*, 1970, **9**, 232.
33. F. Begemann and I. Friedman, *J. Geophys. Res.*, 1968, **73**, 1149.
34. B. D. Gunter and B. C. Musgrave, *Geochim. Cosmochim. Acta*, 1971, **35**, 113.
35. Y. Kiyosu, *Earth Planet. Sci. Lett.*, 1983, **62**, 41.
36. I. Friedman and T. G. Scholz, *J. Geophys. Res.*, 1974, **79**, 785.
37. B. Arnason and T. Sigurgeirsson, *Geochim. Cosmochim. Acta*, 1968, **32**, 807.
38. M. I. Krichevsky, I. Friedman, M. F. Newell, and F. D. Sisler, *J. Biol. Chem.*, 1961, **236**, 2520.
39. I. Kita, S. Matsuo, H. Wakita, and Y. Nakamura, *Geochem. J.*, 1980, **14**, 317.
40. W. E. Schiegl and J. C. Vogel, *Earth Planet. Sci. Lett.*, 1970, **7**, 307.
41. S. Epstein and C. J. Yapp, *Earth Planet. Sci. Lett.*, 1976, **30**, 252.
42. J. Hoefs, 'Stable Isotope Geochemistry', Springer-Verlag, Berlin, 1980.
43. H. Craig, *Science*, 1961, **133**, 1702.
44. W. Dansgaard, *Tellus*, 1964, **16**, 4.
45. M. Kakiuchi, K. Tanaka, and K. Kigoshi, *Appl. Radiat. Isot.*, 1991, **42**, 741.
46. S. kaufman and W. F. Libby, *Phys. Rev.*, 1954, **93**, 1337.
47. H. G. Ostlund and E. Werner, 'Tritium in the Physical and Biological Science', IAEA, Vienna, 1962, Vol. 1, p. 95.
48. W. B. Clarke, W. J. Jenkins, and Z. Top, *Appl. Radiat. Isot.*, 1976, **27**, 515.
49. B. M. Oliver, H. Farrar IV, and M. M. Bretscher, *Appl. Radiat. Isot.*, 1987, **38**, 959.
50. M. P. Unterweger, B. M. Coursey, F. J. Schima, and W. B. Mann, *Appl. Radiat. Isot.*, 1980, **31**, 611.
51. P. Jean-Baptiste, F. Mantisi, A. Dapoigny, and M. Stievenard, *Appl. Radiat. Isot.*, 1992, **43**, 881.
52. Proceedings of a Symposium San Francisco, 16–20 October 1978 jointly organized by the IAEA and UEA (OECD) 'Behaviour of Tritium in the Environment', IAEA, Vienna, 1979.
53. F. Begemann and I. Friedman, *Z. Naturforsch., Teil A*, 1959, **14a**, 1024.
54. H. G. Ostlund and A. S. Mason, *Tellus*, 1974, **26**, 91.
55. K. Kigoshi and K. Yoneda, *J. Geophys. Res.*, 1970, **75**, 2981.
56. W. D. Robertson and J. A. Cherry, *Water Resour. Res.*, 1989, **25**, 1097.
57. F. H. Westheimer, *Chem. Rev.*, 1961, **61**, 265.
58. C. G. Swain and R. F. W. Bader, *Tetrahedron*, 1960, **10**, 182.
59. W. A. Van Hook, *J. Phys. Chem.*, 1968, **72**, 1234.
60. G. Nemethy and H. A. Scheraga, *J. Chem. Phys.*, 1964, **41**, 680.
61. M. Kakiuchi and S. Matsuo, *Geochem. J.*, 1979, **13**, 307.
62. M. Majoube, *J. Chim. Phys.*, 1971, **68**, 1423.
63. L. Merlivat, R. Botter, and G. Nief, *J. Chim. Phys.*, 1963, **60**, 56.
64. L. Merlivat and G. Nief, *Tellus*, 1967, **19**, 122.
65. J. Bigeleisen, *J. Chem. Phys.*, 1963, **39**, 769.
66. J. Bigeleisen, *J. Chem. Phys.*, 1961, **34**, 1485.
67. E. M. Arnett and D. R. Mckelvey, in 'Solute Solvent Interactions', eds. J. F. Coetzee and C. D. Ritchie, Dekker, New York, 1969, Chap. 6, p. 343; H. L. Friedman and C. V. Krishnan, in 'Water: A Comprehensive Treatise', ed. F. Franks, Plenum Press, New York, 1973, Vol. 3, Chap. 1, p. 81.
68. J. Greyson, *J. Phys. Chem.*, 1967, **71**, 259, 2210.
69. J. Pupezin, G. Jakli, G. Jancso, and W. A. Van Hook, *J. Phys. Chem.*, 1972, **76**, 743.
70. G. Jakli, T. C. Chan, and W. A. Van Hook, *J. Solution Chem.*, 1975, **4**, 71.

71. G. Jakli and W. A. Van Hook, *J. Phys. Chem.*, 1981, **85**, 3480.
72. M. Kakiuchi, *Z. Naturforsch., Teil A*, 1988, **43A**, 449.
73. M. K. Stewart and I. Friedman, *J. Geophys. Res.*, 1975, **80**, 3812.
74. M. Kakiuchi, *J. Solution Chem.*, 1994, **23**, 1073.
75. M. Kakiuchi and S. Matsuo, *J. Phys. Chem.*, 1985, **89**, 4627.
76. H. Taube, *J. Phys. Chem.*, 1954, **58**, 523; Z. Sofer and J. R. Gat, *Earth Planet. Sci. Lett.*, 1972, **15**, 232; 1975, **26**, 179; A. H. Truesdell, *Earth Planet. Sci. Lett.*, 1974, **23**, 387; P. Bopp, K. Heinzinger, and K. Klemm, *Z. Naturforsch., Teil A*, 1977, **32A**, 1419.
77. J. Horita, D. J. Wesolowski, and D. R. Cole, *Geochim. Cosmochim. Acta*, 1993, **57**, 2797.
78. H. K. Mao and R. J. Hemley, *Science*, 1989, **244**, 1462.
79. B. Siegel, *J. Chem. Educ.*, 1961, **38**, 496.
80. J. J. Zuckerman ed., ‘Inorganic Reactions and Methods’, VCH, 1986, Vols. 1 and 2.
81. B. R. Puri, S. S. Tulsi, and R. C. Bansal, *Indian J. Chem.*, 1966, **4**, 7.
82. S. D. Robertson, N. Mulder, and R. Prins, *Carbon*, 1975, **13**, 348; M. Qayyum and D. A. Reeve, *Carbon*, 1976, **14**, 199.
83. E. Wiberg and E. Amberger, ‘Hydrides of the Elements of Main Groups I-IV’, Elsevier, Amsterdam, 1971; W. M. Mueller, J. P. Blackledge, and G. G. Libowitz, ‘Metal Hydrides’, Academic Press, New York, 1968; G. Bambakidis ed., ‘Metal Hydrides’, Plenum Press, New York, 1981.
84. F. A. Cotton and G. Wilkinson, ‘Advanced Inorganic Chemistry’, 4th edn., Wiley, New York, 1980, Chap. 6, p. 247.
85. M. W. Roberts and C. S. Mckee, ‘Chemistry of the Metal-Gas Interface’, Clarendon Press, Oxford, 1978, Chap. 10, p. 382.
86. G. Heiland and H. Luth, in ‘The Chemical Physics of Solid Surfaces and Heterogeneous Catalysis’, eds. D. A. King and D. P. Woodruff, Elsevier, Amsterdam, 1984, Vol. 3, Chap. 4, p. 137.
87. R. H. Williams and I. T. McGovern, in ‘The Chemical Physics of Solid Surfaces and Heterogeneous Catalysis’, eds. D. A. King and D. P. Woodruff, Elsevier, Amsterdam, 1984, Vol. 3, Chap. 6, p. 267.
88. A. Seidell, ‘Solubilities of Inorganic Compounds and Metal Organic Compounds’, 3rd edn., Van Nostrand, New York, 1940, Vol. 1, p. 553.
89. R. Wiebe and T. H. Tremearne, *J. Am. Chem. Soc.*, 1934, **56**, 2357; R. Wiebe and V. L. Gaddy, *J. Am. Chem. Soc.*, 1937, **59**, 1984.
90. R. L. Mills and A. F. Schuch, *Phys. Rev. Lett.*, 1965, **15**, 722.
91. C. S. Barrett, L. Meyor, and J. Wasserman, *J. Chem. Phys.*, 1966, **45**, 834.
92. G. F. Bassani, M. Inguscio, and T. W. Hansch eds, ‘The Hydrogen Atom’, Springer-Verlag, Berlin, 1989.
93. T. W. Hansch, A. L. Schawlow, and G. W. Series, *Sci. Am.*, 1979, **240**, 72.
94. Y. Hatano, in ‘Dynamics of Excited Molecules’, ed. K. Kuchitsu, Elsevier, Amsterdam, 1994, Chap. 6.
95. N. Kouchi, N. Terazawa, Y. Chikahiro, M. Ukai, K. Kameta, Y. Hatano, and K. Tanaka, *Chem. Phys. Lett.*, 1992, **190**, 319; S. Arai, T. Kamosaki, M. Ukai, K. Shinsaka, Y. Hatano, Y. Ito, H. Koizumi, A. Yagishita, K. Ito, and K. Tanaka, *J. Chem. Phys.*, 1988, **88**, 3016.
96. W. F. Giauque, *J. Am. Chem. Soc.*, 1930, **52**, 4816.
97. H. L. Johnston and E. A. Long, *J. Chem. Phys.*, 1934, **2**, 389.
98. E. W. Albers, P. Harteck, and R. R. Reeves, *J. Am. Chem. Soc.*, 1964, **86**, 204.
99. G. Ahlers, *J. Chem. Phys.*, 1963, **40**, 3123.
100. M. Rall, J. P. Brison, and N. S. Sullivan, *Phys. Rev. B*, 1991, **44**, 9932.
101. R. E. Roberts, *J. Chem. Phys.*, 1971, **54**, 1422; M. Menzinger, *Chem. Phys. Lett.*, 1971, **10**, 507; L. P. Walkouskas and F. Kaufman, *J. Chem. Phys.*, 1976, **64**, 3885; D. N. Mitchell and D. J. Leroy, *J. Chem. Phys.*, 1977, **67**, 1042.
102. Y. M. Xiao, S. Buchman, L. Pollack, D. Kleppner, and T. J. Greytak, *J. Chem. Phys.*, 1992, **96**, 4032.
103. ‘Hydrogen in Semiconductors: Bulk and Surface Properties’ proceeding of the Sixth Trieste IUPAP-ICTP Semiconductor Symposium. International Centre for Theoretical Physics Trieste, Italy, 27–31 August 1990, eds. M. Stutzmann and J. Chevallier.
104. N. Getoff, *Int. J. Hydrogen Energy*, 1990, **15**, 407.
105. M. Fleischmann, S. Pons, and H. Hawkins, *J. Electroanal. Chem.*, 1989, **261**, 301; M. Fleischmann, S. Pons, and H. Hawkins, *J. Electroanal. Chem.*, 1989, **263**, 187.

Hydrogenation & Isomerization of Alkenes

Fred H. Jardine
Washington State University, Pullman, WA, USA

1	Introduction	1
2	Isomerization	3
3	Hydrogenation of Alkenes	9
4	Related Articles	18
5	References	19

Glossary

Anti-Markovnikov addition: the addition of HX across a C=C bond such that the hydrogen is added to the carbon bound to the lesser number of hydrogen atoms (cf. Markovnikov addition below)
Diffusion control: this occurs when the rate of diffusion of a reactant to the site of the reaction is significantly slower than the rate of reaction
Homogeneous hydrogenation: a hydrogenation reaction in which the substrate, hydrogen, and catalyst are all dissolved in the same solution. These systems can be distinguished from the traditional heterogeneous systems by their ability to hydrogenate insoluble polymeric substrates
Markovnikov addition: the addition of HX across a C=C bond such that the hydrogen is added to the carbon bound to the greater number of hydrogen atoms (cf. anti-Markovnikov addition above)
Metallocycle: a chain of carbon atoms bound at each end to the same metal ion to form a cyclic compound
Radical: a species containing an unpaired electron (e.g. $CH_3\cdot$, Fe^{3+})
Radical scavenger: a compound, often a relatively stable radical, that reacts preferentially with the radicals generated in the system. This reaction is also known as trapping
Sigmatropic rearrangement: a concerted reaction in which an initially σ-bonded group migrates within a π-bonded framework (e.g. an alkene or alkadiene) and reforms its sigma bond elsewhere [1,3]-Sigmatropic rearrangement: a reaction of the type YC–C=C → C=C–CY [3,3]-Sigmatropic rearrangement: a reaction of the type C=C–CY–C–C=CX → YC=C–C–CX–C=C

1 INTRODUCTION

Alkene complexes of late transition metals have been known for over a century. Transition metal hydrido complexes were first characterized nearly 60 years ago. These two types of complex hold the keys to two important catalytic processes: alkene isomerization and hydrogenation. Many complexes catalyze both processes and the catalytic reactions of some of the more active complexes have long been known.[1–3]

Except in radical reactions, the transition metal complex must coordinate with unsaturated organic compounds in order to bring about their transformations. However, since alkenes, and in particular substituted alkenes, do not readily displace other ligands from transition metal complexes, the catalytically active complexes are usually coordinatively unsaturated. Transition metal complexes normally only catalyze the formation of organic molecules of greater thermodynamic stability. There are, therefore, no thermodynamic problems in converting alkenes or alkynes to alkanes. However, once equilibrium has been achieved, alkene isomerizations will usually give mixtures of products, with the thermodynamically most stable predominating.

Three fundamental types of isomerization may be distinguished. The first is double-bond migration, as in the isomerization of pent-1-ene to (Z)-pent-2-ene. The second involves skeletal rearrangements, such as the conversion of bicyclo[3.1.0]hex-2-ene derivatives to the corresponding cyclohexadienes. The third, and possibly most useful type, is the catalysis of group migrations, particularly in the Cope- and Claisen rearrangements.

There are two principal mechanisms by which double-bond migration may occur. The first, the η^3-allylic mechanism, is more often proposed than encountered. In this, the alkene interacts with the transition metal and forms an η^3-allyl hydrido complex. The hydride is then transferred back to the η^3-allyl to complete a 1,3 hydride shift. This occurs in the $[PdCl_2(PhCN)_2]$ system. In the second, which is much more common, a hydrido complex (e.g. $[NiH\{P(OEt)_3\}_4]$) reacts with an alkene to form an alkyl complex. The alkyl complex then reverts to an isomeric alkene and the hydrido complex by undergoing a β-hydride abstraction reaction.[4] Reactions of the latter type are frequently responsible for by-product formation in homogeneous catalytic hydrogenation, deuteriation, Hydroformylation, or Hydrosilation. This type of rearrangement is one of the few cases where synthetic use has been made of catalytic isomerization by transition metal complexes. The double-bond migrations that occur in acyclic alkenes are usually regarded as unmitigated nuisances since they ultimately convert commercially desirable terminal alkenes to internal (E)-alkenes of low reactivity and value. However, the conversion of allyl protecting groups to prop-2-enyl groups by catalytic isomerization facilitates their hydrolytic removal in carbohydrate chemistry. The reaction shown in equation (1) demonstrates that allyl groups are selectively isomerized. However, side reactions make the yields of prop-2-enyl esters slightly less than optimum.[5]

Skeletal rearrangements can be more precisely defined as rearrangements resulting from either decyclization or annulation reactions that do not involve migration of ring substituents. These rearrangements arise from interactions between strained, cyclic organic compounds and the dz^2 orbital of a square-planar transition metal complex. A metallocycle is formed by oxidative addition of the organic species. Extrusion of a metal complex from this may result in ring expansion of polycyclic substrates or acyclic alkene production as a result of decyclization. The least common rearrangement involves transannular reactions of large cycloalkenes to form bi- or polycyclic products.

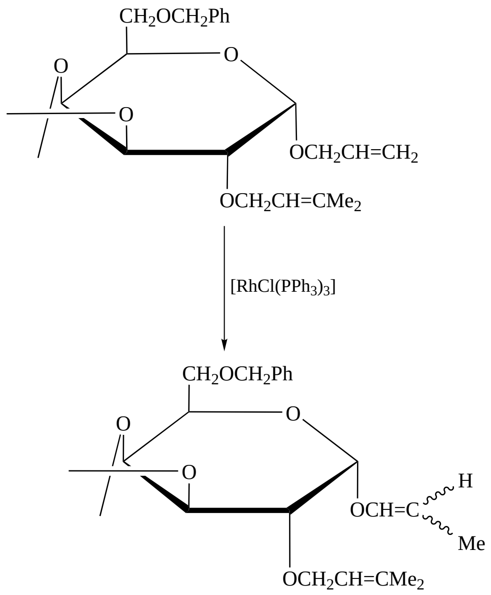

(1)

The Cope- and Claisen rearrangements are also catalyzed by square-planar transition metal complexes. Palladium complexes have been responsible for spectacular increases in the rates of Cope rearrangements by factors of up to 10^8. Certain other sigmatropic rearrangements are also catalyzed by transition metal complexes.

Three major mechanisms of catalytic hydrogenation are known.[6] These are differentiated by the order in which the two reactants are activated and are further distinguished, and named, by the reagent activating molecular hydrogen (Scheme 1).

The two most important mechanisms involve the reaction of an alkene with dihydrido complexes or, the reverse of this, the reaction of dihydrogen with an alkene complex. The third process, known as the *alkyl route*, is of limited applicability and may give rise to substantial quantities of by-products.

The main advantage of catalysis by transition metal complexes is that the reactions may be carried out in solution (i.e. the reactions are homogeneous) and they therefore depend neither upon the state of subdivision nor the surface properties of the heterogeneous metal catalyst. The greater selectivity of the homogeneous catalysts can also be used to advantage when other functional groups are present in the substrate. Normally, homogeneous catalysts are selective towards the least sterically hindered C=C bond and do not catalyze the hydrogenation of other multiple interatomic bonds.

It is also possible to hydrogenate alkenes by transferring hydrogen from another organic compound (transfer hydrogenation). Many transition metal complexes, particularly those

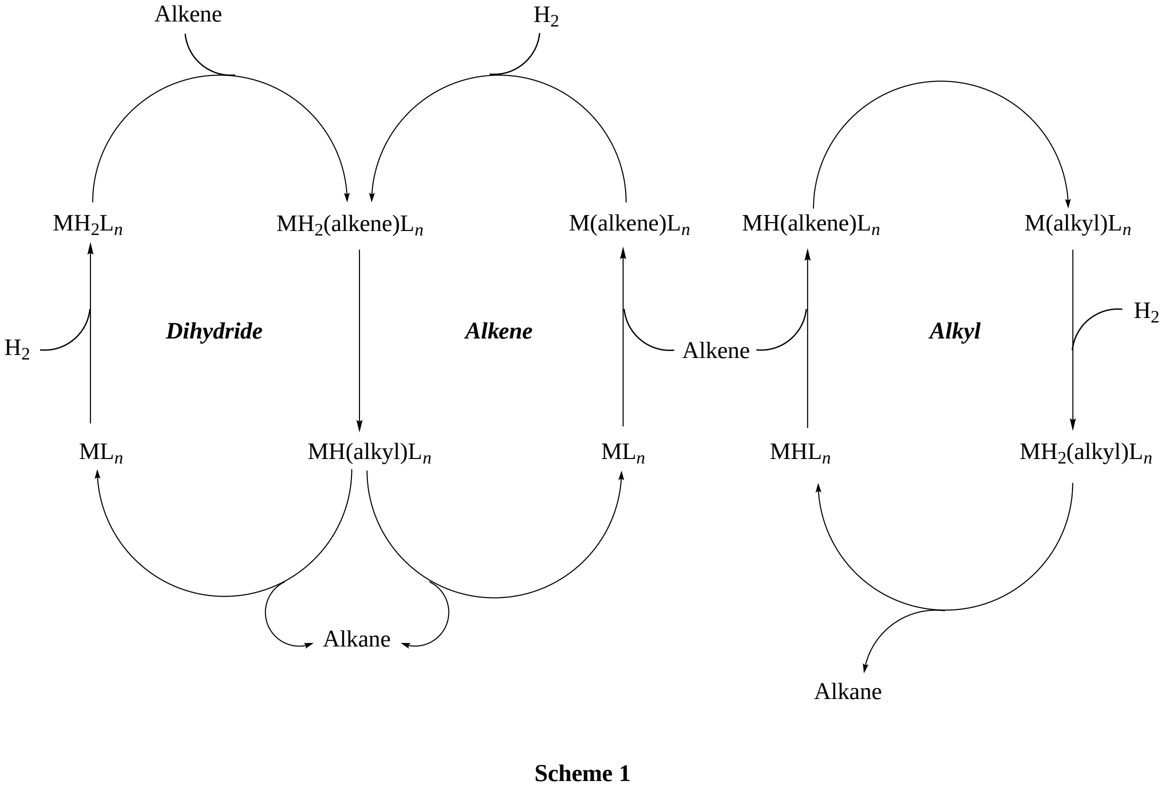

Scheme 1

of ruthenium,[2] catalyze this stoichiometrically simple reaction (equation 2). The mechanism of the reaction is complicated because of the need to activate the reactants in the correct order.

$$\mathrm{RCH{=}CH_2 + Me_2CHOH \xrightarrow{ML_n} RCH_2CH_3 + Me_2CO} \qquad (2)$$

2 ISOMERIZATION

2.1 Isotope Exchange and Double-bond Migration

Monohydrido transition metal complexes are the most active catalysts in double-bond migration reactions. These complexes form alkyl complexes when allowed to react with alkenes. The relatively long lifetimes of alkyl complexes in these systems allows them to undergo β-hydride abstraction reactions before they can react with the other reagents present. The mechanism of the reaction is shown in Scheme 2.

Anti-Markovnikov addition of hydrogen to the alkene forms a 1-alkyl complex from the alk-1-ene substrate. This alkyl complex can either react with other reagents or revert to the original alkene and hydrido complex. If the reaction is carried out using a deuterio complex as shown in Scheme 2, then there is a 50% chance of isotopic exchange occurring upon reversion.

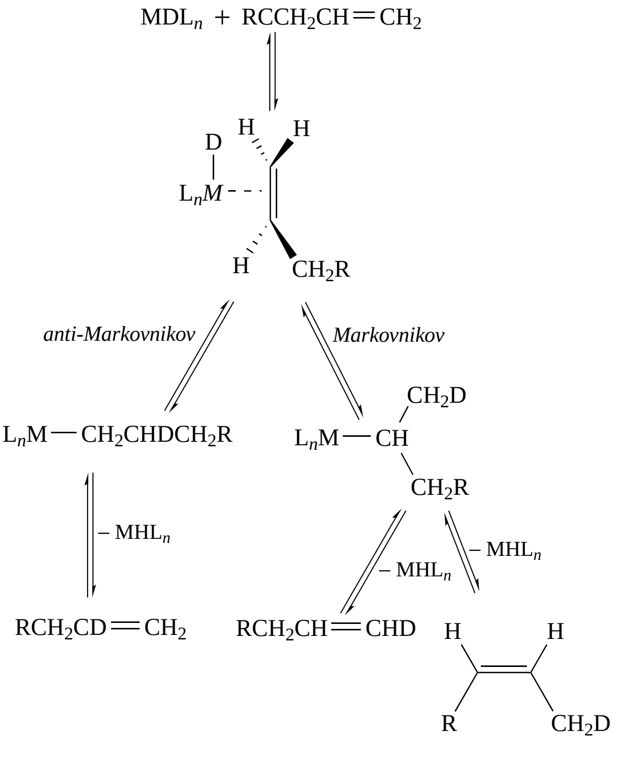

Scheme 2

Markovnikov addition of hydrogen to the alk-1-ene forms a 2-alkyl complex. Thermodynamically it is less likely that this 2-alkyl complex will revert to the original alk-1-ene than be converted to an alk-2-ene as a result of competing β-hydride abstraction reactions.

An alternative explanation is that reforming the alk-1-ene involves breaking a primary C–H bond, which requires more energy than breaking a secondary C–H bond, to form the (Z)-alk-2-ene. If the isomerization reaction is allowed to continue, eventually, by repetition of the catalytic cycle shown in Scheme 2, the alk-1-ene will be further converted into a mixture of alk-2-enes and alk-3-enes. The equilibrium is only slowly achieved because the low-binding constants of internal alkenes make it difficult for them to enter the catalytic cycle.

Isomerization in the absence of a hydrido complex or added hydrogen is frequently and incorrectly assigned an η^3-allylic mechanism. This facile assignment overlooks the possibility of hydrido complexes being formed from reactions with alcohols or other solvents or reagents during the reaction.

Several isomerizations brought about by $[\mathrm{RhCl(PPh_3)_3}]$ fall into this category. Hydrolysis of added $\mathrm{SnCl_2{\cdot}2H_2O}$ forms HCl, which adds to the catalyst forming the pentacoordinate monohydride $[\mathrm{RhHCl_2(PPh_3)_2}]$, which can bring about the isomerization of polyunsaturated carboxylic acids and their esters. The isomerization can be inhibited by the addition of lithium carbonate, which, by removing the HCl formed, prevents the formation of the hydrido complex. Deuteride formation from alkan(^{2}H)ol solvents and the subsequent incorporation of deuterium into the ester has also been observed.

Another way in which hydrido complexes can be formed is by Orthometalation. It has been demonstrated that $[\mathrm{RuCl_2(PPh_3)_3}]$ is particularly susceptible to this reaction. The hydrido complex $[\mathrm{RuHCl\{(2\text{-}C_6H_4)PPh_2\}(PPh_3)_2}]$ may well catalyze the many isomerizations brought about by the ruthenium catalyst. Indeed, the ruthenium complex is a more active catalyst than many other transition metal complexes in the isomerization of allyl groups. It usually isomerizes allyl groups to (E)-prop-2-enyl substituents, but allyl 2,6-dimethylphenyl ether forms mainly the (Z)-product (equations 3 and 4).

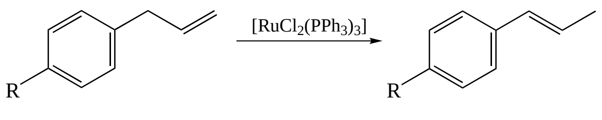

(3)

Peroxides may either be deliberately added or be present in alkenes that have been exposed to the air. The low concentrations of these species are of the same order as those of the catalytic complexes and can convert the catalysts to more active species. Mixtures of peroxides, 4-vinylcyclohexene, and $[\mathrm{RuCl_2(PPh_3)_3}]$ form the complex $[\mathrm{RuCl_2(PPh_3)_2(CO)(C_8H_{12})}]$. The carbonyl complex is the true catalyst since it can isomerize pure 4-vinylcyclohexene.

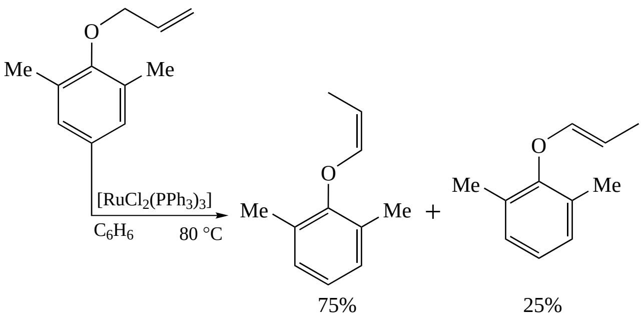

(4)

Genuine η^3-allylic mechanisms give different product distributions from β–hydride abstraction mechanisms, particularly in the case of isotopically labeled substrates. One of the few unambiguous demonstrations of the η^3-allylic mechanism occurs in the [RuCl$_2$(PPh$_3$)$_3$] catalyzed isomerization of a dihydropyridazine derivative (equation 5). Both polyhydrido ruthenium complexes and [RuHCl(PPh$_3$)$_3$] were inferior catalysts for the reaction, and the addition of ethanol to the reaction mixture reduced the yield by a factor of 25. All these observations lead to the conclusion that hydrido complexes, and by implication the β-hydride mechanism, were not involved.[7] It has also been proposed that the isomerization shown in equation (4), which is catalyzed by a wide variety of transition metal complexes including several nonhydridic species, occurs by an η^3-allylic mechanism because substituents on the allyl group hinder the rearrangement.[8]

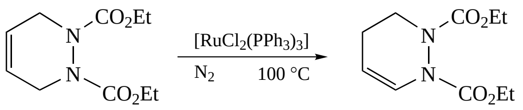

(5)

Double-bond migration also occurs in dienes. Again the isomerization gives rise to more stable products usually containing conjugated double bonds. Possibly one of the most simple reactions is the $(Z) \rightarrow (E)$ conversion of penta-1,3-diene by [Fe(CO)$_5$].[9]

However, the usual course of events in the isomerization of cycloalkadienes is to achieve conjugation where coordination is impossible. Thus cyclohexa-1,4-diene is isomerized to cyclohexa-1,3-diene by [RuCl(PPh$_3$)$_3$]. Nevertheless, RhCl$_3$·3H$_2$O isomerizes cycloocta-1,3-diene, the most stable isomer, to a chelated cycloocta-1,5-diene complex (equation 6). Since no intermediate cycloocta-1,4-diene can be observed in the reaction, it was presumed to proceed via an η^3-intermediate.[10]

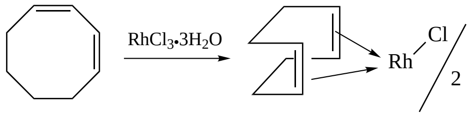

(6)

The chiral, cationic complexes [Rh(BINAP)$_2$]$^+$ catalyze the conversions of N,N-diethylaminoterpenes in good optical yields (Scheme 3).[11]

2.2 Decyclization and Annulation Reactions

Cyclopropane compounds are the most strained carbocyclic species and should, therefore, be the most susceptible to decyclization reactions.

Vinylcyclopropane is converted to (3E)-penta-1,3-diene and 2-methylbuta-1,3-diene by catalytic quantities of [RhCl(CO)$_2$]$_2$. Its homolog, 2-cyclopropylpropene, is similarly converted to (3E)-2-methylpenta-1,3-diene and 2,3-dimethylbuta-1,3-diene. Although the same catalyst converts either (E)- or (Z)-1-methyl-2-phenylcyclopropane to identical mixtures of 1-phenyl-2-methylpropene and 1-phenylbut-2-ene, the reactions proceed at different rates. It has been proposed that ring opening and rhodium coordination to C-1 occurs first, followed by hydride migration to form the products.

Fused cyclopropane rings can also be opened. The main product from the reaction between [RhCl(cod)]$_2$ and (Z)-bicyclo[4.1.0]hept-3-ene is 1-methylcyclohexa-1,3-diene.[11] An allylic radical mechanism has been proposed to account

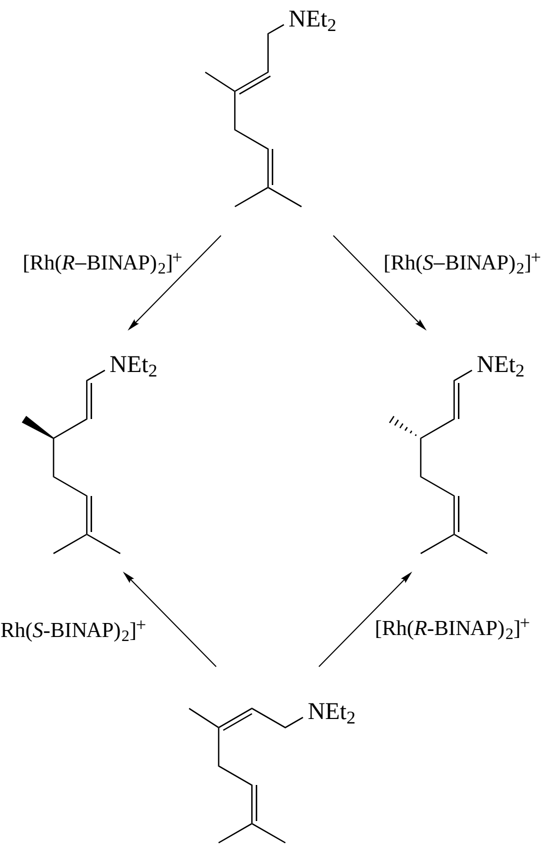

Scheme 3

for the isomerization of 1-cyanobicyclo[1.1.0]butane in the presence of tetraphenylporphyrincobalt(II). The decyclization of the tetradeutero substrate is shown in equation (7), and demonstrates how deuterium migration may occur.

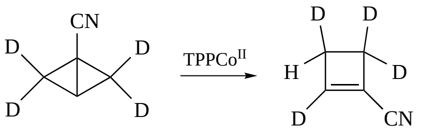

(7)

Trisubstituted cyclopropanes are also catalytically converted to alkenes (equation 8). Rhodium(II) ethanoate or $[RhCl(CO)_2]_2$ catalyze the reaction, but both catalysts form twice as much (E)- as (Z)-isomer.

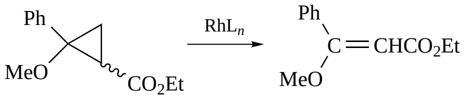

(8)

Quadricyclane effectively contains two cyclopropyl rings and it can be converted to bicyclo[2.2.1]hepta-2,5-diene when treated with numerous transition metal complexes (equation 9). The reaction is of current interest as an energy storage system since bicyclo[2.2.1]hepta-2,5-diene can be photolyzed to quadricyclane.**12** The most likely mechanism for the decyclization reaction is initial interaction between the strained cyclopropyl rings and the transition metals' d_{z^2} orbitals followed by formation of the metallocycle (**1**). The isomerizations of heavily substituted quadricyclanes (equation 10) are slow.**13**

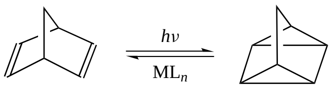

(9)

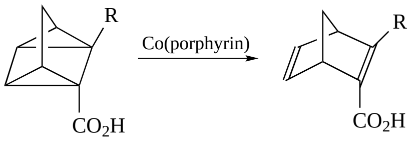

(10)

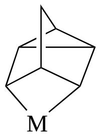

(**1**)

Isolated cyclobutane rings are too stable to undergo catalytic decyclizations. However, bicyclo[2.2.0]hexane and its tetradeutero isotopomer are converted to cyclohexene (equation 11) by catalytic quantities of $[RhCl(CO)_2]_2$. The complex is inserted across the bridge and an intermediate acyl complex can be detected. Unless the reaction is carried out at 5 °C it is not possible to isolate an acyl intermediate in the isomerization of tricyclo[4.2.0.0^{2,5}]octane when the carbonylrhodium(I) complex is used stoichiometrically. The reaction, shown in equation (12), is catalyzed by $[RhCl(nbd)]_2$.

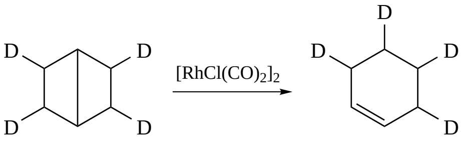

(11)

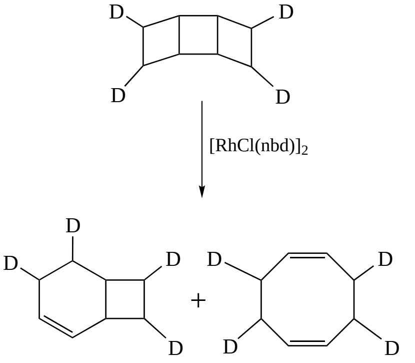

(12)

Fused cyclobutene rings are easily opened. Hexamethyl(Dewar)benzene (HMDB) is thermolyzed to hexamethylbenzene at 100–140 °C, but $[RhCl(HMDB)]_2$ catalyzes the conversion at <70 °C. Since the catalyst itself is stable at 100 °C, it has been suggested that the catalyst is cleaved by excess substrate and that the rate-determining step is the elimination of hexamethylbenzene from $[RhCl(HMDB)_2]$.

Cubanes are partially decyclized to tricyclooctadienes when allowed to react with catalytic quantities of $[RhCl(LL)]_2$ complexes (LL = cod, nbd). Monosubstituted cubanes form two products, as shown in equation (13). Homocubanes (equation 14) react similarly. If methyloxyphosphahomocubane is decomposed, two isomeric products are obtained (equation 15). *Endo*- and *exo* isomers are obtained from the catalytic isomerization of 9,10-dimethoxycarbonyl bishomocubane (equation 16). Sundry palladium(II) complexes, $AgNO_3$, or $PdCl_2$ form significant quantities of (**2**).

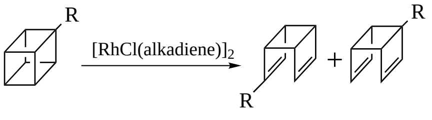

(13)

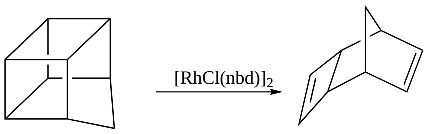

(14)

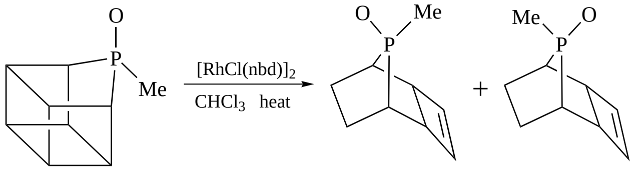

(15)

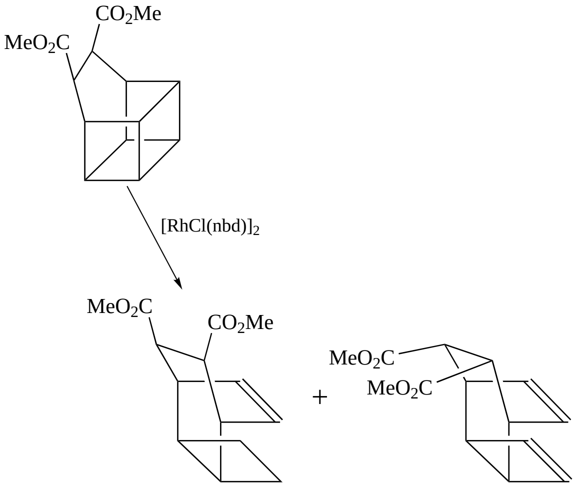

(16)

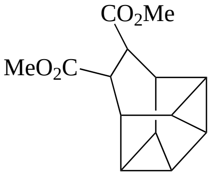

(**2**)

Ring expansion reactions of the type shown in equations (17) and (18), in which a more equitable distribution of carbon atoms between two rings of a polycyclic hydrocarbon is produced, provide the link between the decyclization reactions above and the annulation reactions considered later. It would seem that the greater the strain in the reactant, the larger the number of potential catalysts. The complexes of seven different metals catalyze the reaction shown in equation (17). Of the possible catalysts, only the silver (I) salts bring about any by-product formation.**14** The isomerization of [1.1.1]propellane (equation 18) is catalyzed by $[RhCl(PPh_3)_3]$.**15**

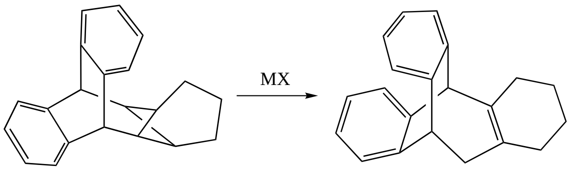

(17)

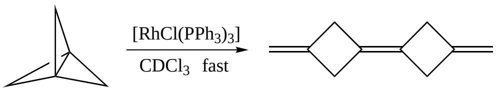

(18)

It seems unlikely, on the basis of deuterium-labeling experiments, that a metallocycle is involved in the ring expansion of (1-methylcyclopropyl)methanol catalyzed by $[RhCl(CO)_2]_2$. Further, if the reaction is carried out in the presence of carbon monoxide, no carbonyl group is incorporated in the organic product.

The formation of a cyclic compound from purely alicyclic reagents is relatively rare but it has been achieved in the case of certain diallylic compounds (equation 19). The same catalyst also brings about the conversion of *N*-methyltrihydropyridine compounds to fused ring systems containing *N*-methylperhydroquinoline rings (equation 20).

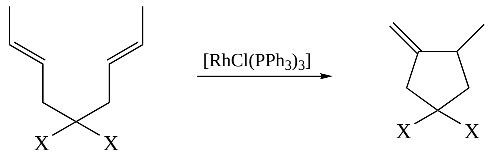

(19)

(X = CO_2Me, CO_2Et, COPh, $^1/_2$(5,5-cyclohexa-1,3-dienyl))

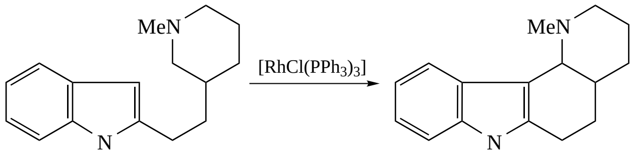

(20)

Suitable α,ω-enynes can be cyclized when allowed to react with catalytic quantities of $[RhCl(PPh_3)_3]$. Alken-2-ynes do not react and the yield is greatly diminished in the case of alk-2-enyne substrates. However, substitution of the alkene bond does not appear to inhibit the dicyclization of dienynes or the cyclization of alkynenones.**16** The dienyne's reaction, shown in equation (21), is catalyzed more effectively by rhodium(I) complexes containing tertiary phosphite ligands. Under similar conditions, trienes can also be cyclized.**17** The cyclopropyl ring can serve as an alkene bond precursor in cyclizations (equation 22).**18**

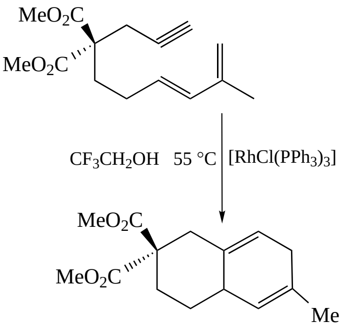

(21)

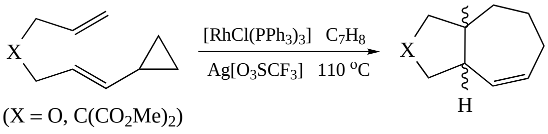

(22)

(X = O, $C(CO_2Me)_2$)

The cyclization of pent-4-enals and related compounds to cyclopentanones is catalyzed by $[RhCl(PPh_3)_3]$ in a reaction that involves oxidative addition of the –CHO group to the rhodium(I) catalyst. This reaction has much in common with the decarbonylation that most aldehydes undergo in the presence of this catalyst (*see* ***Decarbonylation Catalysis***).

More commonly, side chains can be incorporated in existing rings. Thus 2-propenylazirines can be converted to pyrroles and pyridines when treated with catalytic quantities of $[Pd(PPh_3)_4]$. The mechanism of the reaction involves an η^3-allylic species that can give rise to either product.[19]

The least common type of isomerization involves transannular reactions of large rings. Cycloocta-1,5-diene forms varying quantities of bicyclo[3.3.0]oct-2-ene when allowed to react with either $[RuCl_2(PPh_3)_3]$ or $[NiBr_2(PPh_3)_2]$ (equation 23). A hydridonickel complex derived from nickel(II) carboxylates and $AlCl_2Et$ gives the best yield. The various dimethylcycloocta-1,5-dienes form methylated bicyclo[3.3.0]oct-2-enes when allowed to react with the nickel catalyst in benzene, but tricyclooctanes are initially formed if the reactions are carried out in hexane (equations 24–26).[20]

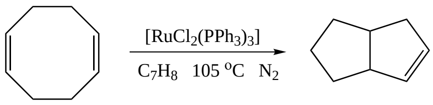

(23)

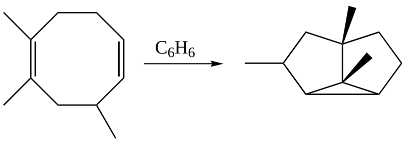

(24)

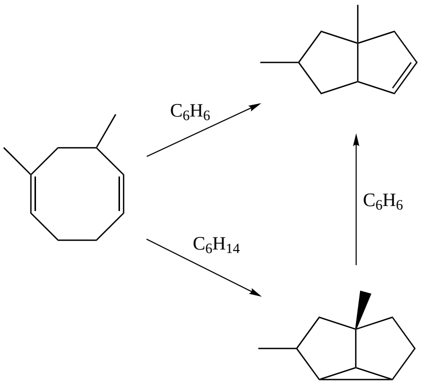

(25)

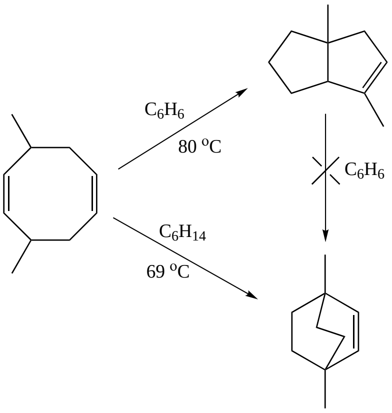

(26)

2.3 Group Migrations

The most important reactions involving skeletal changes together with substituent group migration are the Cope- and Claisen rearrangements. These are both classified as [3,3]-sigmatropic rearrangements. The two reactions are very similar in nature, as can be seen from equation (27). They are catalyzed by various transition metal complexes and other inorganic species, but can also occur as uncatalyzed thermal rearrangements.

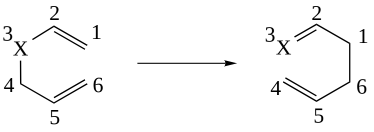

(27)

(Cope X = CH_2; Claisen X = O, N, S)

In particular, palladium(II) complexes are capable of greatly increasing the rates of these rearrangements. The selectivity observed in those catalyzed reactions where more than one product can be obtained may differ from that prevailing in the thermal reactions.

The catalyst need not necessarily be a d^8 square-planar complex, since the potential of the catalyzed rearrangement was first revealed by nickel(0) complexes or mercury(II) trifluoroacetate, both d^{10} species. The pioneering work in this area has been the subject of two reviews.[21,22]

The Cope rearrangement takes place with hydrocarbon substrates. Nickel(0) and palladium(II) species were first demonstrated to show opposite effects in the rearrangement, the nickel(0) catalyst being responsible for ring expansion (equation 28) and the palladium(II) complex for ring contraction (equation 29). The reaction shown in equation (29) is catalyzed less effectively by $H_2[PtCl_4]$.

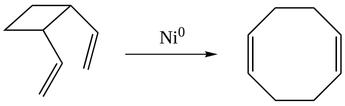

(28)

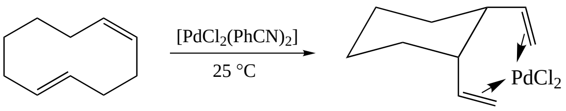

(29)

It was later demonstrated that both Ni^0 and Pd^{II} species catalyzed the conversion of 1-methyl-2-vinyl-3-prop-2-enylcyclobutanes to (E)-3,7-di-ethylcycloocta-1,5-diene. However, as shown in Scheme 4, $[PdCl_2(PhCN)_2]$ forms an equal quantity of the (Z)-isomer, the sole product of the thermal rearrangement. A side reaction in the Ni^0-catalyzed reaction clearly demonstrates the scission of the C–C bond required in the rearrangement, by producing penta-1,3-diene in low yield.

A major practical disadvantage of the palladium-catalyzed rearrangement is the need to disgorge the $PdCl_2$ residue from the product diene by treating it with KCN. Fortunately, as the reaction shown in equation (30) demonstrates, more crowded substrates do not give products containing palladium. The selectivity of this reaction is an improvement over the

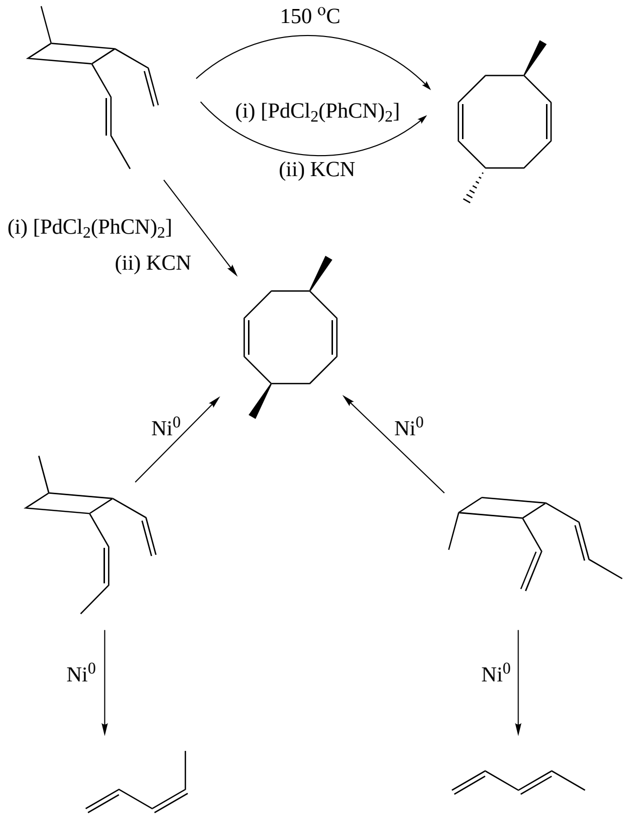
150 °C
(i) [PdCl₂(PhCN)₂]
(ii) KCN
(i) [PdCl₂(PhCN)₂]
(ii) KCN
Ni⁰
Ni⁰
Ni⁰
Ni⁰

Scheme 4

thermal rearrangement, which, carried out at 180 °C for 13 h, produces the (*E*)-isomer in 75% yield. Other reactants of this type are isomerized similarly. The retention of configuration during the migrations shown in equation (31) is of great potential importance.[23] Transfer of chirality also occurs in the $[PdCl_2(PhCN)_2]$-catalyzed [1,3]-sigmatropic rearrangements of steroidal allylic side chains. The stereoselectivity shown in equations (32) and (33) arises from the steroid shielding one side of the double bond and requiring the palladium complex to attack from the other.[24]

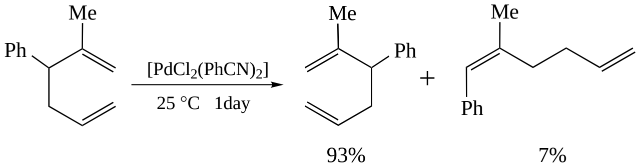
Me
Ph
[PdCl₂(PhCN)₂]
25 °C 1day
Me
Ph
+
Me
Ph
93%
7%

(30)

Unfortunately, more heavily substituted hexadienes than those shown in equation (30) do not undergo the rearrangement, presumably because they have very low binding constants with catalytic palladium(II) species. Nevertheless, the Claisen rearrangement of allyl vinyl ethers can only take place provided palladium coordination to the vinyl group is prevented by alkyl substituents.[25]

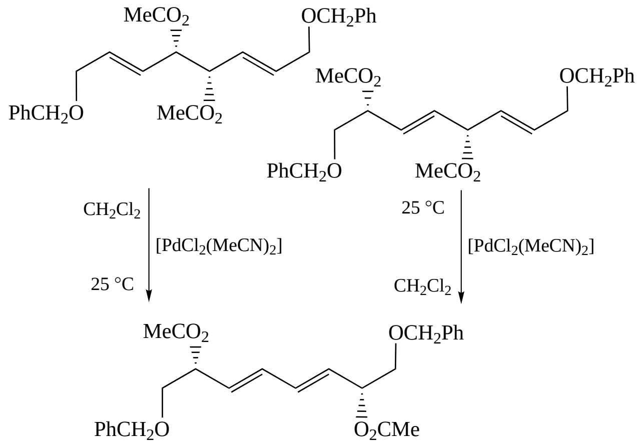
MeCO₂
OCH₂Ph
PhCH₂O
MeCO₂
MeCO₂
OCH₂Ph
PhCH₂O
MeCO₂
CH₂Cl₂
[PdCl₂(MeCN)₂]
25 °C
25 °C
[PdCl₂(MeCN)₂]
CH₂Cl₂
MeCO₂
OCH₂Ph
PhCH₂O
O₂CMe

(31)

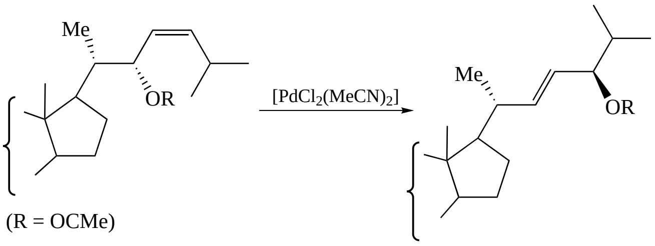
Me
OR
(R = OCMe)
[PdCl₂(MeCN)₂]
Me
OR

(32)

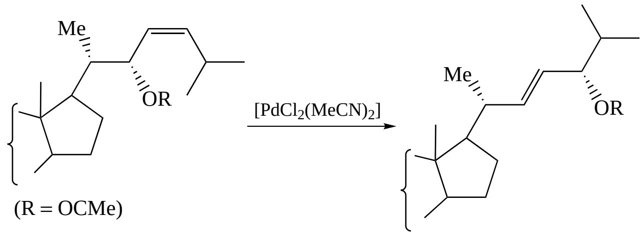
Me
OR
(R = OCMe)
[PdCl₂(MeCN)₂]
Me
OR

(33)

Potentially, the Claisen rearrangement is of greater synthetic utility merely because it is not confined to hydrocarbon substrates. However, no palladium-catalyzed thio-Claisen rearrangements have been observed, possibly owing to sulfur poisoning the catalysts. Nevertheless, thioimidates have been rearranged in the presence of catalytic quantities of $[PdCl_2(PhCN)_2]$.

Although rhodium(I) and ruthenium(II) complexes have been widely used to isomerize allyl ethers to prop-2-enyl ethers (see Sect. 2.1), an ill-defined $[Pt(PPh_3)_n]$ complex brings about the Claisen rearrangement of the naphthyl ether, shown in equation (34). The cleavage of the allyl group required in the reaction was believed to yield allylplatinum cations and aryloxy anions. An interesting variant of the reaction is shown in equation (35). The products are formed in approximately equal yields and the cyclopentanone results from a [1,3]-rearrangement. At 140 °C, $M_2[PtCl_6]$ (M = H, Na) brings about the rearrangement of 2-allyloxypyridine (equation 36). The thermal rearrangement gave low yields of several products.

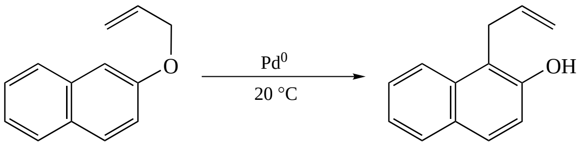

(34)

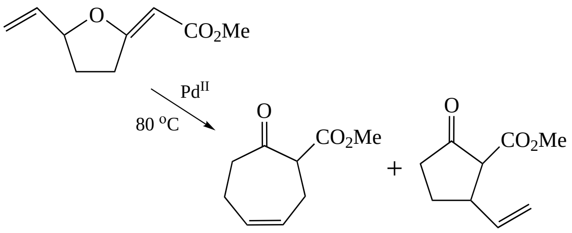

(35)

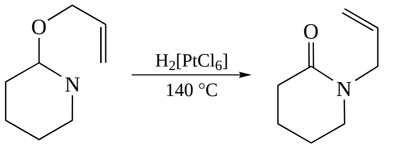

(36)

Palladium(II) complexes also catalyzed the rearrangements of allylic esters. However, as illustrated in Scheme 5, when palladium(0) complexes are used the stereochemical course of the rearrangement is different. It should be noted that the palladium(II)-catalyzed rearrangement occurs preferentially at the (E)-disubstituted double bonds. Again, the selectivity of the palladium(II) complex arises from it forming σ-bonded intermediates.**26**

Alkynyl esters are isomerized by silver(I) or copper(I) compounds in another [3,3]-sigmatropic rearrangement although the reaction is not of wide synthetic application. Copper(I) chloride requires harsher conditions than $AgBF_4$ to effect the transformation shown in equation (37).

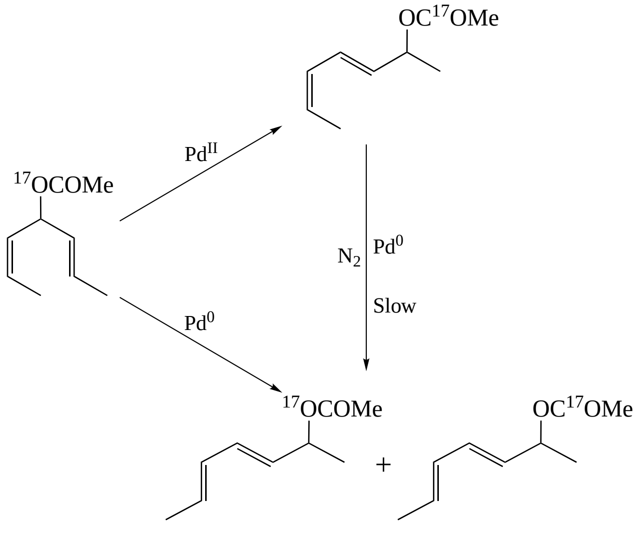

Scheme 5

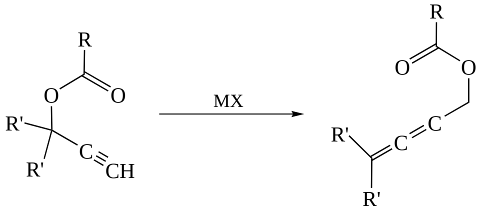

(37)

(MX = $AgBF_4$, R = 4-$C_6H_4NO_2$, R' = Et; MX = CuCl , R = R' =Me)

Palladium(II) complexes appear to be the only metal complexes capable of catalyzing the rearrangements of sulfur–nitrogen or sulfur–oxygen substrates. A very similar reaction takes place with both *S*-allyl thioimidates and *S*-allyl iminothiocarbonates (equation 38). In the latter case, low yields are obtained if there is no substituent on the allyl group (i.e. $R^2 = H$).

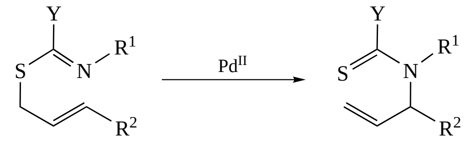

(38)

(Y = Ph, $R^1 = R^2$ = Me; Y = OR, R^1 = H, R^2 = H, Me, Ph, Bz)

Although most catalysts for the various rearrangements are complexes of the late transition metals, $TiCl_4$ catalyzes the amino-Claisen rearrangement shown in equation (39). In this case, the thermal rearrangement gives identical product yields.

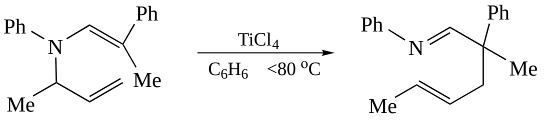

(39)

3 HYDROGENATION OF ALKENES

3.1 Introduction

The ability of finely divided late transition metals to catalyze the heterogeneous hydrogenation of alkenes to alkanes has long been known and there are many industrial and laboratory applications of this reaction. However, the knowledge of the mechanism does not fully reflect the extensive efforts made in studying the reaction. The heterogeneity of the reaction debars many of today's powerful instrumental techniques commonly used to investigate reaction mechanisms. Additionally, it is apparent that there are several side reactions occurring during heterogeneous hydrogenation. Isomerization and isotope exchange in particular make study of the hydrogenation reaction difficult.

Homogeneous catalysts do not suffer from these disadvantages and are much more amenable to study. However, not every late transition metal complex can function as a homogeneous hydrogenation catalyst. In order to exhibit catalytic activity, the complex must possess certain properties. First, the complex must not be reduced to the metal by hydrogen. The earliest attempts to bring about the homogeneous hydrogenation of alkenes, by mixing a transition metal complex, hydrogen, and alkene, were unsuccessful because the systems soon became heterogeneous as the result of metal formation.

Second, the catalytic complex must form a labile-alkene complex. If no alkene complex is formed then the metal complex cannot transfer hydrogen to the alkene. A very stable alkene complex is also disadvantageous since an essential property of catalytic species is their lability.

A third factor, often overlooked but of great practical importance, is sufficient solubility of the catalyst in organic solvents, since alkenes and the majority of their derivatives are insoluble in water. This requirement disqualifies most classical complexes from acting as hydrogenation catalysts.

These requirements are fulfilled by certain tertiary phosphine complexes of the late transition metals, such as $[RhCl(PPh_3)_3]$, $[RuCl_2(PPh_3)_3]$, and $[RhH(CO)(PPh_3)_3]$. Steric crowding induces one of the large triphenylphosphine ligands to dissociate and its place in the coordination sphere can be occupied by an alkene ligand. Dissociation of an acido ligand can also provide a vacant coordination site for alkene coordination. The loss of the perchlorato ligand from $[Rh(OClO_3)(CO)(PPh_3)_2]$ when dissolved in unsaturated dinitriles allows hydrogenation of the solvents to occur.[27]

It will also be noticed that all the above catalysts contain second transition series metals. Generally, the slower reactions of the third transition series elements are not normally conducive to catalytic efficiency, although some very active iridium catalysts are now known. First transition series metals seldom form stable, lower oxidation state tertiary phosphine complexes.

Although all homogeneous hydrogenation catalysts have the above properties in common, four different mechanisms of catalytic hydrogenation have been identified to date. The radical mechanism does not necessarily involve metal–carbon bonds and thus differs from the remaining three mechanisms. The latter mechanisms take their names from the way the catalyst activates dihydrogen. In the first, the catalytic complex activates dihydrogen and participates in the dihydride route. The alkene complex performs this task in the second and hydrogenation is said to occur via the alkene route. Monohydrido catalysts usually follow the alkyl route in which the alkyl intermediate activates dihydrogen. All these mechanisms will be discussed in more detail below. It is often difficult to determine the mechanisms of the reactions, particularly in the case of the dihydride and alkene routes, which share a common intermediate. Many workers have disregarded James' observation that the form of the rate equation is independent of the mechanism.[28] Indeed, the rate equation is similar to that found in Michaelis–Menten enzyme reactions.

3.2 Activation of Reactants

It was quickly realized that both the hydrogenation of alkenes and the reduction of the complex to the metal were brought about by hydrido species. It was therefore essential that the catalysts should be resistant to the autoreduction reaction. At the time of this discovery, many stable hydrido complexes containing π-acid ligands, such as tertiary phosphines, were being isolated, so the search for homogeneous catalysts concentrated on these.

Unfortunately, many of these complexes do not react with hydrogen and therefore cannot act as hydrogenation catalysts. The complexes that did react with hydrogen were usually low oxidation state complexes. The tertiary phosphine ligands also stabilized these low oxidation states and could often be used as the reducing agents in their formation from higher-valent metal salts.

It is now believed that dihydrogen initially adds to many transition metal complexes in the form of a σ-complex. The bond between the hydrogen atoms is broken upon addition to the transition metal complex and homogeneous hydrogenation catalysts can equilibrate mixtures of ortho- and parahydrogen.

The principal modes of conversion to hydrido complexes,[29] oxidative addition, homolysis, and heterolysis, are shown in equations (40–42), respectively. Oxidative addition of hydrogen to a transition metal complex at some stage in the catalytic cycle is essential to its activity. This requires that the metal has two accessible oxidation states corresponding to d^n and d^{n-2} electronic configurations or d^n and d^{n-1} for dinuclear oxidative addition. Hence, only those metals whose complexes meet this criterion may act as catalysts.

$$[Rh^{I}Cl(PPh_3)_3] + H_2 \longrightarrow [Rh^{III}H_2Cl(PPh_3)_3] \quad (40)$$

$$[Ru^{II}Cl_2(PPh_3)_3] + H_2 + NEt_3 \longrightarrow [Ru^{II}HCl(PPh_3)_3] + [NHEt_3]Cl \quad (41)$$

$$[Co(CO)_8] + H_2 \rightleftharpoons 2[CoH(CO)_4] \quad (42)$$

Alkene activation is synonymous with coordination. Alkenes normally have low-binding constants, and they do not readily displace other ligands from the coordination sphere. It has been found that the sterically driven dissociation of bulky tertiary phosphine ligands to form coordinatively unsaturated complexes allows alkenes to enter the coordination sphere. Alkenes with large substituents or the less favorable trans stereochemistry at the double bond bind less well. This can be used to advantage, since hydrogenation of the more sterically favored double bond will occur. The electronically favored double bond is preferentially hydrogenated in heterogeneous catalysis.

Paradoxically, alkenes with high-binding constants are often unsuitable substrates in homogeneous catalytic hydrogenation. This is particularly the case with chelating alkadienes, which occupy two coordination sites and thereby form complexes unable to activate dihydrogen. This may arise either from the alkadiene complex being coordinatively saturated or, because of the π-acidity of the alkadiene ligand, it may have electronic origins. Sometimes this increased π-acidity may be beneficial in preventing reduction of the metal. For example, in the $PdCl_2$-catalyzed reduction of methyl sorbate, palladium is not precipitated until all the diene has been reduced. Even when diene complexes do bind H_2, the inability of the diene to undergo face rotation can prevent them achieving the coplanar M(C=C)H arrangement required for insertion.

3.3 Radical Hydrogenation of Alkenes

This is the least common and least important mechanism of alkene hydrogenation. There have been very few unambiguous demonstrations of this mechanism. Experiments purporting to show that hydrogenation has been inhibited by the addition of a radical scavenger have frequently ignored the fact that these scavengers are often excellent ligands that poison the catalysts used by occupying a coordination site required in one of the more common mechanisms discussed in Sections 3.4–3.6.

In the hydrogenation of α-cyclopropylstyrene by various monohydridocarbonyl complexes, a radical mechanism has been proposed to account for the opening of the cyclopropyl ring in one of the competing reactions. The organic radicals can be trapped by $[Co^{II}(dmgH)(PBu_3)]$, but more conventional radical scavengers react preferentially with the hydrido complexes present.[30]

A second example of an undoubted radical mechanism occurs during the vitamin B_{12s} reduction of either (E)- or (Z)-butendioic acid in aqueous solution. However, the point is better illustrated by the reduction of butyndioic acid[31] to (E)-butendioic acid by two molecules of vitamin B_{12s}. This cobalt (I) species is oxidized to vitamin B_{12r} which contains cobalt (II). The course of the reaction is shown in Scheme 6. The formation of the (E)-alkene is strongly indicative of a radical process since more conventional homogeneous catalysts invariably form (Z) products (see below).

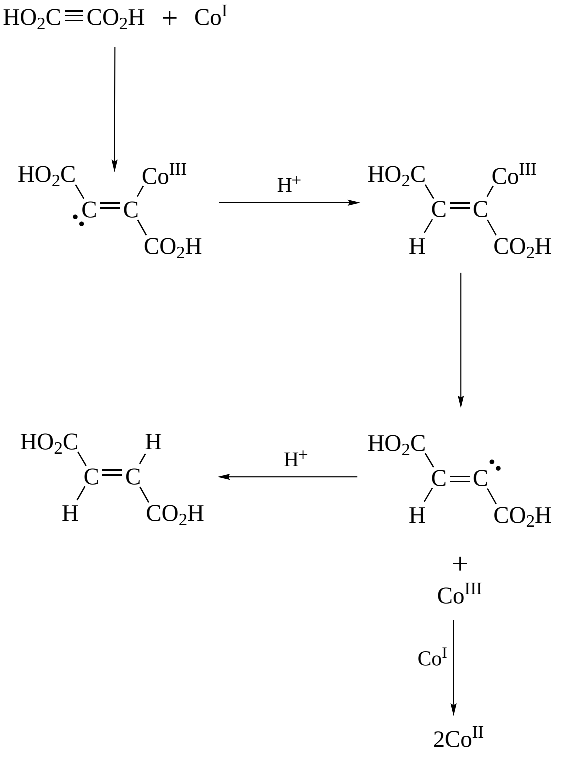

Scheme 6

3.4 The Dihydride Route

By contrast with the radical systems, this mechanism is the most common and most studied. It is also historically important for giving the first practical demonstration of catalytic homogeneous hydrogenation of alkenes.

The most important catalyst in this class is Wilkinson's Catalyst, chlorotris(triphenylphosphine)rhodium(I).[1] The catalytic cycle of this complex is shown in Scheme 7. The basic catalytic cycle is very simple, but parasitic side reactions make its study more difficult.

The key component of the catalytic cycle is the intermediate $RhCl(PPh_3)_2$. This highly reactive, 14-electron species can undergo three possible reactions. The least productive of these is dimerization to $[RhCl(PPh_3)_2]_2$. The dimer is catalytically inactive, but can be formed near the end of batch hydrogenations when the concentrations of the remaining alkene and hydrogen are low. The monomer may also react reversibly with the alkene present to form a 16-electron alkene complex, $[RhCl(PPh_3)_2(alkene)]$. Theoretically, there is no reason why this alkene complex should not undergo oxidative addition of dihydrogen to form the rhodium(III) intermediate, $[RhH_2Cl(PPh_3)_2(alkene)]$. However, it will be shown below that this is very unlikely. Consequently the only productive path that the tricoordinate species can follow is the oxidative addition of dihydrogen to form $[RhH_2Cl(PPh_3)_2]$. The fluxional, dihydridorhodium(III) complex, being coordinatively unsaturated, takes up a molecule of alkene to form $[RhH_2Cl(PPh_3)_2(alkene)]$ in what appears to be the rate-determining step of the catalytic cycle. Molecular modeling has shown that only those species in which the alkene is coordinated cis- to two cis-hydrido ligands can undergo successive hydrido ligand transfer to the alkene.[32] An alkyl complex is first formed and reductive elimination of the alkane takes place once the second hydrido ligand is transferred.

The actual course of events is more complicated than the simple resumé of the catalytic cycle given above. First, there is the competition between alkene and dihydrogen for the

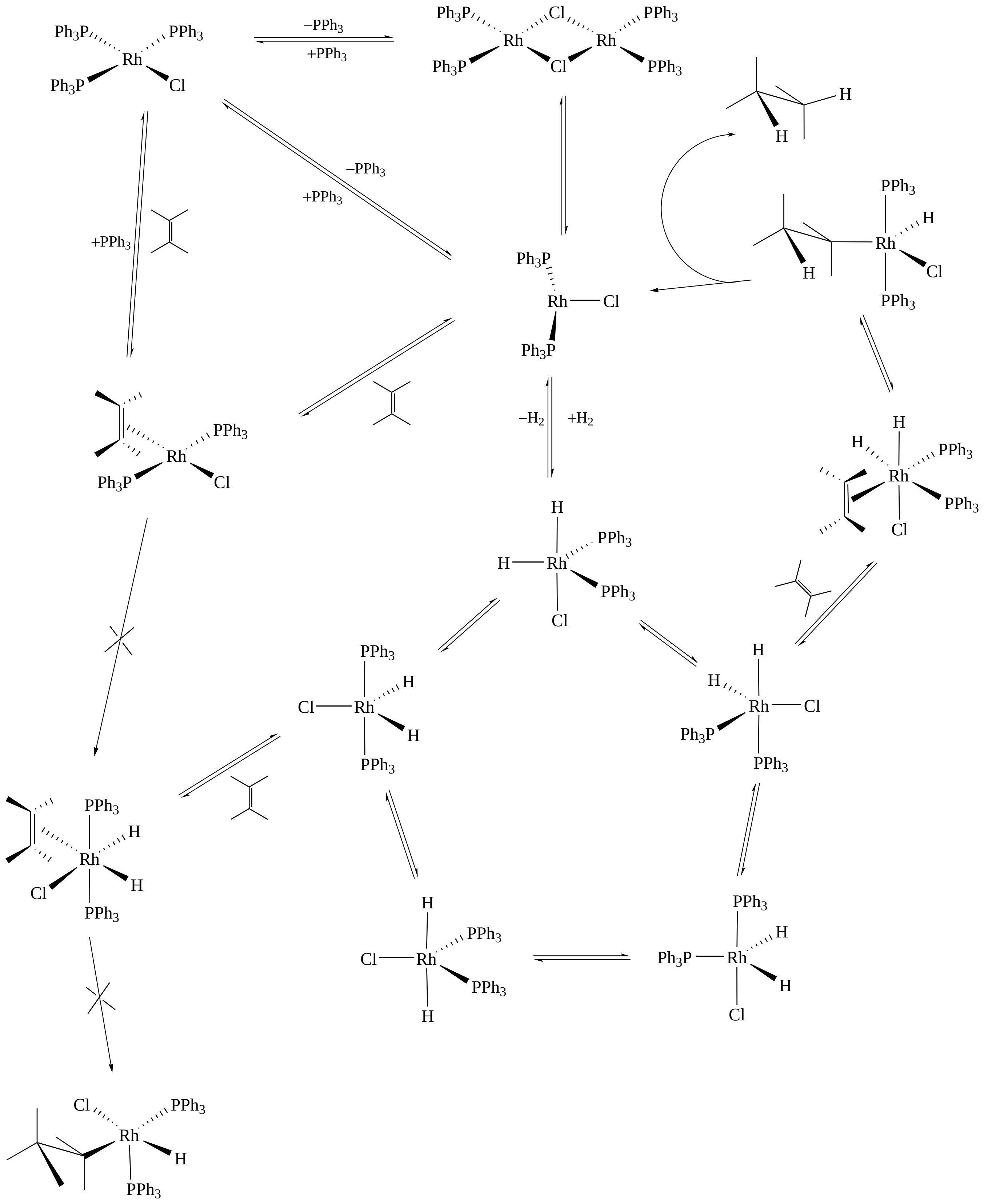
Ph_3P
PPh_3
Rh
Ph_3P
Cl
$-PPh_3$
$+PPh_3$
Ph_3P
Cl
PPh_3
Rh
Rh
Ph_3P
Cl
PPh_3
H
H
$-PPh_3$
$+PPh_3$
PPh_3
H
Rh
H
Cl
PPh_3
$+PPh_3$
Ph_3P
Rh
Cl
Ph_3P
$-H_2$
$+H_2$
PPh_3
Rh
Ph_3P
Cl
H
H
PPh_3
Rh
PPh_3
Cl
H
H
Rh
PPh_3
PPh_3
Cl
PPh_3
H
Cl
Rh
H
PPh_3
H
H
Rh
Cl
Ph_3P
PPh_3
PPh_3
H
Rh
Cl
H
PPh_3
H
Cl
Rh
PPh_3
PPh_3
H
PPh_3
H
Ph_3P
Rh
H
Cl
Cl
PPh_3
Rh
H
PPh_3

Scheme 7

intermediate $RhCl(PPh_3)_2$. It can be demonstrated that there are two reasons why the catalytic cycle proceeds slowly. The rate of alkane formation may be slow because of the alkene's unfavorable geometry, or because the concentration of the dihydrido species is low. The first possibility is exemplified by the difficulty of coordinating (*E*)-1,2-diphenylethene to rhodium. The second occurs when the alkene has a very high binding constant. Ethylene reacts rapidly with the preformed dihydrido complex to form ethane, but, under the competitive conditions of the catalytic cycle, the reaction soon ceases. It is not possible to form ethane by adding dihydrogen to the ethylene complex $[RhCl(PPh_3)_2(C_2H_4)]$ in equilibrium with dissolved ethylene. Effectively ethylene poisons its own reduction just as it does in heterogeneous systems employing copper metal catalysts. This is because the ethylene complex is incapable of activating dihydrogen. The attack of ethylene upon $[RhH_2Cl(PPh_3)_2]$ shows that the common intermediate $[RhH_2Cl(PPh_3)_2(C_2H_4)]$ can be formed and that transfer of hydrogen to ethylene can occur. The poisoning of the system by ethylene can also be demonstrated by adding ethylene during the reduction of cyclohexene. The addition of ethylene stops the reaction, whereas the addition of (*E*)-1,2-diphenylethylene (which coordinates to rhodium only with difficulty) has no effect upon the rate of formation of cyclohexane.

The stereochemistry of the addition has been shown to be cis. This can be demonstrated by the deuteration of (*E*)- or (*Z*)-butendioic acids to form (*R*,*R*)- and (*S*,*S*)-2,3-dideuterobutandioic acid or (*R*,*S*)-2,3-dideuterobutandioic acid, respectively (equations 43 and 44). The deuteration of other (*E*)-alkenes to *threo*-alkanes and (*Z*)-alkenes to *erythro* products also demonstrates that cis addition occurs.

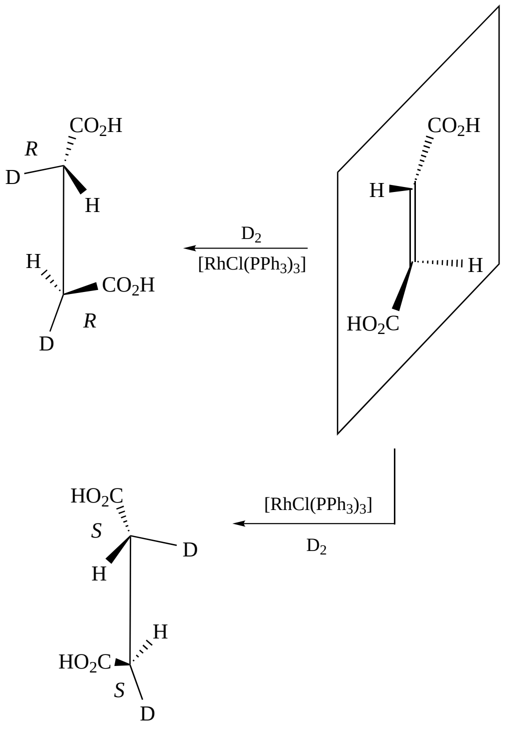

(43)

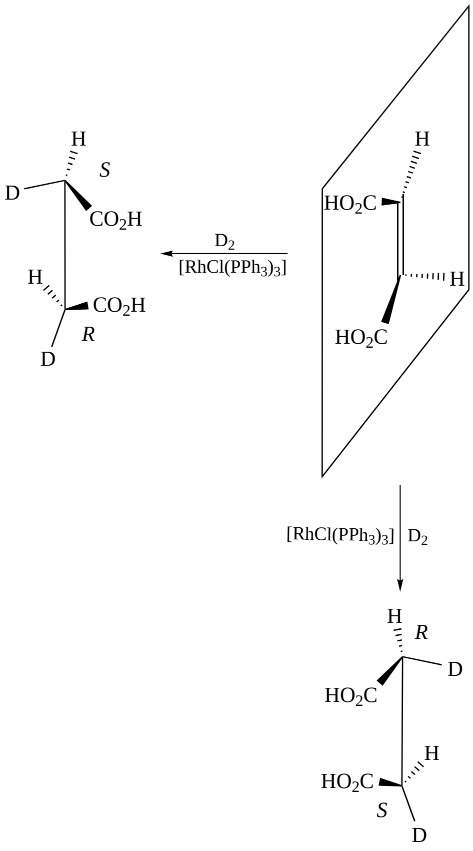

(44)

It was once thought that the exclusively cis addition was a consequence of the simultaneous addition of both hydrogen atoms. However, it has since been demonstrated that the hydrido ligands are transferred successively to the alkene and that a relatively long-lived intermediate alkyl complex is formed. The best evidence for the participation of the alkyl complex comes from hydroisomerization side reactions (equation 45), and the scrambled addition of deuterium to medium-sized cycloalkenes.[33]

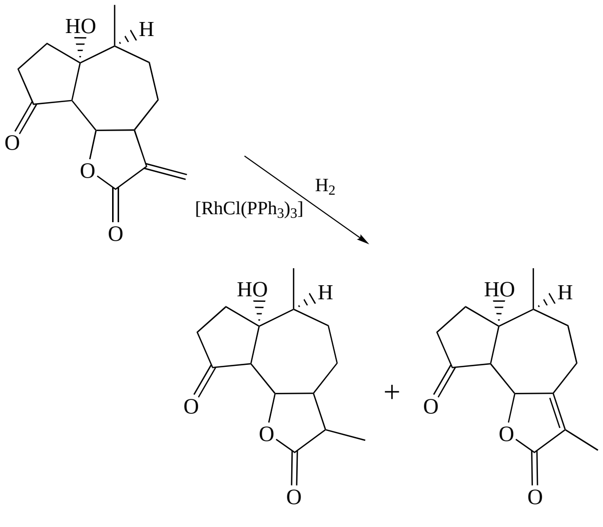

(45)

If more than two deuterium atoms are added to cyclooctene, then isotope exchange must have taken place, and if more than four atoms of deuterium are added, then double-bond migration must also have occurred. The incorporation of excess deuterium can readily be explained by the participation of intermediate alkyl complexes that undergo β–hydride abstraction reactions.

Normally $[RhCl(PPh_3)_3]$ is a very good deuteration catalyst, giving little scrambled or polydeuteration. It is far superior to heterogeneous catalysts in this respect and has been used to tritiate alkenes at the double bond.

Alk-1-ene substrates can form either 1-alkyl or 2-alkyl complexes, the latter as a result of Markovnikov addition. The 2-alkyl complexes are less stable than the 1-alkyl complexes because they are more sterically hindered. As a consequence, they undergo β-hydride abstraction reactions more readily and are more likely to give polydeuterated products. Changing the chloro ligand for the larger iodo ligand ensures that alk-1-enes are more likely to form 1-alkyl intermediates and form dideuteroalkenes. However, when cyclic or internal alkenes, which must form secondary alkyl intermediates, undergo deuteration, the chloro complex should be used to lessen the steric hindrance in the intermediate alkyl complex.

The stability of the intermediate alkyl also depends upon the neutral ligands present. Its stability can be increased by using $P(4\text{-}C_6H_4F)_3$ ligands in place of triphenylphosphine. These reduce the electron density on rhodium and make β-hydride abstraction reactions less likely to occur.

Another of the major advantages of homogeneous catalytic hydrogenation is the facility to hydrogenate molecules containing other multiple interatomic bonds exclusively at the site of the C=C bond. Heterogeneous catalysts usually hydrogenate all the multiple bonds present. They are thus unsuitable for the catalytic hydrogenation of alkenals, nitroalkenes, or unsaturated nitriles.

The accessibility and effectiveness of $[RhCl(PPh_3)_3]$ has done little to encourage the employment of other dihydride route catalysts except for directed and enantioselective hydrogenation and reactions with very hindered substrates where $[RhCl(PPh_3)_3]$ is not successful and cationic iridium- and rhodium catalysts are used. Replacement of the chloro ligand by a heavier halide increases the rate of hydrogenation. Homologous complexes can be prepared from $[RhCl(C_2H_4)_2]_2$ and triarylphosphines. Those ligands containing electron-donating substituents increase the rate of hydrogenation, while the converse is true for those neutral ligands containing electron-withdrawing groups.

The stereochemistry of the neutral ligand also affects the properties of the catalyst. Although $[RhCl\{P(2\text{-}C_6H_4OMe)_3\}_3]$ initially reduces alkenes rapidly, the reaction ceases before all the alkene has been consumed because of the formation of the coordinatively saturated complex (**3**).

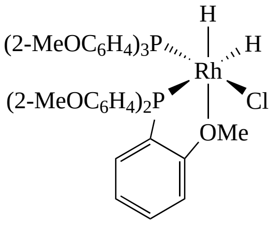

(**3**)

Nevertheless, replacing triarylphosphines by trialkylphosphines destroys the catalytic properties of the complex, since the resulting $[RhH_2Cl(PR_3)_3]$ complex is coordinatively saturated and cannot activate the alkene. The greater stability of dihydridoiridium(III) complexes means that $[IrCl(PPh_3)_3]$ fails to show the activity of its rhodium analog.

Biologically important substrates can be hydrogenated in aqueous solution by using sulfonated triarylphosphine ligands that confer water solubility upon the catalyst.**[34]** However, it was later reported that rhodium metal was formed from these complexes in the presence of hydrogen. It was claimed that the role of the ligands is merely to prevent aggregation of the rhodium colloid produced.**[35]**

Several *cis*-dihydridoruthenium(II) complexes of general formula $[RuH_2L_4]$ have been claimed to follow the dihydride route merely because of their stoichiometry. Since these complexes are coordinatively saturated, they must lose the neutral ligand trans to a hydrido ligand to allow alkene coordination to take place. This would then allow the formation of an alkyl complex since the alkene would be coordinated cis to the second hydride. Since both alkene isomerization and H/D exchange can be observed in the system, the alkyl complex must have a long lifetime.**[36]**

More active catalytic systems in which a significant degree of hydroisomerization is observed are those employing $[IrH_5(PR_3)_2]$ (which may be lower-valent iridium species containing σ-bound H_2) or $[(cod)IrL_2]BF_4$ complexes. The hydroisomerization may arise from the minimal steric constraints present, which allow 2-alkyl intermediates to be formed. The low-steric demands imposed by the catalyst have been exploited in the hydrogenation of the substituted alkenes 1-methylcyclohexene and 2,3-dimethylbut-2-ene. The hydrogenations of these substrates are very slow when other homogeneous catalysts are employed.**[37]**

3.5 The Alkene Route

The first catalysts to be shown to follow the alkene route were the cationic $[Rh(PPh_3)_2(diene)]ClO_4$ complexes.**[38]** These complexes, unlike their neutral $[RhCl(PPh_3)(diene)]$ counterparts, can activate dihydrogen in solution. However, the diene complexes are converted into the true catalysts when allowed to react with hydrogen. The diene is converted to alkene in a stoichiometric reaction that must follow the alkene route. The highly coordinatively unsaturated $[Rh(PPh_3)_2(solvent)_2]^+$ complex can then react with either alkene or dihydrogen and follow the alkene or dihydride route, respectively. There is considerable evidence for the belief that both hydrogenation routes may be followed simultaneously. The alkene route is shown in Scheme 8.

The predominant route depends upon the nature of the substrate. Nonchelating substrates probably follow the dihydride route, but dienes or alkenes containing a substituent group capable of chelating to rhodium may follow the alkene route.

The iridium complex [Ir(cod)PCy_3(py)]PF_6 is a remarkably active and selective hydrogenation catalyst for the reduction of terpinen-4-ol. The trisubstituted alkene bond is very rapidly reduced and the addition of hydrogen occurs to the more shielded face of the alkene to form (**4**) at least 1000 times more rapidly than its stereoisomer, the weakly preferred product in heterogeneous catalysis. The tricyclohexylphosphineiridium(I) catalyst is also more active than $[Ir(cod)(PPh_3)_2]^+$ or the rhodium analog of the latter.**39** High selectivity has also been observed with other cyclohexenol substrates.**40**

The two tertiary phosphine ligands may be replaced by a chelating ditertiary phosphine. The greatest application of the alkene route comes in asymmetric synthesis when chiral, ditertiary phosphine ligands are used. This topic is discussed more fully in (*see* ***Asymmetric Synthesis by Homogeneous Catalysis***).

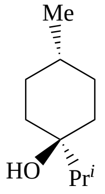

(**4**)

3.6 The Alkyl Route

Chlorohydridotris(triphenylphosphine)ruthenium(II) was the first complex in which homogeneous hydrogenation of alkenes was shown to follow the alkyl route.**41** It can be prepared from dihydrogen and $[RuCl_2(PPh_3)_3]$ in the presence of base (equation 41). Most other alkyl route catalysts are also monohydrido complexes. They are usually specific for terminal alkenes. The behavior of several *exo-nido*-dicarbaborane complexes of rhodium has been reviewed.**42**

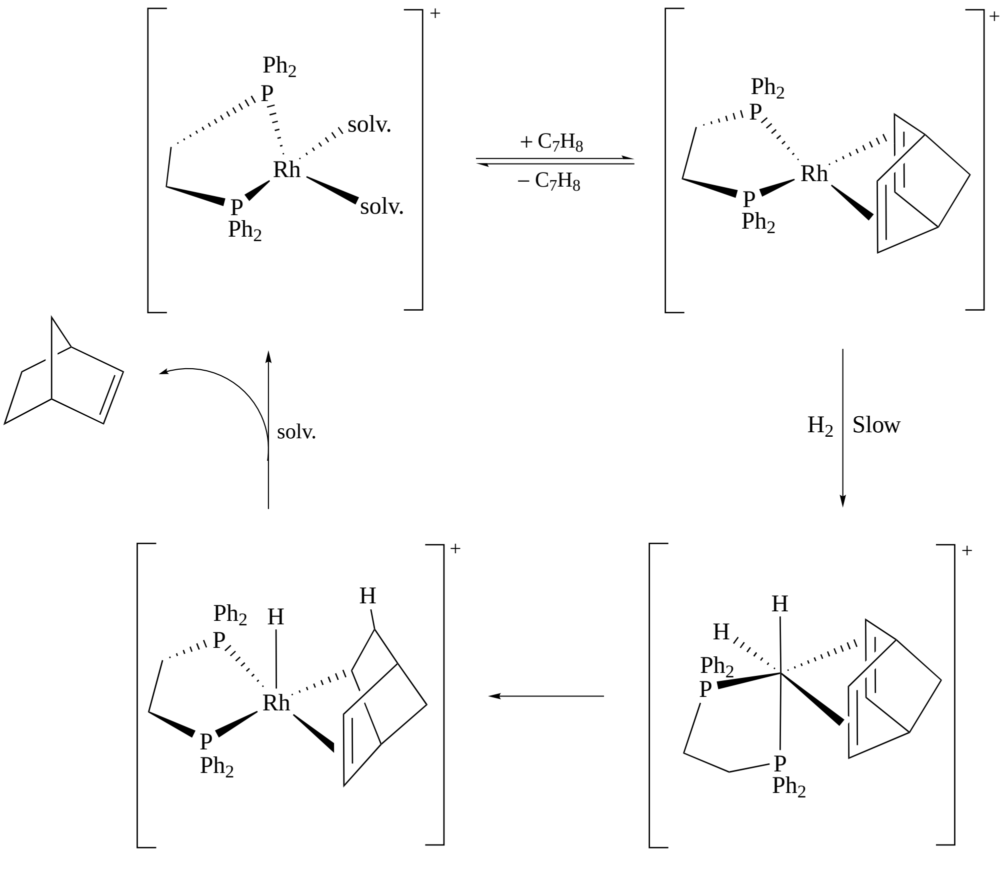

Scheme 8

During deuteration reactions, considerable isotope exchange and a little isomerization are observed. All these properties are characteristic of a catalytic cycle involving a relatively long lived alkyl complex.

In the catalytic cycle shown in Scheme 9, the rate-determining step is the oxidative addition of dihydrogen to the 1-alkyl complex. σ-Bond metathesis is an alternative pathway for hydrogenolysis of the metal alkyl. Any 2-alkyl complexes that may be formed by the Markovnikov addition of the hydrido ligand to the alkene are unstable and are very likely to decompose before the slow oxidative addition of dihydrogen and the transfer of a second hydrido ligand can occur. Their instability has steric origins, and consequently this type of catalyst exhibits high selectivity towards terminal alkenes since internal alkenes must form unstable secondary alkyl complexes.

The ruthenium complex is such an exceedingly active catalyst that, at higher catalyst concentrations, orthometalation of the catalyst by the alkene present may occur if local hydrogen starvation is encountered. (equation 46).

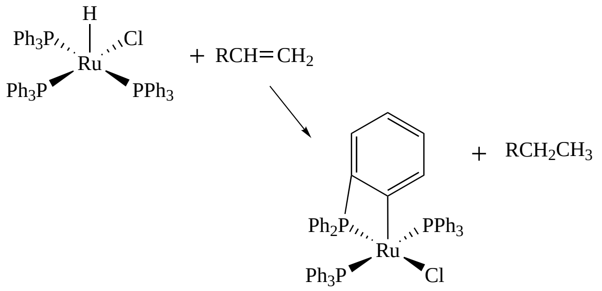
H
Ph3P
Cl
Ru
Ph3P
PPh3
+ RCH=CH2
+ RCH2CH3
Ph2P
PPh3
Ru
Ph3P
Cl

(46)

Accordingly the less active, but more amenable, complex $[RhH(CO)(PPh_3)_3]$ is usually selected to exemplify hydrogenation by the alkyl route.**3** One of the great advantages of this system has been the isolation of several intermediates in the catalytic cycle from stoichiometric reactions. The two principal reactions are shown in equations (47) and (48).

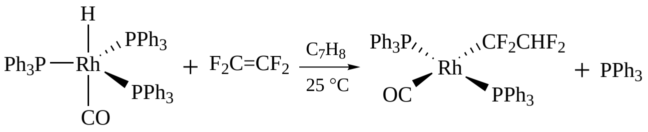
H
PPh3
Ph3P
Rh
PPh3
CO
+ F2C=CF2
C7H8
25 °C
Ph3P
CF2CHF2
Rh
OC
PPh3
+ PPh3

(47)

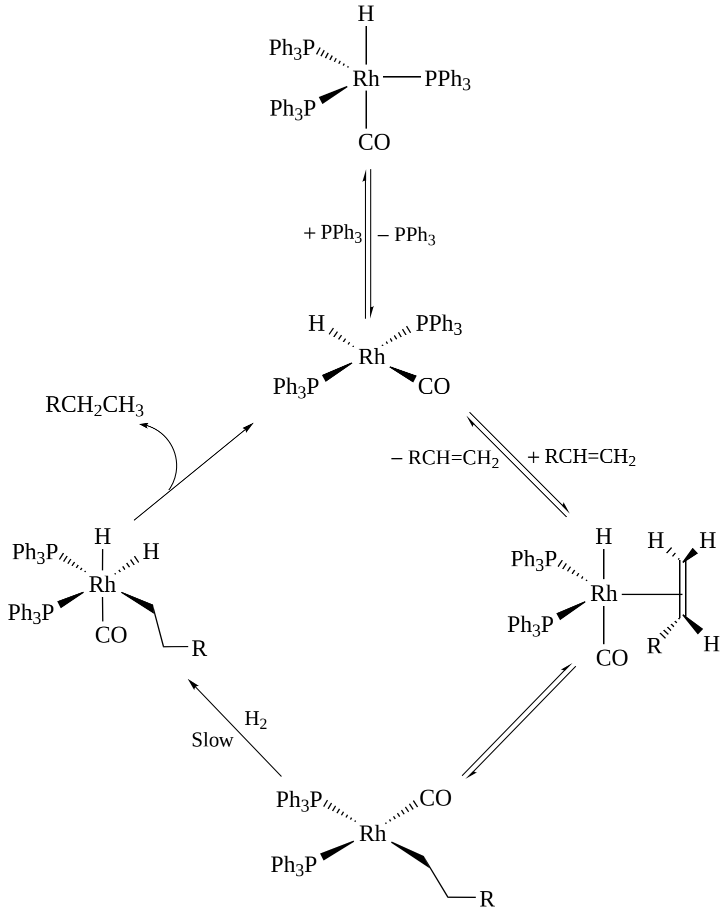
H
Ph3P
Rh
PPh3
Ph3P
CO
+ PPh3
− PPh3
H
PPh3
Rh
Ph3P
CO
RCH2CH3
− RCH=CH2
+ RCH=CH2
H
Ph3P
H
Rh
Ph3P
CO
R
H
Ph3P
Rh
Ph3P
CO
H
H
R
H
H2
Slow
Ph3P
CO
Rh
Ph3P
R

Scheme 9

It was noted above that the crowded alkyl complex was the source of the regioselectivity exhibited by this class of catalyst. However, at lower catalyst concentrations or higher hydrogen pressures the catalyst is much less selective. In the latter case, the higher concentration of hydrogen results in a 2-alkyl complex being hydrogenated before decomposition. In the former case, a second triphenylphosphine ligand can be lost and the relaxation of steric constraints allows more stable, possibly solvated, [Rh(CO)(2-alkyl)(PPh_3)] complexes to be formed.

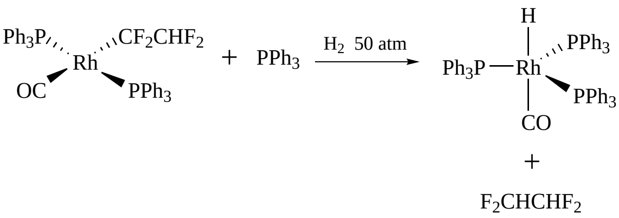

(48)

For example, at 50 °C and under 10 atm pressure, cyclohexene can be hydrogenated to cyclohexane. The reaction proceeds if the catalyst concentration is less than 0.75 mM, and shows an inverse dependence upon catalyst concentration down to 0.25 mM. This behavior indicates the importance of triphenylphosphine dissociation. Removing one PCy_3 ligand by acidification from the similar ruthenium catalyst [RuHCl(CO)(PCy_3)$_2$] brings about a decrease in selectivity and an increase in hydrogenation rates. This catalyst also brings about hydroisomerization since the pentacoordinate intermediate [RuCl(alkyl)(CO)(PCy_3)$_2$] must lose a PCy_3 ligand before activating H_2.[43]

Two acetatoruthenium catalysts have been shown to form alkyl complexes when allowed to react with alkene and hydrogen. However, a second molecule of hydrogen is not responsible for converting the alkyl complex to alkene. Instead, the alkyl complexes are decomposed by a proton from the carboxylic acid solvents.[44]

3.7 Alkyne Hydrogenation

Alkyne hydrogenation remains a largely forgotten area of homogeneous catalytic hydrogenation. There are clear commercial benefits to be obtained in the conversion of alkynes to alkenes; however, homogeneous catalysts are not usually sufficiently selective towards the alkene intermediate.

There seems no reason why any of the mechanisms discussed in Sections 3.4–3.6 cannot function in the conversion of alkynes to alkenes. The alkene route of hydrogenation is frequently encountered because alkynes complex more strongly to transition metals than alkenes and their complexes are formed preferentially in competition with the oxidative addition of dihydrogen. Internal alkynes coordinate to bis(arylimino)acenaphthene complexes of palladium and the tricoordinate species activate molecular hydrogen. Transfer of both atoms of hydrogen forms a Z–alkene complex that is decomposed by a second molecule of internal alkyne to restart the catalytic cycle.[45]

Unfortunately, several complexes, capable of catalyzing the hydrogenation of alkenes by the dihydride route, fail to hydrogenate alkynes since they form alkyne complexes that are incapable of activating dihydrogen. Hex-2-yne coordinates to [RhH_2(nbd)($PPhMe_2$)]$^+$ cations more readily than hex-1-yne and is more selectively reduced to Z-hex-2-ene as a consequence.[38]

Some catalysts suffer a different type of alkyne poisoning. Chlorotris(triphenylphosphine)rhodium(I) is an effective terminal alkyne polymerization catalyst.[1] When this complex is used in the reduction of these alkynes, it gradually loses its activity because of the competing polymerization reaction. Even initially the rate of alkyne hydrogenation is much slower than that of the corresponding alkene because of the greater binding constant of the former substrate.

Addition of alkyne to [RuHCl(PPh_3)$_3$] brings about a color change, presumably due to formation of a vinyl complex. These undergo hydrogenolysis and form alkenes. Normally the alkenes are reduced more rapidly than the alkyne and the selectivity of the method is low. However, although some internal alkynes are hydrogenated to alkanes, sterolic acid is reduced to oleic acid. The formation of the (Z)-alkenoic acid shows that the addition of hydrogen to the alkene is cis.

Most catalysts also bring about the cis addition of hydrogen to alkynes. For example, [RhCl(PPh_3)$_3$] catalyzes the initial formation of (Z)-but-2-enoic acid from but-2-ynoic acid.

3.8 Transfer Hydrogenation

Dihydrogen is not used as a reactant in transfer-hydrogenation reactions. Instead, the hydrogen required for alkene reduction is abstracted from an organic molecule. Secondary alcohols have proved to be the most generally useful hydrogen sources.

The mechanism of transfer hydrogenation is complicated because of the need to activate the reagents in the correct order. Since several of the more successful transfer-hydrogenation catalysts are monohydride complexes, deuterium-labeling experiments to ascertain the source and destination of the transferred hydrogen are subject to some uncertainty. This complication arises from the simultaneous isotope exchange reactions that occur.

The catalytic cycle involving [$RuCl_2$(PPh_3)$_3$], one of the more active transfer-hydrogenation catalysts, is shown in Scheme 10.[2] The catalyst first forms an alkoxido complex, with elimination of HCl, when allowed to react with the secondary alcohol. This pentacoordinate complex forms an 18-electron species by coordinating a molecule of alkene. The alkoxido ligand transfers its α-deuterium atom to the metal, after which the ketone oxidation product of the secondary alcohol is eliminated. The steps are believed to occur in

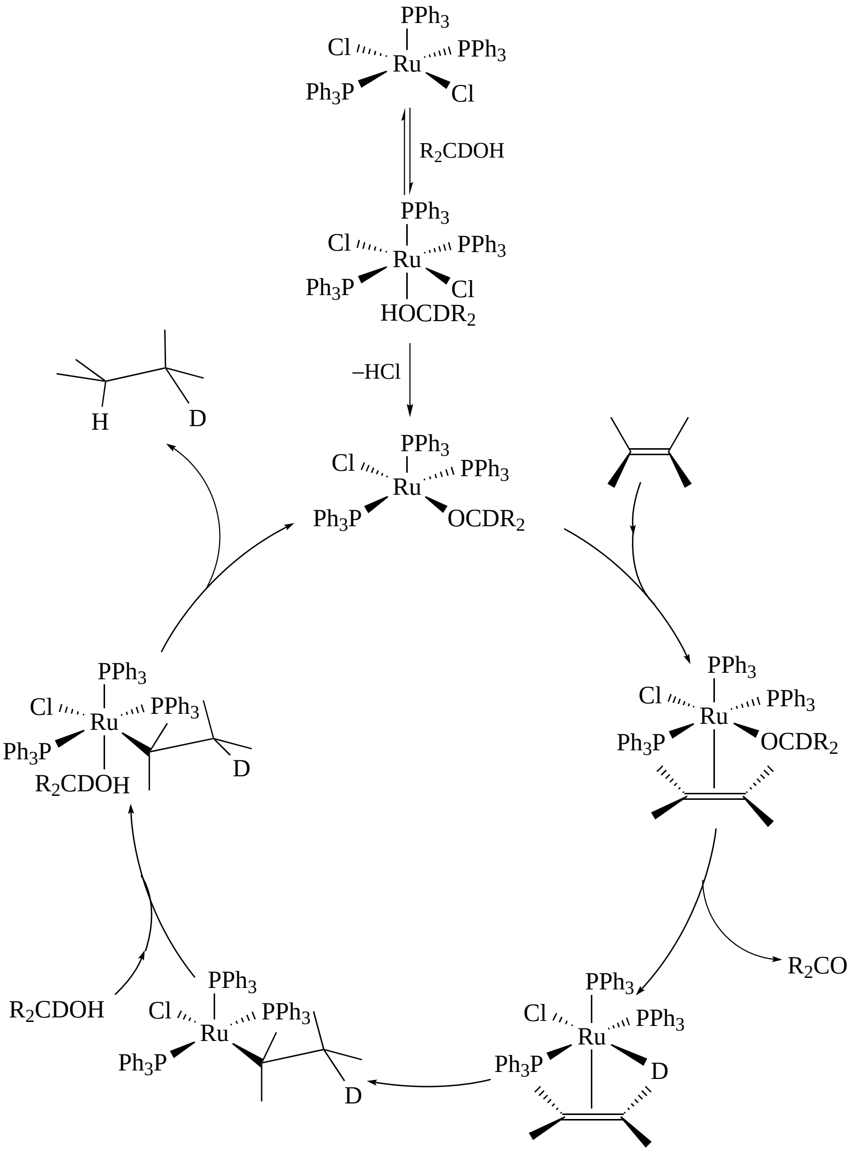

Scheme 10

this order since the presence of a chiral alkoxido ligand is required to account for the selectivity shown in the reactions of prochiral alkenes when chiral secondary alcohols are used as the hydrogen source.

In Scheme 10, transfer of the deuterium marker to the alkene forms a 2-deutero-1-alkyl complex. To complete the catalytic cycle, this complex coordinates a second molecule of the labeled alcohol. The hydroxyl proton of this is transferred to the alkyl ligand and reductive elimination of the monodeuteroalkane ensues. The alkoxido complex resulting can then activate a further molecule of alkene in the next revolution of the catalytic cycle.

The results of several stoichiometric reactions of labeled compounds have led to the proposals put forward in the catalytic cycle.

Transfer hydrogenation is usually carried out under harsher conditions than would be required to add molecular hydrogen across the same alkene bond.

4 RELATED ARTICLES

Cobalt: B_{12} Enzymes & Coenzymes; Copper: Hemocyanin/Tyrosinase Models; Heterogeneous Catalysis by Metals; Hydride Complexes of the Transition Metals; Hydrocyanation by Homogeneous Catalysis; Hydrogen: Inorganic Chemistry; Mechanisms of Reaction of Organometallic Complexes; Nickel: Organometallic Chemistry; Oligomerization & Polymerization by

Homogeneous Catalysis; P-donor Ligands; Palladium: Organometallic Chemistry; Rhodium: Organometallic Chemistry; Ruthenium: Organometallic Chemistry.

5 REFERENCES

1. F. H. Jardine, *Prog. Inorg. Chem.*, 1981, **28**, 63.
2. F. H. Jardine, *Prog. Inorg. Chem.*, 1984, **31**, 275.
3. F. H. Jardine, *Polyhedron*, 1982, **1**, 569.
4. X. Wang and L. K. Woo, *J. Mol. Catal. (A)*, 1998, **130**, 171.
5. C. D. Warren and R. W. Jeanloz, *Carbohydr. Res.*, 1977, **53**, 67.
6. F. H. Jardine, in 'The Chemistry of the Metal – Carbon Bond', ed. F. R. Hartley, Wiley, New York, 1987, p. 1049.
7. G. Menchi, U. Matteoli, A. Serivanti, S. Paganelli, and C. Botteghi, *J. Organomet. Chem.*, 1988, **354**, 215.
8. P. Golborn and F. Scheinman, *J. Chem. Soc., Perkin Trans. 1*, 1973, 2870.
9. G. F. Emerson, J. E. Mahler, R. Kochlar, and R. Petit, *J. Org. Chem.*, 1964, **29**, 3620.
10. R. E. Reinhardt and J. S. Lasky, *J. Am. Chem. Soc.*, 1964, **86**, 2516.
11. K. Tani, T. Yamagata, T. Tatsuno, Y. Yamagata, K. Tomita, S. Akutagawa, H. Kumobayashi, and C. Otsuka, *Angew. Chem., Int. Ed. Engl.*, 1985, **24**, 217.
12. T. B. Patrick and D. S. Bechtold, *J. Org. Chem.*, 1984, **49**, 1935.
13. K. Maruyama and H. Tamiaki, *J. Org. Chem.*, 1986, **51**, 602.
14. K. Baumgart, H. Harnisch, U. Szeimes-Seebach, and G. Szeimes, *Chem. Ber.*, 1985, **118**, 2883.
15. K. B. Wiberg and S. T. Waddell, *J. Am. Chem. Soc.*, 1990, **112**, 2194.
16. Y. Tong, Z. Zhang, and X. Zhang, *J. Am. Chem. Soc.*, 2003, **125**, 6370.
17. S. Jolly, G. Luedtke, D. Sheehan, and T. Livinghouse, *J. Am. Chem. Soc.*, 1990, **112**, 4965.
18. P. A. Wender, C. O. Husfeld, E. Langkopf, J. A. Love, and N. Pleuss, *Tetrahedron*, 1998, **54**, 7203.
19. T. Izumi and H. Alper, *Organometallics*, 1982, **1**, 322.
20. M. Mallien, E. T. K. Haupt, and H. tom Dieck, *Angew. Chem., Int. Ed. Engl.*, 1988, **27**, 1062.
21. R. P. Lutz, *Chem. Rev.*, 1984, **84**, 205.
22. L. E. Overman, *Angew. Chem., Int. Ed. Engl.*, 1984, **23**, 579.
23. S. Saito, A. Kuroda, H. Matsunaga, and S. Ikeda, *Tetrahedron*, 1996, **52**, 13919.
24. S. Takatsuto, M. Ishiguro, and N. Ikekawa, *Chem. Commun. (Cambridge)*, 1982, 258.
25. J. L. van der Baan and F. Bickelhaupt, *Tetrahedron Lett.*, 1986, **27**, 6267.
26. E. Curzon, B. T. Golding, C. Pierpoint, and B. W. Waters, *J. Organomet. Chem.*, 1984, **262**, 263.
27. H. K. Park, I. B. Kim, and C. S. Chin, *J. Organomet. Chem.*, 1987, **326**, 431.
28. B. R. James, in 'Comprehensive Organometallic Chemistry', eds. G. Wilkinson, F. G. A. Stone, and E. W. Abel, Pergamon Press, Oxford, 1982, Vol. 8, p. 285.
29. P. Brothers, *Prog. Inorg. Chem.*, 1981, **28**, 1.
30. R. M. Bullock and E. G. Samsel, *J. Am. Chem. Soc.*, 1990, **112**, 6886, and references therein.
31. G. C. Pillai, J. W. Reid, and E. S. Gould, *Inorg. Chem.*, 1986, **25**, 3734.
32. J. M. Brown, P. L. Evans, and A. R. Lucy, *J. Chem. Soc., Perkin Trans. 2*, 1987, 1589.
33. M. Güngör, F. H. Jardine, and J. D. Wheatley, *J. Chem. Soc., Dalton Trans.*, 1988, 1653.
34. C. Larpent and H. Patin, *J. Organomet. Chem.*, 1987, **335**, C13.
35. C. Larpent and H. Patin, *J. Mol. Catal.*, 1988, **44**, 191.
36. J. M. Bray and R. J. Mawby, *J. Chem. Soc., Dalton Trans.*, 1987, 2989.
37. R. H. Crabtree, H. Felkin, and G. E. Morris, *J. Organomet. Chem.*, 1977, **141**, 205.
38. R. R. Schrock and J. A. Osborn, *J. Am. Chem. Soc.*, 1976, **98**, 2143.
39. R. H. Crabtree and M. W. Davies, *Organometallics*, 1983, **2**, 681.
40. R. H. Crabtree and M. W. Davies, *J. Org. Chem.*, 1986, **51**, 2655.
41. P. S. Hallman, B. R. McGarvey, and G. Wilkinson, *J. Chem. Soc. (A)*, 1968, 3143.
42. F. Texidor, R. Nùñez, M. A. Flores, A. Demonceau, and C. Viñas, *J. Organomet. Chem.*, 2000, **614–615**, 48.
43. C. S. Yi, D. W. Lee, Z. He, A. L. Rheingold, K.-C. Lam, and T. E. Concolino, *Organometallics*, 2000, **19**, 2909.
44. A. J. Lindsay, G. McDermott, and G. Wilkinson, *Polyhedron*, 1988, **7**, 1239.
45. M. W. van Laren and C. J. Elsevier, *Angew. Chem., Int. Ed. Engl.*, 1999, **38**, 3715.

Hydrosilation Catalysis

Christoph Marschner
Technische Universität Graz, Graz, Austria

Based in part on the article Hydrosilation Catalysis by John F. Harrod which appeared in the Encyclopedia of Inorganic Chemistry, First Edition.

1 Introduction 1
2 Radical and Other Nontransition Metal Catalyzed Hydrosilation 1
3 Catalysis by Transition Metal Compounds 2
4 Mechanisms of Metal Complex Catalyzed Hydrosilation 2
5 Substrate Types 4
6 Enantioselective Catalytic Hydrosilation 8
7 Related Reactions of Silanes 9
8 Transition Metal-silyl Complexes 10
9 Related Articles 10
10 References 10

Glossary

Coordination catalysis: a catalytic process which takes place in the coordination sphere of a metal complex
Dehydrosilylation: a condensation reaction between a hydrosilane and another hydride, E–H, with formation of an Si–E bond and hydrogen
Hydroelementation: a reaction in which an element–hydrogen bond adds across an unsaturated molecule

1 INTRODUCTION

The term hydrosilation (or hydrosilylation) refers to the addition of a molecule containing a Si–H bond across the multiple bond of a substrate, usually an alkene, alkyne, or carbonyl compound (equation 1).[1–4] The reaction can be promoted by UV-light, radiation (γ- and X rays), radical initiators, Lewis acids, nucleophiles, or, most importantly, transition metal catalysts. Hydrosilation is related to the important processes of hydrogenation (*see Hydrogenation*) and hydroboration (*see Hydroboration*), all of which belong to the general reaction class of hydroelementation.

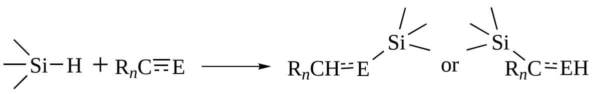
(1)

The first example of a hydrosilation reaction was the peroxide catalyzed addition of trichlorosilane across 1-octene, reported by Sommer in 1947.[5] The discovery of the transition metal catalyzed variant of the reaction by Speier[6] in 1957 initiated a broad interest in the reaction. This interest has grown further even in recent years. With increasing importance of organosilanes in organic synthesis and especially material science, the value of Si–C bonding reactions was very well recognized. The finding that essentially every known metal in some ligand framework can catalyze the hydrosilation reaction brought about very different chemo- and regioselectivities. As conversion and yields are usually very good, the reaction enjoys a wide acceptance in academic and industrial[7] environments.

2 RADICAL AND OTHER NONTRANSITION METAL CATALYZED HYDROSILATION

As the Si–H bond is relatively weak (ca. 300–400 kJmol^{-1}) silyl radicals can be easily generated. Using a radical initiator such as azobisisobutyronitrile (AIBN) or organic peroxides the hydrosilation process can take place as a radical chain reaction (Scheme 1).[8,9]

The addition of the tris(trimethylsilyl)silyl radical to alkenes and alkynes was found to be highly stereoselective (*see Stereoselectivity*) and constitutes an interesting method in organic synthesis.[10] Compared to the transition metal (*see Transition Metals*) catalyzed process the radical reaction is often plagued by severe disadvantages. Radical reactions are frequently less selective and tend to give side-products such as telomers, which are formed by the reaction of an intermediate radical with another unsaturated substrate rather than with a hydrosilane. A large excess of the silane component can occasionally suppress this unwanted side reaction. In cases of higher substituted alkenes as substrates, however, hydrosilation using radical conditions can be useful. Transition metal catalysts frequently cannot be used with tri- and tetrasubstituted alkenes.

Aluminum trichloride catalyzed hydrosilation provides an interesting alternative to the free radical process. The addition of the silane was found to occur regioselectively at trisubstituted alkenes in a *trans*-fashion.[11] Mechanistically it was concluded that the reaction proceeds via the addition of a silylenium cation to the multiple bond, generating the more stable (more substituted) carbocation, which abstracts a hydride from another molecule of hydrosilane (Scheme 2).[12]

A similar *trans*-selectivity was also found for the aluminum trichloride catalyzed hydrosilation of alkynes. Z-Vinylsilanes can be obtained by this method as the exclusive products.[13]

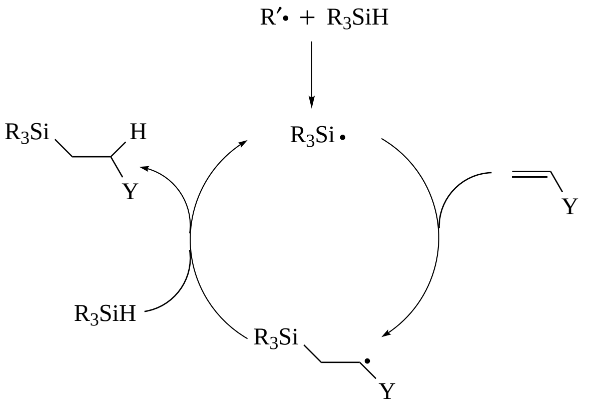

Scheme 1 Radical chain hydrosilation reaction

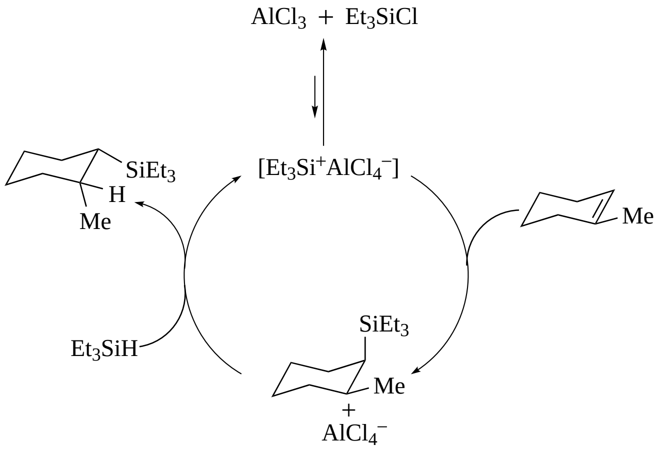

Scheme 2 Aluminum chloride catalyzed hydrosilation reaction

3 CATALYSIS (*See Catalysis*) BY TRANSITION METAL COMPOUNDS

Most hydrosilation reactions are catalyzed by transition metal compounds. Among the known catalyst systems, hexachloroplatinic acid ($H_2PtCl_6 \cdot 6H_2O$) in isopropanol (Speier's catalyst)**[14]** still holds paramount position. The usefulness of this system is illustrated by its high rates and the fact that cases with substrate/catalyst ratios of 10^8 are known to work on industrial scale.**[14]** Besides Speier's catalyst, the Karstedt catalyst system, which is obtained by treatment of hexachloroplatinic acid with vinylsiloxane, enjoys widespread popularity.**[15]** Besides these two, a whole array of other Pt catalysts has been investigated. It is assumed that Pt(II) species are the most effective catalysts.**[4]** A controversy over the active catalytic species in Speier's catalyst being actually metallic platinum seems to have been resolved in favor of a homogeneous mechanism.**[16]** Nevertheless, platinum metal on heterogeneous support materials is an active hydrosilation catalyst also.

Among metals other than platinum, rhodium is probably the most important with respect to hydrosilation catalysis. Mainly Rh(I) compounds, with Wilkinson's complex $(Ph_3P)_3RhCl$ (*see Wilkinson's Catalyst*) being the most investigated, have been found to be active catalysts. While the use of Rh-catalysts seems not to be advantageous in the case of alkene hydrosilation, it offers interesting selectivities in the hydrosilation reactions of alkynes and carbonyl compounds (*vide infra*). Nickel compounds, although in general less active, have been found to react very selectively in certain cases. The hydrosilation/dehydrosilation of alkynes gives 1,2-bissilylalkenes along with the normal hydrosilated products (equation 2).**[17]**

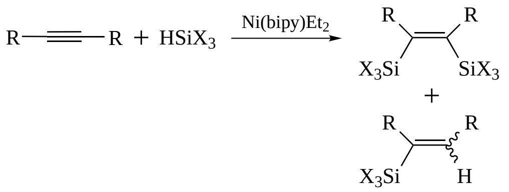

(2)

Nickel and palladium compounds have also been found to exhibit an interesting reactivity pattern in the hydrosilation of diynes (vide infra).

Other late transition metals used in special cases of hydrosilation include cobalt, iron, ruthenium (vide infra for reactions with alkynes), osmium, chromium, molybdenum, tungsten and copper.**[4]** Metallocenes (*see Metallocene Complexes*) of early transition metals and lanthanides have also been found to catalyze the hydrosilation of a number of unsaturated compounds including alkenes and esters (vide infra).

4 MECHANISMS OF METAL COMPLEX CATALYZED HYDROSILATION

Chalk and Harrod provided the first mechanistic explanation for the transition metal catalyzed hydrosilation as early as in 1965.**[18]** Their mechanism was derived from studies with Speier's catalyst and provided a general scheme, which could be used also for other transition metals. The catalytic cycle consists of an initial oxidative addition (*see Oxidative Addition*) of the Si–H bond, followed by coordination of the unsaturated molecule, a subsequent migratory insertion (*see Insertion*) into the metal-hydride bond and eventually a reductive elimination (*see Reductive Elimination*) (Scheme 3 lower cycle). The scheme provides an explanation for the observed Z-geometry in the hydrosilation of alkynes, which is a consequence of the *syn*-addition mechanism. The observation of silated alkenes as by-products in the hydrosilation of alkenes along with the lack of well-established stoichiometric examples of reductive elimination of alkylsilanes from alkyl silyl metal complexes

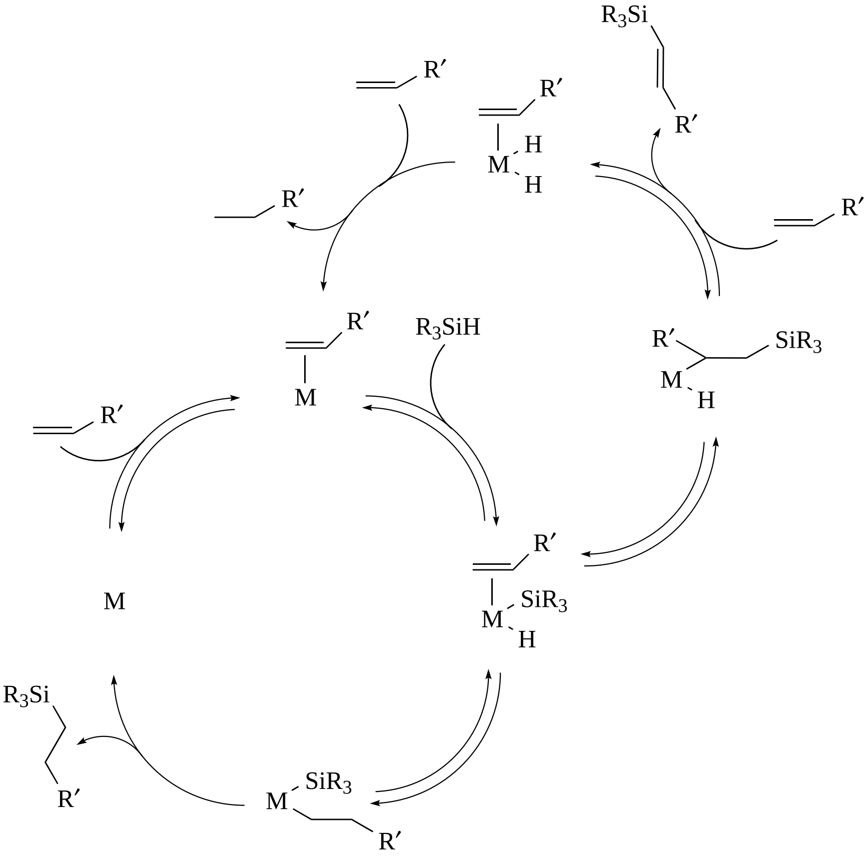

Scheme 3 The Chalk–Harrod mechanism for hydrosilation and a modified version

promoted the formulation of a modified Chalk–Harrod mechanism (Scheme 3 upper cycle).[19] The modification brings about the migratory insertion of the alkene into the metal-silyl bond. While a final reductive elimination of the thus formed β-silylalkyl metal hydride leads to the formation of the same hydrosilation product as in the original mechanistic proposal, a β-hydride elimination of this intermediate yields a silated alkene. The resulting metal dihydride is subsequentially functioning as a hydrogenation catalyst of alkenes present.

More recent studies have shown that a number of other mechanisms are operative in the hydrosilation process for different metals. Mechanistic proposals for early metals, lanthanides and actinides have been elaborated on. These involve a Chalk–Harrod like initial migratory insertion into a metal-hydride bond, followed by a σ-bond metathesis step (Scheme 4).[20] An alternative mechanism, however, was proposed for Group 4 metallocene catalysis, which involves a coordinated olefin, which undergoes σ-bond metathesis with the hydrosilane.[21]

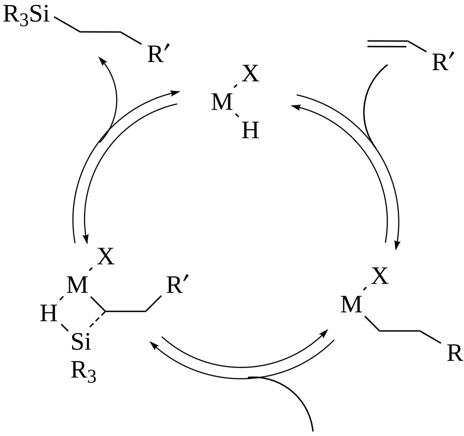

Scheme 4 Early metal hydrosilation mechanism involving σ-bond metathesis

Most recently an example of a ruthenium catalyzed selective addition of primary silanes to alkenes was shown to involve ruthenium silylenes as intermediates (Scheme 5).[22] A remarkable feature of this mechanism is, that the insertion of the alkene does not occur either into a metal-hydride or metal-silyl bond but directly into the Si–H bond of an activated silylene. The mechanism therefore resembles a hydroboration reaction and as a consequence displays anti-Markownikow selectivity.

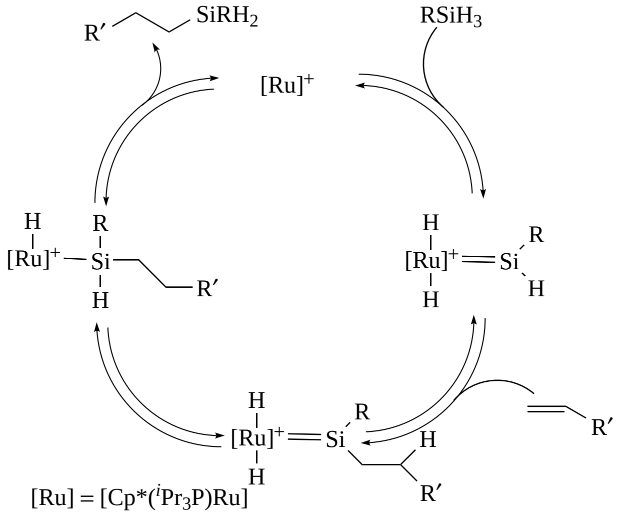

Scheme 5 Ruthenium silylene catalyzed hydrosilation of primary silanes[22]

5 SUBSTRATE TYPES

5.1 Alkenes

Alkenes are most easily hydrosilated by Speier's catalyst. The reaction of trichlorosilane with 1-alkenes usually gives terminal silanes in high yields. 2-Silylalkanes, as products of an initial double bond isomerization, are rarely encountered. Internal alkenes, however, give the expected internally silated product only as minor components as well as the 1-silylalkane. Interestingly, this alkene isomerization is not encountered when dimethylchlorosilane is used as the silating agent.[23] The importance of the right catalyst and ligand framework is illustrated in the reaction of trichlorosilane with styrene. This gives a mixture of α- and β-silyl isomers (35:65)[24] when catalyzed with $H_2PtCl_6 \cdot 6H_2O$. The addition of triphenylphosphane or pyridine to the same catalyst gives 92–95% of the β-isomer.[25] The α-isomer can be obtained almost exclusively employing either $[CpNi(CO)]_2$[26] or $NiCl_2 \cdot 2PPh_3 \cdot CuCl$.[24]

The hydrosilation reaction is highly compatible with a number of functional groups including ether, epoxide, acetal, ketone, ester, nitrile, amine, amide, nitro, carbamate, isocyanate, phosphate, sulfide, sulfone, and others.[4] As a consequence, it is a very attractive reaction for the construction of complex organic molecules. Sometimes allylic displacement is observed as a side reaction, especially in the reaction of allyl halides.[27]

Intramolecular hydrosilation was found to be a useful method for 1,2- or 1,3-chirality transfer. The hydrosilyl moiety is easily attached to a heteroatom such as oxygen or nitrogen and subsequently an intramolecular hydrosilation can be achieved. Depending on the substituents on the substrate and the catalyst used, either four- or five-membered rings can be obtained. Subsequent Tamao oxidation can be used to transform the Si–C bond into an alcohol (equation 3).[28,29]

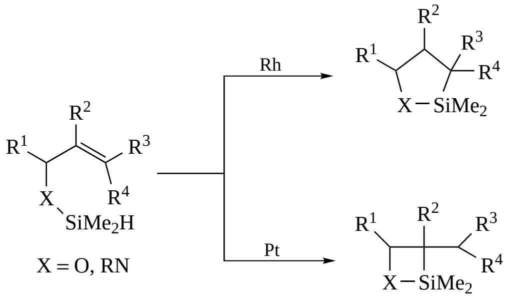

(3)

5.2 Alkynes

Alkynes can be advantageously hydrosilated to give vinylsilanes. The reaction with the triple bond is much faster than with an olefin, therefore a subsequent hydrosilation step to the disilylalkane is usually not encountered. This different reactivity can be exploited in the hydrosilation of vinylacetylene, where 1-silyl-1,3-butadiene is formed chemoselectively (equation 4).[30]

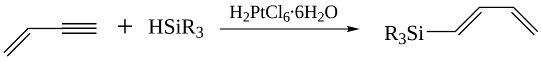

(4)

The hydrosilation of 1-alkynes can give either Z- or E-isomers (*see (E) & (Z) Isomers*) of the linear vinylsilane or the Markownikow product (equation 5). Reaction of 1-hexyne with trichlorosilane under platinum catalysis conditions gives a mixture of 1- and 2-silyl-1-hexene (78:22).[31] From the E-stereochemistry of the 1-silyl isomer, a *syn*-addition mechanism can be assumed.

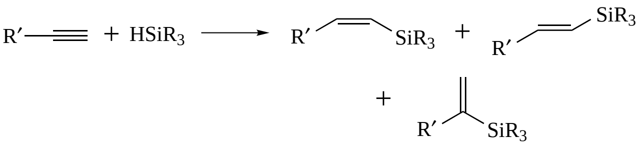

(5)

When employing Rh-COD catalysts, the choice of solvent and cocatalyst allows very good selectivities for either Z- or E-vinylsilanes (Table 1).[32]

A mechanistic rationale for the apparent *trans*-addition in some of these processes is shown in Scheme 6. Initial insertion of the alkyne into the metal-silyl bond yields an intermediate with an unfavorable interaction between the metal and the silyl group. Coordination of the vinyl part to the metal gives formally a metallacyclopropene.

Table 1 Hydrosilation of 1-hexyne with triethylsilane in the presence of rhodium catalysts[32]

Catalyst	Solvent (%)	Z (%)	E (%)	iso (%)
$[Rh(COD)Cl]_2$	DMF	97	1	2
$[Rh(COD)Cl]_2$	EtOH	94	4	2
$[Rh(COD)Cl]_2$	MeCN	36	33	31
$[Rh(COD)Cl]_2/2PPh_3$	MeCN	2	97	1
$[Rh(COD)_2]BF_4/2PPh_3$	MeCN	2	95	3
$[Rh(COD)_2]BF_4/2PPh_3$	EtOH	5	95	0
$[Rh(COD)_2]BF_4/2PPh_3$	Acetone	1	99	0

A consequence of this coordination mode is that the hybridization (*see Hybridization*) at the silyl bearing carbon changes from sp^2 to sp^3. In the course of de-coordination, the change back to sp^2 hybridization gives the sterically less hindered metal vinyl complex with E-geometry of the metal and the silyl group.[33,34] Final reductive elimination eventually yields the thermodynamically less stable Z-alkene.

Use of the cationic $CpRu(MeCN)_3PF_6$ catalyst allows very selective formation of the Markownikow product.[35] The same catalyst has also been applied with triethoxysilane and a desilylating agent (CuI/TBAF, AgF) as a method to convert internal alkynes to E-alkenes (equation 6).[36,37]

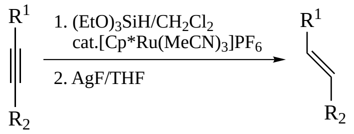

(6)

5.3 Carbonyl Compounds

The discovery of facile hydrosilation of carbonyl compounds employing Wilkinson's complex[38] $RhCl_3(PPh_3)_3$ initiated a broad interest in this synthetically useful reaction (equation 7).

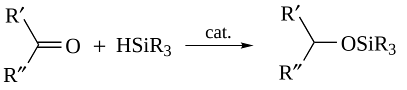

(7)

For aldehydes and ketones $RhCl_3(PPh_3)_3$ serves as an excellent catalyst.[39]

Some alkali metal and trialkylammonium salts also work as efficient catalysts for the reduction of aldehydes, ketones and esters with monohydrosilanes.[40,41] Among those salts CsF was found most effective. Esters are reduced to the alcohols (equation 8).

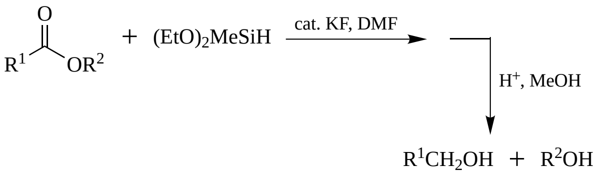

(8)

Transition metal catalyzed reduction of esters either to the silyl acetal ($R^1CH(OSiR)OR^2$) or complete reduction to the respective ethers could be accomplished using a manganese catalyst $[(Ph_3P)(CO)_4MnCOCH_3]$ and either a tertiary or a

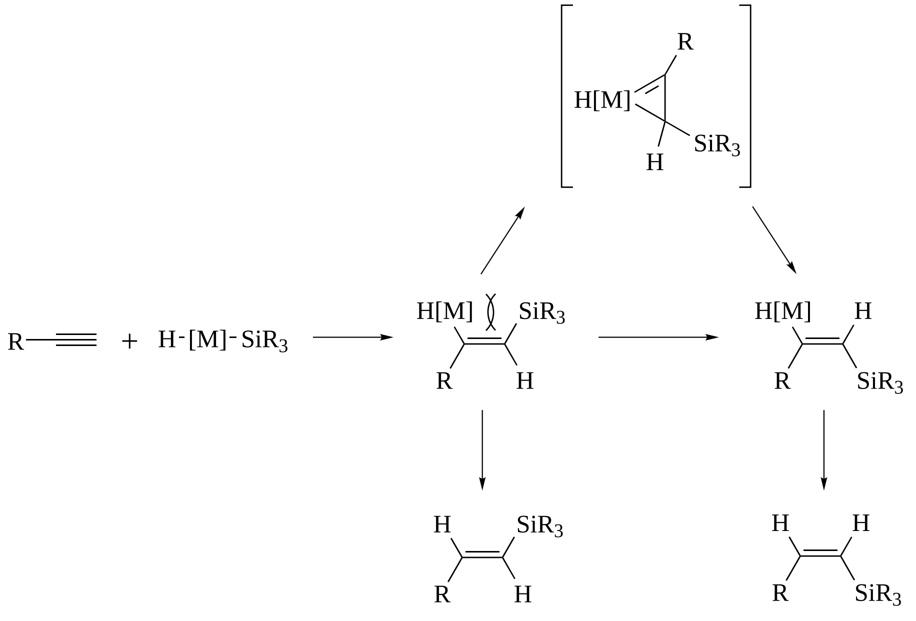

Scheme 6 Explanation for the formation of Z-vinylsilanes

primary silane (equation 9).[42]

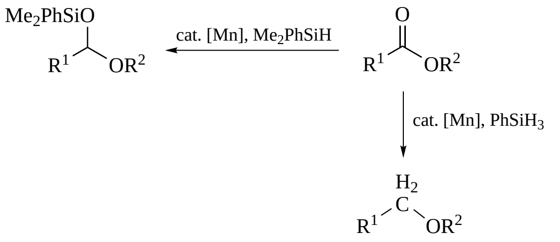
(9)

5.4 Unsaturated Nitrogen Containing Substrates

Substrates containing carbon nitrogen multiple bonds have received somewhat less attention. Nevertheless, imines can be converted to N-silylamines, again with $RhCl_3(PPh_3)_3$ being one of the most effective catalysts (equation 10).[2]

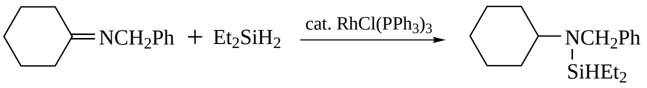
(10)

Oximes can also be reduced to N-silylamines under similar conditions.[43] The $PdCl_2$ catalyzed reaction of isocyanates with triethylsilane depends on the structure (R = alkyl or aryl) of the isocyanate. Either N- or C-silylformamides can be obtained (equation 11).[44]

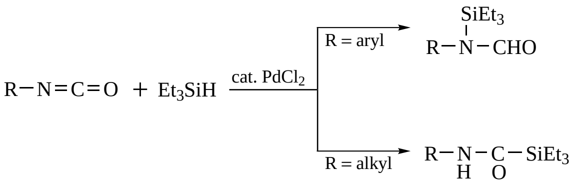
(11)

Carbodiimides can be converted to N-silylformamidines at elevated temperatures with $PdCl_2$ or with $RhCl_3(PPh_3)_3$ catalysts.[45]

The hydrosilation of aromatic nitriles is promoted by $Co_2(CO)_8$ to give *N*,*N*-bis(silyl)benzylamines (equation 12).[46] Aliphatic nitriles require higher temperatures. α,β-Unsaturated nitriles with substituents in α- and/or β-positions give *N*,*N*-bis(silyl)enamines as major products.[47]

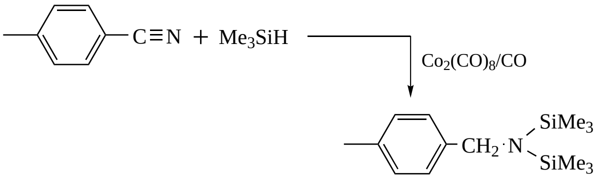
(12)

5.5 Conjugated Compounds

The hydrosilation of 1,3-dienes with Speier's catalyst often gives product mixtures of 1,2 and 1,4-addition, with the latter usually being the main product.[48] In contrast to this, the palladium-catalyzed reaction with trichlorosilane gives the 1,4-addition product exclusively. If trimethylsilane is used, an adduct with two equivalents of diene can be obtained with an excellent yield (equation 13).[49,50]

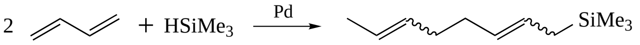
(13)

Cyclic dienes are hydrosilated by 1,4-addition using Pd[51] or Ni[52] catalysts (equation 14).

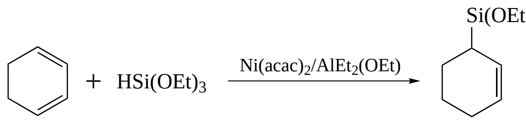
(14)

The hydrosilation of 1,4-bis(trimethylsilyl)-1,3-butadiyne gives either enynes as the product of monohydrosilation or allenes as deriving from di-hydrosilation (equation 15).[53]

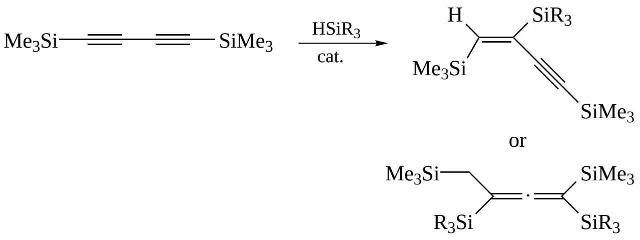
(15)

α,β-Unsaturated carbonyl compounds can be hydrosilated either in 1,2- or 1,4-addition to give either silyl enol ethers or silyl allyl ethers. Using Wilkinson's catalyst, it was found that the regioselectivity (*see Regioselectivity*) of this reaction was mainly governed by the silane used. While monohydrosilanes promote 1,4-addition, the 1,2-addition process is observed with di- and trihydrosilanes (equation 16).[54]

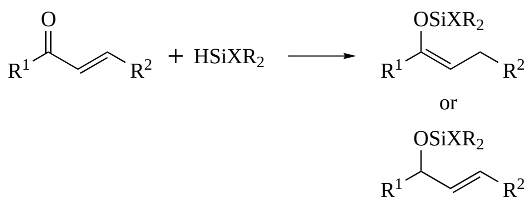
(16)

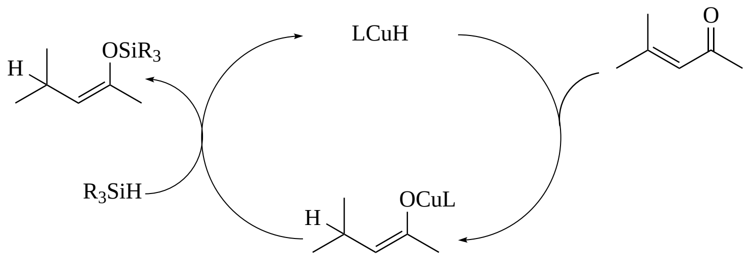

Scheme 7 Copper promoted formal enolate addition of hydrosilane

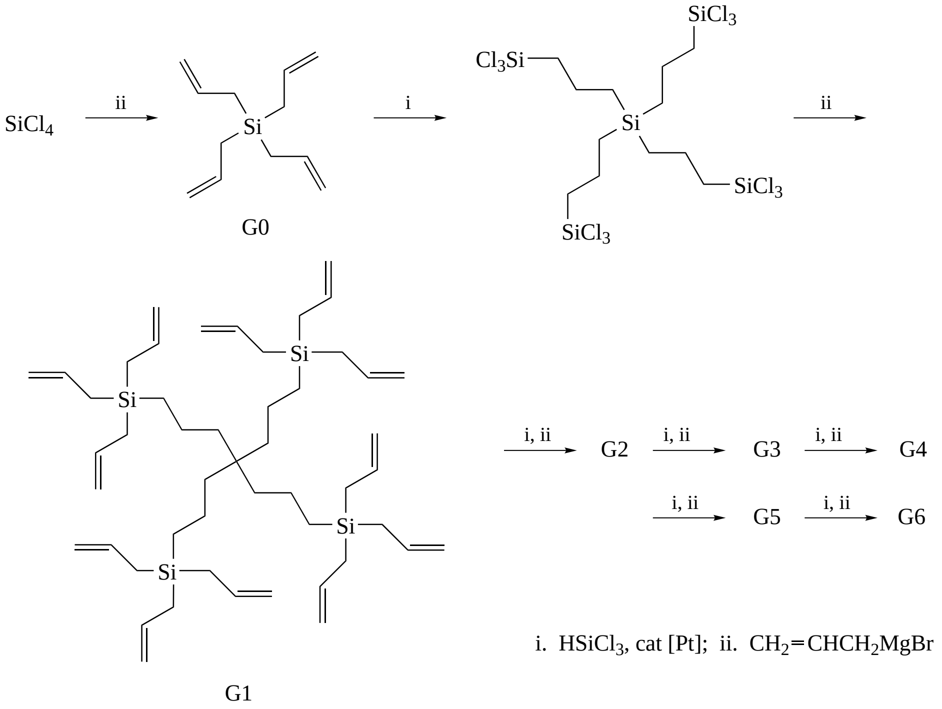

Scheme 8 Dendrimer synthesis employing hydrosilation/allylation chemistry

The use of copper catalysts in the presence of silanes provides another possibility to achieve 1,4-addition selectively.[55,56] The active species is likely to be a copper hydride, which reacts to give a copper enolate, which undergoes a σ-bond metathesis step with the hydrosilane (Scheme 7).[57]

5.6 Dendrimers, Polymers (*See Polymer*) and Other Macromolecules

The high degree of completion and selectivity and the high yields make the hydrosilation reaction an ideal candidate for the buildup of dendrimeric structures. The combination with allylation, vinylation, and alkynylation reactions provides very efficient syntheses of carbosilane dendrimers (Scheme 8).[58]

Numerous examples are known in which hydrosilation reactions are used to prepare monomers for polymerization experiments. The reaction itself can also be used for a polymerization process. This can be accomplished as the hydrosilation of alkenes either using a single-source precursor (equation 17)[59] or a two-component mixture (equation 18).[60]

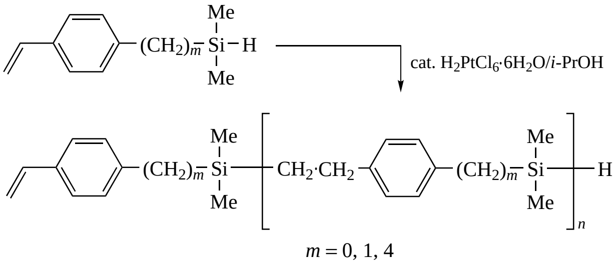

$$\text{CH}_2{=}\text{CH}{-}C_6H_4{-}(CH_2)_m{-}\overset{\text{Me}}{\underset{\text{Me}}{\text{Si}}}{-}H \xrightarrow{\text{cat. } H_2PtCl_6{\cdot}6H_2O/i\text{-PrOH}} \text{CH}_2{=}\text{CH}{-}C_6H_4{-}(CH_2)_m{-}\overset{\text{Me}}{\underset{\text{Me}}{\text{Si}}}\left[{-}CH_2{\cdot}CH_2{-}C_6H_4{-}(CH_2)_m{-}\overset{\text{Me}}{\underset{\text{Me}}{\text{Si}}}{-}\right]_n H$$

$m = 0, 1, 4$

(17)

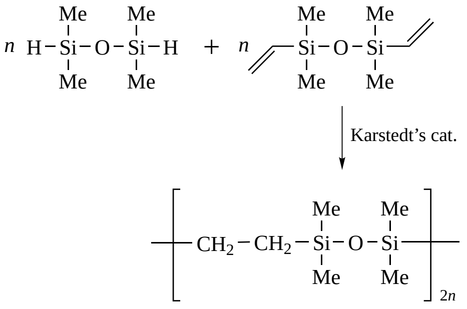

(18)

Also silylacetylenes undergo self-polymerization under hydrosilation conditions to give high molecular weight polymers (equation 19).[61]

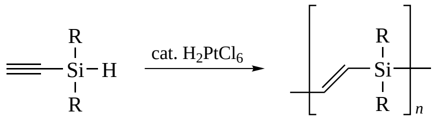

(19)

The functionalization of polymers is another useful feature of the hydrosilation reaction. The introduction of highly fluorinated alkyl chains by the hydrosilation of Si–H groups of the polymer with fluorinated alkenes is a typical example.[62]

Poly(phenylsilanes) obtained by the dehydrocoupling polymerization of phenylsilane undergo AIBN initiated free radical hydrosilation with alkenes, ketones and aldehydes.[63] Cross-linking and branching of polymers can also be easily accomplished using hydrosilation.

Treatment of C_{60} with poly(hydrosiloxane) in the presence of Karstedt's catalyst proceeds to give C_{60}-polysiloxanes (equation 20).[64]

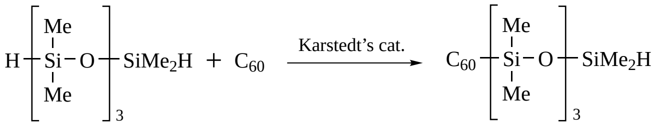

$$H\left[\overset{\text{Me}}{\underset{\text{Me}}{\text{Si}}}-\text{O}\right]_3\text{SiMe}_2\text{H} + C_{60} \xrightarrow{\text{Karstedt's cat.}} C_{60}\left[\overset{\text{Me}}{\underset{\text{Me}}{\text{Si}}}-\text{O}\right]_3\text{SiMe}_2\text{H} \quad (20)$$

6 ENANTIOSELECTIVE CATALYTIC HYDROSILATION

During the process of hydrosilation two prochiral sp^2 hybridized atoms are converted to potentially chiral (*see Chiral*) sp^3 atoms. This opens up the possibility for asymmetric catalysis. The use of prochiral silanes of the type $RR'SiH_2$ also allows for the generation of chiral silanes.

6.1 Enantioselective (*See Enantioselectivity*) Hydrosilation of Alkenes

The asymmetric hydrosilation of prochiral alkenes has been a challenging subject, which eventually experienced a breakthrough with the introduction of a palladium catalyst, which employs the MOP-ligand (**1**).[65]

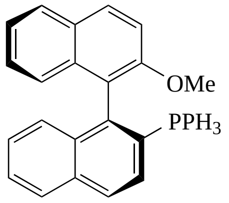

(**1**)

Using this system, 1-alkenes can be hydrosilated with excellent enantioselectivities (e.e. 91–97%). Subsequent Tamao oxidation to the respective secondary alcohol occurs under retention of configuration (equation 21).

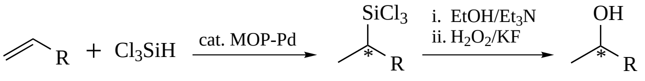

(21)

Also norbornene and related systems,[66] as well as dihydrofuranes,[67] have been hydrosilated with good enantioselectivities with similar MOP ligands. Intramolecular rhodium catalyzed asymmetric hydrosilations have been achieved with good enantioselectivities, for example with *meso*- or other allylsilylethers.[68,69]

6.2 Enantioselective Hydrosilation of Ketones and Other Carbonyl Compounds

Asymmetric hydrosilation of prochiral ketones constitutes a formal reduction of the ketone to the secondary alcohol. Initial studies were driven by the apparent similarity of the hydrosilation with hydrogenation. Accordingly similar ligands such as DIOP, Chiraphos and BINAP related compounds (*see* ***P-donor Ligands***) were used. A breakthrough was achieved using bis(oxazolinyl)pyridine (**2**) ligands and Rh(III) catalysts.[70] A chiral titanocene catalyst (*R*,*R*)-(EBTHI)Ti$(OR)_2$ (**3**) was also found to give good to excellent enantioselectivities.[71]

The synthesis of optically active amines by hydrosilation of imines was achieved in excellent e.e.s using a related catalyst system: (*R*,*R*)-(EBTHI)TiH. This is conveniently generated

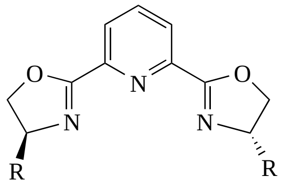

(**2**)

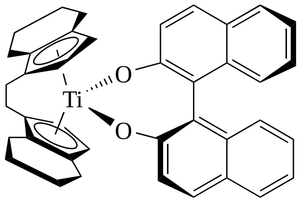

(**3**)

from (R,R)-(EBTHI)TiF_2 by reduction with $PhSiH_3$.[72] Hydrosilation of prochiral imine N-oxides (nitrones) through the use of a Ru-binap catalyst system gives the respective hydroxylamines in high enantiomeric purity.[73] The attachment of a phosphinyl moiety to an imine nitrogen provides excellent asymmetric induction in the reduction to the amine when using a copper-hydride catalyst and a chiral phosphine.[74]

6.3 Enantioselective Hydrosilation of Conjugated Systems

Palladium-catalyzed asymmetric hydrosilation of cyclic and linear 1,3-dienes proceeds as 1,4-addition with moderate to good enantioselectivities.[75] α-Ketoesters such as pyruvates can be hydrosilated with Rh(I)-(+)-DIOP catalysts to yield lactates with much better optical purity than simpler ketones (equation 22).[76] This effect is likely to be caused by a ligand function of the ester moiety in the transition state.

$$\mathrm{MeCOCOOPr}^n \xrightarrow{\substack{\alpha\text{-NpPhSiH}_2\\ (-)\text{-DIOP-Rh(I)}}} \xrightarrow{\mathrm{H^+/MeOH}} \underset{85\%\ \text{e.e.}}{\overset{*}{\mathrm{MeCH(OH)COOPr}^n}} \qquad (22)$$

Asymmetric reduction of α, β-unsaturated esters, lactones or lactames can be effected with copper-hydride catalysts and chiral phosphanes such as various BINAP related compounds in excellent yields and enantioselectivities (equation 23).[77,78] As the hydrosilane component, polymethylhydrosiloxane (PMHS) is frequently used for this reaction.

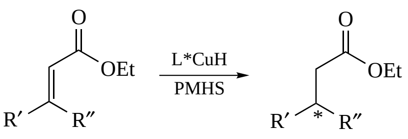

(23)

6.4 Asymmetric Synthesis of Chiral Silanes

The use of prochiral secondary silanes in the asymmetric hydrosilation can give an optically pure silylether, which can be alkylated with a Grignard reagent with retention of the configuration (equation 24).[79]

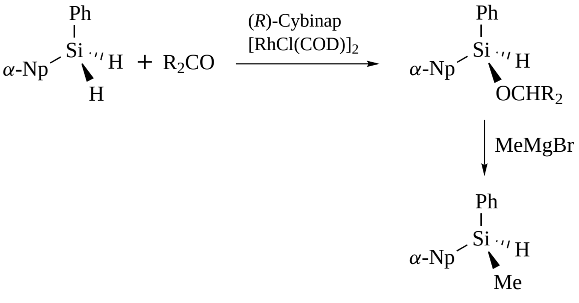

98–99% e.e.

(24)

7 RELATED REACTIONS OF SILANES

The main side reaction of the hydrosilation reaction is the dehydrogenating silation reaction. Under certain conditions this reaction can be the main or even the exclusive reaction. The reaction can occur, not only with alkenes, but also with almost all known substrates. It achieves vinylsilanes from alkenes,[80] silylalkynes from alkynes,[81] and silyl enol ethers from ketones.[82]

Strained silacarbocycles exhibit a similar reactivity as an unsaturated molecule. Therefore the addition of a hydrosilane to a Si–C σ-bond can be accomplished giving rise to the stereospecific formation of trisilanes (equation 25).[83]

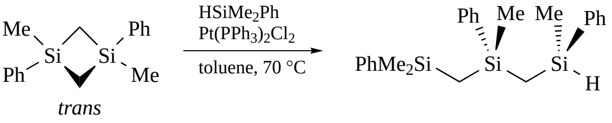

(25)

The dehydrogenating polymerization of hydrosilanes was found to be catalyzed by Group 4 metallocene alkyl and silyl derivatives (equation 26).[84] For zirconocene and hafnocene catalysts, the reaction was found to proceed via σ-bond metathesis steps.[85]

$$n\mathrm{PhSiH_3} \xrightarrow[-(n-1)\mathrm{H_2}]{\text{cat. }\mathrm{Cp_2TiMe_2}} n\mathrm{PhSiH_2}\!-\!(\mathrm{PhSiH})_{n-2}\mathrm{SiH_2Ph} \qquad (26)$$

Similar coupling reactions have also been reported with late metals such as platinum and nickel.[86,87]

As the hydrosilation reaction is related to hydrogenation, it also bears a certain relationship to the hydroformylation (*see Hydroformylation*) reaction. The $Co_2(CO)_8$ catalyzed process, which formylates an alkene in the presence of a hydrosilane instead of hydrogen, gives silyl enol ethers in excellent yields (equation 27).[88] The hydrosilane/CO system can also react with cyclic ethers or aldehydes to give ω- or

α-silyloxyaldehydes (equation 28).[89,90]

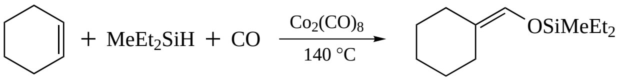

(27)

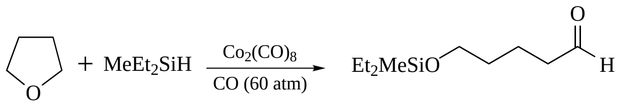

(28)

8 TRANSITION METAL-SILYL COMPLEXES

The discovery of the hydrosilation reaction has greatly stimulated research on transition metal-silyl complexes. Currently, there are examples of silyl complexes with almost every transition metal.[91–93] Silyl hydride complexes are of special interest with respect to the chemistry of the hydrosilation reactions.[94] Such compounds can be seen as the products of oxidative addition into the Si–H bond and thus are intermediates in hydrosilation reactions following the Chalk–Harrod mechanism.

9 RELATED ARTICLES

Asymmetric Synthesis by Homogeneous Catalysis; Coordination & Organometallic Chemistry: Principles; Hydroboration Catalysis; Hydrogenation & Isomerization of Alkenes; Mechanisms of Reaction of Organometallic Complexes; Silicon: Organosilicon Chemistry.

10 REFERENCES

1. B. Marciniec, *Silicon Chem.*, 2002, **1**, 155.
2. I. Ojima, in 'The Chemistry of Organic Silicon Compounds', eds. Z. Rappoport and Y. Apeloig, Wiley, New York, 1998, Vol. 2, Chap. 29.
3. B. Marciniec ed., 'Comprehensive Handbook on Hydrosilylation', Pergamon Press, Oxford, 1992.
4. I. Ojima, in 'The Chemistry of Organic Silicon Compounds', eds. S. Patai and Z. Rappoport, Wiley, New York, 1989, Chap. 25.
5. L. H. Sommer, E. W. Pietrusza, and F. C. Whitmore, *J. Am. Chem. Soc.*, 1947, **69**, 188.
6. J. L. Speier, J. A. Webster, and G. H. Barnes, *J. Am. Chem. Soc.*, 1957, **79**, 974.
7. B. Marciniec, in 'Applied Homogeneous Catalysis with Organometallic Compounds', 2nd edn., eds. B. Cornils and W. A. Herrmann, Wiley-VCH, Weinheim, 2002, Vol. 1, Chap. 2.6.
8. H. Sakurai, in 'Free Radicals', ed. J. K. Kochi, Wiley, New York, 1973, Vol. 2, p. 741.
9. C. Chatgilialoglu, 'Organosilanes in Radical Chemistry', Wiley, Chichester, 2004.
10. C. Chatgilialoglu, C. Ferreri, and T. Gimisis, in 'The Chemistry of Organic Silicon Compounds', eds. Z. Rappoport and Y. Apeloig, Wiley, New York, 1998, Vol. 2, Chap. 25.
11. K. Yamamoto and M. Takemae, *Synlett*, 1990, 259.
12. Y.-S. Song, B. R. Yoo, G.-H. Lee, and I. N. Jung, *Organometallics*, 1999, **18**, 3115.
13. N. Asao, T. Sudo, and Y. Yamamoto, *J. Org. Chem.*, 1996, **61**, 7654.
14. J. L. Speier, *Adv. Organomet. Chem.*, 1979, **17**, 407.
15. B. Karstedt, US Patent 3 775 452, 1973.
16. R. A. Benkeser, S. Dunny, G. S. Li, P. G. Nerlekar, and S. D. Work, *J. Am. Chem. Soc.*, 1968, **90**, 1871.
17. K. Tamao, N. Miyake, Y. Kiso, and M. Kumada, *J. Am. Chem. Soc.*, 1975, **97**, 5603.
18. A. J. Chalk and J. F. Harrod, *J. Am. Chem. Soc.*, 1965, **87**, 16.
19. S. B. Duckett and R. H. Perutz, *Organometallics*, 1992, **11**, 90.
20. T. I. Gountchev and T. D. Tilley, *Organometallics*, 1999, **18**, 5661.
21. M. R. Kesti and R. M. Waymouth, *Organometallics*, 1992, **11**, 1095.
22. P. B. Glaser and T. D. Tilley, *J. Am. Chem. Soc.*, 2003, **125**, 13640.
23. R. A. Benkeser and W. C. Muench, *J. Am. Chem. Soc.*, 1973, **95**, 285.
24. E. W. Bennet and P. J. Orenski, *J. Organomet. Chem.*, 1971, **28**, 137.
25. M. Capka, P. Svoboda, and J. Hetflejs, *Collect. Czech. Chem. Commun.*, 1973, **38**, 3830.
26. P. Svoboda, P. Sedlmayer, and J. Hetflejs, *Collect. Czech. Chem. Commun.*, 1973, **38**, 1783.
27. V. F. Mironov and V. V. Nepomnina, *Izv. Akad. Nauk SSSR, Ser. Khim.*, 1960, 2140.
28. K. Tamao, Y. Nakagawa, and Y. Ito, *Organometallics*, 1993, **12**, 2297.
29. K. Tamao, Y. Nakagawa, and Y. Ito, *J. Org. Chem.*, 1990, **55**, 3438.
30. A. D. Petrov and S. I. Sadykh-Zade, *Izv. Akad. Nauk SSSR, Ser. Khim.*, 1958, 513.
31. R. A. Benkeser, R. F. Cunico, S. Dunny, P. R. Jones, and P. G. Nerlekar, *J. Org. Chem.*, 1967, **32**, 2634.
32. R. Takeuchi and N. Tanouchi, *J. Chem. Soc., Perkin Trans. 1*, 1994, 2909.
33. I. Ojima, N. Clos, R. L. Donovan, and P. Ingallina, *Organometallics*, 1990, **9**, 3127.

34. R. S. Tanke and R. H. Crabtree, *J. Am. Chem. Soc.*, 1990, **112**, 7984.

35. B. M. Trost and Z. T. Ball, *J. Am. Chem. Soc.*, 2001, **123**, 12726.

36. B. M. Trost, Z. T. Ball, and T. Jöge, *J. Am. Chem. Soc.*, 2002, **124**, 7922.

37. A. Fürstner and K. Radkowski, *J. Chem. Soc., Chem. Commun.*, 2002, 2182.

38. I. Ojima, M. Nihonyanagi, and Y. Nagai, *J. Chem. Soc., Chem. Commun.*, 1972, 938.

39. I. Ojima, M. Nihonyanagi, T. Kogure, M. Kumagai, S. Horiuchi, and K. Nakatsugawa, *J. Organomet. Chem.*, 1975, **94**, 449.

40. J. Boyer, R. J. P. Corriu, R. Perz, M. Porier, and C. Reye, *Synthesis*, 1981, 558.

41. C. Chuit, R. J. P. Corriu, R. Perz, and C. Reye, *Synthesis*, 1982, 981.

42. Z. Mao, B. T. Gregg, and A. R. Cutler, *J. Am. Chem. Soc.*, 1995, **117**, 10139.

43. H. Brunner and R. Becker, *Angew. Chem., Int. Ed. Engl.*, 1985, **23**, 222.

44. I. Ojima and S. Inaba, *J. Organomet. Chem.*, 1977, **140**, 97.

45. I. Ojima, S. Inaba, and Y. Nagai, *J. Organomet. Chem.*, 1974, **72**, C11.

46. T. Murai, T. Sakane, and S. Kato, *Tetrahedron Lett.*, 1985, **26**, 5145.

47. T. Murai, T. Sakane, and S. Kato, *J. Org. Chem.*, 1990, **55**, 449.

48. Z. V. Belyakova, M. G. Pomerantseva, K. K. Popkov, L. A. Efemova, and S. A. Golubtsov, *Zh, Obshch. Khim.*, 1972, **42**, 889.

49. K. Yamamoto, T. Hayashi, and M. Kumada, *J. Organomet. Chem.*, 1971, **28**, C37.

50. W. Fink, *Helv. Chim. Acta*, 1971, **54**, 1304.

51. I. Ojima, M. Kumagai, and Y. Miyazawa, *Tetrahedron Lett.*, 1977, **18**, 1385.

52. A. J. Cornish, M. F. Lappert, and T. A. Nile, *J. Organomet. Chem.*, 1977, **132**, 133.

53. T. Kusumoto, K. Ando, and T. Hiyama, *Bull. Chem. Soc. Jpn.*, 1992, **65**, 1280.

54. I. Ojima, T. Kogure, and Y. Nagai, *Tetrahedron Lett.*, 1972, **13**, 5035.

55. B. H. Lipshutz, J. Keith, P. Papa, and R. Vivian, *Tetrahedron Lett.*, 1998, **39**, 4627.

56. A. Mori, A. Fujita, H. Kajiro, Y. Nishihara, and T. Hiyama, *Tetrahedron*, 1999, **55**, 4573.

57. D. H. Appella, Y. Moritani, R. Shintani, E. M. Ferreira, and S. L. Buchwald, *J. Am. Chem. Soc.*, 1999, **121**, 9473.

58. A. W. van der Made and P. W. N. M. van Leeuwen, *J. Chem. Soc., Chem. Commun.*, 1992, 1400.

59. S. Itsuno, D. Chao, and K. Ito, *J. Polym. Sci., Part A: Polym. Chem.*, 1993, **31**, 287.

60. P. R. Dvornic, V. V. Gerov, and M. M. Govedarica, *Macromolecules*, 1994, **27**, 9595.

61. Y. Pang, S. Ijadi-Magsoodi, and T. J. Barton, *Macromolecules*, 1993, **26**, 5671.

62. Y. Chujo and J. E. Mcgrath, *J. Macromol. Sci., Pure, Appl. Chem.*, 1995, **A32**, 29.

63. Y.-L. Hsiao and R. M. Waymouth, *J. Am. Chem. Soc.*, 1994, **116**, 9779.

64. R. West, M. Miller, H. Takahshi, T. Gunji, and K. Oka, *Polym. Prepr. (Am. Chem. Soc., Div. Polym. Chem.)*, 1993, **34**, 227.

65. Y. Uozumi and T. Hayashi, *J. Am. Chem. Soc.*, 1991, **113**, 9887.

66. Y. Uozumi, S. Y. Lee, and T. Hayashi, *Tetrahedron Lett.*, 1992, **33**, 7185.

67. Y. Uozumi and T. Hayashi, *Tetrahedron Lett.*, 1993, **34**, 2335.

68. K. Tamao, T. Tohma, N. Inui, O. Nakayama, and Y. Ito, *Tetrahedron Lett.*, 1990, **31**, 7333.

69. S. H. Bergens, P. Noheda, J. Whelan, and B. Bosnich, *J. Am. Chem. Soc.*, 1992, **114**, 2121.

70. H. Nishiyama, M. Kondo, T. Nakamura, and K. Itoh, *Organometallics*, 1991, **10**, 500.

71. M. B. Carter, B. Schiøtt, A. Gutiérrez, and S. L. Buchwald, *J. Am. Chem. Soc.*, 1994, **116**, 11667.

72. X. Verdaguer, U. E. W. Lange, M. T. Reding, and S. L. Buchwald, *J. Am. Chem. Soc.*, 1996, **118**, 6784.

73. S. Murahashi, S. Watanabe, and T. Shiota, *J. Chem. Soc., Chem. Commun.*, 1994, 725.

74. B. H. Lipshutz and H. Shimizu, *Angew. Chem.*, 2004, **116**, 2278.

75. T. Hayashi, Y. Matsumoto, I. Morikawa, and Y. Ito, *Tetrahedron: Asymmetry*, 1990, **1**, 151.

76. I. Ojima, T. Kogure, and M. Kumagai, *J. Org. Chem.*, 1977, **42**, 1671.

77. G. Hughes, M. Kimura, and S. L. Buchwald, *J. Am. Chem. Soc.*, 2003, **125**, 11253.

78. B. H. Lipshutz, J. M. Servesko, and B. R. Taft, *J. Am. Chem. Soc.*, 2004, **126**, 8352.

79. T. Ohta, M. Ito, A. Tsuneto, and H. Takaya, *J. Chem. Soc., Chem. Commun.*, 1994, 2525.

80. Y. Seki, K. Takeshita, K. Kawamoto, S. Murai, and N. Sonoda, *J. Org. Chem.*, 1986, **51**, 3890.

81. M. A. Esteruelas, M. Oliván, L. A. Oro, and J. I. Tolosa, *J. Organomet. Chem.*, 1995, **487**, 143.

82. H. Sakurai, K. Miyoshi, and Y. Nakadaira, *Tetrahedron Lett.*, 1977, **18**, 2671.

83. K. Hayakawa, M. Tachikawa, T. Suzuki, N. Choi, and M. Murakami, *Tetrahedron Lett.*, 1995, **36**, 3181.

84. C. Aitken, J. F. Harrod, and E. Samuel, *J. Organomet. Chem.*, 1985, **279**, C11.

85. T. D. Tilley, *Acc. Chem. Res.*, 1993, **26**, 22.

86. B. P. S. Chauhan, T. Shimizu, and M. Tanaka, *Chem. Lett.*, 1997, 785.
87. L. F. Groux and D. Zargarian, *Organometallics*, 2001, **20**, 3811.
88. S. Murai and N. Sonoda, *Angew. Chem., Int. Ed. Engl.*, 1979, **18**, 837.
89. Y. Seki, S. Murai, Y. Yamamoto, and N. Sonoda, *Angew. Chem., Int. Ed. Engl.*, 1977, **18**, 789.
90. S. Murai, T. Kato, N. Sonoda, Y. Seki, and K. Kawamoto, *Angew. Chem., Int. Ed. Engl.*, 1977, **18**, 393.
91. M. S. Eisen, in 'The Chemistry of Organic Silicon Compounds', eds. Z. Rappoport and Y. Apeloig, Wiley, New York, 1998, Vol. 2, Chap. 35.
92. T. D. Tilley, in 'The Silicon-Heteroatom Bond', eds. S. Patai and Z. Rappoport, Wiley, New York, 1991, Chap. 10.
93. T. D. Tilley, in 'The Chemistry of Organic Silicon Compounds', eds. Z. Rappoport and Y. Apeloig, Wiley, New York, 1989, Chap. 24.
94. J. Y. Corey and J. Braddock-Wilking, *Chem. Rev.*, 1999, **99**, 175.

Hypervalent Compounds

G. Sean McGrady[1] & Jonathan W. Steed[2]
[1]*University of New Brunswick, Fredericton, NB, Canada*
[2]*University of Durham, Durham, UK*

Based in part on the article Hypervalent Compounds by Michael Lattman which appeared in the Encyclopedia of Inorganic Chemistry, First Edition.

1	Introduction and Background	1
2	The Hypervalent Bond: Geometry and Description	2
3	Synthesis and Stability of Hypervalent Compounds	5
4	Spectroscopy and Diffraction as Structural Probes	9
5	Pentacoordinate and Related Structures	10
6	Reactivity of Hypervalent Compounds	12
7	Hypervalent Intermediates and Transition States	14
8	Inter-ligand Hypervalent Interactions	17
9	Other Hypervalent Species	18
10	Related Articles	19
11	References	19

Glossary

Phosphoranes: tbp 10-P-5 phosphorus(V) molecules
Phosphoranides: pseudo-tbp 10-P-4 phosphorus(III) anions
Pseudo-oct: a structure in which one or two legs of the oct is occupied by lone pairs of electrons
Pseudo-tbp: a structure in which one, two, or three legs of the tbp is occupied by lone pairs of electrons
Sulfuranes: pseudo-tbp 10-S-4 sulfur(IV) molecules

Abbreviations

ap = Apical; ax = Axial; ba = Basal; 3c/4e = Three-center/four-electron; eq = Equatorial; MO = Molecular orbital; NBS = *N*-bromosuccinimide; oct = Octahedron or octahedral; R_f = Perfluorinated hydrocarbon; sp = Square pyramid or square pyramidal; tbp = Trigonal bipyramid or trigonal bipyramidal; VB = Valence bond.

---

1 INTRODUCTION AND BACKGROUND

Hypervalent molecules and ions are fascinating species, since they appear to violate the traditional Lewis–Langmuir theory of bonding by expanding the valence shell of a main group element. Although species such as PCl_5, ICl_3, and $SeCl_4$ were first reported almost two centuries ago, appropriate models to describe the bonding in these molecules have only been developed recently.[1] Whilst the term hypervalent is widely used – and often misused – there is currently no universally accepted definition of the word. Thus, it is instructive briefly to explain the origin of the term before giving the working definition for this article.

1.1 The Phenomenon of Hypervalency

In his 1923 monograph, Lewis[2] defined the valence of an atom in a molecule as '... the number of electron pairs which it shares with other atoms'. Lewis recognized that, through a combination of lone or nonbonding pairs and shared or bonding pairs, many atoms (other than hydrogen) in molecules achieve a total of eight electrons in the outermost shell; he called this the 'rule of eight'. Langmuir coined the now more familiar term 'octet'.[2,3]

Since it was proposed, the octet rule has caused misunderstanding and confusion about the status of hypervalent molecules, and is often taken to imply that the bonding in hypervalent molecules is distinct from that in those that obey the rule. It is an empirical rule based on the formulas of most compounds known in the early part of last century, and there is no reason why there should not be exceptions such as SF_6 and PCl_5, as was indeed recognized by Lewis.

The term hypervalent was introduced in a classic paper by Musher[1] in 1969 to categorize 'molecules and ions formed by elements in Groups 15–18 of the periodic table in any of their valences other than their lowest stable chemical valence of 3, 2, 1, and 0 respectively'. This paper led to a surge of interest in both the theoretical and experimental aspects of species that appear to have 'expanded octets.'According to Musher, these species involve atoms '... which exceed the number of valences allowed them by the traditional theory, and thus utilize more electron pairs of bonding than provide stability in the Lewis–Langmuir theory'. Thus, molecules such as SF_6 and PCl_5 are hypervalent. In addition, according to this definition, F_3PO, F_2SO, and even Me_3NO, are also hypervalent.

If hypervalent literally means exceeding the lowest chemical valence, then even NH_4^+ is hypervalent, despite the fact that the Lewis–Langmuir theory easily accounts for its stability. Furthermore, if the definition of hypervalency is restricted to Groups 15–18, then this artificially excludes species such as SiF_5^- and SiF_6^{2-}, which are isoelectronic and isostructural with PF_5 and SF_6, respectively. The ambiguities in the original definition have led to several changes. Today, no one would regard NH_4^+ as hypervalent, while those that consider PF_5 and SF_6 hypervalent would classify SiF_5^- and SiF_6^{2-} in the same way.

At this point, it is clear that whether or not a species is hypervalent depends not just on valence, but on the total number of valence electrons: a hypervalent molecule or ion features an atom surrounded by a total of more than eight valence electrons – both bonding and nonbonding. This definition is consistent with the word hypervalent, since the expanded octet is a result of increased valence or bond formation. The major difficulty in this definition is how to count electrons.

Can we use the Lewis structure as the determining factor? If so, there can be no doubt about the hypervalency of PF_5 (**1**) and SF_6 (**2**). But what about F_3PO (**3**) and F_2SO (**4**)?

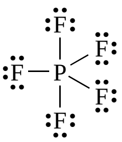
(**1**)

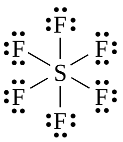
(**2**)

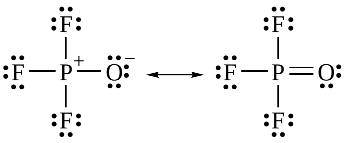
(**3**)

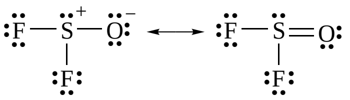
(**4**)

While many chemists would draw double bonds to oxygen because of their knowledge of structure and reactivity, perfectly acceptable nonhypervalent (octet-obeying) Lewis structures can also be drawn. In addition, the Lewis structure of $SO_4{}^{2-}$ (**5**) can be drawn with only single bonds between sulfur and oxygen; however, there is little doubt that significant sulfur–oxygen π-bonding exists. An extreme example of this conundrum is the conclusion that the ion $[F_3CO]^-$ is hypervalent.**4** The carbon–oxygen bond in this ion is very short, and ab initio molecular orbital (MO) calculations show negative hyperconjugation and high polarity in this bond, implying significant double bond character and a structure for the ion that can be represented as $[F_3C{=}O]^-]$.

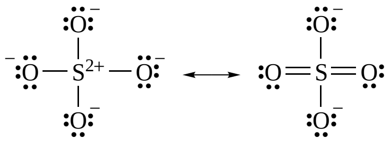
(**5**)

1.2 Definition of Hypervalency

Initially, hypervalent molecules like PCl_5 and SF_6 were described in terms of sp^3d^n hybrid orbitals, in an extension of the sp^n orbital description used to characterize molecules that obey the octet rule. However, ab initio calculations have shown that d orbitals play only a minor role in the bonding of hypervalent molecules.**5** An alternative approach proposed by Pauling invoked combinations of resonance structures involving four covalent bonds and one or more additional ionic bonds, as shown in Scheme 1 for PF_5.

Perhaps the most useful definition of hypervalency makes use of the three-center/four-electron (3c/4e) bond.**6** Indeed, Musher in his original paper detailed this type of bonding based on the models of Rundle and Pimentel. The 3c/4e bond approach has several advantages: (1) it is easily recognizable from geometries derived from simple single-bonded Lewis structures based on Valence-Shell Electron Pair Repulsion Model rules (VSEPR) (*see Valence Shell Electron Pair Repulsion Model*); (2) strategies to stabilize hypervalent bonding are similar for each group; and (3) most inorganic chemists recognize this type of bond.

The 3c/4e hypervalent bond is used to classify the molecules and ions discussed throughout most of this article. Section 9.3 briefly mentions some common species referred to as hypervalent that do not fall into this classification.

2 THE HYPERVALENT BOND: GEOMETRY AND DESCRIPTION

2.1 Theoretical Description

The hypervalent bond is found in molecules and ions in which an atom is formally surrounded by more than an octet of electrons and contains a linear three-center arrangement of atoms. One example is PF_5, which has a trigonal bipyramidal (tbp) geometry. The traditional valence bond (VB) approach

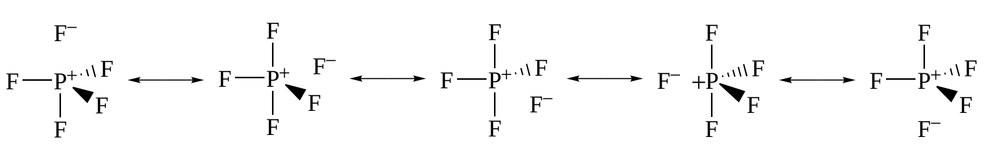
Scheme 1

to describing the bonding in PF_5 is to expand the valence shell of the central atom to accommodate the extra electrons by *Hybridization*. One of the 3s electrons in the ground-state $[Ne]3s^2 3p^3$ electronic configuration of the phosphorus atom is promoted to a 3d orbital. Combining the one 3s, three 3p, and one 3d orbitals gives rise to five sp^3d hybrid atomic orbitals, which are disposed in a tbp arrangement. These hybrid orbitals overlap with the fluorine 2p orbitals to form five 2c/2e P–F covalent bonds. Indeed, this explanation is the only one given in most first-year college chemistry textbooks.

An alternative explanation, one that employs a highly ionic model neglecting d orbital participation, has been proposed. Described originally by Musher in VB terms, it has an equivalent MO description, which is given here.[7] It is in this model that the hypervalent bond is clearly seen. The essential features of the MO model in its most rudimentary form are (1) the central atom uses only valence s and p orbitals; (2) only one p orbital on the central atom is involved in bond formation in the linear three-center atomic arrangement; (3) the remaining central atom valence orbitals bind other atoms in 'normal' bonds or contain lone pairs. The MO description of the hypervalent bond is illustrated in Figure 1 for PF_5. (Not shown is the bonding in the *xy* plane in which phosphorus uses the 3s, $3p_x$, and $3p_y$ orbitals to form three sp^2 hybrid orbitals that bind the three fluorine atoms.) The three p_z atomic orbitals combine to give three MOs. The in-phase combination of fluorine $2p_z$ orbitals is orthogonal to the phosphorus $3p_z$ orbital and gives rise to the nonbonding Ψ_nMO. The out-of-phase combination of fluorine $2p_z$ orbitals overlaps with the phosphorus $3p_z$ orbital to give the bonding and antibonding MOs, Ψ_b and Ψ_a, respectively. Ten valence electrons fill the MOs: six go into the three P–F bonding orbitals in the *xy* plane, and the remaining four fill Ψ_b and Ψ_n. Ψ_b and Ψ_n, when filled, comprise the 3c/4e hypervalent bond (*see* ***Electronic Structure of Main-group Compounds*** and ***Molecular Orbital Theory***).

This model can account for the bonding not only in a tbp geometry but also in *pseudo*-tbp structures in which one or more lone pairs occupy vertices of the tbp (Figure 2) (*see also* ***Coordination Numbers & Geometries***). For *pseudo*-oct geometries, such as square pyramidal (sp) IF_5 and square-planar XeF_4, there are two sets of hypervalent bonds for each molecule. Only in the case of an octahedron or octahedral (oct) geometry, in which the central atom is surrounded by 12 valence electrons (such as SF_6), is the description slightly different.[7] Here, the sulfur 3s orbital contributes to the bonding and is filled. The three Ψ_b MOs are filled; this leaves only two Ψ_n MOs, and these are also occupied. However, for the oct $SeCl_6^{2-}$, where 14 valence electrons surround selenium, there are three filled Ψ_b MOs and three filled Ψ_n MOs; the remaining two electrons reside in a stereochemically inactive 4s orbital.

This description is overly simplified, and quantum chemical calculations have revealed a degree of involvement from s and/or d orbitals. Furthermore, π-bonding and

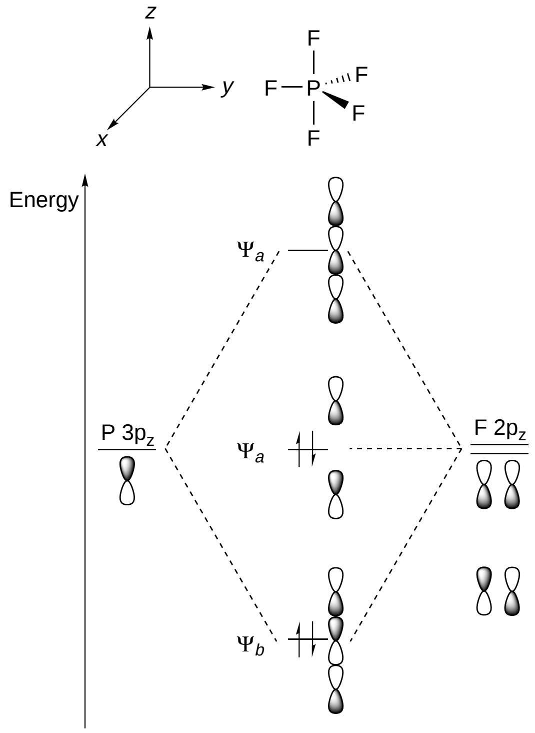

Figure 1 MO description of the 3c/4e hypervalent bond in PF_5. The bonding in the *xy* plane is not shown

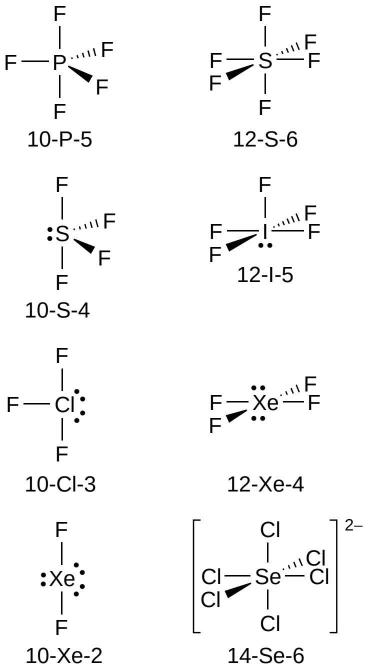

Figure 2 Examples of various geometries based on VSEPR rules. Also given is the N-X-L notation (Section 2.3). Note that the lone pair of electrons in $SeCl_6^{2-}$ is in a stereochemically inactive 4s orbital

hyperconjugation may also be important to account fully for the bonding in these derivatives.[4] Indeed, one well-regarded inorganic chemistry text has called the complete neglect of s and d orbitals in this bonding model 'a ruthless approximation'.[8] Nevertheless, this model has served to explain many structural and chemical features of hypervalent species. For example, the nonbonding component of the 3c/4e EX_2 bond (Ψ_n) is localized on the X groups or ligands, and has no contribution from the central E atom. This buildup of charge is best accommodated by electronegative substituents (*see Electronegativity*) and, in fact, most of these molecules and ions contain electronegative groups at these positions, specifically the axial positions in a tbp (or pseudo-tbp) and the basal positions of a square pyramid (sp). The less electronegative groups will usually prefer the equatorial sites for the tbp (**6**) and apical sites for the sp (**7**). The bonding model is also in agreement with the usual experimental findings that the 3c/4e hypervalent bonds are longer (and weaker) than the 2c/2e bonds.

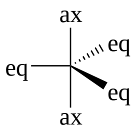

(**6**) tbp

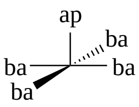

(**7**) sp

Both the ionic resonance structures of Pauling (q.v.), and the 3c/4e bonds proposed by Musher, are consistent with the octet rule, and also take account of the natural polarity of E–X bonds. They explain the paradox whereby the E atom in a molecule EX_n appears to have more than eight valence electrons by recognizing that these bonds are polar. In formulating the octet rule, Lewis implicitly assumed that each bonding pair of electrons contributes fully to the valence shell of both atoms between which it is shared, irrespective of the polarity of the bond. Ionic resonance structures and 3c/4e bonds each locate the excess electron density on the peripheral X atoms. In practice, most hypervalent molecules possess electronegative X atoms or groups that stabilize this redistribution of charge. Thus, when bond polarity is taken into account, the octet rule may be reformulated so that the valence shell of an atom may contain no more than eight electrons. Hence the rule may be obeyed by a hypervalent atom if the ligands are sufficiently electronegative to remove from it a substantial amount of electron density in the form of polar E–X bonds.

It is significant to note that this model places the 'extra' electrons on the ligands attached to the central atom and not on the central atom. Thus the octet may only be expanded in a formal sense.

2.2 What About Period 2 Elements?

A natural question arises for a bonding model that neglects d orbitals. If d orbitals are unimportant, why is it that elements of period 2 (the first row) do not form hypervalent derivatives? First of all, there is good evidence that they do in some cases, although under more restrictive circumstances than elements of periods 3 and below (see Section 9.2). Importantly, the size of period 2 elements may be too small to accommodate the extra electron density and increased coordination numbers; there would be too much ligand–ligand repulsion, except in unusual environments. Experimental and theoretical evidence suggests that the tbp geometry in the nucleophilic displacement mechanism at tetravalent carbon is a transition state, whereas for silicon it is an intermediate.[9] Quantum chemical calculations[10] have added another dimension to the relative stabilities of hypervalent period 2 and 3 elements. These suggest that delocalization of electron density from the axial bonds into the σ^* orbitals of the equatorial bonds results in a significant stabilization for tbp SiH_5^-. For CH_5^-, this interaction is destabilizing. Incidentally, SiH_5^- has been observed experimentally[11] and is the only hypervalent species known that possesses just hydrogen atoms as ligands.

2.3 Recent Developments

Since about 1990, the availability of fast, high-level computing power has led to a range of theoretical studies of formally hypervalent compounds, and of the phenomenon of hypervalency. Ab initio calculations were carried out by Schleyer, and bond orders were obtained for a large number of hypervalent molecules.[4] In all systems studied, the total bond order was found to be less than 4.0; that is, the central atom possessed fewer than eight valence electrons, with electronegative ligands like O and F producing the lowest values. Subsequently, Cioslowski determined bond orders using a different method,[12] but reached the same conclusions; namely that in molecules like SF_6, the S–F bond order is low (0.64), so that the sulfur atom only contains 7.68 electrons in its valence shell. Gillespie used the electron localization function (ELF) to study the same phenomenon.[13] The ELF partitions electron density in the molecule into regions where there is a high probability of finding a pair of electrons of opposite spin: these regions then correspond to bonding or nonbonding electron pairs, and the polarity of bonds is revealed in the unequal partitioning of bonding pairs between the atoms

Table 1 Valence-shell electron populations in a variety of formally hypervalent compounds

Molecule	Valence shell pop.	Molecule	Valence shell pop.
PF_5	5.33	SF_6	6.18
PCl_5	7.13	SeF_6	2.18
PMe_5	9.42	$SeMe_6$	10.98

involved. Analysis of the ELF in a range of systems in fact revealed that most hypervalent molecules have a valence shell containing a total of eight or fewer electrons. However, some compounds possessing less electronegative ligands do exceed a total of eight electrons in their valence shell, as detailed in Table 1. Gillespie concluded that the bonding in hypervalent molecules does not differ in any significant way from that in molecules that obey the octet rule, and reiterated that the Lewis model is an empirical observation with no grounding in theory.

2.4 N-X-L Notation

At this point, it is instructive to introduce a system to classify the bonding around an atom: the N-X-L system.[14] First suggested in 1980, it is particularly useful for the species discussed in this article. In this classification scheme, N is the number of valence-shell electrons formally assigned to the central atom X; and L is the number of ligands directly bonded to X. The N-X-L designations are illustrated in Figure 2 for each species listed.

2.5 VSEPR Theory Basics

It is also useful to review briefly the rules of VSEPR theory with respect to the two simple molecules PF_5 and SF_4 (Figure 3). Only when the central atom possesses no lone pair electrons and is surrounded by simple, identical ligands is an ideal geometry realized. Thus, PF_5 will have an exact tbp geometry. However, the *pseudo*-tbp geometry of SF_4 shows distortions caused by repulsion from the sulfur lone pair. The spatially more demanding lone pair occupies an equatorial site, which provides it with more space than an axial site would allow. Note that both the F_{ax}–S–F_{ax} and F_{eq}–S–F_{eq} bond angles are contracted from the 'ideal' angles of 180° and 120°, respectively. However, the equatorial angle is contracted to a greater extent. This contraction will have significance when 10-X-5 and 10-X-4 geometries are compared in Section 5.4 for more complex ligands.

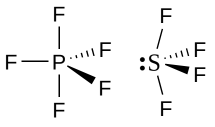

Angle F_{ax}–X–F_{ax} (deg)	180	173.1
Angle F_{eq}–X–F_{eq} (deg)	120	101.6
Distance F_{ax}–X (pm)	158	164.6
Distance F_{eq}–X (pm)	153	154.5

Figure 3 Structures of PF_5 and SF_4

2.6 Primary Literature References

Aspects of hypervalent silicon,[15] tin,[16] phosphorus,[17] arsenic,[18] sulfur,[19] halogens,[20] noble gases,[21] and pentacoordination[22] have been reviewed previously. In addition, comprehensive reviews on organic,[23] organometallic,[24,25] and coordination chemistry[26,27] are useful. Several inorganic texts[8,28] have a wealth of information, particularly relating to halogenated hypervalent molecules and ions. More recent reviews have been published on hypervalent iodine[29–31] and boron/aluminum[32] chemistry in organic synthesis, hypervalent silicates as organocatalysts,[33] bonding descriptions of hypervalent compounds,[13,34,35] inter-ligand hypervalent interactions,[36,37] cyclic aromatic systems with hypervalent centers,[38] hypervalent xenon chemistry,[39] hypervalent tin[40] and crystal engineering using hypervalent interactions.[41] The topics of hypervalent chalcogen stereochemistry,[42] hypervalent transition metal catalysed ligand coupling reactions,[43] and low coordinate hypervalent phosphorus[44] have also been covered.

3 SYNTHESIS AND STABILITY OF HYPERVALENT COMPOUNDS

3.1 Primary Factors Stabilizing the Hypervalent Bond

There are two main principles for the stabilization of the hypervalent bond. The first has already been stated: electronegative groups stabilize the hypervalent bond. This is illustrated by reference to equations (1–6), where a halogen or halide source reacts with a nonhypervalent species to produce a hypervalent product; for tbp or pseudo-tbp geometries, the halogen occupies the axial positions.[15,17,19,20,28] Addition may or may not be accompanied by oxidation of the central atom. Moreover, addition is not limited to halogens; for example, nitrogen and oxygen bases are perfectly suitable (equations 7 and 8).[27]

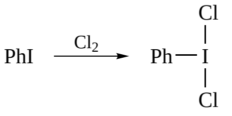

$$\mathrm{PhI} \xrightarrow{\mathrm{Cl_2}} \mathrm{Ph{-}I(Cl)_2} \qquad (1)$$

10-I-3

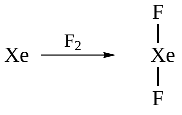

$$\mathrm{Xe} \xrightarrow{\mathrm{F_2}} \mathrm{F{-}Xe{-}F} \qquad (2)$$

10-Xe-2

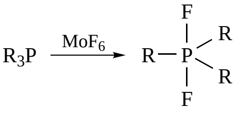

$$\mathrm{R_3P} \xrightarrow{\mathrm{MoF_6}} \mathrm{R_3PF_2} \qquad (3)$$

10-P-5

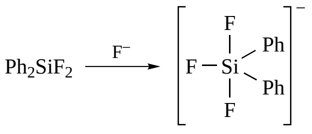
Ph2SiF2
F−
F
Ph
F
Si
Ph
F
−

10-Si-5

(4)

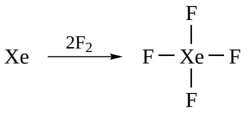
Xe
2F2
F
F
Xe
F
F

12-Xe-4

(5)

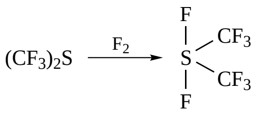
(CF3)2S
F2
F
CF3
S
CF3
F

10-S-4

(6)

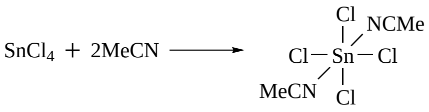
SnCl4 + 2MeCN
Cl
NCMe
Cl
Sn
Cl
MeCN
Cl

12-Sn-6

(7)

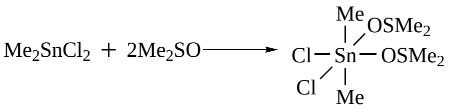
Me2SnCl2 + 2Me2SO
Me
OSMe2
Cl
Sn
OSMe2
Cl
Me

12-Sn-6

(8)

Substituent site preferences in a tbp are based on (what is commonly referred to as) an apicophilicity scale which takes into account several factors, so the ordering of axial/equatorial site preferences may not always strictly follow electronegativity expectations (Section 5.1). For a sp geometry, the more electronegative groups occupy the basal positions.

The second principle may be even more important than the first: the hypervalent bond is stabilized by the steric constraints of small rings. Specifically, this usually means the incorporation of the central atom into four- and five-membered rings. These rings stabilize 90° bond angles about the central atom, and such an orientation introduces the least strain in the ring. This principle is often stated as the preference of four- and five-membered rings to span axial/equatorial positions in a tbp. Equations (9–11) illustrate the principle for reactions involving the synthesis of hypervalent products from nonhypervalent reactants.[15,17] Rings can also be incorporated via substitution reactions using hypervalent starting materials (equations 12 and 13).[17,19]

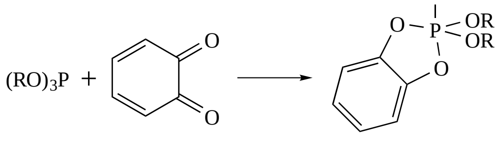
(RO)3P +
O
O
OR
O
P
OR
OR
O

10-P-5

(9)

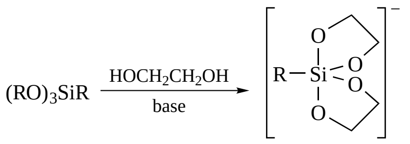
(RO)3SiR
HOCH2CH2OH
base
O
R
Si
O
O
O
−

10-Si-5

(10)

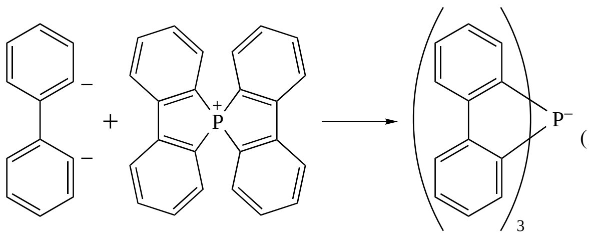

12-P-6

(11)

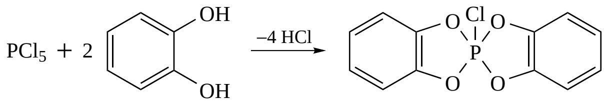
PCl5 + 2
OH
OH
−4 HCl
O
Cl
O
P
O
O

10-P-5

(12)

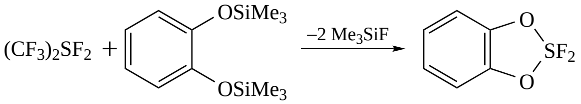
(CF3)2SF2 +
OSiMe3
OSiMe3
−2 Me3SiF
O
SF2
O

10-S-4

(13)

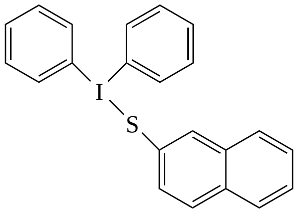

(**8**)

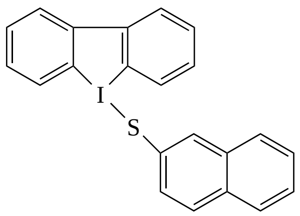

(**9**)

The importance of rings in supporting these hypervalent systems is clearly shown by the relative stabilities of cyclic versus acyclic structures. For example, (**8**) undergoes slow decomposition at ambient temperature, while (**9**) shows no decomposition over several months.[20] A more dramatic demonstration of the stability introduced by rings is illustrated for sulfuranes (**10**) and (**11**) in equations (14) and (15).[6] However, recently the first noncyclic 10-S-5 sulfuranide dioxide anion, $[(CF_3)_3SO_2]^-$ has been reported and structurally characterized. The compound exhibits a tbp structure with equatorial oxygen atoms.[45]

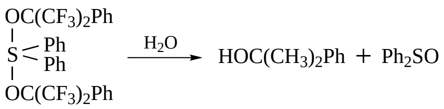
OC(CF3)2Ph
S
Ph
Ph
OC(CF3)2Ph
H2O
HOC(CH3)2Ph + Ph2SO

$$\mathrm{Ph_2S(OC(CF_3)_2Ph)_2} \xrightarrow{H_2O} \mathrm{HOC(CH_3)_2Ph + Ph_2SO}$$

(**10**)

(14)

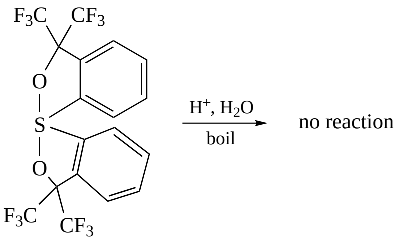

(15)

(**11**)

Judicious choice of ring systems can even overcome the usual preference of electronegative ligands for axial sites. For example, it is well known that the usually tetrahedral 8-Si-4 silanes can function as Lewis acids, particularly when very electronegative substituents are attached to silicon. Molecule (**12**) illustrates the formation of a five-membered ring through intramolecular coordination.[15] Here, the steric requirements of the ring to span axial/equatorial positions outweigh the electronegativity preferences, and one of the two fluorine substituents is forced into an equatorial site.

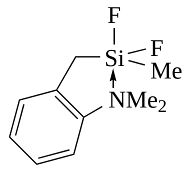

(**12**)

Polydentate ligands also lead to isolation of derivatives with hypervalent bonds. Examples of tetradentate-ligated species are the ‘atranes’ (**13**)[22,46,47] and porphyrins (**14**).[48] Various linkages, both saturated and unsaturated, can connect the oxygen and nitrogen ligand atoms in the atranes, and the R substituent on the porphyrin ring can be varied systematically. Planar tridentate-ligated examples are (**15**)[6] and (**16**).[49] In fact, 10-X-3 (X = P, As, Sb) species can only be isolated under the severe constraints of the ligand illustrated. A striking example of the delicate balance that exists between ligand and product is shown for (**17**) in equation (16).[50]

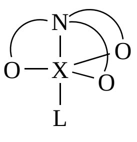

(**13**) X = Al, Si, P

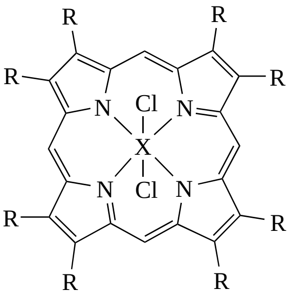

(**14**) X = Sn, Ge

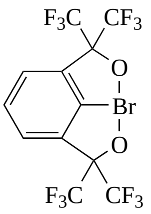

(**15**)

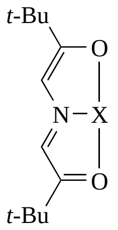

(**16a**) X = P
(**16b**) X = As
(**16c**) X = Sb

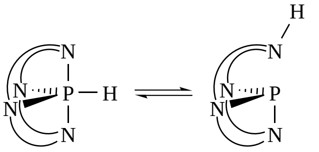

(16)

10-P-5 8-P-3
(**17a**) (**17b**)

Compound (**17**) is synthesized by the treatment of the appropriate cyclic amine with tris(dimethylamino)phosphine at 100 °C, resulting in the elimination of three moles of dimethylamine. The products obtained are dependent on the number of methylene groups bridging the nitrogen atoms. When all four bridges are ethylene, $(CH_2)_2$, only (**17a**) is observed; when all are trimethylene, $(CH_2)_3$, only (**17b**) is found. When there are two of each type, both tautomers are present.

3.2 Other Stabilizing Factors

The above principles are the most important factors in the stabilization of the hypervalent bond. However, there are other general considerations to take into account.[6] One is the preference for a relatively electropositive central atom: a positive charge develops at this center, and is most easily accommodated by such an atom. In addition, an electropositive equatorial ligand will assist in stabilizing this positive charge at the hypervalent center. Other factors, primarily governing site preference and orientation in tbp and pseudo-tbp geometries, have significance, and these are elaborated in Section 5.

3.3 Periodic Trends

There are few periodic generalizations that can be made concerning hypervalent molecules, since the factors contributing to stability, such as oxidation potential, central atom size, type of ligands, and ionic versus covalent bonding type, all interact in a complex manner. However, some general trends are evident.

3.3.1 *Inert Pair and Alternation Effects*

Electronegativity generally decreases down a group in the p-block, and it may be thought that higher oxidation states are therefore more stable for the heavier congeners in a group. However, this is not the case, as insertion of the first row of transition elements and of the lanthanide elements in the third and fifth periods causes the p-block elements directly following these changes to have a higher electronegativity than would otherwise be the case. Group 15 exemplifies this phenomenon admirably: the electronegativity of As (2.2) is identical to that of phosphorus, and that of Bi (2.0) is almost the same as that of Sb (2.1). This Alternation Effect in electronegativity down the Group affects the stability of higher oxidation states for As and Bi: a reduction in ionic resonance energy accompanies the increase in electronegativity and is reflected in weaker bonds to F, O and Cl than would otherwise be the case. Thus, PCl_5 and $SbCl_5$ are stable molecules at ambient temperatures, whereas $AsCl_5$ decomposes above −50 °C, and $BiCl_5$ has never been reported. Operating in tandem with this phenomenon is the *Inert Pair Effect*, whereby a monotonic decrease in bond strengths down a group serves to destabilize higher oxidation states for the heavier congeners. The two effects conspire in the fifth period, and hypervalent compounds of bismuth form only under the most forcing conditions.

3.3.2 *Increase of Coordination Number with Size*

The ability to increase coordination number with central atom size within a group is perhaps the most generally reliable periodic trend. The increased coordination shows up distinctly in period 5. For example, no complex forms between pyridine and Me_3SiCl, while Me_3SnCl· pyridine is stable.[27] In addition, trialkyltin halides have a much greater tendency to associate in the solid state than do their silicon and germanium analogs; for example, trimethyltin fluoride (**18**) is associated in the solid state. Even in solution, tributyltin fluoride associates to give polymeric structures. Likewise, PF_5 and AsF_5 are both monomeric, but SbF_5 is associated, even in the gas phase. SF_4 and SeF_4 are monomeric; TeF_4 in the solid state forms polymeric 12-Te-5 pseudo-octahedra via fluoride bridges. Size is also a factor for the linear trihalide monoanions X_3^-: in general, their thermal stabilities increase with increasing central atom size.[47]

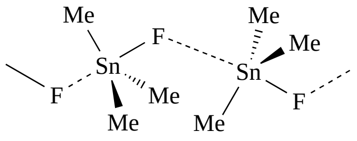

(**18**)

3.3.3 *Oxidizability of the Central Atom*

For hypervalent molecules formed by oxidation, the ability to remove electrons from the central atom is a key factor. The formation of noble gas derivatives,[47] such as XeF_2, is related to the ionization energy of the element in a rather straightforward manner. In fact, Bartlett originally reasoned that since PtF_6 oxidized molecular oxygen to give $O_2^+\ PtF_6^-$, xenon should be similarly oxidized, since the ionization energies of O_2 and xenon are comparable. The ionization energies of the noble gases above krypton are prohibitively high to allow this kind of chemistry. Indeed, although argon has now been activated photochemically at 10 K to form HArF,[51] only xenon and krypton form tractable compounds. (*see* ***Noble Gases: Inorganic Chemistry***). The formation of hypervalent organoiodine(III) dihalides (**19**) is directly related to the oxidizing ability of the ligating halogen (equation 17).[20] This equilibrium is shifted to the left for L = Cl and to the right for L = Br and I.

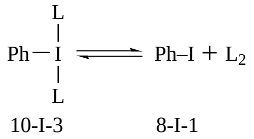

$$\mathrm{Ph{-}I(L)_2} \rightleftharpoons \mathrm{Ph{-}I} + \mathrm{L_2} \qquad (17)$$

(**19**)

3.3.4 *Central Atom Charge*

Central atom charge is also important, particularly for hypervalent species formed by simple addition. This is best illustrated by trends in the Group 14 derivatives $R_{4-n}ML_n$ (M = Si, Ge, Sn, Pb; L = I, Br, Cl, F). In general, the Lewis acidity of the central atom increases in the order $L = I < Br < Cl < F$, and $n = 1 < 2 < 3 < 4$. For $n = 1$, complexes appear to be limited to tbp 1:1 adducts, while for $n > 1$, oct 1:2 adducts are common.[27]

3.3.5 *Covalent Versus Ionic Bonding*

The tendency to form covalent rather than ionic bonds is crucial in the formation of hypervalent compounds. Incorporation of fluoride as a ligand usually stabilizes covalent species. For example, PF_5 is covalent. However, PCl_5 is characterized by the equilibria shown in equations (18) and (19). In the gas and liquid phases, the molecular form exists, while in the solid state it is ionic, consisting of PCl_4^+ and PCl_6^- ions. In solution in nonpolar solvents, the molecular form is favored, while the ionic form described in equation (18) predominates in polar solvents. At low concentrations, some PCl_4^+ and Cl^- may be present owing to the equilibrium in equation (19). For equation (20) (R = alkyl and aryl), if L is a reasonably basic anion such as Cl, Br, I, or OPh, the ionic phosphonium salt (**20**) is favored. With L = F or *O*-alkyl, the pentacoordinate species (**21**) is observed.[52,53]

$$2PCl_5 \rightleftharpoons PCl_4^+ + PCl_6^- \tag{18}$$

$$PCl_5 \rightleftharpoons PCl_4^+ + Cl^- \tag{19}$$

$$\underset{\substack{\text{8-P-4}\\ (\mathbf{20})}}{R_4P^+L^-} \rightleftharpoons \underset{\substack{\text{10-P-5}\\ (\mathbf{21})}}{R_4PL} \tag{20}$$

4 SPECTROSCOPY AND DIFFRACTION AS STRUCTURAL PROBES

4.1 Diffraction Techniques

Leaving aside single-crystal X-ray diffraction, which has produced the vast majority of structural data for compounds of all types, gas-phase electron diffraction deserves special mention in the study of hypervalent molecules. Many hypervalent p-block species are gases or volatile liquids at ambient temperatures, and hence are not amenable to study by conventional X-ray diffraction techniques. Main group molecules like PF_5, SF_4, and ClF_3, and noble gas compounds like XeF_6 were structurally determined by electron diffraction during the 1960s, and these studies were expanded to encompass important mixed-ligand species like the methyl and chloro-substituted derivatives of PF_5. These gas-phase studies produced the main body of evidence around which VSEPR theory developed.[54]

4.2 Vibrational Spectroscopy

IR and Raman spectroscopy are extremely useful for the determination of structures of hypervalent species, particularly for simple molecules where complete spectral assignments can be made.[55] For mixed halide systems in tbp or pseudo-tbp geometries, such as PF_2Cl_3 or SF_2Cl_2, vibrational data can discriminate unambiguously between possible isomers. The fast timescale of vibrational spectroscopy proved particularly useful in showing that the 14-X-6 species BrF_6^- is octahedral in solution; in contrast to IF_6^-, where the nonbonding electron pair displays stereochemical activity.[56] For high-symmetry molecules, rotational-vibrational spectroscopy can afford accurate molecular constants that permit a full structural determination of molecular structure, as was demonstrated elegantly for H_3PF_2 (Figure 4).[57]

4.3 NMR Spectroscopy

Multinuclear NMR spectroscopy is indispensable to the study of hypervalent species for several reasons. First of all, exchange processes can be identified and measured. For example, the ^{19}F NMR spectrum of SF_4 shows two types of fluorine resonances at low temperature; these coalesce to a single feature at higher temperatures. For PF_5 and $RSiF_4^-$, only one resonance is observed, even at low temperatures. However, for the derivatives RPF_4 and $R_2SiF_3^-$, behavior similar to SF_4 is observed. Exchange mechanisms have been advanced to explain this fluxional behavior (see Section 5.2). Secondly, the chemical shift can usually be correlated with coordination number: higher coordination leads to resonances at higher fields. For example, 31P the chemical shift values for PCl_3, PCl_4^+, PCl_5, and PCl_6^- are 219, 96, −80, and −281 ppm, respectively. However, this trend is highly substituent-dependent, and similar ligands must be present to rely on such a correlation. A third application is the use of coupling constants to assign substituent sites in a tbp or pseudo-tbp. Coupling constants are dependent on the amount of s character in a bond: the greater the s character, the larger the coupling constant. A dramatic illustration of this phenomenon is found in the low-temperature ^{13}C NMR spectrum of $Me(CF_3)_3PF$ (**22**), a tbp molecule that has one fluorine and one CF_3 group occupying axial positions. The one-bond P–C coupling to the equatorial CF_3 groups is 258 Hz whereas that to the axial CF_3 is only 17 Hz.[58]

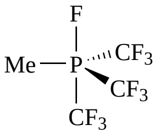

(**22**)

4.4 Other Spectroscopic Techniques

Although less important than gas-phase electron diffraction, microwave spectroscopy is a valuable technique for the structural characterization of gases and volatile liquids. For example, HPF_4 and H_2PF_3 (Figure 4) were shown in a combined electron diffraction and microwave spectroscopy study to be tbp species in which the hydride ligands occupy equatorial sites.[59]

Mössbauer Spectroscopy has also proved useful for the study of hypervalent species, since many of the central atoms, such as Sn, Sb, Te, I, and Xe, are suitable for study by this technique.[60] Gas-phase UV photoelectron spectroscopy, while not particularly important for geometry elucidation, has

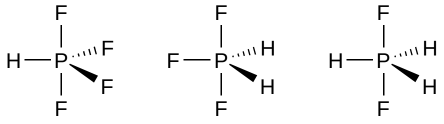

Figure 4 Equatorial H atoms in tbp hydrido derivatives of PF_5

been used to obtain information on the electronic structures of hypervalent molecules.[61] X-ray photoelectron spectroscopy is also useful for determining charge distributions, particularly in demonstrating the greater negative charge on the axial substituents in a tbp.[62]

5 PENTACOORDINATE AND RELATED STRUCTURES

The greatest body of work in hypervalent chemistry has been carried out on 10-X-5 structures, most often tbp phosphoranes. However, the results have been generalized in most cases to include all pentacoordinate main group elements. They also have implications for pseudo-tbp structures such as the 10-S-4 sulfuranes. Some of the more important aspects are described in this Section.

5.1 Apicophilicity

Apicophilicity can be defined as the change in energy when an apical (or axial) ligand and an equatorial ligand in a tbp structure are exchanged; the more apicophilic ligand prefers the axial site. This relative scale has been constructed and quantified by experimental and theoretical techniques. For example, Trippet[63] devised a scale based on dynamic NMR measurements of pentacoordinate phosphoranes. Apicophilicity is dependent on several factors such as electronegativity, π-bonding ability, and size of the ligand. This scale has been examined by many researchers, and no two approaches give exactly the same ordering. However, the following is a general ordering of decreasing apicophilicity: $F > H > CF_3 > OPh > Cl > SMe > OMe > NMe_2 > Me > Ph$. Caution is necessary in using this scale: some results imply that Cl may be more apicophilic than F in certain systems.[64]

Theoretical work on the model phosphorane PH_5 has shown that π-acceptor ligands prefer axial sites and π-donors favor equatorial positions in a tbp.[65] However, a significant difference is observed when the orientation of a π-donor p orbital at an equatorial site is examined for a 10-P-5 phosphorane and a 10-S-4 sulfurane.[66] For the phosphorane, the preferred orientation is in the equatorial plane (**23**), while for the sulfurane it is perpendicular to it (**24**). The difference arises from the interaction of the ligand donor orbital with the sulfurane lone pair.

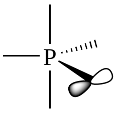

(**23**)

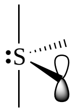

(**24**)

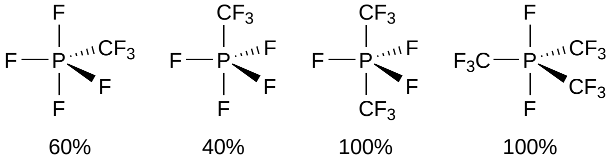

Figure 5 Trifluoromethyl derivatives of PF_5

One particularly intriguing family of molecules is the trifluoromethyl derivatives of PF_5, illustrated in Figure 5. The structure adopted by these molecules depends strongly on their makeup: three CF_3 groups occupy the equatorial sites in a tbp, two occupy the axial ones, and a single CF_3 moiety occupies either position with statistical probability.[67] The CF_3 ligand has a group electronegativity comparable to that of Cl, and so electronic factors would place it preferentially in an axial site. However, the steric bulk of the ligand appears to override these considerations, so that these phosphoranes adopt structures that minimize contacts between CF_3 groups. This series of molecules demonstrates that apicophilicity is a complicated phenomenon, and that each case should be judged on its merits.

5.2 Site Exchange: Pseudorotation

One of the unique aspects of hypervalent chemistry is the fact that two different types of bonds can exist in one molecule (for example, the axial and equatorial P–F bonds in PF_5) and that these bonds may interconvert by an isomerization process. On account of its slow timescale, NMR spectroscopy is the ideal method to study such exchange processes, and PF_5 was one of the first pentacoordinate molecules to be studied using this technique. Only one resonance (a doublet due to ^{31}P coupling) is observed in the ^{19}F NMR spectrum down to −190 °C. However, RPF_4 derivatives display temperature-dependent spectra: at ambient temperatures only one fluorine resonance is seen, while at low temperatures resonances owing to inequivalent fluorine atoms are observed. Berry[68] first proposed an intramolecular exchange process to account for these observations. He showed that, in a tbp (Figure 6(a)), bending two of the equatorial atoms away from each other and the two axial atoms toward each other equilibrates these atoms at the basal sites of a sp transition state (b). Continuing this deformation results in an interchange of the atoms at the axial and equatorial positions (c). This process is known

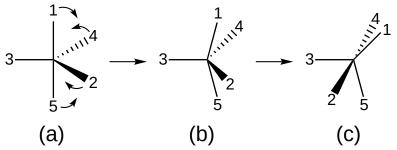

Figure 6 The Berry pseudorotation process

as the *Berry pseudorotation* (or simply *pseudorotation, see Pseudorotation*). Note that one of the equatorial atoms, 3, remains fixed in this scheme and acts as the fulcrum for the process. Continuation of this process with different equatorial pivot atoms results in an equilibration of all five atoms. The energy barrier to this process is very low and for PF_5 cannot be measured by NMR spectroscopy; however, introduction of other substituents (as in RPF_4) raises the exchange barrier to a point where it can be frozen out on the NMR timescale. For some species of the type R_2PF_3, exchange does not occur even at ambient temperature, owing to the necessity of placing one or more R group in an energetically unfavorable axial position.

Pseudorotation has also been shown to be important in 10-S-4 and 10-Si-5 species such as SF_4[19] and $R_2SiF_3^-$.[15]

While pseudorotation is usually invoked to explain the observed exchange phenomena, alternative intramolecular processes have been proposed, such as the *Turnstile Mechanism*.[52] This involves rotation of a pair of ligands on one side of the tbp and the remaining three on the other side. Both Berry and turnstile mechanisms result in a similar exchange, albeit via different transition states. It is difficult to differentiate these mechanisms experimentally; however, the structural data described in the next Section appear to support the Berry process.

5.3 Structural Distortions in the Solid State

The low barrier to exchange of axial and equatorial substituents suggests that structural distortions of 10-X-5 derivatives from a tbp might be observed in ground-state geometries as well. Calculations show that the lowest energy arrangement of five points on a sphere is a tbp; however, the sp is only slightly less stable, and certain substituents might prefer this geometry. The idealized angles for the sp are 105° (ap/ba), 150° (trans-ba/ba), and 86° (cis-ba/ba), as depicted in structure (**25**).[17]

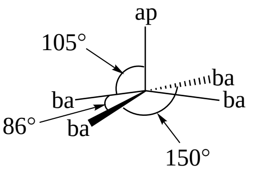

(**25**)

It is important to note that the sp of (**25**) is related to the IF_5 sp (see Figure 2) in the sense that the ligands attached to the central atom are disposed at the vertices of a similar polyhedron. However, they differ electronically, since the sp of (**25**) is a 10-X-5 species and that of IF_5 is 12-X-5. The central atom in the sp of a 10-X-5 species will lie above the basal plane, while that in a 12-X-5 species will lie below the basal plane owing to lone pair/bond pair repulsion.

The most detailed structural work on pentacoordinate structures has been carried out and compiled by Holmes,[17,22] and some of his findings are summarized here. Basic VSEPR rules can account qualitatively for geometries with simple acyclic ligands; for example, the series Me_nPF_{5-n} ($n = 1-3$). However, as ligands become more complex, other factors predominate. Preference rules have been derived for both the tbp and sp geometries and are listed here in order of probable importance.

For the tbp:

1. Four- or five-membered cyclic systems preferentially span axial/equatorial positions.
2. The most electronegative ligands preferentially occupy axial sites.
3. π-Donor ligands, in general, are positioned at equatorial sites.
4. Steric effects are minimized by locating bulky groups in equatorial positions.

For the sp:

1. Four- or five-membered cyclic systems preferentially span cis basal positions.
2. The most electronegative ligands preferentially occupy basal sites.
3. π-Donor ligands, in general, are positioned at the apical site.
4. Steric effects are minimized by locating a bulky group in the apical position.

In addition, factors favoring the sp over the tbp have been identified. The most important appears to be the incorporation of unsaturated five-membered rings into 10-X-5 species. Apparently, less ring strain is introduced when such rings span cis basal positions in a sp rather than axial/equatorial sites in a tbp. In fact, the sp geometry predominates when two such rings are present, as in structure (**26**).

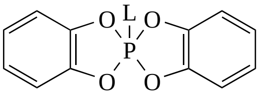

(**26**)

Referring to geometries like (**26**) as a sp or RPF_4 as a tbp are only approximations, since only a species with all five substituents identical (like PF_5) will exhibit an exact tbp geometry. In fact, the geometry of (**26**) is close to a sp and that of RPF_4 is close to a tbp. But how close? A simple metric plots the axial and equatorial angles, versus a measure of the distortion coordinate, the dihedral angle between faces 124 and 245 (see Figure 6(a)). A more complicated scheme involves determining all of the dihedral angles.[17,22] No matter which method is used, the findings are essentially the same. Virtually all of the known structures of 10-P-5 molecules are either close to a tbp or sp geometry, or show distortions that lie along the Berry pseudorotation coordinate (the conversion of (a) to (b) in Figure 6). This has now been extended to most other 10-X-5 species, both neutral and ionic. The fact that these ground-state geometries closely approximate the Berry coordinate lends support to the pseudorotation exchange mechanism described in Section 5.2.

5.4 Apicophilicity ‘Anomalies’ in 10-S-4 Sulfuranes

In general, the trends found in 10-X-5 derivatives find parallels in 10-X-4 species; however, the presence of a nonbonding pair of electrons on the central atom can alter certain aspects, such as the equatorial lone pair orientation described in Section 5.1. More importantly, the F_{ax}–S–F_{ax} angle in SF_4 (Figure 3) suggests that the ring strain introduced by having a small ring span two equatorial positions should be less important than in 10-X-5 species. In fact, sulfurane (**27**) has the ring spanning equatorial sites.[69]

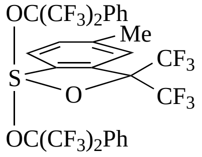

(**27**)

5.5 The Puzzling $SbPh_5$ Structure[8,47]

The vast majority of pentacoordinated molecules unperturbed by rings adopt regular or approximate tbp structures: for example, the organic derivatives Ph_5P, Ph_5As, Me_5As, and Me_5Sb. However, Ph_5Sb is sp in the solid state and appears to retain this geometry in solution. No adequate explanation for this behavior has been advanced. Even (p-$MeC_6H_4)_5Sb$ is tbp. The only other simple species shown unambiguously to favor a sp over a tbp structure is $InCl_5^{2-}$ as the NEt_4^+ salt,[70] although this appears to be highly dependent on crystal packing since the analogous PPh_4^+ and $PPh_2Cl_2^+$ salts each contain tbp $InCl_5^{2-}$.[71,72]

6 REACTIVITY OF HYPERVALENT COMPOUNDS

6.1 General

Sterically unsaturated hypervalent halides are quite reactive. Typical reactions involve the transfer of halogen and a reduction in coordination number. For example, hydrolysis is usually facile and sometimes violent (equations 21 and 22). Many of the fluorides are excellent fluorinating reagents. SF_4 is useful for the conversion of ketones and carboxylic acids to CF_2 and CF_3 groups, respectively (equations 23 and 24).[73] ClF_3 is a powerful fluorinating agent for inorganic chlorides and oxides (equations 25 and 26).

$$PCl_5 + 4H_2O \longrightarrow H_3PO_4 + 5HCl \qquad (21)$$

$$SF_4 + 2H_2O \longrightarrow SO_2 + 4HF \qquad (22)$$

$$Me_2CO + SF_4 \longrightarrow Me_2CF_2 + F_2SO \qquad (23)$$

$$PhCO_2H + 2SF_4 \longrightarrow PhCF_3 + 2F_2SO + HF \qquad (24)$$

$$AgCl + ClF_3 \longrightarrow AgF_2 + \tfrac{1}{2}Cl_2 + ClF \qquad (25)$$

$$NiO + \tfrac{2}{3}ClF_3 \longrightarrow NiF_2 + \tfrac{1}{3}Cl_2 + \tfrac{1}{2}O_2 \qquad (26)$$

Octahedral hypervalent halides, on the other hand, are much less reactive (*see Coordinative Saturation & Unsaturation*). For example, PF_6^- is a widely used noncoordinating anion (*see Noncoordinating Anion or Cation*); $SiF_4\cdot$ bipyridine is stable in the presence of moisture; and SF_6 is remarkably inert: it can be treated with steam at 500 °C or with molten KOH without any effect. It is nontoxic and used as an insulating gas in high voltage applications.

Many coordinatively unsaturated species are good Lewis acids, owing to the positive charge induced on the central atom as a result of electronegative substituents. For example, PF_5, and to an even greater extent AsF_5 and SbF_5, are excellent fluoride ion acceptors, yielding robust XF_6^- anions that stabilize such acidic cations as S_4^{2+} and XeF_5^+.

Oxidative Addition is also common for those central atoms that can increase their oxidation state (*see Oxidation Number*) (equations 27 and 28). Substitution of halogen by organic groups is useful for the preparation of organo derivatives, as mentioned in Section 3.1 (equations 12 and 13).

$$\underset{\text{10-S-4}}{SF_4} + ClF \longrightarrow \underset{\text{12-S-6}}{SF_5Cl} \qquad (27)$$

$$\underset{\text{10-Cl-3}}{ClF_3} + F_2 \longrightarrow \underset{\text{12-Cl-5}}{ClF_5} \qquad (28)$$

6.2 Silicon in Organic Synthesis[15]

Hypervalent silicon compounds have found wide utility in organic synthesis. In general, pentacoordinated anionic silicates are more reactive toward nucleophiles than are tetracoordinated silanes. For example, Mes_2SiF_2 is unreactive toward water, while (the 18-crown-6 potassium salt of) $Mes_2SiF_3^-$ is completely hydrolyzed within minutes. Similarly, the pentacoordinate anion $HSi(OEt)_4^-$ is an effective reducing agent for aldehydes, ketones, and esters at or below room temperature (Scheme 2); no such reaction occurs with $HSi(OEt)_3$. The difference in relative reactivities of hypervalent and nonhypervalent species is relevant to the intermediates proposed in Section 7.6.

The oct 12-Si-6 dianion $RSiF_5^{2-}$ has been carefully studied, and reactions with this reagent are stereospecific. Some of

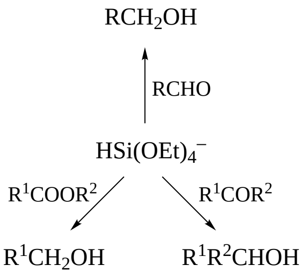
RCH2OH
RCHO
HSi(OEt)4−
R1COOR2
R1COR2
R1CH2OH
R1R2CHOH

Scheme 2

these are illustrated in Scheme 3. For R = alkyl, treatment with *N*-bromosuccinimide (NBS), bromine, or copper(II) bromide yields alkyl halides with inversion of configuration at carbon. For R = alkenyl, cleavage by halogens leads to alkenes with retention of configuration. By comparison, 8-Si-4 alkenyltrimethylsilanes proceed with inversion of configuration under similar conditions. This is a result of the usual trans addition and anti elimination in the latter case, while direct electrophilic displacement may account for the stereochemistry in the former. Reaction of $RSiF_5^{2-}$ with other metal salts (Ag^+, Cu^+, P^{2+}) can lead to reductive coupling.

6.3 Hypervalent Iodine Reagents

Hypervalent organoiodine compounds have found wide utility in organic synthesis. Primary and secondary alcohols can be oxidized to aldehydes and ketones with the 12-I-5 compound (**28**), according to equation (29).[74] α-Hydroxy dimethyl acetals can be synthesized under basic conditions with the 10-I-3 reagent $PhI(OAc)_2$ (equation 30).[75] The topic has been recently reviewed.[29–31,76]

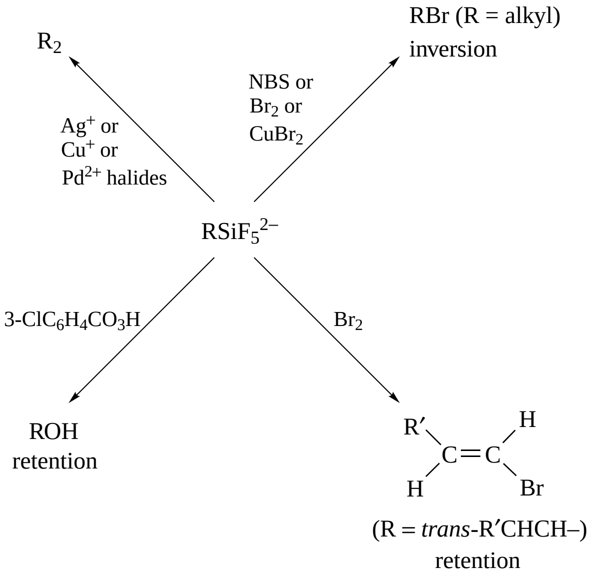
R2
Ag+ or
Cu+ or
Pd2+ halides
NBS or
Br2 or
CuBr2
RBr (R = alkyl)
inversion
RSiF5 2−
3-ClC6H4CO3H
Br2
ROH
retention
R′
H
C=C
H
Br
(R = trans-R′CHCH–)
retention

Scheme 3

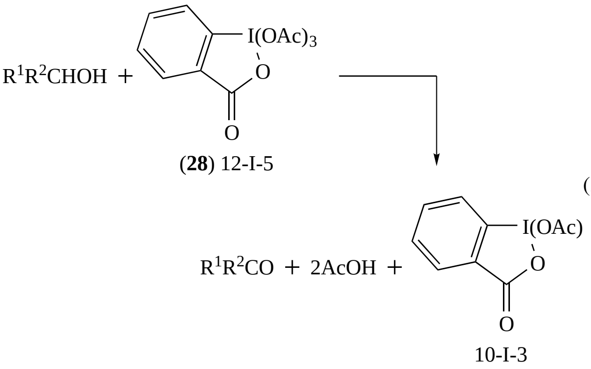
R1R2CHOH +
I(OAc)3
O
O
(28) 12-I-5
R1R2CO + 2AcOH +
I(OAc)
O
O
10-I-3

(29)

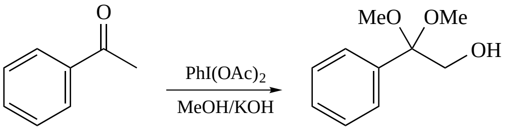
O
PhI(OAc)2
MeOH/KOH
MeO
OMe
OH

(30)

6.4 Basicity of Hypervalent Lone Pairs

10-X-4 derivatives possess lone pairs of electrons in an equatorial position that may show donor ability toward metals and other Lewis acids. For example, SF_4 can be oxidized to OSF_4; however, the BF_3 complex of SF_4 exists as the ionic salt $[SF_3][BF_4]$. The high degree of s character in the equatorial lone pair orbitals of 10-S-4 sulfuranes and 10-P-4 phosphoranide anions should lower their donor ability relative to the excellent ligands R_2S and R_3P. In addition, the presence of very electronegative groups might reduce their basicities; however, since PF_3 is an excellent ligand, the presence of electronegative groups should not ipso facto diminish coordinating ability. Compounds that can be formally considered complexes of phosphoranides exist, (**29**) and (**30**), but they are usually prepared by routes other than simple coordination, such as nucleophilic attack on pentacoordinated phosphorus[77] and oxidative addition of fluorine to a metallated difluorophosphine[78] (equations 31 and 32). Note the use of the hypervalent fluorinating reagent in the latter reaction. Perhaps these are best viewed as metallasubstituted phosphoranes. However, the 10-X-3 species (**16**) show excellent donor properties,[79,80] and both lone pairs can be coordinated under suitable conditions (Scheme 4).

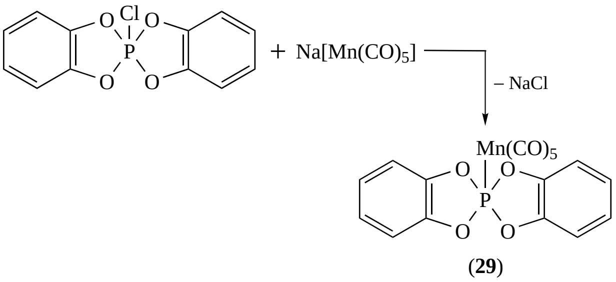
O
Cl
O
P
O
O
+ Na[Mn(CO)5]
− NaCl
Mn(CO)5
O
O
P
O
O

(**29**)

(31)

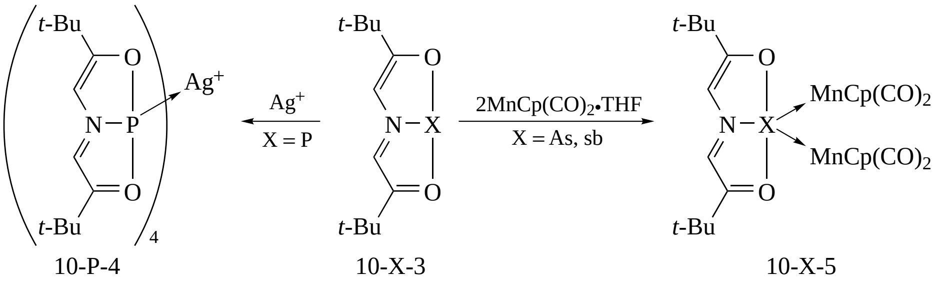
t-Bu
O
N
P
Ag+
4
10-P-4
Ag+
X = P
X
10-X-3
2MnCp(CO)2•THF
X = As, sb
MnCp(CO)2
MnCp(CO)2
10-X-5

(**16a**) X = P
(**16b**) X = As
(**16c**) X = Sb

Scheme 4

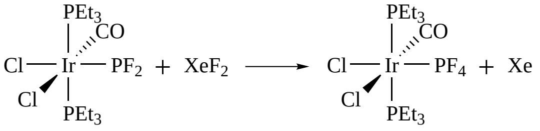

$$\mathrm{Cl_2Ir(CO)(PEt_3)_2PF_2 + XeF_2 \longrightarrow Cl_2Ir(CO)(PEt_3)_2PF_4 + Xe} \quad (32)$$

(**30**)

7 HYPERVALENT INTERMEDIATES AND TRANSITION STATES

7.1 General Considerations for Intermediates

Some of the most important hypervalent species are the reactive intermediates formed by nucleophilic attack at the central atom of a tetracoordinated molecule or ion. Indeed, many 10-P-5 and 10-Si-5 species can be considered as stabilized intermediates formed through such a process. Usually, it is assumed that the attacking group enters at an axial position, and the leaving group leaves from an axial position. Pseudorotation may occur in the tbp intermediate to place the leaving group at an axial position. For phosphorus, this is a well documented process. For silicon, the entry position appears to be usually axial, but some data suggest equatorial entry for organometallic reagents. Since the axial bonds are longer and weaker, it is reasonable that a group will leave from this position.

The possible pathways for reactions at tetracoordinated phosphorus and silicon are summarized in Figure 7. Path 1 is directly analogous to carbon chemistry, in which

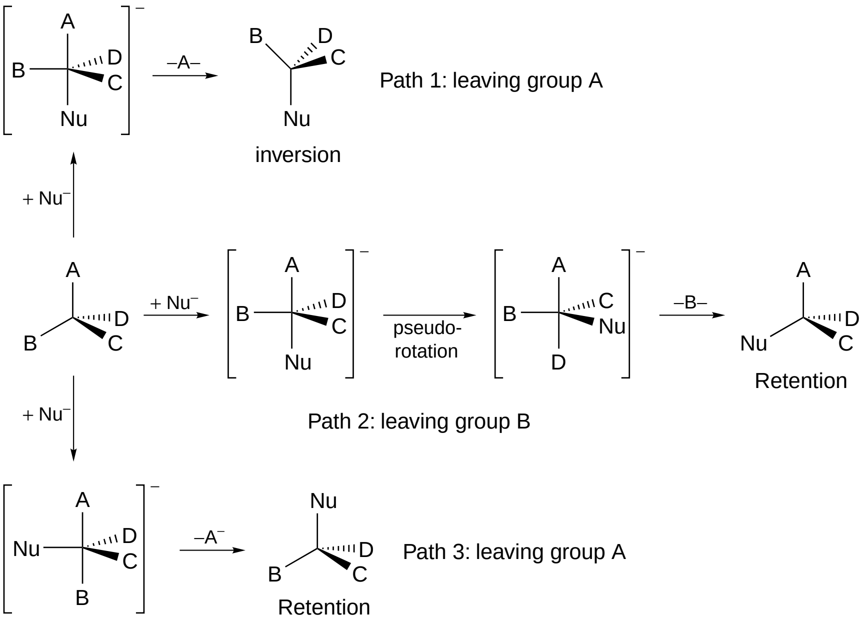
A
B
D
C
Nu
–A–
inversion
Path 1: leaving group A
+ Nu–
pseudo-
rotation
–B–
Retention
Path 2: leaving group B
–A–
Path 3: leaving group A

Figure 7 Pathways for nucleophilic substitution at tetracoordinated phosphorus and silicon. Path 3 is postulated for silicon only[81]

inversion of configuration is observed; however, for carbon the pentacoordinate structure is a transition state, not an intermediate. Path 2 involves pseudorotation of the intermediate and leads to retention of configuration. Only for silicon has equatorial entry been suggested via Path 3. Some very important reactions proceed through 10-P-5 intermediates, such as the Wittig reaction.[52,53] Several specific examples from phosphorus, silicon, and sulfur chemistry are discussed below to illustrate the principles stated above and to demonstrate the importance of reactions involving hypervalent intermediates.

7.2 Hydrolysis of Cyclic Phosphate Esters

Cyclic phosphate esters containing five-membered rings hydrolyze 10^5–10^8 times faster than their acyclic analogs. However, for six- and seven-membered rings, hydrolysis rates are comparable to those of their acyclic congeners. From the principles already discussed, these data suggest that the preference for five-membered rings to span axial/equatorial positions in a tbp may be a factor in the rate enhancement. In fact, Westheimer[82] developed a now well-established mechanism based on this fact; one that not only accounts for the observed rate enhancement but also for product distributions where pseudorotation of an intermediate occurs. For example, the acid-catalyzed hydrolysis of (**31**) gives two phosphorus products; one ring opened and the other with the ring intact. X-ray diffraction analysis of (**31**) and other related cyclic systems shows the O–P–O angle in the ring to be 99°; hence spanning the axial/equatorial positions in a tbp relieves about 9° of ring strain. The proposed mechanism (Scheme 5) involves initial nucleophilic attack by water to give (**32**). If displacement from this intermediate occurs, (**34**) is formed. However, pseudorotation of (**32**) can occur to give (**33**), and this would lead to the final product (**35**). For the specific case of hydrolysis of (**31**), the products (**34**) and (**35**) are produced in an approximate 60:40 ratio. The exact mechanism is somewhat more complicated, but the key points are that the intermediates are stabilized by the ring orientation (leading to enhanced rates), and that formation of (**35**) can only occur via pseudorotation.

7.3 Acyclic Phosphonium Salts

In general, hydrolysis of acyclic phosphonium salts leads to inversion products via Path 1. The incoming group will attack at the tetrahedral face, resulting in a tbp with the leaving group at the opposite axial position. This mechanism can be modified by increasing the steric bulk of substituents. For example, base hydrolysis of (**36**) leads to retention of configuration. The *t*-butyl group effectively prevents the incoming nucleophile from attacking at a face that would put the preferred group (CH_2Ph, owing to electronegativity and leaving ability) in an axial position. Thus, the initial intermediate formed is (**37**), in which the bulky *t*-butyl group is in an unfavored axial position. Instead, pseudorotation places the leaving group ($PhCH_2$) in the preferred axial position for elimination of toluene via Path 2, which gives the final inverted product, (*t*-Bu)(Ph)MeP=O.

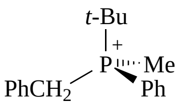

(**36**)

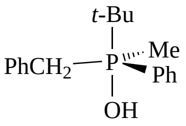

(**37**)

7.4 Enzyme Systems[17,22]

The wealth of structural and mechanistic information available for pentacoordinated phosphorus has provided a firm foundation upon which to explore more complicated

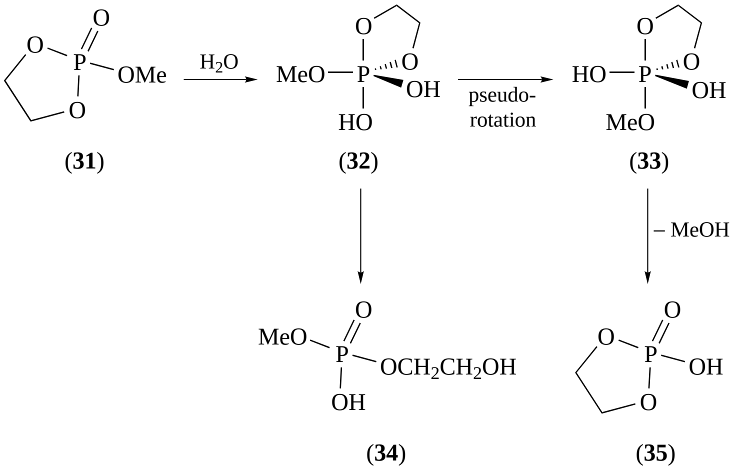

Scheme 5

systems where pentacoordinated phosphorus may play a key role. There are several important biological reactions that are catalyzed by phosphoryl- and nucleotidyl-transfer enzymes. Many of these are postulated to go through ‘in-line’ pentacoordinated mechanisms, in which both the incoming and departing groups are axial. For example, the transphosphorylation step of ribonuclease action on a dinucleotide substrate is suggested to go through a transition state that resembles the intermediates in Scheme 5.

7.5 Halosilanes

Nucleophilic attack at the silicon atom in halosilanes can lead to inversion or retention of configuration, depending on the nature of the leaving group.[81] When the leaving group is chloride, inversion is the usual course. Since fluoride is a poorer leaving group, both retention and inversion are observed with this halide, depending on various other factors. As usual, the incorporation of rings can alter the usual inversion path; retention is observed in equation (33).

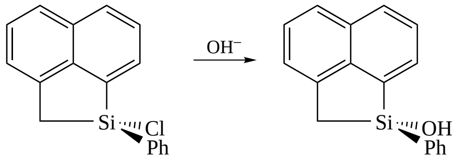

(33)

7.6 Catalytic Activation of Organosilicon Reagents by Nucleophiles[15]

This is one of the most useful applications of organosilicon reagents in organic chemistry, and ionic fluorides are the most common catalysts for this purpose. For example, the reduction of carbonyl groups is proposed to go through both a 10-Si-5 and a 12-Si-6 intermediate, as shown in Scheme 6. Many other reactions, such as the activation of enoxysilanes for the synthesis of carbon–carbon bonds, are believed to proceed through hypervalent intermediates. With the knowledge that many 10-Si-5 silicates are significantly more reactive than their 8-Si-4 counterparts (Section 6.2), these mechanisms appear highly plausible.

7.7 Hypervalent Intermediates in Sulfur Chemistry[19,23]

Evidence for hypervalent intermediates in sulfur chemistry is less well established than in phosphorus and silicon chemistry. Racemization and reduction of sulfoxides each appear to go through hypervalent 10-S-4 sulfurane intermediates. In addition, pathways for the reaction of sulfonium salts with organometallics involve plausible hypervalent intermediates (Scheme 7). Ligand coupling with retention of configuration is presumed to occur via a sulfurane intermediate

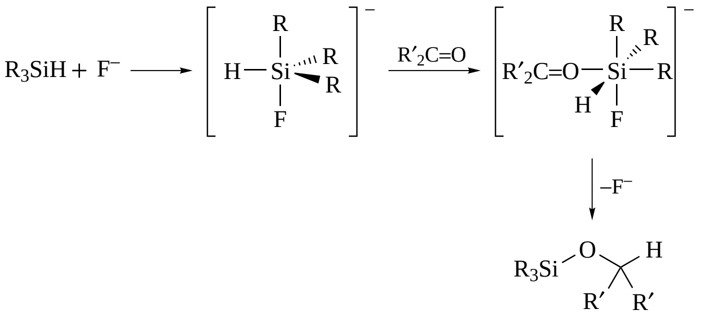

Scheme 6

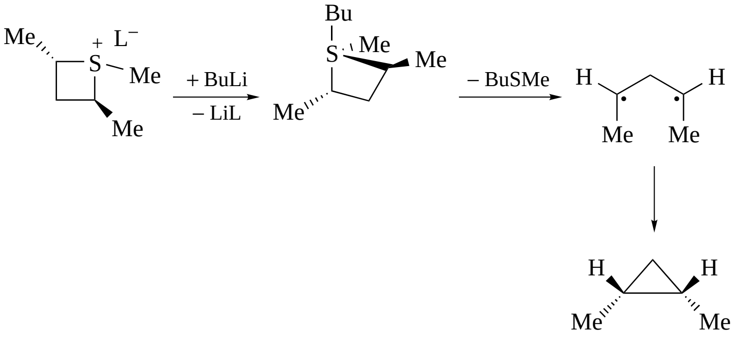

Scheme 7

(equation 34).[83]

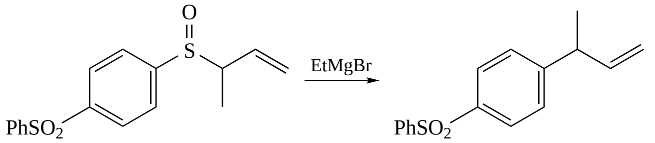

(34)

7.8 Transition State Model for Edge Inversion at 8-X-3 (X = Group 15 Element) Centers[84–86]

The isolation of stable 10-X-3 (X = P, As, Sb) derivatives (**16**) led to the idea that this geometry might represent the inversion transition state for trivalent XL_3 molecules. Inversion of these species had been considered to proceed in a similar manner to NH_3; that is, a vertex pathway whereby a vertex is inverted through the center of a tetrahedron via a trigonal planar transition state. In an edge inversion mechanism, the edges of a tetrahedron are inverted via a square-planar transition state. These processes are illustrated in Figure 8. Of course, vertex inversion is highly unlikely when all four substituents are atoms or ligands. However, when one of the substituents is a nonbonding pair of electrons (substituent A in Figure 8), both mechanisms are possible. Many factors are involved in the choice of one path over the other, but the transition state for the edge inversion process involves a 3c/4e hypervalent bond with ligands C and D. Calculations have predicted that PH_3 and PH_2F invert via the vertex process, while PHF_2 and PF_3 favor the edge pathway. Note that the crossover occurs when two highly electronegative substituents are attached. In an elegant study, (**38**) was synthesized and its inversion barrier measured by NMR magnetization transfer experiments. Such a molecule has to invert by the edge mechanism, and calculations based on this mechanism produced results in good agreement with the experimental values.

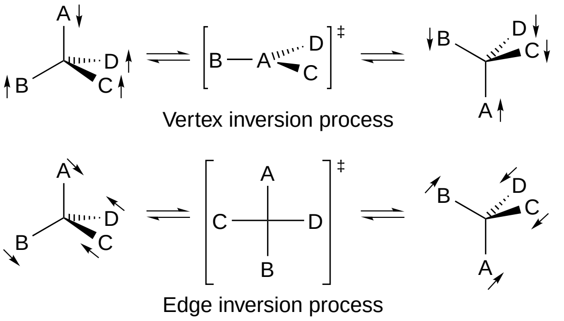

Figure 8 The vertex and edge inversion processes for 10-X-3 XL_3 (X = Group 15 element) molecules; A is the lone pair; L are B, C, D

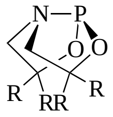

(**38**)

8 INTER-LIGAND HYPERVALENT INTERACTIONS

The development of the discipline of organometallic chemistry over the past several decades is due in large part to the way in which transition metals can bind and preorganize substrates for further reaction. It is quite common for two apparently distinct ligands to engage in reactions with each other, or to show structural features indicative of strong interactions, leading to nonclassical structures and bonding arrangements. The undoubted champion in this respect is the hydride ligand; with its absence of core electrons and a 1s valence orbital, hydrogen forms strong bonds with many elements. M–H bonds engage in a wide spectrum of secondary bonding interactions with other M–L moieties[37] (*see Agostic Bonding*; *Activation*). These may generally be termed Inter-Ligand Hypervalent Interactions.

As long ago as 1988, Crabtree proposed that the silane σ-bond complex $[CpMn(CO)_2(HSiFPh_2)]$ (**39**) was better formulated as a classical silyl hydride.[87] This complex displays a long Si–F bond; Crabtree suggested that this arose from donation of electron density from the Mn–H bond into the suitably disposed Si–F σ^* orbital (**40**), with the Si atom adopting a tbp geometry. Thus, instead of viewing the M-Si-H moiety as resulting from arrested oxidative addition, addition is considered to be complete and a secondary back-interaction occurs between the resulting silane and hydride ligands.

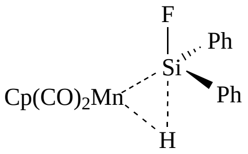

(**39**)

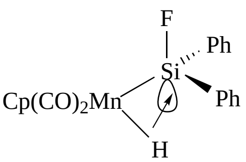

(**40**)

A neutron diffraction structure of the dihydrogen-hydride complex $[(EtPh_2P)_3Fe(H)(\eta^2\text{-}H_2)]$ (**41**) provided accurate positions for the three ligand hydrogen atoms, and revealed the H_2 ligand to be twisted from the expected arrangement so as to bring one of its hydrogen atoms into close proximity with the unique hydride H atom. An attractive interaction appears to occur between the (η^2-H_2) and H ligands. This interaction seems to be different in nature to that proposed for representation (**40**), with little or no changes evident in the bond lengths of the (η^2-H_2) and M–H moieties. Rather is it probably an electrostatic interaction, with the negatively charged hydride H atom being attracted to the somewhat positive dihydrogen moiety. However, a distinct type of interaction occurs in trihydride complexes such as $[CpIr(PR_3)H_3]^+$. Here it is impossible to discern individual hydride and dihydrogen moieties. Although neutron diffraction has shown the H$\cdots$H distances in this complex to be too long for significant bonding interactions to exist, the ^{1}H NMR spectrum displays massive couplings between the three hydride nuclei: these can be as high as 45 000 Hz. This phenomenon puzzled chemists for several years, until it was realized that the effect was quantum mechanical in origin, with the close hydrogen nuclei exchanging sites by a tunneling mechanism.[88]

The complex $[(PCy_3)_2RuH_2(\eta^2\text{-}H_2)(\eta^2\text{-}HSiPh_3)]$ (**42**) was reported to contain two different σ-bond ligands, namely molecular hydrogen and triphenylsilane.[89] Closer inspection revealed, however, that the Si$\cdots$H 'nonbonded' distance was only 6% longer than the Si–H 'bonded' one; in other words the two H atoms trans to the phosphine ligands are virtually indistinguishable, and both are clearly interacting with the Si atom. In such a situation, it is more realistic to consider a single group $[H_2SiPh_3]^-$ acting as a tridentate ligand in this Ru complex, with a 3c/4e bond holding the H-Si-H moiety together. The ligand is then a pentacoordinate, hypervalent silicon species, which may be considered an analog of the trihydrogen anion, $[H_3]^-$. It is noteworthy in this respect that the recently reported complex $[K(18\text{-crown-}6)][H_2SiPh_3]$ contains an uncoordinated 10-Si-5 $[H_2SiPh_3]^-$ ion, in which the hydride ligands occupy the axial sites in a tbp structure.[90] Analogous behavior has also been reported for the borohydride ligand in a transition metal hydride complex. Thus, while the two metal centers in the bimetallic ruthenium complex $[(triphos)Ru(H)(BH_4)(H)Ru(triphos)]^+$ are bridged by BH_4^-, the analogous iron species is formulated instead as $[(triphos)Fe(BH_6)Fe(triphos)]^+$. The bridging moiety here is formally $[BH_6]^{3-}$; a 12-B-6 entity: all B–H distances are statistically equivalent, and only a single ^{1}H resonance is discernable in the hydride region of the NMR spectrum.[91,92]

Since the mid-1990s, a wide range of silyl hydride metallocene complexes of Nb and Ta has been reported by Nikonov, with one example shown in (**43**). These exhibit short Si–H distances, and show large Si, H coupling constants in their NMR spectra.[36] The Si atom adopts a tbp geometry, with a ligand such as Cl trans to the interacting hydride. Donation of electron density from the M–H bond can then occur into the Si–Cl σ^* orbital, in the manner described above for (**40**). Example (**43**), in which an M–H unit simultaneously interacts with two Si centers, can also be considered to be held together by a 5c/6e bond (q.v.).

What is clear from all these examples is that hydrogen can participate in a wide variety of strong secondary interactions with neighboring ligands in transition metal complexes. IHIs constitute a distinct type of nonclassical bonding that is different from other types, such as in σ-bond complexes and agostic interactions (*see Agostic Bonding*). IHIs are important, as major catalytic processes like migratory insertions proceed through a transition state in which a close approach and interaction of the ligands involved leads to a redistribution of bonding. Whilst such inter-ligand hypervalent interactions have been intimated in reaction schemes for several decades, it is only recently that they have been observed in the ground state of transition metal complexes.

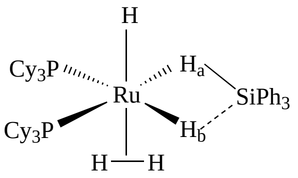

(**42**)

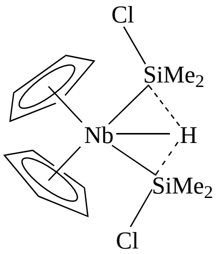

(**43**)

9 OTHER HYPERVALENT SPECIES

9.1 5c/6e Hypervalent Bonding[93]

Theoretically, the concept of hypervalent bonding can be expanded by adding two centers and two electrons at a time in a linear array. Practically, however, the limit may be reached at a 5c/6e system. There are several species of this type known, such as $[R_f\text{–}I\text{–}F\text{–}I\text{–}R_f]^-$ and $[F\text{–}Xe\text{–}F\text{–}Xe\text{–}F]^+$. Pentahalide monoanions like Br_5^- are bent and hence do not conform to this 5c/6e model. The addition of two atoms introduces two more σ atomic orbitals to the scheme, which give rise to a total of five MOs. The lowest three of these are occupied in the hypervalent bonding scheme. The lowest energy MO is bonding with respect to all five atoms; the next is bonding for the first and second and the fourth and fifth atoms, with a node at the central atom; the highest occupied MO is totally nonbonding with nodes at the second and fourth atoms.

9.2 Hypervalent Compounds of Period 2

The vast majority of hypervalent species, whether isolable and stable or proposed as reactive intermediates (rather than transition states), contain a central atom from period 3 or below. However, there is indisputable evidence that elements of period 2 can form species with hypervalent bonds. In fact, hydrogen bonding can be considered a form of hypervalent bonding for a first period element, in which hydrogen exceeds its 'duet'. For example, the well-known symmetrical ion $[F\text{–}H\text{–}F]^-$ has a very similar σ-bonding scheme to that illustrated in Figure 1, except that hydrogen uses an s orbital rather than a p orbital,[94] and the IHIs described in Section 8 require hydrogen to be formally hypervalent.

Nitrogen(V) is an accessible and common oxidation state, which occurs in such everyday laboratory species as nitric acid

HNO_3 and the nitrate ion NO_3^-. Nitrogen is precluded from forming sp^3d^n hybrid orbitals, and this caused early conceptual resistance to the idea that these molecules were hypervalent, with the nonexistence of NF_5 being cited as a counterexample. In fact, it is now clear that the instability of NF_5 owes more to the steric interactions that this pentacoordinate molecule would suffer:[95] the conjugate cation NF_4^+ is accessible and has been stabilized in a variety of salts. Furthermore, the surprisingly unreactive isoelectronic molecule ONF_3 has a short nitrogen–oxygen distance, which can only be categorized as a N=O bond, and hence is clearly a hypervalent N(V) species. Although nitrogen does not possess valence d orbitals, all these compounds can be easily accommodated using 3c/4e bonding schemes or resonance structures, as described in Section 1.

The carbon atoms found at the center of a tbp cage, examples of which are the theoretical CLi_5[96] and the isolated cation $C[AuPPh_3]_5^+$,[97] might be considered hypervalent on first inspection. However, cage bonding (forming Li–Li and Au–Au linkages) is the key factor in the stability of these molecules. The first hypervalent fluorine species was reported in 1976 by Ault and Andrews;[98] the F_3^- ion trapped in an argon matrix. The mutual exclusion rule for IR and Raman spectroscopy was convincing evidence for the linear, symmetrical arrangement of the three fluorine atoms with a Cs^+ counter ion. In 1984, Lee and Martin[99] used NMR spectroscopy to show that several boron compounds, such as (**44**) and (**45**), were authentic 10-B-5 and 12-B-6 species in solution. The first report of hypervalent 10-C-5 carbon (**46**) came in 1979 by Forbus and Martin.[100] This work was expanded in a series of papers in 1993,[9,101,102] which presented NMR and electrochemical evidence for isolation of the first molecule, which is a model for the transition state for an S_N2 reaction at a tetrahedral carbon center.

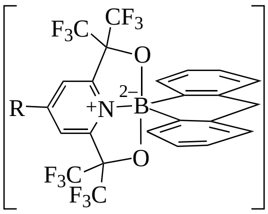

10-B-5

(**44**) Overall monoanion

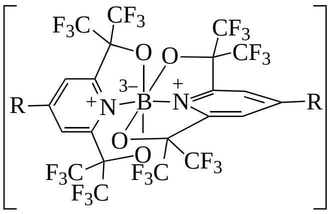

12-B-6

(**45**) Overall monoanion

9.3 Other Species Considered as Hypervalent

Although coordination numbers higher than six were not explicitly considered above, certain species, such as the seven-coordinate 14-I-7 molecule IF_7 in a pentagonal bipyramid geometry, contain a linear F–I–F 3c/4e hypervalent bond.

Hypervalent bonding has also been extended to species that are generally drawn to include double bonds to oxygen or CR_2, such as the organic sulfoxides R_2SO, sufones R_2SO_2, sulfur ylides R_2SCR_2, phosphine oxides R_3PO, and phosphorus ylides R_3PCR_2. Virtually any molecule or ion for which a reasonable Lewis structure can be written with multiple bonds such that the central atom will expand its octet may reasonably be thought of as hypervalent (see Section 1). This includes all noble gas molecules and complex ions, as well as high-valent halogenated derivatives.

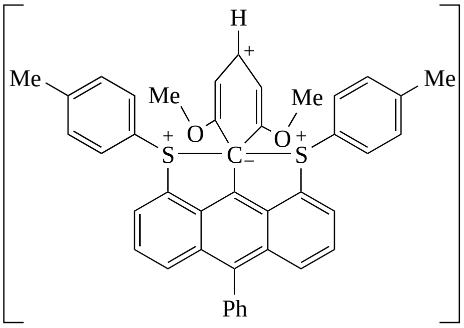

10-C-5

(**46**) Overall monoanion

10 RELATED ARTICLES

Chlorine, Bromine, Iodine, & Astatine: Inorganic Chemistry; Coordination Numbers & Geometries; Electronic Structure of Main-group Compounds; Molecular Orbital Theory; Noble Gases: Inorganic Chemistry; Phosphorus: Inorganic Chemistry; Silicon: Inorganic Chemistry; Sulfur: Inorganic Chemistry.

11 REFERENCES

1. J. I. Musher, *Angew. Chem., Int. Ed. Engl.*, 1969, **8**, 54.
2. G. N. Lewis, ‘Valence and the Structure of Atoms and Molecules’, Chemical Catalog Co., New York, 1923.
3. I. Langmuir, *J. Am. Chem. Soc.*, 1919, **41**, 868.
4. A. E. Reed and P. V. Schleyer, *J. Am. Chem. Soc.*, 1990, **112**, 1434.
5. W. Thiel and A. A. Voityuk, *Int. J. Quantum Chem.*, 1992, **44**, 807.
6. J. C. Martin, *Science*, 1983, **221**, 509.
7. V. B. Koutecky and J. I. Musher, *Theor. Chim. Acta*, 1974, **33**, 227.
8. F. A. Cotton and G. Wilkinson, ‘Advanced Inorganic Chemistry’, 5th edn., John Wiley & Sons, New York, 1988, p. 28.
9. T. R. Forbus and J. C. Martin, *Heteroat. Chem.*, 1993, **4**, 113.

10. G. Sini, G. Ohanessian, P. C. Hiberty, and S. S. Shaik, *J. Am. Chem. Soc.*, 1990, **112**, 1407.
11. D. J. Hajdasz and R. R. Squires, *J. Am. Chem. Soc.*, 1986, **108**, 3139.
12. J. Cioslowski and S. T. Mixon, *Inorg. Chem.*, 1993, **32**, 3209.
13. R. J. Gillespie and B. Silvi, *Coord. Chem. Rev.*, 2002, **233**, 53.
14. C. W. Perkins, J. C. Martin, A. J. Arduengo III, W. Lau, A. Alegria, and J. K. Kochi, *J. Am. Chem. Soc.*, 1980, **102**, 7753.
15. R. J. P. Corriu and J. C. Young, in ‘The Silicon-Heteroatom Bond’, eds. S. Patai and Z. Rappoport, John Wiley & Sons, Chichester, 1991, p. 1 and p. 49.
16. I. Omae, ‘Organotin Chemistry’, 1st edn., Elsevier, Amsterdam, 1989.
17. R. R. Holmes, ‘Pentacoordinated Phosphorus’, 1st ed., American Chemical Society, Washington, DC, 1980.
18. R. Bohra and H. W. Roesky, *Adv. Inorg. Chem.*, 1984, **28**, 203.
19. A. Senning, ed., ‘Sulfur in Organic and Inorganic Chemistry’ Marcel Dekker, New York, 1982.
20. G. F. Koser, in ‘The Chemistry of Halides, Pseudo-halides, and Azides’, eds. S. Patai and Z. Rappoport, John Wiley & Sons, Chichester, 1983, p. 721.
21. K. Seppelt and D. Lentz, *Prog. Inorg. Chem.*, 1982, **29**, 167.
22. R. R. Holmes, *Prog. Inorg. Chem.*, 1984, **32**, 119.
23. D. H. R. Barton ed., ‘Comprehensive Organic Chemistry’, Pergamon Press, Oxford, 1979.
24. E. W. Abel, F. G. A. Stone, and G. Wilkinson eds, ‘Comprehensive Organometallic Chemistry II’, Pergamon Press, Oxford, 1995.
25. G. Wilkinson ed., ‘Comprehensive Organometallic Chemistry’, Pergamon Press, Oxford, 1982.
26. J. A. McCleverty and T. J. Meyer eds, ‘Comprehensive Coordination Chemistry II’, Elsevier, Amsterdam, 2003.
27. G. Wilkinson, ed., ‘Comprehensive Coordination Chemistry’, Pergamon Press, Oxford, 1987.
28. N. N. Greenwood and A. Earnshaw, ‘Chemistry of the Elements’, Pergamon, Oxford, 1984.
29. T. Wirth, Hypervalent Iodine Chemistry – Modern Developments in Organic Synthesis – Introduction and General Aspects, in ‘Hypervalent Iodine Chemistry: Modern Developments in Organic Synthesis’; *Top. Curr. Chem.*, 2002, **224**, 1.
30. H. Tohma and Y. Kita, Synthetic Applications (total synthesis and natural product synthesis), in ‘Hypervalent Iodine Chemistry: Modern Developments in Organic Synthesis’; *Top. Curr. Chem.*, 2002, **224**, 209.
31. T. Kitamura and Y. Fujiwara, *Org. Prep. Proced. Int.*, 1997, **29**, 409.
32. D. Uraguchi, T. Ooi, and K. Maruoka, *J. Synth. Org. Chem., Jpn.*, 2000, **58**, 14.
33. M. Nakajima, *J. Synth. Org. Chem., Jpn.*, 2000, **58**, 839.
34. R. D. Harcourt and T. M. Klapotke, *J. Fluor. Chem.*, 2003, **123**, 5.
35. A. I. Boldyrev and L. S. Wang, *J. Phys. Chem. A*, 2001, **105**, 10759.
36. G. I. Nikonov, *J. Organomet. Chem.*, 2001, **635**, 24.
37. G. S. McGrady and G. Guilera, *Chem. Soc. Rev.*, 2003, **32**, 383.
38. V. I. Minkin and R. M. Minyaev, *Chem. Rev.*, 2001, **101**, 1247.
39. H. J. Frohn and V. V. Bardin, *Organometallics*, 2001, **20**, 4750.
40. C. E. Holloway and M. Melnik, *Main Group Met. Chem.*, 2000, **23**, 1.
41. E. R. T. Tiekink, *Rigaku J.*, 2002, **19**, 14.
42. J. Drabowicz and G. Halaba, *Rev. Heteroat. Chem.*, 2000, **22**, 1.
43. T. Negoro and S. Oae, *Rev. Heteroat. Chem.*, 1995, **13**, 235.
44. A. J. Arduengo III and C. A. Stewart, *Chem. Rev.*, 1994, **94**, 1215.
45. D. V. Sevenard, A. A. Kolomeitsev, B. Hoge, E. Lork, and G. V. Roschenthaler, *J. Am. Chem. Soc.*, 2003, **125**, 12366.
46. M. G. Voronkov, V. M. Dyakov, and S. V. Kirpichenko, *J. Organomet. Chem.*, 1982, **233**, 1.
47. M. A. H. Laramay and J. G. Verkade, *Z. Anorg. Allg. Chem.*, 1991, **605**, 163.
48. K. M. Kadish, C. Swistak, B. Boisselier-Cocolios, J. M. Barbe, and R. Guilard, *Inorg. Chem.*, 1986, **25**, 4336.
49. A. J. Arduengo III, C. A. Stewart, F. Davidson, D. A. Dixon, J. Y. Becker, S. A. Culley, and M. B. Mizen, *J. Am. Chem. Soc.*, 1987, **109**, 627.
50. T. J. Atkins and J. E. Richman, *Tetrahedron Lett.*, 1978, 5149.
51. L. Khriachtchev, M. Pettersson, N. Runeberg, J. Lundell, and M. Rasanen, *Nature*, 2000, **406**, 874.
52. J. Emsley and D. Hall, ‘The Chemistry of Phosphorus’, John Wiley & Sons, New York, 1976.
53. D. E. C. Corbridge, ‘Phosphorus’, 3rd edn., Elsevier, Amsterdam, 1985.
54. R. J. Gillespie and I. Hargittai, ‘The VSEPR Model of Molecular Geometry’, Alleyn and Bacon, Boston, MA, 1991.
55. K. Nakamoto, ‘Infrared and Raman Spectra of Inorganic and Coordination Compounds’, 4th edn., John Wiley & Sons, New York, 1986.
56. K. O. Christe and W. W. Wilson, *Inorg. Chem.*, 1989, **28**, 3275.
57. H. Beckers, J. Breidung, H. Burger, R. Kuna, A. Rahner, W. Schneider, and W. Thiel, *J. Chem. Phys.*, 1990, **93**, 4603.
58. J. G. Verkade and L. D. Quin eds, ‘Phosphorus-31 NMR Spectroscopy in Stereochemical Analysis’, VCH, Deerfield Beach, 1987.
59. D. Christen, J. Kadel, A. Liedtke, R. Minkwitz, and H. Oberhammer, *J. Phys. Chem.*, 1989, **93**, 6672.

60. R. H. Herber, ed., ‘Chemical Mossbauer Spectroscopy’, Plenum, New York, 1984.
61. A. H. Cowley, M. Lattman, and M. L. Walker, *J. Am. Chem. Soc.*, 1979, **101**, 4074.
62. R. W. Shaw, T. X. Carroll, and T. D. Thomas, *J. Am. Chem. Soc.*, 1973, **95**, 5870.
63. S. Trippet, *Pure Appl. Chem.*, 1974, **40**, 595.
64. J. A. Deiters, R. R. Holmes, and J. M. Holmes, *J. Am. Chem. Soc.*, 1988, **110**, 7672.
65. R. Hoffmann, J. M. Howell, and E. L. Muetterties, *J. Am. Chem. Soc.*, 1972, **94**, 3047.
66. M. M. L. Chen and R. Hoffmann, *J. Am. Chem. Soc.*, 1976, **98**, 1647.
67. H. Oberhammer, J. Grobe, and D. Le Van, *Inorg. Chem.*, 1982, **21**, 275.
68. R. S. Berry, *J. Chem. Phys.*, 1960, **32**, 933.
69. L. D. Martin, E. F. Perozzi, and J. C. Martin, *J. Am. Chem. Soc.*, 1979, **101**, 3595.
70. D. S. Brown, F. W. Einstein, and D. G. Tuck, *Inorg. Chem.*, 1969, **8**, 14.
71. W. Bubenheim, G. Frenzen, and U. Muller, *Acta Crystallogr. Sect. C: Cryst. Struct. Commun.*, 1995, **51**, 1120.
72. J. Taraba and Z. Zak, *Inorg. Chem.*, 2003, **42**, 3591.
73. W. C. Smith, *Angew. Chem., Int. Ed. Engl.*, 1962, **1**, 467.
74. D. B. Dess and J. C. Martin, *J. Organomet. Chem.*, 1983, **48**, 4155.
75. R. M. Moriarty and O. Prakash, *Acc. Chem. Res.*, 1986, **19**, 244.
76. T. Wirth, Oxidations and rearrangements in ‘Hypervalent Iodine Chemistry: Modern Developments in Organic Synthesis’; *Top. Curr. Chem.*, 2002, **224**, 185.
77. M. Lattman, B. N. Anand, D. R. Garrett, and M. A. Whitener, *Inorg. Chim. Acta*, 1983, **76**, L139.
78. E. A. V. Ebsworth, J. H. Holloway, N. J. Pilkington, and D. W. H. Rankin, *Angew. Chem., Int. Ed. Engl.*, 1984, **23**, 630.
79. A. J. Arduengo III, M. Lattman, H. V. R. Dias, J. C. Calabrese, and M. Kline, *J. Am. Chem. Soc.*, 1991, **113**, 1799.
80. A. J. Arduengo III, H. V. R. Dias, and J. C. Calabrese, *J. Am. Chem. Soc.*, 1991, **113**, 7071.
81. R. R. Holmes, *Chem. Rev.*, 1990, **90**, 17.
82. F. H. Westheimer, *Acc. Chem. Res.*, 1968, **1**, 70.
83. S. Oae and Y. Uchida, *Acc. Chem. Res.*, 1991, **24**, 202.
84. A. J. Arduengo III and D. A. Dixon, in ‘Heteroatom Chemistry: ICHAC-2’, ed. E. Block, VCH: New York, 1990, p. 47.
85. A. J. Arduengo III, D. A. Dixon, and D. C. Roe, *J. Am. Chem. Soc.*, 1986, **108**, 6821.
86. D. A. Dixon, A. J. Arduengo, and T. Fukunaga, *J. Am. Chem. Soc.*, 1986, **108**, 2461.
87. R. H. Crabtree and D. G. Hamilton, *Adv. Organomet. Chem.*, 1988, **28**, 299.
88. F. Maseras, A. Lledos, E. Clot, and O. Eisenstein, *Chem. Rev.*, 2000, **100**, 601.
89. K. Hussein, C. J. Marsden, J. C. Barthelat, V. Rodriguez, S. Conejero, S. Sabo-Etienne, B. Donnadieu, and B. Chaudret, *Chem. Commun.*, 1999, 1315.
90. M. J. Bearpark, G. S. McGrady, P. D. Prince, and J. W. Steed, *J. Am. Chem. Soc.*, 2001, **123**, 7736.
91. G. S. McGrady, G. Guilera, J. W. Steed, and N. Kaltsoyannis, *New J. Chem.*, 2004, **28**, 444.
92. A. C. Hillier, H. Jacobsen, D. Gusev, H. W. Schmalle, and H. Berke, *Inorg. Chem.*, 2001, **40**, 6334.
93. D. A. Dixon, A. J. Arduengo III, and W. B. Farnham, *Inorg. Chem.*, 1989, **28**, 4589.
94. J. Emsley, *Chem. Soc. Rev.*, 1980, **9**, 91.
95. K. O. Christe, W. W. Wilson, G. J. Schrobilgen, R. V. Chirakal, and G. A. Olah, *Inorg. Chem.*, 1988, **27**, 789.
96. P. V. Schleyer, E. U. Wurthwein, E. Kaufmann, T. Clark, and J. A. Pople, *J. Am. Chem. Soc.*, 1983, **105**, 5930.
97. F. Scherbaum, A. Grohmann, G. Muller, and H. Schmidbaur, *Angew. Chem., Int. Ed. Engl.*, 1989, **28**, 463.
98. B. S. Ault and L. Andrews, *Inorg. Chem.*, 1977, **16**, 2024.
99. D. Y. Lee and J. C. Martin, *J. Am. Chem. Soc.*, 1984, **106**, 5745.
100. T. R. Forbus and J. C. Martin, *J. Am. Chem. Soc.*, 1979, **101**, 5057.
101. T. R. Forbus and J. C. Martin, *Heteroat. Chem.*, 1993, **4**, 129.
102. T. R. Forbus, J. L. Kahl, L. R. Faulkner, and J. C. Martin, *Heteroat. Chem.*, 1993, **4**, 137.

Indium: Inorganic Chemistry

Yanbao Zhao & Zhijun Zhang
Henan University, Kaifeng, China

Based in part on the article Indium: Inorganic Chemistry by Dennis G. Tuck which appeared in the Encyclopedia of Inorganic Chemistry, First Edition.

1 Introduction 1
2 Indium (I) Chemistry 1
3 Indium (II) Chemistry 4
4 Indium (III) Chemistry 4
5 Indium Precursors for CVD 8
6 Indium Nanomaterials 9
7 Intermetallic Compounds 11
8 Indium Catalyzed Organic Synthesis 12
9 References 14

1 INTRODUCTION

Indium is a very soft, silvery–white metal with a brilliant luster, rather like tin in appearance, located behind gallium in the periodic table of the elements. It is considered a nontoxic metal, and is ductile, malleable and diamagnetic. The pure metal gives a high-pitched 'scream' when bent. It wets glass, as does gallium, and so it can be used to seal glass to metals. It can form alloys with extremely low-melting points, down to below room temperature (The alloy of 24% indium and 76% gallium is liquid at room temperature). It is used for electric fuses, safety plugs for storage tanks, and mainly for the automatic release of fire alarm and sprinkler systems, and also for cooling and as a heat-exchange medium in nuclear technology. The majority of the world's supply of indium is produced in Canada, where it would not normally be made in laboratory as it is commercially available. Indium is a by-product of the formation of lead and zinc. Indium metal is isolated by the electrolysis of indium salts in water. Further processes are required to make very pure indium for electronics purposes.

Indium is stable in air or in oxygen at room temperature, and does not react with water even at the boiling point but on heating goes to the oxide.[1] Indium oxide, an n-type semiconductor with a wide band gap of about 3.6 eV, is an ideal material for flat-panel displays owing to its high electrical conductivity and optical transparency, and also is used for gas sensors and conducting glass.[2] When heated, elemental indium easily reacts with the halogens to form the corresponding halide, and with sulfur, selenium, nitrogen, and phosphorous to give the corresponding indium-containing III-V/VI compounds that are well-known semiconductor materials and have technological importance for blue/violet light-emitting diodes (LEDs), laser diodes, solar cells and other optoelectronic devices. In addition, indium and its compounds are also used to promote some organic synthesis.[3]

The inorganic chemistry of indium during the past decade has received unbroken attention that originates from two aspects. One stems from the resurgence of the chemistry of low-valent indium, which is currently extended to various fields. A special highlight is the use of CpIn ($Cp = C_5H_5$), R_4In_4 ($R = Cp$, $C(SiMe_3)_3$, $Si(SiMe_3)_3$), and R_4In_2 ($R = SiBu^t{}_3$, $CH(SiMe_3)_2$) compounds to further prepare new compounds and clusters, which illustrate the lively development and the current trends in this field.[4,5] The other is from the understanding that indium compounds are potential precursors for applications in the field of new materials. In addition, the development of nanotechnology and the utility of indium reagents in organic synthesis present new and exciting opportunities for indium chemistry.

2 INDIUM (I) CHEMISTRY

2.1 Introduction

The current interest in monovalent indium compounds originates from the understanding of the structures and properties of these novel compounds, with particular focus on InX, CpIn, and In_4R_4 complexes. Indium (I) halides can be used as starting materials to prepare other indium (I) compounds and play an important role in the study of the oxidation chemistry of indium (I). The cyclopentadienylindium (I) (CpIn), obtained from the reaction of indium halide with LiCp, is another starting point for the synthesis of a number of indium (I) derivatives. The third approach to obtain indium (I) compounds depends on the tetraalkyltetraindium (I) compounds In_4R_4 ($R = C(SiMe_3)_3$, $Si(SiMe_3)_3$) as a source of In (I) compounds, which exhibits a distinctive chemical reactivity (Scheme 1).[4] The monomer fragment InR has similar frontier orbitals to carbon monoxide, and can form transition metal compounds analogous to metal carbonyls with bridging or terminal InR ligands. Furthermore, In_4R_4 can be oxidized with oxygen, sulfur, selenium, or halide to form heterocubane-type structures containing four indium atoms. These reactions open a new route to organometallic compounds and lead to novel compounds with unusual structures.

2.2 Halogen Derivatives

Indium (I) halides can be prepared by dissolving an excess of indium in hydrohalide acid or reduction of trihalides with metal. The structures of the bromides have been

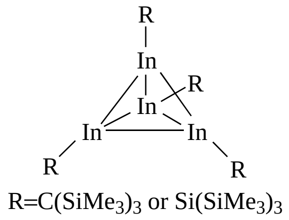

Scheme 1 The molecule structure of In_4R_4 with R = $C(SiMe_3)_3$ and $Si(SiMe_3)_3$, Ref. 4

reinvestigated.[6] Some theoretic calculations indicate that the reduced phases (InBr, In_2Br_3, and In_3Br_7), among the binary indium bromides, are 'soft' and easy to perturb upon chemical reaction, and the coordination polyhedra around In^+ ions are highly irregular. The total In–Br bonding interaction is weak, but in none of the cases has there been found a directed electron 'lone-pair' effect for In^+.[7] The bromide In_5Br_7 exists in two polymorphs, both of which have a layer structure and consist of the structure fragments $[In^I_6Br_2]^{4+}$ and $[In^{II}_4Br_{12}]^{4-}$. The latter is composed of two ethane-like $[In^{II}_2Br_6]^{2-}$ units, which contain In–In bonds.[8] The mixed-valence species also are found in the compounds In_4Br_7 and In_7Br_9, which can be described as $(In^{3+})_3(In^+)_5\,(Br^-)_{14}$ and $(In^+)_6(In^{3+})\,(Br^-)_9$ respectively.[9]

The mixed transition metal indium bromides $InMBr_3$ (M = Fe, Mn), In_2MBr_6 (M = Th, Zr), and $In_3Ti_2Br_9$ are known. In_2ThBr_6 adopts monoclinic crystal structure, which is built up from three- dimensional (3D) interconnected $ThBr_8{}^{4-}$ bisdisphenoids and $InBr_9{}^{8-}$ monocapped cubes, the latter polyhedra being significantly distorted. Within $InMBr_3$, the transition metal cations are octahedrally coordinated by Br^- anions; monovalent indium cations are found in strongly distorted trigonal Br^- prisms, which are tricapped by additional Br^- anions.[10,11]

Fluoride compound, $PtIn_7F_{13}$ is prepared by reduction of InF_3 with In powder, which is built up from the $[PtIn_6]$ octahedra. These units are stacked in a alternating fashion together with $[InPt_6]$ octahedra along [001]. Within the $[InPt_6]$ cluster, platinum centers are octahedrally coordinated by six In atoms. The Pt–In bond lengths are significantly shorter than that in intermetallic phases with sixfold coordinated Pt atoms, and the In–In distances are only slightly longer than in elemental In or molecular In clusters.[12] The compound $InBF_4$ is isotypical to KBF_4.

Indium (I) halides insert into nickel halogen bonds of carbonyl group free organonickel complexes to form Ni–In bond compounds, which can be viewed as derivatives of trimethylindium or indiumtrihalides.[13]

2.3 Reaction of In_4R_4 (R = $C(SiMe_3)_3$)

The tetrahedral tetraindium (I) compound In_4R_4 (R = $C(SiMe_3)_3$) is readily available by the reaction of indium monohalides with LiR (R = $C(SiMe_3)_3$). The monomeric fragments, possessing two empty p orbitals perpendicular to the In–C bond axis and an electron lone pair, thus making it isolobal to carbon monoxide. It can be used to form transition metal compounds that are similar to the metal carbonyls. The cubane In_4R_4 reacts with $(CO)_5Mn–Mn(CO)_5$ to form bis {μ-[tris(trimethylsily)methyl]indanyl}-di- manganese, in which two CO ligands are replaced by two InR fragments. Thus, two $Mn(CO)_4$ groups are bridged by two monoalkylindium units and a planar Mn_2In_2 molecular center.[14] Reaction with tricarbonyl- ironcyclooctatetraene produces $Fe_2(CO)_6\,(InR)_3$, which is one of the very rare examples of a compound with two $Fe(CO)_3$ fragments symmetrically bridged by three main-group elements. It involves a trigonal-bipyramidal Fe_2In_3 moiety with all indium atoms in equatorial positions (Scheme 2).[15] Similar replacements of CO ligands by InR is also demonstrated for $Ni_2Cp_2(\mu\text{-}CO)_2$, $Fe_2(CO)_9$, and $Fe_3(CO)_{12}$ by insertion of InR into the M–M bond and further replacement of one or both bridging carbonyl complexes.[16,17] The reaction of In_4R_4 with bis(cyclooctadiene) nickel (0) gives $Ni(InR)_4$, which is an analogoue of the thermally unstable carbonyl complex $Ni(CO)_4$ with a nickel atom tetrahedrally coordinated by four InR ligands. The Ni-In-C units with two-coordinated In atoms are exactly linear (Ni-In-C, 180.0°).[18] Similar reaction with bis(cyclooctadiene) platinum (0) also gives $Pt(InR)_4$ complex (Scheme 3).[19] In addition, CpIn is also isolobal to CO and displays transition metal carbonyl fragments. The structure of $Pd_3(InCp)_4(\mu_2\text{-}InCp)_4$ exhibits three edge-bridging $PdIn_4$ tetrahedrons. The three central palladium atoms are arranged with only a small deviation from linearity of 10°. The distortion of the $PdIn_4$ tetrahedrons is expressed in the In–Pd–In angles, which are smaller than 109° for the terminal In atoms and larger than 109° for the bridging In atoms.[20]

The In_4 cluster can be completely or partial oxidized with halogen or chalcogen to form In_4X_4 heterocubanes or mixed-valence compounds. The complex $In_4[C(SiMe_3)_3]_4$ abstracts O from *o*-nitrosotoluene forming the extremely

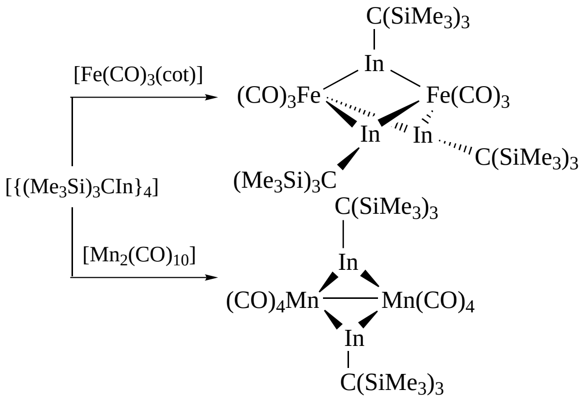

Scheme 2 Reaction of In_4R_4 (R = $C(SiMe_3)_3$) with $Fe(CO)_3(cot)$ and $Mn_2(CO)_{10}$. cot = cyclooctatetraene, Refs. 14,15

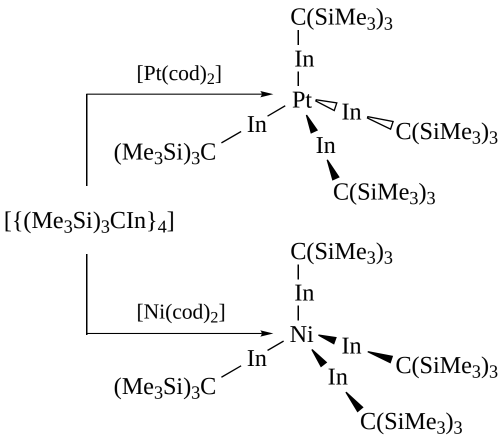

Scheme 3 Reaction of In_4R_4 ($R = C(SiMe_3)_3$) with $Pt(cod)_2$ and $Ni(cod)_2$. cod = cyclooctadiene, Refs. 18,19

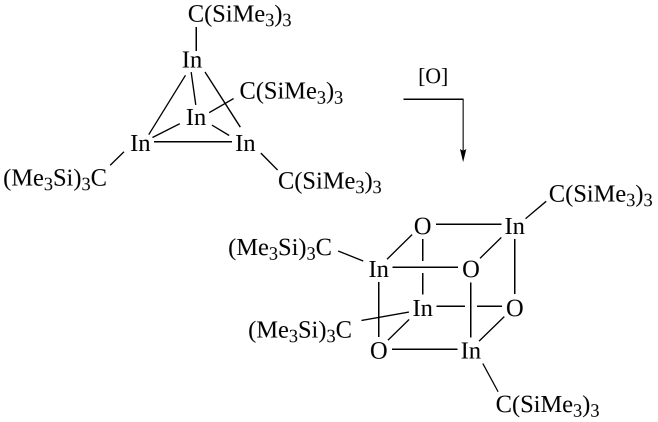

Scheme 4 The oxidization reaction of $[InC(SiMe_3)_3]_4$ to produce $In_4O_4[C(SiMe_3)_3]_4$, Ref. 21

hygroscopic $In_4O_4[C(SiMe_3)_3]_4$ (Scheme 4). The structure exhibits a distorted In_4O_4 moiety with normal In–O bond lengths, but short intracage In to In and O to O distances.[21] The reaction with chalcogen gives the compounds $In_4X_4R_4$, which adopt a slightly distorted In_4X_4 heterocubane structure with an alternating arrangement of In and X atoms (X = chalogen atom).[22] Partial oxidation of In_4R_4 with the sulfur atom donor yields the mixed-valent compound $[In_4S\{C(SiMe_3)_3\}_4]$, in which only one face of the In_4 tetrahedron of In_4R_4 is bridged by a sulfur atom. Partial oxidation of In_4R_4 with halogen donors affords novel alkylindium halides $In_2X_2R_2$ ($R = C(SiMe_3)_3$, $X = Cl$ or Br) and $In_3I_2R_3$, in which the indium atoms still possess low oxidation states. The tetrahedral arrangement of four indium atoms in a cluster is retained in the compound $In_4Br_2R_4$, in which one bromine atom occupied a μ_3-bridging position above one triangular face of the In_4 tetrahedron, and one edge of that triangle is bridged by the second bromine atom.[4]

2.4 In Cluster Compounds

Several interesting new forms of indium cluster compounds have been described during the last decade. The compound $(Bu^t{}_3Si)_6In_8$, prepared by the reaction of CpIn with $Bu^t{}_3SiNa$, has a novel eight-indium cluster framework in which a distorted cube of indium atoms is surrounded by the silyl groups;[23] the compound $[(Bu^t{}_3Si)_8In]_{12}$ possesses an In_{12} deltahedral framework with 20 triangular faces and 12 In atoms. The compound is not spherical, but resembles a stretched ellipsoid.[24] The reaction of LiC_6H_3-2,6-mes_2 ($mes = C_6H_2$-2,4,6-Me_3) with InCl produces the complex $In_8(C_6H_3$-2,6-$mes_2)_4$, possessing a distorted cubane arrangement of eight indium atoms, in which only four atoms of the metal carry a terphenyl substituent.[25]

2.5 Indium–Boron/Phosphorous Compounds

The most interesting aspect of the pyrazolylborates (pz) for indium is their ability to stabilize the univalent indium oxidation state. Thus, bulky poly(pyrazolyl)borate ligands such as $[HB(3\text{-}Bu^t pz)_3]^-$, $[HB(3\text{-}Phpz)_3]^-$, $[HB(3,5\text{-}Bu^t pz)_3]^-$, and $[HB(3,5\text{-}(CF_3)_2pz)_3]^-$ are used to stabilize the indium (I) species.[26,27] The complex $(3,5\text{-}Bu^t pz)In$ is synthesized by the treatment of $Na(3,5\text{-}Bu^t pz)$ with InCl, in which the $3,5\text{-}Bu^t pz$ ligand adopts a highly twisted configuration owing to steric interactions of the *tert*-butyl substituents in the 5 positions of the pyrazolyl groups. The compound $(3,5\text{-}Bu^t pz)In$ can undergo oxidative-addition reactions with I_2 and S_8 to give the complex $(3,5\text{-}Bu^t pz)InI_2$ and $(3,5\text{-}Bu^t pz)In(\mu^2\text{-}S_4)$, respectively. In addition, $[In(\eta^5\text{-}P_2C_3Bu^t{}_3)]$ and $[In(\eta^5\text{-}P_3C_2Bu^t{}_2)]$ are also prepared, which have a half-sandwich structure, similar to the η^5-coordination mode $[In(\eta\text{-}C_5H_5)]$ or InCp.[28]

2.6 Aqueous Solution Chemistry

Solutions of indium (I) can be prepared by treatment of indium amalgam with silver triflate in dry acetonitrile in the absence of oxygen, and then diluted with water to give the low-concentration aqueous solution, which plays a sizable role in the study of the details of intermolecular electron transfer processes in solution.[29] Aqueous In(I) solution has been used to examine the behavior of this hypovalent center in inorganic redox transformations. Reactions with complexes of the type $[(NH_3)_5Co^{III}(Lig)]$ and $[(NH_3)_5Ru^{III}(Lig)]$ ($Lig = Cl^-$, Br^-, I^- or $HC_2O_4{}^-$) show two consecutive one-electron reactions initiated by the formation of the metastable state In^{II}, which is then rapidly oxidized to In^{III}, and the first of which is predominating an inner-sphere mechanism.[30,31]

3 INDIUM (II) CHEMISTRY

3.1 Introduction

Most of the divalent indium compounds appear in the dimeric form, which involves an indium–indium bonded species or R_4In_2. The structure of the indium (II) halides has been identified, in which the divalent In^{2+} ions is present in the dimeric species $[In_2X_6]^{2-}$.**32** A special highlight is the compound R_4In_2 ($R = CH(SiMe_3)_2$, $SiBu^t{}_3$, $SiBu^t{}_2Ph$), which has a remarkable reactivity and is used in the preparation of various indium complexes including indium cluster compounds.**33**

3.2 Halogen Derivatives

The halides of indium (II) can be prepared by heating together the appropriate mixture of elements, or by reduction of the trihalides with indium metal. In the compounds In_2Br_3 and In_5Br_7, the divalent In^{2+} ions are bonded within the dimeric species $[In_2Br_6]^{2-}$, in which each In^{2+} ion is threefold coordinated by Br^- ions, with a mean distance of 257 pm. The other In^{2+} ion augments the coordinating geometry via an In^{2+}-In^{2+} single bond (270 pm) to form a distorted tetrahedron.**7,8** $KInBr_3$ is the first ternary indium bromide containing divalent indium. The divalent In^{2+} ions are found in an $[In_2Br_6]^{2-}$ unit in an eclipsed ethane structure, while potassium ions are located in two different polyhedra.**32** The ethane analogous In_2X_6 (X = S, Se) units are also found in the structures of $MIn_5\,S_7$ (M = Na, K, Tl), MIn_5S_6 (M = K, Tl), and MIn_7X_9 (M = Rb, Cs; X = S, Se).**34**

3.3 Synthesis of R_4In_2 Derivatives

Diindanes R_2InInR_2 ($R = SiBu^t{}_3$) can be prepared by the reactions of NaR ($R = SiBu^t{}_3$) with InX_3 (X = Cl, Br) through $RInX_2$ and R_2InX intermediate process.**5** The reactions of NaR ($R = SiBu^t{}_3$, $SiBu^t{}_2Ph$) with InX ($X = N(SiMe_3)_2$, C_5H_5, C_5Me_5) also produces R_2InInR_2.**22** R_2InInR_2 ($R = CH(SiMe_3)_2$) is also prepared by the reaction of $[LiN(SiMe_3)_2]$ with C_5H_5In, whereas the reaction of $InCl_3$ and $LiSi(SiMe_3)_3$ gives $[(Me_3Si)_3Si]_4In_2$ (Scheme 5).**35** The reaction of $In_2Br\cdot 2TMEDA$ (TMEDA = tetramethylethylenediamine) with $[LiCH(SiMe_3)_2]$ can lead to $[(Me_3Si)_2CH]_4In_2$. The reaction of indium metal with $Pr^n{}_3PI_2$ also yields the ‘subvalent’ indium (II) complex $In_2I_4(PPr^n)_2$, which is the first example of an indium tertiary phosphine complex containing an indium–indium bond.**36**

3.4 Reaction of R_4In_2 Derivatives

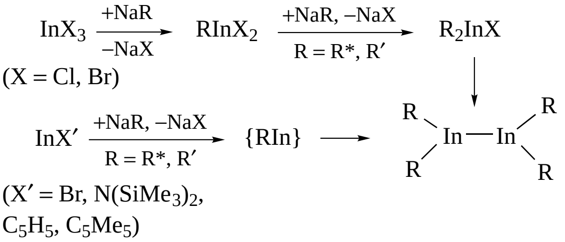

Scheme 5 Syntheses of ditrielanes R_4In_2 with $R = R^* = SitBu_3$ and $R = R' = SitBu_2Ph$, Refs. 5,22,35

Reaction of R_2In–InR_2 ($R = CH(SiMe_3)_2$) with the chalcogen compounds can give the corresponding homoleptic compounds $R_2InEInR_2$ (E = S, Se or Te) by insertion of chalcogen atoms into the In–In bond, while reaction with lithium phenylethynide produces, by the addition of one ethynido ligand to one of the central In atoms, the anionic adducts with intact In–In single bonds.**33** R_2In–InR_2 reacts with $LiCH_2SMe$ to afford $[R_2In(CH_2SMe)_2][Li(TMEDA)]$ probably formed by a metal exchange reaction.**37** Reaction with trimethylamine N-oxide by the insertion of oxygen atoms in their In–In single bonds produces R_2In–O–InR_2, which is monomeric in the solid state owing to the high steric shielding by the voluminous bis(trimethylsilyl)methyl groups,**38** while with protic reagents results in the cleavage of the In–In bond and precipitation of element indium.**39**

R_4In_2 ($R = SiBu^t{}_3$) can transform, with excess hydrogen bromide, into $RInBr_2$ and RH (molar ratio 1:1). Here R_4In_2 behaves as a Lewis base against HBr. R_4In_2 can be oxidized (e.g. with halogens or chalcogens) or reduced with metal. Bromination of R_4In_2 into $RInBr_2$ may proceed either by In–In or by In–Si bond cleavage via R_2InBr or $R_2In_2Br_2$. Fluorination of R_4In_2 with AgF_2 also produces $RInF_2$. The reaction of R_4In_2 with selenium can produce the heterocubane $R_4In_4Se_4$.**5**

4 INDIUM (III) CHEMISTRY

4.1 Introduction

The main development of the indium chemistry during the last decade has centered on the indium (III) compounds, particularly InH_3, InX_3, and R_3In. Indium hydride (InH_3 or $In_2\,H_6$) is unstable in the gas phase or solid state, but the stable indium trihydride complexes can be obtained in the form of adducts.**40** InX_3 and R_3In compounds are electron deficient and can accept pairs of electrons and form their neutral adducts or coordination compounds with the electron-pair donator ligands. This is potentially relevant to the fabrication of the III-V/VI semiconductor materials. The behavior of In^{3+} in solution has been investigated and a large number of stable and soluble In^{3+} complexes are obtained, which can be used as dyes, diagnostic radiopharmaceuticals, and other applications in materials sciences.

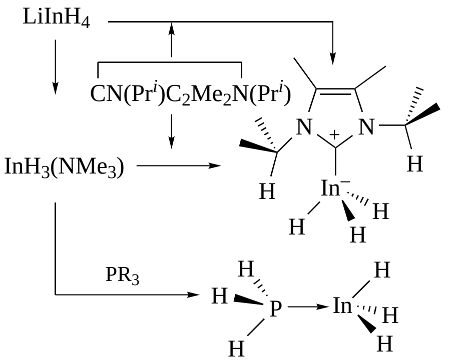

(R = Cy, Cy^p,Ph,Bu^t,Mes, Et)

Scheme 6 Syntheses of Indium hydride compounds, Refs. 43,44

4.2 Hydrides and Related Compounds

Indium hydrides are thermodynamically unstable, and $Me_2InB_3H_8$ is the first reported example of a volatile indium hydride.[41] Reaction of $InCl_3$ with $HSnBu_3$ generates the compound $HInCl_2$, which is stable up to ambient temperature.[42] The thermally stable indium trihydride complexes are obtained with phosphines or carbenes. $LiInH_4$ with $NMe_3{\cdot}HCl$ gives the adduct $InH_3(NMe_3)$, and further reacts with the stable carbene [**:**$CN(Pr^i)C_2Me_2N(Pr^i)$] to afford the carbene-metal trihydride complex $[InH_3\{:CN(Pr^i)C_2Me_2N(Pr^i)\}]$ (Scheme 6).[43] The reaction of $InH_3(NMe_3)$ with PR_3 ($R = $ cyclohexyl (Cy), cyclopentyl (Cp) or phenyl) affords the indium trihydride complexes $[InH_3(PR_3)]$ and $[InH_3(PCy_3)_2]$. The first phosphido-indium hydride complex $[\{InH_2(PCy_2)\}_3]$ is obtained by the treatment of $[InH_3(NMe_3)]$ with $LiPCy_2$. These complexes possess remarkable stability that may be attributed to the phosphone ligand's steric bulk and nucleophilicity. The complex $[InH_3(PCy_3)]$ is used to prepare a range of monomeric indium chalogenolato complexes $[In(Eph)_3(PCy_3)]$ ($E = S$, Se or Te) (Scheme 6).[44,45]

4.3 Indium (III) Halides and their Derivatives

Indium trihalides can be easily prepared from the reaction of indium metal with halide acids, which can form various complexes with water molecules and other ligands. *Trans*-$[InCl_2(H_2O)_4]^+$ and *trans*-$[InCl_4(H_2O)_4]^-$ species are isolated for the first time as parts of supramolecular adducts with cucurbituril are isolated from aqueous solutions and structurally characterized.[46] The behavior of Br_2 $InCH_2Br$ as Lewis acid against NEt_4Br, 1,4-dioxane and $THF(OC_4H_8)$ is examined, which shows that by complete intramolecular tautomeric transfer of the bromide it is possible to obtain $[Br_3$ $InCH_2]^-$ as an anion.[47] Reduction of R_3PI_2 ($R = Ph, Pr^i$) with indium powder produces the four- and five-coordinate complex $InI_3(PPh_3)_2{\cdot}InI_3(PPh_4)$ and the monomeric tetrahedral indium (III) complex $InI_3(PPr^i{}_3)$, which illustrates the subtle effect of the organic substituents on the phosphorus atom for the reaction of R_3PI_2 with indium metal.[37]

4.4 Adducts of InX_3

The adducts of the indium trihalides are readily prepared by simple nonaqueous phase reactions. A series of adducts of $InBr_3$ has been obtained from the treatment of $InBr_3$ with THF (tetrahydrofuran), DMF (dimethyl formamide), and other ligands, which have a pyramidal coordination sphere.[48] In a similar fashion, the coordination geometry of the adduct $InCl_3(THF)_2$ also is a trigonal bipyramid with three Cl atoms in equatorial positions and two axial THF ligands. Reaction of $InBr_3$ with $HN(SiMe_3)_2$ gives stable adducts $Br_3In{\cdot}H_2NSiMe_3$ and $Br_3In{\cdot}HN(SiMe_3)_2$;[49] with $LiR{\cdot}(THF)_n$ ($R = C(SiMe_3)_3$, $THF = OC_4H_8$), it produces $[Li(THF)_4][RInBr_3]$ in good yield.[50] $InCl_3$ with amines can give the corresponding adducts, in which In atoms have a trigonal-bipyramidal coordination sphere with the amines in apical position.[51] The complex $[(Me)_2ATI]_2InCl$ (ATI = aminotroponiminate) was prepared and characterized, showing fluxional behavior in solution at room temperature and adopting trigonal-bipyramidal geometry around the metal center with the halide occupying an equatorial site.[52] The complex $(PPh_3)_4Pt_2(\mu^3\text{-}S)InCl_3$ represents the first report of a square-based pyramidal structure of a five-coordinated adduct of InX_3.[53]

The reactions of indium trihalides with DP or TP ligands ($DP = 1,2$-bis-(diphenylphophanyl) benzene, TP = bis[(2-diphenylphosphanyl)phenyl] phenylphosphane) lead to a variety of molecular and ionic complexes, such as $[(DP)_2InCl_2]^+$ $[InCl_4]^-$, $(DP)InX_3$, $[(DP)InX_2]^+$ $[InX_4]^-$ ($X = Br$, I), and $[(TP)InX_2]^+$ $[InX_4]^-$ ($X = I$). The environment of the metal center is octahedral, square pyramidal, and tetrahedral in the cations respectively.[54]

4.5 Indium Alkoxides

The reaction of Me_3In with ROH ($R = PhCH_2$, Hex and Bu^t) leads to tetranuclear complex $[In\{(RO)_2InMe_2\}_3]$, described also as $[\{Me_2InOR\}_2\{MeIn(OR)_2\}_2]$, then at higher temperature forms an O-centered corner-cut rhombic dodecahedron, $[(MeIn)_5(OR)_8O]$, in which the four μ_2-bridging oxygen atoms form a basal plane and the In-O skeleton can be degraded with elemental cesium to a hexa- and heteronuclear complex $[Cs\{Cs(THF)\}\{[MeIn(OR)_2]_4O\}]$ (Scheme 7).[55,56] The compound $[In(OBu^t)_3]_2$ is the first example of a homoleptic and homometallic indium alkoxide, which is obtained by alcoholysis of $In(N(SiMe_3)_2)_3$ with Bu^tOH.[57] The N,O-5 chelates $[Me_2In(\mu\text{-}ORNMe_2)]_2$ ($R = CH_2CHR'$; $R' = Me$, Pr^i, Bu^t) are synthesized from trimethylindium and the dimethylamino alcohols by elimination of methane. The coordinative $N \rightarrow In$ bonds of the five-coordinate indium complexes show dynamic dissociation/association processes.[58]

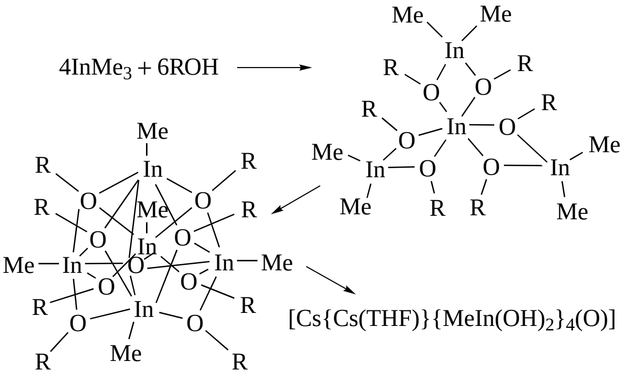

Scheme 7 Syntheses of Indium alkoxides, Refs. 55,56

The reaction of InX_3 (X = Cl, Br) with sodium alkyloxistannate gives $THF\cdot X_2In(OR)_3Sn$ (X = Cl, Br; R = Bu^t), in which the indium atoms are in the centers of distorted octahedral from 4 oxygen and 2 halogen atoms whereas the tin atoms are coordinated by three oxygen atoms in a trigonal pyramidal fashion.[59] Reaction of $InMe_3$ or $InCl_3$ with the Li+ salt of S-BINOLate (S-BINOL = (S)-(−)-2,2′-dihydroxy-1,1-binaphthyl) gives alkoxides with a tetranuclear InO_6Li_3 skeleton, which forms a distorted octahedral coordination sphere around In atoms, built up by three BINOLate ligands, the three Li+ counterions acting as bridging units by metal−oxygen coordination.[60]

4.6 $InMe_3$ Adducts and Derivatives

The Me_3In adducts also have the similar bipyramidal structure to that of InX_3 adducts. The adduct $Me_3In\cdot 2$(mbda) (mbda=*N*,*N*,*N*′,*N*′-tetramethyl-4′,4′-methylene-bis-aniline), with a trigonalbipyramidal In, is said to have the longest known In–N bonds.[61] Me_3In reacting with isocyanides CNR (R = *p*-MeC_6H_4, *p*-$MeOC_6H_4$) gives the corresponding adducts Me_3InCNR, then reacts with pyrrolidine by insertion of the isocyanide into the In–N–Pyr bond to form $[Me_2InC(=NR)(Pyr)]$ (Pyr = conjugate base of pyrrolidine).[62]

The adducts $InMe_3\cdot C_3H_6N_3R_3$ (R = Me, Pr^i or Bu^t) are prepared by simple mixing of the Lewis acid and base in diethylether solution and the adducting bonding of three lone pairs is slightly stronger than a standard one lone-pair adduct bond.[63] Reaction of Me_3In with $[(\eta^5\text{-}C_5Me_5)(CO)_2FeE{=}(NMe_2)_2]$ (E = P and As) affords the adducts $[(\eta^5\text{-}C_5Me_5)(CO)_2FeE\{InMe_3\}(NMe_2)_2]$, which feature η^1-coordination of the phosphaalkene or the arsaalkene ligand towards the Lewis acid via the pnictogen atom.[64]

4.7 Indium–Nitrogen Compounds

Reactions of InX_3 (X = Cl, Br) with various amines give the corresponding neutral or ionic complexes in which indium atoms locate in trigonal-bipyramidal, trigonal planar, or distorted tetrahedral environments. In the structure of $[ClIn(NMeSiMe_2)_2NMe]_2$, a chloride and one amide group of $[MeN(SiMe_2NMe)_2]^{2-}$ ligand are bonded to each In atom in terminal positions and the other amide group of the chelating ligand is shared between two In atoms.[65] Reaction of $[RNC(R')NR]Li$ with $InCl_3$ affords a novel family of monomeric five-coordinate compounds $In[RNC(R')NR]_2Cl$ (R = cyclohexyl, $SiMe_3$; R′ = Me, Bu^t), possessing a distorted trigonal-bipyramidal coordination.[66]

The first azaindatrane $[N(CH_2CH_2NMe)_3In]_2$ is prepared by the reaction of $[In(NEt_2)_3]_2$ with $N(CH_2CH_2NMeH)_3$, in which both indium atoms are pentacoordinate, with widely differing In–N distances.[67] Within $[py_2Na][py_2In(N_3)]_4$, the In and Na atoms are each hexacoordinated by four azido group and two additional solvent molecules.[68]

The reaction of $RSi(NH_2)_3$ (R = 2,6-$\mathrm{Pr}^i{}_2C_6H_3NSiMe_2\mathrm{Pr}^i$) with InR_3 (R = Me, Et) leads to Si–NH–In cage molecules, which may be regarded as a model system for In metal-containing iminosilicates. Further functionalization without cleavage of the cage molecule is achieved by reaction with elemental bromide and iodine.[69]

Indium diphthalocyanine $In(Pc)_2$ contains sandwich-type molecules in which the indium atom is eight-coordinate by the isoindole nitrogens of two phthalocyanie rings. The distance between the phthalocyanie planes in this sandwich macromolecule is equal to 274.1 pm, and the two phthalocyaninato moieties are rotated about 41.2(4)° with respect to each other.[70]

The chloro(phthalocyaninato or naphthalocyaninato) indium $R^1{}_4R^2{}_4PcInCl$ or $R^1{}_4R^2{}_4NcInCl$ react with R^3MgBr to produce the axially substituted aryl (phthalocyaninato or naphthalocyaninato) indium compound, $R^1{}_4R^2{}_4PcInR^3$ or $R^1{}_4R^2{}_4NcInR^3$, which has high solubility owing to steric crowding arising from the new unsymmetrical peripheral substitution pattern and the bulky electron-withdrawing axial liangs.[71,72]

The structure of $In_4X_4(N\mathrm{Bu}^t)_4$ (X = Cl, Br, I) contains heterocubane In_4N_4 cores with an alternating arrangement of In and N atoms. The In atoms are coordinated nearly tetrahedrally by three N atoms and a terminal halogen atom. $In_3Br_4(N\mathrm{Bu}^t)(HN\mathrm{Bu}^t)_3$ contains a tricyclic In_3N_4 core, which can be formally derived from an In_4N_4 heterocubane by removing one In atom.[73]

MeCN can be trimerized in the presence of $InMe_3$ and a trace of CsF to form the InN_2C_3 heterocycle $[Me_2In\{HNC(Me)\}_2C(CN)]$, which forms an infinite chain-like coordination polymer, $[Me_2In\{HNC(Me)\}_2C(CN)]_n$, along [001] by the cooperative interactions of In···N contacts and N–H···N bridges.[74]

4.8 Indium–Phosphorous Compounds

The organoindium phosphides are dimeric, trimeric, and tetrameric in benzene solution. The compounds

$[Pr^i{}_2InPPh_2]$ and $[(PhCH_2)_2InPPh_2]$ exist as a monomer-dimer equilibrium mixture in solution and a trimer in the solid state. The dimer $[\{InPR_2(CH_2CMe_3)_2\}_2]$ ($R = Et, Pr^i$) contains a planar In_2P_2 core, and the trimer $[\{InP(H)(C_6H_{11})(CH_2CMe_3)_2\}_3]$ has an In_3P_3 six-membered ring in a boat conformation. The similar In_3P_3 six-membered rings are also observed in the trimers $[Pr^i{}_2InPPh_2]_3$, $[Me_2InP(SnMe_3)_2]_3$ and $[(PhCH_2)_2InPPh_2]_3{\cdot}OEt_2$. The compound $[(mes)InP(mes)]_4$ is tetrameric in solution, but crystallized as $[(mes)InP(mes)]_4{\cdot}4.5THF$, a heterocubane with an In_4P_4 core shield by the bulky organic groups.[75] The analogous heterocubanes with an In_4P_4 core is also observed in compound $[EtInPSiPr^i{}_3]_4$. The four-membered-ring compounds $[R_2InPBu^t{}_2]_2$ (R = vinyl, allyl, or benzyl) could absorb light at relatively long wavelengths with cutoffs ranging from ~300 nm to 330 nm depending on R groups.[76] The central structural motif of $[Pr^i{}_2Si\{P(H)InEt_2\}_2]_2$ is an adamantine-like cage composed of four indium, four phosphorous, and two silicon atoms, which is the first ternary cluster with combinations of these elements.[77] The one-dimensional compound $[Ph_4][In(P_2Se_6)]$ contains infinite $[In(P_2Se_6)]_n{}^-$ chains with a structure related to that of $K_2FeP_2Se_6$.[78]

4.9 Indium Phosphate Compounds

A new series of layered indium phosphate complexes have potential applications in the areas of sorption, ion exchange, and sensors. The first organically templated indium phosphate is prepared as single crystals from a nonaqueous pyridine-butan-2-ol medium and has a unique two-dimensional (2D) structure consisting of $[Hpy][In(HPO_4)(H_2PO_4)_2]^-$ layers held together by hydrogen bonding to generate cavities containing the pyridium cations. The layers consist of corrugated sheets constructed from ribbons of edge-sharing four-membered rings of alternating InO_6 and PO_4 units linked via $PO_2(OH)_2$ groups.[79] The layered structure also exists in the complexes, $In(O_3PR)(O_2P)(OH)R){\cdot}H_2O$ ($R = C_6H_5$ or $CH_2C_6H_5$) and $In(O_2P(H)C_6H_5)_3$, in which the ligand is present as both a mono- and dianion.[80] A pillared layer structure of the indium phosphate, $[In_8(HPO_4)_{14}(H_2O)_6(H_2O)_5(H_3O)(C_3N_2H_5)_3]$, consists of layers assembled from InO_6 and $InO_5(H_2O)$ octahedra and $PO_3(OH)$ tetrahedra which are pillared through InO_6 octahedra to produce a 3D framework. The framework contains a 2D array of channels in which sit imidazolium cations, hydroxonium ions, and water molecules.[81] The similar pillared layer structure is observed in complexes $[In_4(4,4'\text{-bipy})_3(HPO_4)_4(H_2PO_4)_4]{\cdot}4H_2O$ and $[In_4(4,4'\text{-bipy})_3(HPO_4)_4(H_2PO_4)_4]$. The structure of $PbIn(OH)PO_4$ consists of spirals of *cis* corner-sharing InO_6 octahedra with hydroxyl O as the bridging atom, and the In–O–In bonds nearly equidistant.[82] The framework of $Ca_2(In_{1-x}Fe_x)(PO_4)(HPO_4)_2{\cdot}H_2O$ is based on linear chains formed by (MO_6) octahedral and $(PO_4)(HPO_4)$ tetrahedral sharing corners. The (HPO_4) groups and water molecules link the chains through hydrogen bonding to form layers stacked perpendicular to the c axis. The calcium cations are located between the layers and are coordinated by nine oxide anions.[83]

4.10 Indium Chalcogenide Compounds

The indium chalcogenide compounds may be prepared by the insertion of chalcogenide into either an In–C or In–S bond. The reaction of InR_3 ($R = Bu^t$, Bu^n or CMe_2Et) with selenium or tellurium yields the corresponding compounds $[\{RIn(\mu_3\text{-}E)\}_4]$ (E = Se or Te).[84] Reaction of $[In(mes)_3]$ (mes = 2, 4, 6-trimethylphenyl) with various A(ER) (A = H or Li; E = S or Se; $R = Bu^t$, *tert*-amyl, 2-*t*-BuC$_6$ H$_4$, SiPh$_3$) gives $[\{In(mes)_2(\mu\text{-}ER)\}_2]$. A trimeric indium thiolate, $[\{InMe_2(\mu\text{-}SSiPh_3)\}_3]$, is isolated from the reaction of $InMe_3$ with $HSSiPh_3$.[85] Similar selenium compounds are also described as $[InMe(\mu\text{-}SePh)(SePh)]_\infty$, a spiral chain composed of alternative four-coordinate indium atoms and three-coordinate selenium atoms.[86]

Homoleptic chalcogenolates $In[ESi(SiMe_3)_3]_3$ (E = Se, Te) are also prepared by chalcogenolysis of $InCp_3$. Addition of L ligand (L = THF, TMEDA (N,N,N',N'-tetramethyl ethylene diamine), or DMPE (1,2-bis(dimethylphosphino)ethane)) to $In[SeSi(SiMe_3)_3]_3$ gives 1:1 adducts (L) $In[SeSi(SiMe_3)_3]_3$.[87] The SePy (SePy = 2-Se–NC_5H_4) and SePy* (SePy* = 3-Me_3Si–Se–NC_5H_4) ligands form air-stable homoleptic coordination compounds of indium (III) $[In(SePy)_3]$ and $[In(SePy^*)_3]$, which are distorted fac-octahedra molecules with chelating SePy ligands and are useful low-temperature precursors to In_2Se_3.[88]

The tellurides $K_6In_2Te_6{\cdot}4en$ (en = $C_2H_8N_2$) and $(Ph_4P)_2$ In_2Te_6 are known. The former possesses a highly charged dimeric $[In_2Te_6]^{6-}$ anion, which is composed of two edge-sharing $InTe_4$ tetrahedra. The $InTe_4$ tetrahedra are linked together by sharing two Te corners and by joining the two other Te corners to form two $Te_2{}^{2-}$ units with neighboring tetrahedra.[89] The complex $[InCl\{Ph_2P(Se)NP\ (S)Ph_2\text{–}Se,S\}$ exhibits a very distorted trigonal-bipyramidal geometry at indium, where both the selenium and chlorine atoms are in equatorial positions, while the sulfur atoms are in axial positions.[90]

The reaction of $InCl_3$ with $PhC\{O\}S^-\ A^+$ (A = Li, Na, and K) in the molar ratio 1:4 gives the corresponding ionic complexes $[A(MeCN)_x\{In(SC\{O\}Ph)_4\}]$, (A = Li, X = 0; A = Na, X = 1; A = K, X = 2), which have a one-dimensional polymeric structure. The structural variations may be attributed to the change in the alkali metal ion from Li to Na to K.[91]

Thioindates of alkali metal compounds can be prepared by starting from stoichiometric mixtures of the elements, and several compounds MIn_3S_5 (M = Rb, Cs), KIn_5S_6, MIn_5S_7 (M: Na, K), and MIn_7X_9 (M = Rb, Cs; X = S, Se) are known. MIn_3S_5 (M = Rb, Cs) represents a new type of ternary chalcogenide. On the quasi binary section M_2S–In_2S_5 with the two binary phases in a molar ratio of 1:3, in which the indium atoms are coordinated by sulfur atoms with tetrahedral as well as octahedral arrangement, the coordination numbers of the independent M atoms are nine or ten, and the sulfur and alkali metal atoms are in slightly distorted ccp arrangement.[92,93]

5 INDIUM PRECURSORS FOR CVD

5.1 Introduction

The recent interest in organoindium compounds stems from the finding that organoindium compounds are potential precursors for a wide variety of applications in material science. The deposition of In-containing semiconductor layers is important to diverse areas of research. Generally, the preparation of these thin films involves metal organic chemical vapor deposition (MOCVD). Despite its commercial use, several precursor issues are associated with the conventional MOCVD method, such as safe precursor handling and ‘snowing’ of the films. Moreover, under the condition of separate precursors, the composition control of such multinary films is affected by a precise adjustment of the mole fractions of the different precursors for the film constituting components in the gas phase. This makes it very difficult to obtain multinary films owing to the differences of precursors in volatility, thermal reactivity, and surface mobility.

An alternative route to make the films is the use of a precursor that contains the required atoms in a single molecule. The process control is shifted to the constitutional and structural optimization of the precursor. Therefore, single-source precursors have considerable advantages over conventional separate sources.

5.2 Intermetallic Phase Precursor Compounds

Indium-containing intermetallic phases are especially suitable as epitaxial metallizations, being inert against unwanted interface reactions and useful for Schottky barriers for semiconductor techniques. Thus, MOCVD processes are of interest for these materials and many organoindium precursors have been synthesized for this end. A special highlight is the compound $[\mathrm{Ni(InR)_4}]$ ($\mathrm{R = C(SiMe_3)_3}$), a first example for the existence of compounds that are homoleptic with regard to an earth metal as ligator, which can be used as a single-source precursor for NiIn films.[94] Ni/In films can also be prepared from the compounds $\{[\mathrm{Cp(PEt_3)Ni}]_2\mathrm{InCl}\}_2$, $[\mathrm{Cp(PEt_3)Ni}]_3\mathrm{In}$, and $\mathrm{Cp(PEt_3)NiInI_2}$. In the Co/In system, only $\mathrm{CoIn_2}$ and $\mathrm{CoIn_3}$ are stable. $\mathrm{(CO)_4CoInR_2}$ ($\mathrm{R = CH_2CH_2CH_2NMe_2}$) can give CoIn films with Ni/In = 3.0 to 1.0 depending on the substrate temperature, which can be assigned to these phases; $[\mathrm{Cp(CO)CoInR_2}]$ at 350 °C can provide single-phase films with the hexagonal ε-NiIn phase. This is an example of an unexpected Cp transferring to the In atom, leading to stable CpIn that desorbs and gets into the exhaust gas.[95] In the case of $\mathrm{Cp(CO)_2Fe{-}InR_2}$, the deposition of Fe/In films is proceeded by the release of ferrocene.[96]

In addition, Cr/In, W/In, Mn/In, and Au/In films have also been obtained from the corresponding organometal compounds respectively, which indicate lively development in this field.

5.3 Indium Chalcogenide Precursor Compounds

Indium chalcogenides are potentially useful as single-source precursors for the synthesis of III-VI semiconductor materials. The complex $[\mathrm{InMe_2(S_2CNEt_2)}]$ is the ideal precursor for deposition of indium sulfide (InS and $\mathrm{In_6S_7}$ phases) films, and $[\mathrm{InEt_2(S_2CNEt_2)}]$ can give single phase, cubic β-$\mathrm{In_2S_3}$ films at a temperature of 325–400 °C.[97] β-$\mathrm{In_2S_3}$ films can also be prepared from $[\mathrm{In(SOCNEt_2)_3}]$ and $[\mathrm{In(SOCNPr_2)_3}]$ respectively.[98,99] The deposition of α-$\mathrm{In_2S_3}$ films can be obtained from the precursor, $[\mathrm{In(S_2COPr)_3}]$ or $[\mathrm{In(S_2CNEt_2)_3}]$.[100] $[\mathrm{mes_2In}(\mu\text{-SR})]_2$ (mes = 2, 4, 6-trimethylphenyl, R = t-Bu, t-amyl, $\mathrm{SiPh_3}$) and $[\mathrm{Me_2In}(\mu\text{-SSiPh_3})]_3$ are also used as a single-source precursor for deposition of indium sulfide films.[101] In addition, $[\mathrm{HL}][\mathrm{In(SCOMe)_4}]$ is also used to deposit tetragonal β-$\mathrm{In_2S_3}$ films.

Indium selenide films can be produced from the corresponding compounds containing selenium by MOCVD, and the film quality is dependent on the growth temperature. $[\mathrm{In}^t\mathrm{Bu_2}(\mathrm{Se}\,{}^t\mathrm{Bu})]_2$ gives indium-rich films at a temperature of 230–420 °C, and $[\mathrm{In(CEtMe_2)}(\mu_3\text{-Se})]_4$ produces crystalline InSe films.[102] Pyrolysis of $\mathrm{In(SePh)_3}$ can form hexagonal $\mathrm{In_2Se_3}$ films at 470–530 °C, and of $[\mathrm{Me_2EtC]InSe]_4}$ can provide hexagonal InSe films at temperatures between 290–350 °C.[103] The cubic $\mathrm{In_2Se_3}$ films can be obtained from $[\mathrm{In(Se_2CNMe}\,{}^n\mathrm{Hex)_3}]$ and $[\mathrm{In\{SeC(SiMe_3)_3\}_3}]$, respectively.

Films of chalcopyrite $\mathrm{CuInE_2}$ are formed by MOCVD from the precursor $[\mathrm{(Ph_3P)_2Cu}(\mu\text{-ER})_2\mathrm{In(ER)_2}]$ (E = S or Se and R = Et or ^{i}Bu).[104] The compound $[\mathrm{Bu_2In(SPr)Cu(S_2CNPr_2)}]$ is also reported to deposit $\mathrm{CuInS_2}$ films by MOCVD. $[(n\text{-}\mathrm{Bu_3P})_2\mathrm{Cu(SR)_2In(SR)_2}]$ (R = Et and n-Pr) and $[\mathrm{Bu_2In(SPr)Cu\ (S_2CNPr_2)}]$ are also used to deposit $\mathrm{CuInS_2}$ films.[105] The thiocarboxylates, $[\mathrm{(Ph_3P)_2AgIn(SC(O)R_4)}]$ (R = Me, Ph), were excellent single-source precursors for $\mathrm{AgInS_2}$ and $\mathrm{AgIn_5S_8}$ films by MOCVD.[106]

5.4 Indium Nitride Precursor Compounds

The first adduct stabilized, volatile covalent indium bis-azide compound, $[\mathrm{(InN_3)_2\ (CH_2CH_2CH_2NMe_2)}]$, has been characterized by single crystal X-ray diffraction. It has been used as a precursor for indium nitride thin films.[107] Other azide derivatives of indium, such as $[\mathrm{Cl_2InN_3}]$, $[\mathrm{Br_2InN_3}]$, $[\mathrm{py_2Na}][\mathrm{py_2In(N_3)_4}]$, pyridine, and tetrahydrofuran adducts, are also being studied as precursors for InN materials.[108] Amido derivatives of indium compounds are also important in the preparation of InN materials. Synthesis and characterization of $[H_2InNH_2]$, $[N(CH_2CH_2NMe)_3In]_2$, $[InNH_2CH_3]$, and $[InNH(CH_3)_2]$, which are potential precursors for InN materials, have been reported.[109,110] The reaction of $[Li(Me_3Si)N\text{–}NHBu^t]$ with [MeInCl] can give different hydrazine derivatives of indanes, which are dependent on the solvent. With hexane as a solvent, the dimeric compound $[Me_3In(Li)(Me_3Si)N\text{-}NHBu^t]_2$ is produced. In diethyl ether, the cage compound $[MeIn\{N(SiMe_3)LiN(SiMe_3)NHBu^t\}]$, which can be regarded as an $(Me_3SiN{=}InMe)_2$ adduct with $[Li(Me_3Si)N\text{–}NHBu^t]_2$, is isolated. These compounds are good single-source precursors in MOCVD processes for InN thin films.[111]

The thermally stable In(I) compounds $[In(\eta^5\text{-}P_3C_2Bu^t{}_2)]$ and $[In(\eta^5\text{-}P_2C_3Bu^t{}_3)]$ have a half-sandwich structure, and are potential single sources for chemical vapor deposition of InP semiconductors.[28] The reaction of R_3PI_2 with indium metal produces a variety of novel indium compounds $[InI_3(PPh_3)_2{\cdot}InI_3(PPh_3)]$, $In_2I_4(PPr^n{}_3)_2$, and $InI_3(PPh^i{}_3)$, which may have applications in the microelectronics industry as precursors for MOCVD.[37] A key feature of $[R_2InPBu^t{}_2]$ (R = vinyl, allyl, and benzyl) is the presence of alkyl groups that are capable of facile β-hydride and/or alkyl radical elimination reactions, thus lowering deposition temperature into the range 400–590 °C.[76] In addition, $\{Et_2InSb(SiMe_3)_2\}_3$ is also used as precursor for the CVD of indium antimonide materials.[112]

6 INDIUM NANOMATERIALS

6.1 Introduction

Inorganic nanomaterials have attracted considerable attention owing to their novel physical and chemical properties that arise from size reduction and the potential applications in diverse areas. Moreover, these materials can also be used as ‘building blocks’ to assemble new generations of nanoscale electronic and optical devices. Indium, a low-melting metal, is easily alloyed and converted to InP, InAs, and InS, which are III-V/VI semiconductors that display interesting optoelectronic properties. Indium is easily oxidized to In_2O_3, which can be used as a sensor and light-emitting material. Indium oxides can form with SnO_2 the mixed indium tin oxide (ITO), a conducting glass.[2] Therefore, various indium-containing nanomaterials have been prepared in the last ten years.

6.2 Indium Nanomaterials

Indium nanoparticles can be prepared by metal vapor deposition, by evaporation of metal into a polymerizable monomer, or by reduction of $InCl_3$ with the appropriate quantity of alkalides or electrides.[113,114] In the latter, the indium particles often display an oxidized surface. The monodispersed indium nanoparticles can be obtained by thermal decomposition of organometal precursor $[In(\eta^5\text{-}C_5H_5)]$ using polyvinylpyrolidone (PVP) or trioctylphosphane oxide (TOPO) as a ligand. These particles can be further oxidized into well-crystallized In_2O_3 particles with unchanged morphology.[115,116] The bare indium nanoparticles have been prepared by solution dispersion route from bulk indium granules, which may be the simplest and cheapest method for making indium nanoparticles (Figure 1).[117] The cationic indium nanoparticles are also synthesized in a single crystal of zeolite X through an indium-exchanging process.[118]

The organometallic route can be extended to the formation of one-dimensional indium materials. On the use of long-chain amines as templates, In and In_3Sn nanowires have been prepared from the organometallic precursors InCp ($Cp = C_5H_5{}^-$) in the presence of UV irradiation. In this case, irradiation is crucial for the formation of the wires. In nanowires are also produced in the metal organic chemical vapor deposition grown InGaN layers.[119,120]

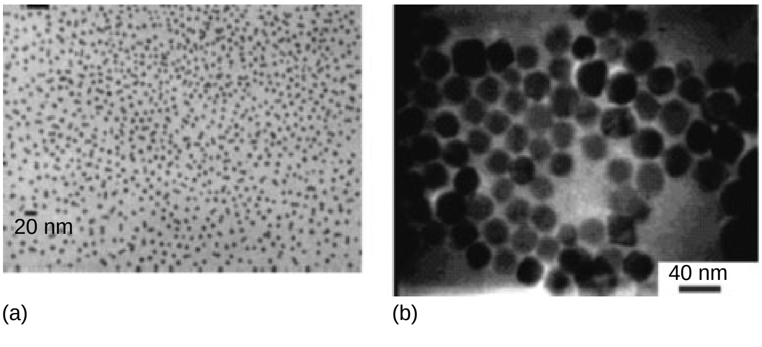

Figure 1 Transmission electron microscopy (TEM) images of indium nanoparticles. ((a) Reproduced from Ref. 115 by permission of Wiley-VCH; (b) Reprinted with permission from Ref. 117. © 2074 American Chemical Society)

6.3 Indium Oxide Nanomaterials

Indium oxide, an n-type semiconductor with a wide band gap of about 3.6 eV, has been widely used as microelectronic device materials in solar cells, sensors, and conducting glasses. In_2O_3 nanoparticles can be prepared by sol-gel processes, or by thermal decomposition of $In(acac)_3$ precursors in the presence of a surfactant.[121] Oxidation of indium nanoparticles also gives In_2O_3 nanoparticles.[116] Without the presence of catalyst, the evaporation of In_2O_3 powders at 1400 °C can yield In_2O_3 nanobelts, which are single crystalline and grow along the 100 plane, with the surfaces being enclosed by {100} (Figure 2).[122] Under an H_2O/oxygen-containing argon atmosphere, thermal evaporation of indium granules also yields In_2O_3 nanowires. In this case, the growth of In_2O_3 nanowires is more likely to be controlled by the vapor–solid process.[123] In_2O_3 nanofibers are also obtained by annealing InOOH nanofibers at 490 °C. The InOOH nanofibers are prepared by controlling hydrolysis of $InCl_3$ at 190–240 °C.[124] Under argon/oxygen atmosphere, rapidly heating an indium-containing target covered with a thin Au layer can also give In_2O_3 nanowires. In this case, Au nanoclusters play a crucial role in directing the growth of In_2O_3 nanowires.[125]

In_2O_3 nanotubes have been synthesized by a sol-gel porous alumina templating method. The length and diameters of nanotubes can be varied by selecting the template dimensions and sol immersion time.[126] Evaporation of a mixture of In/In_2O_3 under vacuum also gives In_2O_3 nanotubes. Interestingly, the In_2O_3 nanotubes are filled with metallic indium, and the length and the position of In fillings can be modified by electron-beam irradiation.[127] Under argon/oxygen atmosphere, heating an indium–tin mixture also produces ITO nanofibers. The tin plays a crucial role in directing the growth of the ITO nanofibers based on the vapor-liquid-solid mechanism.[128]

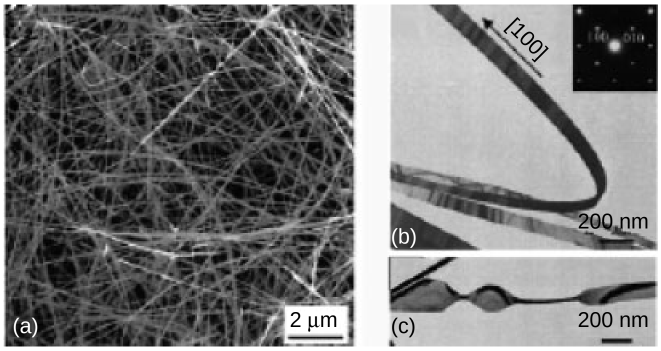

Figure 2 TEM images of In_2O_3 nanobelts and an electron diffraction pattern (insert). (Reprinted with permission from Z.W. Pan, Z.R. Dai, and Z.L. Wang, *Science*, 2001, **291**, 1947. © 2001 AAAS)

6.4 Indium Nitride Nanomaterials

Indium nitride plays an important role in blue/violet light-emitting diodes and laser diodes. Nanocrystalline InN can be prepared by the reaction of azido-indium compounds such as $i\mathrm{Pr_2InN_3}$ or $t\mathrm{Bu_2InN_3}$ with H_2NNMe_2 used as a reductant at 203 °C. H_2NNMe_2 not only serves as a stoichiometric hydrogen-atom donor to assist alkane elimination, but also can reduce some of the azido precursor to form metallic indium, which should promote both precursor decomposition and crystal-lattice construction.[129] A benzene thermal conversion route has been developed to prepare nanocrystalline indium nitride through the reaction of In_2S_3 with Na_2S at 180–200 °C. This may be the lowest temperature at which crystalline InN has been obtained.[130] In addition, crystalline InN powders with the size of 50–300 nm are also prepared by the nitridation of In_2O_3 and $In(OH)_3$ with NH_3 gas.[131]

InP nanocrystals can be made by dehalosilylation of $InCl_3$ and $(Me_3Si)_3P$ with subsequent thermolysis at 200–400 °C.[132] Monodisperse and soluble InP nanocrystals are obtained by thermolysis reactions in trioctylphosphine oxide. InP nanoparticles can also be obtained by the decomposition of organometallic precursors.[133,134] A novel route has been developed to prepare nanocrystalline InP by the reaction of $InCl_3$, P_4, and KBH_4 at temperatures as low as 80 °C, which is the lowest temperature reported for InP nanocrystals.[135] The synthesis of InP nanotubes by laser ablation is also reported.[136]

Nanocrystalline InAs is obtained by the reaction of $(Me_3Si)_3As$ with $InCl_3$ or by reaction of $InCl_3$ with Na_3As, respectively. A solvothermal route has been proposed to prepare InAs nanocrystals, which involves co-reduction of $InCl_3$ and $AsCl_3$ by Zn.[137] The high quality nanocrystalline InAs can be obtained by the thermolysis of a mixture of $InCl_3$ and $As(NMe_2)_3$.[138] In addition, InSb nanocrystals can also be obtained by the solvothermal reduction route.[139]

6.5 Indium Chalcogenide Nanomaterials

Copper indium chalcogenides $CuInE_2$ (where E = S, Se, and Te) are ternary semiconductors, which have emerged as a leading material for high efficiency and radiation-hard solar cell applications. $CuInS_2$ nanocrystals are prepared by a simple colloidal route, using $InCl_3$, CuI, and bis(trimethylsilyl) sulfide as starting materials and TTP (triphenyl phosphite) as surfactant. In this case, the particle surface is shielded by a surfactant.[140] $CuInSe_2$ nanocrystals are also prepared using a two-step reaction from $InCl_3$ and CuCl in a suitable solvent, followed by the addition of trioctylphosphine selenide.[141] Solvothermal routes are also used in the synthesis of $CuInSe_2$, $AgInS_2$, and $CdIn_2S_4$ nanocrystals.[142–144]

7 INTERMETALLIC COMPOUNDS

7.1 Introduction

The development of new intermetallic compounds demands greater understanding of the relationship among structure, bonding, and properties. The Zintl concept provides an effective way to describe the structures of compounds formed between electropositive metals and main-group elements, in which the electropositive atoms serve to donate their valence electrons to main-group atoms. Elements to the right of the Zintl border (separating group 13 and 14) with electropositive metals usually form valence compounds (Zintl compounds), with narrow ranges of composition and the valence electron concentration per atom (vec) exceeding 4. On the other hand, the compounds with elements to the left of the Zintl border behave like traditional intermetallic compounds (Hume-Rothery phases) with wide ranges of homogeneity for different structures and vec values between 1 and 2. There are no clear classification schemes for the range between 2 and 4. Furthermore, many indium-containing intermetallic compounds have a vec near 3 and the degree of In–In bonding in these compounds depends strongly on the indium content as well as the electron count.[145] Therefore, much attention has been directed to understanding the indium-containing compounds ‘between’ Hume-Rothery and Zintl phases in the past ten years.

7.2 Binary Compounds

The binary indium-rich transition metal compounds show a variety of different indium networks. In the structures of T_2In_5 (T = Ti, Hf), the indium atoms form infinite two-dimensional (2D) planar networks, which can be described as a tessalation of triangles, squares, and pentagons. The 2D network is also found in the structures of the La_3In_5 compounds, which contain well-defined indium square pyramids and some intercluster indium–indium distances that are only 11–15% greater than the average intracluster bond lengths. The apparent In_5^{9-} cluster in La_3In_5 can be described as a closed shell nido-deltahedron, and the compound structurally as a Zintl phase. The β-Y_3In_5 compounds with a similar structure to La_3In_5 present a slow first-order phase transition to α-Y_3In_5 at high temperature. Clusters in the low-temperature α-Y_3In_5 phase are twisted and joined by short bonds at trans-basal positions into chains that are more weakly interconnected into a three-dimensional structure.[146]

The 3D network of indium atoms is found in the TIn_3 (T = Co, Rh, and Ir) compounds. The compounds TIn_3 (T = Co, Rh, and Ir) belong to a large family and are built up from tungsten-like building blocks of indium atoms and AlB_2-like slabs of compositions $In\square Co$, $In\square Rh$, and $In\square Ir$, respectively, where □ represents the vacancies in the AlB_2 fragments of TIn_3. $RhIn_3$ shows evident antibonding Rh–Rh interactions, and three compounds display similar bonding characteristics to $RuIn_3$.[147]

7.3 Alkaline Earth-transition Metal–Indium Compounds

The main features of ternary alkaline earth-transition metal–indium compounds are 2D or 3D infinite transition metal–indium polyanions in which the degree of In–In bonding strongly depends on the indium content and the structure type. CaAuIn compounds adopt the KHg_2-type structure with an ordered arrangement of gold and indium atoms on the mercury position. Each calcium atom has a distinctly ordered near-neighbor environment of six gold and six indium atoms in the form of two Au_3In_3 hexagons.[148] Within SrPtIn, the indium atoms have a distorted tetrahedral platinum coordination. These $InPt_{4/4}$ tetrahedra are edge- and corner-shared, forming a 3D [PtIn] polyanion in which the strontium atoms are embedded.[149] The CaRhIn structure also consists of strongly puckered Rh_3In_3 hexagons in which each rhodium atom has a distorted tetrahedral indium environment and the calcium atoms fill the channels within the 3D [RhIn] polyanion.[150]

The structures of $CaTIn_2$ (T = Pd, Pt, Au) are transition metal (T)-centered trigonal prisms formed by the calcium and indium atoms. The transition metal and indium atoms form a 3D $[TIn_2]$ polyanion in which the large alkaline earth metal atoms occupy one-dimensional pentagonal tubes, and the strongest bonding interactions are found for the In–In and T–In contacts.[150,151]

The 3D $[TIn_4]$ polyanions are also found in the structure of $CaTIn_4$ (T = Rh, Pd, Ir), in which the calcium atoms occupy distorted pentagonal tubes formed by indium and transition metal.[152] The main motifs of both $Ca_2Au_3In_4$ and $Sr_2Pt_3In_4$ are condensed, platinum (gold)-centered trigonal prisms formed by the alkaline earth and indium atoms. The platinum (gold) and indium atoms form complex 3D $[Pt_3In_4]$ and $[Au_3In_4]$ polyanions respectively, and the alkaline earth cations are located in distorted hexagonal tubes.[149]

7.4 Rare Earth-transition Metal–Indium Compounds

The ternary rare earth-transition metal–indium compounds display a pronounced tendency for clustering of the transition metal atoms and a 2D and sometimes 3D indium substructure depending on the relative content of indium. The structures of $(RE)In_{1-x}Sb_2$ (RE = La–Nd) is built up of alternating layers of compositions $[Sb]_m$ and $[In_{0.8}Sb]_m$ ($m = 2 \sim \infty$), separated by the La atoms. The $[Sb]_m$ layer is described as a nearly square net of Sb atoms held by weak one-electron bonds, while the $[In_{0.8}Sb]_m$ layer is derived from an edge-sharing $[InSb_4]$ tetrahedron distorted in such a way as to produce In–In zigzag chains.[153] The one-dimensional $[Ni_7]$ clusters are observed in the compound $LaNi_7In_6$.[154]

The complexes (RE)TIn_2 (RE = Eu, Yb; T = Pd, Au) also form transition metal (T)-centered trigonal prisms by the rare earth metal and indium atoms. The transition metal and indium atoms form a 3D [TIn_2] polyanion in which the large rare earth metal atoms occupy one-dimensional pentagonal tubes.**155** The strongest bonding interactions are found for the In–In and Pd–In contacts; the Eu–Pd and Eu–In interactions are much weaker.

The structural motifs of $LaPtIn_3$ are condensed distorted trigonal [$PtIn_6$] prisms, and Pt–In and In–In bonding play an important role in the structure. The La atoms occupy large cavities within the polyhedral network.**156** Within $LaPtIn_4$ or $YbPtIn_4$, together with indium atoms platinum atoms form a complex 3D [$PtIn_4$] polyanion in which the lanthanum or ytterbium atoms occupy large hexagonal tubes.**157** In the structure of $LaNiIn_4$, the nickel and indium atoms also form a 3D [$NiIn_4$] polyanion and the indium substructure consists of distorted bcc-like indium cubes.**154**

Within $YbCoIn_5$ and $YbRhIn_5$, the transition metal atoms have eight indium neighbors in a square prismatic coordination by indium atoms; these prisms are condensed via common edges, forming layers. The ytterbium and additional indium atoms are located between these layers. The ytterbium atoms are cubooctahedrally coordinated by 12 indium atoms.**157**

The gold and indium atoms in $La_3Au_4In_7$ build a 3D [Au_4In_7] polyanion in which the lanthanum atoms fill distorted pentagonal and hexagonal channels. Within the polyanion, short Au–In and In–In distances are indicative of strongly bonding Au–In and In–In interactions.**158** Within $EuRh_2In_8$, the rhodium and indium atoms together build a complex 3D [Rh_2In_8] polyanion in which the europium atoms are located within distorted pentagonal channels. In $RE_4Pd_{10}In_{21}$ (RE = La, Ce, Pr, Nd, Sm), all palladium atoms have a trigonal prismatic coordination. The strongest bonding interactions occur for the Pd–In and In–In contacts. The structures are composed of covalently bonded three-dimensional [$Pd_{10}In_{21}$] networks in which the rare earth metal atoms fill distorted pentagonal channels.**159,160** In addition, the 3D [$Pt_{12}In_{32}$] network is also observed in the structures of $Gd_3Pt_4In_{12}$ and $Tb_3Pt_4In_{12}$.**161**

7.5 Multinary Compounds

The compound $Cs_7NbIn_3As_5$ contains an unprecedented anion, $[\{In_3As_4Nb\}-As]^{7-}$, a cubane made of three indium, four arsenic, and one niobium atom and a 'handle' composed of an arsenic atom that is multiply bonded to the niobium corner (Scheme 8).**162**

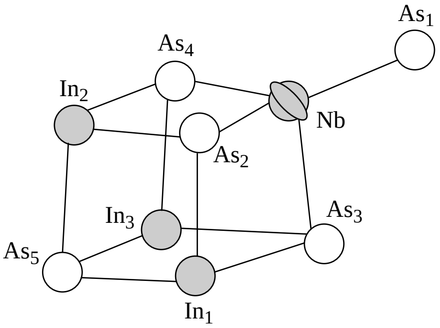

Scheme 8 Structure of the cubane with a 'handle' $[\{As(InAs)_3\}Nb–As]^{7-}$, Ref. 162

The structure of $[PtIn_6][GaO_4]_2$ contains the [$PtIn_6$] octahedral, which are linked via $[GaO_4]^{5-}$ tetrahedral to a 3D network. Starting from $[PtIn_6][GaO_4]_2$, the substitution of Ga^{3+} ions by larger In^{3+} ions leads to the formation of a solid solution series according to the general formula $[PtIn_6][GaO_4]_{2-x}[InO_4]_x$ and becomes apparent in an increase of the lattice parameter.**163**

The first compound representing the next stage of a structural hierarchy, that is supertetrahedra of supertetrahedra, specifically is a T2 supertetrahedron of T4, a discrete anionic cluster of 214 atoms and 80 tetrahedral centers. The structure contains the finite tetrahedral anionic units of $[Cd_{16}In_{64}S_{134}]^{44-}$ that have an underlying T2 type of structure in which the individual tetrahedra have each been replaced by a T4 supertetrahedron forming a super-supertetrahedron.**164**

In the compound $Ba_6ZnIn_2Cl_{20}$, Zn^{2+} is surrounded tetrahedrally and In^{3+} octahedrally by chloride ions. Half of the [$InCl_6$] octahedra are isolated from each other; the other half share common edges to form [In_2Cl_{10}] double octahedra. Ba^{2+} has coordination numbers of eight and nine.**165**

$Na_3K_{23}Cd_{12}In_{48}$ is obtained by stoichiometric fusion of the elements and is composed of indium icosahedra, indium triangular clusters, and the novel $Cd_{12}In_6$ tubular cluster. The latter contains two Na^+ ions and a 96-atom polyhedra (fullerane), and is sheathed by 20 K^+ and 12Na^+. The clusters are linked together through two-center two-electron bonds with a 3D anionic network.**166**

8 INDIUM CATALYZED ORGANIC SYNTHESIS

8.1 Introduction

Since the discovery of the indium-mediated Barbier–Grignard reaction in 1991, indium reagents have become more popular in organic synthesis.**167** The attraction of indium catalysis is that it provides the ability to perform organic reactions in water. During the last decade, a large proportion of this work has been focused on the use of indium reagents to promote organic reactions in aqueous media. Moreover, indium-assisted reactions often display a low heterophilicity and low nucleophilicity that imparts high regio- and chemoselectivity in various chemical transformations of groups of similar reactivity, without protecting other groups.

The recent emergence of indium halides as efficient Lewis acid catalysts presents new and exciting opportunities for indium chemistry.[168]

8.2 Allylation

The indium-mediated allylation reaction is an aldol-type reaction where the nucleophile is an allylindium species usually generated from allylic halide and indium. By far the greatest number of indium-mediated organic reactions involves the allylation of unsaturated compounds, and the list of indium-mediated allylations is formidable. In principle, there are five types of indium-mediated allylation reactions depending on the unsaturated functional groups (Scheme 9). (a) Treatment of allylindium reagents with carbonyl compounds can produce the corresponding allylalcohols;[169–171] (b) Reaction with terminal epoxides affords the corresponding bishomoalcohols;[172] (c) Allylation of aldimines gives the corresponding homoallylic amines;[173,174] (d) Reaction with alkenes or terminal alkynes gives the corresponding alkenes and 1,4-dienes respectively;[175,176] (e) Aromatic sulfonyl halides react with allyl indium reagents to give the corresponding sulfones.[177]

In general, solvent effect can play a significant role in the reactions and the regio- and stereo-selectivity of allylations is determined by the location of other functional groups in the molecules and the reaction solvents; several reports on the effect of other functional groups and solvents on the selectivity are published. Araki's group has noted that hydroxy-bearing cyclopropens can be allylated both in organic and aqueous media, but the regio- and stereo-selectivity can be regulated by both the location of the hydroxyl group in the molecules and the reaction solvents.[178]

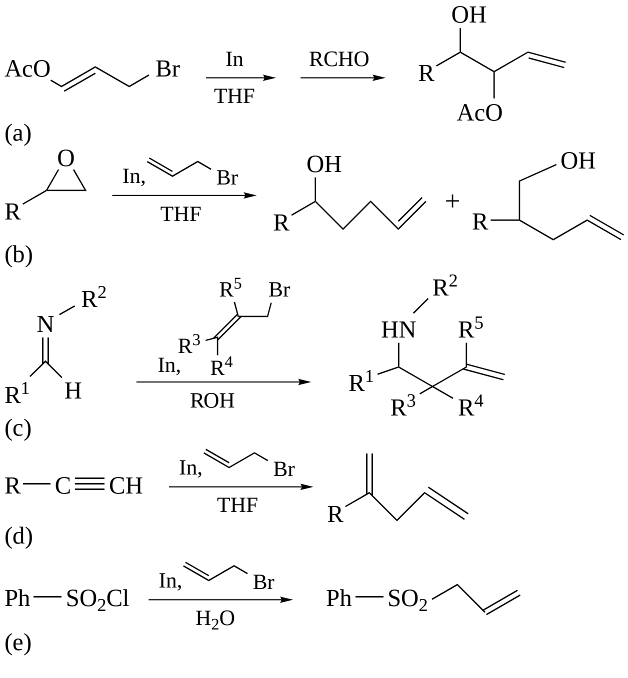

Scheme 9 Indium-mediated allylation reactions

8.3 Acylation

The acylation of alcohols and amines is one of the most frequently used transformations in organic synthesis as it provides an efficient and inexpensive means for protecting hydroxy and amino groups in a multistep synthetic process. The Lewis acid catalyzed acylation is a mild alternative to conventional acidic or basic catalyst. The extremely efficient acylation of a diverse range of substrates has been noted using indium halides. Using this method, acylation of a primary OH group in the presence of secondary and phenolic OH groups, and of a primary NH_2 in the presence of secondary NH and primary OH, has been achieved with high selectivity. The practical utility of indium halides is reflected in the high-yielding acylation of polyhydroxy compounds.[179,180]

8.4 Addition to Imines

α-Aminophosphonates have been the subject of considerable recent interest owing to their structural analogy to α-amino acids, and several synthetic methods for the compounds have been developed. Of these, the nucleophilic addition of phosphates to imines, catalyzed by Lewis acids such as $SnCl_2$, $ZnCl_2$, and $MgBr_2$, is the most convenient. However, these reactions cannot be carried out in a one-pot operation starting from a carbonyl compound, an amine, and dialkyl phosphite because the amines and water present during imine formation are likely to decompose or deactivate Lewis acids. To circumvent this disadvantage, an elegant procedure has been developed employing indium (III) chloride as catalyst from the reaction of a carbonyl compound, amine, and diethyl phosphite. The method is operationally simple and applicable to aldehydes and ketones. The reaction is tolerant of sensitive functional groups and chelating groups.[181] In this way, a wide range of structurally diverse carbonyl compounds was converted into the corresponding α-Aminophosphonates in high yields.[3,182] In addition, indium agents are also effective for the conversion of azides to carbamates.[183]

8.5 Reduction

Indium is reported to be an efficient catalyst for the debromination processes of vic-dibromides. An illustration of the utility of this method is in the debromination of aryl-substituted vic-dibromides to produce the corresponding (E)-alkenes with indium metal in MeOH. In general, the reaction proceeds via a common, relatively stable radical intermediate, collapse of which leads directly to the (E)-alkenes, and methanol is found to be the best solvent for this reaction.[184]

Indium metal is equally effective for the reductive of α-halocarbonyl compounds as demonstrated by the transformation of $PhCOCH_2Br$ to the dehalogenated product $PhCOCH_3$.[185] A wide range of structurally diverse α-halo ketones and esters has been reduced according to this procedure to provide the corresponding dehalogenated carbonyl compounds.[186]

8.6 Other Reaction

A catalytic amount of indium metal effectively promotes the homocoupling of alkyl and aryl halides to provide the corresponding bialkyls and biaryls.[187] Ranu's group has reported that indium (III) chloride is very effective in effecting the rearrangement of epoxides in THF solution to give the corresponding carbonyl compounds very selectively.[188] Indium (III) chloride is effective in catalyst amounts for the Michael reaction between amines and α,β-ethylenenic compounds in water,[189] Diels–Alder reaction between various dienes and dienophiles in water,[190] and the synthesis of alkyl and aryl 2,3-unstaturated C-glycosides through the Ferrier rearrangement.[191] The combination of indium catalyst and other catalyst is extremely effective for deoxygenation process. For example, treatment of tetralone with Me_2SiClH in the presence of indium (III) chloride at room temperature produces tetralin in excellent yields.[192] In addition, $InBr_3$, indium (III) triflate, and In (I) compounds used for catalyst also are reported.[193]

9 REFERENCES

1. L. Dai, X. L. Chen, J. K. Jian, M. He, T. Zhou, and B. Q. Hu, *Appl. Phys. A*, 2002, **75**, 687.
2. J. Cui, A. Wang, N. L. Edleman, J. Ni, P. Lee, N. R. Armstrong, and T. J. Marks, *Adv. Mater.*, 2001, **13**, 1476.
3. B. C. Ranu, *Eur. J. Org. Chem.*, 2000, 2347.
4. W. Uhl and S. Melle, *Chem. – Eur. J.*, 2001, **7**, 4216.
5. N. Wiberg, T. Blank, K. Amelunxen, H. Nöth, H. Schnöckel, E. Baum, A. Purath, and D. Fenske, *Eur. J. Inorg. Chem.*, 2002, 341.
6. R. Dronskowski, *Inorg. Chem.*, 1994, **33**, 5960.
7. R. Dronskowski, *Inorg. Chem.*, 1994, **33**, 6201.
8. M. Ruck and H. Bärnighausen, *Z. Anorg. Allg. Chem.*, 1999, **625**, 577.
9. R. Dronskowski, *Angew. Chem., Int. Ed. Engl.*, 1995, **34**, 1126.
10. R. Dronskowski, *Inorg. Chem.*, 1994, **33**, 5927.
11. R. Dronskowski, *Inorg. Chem.*, 1995, **34**, 4991.
12. J. Köhler and J. H. Chang, *Angew. Chem., Int. Ed. Engl.*, 2000, **39**, 1998.
13. J. Weiss, T. Priermeier, and R. A. Fischer, *Inorg. Chem.*, 1996, **35**, 71.
14. W. Uhl, S. U. Keimling, W. Hiller, and M. Neumayer, *Chem. Ber.*, 1995, **128**, 1137.
15. W. Uhl and M. Pohlmann, *Organometallics*, 1997, **16**, 2478.
16. W. Uhl, S. Melle, G. Frenking, and M. Hartmann, *Inorg.Chem.*, 2001, **40**, 750.
17. W. Uhl, S. U. Keimling, M. Pohlmann, S. Pohl, W. Saak, W. Hiller, and M. Neumayer, *Inorg. Chem.*, 1997, **36**, 5478.
18. W. Uhl, M. Pohlmann, and R. Wartchow, *Angew. Chem., Int. Ed. Engl.*, 1998, **37**, 961.
19. W. Uhl and S. Melle, *Z. Anorg. Allg. Chem.*, 2000, **626**, 2043.
20. T. Steinke, C. Gemel, M. Winter, and R. A. Fischer, *Angew. Chem., Int. Ed. Engl.*, 2002, **41**, 4761.
21. W. Uhl and M. Pohlmann, *Chem. Commun.*, 1998, 451.
22. W. Uhl, R. Graupner, W. Hiller, and M. Neumayer, *Angew. Chem., Int. Ed. Engl.*, 1997, **36**, 62.
23. N. Wiberg, T. Blank, A. Purath, G. Stöβer, and H. Schnöckel, *Angew. Chem., Int. Ed. Engl.*, 1999, **38**, 2563.
24. N. Wiberg, T. Blank, H. Nöth, and W. Ponikwar, *Angew. Chem., Int. Ed. Engl.*, 1999, **38**, 839.
25. B. E. Eichler, N. J. Hardman, and P. P. Power, *Angew. Chem., Int. Ed. Engl.*, 2000, **39**, 383.
26. H. V. R. Dias, L. Huai, W. Jin, and S. G. Bott, *Inorg. Chem.*, 1995, **34**, 1973.
27. H. V. R. Dias and W. Jin, *Inorg. Chem.*, 1996, **35**, 267.
28. G. K. B. Clentsmith, F. G. N. Cloke, M. D. Francis, J. C. Green, P. B. Hitchcock, J. F. Nixon, J. L. Suter, and D. M. Vickers, *J. Chem. Soc., Dalton Trans.*, 2000, **1**, 1715.
29. S. K. Chandra and E. S. Gould, *Chem. Commun.*, 1996, 809.
30. S. K. Chandra, P. C. Paul, and E. S. Gould, *Inorg. Chem.*, 1997, **36**, 4684.
31. S. K. Chandra and E. S. Gould, *Inorg. Chem.*, 1997, **36**, 3485.
32. M. Scholten, R. Dronskowski, T. Staffel, and G. Meyer, *Z. Anorg. Allg. Chem.*, 1998, **624**, 1741.
33. W. Uhl and T. Spies, *Z. Anorg. Allg. Chem.*, 2000, **626**, 1059.
34. H. J. Deiseroth and C. Reiner, *Z. Anorg. Allg. Chem.*, 1998, **624**, 1839.
35. R. Wochele, W. Schwarz, K. W. Klinkhammer, K. Locke, and J. Weidlein, *Z. Anorg. Allg. Chem.*, 2000, **626**, 1963.
36. S. M. Godfrey, K. J. Kelly, P. Kramkowski, C. A. McAuliffe, and R. G. Pritchard, *Chem. Commun.*, 1997, 1001.
37. W. Uhl, R. Gerding, and F. Hannemann, *Z. Anorg. Allg. Chem.*, 1998, **624**, 937.
38. W. Uhl, R. Graupner, I. Hahn, and W. Saak, *Z. Anorg. Allg. Chem.*, 1999, **625**, 1113.
39. W. Uhl, R. Graupner, I. Hahn, T. Spies, and W. Frank, *Eur. J. Inorg. Chem.*, 1998, 355.
40. P. Hunt and P. Schwerdtfeger, *Inorg. Chem.*, 1996, **35**, 2085.
41. S. Aldridge, A. J. Downs, and S. Parsons, *Chem. Commun.*, 1996, 2055.

42. T. Miyai, K. Inoue, M. Yasuda, I. Shibata, and A. Baba, *Tetrahedron Lett.*, 1998, **39**, 1929.

43. M. D. Francis, D. E. Hibbs, M. B. Hursthouse, C. Jones, and N. A. Smithies, *J. Chem. Soc., Dalton Trans.*, 1998, **1**, 3249.

44. M. L. Cole, D. E. Hibbs, C. Jones, and N. A. Smithies, *J. Chem. Soc., Dalton Trans.*, 2000, **1**, 545.

45. C. Jones, *Chem. Commun.*, 2001, 2293.

46. D. G. Samsonenko, M. N. Sokolov, A. V. Virovets, N. V. Pervukhina, and V. P. Fedin, *Eur. J. Inorg. Chem.*, 2001, 167.

47. A. B. de Carvalho, M. A. M. A. de Maurera, J. A. Nobrega, C. Peppe, M. A. Brown, D. G. Tuck, M. Z. H. Longo, and F. R. Sensato, *Organometallics*, 1998, **17**, 99.

48. G. R. Willey, D. R. Aris, J. V. Haslop, and W. Errington, *Polyhedron*, 2001, **20**, 423.

49. S. Kühner, H. D. Hausen, and J. Weidlein, *Z. Anorg. Allg. Chem.*, 1998, **624**, 13.

50. A. Walz, K. W. Klinkhammer, and J. Weidlein, *Z. Anorg. Allg. Chem.*, 1998, **624**, 4.

51. J. Pauls, S. Chitsaz, and B. Neumüller, *Z. Anorg. Allg. Chem.*, 2001, **627**, 1723.

52. H. V. R. Dias and W. Jin, *Inorg.Chem.*, 1996, **35**, 6546.

53. M. Zhou, Y. Xu, C. F. Lam, P. H. Leung, L. L. Koh, K. F. Mok, and T. S. A. Hor, *Inorg.Chem.*, 1994, **33**, 1572.

54. M. Sigl, A. Schier, and H. Schmidbaur, *Eur. J. Inorg. Chem.*, 1998, 203.

55. S. Chitsaz, E. Iravani, and B. Neumüller, *Z. Anorg. Allg. Chem.*, 2002, **628**, 2279.

56. S. Chitsaz and B. Neumüller, *Z. Anorg. Allg. Chem.*, 2001, **627**, 2451.

57. B. Neumüller, *Chem. Soc. Rev.*, 2003, **32**, 50.

58. H. Schumann, J. Kaufmann, B. C. Wassermann, F. Girgsdies, N. Jaber, and J. Blum, *Z. Anorg. Allg. Chem.*, 2002, **628**, 971.

59. M. Veith, S. Hill, and V. Huch, *Z. Anorg. Allg. Chem.*, 2001, **627**, 1495.

60. J. Pauls, S. Chitsaz, and B. Neumüller, *Z. Anorg. Allg. Chem.*, 2000, **626**, 2028.

61. K. M. Coward, A. C. Jones, A. Steiner, J. F. Bickley, L. M. Smith, and M. E. Pemble, *J. Chem. Soc., Dalton Trans.*, 2001, 41.

62. R. Bertani, L. Crociani, G. D. Arcangelo, G. Rossetto, P. Traldi, and P. Zanella, *J. Organomet. Chem.*, 2001, **626**, 11.

63. D. C. Bradley and I. S. Harding, *J. Chem. Soc., Dalton Trans.*, 1997, 4637.

64. L. Weber, M. H. Scheffer, H. G. Stammler, and A. Stammler, *Eur. J. Inorg. Chem.*, 1999, 1607.

65. J. Kim, S. G. Bott, and D. M. Hoffman, *J. Chem. Soc., Dalton Trans.*, 1999, 141.

66. Y. Zhou and D. S. Richeson, *Inorg. Chem.*, 1996, **35**, 1423.

67. P. L. Shutov, S. S. Karlov, K. Harms, O. K. Poleshchuk, J. Lorberth, and G. S. Zaitseva, *Eur. J. Inorg. Chem.*, 2003, 1507.

68. H. Sussek, F. Stowasser, H. Pritzkow, and R. A. Fischer, *Eur. J. Inorg. Chem.*, 2000, 455.

69. C. Rennekamp, P. Müller, J. Prust, H. Wessel, H. W. Roesky, and I. Usón, *Eur. J. Inorg. Chem.*, 2000, 1861.

70. J. Janczak, R. Kubiak, and A. Jezierski, *Inorg. Chem.*, 1995, **34**, 3505.

71. M. Hanack and H. Heckmann, *Eur. J. Inorg. Chem.*, 1998, 367.

72. T. Schneider, H. Heckmann, M. Barthel, and M. Hanack, *Eur. J. Inorg. Chem.*, 2001, 3055.

73. T. Grabowy and K. Merzweiler, *Z. Anorg. Allg. Chem.*, 2000, **626**, 736.

74. M. R. Kopp and B. Neumüller, *Z. Anorg. Allg. Chem.*, 1999, **625**, 1246.

75. B. Werner and B. Neumüller, *Organometallic*, 1996, **15**, 4258.

76. R. D. Culp, A. H. Cowley, A. Decken, R. A. Jones, M. R. Bond, L. M. Mokry, and C. J. Carrano, *Inorg. Chem.*, 1997, **36**, 5165.

77. C. V. Hänisch, *Eur. J. Inorg. Chem.*, 2003, 2955.

78. K. Chondroudis, D. Chakrabarty, E. A. Axtell, and M. G. Kanatzidis, *Z. Anorg. Allg. Chem.*, 1998, **624**, 975.

79. A. M. Chippindale and S. J. Brech, *Chem. Commun.*, 1996, 2781.

80. J. Morizzi, M. Hobday, and C. Rix, *J. Mater. Chem.*, 2000, **10**, 1693.

81. A. M. Chippindale, S. J. Brech, A. R. Cowley, and W. M. Simpson, *Chem. Mater.*, 1996, **8**, 2259.

82. K.-H. Lii, *J. Chem. Soc., Dalton Trans.*, 1996, 815.

83. X. Tang, A. Jones, A. Lachgar, B. J. Gross, and J. L. Yanger, *Inorg. Chem.*, 1999, **38**, 6032.

84. S. L. Stoll, S. G. Bott, and A. R. Barron, *J. Chem. Soc., Dalton Trans.*, 1997, 1351.

85. H. Rahbarnoohi, M. Taghiof, M. J. Heeg, D. G. Dick, and J. P. Oliver, *Inorg. Chem.*, 1994, **33**, 6307.

86. H. Rahbarnoohi, R. Kumar, M. J. Heeg, and J. P. Oliver, *Organometallic*, 1995, **14**, 3869.

87. S. P. Wuller, A. L. Seligson, G. P. Mitchell, and J. Arnold, *Inorg. Chem.*, 1995, **34**, 4854.

88. Y. Cheng, T. J. Emge, and J. G. Brennan, *Inorg. Chem.*, 1996, **35**, 7339.

89. C. Wang and R. C. Haushalter, *Inorg. Chem.*, 1997, **36**, 3806.

90. R. Cea-Olivares, R. A. Toscano, S. Hernández-Ortega, J. Novosad, and V. García-Montalvo, *Eur. J. Inorg. Chem.*, 1999, 1613.

91. T. C. Deivaraj, W. H. Lye, and J. J. Vittal, *Inorg. Chem.*, 2002, **41**, 3755.

92. H. J. Deiseroth, C. Reiner, M. Schlosser, and L. Kienle, *Z. Anorg. Allg. Chem.*, 2002, **628**, 1641.

93. H. J. Deiseroth and C. Reiner, *Z. Anorg. Allg. Chem.*, 1998, **624**, 1839.
94. W. Uhl, M. Pohlmann, and R. Wartchow, *Angew. Chem., Int. Ed. Engl.*, 1998, **37**, 961.
95. R. A. Fischer, M. Kleine, O. Lehmann, and M. Stuke, *Chem. Mater.*, 1995, **7**, 1863.
96. R. A. Fischer, E. Herdtweck, and T. Priermeier, *Inorg. Chem.*, 1994, **33**, 934.
97. S. W. Haggata, M. A. Malik, M. Motevalli, P. O'Brien, and J. C. Knowles, *Chem. Mater.*, 1995, **7**, 716.
98. G. A. Horley, P. O. Brien, J.-H. Park, A. J. P. White, and D. J. Williams, *J. Mater. Chem.*, 1999, **9**, 1289.
99. G. A. Horley, M. Chunggaze, P. O'Brien, A. J. P. White, and D. J. Williams, *J. Chem. Soc., Dalton Trans.*, 1998, 4205.
100. V. G. Bessergenev, E. V. Ivanona, Y. A. Kovalevskaya, S. A. Gromilov, V. N. Kirichenko, and S. V. Larionov, *Inorg. Mater.*, 1996, **6**, 1639.
101. H. Rahbarnoohi, M. Taghiof, M. J. Heeg, D. G. Dick, and J. P. Oliver, *Inorg. Chem.*, 1994, **33**, 6307.
102. S. L. Stoll and A. R. Barron, *Chem. Mater.*, 1998, **10**, 650.
103. H. Rahbarnoohi, R. L. Wells, L. M. Liable-Sands, G. P. A. Yap, and A. L. Rheingold, *Organometallics*, 1997, **16**, 3959.
104. J. A. Hollingsworth, A. F. Hepp and W. E. Buhro, *Chem. Vap. Dep.*, 1999, **5**, 105.
105. K. K. Banger, J. Cowen, and A. F. Hepp, *Chem. Mater.*, 2001, **13**, 3827.
106. T. C. Deivaraj, J.-H. Park, M. Afzaal, P. O'Brien, and J. J. Vittal, *Chem. Commun.*, 2001, 2304.
107. A. Devi, W. Rogge, A. Wohlfart, F. Hipler, H. W. Becker, and R. A. Fischer, *Chem. Vap. Dep.*, 2000, **6**, 245.
108. C. Steffek, J. McMurran, B. Pleune, J. Kouvetakis, T. E. Concolino, and A. L. Rheingold, *Inorg. Chem.*, 2000, **39**, 1615.
109. H. J. Himmel, A. J. Downs, and T. M. Greene, *Chem. Commun.*, 2000, 871.
110. G. K. Rothschopf, S. Li, J. S. Perkins, and D.-S. Yang, *J. Chem. Phys.*, 2001, **115**, 4565.
111. H. Nöth and T. Seifert, *Eur. J. Inorg. Chem.*, 2002, 602.
112. E. E. Foos, R. J. Jouet, R. L. Wells, and P. S. White, *J. Organomet. Chem.*, 2000, **598**, 182.
113. Q. Chen, M. Tanaka, and K. Furuya, *J. Surf. Anal.*, 1999, **5**, 348.
114. G. T. Cardenas, E. C. Salgado, J. Morales, and H. Z. Soto, *J. Appl. Polym. Sci.*, 1999, **73**, 1239.
115. K. Soulantica, A. Maisonnat, M.-C. Fromen, M. J. Casanove, P. Lecante, and B. Chaudret, *Angew. Chem., Int. Ed. Engl.*, 2001, **40**, 448.
116. K. Soulantica, L. Erades, M. Sauvan, F. Senocq, A. Maisonnat, and B. Chaudret, *Adv. Funct. Mater.*, 2003, **13**, 553.
117. Y. B. Zhao, Z. J. Zhang, and H. X. Dang, *J. Phys. Chem. B*, 2003, **107**, 7574.
118. N. H. Heo, J. S. Park, Y. J. Kim, W. T. Lim, S. W. Jung, and K. Seff, *J. Phys. Chem. B*, 2003, **107**, 1120.
119. K. Soulantica, A. Maisonnat, F. Senocq, M.-C. Fromen, M.-J. Casanove, and B. Chaudret, *Angew. Chem., Int. Ed. Engl.*, 2001, **40**, 2984.
120. A. Krost, J. Bläsing, H. Protzmann, M. Lünenbürger, and M. Heuken, *Appl. Phys. Lett.*, 2000, **76**, 1395.
121. W. S. Seo, H. H. Jo, K. Lee, and J. T. Park, *Adv. Mater.*, 2003, **15**, 795.
122. Z. W. Pan, Z. R. Dai, and Z. L. Wang, *Science*, 2001, **291**, 1947.
123. X. P. Peng, Y. W. Wang, J. Zhang, X. F. Wang, L. X. Zhao, G. W. Meng, and L. D. Zhang, *Appl. Phys. A*, 2002, **74**, 437.
124. D. Yu, S. H. Yu, S. Zhang, J. Zuo, D. Wang, and Y. Qian, *Adv. Funct. Mater.*, 2003, **13**, 497.
125. C. Li, D. Zhang, S. Han, X. Liu, T. Tang, and C. Zhou, *Adv. Mater.*, 2003, **15**, 143.
126. B. Cheng and E. T. Samulski, *J. Mater. Chem.*, 2001, **11**, 2901.
127. Y. Li, Y. Bando, and D. Golberg, *Adv. Mater.*, 2003, **15**, 581.
128. X. P. Peng, G. W. Meng, X. F. Wang, Y. W. Wang, J. Zhang, X. Liu, and L. D. Zhang, *Chem. Mater.*, 2002, **14**, 4490.
129. S. D. Dingman, N. P. Rath, P. D. Markowitz, P. C. Gibbons, and W. E. Buhro, *Angew. Chem.*, 2000, **112**, 1530.
130. J. Xiao, Y. Xie, R. Tang, and W. Luo, *Inorg. Chem.*, 2003, **42**, 107.
131. L. Gao, Q. Zhang, and J. Li, *J. Mater. Chem.*, 2003, **13**, 154.
132. R. L. Wells, S. R. Aubuchon, S. S. Kher, M. S. Lube, and P. S. White, *Chem. Mater.*, 1995, **7**, 793.
133. T. J. Trentler, S. C. Goel, K. M. Hickman, A. M. Viano, M. Y. Chiang, A. M. Beatty, P. C. Gibbons, and W. E. Buhro, *J. Am. Chem. Soc.*, 1997, **119**, 2172.
134. M. Green and P. O. Brien, *Chem. Commun.*, 1998, 2459.
135. P. Yan, Y. Xie, W. Wang, F. Liu, and Y. Qian, *J. Mater. Chem.*, 1999, **9**, 1831.
136. E. P. A. M. Bakkers and M. A. Verheijen, *J. Am. Chem. Soc.*, 2003, **125**, 3440.
137. Y.-D. Li, X.-F. Duan, Y.-T. Qian, L. Yang, M.-R. Ji, and Cheng-Wei Li, *J. Am. Chem. Soc.*, 1997, **119**, 7869.
138. M. Green, S. Norager, P. Moriarty, M. Motevalli, and P. O'Brien, *J. Mater. Chem.*, 2000, **10**, 1939.
139. Y. Li, Z. Wang, X. Chuan, G. Zhang, and C. Wang, *Adv. Mater.*, 2001, **13**, 145.
140. E. Arici, N. S. Sariciftci, and D. Meissner, *Adv. Funct. Mater.*, 2003, **13**, 165.
141. M. A. Malik, P. O'Brien, and N. Revaprasadu, *Adv. Mater.*, 1999, **11**, 1441.
142. B. Li, Y. Xie, J. Huang, and Y. Qian, *Adv. Mater.*, 1999, **11**, 1456.
143. J. Q. Hu, B. Deng, K. B. Tang, C. R. Wang, and Y. T. Qian, *J. Mater. Res.*, 2001, **16**, 3411.

144. J. Q. Hu, B. Deng, W. X. Zhang, K. B. Tang, and Y. T. Qian, *Inorg. Chem.*, 2001, **40**, 3130.

145. K. J. Nordell and G. J. Miller, *Inorg. Chem.*, 1999, **38**, 579.

146. J.-T. Zhao and J. D. Corbett, *Inorg. Chem.*, 1995, **34**, 378.

147. R. Pöttgen, R.-D. Hoffmann, and G. Kotzyba, *Z. Anorg. Allg. Chem.*, 1998, **624**, 244.

148. D. Kuβmann, R.-D. Hoffmann, and R. Pöttgen, *Z. Anorg. Allg. Chem.*, 1998, **624**, 1727.

149. R.-D. Hoffmann and R. Pöttgen, *Z. Anorg. Allg. Chem.*, 1999, **625**, 994.

150. R.-D. Hoffmann and R. Pöttgen, *Z. Anorg. Allg. Chem.*, 2000, **626**, 28.

151. R.-D. Hoffmann, R. Pöttgen, G. A. Landrum, R. Dronskowski, B. Künnen, and G. Kotzyba, *Z. Anorg. Allg. Chem.*, 1999, **625**, 789.

152. R.-D. Hoffmann and R. Pöttgen, *Chem. – Eur. J.*, 2000, **6**, 600.

153. M. J. Ferguson, R. E. Ellenwood, and A. Mar, *Inorg. Chem.*, 1999, **38**, 4503.

154. fnm. Y. M. Kalychak, V. I. Zaremba, Y. V. Galadzhun, K. Y. Miliyanchuk, R.-D. Hoffmann, and R. Pöttgen, *Chem. – Eur. J.*, 2001, **7**, 5343.

155. Y. V. Galadzhun, R.-D. Hoffmann, G. Kotzyba, B. Künnen, and R. Pöttgen, *Eur. J. Inorg. Chem.*, 1999, 975.

156. Y. V. Galadzhun and R.-D. Hoffmann, *Z. Anorg. Allg. Chem.*, 1999, **625**, 481.

157. V. I. Zaremba, U. C. Rodewald, R.-D. Hoffmann, Y. M. Kalychak, and R. Pöttgen, *Z. Anorg. Allg. Chem.*, 2003, **629**, 1157.

158. Y. V. Galadzhun, V. I. Zaremba, Y. M. Kalychak, R.-D. Hoffmann, and R. Pöttgen, *Z. Anorg. Allg. Chem.*, 2000, **626**, 1773.

159. R. Pöttgen and D. Kußmann, *Z. Anorg. Allg. Chem.*, 2001, **627**, 55.

160. V. I. Zaremba, U. C. Rodewald, Y. M. Kalychak, Y. V. Galadzhun, D. Kaczorowski, R.-D. Hoffmann, and R. Pöttgen, *Z. Anorg. Allg. Chem.*, 2003, **629**, 434.

161. U. C. Rodewald, V. I. Zaremba, Y. V. Galadzhun, R.-D. Hoffmann, and R. Pöttgen, *Z. Anorg. Allg. Chem.*, 2002, **628**, 2293.

162. F. Gascoin and S. C. Sevov, *Angew. Chem., Int. Ed. Engl.*, 2002, **41**, 1232.

163. H. A. Friedrich and J. Köhler, *Z. Anorg. Allg. Chem.*, 2001, **627**, 144.

164. H. Li, J. Kim, M. O'keeffe, and O. M. Yaghi, *Angew. Chem. Int. Ed. Engl.*, 2003, **42**, 1819.

165. S. Masselmann and G. Meyer, *Z. Anorg. Allg. Chem.*, 1999, **625**, 269.

166. D. M. Flot, M. M. Tillard-Charbonnel, and C. H. E. Belin, *J. Am. Chem. Soc.*, 1996, **118**, 5229.

167. C. J. Li and T. H. Chan, *Tetrahedron Lett.*, 1991, **32**, 7017.

168. G. Hilt and K. I. Smolko, *Angew. Chem., Int. Ed. Engl.*, 2001, **40**, 3399.

169. U. Anwar, R. Grigg, M. Rasparini, V. Savic, and V. Sridharan, *Chem. Commun.*, 2000, 645.

170. J. A. Shin, J. H. Cha, A. N. Pae, K. I. Choi, H. Y. Koh, H. Y. Kang, and Y. S. Cho, *Tetrahedron Lett.*, 2001, **42**, 5489.

171. J. S. Kwon, A. N. Pae, K. I. Choi, H. Y. Koh, H. Y. Kang, and Y. S. Cho, *Tetrahedron Lett.*, 2001, **42**, 1957.

172. J. S. Yadav, S. Anjaneyulu, M. M. Ahmed, and B. V. S. Reddy, *Tetrahedron Lett.*, 2001, **42**, 2557.

173. T. Vilaivan, C. Winotapan, T. Shinada, and Y. Ohfune, *Tetrahedron Lett.*, 2001, **42**, 9073.

174. B. K. Banik, A. Ghatak, and F. F. Becker, *J. Chem. Soc., Perkin Trans.*, 2000, **1**, 2179.

175. B. C. Ranu and A. Majee, *Chem. Commun.*, 1997, 1225.

176. S. Araki, T. Kamei, Y. Igarashi, T. Hirashita, H. Yamamura, and M. Kawai, *Tetrahedron Lett.*, 1999, **40**, 7999.

177. L. Wang and Y. Zhang, *J. Chem. Res. (S)*, 1998, **9**, 588.

178. S. Araki, F. Shiraki, T. Tanaka, H. Nakano, K. Subburaj, T. Hirashita, H. Yamamura, and M. Kawai, *Chem. – Eur. J.*, 2001, **7**, 2784.

179. B. C. Ranu, P. Dutta, and A. Sarkar, *J. Chem. Soc., Perkin Trans.*, 2000, **1**, 2223.

180. K. K. Chauhan and C. G. Frost, *J. Chem. Soc., Perkin Trans.*, 2000, **1**, 3015.

181. B. C. Ranu, A. Hajra, and U. Jana, *Org. Lett.*, 1999, **1**, 1141.

182. C. Qian and T. Huang, *J. Org. Chem.*, 1998, **63**, 4125.

183. J. S. Yadav, B. V. S. Reddy, and G. S. K. K. Reddy, *New J. Chem.*, 2000, **24**, 571.

184. B. C. Ranu, S. K. Guchhait, and A. Sarkar, *Chem. Commun.*, 1998, 2113.

185. B. C. Ranu, P. Dutta, and A. Sarkar, *J. Chem. Soc., Perkin Trans.*, 1999, **1**, 1139.

186. L. Park, G. Keum, S. B. Kang, K. S. Kim, and Y. Kim, *J. Chem. Soc., Perkin Trans.*, 2000, **1**, 4462.

187. V. Penalva, J. Hassan, L. Lavenot, C. Gozzi, and M. Lemaire, *Tetrahedron Lett.*, 1998, **39**, 2559.

188. B. C. Ranu and U. Jana, *J. Org. Chem.*, 1998, **63**, 8212.

189. B. S. Babu and K. K. Balasubramanian, *Tetrahedron Lett.*, 2000, **41**, 1271.

190. T. P. Loh, J. Pei, and M. Lin, *Chem. Commun.*, 1996, 2315.

191. B. C. Ranu and U. Jana, *J. Org. Chem.*, 1998, **63**, 8212.

192. T. Miyai, M. Ueba, and A. Baba, *Synlett*, 1999, 182.

193. S. Gadhwal and J. S. Sandhu, *J. Chem. Soc., Perkin Trans.*, 2000, **1**, 2827.

Indium: Organometallic Chemistry

Kulbinder Kumar Banger
Ohio Aerospace Institute & NASA Glenn Research Center, Cleveland, OH, USA

1	Introduction	1
2	Alkyl and Aryl Derivatives, InR_3	1
3	Organoindium Halides	4
4	Organoindium Pnictogens	5
5	Organoindium Chalcogenides	7
6	Organoindium Hydrides	38
7	Organoindium Metal Complexes	39
8	Organoindium Low Valency Compounds	40
9	Organoindium Anionic Derivatives	43
10	Related Articles	44
11	Further Reading	44
12	References	44

---

1 INTRODUCTION

The importance of organoindium derivatives has been perpetuated in the last decade by their application as precursors to materials for advanced technologies, in particular, for fabricating multi-component alloys classified as III-V and I-III-VI semiconductors. Key areas that have helped advance the drive for new indium derivatives are thin-film technologies and, more recently, nanotechnology. A number of reviews and reports have been published that discuss in whole, or in part, organometallic compounds of indium.[1–15] Furthermore, general overviews of the chemistry of organoindium compounds related to thin-film technology were presented in books and annual reviews.[16–32] Another area where the use of indium organometallics has found increased use is for organic synthesis, more precisely the formation of indium organometallics *in situ* from elemental indium.[33–38] An area of interest that has gathered considerable interest is the indium meditated coupling of allyl and propargyl halides with aldehydes to give the corresponding alcohols in high yields.[39] An important aspect of this reaction is the ability to obtain good regioselectivity and diastereoselectivity by steric or chelation control.[37]

2 ALKYL AND ARYL DERIVATIVES, InR_3

2.1 Synthesis

The established method of choice for synthesizing indium derivatives follows those classically defined and used for generic organometallic synthesis. These are (a) Metathesis: equations (1), (2), and (3); (b) Transmetallation/Mercuration: equation (4); (c) Mixed metal Synthesis (direct): equation (5); (d) Metal plus organic halide (direct): equation (6).

$$InX_3 + 3RMgX \xrightarrow{Et_2O} InR_3(Et_2O) + 3MgX_2 \quad (1)$$

$$InX_3 + 3RLi \xrightarrow{Et_2O} InR_3(Et_2O) + 3LiX \quad (2)$$

$$InX_3 + 3R_3Al \longrightarrow InR_3 + 3R_2AlX \quad (3)$$

$$2In + 3R_2Hg \longrightarrow 2InR_3 + 3Hg \quad (4)$$

$$2In + 3Mg + 6RX \xrightarrow{Et_2O} 2InR_3(Et_2O) + 3MgX_2 \quad (5)$$

$$In + 3.5RX \xrightarrow[R = Me,\ 3.5Li]{hexane} InR_3 + 3LiX \quad (6)$$

A limiting factor for the use of group I organometallic reagents for the preparation of InR_3 from InX_3 (equation 2) is that many sodium or lithium reagents often act as reducing agents, affording In(I)R derivatives in poor to good yields instead of the desired In(III) organometallics. The use of Grignard reagents (RMgX) or AlR_3 does circumvent reduction of In(III) to In(I). With the exception of the metathesis route using AlR_3, both group I and Grignard reagents require the synthesis to be conducted in a coordinating solvent that subsequently forms an adduct to the desired product, e.g. $[InR_3{\cdot}(OEt_2)]$. However, repeated vacuum distillation, or azeotropic distillation with noncoordinating aromatic/aliphatic solvents results in the removal of the diethyl ether. Alternatively, it has recently been shown that thermal decomposition of $[InR_3{\cdot}(OEt_2)]$ in the presence of CsF affords the adduct free $InMe_3$ in very high yields.[40]

The use of mercurating agents (R_2Hg) has become obsolete owing to extended reaction times and elevated reaction temperatures, but more importantly due to the associated toxicity of mercury compounds. Mixed metal synthesis (equation 5) has proved to be versatile and is widely used owing to the high product yields and purity.[41] The propensity for ultra-high purity InR_3 via mixed metal synthesis has largely been driven by the semiconductor industry and its need to eliminate extrinsic dopants during synthesis (equation 6). This has warranted numerous patents for the preparation of InR_3.[41–51] The use of photoexcited indium atoms and their reaction with CH_4 to afford low-valent In(I) and In(II) has also been studied, and is expanded in Section 8.

Limited heteroleptic organoindium examples are known since they have a tendency to rearrange to form the more stable symmetrical derivatives. The preparation of the majority of the heteroleptic compounds has been investigated via (a) ligand redistribution (equation 7–8), (b) metathesis (equation 9), or (c) methane elimination (equation 10);

$$InR_3 + 2InR'_3 \longrightarrow 3RInR'_2 \quad (7)$$

$$2InR_3 + InR'_3 \longrightarrow 3R_2InR' \tag{8}$$

$$R_2InX + LiR' \longrightarrow R_2InR' + LiX \tag{9}$$

$$In(CH_3)_3 + H\text{-}R' \xrightarrow{\text{Heat}} (CH_3)_2InR' + CH_4 \tag{10}$$

The synthesis of mixed alkyl indium organometallics has again been driven by the need for more volatile and enhanced properties for use in CVD and related areas. This has been a subject of recent review and discussion with attention being focused on the existence of liquid ethyldimethylindium (EtInMe$_2$).[27] Although two patents currently exist for the preparation of high purity EtInMe$_2$,[48,51] an early study by two independent research groups demonstrated that EtInMe$_2$ was indeed a mixture of InMe$_3$ and InEt$_3$ (equation 11).

$$3EtInMe_2 \rightleftharpoons 2InMe_3 + InEt_3 \tag{11}$$

The most definitive examples of heteroleptic organoindium (III) compounds are generally found for mixed alkyl-cyclic systems. Ligand redistribution reactions between InCp$_3$ and InR$_3$ (R = Me and CH$_2$CMe$_3$) in THF solution provided R$_2$In(C$_5$H$_5$) and RIn(C$_5$H$_5$)$_2$.[52] These heteroleptic organoindium(III) compounds were isolated as analytically pure crystalline solids; however, in THF solution, the compounds underwent a redistribution mechanism to afford equilibrium mixtures of the THF-adducts of InR$_3$, R$_2$In(C$_5$H$_5$), RIn(C$_5$H$_5$)$_2$, and In(C$_5$H$_5$)$_3$. Single-crystal X-ray structural studies unequivocally showed the existence of the mixed alkyl-cyclic derivative [(Me$_3$CCH$_2$)$_2$In(C$_5$H$_5$)], which revealed the compound to exist as a polymer with cyclopentadienide units bridging In(CH$_2$CMe$_3$)$_2$ moieties (Figure 1).

Heteroleptic derivatives have also been prepared via metathesis and methane elimination reactions as illustrated by the synthesis of [Me$_2$In(C$_5$H$_5$)], which was obtained by the reaction between [Me$_2$InCl] and Li(C$_5$H$_5$) in THF at 145–160 °C.[53] An X-ray structural study identified an infinite linear polymer with cyclopentadienide units bridging InMe$_2$ moieties through the 1 and 3 positions of the ring (Figures 2 and 3).

Like most heteroleptic derivatives, [Me$_2$In(C$_5$H$_5$)] when dissolved in THF exists as an equilibrium mixture of components [Me$_2$In(C$_5$H$_5$)]·THF, [MeIn(C$_5$H$_5$)$_2$]·THF, and [InMe$_3$]·THF.

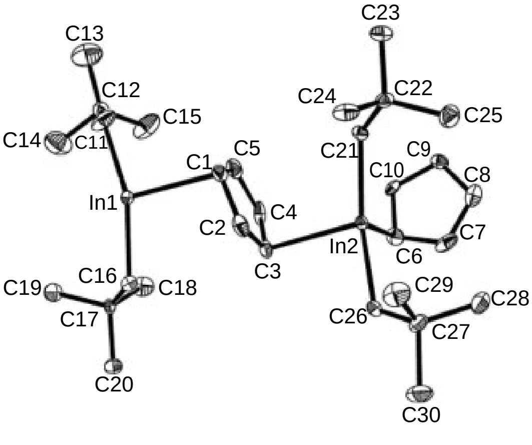

Figure 1 Single-crystal structure of [(Me$_3$CCH$_2$)$_2$In(C$_5$H$_5$)]$_n$

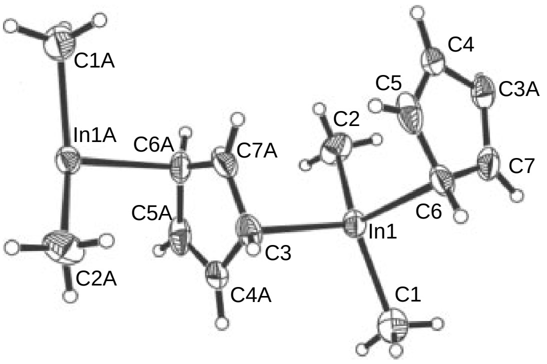

Figure 2 Polymeric chain of [Me$_2$In(C$_5$H$_5$)]$_n$

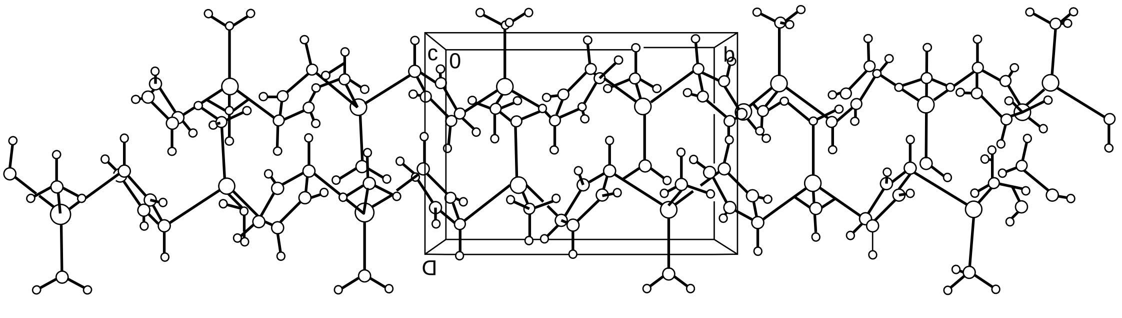

Figure 3 Unit cell of [Me$_2$In(C$_5$H$_5$)]$_n$

Table 1 Selective reported physical properties of some organoindium compounds

Compound	Phase	Mp (°C)	Bp (°C) (torr)	Sub. (°C) (torr)	Vapor press
$InMe_3$	Solid	89	136 66–67(12)		
$InEt_3$	liquid	−32	184 83–84(12)		$\log p = 2790/T + 8.98$
$InPr_3$	liquid	−51	178 97(12)		$\log p = -3051/T + 9.20$
$In(i\text{-}Pr)_3$	liquid	–	88 (12)		
$InBu_3$	liquid	–	85–6(1)		$\log p = 3124/T + 8.72$
$In(i\text{-}Bu)_3$	liquid	–	71–2(0.05)		$\log p = -3009/T + 8.81$
$In(s\text{-}Bu)_3$	solid	–	70–2(0.1)		
$In(t\text{-}Bu)_3$	solid	53–57		$30(10^{-2})$	
$InCp_3$	yellow solid	∼160–164 dec.			
InCp	Pale yellow solid	169–170 dec. 170–171 dec.		50(0.01)	
Me_2InCp	Colorless Solid	190–196 dec. 195–200 dec.			
$MeInCp_2$	Yellow Solid	151–160			
$In(Ph)_3$	Solid	212	–		
$In(C_6F_5)_3$	Solid	176–178			
$InNp_3$	Solid	54–55	–	27(0.01)	
Np_2InCp	Solid	188–190 dec.			
$NpInCp_2$	Yellow Solid	126–127 dec.			
$In(C{\equiv}Ct\text{-}Bu)_3{\cdot}NEt_3$	Solid	220[57]			

2.2 Properties

Indium organometallics are generally pyrophoric and sensitive to air and moisture, with some exceptions.[54] The thermal decomposition pathway has been studied largely in order to understand how to achieve derivatives that will pyrolyze at lower temperatures with minimal impurities such as carbon. InR_3 with β-hydrogen's have been shown to decompose via a β-hydride elimination pathway to give the respective olefins and metal hydride.[54] Generally the possibility of β-elimination lowers the decomposition temperature of the metal alkyls, and in addition some branching at the β position weakens the In–C bond. Furthermore, the onset for the decomposition temperature decreases upon introduction of increased alkyl chain length and steric encumbrance.[27,55] In contrast, thermal solution decomposition studies of indium trialkyls possessing an α-branch, for example, $[In(s\text{-}Bu)_3]$ and $[In(i\text{-}Pr)_3]$, have demonstrated decomposition to occur predominately through an α-fission pathway to selectively give the corresponding alkyl radicals.[54]

A recent study on the stability of various indium alkyl derivatives has been performed using differential scanning calorimetry (DSC), which provides a comprehensive thermal ''fingerprint'' of the compounds.[55] In addition, when this method of thermal analyses is used in conjunction with thermogravimetric analysis coupled to FTIR and/or GCMS evolved gas analysis, it can provide a complete mechanism for the decomposition pathway of prospective compounds.[56]

Selective physical properties of some organoindium compounds are listed in Table 1.

Studies on the properties of trialkyl indium derivatives and their designated use in MOCVD have also been reported,[58,59] and for the first time a detailed study on the vibrational spectrum for $InMe_3$ has been reported.[60]

2.3 In(III) Adducts

Organoindium derivatives behave as Lewis acids, readily forming adducts with electron-donating species. A large number of organoindium chelating compounds have been identified and studied.[55] One of the most noticeable differences between chelated and nonchelated InR_3 is the associated reduced reactivity due in part to the saturation of the indium-metal coordination sphere. A novel use of alkyl indium chelate chemistry is for the purification of InR_3 by removal of extrinsic impurities for the semiconductor industry. This method is in commercial practice by Epichem. The method involves reacting InR_3 with an ultra-pure Lewis base to afford the trialkyl indium chelate as a stabilized nonvolatile adduct. This can subsequently be purified via recrystalization or distillation. The purified InR_3 is then obtained by controlled thermal dissociation of the adduct.[55] $InMe_3$ purified via this technique has been shown to have reduced silicon impurities by a factor of 100 and when used to fabricate III–V semiconductors thin films, enhanced carrier concentration and mobility were recorded.[27]

3 ORGANOINDIUM HALIDES

3.1 Synthesis

Organoindium halides can readily be prepared by many of the synthetic methods outlined for the preparation of organoindium derivatives, but with stoichiometric control to afford the organoindium halide derivative.[61–73] For example, (a) reaction of InX_3 with less than three equivalents of a lithium or Grignard reagent (equations 12–13), (b) reaction of R_3In with HX, which proceeds by elimination of a simple organic moiety (equation 14), (c) a redistribution reaction between InX_3 and R_3In (equations 15–16).

$$InX_3 + nRMgX \xrightarrow{n = 1,2} R_nInX_{(3-n)} + nMgX_2 \quad (12)$$

$$InX_3 + nLiX \xrightarrow{n = 1,2} R_nInX_{(3-n)} + nLiX \quad (13)$$

$$InR_3 + nHX \xrightarrow{n = 1,2} R_{(3-n)}InX_n + nR\text{-}H \quad (14)$$

$$InX_3 + 2InR_3 \longrightarrow 3R_2InX \quad (15)$$

$$3InX_3 + 3R_2InX \longrightarrow 6RInX_2 \quad (16)$$

Specialized methods include (a) reaction of halogens with R_3In to yield R_nInX_{3-n} compounds, and (b) reaction of an indium(I) or indium(II) halide with an organic halide via *Oxidative Addition* (equations 17–18).[74–76]

$$InX + CH_2X_2 \xrightarrow[X = I,\ Br]{R = Alkyl} X_2InCH_2X \quad (17)$$

$$In_2Cl_4 + CH_2Cl_2 \longrightarrow Cl_2InCH_2InCl_2 \quad (18)$$

These indium halomethyl derivatives possess two-electron donor sites, namely the indium atom and the CH_2 group where coordination may occur. Anionic ligands preferentially coordinate to indium atom (e.g. $[R_4N]^+[X_3InCH_2X]^-$), while neutral ligands attack the CH_2 group via nucleophilic substitution of the methlyene halide following concomitant halide transfer to the indium atom to give X_3InCH_2L.[77] The potential application as indium metal ylids was also investigated for adducts with group 16 ligands.[77] An extension to the novel preparation of indium(III) halomethyl derivatives via oxidative insertion of InX into the carbon–halide bond of methylene dihalides ($X\text{-}CH_2X$) (equation 17) has now been demonstrated to be feasible for haloforms (CHX_3) for the preparation of X_2InCHX_2 compounds (equation 19).[78]

$$InX + CHX_3 \xrightarrow{X = I,\ Br} X_2InCHX_2 \quad (19)$$

The reactivity of X_2InCHX_2 with anionic ligands is analogous to X_2InCH_2X, where the corresponding salts $[X_3InCHX_2]^-$ and $[X_3InCH_2X]^-$ can be isolated respectively. However, unlike X_2InCH_2X, when X_2InCHX_2 derivatives undergo reaction with neutral ligands (L) the associated adduct of InX_3 is formed. This suggests that the decomposition of the dihalomethyl indium compounds (X_2InCHX_2) proceeds via carbene elimination (equation 20).

$$X_2InCH_2X + L \longrightarrow InX_3L + :CHX \quad (20)$$

The transmetalation of organotin derivatives to their indium counterparts (Scheme 1) has recently been used to investigate a new route to Group 13 polyfunctional Lewis acids, which are becoming important in catalysis, molecular recognition, and materials synthesis.[79–82]

As synthetic reagents, sterically encumbered organoindium halides have been used in transmetalation reactions to prepare the first example of a monomeric base-free group 13 hydride complex (Scheme 2).[83]

The first example of the indium carbene complexes have been reported using the stable imidazolyidene carbene derivatives (Scheme 3).[84–86]

The indium carbene derivatives were prepared from a THF solution at room temperature. The reaction of excess carbene to the InX_3 (5:1) only afforded the 2:1 adduct and unreacted carbene, which suggested that higher adduct formation was not sterically viable. X-ray crystallography showed the 1:1 indium bromide adduct to be monomeric and tetrahedral

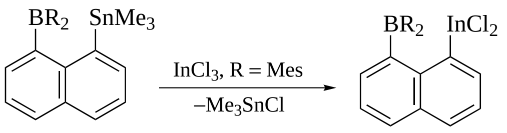

Scheme 1 Transmetalation of organotin to organoindium derivatives

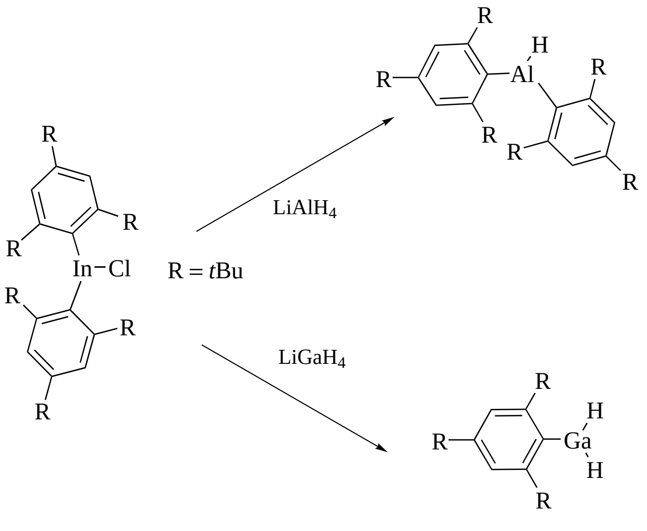

Scheme 2 Preparation of a monomeric base- free group 13 hydride complexes

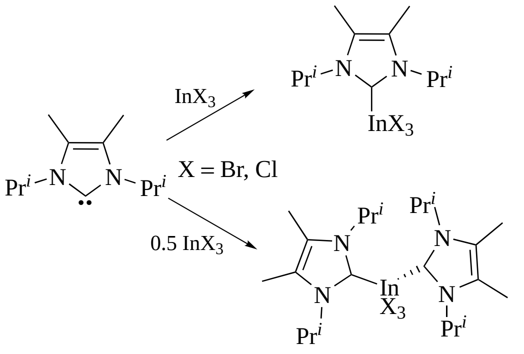

Scheme 3 Formation of organoindium carbene halide derivatives

and both bromo and chloro 2:1 adducts to have a trigonal-bipyramidal geometry, and surprisingly two axial halides and one equatorial. The treatment of the indium halide with one equivalent of the carbene in the presence of water was found adventitiously to afford a novel ionic indium imidazolium species (Scheme 4).[84,87] Additional indium analogues with increasing steric encumbrance provided by the carbene moiety have been investigated to determine the stabilizing effect on the indium coordination sphere.[85,86]

The preparation of ''inert'' organoindium halides with sterically demanding ligands such as Mes (2,4,6-$Me_3C_6H_2$), Trip (2,4,6-$i$$Pr_3C_6H_2$), or Mes* (2,4,6-$t$$BuC_6H_2$), and so on has become a recent trend.[88–90] Most of these derivatives are prepared via the normal synthetic routes outlined earlier. A key property provided by the added steric protection from the ligands is the lack of dimerization, and association of the reaction solvent such as THF or ether (e.g. [In(Mes*)X_2], Figure 4).[89,90]

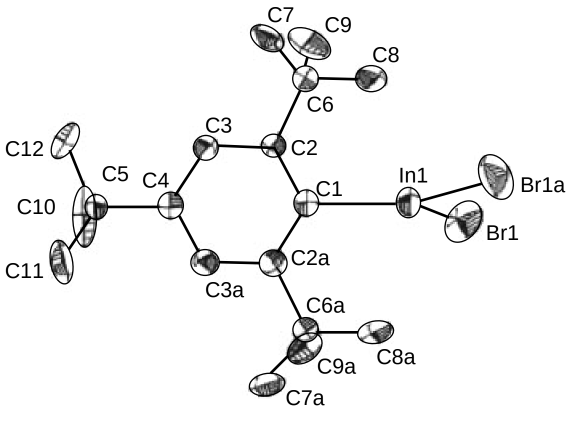

Figure 4 Structure of [In(Mes*)X_2], X = Br, Cl

4 ORGANOINDIUM PNICTOGENS

The number of indium and other Group 13 inter and intra pnictogen adducts have been attributed to an investigation of their coordination chemistry, kinetic reactivity, and application as single-source precursors to binary III-V semiconductors and catalysis. Organometallic adducts of Group 13 have been largely dominated by tetrahedral coordination mode. However, there has been a strong impetus to synthesize and characterize organoindium derivatives of higher coordination number, which can be achieved with bulky substituents, the aspiration being to form derivatives with a monomeric nature and inert or reduced kinetic reactivity, and compounds free from reaction solvent incorporation.

There are three main bonding modes which are prevalent for organoindium pnictogens: (a) inter-datively, (b) intra-datively, and (c) direct. In addition, mixed bonding modes (d) are also commonplace (Scheme 5).

The mixed bonding mode generally occurs for indium pnictogen adducts with reduced steric demand, leading to the formation of the heterocyclic $[Me_2InL(SiR_3)_2]_x$ compounds. These III-V heterocycles are made up of the amphoteric $R_2M\text{-}LR_2$ moiety, which simultaneously reacts as a Lewis acid (In) and a Lewis base (pnictogens). The lone pair character of the heavier pnictogen and the presence of an adjacent empty orbital of indium ensure that associated species with ''head to tail'' ring-coordinate centers are normally observed. Additionally, the affinity of both In and the pnictogen groups toward attaining tetrahedral coordination geometry limits monomeric compound formation ($R_2M\text{-}ER_2$), which is realized by the use of highly sterically demanding substituents.

4.1 Synthesis

Intermolecular adducts of organoindium can be prepared in a hydrocarbon solvent by reaction with a Lewis base[91,92] (equation 21), or via displacement of more labile adducts

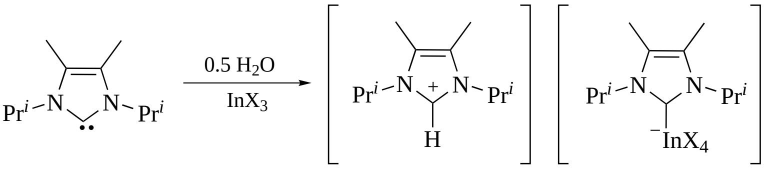

Scheme 4 Formation of ionic indium imidazolium species

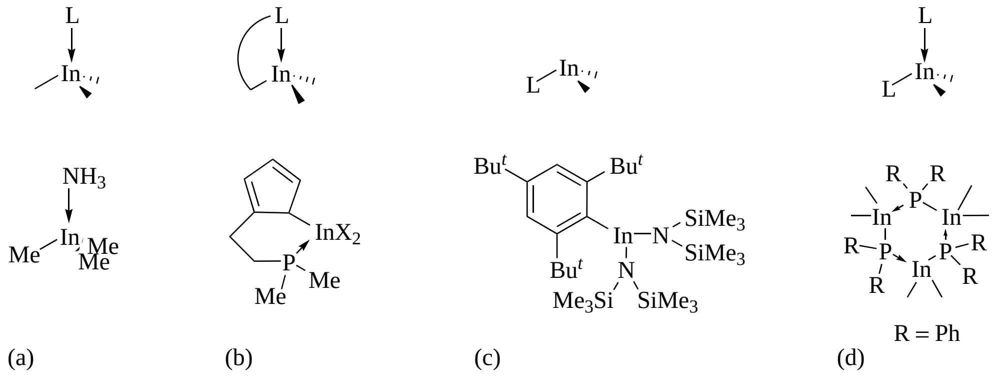

Scheme 5 Bonding modes for organoindium pnictogens

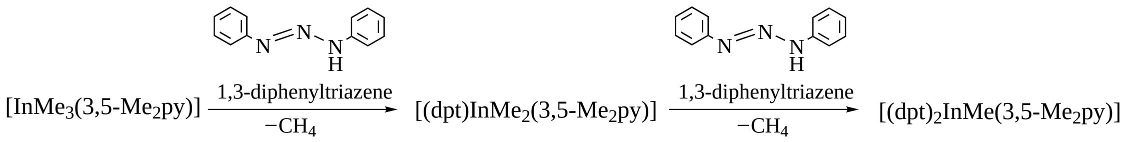

Scheme 6 Synthesis of organoindium compounds via methane elimination

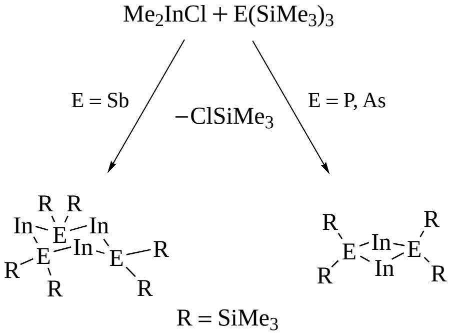

Scheme 7 Dehalosilyation synthetic pathway

such as etherates[93] (equation 22). Adduct formation can generally be reversed cleanly by controlled distillation to obtain adduct free derivatives.[27,55,93] Intramolecular adducts can be formed by metathesis type reactions between organoindium halides with lithium[94–115] and Grignard[93,116–119] reagents (equations 23–24) or by elimination of small gaseous molecules[120–151] (equation 25, e.g. Scheme 6).[137,151]

Additionally, the use of metal halides has been shown to accelerate alkane elimination and product formation, for example, the reaction of phenylacetonitrile with $InMe_3$. The introduction of CsF has been perceived to act as a catalyst by forming intermediate metalates of the types $[XMMe_3]^-$ and $[Me_3MXMMe_3]^-$.[120]

$$R_3M + L \longrightarrow R_3InL \qquad (21)$$

$$R_3M(Et_2O) + L \xrightarrow[-Et_2O]{} R_3InL \qquad (22)$$

$$R_2MX + LiR'LR_2 \xrightarrow[-LiX]{} R_2In\text{-}R'LR_2 \qquad (23)$$

$$R_2MX + XMg(R'LR_2) \longrightarrow R_2In\text{-}R'LR_2 \qquad (24)$$

$$R_3M + R_2LH \longrightarrow R_2InL + CH_4 \qquad (25)$$

$$R_2InX + L(SiR_3)_3 \longrightarrow R_2In\text{-}L(SiR_3)_2 + XSiR_3 \qquad (26)$$

Dehalosilyation reactions involving $L(SiR_3)_x$ and $XInR_2$ also prove to be a versatile synthetic pathway.[152–156] The driving force for the reaction is the high propensity for Si–X bond formation (381 kJ mol^{-1}, X = Cl), resulting in the elimination of $R_3Si\text{-}X$ (equation 26, Scheme 7).

The dehalosilylation route, however, has not been utilized for the preparation of the analogous $[(Me_2In)Bi(SiMe_3)_2]_3$ owing to the lack of stable In-Bi reagents. This has been recently overcome by the low-temperature (−50 °C) metathesis reaction involving $[(Me_2Al)Bi(SiMe_3)_2]_3$ and the Indium Lewis base adduct $[InMe_3(dmap)]$, (dmap = 4-dimethylaminopyridine).[157] The key factor in the reaction pathway is the presence of the strong Lewis base, which increases the reactivity of $[(Me_2Al)Bi(SiMe_3)_2]_3$ by Al-Bi cleavage of the Al-Bi heterocycle. The concerted coordination of $InMe_3$ affords the Lewis base stabilized intermediate $[InMe_3(Me_3Si)_2BiAlMe_2(dmap)]$, which rearranges to give $[(Me_2In)Bi(SiMe_3)_2]_3$.[124,157] In the absence of the Lewis base, no reaction was found to occur. Furthermore, this reaction pathway has also been successfully implemented for the preparation of other Group 13 adducts of group 15 (Scheme 8).[152]

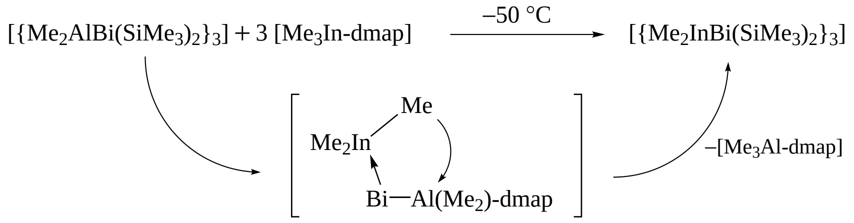

Scheme 8 Formation of In-Bi hetrocyclic derivatives

4.2 Mixed Organoindium Pnictogens

The only example of a mixed organoindium pnictogen was obtained by equilibration of $[(\mathrm{Me_3SiCH_2})_2\mathrm{InP}(\mathrm{SiMe_3})_2]_2$ with $[(\mathrm{Me_3SiCH_2})_2\mathrm{InAs}(\mathrm{SiMe_3})_2]_2$ in a 1:1 mol ratio.[158] The formation of the $[(\mathrm{Me_3SiCH_2})_2\mathrm{InAs}(\mathrm{SiMe_3})_2\mathrm{In}(\mathrm{CH_2SiMe_3})_2\mathrm{P}(\mathrm{SiMe_3})_2]$ was confirmed by X-ray crystallography, which showed the In-As-In-P ring to be planar (Table 2). In addition, a combination of elemental analysis, multinuclear NMR, and EI-MS shows no residual indication that the product is a mixture of the starting reagents. Attempts to prepare the mixed indium pnictogen via the reaction between $[(\mathrm{Me_3SiCH_2})_2\mathrm{InAs}(\mathrm{SiMe_3})_2\mathrm{In}(\mathrm{CH_2SiMe_3})_2\mathrm{Cl}]$ and $(\mathrm{Me_3Si})_2\mathrm{AsLi}$ failed to give the desired compound, but rather $[(\mathrm{Me_3SiCH_2})_3\mathrm{In}{\cdot}\mathrm{As}(\mathrm{SiMe_3})_3]$, Scheme 9.

4.3 Structures

The structural motifs of organoindium pnictogens bear consequence to the large coordination sphere of the indium center and good overlap between metal and ligand orbitals.[162–166] Variation in the geometric structures can also be influenced by the peripheral groups attached to the pnictogens.[167] For example, in the reaction between $\mathrm{InEt_3}$ and $\mathrm{R_3SiPH_2}$, $[\mathrm{EtInPSi}(\mathrm{Pr}^i)_3]$ is cubane,[168] $[\mathrm{EtInPSiCMe_2}(\mathrm{Pr}^i)]$ is hexagonal prismatic,[168] and $[\mathrm{EtInPSiCMe_3})]$ is a cyclic structure.[169] As a result, organoindium derivatives can form elaborate geometric structures such as hetrocyclic rings in planar, boat, or chair conformation, in addition to hetrocubane and clusters (Table 2). Additionally, a good understanding of the geometric conformation is sought after for use in MOCVD thin film and nanocrystallite III-V fabrication processes.[27,170–172] Two reported indium hetrocubanes have been prepared by two differing routes. The first by reaction between haloorganoindium derivatives with a lithium phosphide,[115] whilst the second route entailed intramolecular methane elimination of the indiumamino derivative $[(\mathrm{C_6F_5})\mathrm{NHInMe_2}]$.[150] In both cases, the ‘In–P’ and ‘In–N’ angles of P–In–P 88.8(1), In–P–In 91.2(1)°, N–In–N 84.3(4), and In–N–In 95.5(4)° respectively deviate from those of an ideal cube; however, this is more prevalent in the In–N cubane owing to the larger difference in III-V atomic radii (see Table 2 for structures).

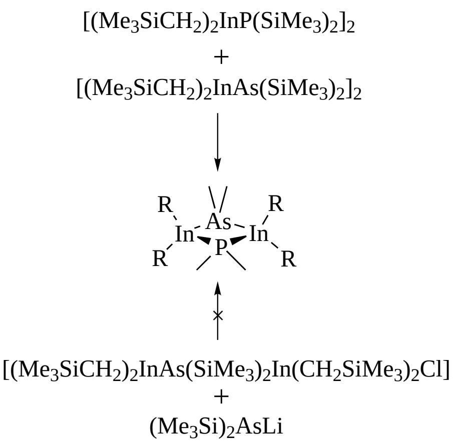
[(Me3SiCH2)2InP(SiMe3)2]2
+
[(Me3SiCH2)2InAs(SiMe3)2]2
R
R
In
As
In
P
R
R
×
[(Me3SiCH2)2InAs(SiMe3)2In(CH2SiMe3)2Cl]
+
(Me3Si)2AsLi

Scheme 9 Preparation of mixed indium pnictogen

5 ORGANOINDIUM CHALCOGENIDES

Without question, the predominant organoindium chalcogenides prepared and studied are the oxygen-containing derivatives (O-In-C), which are notable for their use as precursors for the fabrication of thin-film $\mathrm{In_2O_3}$. Many of the O-In-C compounds bear the diketone,[121,123,173–175] Schiff base,[130,134,136,140,176] carboxylate, or alkoxide[177–179] ligands. The heavier organoindium chalcogenides are now receiving greater attention for their use in attaining thin film or nanocrystallite-semiconducting $\mathrm{In_2S_3}$ phases, which amongst other things are highly important for third generation solar cell hetrojunction formation.[180–190] Deposition of $\mathrm{In_2S_3}$ phases has been realized by using precursors such as the heteroleptic dithiocarbamate complexes $[\mathrm{R_2InS_2CNMe}(\mathrm{CH_2})_3\mathrm{NMe_2}]$ (R = Me, Et, naphthyl, $\mathrm{C_5H_{11}}$)[188,189] or thiocarboxylate and thiolate complexes.[190]

Organoindium oxygen derivatives have also been determined to be valuable catalysts in organic synthesis.[191–194] Chiral organoindium chalcogenides have been utilized as catalysts in asymmetric ring openings of cyclohexene norbonylene, and cyclooctene oxides with TMSCN (Scheme 10). The expected β-isocyanohydrins were obtained in yields varying from 45% to 80%, with the enantioselectivity varying from

Table 2 Selected bond lengths and angles for organoindium pnictogens

Compound	M–V Bond length (Å)	M–V–C Bond angle (° Deg)	Ref.
In–N			
2-Amino-1-[$Me_2In(TMEDA)$]-4-amino-3,5-diphenyl-6-benzylpyridine 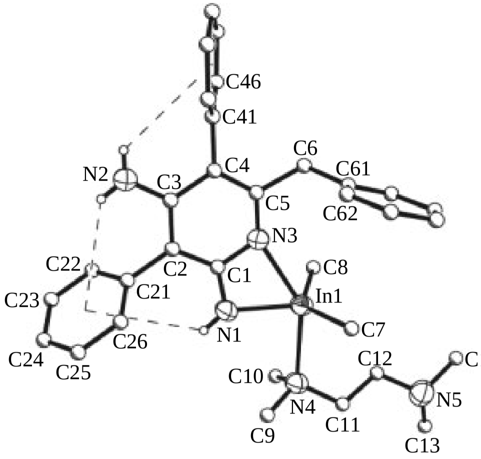 C46 C41 C6 C61 N2 C3 C4 C5 C62 N3 C8 C22 C2 C1 In1 C23 C21 C7 N1 C26 C12 C14 C24 C25 C10 N5 N4 C9 C11 C13	**In–N** In(1)-N(1) 2.180(3) In(1)-N(3) 2.439(3) In(1)-N(4) 2.523(3)	**N–In–C** N(1)-In(1)-C(7) 112.6(1) N(1)-In(1)-C(8) 114.5(2) N(3)-In(1)-C(8) 93.1(1) **Other** N(1)-In(1)-N(3) 57.72(9) N(1)-In(1)-N(4) 90.01(9)	21
[$Ph_2C{=}C{=}NInMe_2(THF)$]$_2$ 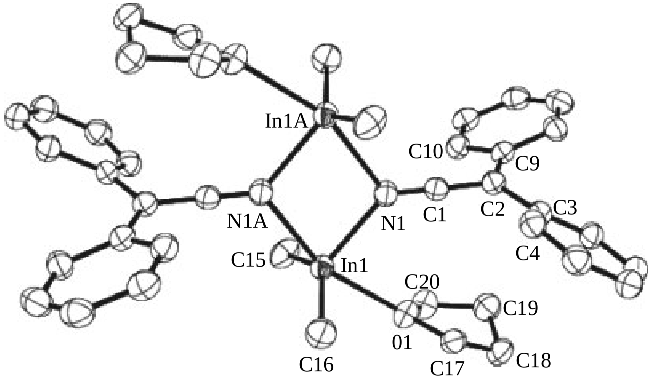 In1A C10 C9 C3 N1A N1 C1 C2 C4 C15 In1 C20 C19 01 C18 C16 C17	**In–N** In(1)-N(1) 2.252(3) In(1)-N(1A) 2.458(3)	**N–In–C** N(1)-In(1)-C(15) 112.2(2) N(1)-In(1)-C(16) 108.2(2) **Other** N(1)-In(1)-N(1A) 73.9(1)	21

$[Me_2InNH(t\text{-}Bu)]_2$ 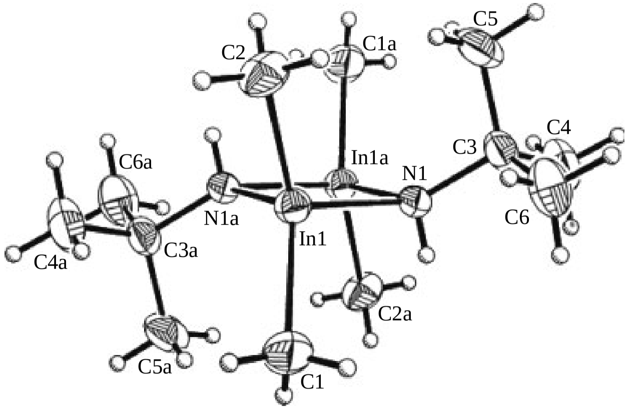 C5 C2 C1a C4 C6a In1a C3 N1 N1a In1 C6 C4a C3a C2a C5a C1	**In–N** In(1)-N(1) 2.230(3) In(1a)-N(1) 2.220(3) In(1)-N(1A) 2.220(3) **In–C** In(1)-C(2) 2.157(4) In(1)-C(1) 2.160(4) In(1)· · ·In(1A) 3.335(2) **Other** N-H 0.81(3)	**N–In–C** N(1)-In(1)-C(1) 106.6(1) N(1)-In(1)-C(2) 116.1(1) **Other** N(1)-In(1)-N(1A) 82.9(1) N(1)-In(1)· · ·In(1A) 41.3(1)	121
$[InMe_2(OC(CF_3)_2CH_2NH(CH_2CH_2OMe))]_2$ 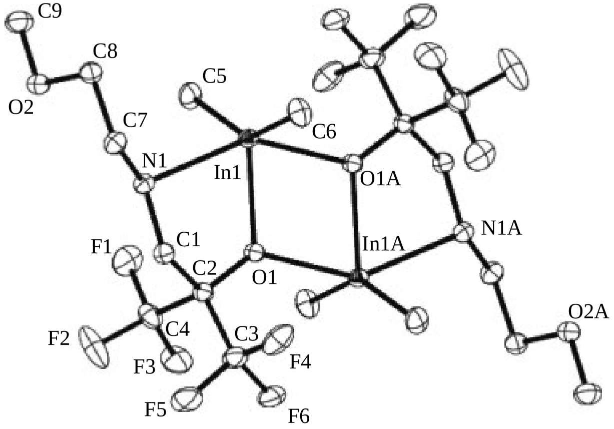 C9 C8 C5 O2 C7 C6 N1 In1 O1A N1A F1 C1 In1A C2 O1 O2A F2 C4 C3 F3 F4 F5 F6	**In–N** In(1)-N(1) 2.4655(10) **In–C** In(1)-C(5) 2.1397(14)	**N–In–C** C(5)-In(1)-N(1) 93.20(5) **Other** O(1)-In(1)-N(1) 73.79(3) O(1A)-In(1)-N(1)147.58(3)	122

(cont’d overleaf)

Table 2 cont'd

Compound	M–V Bond length (Å)	M–V–C Bond angle (° Deg)	Ref.
$[InMe_2(OC(CF_3)CH_2C(CF_3){=}NCH_2CH_2NMe_2)]$ 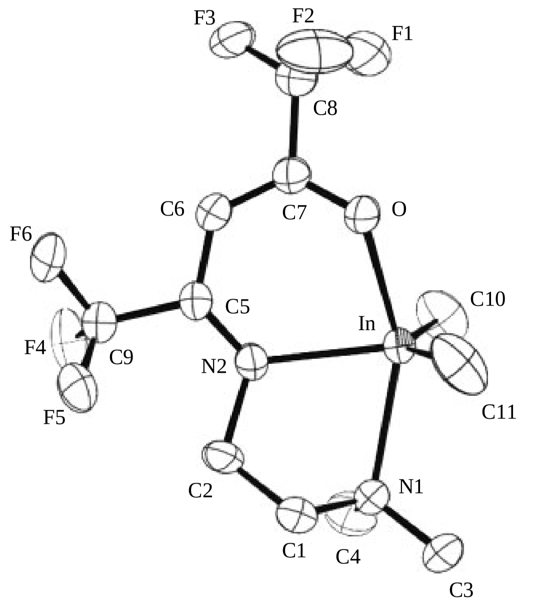 F3 F2 F1 C8 C6 C7 O F6 C5 C10 In F4 C9 N2 C11 F5 C2 N1 C1 C4 C3	**In–N** In-N(1) 2.428(2) In-N(2) 2.321(2) **In–C** In-C(11) 2.142(2) In-C(10) 2.141(2) **Other** In-O 2.251(3)	**N–In–C** C(10)-In-N(2) 111.2(1) C(11)-In-N(2) 112.9(1) N(1)-In-C(10) 96.1(1) **Other** O-In-N(1) 153.3(1) O-In-N(2) 80.4(1) C(10)-In-C(11) 135.9(11)	122
$[Me_2In(saldPh)]_2$ (*N*-phenylsalicylideneimine (HsaldPh)) 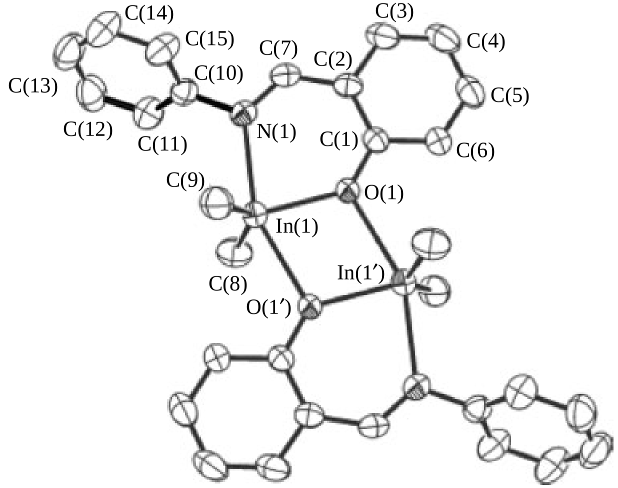 C(14) C(15) C(3) C(7) C(2) C(4) C(10) C(13) C(5) C(12) C(11) N(1) C(1) C(6) C(9) O(1) In(1) In(1′) C(8) O(1′)	**In–N** In(1)-N(1) 2.366(3) **In–C** In(1)-C(8) 2.137(5) In(1)-C(9) 2.133(5) **Other** In(1)-O(1′) 2.477(3)	**Other** O(1)-In(1)-N(1) 82.01(11) O(1)-In(1)-O(1′) 74.51(11) N(1)-In(1)-O(1′) 156.23(11) In(1)-O(1)-In(1) 105.49(11)	123

$Ar'InNAr''$ ($Ar' = C_6H_3$-2,6-$Dipp_2$, Dipp = C_6H_3-2,6-Pr^i_2, $Ar'' = C_6H_3$-2,6(Xyl-4-Bu^t)$_2$) 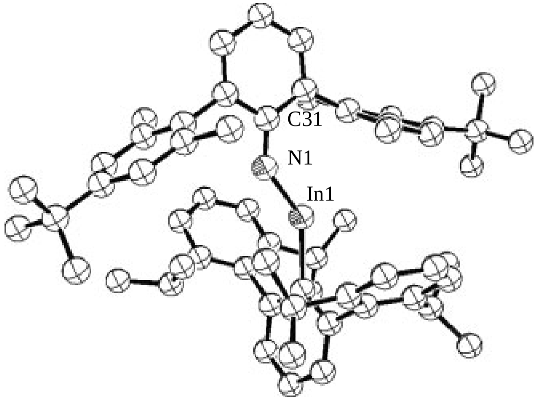	**In–N** In-N 1.928(3) **In–C** In-C 2.127(3) **Other** N-C 1.355(4)	**N–In–C** N-In-C 142.2(1) In-N-C 134.9(2) C-In-N-C 173.5(3)	127
$[(Li^+)_2\cdot(\text{dioxane})_7]_{0.5}$ $[2,6\text{-}i\text{Pr}_2C_6H_3N(SiMe_3)In(C{\equiv}CSiMe_3)_3{}^-]\cdot 1.5$ dioxane 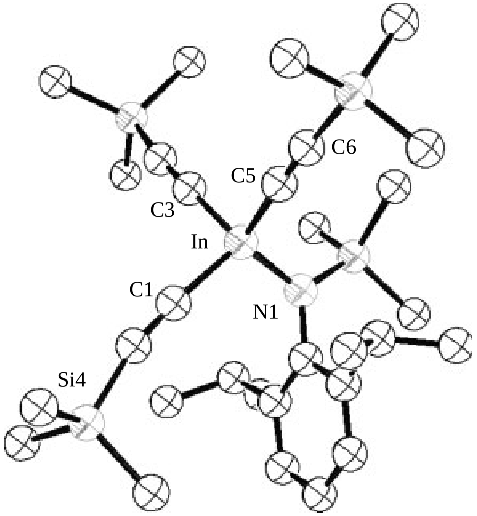	**In–N** In-N(1) 2.113(2) **In–C** In-C(1) 2.148(2) In-C(3) 2.154(2) In-C(5) 2.169(2)	**Other** In-C(1)-C(2) 170.9(2) In-C(3)-C(4) 169.0(2) In-C(5)-C(6) 168.1(2) C(1)-In-C(3) 112.5(7) C(1)-In-C(5) 106.9(7) C(3)-In-C(5) 112.5(7)	57

(cont'd overleaf)

Table 2 cont'd

Compound	M–V Bond length (Å)	M–V–C Bond angle (° Deg)	Ref.
[{$NC_4H_2(CH_2NMe_2)_2$-2,5}$InMe_2$] 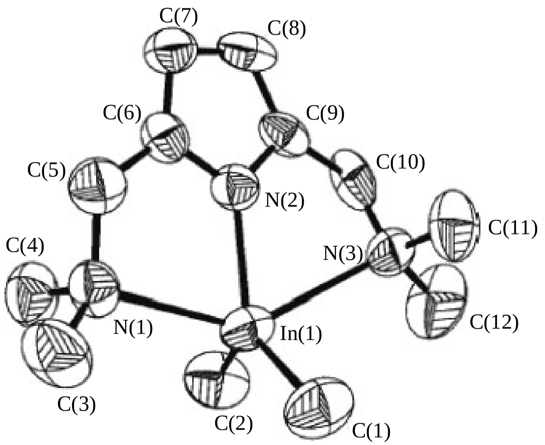 C(7) C(8) C(6) C(9) C(10) C(5) N(2) C(11) C(4) N(3) C(12) N(1) In(1) C(3) C(2) C(1)	**In–N** In(1)-N(2) 2.108(5) In(1)-N(1) 2.519(5) In(1)-N(3) 2.681(6) **In–C** In(1)-C(1) 2.187 (6) In(1)-C(2) 2.173(6)	**N–In–C** N(2)-In(1)-C(2) 113.1(2) N(2)-In(1)-C(1) 121.2(2) C(2)-In(1)-N(1) 105.4(2) C(1)-In(1)-N(1) 101.3(2) C(2)-In(1)-N(3) 94.5(3) C(1)-In(1)-N(3) 94.0(2) **Other** N(2)-In(1)-N(3) 69.5(2) N(1)-In(1)-N(3) 140.96(19) C(2)-In(1)-C(1) 124.6(3) N(2)-In(1)-N(1) 71.9(2)	96
[{[$C_4H_2N(CH_2NMe_2)_2$-2,5]$InCl_2$}$_2$(μ-OH_2)] 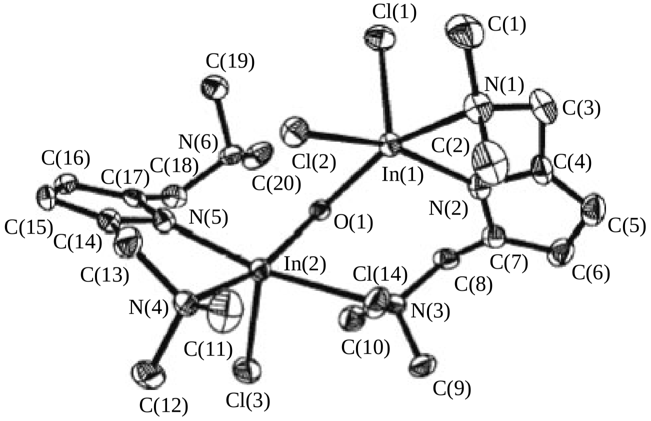 Cl(1) C(1) C(19) N(1) C(3) N(6) C(16) C(18) Cl(2) C(2) C(4) C(17) C(20) In(1) N(2) N(5) O(1) C(5) C(15) C(14) In(2) C(7) C(13) Cl(14) C(8) C(6) N(4) N(3) C(11) C(10) C(9) C(12) Cl(3)	**In–N** In(1)-N(2) 2.167(5) In(1)-N(1) 2.334(5) In(2)-N(5) 2.146(5) In(2)-N(4) 2.366(5) **Other** In(1)-O(1) 2.136(4) In(1)-Cl(1) 2.434(2) In(1)-Cl(1) 2.519(2) In(2)-O(1) 2.175(4) In(2)-Cl(3) 2.462(2) In(2)-Cl(4) 2.4750(14)	**Other** N(2)-In(1)-N(1) 78.7(2) N(5)-In(2)-N(4) 77.6(2) O(1)-In(1)-N(2) 97.5(2) O(1)-In(1)-N(1) 156.9(2) N(1)-In(1)-Cl(1) 96.4(1) O(1)-In(1)-Cl(2) 84.7(1)	96

<table>
<tr><td>

cis-$[(CH_3)_2In\text{-}N(H)\textit{i}-C_3H_7]_2$

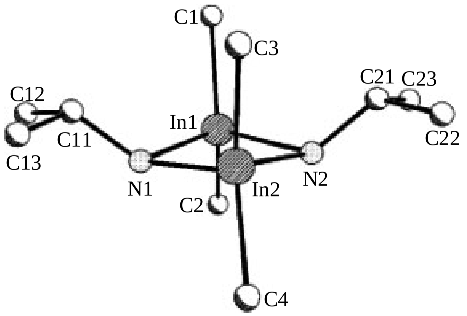
C1
C3
C12
C11
C13
In1
N1
C2
In2
N2
C21
C23
C22
C4

</td><td>

In–N
In(1)-N(1) 2.218(4)
In(1)-N(2) 2.211(4)
In(2)-N(1) 2.214(4)
In(2)-N(2) 2.200(4)

In–C
In(1)-C(1) 2.144(5)
In(1)-C(2) 2.144(5)

</td><td>

Other
N(1)-In(1)-N(2) 83.92(14)
N(2)-In(2)-N(1) 84.16(14)
In(2)-N(1)-In(1) 95.0(2)
In(2)-N(2)-In(1) 95.5(2)
C(1)-In(1)-C(2) 129.2(2)
C(3)-In(2)-C(4) 129.8(2)

</td><td>128</td></tr>
<tr><td>

trans-$[(CH_3)_2In\text{-}N(H)\textit{i}-C_3H_7]_2$

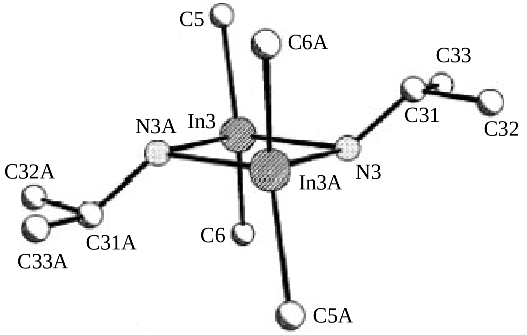
C5
C6A
C33
C31
C32
N3A
In3
C32A
In3A
N3
C31A
C33A
C6
C5A

</td><td>

In–N
In(3)-N(3) 2.221(4)
In(3)-N(3A) 2.229(5)

In–C
In(3)-C(5) 2.140(7)
In(3)-C(6) 2.134(7)

Other
In(3)-In(3A)
3.2828(8)

</td><td>

N–In–C
In(3)-N(3)-C(31) 119.8(4)
In(3A)-N(3)-C(31) 122.5(4)

Other
N(3)-In(3)-N(3A) 84.9(2)
In(3)-N(3)-In(3A) 95.1(2)
C(5)-In(3)-C(6) 131.5(3)

</td><td>128</td></tr>
<tr><td>

$[HC\{C(Me)N(C_6H_3\text{-}2,6\text{-}\textit{i}\text{-}Pr_2)\}_2MI_2]$

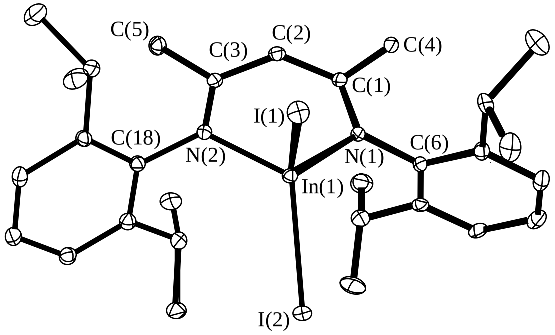
C(5)
C(3)
C(2)
C(4)
C(1)
I(1)
C(18)
N(2)
N(1)
C(6)
In(1)
I(2)

</td><td>

In–N
In(1)-N(1) 2.121(2)
In(1)-N(2) 2.147(1)

Other
In(1)-I(1) 2.7008(2)
In(1)-I(2) 2.6050(2)

</td><td>

Other
In(1)-N(1)-C(1) 118.9(1)
In(1)-N(2)-C(3) 118.9(1)
N(1)-In(1)-N(2) 92.42(5)
I(1)-In(1)-I(2) 111.748(6)
N(1)-C(1)-C(2) 125.0(2)
C(1)-C(2)-C(3) 131.3(2)
C(2)-C(3)-N(2) 125.1(2)

</td><td>97</td></tr>
</table>

(cont’d overleaf)

Table 2 cont'd

Compound	M–V Bond length (Å)	M–V–C Bond angle (° Deg)	Ref.
[((Me$_3$Si)$_2$C(Ph)C(Me$_3$Si)N)InBr]$_2$ 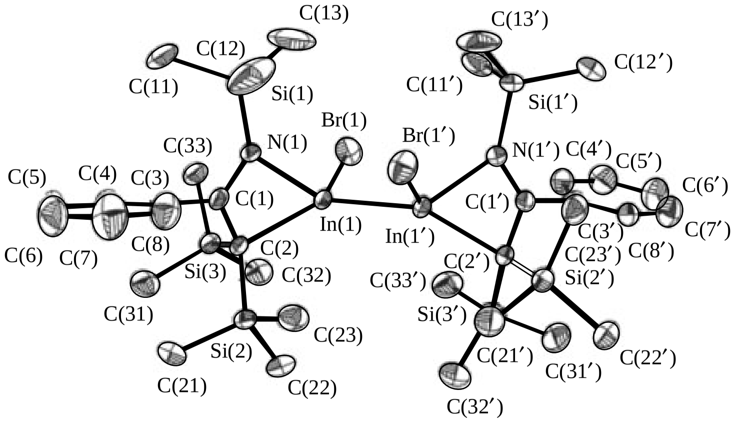 C(13) C(12) C(11) Si(1) Br(1) C(33) N(1) C(5) C(4) C(3) C(1) In(1) C(6) C(7) C(8) C(2) Si(3) C(32) C(31) Si(2) C(23) C(21) C(22) C(13′) C(11′) C(12′) Si(1′) Br(1′) N(1′) C(4′) C(5′) C(6′) C(1′) In(1′) C(3′) C(7′) C(2′) C(23′) C(8′) C(33′) Si(2′) Si(3′) C(21′) C(31′) C(22′) C(32′)	**In–N** In(1)-N(1) 2.254(5) In(1′)-N(1′) 2.251(5) **In–C** In(1′)-C(2′) 2.279(6) In(1′)-C(1′) 2.635(6) In(1)-C(2) 2.281(6) In(1)-C(1) 2.633(6) **Other** In(1′)-Br(1′) 2.561(2) In(1)-Br(1) 2.567(4) In(1)-In(1′) 2.728(4)	**N–In–C** N(1)-In(1)-C(2) 63.1(2) N(1′)-In(1′)-C(2′) 63.4(2) **Other** C(2)-In(1)-Br(1) 121.9(2) N(1)-In(1)-In(1′) 113.5(2) Br(1)-In(1)-In(1′) 106.8(10) C(2′)-In(1′)-Br(1′) 119.6(2) N(1′)-In(1′)-In(1) 117.4(2) Br(1′)-In(1′)-In(1) 107.4(10) N(1)-In(1)-Br(1) 110.2(2)	98
(Me$_3$Si)$_2$NMeIn(O-*t*Bu)$_2$ 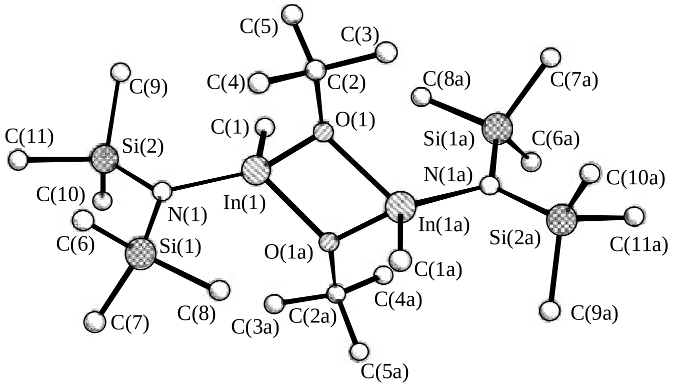 C(5) C(3) C(9) C(4) C(2) C(8a) C(7a) C(11) Si(2) C(1) O(1) Si(1a) C(6a) C(10) N(1) In(1) N(1a) C(10a) C(6) Si(1) O(1a) In(1a) Si(2a) C(11a) C(1a) C(7) C(8) C(3a) C(2a) C(4a) C(9a) C(5a)	**In–N** In(1)-N(1) 2.093(4) **In–C** In(1)-C(1) 2.160(5) **Other** In(1)-O(1) 2.138(3) O(1)-C(2) 1.459(5) In(1)-O(1a) 2.153(3) O(1)-In(1a) 2.153(3) In(1)-In(1a) 3.405(9)	**N–In–C** N(1)-In(1)-C(1) 119.5(2) **Other** N(1)-In(1)-O(1) 113.2(1) O(1A)-In(1)-C(1) 109.3(2) N(1)-In(1)-O(1a) 117.7(1) N(1)-In(1)-In(1a) 122.8(1) Si(1)-N(1)-In(1) 125.1(2) O(1)-In(1)-O(1a) 75.0(1) C(1)-In(1)-In(1a) 117(1) O(1)-In(1)-C(1) 114.1(2) In(1)-O(1)-In(1a) 105.0(1)	101

[(InEt$_2$)4(di-2-pyridyl-amido)2(μ^4-O)] 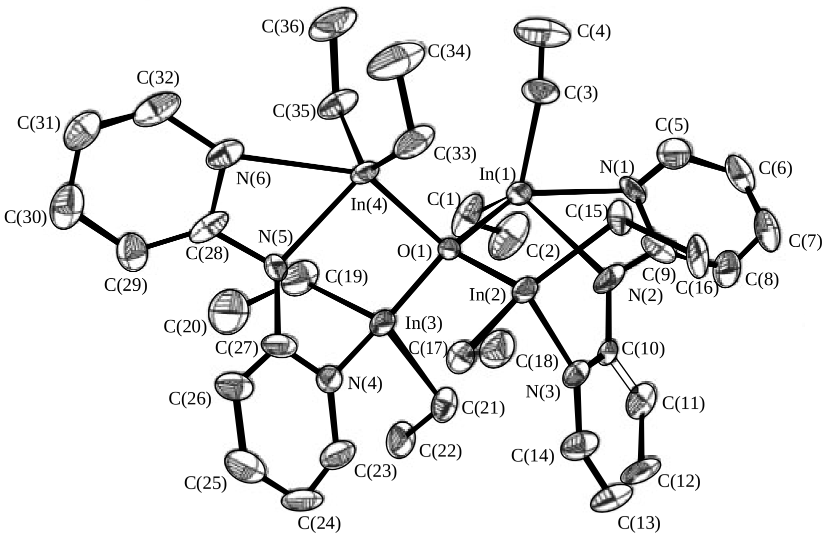 C(36) C(34) C(4) C(3) C(32) C(35) C(33) C(31) N(6) In(4) In(1) N(1) C(5) C(6) C(1) C(15) C(30) N(5) O(1) C(2) C(7) C(28) C(19) In(2) C(9) C(16) C(8) C(29) N(2) In(3) C(20) C(17) C(10) C(27) C(18) N(3) C(11) C(26) N(4) C(21) C(22) C(14) C(12) C(25) C(23) C(24) C(13)	**In–N** In(1) – N(2) 2.361(4) In(1) – N(1) 2.431(5) In(2) – N(3) 2.240(4) In(4) – N(5) 2.299(6) In(4) – N(6) 2.546(5) **In–C** In(1) – C(1) 2.145(6) In(2) – C(15) 2.129(5) In(1) – C(3) 2.172(6) In(4) – C(35) 2.182(4) **Other** In(4) – O(1) 2.273(3) In(3) – O(1) 2.175(4) In(2) – O(1) 2.160(3)	**N–In–C** C(3) – In(1) – N(2) 115.3(2) C(3) – In(1) – N(1) 90.1(2) C(1) – In(1) – N(1) 94.8(2) **Other** O(1) – In(1) – O(1) 91.6(2) N(2) – In(1) – N(1) 54.1(2) In(2) – O(1) – In(4) 105.94(14) In(2) – O(1) – In(3) 120.0(2)	144
[(THF·Me$_2$In)$_2$CH$_2$(MeCNNC(S)NMe)$_2$InMe] 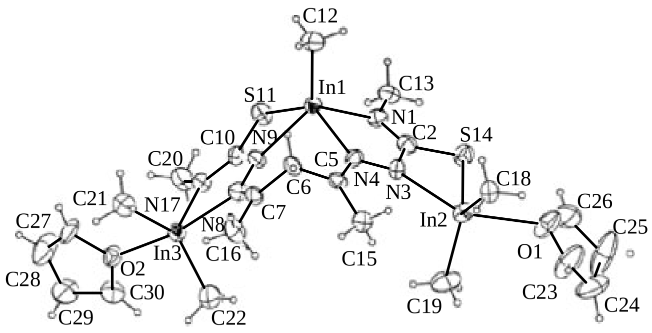 C12 In1 C13 S11 N1 C10 N9 C2 S14 C20 C5 C6 N4 N3 C18 C21 N17 C7 C26 C27 N8 In2 C25 In3 C16 O1 C28 O2 C30 C15 C29 C22 C19 C23 C24	**In–N** In(1)-N(1) 2.16(1) In(1)-N(4) 2.30(1) In(1)-N(9) 2.271(9) In(2)-N(3) 2.33(1) In(3)-N(17) 2.19(1) **In–C** In(1)-C(12) 2.17(4) In(3)-C(21) 2.13(1) **Other** In(2)-O(1) 2.57(1) In(1)-S(11) 2.550(4) In(2)-S(14) 2.561(4)	**Other** N(9)-In(1)-N(1) = 124.0(4) S(11)-In(1)-N(4) = 132.4(2) S(14)-In(2)-C(19) = 112.5(5) O(1)-In(2)-N(3) = 145.8 (4) O(2)-In(3)-N(8) = 161.4(3)	145

(cont’d overleaf)

Table 2 cont'd

Compound	M–V Bond length (Å)	M–V–C Bond angle (° Deg)	Ref.
[$(Me_2In)_2(NC_5H_4CMeNNC(S)NC_6H_5)_2InMe$]·THF 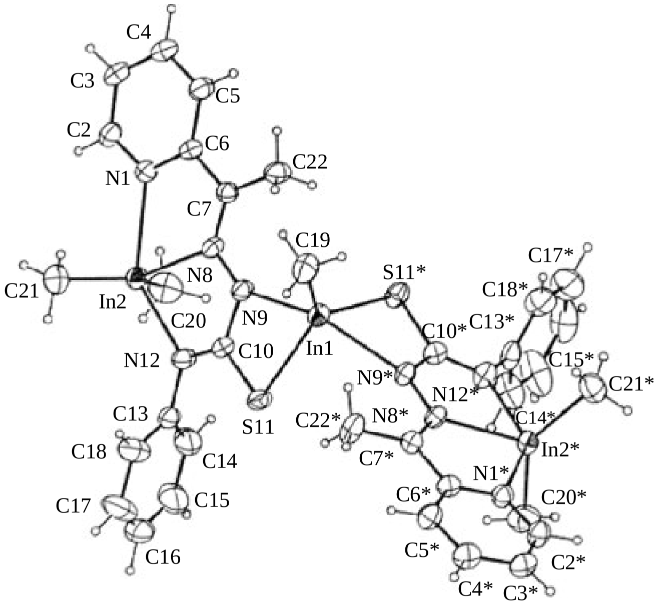	**In–N** In(1)-N(9) 2.394(4) In(2)-N(1) 2.418(4) In(2)-N(8) 2.317(4) In(2)-N(12) 2.298(4) **In–C** In(1)-C(19) 2.10(1) In(2)-C(20) 2.151(7) In(2)-C(21) 2.143(7) **Other** In(1)-S(1) 2.491(2)	**N–In–C** N(8)-In(2)-C(20) = 111.2(2) **Other** N(9)-In(1)-N(9*) 144.1(2) S(11)-In(1)-S(11*) 109.38(8) N(1)-In(2)-N(12) 137.4(1)	145
[$(t\text{-}Bu)_2InN(2,6\text{-}i\text{-}Pr_2C_6H_3)SiPh_3$] (A) [$In(N(SiMe_3)_2)_3$] (B)	**In–N** In-N 2.104 (3) (A) In-N 2.049 (1) (B)	–	108

C4
C3
C5
C2
C6
C22
N1
C7
C19
C17*
N8
S11*
C21
In2
C18*
C20
N9
C10*
C13*
C10
In1
C15*
N12
N9*
C21*
N12*
C13
C22*
N8*
C14*
S11
In2*
C18
C14
C7*
N1*
C6*
C20*
C17
C15
C5*
C2*
C16
C4*
C3*

$[(C_6F_5NInMe)_4]$ 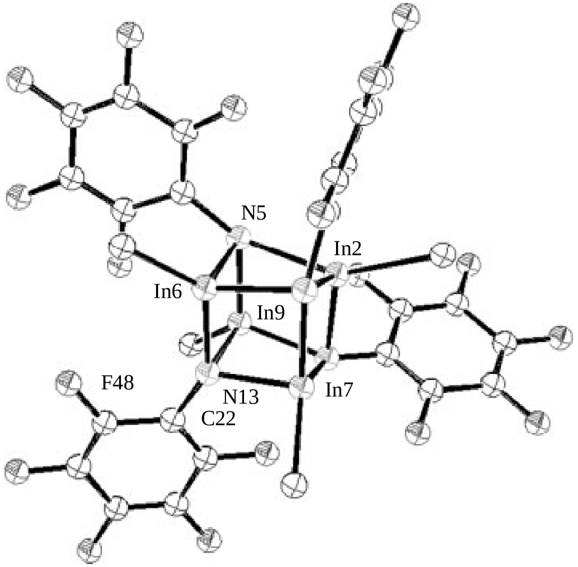 N5 In2 In6 In9 F48 N13 In7 C22	**In–N** In(1)-N(3) 2.202(9) In(3)-N(2) 2.167(10) In(4)-N(2) 2.227(10) **In–C** In(1)-C(1) 2.115(12) In(4)-C(4) 2.09.9(14) **Other** In-In 3.26 N-N 2.96 (average)	**Other** N(1)-In(1)-N(3) 85.4(3) In(1)-N(1)-In(3) 94.9(4)	150
$[Me_2InN(H)Ph']_2$ 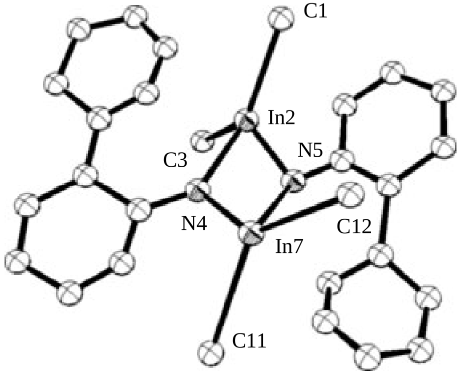 C1 In2 C3 N5 N4 C12 In7 C11	**In–N** In(2)-N(4) 2.242(7) In(2)-N(5) 2.236(5) In(7)-N(4) 2.238(4) In(7)-N(5) 2.255(7) **In–C** In(2)-C(1) 2.135(9) In(7)-C(12) 2.117(9) In(2)-In(7) 3.3275(9)	**N–In–C** N(4)-In(2)-C(1) 107.6(3) N(4)-In(7)-C(11) 111.7(3) N(5)-In(2)-C(1) 111.8(3) N(5)-In(7)-C(12) 101.5(3) **Other** In(2)-N(4)-In(7) 95.9(2) In(2)-N(5)-In(7) 95.6(2) N(4)-In(2)-N(5) 82.6(2) N(4)-In(7)-N(5) 82.3(2)	149

(cont'd overleaf)

Table 2 cont'd

Compound	M–V Bond length (Å)	M–V–C Bond angle (° Deg)	Ref.
[InMe$_2$(dpt)(3,5-Me$_2$py)] 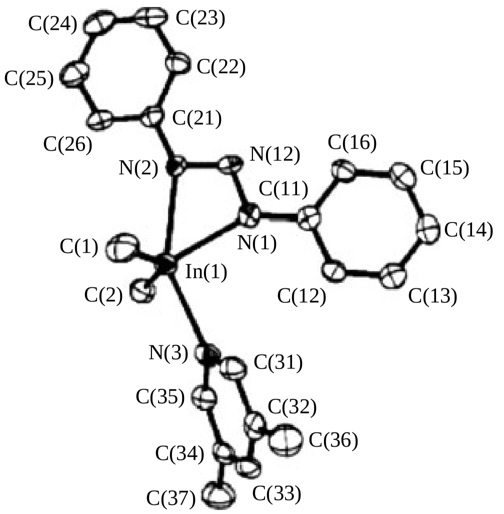 C(24) C(23) C(22) C(25) C(21) C(26) N(2) N(12) C(16) C(15) C(11) N(1) C(14) C(1) In(1) C(2) C(12) C(13) N(3) C(31) C(35) C(32) C(36) C(34) C(37) C(33)	**In–N** In(1)-N(1) 2.293(4) In(1)-N(3) 2.425(4) In(1)-N(2) 2.430(4) **In–C** In(1)-C(1) 2.147(6) In(1)-C(2) 2.153(6) **Other** N(1)-C(l1) 1.407(7) N(2)-C(21) 1.404(6) N(1)-N(12) 1.324(5) N(2)-N(12) 1.292(6)	**N–In–C** C(1)-In(1)-N(1) 110.1(2) C(1)-In(1)-N(2) 96.3(2) C(1)-In(1)-N(3) 94.4(2) **Other** In(1)-N(1)-C(l1) 145.4(3) N(l)-In(1)-N(3) 95.8(1) N(2)-In(1)-N(3) 149.7(1) N(1)-N(12)-N(2) 110.1(4) In(1)-N(1)-N(12) 100.8(3) C(l)-In(l)-C(2) 137.1(2)	151
[InMe(dpt)$_2$(3,5-Me$_2$py)] 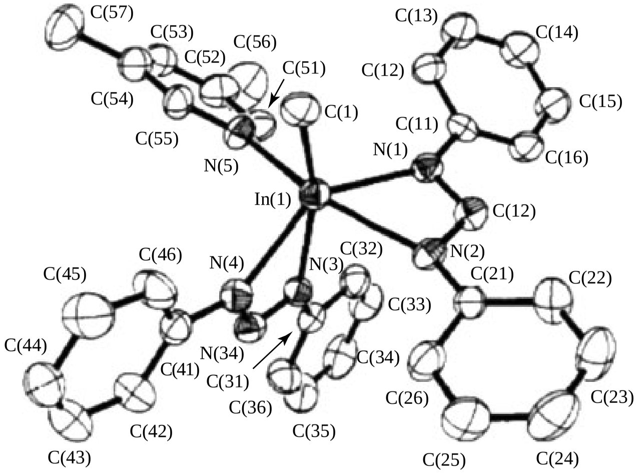 C(57) C(53) C(56) C(52) C(51) C(13) C(14) C(12) C(54) C(1) C(15) C(11) C(55) N(1) C(16) N(5) In(1) C(12) C(46) N(4) C(32) N(3) N(2) C(21) C(22) C(45) C(33) C(44) N(34) C(34) C(41) C(31) C(23) C(36) C(26) C(42) C(35) C(43) C(25) C(24)	**In–N** In(1)-N(2) 2.311(6) In(1)-N(4) 2.250(7) In(1)-N(1) 3.204(6) In(1)-N(3) 2.428(7) In(1)-N(5) 2.351(7) **In–C** In(1)-C(1) 2.179(9)	**N–In–C** C(1)-In(1)-N(1) 105.8(3) C(1)-In(1)-N(3) 164.0(3) C(1)-In(1)-N(5) 95.3(3) C(1)-In(1)-N(2) 101.4(3) C(l)-In(l)-N(4) 111.1(3) N(1)-In(1)-N(2) 55.2(2) **Other** N(1)-In(1)-N(3) 90.2(2) N(1)-In(1)-N(4) 138.7(2) N(1)-In(1)-N(5) 99.2(2) N(2)-In(1)-N(3) 87.5 (2) N(2)-In(1)-N(4) 98.9(2) N(2)-In(l)-N(5) 152.3(2) N(3)-In(1)-N(4) 53.8 (2) N(3)-In(l)-N(5) 82.0(2) N(4)-In(1)-N(5) 95.3(2) In(1)-N(1)-N(l2) 98.0(5) N(1)-N(12)-N(2) 108.9(6)	151

$[In(dpt)_3]$	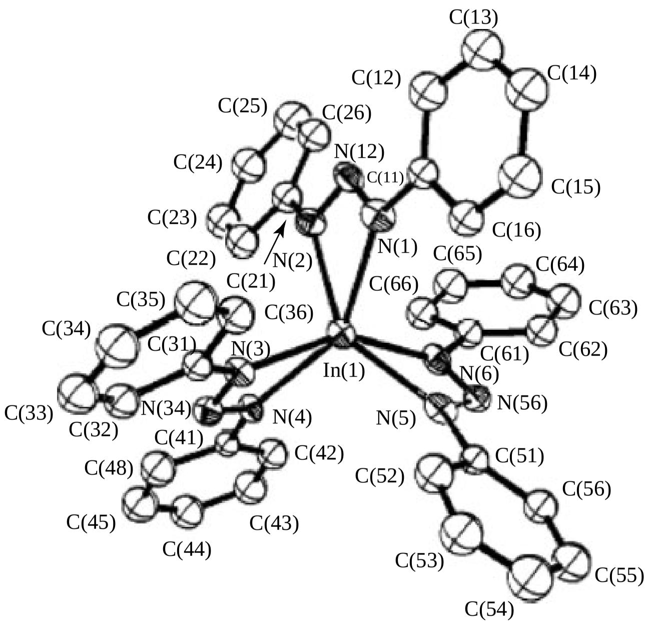	**In–N** In(1)-N(1) 2.259(9) In(1)-N(2) 2.26(1) In(1)-N(3) 2.22(1) In(1)-N(4) 2.23 l(9) In(1)-N(5) 2.24(1) In(1)-N(6) 2.21(1)	**Other** N(l)-In(l)-N(2) 55.2 (4) N(l)-In(l)-N(3) 105.6(4) N(1)-In(1)-N(4) 148.9(4) N(l)-In(l)-N(5) 102.0(3) N(1)-In(1)-N(6) 99.7(4) N(2)-In(l)-N(3) 107.8(4) N(2)-1n(1)-N(4) 102.9(4) N(2)-In(1)-N(5) 144.1 (4) N(56)-N(6)-C(61) 117(1) N(l)-N(12)-N(2) 109(1) In(1)-N(1)-C(l1) 143.6(9) N(12)-N(1)-C(11) 118(1)	151
$[Me_2In\{HNC(Me)\}_2C(CN)]$	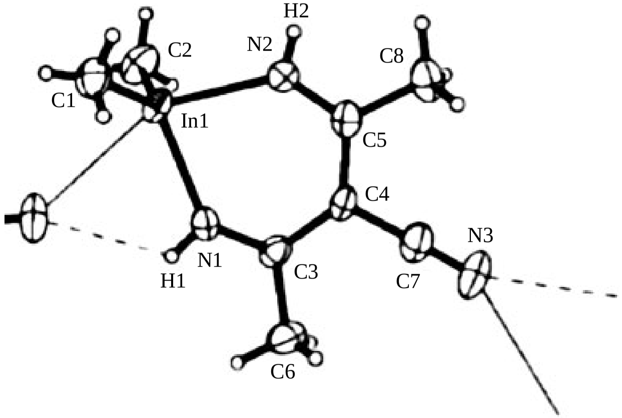	**In–N** In(1)-N(1) 2.179(2) In(1)-N(2) 2.229(2) **In–C** In(1)-C(1) 2.149(4) In(1)-C(2) 2.147(4)	**N–In–C** N(2)-In(1)-C(1) 105.0(1) N(1)-In(1)-N(2) 80.91(9) N(1)-In(1)-C(1) 112.3(1) N(1)-In(1)-C(2) 111.6(1) N(2)-In(1)-C(2) 103.4(1) **Other** C(1)-In(1)-C(2) 130.6(2)	141

C(13)
C(12)
C(14)
C(25)
C(26)
N(12)
C(11)
C(24)
C(15)
C(23)
C(16)
N(2)
N(1)
C(22)
C(65)
C(64)
C(21)
C(66)
C(63)
C(35)
C(36)
C(34)
C(31)
N(3)
In(1)
C(61)
C(62)
N(6)
C(33)
C(32)
N(34)
N(4)
N(5)
N(56)
C(41)
C(42)
C(51)
C(48)
C(52)
C(56)
C(45)
C(43)
C(44)
C(53)
C(55)
C(54)

H2
C2
N2
C8
C1
In1
C5
C4
N3
N1
C3
C7
H1
C6

(cont’d overleaf)

Table 2 cont'd

Compound	M–V Bond length (Å)	M–V–C Bond angle (° Deg)	Ref.
$[(C_6F_5)_2In(CH_2)_3NMe_2]$ 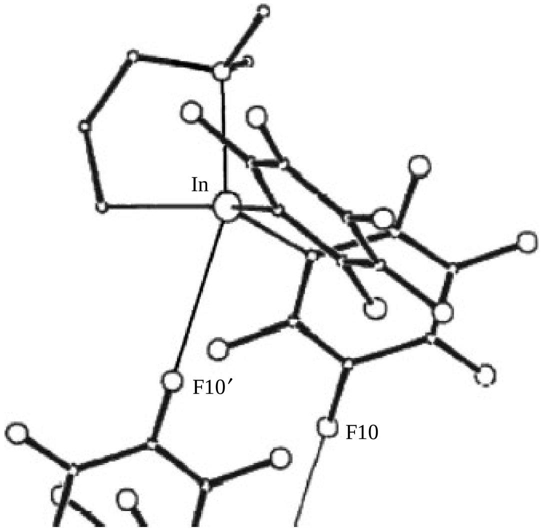 	**In–N** In-N 2.310(5) **In–C** In-C(12) 2.196(8) In-C(13) 2.151(6) In-C(6) 2.194(9) **Other** In-F(10)′ 3.175(5)	**N–In–C** C(6)-In-N 107.3(2) **Other** C(6)-In-C(12) 109.0(3)	109
In–P			
$[(Me_3CCH_2)_2InP(i\text{-}Pr)_2]_2$ 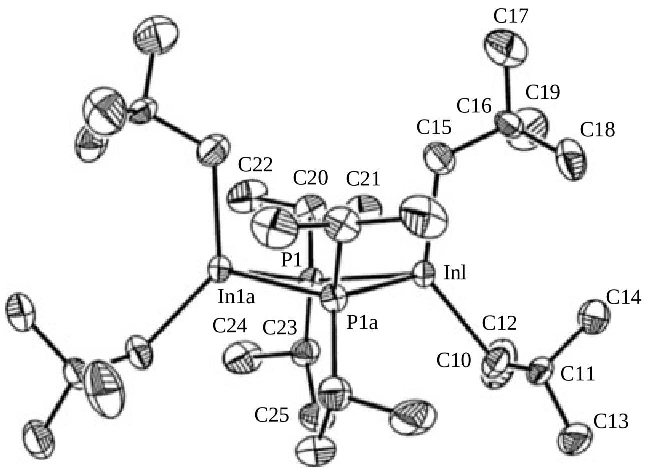 C17 C16 C19 C15 C18 C22 C20 C21 P1 Inl In1a C14 C24 C23 P1a C12 C10 C11 C25 C13	**In–P** In(1)-P(1) 2.638(2) In(1)-P(1A) 2.664(2) In(2)-P(2) 2.663(2) In(2)-P(2A) 2.631(3) **In–C** In(1)-C(10) 2.201(9) In(1)-C(15) 2.248(9) In(2)-C(30) 2.206(9) In(2)-C(35) 2.222(20)	**P–In–C** P(1)-In(1)-C(10) 117.3(2) P(1)-In(1)-C(15) 102.9(2) C(10)-In(1)-P(1A) 108.0(2) C(15)-In(1)-P(1A) 98.6(3) P(2)-In(2)-C(30) 99.7(3) P(2)-In(2)-C(35) 104.7(5) C(30)-In(2)-P(2A) 100.9(3) C(35)-In(2)-P(2A) 117.6(6) **P–In–P** P(1)-In(1)-P(1A) 83.6(1) P(2)-In(2)-P(2A) 83.3(1)	133

[$Me_2InP(SiMe_3)_2$] 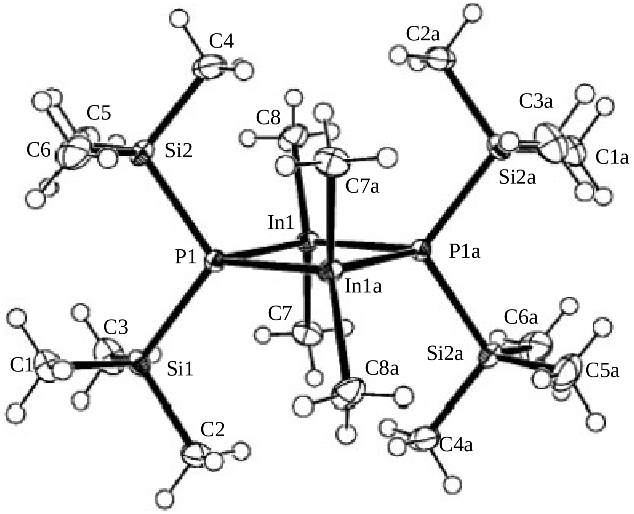 C4 C5 C6 Si2 C8 C7a In1 P1 In1a P1a C2a C3a Si2a C1a C7 C3 C1 Si1 C8a Si2a C6a C5a C2 C4a	**In–P** In(1)-P(1) 2.632(1) In(1)-P(1a) 2.628(1) **In–C** In(1)-C(7) 2.173(2) In(1)-C(8) 2.174(2) **Other** P(1)-Si(1) 2.251(1) P(1)-Si(2) 2.251(1)	**P–In–P** P(1)-In(1)-P(1a) 86.7(1) **Other** In(1)-P(1)-In(1a) 93.3(1) C(7)-In(1)-C(8) 116.9(1) Si(1)-P(1)-Si(2) 109.8(1)	152
[$In(\eta^5\text{-}P_3C_2Bu^t_2)$] 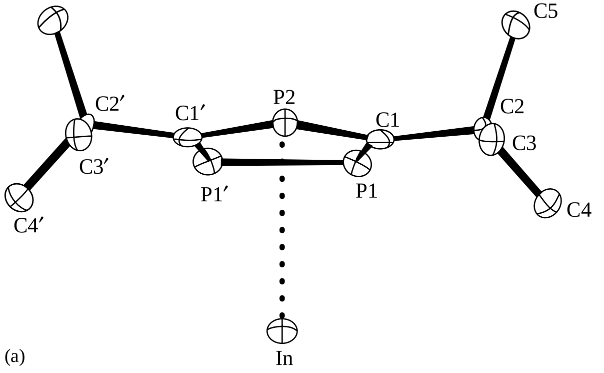 C5′ C2′ C1′ P2 C1 C2 C5 C3′ P1′ P1 C3 C4′ C4 In (a)	**In–P** In-P(1) 3.035(3) In-P(2) 3.108(4) **In–C** In-C(1) 2.981(9) **Other** P(1)-C(1) 1.748(10) P(1)-P(1′) 2.111(5) In-centroid 2.598(9) P(2)-C(1) 1.781(10)	C(1)-P(1)-P(1′) 100.2(3) C(2)-C(1)-P(1) 119.8(6) P(1)-C(1)-P(2) 119.8(6) C(1)-P(2)-C(1′) 100.0(7)	159

(cont’d overleaf)

Table 2 cont'd

Compound	M–V Bond length (Å)	M–V–C Bond angle (° Deg)	Ref.
[(allyl)$_2$InP(t-Bu)$_2$]$_2$ 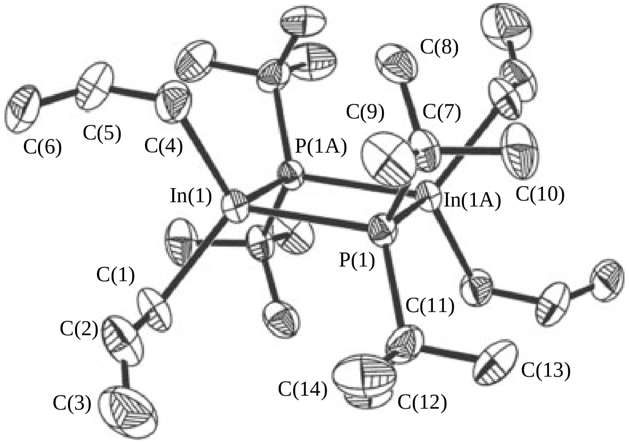 C(8) C(9) C(7) C(6) C(5) C(4) P(1A) In(1) In(1A) C(10) P(1) C(1) C(11) C(2) C(13) C(14) C(3) C(12)	**In–P** In(1)-P(1) 2.639(1) In(1)-P(1A) 2.645(1) **In–C** In(1)-C(1) 2.204(4) In(1)-C(4) 2.218(4) **Other** P(1)-C(7) 1.895(4) P(1)-C(11) 1.898(4)	**P–In–P** P(1)-In(1)-P(1A) 86.34(3) **Other** In(1)-P(1)-In(1A) 93.66(3) C(1)-In(1)-C(4) 107.3(2) C(7)-P(1)-C(11) 112.2(2)	102
[(benzyl)$_2$InP-t-Bu$_2$]$_2$ 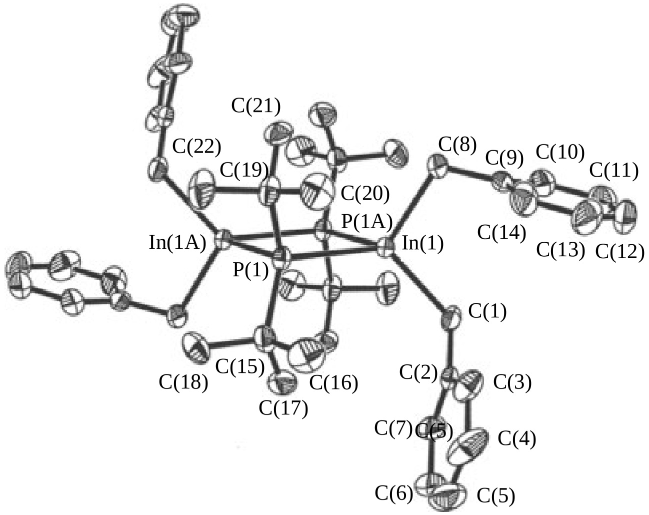 C(21) C(22) C(19) C(8) C(9) C(10) C(11) C(20) P(1A) C(14) In(1A) In(1) C(13) C(12) P(1) C(1) C(18) C(15) C(16) C(2) C(3) C(17) C(7) C(5) C(4) C(6) C(5)	**In–P** In(1)-P(1) 2.637(2) In(1)-P(1A) 2.649(2) **In–C** In(1)-C(1) 2.212(7) In(1)-C(8) 2.228(7) **Other** P(1)-C(15) 1.889(8) P(1)-C(19) 1.892(8)	**P–In–P** P(1)-In(1)-P(1A) 85.11(6) **Other** In(1)-P(1)-In(1A) 94.89(6) C(1)-In(1)-C(8) 105.0(3) C(15)-P(1)-C(19) 112.8(4) C(1)-In(1)-P(1) 125.9(2) C(1)-In(1)-P(1A) 113.6(2) C(8)-In(1)-P(1) 112.7(2) C(8)-In(1)-P(1A) 113.8(2) C(2)-C(1)-In(1) 121.5(5) C(9)-C(8)-In(1) 111.5(5)	102

[(vinyl)$_2$InP-*t*-Bu$_2$]$_2$ 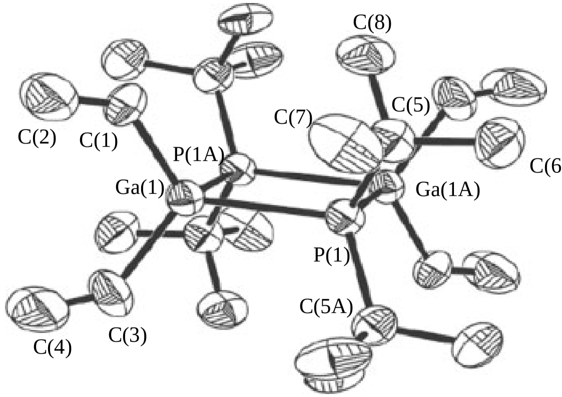 C(8) C(7) C(5) C(2) C(1) P(1A) C(6) Ga(1) Ga(1A) P(1) C(5A) C(4) C(3)	**In–P** In(1)-P(1) 2.6211(8) **In–C** In(1)-C(1) 2.166(6) In(1)-C(3) 2.163(6) **Other** P(1)-C(5) 1.894(3)	**P–In–P** P(1)-In(1)-P(1A) 86.42(3) **Other** In(1)-P(1)-In(1A) 93.58(3) C(5)-P(1)-C(5A) 112.5(2) C(2)-C(1)-In(1) 131.1(7) C(4)-C(3)-In(1) 131.2(7) C(1)-In(1)-C(3) 110.3(3)	102
[(Me$_3$CCH$_2$)$_2$InPEt$_2$]$_2$ 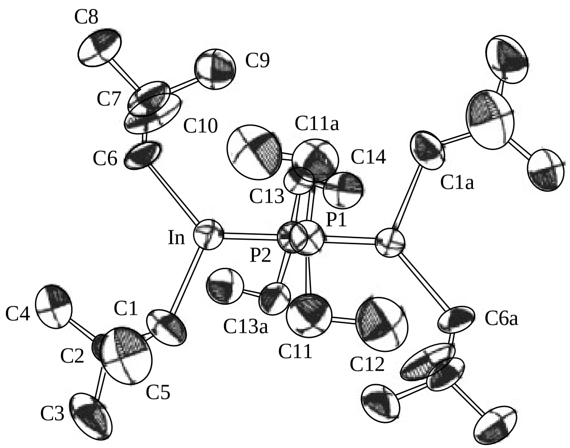 C8 C9 C7 C10 C11a C6 C14 C13 C1a P1 In P2 C4 C1 C6a C13a C2 C11 C12 C5 C3	**In–P** In-P(1) 2.623(2) In-P(2) 2.641(2) **In–C** In-C(1) 2.211(8) In-C(6) 2.17(2)	**P–In–P** P(l)-In-P(2) 82.91(6) **Other** P(l)-In-C(l) 111.1(2) P(l)-In-C(6) 115.7(4) P(l)-In-C(6)′ 101.2(7) P(2)-In-C(1) 100.5(2) P(2)-In-C(6) 124.6(4) P(2)-In-C(6)′ 118.1(6)	146

(cont’d overleaf)

Table 2 cont'd

Compound	M–V Bond length (Å)	M–V–C Bond angle (° Deg)	Ref.
$[(MesCCH_2)_2InP(H)(C_6H_{11})]_3$ 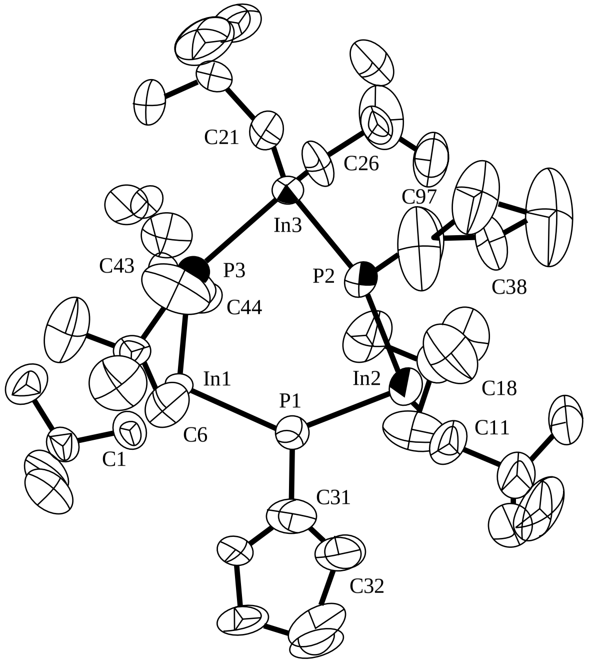	**In–P** In(1)-P(l) 2.644(3) In(1)-P(3) 2.613(3) In(2)-P(2) 2.645(3) In(2)-P(1) 2.637(3) In(3)-P(3) 2.659(2) In(3)-P(2) 2.625(3) **In–C** In(1)-C(1) 2.195(8) In(l)-C(6) 2.22(1) In(2)-C(11) 2.20(1) In(2)-C(16) 2.19(2) In(3)-C(21) 2.188(9) In(3)-C(26) 2.16(1)	**P–In–P** P(1)-In(1)-P(3) 101.18(9) P(1)-In(2)-P(2) 92.85(8) P(2)-In(3)-P(3) 93.69(8) **Other** P(1)-In(l)-C(1) 98.1(3) P(3)-In(l)-C(l) 106.5(3) P(l)-In(l)-C(6) 104.4(3) P(3)-In(l)-C(6) 113.3(3) P(1)-In(2)-C(11) 105.5(3) P(2)-In(2)-C(11) 104.5(3) P(l)-In(2)-C(l6) 118.3(4) P(2)-In(2)-C(16) 103.5(5) P(2)-1n(3)-C(21) 98.4(3) P(3)-In(3)-C(21) 108.0(3) P(2)-In(3)-C(26) 113.9(3)	146
$(Me_3SiCH_2)_3InP(SiMe_3)_3$ 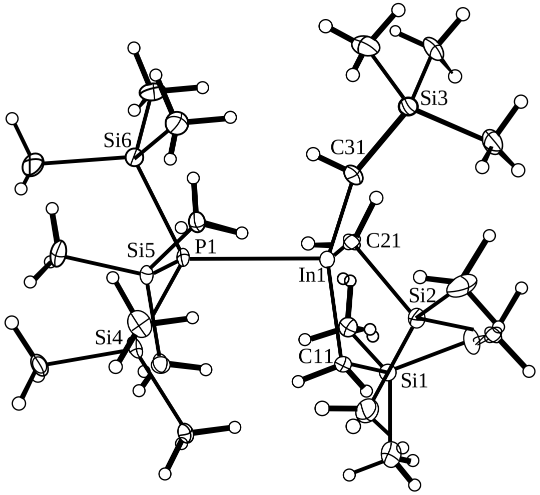	**In–P** In(1)-P(1) 2.7713(15) **In–C** In(1)-C(31) 2.207(6) In(l)-C(11) 2.206(6) In(1)-C(21) 2.218(6) **Other** P(1)-Si(5) 2.2809(23)	**P–In–C** P(l)-In(l)-C(11) 98.45(16) **Other** P(1)-Si(4)-C(42) 109.39(20) C(lI)-In(l)-C(31) 117.53(22) In(I)-P(l)-Si(5) 112.73(7) In(l)-C(3l)-Si(3) 117.7(3)	160

C21
C26
C97
In3
C43
P3
P2
C38
C44
In1
P1
In2
C18
C6
C11
C1
C31
C32

Si6
Si3
C31
C21
Si5
P1
In1
Si2
Si4
C11
Si1

(t-$Bu_2PCH_2CH_2C_5H_4$)$InCl_2$ 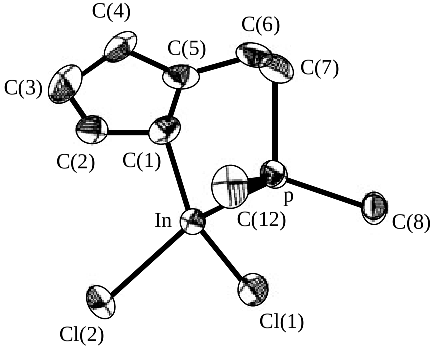 C(4) C(5) C(6) C(7) C(3) C(2) C(1) p In C(12) C(8) Cl(2) Cl(1)	**In–P** In-P 2.595(2) **In–C** In-C(l) 2.202(9) **Other** P-C(7) 1.843(9) P-C(8) 1.860(9) P-C(12) 1.854(10) In-Cl(1) 2.383(3) In-Cl(2) 2.364(3)	**P–In–C** P-In-C(l) 104.2(2) **In–P–C** In-P-C(7) 103.7(3) In-P-C(8) 112.3(3) In-P-C(12) 111.4(3) **Other** Cl(l)-In-C(l) 108.2(3) C1(2)-In-C(1) 118.6(2) Cl(l)-In-C1(2) 101.9(1) P-In-Cl(1) 113.0(1) P-In-Cl(2) 111.2(1)	105
$[Me_2InPPh_2]_3$ 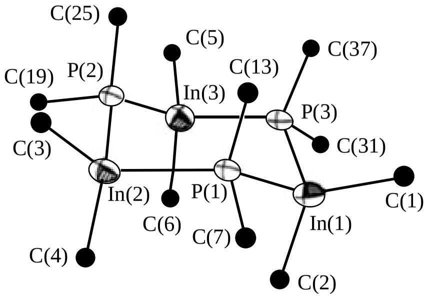 C(25) C(5) C(37) C(19) P(2) C(13) In(3) P(3) C(3) C(31) In(2) P(1) C(1) C(6) C(7) In(1) C(4) C(2)	**In–P** In(1)-P(1) 2.593(1) In(1)-P(3) 2.625(2) In(2)-P(1) 2.622(1) In(2)-P(2) 2.612(2) In(3)-P(2) 2.633(2) In(3)-P(3) 2.628(2) **In–C** In(l)-C(l) 2.172(6) In(l)-C(2) 2.151(6) In(2)-C(3) 2.178(7) In(2)-C(4) 2.172(7) In(3)-C(5) 2.168(9) In(3)-C(6) 2.156(7)	**P–In–P** P(l)-In(l)-P(3) 104.0(1) P(l)-In(2)-P(2) 99.8(1) P(2)-In(3)-P(3) 102.5(1) **Other** In(1)-P(3)-In(3) 118.2(1) P(1)-In(1)-C(1) 106.7(2) P(1)-In(2)-C(4) 109.0(2) P(2)-In(3)-C(5) 108.0(2)	147

(cont’d overleaf)

Table 2 cont'd

Compound	M–V Bond length (Å)	M–V–C Bond angle (° Deg)	Ref.
$[Me(Me_3CCH_2)In\text{-}P(SiMe_3)_2]_2$ 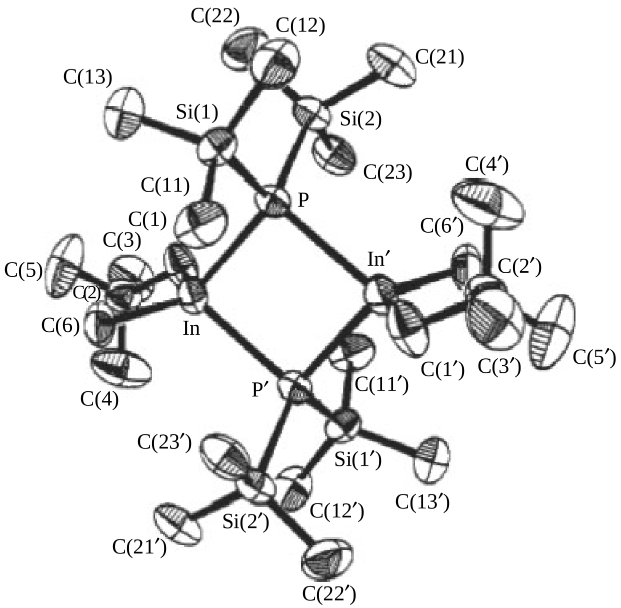 C(22) C(12) C(21) C(13) Si(1) Si(2) C(23) C(4′) C(11) P C(1) C(6′) C(3) In′ C(2′) C(5) C(2) C(6) In C(5′) C(1′) C(3′) P′ C(11′) C(4) C(23′) Si(1′) C(13′) C(12′) Si(2′) C(21′) C(22′)	**In–P** In-P 2.630(2) In-P′ 2.643(2) **In–C** In-C(l) 2.17(1) In-C(6) 2.17(1) **Other** P-Si(1) 2.251(4) P-Si(2) 2.257(4)	**P–In–P** P-In-P′ 86.0(1) **Other** C(1)-In-C(6) 120.2(4) In-P-In′ 94.0(1) Si(l)-P-Si(2) 108.2(2)	161
$(Me_3CCH_2)_2InP(SiMe_3)_2In(CH_2CMe_3)_2Cl$ 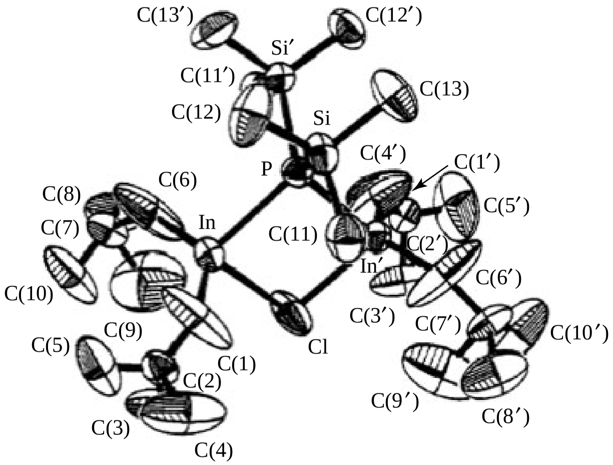 C(13′) C(12′) Si′ C(11′) C(13) C(12) Si C(4′) C(1′) P C(8) C(6) C(5′) C(7) In C(11) C(2′) In′ C(6′) C(10) C(3′) C(7′) C(10′) C(9) Cl C(5) C(1) C(2) C(9′) C(8′) C(3) C(4)	**In–P** In-P 2.622(5) **In–C** In-C(1) 2.560(7) In-C(1) 2.14(4) In-C(6) 2.09(4) **Other** P-Si 2.260(7)	C(l)-In-C(6) 133(2) In-P-In′ 92.8(2) Si-P-Si′ 106.8(3) In-C1-In′ 95.8(3) P-In-Cl 85.7(2)	161

$(Me_3CCH_2)_2InP(SiMe_3)_2In(CH_2CMe_3)_2PH(SiMe_3)$ 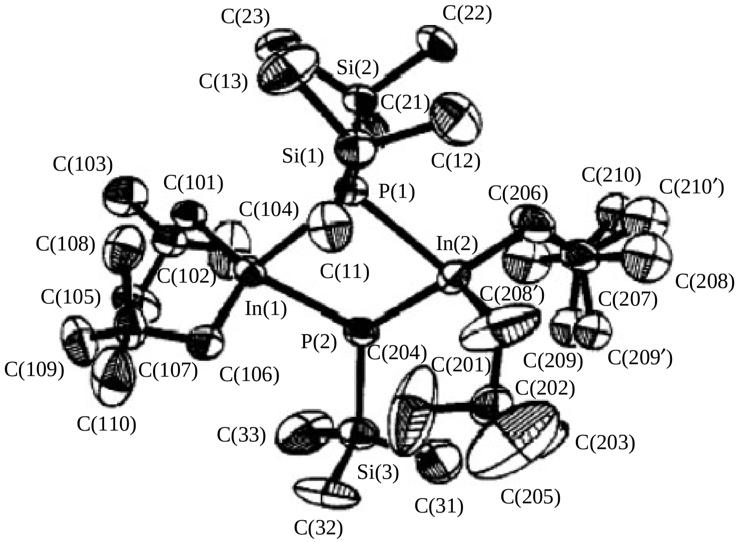 C(23) C(22) Si(2) C(13) C(21) Si(1) C(12) C(103) C(101) P(1) C(104) C(206) C(210) C(210′) C(108) In(2) C(102) C(11) C(208) C(105) In(1) C(208′) C(207) P(2) C(204) C(201) C(209) C(209′) C(109) C(107) C(106) C(202) C(110) C(33) C(203) Si(3) C(31) C(205) C(32)	**In–P** In(l)-P(l) 2.669(2) In(l)-P(2) 2.650(3) In(2)-P(1) 2.644(3) In(2)-P(2) 2.638(2) **In–C** In-C 2.17(1)-2.25(2) **Other** P(l)-Si(l) 2.252(4) P(l)-Si(2) 2.248(3) P(2)-Si(3) 2.248(4)	**P–In–P** P(l)-In(l)-P(2) 82.43(7) P(l)-In(2)-P(2) 83.12(7) **In–P–In** In(l)-P(l)-In(2) 94.52(7) In(l)-P(2)-In(2) 95.08(7) **Other** C(101)-In(l)-C(106) 124.8(4) C(201)-In(2)-C(206) 112.8(8) In(l)-P(2)-Si(3) 123.0(1) In(2)-P(2)-Si(3) 127.9(1)	161
$[i\text{-}Pr(i\text{-}Pr_2P)In(\mu\text{-}P(i\text{-}Pr)_2]_2$ 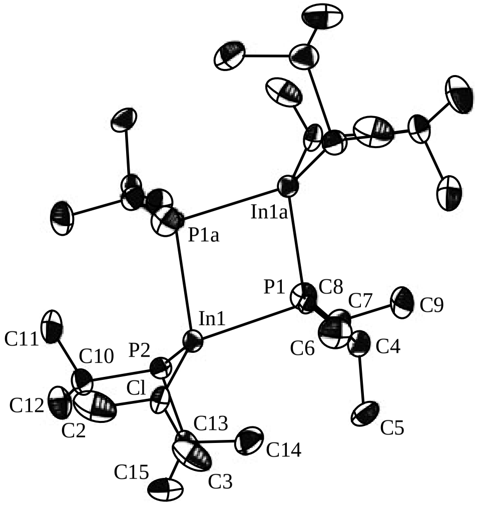 P1a In1a P1 C8 C7 C9 In1 C6 C4 C11 P2 C10 Cl C12 C2 C13 C14 C5 C15 C3	**In–P** In(1)-P(1) 2.642(1) Endo In(1)-P(2) 2.574(1) Exo **In–C** In(l)-C(l) 2.302(5) **Other** P(1)-C(7) 1.856(5) P(2)-C(l0) 1.873 (6) P(2)-C(13) 1.883(6)	**P–In–P** P(1)-In(1)-P(1)′ 107.3(8) P(l)-In(l)-P(2) 111.83(5) **In–P–In** In(1)-P(1)-In(1)′ 72.6(1) **Other** P(1)-In(l)-C(l) 117.7(2) P(2)-1n(l)-C(l) 118.0(1) In(l)-P(l)-C(4) 112.0(2)	114

(cont’d overleaf)

Table 2 cont'd

Compound	M–V Bond length (Å)	M–V–C Bond angle (° Deg)	Ref.
[i-PrIn(μ^3-PSiPh$_3$)]$_4$ 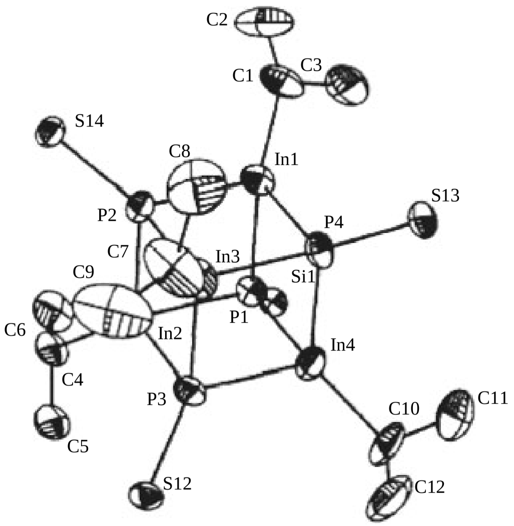 C2 C1 C3 S14 C8 In1 S13 P2 P4 C7 In3 C9 Si1 P1 C6 In2 In4 C4 P3 C10 C11 C5 S12 C12	**In–P** In(l)-P(2) 2.599(4) In(2)-P(2) 2.595(4) In(3)-P(2) 2.60(4) In(3)-P(4) 2.590(4) In(4)-P(1) 2.582(4) In(4)-P(4) 2.583(4)	**P–In–P** P(l)-In(1)-P(2) 89.7(1) P(2)-In(3)-P(3) 89.3(l) P(3)-In(3)-P(4) 89.4(l) P(l)-In(4)-P(4) 87.6(l) P(3)-In(3)-P(4) 89.4(l) P(l)-In(4)-P(4) 87.6(l) P(3)-In(3)-P(4) 89.4(l) P(l)-In(4)-P(4) 87.6(l) P(2)-In(1)-P(4) 89.4(l)	115
[Ph$_2$InP(SiMe$_3$)$_2$]$_2$ 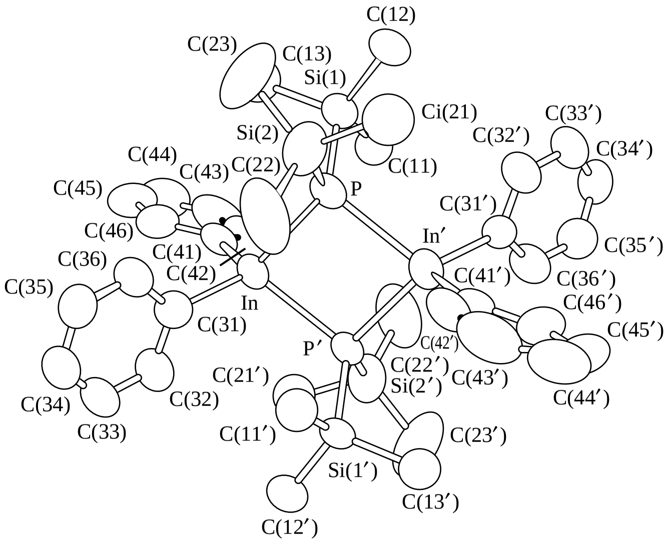 C(12) C(23) C(13) Si(1) Ci(21) C(33′) Si(2) C(32′) C(34′) C(44) C(43) C(22) C(11) C(45) P C(31′) C(46) In′ C(35′) C(36) C(41) C(41′) C(36′) C(42) C(35) In C(46′) C(31) C(45′) P′ C(42′) C(22′) C(21′) Si(2′) C(43′) C(32) C(44′) C(34) C(33) C(11′) C(23′) Si(1′) C(13′) C(12′)	**In–P** P-In 2.612(l) P′-In 2.612(l) **In–C** In-C(31) 2.178(6) In-C(41) 2.185(5) **Other** P-Si(1) 2.262(2) P-Si(2) 2.261(3)	**P–In–P** P-In-P′ 87.03(4) **In–P–In** In-P-In′ 92.97(4)	156

In–As

[$Me_2InAs(SiMe_3)_2$]

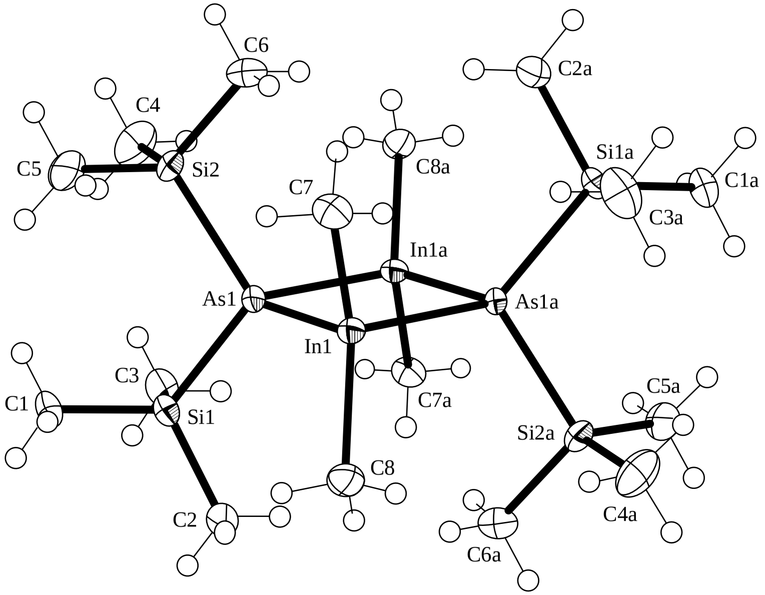
C6
C2a
C4
C5
Si2
C8a
Si1a
C1a
C7
C3a
In1a
As1
As1a
In1
C3
C5a
C1
Si1
C7a
Si2a
C8
C4a
C2
C6a

In–As
In(1)-As(1) 2.703(1)
In(1a)-As(1) 2.170(2)

In–C
In(1)-C(7) 2.168(2)
In(1)-C(8) 2.170(2)

Other
As(1)-Si(1) 2.343(1)
As(1)-Si(2) 2.341(1)

As–In–As
As(1a)-In(1)-As(1) 85.5(1)

In–As–In
In(1a)-As(1)-In(1) 94.5(1)

Other
C(7)-In(1)-C(8) 118.8(1)
Si(1)-As(1)-Si(2) 109.4(1)

152

(cont'd overleaf)

Table 2 cont'd

Compound	M–V Bond length (Å)	M–V–C Bond angle (° Deg)	Ref.
$[(Me_3CCH_2)_2InAs(SiMe_3)_2]_2$ 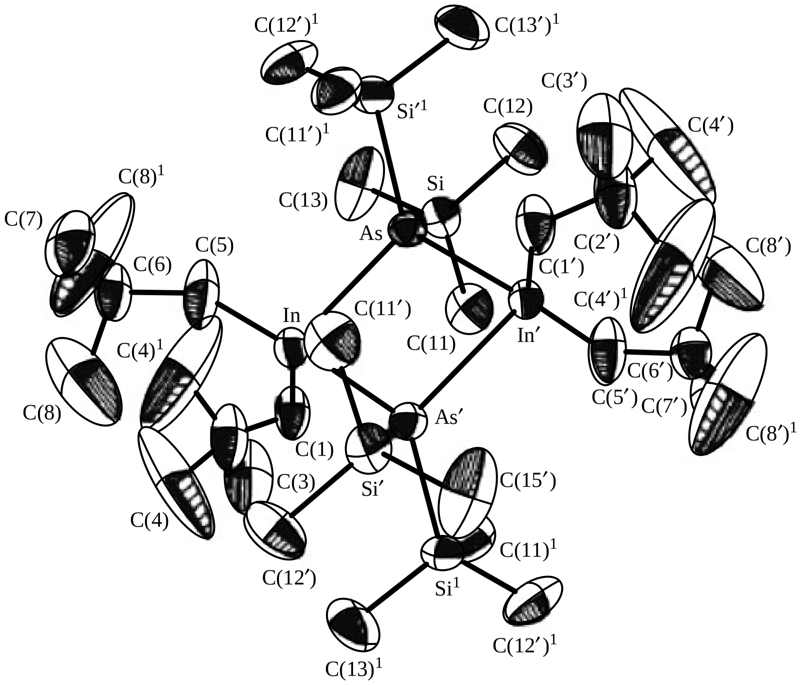	**In–As** In-As 2.752 (1) **In–C** In-C(l) 2.17(1) In-C(5) 2.17(2) **Other** As-Si 2.350(3)	**As–In–As** As-In-As′ 83.46(2) **In–As–In** In-As-In′ 96.54(3) **Other** As-In-C(1) 106.2 (1) In-As-Si 112.91(5) As-In-C(5) 105.4(2) In-As-Si′′ 114.91(2) C(l)-In-C(5) 137.2(4) Si-As-Si′′ 105.0 (1) In-C(1)-C(2) 128(1) In-C(5)-C(6) 133(1)	153

C(12′)^1
C(13′)^1
C(3′)
Si′^{1}
C(12)
C(4′)
C(11′)^1
C(8)^1
Si
C(13)
C(7)
As
C(2′)
C(8′)
C(5)
C(6)
C(1′)
In
C(11′)
C(4′)^1
C(11)
In′
C(4)^1
C(6′)
C(5′)
C(7′)
C(8)
As′
C(8′)^1
C(1)
C(3)
Si′
C(15′)
C(4)
C(11)^1
C(12′)
Si^1
C(12′)^1
C(13)^1

$(Me_3CCH_2)_2InAs(SiMe_3)_2In(CH_2CMe_3)_2Cl\cdot$ 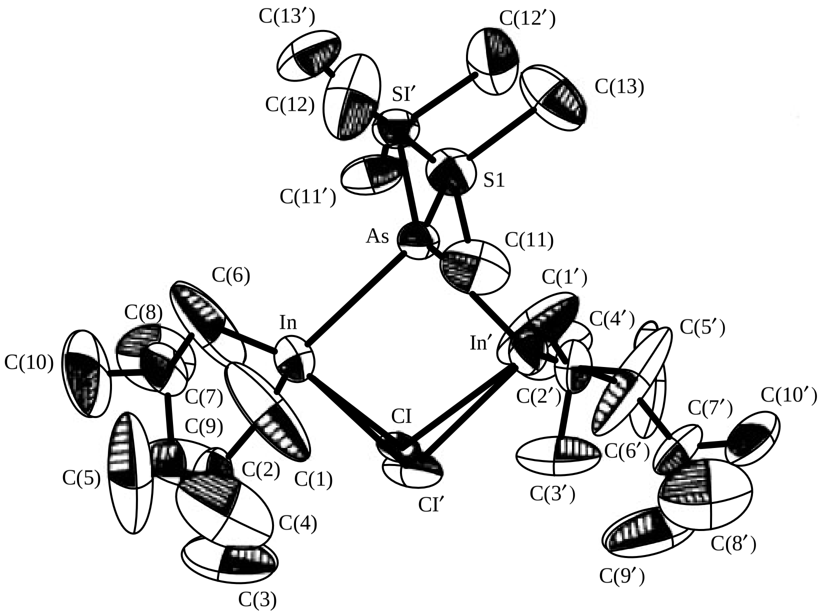 C(13′) C(12′) C(13) C(12) SI′ S1 C(11′) As C(11) C(6) C(1′) C(8) In C(4′) C(5′) C(10) In′ C(7) C(2′) CI C(7′) C(10′) C(9) C(6′) C(5) C(2) C(1) CI′ C(3′) C(4) C(8′) C(9′) C(3)	**In–As** In-As 2.694(3) **In–C** In-C(l) 2.30(4) In-C(6) 2.28(4) **Other** In-Cl 2.639(12) In-Cl′ 2.574(14) As-Si 2.346(8)	**In–As–In** In-As-In′ 91.8(1) **Other** As-In-C1 84.6(3) As-In-C1′ 85.9(3) In-As-Si′ 116.1(2) As-In-C(1) 108(1) As-In-C(6) 107(1) In-Cl-In′ 95.8(4) Cl-In-Cl(1) 113(1) As-Si-C(I1) 109(1) CI-In-C(6) lOl(1) Cl-In-Cl(1) 113(1) C(l)-In-C(6) 133(1)	153
$(Me_3SiCH_2)_2InAs(SiMe_3)_2In(CH_2SiMe_3)_2P(SiMe_3)_2$ 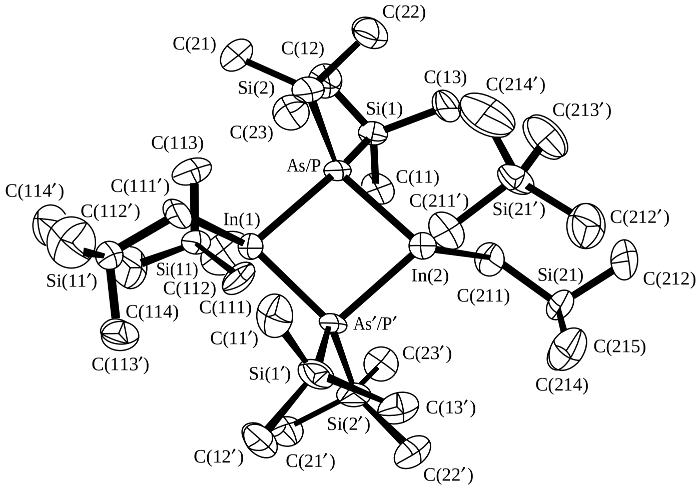 C(22) C(21) C(12) Si(2) C(13) C(214′) Si(1) C(213′) C(23) C(113) As/P C(11) C(114′) C(111′) C(211′) Si(21′) C(112′) In(1) C(212′) Si(11′) Si(11) C(112) C(111) In(2) Si(21) C(212) C(114) C(211) As′/P′ C(11′) C(113′) C(23′) C(215) Si(1′) C(214) C(13′) Si(2′) C(12′) C(21′) C(22′)	**In–(As,P)** (V)-In(1) 2.690(2) (V)-In(2) 2.692(2) **In–C** In(1)-C(111) 2.159(15) In(2)-C(211) 2.205(13) **Other** (V)-Si(1) 2.304(4) (V)-Si(2) 2.308(4) V = (As, P)	**(As,P)–In–(As,P)** (V)-In(1)-(V) 85.9(1) (V)-In(2)-(V′) 85.8(1) **In–(As,P)–In** In(1)-(V)-In(2) 94.1(1) **Other** In(1)-(V)-Si(l) 120.7(1) In(l)-(V)-Si(2) 110.9(1) In(2)-(V)-Si(l) 110.8(1) (V)-In(l)-C(111′) 105.0(4) (V)-In(2)-C(211) 106.4(4) (V)-In(2)-C(211′) 113.3(4) (V)-In(1)-C(111) 115.8(4) C(211)-In(2)-C(211′) 125.0(5) C(111)-In(1)-C(111′) 123.4(5)	153

(cont’d overleaf)

Table 2 cont'd

Compound	M–V Bond length (Å)	M–V–C Bond angle (° Deg)	Ref.
$[Ph_2InAs(SiMe_3)_2]_2$ 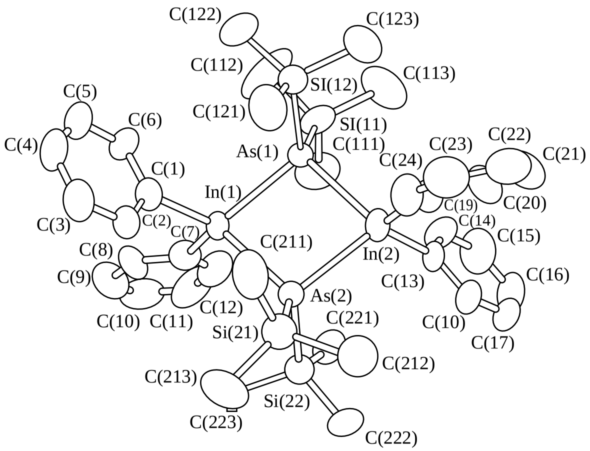 C(122) C(123) C(112) SI(12) C(113) C(5) C(121) SI(11) C(6) C(111) C(4) As(1) C(23) C(22) C(1) C(24) C(21) In(1) C(19) C(20) C(3) C(2) C(14) C(7) C(15) C(8) C(211) In(2) C(9) C(13) C(16) As(2) C(12) C(221) C(10) C(11) Si(21) C(10) C(17) C(212) C(213) Si(22) C(223) C(222)	**In–As** As(1)-In(1) 2.689(1) As(2)-In(1) 2.689(1) As(1)-In(2) 2.683(l) As(2)-In(2) 2.682(1) **In–C** In(l)-C(l) 2.19(l) In(2)-C(13) 2.17(l) In(l)-C(7) 2.17(l) In(2)-C(19) 2.17(l) **Other** As(1)-Si(11) 2.344(4) As(2)-Si(21) 2.370(4) As(l)-Si(l2) 2.352(2) As(2)-Si(22) 2.353(2)	**In–As–In** In(l)-As(1)-In(2) 93.47(4) In(l)-As(2)-In(2) 93.48(4) **As–In–As** As(l)-In(l)-As(2) 86.22(4) As (l)-In(2)-As(2) 86.49(3) **Other** In(l)-As(2)-Si(21) 121.6(l) In(1)-As(2)-Si(22) 107.8(1) In(2)-As(2)-Si(21) 116.6(l) In(2)-As(2)-Si(22) 111.3(l) In(l)-As(l)-Si(l1) 119.8(l) In(l)-As(l)-Si(l2) 110.3(l) In(2)As(1)-Si(11) 118.2(l) In(2)-As(l)-Si(l2) 107.5(l)	156
In–Sb			
$[Me_2InSb(SiMe_3)_2]$ 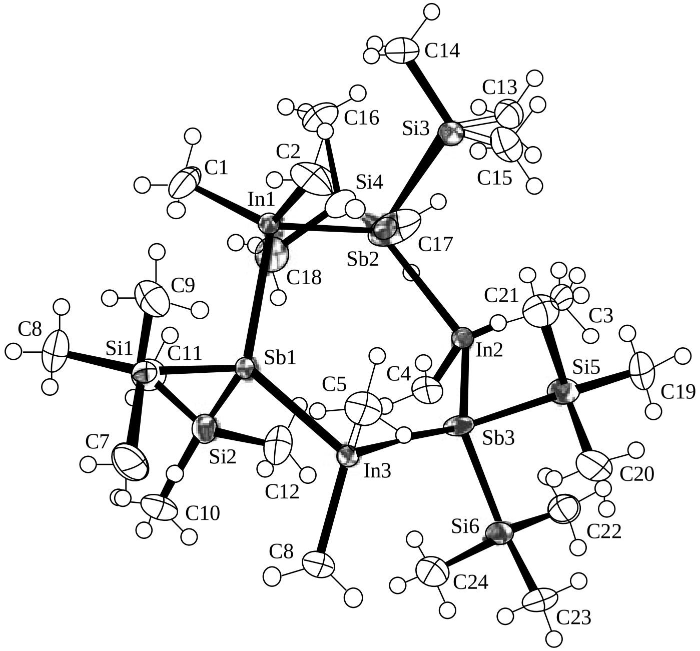 C14 C13 C16 Si3 C2 C1 Si4 C15 In1 Sb2 C17 C9 C18 C21 C3 C8 Si1 C11 Sb1 In2 C5 C4 Si5 C19 Sb3 C7 Si2 In3 C20 C12 C10 Si6 C22 C8 C24 C23	**In–Sb** In(1)-Sb(1) 2.844(1) In(2)-Sb(2) 2.847(1) In(3)-Sb(1) 2.845(1) In(1)-Sb(2) 2.851(1) In(2)-Sb(3) 2.861(1) In(3)-Sb(3) 2.870(1) **In–C** In(1)-C(1) 2.168(3) In(1)-C(3) 2.180(3) In(3)-C(5) 2.176(3) **Other** Sb(1)-Si(1) 2.553(1) Sb(2)-Si(3) 2.563(1) Sb(3)-Si(5) 2.563(1)	**In–Sb–In** In(1)-Sb(2)-In(1) 126.0(1) In(2)-Sb(2)-In(1) 126.0(1) In(2)-Sb(3)-In(3) 127.0(1) **Sb–In–Sb** Sb(1)-In(1)-Sb(2) 102.8(1) Sb(2)-In(2)-Sb(3) 106.8(1) Sb(2)-In(3)-Sb(3) 102.7(1) **Other** C(1)-In(1)-C(2) 122.6(2) C(1)-In(2)-C(4) 114.1(2) Si(20-Sb(1)-Si(1) 103.9(1)	152

[(Me$_3$SiCH$_2$)$_2$InSbMe$_2$]$_3$ 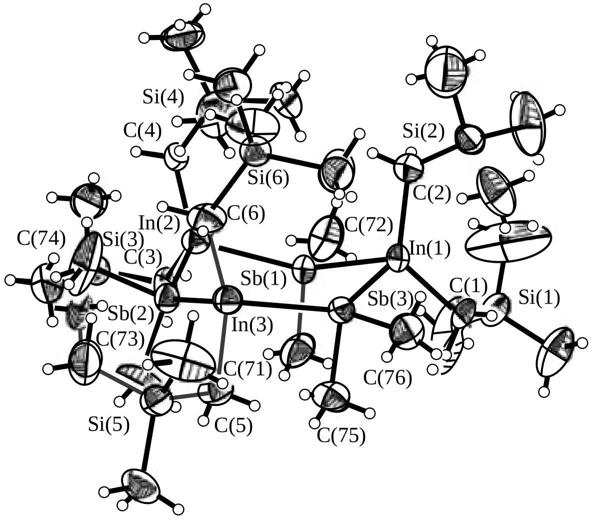	**In–Sb** Sb(1)-In(1) 2.8693(5) Sb(1)-In(2) 2.8604(6) Sb(2)-In(2) 2.8677(6) Sb(2)-In(3) 2.8541(6) Sb(3)-In(1) 2.8653(6) Sb(3)-In(3) 2.8519(6)	**In–Sb–In** In(2)-Sb(1)-In(1) 131.58(2) In(3)-Sb(2)-In(2) 129.22(2) In(3)-Sb(3)-In(1) 137.68(2) **Sb–In–Sb** Sb(3)-In(1)-Sb(1) 92.38(2) Sb(1)-In(2)-Sb(2) 98.56(2) Sb(3)-In(3)-Sb(2) 96.87(2) **Other** C(2)-In(1)-C(1) 126.1(2) C(4)-In(2)-C(3) 124.6(2) C(6)-In(3)-C(5) 120.2(2)	143
In–Bi [{Me$_2$InBi(SiMe$_3$)$_2$}$_3$] 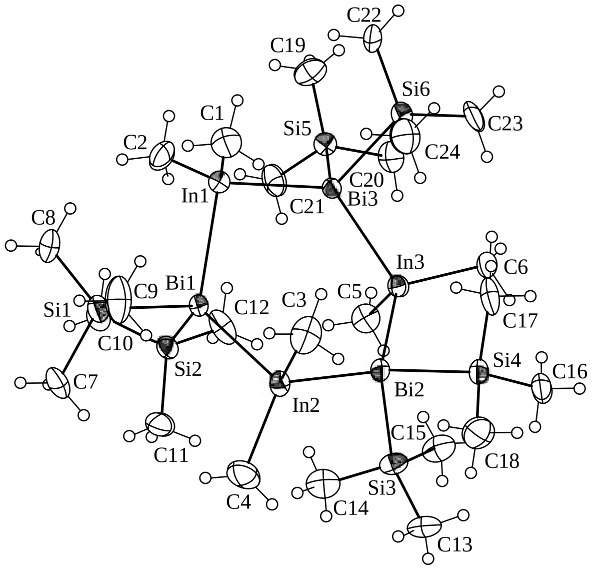	**In–Bi** Bi1-In1 2.907(1) Bi1-In2 2.903(1) Bi2-In2 2.914(1) Bi2-In3 2.911(1) Bi3-In1 2.935(1) Bi3-In3 2.920(1)	**In–Bi–In** In1-Bi1-In2 123.0(1) In2-Bi2-In3 129.1(1) In1-Bi3-In3 129.2(1) **Bi–In–Bi** Bi1-In1-Bi3 99.7(1) Bi1-In2-Bi2 99.4(1)	157

Si(4)
C(4)
Si(6)
Si(2)
C(2)
C(6)
In(2)
C(74)
Si(3)
C(3)
C(72)
In(1)
Sb(1)
C(1)
Si(1)
Sb(2)
Sb(3)
In(3)
C(73)
C(71)
C(76)
Si(5)
C(5)
C(75)

C22
C19
Si6
C23
C1
Si5
C2
C24
C20
In1
C21
Bi3
C8
In3
C6
C3
C5
C9
Bi1
C12
C17
Si1
C10
Si2
Si4
C16
C7
In2
Bi2
C15
C11
C18
Si3
C4
C14
C13

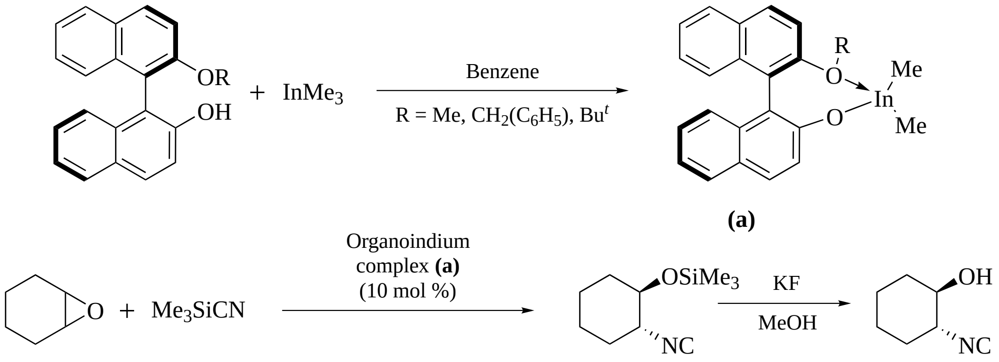

Scheme 10 Use of asymmetric indium catalysts in organic synthesis

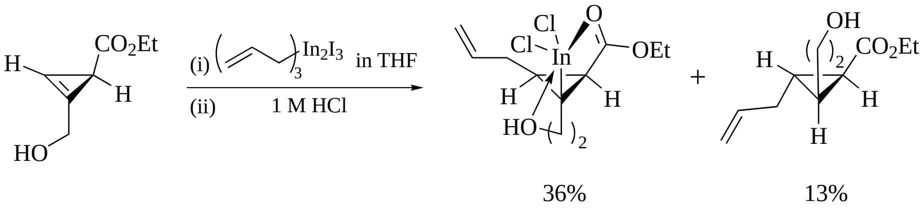

Scheme 11 Allylindation of cyclopropenes using allylindium reagents

10% to 95% depending on the nature of the epoxide and the catalyst used. Although the gallium complexes were found to give better enantioselectivities, they gave lower yields than indium complexes (Scheme 10).[191]

Hydroxy-bearing cyclopropenes have been shown to react with allylindium reagents to undergo clean allylindation, in which the chelation of the hydroxyl group to indium plays the central role. The regio- and stereoselectivity is regulated both by the location of the hydroxyl group in the cyclopropenes and the reaction solvent. In particular, the allylindation in water shows marked differences from that in organic solvents.[192] Consequently, hydrolysis stable cyclopropylindium derivatives have been isolated from the reaction of 1-(ω-hydroxyalkyl)cyclopropenes and the structure for 3-Allyl-2-ethoxycarbonyl-1-(2-hydroxyethyl)]cyclopropylindium dichloride has been resolved by X-ray crystallography.[192] Allylindation of these cyclopropenes was conducted with allylindium reagents prepared *in situ* (Grignard-type reaction) or, more conveniently, by mixing allyl halides, indium, and the cyclopropenes together (Barbier-type reaction) with both methods giving almost identical results (Scheme 11).

5.1 Synthesis

The preparation of the organoindium chalcogenides resembles that outlined for the organoindium pnictogens. In general, by elimination of gaseous molecules[144,174,178,195–198] (e.g. cyclopentadiene,[121,195] equation 27), which can be cross-defined as alcoholysis, or by reacting organoindium halides with lithium chalogenides,[57,199,200]

$$\mathrm{In(C_5H_5)_3 + HOBu^{\mathit{t}} \longrightarrow \tfrac{1}{2}[(C_5H_5)_2InOBu^{\mathit{t}}]_2 + C_5H_6} \tag{27}$$

The cyclopentadiene elimination reaction has proven extremely useful for the synthesis of organoindium(III) chalcogenide derivatives. Products of the types $\mathrm{R_2InLR}$ ($\mathrm{R = Me, CH_2CMe_3}$; $\mathrm{L = O, S}$) have been formed in nearly quantitative yields and in excellent purity.[121,195] Interestingly, although $\mathrm{R_2In(C_5H_5)}$ incorporates two different organic ligands, only the cyclopentadiene is preferentially eliminated over the more thermodynamically stable compounds, $\mathrm{CH_4}$ or $\mathrm{CMe_4}$, (equation 28). Thus, it is believed that the cyclopentadiene elimination reaction must be controlled by kinetic rather than thermodynamic factors.[195]

$$\mathrm{R_2In(C_5H_5) + H\text{-}LR \longrightarrow \tfrac{1}{2}[R_2In - LR]_2 + C_5H_6} \tag{28}$$

Attempts to prepare the heteroleptic cyclopentadienide-indium-diketonate derivatives $[\mathrm{(C_5H_5)_{3-\mathit{x}}In(acac)_{\mathit{x}}}]$ (acac = $\mathrm{CH_3COCH_2COCH_3}$; $x = 1,2$) products via cyclopentadiene elimination reactions from $[\mathrm{In(C_5H_5)_3}]$ and acac fail to yield the expected products, since both $[\mathrm{(C_5H_5)_2In(acac)}]$ and $[\mathrm{(C_5H_5)In(acac)_2}]$ are unstable and undergo ligand redistribution reactions to form $[\mathrm{In(C_5H_5)_3}]$ and $[\mathrm{In(acac)_3}]$, respectively.[121]

The preparation of organoindium Schiff base derivatives also encompasses the mechanistic pathway of hydrocarbon elimination and has received a renewed interest in part owing to their low costs and ease of ligand synthesis. Furthermore, the ligands can be readily engineered to cause change in both steric and electronic properties by directed functionalization. This area has recently been comprehensively reviewed.[176]

The reaction between lithium tetramethylindate Li[$InMe_4$] and disilanol [$(Ph_2SiOH)_2O$] yields the rare Lithium indium siloxane [$InMe\{(OPh_2Si)_2O\}_2$-μ-$\{Li(THF)_2\}_2$], which can also be synthesized from $Ph_2Si(OH)_2$ and Li[$InMe_4$] in good yields.[201] The solid-state structure determined by single-crystal X-ray crystallography reveals that the central indium atom is surrounded by four oxygen atoms of the two disilanolate ligands and a methyl group in a square-pyramidal geometry. The InO_4C coordination environment observed is rare among organometallic compounds of indium (Scheme 12).

An example of methane elimination preparation is the reaction between $InMe_3$ with two equivalents of $HO(C_6H_{11})$ in toluene.[177] The reaction was predicted to afford the expected stoichiometric driven product [$MeIn(O(C_6H_{11}))_2]_n$, but instead yielded only the sesquialkoxide [$In\{Me_2In(OCH_2Ph)_2\}_3$], which can be described also as [$\{Me_2In(O(C_6H_{11}))\}_2\{$-$MeIn(O(C_6H_{11}))_2\}_2$] (Scheme 13).

Only a limited number of S, Se, or Te organoindium derivatives are known, the majority of which have been prepared and isolated with large sterically demanding ligands. The supermesityl ligand (Mes* = 2,4,6-$Bu^t_3(C_6H_2)$) and mesityl ligand (Mes = 2,4,6-$Me_3(C_6H_2)$) have been effectively used to prepare several stabilized organoindium derivatives owing to the kinetic stabilization effect these ligands have on the metal center. [$Mes^*In(SePh)_2$] has been prepared via Grignard synthesis and isolated as a monomer and base-free ligand.[62] The reaction of $In(Mes)_3$ with diselenides R_2Se_2 (R = Me, Ph) at room temperature yields [$Mes_2In(\mu$-$SeR)]_2$ (R = Me, Ph) and [$Mes_2In(\mu$-$SeMes)]_2$ can be synthesized by the reaction of $In(Mes)_3$ with elemental Se in refluxing toluene. However, under similar conditions, the reaction of $InMe_3$ with Ph_2Se_2 failed to give the target product, but afforded the rearranged product [$MeIn(\mu$-$SePh)(SePh)]_n$. Single-crystal analysis of the structures revealed that both [$Mes_2In(\mu$-$SePh)]_2$ and [$Mes_2In(\mu$-$SeMes)]_2$ were dimeric with planar $(In$-$Se)_2$ rings,[62] (see Table 3).

The analogous organotellurolates [$Mes_2In(\mu$-$TePr)]_2$ and [$Mes_2In(\mu$-$TePh)]_2$ can also be prepared via a similar reaction using the ditellurides (Pr_2Te_2) and Ph_2Te_2 as starting reagents. Like their Se congeners, the organotellurolates have a dimeric configuration with a planar $(InTe)_2$ ring. An advantage of this synthetic route is that it avoids the requirement of organochalcogenide protic compounds (REH), which is generally unstable, thus providing a simple synthetic pathway to binary single-source precursors capable of delivering III-VI materials upon pyrolysis.[62]

5.2 Structures

The organoindium chalcogenides also exhibit extended ring, cage, and cluster-like structures as is commonly found for III-V derivatives. For example, intra-dative coordination is demonstrated by [$Me_2InCH_2SMe)_2$], which adopts conformations where the S-bound Me groups are placed in equatorial positions of the chair-like six-membered ring systems.[95]

Cage structures are exemplified by the first reported polyhedral indium siloxanes synthesized when $RSi(OH)_3$ (R = 1,3-$Pr^i_2C_6H_3$) is reacted with $InMe_3$ in a 1:2 ratio via partial elimination of the CH_3 groups, leading to a drum-shaped indium siloxane.[198] Complete elimination of all

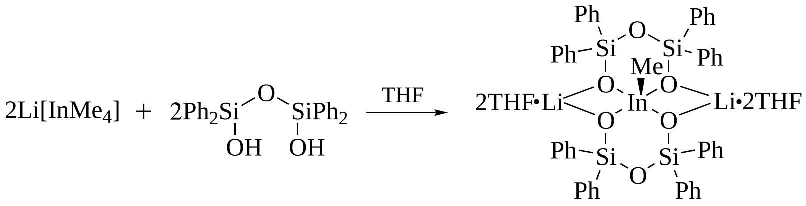

Scheme 12 Indium siloxane [$InMe\{(OPh_2Si)_2O\}_2$-μ-$\{Li(THF)_2\}_2$]

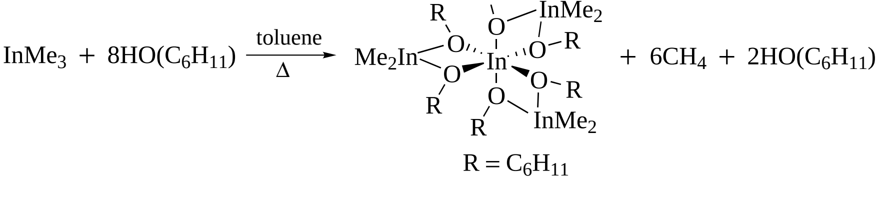

Scheme 13 Sesquialkoxide [$In\{Me_2In(OCH_2Ph)_2\}_3$]

Table 3 Selected bond angles and lengths for organoindium chalcogenides

Organoindium chalcogenides	Bond distances (Å)	Angles (deg)	Ref.
	In–O	**O–In–C**	
[$Me_2In(acac)$]	2.198(1) 2.551(1) 2.256(1)	105.67(7) 90.97(6)	121
[$(Me_3CCH_2)_2In(acac)$]	2.195(1) 2.203(1)	106.42(7) 103.53(7) 109.23(7) 103.36(7)	121
[$(Me)(Me_3CCH_2)In(acac)$]	2.206(2) 2.262(2) 2.569(2)	107.38(8) 93.12(8)	121
[$InMe_2(OC(CF_3)_2CH_2NHCH_2CH_2OMe)]_2$	2.2034(8) 2.3959(8)	110.94(5) 105.19(5)	122
[$InMe_2(OC(CF_3){=}CHC(CF_3){=}NCH_2CH_2NMe_2)$]	2.251(3)	100.4(1) 86.9(1)	141
[$Me_2In(saldPh)]_2$	2.158(3) 2.477(3)	110.58(16) 108.29(17)	123
[$(C_5H_5)_2InO(t\text{-Bu})]_2$	2.118(2) 2.141(2)	118.26(7) 111.96(7)	195
[$InMe\{(OPh_2Si)_2O\}_2\text{-}\mu\text{-}\{Li(THF)_2\}_2$]	2.186(4)	109.1(2) 110.8(2) 109.4(2)	201
[$\{Me_2In(OCy)\}_2\{MeIn(OCy)_2\}_2$]	2.145(4) 2.151(4) 2.149(3) 2.139(3) 2.147(3) 2.155(3)	112.3(2) 107.2(2) 108.9(2) 112.4(2) 115.0(2) 104.7(2)	177
[$In\{(PhCH_2O)_2InMe_2\}_3$]	2.174(2) 2.147(2) 2.162(4) 2.141(2)	108.2(1) 108.8(1) 107.4(1) 109.5(2)	196
[(3-Allyl-2-ethoxycarbonyl-1-(2-hydroxyethyl)]cyclopropylindium dichloride $C_{11}H_{17}Cl_2InO_3$	2.521(8) (OH) 2.532(7)	87.6(2) 84.0(2) 92.0(2)	192
[$C_{42}H_{50}In_2N_4O_8$]	2.199(2) 2.172(2) 2.517(3)	91.0(2) 104.2(1)	132
$Br_2In[OP(C_6H_5)_3]_2CH_2Br$	2.281(6)	89.2(3) Mean values	74
[$(Me_2In)(OC_4H_3CHNNC_6H_5)]_2O$	2.182(7) 2.189(6)	–	137
[$(\mu\text{-}9\text{-}BBN\text{-}9\text{-}O)InMe_2]_2$ $\{C_{20}H_{40}B_2In_2O_2\}$	2.174(10) 2.177(7)	–	203
[$ClMeIn(OBu^t)$]	2.109(3) 2.122(4) 2.109(3)	122.9(2)	61
[$BrMeIn(OBu^t)]_2$	2.114(7) 2.129(8) 2.113(7)	121.8(5) 115.4(4)	61

Table 3 cont'd

Organoindium chalcogenides	Bond distances (Å)	Angles (deg)	Ref.
$[\mathrm{ClMeIn(OC_6H_4OMe)}]_2$	2.136(4) 2.204(4) 2.406(5) 2.204(4)	129.2(3) 110.2(3) 95.7(3)	61
$[(\mathrm{N(SiMe_3)_2})\mathrm{MeInO}t\mathrm{Bu}]_2$	2.138(3) 2.153(3)	114.1(2) 109.3(2)	61
$[\mathrm{MeIn(OBu}^t)_2]_2$	2.006(4) 2.126(4) 2.131(4)	129.0(3) 116.8(3) 117.3(3)	61
$[(\mathrm{Me_3SiCH_2})_2\mathrm{In})_2\mathrm{O}]$	1.989(2) 1.981(2) (Bridging)	–	204
$[\{(\mathrm{CH_3})_3\mathrm{Si}\}_3\mathrm{C(C_3H_7)In}(\mu\text{-OH})]_3$	2.162(2) 2.167(2) 2.160(2) 2.166(2) 2.155(2) 2.171(2)	–	200
$[(\mathrm{InEt_2})_4(\textit{di}\text{-2-pyridylamido})_2(\mu^4\text{-O})]$	2.252(3) 2.160(3) 2.175(4) 2.273(3)	110.73(14) 116.4(2) 101.8(2) 129.1(2) 104.69(14)	144
$[(o\text{-}\mathrm{C_6H_4(InBr(THF)_2)})_2]$	2.407(3) 2.492(3)	–	32
$[(\mathrm{Ph_2InOSiMe_3})_2]$	2.159(7) 2.149(8)	–	179
$[\mathrm{C_{36}H_{70}In_4N_2O_6Si_4}]$	2.148(6) 2.150(6) 2.033(6)	–	198
	In–S	**S–In–C**	
$[(\mathrm{Me_2In})_2\{\mathrm{NC_5H_4CMeNNC(S)NC_6H_5}\}_2(\mathrm{InMe})]\cdot\mathrm{THF}$	2.491(2)	125.31(4)	145
$[((\mathrm{THF})\mathrm{Me_2In})_2\{\mathrm{CH_2(MeCNNC(S)NMe)_2}\}(\mathrm{InMe})]$	2.550(4) 2.561(4)	119.5(4)	145
$[\mathrm{Mes_2In}(\mu\text{-SBu}^t)]$	2.622(5) 2.615(5)	–	205
$[\mathrm{Mes_2In}(\mu\text{-Samy1}^t)]_2$	2.595(4) 2.598(4)	–	205
$[\mathrm{Mes_2In}(\mu\text{-SSiPh_3})]_2$	2.698(1) 2.172(3)	–	205
$\mathrm{Me_2In}(\mu\text{-SSiPh_3})]_3$	2.644(3) 2.617(3) 2.627(3)	–	205
	In–Se	**Se–In–C**	
$[(2,4,6\text{-}^t\mathrm{Bu_3(C_6H_2)})\mathrm{In(SePh)_2}]$	2.5261(12) 2.5507(11)	134.9(2) 121.8(2)	164
$[(2,4,6\text{-}^t\mathrm{Bu_3(C_6H_2)})_2\mathrm{In}(\mu\text{-SePh})]_2$	2.7272(7) 2.7369(8)	97.64(12) 105.09(14)	206
$[(2,4,6\text{-}^t\mathrm{Bu_3(C_6H_2)})_2\mathrm{In}(\mu\text{-Se(Mes)}]_2$	2.705(3) 2.728(3)	117.5(5) 109.3(6)	206
$[\mathrm{MeIn}(\mu\text{-SePh})(\mathrm{SePh})]_n$	2.640(3) bridging 2.726(4) bridging 2.633(4) terminal 2.542(3) terminal 2.541(4) terminal	–	206

(cont'd overleaf)

Table 3 cont'd

Organoindium chalcogenides	Bond distances (Å)	Angles (deg)	Ref.
$[(2,4,6\text{-}{}^t\mathrm{Bu}_3(\mathrm{C}_6\mathrm{H}_2))\mathrm{In}(\mathrm{SePh})_2]$	2.5261(12) 2.5507(11)	134.9(2) 121.8(4)	206
	In–Te	**In–Te–C**	
$[\mathrm{Mes}_2\mathrm{In}(\mu\text{-TePr})]_2$	2.906(1) 2.911(1)	93.8(2) 92.8(2)	207
$[\mathrm{Mes}_2\mathrm{In}(\mu\text{-TePh})]_2$,	2.919(1) 2.911(1)	103.0(2) 95.2(2)	207

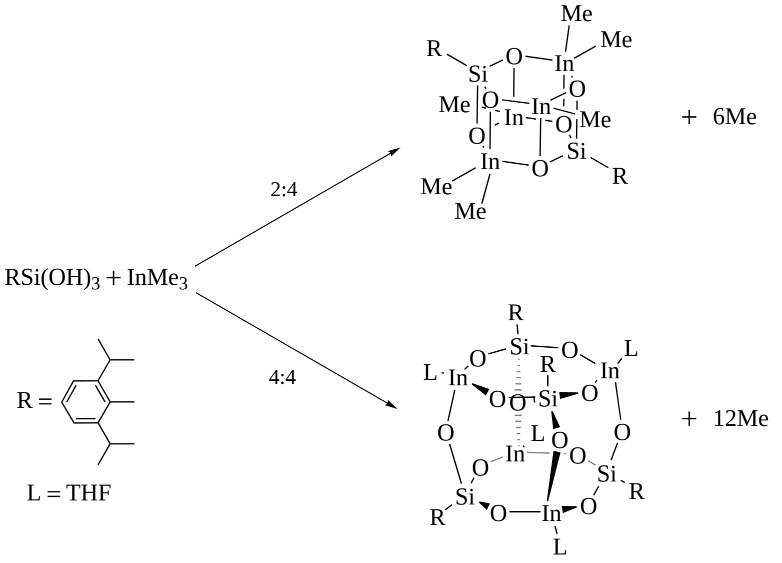

Scheme 14 Synthesis of indium siloxanes

the CH_3 groups can also be performed when the reaction is carried out in a 1:1 ratio, affording the cube shaped indium siloxane (Scheme 14). These indium siloxanes are considered to be important catalysts in the reduction of nitrogen oxides.

A detailed computational study using density functional theory has been used to examine the structural properties of a combination of group 13 and group 16 chalcogenide heterocubanes $[\mathrm{RM}(\mu_3\text{-E})]_4$ ($\mathrm{R} = \mathrm{H}, \mathrm{CH}_3$; $\mathrm{M} = \mathrm{Al}, \mathrm{Ga}, \mathrm{In}$; $\mathrm{E} = \mathrm{O}, \mathrm{S}, \mathrm{Se}, \mathrm{Te}$). Geometries and thermodynamic properties were computed at the B3LYP/SRLC level and all structures were found to be true minima with at most a deviation of 0.08 Å and 2.5° in bond lengths and angles respectively from the experimental geometries reported in Table 3. The M_4E_4 core for each structure proved to be insensitive to ligand choice for the group 13–16 heterocubanes. Density functional theory also suggested that the difficulty for the preparation and isolation of earlier group 13 derivatives $[\mathrm{RM}(\mu_3\text{-O})]_4$ can be attributed to the synthesis being favored by enthalpy but disfavored by entropy; thus, the products might be achievable when prepared at low temperatures.[202]

6 ORGANOINDIUM HYDRIDES

Only an exclusive number of organoindium hydrides are known owing to the inherently weak In–H bond, thus making their synthesis and isolation difficult. Two groups of organoindium hydrides have been characterized, bridging (C-In-H-In) and terminal (C-In-H). The reaction of either $\mathrm{InMe_3{\cdot}Et_2O}$ or $\mathrm{InMe_2Cl}$ with an excess of LiH at reduced temperatures followed by treatment with TMEDA affords the bridged hydride derivative $[\mathrm{Li(TMEDA)_2}][\mathrm{Me_3In(H)InMe_3}]$.[208] The compound is stable in solution or solid state for extended periods when kept below 0 °C, above which it auto catalytically decomposes to $[\mathrm{Li(TMEDA)_2}][\mathrm{InMe_4}]$, indium metal, and gaseous byproducts, (equation 29).

$$\mathrm{InMe_3{\cdot}Et_2O} + \text{xs LiH} \xrightarrow[\text{tmeda}]{0\,^\circ\mathrm{C},\ 16\,\mathrm{h}} [\mathrm{Li(tmeda)_2}]^+[\mathrm{Me_3In\text{-}H\text{-}InMe_3}]^-$$
$$\xrightarrow{>0\,^\circ\mathrm{C}} [\mathrm{Li(tmeda)_2}]^+[\mathrm{InMe_4}]^- + \mathrm{In} + \text{byproducts} \qquad (29)$$

An interesting feature of $[Li(TMEDA)_2][Me_3In(H)InMe_3]$ as determined from its crystallographic structure is the presence of a bent hydride bridge formation, this is in contrast to its aluminum analogue, which possesses a linear structure.[208] Examples of organoindium with terminal hydride have been pioneered recently by the use of bulky carbene ligands such as $\{:CN(Mes)C_2H_2N(Mes)\}$ or $\{:CN(Pr^i)C_2(R)_2CN(Pr^i)\}$, where R = Me, H, these have been described as ''Arduengo-type'' carbenes[209–212] (Scheme 15).

The organoindium carbene hydrides are synthesized by reacting either $LiInH_4$ or $[InH_3(NMe_3)]$ with the Arduengo-type carbene $\{:CN(R')C_2(R)_2CN(R')\}$ at low temperatures, to afford the indium trihydride complexes $[InH_3\{CN(R')C_2(R)_2N(R')\}]$. The thermal stability of these derivatives can be tailored via the substituents on the ring system. In the case of $[InH_3\{CN(Pr^i)C_2Me_2CN(Pr^i)\}]$, the compound decomposes in the solid state at temperatures $>-5\,°C$ and in solution at $>-20\,°C$.[210] In contrast, in the use of the more sterically demanding groups where $R' = Mes = C_6H_2Me_3$-2,4,6, the indium hydride has exceptionally solid-state stability (dec. $>115\,°C$).[209] Additionally, its decomposition in solution was found to be solvent dependent. For example, in toluene decomposition results in liberation of the free carbene and precipitation of In metal, whilst in THF, H transfer occurs to give $H_2CN(Mes)C_2H_2N(Mes)$ and In metal. In dichloromethane, chloride abstraction occurs from the solvent to yield the trihalide, $[InCl_3\{CN(Mes)C_2H_2N(Mes)\}]$. In addition, a mixed indium hydride halide complex $[InH_2Cl\{CN(Mes)C_2H_2N(Mes)\}]$ can be prepared by the reaction of the carbene organoindium hydride with HCl·quinuclidine ($C_7H_{13}N\cdot HCl$).

The use of bidentate chelating carbene has also been investigated (Scheme 16); however, in thermal stability studies of the organoindium carbene hydride derivative, the bidentate ligand was found not to enhance stability (dec. 10–12 °C).[212]

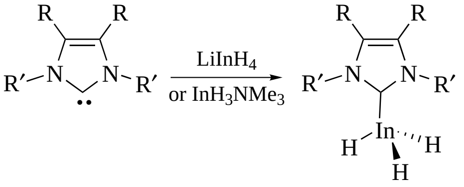

Scheme 15 Synthesis of organoindium carbene hydrides

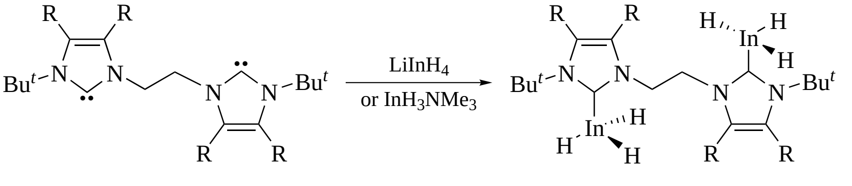

Scheme 16 Bidentate carbene organoindium hydride derivative

7 ORGANOINDIUM METAL COMPLEXES

Most of the reported intermetallic indium complexes are those where the indium is in low oxidation state and are hence discussed in Section 8. Examples where the indium metal center is in higher oxidation states are given below. The intermetallic *bis*(dialkylaminomethyl)-phenylindium derivative is synthesized via metathesis as outlined in Scheme 17.[213] The compound exists as a distorted trigonal bipyramid since the N–In–N angle of 143.1(2) falls considerably short of an ideal trigonal bipyramid (180°).

In similar investigative studies for bimetallic single-source precursors, an iron indane derivative was synthesized by the reaction $Na[(Cp)(CO)_2Fe]0.5THF$ with $BrIn[(CH_2)_3NMe_2]_2$ in THF (Scheme 18)). The analogous Ni, Co, and Mn intermetallic complexes were also successfully prepared with either cyclopentadiene or carbonyl ligands.[214] Photolysis of the indium-iron derivative $[\{Cp(CO)_2Fe\}_2In(CH_2)_3NMe_2)_2]$

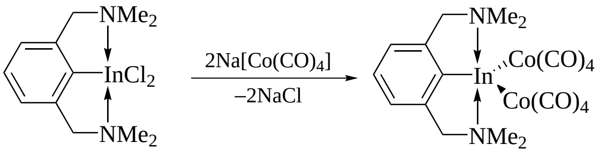

Scheme 17 Synthetic route to intermetallic *bis*(dialkylamino-methyl)-phenylindium derivative

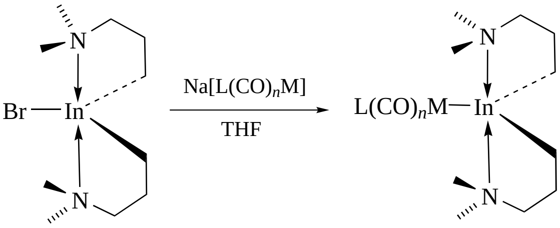

Scheme 18 (M = Fe, L = Cp, $n = 2$; M = Ni, L = Cp, $n = 1$; M = Mn, L = CO, $n = 4$; M = Co, L = CO, $n = 3$)

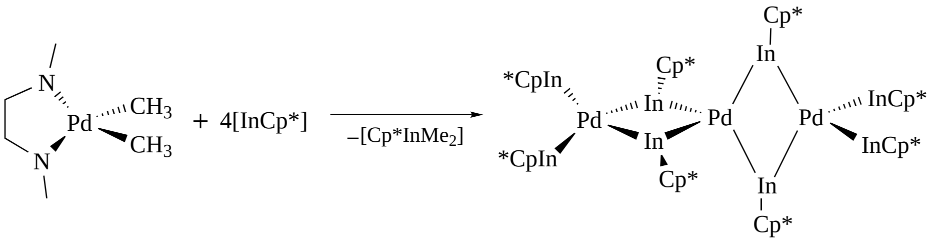

Scheme 19 Formation of low-valent In–M bonds via ligand displacement

in daylight leads to the rearrangement product [(μ-CO) (μ-In$(CH_2)_3NMe_2$){Cp(CO)Fe$_2$}$_2$].

Attempts to prepare the analogous indium derivative of [$((Me_3)_3SiCH_2)_2$Ga{Co$(CO)_4$}] failed to yield the desired product from the reaction between [$((Me_3)_3SiCH_2)_2$InCl] and Na[$(CO)_3$Co], but instead gave the unexpected indane cobaltate product [{$(CO)_4$Co}$_2$In(CH_2SiMe_3)(THF)].[214] In all cases, these bimetallic compounds were studied to see if they could be viable candidates in CVD process to afford bimetallic thin films.

8 ORGANOINDIUM LOW VALENCY COMPOUNDS

The paucity of organoindium(I) and (II) derivatives is evidenced by the limited number of articles in this area in comparison to those for organoindium(III). This is largely due to the high propensity for In(I) to disproportionate to In(III) and elemental indium.[215] The bulk of low-valent organoindium compounds have been derived with cyclic groups such as Cp, Cp*, etc and functionalized derivatives thereof. The main preparative routes for these species are reduction of InX_3 with alkali salts, controlled reaction of organolithium, or Grignard reagents with of InX, co-condensation of indium vapor with the respective organic moiety and matrix isolation. The area of lower oxidation state indium derivatives has been extensively reviewed, and their synthesis, reactivity, and properties examined;[215] thus, this section will be an overview with recent additions. Again the two areas which have perpetuated the increase for organoindium(I) derivatives are the semiconductor industry and the search for intermetallic precursors to thin films and nanocrystallites,[216–218] and organic synthesis, which reported an organoindium(I) derivative (InCp) as an effective reagent for the preparation of highly functionalized organic cyclopentadienes in aqueous media, thus paving the way for a new role for organoindium(I) derivatives.[219]

8.1 Intermetallic Organoindium Derivatives

The most common synthetic pathway for the formation of low-valent In–M bonds is the replacement of labile ligands on the incoming metal with InR.[112,220–225] For example, the labile COD ligands in [Pt$(COD)_2$] and [Ni$(COD)_2$] are readily replaced by InC$(SiMe_3)_3$, InCp* and other group 13 derivatives (i.e. GaCp*, GaC$(SiMe_3)_3$), yielding monomeric complexes of the type [M$(InR)_4$] (M = Pt, Ni) (equation 30). Elimination reactions have also been employed to prepare novel In-M derivatives (Scheme 19).[221]

$$[\mathrm{Pt(COD)_2}] + \mathrm{InL} \xrightarrow{-2\mathrm{COD}} [\mathrm{Pt(InL)_4}] \qquad (30)$$

Another successful synthetic route to indium-metal species is via insertion of organoindium(I) compounds into metal-halide or metal–metal bonds.[225–227] The organo indium subhalide [R(Cl)In-In(Cl)R]$_2$ [R=C$(SiMe_3)_3$] reacts with Na_2[$Fe_2(CO)_8$] to form an iron-indium coordination compound, which is isolated as the NaCl adduct [Na$(THF)_4Fe_2(CO)_6$(μ-CO)(μ-InR)$_2$Cl].[226] The iron atoms are bridged by a CO ligand and two InR groups, and the indium atoms are further connected by the μ^2-bridging chlorine atom. Similarly, the insertion of InR (R = Cp*, C$(SiMe_3)_3$ into the Rh–Cl bond of [(Cp*RhCl$_2$)$_2$] affords the intermetallic derivatives [(Cp*Rh{InCp*}$_3$Cl$_2$] and [(Cp*Rh(μ^2-Cl$_2$){In-C$(SiMe_3)_3$}$_3$] (Scheme 20).[227]

A very interesting feature determined from the single-crystal structure for [(Cp*Rh{InCp*}$_3$Cl$_2$] is the difference in bonding of the Cp* rings to indium, varying from a sigma bonded mode (InCp*Cl$_2$) to a hapticity of η^5, and one between η^{2-3}, Figure 5.

As is the case for most indium-metallic derivatives in solution, rapid fluxional exchanges are prevalent as can be

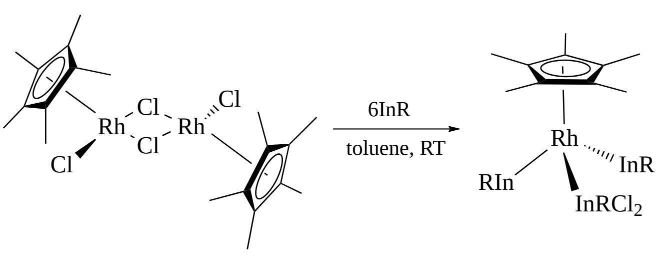

Scheme 20 Synthetic route to [(Cp*Rh{InCp*}$_3$Cl$_2$] and [(Cp*Rh(μ^2-Cl$_2$){In-C$(SiMe_3)_3$}$_3$]

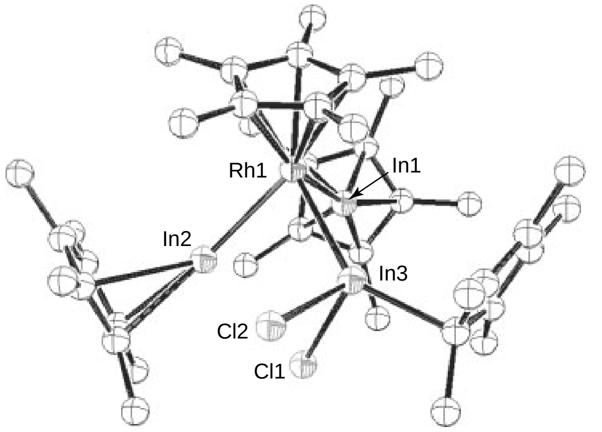

Figure 5 Single-crystal structure for $[(Cp^*Rh\{InCp^*\}_3Cl_2]$

observed by NMR spectroscopic studies. In the case of both the In-Rh derivatives, ^{1}H-NMR of both complexes shows chemical shifts for only one InR entity and not the three as expected; thus, rapid exchange between the chloride and the In(I) and In(III) centers is occurring.[227]

8.2 In(0), In(I) and In(II) Organo Derivatives

Matrix isolation provides a unique insight into otherwise unattainable compounds by isolating the trapped molecule in a rigid and inert matrix such as argon, which is non-invasive during spectroscopic measurements. This novel technique has been used successfully for the fabrication and spectroscopic study of In(0) derivatives, namely In(CO), In·In(CO), $In(CO)_2$, and $In(CO)_2{\cdot}In$ (Scheme 21).[228] Additionally, InMe and GaMe have been reported via the reaction of the respective group 13 atoms with methane in solid Ar matrix.[229] The products are formed via UV photolysis ($\lambda = 200-400$ nm) to give the alkylmetalhydride followed by photodissociation on broad-band irradiation ($\lambda = 200-800$ nm) to yield MeM(I) derivative.[229,230]

Co-condensation of indium vapor and *tert*-butylphosphaethyne at 77 K yields the volatile In(I) complexes $[In(\eta^5\text{-}P_3C_2Bu^t_2)]$ and 1,3-diphosphacyclopentadienyl complex $[In(\eta^5\text{-}P_2C_3Bu^t_3)]$.[159] Single-crystal x-ray diffraction studies for $[In(\eta^5\text{-}P_3C_2Bu^t_2)]$ reveals a discrete molecular structure, involving half-sandwich coordination of the $P_3C_2Bu^t_2$ ring around the indium center. Cyclization of the $Bu^tC{\equiv}P$ ligand to afford the cyclic ring is thought to occur by the ''naked'' indium atoms. The crystal structure of $[In(\eta^5\text{-}P_3C_2Bu^t_2)]$ (see Table 2) confirms that the ring is coordinated to the indium metal center with a η^5-hapacity. In contrast to $[In(\eta^5\text{-}C_5H_4R)]$ derivatives, where polymeric zigzag chains are evident, the greater steric bulk of the phosphine substituted ring affords discrete molecular units with no aggregation (intermonomer distance = 3.526 Å).[159] Coincidentally, $[In(\eta^5\text{-}P_3C_2Bu^t_2)]$ can also be synthesized in good yields by treating InI with the base-free ligand salt $K(P_3C_2Bu^t_2)$ (Scheme 22). A study of the molecular and electronic structure of these indium(I) phospholyls including computational modeling has been performed.[231]

Low oxidation state derivatives also have the tendency to be isolated in cage like structures; for example, the tetrahedral derivative $In_4[C(SiMe_3)_3]_4$ is readily prepared from the reaction between InBr and $Li[C(SiMe_3)_3]$.[232,233] $In_4[C(SiMe_3)_3]_4$ is a highly versatile synthon to many other novel organoindium compounds (Scheme 23). For example, reaction with elemental Se affords the unique In-Se hetrocubane,[232] and halogenation studies of $In_4[C(SiMe_3)_3]_4$ afford novel alkylindium(I) halides,[234,235] while reaction with bimetallic species demonstrates its ability to be inserted into the metal–metal bond.[236] The main by-product from the reaction of InBr with the THF adduct of $LiC(SiMe_3)_3$ is $[In_3Br_3\{C(SiMe_3)_3\}_3]^-[Li(THF)_3]^+$ whose geometrical configuration is analogous to that of $In_3I_2[C(SiMe_3)_3]_3$, except the inner In atom is attached to a bromide ion which bridges the In_3 chain and the counterion $[Li(THF)_3]^+$.[237]

A clear example of how ligand steric encumbrance has been implemented to control geometrical conformation for organoindium(I) species from monomeric to aggregated is

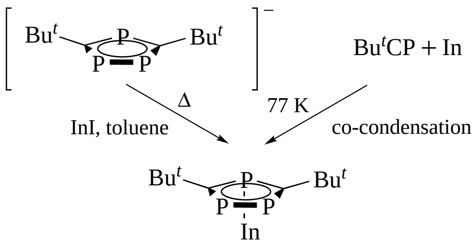

Scheme 22 Preparative routes to these indium(I) phospholyls

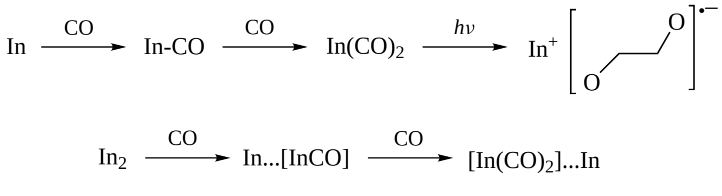

Scheme 21 Pathways for matrix reactions of Indium with CO

the reaction of InX with lithium-terphenyls of various sizes. Molecular In(I) derivatives of monodentate ligands of any kind are limited; however, the use of the sterically demanding *o*-terphenyl ligand {–C_6H_3-2,6-$Trip_2$ (Trip = C_6H_2-2,4,6-$Pr^i{}_3$)}, the monomeric compound InC_6H_3-2,6-$Trip_2$, has been prepared and isolated, (Figure 6a).[112] The modified terphenyl ligand –C_6H_3-2,6-$Dipp_2$ (Dipp = C_6H_3-2,6-Pr^i_2) enables the isolation of a stable dimeric group 13 ''dimetallene'' species ArInInAr (Ar = C_6H_3-2,6-$Dipp_2$) (Figure 6b),[238] whereas using the less crowded ligand –C_6H_3-2,6-Mes_2 (Mes = C_6H_2-2,4,6-Me_3) affords the aggregated distorted cubane $In_8(C_6H_3\text{-}2,6\text{-}Mes_2)_4$ (Figure 6c).[239]

A common trait of organoindium(II) complexes is the presence of In–In bonding. The preparation of the first carbene and diazabutadiene In(II) compound has been achieved by the reaction of {:CN(Mes)C_2H_2N(Mes)} with InBr in either a 1:1 or 1:2 ratio, and $((C_6H_3Pr^i_2\text{-}2,6)N{=}CH)_2$ with InCl in a 3:2 ratio.[240] Structural characterization reveals In–In bond lengths of 2.7436(7) and 2.7280(9) respectively. A comparison with reported In–In bond distances (Table 4) shows that In–In bond distances fall within the reported range since the In–In bond length is known to vary owing to the steric demand of substituents on the ligands.[98]

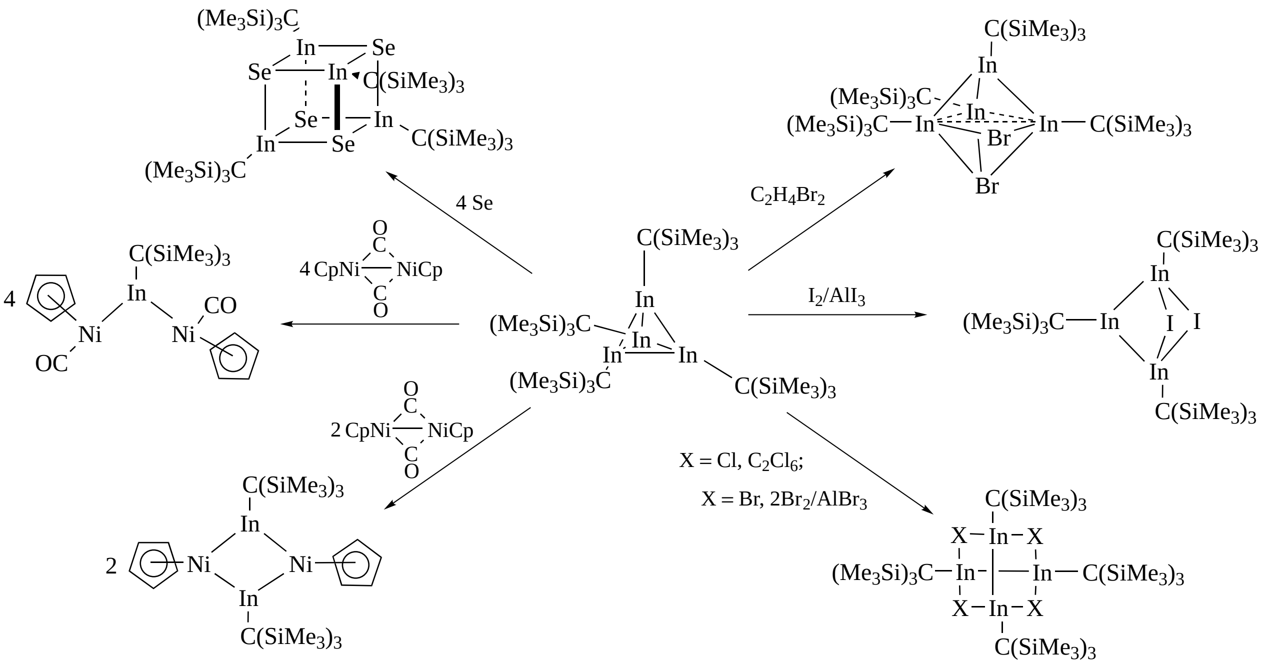
4 Se
$C_2H_4Br_2$
I_2/AlI_3
4 CpNi(CO)₂NiCp
2 CpNi(CO)₂NiCp
X = Cl, C_2Cl_6;
X = Br, $2Br_2/AlBr_3$
4
2
$(Me_3Si)_3C$
$C(SiMe_3)_3$
In
Se
Br
I
Ni
CO
OC
X

Scheme 23 Reaction pathways for $In_4[C(SiMe_3)_3]_4$

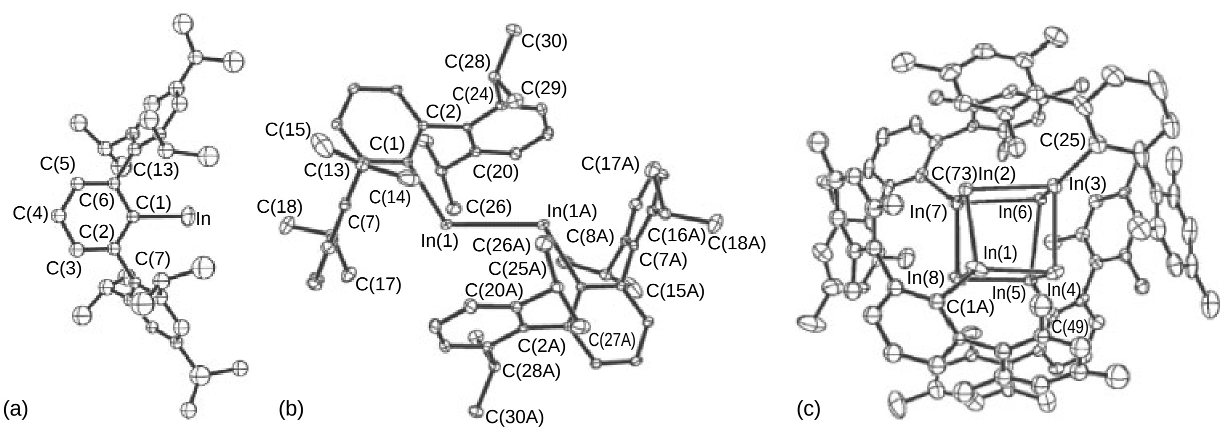
C(5)
C(13)
C(6)
C(1)
C(4)
In
C(2)
C(3)
C(7)
(a)
C(30)
C(28)
C(24)
C(29)
C(2)
C(15)
C(1)
C(13)
C(20)
C(17A)
C(14)
C(18)
C(26)
In(1A)
C(7)
In(1)
C(26A)
C(8A)
C(16A)
C(18A)
C(25A)
C(7A)
C(17)
C(20A)
C(15A)
C(2A)
C(27A)
C(28A)
(b)
C(30A)
C(25)
C(73)In(2)
In(3)
In(7)
In(6)
In(1)
In(8)
In(5)
In(4)
C(1A)
C(49)
(c)

Figure 6 Organoindium-terphenyl complexes

Table 4 Metal–metal bond lengths of structurally characterized organoindium derivatives

Compound	In–In bond length (Å)	Ref.
$[In_2Br_4(IMes)_2]$	2.7436(7)	240
$[In_2Cl_2(DAB\cdot)_2]$	2.7280(9)	240
$[((Me_3Si)_2C(Ph)C(Me_3Si)N)InBr]_2$	2.728(4)	98
$[(2,4,6\text{-}Pr^i_3C_6H_2)_2In]_2$	2.775(2)	241
$[(2,4,6\text{-}(CF_3)_3C_6H_2)_2In]_2$	2.744(2)	242
$[(Me_3Si)_3CIn]_4$	3.002(1)	232
$[(EtMe_2Si)_3CIn]_4$	3.004(1)	101
$[(Pr^iMe_2Si)_3CIn]_4$	3.145(1)	101
$[(Me_3Si)_2CHIn]_2$	2.8534(4)	243
$[(2,6\text{-}Dipp_2C_6H_3)_2In]_2$	2.9786(5)	238
$[In_8(C_6H_3\text{-}2,6\text{-}Mes_2)_4]$	2.8754(13)–2.9328(13)	239

9 ORGANOINDIUM ANIONIC DERIVATIVES

The reaction of organoindium derivatives with alkali metals[54,244,245] results in the isolation of the appropriate tetraorgano anionic complex $M[InR_4]$ ($M = K$, Rb, Cs; $R = Me$ and $M = Li$, Na, K, Rb, Cs; $R = Ph$) (equation 31), and they prove to be valuable synthons for the preparation of indium compounds.

$$3M + 4R_3In \longrightarrow 3M[InR_4] + In \qquad (31)$$

$$[(Bu^tCH_2)_3In] \xrightarrow{\text{xs KH}} K[(Bu^tCH_2)_3InH] \qquad (32)$$

$$[(Bu^tCH_2)_3In] + K[(Bu^tCH_2)_3InH] \longrightarrow K[\{(Bu^tCH_2)_3In\}_2H] \qquad (33)$$

$$R_3In + [NR'_4]X \longrightarrow [NR'_4][R_3InX] \qquad (34)$$

$$2R_3In + [NR'_4]X \longrightarrow [NR'_4][R_3InXInR_3] \qquad (35)$$

Organoindium anionic compounds in which indium coordinates to both alkyl and hydride ligands have been synthesized via the reaction of R_3In with KH (equation 32); the product, however, combines with unreacted trialkyl to give $K[\{(t\text{-}BuCH_2)_3In\}_2H]$ (equation 33).[54] Complexes in which indium coordinates to both alkyl and halide ligands can be prepared by the reaction of R_3In with $[NR'_4]X$ ($X = F$, Cl, Br) (equation 34). If two equivalents of R_3In are used, the products are dimeric with bridging halides (equation 35).

An example of a novel synthesis to triple stacked InCp cations is via the reaction of $[InCp^*]_6$ with an equimolar mixture of $B(C_6F_5)_3$ and $H_2O{\cdot}B(C_6F_5)_3$ in toluene to afford $[(\eta^6\text{-}C_7H_8)In(\mu\text{-}\eta^5\text{-}C_5Me_5)In(\eta^6\text{-}C_7H_8)]^+$ $[(C_6F_5)_3BO(H)B(C_6F_5)_3]^-$.[246] Given the very long indium-ring-centroid distances of 3.490(4) and 3.325(4) Å in conjunction with molecular orbital calculations, the authors view the molecule as an inverse sandwich cation.[247] Ionic cage structures are exemplified by an extension to the first reported polyhedral indium siloxanes[198] when $RSi(OH)_3$ ($R = 1,3\text{-}Pr^i_2C_6H_3$) is reacted with $M[InMe_4]$ ($M = Li$, Na) in a 4:4 ratio via elimination of the CH_3 groups, leading to a ionic poly-organoindium siloxane (Scheme 24).[198]

In another example, the reaction of CsF with organoindium compounds in acetonitrile provides a novel route to the respective cesium organoindium heterocubane in high yields (Figure 7).[248,249] In contrast to $Cs[InMe_4]$, no short intra- and intermolecular Cs···C contacts are noted for $[Cs\{Pr^i_3In\}]_4$, thus indicating that there are no significant intermolecular interactions between the heterocubane units.

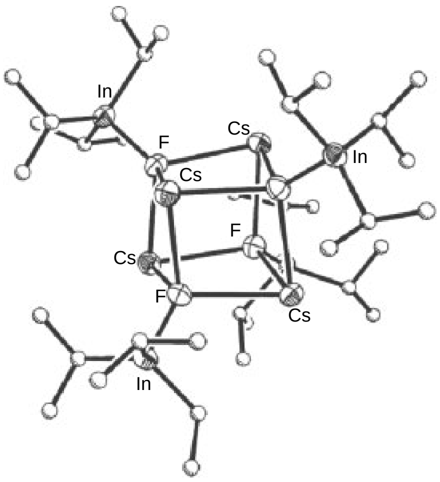

Figure 7 Single-crystal structure of the ionic heterocubane $[Cs\{Pr^i_3In\}]_4$

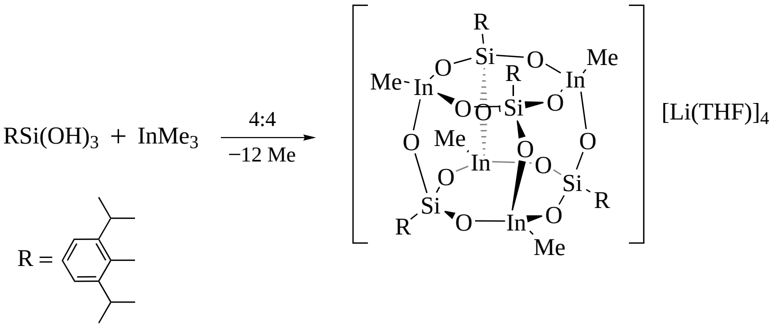

Scheme 24 Ionic polyhedron organoindium siloxane

10 RELATED ARTICLES

Alloys; Aluminum: Inorganic Chemistry; Coordination & Organometallic Chemistry: Principles; Gallium: Inorganic Chemistry; Gallium: Organometallic Chemistry; Indium: Inorganic Chemistry; Organic Synthesis Using Metal-mediated Coupling Reactions; Organic Synthesis Using Metal-mediated Metathesis Reactions.

11 FURTHER READING

C. J. Carmalt, N. C. Norman, R. F. Pember, and L. J. Farrugia, *Polyhedron*, 1995, **14**(3), 417.

K.-N. Tu, J. W. Mayer, and L. C. Feldman, ‘Electronic Thin Film Science for Electrical Engineers & Material Scientists’, 1st edition, Prentice Hall College Div; 1996, p. 127.

K.-N. Tu, J. W. Mayer, and L. C. Feldman, ‘Electronic Thin Film Science for Electrical Engineers & Material Scientists’, 1st edition, Prentice Hall College Div; 1996, p. 157.

K.-N. Tu, J. W. Mayer, and L. C. Feldman, ‘Electronic Thin Film Science for Electrical Engineers & Material Scientists’, 1st edition, Prentice Hall College Div; 1996, p. 194.

D. G. Tuck, *Studies of the Chemistry of Indium I and II Compounds, Chemical Institute of Canada*, 1990, **42**(8), 25.

Wikipedia, the free encyclopedia, 2004, http://en.wikipedia.org/wiki/Indium

M. Winter, 2004, Webelements, Indium, http://www.webelements.com/webelements/elements/text/In/key.html

12 REFERENCES

1. B. Neumueller, *Chem. Soc. Rev.*, 2003, **32**(1), 50.
2. M. J. Almond, *Organomet. Chem.*, 2002, **30**, 128.
3. P. J. Shapiro, *ACS Symp. Ser.*, 2002, **822**, 31.
4. M. J. Almond, *Organomet. Chem.*, 2001, **29**, 127.
5. M. J. Almond, *Organomet. Chem.*, 2000, **28**, 107.
6. M. J. Almond, *Organomet. Chem.*, 1999, **27**, 380.
7. M. J. Almond, *Organomet. Chem.*, 1998, **26**, 74.
8. B. Neumuller, *Coord. Chem. Rev.*, 1997, **158**, 69.
9. M. J. Almond, *Organomet. Chem.*, 1996, **25**, 50.
10. N. Auner, *Synth. Methods Organomet. Inorg. Chem.*, 1996, **2**, 63.
11. K. C. Molloy, *Organomet. Chem.*, 1995, **24**, 48.
12. J. P. Oliver, *J. Organomet. Chem.*, 1995, **500**(1–2), 269.
13. K. C. Molloy, *Organomet. Chem.*, 1994, **23**, 41.
14. D. G. Tuck, *Chem. Soc. Rev.*, 1993, **22**(4), 269.
15. W. Uhl, *Angew. Chem., Int. Ed. Engl. A.*, 1993, **32**(10), 1386.
16. J. P. Maher, *Annu. Rep. Prog. Chem., Sec. A: Inorg. Chem.*, 2003, **99**, 43.
17. J. P. Maher, *Annu. Rep. Prog. Chem., Sec. A: Inorg. Chem.*, 2002, **98**, 45.
18. J. P. Maher, *Annu. Rep. Prog. Chem., Sec. A: Inorg. Chem.*, 2001, **97**, 49.
19. W. Hermann, ed., ‘Synthetic Methods of Organometallic and Inorganic Chemistry’, Thieme Medical Pub., Transition Metals Part 3, 2000 Vol. 9, ISBN 0865778000.
20. J. P. Maher, *Annu. Rep. Prog. Chem., Sec. A: Inorg. Chem.*, 2000, **96**, 45.
21. R. A. Fischer and A. Devi, *Recent Res. Dev. Cryst. Growth Res.*, 2000, **2**, 61.
22. J. P. Maher, *Annu. Rep. Prog. Chem., Sec. A: Inorg. Chem.*, 1999, **95**, 45.
23. J. P. Maher, *Annu. Rep. Prog. Chem., Sec. A: Inorg. Chem.*, 1998, **94**, 43.
24. P. Zanella, G. A. Battiston, G. Carta, R. Gerbasi, M. Porchia, and G. Rossetto, *Mater. Sci. Foru.*, 1998, **282–283**, 123.
25. J. P. Maher, *Annu. Rep. Prog. Chem., Sec. A: Inorg. Chem.*, 1997, **93**, 45.
26. J. P. Maher, *Annu. Rep. Prog. Chem., Sec. A: Inorg. Chem.*, 1996, **92**, 41.
27. A. C. Jones and P. O’Brien, ‘CVD of Compound Semiconductors: Precursor Synthesis, Development and Applications’, VCH Press, New York, 1996 ISBN 3-527-29294-2.
28. A. C. Jones, C. R. Whitehouse, and J. S. Roberts, *Chem. Vap. Dep.*, 1995, **1**(3), 65.
29. P. Cintas, *Synlett*, 1995, **11**, 1087.
30. J. P. Maher, *Annu. Rep. Prog. Chem., Sec. A: Inorg. Chem.*, 1995, **91**, 41.
31. J. P. Maher, *Annu. Rep. Prog. Chem., Sec. A: Inorg. Chem.*, 1994, **90**, 25.
32. S. Jena and K. C. Dash, *Indian J. Chem., Sect. A: Inorg., Bio-inorg., Phys., Theor. Anal. Chem.*, 1994, **33A**(8), 699.
33. C. Keh and C. Li, *Chemtracts*, 1999, **12**(11), 813.
34. A. Hashmi and K. Stephen, *J. Prakt. Chem./Chem.-Ztg.*, 1998, **340**(1), 84.
35. J. Auge, N. Lubin-Germain, S. Marque, and L. Seghrouchni, *J. Organomet. Chem.*, 2003, **679**(1), 79.
36. A. G. Fallis, P. Forgione, S. Woo, S. Legoupy, S. Py, C. Harwig, and T. Rietveld, *Polyhedron*, 2000, **19**(5), 533.
37. M. Reetz and H. Haning, *J. Organomet. Chem.*, 1997, **541**(1–2), 117.
38. D. Laine, *Synlett*, 1999, **8**, 1331.
39. W. Miao, W. Lu, and T. H. Chan, *J. Am. Chem. Soc.*, 2003, **125**(9), 2412.
40. V. I. Bregadze, L. M. Golubinskaya, and B. I. Kozyrkin, *J. Cluster Sci.*, 2002, **13**(4), 631.
41. H. Oosaki and M. Ohshima, Preparation of Organoindium Compounds for Manufacture of Semiconductors by MOCVD, Jpn. Kokai Tokkyo Koho, 1999, JP 11012284 A2.
42. D. V. Shenai-Khatkhate, M. B. Power, and R. L. Dicarlo, Trialkylindium Preparation, U.S. Pat. Appl. Publ. US 2003191333, 2003.

43. H. Osaki and M. Oshima, Preparation of Organoindium Compounds for Manufacture of Semiconductors by MOCVD, Jpn. Kokai Tokkyo Koho, JP 11012283 A2 1999.
44. H. Oosaki, Preparation of Organoindium Compounds for Manufacture of Semiconductors by MOCVD, Jpn. Kokai Tokkyo Koho, JP 11012282 A2, 1999.
45. M. B. Power and D. V. Shenai-Khatkhate, Preparation of High-Purity Trimethylindium, Cont.-in-part of U.S. Series No. 881,907., US 5756786, 1998.
46. R. Kanjolia and C. Benjamin, Liquid Indium Source, Can. Pat. Appl., CA 2124052 AA, 1995.
47. K. Asakura, T. Ishihara, H. Oosaki, K. Sato, and I. Kaneko, Recovery of Organometallic Compounds, Jpn. Kokai Tokkyo Koho, JP 06009651, 1994.
48. K. Asakura, T. Ishihara, H. Oosaki, K. Hiromi, and S. K. Isao, Preparation of Organoindium Compounds, Jpn. Kokai Tokkyo Koho, JP 06073068, 1994.
49. C. J. Smit, A. J. Van der Lee, and E. Van, Process for the Preparation of Trialkyl Compounds of Group 3A Metals, PCT Int. Appl., WO 9401438 A1, 1994.
50. T. Krafft, Method for the Synthesis of Metal Alkyls and Metal Aryls, PCT Int. Appl., WO 9418145 A1, 1994.
51. B. C. Hui, J. Lorberth, and A. A. Melas, Hybrid Organometallic Compounds for Metal-Organic Chemical-Vapor Deposition, Eur. Pat. Appl., EP 181706 A1, 1986.
52. O. T. Beachley Jr, D. J. MacRae, A. Y. Kovalevsky, Y. Andrey, Y. Zhang and X. Li, *Organometallics*, 2002, **21**(22), 4632.
53. O. T. Beachley Jr, E. S. Robirds, D. A. Atwood and P. Wei, *Organometallics*, 1999, **18**(13), 2561.
54. J. T. Leman and A. R. Barron, Indium: Organometallic Chemistry, in ‘Encyclopedia of Inorganic Chemistry’, ed. R. King, John Wiley & Sons, New York, 1993, p. 1531.
55. S. Duffy, P. F. Nolan, S. A. Rushworth, A. Simon, B. A. Leese, and A. C. Jones, *Adv. Mater. Opt. Electron.*, 1997, **7**(5), 233.
56. K. K. Banger, J. Cowen, and A. F. Hepp, *Chem. Mater.*, 2001, **13**(11), 3827.
57. M. Schiefer, D. N. Reddy, H.-J. Ahn, A. Stasch, H. W. Roesky, C. A. Schlicker, H.-G. Schmidt, M. Noltemeyer, and D. Vidovic, *Inorg. Chem.*, 2003, **42**(16), 4970.
58. R. J. Creighton, G. T. Wang, W. G. Breiland, and M. E. Coltrin, *J. Cryst. Growth*, 2004, **261**(2–3), 204.
59. B. H. Cardelino, C. E. Moore, C. A. Cardelino, D. O. Frazier, and K. J. Bachmann, *J. Phys. Chem. A*, 2001, **105**(5), 849.
60. A. P. Kurbakova, S. S. Bukalov, L. A. Leites, L. M. Golubinskaya, and V. I. Bregadze, *J. Organomet. Chem.*, 1997, **536/537**(1–2), 519.
61. M. Veith, S. Hill, and V. Huch, *Eur. J. Inorg. Chem.*, 1999, **8**, 1343.
62. H. Rahbarnoohi, R. L. Wells, L. M. Liable-Sands, and A. L. Rheingold, *Organometallics*, 1996, **5**(18), 3898.
63. D. L. Reger, M. J. Pender, D. L. Caulder, L. B. Reger, A. L. Rheingold, and L. M. Liable-Sands, *J. Organomet. Chem.*, 1996, **512**(1–2), 91.
64. A. Meller, C. Kuemmel, and M. Noltemeyer, *Z. Naturforsch., B: Chem. Sci.*, 1996, **51**(1), 107.
65. B. Werner, T. Kraeuter, and B. Neumueller, *Z. Anorg. Allg. Chem.*, 1995, **621**(3), 346.
66. A. H. Cowley, C. S. King, and A. Decken, *Organometallics*, 1995, **14**(1), 20.
67. H. Schumann, T. D. Seuss, O. Just, R. Weimann, H. Hemling, and F. H. Goerlitz, *J. Organomet. Chem.*, 1994, **479**(1–2), 171.
68. L. J. Jones III, A. T. McPhail, and R. L. Wells, *Organometallics*, 1994, **13**(9), 3634.
69. H. Rahbarnoohi, M. J. Heeg, and J. P. Oliver, *Organometallics*, 1994, **13**(5), 2123.
70. K. Merzweiler, L. Brands, and J. Spohn, *Z. Naturforsch., B: Chem. Sci.*, 1993, **48**(10), 1315.
71. R. L. Wells, A. T. McPhail, and M. F. Self, *Organometallics*, 1993, **12**(8), 3363.
72. G. Rossetto, N. Brianese, A. Camporese, M. Porchia, and P. Zanella, *Gazz. Chim. Ital.*, 1993, **123**(5), 279.
73. B. Neumueller, *Chem. Ber.*, 1993, **126**(1), 11.
74. C. Peppe, J. A. Nobrega, M. Z. Hernandes, R. L. Longo, and D. G. Tuck, *J. Organomet. Chem.*, 2001, **626**(1–2), 68.
75. W. Tyrra and M. S. Wickleder, *J. Organomet. Chem.*, 2003, **677**(1–2), 28.
76. A. B. De Carvalho, M. A. De Maurera, J. A. Nobrega, C. Peppe, M. A. Brown, D. G. Tuck, M. Z. Hernandes, E. Longo, and F. R. Sensato, *Organometallics*, 1999, **18**(1), 99.
77. J. A. Nobrega, C. Peppe, M. A. Brown, and D. G. Tuck, *Chem. Commun.*, 1998, **3**, 381.
78. J. Estrela dos Santos, C. Peppe, M. A. Brown, and D. G. Tuck, *Organometallics*, 1996, **15**(9), 2201.
79. J. D. Hoefelmeyer, M. Schulte, M. Tschinkl, and F. P. Gabbai, *Coord. Chem. Rev.*, 2002, **235**(1–2), 93.
80. M. Schulte and F. P. Gabbai, *Chem. – Eur. J.*, 2002, **8**(16), 3802.
81. J. D. Hoefelmeyer, M. Schulte, and F. P. Gabbaie, *Inorg. Chem.*, 2001, **40**(15), 3833.
82. F. P. Gabbai, A. Schier, J. Riede, and D. Schichl, *Organometallics*, 1996, **15**(20), 4119.
83. A. H. Cowley, H. S. Isom, and A. Decken, *Organometallics*, 1995, **14**(5), 2589.
84. S. J. Black, D. E. Hibbs, M. B. Hursthouse, C. Jones, A. K. Malik, and N. A. Smithies, *J. Chem. Soc., Dalton Trans.*, 1997, 4313.
85. R. J. Baker, R. D. Farley, C. Jones, M. Kloth, and D. M. Murphy, *Chem. Commun.*, 2002, 1196.
86. R. J. Baker, M. L. Cole, C. Jones, and M. F. Mahon, *J. Chem. Soc., Dalton Trans.*, 2002, 1992.

87. D. E. Hibbs, M. B. Hursthouse, C. Jones, and N. A. Smithies, *Main Group Chem.*, 1998, **2**(4), 293.
88. G. S. Hair, S. L. Battle, A. Decken, A. H. Cowley, and R. A. Jones, *Inorg. Chem.*, 2000, **39**(1), 27.
89. M. A. Petrie, P. P. Power, H. V. Dias, K. Ruhlandt-Senge, K. M. Waggoner, and R. J. Wehmschulte, *Organometallics*, 1993, **12**(4), 1086.
90. S. Schulz, S. Pusch, E. Pohl, S. Dielkus, R. Herbst-Irmer, A. Meller, and H. W. Roesky, *Inorg. Chem.*, 1993, **32**(15), 3343.
91. R. Bertani, L. Crociani, G. D'Arcangelo, G. Rossetto, P. Traldi, and P. Zanella, *J. Organomet. Chem.*, 2001, **626**(1–2), 11.
92. V. Souliere, P. Abraham, M. Sacilotti, M. P. Berthet, J. Bouix, and Y. Monteil, *Mater. Sci. Eng., B*, 1993, **B17**(1–3), 34.
93. F. Thomas, T. Bauer, S. Schulz, and M. Nieger, *Z. Anorg. Allg. Chem.*, 2003, **629**(11), 2018.
94. M. Schiefer, D. N. Reddy, H.-J. Ahn, A. Stasch, H. W. Roesky, C. A. Schlicker, H.-G. Schmidt, M. Noltemeyer, and D. Vidovic, *Inorg. Chem.*, 2003, **42**(16), 4970.
95. C. Lustig and N. W. Mitzel, *Organometallics*, 2003, **22**(2), 242.
96. P.-C. Kuo, J.-H. Huang, C.-H. Hung, G.-H. Lee, and S.-M. Peng, *Eur. J. Inorg. Chem.*, 2003, **7**, 1440.
97. M. Stender, B. E. Eichler, N. J. Hardman, P. P. Power, J. Prust, M. Noltemeyer, and H. W. Roesky, *Inorg. Chem.*, 2001, **40**(12), 2794.
98. K. S. Klimek, C. Cui, H. W. Roesky, M. Noltemeyer, and H.-G. Schmidt, *Organometallics*, 2000, **19**(16), 3085.
99. O. T. Beachley Jr and S. L. Chao, *Organometallics*, 2000, **19**(14), 2820.
100. E. Hecht, *Z. Anorg. Allg. Chem.*, 2000, **626**(3), 759.
101. W. Uhl, A. Jantschak, W. Saak, M. Kaupp, and R. Wartchow, *Organometallics*, 1998, **17**(23), 5009.
102. R. D. Culp, A. H. Cowley, A. Decken, R. A. Jones, M. R. Bond, L. M. Mokry, and C. J. Carrano, *Inorg. Chem.*, 1997, **36**(23), 5165.
103. D. L. Reger, M. J. Pender, D. L. Caulder, L. B. Reger, A. L. Rheingold, and L. M. Liable-Sands, *J. Organomet. Chem.*, 1996, **512**(1–2), 91.
104. L. Contreras, A. H. Cowley, F. P. Gabbai, R. A. Jones, C. J. Carrano, and R. Marcus, *J. Organomet. Chem.*, 1995, **489**(1–2), C1.
105. A. H. Cowley, C. S. King, and A. Decken, *Organometallics*, 1995, **14**(1), 20.
106. H. Schumann, T. D. Seuss, O. Just, R. Weimann, H. Hemling, and F. H. Goerlitz, *J. Organomet. Chem.*, 1994, **479**(1–2), 171.
107. M. F. Self, A. T. McPhail, L. J. Jones, III, and R. L. Wells, *Polyhedron*, 1994, **13**(4), 625.
108. M. A. Petrie, K. Ruhlandt-Senge, H. Hope, and P. P. Power, *Bull. Soc. Chim. Fr.*, 1993, **130**(6), 851.
109. H. Schumann, O. Just, T. D. Seuss, F. H. Goerlitz, and R. Weimann, *J. Organomet. Chem.*, 1994, **466**(1–2), 5.
110. G. Mueller and J. Lachmann, *Z. Naturforsch., B: Chem. Sci.*, 1993, **48**(11), 1544.
111. K. M. Simpson, R. W. Gedridge Jr, and K. T. Higa, *J. Organomet. Chem.*, 1993, **456**(1), 31.
112. S. T. Haubrich and P. P. Power, *J. Am. Chem. Soc.*, 1998, **120**(9), 2202.
113. R. L. Wells, A. T. McPhail, and M. F. Self, *Organometallics*, 1993, **12**(8), 3363.
114. D. A. Atwood, V. O. Atwood, A. H. Cowley, H. R. Gobran, R. A. Jones, T. M. Smeal, and C. J. Carrano, *Organometallics*, 1993, **12**(9), 3517.
115. D. A. Atwood, A. H. Cowley, R. A. Jones, and M. A. Mardones, *J. Organomet. Chem.*, 1993, **449**(1–2), C1.
116. S. Vagin, M. Barthel, D. Dini, and M. Hanack, *Inorg. Chem.*, 2003, **42**(8), 2683.
117. O. V. Mal-chugina and P. A. Stuzhin, *Russ. Chem. Bull.*, 2002, **51**(12), 2261.
118. A. C. Jones, S. A. Rushworth, T. Martin, T. J. Whittaker, and R. W. Freer, Metalorganic Compounds, PCT Int. Appl., WO 9607660 A1, 1996.
119. W. Tyrra and M. S. Wickleder, *J. Organomet. Chem.*, 2003, **677**(1–2), 28.
120. E. Iravani and B. Neumueller, *Organometallics*, 2003, **22**(20), 4129.
121. O. T. Beachley, Jr, D. J. MacRae, M. R. Churchill, A. Y. Kovalevsky and E. S. Robirds, *Organometallics*, 2003, **22**(20), 3991.
122. T.-Y. Chou, Y. Chi, S.-F. Huang, C.-S. Liu, A. J. Carty, L. Scoles, and K. A. Udachin, *Inorg. Chem.*, 2003, **42**(19), 6041.
123. J. Lewinski, J. Zachara, K. B. Starowieyski, Z. Ochal, I. Justyniak, T. Kopec, P. Stolarzewicz, and M. Dranka, *Organometallics*, 2003, **22**(18), 3773.
124. F. Thomas, S. Schulz, H. Mansikkamaeki, and M. Nieger, *Organometallics*, 2003, **22**(17), 3471.
125. T. Bauer, S. Schulz, M. Nieger, and U. Kessler, *Organometallics*, 2003, **22**(15), 3134.
126. F. X. Gao, C. J. Zhu, F. Yuan, Y. H. Zhu, and Y. Pan, *Chin. Chem. Lett.*, 2003, **14**(2), 138.
127. R. J. Wright, A. D. Phillips, T. L. Allen, W. H. Fink, and P. P. Power, *J. Am. Chem. Soc.*, 2003, **125**(7), 1694.
128. F. Cordeddu, H.-D. Hausen, and J. Weidlein, *Z. Anorg. Allg. Chem.*, 2002, **628**(3), 529.
129. E. K. Styron, C. H. Lake, D. H. Powell, L. K. Krannich, and C. L. Watkins, *J. Organomet. Chem.*, 2002, **649**(1), 78.
130. Y.-M. Hu, X.-H. Huang, B.-H. Du, X.-R. Wang, and Z.-W. Ye, *Anhui Jidian Xueyuan Xuebao*, 2001, **16**(4), 37.
131. M. J. Plater, A. Jeremiah, and G. Bourhill, *J. Chem. Soc., Perkin Trans. 1*, 2002, **1**, 91.

132. Y. Yuan, Z. Cao, N. Fu, J. Wang, L. Weng, A. Bezerra de Carvalho, and C. Peppe, *J. Organomet. Chem.*, 2001, **637–639**, 631.
133. O. T. Beachley Jr, S. L. Chao, M. R. Churchill, and C. H. Lake, *Organometallics*, 2001, **20**(23), 4896.
134. M. S. Hill, A. R. Hutchison, T. S. Keizer, S. Parkin, M. A. VanAelstyn, and D. A. Atwood, *J. Organomet. Chem.*, 2001, **628**(1), 71.
135. C. Von Hanisch, *Z. Anorg. Allg. Chem.*, 2001, **627**(1), 68.
136. Y.-Z. Shen, H. Gu, Y. Pan, G. Dong, T. Wu, X.-P. Jin, X.-Y. Huang, and H. Hu, *J. Organomet. Chem.*, 2000, **605**(2), 234.
137. S.-J. Kim, N. Yang, D.-H. Kim, S. O. Kang, and J. Ko, *Organometallics*, 2000, **19**(20), 4036.
138. Y.-Z. Shen, Y. Pan, H.-W. Gu, T. Wu, X.-Y. Huang, and H.-W. Hu, *Main Group Met. Chem.*, 2000, **23**(8), 423.
139. A. Schaller, H.-D. Hausen, W. Schwarz, G. Heckmann, and J. Weidlein, *Z. Anorg. Allg. Chem.*, 2000, **626**(5), 1047.
140. M. S. Hill and D. A. Atwood, *Main Group Chem.*, 1998, **2**(3), 191.
141. M. R. Kopp and B. Neumuller, *Z. Anorg. Allg. Chem.*, 1999, **625**(8), 1246.
142. Z.-H. Choi and W. Tyrra, *Z. Anorg. Allg. Chem.*, 1998, **624**(12), 2015.
143. H. J. Breunig, M. Stanciu, R. Roesler, and E. Lork, *Z. Anorg. Allg. Chem.*, 1998, **624**(12), 1965.
144. Q. Zhao, H.-S. Sun, W.-Z. Chen, Y.-J. Liu, and X.-Z. You, *J. Organomet. Chem.*, 1998, **556**(1–2), 159.
145. C. Paek, S. O. Kang, J. Ko, and P. J. Carroll, *Organometallics*, 1997, **16**(21), 4755.
146. O. T. Beachley Jr, J. D. Maloney, M. A. Banks, and R. D. Rogers, *Organometallics*, 1995, **14**(7), 3448.
147. J. A. Burns, M. D. B. Dillingham, J. B. Hill, K. D. Gripper, W. T. Pennington, and G. H. Robinson, *Organometallics*, 1994, **13**(4), 1514.
148. R. Hasselbring, H. W. Roesky, A. Heine, D. Stalke, and G. M. Sheldrick, *Z. Naturforsch., B: Chem. Sci.*, 1994, **49**(1), 43.
149. M. D. B. Dillingham, J. B. Hill, B. Lee, S. J. Schauer, W. T. Pennington, G. H. Robinson, and D. C. Hrncir, *J. Coord. Chem.*, 1993, **28**(3–4), 337.
150. T. Belgardt, H. W. Roesky, M. Noltemeyer, and H. G. Schmidt, *Angew. Chem., Int. Ed. Engl.*, 1993, **32**(7), 1056.
151. J. T. Leman, H. A. Roman, and A. R. Barron, *Organometallics*, 1993, **12**(8), 2986.
152. F. Thomas, S. Schulz, and M. Nieger, *Z. Anorg. Allg. Chem.*, 2002, **628**(1), 235.
153. L. J. Jones III, A. T. McPhail, and R. L. Wells, *Organometallics*, 1994, **13**(9), 3634.
154. K. Merzweiler, L. Brands, and J. Spohn, *Z. Naturforsch., B: Chem. Sci.*, 1993, **48**(10), 1315.
155. R. L. Wells, A. T. McPhail, and M. F. Self, *Organometallics*, 1993, **12**(8), 3363.
156. R. L. Wells, A. T. McPhail, L. J. Jones, and M. F. Self, *Polyhedron*, 1993, **12**(2), 141.
157. F. Thomas, S. Schulz, H. Mansikkamaeki, and M. Nieger, *Angew. Chem., Int. Ed. Engl.*, 2003, **42**(45), 5641.
158. L. J. Jones III, A. T. McPhail, and R. L. Wells, *Organometallics*, 1994, **13**(6), 2504.
159. C. Callaghan, G. K. B. Clentsmith, G. F. N. Cloke, P. B. Hitchcock, J. F. Nixon, and D. M. Vickers, *Organometallics*, 1999, **18**(4), 793.
160. R. L. Wells, R. A. Baldwin, and P. S. White, *Organometallics*, 1995, **14**(4), 2123.
161. R. L. Wells, A. T. McPhail, L. J. Jones, III, and M. F. Self, *J. Organomet. Chem.*, 1993, **449**(1–2), 85.
162. C. J. Carmalt, *Coord. Chem. Rev.*, 2001, **223**, 217.
163. P. P. Power, *J. Chem. Soc. Dalton Trans.*, 1998, 2939.
164. P. J. Brothers and P. P. Power, *Adv. Organomet. Chem.*, 1996, **39**, 1.
165. P. P. Power, *Chem. Rev.*, 1999, **99**(12), 3463.
166. D. L. Reger, *Coord. Chem. Rev.*, 1996, **147**, 571.
167. C. von Haenisch, *Eur. J. Inorg. Chem.*, 2003, **16**, 2955.
168. C. von Haenisch and B. Rolli, *Z. Anorg. Allg. Chem.*, 2002, **628**(11), 2255.
169. C. von Haenisch, *Z. Anorg. Allg. Chem.*, 2001, **627**(1), 68.
170. T. J. Trentler, S. C. Goel, K. M. Hickman, A. M. Viano, M. Y. Chiang, A. M. Beatty, P. C. Gibbons, and W. E. Buhro, *J. Am. Chem. Soc.*, 1997, **119**(9), 2172.
171. T. J. Trentler, K. M. Hickman, S. C. Goel, A. M. Viano, P. C. Gibbons, and W. E. Buhro, *Science*, 1995, **270**(5243), 1791.
172. M. A. Malik, S. W. Haggata, M. Motevalli, and P. O'Brien, *J. Organomet. Chem.*, 1996, **524**(1–2), 95.
173. X.-H. Huang and X.-R. Wang, *Anhui Jidian Xueyuan Xuebao*, 2001, **16**(4), 26.
174. Y.-M. Hu, X.-H. Huang, Z.-W. Ye, X.-R. Wang, J.-S. Gu, and J. Sun, *Chin. J. Chem.*, 2001, **19**(1), 109.
175. J.-H. Park, G. A. Horley, P. O'Brien, A. C. Jones, and M. Motevalli, *J. Mater. Chem.*, 2001, **11**(9), 2346.
176. D. A. Atwood and M. J. Harvey, *Chem. Rev.*, 2001, **101**(1), 37.
177. S. Chitsaz, E. Iravani, and B. Neumuller, *Z. Anorg. Allg. Chem.*, 2002, **628**(11), 2279.
178. D. A. Robson, S. Y. Bylikin, M. Cantuel, N. A. H. Male, L. H. Rees, P. Mountford, and M. Schroder, *J. Chem. Soc. Dalton Trans.*, 2001, 157.
179. M. F. Self, A. T. McPhail, and R. L. Wells, *J. Coord. Chem.*, 1993, **29**(1–2), 27.
180. N. Barreau, S. Marsillac, J. C. Bernede, and A. Barreau, *Appl. Surf. Sci.*, 2000, **161**(1–2), 20.

181. N. Barreau, J. C. Bernede, H. Maliki, S. Marsillac, X. Castel, and J. Pinel, *Solid State Commun.*, 2002, **122**(7–8), 445.

182. S. Spiering, D. Hariskos, M. Powalla, N. Naghavi, and D. Lincot, *Thin Solid Films*, 2003, **431–432**, 359.

183. K. Govender, D. S. Boyle, and P. O'Brien, *J. Mater. Chem.*, 2003, **13**(9), 2242.

184. M. Nanu, J. Schoonman, and A. Goossens, *Adv. Mater.*, 2004, **16**(5), 453.

185. M. Lazell, P. O'Brien, D. J. Otway, and J.-H. ParkHo, *J. Chem. Soc., Dalton Trans.*, 2000, 4479.

186. M. Afzaal, M. A. Malik, and P. O'Brien, *Chem. Commun.*, 2004, 334.

187. M. Afzaal, D. Crouch, P. O'Brien, and J.-H. Park, *J. Mater. Sci.: Mater. Electron.*, 2003, **14**(9), 555.

188. G. A. Horley, M. Chunggaze, P. O'Brien, A. J. P. White, and D. J. Williams, *J. Chem. Soc., Dalton Trans.*, 1998, 4205.

189. S. W. Haggata, M. A. Malik, M. Motevalli, P. O'Brien, and J. C. Knowles, *Chem. Mater.*, 1995, **7**(4), 716.

190. S. Suh and D. M. Hoffman, *Inorg. Chem.*, 1998, **37**, 5823.

191. C. Zhu, F. Yuan, W. Gu, and Y. Pan, *Chem. Commun.*, 2003, **6**, 692.

192. S. Araki, F. Shiraki, T. Tanaka, H. Nakano, K. Subburaj, T. Hirashita, H. Yamamura, and M. Kawai, *Chem. – Eur. J.*, 2001, **7**(13), 2784.

193. S. Araki, T. Tanaka, T. Hirashita, and J. Setsune, *Tetrahedron Lett.*, 2003, **44**(43), 8001.

194. M. Shenglof, D. Gelman, B. Heymer, H. Schumann, G. A. Molander, and J. Blum, *Synthesis*, 2003, **2**, 302.

195. O. T. Beachley Jr, D. J. MacRae, and A. Y. Kovalevsky, *Organometallics*, 2003, **22**(8), 1690.

196. S. Chitsaz and B. Neumuller, *Z. Anorg. Allg. Chem.*, 2001, **627**(11), 2451.

197. E. Hecht, T. Gelbrich, K.-H. Thiele, and J. Sieler, *Main Group Chem.*, 2000, **3**(2), 109.

198. A. Voigt, M. G. Walawalkar, R. Murugavel, H. W. Roesky, E. Parisini, and P. Lubini, *Angew. Chem., Int. Ed. Engl.*, 1997, **36**(20), 2203.

199. E. Iravani, D. Dashti-Mommertz, and B. Neumueller, *Z. Anorg. Allg. Chem.*, 2003, **629**(7–8), 1136.

200. A. Walz, M. Niemeyer, and J. Weidlein, *Z. Anorg. Allg. Chem.*, 1999, **625**(4), 547.

201. M. G. Walawalkar, *Organometallics*, 2003, **22**(4), 879.

202. C. J. Barden, P. Charbonneau, and H. F. Schaefer, III, *Organometallics*, 2002, **21**(17), 3605.

203. R. Anulewicz-Ostrowska, S. Lulinski, and J. Serwatowski, *Inorg. Chem.*, 1999, **38**(17), 3796.

204. W. Wahl, R. Graupner, I. Hahn, and W. Saak, *Z. Anorg. Allg. Chem.*, 1999, **625**(7), 1113.

205. H. Rahbarnoohi, M. Taghiof, M. J. Heeg, D. G. Dick, and J. P. Oliver, *Inorg. Chem.*, 1994, **33**(26), 6307.

206. H. Rahbarnoohi, R. Kumar, M. J. Heeg, and J. P. Oliver, *Organometallics*, 1995, **14**(8), 3869.

207. H. Rahbarnoohi, R. Kumar, M. J. Heeg, and J. P. Oliver, *Organometallics*, 1995, **14**(1), 502.

208. D. E. Hibbs, M. B. Hursthouse, C. Jones, and N. A. Smithies, *Organometallics*, 1998, **17**(14), 3108.

209. C. D. Abernethy, M. L. Cole, and C. Jones, *Organometallics*, 2000, **19**(23), 4852.

210. M. D. Francis, D. E. Hibbs, M. B. Hursthouse, C. Jones, and N. A. Smithies, *J. Chem. Soc., Dalton Trans.*, 1998, 3249.

211. D. E. Hibbs, M. B. Hursthouse, C. Jones, and N. A. Smithies, *Chem. Commun.*, 1998, 869.

212. R. J. Baker, M. L. Cole, C. Jones, and M. F. Mahon, *J. Chem. Soc., Dalton Trans.*, 2002, 1992.

213. C. A. Olazabal, F. P. Gabbai, A. H. Cowley, C. J. Carrano, L. M. Mokry, and M. R. Bond, *Organometallics*, 1994, **13**(2), 421.

214. R. A. Fischer, J. Behm, T. Priermeier, and W. Scherer, *Angew. Chem., Int. Ed. Engl.*, 1993, **32**(5), 746.

215. D. G. Tuck, *Chem. Soc. Rev.*, 1993, **22**(4), 269.

216. K. Soulantica, L. Erades, M. Sauvan, F. Senocq, A. Maisonnat, and B. Chaudret, *Adv. Funct. Mater.*, 2003, **13**(7), 553.

217. K. Soulantica, A. Maisonnat, F. Senocq, M.-C. Fromen, M.-J. Casanove, and B. Chaudret, *Angew. Chem., Int. Ed. Engl.*, 2001, **40**(16), 2984.

218. K. Soulantica, A. Maisonnat, M.-C. Fromen, M.-J. Casanove, P. Lecante, and B. Chaudret, *Angew. Chem., Int. Ed. Engl.*, 2001, **40**(2), 448.

219. Y. Yang and T. H. Chan, *J. Am. Chem. Soc.*, 2000, **122**(2), 402.

220. C. Gemel, T. Steinke, D. Weiss, M. Cokoja, M. Winter, and R. A. Fischer, *Organometallics*, 2003, **22**(13), 2705.

221. T. Steinke, C. Gemel, M. Winter, and R. A. Fischer, *Angew. Chem., Int. Ed. Engl.*, 2002, **41**(24), 4761.

222. D. Weiss, M. Winter, K. Merz, A. Knufer, and R. A. Fischer, *Polyhedron*, 2002, **21**(5–6), 535.

223. W. Uhl and S. Melle, *Z. Anorg. Allg. Chem.*, 2000, **626**(10), 2043.

224. P. Jutzi, B. Neumann, G. Reumann, L. O. Schebaum, and H.-G. Stammler, *Organometallics*, 1999, **18**(13), 2550.

225. R. A. Fischer and J. Weiss, *Angew. Chem., Int. Ed. Engl.*, 1999, **38**(19), 2831.

226. W. Uhl, F. Schmock, and W. Petz, *Z. Naturforsch., B: Chem. Sci.*, 2003, **58**(5), 385.

227. T. Steinke, C. Gemel, M. Cokoja, M. Winter, and R. A. Fischer, *Chem. Commun.*, 2003, 1066.

228. A. J. Downs, H.-J. Himmel, and L. Manceron, *Polyhedron*, 2002, **21**(5–6), 473.

229. H. J. Himmel, A. J. Downs, T. M. Greene, and L. Andrews, *Chem. Commun.*, 1999, 2243.

230. H. J. Himmel, A. J. Downs, T. M. Greene, and L. Andrews, *Organometallics*, 2000, **19**(6), 1060.

231. G. K. B. Clentsmith, G. N. Cloke, M. D. Francis, J. C. Green, P. B. Hitchcock, J. F. Nixon, J. L. Suter, and D. M. Vickers, *J. Chem. Soc., Dalton Trans.*, 2000, **11**, 1715.

232. W. Uhl, R. Graupner, M. Layh, and U. Schuetz, *J. Organomet. Chem.*, 1995, **493**(1–2), C1.

233. R. D. Schluter, A. H. Cowley, D. A. Atwood, R. A. Jones, and J. L. Atwood, *J. Coord. Chem.*, 1993, **30**(1), 25.

234. W. Uhl and S. Melle, *Chem. – Eur. J.*, 2001, **7**(19), 4216.

235. W. Uhl, S. Melle, G. Geiseler, and K. Harms, *Organometallics*, 2001, **20**(15), 3355.

236. W. Uhl, S. Melle, G. Frenking, and M. Hartmann, *Inorg. Chem.*, 2001, **40**(4), 750.

237. W. Uhl, F. Schmock, G. Geiseler, *Z. Anorg. Allg. Chem.*, 2002, **628**(9–10), 1963.

238. R. J. Wright, A. D. Phillips, N. J. Hardman, and P. P. Power, *J. Am. Chem. Soc.*, 2002, **124**(29), 8538.

239. B. E. Eichler, N. J. Hardman, and P. P. Power, *Angew. Chem., Int. Ed. Engl.*, 2000, **39**(2), 383.

240. R. J. Baker, R. D. Farley, C. Jones, M. Kloth, and D. M. Murphy, *Chem. Commun.*, 2002, 1196.

241. P. J. Brothers, K. Huebler, U. Huebler, B. C. Noll, M. M. Olmstead, and P. P. Power, *Angew. Chem., Int. Ed. Engl.*, 1996, **35**(20), 2355.

242. R. D. Schluter, A. H. Cowley, D. A. Atwood, R. A. Jones, M. R. Bond, and C. J. Carrano, *J. Am. Chem. Soc.*, 1993, **115**(5), 2070.

243. W. Uhl and T. Spies, *Z. Anorg. Allg. Chem.*, 2000, **626**(5), 1059.

244. F. Gahlmann and B. Neumueller, *Z. Anorg. Allg. Chem.*, 1994, **620**(5), 847.

245. B. Neumueller and F. Gahlmann, *Z. Anorg. Allg. Chem.*, 1993, **619**(11), 1897.

246. A. H. Cowley, C. L. B. Macdonald, J. S. Silverman, J. D. Gorden, and A. Voigt, *Chem. Commun.*, 2001, **2**, 175.

247. J. N. Jones, C. L. B. Macdonald, J. D. Gorden, and A. H. Cowley, *J. Organomet. Chem.*, 2003, **666**(1–2), 3.

248. B. Werner, T. Kraeuter, and B. Neumueller, *Inorg. Chem.*, 1996, **35**(10), 2977.

249. B. Neumueller and F. Gahlmann, *Z. Anorg. Allg. Chem.*, 1993, **619**(4), 718.

Cluster Compounds: Inorganometallic Compounds Containing Transition Metal & Main Group Elements

Professor Thomas P. Fehlner
University of Notre Dame, Notre Dame, IN, USA

1 Introduction 1
2 Heteronuclear Cluster Bonding 1
3 Transition Metal versus Main Group Elements in a Cluster Environment 8
4 Cluster Composition and Structure Types 12
5 Cluster Reactivity 13
6 Related Articles 19
7 References 19

Glossary

Electron precise: refers to an atom or fragment that possesses the same number of valence functions and valence electrons
Exo- and endo-: define cluster regions lying outside and inside respectively, the sphere defined by the cluster core atoms
Orbitally rich: refers to an atom or fragment that possesses more valence functions than valence electrons
't_{2g}' levels: three metal-based d-functions in a transition metal fragment that are often considered to be nonbonding with respect to a cluster network

Abbreviations

$Cp = \eta^5\text{-}C_5H_5$; $Cp^* = \eta^5\text{-}C_5Me_5$; triphos = $MeC(CH_2PPh_2)_2$; etriphos = $MeC(CH_2PEt_2)_2$.

1 INTRODUCTION

Inorganic chemistry can be usefully approached from a number of points of view. One can take an element orientation, for example, boron chemistry;[1] a phase orientation, for example, solid-state chemistry;[2] a function orientation, for example, bioinorganic chemistry;[3] a technique orientation, for example, photochemistry;[4] a mechanistic orientation, for example, electron transfer reactions;[5] a bond-type orientation, for example, quadruple bond chemistry;[6] or even a practical orientation, for example, materials chemistry.[7] All these views of inorganic chemistry are interwoven in a number of ways and are far from mutually exclusive. In the case of this chapter, there is both an element orientation (transition metal and main group elements) and a bonding orientation (clusters containing bonding between transition metal and main group elements).

The rationale for this choice is straightforward. The development of organometallic chemistry, which is essentially the study of the chemistry of the metal–carbon bond, into a full discipline of chemistry is well documented. A substantial subsection of organometallic chemistry is cluster chemistry (*see* ***Polynuclear Organometallic Cluster Complexes***). Carbon, however, is only one of the p-block elements that form covalent bonds to transition metals, and this chapter is concerned with a substantial part of the 'otherside' of organometallic chemistry. This chemistry associated with the transition metal–main group element bond (excluding carbon) has been called *Inorganometallic Chemistry*[8] in order to emphasize similarities to organometallic chemistry without neglecting the differences. Herein, we restrict ourselves to that part of inorganometallic chemistry found in clusters – three-dimensional element catenation. The intercomparison of this chemistry with the analogous organometallic chemistry provides a better understanding of both systems.

This chapter is divided into two parts that are complementary but sufficiently self-contained to be consulted separately if desired. First, in Sections 2 and 3, the essential aspects of cluster structure and bonding using inorganometallic examples are presented and illustrated with real clusters. This primarily serves to outline the possibilities of an area that is rapidly developing. The second part (Sections 4 and 5) contains a more complete description of the structural and reaction chemistry of selected cluster types. Emphasis is placed on the possibilities generated by element variation within a structure type. Sufficient information now exists to show that this not only permits rational variation of structure but also provides access to reactivity types not seen in the homonuclear cluster systems. The goal is to illustrate the possibilities and there is no attempt to be complete either globally or specifically. This is an introduction to a developing area and references to more general sources of information will be found at appropriate points.

2 HETERONUCLEAR CLUSTER BONDING

Mixed transition metal–main group element clusters are ultimately related to either homonuclear metal or main group element clusters.[9] Although there are similarities between the bonding within these two limiting types of clusters, there are also significant differences. It is these differences in the mixed systems, which can give rise to major changes in both structural aspects as well as properties. In a situation in which a main group fragment cannot mimic a transition metal fragment or, conversely, where a transition metal fragment cannot mimic a main group fragment, what are the consequences in structure and reactivity? Before this question can be sensibly addressed, it is necessary to have a clear understanding of cluster bonding (*see* ***Electronic Structure of Clusters***) as well as the ways in which transition metal and main group fragments combine to generate cluster systems.

2.1 Geometric Considerations

Homonuclear cluster formation, a form of catenation, reflects intrinsic properties of the fragments that make up the compound (*see* ***Boron Hydrides*** and ***Boron: Polyhedral Carboranes***). In a 'leggo' or 'tinkertoy' style approach, it is easily seen that chains and rings can form from two-connect units, whereas clusters can only form from units that can make three or more connections. Thus, a simple geometric definition of a cluster is a three-dimensional array of units in which each is bonded to three or more nearest neighbors. This is a more logical, albeit more limiting, definition than is sometimes used, that is, trinuclear metal systems have been described as clusters, whereas here we consider them as three-member rings.[10]

2.2 Electronic Considerations

Geometric and electronic structures are inseparable. The heavy, slow nuclei are easier to deal with, and the first source of information on the distribution of electrons on a nuclear framework is the lowest energy geometry of this framework. With the advent of routine single crystal X-ray structure determinations, measured geometric parameters serve as a rich source of information on cluster bonding – an elementary description of electronic structure that partitions electron density on a nuclear framework to account for the stability of a set of atoms in the observed geometry. Rationalization of observed cluster geometry as a function of composition leads to a bonding model, which, in turn, is used to make predictions, that is, an experimental composition permits a limited set of structures to be postulated, which can then be tested against spectroscopic observations. Models used range from the qualitative (usually simple and often of some generality), for example, electron counting, to the quantitative (usually complex and more specific), for example, quantum chemical calculations. In an impressive advance, the latter approach permits the definition of geometries by the comparison of calculated NMR shifts with observed shifts;[11,12] thus, for compounds not amenable to X-ray determination, for example, intermediates in reactions, good structures are determined and structural controversies in the literature can be resolved. Presently, this technique is restricted to main group cages; however, when the capability to calculate systems with multiple metal atoms of similar accuracy becomes generally available, fruitful application to metal cluster systems is anticipated.

2.2.1 Electron-precise Clusters

Two limiting types of cluster bonding can be distinguished and are presented. In electron-precise clusters, each edge of the polyhedron-defining cluster geometry corresponds to a two-center two-electron bond and the 18- or 8-electron rule (*see* ***Electronic Structure of Clusters*** and ***Electronic Structure of Organometallic Compounds***) is often satisfied for the transition metal and main group atoms, respectively.[13] The shapes exhibited are constructed with three-connect vertices. For example, P_4 (**1**) and $Co_4(CO)_{12}$ (**2**) are examples of main group and transition metal clusters of this type. $Co_3(CO)_9P$ (**3**) is an inorganometallic example in which both geometry (tetrahedron) and bonding structure are analogous to those in the homonuclear example. For (**3**), the reader can easily verify that the 8-electron rule for the main group center and the 18-electron rule for the transition metal centers are both satisfied. Although the bonding may be analogous (two-center two-electron bond on each edge of the tetrahedron), compound properties depend on more than the type of bonding within the cluster core – the external ligand bonds as well as the high-lying partially filled d orbitals on the metal centers play a significant role.

Note that for clarity as well as emphasis, only the cluster geometry and cluster core composition are shown in the structural drawings. The ligands, if any, associated with the transition metal and main group atoms should be clear from the molecular formula for any given compound. The structural abbreviation can be seen in the comparison of the full structural drawing given for (**3**) versus the shorthand one. The reader should note that these ancillary ligands do affect cluster properties via the bonding properties of the main group or metal fragment. On the other hand, endo-cluster hydrogens and interstitial atoms (see below) are shown in the drawings,

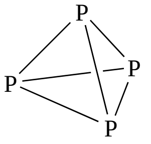

(**1**)

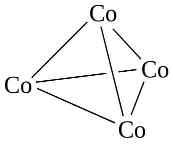

(**2**)

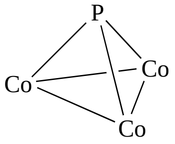

(**3**)

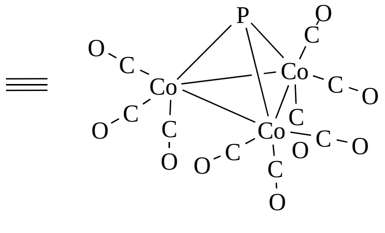

as they are considered essential parts of the cluster network bonding.

Electron-precise cluster systems can be seen to be a more complex version (three-connect units) of chains (one-connect units) and rings (two-connect units), leading up to an extended solid (four-connect units, e.g. the diamond structure). This is most easily appreciated for homonuclear examples, for example, (**1**) and (**2**). For the mixed systems like (**3**), two distinct descriptions are possible – as a 4-atom cluster or as a trinuclear metal complex with a μ_3-P cap. In many cases, the difference is of little consequence; however, in others, proper choice of description can lead to analyses of significant conceptual value.

The $L_{4n}M_4E_4$, M = transition metal, E = p-block element, cluster systems (**4**) provide an example. The elegant experimental work of Dahl and coworkers generated M_4E_4 clusters in which the M_4 unit changed smoothly from a fully bonded tetrahedron with capping E fragments to a fully nonbonding tetrahedron in which the M and E fragments occupy nonadjacent vertices of a cube.**14** Dahl described the bonding and the related spin multiplicities using a molecular orbital model based on fragmenting a given cubane cluster into a M_4E_4 unit to which the external ligands are then appended at the metal sites (*see* ***Paramagnetic Organometallic Complexes***). Harris later showed that an equivalent description is one in which four E_3 ML_n fragments of characteristic coordination geometry condense into $L_{4n}M_4E_4$ by elimination of 8 E moieties.**15** Although equivalent, the latter description has the added conceptual benefit that the basics of the electronic structure follows easily from that of mononuclear Werner complexes, a topic of undergraduate chemistry. (*see* ***Coordination & Organometallic Chemistry: Principles***) A transparent 'back of the envelope' analysis connects Werner models to cubane structure, readily suggesting new variations for synthesis.

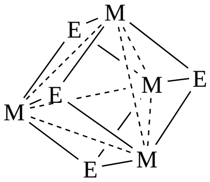

(**4**)

A valuable corollary results from the Harris treatment. Although the cluster bonding is electron precise (two-center two-electron bonds), the electronic structure possesses intrinsic complexity due to the metal centers that constitute part of the cluster framework fragments. Werner complexes need not obey the 18-electron rule; thus, these clusters need not do so either, thereby qualitatively accounting for their interesting metal bond orders and paramagnetism. This example again emphasizes the fact that bridging ligands (E) can be considered as ligands or cluster fragments. In Dahl's picture, they constitute part of the cubane-like cluster even for the fully bonded tetrahedron, whereas in Harris's picture, the focus is exclusively on the metal atoms. The same ambiguity arises for an intrinsically different type of cluster described in the following section.

2.2.2 *Orbitally Rich Clusters*

In the second type of cluster, there are insufficient skeletal bonding electrons (electrons formally assigned to cluster bonding, e.g. after accounting for lone pairs, electrons involved in bonding terminal H atoms or other ligands external to the cluster, the electrons that remain are assigned to cluster bonding) to allow two-center two-electron bonds on all of the edges of the cluster polyhedron. Consequently, the 8- or 18-electron rules are not obeyed in any simple fashion, and localized bonding models are inadequate. Attempts to use them in the past resulted in such bizarre structures (as seen with hindsight) such as 'no-bond' resonance structures. Multicenter bonding, for example, three-center two-electron bonds, of some type is required (*see* ***Molecular Orbital Theory***).

The shapes adopted possess at least one vertex of connectivity four. For example, 1,2-$C_2B_4H_6$ (**5**), $[Ru_6(CO)_{18}]^{2-}$ (**6**), and $C(Me)CHBHFe_3(CO)_9$ (**7**), all have octahedral structures with vertices of connectivity four and 12 equivalent edges – if one is bonding they all are. After localized exo-cluster bonding and the six electrons associated with the nonbonding 't_{2g}' orbitals on the metal centers are accounted for, only seven pairs remain to be distributed between the 12 bonding edges, that is, (**5**) has 26 cluster valence electrons 12 of which are associated with exo-cluster bonding to the hydrogen atoms, leaving 14 for cluster bonding; (**6**) has 86 cluster valence electrons (each CO ligand is counted as 2) 72 of which are associated with exo-cluster bonding or nonbonding electrons at the metal center (36 for 18 CO's, 36 for 6 Fe's), leaving 14 for cluster bonding; whereas (**7**) has 56 cluster valence electrons 42 of which are associated with exo-cluster bonding or nonbonding electrons at the metal centers (18 for 9 CO's,

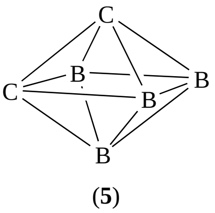

(**5**)

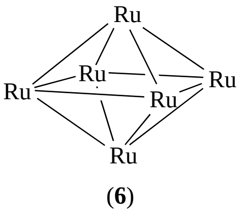

(**6**)

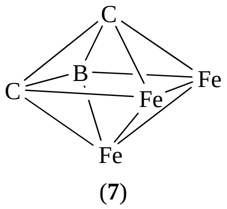

(**7**)

18 for 3 Fe's, 1 for Me, 2 for terminal H, 2 for cluster C atoms, and 1 for cluster B atom), leaving 14 for cluster bonding.

Note that for each metal vertex replaced by a main group atom, the total number of cluster valence electrons decreases by 10. In this counting scheme (Mingos),[13,16,17] the valence electron count associated with a given shape depends on the main group/transition metal numbers, whereas the number of electrons associated with cluster bonding (Wade)[18–20] remains the same. These counting methodologies are to orbitally rich clusters as the 8-, 18-electron rules are to chains, rings, and electron-precise clusters. As it connects the composition to structure in a simple way, the method can both rationalize known compounds and predict cluster shape. The approach is formalized in the empirical skeletal electron counting rules of Wade and Mingos (*see* ***Electronic Structure of Clusters***). A theoretical derivation of these rules for spherical clusters of p-block elements has been presented by Stone.[21]

These counting rules follow from a single essential hypothesis that is correct for a spherical cluster. For a closed deltahedral structure with n vertices, the number of skeletal bonding electron pairs (SEP) associated with cluster is $n + 1$. Thus, clusters (**5**)– (**7**) have closed (all vertices occupied) 6-vertex deltahedral structures (often called closo) with seven sep associated with delocalized cluster-bonding orbitals (see below for further examples). An important caveat is that, contrary to the σ/π separation employed in organic aromatic systems, the separation of cluster-bonding orbitals from the rest is never one that is derived from the symmetry of the cluster. This is true even for the high-symmetry octahedral $[B_6H_6]^{2-}$, where mixing of exo-B–H bonding with endo-B–B bonding orbitals of the same point group symmetry is large.

2.2.3 Cluster Reduction

For either cluster type, the addition of electrons, either by ligand addition to the cluster or by a change in cluster composition, changes the cluster valence electron count and sep. On the basis of the electron counting rules, a change in shape is required. The electron-precise tetrahedral $Fe_2(CO)_6S_2$ (**8**), with six pairs for the six cluster edges, exhibits an opened 'butterfly' shape when it is reduced to $[Fe_2(CO)_6S_2]^{2-}$ (**9**) with seven pairs.[22] The seventh pair enters a S–S antibonding orbital and the edge bond between the S atoms is ruptured. On the other hand, addition of a pair of electrons to clusters (**5**)– (**7**) yields eight sep clusters and a pentagonal bipyramidal shape (the geometry is based on a closed 7-vertex deltahedron). As there are only six cluster fragments, one vertex must remain empty. Thus, for example, *nido* 2,3-$C_2B_4H_8$ (**10**) exhibits a pentagonal pyramidal shape. Usually, it is assumed that the vertex of highest connectivity is removed in forming a nido structure from its closo parent. However, recently, a pair of noninterconverting metallacarboranes isomers, which differ only in the vertex removed from the parent pentagonal bipyramid, have been isolated from two different routes.[23] This suggests that the balance in energies between the two different shapes is less than that previously considered, at least for clusters containing transition metals.

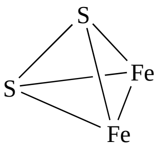

(**8**)

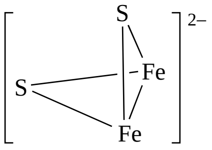

(**9**)

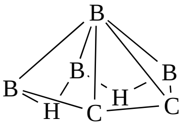

(**10**)

Alternatively, (**10**) formally arises by the addition of 2H to octahedral (**5**), thereby causing it to open. Continued cluster reduction will result in the generation of rings or chains. It should be clear that the overall process is conceptually more difficult to represent than that for the electron-precise cluster. In both electron-precise and orbitally rich clusters, the average connectivity of the cluster decreases on sep increase. There is a difference in that in the latter more than a single bonding edge is ruptured, for example, in going from an octahedron to a pentagonal pyramid, the number of bonded edges goes from 12 to 10. The principles involved have been discussed by Mingos in the context of cluster rearrangements, which require cluster opening in the transition state or high energy intermediate.[13] The barrier for positional isomerization depends on cluster shape, which implies significant differences in the rigidity of the various cluster shapes. With metal clusters, a complex distortion of cluster geometry is a possible alternative to edge bond rupture.[24]

It is worthwhile pointing out that the electron counting rules can lead to apparent ambiguities. Thus, closed (**8**) can be viewed as a nido-cluster (six cluster pairs with a structure based on a trigonal bipyramid with an axial vertex unoccupied) and (**9**) can be viewed as an arachno cluster (seven cluster pairs with a structure based on an octahedron, with two adjacent vertices unoccupied). Little profit is gained in debating which view is 'right,' and most ambiguities of this type cause little problem. Finally, clusters without external ligands,[25] as well as clusters formed from elements with fewer than four valence functions,[26] present interesting variations not discussed here.

2.2.4 Role of Hydrogen Ligands

Two types of hydrogen atoms can be distinguished in clusters. Terminal hydrogens (*see* ***Hydride Complexes of the Transition Metals***) are considered external to the cluster bonding, whereas hydrogens that lie on, or within, the surface defined by the cluster core atoms, that is, bridging hydrogens, are considered to contribute their electrons to cluster bonding. On the other hand, the hydrogen positions are not counted as cluster vertices. This holds true for transition metal, main group, and mixed element clusters. For example, like (**1**)– (**3**), both $Co_3(CO)_9GeR$ (**11**) and $HFe_3(CO)_9(\mu\text{-}H)_3BH$ (**12**) have six electron pairs associated with cluster bonding.

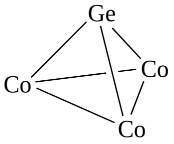

(**11**)

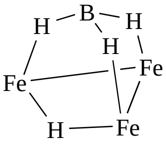

(**12**)

2.2.5 *Role of Interstitial Atoms*

There is a related complicating factor found only to date in transition metal cluster systems. Because of the larger size of transition metal clusters, a main group or transition metal atom may be found within the interstitial space of the cluster.[27] These interstitial atoms are considered to contribute all their valence electrons to cluster bonding but, like bridging hydrogen atoms, they are not considered as occupying a cluster vertex. For example, as with (**5**) and (**6**), $[Co_6(CO)_{13}N]^-$ (**13**) and $HRu_6(CO)_{17}B$ (**14**) are considered to be 6-vertex closed clusters with seven pairs of electrons associated with cluster bonding with the N and B atoms contributing five and three electrons respectively.

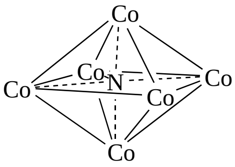

(**13**)

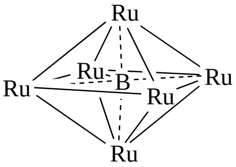

(**14**)

2.3 Role of Element Properties

Superimposed on these fundamental cluster-bonding principles are the valence properties of the main group and transition metal elements and fragments that make up the compound. Just as the polarity changes for the 10 valence electron diatomics, N_2, CO, and BF, so too does the charge distribution within a cluster framework change with composition as well as shape.

2.3.1 *Main Group Elements*

First, the number of valence functions (or frontier orbitals) and valence electrons (frontier orbital occupancy) determines the tendency toward cluster bonding. It is instructive to recall that the structural motif in elemental boron is the icosahedron with six-connected boron atoms (*see* ***Borides: Solid-state Chemistry***); it is the tetrahedral carbon atom in the diamond form of elemental carbon with four-connected carbon atoms; and it is three-connected phosphorus atoms in the sheets of elemental black phosphorus (*see* ***Phosphides: Solid-state Chemistry***). Boron has more valence orbitals than valence electrons, naturally leading to orbitally rich cluster formation; for example, BH has three orbitals and two electrons and forms the very stable $[B_{12}H_{12}]^{2-}$ ion with an icosahedral structure and 13 skeletal bonding pairs. Carbon has the same number of valence orbitals as valence electrons, leading naturally to three-connect units that form electron-precise clusters, for example, CR is found in tetrahedrane, R_4C_4. With a lone pair, a phosphorus atom also constitutes a three-connect unit and P_4 (**1**) is analogous to tetrahedrane.

This does not mean that CH or P units are not found in orbitally rich clusters or that boron is not found in electron-precise clusters, for example, (**7**) and (**12**). Electron-precise clusters will tend to form from three orbital (three-connect) atoms or fragments when the average number of electrons per fragment is three. Likewise, there will be a tendency for orbitally rich clusters when the average number of electron pairs per fragment approaches $(n+1)/n$, where n is the number of fragments in the cluster. An example is instructive. (**15**), an isomer of (**5**), possesses 7 cluster-bonding pairs (exactly the $(n+1)/n$ limit) for the octahedral shape it exhibits. The only reasonable description of the cluster bonding is via bonding orbitals delocalized over all of the six cluster atoms.

On the other hand, B_5H_9 (**16**) also has 7 skeletal bonding electron pairs and, in accord with the electron counting rules, the cluster geometry is based on an octahedron but with one vertex unoccupied. Consequently, the average number of electrons per vertex is higher and B_5H_9 can be viewed as a hybrid of the two cluster types, that is, one can consider B_5H_9 as derived from $[B_5H_5]^{4-}$ (**17**) and use four of the skeletal pairs to bond the four basal edges of the square pyramid with two-center two-electron bonds. This leaves three pairs in delocalized orbitals bonding the apical vertex to the square base. Likewise, B_4H_{10} can be derived from $[B_4H_4]^{6-}$. Once the six BH bonds are taken care of, five pairs remain to bond the five edges of the butterfly structure generated by removing two adjacent vertices from the parent octahedron. The more electrons added to an orbitally rich cluster, the closer the bonding approaches that of electron-precise systems.[28]

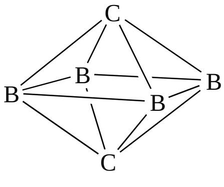

(**15**)

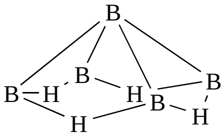

(**16**)

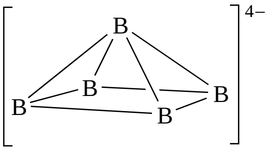

(**17**)

2.3.2 Transition Metal Elements

The transition metal elements also have partially filled valence levels but now fragments formed from a metal atom and one or more ligands need be considered. The isolobal principle[29] provides a transparent method for applying the ideas developed from the p-block elements above to fragments derived from d-block elements. Thus, $Mn(CO)_5$ (17 electron), $Fe(CO)_4$ (16 electron), and $Co(CO)_3$ (15 electron) fragments are isolobal with CH_3 (7 electron), CH_2 (6 electron), and CH (5 electron) fragments respectively.[30] It follows, then, that metal fragments with three frontier functions and three electrons will have a tendency to form electron-precise clusters, for example, four $Co(CO)_3$ fragments yield (**2**). Likewise, fragments with three orbitals and less than three electrons will tend to form orbitally rich clusters, for example, $Fe(CO)_3$ and CpCo are isolobal with BH (Figure 1). Thus, with six $Ru(CO)_3$ fragments and a charge of 2^-, (**5**) is analogous to $[B_6H_6]^{2-}$.

Recall that bridging hydrogens and interstitial atoms provide a means of increasing the average number of electrons per vertex. Thus, $H_4Fe_4(CO)_{12}$ (**18**) is analogous to (**2**). Note that in contrast to hydrogen, a CO ligand can be bridging or terminal with no consequence in terms of counting cluster electrons or vertices.

Similar to the main group clusters, the addition of electrons to metal clusters causes a transition from orbitally rich cluster bonding toward electron-precise bonding. $[Co_6(CO)_{15}N]-$ (**19**) has two more skeletal electron pairs than (**6**) and the structure adopted has a three-connect trigonal prismatic geometry rather than four-connect octahedral geometry. Although the number of skeletal pairs matches the number of edges of the trigonal prismatic geometry, it would be misleading to consider this completely as an electron-precise cluster as the phosphorus atom is certainly strongly involved in the cluster bonding even though it is not considered a cluster vertex.

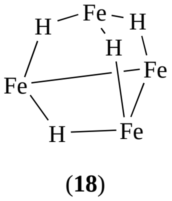
(**18**)

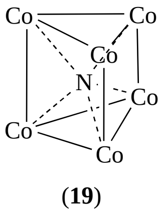
(**19**)

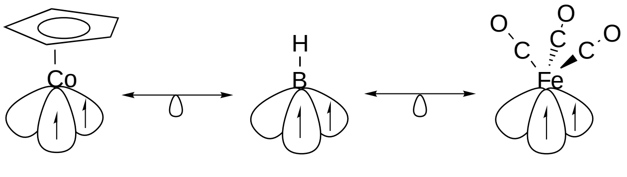

Figure 1 Schematic drawings indicating the isolobal relationship between η^5-C_5H_5Co, BH, and $Fe(CO)_3$ fragments

2.4 Variation in External Ligands

Valence properties of the transition metal or main group element fragments can be changed by variation of element identity and by changing the external ligands.

2.4.1 Main Group Elements

Variation of the external ligand on the main group element changes the number of electrons contributed by the fragment to cluster bonding. For example, contrast BH in $HFe_3(CO)_9(\mu$-$H)_3BH$ (**12**) with BCO in $H_3Os_3(CO)_9BCO$ (**20**) and P in $Co_3(CO)_9P$ (**3**) with PPh in $H_2Ru_3(CO)_9PPh$ (**21**). Replacing the terminal H on B with CO makes BCO a three-electron fragment (as opposed to two for BH), whereas adding a one-electron ligand to P makes PR a four-electron fragment (as opposed to three for P).

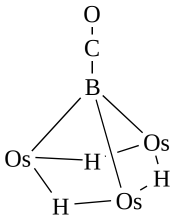
(**20**)

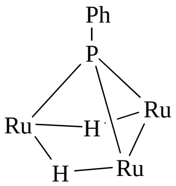
(**21**)

2.4.2 Transition Metal Elements

External ligand variation is more commonly observed for the transition metal fragments. $HRu_6(CO)_{17}B$ (**14**) might be considered to be made up of five $Ru(CO)_3$ fragments (10 electrons) and one $Ru(CO)_2$ fragment (zero electrons) with the interstitial boron and bridging hydrogen providing the four additional electrons needed. Changing from a $Fe(CO)_3$ to a CpFe fragment, for example, also reduces the number of electrons contributed to cluster bonding. In this case, it follows from Figure 1 that the latter fragment will be a three-orbital one-electron fragment.

Group 18 and 19 metals are often found in clusters as carbonyl and Cp derivatives. With these π-acceptor ligands, the 't_{2g}' levels in the fragment are sufficiently stabilized such that they are effectively nonbonding with respect to the cluster. An interesting development in organometallic cluster chemistry is the observation that π-donor ligands such as alkoxy ligands change the role of the 't_{2g}' levels.[31] The p-donor ligands destabilize the 't_{2g}' levels and push them into the valence region. Thus, the $W(OR)_3$ fragment in $W_3(OR)_9CR$ (**22**) has three valence 't_{2g}' orbitals containing three electrons, and is considered to be analogous to the $Co(CO)_3$ fragment in $Co_3(CO)_9CR$ (**23**). $Co(CO)_3$ and $W(OR)_3$ can be considered to be isolobal (surrogates for CH) even though they are not isoelectronic.

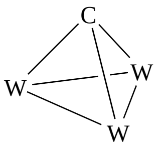

(**22**)

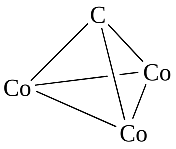

(**23**)

The group 10 metals also provide an interesting complication. The increasing gap between the nd band and $(n + 1)$p band that gives rise to the observation of stable 16 electron complexes leads, for example, to $Pt(PPh_3)_2$ fragments that can behave in an isolobal manner to CH_2, BH, or $[CH]^-$.[13] Clearly, ligand variation on the transition metal in terms of number and geometric arrangement, as well as the transition metal itself, permits a metal fragment to mimic a range of main group fragments.

2.5 Structural Role of Bridging Hydrogens

As noted several times, bridging hydrogens are found in all types of clusters. Thus far, they have been considered as of no consequence structurally as far as the cluster bonding is concerned. The experimental evidence suggests that this is an oversimplified view.

2.5.1 Main Group Elements

There is evidence from quantum chemical calculations that bridging hydrogens play a structural role in main group clusters.[32] For example, if $[B_4H_4]^{6-}$ is considered as a 7 skeletal pair arachno cluster with a structure based on an octahedron with two unoccupied vertices, then the electron counting rules allow two isomeric forms, (**24**) and (**25**). Calculations suggest that the planar isomer is the lower energy form, and that the observation that B_4H_{10} adopts the second less stable isomeric form results from a real structural role for the bridging hydrogens.[33] Note also that $[B_6H_6]^{2-}$ decomposes on protonation and calculations suggest that protonation leads to destabilization of the octahedral cluster bonding network.[34] Only face bridging hydrogens are possible on an octahedron and these have only been observed in metal or metallaborane cluster systems. In the latter case, only triangular faces containing a metal atom or atoms are found to be capped.

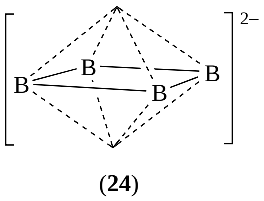

(**24**)

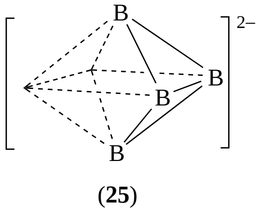

(**25**)

2.5.2 Transition Metal Elements

In transition metal systems, bridging hydrogens play an experimentally defined structural role. Two factors permit this behavior. First, the hydrogen ligand occupies space. Second, the metal–metal interactions are weaker than the metal–ligand interactions. Thus, protonation of an anion can lead to observable cluster structure rearrangement as illustrated by (**26**) and (**27**).[35] Capped structures have the same skeletal count as the parent cluster (*see* ***Electronic Structure of Clusters***) and, consequently, the two structures are cluster geometric isomers. Such capped structures do not appear viable for purely main group clusters but they are observed in the mixed main group–transition metal systems, for example, $Co_3Cp_3B_4H_4$ (**28**).

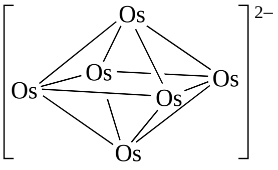

(**26**)

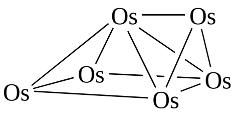

(**27**)

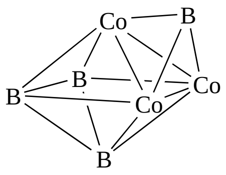

(**28**)

2.6 Fused Clusters

Larger clusters can be formed from two or more cluster fragments by sharing one or more cluster atoms in common. For example, $Co_4(CO)_{11}Bi_2$ (**29**) can be considered as two Co_4Bi_2 tetrahedra sharing a common Bi–Bi edge. Likewise, the condensation of $[Co_6(CO)_{13}N]^-$ (**19**) to give $[Co_{14}(CO)_{26}N_3]^-$ (**30**) can be viewed as the fusion of three trigonal prismatic Co_6N clusters.

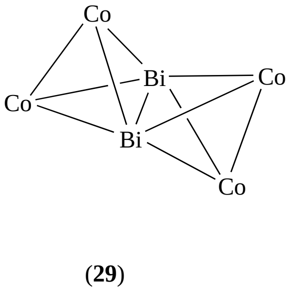

(**29**)

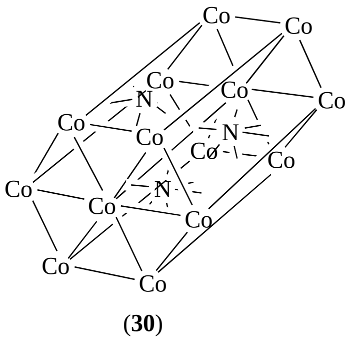

(**30**)

A generalization of the electron counting rules for clusters to accommodate various types of fused cluster structures with common cluster vertices has appeared.[36] The wide variety of examples already known illustrates a richness of cluster structure greatly exceeding that of the single cluster (*see* ***Electronic Structure of Clusters***). Indeed, these ideas provide new insight into the structures of elemental boron in which complex fused cages are observed, and one can see that cluster versions of, for example, metal chains (**31**), are possible.[37]

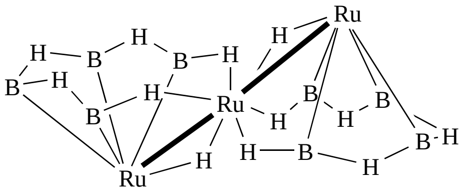

(**31**)

2.7 Hydrogen Analogs

Metal hydrides can often be replaced with the $AuPR_3$ fragment and the $[AuPR_3]^+$ fragment is considered isolobal with a proton (*see* ***Gold: Organometallic Chemistry***). However, the gold fragments need not occupy the same positions as the protons they replace and, depending on the phosphine used, are subject to disproportionation reactions. Pure gold clusters have a characteristic structural chemistry that obeys modified cluster counting rules as the orbital contribution of such a fragment to cluster bonding is no longer three.[13]

3 TRANSITION METAL VERSUS MAIN GROUP ELEMENTS IN A CLUSTER ENVIRONMENT

The significant differences in the cluster bonding tendencies of main group and transition metal elements give rise to distinct behaviors that compete in the mixed clusters.

3.1 Differences in Coordination Number

Geometrically, the main group element tends to retain a tetrahedral nearest neighbor environment, whereas the transition metal element tends to retain an octahedral environment. As a consequence, transition metal clusters with more than six metal atoms have a tendency toward ligand loss, leading to the formation of condensed clusters (multiple interstitial metal atoms). This leads eventually to close-packed structures that mimic bulk metal structures (*see* ***Polynuclear Organometallic Cluster Complexes***). On the contrary, the premier cluster-forming element, boron, tends to form single cages without interstitial atoms. In the absence of metal atoms, 12 was the limit of single-cluster nuclearity until recently, even though theoretical evidence of stability beyond 12 vertices has been put forward more than once in the past. A breakthrough this year resulted in the isolation of a single-cage 13-vertex carborane, which resulted from a clever synthetic strategy.[38] Although rare, clusters containing many transition metals can be found in an icosahedral geometry. With the addition of an interstitial atom or main group fragment of appropriate size, icosahedral transition metal clusters have been characterized, for example, $[Ni_{12}(CO)_{22}Ge]^{2-}$ (**32**) and $[Ni_{10}(CO)_{18}(AsR)_2]^{2-}$ (**33**) with 13 skeletal pairs each as expected.

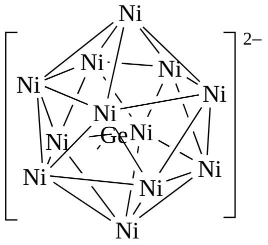

(**32**)

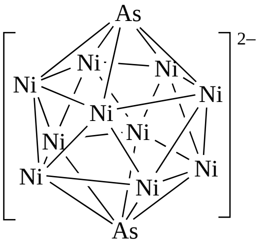

(**33**)

3.2 Steric Interactions

Because metal fragments in general have more than one ancillary ligand, the space demanded by the exo-cluster ligands limits the scope of clusters that are viable. For example, the icosahedral metal clusters just discussed involve a late transition metal that minimizes the number of CO ligands and, hence, intramolecular steric interactions. Even though the $Ni(CO)_2$ and $Fe(CO)_3$ fragments are equivalent in terms of electrons contributed to cluster bonding, it is unlikely that an icosahedral $[Fe_{12}(CO)_{34}Ge]^{2-}$ cluster could be prepared. The concept of a cluster fragment cone angle is useful in estimating possible cluster geometries for a given metal fragment.[39] As the main group fragment usually has a single small ligand or no ligand, steric considerations are a less-important consideration. On the other hand, bulky ligands are important in some instances such as for the isolation of icosahedral $[Al_{12}(^{t}Bu)_{12}]^{2-}$ (*see* ***Aluminum: Inorganic Chemistry***; ***Aluminum: Organometallic Chemistry***).[40]

3.3 Relative Electronegativities

An important factor in the bonding and reactivity of clusters, as well as all chemical entities, is the effective electronegativity of the atoms or fragments that make up the cluster.[41] In terms of assembling a cluster from a set of fragments, electronegativity differences affect the mutual compatibility of the frontier orbitals of fragment types, that is, if the fragment orbitals are poorly matched in terms of energy or spatial extent, any covalent interaction will be weakened and the polarity of the cluster will be increased. This is important in considerations of reactivity as well as in the spatial distribution of cluster bridging hydrogens.[42] Note that it is fragment electronegativity that is important and that the ligands on the main group or transition element fragment play a large, albeit difficult to measure, role in determining the value of this parameter.

3.4 Variation of the Transition Metal/Main Group Element Ratio in a Cluster Environment

Consider two examples in which there is a continuous variation in E/M (E, M = main group and transition metal element, respectively) ratio. The first is a series of clusters beginning with a main group element cluster and proceeding via the mixed element clusters to a transition metal cluster. A four-atom cluster system, the E_nM_{4-n} cluster is chosen because examples of all of the possible members of the series for E = B and M = Fe are known.[43] The clusters and their structures are schematically illustrated in Figure 2. For $n = 4$ and 3, clusters with 7 skeletal pairs have been characterized, whereas for $n = 2$–0, clusters with 6 skeletal pairs are known. Examples of clusters with 6 skeletal pairs for the former or 7 skeletal pairs for the latter are not presently known. However, there is evidence for B_4H_8 as a transient intermediate, and the other compounds may well be identified once suitable routes to their formation are discovered. Even so, the change in cluster behavior in going from one to two metals in the cluster is real and illustrates competition between the different structural tendencies of main group and transition metal fragments. Thus, hybrid behavior even in gross structure should not be unexpected for mixed transition metal–main group element clusters.

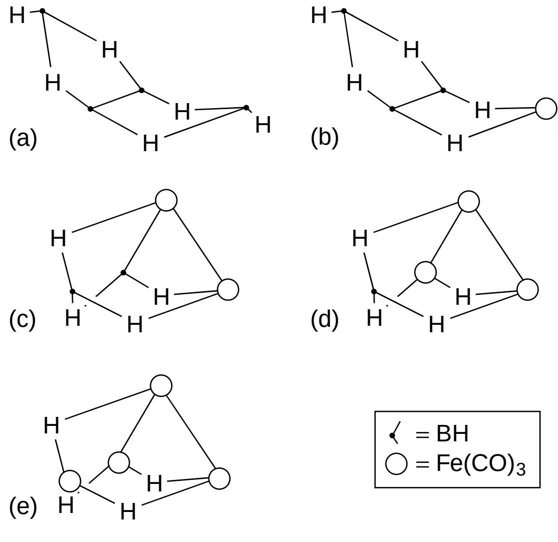

Figure 2 The observed structures of series of clusters B_nFe_{4-n}, (a) $n = 4$, (b) 3, (c) 2, (d) 1, and (e) 0, which run from the boron hydride to the metal hydride

The second example comes from solid-state chemistry, and the connection with cluster chemistry is less obvious. Despite this, it is an excellent example of how E/M variation can lead to systematic variation in structure and, consequently, to properties. Although the example is taken from solid-state metal borides, the silicides (*see* ***Silicon: Inorganic Chemistry***) and phosphides (*see* ***Phosphides: Solid-state Chemistry***) could have been used.

Examples of metal borides (*see* ***Borides: Solid-state Chemistry***) with B/M ratios ranging from large to small have been characterized, although not for the same metal.[44] The boron-rich borides often exhibit boron polyhedra in their structures. In these compounds, the preferred bonding motif of boron is dominant. One view of such compounds is a cluster network with metal ions in the network holes. Indeed, it was a consideration of the electronic structure of these borides that led to the early calculations on $[B_{12}H_{12}]$ and the famous prediction of the stability of this species as a dianion.[45] This prediction was later confirmed experimentally, and these observations eventually gave rise to the cluster electron counting rules. The relationship of CaB_6, which contains a network of octahedral B_6 clusters with intercluster B–B bonds from each vertex, and $[B_6H_6]^{2-}$ (**34**) is clear. Each H on the latter is replaced by a single bond to another B_6 cage, and the net 2− charge required for cluster bonding is derived from the s-block metal, that is, CaB_6 is viewed as a Zintl salt $[Ca^{2+}][B_6{}^{2-}]$.

Going to the opposite extreme, the metal-rich borides have structures most easily identified with close-packed metal structures. Now it is the boron atoms that are found in the interstitial holes. Clearly, it is the requirements of the transition metal atoms that are first met. Often, the holes in which the boron atoms reside have a trigonal prismatic geometry defined by the metal atoms. The same type of geometry is found in the cluster, $[H_2Ru_6(CO)_{18}B]^-$ (**35**).[46] However, there is no simple way of relating the solid state and discrete cluster structures. On the other hand, for an E/M = 1 boride, just such a relationship has been described.[47] Thus, for FeB and CrB, the solid-state structures have been described in terms of the packing of chains of M_2B_2 tetrahedra. It is interesting to note, then, that a distorted chain of this type containing four boron atoms is found in the compound $B_4H_8Fe_4(CO)_{12}$ (**36**) containing equal numbers of metal and main group atoms.

3.5 The Main Group Element Fragment as a Ligand

For completeness, it is necessary to briefly mention a popular competing view of a transition metal–main group element cluster. This description will certainly be encountered if the topic is pursued in the literature and, indeed, has already been mentioned in Section 2.2.1. The main group element fragment can be viewed as a ligand, albeit often an exotic one, coordinated to the transition metal center or centers.[48]

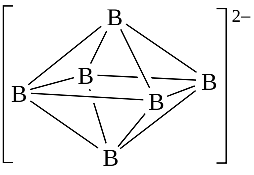

(**34**)

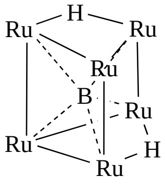

(**35**)

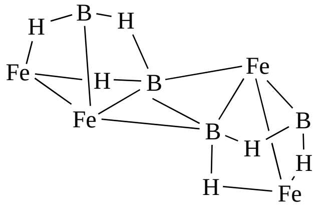

(**36**)

This view is favored by practitioners who have entered the area with a background in transition metal chemistry and can be a more useful approach in some instances. Contrasting the two views with examples highlights the differences. Thus, $Fe(CO)_3B_4H_8$ (**37**) and $CpNb(CO)_2P_4$ (**38**) can be viewed as either clusters (structure drawing at the left) or as metal complexes (structure drawing on the right).

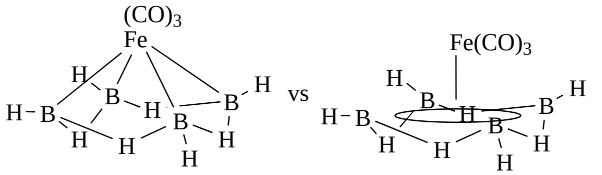

(**37**)

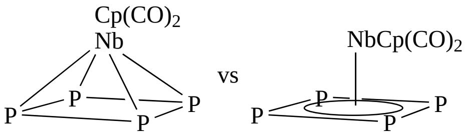

(**38**)

The cluster view is as a 7 skeletal pair, 5 fragment skeleton based on an octahedron, whereas the metal–ligand complex view is as a dianionic η^4-ligand donating six electrons to the metal center in the same manner as η^4-$[C_4H_4]^{2-}$. In the second representation, the compounds are not considered as clusters and would not be classified as such unless the ligand itself is a cluster, for example, the η^5-$[C_2B_9H_{11}]^{2-}$ open cage is a ligand analog of η^5-$[C_5H_5]^{2-}$ (*see* ***Boron: Metallacarbaboranes*** and ***Boron: Polyhedral Carboranes***). Alternatively, the metal fragment can have a nuclearity greater than one, for example, $HFe_3(CO)_9(\mu\text{-}H)_3BH$ (**12**) can be considered as a trimetallic ring with a μ_3-bridging $[BH_4]^-$ ligand. In the examples given, both views are equally useful.

For $CpNb(CO)_2P_4$ (**38**), the ligand view is more realistic because of the greater difference in electronegativities between the transition metal and main group elements. On the other hand, viewing the borane fragment in $Fe(CO)_3B_4H_8$ (**37**) as an η^4-ligand hides its close relationship to $Fe_2(CO)_6B_3H_7$ (**39**) and $Ru_3(CO)_9B_2H_6$ (**40**). All three are 7 skeletal pair, 5 fragment clusters whose main group element parent is B_5H_9 (**16**) or $[B_5H_5]^{4-}$ (**15**). Further, although the $[B_3H_7]^{2-}$ ligand in $Fe_2(CO)_6B_3H_7$ (**39**) is isoelectronic with the allyl ligand, the geometry and bonding in the compound do not correspond to any known allyl metal complex.[**49**] This makes the ligand view an artificial one. Finally, the ligand view hides the possibility of structural isomerism. Thus, 1-$CpCoB_4H_8$ (**41**) is reasonably considered analogous to $CpCo(\eta^4\text{-}C_4H_4)$ (**42**) but in fact 2-$CpCoB_4H_8$ (**43**) is also stable – a possibility that an organometallic chemist does not consider for $CpCo(\eta^4\text{-}C_4H_4)$. Indeed, the barrier for the conversion of the hypothetical 2-isomer to the 1-isomer is calculated to be very low and even if formed would not be isolated. This is not the case for the boron analog.

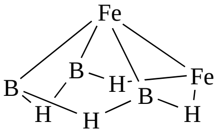

(**39**)

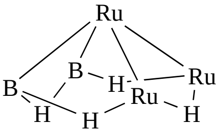

(**40**)

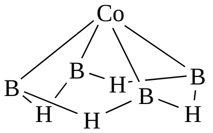

(**41**)

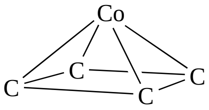

(**42**)

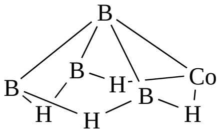

(**43**)

The relationship between the metallaborane structural isomers is clear in the cluster view but less so in the ligand view. In summary, the ligand view will be most useful for compounds containing one, or perhaps two, metal atoms bound to a contiguous main group fragment possessing a substantially higher effective electronegativity than the metals.

3.6 Element Substitution

In main group chemistry, element substitution constitutes a major perturbation, for example, C_2H_6 to B_2H_6 have very different structures and properties. The latter is more closely related to C_2H_4, that is, in order to draw a parallel between the E–E interactions, the number and/or type of ligands on the main group framework need to be changed. In transition metal chemistry, the perturbation is still significant but potentially a more subtle one. Thus, $[CpMo(CO)_2]_2$ and $[CpFe(CO)_2]_2$ have the same composition but very different M–M interactions: the former has a triple bond and the latter a single bond.[50] This is possible because 10 metal atom valence functions versus four main group atom valence functions permits changes in the metal–metal interaction to accommodate differing numbers of metal valence electrons for the same ligand set. Similar comparisons in inorganometallic complexes become interesting in the sense of exactly how this plays out in a cluster bonding environment.

3.6.1 Variation in Main Group Identity

Early examples of inorganometallic compounds benefited greatly from comparison with known organometallic complexes or clusters. Thus, $HFe_2(CO)_{12}EH_n$, E = B, $n = 2$; C, $n = 1$; N, $n = 0$, (**44–46**) provide three isoelectronic compounds that are isostructural if one ignores the hydrogen atoms associated with the main group atom. They are analogous in the same sense as ethylene and diborane.[27]

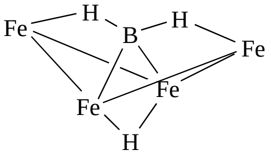

(**44**)

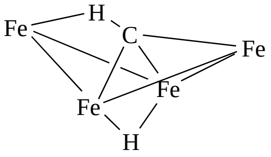

(**45**)

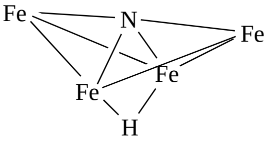

(**46**)

More examples of this type are known,[51] and each structural relationship found generates curiosity concerning the reaction chemistries. The latter is largely unrealized for inorganometallic compounds where identification and structural characterization remain the focus of the vast majority of studies. But much of the impetus behind the study of Inorganometallic Chemistry lies in the possibilities of structural and reaction chemistry that differs from that of organometallic analogs. It was already pointed out above that inorganometallic analogs of organometallic compounds, particularly metallaboranes, exhibit a more varied structural chemistry for a given composition than the organometallic analog. For example, the bridged dimetal compounds $(CO)_6Fe_2(E_2H_n)$, E = B, $n = 3$; E = P, $n = 1$ (^{t}Bu not H); E = S, $n = 0$ all exist, but the carbon compound, E = C, $n = 2$, has not been reported.

An example illustrating the possibility of significantly different reactivity is pertinent here (see also Section 5). A comparison of the photon driven reaction of alkynes with $(CO)_3Fe(\eta^4\text{-}E_4H_4)$, E = C, BH (**39**) has been reported.[52] The former yields substituted benzenes, whereas the latter generates predominantly carbon-rich carboranes, $C_nH_nB_4H_4$, $n = 2, 4, 9$, where the tetracarbon carborane is the primary product.

3.6.2 Variation in Transition Metal Identity

Two series are illustrative. It is important to note that this kind of comparison has only become possible recently because of progress in the synthesis of inorganometallic clusters of boron. The development of the reaction of monocyclopentadienyl metal hydrides with monoboranes has permitted metallaboranes to be generated containing Cp*M fragments of transition metals ranging from groups 5 to 9. For groups 6 and 9, metallaboranes representing all three rows are accessible. In several cases, series with constant or near-constant stoichiometry have been synthesized and characterized, thereby permitting the role of the metal atom in cluster structure to be explicitly defined. The series $Cp^*_2M_2B_4H_8$ for M = Ir, Ru, Cr, Re (**47–50**) is particularly interesting.[53]

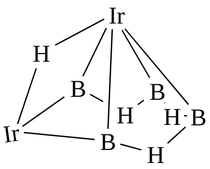

(**47**)

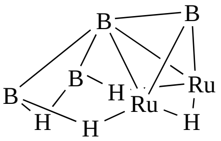

(**48**)

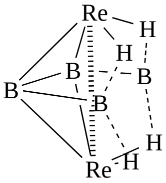

(**49**)

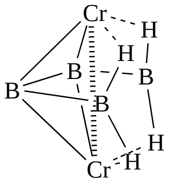

(**50**)

Formally, these compounds contain 8, 7, 6, and 5 cluster bonding pairs. In agreement with the electron counting rules, the structure of the Ir compound is based on a 7-vertex deltahedron with an axial vertex vacant (pentagonal pyramid). For Ru, the structure predicted is an octahedron; however, an alternative structure possible when there are at least two metals in the cluster, namely, a capped square pyramid, is the observed structure. Continuing the capping motif, the Re compound is considered as a bicapped tetrahedron requiring six pairs. The Cr compound appears to possess the same structure as that for Re and, thus, is not in conformance with the counting rules.[54] A detailed examination of its electronic structure shows the compound to be electronically unsaturated.

Unlike $[CpMo(CO)_2]_2$ in which unsaturation generates localized metal–metal multiple bonding, here the unsaturation is spread out over the entire six-atom cluster system; a conclusion supported by the difference in geometric parameters between the Cr and Re compounds as well as by molecular orbital modeling. Because of the invariant stoichiometry, these observed geometry changes can only be attributed to the change in metal.

3.6.3 Variation in Borane Fragment Size for a Group 7 Metal

A description of an unusual type of cluster bonding results from the synthesis and characterization of the series of closed clusters $Cp^*_2Re_2B_nH_n$, $n = 6–10$, (**51–55**) (Note: The Re–B bonding interactions have been omitted for clarity and for the $n = 6$ member, only the dichloro derivative was isolated).[55] These clusters all exhibit flattened spherical shapes with cross-cluster metal–metal bonding. Formally, they lack 3 cluster bonding electron pairs to satisfy the cluster electron counting rules for closed clusters possessing 8 to 12 vertices. This must be a consequence of the properties of the elements making up the cluster.

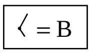

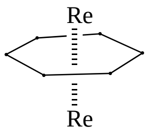

(**51**)

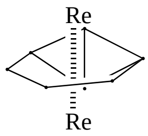

(**52**)

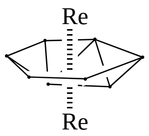

(**53**)

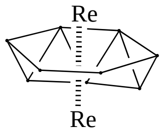

(**54**)

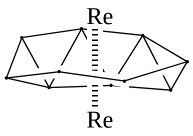

(**55**)

Years earlier in the development of metallaborane and metallacarborane cluster chemistry, structures were found in which the electron count was one less than that demanded by the observed shape. Named ‘isocloso’ (or ‘isonido’ for more open shapes) by their discoverers, these compounds were shown to possess metals at vertices of higher connectivity than expected on the basis of the shape of the equivalent borane. Two explanations were proffered albeit individually and not as alternatives. The ‘iso-’ nomenclature was said to reflect the fact that the metal centers were effectively in a higher oxidation state due to a contribution of two additional electrons to cluster bonding over and above those expected on the basis of an isolobal main group fragment (the ‘missing’ electrons localized at the metal). The competitive explanation produced the prefix ‘hyper,’ reflecting an explanation in terms of a low electron count, leading to a change in shape (‘missing’ electrons delocalized throughout the cluster framework).[56,57] Although the number of such compounds continually grew, they were considered by many as exceptions to the electron counting rule.

The series of Re clusters, used to introduce this section, established the fact that for the right transition metal, this qualitative behavior is the rule not the exception. Consider the principal observations. Each compound characterized possesses a structure compressed along the Re–Re axis that has a distance corresponding to a Re–Re single bond. Of necessity, the equator bulges out. Likewise, the metal vertices are of higher connectivity and the boron vertices are of lower average connectivity than those for borane clusters of nuclearity $n + 2$. These differences do not change the overall connectivity for a given nuclearity. The generation of a Re–Re cross cage bond, the reduction of the B–B bonding and increase in Re–B bonding conspire to empty three orbitals that would be filled in the B_{n+2} core. The electronic mechanism to achieve this situation is equivalent to that developed for families of triple-decker complexes of which $Cp^*_2Re_2B_6H_6$ is a member.

Recent work on related Ru clusters suggests that both the ‘iso-’ or ‘hyper-’ nomenclature (and associated description of the location of the ‘missing’ electrons) are too restrictive. A more general nomenclature, ‘hypo-electronic’ accommodates both possibilities, which, in fact, are known in related solid-state systems.[58] Moreover, this view suggests that the proper origin of the effect is the metal and is an expression of the variation of metal properties with group number. It was only when metallaboranes substantially different from the commonly studied group 9–10 compounds could be synthesized that the role of the metal center could be distinguished from variations due to ancillary ligand differences.[59]

4 CLUSTER COMPOSITION AND STRUCTURE TYPES

4.1 Limiting Factors

The model-based discussion of Sections 2 and 3 suggests two distinct categories of mixed transition metal–main group element clusters. The first includes main group or transition metal atoms or fragments, which do not necessarily form clusters on their own, incorporated into cluster networks. The formation of the cluster is driven by the cluster-forming tendencies of either the transition metal or the main group element fragments. Thus, these clusters will be transition metal–rich in one case and main group element–rich in the other, somewhat analogous to the borides discussed in Section 3.4. The second category consists of compounds that contain equal or nearly equal numbers of transition metal and main group elements both of which usually meet the requirements of cluster bonding. In this section, these predictions are tested against a range of cluster compositions and isomeric structural forms that have been characterized.

The examples presented illustrate three points already presented in Sections 2 and 3. The formation of a cluster structure containing specified transition metal and main group atoms depends on (1) the skeletal electron count, (2) the identity of the elements chosen, and (3) the number and type of ligands on the cluster atoms. In addition, the following dramatically shows the wide variety of cluster isomers and stoichiometries that remain to be discovered.

4.2 Examples of Cluster Structures

The compilation of transition metal–main group element compounds is given in Table 1, using Figure 3 to define core cluster structure type. To make the discussion tractable, only three types of clusters having core stoichiometries with varying E/M ratio are considered, that is, 4-, 5-, and 6-atom clusters are discussed. Many more cluster types will be found in the literature but similar organization is possible using the examples given here as a guide (see Sections 2 and 3 for selected examples of other cluster types). The first type discussed is electron precise, while the other two are orbitally rich clusters (see Section 2.2). Both fully closed (closo) and partially opened (nido) clusters are included but, again, more open clusters are known.

The examples given have been characterized mainly by crystallographic techniques. Further discussion of many of these compounds, as well as other related compounds, will be found in the book *Inorganometallic Chemistry* along with references to the primary literature.[8] Many of these same structure types have been observed for carbon as the main group element (*see* ***Polynuclear Organometallic Cluster Complexes***), and are so indicated in Figure 3 by an asterisk. The end members of each series (pure transition metal or pure main group element) are not given but several can be found in chapters devoted to specific elements. Note also that although $HRu_6(CO)_{17}B$ (**14**) can be considered as a 7-atom transition metal, main group element cluster system, electronically it is more usefully considered as a 6-atom metal cluster with an interstitial boron atom. Hence, it too provides an all-metal cluster for the closo-6-atom series.

The organization of Table 1 and Figure 3 is best appreciated by means of an example. $Fe_2(CO)_6B_3H_7$ (**39**) will be found in the table as $\{BH\}_3\{Fe(CO)_3\}_2H_4$, emphasizing that the cluster core contains 3 BH fragments and 2Fe(CO)$_3$ fragments with 4 H atoms associated with cluster bonding. The skeletal electron count is $(3 \times 2) + (2 \times 2) + 4 = 14$. Thus, the cluster structure is based on a $(14/2) - 1 = 6$ vertex deltahedron (octahedron) with one vertex unoccupied. There is only one possibility: the square pyramidal shape. However, a square pyramidal cluster has three possible ways for the distribution of 3 BH and 3 Fe(CO)$_3$ fragments over the five vertices. Of these three isomeric forms, the one observed for this compound is indicated by reference to Figure 3, that is, structure 5q. But now that many metals may be incorporated into such a framework, examples of all three possible isomers are known for this structure type. Indeed, two have been isolated for Rh, and in this case, the relative stabilities of the two isomers were determined to be 5p > 5q.[60] If one assumes that the isomeric form isolated in the other cases corresponds to the most stable one, then isomer stability is seen to depend on the nature of the metal and its ancillary ligands. The properties of the transition metal are expressed in structure.

The information in Table 1 and Figure 3 defines some interesting trends. More than 100 compounds are listed for just these three cluster types. For the 4-atom electron-precise cluster, at least one example of all possible isomers is known. There are more than 30 examples of the tetrahedral M_3E core, with E from groups 13–16 and M from groups 6–9. The E atom usually has a one-electron ligand (H, R, or a 17-electron metal fragment) but examples with no ligand, a two-electron donor (CO), or a two-electron acceptor (see Section 5.3) are known. The M atom usually has three coordination positions occupied by exo-cluster ligands (3CO or Cp are most common). The number of hydrogens bound to the cluster in edge-bridging positions range from none to four. These observations are completely in accord with the limitations on cluster composition imposed by the requirements of cluster bonding and steric considerations (see Section 2).

The 5- and 6-atom cluster systems shown in Figure 3 and Table 1 have more compositional and isomeric possibilities, but relatively fewer examples are known. Thus, although some structural types are well represented, about half of the possibilities remain to be characterized. If barriers for rearrangement of isomeric forms are low, the isolation of the less stable forms will be very difficult (see Section 5.2). However, the unrepresented structures in Figure 3 are probably due more to lack of appropriate synthetic routes than to any intrinsic factors. Thus, for all three-cluster sizes, it would be dangerous to draw any interpretations from the differences in the numbers of examples for differing E and M core compositions. Certainly, one expects differences but what is required is a comparison of series containing differing numbers of the same E and M atoms (see Section 3.4). The missing compounds constitute attractive synthetic goals for future work.

5 CLUSTER REACTIVITY

The complement of structure is reactivity. Studies of reactivity usually follow advances in synthesis, which, in turn, are often stimulated by serendipitous characterization of novel compounds. Progress in understanding reactivity, even at the most elementary mechanistic level, is very important. New compounds, despite novel and interesting structures, find little use unless their chemical origins and ultimate chemical

Table 1 Known closo and nido inorganometallic clusters[a] of core nuclearity four to six

Size and structure type	Cluster fragment composition	Size and structure type	Cluster fragment composition
4a	$\{BH\}\{Fe(CO)_3\}_3H_4$	5d	$\{BH\}_2\{Cp^*Co\}_3H_2$
4a	$\{BH\}\{Ru(CO)_3\}_3H_4$	5d	$\{BPh\}\{PPh\}\{CpCo\}_3$
4a	$\{BH\}\{Fe(CO)_3\}_3(H)_2CO$	5d	$\{SnFeCp(CO)_2\}_2\{Fe(CO)_3\}_3$
4a	$\{BCO\}\{Os(CO)_3\}_3H_3$	5d	$\{PCr(CO)_5\}_2\{Fe(CO)_3\}_3$
4a	$\{SiCo(CO)_4\}\{Co(CO)_3\}_3$	5d	$\{As\}_2\{Fe(CO)_3\}_3$
4a	$[\{GeFe(CO)_4\}\{Fe(CO)_3\}_3CO]^-$	5d	$\{SbCr(CO)_5\}_2\{Fe(CO)_3\}_3$
4a	$\{GeR\}\{Co(CO)_3\}_2\{CpW(CO)_2\}$	5d	$\{Bi\}_2\{Fe(CO)_3\}_3$
4a	$\{GeR\}\{Co(CO)_3\}_3$	5d	$\{Bi\}_2\{Ru(CO)_3\}_3$
4a	$\{NH\}\{Fe(CO)_3\}_3CO$	5d	$[\{S\}_2\{Ni(PEt_3)_2\}_3]^{2+}$
4a	$\{NPh\}\{Ru(CO)_3\}_3H_2$	5d	$[\{S\}_2\{Rh(CO)_2\}_3]^-$
4a	$\{PPh\}\{Ru(CO)_3\}_3H_2$	5d	$[\{Se\}_2\{Ir(CO)_2\}_3]^-$
4a	$\{P\}\{Co(CO)_3\}_3$	5d	$[\{Se\}_2\{Rh(CO)_2\}_3]^-$
4a	$\{AsMe\}\{Fe(CO)_3\}_2\{Co(CO)_3\}$	5f	$\{P\}_3\{Co(triphos)\}\{Fe(etriphos)\}$
4a	$\{As\}\{Co(CO)_3\}_3$	5l	$\{PPh\}\{Ru(CO)_3\}_4CO$
4a	$\{As\}\{Co(CO)_3\}_3$	5l	$\{AsPh\}\{Os(CO)_3\}_4H_2$
4a	$\{Bi\}\{Fe(CO)_3\}_3H_3$	5n	$\{BH\}_2\{Ru(CO)_3\}_3H_3$
4a	$\{Bi\}\{Ru(CO)_3\}_3H_3$	5n	$\{NEt\}_2\{Fe(CO)_3\}_3$
4a	$\{Bi\}\{Os(CO)_3\}_3H_3$	5o	$\{NEt\}_2\{Fe(CO)_3\}_3$
4a	$\{Bi\}\{Co(CO)_3\}_3$	5o	$\{NPh\}_2\{Ru(CO)_3\}_3$
4a	$\{Bi\}\{Ir(CO)_3\}_3$	5o	$\{PPh\}_2\{Fe(CO)_3\}_3$
4a	$[\{Bi\}\{Fe(CO)_3\}_3CO]^-$	5o	$\{AsPh\}_2\{Fe(CO)_3\}_3$
4a	$[\{OH\}\{Re(CO)_3\}_3H_3]^-$	5o	$[\{SbCr(CO)_5\}_2\{Fe(CO)_3\}_3]^{2-}$
4a	$[\{O\}\{Cp^*Ru\}_3H_3]^+$	5o	$[\{Bi\}_2\{Fe(CO)_3\}_3]^{2-}$
4a	$[\{O\}\{Fe(CO)_3\}_3]^{2-}$	5o	$\{S\}_2\{Os(CO)_3\}_3$
4a	$\{O\}\{CpCo\}_3CO$	5o	$\{Se\}_2\{Fe(CO)_3\}_3$
4a	$[\{SR\}\{Fe(CO)_3\}_3]^-$	5o	$\{Te\}_2\{Fe(CO)_3\}_3$
4a	$[\{S\}\{Fe(CO)_3\}_3]^{2-}$	5o	$\{Te\}_2\{Os(CO)_3\}_3$
4a	$\{S\}\{Os(CO)_3\}_3H_2$	5q	$\{BH\}_3\{Fe(CO)_3\}_2H_4$
4a	$\{S\}\{Ru(CO)_3\}_3H_2$	5p,q	$\{BH\}_3\{Cp^*Rh\}_2H_4$
4a	$\{Se\}\{Os(CO)_3\}_3H_2$	5r	$\{BH\}_3\{Cp^*Co\}_2H_4$
4a	$\{Te\}\{Os(CO)_3\}_3H_2$	5s	$\{BH\}_4\{CpCo\}H_4$
4b	$\{BH\}_2\{CpTa\}_2(H)_4Br_2$	5s	$\{BPr\}_2\{N(t\text{-}Bu)\}_2\{CpCo\}$
4b	$\{BH\}_2\{Fe(CO)_3\}_2H_4$	5s	$\{C(t\text{-}Bu)\}_2\{P\}_2\{Cp^*Co\}$
4b	$\{NH\}\{S\}\{Fe(CO)_3\}_2$	5s	$\{P\}_4\{Cp^*(CO)_2Nb\}$
4b	$\{PR_2\}_2\{Fe(CO)_3\}_2$	5t	$\{BH\}_4\{CpCo\}H_4$
4b	$\{P\}_2\{Co(CO)_3\}_2$	5u	$\{P_4\}\{Rh(PPh_3)_2Cl\}$
4b	$\{AsCr(CO)_5\}_2\{Cp(CO)_2W\}_2$	6a	$\{B\}\{Ru(CO)_3\}_5\{AuPPh_3\}$
4b	$\{S\}_2\{Fe(CO)_3\}_2$	6a	$[\{N\}\{Ru(CO)_3\}_3\{Ru(CO)_2\}_2CO]^-$
4c	$\{BH\}_3\{Mn(CO)_3\}H_5$	6a	$\{N\}\{Fe(CO)_3\}_3\{Fe(CO)_2\}_2(H)CO$
4c	$\{P\}_3\{Co(triphos)\}$	6a	$\{PPh\}\{Ru(CO)_3\}_5$
4c	$[\{Te\}_3\{W(CO)_4\}]^{2+}$	6a	$\{S\}\{Os(CO)_3\}_5$
4d	$\{SnR_2\}\{Os(CO)_3\}_3CO$	6a	$\{S\}\{Ru(CO)_3\}_5$
4d	$\{SEt\}\{Os(CO)_3\}_3(H)CO$	6b	$\{BH\}_2\{CpCo\}_4H_2$
4e	$\{As(p\text{-}tolyl)\}\{Os(CO)_3\}_3\{C_6H_3Me\}$	6b	$\{BH\}_2\{CpCo\}_4H_2$
4e	$\{SSiMe_3\}\{Os(CO)_3\}_3$	6b	$\{Bi\}_2\{Os(CO)_3\}_4$
4f	$\{BH\}_2\{PPh_2\}\{CpCo\}_2H_3$	6c	$\{GeCo(CO)_4\}_2\{Co(CO)_3\}\{Co(CO)_2\}_2CO$
4g	$\{SiPhCl\}_2\{Pt(PEt_3)_2\}_2$	6c	$\{PPh_2\}_2\{Co(CO)_2\}_4(CO)_2$
4h	$\{SiR_2\}_2\{Mn(CO)_4\}_2$	6c	$\{PPh_2\}_2\{Fe(CO)_3\}_2\{Fe(CO)_2\}_2(CO)$
4h	$\{PR_2\}_2\{Fe(CO)_3\}_2$	6c	$\{PPh_2\}_2\{Ru(CO)_3\}_2\{Ru(CO)_2\}_2(CO)$
4h	$\{As\}_2\{Cp^*Mn(CO)_2\}_2$	6c	$\{Bi\}_2\{Ru(CO)_3\}_4$
4h	$[\{S\}_2\{Fe(CO)_3\}_2]^{2-}$	6c	$\{Se\}_2\{CpNi\}_4$
4h	$\{Se\}_2\{CpCr(CO)_2\}_2$	6c	$\{Te\}_2\{CpNi\}_4$
4h	$[\{Te\}\{Te_2\}\{Fe(CO)_3\}_2]^{2-}$	6d	$\{BH\}\{CH\}\{Cme\}\{Fe(CO)_3\}_3$
4i	$\{BH\}_3\{Mn(CO)_4\}H_5$	6f	$\{BH\}_4\{CpCo\}_2H_2$
4j	$\{BH\}\{BH_2\}_2\{Pt(PR_3)_2\}H_2$	6d	$\{BH\}_3\{CpCo\}_3H_2$
5a	$\{S\}\{Os(CO)_3\}_4$	6h	$\{BH\}_3\{BCO\}_2\{Fe(CO)_3\}$
5b	$\{B\}\{Fe(CO)_3\}_4H_3$	6u	$\{BH\}_5\{Mn(CO)_3\}H_5$
5b	$\{B\}\{Ru(CO)_3\}_4H_3$	6u	$\{BH\}_5\{Fe(CO)_3\}H_4$
5b	$\{N\}\{Fe(CO)_3\}_4H$	6u	$\{BH\}_5\{Co(CO)_3\}H_3$
5b	$\{N\}\{Os(CO)_3\}_4H$	6v	$\{BH\}_5\{CpFe\}H_5$
5b	$\{N\}\{Ru(CO)_3\}_4H$	6v	$\{P\}_5\{Cp^*Fe\}$
5b	$[\{O\}\{Mn(CO)_3\}\{Fe(CO)_3\}_3]^-$		

[a] Organized according to framework size, skeleton type (see Figure 3), main group atom, and transition metal atom.

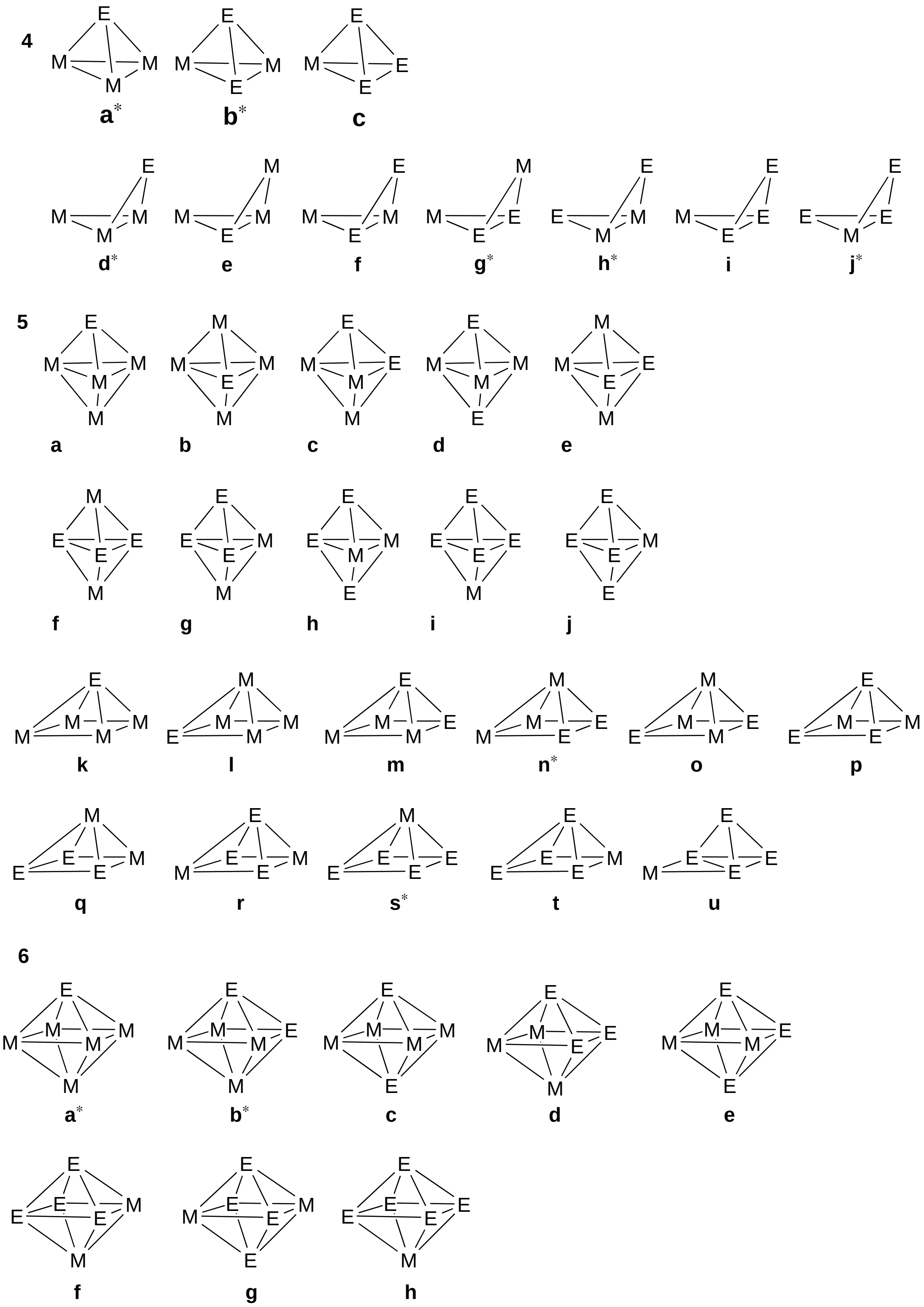

Figure 3 Isomeric possibilities for structures for E_nM_{x-n}, $n = (x - 1) - 1$, $x = 4$–6. Only the geometry of highest total vertex connectivity (usually denoted as closo but note the ambiguity for $x = 4$) and that of next highest (usually denoted as nido) are shown for economy of space. Likewise, only the binary E and M clusters are enumerated. Clearly, many more structures are possible if more open structures are allowed or more than one type of main group or transition metal element is used in the compound

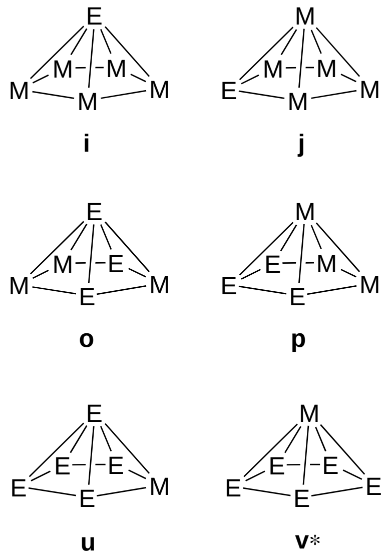

Figure 3 cont'd

destinations are understood. This information not only aids the development of new synthetic routes but can also lead to applications. Thus, it can be argued that if organometallic chemistry had not developed beyond the bizarre (at the time) structures of ferrocene and olefin π-complexes, it would never have had the large impact already demonstrated. Transition metal–main group cluster chemistry remains rich in structure and poor in reactivity. But progress continues to be made, and a brief introduction to reaction types characteristic of the area is presented. It is highly selective but illustrates the mutual effects of main group and transition elements on reactivity. Of course, element properties are important, but the emphasis in the following is on the reactivity derived from or modified by cluster structure properties. For example, element properties make the hydrogen of a B–H bond hydridic, but when a B–H bonding interaction is found as part of a cluster edge-bridge, it also exhibits protonic character.[61]

5.1 Addition or Loss of a Proton

Boron hydride (equation 1)[62] and transition metal clusters (equation 2)[63] containing bridging hydrogens can be deprotonated by bases (*see* ***Boron Hydrides***; ***Boron: Polyhedral Carboranes***; ***Hydride Complexes of the Transition Metals***, and ***Polynuclear Organometallic Cluster Complexes***). The resulting anionic conjugate bases are often nucleophilic in character and more reactive than the neutral clusters (see below). For the boranes, it has been demonstrated that the acidity of a bridging hydrogen increases as the cluster size increases, whereas for transition metal clusters, it is the ligands on the metal atoms that have the dominant effect. In general, the boranes are weaker Brönsted acids than the metal cluster hydrides, and the anions are consequently more reactive. An important factor here is that the metal clusters are much more effective at delocalizing the anionic charge generated on deprotonation, particularly when the metal centers contain carbonyl ligands.

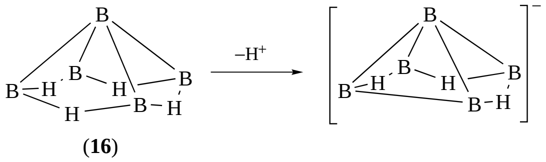

(**16**) (1)

$$(\mu\text{-H})_2\text{Re}_3(\text{CO})_{12} \xrightarrow{-\text{H}^+} [(\mu\text{-H})_2\text{Re}_3(\text{CO})_{12}]^- \qquad (2)$$

From this, it follows that transition metal–main group element clusters with bridging hydride ligands will also serve as Brönsted acids but with acidities intermediate between those of the homonuclear clusters of the same structure type. Thus, the isolobal analog of B_5H_9 (**16**), $Fe_2(CO)_6B_3H_7$ (**39**), is more easily deprotonated than B_5H_9 (equation 3), and it is one of the FeHB protons that is lost rather than a BHB proton.[64] Deprotonation of $HFe_3(CO)_9(\mu\text{-H})_3BH$ (**10**) yields $[HFe_3(CO)_9(\mu\text{-H})_2BH]^-$, again with the loss of a B–H–Fe proton. However, the Fe–H–Fe and remaining Fe–H–B hydrogens are fluxional on the NMR timescale and, thus, the difference in proton affinities of the Fe–Fe and Fe–B edges must be small.[65]

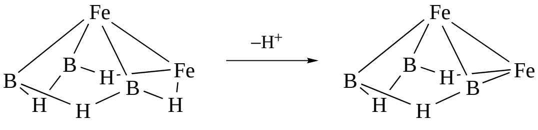

(**39**) (3)

The removal of a cluster bridging hydrogen as a proton yields a semilocalized bonding orbital that, in the reverse process, serves as a site of available electron density. It follows that an unbridged edge of neutral clusters is a potential site of protonation provided that there is a high-lying cluster orbital associated predominantly with that edge. Thus, B_6H_{10} and $Os_3(CO)_{12}$ can be protonated (equations 4 and 5) to yield cationic species.**[66,67]** In both cases, the added proton becomes a bridging 'hydride.' Because cluster bonding is often highly delocalized, cationic clusters like these are rare.

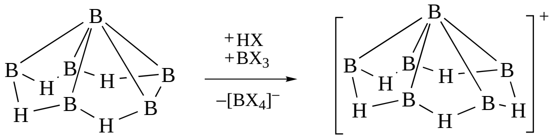

(4)

$$Os_3(CO)_{12} \xrightarrow{+H^+} [(\mu\text{-H})Os_3(CO)_{12}]^+ \quad (5)$$

When there are exo-cluster ligands with lone pairs as well as metal–metal edges, an incoming proton is presented with two possible basic sites with differing proton affinities. Because the metal–metal edges are sterically shielded by the ligands on the metal centers, the exo-cluster lone pair is more accessible. An interesting example of such behavior is shown in equation (6).**[68]** For our purposes, $[Ru_3(CO)_{10}NO]^-$ can be viewed as the $[Ru_3(CO)_{10}N]^-$ tetrahedral cluster with the lone pair of the N atom coordinated to the Lewis acid oxygen (see Section 5.3). The first product formed is the O protonated product, which then rearranges to the Ru–Ru edge protonated product. Steric control generates the kinetic product but, at least in this case, the greater basicity of the metal site controls the identity of the final product.

$$[Ru_3(CO)_{10}NO]^- \xrightarrow{+H^+} Ru_3(CO)_{10}NOH \longrightarrow (\mu\text{-H})Ru_3(CO)_{10}NO \quad (6)$$

5.2 Addition or Loss of a Lewis Base

Clusters, particularly those described in Section 2.2 as orbitally rich, can act as Lewis acids. Addition of a Lewis base formally adds two electrons to the cluster bonding system. For some clusters, this causes an opening of the cluster, for example, closo to nido interconversion of $B_3H_8Mn(CO)_3$ and $B_3H_8Mn(CO)_4$ by the addition and loss of CO (equation 7).**[69]** If the cluster is formally unsaturated with respect to the electron counting rules, no change in the core structure takes place, for example, the interconversion of $Fe_4(CO)_{11}(PPh)_2$ and $Fe_4(CO)_{12}(PPh)_2$ (equation 8).**[70]** The base pair may be supplied by a conventional Lewis base (equation 7 or 8), but also can come from bond pairs, for example, H_2 (equation 9).**[71]** The latter is equivalent to oxidative addition in mononuclear systems (*see* ***Hydride Complexes of the Transition Metals***).

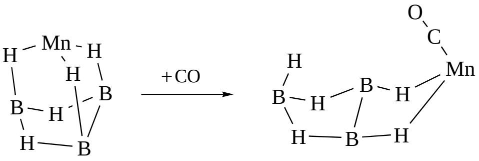

(7)

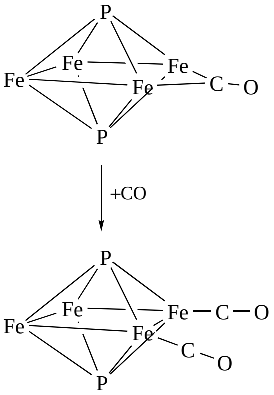

(8)

$$Os_4(CO)_{11}(\mu_4\text{-S})(\mu_4\text{-HC}_2CO_2Me) \xrightarrow{+H_2} Os_4(CO)_{11}(\mu_3\text{-S})(\mu\text{-HC}_2CO_2Me)(\mu\text{-H})_2 \quad (9)$$

In transition metal–main group element clusters, there is the possibility of ligand substitution at either type of element center. Displacement of an exo-cluster ligand on one of the metal centers (equation 10) is to be expected (*see* ***Mechanisms of Reaction of Organometallic Complexes***).**[72]** However, displacement at a main group cluster site has also been observed (equation 11).**[73]** Indeed, phosphine substitution takes place exclusively at the boron atom, and the osmium-substituted BCO complex can only be prepared by synthesizing it from the phosphine-substituted osmium carbonyl starting material.

It is interesting to note that the base displaced need not be a simple one, that is, dihydrogen is exclusively displaced from $[HFe_3(CO)_9(\mu\text{-H})_2BH]^-$ (equation 10). Indeed, a comparison of equations (10) and (11) demonstrates that cluster composition is important in determining the outcome of a Lewis base displacement reaction on a transition metal–main group element cluster. This implies that control of electronic structure via cluster element composition is a viable means of controlling reactivity.

$$Fe_3(CO)_9(\mu\text{-CO})(\mu_3\text{-HBH})^- \xrightarrow[-CO]{+PR_3} Fe_3(CO)_8(PR_3)(\mu\text{-CO})(\mu_3\text{-HBH})^-$$

$$(\mu\text{-H})Fe_3(CO)_9(\mu_3\text{-HBH})^- \xrightarrow[-H_2]{+PR_3} Fe_3(CO)_8(PR_3)(\mu\text{-CO})(\mu_3\text{-HBH})^- \quad (10)$$

$$(\mu\text{-H})_3Os_3(CO)_9(\mu_3\text{-BCO}) \xrightarrow[-CO]{+PR_3} (\mu\text{-H})_3Os_3(CO)_9(\mu_3\text{-BPR}_3) \quad (11)$$

It should be clear from the discussion of Section 2 that all of these clusters can be unstable with respect to cluster degradation in the presence of Lewis bases with the formation of saturated fragment species (*see* ***Boron Hydrides*** and ***Polynuclear Organometallic Cluster Complexes***). Thus, in the presence of an excess of phosphine, the reaction of $[HFe_3(CO)_9(\mu\text{-H})_2BH]^-$ changes from that shown in equation (10) to that shown in equation (12). The mononuclear boron and iron products demonstrate that both transition metal and main group element vertices are removed by base and the cluster is degraded.[72]

$$(\mu\text{-H})Fe_3(CO)_9(\mu_3\text{-HBH})^- \xrightarrow{+PR_3\text{ excess}} BH_3PR_3 + Fe(CO)_3(PR_3)_2 + Fe_3(CO)_9(PR_3)_{2-} \quad (12)$$

The variety of cluster structure isomers shown in Figure 3 suggest that geometrical isomerization should be a substantial feature of the reaction chemistry of transition metal–main group element clusters. It may well be, but at present there are only a few established examples of isomerization reactions. Consistent with the high main group character of the cluster bonding, the isomerization of 2-$CpCoB_4H_8$ (**40**) (equation 13) requires high temperatures.[74] However, the rearrangement of 1,2-$(Cp^*Rh)_2B_3H_7$ to the 2,3-isomer takes place on mild heating and that of 1-$Cp^*WH_3B_4H_8$ to 2-$Cp^*WH_3B_4H_8$ takes place below 0 °C.[75] As all these clusters have the same square pyramidal geometry, not only is the number of metal fragments important but also the type of metal fragments is important in determining the flexibility of the skeleton toward rearrangement. Cluster geometry can play a role that has been delineated via calculations. Thus, the octahedral cluster system appears to be one that possesses a large barrier for unimolecular rearrangement compared to other less symmetrical cluster geometries.[76] Note, however, that coordination of a Lewis base, thereby opening the structure, can catalyze rearrangement of rigid frameworks under mild conditions.[77]

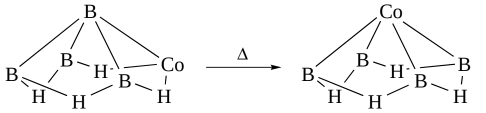

(**43**) (**41**)

(13)

5.3 A Cluster as a Lewis Base

The conjugate base of a cluster generated by deprotonation (see Section 5.1) is a Lewis base. Any metal–metal, metal–boron, or boron–boron bond is a potential Lewis base. The former have considerable nucleophilic character if anionic and effectively interact with electrophiles more complex than the proton. As the site of basicity is associated with framework bonding, this reaction type results in cluster building, for example, with metal fragment sources (equation 14).

$$(\mu\text{-H})Fe_3(CO)_9(\mu_3\text{-HBH})^- \xrightarrow{+Fe_2\,(CO)_9} (\mu\text{-H})Fe_4(CO)_{12}(\mu_4\text{-BH})^- \quad (14)$$

As noted in Section 2, clusters with ‘bare’ main group atoms possess a lone pair not formally involved in cluster bonding, for example, $Co_3(CO)_9P$ (**3**). Such clusters can act as ligands to main group or metal centers. Thus, for example, loss of CO from (**3**) takes place and leads to the formation of a trimer (equation 15).[78]

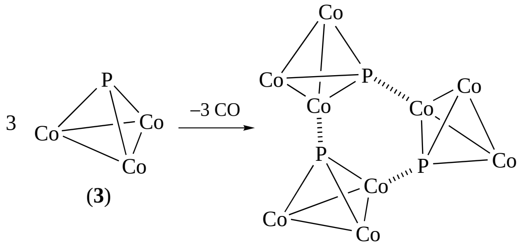

(**3**)

(15)

The coordination of a cluster to an oxidized metal center is a crucial part of the oxidative fusion reaction, whereby large clusters are generated from smaller ones in a single reaction procedure (equation 16).[79] Recently, this approach has been extended to a metallaborane system as illustrated in equation 17.[80] Although the presumed coordinated Fe^{II} intermediate has not been isolated, the fact that the reaction requires Fe^{2+} strongly suggests its formation.

$$R_2C_2B_4H_4{}^{2-} \xrightarrow{Mn^+} H_xM\{R_2C_2B_4H_4\}_2 \xrightarrow{[O]} R_4C_4B_8H_8 \quad (16)$$

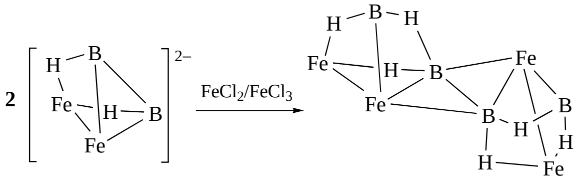

(**36**)

(17)

5.4 Metallacarboranes via Metallaboranes

Metallacarboranes historically have been prepared from carboranes and metal fragment sources. The recent ready availability of metallaboranes permits the generation of metallacarboranes from the reaction of alkynes with metallaboranes. An advantage of such an approach arises from the fact that one forms weaker M–B bonds before stronger B–C bonds, which, in principle, permits milder reaction conditions and more control of reactivity. Indeed, such appears to be the case. For example, the reaction of $(Cp^*RuH)_2B_3H_7$ with MeC≡CMe permits the generation of several previously unprecedented metallacarborane structures.[81] As shown in Figure 4, among other compounds, two isomers of identical

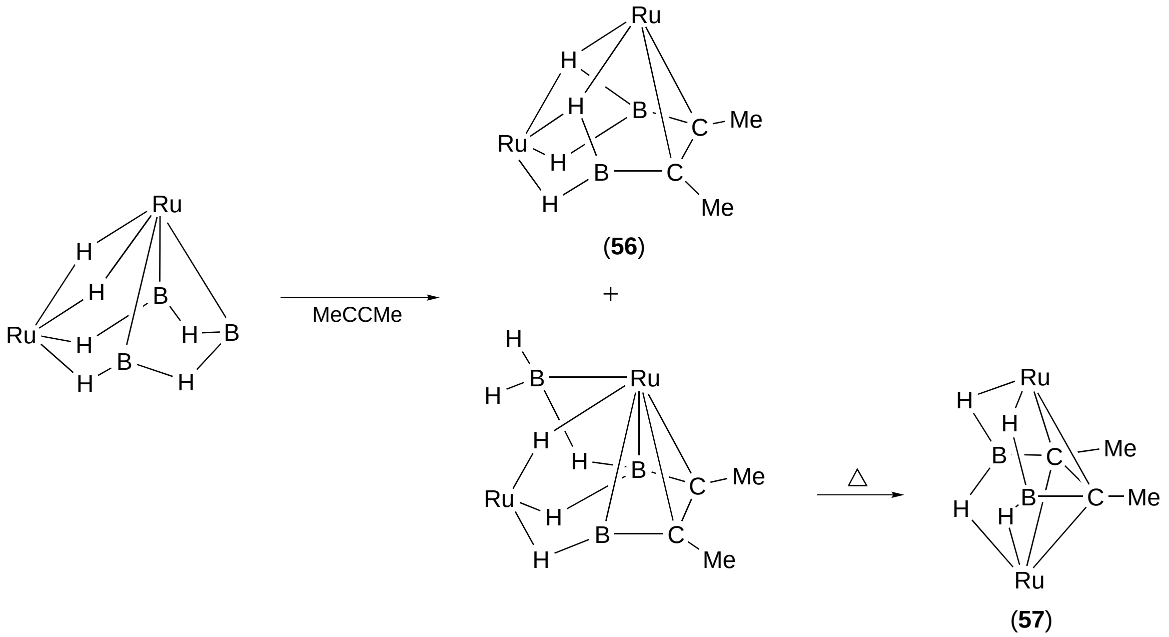

Figure 4 The reaction of a nido-diruthenapentaborane with an alkyne, ultimately generating two clusters of identical composition in which the geometric isomerism is associated with the type of unoccupied vertex in the pentagonal bipyramidal shape upon which both structures are based

composition, (**56**) and (**57**), are produced – isomers in the sense that the observed nido structures are based on the same pentagonal pyramid with either apical (**56**) or basal (**57**) vertices remaining vacant. These two species are to cluster chemistry as cis and trans olefins are to organic chemistry. Also, reminiscent of olefin isomers, the two species do not interconvert readily by thermal activation, showing that access to such species only arises from control of the reaction chemistry. Note that this isomerism is distinctly different from that associated with different distributions of the metal and main group atoms on a given framework geometry. This constitutes one more example that the prospects for the future development of inorganometallic chemistry are excellent.

6 RELATED ARTICLES

Aluminum: Inorganic Chemistry; Arsenic: Organoarsenic Chemistry; Borides: Solid-state Chemistry; Boron Hydrides; Boron: Inorganic Chemistry; Boron: Metallacarbaboranes; Boron: Polyhedral Carboranes; Carbonyl Complexes of the Transition Metals; Dinuclear Organometallic Cluster Complexes; Electronic Structure of Main-group Compounds; Electronic Structure of Organometallic Compounds; Electronic Structure of Clusters; Germanium: Organometallic Chemistry; Hydride Complexes of the Transition Metals; Hydroboration Catalysis; Iron–Sulfur Models of Protein Active Sites; Molecular Orbital Theory; Phosphorus: Inorganic Chemistry; Polynuclear Organometallic Cluster Complexes.

7 REFERENCES

1. E. L. Muetterties ed., ‘Boron Hydride Chemistry’, Academic Press, New York, 1975.
2. A. R. West, ‘Solid State Chemistry and its Applications’, John Wiley & Sons, New York, 1984.
3. R. W. Hay, ‘Bioinorganic Chemistry’, Ellis Horwood, New York, 1984.
4. A. W. Adamson and P. D. Fleischauer, ‘Concepts of Inorganic Photochemistry’, John Wiley & Sons, New York, 1975.
5. R. G. Wilkins, ‘Kinetics and Mechanism of Reactions of Transition Metal Complexes’, VCH Publishers, Weinheim, 1991.
6. F. A. Cotton and R. A. Walton, ‘Multiple Bonds Between Metal Atoms’, John Wiley & Sons, New York, 1983.
7. D. C. Bradley, *Chem. Rev.*, 1989, **89**, 1317.
8. T. P. Fehlner ed., ‘Inorganometallic Chemistry’, Plenum Publishing, New York, 1992.
9. H. W. Roesky ed., ‘Rings, Clusters and Polymers of Main Group and Transition Elements’, Elsevier, Amsterdam, 1989.

10. F. A. Cotton, M. Shang, and A.-S. Sun, *J. Am. Chem. Soc.*, 1991, **113**, 6917.
11. M. Bühl and P. v. R. Schleyer, *J. Am. Chem. Soc.*, 1992, **114**, 477.
12. J. W. Bausch, G. K. S. Prakash, M. Bühl, P. v. R. Schleyer, and R. E. Williams, *Inorg. Chem.*, 1992, **31**, 3060.
13. D. M. P. Mingos and D. J. Wales, 'Introduction to Cluster Chemistry', Prentice Hall, New York, 1990.
14. B. K. T. Trinh-Toan, J. A. Ferguson, T. J. Meyer, and L. F. Dahl, *J. Am. Chem. Soc.*, 1977, **99**, 408.
15. S. Harris, *Polyhedron*, 1989, **8**, 2843.
16. D. M. P. Mingos and R. L. Johnston, *Struct. Bonding*, 1987, **68**, 29.
17. D. M. P. Mingos and A. S. May, in 'The Chemistry of Metal Cluster Complexes', eds. D. F. Shriver, H. D. Kaesz, R. D. Adams, VCH Publishers, New York, 1990.
18. K. Wade, *Inorg. Nucl. Chem. Lett.*, 1972, **8**, 559.
19. K. Wade, *New Sci.*, 1974, **62**, 615.
20. K. Wade, *Adv. Inorg. Chem. Radiochem.*, 1976, **18**, 1.
21. A. J. Stone, *Mol. Phys.*, 1980, **41**, 1339.
22. D. Seyferth, R. S. Henderson, and L.-C. Song, *Organometallics*, 1982, **1**, 125.
23. H. Yan, A. M. Beatty, and T. P. Fehlner, *Angew. Chem., Int. Ed. Engl.*, 2002, **41**, 2578.
24. D. F. Shriver, H. D. Kaesz, and R. D. Adams eds., 'The Chemistry of Metal Cluster Complexes', VCH Publishers, New York, 1990.
25. D. M. P. Mingos, T. Slee, and L. Zhenyang, *Chem. Rev.*, 1990, **90**, 383.
26. N. J. Clayden, C. M. Dobson, K. P. Hall, D. M. P. Mingos, and D. J. Smith, *J. Chem. Soc., Dalton Trans.*, 1985, 1811.
27. C. E. Housecroft, *Chem. Soc. Rev.*, 1995, 215.
28. R. W. Rudolph, *Acc. Chem. Res.*, 1976, **9**, 446.
29. R. Hoffmann, *Angew. Chem., Int. Ed. Engl.*, 1982, **21**, 711.
30. T. A. Albright, J. K. Burdett, and H.-H. Whangbo, 'Orbital Interactions in Chemistry', John Wiley & Sons, New York, 1985.
31. M. C. Chisholm, D. L. Clark, M. J. Hampden-Smith, and D. H. Hoffman, *Angew. Chem., Int. Ed. Engl.*, 1989, **28**, 432.
32. M. A. Cavanaugh, T. P. Fehlner, R. Stramel, M. E. O'Neill, and K. Wade, *Polyhedron*, 1985, **4**, 687.
33. W. W. Porterfield, M. E. Jones, and K. Wade, *Inorg. Chem.*, 1990, **29**, 2923.
34. P. Brint, E. F. Healy, T. R. Spalding, and T. Whelan, *J. Chem. Soc., Dalton Trans.*, 1981, 2515.
35. C. R. Eady, P. F. Jackson, B. F. G. Johnson, J. Lewis, C. R. Malatesta, M. McPartlin, and W. J. H. Nelson, *J. Chem. Soc., Dalton Trans.*, 1980, 383.
36. E. D. Jemmis, M. M. Balakrishnarajan, and P. D. Pancharatna, *J. Am. Chem. Soc.*, 2001, **123**, 4313.
37. X. Lei, M. Shang, and T. P. Fehlner, *Angew. Chem., Int. Ed. Engl.*, 1999, **38**, 1986.
38. N. M. M. Wilson, D. Ellis, A. S. F. Boyd, B. T. Giles, S. A. Macgregor, G. M. Rosair, and A. J. Welch, *Angew. Chem., Int. Ed. Engl.*, 2003, 464.
39. D. M. P. Mingos, *Inorg. Chem.*, 1982, **21**, 464.
40. W. Hiller, K.-W. Klinkhammer, W. Uhl, and J. Wagner, *Angew. Chem., Int. Ed. Engl.*, 1991, **30**, 179.
41. Y.-R. Luo and S. W. Benson, *Inorg. Chem.*, 1991, **30**, 1676.
42. T. P. Fehlner, *Polyhedron*, 1990, **9**, 1955.
43. C. E. Housecroft, 'Boranes and Metalloboranes', Ellis Horwood, Chichester, 1990.
44. T. Lundström, in 'Boron and Refractory Borides', ed. V. I. Matkovich, Springer-Verlag, Berlin, 1977.
45. H. C. Longuet-Higgins and M. D. Roberts, *Proc. R. Soc. London*, 1955, **A230**, 110.
46. C. E. Housecroft, D. M. Matthews, and A. L. Rheingold, *Organometallics*, 1992, **11**, 2959.
47. V. I. Matkovich, *Pure Appl. Chem.*, 1974, **39**, 525.
48. R. N. Grimes, in 'Metal Interactions with Boron Clusters', ed. R. N. Grimes, Plenum Publishing, New York, 1982, p. 269.
49. C. E. Housecroft and T. P. Fehlner, *Inorg. Chem.*, 1982, **21**, 1739.
50. R. Hoffmann, *Science*, 1981, **211**, 995.
51. T. P. Fehlner, *New J. Chem.*, 1988, **12**, 307.
52. T. P. Fehlner, *J. Am. Chem. Soc.*, 1980, **102**, 3424.
53. T. P. Fehlner, *PINSA*, 2002, **68A**, 579.
54. T. P. Fehlner, *J. Chem. Soc., Dalton Trans.*, 1998, 1525.
55. T. P. Fehlner, *Adv. Inorg. Chem.*, 2002, **822**, 49.
56. R. L. Johnston and D. M. P. Mingos, *Inorg. Chem.*, 1986, **25**, 3321.
57. R. L. Johnston, D. M. P. Mingos, and P. Sherwood, *New J. Chem.*, 1991, **15**, 831.
58. S. C. Sevov and J. D. Corbett, *Inorg. Chem.*, 1991, **30**, 4875.
59. H. Wadepohl, *Angew. Chem., Int. Ed. Engl.*, 2002, **41**, 4220.
60. H. Yan, A. M. Beatty, and T. P. Fehlner, *Organometallics*, 2002, **21**, 5029.
61. G. B. Jacobsen, E. L. Andersen, C. E. Housecroft, F.-E. Hong, M. L. Buhl, G. J. Long, and T. P. Fehlner, *Inorg. Chem.*, 1987, **26**, 4040.
62. H. D. Johnson II, R. A. Geanagel, and S. G. Shore, *Inorg. Chem.*, 1970, **9**, 908.
63. B. F. G. Johnson and J. Lewis, *Adv. Inorg. Chem. Radiochem.*, 1981, **24**, 225.
64. C. E. Housecroft, *Inorg. Chem.*, 1986, **25**, 3108.
65. J. C. Vites, C. E. Housecroft, C. Eigenbrot, M. L. Buhl, G. J. Long, and T. P. Fehlner, *J. Am. Chem. Soc.*, 1986, **108**, 3304.

66. H. D. Johnson II, V. T. Brice, G. L. Brubaker, and S. G. Shore, *J. Am. Chem. Soc.*, 1972, **94**, 6711.
67. J. Knight and M. J. Mays, *J. Chem. Soc. A*, 1970, 711.
68. R. E. Stevens, R. D. Guettler, and W. L. Gladfelter, *Inorg. Chem.*, 1990, **29**, 451.
69. S. J. Hildebrandt, D. F. Gaines, and J. C. Calabrese, *Inorg. Chem.*, 1978, **17**, 790.
70. H. Vahrenkamp and D. Walter, *Organometallics*, 1982, **1**, 874.
71. R. D. Adams and S. Wang, *Organometallics*, 1986, **5**, 1272.
72. C. E. Housecroft and T. P. Fehlner, *J. Am. Chem. Soc.*, 1986, **108**, 4867.
73. S. G. Shore, D.-Y. Jan, L.-Y. Hsu, and W.-L. Hsu, *J. Am. Chem. Soc.*, 1983, **105**, 5923.
74. V. R. Miller, R. Weiss, and R. N. Grimes, *J. Am. Chem. Soc.*, 1977, **99**, 5646.
75. A. S. Weller, M. Shang, and T. P. Fehlner, *Organometallics*, 1999, **18**, 53.
76. D. J. Wales, D. M. P. Mingos, and L. Zhenyang, *Inorg. Chem.*, 1989, **28**, 2754.
77. D. F. Gaines, *Acc. Chem. Res.*, 1973, **6**, 416.
78. A. Vizi-Orosz, *J. Organomet. Chem.*, 1976, **111**, 61.
79. R. N. Grimes, *Adv. Inorg. Chem. Radiochem.*, 1983, **26**, 55.
80. C.-S. Jun, D. R. Powell, K. J. Haller, and T. P. Fehlner, *Inorg. Chem.*, 1993, **32**, 5071.
81. H. Yan, A. M. Beatty, and T. P. Fehlner, *J. Organomet. Chem.*, 2003, **680**, 66.

Intercalation Chemistry

Allan J. Jacobson[1] **& Linda F. Nazar**[2]
[1]*University of Houston, Houston, TX, USA*
[2]*University of Waterloo, Waterloo, ON, Canada*

1 Introduction 1
2 Insulating Host Lattices 5
3 Conducting Host Lattices 14
4 Related Articles 33
5 References 33

Abbreviations

FAU = Faujasite; LTA = Zeolite A; meq = Milliequivalent; NMF = *N*-methylformamide; α-ZrP = α-Zr(HPO$_4$)$_2$·H$_2$O.

1 INTRODUCTION

The term 'intercalation' refers to a process whereby a guest molecule or ion is inserted into a host lattice. The structure of the guest–host or intercalation compound is only slightly perturbed from the host structure and the reaction used to form the compound is either chemically or thermally reversible. Other terms such as *Insertion*, inclusion, and *Topotactic* reaction are also often used but fall under this general definition. Intercalation compounds have been known since the last century, but in the last three decades have attracted significant attention from the scientific community. The term intercalation was originally used for reactions of layered host lattices but it has been recognized for some years that structures with other dimensionalities can also fall under the same general definition. The more general approach will be taken here, though detailed coverage of all the guest–host combinations that have been studied is beyond the scope of the article. A more detailed view of the extensive scientific literature that covers a wider range of different host lattices and guest molecules and ions and the many different facets of synthesis, reactivity, and physical properties can be found in the references.**[1–8]**

Intercalation reactions and intercalation compounds have attracted attention for several reasons. Reactions provide routes for the synthesis of new solids with kinetic rather than thermodynamic stability and permit controlled systematic changes in physical properties, particularly the electronic, magnetic, and optical properties of the host lattice. Chemical properties may also be finely tuned by incremental changes in composition through *Ion Exchange* reactions. The ability to tailor specific properties by intercalation has been one of the major reasons for interest in the area. This 'tunability' makes it possible to design materials for a variety of applications, for example, catalysts, sorbents, solid electrolytes, sensors, electrochromic displays, and batteries.

Intercalation reactions leave the structure of the host lattice largely unchanged and are therefore different from normal solid-state reactions that involve extensive bond breaking and structural reorganization. Host lattices suitable for intercalation are inherently anisotropic in their chemical bonding. One part of the structure has a strongly bonded lattice of atoms that is largely unchanged when guest molecules or ions are inserted. Intercalation of the guest species occurs in other parts of the structure that contain a connected network of vacant lattice sites or of mobile ionic species. Intercalation of a mobile guest species (G) into a host lattice (H) with interconnected vacant lattice sites (□) can be represented by equation (1), and exchange reactions where the host lattice contains a connected network of mobile ions by equation (2).

$$x\mathrm{G} + \square_x[\mathrm{H}] \Longleftrightarrow \mathrm{G}_x[\mathrm{H}] \qquad (1)$$

$$x\mathrm{G}'' + \mathrm{G}_x{}'[\mathrm{H}] \Longleftrightarrow \mathrm{G}_x{}'[\mathrm{H}] + x\mathrm{G}'' \qquad (2)$$

As indicated, intercalation reactions are usually reversible. In many cases, reactions occur near ambient temperature, but in general the reaction temperature should be high enough to ensure mobility of the guest species but not so high that the strong bonds are broken and the structure of the host lattice is rearranged. Many intercalation compounds are metastable because of the inherent anisotropy in the chemical bonding.

The structural requirement described above places restrictions on the types of host lattices that are suitable for intercalation reactions. Nevertheless, many examples of one-, two-, and three-dimensional structures can be found with suitable properties. Studies of alkali metal reactions with C$_{60}$ (*see* ***Carbon: Fullerenes***) have been discussed in terms of intercalation in a host lattice of effectively zero dimensionality.**[9]** The different types of host lattice geometry are shown in Figure 1.

In three-dimensional systems, the sizes of the guest species that can access the host lattice are constrained. In lower dimensional systems, no such restriction exists and the strongly bonded components (layers, chains, C$_{60}$ molecules) can adjust their separation freely to accommodate guest species of different sizes. With increasing guest size, the structural correlation between layers or chains is diminished and compounds become more difficult to characterize. In the limiting case, complete separation of single layers or chains occurs in solution, resulting in the formation of colloidal dispersions.

In addition to dimensionality, host lattices can be classified as electronic insulators (*see Insulator*) or conductors. Insulating lattices undergo reactions that involve ion exchange, acid–base chemistry (*see Acids & Acidity*), and solvent exchange. Sorption of neutral molecules from the gas phase is

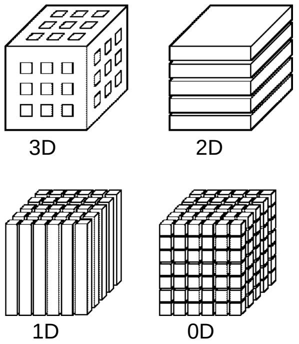

Figure 1 A schematic illustration of different host lattice geometries for intercalation

also an important property, particularly for three-dimensional structures with large pores (e.g. zeolites, *see* ***Zeolites***) and the layered compounds. Sorption of organic molecules forms the basis for the application of these compounds in separations and in catalytic conversions (*see Catalysis*) of hydrocarbons to fuels and chemicals. The major classes of three- and two-dimensional insulating host lattices are listed in Table 1; examples of one-dimensional systems are rare. Most of the examples contain mobile cationic species in negatively charged lattices. The layered double hydroxides, such as $Zn_2Cr(OH)_6Cl{\cdot}2H_2O$, form the only major class of anion exchangers.

The major classes of conducting host lattices are summarized in Table 2. Of these, graphite and the layered transition metal dichalcogenides (*see* ***Chalcogenides: Solid-state Chemistry***) have been investigated in the greatest detail. The conducting host lattices have the feature that the concentration of ionic guest species can be altered by oxidation or reduction of the host lattice. In contrast, in the insulating lattices the concentration of ionic guests is fixed by the chemical composition and remains unchanged throughout subsequent reactions. The chemistry of most of the compound classes in Table 2 involves reduction reactions and cation insertions. The major exception is graphite, which can be both reductively intercalated with cations and oxidized with anion insertion. The two types of reactions can be represented by equations (3) and (4).

Table 1 Insulating host lattices for intercalation

Three-dimensional structures
Zeolites $M_x^+(Al_xSi_{2-x}O_2){\cdot}nH_2O$
$AlPO_4$-*n*, SAPO-*n*
Zeotypes: phosphates and silicates containing transition metal ions.
Pyrochlores: $Ca_2Nb_2O_7$, $KNbWO_6$, W_2O_6
$KsbO_3$, $LiNbO_3$
β-Alumina
Two-dimensional structures
Clays and layered silicates
Kaolinite $Al_2Si_2O_5(OH)_4$
Hectorite $Na_x(Mg_{3-x}Li_x)Si_4O_{10}(OH)_2{\cdot}mH_2O$
Montmorillonite $Na_x(Al_{2-x}MG_x)Si_4O_{10}(OH)_2{\cdot}mH_2O$
Niobates and tantalates
$K[Ca_2Na_{n-3}Nb_nO_{3n+1}]$, $3 \leq n \leq 7$; $K_2Ti_4O_9$, $KtiNbO_3$
Acid phosphates
$M(HPO_4)_2{\cdot}H_2O$; M = Ti, Zr, Hf, Ce, Sn
Hydrous oxides
$A_xUO_2XO_4{\cdot}mH_2O$
Layered double hydroxides
$LiAl_2(OH)_6OH{\cdot}2H_2O$, $Zn_2Cr(OH)_6Cl{\cdot}2H_2O$
$Ni(CN)_2$

Table 2 Redox-active host lattices for intercalation

Three-dimensional structures
Intersecting channels
Chevrel phases $M_xMo_6X_8$ (X = S, Se)
Perovskite related oxides WO_3, ReO_3, V_6O_{13}
Tunnel structures
Nb_3X_4 (X = S, Se); Ti_3S_4, $Tl_xV_6S_8$
Rutile oxides MO_2 (M = Ti, Mn, Cr, Mo, W, Ru, Os, Ir)
h-WO_3
Two-dimensional structures
Graphite
Dichalcogenides
MX_2 (M = Ti, Zr, Hf, V, Nb, Ta, Mo, W; X = S, Se, Te)
Metal phosphorus trichalcogenides
MPX_3 (M = Mg, V, Mn, Fe, Co, Ni, Zn, Cd, In; X = S, Se)
Metal oxyhalides
MOX (M = Ti, V, Cr, Fe; X = Cl, Br)
Metal Nitride Halides
MNX (M = Zr, Hf; X = Cl, Br, I)
Ternary chalcogenides
AMX_2 (A = Group 1; M = Ti, V, Cr, Mn, Fe, Co, Ni; X = O, S)
$MOXO_4$ (M = V, Nb, Ta, Mo; X = P, As)
MoO_3; V_2O_5
One-dimensional structures
Carbon nanotubes
MX_3 (M = Ti, Zr, Hf, Nb, Ta; X = S, Se)
$AFeS_2$ (A = Na, K, Rb, Cs)
AMo_3X_3 (A = Group 1; X = S, Se)

$$xG^+ + xe' \text{ to } [H] \Longleftrightarrow G_x^+[H]^{x-} \tag{3}$$

$$xG^- + xe' \text{ from } [H] \Longleftrightarrow [H]^{x+}G_x^- \tag{4}$$

The simplest model for redox intercalation involves the quantitative transfer of electrons between the intercalating species and the lowest energy level of the host lattice. A rigid band description is generally assumed to give a reasonable account of the variation of the composition and the properties of the intercalation compound. Once an intercalation compound has been formed by a redox process, then ion and solvent exchange reactions of the type observed in insulating lattices are possible. A redox intercalation reaction of a layered compound is shown schematically in Figure 2 for the reaction of lithium with TiS_2. The titanium disulfide layers are reduced and lithium cations diffuse into empty octahedral sites between the sulfur layers. The reaction begins at the crystal edges and the reaction front moves into the center of

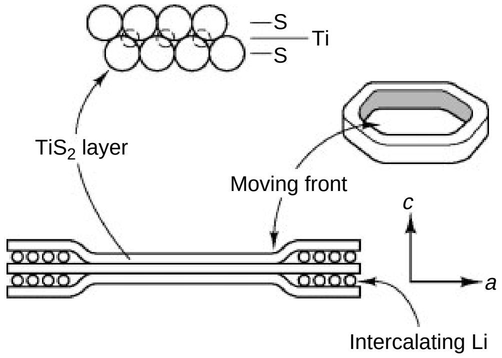

Figure 2 Schematic representation of the process of lithium intercalation into layered titanium disulfide. (Reprinted from Ref. 10. © 1976, with permission from Elsevier)

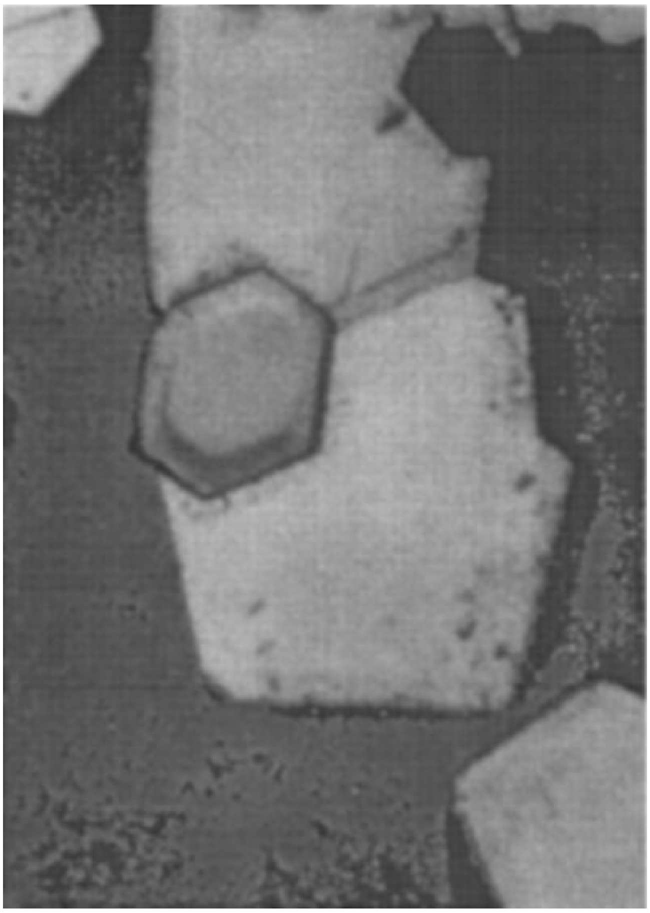

Figure 3 Optical micrograph of a partially intercalated TiS_2 crystal. (Reprinted from Ref. 10. © 1976, with permission from Elsevier)

the crystal as the reaction proceeds. The intermediate stage shown schematically in Figure 2 is clearly visible in the optical micrograph of a partially reacted crystal (Figure 3).[10]

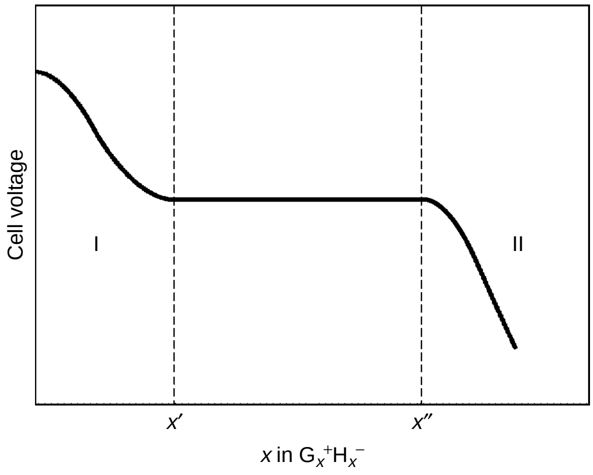

Figure 4 Schematic of the variation of cell voltage with composition for the electrochemical intercalation of a guest ion (G) into a host lattice (H)

Electrochemical techniques have been widely used to study redox reactions. They provide important quantitative information about the extent of total charge transfer and details of phase equilibria. For a reaction expressed by equations (3) and (4) a schematic diagram of the variation of voltage versus charge transferred is shown in Figure 4 for a typical system at equilibrium.[2b] The smooth variations of V versus x in regions I and II are indicative of single phases with varying compositions. The variation in voltage is directly proportional to the partial molar free energy (*see Gibbs Energy*) of solution of the guest species in the host lattice. Regions where the cell voltage is constant with x correspond to regions where two solid phases coexist. For example, in Figure 4, phase I is converted to phase II between x' and x''. Interpretation of such data assumes that equilibrium has been obtained, a situation that can be difficult to achieve at lower temperatures for larger guest species. Apparent plateaux in V versus x data may also be observed in cases where electron transfer involves a region where the density of states is very large.[11]

Chemical reagents can also be used to carry out redox intercalation reactions. Alkali metals in liquid ammonia[12] and organometallic reagents such as n-butyllithium[13] were among the earliest used. Other chemical reagents can be used to provide different effective activities of the alkali metal relative to the pure metal. A convenient summary, developed for comparison of the reduction potentials for some common lithium reagents and common host lattices, is shown in Figure 5.[14]

1.1 Mechanisms of Intercalation

Intercalation is a complex process. Reactions involve adsorption of guest species on host crystals, exchange or insertion at the host surface, the formation of intermediate stages in layered compounds, and transport within the host lattice. Macroscopic effects such as variations in crystal size,

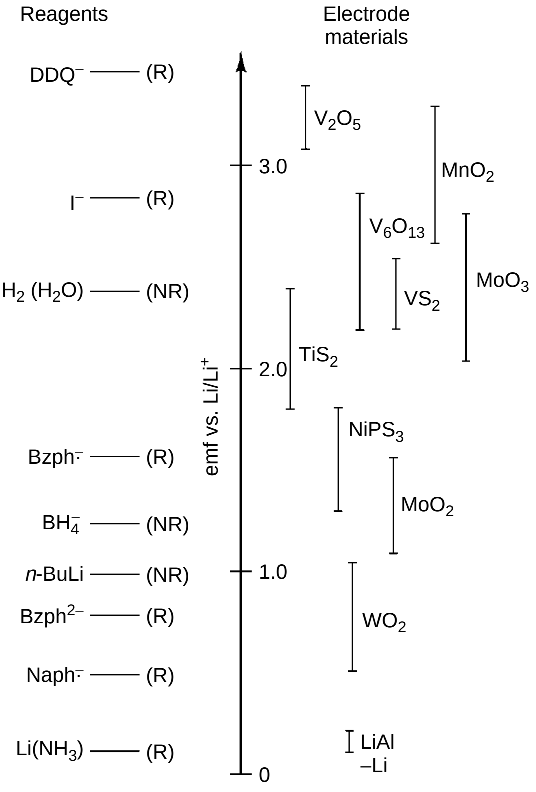

Figure 5 Reduction potentials for some common host lattices relative to some common lithium reagents. (Reprinted with permission from D.W. Murphy and P.A. Christian, *Science*, 1979, **205**, 651. © 1979 AAAS)

dislocations, stacking faults, and pore mouth blockage can strongly influence the kinetics of intercalation. In layered compounds, interlayer defects (*see* ***Defects in Solids***) such as crosslinks in graphite and interstitial metal atoms in dichalcogenides further complicate the situation. Reaction mechanisms have been studied in some detail for layered structures, but some aspects remain poorly understood. Recent advances in in situ studies using energy dispersive X-ray diffraction with synchrotron radiation have added significantly to our general understanding of intercalation mechanisms.[15]

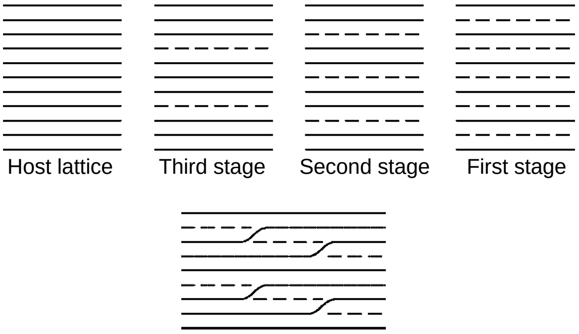

Figure 6 Schematic representation of staging in intercalation compounds. The lower part represents the isolated island or domain model. The continuous line represents the host layer, the dashed line a guest layer

Redox intercalation reactions of layered host lattices show two extreme kinds of behavior at low guest concentrations where the interlayer sites are only partially occupied. Some reactions proceed by insertion of the guest species into all the interlayers. At intermediate compositions each interlayer has the same concentration of guest species distributed randomly over the available interlayer sites. Two-phase behavior is observed up to some critical concentration of guest species, implying that a minimum energy of reaction is required to open up the van der Waals gap between the layers. Other reactions occur *via* staging, which provides a mechanism to minimize the energy associated with separating the layers. Ideally, staging results in the formation of compounds with alternating sequences of filled or empty interlayer sites, as shown in Figure 6. The facile transformations between odd and even numbered stages that are observed in graphite intercalation compounds are not easily explained with this simple model. Consequently, Daumas and Hérold proposed a model in which the stages are assumed to exist in the crystal in the form of local domains.[16] The existence of staging indicates that at low guest concentrations the energy associated with a homogeneous distribution of cations throughout the interlayer space is higher than when the guests are concentrated in a fraction of the interlayer sites. Communication between layers in staged systems involves deformation of the layers and is most commonly observed in compounds where the layers are flexible. The origin of the effect has been discussed in detail for graphite intercalation compounds.[17] A related phenomenon occurs in ion-exchange reactions of layered compounds with two cations of different sizes. Some synthesis conditions can result in a random distribution of both cations over the interlayer sites. The random distribution is, however, unstable with respect to a distribution in which cations of different sizes are segregated into different interlayers.

Uptake isotherms measured for the intercalation of gaseous species by layered structures generally show the sigmoidal behavior characteristic of a nucleated process. These curves may also show plateaux as a consequence of the formation of intermediate stages. Early experiments by Hooley[18] showed that basal plane adsorption plays a critical role. In a study of the reaction of graphite with bromine, intercalation did not occur when the basal surfaces of a graphite cylinder were isolated from the bromine by glass caps. When the basal surfaces were exposed, intercalation proceeded with the greatest physical expansion of the specimen observed nearest the ends. The experiments were interpreted in terms of basal plane adsorption weakening the interaction between the first two layers and permitting intercalation to occur. Once the process begins, then the effect is transmitted layer to layer.

Involvement of higher stages at the early stages of intercalation has been shown in several experiments. For example, intercalation of ammonia in TaS_2 was shown by in situ neutron diffraction (*see* ***Diffraction Methods in Inorganic Chemistry***) of a bulk polycrystalline sample to proceed through the formation of higher stages, which coexist in the powder sample.[19] A single-crystal study of the intercalation of silver in TiS_2 was shown to involve the initial formation of a first stage phase on electrochemical reaction. Analysis of the penetration of silver into the crystal showed that a stage 1 region was formed near to the crystal edge. Further inside the crystal, the stage 1 region transformed into a stage 2 zone that was followed by unintercalated host. When the electrochemical insertion was stopped and the crystal allowed to equilibrate, the stage 1 region rapidly converted to stage 2 without further treatment and the overall reaction front moved further into the crystal. The result supports the Daumas–Hérold model of staging (see Figure 6) and gives for this specific case an estimate of 130 Å for the dimension of the islands.[20] A similar study of lithium intercalation in 2H-TaS_2 by measurement of the ^{181}Ta quadrupole interaction also showed the existence of phase boundaries between regions of different composition, which gradually diffused into the center of the crystal. In this case, three different regions were identified: stage 1, a dilute stage 1 with the composition $Li_{1/3}TaS_2$, and an intermediate improper stage 2 made up of alternating layers of the two first stage compositions.[21] Crystal size plays an important role in all of these experiments. Intercalation of hydrated sodium ions under nonequilibrium conditions carried out either electrochemically or by using sodium dithionite as a chemical reductant, shows the same staging type of behavior as that described above, together with the additional feature that a monolayer hydrate region precedes the stable bilayer configuration into the crystal. In contrast, no staged intermediates are observed with polycrystalline material and the reaction occurs as a simple two-phase process.[22]

As mentioned above, the rigidity of the layers is an important parameter in directing the mechanism of intercalation. The concept of layer rigidity has been quantified by Solin and coworkers.[23] For an intercalation compound with the general composition $G_xG'_{1-x}H$ where G and G′ are either two different guests or a guest and a vacant site, the normalized interlayer separation as a function of the mole fraction x of the guest species can be written as $d_n(x) = 1 - (1-x)^p$ where p is a parameter that characterizes the layer rigidity. The normalized interlayer separation is defined as $d_n(x) = [d(x) - d(0)]/[d(0) - d(1)]$. By measuring the composition dependence of the normalized interlayer separation the rigidity parameter of the host structure can be determined. This technique has been applied to several systems including Cs_xRb_{1-x}-vermiculite ($p = 7$), Li_xTiS_2 ($p = 5$) and Li_xC_6 ($p = 2$). As shown by the values of p, the layer rigidity of vermiculite is higher than that of TiS_2, which in turn is higher than that of graphite. An assumption of the layer rigidity model is that the guest ions do not deform. For hosts such as the layer perovskites, with layers that are even more rigid than those of 2:1 clays, this condition does not hold and an alternative model was developed to account for the observed variation of the interlayer spacing as a function of composition.[24] The rigidity of the layer is an important factor in determining whether or not staging will occur. Layered compounds with rigid layers such as clays and layered perovskites do not show staging behavior unlike the intercalation compounds of graphite and the layered dichalcogenides.

2 INSULATING HOST LATTICES

The major classes of insulating host lattices are given in Table 1. A very diverse range of compositions and structure types is included and it is beyond the scope of this article to describe all the structures and their associated chemistry in any detail. Some general comments concerning a few typical compounds will be made to illustrate the types of intercalation compounds and reactions that are known.

2.1 Three-dimensional Structures

2.1.1 Zeolites[25,26]

Zeolites and the related aluminophosphates form the most extensive class of insulating three-dimensional solids. Zeolites are three-dimensional framework structures with the general composition $M_{x/n}{}^{n+}[Al_xSi_{1-x}O_2]\cdot nH_2O$. The frameworks consist of AlO_4 and SiO_4 tetrahedra (*see Tetrahedral*) linked by corner-sharing oxygen atoms to build open structures illustrated in Figure 7 for two important materials, zeolite A (LTA) and *Faujasite* (FAU, also called zeolite X or Y depending on the Si:Al ratio). The vertices show the positions of the Si or Al (T) atoms; oxygen atoms are not shown. Frameworks are constructed so that there are no Al–O–Al bonds (Lowenstein's Rule[27]) and consequently Si:Al $\geq$ 1.0. The substitution of Al atoms for some Si atoms introduces a net negative charge on the MO_2 framework, which is compensated

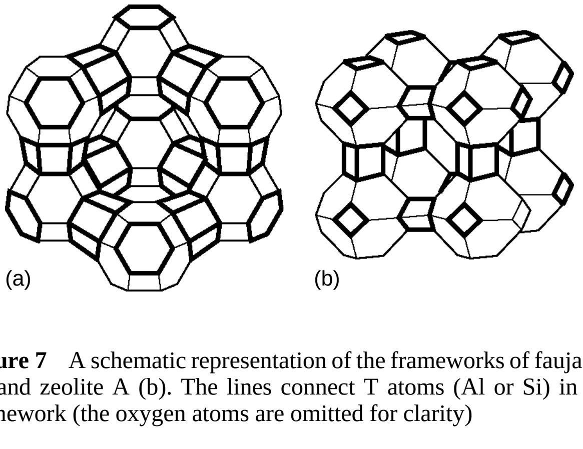

Figure 7 A schematic representation of the frameworks of faujasite (a) and zeolite A (b). The lines connect T atoms (Al or Si) in the framework (the oxygen atoms are omitted for clarity)

by the presence of nonframework cations. Nonframework cations are either solvated or bonded to the framework oxygen atoms when the zeolite is anhydrous. Zeolites are very low density metastable phases. The intracrystalline pore volumes of FAU and zeolite LTA are 0.53 and 0.47 cm^3 liq H_2O/cm^3 crystal, respectively. Consequently, zeolites can adsorb large amounts of gaseous atomic or molecular species. Adsorption isotherms and kinetics and thermodynamics of sorption have been investigated for a wide range of polar and nonpolar molecules. The adsorption of molecules is restricted to those that are smaller than the narrowest free diameter of the channel structure. This diameter is controlled by the topology of the specific zeolite, by the narrowest ring of tetrahedra, and also by the nonframework cations. In LTA, the smallest diameter is defined by eight tetrahedra, whereas FAU contains a 12-ring. The aperture of LTA is large enough to permit access by paraffins, whereas FAU will sorb single ring aromatics. Until the discovery of the $AlPO_4$ family of structures,**[28,29]** 12-rings were the largest known. Compounds are now known with larger ring sizes, for example, 18 in the aluminum phosphate VPI-5**[30]** and in the aluminosilicate ECR-34.**[31]**

The energetics of molecule sorption depend on the guest molecule or atom, the specific cations present in the framework, and the Si:Al ratio. Frameworks with low levels of aluminum substitution and few nonframework cations have relatively low affinities for polar molecules.

In addition to molecule sorption, zeolites also exhibit extensive ion-exchange behavior. Ion mobilities in anhydrous phases are very low, but increase when polar molecules or water are present in the structure. Ion exchange is an important property of zeolites. The ion-exchange capacity is determined by the Si:Al ratio and exchange rates are usually fast. Synthetic zeolite A (Na-LTA) is widely used for water treatment by selective ion exchange of Ca and Mg for Na ions. Ion-exchange reactions also make possible the introduction of a wide range of cations that modify the sorption and catalytic properties. For example, the Na exchanged form of zeolite A (often called zeolite 4A) has an effective pore diameter of 4 Å, whereas in the potassium exchanged form this diameter is reduced to 3 Å. The K-LTA (zeolite 3A) will sorb water but will not sorb larger molecules such as alkanes, and consequently is widely used for drying solvents and gases. Exchange of Na^+ by Ca^{2+} (zeolite 5A) increases the effective pore diameter sufficiently to permit sorption of n-alkanes. Zeolite 5A is used commercially for separating straight chain from branched alkanes.

Zeolites find major applications in catalysis. A form of the zeolite FAU is, for example, an active catalyst component in catalytic cracking of heavy hydrocarbons to produce motor gasoline and diesel. The catalyst activity arises from its Brønsted acidity, which in turn comes from the presence in the structure of protons attached to bridging oxygen atoms. Protons can be introduced by ion exchange of ammonium cations, followed by calcination to remove NH_3 and generate the acid form of the zeolite. The process is more complex in practice because of the instability of the acid form of the zeolite. Some decomposition invariably occurs, resulting in aluminum removal from the framework sites (dealumination).

Zeolite catalysts containing platinum and other precious metals are prepared by ion exchange of species such as $Pt(NH_3)_4{}^{2+}$, for example, the catalyst Pt/zeolite KL that catalyzes hexane aromatization to selectively form benzene.

2.1.2 Other Structures[32–35]

In addition to the zeolites and the $AlPO_4$-*n* structures, many other synthetic materials now are known with pores big enough to permit access of molecules larger than water. These include phosphates of main group elements, such as Ga, In, and Sn, and a number of transition metal phosphates, including systems based upon V, Mo, Fe, Co, and Ni. The nickel phosphate, VSB-5, $Ni_{20}[(OH)_{12}(H_2O)_6][(HPO_4)_8(PO_4)_4]\cdot 12H_2O$, is an example of a framework that is porous, has good thermal stability and catalytic activity for hydrogenation and base-catalyzed reactions.**[36]** Synthesis of novel microporous materials that have mixed octahedral-tetrahedral frameworks has been extended to include transition metal silicates, particularly those of titanium, vanadium, and copper.**[33,34]**

In addition to the synthetic materials, several naturally occurring phases formed under hydrothermal conditions are known with very large intracrystalline volumes and pore openings. Examples include cacoxenite, $AlFe_{24}O_6(OH)_{12}(PO_4)_{17}(H_2O)_{17}\cdot 51H_2O$, which has 14.2 Å pores,**[37]** and wightmanite ('natural drainpipe'), $Mg_5(BO_3)O(OH)_5\cdot nH_2O$, which has elliptical channels with maximum and minimum free diameters of 6.0 and 4.0 Å.**[38]** Both phases contain octahedrally coordinated cations connected by other units.

The wide range of structural units exhibited by the natural and synthetic phases suggests that many new open frameworks with ion-exchange and sorption properties can be obtained. Exploratory synthesis of novel microporous solids is currently an active research area.

Other three-dimensionally connected oxide structures show ion-exchange chemistry and sorption of small molecules such as water or ammonia. These include oxides with the $A_2B_2O_7$ pyrochlore structure,**[39]** $KSbO_3$ related phases,**[40]** and $LiNbO_3$.**[41]** Compositions with these structure types can be exchanged in mineral acids or in molten salts.

The pyrochlore structure can be described as a three-dimensional connected network of BO_6 octahedra that share all corners (Figure 8). Interpenetrating the B_2O_6 network is a tetrahedral A_2O' lattice oriented so that the A cations are located in rings formed by six oxygen atoms from the B_2O_6 lattice and two O′ oxygen atoms from the A_2O' lattice. The A_2O' lattice is not necessary for the stability of the structure, and defect pyrochlore compositions are known in which all or part of the A_2O' lattice is missing. Examples include $Ca_2Nb_2O_7$, $Tl_2Nb_2O_6$, and $KNbWO_6$.**[42,43]** The last-named compound is anhydrous when prepared by reaction of

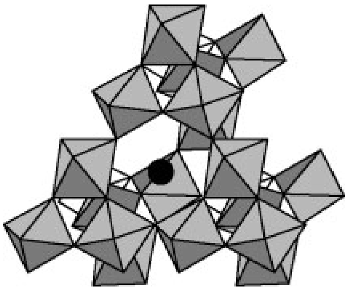

Figure 8 The B_2O_6 framework of pyrochlore represented as BO_6 octahedra sharing corners. The filled circle corresponds to the position of the water molecule in $W_2O_6{\cdot}H_2O$

$KNbO_3$ and WO_3 at high temperature, but readily hydrates in ambient conditions to form $KNbWO_6{\cdot}H_2O$. All three niobates form the corresponding proton exchange forms $H_2Nb_2O_6{\cdot}H_2O$ when ion exchanged in acid with retention of the pyrochlore structure. Recently, the series has been extended to include synthesis of the pyrochlore $W_2O_6{\cdot}H_2O$ by ion exchange of an alkali metal tungstate.[44] The water molecule is only weakly bound in the pyrochlore WO_3 compared with $KNbWO_6$ or zeolitic frameworks where significant interactions with nonframework cations are present.

The $KSbO_3$ structure contains pairs of edge-shared SbO_6 octahedra that share corners to form the cubic network with K^+ ions in three-dimensionally connected channels. The structure was originally investigated as a candidate for fast ion conductivity (*see* ***Ionic Conductors***). The K atoms are readily exchanged in excess molten nitrates to form the phases $MSbO_3$ (M = Li, Na, Rb, Tl, and Ag). The hydronium phase $HSbO_3{\cdot}H_2O$ has been synthesized by acid exchange and found to have lower proton conductivity than the same composition with the pyrochlore structure.[45]

Ion-exchange reactions in aqueous acid of $LiNbO_3$ and $LiTaO_3$ to form $HNbO_3$ and $HTaO_3$ have also been reported. A transformation from the hexagonal close-packed oxygen lattice to the perovskite structure occurs during reaction. The transformation appears surprising at first glance, but can occur by deformation of the lattice without bond breaking. The reverse transformation is observed in lithium intercalation of ReO_3 (see Section 3.6.1). Lithium niobate has important nonlinear optical properties, and ion-exchange reactions have been used to modify the surface of crystals for optical devices.

2.2 Two-dimensional Structures

The sheet silicates or *Clay Minerals* constitute the largest group of the two-dimensional structures in Table 1.[25,46,47] All the two-dimensional materials show ion exchange and sorption of neutral molecules like the three-dimensional structures, but with the added feature that the interlayer separation can adjust freely to accommodate large guest species. Shape selective sorption or molecular sieving is not generally observed except in a special class of materials usually referred to as pillared layered compounds.

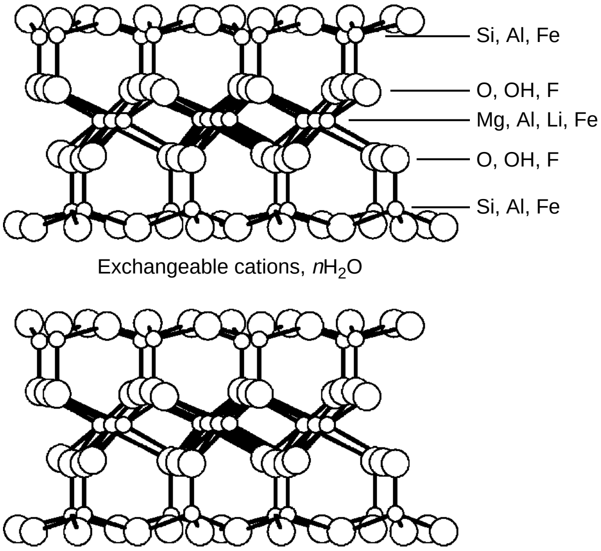

Figure 9 Schematic diagram of the structure of a three-layer silicate

2.2.1 *Clay Minerals*

Clay minerals have structures comprising complex layers made by condensing two types of sublayers. In one type, silicon is tetrahedrally coordinated, $Si_2O_3(OH)_2$, and in the other aluminum is octahedral, $Al(OH)_6$ (see Figure 9). The sublayers are connected to produce two different structure types that are illustrated by kaolinite, which has the ideal composition $Al_2Si_2O_5(OH)_4$ and contains one octahedral and one tetrahedral layer (1:1), and pyrophyllite, $Al_2(Si_4O_{10})(OH)_2$, which has one octahedral and two tetrahedral layers (2:1). Compounds are also known in which three Mg^{2+} cations replace two Al^{3+} cations to give serpentine, $Mg_3Si_2O_5(OH)_4$, or talc, $Mg_3(Si_4O_{10})(OH)_2$.

The compositions of the layers in the ideal end members have no charge and are not reducible. Consequently their intercalation chemistry is very restricted. *Hydrogen Bonding* interactions exist between the layers in kaolinite, and some intercalation reactions occur with guest molecules that can themselves hydrogen bond. For example, kaolinite intercalation compounds are known with urea, formamide, acetamide, and hydrazine. The hydrogen bonding network in the compound of formamide with dickite (a crystallographic modification of kaolinite with the same composition) has been determined by single-crystal *X-Ray Diffraction*. The compound is an unusual example of intercalation of a neutral guest between neutral layers and where the product is sufficiently crystalline for a complete structure determination.

As in zeolites, negative charges on the layers can be introduced by chemical substitution. Substitutions can be made in either the tetrahedral or the octahedral positions with ions of comparable radii. Thus aluminum may replace silicon in the tetrahedral layers and Li^+ can replace Mg^{2+} or Fe^{2+}/Fe^{3+} can replace Al^{3+} in the octahedral sites. The flexibility that results by substitution with many different cations leads to an extraordinary diversity of phases, beyond the scope of this section.[25,46,47] The micas, with very high layer charges (24 Å^2 per e^-), represent the opposite extreme of behavior to that shown by the neutral layers. Muscovite, $KAl_2(Si_3AlO_{10})(OH)_2$, is the analog of pyrophyllite. One tetrahedral layer silicon atom is substituted by aluminum and K^+ interlayer cations balance the layer charge. Similarly phlogopite, $KMg_3(AlSi_3O_{10})(OH)_2$, is the mica analog of talc. Solvent molecules cannot usually be intercalated into micas because of the strong electrostatic forces between the layers.

In clay chemistry, the layer charge density is often expressed in terms of the cation exchange capacity in milliequivalents per gram of solid (e.g. muscovite 252 meq g^{-1} and phlogopite 240 meq g^{-1}). Pyrophyllite and talc ideally have zero ion-exchange capacities. The interesting intercalation chemistry in the clays occurs in the intermediate range of layer charges (60–165 meq g^{-1}) for compounds described as smectites (60–100 meq g^{-1}) or vermiculites (100–165 meq g^{-1}). Idealized compositions of some examples are given below:

montmorillonite	$Na_x(Al_{2-x}Mg_x)(Si_4O_{10})(OH)_2 \cdot mH_2O$
Beidellite	$Na_x(Al_2)(Al_xSi_{4-x}O_{10})(OH)_2 \cdot mH_2O$
hectorite	$Na_x(Mg_{3-x}Li_x)(Si_4O_{10})(OH)_2 \cdot mH_2O$
vermiculite	$(Na, Ca)Mg_3(Al_xSi_{4-x}O_{10})(OH)_2 \cdot mH_2O$

Interlayer water molecules that solvate the interlayer alkali or alkaline earth metal are present in all compositions.

The smectites and vermiculites show reversible intercalation behavior with a wide range of neutral molecules. Two features are worth noting. In molecule sorption by zeolites, minimal changes in the framework structure occur. In layered systems, however, energy has to be expended to separate the layers on intercalation, with the consequence that reactions with vapor-phase guests generally have threshold pressures for intercalation and hysteresis is observed on deintercalation. The hysteresis loops are a measure of the energy needed to expand and contract the interlayer spacing. Secondly, when in contact with an electrolyte solution the interlayer separation depends on the solvent activity. As the electrolyte concentration is lowered, the layer separation is increased as increasing numbers of solvent molecules are intercalated. At lower layer charges, this process can ultimately lead to complete delamination (exfoliation) and the formation of colloidal solutions or gels at higher solid concentrations.

Three areas of the intercalation chemistry of clays have received very detailed study and will be described further: (a) intercalation of organic cations and neutral organic molecules; (b) pillaring reactions; and (c) clay–polymer nanocomposites.

Organic Cations. Intercalation reactions of long chain alkylamines and alkanols have been studied in many different classes of insulating host lattices.[48,49] Ordered bilayer structures are formed because of the high van der Waals interaction energies (*see van der Waals Forces*) between the alkyl chains (4.2 kJ per CH_2). The compounds provide model systems for study of structure and phase transitions in ordered bilayers related to lipid layers in biological membranes and ordered monomolecular films on surfaces. In sheet silicates, particularly uniform structures are obtained when ion exchange of the inorganic cations by alkylammonium cations is followed by intercalation of neutral alkanol molecules. When the alkyl chains in the alkylammonium cations and in the alkanol are about the same length, two alkyl groups per Si_4O_{10} unit are intercalated. The stoichiometry corresponds to one polar head group for each hexagonal hole in the layer surface. The ratio of alkylamine to alkanol varies with the layer charge and the packing density is in the range 23–23.5 Å^2 per chain, somewhat less than the value of 19 Å^2 per chain observed in paraffins or polyethylene. At ambient temperature the alkyl chains are perpendicular to the layers and have all trans conformations (see Figure 10). However, as the temperature is raised, decreased interlayer separations are observed corresponding to the conformational changes from trans to gauche. The introduction of regular sequences of trans and gauche bonds produces kinks in the chains, which reduces the interlayer separation in steps of 1.27 Å. The regular decrease in the interlayer spacing implies a concerted rearrangement of the chains in order to fit adjacent chains together. Such packing results in the formation of kink blocks (Figure 10). At higher temperatures, loss of the intercalated alkanol molecules results in a lower packing density of the remaining alkyl chains and a large drop in the interlayer spacing is observed. The changes in interlayer spacing are harder to interpret in this region, but generally involve the formation of gauche blocks.

The formation of different types of ordered arrangements generally correlates with the chain packing density. At high chain packing densities (closest packing $\leq$20 Å^2) the energy required to nucleate a kink is $\geq$30 kJ mol^{-1}, but for 24 Å^2 it is only about 3 kJ mol^{-1}. Consequently, regular kink block structures are favored in the range of 22–25 Å^2 and gauche blocks at packing densities of 33–40 Å^2 per chain. Similar

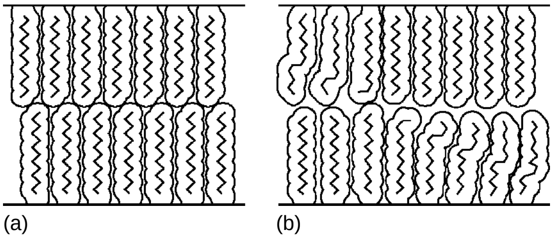

Figure 10 Schematic diagram of organic bilayer structures in layered compounds; all trans conformation (a), kink blocks (b)

results are observed in alkyl chain structures in other insulating layered systems including titanates, niobates, and molybdates.

Pillaring Reactions. In zeolite and other three-dimensional structures, the frameworks remain porous in the absence of guest molecules. In smectites and vermiculites, on the other hand, the layer separation is reduced as intercalated solvent molecules are removed and the materials have no permanent porosity. The introduction of large cations by ion exchange can, however, provide permanent intracrystalline porosity. Organic cations, for example, mono-, di-, tri-, and tetra-alkylammonium cations, were shown to introduce porosity characterized by no additional increase in separation of the layers on sorption of small molecules. Larger molecules produce an increase in interlayer separation and characteristic hysteresis in the sorption isotherms. Dications such as en^{2+} are even more effective, since only half as many are required to neutralize the layer charge. Significant amounts of guest molecules can be intercalated and selective molecule separations characteristic of materials with permanent and well-defined porosity are observed. An interesting example is the separation of benzene and toluene by ethylenediammonium fluorohectorite.[50]

The organic pillared layered compounds are of considerable interest for intercalation chemistry at lower temperatures, but are not stable at the higher temperatures where clays have been used as catalysts. Inorganic pillared clays were studied by Vaughan, Lussier, and Magee[51] with a view to extending the temperature stability range. A large inorganic cation is introduced by ion exchange into the interlamellar space to separate the layers. The inorganic pillars are then fixed in place by calcination to form a stable pillared clay with permanent microporosity.[52] The initial work and many subsequent studies have used the complex aluminum polyoxocations present either in commercially available chlorhydrol solutions or solutions of aluminum chloride partially hydrolyzed with sodium hydroxide. Both reagents have been shown by nuclear magnetic resonance (NMR) to contain the polyoxocation $[Al_{13}O_4(OH)_{24}\cdot 12H_2O]^{7+}$, first identified crystallographically by Johansson.[53] Ion exchange of smectite layers with such solutions produces an interlayer expansion of about 9 Å, consistent with the incorporation of the Al_{13} cation. The amount incorporated depends on the layer charge, but is somewhat variable since the polyoxocation charge may change by further hydrolysis reactions. On heating, the Al_{13} cationic species dehydrates and becomes permanently attached to the silicate layers through the formation of Si–O–Al bonds, producing a permanent microporous solid. The pore size distribution is not as sharp as that observed in crystalline zeolites, but pillared clays do show characteristic molecular sieving properties. Similar pillaring reactions with a variety of other inorganic cations including zirconium, bismuth, silicon, and niobium halide clusters have also been reported.[54]

Clay – Polymer Nanocomposites. Polymer intercalation into layered compounds has become an important route to the synthesis of organic-inorganic hybrid materials and composites. A variety of layered systems have been investigated but much of the work has focused on the sheet silicates, in part because of the discovery of exceptional mechanical properties of clay nanocomposites formed between organocation exchanged montmorillonites and nylon-6 by Toyota researchers.[55–57] In general, these polymer-clay composites can be described as either intercalated or exfoliated. In the former, polymer chains are intercalated into the host lattice to give a well ordered multilayer structure. In contrast, in an exfoliated composite, individual 10 Å thick clay layers are dispersed in a continuous polymer matrix and separated at average distances that depend on the volume fraction of clay. The general synthesis approach to these systems involves preintercalation of a cationic surfactant such as a long chain primary alkylammonium cation, as discussed in Section Organic Cations, in order to make the silicate sufficiently organophilic to intercalate either monomers or polymers in a second step. A wide range of polymer systems including, for example, poly(styrene), poly(isoprene), poly(methyl methacrylate), poly (L-lactic acid), and poly(ethylene oxide) have been studied.

Intercalation of poly(ethylene oxide) into a lithium-ion exchanged clay gives an interesting class of layered silicate nanocomposites that are lithium-ion electrolytes.[58,59] Compounds have been prepared by intercalation from methanol/water solutions and by melt intercalation. Melt intercalation typically gives samples with higher polymer contents than the solution method and with higher lithium-ion conductivity though the conductivity is probably still too low for practical applications.

2.2.2 *Layered Double Hydroxides*[60,61]

The layered double hydroxides are derived by partial substitution of a trivalent cation for a divalent cation in a hydroxide with the $Mg(OH)_2$ brucite structure. The natural mineral hydrotalcite, with the approximate formula $Mg_6Al_2(OH)_{16}CO_3\cdot 4H_2O$, is the best known example. Substitution results in a general composition $M_{1-x}M'_x(OH)_2\cdot A_{x/n}\cdot mH_2O$, where the positive charge introduced into the hydroxide layers is compensated by a solvated interlayer anion (A). Compounds with a wide range of cations, for example, $M^{2+} = $ Mg, Zn, Fe, or Co and $M'^{3+} = $ Cr, Al, Mn, or Fe, can be synthesized by direct precipitation from aqueous solutions with hydroxide or carbonate ions. The precipitates have broad X-ray diffraction patterns, indicating small particles. Crystallinity can be improved by mild hydrothermal treatment. The amount of trivalent cation substituted in the $M(OH)_2$ layer typically corresponds to either $x = 0.25$ or $x = 0.33$. In the Mg–Al and Ni–Al systems, some evidence exists for a more continuous range of composition. One interesting synthesis variant is found for

$Zn_{2/3}Cr_{1/3}(OH)_2{\cdot}A_{1/3}{\cdot}mH_2O$. This phase is formed directly by reaction of 60 °C of ZnO with a solution of $CrCl_3$ at $pH = 4$.[62] The specific interlayer anion is determined by the synthesis method, but can easily be exchanged after the compound is formed. Ion-exchange isotherms have been determined for several combinations of simple ions (e.g. $OH^-{-}NO_3^-$, $NO_3^-{-}X^-$ ($X = F, Cl, Br, I$), $NO_3^-{-}SO_4^{2-}$, $NO_3^-{-}CO_3^{2-}$). Ion selectivities are generally found to be in the order $OH^- > F^- > Cl^- > Br^- > NO_3^- > I^-$.[63]

The layered double hydroxides will also intercalate organic anions such as *n*-alkylsulfates to give phases with large basal spacings that undergo further swelling by intercalation of *n*-alkanols and *n*-alkylamines analogous to the behavior of the layered silicates.[62] Exchange of interlayer ions by aliphatic carboxylate anions with different chain lengths gives intercalation compounds in which the interlayer separation increases regularly with the increase in the number of carbon atoms. In situ X-ray diffraction has been used to study dicarboxylate intercalation reactions in $[LiAl_2(OH)_6]Cl{\cdot}H_2O$.[61] The reaction proceeds via the formation of a second stage intermediate, which then transforms into a single-phase first stage compound. Intercalation of ammonia in TaS_2 shows similar behavior (see Section 1.1). In situ X-ray diffraction has also been used to study the competition between exchange reactions of terephthalate and phthalate in $[Ca_2Al(OH)_6]NO_3{\cdot}2H_2O$. Exchange of both anions occurs initially but with time the phthalate phase is replaced by the more stable terephthalate intercalation compound.

The layered double hydroxides have been of interest as anion exchangers, basic catalysts, and catalyst precursors. Pillared derivatives of the type discussed earlier for the clays have been synthesized by ion exchange with polyoxometallate anions but have lower thermal stability.[52] Several authors have reported synthesis of layered double hydroxides pillared with the $V_{10}O_{28}{}^{6-}$ ion by direct ion exchange or by techniques that involve preswelling the layer structure with an organic anion. For example, the terephthalate anion was used in the synthesis of $V_{10}O_{28}{}^{6-}$ and $Mo_7O_{24}{}^{6-}$ intercalated phases.

In other recent developments, the intercalation of biologically active materials in layered double hydroxides has been investigated. For example, large biological molecules such as DNA, ATP, and nucleosides were intercalated into $[Mg_2Al(OH)_6]NO_3{\cdot}1.2H_2O$ and shown to remain structurally intact. Similarly, anionic drug molecules have been intercalated into a variety of layered double hydroxides, in order to determine the possible use of these intercalation compounds for controlled drug release.

Somewhat surprisingly, intercalation reactions of certain layered double hydroxides show shape selectivity. For example, a strong preference for 1,5-naphthalenedisulfonate over 2,6-naphthalenedisulfonate is found on intercalation of an equimolar mixture into $[LiAl_2(OH)_6]Cl{\cdot}H_2O$ at 100 °C. Perhaps even more remarkably, the rate of intercalation into $[Mg_{0.7}Al_{0.3}(OH)_2](Cl)_{0.3}nH_2O$ of L-histidine was shown to be larger than that of D-histidine and that stereoselective intercalation of the L-histidine was achieved by an optically inactive host lattice.[64]

2.2.3 *Tetravalent Acid Phosphates*[52,65]

Because of their selectivity, stability in acid solutions, thermal stability, and resistance to radiation, the acid phosphates, $M^{IV}(HXO_4)_2{\cdot}nH_2O$ ($X = P$, As), have been investigated as ion exchangers for applications where organic ion-exchange resins cannot be used. The layered structures exist in two modifications, α and γ. The structure of α-$Zr(HPO_4)_2{\cdot}H_2O$ (α-ZrP), was first determined by Clearfield and Smith (Figure 11).[66] Each layer contains zirconium atoms octahedrally coordinated by oxygen atoms and bridged by the phosphate groups. Three oxygen atoms of each phosphate group are shared by three zirconium atoms. The fourth oxygen atom is directed into the interlayer space and carries a proton. Adjacent layers are displaced relative to each other to form a cavity between the layers that contains the H_2O molecule. Zirconium hydrogen phosphate can be prepared by adding a soluble zirconium salt to concentrated phosphoric acid, and refluxing the mixture before separating the precipitate. Larger crystals can be prepared by slow crystallization from fluoride containing solutions. Other tetravalent metal cations also form the α structure. Examples include Ti, Hf, Ge, Sn, and Pb phosphates and Ti, Zr, and Sn arsenates.

The intercalation chemistry of α-$Zr(HPO_4)_2{\cdot}H_2O$ includes ion-exchange reactions, acid–base reactions, and layer derivatization. The protons of the P–OH groups can be partially or completely replaced with counterions by exchange reactions. The exchange reaction equilibrium greatly favors the proton form of the exchanger, so that exchange requires the addition of base. Titration curves for alkali metal hydrogen ion exchange are shown in Figure 12. For exchange with sodium ions, the data show that the exchange proceeds in two steps as OH^- ions are added at constant $[Na^+]$, as in equation (5).

$$\underset{(7.65\text{Å})}{Zr(HPO_4)_2{\cdot}H_2O} \longrightarrow \underset{(11.8\text{Å})}{ZrNaH(PO_4)_2{\cdot}5H_2O} \longrightarrow \underset{(9.8\text{Å})}{Zr(NaPO_4)_2{\cdot}3H_2O} \qquad (5)$$

The interlayer separation directly depends on the number of water molecules present between the layers. In the anhydrous phases $ZrM(PO_4)_2$ ($M = Mg$, Ca, Sr, or Ba) and the half exchanged phases $ZrHM(PO_4)_2$ ($M = Li$, Na, K, Rb, or Cs) the interlayer separation is independent of cation size, indicating that the interlayer cavity, which contains one water molecule in the unexchanged compound, is sufficiently large to accommodate a single cation. In contrast, in the fully exchanged alkali metal ion compositions, the interlayer separation increases with increasing cation radius.

The acid phosphates, as the name suggests, also show acid–base intercalation reactions. For example, ammonia is intercalated from very dilute aqueous solutions to form

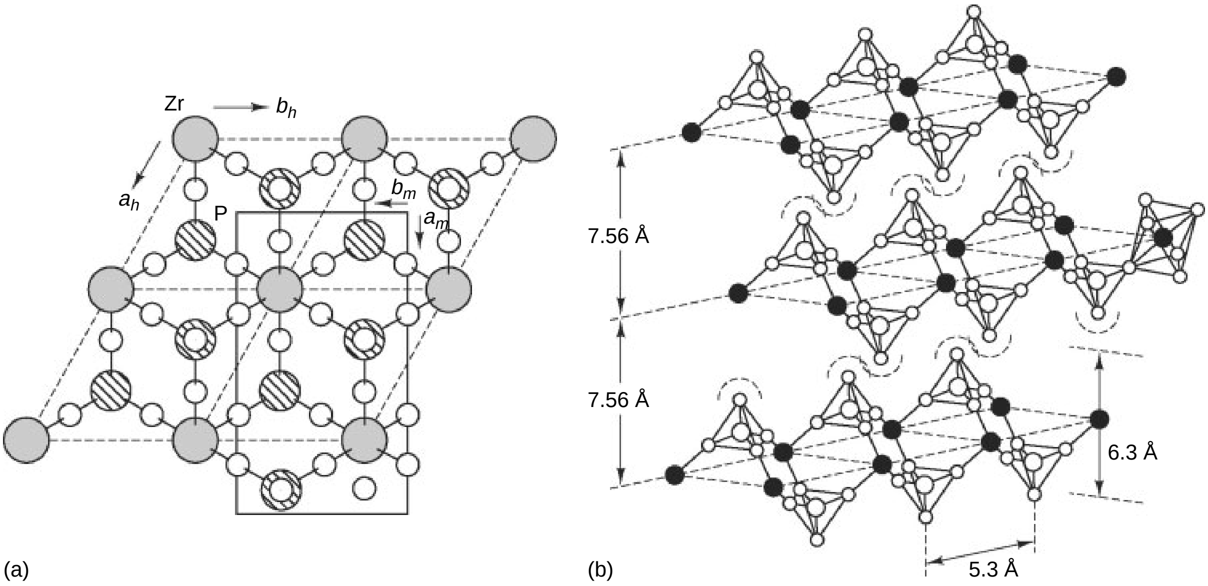

Figure 11 The structure of α-Zr(HPO$_4$)$_2$·H$_2$O looking down on the layers (a); edge on (b). (Reprinted with permission from Ref. 65. © 1969 American Chemical Society)

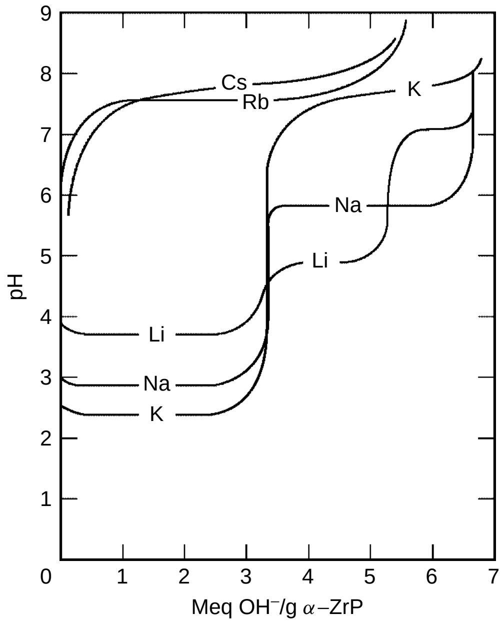

Figure 12 Ion-exchange isotherms for alkali cation exchange with Zr(HPO$_4$)$_2$·H$_2$O. (Reprinted with permission from Ref. 66. © 1981 American Chemical Society)

Zr(PO$_4$NH$_4$)$_2$·H$_2$O. The same compound is formed by ammonium ion exchange with α-Zr(PO$_4$)$_2$K$_2$·H$_2$O. Heat treatment of the ammonium exchanged form at 300 °C gives back the hydrogen phosphate. Primary alkylamines react very readily to form bilayer intercalation compounds analogous to those formed by clays (the layer area per proton is 24 Å^2). The chain packing density is not close packed, but falls in the range where regular kink blocks are observed. Diamines and secondary and tertiary *n*-alkylamines have also been studied.

The mechanism of amine intercalation has been investigated by measuring the change in pH as amine is added to a suspension of α-ZrP. Several intermediate compositions are observed en route to the fully exchanged phase. When *n*-propylamine is used in this reaction, at a point when about one half of the protons have been titrated, the α-ZrP layers spontaneously exfoliate. Presumably the hydrogen bonding interlayer interactions are reduced and not compensated by interchain van der Waals forces. Addition of more propylamine causes the layers to reflocculate.

In addition to the α form of Zr(HPO$_4$)$_2$·H$_2$O, a second modification, γ-Zr(HPO$_4$)$_2$·2H$_2$O, is also known. The γ phase contains an additional water molecule and has a correspondingly larger interlayer separation (9.5 Å vs. 7.65 Å). Similar ion-exchange and intercalation chemistry of amines and polar molecules is observed, though the layer charge density is apparently 30% higher than that in the α phase. The formation of organic derivatives of ZrP using the γ form was investigated by Yamanaka and coworkers.[67] They showed that reactions with ethylene and propylene oxide resulted in simultaneous intercalation and reaction with P–OH groups to form P–O–C ester linkages on the internal surfaces of the layers. Compounds are formed with compositions illustrated by γ-Zr(HOCH$_2$CH$_2$OPO$_3$)$_2$·H$_2$O. A large number of organic derivatives with the general composition Zr(RPO$_3$)$_2$ can be synthesized by direct reaction of a zirconium source with an organophosphonic acid. The organic R group can be an alkyl or an aryl group and may itself be functionalized with, for example, SO$_3$H, CO$_2$H, or NMe$_3$Cl. Reaction chemistry of the organic groups attached to the layer has been studied. Compounds analogous to amine intercalation compounds are obtained by the reaction shown in equation (6), where $X = NH$ or O, and $R = n$-alkyl; the alkyl group is attached to the layers through a covalent bond.[68]

$$Zr(O_3PCH_2CH_2COCl)_2 + 2HXR \longrightarrow Zr(O_3PCH_2CH_2COXR)_2 + 2HCl \qquad (6)$$

The development of organic derivatives of zirconium phosphate has led to wide interest in other examples of layered metal organophosphonates. For example, VO^{2+}, M^{2+}, and M^{3+} phases have been synthesized with a variety of different layer connectivities and interlayer chemistry.[69]

2.2.4 *Intercalation and delamination of layered oxides*

Many high-temperature ternary oxides are known that have structures made up of layers of transition metal–oxygen atom octahedra separated by large alkali metal cations or layers of composition $Bi_2O_2{}^{2+}$. These layered oxides often can undergo ion-exchange reactions in molten salts and sometimes in aqueous solutions. The relationship between the ionic conductivity, structure, and ion-exchange properties has been discussed.[70] Of particular interest are the ion-exchange reactions in aqueous acids that generate the protonic or hydronium forms of the oxides. The proton exchanged forms are good starting materials both for the synthesis of other cationic exchange forms and for the synthesis of novel oxides by dehydration–dehydroxylation. The proton exchange forms can be intercalated by organic bases and under appropriate conditions complete exfoliation of the layers can be induced.

Alkali Metal Titanates and Niobates.[71,72] The structures of the titanates and titanium niobates with the general formula $A_mM_nO_{2n+1}$, where A is the interlayer cation and M is the transition metal atom, contain double chains of edge-shared octahedra, which are joined by corner sharing to form puckered layers; n describes the number of edge-sharing octahedra in each chain. The end member of this series has the layer composition MO_3 and the structure is that of MoO_3. The structures of some examples of the alkali metal-containing phases synthesized at high temperature are shown in Figure 13. The proton exchanged forms of the oxides dehydroxylate on heating above 300–350 °C to form metastable oxides with structures that bear a strong relationship to the original layers. For example, $HTiNbO_5$ dehydroxylates to $Ti_2Nb_2O_9$, a tunnel structure formed by crosslinking the starting layers. Similarly on dehydroxylation, $H_2Ti_4O_9$ first forms $H_2Ti_6O_{17}$ and then, at higher temperatures, $TiO_2(B)$. The second transformation is not topotactic because $TiO_2(B)$ is also obtained on heating $H_2Ti_3O_7$ and $H_2Ti_5O_{11}$.

The proton exchanged form of the titanates and titanium niobates are Brønsted acids and intercalate bases in the same way as described above for zirconium hydrogen phosphate. All compounds intercalate strong bases such as primary amines. The titanium niobates, however, are somewhat stronger acids than the pure titanates. Thus $HTiNbO_5$ will intercalate bases with pK_a values greater than 6, whereas pK_a values greater than 9 are required for bases to intercalate $H_2Ti_4O_9$. It is interesting to note that $HTiNbO_5$, like $Zr(HPO_4)\cdot H_2O$, exfoliates when treated with short chain primary alkylamines.

Compounds Containing Perovskite Layers. A second class of layered oxides have structures related to the three-dimensional perovskite lattice and include the Aurivillius phases,[73] the Ruddlesden–Popper phases[74] and the Dion–Jacobson phases.[75,76] The general composition can be written $M_a[A_{n-1}B_nO_{3n+1}]$ where A is an alkaline or rare earth metal, and B is niobium or titanium. In the Aurivillius phases $M_a = Bi_2O_2{}^{2+}$, whereas M is an alkali metal cation in the ion-exchangeable Ruddlesden–Popper ($a = 2$) and Dion–Jacobson ($a = 1$) phases. The relationships between the three structure types is shown in Figure 14. The intercalation chemistry of the Dion – Jacobson phases was the first to be studied.

The first examples with $n = 3$ were synthesized by Dion *et al.*[75] and later extended to compounds with $n = 7$.[75,76] The ion-exchange properties and intercalation chemistry are generally similar to the titanium niobates (above) and have been discussed in detail by Jacobson.[77] Ion exchange is facile in molten alkali metal nitrates and the proton containing phases are formed by reaction in mineral acids. The proton exchanged phases are much stronger Brønsted acids and will intercalate bases as weak as pyridine. One of the most unusual features of the layered perovskites is that the layers are extremely thick and are presumably very rigid. Layer thicknesses range from 10 to 30 Å for compounds with $n = 1$ to 7, though this apparently has little effect on the general features of the intercalation chemistry.

The earlier studies of the Dion–Jacobson phases have been extended to the other layered perovskites.[78] Specifically, Ruddlesden-Popper phases with interlayer alkali metal cations have been synthesized, for example, $K_2La_2Ti_3O_{10}$, $K_2CaNaTa_3O_{10}$ ($n = 3$) and $K_2SrTa_2O_7$ ($n = 2$). The interlayer alkali metal cations in these compounds can be exchanged for protons. The protonated compounds are particularly interesting because they undergo topochemical dehydration to form three-dimensional perovskites. Thus on heating $H_2La_2Ti_3O_{10}$ at 350 and 500 °C, water is lost and the structure collapses to form the three-dimensional perovskite $La_2Ti_3O_9$. The perovskite has 1/3 of the A sites vacant and preserves the original A site distribution so that the A site cations (La) and vacancies (V) are ordered in the sequence La-La-V. This reaction does not occur for the Dion-Jacobson phases that contain only half of the number of interlayer protons. Aurivillius phases can also be converted to the proton form of the corresponding Ruddlesden–Popper phase by selectively dissolving the interlayer bismuth oxide in acid.

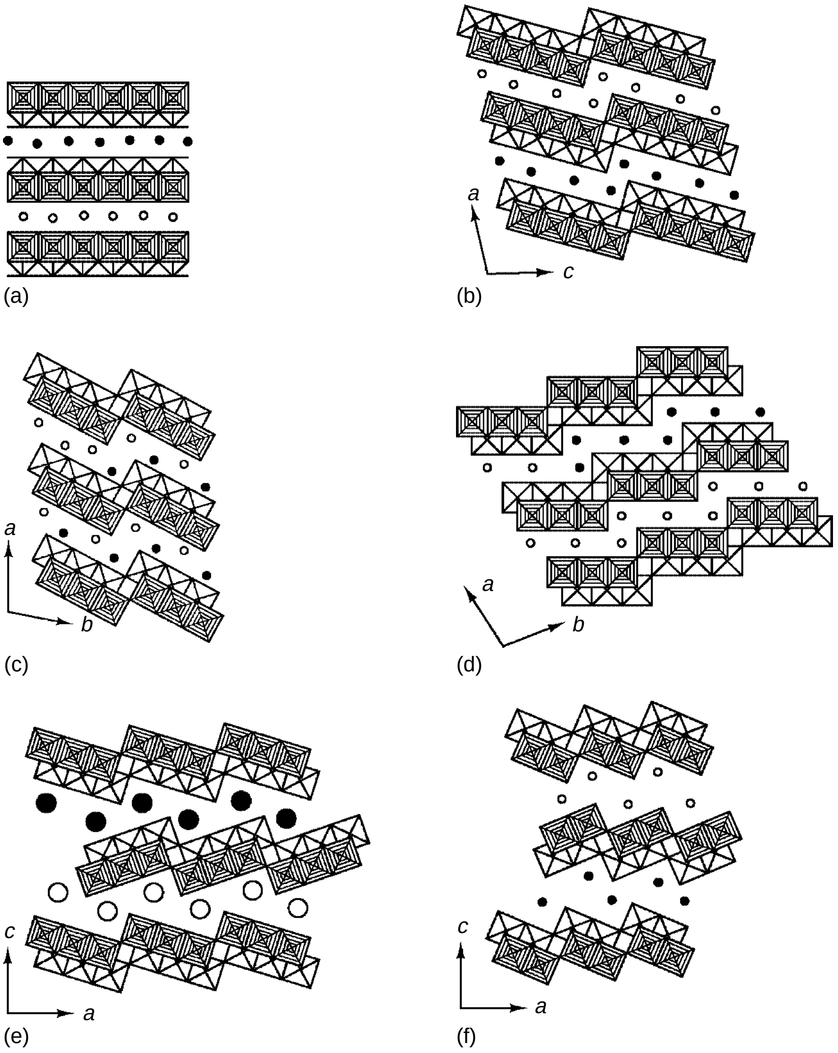

Figure 13 Schematic representations of the layer structures of (a) $A_xTi_{2-x}M_xO_4$, (b) $Tl_2Ti_4O_9$, (c) $Na_2Ti_3O_7$, (d) $K_3Ti_5NbO_{14}$, (e) $CsTi_2NbO_7$, (f) $KTiNbO_5$[72]

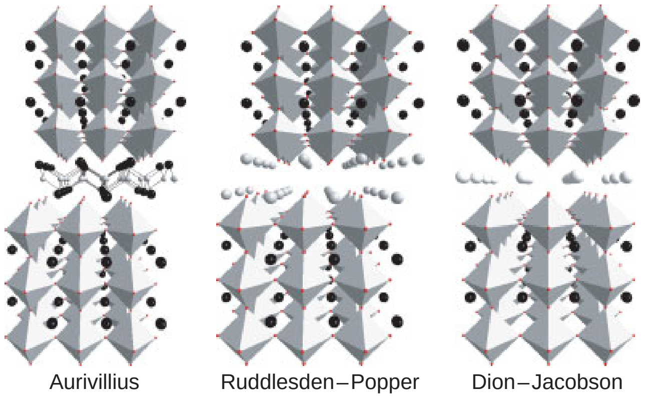

Figure 14 The triple layer structures of the Aurivilius, Ruddlesden–Popper, and Dion–Jacobson perovskite phases

For example, the Aurivillius phase $Bi_2O_2[SrNaNb_3O_{10}]$ reacts with HCl with removal of the interlayer $Bi_2O_2{}^{2+}$ forming the Ruddlesden–Popper phase $H_2SrNaNb_3O_{10}$. The protonated Ruddlesden–Popper compounds in general do not intercalate organic bases though some exceptions have been found. Specifically, $H_2SrNaNb_3O_{10}$ reacts with *n*-butylamine and *n*-octylamine and some tantalates such as $H_2CaNaTa_3O_{10}$ and $H_2Ca_2Ta_2TiO_{10}$ also intercalate alkylamines. A new series of layered oxyhalide perovskites were prepared by reaction of the Dion–Jacobson phases ($ALaNb_2O_7$, A = Li, Na, K, or Rb) with anhydrous metal halides under mild reaction conditions (<400 °C).[79] The compounds have the composition $(MCl)LaNb_2O_7$ (M = Cr, Mn, Fe, Co, Cu). The reaction is topochemical and results in the formation of a two dimensional metal halide sheet in the perovskite interlayer in which MO_2X_4 octahedra corner-share with NbO_6 octahedra from the perovskite slab and edge-share with each other along all four equatorial edges. The interrelation of all of the ion exchange, amine intercalation and dehydration reactions of this family of oxides has been reviewed by Schaak and Mallouk.**[80]**

Exfoliation of the perovskite related layer structures is more difficult than for the clays and acid phosphates discussed earlier but can be achieved by intercalation of large bulky amines. Treacy *et al.* reported that the layered perovskite $HCa_2Nb_3O_{10}$ could be made to form unilamellar sheets by first intercalation of an amine polyether.**[81,82]** Spontaneous exfoliation of the layers occurs on subsequent exposure of the intercalated phase to a suitable solvent. Exfoliation techniques have been extended to other systems using tetra(n-butyl)-ammonium hydroxide (TBAOH) by Mallouk and others.**[78]** A number of examples of the protonated layered perovskite phases that intercalate bases have been exfoliated. The Dion–Jacobson phases typically exfoliate to form plates but others including Ruddlesden–Popper tantalates curl to form tubular ‘scrolls’. Part of the interest in these single layer dispersions arises from their use as building blocks in the layer-by-layer self-assembly of thin films. Single layers derived from exfoliated perovskites can be attached to or alternately stacked with polycationic layers to produce thin films. Tiled monolayer structures and multilayer perovskite heterostructures result from the self-assembly.

3 CONDUCTING HOST LATTICES

Conducting host lattices have been intensively investigated since graphite intercalation attracted the attention of physicists and chemists in the 1950s and dichalcogenide intercalation reactions were discovered in 1969. Intercalation chemistry in layered structures has received the most attention and will be described first. A summary of the analogous chemistry for the smaller number of one and three-dimensional compounds will be given for comparison.

3.1 Graphite Intercalation

Graphite is the simplest of the two-dimensional structures that show intercalation chemistry. The formation of the earliest reported intercalation compound, graphite sulfate, was described by Schauffaütl in 1841**[83]** as resulting from the reaction of single-crystal graphite flakes in H_2SO_4/HNO_3 mixtures. Since then detailed studies have been made both of the intercalation chemistry of a variety of guest species and of the physics (structure, dynamics, transport, and electronic properties) of graphite intercalation compounds. The physics and chemistry of graphite intercalation are described in several review articles and in a comprehensive survey edited by Zabel and Solin.**[84]** The focus of this section is on the chemistry of graphite intercalation.

Graphite intercalation compounds have received widespread interest for two main reasons. First, intercalation results in compounds that have metallic conductivity. The electrical conductivity can approach that of copper metal and is highly anisotropic: ratios of the conductivity in-plane to that along the c axis can be six orders of magnitude at room temperature. Secondly, graphite is a unique host lattice in that intercalation compounds can be formed with either electron donors or electron acceptors as guest species.

3.1.1 *Structure*

Graphite is structurally the simplest host lattice (Figure 15). The stable hexagonal form is obtained by stacking planar sheets of carbon atoms in an ABAB arrangement. Adjacent sheets are separated by a van der Waals gap of 3.35 Å. Each individual sheet is a regular hexagonal network of sp^2 hybridized carbon atoms. The p_z orbitals perpendicular to the sheets overlap to form a filled *Valence Band* (bonding π orbitals) and an empty *Conduction Band* (*Antibonding*) π orbitals, (*see π-Bond*). The C–C bond length is 1.42 Å, longer than in benzene (1.39 Å) because each p_z orbital interacts with three rather than two neighbors. For an isolated graphite sheet the *Band Gap* would be exactly zero, but in the three-dimensional structure some interaction between adjacent sheets results in a small overlap (0.04 eV) of the valence and conduction bands. A small number of electrons in the conduction band and holes in the valence band result and the pristine material has significant conductivity.

Intercalation studies of graphite have used a variety of different types of material with different degrees of perfection.

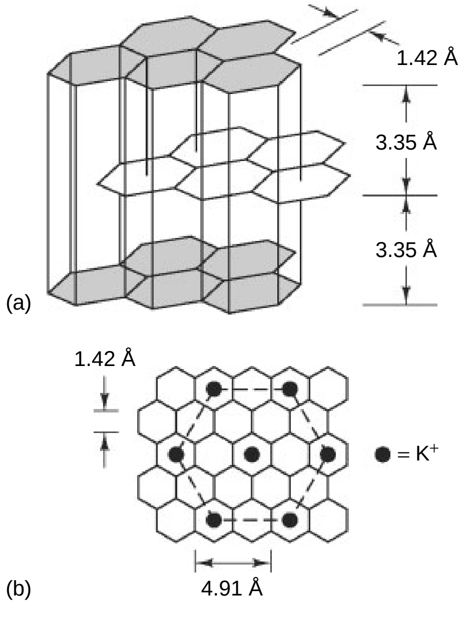

Figure 15 Layer structure of graphite (a) and the arrangement of alkali metal atoms in MC_8 (b)

Some studies have used single crystals obtained naturally from coal or lead mines or synthetic (Kish) graphite. Most work has, however, been carried out using highly oriented pyrolytic graphite, which is a textured polycrystalline material. The *ab* orientation of the graphite layers is random, but the *c* axis is well defined. Intercalation reactions of graphite commonly lead to staging (see Section 1.1). Adjacent carbon layers present in higher stages are stacked in the same way as in graphite but graphite layers containing a guest species are usually eclipsed. A shorthand description of a stage 2 intercalation compound where the guest species is represented by/is then given by – A/AB/BC/CA–. This simple description of staging was modified by Daumas and Hérold,[16] who proposed the isolated island (domain) model to account for transformations between odd and even numbered stages (see Figure 6). Direct experimental evidence for the existence of islands has been obtained by high-resolution *Transmission Electron Microscopy* studies of $FeCl_3$ intercalation compounds.

Within a domain, several different arrangements of the guest species have been identified. The guest species may form an ordered structure that is commensurate with the graphite lattice. This may result in an ideal composition in which the carbon:guest ratio is a rational fraction, such as LiC_6 or KC_8. Incommensurate ordered arrangements with more complex compositions, where the lattice formed by the guest species and the graphite lattice are not simply related, are also known. At higher temperatures, the intercalated layers have two-dimensional liquid structures.

3.1.2 *Intercalation with Graphite Reduction*

Donor intercalation compounds, where charge is transferred from the guest to the graphite layers, include the alkali metal, alkaline earth metal, and rare earth metal phases. The compounds with K, Rb, or Cs are the easiest to prepare and can be obtained by reaction with the elements in sealed tubes at 200 °C. Formation of compounds with Li, Na, the alkaline earth metals (Ca, Sr, Ba), and rare earth metals (Sm, Eu, Yb, Tm) requires higher reaction temperatures (500–600 °C) and is complicated by side reactions that lead to the formation of carbides. The first stage compounds of K, Rb, and Cs have compositions MC_8 and higher stages MC_{12n}, where n is the stage number. The other metals form first stage compounds MC_6, but higher stage compounds are not well defined. Figure 15 shows the in-plane ordered arrangement of alkali metal atoms observed for KC_8 and RbC_8 relative to the graphite lattice. Table 3 shows structural and conductivity data for several different alkali metal phases.

Intercalation compounds containing two metals can be prepared by reaction of binary alloys of K, Rb, and Cs and also with alloys of metals that intercalate easily combined with those that do not. For example, Billaud and Hérold[85] prepared a compound Na_2BaC_8 by reaction with a NaBa alloy. The interlayer separation implies a sandwich structure comprising a layer of barium atoms with layers of sodium on either side. Triple layer structures for $KHgC_4$ and more complex compositions containing Tl and Bi have been described by Lagrange.[86,86] Several of these phases show ***Superconductivity*** in the range 1–4 K, significantly higher than observed in the ambient pressure binary phases (e.g. KC_8; $T_c = 0.13\,K$).

Table 3 Graphite–alkali metal intercalation compounds

Compound	Stage	Color	Interlayer separation (Å)	σ ($S\,cm^{-1} \times 10^4$)	r
C_8K	1	Gold	5.41	11, 9	2.06
$C_{24}K$	2	Blue	8.77	12	2.07
$C_{36}K$	3	Blue	12.15	17	2.07
C_8Rb	1	Gold	5.65	8	2.30
$C_{24}Rb$	2	Blue	8.97	–	2.27
C_8Cs	1	Gold	5.94	11, 8	2.59
$C_{24}Cs$	2	Blue	9.25	12	2.55

Intercalation compounds containing solvated cations are also well known and are obtained from metal ammonia solutions, alkali metal naphthalides, or by electrochemical intercalation.

3.1.3 *Intercalation with Graphite Oxidation*

Intercalation compounds with electron acceptors form a large class of compounds with several distinct types of guest, including anions of strong acids, halogens and halides, and oxides.

Graphite intercalation compounds can be synthesized with guest anions of strong inorganic and organic acids. Direct intercalation reactions occur with oxidizing acids (HNO_3, $HClO_4$), but generally electrochemical oxidation of graphite has been used. Electrochemical synthesis is necessary for nonoxidizing systems. Some examples of stage 1 compounds include (interlayer separation in parentheses) $C_{24}(HSO_4)(H_2SO_4)_2$ (7.98 Å), $C_{21}SO_3F(HSO_3F)_2$ (7.73 Å), $C_{24}ClO_4(HClO_4)_2$ (7.85 Å), and $C_{25.8}NO_3(HNO_3)_5$ (7.8 Å). The interlayer separation for the tetrahedral anions implies a double layer of oxygen atoms between graphite layers. The maximum packing density would correspond to two close-packed oxygen layers, but lower density packings can be envisaged, for example, with the C_2 axis of the tetrahedron perpendicular to the graphite layers. The interlayer separation of the nitrate intercalation compound is consistent with a bilayer of nitrate groups with their C_3 axes along c or a monolayer with C_3 parallel to the graphite planes.

Bromine readily reacts with graphite from the vapor phase at ambient temperature to form a second stage phase with composition C_8Br. Higher stage compositions are formed by reaction above 50 °C. Several studies show that complete charge transfer from graphite to bromine does not occur, but that polybromide species, Br_n^-, are present in the interlayer. The oxidizing power of bromine, even with the additional stabilization provided by the formation of polybromide species, is insufficient for stage 1 formation. Chlorine intercalation compounds have lower stability and iodine compounds do not form. However, intercalation compounds with ICl and IBr are known, presumably owing to additional stabilization provided by the formation of ICl_2^- and IBr_2^- species in the interlayers. Intercalation compounds are not formed with fluorine, which reacts with graphite to form either black C_2F (at temperatures in the range 350–450 °C) or white CF (near 600 °C).

Metal and nonmetal halides also form acceptor intercalation compounds with graphite. Compounds fall into several classes: halides that are strong enough electron acceptors to oxidize graphite; halides that undergo *Disproportionation* reactions; and halides that can only intercalate in the presence of a separate oxidizing agent. Bartlett and McQuillan[1] have reviewed direct intercalation of metal hexafluorides and shown that spontaneous reaction requires an *Electron Affinity* greater than 108 kcal mol^{-1}. The hexafluorides, MF_6 (M = Os, Ir, Pt, Mo, U), all meet this criterion and form first stage compounds with compositions in the range C_8–C_{12}. Higher stages are formed with the composition $C_{12n}MF_6$ at higher temperatures and pressures.

Other metal fluoride intercalation compounds can be formed in the presence of fluorine, where the formation of MF_{n+1}^- complexes from MF_n adds to the overall stability. Examples include the intercalation of WF_6 and ReF_6 in the presence of F_2 via formation of MF_7^- guest species, C_8MF_6 (M = P, As), and C_nBF_4 compounds. Direct intercalation of AsF_5 occurs by a different mechanism (see below). Metal chlorides react similarly. Thus $AlCl_3$ and $NiCl_2$ can form intercalation compounds in the presence of Cl_2 through formation of the complex anions $AlCl_4^-$, $NiCl_3^-$, or $NiCl_4^{2-}$.

Molecular halides (e.g. AsF_5, SbF_5, and $SbCl_5$) can also form intercalation compounds by *Disproportionation* reactions. Intercalation of AsF_5 has been extensively studied, because of the high electrical conductivity of the resulting compound. Early studies indicated conductivities at room temperature comparable to that of copper, but subsequent measurements have indicated lower values more comparable to aluminum metal. The direct reaction with AsF_5 proceeds via disproportionation of the neutral fluoride according to equation (7), and both hexafluoride and trifluoride species are present in the interlayer. The composition corresponds to C_8AsF_5 for the first stage compound. The AsF_3 component can be removed by vacuum and reintroduced into the lattice from the gas phase without any change in the stage or significant change in conductivity. The AsF_3 species can be replaced by AsF_5 by repeated exposure to AsF_5 and evacuation. The composition is gradually modified to form C_8AsF_6 analogous to the low conductivity phase prepared from AsF_5/F_2.

$$2e^- + 3AsF_5 \longrightarrow 2AsF_6^- + AsF_3 \tag{7}$$

Several oxides and oxyhalide intercalation compounds have been reported, but detailed reaction mechanisms and stoichiometries are available in only a few cases. Reactions with N_2O_5, Cl_2O_7, and SO_3 proceed with evolution of NO_2, Cl_2O_6, and SO_2 respectively. These species are both strong oxidants and Lewis acids and intercalate by the reactions shown in equations (8) and (9). In the case of SO_3, the formation of polymeric guest species based on corner-shared chains of tetrahedral SO_4 terminated with SO_4^{2-} anions has been proposed.

$$N_2O_5 + e^-(\text{graphite}) \longrightarrow NO_3^- + NO_2 \tag{8}$$

$$2Cl_2O_7 + 2e^-(\text{graphite}) \longrightarrow 2ClO_4^- + Cl_2O_6 \tag{9}$$

The disproportionation reactions with graphite of oxidants that are also strong Lewis acids parallel the intercalation of molecular species into the layered dichalcogenides, which are reductants and Lewis bases (see Section 3.2.1).

3.1.4 Alkali Metal Intercalation in C_{60}

The molecule C_{60} was first observed in the mass spectrum of laser evaporated carbon by Kroto *et al.*,[87] who proposed the now familiar 'soccer ball' structure. Subsequently, macroscopic quantities were synthesized.[88] In the solid state, C_{60} adopts a face-centered cubic (fcc) structure, which can be considered to be based on the close packing of spheres with a radius of 5 Å. Two tetrahedral sites and one octahedral site with radii 1.12 and 2.06 Å are present in the structure. The availability of these empty sites and the electronegativity of C_{60} make it a suitable host lattice for reductive intercalation by electropositive cations such as the alkali metals. The octahedral site is larger than any of the alkali cations, but the tetrahedral site is about the same size as Na^+. The discovery of ***Superconductivity*** in K_xC_{60} ($T_c = 18\,K$) has focused considerable interest on these materials. Intercalation compounds can be prepared by direct reaction of the alkali metal with C_{60} to form compositions A_xC_{60} ($x = 2$, 3, 4, or 6) depending on the specific A cation. Direct reaction of C_{60} with the alkali metals is the most convenient route to the A_6C_{60} phases; other compositions can be prepared by use of the appropriate stoichiometry or by reaction of A_6C_{60} with C_{60}. Other alkali metal reagents such as Na_5Hg_2 and NaH have also been used.[89]

The structures of the alkali metal fullerides may be considered to be intercalation compounds of the fcc lattice of the C_{60} host formed by filling the interstitial sites. Superconductivity has been investigated in detail for the alkali metal and mixed alkali metal phases of composition A_3C_{60} where the conduction band is half filled. Critical temperatures as high as 31.3 K (in Rb_2CsC_{60}) have been observed. A clear correlation between unit cell size and T_c is observed, and it has been suggested that the conduction bandwidth controlled by the separation between the molecules is the dominant factor in determining T_c.

It is interesting to compare the intercalation chemistries of C_{60} and graphite. The different electronic structures produce quite different intercalation chemistry. As discussed above graphite is a *Semimetal* and is amphoteric (*see Amphoterism*), forming both acceptor and donor intercalation compounds. In contrast, C_{60} is more electronegative than graphite, and forms much more stable intercalation compounds with alkali metals. No stable acceptor compounds are formed by C_{60}, $(I_2)_2C_{60}$ being the closest example. Addition reactions occur with more oxidizing halogens, analogous to the formation of C_2F and CF in reactions of graphite with fluorine.

3.1.5 Intercalation Chemistry of Single-walled Carbon Nanotubes

Single-walled carbon nanotubes comprise rolled sheets of sp^2 graphene carbon, which form well-defined cylinders with diameters in the range 1 to 2 nm. The diameter depends on the synthesis conditions as does the orientation of the six-membered carbon rings with respect to the nanotube axis. Achiral zigzag, achiral armchair, or chiral nanotubes can be obtained as illustrated in Figure 16.**[90]**

Single-walled carbon nanotubes self-assemble during growth into partially ordered two-dimensional bundles, or 'ropes', which consist of 100 to 500 nanotubes in a two-dimensional triangular lattice with a lattice spacing of 17 Å.**[92]**

Intercalation reactions can occur either by insertion of guest species into the channels between the tubes**[93,94]** or by insertion into individual tube after the ends have been open by oxidation.**[91,95,96]** Intercalation reactions of species between the tubes are accompanied by charge exchange between host and guest and are similar to those observed for graphite and C_{60} host lattices. Both oxidative intercalation with bromine and iodine and reductive intercalation with the alkali metals can occur. Reaction with alkali metals vapors give intercalation compounds with the composition MC_8 (M = K, Rb, Cs) comparable to those observed for the corresponding graphite intercalation compounds (Table 3). Intercalation leads to expansion of the two-dimensional lattice of the nanotubes so that the alkali metals are intercalated in between the tubes within the bundles. Disordered lattices are observed after intercalation of Rb and Cs ions. Simulations of the X-ray powder data for potassium intercalation compounds indicate that three K ions occupy the triangular cavities between the tubes. Various physical measurements including in situ measurements of the resistivity show a large drop in the resistance on intercalation and the temperature dependence suggests metallic behavior.

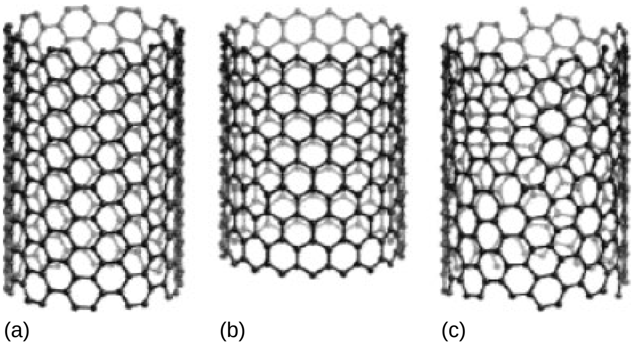

Figure 16 Schematic representation of (a) armchair, (b) zigzag and (c) chiral single-walled nanotubes. (Reprinted with permission from Ref. 91. © 2002 American Chemical Society)

Carbon nanotube bundles can also be intercalated electrochemically in nonaqueous cells. Intercalation of lithium ions has been investigated in some detail because of the possible use of carbon nanotubes as anodes in reversible lithium batteries. On electrochemical intercalation of lithium ions, the composition approaches LiC_6 and a significant amount of the intercalated lithium can be removed on reoxidation though there is also a large irreversible component. No well-defined redox potential for lithium insertion or removal in the nanotube lattice is observed in galvanostatic charge-discharge and the loss in crystallinity that is observed by in situ X-ray diffraction suggests that solvent molecules are cointercalated.

In the second class of intercalation reaction, guest species are encapsulated inside individual single-walled nanotubes rather than between them. Guest compounds are introduced into the nanotubes by capillary filling with molten salts and crystals are formed that have structures typically with different coordination environments compared to the bulk. Metal halides have been studied in most detail though several examples of inorganic oxides have also been reported.

Confining either halides or oxides inside nanotubes leads to structures that are strongly influenced by the restricted dimensionality. As an example, the structure of a 2 × 2 KI crystal formed within a 1.4 nm-diameter carbon nanotube is shown in Figure 17. Electron microscopy shows pairs of identical dark spots along the axis of the tube, each representing an individual KI column viewed in projection. All of the ions in this 2 × 2 structure have a 4:4 coordination environment that is reduced from the 6:6 coordination found in the bulk crystal. The KI lattice is also expanded across the tube relative to the bulk. Single-walled nanotubes can also be filled with C_{60} molecules to give so-called 'peapod' structures.**[96]** Further intercalation reactions of the peapods using both donor (K) and acceptor ($FeCl_3$) guest species have been studied.

3.2 Transition Metal Dichalcogenides[1–8,97–100]

3.2.1 Structures

The transition metal dichalcogenides of groups 14, 15, and 16 have layered structures in which the transition metal (M) occupies either octahedral (trigonal antiprismatic, TAP) or trigonal prismatic (*see Trigonal Prism*) sites between two layers of chalcogen atoms (X). Each chalcogen layer

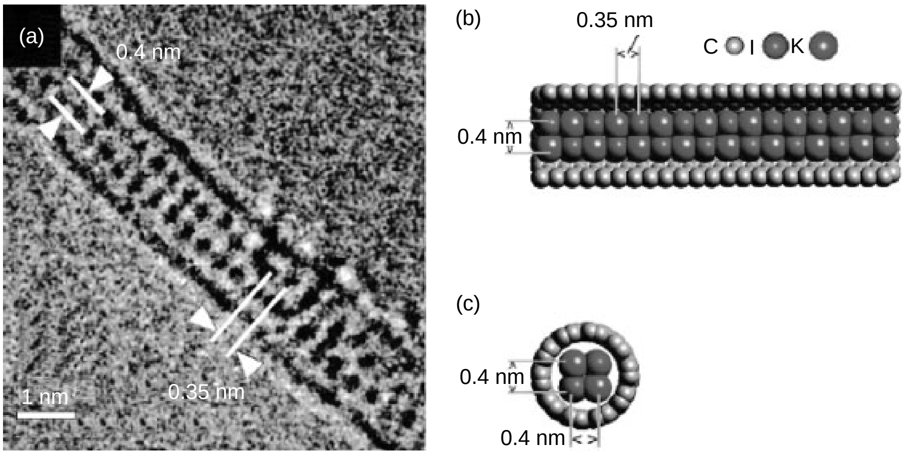

Figure 17 (a) High-resolution electron micrograph of a 2 × 2 KI crystal inside a single-walled carbon nanotube; (b,c) side and end views of the 2 × 2 KI crystal showing the lattice dimensions. (Reprinted with permission from Ref. 91. © 2002 American Chemical Society)

is close packed and the X–M–X sandwiches are stacked in a direction perpendicular to the chalcogen layers to complete the structure. Bonding within a layer is strong whereas, the van der Waals interactions between layers are weak. Different combinations of octahedral and trigonal prismatic coordination for M and different stacking sequences of the layers give rise to a variety of polymorphs (*see Polymorph*) and polytypes. Several commonly occurring stacking arrangements are shown in Figure 18, and a summary of examples of different stacking sequences and different transition metal coordinations is given in Table 4. In general, the group 14 metals and vanadium are octahedrally coordinated, whereas trigonal prismatic sites are occupied by the group 16 elements. Niobium and tantalum are found in both coordinations and the number of possible structures for the dichalcogenides of these elements is greatly increased by the possibility of alternating octahedral and trigonal prismatic layers. An example of a mixed layer sequence, 4Hb, which is observed for both TaS_2 and $TaSe_2$ is shown in Figure 18.

In an intercalation reaction, guest species are inserted into the octahedral, tetrahedral, or trigonal prismatic sites between the chalcogenide layers. Intercalation often produces a change in the layer stacking sequence.

3.2.2 Alkali Metal Intercalation

Intercalation reactions of the dichalcogenides with alkali metals are redox reactions in which the host lattice is reduced by electron transfer from the alkali metal. Lithium and sodium intercalation reactions, for example, have been studied using cells of the type $Li/LiClO_4$–dioxolane/MX_2 and Na/NaI–propylene carbonate/MX_2. The reactions proceed spontaneously to form the intercalation compound if the cell is short circuited; alternatively, a reverse potential can be applied to control the composition of the final product. Apart from their application in synthesis, such electrochemical cells can be used to obtain detailed thermodynamic information and to establish phase relations by measuring the dependence of the equilibrium cell voltage on composition (see Figure 4).

A variety of chemical reagents may also be used to form alkali metal intercalation compounds. The first compounds of the dichalcogenides were prepared by Rüdorff,[12] who reacted the host lattices with liquid ammonia solutions of the alkali

Table 4 Structure of layered dichalcogenides[a]

Designation[b]	Sequence	Space group	Examples	M coordination[b]
1T	AbC|	*P3m1*	MX_2 (M = Ti, Zr, Hf, V; X = S, Se, Te)	TAP
2Ha	BaB|CaC	$P6_3/mmc$	MX_2 (M = Ta, Nb; X = S, Se)	TP
2Hb	BaB|CbC	$P6m2$	$TaSe_2$, $NbSe_2$	TP
2Hc	BcB|CbC	$P6_3/mmc$	MX_2 (M = Mo, W; X = S, Se), $MoTe_2$	TP
3R	BcB|CaC|AbA	*R3m*	MX_2 (M = Ta, Nb, Mo; X = S, Se), WS_2	TP
4Hb	aB|CaC|BaC|BaB|Ca	$P6_3/mmc$	TaS_2, $TaSe_2$	TP, TAP

[a] In the notation used, A, B, C and a, b refer to chalcogen and transition metal layers, respectively. The layers are stacked at (0, 0, 0), (2/3, 1/3, z), and (1/3, 2/3, z) and, for example, AbA and AbC represent trigonal and octahedral sites. [b] T = trigonal, H = hexagonal, R = rhombohedral, TAP = trigonal antiprismatic (octahedral), TP = trigonal prismatic.

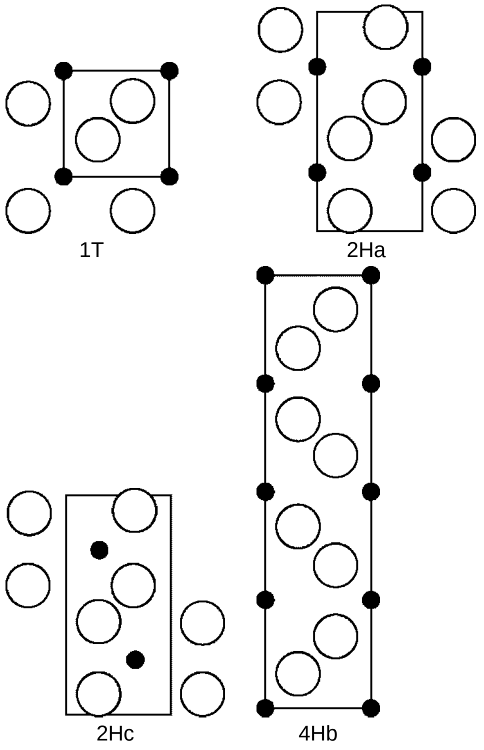

Figure 18 Stacking sequences for chalcogenide layers. (Reprinted with permission from Ref. 4, by permission of Oxford University Press)

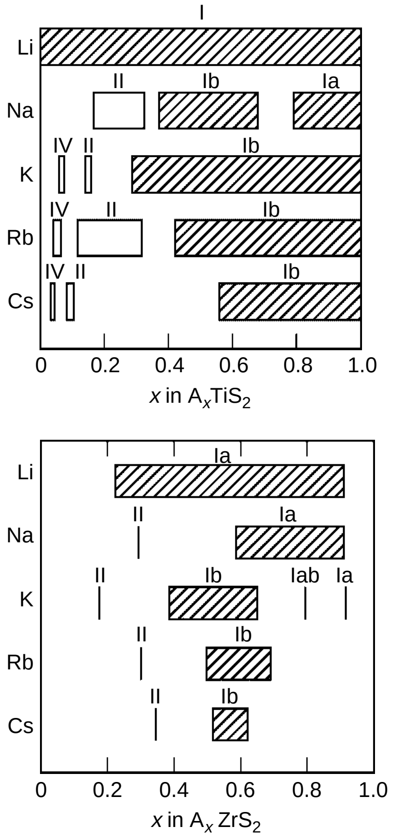

Figure 19 Compositions of the alkali metal intercalation compounds of TiS_2 and ZrS_2. (Reprinted with permission from Ref. 4, by permission of Oxford University Press). The numerals refer to the stage, and a, b to different layer stackings (see text)

metals. The compounds formed by this procedure contain cointercalated ammonia molecules that are difficult to remove completely and the high thermodynamic activity of the alkali metal can lead to destructive side reactions. However, the method is applicable to all of the alkali metals and has been used successfully for the synthesis of a variety of compounds including the low stability A_xMoS_2 phases (A = K, Rb, Cs).

Other chemical reagents that give lower alkali metal activities, for example, sodium and potassium naphthalide and benzophenone solutions in tetrahydrofuran (THF), have been used Examples of lithium reagents with different activities are shown in Figure 5.

The phase relations for the alkali metal–TiS_2 and –ZrS_2 systems (Figure 19) illustrate most of the general features of alkali metal dichalcogenide systems. The simplest system is Li_xTiS_2, which is a single phase over the entire composition range as indicated by the smooth variation of the c axis lattice parameter with composition and by the equilibrium electrochemical data.[100] The intercalation reaction leads to occupation of the octahedral interlayer sites and the final product, $LiTiS_2$, is isostructural with the high-temperature phases $LiVS_2$ and $LiCrS_2$. The intercalation compounds formed by the other alkali metals are more complex and show two-phase behavior up to some low value of x, implying that a minimum energy of reaction is required to open up the van der Waals gap. Staging can provide a mechanism to minimize this energy and is observed for all of the alkali metal compounds at low x values except for those of lithium. In the TiS_2 systems, second stage compounds are formed for all alkali metals except lithium, and fourth stage phases occur with K, Rb, and Cs (see Figure 19).

The structures of the first stage compounds (I, Ia, Ib) illustrate how the dichalcogenide layers are restacked to optimize the guest coordination and the interlayer interactions. Structure I is observed for $LiTiS_2$ and has the same hexagonal sulfur stacking as TiS_2. Structure type Ia, in contrast, involves a restacking such that the chalcogen layers become cubic close packed. The alkali metals in Ia are in octahedral interlayer sites. Structure Ib is also restacked but in this case the rearrangement results in trigonal prismatic coordination for the alkali cations.

The alkali metal coordination depends on its ionic radius and also on the particular composition and the ionicity of the specific host lattice. Chalcogen–chalcogen repulsions destabilize trigonal prismatic coordination and are larger at higher layer charges and greater *Ionic Character* in the transition metal–chalcogen bond. Consequently, the alkali cation coordination generally changes from trigonal to octahedral as the layer charge increases.

The alkali metal intercalation compounds of the dichalcogenides readily form hydrated phases on exposure to water (equation 10). The value of x varies with host lattice, and depends on the reducing power of the intercalated host relative to water. For example, approximate x values of 0.5, 0.33, and 0.1 are found for hydration of the sodium intercalation compounds of TiS_2, TaS_2, and MoS_2, respectively. Hydrated phases may be prepared by several other procedures, including electrochemical reduction in the corresponding aqueous electrolyte and chemical reduction using aqueous reducing agents such as sulfide, borohydride, and dithionite.

$$\begin{aligned} \mathrm{AMX_2 + H_2O} &\longrightarrow \mathrm{A}_x\mathrm{(H_2O)}_y\mathrm{MX_2} + (1-x)\mathrm{A^+} \\ &\quad + (1-x)\mathrm{OH^-} + \tfrac{1}{2}(1-x)\mathrm{H_2} \qquad (10) \end{aligned}$$

The water content (y) depends on the ambient water pressure and on the hydration energy of the interlayer cation. At low water partial pressures or for cations with low hydration energies (small charge/radius ratio) a monolayer of water molecules is present between the chalcogen layers. At higher pressures or at a higher cation charge:radius ratio, a bilayer structure is observed.

In solvents with high dielectric constants, for example, *N*-methylformamide (NMF), the application of weak shear forces to solvated alkali metal systems results in complete dispersion of the solid intercalation compound and the formation of homogeneous dispersions or colloidal solutions of negatively charged dichalcogenide layers. Colloidal dispersions can be reflocculated by addition of electrolyte solutions of other cations. Ion exchange occurs at the same time. The reaction provides a good way of circumventing problems with the ion-exchange kinetics of large guest species. For example, an intercalation compound of the large cluster cation $[Fe_6S_8(PEt_3)_6]^{2+}$ was synthesized by flocculation of a colloidal solution of $Na_{1/3}TaS_2$ in NMF/H_2O.[101]

3.2.3 *Molecular Guests*

Intercalation compounds of the dichalcogenides can be formed with organic guest molecules under strictly anhydrous conditions by direct reaction at temperatures up to about 200 °C. Early studies of the transition metal dichalcogenides largely focused on this type of reaction after the initial discovery of amide intercalation in TiS_2[102] and the subsequent observation of the increase in the superconducting transition temperature of 2H-TaS_2 on intercalation of primary organic amines.[103] Since the early work, a large number of compounds with several different general classes of organic molecule (amines, phosphines, amides, and N-heterocycles) have been synthesized. Several studies of the physical properties of organic intercalation compounds such as optical spectra and magnetic susceptibilities have established charge transfer from the organic guest to the host layers. The charge transfer in most cases occurs through redox chemistry involving reactions of the guest molecules.[104] Ammonia, for example, may be intercalated into TaS_2 or the other dichalcogenides by direct reaction at ambient temperature. The reaction proceeds to a limiting composition NH_3MX_2, which is a first stage compound. The first stage composition is not very stable and readily converts to a second stage phase of composition $(NH_3)_{0.5}MX_2$ under vacuum at room temperature.

The ammonia molecules occupy trigonal prismatic sites between the dichalcogen layers and NMR measurements show that they are oriented with the threefold axis parallel to the dichalcogenide layers, indicating only weak *Lone Pair* interactions with the layers. Careful study of the reaction stoichiometry, prompted by this observation, led to the conclusion that ammonia oxidation was involved and that the overall mechanism of reaction could be summarized by equation (11). The reaction product has x in the range 0.1–0.3 and contains ammonium ions solvated by neutral ammonia molecules.

$$\left(1+\frac{x}{3}\right)\mathrm{NH_3} + \mathrm{TaS_2} \longrightarrow \mathrm{(NH_4)}_x\mathrm{(NH_3)}_{1-x}\mathrm{TaS_2} + \frac{x}{6}\mathrm{N_2} \qquad (11)$$

While ammonia can be taken as a model system for intercalation of primary organic amines, pyridine represents the simplest N-heterocyclic Lewis base. The general chemistry is closely analogous to that shown by ammonia. Direct reaction of the dichalcogenide, for example, 2H-TaS_2, with pyridine at elevated temperature (200 °C) leads to the formation of a first stage intercalation compound with limiting composition $(py)_{0.5}TaS_2$. Structural measurements have shown that pyridine is oriented with the long C–N axis, and hence the nitrogen lone pair, parallel to the layers. Chemical studies established that intercalation involved redox chemistry of the guest molecules, leading to the formation of bipyridines. The oxidation of pyridine by TaS_2 is analogous to the oxidation of ammonia, and the product of the reaction contains pyridine and pyridinium cations.

A second class of molecular intercalation compounds that can be prepared by direct reaction with the dichalcogenides are those formed with certain organometallic molecules. Compounds with *Chromocene* and *Cobaltocene* were the first examples.[105] All of the organometallic molecules known to form intercalation compounds are good reducing agents and form stable cations. Compounds may be prepared by direct reaction with a solution of the organometallic molecule or alternatively by electrochemical or ion-exchange methods. Electrochemical intercalation of $Co(\eta\text{-}C_5H_5)_2{}^+$ into TaS_2 gives a compound with the same stoichiometry as that obtained for the compound prepared by direct reaction with neutral cobaltocene and confirms the redox nature of the process. The *Magnetic Susceptibility* of $[Co(\eta\text{-}C_5H_5)_2]_{1/4}TaS_2$ and of $[Cr(\eta\text{-}C_5H_5)_2]_{1/4}TaS_2$ are also consistent with complete electron transfer to the TaS_2 layers. The electron transfer mechanism accounts for the correlation that exists between the reducing power of the organometallic (measured in a relative way by its first ionization potential, IP) and its ability to intercalate specific host lattices. For example, $Co(\eta\text{-}C_5H_5)_2$ with an IP of 5.56 eV will intercalate both TaS_2 and FeOCl, but *Ferrocene*, which is less reducing (IP is 6.88 eV), will only intercalate the more oxidizing host lattice, FeOCl (see Section 3.4).

3.3 Metal Phosphorus Trisulfides[106]

The metal phosphorus trisulfide phases, MPS_3, form layered structures with M = Mg, V, Mn, Fe, Co, Ni, Zn, Pd, and Cd. All of the first transition series sulfides adopt the $FePS_3$ structure that is based on a cubic close-packed anion array with alternate layers of cation sites vacant. Within a layer, the cation sites are occupied by M^{2+} cations and P_2 pairs, as shown in Figure 20. The two different types of octahedra are ordered so that each P_2S_6 octahedron is surrounded by six MS_6 octahedra and each MS_6 octahedron has three each of MS_6 and P_2S_6 neighbors. To emphasize the structural relationship to the dichalcogenides, the composition can be written $M_{2/3}(P_2)_{1/3}S_2$.

The MPS_3 host lattices are ***Semiconductors*** or insulators, and the transition metal compounds have magnetic properties characteristic of high-spin octahedral cations (*see High-spin & Low-spin Compounds*). At low temperatures, antiferromagnetic order (*see Antiferromagnetism*) is observed but the susceptibility maxima are broad, indicative of the strong two-dimensional nature of the magnetic interactions.

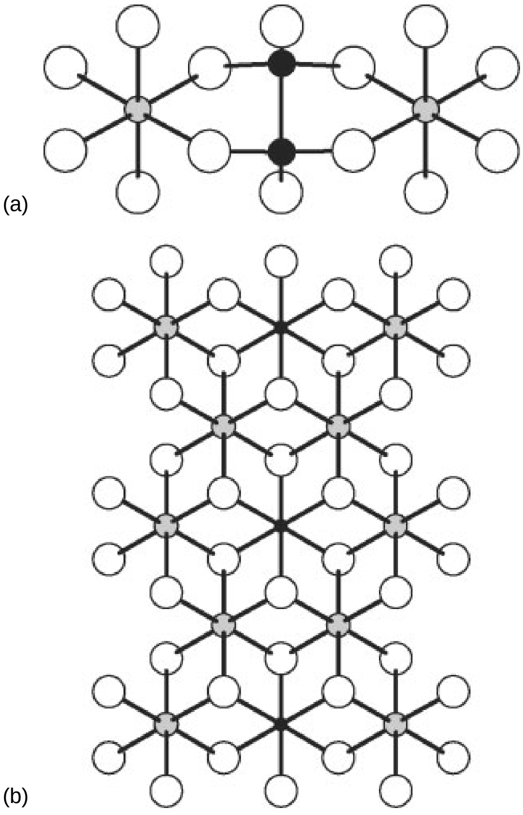

Figure 20 The iron phosphorus trisulfide structure showing the connection of P_2S_6 and FeS_6 octahedra (a) and the ordered arrangement within a single layer (b). The speckled circles are iron and the filled circles phosphorus

Redox intercalation reactions analogous to those of the dichalcogenides are observed for the MPS_3 phases with lower band gaps, that is, MPS_3 (Fe, 1.5 eV; Ni, 1.6 eV) and $FePSe_3$ (1.3 eV). Most work has focused on reactions of the MPS_3 (particularly $NiPS_3$) compounds with lithium because of interest in the application of the materials as cathodes in secondary batteries. The intercalation reactions are significantly more complex than those of the dichalcogenides. The reaction of $NiPS_3$, for example, with excess n-butyllithium in hexane results in compositions Li_xNiPS_3, with $x \leq 3$. Complete occupation of the interlayer sites corresponds to a maximum value of $x = 1.5$, indicating that degradation of the host lattice occurs with the formation of lithium sulfide. Irreversible behavior beyond $x = 1.5$ is confirmed by electrochemical intercalation of lithium in $NiPS_3$. Detailed studies using physical techniques (e.g. NMR and *Extended X-ray Absorption Fine Structure*) and theoretical calculations have led to an understanding of the reaction mechanism and the nature of the host acceptor levels.

Both $FePS_3$ and $NiPS_3$ react with toluene solutions of cobaltocene to give intercalation compounds that are similar in compositions and interlayer separations to the corresponding phases formed by the transition metal dichalcogenides. However, in studies of the direct intercalation reaction of metallocenes with some wide band gap host lattices ($MnPS_3$, 3.0 eV; $ZnPS_3$, 3.4 eV; $CdPS_3$, 3.5 eV), similar intercalation compounds were formed by reaction with solutions of metallocene salts, for example, with cobaltocenium iodide. This reaction is an example of a different intercalation mechanism involving removal of M^{2+} cations from the layers and is unique to the MPX_3 compounds. Intercalation involves an ion-exchange process whereby loss of M cations from the MPX_3 layers into the solution phase maintains charge balance on intercalation of cations between the layers. The intercalation compounds have the general stoichiometry $G_{2x}[M_{1-x}[\cdot]_xPS_3]\cdot yH_2O$.

After the initial reaction, additional compositions can be made by cation exchange with the interlayer cations. A particularly interesting example is the exchange of $Ni(H_2O)_6{}^{2+}$ with $K_{0.4}[Mn_{0.8}PS_3]\cdot 0.9H_2O$. Complete exchange of the potassium ions followed by dehydration gives the compound $Ni_{0.28}Mn_{0.72}PS_3$, which has identical lattice constants and magnetic properties to the phase prepared by direct reaction of the elements at high temperature. The experiment demonstrates that the ion-exchange process with the layer cations is reversible. The MPS_3 lattices differ in their relative abilities to form vacant sites in the layers by direct ion-exchange reactions. Ion-exchange reactions readily occur for Mn, Cd, and Zn. In contrast, $NiPS_3$ does not undergo ion exchange and $FePS_3$ does so with difficulty and only in the presence of a complexing agent like ethylenediaminetetraacetic acid (EDTA).

The two distinct types of interlayer reaction observed in the MPS_3 compounds (electron transfer to the layers and ion transfer from the layers into the reactant solution) are partially reversible and occur with simultaneous intercalation of cationic species into the interlayer spaces. The balance between the two different reaction pathways appears to depend on the band gap of the particular solid. Ion transfer reactions are easier in the larger band gap compounds (for example, with M = Zn, Cd, and Mn) where the layers appear to behave as M^{2+} cations weakly coupled to $P_2S_6{}^{2-}$ units. The MPS_3 lattices behave very differently from the dichalcogenides where the strong covalent interactions between formally M^{4+} cations and S^{2-} anions preclude any ion transfer chemistry involving the layers.

3.4 The Transition Metal Oxyhalides[1,107]

The transition metal oxyhalides occur with four main structure types (FeOCl, AlOCl, SmSI, and PbFCl) but only the FeOCl structure undergoes topotactic redox reactions. A layer of the orthorhombic FeOCl structure is shown in Figure 21. The structure is characterized by double sheets of distorted octahedra that share edges. Each iron atom is coordinated to four oxide anions and two chloride ions, with the two chloride ions in cis octahedral positions on the outside of the layer. The arrangement of octahedra within a layer is similar to that found in γ-FeOOH and γ-AlOOH.

The redox intercalation chemistry of FeOCl with inorganic, organic, and organometallic guest cations is very similar to that of the dichalcogenides. For example, some degree of reversible intercalation occurs in electrochemical or chemical reactions with n-butyllithium to form Li_xFeOCl. In aqueous systems, hydrated alkali intercalation compounds can be prepared using chemical reducing agents, but reactions are complicated by the tendency of FeOCl to topochemically hydrolyze to γ-FeOOH. The alkali metal systems $M_{0.14}(H_2O)_yFeOCl$ (M = Li, Na, K, Cs), prepared using $Fe(CN)_6{}^{4-}$ as the reducing agent, show large interlayer spacings that are very dependent on the water activity. For example, the interlayer spacing in the potassium compound changes from 11.47 to 22.84 Å when the contacting liquid is changed from 3 M KCl solution to pure water. This behavior is in marked contrast to that of the dichalcogenides, where the spacings primarily reflect cation hydration effects. The behavior of FeOCl indicates much stronger interactions between solvating water molecules with either the chloride layers or with partially hydrolyzed layers in which some Cl^- has been replaced by OH^-.

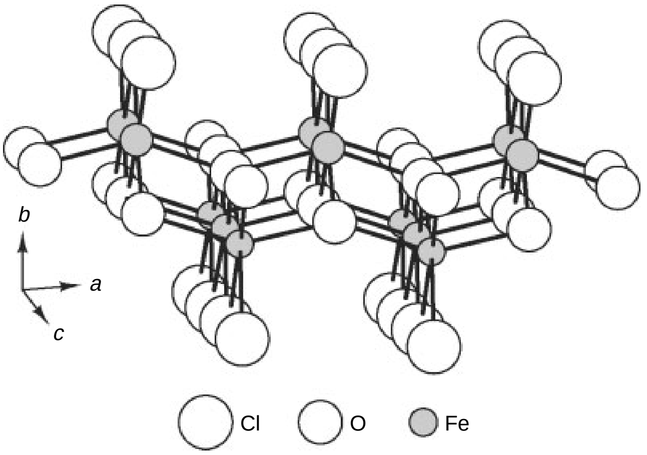

Figure 21 The arrangement of atoms in a single layer of FeOCl

Much more is known about the reactions of FeOCl with organic and organometallic cations than with the simple inorganic ions. The chemistry is generally similar to that of the dichalcogenides, but because FeOCl is more oxidizing, a wider range of organic and organometallic compounds can form by direct reaction. Unlike any of the dichalcogenide or MPS_3 phases, FeOCl will oxidize ferrocene to ferrocenium and form an intercalation compound. The formation of $[(\eta\text{-}C_5H_5)_2Fe]_{1/6}FeOCl$ has been studied in detail by Mössbauer Spectroscopy.[108] Resonances characteristic of the ferrocenium cation, two types of lattice Fe^{3+} that differ in the number of Fe^{2+} neighbors, and lattice Fe^{2+} are observed. Quantitative measurements confirm that intercalation occurs with complete electron transfer from the guest to the host lattice.

Intercalation compounds are also formed by reaction of FeOCl with organic compounds that are good electron donors. Several systems have been synthesized with organic molecules such as tetrathiofulvalene (TTF), tetrathionaphthalene (TTN), and tetrathiotetracene (TTT). The organic intercalation compounds have interlayer separations and stoichiometries consistent with near close packing of the guests. Part of the interest in these systems stems from the possibility of obtaining very high conductivities via properly oriented organic guests.[109]

Reactions with Lewis bases are the other major class of redox intercalation reactions that have been explored with the FeOCl lattice. Pyridine, for example, reacts with FeOCl to form two compounds, $(py)_{1/4}FeOCl$ and $(py)_{1/3}FeOCl$.[110] Reactions of FeOCl with ammonia and alkylamines are among the earliest reported intercalation reactions of compounds with neutral layers.[111]

$$FeOCl + 2RNH_2 \longrightarrow FeONHR + RNH_3Cl \qquad (12)$$

FeOCl also shows a type of interlayer reactivity not found in other systems. Irreversible topochemical substitution reactions are observed where the outer halide layers of the FeOCl lattice are replaced by other groups. Examples of this type of substitution were first observed in reactions of ammonia and methylamine with FeOCl at ambient temperature. Reaction occurs with two moles of ammonia or methylamine according to equation (12), where R = H or Me. The products of the substitution reaction are X-ray amorphous, but strong evidence for their formation comes from chemical analysis and infrared (IR) measurements.

Other substitution reactions lead to more crystalline phases. Reaction of (4-aminopyridine)$_{1/4}$FeOCl with methanol at 100 °C, for example, gives crystalline FeOOMe. Reactions with aliphatic and aromatic alkoxides and acids, of the type shown in equations (13) and (14), have also been studied.[112] More rigid and longer molecules, such as 4-hydroxybenzoic acid, can crosslink the iron oxide layers. An initial intercalation step that causes an expansion of the FeOCl interlayer distance is followed by a second substitution step leading to layer crosslinking.

$$\mathrm{KR} + \mathrm{FeOCl} \longrightarrow \mathrm{KCl} + \mathrm{FeOR} \qquad (13)$$

$$\mathrm{K_2R} + 2\mathrm{FeOCl} \longrightarrow 2\mathrm{KCl} + (\mathrm{FeO})_2\mathrm{R} \qquad (14)$$

Layer derivatization reactions have yet to be fully explored for the layered oxyhalides but the compounds are examples of a growing class of layered compounds with alternating organic and inorganic layers where the organic group is attached to the inorganic layer by a covalent bond. The organophosphonates of zirconium, Zr(RPO$_3$)$_2$, and vanadium, VORPO$_3$, are other examples (see Section 2.2.3).

3.5 Alkali Metal Intercalated Nitride Halides MNX (M = Zr, Hf; X = Cl, Br, I)

Superconductivity has been observed in the intercalated layered nitride halides of general composition MNX (M = Zr, Hf; X = Cl, Br, I). On intercalation, β-ZrNCl and β-HfNCl, become superconductors with transition temperatures of 13 and 25.5 K, respectively.[113–116] The transition temperature of the electron doped β-HfNCl is higher than that observed in any intermetallic compound.

The structure of β-ZrNCl contains ZrN double layers sandwiched between close-packed layers of chlorine ions that are stacked as in either CdCl$_2$ or CdI$_2$ or with a random mixture of both sequences. Synthetic techniques have been developed to prepare highly crystalline β-ZrNCl with the CdCl$_2$ arrangement and this structure has been well determined. The stacking sequence is –BABACBCBACACB– for the layers –N Cl Cl N N Cl Cl N N Cl Cl N N– so that the chlorine ions are stacked in a hexagonal arrangement as found in the structure of SmSI.[117] The stacking sequence changes on alkali metal intercalation to that of the YOF structure in which all of the individual layers adopt cubic stacking.

Both β-ZrNCl and β-HfNCl form intercalation compounds that are very similar to those of transition metal dichalcogenides. In the interlayer space between the chloride layers one octahedral and one tetrahedral vacant site per 2ZrNCl formula units are available for guest molecules. Alkali cations can occupy both positions since compositions are observed with $x > 0.5$ in A$_x$ZrNCl (A = Li, Na).

When pale yellow-green β-ZrNCl is allowed to react with n-butyllithium in hexane, lithium atoms are intercalated to give black Li$_{0.16}$ZrNCl an interlayer separation of 9.3 Å only slightly larger than that of β-ZrNCl (9.2 Å). The intercalation compound shows metallic conductivity and becomes a superconductor at 13 K. When Li$_{0.16}$ZrNCl is stirred in THF or PC (propylene carbonate), the interlayer separation increases to 14.9 and 22.2 Å, respectively owing to cointercalation of solvent molecules.

Higher concentrations of lithium ions and other alkali metal (Na, K) intercalated compounds can be prepared by using the corresponding alkali metal naphthalide solutions in THF. THF molecules are cointercalated with lithium and potassium ions but not with the Na intercalation compound, Na$_{0.40}$ZrNCl. PC can, however, form cointercalation compounds with all of the alkali metal intercalated β-ZrNCl phases. The basal spacing varies depending on the alkali metals content intercalated: single layer arrangements are observed at low concentrations and double layers at high concentrations. Cointercalation compounds with other polar solvents, including dimethylformamide, dimethylsulfoxide, and acetonitrile has also been reported.

Reductive intercalation compounds of β-ZrNCl with cobaltocenes have been reported where the metallocene molecules are believed to be oriented with the molecular axes parallel to the layers.[118] The metallocene intercalation compounds also show superconductivity at 14 K.

Alkali metals can be electrochemically intercalated into β-ZrNCl. The results are generally in agreement with those from chemical intercalation with respect to interlayer separations and degree of intercalation. For example, the electrochemical data for the cell Li | LiClO$_4$/THF| –ZrNCl is consistent with the difference in the degree of reduction obtained using n-BuLi and Li-naphthalide.

As mentioned above, Li$_{0.16}$ZrNCl becomes superconducting below 13 K. On lithium intercalation of β-HfNCl with lithium naphthalide/THF the color of the crystals changes from white to black, and the interlayer separation increases from 9.23 Å to either 14.0 and 18.7 Å, corresponding to single or bilayer arrangements of THF molecules. Resistivity data for the 18.7 Å phase of Li$_{0.48}$(THF)$_y$HfNCl show a sharp drop at 25.5 K and zero resistance at 24.5 K. Superconductivity is confirmed by magnetic susceptibility measurements, which indicate that the compound is a bulk type II superconductor. The composition Li$_{0.48}$(THF)$_y$HfNCl has the highest transition temperature in this class of superconductors.

The MNX α-polymorphs adopt the FeOCl type layered structure (see Section 3.4) and exist for all combinations of MNX (M = Zr, Hf; X = Cl, Br, I) and for TiNX (X = Cl, Br, I). Superconductivity at 11 K is observed on intercalation of lithium in α-ZrNBr and α-ZrNI using BuLi.[119] Intercalation of pyridine into TiNCl gives pyridine$_{1/3}$ TiNCl, which superconducts at 4–6 K. The latter is reminiscent of the effect of intercalation of organic bases into the superconducting dichalcogenides.

3.6 Layered Transition Metal Oxides[4,5]

Simple layered structures with true van der Waals gaps are found only for the oxides of high oxidation state transition metal cations that form strong multiple covalent bonds to oxygen, such as MoO_3, V_2O_5, and $VOPO_4$. In the absence of this strong covalent bonding, oxide layer structures are destabilized by electrostatic repulsions between layers of negatively charged oxide ions, which are not offset by sufficiently strong attractive van der Waals forces. Transition metal oxide layers may be stabilized when the electrostatic repulsion is reduced by the presence of interlayer cations or hydrogen bonding. The three types of situation that are encountered are illustrated schematically in Figure 22. Intercalation reactions of type I oxides involve reduction of the transition metal whereas, the reaction chemistry of type II oxides involves mainly ion-exchange and oxidative deintercalation.

3.6.1 High Oxidation State Oxides

The compounds MoO_3, V_2O_5, and $VOPO_4{\cdot}H_2O$ each contain a transition metal ion in a strongly distorted octahedral environment arising from $d_\pi - p_\pi$ covalent M=O bonding. The structure of molybdenum trioxide is shown in Figure 23 as an example. The layers of double octahedra are anisotropic. Along the *c* axis the octahedra share cis edges, whereas along the *a* direction they share corners. The octahedra are far from ideal and have two short distances cis to each other, one pointing into the interlayer space and one along the *c* axis. Individual layers in MoO_3 are separated by a true van der Waals gap and consequently the oxide shows the full range of topotactic redox chemistry outlined for the dichalcogenides. Molybdenum trioxide is insulating and white in color when fully oxidized, but reductive intercalation produces both a large increase in electronic conductivity and a dramatic change in color to metallic blue-black, even for small amounts of reduction.

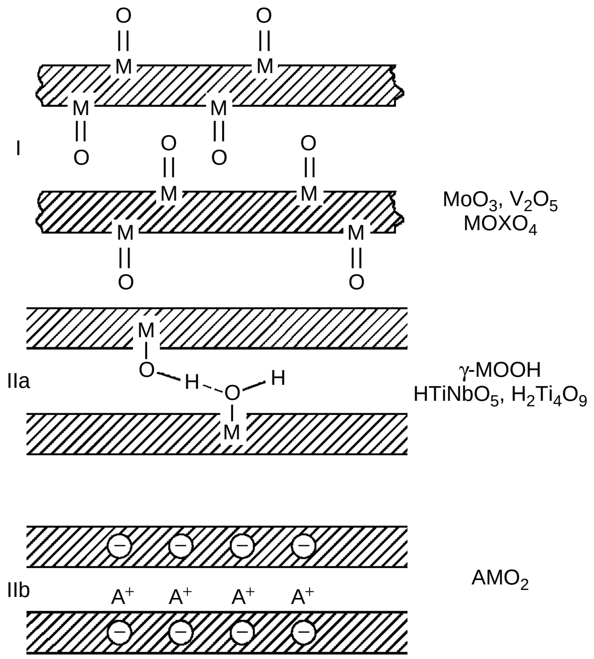

Figure 22 Schematic representation of the different types of layered metal oxides. (Reprinted with permission from Ref. 4 by permission of Oxford University Press (www.oup.com))

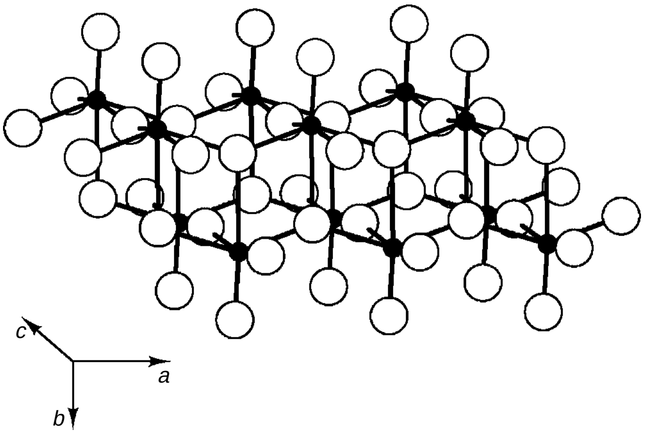

Figure 23 The structure of a single layer of MoO_3; filled and open circles are molybdenum and oxygen atoms, respectively

The intercalation of MoO_3 by hydrogen is the most extensively investigated of its redox reactions. Chemical reduction of MoO_3 in aqueous acid was first shown by Glemser and coworkers[120] to result in the formation of a series of compounds that could be formulated H_xMoO_3. The hydrogen bronzes can be prepared by electrochemical reduction in acid solution and by chemical reduction ('hydrogen spillover') with hydrogen and a platinum metal catalyst. Four distinct hydrogen bronze phases are formed: blue I ($0.23 < x < 0.40$), blue II ($0.85 < x < 1.04$), red ($1.55 < x < 1.72$), and green ($x = 1.99$).[121] All the H_xMoO_3 phases show metallic conductivity and weak temperature independent paramagnetism. The hydrogen intercalation compounds are Brønsted acids and react with Lewis bases (L) to form intercalation compounds of general composition $L_yH_xMoO_3$, for example, $(py)_{0.3}H_{0.5}MoO_3$.

In other respects the intercalation chemistry of MoO_3 closely resembles that of the dichalcogenides. Reduction in neutral aqueous electrolytes leads to the formation of hydrated cation intercalation compounds with the general composition $A_x{}^+(H_2O)_y[MoO_3]^{x-}$ (A = Na, K, Rb, Cs, NH_4, etc.), which can exchange ions or solvent molecules easily. Cation exchange reactions in aqueous solution are rapid at room temperature and interlayer separations are found to depend on the hydration energy of the interlayer cation, but there is no simple correlation between layer spacing and cation charge:radius ratio as observed for the dichalcogenides.

In the structure of V_2O_5, layers of vanadium–oxygen square pyramids (*see Square Pyramidal*) are connected by $V = O\cdots V = O$ bonds. Unlike MoO_3, these interlayer interactions are sufficiently strong that V_2O_5 behaves more like a three-dimensional lattice and intercalation compounds are formed only with the smallest cations, H^+ and Li^+.[122]

Vanadium pentoxide is more strongly oxidizing than MoO_3 and can be reduced by mild reducing agents such as acetonitrile solutions of lithium iodide. More strongly reducing reagents such as n-butyllithium give poorly crystalline products that are not well characterized. Both chemical and electrochemical reactions with lithium at ambient temperature give a series of phases, $Li_xV_2O_5$ with $x < 2.0$.[122]

Hydrogen intercalation compounds of V_2O_5 can be prepared by the same techniques used for MoO_3, and are structurally similar to their molybdenum analogs. Hydrogen 'spillover' gives the composition $H_xV_2O_5$ ($x = 3.8$), but unlike the high hydrogen content molybdenum bronzes the vanadium compounds are X-ray amorphous and semiconducting. Gels of vanadium pentoxide can be prepared by polycondensation of decavanadic acid. Removal of excess water results in a solid gel with approximate composition $V_2O_5{\cdot}1.6H_2O$. X-ray diffraction studies of oriented films show that the gels have a layered structure. Unlike crystalline V_2O_5, vanadium pentoxide gels can form intercalation compounds with large guests (e.g. ammonium, alkylammonium, ferrocenium, and cobaltocenium cations).[123]

Vanadium phosphate shows a wide range of intercalation reactions that parallel in many respects the chemistry of MoO_3. The α form of $VOPO_4$ is a layered compound and is one member of a series of complex oxides of general formula $MOXO_4$ ($M = V$, Nb, Ta, Mo; $X = P$, As, S) that are isostructural. The tetragonal layer structure of these compounds is made up of distorted MO_6 octahedra and XO_4 tetrahedra, which are linked by corner-sharing oxygen atoms. Each octahedron is joined to four tetrahedra and the layers are joined along the c axis by corner sharing the remaining two trans vertices of the octahedron. The vanadium coordination is consequently better represented as square pyramidal, and is similar to the vanadium atom coordination in V_2O_5. An important difference between V_2O_5 and $VOPO_4$ is the number per unit area of interlayer interactions of the type $V = O\cdots V$, which is reduced in $VOPO_4$ by the presence of the phosphate groups. Consequently, the interlayer interactions in $VOPO_4$ are much weaker and $VOPO_4$ behaves in its chemistry like a two-dimensional system. An immediate indication of the layered nature of the structure is the ease with which it forms mono- and dihydrates. Structural studies of the dihydrate show that one water molecule is coordinated to the vanadium atom and that the second is located in the interlayer space. The intercalation and deintercalation of water between $VOPO_4$ and $VOPO_4{\cdot}H_2O$ can be viewed as a special type of intercalation reaction in which coordination of the guest species to a metal center provides the driving force. Similar reactions have been described for larger donor ligands such as straight chain alcohols and for stronger Lewis bases such as pyridine and 4,4′-bipyridine.[124] With 4,4′-bipyridine, the stoichiometry is $VOPO_4$(bipy)0.5 and adjacent layers are crosslinked or 'pillared' by the bifunctional ligand.

Vanadium phosphate dihydrate readily undergoes redox intercalation reactions with alkali metal and alkaline earth metal cations in the presence of a mild reducing agent.[125] The reactions are analogous to those used to prepare lithium intercalation compounds of V_2O_5; iodide is oxidized to iodine, V^V is partially reduced to V^{IV}, and the metal cation present in solution is inserted between the layers. An important difference between $VOPO_4{\cdot}2H_2O$ and the other oxide lattices discussed above is that the layers have low electronic conductivity. Redox intercalation generally requires both ionic transport of the guest species in the interlayer region and electronic transport in the host lattice. Consequently, it has been proposed that the reductant, I^-, itself is intercalated into the interlayer space of $VOPO_4{\cdot}2H_2O$ and subsequently expelled in oxidized form.

3.6.2 Intercalation in Oxides Containing Bi–O Double Layers

Oxides containing bismuth oxygen atom double layers include the bismuth calcium copper oxide series of superconductors exemplified by $Bi_2Sr_2CaCu_2O_8$ (Bi-2212) and the beta phase oxide ion conductors based on the composition $Sr_xBi_{9-x}O_{(27-x)/2}$. While the details of these two structure types are quite different, they have the common feature of containing Bi–O double layers that are only weakly bonded. In Bi-2212, the bismuth atoms are four + one coordinated by oxygen atoms whereas, in $Sr_xBi_{9-x}O_{(27-x)/2}$ they are three + one coordinated and form square and hexagonal layers of Bi–O bonds. Both classes of compounds and be intercalated by iodine atoms that are inserted between the Bi–O double layers.

Iodine intercalation of Bi-2212 via reaction with iodine vapor was first shown to form a stage-1 compound with the composition, $IBi_2Sr_2CaCu_2O_8$.[126] Subsequently, it was shown that by varying the temperature at which the intercalation reaction was carried led to the formation of higher stage compounds with the general composition $IBi_{2n}Sr_{2n}Ca_nCu_{2n}O_{8n}$. Stage 1 and 2 compounds have been obtained as pure phases and stages up to $n = 5$ have been seen in high-resolution transmission electron micrographs.[127] Each intercalated iodine layer produces an expansion of 3.6 Å. Similar compounds were formed with other members of the bismuth superconducting family including $Bi_2Sr_2CuO_6$ (Bi 2:2:0:1) and $Bi_2Sr_2Ca_2Cu_3O_{10}$ (Bi 2:2:2:3).[128] The lowering of the superconducting transition temperature upon intercalation was thought to be primarily due to the change in interlayer coupling owing to the expansion of the lattice in the c-axis direction. Micro-Raman spectroscopy, however, provided information that iodine was present between the layers in the form of I_3^- suggesting significant charge transfer.[129] Evidence for electron hole transfer from iodine to the copper-oxygen sheets is suggested by the observation that $Bi_2Sr_2Y_{0.5}Ca_{0.5}Cu_2O_8$ becomes superconducting on intercalation of iodine.[130] More recently several other guest species including Br_2, IBr, HgI_2, and AgI have been intercalated into Bi-2212.[131]

The layered oxide ion conductors $Sr_xBi_{9-x}O_{(27-x)/2}$ and $BaBi_8O_{13}$ show similar intercalation reactions with iodine.[132] The iodine atoms intercalate into the van der Waals gap between adjacent Bi–O sheets to form stage 1 compounds. The spacing between adjacent Bi–O layers increases by 3 Å corresponding to the intercalation of a monolayer of iodine atoms. Micro-Raman spectroscopy shows that the intercalated iodine species is predominantly I_3^-. Ag–I intercalated $Sr_{1.5}Bi_{7.5}O_{12.75}$, was synthesized by reaction with iodine and then in a second step with silver metal.[133] Intercalation of lithium iodide into the ferroelectric layered compound $Bi_4Ti_3O_{12-x}$ has also been reported.[134]

3.6.3 The Layered AMO$_2$ Oxides[134,135]

The layered oxides AMO_2 ($A = Li$, Na; $M = V$, Cr, Mn, Fe, Co, Ni) comprise alternating layers of edge-shared MO_6 octahedra and layers of alkali metal cations, and are structurally similar to the alkali−transition metal dichalcogenides. Nonstoichiometric phases A_xMO_2 can be synthesized at high temperatures by substitution of a tetravalent cation of a different metal or partial oxidation of the trivalent M cation. In general, stable phases cannot be synthesized at high temperature for $x < 0.5$.

The structures of the A_xMO_2 oxides, like those of the alkali metal dichalcogenides, depend on composition, the alkali cation size, and on the ionicity of the M–O bond, but there are important differences. For example, the transition metal is octahedrally coordinated in almost all cases and the pure MO_2 phases cannot be prepared even at low temperature because some alkali metal content is necessary to stabilize the layer structure. Staging is not observed because the interlayers cannot be completely emptied of cations.

Most of the reaction chemistry of the alkali−transition metal oxides involves oxidation of the host lattice, either electrochemically or with chemical reagents such as iodine or bromine in acetonitrile. The chemical reactions are analogous to, for example, the oxidation of $LiVS_2$ to form VS_2 using I_2, though generally the transition metal oxides are much harder to oxidize than the sulfides. In electrochemical oxidation the applied cell voltages are limited only by electrolyte stability, whereas chemical oxidations depend on the particular redox couple chosen. Not all of the alkali metal cations can be removed by either synthetic method without irreversible structural rearrangement. In lithium systems the formation of the three-dimensional spinel structure in preference to the layer structure is particularly favorable. Correspondingly, lithium intercalation of oxide spinels is quite facile and has been studied in its own right by several groups.[136]

The intercalation and deintercalation chemistry of the $LiMO_2$ ($M = Ni$, Co) phases forms the basis for the operation of lithium-ion batteries and is discussed in more detail in Section 3.7.1. Sodium ions also can be deintercalated from the host lattices Na_xMO_2 ($M = Ti$, Cr, Mn, Co, Ni) by electrochemical oxidation but the electrochemical behavior is very complicated. Limited ranges of solid solution and large numbers of intermediate phases are observed.

Sodium Cobalt Oxide. The general features of the intercalation chemistry of the layered AMO_2 oxides are described above in Section 3.6.3. Recently superconductivity with a transition temperature $T_c \sim 5\,K$ was observed in the compound $Na_xCoO_2{\cdot}yH_2O$ ($x < 0.35$, $y < 1.3$).[137] The hydrated sodium ion containing phase was prepared from $Na_{0.7}CoO_2$ by oxidative deintercalation using a solution of bromine in acetonitrile followed by washing in water. Analysis of the X-ray powder diffraction pattern showed that the structure contained a bilayer of water molecules. Subsequent studies confirmed the presence of superconductivity and also examined the variation of T_c with sodium ion content.[138] Samples were prepared by the same chemical method but used varying amounts of bromine from stoichiometric to a one hundred fold excess. The results show that like the high-T_c copper oxides, the highest superconducting transition temperature occurs in a narrow composition range and decreases for both underdoped and overdoped materials. Most recently, superconducting single crystals of $Na_xCoO_2{\cdot}yH_2O$ were prepared by electrochemical deintercalation of single crystals of $Na_{0.75}CoO_2$ in 1 M NaOH.[139] After deintercalation large single crystals break up into smaller pieces (∼5 × 5 × 2 mm) and are a mixture of hydrated and partially hydrated phases. After careful hydration, nearly single-phase crystals are obtained in which over 90% of the sample volume corresponds to the superconducting $Na_{0.3}CoO_2{\cdot}1.3H_2O$ structure.

3.7 Lithium Intercalation in Transition Metal Oxides and Phosphates

Reversible electrochemical lithium deintercalation from 2D and 3D materials is important for applications in lithium-ion batteries. New developments have been realized in two classes of materials that show exceptionally promising properties as cathode materials. The first includes mixed layered oxides exemplified by $Li[Mn_xNi_yCo_z]O_2$, where the Mn remains inert to oxidation/reduction and acts as a framework ‘stabilizer’ while the other elements carry the redox load. Another class that shows much potential is metal phosphates, which includes olivine-type $LiFePO_4$, and the NASICON-related frameworks $Li_3M_2(PO_4)_3$.

3.7.1 Lithium Transition Metal Oxides

Various advances in this area during the past decade have been recently reviewed,**[140]** and highlights are summarized here. The layered $LiMO_2$ structure adopted by $LiCoO_2$ described in Section 3.6.3 (α-$NaFeO_2$ type, or 'O3'), is a versatile intercalation host. Isostructural alternatives that target less costly materials were initially based on substitution of $M = Co$ with M^{3+} ions (Ni, Mn, and Al) aimed to reduce the Co content, and stabilize the structure to reversible lithium extraction. Materials with high nickel content $LiNi_{1-x-y}M^1{}_xM^2{}_yO_2$ are appealing,**[141]** but suffer from oxidation reactions with the electrolyte at elevated temperature/voltage as does $LiNiO_2$. Band structure considerations indicate that extraction of oxygen from the lattice competes with removal of Li^+ at high potential, in the order $Ni > Co > Mn$.**[140]**

Mn oxides are especially attractive:**[140,142]** the most extensively studied of these is the spinel $LiMn_2O_4$. Lithium can be deintercalated from or inserted into the 3D structure to give $Li_{1\pm x}Mn_2O_4$ ($x \leq 1$). Pronounced Jahn–Teller structural distortions in the range $Li_{1+x}Mn_2O_4$ ($Mn^{3.5+} \longleftrightarrow Mn^{3+}$) limit practical reversible (de)intercalation to $Li_{1-x}Mn_2O_4$. Metal dopants act as structural stabilizers, but do not inhibit dissolution of Mn that occurs from disproportionation of $Mn^{3+} \longleftrightarrow Mn^{2+} + Mn^{4+}$. Layered 'O3′ $LiMnO_2$ is not thermodynamically stable: compositions of this stoichiometry crystallize as an orthorhombic phase o-$LiMnO_2$. This unique structure contains Li and Mn ions that occupy octahedral sites arranged in an alternative zigzag configuration. Its electrochemical intercalation properties have been investigated by various groups, and shown to be poor. Reduction of crystallite size (to less than 0.3 µm) facilitates (de)intercalation, but repeated cycling of lithium within the structure results in spinel formation. Surprisingly, little intercalation capacity loss is observed and has been attributed to the formation of antiphase nanodomains that arise from the nucleation of the spinel at different points in the orthorhombic structure.**[143]** The high density of phase boundaries provide elasticity that can accommodate transformation strain arising from intercalation over a wide range of lithium content. Metastable layered $LiMnO_2$ was reported recently, with a structure analogous to that of $LiCoO_2$.**[144]** The Jahn–Teller effect of the Mn^{3+} ions result in monoclinic distortion from the ideal rhombohedral O3 structure. The material is accessed via a 'chemie douce' route, involving ion exchange of O3-type $NaMnO_2$ with $LiNO_3$ in hexanol or propanol at elevated temperature. During repeated lithium deintercalation/intercalation, transformation to the spinel phase is also observed, although this is advantageous rather than detrimental. As in orthorhombic $LiMnO_2$, nanostructures of spinel/layered oxide intergrowth regions are sustained, and enhance the reversible Li intercalation process by inhibiting strain and stress within the 'splayered' materials.**[145]**

In a new group of layered metal oxides, Jahn–Teller distortion effects are circumvented by using a combination of Mn^{4+} with a second element as the redox-active species. The first materials to utilize this concept were based on chromium substitution in the ordered rock salt structure Li_2MnO_3.**[146]** A line phase within the solid solution of Li_2MnO_3 (or $Li[Li_{1/3}Mn_{2/3}]O_2$) and $LiCrO_2$; that is, $[Li_{0.2}Cr^{III}_{0.4}Mn^{IV}_{0.4}]O_2$ was reported to have particularly good properties. Extraction of lithium from this material is concommitant with reversible oxidation of Cr^{3+} to Cr^{6+}, with the Mn^{4+} remaining inert.**[147]** The redox-inactive Mn^{4+} in the lattice forms an electronically conductive framework, and facilitates the 3-electron redox process at the Cr center. The restriction of Mn to the +4 state provides high stability, as more reduced valence states of Mn are prone to migration.

The high toxicity of Cr^{6+} led to the development of isostructural Mn oxides that incorporate the $Ni^{2+} \longleftrightarrow Ni^{4+}$ redox couple. These can be described as a solid solution between $Ni^{II}O$, and $Li_2Mn^{IV}O_3$. A wide range of compositions have been reported with the general stoichiometry $Li[Li_{1/3-2x/3}Ni^{II}_xMn^{IV}_{2/3-x/3}]O_2$ ($x = 0.5- >$).**[148]** The end member of the series, $Li[Ni_{0.5}Mn_{0.5}]O_2$ is particularly intriguing. The first reports showed poor intercalation capacity retention**[37,140]** but improvements in synthesis methods yield materials that demonstrate good stability.**[149]** Control of stoichiometry, morphology, and cation ordering within the lattice is paramount to achieving excellent reversible intercalation properties. Samples are prepared using a mixed hydroxide method, involving first a precipitation to form homogenously mixed $[Ni,Mn](OH)_2$, which is allowed to react with Li_2O at high temperature (1000 °C) to form the desired composition. Sol-gel methods utilizing a solution-based technique to achieve homogeneous mixing have also been reported. Electrochemical data show that 80% of the lithium can be reversibly deintercalated from optimized materials below 4.7 V.**[150]** The size of Ni^{2+} (0.83 Å) is similar to that of Li^+ (0.86 Å), making it prone to mix with the Li layer thereby impeding Li^+ ion diffusion. Correlation of mixing with intercalation capacity has been established, with the best materials exhibiting as little as 8% Li/Ni exchange. ^6Li NMR studies are able to differentiate the Li^+ ions within the lithium layer from those within the transition metal layer, and also reveal that Li^+ ions in both sites are subject to deintercalation.**[151]** The invariance of the Mn^{+4} valence state during (de)intercalation has been confirmed by X-ray absorption studies, which furthermore suggest the oxidation of Ni^{2+} to Ni^{4+} is a two-step process that occurs via Ni^{3+}.**[152]**

Triple solutions of $LiCoO_2$, NiO, and $Li[Li_{1/3}Mn_{2/3}]O_2$ show equal, if not greater promise as intercalation hosts. Compositions close to $LiNi_{1/3}Co_{1/3}Mn_{1/3}O_2$ prepared by sol-gel methods using citric acid as a chelating agent exhibit very little (<3%) undesirable cation mixing, and excellent intercalation properties, whereas less well ordered materials display poor reversible lithium intercalation capacity.**[153]** X-ray absorption near-edge studies show the valence states of Ni, Co, and Mn are +2, +3 and +4 in good agreement with calculated valence states.**[154]**

The success of the $Li[Ni^{2+}, Mn^{4+}]O_2$ materials has prompted investigation into analogous Ti^{4+} materials. Direct high-temperature synthesis of $Li_x[Ni_{1-y}Ti_y]O_2$ yields a disordered rock salt structure for $y > 0.4$; although an ordered layered structure $Li_{0.9}[Ni_{0.45}Ti_{0.55}]O_2$ can be synthesized by means of ion exchange from the sodium compound.[155] In contrast to the Ni, Mn oxides, partially disordered phases show better intercalation capacity then the least disordered. Nonetheless, the migration of Ti^{4+} into the Li^+ layer during electrochemical oxidation/reduction and the poor electronic conductivity of the material ultimately results in low lithium extractability.

3.7.2 Lithium Transition Metal Phosphates

Lithium transition metal phosphates are potentially very versatile and practical hosts for lithium intercalation, owing to their framework structures built of ${PO_4}^{3-}$ tetrahedra and ${MO_6}^{n+}$ octahedra that house highly mobile interstitial Li^+ ions. Much recent interest has been devoted to $LiFePO_4$, the most prominent member of this family. The promise of these materials is based on the 'inductive effect', described by Goodenough as the withdrawal of electron density from the metal centre owing to strong covalent bonding in the ${PO_4}^{3-}$ moiety. The inductive effect results in a very favorable increase in the Li (de)intercalation potential compared to the corresponding oxide. The raising of the $M^{n+}/M^{(n+1)+}$ redox couple is particularly advantageous for iron phosphates, where the potential of the Fe^{3+}/Fe^{2+} couple lies between 2.8 and 3.4V depending on the structural features of the framework. The metal phosphates also exhibit remarkably stable intercalation behavior, and resistance to oxygen loss.

Olivine-type $LiFePO_4$ was first reported by Goodenough in 1997.[156] Phosphates of this type ($LiMPO_4$; M = Fe, Ni, Co, Mn) adopt a common structure displayed by silicate minerals such as $MgFeSiO_4$, that constitute a large fraction of the earth's crust. The olivine architecture comprises a network of MO_6 octahedra connected to SiO_4 or PO_4 tetrahedra. The mobile alkali ions, that is, Li^+, form one-dimensional chains in the structure. These run parallel to planes of corner-shared MO_6 octahedra that are separated by connecting sheets of phosphate tetrahedra. Whereas the lithium-ion mobility along the chain direction is thought to be high based on recent calculations;[157] the electronically insulating tetrahedral phosphate groups on which the inductive effect relies partially isolate the redox centers within the lattice. Thus, the moiety that raises the cell voltage also limits the electronic conductivity. The pristine compound can be classified as a very poor semiconductor ($\sigma \sim 10^{-9}$ S cm^{-1}).

Initially it was reported that only 60% of the Li^+ could be reversibly deintercalated from the structure, even at very slow rates. Goodenough *et al.* proposed that this reversibility was also limited by the migration of the $LiFePO_4/FePO_4$ interface. On oxidation, lithium extraction is initiated from the surface of the particle and moves inwards behind a two-phase $LiFePO_4/FePO_4$ interface. As delithiation proceeds, the surface area of the interface shrinks. For a constant rate of lithium transport per unit area across the interface, a critical surface area is reached where the interface is no longer able to sustain the transport.[140]

The consequence of grain boundary and electronic transport limitations has led to several efforts worldwide to overcome them. These rely on a combination of reducing path length for Li ion/grain boundary diffusion (by restricting particle size) and adding conductive materials to provide good electronic contact to the crystallite surfaces. They include methods to coat the phosphate particles with carbon,[158] embed them in a carbon matrix,[159] and lay down metal particles within the mixture.[160] The latter have all resulted in increase of the working capacity of the material to approach 90–95% theoretical intercalation capacity at relatively fast rates of extraction and insertion in the material. An intriguing report suggested that doping the structure with supervalent cations could result in high inherent bulk electronic transport owing to Fe^{3+} 'hole carriers'.[161] The high conductivity has recently been shown to be due, however, to the formation of highly conductive iron carbophosphides on the nanocrystallite surfaces under certain processing conditions. The resultant nanonetwork gives rise to efficient electron transport at the grain boundaries, and bulk conductivities that approach 10^{-2} S cm^{-1}.[162]

The renewed interest in lithium metal phosphates has led to the investigation of many other important polyanion frameworks. These have been comprehensively reviewed[140] and include, amongst others: $Li_3M_2(PO_4)_3$ (M = Fe, V);[163,164] various $VOPO_4$ phases;[165] and analogous sulfates. Their working potentials also lie in the 3–4 V range depending on the anion, and the choice of the redox couple M^{n+}/M^{n+1}. The $Li_3M_2(PO_4)_3$ phases show rich chemistry. Two polymorphs are known: the rhombohedral framework that $Na_{1+x}Zr_2Si_xP_{3-x}O_{12}$ (NASICON) adopts, and a monoclinic modification that has a related, but slightly more compact structure. Lithium cannot be deintercalated from $Li_3Fe_2(PO_4)_3$ owing to the inaccessibility of the $Fe^{3+/4+}$ redox couple, although the structure can accommodate two additional Li ions utilizing the $Fe^{3+/2+}$ couple. The monoclinic lithium vanadium phosphate, α-$Li_3V_2(PO_4)_3$, possesses both excellent ion mobility and high lithium capacity owing to the ability to reversibly extract all three lithium ions from the lattice. It displays particularly complex and unusual behavior characterized by a series of two-phase transformations on deintercalation, followed by classic solid solution behavior on re-intercalation. A combination of neutron diffraction and ^{7}Li magic angle spinning (MAS) NMR studies revealed that a combination of charge ordering on the vanadium $V^{3+/4+/5+}$ sites and lithium ordering/disordering amongst lattice sites is responsible for the hysteresis.[166] Subtle ion–ion interactions in the solid dictate the intercalation sites that are emptied or filled.

3.8 Other Dimensional Structures

3.8.1 Three-dimensional Structures

The three-dimensional structures comprise two groups, those with intersecting channels (e.g. V_6O_{13}[14] and the *Chevrel Phases*[167,168]) and the one-dimensional channel structures. The intercalation chemistry of both groups is restricted to the insertion of small ions or molecules (H_2O, NH_3) because the sites that form a connected network, internal to the crystal, are nearly fixed in size.

Chevrel Phases.[2b,167] The ternary chalcogenides of molybdenum, $M_x{}^{m+}Mo_6X_8$ (X = S, Se, Te; M is an alkali, alkaline, rare earth metal, or transition metal cation, or Cd, Sn, Pb), have been of great interest because of their electronic properties, particularly *High Temperature Superconductivity*. The structures can be viewed as an assembly of Mo_6X_8 units, which can be described as X_8 cubes with molybdenum atoms at the centers of the six faces. The Mo_6X_8 cubes are joined by Mo–X bonds between units to form a three-dimensional lattice containing intersecting channels that are occupied by the M cations (Figure 24).

The $M_xMo_6X_8$ phases are obtained by high-temperature reaction of the elements in sealed tubes. The empty frameworks, Mo_6X_8, can be prepared from suitable $M_xMo_6X_8$ phases by either chemical or electrochemical oxidation. For example, Mo_6S_8 can be obtained from $Cu_2Mo_6S_8$ by oxidation with a solution of iodine in acetonitrile at 60 °C. Similarly, Mo_6S_8 can be obtained by electrochemical oxidation of $Cu_xMo_6S_8$ or $Ni_xMo_6S_8$ in nonaqueous electrolytes. Once formed the empty lattices can be intercalated with a wide variety of simple cations, though the three-dimensional nature of the structure places restrictions on cation sizes. Schöllhorn has examined many examples and shown that the critical radius for guest cations in Mo_6S_8 is in the range 0.96–1.26 Å, whereas it is 1.26–1.33 Å for Mo_6Se_8 phases. A typical example is the intercalation of lithium ions. Reaction of Mo_6S_8 with excess *n*-butyllithium in hexane gives a limiting composition of $Li_4Mo_6S_8$, but intermediate phases are observed by electrochemical intercalation. The compositions of the phases formed and the maximum extent of intercalation depend on the details of the electronic structure and the availability of suitable sites for the intercalating cation. The maximum value of electron transfer (4e) to the host lattice is supported by band structure calculations.

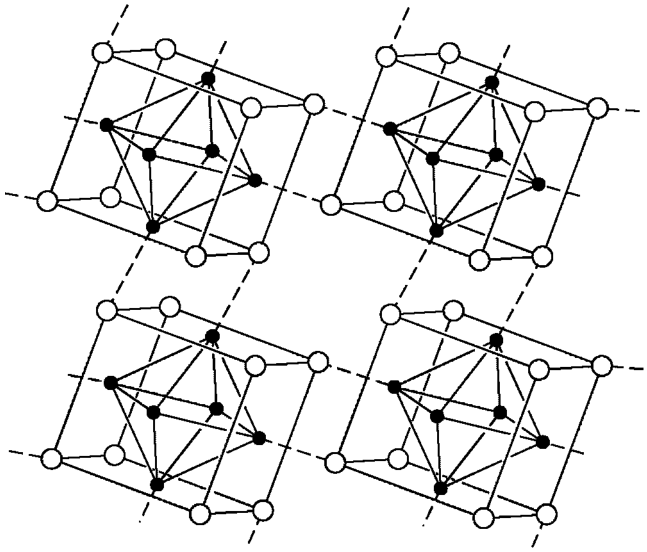

Figure 24 A schematic representation of the Mo_6S_8 cluster arrangement in the Chevrel phases. The filled and open circles are Mo and S atoms, respectively; the M atoms are not shown. (Reprinted with permission from Ref. 168. © 1983 American Chemical Society)

Perovskite Oxides.[2b,14,44,169] The perovskite lattice consists of a three-dimensional network of BO_6 octahedra in which each oxygen atom is shared between two B atoms. The 12 oxygen atoms in each unit cell describe a cubo-octahedral site that is occupied by the large A cation in perovskite, ABO_3. Rhenium trioxide and one form of WO_3 have the parent framework structure and can be intercalated with lithium though not with larger alkali metals. Reaction of WO_3 with *n*-butyllithium gives a phase with a limiting composition $Li_{0.67}WO_3$. In contrast, ReO_3 forms three distinct phases on lithium intercalation: cubic $Li_{0.35}ReO_3$, rhombohedral $LiReO_3$, and Li_2ReO_3. In the rhombohedral structures the octahedra rotate to give a structure with nearly hexagonal close-packed oxygens. The transformation is the same as that noted earlier for the ion-exchange reaction $LiNbO_3 \Leftrightarrow HNbO_3$. Both Li_xWO_3 and Li_xReO_3 can readily be reconverted to the parent oxides by electrochemical oxidation, but the reactions are slow.

Empty perovskite lattices can also form oxygen deficient phases by a process known as *Crystallographic Shear*, which introduces edge-sharing octahedra in addition to corner sharing. Examples include the reduced molybdenum oxides Mo_8O_{23}, Mo_9O_{26}, and V_6O_{13}. The latter is a metallic phase with substantial reversible capacity for electrochemical lithium intercalation between 2.8 and 2.2 V with respect to lithium metal.

One-dimensional Channel Structures.[2b] The chalcogenides Nb_3S_4, Ti_3S_4, and $Tl_{0.6}V_6S_8$ have one-dimensional channel structures in which MS_6 octahedra share edges and faces. A similar though more open structure is adopted by TlV_5S_8. The oxidative deintercalation reactions of the thallium ions from both structures are interesting exceptions to the simple electron transfer to and from the host lattice normally observed for redox reactions. The electrochemical results indicate a continuous nonstoichiometric phase from $Tl_{0.6}V_6S_8$ to a composition of $Tl_{0.2}V_6S_8$. The oxidation reaction, however, requires 0.8e (determined by coulometric titration), implying that at least some Tl^+ cations are oxidized to Tl^{3+} cations as they cross the solid–electrolyte interface. Oxidation of TlV_5S_8

also occurs with oxidation of the guest species according to equation (15). The reaction is electrochemically reversible between the composition limits shown. In this case, the ^{51}V NMR data indicate that the charge on the V_5S_8 lattice does not change. Instead the intercalation occurs by changing the oxidation state of the guest species from Tl^+ in TlV_5S_8 to Tl^{3+} in $Tl_{1/3}V_5S_8$.

$$Tl^{I}V_5S_8 \longrightarrow Tl^{III}{}_{1/3}V_5S_8 + \frac{2}{3}Tl^{3+} + 2e^- \qquad (15)$$

The intercalation behavior of some one-dimensional oxide structures has also been investigated, particularly oxides with the rutile structure[170] and the hexagonal form of WO_3.[171] The rutile oxides include MnO_2, which undergoes topochemical reactions with H^+ ions and is of considerable importance in primary battery systems. The ideal rutile structure is derived from edge-shared chains of octahedra that are corner linked to form four sided tunnels (see Figure 25). The structure is the end member of a series of phases with tunnels of different dimensions derived from single, double, and triple rutile chains connected by corner sharing. These structures are found in manganese oxide minerals (see Figure 25),[172] but can be synthesized with manganese or other elements. The difficulty of synthesis increases with increasing tunnel size, though todorokite (3 × 3) was recently obtained in microcrystalline form.[173] Intercalation of rutile phases has received the most attention. The ion-exchange properties and ionic conductivity of insulating hollandite phases have also been investigated. Lithium intercalation of several rutile phases has been studied by chemical reaction with *n*-butyllithium and electrochemically. The metallic phases MoO_2, WO_2, RuO_2, OsO_2, and IrO_2 give the highest lithium uptakes, in the range of 1–1.5 per metal atom. The first transition series phases react less readily either because they are difficult to reduce (Ti), the available sites are too small, or other structures are competitive, as in the rock salt related structure of $LiMnO_2$.

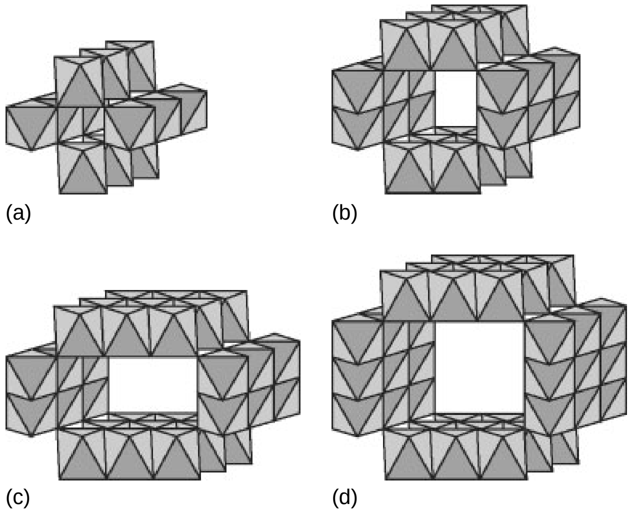

Figure 25 Schematic diagram of tunnel structures built from rutile chains: 1 × 1, rutile; 2 × 2, hollandite; 2 × 3, romanèchite; 3 × 3, todorokite. (Reprinted with permission from S. Turner and P.R. Buseck, *Science*, 1981, **212**, 1024. © 1981 AAAS)

The final example of a three-dimensional tunnel structure is that of hexagonal WO_3.[44] Alkali metal tungsten bronzes (M = K, Rb, Cs) with this structure type have been known for many years and are metallic conductors and in a few cases superconductors. Only recently, however, has the fully-oxidized parent framework been known. It has been synthesized by careful dehydration of $WO_3{\cdot}1{:}3H_2O$ or by oxidation of $(NH_4)_xWO_3$ at low temperatures. Once formed, the structure may readily be intercalated by reaction with *n*-butyllithium, sodium, and potassium naphthalides in THF. The larger alkali metal cations form the stable known high-temperature phases on intercalation. Metastable phases, such as $Na_{1/3}WO_3$, previously synthesized only at high pressure, are obtained with Li and Na. Very high uptakes of Li and Na cations occur on electrochemical reaction, but the crystallinity of the phase is lost and eventually the structure becomes completely amorphous. H_xWO_3 with the hexagonal bronze structure and $x \leq \approx 0.5$ has been synthesized electrochemically, by reaction with Zn/HCl, and by hydrogen spillover. Hydrogen intercalation causes a reversible color change from white to blue and, like WO_3 with the perovskite structure, the compound has been considered as a candidate material for electrochromic displays.

3.8.2 One-dimensional Systems

Only a few studies have been made of intercalation of linear chain systems. Like the layered structures, no restrictions are imposed by the structure on the size of guest species. The interchain distance can adjust to accommodate large guest molecules or ions. Unfortunately, intercalation often leads also to loss of correlation between adjacent chains along their length and compounds are difficult to structurally characterize.

The transition metal trichalcogenides MX_3 (M = Ti, Zr, Hf, Nb, Ta; X = S, Se) have been studied in some detail.[3,98] All the trichalcogenides contain anion–anion bonding and consequently a redox competition exists between electron transfer to the metal center and electron transfer to the anions. The situation is the converse of the deintercalation of the thallium vanadium sulfides, where the competition is between oxidation of Tl^+ cations and that of the metal sulfur framework.

The structure of $NbSe_3$, shown in Figure 26, is built up from infinite chains of $NbSe_6$ trigonal prisms. The chains interact through additional niobium–selenium bonds. Each unit cell contains three types of chain that are characterized by three different Se–Se distances (2.37, 2.48, and 2.91 Å). The distances suggest that the 2.37 Å chain corresponds to an electron distribution $Nb^{4+}(d^1)Se^{2-}(Se_2)^{2-}$ (metallic), the 2.91 Å corresponds to $Nb^{5+}(d^0)$ and is insulating, and

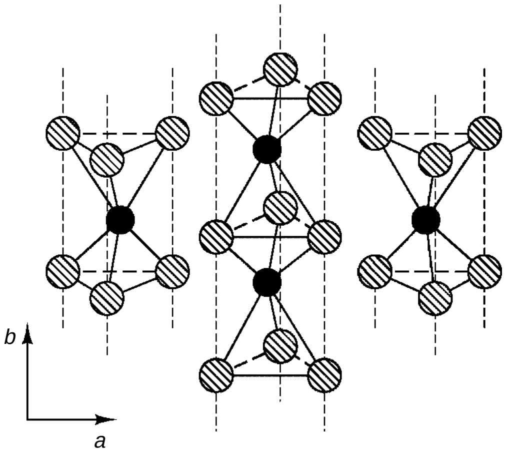

Figure 26 The chain structure of $NbSe_3$. Filled and shaded circles are Nb and Se, respectively. (Ref. 5. Reproduced by permission of John Wiley & Sons, Ltd)

the third chain is intermediate. Electrochemical lithium intercalation gives a maximum composition of $Li_{2.5}NbSe_3$. The electrochemical reaction occurs smoothly over the whole range and is reversible. Changes in slope of the voltage with increasing x have been correlated with the calculated band structure. Similar intercalation reactions occur for the trisulfides, but reactions cleave the $(S–S)^{2-}$ bonds and are not reversible.

Other aspects of intercalation of chain structures are illustrated by $KFeS_2$ and the $M_2Mo_6X_6$ ($X = S$, Se, Te) phases. Both these structure types have interesting ion-exchange properties. In the structure of $KFeS_2$, the potassium ions occupy eight-coordinate sites between infinite chains of edge-shared FeS_4 tetrahedra. Ion exchange with aqueous solutions of alkaline earth halides gives compounds with compositions $M_{1/2}FeS_2$. Exchange with Li^+ and Na^+ is also facile, but leads to complete separation of the chains and the formation of colloidal dispersions in dilute solutions. Chains of significant length are present in these dispersions. Increasing the electrolyte concentration causes reprecipitation of a crystalline solid phase with the same structure. In the case of sodium ion exchange, the solid phase has the composition $NaFeS_2{\cdot}2H_2O$ and is isostructural with the mineral erdite. Ion exchange with Ag^+ and Cu^{2+} ions under similar conditions causes considerable structural rearrangement and formation of the zinc blende related structures $AgFeS_2$ and $CuFeS_2$. Structural rearrangement also occurs in the electrochemical intercalation of $KFeS_2$ with lithium. A layered compound, $KLiFeS_2$, is formed with Li and Fe atoms occupying tetrahedral sites within a layer; the large K^+ ions fill all the interlayer sites.[174]

The $M_2Mo_6X_6$ ($M = S$, Se, Tl) compounds are closely related to the three-dimensional Chevrel phases $M_xMo_6X_8$ described in Section 3.6.1. The structures can be thought of as a condensation of the Mo_6S_8 units along the threefold axis of the Mo_6 octahedron to form $[Mo_3X_3]$ chains. The M cations occupy interchain sites. High-temperature reactions have been used to prepare these compounds, which are known for Na, K, In, Tl (Se, Te) and K, Rb, Cs (S). Other alkali metal systems can be prepared from $In_2Mo_6X_6$ compounds by ion exchange, in molten alkali metal iodides or by reductive intercalation with *t*-butyllithium.[175] Metastable phases such as $Li_2Mo_6Se_6$ and $Na_2Mo_6Se_6$ have been prepared by these routes. In polar solvents such as N-methylformamide or dimethylsulfoxide (NMF or DMSO), behavior like that noted above for $NaFeS_2{\cdot}2H_2O$ is observed. The chains completely separate to form colloidal solutions, but remain intact as shown by *Transmission Electron Microscopy* and light scattering.

3.9 Oxygen Intercalation

With the exception of the reactions of graphite with electron acceptors, the previous discussion has focused on reactions that involve intercalation of cations or solvated cations. Reactions of solids with oxygen that involve intercalation of oxide ions can also be considered to fall under the general definition of intercalation. In most cases, oxide ion diffusion is slow at ambient temperature and consequently somewhat higher temperatures ($<400-500$ °C) are generally required to achieve reasonable rates. In a few special cases, reactions occur at ambient temperature. The topic has acquired particular importance since the discovery of High-Temperature Superconductivity in cuprates with perovskite related structures. In the cuprates, oxygen stoichiometry can vary by changing the formal oxidation state of copper from $+1$ to $+3$ and the Cu–O coordination from linear → square planar → square pyramidal → octahedral as the coordination number and oxidation state increase. Changes in the stoichiometry play a critical role in determining the electronic properties in this class of materials.

Oxygen intercalation was first discussed explicitly in relation to reactions of mixed valence copper oxides with perovskite related structures.[176] Michel and Raveau showed that for three systems ($La_3Ba_3Cu_6O_{14+\delta}$, $La_{2-x}A_{1+x}Cu_2O_{6+\delta}$ ($A = Sr$, Ca), and $La_{2-x}A_xCuO_{4-\delta}$), oxygen could be reversibly intercalated and deintercalated into the structures at 400 °C by varying the oxygen partial pressure between 1 and 10^{-3} atm. The intercalation of oxide ions occurs by filling vacant lattice sites without significant rearrangement of the structure. An example in which the relationship between composition, structure, and physical properties has been well worked out is that of the 91 K superconductor $YBa_2Cu_3O_{7-\delta}$. Samples prepared at high temperatures with the stoichiometry $YBa_2Cu_3O_6$ can be oxidized in oxygen at temperatures ca. 350 °C. The structural changes that occur are shown in Figure 27. Initially, the structure contains two distinct Cu ion coordination types, CuO_5 square pyramids and CuO_2 linear units. As the oxygen content is increased, the sites shown stippled in Figure 27 are filled in a disordered manner, but eventually become ordered with formation of chains of

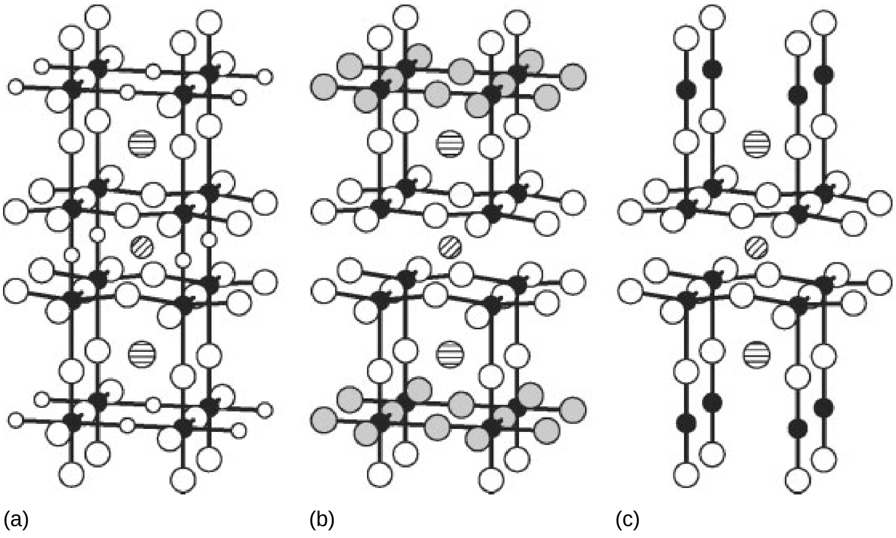

Figure 27 The structure of $YBa_2Cu_3O_{7-x}$ for $x = 0$ (a), $x = 0.6$ (b), and $x = 1.0$ (c). The filled, open, and stippled circles are copper, oxygen, and partially occupied oxygen atom positions, respectively. Yttrium and barium atom positions are shaded. (Ref. 177. Reproduced by permission of Blackwell)

square-planar CuO_4 units sharing corners at the composition $YBa_2Cu_3O_7$. Deintercalation from oxidized phases can be achieved by reduction of the oxygen partial pressure, by equilibration with a sample with a lower oxygen content, or by reaction in a sealed tube with a metal such as zirconium. Intermediate compositions are not completely disordered, but subtle differences in oxygen vacancy distributions are introduced that depend on the precise synthesis conditions used. Short range or intermediate range order shows up in different variations of the superconducting transition temperatures with composition for samples prepared by different procedures.[177]

In addition to the cuprates, oxides with perovskite related structures containing other transition metals or B metal cations show similar behavior. For example, the compounds $BaBiO_{3-x}$ $(0 \leq x \leq 0.5)$ and La_2NiO_{4+x} $(0 < x < 0.18)$ are other oxides that show wide ranges of oxygen nonstoichiometry. In La_2NiO_4 the excess oxygen is introduced as an interstitial oxide ion between layers in the K_2NiF_4 structure, coordinated by four lanthanum cations. Energy has to be expended in separating the layers in order to form the interstitial site, and consequently a two-phase region is observed up to $x = 0.06$ when the energy of intercalation is sufficient to compensate for that lost in separating the layers.

Several oxides with perovskite related structures can also be intercalated with oxygen ions by an electrochemical method.[178,179] The oxide $Sr_2Fe_2O_5$ with the brownmillerite structure has been electrochemically oxidized to $SrFeO_3$. The reaction was carried out by controlled potential electrolysis at a potential below that for oxygen evolution in 1 M aqueous KOH at room temperature. Bulk oxidation was confirmed by Mössbauer spectroscopy and X-ray diffraction. Similar results have been obtained for electrochemical oxidation of $Sr_2Co_2O_5$, $SrFe_{1-x}Co_xO_3$ $(O < x < 1)$, La_2CuO_4, and La_2NiO_4. The electrochemically oxidized materials are similar to compounds prepared by oxidation in oxygen. For example, La_2CuO_4 can be oxidized electrochemically to a superconducting phase $La_2CuO_{4+\delta}$ with a T_c similar to that obtained by oxidation in high-pressure oxygen. The phase behavior of the 214 compounds $La_2CuO_{4+\delta}$ and $La_2NiO_{4+\delta}$ have been investigated by both electrochemical and diffraction techniques. Neutron diffraction studies show that phase separation occurred near room temperature, implying high oxygen ion mobility consistent with the electrochemical data.

A particularly interesting example of electrochemical oxygen intercalation has been described for epitaxial thin films of La_2CuO_4. The electrochemical experiments were performed at room temperature in 1 M KOH solution with a Hg/HgO reference electrode.[180] For films deposited on $SrTiO_3$, oxygen can be intercalated electrochemically into the grown c-axis thin film. Superconductivity is observed with a double transition with a resistivity drop at 55–58 K, suggesting a more strongly oxidized phase, and a zero-resistance state at 42 K. Films on $SrLaAlO_4$ could not be studied, as they decompose during the anodic polarization. An electrochemical oxidation mechanism that occurs in two steps was proposed. First oxygen is transported into the film by intercalation into the planar defects, and then slower oxygen diffusion into the interstitial sites occurs along the *ab* planes. A similar mechanism for oxygen intercalation into c axis oriented $YBa_2Cu_3O_{7-d}$ (YBCO) has been proposed.[181]

Renewed interest in the superconductivity of cuprate films was generated by the observation that T_c for an epitaxial film of $La_{1.9}Sr_{0.1}CuO_4$ deposited on $SrLaAlO_4$ was 49 K, roughly double the bulk value of 25 K. The increase was initially attributed to the effects of compressive epitaxial strain.[182]

Recent detailed studies of a large number of $La_{2-x}Sr_xCuO_4$ films under both compressive and tensile epitaxial strain that were subjected to post annealing in various partial pressures of oxygen and in ozone suggest, however, that T_c cannot be increased by compressive epitaxial strain alone.[183] The results show that extra oxygen can be intercalated easily into underdoped $La_{2-x}Sr_xCuO_4$ films, even at 150 °C, and that the sensitivity to the intercalated oxygen atom concentration is the primary cause of the large variations of T_c in such films.

As discussed above, oxygen deintercalation from complex oxides at <300 °C can occur topotactically by reduction with molecular hydrogen or by heating samples in sealed systems with zirconium metal as a getter. At lower temperatures, ∼200 °C, sodium hydride is an effective reducing agent for oxide deintercalation reactions. For example, the Ni(III) perovskite $LaNiO_3$ can be reduced topotactically to $LaNiO_2$, isostructural with the 'infinite layer' cuprates, using solid sodium hydride between 190 and 210 °C.[184] Structural characterization indicates the presence of some incompletely reduced regions, with five-coordinate Ni centers due to the presence of a small number of oxide anions between the $NiO_2{}^{3-}$ sheets. Neutron powder diffraction and magnetization measurements indicate that the lamellar Ni(I) phase does not show the long-range antiferromagnetic ordering characteristic of isoelectronic Cu(II) oxides. By using the same technique, a new Co(II) phase, $LaSrCoO_{3.38}$, was prepared at 200 °C from $LaSrCoO_4$ by oxygen deintercalation using NaH.[185] Substantial concentrations of Co(I) are present in contrast to higher temperature reduction with molecular hydrogen where the product contains only Co(II).

NaH decomposes at 210 °C and therefore above this temperature the reaction becomes equivalent to using hydrogen gas. To study deintercalation by hydride at higher temperatures the more thermally stable CaH_2 has been used. Reaction of $LaSrCoO_4$ at 450 °C with CaH_2 leads to the formation of an unusual transition metal oxide hydride, $LaSrCoO_3H_{0.7}$.[186]

This compound was shown by neutron powder diffraction to adopt an unprecedented structure in which chains of CoO_4 squares share corners to form chains that are linked to form a layer by H–bridges. The average cobalt oxidation state is $1.7+$ and the CoO_2 sheets in the starting material have been replaced with $CoOH_{0.7}$ sheets in the oxide hydride product, which is consistent with a mechanism in which oxide vacancies created by oxide ion deintercalation are filled by intercalation of hydride ions.

4 RELATED ARTICLES

Carbon: Fullerenes; Chalcogenides: Solid-state Chemistry; Defects in Solids; Diffraction Methods in Inorganic Chemistry; Ionic Conductors; Semiconductors; Superconductivity; Zeolites.

5 REFERENCES

1. M. S. Whittingham and A. J. Jacobson eds., 'Intercalation Chemistry', Academic Press, New York, 1982.
2. (a) T. Iwamoto, in 'Inclusion Compounds', eds. J. L. Atwood, J. E. D. Davies, and D. D. MacNicol, Academic Press, New York, 1984, p. 29; (b) R. Schöllhorn, in 'Inclusion Compounds', eds. J. L. Atwood, J. E. D. Davies, and D. D. MacNicol, Academic Press, New York, 1984, p. 249; (c) R. M. Barrer, in 'Inclusion Compounds', eds. J. L. Atwood, J. E. D. Davies, and D. D. MacNicol, Academic Press, New York, 1984, p. 191.
3. (a) F. Levy ed., 'Physics and Chemistry of Materials with Layer Structures', Reidel, Holland, 1976, Vol. 2; (b) F. Hülliger, 'Physics and Chemistry of Materials with Layer Structures', Reidel, Holland, 1976, Vol. 5; (c) C. V. Subba Rao and M. W. Shafer, 'Physics and Chemistry of Materials with Layer Structures', Reidel, Holland, 1979, Vol. 6, p. 99; (d) J. Rouxel, 'Physics and Chemistry of Materials with Layer Structures', Reidel, Holland, 1979, Vol. 6, p. 201.
4. A. J. Jacobson, in 'Solid State Chemistry: Compounds', eds. A. K. Cheetham and P. Day, Oxford University Press, Oxford, 1992, Chap. 6, p. 162.
5. D. O'Hare, in 'Inorganic Materials', eds. D. W. Bruce and D. O'Hare, Wiley, Chichester, 1992, p. 165.
6. M. Dresselhaus ed., 'Intercalation in Layered Materials', NATO ASI Series B 148, Plenum, New York, 1986.
7. A. P. Legrand and S. Flandris eds, 'Chemical Physics of Intercalation', NATO ASI Series B172, Plenum, New York, 1987.
8. J. E. Fischer, P. Bernier, S. Roth, and S. A. Solin eds, 'Chemical Physics of Intercalation II', NATO ASI Series B 305, Plenum, New York, 1993.
9. D. W. Murphy in 'Chemical Physics of Intercalation II', NATO ASI Series B 305, eds. J. E. Fischer, P. Bernier, S. Roth, and S. A. Solin Plenum, New York, 1993, p. 73.
10. R. R. Chianelli, *J. Crystal Growth*, 1976, **34**, 239; R. R. Chianelli, J. C. Scanlon, and B. M. L. Rao, *J. Solid State Chem.*, 1979, **29**, 323.
11. J. Rouxel, in 'Chemical Physics of Intercalation', NATO ASI Series B172, eds. A. P. Legrand and S. Flandris Plenum, New York, 1987, p. 127.
12. W. Rüdorff, *Chimia*, 1965, **19**, 489.
13. M. B. Dines, *Mater. Res. Bull.*, 1975, **10**, 287; M. S. Whittingham and M. B. Dines, *J. Electrochem. Soc.*, 1977, **124**, 1387.
14. D. W. Murphy and P. A. Christian, *Science*, 1979, **205**, 651.
15. J. O. Evans and D. O'Hare, *Advanced Materials*, 1994, **6**, 646.
16. N. Daumas and A. Hérold, *C. R. Acad. Sci. Ser. C*, 1969, **268**, 373.
17. S. A. Safran and D. R. Hamann, *Phys. Rev. Lett.*, 1979, **42**, 1410.
18. J. G. Hooley, *Mater. Sci. Eng.*, 1977, **31**, 17.

19. C. Riekel and C. O. Fischer, *J. Solid State Chem.*, 1979, **29**, 181.
20. D. Kaluarachchi and R. F. Frindt, *Phys. Rev. B*, 1983, **28**, 3663; D. Kaluarachchi and R. F. Frindt, *Phys. Rev. B*, 1985, **31**, 3648.
21. T. Butz, A. Lerf, and J. O. Besenhard, *Rev. Chim. Miner.*, 1984, **21**, 556.
22. R. Schöllhorn, in 'Chemical Physics of Intercalation', NATO ASI Series B172, eds. A. P. Legrand and S. Flandris Plenum, New York, 1987, p. 149.
23. S. A. Solin, *Ann. Rev. Mater. Sci.*, 1997, **27**, 89.
24. S. A. Solin, D. Hines, A. J. Jacobson, and S. D. Mahanti, *Solid State Commun.*, 1996, **100**, 143.
25. R. M. Barrer, 'Zeolites and Clay Minerals', Academic Press, New York, 1978.
26. J. M. Newsam in 'Solid State Chemistry: Compounds', eds. A. K. Cheetham and P. Day, Oxford University Press, Oxford, 1992, Chap. 6, p. 234.
27. W. Loewenstein, *Am. Mineral.*, 1954, **39**, 92.
28. S. T. Wilson, B. M. Lok, C. A. Messina, T. R. Cannan, and E. M. Flanigen, *J. Am. Chem. Soc.*, 1982, **104**, 1146.
29. B. M. Lok, C. A. Messina, R. L. Patton, R. T. Gajek, T. R. Cannan, and E. M. Flanigen, *J. Am. Chem. Soc.*, 1984, **106**, 6092.
30. M. E. Davis, C. Saldarriaga, J. Garces, and C. Crowder, *Nature*, 1988, **331**, 698.
31. K. G. Strohmaier and D. E. W. Vaughan, *J. Am. Chem. Soc.*, 2003, **125**, 16035.
32. A. K. Cheetham, G. Férey, and T. Loiseau, *Angew. Chem.*, 1999, **38**, 3268.
33. J. Rocha and M. W. Anderson, *Eur. J. Inorg. Chem.*, 2000, **5**, 801.
34. X. Wang, L. Liu, and A. J. Jacobson, *J. Amer. Chem. Soc.*, 2002, **124**, 7812.
35. R. C. Haushalter and L. A. Mundi, *Chem. Mater.*, 1992, **4**, 31.
36. N. Guillou, Q. Gao, P. M. Forster, J.-S. Chang, M. Nogues, S.-E. Park, G. Férey, and A. K. Cheetham, *Angewandte Chemie*, 2001, **40**, 2831.
37. P. B. Moore and J. Shen, *Nature*, 1983, **306**, 356.
38. P. B. Moore and T. Araki, *Nature*, 1972, **239**, 25.
39. M. A. Subramanian, G. Aravamudan, and G. V. Subba Rao, *Prog. Solid State Chem.*, 1983, **15**, 55.
40. H. Y.-P. Hong, J. A. Kafalas, and J. B. Goodenough, *J. Solid State Chem.*, 1974, **9**, 345.
41. C. E. Rice and J. L. Jackel, *J. Solid State Chem.*, 1982, **41**, 308.
42. J. T. Lewandowski, I. J. Pickering, and A. J. Jacobson, *Mater. Res. Bull.*, 1992, **27**, 981.
43. B. Darriet, M. Rat, J. Galy, and P. Hagenmuller, *Mater. Res. Bull.*, 1971, **6**, 1305.
44. M. Figlarz, *Prog. Solid State Chem.*, 1989, **19**, 1.
45. U. Chowdhry, J. R. Barkley, A. D. English, and A. W. Sleight, *Mater. Res. Bull.*, 1982, **17**, 917.
46. A. C. D. Newman ed., 'Chemistry of Clays and Clay Minerals', Wiley, New York, 1987.
47. F. Liebau, 'Structural Chemistry of Silicates', Springer-Verlag, Berlin, 1985.
48. G. Lagaly, *Angew. Chem., Int. Ed. Engl.*, 1976, **15**, 575.
49. G. Lagaly, *Naturwissenschaften*, 1981, **68**, 82.
50. R. M. Barrer, *Philos. Trans. R. Soc. London*, 1984, **311**, 333.
51. D. E. W. Vaughan, R. J. Lussier, and J. S. Magee, *US Pat.* 4 176 090, Nov. 1979.
52. A. Clearfield and M. Kuchenmeister, in 'Supramolecular Architecture', ACS Symposium Series 499, ed. T. Bein, American Chemistry Society, Washington, DC, 1992, p. 128.
53. G. Johansson, *Acta Chem. Scand.*, 1960, **14**, 771.
54. T. J. Pinnavaia, *Science*, 1983, **220**, 365.
55. A. Usuki, M. Kawasumi, Y. Kojima, A. Okada, T. Kurauchi, and O. Kamigaito, *J. Mater. Res.*, 1993, **8**, 1174.
56. T. Lan and T. J. Pinnavaia, *Chem. Mater.*, 1994, **6**, 2216.
57. R. Krishnamoorti, R. A. Vaia, and E. P. Giannelis, *Chem. Mater.*, 1996, **8**, 1728.
58. P. Aranda and E. Ruiz-Hitzky, *Chem. Mater.*, 1992, **4**, 1395.
59. M. M. E. Jacob, E. Hackett, and E. P. Giannelis, *J. Mater. Chem.*, 2003, **13**, 1.
60. R. Allmann, *Chimia*, 1970, **24**, 99.
61. A. I. Khan and D. O'Hare, *J. Mater. Chem.*, 2002, **12**, 3191.
62. H. P. Boehm, J. Steinle, and C. Vieweger, *Angew. Chem., Int. Ed. Engl.*, 1977, **16**, 265.
63. S. Miyata, *Clays Clay Min.*, 1975, **23**, 369.
64. T. Ikeda, H. Amoh, and T. Yasunaga, *J. Am. Chem. Soc.*, 1984, **106**, 5772.
65. A. Clearfield and G. D. Smith, *Inorg. Chem.*, 1969, **8**, 431.
66. L. Kullberg and A. Clearfield, *J. Phys. Chem.*, 1981, **85**, 1585.
67. S. Yamanaka, *Inorg. Chem.*, 1976, **15**, 2811.
68. G. Alberti, U. Costantino, S. Allulli, and N. Tomassini, *J. Inorg. Nucl. Chem.*, 1978, **40**, 1113.
69. G. Huan, A. J. Jacobson, J. W. Johnson, and D. P. Goshorn, *Chem. Mater.*, 1992, **4**, 661, and references therein.
70. W. A. England, J. B. Goodenough, and P. J. Wiseman, *J. Solid State Chem.*, 1983, **49**, 289.
71. M. Tournoux, R. Marchand, and L. Brohan, *Prog. Solid State Chem.*, 1986, **17**, 33.
72. B. Raveau, *Rev. Chim. Miner.*, 1984, **21**, 391.
73. (a) B. Aurivillius, *Ark. Kemi*, 1949, **1**, 463; (b) B. Aurivillius, *Ark. Kemi.*, 1949, **1**, 499.
74. (a) S. N. Ruddlesden and P. Popper, *Acta Crystallogr.*, 1957, **10**, 538; (b) S. N. Ruddlesden, and P. Popper, *Acta Crystallogr.*, 1958, **11**, 54.
75. M. Dion, M. Ganne, and M. Tournoux, *Mater. Res. Bull.*, 1981, **16**, 1429.

76. A. J. Jacobson, J. W. Johnson, and J. T. Lewandowski, *Inorg. Chem.*, 1985, **24**, 3727.
77. A. J. Jacobson, in ‘Chemical Physics of Intercalation II’, NATO ASI Series B 305, eds. J. E. Fischer, P. Bernier, S. Roth, and S. A. Solin Plenum, New York, 1993, p. 117.
78. R. E. Schaak and T. E. Mallouk, *Chem. Mater.*, 2000, **12**, 3427.
79. T. A. Kodenkandath, J. N. Lalena, W. L. Zhou, E. E. Carpenter, C. Sangregorio, A. U. Falster, W. B. Simmons Jr, C. J. O’Connor, and J. B. Wiley, *J. Am. Chem. Soc.*, 1999, **121**, 10743.
80. R. E. Schaak and T. E. Mallouk, *Chem. Mater.*, 2002, **14**, 1455.
81. M. M. J. Treacy, S. B. Rice, A. J. Jacobson, and J. T. Lewandowski, *Chem. Mater.*, 1990, **2**, 279.
82. A. J. Jacobson, in ‘Comprehensive Supramolecular Chemistry’, eds. G. Alberti and T. Bein, Pergamon, 1996, Vol. 7, p. 315.
83. P. Schauffaütl, *J. Prakt. Chem.*, 1841, **21**, 155.
84. H. Zabel and S. Solin eds, ‘Graphite Intercalation Compounds’, Springer Series in Materials Science 18, Springer-Verlag, Berlin, 1992.
85. D. Billaud and A. Hérold, *Bull. Soc. Chim. Fr.*, 1978, 131.
86. M. El Makrini, P. Lagrange, D. Guerard, and A. Hérold, *Carbon*, 1980, **18**, 211.
87. H. W. Kroto, J. R. Heath, S. C. O’Brien, R. F. Curl, and R. E. Smalley, *Nature*, 1985, **318**, 162.
88. W. Krätschmer, L. D. Lamb, K. Fostiropoulos, and D. M. R. Huffman, *Nature*, 1990, **347**, 354.
89. D. W. Murphy, M. J. Rosseinsky, R. M. Fleming, R. Tycko, A. P. Ramirez, R. C. Haddon, T. Siegrist, G. Dabbagh, J. C. Tully, and R. E. Walstedt, *J. Phys. Chem. Solids*, 1992, **53**, 1321.
90. S. Iijima, *Nature*, 1991, **354**, 56.
91. J. Sloan, A. I. Kirkland, J. L. Hutchison, and M. L. H. Green, *Acc. Chem. Res.*, 2002, **35**, 1054.
92. A. Thess, R. S. Lee, P. Nikolaev, H. Dai, P. Petit, J. Robert, C. Xu, H. Lee, S. G. Kim, D. T. Colbert, G. Scuseria, D. Tomanek, J. E. Fischer, and R. E. Smalley, *Science*, 1996, **273**, 483.
93. J. E. Fischer, *Acc. Chem. Res.*, 2002, **35**, 1079.
94. A. S. Claye, J. E. Fischer, C. B. Huffman, A. G. Rinzler, and R. E. Smalley, *J. Electrochem. Soc.*, 2000, **147**, 2845.
95. R. R. Meyer, J. Sloan, R. E. Dunin-Borkowski, A. I. Kirkland, M. C. Novotny, S. R. Bailey, J. L. Hutchison, and M. L. G. Green, *Science*, 2000, **289**, 1324.
96. B. W. Smith and D. E. Luzzi, *Chem. Phys. Lett.*, 2000, **321**, 169.
97. R. Schöllhorn, *Angew. Chem., Int. Ed. Engl.*, 1980, **19**, 983.
98. J. Rouxel, *Rev. Inorg. Chem.*, 1979, **1**, 245; J. Rouxel and R. Brec, *Annu. Rev. Mater. Sci.*, 1986, **16**, 137.
99. R. Schöllhorn, *Pure Appl. Chem.*, 1984, **56**, 1739.
100. M. S. Whittingham, *Prog. Solid State Chem.*, 1978, **12**, 41.
101. L. F. Nazar and A. J. Jacobson, *J. Chem. Soc., Chem. Commun.*, 1986, 570.
102. A. Weiss and R. Ruthardt, *Z. Naturforsch.*, 1969, **24b**, 355 and 1066.
103. F. R. Gamble, F. J. DiSalvo, R. A. Klemm, and T. H. Geballe, *Science*, 1970, **168**, 568.
104. M. J. McKelvey and W. S. Glaunsinger, *Annu. Rev. Phys. Chem.*, 1990, **41**, 497.
105. M. B. Dines, *Science*, 1975, **188**, 1210.
106. R. Brec, *Solid State Ionics*, 1986, **22**, 3.
107. P. Palvadeau, J. Rouxel, M. Queignec, and B. Bujoli, in ‘Supramolecular Architecture’, ACS Symposium Series 499, ed. T. Bein, American Chemistry Society, Washington, DC, 1992, p. 114.
108. P. Palvadeau, L. Coic, J. Rouxel, F. Menil, and L. Fournes, *Mater. Res. Bull.*, 1981, **16**, 1055.
109. B. A. Averill and S. M. Kauzlarich, *Mol. Cryst. Liq. Cryst.*, 1984, **107**, 55.
110. H. Eckert and R. Herber, *J. Chem. Phys.*, 1984, **80**, 4526.
111. P. Hagenmuller, J. Rouxel, and J. Portier, *C. R. Acad. Sci. Paris*, 1962, **254**, 2000.
112. J. Villieras, R. Chiron, P. Palvadeau, and J. P. Venien, *Rev. Chim. Miner.*, 1985, **22**, 209.
113. S. Yamanaka, H. Kawaji, K. Hotehama, and M. Ohashi, *Adv. Mater.*, 1996, **8,**, 771.
114. S. Yamanaka, K. Hotehama, and H. Kawaji, *Nature*, 1998, **392**, 580.
115. S. Yamanaka, *Annu. Rev. Mater. Sci.*, 2000, **30**, 53.
116. S. Yamanaka and H. Tou, *Cur. Opini. Solid State Mater. Sci.*, 2001, **5**, 545.
117. A. M. Fogg, J. S. O. Evans, and D. O’Hare, *Chem. Commun.*, 1998, 2269.
118. A. M. Fogg, V. M. Green, and D. O’Hare, *Chem. Mater.*, 1999, **11**, 216.
119. A. M. Fogg, V. M. Green, and D. O’Hare, *J. Mater. Chem.*, 1999, **9**, 1547.
120. O. Glemser and G. Hutz, *Z. Anorg. Allg. Chem.*, 1951, **264**, 17.
121. J. J. Birtill and P. G. Dickens, *Mater. Res. Bull.*, 1978, **13**, 311.
122. D. W. Murphy, P. A. Christian, F. J. DiSalvo, and J. V. Waszczak, *Inorg. Chem.*, 1979, **18**, 2800.
123. P. Aldebert, N. Baffier, N. Gharbi, and J. Livage, *Mater. Res. Bull.*, 1981, **16**, 949.
124. J. W. Johnson, A. J. Jacobson, J. F. Brody, and S. M. Rich, *Inorg. Chem.*, 1982, **21**, 3820.
125. A. J. Jacobson, J. W. Johnson, J. F. Brody, and J. T. Lewandowski, *Inorg. Chem.*, 1985, **24**, 1782.
126. X. D. Xiang, S. McKernan, W. A. Vareka, A. Zettl, J. L. Corkill, T. W. Barbee III, and M. L. Cohen, *Nature*, 1990, **348**, 145.

127. X. D. Xiang, W. A. Vareka, A. Zettl, J. L. Corkill, T. W. Barbee III, M. L. Cohen, N. Kijima, and R. Gronsky, *Science*, 1991, **254**, 1487.

128. X. D. Xiang, A. Zettl, W. A. Vareka, J. L. Corkill, T. W. Barbee III, and M. L. Cohen, *Phys. Rev. B*, 1991, **43**, 11496.

129. P. V. Huong and A. L. Verma, *Phys. Rev. B*, 1993, **48**, 9869.

130. M. A. Subramanian, *J. Solid State Chem.*, 1994, **110**, 193.

131. J.-H. Choy, S.-J. Kwon, S.-J. Hwang, Y.-I. Kim, and W. Lee, *J. Mater. Chem.*, 1999, **9**, 129.

132. D. P. Scarfe, S. Bhavaraju, and A. J. Jacobson, *Chem. Commun.*, 1997, 313; D. P. Scarfe and A. J. Jacobson, *Chem. Mater.*, 1997, **9**, 3107.

133. M. Matsuda, K. Abe, and M. Miyake, *Solid State Ionics*, 2002, **154–155**, 413.

134. T. Kijima, S. Kimura, Y. Kawahara, K. Ohe, M. Yada, and M. Machida, *J. Solid State Chem.*, 1999, **146**, 60.

135. C. Delmas, J.-J. Braconnier, A. Maazaz, and P. Hagenmuller, *Rev. Chim. Miner.*, 1982, **19**, 343.

136. M. M. Thackeray, S. D. Baker, K. T. Adendorff, and J. B. Goodenough, *Solid State Ionics*, 1985, **17**, 175.

137. K. Takada, H. Sakurai, E. Takayama-Muromachi, F. Izumi, R. A. Dilanian, and T. Sasaki, *Nature*, 2003, **422**, 53.

138. R. E. Schaak, T. Klimczuk, M. L. Foo, and R. J. Cava, *Nature*, 2003, **424**, 527.

139. F. C. Chou, J. H. Cho, P. A. Lee, E. T. Abel, K. Matan, and Y. S. Lee, *Phys. Rev. Lett.*, 2004, **92**, 157004/1.

140. G.-A. Nazri and G. Pistoia eds, 'Lithium Batteries: Science and Technology', Academic Publishers, USA and the Netherlands, 2004.

141. C. Pouillerie, L. Croguennec, Ph. Biensan, P. Willmann, and C. Delmas, *J. Electrochem. Soc*, 2000, **147**, 2061.

142. B. Ammundsen and J. Paulsen, *Adv. Mater.*, 2001, **13**, 943.

143. Y. I. Jang, B. Huang, H. Wang, D. R. Sadoway, and Y. M. Chiang, *J. Electrochem. Soc.*, 1999, **146**, 3217.

144. F. Capitaine, P. Gravereau, C. Delmas, *Solid State Ionics*, 1996, **89**, 197; A. R. Armstrong and P. G. Bruce, *Nature*, 1996, **381**, 499.

145. A. R. Armstrong, A. J. Paterson, A. D. Robertson, and P. G. Bruce, *Chem. Mater.*, 2002, **14**, 710.

146. C. Storey, I. Kargina, Y. Grincourt, I. J. Davidson, Y. Yoo, and D. Y. Seung, *J. Power Sources*, 2001, **97–98**, 541.

147. B. Ammundsen, J. Paulsen, I. Davidson, R.-S. Liu, C.-H. Shen, J.-M. Chen, J.-Y. Jang, and J.-F. Lee, *J. Electrochem. Soc.*, 2002, **149**, A431.

148. Z. Lu, D. MacNeil, and J. R. Dahn, *Electrochem. Solid-State Lett.*, 2001, **4**, A191.

149. T. Ohzuku and Y. Makimura, *Chem. Lett.*, 2001, 744.

150. Y. Makimura and T. Ohzuku, *J. Power Sources*, 2003, **119**, 156.

151. W.-S. Yoon, Y. Paik, X.-Q. Yang, M. Balasubramanian, J. McBreen, and C. P. Grey, *Electrochem. Solid-State Lett.*, 2002, **5**, A263.

152. W.-S. Yoon, C. P. Grey, M. Balasubramanian, X.-Q. Yang, and J. McBreen, *Chem. Mater.*, 2003, **15**, 3161.

153. B. J. Hwang, Y. W. Tsai, D. Carlier, and G. Ceder, *Chem. Mater.*, 2003, **15**, 3676.

154. W.-S. Yoon, C. P. Grey, M. Balasubramanian, X.-Q. Yang, D. A. Fischer, and J. McBreen, *Electrochem. Solid-State Lett.*, 2004, **7**, A53.

155. K. Kang, D. Carlier, J. Reed, E. Arroyo, G. Ceder, L. Croguennec, and C. Delmas, *Chem. Mater.*, 2003, **15**, 4503.

156. A. K. Padhi and J. B. Goodenough, *J. Electrochem. Soc.*, 1997, **144**, 1188.

157. D. Morgan, A. van der Ven, and G. Ceder, *Electrochem. Solid-State Lett*, 2004, **7**, A30.

158. N. Ravet, Y. Chouinard, J. F. Magnan, S. Besner, M. Gauthier, M. Armand, *J. Power Sources*, 2001, **97–98**, 503.

159. H. Huang, S.-C. Yin, and L. F. Nazar, *Electrochem. Solid-State Lett.*, 2001, **4**, A170.

160. F. Croce, A. D'Epifanio, J. Hassoun, A. Deptula, T. Olczac, and B. Scrosati, *Electrochem. and Solid-State Lett.*, 2002, **5**, A47.

161. S. Y. Chung, J. T. Bloking, and Y. M. Chiang, *Nat. Mater.*, 2002, **1**, 123.

162. S. Herle, B. Ellis, N. Coombs, and L. F. Nazar, *Nat. Mater.*, 2004, **2**, 147.

163. C. Masquelier, A. K. Padhi, K. S. Nanjundaswamy, and J. B. Goodenough, *J. Solid State Chem.*, 1998, **135**, 228.

164. M. Sato, H. Ohkawa, K. Yoshida, M. Saito, K. Uematsu, and K. Toda, *Solid State Ionics*, 2000, **135**, 137; J. Gaubicher, C. Wurm, G. Goward, C. Masquelier, and L. F. Nazar, *Chem. Mater.*, 2000, **12**, 3240.

165. T. A. Kerr, J. Gaubicher, and L. F. Nazar, *Electrochem. Solid-State Lett.*, 2000, **3**, 460; N. Dupre, J. Gaubicher, T. Le Mercier, G. Wallez, J. Angenault, and M. Quarton, *Solid State Ionics*, 2001, **140**, 209; N.-G. Park, K. M. Kim, S. H. Chang, *Electrochem. Commun.*, 2001, **3**, 553.

166. S.-C. Yin, H. Grondey, P. Strobel, M. Anne, and L. F. Nazar, *J. Am. Chem. Soc.*, 2003, **125**, 10402.

167. M. Potel, P. Gougeon, R. Chevrel, and M. Sergent, *Rev. Chim. Miner.*, 1984, **21**, 509.

168. T. Hughbanks and R. Hoffmann, *J. Am. Chem. Soc.*, 1983, **105**, 1150.

169. K. H. Cheng and M. S. Whittingham, *Solid State Ionics*, 1980, **1**, 151.

170. D. W. Murphy, F. J. DiSalvo, J. N. Carides, and J. V. Waszczak, *Mater. Res. Bull.*, 1978, **13**, 1395.

171. K. H. Cheng, A. J. Jacobson, and M. S. Whittingham, *Solid State Ionics*, 1981, **5**, 355.

172. S. Turner and P. R. Buseck, *Science*, 1981, **212**, 1024.

173. D. C. Golden, C. C. Chen, and J. B. Dixon, *Science*, 1986, **231**, 717.

174. A. J. Jacobson, M. S. Whittingham, and S. M. Rich, *J. Electrochem. Soc.*, 1979, **126**, 887.

175. J. H. Golden, F. J. DiSalvo, and J. M. J. Frechet, *Mater. Sci. Forum*, 1994, **152–153**, 209.

176. C. Michel and B. Raveau, *Rev. Chim. Miner.*, 1984, **21**, 407.

177. See, for example, A. J. Jacobson, J. M. Newsam, D. C. Johnston, J. P. Stokes, S. Bhattacharya, J. T. Lewandowski, D. P. Goshorn, M. J. Higgins, and M. S. Alvarez, in ‘Chemistry of Oxide Superconductors’, ed. C. N. R. Rao, Blackwell, Oxford, 1988.

178. J. C. Grenier, A. Wattiaux, J. P. Doumerc, P. Dordor, L. Fournes, J. P. Chaminade, and M. Pouchard, *J. Solid State Chem.*, 1992, **96**, 20.

179. J. C. Grenier, M. Pouchard, and A. Wattiaux, *Curr. Opin. Solid State Mater. Sci.*, 1996, **1**, 233.

180. F. Arrouy, J.-P. Locquet, E. J. Williams, E. Mächler, R. Berger, C. Gerber, C. Monroux, J.-C. Grenier, and A. Wattiaux, *Phys. Rev. B*, 1996, **54**, 7512.

181. L. Chen, C. Chen, and A. J. Jacobson, *IEEE Trans. Appl. Superconduct.*, 2003, **13**, 2882.

182. J.-P. Locquet, J. Perret, J. Fompeyrine, E. Mächler, J. W. Seo, and G. Van Tendeloo, *Nature*, 1998, **394**, 453.

183. I. Bozovic, G. Logvenov, I. Belca, B. Narimbetov, and I. Sveklo, *Phys. Rev. Lett.*, 2002, **89**, 100701.

184. M. A. Hayward, M. A. Green, M. J. Rosseinsky, and J. Sloan, *J. Am. Chem. Soc.*, 1999, **121**, 8843.

185. M. A. Hayward and M. J. Rosseinsky, *Chem. Mater.*, 2000, **12**, 2182.

186. M. A. Hayward, E. J. Cussen, J. B. Claridge, M. Bieringer, M. J. Rosseinsky, C. J. Kiely, S. J. Blundell, I. M. Marshall, and F. L. Pratt, *Science*, 2002, **295**, 1882.

Ionic Conductors

Martha Greenblatt
Rutgers, the State University of New Jersey, Piscataway, NJ, USA

1	Introduction	1
2	General Features of Solids with High Ionic Conductivity: Theory	3
3	Crystalline Electrolyte Materials	5
4	Amorphous Glass Electrolytes	18
5	Applications	22
6	Related Articles	29
7	References	29

1 INTRODUCTION

Electrical conduction occurs by the long-range diffusion of either electrons or ions. Usually conduction by one or the other type of charge-carrier predominates, but in some inorganic materials both ionic and electronic conduction are significant.

Migration of ions at normal temperatures does not occur to any appreciable extent in most ionic and covalent-bonded solids such as oxides and halides. For example, NaCl is an insulator at room temperature with a conductivity of only $\sim 10^{-15}\,\mathrm{S\,cm^{-1}}$.

The idea that ions can diffuse as rapidly in a solid as in an aqueous solution or in a molten salt may seem astonishing. However, since the 1960s, a variety of solids that include crystalline compounds, glasses, polymers, and composite materials with exceptionally high ionic conductivities have been discovered. Materials that conduct anions (e.g. F^- and O^{2-}) and cations including monovalent (e.g. H^+, Li^+, Na^+, Cu^+, Ag^+), divalent, and even trivalent and tetravalent ions have been synthesized. A variety of names that have been used for these materials include solid electrolytes, superionic conductors, and fast-ionic conductors. 'Solid electrolytes' arguably provides the least misleading and broadest description for this class of materials.

In Figure 1, the electrical conductivities of several common substances and representative solid electrolytes are shown at the temperature where the materials have potential application. The solid electrolytes have conductivities that fall between those of a typical semiconductor, silicon, and a typical aqueous electrolyte, sodium chloride.

Research in the area of fast-ion transport in solids has been extremely active in recent years, partly because of the many potential technological applications of solid electrolytes. These applications include high-energy-density batteries, fuel cells, sensors, electrochromic materials for both optical display and 'smart window' devices, low-cost electrolysis of water, and selective atomic filters. Devices using solid electrolytes are already available commercially: oxygen detectors for automotive pollution-control systems employ solid O^{2-} conductors, solid-state batteries with solid electrolytes are employed in heart pacemakers and lithium batteries commercially available since 1990 and widely used in laptop computers and other portable electronic devices employ electrolytes that are highly viscous; the goal is to develop all solid-state electrochemical devices with appropriate solid electrolytes.

1.1 Brief History

Interest in solids with highly mobile ionic species is not new. In 1839, Michael Faraday reported measurements on several materials including lead fluoride (PbF_2) that showed an unusual increase in the electrical conductivity at elevated temperatures, contrary to that found in normal metals.[2] This finding was a surprising discovery, since most simple salts are not good conductors of electricity.

Although Faraday discovered the unusual electrical properties of lead fluoride, he did not explain his observations. It is now known that the high electrical conductivity of PbF_2 is due to the motion of F^- ions, not electrons. At 500–700 °C, fluoride ions diffuse rapidly through the PbF_2 lattice. PbF_2 was the first example of a solid with high ionic conductivity.

In 1914, Tubandt and Lorenz[3] showed that the ionic conductivity of the high temperature α phase of silver iodide, AgI was even higher than that of the molten material. Tuband and coworkers presented evidence for the first time that ions can carry electrical current in solids.[4,5] In a simple experiment, based on Faraday's law (Figure 2), they proved that the conductivity of AgI above 147 °C results from the motion of Ag^+ ions. In Tubandt's electrochemical cell shown in Figure 2, silver electrodes were placed in contact with both sides of an AgI pellet. After a known amount of electrical charge was passed through the cell, the electrodes were removed and weighed; the amount of silver lost from the anode and deposited on the cathode corresponded almost exactly to that expected if the charge carriers through AgI were Ag^+ ions.

Subsequent findings that even conventional ionic solids, such as sodium chloride, have measurable conductivities that are not electronic stimulated the development of theories for ionic motion in solids. Early in this century, Joffe introduced the concept of interstitial ions and vacancies (*see* ***Defects in Solids***), which was the starting point of the theory of defects.[6] Frenkel and Schottky used these theories to develop their classic mechanisms to explain how electricity can be conducted through ionic solids by the flow of ions (*see Frenkel Defects*; *Schottky Defects*).[7,8] They proposed that ionic solids are not perfect, with every lattice site occupied by its appropriate ions, but contain defects in which either ions

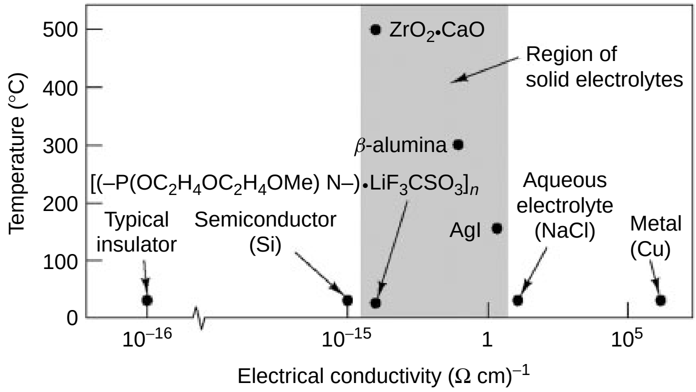

Figure 1 Electrical conductivities of selected common substances and representative solid electrolytes. (Reprinted from Ref. 1. Published 1985 American Chemical Society)

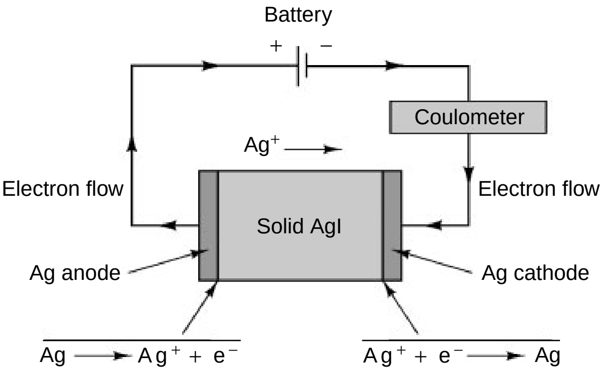

Figure 2 Tubandt's electrochemical cell. (Reprinted from Ref. 1. Published 1985, American Chemical Society)

are located in interstitial sites or vacancies occur in normally filled sites. The hopping of ions from normal lattice sites to interstitial sites and/or through a series of interstitial sites (Frenkel disorder, Figure 3), or the hopping of vacancies among normal lattice sites (Schottky disorder, Figure 3), established a clear structural basis for the occurrence of ionic conductivity in crystalline solids.

Around the same time, the development of *X-Ray Diffraction* methods made it possible to investigate directly the disorder of mobile ions in crystalline conducting solids. In 1934, Strock, on the basis of X-ray diffraction observations, postulated that the silver ions in α-AgI are distributed over a large number of lattice sites, which are energetically equivalent, while the iodide ions form a rigid framework structure.[10] Latter, Wuensch, and Cava confirmed unambiguously that the large (ca. four orders of magnitude) conductivity increase at the β-AgI → α-AgI transition at 147 °C is due to 'sublattice melting'.[11] That is, below 147 °C the Ag^+ ions occupy specific tetrahedral sites in a body-centered cubic arrangement of iodide ions. Both filled and vacant tetrahedral sites exist in the low-temperature structure. Above 147 °C, the silver ions distribute themselves over all the tetrahedral sites in a 'quasi-molten' or 'liquid-like' state (Figure 4) and they can move almost freely in three dimensions (3D). This pre-melting of the cation sublattice of silver iodide was also supported by the anomalously low value of the entropy of fusion ($11.3\,J\,K^{-1}\,mol^{-1}$) relative to the mean value of $24.5\,J\,K^{-1}\,mol^{-1}$ for alkali halides. The value of the transition entropy of AgI, $14.5\,J\,K^{-1}\,mol^{-1}$ at 147 °C, also suggested that the silver ion sublattice might be considered to melt at 147 °C while the remaining iodide sublattice collapses at 557 °C (the melting temperature of AgI).[12–14] Theoretical calculations indicate that the energy barriers at the 'bottlenecks' (i.e. the smallest openings) through

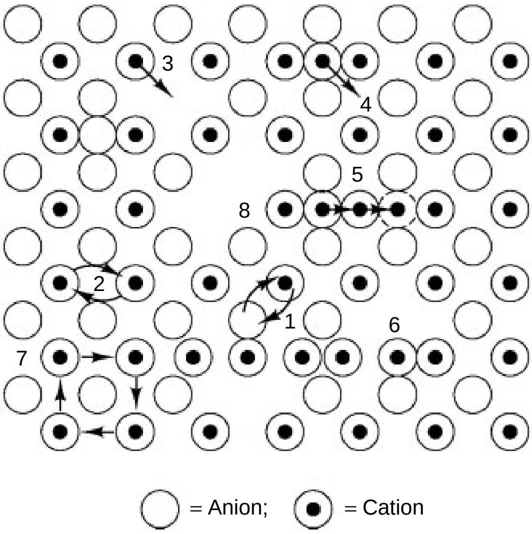

Figure 3 Defects and associated diffusion mechanism: 1 and 2, diffusion mechanism by direct exchange; 3, diffusion through vacancy; 4, direct interstitial mechanism; 5, indirect interstitial or caterpillar mechanism; 6, Frenkel defect; 7, indirect exchange; 8, Schottky defect. (Ref. 9. Reproduced by permission of Cambridge University Press)

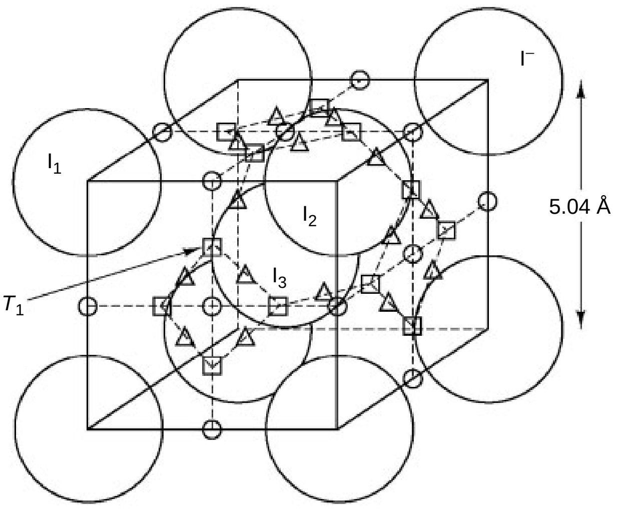

Figure 4 The unit cell of α-AgI depicted as a bcc sublattice of I^- and the Ag^+ sites at: ○, 6b, octahedral sites; □, 12d, tetrahedral sites; △, 24h, trigonal bipyramidal sites

which the diffusing Ag^+ ions must pass are low, because of small distortions of the iodide ions from their equilibrium crystallographic positions and because of the polarization of the electron clouds of both the Ag^+ and I^- ions.[15–17]

In an attempt to stabilize the highly conducting α-AgI phase at lower temperatures, various anionic and cationic substitutions have been tried.[18] The most successful so far has been the replacement of silver by rubidium in $RbAg_4I_5$. This material has the highest ionic conductivity at room temperature of any known crystalline substance ($0.27\,S\,cm^{-1}$) with an activation energy of 0.07 eV. The electronic conductivity of $RbAg_4I_5$ is negligibly small ($\sim 10^{-9}\,S\,cm^{-1}$).

Although the details differ from compound to compound, most crystalline inorganic electrolytes show behavior similar to that described for AgI. Each has a low-conductivity phase in which ions are ordered (or disordered) in a subset of lattice sites.

Over some higher temperature range, the ions become disordered (or more disordered) among the sites and ionic conductivity is high. More generally, all classes of solid electrolytes share an important characteristic in that they all owe their conductivities to highly disordered regions in their structures. These regions may encompass an entire crystal (e.g. AgI), be restricted to specific interfaces of a composite (e.g. Al_2O_3 dispersed in LiI,[19,20]) occur as highly disordered regions in a crystal (e.g. on two-dimensional (2-D) planes (β-aluminas)[1,21–24] or in one-dimensional (1-D) tunnels (hollandite),[25]) or involve liquidlike disorder of an amorphous material (glasses)[26–28] and polymers.[29–31]

Intercalation and insertion compounds are another class of ionically conducting solids. These materials are mixed ionic and electronic conductors and are also covered by a separate article (*see* ***Intercalation Chemistry***).

The great acceleration of interest in solids with high ionic conductivity was stimulated by the report of Yao and Kummer[32] in 1967 that sodium β-alumina has a sodium ion conductivity at room temperature comparable to that of an aqueous sodium chloride solution. The simultaneous invention of the sodium/β-alumina/sulfur battery by the same group intensified interest in the commercial application of solids with high ionic conductivity.

2 GENERAL FEATURES OF SOLIDS WITH HIGH IONIC CONDUCTIVITY: THEORY

2.1 Conductivity

The electrical conductivity of a single-phase material is the sum of the electronic and ionic contribution (equation 1):

$$\sigma = \sum n_i Z_i \mu_i \tag{1}$$

where n_i is the concentration of the charge carriers with charge Z_i and mobility μ_i. In solid ionic conductors with negligible electronic conductivity, the electrical conductivity follows Arrhenius-type temperature dependence (equation 2):

$$\sigma = \frac{C}{kT}\exp\left(\frac{-E_a}{kT}\right) \qquad \text{or} \qquad \sigma = \frac{\sigma_0}{T}\exp\left(\frac{-E_a}{kT}\right) \tag{2}$$

where E_a is the activation energy for conduction, and C or σ_0 (differing only by a factor $k =$ Boltzmann constant) is called the pre-exponential term.

Fast ion conduction generally results from low activation energies (a fraction of an electron volt, eV). A model of diffusion by isolated jumps with random walk of the mobile species is generally used to account for this behavior.

To be able to diffuse, an atom must surmount the energy barrier for migration E_m presented by its neighbors. If ν_0 is a characteristic atomic vibrational frequency, the probability for jump per second, ν, is expressed as $\nu = \nu_0 \exp(-E_a/kT)$. The atom makes ν_0 passes at the barrier with a probability $\exp(-E_m/kT)$ on each try of surmounting it by thermal energy (ν_0 is the so-called attempt frequency).

The diffusion constant D depends on the jump distance d and on a geometrical factor α (equation 3):

$$D = \alpha d^2 \nu_0 \exp\left(\frac{-E_m}{kT}\right) \tag{3}$$

The mobility μ, and hence the ionic conductivity, are directly related to the diffusion through the Nernst–Einstein equation, $\mu kT = ZeD$, giving equation (4):

$$\sigma = nZe\mu = \alpha n(Ze)^2 \nu_0 d^2 (kT)^{-1} \exp\left(\frac{-E_m}{kT}\right) \tag{4}$$

The specific character of a fast ionic conductor (FIC) arises from the value n of the concentration of the charge carriers with respect to n_0 the total number of ions.

In normal ionic materials the number of charge carriers (Frenkel or Schottky defects) is only determined by thermal generation (equation 5):

$$n = n_0 \exp\left(\frac{-E_{\mathrm{f}}}{kT}\right) \tag{5}$$

where E_{f} is the energy of defect formation. The conductivity then becomes (equation 6):

$$\sigma = \alpha n_0 (Ze)^2 \nu_0 d^2 (kT)^{-1} \exp\left\{\frac{-(E_{\mathrm{m}} + E_{\mathrm{f}})}{kT}\right\} \tag{6}$$

In FICs, the number of charge carriers represents an important fraction of the potentially mobile ions because of the presence of structurally inherent vacant positions (equation 7):

$$n = \beta n_0 \qquad \text{and} \qquad \sigma = \alpha\beta n_0 (Ze)^2 \nu_0 d^2 (kT)^{-1} \exp\left(\frac{-E_{\mathrm{m}}}{kT}\right) \tag{7}$$

Normal ionic compounds contain a limited number of charge carriers, and their activation energy for conduction is the sum of both the energy for defect formation (usually a few electron volts) and the energy for defect migration. In contrast, FICs have a large number of moving species with an activation energy representing only the energy for migration of defects. This last term may be only a fraction of an electron volt and has the same order of magnitude as observed activation energies in FICs.

Nevertheless, such a simple model that assumes the harmonic vibration of an isolated particle in a rigid potential well cannot take into account anharmonicity, polarization effects, and correlation between moving species, which are influential factors in fast-conducting materials.

Atomic vibrations with a large anharmonic character have been found to be responsible for fast conduction. There are numerous examples of studies of FICs by diffraction techniques that show unambiguously large thermal parameters for the mobile ion and/or diffuse/smeared-out electron density corresponding to the mobile species.

The lattice polarizability strongly influences the ionic conduction. A large amount of local polarization is unfavorable for migration: when hopping, the ion has to carry its polarization cloud with it. This ionic *Polaron* behavior[33] seems to be of major importance in FICs. Highest ionic conductivity values are obtained for migration of highly polarizable ions (Ag^+ and Cu^+ are the most mobile ions) in a deformable framework (iodides or derivatives). Compounds involving Pb^{2+} or Bi^{3+} give rise to higher anionic conduction than homolog phases containing less polarizable cations (like alkaline earth or rare earth cations) of comparable size. For example, β-PbF_2 exhibits a higher conductivity by fluorine migration than the alkaline earth fluorides with the same structure.[34]

For nonstoichiometric phases the stabilization of ‘extended defects’ depends on the ion polarizability.[35] The formation of extended defects is associated with a drastic decrease in the ionic conductivity, as for instance in calcia-stabilized zirconia (Section 3.2.1).

Correlation between the moving species is another important factor to consider, as all the atoms of a given sublattice (i.e. cationic in α-AgI, anionic in fluorites) or all the atoms of the conducting plane (β-alumina) may be involved in the conduction process.

In recent years, computer simulation (*see* ***Solids: Computer Modeling***) methods have been used successfully to examine the relationship between structural properties and transport mechanism in crystalline amorphous and polymeric materials.[36–41]

2.2 Structural Features

In the search for new inorganic crystalline solid electrolytes, a set of guidelines which show likely structural characteristics for high ionic conductivity has been established.[42,43]

1. A large number of the ions of one species should be mobile (i.e. a large value of n in $\sigma = ne\mu$).
2. There should be a large number of empty sites for the mobile ions to jump into.
3. The empty and occupied sites should have similar potential energies with a low activation energy barrier for jumping between neighboring sites (i.e. there is no use having a large number of available empty sites if the ion does not have enough energy to get into them).
4. The structure should have a framework (a rigid subarray or ‘skeleton’) with interconnected interstitial space (open channels) in which ions move preferably in three dimensions.
5. The anion framework should be highly polarizable.
6. Retain a negligible electronic conductivity σ at the operating temperature, T_{op} under operating atmospheres, that is, retain a transport number

   $$\mathrm{t} = \frac{\sigma_i}{\sigma} \tag{8}$$

   where the total conductivity is $\sigma = \sigma_i + \sigma_{\mathrm{e}}$ where σ_i is the conductivity due to only the mobile ions, and σ_{e} is the electronic conductivity.
7. Chemical stability in the working environment, which includes reactions at electrode/electrolyte as well as reactant/electrolyte interfaces. Thermodynamic stability vis à vis the reactants is achieved only by placing the bottom of the electrolyte conduction band above the highest occupied molecular orbital (HOMO) of the reductant and the top of the electrolyte valence band below the lowest unoccupied molecular orbital (LUMO)

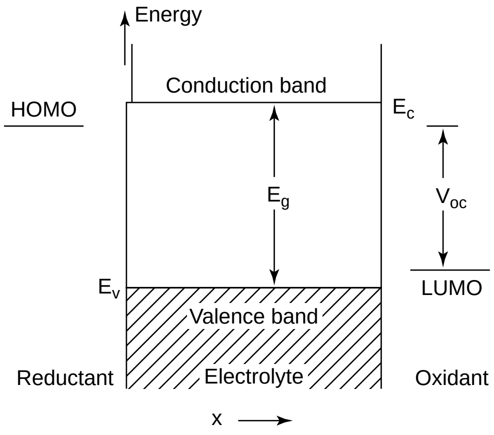

Figure 5 Placement of reactant energies relative to the edges of the electrolyte conduction and valence bands in a thermodynamically stable electrochemical cell at flat-band potential. (Reprinted, with permission, from the Annual Review of Materials Research, Volume 33 © 2003 by Annual Reviews www.annualreviews.org)

of the oxidant as illustrated in Figure 5. Note: The Fermi energies of the metallic electrodes should also lie in the energy gap E_g of the electrolyte, with that of the anode rising to the HOMO of the reductant and that of the cathode falling to the LUMO of the oxidant under operating conditions.

8. Mechanical stability against thermal cycling between ambient temperature and T$_{op}$ requires matching of thermal-expansion coefficients of the electrolyte and electrodes, the interconnects, and the seals. Note: Ceramic strength is improved where cell design retains the ceramic membrane under a compressive stress.
9. Costs of material and fabrication as well as operational life are always considerations.

In addition, alkali-ion transport is governed physically by the size of the 'bottlenecks' (i.e. smallest opening at the site interface) between interstitial alkali-ion positions and chemically by the bonding energy between the mobile ions and the network anions. The shortest diameter of the bottlenecks should be larger than twice the sum of the mobile-ion and anion radii. The covalent bonding between the mobile ion and the anion network should be as weak as possible, which may be achieved if the anion forms a strong covalent complex with the network cations and/or if the anion is bonded to more than two of these cations.[44]

3 CRYSTALLINE ELECTROLYTE MATERIALS

As mentioned in the Introduction, a large variety of solid electrolytes have been synthesized and characterized in recent years. In addition to a good number of fairly recent review articles[41,43,45–51] and books on the subject,[9,52–61] publications dealing with research in this area appear regularly in the journals including *Solid State Ionics, Ionics, Chemistry of Materials, Materials Research Bulletin, J. Solid State Chem., J. of Materials Chemistry, J. Electrochemistry, J. Power Sources, Sensors and Actuators, Solid State Sciences, MRS Symposium Proceedings on Solid State Ionics, Annual Reviews of Materials Research, and Annual Review of Material Science.*

Some examples of solid electrolytes are presented in Table 1. In the limited scope of this article, only a few examples of some of the most important (i.e. for potential commercial applications) monovalent cation (Li^+, Na^+, and H^+) and anion (oxide and fluoride) conductors will be discussed. Amorphous materials, glasses, and polymers are treated in Section 4. However, it should be noted that relatively good ionic conductors are known with many other monovalent ions including K^+, Rb^+, Cu^+, Tl^+, and Ag^+, divalent ions, for example, Pb^{2+}, Ca^{2+}, Ba^{2+}, Zn^{2+}, Sn^{2+} in β'-alumina,[62] and even trivalent cations,[23,63,64] and tetravalent cations.[65] In Section 5, the application of some of these materials in electrochemical devices including batteries, sensors, smart windows and fuels cells are discussed.

3.1 Cation Conductors

3.1.1 Sodium Ion Conductors

β- and β''-aluminas. The β-aluminas are one of the most important and widely investigated family of solid electrolytes. They permit not only fast Na^+ diffusion, but also the diffusion of other alkali ions, protonic species, divalent and even trivalent cations. The β-aluminas combine interesting chemistry with wide-ranging potential technological applications.

Sodium β- and β''-alumina are nonstoichiometric aluminates that are typically synthesized from sodium oxide (Na_2O) and alumina (Al_2O_3) at high temperature.[66,67] More recently synthesis of β- and β''-alumina by microwave processes could lead to a high density stoichiometric maore cost-effective product.[68] Single crystals can be grown by the Czochralski method from excess Na_2O melt.[69–71] Both can be thought of as derivatives of the yet-unknown stoichiometric sodium aluminate $NaAl_{11}O_{17}$. Both contain excess Na^+ compared to this composition. The general formula of β-alumina is $Na_{1+x}Al_{11}O_{17+x/2}$ with x being typically 0.2. Structural studies show that the excess sodium content is compensated for by oxygen ions in interstitial sites.[72–74] It is now clear that β- and β''-alumina are particular examples of a larger family of complex oxides with the general formula, $A_2O{\cdot}nM_2O_3$, where A is most commonly a monovalent alkali cation and M is Al, Fe, or Ga.

The crystal structure of β-alumina with nearly ideal composition was elucidated in 1937, about 30 years before

Table 1 Selected ionic conductors[9,31,43,48,54–57]

Compound[a]	Ionic charge carrier	Dimensionality[b]	σ_T[e] (Ω^{-1} cm^{-1})	T[d] (°C)	E_a[c] (eV)	E_G[g] (eV)	σ_e[f] (Ω^{-1} cm^{-1})
Cations							
Na-β-Al_2O_3	Na^+	2D	3×10^{-2}	RT	0.16	6	10^{-8}
$Na_3Zr_2Si_2PO_{12}$ (NASICON)	Na^+	3D	10^{-1}	300	0.15	–	–
NASICON (glassy)	Na^+	3D	10^{-4}	600	0.65	–	–
$LiAlSiO_4$	Li^+	1D	10^{-3}	RT	1	–	–
$LiAlSiO_4$ (glassy)	Li^+	3D	10^{-9}	RT	–	–	–
Li_3N	Li^+	2D	5×10^{-3}	RT	0.3	2.2	$<10^{-4}$
$Li_{5-x}Al_{1-x}Si_xO_4$	Li^+	3D	1×10^{-3}	300	0.4	–	–
K-β''-Al_2O_3	K^+	2D	10^{-1}	RT	0.21	–	–
$K_{2x}Mg_xTi_{8-x}O_{16}$ (hollandite)	K^+	1D	2×10^{-2}	RT	0.22	–	–
Ag_4RbI_5	Ag^+	3D	3×10^{-1}	RT	0.1	3.2	–
α-AgI	Ag^+	3D	1.9	200	0.1	–	–
$0.75AgI-0.25Ag_2SeO_4$ (glassy)	Ag^+	3D	6×10^{-2}	RT	–	–	–
$0.67AgI-0.25Ag_2O-0.08P_2O_5$ (glassy)	Ag^+	3D	10^{-2}	RT	–	–	–
$Cu_4RbCl_3I_2$	Cu^+	3D	5×10^{-1}	RT	0.15	–	–
Pb-β''-Al_2O_3	Pb^{2+}	2D	4×10^{-3}	RT	–	–	–
$Sc_2(WO_4)_3$	Sc^{3+}	3D	6×10^{-5}	600	–	–	–
$ZrNb(PO_4)_3$	Zr^{4+}	3D	10^{-4}	600	–	–	–
Anions							
PbF_2	F^-	3D	10^{-4}	100	0.45	–	–
ZrO_2:10%Y_2O_3	O^{2-}	3D	5×10^{-2}	700	0.8	–	–
CeO_2:10%Gd_2O_3	O^{2-}	3D	5×10^{-2}	500	0.5	–	–
$La_{0.9}Sr_{0.1}Ga_{0.8}Mg_{0.2}O_{2.85}$	O^{2-}	3D	5×10^{-2}	550	–	–	–
δ-Bi_2O_3	O^{2-}	3D	2.3	800	–	–	–
$La_2Mo_2O_9$	O^{2-}	3D	6×10^{-2}	800	–	–	–
Polymers							
$PPO-NaCF_3SO_4$ (amorphous)	Na^+	3D	10^{-5}	37	–	–	–
MEEP–LiSCN (amorphous)	Li^+	3D	–	–	–	–	–
$(MEEP)_4LiCF_3SO_3$	Li^+	3D	10^{-4}	300	1.6	–	–
$PEO-LiClO_4$	Li^+	3D	$10^{-6}/10^{-7}$	RT	0.31	–	–
$(PEO)_4-AgClO_4$	Ag^+	3D	$10^{-3}/10^{-5}$	RT	1.02	–	–
Nafion	H^+		10^{-1}	RT			

[a] PEO, poly(ethylene oxide); MEEP, $-[N{=}P(OC_2H_4OC_2H_4OMe)_2]_n$, poly(bis(methoxyethoxyethoxide)phosphazene); PPO, poly(propylene oxide). [b] Dimensionality of the conduction: (1-D) mono-, (2-D) bi-, (3-D) tridimensional. [c] E_a, activation energy. [d] RT, room temperature. [e] σ_T, total conductivity. [f] σ_e, electronic conductivity. [g] E_G, band gap.

the discovery of its fast ionic conductivity.[75] It crystallizes with hexagonal symmetry ($a = 5.38$, $c = 22.53$ Å) where the $Al_{11}O_{16}$ layer with basically the same atomic arrangement as that of spinel ($MgAl_2O_4$, *see* ***Oxides: Solid-state Chemistry***) sandwiches the Na–O layer as shown in Figure 6(a). The spinel blocks are connected by Al–O–Al bonds. The connecting oxygens are referred to as bridging or column oxygens. The packing of the O^{2-} in the spinel layer is close (ccp), while quite open in the inter-spinel Na–O 'conduction planes'. In the latter there are three kinds of sites for the Na^+ ions, as shown in Figure 6(b), called the BR (Beevers–Ross), aBR (anti-Beevers–Ross), and mO (mid-oxygen) sites. At low temperature the Na^+ ions are preferentially located at the BR sites. At higher temperature, however, the Na^+ ions are statistically distributed over the three sites, because the potential energy difference among the sites becomes negligible. This situation can be regarded as a 'half-fused' state of the Na^+ lattice. Thus the Na^+ ions can be easily transported in the 2D honeycomb-like pathways around the column oxygens, perpendicular to the c-axis, in a similar way as previously seen in α-AgI.

Sodium β'-alumina has the general formula $Na_{1+x}M_xAl_{11-x}O_{17}$ in which M is a divalent cation such as Mg^{2+}, Ni^{2+}, or Zn^{2+}. A typical composition of sodium β''-alumina is $Na_{1.67}Mg_{0.67}Al_{10.33}O_{17}$. β''-Aluminas have a structure[67] similar to the β-aluminas, except that there are three spinel blocks in the β'- and only two in the β-aluminas. The β''-phase contains a greater number of sodium ions than the β-phase, therefore exhibiting greater conductivity. The excess sodium charge is compensated for by substituting the divalent or monovalent cation into a lattice site normally occupied by Al^{3+}. The relationship between the charge compensation mechanism and ion transport in β''-alumina has been studied by single crystal X-ray diffraction.[77,78]

Ionic conductivity in β- or β''-aluminas is anisotropic, because it takes place along the planes sandwiched between

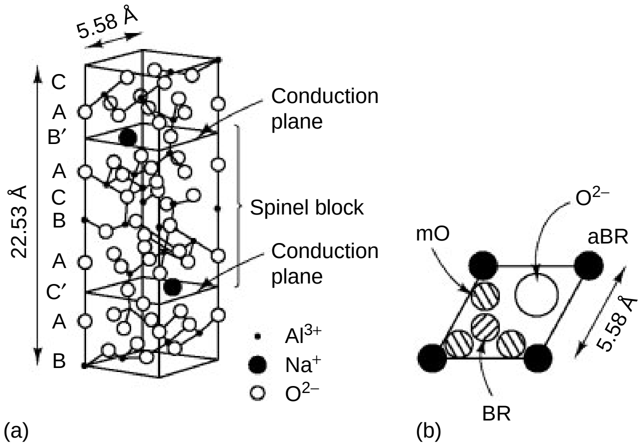

Figure 6 Crystal structure of β-alumina and sodium sites in the conduction plane: (a) unit cell structure; (b) site model of conduction plane. (Reprinted from Ref. 76 © 1978, with permission from Elsevier)

the spinel layers (Figure 6). Ionic conductivity measurements on single crystals of β-alumina show conductivity as large as $\sim 10^{-2}\,\mathrm{S\,cm^{-1}}$ at 25 °C perpendicular to the crystallographic c-axis,**[79]** while it is several orders of magnitude lower in the direction parallel to c. The temperature dependence of the ionic conductivity measured for single crystal samples in a wide range from −190 to 800 °C follows Arrhenius behavior with $E_a = 0.16\,\mathrm{eV}$.**[80]** Sintered, polycrystalline pressed-pellet samples show isotropic conduction with $\sigma \approx 10^{-3}\,\mathrm{S\,cm^{-1}}$ at 25 °C.**[81]** However, conductivities reported for sintered pellets are very diverse and appear to depend strongly on sample density and structure and/or composition at the grain-boundary layer.

Sodium β- and β''-alumina have a fascinating *Ion Exchange* chemistry.**[62]** The sodium-ion content in a crystal or polycrystalline sample can be replaced by a large variety of monovalent cations, including K^+, Cs^+, Rb^+, Ag^+, Cu^+, and Tl^+. The ion exchange reactions are straightforward. For example, when a small ($\sim 2 \times 2 \times 0.5\,\mathrm{mm^3}$) crystal of sodium β-alumina is immersed in molten potassium nitrate (KNO_3) at 400 °C, the sodium ions are replaced entirely by potassium ions in a few minutes. Ion exchange takes place also in aqueous solution to yield proton conductors. Of the monovalent cation β- and β''-aluminas, the sodium analogs exhibit the highest ionic conductivity and the lowest activation energy. This is probably because the spacing between the spinel layers is optimal for Na^+ ion mobility. In contrast, Li^+ is too small and too polarizing, so its mobility is diminished, while the others are too large for the conduction path. Tables 1–3 show the ionic conductivity of various β- and β''-aluminas.

Sodium Ion Conductors with Framework Structures. The so-called NASICON (Na super ionic conductors) materials, with the general formula $Na_{1+x}Zr_2P_{3-x}Si_xO_{12}$ ($0 \le x \le 3$), are another important class of Na^+ ionic conductors under intense investigation. These materials may be regarded as solid solutions of $NaZr_2(PO_4)_3$ and $Na_4Zr_2(SiO_4)_3$.**[44,85]** The host compound, $NaZr_2(PO_4)_3$, has a rhombohedral 3-D network structure built up of corner sharing PO_4 tetrahedra and ZrO_6 octahedra with interconnected tunnels (Figure 7). The conductivity is not very high, because Na^+ occupies one of three sites preferentially. In solid solutions, all the Na sites are occupied partially and the conductivity improves. The maximum conductivity of $2 \times 10^{-2}\,\mathrm{S\,cm^{-1}}$ at 300 °C is observed around the $x = 2$ composition of $Na_3Zr_2PO_4(SiO_4)_2$ (monoclinic system) and is comparable to that of Na β''-alumina. The conductivity decreases if x exceeds 2 as the Na sites become increasingly occupied. The synthesis of NASICON materials either by hydrothermal or sol–gel methods (*see* ***Sol–Gel Synthesis of Solids***) requires a final high-temperature (>900 °C) sintering to result in crystalline materials.**[86]** This high-temperature treatment leads to loss of Na and P content, because Na_2O and P_2O_5 are highly volatile, and an uncertain composition of the final product. Although the conductivity of the

Table 2 Conductivity characteristics of selected lithium ion conductors**[48,55,56,82]**

Compound	Dimensionality	σ_T ($\Omega^{-1}\,\mathrm{cm^{-1}}$)	T (°C)	E_a (eV)
Li-β-alumina	2D	1.3×10^{-3}	200	0.19
$Li_{14}Zn(GeO_4)_4$	3D	1.7×10^{-4}	200	0.50
$Li_{4.4}Si_{0.6}Al_{0.4}O_4$	3D	8×10^{-3}	300	0.59
$Li_{3.6}Si_{0.6}P_{0.4}O_4$	3D	3×10^{-2}	300	0.55
$Li_{3.75}Si_{0.75}P_{0.25}O_4$	3D	1×10^{-2}	300	0.60
$Li_{3.5}P_{0.5}Si_{0.5}O_4$	3D	3×10^{-2}	300	0.55
$Li_{3.5}Zn_{0.25}GeO_4$	3D	1.3×10^{-1}	300	0.24
$Li_{3.6}Ge_{0.6}V_{0.4}O_4$	3D	1×10^{-2}	190	0.44
$Li_{3.4}Si_{0.4}As_{0.6}O_4$	3D	2×10^{-4}	300	0.44
Li_4SiO_4	3D	2.2×10^{-3}	400	0.74
$LiTaAl(PO_4)_3$	3D	1×10^{-2}	300	0.47
$Li_{0.3}La_{0.57}\square_{0.13}TiO_3$	3D	1×10^{-3}	300	0.4
$LiSr_{1.65}\square_{0.35}Ti_{1.3}Nb_{1.7}O_9$	3D	1×10^{-2}	360	0.34

Table 3 Selected proton ionic conductors[57,83,84]

Material	σ_{RT} (Ω^{-1} cm^{-1})	E_a (eV)	Assumed mechanisms
β-$Al_{11}O_{16}(1+x)M_2O$			
$M = NH_4{}^+$, $x = 0.25$	1.5×10^{-6}	0.5	Ion jump
$M = H_3O^+$, $x = 0.25$	$\sim 10^{-10}$	0.8	Ion jump
β''-$Al_{11-y}O_{17}Mg_yM_{1+y}$			
$M = H^+(H_2O)_2$, $y = 0.66$	7×10^{-6}	0.17	Ion jump + Grotthus
β''-Al_2O_3	$\geq 10^{-3}$	0.2	Surface (liquidlike)
$H_3OZr_2(PO_4)_3$ (NASICON)	$< 10^{-6}$	0.56	Ion jump
Zeolite ($NH_4{}^+$)	$0.5/2.5 \times 10^{-5}$	0.36/0.84	
$HSbO_3 \cdot 1-2H_2O$ (pyrochlore)	3×10^{-3}	0.20	
H^+-montmorillonite	$\sim 10^{-4}$	–	
$H_3Sb_3P_2O_{14} \cdot 10H_2O$	4×10^{-3}	0.33	
$H_3AlP_3O_{10} \cdot nH_2O$ (600 K)	10^{-2}	–	
$H_3PW_{12}O_{40} \cdot 28/29H_2O$	$\sim 10^{-4}$	0.15/0.25	
$H_3PMo_{12}O_{40} \cdot 29H_2O$	1.7×10^{-1}	0.15	
$Zr(HPO_4)_2 \cdot nH_2O$	$10^{-3}-10^{-8}$	0.3–0.0	Surface and bulk
$H_3OUO_2AsO_4 \cdot 3H_2O$	5×10^{-3}	0.27	Ion/water jump
$H_3OU_2PO_4 \cdot 3H_2O$			
$UO_2(H_2PO_4)_2 \cdot 3H_2O$	5×10^{-5}	0.20	
$ZrO_2 \cdot 1.75H_2O$	2×10^{-5}	0.34	Surface (liquidlike)
$SnO_2 \cdot 2H_2O$	4×10^{-4}	0.20	Surface (liquidlike)
$CsHSO_4$ (~250 °C)	10^{-2}		Bulk
$SrCeO_3$:Yb (500 K)	10^{-6}	0.63	Bulk
$BaCeO_3$:Y (500 K)	10^{-2}	0.51	Bulk
$BaZrO_3$:Y (300 K)	10^{-2}	–	bulk

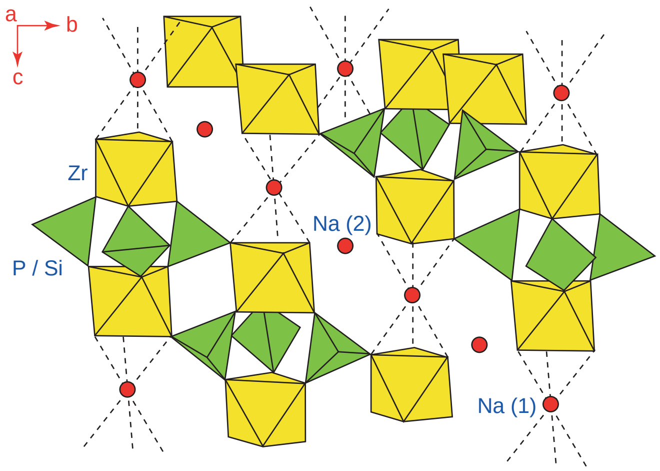

Figure 7 Schematic structure of NASICON

$x = 2$ NASICON is quite comparable to that of the β-aluminas in the temperature range 300–400 °C (the expected working temperature of the Na/S battery), some problems (including the chemical stability to fused Na) still remain for NASICON.

A series of compounds $Na_5MSiO_4O_{12}$ (M = Fe, In, Sc, lanthanides) with NASICON-like structure also exhibit high ionic conductivity; of these, Na_2GdSiO_{12} shows conductivity of 0.26 S cm^{-1} at 300 °C, which is higher than that of NASICON.[87]

3.1.2 Li$^+$ Ion Conducting Solid Electrolytes

Lithium is the most electropositive metal and the lightest; consequently there has been a lot of interest in electrochemical devices using components that include Li metal electrodes and Li$^+$ conducting solid electrolytes. Hundreds of materials have been studied for applications as potential lithium conducting solid electrolytes. Tables 1 and 2 give representative examples of the more important Li$^+$ solid electrolytes, some of which are discussed in this section.

All LiX (X = F, Cl, Br, I) form with the NaCl structure. Except for LiI they are all almost perfect ionic crystals and insulators at room temperature. The bonding in LiI is partly covalent because of the large polarizability of I$^-$,[88] giving it a Li$^+$ conductivity of 5.5×10^{-7} S cm^{-1} at 30 °C.[89] It is noteworthy that LiI was the first solid electrolyte used practically in a LiI/I_2 (complex) battery in 1972 (e.g. heart pacemaker battery). The many efforts to improve the ionic conductivity of LiX-based solid electrolytes led to the discovery of LiI–Al_2O_3 composites[19] with dramatic improvement of the conductivity. Merely dispersing fine particles of Al_2O_3 in LiI (at an experimentally determined optimal concentration) improves the conductivity by two orders of magnitude. The mechanism of conductivity in LiI–Al_2O_3 composites is not certain, but it is explained by the formation of a space-charge layer consisting of either Li$^+$ ion vacancies or interstitials at the interface between the host and the dielectric particles of Al_2O_3.[90] LiI–Al_2O_3 is one of the few solid electrolytes that has been put to practical use. Moreover, the dispersion effect found in this system is also useful for developing other useful high-conductive solid electrolytes, because the effect should be universally applicable to other/similar component systems.

Complex metal halides with the inverse spinel structure (*see **Oxides: Solid-state Chemistry***), Li_2MCl_4 with M = Mg, Cr, Mn, Fe, Co, and Cd, are also examples of halide-type Li^+ conductors; these materials have conductivities of the order of 10^{-2} S cm^{-1} at ∼300 °C.[91]

Lithium nitride, Li_3N, is an ionic crystalline compound; it is synthesized by the direct reaction of Li metal with nitrogen. The structure of Li_3N consists of alternating layers of $Li(2)_2N$ and Li(1).[92] Conduction takes place primarily in the Li(1) layers, as demonstrated by single crystal experiments. The conductivity at room temperature is $\sim 10^{-3}$ S cm^{-1} in the *ab* plane and $\sim 10^{-5}$ S cm^{-1} in the direction along *c*, while in polycrystalline samples it is $\sim 10^{-4}$ S cm^{-1}. Thus the conductivity of Li_3N is several orders of magnitude higher than those of the LiX-based materials. However, its application is limited by its low decomposition voltage 0.445 V (i.e. free energy of formation of Li_3N), since a battery with an emf greater than this value, at least theoretically, cannot be constructed. To overcome the decomposition problem, various systems based on Li_3N have been investigated. Of these, a Li_3N–LiI–LiOH (1:2:0.77 in molar ratio) ternary system, prepared by sintering the components at 500 °C in N_2 for 3 h, is the most successful. This composite has nearly as high a conductivity as Li_3N, and its decomposition voltage is as high as 1.6–1.8 V.[93]

In Table 2, the Li^+ ionic conductivities of some representative compounds based on Li_4SiO_4 and its solid solutions are shown. The highest conductivity is exhibited by those phases that crystallize with the γ-Li_3PO_4 structure[94] with orthorhombic symmetry. In this structure the oxygens are packed in an array intermediate between hcp and tetragonal packing (*see **Oxides: Solid-state Chemistry***), with the cations distributed over various tetrahedral sites. These phases are sometimes also called lithium ion conducting solid electrolytes (LISICONS). Li^+ diffusion can occur via vacant interstices. However, in the ideal γ-Li_3PO_4 structure all the Li^+ are used to build the framework structure; hence the ionic conductivity is only significant at very high temperatures. Li^+ ion mobility can be facilitated by introducing vacant interstices by aliovalent substitutions. Thus the highest conductivity is achieved in xLi_3PO_4–$(1-x)Li_4SiO_4$, which may be formulated in the γ-type defective structure as $Li^*_{1-x}Li_3Si_{1-x}P_xO_4$, where Li* corresponds to the mobile Li ions. The conductivities are maximized (4×10^{-6} S cm^{-1} at 25 °C) when $x = 0.5$, which means that only half of the cation sites in the conducting plane are occupied.

LISICON, $Li_{14}Zn(GeO_4)_4$, is an interstitial solid solution based on the HT γ-Li_2ZnGeO_4 structure with the substitution mechanism $2Li \longleftrightarrow Zn$.[44,95] $Li_{14}Zn(GeO_4)_4$ has very high conductivity at high temperature (HT) (0.13 S cm^{-1} at 300 °C), but at room temperature (RT) the conductivity is low 10^{-7} S cm^{-1} owing to lithium ion trapping. Moreover, this composition is thermodynamically unstable below ∼630 °C and reacts with atmospheric CO_2 and violently with molten Li.[96] However, the composition $Li_3Zn_{0.5}GeO_4$ in this system retains its high conductivity at HT and is thermodynamically stable down to RT.

A variety of other γ-type phases with high Li^+ conductivity are derived from the Li_3XO_4 phases with X = P, As, or V. The substitution mechanisms are of the type $X \longleftrightarrow$ (Si, Ge, Ti) + Li, and lead to the creation of interstitial Li^+ ions which are responsible for the high ionic conductivity. The highest conductivity at room temperature, 4×10^{-5} S cm^{-1}, is found in the series $Li_{3+x}(Ge_xV_{1-x})O_4$.[97] Neutron diffraction has been used to locate the interstitial lithium ions, to determine their site occupancy, and correlate the high ionic conductivity with the connectivity of the interstitial sites.[98]

Li_2SO_4 and related materials have been studied for many years by Kvist, Lunden, and coworkers.[99] The high temperature, cubic, α-form of Li_2SO_4 has very high ionic conductivity, ∼ 1 S cm^{-1} between 575 °C and its melting point (879 °C), which makes this potentially a very interesting solid electrolyte. The low-temperature, monoclinic β-form of Li_2SO_4 has much lower conductivity. Many attempts have been made to reduce the temperature of the $\beta \longrightarrow \alpha$ transition by various substitutions, but without much success so far. There is little change in the ionic conductivity of Li_2SO_4 upon melting; it appears that the Li^+ ions in crystalline α-Li_2SO_4 are in an essentially liquidlike environment. The precise mechanism of conductivity in Li_2SO_4 is a topic of some current controversy.[100–103] The key issue concerns the rotation of the $SO_4{}^{2-}$ groups: are they rigidly fixed in the structure, or do they undergo small rotational motion, or are they in free rotational motion? There is evidence for rotational disorder of the sulfate groups from neutron diffraction, which suggests rapidly reorienting $SO_4{}^{2-}$ ions which effectively gate the movement of Li^+ ions, that is, a 'paddle-wheel' mechanism,[103] however report of the increase of conductivity with substitution of $WO_4{}^{2-}$ for $SO_4{}^{2-}$ is consistent with the interpretation of fast ion transport in Na_2SO_4-based compounds via a percolation-type mechanism where lattice free volume plays a predominant role.[101,102]

Li β-alumina, prepared from Na β-alumina by ion exchange in LiCl at 650 °C, has the one of the highest Li^+ conductivities reported in a crystalline material, 3×10^{-3} S cm^{-1} at 25 °C in a single crystal sample.

Some of the other important Li^+ solid electrolytes with reasonably high conductivities include: $Li_{5+x}Al_{1-x}Si_2O_8$ with a γ-$LiAlO_2$ structure;[104] lithium analogs of NASICON, $Li_{1+x}Zr_2Si_xP_{1-x}O_{12}$; substituted framework silicates, $LiAlSiO_4$ with good 1D Li^+ conductivity;[105] $Li_4B_7O_{12}(Cl,Br)$ and $Li_5B_7O_{12}S$ with 3D cagelike structures;[106] $Li_{5+x}M_{1-x}M'_xO_4$ (M = Al, Ga; M′ = Zn) phases with the antifluorite structure and high vacancy contents.[107]

A recent review article by Sebastian and Gopalakrishnan[48] surveys high lithium ion conducting oxides based on ionic conductivity, redox insertion/deinsertion and ion exchange properties. In addition to the wide variety of compounds discussed above, the review includes compounds with mixed ionic and electronic conductivity. The survey shows that considerable lithium ion mobility occurs in close packed (CP) structures including rock salt type (α-AMO_2, A = Li, M=V, Cr, Mn, Co, Ni); Figures 8 (a–c). It is now well established that the β and γ polymorphs of these compounds, where the A and M cations are not ordered in the 111 planes of the cubic close packed (CCP) oxide lattice (Figure 8c) do not undergo facile ion exchange are poor ion conductors in general, and also do not undergo Li insertion/deinsertion readily. Hence the correlation between a layered structure, ion exchange, and redox insertion/extraction in α-AMO_2 phases is clear. Other examples of CP oxides with high Li mobility are the spinels, namely AB_2O_4 compounds in which the A and B cations partially occupy tetrahedral and octahedral sites of the CP lattice of oxygens (Figure 8(d)). Typically Li^+ ions in partially occupied tetrahedral sites can diffuse in the 3D pathways provided by the interconnected empty tetrahedral and octahedral sites. $LiMn_2O_4$ spinel, a mixed conductor and various substituted analogs are currently researched for application as cathode material in lithium batteries.[108] Other CP oxides with hexagonal close packed (HCP) structures with high Li^+ion mobility include $LiMO_3$ phases (M = Nb, Ta, Sb), the trirutiles, $LiMM'O_6$ (M = Nb/Ta; M′ = W/Mo), $LiFePO_4$ and the above described LISICONS, Li_2ZnGeO_4 and Li_3VO_4 solid solutions.

3D (Li,La)TiO_3 perovskite-type phases, first reported by Belous *et al.*[109] exhibit high Li^+ion conductivity, $\sim 1 \times 10^{-3}\,S\,cm^{-1}$ at room temperature.[110] This remarkable result initiated extensive research in these A-cation deficient ABO_3 perovskite materials. In the perovskite structure, a 3D network structure is built up by corner sharing BO_6 octahedra where the A cations occupy the 12 coordinated interconnected interstitial sites (Figure 9). Thus, in (Li,La)TiO_3, the Li and La ions partially occupy the A site, which provides the 3D pathway for the high mobility of Li^+ ions. Stramare *et al.*[82] in a recent review survey most of these materials and show that $Li_{3x}La_{2/3-x}\square_{1/3-2x}TiO_3$ with $x = 0.1$ has the highest bulk lithium-ion-conductivity, $\sigma(RT) \sim 1 \times 10^{-3}\,S\,cm^{-1}$ and $E_a = 0.40\,eV$ in this series. A major problem with the possible use of these materials as solid electrolytes in lithium batteries is the reduction of Ti^{4+} at relatively low potentials (~2V), with the onset of electronic conductivity and short-circuiting. Thus analogous materials with similar high Li mobility, but suitable nonreducible B cations are necessary for applications. In an effort to achieve that various compositions including $LiABB'O_6$ and $LiA_2B_2B'O_9$ with A = Ca, Sr, Ba; B = Ti, Zr; and B′ = Nb, Ta were investigated.[48]

NASICON ($Na_3Zr_2PSi_2O_{12}$) is a well-known framework oxide (Figure 7) with high Na^+-conductivity.[111] The substitution of $2Zr^{4+} \rightarrow M^{5+} + M^{3+}$ in NASICON is possible, yielding A $M^{5+}M^{3+}(PO_4)_3$ (A = Na, Li; M^{5+} = Nb, Ta; M^{3+} = Ti, V, Cr, Fe, Al). An investigation of the ionic conductivity of the Li derivatives showed that $LiTaAl(PO_4)_3$ exhibits the

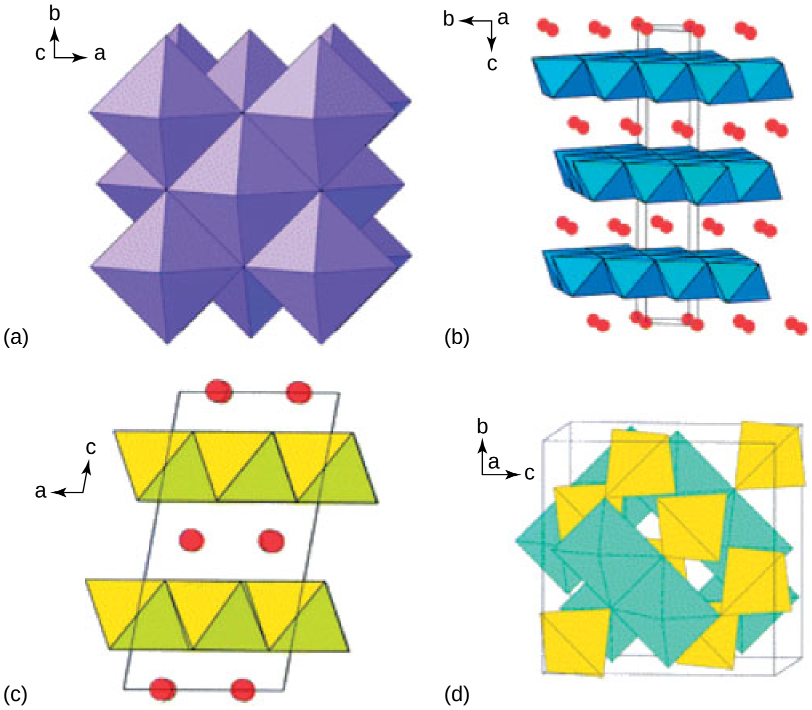

Figure 8 Structures based on cubic close-packed anion arrays: (a) rocksalt; (b) a-$NaFeO_2$; (c) b-Li_2SnO_3; (d) spinel. In (b) and (c), the red circles denote interlayer alkali metal ions.[48] (Reproduced by permission of Royal Society of Chemistry)

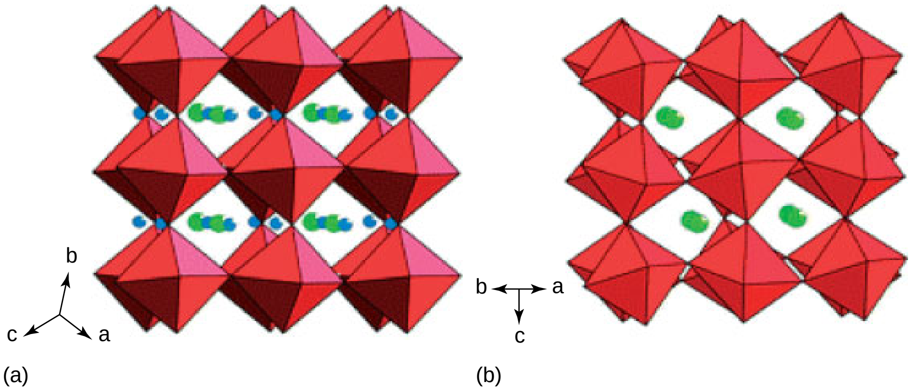

Figure 9 Structures of perovskite lithium ion conductors: (a) (Li, La)TiO_3; (b) $LiCa_{1.65} * **_{0.35}Ti_{1.3}Nb_{1.7}O_9$. ($\sigma_{800\,°C} = 3.1 \times 10^{-3}$ S cm^{-1}; $E_a = 0.71$ eV). In (a), the green and blue circles denote La and Li, respectively. In (b), the green circles denote Li and Ca in the $GdFeO_3$ structure.[48] (Reproduced by permission of Royal Society of Chemistry)

highest conductivity, ~1 × 10^{-2} S cm^{-1} with $E_a = 0.47$ eV.[48] Recently Goodenough *et al.* investigated various transition metal analogs and found that $Li_2NaV_2(PO_4)_3$ and $Li_3V_2(PO_4)_3$ insert/deinsert Li at 3.7 V.[112,113] The NASICON framework is indeed unique in that it exhibits all three properties: high ionic conductivity, ion exchange, and redox insertion/extraction, that characterize high Li mobility in solids.

3.1.3 Proton Conductors

Development of good proton conductors has recently acquired great significance, primarily because of their potential application as solid electrolytes in fuel cells, batteries sensors and other electrochemical devices. In general, the term proton conductor refers not only to H^+ ion transport, but also includes materials with complex ion transporting groups such as $NH_4{}^+$, H_3O^+, OH^-, and so on. There have been many reviews on the subject[9,83,114–120] including several International Conference Proceedings.[121–128]

Mechanism. Because of the small radius of the free proton, 'isolated' H^+ ions are not present in solids under equilibrium conditions. Owing to its strongly polarizing power, H^+ is covalently bonded to one or two electronegative atom/ions of its surroundings, for example, hydrogen bonds. Tunneling effects may explain some of the low-temperature conductivity of proton conductors, for example, $HTaWO_9{\cdot}H_2O$;[129] however, at room temperature and above, thermally activated processes will dominate the conductivity. An excellent discussion of the different transport modes has been given by Kreuer *et al.*[84,130,131] At least three bonding situations for the proton are relevant: (1) the acceptor site may be an ion of the immobile lattice, for example, formation of a hydroxo group; (2) the proton may be attached to a mobile ion, for example, oxide ion, thus forming an OH^- group; (3) the proton is attached to a mobile molecule, for example, water or ammonia, thus forming a hydronium ion or ammonium ion. The question is: how is the proton delivered from one site to another in the direction of the field? In the first case, proton conduction can only take place by a simple hopping mechanism of the proton to an adjacent acceptor site, followed by the rotation of the new H-acceptor bond in the direction of the field. The mechanism may be described as a 'point defect migration' with rapid exchange of cations between filled and empty sites in a disordered cation sublattice. This mechanism, sometimes referred to as the Grotthuss, or free-proton mechanism (Figure 10). This is the accepted mechanism for proton conduction in the high-temperature (>500 °C) proton conductors such as the proton-containing doped pervoskite-type phases, $MCeO_3$ (M = Ca, Sr, Ba), $BaZrO_3$ and $MTaO_3$.[84]

When the proton is attached to a mobile ion, two modes of transport have been proposed. (1) Polyatomic ions like H_3O^+ or $NH_4{}^+$ may migrate by a simple jump from site to site in the lattice, as has been claimed in the β-aluminas[132] and in the zeolites.[133] (2) A more involved mechanism based on the simultaneous diffusion of two types of polyatomic units, the so-called 'vehicular' mechanism, was suggested

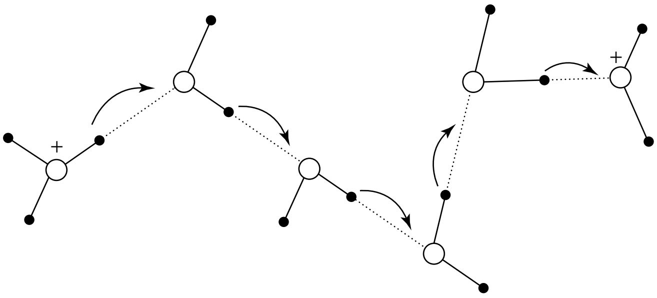

Figure 10 Proton conductivity according to the Grotthuss mechanism. (Reprinted from Ref. 131 © 2003, with permission from Elsevier)

by Kreuer *et al.*[134] The proton travels through the lattice on a 'vehicle', which may itself be neutral or charged; there must be a counter diffusion of the vehicles, for example, H_3O^+ in one direction and H_2O in the opposite direction. The mechanism involving polyatomic ions can be often ruled out by structural considerations, that is, if the bottlenecks are too small to allow the passage of the relatively large polyatomic ions. Positive indication for transport mechanism involving polyatomic species is the absence of an *Isotope Effect* when the conductivity of the protonic and the fully deuterated analogs are compared. If H^+ and D^+ are the mobile species, the conductivities should be approximately in the ratio of $\sqrt{2}:1$. If this is not the case, or a very small isotope effect is observed, then it may be assumed that the H/D is part of a larger ion and the mass difference is 'drowned'.

Surfaces of crystals and the grain boundaries may have disordered regions where proton transport is facilitated. Adsorbed water or electrolyte solution trapped between the grains will also increase the conductivity and give rise to false conclusions concerning the solid-state nature of conductivity. Surface or liquidlike conductivity has a low activation energy ($E_a \approx 0.1–0.4$ eV), approaching the E_a of aqueous acidic solutions (0.1–0.15 eV)

Materials. In Table 3, the conductivities of selected proton conducting materials are presented. There are a diversity of proton conducting materials, sometimes classified according to the mechanism of H^+ motion as bulk conductors and surface conductors.[135] Many solid protonic conductors have liquid, or liquidlike regions, or layers of water, and thus substantial water contents. Such materials maybe borderline between solid and liquid phase, or maybe two-phase systems. The materials with the highest protonic conductivities are found in the group of heteropolyacid hydrates, for example, $H_3[PW_{12}O_{40}]\cdot 29H_2O$, which has a conductivity of 2×10^{-2} S cm^{-1} at 25 °C.[9] This material has a diamond-type lattice of clustered ions, $[H_3\cdot 29H_2O]^{3+}$ and $[PW_{12}O_{40}]^{3-}$, interpenetrated by each other in which a hydrogen bonding network spreads over the entire crystal. The high conductivity may be due to H^+ transport via molecular H_3O rotation. The Mo analog has similar properties. Hydrogen uranyl phosphate (HUP, $HUO_2PO_4\cdot 4H_2O$) and arsenate (HUAs, $HUO_2AsO_4\cdot 4H_2O$) are layered materials and also among the best proton conducting hydrates. The room temperature conductivities are high ($\sim 10^{-3}$ S cm^{-1}) and are attributed to H^+ migration through a hydrogen bonding network in the layers similar to that in $H_3[PW_{12}O_{40}]\cdot 29H_2O$.[9] In HUAs there is evidence for direct diffusion of H_3O^+. The α-$M(HPO_4)_2\cdot nH_2O$ (M = Zr, Ti, Ce) are another class of layered materials with relatively high proton conductivity ($\sim 10^{-3}$ S cm^{-1} at 25 °C) that have been investigated thoroughly.[136]

The close connection between ion exchange properties of solids and solid electrolyte behavior was stressed by England *et al.*,[135] who were also among the first to explain proton conduction in particle hydrates, such as $ZrO_2\cdot nH_2O$ and $SnO_2\cdot nH_2O$, where adsorbed hydrous layers on each grain provide the proton conductive medium.

The β- or β''-aluminas exhibit H^+ conductivity when the Na^+ ions are replaced by H_3O^+ or NH_4^+ by ion exchange. Of these materials, the best conductivity of 10^{-4} S cm^{-1} at 25 °C is found in $(NH_4^+)(H_3O^+)_{2/3}Mg_{2/3}Al_{31/3}O_{17}$, derived from the β''-phase.[137] Ammonium exchanged zeolites (*see* ***Zeolites***) also show high H^+ conductivity. One of the highest room temperature conductivities, 2×10^{-3} S cm^{-1}, has been reported for the fully hydrated NH_4-zeolite-A.[138] A dehydrated H-analog of NASICON, prepared by deammoniation of a hydrothermally prepared $NH_4Zr_2P_3O_{12}$ sample, also shows excellent proton conducting properties for potential applications.[139] In these network structures sufficiently large bottlenecks allow the direct diffusion of NH_4^+ or H_3O^+ charge carriers.

Most proton conducting solids until fairly recently were inorganic hydrates and stable conductivities much above 150 °C in such materials are seldom found (i.e. after the water is lost, conductivity disappears); moreover, the conductivity is highly dependent on the water content, including the surface water of the material. Thus there is a need to develop proton conductors for various applications in the higher temperature range, which are not dependent on water content.

The most prominent high-temperature proton conducting materials are the perovskites, of doped ABO_3 type (*see* ***Oxides: Solid-state Chemistry***), exemplified by Yb-doped $SrCeO_3$, first studied by Iwahara and his group since 1980.[140] When a trivalent ion replaces Ce^{4+}, the material may be formulated as $SrCe_{1-x}Yb_xO_{3-\delta}$ under dry conditions in air, but when heated in water vapor it becomes $SrCe_{1-x}Yb_xH_yO_{3-\delta}$ with $\delta = x/2$ and $y = x$. A typical dopant concentration is $x = 0.05$. The value of y is dependent on the synthetic conditions and the x content. The material is a p-type semiconductor in air at ∼1000 °C; however, in a H_2O atmosphere the conductivity is $\sim 10^{-2}$ S cm^{-1} at 900 °C and occurs by protons. Thus protonic defects are formed by the dissociation of gaseous water into a hydroxide ion and a proton; the OH^- ion fills an oxide ion vacancy and the H^+ covalently attaches to a lattice oxygen. This reaction may be represented according to: $H_2O + h^+ \longleftrightarrow 2H^+ + 0.5O$, or in Kröger–Vink notation as: $O_O + V^{\bullet\bullet}{}_O + H_2O \longleftrightarrow 2OH_O$, where O_O is a normal oxygen site, $V_O^{\bullet\bullet}$ is an oxygen vacancy, and $OH_O^{\cdot}$ is an OH ion in the normal oxygen site. In general, this reaction is exothermic, so protons rule at low temperatures and oxygen vacancies at high temperatures. Transport in the doped $M^{II}CeO_3$ perovskites by H^+ ions was well established by the work of Iwahara[140] and others.[141,142] In the past decade, a great deal of work has been carried out on a large variety of substituted proton conducting oxides mostly with the perovskite structure.[84] Figure 11 shows that one of the best proton conductors is Y-doped $BaCeO_3$; this perovskite has the highest molar volume and compared with the $SrCeO_3$ analog, its deviation from the ideal cubic perovskite structure is smaller. Data for $Ba_2YSnO_{5.5}$[143] and

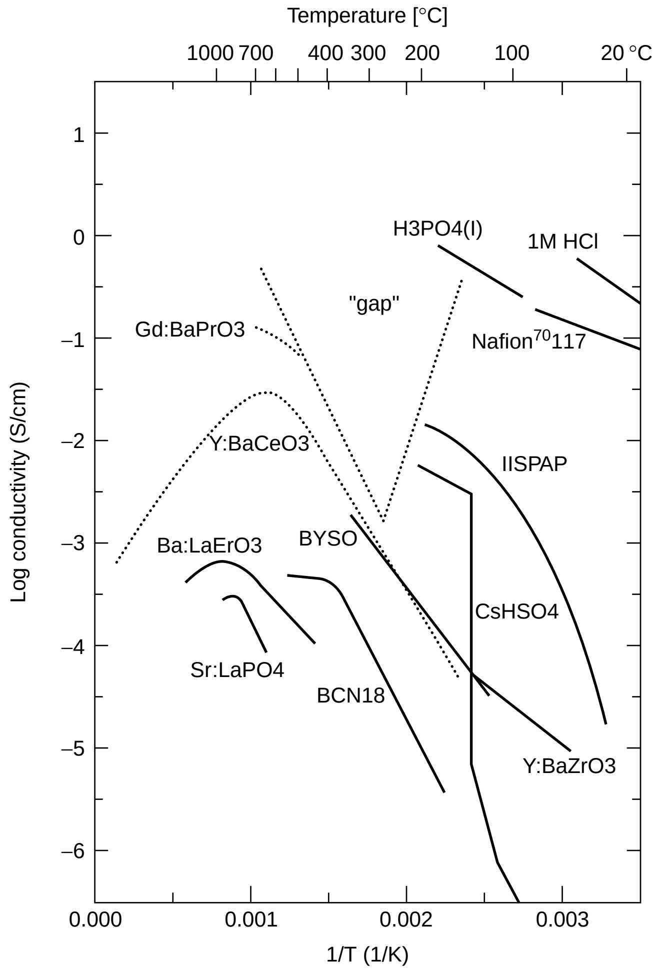

Figure 11 Selected literature data for proton conductivity as a function of inverse temperature. Imidazole-intercalated sulfonated polyaromatic polymer (IISPAP); $Ba_2YSnO_{5.5}$ (BYSO); $Ba_3Ca_{1.18}Nb_{1.82}O_{8.73}$ (BCN18), the curve for Y:$BaCeO_3$ is a calculated estimate. The interpretation of the conductivity of Gd:$BaPrO_3$ as protonic is somewhat ambiguous at present. For further explanation and discussion, see Ref. 119. (Reprinted from Ref. 119 © 1999, with permission from Elsevier)

Y-doped $BaZrO_3$ show that these compete in terms of proton conductivity with Y-doped $BaCeO_3$. The principal features of the transport mechanism are rotational diffusion of the protonic defect and proton transfer towards a neighboring oxide ion. The first has been shown experimentally[144] and by quantum MD simulations[145] to be fast with activation barriers below 0.1 eV, which suggests that the proton transfer reaction is the rate-limiting step. On the other hand, the strong, red-shifted OH-stretching absorptions in the IR spectra are indicative of strong hydrogen bond interactions, which favor fast proton transfer reactions rather than fast reorientation processes, the latter requiring the breaking of such strong bonds.[146]

It is clear from Figure 11 that, at present, proton conductors do not parallel the best oxygen ion conductors (i.e. $\sigma > 1\ \mathrm{S\,cm^{-1}}$).

However proton conductors, in general, work at substantially lower temperatures and may offer the highest conductivities at intermediate or low temperature. Nevertheless, there are no solid proton conductors working in the range between ∼200–500 °C (Figure 11). This range is the most desirable operating temperature for both chemical processes and energy conversion processes. Thus finding new materials with proton conductivity in this temperature range is critical for practical applications for example in fuel cells.

Solid acid compounds with a fixed crystallographic proton including $CsHSO_4$, $CsHSeO_4$ and CsH_2PO_4 and CsH_2AsO_4 have been intensely investigated recently as inorganic proton conducting solid electrolytes for low temperature applications in fuel cells and other devices. These compounds are made up of hydrogen-bonded tetrahedral oxyanions, (i.e. SO_4, SeO_4, PO_4, and AsO_4), and metal cations (e.g. Cs), which provide overall charge balance to the hydrogen bonded network. Several solid acids exhibit an ordered arrangement of hydrogen bonds at room temperature and, upon slight heating, become structurally disordered. A typical example is $CsHSO_4$, which transforms from a monoclinic to a tetragonal structure at 141 °C.[147] Accompanying this transformation is an increase in proton conductivity of two to three orders of magnitude, reaching values as high as $10^{-2}\ \mathrm{S\,cm^{-1}}$. Recently Haile and her group have demonstrated that CsH_2PO_4 is a 'superprotonic' conductor, which does not decompose, or become reduced (as do the corresponding S and Se analogs) up to ∼270 °C, and have many advantages over the proton conducting polymer film electrolyte Nafion used in similar fuel cells.[148]

3.1.4 Multivalent Ion Conductors

Divalent cations (as monovalent ones) also can exchange for sodium in β-alumina, but the reactions are slow, and the resulting divalent β-aluminas are not good ionic conductors. However, cation exchange of divalent ions in β''-aluminas is much more rapid; the ionic conductivity of divalent β-aluminas at room temperature can be as high as $10^{-3}\ \mathrm{S\,cm^{-1}}$ for Pb^{2+}-β-alumina, although most are in the range of $10^{-7}\ \mathrm{S\,cm^{-1}}$ (e.g. Ba^{2+}, Ca^{2+}, among others).[149] The sodium ions in β'-alumina can also be replaced by trivalent cations, such as the lanthanides. For example, almost total replacement of Na^+ by Eu^{3+} occurs in a small crystal of β''-alumina by heating it in $EuCl_3$ powder at 650 °C (mp of $EuCl_3$, 850 °C) for 24 h.[150] Similar ion exchange via vapor phase takes place between β''-alumina and rare earth chlorides such as $NdCl_3$, $EuCl_2$, $SmCl_3$, or $TbCl_3$.

Although the conductivity of the trivalent-ion β''-aluminas is too low for solid electrolyte applications (e.g. batteries, sensors), they have potential use in optics, phosphors, and lasers because they can serve as single crystal or powder hosts for the optically active lanthanide ions. For example, Eu^{3+}-β''-alumina emits red luminescence when excited by UV rays.[151] A Nd^{3+}-β''-alumina single crystal shows luminescent characteristics similar to those of YAG:Nd^{3+}.[152] The Er^{3+} and Ho^{3+} analogs have similar encouraging laser application properties. Another example of controlled valence and composition by ion exchange techniques in β''-alumina is the doping of this material by Cu^{I}, which emits in the blue–green region of the spectrum. Cu(I) with another 'codopant' ion (e.g. Ca^{2+}, Ag^{+}) produces materials that exhibit tunable emission over much of the visible spectrum.[153] These and similar promising optical data are accelerating the development of phosphors and/or laser materials based on rare earth incorporated β''-aluminas.[154]

The multivalent β''-aluminas are the first family of high-conductivity solid electrolytes with multivalent cations. They demonstrate that fast ion transport is not limited to a few monovalent cations, but occurs with many different cations.

More recently Adachi and Imanaka[155–158] have been investigated a variety of network oxides with tri- and tetra-valent ion mobility. For example the conductivity, $\sigma_{600\,°C} \sim 10^{-5}\,S\,cm^{-1}$ of trivalent cations in NASICON-like compounds, $R_{1/3}Zr_2(PO_4)_3$ ($R = Sc^{3+}$, Y^{3+}, Er^{3+}, Tm^{3+}, Lu^{3+}) was observed;[159] similarly in solid solutions of $Sc_2(WO_4)_3$-$Gd(WO_4)_3$, Sc^{3+} and Gd^{3+} ions exhibit $\sigma_{600\,°C} \sim 6 \times 10^{-5}\,S\,cm^{-1}$ (Ref. 160); and in $MNb(PO_4)_3$ ($M = Zr^{4+}$, Hf^{4+}), the tetravalent ions show $\sigma_{600\,°C} \sim 10^{-4}\,S\,cm^{-1}$ (Ref. 161).

3.2 Anion Conductors

Propagation of an ion in a solid involves the diffusion of a rather large species through a structure, which is densely populated. Therefore the motion of smaller ions, the cations, is expected to be more likely than those of the larger anions. While this indeed is the trend, fast anionic conduction in solids can be observed at high temperature with conductivities of the order of $1\,S\,cm^{-1}$.

Fast anionic conduction is found mainly in solids of the fluorite (CaF_2) and fluorite-related structures. It is also observed in solids with the perovskite, YF_3, tysonate (LaF_3), and simple cubic structures (for these structures, *see* ***Oxides: Solid-state Chemistry*** and ***Fluorides: Solid-state Chemistry***). The smaller anions O^{2-} ($r \sim 1.4\,Å$) and F^- ($r \sim 1.2\,Å$) show the fastest conduction; however, good anionic conductivity is also found for Cl^-($r \sim 1.7\,Å$), Br^-($r \sim 1.8\,Å$), I^-($r \sim 2.1\,Å$), and for S^{2-}($r \sim 1.7\,Å$).

The highest anionic conductivity is found in δ-Bi_2O_3 and doped Bi_2O_3, with an oxygen-deficient fluorite structure, with $\sigma \approx 1\,S\,cm^{-1}$ at 800 °C and $E_a = 0.47\,eV$. The best F^- ion conductors are $RbBiF_4$, $KBiF_4$, and $Pb_{0.75}Bi_{0.25}F_{2.25}$ with $\sigma \approx 1\,S\,cm^{-1}$ at ~300 °C and $E_a \approx 0.39\,eV$.

A number of good reviews have been published in the past several years on oxide ion conductors, and they provide more detail on this subject.[43,46,162–166]

The materials that display oxygen ion conductivity have highly unusual crystal structures with partially occupied oxygen sites and, hence, the number of oxides we need to consider is relatively small. Figure 12 shows selected oxide ion conductors (with the exception of $BaZr_{0.9}Y_{0.1}O_3$ which is a proton conductor as discussed above) that are the focus of major research and development for application as electrolyte membranes in fuel cells.

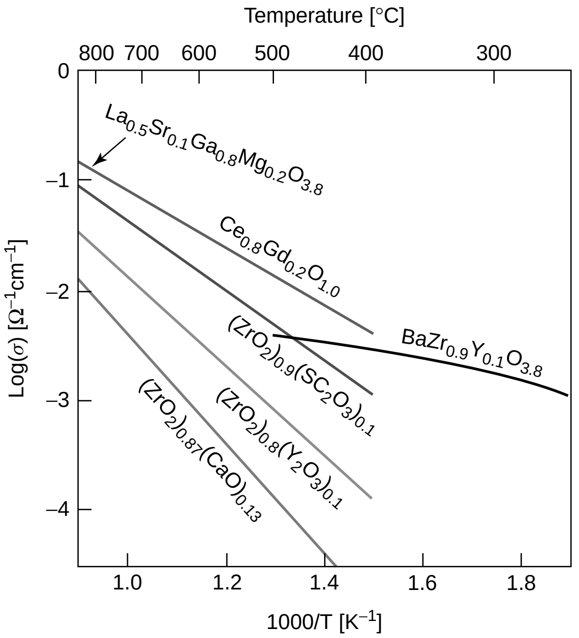

Figure 12 Conductivities of selected oxides as a function of temperature. Doped ceria and zirconia, and lanthanum gallate are oxide ion conductors, while barium zirconate is a proton conductor (From S.M. Haile Materials for fuel cells, *Materials Today* **6**: 24–29 (March 2003)). (Reprinted from Ref. 148. © 2003, with permission from Elsevier)

In order to obtain a material that is a 'pure' oxygen ion conductor (a solid electrolyte), the level of any electronic contribution to the total electrical conductivity must be negligible. This, again, is not easy to achieve. Even very low concentrations of electronic carriers will give rise to a significant electronic component because of the very high mobility of electrons and holes in comparison with the ionic mobilities. Most oxygen ion conductors are, in fact, mixed conductors and only very few are capable of being classed as 'pure' ionic conductors.

3.2.1 *Oxide Ion Conductors in Fluorite-type Solid Solutions*

The fluorite oxides are the classical oxygen ion conducting oxide materials; the study of these materials as electrolytes derives from the early investigations of Walther Nernst ~1900. The fluorite structure illustrated in Figure 13 is best described for the purposes of the present discussion as a primitive cubic array of anions (O^{2-}) with half the cube centers occupied by cations; the latter form a face-centered-cubic (fcc) arrangement of the cation sublattice. The unoccupied cube centers play a central role in the defect physics and ionic conductivity of fluorites, because they

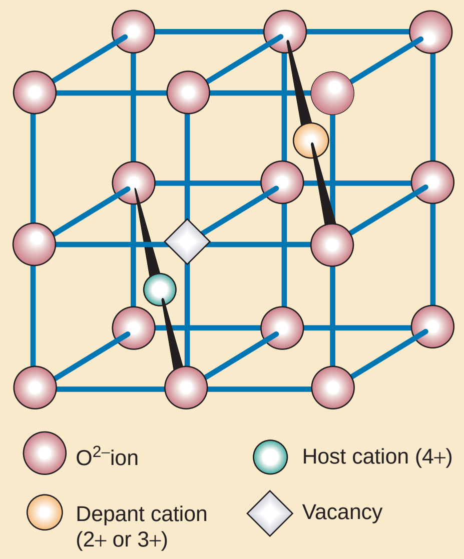

Figure 13 The ideal fluorite, AO_2 oxide structure; oxides with this structure have high-ionic conductivity when the host cations (such as A = Zr^{4+} or Ce^{4+}) are replaced by lower-valent cations such as Y^{3+} for Zr^{4+} in YSZ and Gd^{3+} for Ce^{4+} in $Ce_{1-x}Gd_xO_{2-x/2}$. (Ref. 167. Reproduced by permission of Nature Publishing Group (www.nature.com))

provide effective sites for the interstitial ions. It is indeed the availability of these sites that leads to anion Frankel disorder, responsible for the anion mobility in the fluorite structure. Anion transport in fluorites can be affected by both vacancy and interstitial mechanisms. A combination of experimental studies based on conductivity, NMR, and diffusion measurements and calculations established that E_a for vacancy migration (~0.40 eV) is about half of that for interstitial motion. Thus high mobility of anion vacancies is the most important single factor leading to fast ionic conductivity in anion conductors with the fluorite structure.

Of the oxides, ZrO_2, HfO_2, CeO_2, PrO_2, TbO_2, ThO_2, UO_2, PuO_2, δ-Bi_2O_3 with the fluorite-type structure, CeO_2, and ThO_2 form with the cubic fluorite structure shown in Figure 13. The other oxides form with a distorted fluorite-type lattice. These oxides form solid solutions with alkaline earth and rare earth oxides over a fairly wide range of composition. ZrO_2 is a refractory material with a melting point of 2700 °C; in its pure form, it is monoclinic at room temperature, tetragonal at ~1500 °C, and cubic only at higher temperatures. However, incorporation of as little as 8% (mol) of CaO in $Zr_{1-x}Ca_xO_{2-x}$ $(V^{\bullet\bullet}{}_O)_x$, or ~ same doping by Y $Zr_{1-x}Y_xO_{2-x/2}$ $(V_O^{\bullet\bullet})_{x/2}$ stabilizes the cubic fluorite structure. The ZrO_2–CaO or ZrO_2–Y_2O_3 system is the so-called calcia- or yttria-stabilized zirconia (CSZ or YSZ). Thus, substitution of a divalent cation (Ca^{2+}) for Zr^{4+} generates x amount of vacancies, while a trivalent cation (Y^{3+}) will generate $x/2$ vacancies in these fluorite-type oxides. The major reason for the high ionic conductivity of fluorite-type solid solutions is the high concentration of vacancies ($V_O^{\bullet\bullet}$), via solid solution formation, through which O^{2-} ion can diffuse.

These solid solutions have been prepared by many synthetic routes; for example, by firing appropriate amounts of the component oxide mixtures at high temperature (>1000 °C). A transparent sintered, high-density body of yttria-stabilized zirconia can be obtained by sintering a coprecipitated powder of $Zr(OC_3H_7)_4$ and $Y(OC_3H_7)_3$ at 1000 °C for ~30 min.[168]

The oxygen ion transport properties of CeO_2 have long been known; the ionic conductivity of Gd-doped CeO_2 ($Ce_{1-x}Gd_xO_{2-x/2}$; GDC) is significantly greater than that of the conventional solid oxide fuel cell (SOFC) electrolyte, yttria-stabilized zirconia (YSZ; Figure 12), but CeO_2 had not been considered viable for fuel cell applications because of its high electronic conductivity. However, at temperatures below ~700 °C (and at 10^{-18} atm O_2 partial pressure), the ionic transference of CeO_2 is greater than ~0.9, a value that results in good fuel cell efficiency.[169]

A simple analysis would predict that the conductivity should be a maximum when half the oxygen lattice sites are vacant; however, this is not the case. In Figure 14, the effect of various rare earth dopants on the properties of CeO_2 show that the ionic conductivity is highly dependent on the ionic radius of the dopant. Moreover, the conductivity increases and then decreases across the rare earth dopant series[170] from Yb to La, peaking at Gd (Figure 14). A similar observation has been made for Zr, with the peak occurring at Sc. It is clear that the conductivity drops with relatively modest additions of the rare earth ion, when the vacancy concentration is only a few percent.

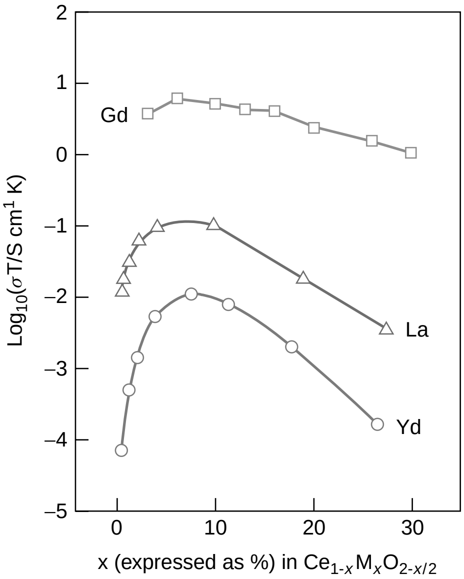

Figure 14 The isothermal conductivity of selected $Ce_{1-x}M_xO_2$ at ~200 °C. (Reprinted from Ref. 171. © 2003, with permission from Elsevier)

This conductivity maximum is common to all the classical ionic conductors studied and has been the subject of debate. However it is now well established, from a combination of atomistic modeling[172,173] and experimental studies,[174] that the maximum is caused by the interaction of the substitutional rare earth ion and the oxygen vacancy. Originally, it was thought that this was a Coulombic effect, as both the substitutional ion and the vacancy act as if they were oppositely charged species within a neutral lattice. However, if this were the case, then all substitutional ions of the same charge would give rise to exactly the same level of conductivity, which is clearly not the case as Figure 14 sOChows. The modeling has clearly shown that the major interaction between these point defects is through the elastic strain introduced into the crystal lattice by a mismatch between the size of the dopant ion and the ion that it replaces. Thus to make good oxygen ion conductors, it appears that in addition to introducing vacancies, leaving the crystal lattice as undisturbed as possible is highly desirable. This explains why some of the best oxygen ion conductors are materials such as zirconia-scandia, $Zr_{1-x}Sc_xO_{2-\delta}$, and ceria-gadolinia $Ce_{1-x}Gd_xO_{2-\delta}$ where the host and dopant ions are very close in size.[174] Zirconia-scandia is often ruled out on cost grounds, but the next best material, YSZ, is a standard material for use in high temperature SOFCs and GDC is a strong candidate for use in lower temperature cells operating at temperatures as low as 550 °C.

3.2.2 *Bi_2O_3-based Oxide Ion Conductors*

The highly conducting high-temperature (>730 °C) cubic phase of δ-Bi_2O_3 forms with the fluorite structure in which one quarter of the anion sites are vacant (i.e. $Bi_4O_6\square_2$). The δ-phase can be stabilized at room temperature by rare-earth ion substitution; for example, for $(Bi_2O_3)_{1-x}(Y_2O_3)_x$ with $x \geq 0.25$ the O^{2-} conductivity is $1.3 \times 10^{-3}\,S\,cm^{-1}$ at 500 °C, vs. that of $5 \times 10^{-4}\,S\,cm^{-1}$ for CSZ at the same temperature. However the Bi_2O_3-based materials are unstable to a reducing atmosphere at even moderate temperatures, and therefore are not considered for SOFC application.[166]

3.2.3 *Perovskite-based Materials*

Pure oxygen conducting materials based on oxygen deficient $LaGaO_3$ were developed by Huang *et al.*[175] and Ishihara;[176] the optimized material with the composition, $La_{0.9}Sr_{0.1}Ga_{0.8}Mg_{0.2}O_{2.85}$ has an oxide-ion conductivity of $\sigma > 10^{-2}\,S\,cm^{-1}$ at 600 °C with a transport number $t \sim 1$ over an oxygen pressure range $10^{-20} < p_{O2} < 0.4$ atm. However it is difficult to prepare single-phase materials and nonconducting $SrLaGa_3O_7$ and $La_4Ga_2O_9$ impurity phases are often detected in the grain boundaries. It has been shown that a single phase stable cubic form $La_{0.8}Sr_{0.2}Ga_{0.83}Mg_{0.17}O_{2.85}$ operating at 800 °C in a

$$SrCo_{0.8}Fe_{0.2}O_{3-\delta}/La_{0.8}Sr_{0.2}Ga_{0.83}Mg_{0.17}O_{2.85}$$
$$/La_{0.4}Ce_{0.6}O_{1.8} + NiO$$

dry H_2 and air fuel cell gave comparable performance with that of an yttria-stabilized zirconia as an electrolyte.[43]

The high oxygen diffusivity, even at room temperature, of the 90 K high-temperature superconductor $YBa_2Cu_3O_{7-\delta}$ $(0 \leq \delta \leq 1)$ is one of its remarkable properties. The large concentration of anion vacancies of the perovskite-related structure (i.e. $A_3B_3O_{9-2}$) is responsible for the high O^{2-} mobility of this phase.

3.2.4 *Aurivillius Phases*

$Bi_2VO_{5.5}$ has an oxygen-deficient Aurivillius intergrowth structure of $(Bi_2O_2)^{2-}$ sheets alternating with perovskite $(A_{n-1}B_nO_{3n+1})^{2-}$ layers.[177,178] On heating, $Bi_2VO_{5.5}$ $(n = 1)$ undergoes two transitions, from a monoclinic α to an orthorhombic β phase at 450 °C, and from the β phase to a tetragonal γ phase at 570 °C. Abraham *et al.*[179] found a high oxide-ion conductivity in the tetragonal γ phase; they subsequently stabilized the tetragonal, vacancy-disordered phase to room temperature by substituting other elements for vanadium. Various doped compositions of γ-$Bi_2V_{0.9}Cu_{0.1}O_{5.5}$ (Ref. 180) γ-$Bi_2V_{0.85}Ti_{0.15}O_{5.5}$ (Ref. 181), so called BIMEVOX materials, where ME represents the substituted metal atom, for example, BICUVOX-10 for $Bi_2V_{0.9}Cu_{0.1}O_{5.5}$, were shown to have excellent oxide ion conductivity at low temperature ($\sigma \sim 10^{-4}\,S\,cm^{-1}$ at 227 °C). In air BICUVOX-10 has transfer number $t \sim 1$ and was shown to separate oxygen from air at 437 °C with 100% efficiency.[182] However at ~500 °C and an oxygen partial pressure, $p_{O2} < 10^{-2}$ atm these materials are reduced, and in the reducing atmosphere at the anode of a SOFC, irreversible reduction to other phases occurs.

3.2.5 *Apatite-based Oxide Ion Conductors*

$La_{10-x}Ge_6O_{26+y}$ and $La_{10-x}Al_6O_{26+y}$ with the apatite structure have been synthesized by several groups.[183–190] The highest oxide-ion conductivity ($\sigma = 0.14\,S\,cm^{-1}$ at 950 °C) was achieved in $La_9SrGe_6O_{26+y}$.[189]

3.2.6 *LAMOX Phases*

Lacorre and his group[191–193] developed the LAMOX family of oxide ion conductors. Theses materials are based on the $La_2Mo_2O_9$ parent compound and are competitive with existing electrolytes at temperatures above the α-to-β first-order structural phase transition, at ~580 °C. Associated with this transition is a dramatic improvement in the ionic conductivity to $\sim 10^{-2}\,S\,cm^{-1}$ at ~720 °C. The structure of

$La_2Mo_2O_9$ is made up of isolated $(MoO_4)^{2-}$ units in a 3D matrix of $(La_2O)^{4+}$. It was proposed that $La_2Mo_2O_9$ could be viewed as β-$SnWO_4$ ($Sn_2W_2O_8$) substituted by La for Sn and for Mo by W. In this case, the $5s^2$ lone pair electrons of Sn^{2+} in β-$SnWO_4$ are substituted by one oxygen ion and one oxygen vacancy, and it is the disordering of the lattice oxygens on the two sites in the β-phase that results in the high oxygen mobility. Substitution for La and Mo stabilizes the high-temperature phase of $La_2Mo_2O_9$. Lacorre and his coworkers suggests a similar 'lone pair substitution' principle as a novel approach for searching for new oxygen conductors. The Mo (or other transition metal) content of this material leaves it susceptible to reduction and, therefore, significant development of this material is needed before it is commercially useful, either as an electrolyte in fuel cells or as an oxygen separator. There have been limited studies with doping strategies to overcome the reducibility of the material and to stabilize the high temperature phase.[194–196]

3.2.7 *Fluoride Ion Conductivity*

Calcium fluoride, CaF_2, is fluorite itself. Hence, similar to CSZ, F^- can conduct through vacancies ($V_F^{\bullet}$) generated by the partial replacement of Ca^{2+} with a monovalent cation such as Na^+. Thus CaF_2:1%NaF has a conductivity of 10^{-3} S cm^{-1} at 400 °C, which is several orders of magnitude larger than that of CSZ at the same temperature.

β-PbF_2 with the same fluorite structure was discovered by Faraday to have substantial conductivity (10^{-6} S cm^{-1}), even at room temperature, and the conductivity is as large as 1 S cm^{-1} at 400 °C without alleo-valent dopants. Neutron diffraction studies show the presence of significant concentrations of interstitial F^- in β-PbF_2 and the high conductivity observed at low temperature is attributed to the hopping of these Frankel defects. At about 300 °C, there is a diffuse transition from a low conducting to a high conducting state with the conductivity being almost as large as in fused PbF_2 (mp 818 °C). It has been confirmed by high-temperature diffraction methods, which show evidence of anharmonic large temperature factors for F^- in β-PbF_2, that in the high-temperature phase the high conductivity is associated with the disordering of the anion sublattice, similar to that of the fusion of the cation sublattice of α-AgI.

Fluorite-type fluorides (CaF_2, SrF_2, and BaF_2) also form a wide range of solid solutions with higher valent cations like LaF_3 that are also very good F^- ionic conductors. For example, in $Ca_{1-x}La_xF_{2+x}$ the excess F^- ions occupy the interstitial sites of the fluorite structure. At high concentration of the rare earth ion (up to 40 mol%), the conductivity is low owing to the formation of defect clusters between the dopant cations and their charge-compensating F^- interstitials. A great deal of attention has been paid to the nature of the structure of these clusters. The problem has been investigated by computer modeling and magnetic resonance techniques. It is now well established that a wide range of cluster structures are possible from the simple dopant–interstitial pairs to the complex, celebrated, so-called '2:2:2' cluster shown in Figure 15.

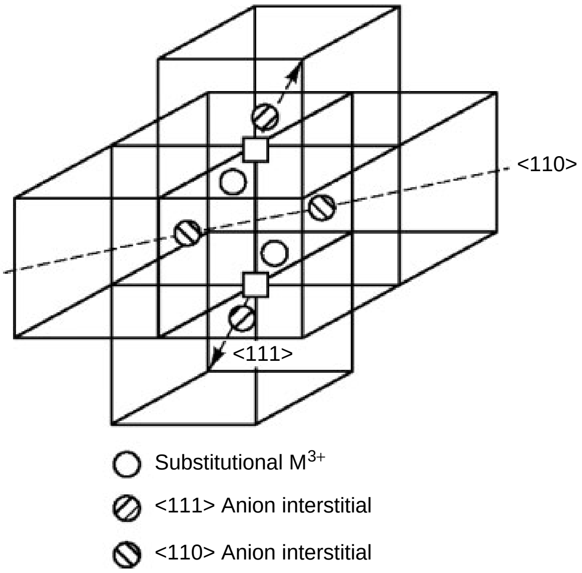
<110>
<111>
○ Substitutional M^{3+}
⊘ <111> Anion interstitial
⊘ <110> Anion interstitial

Figure 15 The '2:2:2' cluster. (Ref. 163. Reproduced by permission of Springer)

3.3 Mixed Oxide and Electron Conductors

3.3.1 *Perovskite-based Materials*

Significant developments have been made in the field of perovskite and perovskite-related mixed ionic-electronic conductors for use as cathodes in SOFCs.[197] Both YSZ- as high-temperature (~800–1000 °C) and GDC as intermediate-temperature (~650 °C) electrolytes have been considered. The $La_{1-x}Sr_xCoO_{3-\delta}$ lanthanum strontium cobalt (LSC) perovskite, is among the highest oxide-ion conductors, with only δ-Bi_2O_3 with a higher conductivity over the temperature range of 600–1000 °C.[198] In contrast to the high ionic conductivity of LSC, the electronic conductivity was found to be relatively low, whereas the Mn analog, $La_{1-x}Sr_xMnO_{3-\delta}$ lanthanum strontium manganese (LSM) was found to have electronic conductivity of the order of 300 S cm^{-1}, but poor oxide ion conductivity.[199,200] However, the thermal expansion of the LSC/LSM materials are too high ($\geq$ 20 ppm K^{-1}) and not compatible with those of the electrolytes. Co-doping on the B-site with Fe in $La_{1-x}Sr_xCo_{1-y}Fe_yO_{3-\delta}$ was found to reduce the thermal expansion coefficient of the cathode material and match with that of the electrolytes.[201–203] Among the attractive alternatives to the perovskites mentioned above for application as fuel cell cathodes are the Gd- and Sm-based perovskites, and the compositions $Sm_{1-x}Sr_xCoO_{3-\delta}$ (SSC) have been demonstrated to operate at temperatures as low as 500 °C.

Other developments of perovskite-type oxides as cathode materials for fuel cells have been discussed in detail in the reviews by Skinner[204] and Brandon.[205]

Despite the many problems that still exist with these perovskite cathodes, several commercial developers including Siemens–Westinghouse, Rolls Royce, and Sulzer–Hexis have adopted the LSM material for use in current devices and they are likely to be incorporated in first generation commercial SOFCs.

3.3.2 *K_2NiF_4-type Oxides*

Perovskite-related oxides of the K_2NiF_4 ($A_2BO_{4+\delta}$; B-transition metal ion) structure (Figure 16) have been investigated by several groups as alternative mixed conductors for SOFC.

In this structure there are perovskite layers of ABO_3 separated by AO rock salt layers. It is this layered structure that allows great flexibility in the oxygen stoichiometry of these materials. It is possible to incorporate excess oxygen ($\delta > 0$) in the unusual form of *interstitial* oxygens, which provide an alternative to the vacancy-based conduction mechanism present in the perovskite and fluorite oxides, where the dopant-vacancy interactions can limit the observed conductivity. The mobility of the oxide ions in these materials occurs mainly through an interstitialcy mechanism in the *ab*-plane, although evidence of low E_a for the conduction in the *c*-direction via a Frenkel mechanism has also been reported.[206]

Preliminary work on these materials indicates that the permeation properties of these oxides are competitive with those of the perovskite discussed above; for example, both $La_2Ni_{1-x}Fe_xO_{4+\delta}$ and $La_2Cu_{1-x}CoO_{4+\delta}$ exhibit a maximum flux density of 10^{-7} mol s^{-1} cm^{-2} at 850 °C.[205–210]

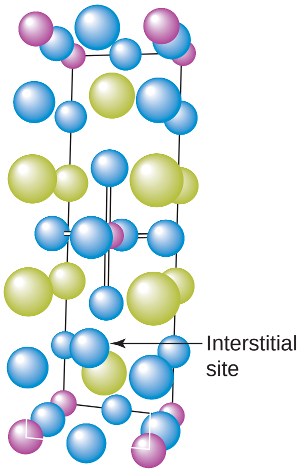

Figure 16 Representation of the $A_2BO_{4+\delta}$ structure, where the red spheres represent the B-cations, the blue spheres represent oxygen ions, and the yellow spheres represent A-cations. An interstitial oxygen ion is also shown

4 AMORPHOUS GLASS ELECTROLYTES

4.1 Glasses (*see Noncrystalline Solids*)

Although initially crystalline materials were more widely investigated, more recently great efforts have been directed towards the study of glassy FIC, because of the unique properties specific to the glassy state. The advantages over crystalline solid electrolytes include: isotropic conduction; ease of fabrication into films or complex shapes; wide compositional flexibility, allowing control and optimization of electrolyte properties through composition; absence of grain boundaries; and high ionic conductivity coupled with low electronic conductivity which often results in good redox stability.

Hundreds of FIC glasses have been prepared by melt quench techniques and in the last three decades by the sol–gel method (*see* ***Sol–Gel Synthesis of Solids***). Several excellent reviews have been published in the past[26–28,55,56,58] and more recently.[211–214]

In Table 4 are some representative FIC oxide and sulfide glasses. Most of these glasses have a simple composition consisting of a network-forming oxide (sulfide), for example, SiO_2, B_2O_3, P_2O_5, (GeS_2), and a network-modifying oxide (sulfide), for example, Li_2O, Na_2O, Ag_2O, (Na_2S). A 2-D

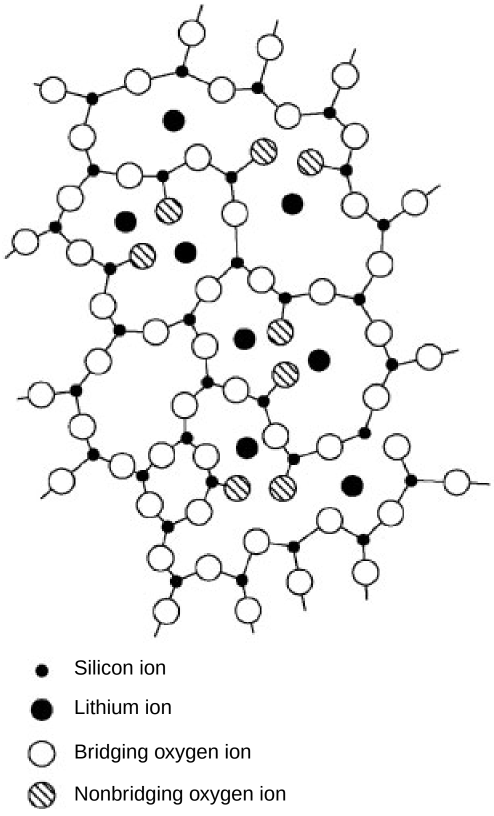

Figure 17 Structure of lithium silicate glass

Table 4 Ionic conductivity of selected glasses[28]

Composition (at maximum conductivity)	Ionic charge carrier	T_g (°C)	Log σ_o	E_a (eV)	σ_{RT} (S cm^{-1})
$60AgI{\cdot}30Ag_2O{\cdot}10B_2O_3$	Ag^+	–	–	–	8.5×10^{-3}
$40AgCl{\cdot}30Ag_2O{\cdot}30B_2O_3$	Ag^+	–	–	–	6.3×10^{-4}
$45GeS_2{\cdot}55AgS$	Ag^+	–	2.64	0.32	1.4×10^{-3}
$62Li_2O{\cdot}38SiO_2$	Li^+	–	–	0.48	$\sim 10^{-5}$
$30LiCl{\cdot}41Li_2O{\cdot}29P_2O_5$	Li^+	215	–	0.53	4.8×10^{-7}
$30LiBr{\cdot}41Li_2O{\cdot}29P_2O_5$	Li^+	–	–	0.52	$\sim 10^{-6}$
$30LiI{\cdot}41Li_2O{\cdot}29P_2O_5$	Li^+	200	–	0.46	$\sim 3 \times 10^{-6}$
$Li_2B_4O_7$					
crystal	Li^+	917 (T_m)	–	1.3	9×10^{-8} (573 K)
glass	Li^+	500	–	0.74	1×10^{-4} (573 K)
$61B_2O_3{\cdot}34.1Li_2O{\cdot}4.9LiCl$	Li^+	–	–	0.60	1×10^{-3} (573 K)
$61B_2O_3{\cdot}34.1Li_2O{\cdot}4.9LiI$	Li^+	–	–	0.52	3.2×10^{-3} (573 K)
$40Li_2O{\cdot}60B_2O_3$	Li	–	–	0.99	5.5×10^{-8} (455 K)
$37Li_2S{\cdot}18P_2S_5{\cdot}45LiI$	Li^+	120	–	0.31	$\sim 10^{-3}$
$50Li_2S{\cdot}50GeS_2$	Li^+	310	4.21	0.51	4×10^{-5}
$Na_2O{\cdot}SiO_2$	Na^+	–	–	0.63	2.8×10^{-5} (373 K)
$50Na_2O{\cdot}18.75Al_2O_3{\cdot}31.25B_2O_3$	Na^+	350	–	0.58	5.0×10^{-4} (573 K)
$40Na_2O{\cdot}50SiO_2{\cdot}10B_2O_3$	Na^+	415	–	0.54	2×10^{-3} (573 K)
$Na_2O{\cdot}GeO_2$	Na^+	–	–	0.69	5.0×10^{-6} (373 K)
$60Na_2S{\cdot}40GeS_2$	Na^+	–	2.14	0.44	1.5×10^{-4} (373 K)

representation of a silicate glass is shown in Figure 17. Ionic conductivity is the result of the motion of cations (i.e. hopping of Li^+ from one nonbridging – SiO^-Li^+ site to another) through the random network of these disordered materials where the mobile carriers are produced from the dissociation of the 'electrolyte' M_2O in the 'solvent' network-forming oxide, SiO_2 for example. The general principles required for good ionic conductivity outlined in Section 2 apply to glasses as well. Table 4 indicates that the ionic conductivities of Ag glasses are the highest, approaching $\sim 10^{-2}$ S cm^{-1} at room temperature. Sulfide glasses often have a conductivity several orders of magnitude higher than their oxide analogs (e.g. $\sigma(Na_2O\text{–}SiO_2)_{25\,°C} \approx 10^{-7}$ vs. $\sigma(Na_2S\text{–}SiS_2)_{25\,°C} \approx 10^{-5}$ S cm^{-1}), which is attributed to the higher polarizability of the sulfide network (i.e. the greater ease of deforming the lattice, or the electron cloud, when the cation changes site).

Glasses that have higher ionic conductivity than crystalline materials of the same composition are fairly common. A case in point is the room-temperature conductivity of glassy $Li_2B_4O_7$, which is many orders of magnitude higher than that of the crystalline material of the same composition (Table 4).

In the past thirty years, much research has been done on the characteristics that lead to high conductivity in glasses. Addition of alkali metal salts (AgI, LiI, LiCl) with anions of high polarizability often increases the cation conductivity of the glass. For example, with glasses of the composition $LiX\text{–}Li_2O\text{–}B_2O_3$ the conductivity increases as X is changed from the least polarizable halogen, fluorine, to the most polarizable one, iodine (Table 4). Many researchers have investigated glasses with various proportions of two different alkali metals. The rather unexpected observation that the conductivity passes through a minimum as one alkali metal is substituted for another is called the 'mixed-alkali effect' and it is most pronounced with alkali metal ions having very different radii, such as Li^+ and Rb^+. Several models have been proposed to explain the mixed-alkali effect, but none are entirely satisfactory.

Only a small number of anionic conductive glasses are known. The most conductive are ZrF_4-based glasses with $\sigma \approx 10^{-6}$ S cm^{-1} at 200 °C.

Theoretical models for ion transport in glasses must take into account the disorder inherent in the glass structure. The determination of equilibrium sites for cations and ion-conduction paths in glasses is complicated by the random structures of the framework and the resulting lack of precise structural information.

Recent models for ion transport in glasses include the 'weak electrolyte', the 'random site', and the Anderson and Stuart models.[26–28,44,45,48,215,216]

4.2 Solid Polymeric Electrolytes (SPE)

Solid polymer electrolytes (SPE) represent the newest and one of the most important (i.e. as far as potential applications are concerned) class of FIC solids. The area of polymer/salt complexes became extremely active following the work of Wright,[165] who first reported that PEO is an excellent polymer host for a number of salts and that the resulting polymer/salt complexes have significant electrical conductivities near room temperature. Armand[29,54] extended the investigation of the electrical properties of the polymer/salt electrolytes and recognized that these solvent-free polymer/salt complexes might be excellent electrolytes for high-energy-density batteries and other electrochemical devices.

The subject is now too vast to be covered in any detail here; extensive reviews[9,29,30,52–58] in the past and a complete book[31] on the subject are recommended for further information.

These materials consist of alkali-metal salts dissolved in a solid polar polymer, which can be denoted by equation (9):

$$\mathrm{p(ru)} + \mathrm{MX(s)} \longrightarrow \mathrm{p[(ru)}_n\cdot\mathrm{MX]} \qquad (9)$$

where p stands for poly, ru is the repeat unit of the polymer structure, and MX is the salt. Most of the materials studied involve univalent salts, with $M = H^+$, Li^+, Na^+, K^+, Ag^+, and $X = CNS^-$, $CF_3SO_3{}^-$, I^-. In the earlier materials, the polymer repeat units always contained backbone oxygens or nitrogens, which acted as Lewis-base sites to complex the alkali. There are several criteria now established for the formation of stable polymer/salt complexes. (1) The polymer host must have low cohesive energy density, high flexibility, and a high density of Lewis-base sites. (2) The salt involved must have a relatively low lattice energy, that is, the lattice energy of the MX salt must be overbalanced by the solvation energy of the p(ru) host, so that the formation reaction will proceed to the right.

SPE can be prepared by dissolving the polymer and an alkali metal salt in a mutual solvent and then evaporating the solution on a teflon fluorocarbon resin plate in a dry atmosphere. SPE films are obtained by casting the solution and heating at relatively low temperatures (~150 °C) under vacuum. The existence of a polymer/salt complex, however, is no guarantee that the material will be a good ionic conductor.

The ionic conductivities of selected polymer electrolytes given in Table 1 show that these materials are poorly conducting compared to the best inorganic/ceramic crystalline or glassy materials. Moreover, the nature of the transport mechanism in the SPE is quite different from that of the ceramic materials. The SPE can transport charge only above their glass transition temperature where, on a microscopic scale, the material is molten. Thus ion transport in SPE is more similar to liquid electrolytes than ceramic conductors. Indeed, more detailed mechanistic studies indicated clearly that ionic motion in these materials does not occur by hopping in a locally crystalline region, but rather by a liquidlike mechanism in which the local motion of the polymer assists the migration of the ion through the solid. This liquidlike migration of a lithium ion assisted by the large-amplitude motion of the polymer, shown schematically in Figure 18, is drastically reduced if the polymer chains are crystallized. To prevent crystallization, cross-linked polymers based on poly(ethylene oxide), $(\text{–}CH_2CH_2O\text{–})_n$ (PEO), poly(propylene oxide) $(\text{–}CHMeCH_2O\text{–})_n$ (PPO), and others have been synthesized. Such cross-linked polymer/salt complexes, in addition to exhibiting higher ionic conductivity, have the advantage of better mechanical and thermal stability, which is important for applications.

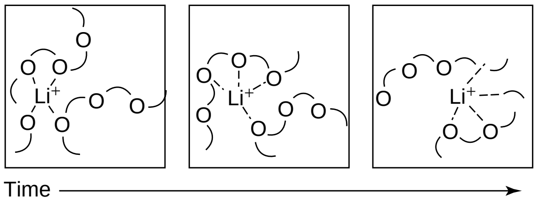

Figure 18 Scheme of ion transport in a polymer electrolyte: Li^+ motion is assisted by the local motion of the polymer chains. (Reprinted from Ref. 1. Published 1985, American Chemical Society)

Typical polymer hosts have Lewis-base sites and include the simple linear polymers: PEO, PPO, and poly(ethyleneimine), and a number of comb polymers, in which oligoether side chains are built on a flexible backbone. A tremendous variety of polymer electrolytes can be prepared. Not only can the anion and cation of the salt be varied, but a wide range of polar polymers that might be suitable hosts for salts can be envisioned.

This provides many opportunities for controlling electrical, mechanical, and chemical properties. For example, the recognition that polymer flexibility promotes high conductivity has led to the synthesis of a new electrolyte based on a highly flexible polyphosphazene (*see* ***Polyphosphazenes***) backbone to which short-chain polyether groups are attached (see **1**). This polymer forms complexes with a wide variety of salts, and the resulting complexes have room-temperature conductivities that are about 1000 times greater than those of their poly(ethylene oxide) analogs.

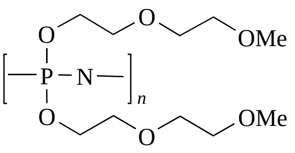

(**1**)

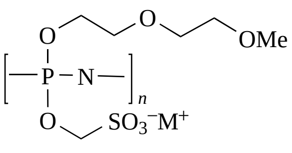

(**2**)

New rubbery ‘polymer-in-salt’ solid electrolytes in which lithium salts are mixed with PEO or PPO have been reported initially with conductivities as high as 10^{-2} S cm^{1} at room temperature.[217] More recently Xu *et al.*[218] report on a plasticized and crosslinked poly(lithium oligo-etherato mono-oxalato borate) and (lithium polyMOB). In heavily plasticized forms of both polyMOB, and a LiBH4-crosslinked polyMOB, the ionic conductivity reached 10^{-3} S cm^{-1} at room temperature, while single ion conductivity is automatically retained. The electrochemical stability window of the electrolytes is up to 5 V, for stainless steel (SS) electrodes. The plasticized forms are fluid, not gel like, owing to the low molecular weight of the polyanions. Free-standing gel electrolytes with high single ionic conductivity of 10^{-4} S cm^{-1} at ambient temperature can be obtained by incorporation of high molecular weight poly(Me methacrylate) (PMMA) into the solution. Electrochemical cells with these electrolytes will not experience concentration polarization problems. Also from Austin's group, hybrid polymers combining P_2S_5 moieties with oligoether spacers were reported to be highly viscous, but not rubbery.[219] A high ambient temperature conductivity of $\sim 10^{-4}\,\mathrm{S\,cm^{-1}}$ was measured with LiTFSI dissolved in the P_2S_5-PEO matrix, i.e, in salt-in-polymer materials. The decoupling of Li^+ motions from polymer segmental motions was demonstrated, suggesting that, in certain cases, the transport number for Li^+ ions in the phosphorus sulfide-PEO matrix will be much higher than in a typical PEO-based salt-in-polymer system.[219]

The polymer/salt electrolytes discussed above generally exhibit both cation and anion mobilities; this makes the study of single-ion transport difficult and can lead to polarization in static electrochemical applications. Another class of polymer electrolytes consists of high-mobility charged backbone species, or polyelectrolytes (**2**).[30] Both cationic and anionic transport is possible, depending on whether the backbone charge is positive or negative. These polyelectrolytes exhibit transference numbers of unity for a small counter ion, and are therefore promising for electrolyte application.

The most successful 'solid' protonic membrane for fuel cell use is 'NAFION®' membrane (saturated with aqueous acid solution) used in kW-size fuel cells in the US Gemini space program up to 150 °C. NAFION is a perfluorinated polymer with sulfonic acid groups.

Unlike hard inorganic electrolytes, polymer electrolytes can deform under stress. This makes them extremely promising materials for use as electrolytes in solid state batteries. The chief difficulty in making a successful solid state battery arises from dimensional changes in the electrodes during charging and discharging. In a typical high-energy-density battery, lithium might be used as the negative electrode (see Section 5). As the battery discharges, oxidation of the electrode gradually strips lithium metal away from the metal/electrolyte interface. Unless the interface can deform so that lithium/electrolyte contact is maintained, the battery will cease to function. Similarly, the insertion/deinsertion of Li^+ into the cathode material, swells/shrinks the lattice volume of the cathode material, which is deleterious for contact at that interface. Many all-solid-state batteries using hard, crystalline solid electrolytes have been proposed but have been unsuccessful because interfacial contact is not maintained as the battery is operated. The polymer electrolytes can flow and thus may be able to better maintain interfacial contact with the electrodes.

Polymer electrolytes also are attractive because they can be cast as thin films. Thin films minimize the resistance of the electrolyte and reduce its volume and weight. Although an electrolyte is essential for a battery, it adds weight and occupies space, it therefore reduces the energy stored per unit weight and volume that might otherwise be devoted to the active electrodes.

For battery application, SPE can be classified into three types:[220] dry SPE, gelled SPE[221,222] and porous SPE.[223] Figure 19 shows the concept of gelled SPE and Figure 20 shows the improvement of ionic conductivity of these three categories of SPEs.

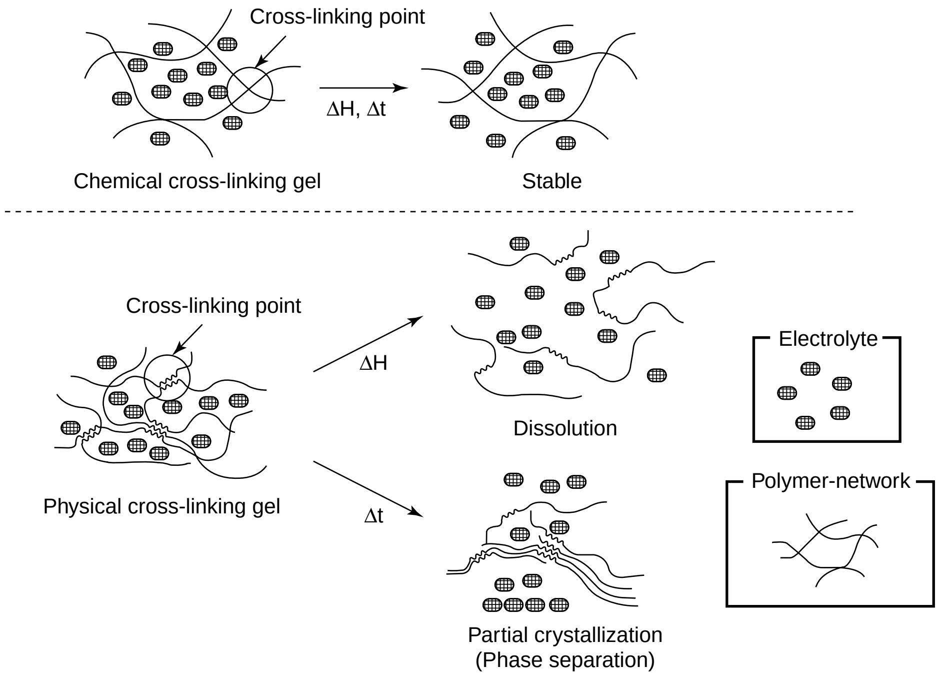

Figure 19 Gelled SPE model-top chemically[221] and bottom physically[222] cross-linked polymer. (Reprinted from Ref. 220. © 2000, with permission from Elsevier)

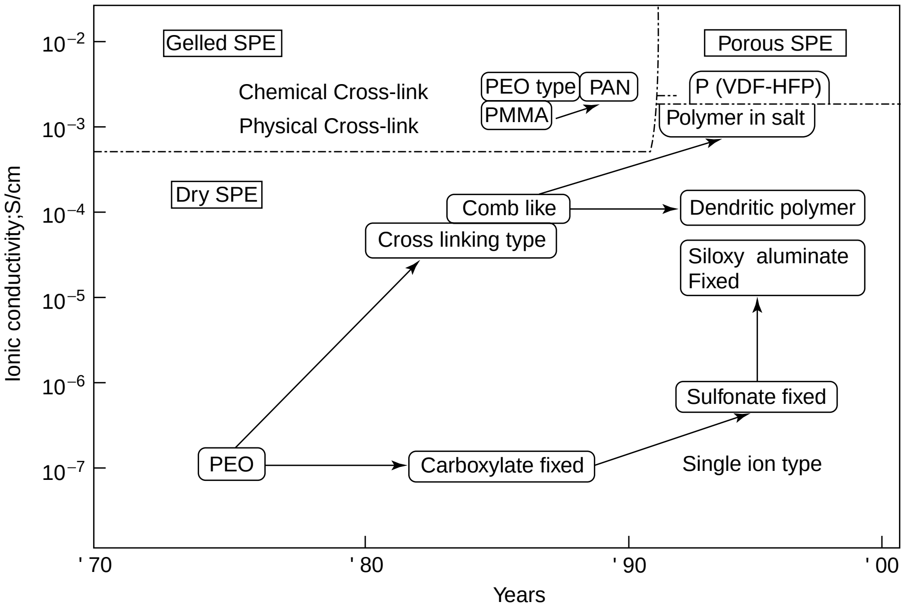

Figure 20 History of ionic conductivity improvement of SPE. (Reprinted from Ref. 220. © 2000, with permission from Elsevier)

The improvement of the performance of the dry SPE has been carried out along two approaches: (I) enhancement of the mobility of the polymer chains, and (II) an increase in the carrier density. With the combination of the above (I) and (II), the ionic conductivity at room temperature is now about $1 \times 10^{-4}\,\mathrm{S\,cm^{-1}}$, while with the polymer-in-salt based on the above (II), it is now about $1 \times 10^{-3}\,\mathrm{S\,cm^{-1}}$, and with the single ion conductor approach, it is about $1 \times 10^{-6}\,\mathrm{S\,cm^{-1}}$. In considering the use of a battery at a lower temperature, $1 \times 10^{-3}\,\mathrm{S\,cm^{-1}}$ is probably needed for SPE, except for the single-ion conductor type, which probably requires $1 \times 10^{-4}\,\mathrm{S\,cm^{-1}}$. Although the polymer-in-salt now shows $1 \times 10^{-3}\,\mathrm{S\,cm^{-1}}$ at room temperature, it tends to crystallize at lower temperature, which prevents its practical use. Therefore, the future needs are as follows: 1. A high-mobility polymer by increasing the mobility of the interpenetrated polymer in SPE and/or increasing the mobility of the polymers in the dendritic polymer system; 2. a single ion conductor with increasing number of dissociating lithium ions; 3. the polymer-in-salt polymer with molten salt; 4. preventing crystallization below $-10\,^{\circ}\mathrm{C}$, and 5. molten salt with a wide stability window.

Recently, studies on the porous SPE with similar performance as liquid electrolyte are active. Considering leak-proof and safety, however, SPE should preferentially have a homogeneous macro-structure, which physically prevents separation of the matrix polymer and the electrolyte. For leak-proof in particular, retention of sufficient osmosis pressure is important. Thus the design of a gelled SPE with good ionic conductivity, should have a structure with a large domain (a matrix with a long molecular chain length and coarse cross-linking) composed of polymers with less interaction with lithium ions, or a micro-phase separation type, is favorable. In addition, a gelled structure composed of the matrix polymer, which has affinity for anions and solvents, but repels lithium ions might bring about an ionic conductivity comparable, or superior to that of liquid electrolyte. Figure 21 summarizes recent improvements in the conductivity of various polymer electrolytes.

5 APPLICATIONS

An electrolyte is an essential component of an electrochemical cell, be it a battery or fuel cell for producing electrical energy or a sensor for determining the concentration of a specific ion or molecule. The primary electrochemistry occurs at the interface between the electrolyte and the electrodes. At this interface, a metal atom on the surface of an electrode might be oxidized to a metal ion, which then enters the electrolyte. At the other electrode, metal ions from the electrolyte might be incorporated into a solid such as a layered transition metal oxide ($\mathrm{LiCoO_2}$) or chalcogenide ($\mathrm{TiS_2}$). Thus the function of the electrolyte is to provide a path for the migration of ions from one electrode to the other. The flow of charge by ions through the electrolyte is balanced by the electrons flowing through an external circuit.

If the cell is a battery, it is desirable to channel all of the electron flow through the external circuit, where it can perform a useful function. The electrolyte must not conduct electrons. If electronic current were to flow through the electrolyte, it would be unavailable to carry out useful functions in the external circuit. Electronic conductivity in the electrolyte also would cause a battery to discharge as it stands unused.

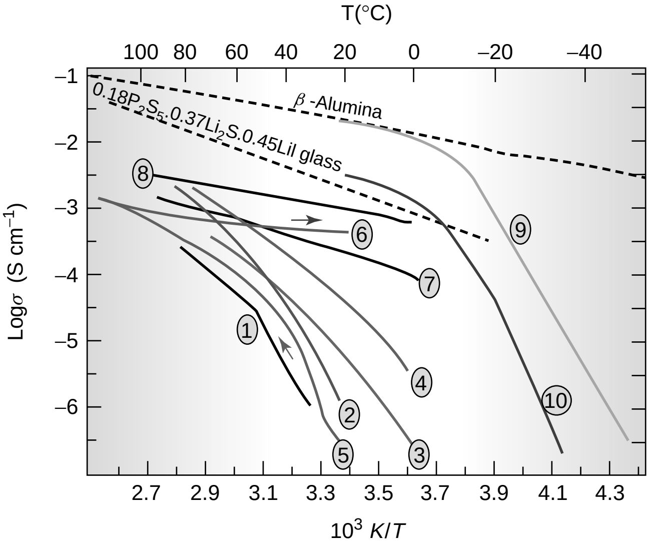

Figure 21 Arrhenius plot of conductivity for various solid electrolytes. 1, First generation PEO-$LiCF_3SO_3$; 2, new solutes with high-dissociation PEO-$Li[(CF_3SO_2)_2N]$; 3, low-Tg combination polymer; 4, plasticized polymer electrolyte PEO-$Li[(CF_3SO_2)_2N]$ & 25% w/w PEG-dimethylether (molecular weight, 250); liquid crystalline polymer electrolytes; 5, heating curves; 6, cooling curve64; 7, gel-type polymer (X-linked PEO-dimethacrylate-$Li[(CF_3SO_2)_2N]$-PC 70%); 8, liquid electrolyte PC/DME $LiCF_3SO_3$; 9, liquid electrolyte EC/DMC-LiPF6 at low temperature61; 10, gel electrolyte P(VDF-HFP)/EC/DMC-$LiPF_6$. (Ref. 47. Reproduced by permission of Nature Publishing Group (www.nature.com))

For these reasons, a minimum requirement of a battery electrolyte is that it must be a good ionic conductor and a poor electronic conductor.

Because all electrochemical devices such as batteries, fuel cells, sensors, and electrochromics require an electrolyte, the potential applications for ionic conductors are enormous. In addition to these more conventional applications, solid electrolyte materials are investigated for use as electrochemical memory devices, oxygen pumps, gas phase electrolyzers, and thermoelectric generators.[57]

Among the various electrolytes, yttrium stabilized zirconia (YSZ) has been developed, for use in high-temperature fuel cells and oxygen sensors; similarly, various $\beta(\beta'')$-alumina materials are in development for sodium–sulfur batteries.

5.1 Sodium Sulfur Battery

Since the principle of the sodium–sulfur battery was established in 1967, it has been under development throughout the world. The schematic set-up of a sodium–sulfur battery, operated at 300–350 °C, is shown in Figure 22. Molten sodium, the anode active material, is placed in a sintered β-alumina solid electrolyte tube, and molten sulfur impregnated in the porous graphite cathode, outside. The ceramic electrolyte serves as ionic conductor and heat-resistive separator of the very active electrode materials at the same time. The anode and cathode reactions of the cell are expressed in equations (10) and (11).

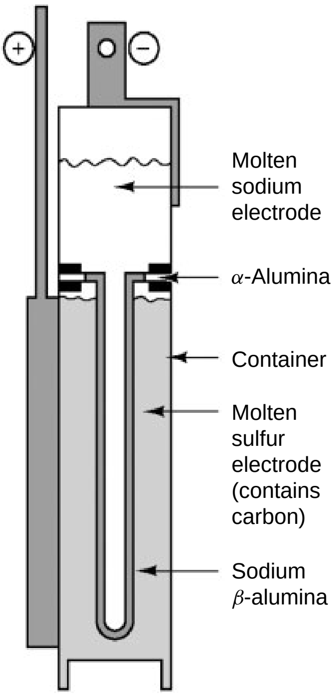

Figure 22 The sodium/β-alumina/sulfur battery. (Reprinted from Ref. 1. Published 1985, American Chemical Society)

$$\text{anode}: \quad \mathrm{Na} \longrightarrow \mathrm{Na}^+ + \mathrm{e}^- \tag{10}$$

$$\text{cathode}: \quad \mathrm{Na}^+ + \frac{x}{2}\mathrm{S} + \mathrm{e}^- \longrightarrow \frac{1}{2}\mathrm{Na_2S}_x \tag{11}$$

During discharge, Na is oxidized at the molten Na/β-alumina interface. It is then transported through the solid electrolyte as Na^+ ion and is combined with reduced sulfur in the outer chamber to form sodium polysulfide, Na_2S_x. These processes are reversed during charging. The cell generates 2.1 V and is rechargeable for $x \leq 3$. Sodium–sulfur batteries feature high energy densities (storageable energy per battery weight or volume); the theoretical density by weight is $790\,\mathrm{W\,h^{-1}\,kg^{-1}}$ for $x = 3$, which is 4.7 times greater than that of the lead–acid battery. The power density (peak or average wattage per cell weight or volume) is also high, $\sim 50\,\mathrm{W\,kg^{-1}}$. These are very favorable properties for the development of sodium–sulfur batteries as the power source for electrical vehicles and power storage systems. However, presently, economical techniques for the production of crack-free β-alumina, and a container for the highly corrosive electrode materials required for the safe operation of such batteries, have not been established.

5.2 Oxygen Sensors

The principle of the emf-type oxygen sensor using a CSZ oxide conductor in the form of an open ended tube is illustrated by the oxygen concentration cell in Figure 23. Inside the tube is a reference gas such as air. The tube is coated with porous Pt electrodes to allow the absorption and liberation of oxygen gas. If the partial pressure of oxygen gas that is to be measured, P'_{O2}, is less than the reference pressure, P''_{O2}, the electrode reactions shown in Figure 23(b) take place and O^{2-} ions migrate through the solid electrolyte from right to left. The Nernst equations for the reactions at each electrode may be combined into a single equation (equation 12) that relates the oxygen partial pressures in the two compartments of the cell to the cell voltage.

$$E = \left(\frac{RT}{4F}\right) \ln \left(\frac{P''_{O_2}}{P'_{O_2}}\right) \tag{12}$$

Therefore, P'_{O2} can be determined by measuring E and T. Partial pressures of oxygen as low as 10^{-16} atm can be determined with the CSZ sensor.

Such stabilized zirconia sensor devices are widely used for combustion control in automobiles. All new cars sold in the US contain one of these devices in the exhaust system to sense the partial pressure of oxygen. This sensor is a key component in the carburetor control of pollution. Other applications of such devices are as oxygen sensors in steelmaking.

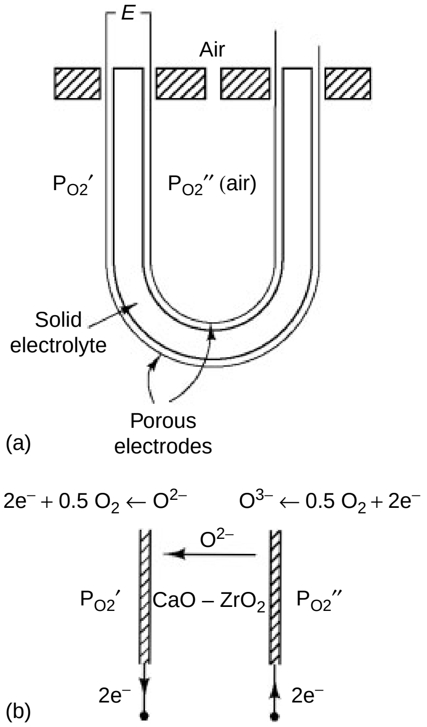

Figure 23 The oxygen concentration cell with calcium-stabilized zirconia solid electrolyte. (Ref. 42. Reproduced by permission of John Wiley & Sons, Inc.)

5.3 Fuel Cells

Fuel cells convert chemical energy into electrical energy, and are already used as power sources in spacecraft. Fuel cells are efficient (more than conventional energy sources, for example, the combustion engine, whose efficiency is thermodynamically limited) and environmentally friendly. Currently, there are large government supported efforts in the US (SECA) and in Europe to develop fuel cells for applications (large power sources, automobiles, energy for houses etc.) by the year 2010. There are already experimental electrical cars powered by fuel cells. The various fuel cell types, including solid oxide (SOFC), molten carbonate (MCFC), phosphoric-acid (PAFC), polymeric-electrolyte-membrane (PEMFC), and alkaline (AFC) fuel cells currently in development are illustrated in Figure 24. Here only SOFC will be discussed in any detail.

Oxide- or proton-conducting materials (discussed in Sections 3 and 4) can be used as the solid electrolyte or separator in high-temperature fuel cells in a configuration similar to a concentration cell. In SOFC the two compartments contain air or O_2 and a fuel gas, H_2 and/or CO, respectively. The H_2/CO fuel on the anode side could come directly from a hydrogen storage device, or from internal reformation of natural gas (CH_4) as shown in Figure 25. The solid electrolyte is coated with a porous mixed (electron and ion) conductor as the electrodes and the cell reaction produces water as shown in Figure 25. The best component materials currently under development for SOFC are shown in Figure 26. With the YSZ electrolyte, the cathode material is $La_{1-x}Sr_xMnO_3$, the anode is Ni/YSZ cermet, and the interconnect between the individual fuel cells is a conducting oxide, $La_{1-x}Ca_xCrO_3$.

Although SOFCs are in advanced development as promising sources of energy, there are still many problems to be worked out in the materials research and development stage as discussed earlier. Moreover, the operating temperature of the SOFC with YSZ is high, because of the low ionic conductivity of this electrolyte. Lowering the operating temperature of the SOFC is desirable for several reasons; at lower operating temperature, reactions at the interface are less serious, matching of the thermal coefficients of the materials at the interface is less critical and of course the cell is economically more efficient. In addition, problems with the large-scale production of hydrogen and hydrogen-storage materials will have to be solved for a 'hydrogen economy' to be realized.

5.4 Lithium Batteries

Rechargeable Li-ion cells are key components of the portable computing and telecommunication equipment required by today's information-rich, mobile society. A battery is composed of several electrochemical cells that are connected

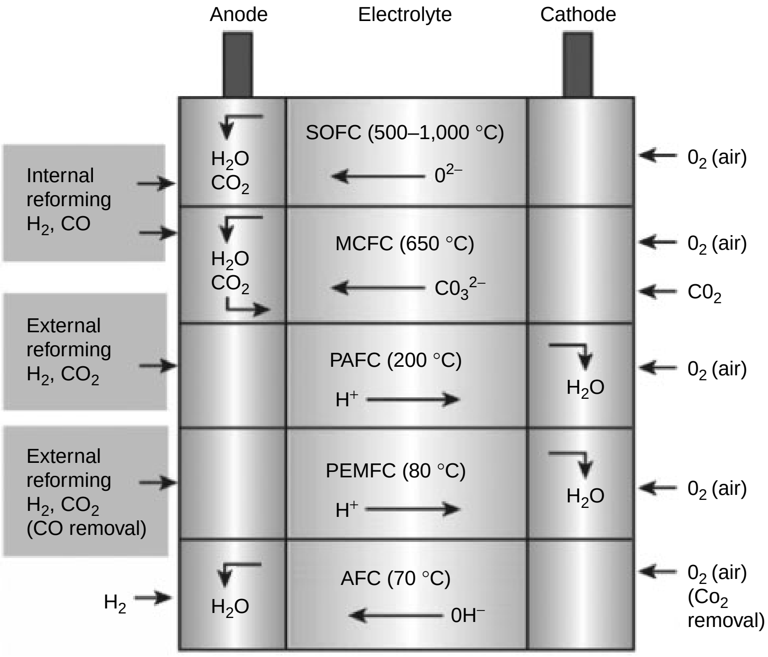
Anode
Electrolyte
Cathode
Internal reforming H2, CO
H2O CO2
SOFC (500–1,000 °C)
0²⁻
0₂ (air)
MCFC (650 °C)
C0₃²⁻
0₂ (air)
C0₂
External reforming H2, CO2
PAFC (200 °C)
H⁺
H2O
0₂ (air)
External reforming H2, CO2 (CO removal)
PEMFC (80 °C)
H⁺
H2O
0₂ (air)
H2
H2O
AFC (70 °C)
0H⁻
0₂ (air) (Co₂ removal)

Figure 24 Summary of fuel-cell types. The oxidation reaction takes place at the anode (+) and involves the liberation of electrons (for example, $O^{2-} + H_2 = H_2O + 2e^-$ or $H_2 = 2H^+ + 2e^-$). These electrons travel around the external circuit producing electrical energy by means of the external load, and arrive at the cathode (−) to participate in the reduction reaction (for example, $1/2O_2 + 2e^- = O^{2-}$ or $1/2O_2 + 2H^+ + 2e^- = H_2O$). It should be noted that as well as producing electrical energy and the reaction products (for example, H_2O and CO_2), the fuel-cell reactions also produce heat. The reaction products are formed at the anode for SOFC, MCFC and AFC types, and at the cathode for PAFC and PEMFC types. This difference has implications for the design of the entire fuel-cell system, including pumps and heat exchangers. To maintain the composition of the electrolyte component in the MCFC system, CO_2 has to be re-circulated from the anode exhaust to the cathode input. Additionally, the composition of the polymeric-membrane electrolyte has to be carefully controlled during operation by an appropriate 'water management' technology. (Ref. 197. Reproduced by permission of Nature Publishing Group (www.nature.com))

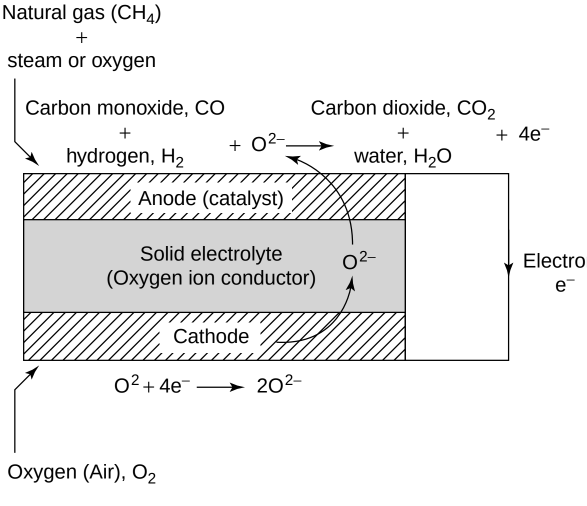
Natural gas (CH4) + steam or oxygen
Carbon monoxide, CO + hydrogen, H2
+ O²⁻
Carbon dioxide, CO2 + water, H2O
+ 4e⁻
Anode (catalyst)
Solid electrolyte (Oxygen ion conductor)
O²⁻
Electrons e⁻
Cathode
O² + 4e⁻ → 2O²⁻
Oxygen (Air), O2

Figure 25 Schematic diagram showing the operating principles of a SOFC running on natural gas (R. Mark Ormerod 'Solid oxide fuel cells' *Chemical Society Reviews* 32: 17–28 (2003). Reprinted with permission of The Royal Society of Chemistry)

in series and/or in parallel to provide the required voltage and capacity, respectively. The amount of electrical energy, expressed either per unit of weight (W h kg^{-1}) or per unit of volume (W h l^{-1}), that a battery is able to deliver is a function of the cell potential (V) and capacity (A h kg^{-1}), both of which are linked directly to the chemistry of the system. Among the various battery technologies (Figure 27), Li-based batteries, because of their high energy density and design flexibility, currently outperform other systems.

The principle of the rechargeable Li-battery is illustrated in Figure 28(a), as it was originally conceived. The preferred anode is Li, the most electropositive (−3.04 V) versus standard hydrogen electrode as well as the lightest metal, which on discharge will donate an electron according to

$$xLi \longrightarrow xLi^+ + xe^- \qquad (13)$$

where Li^+ enters the electrolyte, and the electron exits the anode to the external circuit to power the load. The Li^+ ions move through the electrolyte; because Li is more electropositive than hydrogen, the electrolyte must be nonaqueous and aprotic. A representative nonaqueous liquid electrolyte is a solution (1:1 by volume) of ethylene or propylene carbonate with a lithium salt (at a concentration of ~1M) such as lithium hexafluorophosphate, $LiPF_6$. At

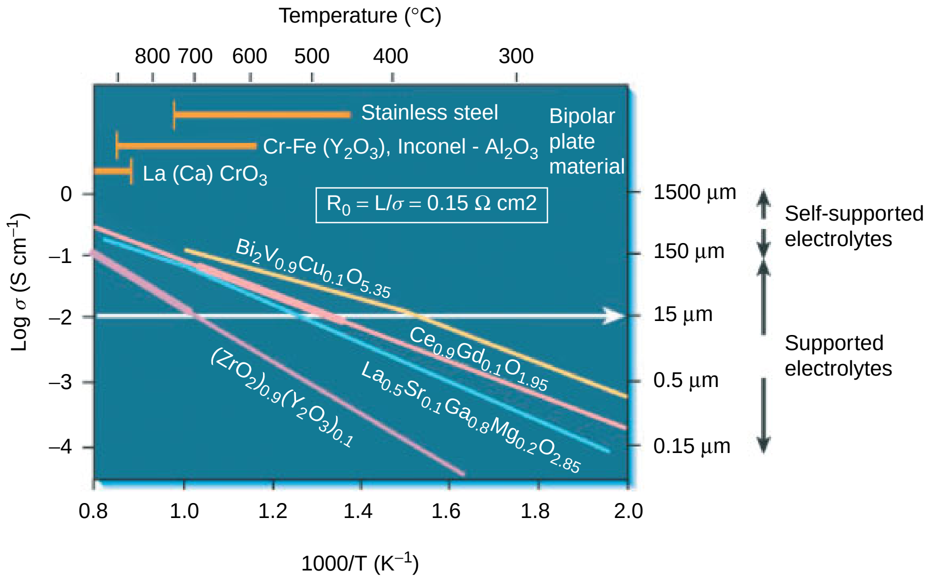

Figure 26 Specific conductivity versus reciprocal temperature for selected solid-oxide electrolytes. To ensure that the total internal resistance (that is, electrolyte + electrodes) of a fuel cell is sufficiently small, the target value for the area specific resistivity (ASR) of the electrolyte is set at $0.15\ \Omega cm^2$. Films of oxide electrolytes can be reliably produced using cheap, conventional ceramic fabrication routes at thicknesses down to ~15 μm. It follows that the specific conductivity of the electrolyte must exceed 10^{-2} S cm^{-1}. This is achieved at 500 °C for the electrolyte $Ce_{0.9}Gd_{0.1}O_{1.95}$, and at 700 °C for the electrolyte $(ZrO_2)_{0.9}(Y_2O_3)_{0.1}$. Although the electrolyte $Bi_2V_{0.9}Cu_{0.1}O_{5.35}$ exhibits higher conductivities, it is not stable in the reducing environment imposed by the fuel in the anode compartment of a fuel cell. (Ref. 197. Reproduced by permission of Nature Publishing Group (www.nature.com))

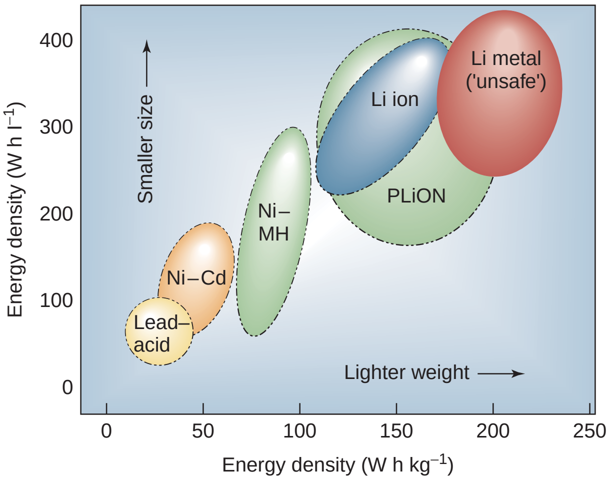

Figure 27 Comparison of the different battery technologies in terms of volumetric and gravimetric energy density. The share of worldwide sales for Ni–Cd, Ni–MeH and Li-ion portable batteries is 23, 14, and 63%, respectively. The use of Pb–acid batteries is restricted mainly in automobiles or standby applications, whereas Ni–Cd batteries remain the most suitable technologies for high-power applications (for example, power tools). (Ref. 47. Reproduced by permission of Nature Publishing Group (www.nature.com))

the cathode, Li^+ ions are inserted topotactically in the open cavities of the host lattice, which calls for compensating electrons, and the cathode also accepts electron via the external circuit and is reduced according to

$$xLi^+ + xe^- + MO_y \longrightarrow Li_xMO_y \qquad (14)$$

where MO_y is a transition metal oxide with either a layered structure (e.g. $LiMO_2$ M = Co, Ni) or a framework structure (e.g. V_6O_{13}, V_2O_5) as illustrated (Figure 28).

Thus the net reaction is:

$$xLi + MO_y \rightleftharpoons Li_xMO_y \qquad (15)$$

If the battery is to be rechargeable, the reaction must be reversible, and if the load is replaced by a power supply, the reaction in equation (15) is reversed, or the cathode and anode reaction go in the reverse direction. The system depicted in Figure 28(a) was not viable, because of the uneven (dendritic) growth of Li metal upon subsequent discharge-recharge cycles, which lead to explosion hazards.

To circumvent the safety issues related to use of Li metal, anodes that were also Li-insertion materials were introduced[224,225] and led by the early 1990s to the development of so-called rocking–chair technology as illustrated in Figure 27(b). This concept was exploited by Sony Inc. in their first commercialized rechargeable Li-battery with a C/$LiCoO_2$ rocking-chair cell.[226] This cell has a potential exceeding 3.6 V (three times that of alkaline systems), and an energy density of 120–150 $Whkg^{-1}$ (two to three times those of usual Ni-Cd

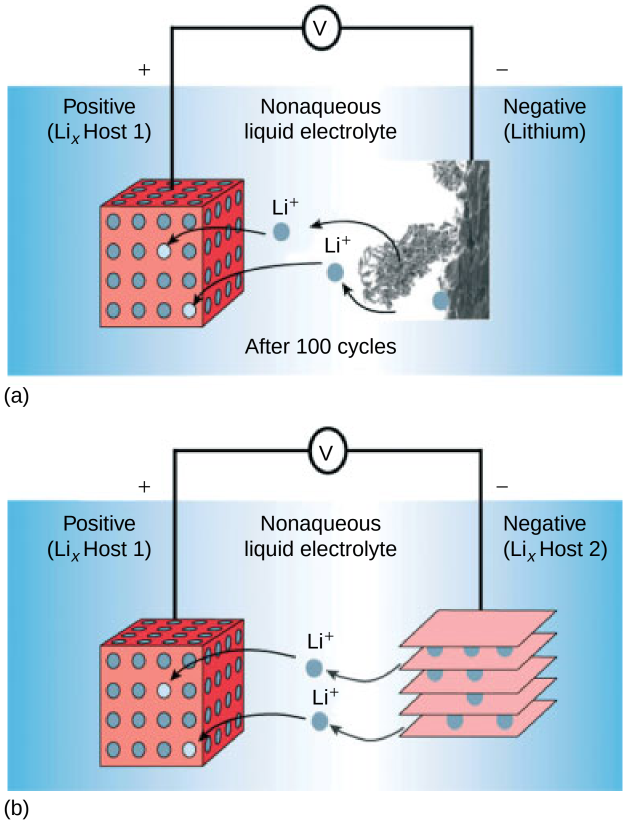

Figure 28 Schematic representation and operating principles of Li batteries. (a) Rechargeable Li-metal battery (the picture of the dendrite growth at the Li surface was obtained directly from in situ scanning electron microscopy measurements), (b) Rechargeable Li-ion battery. (Ref. 47. Reproduced by permission of Nature Publishing Group (www.nature.com))

batteries) found in most of today's high-performance portable electronic devices.

As discussed earlier, the polymer electrolytes were developed primarily to replace the liquid electrolyte by a dry polymer electrolyte in Li-batteries, leading to the so-called Li-solid polymer electrolyte battery. This technology is restricted to stationary power generation, and not portable devices, as it operates only at relatively high temperature (~80 °C). Subsequently a Li hybrid polymer electrolyte (Li-HPE) battery was developed, where the 'hybrid' electrolyte included three components: a polymer matrix swollen with liquid solvent and a Li-salt. The HPE concept never materialized, as Li-metal dendrites were still a safety issue. Bellcore researchers introduced polymeric electrolytes in a liquid Li-ion system and developed the first practical rechargeable Li-ion HPE battery, called plastic Li-ion (PLiON) in 1996,[227] which allowed the development of thin film technology in addition to usual coin-, cylindrical- and prismatic-type cell configurations (Figure 29).

The 'PliON' thin-film battery technology has been in development since 1999, and has many potential advantages including shape versatility, flexibility, lightness, and miniaturization. Currently commercial Li-ion polymer batteries use a gel-coated, microporous poly-olefin separator bonded to the electrodes (also gel-laden), rather than the P(VDF-HFP)-based membrane (i.e. copolymer of vinylidine difluoride with hexafluorpropylene) used in the plastic Li-ion cells.

Li-based battery technologies continue to be developed. The materials research aspect is particularly intense; new and better electrolyte and electrode materials are designed and investigated (see Li-ion conductors in Section 3) to minimize deleterious reactions occurring at the electrode-electrolyte interface – the critical phase of all electrochemical systems.

Very recently, new reports of inexpensive and nontoxic nanomaterials based on inexpensive and environmentally safe Fe-based compounds promise to revolutionize Li-battery technology.[228–231]

5.5 Electrochromism

A highly important application of solid state ionic materials is in electrochromic devices referred to as 'smart windows'.[232,233] Intelligent glass facades and smart windows are attracting much interest in modern architecture. These windows have the ability to modulate the incoming light and solar energy. Electrochromism[232] is a well-known phenomenon capable of providing the required variation in the optical properties, and presently some full-scale electrochromic smart windows are undergoing practical testing in buildings. An electrochromic material is characterized by its ability to sustain reversible and persistent changes of the optical properties when a voltage is applied to it. The electrochromic phenomenon was discovered in tungsten oxide, WO_3 thin films and this material remains the most promising candidate for electrochromic devices. It is convenient to introduce electrochromism in WO_3 by reference to the simple reaction

$$\mathrm{WO_3} + x\mathrm{M^+} + x\mathrm{e^-} \longrightarrow \mathrm{M}_x\mathrm{WO_3} \qquad (16)$$

with $M^+ = H^+$, Li^+, Na^+, or K^+ and e^- denoting electrons. Thus when WO_3, which is transparent as a thin film, incorporates electrons and charge-balancing ions it can be reversibly transformed to a material with radically different properties, being absorbing and blue, if the material is heavily disordered and infrared-reflecting if it is sufficiently crystalline.

An electrochromic device embodies a number of superimposed layers on a transparent substrate or between two transparent substrates, and optical transmittance is altered when an electrical potential is applied so that charge is shuttled between layers serving in the same way as anodes and cathodes in an electrical battery. One specific design with a five-layer construction shown in Figure 30 uses cathodically coloring WO_3 and anodically coloring nickel oxide joined by an ion-conducting electrolytic laminate. A potential of a few volts, preferably supplied by solar cells, is applied between

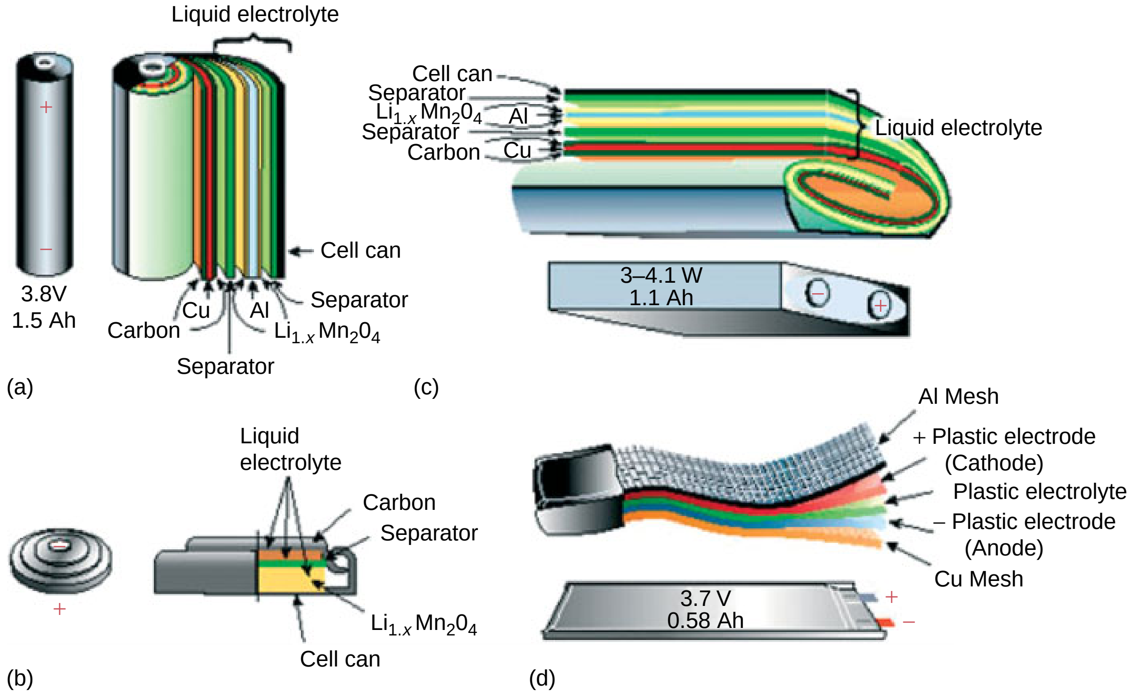
Liquid electrolyte
3.8V
1.5 Ah
Cell can
Separator
Carbon
Cu
Al
$Li_{1.x}Mn_20_4$
Separator
(a)
Cell can
Separator
$Li_{1.x}Mn_20_4$
Al
Separator
Carbon
Cu
Liquid electrolyte
3–4.1 W
1.1 Ah
(c)
Liquid electrolyte
Carbon
Separator
$Li_{1.x}Mn_20_4$
Cell can
+
(b)
Al Mesh
+ Plastic electrode (Cathode)
Plastic electrolyte
– Plastic electrode (Anode)
Cu Mesh
3.7 V
0.58 Ah
+
–
(d)

Figure 29 Schematic drawing showing the shape and components of various Li-ion battery configurations: (a) cylindrical, (b) coin, (c) prismatic, and (d) thin and flat. Note the unique flexibility of the thin and flat plastic LiION configuration; in contrast to the other configurations, the 'PLiION' technology does not contain free electrolyte. (Ref. 47. Reproduced by permission of Nature Publishing Group (www.nature.com))

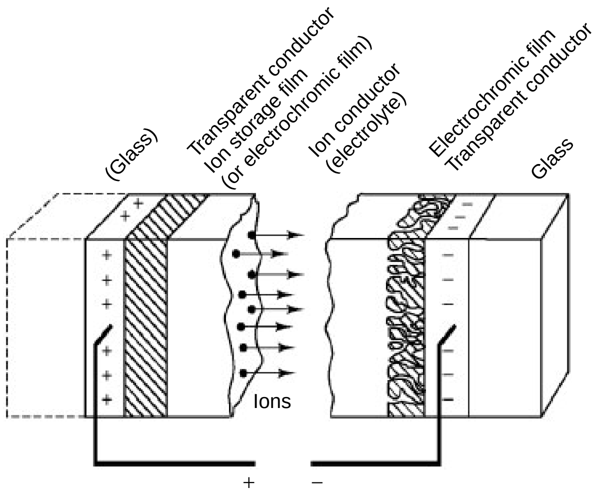
(Glass)
Transparent conductor
Ion storage film
(or electrochromic film)
Ion conductor
(electrolyte)
Electrochromic film
Transparent conductor
Glass
Ions
+
–

Figure 30 Schematic diagram of an electrochromic device

transparent and electrically conducting layers of In_2O_3:Sn (known as indium tin oxide ITO) on the glass. The spectral transmittance of this device in fully colored and bleached states is shown in Figure 31; the luminous transmittance – obtained by integration over the eye's sensitivity curve – lies between 74 and 7%. Devices of a similar type, with films of tungsten oxide and nickel oxide operating in concert, have been subject to several recent investigations.[232–241]

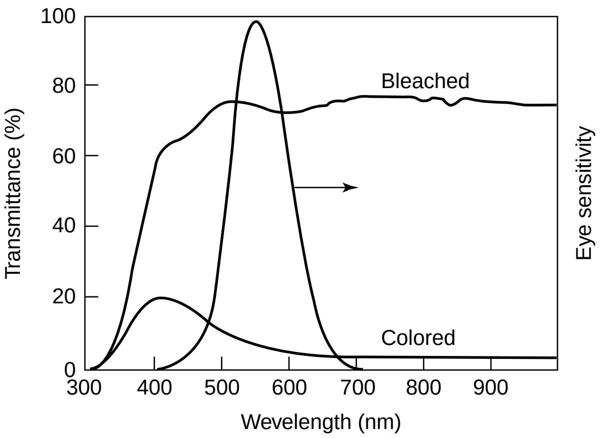

Figure 31 Spectral transmittance of an electrochromic foil in fully darkened and bleached states. Also shown is the sensitivity of the human eye. The visible transmittance is 73.5/7.1% in the bleached colored state. (Ref. 235. Reproduced by permission of Springer Verlag)

When a potential is applied across a smart window, the electrochemical process, indicated in equation (16), changes the window to nearly opaque (Figure 31). The process can be reversed and repeated many times. Smart windows may be used to selectively block sunlight in automobiles, airplanes, and buildings if the environmental stability of the device is made satisfactory. Smart windows may find large-scale application as architectural glass when the cost of this technology is made economical.

The two active material films, tungsten oxide and nickel oxide (Figure 30), must survive many thousands of cycles of reactions. However, WO_3 is stable in a moderately acidic environment, and rapidly dissolves in a basic electrolyte, while NiO is stable in a basic environment, but unstable in an acidic one. Stability can be accomplished by putting a thin layer of tungsten oxide on top of the nickel oxide counterelectrode;[241] the tungsten oxide film has two different functions: it protects the underlying film in acidic electrolytes, and exhibits electrochromic properties. Figure 32 show highly schematic electron density-of-states (DOS) diagrams: the nickel oxide film may be considered a Mott insulator with a wide band gap due to the large correlation between the Ni 3d electrons.[242] In the bleached state, the Fermi energy, E_F, is expected to lie slightly above the valence band edge.[243] For tungsten oxide, E_F lies in the band gap separating a valence band dominated by O 2p states from a conduction band dominated by W 5d states.[242] When a voltage, U_{col}, is applied between the nickel oxide and tungsten oxide films – as indicated in the right-hand part of Figure 32 – their E_F are separated. Electrons enter the W 5d states, where they may cause strong polaron absorption[232,244] provided that the tungsten oxide film is heavily disordered. A corresponding charge is subtracted from the top of the valence band of the nickel oxide film, thereby rendering this material absorbing by a mechanism that appears to be nonpolaronic but is not known in detail.[245] Hence the initially transparent device turns absorbing (i.e. colored) by a combination of anodic electrochromism in nickel oxide and cathodic electrochromism in tungsten oxide. Thus, if an absorbing device combining nickel oxide and tungsten oxide is electrically shorted it turns transparent, implying that the bottom of the conduction band of tungsten oxide lies at a higher energy than the top of the valence band for nickel oxide. Figure 32 assumes rigid-band behavior for the DOS, which appears well-founded for tungsten oxide,[242] but is less established for nickel oxide. The protective tungsten oxide layer in the device is always transparent and does not contribute to device coloration at any stage, although it may impart chemically desirable surface properties to the anodically coloring electrochromic nickel oxide film.[235]

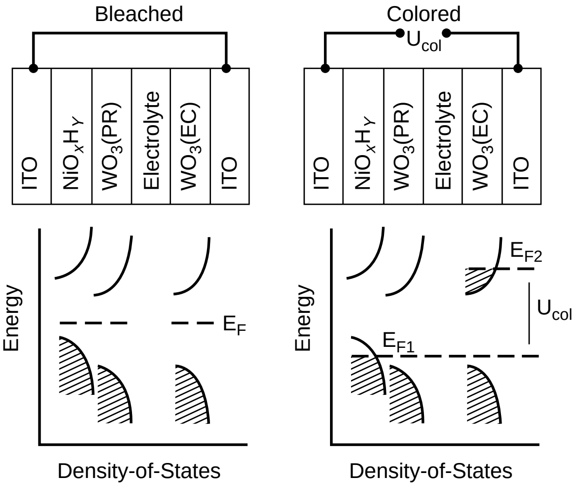

Figure 32 Schematic electron density-of-states diagrams for electrochromic, EC, multilayer design. The materials include In_2O_3:Sn (ITO), nickel oxide (presumably hydrous), tungsten oxide (also presumably hydrous) prepared so that the EC and chemically protective (PR) properties are emphasized, and an electrolyte. The Fermi energy is denoted E_F, with E_{F1} and E_{F2} pertaining to the case of an applied potential, U_{col} filled states are denoted by shadings. (Ref. 235. Reproduced by permission of Springer Verlag)

6 RELATED ARTICLES

Defects in Solids; Dielectric Polarizabilities of Oxides & Fluorides; Diffraction Methods in Inorganic Chemistry; Electronic Structure of Solids; Fluorides: Solid-state Chemistry; Halides: Solid-state Chemistry; Intercalation Chemistry; Noncrystalline Solids; Oxides: Solid-state Chemistry; Phosphates: Solid-state Chemistry; Polyphosphazenes; Sol–Gel Synthesis of Solids; Solids: Computer Modeling; Structure & Property Maps for Inorganic Solids; Zeolites.

7 REFERENCES

1. D. F. Shriver and G. C. Farrington, *Chem. Eng. News*, 1985, **63**(20), 42.
2. M. Faraday, ‘Experimental Researches in Electricity’, Taylor & Francis, London, 1839.
3. C. Tubandt and E. Lorenz, *Z. Phys. Chem.*, 1914, **87**, 513.
4. C. Tubandt, *Z. Anorg. Allg. Chem.*, 1921, **115**, 105.
5. C. Tubandt and H. Rheinhold, *Z. Electrochem.*, 1923, **29**, 313.
6. A. Joffe, *Ann. Phys. (Leipzig)*, 1923, **72**, 461.
7. J. Frenkel, *Z. Phys.*, 1926, **35**, 652.
8. W. Schottky, *Z. Phys. Chem.*, 1935, **B29**, 335.
9. P. Colomban and A. Novak, Defect, Non-stoichiometry and Phase Transitions, in ‘Proton Conductors – Solids, Membranes and Gels – Materials and Devices’, ed. P. Colomban, Cambridge University Press, Cambridge, MA, 1992, Chap. 4.
10. L. W. Strock, *Z. Phys. Chem.*, 1934, **B25**, 441; L. W. Strock, *ibid.*, 1935, **B31**, 132.
11. R. J. Cava, F. Reidinger, and B. J. Wuensch, *Solid State Commun.*, 1977, **24**, 411.
12. M. O’Keefe, in ‘Fast Ion Transport in Solids’, ed. W. van Gool, North Holland, Amsterdam, 1973, p. 233.
13. W. van Gool, in ‘Solid Electrolytes’, eds. P. Hagenmuller and W. van Gool, Academic Press, New York, 1974, p. 9.

14. M. O'Keefe and B. G. Hyde, *Philos. Mag.*, 1976, **33**, 219.
15. K. Funke, J. Kalus, and R. E. Lechner, *Solid State Commun.*, 1974, **14**, 1012.
16. K. Funke, in 'Superionic Conductors', eds. G. D. Mahan and W. L. Roth, Plenum, New York, 1976, p. 183.
17. K. Funke, in 'Solid Electrolytes', eds. P. Hagenmuller and W. van Gool, Academic Press, New York, 1978, p. 77.
18. S. Geller, *Acc. Chem. Res.*, 1978, **11**, 87.
19. C. C. Liang, *J. Electrochem. Soc.*, 1973, **120**, 1289.
20. J. B. Wagner Jr, in 'Solid State Batteries', eds. C. A. C. Sequeira and A. Hopper, Nijhoff, Dordrecht, 1985, p. 77.
21. J. B. Bates, J. C. Wang, and N. J. Dudney, *Phys. Today*, 1982, **35**, 46.
22. G. C. Farrington and J. L. Briant, *Science*, 1979, **204**, 1371.
23. G. C. Farrington, B. Dunn, and J. O. Thomas, *Appl. Phys.*, 1983, **A32**, 159.
24. B. Dunn, G. C. Farrington, and J. O. Thomas, *MRS Bull.*, 1989, **14**, 22.
25. H. U. Beyeler and P. Bruesch, in 'Crystal Growth and Materials', eds. E. Kaldis and H. J. Scheel, North Holland, Amsterdam, 1977, p. 766.
26. J. L. Souquet, *Annu. Rev. Mater. Sci.*, 1981, **11**, 211.
27. C. A. Angell, *Annu. Rev. Chem.*, 1992, **43**, 693.
28. F. A. Fusco and H. L. Tuller, in 'Superionic Solids and Solid Electrolytes – Recent Trends', eds. A. L. Laskar, and S. Chandra, Academic Press, Boston, MA, 1989, p. 43.
29. M. B. Armand, *Annu. Rev. Mater. Sci.*, 1986, **16**, 245.
30. M. A. Ratner and D. F. Shriver, *MRS Bull.*, 1989, **14**, 39.
31. J. R. MacCallum and C. A. Vincent, 'Polymer Electrolyte Reviews', Elsevier Applied Science, London, 1987.
32. Y. F. Y. Yao and J. T. Kummer, *J. Inorg. Nucl. Chem.*, 1967, **29**, 2453.
33. W. J. Pardee and G. D. Mahan, *J. Solid State Chem.*, 1975, **15**, 310.
34. J. M. Reau and J. Portier, in 'Solid Electrolytes', eds. P. Hagenmuller and W. Van Gool, Academic Press, London, 1978, p. 543.
35. C. R. A. Catlow and A. James, *Nature*, 1978, **272**, 603.
36. C. R. A. Catlow, *Solid State Ionics*, 1992, **53–56**, 955.
37. M. Saiful Islam, *Solid State Ionics*, 2002, **154–155**, 75.
38. W. Münch, K. D. Kreuer, G. Seifert, and J. Maier, *Solid State Ionics*, 2000, **136–137**, 183.
39. C. Cramer, S. Brunklaus, Y. Gao, and K. Funke, *J. Phys.: Condens. Matter*, 2003, **15**, S2309.
40. W. Dieterich, Solid State Ionics: Trends in the New Millennium, in 'Proceedings of the Asian Conference, 8th, Langkawi', ed. B. V. R. Chowdari, World Scientific Publishing Co. Pte. Ltd., Singapore, 2002, Dec. 15 – 19, p. 689.
41. S. J. Paddison, *Annu. Rev. Mater. Res.*, 2003, **33**, 289.
42. A. R. West, 'Solid State Chemistry and its Applications', Wiley, New York, 1984, p. 479.
43. J. B. Goodenough, *Annu. Rev. Mater. Res.*, 2003, **33**, 91.
44. H. Y.-P. Hong, *Mater. Res. Bull.*, 1978, **13**, 117.
45. *MRS Bull.*, 1989, **14**, 18.
46. R. Collongues, A. Kahn, and D. Michel, *Annu. Rev. Mater. Sci.*, 1979, **9**, 123.
47. J.-M. Tarascon and M. Armand, *Nature*, 2001, **414**, 359.
48. L. Sebestian and J. Gopalakrishnan, *J. Mater. Chem.*, 2003, **13**, 433.
49. B. Owens, *J. Power Sources*, 2000, **90**(1), 2.
50. G. Alberti and M. Casciola, *Solid State Ionics*, 2001, **145**, 3.
51. J. Schoonman, *Solid State Ionics*, 2000, **135**, 5.
52. G. Nazri, R. A. Huggins, and D. F. Shriver eds, 'Solid State Ionics', MRS, Pittsburgh, PA, 1989, p. 135.
53. G. Nazri, D. F. Shriver, R. A. Huggins, and M. Balkanski eds, 'Solid State Ionics II', MRS, Pittsburgh, PA, 1991, p. 210.
54. G. Nazri, J.-M. Tarascon, and M. Armand eds, 'Solid State Ionics III', MRS, Pittsburgh, PA, 1993, p. 293.
55. T. Takahasi ed., 'High Conductivity Solid Ionic Conductors – Recent Trends and Applications', World Scientific, Singapore, 1989.
56. A. L. Laskar and S. Chandra eds, 'Superionic Solids and Solid Electrolytes – Recent Trends', Academic Press, Boston, MA, 1989.
57. T. Kudo and K. Fueki, 'Solid State Ionics', Kodansha, 1990.
58. H. Tuller and M. Balkanski eds, 'Science and Technology of Fast Ion Conductors', Plenum Press, New York, 1989.
59. J. Larminie and A. Dicks, 'Fuel Cell Systems Explained', 2nd edn., John Wiley & Sons, 2000, p. 428.
60. S. C. Singhal and K. Kendall eds, 'High-temperature Solid Oxide Fuel Cells: Fundamentals, Design and Applications', Elsevier Advanced Technology, 2000, p. 512.
61. 'MRS-Proceedings on the Symposium on e.g., ''Solid State Ionics IV'' ', eds. G.-A. Nazri, J.-M. Tarascon, M. Schveiber Materials Research Society-yearly or bi-yearly publications, Boston, MA, 1994.
62. G. C. Farrington and B. Dunn, *Solid State Ionics*, 1982, **7**, 267.
63. Y. Kobayashi, T. Egawa, Y. Okazaki, S. Tamura, N. Imanaka, and G. Adachi, *Solid State Ionics*, 1998, **111**, 59.
64. S. Tamura, N. Imanaka, and G. Adachi, *Solid State Ionics*, 2002, **154–155**, 767.
65. N. Imanaka, M. Itaya, T. Ueda, and G. Adachi, *Solid State Ionics*, 2002, **154–155**, 3190.
66. J. T. Kummer, *Prog. Solid State Chem.*, 1972, **7**, 141.
67. M. Bettman and C. R. Peters, *J. Phys. Chem.*, 1969, **73**, 1774.
68. R. Subasri, T. Mathews, O. M. Sreedharan, and V. S. Raghunathan, *Solid State Ionics*, 2003, **158**, 199.

69. R. J. Baughman and R. E. Lofever, *Mater. Res. Bull.*, 1975, **10**, 106.
70. K. G. Frase, J. O. Thomas, and G. C. Farrington, *Solid State Ionics*, 1983, **9/10**, 307.
71. J. L. Briant and G. C. Farrington, *J. Solid State Chem.*, 1980, **33**, 385.
72. C. Peters, M. Bettman, J. Moore, and M. Glick, *Acta Crystallogr.*, 1971, **B27**, 1826.
73. W. L. Roth, *J. Solid State Chem.*, 1972, **4**, 62.
74. W. L. Roth, F. Reidinger, and S. LaPlaca, in 'Superionic Conductors', eds. W. L. Roth and G. D. Mahan, Plenum Press, New York, 1976.
75. C. A. Beevers and M. A. Ross, *Z. Kristallogr.*, 1937, **97**, 59.
76. R. Collongues, J. Thery, and J. P. Boilot, in 'Solid Electrolytes', ed. P. Hagenmuller, Academic Press, New York, 1978, p. 253.
77. J. O. Thomas and G. C. Farrington, *Acta Crystallogr.*, 1983, **B39**, 227.
78. J. O. Thomas, M. Alden, and G. J. McIntyre, *Acta Crystallogr.*, 1984, **B40**, 208.
79. M. S. Whittingham and R. A. Huggins, *J. Chem. Phys.*, 1971, **54**, 414.
80. M. S. Whittingham and R. A. Huggins, *Natl. Bur. Stand. (NBS) Spec. Publ.*, 1972, **364**, 139.
81. K. W. Powers and S. P. Mitoff, GE Report No. CRD 082, 1974.
82. S. Stramare, V. Thangadurai, and W. Weppner, *Chem. Mater.*, 2003, **15**, 3974.
83. T. Norby and Y. Larring, *Curr. Opin. Solid State Mater. Sci.*, 1997, **2**, 593.
84. K. D. Kreuer, *Annu. Rev. Mater. Res.*, 2003, **33**, 333.
85. J. B. Goodenough, H. Y.-P. Hong, and J. A. Kafalas, *Mater. Res. Bull.*, 1976, **11**, 203.
86. P. Colomban, *Solid State Ionics*, 1986, **21**, 97.
87. J. J. Bentzen and P. S. Ivicholson, *Mater. Res. Bull.*, 1980, **15**, 1737.
88. T. Moeller, 'Inorganic Chemistry', Wiley, New York, 1961, p. 831.
89. C. R. Schlaikjer and C. C. Liang, in 'Fast Ion Transport in Solids', ed. W. van Gool, North Holland, Amsterdam, 1973, p. 685.
90. T. Jow and J. B. Wagner, *J. Electrochem. Soc.*, 1979, **126**, 1963.
91. R. Kanno, Y. Takeda, and O. Yamamoto, *Mater. Res. Bull.*, 1981, **16**, 999.
92. R. A. Huggins, *Electrochim. Acta*, 1977, **22**, 774.
93. H. Obayashi, R. Nagai, A. Gotch, S. Mochizuki, and T. Kudo, *Mater. Res. Bull.*, 1981, **16**, 587.
94. A. R. West, *Z. Kryst.*, 1975, **141**, 422.
95. P. G. Bruce and A. K. West, *Mater. Res. Bull.*, 1980, **15**, 379.
96. Von U. Alpen, M. F. Bell, W. Wichelhaus, K. Y. Cheung, and G. J. Dudley, *Electrochim. Acta*, 1978, **23**, 1395.
97. J. Kuwano and A. R. West, *Mater. Res. Bull.*, 1980, **15**, 1661.
98. I. Abrahams, P. G. Bruce, A. R. West, and W. I. F. David, *J. Solid State Chem.*, 1988, **75**, 390.
99. A. Z. Lunden, *Solid State Ionics*, 1987, **25**, 231.
100. L. Borjesson and L. M. Torell, *Solid State Ionics*, 1986, **18/19**, 582.
101. E. A. Secco, *Solid State Commun.*, 1988, **66**, 921.
102. A. C. Stewart, K. G. MacDonald, E. A. Secco, *J. Solid State Chem.*, 1989, **81**, 65.
103. R. Kaber, L. Nilsson, N. Andersen, L. Hessel, T. Arnold, and O. John, *J. Phys.: Condens. Matter*, 1999, **4**, 1925.
104. A. Garcia, G. Torres-Trevino, and A. R. West, *Solid State Ionics*, 1990, **40/41**, 13.
105. Von. U. Alpen, H. Schultz, G. H. Talat, and H. Bohm, *Solid State Commun.*, 1977, **23**, 911.
106. R. D. Shannon, B. E. Taylor, A. D. English, and T. Berzins, *Electrochim. Acta*, 1977, **22**, 783.
107. T. Esaka and M. Greenblatt, *J. Solid State Ionics*, 1986, **21**, 255.
108. J. B. Goodenough, M. M. Theckeray, W. I. F. David, and P. G. Bruce, *Rev. Chim. Miner.*, 1984, **21**, 435.
109. A. G. Belous, G. N. Novitskaya, S. V. Polyanetskaya, and Yu. I. Gornikov, *Izv. Akad. Nauk SSSR, Neorg. Mater.*, 1987, **23**, 4700.
110. Y. Inaguma, Y. Matsui, Y.-J. Shan, and T. Nakamura, *Solid State Ionics*, 1995, **79**, 91.
111. J. B. Goodenough, *Proc. R. Soc. London, Ser. A*, 1984, **393**, 215.
112. K. S. Nunjundaswamy, A. K. Padhi, J. B. Goodenough, S. Okada, H. Ohtsuka, H. Arai, and J. Yaamaki, *Solid State Ionics*, 1996, **92**, 1.
113. B. L. Cushing and J. B. Goodenough, *J. Solid State Chem.*, 2001, **162**, 176.
114. L. Glasser, *Chem. Rev.*, 1975, **75**, 21.
115. S. Chandra, in 'Superionic Solids and Solid Electrolytes – Recent Trends', eds. A. L. Laskar and S. Chandra, Academic Press, Boston, MA, 1989, p. 185.
116. F. W. Poulsen, in 'High Conductivity Solid Ionic Conductors – Recent Trends and Applications', ed. T. Takahashi, World Scientific, Singapore, 1989, p. 166.
117. Ph. Colomban and J. Tomkinson, *Solid State Ionics*, 1997, **97**, 123.
118. T. Norby and N. Christiansen, *Solid State Ionics*, 1995, **77**, 240.
119. T. Norby, *Solid State Ionics*, 1999, **125**, 1.
120. K. D. Kreuer, *Chem. Mater.*, 1996, **8**, 610.
121. J. Jensen and M. Kleitz eds, 'Solid State Protonic Conductors I – for Fuel Cells and Sensors', Odense University Press, Odense, 1982.

122. J. B. Goodenough, J. Jensen, and M. Kleitz eds, ‘Solid State Protonic Conductors II – for Fuel Cells and Sensors’, Odense University Press, Odense, 1983.

123. J. B. Goodenough, J. Jensen, and A. Potier eds, ‘Solid State Protonic Conductors III – for Fuel Cells and Sensors’, Odense University Press, Odense, 1985.

124. Proceedings of the IVth International Conf. for Fuel Cells and Sensors, Odense University Press, 1986.

125. Proceedings of the 8th International Conference, Storefjell, Gol, Norway, August 18 – 23, 1996.

126. Proceedings of the 9th International Conference on Solid State Protonic Conductors, Golf Hotel, Bled, Slovenia, August 17 – 21, 1998.

127. Proceedings of the 10th International Conference on Solid State Protonic Conductors (SSPC10), Montpellier, 24 – 28 September, 2000.

128. Proceedings of the 11th International Conference on Solid State Protonic Conductors (SSPC-11), Guildford, 27 – 30 August, 2002.

129. M. A. Butler and R. M. Biefield, *Phys. Rev.*, 1979, **B19**, 5455.

130. K. D. Kreuer, A. Rabenau, and R. Messer, *Appl. Phys.*, 1983, **A32**, 45.

131. K. D. Kreuer, *Solid State Ionics*, 2003, **94**, 55.

132. H. Arribart, H. Carlos, and B. Sapoval, *Solid State Ionics*, 1981, **5**, 253.

133. E. K. Anderson, I. G. Krogh Andersen, E. Skou, and S. Yde-Andersen, *Solid State Ionics*, 1986, **18/19**, 1170.

134. K.-D. Kreuer, A. Rabenau, and W. Weppner, *Angew. Chem., Int. Ed. Engl.*, 1982, **21**, 208.

135. W. A. England, M. G. Cross, A. Hamnett, P. J. Wiseman, and J. B. Goodenough, *Solid State Ionics*, 1980, **1**, 231.

136. G. Alberti, M. Casciola, U. Constantino, and M. Leonardi, *Solid State Ionics*, 1984, **14**, 289.

137. G. C. Farrington and J. L. Briant, *Science*, 1979, **204**, 1371.

138. K.-D. Kreuer, W. Weppner, and A. Rabenau, *Mater. Res. Bull.*, 1982, **17**, 501.

139. S. Feng and M. Greenblatt, *Chem. Mater.*, 1992, **4**, 1257; S. Feng and M. Greenblatt, *ibid.*, 1993, **5**, 1277.

140. T. Yajima and H. Iwahara, *Solid State Ionics*, 1992, **53–56**, 983.

141. T. Scherban and A. S. Nowick, *Solid State Ionics*, 1989, **35**, 189; T. Scherban and A. S. Nowick, *ibid.*, 1992, **53–56**, 1004.

142. N. Bonanos, *Solid State Ionics*, 1992, **53–56**, 967.

143. P. Murugaraj, K. D. Kreuer, T. He, E. Schober, and J. Maier, *Solid State Ionics*, 1997, **98**, 1.

144. T. He, K. D. Kreuer, and J. Maier, *Solid State Ionics*, 1997, **95**, 301.

145. W. Münch, K. D. Kreuer, S. Adams, G. Seifert, and J. Maier, *Phase Transit.*, 1999, **68**, 567.

146. K. D. Kreuer, *Solid State Ionics*, 1997, **97**, 1.

147. A. I. Baranov, L. A. Shuvalov, and N. M. Shchagina, *JETP Lett.*, 1982, **36**, 459.

148. D. A. Boysen, T. Uda, C. R. I. Chisolm, and S. Haile, *Science*, 2004, **303**, 68.

149. B. Dunn and G. C. Farrington, *Mater. Res. Bull.*, 1980, **15**, 1773.

150. G. C. Farrington and B. Dunn, *Solid State Ionics*, 1982, **7**, 267.

151. W. Carrillo-Cabrera, J. O. Thomas, and G. C. Farrington, *Solid State Ionics*, 1986, **18/19**, 645.

152. M. Jansen, A. J. Alfrey, O. M. Stafsudd, D. L. Yang, B. Dunn, and G. C. Farrington, *Opt. Lett.*, 1984, **9**, 119.

153. J. D. Berrie, B. Dunn, O. M. Stafsudd, and P. Nelson, *J. Lumin.*, 1987, **37**, 303.

154. J. D. Berrie and B. Dunn, *Solid State Ionics*, 1992, **53–56**, 496.

155. G. Adachi and N. Imanaka, *Inorg. Chem. Highlights*, 2002, **71**.

156. Y. Hasegawa, N. Imanaka, and G. Adachi, *J. Solid State Chem.*, 2003, **171**, 387.

157. N. Imanaka, Y. Hasegawa, M. Yamaguchi, M. Itaya, S. Tamura, and G. Adachi, *Chem. Mater.*, 2002, **14**, 4481.

158. N. Imanaka, S. Tamura, and G. Adachi, *Mater. Integration*, 2000, **14**, 29.

159. S. Tamura, N. Imanaka, and G. Adachi, *Solid State Ionics*, 2002, **154–155**, 767.

160. Y. Kobayashi, T. Egawa, Y. Okazaki, S. Tamura, N. Imanaka, and G. Adachi, *Solid State Ionics*, 2002, **154–155**, 59.

161. N. Imanaka, M. Itaya, T. Ueda, and G. Adachi, *Solid State Ionics*, 2002, **154–155**, 319.

162. B. C. H. Steele, in ‘High Conductivity Solid Ionic Conductors – Recent Trends and Applications’, ed. T. Takahasi, World Scientific, Singapore, 1989, p. 402.

163. I. Riess, in ‘Science and Technology of Fast Ion Conductors’, eds. H. L. Tuller and M. Balkanski, Plenum Press, New York, 1989, p. 23.

164. J. A. Kilner and B. C. H. Steele, in ‘Nonstoichiometric Oxides’, ed. P. T. Sorensen, Academic Press, New York, 1981, p. 233.

165. P. V. Wright, *Br. Polym. J.*, 1975, **7**, 319.

166. P. Shuk, H.-D. Wiemhofer, U. Guth, W. Gopel, and M. Greenblatt, *Solid State Ionics*, 1996, **89**, 179.

167. J. B. Goodenough, *Nature*, 2000, **404**, 821.

168. C. R. A. Catlow, in ‘Superionic Solids and Solid Electrolytes Recent Trends’, eds. A. L. Laskar and S. Chandra, Academic Press, Boston, MA, 1989, p. 339.

169. C. Milliken and S. Guruswamy, *J. Am. Ceram. Soc.*, 2002, **85**, 2479.

170. K. Eguchi, T. Setoguchi, T. Inoue, and H. Arai, *Solid State Ionics*, 1992, **52**, 165.

171. S. Skinner and J. A. Kilner, ‘Materials Today’, 2003, Vol. 6, p. 30.

172. V. Butler, C. R. A. Catlow, B. E. F. Fender, and J. H. Harding, *Solid State Ionics*, 1983, **8**, 109.
173. L. Minervini, M. O. Zacate, and R. W. Grimes, *Solid State Ionics*, 1999, **116**, 339.
174. J. A. Kilner, *Solid State Ionics*, 2000, **129**, 13.
175. K. Huang, M. Feng, and J. B. Goodenough, *J. Electrochem. Soc.*, 1997, **144**, 3620.
176. T. Ishihara, *J. Mater. Sci.*, 2001, **36**, 1125.
177. A. A. Bush and Y. N. Venetsev, *Russ. J. Inorg. Chem.*, 1986, **31**, 769.
178. A. F. Debreuille-Gresse, Synthese, Structure et propri'et de Compos'es du Bismuth et d'anions Phosphate ou Vanadate, PhD thesis, University de Lille, 1986, 141.
179. F. Abraham, A. F. Debreuille-Gresse, G. Mairesse, and G. Nowogrocki, *Solid State Ionics*, 1988, **28–30**, 529.
180. J. B. Goodenough, A. Manthiram, M. Paranthaman and Y. S. Zhen, in 'Solid State Ionics, Proc. Symp. A2, Int. Conf. Advanced Materials', eds. M Balkanski, T. Takahasi, and H. L. Tuller, North-Holland, Amsterdam, 1992, p. 79.
181. J. Yan and M. Greenblatt, *Solid State Ionics*, 1995, **81**, 225.
182. J. C. Boivin, G. Nowogrocki, G. G. Mairesse, P. Labrune, G. Lagrange, *11th Int. Conf. Solid State Ionics*, Honolulu, 1997.
183. S. Nakayama, *et al*., *Chem. Lett.*, 1995, 431.
184. S. Nakayama and M. Sakamoto, *J. Eur. Ceram. Soc.*, 1998, **18**, 1413.
185. S. Nakayama, *et al*. *J. Eur. Ceram. Soc.*, 1999, **19**, 507.
186. S. Tao and J. T. S. Irvine, *Mater. Res. Bull.*, 2001, **36**, 1245.
187. J. E. H. Sansom, D. Richings, and P. R. Slater, *Solid State Ionics*, 2001, **139**, 205.
188. E. J. Abram, D. C. Sinclair, and A. R. West, *J. Mater. Chem.*, 2001, **11**, 1978.
189. H. Arikawa, H. Nishiguchi, T. Ishihara, and Y. Takita, *Solid State Ionics*, 2000, **136–137**, 31.
190. J. McFarlane, *et al*. *Ionics*, 2002, **8**, 149.
191. P. Lacorre, F. Goutenoire, O. Bohnke, R. Retoux, and Y. Laligant, *Nature*, 2000, **404**, 856.
192. F. Goutenoire, O. Isnard, R. Retoux, and P. Lacorre, *Chem. Mater.*, 2000, **12**, 2575.
193. F. Goutenoire, O. Isnard, E. Suard, O. Bohnke, Y. Laligant, R. Retoux, and P. Lacorre, *J. Mater. Chem.*, 2001, **11**, 119.
194. Z. S. Khadasheva, *et al*. *Inorg. Mater.*, 2000, **38**, 1168.
195. X. P. Wang, Q. F. Fang, Z. S. Li, G. G. Zhang, and Z. G. Yi, *Appl. Phys. Lett.*, 2002, **81**, 3434.
196. J. A. Collado, M. A. G. Aranda, A. Cabeza, P. Olivera-Pastor, and S. Bruque, *J. Solid State Chem.*, 2002, **167**, 80.
197. B. C. H. Steele, A. Heinzel, *Nature*, 2001, **414**, 345.
198. A. A. Yaremchenko, V. V. Kharton, E. N. Naumovich, and A. A. Tonoyan, *Mater. Res. Bull.*, 2000, **35**, 515.
199. R. A. De Souza and J. A. Kilner, *Solid State Ionics*, 1998, **106**, 175.
200. R. A. De Souza, J. A. Kilner, and J. F. Walker, *Mater. Lett.*, 2000, **43**, 43.
201. B. C. H. Steele, *J. Power Sources*, 1994, **49**, 1.
202. L.-W. Tai, M. M. Nasrallah, H. U. Anderson, D. M. Sparlin, and S. R. Sehlin, *Solid State Ionics*, 1995, **76**, 259.
203. L.-W. Tai, M. M. Nasrallah, H. U. Anderson, D. M. Sparlin, and S. R. Sehlin, *Solid State Ionics*, 1995, **76**, 273.
204. N. P. Brandon, S. Skinner, and B. C. H. Steele, *Annu. Rev. Mater. Res.*, 2003, **33**, 183.
205. S. J. Skinner and J. A. Kilner, *Solid State Ionics*, 2000, **131**, 709.
206. S. J. Skinner and J. A. Kilner, *Ionics*, 1999, **5**, 171.
207. J. A. Kilner and C. K. M. Shaw, *Solid State Ionics*, 2002, **154–155**, 523.
208. V. V. Kharton, A. P. Viskup, E. N. Naumovich, and F. M. B. Marques, *J. Mater. Chem.*, 1999, **9**, 2623.
209. V. V. Kharton, V. V. Kharton, A. P. Viskup, A. V. Kovalevsky, E. N. Naumovich, and F. M. B. Marques, *Solid State Ionics*, 2001, **143**, 337.
210. V. V. Vashook, S. P. Tolochko, I. I. Yushkevich, L. V. Makhnach, I. F. Kononyuk, H. Altenburg, J. Hauck, and H. Ullmann, *Solid State Ionics*, 1998, **110**, 245.
211. W. Dieterich and P. Maass, *Adv. Sci. Technol. (Faenza, Italy)*, 2003, **37**, 159.
212. B. Roling, *J. Chem. Phys.*, 2000, **117**(3), 1320.
213. H. Eckert, E. Ratai, T. Torbrugge, and M. Witschas, *NATO Sci. Ser., II: Math., Phys. Chem.*, 2000, **76**, 15.
214. M. Ribes, E. Bychkov, and A. Pradel, *J. Optoelectron. Adv. Mater.*, 2000, **3**(3), 665.
215. K. Funke, *Prog. Solid State Chem.*, 1993, **22**, 111.
216. C. Cramer, S. Brunklaus, Y. Gao, and K. Funke, *J. Phys.: Condens. Matter*, 2000, **15**(31), S2309.
217. C. A. Angell, C. Liu, and E. Sanchez, *Nature*, 1993, **362**, 137.
218. W. Xu, L.-M. Wang, and C. A. Angell, *Electrochim. Acta*, 2000, **48**(14–16), 2037.
219. A. Hayashi, L. Wang, and C. A. Angell, *Electrochim. Acta*, 2003, **48**(14–16), 2003.
220. K. Murata, S. Izuchi, and Y. Yoshihisa, *Electrochim. Acta*, 2000, **45**, 1501.
221. T. Iijima, Y. Toyoguchi, and N. Eda, *Denki Kagaku*, 1985, **63**, 619.
222. H. Takahashi and H. Ashitaka, Extended Abstracts of 31st Japanese Battery Symposium, 1990, Vol. 1A16, 35.
223. J.-M. Tarascon, A. S. Gozdz, C. Schmutz, and F. Shokoohi, *Solid State Ionics*, 1996, **86**, 49.
224. D. W. Murphy, F. J. DiSalvo, J. N. Carides, and J. V. Waszczak, *Mater. Res. Bull.*, 1978, **13**, 1395.
225. M. Lazzari and B. Scrosati, *J. Electrochem. Soc.*, 1980, **127**, 773.
226. T. Nagaura and K. Tozawa, *Prog. Batt. Solar Cells*, 1990, **9**, 209.

227. J.-M. Tarascon, A. S. Gozdz, C. Schmutz, F. Shokoohi, and P. C. Warren, *Solid State Ionics*, 1996, **86–88**, 49.

228. V. Pralong, J.-B. Leriche, B. Beaudoin, E. Naudin, M. Morcrette, and J.-M. Tarascon, *Solid State Ionics*, 2004, **166**, 295.

229. F. Badway, N. Pereira, F. Cosandey, and G. G. Amatucci, *J. Electrochem. Soc.*, 2003, **150**(9), A1209.

230. N. Pereira, L. C. Klein, and G. G. Amatucci, *Solid State Ionics*, 2004, **167**(1–2), 29.

231. P. E. Stallworth, J. J. Fontanella, M. C. Wintersgill, C. D. Scheidler, J. J. Immel, S. G. Greenbaum, and A. S. Gozdz, *J. Power Sources*, 1999, **81**, 739.

232. C. G. Granquist, 'Handbook of Inorganic Electrochromic Materials', Elsevier, Amsterdam, 1995.

233. C. G. Granquist, *Sol. Energy Mater. Sol. Cells*, 2000, **60**, 201.

234. C. G. Granquist, *Solid State Ionics*, 1992, **53–56**, 479.

235. A. Azens and C. G. Granquist, *J. Solid State Electrochem.*, 2003, **7**, 64.

236. A. Azens, L. Kullman, G. Vaivars, H. Nordborg, and C. G. Granqvist, *Solid State Ionics*, 1998, **113–115**, 449.

237. R. Lechner and L. K. Thomas, *Sol. Energy Mater. Sol. Cells*, 1999, **54**, 139.

238. J. Nagai, G. D. McMeeking, and Y. Saitoh, *Sol. Energy Mater. Sol. Cells*, 1999, **56**, 309.

239. J. Karlsson and A. Roos, *Sol. Energy*, 2000, **68**, 493.

240. A. Azens, G. Vaivar, M. Veszelei, L. Kullman, and C. G. Granqvist, *J. Appl. Phys.*, 2001, **89**, 7885.

241. P. K. Shen, H. T. Huang, and A. C. C. Tseung, *J. Mater. Chem.*, 1992, **2**, 479.

242. A. Hjelm, C. G. Granqvist, and J. M. Wills, *Phys. Rev. B*, 1996, **54**, 2436.

243. S. Hufner, *Adv. Phys.*, 1994, **43**, 183.

244. C. G. Granqvist, *Sol. Energy Mater. Sol. Cells*, 2000, **60**, 201.

245. T. M. J. Nilsson and G. A. Niklasson, *Proc. Soc. Photo-Opt. Instrum. Eng.*, 1990, **129**, 1272.

Iridium: Inorganic & Coordination Chemistry

Catherine E. Housecroft
University of Basel, Basel, Switzerland

1	Introduction	1
2	Oxidation States and Geometries	1
3	Solid-State Compounds Excluding Halides	1
4	The Higher Oxidation States: Iridium(V) and Iridium(VI)	2
5	Mononuclear Complexes of Iridium(IV)	3
6	Mononuclear Complexes of Iridium(III)	4
7	The Lower Oxidation States: Mononuclear Complexes	12
8	Dinuclear and Multinuclear Iridium Complexes	14
9	Related Articles	17
10	References	17

1 INTRODUCTION

Iridium is a third-row d-block metal and is the heaviest element in group 9. It is a hard, lustrous, silvery metal, discovered by Tennant in 1803; the name iridium derives from the Latin *iris* (rainbow). The element occurs as a native platinum alloy and in osmiridium (a native alloy of osmium, 15–40%, and iridium, 50–80%). Selected physical and chemical properties of Ir are given in Table 1. It is considered both as a 'platinum metal' and as a precious metal. At room temperature, Ir is particularly resistant to corrosion.

In elemental analysis, the presence of Ir in a compound can be quantified by use of atomic absorption and emission spectroscopies. Both natural isotopes (*see Isotopes & Isotope Labeling*) of Ir possess nuclear spins ($I = 3/2$), but their use in NMR spectroscopy is limited by a large quadrupole moment (^{191}Ir, $Q = 1.5 \times 10^{-28}\,\mathrm{m}^2$; ^{193}Ir, $Q = 1.4 \times 10^{-28}\,\mathrm{m}^2$), low sensitivity (^{191}Ir, 0.023; ^{193}Ir, 0.050 with respect to ^{13}C), and low frequencies of observation (^{191}Ir, 6.87 Hz; ^{193}Ir, 7.48 Hz with respect to $^1\mathrm{H} = 400$ Hz). The ^{193}Ir nucleus is suitable for Mössbauer spectroscopy.

Iridium metal has a cubic close-packed structure at 298 K and is stable in air and water. It is inert toward acids but reacts with fused alkalis. In many respects, the chemistry of its compounds resembles that of its group 9 congener Rh (*see* ***Rhodium: Inorganic & Coordination Chemistry***).

Simple inorganic compounds commonly used as precursors to *Coordination Complexes* and that are commercially available include those listed in Table 2. The dark green hydrate of iridium(III) chloride is usually more reactive than the black anhydrous form.

General sources of reference are as follows: a survey of the chemistry of iridium (pre-1967);**[1]** compounds of the high oxidation states of Ir;**[2]** a detailed chemistry of elemental Ir and its alloys, solid-state compounds, and coordination complexes;**[3]** coordination chemistry of Ir;**[4–6]** organometallic complexes of Ir including complexes with inorganic ligands;**[7,8]** general chemistry of Rh and Ir along with that of other precious metals;**[9]** aspects of the chemistry of the platinum group metals;**[10]** structural aspects of elemental Ir and its binary compounds;**[11]** sources of reference for individual inorganic compounds of Ir;**[12]** chloro and bromo complexes of Ir(III) and Ir(IV);**[13,14]** halo complexes;**[15]** and phosphine, arsine, and stibine complexes.**[16]**

2 OXIDATION STATES AND GEOMETRIES

The ground-state electronic configuration of Ir is 6s^2 5d^7 (Table 1), and oxidation states (*see Oxidation Number*) in its compounds range from −I to +VI (Table 3). Of these, Ir in formal oxidation states −I, 0, and +I is stabilized by π-acceptor ligands (*see* ***Iridium: Organometallic Chemistry***). This article deals with compounds in which Ir is in formal oxidation state II, III, IV, V, or VI, as well as those complexes of Ir(I) that possess nonorganometallic features of significant interest. Table 3 also lists typical geometrical environments observed for iridium.

3 SOLID-STATE COMPOUNDS EXCLUDING HALIDES

The most stable oxide is the black iridium(IV) oxide, IrO_2; it forms when Ir is heated in oxygen or by controlled hydrolysis of alkaline solutions of $[IrCl_6]^{2-}$, and it crystallizes with a rutile structure. Pure crystalline IrO_2 can be prepared by slow, basic hydrolysis of $IrCl_3{\cdot}2.6H_2O$ at room temperature, followed by calcination at 900 °C.**[17]** Of practical importance is the fabrication of IrO_x pH electrodes, which have long-term stability; the method involves coating the surface of an Ir metal wire with iridium oxide by oxidizing the wire in a carbonate melt.**[18]**

High-temperature solid-state reactions**[3]** lead to mixed metal oxides (metal iridates) such as Na_2IrO_3 (from the reaction of Ir and Na_2CO_3 above 600 °C), $Bi_2Ir_2O_7$ (from IrO_2 and Bi_2O_3), $CaIrO_3$ (from 1:1 $IrO_2 : CaCO_3$), Ca_2IrO_4 (from 1:2 $IrO_2 : CaCO_3$), and the strontium iridates $SrIrO_3$, Sr_2IrO_4, and Sr_4IrO_6 (from $SrCO_3$ and IrO_2). Ca_2IrO_4 possesses a hexagonal structure with rutile-like chains held together by Ca^{2+} ions. In Sr_4IrO_6, each Ir atom is octahedrally sited and

Table 1 Physical properties of the element iridium

Atomic number	77
Atomic mass	192.22
Natural isotopes	^{191}Ir (37.3%); ^{193}Ir (62.7%)
Electronic configuration	[Xe] $4f^{14}6s^25d^7$
Melting point (°C)	2410
Boiling point (°C)	4130
$\Delta_{\mathrm{fus}}H$(mp) (kJ mol^{-1})	26.4
$\Delta_{\mathrm{vap}}H$(bp) (kJ mol^{-1})	612.1
Metallic radius (12-coordination) (Å)	1.36
Ionic radius $\mathrm{Ir^{2+}}$ (Å)	0.89
Ionic radius $\mathrm{Ir^{3+}}$ (Å)	0.75
Electronegativity (Pauling)	2.20

Table 2 Some commercially available precursors to inorganic compounds of iridium

Compound name	Formula
Iridium(III) chloride	$\mathrm{IrCl_3}$
Iridium(III) chloride hydrate	$\mathrm{IrCl_3}\cdot x\mathrm{H_2O}$
Sodium hexachloroiridate(IV) trihydrate	$\mathrm{Na_2[IrCl_6]\cdot 3H_2O}$
Potassium hexachloroiridate(IV)	$\mathrm{K_2[IrCl_6]}$
Sodium hexachloroiridate(III) hydrate	$\mathrm{Na_3[IrCl_6]}\cdot x\mathrm{H_2O}$
Potassium hexachloroiridate(III)	$\mathrm{K_3[IrCl_6]}$
Iridium(III) oxide hydrate	$\mathrm{Ir_2O_3}\cdot x\mathrm{H_2O}$
Iridium(IV) oxide	$\mathrm{IrO_2}$
Iridium(IV) chloride hydrate	$\mathrm{IrCl_4}\cdot x\mathrm{H_2O}$
Dihydrogen hexachloroiridate(IV) hydrate (chloroiridic acid)	$\mathrm{H_2IrCl_6}\cdot x\mathrm{H_2O}$

the $\mathrm{IrO_6}$ units are linked by $\mathrm{Sr^{2+}}$ ions. The iridate $\mathrm{KIrO_3}$ is prepared from $\mathrm{KO_2}$ and Ir metal. Quaternary oxides include $\mathrm{Ba_6ZnIr_4O_{15}}$ and $\mathrm{Ba_6CuIr_4O_{15}}$.**19**

At atmospheric pressure, Ir combines with sulfur to yield $\mathrm{IrS_2}$, which has an orthorhombic structure; it is isostructural with $\mathrm{IrSe_2}$. If the ratio of S:Ir is raised to ≈3:1, the sulfide formed has a pyrite structure with cation vacancies balancing the charge of the $\mathrm{Ir^{3+}}$ ions. At 60 kbar and 1500 °C and with a ratio of S:Ir = 3:1, the product has the stoichiometry $\mathrm{IrS_{2.9}}$; with a 2:1 ratio (60 kbar, 1500 °C), a new pyrite phase $\mathrm{IrS_{1.9}}$ is formed. Iridium(III) sulfide, $\mathrm{Ir_2S_3}$, possesses a solid-state structure in which pairs of face-sharing octahedra are joined to give an extended structure.

Iridium(VI) selenide, $\mathrm{IrSe_3}$, and the corresponding telluride, $\mathrm{IrTe_3}$, are made from $\mathrm{IrCl_3}$ and Se or Te, respectively. The Ir(IV) compounds $\mathrm{IrSe_2}$ and $\mathrm{IrTe_2}$ can be prepared from the respective elements or by reducing the corresponding Ir(VI) selenide or telluride with $\mathrm{H_2}$. In $\mathrm{IrSe_2}$, each Ir atom is octahedrally sited; half the Se atoms are each surrounded by three Ir atoms at the corners of a distorted tetrahedron, the fourth corner being occupied by a Se atom. The selenide $\mathrm{Ir_2Se_3}$ is prepared from $\mathrm{IrCl_3}$ and $\mathrm{H_2Se}$. The mixed chalcogenides IrSSe and $\mathrm{IrSe_{1.5}Te_{0.5}}$ are ***Semiconductors***.

The phosphide $\mathrm{IrP_2}$ is isomorphous with $\mathrm{RhP_2}$; $\mathrm{Ir_2P}$ and $\mathrm{IrP_3}$ adopt the *anti*-$\mathrm{CaF_2}$ and skutterudite structures, respectively. Crystalline $\mathrm{IrAs_3}$ and $\mathrm{IrSb_3}$ also possess a skutterudite structure. Ternary phosphides and arsenides include $\mathrm{Ca_2Ir_{12}P_7}$ and $\mathrm{Ca_5Ir_{19}P_{12}}$.**20**

4 THE HIGHER OXIDATION STATES: IRIDIUM(V) AND IRIDIUM(VI)

The highest oxidation states for Ir are VI and V, stabilized by ligands such as $\mathrm{F^-}$. $\mathrm{IrF_6}$ (a yellow crystalline solid, $\mu_{\mathrm{eff}} = 2.9\,\mu_{\mathrm{B}}$ at 300 K) is formed by the direct fluorination of Ir metal. Molecules of $\mathrm{IrF_6}$ are octahedral, and the structure has been studied in the gas phase by electron diffraction**21** and in the solid phase by EXAFS.**22** $\mathrm{IrF_6}$ is hydrolyzed by water, and reactions (1–4) illustrate its general reactivity. Reaction four represents the formation of the first binary, tripositive metal carbonyl complex.**23**

$$\mathrm{IrF_6} \xrightarrow{\mathrm{N_2O_4}} \mathrm{[NO]_2[IrF_6]} \qquad (1)$$

Table 3 Oxidation states and geometries of iridium in its compounds[a]

Oxidation state	Electronic configuration	Coordination number	Characteristic geometry	Example
−I	d^{10}	4	Tetrahedral	$\mathrm{[Ir(CO)_3(PPh_3)]^-}$
0	d^9			Cluster compounds, e.g. $\mathrm{Ir_4(CO)_{12}}$
I	d^8	4	Square planar	Vaska's compound = *trans*-$\mathrm{IrCl(CO)(PPh_3)_2}$
		5	Trigonal bipyramidal	$\mathrm{[Ir(dppe)_2(CNMe)]^+}$
II	d^7	4	Square planar	*trans*-$\mathrm{Ir(}t\mathrm{\text{-}Bu_2PC_6H_4O)_2}$
III	d^6	5	Trigonal bipyramidal	$\mathrm{IrH_3(AsPh_3)_2}$
		6	Octahedral	$\mathrm{[IrCl_6]^{3-}}$; $\mathrm{[Ir(CN)_6]^{3-}}$
IV	d^5	6	Octahedral	$\mathrm{[IrCl_6]^{2-}}$; $\mathrm{[Ir(C_2O_4)_3]^{2-}}$
V	d^4	6	Octahedral	$\mathrm{[IrF_6]^-}$
		5	Pentagonal bipyramidal	$\mathrm{IrH_5(PR_3)_2}$
VI	d^3	6	Octahedral	$\mathrm{IrF_6}$

[a] The boundary between organometallic and inorganic coordination complexes is not a precise one; note the borderline behavior of iridium(I).

$$IrF_6 \xrightarrow{SO_3} \underset{\text{Blue}}{IrF_4{\cdot}3SO_3} \qquad (2)$$

$$IrF_6 \xrightarrow{SO_2} \underset{\text{Orange-brown}}{IrF_5{\cdot}SO_2} \qquad (3)$$

$$IrF_6 \xrightarrow{\text{CO in liquid } SbF_5} [Ir(CO)_6][Sb_2F_{11}]_3 \qquad (4)$$

Few complexes of iridium(V) are known. Before 1965, literature references to 'IrF_4' actually refer to IrF_5. Reduction of IrF_6 by H_2 at 60 °C gives IrF_5; at 100 °C, further reduction leads to Ir metal. IrF_5 is a yellow crystalline solid ($\mu_{eff} = 1.32\,\mu_B$ at 296 K) with a tetrameric structure (**1**). It is moisture sensitive (equation 5). Other iridium(V) compounds include salts of the type (M)[IrF_6] ($M^+ = NO^+, K^+, Na^+, Rb^+, Cs^+, Ag^+, XeF^+, Xe_2F_{11}{}^+, ClO_2{}^+, Cl_4{}^+$). $KIrF_6$ and $CsIrF_6$ exhibit temperature-independent paramagnetism.

$$IrF_5 \xrightarrow{H_2O} IrO_2{\cdot}xH_2O + 5HF \qquad (5)$$

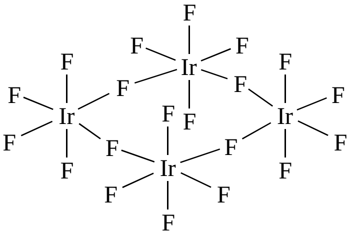

(**1**)

Hydride ligands (*see* ***Hydride Complexes of the Transition Metals***) stabilize iridium(V), for example, in the pentagonal bipyramidal complex $IrH_5(PMe_3)_2$,**[24]** which is characterized in the IR spectrum by an absorption at $1920\,cm^{-1}$ assigned to ν(Ir–H). The hydride complex $IrH_5(P(^iPr)_3)_2$ is an effective catalyst precursor for transfer hydrogenation reactions, including alkane dehydrogenation. The ligand $[C(Ph_2PO)_3]^-$ also stabilizes Ir(V), as observed in the complex $IrH_2\{C(Ph_2PO)_3\}(SiR_3)_2$.**[25]**

5 MONONUCLEAR COMPLEXES OF IRIDIUM(IV)

Among the halo complexes of iridium, the anions $[IrX_6]^{2-}$ (X = F, Cl, Br) containing Ir(IV) are the most stable. The white salts $M_2[IrF_6]$ ($M^+ = Na^+, K^+, Rb^+, Cs^+, NH_4{}^+, NO^+$) can be made by the reduction of M[IrF_6] using water; the Na^+ or $NH_4{}^+$ salts can be prepared by reacting $H_2[IrF_6]{\cdot}xH_2O$ with NaOH or NH_4OH. In neutral or acidic solutions, $[IrF_6]^{2-}$ is stable, but it decomposes in basic media. Electrochemical data for $[IrF_6]^{2-}$ in MeCN show an $[IrF_6]^{-/2-}$ process at +1.29 V and an irreversible $[IrF_6]^{2-/3-}$ process at 1.5 V(vs. SCE).**[26]**

Chloroiridic acid (Table 2), $H_2[IrCl_6]{\cdot}xH_2O$, is a deliquescent purple–black solid prepared by the dissolution of $K_2[IrCl_6]$ or $(NH_4)_2[IrCl_6]$ in aqua regia. Salts of $[IrCl_6]^{2-}$ can be made by chlorination of an MCl/Ir (M = alkali metal) mixture, or by reacting MCl with IrO_2 in hydrochloric acid. Oxidation of $[IrCl_6]^{3-}$ in acidic solution gives $[IrCl_6]^{2-}$ (equation 6). The ^{35}Cl and ^{37}Cl NQR frequencies and spin-lattice relaxation times in $Cs_2[IrCl_6]$ and $(NH_4)_2[IrCl_6]$ have been measured over the temperature range 4 to 350 K.**[27]** The ion $[IrCl_6]^{2-}$ is reduced quantitatively by KI or $Na_2C_2O_4$ to $[IrCl_6]^{3-}$, and is used as an oxidizing agent in some organic reactions. $Na_2[IrCl_6]$ is a water-soluble, black crystalline solid. It is an important precursor to a variety of coordination complexes of iridium (Scheme 1); note the predominance of iridium(III) products. Heating $(Et_4N)_2[IrCl_6]$ with CF_3CO_2H leads to the formation of $[Ir_2Cl_{10}]^{2-}$ (D_{2h}).**[28]**

$$4[IrCl_6]^{3-} + O_2 + 4H^+ \longrightarrow 4[IrCl_6]^{2-} + 2H_2O \qquad (6)$$

A series of aquachloro complexes, $[IrCl_x(H_2O)_{6-x}]^{(x-4)-}$ is known; *cis* and *trans* isomers (for $x = 2$) and *mer* and *fac* isomers (for $x = 3$) are prepared by oxidation of the corresponding Ir(III) complexes. In alkaline solutions, red–brown $[IrCl_6]^{2-}$ salts are unstable and the ion is reduced to yellow–green $[IrCl_6]^{3-}$. In the pH range 2.5–6.5, solutions of $[IrCl_6]^{2-}$ contain hydroxy species $[IrCl_x(OH)_{6-x}]^{2-}$; equilibrium constants (*see Equilibrium Constant*) are given in Table 4.

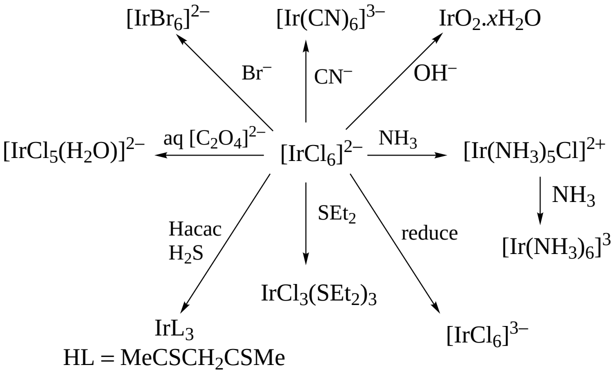

Scheme 1

Table 4 Formation of $[IrCl_x(OH)_{6-x}]^{2-}$ and equilibrium constants at 298 K

Equilibrium	Equilibrium constant, *K*
$[IrCl_6]^{2-} + OH^-[IrCl_5(OH)]^{2-} + Cl^-$	1.2×10^7
$[IrCl_5(OH)]^{2-} + OH^-\ [IrCl_4(OH)_2]^{2-} + Cl^-$	2.8×10^6
$[IrCl_4(OH)_2]^{2-} + OH^-[IrCl_3(OH)_3]^{2-} + Cl^-$	1.1×10^6
$[IrCl_3(OH)_3]^{2-} + OH^-[IrCl_2(OH)_4]^{2-} + Cl^-$	1.5×10^5

In 1953, the potassium salt $K_2[IrCl_6]$ was the subject of a classic electron spin resonance experiment.**[29]** Results were consistent with the presence of one unpaired electron ($5d^5$ low-spin) delocalized over all the ligands. This was one of the first pieces of evidence for the existence of metal–ligand π-bonding (*see π-Bond*). Significant π-bonding is also observed between the Ir(IV) center and nitrate ligands (Ir d $\rightarrow NO_3\ \pi^*$) in $K_2[Ir(NO_3)_6]$. Salts of $[IrBr_6]^{2-}$ may be made from $IrO_2{\cdot}xH_2O$ and HBr in the presence of a suitable cation, or by the reaction of $[IrCl_6]^{2-}$ with HBr. Reaction of $[IrCl_6]^{2-}$ with NaSCN results in reduction of Ir and formation of linkage isomers of *trans*-$[IrCl_2(SCN)_4]^{3-}$.**[30]** Heating $[NH_4]_2[Ir^{IV}Cl_6]$ with NH_4Cl in a sealed ampoule yields $[NH_4]_2[Ir^{III}(NH_3)Cl_5]$; changing the reaction conditions allows for isolation of $[Ir^{III}(NH_3)_5Cl]Cl_2$ and *trans*-$[Ir^{IV}(NH_3)_4Cl_2]Cl_2$.**[31]**

Mononuclear iridium(IV) compounds involving O-donor ligands are few. The hydroxide $Ir(OH)_4$ is formed when aqueous $K_2[IrBr_6]$ is treated with carbonate ions. Reaction of $Na_2[IrCl_6]$ with KOH at 120 °C leads to the red salt $K_2[Ir(OH)_6]$, and heating this salt to 270 °C converts it to $K_2[IrO_2(OH)_2]$. The reaction of N_2O_5 with $K_2[IrBr_6]$ (or the corresponding Cs^+ or Rb^+ salt) produces $K_2[Ir(NO_3)_6]$. The complex $[Ir(C_2O_4)_3]^{2-}$ is produced by oxidizing the corresponding Ir(III) species.

Iridium(IV) complexes with group 15 ligands include *trans*-$IrCl_4(PPr_3)_2$ and *trans*-$IrCl_4(AsPh_3)_2$. These complexes are potential oxidizing agents for organic transformations. An apparently similar iodo complex $IrI_4(PPh_2Me)_2$ is actually the Ir(III) complex $[Ir_2I_5(PPh_2Me)_4][I_3]$ (**2**).**[32]**

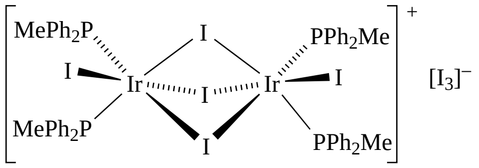

(**2**)

6 MONONUCLEAR COMPLEXES OF IRIDIUM(III)

The Ir(III) ion has a d^6 configuration. In octahedral complexes, the low-spin state ($t_{2g}{}^6$) is favored and the Ir center is kinetically inert.

6.1 Complexes with Halide and Related Ligands

Iridium(III) fluoride is a dark brown solid, insoluble in water and dilute acids. It is prepared by heating Ir metal with IrF_6 and N_2 at 500 °C. Direct fluorination of Ir in the correct stoichiometric ratio gives a mixture of IrF_3 and IrF_5. Iridium(III) chloride is dimorphic: the α-form (made from Ir and Cl_2 at 600 °C) is brown and the β-form (made by heating α-$IrCl_3$) is red. Other color variations are observed under varying preparative conditions. Both forms of anhydrous $IrCl_3$ are insoluble in water. The hydrated complex $IrCl_3{\cdot}xH_2O$ is dark green and is water soluble; $IrCl_3{\cdot}xH_2O$ is a precursor to a range of Ir(III) complexes, examples of which are given in Scheme 2. Insoluble $IrBr_3$ can be made from Ir and Br_2 (8 atm) at 540 °C. Early reports of $IrBr_3$ may refer to Ir_2OBr_6. Critical discussions of various forms of iridium(III) halides are available.**[1,3,4,15]** In addition, chloro and bromo complexes of Ir(III) have been reviewed.**[13,14]**

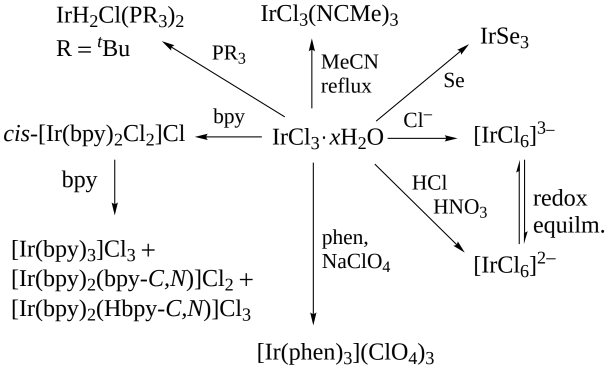

Scheme 2

The reduction of octahedral $[IrCl_6]^{2-}$ (Scheme 1) by oxalate or nitrite ion gives octahedral $[IrCl_6]^{3-}$. Alternative routes to particular salts include heating Ir metal with NaCl and Cl_2 to give $Na_3[IrCl_6]$, or the reduction of $M_2[IrCl_6]$ ($M^+ = K^+$ or $NH_4{}^+$) with H_2 to give $M_3[IrCl_6]$. The use of $[IrCl_6]^{3-}$ as a precursor to a variety of Ir(III) complexes is illustrated in Schemes 3–6. Complexes of Ir(III) with ligands other than halides are discussed in more detail in later sections. The $[IrCl_6]^{3-}$ anion hydrolyzes to give $[IrCl_5(H_2O)]^{2-}$, $[IrCl_4(H_2O)_2]^-$, and $IrCl_3(H_2O)_3$; a dissociative mechanism has been proposed for this hydrolysis.

The cyanide ligand**[33]** is often considered as a pseudohalide (*see Pseudohalide*). Fusion of $(NH_4)_3[IrCl_6]$ with KCN gives $K_3[Ir(CN)_6]$, which can be isolated as pale yellow crystals after recrystallization from water. Derivative anions of the type $[Ir(CN)_5X]^{n-}$ (X = halide or hydroxide, $n = 3$; X = MeCN, $n = 2$) can be prepared as shown in Scheme 7.

6.2 Complexes with Nitrogen Donor Ligands

Methods of preparing nitrito complexes of Ir(III) are shown in Scheme 3. Structural characterization of $(NH_4)_3[Ir(NO_2)_6]$ shows that each $NO_2{}^-$ ligand coordinates through the nitrogen atom (Ir–N = 2.060 Å). The coordination of thiocyanate ligands (NCS^-) is discussed in Section 6.6; in $[Ir(NCS)_6]^{3-}$, the ligand exhibits *Linkage Isomerism* and

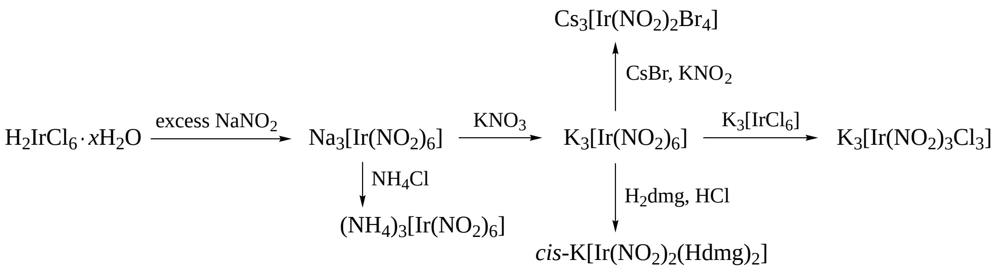
Cs3[Ir(NO2)2Br4]
CsBr, KNO2
H2IrCl6·xH2O
excess NaNO2
Na3[Ir(NO2)6]
KNO3
K3[Ir(NO2)6]
K3[IrCl6]
K3[Ir(NO2)3Cl3]
NH4Cl
(NH4)3[Ir(NO2)6]
H2dmg, HCl
cis-K[Ir(NO2)2(Hdmg)2]

Scheme 3

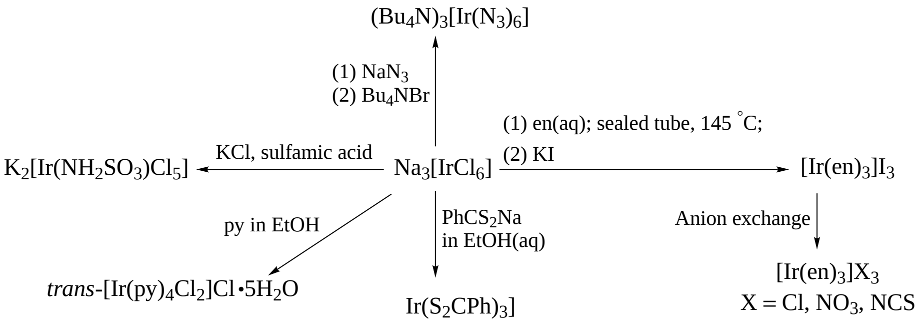
(Bu4N)3[Ir(N3)6]
(1) NaN3
(2) Bu4NBr
(1) en(aq); sealed tube, 145 °C;
(2) KI
K2[Ir(NH2SO3)Cl5]
KCl, sulfamic acid
Na3[IrCl6]
[Ir(en)3]I3
py in EtOH
PhCS2Na
in EtOH(aq)
Anion exchange
trans-[Ir(py)4Cl2]Cl•5H2O
Ir(S2CPh)3]
[Ir(en)3]X3
X = Cl, NO3, NCS

Scheme 4

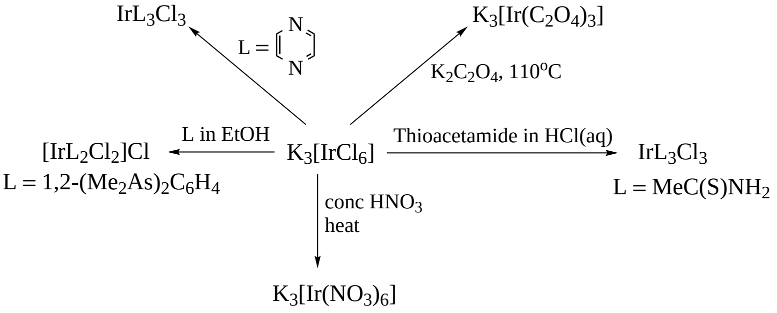
IrL3Cl3
L =
N
N
K3[Ir(C2O4)3]
K2C2O4, 110°C
[IrL2Cl2]Cl
L = 1,2-(Me2As)2C6H4
L in EtOH
K3[IrCl6]
Thioacetamide in HCl(aq)
IrL3Cl3
L = MeC(S)NH2
conc HNO3
heat
K3[Ir(NO3)6]

Scheme 5

the mixture of isomers can be separated by ion-exchange chromatography.[34]

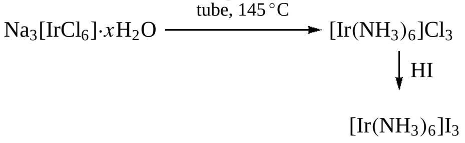
Na3[IrCl6]·xH2O
NH3(aq) in sealed
tube, 145 °C
[Ir(NH3)6]Cl3
HI
[Ir(NH3)6]I3

(7)

Syntheses of octahedral Ir(III) hexammine complexes are shown in equation (7). The cation $[Ir(NH_3)_5(H_2O)]^{3+}$ can be made indirectly (Scheme 8) or by photolyzing (254 or 313 nm) $[Ir(NH_3)_6]^{3+}$ in aqueous solution. A high-yield route to $Ir(NH_3)_3Cl_3$ involves the reaction of $IrCl_3\cdot xH_2O$ with 12 M

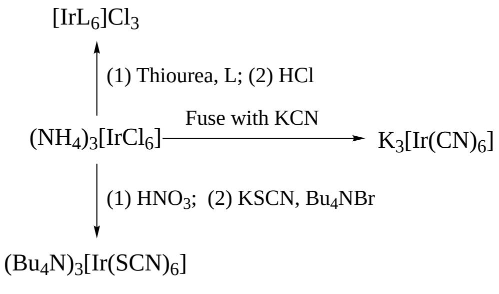
[IrL6]Cl3
(1) Thiourea, L; (2) HCl
(NH4)3[IrCl6]
Fuse with KCN
K3[Ir(CN)6]
(1) HNO3; (2) KSCN, Bu4NBr
(Bu4N)3[Ir(SCN)6]

Scheme 6

NH_3 at 150 °C.[35] The introduction of 1,2-ethanediamine (en) gives $[Ir(en)_3]^{3+}$ (Scheme 4). Both *cis* and *trans* isomers of

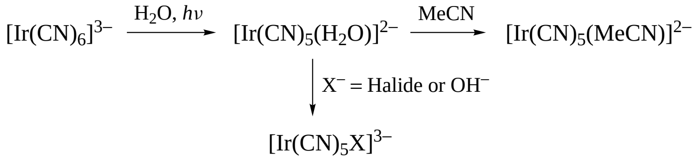

$$\begin{tikzcd} {[Ir(CN)_6]^{3-}} \arrow[r, "H_2O,\ h\nu"] & {[Ir(CN)_5(H_2O)]^{2-}} \arrow[r, "MeCN"] \arrow[d, "X^- = \text{Halide or OH}^-"] & {[Ir(CN)_5(MeCN)]^{2-}} \\ & {[Ir(CN)_5X]^{3-}} & \end{tikzcd}$$

Scheme 7

$[IrX_2(en)_2]^+$ have been prepared for X = halide; the complex cations *trans*-$[Ir(X)(Cl)(en)_2]^+$ are known for X = Br^-, I^-, OH^-, NCS^-, $NO_2{}^-$. A halide ligand in *trans*-$[IrX_2(en)_2]^+$ is rapidly substituted by H_2O when the complex is irradiated (350 nm). This reaction gives a useful route to several other complexes of the general type *trans*-$[Ir(X)(Y)(en)_2]^{n+}$ (equation 8). Although less common than a didentate mode, the en ligand can also act as a monodentate ligand, for example, in *mer*-$IrCl_3(en)_2$ (**3**).**[36]**

$$\begin{tikzcd} trans\text{-}[IrCl_2(en)_2]^+ \arrow[r, "h\nu,\ I^-"] & trans\text{-}[IrCl(I)(en)_2]^+ \arrow[d] \\ & trans\text{-}[IrI_2(en)_2]^+ \end{tikzcd} \qquad (8)$$

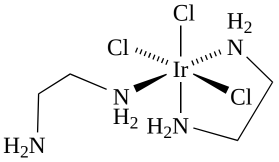

(**3**)

The azide ion coordinates to Ir(III) in complexes such as $[Ir(N_3)_6]^{3-}$ (Scheme 4), *trans*-$[Ir(en)_2(N_3)_2]^+$ (equation 9), and $[Ir(N_3)(NH_3)_5]^{2+}$. Both *trans*-$[Ir(en)_2(N_3)_2]^+$ and $[Ir(N_3)(NH_3)_5]^{2+}$ liberate N_2 on addition of acid; a mechanism via a nitrene intermediate has been proposed.**[4]** The complex *trans*-$[Ir(en)_2(NH_2Cl)_2]Cl_3$ is formed when *trans*-$[Ir(en)_2(N_3)_2]Cl$ reacts with HCl.

$$trans\text{-}[Ir(en)_2Cl_2]^+ + 2N_3{}^- \xrightarrow[\text{tube, 140 °C}]{\text{aq, sealed}} trans\text{-}[Ir(en)_2(N_3)_2]^+ + 2Cl^- \qquad (9)$$

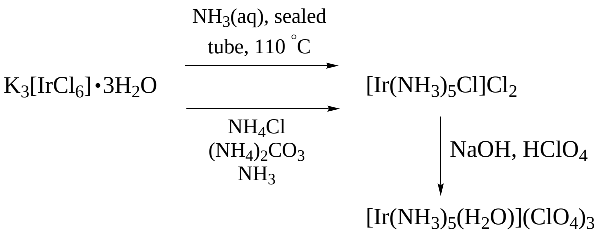

$$\begin{tikzcd} K_3[IrCl_6]\cdot 3H_2O \arrow[r, "\text{NH}_3\text{(aq), sealed tube, 110 °C}"] \arrow[r, shift right=3, "\text{NH}_4\text{Cl, (NH}_4)_2\text{CO}_3\text{, NH}_3"'] & {[Ir(NH_3)_5Cl]Cl_2} \arrow[d, "\text{NaOH, HClO}_4"] \\ & {[Ir(NH_3)_5(H_2O)](ClO_4)_3} \end{tikzcd}$$

Scheme 8

Coordination of N_2H_4 is exemplified in $Ir(N_2H_4)_3Br_3\cdot 0.5\,H_2O$ (equation 10). The coordination of diazonato ligands is well established; diazonato complexes are useful models for catalytic intermediates in the activation of N_2. Vaska's compound, *trans*-$IrCl(CO)(PPh_3)_2$, reacts with $[ArN{=}N](BF_4)$ in the presence of LiCl to give octahedral $IrCl_2(CO)(N{=}NAr)(PPh_3)_2$ in which the diazonato ligand has a bent geometry. In the absence of LiCl, the five-coordinate complex (**4**) is obtained. Conditions for the reaction are important: in EtOH, Vaska's compound reacts with $[ArN{=}N]^+$ to give the cyclometalated product (**5**) (*see Cyclometalation*), in addition to complex (**6**).

$$K[Ir(NO)Br_5] + N_2H_4\cdot nH_2O \longrightarrow Ir(N_2H_4)_3Br_3\cdot 0.5H_2O \qquad (10)$$

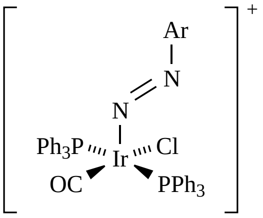

(**4**)

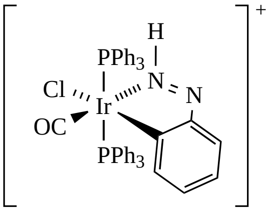

(**5**)

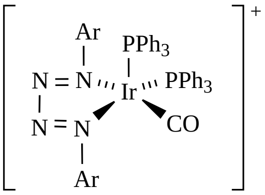

(**6**)

Complex (**7**) is an unusual example of a nitroxyl derivative, formed from the reaction of $Ir(NO)(PPh_3)_3$ with anhydrous HCl.**[37]**

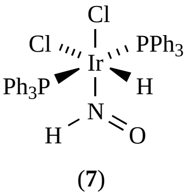

(**7**)

Many Ir(III) complexes containing heterocyclic N-donor ligands are known. Pyridine (py) reacts with $Na_3[IrCl_6]$ (Scheme 4) to yield *trans*-$[Ir(py)_4Cl_2]Cl{\cdot}5H_2O$. Photolysis of this complex in py gives *mer*-$Ir(py)_3Cl_3$ which, in a $CHCl_3$ solution in light, converts to $[Ir(py)_2Cl_3]_n$ and other products. The Ir(IV) complex $(NH_4)_2[IrCl_6]$ reacts with $[C_2O_4]^{2-}$ and py to give $[pyH][Ir(py)_2Cl_4]$; both the *trans* (red) and *cis* (yellow) isomers are formed, and the $[pyH]^+$ cation can be exchanged for Na^+ or $NH_4{}^+$. Water exchanges for a chloride ligand in the *trans* isomer without disruption of the *trans* arrangement of the py ligands; in the *cis* isomer, the H_2O-for-Cl^- exchange results in a mixture of isomers of $Ir(py)_2Cl_3(H_2O)$. Structures (**8**) to (**10**) show the three isomers of $Ir(py)_2Cl_3(H_2O)$. Complex (**8**) is prepared from *cis*-$(NH_4)[Ir(py)_2Cl_4]$ with py in water (110 °C). Complex (**9**) is made by photolyzing *cis*-$K[Ir(py)_2Cl_4]{\cdot}H_2O$, and (**10**) is formed from *trans*-$Na[Ir(py)_2Cl_4]$ in water. Related monodentate ligands that complex to Ir(III) are substituted pyridines, pyrazine, pyridazine, and pyrimidine.

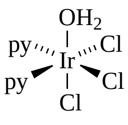

(**8**)

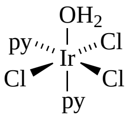

(**9**)

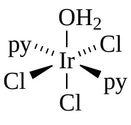

(**10**)

Over the years, reports of '$[Ir(bpy)_3]^{3+}$' (bpy = 2,2′-bipyridine) have been unclear.[38] Early studies most probably refer to $[Ir(bpy)_2Cl_2]^+$ rather than the tris-bpy complex. Under chloride-free conditions, a complex containing three bpy ligands was isolated, but it exhibited properties that were unexpected for an N_6-donor set. X-ray diffraction data confirmed that one bpy ligand was C,N- rather than N,N'-bound to Ir(III), that is, $[Ir(bpy\text{-}N,N')_2(bpy\text{-}C,N)]^{2+}$ (**11**) formed after cyclometallation had occurred.[39] The dication (**11**) can be prepared from bpy and a mixture of $K_2[IrCl_6]$ and $K_3[IrCl_6]$; the presence of Ir(IV) facilitates cyclometallation. The uncoordinated N atom in (**11**) can be protonated to give trication (**12**). Interest in the bipyridine complexes of this family arises in part from their particular photochemical and photophysical properties. The noncyclometalated complex $[Ir(bpy)_3]^{3+}$ can be prepared by treating $[Ir(bpy)_2(O_3SCF_3)_2]^+$ with bpy, and the presence of three N,N'-bound ligands has been confirmed crystallographically. Ligands related to bpy are 1,10-phenanthroline, (phen, **13**), and oligopyridines. Again, the literature is not definitive. Although complexes with phen are reported to exhibit anomalous behavior related to that of the bpy complexes, this clearly cannot originate from cyclometallation because the phen ligand, unlike bpy, is not flexible enough to adopt the conformation needed to become an N,C-chelate. The luminescent properties of Ir(III) polyimine complexes (with charge-transfer or ligand-centered emissive states) have stimulated a range of studies, which have been reviewed.[40] The lifetimes of the Ir(III) excited states range from nanoseconds to microseconds. Complexes with $IrN_6{}^{3+}$ units behave as photooxidants; in contrast, those with cyclometalated IrN_3C_3 units are photoreductants. The luminescent, cyclometalated complexes $[Ir(ppy)_2(phen\text{-}NCS)]^+$ and $[Ir(ppy)_2(phen\text{-}NHCOCH_2I)]^+$ (Hppy = 2-phenylpyridine, phen-NCS = 5-isothiocyanato-1,10-phenanthroline, $phenHNCOCH_2I$ = 5-(iodoacetamido)-1,10-phenanthroline) and related complexes have been used to label modified oligonucleotides and proteins, thereby producing luminescent bioconjugates.[41,42] The long-lived luminescence of bis-tpy (tpy = **14**) complexes of Ir(III) in which the tpy ligands carry N-methylpyridyl substituents is quenched by Cl, providing the basis for a chloride ion sensor.[43]

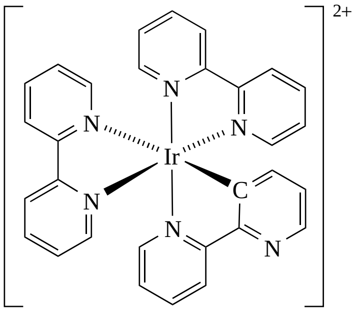

(**11**)

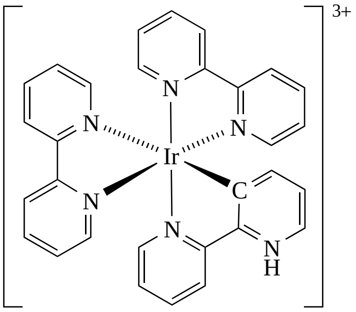

(**12**)

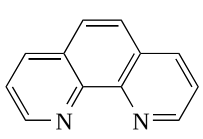

(**13**)

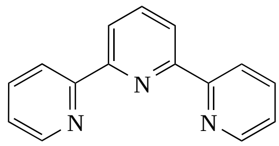

(**14**)

An overview of trispyrazolylborate (**15**) complexes of iridium has been included in a wider review of Rh and Ir complexes including these and derivative ligands.[44]

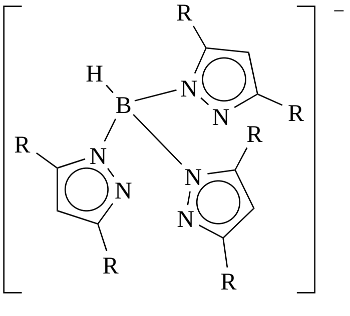

R = H, Me

(15)

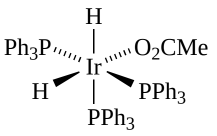

(16)

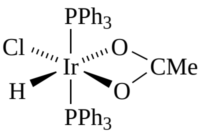

(17)

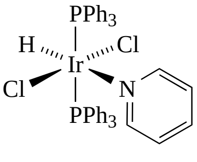

(18)

6.3 Complexes with Phosphorus Donor Ligands

Since phosphine ligands[16] stabilize low oxidation states of d-block metals, it is not surprising that a large number of phosphine-containing complexes of iridium exhibit the metal in oxidation states +1 and below. Nonetheless, there is a large group of complexes of general formula $Ir(PR_3)_3H_3$, $Ir(PR_3)_3H_2X$, $Ir(PR_3)_3HX_2$ and $Ir(PR_3)_3X_3$ (X = halide ligand; R = alkyl or aryl substituent) that formally contain Ir(III).[3,4] Selected syntheses are given in equations (11–14). Related species in which other ligands take the place of the halides include $Ir(PPh_3)_3H_2(O_2CMe)$ (**16**), $Ir(PPh_3)_2HCl(O_2CMe)$ (**17**), and $Ir(PPh_3)_2HCl_2(py)$ (**18**). The entire range of complexes known is too varied[3,12] to describe in detail here. Some of these iridium(III) complexes are used as catalysts, for example, $Ir(PEt_2Ph)_3HCl_2$ is a catalyst for the isomerization of dienes and of 1-octene, and $Ir(PPh_3)_2H_2(O_2CR)$ (R = Me, Et, Pr) catalyzes the homogeneous hydrogenation of nonactivated α-alkenes. Complexes $[Ir(PR_3)_2H_2L_2]^+$ containing *trans*-PR_3 and *cis*-H are known, for example, L = MeI, H_2, Me_2CO, R_3SiH, and H_2O. The anionic complex $[Ir(P^iPr_3)_2HI_3]^-$ forms when $Ir(P^iPr_3)_2HI_2$ dissolves in Bu_4NI; $[Ir(P^iPr_3)_2HCl_3]^-$ has also been prepared and characterized.[45]

$$Ir(PMe_3)_2H_5 \xrightarrow{\text{PMe}_3\text{ in benzene}} fac\text{-}Ir(PMe_3)_2H_3 \qquad (11)$$

$$\underset{\text{R = Et, Pr}}{mer\text{-}Ir(PR_3)_3Cl_3} \xrightarrow{\text{EtOH, KOH (aq)}} mer\text{-}Ir(PR_3)_3Cl_2H \qquad (12)$$

$$\left.\begin{array}{l} Na_2[IrCl_6]\cdot xH_2O \\ IrCl_3\cdot xH_2O \end{array}\right\} \xrightarrow{\text{PPh}_3\text{/NaBH}_4\text{/EtOH}} \begin{array}{c} mer\text{-}Ir(PPh_3)_3H_3 \\ + \\ fac\text{-}Ir(PPh_3)_3H_3 \end{array} \qquad (13)$$

An interesting property of *mer*-$Ir(PMe_3)_3Cl_3$ and *mer*-$Ir(PMe_2Ph)_3Cl_3$ is their reactions with strong bases such as $^iPr_2NLi$ or BuLi (equation 15). When the cyclometalated product with R=Ph is treated with Cl_2, ring opening occurs to yield *mer*-$IrCl_3(PMe_2Ph)_2(PMePhCH_2Cl)$, which rearranges to the *fac* isomer.

$$\begin{tikzcd} H_2[IrCl_6]\cdot xH_2O \arrow[r, "\text{PMe}_2\text{Ph, HCl}", "\text{in MeOCH}_2\text{CH}_2\text{OH}"'] & mer\text{-}Ir(PMe_2Ph)_3Cl_3 \arrow[d, "\text{reflux in CCl}_4"] \\ & fac\text{-}Ir(PMe_2Ph)_3Cl_3 \end{tikzcd} \qquad (14)$$

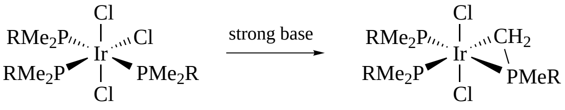

(15)

The coordination of didentate phosphine ligands to Ir(III) is illustrated by the formation of *cis*-$[Ir(dppe)_2H_2]X$ (prepared by the *Oxidative Addition* of H_2 to $[Ir(dppe)_2]X$), where X = Br or Cl; *cis*-$[Ir(dppe)_2HCl]Cl$ (by the oxidative addition of HCl to $[Ir(dppe)_2]Cl$); and $[Ir(dppp)_2HCl](PF_6)$ (from the oxidative addition of HCl to $[Ir(dppp)_2]Cl$ in the presence of HPF_6). Complexes containing multidentate phosphine ligands include IrL^1Cl_3 (L^1 = **19**) (prepared from $H_2[IrCl_6]\cdot xH_2O$ and L^1), IrL^2Cl_3 (L^2 = **20**) (prepared from $Na_2[IrCl_6]\cdot 6H_2O$ and L^2 in ethanolic HCl), IrL^2H_3 (made from IrL^2Cl_3), $[Ir(L^3)HBr](BPh_4)$ (L^3 = **21**) (from $Ir(PPh_3)_3HBr_2$ and L^3, with anion exchange), and $[Ir(L^3)Br_2](BPh_4)$ (prepared from $[Ir(L^3)HBr]Br$ and Br_2 in the presence of $[BPh_4]^-$). Other related systems have been prepared.[3,4,12] The formation of bridged multinuclear complexes may also be a possibility.

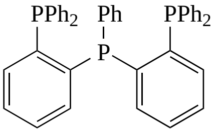

(19)

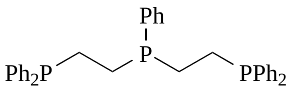

(20)

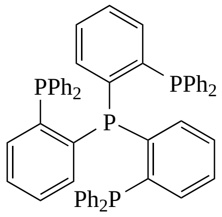

(21)

6.4 Complexes with Arsenic or Antimony Donor Ligands

Complexes of the type $Ir(AsR_3)_3X_3$ (X = halide)[3] are fairly large and selected synthesis methods are given in equations (16) to (18); most compounds are either yellow, orange, or brown. Complexes of the general formula $Ir(AsR_3)_3HX_2$ (X = halide)^3 tend to be white, yellow, or orange. Several complexes exist in both the isomeric forms shown in (**22**) and (**23**), but the tendency for isomerization from (**22**) to (**23**) is less for the arsine complexes than for the corresponding phosphine derivatives. The complexes *fac*-$Ir(AsEt_2Ph)_3H_3$, *fac*-$Ir(AsPh_3)_3H_3$, and *mer*-$Ir(AsPh_3)_3H_3$ can be prepared from corresponding halo complexes $Ir(AsPh_3)_3HX_2$ using $[BH_4]^-$ or $[AlH_4]^-$ as the hydride source.

$$H_2[IrCl_6]\cdot xH_2O \xrightarrow{\text{AsEt}_3\text{, HCl in EtOH}} mer\text{-}Ir(AsEt_3)_3Cl_3 \qquad (16)$$

$$Na_3[IrCl_6]\cdot xH_2O \xrightarrow{\text{AsMePh}_2\text{, HI in EtOH}} Ir(AsMePh_2)_3I_3 \qquad (17)$$

$$Ir(AsPh_3)_3H_3 \xrightarrow{\text{Br}_2\text{, benzene}} Ir(AsPh_3)_3Br_3 \qquad (18)$$

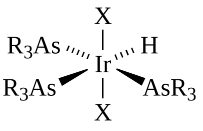

(**22**)

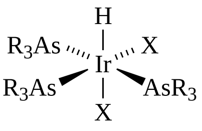

(**23**)

Multidentate arsine ligands that coordinate to Ir(III) include $Ph_2AsCH_2CH_2AsPh_2$, 1,2-$(AsMe_2)_2C_6H_4$ (Scheme 5), $PhAs(C_6H_4AsPh_2\text{-}2)_2$, and $As(C_6H_4AsPh_2\text{-}2)_3$.

Only a few complexes exhibiting stibine ligands have been prepared and characterized. Amongst them are *mer*- and *fac*-$Ir(SbPh_3)_3Cl_3$, $Ir(SbPh_3)(PEt_2Ph)_2H_3$, $[Ir(SbPh_3)_2Cl_4]^-$, $Ir(SbPh_3)_3HCl_2$, $Ir(SbPh_3)_3H_2Cl$, and related bromo complexes.**[3]**

6.5 Complexes with Oxygen Donor Ligands

The hexaaqua ion $[Ir(H_2O)_6]^{3+}$ is air sensitive. It is prepared (with difficulty) from the hydrolysis product of $(NH_4)_2[Ir^{IV}Cl_6]$ but is not a well-characterized ion. Iridium(III) hydroxide is formed as an olive-green precipitate by hydrolyzing $H_2[IrCl_6]$ with NaOH in ethanol (at pH 12, 40 °C), by treating $K_3[IrCl_6]$ with KOH under a CO atmosphere, or by dissolving $IrO_2\cdot xH_2O$ in sulfuric acid and adding NaOH. It is not well characterized but can be used to prepare other complexes, for example, yellow $Ir(acac)_3$ (equation 19) and orange–yellow IrL_3, where HL = $CF_3COCH_2COCF_3$. The structures of $Ir(acac)_3$ and $Ir(acacX)_3$ (X = Cl, Br, and I in the γ-position) have been determined.**[46]**

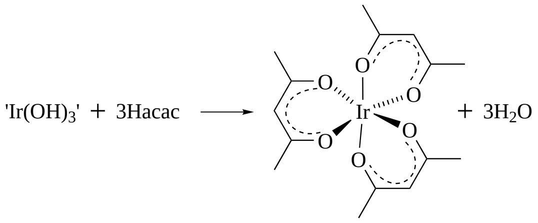

(19)

Scheme 5 shows a route to the violet-colored $K_3[Ir(NO_3)_6]$. The reaction of HNO_3 with $K_3[Ir(NO_2)_6]$ leads to $K_3[Ir(NO_3)_3(NO_2)_3]$. A range of mixed ligand complexes involving coordinated NO_3^- or NO_2^- anions is known,**[3,4]** for example, $[Ir(NO_2)_2(en)_2]^+$, $[Ir(NO_2)_3Cl_3]^{3-}$, $[Ir(NO_2)_2(C_2O_4)_2]^{3-}$, $IrCl(NO_3)_2(CO)(PPh_3)_2$, and $Ir(NO_2)(NO_3)_2(CO)(PPh_3)_2$. The NO_2^- ligand can be O- or N-bonded (the structure of $[Ir(NO_2)_6]^{3-}$ is described later); the NO_2^- ligand in the complex $[Ir(NH_3)_5(NO_2)]^{2+}$ undergoes a change from O- to N-coordination in aqueous basic solution.

Coordination of sulfate ligands to Ir(III) often leads to multinuclear complexes (see Section 8), and a similar trend is observed for carboxylate complexes. In equation (20), acetate acts as a monodentate ligand; structures (**16**) and (**17**) give examples of monodentate and didentate modes. Iridium(III) complexes of the type $Ir(H)X(CO)(PR'_3)_2(O_2CR)$ are formed via the oxidative addition of RCO_2H (e.g. R = H, Me, Ph) to $Ir^IX(CO)(PR'_3)_2$ (X = Cl, Br, I; e.g. R′ = Et, Ph). The complexes $IrCl(PR'_3)_2(O_2CR)_2$ (e.g. R = R′ = Ph; R = Me, R′ = Ph) are formed by the reaction of $IrCl(PR'_3)_2(CO)$ or $IrCl(PR'_3)_2(N_2)$ with RCO_3H (a peroxycarboxylic acid) and possess both mono- and didentate carboxylates (**24**).

$$[Ir(NH_3)_5(OH)]^{2+} + MeCO_2H \longrightarrow [Ir(NH_3)_5(MeCO_2)]^{2+} + H_2O \qquad (20)$$

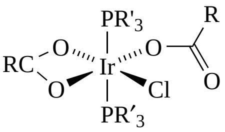

(**24**)

The complex anion $[Ir(C_2O_4)_3]^{3-}$ may be prepared from Ir(III) or Ir(IV) precursors (Scheme 5, and equations 21 and 22). Studies on the complex have been quite extensive.**[4]** The structures of optically active $K_3[Ir(C_2O_4)_3]\cdot 2H_2O$ and racemic $K_3[Ir(C_2O_4)_3]\cdot 4.5H_2O$ have been crystallographically determined; Ir is octahedral as expected (Ir–O = 1.96 Å in $K_3[Ir(C_2O_4)_3]\cdot 2H_2O$).

$$K_2[IrCl_6] \xrightarrow{K_2C_2O_4\text{ heat in aq. slurry}} K_3[Ir(C_2O_4)_3]\cdot 4H_2O \qquad (21)$$

$$IrO_2\cdot nH_2O \xrightarrow[\text{2. Ca}^{2+}]{\text{1. H}_2\text{C}_2\text{O}_4\text{/KHCO}_3} Ca_3[Ir(C_2O_4)_3]_2 \qquad (22)$$

Iridium(III) complexes incorporating β-diketonate ligands include $Ir(acac)_3$ (equation 19), γ-halogenated derivatives,**[46]** and IrL_3 (HL = $CF_3C(O)CH_2C(O)CF_3$) (see above). The reaction of $Ir(PPh_3)_2H_3$ with Hacac leads to complex (**25**); similar reactions occur with other β-diketones.

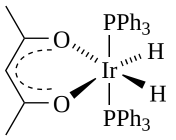

(**25**)

6.6 Complexes with Sulfur Donor Ligands

The thiocyanate ion, NCS^-, may be N-bonded (thiocyanate ligand) or S-bonded (isothiocyanate ligand) to a transition metal ion (*see d–d Transitions*), and in the absence of X-ray diffraction results, IR spectroscopic data are an important means of assigning the coordination mode. Linkage isomers of $[Ir(SCN)_6]^{3-}$ can be separated by ion-exchange chromatography.[34] In $(NH_4)_3[Ir(SCN)_6]$ (Scheme 6), IR spectral data are consistent with S-bonded ligands (ν_{CN} = 2127, 2098 cm^{-1}, ν_{CS} = 822, 693 cm^{-1} in the solid state) and this has been confirmed by X-ray diffraction data.[34] $[Ir(NH_3)_5(H_2O)]^{3+}$ reacts with aqueous NaSCN to yield $[Ir(NH_3)_5(SCN)]^{2+}$. Both linkage isomers are observed; the N-bonded isomer dominates and crystallizes out before the S-bonded complex.

A variety of Ir(III) complexes with SR^- (R = H, alkyl, or aryl) ligands are known. The oxidative addition of H_2S to Ir(I) is shown in equation (23); similar oxidative addition reactions between $Ir(PPh_3)_3Cl$ and RSH lead to complexes of the type $Ir(SR)(H)Cl(PPh_3)_2$. Arsine analogs are also known. $Cp^*IrCl_2(PMe_3)$ reacts with NaSH and H_2S to give $Cp^*Ir(SH)_2(PMe_3)$. Dialkyl or diaryl sulfide ligands can be introduced as in equation (24) and Scheme 9. The red product gained after chloroform extraction in Scheme 9 has been referred to in the literature as '*trans*-$Ir(SEt_2)_3Cl_3$', but in a $MeNO_2$ solution, it is a 1:1 electrolyte.

$$\begin{tikzcd}
(NH_4)_2[IrCl_6] \arrow[r, "\text{Et}_2\text{S in EtOH reflux}"] & {} \arrow[r, "\text{Extract in C}_6\text{H}_6"] \arrow[d, "\text{Extract in CHCl}_3"] & mer\text{-}Ir(SEt_2)_3Cl_3\ \text{yellow} \\
& {[trans\text{-}Ir(SEt_2)_4Cl_2][trans\text{-}Ir(SEt_2)_2Cl_4]}\ \text{Red } trans \text{ isomer} \arrow[d, "AgNO_3"] & \\
& {[trans\text{-}Ir(SEt_2)_4Cl_2](NO_3) + Ag[trans\text{-}Ir(SEt_2)_2Cl_4]} &
\end{tikzcd}$$

Scheme 9

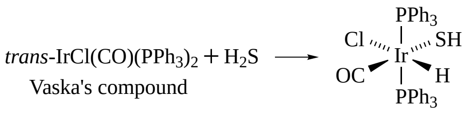

(23)

$$\begin{tikzcd}
H_2[IrCl_6]\cdot xH_2O \arrow[r, "Me_2S"] & mer\text{-}Ir(SMe_2)_3Cl_3 \arrow[d, "LiBr"] \\
& mer\text{-}Ir(SMe_2)_3Br_3
\end{tikzcd} \qquad (24)$$

Iridium(III) complexes containing thiourea, thioacetamide, and dithioacetylacetonate ligands are known (Schemes 1, 5 and 6), and Ir(III) dithiocarbamate complexes $Ir(S_2CNR_2)_3$ (**26**) have been prepared from either $Na_2[Ir^{IV}Cl_6]$ or $(NH_4)_3[Ir^{III}Cl_6]$ with the appropriate sodium dithiocarbamate. Hydride transfer from $Ir(H)Cl_2(PPh_3)_3$ to CS_2 yields the dithioformato ligand and complex (**27**). The hydrido analog of (**27**), $Ir(S_2CH)H_2(PPh_3)_2$, is prepared by the reaction of CS_2 with *mer*-$IrH_3(PPh_3)_3$.

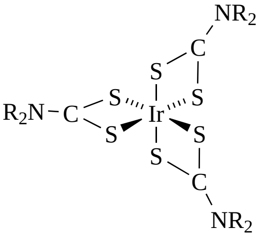

(**26**)

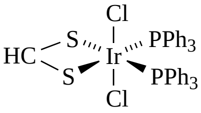

(**27**)

The reaction of RSO_2Cl (e.g. R = Me, Et, Pr) with Vaska's complex (an oxidative addition, equation 25) gives an S-bound sulfinato ligand. (See Section 6.7 for the oxidative addition of CX_2 (X = S or Se) to Vaska's compound.)

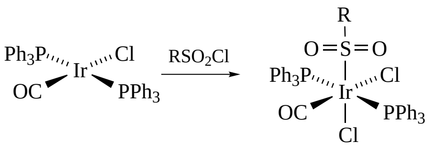

(25)

Polysulfide complexes of iridium(III) include $[Ir(S_5)_3]^{3-}$ and $[Ir(S_6)_3]^{3-}$, the latter being prepared from the reaction of $IrCl_3\cdot xH_2O$ with aqueous $(NH_4)_2S_n$.[47]

6.7 Complexes with Selenium Donor Ligands

Relatively few nonorganometallic, seleno complexes of Ir(III) have been synthesized and characterized. Treating $(NH_4)_2[IrCl_6]$ with Et_2Se in refluxing ethanol leads to $Ir(SeEt_2)_3Cl_3$, for which a *fac* arrangement of ligands is suggested (compare Scheme 9). The oxidative addition of CSe_2 to *trans*-$IrCl(CO)(PPh_3)_2$ gives an octahedral complex (**28**); similar reactions with CS_2 have also been reported. The tripodal ligand (**29**) forms the octahedral complex $[Ir(\mathbf{29})_2]^{3+}$.[48]

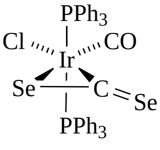

(**28**)

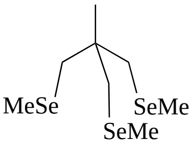

(**29**)

Complex (**26**) and its seleno analogs react with $AgBF_4$ to give $[Ag\{IrL_3\}_2][BF_4]$ (L = dithiocarbamate or diselenocarbamate) in which two octahedral IrL_3 act as ligands to Ag^+ to give a trinuclear complex.[49] Iridium(III) complexes involving polyselenide ligands are represented by $[Ir(Se_4)_3]^{3-}$ (**30**) and $[Ir(Se_4)_2(MeCN)_2]^-$. In the solid-state structure of $[K(2.2.2\text{-cryptand})]_3[Ir(Se_4)_3]\cdot$toluene, the anion exists as a $\Delta\lambda\lambda\delta/\Lambda\delta\delta\lambda$ racemate.[47]

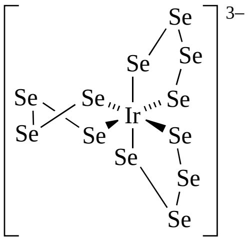

(**30**)

Related complexes with formally $O_2{}^{2-}$, $S_2{}^{2-}$, or $Se_2{}^{2-}$ ligands are considered together here. Dioxygen binds in a 'side-on' fashion in $[Ir(dppe)_2(\eta^2\text{-}O_2)]^+$, formed when O_2 reacts with $[Ir(dppe)_2]^+$; the IR spectrum exhibits an absorption at 830 cm^{-1} assigned to ν(O–O), and structural data give an O–O bond length of 1 to 52 Å.[50] The potential for this and related peroxo complexes to undergo photochemical elimination of singlet oxygen has been investigated.[51] Reactions of $[Ir(dppe)_2]^+$ or $[Ir(Me_2PCH_2CH_2PMe_2)_2]^+$ with S_8 or Se_8 give $[IrL_2(\eta^2\text{-}E_2)]^+$. Characteristic IR spectroscopic absorptions are $\nu_{SS} = 510$ to 550 cm^{-1} and $\nu_{SeSe} = 300$ to 310 cm^{-1}.[52] Members of this group of complexes are photochromic.[53]

6.8 Macrocyclic Ligands

Octaethylporphyrin, H_2OEP, reacts with $[IrCl(CO_3)]_2$ to give Ir(OEP)Cl(CO) in which the four N-donors of the OEP^{2-} ligand lie in the equatorial plane of the octahedral Ir(III). Ir(OEP)Cl(CO) is a precursor to other complexes containing the Ir(OEP) unit (Scheme 10).

Macrocyclic ligands (**31**) encapsulate Ir^{3+} to give octahedral $[Ir(\mathbf{30})(Cl)(Et)]^+$ in which the Et and Cl^- ligands are in axial sites.[54]

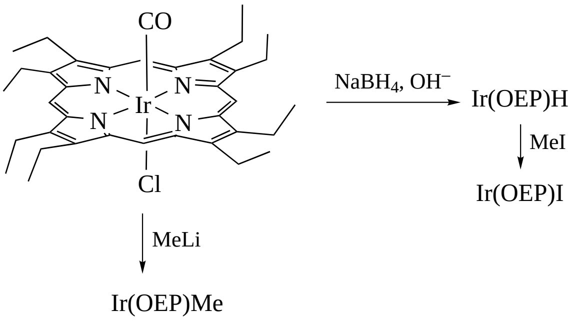

Scheme 10

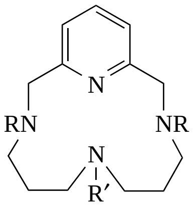

R = R' = Me
R = R' = H
R = H, R' = Me

(**31**)

Several Ir(III) complexes with macrocyclic ligands containing S-donors have been prepared and characterized.[55] The macrocyclic thioether (**32**) reacts with $[(C_8H_{14})IrCl]_2$ (C_8H_{14} = cyclooctene) to give $[Ir(\mathbf{32})_2(H)]^{2+}$ (**33**), isolated and structurally characterized as the $[PF_6]^-$ salt. The presence of the hydride ligand forces one S-donor to be uncoordinated. In (**34**), the two macrocyclic ligands act as S_3-donor sets (average Ir–S distance = 2.340 Å). Ligand (**35**) reacts with $IrCl_3\cdot xH_2O$ to give *cis*-$[IrCl_2(\mathbf{35})]^+$. The selenoether macrocycle (**36**) forms the complex *trans*-$[Ir(\mathbf{36})Br_2]^+$.[56]

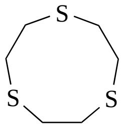

(**32**)

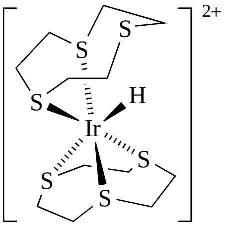

(**33**)

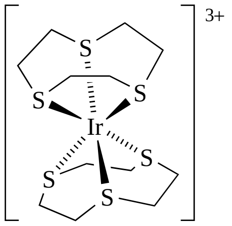

(**34**)

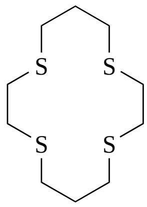

(**35**)

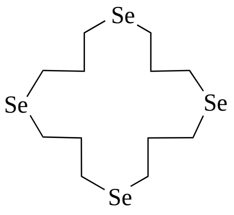

(**36**)

7 THE LOWER OXIDATION STATES: MONONUCLEAR COMPLEXES

Iridium(II) is not a common oxidation state for the metal and the d^7 electronic configuration leads to *Paramagnetism* in mononuclear complexes. A representative example is square planar (**37**).

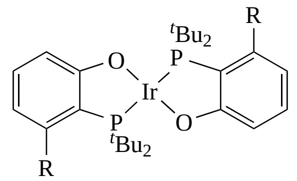

(**37**) R = H, OMe

The iridium(I) state is commonly observed in an organometallic environment[7,8] (*see* ***Iridium: Organometallic Chemistry***). Thus, only selected Ir(I) complexes are considered here. The Ir(I) state is not usually stabilized by ligands that are unable to act as π-acceptors. Therefore, simple complexes such as $[IrL_4]^+$, where L = H_2O or NH_3; or $[IrL_4]^{3-}$, where L = F^-, Cl^-, Br^-; or OH^- are not known. There is some evidence for the existence of the binary halides IrCl, IrBr, and IrI. In $Mg_6Ir_2H_{11}$, the square pyramidal $[IrH_5]^{4-}$ hydrido complex is present along with $[IrH_4]^{5-}$.[57]

Common precursors for the formation of iridium(I) complexes are *trans*-$IrCl(CO)(PPh_3)_2$ (Vaska's compound), $[IrCl(CO)_3]_n$, $[IrCl(C_8H_{14})_2]_2$ (C_8H_{14} = cyclooctene), and $[(cod)IrCl]_2$ (cod = cycloocta-1,5-diene). Complexes of Ir(I) are usually either four-coordinate (square planar) or five-coordinate (trigonal bipyramidal). In solution, five-coordinate complexes are typically stereochemically nonrigid (*see Fluxional Molecule*). Although low oxidation state d-block metal complexes are typically expected to obey the 18-electron rule (*see Effective Atomic Number Rule*), square-planar iridium(I) complexes, in particular, are stable with a 16-electron configuration, for example, in $IrCl(CO)(PPh_3)_2$. It follows that such complexes tend to undergo oxidative addition reactions in which the Ir(I) is oxidized to Ir(III) (*see* ***Mechanisms of Reaction of Organometallic Complexes***).

The reaction of $[IrCl(CO)_3]_n$ with an isocyanide, CNR (R = alkyl or aryl), leads to the square-planar $[Ir(CNR)_4]^+$ representative oxidative additions, which are given in equation (26).[4,7]

$$[Ir(CNR)_4]^+ \xrightarrow{MeI} [IrI(Me)(CNR)_4]^+$$
$$\xrightarrow{X_2\text{ (halogen)}} [IrX_2(CNR)_4]^+ \qquad (26)$$

Complexes (**38**) to (**41**) illustrate mononuclear Ir(I) complexes with N-donor ligands. The N_2 ligand in (**38**) is introduced by the reaction of ArC(O)NNN with *trans*-$IrCl(CO)(PPh_3)_2$, and it is bound in an 'end-on' fashion (*see End-On Coordination*).[58] Cation (**39**) contains Ir(III) and is formed from the neutral triazenido Ir(I) complex $Ir(CO)(PPh_3)(ArNNNAr)$ (Ar = aryl).[59] The tetrazene ligand in (**38**) is a 4-electron donor, and complex (**38**) is an 18-electron complex.[60] Pyrazine can act as a monodentate (**41**) or a bridging (**42**) ligand.[61]

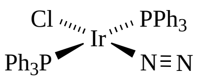

(**38**)

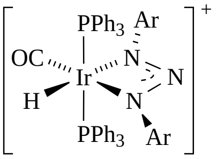

(**39**)

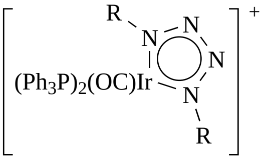

(**40**)

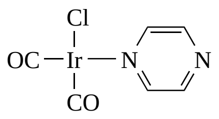

(**41**)

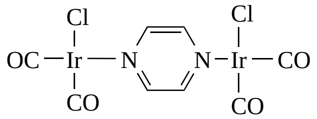

(**42**)

There are many Ir(I) complexes containing phosphine ligands (*see* ***P-donor Ligands***).[16] Phosphorus trifluoride is a π-acid ligand and coordinates to low oxidation state d-block metals (e.g. Scheme 11). Some cationic complexes of the type $[Ir(PR_3)_4]^+$ for $R \neq F$ have also been prepared. The crystal structure of $[Ir(PPh_2Me)_4](BF_4)$ shows a distorted square planar Ir(I), the distortion being toward tetrahedral.[62] The $[Ir(PPh_2Me)_4]^+$ cation undergoes oxidative additions. For addition of I_2, a complex of stoichiometry IrL_2I_4 is obtained; structural characterization shows it to be the dinuclear complex $[Ir_2L_4I_2(\mu\text{-}I)_3][I_3]$, (**2**).[32,63] Related complex cations with secondary phosphines are $[Ir(PEt_2H)_4]^+$ and $[Ir(PPh_2H)_4]^+$, prepared from $\{IrCl(C_8H_{14})_2\}_2$ and the phosphine. The reaction of $IrH_3(PPh_3)_3$ with $P(OPh)_3$ results in reduction of the metal (equation 27); $IrH\{P(OPh)_3\}_4$ is a catalyst for the reduction of alkenes and acetylenes by formic acid or formates.

$$IrH_2(PPh_3)_3 \xrightarrow{P(OPh)_3,\ 110\,^\circ C} IrH\{P(OPh)_3\}_4 \qquad (27)$$

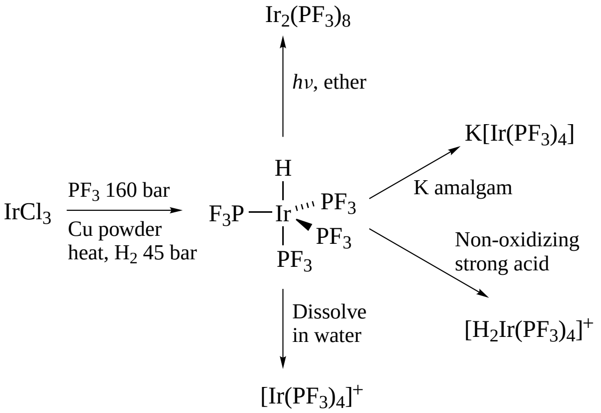
Ir2(PF3)8
hν, ether
K[Ir(PF3)4]
K amalgam
H
IrCl3
PF3 160 bar
Cu powder
heat, H2 45 bar
F3P
Ir
PF3
PF3
PF3
Non-oxidizing
strong acid
[H2Ir(PF3)4]+
Dissolve
in water
[Ir(PF3)4]+

Scheme 11

$$\begin{tikzcd}
Ir(CO)_3Cl \arrow[r, "dppe"] & {[Ir(dppe)_2]^+} \arrow[r, "PF_3"] \arrow[d, "Cl_2\text{ (Oxidative addition)}"] & {[Ir(PF_3)(dppe)_2]^+} \\
 & {[IrCl_2(dppe)_2]^+} &
\end{tikzcd}$$

Scheme 12

Iridium(I) complexes incorporating multidentate phosphine ligands are varied. The simplest are the square-planar $[IrL_2]^+$ cations, where, for example, L = dppe (Scheme 12), dppp, and the *Chiral* ligands (**43**) and (**44**). The complex $[Ir(dppp)_2]Cl$ is made from Vaska's compound and dppp; $[Ir(\mathbf{43})_2](BPh_4)$ is prepared from $[IrCl(cod)]_2$ and (**43**). The reaction of (**44**) with $[IrCl(cod)]_2$ in the presence of $AgBF_4$ gives $[Ir(cod)(\mathbf{44})][BF_4]$; using enantiomerically pure ligand (**44**), the enantiomerically pure $[Ir(cod)(\mathbf{44})]^+$ can be isolated.**64** The complex cation $[Ir(\mathbf{43})_2]^+$ is a precursor to optically active hydrido complexes, and $[Ir(dppe)_2]Cl$ catalyzes the homogeneous oxidation of styrene. Ligand (**21**) forms the complexes Ir(**21**)Cl and Ir(**21**)Br, and $Ph_2P(CH_2)_2P(Ph)(CH_2)_2P(Ph)(CH_2)_2PPh_2$ (L) forms IrLCl. In contrast to the chelating nature of theses ligands, dppm ($Ph_2PCH_2PPh_2$) tends to bridge two metal centers (see Section 8.5). Ligand (**45**) draws together two iridium atoms such that each is coordinated to three phosphorus atoms in the complex ClIr(μ-L)IrCl.**65**

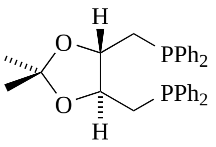
H
O
PPh2
O
PPh2
H

(**43**)

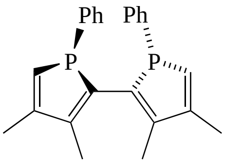

(**44**)

The ligand $N(CH_2CH_2PPh_2)_3$ is potentially tetradentate, and it reacts with $[IrCl(cod)]_2$ to give (**46**). Oxidative addition of a C–H bond of cod occurs in the reaction of (**46**) with cod to give the Ir(III) complex (**47**).**66**

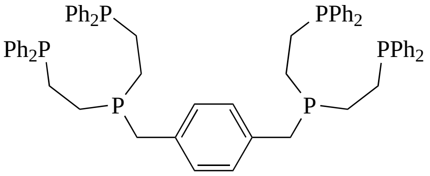
Ph2P
Ph2P
PPh2
PPh2
P
P

(**45**)

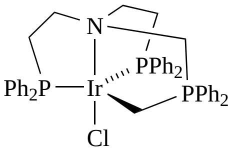
N
PPh2
Ph2P
Ir
PPh2
Cl

(**46**)

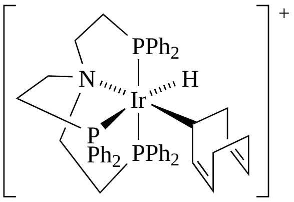
+
PPh2
N
H
Ir
P
Ph2
PPh2

(**47**)

Oxygen donor ligands on their own do not stabilize iridium(I) but can do so in the presence of suitable π-acceptor ligands, for example, (**48**).

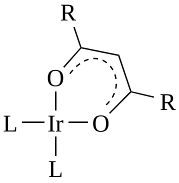

L = alkene or CO

R = Me, CF_3 or Ph

(**48**)

The reaction of *trans*-$IrCl(CO)(PPh_3)_2$ with carbon disulfide in the presence of $NaBPh_4$ yields $[(\mathbf{49})](BPh_4)$ in which the S-donor ligand is the zwitterion $S_2C^-PPh_3{}^+$.**67** Sulfur dioxide is S-bonded to an iridium(I) atom in the trigonal bipyramidal complex $IrH(PPh_3)_2(CO)(SO_2)$; in the related chloro complex (**50**), the Ir–S distance is 2.45 Å.**68**

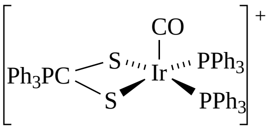
+
CO
Ph3PC
S
Ir
PPh3
S
PPh3

(**49**)

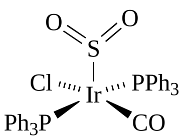
O
O
S
Cl
Ir
PPh3
Ph3P
CO

(**50**)

Examples of the interaction between Ir(I) and macrocyclic ligands include $(CO)_3Ir(\mu\text{-TPP})Ir(CO)_3$ (H_2TPP = tetraphenylporphyrin). The complex undergoes three irreversible electrochemical oxidations leading to $[Ir(TPP)]^+$.**69**

Softer donor atoms are involved in the following examples. Reaction of $Ir_2(C_8H_{14})_4Cl_2$ (C_8H_{14} = cyclooctene) or $Ir(C_2H_4)_4Cl$ with 1,4,7-trithiacyclononane, L, gives $[IrL(C_8H_{14})_2]^+$ and $[IrL(C_2H_4)_2]^+$.[70] Ligand (**51**), H_2L, reacts with $[Ir(CO)_3Cl]_n$ to give $L\{Ir(CO)_2\}_2$ in which the deprotonated ligands bind two $Ir(CO)_2{}^+$ units through coordination to N,N'-donor sites.[71]

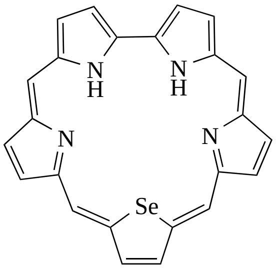

(**51**)

The area of metallamacrocycles, in which the metal centers are an integral part of the cyclic structure, is rapidly expanding. Complexes (**52**) and (**53**) involve Ir(I) centers.[72]

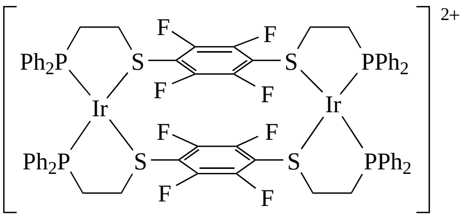

(**52**)

8 DINUCLEAR AND MULTINUCLEAR IRIDIUM COMPLEXES

The control of molecular assemblies through ligand design is of active interest, and this theme has been addressed in a review concerned specifically with low nuclearity Rh and Ir complexes.[73]

8.1 Halide Ligands

Halide ions and common bridging ligands (*see Bridging Ligand*), examples of bridging fluoride and iodide ligands in (**1**) and (**2**), respectively. When $(Et_4N)_2[IrCl_6]$ is heated with CF_3CO_2H, the $[Ir_2Cl_{10}]^{2-}$ (D_{2h}) ion forms.[74] Chloro bridges are present in a variety of organometallic complexes, for example, $[Ir(\mu\text{-}Cl)(C_8H_{14})_2]_2$, $[(cod)Ir(\mu\text{-}Cl)]_2$, and $[Ir(CO)_2(\mu\text{-}Br)]_2$; the latter catalyzes the carboxylation of alkenes. A wide range of Ir(III) complexes possess halide bridges, for example, $[CpIrCl(\mu\text{-}Cl)]_2$ and the hydrotris(3,5-dimethylpyrazolyl)borato complex (**54**), which is a precursor to related complexes. In some cases, the loss of a ligand may induce bridge formation, for example, during the photolysis of the mononuclear iridium(III) complex *mer*-$IrCl_3(SEt_2)_3$ (equation 28). Iodo-bridges support the two square-planar Ir(I) centers in $Ir_2(\mu\text{-}I)_2({}^tBu_2PCH_2P^tBu_2)_2$.[75]

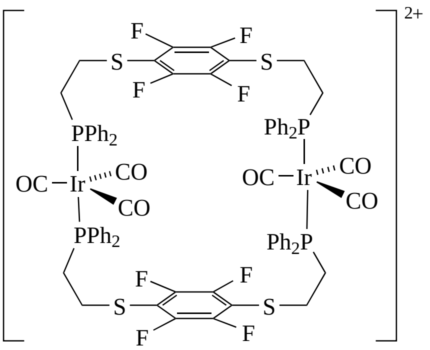

(**53**)

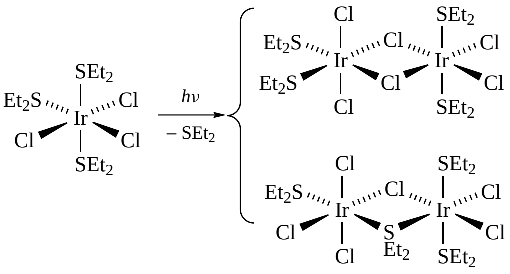

(28)

8.2 Sulfur Donor Ligands

Sulfur-containing bridges are typically S^{2-}, SR^-, or SR_2 (e.g. equation 28) (*see d–d Transitions*). Derivatives of the type $Ir_2H_2Cl_2(SAr)_2(PAr_3)_4$ (Ar = aryl) react in $CHCl_3$ to give triply bridged complexes $[Ir_2H_2(PAr_3)_4(\mu\text{-}Cl)(\mu\text{-}SAr)_2]^+$, although triple-bridge formation is not observed when $PAr_3{=}P(C_6H_4\text{-}4\text{-}F)_3$.[76] The reaction of $[Cp^*IrCl_2]_2$ with $(NH_4)_2[WS_4]$ and $NaBH_4$ yields the double (but incomplete) iridium(III)/tungsten(VI) cubane (**55**) in which the sulfido ligands support the framework.[77]

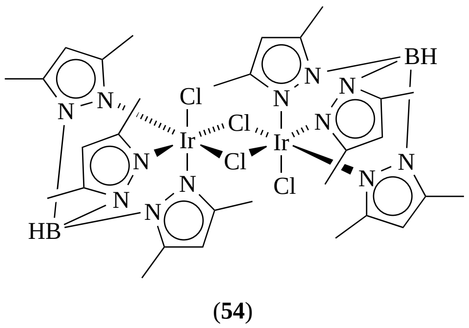

(**54**)

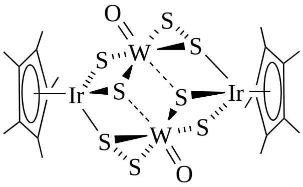

(**55**)

8.3 Oxygen Donor Ligands

Ligands such as carboxylate, nitrate, and sulfate ions stabilize a number of trinuclear iridium complexes.[78] Each complex contains a triangular Ir_3, supported by bridging O,O′-donor ligands and a capping (μ_3) ligand. The reaction of iridium(III) bromide with N_2O_5 gives $[Ir_3(NO_3)_9(\mu_3\text{-}O)](NO_3)$,[79] which is a deep purple, paramagnetic complex, soluble in HNO_3; it is a deliquescent solid and is hydrolyzed to $IrO_2 \cdot nH_2O$. The structure of $[Ir_3(NO_3)_9(\mu_3\text{-}O)]^+$ (**56**) has similar features to that of $[Ir_3(SO_4)_9(\mu_3\text{-}O)]^{10-}$. The blue−green salt $K_{10}[Ir_3(SO_4)_9(\mu_3\text{-}O)] \cdot H_2O$ is prepared from $Na_2[IrCl_6] \cdot 6H_2O$ by treatment with H_2SO_4 and K_2SO_4; known as 'Boisbaudron's blue salt', $K_{10}[Ir_3(SO_4)_9(\mu_3\text{-}O)]$ was originally formulated as '$K_3[Ir(SO_4)_3] \cdot H_2O$'. The $[Ir_3(SO_4)_9(\mu_3\text{-}O)]^{10-}$ anion exhibits one Ir(IV) and two Ir(III) centers. In 1906, Delépine discovered the green salt $K_4[Ir_3(SO_4)_6(H_2O)_3(\mu_3\text{-}N)]$; this complex can be formed by the reaction of $K_3[Ir(C_2O_4)_3] \cdot 4.5H_2O$ with concentrated sulfuric acid and ammonium sulfate. The structure of $(NH_4)_4[Ir_3(SO_4)_6(H_2O)_3(\mu_3\text{-}N)]$ has been determined,[80] as have the structures of related salts.[81] The terminal water ligands are quite labile and can be replaced by Cl^-, Br^-, N_3^-, OH^-, or NCS^- ligands. Acetate ligands feature in a series of complexes of the type $[Ir_3(O_2CMe)_6(\mu_3\text{-}O)L_3]^{x+}$ (Scheme 13), and structural studies include those of salts of $[Ir_3(O_2CMe)_6(\mu_3\text{-}O)(H_2O)_3]^+$.[82] The related nitrido-capped complex $[Ir_3(O_2CMe)_6(\mu_3\text{-}N)(py)_3]^+$ has been the subject of detailed electrochemical studies,[83] the results of which are compared with those of the analogous oxo-capped species.[83,84]

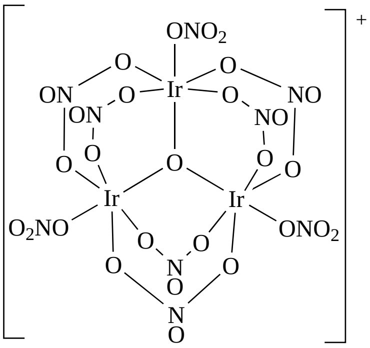

(**56**)

Carboxylate ligands also support several dinuclear complexes of iridium, for example, $[Cp^*Ir(\mu\text{-}O_2CCF_3)(\mu\text{-}H)_2IrCp^*]^+$ and $[Cp^*Ir(\mu\text{-}O_2CCF_3)_2(\mu\text{-}H)IrCp^*]^+$, which are moderately air-stable crystalline solids. The reaction of H_2IrCl_6 with $MeCO_2Li$ under O_2 in acetic acid/acetic anhydride gives $[Ir_2(\mu\text{-}O_2CMe)_2Cl_2(CO)_2]$ to which axial ligands can be added (**57**).[85]

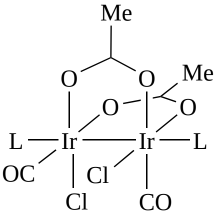

e.g. L = MeCN, DMSO, py

(**57**)

The hydroxide ion is a well-established bridging ligand, and hydroxo-bridged complexes of iridium(III) have been reviewed.[86] Among the dinuclear iridium(I) complexes that have structures supported by OH^- ligands is $[Cp^*Ir(\mu\text{-}OH)_3IrCp^*]^+$, and closely related to this is $(cod)Ir(\mu\text{-}OPh)_2Ir(cod)$. The presence of the three OH

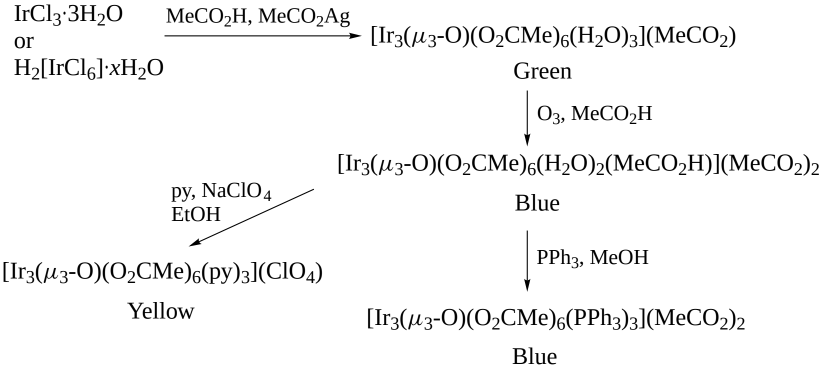
IrCl3·3H2O
or
H2[IrCl6]·xH2O
MeCO2H, MeCO2Ag
[Ir3(μ3-O)(O2CMe)6(H2O)3](MeCO2)
Green
O3, MeCO2H
[Ir3(μ3-O)(O2CMe)6(H2O)2(MeCO2H)](MeCO2)2
Blue
py, NaClO4
EtOH
[Ir3(μ3-O)(O2CMe)6(py)3](ClO4)
Yellow
PPh3, MeOH
[Ir3(μ3-O)(O2CMe)6(PPh3)3](MeCO2)2
Blue

Scheme 13

units in $[Cp^*Ir(\mu\text{-}OH)_3IrCp^*]^+$ draws the Ir atoms relatively close together, for example, Ir–Ir = 3.07 Å in the hydrated acetate salt;[87] the dichromate salt displays a hydrogen-bonded 2-D–network in the solid state.[88] In $\Delta,\Lambda\text{-}[(H_2O)(en)_2Ir(\mu\text{-}OH)Ir(en)_2(OH)]^{4+}$, the terminal OH^- ligand on one Ir atom is associated with the H_2O ligand on the second Ir atom via a hydrogen bridge.[89] This fixes the conformation of the complex. A feature of $\Lambda,\Lambda\text{-}[(H_2O)(en)_2Ir(\mu\text{-}OH)Ir(en)_2(H_2O)]^{5+}$ is that the acid dissociation constants (i.e. dissociation of H^+ from coordinated H_2O) are greater ($pK_{a1} = 1.91$) and smaller ($pK_{a2} = 9.04$) than predicted on the basis of values of pK_a for related mononuclear complexes. Equilibration between *cis*-$[Ir(NH_3)_4(H_2O)_2]^{3+}$ and *cis,cis*-$[(H_2O)(NH_3)_4Ir(\mu\text{-}OH)Ir(NH_3)_4(H_2O)]^{5+}$ and $[(NH_3)_4Ir(\mu\text{-}OH)_2Ir(NH_3)_4]^{4+}$ (and for analogous en complexes) has been studied.[90]

8.4 Nitrogen Donor Ligands

Nitrogen donor ligands supporting dinuclear complexes include amido (NR_2^-) groups, diazonato ligands, and a range of heterocyclic N-donors. The flexibility of the diazonato ligand is seen in $[Cp^*Ir(\eta^2\text{-}C_2H_4)(NNAr)]^+$.[91] Here, the diazonato ligand coordinates in a monodentate mode, but when $[Cp^*Ir(\eta^2\text{-}C_2H_4)(NNAr)]^+$ reacts with $Cp^*Ir(CO)_2$, the diazonato group converts to a bridging mode as shown in (**58**).[92]

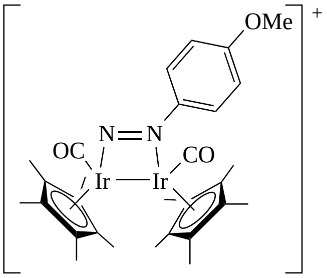

(**58**)

Pyrazoles (Hpz) react with $[Cp^*Ir(\mu\text{-}OH)_3IrCp^*]^+$ in Me_2CHOH to give $[Cp^*Ir(\mu\text{-}H)_2(\mu\text{-}pz)IrCp^*]^+$.[93] This is one of a number of ways of introducing the bridging pz ligand. An alternative route is via deprotonation of the mononuclear $IrH_2(PPh_3)_2(OCMe_2)(Hpz)$ using KOH to give $H_2(PPh_3)_2Ir(\mu\text{-}pz)Ir(PPh_3)_2H_2$. Reaction of this with HBF_4 reprotonates the bridging ligand, generating the five-coordinate $IrH_2(PPh_3)_2(Hpz)$.[94] The doubly bridged complex $(^tBuNC)_2Ir(\mu\text{-}pz)_2Ir(^tBuNC)_2$ reacts with HCl to give $[(H)Cl(^tBuNC)_2Ir(\mu\text{-}pz)_2Ir(^tBuNC)_2Cl(H)]$, which in solution loses Cl^- with concomitant movement of the remaining terminal Cl^- ligand into a bridging site.[95] When equimolar amounts of $(^tBuNC)_2Ir(\mu\text{-}pz)_2Ir(^tBuNC)_2$ and $[(MeCN)(^tBuNC)_2Ir(\mu\text{-}pz)_2Ir(^tBuNC)_2(MeCN)]^{2+}$ react together, a redox condensation occurs to yield tetranuclear, blue complexes ('iridium blues').[96]

While Rh(II) chemistry has many examples of $Rh_2(\mu\text{-}L)_4$-type complexes (e.g. $L^- = RCO_2^-$), related examples within iridium chemistry are rare. Scheme 14 shows the formation of the first example of an $Ir^{II}{}_2(\mu\text{-}L)_4$ complex.[97] Reaction of $IrCl_3$ with Hhpp ($hpp^- =$ **59**) in EtOH at reflux leads to $Ir_2(\mu\text{-}hpp)_4Cl_2$ (Ir–Ir = 2.495 Å), the first 'paddle-wheel' complex with an $Ir_2{}^{6+}$ core.[98]

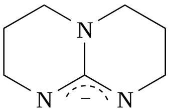

(**59**)

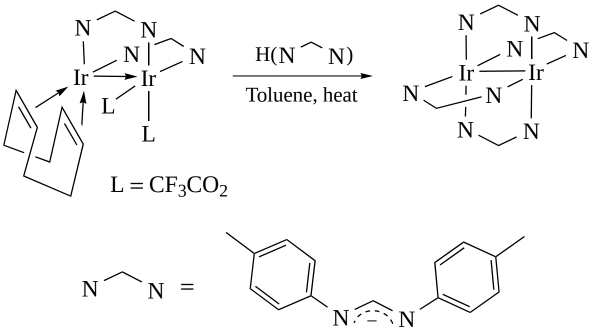

Scheme 14

8.5 Phosphine Ligands Including 'A-Frame' Complexes

Many multidentate phosphorus ligands have the ability to chelate to a single metal center or bridge between two or more metal centers.[16] The ligand dppm stabilizes the so-called 'A-frame' complexes, for example, the diiridium(I) complex (**60**) in which the Ir atoms are not directly bonded. The $Ir_2(dppm)_2$ framework is quite robust; oxidative addition of H_2 leads to the formation of an Ir–Ir bond in complex (**61**). A range of related hydrido complexes is known; these and other polynuclear hydrido complexes of iridium have been reviewed[99] (*see* ***Hydride Complexes of the Transition Metals***). Heterometallic 'A-frame' complexes in which one metal is iridium are also known. By choosing appropriate ligands, the framework can be extended, for example, $Ph_2PCH_2As(Ph)CH_2PPh_2$ has a P,As,P′-donor set that has the same ligand 'bite' (*see Bite Angle*) as two adjacent dppm ligands.

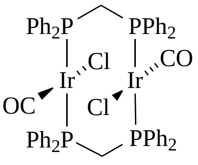

(**60**)

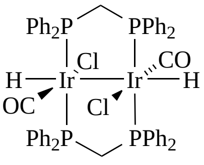

(**61**)

9 RELATED ARTICLES

Hydride Complexes of the Transition Metals; Iridium: Organometallic Chemistry; Luminescence; Macrocyclic Ligands; Rhodium: Inorganic & Coordination Chemistry.

10 REFERENCES

1. W. P. Griffith, 'The Chemistry of the Rarer Platinum Metals (Os, Ru, Ir and Rh)', John Wiley & Sons, London, 1967.
2. D. J. Gulliver and W. Levason, *Coord. Chem. Rev.*, 1982, **46**, 1.
3. (a) 'Gmelin Handbuch der Anorganischen Chemie: Iridium', Springer-Verlag, Berlin, 1978, System-Nummer 67, Ergänzungsband 1 and 2; (b) 'Gmelin Handbuch der Anorganischen Chemie: Iridium', Verlag Chemie, Berlin, 1939, System-Nummer 67.
4. N. Serpone and M. A. Jamieson, in 'Comprehensive Coordination Chemistry', G. Wilkinson, R. D. Gillard, and J. A. McCleverty, eds. Pergamon, Oxford, 1987, Vol. 4, p. 1097.
5. K. Macnamara and L. J. Yellowlees, in 'Comprehensive Coordination Chemistry II', eds. J. A. McCleverty and T. Meyer, Elsevier, Oxford, 2003, Vol. 6.
6. M. J. Hannon, *Coord. Chem. Rev.*, 1996, **152**, 393.
7. G. J. Leigh and R. L. Richards, in 'Comprehensive Organometallic Chemistry', eds. G. Wilkinson, F. G. A. Stone, and E. W. Abel, Pergamon, Oxford, 1987, Vol. 5, p. 541.
8. J. D. Atwood, in 'Comprehensive Organometallic Chemistry II', eds. E. W. Abel, F. G. A. Stone, and G. Wilkinson, Pergamon, Oxford, 1995, Vol. 8, p. 303.
9. S. A. Cotton, 'Chemistry of Precious Metals', Blackie, London, 1997.
10. F. R. Hartley ed., 'Chemistry of the Platinum Group Metals: Recent Developments', Elsevier, Oxford, 1991.
11. A. F. Wells, 'Structural Inorganic Chemistry', 5th edn., Oxford University Press, Oxford, 1985.
12. J. E. Macintyre ed., 'Dictionary of Inorganic Compounds', Chapman & Hall, London, 1992.
13. J. E. Fergusson and D. A. Rankin, *Aust. J. Chem.*, 1983, **36**, 863.
14. D. A. Rankin, B. R. Penfold, and J. E. Fergusson, *Aust. J. Chem.*, 1983, **36**, 871.
15. J. H. Canterford and R. Colton, 'Halides of the Second and Third Row Transition Metals', John Wiley & Sons, London, 1968, p. 346.
16. C. A. McAuliffe and W. Levason, 'Phosphine, Arsine and Stibine Complexes of the Transition Elements', Elsevier, Amsterdam, 1979.
17. N. Bestaoui and E. Prouzet, *Chem. Mater.*, 1997, **9**, 1036.
18. M. Wang, S. Yao, and M. Madou, *Sens. Actuators B*, 2002, **81**, 313.
19. P. D. Battle, G. R. Blake, J. Darriet, J. G. Gore, and F. Weill, *J. Mater. Chem.*, 1997, **7**, 1559.
20. A. Wurth, A. Löhken, and A. Mewis, *Z. Anorg. Allg. Chem.*, 2002, **628**, 661.
21. A. D. Richardson, K. Hedberg, and G. M. Lucier, *Inorg. Chem.*, 2000, **39**, 2787.
22. A. K. Brisdon, J. H. Holloway, E. G. Hope, W. Levason, J. S. Ogden, and A. K. Saad, *J. Chem. Soc., Dalton Trans.*, 1992, 139.
23. B. von Ahsen, C. Bach, H. Pernice, H. Willner, and F. Aubke, *J. Fluorine Chem.*, 2000, **102**, 243.
24. E. K. Barefield, *Inorg. Synth.*, 1974, **15**, 34.
25. R. S. Tanke and R. H. Crabtree, *Organometallics*, 1991, **10**, 415.
26. S. A. Macgregor and K. H. Moock, *Inorg. Chem.*, 1998, **37**, 3284.
27. H. Miyoshi, K. Horiuchi, and R. Ikeda, *Z. Naturforsch. A*, 2002, **57**, 431.
28. P. Hollmann and W. Preetz, *Z. Naturforsch. B*, 1992, **47**, 1115.
29. J. Owen and K. W. H. Stevens, *Nature*, 1953, **171**, 836.
30. J. U. Rohde and W. Preetz, *Z. Anorg. Allg. Chem.*, 1997, **623**, 1774.
31. V. M. Deflon, C. M. Mössmer, and J. Strähle, *Z. Anorg. Allg. Chem.*, 1999, **625**, 2186.
32. M. J. Nolte, E. Singleton, and E. van der Stok, *Acta Crystallogr., Sect. B*, 1978, **34**, 1684.
33. A. G. Sharpe, 'The Chemistry of Cyano Complexes of the Transition Metals', Academic Press, London, 1976.
34. J.-U. Rohde and W. Preetz, *Z. Anorg. Allg. Chem.*, 1998, **624**, 1319.
35. F. Galsbøl, S. K. Hansen, and K. Simonsen, *Acta Chem. Scand.*, 1990, **44**, 796.
36. F. Galsbøl, T. Glowiak, A. Hammershøi, B. S. Hammershøi, S. Larsen, and M. Wilgocki, *Acta Chem. Scand.*, 1990, **44**, 31.
37. R. Melenkivitz and G. L. Hillhouse, *Chem. Commun.*, 2002, 660.
38. E. C. Constable, *Adv. Inorg. Chem.*, 1989, **34**, 1.
39. E. C. Constable, *Polyhedron*, 1984, **3**, 1037.
40. I. M. Dixon, J.-P. Collin, J.-P. Sauvage, L. Flamigni, S. Encinas, and F. Barigelletti, *Chem. Soc. Rev.*, 2000, **29**, 385.
41. K. K.-W. Lo, D. C.-M. Ng, and C.-K. Chung, *Organometallics*, 2001, **20**, 4999.
42. K. K.-W. Lo, C.-K. Chung, D. C.-M. Ng, and N. Zhu, *New J. Chem.*, 2002, **26**, 81.
43. W. Goodall and J. A. G. Williams, *J. Chem. Soc., Dalton Trans.*, 2000, 2893.
44. C. Slugovc, I. Padilla-Martínez, S. Sirol, and E. Carmona, *Coord. Chem. Rev.*, 2001, **213**, 129.
45. R. D. Simpson, W. J. Marshall, A. A. Farischon, D. C. Roa, and V. V. Grushin, *Inorg. Chem.*, 1999, **38**, 4171.

46. V. G. Isakova, I. A. Baidini, N. B. Morozova, and I. K. Igumenov, *Polyhedron*, 2000, **19**, 1097.
47. T. E. Albrecht-Schmitt and J. A. Ibers, *Inorg. Chem.*, 1996, **35**, 7273.
48. W. Levason, S. D. Orchard, and G. Reid, *Inorg. Chem.*, 2000, **39**, 3853.
49. A. M. Bond, R. Colton, B. M. Gatehouse, and Y. A. Mah, *Inorg. Chim. Acta*, 1997, **260**, 61.
50. M. J. Nolte, E. Singleton, and M. Laing, *J. Am. Chem. Soc.*, 1975, **97**, 6396.
51. M. Seip and H.-D. Brauer, *J. Photochem. Photobiol., Sect. A*, 1994, **79**, 19.
52. A. P. Ginsberg and W. E. Lindsell, *J. Chem. Soc., Chem. Commun.*, 1971, 232.
53. A. P. Ginsberg, R. L. Harris, B. Batlogg, J. H. Osborne, and C. R. Sprinkle, *Inorg. Chem.*, 1985, **24**, 4192.
54. P. Moore, H. A. A. Omar, N. W. Alcock, and G. A. Pike, *J. Chem. Soc., Chem. Commun.*, 1990, 280.
55. A. J. Blake and M. Schröder, *Adv. Inorg. Chem.*, 1990, **35**, 2.
56. W. Levason, J. J. Quirk, and G. Reid, *J. Chem. Soc., Dalton Trans.*, 1996, 3713.
57. R. Eerný, J.-M. Joubert, H. Kohlmann, and K. Yvon, *J. Alloys Compd.*, 2002, **340**, 180.
58. G. P. Rosini, F. Liu, K. Krogh-Jespersen, A. S. Goldman, C. Li, and S. P. Nolan, *J. Am. Chem. Soc.*, 1998, **120**, 9256.
59. L. Toniolo and G. Cavinato, *Inorg. Chim. Acta*, 1979, **35**, L301.
60. A. B. Gilchrist and D. Sutton, *Can. J. Chem.*, 1974, **52**, 3387.
61. C. Dragonetti, M. Pizzotti, D. Roberto, and S. Galli, *Inorg. Chim. Acta*, 2002, **330**, 128.
62. G. R. Clark, B. W. Skelton, T. N. Waters, and J. E. Davies, *Acta Crystallogr., Sect. C*, 1987, **43**, 1708.
63. M. J. Nolte, E. van der Stok, and E. Singleton, *Inorg. Chim. Acta*, 1976, **19**, L51.
64. O. Tissot, M. Gouygou, F. Dallemer, J.-C. Daran, and G. G. A. Balavoine, *Eur. J. Inorg. Chem.*, 2001, 2385.
65. M. M. T. Khan and A. E. Martell, *Inorg. Chem.*, 1975, **14**, 676.
66. C. Bianchini, D. Masi, A. Meli, M. Peruzzini, M. Sabat, and F. Zanobini, *Organometallics*, 1986, **5**, 2557.
67. S. M. Boniface and G. R. Clark, *J. Organomet. Chem.*, 1980, **188**, 263.
68. A. J. Blake, E. A. V. Ebsworth, S. G. D. Henderson, H. M. Murdoch, and L. J. Yellowlees, *Z. Kristallogr.*, 1992, **290**, 199.
69. K. M. Kadish, Y. J. Deng, C. L. Yao, and J. E. Anderson, *Organometallics*, 1988, **7**, 1979.
70. A. J. Blake, M. A. Halcrow, and M. Schröder, *J. Chem. Soc., Dalton Trans.*, 1994, 1631.
71. J. Lisowski, J. L. Sessler, and V. Lynch, *Inorg. Chem.*, 1995, **34**, 3567.
72. M. S. Masar, M. V. Ovchinnikov, C. A. Mirkin, L. N. Zakharov, and A. L. Rheingold, *Inorg. Chem.*, 2003, **42**, 6851.
73. L. A. Oro, M. A. Ciriano, J. J. Pérez-Torrente, and B. E. Villarroya, *Coord. Chem. Rev.*, 1999, **193–195**, 941.
74. P. Hollmann and W. Preetz, *Z. Anorg. Allg. Chem.*, 1992, **47**, 1115.
75. P. Hofmann, C. Meier, A. Maier, O. Steck, V. Sporys, and F. Rominger, *Z. Kristallogr.*, 2000, **215**, 609.
76. T. L. Kelly and C. V. Senoff, *Can. J. Chem.*, 1976, **54**, 1860.
77. Y. Ozawa, Y. Hayashi, and K. Isobe, *Chem. Lett.*, 1990, 249.
78. R. D. Cannon and R. P. White, *Prog. Inorg. Chem.*, 1988, **36**, 195.
79. B. Harrison and N. Logan, *J. Chem. Soc., Dalton Trans.*, 1972, 1587.
80. A. C. Skapski, M. Ciechanowicz, W. P. Griffith, D. Pawson, and M. J. Cleare, *J. Chem. Soc., Chem. Commun.*, 1971, 876.
81. V. I. Korsunskii, T. A. Fomina, and N. N. Chalisova, *Zh. Neorg. Khim.*, 1988, **33**, 2594.
82. O. Almog, A. Bino, and D. Garfinkel-Shweky, *Inorg. Chim. Acta*, 1993, **213**, 99.
83. N. A. Ezerskaya, E. S. Toropchenova, I. N. Kiseleva, and R. D. Cannon, *Russ. J. Coord. Chem.*, 2000, **26**, 433.
84. K. Takashi, K. Umakoshi, A. Kikuchi, Y. Sasaki, M. Tominaga, and I. Taniguchi, *Z. Naturforsch., B*, 1995, **50**, 551.
85. N. Kanematsu, M. Ebihara, and T. Kawamura, *J. Chem. Soc., Dalton Trans.*, 1999, 4413.
86. J. Springborg, *Adv. Inorg. Chem.*, 1988, **32**, 55.
87. A. Nutton, P. M. Bailey, and P. M. Maitlis, *J. Chem. Soc., Dalton Trans.*, 1997, 1981.
88. J. T. Park, T. Nishioka, T. Suzuki, and K. Isobe, *Bull. Chem. Soc. Jpn.*, 1994, **67**, 1968.
89. F. Galsbøl, S. Larsen, B. Rasmussen, and J. Springborg, *Inorg. Chem.*, 1986, **25**, 290.
90. F. Galsbøl, K. Kaas, B. Nielsen, and J. Springborg, *Acta Chem. Scand.*, 1995, **49**, 44.
91. X. Yan, F. W. B. Einstein, and D. Sutton, *Can. J. Chem.*, 1995, **73**, 939.
92. F. W. B. Einstein, X. Yan, and D. Sutton, *J. Chem. Soc., Chem. Commun.*, 1990, 1466.
93. L. A. Oro, D. Carmona, M. P. Puebla, M. P. Lamata, C. Foces-Foces, and F. H. Cano, *Inorg. Chim. Acta*, 1986, **112**, L11.
94. M. P. García, M. A. Esteruelas, M. Martín, and L. A. Oro, *J. Organomet. Chem.*, 1994, **467**, 151.
95. C. Tejel, M. A. Ciriano, M. Millaruelo, J. A. López, F. J. Lahoz, and L. A. Oro, *Inorg. Chem.*, 2003, **42**, 4750.
96. C. Tejel, M. A. Ciriano, and L. A. Oro, *Chem. Eur. J.*, 1999, 1131.
97. F. A. Cotton and R. Poli, *Polyhedron*, 1987, **6**, 1625.
98. F. A. Cotton, C. A. Murillo, and D. J. Timmons, *Chem. Commun.*, 1999, 1427.
99. T. M. Gomes Carneiro, D. Matt, and P. Braunstein, *Coord. Chem. Rev.*, 1989, **96**, 49.

Iridium: Organometallic Chemistry

Joseph S. Merola
Virginia Polytechnic Institute and State University, Blacksburg, VA, USA

1	Introduction	1
2	Iridium Olefin Complexes	1
3	Iridium Arene and Cyclopentadienyl Complexes	3
4	Iridium Alkyne and Related Complexes	5
5	Iridium Carbonyl Complexes	6
6	Iridium Alkyl and Aryl Complexes	8
7	Iridium Carbene and Carbyne Complexes	10
8	Catalysis	11
9	C–H Activation	13
10	HDS Chemistry	15
11	Summary	15
12	Related Articles	15
13	References	16

Abbreviations

Cp = η^5-Cyclopentadienyl; Cp* = η^5-Pentamethylcyclopentadienyl; Ind = Indenyl; COD = 1, 5-cyclooctadiene; COE = cyclooctene; Tp = Tris-pyrazolylborate; Tp* = Tris-(3,5-dimethylpyrazolyl)borate; tfb = Tetrafluorobenzobarrelene.

1 INTRODUCTION

The organometallic chemistry of iridium is rich in both numbers of investigations as well as in the breadth of the areas explored. Iridium complexes possess an incredible array of properties that make them ideal for quite a number of bond-breaking and bond-making reactions. On a large scale, which clearly must involve organometallic chemistry at some point, iridium has found use in petroleum refining catalysis, especially reforming.[1,2] Although rhodium has found greater application in catalysis, a great deal of attention has been focused on iridium complexes as models for the reaction chemistry of other systems since many iridium(I) and iridium(III) complexes with ligand sets similar to those proposed in rhodium chemistry can be isolated more readily. Special attention has been paid to iridium for C–H activation chemistry and the implications that chemistry has for potentially valuable catalytic applications. This article simply cannot provide an exhaustive and detailed coverage of the field of organoiridium chemistry nor can it provide much detail in those areas it does cover. Rather it will attempt to survey a few important areas in the organometallic chemistry of iridium and point the reader to sources that will provide them with further detail. (Since the chemistry of iridium closely parallels that of rhodium, the reader should also *see* ***Rhodium: Organometallic Chemistry***.) Some important monographs[3–5] and reviews[6–10] dealing with the organometallic chemistry of iridium are available. There are some journals that have had periodical reviews and surveys of the chemistry of iridium.[11–15] Excellent texts are available that cover the general aspects of the organometallic chemistry of the transition elements including iridium.[16,17] The bond-making and bond-breaking capabilities of iridium and their relevance to organic synthesis have been reviewed.[18] Where a particular area of research has been investigated in depth by a research group, several key references are provided with the expectation that additional references to that group's work can easily be found from references within those articles.

In the following sections, general classes of organoiridium compounds will be discussed followed by brief reviews of some important types of reactions involving organoiridium compounds.

2 IRIDIUM OLEFIN COMPLEXES

Olefin complexes (*see Alkene Complexes*) of iridium play a very important role in the organic chemistry of iridium since, in addition to being the simplest of the organic compounds of iridium to prepare, they are the starting point for the preparation of many other complexes. The two most often utilized complexes are the cyclooctadiene complex $[Ir(COD)Cl]_2$ (**1**) and the bis-cyclooctene complex $[Ir(COE)_2Cl]_2$ (**2**). Interestingly, the pricey iridium cyclooctadiene complex has made its way into the undergraduate chemistry curriculum.[19] Both of these may be prepared from either $IrCl_3{\cdot}3H_2O$ or $[NH_4][IrCl_6]$ and the olefin in refluxing alcoholic solvent.[20,21] Unlike the corresponding rhodium complex, $[Ir(C_2H_4)_2Cl]_2$ (**3**) cannot be prepared by this direct reaction but can be synthesized via (**2**). For this reaction, the first product that is formed is the mononuclear $[Ir(C_2H_4)_4Cl]$ (**4**), which is only stable at low temperatures under an ethylene atmosphere. When this is allowed to warm up, it decomposes into the red dimeric (**3**).[22] Although the rhodium norbornadiene complex may be synthesized, the norbornadiene complex of iridium cannot be prepared and the product obtained when attempting to make such a complex apparently contains norbornene fragments coupled by carbon−carbon bonds. However, the similar tetrafluorobenzobarrelene (**5**) can be used as a diolefin ligand and a rich chemistry

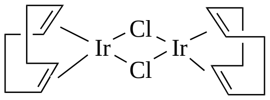

(**1**)

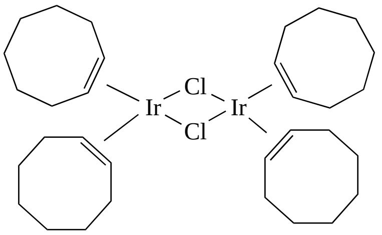

(**2**)

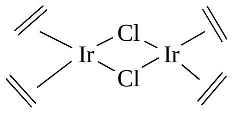

(**3**)

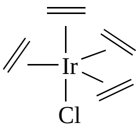

(**4**)

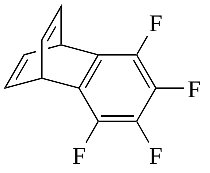

(**5**)

has been developed with iridium tetrafluorobenzobarrelene complexes.[23]

The iridium olefin complexes provide the entryways into a number of other complexes of iridium. The simplest reactions that the dinuclear complexes undergo are bridge-splitting reactions with phosphine and nitrogen donor ligands (*see **P-donor Ligands***). The exact nature of the product obtained depends on the ligand, the stoichiometry, and the reaction conditions employed. With large, bulky phosphines employing a 1:1 PR_3: Ir ratio at room temperature, the bridge may be split with no further reaction taking place. Thus, $[Ir(COD)Cl]_2$ (**1**) will react with one equivalent of triphenylphosphine per iridium at room temperature in hydrocarbon solvent to yield $Ir(COD)(PPh_3)Cl$ (**6**). However, if larger ratios of PPh_3 to iridium are employed at higher reaction temperatures, ''$Ir(PPh_3)_3Cl$'' is produced but rapidly converts to an orthometallated (*see Orthometalation*) form (**7**). On the other hand, if dichloromethane is employed as the reaction medium, the bis-phosphine product $Ir(COD)(PPh_3)_2Cl$ (**8**) is prepared.[24] With cold alcohol as the solvent, $[Ir(COD)(PR_3)_2]^+$ (**9**) or even $[Ir(COD)(PR_3)_3]^+$ (**10**) complexes are obtained, the number of phosphines attached dependent upon the size of the ligand.[25] If the ligand is very small, such as in the case of PMe_3, tri-substitution to form $[Ir(COD)(PMe_3)_3]Cl$ (**11**) occurs readily at room temperature even in nonpolar solvents.[26] Various tripodal tris-phosphine ligands have also been shown to attach all three phosphorus atoms providing $[Ir(COD)P_3]^+$ compounds.[26–28]

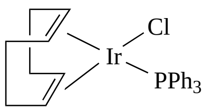

(**6**)

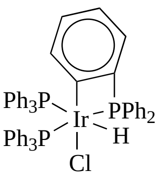

(**7**)

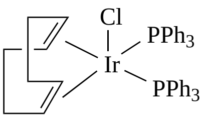

(**8**)

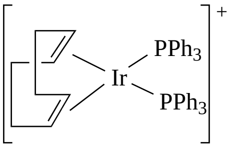

(**9**)

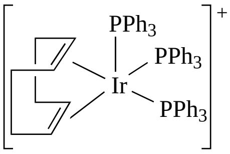

(**10**)

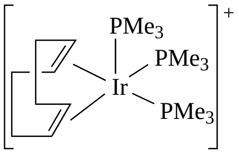

(**11**)

For the most part, displacement of the chelating COD ligand (*see Chelating Ligands*) is difficult to achieve as a simple substitution under mild conditions. So, the cyclooctene complex $[Ir(COE)_2Cl]_2$ (**2**) is typically employed as a starting material for the preparation of $[Ir(COE)(PR_3)_3]$ (**12**) or $[Ir(PR_3)_3Cl]$ (**13**) complexes.[29] In the case of $PR_3 = PMe_3$, these complexes are extremely reactive and undergo a number of oxidative addition reactions (*see Oxidative Addition*).

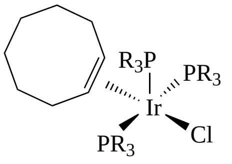

(**12**)

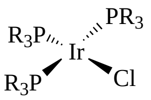

(**13**)

Bianchini's group has been investigating the chemistry of iridium with tripodal (*see Tripodal Ligand*) phosphine ligands.[30] One very interesting olefin complex, which provides a starting point for a number of their studies, is the ethylene complex $(tripod)IrCl(C_2H_4)$ (**14**) where tripod $= HC(CH_2PPh_2)_3$.[31] This particular ethylene complex has been a rich source of unusual iridium chemistry. An intriguing variant of the tripod ligand is one in which the tertiary carbon is replaced by boron yielding tripod B $= PhB(CH_2PPh_2)_3{}^-$. Since the ligand is overall negatively charged, iridium(I) compounds with this ligand are zwitterionic, which leads to some subtle differences in chemistry of compounds such as (**15**).[28]

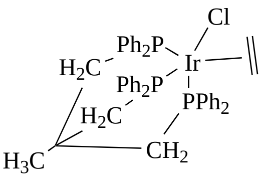

(**14**)

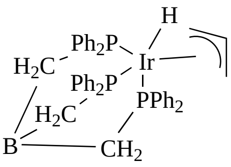

(**15**)

The reactions of iridium olefin complexes are not restricted to reactions with phosphines. Amines have also employed in bridge-splitting and substitution reactions with $[Ir(COD)Cl]_2$, especially chelating diamines. The reactions proceed to yield $[Ir(COD)N–N]_2$ compounds.**[32]** A fertile chemical area involves the *tris*(pyrazolyl)borate (*see Tris(pyrazolyl)borates*) family of compounds with the monoethylene and bisethylene complexes serving as reactive entries in this field.**[33–37]**

The bridging chloride ligands in these $[Ir(olefin)_2Cl]_2$ compounds are susceptible to metathesis reactions, yielding new dimeric compounds of the form $[Ir(olefin)_2B]_2$ where 'B' represents a new bridging ligand. Alkoxides, thiolates, and carboxylates have all been employed successfully in the replacement of chloride. The complexes with B = Br, I have also been prepared, both by metathesis reactions and by direct reaction of cyclooctene or cyclooctadiene with $IrBr_3$ or IrI_3.**[22]** The olefin complexes also provide excellent starting materials for the syntheses of arene and cyclopentadienyl iridium complexes, a subject that will be discussed in the next section.

3 IRIDIUM ARENE (*See Arene Complexes*) AND CYCLOPENTADIENYL (*See Cyclopentadienyl*) COMPLEXES

In this section, the syntheses and some chemistry of two important classes of π-ligand complexes of iridium are described (*see* ***Organic Synthesis using Transition Metal Complexes Containing π-Bonded Ligands***).

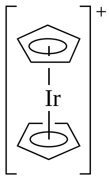

(**16**)

3.1 Cyclopentadienyl Complexes

Historically, pentahapto (*see Hapticity*) cyclopentadienyl complexes of iridium have been a very popular area for research, with many examples of cyclopentadienyl and substituted cyclopentadienyl compounds having been synthesized. The iridium analog of cobaltacinium, $[Cp_2Ir]^+$ (**16**), may be prepared via the reaction between a suitable iridium(III) precursor such as $IrCl_3$ and cyclopentadienyl magnesium chloride. Other ring substituted derivatives have also been prepared, but attempts to prepare neutral iridacene have been unsuccessful. More commonly investigated are the mono-cyclopentadienyl or half-sandwich (*see Half-sandwich Complexes*) complexes of iridium. Again, using $[Ir(olefin)_2Cl]_2$ complexes as starting materials, reactions with cyclopentadienylating reagents lead to the formation of $CpIr(olefin)_2$ compounds (**17**) (equation 1). These may be used to synthesize additional compounds via substitution of the olefin ligands, but in general this substitution is sluggish and forcing conditions are required in order to carry out these substitutions. A better route to substituted CpIr complexes is via the $[CpIrCl_2]_2$ family of compounds.

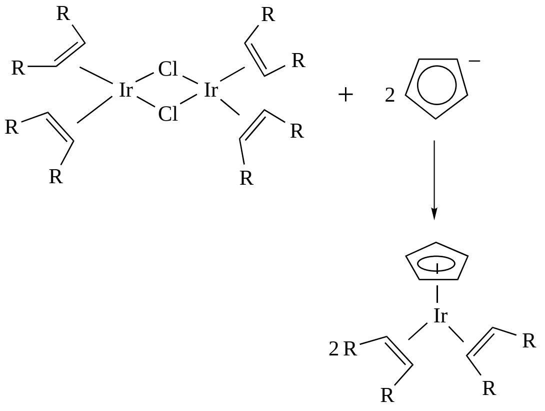

(1)

(**17**)

Initially, $[Cp^*IrCl_2]_2$ (**18**) was synthesized via the reaction between hexamethyldewarbenzene and $IrCl_3{\cdot}H_2O$ (equation 2).**[38]** However, a more convenient and efficient synthesis is via direct reaction between pentamethylcyclopentadiene and $IrCl_3{\cdot}H_2O$.**[39]** The chloride bridge may then be split with donor ligands such as phosphines to yield $Cp^*Ir(PR_3)Cl_2$ compounds. The chloride ligands may then be replaced by alkyl or hydrido groups in further transformations. Reduction of (**18**) in the presence of CO and other donors will produce the iridium(I) bis-ligand complexes (**19**) (equation 3). Using a combination of the above reactions, quite a variety of half-sandwich (*see Half-sandwich Complexes*) iridium complexes may be synthesized.**[40]**

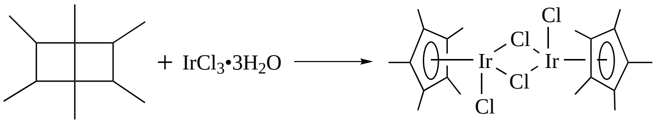

(**18**)

(2)

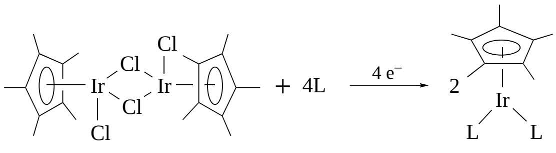

(**18**) (**19**)

(3)

From $[Cp^*IrCl_2]_2$, removal of the chloride ligands in the presence of weakly coordinating solvents leads to the production of a host of $[Cp^*IrS_3]^{2+}$ compounds that provide an easy entry into the chemistry of the Cp^*Ir^{2+} fragment as well as an excellent starting material for other Cp*Ir complexes.**[41]** A very large body of work has been added to this field by the Maitlis group.**[42–44]**

An interesting variant in the family of cyclopentadienlyiridium complexes are those containing η^5-indenyl ligands. It had been shown by Mawby and coworkers that indenyl metal complexes are far more reactive with respect to ligand substitution chemistry than their cyclopentadienyl analogues.**45** Basolo quantified this greatly accelerated reaction chemistry for a number of indenyl metal systems and dubbed this acceleration the 'indenyl effect'.**46–48** The indenyl effect also appears to play an important role in the chemistry of indenyl iridium complexes. Indenyliridium complexes may be prepared in much the same way as the cyclopentadienyl and pentamethylcyclopentadienyl iridium complexes. However, once formed, they are far more reactive in terms of substitution chemistry.

For example, $CpIr(C_2H_4)_2$ only reacts with phosphines at elevated temperatures for long reaction times to produce $CpIr(PR_3)_2$ complexes. On the other hand, $IndIr(C_2H_4)_2$ (**20**) reacts with phosphine ligands rapidly at room temperature to produce $IndIr(PR_3)_2$ (**21**) (equation 4). In this area, the first example of an η^5 to η^3 ring-slip (*see Slip Processes in Ligands*) transformation was demonstrated and the crystal structure of η^3-$IndIr(PMe_3)_3$ (**22**) has been reported.**49** Perhaps one of the more unusual manifestations of the reactivity of the indenyl ligand was found in the chemistry of IndIr(COD) (**23**). Here, reaction with PMe_3 led to the displacement of the indenyl ligand (as indenide) from the iridium followed by nucleophilic attack of the indenide on the coordinated COD yielding the unusual cyclooctenyl structure (**24**) shown (equation 5).**50** (See Section 7 of this article on an important utilization of the indenyl effect in C–H activation chemistry.)

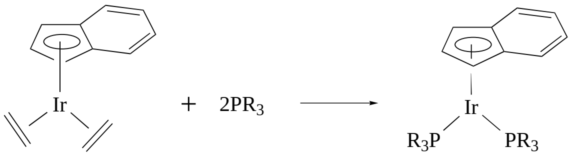

(4)

(**20**) (**21**)

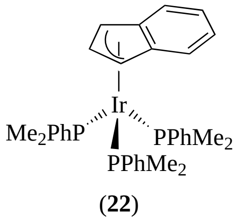

(**22**)

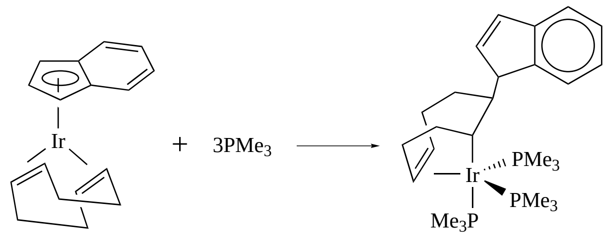

(5)

(**23**) (**24**)

3.2 Arene Complexes

Sandwich (*see Sandwich Compound*) and half-sandwich (*see Half-sandwich Complexes*) complexes of iridium may also be readily prepared by the reaction of an arene with an iridium complex possessing three labile ligands.**51,52** So, $[Ir(COD)]^+$ (solvated) will react with an arene to form $[Ir(COD)(arene)]^+$ through displacement of the loosely bound solvates. Iridium may also catalyze the disproportion of cyclohexadiene to cyclohexene and in the process produce an arene complex. Thus, $IrCl(1,3\text{-}C_6H_8)_2$ (**25**) will undergo a transformation to $[Ir(\eta^6\text{-}C_6H_6)(h^4\text{-}C_6H_4)]^+$ (**26**) upon removal of the chloride by Ag^+ (equation 6).**44** The coordinated benzene can then be displaced by other arenes providing a route to additional arene complexes. Crabtree also discovered that arene complexes may be obtained from an iridium system active for the dehydrogenation of alkanes when a C_6 cycloalkane capable of converting into an arene was used as the substrate.**53–55** Arene compounds with three very loosely solvated ligands may be prepared from $[(Arene)IrCl_2]_2$ compounds via the removal of chloride in the presence of weekly coordinating ligands.**56**

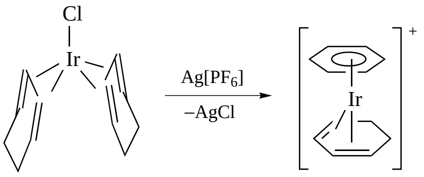

(6)

(**25**) (**26**)

More commonly encountered are the arene complexes also containing Cp or Cp* ligands. Since $[Cp^*IrCl_2]_2$ (**18**) may be prepared so readily (see above), this provides a useful starting material for the formation of $[Cp^*Ir(\eta^6\text{-}arene)]^{+2}$ compounds.**40** (**18**) may be easily converted into $[Cp^*Ir(acetone)_3]^{+2}$ by dissolution in acetone and treatment with $Ag[PF_6]$. Maitlis has shown in a number of cases that this dication will then react with a variety of arenes including benzene, toluene, xylene, and naphthalene to yield arene complexes (**27**) by displacement of the acetones (equation 7). Maitlis has also used $[Cp^*Ir(OAc)_2(OH_2)]$ and $[Cp^*Ir(NCCH_3)_3]^{+2}$ as sources of iridium.

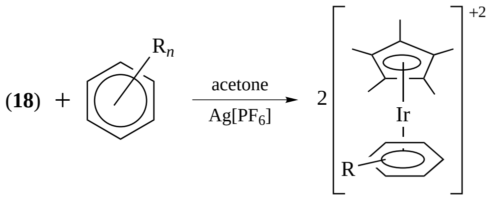

(7)

(**27**)

Arenes bound to iridium are susceptible to nucleophilic attack to form first cyclohexadienyl and then cyclohexadiene complexes. For example, Maitlis showed that $[Cp^*Ir(\eta^6\text{-}toluene)]^{+2}$ reacts with $NaBH_4$ yielded the cyclohexadiene complex with H attack always occurring exo. Treatment of the cyclohexadiene complex with HCl liberated the organic fragment as cyclohexene. Bianchini and Caulton *et al.* have shown that reaction between (triphos)Ir(Cl)(C_2H_4) (**14**) and acetylene in the presence of Tl[PF_6] yields an η^4-benzene complex (**28**) via cyclotrimerization (*see Cyclodimerization & -trimerization Reactions*) of the alkyne (see Section 4) (equation 8).[57] In a series of H^+, H^- addition sequences, it was shown that the η^4-benzene can be reduced to cyclohexene.[58] Arene iridium complexes have been exploited for their catalytic activity.[59,60]

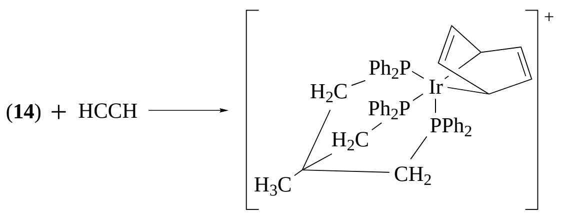

(**28**)

(8)

Heteroatom containing arenes have also been made to complex with transition metals, including iridium. For example, borabenzene has been shown to complex to iridium and iron in a single complex.[61]

4 IRIDIUM ALKYNE AND RELATED COMPLEXES (*See Alkyne Complexes*)

Simple alkyne adducts of iridium may be readily formed with a variety of ancillary ligands.[62] Reaction between Vaska's compound Ir(CO)Cl(PPh_3)$_2$ (**29**) (*see Vaska's Complex*) and electron-deficient alkynes results in the formation of simple adducts. For example, (**29**) and $F_3CC{\equiv}CCF_3$ react to form Ir(CO)Cl(PPh_3)$_2$($F_3CC{\equiv}CCF_3$) (**30**). With chlorophenylacetylene there is a competition between making the simple adduct Ir(CO)Cl(PPh_3)(ClC≡CPh) (**31**) and forming an acetylide complex (**32**) via oxidative addition of the C–Cl bond (equation 9). Werner has prepared trans-$[IrCl(RC{\equiv}CR)(PPr^{i}_{3})_2]$ complexes (**33**) (R = H, Me, Ph) from the reaction of the alkyne with $[IrCl(PPr^{i}_{3})_2]$ prepared in situ. Further reaction of these alkyne complexes with Cp^- leads to the formation of $CpIr(RC{\equiv}CR)(PPr^{i}_{3})$ (**34**) compounds (equation 10).[63]

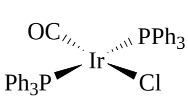

(**29**)

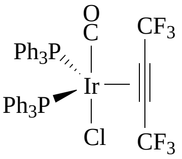

(**30**)

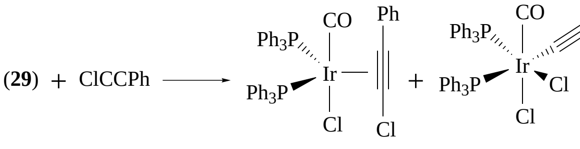

(**31**) (**32**)

(9)

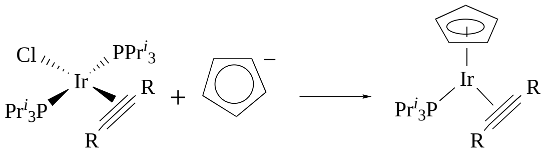

(**33**) (**34**)

(10)

The interaction of alkynes with iridium hydride complexes can lead to a number of different alkyne complexes. Reaction between two equivalents of 2-butyne and $[IrH_4(PPhMe_2)_3]^+$ produces one equivalent of butene and the butyne complex $[Ir(MeC{\equiv}CMe)(PPhMe_2)_3]^+$ (**35**) with a structure that differs from the expected square planar. Reaction between the same iridium complex and dimethylacetylenedicarboxylate produces a bis-alkyne complex (**36**).[64,65]

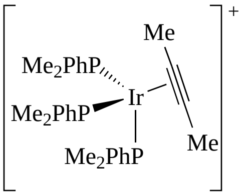

(**35**)

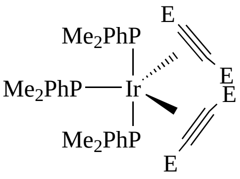

(**36**) E = CO_2Me

When the alkyne is a terminal one, a common reaction path is the formation of a vinylidene iridium complex. Werner's group has extensively studied the chemistry of iridium with bulky phosphine ligands and their ability to form vinylidene complexes. For example, the reaction between $IrH_2Cl(PMeBu^{t}_{2})_2$ (**37**) and acetylene yields the vinylidene complex $Ir(C{=}CH_2)Cl(PMeBu^{t}_{2})_2$ (**38**) (equation 11).[66,67] The square-planar vinylidene complexes $IrCl(C{=}CHR)(PPr^{i}_{2})_2$ (**39**) were also prepared by Werner's group. A particularly interesting discovery was that these square-planar vinylidene complexes are quantitatively protonated to form $[HIrCl(C{=}CHR)(PPr^{i}_{2})_2]^+$ (**40**) species, which appear to be in equilibrium with the corresponding iridium carbyne complexes $[IrCl(CCH_2R)(PPr^{i}_{2})_2]^+$ (**41**) (equation 12).[68]

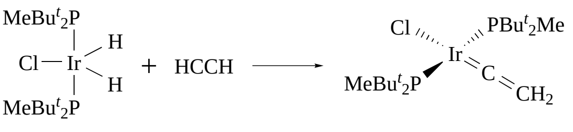

(**37**) (**38**)

(11)

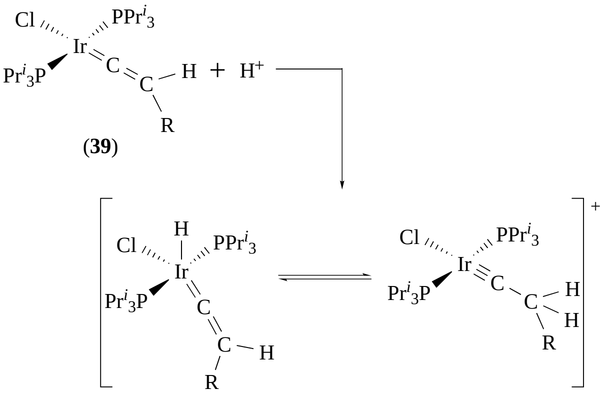

(**39**) (**40**) (**41**) (12)

Coupling of multiple alkynes at one iridium center can proceed through any one of quite a number of different reaction paths. In some cases, alkynes react with iridium complexes to undergo cyclotrimerization to form arenes. Such a reaction was discussed above concerning the formation of the η^4-benzene complex (**28**).[57] In general, the iridium compounds are not as reactive as some metals for the cyclotrimerization reaction, but the stability of various intermediates along the way has made these systems valuable for studying the steps involved. Common among these reactions is oxidative coupling (*see Oxidative Coupling*) of alkynes to yield iridacyclopentadiene complexes. For example, $Ir(CO)Cl(PMePh_2)_2$ reacts with $F_3CC{\equiv}CCF_3$ to yield metallacycle (**42**, *see Metallacycle*) while $Ir(CO)Cl(PPh_3)_2$ reacts with dimethylacetylene dicarboxylate to form metallacyclopentadiene (**43**).

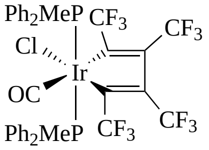

(**42**)

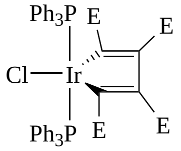

(**43**) $E = CO_2Me$

Metal compounds are often used to stabilize reactive organic fragments via complexation and intriguing 'alkyne' ligand in this classification is benzyne. A series of iridium benzyne complexes has been made with compound (**44**) as an example and the reaction chemistry of coordinated benzyne has been explored.[69–71]

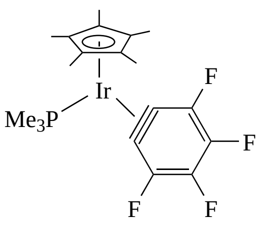

(**44**)

5 IRIDIUM CARBONYL COMPLEXES

The carbonyl complexes of iridium have perhaps not been as extensively studied as those of some other metals (*see* ***Carbonyl Complexes of the Transition Metals***; ***Carbonylation Processes by Homogeneous Catalysis***, and ***Organic Synthesis using Transition Metal Carbonyl Complexes***). Nevertheless some interesting findings in this area both in terms of structure and reactivity have been reported.

5.1 Mononuclear Carbonyl Complexes (*See Metal Carbonyls*)

Several mononuclear carbonyl complexes may be synthesized with iridium(I), but most intriguing of those are the binary carbonyls. $[Ir(CO)_4]^-$ (**46**) may be synthesized by the reduction of $Ir_4(CO)_{12}$ (**45**) with sodium under an atmosphere of carbon monoxide. More vigorous reduction of (**45**) with sodium can also yield the very reactive trianion, $[Ir(CO)_3]^{3-}$ (**47**) (equation 13). These anions may then be used for the synthesis of other mono and polynuclear (*see Polynuclear Complexes*) carbonyl compounds of iridium.

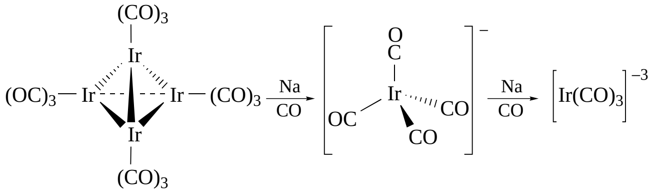

(**45**) (**46**) (**47**)

(13)

Chloro- and other halo- containing carbonyl compounds of iridium may also be synthesized under mild conditions. Unlike $[Rh(CO)_2Cl]_2$, $[Ir(CO)_2Cl]$ is not obtainable by the direct reaction of an iridium chloride solution with CO. Instead, $[Ir(CO)_2Cl_2]_n$ (**48**) is obtained in low yields by reaction between $IrCl_3{\cdot}H_2O$ and carbon monoxide. The predominant mononuclear compound obtained upon carbonylation of iridium chloride salts is the tricarbonyl $[Ir(CO)_3Cl]_n$ (**49**), which appears in the solid state to be a polymeric array consisting of stacking square-planar $Ir(CO)_3Cl$ units with short Ir–Ir bonds. Even though $[Ir(CO)_3Cl]_n$ is polymeric, it is sublimable and is still a convenient source of iridium(I) containing carbon monoxide. (**49**) will react with a number of nucleophiles to form mononuclear iridium carbonyl complexes.

The arena of mononuclear carbonyl complexes of iridium is dominated by Vaska's compound,[72] $[IrCl(CO)(PPh_3)_2]$ (**29**), and its variants. The most common variation found in the literature comes from replacement of the chloride ligand with other monoanionic ligands such as halides and pseudohalides. Infrared spectroscopy has been used (by examining

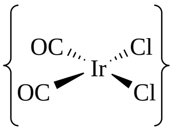

(**48**)

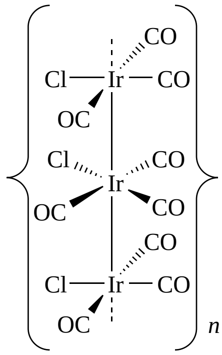

(**49**)

ν_{CO}) to determine the electron donor/acceptor properties of various X ligands in $[IrX(CO)(PPh_3)_3]$ compounds. In addition, it is possible to replace the PPh_3 ligands by other phosphine donors thereby widely extending the range of these compounds that can be synthesized. By far the largest number of investigations into the reaction chemistry of Vaska-type compounds delved into their oxidative addition reactions. A large number of X–Y bonds have been added to iridium including C–Br, C–I, H–Cl, H–Br, H–I and H–H. In addition, O_2 adds to Vaska's complex to form a stable O_2 adduct. Because of the relative ease with which oxidative addition reactions take place with the iridium(I) center in Vaska-type complexes, these complexes have been used extensively to model reactions where the oxidative addition step is believed to be an important one. One indication of the reactivity of Vaska-type compounds is a reaction between C_{60} (fullerene, *see Buckminsterfullerene*) and $Ir(CO)Cl(PMe_2Ph)_2$ to yield a C_{60} core with two $Ir(CO)Cl(PMe_2Ph)_2$ moieties bound (**50**) with similar unusual chemistry with C_{70}.[73–75]

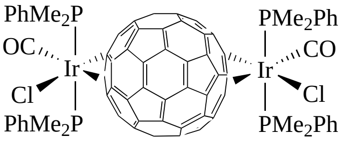

(**50**)

Although there is no stable free S analog of CO, nevertheless, several CS compounds of iridium have been synthesized by multistep methods and their reaction chemistry has been investigated.[76–80]

5.2 Polynuclear Iridium Carbonyl Clusters (*See Metal Carbonyl Clusters*)

Because of the great strength of iridium–iridium bonds, there is a wealth of information on polynuclear metal-carbonyl cluster compounds of iridium (*see* ***Dinuclear Organometallic Cluster Complexes*** and ***Polynuclear Organometallic Cluster Complexes***). $Ir_4(CO)_{12}$ (**45**) may be synthesized from $IrCl_3{\cdot}H_2O$ via reduction with zinc metal under a carbon monoxide atmosphere. A number of other syntheses involving both high pressures of carbon monoxide as well as involving atmospheric pressures of carbon monoxide have been reported. $Ir_4(CO)_{12}$ (**45**) is a yellow–orange air stable molecule with a tetrahedral arrangement of iridium atoms with only terminal carbonyl ligands.[81,82] $Ir_4(CO)_{12}$ (**45**) serves as a starting point for a number of other cluster compounds of iridium such as $Ir_6(CO)_{16}$ (**51**) via reductive routes. Each of these clusters is susceptible to ligand substitution chemistry not only by phosphines but also by a large number of other neutral and anionic nucleophiles. Higher nuclearity clusters of iridium have been formed including a heptanuclear cluster, $[Ir_7(CO)_{12}(COD)(C_6H_{11})]$ (**52**) and the octanuclear clusters $[Ir_8(CO)_{22}]^{-2}$ (**53**) and $[Ir_8(CO)_{20}]^{-2}$ (**54**). Garlaschelli and coworkers have reported on extensive investigations into the chemistry of $Ir_6(CO)_{16}$ (**51**) as well as that of $[Ir_6(CO)_{15}]^{-2}$ (**52**). In one reaction they find a nonanuclear cluster, $[Ir_9(CO)_{20}]^{3-}$ (**53**), as a by-product.[83] The same group reported on the structure of $[Ir_{11}(CO)_{23}]^{3-}$ (**54**).[84]

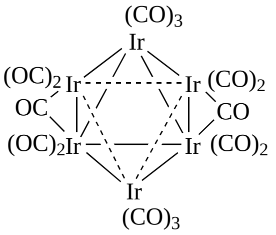

(**51**)

An interesting variant in the study of iridium carbonyl cluster compounds comes from studies on inorganic surfaces. From one direction, there have been studies involving the preparation of catalysts by the deposition of discrete metal-carbonyl clusters (*see* ***Heterogeneous Catalysis by Metals***). The deposition of $Ir_4(CO)_{12}$ on SiO_2 yields a catalyst for the isomerization of 1,5-cyclooctadiene. Infrared spectroscopy and thermal analysis have been used to study the nature of the species generated when $Ir_4(CO)_{12}$ is adsorbed onto SiO_2 and MgO. Yet another twist on the supported metal-cluster area is the use of $AlCl_3$/NaCl melts containing $Ir_4(CO)_{12}$. The subject of metal clusters on zeolites has been reviewed.[85]

From the other directions, there have been a number of studies of the cluster species that are formed when mononuclear iridium precursors are deposited onto inorganic supports and then subjected to carbon monoxide pressures. Gates and coworkers have shown that $Ir(CO)_2(acac)$ will form higher nuclearity iridium carbonyl clusters, the exact nature of which depends on the substrate and the carbonylation conditions.[86,87] For zeolite NaY, they have observed that $Ir(CO)_2(acac)$ will yield both $Ir_4(CO)_{12}$ (**45**) and $Ir_6(CO)_{16}$ (**51**). Using zeolite NaX, they find that the predominant species that may be removed from the zeolite is $[Ir_6(CO)_{15}]^{-2}$ (**52**). On the other hand, $Ir(CO)_2(acac)$ (**55**) on MgO typically yields $[HIr_4(CO)_{11}]^-$ (**56**) and $[Ir_8(CO)_{22}]^{-2}$ (**57**). Deposition of $IrCl_3$ onto MgO apparently yields only $[Ir(CO)_3Cl]_n$ (**49**) upon carbonylation while silica gel can be used for the syntheses of a number of carbonyl clusters.[88]

Mixed-metal clusters containing iridium also have been formed combining iridium with a number of other metals such as rhodium, rhenium, nickel, copper, and gold. A variety of structures have been reported from these studies. The most unusual of 'mixed-metal' complexes involving iridium are those that contain an 'early-late' metal combination. A driving force for the syntheses of such compounds is the potential synergistic effect of having an electron-deficient (*see Electron Deficient Compound*), Lewis-acidic metal (*see Lewis Acids & Bases*) in combination with an electron-rich, Lewis-basic metal (*see Lewis Acids & Bases*) for unusual organic transformations. A methylene bridged tantalum–iridium carbonyl compound (**58**) has been reported by Bergman and it has very interesting catalytic properties.

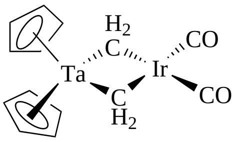

(**58**)

6 IRIDIUM ALKYL (*See Alkyl Complexes*) AND ARYL COMPLEXES

6.1 Iridium(I)

In general, iridium(I) alkyl complexes are easily prepared via the reaction between an iridium halide and a suitable alkylating or arylating reagent, the stability of the complex depending on the nature of the other ligands on iridium. $H_3C–Ir(PPh_3)_3$ (**59**) may be prepared by treating $IrCl(PPh_3)_3$ (**7**) with H_3CMgX (equation 14) but is not very thermally stable decomposing via a presumed radical pathway. $(Me_3P)_3IrCH_2C(CH_3)_3$ (**60**) is stable at -20 °C but decomposes rapidly at 0 °C to form a cyclometallated (*see Cyclometalation*) product (**61**) (equation 15). The analogous silyl compound, $(Me_3P)_3IrCH_2Si(CH_3)_3$ (**62**), is somewhat more stable but still cyclometallates at room temperature.[89–91]

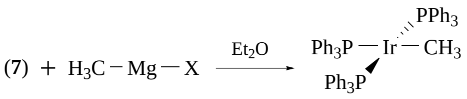

(**59**) (14)

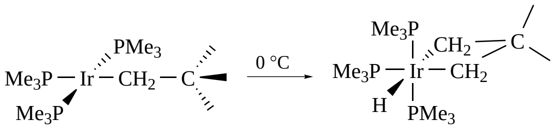

(**60**) (**61**) (15)

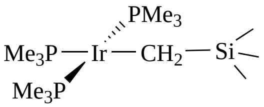

(**62**)

Treatment of $Ir(CO)Cl(PPh_3)_2$ (**29**) with alkyl or aryl grignard reagents produces the corresponding alkyl or aryl iridium complexes $R–Ir(CO)(PPh_3)_2$ (**63**). These compounds are substantially more stable than the fully phosphinated alkyl iridium compounds. The stability of these compounds also increases in the order aryl > alkyl with the fluoro substituted aryl complexes being the most stable.

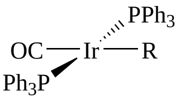

(**63**) R = alkyl, aryl

Alkyl complexes with both phosphine ligands and COD have been extensively studied, especially their dynamic processes (*see* ***Stereochemical Nonrigidity of Organometallic Complexes***) in solution. Treating $[Ir(COD)Cl]_2$ (**1**) with two equivalents of PR_3 per iridium followed by an equivalent of an alkyl grignard reagents leads to the formation of $R–Ir(COD)(PR_3)_2$ (**64**) complexes (equation 16). These compounds appear to be quite stable, especially for $R = CH_3$ and CH_2Ph. A number of structural studies on these compounds were carried out by Churchill and coworkers showing them to be trigonal bipyramidal molecules. Shapley and Osborn studied their dynamic NMR processes and found them to be consistent with Berry pseudo-rotation.

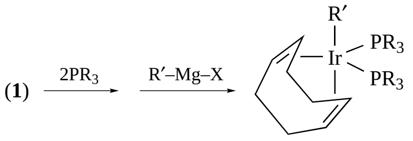

(**64**) (16)

Alkyl iridium compounds are also accessible via insertion (*see Migratory Insertion*) of alkenes into Ir–H bonds. Analogously, alkenyl iridium compounds may be formed via insertion of alkynes into Ir–H bonds. These types of reactions have been studied to shed light on the mechanism of alkene and alkyne hydrogenation processes. For example, $HIr(CO)(PPh_3)_2$ (**65**) will react with ethylene and higher olefins to produce the alkyl iridium compounds (equation 17).

These are reversible reactions with β-hydride elimination (*see β-Hydride Elimination*) competing with insertion and the alkyl complexes are generally only stable in the presence of excess olefin.

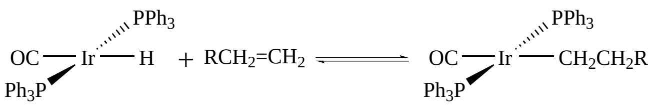

(**65**)

(17)

6.2 Iridium(III)

There are quite a number of routes available for the production of iridium(III) alkyl compounds. In addition to the halide displacement and olefin insertion pathways noted above for iridium(I) compounds, oxidative addition of C–H bonds to iridium(I) to form iridium(III) hydrido alkyl complexes is also a possibility. This subject will be covered in detail in Section 9 and will not be discussed here. However, there are other oxidative addition routes that lead to the formation of iridium(III) alkyls. First, oxidative addition of O_2 or HCl to some alkyl and aryl iridium(I) complexes can produce iridium(III) alkyl or aryl compounds. In some cases, $HgCl_2$ can add, but this appears to lead to tractable products only for the very stable pentafluorophenyl complex. Of course, oxidative addition (*see Oxidative Addition*) of alkyl halides such as H_3CI will also yield alkyl iridium(III) compounds. Addition of MeI to Vaska's compound yields a stable iridium(III) complex, but addition of EtI does not produce a stable compound, presumably due to subsequent β-hydride elimination (*see β-Hydride Elimination*). A number of mechanistic studies have been done on the oxidative addition of alkyl halides to iridium(I), especially Vaska's complex (*see Vaska's Complex*).

$[Ir(PMe_3)_4]Cl$ (**66**) is a very reactive iridium(I) species, which undergoes oxidative addition reactions with a number of substrates. Reactions between (**66**) and ethylene oxide remarkably lead to the formation of formylmethyl iridium(III) complex (**67**) (equation 18).**92**

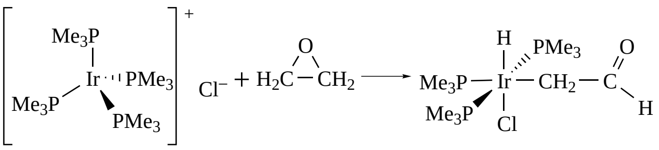

(**66**) (**67**)

(18)

The synthesis of iridium(III) alkyl and aryl compounds via nucleophilic displacement is straightforward starting from a suitable L_3IrX_3 complex with X most commonly being chloride. Chatt and Shaw carried out early work on the syntheses of iridium(III) alkyl complexes showing that fac$[IrMe_3(PR_3)_3]$ (**69**) could be formed by reaction between $[IrCl_3(PR_3)_3]$ (**68**) and methyl grignard (equation 19). The homoleptic (*see Homoleptic Compound*) metal aryl and alkyl compounds have also been described. Reaction of $IrCl_3(THT)$ (**70**) (THT = tetrahydrothiophene) with mesitylmagnesium bromide yields the tris-mesityliridium complex (**71**) free of other ligands (equation 20).**93** Reaction of (**70**) with methyllithium followed by addition of (tetramethylethylenediamine) TMEDA yields the hexamethyliridium(III) complex (**72**) (equation 21).**94**

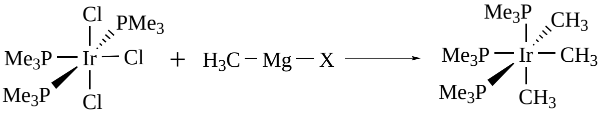

(**68**) (**69**)

(19)

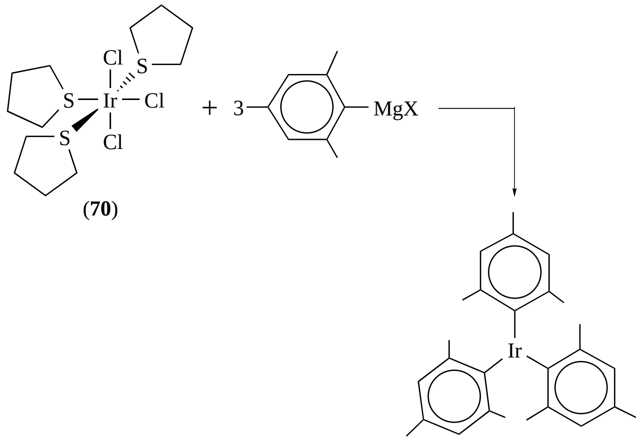

(**70**)

(**71**)

(20)

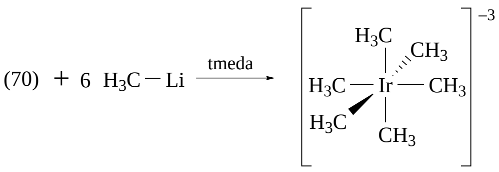

(**72**)

(21)

6.3 Iridium(V) Complexes

As a third-row transition element, iridium does have a propensity to attain higher oxidation states than the first and second row congeners. Thus, it is possible to isolate and study a variety of Ir(V) alkyl compounds.**93,95**

6.3.1 *Iridium Fullerene Complexes*

With the discovery of C_{60} and other fullerenes (*see* ***Carbon: Fullerenes***), it was not long before investigations into the possible reactions of fullerenes and iridium complexes were undertaken. Quite a variety of exohedral iridium fullerene compounds have been characterized including complexes of

C_{60}, C_{70}, C_{84} and nanotubes.[96–98] An example of such a complex was shown earlier in compound (**50**).

7 IRIDIUM CARBENE AND CARBYNE (*See Carbyne Complexes*) COMPLEXES[99–101]

Carbene and related complexes have been shown to be important players in a number of catalytic processes, including olefin metathesis (*see* ***Organic Synthesis Using Metal-mediated Metathesis Reactions***). The following briefly surveys some of the structural types found in iridium chemistry.

7.1 Mononuclear Systems[102]

An early synthesis of an iridium carbene complex (**74**) involved the three fragment oxidative addition reaction of $[Me_2NHCl]Cl$ with $Ir(N_2)(Cl)(PPh_3)_2$ (**73**) (equation 22). A related complex containing a thiazolidinylidene ligand (**75**) has also been synthesized, although in this case it is unclear how much carbene character the Ir–C bond possesses. Lappert and coworkers performed a number of studies on the reactions between electron-rich alkenes and iridum complexes that yielded iridium carbene complexes. A sulfur stabilized carbene complex of iridium may be prepared via the alkylation of an iridium thiocarbonyl (*see Thiocarbonyl*) compound with MeI. A dichlorocarbene complex was prepared by Roper's group via the reaction between $IrHCl_2(PPh_3)_3$ and $Hg(CCl_3)_2$.

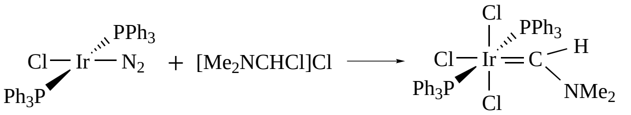

(**73**) (**74**)

(22)

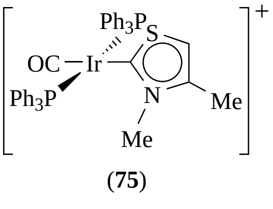

(**75**)

Another route to heteroatom stabilized carbenes involves first the interaction of a terminal alkyne with an iridium complex to yield an iridium vinylidene compound. The vinylidene complex then reacts with nucleophiles, typically alcohols, to form oxa stabilized carbene complexes. O'Connor extended this strategy to form a carbene ligand on the same iridium center as a metallacycle (**76**)[103] and was also able to synthesize a bis-carbene complex of iridium (**77**).[104] Carmona and coworkers have reported that similar cyclic carbene ligands may be prepared from $Tp^*Ir(H)(CH{=}CH_2)(C_2H_4)$ (**78**) (where $Tp^* =$ tris-(3,5-dimethylpyrazolyl)borate) and THF, where a double C–H activation is invoked to account for the formation of the carbene complex (**79**) (equation 23).[105]

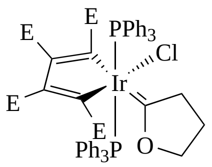

(**76**) $E = CO_2Me$

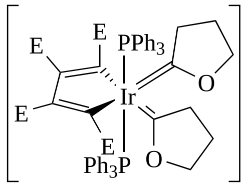

(**77**) $E = CO_2Me$

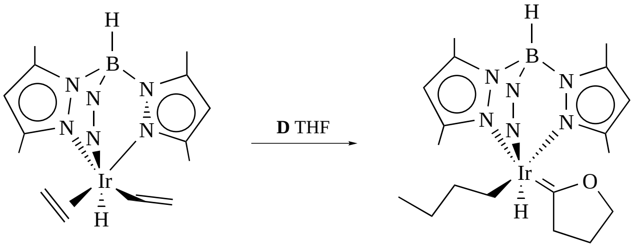

(**78**) (One pyrazolyl ring removed for clarity) (**79**)

(23)

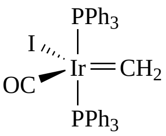

(**80**)

Unsubstituted iridium carbene complexes have been formed in several different ways. Roper found that addition of diazomethane to $IrI(CO)(PPh_3)_2$ yielded the terminal methylene complex $Ir(CH_2)(I)(CO)(PPh_3)_2$ (**80**). Bergman and Klein prepared $Cp^*Ir(PMe_3)(CH_2)$ (**82**) via photolysis of an oxametallacycle of iridium (**81**), but this is only stable in solution below −40 °C (equation 24). Although it was not isolated, a terminal methylene complex of iridium was prepared by Thorn from the reaction between $MeIrBr(CH_2OMe)(PMe_3)_3$ and H^+ and trapped by pyridine to form (**83**) (equation 25).[106]

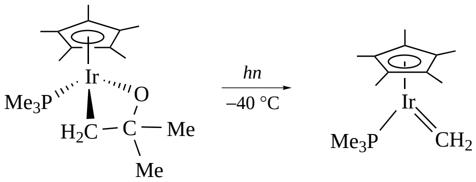

(**81**) (**82**)

(24)

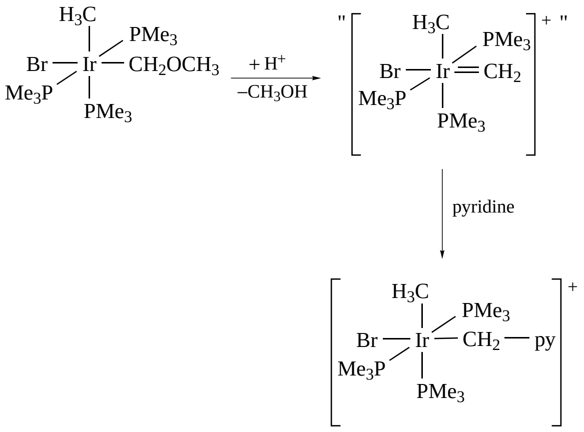

(25)

(**83**)

7.2 Polynuclear Compounds

Complexes with bridging carbene or carbyne ligands have been prepared with the ligands bridging a number of different metals (*see* ***Dinuclear Organometallic Cluster Complexes*** and ***Polynuclear Organometallic Cluster Complexes***). F. G. A. Stone and coworkers have published numerous papers on bridging carbene and carbyne ligands in polynuclear compounds. The simplest complex containing methylene bridging two iridium centers would appear to be (COD)Ir(μ-CH_2)$_2$Ir(COD) (**84**) formed by reaction between $[Ir(COD)Cl]_2$ and methyllithium.[107]

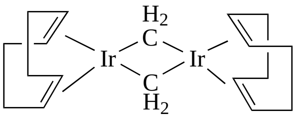

(**84**)

8 CATALYSIS (*See Catalysis*)

Results from studies on organoiridium compounds have made significant contributions in the area of catalysis. In some transformations, organometallic iridium compounds are the most active catalysts available. In others, where iridium may not yield the most active catalysts, iridium complexes nevertheless yield important information about the structure and reactivity of important catalytic intermediates. The following sections attempt to briefly cover some of the most important homogeneous catalytic process where iridium chemistry has had some impact.

8.1 Hydrogenation[108,109]

Since iridium(I) readily undergoes oxidative addition with H_2, studying hydrogenation catalysis with iridium complexes was a natural progression (*see* ***Hydrogenation & Isomerization of Alkenes*** and ***Hydride Complexes of the Transition Metals***). Vaska's complex has been shown to be an active catalyst for the hydrogenation of unsaturated compounds. While there have been numerous studies of hydrogenation with iridium catalysts, the most active catalysts are formed via the hydrogenation of cationic $[Ir(COD)L_2]^+$ complexes in noncoordinating solvents. This process yields highly coordinatively unsaturated iridium complexes that are among the most active for olefin hydrogenation even for hindered double bonds. The most active complex would appear to be of the form $[Ir(COD)LL']^+$ where L = a bulky phosphine such as tricyclohexylphosphine or triisopropylphosphine and L′ = pyridine.[110] These catalysts show activities several orders of magnitude higher than $RhCl(PPh_3)_3$ and can hydrogenate even very hindered olefins. The general method of generating cationic iridium complexes for hydrogenation has been applied to a number of systems for the hydrogenation of olefins, the hydrogenation of ketones, the hydrogenation of nitriles and the hydrogenation of imines. There have also been a number of systems that are capable of carrying out asymmetric hydrogenation of pro-chiral olefins with the use of chiral bis-phosphine ligands.[111]

8.2 Hydroformylation (*See Hydroformylation*)

Unlike the hydrogenation catalysts, most iridium catalysts studied for hydroformylation chemistry are not particularly active and are usually much less active than their rhodium counterparts (*see* ***Carbonylation Processes by Homogeneous Catalysis***). However, this lower activity was useful in utilizing iridium complexes to study separate steps in the hydroformylation mechanism. Using iridium complexes, several steps important in the hydroformylation cycle such as alkyl migration to carbon monoxide were studied. Another carbonylation reaction in which iridum catalysis appears to be commercially viable is in the carbonylation of methanol.[112]

8.3 Hydrosilation (*See Hydrosilation*)

Hydrogenation may be considered a specific case of the addition of H–X molecules to unsaturates where X = H. There has been of late considerable interest in developing systems for which X can be a number of other elements. One of the goals of research into C–H activation (discussed in the next section) is to develop catalysts for the addition of C–H bonds to unsaturates. While this goal has not been met, the addition of Si–H bonds to unsaturates may be accomplished with a number of iridium complexes as catalysts. Although iridium complexes are not among the most active for hydrosilation, there are a number of active ones and studies into the interactions of iridium with silanes has provided useful information about important steps in catalytic hydrosilation.

Many of the systems investigate for hydrosilation chemistry are, not surprisingly, similar to those found for hydrogenation chemistry. Complexes that have shown activity for hydrosilylation include $[Ir(COE)_2Cl]_2$ (**2**), $Ir_4(CO)_{12}$ (**45**), $[IrCl(COD)(PPh_3)]$ (**6**), $IrH_2(SiEt_3)(COD)(AsPh_3)$ (**85**), and $Ir(CO)Cl(PPh_3)_2$ (**29**). Bergman has shown that a heterobimetallic complex of tantalum and iridium discussed previously (**58**) is also an active catalyst for olefin hydrosilylation.[113] In a combined reaction similar to hydroformylation (*see Hydroformylation*), hydrosilylation has been combined with carbonylation chemistry using an $[Ir(CO)_3Cl]_n$ (**49**) catalyst to form silyl enol silyl ethers (equation 26).[114]

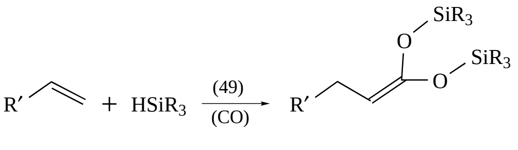

(26)

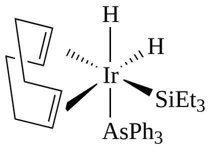

(**85**)

8.4 Hydroboration (*See Hydroboration*)

While the hydroboration of unsaturates is a powerful synthetic tool that does not require the use of a catalyst, research has shown a number of circumstances where a catalyst may improve the speed or the chemoselectivity of the uncatalyzed reaction (*see **Hydroboration Catalysis***). Asymmetric hydroboration may also be induced with achiral R_2BH reagents with the use of an appropriate chiral ligand on the metal (*see **Asymmetric Synthesis by Homogeneous Catalysis***). Evans *et al.* have shown that $[Ir(COD)(PCy_3)(py)]^+$ (**86**) (one of the most active hydrogenation catalysts) is also effective for catalyzing the addition of catecholborane tounsaturates.[115] Merola and Knorr characterized the product of the addition of catecholborane to $Ir(COE)(PMe_3)_3Cl$ as complex (**87**). This complex, while not a very active catalyst, would react with alkynes to yield isolable alkenyliridiumborane complexes (**88**) and thus serves as a model for the steps in catalytic hydroboration (equation 27).[116] Along these lines Marder, Baker and coworkers have investigated the reactions of a number of boranes with iridium and have characterized a number of fascinating structures with unusual modes of iridium–boron bonding.[117,118]

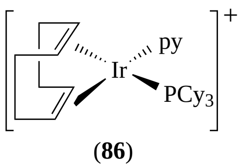

(**86**)

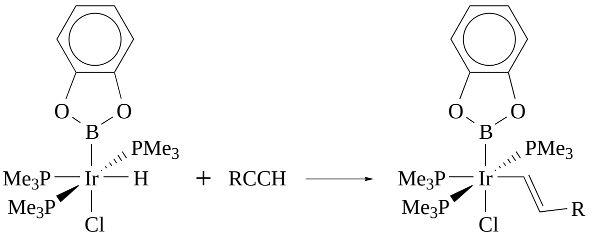

(**87**) (**88**)

(27)

In addition to using boron-hydrides as the reactive reagent in hydroboration chemistry, compounds with B–B bonds have also been utilized successfully.[119]

8.5 Iridium Catalysts with Oxygen Ligand Environment

Most of the catalysis using iridium compounds has typically exploited iridium with neutral, soft donor ligands such as phosphines, arsines, olefins, and carbon monoxide. Recent investigations into the chemistry of iridium in atypical environments has shown that oxygen ligand environments can support some very active iridium catalysts and may actually be more akin to the environment that exists around a metal when it is supported on an oxide support (*see **Water & O-donor Ligands*** and ***Oxides: Solid-state Chemistry***).

Finke's group has synthesized $[(COD)Ir{\cdot}P_2W_{15}Nb_3O_{62}]^{-8}$ (**89**) in which the iridium is bound, in addition to the COD, to three oxygens from the polyoxoanion (*see **Polyoxometalates***). NMR evidence (from ^{17}O NMR) indicates that the iridium is bound to the polyoxoanion at the NbO_3 portion. Under hydrogen, this material converts into a complex that is active for the catalytic hydrogenation of olefins. While the nature of the actual catalyst is not known, evidence suggest that the iridium must still be attached to the polyoxoanion.[120–122]

Klemperer's group has also attached iridium to various polyoxoanions.[123] They have synthesized and characterized such complexes as $[\{(COD)Ir\}_2V_4O_{12}]^{-2}$ (**90**), $[\{(COD)Ir\}V_4O_{12}]_{-3}$ (**91**), $[\{(COD)Ir\}_5\{Nb_2W_4O_{19}\}_2]^{-5}$ (**92**), $[(COD)IrP_3O_9]^{-2}$ (**93**), and $[(OC)_2IrP_3O_9]^{-2}$ (**94**). The most intriguing result from this work shows the potential to carry out oxidative reactions as well as the more commonly found reductive reactions using iridium catalysts. They found that the COD ligand in $[(COD)IrP_3O_9]^{-2}$ (**93**) reacts with molecular oxygen to yield a compound containing an oxometallacyclobutane unit derived from insertion of oxygen into a metal–carbon bond. This suggests that placing iridium into this oxygen environment may provide the platform for more unusual catalytic reactions.

Crabtree has also investigated the effect of an oxygen environment on iridium chemistry. Here, using the anion derived from the deprotonation of $HC(Ph_2P{=}O)_3$ (studied also by Grim), which is dubbed 'triso', Crabtree's group showed that this ligand could stabilize not only the +1 oxidation state but also the +3 and the +5 as well. They found that they could synthesize $(triso)Ir(olefin)_2$ (iridium(I)) compounds (**95**) and then react those with silanes to yield (triso)Ir($SiPh_3$)(H)(ethylene) (**96**) (iridium(III)) as well as (triso)Ir$(H)_2(SiPh_2Me)_2$ (**97**) (iridium(V)). This system was found to be active for the catalytic hydrosilation (*see Hydrosilation*) of olefins.[124,125]

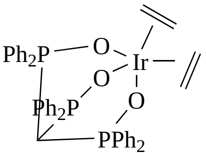

(**95**)

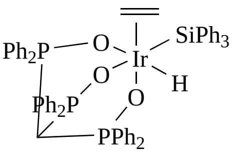

(**96**)

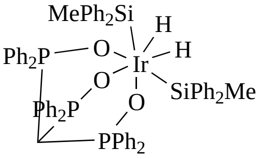

(**97**)

A relatively recent development in catalysis by iridium with an oxygen-donor environment comes in the form of catalysis by iridium with aquo ligands and in aqueous solvent. Water-soluble compounds of iridium, either by virtue of attachment of water-soluble ligands or by direct interaction of water with the metal, are receiving a great deal of attention because of their potential as catalysts in aqueous solution.[126,127]

9 C–H ACTIVATION[128–130]

Since 1984, the single largest driving force in iridium chemistry has been the lure of finding a system capable of functionalizing hydrocarbons via C–H activation processes.1984 saw the publication of a report by Bergman and Janowicz on the oxidative addition of C–H bonds to ''Cp*Ir(PMe_3)''(**98**) to yield the alkyliridiumhydride complex Cp*Ir(H)(R)(PMe_3).[131] This was something akin to finding the holy grail: the firm establishment that alkane C–H bonds were reactive with the proper metal complex. Yet, well before this report there was significant evidence of iridium's ability to react with C–H bonds.

The first indications came from reactions of C–H bonds in coordinated ligands with iridium centers. Prominent among this type of reaction are the ortho-metallation (*see Orthometalation*) reactions, especially of arylphosphine ligands in which a C–H bond ortho to the phosphorus adds to the iridium. Beyond this, however, there were also examples of C–H bonds of alkyl chains adding to low-valent iridium centers. These intramolecular C–H reactions seemed to be induced when the alkyl backbone of a chelating ligand place the C–H bond in very close proximity to the metal.

Beyond these intramolecular C–H additions, there were several examples of C–H 'disproportionation' reactions (*see Disproportionation*) that could be induced by iridium. For example, cyclohexadiene could be transformed into benzene and cyclohexane under the influence of an iridium complex. Clearly, C–H bond-making and breaking processes were taking place in these transformations. Reasoning that C–H activation is just the reverse of olefin hydrogenation, Crabtree undertook a detailed investigation into the chemistry of iridium complexes that he had demonstrated were among the most active available, with the goal of finding systems that would catalyze C–H activation processes. Indeed, his group discovered that with the proper choice of H_2 acceptor (3,3-dimethyl-1-butene), iridium complexes could catalyze the dehydrogenation of a number of alkanes to yield the unsaturated organic compound.[132,133]

In the Crabtree work, while it was clear that C–H bond-breaking processes must be taking place, there was a general belief that the isolation of a complex that resulted from the oxidative addition of a C–H bond would be required to truly demonstrate that C–H activation was indeed occurring with homogeneous transition metal systems. Bergman and Janowicz were the first the show that such reactions were indeed possible.[134] Using Cp*Ir(PMe_3)H_2 (**99**) as the source of iridium, they discovered that photolysis of this complex induced the elimination of H_2 creating a very reactive, coordinatively unsaturated iridium(I) complex. This complex would then react with alkane C–H bonds to yield alkylhydride iridium complexes of the form Cp*Ir(PMe_3)(R)(H) (**100**) (equation 28). Subsequent studies by the Bergman group on the Cp*Ir(PMe_3)H_2 system delved into the relative reactivities of various C–H bonds and the thermodynamics and mechanism of the C−H activation process.[135]

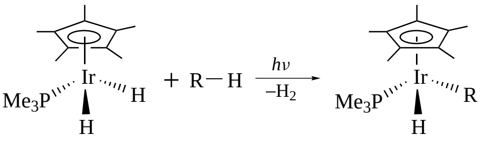

(**99**) (**100**) (28)

The iridium center utilized by the Bergman group contained both PMe_3 and Cp* ligands, both very electron donating. Initially, it was reasoned that in order to effect the oxidative addition of the relatively unreactive C–H bonds to iridium, the iridium center would have to be extremely electron rich and ligands such as PMe_3 and Cp* would be essential. Graham and coworkers, however, showed that the C–H addition of alkanes proceeded well for the less electron-rich carbonyl complexes Cp*Ir$(CO)_2$ (**101**) or even CpIr$(CO)_2$. In the case of the carbonyl complexes, photolysis was also required for the removal of the CO ligand to generate a coordinatively unsaturated mono-carbonyl intermediate, which would then react with the alkyl C–H bonds to yield complexes of the form

(**102**) (equation 29).

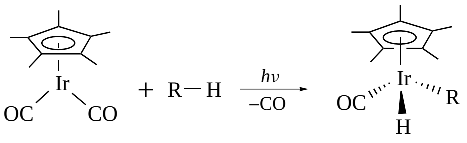

(**101**) (**102**)

(29)

Since those initial reports, there have been a number of reports of C–H activation with iridium complexes, induced both thermally and photochemically. Werner has demonstrated a number of iridium systems with bulky ligands that are capable of adding C–H bonds.[136] [Ir(COD)(PMe$_3$)$_3$]Cl (**11**) will react with aromatic C–H bonds thermally to yield octahedral iridium(III) complexes of the form mer-(Me$_3$P)$_3$Ir(H)(Ar)(Cl) (**103**).[137,138]

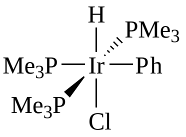

(**103**)

Once the C–H activation step was demonstrated, the search was on to find systems that would not only add the C–H bond, but could also be induced to proceed further down a reaction path that would result in the functionalization of the added hydrocarbon. Unfortunately, with most systems, it is difficult to achieve further reaction beyond the C–H addition step since most conditions employed to effect further reaction usually lead to nonproductive reductive elimination of the hydrocarbon. The Merola group was able to show that for a specific case of benzene C–H addition yielding mer-(Me$_3$P)$_3$Ir(H)(Ph)(Cl) (**103**), further reaction was available. In this case, a site of coordinative unsaturation was opened on the metal by removing the bound chloride with Tl[PF$_6$]. This yielded a highly energetic 16-electron complex that would react with alkynes with the exact product dependent on the structure of the alkyne. When the alkyne contained hydrogens on carbon α to the triple bond, the resulting product was the allyliridium complex (**104**, *see Allyl Complexes*).[139] However, with *t*-butylacetylene, where an arrangement to an allylic ligand was not possible, an unusual dimerization reaction occurred to yield a cyclobutadienyliridium complex (**105**) with the sixth coordination site of the metal being occupied by a δ-agostic (*see Agostic Bonding*) interaction.[140]

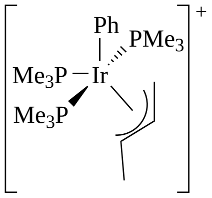

(**104**)

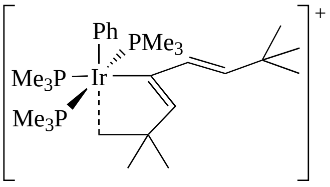

(**105**)

More intriguing is that the product of furan addition to [Ir(COD)(PMe$_3$)$_3$]Cl (**106**), undergoes an insertion reaction with *t*-butylacetylene, not into the Ir–H bond but into the Ir–C bond (equation 30).[138]

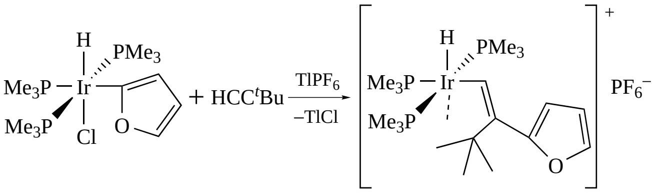

(**106**) (**107**)

(30)

Another approach to developing alkyliridium hydride complexes that would be more reactive toward further substitution reactions utilizes the indenyl effect (see Section 3). Bergman and Foo synthesized the indenyl analogs of the Cp*Ir(PMe$_3$)H$_2$ (**99**) system for C–H activation and discovered that IndIr(PMe$_3$)H$_2$ (**108**) is also capable of activating C–H bonds upon photolysis yielding indenyliridium alkyl hydride compounds (**109**).[141] However, in the case of the indenyl complexes, the η^5 to η^3 indenyl transformation allows reagents to enter the iridium coordination sphere under mild conditions and insert into the Ir–H bond to yield (**110**) (equation 31).[142]

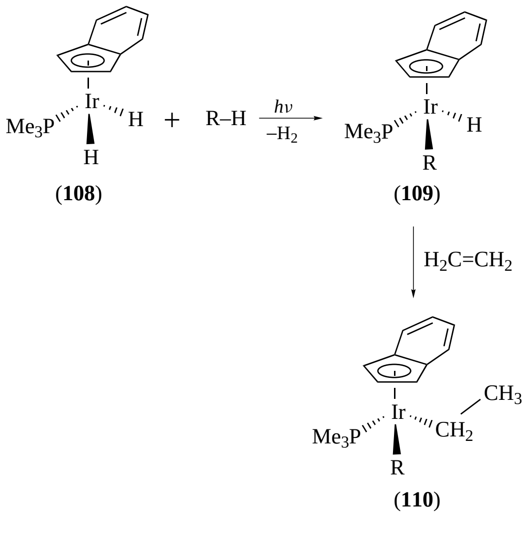

(**108**) (**109**) (**110**)

(31)

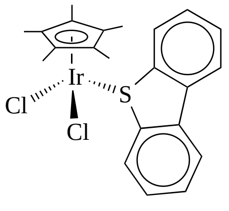

(**111**)

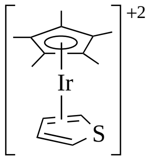

(**112**)

10 HDS CHEMISTRY[143]

Hydrodesulfurization (HDS) is the process for the removal of sulfur from petroleum feedstocks (*see* ***Hydrodesulfurization & Hydrodenitrogenation***). While iridium is not used in commercial HDS catalysts, organometallic complexes of iridium have nevertheless played an important role in developing an understanding of the mechanism of HDS chemistry. Since sulfur is present in petroleum feedstocks primarily as thiophenic sulfur, there have been many investigations into the coordination chemistry of thiophene. While a number of different metals have been examined to synthesize compounds that may serve as models for HDS chemistry, iridium has provided some unusual insights into possible reactions of thiophenic molecules. One mode of coordination of thiophenic molecules is simple bonding through sulfur. Angelici has reported that $[Cp^*IrCl_2]_2$ (**18**) may be split by dibenzothiophene to yield $Cp^*IrCl_2(\eta^1$-dibenzothiophene) (**111**). Angelici has also shown that π-bonded thiophene and benzothiophene complexes of iridium may be synthesized including $[Cp^*Ir(\eta^5$-thiophene$)]^{+2}$ (**112**). His group also found that thiophene and benzothiophene coordinated to iridium is susceptible to nucleophilic attack (*see Nucleophilic Addition: Rules for Predicting Direction*) by H^-, MeO^-, EtS^- and phosphines. The η^5 complexes may be converted into η^4 complexes by a two-electron reduction.[144] Thus, $[Cp^*Ir(\eta^5$-dimethylthiophene$)]^{+2}$ (**113**) is transformed into $Cp^*Ir(\eta^4$-dimethylthiophene) (**114**) where the iridium is bound to the four carbons of the thiophene ring and not to the sulfur atom. This η^4 complex is further transformed via isomerization over alumina into an unusual thiairidametallacycle (*see Inorganic Heterocycle*) complex (**115**)[145] (equation 32). This metallacycle would appear to have considerable aromatic character based on both crystallographic and NMR data.

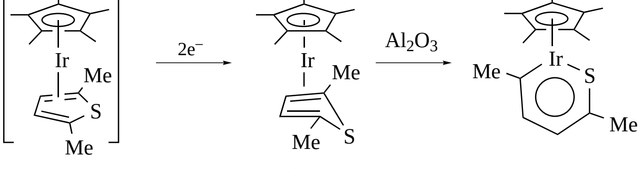

(**113**) (**114**) (**115**)

(32)

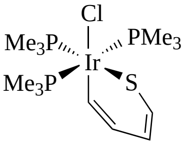

(**116**)

Merola also has shown that thiophene and benzothiophene will undergo a ring-opening C–S addition reaction with $[Ir(COD)(PMe_3)_3]Cl$ (**10**) to yield (**116**).[139] Unlike the Angelici complex, this thiairidacycle does not have aromatic character, although it is a planar six-membered ring. In both of these cases, it is unclear how much of a connection there is between these models and the actual intermediates in HDS catalysis. Nevertheless, these models have shed a great deal of light on the possible modes of bonding and reactivity of thiophenic molecules with metal centers.

11 SUMMARY

This review of some aspects of the organometallic chemistry of iridium is certainly not exhaustive. There have been some types of complexes that have receive little notice such as those containing polyolefinic ligands and related compounds. Also, there are other organic transformations that may be catalyzed by iridium complexes. However, throughout this chapter the reader has been directed to a number of primary references as well as a number of review articles that will delve into some areas of iridium organometallic chemistry more deeply.

12 RELATED ARTICLES

Ammonia & N-donor Ligands; Asymmetric Synthesis by Homogeneous Catalysis; Boron Hydrides; Carbene Complexes; Carbonyl Complexes of the Transition Metals; Carbonylation Processes by Homogeneous Catalysis; Coordination & Organometallic Chemistry: Principles; Dinuclear Organometallic Cluster Complexes; Hydride Complexes of the Transition Metals; Hydroboration Catalysis; Hydrodesulfurization & Hydrodenitrogenation; Hydrogenation & Isomerization of Alkenes; Hydrosilation Catalysis; Iridium: Inorganic & Coordination Chemistry; Organic Synthesis Using Metal-mediated Metathesis Reactions; Organic Synthesis using Transition Metal Carbonyl Complexes; Organic Synthesis using Transition Metal Complexes Containing π-Bonded Ligands; P-donor Ligands; Polynuclear Organometallic Cluster Complexes; Polyoxometalates; Rhodium: Organometallic Chemistry; Water & O-donor Ligands.

13 REFERENCES

1. T. Gjervan, R. Prestvik, and A. Holmen, *Springer Ser. Chem. Phy.*, 2004, **75**, 127.
2. M. Grehl and H. Meyer, Conference Proceedings – International Precious Metals Institute, 27th, Dorado, Puerto Rico, PR, 2003, 63.
3. R. S. Dickson, 'Organometallic Chemistry of Rhodium and Iridium', Academic Press, London, 1983, p. 421.
4. R. S. Dickson, in 'Homogeneous Catalysis with Compounds of Rhodium and Iridium', D. Reidel Publishing Company, Dordrecht, 1985, p. 278.
5. S. A. Cotton, 'Chemistry of Precious Metals', Blackie, London, 1997, p. 452.
6. A. Segnitz, Organometallic Compounds of Cobalt, Rhodium, Iridium, Nickel, Palladium, 'Houben-Weyl Methods of Organic Chemistry', 4th edn., Houben-Weyl, Stuttgart, Fed. Rep. Ger., 1984, Vol. 13, Pt. 9B, p. 1062.
7. G. J. Leigh and R. L. Richards, Iridium, in 'Comprehensive Organometallic Chemistry', eds. G. Wilkinson, F. G. A. Stone, and E. W. Abel, Pergamon, Oxford, 1982, Vol. 5, Chap. 36, p. 541.
8. F. H. Jardine, *Stud. Inorg. Chem.*, 1991, **11**, 407.
9. J. D. Atwood, Iridium, in 'Cobalt, Rhodium and Iridium', ed. J. D. Atwood, Pergamon, Oxford, 1995, Vol. 8, p. 585.
10. J. M. O'Connor, *Sci. Synth.*, 2002, **1**, 617.
11. L. J. Yellowlees and K. G. MacNamara, *Compr. Coord. Chem. II*, 2004, **6**, 147.
12. P. Thornton, *Annu. Rep. Prog. Chem., Sect. A: Inorg. Chem.*, 1999, **95**, 213.
13. M. A. Halcrow, *Annu. Rep. Prog. Chem., Sect. A: Inorg. Chem.*, 1998, **94**, 255.
14. C. E. Housecroft, *Coord. Chem. Rev.*, 1996, **152**, 141.
15. C. E. Housecroft, *Coord. Chem. Rev.*, 1995, **146**,(Pt 1), 269.
16. R. H. Crabtree, 'The Organometallic Chemistry of the Transition Metals', 3rd edn., Wiley-Interscience, 2000.
17. C. Elschenbroich and A. Salzer, 'Organometallic Chemistry: A Short Introduction', VCH, New York, 1993, p. 562.
18. J. S. Merola, *Curr. Org. Chem.*, 1997, **1**(3), 235.
19. J. W. Logan and M. Wicholas, *J. Chem. Educ.*, 2001, **78**(9), 1272.
20. J. L. Herde, J. C. Lambert, and C. V. Senoff, *Inorg. Synth.*, 1974, **15**, 18.
21. R. H. Crabtree, J. M. Quirk, H. Felkin, and T. Fillebeen-Khan, *Synth. React. Inorg. Met.-Org. Chem.*, 1982, **12**(4), 407.
22. A. L. Onderdelinden and A. Van der Ent, *Inorg. Chim. Acta*, 1972, **6**(3), 420.
23. M. A. Esteruelas and L. A. Oro, *Coord. Chem. Rev.*, 1999, **193–195**, 557.
24. R. J. Restivo, G. Ferguson, T. L. Kelly, and C. V. Senoff, *J. Organomet. Chem.*, 1975, **90**(1), 101.
25. R. H. Crabtree and G. E. Morris, *J. Organomet. Chem.*, 1977, **135**(3), 395.
26. J. F. Frazier and J. S. Merola, *Polyhedron*, 1992, **11**(22), 2917.
27. H. A. Mayer, H. Otto, H. Kuehbauch, R. Fawzi, and M. Steimann, *J. Organomet. Chem.*, 1994, **472**(1–2), 347.
28. J. D. Feldman, J. C. Peters, and T. D. Tilley, *Organometallics*, 2002, **21**(20), 4050.
29. T. Herskovitz, *Inorg. Synth.*, 1982, **21**, 99.
30. C. Bianchini, K. G. Caulton, C. Chardon, M.-L. Doublet, O. Eisenstein, S. A. Jackson, T. J. Johnson, A. Meli, M. Peruzzini, W. E. Streib, A. Vacca, and F. Vizza, *Organometallics*, 1994, **13**(5), 2010.
31. P. Barbaro, C. Bianchini, A. Meli, M. Peruzzini, A. Vacca, and F. Vizza, *Organometallics*, 1991, **10**(7), 2227.
32. S. Burling, L. D. Field, B. A. Messerle, K. Q. Vuong, and P. Turner, *J. Chem. Soc., Dalton Trans.*, 2003, (21), 4181.
33. M. A. Arthurs, J. Bickerton, S. R. Stobart, and J. Wang, *Organometallics*, 1998, **17**(13), 2743.
34. W. J. Oldham Jr, A. S. Hinkle, and D. M. Heinekey, *J. Am. Chem. Soc.*, 1997, **119**(45), 11028.
35. C. Slugovc, I. Padilla-Martinez, S. Sirol, and E. Carmona, *Coord. Chem. Rev.*, 2001, **213**, 129.
36. D. M. Tellers and R. G. Bergman, *Organometallics*, 2001, **20**(23), 4819.
37. D. M. Tellers and R. G. Bergman, *Can. J. Chem.*, 2001, **79**(5/6), 525.
38. J. W. Kang, K. Moseley, and P. M. Maitlis, *J. Am. Chem. Soc.*, 1969, **91**(22), 5970.
39. C. White, A. Yates, P. M. Maitlis, and D. M. Heinekey, *Inorg. Synth.*, 1992, **29**, 228.
40. P. M. Maitlis, *Coord. Chem. Rev.*, 1982, **43**, 377.
41. C. White, S. J. Thompson, and P. M. Maitlis, *J. Chem. Soc., Dalton Trans.*, 1978, (10), 1305.
42. O. V. Gusev, S. Sergeev, I. M. Saez, and P. M. Maitlis, *Organometallics*, 1994, **13**(5), 2059.
43. J. E. Hamlin, K. Hirai, V. C. Gibson, and P. M. Maitlis, *J. Mol. Catal.*, 1982, **15**(3), 337.
44. P. M. Maitlis, *Chem. Soc. Rev.*, 1981, **10**(1), 1.
45. A. J. Hart-Davis and R. J. Mawby, *J. Chem. Soc. A*, 1969, 16, 2403.
46. M. E. Rerek and F. Basolo, *J. Am. Chem. Soc.*, 1984, **106**(20), 5908.
47. A. K. Kakkar, N. J. Taylor, T. B. Marder, J. K. Shen, N. Hallinan, and F. Basolo, *Inorg. Chim. Acta*, 1992, **198–200**, 219.
48. J. M. O'Connor and C. P. Casey, *Chem. Rev.*, 1987, **87**(2), 307.
49. J. S. Merola, R. T. Kacmarcik, and D. Van Engen, *J. Am. Chem. Soc.*, 1986, **108**(2), 329.
50. J. S. Merola and R. T. Kacmarcik, *Organometallics*, 1989, **8**(3), 778.

51. A. C. Sievert and E. L. Muetterties, *Inorg. Chem.*, 1981, **20**(7), 2276.
52. A. C. Sievert and E. L. Muetterties, *Inorg. Chem.*, 1981, **20**(2), 489.
53. R. H. Crabtree, C. P. Parnell, and R. J. Uriarte, *Organometallics*, 1987, **6**(4), 696.
54. R. H. Crabtree, M. F. Mellea, and J. M. Quirk, *J. Chem. Soc., Chem. Commun.*, 1981, (23), 1217.
55. R. H. Crabtree and C. P. Parnell, *Organometallics*, 1985, **4**(3), 519.
56. M. I. Rybinskaya, A. R. Kudinov, and V. S. Kaganovich, *J. Organomet. Chem.*, 1983, **246**(3), 279.
57. C. Bianchini, K. G. Caulton, C. Chardon, O. Eisenstein, K. Folting, T. J. Johnson, A. Meli, M. Peruzzini, D. J. Rauscher, W. E. Streib, and F. Vizza, *J. Am. Chem. Soc.*, 1991, **113**(13), 5127.
58. C. Bianchini, K. G. Caulton, K. Folting, A. Meli, M. Peruzzini, A. Polo, and F. Vizza, *J. Am. Chem. Soc.*, 1992, **114**(18), 7290.
59. F. Torres, E. Sola, M. Martin, J. A. Lopez, F. J. Lahoz, and L. A. Oro, *J. Am. Chem. Soc.*, 1999, **121**(45), 10632.
60. F. Torres, E. Sola, M. Martin, C. Ochs, G. Picazo, J. A. Lopez, F. J. Lahoz, and L. A. Oro, *Organometallics*, 2001, **20**(13), 2716.
61. U. Behrens, T. M. Meyer-Friedrichsen, and J. Heck, *Z. Anorg. Allg. Chem.*, 2003, **629**(7–8), 1421.
62. M. R. Churchill, J. C. Fettinger, W. M. Rees, and J. D. Atwood, *J. Organomet. Chem.*, 1986, **301**(1), 99.
63. H. Werner and A. Hoehn, *J. Organomet. Chem.*, 1984, **272**(1), 105.
64. G. Marinelli, I. E. I. Rachidi, W. E. Streib, O. Eisenstein, and K. G. Caulton, *J. Am. Chem. Soc.*, 1989, **111**(6), 2346.
65. G. Marinelli, W. E. Streib, J. C. Huffman, K. G. Caulton, M. R. Gagne, J. Takats, M. Dartiguenave, C. Chardon, S. A. Jackson, and O. Eisenstein, *Polyhedron*, 1990, **9**(15), 1867.
66. A. Hoehn and H. Werner, *Angew. Chem.*, 1986, **98**(8), 745.
67. A. Hoehn and H. Werner, *J. Organomet. Chem.*, 1990, **382**(1), 255.
68. F. J. Garcia Alonso, A. Hoehn, J. Wolf, H. Otto, and H. Werner, *Angew. Chem.*, 1985, **97**(5), 401.
69. R. P. Hughes, A. Williamson, R. D. Sommer, and A. L. Rheingold, *J. Am. Chem. Soc.*, 2001, **123**(30), 7443.
70. R. P. Hughes, R. B. Laritchev, A. Williamson, C. D. Incarvito, L. N. Zakharov, and A. L. Rheingold, *Organometallics*, 2002, **21**(22), 4873.
71. R. P. Hughes, R. B. Laritchev, A. Williamson, C. D. Incarvito, L. N. Zakharov, and A. L. Rheingold, *Organometallics*, 2003, **22**(10), 2134.
72. L. Vaska and J. Peone, *Inorg. Synth.*, 1974, **15**, 64.
73. A. L. Balch, J. W. Lee, and M. M. Olmstead, *Angew. Chem.*, 1992, **104**(10), 1400; See also *Angew. Chem., Int. Ed. Engl.*, 1992, **31**(10), 1356.
74. A. L. Balch, J. W. Lee, B. C. Noll, and M. M. Olmstead, *J. Am. Chem. Soc.*, 1992, **114**(27), 10984.
75. A. L. Balch, J. W. Lee, B. C. Noll, and M. M. Olmstead, *Inorg. Chem.*, 1994, **33**(23), 5238.
76. M. Kubota and C. R. Carey, *J. Organomet. Chem.*, 1970, **24**(2), 491.
77. M. J. Mays and F. P. Stefanini, *J. Chem. Soc. A*, 1971, (17), 2747.
78. M. Kubota and C. J. Curtis, *Inorg. Chem.*, 1974, **13**(9), 2277.
79. A. F. Hill and J. D. E. T. Wilton-Ely, *Organometallics*, 1996, **15**(18), 3791.
80. A. F. Hill, J. D. E. T. Wilton-Ely, B. K. Breedlove, and C. P. Kubiak, *Inorg. Synth.*, 2002, **33**, 244.
81. L. Malatest, G. Caglio, and M. Angoletta, *Inorg. Synth.*, 1971, **13**, 95.
82. C. S. Chin, B. Lee, and Y. Kim, *Synth. React. Inorg. Met.-Org. Chem.*, 1995, **25**(3), 463.
83. R. Della Pergola, F. Demartin, L. Garlaschelli, M. Manassero, S. Martinengo, N. Masciocchi, and D. Strumolo, *Inorg. Chem.*, 1991, **30**(4), 846.
84. R. D. Pergola, L. Garlaschelli, M. Manassero, and M. Sansoni, *J. Cluster Sci.*, 1999, **10**(1), 109.
85. G. Schulz-Ekloff, *Compr. Supramol. Chem.*, 1996, **7**, 549.
86. S. Kawi and B. C. Gates, *Inorg. Chem.*, 1992, **31**(13), 2939.
87. S. Kawi and B. C. Gates, *J. Chem. Soc., Chem. Commun.*, 1992, (9), 702.
88. E. Cariati, D. Roberto, and R. Ugo, *J. Cluster Sci.*, 1998, **9**(3), 329.
89. T. H. Tulip and D. L. Thorn, *J. Am. Chem. Soc.*, 1981, **103**(9), 2448.
90. J. C. Calabrese, M. C. Colton, T. Herskovitz, U. Klabunde, G. W. Parshall, D. L. Thorn, and T. H. Tulip, *Ann. N.Y. Acad. Sci.*, 1983, **415**, 302.
91. T. G. P. Harper, P. J. Desrosiers, and T. C. Flood, *Organometallics*, 1990, **9**(9), 2523.
92. D. Milstein and J. C. Calabrese, *J. Am. Chem. Soc.*, 1982, **104**(13), 3773.
93. R. S. Hay-Motherwell, G. Wilkinson, B. Hussain-Bates, and M. B. Hursthouse, *J. Chem. Soc., Dalton Trans.*, 1992, (24), 3477.
94. R. S. Hay-Motherwell, G. Wilkinson, B. Hussain, and M. B. Hursthouse, *J. Chem. Soc., Chem. Commun.*, 1989, (19), 1436.
95. R. S. Hay-Motherwell, G. Wilkinson, B. Hussain-Bates, and M. B. Hursthouse, *Polyhedron*, 1993, **12**(16), 2009.
96. A. L. Balch, J. W. Lee, and M. M. Olmstead, *Angew. Chem.*, 1992, **104**(10), 1400; See also *Angew. Chem., Int. Ed. Engl.*, 1992, **31**(10), 1356).

97. A. L. Balch, J. W. Lee, B. C. Noll, and M. M. Olmstead, *J. Am. Chem. Soc.*, 1992, **114**(27), 10984.
98. G. Lee, Y.-J. Cho, B. K. Park, K. Lee, and J. T. Park, *J. Am. Chem. Soc.*, 2003, **125**(46), 13920.
99. E. Carmona, M. Paneque, and M. L. Poveda, *J. Chem. Soc., Dalton Trans.*, 2003, (21), 4022.
100. H. Werner, K. Ilg, R. Lass, and J. Wolf, *J. Organomet. Chem.*, 2002, **661**(1–2), 137.
101. M. A. Gallop and W. R. Roper, *Adv. Organomet. Chem.*, 1986, **25**, 121.
102. R. H. Crabtree, *Pure Appl. Chem.*, 2003, **75**(4), 435.
103. J. M. O’Connor, L. Pu, and A. L. Rheingold, *Organometallics*, 1988, **7**(9), 2060.
104. J. M. O’Connor, L. Pu, and A. L. Rheingold, *J. Am. Chem. Soc.*, 1989, **111**(11), 4129.
105. O. Boutry, E. Gutierrez, A. Monge, M. C. Nicasio, P. J. Perez, and E. Carmona, *J. Am. Chem. Soc.*, 1992, **114**(18), 7288.
106. D. L. Thorn and T. H. Tulip, *Organometallics*, 1982, **1**(12), 1580.
107. J. Mueller, B. Passon, and J. Pickardt, *J. Organomet. Chem.*, 1982, **228**(2), C51.
108. J. D. Atwood, *Coord. Chem. Rev.*, 1988, **83**, 93.
109. R. Crabtree, *Acc. Chem. Res.*, 1979, **12**(9), 331.
110. R. H. Crabtree and M. W. Davis, *J. Org. Chem.*, 1986, **51**(14), 2655.
111. G. Zassinovich, G. Mestroni, and S. Gladiali, *Chem. Rev.*, 1992, **92**(5), 1051.
112. C. M. Thomas and G. Suss-Fink, *Coord. Chem. Rev.*, 2003, **243**(1–2), 125.
113. M. J. Hostetler and R. G. Bergman, *J. Am. Chem. Soc.*, 1990, **112**(23), 8621.
114. N. Chatani, S. Ikeda, K. Ohe, and S. Murai, *J. Am. Chem. Soc.*, 1992, **114**(24), 9710.
115. D. A. Evans and G. C. Fu, *J. Am. Chem. Soc.*, 1991, **113**(10), 4042.
116. J. R. Knorr and J. S. Merola, *Organometallics*, 1990, **9**(12), 3008.
117. R. T. Baker, D. W. Ovenall, J. C. Calabrese, S. A. Westcott, N. J. Taylor, I. D. Williams, and T. B. Marder, *J. Am. Chem. Soc.*, 1990, **112**(25), 9399.
118. S. A. Westcott, T. B. Marder, R. T. Baker, and J. C. Calabrese, *Can. J. Chem.*, 1993, **71**(7), 930.
119. T. Ishiyama and N. Miyaura, *Chem. Rec.*, 2004, **3**(5), 271.
120. M. Pohl and R. G. Finke, *Organometallics*, 1993, **12**(4), 1453.
121. D. K. Lyon and R. G. Finke, *Inorg. Chem.*, 1990, **29**(10), 1787.
122. R. G. Finke, D. K. Lyon, K. Nomiya, S. Sur, and N. Mizuno, *Inorg. Chem.*, 1990, **29**(10), 1784.
123. V. W. Day, W. G. Klemperer, S. P. Lockledge, and D. J. Main, *J. Am. Chem. Soc.*, 1990, **112**(5), 2031.
124. R. S. Tanke and R. H. Crabtree, *J. Am. Chem. Soc.*, 1990, **112**(22), 7984.
125. R. S. Tanke and R. H. Crabtree, *Organometallics*, 1991, **10**(2), 415.
126. J. S. Merola, T. L. Husebo, K. E. Matthews, M. A. Franks, R. Pafford, and P. Chirik, *NATO ASI Ser., Ser. 3: High Technol.*, 1995, **5**, 33.
127. J. S. Merola, Variation of Central Atoms, ‘Aqueous-Phase Organometallic Catalysis’, ed., B. Cornils and W. A. Herrmann, Wiley-VCH Verlag GmbH, 1998, p. 59.
128. A. H. Janowicz, R. A. Periana, J. M. Buchanan, C. A. Kovac, J. M. Stryker, M. J. Wax, and R. G. Bergman, *Pure Appl. Chem.*, 1984, **56**(1), 13.
129. R. G. Bergman, *Adv. Chem. Ser.*, 1992, **230**, 211.
130. A. A. Bengali, B. A. Arndtsen, P. M. Burger, R. H. Schultz, B. H. Weiller, K. R. Kyle, C. B. Moore, and R. C. Bergman, *Pure Appl. Chem.*, 1995, **67**(2), 281.
131. A. H. Janowicz and R. G. Bergman, *J. Am. Chem. Soc.*, 1983, **105**(12), 3929.
132. R. H. Crabtree, *CHEMTECH*, 1982, **12**(8), 506.
133. H. Gerard, O. Eisenstein, D.-H. Lee, J. Chen, and R. H. Crabtree, *New J. Chem.*, 2001, **25**(9), 1121.
134. A. H. Janowicz and R. G. Bergman, *J. Am. Chem. Soc.*, 1982, **104**(1), 352.
135. P. O. Stoutland, R. G. Bergman, S. P. Nolan, and C. D. Hoff, *Polyhedron*, 1988, **7**(16–17), 1429.
136. M. Schulz and H. Werner, *Organometallics*, 1992, **11**(8), 2790.
137. J. S. Merola, *Organometallics*, 1989, **8**(12), 2975.
138. H. E. Selnau and J. S. Merola, *Organometallics*, 1993, **12**(10), 3800.
139. H. E. Selnau and J. S. Merola, *Organometallics*, 1993, **12**(5), 1583.
140. H. E. Selnau and J. S. Merola, *J. Am. Chem. Soc.*, 1991, **113**(10), 4008.
141. T. Foo and R. G. Bergman, *Organometallics*, 1992, **11**(5), 1801.
142. T. Foo and R. G. Bergman, *Organometallics*, 1992, **11**(5), 1811.
143. J. Chen and R. J. Angelici, *Coord. Chem. Rev.*, 2000, **206–207**, 63.
144. J. Chen and R. J. Angelici, *Organometallics*, 1989, **8**(9), 2277.
145. J. Chen, L. M. Daniels, and R. J. Angelici, *J. Am. Chem. Soc.*, 1990, **112**(1), 199.

Iron: Heme Proteins & Dioxygen Transport & Storage

Takashi Hayashi
Osaka University, Yamadaoka, Japan

Based in part on the article Iron: Heme Proteins & Dioxygen Transport by Harold M. Goff which appeared in the Encyclopedia of Inorganic Chemistry, First Edition.

1 Introduction 1
2 General Features of Myoglobin and Hemoglobin 1
3 Mechanism of O_2 Binding by Myoglobin and Hemoglobin 4
4 Improvement of O_2 Affinity in Heme Proteins 6
5 Cooperativity of O_2 Binding for Hemoglobin 8
6 Modulation of O_2 Binding by Small Molecules 10
7 Other Aspects of Myoglobins and Hemoglobins 10
8 Related Articles 12
9 References 12

1 INTRODUCTION

Myoglobin and hemoglobin have been studied intensively for over 100 years and are two of the most well-known metalloproteins, because they were the first two proteins for which 3D structures were determined by X-ray crystallography in 1958 and 1960, respectively (Figure 1).[1,2] As a result, they have always been described in inorganic chemistry and biochemistry text books.[3,4] The physiological functions of myoglobins and vertebrate hemoglobins are O_2 storage and transport, respectively. Particularly, hemoglobins are the most widely distributed family of O_2 carriers (*see* ***Iron Proteins with Dinuclear Active Sites***; ***Copper Proteins with Dinuclear Active Sites***), although the role of some hemoglobins is still not clear. They can bind O_2 reversibly at a heme prosthetic group, a protoporphyrin IX iron complex (Figure 2), in their protein matrix (equation 1; P = porphyrin ring). Thus, it is of particular interest not only for biologists but also for chemists to understand the molecular mechanism of O_2-binding and its stabilization.[5]

$$\text{PFe(II)} + O_2 \rightleftharpoons \text{PFe(II)}\cdot O_2 \qquad (1)$$

Myoglobin consists of a single peptide chain of 150–160 amino acids and one heme with a molecular weight of approximately 17 500, and more than three-fourths of the amino acid residues are involved in eight (A–H) helices as shown in Figure 1(a).[6] The prefix 'myo' means muscle in Greek, because myoglobin is mainly located in skeletal and cardiac muscle cells for respiration. O_2 is bound to a ferrous pentacoordinated heme along the Langmuir adsorption isotherm. On the other hand, vertebrate hemoglobins are tetrameric proteins that consist of two α- and two β-globins, and the total molecular weight is approximately 64 000 as shown in Figure 1(b).[7] Each globin has one protoheme; therefore, one hemoglobin can bind a total of four O_2 molecules. The tertiary structure of the globin is mostly identical to that of myoglobin; however, each of the O_2-binding sites is mutually dependent due to the strong interaction between globins. Therefore, hemoglobin can exhibit cooperative O_2-binding behavior with a homotropic allosteric interaction (vide infra). Hemoglobin is located in the erythrocyte, the red blood cell, and 150 g of hemoglobin exists in 1000 mL of blood to solubilize O_2, because the solubility of O_2 in blood plasma is too low to carry sufficient O_2 to target tissues without any O_2 carrier.[8]

In chemistry, it is well known that O_2 can be strongly bound to a ferrous iron porphyrin in solvents without any protein matrix; however, the oxygenated states of most simple iron porphyrins are irreversibly converted into μ-oxodimers (equation 3), PFe(III)–O–PFe(III), via peroxo and ferryl intermediates (equation 2). The μ-oxodimer is usually very stable in solvents, so it is sometimes called a thermodynamic sink. In addition, autoxidation of PFe(II)•O_2 to an inert ferric porphyrin easily occurs under aerobic conditions (equation 4). Thus, it is clear that the heme pockets of myoglobin and hemoglobin play an important role in protecting the O_2-bound heme from dimerization and autoxidation.

$$\text{PFe(II)}\cdot O_2 \rightleftharpoons \text{PFe(III)–O–O–PFe(III)} \rightleftharpoons 2\text{PFe(IV)=O} \qquad (2)$$

$$\text{PFe(IV)=O} + \text{PFe(II)} \rightleftharpoons \text{PFe(III)–O–PFe(III)} \qquad (3)$$

$$\text{PFe(II)}\cdot O_2 \rightleftharpoons \text{PFe(III)} + O_2^{\bullet -} \qquad (4)$$

This article focuses on the salient physiological and chemical features of myoglobin and hemoglobin and additional current topics that could serve as a new way to modify the functions of the heme proteins.

2 GENERAL FEATURES OF MYOGLOBIN AND HEMOGLOBIN

2.1 Structural and Electronic Properties of Oxyheme Proteins

The prosthetic group of myoglobin and hemoglobin is a heme-b, protoheme-IX (Figure 2), which is the same as that found in several peroxidases, catalases, and cytochromes. The heme is linked noncovalently at the heme pocket of the protein

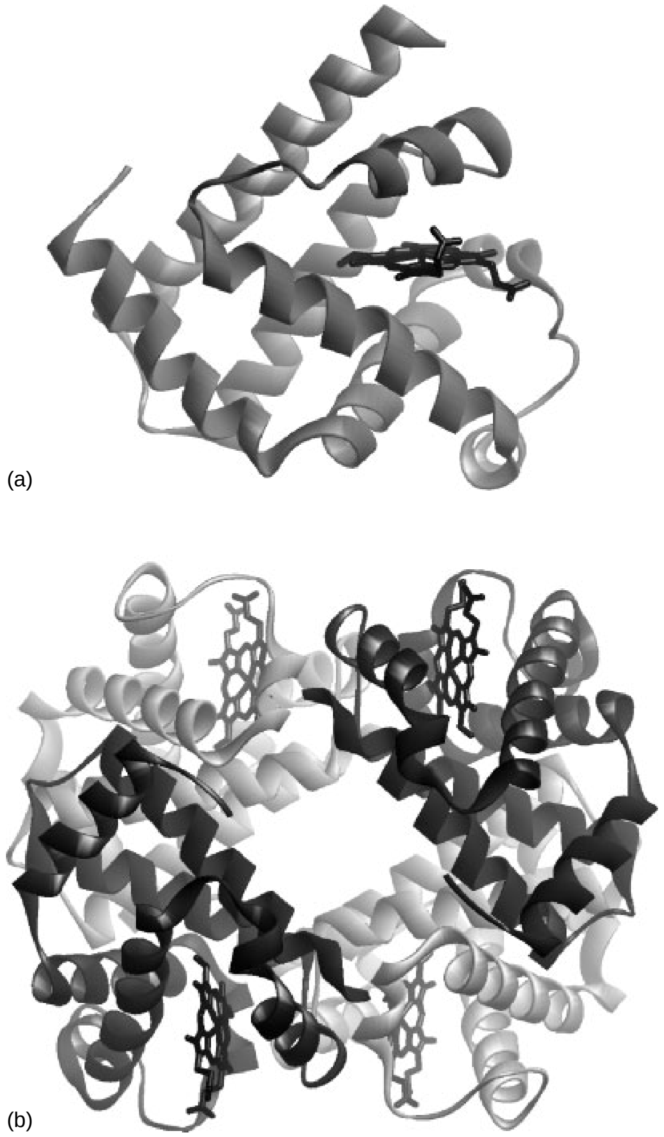

Figure 1 Three-dimensional structures of myoglobin and hemoglobin. (a) Deoxymyoglobin from sperm whale (1A6N) and (b) deoxyhemoglobin from human (1BZ0). Black and gray stick molecules are protoheme-IX. Hemoglobin consists of two $\alpha\beta$ dimers, dark and light gray pairs

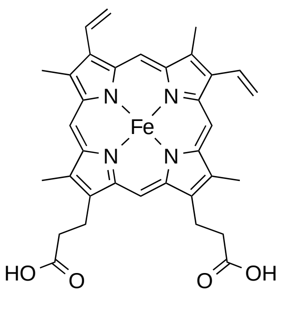

Figure 2 Structural formula of protoheme-IX

matrix through multiple interactions. The heme pocket has two characteristic histidines, the proximal and distal histidines, and the imidazole Nε of the former histidine is coordinated to heme-iron directly, whereas the latter histidine plays an important role in the stabilization of heme-bound dioxygen via hydrogen bonding (Figure 3). The heme is furthermore fixed in the protein matrix through a salt bridge between the heme-propionate side chains and amino acid residues near the heme pocket. In addition, the asymmetric peripheral heme side chains at the β-pyrrolic carbons of the A and B pyrrole rings, two vinyl and two methyl groups, contact the hydrophobic amino acid residues in the heme pocket and determine the orientation of the heme plane. The ratio of normal and backward porphyrin planes is approximately 11:1 for sperm whale myoglobin.**[9]**

The characteristic property of the oxygenated species of heme protein has been discussed for a long time. O_2 is reversibly bound to a ferrous high-spin heme-iron ($S = 2$) species to form the diamagnetic oxygenated species ($S = 0$) in biological systems. In general, the reduced Fe(II) state and the O_2-bound state are described as the deoxy and oxy species, respectively, whereas the functionally inactive oxidized Fe(III) form is referred to as the met species. The argument on the structural and electronic properties of the oxygenated heme complex in the protein matrix began in 1936 when Pauling and Coryell suggested the nature of the PFe(II)•O_2 species was the combination of low-spin Fe(II) and singlet oxygen with a σ donor and a π acceptor character, by measuring the magnetic moment of oxyhemoglobin.**[10]** In addition, a bent end-on geometry of the Fe–O–O species was proposed by Pauling and Weiss in 1964.**[11]** Moreover, Weiss has reported an alternative formulation, Fe(III)$-O_2{}^{\bullet -}$, which is regarded as a single-electron transfer from Fe(II)

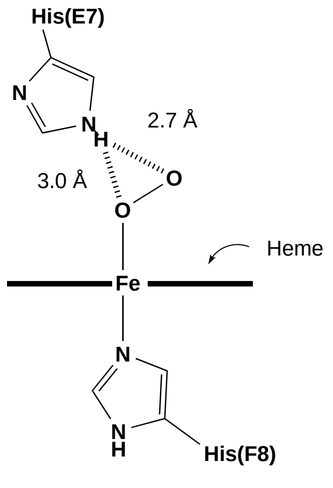

Figure 3 Simplified structure of the oxyheme unit in myoglobin and hemoglobin. There are two characteristic histidines in the heme pocket, proximal (F8) and distal (E7) histidines. The latter histidine strongly stabilizes the iron-bound O_2 via hydrogen-bonding interaction

to the bound O_2.[12] This charge-separated species, which is a combination of low-spin Fe(III) and superoxide, seems to show strong antiferromagnetic coupling between iron and O_2. The Fe–O–O geometry in the protein matrix was first demonstrated by Phillips in 1978, and his data supported the nonlinear Fe–O–O geometry proposed by Pauling and Weiss.[13] The crystal structural data also suggest the charge-separated character of oxygenated heme proteins. For example, the O–O distance of the O_2 bound onto the heme-iron in the proteins was determined to be 1.2–1.3 Å by X-ray crystal-structure analysis, which is comparable with that observed for a metal-superoxide. From recent results at 1.0 Å resolution in sperm whale myoglobin, the O–O bond length is 1.24 Å, which is slightly longer than that of molecular oxygen.[14] In addition, the O–O stretching mode in the oxygenated complex by IR and resonance Raman spectroscopies appears at $1130-1140\,\mathrm{cm^{-1}}$, which is a lower frequency compared to that observed for molecular oxygen (ca. $1550\,\mathrm{cm^{-1}}$).[15–17] These experimental results support the fact that the charge-separated formulation, $\mathrm{Fe(III)-O_2}^{\bullet -}$, is the predominant state in oxygenated heme proteins. Thus, the following equation, the combination between low-spin Fe(III) and superoxide, could be an appropriate representation for the O_2-binding equilibrium in the protein matrix (equation 1′).

$$\mathrm{PFe(II)} + \mathrm{O_2} \rightleftharpoons \mathrm{PFe(III)}\text{•}\mathrm{O_2}^{\bullet -} \qquad (1')$$

2.2 Thermodynamic and Kinetic Properties of O_2 Binding to Heme Proteins

Thermodynamic and kinetic measurements of the O_2 binding process for the heme proteins are essential to discuss their physiological and chemical properties. Representative parameters are depicted in Table 1. The oxygen equilibrium can be directly determined by a polarographic-spectrophotometic method with an O_2 electrode.[18,19] The P_{50} value, the O_2 pressure when half of the heme protein's O_2-binding sites are occupied, is quite often used for the evaluation of O_2 affinity. The P_{50} of sperm whale myoglobin is 0.51 torr, whereas the P_{50}s of the R- and T-states for human hemoglobin A are 0.15–1.5 torr and 9–160 torr, respectively.[8] Kinetic studies on O_2 binding also provide us an important insight into the physiological properties of the heme proteins. The association process for O_2 binding is usually monitored by laser flash photolysis or the T-jump method. From these experiments, the second-order rate constant of O_2 binding, k_{on}, is determined (ca. $10-20\,\mathrm{\mu M^{-1}\,s^{-1}}$ at 20 °C for a series of native myoglobins).[20] On the other hand, the first-order rate constant of O_2 dissociation, k_{off}, is obtained by monitoring the replacement with a CO or NO ligand or mixing of an O_2 scavenger such as ferricyanide or dithionite using a typical rapid-stopped flow apparatus (ca. $10-25\,\mathrm{s^{-1}}$ at 20 °C for a series of wild-type myoglobins).[20] Therefore, O_2 affinity can be calculated from the ratio of $k_{\mathrm{on}}/k_{\mathrm{off}}$, which is in good agreement with the O_2 affinity measured by the equilibrium process described above. These association-dissociation rate constants are very helpful in evaluating the physiological function of a variety of species of heme proteins and/or their mutants.[21] In the case of hemoglobin, ligand-binding kinetics are not simple compared to those of myoglobin, and the analytical method has been summarized in detail elsewhere.[22]

2.3 Models for Heme Proteins

To understand the chemical properties of oxygenated heme in the protein, many inorganic and bioinorganic chemists have devoted their efforts to preparing effective models, which provided many important insights into the molecular mechanisms and structure of oxygenated heme proteins.[23,26–28] One of the representative models is the picket fence iron porphyrin reported by Collman and his coworkers (Figure 4).[29] The picket fence porphyrin as a structural model for myoglobin has four bulky pivaloyl groups at the peripheral positions to prevent two of these iron porphyrins from coming together to form a μ-oxo dimer. The first significant result in their study was to demonstrate the 3D structure of the stable

Table 1 O_2 Binding and autoxidation for a series of myoglobins, hemoglobins, and synthetic models (20 °C, pH 7.0)

Source	k_{on} ($\mathrm{\mu M^{-1}\,s^{-1}}$)	k_{off} ($\mathrm{s^{-1}}$)	K_{O_2} ($\mathrm{\mu M^{-1}}$)	P_{50} (torr)	k_{ox} ($\mathrm{h^{-1}}$)[a]	Ref.
Sperm whale Mb	17	15	1.1	0.51	0.055	20
Horse heart Mb	14	11	1.3	–	0.05[i]	20
Pig Mb	17	14	1.2	–	0.07	20
Human Mb	19	22	0.86	–	0.1	20
Human Hb α-chain	28	12	2.3	–	–	21
Human Hb β-chain	110	22	4.5	–	–	21
Human Hb R-state[b]	–	–	–	0.17	–	23
Human Hb T-state[b]	–	–	–	26	–	23
Fe–ProtoP(chelated-Im)[c,d]	26	47	0.55	1.0	–	24
Fe–TpivPP(1,2-$\mathrm{Me_2}$Im)[e,f]	110	46 000	0.0024	38	–	25
Fe–$\mathrm{(Piv)_3}$(5CIm)PP[g,h]	430	2900	0.15	0.58	–	25

[a] At 37 °C. [b] 25 °C. [c] Chelated protoheme. [d] 22 °C, pH 7.3 in 2% $\mathrm{CetMe_3NBr}$ solution. [e] Fe(II) picket fence porphyrin, [f] 25 °C, in toluene, [1,2-$\mathrm{Me_2}$Im] = 0.1 M. [g] Fe(II) tailed picket fence porphyrin. [h] 25 °C, toluene. [i] pH 7.4.

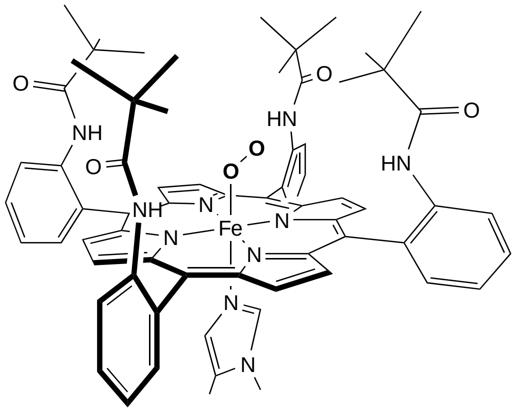

Figure 4 Molecular structure of O_2-bound picket fence iron porphyrin complex. The iron porphyrin has four pivalamide groups forming a hydrophobic cavity for the ligand O_2. The axial ligand is 1,2-dimethylimidazole. X-ray crystal structure shows the end-on and bent coordination of O_2 to the heme-iron

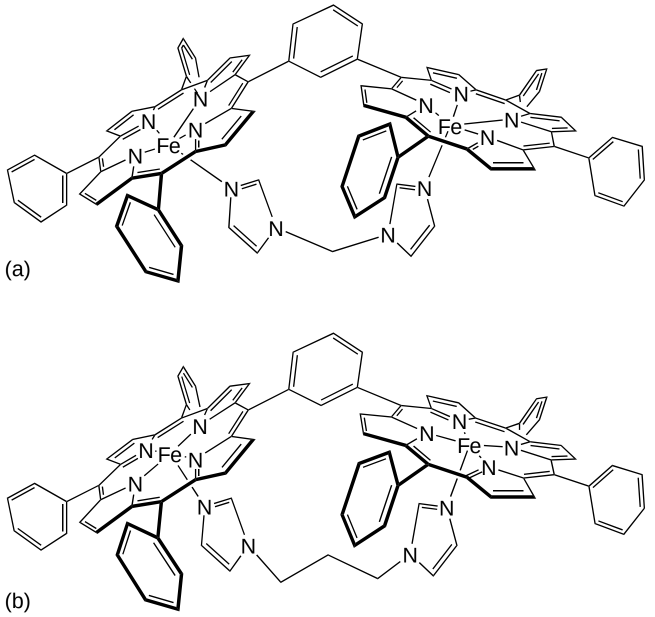

Figure 5 The structure of gable porphyrin diiron(II) complex with ditopic interaction of bisimidazole ligand. (a) T-state model; each iron may be deviated from the porphyrin planes due to 'short' bidentate ligand, bisimidazolylmethane. (b) R-state model; each iron is in-plane because of the sufficient length of bisimidazolylpropane compared to the distance between two Fe atoms

oxygenated iron porphyrin in 1974 before the crystal structure of oxymyoglobin was available. O_2 is bound to the iron porphyrin in end-on style with an Fe–O–O bond angle of 136° and an O–O distance of 1.24 Å, which strongly supported the nonlinear end-on O_2 binding postulated by Pauling and Weiss. Furthermore, the picket fence iron porphyrin was a useful functional model because it was able to bind O_2 reversibly for a long time.[25] In addition, there have been many functionalized iron porphyrins to mimic the function of myoglobins and hemoglobins for over 30 years, and these unique properties have been described in several reviews.[23,26–28] On the other hand, there are a limited number of synthetic models for hemoglobin, because it seems to be difficult to totally mimic the molecular trigger of cooperative oxygenation observed in hemoglobin. For example, Tabushi and his coworkers reported a unique model demonstrating reversible cooperative O_2 binding by a metalloporphyrin dimer and a bidentate bisimidazole ligand (Figure 5).[30,31]

3 MECHANISM OF O_2 BINDING BY MYOGLOBIN AND HEMOGLOBIN

3.1 Molecular Mechanism of O_2 Binding

In the synthetic iron porphyrin, O_2 affinity mainly depends on the strengths of the σ-donation from the lone pair of O_2 to the heme-iron dz^2 orbital and π-back donation from the $d\pi$ orbital on the iron to the π^* orbital of O_2.[32] To evaluate the O_2 affinity and/or O_2 binding dynamics in myoglobin and hemoglobin, O_2–protein interaction is a further important factor. For example, the O_2 dissociation rate constant for oxymyoglobin is relatively smaller than those of O_2 complexes of the synthetic model (e.g. $k_{\mathrm{off}} = 4.6 \times 10^4\ \mathrm{s}^{-1}$ for the picket fence iron porphyrin in the presence of 1,2-dimethylimidazole at 20 °C in toluene).[25] Figure 6 illustrates the heme pocket of sperm whale deoxymyoglobin. The role of each amino acid residue has been nearly clarified by a series of kinetic studies and X-ray crystal-structure analysis of oxy and deoxymyoglobin. Table 2 displays a comparison of kinetic parameters for several mutants with those for the wild type.

On the distal side, there are at least three important moieties to regulate O_2 binding. First, His64 on the distal side strongly stabilizes the bound O_2 via hydrogen-bonding interaction between the imidazole moiety of His64 and polar O_2. In fact, the replacement of His64 with Gly drastically accelerates the O_2 dissociation by more than 100-fold, and the O_2 affinity dramatically decreases to $K_a = 8.8 \times 10^4\ \mathrm{M}^{-1}$.[35] In addition, autoxidation of the H64G oxymyoglobin is more than 500-fold faster than that observed for wild-type myoglobin ($k_{\mathrm{ox}} = 0.055\ \mathrm{h}^{-1}$ for wild-type myoglobin at 37 °C, pH = 7.0).[36] Vertebrate hemoglobins also have a distal histidine (E7) for each heme pocket, and it is well known that the histidine interacts with the heme-bound O_2 via hydrogen bonding. Second, Table 2 shows that the residues Leu29(B10) or Val68(E11) in myoglobin regulate O_2 binding. Olson and his coworkers have carried out site-directed mutagenesis studies systematically on mammalian myoglobin to examine pathways for ligand movement inside the protein and proposed that O_2 is first captured by a part of

Table 2 O_2 Binding parameters for a series of sperm whale myoglobins and human hemoglobins (at 20 °C, pH 7.0)

Protein	k_{on} (μM^{-1} s^{-1})	k_{off} (s^{-1})	K_{O_2} (μM^{-1})	k_{ox} (h^{-1})	Ref.
	Myoglobins				
Wild type	17	15	1.1	0.055	21
H64G	140	1600	0.090	44	21
H64Q	24	130	0.18	0.021	21
L29F	21	1.4	15	0.005	21
L29W	0.25	8.5	0.029	0.18	21
V68S	5.1	31	0.16	–	21
V68I	3.2	14	0.22	0.75	21
S92L[a]	24	5.5	4.5	–	33
S92A[b,c]	22	15	1.5	–	34
	Hemoglobins				
α-chain	28	12	2.3	–	21
β-chain	110	22	4.5	–	21
α (H(E7)G)	220	620	0.40	–	21
β (H(E7)G)	100	37	2.7	–	21
α (H(E11)I)	16	6.8	2.4	–	21
β (H(E11)I)	12	28	0.43	–	21

[a] Pig myoglobin. [b] Human myoglobin. [c] At 25 °C.

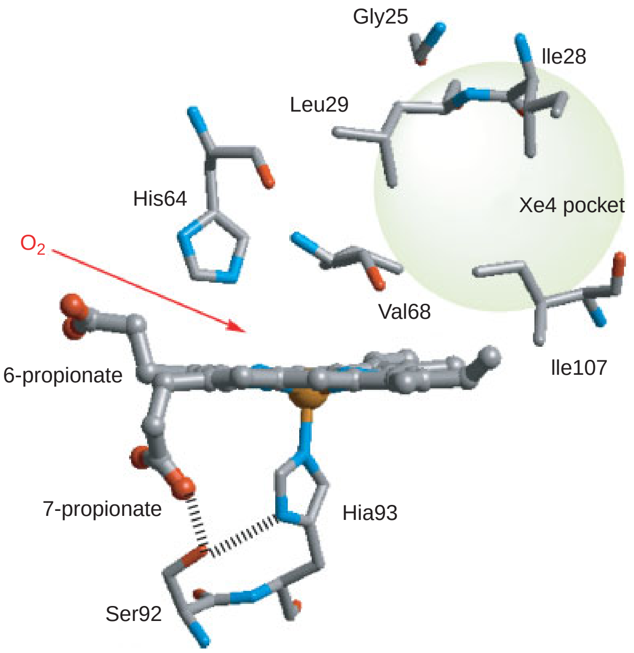

Figure 6 Distal and proximal heme pockets of sperm whale deoxymyoglobin. O_2 enters into the heme pocket and is noncovalently bound at the distal side or hydrophobic Xe4 pocket, and then forms the covalent bond with heme-iron. The iron-bound O_2 is stabilized by His64 via hydrogen-bonding interaction

the heme pocket formed by these hydrophobic residues and then binds to heme-iron.[37,38] In fact, the replacement of several hydrophobic residues on the distal side such as Leu29 and Val68 with more polar or larger residues clearly influences the O_2-binding kinetics parameters and autoxidation process.[39–41] Thus, these residues may serve as an appropriate size and hydrophobicity of the distal pocket to regulate O_2 binding and prevent unfavorable autoxidation. In addition, Scott and Olson pointed out that hydrophobic Xe binding cavities, particularly Xe4 (formed by Gly25, Ile28, Leu29, Val68, and Ile107) as shown in Figure 6 and Xe1 (formed by Leu89, His93, Leu104, and Phe138) behind the proximal side, play a role in the modulation of O_2 binding.[38,42] O_2 can partially diffuse to and from these hydrophobic cavities inside the protein. In contrast, the replacement of the heme-6-propionate side chain with a methyl group enhances the O_2-dissociation (3.1-fold) and the autoxidation of oxymyoglobin (6.2-fold) compared to the reference oxymyoglobin,[43] suggesting that the propionate–residue 45 (Arg or Lys) salt bridge is also important for stabilizing oxygenated heme. In fact, the crystal structure of oxymyoglobin demonstrates that there is a hydrogen-bonding network from the propionate to the bound O_2 via residues 45 and 64; thus, one can expect that the lack of the 6-propionate disrupts the stabilization system of the O_2 complex.[44]

On the proximal side, Ser92 is an important residue modulating O_2 affinity. According to the crystal structure, the hydroxyl group of Ser92 interacts with N_δ–H of the proximal His93 and heme-7-propionate via hydrogen bonding. For the S92L mutant of recombinant pig myoglobin, there is an approximately 1.5-fold increase in the O_2 association rate and a 2.5-fold decrease in the O_2 dissociation rate; thus, the increase in O_2 affinity is 3.8-fold.[33] These kinetic results suggest that the loss of the hydrogen bonding between His93 and Ser92 promotes the proximal histidine flexibility, and heme-iron may then easily return to the plane of the porphyrin ring, although the replacement of Ser92 with Asp or Ala causes no drastic changes in ligand binding.[34]

3.2 O_2/CO Discrimination

Another important debate on the O_2 binding mechanism is how to control the discrimination between O_2 and CO for deoxymyoglobin and deoxyhemoglobin. It is well known that a synthetic pentacoordinated ferrous porphyrin, such as the chelated protoheme reported by Traylor, binds CO more tightly by 1300-fold compared to O_2.[24] This result could be very serious for a biological system if the CO selectivity would be reflected in red blood, because CO is generated by heme degradation of heme oxygenase. Interestingly, the $K\mathrm{co}/K\mathrm{o}_2$ ratio in the hemoproteins is drastically reduced ($K\mathrm{co}/K\mathrm{o}_2 = 25$ for sperm whale Mb and 310 for the R-state of human hemoglobin), because O_2 affinity for the deoxy species clearly increases while CO affinity decreases compared to those observed for the synthetic models.[45] The sharp difference between the heme proteins and the synthetic models is explained as follows. First, the enhancement of O_2 affinity is derived from the remarkably slow dissociation of bound O_2. Thus, the O_2 complexes in myoglobins and hemoglobins are stabilized by hydrogen bonding between the distal histidine and the charge-separated oxyheme, $\mathrm{PFe(III)}{-}O_2{}^{\bullet-}$.[35] Second, the relatively nonpolar Fe–CO species is not strongly stabilized by the distal residue, whereas the bound CO molecule is found to cause steric hindrance to the distal residues, because the Fe–C–O unit prefers a linear geometry owing to the back donation from the iron $d\pi$ orbitals.[14,46,47] Although there are still several arguments about Fe–C–O geometry,[14,48] model studies on CO binding by capped or strapped metal porphyrins also support the steric factors which exhibit CO discrimination in the proteins.[23,26–28,49]

4 IMPROVEMENT OF O_2 AFFINITY IN HEME PROTEINS

4.1 Naturally Occurring Hemoglobins with Unusually High O_2 Affinity

Under physiological conditions, O_2 binding constants for mammalian myoglobins and hemoglobins are 10^5–$10^6\ \mathrm{M}^{-1}$. Some synthetic models for myoglobin also exhibit a similar order of O_2 affinity in water and organic solvents. In contrast, there are special O_2-binding heme proteins, which show extremely high O_2 affinity in nature. One of these proteins is a hemoglobin from *Ascaris suum* which is a family of nematodes.[50] The O_2-binding constant of the *Ascaris* hemoglobin is determined to be $3.7 \times 10^8\ \mathrm{M}^{-1}$. In addition, interestingly, the O_2 affinity is higher than the CO affinity with a $K\mathrm{co}/K\mathrm{o}_2$ of 0.03.[51] Table 3 shows that there is a 350-fold increase in O_2 affinity and 2.5-fold decrease in CO affinity compared with the corresponding parameters for wild-type sperm whale myoglobin. This unusual thermodynamic property is derived from the extremely slow O_2 dissociation as shown in Table 3, because bound O_2 is strongly stabilized by two amino acid residues, Tyr(B10) and Gln(E7), via a hydrogen-bonding network in the distal pocket (Figure 7a and b),[52] although in normal myoglobin and hemoglobin, only a distal histidine stabilizes the bound O_2.

Leghemoglobin, a small monomeric heme protein, is another unique O_2-binding protein with a large O_2 affinity in nature.[58] It is found in the root nodules of leguminous plants, and its physiological function may be O_2 transport as well as O_2 scavenging.[53] The O_2-binding mechanism of leghemoglobin is slightly different from those of other O_2 binding hemoproteins, although it is still not completely clear. Interestingly, the replacement of a distal histidine with several amino acid residues causes no serious decrease in O_2 affinity, suggesting that the hydrogen bonding of the distal histidine to bound O_2 is not essential for the stabilization of oxyleghemoglobin.[59] Table 3 shows that the large O_2 affinity in leghemoglobin is mainly derived from the fast O_2 association with heme-iron. It is likely that the large distal heme pocket reduces the barrier to O_2 association in leghemoglobin compared to myoglobin, whereas O_2 dissociation is modulated from the proximal side.[60]

A heme protein which displays the highest O_2 affinity ever observed in nature is the trematode hemoglobin from *Paramphistonum epiclitum*. Table 3 indicates that the exceptionally high O_2 affinity is due to the combination of high O_2 association rate and very low O_2 dissociation rate.[54,61,62] According to the high-resolution structure of the trematode hemoglobin (Figure 7d), there are two tyrosines

Table 3 Kinetic and thermodynamic parameters for O_2 and CO binding to several heme proteins (20 °C, pH 7.0)

Protein	k_{on} ($\mu\mathrm{M}^{-1}\,\mathrm{s}^{-1}$)	k_{off} (s^{-1})	$K\mathrm{o}_2$ ($\mu\mathrm{M}^{-1}$)	$K\mathrm{co}$ ($\mu\mathrm{M}^{-1}$)	$K\mathrm{co}/K\mathrm{o}_2$	Ref.
Sperm whale Mb	17	15	1.1	27	25	21
Ascaris Hb	1.5	0.004	370	11	0.03	51
LegHb	130	5.6	23	2200	96	53
Trematode Hb[a,b]	90	0.07	1300	250	0.19	54
L29Y/H64Q Mb[c]	2.8	1.6	1.8	5.1	2.8	55
L29F/H64Q Mb	54	30	55	100	1.8	56
Reconstituted Mb[d,e,f]	120	0.11	1100	420	0.38	57

[a] Trematode species from *paramphistomum epiclitum*. [b] At 25 °C, pH 7.0. [c] Sperm whale. [d] Horse heart. [e] Myoglobin reconstituted with an iron porphycene. [f] At 25 °C, pH 7.0.

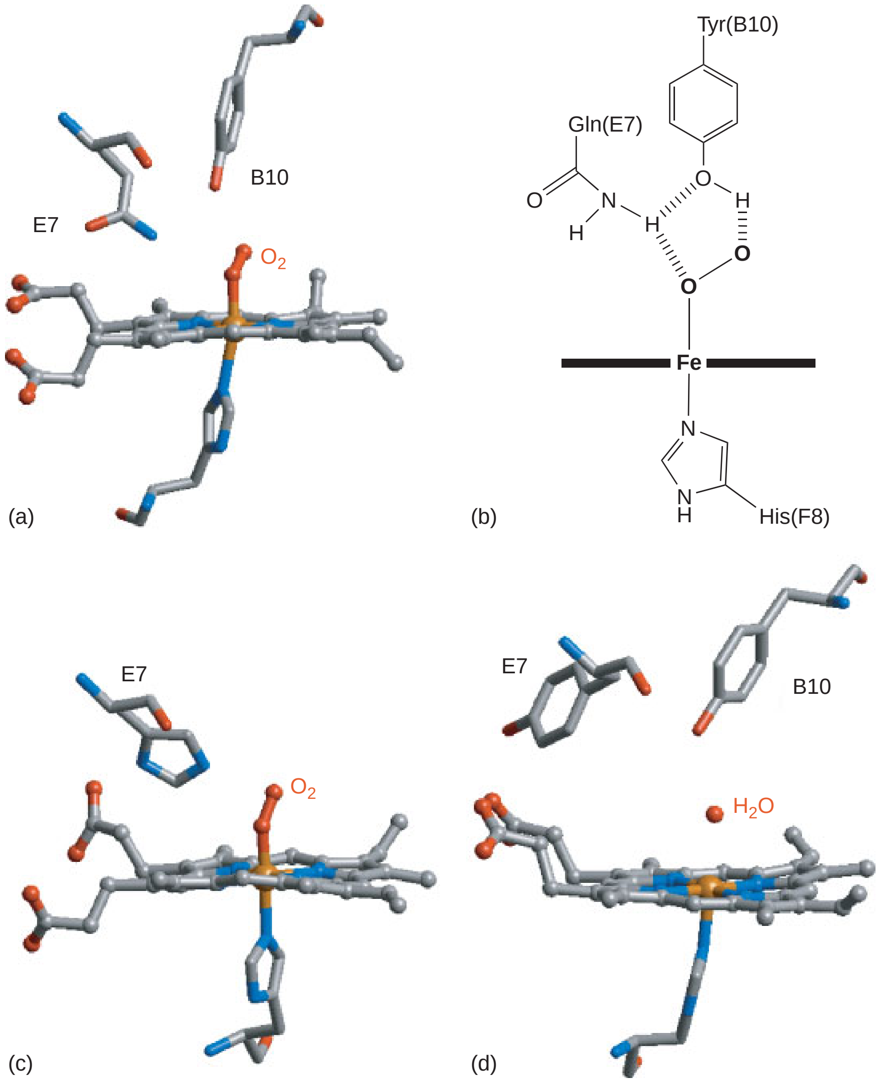

Figure 7 O_2 binding sites and environments in monomeric hemoglobins with unusually high O_2 affinity. (a) O_2 complex of *Ascaris suum* hemoglobin (1ASH). (b) Schematic representation of hydrogen-bonding network between O_2 and two distal residues in *Ascaris suum* hemoglobin. (c) O_2 complex of leghemoglobin from lupin (2GDM). (d) Aquo-met form of a trematode hemoglobin from *Paramphistomum epiclitum* (1H97)

and one histidine in the distal pocket and two tyrosines at the B10 and E7 positions are thought to mainly stabilize O_2 via strong hydrogen-bonding interaction. Tyr(B10) is found at the appropriate position in the distal pocket to make a hydrogen bond with the iron-bound O_2, whereas the hydroxyl group of Tyr(E7) interacts with heme-6-propionate via hydrogen bonding and is not oriented towards the ligand-binding site. In contrast, computer modeling proposes that the one of the plausible structures is different with the structure obtained by X-ray crystallography analysis, where the Tyr(E7) side chain is inside the distal heme pocket and potentially able to make a second hydrogen bond with the iron-bound O_2.[54,61] The crystal structure of trematode oxyhemoglobin will account for the high O_2 affinity of the trematode hemoglobin in the near future.

4.2 Artificial Modification of Myoglobins to Increase O_2 Affinity

For over a decade, there have been various trials to obtain a special myoglobin with high O_2 affinity. Particularly, several groups have modified the distal side of myoglobin by a mutagenetic approach to mimic the structure found in *Ascaris* hemoglobin.[55,56] Although L29Y/H64Q sperm whale myoglobin was a good candidate, the double mutant to mimic the distal site of the *Ascaris* hemoglobin did not clearly enhance the O_2 binding as shown in Table 3.

In contrast, another approach to the improvement of O_2 affinity is the replacement of the native heme with an artificially created prosthetic group. This method is called ‘reconstitution’ (Scheme 1).[63] Although this method

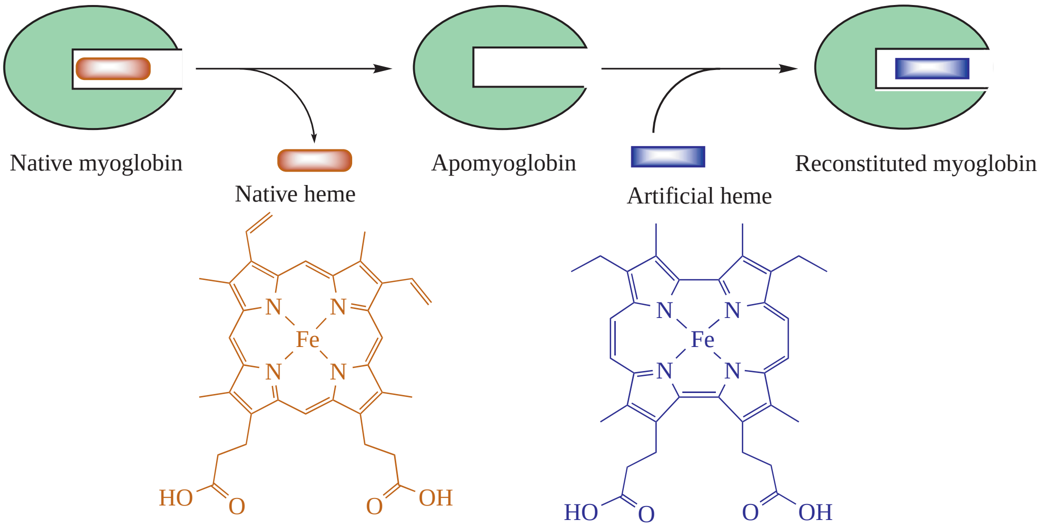

Scheme 1 Reconstitution of myoglobin with an artificially created heme

could be effective in modulating the physiological function in heme proteins, only a limited number of studies are available on reconstituted myoglobins actually improving O_2 affinity.[64–69] For example, the replacement of native heme with an iron porphycene, a structural isomer of mesoheme, in horse heart myoglobin markedly enhances O_2 affinity, $K\text{o}_2 = 1.1 \times 10^9\ \text{M}^{-1}$, due to the slightly faster O_2 association and dramatically slower O_2 dissociation.[57] In this case, the O_2/CO selectivity of the reconstituted myoglobin is completely different from that observed for the native protein. The ratio $K\text{co}/K\text{o}_2$ for the reconstituted myoglobin with the iron porphycene is less than 1. The artificially created prosthetic group stabilizes the bound O_2 due not only to the strong hydrogen bonding with the distal histidine but also to an increase in the strength of the O_2–Fe σ-bond because of the lower-energy dz^2 orbital of the porphycene iron.

5 COOPERATIVITY OF O_2 BINDING FOR HEMOGLOBIN

Hemoglobin is a tetrameric protein, which contains two identical α-subunits and two identical β-subunits. Furthermore, these subunits are paired as two dimers, $\alpha_1\beta_1$ and $\alpha_2\beta_2$, and each subunit has one heme, which can bind O_2 reversibly. The structures of the four subunits are similar to each other and to that of myoglobin. The most essential physiological function of hemoglobin is cooperative O_2 binding; that is, O_2 binding in hemoglobin exhibits a sigmoidal behavior versus O_2 concentration (Figure 8). When we define Y as a fractional saturation of O_2, this cooperativity is represented as follows:

$$\frac{Y}{(1-Y)} = K(P\text{o}_2)^n \tag{5}$$

where K and $P\text{o}_2$ are the association constant and partial pressure of O_2, respectively. The equation is further modified to

$$\log\left[\frac{Y}{(1-Y)}\right] = \log K + n\log(P\text{o}_2) \tag{6}$$

Figure 8(b) is called a Hill plot which represents the oxygen equilibrium curve according to equation (6), and n is a Hill coefficient number. The larger the n value is, the more strongly is the curve sigmoidal; that is, the n value indicates the degree of cooperativity. In the case of myoglobin, the n value is 1 and the Hill plot is linear, whereas the curve for human hemoglobin shows a typical sigmoidal curve with an n value of 2.8.

The O_2 binding properties of hemoglobin have been mainly represented by two methods as shown in Figure 9. First, the model proposed by Adair and Koshland uses four successive O_2 affinity constants (K_1, K_2, K_3, and K_4) and the partial O_2 pressure, $P\text{o}_2$, to describe the fractional oxygen saturation;[70,71]

$$Y = \frac{K_1P\text{o}_2 + 3K_1K_2P\text{o}_2{}^2 + 3K_1K_2K_3P\text{o}_2{}^3 + K_1K_2K_3K_4P\text{o}_2{}^4}{1 + 4K_1P\text{o}_2 + 6K_1K_2P\text{o}_2{}^2 + 4K_1K_2K_3P\text{o}_2{}^3 + K_1K_2K_3K_4P\text{o}_2{}^4} \tag{7}$$

This equation assumes that each of the four binding sites is identical.

In contrast, Monod, Wyman, and Changeux proposed a simple model, which is called the MWC two-state concerted model.[72] They defined two quaternary T and R states; the T (tense) state exhibits low affinity whereas the R (relaxed) state exhibits high affinity. This model assumes that each

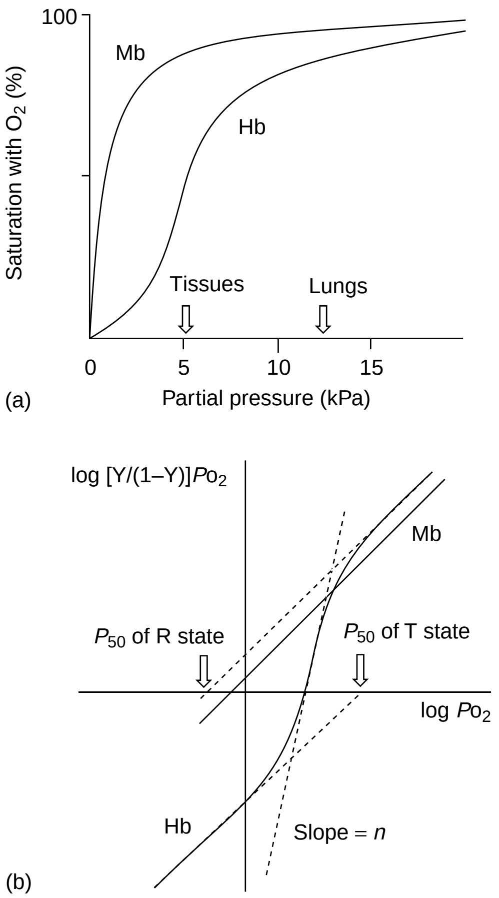

Figure 8 Cooperative and noncooperative binding of O_2. (a) Binding curves of myoglobin and hemoglobin. (b) Hill plot of binding curves. The Hill coefficient number is determined from the first derivative (slope) of the Hill plots

subunit possesses only two conformations, T or R, regardless of the number of bound O_2 molecules. When T_0 and R_0 are defined as the ligand-free T- and R-states, respectively, the equilibrium constant, L_0, between the two states is described as follows:

$$L_0 = \frac{[T_0]}{[R_0]} \tag{8}$$

Therefore, the fractional O_2 saturation value Y is given as

$$Y = \frac{L_0 K_T Po_2(1 + K_T Po_2)^3 + K_R Po_2(1 + K_R Po_2)^3}{L_0(1 + K_T Po_2)^4 + (1 + K_R Po_2)^4} \tag{9}$$

where K_T and K_R are O_2 binding constants for the T_0 and R_0 states, respectively. In addition, K_T and K_R can be estimated from the lower and upper asymptotes in Figure 9 and are approximately equal to K_1 and K_4 determined by the Adair and Koshland method; the K_R/K_T, cooperativity factor, is 30–40 in human hemoglobin. Furthermore, the equilibrium constants, L_0, L_2, and L_4, are roughly estimated to be 10^3, 1, and 10^{-3}, respectively.[73] The MWC two-state concerted model has recently been accepted as the practical allosteric model of hemoglobin.

The 3D structure of hemoglobin suggests a difference in the two quaternary conformations, T and R.[74] The four heme groups are well separated from each other in the tetramer with an Fe–Fe distance of 24–40 Å. The deoxy and oxy forms may be assigned to the T and R states, respectively. Comparison of the structures between the T and R states is indicative of the drastic quaternary conformational change which consists of a rotation of one pair of $\alpha\beta$ dimer relative to the other by 15°. The driving force for the rotation of the α–β subunit pair seems to be adjustments in the tertiary structure upon O_2 binding. X-ray data show that the heme-iron

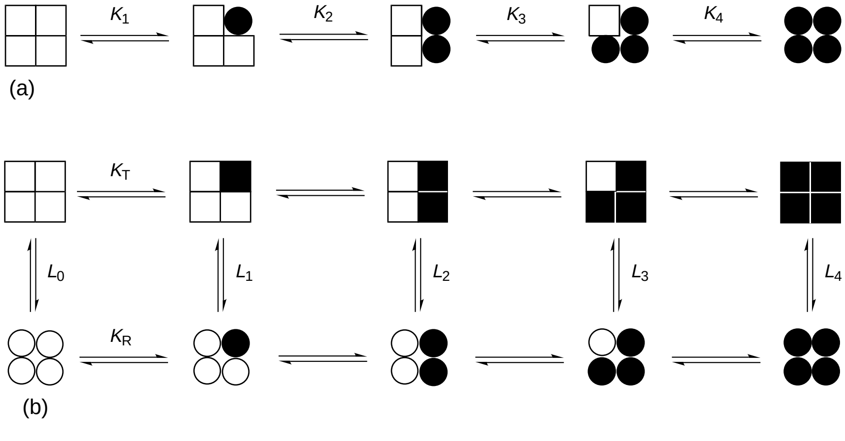

Figure 9 Two proposed models for allosteric interaction observed in hemoglobin. (a) A sequential model of allosteric interaction. When one O_2 molecule binds to a subunit in the T-state, the subunit shifts to R-state and affects the affinity of neighboring subunits for the ligand binding. (b) An MWC two-state concerted model of allosteric interaction. When one O_2 molecule binds to a subunit in all T-states, a concerted conformational change occurs to produce a protein with all R-state subunits. Square and circle represent T- and R-state subunits, respectively. Moreover, opened and closed diagrams represent free and O_2 bound subunits, respectively

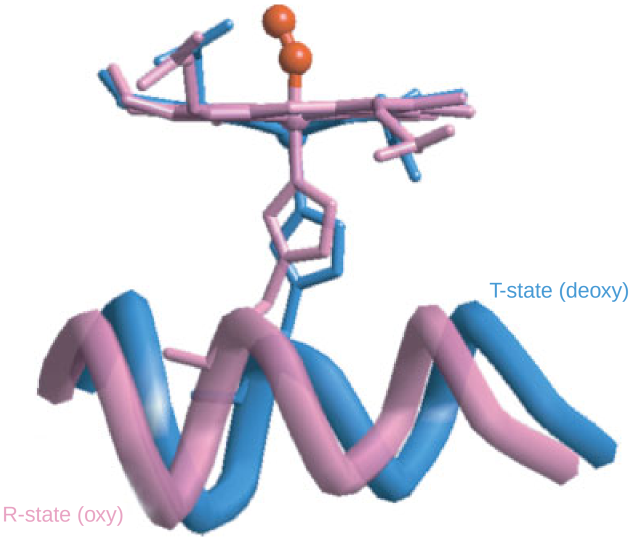

Figure 10 Conformational changes in human hemoglobin upon the O_2 binding. The proximal histidine is pulled toward the porphyrin ring by oxygenation, and then the F-helix shifts position. Purple and blue units represent oxy (R-state) and deoxy (T-state) proteins and hemes, respectively

which is located about 0.4 Å away from the porphyrin plane in the T-state shifts to inside the porphyrin core in the R-state owing to the decrease in ion radius of the oxygenated heme-iron (Figure 10). As a result of this movement, the proximal histidine F8 is pulled along with the heme-iron, and the shift in the F-helix is then thought to be induced. The corresponding conformational shift in the F8-containing α-helix requires rearrangement of the $\alpha_1\beta_1$–$\alpha_2\beta_2$ interface. According to a comparison of the 3D structure between the T and R states, the interface formed by several sets of salt-bridges and hydrogen bonds between the α_1 and β_2 or α_2 and β_1 subunits in the T-state is disrupted, and only one new interaction between the subunits is generated. The arguments on the thermodynamic aspects of the transformation between the T and R states are still continuing, because the apparent free energy changes in cooperative interactions are relatively small ($\Delta G_{\text{T-R}}$ = ca. 1.9 kcal mol^{-1}). However, several spectroscopic data clearly support Perutz's stereochemical mechanism that the heme-iron movement upon O_2 binding directly induces the structural perturbation of other subunits to regulate cooperatively the next ligand binding.[75]

6 MODULATION OF O_2 BINDING BY SMALL MOLECULES

It is well known that the O_2 affinity of vertebrate hemoglobin affects several physiological effectors such as H^+, CO_2 or 2,3-diphosphoglycerate (2,3-DPG).[5] Particularly, H^+ and CO_2 play a physiologically important role in the regulation of O_2 binding for hemoglobin in the lungs and tissues. This is called the Bohr effect. The negatively charged 2,3-DPG is present in red blood cells and acts as an allosteric effector. According to 3D structure data for the deoxy form in the presence of 2,3-DPG, one molecule of 2,3-DPG preferentially binds to the T-state of hemoglobin via electrostatic interaction and fixes the T-state more tightly, whereas the bound 2,3-DPG is driven away upon O_2 binding, because the 2,3-DPG binding site collapses upon transition from the T- to the R-state.[76] Hill plots of the O_2 binding equilibrium shows that 2,3-DPG mainly decreases the K_T value.[77]

Recently, several heterotropic allosteric effectors have been found such as bezafibrate (BZF) and inositol hexaphosphate (IHP).[78,79] O_2 equilibrium measurements in the presence of these effectors demonstrate that the addition of these effectors particularly reduces K_R (max. 2000-fold). This finding suggests that the effectors can bind not only the T-state but also the R-state tightly, although the binding site of the effectors in the R-state could be different from that of the T-state. The binding of the effectors for the R-state is also estimated by spectroscopic evidence.[79] This finding suggests that the effectors have the potential to drastically modulate the O_2 binding of hemoglobin without any mutation of amino acid residues.

7 OTHER ASPECTS OF MYOGLOBINS AND HEMOGLOBINS

Iron porphyrin as a prosthetic group of heme proteins undergoes a variety of ligand binding and other reactions. Thus, it is no wonder that myoglobin and hemoglobins exhibit multiple functions in vivo and/or in vitro. In the final section of this article, two other reactions of myoglobin and hemoglobin are briefly reviewed.

7.1 NO Binding

In the last decade, nitric oxide (NO) chemistry for biological systems has attracted considerable attention, because NO is not only a toxic agent for organisms but also an important messenger in many vertebrate signal-transduction processes (*see* ***Nitrogen Monoxide (Nitric Oxide): Bioinorganic Chemistry***). For example, a soluble guanylyl cyclase is a famous heme protein which is activated upon NO binding.[80] NO binding to ferrous heme-iron in myoglobin and hemoglobin is very strong with a binding constant of 2×10^7 M^{-1} for wild-type sperm whale myoglobin,[81] whereas NO can also bind to ferric heme-iron in the heme proteins in the range of 10^3–10^4 M^{-1}.[82] In addition, it is of particular interest to compare the ligand-binding structure between O_2 and NO in the heme proteins. Based on several spectroscopic studies, upon NO binding, the Fe–His(E7) bond in the α-subunit of

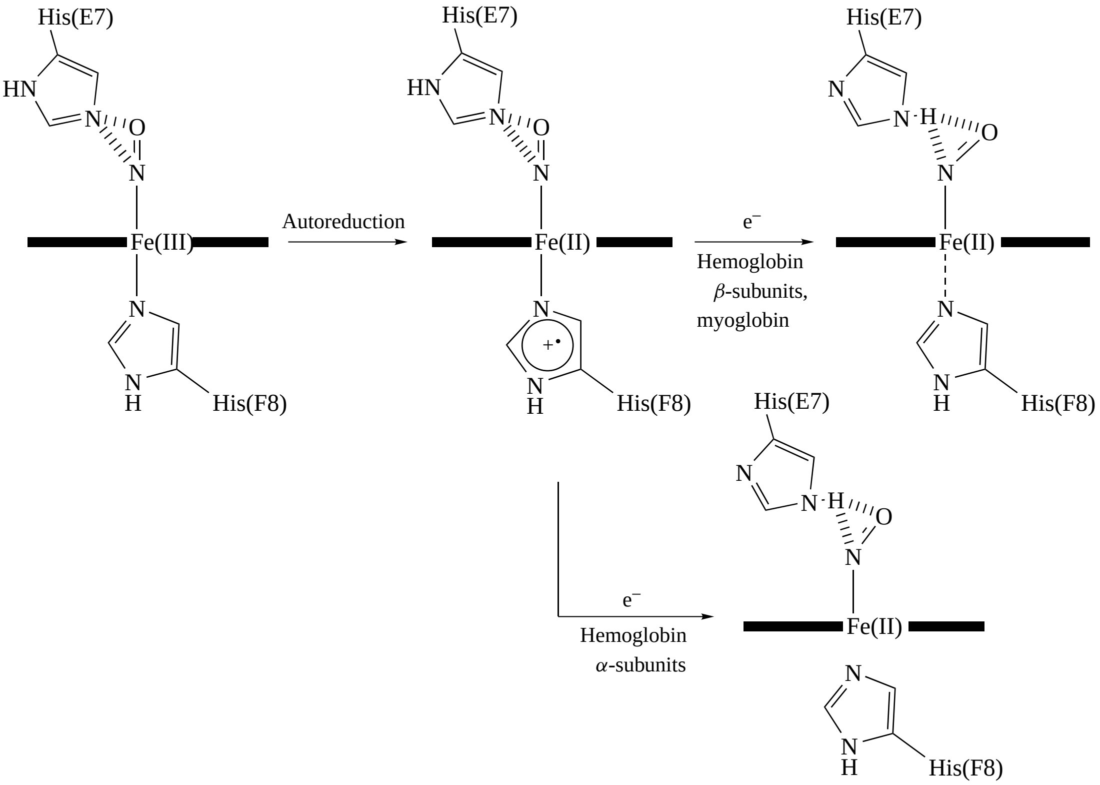

Scheme 2 NO binding behavior in heme proteins

hemoglobin is ruptured to form a pentacoordinate Fe–NO species, while the corresponding Fe–His bond in myoglobin and the β-subunits of hemoglobin weakens due to a repulsive trans effect as shown in Scheme 2.[83–86] The secondary physiological function of myoglobin is now considered to be a scavenger or reservoir for NO; for example, deoxymyoglobin or oxymyoglobin may prevent NO from inhibiting the cytochrome *c* oxidase reaction.[87] In the case of hemoglobins, the interaction of NO with the protein is more complicated, because NO binds to a β-93 cysteinyl residue as well as heme-iron in hemoglobin and forms an *S*-nitrosothiol.[88–90] Although NO can be transported by hemoglobin linked with O_2 transport, the molecular mechanisms of NO to explain the physiological function of hemoglobin are still being discussed.[91–93]

7.2 Peroxidase Activity of Myoglobin

Myoglobin has the same prosthetic group as some peroxidases, such as horseradish peroxidase (HRP) or cytochrome *c* peroxidase, and reacts with H_2O_2 to produce a ferryl species, PFe(IV)=O, observed in the native peroxidase (*see* ***Iron: Heme Proteins, Peroxidases, Catalases & Catalase-peroxidases***). However, the catalytic activity of myoglobin toward substrate oxidation is very low, because the structure of the distal side of myoglobin is slightly different from that of HRP, and myoglobin has no substrate-binding site. To convert myoglobin into a peroxidase or peroxygenase, some groups have modified several residues on the distal side by site-directed mutagenesis.[94–98] For example, the F43H/H64L mutant, which resembles cytochrome *c* peroxidase in distal structure, exhibits high peroxygenase activity toward thioanisole and styrene oxidation; there is a 360-fold increase in turnover of thioanisole oxidation relative to that of wild-type myoglobin.[99] Furthermore, upon the addition of H_2O_2 to the ferric H64D, a transient compound I with a porphyrin ring cation radical, $P^{+\bullet}Fe(IV){=}O$, was directly observed by UV-vis spectroscopy at 4 °C, although no evidence of the formation of compound I has been obtained with wild-type sperm whale myoglobin.[100] In contrast, horse heart myoglobin reconstituted with a chemically modified heme having two benzene moieties bound to the terminal propionates has been reported to exhibit 13-fold greater specificity than native myoglobin in the oxidation of guaiacol, because the two benzene moieties located at the exit of the heme pocket will form a substrate-binding domain on the protein surface.[101] In addition, hybridization of the modified heme and an appropriate mutant such as H64D remarkably enhances peroxidase activity toward guaiacol oxidation by ca. a 430-fold increase in the $k_{\mathrm{cat}}/K_{\mathrm{m}}$ value relative to wild-type myoglobin.[102]

8 RELATED ARTICLES

Iron: Heme Proteins, Mono- & Dioxygenases; Iron: Heme Proteins, Peroxidases, Catalases & Catalase-peroxidases; Iron Porphyrin Chemistry.

9 REFERENCES

1. J. C. Kendrew, G. Bodo, H. M. Dintzis, R. G. Parrish, H. Wyckoff, and D. C. Phillips, *Nature*, 1958, **181**, 662.
2. M. F. Perutz, M. G. Rossmann, A. F. Cullis, H. Muirhead, G. Will, and A. C. T. North, *Nature*, 1960, **185**, 416.
3. F. A. Cotton, G. Wilkinson, C. A. Murillo, and M. Bochmann, 'Advanced Inroganic Chemistry', 6th edn., Wiley, New York, 1999.
4. J. M. Berg, J. L. Tymoczko, and L. Stryer, 'Biochemistry', 5th edn., Freeman, New York, 2002.
5. E. Antonini and M. Brunori, 'Hemoglobin and Myoglobin in their Reactions with Ligands', North-Holland, Amsterdam, NY, 1971.
6. G. N. Phillips Jr, in 'Handbook of Metalloproteins', eds. A. Messerschmidt, R. Huber, T. Poulos, and K. Wieghardt, Wiley, Chichester, 2001, Vol. I, p. 5.
7. M. Paoli and K. Nagai, in 'Handbook of Metalloproteins', eds. A. Messerschmidt, R. Huber, T. Poulos, and K. Wieghardt, Wiley, Chichester, 2001, Vol. I, p. 16.
8. G. B. Jameson and J. A. Ibers, in 'Bioinorganic Chemistry', eds. I. Bertini, H. B. Gray, S. J. Lippard, and J. S. Valentine, University Science Books, Mill Valley, 1994, p. 167.
9. G. N. La Mar, H. Toi, and R. Krishnamoorthi, *J. Am. Chem. Soc.*, 1984, **106**, 6395.
10. L. Pauling and C. D. Coryell, *Proc. Natl. Acad. Sci. U.S.A.*, 1936, **22**, 210.
11. L. Pauling and J. J. Weiss, *Nature*, 1964, **203**, 182.
12. J. J. Weiss, *Nature*, 1964, **202**, 83.
13. S. E. V. Phillips, *Nature*, 1978, **273**, 247.
14. J. Vojtechovsky, K. Chu, J. Berendzen, R. M. Sweet, and I. Schlichting, *Biophys. J.*, 1999, **77**, 2153..
15. W. T. Potter, M. P. Tucker, R. A. Houtchens, and W. S. Caughey, *Biochemistry*, 1987, **26**, 4699.
16. L. M. Miller and M. R. Chance, *Biochemistry*, 1995, **34**, 10170.
17. T. K. Das, M. Couture, Y. Ouellet, M. Guertin, and D. L. Rousseau, *Proc. Natl. Acad. Sci. U.S.A.*, 2001, **98**, 479.
18. K. Imai, 'Allosteric Effects in hemoglobin', Cambridge University Press, Cambridge, 1982.
19. K. Imai, H. Morimoto, M. Kotani, H. Watari, W. Hirata, and M. Kuroda, *Biochim. Biophys. Acta*, 1970, **200**, 189.
20. E. E. Scott, E. V. Paster, and J. S. Olson, *J. Biol. Chem.*, 2000, **275**, 27129.
21. B. A. Springer, S. G. Sligar, J. S. Olson, and G. N. Phillips Jr, *Chem. Rev.*, 1994, **94**, 699.
22. J. S. Olson, E. W. Foley, D. H. Maillett, and E. V. Paster, in 'Hemoglobin Disorders', ed. R. L. Nagel, Humana Press, Totowa, 2003, p. 65.
23. M. Momenteau and C. A. Reed, *Chem. Rev.*, 1994, **94**, 659.
24. T. G. Traylor, D. K. White, D. H. Campbell, and A. P. Berzinis, *J. Am. Chem. Soc.*, 1981, **103**, 4932.
25. J. P. Collman, J. I. Brauman, B. L. Iverson, J. L. Sessler, R. M. Morris, and Q. H. Gibson, *J. Am. Chem. Soc.*, 1983, **105**, 3052.
26. K. S. Suslick and T. J. Reinert, *J. Chem. Educ.*, 1985, **62**, 974.
27. J. P. Collman and L. Fu, *Acc. Chem. Res.*, 1999, **32**, 455.
28. J. P. Collman, R. Boulatov, C. J. Sunderland, and L. Fu, *Chem. Rev.*, 2004, **104**, 561.
29. J. P. Collman, R. R. Gagne, C. A. Reed, W. T. Robinson, and G. A. Rodley, *Proc. Natl. Acad. Sci. U.S.A.*, 1974, **71**, 1326.
30. I. Tabushi, S. Kugimiya, and T. Sasaki, *J. Am. Chem. Soc.*, 1985, **107**, 5159.
31. I. Tabushi and S. Kugimiya, *J. Am. Chem. Soc.*, 1986, **108**, 6926.
32. C. A. Reed and S. K. Cheung, *Proc. Natl. Acad. Sci. U.S.A.*, 1977, **74**, 1780.
33. S. J. Smerdon, S. Krzywda, A. J. Wilkinson, R. E. Brantley Jr, T. E. Carver, M. S. Hargrove, and J. S. Olson, *Biochemistry*, 1993, **32**, 5132.
34. Y. Shiro, T. Iizuka, K. Marubayashi, T. Ogura, T. Kitagawa, S. Balasubramanian, and S. G. Boxer, *Biochemistry*, 1994, **33**, 14986.
35. R. J. Rohlfs, A. J. Mathews, T. E. Carver, J. S. Olson, B. A. Springer, K. D. Egeberg, and S. G. Sligar, *J. Biol. Chem.*, 1990, **265**, 3168.
36. R. E. Brantley Jr, S. J. Smerdon, A. J. Wilkinson, E. W. Singleton, and J. S. Olson, *J. Biol. Chem.*, 1993, **268**, 6995.
37. J. S. Olson and G. N. Phillips Jr, *J. Biol. Chem.*, 1996, **271**, 17593.
38. E. E. Scott, Q. H. Gibson, and J. S. Olson, *J. Biol. Chem.*, 2001, **276**, 5177.
39. K. D. Egeberg, B. A. Springer, S. G. Sligar, T. E. Carver, R. J. Rohlfs, and J. S. Olson, *J. Biol. Chem.*, 1990, **265**, 11788.
40. T. E. Carver, R. E. Brantley Jr, E. W. Singleton, R. M. Arduini, M. L. Quillin, G. N. Phillips Jr, and J. S. Olson, *J. Biol. Chem.*, 1992, **267**, 14443.
41. T. Li, M. L. Quillin, G. N. Phillips Jr, and J. S. Olson, *Biochemistry*, 1994, **33**, 1433.
42. E. E. Scott and Q. H. Gibson, *Biochemistry*, 1997, **36**, 11909.
43. T. Hayashi, T. Matsuo, Y. Hitomi, K. Okawa, A. Suzuki, Y. Shiro, T. Iizuka, Y. Hisaeda, and H. Ogoshi, *J. Inorg. Biochem.*, 2002, **91**, 94.
44. T. E. Carver, J. S. Olson, S. J. Smerdon, S. Krzywda, A. J. Wilkinson, Q. H. Gibson, R. S. Blackmore, J. D. Ropp, and S. G. Sligar, *Biochemistry*, 1991, **30**, 4697.

45. J. S. Olson and G. N. Phillips Jr, *J. Biol. Inorg. Chem.*, 1997, **2**, 544.
46. G. S. Kachalova, A. N. Popov, and H. D. Bartunik, *Science*, 1999, **284**, 473.
47. G. N. Phillips Jr, M. L. Teodoro, T. Li, B. Smith, and J. S. Olson, *J. Phys. Chem. B*, 1999, **103**, 8817.
48. T. G. Spiro and P. M. Kozlowski, *Acc. Chem. Res.*, 2001, **34**, 137.
49. C. Slebodnick and J. A. Ibers, *J. Biol. Inorg. Chem.*, 1997, **2**, 521.
50. D. E. Goldberg, *Chem. Rev.*, 1999, **99**, 3371.
51. Q. H. Gibson and M. H. Smith, *Proc. R. Soc. Lond., B, Biol. Sci.*, 1965, **163**, 206.
52. J. Yang, A. P. Kloek, D. E. Goldberg, and F. S. Mathews, *Proc. Natl. Acad. Sci. U.S.A.*, 1995, **92**, 4224.
53. M. S. Hargrove, J. K. Barry, E. A. Brucker, M. B. Berry, G. N. Phillips Jr, J. S. Olson, R. Arredondo-Peter, J. M. Dean, R. V. Klucas, and G. Sarath, *J. Mol. Biol.*, 1997, **266**, 1032.
54. A. Pesce, S. Dewilde, L. Kiger, M. Milani, P. Ascenzi, M. C. Marden, M.-L. Van Hauwaert, J. Vanfleteren, L. Moens, and M. Bolognesi, *J. Mol. Biol.*, 2001, **309**, 1153.
55. F. Draghi, A. E. Miele, C. Travaglini-Allocatelli, B. Vallone, M. Brunori, Q. H. Gibson, and J. S. Olson, *J. Biol. Chem.*, 2002, **277**, 7509.
56. C. Travaglini-Allocatelli, F. Cutruzzolà, A. Brancaccio, B. Vallone, and M. Brunori, *FEBS Lett.*, 1994, **352**, 63.
57. T. Hayashi, H. Dejima, T. Matsuo, H. Sato, D. Murata, and Y. Hisaeda, *J. Am. Chem. Soc.*, 2002, **124**, 11226.
58. M. J. Davies, C. Mathieu, and A. Puppo, in 'Advances in Inorganic Chemistry', ed., A. G. Sykes, Academic Press, San Diego, CA, 1999, Vol. 46, p. 495.
59. S. Kundu and M. S. Hargrove, *Proteins*, 2003, **50**, 239.
60. S. Kundu, B. Snyder, K. Das, P. Chowdhury, J. Park, J. W. Petrich, and M. S. Hargrove, *Proteins*, 2002, **46**, 268.
61. A. K. Rashid, M.-L. Van Hauwaert, M. Haque, A. H. Siddiqi, I. Lasters, M. De Maeyer, M. Griffon, M. C. Marden, S. Dewilde, J. Clauwaert, S. N. Vinogradov, and L. Moens, *J. Biol. Chem.*, 1997, **272**, 2992.
62. L. Kiger, A. K. Rashid, N. Griffon, M. Haque, L. Moens, Q. H. Gibson, C. Poyart, and M. C. Marden, *Biophys. J.*, 1998, **75**, 990.
63. T. Hayashi and Y. Hisaeda, *Acc. Chem. Res.*, 2002, **35**, 35.
64. B. M. Hoffman and D. H. Petering, *Proc. Nat. Acad. Sci. U.S.A.*, 1970, **67**, 637.
65. D. R. Paulson, A. W. Addison, D. Dolphin, and B. R. James, *J. Biol. Chem.*, 1979, **254**, 7002.
66. C. K. Chang, B. Ward, and S. Ebina, *Arch. Biochem. Biophys.*, 1984, **231**, 366.
67. S. Neya, T. Kaku, N. Funasaki, Y. Shiro, T. Iizuka, K. Imai, and H. Hori, *J. Biol. Chem.*, 1995, **270**, 13118.
68. S. Neya, K. Imai, H. Hori, H. Ishikawa, K. Ishimori, D. Okuno, S. Nagatomo, T. Hoshino, M. Hata, and N. Funasaki, *Inorg. Chem.*, 2003, **42**, 1456.
69. M. C. Marden, L. Kiger, C. Poyart, A. K. Rashid, J. Kister, F. Stetzkowski-Marden, G. Caron, M. Haque, and L. Moens, *FEBS Lett.*, 2000, **472**, 221.
70. G. S. Adair, *J. Biol. Chem.*, 1925, **63**, 529.
71. D. E. Koshland Jr, G. Némethy, and D. Filmer, *Biochemistry*, 1966, **5**, 365.
72. J. Monod, J. Wyman, and J. P. Changeux, *J. Mol. Biol.*, 1965, **12**, 88.
73. T. Yonetani and A. Tsuneshige, *C. R. Biol.*, 2003, **326**, 523.
74. M. F. Perutz, G. Fermi, B. Luisi, B. Shaanan, and R. C. Liddington, *Acc. Chem. Res.*, 1987, **20**, 309.
75. W. A. Eaton, E. R. Henry, J. Hofrichter, and A. Mozzarelli, *Nat. Struct. Biol.*, 1999, **6**, 351.
76. A. Arnone, *Nature*, 1972, **237**, 146.
77. K. Imai and T. Yonetani, *J. Biol. Chem.*, 1975, **250**, 7093.
78. M. Coletta, M. Angeletti, P. Ascenzi, A. Bertollini, S. Della Longa, G. De Sanctis, A. M. Priori, R. Santucci, and G. Amiconi, *J. Biol. Chem.*, 1999, **274**, 6865.
79. T. Yonetani, S. Park, A. Tsuneshige, K. Imai, and K. Kanaori, *J. Biol. Chem.*, 2002, **277**, 34508.
80. K. A. Lucas, G. M. Pitari, S. Kazerounian, I. Ruiz-Stewart, J. Park, S. Schulz, K. P. Chepenik, and S. A. Waldman, *Pharmacol. Rev.*, 2000, **52**, 375.
81. T. G. Traylor and V. S. Sharma, *Biochemistry*, 1992, **31**, 2847.
82. M. Hoshino, K. Ozawa, H. Seki, and P. C. Ford, *J. Am. Chem. Soc.*, 1993, **115**, 9568.
83. S. M. Decatur, S. Franzen, G. D. DePillis, R. B. Dyer, W. H. Woodruff, and S. G. Boxer, *Biochemistry*, 1996, **35**, 4939.
84. N.-L. Chan, J. S. Kavanaugh, P. H. Rogers, and A. Arnone, *Biochemistry*, 2004, **43**, 118.
85. K. B. Killday, M. S. Tempesta, M. E. Bailey, and C. J. Metral, *J. Agric. Food Chem.*, 1988, **36**, 909.
86. L. M. Miller, A. J. Pedraza, and M. R. Chance, *Biochemistry*, 1997, **36**, 12199.
87. J. K. S. Møller and L. H. Skibsted, *Chem. Rev.*, 2002, **102**, 1167.
88. L. Jia, C. Bonaventura, J. Bonaventura, and J. S. Stamler, *Nature*, 1996, **380**, 221.
89. J. S. Stamler, L. Jia, J. P. Eu, T. J. McMahon, I. T. Demchenko, J. Bonaventura, K. Gernert, and C. A. Piantadosi, *Science*, 1997, **276**, 2034.
90. N.-L. Chan, P. H. Rogers, and A. Arnone, *Biochemistry*, 1998, **37**, 16459.
91. U. Flögel, M. W. Merx, A. Gödecke, U. K. M. Decking, and J. Schrader, *Proc. Natl. Acad. Sci. U.S.A.*, 2001, **98**, 735.

92. X. Xu, M. Cho, N. Y. Spencer, N. Patel, Z. Huang, H. Shields, S. B. King, M. T. Gladwin, N. Hogg, and D. B. Kim-Shapiro, *Proc. Natl. Acad. Sci. U.S.A.*, 2003, **100**, 11303.
93. A. Fago, A. L. Crumbliss, J. Peterson, L. L. Pearce, and C. Bonaventura, *Proc. Natl. Acad. Sci. U.S.A.*, 2003, **100**, 12087.
94. S. Ozaki, M. P. Roach, T. Matsui, and Y. Watanabe, *Acc. Chem. Res.*, 2001, **34**, 818.
95. R. A. Tschirret-Guth and P. R. Ortiz de Montellano, *Arch. Biochem. Biophys.*, 1996, **335**, 93.
96. L. Wan, M. B. Twitchett, L. D. Eltis, A. G. Mauk, and M. Smith, *Proc. Natl. Acad. Sci. U.S.A.*, 1998, **95**, 2825.
97. P. K. Witting, A. G. Mauk, and P. A. Lay, *Biochemistry*, 2002, **41**, 11495.
98. R. Roncone, E. Monzani, M. Murtas, G. Battaini, A. Pennati, A. M. Sanangelantoni, S. Zuccotti, M. Bolognesi, and L. Casella, *Biochem. J.*, 2004, **377**, 717.
99. S. Ozaki, T. Matsui, and Y. Watanabe, *J. Am. Chem. Soc.*, 1997, **119**, 6666.
100. T. Matsui, S. Ozaki, and Y. Watanabe, *J. Am. Chem. Soc.*, 1999, **121**, 9952.
101. T. Hayashi, Y. Hitomi, T. Ando, T. Mizutani, Y. Hisaeda, S. Kitagawa, and H. Ogoshi, *J. Am. Chem. Soc.*, 1999, **121**, 7747.
102. H. Sato, T. Hayashi, T. Ando, Y. Hisaeda, T. Ueno, and Y. Watanabe, *J. Am. Chem. Soc.*, 2004, **126**, 436.

Iron: Heme Proteins & Electron Transport

Bill Durham & Francis S. Millett
University of Arkansas, Fayetteville, AR, USA

1	Introduction	1
2	Function of Cytochromes	1
3	Structure and Mechanism of Cytochrome *c*	4
4	Structure of Cytochrome b_5	6
5	Experimental Methods for Studying Electron Transfer Reactions	7
6	The Cytochrome b_5–Cytochrome *c* Reaction	9
7	Cytochrome *c*–Cytochrome *c* Peroxidase Reaction	10
8	Cytochrome *c*–Cytochrome bc_1 Reaction	13
9	Cytochrome *c*–Cytochrome *c* Oxidase Reaction	16
10	References	18

Abbreviations

cyt = Cytochrome; Cc = Cytochrome *c*; yCc = Yeast iso-1- cytochrome *c*; CcP = Cytochrome *c* peroxidase; CcO = Cytochrome oxidase; 2Fe2S = Rieske iron-sulfur center; Ru-39-Cc = Ru(bpy)$_2$dmb-Cys-39-(H39C;C102T)-yCc; bpy = 2,2′-bipyridine; bpz = 2,2′-bipyrazine; bphb = 1,4-bis(2,2′-bipyridyl-4′-yl)benzene; qpy = 2,2′:4′,4″:2″,2‴-quaterpyridine; CDNP = 4-carboxy-2,5-dintrophenyl; TFA = Trifluoroacetyl; TFC = M-trifluoromethylphenylcarbamoyl.

1 INTRODUCTION

The cytochromes are a class of iron-containing heme proteins that are primarily involved in biological electron-transfer reactions. MacMunn[1] first discovered spectral evidence for the cytochromes in 1886 using a microspectroscope. He found that reduction of a variety of tissues from different organisms with ammonium hydrosulfide led to the appearance of a four-banded spectrum with absorption maxima at 604 nm, 566 nm, 550 nm, and 520 nm (Figure 1). These spectral features disappeared upon oxidation with hydrogen peroxide or ferricyanide. He named the material responsible for these spectral bands ‘‘histohematin’’. However, Levy[2] reported that many of these spectroscopic features could be mimicked by mixtures of hemoglobin derivatives. The influential chemist and editor Hoppe–Seyler[3] supported Levy's position and rejected MacMunn's discovery of a new class of compounds. It was not until 1925 that Keilin confirmed MacMunn's spectroscopic studies and named the new class of compounds ‘‘cytochromes’’, which means cellular pigments. In an elegant series of experiments, he found that the four-banded spectrum rapidly appeared in the flight muscles of a live wax moth during muscular activity, and then disappeared when the moth rested. Keilin's experiments were the first to establish a direct correlation between the chemical state of a cellular component and the physiological state of the organism. Keilin identified the absorption bands at 604 nm, 566 nm, and 550 nm as the α-bands of three different cytochromes, *a*, *b*, and *c*, respectively. The broadband at 520 nm is due to overlapping β-bands of the three cytochromes. A more detailed account of the discovery of cytochromes can be found in Keilin.[4]

The first isolation of cytochrome *c* (Cc) from yeast[5] was followed by more efficient isolation procedures to obtain highly purified Cc from beef heart with an iron content of 0.43%, corresponding to a MW of 12 600.[6] The interested reader should consult Moore and Pettigrew[7] and Scott and Mauk[8] for recent books on Cc. Mitochondrial Cc has a single iron-containing porphyrin (Figure 2) covalently attached to a polypeptide chain of 103–113 amino acids by thioether bridges to two cysteine sulfhydryl residues (Figure 3). The iron atom is ligated by the nitrogen atom of a histidine residue, and the sulfur atom of a methionine residue. In oxidized ferricytochrome c the Fe(III) has a single unpaired electron and the heme has a formal charge of +1, while in reduced ferrocytochrome *c* Fe(II) has no unpaired electrons and the heme has no formal charge. The reduction potential of mitochondrial Cc is +260 mV versus NHE. Cytochromes *c* have also been isolated from a wide variety of nonmitochondrial sources including bacteria, algae, plants, and animals. These Cc have as many as four heme groups, and reduction potentials ranging from −290 to +400 mV. The amino acid sequences of over 96 Cc have now been determined, more than for any other protein.

The *b* cytochromes contain noncovalently-attached protoheme in which the cysteine bridges are replaced by vinyl groups. The iron atom in most *b* cytochromes is ligated by two histidine nitrogen atoms, and has a redox potential of about 0 V. The 604 nm absorption band in reduced mitochondria is due to two *a*-type cytochromes, cyt *a* and cyt a_3, which are components of cytochrome oxidase (CcO) (*see* ***Cytochrome Oxidase***). A number of other classes of cytochromes have been discovered, including cytochrome peroxidases (CcP) (*see* ***Iron: Heme Proteins, Peroxidases, Catalases & Catalase-peroxidases***), cytochrome P-450, and cytochrome o (*see* ***Iron: Heme Proteins, Mono- & Dioxygenases***).

2 FUNCTION OF CYTOCHROMES

Eugene Kennedy and Albert Lehninger[9] discovered in 1948 that mitochondria are responsible for carrying out oxidative

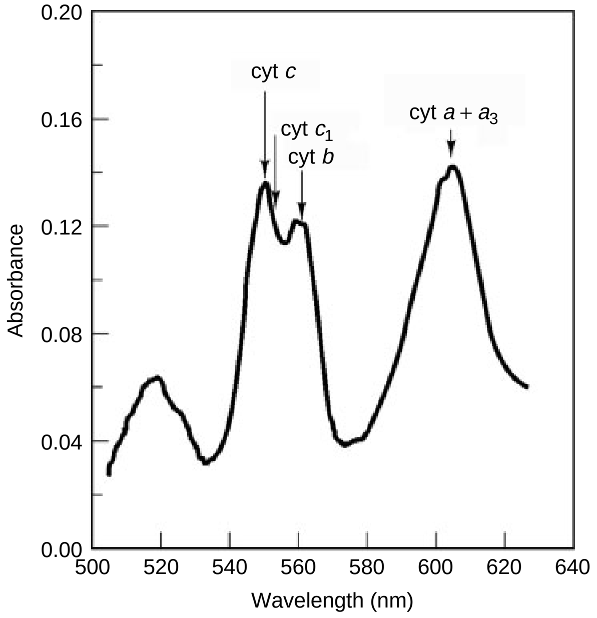

Figure 1 Visible absorption spectrum of cytochromes in beef heart mitochondria. The mitochondria were suspended at a concentration of 1 mg mL^{-1} and the reduced minus oxidized difference spectrum recorded. (Figure 5 (p. 14) from ''Mitochondria: A Practical Approach'' edited by Darley-Usmar *et al*. (1989). By permission of Oxford University Press)

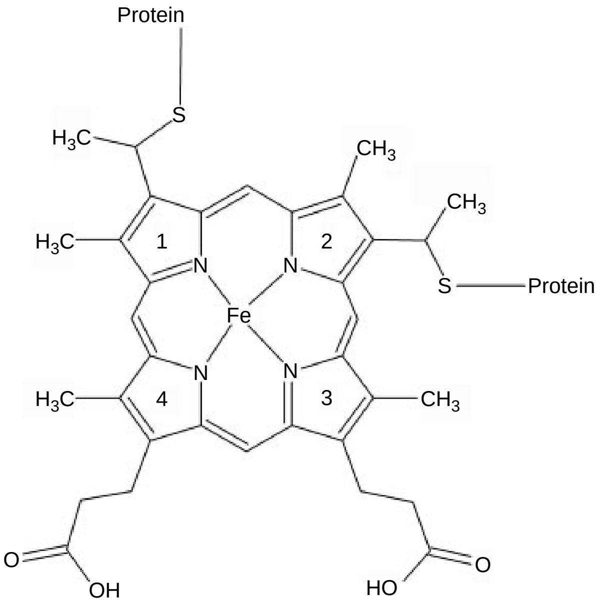

Figure 2 Iron-containing porphyrin (heme group) from cytochrome *c*

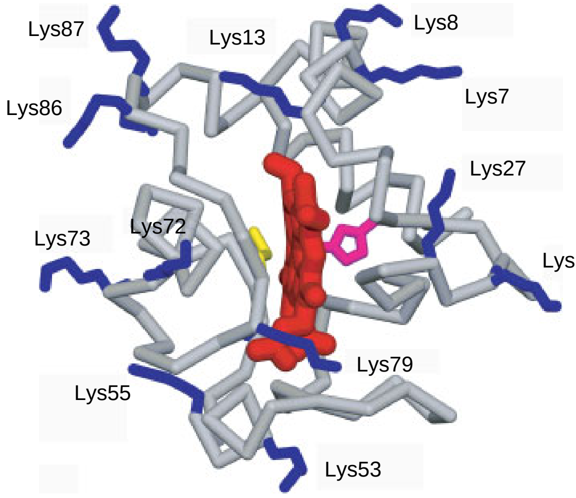

Figure 3 X-ray crystal structure of horse heart cytochrome *c*. Lysine residues surrounding the heme crevice are blue, and the heme is red

phosphorylation, the major energy transduction process in eukaryotic cells. Mitochondria are small organelles that are believed to have evolved from aerobic bacteria that established a symbiotic relationship inside primitive anaerobic eukaryotic cells. Mitochondria typically have a length of 1 to 2 µm, and have two membranes (Figure 4). The outer membrane is unfolded and is permeable to ions and molecules smaller than about 5000 Da. The inner membrane is highly folded into cristae, and is impermeable to most small molecules and ions. The inside aqueous phase, or matrix, is a very concentrated solution of proteins including the citric acid cycle enzymes, fatty acid oxidation enzymes, as well as many others. The mitochondrial respiratory chain consists of four large protein complexes that are an integral part of the inner mitochondrial membrane. The transport of two electrons from nicotinamide adenine dinucleotide (NADH) to oxygen by this respiratory chain is accompanied by the translocation of about 11 protons from the inside to the outside of the inner mitochondrial membrane. The stored free energy of the resulting proton gradient is then used to translocate protons across the ATP synthase complex, resulting in the synthesis of one molecule of ATP for every three protons transported. Enormous progress has been made in our understanding of the molecular mechanism of the mitochondrial electron-transport chain over the past decade. X-ray crystal structures have been determined for three of the four electron-transfer complexes: succinate–ubiquinone reductase, cytochrome bc_1, and CcO. The X-ray crystal structure has also been determined for the F_1 component of ATP synthase, as well as a portion of the F_o component. The roles of many individual amino acids in these complexes have been determined by site-directed mutagenesis studies, and powerful new techniques have been developed to study rapid electron-transfer reactions within and between the complexes.

The first complex in the respiratory chain, NADH:ubiquinone oxidoreductase (complex I), transfers two electrons from matrix NADH to ubiquinone to form ubiquinol. This

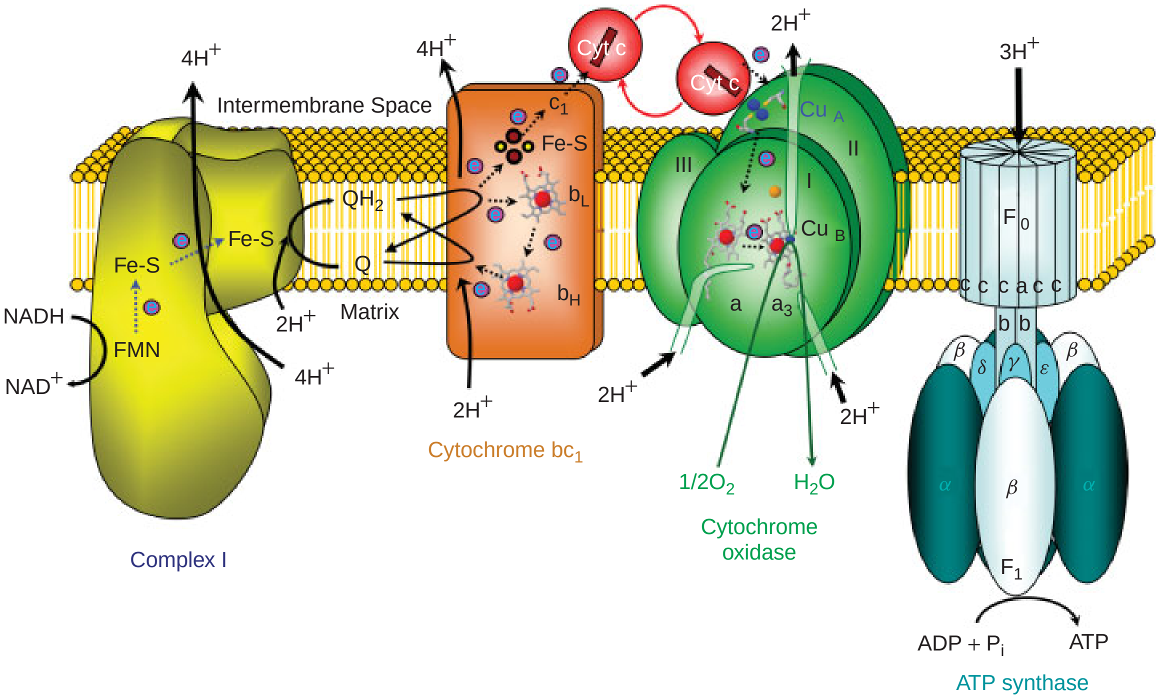

Figure 4 Mitochondrial electron-transport chain

electron-transfer reaction is coupled to the translocation of 4 protons across the inner mitochondrial membrane. NADH:ubiquinone oxidoreductase is the largest and least understood complex of the mitochondrial respiratory chain, containing 45 polypeptide chains, seven iron–sulfur centers, and one flavin mononucleotide (FMN), with a total molecular weight of nearly 1 million Da. The cyt bc_1 complex is perhaps the most universal electron-transfer complex, and is found in many prokaryotes and photosynthetic bacteria as well as eukaryotic mitochondria.**[10]** The X-ray crystal structure has been determined for cyt bc_1 from bovine, chicken, and yeast mitochondria.**[11–14]** The enzyme from bovine mitochondria is a dimer with 11 polypeptide chains and molecular weight of 250 000 Da monomer. The complex contains two b cytochromes ($\mathrm{b_L}$ and $\mathrm{b_H}$) located on a single transmembrane polypeptide chain, and cyt c_1 and the Rieske iron–sulfur protein (2Fe2S) located on the cytoplasmic side of the membrane. Electron transfer through the complex involves a Q-cycle mechanism in which four protons are translocated to the positive (P) side of the membrane per two electrons transferred from ubiquinol to Cc (see Section 8). The major function of Cc is to transport electrons from the cyt bc_1 complex to CcO. It is a very positively charged protein, and is known to bind to both cyt c_1 and CcO by means of electrostatic interactions. Detailed chemical modification experiments in three separate laboratories have shown that the lysine amino groups immediately surrounding the heme crevice of Cc are involved in binding to negatively charged domains on both cyt c_1 and CcO (see Section 3.). Since the binding domain on Cc for these two proteins is nearly identical, Cc must function as a mobile electron shuttle during electron transport. Cytochrome *c* oxidase, the terminal member of the mitochondrial electron-transport chain, sequentially accepts four electrons from Cc and uses them to reduce molecular oxygen to water. This electron-transfer reaction is coupled to the pumping of four protons across the mitochondrial membrane. CcO from bovine heart is a dimer with 13 subunits and a molecular weight of 200 000 Da per monomer. The enzyme contains four redox centers, $\mathrm{Cu_A}$, heme a, heme $\mathrm{a_3}$, and $\mathrm{Cu_B}$. The X-ray crystal structure has been determined for CcO from bovine heart and *Paracoccus denitrificans* (*P. denitrificans*).**[15,16]** (see Section 9; *see* ***Cytochrome Oxidase***).

A number of other cytochromes are located in the intermembrane space and the inner surface of the outer mitochondrial membrane. Cyt b_5 (cytochrome b_5) is a small heme protein with a hydrophilic domain of about 95 amino acids and a carboxyl terminus of about 45 hydrophobic amino acids that serve to anchor the protein to the inner surface of the outer mitochondrial membrane.**[17]** Cyt b_5 is reduced by NADH-cyt b_5 reductase, also located on the inner surface of the outer membrane. Under conditions of high intermembrane ionic strength, Cc is released from the inner membrane, and can transport electrons from cyt b_5 on the outer membrane to CcO on the inner membrane. Cyt b_5 contains protoheme *b* with the iron atom ligated by two histidine nitrogen atoms. The heme group has a reduction potential of +10 mV versus NHE. Cyt b_5 is also found on the liver endoplasmic reticulum membrane, where it transfers electrons from NADH-cyt b_5

reductase to fatty acid desaturase and cytochrome P-450. A form of cyt b_5 lacking the hydrophobic tail is found in red blood cells, where it reduces the ferric iron of Met-hemoglobin back to the ferrous state that is active in oxygen transport.

Several larger enzymes present in the intermembrane space contain a cyt *b* domain that is homologous to cyt b_5. Sulfite oxidase located in the intermembrane space of liver mitochondria carries out the terminal step in the degradation of sulfur amino acids, the oxidation of sulfite to sulfate accompanied by the reduction of two molecules of Cc.[18] Sulfite oxidase is a dimer of two identical chains of 60 000 Da. Each subunit contains two domains, a large domain of 50 000 Da containing a molybdenum prosthetic group, and a small domain of 10 000 Da containing cyt *b*. The small cyt *b* domain can be released from the large domain by tryptic hydrolysis, and is quite homologous to cyt b_5 in terms of amino acid composition and redox properties. In the reaction of this enzyme, sulfite is oxidized to sulfate by the molybdenum cofactor, and the electrons are then transferred to cyt *b*. Cc present in the intermembrane space then transports electrons from cyt *b* of sulfite oxidase to CcO. Flavocytochrome b_2 located in the intermembrane space of yeast mitochondria catalyzes the two-electron oxidation of L-lactate to pyruvate followed by reduction of two molecules of Cc. It is a tetramer of identical subunits, each with a molecular weight of 57 500. The crystal structure[19] revealed that each subunit is composed of two domains, one binding an FMN prosthetic group and the second binding cyt *b*. The cyt *b* domain is quite homologous to cyt b_5. Lactate is oxidized by FMN, and the electrons are then transferred to cyt *b*. Cc then transports the electrons from cyt *b* to CcO. The intermembrane space of yeast mitochondria also contains cytochrome *c* peroxidase, which carries out the two-electron reduction of hydrogen peroxide to water accompanied by the oxidation of two molecules of ferrocytochrome *c* (see Section 7; *see* ***Iron: Heme Proteins, Peroxidases, Catalases & Catalase-peroxidases***). Cc plays a central role as a mobile shuttle in transporting electrons between the outer membrane, the intermembrane space, and the inner membrane. In addition, release of Cc from the mitochondrial membrane triggers the process of apoptosis, or programmed cell death. A wide variety of different cytochromes are found in other organisms and tissues.

3 STRUCTURE AND MECHANISM OF CYTOCHROME *c*

High-resolution X-ray crystal structures have been determined for cytochrome *c* from many different organisms, including yeast (*S. cerevisiae*, iso-1-cyt *c*),[20] rice,[21] horse,[22] tuna,[23] and bonita.[24] Cc from these organisms contains one heme group bound to the protein matrix by two thioether links from the edge of the porphyrin ring to Cys14 and Cys17. The axial positions of the iron are bound to His18 and Met80. Cc from these organisms contain between 103–111 amino acids and share many of the same structural features (Figure 3). They are globular in shape with slightly less than half of the amino acids organized into five α-helices (3–12, 50–55, 61–69, 70–75, and 88–101). The α-helices are separated by six type II 3_{10} bends (21–24, 32–35, 35–38, 39–42, 43–46, and 75–78) and 4 Ω loops (18–32, 34–43, 40–54, and 70–84) with no β-stranded structures. The heme is almost completely buried in the folded protein with only about 4% exposed to the protein surface. A relatively large number of hydrogen bonds in addition to those contributing the α-helical structures provide added stability to the overall structure. Moore and Pettigrew have reviewed the structural features in detail.[7] The amino acids in van der Waals contact with the buried heme macrocycle provide a very hydrophobic environment for the iron, which plays an important role in controlling the redox potential of the heme and the energetics of electron transfer. Interestingly, there are two propionate groups on the heme that are completely buried inside the protein, and at least one of these is probably deprotonated at pH 7. The X-ray structures indicate that there are several amino acid side chains, which could potentially interact through hydrogen bonds or salt bridges with the propionates.

The surface residues of Cc are divided nearly equally between hydrophobic and hydrophilic types. The charged hydrophilic residues are mainly lysines and these tend to cluster around the exposed heme edge and along the sides as indicated in Figure 5. The segregation of charged residues is not totally exclusive. A few carboxylates are scattered over the periphery of the front surface and some lysines are on the back surface. The overall protein is basic with an isoelectric point of 10 and a net charge of +7 at pH 7. Cytochome *c* undergoes significant but reversible changes in conformation at the extremes in pH. Theorell and Akesson[25] have shown that the oxidized form exists in at least five different conformational states over the range of pH from 0 to 13 and the reduced form exists in at least three different conformations. Some of the conformational changes found at high pH appear to involve changes in coordination of the iron, for example, displacement of Met80. The conformation changes are extremely complex and the interested reader should consult Moore and Pettigrew[7] and the extensive list of references cited.

An important question related to the function of Cc is whether or not there are significant differences in the structures of the oxidized and reduced forms of the protein. Structural differences could lead to energetic barriers to electron transfer in the form of reorganizational energies or conformational changes which could regulate the electron-transfer process. There are many chemical differences between the redox states of Cc but it is not clear that these are of consequence in the biological function of Cc.[7,26] For example, under a number of potentially denaturing conditions the oxidized form appears to be less stable than the reduced form. Ferrocytochrome c appears to be resistant to trypsin

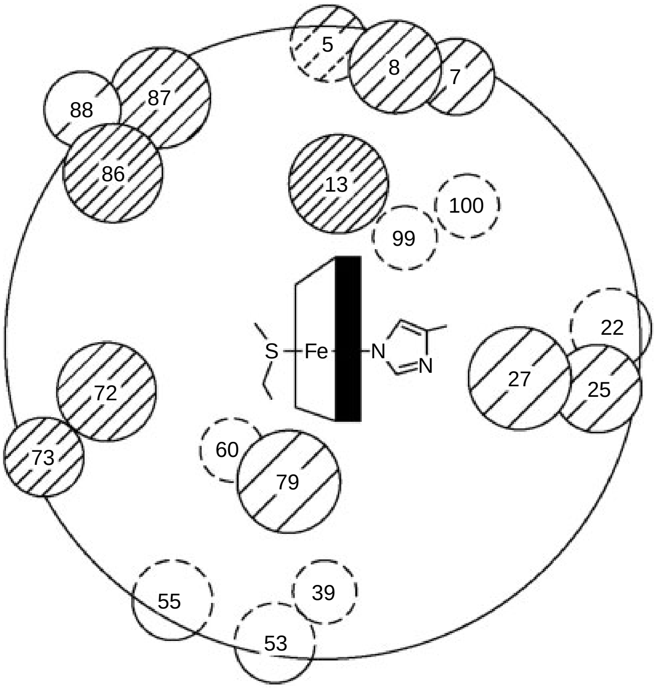

Figure 5 A schematic diagram of horse heart cytochrome *c* viewed from the front of the heme crevice. The approximate positions of the β-carbon atoms of the lysine residues are indicated by *closed* and *dashed* circles for residues located toward the front and back of Cc, respectively. The electrostatic free energy contribution of lysine i, V_i, is indicated by the number of diagonal marks in the circle, with $-0.4\,\mathrm{kJ\,M^{-1}}$ per hatch mark. The binding domain is essentially the same for CcO and cytochrome bc_1

digestion whereas ferricytochrome *c* is not. The binding of small ions and interaction with chromatographic materials appear to be redox-state dependent. Ferricytochrome *c* and ferrocytochrome *c* have different crystal forms and the two cannot be interconverted without damaging the crystals. The X-ray crystal structures indicate that there is little difference in the coordination of the iron between the two redox forms, and the heme is low spin in both oxidation states. Moore and Pettigrew[7] indicate that the differences in iron displacement out of the porphyrin ring plane in mitochondrial Cc are much smaller than those observed in simple porphyrin complexes. Evidence regarding the changes in the remainder of the protein is more ambiguous. X-ray crystallographic studies have indicated that there are no substantial differences in the structures of Fe(III) and Fe(II) forms of horse Cc.[27,28] However, small differences (on the order of an angstrom or less) were noted in the locations of some of the side chains which are consistent with NMR studies. X-ray studies of the bacterial cytochromes *Rhodospirillum rubrum* c_2[29] and *Pseudomonas Aeruginosa* *c*-551[30] show little difference in structure for oxidized and reduced forms.

The mechanism by which Cc transports electrons from the cyt bc_1 complex to CcO is very complicated. An important question posed in the early 1970s is whether Cc binds to cyt bc_1 and CcO at separate sites, or instead has a single binding site for both proteins, and functions as a mobile electron shuttle. It was known that Cc binds to both proteins by means of electrostatic interactions, so the search for binding sites focused on the positively charged domains of Cc. Upon examining the crystal structure, Takano *et al.*[31] proposed that the cyt bc_1 complex might bind to the ''left channel'' of Cc defined by residues 55 to 75 that form a loop surrounding hydrophobic residues that lead from the surface of the protein to the heme. The eight lysine residues at the periphery of the channel would bind the cyt bc_1 complex electrostatically, while the aromatic residues Tyr74 and Tyr67 would form an electron-transfer pathway. Takano *et al.* also proposed that CcO binds to the ''right channel'' bounded by residues 1 to 20 and 89 to 101. This channel is also surrounded by lysine residues, and contains the aromatic residues Phe10 and Tyr97 that could transfer electrons from the heme to CcO. In contrast, Salemme *et al.*[32] proposed that both the cyt bc_1 complex and CcO bind to the front of Cc, and that electrons are transferred directly through the exposed edge of the heme. The highly conserved lysine amino groups surrounding the heme crevice of Cc would bind to negatively charged residues on the cyt bc_1 complex and CcO.

Several different laboratories addressed this question experimentally in an extensive series of chemical modification studies to map the binding domain on Cc for the partners. These studies focused on preparing derivatives in which single lysine amino groups were modified to form uncharged or negatively charged groups. Margoliash and coworkers[33,34] prepared 12 different derivatives modified at single lysine residues with the negatively charged 4-carboxy-2,5-dinitrophenyl (CDNP) group, while Millett and coworkers[35–37] prepared 17 derivatives modified with a neutral trifluoracetyl (TFA) or trifluoromethylphenylcarbamoyl (TFC) group. Enzyme kinetic studies[38–40] revealed that modification of any of the lysines immediately surrounding the heme crevice inhibited the binding interaction with both the cyt bc_1 complex and CcO (Figure 5). Using a different approach, Rieder and Bosshard[41] found that these lysine residues were protected from acetylation by complex formation with either the cyt bc_1 complex or CcO. The combined results of these three research groups have demonstrated that the binding domain for both proteins is located at the heme crevice, and that the lysines immediately surrounding the heme crevice help bind the redox partners. Since the binding domains for the cyt bc_1 complex and CcO are the same, Cc must function as a mobile shuttle during electron transport.

Smith *et al.*[42] estimated the contribution V_i that a positively charged amino group on lysine *i* makes to the total electrostatic free energy of binding by comparing the decrease in binding strength due to modification of lysine *i* with the neutral TFA or TFC groups, or the negatively charged CDNP group. These V_i values are represented on Figure 5 as the number of hatch marks on the circle for each lysine. Smith *et al.* went on to develop a semi-empirical relationship representing the electrostatic interaction between Cc and its redox partners by specific complementary charge-pair interactions. This relationship agrees quantitatively with the ionic-strength dependence of the reactions of native Cc with CcO and the cyt bc_1 complex. The interaction with the oxidase involves 8 electrostatic interactions, with interaction energies ranging from $-5.0\,\mathrm{kJ\,mol^{-1}}$ to $-1.3\,\mathrm{kJ\,mol^{-1}}$ (Figure 5). The total electrostatic energy of binding is $-25\,\mathrm{kJ\,mol^{-1}}$ at 50 mM ionic strength. The interaction with the cyt bc_1 complex involves 7 electrostatic interactions, with a total electrostatic energy of binding of $-21\,\mathrm{kJ\,mol^{-1}}$ at 0.2 M ionic strength.

The studies reported above lead to the prediction that the interaction site on CcO consists of a cluster of carboxylate residues. Millett *et al.*[43] found that the water-soluble carbodiimide 1-ethyl-3-[3-(dimethylamino)propyl]carbodiimide (EDC) specifically modified five carboxylate groups on subunit II of CcO and inhibited the reaction with Cc. Binding one molecule of Cc to CcO protected Asp112, Glu114, Asp115, and Glu198 from modification by EDC, and prevented the loss in electron-transfer activity. These studies suggest that the negatively charged carboxylate groups on these residues are involved in binding Cc. Glu198 is located between the conserved cysteines 196 and 200 that have been shown to ligand $\mathrm{Cu_A}$.[44] Thus, it is possible that $\mathrm{Cu_A}$ is the initial electron acceptor in CcO. Asp112, Glu114, and Asp115 are located in a highly conserved sequence (104–115) containing alternating acidic and aromatic residues that could serve as an electron-transfer pathway from Cc to cyt *a* or $\mathrm{Cu_A}$. Stonehuerner *et al.*[45] used EDC to identify the binding domain on the cyt bc_1 complex for Cc. EDC selectively labeled carboxylate groups in the sequence 63–81 of cyt c_1, and Cc binding protected these residues from labeling. This highly acidic sequence contains 7 Asp and Glu residues that could be involved in binding Cc. Broger *et al.*[46] have shown that arylazido–lysine 13 Cc is cross-linked to cyt c_1 somewhere in the highly acidic sequence 165–174, suggesting that carboxylate groups in this region are also involved in Cc binding. The highly acidic ‘‘hinge’’ protein in the cyt bc_1 complex is also involved in binding Cc.[47]

4 STRUCTURE OF CYTOCHROME b_5

Cytochrome b_5 exists in a soluble form in erythrocytes and in a membrane bound form in microsomes. A soluble derivative of hepatic cyt b_5 with 93 amino acids can be isolated by treatment of microsomes with pancreatic lipase[48] and this form has essentially the same amino acid sequence as the erythrocyte protein.[49] Further treatment of the soluble form with trypsin cleaves two residues from the N-terminal and seven from the carboxylate-terminal and leaves the heme core with only 84 residues. Rat liver cyt b_5 has been prepared by expression in *Eschericha coli* (*E.coli*). The structure[50] of calf liver cyt b_5 obtained by treatment with pancreatic lipase is illustrated in Figure 6. In contrast to Cc, the porphyrin ring in cyt b_5 is not covalently bound to the protein side chains. The heme is held in a hydrophobic pocket by axial coordination to His63 and His39. As in Cc, most of the residues in van der Waals contact with the porphyrin ring contain bulky hydrophobic side chains. The amino acids of cyt b_5 fold around the porphyrin ring forming six short α-helices separated by a number of β bends. A small region of β-pleated sheet structure can be found near the center of the molecule formed by residues 5–7, 74–80, 27–32, 21–25, and 51–54. The porphyrin ring in cyt b_5 is more exposed to the protein surface than that of Cc. Dixon *et al.*[51] calculated an exposed heme to protein surface area ratio of 0.007 and 0.038 for Cc and cyt b_5, respectively. Both hydrophobic and hydrophilic residues can be found on the surface of cyt b_5. Unlike Cc, however, acidic residues are more dominant than basic residues. The distribution of acidic residues is very uneven with 11 of the 18 carboxylates located on the top half of the protein near the exposed heme edge. The dominance of carboxlate groups gives the protein an overall acidic character with a charge at pH 7 of −9.[52]

An interesting feature of the crystal structure of cyt b_5 are the heme propionate groups shown in Figure 6. One of the propionate groups extends into the solvent while the other folds back and is hydrogen bonded to Ser64. In Cc, the porphyrin ring is turned by 90° such that the propionates are not exposed to the solvent. Single crystals of the oxidized form of cyt b_5 can be reduced with sodium dithionite. Upon reduction, crystals turn from red to orange without cracking and remain isomorphous with the oxidized form. The structures of the oxidized and reduced forms are practically identical.

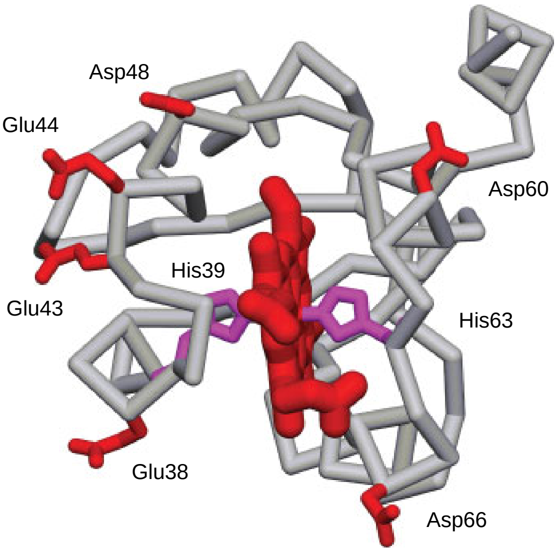

Figure 6 X-ray crystal structure of bovine cytochrome b_5. Acidic residues are red and the heme is red

5 EXPERIMENTAL METHODS FOR STUDYING ELECTRON TRANSFER REACTIONS

The investigation of electron transfer in biological systems over the last two decades can be separated into two general areas: (1) intraprotein electron transfer between metal centers covalently bound to the same protein scaffold and (2) interprotein electron transfer between two separate proteins. The two areas evolved from the realization that many electron-transfer reactions in biological systems appear to take place with large distances separating the metal centers. Thus, the mechanism of long-distance electron transfer became a fundamental component of understanding electron transfer in biological systems. Investigation of intraprotein electron transfer focused initially on artificial systems designed to allow investigators to manipulate the distance between redox centers. Concurrently, many investigators focused on natural systems containing multiple redox centers in the same large protein. The photosynthetic reaction center contains a series of redox centers and is among the most thoroughly investigated.

Photosynthetic reaction centers offer an inherent advantage in the fact that the electron-transfer reactions are activated by light. Thus, very fast laser-based kinetic methods, called laser flash photolysis, can be applied to follow the time course of the reactions. The initial electron transfer step in these systems occurs in approximately 2 ps and is followed by several subsequent steps that are progressively slower. Numerous investigators have focused their attention on these reactions, which are described elsewhere (*see* ***Photosynthesis***).

Three fundamental parameters govern electron transfer: (1) the distance between the redox centers, (2) the difference in the redox potentials of the centers, and (3) the reorganizational barrier, which is related to the difference in the geometries of the oxidized and reduced forms of each of the proteins. Studies of photosynthetic reaction centers have been extremely useful in characterizing the importance of these parameters. In order to further expand this characterization, researchers have developed methods to introduce artificial redox centers into biological systems. The most common strategy involved covalent attachment of ruthenium complexes to specific sites on the surface of small proteins. In other investigations, the iron center of the metalloprotein was changed, commonly to zinc. The results of these studies provided much of our fundamental understanding of the electron-transfer process (*see* ***Long-range Electron Transfer in Biology***).

Surface modification with ruthenium complexes has proven valuable in studies of both interprotein and intraprotein electron transfer in systems that are difficult to study by traditional kinetic tools.[53] The choice of ruthenium complexes in these investigations stems from an extensive photochemistry as well as exceptional thermal stability. The photochemistry provides a means of examining reactions over a time range of nanoseconds to seconds by laser-flash photolysis and the thermal stability allows researchers to covalently bind a wide variety of complexes to proteins with some assurance that the labeled proteins will be stable in subsequent investigations. As a specific example, the use of a ruthenium-labeled cyt b_5 derivative that was designed for the study of both intraprotein- and interprotein electron transfer is described in the following paragraphs.[54,55]

The derivative, Ru-65-cyt b_5, was prepared by the reaction of 4-bromomethyl-4′-methylbipyridine) Ru(bipyridine)$_2{}^{2+}$ with cyt b_5 that was genetically engineered to place a cysteine at residue 65 of the protein backbone.[54] The reaction involves the elimination of HBr and the formation of a thioether linkage between the 4 methylene carbon of the bipyridine and the cysteine sulfur. The ruthenium complex bound to Cys65 is separated by 12 covalent bonds from His63, which ligates the heme iron as shown in Figure 7. Electron transfer is initiated by exposing Ru-65-cyt b_5 to a short laser flash which excites the resting state, designated as $\mathrm{Ru^{II}Fe^{III}}$, to the excited state, $\mathrm{Ru^{II^*}Fe^{III}}$ (Scheme 1). One of the remarkable properties of these ruthenium complexes is the long excited-state lifetime, typically hundreds of nanoseconds under the conditions of the experiment. The natural decay of the excited state is described by k_d. The excited state Ru(II*) is a strong reducing agent

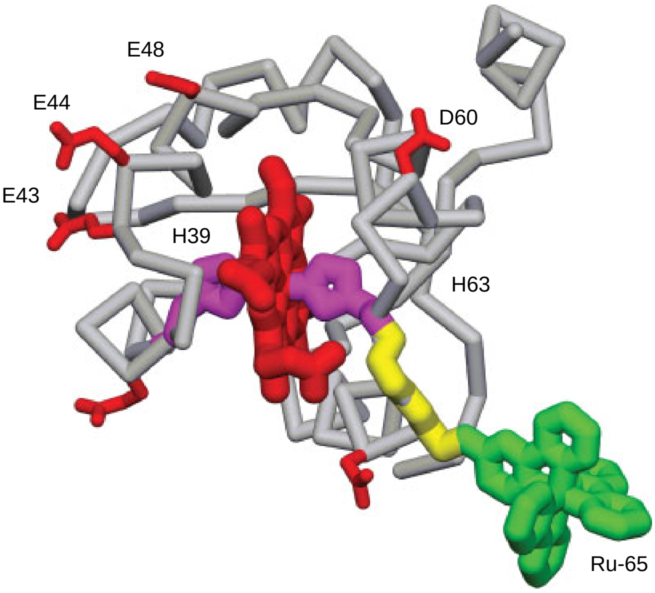

Figure 7 Electron-transfer pathway between ruthenium complex and heme in Ru-65-cyt b_5. The heme group, amino acid residues 63, 64, and 65, and the ruthenium complex are highlighted

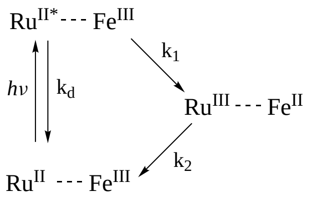
$\mathrm{Ru^{II*}}$ - - - $\mathrm{Fe^{III}}$
k_1
$h\nu$
k_d
$\mathrm{Ru^{III}}$ - - - $\mathrm{Fe^{II}}$
k_2
$\mathrm{Ru^{II}}$ - - - $\mathrm{Fe^{III}}$

Scheme 1

and rapidly reduces the heme Fe(III) to Fe(II). The resulting ground-state Ru(III) is an extremely strong oxidant and rapidly oxidizes Fe(II) to return the system to the original state. Since the system can be initiated with a laser pulse having a duration of only a few nanoseconds, the time course of the reaction can be followed easily by monitoring the absorbance changes at appropriate wavelengths. The transient absorbance change at 556 nm shows the rapid formation of reduced cyt b_5 followed by a slightly slower reoxidation (Figure 8).[55] The measured rate constants are $k_d = 3 \times 10^6\,s^{-1}$, $k_1 = 12 \times 10^6\,s^{-1}$, and $k_2 = 8.5 \times 10^6\,s^{-1}$. These electron-transfer reactions were further examined using a series of ruthenium complexes with different ligands, which altered the redox potentials over a wide range. A study of the dependence of the rate of reaction on the overall driving force was performed using this strategy.[55] The results were interpreted using the Marcus theory of electron transfer, which in its simplest form is given by equation (1):[56]

$$k_{et} = k_o \exp[-\beta(r - r_o)] \exp\left[\left(-\frac{(\Delta G^{\circ\prime} + \lambda)^2}{4\lambda RT}\right)\right] \qquad (1)$$

where r is the distance between the closest macrocycle atoms in the two redox centers, the van der Waals contact distance $r_o = 3.6$ Å, λ is the reorganization energy, $\Delta G^{\circ\prime}$ is the driving force, $\beta = 1.4$ Å^{-1}, and the nuclear frequency $k_o = 10^{13}\,s^{-1}$. Dutton and coworkers have found that a wide range of biological electron-transfer systems can be described by this system using the parameters given above.[57] The driving force dependence of the electron-transfer rate constants for Ru-65-cyt b_5 were fitted to equation (1) with $r = 13$ Å, and $\lambda = 0.94$ eV (Figure 9). The experimental r value is in good agreement with the actual distance between the ruthenium complex and the heme group, while the reorganization energy is in good agreement with the predicted value. Beratan and Onuchic have developed a pathway theory for electron transfer which involves a combination of covalent bond, hydrogen bond, and through-space contributions to the pathway.[58] The kinetic data for Ru-65-cyt b_5 are also in good agreement with this theory, with a pathway consisting of 12 covalent bonds separating the bipyridine ligand of the ruthenium complex and the axial histidine ligand of the heme iron.

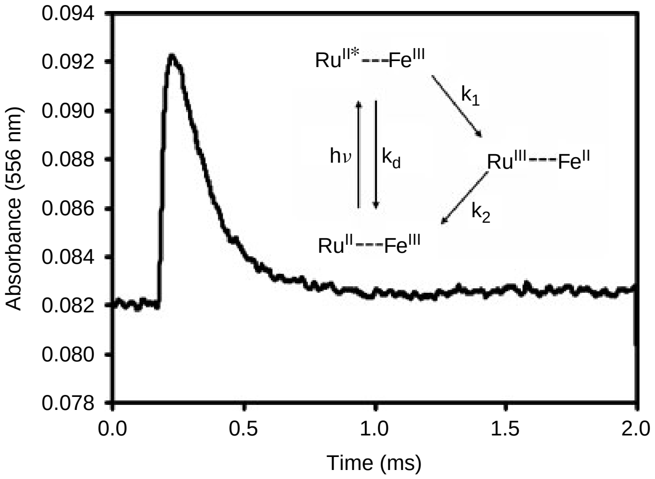

Figure 8 Photoinduced electron transfer in Ru-65-cyt b_5. The transient absorbance at 556 nm was measured following flash photolysis of 12 µM Ru-65-cyt b_5[55]

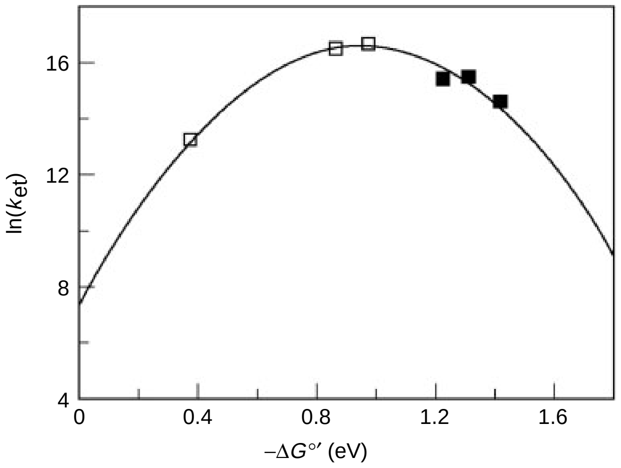

Figure 9 Plot of lnk_{et} as a function of free energy for electron-transfer reactions of Ru-65-cyt b_5 labeled with different ruthenium polypyridine complexes. The solid line shows the theoretical dependence of equation (1) calculated with a reorganizational energy of 0.94 eV and a distance r of 13 Å. The open boxes are for the reactions involving the excited state, $k_{et} = k_1$, and the filed boxes are for the thermal back reactions, $k_{et} = k_2$, all determined at 22 °C. (Reprinted with permission from Ref. 55. © 1993 American Chemical Society)

The interprotein electron-transfer reactions of Ru-65-cyt b_5 can be studied using a sacrificial electron donor such as aniline to reduce Ru(III) and prevent the back reaction k_2, as described in Scheme 2. Appropriate sacrificial electron donors can also reduce Ru(II*) to Ru(I), which then reduces Fe(III) as shown in the top pathway of Scheme 2. Cyt b_5 is rapidly reduced by either pathway, and is then poised to transfer an electron to another protein. The reaction of cyt b_5 with Cc using this methodology will be described in the next section. Covalent labelling of Cc with ruthenium complexes and subsequent flash photolysis has provided a

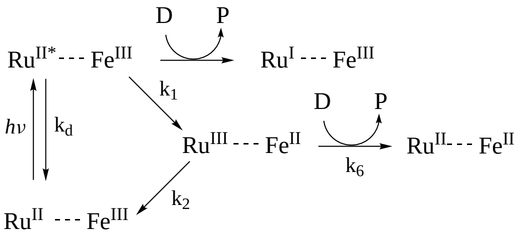

Scheme 2

means of examining the reactions of Cc with CcO, the cyt bc_1 complex, CcP and plastocyanin. More details on these studies are provided in the following sections.

Modification of larger proteins with ruthenium complexes, while possible, have proven difficult. Fortunately, a ruthenium labeled partner such as Cc can be used to rapidly inject or remove an electron from the large protein complex, and thus study internal electron-transfer reactions. In a complementary approach, Nilsson found that the excited state of $Ru(bpy)_3{}^{2+}$ can inject an electron into CcO.[59] The ruthenium complex binds electrostatically to the protein in a location similar to that occupied by Cc. The initial site of electron transfer is the Cu_A site, as it is when Cc is the electron donor. The simplicity of this technique makes it very attractive since it eliminates any modification of the protein which might alter the structure. Sadoski *et al.* showed that significant improvements in the yield of electron transfer could be obtained with ruthenium complexes of higher charge. One specific complex used was the dinuclear complex $[(bpy)_2Ru(qpy)Ru(bpy)_2]^{4+}$ (Figure 10).[60]

6 THE CYTOCHROME b_5–CYTOCHROME c REACTION

The reaction between cyt b_5 and Cc has served as a prototype of biological electron-transfer reactions because both proteins are small, well-characterized, and have known X-ray crystal structures. Ferrocytochrome b_5 rapidly reduces ferricytochrome c in a reaction that proceeds through a bimolecular complex stabilized by electrostatic interactions. In the first molecular modeling study of an electron-transfer complex, Salemme[61] proposed that the two proteins form a 1:1 complex stabilized by complementary charge-pair interactions between negatively charged carboxylate groups surrounding the heme crevice of cyt b_5 and lysine amino groups surrounding the heme crevice of Cc. The heme groups of the two proteins are nearly coplanar in the model, with their edges separated by 8.4 Å. Ng *et al.*[62] found that modification of lysines 13, 25, 27, 72, or 79 surrounding the heme crevice of Cc with TFA or TFC significantly decreased binding to cyt b_5. Rodgers *et al.*[63] found that substitution of Glu48, Asp60, Glu43, or Glu44 on cyt b_5 with glutamine or asparagine residues decreased the binding strength for the complex with Cc by a factor of about 2. A number of other biophysical studies have provided experimental support for Salemme's model[64–68] and indicate that lysines 13, 25, 27, 72, and 79 on Cc form charge-pair interactions with the cyt b_5 carboxylate groups on Asp48, Glu43, Glu44, Asp60, and the most exposed heme propionate group, respectively. NMR and molecular dynamics studies have indicated that the complex is not static as in the original Salemme model, but rather exists in a dynamic equilibrium between several different conformations.[69–71]

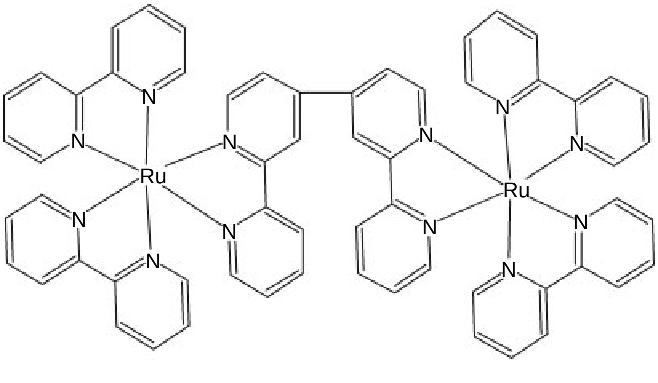

Figure 10 Structure of $[(bpy)_2Ru(qpy)Ru(bpy)_2]^{4+}$

The electron-transfer reaction between ferrocytochrome b_5 and ferricytochrome c has been studied using a number of different methods. Stopped-flow studies indicated that the reaction is second order above 0.1 M ionic strength, and that the rate constant rapidly decreases with increasing ionic strength.[72] McLendon and Miller used pulse radiolysis to measure a rate constant of $1600 \pm 700\,s^{-1}$ for intracomplex electron transfer at low-ionic strength.[73] The reaction between cyt b_5 and Cc has been extensively studied by Willie *et al.*[54] using the ruthenium-based methodology described in Section 5. The labeled derivative Ru-65–cyt b_5 (Figure 11) was designed specifically to investigate the interprotein electron-transfer reactions of cyt b_5. The position of the ruthenium complex on the surface of Ru-65–cyt b_5 was selected to promote rapid photoinduced electron transfer from ruthenium to the heme group, but not interfere with the binding of redox partners such as Cc (Figure 11). Laser excitation of the Ru-65–cyt b_5–horse Cc complex formed at low-ionic strength resulted in rapid electron transfer from Ru^{II*} to the Ru-65–cyt b_5 heme group, followed by biphasic electron transfer to the Cc heme group with rate constants of $4 \times 10^5\,s^{-1}$ and $3 \times 10^4\,s^{-1}$ (Figure 12). Low-ionic strength favors electrostatic interaction between the proteins and formation of a 1:1 protein–protein complex. At high-ionic strength where the proteins do not form a complex, the reaction is second order and dominated by diffusion rather than electron transfer. Under these conditions, the ruthenium methodology yields the same rate constants as for the reaction between unmodified cyt b_5 and Cc. The overall results are consistent with recent ionic-strength calculations by Sivozhelezov.[74]

Wendoloski *et al.*[71] carried out molecular dynamics studies of the complex between cyt b_5 and Cc, and reported that complex formation altered the position of the side chain on Cc residue Phe82 to a new position between the two heme groups. This led to the proposal that the aromatic ring on Phe82 may act as an electron-transfer bridge between the heme groups of cyt b_5 and Cc. However, Willie *et al.* found that substitution of Phe 82 with Tyr, Gly, Leu, or Ile did not change the rate

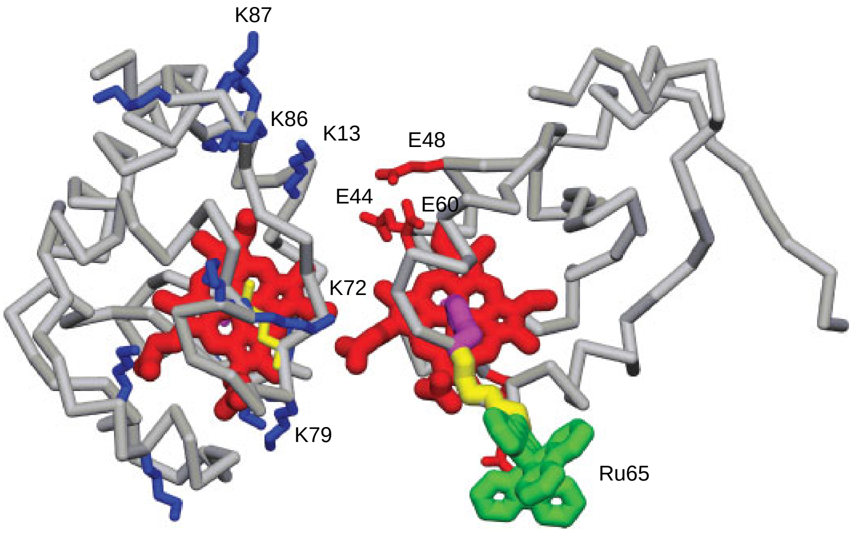

Figure 11 Molecular model of the complex between Ru-65-cyt b_5 and Cc. The geometry of the complex is the same as that of the complex involving native cytochrome b_5 proposed by Salemme. The heme groups (red), and the ruthenium complex (green) are highlighted. The atoms forming an electron-transfer pathway between the ruthenium complex and the heme group of Ru-65-cyt b_5 are colored yellow. The lysine and arginine residues are blue, while aspartate and glutamate residues are red[54]

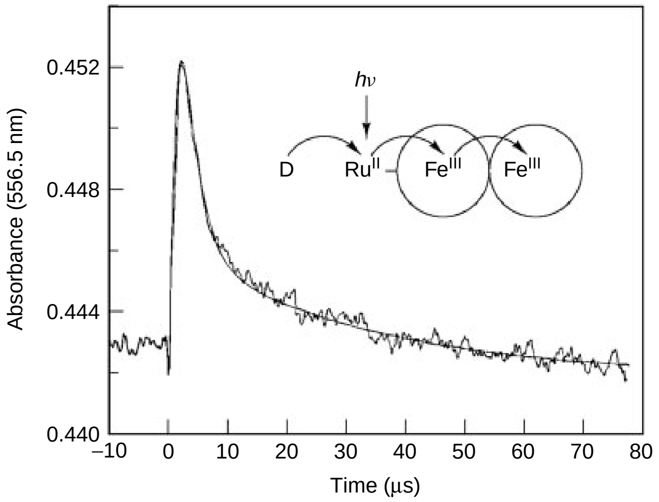

Figure 12 Transient absorption profile recorded at 556.5 nm for electron transfer in a solution containing 20 μM Ru-65-cyt b_5, 26 μM Cc, 1 mM sodium phosphate, pH 7, and 10 mM aniline. The transient was fit to a biexponential function with $k_f = 4.0 \times 10^5\ s^{-1}$ and $k_s = 3.4 \times 10^4\ s^{-1}$. (Reprinted with permission from Ref. 54. © 1992 American Chemical Society)

constant for electron transfer from cyt b_5 to Cc by more than a factor of two.[75] These results demonstrate that an aromatic side chain is not needed at Phe 82 for rapid electron transfer with Cc. The biphasic kinetics observed for the reaction of Ru-65–cyt b_5 with Cc at low-ionic strength indicate that there are at least two different conformational forms of the complex. This is consistent with previous studies indicating that the cyt b_5–Cc complex may exist in dynamic equilibrium between several different forms.[69–71] As the ionic strength increases, the fast-phase rate constant decreases and the slow-phase rate constant increases until a single phase is present at 50 mM ionic strength. This behavior indicates that the two different conformations of the complex interconvert more rapidly with increasing ionic strength.

7 CYTOCHROME *c*–CYTOCHROME *c* PEROXIDASE REACTION

The cytochrome *c*–cytochrome *c* peroxidase system has become an important paradigm for investigating fundamental questions about interprotein electron transfer. Extensive structural data are available for Cc isolated from many different organisms, while the X-ray crystal structure of yeast CcP has been determined for both the resting ferric form of the enzyme, CcP, and the hydrogen peroxide oxidized form Compound I (CMPI)[76,77] (*see* ***Iron: Heme Proteins, Peroxidases, Catalases & Catalase-peroxidases***). Moreover, Pelletier and Kraut have determined the crystal structure of the 1:1 complex between yeast iso-1-cytochrome *c* (yCc) and CcP.[78] In the first step of the reaction, hydrogen peroxide oxidizes ferric CcP to CMPI ($Fe^{IV} = O,R^{\bullet +}$), which contains an oxyferryl heme $Fe^{IV} = O$ and an indolyl radical cation, $R^{\bullet +}$, located on Trp191.[79,80] CMPI is then sequentially reduced to CMPII and CcP in two one-electron steps involving ferrocytochrome *c*. Two forms of the singly oxidized state CMPII have been identified, CMPII($Fe^{IV} = O,R$) containing the oxyferryl heme and CMPII($Fe^{III},R^{\bullet +}$) containing the radical cation.[81] A number of important questions about the reaction mechanism will be addressed here. First, does Cc react initially with $Fe^{IV}=O$ on CMPI($Fe^{IV}=O,R^{\bullet+}$) to form CMPII($Fe^{III},R^{\bullet+}$), or instead with the radical cation to form CMPII($Fe^{IV}=O,R$). Second, what are the true rate constants for electron transfer from Cc to the radical cation and the oxyferryl heme. Third, what binding domain(s) and pathways are used by Cc for electron transfer to the radical cation and the oxyferryl heme. Fourth, what is the mechanism for complete reduction of CMPI by two molecules of Cc under physiological conditions.

A new yeast Ru-Cc derivative, Ru-39-Cc, was designed to study the reaction mechanism with CcP (Figure 13). The sulfhydryl group at Cys39 on the back surface of yeast H39C,C102T iso-1-Cc was labeled with Ru(bpy)$_2$(4-bromomethyl-4′methyl-2.2′-bipyridine) to give Ru-39-Cc.[82] Both the binding constant at low-ionic strength and second-order rate constant at high-ionic strength for the reaction of Ru-39-Cc with CcP are the same as for native yCc.[83] These results indicate that the ruthenium group on the backside of Ru-39-Cc does not affect the interaction with CcP. Electron transfer from Ru(II*) to the heme group in Ru-39-Cc occurred with a rate constant of $5\times10^5\,s^{-1}$. There is good electronic coupling between the ruthenium complex and the heme group involving 13 covalent bonds and one hydrogen bond (Figure 13). The driving force of the reaction, 1.1 eV, is close to the reorganization energy of 0.74–1.0 eV, and thus the rate constant is close to the maximum value (cf. Figure 9).

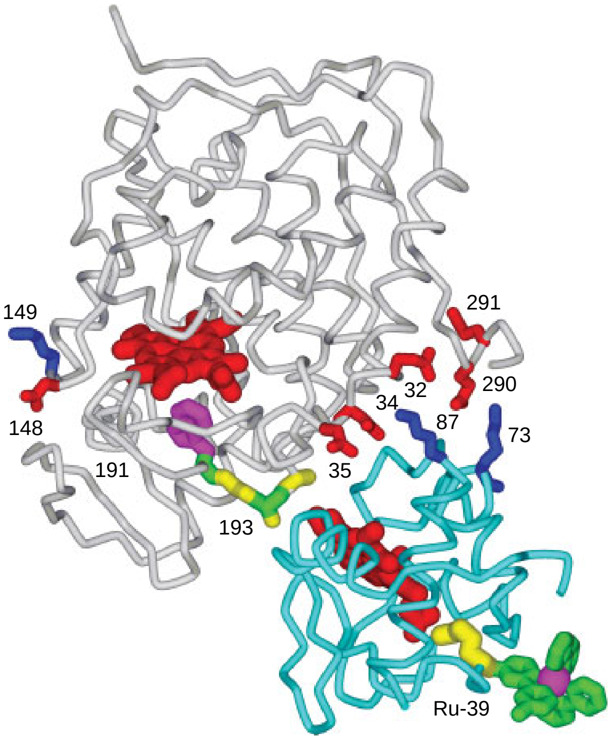

Figure 13 X-ray crystal structure of the CcP-yCc complex.[78] The heme groups are colored red, the Trp191 indole group is purple, the Trp191 backbone and Ala193 are green, Gly192 and Ala 194 are yellow, and Ru39 is green. Cc residues 39–41 between Ru-39 and heme c are colored yellow. The side chains of CcP residues E32, D34, E35, E290, E291, and yCc residues K73 and K87 are labeled. The low-affinity Cc binding site is proposed to be located near D148 and K149, which are labeled

When a 1:1 Ru-39-Cc:CMPI complex was excited with a single laser flash at low-ionic strength, the excited state Ru(II*) rapidly reduced heme c Fe(III), followed by electron transfer from heme c Fe(II) to the Trp191 radical cation in CMPI with rate constant $k_{eta}=2.0\times10^6\,s^{-1}$ (Figure 13; Scheme 3).[83] Excitation with a second laser flash resulted in electron transfer from heme c Fe^{II} to the oxyferryl heme in CMPII($Fe^{IV}=O,R$) with rate constant $k_{etb}=5000\,s^{-1}$. These studies indicate that the Trp191 radical cation is the initial site of reduction in CMPI, rather than the oxyferryl heme. Stopped-flow studies have confirmed that native yeast and horse Cc also initially reduce the Trp191 radical cation in CMPI under a variety of ionic strength and pH conditions.[84]

On the basis of their crystal structure of the complex between yeast iso-1-Cc (yCc) and CcP, Pelletier and Kraut have proposed an electron-transfer pathway that extends from the exposed heme methyl group of Cc through CcP residues Ala194, Ala193, and Gly192 to the indole group of Trp191 (Figure 13). In order to determine whether the reaction domain used in solution is the same as found in the crystal structure, the reaction of Ru-39-Cc with a series of CcP mutants with altered surface residues was examined (Table 1). These studies indicate that the reactions of Ru-39-Cc with both the radical cation and the oxyferryl heme in solution use the binding domain identified in the crystal structure (Table 1, Figure 13).[83] The rate constants k_{eta} and k_{etb} were each decreased 3- to 4-fold by the mutations D34N, E290N, and A193F, while the dissociation constant K_d of the complex

$$c^{II}+(R^{\bullet+},Fe^{IV}{=}O)\underset{k_d}{\overset{k_f}{\rightleftharpoons}}c^{II}{:}(R^{\bullet+},Fe^{IV}{=}O)\xrightarrow{k_{eta}}c^{III}{:}(R,Fe^{IV}{=}O)\underset{k_f}{\overset{k_d}{\rightleftharpoons}}c^{III}+(R,Fe^{IV}{=}O)$$

$$c^{II}+(R,Fe^{IV}{=}O)\underset{k_d}{\overset{k_f}{\rightleftharpoons}}c^{II}{:}(R,Fe^{IV}{=}O)\xrightarrow{k_{etb}}c^{III}{:}(R,Fe^{III})\underset{k_f}{\overset{k_d}{\rightleftharpoons}}c^{III}+(R,Fe^{III})$$

Scheme 3

Table 1 Effect of CcP mutants on reaction with Ru-39-Cc. k_{eta} and k_{etb} were measured at 5 mM and K_{d} at 100 mM ionic strength[83]

Mutant	$k_{\mathrm{eta}} \times 10^{-6}\,\mathrm{s}^{-1}$	$k_{\mathrm{etb}} \times 10^{-3}\,\mathrm{s}^{-1}$	K_{d} (μM)
CcP	2.0	5.0	0.6
E32Q	2.1	4.3	0.9
D34N	0.5	1.2	13
E35Q	0.8	2.3	1.2
E290N	0.9	2.0	11
E291Q	2.0	4.4	0.8
A193F	0.8	1.5	5.1

Table 2 Reaction of Ru-55-Cc with *Rhodobacter Sphaeroides* CcO mutants. The intracomplex rate constant k_{a} for electron transfer from heme c to $\mathrm{Cu_A}$, the dissociation constant K_{d}, and the second-order rate constant k_{2nd} were at 5 mM, 45 mM, and 95 mM ionic strength, respectively, at pH 8 and 23 °C[86]

CcO mutant	k_{a} (s^{-1})	K_{d} (μM)	k_{2nd} ($\mu\mathrm{M}^{-1}\,\mathrm{s}^{-1}$)
Wild type	38 000	1.0	310
W143A	32	0.9	0.6
W143F	85	1.5	1.7
E148Q	15 000	2.3	125
D151N/D152Q	45 000	1.6	192
E157Q	12 000	3.9	58
D188N/E189Q	45 000	1.3	285
D195N	25 000	2.3	152
D214N	700	3.2	37
E254A	10 500	1.0	120

between Ru-39-Cc and CMPI was increased by 10- to 20-fold (Table 2). The negatively charged carboxylates on Asp34 and Glu-290 interact electrostatically with the positively charged yCc lysines 87 and 73, respectively, in the crystalline complex (Figure 13). The methyl group of Ala193 is in van der Waals contact with the heme CBC methyl group at the center of the crystalline binding domain. Since the value of k_{eta} is independent of viscosity and temperature, it is the true rate constant for electron transfer from the Cc heme to the Trp191 radical cation and not rate-limited by conformational gating.[85] The experimental rate constant k_{eta} can thus be compared with predictions of the Marcus theory based on the crystal structure. The distance between the heme group in yCc and the Trp191 indole ring atom in CcP is 16.0 Å in the crystal structure. Since k_{eta} is independent of temperature, it is reasonable to assume that the driving force $-\Delta G^{\circ\prime}$ equals the reorganization energy λ. A theoretical rate constant of $k_{\mathrm{et}} = 3 \times 10^5\,\mathrm{s}^{-1}$ is calculated using equation (1). This theoretical estimate is in reasonable agreement with the experimental value of $k_{\mathrm{eta}} = 2 \times 10^6\,\mathrm{s}^{-1}$. The best pathway between heme *c* and the Trp191 indolyl radical cation consists of 11 covalent bonds and a van der Waals contact of 4.1 Å between the heme CBC methyl group and the Ala193 methyl group.

The reduction of CMPII($\mathrm{Fe^{IV}} = \mathrm{O}$, R) has been found to involve rapid internal electron transfer leading to formation of the radical cation in CMPII($\mathrm{Fe^{III}}$, $\mathrm{R^{\bullet+}}$), which is then reduced by $\mathrm{yCc^{II}}$ in the high-affinity binding site (Scheme 4).[87]

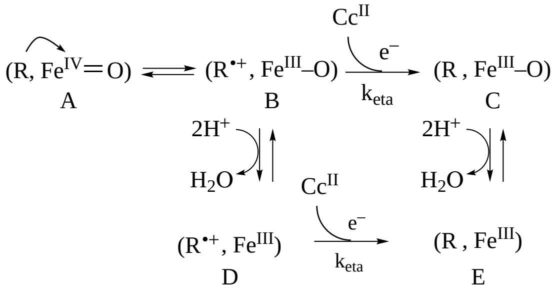

Scheme 4

The steps A → B → D in Scheme 4 have a rate constant of $1100\,\mathrm{s}^{-1}$, which is rate limited by proton transfer to the oxygen atom on the iron. At low concentrations of solution $\mathrm{Cc^{II}}$, reduction of CMPII($\mathrm{Fe^{IV}} = \mathrm{O}$, R) involves steps A → B → D → E with second-order rate constant k_{b}.[83] However, at saturating concentrations of $\mathrm{Cc^{II}}$ the reduction of CMPII($\mathrm{Fe^{IV}} = \mathrm{O}$, R) involves the steps A → B → C → E with rate constant $k_{\mathrm{etb}} = 5000\,\mathrm{s}^{-1}$.[83] This suggests that proton transfer is faster in the C → E step than in the B → D step due to electrostatic repulsion by the radical cation. Mutating Trp191 to Phe decreased the rate of reduction of the oxyferryl heme by $\mathrm{yCc^{II}}$ more than 10 000-fold, showing the essential role of the Trp191 radical cation.[88] Both steps in the complete reduction of CMPI therefore involve electron transfer from $\mathrm{Cc^{II}}$ to the Trp191 radical cation using the binding site and pathway identified in the crystal structure.

A second molecule of yCc binds to a low-affinity site on the 1:1 yCc:CcP complex to form a 2:1 complex at low-ionic strength. $\mathrm{yCc^{II}}$ binding to the low-affinity site significantly increases the rate constant for dissociation of $\mathrm{yCc^{III}}$ from the high-affinity site at low-ionic strength, an example of substrate-assisted product dissociation. Both ruthenium photoreduction and stopped-flow experiments have shown that the low-affinity Cc binding site is not significantly active in direct electron transfer to either the Trp191 radical cation or the oxyferryl heme.[84,89] It is therefore surprising that the excited state of zinc-porphyrin horse Cc, ^{3}Zn-hCc, was found to be active in electron transfer to the ferric heme from the low-affinity site on CcP, but is nearly inactive from the high-affinity site.[90] The reason for this striking difference in reaction pathways is that the Trp191 indole cannot be oxidized to the radical cation by the reductive ^{3}Zn porphyrin, and thus cannot be a redox intermediate in the reaction. The distance between the ^{3}Zn-hCc in the high-affinity site and the CcP heme (26.5 Å metal-to-metal) is too large for efficient electron transfer. ^{3}Zn-hCc binds to the second, low-affinity site close to Asp148 with a metal-to-metal distance of 22–25 Å,[91] which allows a faster rate of electron transfer than from the high-affinity site. These results illustrate that the pathway for electron transfer can depend critically on the reaction mechanism. Electron transfer from ^{3}Zn-hCc to the CcP ferric heme is a pure electron-transfer process that should obey the Marcus relation. In contrast, electron transfer from yCc to the oxyferryl heme is a complex process involving proton transfer to the oxygen atom and release of water, and requiring the use of the Trp191 radical cation as a redox intermediate.

The mechanism for complete reduction of CMPI by two molecules of Cc^{II} involves two complex formation and dissociation steps and two intracomplex electron-transfer steps (Scheme 3). The formation and dissociation rate constants k_f and k_d of the high-affinity complex between yC*c* and CMPI were measured over a wide range of ionic strength using a ruthenium photoreduction technique.[85] The dissociation constant k_d increases from $<5\,s^{-1}$ at low-ionic strength to $4000\,s^{-1}$ at 150 mM ionic strength, while k_f decreases from $>3 \times 10^9\,M^{-1}\,s^{-1}$ at low-ionic strength to $1.3 \times 10^9\,M^{-1}\,s^{-1}$ at 150 mM ionic strength. The rate constants in Scheme 3 are $k_f = 1.3 \times 10^9\,M^{-1}\,s^{-1}$, $k_d = 4000\,s^{-1}$, $k_{eta} = 1.0 \times 10^6\,s^{-1}$, and $k_{etb} = 3000\,s^{-1}$ at physiological ionic strength, estimated to be 150 mM. The rate-limiting step in the overall reaction is product dissociation below 150 mM ionic strength, and substrate complex formation at higher-ionic strength. At physiological ionic strength, the interaction between yC*c* and C*c*P is optimized to facilitate both rapid substrate complex formation and product complex dissociation.

8 CYTOCHROME *c*–CYTOCHROME *bc*$_1$ REACTION

The cytochrome *bc*$_1$ complex (cyt bc_1) is an integral membrane protein in the electron-transport chains of mitochondria and many respiratory and photosynthetic prokaryotes.[10] The complex contains two b cytochromes (b_L and b_H) located on a single transmembrane polypeptide chain, and cyt c_1 and the 2Fe2S protein located on the cytoplasmic side of the membrane. Each cyt *b* iron is ligated by two histidine nitrogen atoms. Cyt c_1 has a relatively large hydrophilic domain located on the cytoplasmic surface of the membrane, and is anchored to the membrane by a single hydrophobic α-helix at the C-terminus. The redox potentials of cyt b_L, cyt b_H, cyt c_1, and the 2Fe2S center are −80 mV, +50 mV, +280 mV, and +280 mV, respectively. Electron transfer through the complex involves a Q-cycle mechanism in which four protons are translocated to the positive (P) side of the membrane per two electrons transferred from ubiquinol to Cc (Scheme 5).[10] The reaction is initiated at the Q_o site where an electron is transferred from ubiquinol to the 2Fe2S center, and then to cyt c_1 and cyt c. The resulting semiquinone in the Q_o site transfers an electron to cyt b_L and then to cyt b_H and ubiquinone in the Q_i site. The resulting ubisemiquinone remains bound in the Q_i site until it accepts a second electron from cyt b_{562} to form ubiquinol. The Rieske iron–sulfur protein has been found in different conformations in different crystal forms of the complex, and in the presence of Q_o-site inhibitors (Figure 14).[11–14] The Rieske iron–sulfur protein is in the ''*b state*'' conformation with 2Fe2S proximal to the cyt b_L heme in the presence of the Q_o-site inhibitor stigmatellin. In the absence of the inhibitor, the 2Fe2S protein is in the ''*c*$_1$ *state*'' conformation with 2Fe2S close to cyt c_1 in bovine $P6_522$ crystals, but is conformationally mobile in bovine $I4_122$ crystals.[11–13] A shuttle mechanism has been proposed in which the Rieske protein changes conformation from the *b* state, where oxidized 2Fe2S accepts an electron

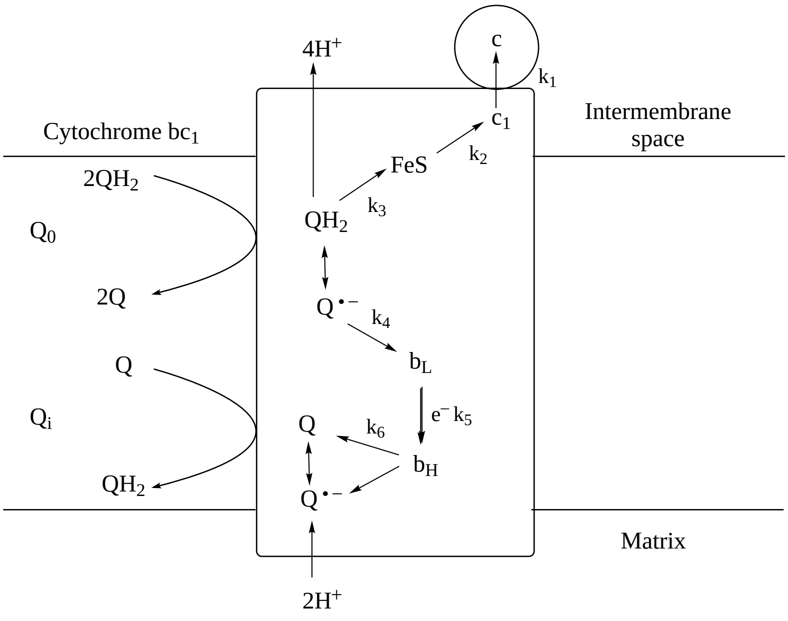

Scheme 5

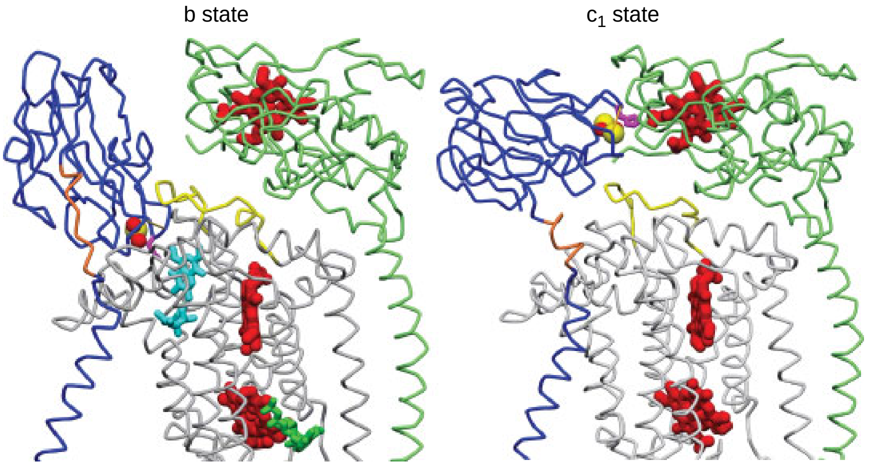

Figure 14 X-ray crystal structures of cytochrome *b*c_1 from chicken in the presence of stigmatellin and antimycin (b state), and in the beef P$6_5$22 crystals (c_1 state).[12,13] The Rieske, cyt c_1, and cyt b subunits are colored blue, green, and grey, respectively. The hemes, the 2Fe2S center, stigmatellin, and antimycin are colored red, red/yellow, cyan, and green, respectively. The Rieske neck region residues 66–72 are colored orange, the ef loop is yellow, and His161 is colored purple

from ubiquinol in the Q_o site, to the c_1 state where reduced 2Fe2S transfers an electron to cyt c_1.[11–13]

Electron transfer within the cyt bc_1 complex has been studied using the binuclear ruthenium complex $[Ru(bpy)_2]_2(qpy)^{4+}$ (Figure 10), which binds with high affinity to the negatively charged binding domain on the surface of cyt c_1 as a surrogate for Cc.[92] Photoexcitation of $[Ru(bpy)_2]_2(qpy)$ to the metal-to-ligand charge transfer state, $[Ru(bpy)_2]_2(qpy)^*$, results in oxidation of cyt c_1 within 1 μs in the presence of a sacrificial electron acceptor as shown in Scheme 6. The reduction of photooxidized cyt c_1 in bovine cyt bc_1 has a fast phase with a rate constant of $k_1 = 16\,000\ \mathrm{s}^{-1}$ due to electron transfer from 2Fe2S to cyt c_1, and a slow phase with a rate constant of $k_2 = 250\ \mathrm{s}^{-1}$ due to electron transfer from QH_2 to 2Fe2S and cyt c_1. This is followed by rapid electron transfer from the semiquinone in the Q_o site to cyt b_L and cyt b_H (Scheme 6). The corresponding rate constants in *R. sphaeroides* cyt bc_1 are $k_1 = 80\,000\ \mathrm{s}^{-1}$ and $k_2 = 1000\ \mathrm{s}^{-1}$. Experiments exploring the effects of temperature, pH, and driving force demonstrated that the electron-transfer reaction from the 2Fe2S center to cyt c_1 is not rate-limited by true electron transfer, but rather by dynamic fluctuations in the conformation of the Rieske protein between the b state and the c_1 state.[93] In the c_1 state, the iron–sulfur ligand His161 forms a hydrogen bond with the heme c_1 propionate oxygen (Figure 14). This provides a direct pathway for electron transfer from the 2Fe2S center to heme c_1 with an edge-to-edge distance of 7.8 Å. The rate constant calculated from the Marcus equation (1) is $3 \times 10^7\ \mathrm{s}^{-1}$, which is considerably faster than the observed value of $16\,000\ \mathrm{s}^{-1}$ for the bovine enzyme or $80\,000\ \mathrm{s}^{-1}$ for the *sphaeroides* enzyme. The experimental rate constant k_1 thus provides a true measure of the rate of the conformational change from the b state to the c_1 state. Additional support for the mobile-shuttle mechanism has been obtained from cross-linking and mutational studies that immobilize the 2Fe2S protein or alter the conformation of the neck region.[94]

Electron transfer from quinol in the Q_o site to the iron–sulfur center has a relatively small rate constant ($1500\ \mathrm{s}^{-1}$ in *R. sphaeroides* cyt bc_1) and a large activation energy. The activation barrier for this process has been shown to occur after formation of a complex between quinol and the oxidized 2Fe2S center that is stabilized by a hydrogen bond between the deprotonated 2Fe2S ligand His161 and quinol.[95]

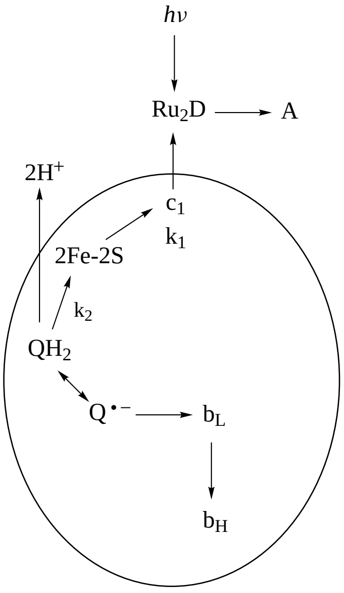

Scheme 6

Electron transfer takes place over a distance of 7 Å from quinol through the bridging ligand His161 to 2Fe2S, and is coupled to proton transfer from the quinol to His161. The slow-rate constant and high-activation energy of this process are due to the proton-coupled electron transfer mechanism.[95] A major unresolved question about the Q-cycle mechanism is how QH_2 in the Q_o site can deliver two electrons sequentially to the high- and low-potential chains, even though thermodynamics would favor delivery of both electrons to the high-potential chain. Crofts *et al.* have suggested that following electron transfer to 2Fe2S, the resulting semiquinone rotates towards cyt b_L, favoring electron transfer to cyt b_L and preventing electron transfer to 2Fe2S.[96] The recent discovery that two quinol molecules reside in the Q_o site may complicate this mechanism, however.[97] It is also possible that the conformational dynamics of the 2Fe2S protein may play a role in preventing electron transfer from the semiquinone in the Q_o site to 2Fe2S. Recent studies on the effect of the Q_o-site inhibitor famoxadone on the conformational dynamics of the iron–sulfur protein are of interest in this regard. Famoxadone binding to the Q_o site of bovine cyt bc_1 was found to decrease the rate constant of the conformation change from the b state to the c_1 state from $16\,000\,s^{-1}$ to $1500\,s^{-1}$.[98] X-ray crystallography studies revealed that famoxadone binding leads to significant conformational changes in three domains on the surface of cyt b, including the *ef* loop which is part of the ISP-docking site (Figure 14).[99] The *ef* loop may play a role in relaying famoxadone-induced conformational changes in the Q_o pocket to the ISP-docking site to decrease the rate of release of the ISP. The linkage between the conformation of the Q_o site and the dynamics of the ISP movement could be a key to how the enzyme promotes the transfer of the first electron from QH_2 to 2Fe-2S, but inhibits the transfer of the second electron from semiquinone to 2Fe-2S.

The electron-transfer reaction from the cyt bc_1 complex to Cc involves three steps: formation of a 1:1 reactant complex between reduced cyt bc_1 and Cc^{3+}, intracomplex electron transfer from cyt c_1^{2+} to Cc^{3+}, and release of Cc^{2+}. The interaction between Cc and cyt bc_1 should stabilize the reactant complex in an optimal orientation for rapid electron transfer, and also allow both rapid reactant complex formation and product complex dissociation. The reaction rate measured by steady state and stopped-flow kinetics decreases with increasing ionic strength, indicating that electrostatic interactions are important to the reaction.[100] Chemical modification studies have indicated that six lysine amino groups surrounding the heme crevice of Cc are involved in the interaction with cyt bc_1.[38,40] Chemical modification and cross-linking studies have indicated that acidic residues on bovine cyt c_1 and subunit 8 are involved in binding Cc.[45–47] The X-ray crystal structures show that the cyt c_1 heme edge on the cytoplasmic surface is surrounded by acidic residues that could form the docking site with Cc.[11–14] Most importantly, the X-ray crystal structure of the complex between yeast Cc and yeast cyt bc_1 has recently been determined to 2.97 Å resolution (Figure 15).[101] Surprisingly, the complex is stabilized largely by nonpolar interactions, including a planar-stacking interaction between yCc Arg13 and Phe230 of cyt c_1. Complementary charged residues are located around the periphery of the binding domain, but only two are close enough to make direct polar interactions. The distance between the edges of the heme *c* and heme c_1 groups is only 9.4 Å, giving an estimated rate constant for electron transfer of 1×10^6 to $8 \times 10^6\,s^{-1}$.

The second-order reaction between Cc and cyt c_1 has been studied by stopped-flow spectroscopy at high-ionic strength, but the reaction becomes too fast to resolve by this technique as the ionic strength is decreased below 200 mM.[100] A new yeast Ru_z-39-Cc derivative was designed to measure intracomplex electron transfer with the cyt bc_1 complex in the physiological direction.[102] The ruthenium complex attached to Cys39 on the surface opposite from the heme crevice of Cc does not affect the interaction with cyt bc_1 (Figure 15). The new $Ru(bpz)_2(dmb)$ complex has a large reduction potential for the $Ru(II^*)/Ru(I)$ transition, and is optimized for photooxidation of the reduced heme *c*. Laser excitation of the reduced Ru_z-39-Cc derivative resulted in electron transfer from heme *c* Fe(II) to $Ru(II^*)$ with a rate constant of $1.5 \times 10^6\,s^{-1}$ to form heme c Fe(III) and Ru(I). Atmospheric oxygen rapidly oxidized Ru(I), preventing the back reaction. The yield of photooxidized heme *c* is 20% in a single flash, which is quite large for this type of derivative. When a 1:1 complex between yeast Ru_z-39-Cc and yeast cyt bc_1 was photoexcited at low-ionic strength, intracomplex electron transfer from cyt c_1^{2+} to photooxidized heme c^{3+} occurred with a rate constant of $14\,000 \pm 3000\,s^{-1}$. In the crystal structure of the yCc:cyt bc_1 complex, the heme *c* and heme c_1 groups are in close proximity with a distance of 17.4 Å between the two iron atoms, and an edge-to-edge distance between the two porphyrin heterocycles of 9.4 Å.[101] With this distance and a reorganization energy λ of 1.0 V, the rate constant estimated from equation (1) is $1.8 \times 10^5\,s^{-1}$. Although the theoretical value is larger than the experimental value of $1.4 \times 10^4\,s^{-1}$, the theory has been applied most extensively to intraprotein electron transfer, with relatively few applications to intracomplex electron transfer between two proteins. There is a through-space jump of 4.5 Å between the two hemes in the crystal structure, which could significantly decrease the rate constant.

As the ionic strength is increased to 200 mM, the fast intracomplex phase of electron transfer disappears indicating complex dissociation, and a slow phase appears due to the bimolecular reaction of solution Ru_z-39-Cc with cyt bc_1. The second-order rate constant decreases with increasing ionic strength above 250 mM, consistent with a reaction between oppositely charged proteins. There is only one electrostatic charge-pair interaction in the binding domain of the yCc:ybc_1 crystallographic complex. However, there are five lysine amino groups on yCc and five carboxylate groups on cyt bc_1 surrounding the interaction domain, which could guide

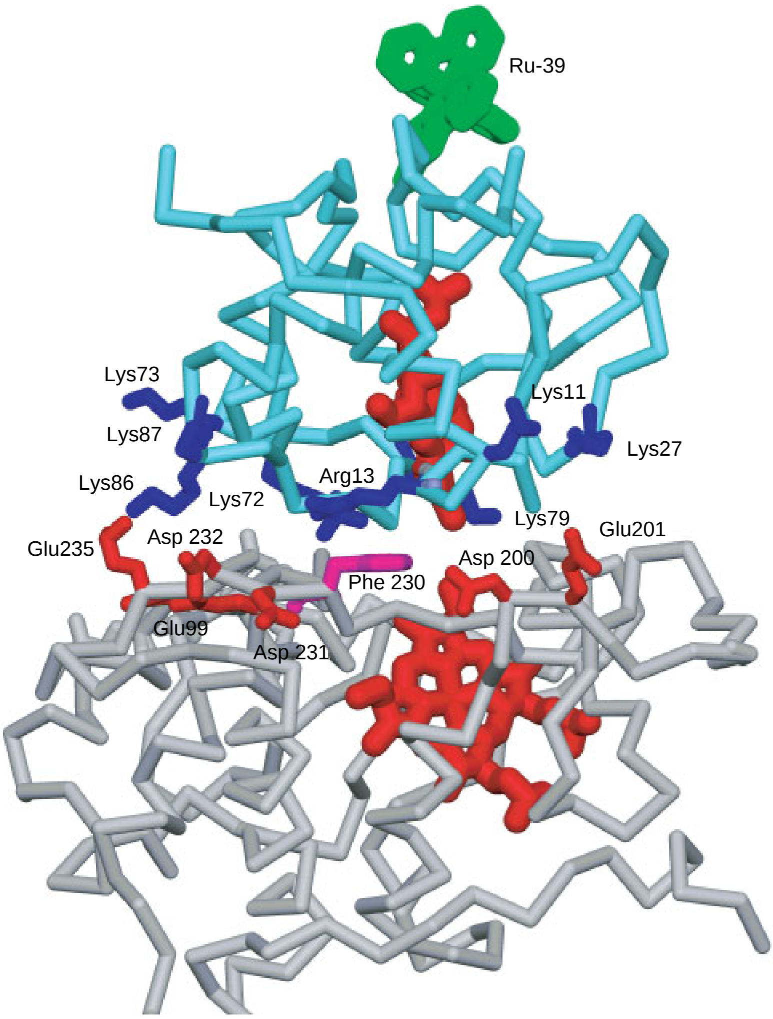

Figure 15 X-ray crystal structure of the complex between yeast cyt bc_1 and yCc.[101] Cyt c_1 is colored grey, yCc is light blue, the heme groups are red, acidic residues on cyt c_1 are red, basic residues on yCc are blue, and Phe230 is purple. The ruthenium complex on Cys39 is green

Cc to the correct binding site during the final stages of the complex formation process (Figure 15).

9 CYTOCHROME *c*–CYTOCHROME *c* OXIDASE REACTION

Cytochrome *c* oxidase (CcO), the terminal member of the mitochondrial electron-transport chain, transfers electrons from Cc to molecular oxygen and pumps protons across the mitochondrial membrane. The determination of the X-ray crystal structures of CcO from both bovine mitochondria and *P. denitrificans* has made it possible to address questions about the mechanism of electron transfer and proton pumping at the molecular level.[15,16] The enzyme from bovine mitochondria has 13 subunits, while *Paracoccus* enzyme has 4 subunits. CcO contains four redox-active metal centers, Cu_A, located in subunit II, and heme a, heme a_3, and Cu_B, located in subunit I. Cu_A consists of two copper atoms bridged by the sulfur atoms of two cysteine residues. Efficient electron transfer from Cc to CcO requires that the binding interaction between the two proteins facilitate rapid formation of a reactant complex with CcO, stabilize the optimal orientation of the complex for rapid electron transfer to the initial acceptor in CcO, and allow rapid dissociation of the product complex to release oxidized Cc. The steady state reaction is limited by product dissociation at low-ionic strength, reaches an optimum at intermediate ionic strength, and is strongly inhibited at high-ionic strength, indicating the importance of electrostatic interactions between the two proteins.[33–36] Chemical modification studies have shown that six lysine amino groups surrounding the heme crevice of Cc interact electrostatically with CcO.[33–37] Steady state and stopped-flow kinetics studies have provided insight into the reaction between Cc and CcO, but did not allow resolution of intracomplex electron transfer. The Ru-39-Cc derivative was designed to measure intracomplex electron transfer to the initial acceptor in CcO, as well as the rate constants for complex formation and dissociation.[82] When a 1:1 complex between Ru-39-Cc and beef CcO was photoexcited at low-ionic strength, the following electron-transfer sequence was observed: Ru(II*) → hemec^{3+} → Cu$_A^{2+}$ → heme a^{3+} with rate constants of $k_1 = 5 \times 10^5\,\mathrm{s}^{-1}$, $k_a = 6 \times 10^4\,\mathrm{s}^{-1}$, and $k_b = 1.8 \times 10^4\,\mathrm{s}^{-1}$, according to Scheme 7 (Figure 16).[82] The initial electron acceptor in CcO was thus identified to be Cu$_A$. When the ionic strength was increased from 40 mM to 100 mM, the fast phase decreased in amplitude due to dissociation of the 1:1 complex, and a slow phase appeared because of the intermolecular reaction between free Ru-39-Cc and CcO. The rate constants for complex formation and dissociation were also determined using the ruthenium photoreduction technique. The complete reaction at physiological ionic strength (100 mM) involves substrate complex formation between Cc^{2+} and CcO with rate constant $k_f = 1.8 \times 10^8\,\mathrm{M}^{-1}\,\mathrm{s}^{-1}$, intracomplex electron transfer from Cc^{2+} to Cu$_A^{2+}$ with rate constant $k_a = 6 \times 10^4\,\mathrm{s}^{-1}$, and product complex dissociation with rate constant $k_d = 8 \times 10^3\,\mathrm{s}^{-1}$ (Scheme 7).[82]

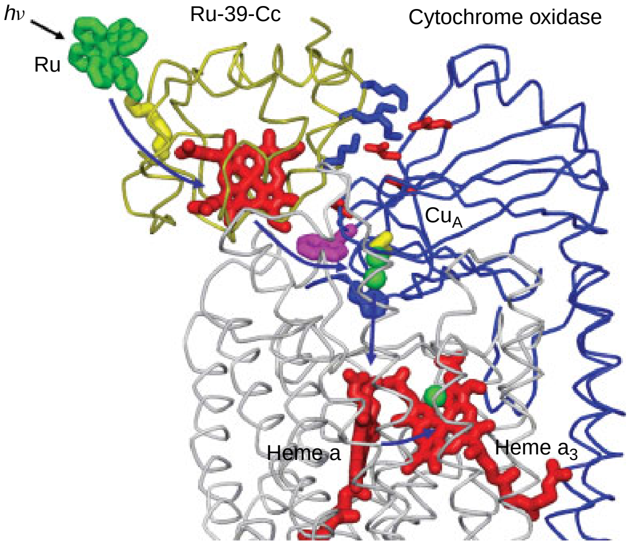

Figure 16 Complex between Ru-39-Cc and CcO. Ru-39-Cc is bound to CcO in the configuration determined by Roberts and Pique.[103] The Cc backbone is colored yellow, CcO subunit I is grey, and CcO subunit II is blue. Subunit II Trp143, Met263, and His260 are colored purple, yellow, and blue, respectively. Cc lysines 8, 13, 72, 86, and 87 are colored blue, while subunit II Glu148, Asp151, Glu157, Asp195, and Asp214 are colored red

The X-ray crystal structures of bovine and *P. denitrificans* CcO reveal a cluster of acidic residues on subunit II near the binuclear Cu$_A$ center.[15,16] The highly conserved aromatic residue, Trp143, at the center of this acidic cluster is in van der Waals contact with the Cu$_A$ center and could be involved in electron transfer with Cc. In order to investigate the location of the binding domain for Cc, a series of *R. sphaeroides* CcO mutants was prepared in which acidic residues were replaced with neutral Asn or Gln residues (Figure 17, Table 2).[86] When the 1:1 complex between Ru-55-Cc and wild-type CcO is photoexcited at low-ionic strength, electron transfer from heme c to Cu$_A$ occurs with an intracomplex rate constant of $k_a = 4 \times 10^4\,\mathrm{s}^{-1}$, followed by electron transfer from Cu$_A$ to heme a with a rate constant of $\mathrm{k_b} = 9 \times 10^4\,\mathrm{s}^{-1}$. The rate constant k_a is decreased to $700\,\mathrm{s}^{-1}$ by the D214N mutation, indicating a significant change in the binding orientation of Ru-55-Cc. The value of k_a was decreased by 2 to 4-fold by the E157Q, E148Q, and D195N mutations. The dissociation constant K_D was significantly decreased by the D214N, E157Q, E148Q, and D195N mutations, indicating that they affect both binding strength and orientation. The k_a, K_D, and k_{2nd} values were not significantly affected by the D151N/E152Q and D188N/E189Q double mutants, indicating that these residues are outside the binding domain. The aromatic residue Trp143 was mutated to Phe or Ala to investigate its role in mediating electron transfer from the heme group of Cc to Cu$_A$. The rate constant k_a was decreased 450-fold and 1200-fold by the mutations W143F and W143A, respectively.[86] It is proposed that these mutations cause a substantial disruption in the pathway for electron transfer rather than simply leading to a change in the orientation of the complex.

The mutational studies indicate that Cc binds to a highly conserved acidic domain on the surface of subunit II involving the negatively charged carboxylates on residues Asp214, Glu157, Glu148, and Asp195. The positively charged lysines 8, 13, 72, 86, and 87 surrounding the heme crevice of Cc have been shown to be involved in the interaction with CcO using a chemical modification approach. A theoretical model for the complex between Cc and CcO determined by Roberts and Pique is consistent with the kinetic studies (Figure 17).[103] The interaction consists of a central hydrophobic domain, surrounded by complementary

$$\begin{tikzcd}
\mathrm{c^{3+}\!:\,(Cu^{2+}\,a^{3+})} \arrow[r, "k_1", "h\nu"'] \arrow[d, shift left, "K_D"] & \mathrm{c^{2+}\!:\,(Cu^{2+}\,a^{3+})} \arrow[r, "k_a"] \arrow[d, shift left, "k_d"] & \mathrm{c^{3+}:\,(Cu^{1+}\,a^{3+})} \arrow[r, shift left, "k_b"] & \mathrm{c^{3+}:\,(Cu^{2+}\,a^{2+})} \arrow[l, shift left, "k_c"] \arrow[d, shift left, "k_d"] \\
\mathrm{c^{3+} + (Cu^{2+}\,a^{3+})} \arrow[u, shift left] \arrow[r, "k_1", "h\nu"'] & \mathrm{c^{2+} + (Cu^{2+}\,a^{3+})} \arrow[u, shift left, "k_f"] & & \mathrm{c^{3+} + (Cu^{2+}\,a^{2+})} \arrow[u, shift left, "k_f"]
\end{tikzcd}$$

Scheme 7

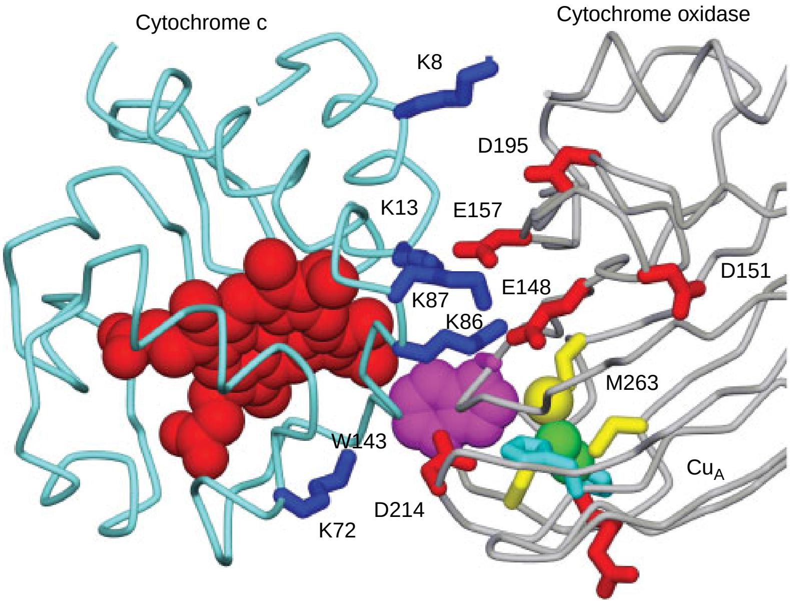

Figure 17 Model for the high-affinity complex between horse Cc and CcO determined by Roberts and Pique.**103** The backbone of horse Cc and CcO subunit II are shown with the side chains of selected lysines and acidic residues colored blue and red, respectively. The residue numbers on subunit II are for *Rhodobacter sphaeroides CcO*. The Cc heme and subunit II Trp143 and Met 263 sulfur atom are represented by CPK models. The Cu_A coppers are represented by green CPK models

electrostatic interactions between Cc lysines 8, 13, 86/87, 72, and CcO Asp195, Glu157, Glu148, and Asp214, respectively. At the center of the hydrophobic domain, the indole ring of Trp143 is in van der Waals contact with the heme CBC methyl group. The edge-to-edge distance between the heme c macrocycle and the Met263 Cu_A ligand is 12.5 Å in the Cc:CcO model complex. A theoretical electron-transfer rate constant of $6 \times 10^4\,s^{-1}$ is calculated from the Marcus equation (1), assuming $r = 12.5$ Å, $\lambda = 0.65$ eV and $\Delta G^{\circ\prime} = -0.03$ eV. This theoretical value is in good agreement with the experimental value of $k_{et} = 6 \times 10^4\,s^{-1}$ for the reaction between Ru-39-Cc and Cu_A. Since the indole ring of Trp143 is in van der Waals contact with both the Cc heme and the Cu_A ligand Met263, there is good electronic coupling between redox centers (Figure 17).

In the novel binuclear Cu_A center of CcO, the two copper atoms are bridged by the sulfur atoms of Cys252 and Cys256. The outer copper atom is also liganded by His217 and Met263 while the inner copper is liganded by His260 and the backbone carbonyl of Glu254. Two *R. sphaeroides* CcO mutants, M263L and H260N, were examined to investigate the mechanism of electron transfer from Cc to Cu_A and heme a.**104** Met263 ligates the copper that is closest to Cc, while His260 ligates the copper that is linked by a hydrogen-bond network to heme a. Two copper atoms are retained at the Cu_A center of these mutants, but the redox potential of Cu_A was increased by 120 mV for the M263L mutant and 90 mV for the H260N mutant. The mixed valence $Cu(1.5)\cdots Cu(1.5)$ state of the wild-type Cu_A center is converted to a state in which the two copper atoms are no longer equivalent. The rate constant for intracomplex electron transfer from heme c to Cu_A is decreased from $40\,000\,s^{-1}$ to $16\,000\,s^{-1}$ by the M263L mutation, and to $11\,000\,s^{-1}$ by the H260N mutation. The rate constants for electron transfer between Cu_A to heme a are $k_b = 4000\,s^{-1}$ and $k_c = 66\,000\,s^{-1}$ for M263L CcO and $k_b = 45\,s^{-1}$ and $k_c = 180\,s^{-1}$ for H260N, compared to $k_b = 90\,000\,s^{-1}$ and $k_c = 17\,000\,s^{-1}$ for wild-type CcO. The effects of the M263L mutation on the kinetics can be explained by the increase in redox potential of the Cu_A center. However, the large decrease in the rate constants for electron transfer between Cu_A and heme a in the H260N mutant must be due to a disruption in the structure between the two centers. The pathway for electron transfer from Cu_A to heme a is thought to involve a hydrogen-bond network through the Cu_A ligand His260, the peptide backbone, and the highly conserved subunit I residue Arg482 to the heme a propionates. Disruption of this pathway by the H260N mutation leads to the large decrease in the rate constants for electron transfer between Cu_A and heme a.

10 REFERENCES

1. C. A. MacMunn, *Proc. R. Soc. London*, 1886, **39**, 248.
2. L. Levy, *Z. Physiol. Chem.*, 1889, **13**, 309.
3. F. Hoppe-Seyler, *Z. Physiol. Chem.*, 1890, **14**, 206.
4. D. Keilin, 'The History of Cell Respiration and Cytochrome', Cambridge University Press, London and New York, 1966.

5. D. Keilin, *Proc. R. Soc.*, 1930, **B106**, 418.
6. H. Theorell and A. Akesson, *J. Am. Chem. Soc.*, 1941, **63**, 1804.
7. G. R. Moore and G. W. Pettigrew, 'Cytochromes c Evolutionary, Structural and Physicochemical Aspect', Springer-Verlag, Heidelberg, 1990.
8. R. A. Scott and A. G. Mauk eds, 'Cytochrome c: A Multidisciplinary Approach', University Science Books, Sausalito, CA, 1996.
9. A. L. Lehninger, 'The Mitochondrion: Molecular Basis of Structure and Function', The Benjamin Company, New York, 1964.
10. B. L. Trumpower and R. B. Gennis, *Ann. Rev. Biochem.*, 1994, **63**, 675.
11. D. Xia, C. A. Yu, H. Kim, J. Z. Xia, A. M. Kachurin, L. Zhang, L. Yu, and J. Deisenhofer, *Science*, 1997, **277**, 60.
12. Z. Zhang, L. Huang, V. M. Shulmeister, Y. I. Chi, K. K. Kim, L. W. Hung, A. R. Crofts, E. A. Berry, and S. H. Kim, *Nature*, 1998, **392**, 677.
13. S. Iwata, J. W. Lee, K. Okada, J. K. Lee, M. Wata, B. Rasmussen, T. A. Link, S. Ramaswamy, and B. K. Jap, *Science*, 1998, **281**, 64.
14. C. Hunte, J. Koepke, C. Lange, T. Rossmanith, and H. Michel, *Structure*, 2000, (*London*) **8**, 669.
15. T. Tsukihara, H. Aoyama, E. Yamashita, T. Tomizaki, H. Yamaguchi, K. Shinzawa-Itoh, R. Nakashima, R. Yaono, and S. Yoshikawa, *Science*, 1995, **269**, 1069.
16. S. Iwata, C. Ostermeier, B. Ludwig, and H. Michel, *Nature*, 1995, **376**, 660.
17. L. Spatz and P. Strittmatter, *Proc. Natl. Acad. Sci. U.S.A.*, 1971, **68**, 1042.
18. W. M. Southerland, D. R. Winge, and K. V. Rajagoplan, *J. Biol. Chem.*, 1978, **253**, 8747.
19. Z. Xia and F. S. Mathews, *J. Mol. Biol.*, 1990, **212**, 837.
20. G. V. Louie, W. L. B. Hutcheon, and G. D. Brayer, *J. Mol. Biol.*, 1988, **199**, 295.
21. H. Ochi, Y. Hata, N. Tanaka, M. Kakudo, T. Sakurai, S. Aihara, and Y. Morita, *J. Mol. Biol.*, 1983, **166**, 407.
22. R. E. Dickerson, T. Takano, D. Eisenberg, O. B. Kallai, L. Samson, A. Cooper, and E. Margoliash, *J. Biol. Chem.*, 1971, **256**, 1511.
23. T. Takano and R. E. Dickerson, *J. Mol. Biol.*, 1981, **153**, 95.
24. Y. Matsuura, Y. Hata, T. Yamaguchi, N. Tanaka, and M. Kakudo, *J. Biochem.*, 1979, **85**, 729.
25. H. Theorell and A. Akesson, *J. Am. Chem. Soc.*, 1941, **63**, 1804.
26. E. Margoliash and A. Schejter, *Adv. Protein Chem.*, 1966, **21**, 113.
27. T. Tsukihara, T. Yamane, N. Tanaka, T. Ashida, and M. Kakudo, *J. Biochem.*, 1973, **73**, 1163.
28. N. Mandel, G. Mandel, B. L. Trus, J. Rosenberg, G. Carlson, and R. E. Dickerson, *J. Biol. Chem.*, 1977, **252**, 4619.
29. F. R. Salemme, S. T. Freer, N. H. Xuong, R. A. Alden, and J. Kraut, *J. Biol. Chem.*, 1973, **248**, 3910.
30. Y. Matsuura, T. Takano, and R. E. Dickerson, *J. Mol. Biol.*, 1982, **156**, 389.
31. T. Takano, O. Kallai, R. Swanson, and R. E. Dickerson, *J. Biol. Chem.*, 1973, **248**, 5234.
32. F. R. Salemme, J. Kraut, and M. D. Kamen, *J. Biol. Chem.*, 1973, **248**, 7701.
33. D. L. Brautigan, S. Ferguson-Miller, and E. Margoliash, *J. Biol. Chem.*, 1978, **253**, 130.
34. N. Osheroff, D. L. Brautigan, and E. Margoliash, *J. Biol. Chem.*, 1980, **255**, 8245.
35. N. Staudenmeyer, M. B. Smith, H. T. Smith, F. K. Spies, and F. Millett, *Biochemistry*, 1976, **15**, 3198; **16**, 600.
36. H. T. Smith, N. Staudenmeyer, and F. Millett, *Biochemistry*, 1977, **16**, 4971.
37. M. T. Smith, G. Stonehuerner, A. J. Ahmed, N. Staudenmeyer, and F. Millett, *Biochim. Biophys. Acta*, 1980, **592**, 303.
38. A. J. Ahmed, H. T. Smith, M. B. Smith, and F. Millett, *Biochemistry*, 1978, **17**, 2479.
39. S. Ferguson-Miller, P. L. Brautigan, and E. Margoliash, *J. Biol. Chem.*, 1978, **253**, 149.
40. S. H. Speck, S. Ferguson-Miller, N. Osheroff, and E. Margoliash, *Proc. Natl. Acad. Sci. U.S.A.*, 1979, **76**, 155.
41. R. Rieder and H. R. Bosshard, *J. Biol. Chem.*, 1980, **255**, 4732.
42. H. T. Smith, A. Ahmed, and F. Millett, *J. Biol. Chem.*, 1981, **256**, 4984.
43. F. Millett, C. deJong, L. Paulson, and R. A. Capaldi, *Biochemistry*, 1983, **22**, 546.
44. J. Hall, A. Moubarak, P. O'Brien, L. P. Pan, I. Cho, and F. Millett, *J. Biol. Chem.*, 1988, **263**, 8142.
45. J. Stonehuerner, P. O'Brian, L. Geren, F. Millett, J. Steidl, L. Yu, and C. A. Yu, *J. Biol. Chem.*, 1985, **260**, 5392.
46. C. Broger, S. Salardi, and A. Azzi, *Eur. J. Biochem.*, 1983, **131**, 349.
47. C. H. Kim and R. E. King, *J. Biol. Chem.*, 1983, **258**, 13543.
48. P. Strittmatter and S. F. Velick, *J. Biol. Chem.*, 1956, **221**, 253.
49. S. R. Slaughter, C. H. Willliams Jr, and D. E. Hultquist, *Biochim. Biophys. Acta*, 1982, **705**, 228.
50. F. S. Mathews, E. W. Czerwinski, and P. Argos, in 'The Porphyrins', ed. D. Dolphin, Academic Press, 1979, Chap. 3.
51. D. W. Dixon, X. Hong, S. E. Woehler, A. G. Mauk, and B. P. Sishta, *J. Am. Chem. Soc.*, 1990, **112**, 1082.
52. L. D. Eltis, R. G. Herbert, P. D. Barker, A. G. Mauk, and S. H. Northrup, *Biochemistry*, 1991, **30**, 3663.
53. F. Millett and B. Durham, *Biochemistry*, 2003, **41**, 11.
54. A. Willie, P. S. Stayton, S. G. Sligar, B. Durham, and F. Millett, *Biochemistry*, 1992, **31**, 7237.

55. J. R. Scott, A. Willie, M. McLean, P. S. Stayton, S. G. Sligar, B. Durham, and F. Millett, *J. Am. Chem. Soc.*, 1993, **115**, 6820.
56. N. Sutin and R. A. Marcus, *Biochim. Biophys. Acta*, 1985, **811**, 265.
57. C. C. Moser, J. M. Keske, K. Warncke, R. S. Farid, and P. L. Dutton, *Nature*, 1992, **355**, 796.
58. D. N. Beratan, J. N. Onuchic, and J. J. Hopfield, *J. Chem. Phys.*, 1987, **86**, 4488.
59. T. Nilsson, *Proc. Natl. Acad. Sci. U.S.A.*, 1992, **89**, 6497.
60. D. Zaslavsky, R. C. Sadoski, K. Wang, B. Durham, R. B. Gennis, and F. Millett, *Biochemistry*, 1998, **37**, 14910.
61. F. R. Salemme, *J. Mol. Biol.*, 1976, **102**, 563.
62. S. Ng, M. B. Smith, and F. Millett, *Biochemistry*, 1977, **16**, 4975.
63. K. K. Rodgers, T. C. Pochapsky, and S. G. Sligar, *Science*, 1988, **240**, 1657.
64. M. R. Mauk, L. S. Reid, and A. G. Mauk, *Biochemistry*, 1982, **21**, 1843.
65. M. R. Mauk, A. G. Mauk, P. C. Weber, and J. B. Mathew, *Biochemistry*, 1986, **25**, 7085.
66. L. Eltis, A. G. Mauk, J. T. Hazzard, M. A. Cusanovich, and G. Tollin, *Biochemistry*, 1988, **27**, 5455.
67. K. K. Rodgers and S. G. Sligar, *J. Mol. Biol.*, 1991, **221**, 1453.
68. M. R. Mauk, P. D. Barber, and A. G. Mauk, *Biochemistry*, 1991, **30**, 9873.
69. A. M. Burch, S. E. J. Rigby, W. D. Funk, R. T. A. MacGillivray, M. R. Mauk, A. G. Mauk, and G. R. Moore, *Science*, 1990, **247**, 831.
70. D. Whitford, Y. Gao, G. J. Pielak, R. J. P. Williams, G. L. McLendon, and F. Sherman, *Eur. J. Biochem.*, 1991, **200**, 359.
71. J. J. Wendoloski, J. B. Matthew, P. C. Weber, and F. Salemme, *Science*, 1987, **238**, 794.
72. L. D. Eltis, R. G. Herbert, P. D. Barker, A. G. Mauk, and S. H. Northrup, *Biochemistry*, 1991, **30**, 3663.
73. G. McLendon and J. R. Miller, *J. Am. Chem. Soc.*, 1985, **107**, 7811.
74. V. Sivozhelezov, *Mol. Eng.*, 1996, **6**, 405.
75. A. Willie, M. McLean, R. Liu, S. Hilgen-willis, A. J. Aunders, G. J. Pielak, S. G. Sligar, B. Durham, and F. Millett, *Biochemistry*, 1993, **32**, 7519.
76. S. L. Edwards, N. G. Xuong, R. C. Hamlin, and J. Kraut, *Biochemistry*, 1987, **26**, 1503.
77. B. C. Finzel, T. L. Poulos, and J. Kraut, *J. Biol. Chem.*, 1984, **259**, 13027; T. L. Poulos and J. Kraut, *J. Biol. Chem.*, 1980, **255**, 10322.
78. H. Pelletier and J. Kraut, *Science*, 1992, **258**, 1748.
79. J. M. Mauro, L. A. Fishel, J. T. Hazzard, T. E. Meyer, G. Tollin, M. A. Cusanovich, and J. Kraut, *Biochemistry*, 1988, **27**, 6243.
80. M. Sivaraja, D. B. Goodin, M. Smith, and B. M. Hoffman, *Science*, 1989, **245**, 738.
81. P. S. Ho, B. M. Hoffman, C. H. Kang, and E. Margoliash, *J. Biol. Chem.*, 1983, **258**, 4356; A. J. W. Coulson, J. E. Erman, and T. Yonetani, *J. Biol. Chem.*, 1971, **246**, 917.
82. L. M. Geren, J. R. Beasley, B. R. Fine, A. J. Saunders, S. Hibdon, G. J. Pielak, B. Durham, and F. Millett *J. Biol. Chem.* 1995, **270**, 2466.
83. K. Wang, H. Mei, L. Geren, M. A. Miller, A. Saunders, X. Wang, J. L. Waldner, G. J. Pielak, B. Durham, and F. Millett, *Biochemistry*, 1996, **35**, 15.
84. H. Mei, L. Geren, M. A. Miller, B. Durham, and F. Millett, *Biochemistry*, 2002, **41**, 3968.
85. H. Mei, K. Wang, N. Peffer, G. Weatherly, D. S. Cohen, M. Miller, G. Pielak, B. Durham, and F. Millett, *Biochemistry*, 1999, **38**, 6846.
86. D. Wang, Y. Zhen, R. Sadosky, S. Grinnell, L. Geren, S. Ferguson-Miller, B. Durham, and F. Millett, *J. Biol. Chem.*, 1999, **274**, 38042.
87. R.-Q. Liu, S. Hahm, M. A. Miller, G. W. Han, L. Geren, S. Hibdon, J. Kraut, B. Durham, and F. Millett, *Biochemistry*, 1994, **33**, 8678.
88. J. M. Mauro, L. A. Fishel, J. T. Hazzard, T. E. Meyer, G. Tollin, M. A. Cusanovich, and J. Kraut, *Biochemistry*, 1988, **27**, 6243.
89. H. Mei, K. Wang, S. McKee, X. Wang, J. L. Waldner, G. J. Pielak, B. Durham, and F. Millett, *Biochemistry*, 1996, **35**, 15800.
90. J. S. Zhou and B. M. Hoffman, *Science*, 1994, **265**, 1693.
91. V. W. Leesch, J. Bujons, A. G. Mauk, and B. M. Hoffman, *Biochemistry*, 2000, **39**, 10132.
92. R. C. Sadoski, G. Engstrom, H. Tian, L. Zhang, C.-A. Yu, L. Yu, B. Durham, and F. Millett, *Biochemistry*, 2000, **39**, 4231.
93. G. Engstrom, K. Xiao, C.-A. Yu, L. Yu, B. Durham, and F. Millett, *J. Biol. Chem.*, 2002, **277**, 31.
94. E. Darrouzet and F. Daldal, *J. Biol. Chem*, 2002, **277**, 3471.
95. S. Hong, N. Ugulava, M. Guergova-kuras, and A. R. Crofts, *J. Biol. Chem.*, 1999, **274**, 33.
96. A. R. Crofts, M. Guergova-Kuras, R. Kuras, N. Ugulava, J. Li, and S. Hong, *Biochim.Biopys. Acta*, 2000, **1459**, 456.
97. S. Bartoschekt, M. Johannson, B. H. Geierstanger, J. G. Okun, C. R. D. Lancaster, E. Humpfer, L. Yu, C.-A. Yu, C. Griesinger, and U. Brandt, *J. Biol. Chem.*, 2001, **276**, 35231.
98. K. Xiao, G. Engstrom, S. Rajagukguk, C. A. Yu, L. Yu, B. Durham, and F. Millett, *J. Biol. Chem.*, 2003, **278**, 11419.
99. X. Gao, X. Wen, C.-A. Yu, L. Esser, S. Tsao, B. Quinn, L. Zhang, L. Yu, and D. Xia, *Biochemistry*, 2002, **41**, 11692.
100. C.-A. Yu, L. Yu, and T. E. King, *J. Biol. Chem*, 1973, **248**, 528.

101. C. Lange and C. Hunte, *Proc. Natl. Acad. Sci. U.S.A.*, 2002, **99**, 2800.

102. G. Engstrom, R. Rajagukguk, A. J. Saunders, C. N. Patel, S. Rajagukguk, R. Merbitz-Zahradnik, K. Xiao, G. J. Pielak, B. Trumpower, C.-A. Yu, L. Yu, B. Durham, and F. Millett, *Biochemistry*, 2003, **42**, 2816.

103. V. A. Roberts and M. E. Pique, *J. Biol. Chem*, 1999, **274**, 38051.

104. K. Wang, L. Geren, Y. Zhen, L. Ma, S. Ferguson-Miller, B. Durham, and F. Millett, *Biochemistry*, 2002, **41**, 2298.

Iron: Heme Proteins, Mono- & Dioxygenases

Luet-Lok Wong & Stephen G. Bell
University of Oxford, Oxford, UK

Based in part on the article Iron: Heme Proteins, Mono- & Dioxygenases by Masanori Sono & John H. Dawson which appeared in the Encyclopedia of Inorganic Chemistry, First Edition.

1 Introduction 1
2 Cytochrome P450 Enzymes are Heme Monooxygenases 3
3 Indoleamine 2,3-dioxygenase 22
4 Related Articles 25
5 References 25

1 INTRODUCTION

Oxygenase enzymes are important components of oxygen biological chemistry that sustains all aerobic life. Oxygen is formed in the four-electron oxidation of two water molecules catalyzed by the photosystem II oxygen-evolving system in plants and photosynthetic microorganisms (*see* ***Manganese: The Oxygen-evolving Complex & Models***). Once inside cells, oxygen is transported by iron- (*see* ***Iron: Heme Proteins & Dioxygen Transport & Storage***) and copper-containing proteins (*see* ***Copper Proteins with Dinuclear Active Sites***) to subcellular compartments and utilized in a myriad of biological functions. The importance of oxygen stems from the thermodynamically favorable nature of reactions that involve reduction and cleavage of the O–O bond (Figure 1) (*see* ***Dioxygen & Related Ligands***). In the mitochondria, cytochrome *c* oxidase catalyzes the highly favorable reduction of oxygen to water ($E^{\circ\prime} = +0.82\,\mathrm{V}$) and couples this electron-transfer reaction to proton translocation across a membrane (*see* ***Cytochrome Oxidase***). The resultant proton gradient is utilized for the synthesis of ATP – the energy source for aerobic organisms. The two-electron reduction of oxygen to hydrogen peroxide ($E^{\circ\prime} = +0.30\,\mathrm{V}$) provides the thermodynamic driving force for oxidase enzymes to oxidize many biological molecules.

Apart from water, all reduced oxygen species (Figure 1) are highly reactive. Superoxide ($O_2^{\bullet-}$), peroxide and especially the hydroxyl radical ($HO^{\bullet}$), cause cellular damage by oxidizing peptides, lipids, and nucleic acids. These reactive oxygen species (ROS) are side products in many reactions inside cells, for example, hydrogen peroxide from oxidase activity. Aerobic organisms have evolved highly active and specific enzymes for ROS removal. The disproportionation of superoxide to oxygen and peroxide is catalyzed by superoxide dismutase (SOD) (*see* ***Copper Proteins with Type 2 Sites***; ***Manganese Proteins with Mono- & Dinuclear Sites***; ***Nickel Enzymes & Cofactors***). Hydrogen peroxide is removed by peroxidases and catalases (*see* ***Iron: Heme Proteins, Peroxidases, Catalases & Catalase-peroxidases***). These enzymes are amongst the most active and efficient biological catalysts.

$$\text{Superoxide dismutase}\qquad 2O_2^{\bullet-} \longrightarrow O_2 + O_2^{2-} \tag{1}$$

$$\text{Peroxidase}\qquad H_2O_2 + 2AH \longrightarrow 2H_2O + 2A \tag{2}$$

$$\text{Catalase}\qquad 2H_2O_2 \longrightarrow 2H_2O + O_2 \tag{3}$$

In the disproportionation of superoxide (equation 1) and hydrogen peroxide (equation 3), the reactant is both the electron donor and electron acceptor, while peroxidases (equation 2) require an external source of electrons. Some organisms have evolved to exploit this property of peroxidases for both the synthesis and oxidative degradation of organic compounds. Higher organisms have actually harnessed the destructive power of ROS in the immune defense system.

1.1 Oxygen is Kinetically Trapped

The reduction of oxygen to water is a highly favorable reaction. When oxygen was first released into the Earth's atmosphere, it was an ecological catastrophe because early organisms lived on the chemistry of lower oxidation state species such as Fe^{2+} and S^{2-}, in an anaerobic world. These vital elements were rapidly oxidized at neutral pHs and suddenly became unavailable. Today anaerobic organisms only survive in special niches that have low levels of oxygen. In an aerobic atmosphere, carbon- and hydrogen-containing compounds that are present in all living things, are thermodynamically unstable to oxidation to carbon dioxide and water. However, the direct oxidation of organic compounds by oxygen is kinetically slow: We live in a metastable world and coexist with oxygen in a kinetic trap.

Molecular oxygen is a kinetically slow oxidant because of its electronic structure, which may be described as $(\sigma 1s)^2(\sigma^*1s)^2\,(\sigma 2s)^2\,(\sigma^*2s)^2(\sigma 2p_z)^2(\pi 2p_{x,y})^4(\pi^*2p_x)^1\,(\pi^*2p_y)^1$ (*see* ***Dioxygen & Related Ligands***). The bond order is two and the highest occupied molecular orbital is the doubly degenerate antibonding π^* orbital. The two π^* electrons have parallel spins, and O_2 is a diradical with a triplet ground state, ${}^3\Sigma_g{}^-$. The first excited state, with both π^* electrons in one orbital, is a singlet (${}^1\Delta_g{}^+$) $23\,\mathrm{kcal\,mol^{-1}}$ above the ground state. In the second excited state, the two electrons are in separate π^* orbitals but their spins are paired, resulting in a singlet state (${}^1\Sigma_g{}^-$) that is a further $14\,\mathrm{kcal\,mol^{-1}}$ above the ${}^1\Delta_g{}^+$ state.

The triplet ground state of oxygen is the principal barrier to direct attack of organic compounds. Essentially all stable

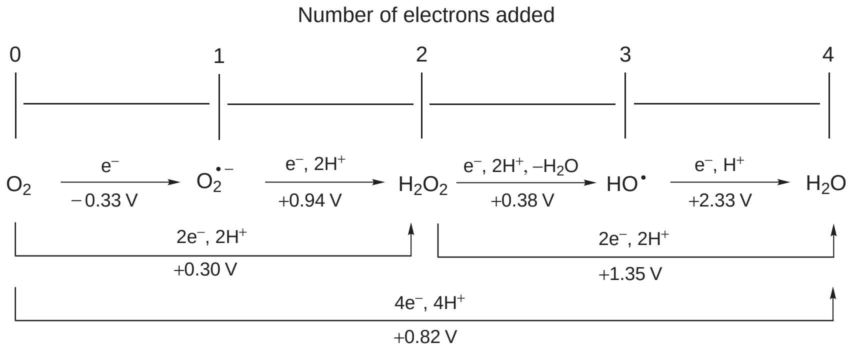

Figure 1 The electrode potentials for the stepwise reduction of oxygen to water. E°′ values are at pH 7.0, 298 K, 1 atm O_2 and unit activity for other components

organic molecules have singlet ground states, and the products of oxidation by oxygen are also singlets. The direct reaction between a triplet molecule (O_2) and a singlet molecule to give a singlet product is spin-forbidden. The reaction to give a triplet product is spin-allowed but requires preactivation of the organic molecule to an excited state, resulting in a high activation barrier. The reaction between singlet O_2 and a singlet organic molecule is spin-allowed. However, the lowest energy singlet state of O_2 is 23 kcal mol^{-1} above the ground state and thus presents a high activation barrier to the reaction. Singlet oxygen can be generated photochemically in the presence of a sensitizer molecule. However, these reactions often give different products from those catalyzed by chemical and biological catalysts.

The high kinetic barrier to reactions with triplet O_2 is overcome in biological systems by the use of transition metals (mainly iron and copper) and electron-rich organic groups. Transition metals readily undergo redox reactions and direct reduction of oxygen is possible, but metal centers in metalloenzymes can bind oxygen. The Fe(II) centers in heme and nonheme iron proteins are high spin ($S = 2$) and the binding of triplet O_2 ($S = 1$) is fast because it is not spin-inhibited. In oxygen transport metalloproteins such as hemoglobin (*see* ***Iron: Heme Proteins & Dioxygen Transport & Storage***) and hemocyanin (*see* ***Copper Proteins with Dinuclear Active Sites***), there is no activation of the metal-bound O_2 molecule. In enzymes, further electron transfer or chemical steps lead to activation and cleavage of the O–O bond and the formation of reactive intermediates that can attack bound substrates. Highly electron-rich organic molecules can also undergo direct reaction with O_2. Compounds such as flavins have singlet ground states but can readily form stable cation radicals. The isoalloxazine double bond in a reduced flavin molecule is electron rich because it has three electron-releasing nitrogen substituents (Figure 2). It readily reduces oxygen to superoxide because the flavin radical cation is resonance-stabilized. These two ions recombine to form a flavin hydroperoxide that can decompose to form hydrogen peroxide or, in the case of flavin monooxygenases, oxidize a bound substrate.

1.2 Oxygen Activation by Oxygenases

Oxygenases activate O_2 to oxidize organic molecules. Mason**[1]** and Hayashi**[2]** were the first to observe oxygenase activity by ^{18}O labeling experiments. The term ‘oxygenase’ was introduced by Hayashi.**[3]** Monooxygenases cleave O_2 to give one molecule of water while inserting the other oxygen atom into the substrate (equation 4, where X is the substrate) while dioxygenases insert both oxygen atoms (equation 5).

$$\text{Monooxygenases} \qquad X + O_2 + 2e^- + 2H^+ \longrightarrow XO + H_2O \quad (4)$$

$$\text{Dioxygenases} \qquad X + O_2 \longrightarrow X(O)_2 \quad (5)$$

Oxygenases contain transition metals, mainly iron (heme and nonheme), copper, and manganese. Organic prosthetic groups (e.g. flavins) are also found in monooxygenases. These enzymes oxidize a very broad range of organic compounds. Dioxygenases are particularly important in the biodegradation of aromatic compounds by microorganisms. The aromatic ring is oxidized by a nonheme iron dioxygenase to the dihydrodiol that is re-aromatized to the catechol. Diol dioxygenases, another class of nonheme iron dioxygenases, then cleave the ring, leading ultimately to mineralization of the organic compound (*see* ***Iron Proteins with Mononuclear Active Sites***).

Monooxygenases usually utilize an external source of electrons (equation 4). However, nonheme iron monooxygenases can also activate oxygen by transferring one oxygen atom to a cofactor. A common cofactor is 2-oxo-glutarate (2-OG), which is converted to succinate in the reaction (Figure 3). 2-OG dependent enzymes are involved in antibiotic biosynthesis and also include the newly discovered oxygen-sensing enzyme hypoxia inducible factor (HIF).**[4–7]** Since the cofactor is also oxygenated, such enzymes could be classified as dioxygenases.

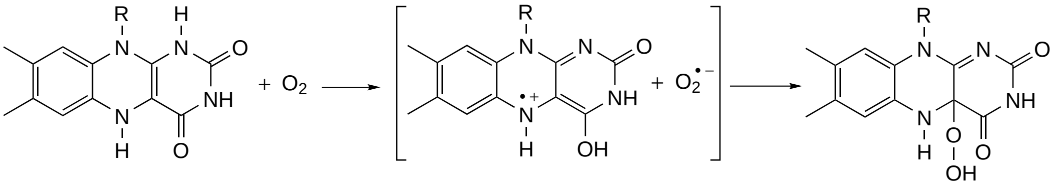

Figure 2 Direct reaction of a flavin group with O_2

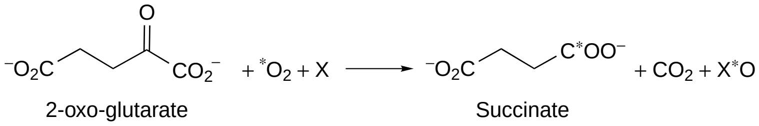

Figure 3 Activation of O_2 by 2-oxo-glutarate dependent nonheme iron monooxygenases

2 CYTOCHROME P450 ENZYMES ARE HEME MONOOXYGENASES

2.1 History of the Cytochrome P450 (CYP) Superfamily

In 1958, Klingenberg[8] and Garfinkel[9] independently reported liver microsomal pigments that showed an unprecedented absorption maximum at 450 nm upon carbon monoxide binding. Omura and Sato showed that these pigments were heme-containing proteins and designated them 'cytochrome P450'.[10,11] P450 enzymes are *b*-type cytochromes, with the iron bound to protoporphyrin IX (Figure 4) (*see* ***Iron Porphyrin Chemistry***) and the porphyrin ring substituents are not covalently bonded to the polypeptide. In *c*-type cytochromes a cysteine thiol group is added across the double bond of each of the porphyrin vinyl groups (*see* ***Iron: Heme Proteins & Electron Transport***). Mason proposed that the unusual spectrum of P450 enzymes arose from thiolate coordination to the heme iron.[12] The importance of cytochrome P450 enzymes became evident when Estabrook and coworkers showed that these microsomal enzymes are monooxygenases that catalyze the hydroxylation of steroids and other organic compounds.[13] As more and more P450 enzymes were discovered, it was found that all eukaryotic enzymes were associated with either the inner mitochondrial or the endoplasmic reticulum membranes, while the vast majority of microbial enzymes were cytosolic and soluble.

Early attempts to solubilize membrane-bound P450 enzymes resulted in loss of activity and shift of the characteristic 450 nm absorption band of the Fe^{II}-CO form to 420 nm. This inactive form was designated 'cytochrome P420'.[11] Liver microsomal P450 enzymes were eventually solubilized in their active forms by Coon and coworkers,[14] and the field of P450 research grew rapidly. New P450 enzymes, often induced by xenobiotics, were isolated from mammals, fungi, plants, and, later, humans. In the late 1960s, Gunsalus and coworkers isolated the soluble enzyme $P450_{cam}$ from the soil bacterium *Pseudomonas putida*.[15–17] The availability of large quantities of this stable and soluble enzyme, and its physiological electron transport cofactor proteins putidaredoxin reductase and putidaredoxin, made possible detailed spectroscopic and mechanistic investigations into P450 catalysis. $P450_{cam}$ was also the first P450 enzyme to be structurally characterized.[18]

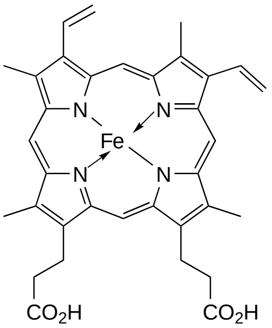

Figure 4 Iron protoporphyrin IX (heme *b*), the prosthetic group of P450 enzymes

As more genes encoding P450 enzymes were sequenced, nomenclature of the P450 superfamily was systematized.[19] The CYP (P450) superfamily was grouped by amino acid sequence identity into families (1, 2, 3...), subfamilies (A, B, C ...) and individual enzymes (1, 2, 3...). Hence, current names include CYP1A2, CYP3A4, CYP2E1, CYP102A2, and so on (see http://drnelson.utmem.edu/CytochromeP450.html). The increasing availability of genome sequences shows that P450 enzymes are found in almost all organisms. Only certain bacteria, such as *Escherichia coli* and *Lactobacillus*, do not synthesize P450s. As of January 2004, there are over 3000 distinct P450 sequences in the data banks. There are about 53 human P450 enzymes, the worm *C. elegans* has 80, fruit fly 83, the plant *A. thaliana* 286, rice 500, but yeast has only 3.

2.2 Physiological Significance

Some P450 enzymes are constitutively expressed and play vital roles in the biosynthesis of endogenous compounds such as steroids and other hormones (e.g. nitric oxide) in mammals,**[20]** and secondary metabolites in plants.**[21]** In microorganisms the substrate hydroxylation activity of P450 enzymes enables the organism to grow on chemically inert compounds such as alkanes as the sole carbon and energy source.**[22,23]** P450 enzymes are also involved in the synthesis of important medicinal antibiotics in microorganisms.**[24]** Many P450 enzymes are induced by xenobiotics and perform vital functions in detoxification pathways.**[25,26]** Hydrophobic and chemically inert exogenous compounds are oxidized to more soluble, polar derivatives that are either excreted directly or conjugated to sugars for transport and excretion.**[20]** This xenobiotic-removal function casts P450 enzymes in a central role in drug metabolism and pharmacokinetics. Indeed P450 enzymes in the human body metabolize over 50% of all pharmaceuticals. P450 enzymes also convert some drugs, for example, losartan, to their active forms, or derivatives that are more active than the parent compound. The circulating concentration and hence efficacy of a medicinal compound may vary between individuals depending on the constitutive expression levels of different P450 isoforms, the inducibility of different P450 enzymes, and gene polymorphism.

The increased reactivity of substrate oxidation products also means that P450 enzymes can transform otherwise inert compounds into reactive derivatives which may be toxic or carcinogenic.**[26]** Thus at an early stage of development, candidate pharmaceutical compounds are subjected to oxidation by a variety of heterologously expressed human P450 enzymes and the products screened for toxicity. The *N*-hydroxylation of nitrosoamines and aromatic amines give metabolites that are toxic and can react with DNA. Procarcinogens such as polycyclic aromatic hydrocarbons (e.g. benzanthracene and benzo[*a*]pyrene) and aflataxin B are converted to carcinogens by P450 enzymes. The active carcinogens that modify DNA are the highly electrophilic epoxides and diol-epoxides (Figure 5). In addition, other oxidation products, especially phenol and hydroquinone derivatives, readily undergo redox cycling to generate ROS such as superoxide and peroxide which cause damage to cells.

2.3 Electron Transport in P450 Enzyme Systems

2.3.1 *Classification of P450 Enzymes*

The two electrons required for the P450 monooxygenase reaction (equation 4) are normally derived from NADH or NADPH and transferred to the P450 enzyme one-at-a-time by

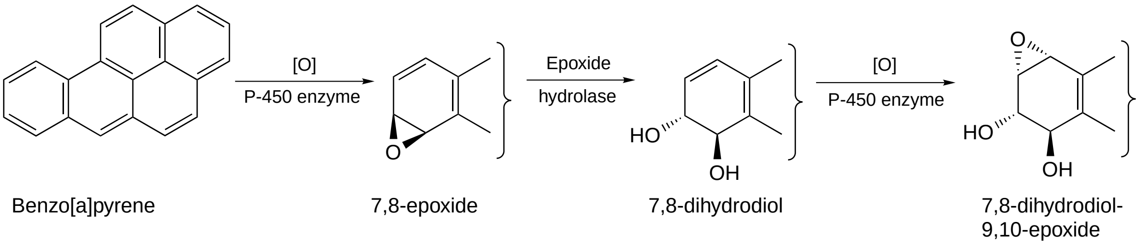

Figure 5 Activation of the procarcinogen benzo[*a*]pyrene by P450 enzymes. The diol-epoxide is the active carcinogen that modifies nucleic acids

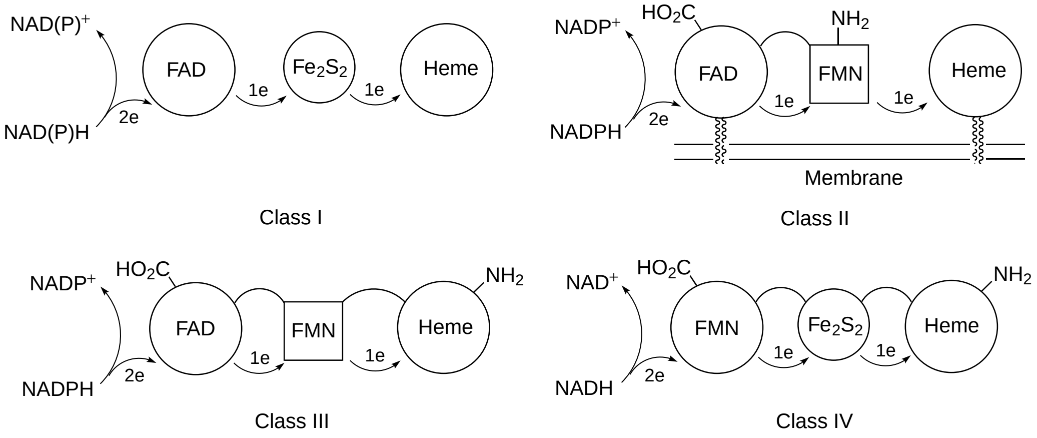

Class I

Class II

Class III

Class IV

Figure 6 The four classes of P450 enzymes distinguished by the nature of their electron transport chains

an electron-transfer protein. Since NAD(P)H is a two-electron reductant, this is a noncomplementary electron-transfer reaction like those found with inorganic complexes. The electron-transfer proteins play the role of a catalyst, analogous to $Ta_6Cl_{12}^{2+}$ in the reduction of Fe^{3+} by Sn^{2+}.

There are four classes of P450 enzymes that are distinguished by the organization of their electron transport chains (Figure 6). NAD(P)H delivers a hydride (2 electrons) to a flavin group. Class I P450 systems, which include mitochondrial and most bacterial P450 enzymes, utilize three-component electron transport chains where a flavin adenine dinucleotide (FAD)-containing reductase transfers an electron to an Fe–S protein which then delivers the electron to the P450 monooxygenase. Class II P450 enzymes are membrane-bound microsomal systems comprised of two proteins. A NADPH-cytochrome P450 reductase, with FAD and FMN groups in separate domains, acts as the electron-transfer shuttle. The FAD group accepts two electrons from NADPH which are transferred to the P450 enzyme via the FMN group. Hence the FMN group performs the role of Fe–S redox centers of Class I systems. The first example of a Class III P450 enzyme was $P450_{BM-3}$ (CYP102A1) from *Bacillus megaterium*. Like their Class II counterparts, Class III systems also have a reductase protein containing FAD and FMN groups in separate domains, but this reductase is fused to the C-terminal of the P450 monooxygenase enzyme. Class III P450s are therefore fused Class II systems and catalytically self-sufficient. More Class III bacterial enzymes are being discovered, and eukaryotic counterparts are also known.[27] The first example of a Class IV enzyme was reported in 2002.[28] Like Class III enzymes, P450RhF from *Rhodococcus* is also self-sufficient. However, the reductase domain contains a flavin mononucleotide (FMN) group which accepts electrons from NADH and transfers them to the P450 enzyme via a Fe_2S_2 group in a separate domain (Figure 6).[29] This Class IV enzyme is essentially a fused Class I system except that FMN is the initial electron acceptor instead of FAD.

2.3.2 *Structure of P450 Electron-transfer Proteins*

The crystal structure of NADPH-cytochrome P450 reductase (CPR), the common electron-transfer protein of Class II eukaryotic P450 systems, was reported in 1997.[30] This was followed by the structures of adrenodoxin reductase (AdR)[31] and adrenodoxin (Adx),[32] the two electron-transfer proteins of the Class I mitochondrial P450 system. The crystal structure of a cross-linked AdR-Adx complex has also been reported.[33,34] Putidaredoxin reductase (PdR) and putidaredoxin (Pd) of the $P450_{cam}$ system have also been structurally characterized.[35,36]

The structure of CPR is significant because this membrane-bound protein mediates electron transfer from NADPH to *all* microsomal P450 enzymes. A soluble form of CPR was generated by limited protease digestion and crystallized. The structure consists of a N-terminal FMN domain linked to the C-terminal FAD domain via a hinge domain (Figure 7). The protein crystallized with the isoalloxazine rings of the flavin cofactors from the different domains in close contact (4 Å), which facilitates electron transfer (*see* ***Long-range Electron Transfer in Biology***). A surface region near the FMN cofactor was suggested to be the recognition site for the binding of P450 enzymes. However, at the present time, there is little experimental data on the recognition and binding interactions between CPR and microsomal P450 enzymes. It is possible that the hinge domain in CPR allows the FMN domain to move away from the FAD domain and bind to P450 monooxygenases.

The crystal structure of the cross-linked AdR-Adx complex (Figure 8) showed that there were changes in the structure of AdR, but not of Adx, upon complex formation.[33,34] The Fe_2S_2 ferredoxin Adx is known to undergo a redox-dependent conformation change that is required for electron transfer (*see* ***Iron–Sulfur Proteins***).[32,37] The structure of Adx in the complex suggests that this is possible in the protein-protein complex. It had been noted from the structures of the separate proteins that the charge distributions of AdR and Adx are highly asymmetric, resulting in large dipoles for the proteins that may facilitate protein-protein recognition and binding. This was observed in the complex where the cluster of basic residues on the surface of AdR formed salt bridge contacts with surface acidic residues on Adx. The closest approach of the AdR isoalloxazine ring to the Adx Fe_2S_2 group was 10 Å, which facilitates electron transfer between the cofactors.

The structure of PdR (Figure 9) is significantly different from that of AdR although both proteins are related to disulfide reductases and other flavin-dependent enzymes. The

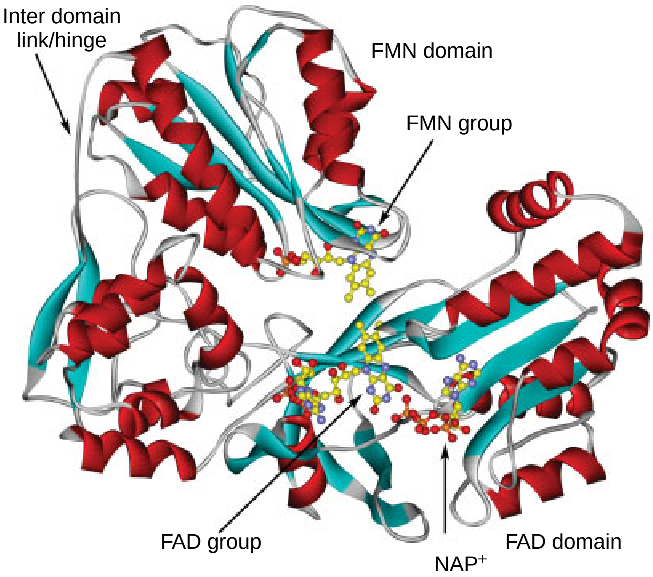

Figure 7 The crystal structure of NADPH-cytochrome P450 reductase (CPR). The FAD and FMN domains are linked by a hinge domain

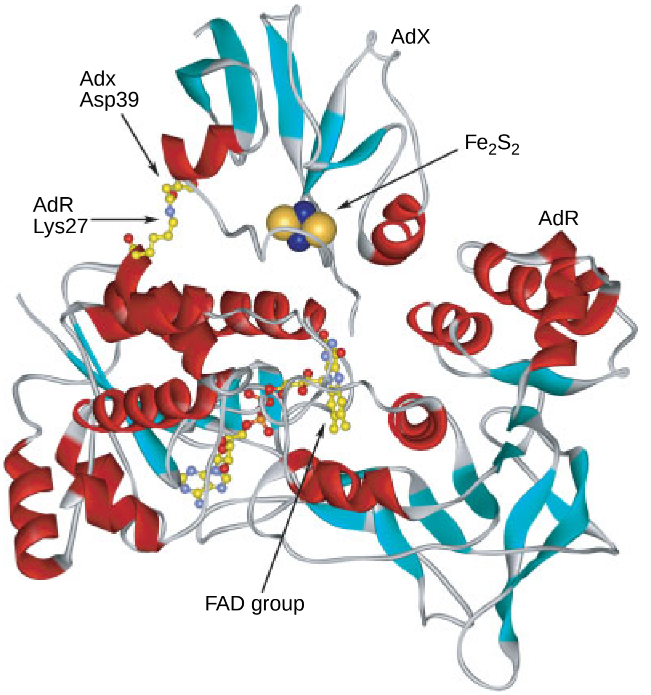

Figure 8 The structures of the FAD-containing adrenodoxin reductase (AdR) and the Fe_2S_2 ferredoxin adrenodoxin (Adx) cross-linked by the side chains of Lys27 of AdR and Asp39 of Adx. The distance of closest approach of the two redox centers is ~10 Å

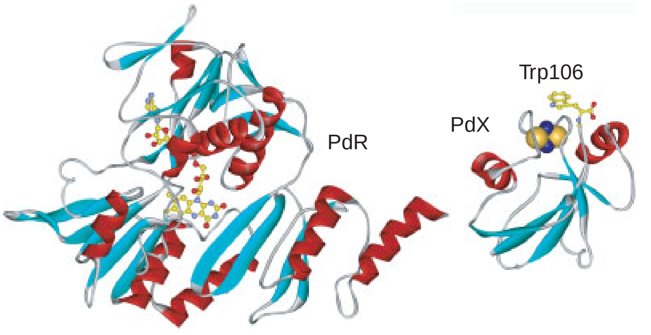

Figure 9 The structure of PdR and Pdx, the electron-transfer proteins of the $P450_{cam}$ system. The PdR molecule is viewed from the *si* side of the flavin from which Pdx is proposed to approach and accept electrons from PdR. The Fe_2S_2 center of Pdx is close to the protein surface, and the C-terminal Trp-106 residue is important for electron transfer

C-terminal FAD-binding domains of the two proteins are different in size and have different secondary structure elements (Figures 8 and 9). The highly asymmetric charge distribution of AdR was absent from PdR, which has a much lower dipole moment. The reductant NADH approaches and binds on the *re* side of the FAD in PdR, indicating that Pdx should bind on the *si* side. Unlike for AdR, the *si* side surface of PdR is much less hydrophilic, suggesting that the PdR/Pdx interaction predominantly involved polar contacts. The structure of Pdx is consistent with these observations. Although Adx and Pdx share the same overall ferredoxin fold, Pdx (Figure 9) is conformationally rigid; it does not have an asymmetric charge distribution; and the immediate vicinity of the Fe_2S_2 redox center is largely neutral. It appears that polar residues on the surface of Pdx are involved in molecular recognition with the *si* side surface of PdR. The different charge distributions, conformational dynamics, and protein recognition interactions observed in these structures have resolved the long-standing puzzle of the poor cross reactivity between these two Class I P450 systems.

2.4 Structure of P450 Enzymes

The first structurally characterized P450 enzyme was $P450_{cam}$ (CYP101) from *Pseudomonas putida*.[18,38] This was followed by the crystal structures of $P450_{BM\text{-}3}$ (CYP102A1) from *Bacillus megaterium*,[39,40] $P450_{terp}$ (CYP108) from a *Pseudomonad*,[41] and $P450_{eryF}$ (CYP107A1) from *Saccharopolyspora erythraea*.[42,43] The structures of other bacterial P450 enzymes have been determined, including the sterol demethylase CYP51 and CYP121 from *Mycobacterium tuberculosis*,[44,45] CYP154A1 and CYP154C1 from *Streptomyces coelicolor*,[46,47] CYP119 from the thermophilic bacterium *Sulfolobus solfataricus*,[48,49] CYP175A1 from another thermophile *Thermus thermophilus*, P450oxyB and P450oxyC from the vancomycin-synthesizing *Amycolatopsis orientalis*,[50,51] and $P450_{epoK}$ which is involved in epothioline synthesis in *Sorangium cellulosum*.[52]

Since bacterial enzymes are soluble and often readily crystallized, we can expect the crystal structures of many more prokaryotic P450 enzymes to be determined in the future. Eukaryotic P450 enzymes are membrane-bound and much more difficult to crystallize. Johnson and coworkers have replaced the N-terminal membrane anchor residues with short hydrophilic peptides and also used mutagenesis to reduce the extent of protein aggregation.[53] Using this method, rabbit CYP2C5 and human CYP2C9 and CYP2B4 have been crystallized and structurally characterized.[54,55]

All of the structures of P450 enzymes show a common overall fold (the P450 fold) and similar secondary structure elements.[56–59] The P450 fold has a helix-rich domain and another domain mainly comprised of β-sheets. The heme is located at the boundary between these two domains and the substrate-binding pocket is defined by residues from both domains. The primary sequences and structures of P450 enzymes show a well-conserved series of helices A–L. The I and L helices contact the heme on the distal and proximal sides, respectively. The B, C, and I helices have extensive contacts with the substrate, and residues in the F and G helices also contribute to substrate binding. However, the structures of P450 enzymes, in particular the crucial substrate-binding pocket on the distal side of the heme, differ dramatically in detail. These differences arise from slightly different lengths and arrangement of helices and β-sheets, and also different packing of the two major domains in the structure.

The P450$_{\text{cam}}$ structure does not show any opening from the heme prosthetic group to the protein surface. Substrate entry must therefore rely on transient conformational fluctuations to open a substrate access channel. Other enzymes do have well-defined substrate access channels, for example, P450$_{\text{BM-3}}$ (CYP102A1) and CYP51,[39,44] or have very open structures with large clefts leading directly from the protein surface to the heme, for example, CYP154C1 and CYP2B4.[46,55] CYP2B4 crystallizes as a dimer with an open cleft that runs from the surface of the protein to the heme. In the absence of a substrate the cleft is partially filled by residues from the other molecule of the dimer, with the imidazole side chain from one residue coordinated to the heme.

2.4.1 Structure of P450$_{cam}$ (CYP101)

Although first reported nearly twenty years ago, the structural features and inferences drawn from the structure of P450$_{\text{cam}}$ remain the basis of much of the current understanding of P450 catalysis, and will do so in future efforts on detailed mechanistic investigations. The structure of P450$_{\text{cam}}$ with camphor bound within its active site is shown in Figure 10.[18] The protein is a trigonal prism with triangular sides of ~60 Å and a thickness of ca. 30 Å. In this 'normal' view of the P450 structure, the helix-rich domain is on the right while the more β-sheet domain is in the top left quadrant. The heme is sandwiched between the two domains and roughly parallel to the triangular faces. The iron is five-coordinate and out of the porphyrin plane towards the proximal cysteine thiolate ligand.

Of the secondary structural elements, helices I and L contact the heme. The L helix provides the proximal Cys-357 ligand to the heme iron, and contains the highly conserved P450 signature sequence FGHGXHXCLG used to identify CYP genes in genomes. The I helix on the distal side is the longest in the molecule and spans the whole structure. It contains two highly conserved residues Asp-251 and Thr-252. There is a characteristic kink in the helix (Figure 11) as a result of a H-bond between the backbone carbonyl of G248 and the alcohol side chain of T252; in a normal helix the hydrogen bond is formed with the amide NH of T252. This kink creates a small pocket or groove which was proposed to be important for oxygen binding. Supporting evidence comes from the structure of the ferrous-carbon monoxide form of the enzyme, in which the oxygen of the CO ligand pointed into this groove.[60] Three ordered water molecules (WAT 523, 566, 687) are found in the vicinity of this groove (Figure 11) and these, together with the D251 and T252 side chains, are believed to be involved in the relay that shuttles protons to the heme-bound O_2 for O–O bond cleavage (see Section 2.5.2).

On the proximal side of the heme, the amide NH protons of L358, G359 and Q360 form H-bonds with the C357 proximal thiolate ligand. Since the Cys-Leu-Gly motif is part of the highly conserved P450 signature sequence, this set of H-bonds occurs in all P450 enzymes and they play crucial roles in moderating the electronic structure and redox properties of the heme. The proximal side of the heme is close to the protein surface (shortest distance ~10 Å), and it is most likely that the physiological electron-transfer protein will deliver the electron from this side of the enzyme. The proximal surface of P450$_{\text{cam}}$ has a number of basic residues that are conserved across the CYP superfamily. The presence of such residues, in particular R72, R112, K344 and R392 in P450$_{\text{cam}}$,[61,62] suggests that basic residues on the proximal surface of P450 enzymes interact with surface acidic residues on the electron-transfer protein.[30,63]

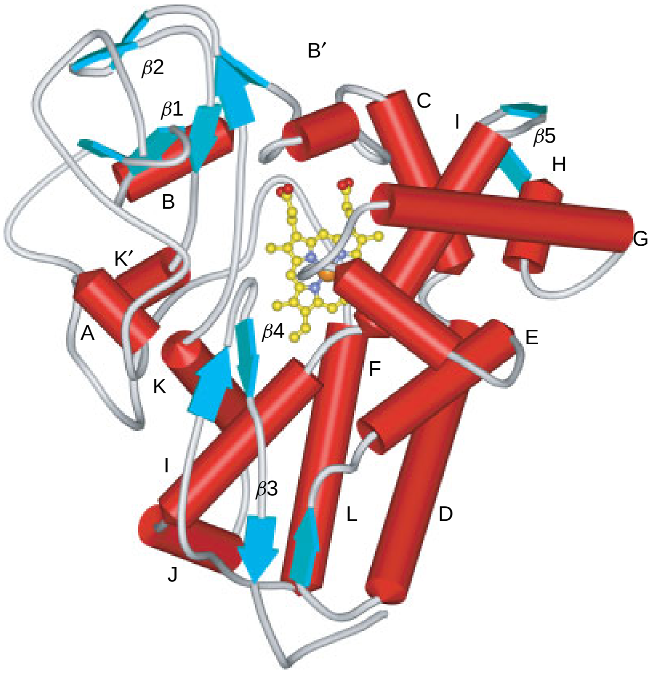

Figure 10 The crystal structure of P450$_{\text{cam}}$ with bound camphor. The secondary structure elements are shown schematically with cylinders representing α helices and ribbon arrows depicting β strands

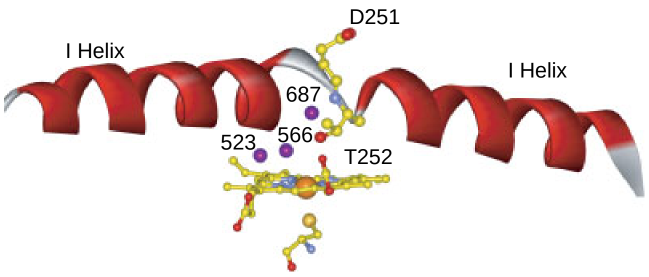

Figure 11 The oxygen-binding groove in the I helix formed by the characteristic kink in the helix. The side chains of Asp-251 and Thr-252, and the three ordered water molecules 523, 566 and 687, are proposed to be involved in oxygen binding and proton shuttling

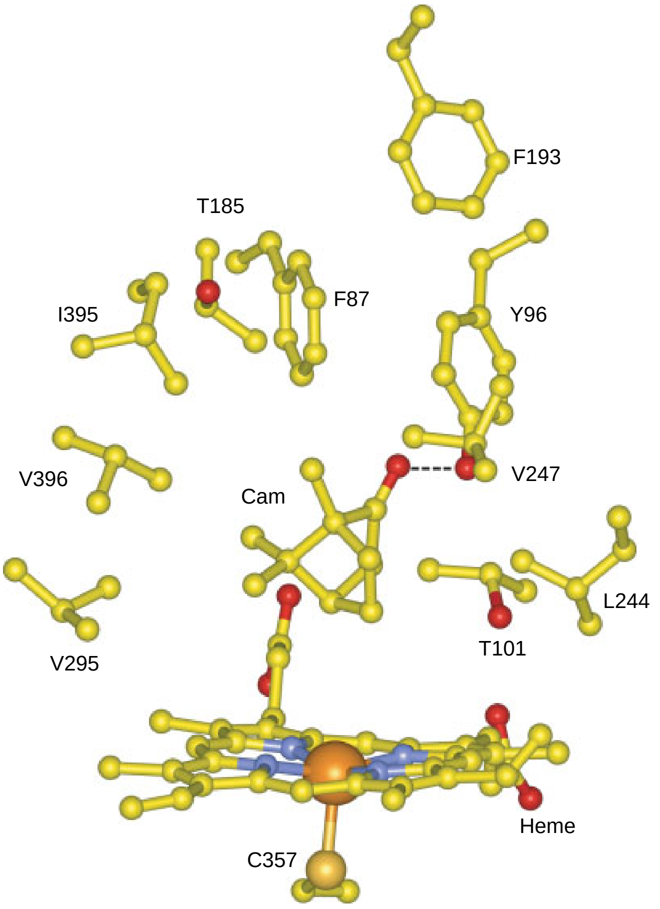

Figure 12 The active structure of P450$_{cam}$ with bound camphor. The amino acid side chains that define the substrate pocket and contact the substrate are shown. The dotted line indicates the hydrogen bond between the camphor carbonyl and the phenol side chain of Tyr-96

The active-site structure of P450$_{cam}$ with bound camphor is shown in Figure 12. There are numerous noncovalent contacts between substrate and protein, and the camphor carbonyl is H-bonded to the phenol side chain of Y96 – the most prominent hydrophilic active-site residue.[18] The contacts between camphor and F87, L244, V247, V295, and V396 contribute to the strength of binding and, together with the H-bond to Y96, hold the orientation of the molecule so that the camphor C-5 is placed ∼4.5 Å from the heme iron and the Cys-S/Fe/C-5 angle is close to 180°. The importance of the camphor-Y96 H-bond has been demonstrated by mutagenesis studies.[64] Sligar also noted that the active-site residues are arranged approximately in tiers above the heme. Tier 1 contains T101, L244, V295, while F87, Y96, F98, V247, I395 and V396 are in Tier 2, and T185 is in tier 3 and appears to serve as a cap on the active site. This Tier model offers a useful framework for discussing the effect of amino acid substitutions on protein substrate recognition and catalytic activity.[65]

Based on multiple sequence alignments, Gotoh has identified six substrate recognition sites (SRS) in P450 sequence space.[66] When mapped onto the P450$_{cam}$ structure (Figures 10 and 12), SRS 1 is in the B′–C loop (around F87, Y96 and T101), SRS 2 and 3 are on the F and G helices (around T185 and F193), SRS 4 is in the distal I helix (around L244 and V247), SRS 5 is between helix K and β strand 1–4 (around V295), while SRS 6 is in β strand 4–2 (around I395 and V396). These SRS regions can be identified in the sequences of P450 enzymes but comparison of the available structures indicates that the locations of these sites in 3-D space are not well conserved.[56–59] Helix movement and different packing of secondary elements as well as changes in the domain contacts can result in varied active-site architecture.

2.4.2 Structure of P450$_{BM\text{-}3}$ (CYP102A1) and CYP2C9

The structure of the heme domain of P450$_{BM\text{-}3}$ with a fatty acid substrate bound shows the characteristic P450 fold and the kink in the distal I helix,[40] and E267 and T268 are equivalent to D251 and T252 in P450$_{cam}$. Two features in the structure are particularly relevant to the present discussion. Firstly P450$_{BM\text{-}3}$ has a well-defined substrate access channel that extends from the surface residues R47 and Y51 at the channel entrance down through to the heme (Figure 13). Secondly, unlike the P450$_{cam}$ structure in which camphor is poised over the heme iron for oxidation at C-5, the terminal carbons of the fatty acid substrate are prevented from approaching the heme iron by the F87 side chain in P450$_{BM\text{-}3}$. Hence there must be a conformational change during catalysis, perhaps associated with an electron-transfer step, to flip the F87 side chain out of the way to allow the substrate carbons to approach the heme iron.

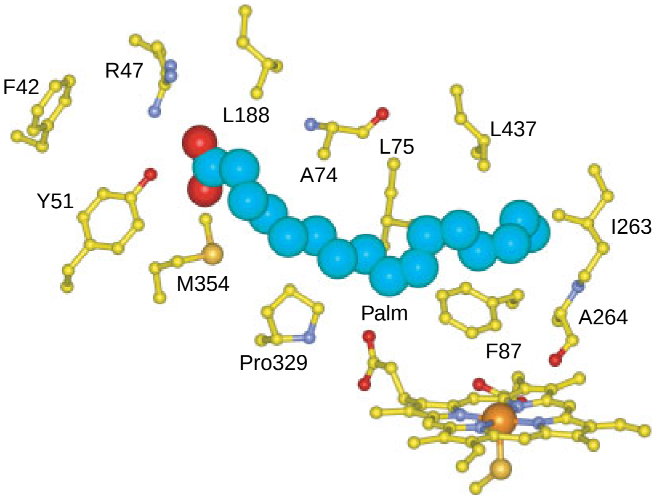

Figure 13 The active-site structure of P450$_{BM\text{-}3}$ with palmitoleic acid bound to the substrate pocket. The fatty acid substrate extends along the substrate access channel to the surface of the protein. The side chains lining the channel are also shown

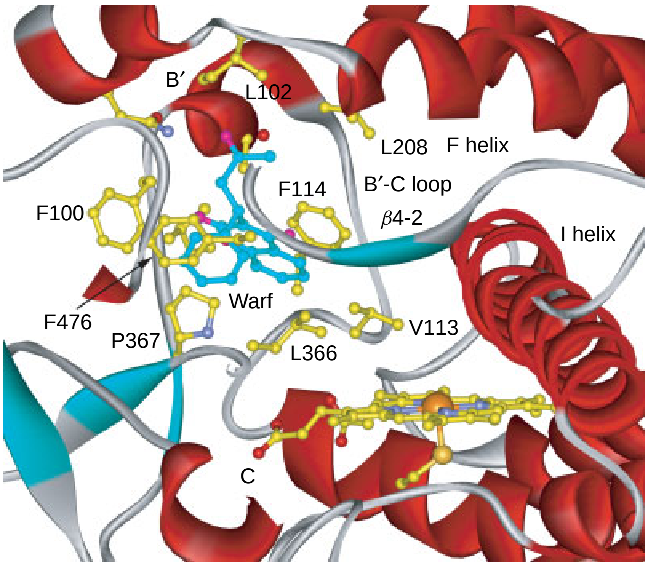

Figure 14 The structure of human CYP2C9 with warfarin (in blue) bound within the active site. There is a large pocket over the heme defined by the B′–C loop, the F and I helices, and the $\beta 4-2$ strand

The structure of CYP2C9, a drug metabolizing human P450 enzyme, with warfarin bound within its active site, is shown in Figure 14.[54] Although the CYP2C9 enzyme is closely related to CYP2C5, another structurally characterized P450 enzyme, their structures are very different. One important observation from the CYP2C9 structure is that the active site is very large and can accommodate more than one substrate. Warfarin is bound to the enzyme by numerous noncovalent and polar contacts with protein side chains. This binding orientation is nonproductive because warfarin is too far away from the heme for efficient oxidation. In addition, even with a large three-ring compound such as warfarin bound, there is space to accommodate another, equally large molecule in the active site. There is a large pocket defined by residues in the B′–C loop (including V113 and F114, Figure 14), the F and I helices, and the $\beta 4-2$ strand. This second pocket extends over the heme, and a substrate bound here may be preferentially oxidized by the enzyme. The presence of multiple potential substrate-binding pockets is a model for drug-drug interactions where one drug can affect the efficacy and toxicity of another simultaneously administered drug.

2.5 Catalytic Cycle and Intermediates of P450 Enzymes

2.5.1 The P450 Catalytic Cycle

The generally proposed P450 catalytic cycle is shown in Figure 15. The overall features of the mechanism have not changed since the early 1970s.[67] However, recent work showed that the nature of the intermediates and rate-limiting step can differ among enzymes, and that protein structure and dynamics play important roles. An overview of the catalytic cycle is provided in this section. More detailed discussions on the intermediates, rate-limiting step and mechanism of aliphatic C–H bond oxidation then follow. The mechanism of aromatic C–H bond oxidation, alkene epoxidation, and atypical activity of P450 enzymes are discussed in Section 2.6.

The resting state **I** of P450 enzymes has a ferric heme, commonly with a water molecule acting as the sixth ligand to the heme iron. The iron center is low spin and out of the porphyrin plane, towards the cysteine thiolate ligand. The heme reduction potential is around −300 mV (vs. NHE). In Step **1** of the catalytic cycle the substrate binds to the active site, on the distal side of the heme and near the iron center. This step is generally accompanied by the expulsion of active-site water molecules, including the heme iron sixth ligand. The five-coordinate iron in the substrate-bound form **II** remains below the porphyrin plane and the heme usually shifts towards the high-spin state. The heme reduction potential of **II** is around −170 mV. Step **2** is the transfer of the first electron by the associated electron-transfer protein to generate the ferrous-deoxy form **III**. This high-spin ferrous center binds oxygen (Step **3**) and forms the low-spin, diamagnetic oxy-P450 **IV** which has a reduction potential ∼0 mV. This $\mathrm{Fe^{II}(Por)\cdot(O_2)}$ complex (see Section 2.5.2) is unstable to auto-oxidation which regenerates **II** and releases superoxide ($\mathrm{O_2^{\bullet -}}$), with a typical half-life of minutes at ambient temperatures.[68–70] In Step **4**, the electron-transfer protein delivers the second electron required for oxygen activation. A ferric-peroxo species (**V**) is formed which is protonated to give the ferric-hydroperoxo intermediate (**VI**). In mammalian P450 systems, cytochrome b_5 (reduction potential ca. −50 mV) can also be the source of the second electron.

The intermediates beyond **VI** have not been observed, and their molecular and electronic structures remain controversial. Clearly a highly reactive species is generated and water is a by-product of the overall reaction. Certain 'oxygen atom' donors can replace the two electrons and $\mathrm{O_2}$ required for the normal catalytic activity of P450 enzymes. These oxygen surrogates include hydrogen peroxide, alkyl hydroperoxides (ROOH), peroxyacids ($\mathrm{RCO_3H}$), chlorite ($\mathrm{ClO_2^-}$), periodate ($\mathrm{IO_4^-}$) and iodosylbenzene (PhIO).[71–75] In this 'peroxide shunt' (Step **13**), the substrate-bound form of the enzyme **II** is converted to the active species **VII**. The ferric heme in peroxidases and catalases reacts with hydrogen peroxide to give a high-valent intermediate called Compound I, which has been characterized in detail as an oxy-ferryl ($\mathrm{Fe^{IV}{=}O}$) porphyrin π-cation radical (*see* ***Iron: Heme Proteins, Peroxidases, Catalases & Catalase-peroxidases***). From indirect evidence, and by analogy with peroxidases, it is generally proposed that the ferric-hydroperoxo intermediate **VI** is protonated at the noniron bound oxygen atom (Step **6**), leading to O–O bond cleavage and release of a water molecule. At this stage, the P450 catalytic cycle can be considered formally as the two-electron reduction and heterolytic cleavage of $\mathrm{O_2}$ to give water

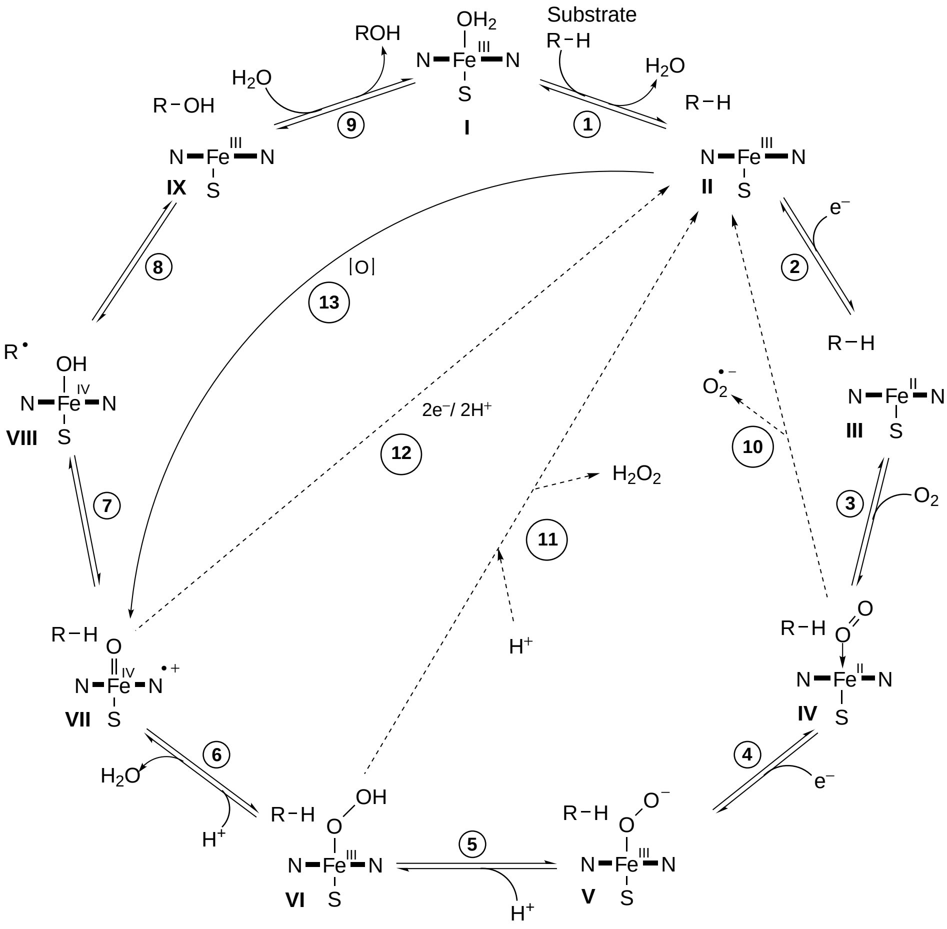

Figure 15 The P450 catalytic cycle including uncoupling side reactions (Steps **10**, **11** and **12**) and the peroxide shunt (Step **13**)

and an oxygen atom (equation 6).

$$O_2 + 2e^- + 2H^+ \longrightarrow H_2O + O \qquad (6)$$

Since the resting state of the enzyme is Fe^{III}, and an oxygen atom requires two electrons to complete its octet, O–O bond cleavage in **VI** and the bonding of an oxygen atom to the heme iron leads to a species which is two oxidizing equivalents above ferric, formally $Fe^{V}{=}O$ or $(Fe{=}O)^{3+}$. The electronic structure of this ferryl intermediate **VII** is not known, but it is commonly depicted as a $Fe^{IV}{=}O$ porphyrin π-cation radical (P450 Compound I, by analogy with peroxidases and catalases). In Step **7**, this reactive intermediate attacks the substrate; it can abstract a hydrogen atom or an electron from the substrate, or indeed form a σ-complex with the substrate via a C–O bond (see Section 2.6). Hydrogen atom abstraction gives a Fe^{IV}–OH species **VIII** and a substrate radical that is held within the active site. These two radicals collapse (Step **8**) to give the alcohol product and return the heme to a ferric state **IX**. The two-step hydrogen abstraction/radical collapse pathway is called the radical rebound mechanism.[76] In the final step of the cycle (Step **9**), the product dissociates from the enzyme. The crystal structure of $P450_{cam}$ with 5-*exo*-hydroxycamphor bound within the active site showed that the alcohol oxygen of this camphor oxidation product is ligated to the ferric heme iron.[77] Since all substrate oxidation products contain an oxygen atom with lone pairs of electrons that can coordinate to the heme, it is not known if P450 enzymes fully return to the true resting state **I** (as shown in Figure 15), or the substrate could displace the product directly from the active site so that the cycle will proceed directly from **IX** to **II**.

2.5.2 Nature of Intermediates in the P450 Catalytic Cycle

Spectroscopic techniques played a major role in characterizing the resting state and intermediates of P450 enzymes before the first crystal structure of a P450 enzyme became available. These techniques included UV-visible absorption, EPR, NMR, MCD, resonance Raman, Mössbauer and EXAFS spectroscopy.[78–80] Recent application of these techniques to transient intermediates generated by stopped-flow and rapid quench methods, and reactions at cryogenic temperatures, have provided important new insights into the structure of intermediates in the P450 catalytic cycle.

The Resting State I. The heme iron is six-coordinate and located out of the porphyrin plane in the substrate-free, low-spin ferric resting state of almost all P450 enzymes. Contradictory arguments have been put forward to account for the low-spin state. The active site of substrate-free $P450_{cam}$ is filled with a cluster of six hydrogen-bonded water molecules.[38] $P450_{cam}$ with adamantane and other camphor analogs bound within the active site are high spin and yet one water remains ligated to the heme iron.[81] It was suggested that substrate-free $P450_{cam}$ was low spin because H-bonding within the water cluster imparted substantial hydroxide (stronger ligand) character to the water ligand. Semiempirical calculations suggested that the isolated Cys–heme–OH_2 complex is high spin, and the protein electrostatic field plays a major role in stabilizing the low-spin state.[82] Studies on porphyrin model compounds also suggested that a water ligand on its own is not sufficient to drive the heme low spin.[83,84] However, when the porphyrin substituent groups are modified to form two H-bonds to the water ligand, the heme iron becomes low spin.[85] The water ligand can also be made hydroxide-like by H-bonding interactions with the protein.[51] It appears that hydroxide-like character of the water ligand is a general requirement for a low-spin resting state. The high-spin resting states of some mammalian P450s[86] may indicate a less hydroxide-like ligand, or a five-coordinate heme iron.

Hydrogen bonding on the proximal side of the heme has emerged as an important factor in determining the properties of P450 enzymes. The thiolate sulfur of the proximal C357 in $P450_{cam}$ forms H-bonds with the amide NH of L358, G359 and Q360.[18] These H-bonding interactions are conserved in other P450 enzymes.[39,42,57] Poulos suggested that proximal H-bonding may stabilize the Fe–S bond and control the heme redox potential.[56] Studies on iron porphyrin model complexes with H-bonds to the proximal RS^- ligand clearly showed that such interactions caused significant positive shifts of the reduction potential and affected the monooxygenase activity.[87–90] Mutagenesis studies have highlighted the role of proximal ligand H-bonding in $P450_{cam}$.[91,92] The L358P, Q360L, and Q360P mutations shifted the heme reduction potential by 35–70 mV to more negative values as well as affecting the $Fe(O_2)$ interaction and kinetics of O–O bond heterolysis. Spectroscopic data indicated that the Q360 mutations mainly altered the Fe–S σ-interaction while the L358P mutation increased S→Fe π-donation. The activity of the Q360 mutants was comparable to the wild type but the L358P mutant showed higher activity for the oxidation of nonnatural substrates such as styrene. NMR studies showed that L358 and Q360 are involved in electron transfer, and that the L358P mutation induced structural changes similar to those induced by putidaredoxin binding.[93,94] Therefore proximal ligand H-bonding not only increases the heme reduction potential to promote electron transfer but also affects the O–O bond activation and substrate oxidation steps.

Deoxy-ferrous P450 III. Detailed spectroscopic studies had shown that the heme in deoxy-ferrous P450 is high spin.[79,80] The crystal structure of deoxy-ferrous $P450_{cam}$ closely resembled that of the ferric form (Figures 10–12), with the iron out of the porphyrin plane.[95]

Oxy-P450 IV. Oxygen binds rapidly to high-spin deoxy-ferrous P450 **III** to give the oxy-P450 species **IV**. Despite extensive studies, the electronic structure of oxy-ferrous heme complexes is not definitely understood. It is well documented that such species can be considered to have two extreme forms: ferrous-oxygen (Fe^{2+}–O_2) and ferric-superoxide (Fe^{3+}–$O_2^{\bullet-}$). The chemical properties of these proteins are consistent with both structures, for example, displacement of the bound oxygen by CO indicates a Fe^{2+}–O_2 structure while substitution by anions such as CN^- and N_3^- to form Fe^{3+}–X, and auto-oxidation to form ferriheme and $O_2^{\bullet-}$, are more readily accounted for by the Fe^{3+}–$O_2^{\bullet-}$ structure. Oxy-heme proteins are diamagnetic. In the Fe^{2+}–O_2 form, the ligand field splitting induced by O_2 binding must be sufficient to drive the d^6 Fe^{2+} center low spin. This occurs because O_2 is a good π-acceptor. On the other hand, even if the ligand field splitting is high in the Fe^{3+}–$O_2^{\bullet-}$ form, there will be an unpaired electron on the d^5 Fe^{3+} center and another on the superoxide anion. These two spins must be strongly coupled by antiferromagnetic coupling to give a diamagnetic state. Whether the Fe^{2+}–O_2 or Fe^{3+}–$O_2^{\bullet-}$ structure is adopted depends on the extent to which an electron is transferred from Fe^{2+} to O_2, which in turn depends on the extent of π-back donation from the iron center. Oxy-heme species are best considered as $Fe^{(2+\delta)+}$–$O_2^{\delta-}$ where δ indicates partial transfer of an electron from Fe^{2+} to O_2. The O–O stretching frequency is indicative of the O–O bond order and hence the extent of back-donation. Resonance Raman spectroscopy detected the O–O stretch for oxy-$P450_{cam}$ **IV** at $1140\,cm^{-1}$,[96] which is $20\,cm^{-1}$ lower than the value found for oxy-hemoglobin and consistent with the anionic thiolato coordination in P450 enzymes compared to the neutral imidazole nitrogen ligand in globins. Hence oxy-$P450_{cam}$ is closer to the Fe^{3+}–$O_2^{\bullet-}$ limit than oxy-globins.

The crystal structure of oxy-$P450_{cam}$ **IV** with bound camphor showed that O_2 is bound end-on (η^1) to the heme iron with the distal oxygen atom pointing towards the side chain of T252.[95] The Fe–O distance was 1.8 Å. Camphor was displaced slightly from its position in the ferric form of the enzyme to create space for O_2 binding but the C-5 of camphor was in van der Waals contact with the proximal oxygen atom. The iron center moved from below the porphyrin plane in the ferric (**II**) and deoxy-ferrous (**III**) forms into the porphyrin plane.

There were changes in the protein and water structure in the oxygen-binding groove between G248 and T252 which may be important in O–O bond activation. Two new water molecules were found in the oxygen-binding groove of oxy-ferrous $P450_{cam}$. The presence of these water molecules induced conformational changes to D251 and T252. One

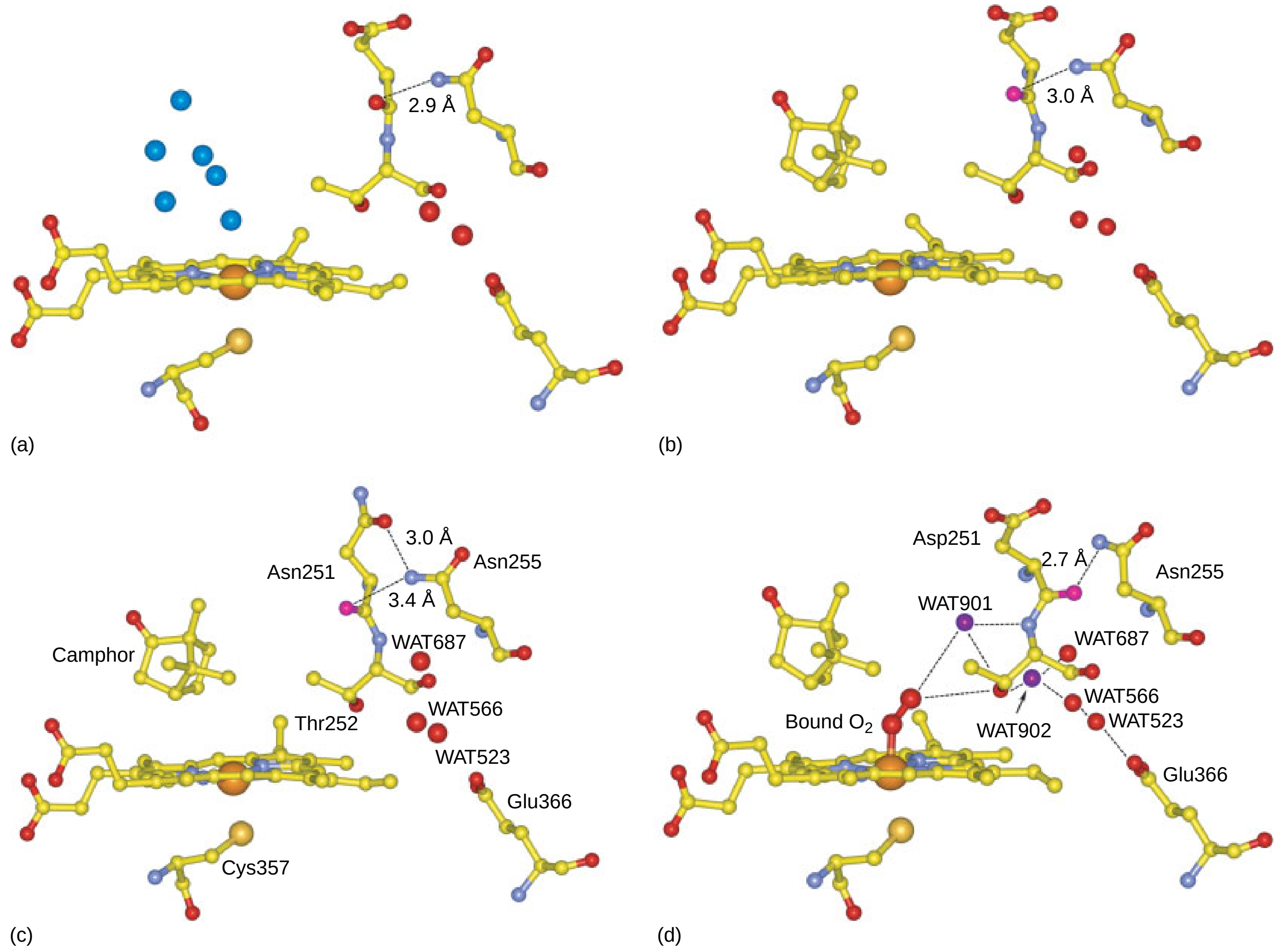

Figure 16 The protein structural dynamics of P450$_{cam}$ up to the O_2 binding step. (a) The structure of substrate-free ferric P450$_{cam}$ showing the cluster of six-water molecules (dark blue) in the substrate-binding pocket and the two waters in the O_2-binding groove in the kink within the I helix. (b) The structure of ferric P450$_{cam}$ with bound camphor; the six-water cluster has been displaced and a new water molecule (WAT687) enters the O_2-binding groove to complete the chain of three water molecules that ends at Glu366. Note the side chains of D251, T252 and N255. (c) The structure of the D251N mutant showing the altered side chain conformation and the H-bond between the N251 carbonyl and side chain NH_2 of N255. (d) The structure of oxy-P450$_{cam}$ with bound camphor. Two new water molecules (901 and 902) are found in the oxy-P450$_{cam}$ structure. The bound O_2 is hydrogen-bonded to WAT901 and the T252 side chain. The flipped conformation of the D251 main chain carbonyl, stabilized by a hydrogen bond to the N255 side chain, creates space to accommodate WAT901. This driving force is not available in the D251N mutant because the N255 side chain is hydrogen-bonded to the N251 side chain

water molecule (WAT901, Figure 16d) formed H-bonds to the distal oxygen atom of the heme-bound O_2, the amide NH and hydroxyl side chain of T252, and other protein groups. The distal oxygen of the bound O_2 also formed a H-bond to the T252 hydroxyl side chain. The other new water molecule (WAT902) formed H-bonds to the hydroxyl side chain of T252, WAT901, WAT687 and other protein groups. Waters 901, 902, 687, 566 and 523 extend in a chain anchored by a H-bond between WAT523 and the carboxylate side chain of E366.

The characteristic kink in the distal I helix of most P450 enzymes was believed to perform the function of an oxygen-binding groove, but the structure of oxy-P450$_{cam}$ suggested that its role may be to accommodate an extra water molecule that forms a H-bond to stabilize O_2 binding. T252 is highly conserved amongst P450 enzymes. Replacement of threonine with serine or an artificial amino acid residue with a methoxy group in place of the alcohol had little effect on the activity,[97] but the T252A mutant showed slow O–O bond cleavage and increased peroxide formation.[98] These activity data, and the structure of oxy-P450$_{cam}$, indicate that the role of T252 is to provide an oxygen atom that can participate in H-bonding in proton delivery for O–O bond cleavage.[95,97]

The requirement of two protons for O–O bond cleavage and the appearance of two new water molecules in oxy-P450$_{cam}$ may be a coincidence. Certainly the chain of water molecules (Figure 16d) does not lead to the protein surface to allow proton delivery. However, the oxy-heme complex has two H-bonds to the distal oxygen and appears to be well set for proton delivery and O–O bond cleavage after the second electron is transferred. The mechanism of proton delivery is not known, but WAT901 and 902 are very likely to be involved and the side chain of D251 is known to play an important role (Figure 16d). The D251N mutation decreased the O–O bond cleavage rate by two orders of magnitude but there was no increased loss of peroxide.**[99,100]** The crystal structure of the D251N mutant showed that the N251 side chain carbonyl formed a H-bond with the side chain NH_2 of N255 (Figure 16c),**[100]** while in the wild-type structure the D251 side chain carboxylate is H-bonded to the K178 side chain. The structure of oxy-P450$_{cam}$ showed that the N255 side chain NH_2 was required for H-bonding to the *backbone* carbonyl oxygen of D251 to flip this carbonyl group and create space for the catalytically important new water molecule WAT901.**[95]** The H-bond between the *side chain* carbonyl of N251 and the N255 side chain NH_2 blocks this critical conformation change, thus slowing proton delivery. Finally the 'closed' nature of the chain of water molecules in oxy-P450$_{cam}$ also suggests that further protein conformational changes, and perhaps the entry of more water molecules, are required to shuttle protons to the water cluster after the second electron transfer.

The Ferric-peroxo (V) and Ferric-hydroperoxo (VI) Intermediates. Stopped-flow studies have not detected any intermediates after the second electron transfer (Step **4**). Sligar, Hoffman, and coworkers have studied the cryoreduction (77 K) of oxy-P450$_{cam}$ by solvated electrons generated by irradiation with a ^{60}Co source. EPR studies showed that the ferric-hydroperoxo species (Fe^{III}–O–OH) **VI** was the first observed product, suggesting fast protonation (Step **5**) of the ferric-peroxo form **V**.**[101]** Consistent with this suggestion was the observation that cryoreduction of the active-site mutant D251N, in which the proton delivery pathway has been disrupted,**[100]** gave the ferric-peroxo species **V** at 77 K and this was transformed to the hydroperoxo form **VI** upon annealing at higher temperatures.**[102]** The sequence of reactions can be summarized as follows: (i) oxy-P450 **IV** has the 'ferric-superoxo' electronic configuration and is stabilized by H-bonding, (ii) the second electron is transferred and becomes localized on the O–O moiety to form the ferric-peroxo species **V**, (iii) the developing negative charge on the distal oxygen is rapidly neutralized by rearrangement of the H-bonding to transfer a proton and give the ferric-hydroperoxo form **VI** in a process that requires the carboxylate side chain of the 251 residue.

No further chemical input is necessary for substrate oxidation to occur once the second electron is transferred. Quantum mechanical calculations have provided insights into the protonation and O–O bond cleavage steps. Density function theory (DFT) calculations on the ferric-peroxo form of P450$_{eryF}$ indicated fast protonation at the distal oxygen by a chain of two water molecules that extended to a serine side chain. The second protonation step, which leads to O–O bond cleavage, was found to be essentially activationless.**[103]** Once the two protons are transferred, formation of the ferryl species was very facile. Interestingly, the calculations also suggested that a single water molecule was not sufficient to protonate the peroxo group.

The Ferryl Compound I Intermediate VII. Cryoreduction of oxy-P450$_{cam}$ with bound camphor in a crystal resulted in partial reaction and disorder, and definitive refinement was not possible. Thawing the crystal gave the product of camphor oxidation.**[95]** Spectroscopic investigations on cryoreduced oxy-P450$_{cam}$ did not detect the Compound I intermediate **VII**.**[102]** Annealing of ferric-hydroperoxo P450$_{cam}$ (**VI**) from 77 K to within a narrow temperature range (180–200 K) gave ferric P450$_{cam}$ with the product of camphor oxidation, 5-*exo*-hydroxycamphor, bound to the heme iron. The data suggest that the Compound I intermediate **VII** is sufficiently reactive that it rapidly attacks camphor to form the product even at 200 K. It was also shown that, while D251 was required for the first protonation of **V** to give **VI**, T252 was critical for the second protonation to give the active intermediate **VII**. Thus the T252A mutation did not interfere with the rapid delivery of the first proton to form **VI**, even at 77 K, but the mutant did not give any product of camphor oxidation upon thawing.

The peroxide shunt has been used to by-pass the electron-stransfer steps and generate the ferryl intermediate directly from ferric P450s. Transient signals have been observed in stopped-flow experiments when ferric P450$_{cam}$ with camphor or other substrates bound was treated with hydrogen peroxide or *m*-chloroperbenzoic acid.**[104,105]** Similar results have been reported for CYP119 from *Sulfolobus solfataricus*.**[106]** However, these spectroscopic intermediates have not been definitively assigned to a ferryl species. The product of the reaction between substrate-free ferric P450$_{cam}$ and peracetic acid has been rapidly freeze-quenched and examined by EPR and Mössbauer spectroscopy.**[107,108]** It was concluded that the reaction gave a Fe^{IV}=O ($S = 1$) species together with a protein-based radical, that is, an analogue to peroxidase Compound II which contains a noncoupled protein radical. This oxidizing equivalent located on the protein is lost to the catalytic reaction of the enzyme. Further EPR and mutagenesis studies showed that the protein radical was based on the phenol side chains of Y75 or Y96. However, when both these residues were replaced with the more inert phenylalanine, the radical signal disappeared without a new signal from the expected porphyrin radical.

DFT calculations on the electronic structure of P450 Compound I models with HS$^-$, MeS$^-$, or cysteinate as the proximal ligand and no substituents on the porphyrin ring show that a number of spin states are close in energy.**[109,110]** The protein medium (in the form of the dielectric constant) and the proximal NH–S hydrogen bonding interactions both have significant effects. Calculations on the bare 'P450 Compound

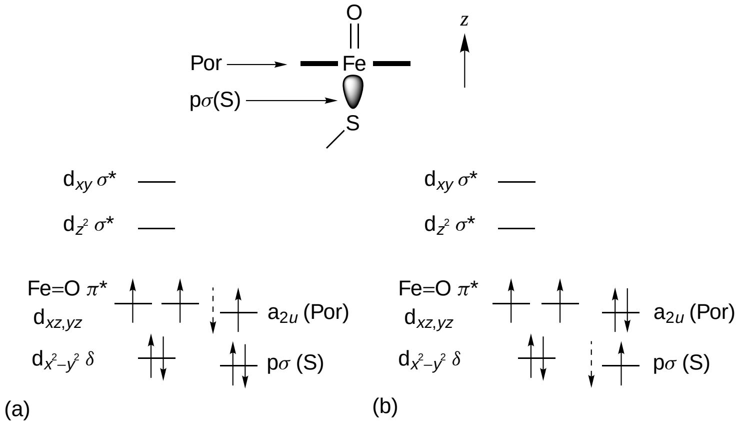

Figure 17 The electronic structure of the P450 Compound I intermediate from density function theory (DFT) calculations. The two unpaired electrons on the Fe(IV) center are in the 3d π^* orbitals while the other unpaired electron may be in the porphyrin a_{2u} π^* orbital (a) or sulfur pσ orbital (b). The solid arrows in the a_{2u} or pσ orbital show the electron spin parallel to those in the 3d π^* orbital (quartet state) while the dotted arrows indicate the doublet state

I' (**VII**) in a vacuum show that it has two unpaired electrons in the degenerate d_{xz},d_{yz} set of Fe=O π^* orbitals, with the other two 3d electrons of the Fe(IV) center in the $d_{x^2-y^2}$ orbital (Figure 17).**[111–116]** The other unpaired electron is spread over the porphyrin and proximal sulfur ligand, but largely localized on the sulfur (Figure 17b).**[112]** In effect, the thiolate has been oxidized to the radical. The Fe–S bond is long (~2.6 Å) and the iron sits above the heme plane. Slightly different calculations suggest that the unpaired electron on sulfur is in a pπ orbital.**[114,115,117,118]**

Introducing the proximal NH–S bonding found in the crystal structure, and applying a low dielectric constant for the medium, shortened the Fe–S distance, pulled the iron into the porphyrin plane, and most importantly shifted the radical from the proximal sulfur to a porphyrin π^* orbital (Figure 17a).**[119,120]** Hence, increasing the polarity around the proximal sulfur ligand stabilized the ionic $-S^-$ over the radical –S· form, and ensured that the other oxidizing equivalent was more localized on the porphyrin π-system. More sophisticated hybrid quantum mechanics-molecular mechanics (QM-MM) calculations further cemented this trend towards a shorter Fe–S bond and greater spin density on the porphyrin, and also indicated that the unpaired electron (oxidizing equivalent) is most likely to be in a porphyrin a_{2u} orbital.**[109,121]** Some spin density was also found on the heme propionate group which formed a salt bridge to an arginine side chain, suggesting that the heme periphery groups and the protein environment modulate the electronic structure of the P450 Compound I intermediate.**[109]** Significantly, the Fe=O dπ^* orbitals containing the two unpaired electrons on iron interact weakly with the porphyrin a_{2u} orbital containing the third unpaired electron. Hence, the P450 Compound I could have doublet or quartet electronic states $^2A_{2u}$ or $^4A_{2u}$, and the exact partition between these two states will vary from one enzyme to another because the electronic structure is sensitive to the micro-architecture of the heme pocket. DFT calculations have given contradictory predictions on the lowest energy spin state from slightly different levels of theory,**[109,121,122]** suggesting that the Compound I doublet and quartet states are very close in energy.

2.5.3 Mechanism of C–H Bond Oxidation

The Radical or Oxygen Rebound Mechanism. The mechanism of C–H bond oxidation by the P450 Compound I intermediate has been debated for over twenty years.**[71,80,110,123]** A simple concerted mechanism (Figure 18) has been disproved by large intramolecular kinetic isotope effects ($k_H/k_D > 10$),**[124]** scrambling of stereochemistry,**[124–126]** and substrate rearrangements.**[76,124,125,127–129]** Deuterium labeling studies in norbornane oxidation by liver microsomal P450 enzymes showed scrambling of stereochemistry.**[124]** Similar labeling at C-5 of camphor showed that the hydrogen in the 5-*exo*-hydroxycamphor product could come from the exo or endo face but only the exo alcohol was formed.**[125]** In 1976, Groves and McClusky put forward a nonconcerted mechanism for C–H bond activation by P450 Compound I that accounted for the isotope effects and rearrangement.**[76,113]** The first step is the abstraction of a hydrogen atom by the ferryl oxygen to give a Fe^{IV}–OH species (**VIII**) and a carbon-based substrate radical that remains bound within the active site (Figure 18). This radical can then recombine with the iron-bound hydroxyl group, abstracting a hydroxyl radical to form the alcohol product and returning the other electron in the Fe^{IV}–OH bond to the iron center. This stepwise pathway has been called the radical rebound (or oxygen rebound) mechanism. The oxygen lone pair of the alcohol product can act as a ligand to the Fe^{III} center (Figure 18). However, radical reactions in solution normally result in scrambling of stereochemistry. The high stereoselectivity and stereospecificity observed in

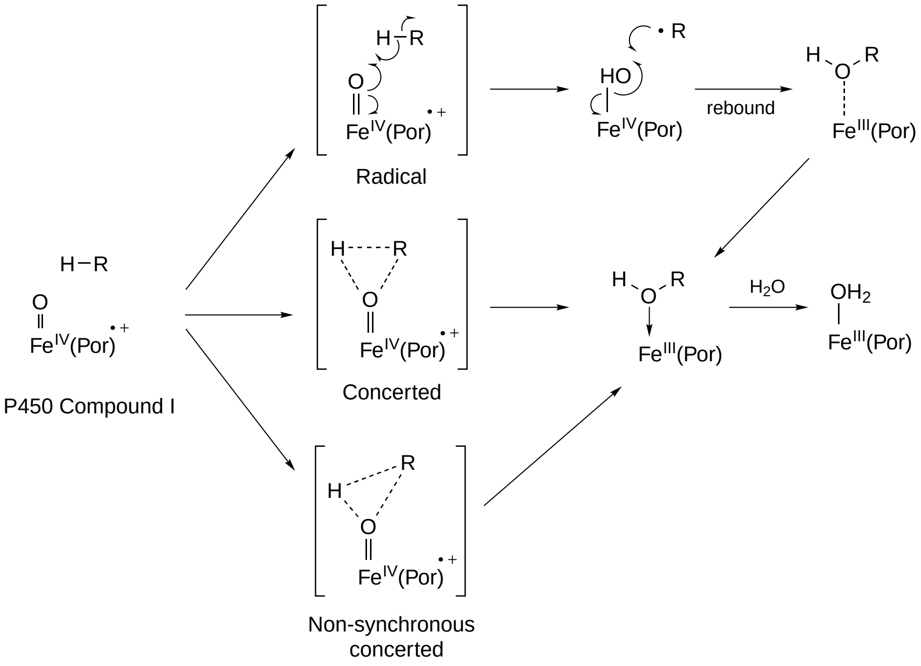

Figure 18 The concerted, nonsynchronous concerted, and radical (oxygen) rebound mechanisms of C–H bond oxidation by the P450 Compound I intermediate

many P450 reactions[83,130,131] suggest that either the radical is short-lived or that substrate motion within the active site is limited. Since some P450 enzymes can oxidize large as well as small molecules it seems that, at least in some cases, the substrate will be mobile and therefore it is likely that the substrate radical will have a short lifetime.

Ortiz de Montellano and Stearns were the first to use a radical clock substrate such as bicyclo[2,1,0]pentane to time the radical rebound reaction.[132] Radical clock substrates contain strained ring systems which undergo rapid ring-opening reactions once the radical is generated (Figure 19). If the rate constants of the ring-opening reactions are known, the ratio of rearranged and unrearranged products from a reaction allows the lifetime of the radical intermediate to be calculated. A radical lifetime of 50 ps was determined for the oxidation of bicyclo[2,1,0]pentane by microsomal P450.

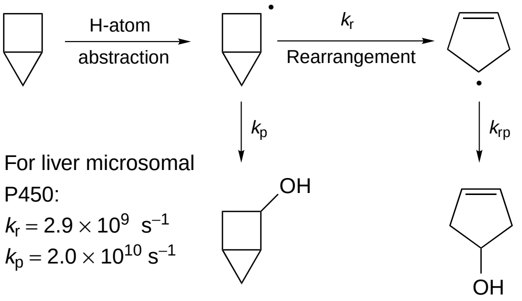
H-atom abstraction
k_r
Rearrangement
k_p
k_{rp}
OH
OH
For liver microsomal P450:
$k_r = 2.9 \times 10^9$ s^{-1}
$k_p = 2.0 \times 10^{10}$ s^{-1}

Figure 19 Structure of bicyclo[2,1,0]pentane and its use as a radical clock for C–H bond oxidation catalyzed by P450 enzymes. The radical intermediate can undergo the rebound step with the Fe^{IV}–OH species before and after ring-opening rearrangement

Newcomb and coworkers used ultrafast radical clock substrates which are also able to detect carbocationic intermediates (Figure 20) to time the radicals in P450 reactions.[133] The apparent radical lifetimes of 70–200 fs were far too short for reaction intermediates and much more like the lifetimes of transition states.[134–137] A nonsynchronous concerted mechanism was proposed to introduce some concerted nature to the rebound mechanism.[135] In this nonsynchronous mechanism the transition state is high asymmetric, with C–H bond breaking and O–H bond formation being much more advanced than C–O bond formation (Figure 18). Some substrates also gave products arising from rearrangement of carbocation intermediates,[136,138,139] which led to the suggestion that two oxidizing species are involved: a Compound I iron-oxo species (**VII**) that inserts an oxygen atom without a radical intermediate and the ferric-hydroperoxo intermediate (**VI**) that inserts HO^+ to form a carbocation intermediate.[133,138,139]

The possibility of the ferric-hydroperoxo species **VI** being the active C–H bond oxidizing intermediate has been investigated. Mutagenesis of T303 in CYP2E1 disrupts proton delivery for O–O bond cleavage, allowing **VI** to accumulate. Allylic C–H bond oxidation of alkenes was found to be slow but the rate of epoxidation was increased.[136] The T252A mutant of $P450_{cam}$ catalyzed the epoxidation of styrene but there was no C–H bond oxidation of the benzene ring, nor

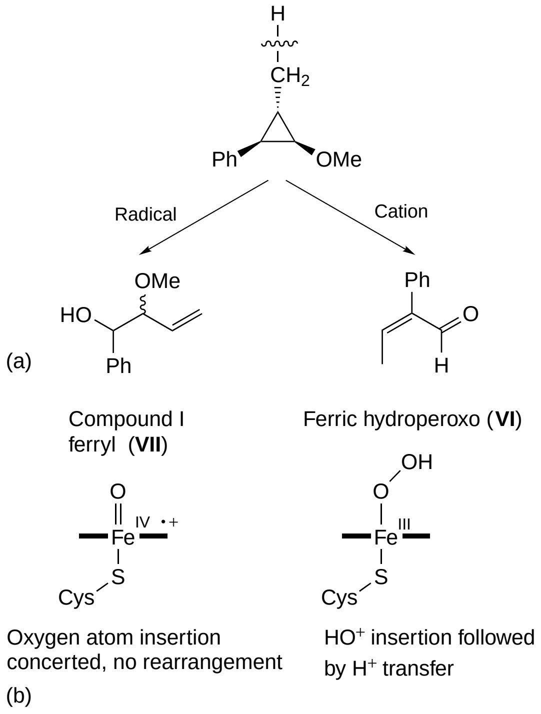

Figure 20 (a) An ultrafast radical clock substrate capable of distinguishing between radical and carbocation intermediates (b) The proposed two-oxidant pathway of C–H bond oxidation by P450 enzymes in which Compound I follows a concerted mechanism with no intermediate while the ferric-hydroperoxo attacks substrates by insertion of HO^+ leading to carbocation intermediates which rearrange to give the alcohol product

was the mutant able to catalyze camphor oxidation.[140] Studies on porphyrin model compounds also showed that the ferric-hydroperoxo species catalyzed slow alkene epoxidation.[141,142] DFT calculations suggest that a hydroperoxo species is at best a slow oxidant for C–H bonds.[122,143] Detailed spectroscopic investigations of intermediates in camphor oxidation at cryogenic temperatures clearly established that the proton abstracted from camphor C-5 became the product hydroxyl proton.[102] Thus, it appears that the ferric-hydroperoxo intermediate **VI** can oxidize alkenes but it is not sufficiently oxidizing to attack C–H bonds.

Based on DFT calculations, Shaik and coworkers proposed a ‘two-state reactivity’ process.[110,113,116,120,143] The doublet and quartet states of P450 Compound I (see Figure 17) have virtually identical reactivity but follow very different pathways. The low-spin doublet state leads to a substrate radical transition state with no barrier to the rebound step, whereas the high-spin quartet state generates a radical with a significant barrier to rebound. In this model, predominance of the low-spin pathway explains the apparently short (~100 fs) radical lifetimes in some radical clock experiments, while the high-spin pathway accounts for the finite radical lifetimes in others. The calculations further suggested that the doublet state did not generate cationic character in the substrate intermediate while the quartet state allowed the build up of significant positive charge on the substrate and is the potential cationic pathway. Since these two states of Compound I are very close in energy, minor changes in the heme environment could change the partition between these pathways, leading to different proportions of products arising from radical/cationic intermediates. Hybrid QM-MM calculations have, however, indicated that the quartet state is the more reactive and the doublet state may not be necessary.[109,122]

Groves made the interesting observation that the oxidation of clock substrates with only methylene C–H bonds (e.g. bicyclo[2,1,0]pentane or the [4,1,0] molecule norcarane) showed finite radical lifetimes and gave only trace amounts of cation rearrangement products.[131] The proportion of cation rearrangement products increased for the oxidation of primary C–H bonds of methyl groups in some ultrafast radical clock substrates (see Figure 20). This partition between radical and cationic pathways was suggested to be the result of competition between radical rebound to form products and electron-transfer oxidation of the radical by the Fe^{IV}–OH intermediate (**VIII**). Such competition had been described for electron transfer from primary alkyl radicals to an Fe^{III}(phen) oxidant against trapping of the radical by a bromine atom.[144,145] The rate of electron transfer was sensitive to the redox potentials of both the iron and alkyl radical centers, and shown to be ca. $10^8\ M^{-1}s^{-1}$ for secondary alkyl radicals. Electron-transfer oxidation of the radical should be faster for the more oxidizing Fe^{IV} species in P450 catalysis and may compete with the rebound rate of ca. $10^{10}\ s^{-1}$. Other important factors are the distance between the substrate C–H bond and the Fe=O oxygen of Compound I, and the mobility of the substrate and radical intermediate within the active site. Primary C–H bonds in a methyl group are less sterically encumbered and can approach closer to the Compound I ferryl oxygen. Both the rebound and electron-transfer oxidation of the substrate radical could be accelerated compared to those for secondary C–H bonds, and hence there may be little to no radical rearrangement (faster rebound) but the proportion of cationic products may be increased (faster electron-transfer oxidation).

The mechanisms of enzymatic aliphatic C–H bond oxidation remain one of the most interesting and challenging areas in chemical biology. Since the proposal of the radical rebound mechanism by Groves and McClusky in 1976,[76] catalysis research has delved further into the intricate detail of the structure of the Compound I species and its reaction with C–H bonds. The protein environment and dynamics have been shown to have subtle but important effects on the redox potential, electronic structure, and reactivity of the heme iron. Nature has evolved mechanisms to exert delicate control over iron bioinorganic chemistry, electron transfer, and to choreograph the binding and movement of substrate and water molecules in the active site at all steps of the P450 catalytic cycle.

2.5.4 Rate-limiting Steps in the P450 Catalytic Cycle

Of the nine steps in the generalized cycle shown in Figure 15, some are obviously fast reactions but essentially any of the other steps could be rate limiting for the overall cycle. The binding of substrate (Step **1**) and O_2 (Step **3**) are probably very fast and diffusion-controlled for all P450 enzymes. The second-order rate constant of O_2 binding to $P450_{cam}$ has been determined to be ca. $10^8\ M^{-1}\ s^{-1}$,**[123]** and for camphor binding, $2.5 \times 10^7\ M^{-1}\ s^{-1}$.**[146]** At a substrate concentration of 100 μM the camphor binding rate is $2\,500\ s^{-1}$, or $150\,000\ min^{-1}$. By comparison, the fastest steady state substrate oxidation rate observed to date for a P450 enzyme is $20\,000\ min^{-1}$ for arachidonic acid oxidation by $P450_{BM\text{-}3}$.**[147]**

It is notable that many P450 enzymes do not have obvious substrate access channels.**[56,57]** However, the diffusion-controlled nature of substrate binding indicates that the structural and conformational changes required for substrate entry to most P450 enzymes must be very fast.**[123,148]** Structural studies on $P450_{cam}$ have shown that, in the absence of a substrate, residues such as F87, F193 and I395 (see Figure 12) which are close to the protein surface, are very mobile and could be part of a cluster of residues that open up to allow substrate entry.**[38]** The structures of $P450_{cam}$ with a number of large inhibitors bound within the active site all showed dramatic movements of protein backbone and side chains, and yet the enzyme was stable.**[149–151]** These observations clearly show that the 'P450 fold' can tolerate large changes in the structure, including those transient fluctuations required for entry of substrates into the active site.

For nearly thirty years, the paradigm of P450 catalysis was that the rate-limiting step of the catalytic cycle was the first electron transfer (Step **2** in Figure 15), and that this was gated by substrate binding (Step **1**) and the associated changes in heme spin state.**[123,152,153]** This paradigm is firmly established for the bacterial enzymes $P450_{cam}$ and $P450_{BM\text{-}3}$. The $P450_{cam}$ heme reduction potential shifts from −300 mV in the absence of substrate to −170 mV when camphor binds to the enzyme.**[152,154]** A similar positive shift of the heme potential by 140 mV upon substrate binding has also been reported for $P450_{BM\text{-}3}$.**[153]** For the $P450_{cam}$ system, the reduction potential of the electron-transfer protein putidaredoxin (Pdx) is −235 mV.**[155]** The proposal was that, in the absence of substrate, reduction of the P450 enzyme by the electron-transfer protein is thermodynamically unfavorable and therefore slow. When substrate binds to the active site, the heme reduction potential rises and the reaction is thermodynamically favorable and fast. Substrate binding serves as a regulatory step or 'gate' so that NADH is not wasted in futile cycling which puts metabolic stress on the organism.

In the absence of substrate, the heme iron of $P450_{cam}$ is six-coordinate and low spin. Camphor binding expels all water molecules from the $P450_{cam}$ active site, and the iron becomes five-coordinate and high spin.**[152,156]** A linear free-energy relationship has been observed between the $P450_{cam}$ spin state equilibrium and heme redox potential.**[157]** The presence of the sixth ligand is expected to stabilize the higher oxidation state of the heme iron and increase the ligand field strength, which accounts for the lower reduction potential and the low-spin iron center in substrate-free $P450_{cam}$. Loss of this ligand upon substrate binding changes the heme spin state and reduction potential and switches on the catalytic cycle. The first electron-transfer step is rate limiting for the overall reaction. This simple and elegant scheme is very attractive and had been the paradigm for nearly 30 years. Early work on microsomal P450s supported gating by substrate binding,**[158–160]** but further work showed that the concentration of the electron-transfer reductase CPR in microsomes or systems reconstituted in lipids might be too low for fast electron-transfer kinetics to be observed.**[161,162]** Detailed analysis of the rates of electron transfer and steady state turnover for many human P450s showed that the rate-limiting step occurs after the electron-transfer reactions.**[162,163]**

Substrate binding does not induce changes to the heme spin state and redox properties for all P450 enzymes. Some mammalian P450s have high-spin heme in the absence of substrate but the heme reduction potential remains low,**[86,164,165]** while others do not show a shift to high-spin heme or an increase in the potential but fast electron transfer is still possible.**[162,164,166]** The bacterial enzyme $P450_{cin}$ does not show a change in heme redox potential when cineol binds to the active site and initiates the catalytic cycle.**[167]** Studies on the oxidation of nonnatural substrate by $P450_{cam}$ and $P450_{BM\text{-}3}$ mutants also gave many examples of the breakdown of the correlation between substrate binding, heme spin state and electron-transfer kinetics.**[168–170]** The accumulated data show that (a) changes in heme spin state and reduction potential upon substrate binding is not a general property of P450 enzymes, (b) the heme spin state is not always linked to the reduction potential or the catalytic activity, and (c) the first electron transfer is rate-limiting for most (if not all) bacterial enzymes but for many mammalian enzymes the rate-limiting step occurs after electron transfer.

When the first electron transfer is rate limiting, it has been suggested that the thermodynamic argument for gating by substrate binding overlooked the effect of O_2 binding.**[171]** The reduction potential of the P450 enzymes (equation 7) are measured under anaerobic conditions. Under turnover conditions, O_2 is present and rapidly binds to the heme Fe(II) center (equation 8).

$$P450_{cam}Fe^{III} + Pdx^{Red} \underset{k_{-1}}{\overset{k_1}{\rightleftharpoons}} P450_{cam}Fe^{II} + Pdx^{Ox} \qquad (7)$$

$$P450_{cam}Fe^{II} + O_2 \underset{k_{-2}}{\overset{k_2}{\rightleftharpoons}} P450_{cam}Fe^{II}(O_2) \qquad (8)$$

The effect of O_2 binding is to stabilize the Fe^{II} state of the heme, and the reduction potential will increase by approximately 60 mV per decade increase in O_2 concentration for both the substrate-free and substrate-bound forms. At the ambient concentration of O_2 in the cytoplasm ($\sim$mM), the reduction potential is likely to be increased sufficiently for the reduction of the substrate-free form of P450 enzymes to become thermodynamically favorable. Since k_2 (equation 8) is large, the turnover rate of the cycle will be determined by k_1. In semiclassical Marcus theory,[172] the rate of electron transfer can be expressed as:

$$k_{\text{et}} \propto (H_{\text{AB}})^2 \exp\left(-\frac{(\lambda + \Delta G^\circ)^2}{4\lambda k_{\text{B}}T}\right) \tag{9}$$

where H_{AB} is the donor–acceptor coupling matrix element, ΔG° is the free-energy change or driving force for the reaction and λ is the reorganization energy, the sum of both inner (changes in metal–ligand bonding) and outer (solvents and other structural changes) sphere components (*see* ***Long-range Electron Transfer in Biology***). For P450 enzymes, the change in heme reduction potentials indicate that the reduction of the substrate-free form of the enzyme is ca. 140 mV less favorable compared to the substrate-bound form if the reorganization energies were the same for both reactions. When the substrate-free form is reduced, the transition from a six- to five-coordinate iron center will introduce a large inner-sphere reorganization barrier (λ_{inn}) to electron transfer because the Fe^{III}–OH_2 bond has to be weakened before electron transfer can occur. When camphor binds to the active site, both the ferric and ferrous forms have five-coordinate heme iron, λ_{inn} is much smaller and electron transfer is greatly accelerated.

The magnitude of λ_{inn} will be as high as 1 eV when a metal–ligand bond has to be broken during electron transfer. In general, the total reorganization energy ($\lambda_{\text{inn}} + \lambda_{\text{out}}$) will be of the order of 0.3–1.3 eV, which is 5 to 10 times the difference in ΔG° between substrate-bound and substrate-free forms of P450_{cam} and other P450 enzymes. The reorganization energy may dominate over the redox potential in the activation energy for electron transfer in equation (9). In addition to changes in the primary coordination sphere of the heme iron, protein conformation changes, such as altered hydrogen bonding, may also contribute to λ.

The importance of donor–acceptor coupling strength (H_{AB}) is often ignored. Electron transfer is facilitated by coupling or overlap of the donor (reductant) and acceptor (oxidant) wavefunctions. This overlap can occur directly or via specific groups in the intervening medium (*see* ***Long-range Electron Transfer in Biology***).[173–176] In general, donor–acceptor coupling, and hence the electron-transfer rate, decreases with distance or if a good pathway through the medium (peptide) is absent. Delocalized prosthetic groups (such as flavins) with more extended wavefunctions can give faster electron transfer. The electron-transfer distance can also vary between different P450 systems. The potential significance of these factors will become clearer when catalytically competent electron-transfer complexes are characterized in the future.

2.5.5 Uncoupling Reactions

Substrate-specific P450 enzymes oxidize their natural substrate with 100% yield based on NAD(P)H consumed, for example, camphor oxidation by P450_{cam}, fatty acid oxidation by $\text{P450}_{\text{BM-3}}$, and in sterol biosynthesis. Each molecule of NAD(P)H leads to the activation of one molecule of O_2 and the formation of one molecule of product. The catalytic reaction follows the cycle from Steps **1**–**9** in Figure 15, with no deviations. These reactions are said to be tightly coupled. However, P450 enzymes do show slightly relaxed substrate specificity, and the oxidation of nonnatural substrates often proceeds with low product yields, sometimes as low as 1%. This is particularly common for P450 enzymes responsible for xenobiotic oxidation. In such reactions the excess reducing equivalents are channeled away from product formation and form hydrogen peroxide and water.

There are three branch points in the P450 catalytic cycle.[65,123] As noted above, oxy-ferrous P450 is unstable to auto-oxidation to form superoxide. During the catalytic cycle, if the second electron transfer is slow or the Fe–O_2 interaction weakened, superoxide dissociation (Step **10**, Figure 15) will compete with substrate oxidation. Superoxide then disproportionates nonenzymatically to O_2 and H_2O_2. In some cases, superoxide can be detected as a direct product during turnover. One mechanism of increased superoxide dissociation is movement of the substrate within the active site, which causes steric interaction with the bound O_2. It is notable that the structure of oxy-P450_{cam} shows the camphor substrate contacting the heme-bound oxygen atom.[95] Clearly, a substrate not bound as specifically as camphor can sterically hinder O_2 binding, and substrate mobility will result in collisions between substrate and the bound O_2.

Another mechanism of H_2O_2 formation is dissociation of the hydroperoxo ligand (Step **11**, Figure 15) from the ferric-hydroperoxo intermediate **VI**. The Fe^{III}–OOH interaction can be weakened by steric hindrance with a substrate bound too close to the heme iron and during movements of a mobile substrate, or by protonation of the heme-bound oxygen atom.[65,81] The neutral H_2O_2 molecule is a much weaker ligand than the anionic hydroperoxide (HO_2^-). Protonation could occur if the substrate does not exclude all water molecules from the active site, and water molecules get access to the proximal oxygen in **VI**. However, DFT calculations showed that an isolated water molecule is not sufficiently acidic to protonate the hydroperoxo group.[103] It is likely that an acidic protein side chain is also involved (see Section 2.5.2).[177]

The third uncoupling pathway, or branch point, occurs at the Compound I species **VII**. If the substrate is bound too far away from the Compound I oxygen, or if the functional group closest to this oxygen is inert to oxidation, the lifetime of **VII** will be increased and electron-transfer reduction of **VII** to **II** can become the dominant reaction. The overall result is the use of two molecules of NAD(P)H to reduce O_2 to two water molecules. This is the reaction catalyzed by oxidases and this oxidase uncoupling pathway has been observed with perfluorohexane and microsomal P450,[178] and 5,5-difluorocamphor with $P450_{cam}$.[179] Mutagenesis studies on $P450_{cam}$ also showed that the oxidase pathway dominates uncoupling if a substrate is manipulated to bind far away from the heme.[65]

2.6 Typical and Atypical Activity of P450 Enzymes

The primary (or typical) activity of P450 enzymes is the oxidation of C–H bonds by the $(FeO)^{3+}$ ferryl (Compound I) intermediate. Alkene epoxidation is also a common reaction. However the highly electrophilic nature of the ferryl species opens up other oxidative reactions such as desaturation, dealkylation, ipso attack, C–C bond cleavage, isomerization, and one-electron oxidation.[180] Other intermediate species in the P450 catalytic cycle can also catalyze chemical transformations. Deoxy-ferrous P450 **III** can act as a reducing agent and the distal oxygen atom of the ferric-hydroperoxo intermediate **IV** can act as a nucleophile. A collection of typical and atypical reactions catalyzed by P450 enzymes is shown in Figure 21.

Alkene Oxidation. The insertion of an oxygen atom into the π bond of an alkene to form an epoxide is a technologically important reaction because optically pure epoxides are valuable intermediates in synthesis. Although at first sight the mechanism might be considered a straightforward concerted insertion of the ferryl oxygen, the product profiles suggest otherwise. Alkene oxidation can give rearrangement products such as aldehydes and ketones, and terminal alkenes can give rise to N-alkylation of the porphyrin ring, leading to enzyme inactivation. These side reactions are not observed when P450 enzymes are treated with the epoxide products, which suggests a stepwise mechanism via radical or carbonium ion intermediates generated by electron-transfer oxidation or direct electrophilic attack by the ferryl oxygen (Figure 22). Rearrangement of a substrate cation radical leads to the allylic alcohol, and this pathway can be distinguished from direct allylic C–H bond oxidation by the kinetic isotope effect. The carbonium ion intermediate can rearrange to give an aldehyde or ketone, or it can attack the porphyrin ring nitrogen.

Arene Oxidation and the NIH Shift. P450 enzymes catalyze the oxidation of aromatic compounds to give phenols, dihydrodiols, and rearrangement products that can be rationalized with an arene oxide intermediate. A common process in aromatic oxidation is the 'NIH shift'.[181,182] This is a rearrangement reaction in which a ring substituent undergoes a 1,2-migration to the adjacent ring carbon to give an *ortho*-substituted phenol, or is displaced by the incoming hydroxo group (Figure 23). The NIH shift and the formation of dihydrodiol products via hydrolysis by epoxide hydrolase are strong evidence for epoxide intermediates. Earlier work assumed a concerted mechanism of oxygen atom insertion into the arene ring. However, evidence for a concerted mechanism is not unequivocal. Guengerich has

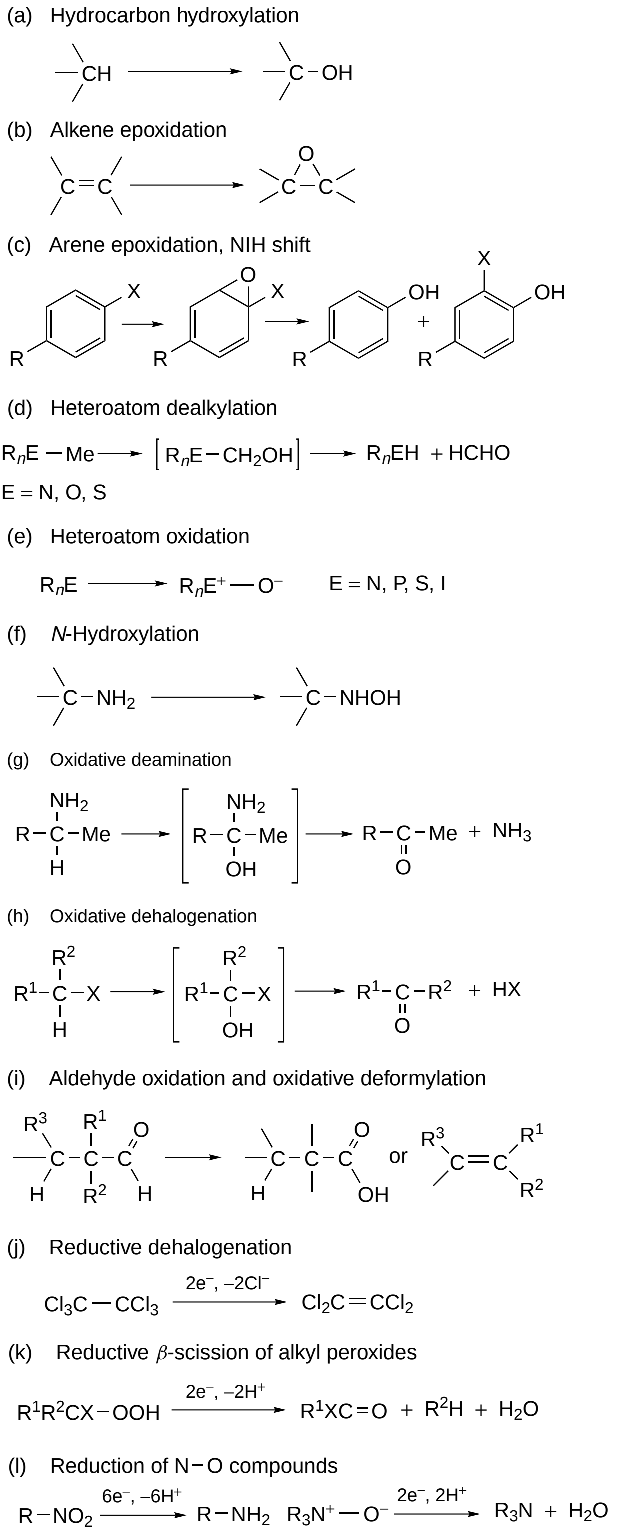
(a) Hydrocarbon hydroxylation
(b) Alkene epoxidation
(c) Arene epoxidation, NIH shift
(d) Heteroatom dealkylation
E = N, O, S
(e) Heteroatom oxidation
E = N, P, S, I
(f) N-Hydroxylation
(g) Oxidative deamination
(h) Oxidative dehalogenation
(i) Aldehyde oxidation and oxidative deformylation
(j) Reductive dehalogenation
(k) Reductive β-scission of alkyl peroxides
(l) Reduction of N–O compounds

Figure 21 Summary of the diverse reactions catalyzed by P450 enzymes

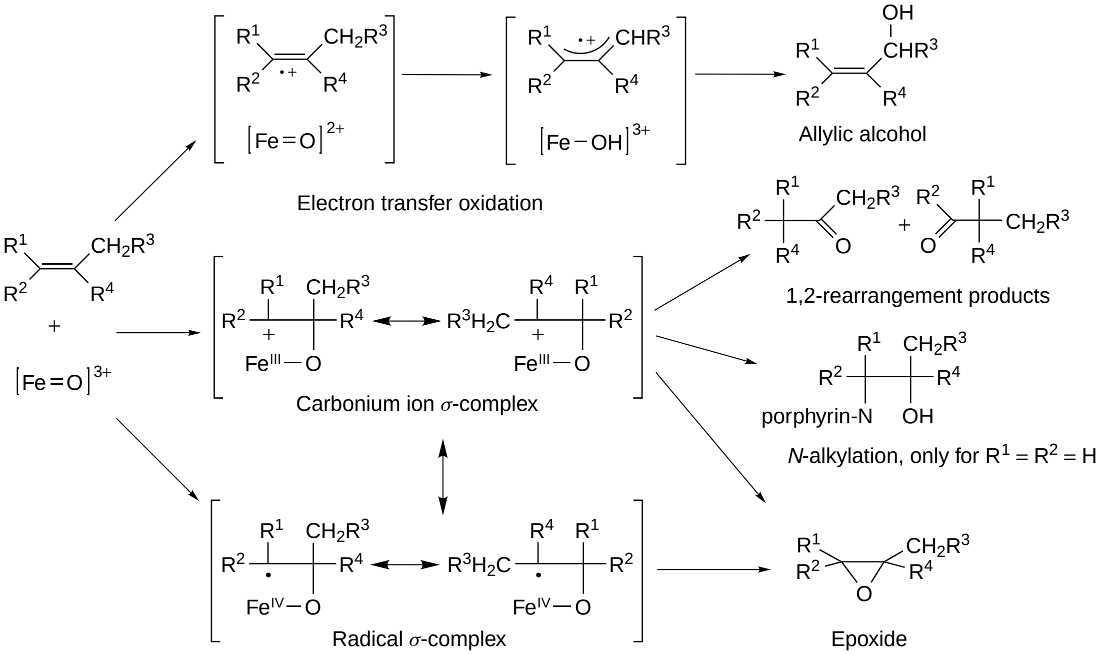
Electron transfer oxidation
Allylic alcohol
1,2-rearrangement products
Carbonium ion σ-complex
porphyrin-N
N-alkylation, only for R1 = R2 = H
Radical σ-complex
Epoxide

Figure 22 The carbocation and radical mechanisms and potential side reactions of alkene oxidation by P450 enzymes

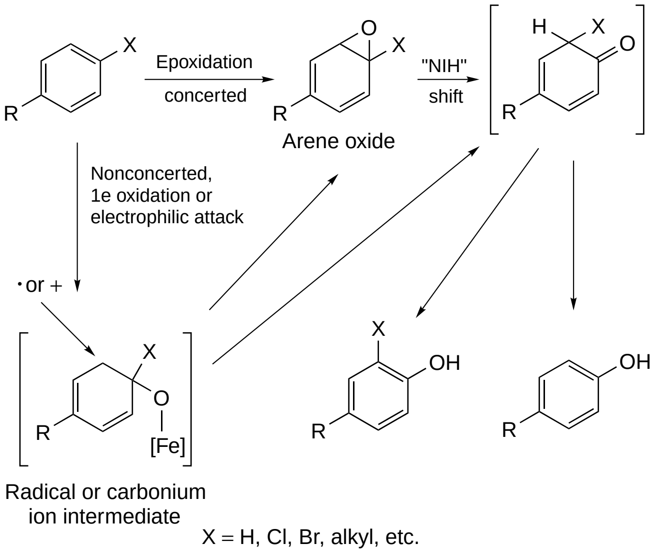
Epoxidation
concerted
"NIH"
shift
Arene oxide
Nonconcerted,
1e oxidation or
electrophilic attack
•or +
Radical or carbonium
ion intermediate
X = H, Cl, Br, alkyl, etc.

Figure 23 The pathways of arene oxidation and the NIH shift

suggested nonconcerted pathways via radical and carbonium ion σ-complexes, as well as electron-transfer oxidation.[183] The exact mechanism will depend on the substrate and the orientation in which it is bound within the enzyme active site. With the larger polyaromatic compounds, and as the number of electron-releasing substituents increases, the electron-transfer oxidation pathway may become dominant. Indeed, a stable polymethoxybenzene cation radical has been observed in P450-catalyzed oxidation.[184] The concerted pathway may dominate if the substrate is bound close to the ferryl oxygen.

Oxygenation and Dealkylation of Heteroatom-containing Compounds. There are two common reactions for P450-catalyzed oxidation of compounds containing heteroatoms. Firstly compounds with N, P, S and I centers can be oxygenated, for example, amine to the *N*-oxide $R_3N^+–O^-$, but P450 Compound I (**VII**) does not oxygenate F, Cl, and O. Secondly, all compounds with a $–CH_2R$ substituent undergo oxidative dealkylation, releasing the alkyl group as the aldehyde (Figure 21). This dealkylation activity is identical to oxidative deamination and dehalogenation, and follows a common pathway of apparent hydroxylation of the α-carbon to form an unstable intermediate, for example, a halohydrin, thioacetal and carbinolamine, that break down with cleavage of the carbon-heteroatom bond.

Guengerich has proposed a unified mechanism based on radical intermediates for this class of reactions (Figure 24).[183] For the oxygenation reaction, direct transfer of the ferryl oxygen atom to the heteroatom is unlikely in view of the bond strengths and electron density distributions. Instead, the Compound I intermediate oxidizes the heteroatom to a radical cation which attacks the $Fe^{IV}{=}O$ species to form the heteroatom-oxygen bond (Figure 24a). The dealkylation reaction can be considered formally to proceed via direct C–H bond hydroxylation followed by breakdown of the intermediate. This is likely when the heteroatom is oxygen, fluorine, and chlorine because the ferryl species cannot oxidize these heteroatoms. Thus *O*-dealkylation of 7-ethoxycoumarin

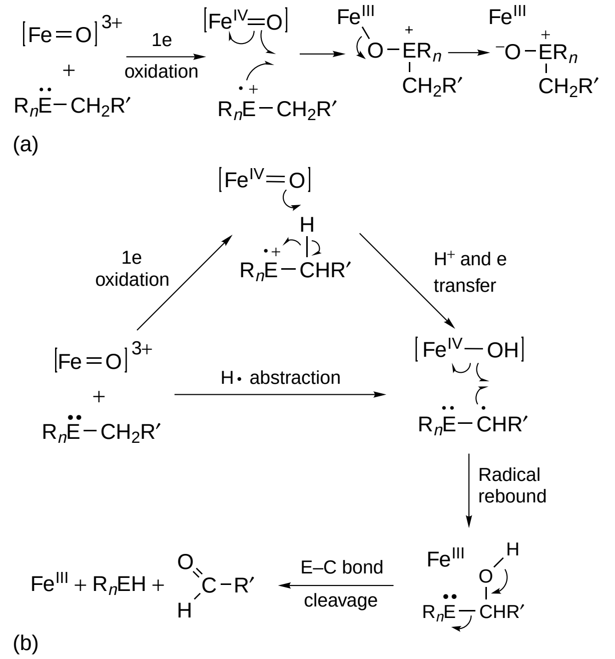

Figure 24 The mechanism of oxidation of heteroatom-containing compounds by P450 enzymes (a) The one-electron oxidation mechanism of heteroatom oxygenation (b) The one-electron and hydrogen atom abstraction mechanisms of heteroatom dealkylation

shows a large kinetic isotope effect ($k_H/k_D \approx 13$), indicative of a hydroxylation mechanism (Figure 24b). With amines, sulfides, and iodides, which have readily oxidized lone pairs of electrons, a stepwise pathway akin to that of heteroatom oxygenation is preferred. One-electron oxidation by the Compound I intermediate gives $Fe^{IV}{=}O$ and a heteroatom cation radical which renders the α-hydrogens more acidic. The $Fe^{IV} = O$ oxygen then abstracts a proton from the α-carbon. As negative charge develops on the α-carbon, an electron is transferred to the cationic heteroatom, resulting in a radical centered on the α-carbon. This intermediate is indistinguishable from that generated via hydrogen atom abstraction by the ferryl intermediate, and similarly undergoes a rebound reaction with the Fe^{IV}–OH species to form the α-hydroxylated intermediate from which the aldehyde is released (Figure 24b). Evidence in support of the stepwise mechanism includes (a) the low kinetic isotope effects ($k_H/k_D = 1.3-3.0$) for the oxidative dealkylation of amines which are similar to isotope effects observed for nonenzymatic electrochemical oxidation,[185] (b) cyclopropylamines give ring-opening products and are mechanism-based inhibitors of P450 enzymes,[186,187] (c) the linear free-energy relationship observed with *para*-substituted *N*,*N*-dimethylanilines,[188,189] (d) preferential demethylation of *N*-methyl,*N*-ethylaniline which showed the importance of the cationic heteroatom radical over the reactivity of the C–H bond,[190] (e) the oxidation of 4-alkyl,1,4-dihydropyridine releases the alkyl group as the radical which attacks the porphyrin.[191,192]

The different mechanisms for oxidizing heteroatom-containing compounds have two main branch points. Firstly, the P450 ferryl intermediate can abstract a hydrogen atom or oxidize the heteroatom. For highly electronegative atoms such as F, O and Cl, the hydroxylation pathway dominates. For more readily oxidized atoms such as N and S, the mechanism shifts to the one-electron pathway. If the amine nitrogen is acetylated, the lone pair is lower in energy and the hydroxylation pathway can compete, and accordingly the kinetic isotope effect is increased.[193] The second branch point is at the $Fe^{IV}{=}O$/cation-radical pair. An E–O bond is formed if no α-hydrogen is present, or if the α-hydrogen is less acidic because the heteroatom cation is not very electron withdrawing. Hence aromatic and other amines without α-hydrogens are *N*-hydroxylated (to N–OH) or oxygenated (to N^+–O^-), while amines with α-hydrogens are dealkylated. On the other hand sulfur-containing compounds are oxygenated even when α-hydrogens are present, for example, dimethylsulfide is oxidized to dimethyl sulfoxide.

Aldehyde Oxidation, Oxidative Deformylation and Other C–C Bond Cleavage Reactions. Aldehyde oxidation was studied intensely because the ‘ferryl mechanism’ does not account for the last step of steroid demethylation in the biosynthesis of estrogens from androgens, that is, the aromatase reaction (Figure 25a). Akhtar proposed that the distal oxygen of the ferric-hydroperoxo intermediate **VI** is sufficiently nucleophilic to attack the aldehyde group.[194–197] The resulting peroxyhemiacetal intermediate can rearrange by an ionic or radical mechanism (Figure 25b), leading to abstraction of a β-hydrogen to form a C=C double bond and loss of formic acid. Strong evidence for the mechanism comes from the observation that hydrogen peroxide and alkyl hydroperoxides can support the reaction with the ferric resting state of the P450 aromatase but not compounds such as iodosylbenzene that provide a single ‘oxygen atom’.[197,198] A related reaction in the steroid biosynthesis pathway is the side chain cleavage of 17-α-hydroxypregnenolone in which an acetyl group is removed and the β-hydrogen is abstracted from an alcohol group, leading to the ketone instead of an alkene (Figure 25c).

The alkyl cleavage reactions proceed via sequential oxidation to the alcohol and then aldehyde or ketone, followed by oxidative C–C bond cleavage. The oxidation of alcohols to aldehydes and ketones can proceed via hydroxylation to the hemiacetal which spontaneously dehydrates to give the product (Figure 26a). A slightly different mechanism of alcohol oxidation has been proposed to operate in the final step of the cholesterol side chain cleavage reaction to form pregnenolone (Figure 26b).[199] The reaction proceeds with two initial C–H bond oxidation steps to form the glycol. In the final step, the ferryl intermediate abstracts a hydrogen atom from one of the alcohol groups. The glycol C–C bond is cleaved homolytically when the alkoxyl radical forms the aldehyde, and the resultant carbon-based radical is oxidized

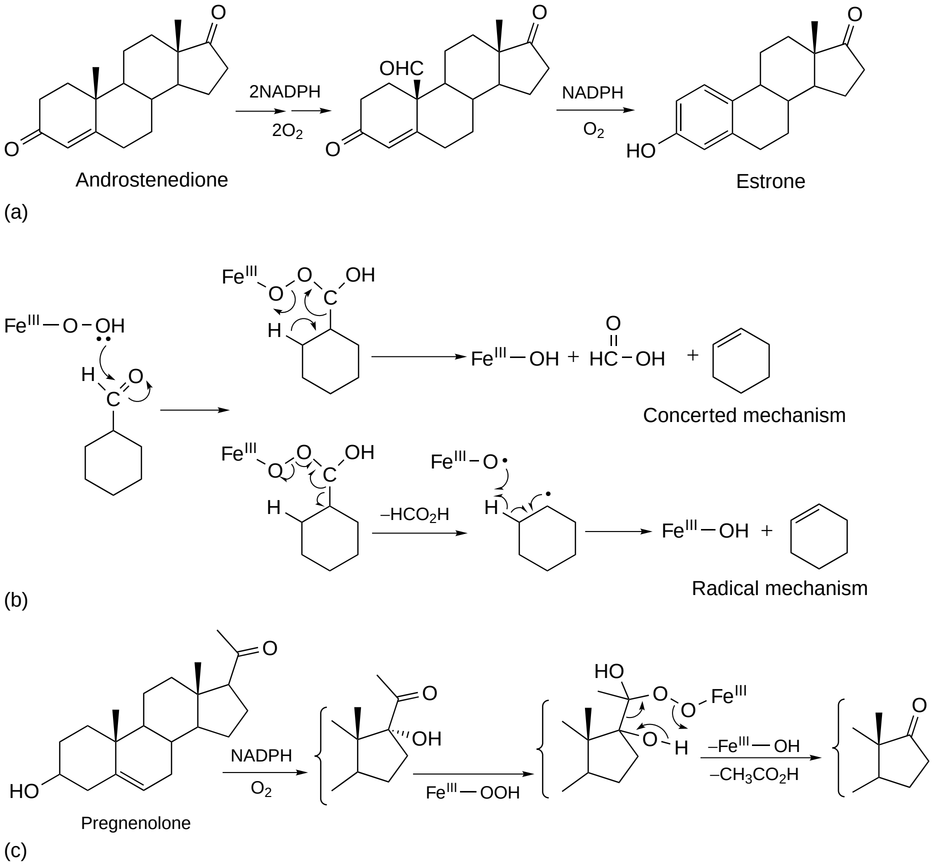

Figure 25 (a) The aromatase activity of P450 enzymes in which androstenedione is converted to estrone via oxidative deformylation (b) The concerted and radical mechanism of deformylation via breakdown of a peroxohemiacetal intermediate formed by nucleophilic attack of the ferric-hydroperoxo intermediate on the aldehyde (c) Abstraction of a β alcohol hydrogen leads to the formation of a ketone rather than a ring C=C double bond

by the Fe^{IV}–OH species to the cation which is deprotonated to form the second aldehyde.

Reductions. P450 enzymes primarily catalyze oxidation reactions using the ferryl and ferric-hydroperoxo intermediates. However, the heme Fe^{III}/Fe^{II} reduction potential is ca. −300 mV in the absence of substrate, and ca. −170 mV if the sixth ligand water is displaced by a bound substrate. If a bound molecule has sufficiently high electron affinity, electron-transfer reduction by the Fe^{II} state can occur. This reaction will be promoted by stabilization of the developing negative charge on the substrate by active-site residues, and retarded by the presence of oxygen which binds rapidly and tightly to the ferrous heme. Nevertheless if the oxygen tension is low or if oxygen binding is weakened, for example, by steric hindrance with a substrate that binds close to the heme iron, substrate reduction can occur even under conditions that are not strictly anaerobic.

Some reduction reactions catalyzed by P450 enzymes are listed in Figure 21. The starting materials are often oxidizing agents and contain electronegative atoms that can accommodate the developing negative charge. The reductive dehalogenation of haloalkanes has been studied extensively because of the potential applications in bioremediation.[200–203] Mammalian P450 enzymes have been reported to catalyze the reductive dehalogenation of polyhalogenated aromatics.[204] The mechanism of hexachloroethane reductive dehalogenation to give tetrachloroethene is shown in Figure 27. Both electron-transfer steps are followed by loss of chloride and the π-bond is formed when the second electron is transferred. The rate-limiting step is the first electron transfer, and the rate increases with the extent of chlorination. Theoretical calculations showed a correlation between the rate of reaction and the electron affinity of the chloroethene.[205]

3 INDOLEAMINE 2,3-DIOXYGENASE

3.1 History, Properties and Physiological Significance

In 1937, Kotake and Ito found that D-Trp-fed rabbits excreted *N*-formyl-D-kynurenine. Later Hayaishi and

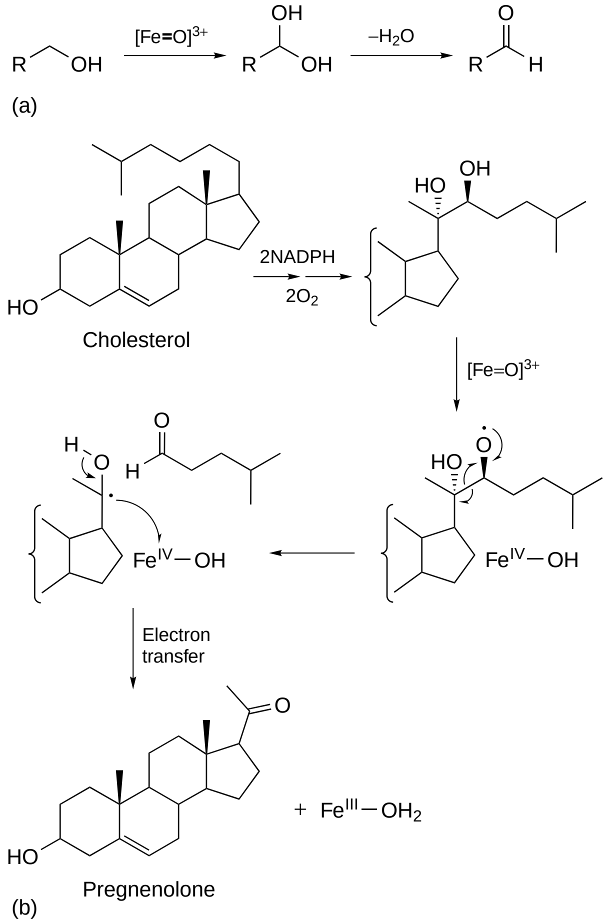

Figure 26 (a) The oxidation of alcohols to aldehydes via an hemiacetal intermediate (b) The sterol side chain cleavage reaction via a diol; note the formation of an O-based radical intermediate

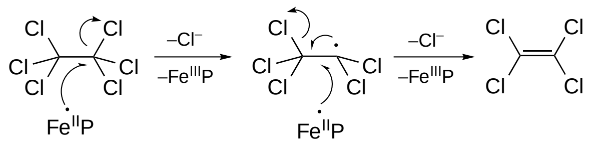

Figure 27 The mechanism of reductive dechlorination of hexachloroethane

coworkers isolated a soluble enzyme from rabbit intestine capable of catalyzing this reaction. The enzyme was found to be a heme-containing protein which could also utilize several other tryptophan derivatives including L-Trp, 5-hydroxy-Trp, tryptamine, and 5-hydroxytryptamine (serotonin).[206,207] It was designated indoleamine 2,3-dioxygenase as only the α-amino group of Trp was found to be essential for Trp derivatives to be substrates of the enzyme.

Indoleamine dioxygenase has been found in many tissues of mammals. It catalyzes the first and rate-limiting step in the main pathway of human tryptophan catabolism, the kynurenine pathway (Figure 28).[208,209] The induction and metabolism of L-Trp along the kynurenine pathway are implicated in a variety of physiological and pathophysiological processes, including antimicrobial and antitumor defense, immunoregulation, neuropathology, and antioxidant activity.[210] Most of the studies on the purified enzyme have been carried out with rabbit indoleamine 2,3-dioxygenase.[211] The human form of the enzyme has recently been cloned and expressed in *E. coli*.[212] Indoleamine 2,3-dioxygenase catalyzes the same reaction as tryptophan dioxygenase but the two enzymes are distinct in several respects which are summarized in Table 1.

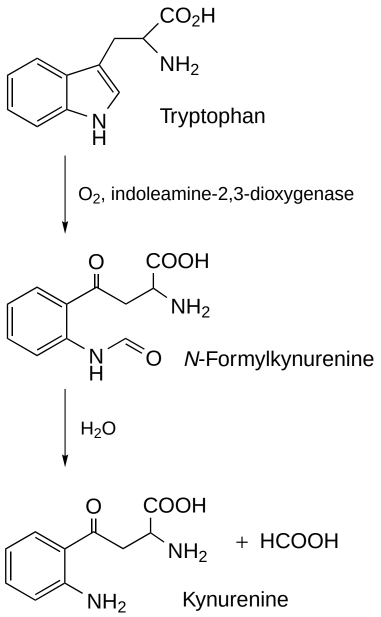

Figure 28 The indoleamine 2,3 dioxygenase pathway of Trp metabolism. Molecular oxygen is incorporated into the pyrrole ring to yield *N*-formylkynurenine which is then degraded to kynurenine and formic acid

3.2 Heme Environment and the Roles of Superoxide Anion ($O_2^{\bullet -}$) and Cofactors Required for in vitro Activation

Only the primary structure of indoleamine 2,3-dioxygenase has been determined. However, extensive equilibrium and spectroscopy studies have been undertaken to investigate the binding properties of both substrate and oxygen and to identify the proximal and distal heme ligands.

MCD spectra of ferric and ferrous indoleamine 2,3-dioxygenase closely resemble those of myoglobin and horseradish peroxidase. Indoleamine 2,3-dioxygenase can bind a variety of relatively large inhibitors indicating a larger substrate-binding pocket than myoglobin.[213–215] On the basis of EPR studies, the proximal ligand of the heme was proposed to be nitrogen, probably from the imidazole of histidine.[207]

Table 1 Comparison of the properties of indoleamine dioxygenase and tryptophan dioxygenase

Properties	Indoleamine dioxygenase	Tryptophan dioxygenase
Molecular weight	42 000–47 000 Da	122 000–167 000 Da
Subunits	1	4 ($\alpha_2\beta_2$)
Prosthetic Group	One protoheme IX	Two protoheme IX
Oxygen source	O_2 (and $O_2^{\bullet-}$)	O_2
Distribution		
Mammals	Ubiquitous (except liver)	Liver
Bacteria	None	*Pseudomonas acidovorans*
Inducers	Influenza virus Lipopolysaccharide Interferons	Tryptophan Kynurenine Hydrocortisone

The distal ligand has also been proposed to be a histidine imidazole nitrogen based on MCD spectroscopy, as found in hemoglobin and myglobin.[216,217]

Resonance Raman studies on human indoleamine 2,3-dioxygenase indicate that the Fe^{III} state is six-coordinate with a distal water/hydroxide ligand (predominantly high spin at neutral pH) whereas the Fe^{II} state displays a peroxidase-like proximal Fe–His bond which moves the iron out of the porphyrin plane preventing the coordination of a weak distal water.[218] This strengthening of the Fe–His bond has been linked to a hydrogen bond between the NH group of the proximal His and the carboxylate group of a nearby aspartate residue which gives the histidine an imidazolate character.[219] These Raman studies also indicate that the binding of substrate appears to lead to significant changes to the conformation of the heme peripheral groups and the chemical environment of the distal pocket.

Sequence alignments of various forms of indoleamine 2,3-dioxygenase and related myoglobins have revealed several highly conserved residues including three histidines. Mutagenesis studies on these conserved residues have shown that H346 in human indoleamine 2,3-dioxygenase was the only one of the three conserved histidine residues essential for heme binding. This strongly suggests that this residue is the proximal histidine ligand (Figure 29).[220]

Both indoleamine dioxygenase and tryptophan dioxygenase are catalytically active only in their Fe^{II} states. Both are isolated as Fe^{III} enzymes and therefore require reduction for activity. For tryptophan dioxygenase this can be achieved by addition of the substrate, Trp. The Trp-enzyme complex appears to be autoreductive. The catalytically active Fe^{II} form of indoleamine dioxygenase readily autoxidizes in the presence of a substrate. A reducing cofactor is therefore required to initiate and sustain enzyme activity. This is usually achieved in vitro using methylene blue and ascorbic acid.[221] The in vivo cofactor remains unknown, but superoxide is one possible candidate as it can activate rabbit indoleamine dioxygenase and is incorporated into L-Trp.[222,223] The Fe^{III} enzyme readily reacts with $O_2^{\bullet-}$ to yield the enzyme-O_2 complex (Fe^{II}–O_2) which is also generated by addition of O_2 to the Fe^{II} form of the enzyme.

3.3 Catalytic Cycle, Intermediates and Reaction Mechanism

Oxygenases commonly bind substrate before dioxygen. This has been shown to be the case with tryptophan 2,3-dioxygenase.[224] Indoleamine 2,3-dioxygenase can bind oxygen to form a relatively stable, catalytically active complex.[225] Later investigation showed that ferrous indoleamine 2,3-dioxygenase binds L-tryptophan followed by molecular oxygen.[226] The reaction mechanism shown in Figure 30 has been proposed.

It should be noted that no redox changes of the heme iron are involved in indoleamine or tryptophan 2,3-dioxygenase

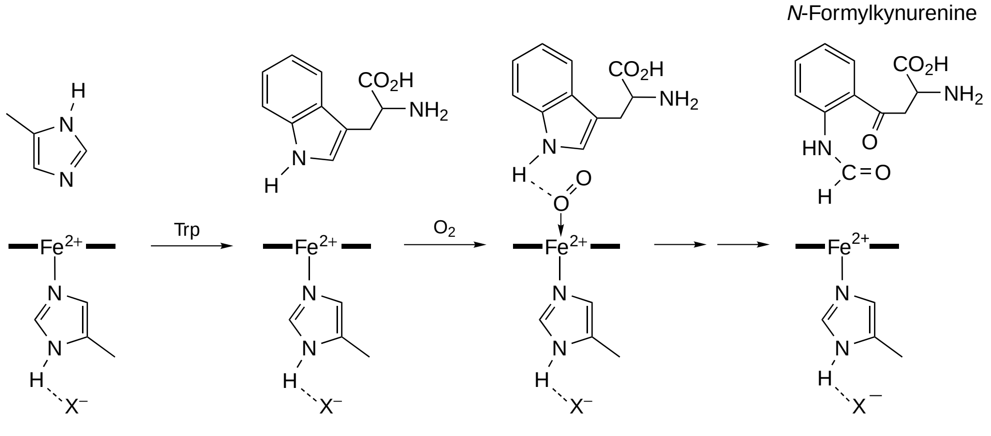

Figure 29 Schematic of the heme environment during the oxidation of Trp by indoleamine dioxygenase. X is probably a carboxylate of aspartate or glutamate

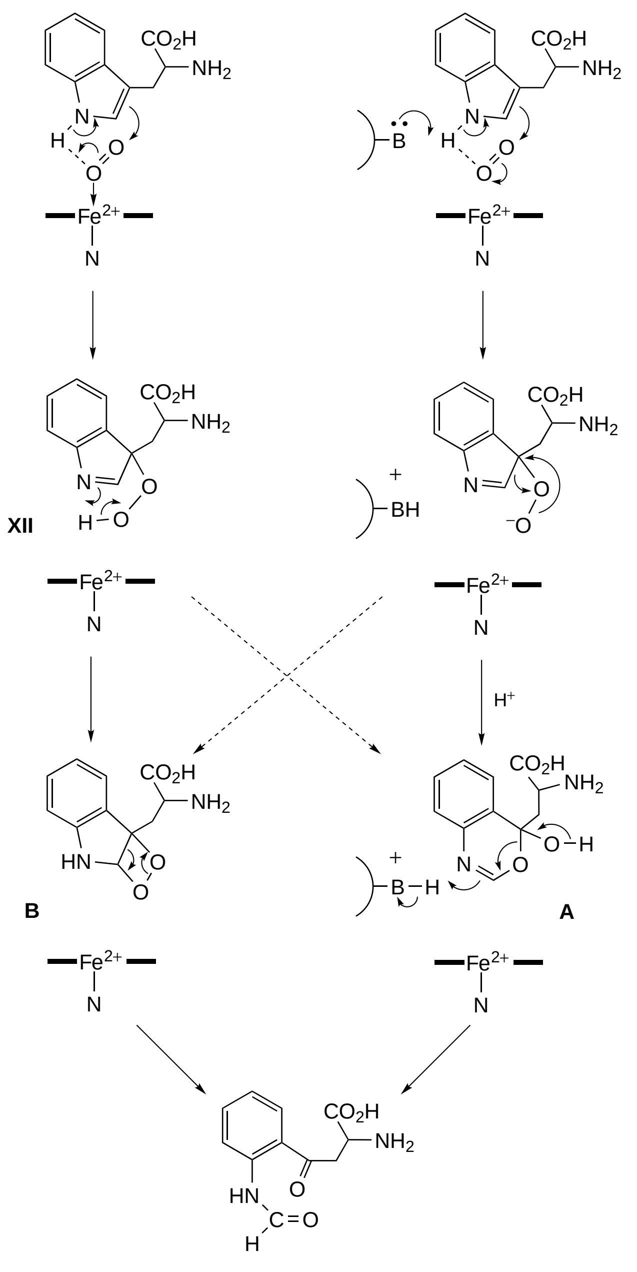

Figure 30 Proposed mechanism for the conversion of Trp to *N*-formylkynurenine catalyzed by indoleamine dioxygenase. Crossover may occur between the two mechanisms as indicated by the dashed lines

activity. Resonance Raman data of the substrate-bound CO complex of human indoleamine 2,3-dioxygenase indicates that strong H-bonding occurs between L-Trp and CO, suggesting a strong interaction between L-Trp and O_2. The electronic effect imposed by this H-bond and the imidazolate character of the strong proximal Fe–His bond is believed to facilitate the electrophilic addition of the dioxygen to the pyrrole ring.[218] This is supported by substrate analogue studies where electron-donating groups at the 5- or 6-position of L-Trp enhance the rate of substrate oxidation but electron-donating groups have the opposite effect.[227] These data suggest an electrophilic reaction involving O_2 attacking the double bond between C-2 and C-3 in indole. The 3-hydroxyperoxyindolenine intermediate (**XII**) has been implicated in chemical studies.[228] An alternative mechanism involves nucleophilic attack of the C-3 of indole on the distal oxygen atom of the bound O_2 coupled with deprotonation.[229] Two pathways to the *N*-formylkynurenine product have been proposed, one involves a Criegee rearrangement-type mechanism (**A**),[229] and the other involves an endoperoxide intermediate (**B**).[230] Further studies are required to establish the exact mechanism of product formation.

4 RELATED ARTICLES

Iron: Heme Proteins, Peroxidases, Catalases & Catalase-peroxidases; Iron Porphyrin Chemistry.

5 REFERENCES

1. H. S. Mason, W. Fawlks, and J. Peterson, *J. Am. Chem. Soc.*, 1955, **77**, 2914.
2. O. Hayashi, M. Katagiri, and S. Rothberg, *J. Am. Chem. Soc.*, 1955, **77**, 5450.
3. O. Hayashi, in ‘Molecular Mechanisms of Oxygen Activation’, ed. O. Hayashi, Academic Press, New York, 1974, p. 1.
4. Z. Zhang, J. Ren, D. K. Stammers, J. E. Baldwin, K. Harlos, and C. J. Schofield, *Nat. Struct. Biol.*, 2000, **7**, 127.
5. M. Ivan, K. Kondo, H. Yang, W. Kim, J. Valiando, M. Ohh, A. Salic, J. M. Asara, W. S. Lane, and W. G. Kaelin Jr, *Science*, 2001, **292**, 464.
6. P. Jaakkola, D. R. Mole, Y. M. Tian, M. I. Wilson, J. Gielbert, S. J. Gaskell, A. Kriegsheim, H. F. Hebestreit, M. Mukherji, C. J. Schofield, P. H. Maxwell, C. W. Pugh, and P. J. Ratcliffe, *Science*, 2001, **292**, 468.
7. K. S. Hewitson, L. A. McNeill, M. V. Riordan, Y. M. Tian, A. N. Bullock, R. W. Welford, J. M. Elkins, N. J. Oldham, S. Bhattacharya, J. M. Gleadle, P. J. Ratcliffe, C. W. Pugh, and C. J. Schofield, *J. Biol. Chem.*, 2002, **277**, 26351.
8. M. Klingenberg, *Arch. Biochem. Biophys.*, 1958, **75**, 376.
9. D. Garfinkel, *Arch. Biochem. Biophys.*, 1958, **77**, 493.
10. T. Omura and R. Sato, *J. Biol. Chem.*, 1962, **237**, 1375.
11. T. Omura and R. Sato, *J. Biol. Chem.*, 1964, **239**, 2370.

12. K. Murakami and H. S. Mason, *J. Biol. Chem.*, 1967, **242**, 1102.
13. R. W. Estabrook, D. Y. Cooper, and O. Rosenthal, *Biochem. Z.*, 1963, **338**, 741.
14. A. Y. Lu and M. J. Coon, *J. Biol. Chem.*, 1968, **243**, 1331.
15. W. H. Bradshaw, H. E. Conrad, E. J. Corey, I. C. Gunsalus, and D. Lednicer, *J. Am. Chem. Soc.*, 1959, **81**, 5507.
16. J. Hedegaard and I. C. Gunsalus, *J. Biol. Chem.*, 1965, **240**, 4038.
17. C.-A. Yu, I. C. Gunsalus, M. Katagiri, K. Suhara, and S. Takemori, *J. Biol. Chem.*, 1974, **249**, 94.
18. T. L. Poulos, B. C. Finzel, and A. J. Howard, *J. Mol. Biol.*, 1987, **195**, 687.
19. D. W. Nebert, D. R. Nelson, M. J. Coon, R. W. Estabrook, R. Feyereisen, Y. Fujii-Kuriyama, F. J. Gonzalez, F. P. Guengerich, I. C. Gunsalus, E. F. Johnson, J. C. Loper, R. Sato, M. R. Waterman, and D. J. Waxman, *DNA Cell Biol.*, 1991, **10**, 1.
20. F. P. Guengerich, in ‘Cytochrome P450: Structure, Mechanism, and Biochemistry’, ed. P. R. Ortiz de Montellano, Plenum Press, New York, 1995, p. 473.
21. M. A. Schuler and D. Werck-Reichhart, *Annu. Rev. Plant Physiol. Plant Mol. Biol.*, 2003, **54**, 629.
22. S. G. Sligar and R. I. Murray, in ‘Cytochrome P450: Structure, Mechanism, and Biochemistry’, ed. P. R. Ortiz de Montellano, Plenum Press, New York, 1986, p. 429.
23. A. W. Munro and J. G. Lindsay, *Mol. Microbiol.*, 1996, **20**, 1115.
24. M. J. Cryle, J. E. Stok, and J. J. De Voss, *Aust. J. Chem.*, 2003, **56**, 749.
25. F. P. Guengerich, *Crit. Rev. Biochem. Mol. Biol.*, 1990, **25**, 97.
26. F. P. Guengerich and T. Shimada, *Chem. Res. Toxicol.*, 1991, **4**, 391.
27. R. De Mot and A. H. Parret, *Trends Microbiol.*, 2002, **10**, 502.
28. G. A. Roberts, G. Grogan, A. Greter, S. L. Flitsch, and N. J. Turner, *J. Bacteriol.*, 2002, **184**, 3898.
29. G. A. Roberts, A. Celik, D. J. Hunter, T. W. Ost, J. H. White, S. K. Chapman, N. J. Turner, and S. L. Flitsch, *J. Biol. Chem.*, 2003, **278**, 48914.
30. M. Wang, D. L. Roberts, R. Paschke, T. M. Shea, B. S. Masters, and J. J. Kim, *Proc. Natl. Acad. Sci. U.S.A.*, 1997, **94**, 8411.
31. G. A. Ziegler, C. Vonrhein, I. Hanukoglu, and G. E. Schulz, *J. Mol. Biol.*, 1999, **289**, 981.
32. A. Müller, J. J. Müller, Y. A. Muller, H. Uhlmann, R. Bernhardt, and U. Heinemann, *Structure*, 1998, **6**, 269.
33. J. J. Muller, A. Lapko, G. Bourenkov, K. Ruckpaul, and U. Heinemann, *J. Biol. Chem.*, 2001, **276**, 2786.
34. A. V. Grinberg, F. Hannemann, B. Schiffler, J. Muller, U. Heinemann, and R. Bernhardt, *Proteins*, 2000, **40**, 590.
35. I. F. Sevrioukova, H. Li, and T. L. Poulos, *J. Mol. Biol.*, 2004, **336**, 889.
36. I. F. Sevrioukova, C. Garcia, H. Li, B. Bhaskar, and T. L. Poulos, *J. Mol. Biol.*, 2003, **333**, 377.
37. A. V. Grinberg, F. Hannemann, B. Schiffler, J. Müller, U. Heinemann, and R. Bernhardt, *Proteins*, 2000, **40**, 590.
38. T. L. Poulos, B. C. Finzel, and A. J. Howard, *Biochemistry*, 1986, **25**, 5314.
39. K. G. Ravichandran, S. S. Boddupalli, C. A. Hasemann, J. A. Peterson, and J. Deisenhofer, *Science*, 1993, **261**, 731.
40. H. Li and T. L. Poulos, *Nat. Struct. Biol.*, 1997, **4**, 140.
41. C. A. Hasemann, K. G. Ravichandran, J. A. Peterson, and J. Deisenhofer, *J. Mol. Biol.*, 1994, **236**, 1169.
42. J. R. Cupp-Vickery and T. L. Poulos, *Nat. Struct. Biol.*, 1995, **2**, 144.
43. J. R. Cupp-Vickery and T. L. Poulos, *Steroids*, 1997, **62**, 112.
44. L. M. Podust, T. L. Poulos, and M. R. Waterman, *Proc. Natl. Acad. Sci. U.S.A.*, 2001, **98**, 3068.
45. D. Leys, C. G. Mowat, K. J. McLean, A. Richmond, S. K. Chapman, M. D. Walkinshaw, and A. W. Munro, *J. Biol. Chem.*, 2003, **278**, 5141.
46. L. M. Podust, Y. Kim, M. Arase, B. A. Neely, B. J. Beck, H. Bach, D. H. Sherman, D. C. Lamb, S. L. Kelly, and M. R. Waterman, *J. Biol. Chem.*, 2003, **278**, 12214.
47. L. M. Podust, H. Bach, Y. Kim, D. C. Lamb, M. Arase, D. H. Sherman, S. L. Kelly, and M. R. Waterman, *Protein Sci.*, 2004, **13**, 255.
48. J. K. Yano, L. S. Koo, D. J. Schuller, H. Li, P. R. Ortiz de Montellano, and T. L. Poulos, *J. Biol. Chem.*, 2000, **275**, 31086.
49. S. Y. Park, K. Yamane, S. Adachi, Y. Shiro, K. E. Weiss, S. A. Maves, and S. G. Sligar, *J. Inorg. Biochem.*, 2002, **91**, 491.
50. K. Zerbe, O. Pylypenko, F. Vitali, W. Zhang, S. Rouset, M. Heck, J. W. Vrijbloed, D. Bischoff, B. Bister, R. D. Sussmuth, S. Pelzer, W. Wohlleben, J. A. Robinson, and I. Schlichting, *J. Biol. Chem.*, 2002, **277**, 47476.
51. O. Pylypenko, F. Vitali, K. Zerbe, J. A. Robinson, and I. Schlichting, *J. Biol. Chem.*, 2003, **278**, 46727.
52. S. Nagano, H. Li, H. Shimizu, C. Nishida, H. Ogura, P. R. Ortiz de Montellano, and T. L. Poulos, *J. Biol. Chem.*, 2003, **278**, 44886.
53. J. Cosme and E. F. Johnson, *J. Biol. Chem.*, 2000, **275**, 2545.
54. P. A. Williams, J. Cosme, A. Ward, H. C. Angove, D. M. Vinkovic, and H. Jhoti, *Nature*, 2003, **424**, 464.
55. E. E. Scott, Y. A. He, M. R. Wester, M. A. White, C. C. Chin, J. R. Halpert, E. F. Johnson, and C. D. Stout, *Proc. Natl. Acad. Sci. U.S.A.*, 2003, **100**, 13196.
56. T. L. Poulos, J. Cupp-Vickery, and H. Li, in ‘Cytochrome P450: Structure, Mechanism, and Biochemistry’, ed. P. R. Ortiz de Montellano, Plenum Press, New York, 1995, p. 125.
57. C. A. Hasemann, R. G. Kurumbail, S. S. Boddupalli, J. A. Peterson, and J. Deisenhofer, *Structure*, 1995, **2**, 41.

58. J. A. Peterson and S. E. Graham-Lorence, in 'Cytochrome P450: Structure, Mechanism, and Biochemistry', ed. P. R. Ortiz de Montellano, Plenum Press, New York, 1995, p. 151.
59. J. A. Peterson and S. E. Graham, *Structure*, 1998, **6**, 1079.
60. R. Raag and T. L. Poulos, *Biochemistry*, 1989, **28**, 7586.
61. P. S. Stayton, T. L. Poulos, and S. G. Sligar, *Biochemistry*, 1989, **28**, 8201.
62. P. S. Stayton and S. G. Sligar, *Biochemistry*, 1990, **29**, 7381.
63. P. A. Williams, J. Cosme, V. Sridhar, E. F. Johnson, and D. E. McRee, *Mol. Cell*, 2000, **5**, 121.
64. W. M. Atkins and S. G. Sligar, *J. Biol. Chem.*, 1988, **263**, 18842.
65. P. J. Loida and S. G. Sligar, *Biochemistry*, 1993, **32**, 11530.
66. O. Gotoh, *J. Biol. Chem.*, 1992, **267**, 83.
67. C. A. Tyson, J. D. Lipscomb, and I. C. Gunsalus, *J. Biol. Chem.*, 1972, **247**, 5777.
68. S. G. Sligar, J. D. Lipscomb, P. G. Debrunner, and I. C. Gunsalus, *Biochem. Biophys. Res. Commun.*, 1974, **61**, 290.
69. F. P. Guengerich, D. P. Ballou, and M. J. Coon, *Biochem. Biophys. Res. Commun.*, 1976, **70**, 951.
70. R. W. Estabrook, A. G. Hildebrandt, J. Baron, K. J. Netter, and K. Leibman, *Biochem. Biophys. Res. Commun.*, 1971, **42**, 132.
71. J. T. Groves and Y.-Z. Han, in 'Cytochrome P-450: Structure, Mechanism and Biochemistry', ed. P. R. Ortiz de Montellano, Plenum Press, New York, 1995, p. 3.
72. P. R. Ortiz de Montellano, in 'Cytochrome P450: Structure, Mechanism, and Biochemistry', ed. P. R. Ortiz de Montellano, Plenum Press, New York, 1995, p. 245.
73. H. Danielsson and K. Wikvall, *FEBS Lett.*, 1976, **66**, 299.
74. E. G. Hrycay, J. A. Gustafsson, M. Ingelman-Sundberg, and L. Ernster, *Biochem. Biophys. Res. Commun.*, 1975, **66**, 209.
75. J. Å. A. Gustafsson, E. G. Hrycay, and L. Ernster, *Arch. Biochem. Biophys.*, 1976, **174**, 440.
76. J. T. Groves and G. A. McClusky, *J. Am. Chem. Soc.*, 1976, **98**, 859.
77. H. Li, S. Narasimhulu, L. M. Havran, J. D. Winkler, and T. L. Poulos, *J. Am. Chem. Soc.*, 1995, **117**, 6297.
78. J. H. Dawson and K. S. Eble, *Adv. Inorg. Bioinorg. Mech.*, 1986, **4**, 1.
79. J. H. Dawson and M. Sono, *Chem. Rev.*, 1987, **87**, 1255.
80. M. Sono, M. P. Roach, E. D. Coulter, and J. H. Dawson, *Chem. Rev.*, 1996, **96**, 2841.
81. R. Raag and T. L. Poulos, *Biochemistry*, 1991, **30**, 2674.
82. D. Harris and G. Loew, *J. Am. Chem. Soc.*, 1993, **115**, 8775.
83. H. Aissaoui, S. Ghirlanda, C. Gmur, and W. D. Woggon, *J. Mol. Catal. A*, 1996, **113**, 393.
84. H. Aissaoui, R. Bachmann, A. Schweiger, and W.-D. Woggon, *Angew. Chem. Int. Ed.*, 1998, **37**, 2998.
85. M. Lochner, M. Meuwly, and W. D. Woggon, *Chem. Commun.*, 2003, 1330.
86. R. O. Juvonen, M. Iwasaki, and M. Negishi, *J. Biol. Chem.*, 1991, **266**, 16431.
87. T. Ueno, Y. Kousumi, K. Yoshizawa-Kumagaye, K. Nakajima, N. Ueyama, T.-A. Okamura, and A. Nakamura, *J. Am. Chem. Soc.*, 1998, **120**, 12264.
88. T. Ueno, N. Nishikawa, S. Moriyama, S. Adachi, K. Lee, T.-A. Okamura, N. Ueyama, and A. Nakamura, *Inorg. Chem.*, 1999, **38**, 1199.
89. N. Ueyama, N. Nishikawa, Y. Yamada, T.-A. Okamura, S. Oka, H. Sakurai, and A. Nakamura, *Inorg. Chem.*, 1998, **37**, 2415.
90. N. Ueyama, N. Nishikawa, Y. Yamada, T.-A. Okamura, and A. Nakamura, *J. Am. Chem. Soc.*, 1996, **118**, 12826.
91. S. Yoshioka, S. Takahashi, K. Ishimori, and I. Morishima, *J. Inorg. Biochem.*, 2000, **81**, 141.
92. S. Yoshioka, T. Tosha, S. Takahashi, K. Ishimori, H. Hori, and I. Morishima, *J. Am. Chem. Soc.*, 2002, **124**, 14571.
93. T. Tosha, S. Yoshioka, H. Hori, S. Takahashi, K. Ishimori, and I. Morishima, *Biochemistry*, 2002, **41**, 13883.
94. T. Tosha, S. Yoshioka, S. Takahashi, K. Ishimori, H. Shimada, and I. Morishima, *J. Biol. Chem.*, 2003, **278**, 39809.
95. I. Schlichting, J. Berendzen, K. Chu, A. M. Stock, S. A. Maves, D. E. Benson, R. M. Sweet, D. Ringe, G. A. Petsko, and S. G. Sligar, *Science*, 2000, **287**, 1615.
96. O. Bangcharoenpaurpong, A. K. Rizos, P. M. Champion, D. Jollie, and S. G. Sligar, *J. Biol. Chem.*, 1986, **261**, 8089.
97. Y. Kimata, H. Shimada, T. Hirose, and Y. Ishimura, *Biochem. Biophys. Res. Commun.*, 1995, **208**, 96.
98. S. A. Martinis, W. M. Atkins, P. S. Stayton, and S. G. Sligar, *J. Am. Chem. Soc.*, 1989, **111**, 9252.
99. N. C. Gerber and S. G. Sligar, *J. Biol. Chem.*, 1994, **269**, 4260.
100. M. Vidakovic, S. G. Sligar, H. Li, and T. L. Poulos, *Biochemistry*, 1998, **37**, 9211.
101. R. Davydov, I. D. G. Macdonald, T. M. Makris, S. G. Sligar, and B. M. Hoffman, *J. Am. Chem. Soc.*, 1999, **121**, 10654.
102. R. Davydov, T. M. Makris, V. Kofman, D. E. Werst, S. G. Sligar, and B. M. Hoffman, *J. Am. Chem. Soc.*, 2001, **123**, 1403.
103. V. Guallar, D. L. Harris, V. S. Batista, and W. H. Miller, *J. Am. Chem. Soc.*, 2002, **124**, 1430.
104. T. Egawa, H. Shimada, and Y. Ishimura, *Biochem. Biophys. Res. Commun.*, 1994, **201**, 1464.
105. S. Prasad and S. Mitra, *Biochem. Biophys. Res. Commun.*, 2004, **314**, 610.
106. D. G. Kellner, S. C. Hung, K. E. Weiss, and S. G. Sligar, *J. Biol. Chem.*, 2002, **277**, 9641.
107. V. Schunemann, C. Jung, J. Terner, A. X. Trautwein, and R. Weiss, *J. Inorg. Biochem.*, 2002, **91**, 586.

108. V. Schunemann, F. Lendzian, C. Jung, J. Contzen, A. L. Barra, S. G. Sligar, and A. X. Trautwein, *J. Biol. Chem.*, 2004, **279**, 10919.
109. V. Guallar, M. H. Baik, S. J. Lippard, and R. A. Friesner, *Proc. Natl. Acad. Sci. U.S.A.*, 2003, **100**, 6998.
110. D. Kumar, S. P. de Visser, P. K. Sharma, S. Cohen, and S. Shaik, *J. Am. Chem. Soc.*, 2004, **126**, 1907.
111. D. L. Harris and G. H. Loew, *J. Am. Chem. Soc.*, 1998, **120**, 8941.
112. M. T. Green, *J. Am. Chem. Soc.*, 1999, **121**, 7939.
113. F. Ogliaro, N. Harris, S. Cohen, M. Filatov, S. P. de Visser, and S. Shaik, *J. Am. Chem. Soc.*, 2000, **122**, 8977.
114. J. Antony, M. Grodzicki, and A. X. Trautwein, *J. Phys. Chem. A*, 1997, **101**, 2692.
115. F. Ogliaro, S. Cohen, M. Filatov, N. Harris, and S. Shaik, *Angew. Chem. Int. Ed.*, 2000, **39**, 3851.
116. F. Ogliaro, S. P. De Visser, J. T. Groves, and S. Shaik, *Angew. Chem. Int. Ed.*, 2001, **40**, 2874.
117. K. Yoshizawa, T. Kamachi, and Y. Shiota, *J. Am. Chem. Soc.*, 2001, **123**, 9806.
118. M. T. Green, *J. Am. Chem. Soc.*, 2000, **122**, 9495.
119. F. Ogliaro, S. Cohen, S. P. de Visser, and S. Shaik, *J. Am. Chem. Soc.*, 2000, **122**, 12892.
120. S. P. de Visser, F. Ogliaro, P. K. Sharma, and S. Shaik, *Angew. Chem. Int. Ed.*, 2002, **41**, 1947.
121. J. C. Schöneboom, H. Lin, N. Reuter, W. Thiel, S. Cohen, F. Ogliaro, and S. Shaik, *J. Am. Chem. Soc.*, 2002, **124**, 8142.
122. T. Kamachi and K. Yoshizawa, *J. Am. Chem. Soc.*, 2003, **125**, 4652.
123. E. J. Mueller, P. J. Loida, and S. G. Sligar, in 'Cytochrome P450: Structure, Mechanism, and Biochemistry', ed. P. R. Ortiz de Montellano, Plenum Press, New York, 1995, p. 83.
124. J. T. Groves, G. A. McClusky, R. E. White, and M. J. Coon, *Biochem. Biophys. Res. Commun.*, 1978, **81**, 154.
125. M. H. Gelb, D. C. Heimbrook, P. Mälkönen, and S. G. Sligar, *Biochemistry*, 1982, **21**, 370.
126. R. E. White, J. P. Miller, L. V. Favreau, and A. Bhattacharyya, *J. Am. Chem. Soc.*, 1986, **108**, 6024.
127. J. T. Groves and D. V. Subramanian, *J. Am. Chem. Soc.*, 1984, **106**, 2177.
128. H. Fretz and W. D. Woggon, *Helv. Chim. Acta*, 1986, **69**, 1959.
129. B. Meunier and J. Bernadou, *Top. Catal.*, 2002, **21**, 47.
130. H. Fretz, W. D. Woggon, and R. Voges, *Helv. Chim. Acta*, 1989, **72**, 391.
131. K. Auclair, Z. Hu, D. M. Little, P. R. Ortiz De Montellano, and J. T. Groves, *J. Am. Chem. Soc.*, 2002, **124**, 6020.
132. P. R. Ortiz de Montellano and R. A. Stearns, *J. Am. Chem. Soc.*, 1987, **109**, 3415.
133. M. Newcomb and P. H. Toy, *Acc. Chem. Res.*, 2000, **33**, 449.
134. M. Newcomb, M.-H. Le Tadic, D. A. Putt, and P. F. Hollenberg, *J. Am. Chem. Soc.*, 1995, **117**, 3312.
135. M. Newcomb, M.-H. Le Tadic-Biadatti, D. L. Chestney, E. S. Roberts, and P. F. Hollenberg, *J. Am. Chem. Soc.*, 1995, **117**, 12085.
136. M. Newcomb, R. Shen, S.-Y. Choi, P. H. Toy, P. F. Hollenberg, A. D. N. Vaz, and M. J. Coon, *J. Am. Chem. Soc.*, 2000, **122**, 2677.
137. M. Newcomb, R. Shen, Y. Lu, M. J. Coon, P. F. Hollenberg, D. A. Kopp, and S. J. Lippard, *J. Am. Chem. Soc.*, 2002, **124**, 6879.
138. P. H. Toy, M. Newcomb, and P. F. Hollenberg, *J. Am. Chem. Soc.*, 1998, **120**, 7719.
139. P. H. Toy, M. Newcomb, M. J. Coon, and A. D. N. Vaz, *J. Am. Chem. Soc.*, 1998, **120**, 9718.
140. S. Jin, T. M. Makris, T. A. Bryson, S. G. Sligar, and J. H. Dawson, *J. Am. Chem. Soc.*, 2003, **125**, 3406.
141. W. Nam, M. H. Lim, H. J. Lee, and C. Kim, *J. Am. Chem. Soc.*, 2000, **122**, 6641.
142. W. Nam, S. E. Park, I. K. Lim, M. H. Lim, J. Hong, and J. Kim, *J. Am. Chem. Soc.*, 2003, **125**, 14674.
143. F. Ogliaro, S. P. de Visser, S. Cohen, P. K. Sharma, and S. Shaik, *J. Am. Chem. Soc.*, 2002, **124**, 2806.
144. J. K. Kochi and H. E. Mains, *J. Org. Chem.*, 1965, **30**, 1862.
145. K. L. Rollick and J. K. Kochi, *J. Am. Chem. Soc.*, 1982, **104**, 1319.
146. B. W. Griffin and J. A. Peterson, *Biochemistry*, 1972, **11**, 4740.
147. S. Graham-Lorence, G. Truan, J. A. Peterson, J. R. Falck, S. Wei, C. Helvig, and J. H. Capdevila, *J. Biol. Chem.*, 1997, **272**, 1127.
148. H. Li and T. L. Poulos, *Biochimie*, 1996, **78**, 695.
149. R. Raag, H. Li, B. C. Jones, and T. L. Poulos, *Biochemistry*, 1993, **32**, 4571.
150. K. Di Gleria, D. P. Nickerson, H. A. O. Hill, L.-L. Wong, and V. Fülöp, *J. Am. Chem. Soc.*, 1998, **120**, 46.
151. A. R. Dunn, I. J. Dmochowski, A. M. Bilwes, H. B. Gray, and B. R. Crane, *Proc. Natl. Acad. Sci. U.S.A.*, 2001, **98**, 12420.
152. S. G. Sligar, *Biochemistry*, 1976, **15**, 5399.
153. S. N. Daff, S. K. Chapman, K. L. Turner, R. A. Holt, S. Govindaraj, T. L. Poulos, and A. W. Munro, *Biochemistry*, 1997, **36**, 13816.
154. I. C. Gunsalus, J. R. Meeks, and J. D. Lipscomb, *Ann. N Y Acad. Sci.*, 1973, **212**, 107.
155. G. S. Wilson, J. C. Tsibris, and I. C. Gunsalus, *J. Biol. Chem.*, 1973, **248**, 6059.
156. R. Tsai, C. A. Yu, I. C. Gunsalus, J. Peisach, W. Blumberg, W. H. Orme-Johnson, and H. Beinert, *Proc. Natl. Acad. Sci. U.S.A.*, 1970, **66**, 1157.
157. M. T. Fisher and S. G. Sligar, *J. Am. Chem. Soc.*, 1985, **107**, 5018.

158. P. L. Gigon, T. E. Gram, and J. R. Gillette, *Mol. Pharmacol.*, 1969, **5**, 109.

159. V. Ullrich, R. W. Estabrook, J. Schadelin, and H. Staudinger, *Hoppe Seylers Z. Physiol. Chem.*, 1968, **349**, 1631.

160. V. Ullrich, *Hoppe Seylers Z. Physiol. Chem.*, 1969, **350**, 357.

161. C. S. Eyer and W. L. Backes, *Arch. Biochem. Biophys.*, 1992, **293**, 231.

162. F. P. Guengerich and W. W. Johnson, *Biochemistry*, 1997, **36**, 14741.

163. H. Zhang, L. Gruenke, D. Arscott, A. Shen, C. Kasper, D. L. Harris, M. Glavanovich, R. Johnson, and L. Waskell, *Biochemistry*, 2003, **42**, 11594.

164. F. P. Guengerich, *Biochemistry*, 1983, **22**, 2811.

165. Y. Y. Huang, T. Hara, S. Sligar, M. J. Coon, and T. Kimura, *Biochemistry*, 1986, **25**, 1390.

166. H. Yamazaki, W. W. Johnson, Y. F. Ueng, T. Shimada, and F. P. Guengerich, *J. Biol. Chem.*, 1996, **271**, 27438.

167. K. F. Aguey-Zinsou, P. V. Bernhardt, J. J. De Voss, and K. E. Slessor, *Chem. Commun.*, 2003, 418.

168. O. Sibbesen, Z. Zhang, and P. R. Ortiz de Montellano, *Arch. Biochem. Biophys.*, 1998, **353**, 285.

169. C. F. Harford-Cross, A. B. Carmichael, F. K. Allan, P. A. England, D. A. Rouch, and L.-L. Wong, *Protein. Eng.*, 2000, **13**, 121.

170. A. B. Carmichael and L. L. Wong, *Eur. J. Biochem.*, 2001, **268**, 3117.

171. M. J. Honeychurch, H. A. O. Hill, and L. L. Wong, *FEBS Lett.*, 1999, **451**, 351.

172. R. A. Marcus and N. Sutin, *Biochim. Biophy. Acta*, 1985, **811**, 265.

173. C. C. Moser, J. M. Keske, K. Warncke, R. S. Farid, and P. L. Dutton, *Nature*, 1992, **355**, 796.

174. J. N. Onuchic, D. N. Beratan, J. R. Winkler, and H. B. Gray, *Annu. Rev. Biophys. Biomol. Struct.*, 1992, **21**, 349.

175. H. B. Gray and J. R. Winkler, *Q. Rev. Biophys.*, 2003, **36**, 341.

176. C. C. Page, C. C. Moser, and P. L. Dutton, *Curr. Opin. Chem. Biol.*, 2003, **7**, 551.

177. S. G. Bell, E. Orton, H. Boyd, J.-A. Stevenson, A. Riddle, S. Campbell, and L.-L. Wong, *Dalton Transactions*, 2003, 2133.

178. V. Ullrich, *Top. Curr. Chem.*, 1979, **83**, 67.

179. S. Kadkhodayan, E. D. Coulter, D. M. Maryniak, T. A. Bryson, and J. H. Dawson, *J. Biol. Chem.*, 1995, **270**, 28042.

180. F. P. Guengerich, *Chem. Res. Toxicol.*, 2001, **14**, 611.

181. G. Guroff, J. W. Daly, D. M. Jerina, J. Renson, B. Witkop, and S. Udenfriend, *Science*, 1967, **157**, 1524.

182. D. M. Jerina and J. W. Daly, *Science*, 1974, **185**, 573.

183. F. P. Guengerich and T. L. MacDonald, *Acc. Chem. Res.*, 1984, **17**, 9.

184. H. Sato and F. P. Guengerich, *J. Am. Chem. Soc.*, 2000, **122**, 8099.

185. F. P. Guengerich, C. H. Yun, and T. L. Macdonald, *J. Biol. Chem.*, 1996, **271**, 27321.

186. F. P. Guengerich, R. J. Willard, J. P. Shea, L. E. Richards, and T. L. Macdonald, *J. Am. Chem. Soc.*, 1984, **106**, 6446.

187. A. Bondon, T. L. Macdonald, T. M. Harris, and F. P. Guengerich, *J. Biol. Chem.*, 1989, **264**, 1988.

188. G. Galliani, M. Nali, B. Rindone, S. Tollari, M. Rocchetti, and M. Salmona, *Xenobiotica*, 1986, **16**, 511.

189. T. L. Macdonald, W. G. Gutheim, R. B. Martin, and F. P. Guengerich, *Biochemistry*, 1989, **28**, 2071.

190. Y. Seto and F. P. Guengerich, *J. Biol. Chem.*, 1993, **268**, 9986.

191. O. Augusto, H. S. Beilan, and P. R. Ortiz de Montellano, *J. Biol. Chem.*, 1982, **257**, 11288.

192. F. P. Guengerich and R. H. Böcker, *J. Biol. Chem.*, 1988, **263**, 8168.

193. L. R. Hall and R. P. Hanzlik, *J. Biol. Chem.*, 1990, **265**, 12349.

194. M. Akhtar, M. R. Calder, D. L. Corina, and J. N. Wright, *Biochem. J.*, 1982, **201**, 569.

195. M. Akhtar, D. Corina, S. Miller, A. Z. Shyadehi, and J. N. Wright, *Biochemistry*, 1994, **33**, 4410.

196. E. S. Roberts, A. D. Vaz, and M. J. Coon, *Proc. Natl. Acad. Sci. U.S.A.*, 1991, **88**, 8963.

197. A. D. N. Vaz, S. J. Pernecky, G. M. Raner, and M. J. Coon, *Proc. Natl. Acad. Sci. U.S.A.*, 1996, **93**, 4644.

198. T. D. Porter and M. J. Coon, *J. Biol. Chem.*, 1991, **266**, 13469.

199. S. G. Sligar, M. H. Gelb, and D. C. Heimbrook, *Xenobiotica*, 1984, **14**, 63.

200. B. A. Mico and L. R. Pohl, *Arch. Biochem. Biophys.*, 1983, **225**, 596.

201. C. E. Castro, R. S. Wade, and N. O. Belser, *Biochemistry*, 1985, **24**, 204.

202. S. Li and L. P. Wackett, *Biochemistry*, 1993, **32**, 9355.

203. K. Rattan, R. Shanker, P. Khanna, and W. M. Atkins, *Biotechnol. Prog.*, 1999, **15**, 958.

204. R. S. Takazawa and H. W. Strobel, *Biochemistry*, 1986, **25**, 4804.

205. B. T. Luke, G. H. Loew, and A. D. McLean, *J. Am. Chem. Soc.*, 1988, **110**, 3396.

206. O. Hayaishi, *J. Biochem.* (*Tokyo*), 1976, **79**, 13.

207. T. Shimizu, S. Nomiyama, F. Hirata, and O. Hayaishi, *J. Biol. Chem.*, 1978, **253**, 4700.

208. O. Takikawa, R. Yoshida, R. Kido, and O. Hayaishi, *J. Biol. Chem.*, 1986, **261**, 3648.

209. N. P. Botting, *Chem. Soc. Rev.*, 1995, **24**, 401.

210. S. R. Thomas and R. Stocker, *Redox Rep.*, 1999, **4**, 199.

211. R. Yoshida and O. Hayaishi, *Methods Enzymol.*, 1987, **142**, 188.

212. T. K. Littlejohn, O. Takikawa, D. Skylas, J. F. Jamie, M. J. Walker, and R. J. W. Truscott, *Protein Expr. Purif.*, 2000, **19**, 22.

213. M. Sono and S. G. Cady, *Biochemistry*, 1989, **28**, 5392.

214. M. Sono, *Biochemistry*, 1989, **28**, 5400.

215. S. G. Cady and M. Sono, *Arch. Biochem. Biophys.*, 1991, **291**, 326.

216. K. Uchida, T. Shimizu, R. Makino, K. Sakaguchi, T. Iizuka, Y. Ishimura, T. Nozawa, and M. Hatano, *J. Biol. Chem.*, 1983, **258**, 2519.

217. M. Sono and J. H. Dawson, *Biochim. Biophy. Acta*, 1984, **789**, 170.

218. A. C. Terentis, S. R. Thomas, O. Takikawa, T. K. Littlejohn, R. J. W. Truscott, R. S. Armstrong, S.-R. Yeh, and R. Stocker, *J. Biol. Chem.*, 2002, **277**, 15788.

219. G. Smulevich, *Adv. Spectros.*, 1993, **20**, 163.

220. T. K. Littlejohn, O. Takikawa, R. J. W. Truscott, and M. J. Walker, *J. Biol. Chem.*, 2003, **278**, 29525.

221. M. Sono, *J. Biol. Chem.*, 1989, **264**, 1616.

222. O. Hayaishi, *Adv. Exp. Med. Biol.*, 1996, **398**, 285.

223. O. Hayaishi, O. Takikawa, and R. Yoshida, *Prog. Inorg. Chem.*, 1990, **38**, 75.

224. Y. Ishimura, M. Nozaki, and O. Hayaishi, *J. Biol. Chem.*, 1970, **245**, 3593.

225. F. Hirata, T. Ohnishi, and O. Hayaishi, *J. Biol. Chem.*, 1977, **252**, 4637.

226. M. Sono, T. Taniguchi, Y. Watanabe, and O. Hayaishi, *J. Biol. Chem.*, 1980, **255**, 1339.

227. M. D. Southan, R. J. W. Truscott, J. F. Jamie, L. Pelosi, M. J. Walker, H. Maeda, Y. Iwamoto, and S. Tone, *Med. Chem. Res.*, 1996, **6**, 343.

228. M. Nakagawa, H. Watanabe, S. Kodato, H. Okajima, T. Hino, J. L. Flippen, and B. Witkop, *Proc. Natl. Acad. Sci. U.S.A.*, 1977, **74**, 4730.

229. G. A. Hamilton, *Adv. Enzymol. Relat. Areas Mol. Biol.*, 1969, **32**, 55.

230. B. Witkop and J. B. Patrick, *J. Am. Chem. Soc.*, 1951, **73**, 2196.

Iron: Heme Proteins, Peroxidases, Catalases & Catalase-peroxidases

B. Bhaskar, Latesh Lad & Thomas L. Poulos
University of California-Irvine, Irvine, CA, USA

Based in part on the article Iron: Heme Proteins, Peroxidases, & Catalases by Ann M. English which appeared in the Encyclopedia of Inorganic Chemistry, First Edition.

1 Introduction 1
2 Class I Peroxidases 2
3 Class II Peroxidases 7
4 Class III Peroxidase 8
5 Bacterial Di-heme Cytochrome *C* peroxidases (BCcP) 10
6 Prostaglandin Endoperoxide H_2 Synthases-1 and 2 (PGHS) 11
7 Mammalian Peroxidases 13
8 Catalases 16
9 References 17

Glossary

Compound I: two-electron oxidized intermediate of heme peroxidases and catalases
Compound II: one-electron oxidized intermediate of heme peroxidases and catalases

Abbreviations

CcP = Cytochrome *c* Peroxidase; BCCP = Bacterial Cytochrome *c* Peroxidases; APX = Soybean or pea or Tobacco Ascorbate Peroxidase; MNP = Manganese Peroxidase; LIP = Lignin Peroxidase; EPO = Eosinophil Peroxidase; LPO = Lactoperoxidase; MPO = Myeloperoxidase; TPO = Thyroid Peroxidase; ARP = *ArthomycesRamosus* Peroxidase; SPO = Salivary Peroxidase; PGHsynthase = Prostaglandin Hsynthase; KatG = Catalase-peroxidase; EPR = Electron Paramagnetic Resonance; RR = Resonance Raman; BHA = Benzhydroxamic Acid; FA = Ferulic Acid; DBNBS = 3,5-dibromo-4-nitrosobenzenesulfonic acid; ABTS = 2,2′-azino-bis(3-ethylbenzothiazoline-6-sulfonic acid); MNPr = Methylnitrosopropane; INH = Isoniazid.

1 INTRODUCTION

The purpose of this article is to review structure–function relationships for heme peroxidases, catalases, and catalase-peroxidases for which detailed crystallographic information is available. Peroxidases catalyze the peroxidation of various substrates and catalases are similar except that a peroxide is both an oxidant and a reductant.

The overall peroxidase cycle is

$$\underset{\text{Resting State}}{Fe^{3+}R + H_2O_2} \longrightarrow \underset{\text{Compound I}}{Fe^{4+} - O\,R^{\bullet} + H_2O} \qquad (1)$$

$$\underset{\text{Compound I}}{Fe^{4+} - O\,R^{\bullet} + S} \longrightarrow \underset{\text{Compound II}}{Fe^{4+} - O\,R + S^{\bullet}} \qquad (2)$$

$$\underset{\text{Compound II}}{Fe^{4+} - O\,R + S} \longrightarrow \underset{\text{Resting State}}{Fe^{3+}R + H_2O + S^{\bullet}} \qquad (3)$$

In the first step (equation 1), peroxide removes two electrons from the protein. One derives from iron and another from an organic group, *R*, giving the well-known compound I. Compound I thus has two fewer electrons than the native enzyme. In most peroxidases, the oxidized organic group is the porphyrin leading to a porphyrin π-cation radical.[1] However, in cytochrome c peroxidase (CcP), a tryptophan residue rather than the porphyrin is oxidized.[2,3]

Both compounds I and II have distinct spectroscopic signatures and very often are relatively long-lived. This, together with the relative ease of obtaining these enzymes, has enabled peroxidases and catalases to occupy a pivotal position in the history of enzymology. Peroxidases played an important role in the development of modern enzymology as early as the 1930s.[4] The formation of distinct spectroscopic intermediates in the peroxidase reaction cycle helped shape the development of rapid reaction kinetic methods pioneered by Britton Chance in the 1940s.[5] Since then, nearly every conceivable sophisticated biophysical tool has been applied to peroxidases, which has resulted in a vast and diverse range of studies.

The most well-known and thoroughly investigated peroxidases are of nonmammalian origin. Establishment of a detailed sequence database enabled Welinder[6] to divide nonmammalian heme peroxidases into three distinct classes. Class I comprises intracellular and/or peroxidases of prokaryotic origin. These include yeast CcP, chloroplast and cytosolic ascorbate peroxidases (APX), and bacterial catalase-peroxidases (KatGs). Class II peroxidases are the secreted fungal peroxidases. Examples include lignin peroxidase (LIP) and manganese peroxidase (MnP) of *Phanerochaete chrysosporium* and the ink cap mushroom peroxidase, ARP from *Coprinius cinerius* (alternate name *Arthomyces ramosus*). Chloroperoxidase from *Caladariomyces fumago*, while also a secreted fungal peroxidase, does not belong to class II owing to its specialized function and lack of either primary or tertiary structural homology with other fungal peroxidases. Class III peroxidases are the classical secretory plant peroxidases such as horseradish peroxidase (HRP), the most well-known and thoroughly investigated class III peroxidase.

2 CLASS I PEROXIDASES

2.1 Yeast Cytochrome *c* Peroxidase (CcP)

CcP is the most well-known and thoroughly studied class I peroxidase and has been recently reviewed.[7,8] CcP is a yeast mitochondrial enzyme that catalyzes the following reaction:

$$2\text{cyt. } c(\text{Fe}^{3+}) + \text{H}_2\text{O}_2 + 2\text{H}^+ \longrightarrow \text{cyt. } c(\text{Fe}^{3+}) + 2\text{H}_2\text{O} \qquad (4)$$

Given the large number of studies centered on CcP, it is surprising that only recently have there been advances in understanding the biological function of CcP. Kwon *et al.*[9] found that yeast CcP levels increase during oxidative stress indicating that the primary function of CcP is to serve as an antioxidant. In addition, yeast CcP may participate in a signaling process during oxidative stress.[10]

2.1.1 Yeast CcP Structure and Mechanism

CcP shares the same overall fold with other class I as well as class II and III peroxidases (Figure 1(a)). CcP contains 10 α-helices with a single β-sheet. The protein is divided into two distinct domains separated by heme *viz.* distal and proximal heme domains. Figure 1(b) shows the active site architecture of CcP with the role of key residues in catalysis, which are typical of most peroxidases. On the distal side of the heme, Arg48, Trp51, and His52 form the catalytic triad and distal heme pocket where exogenous ligands and substrates like hydrogen peroxide bind. On the proximal side of the heme, His175 coordinates the heme iron while Trp191 forms a parallel stacking interaction with His175. Asp235 hydrogen bonds to both His175 and Trp191. The His175-Asp235 H-bond imparts anionic character to the proximal His175, which is important for stabilization of the high oxidation state of iron in compounds I and II.[11,12] As outlined in Figure 1, His52 operates as an acid-base catalyst in promoting heterolytic fission of the peroxide O–O bond while Arg48 helps to stabilize the developing negative charge on the leaving OH group. Mutagenesis studies clearly illustrate the critical role of His52 in CcP[13] and other peroxidases,[14,15] although the effect of changing Arg48 is less dramatic.[16] Similarly mutagenesis of the distal His42 in HRP has demonstrated the critical role of the distal His in peroxidase catalysis.[14,15]

Once compound I is formed, CcP reacts with ferrocytochrome *c* in the following multistep scheme:[17]

1. $\text{Fe}^{4+}\ \text{Trp}^{\bullet+} + \text{cyt. } c\ (\text{Fe}^{2+}) \longrightarrow \text{Fe}^{4+}\text{Trp}^{\bullet+}/\text{cyt. } c\ (\text{Fe}^{2+})$
2. $\text{Fe}^{4+}\ \text{Trp}^{\bullet+}/\text{cyt. } c\ (\text{Fe}^{2+}) \longrightarrow \text{Fe}^{4+}\text{Trp}/\text{cyt. } c\ (\text{Fe}^{3+})$
3. $\text{Fe}^{4+}\ \text{Trp}/\text{cyt.} c\ (\text{Fe}^{3+}) \longrightarrow \text{Fe}^{4+}\text{Trp} + \text{cyt. } c\ (\text{Fe}^{3+})$
4. $\text{Fe}^{4+}\ \text{Trp} \longleftrightarrow \text{Fe}^{3+}\text{Trp}^{\bullet+}$

In step 1, CcP compound I forms a complex with ferrocytochrome *c* followed by electron transfer (step 2) and dissociation (step 3) of oxidized cytochrome *c*. Step 4 represents the intramolecular electron transfer from Trp191 to the iron giving $\text{Fe}^{3+}\text{Trp}^{\bullet+}$, the intermediate required to oxidize the second molecule of ferrocytochrome *c*. In this mechanism, formation of the Trp191 cation radical is essential for both electron transfer steps.

Recent 1.2-Å and 1.3-Å structures of resting state and compound I CcP have provided new insights into the nature and stabilization of compound I.[18] This was possible owing to the unexpected stability of compound I in the X-ray beam. Exposure of metalloprotein crystals to X-rays can often lead to reduction of the metal center,[19] which can be problematic for enzyme intermediates like compounds I and II where the redox potential of the oxyferryl centers are near 1000 mV.[20] Spectroscopic studies of single crystals of resting state and compound I showed that CcP compound I is remarkably stable to X-ray exposure. The oxyferryl center (Fe^{4+}–O) is not affected by X-ray exposure as evidenced by both absorption and single-crystal EPR (electron paramagnetic resonance) spectroscopies.[18] In addition, the single-crystal EPR data indicated that by the end of X-ray diffraction data collection, approximately 50% of the Trp191 π-cationic radical signal remains.

These higher resolution structures have provided insight into small but functionally important conformational differences between resting state CcP and compound I.[18] There are three such regions which occupy two discrete positions in the resting state structure but only one conformation in compound I. The first of these is Arg48 in the distal heme pocket which is considered to be a key residue involved in the formation of compound I.[21,22] In resting state CcP, Arg48 occupies two positions, one '*out*' toward the heme propionate and the other '*in*' toward heme iron. In compound I, Arg48 occupies the '*in*' position which enables Arg48 to hydrogen bond with Fe^{4+}–O oxygen. The '*in*' position is similar to the earlier compound I structures observed at lower resolution[23,24] and in the CcP-fluoride complex.[25] A second region is Met172 in the proximal heme pocket which exists in two conformations in resting state, but becomes more ordered in compound I. In compound I, Met172 occupies a position closer to the His175 ligand (Figure 1). The third region that shows discrete differences between resting state and compound I is the proximal loop region involving residues 190–195 which plays an important role in complex formation with cytochrome *c*. Residues 193–195, including both side chains and the peptide backbone, adopt multiple conformations in the resting state, but become more ordered in compound I. In the single conformation that is observed in compound I, the side chain

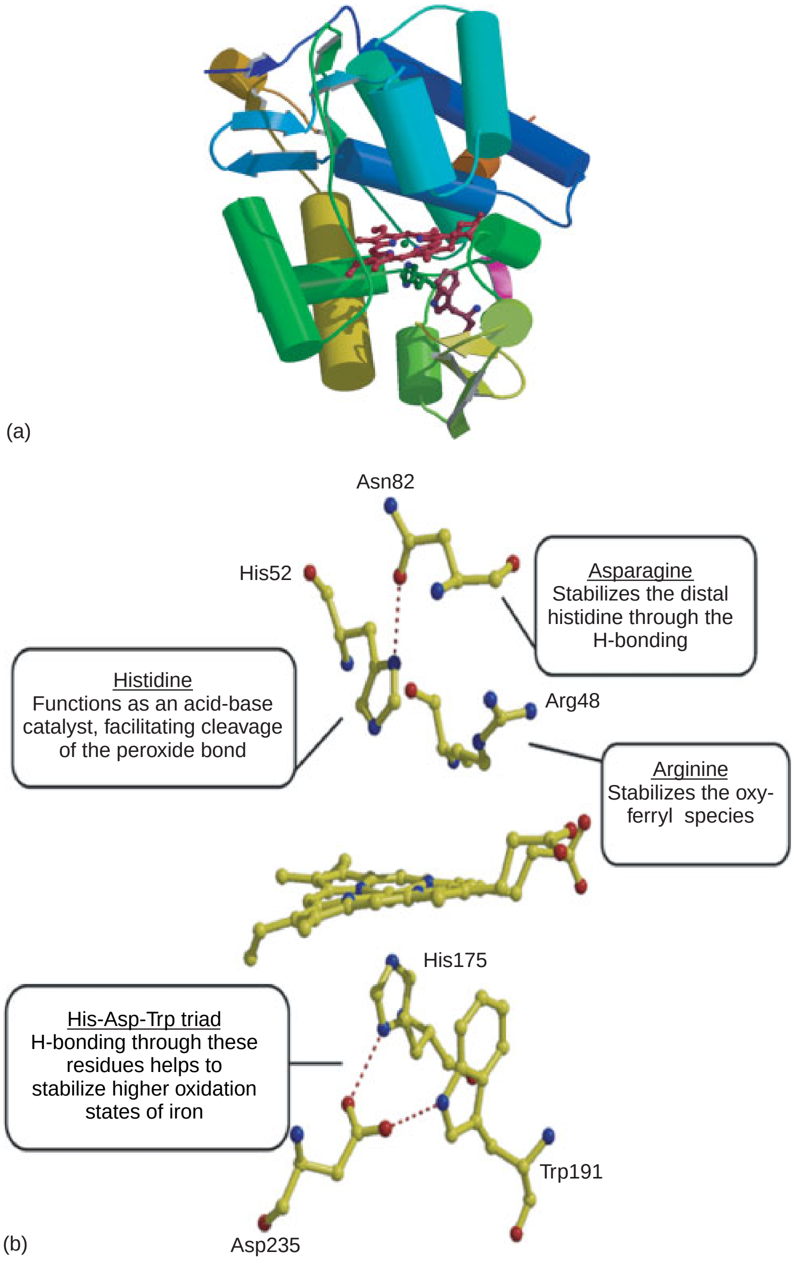
(a)
Asn82
His52
Asparagine
Stabilizes the distal histidine through the H-bonding
Histidine
Functions as an acid-base catalyst, facilitating cleavage of the peroxide bond
Arg48
Arginine
Stabilizes the oxy-ferryl species
His175
His-Asp-Trp triad
H-bonding through these residues helps to stabilize higher oxidation states of iron
Trp191
(b)
Asp235

Figure 1 (a) Schematic representation of yeast cytochrome *c* peroxidase (CcP) structure with heme and key active site residues represented as ball-and-stick models. (b) Active site architecture of yeast cytochrome *c* peroxidase (CcP) showing the role of all the key residues in catalysis. The dashed lines represent hydrogen bonds

of Asn195 is in position to donate a hydrogen bond to the peptide carbonyl oxygen of Gly178. Gly178, in turn, is 4.01 Å away from Trp191. Taken together these changes help to stabilize compound I. The movement of Arg48 provides an extra H-bond to the Fe^{4+}–O center while the movement of Met172 and the Asn195 region places polar groups closer to the Trp191 radical which helps to stabilize the Trp191 cationic radical.

Another important insight in the 1.3-Å compound I structure is the nature of the Fe^{4+}–O bond. There were two previous X-ray studies of CcP compound I,[23,24] both of which were of lower resolution. The Laue diffraction methods employed in the 2.2-Å study of compound I by Fulop *et al.*[24] assigned an Fe^{4+}–O distance ranging from 1.7 to 1.9 Å. The structures of catalase compounds I and II determined at lower resolution (2.7 Å) precluded accurate estimation of Fe^{4+}–O bond distances.[26,27] However, results of some recent studies on compound II of horse heart myoglobin and compounds I and II of HRP are comparable to CcP compound I. In the 1.35-Å myoglobin compound II structure, the Fe^{4+}–O was found to be 1.92 Å.[28] The recent X-ray work on HRP compounds

I and II to 1.6 Å resolution gives Fe^{4+}–O distances of 1.7 Å for compound I and 1.8 Å for compound II.[29] The heme of HRP compound II and the heme of CcP compound I are electronically equivalent. Hence, the longer 1.8-Å Fe^{4+}–O distance in HRP compound II is comparable to the 1.87-Å distance found in CcP compound I. These longer Fe^{4+}–O distances are at odds with some of the early EXAFS work on peroxidases. Chance *et al.*[30] estimated a distance of 1.67 Å in CcP compound I while Penner–Hahn *et al.*[31] estimated a distance of 1.6 Å in HRP compounds I and II. However, Chance *et al.*[30] estimated a Fe^{4+}–O distance of 1.93 Å in HRP compound II which is closer to the 1.8 Å found in the HRP crystal structure. Although EXAFS results differ from that of the recent X-ray results, resonance Raman data more closely match the more current results. Reczek *et al.*[32] assigned a stretching frequency for the Fe^{4+}–O stretch in CcP compound I to be 753 cm^{-1}, compared the 773–779 cm^{-1} for HRP[32–35] indicating a weaker Fe^{4+}–O bond in CcP compound I. It was argued that the lower stretching frequency for the Fe^{4+}–O stretch was due to a strong hydrogen bond to the Fe^{4+}–O oxygen and greater single-bond character of the Fe^{4+}–O bond. This is consistent with the high-resolution CcP compound I structure since both Arg48 and Trp51 form hydrogen bonds with ferryl oxygen and the long 1.87 Å Fe^{4+}–O bond indicates a single bond. Overall, the results of the high-resolution structure of CcP coupled with a wealth of spectroscopic data strongly favor a single Fe^{4+}–O bond. A single bond would also inevitably mean that the ferryl oxygen is protonated. In peroxidases, we know that the peroxide O–O bond undergoes heterolytic cleavage[36] which leaves an oxygen atom with six valence electrons bound to the iron. If both electrons now reside primarily on the Fe-linked O atom, this oxygen atom contains a full complement of eight valence electrons, giving an Fe^{4+}–O center which should be a strong base and exist primarily as a Fe^{4+}–OH center if the Fe^{4+}–O bond is a single bond. The –OH group is stabilized by the motion of Arg48 in the high-resolution structure of CcP compound I.[18] Therefore, the ferryl center of CcP may be best described as a hydroxide ion with a single bond to Fe^{4+} stabilized by hydrogen bonding interactions with Arg48 and Trp51.

2.1.2 Stabilization of the Trp Cation Radical Yeast CcP

A fascinating aspect of CcP chemistry and biochemistry is the formation and stabilization of the Trp191 cationic radical in compound I while other peroxidases form a porphyrin π-cationic radical. A wealth of biochemical, spectroscopic, and structural results are available on several mutants of CcP which have emphasized the importance of Trp191 to enzyme catalysis.[8] Other class I peroxidases like APX and KatG also have a proximal side Trp analogous to yeast CcP Trp191 but these peroxidase do not form a Trp radical. It now appears that the local environment surrounding Trp191 is designed to electrostatically stabilize the extra positive charge on the Trp191 cationic radical. Indeed, the first clue to this puzzle came from several mutagenesis studies that showed that the Trp191Gly mutation resulted in a cavity that binds cations such as potassium and imidazolium.[37–39] These results and electrostatic calculations suggested that the local environment created a negative potential that can stabilize the Trp radical in CcP[37,40,41] and these results have been further corroborated by computational studies of Poulos and coworkers.[42] Further structural comparisons showed that in APX and plant peroxidases, a cation-binding site [a K^+ site for APX (*see* ***Cation-activated Enzymes***) and a Ca^{2+} for most other peroxidases (*see* ***Calcium-binding Proteins***)] is located ∼8 Å away from the Trp/Phe residue, while only a water molecule is present at the same location in CcP.[18,40,43] Therefore, Patterson *et al.*[44] proposed that this cation-binding site may play a role in destabilizing the Trp radical in APX. This hypothesis was tested by engineering a protein whose activity could be modulated by a designed cation site. On the basis of structural homology between APX and CcP, the K^+ binding site of APX was engineered into CcP.[40,45] Crystal structures showed that K^+ binds to the engineered site in CcP exactly as in APX. Moreover, EPR experiments showed that the Trp191 radical becomes increasingly less stable as a function of K^+ concentration while the steady state enzyme activity decreases. These results demonstrated that long-range electrostatic effects can control the reactivity of a redox-active amino acid side chain. Building on this success, further metallo-engineering efforts enabled the selectivity of the engineered site to be switched from K^+ to Ca^{2+}.[46]

2.1.3 CcP-cytochrome c Complex

CcP and cytochrome *c* were the first physiological redox partners where the crystal structure of each partner had been determined. As such, the CcP-cytochrome *c* system has served as a paradigm for both protein–protein interactions and interprotein electron transfer studies. The crystal structure of the CcP-cytochrome *c* complex[47] provided a major advance in our understanding of how CcP works. The complex shows that the cytochrome *c* heme is within ≈3.9 Å from Ala194 in CcP. This provides a direct route of electron transfer from the cytochrome *c* heme to the Trp191 cationic radical. There are few strong charge–charge interactions at the interface which was surprising since the complex is strongly dependent on ionic strength.

Various biophysical probes indicate that CcP has two sites of interaction with cytochrome *c* although it is less clear if both sites are involved in electron transfer. To probe this question, CcP and cytochrome *c* have been site-specifically cross-linked using engineered disulfide bonds[48] to generate a covalent complex that mimics the noncovalent complex. CcP in the covalent complex is unable to accept electrons from free ferrocytochrome *c*. A second cross-link was designed to block the proposed second cytochrome *c* binding site[49,50] but this complex could still accept electrons from ferrocytochrome *c*. Taken together, these results indicate that the covalently attached cytochrome *c* is blocking the one site used by cytochrome *c* for docking and transferring electrons and that this single competent electron transfer site is the same one identified in the crystal structure of the CCP-cytochrome *c* complex.[47]

2.2 Ascorbate Peroxidase (APX)

The primary function of APX is to rid plant cells of toxic peroxides by using ascorbate as the reducing substrate. Pea cytosolic APX is the most thoroughly studied APX and was the first APX crystal structure determined.[43] This now has been followed by the crystal structures of soybean cytosolic[51] and tobacco stromal APX.[52] The overall fold of APX is very similar to CcP except that APX is smaller and contains 250 residues compared to 294 in CcP. The main difference is that APX lacks the β-sheet structure in CcP. APX also exists as a homodimer.

The key elements of the APX active site are the same as in CcP including the homolog to CcP Trp191 (Trp179 in APX) which, in CcP, forms the stable compound I cation radical. However, APX does not form a Trp179 radical but instead forms the more traditional porphyrin π-cation radical.[44] In the absence of reducing substrates, compound I decays to compound I*. Recently Rodriguez–Lopez and coworkers showed by low-temperature EPR and RP-HPLC the existence of a transient Trp cation radical.[53] As noted in Section 2.1.2, this difference has been attributed to the local electrostatic environment of CcP, which is designed to stabilize a Trp191 cation radical.[40,41,43]

Studies on APX provided some of the first evidence that peroxidases can have different substrate binding sites. Early on, it was found that modification of the single Cys in pea APX eliminated enzyme activity but at that time there was insufficient enzyme for more detailed studies. This was followed by work on recombinant APX where both the Cys modified form of APX and the Cys-to-Ser mutant crystal structures led to the hypothesis that the substrate, ascorbate, binds near Cys32 (Figure 2).[54] Moreover, Poulos and coworkers proposed that Arg172 in this region interacts with the ascorbate and helps to hold the substrate in place near the heme propionates.[55] As predicted, mutating Arg172 to other residues blocked the oxidation of ascorbate but not the oxidation of the small phenolic substrate, guaiacol. This led to the view that phenolic substrates interact with APX at a different site near the exposed heme edge. More recently, the crystal structure of the ascorbate-APX complex[51] clearly shows (Figure 2) that the ascorbate is positioned near the propionate edge of the heme where it interacts with Arg172 as predicted by the chemical modification and mutagenesis studies.[55]

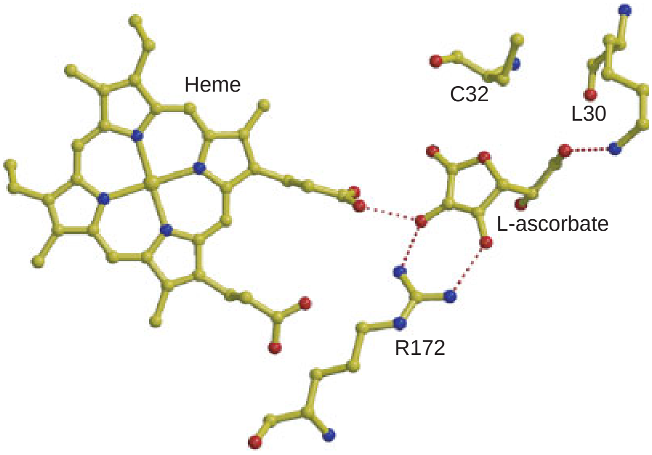

Figure 2 Structure of active site of recombinant soybean ascorbate peroxidase (sAPX) showing the heme, Lys30, Cys32, and Arg172 with the substrate ascorbate (This figure was generated from coordinates of **1OAF** deposited in the *Protein Data Bank*)

2.3 Bacterial Catalase-peroxidases

2.3.1 *Introduction*

Over the last ten years, the catalase-peroxidases have attracted significant interest in the fight against *tuberculosis. Mycobacterium tuberculosis* is a leading pathogen worldwide, infecting an estimated 2–3 million people each year.[56] One of the primary drugs used to treat tuberculosis is isoniazid (INH), a prodrug that is oxidized by the *KatG* (gene encoding catalase-peroxidase) catalase-peroxidase to an activated form that inhibits cell wall synthesis.[57,58] The real surge of interest in catalase-peroxidases started in 1992 when it was confirmed that mutation of *KatG* in *Mycobacterium tuberculosis* confers isoniazid resistance.[59] A putative reaction scheme of catalase-peroxidases is shown in Figure 3(a).

2.3.2 *Structure and Mechanism*

These are difficult enzymes to work with and only recently have crystal structures become available for two catalase-peroxidases: *Haloarcula marismortui* (HMCP)[60] and *Burkholderia pseudomallei* (BpKatG).[61] A typical subunit is approximately 80 kDa in molecular mass, with a single heme *b* prosthetic group. The primary structure of each subunit can be divided into two distinct domains, N terminal and C terminal. The N-terminal domain contains the heme and active site,[62] while the C-terminal domain does not contain a heme binding motif and its function remains unclear. The clear sequence similarity between the two domains suggests gene duplication and fusion.[63] Curiously, despite many years of study, the actual in vivo peroxidatic substrate of the catalase-peroxidases has not been identified.

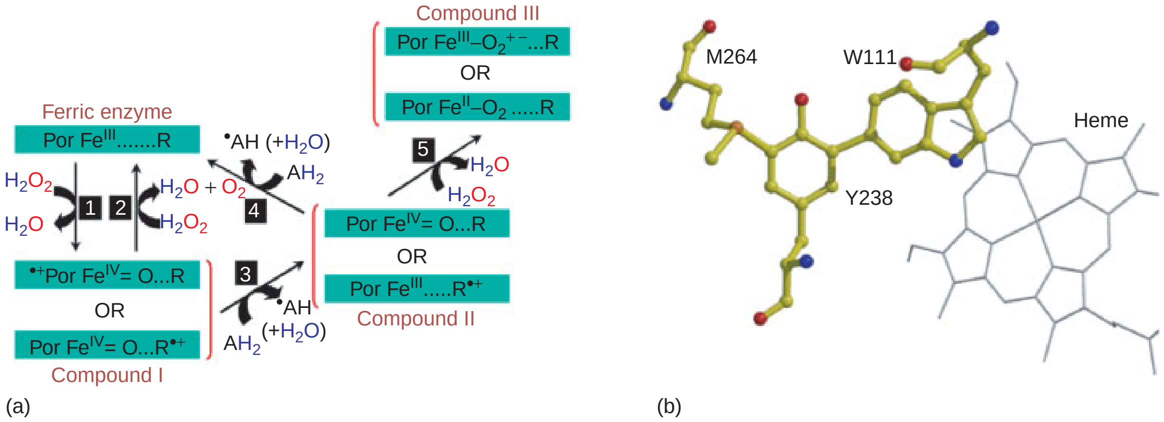

Figure 3 (a) Putative reaction scheme of catalase-peroxidases (KatG). (b) Schematic diagram showing the formation of a novel covalent adduct among side chain of residues Trp111 (Trp95), Tyr238 (Tyr218), and Met264 (Met244) of catalase-peroxidase of *Burkholderia pseudomallei* (BpKatG). The numbers in parenthesis represent the residues of *Haloarcula marismortui* (HMCP) which form a similar adduct. (This figure was generated from coordinates of **1MWV** deposited in the *Protein Data Bank*)

As noted, the N-terminal domain of KatGs exhibits the classic peroxidase fold. Superimposition of the N-terminal segment of either BpKatG or HMCP onto CcP, APX, or HRP give rms deviations of 0.97 Å, 1.22 Å, and 2.03 Å, respectively, for BpKatG and 1.12 Å, 1.31 Å, and 1.99 Å, respectively, for the ten α-helical segments of HMCP. On the other hand, superimposition of the C-terminal region of either BpKatG or HMCP onto the same peroxidase proteins give rms deviations of 3.62 Å, 3.75 Å, and 4.06 Å, respectively, for BpKatG and 3.51 Å, 3.83 Å, and 4.44 Å, respectively, for HMCP.

The organization of the heme active site of both HMCP and BpKatG are almost identical to that of CcP and APX. On the distal side of the heme, Trp, Arg, and His form the peroxide-binding site. On the proximal side, the conserved Asp H-bonds with both the proximal His ligand and proximal side Trp just as in CcP and APX. However, comparison of other residues surrounding the catalase-peroxidase group reveals greater similarity to CcP with decreasing similarity to APX. Most notably, a potassium ion found in APX in a surface loop about 8 Å from the proximal Trp is absent. This same loop forms the Ca^{2+} site in class III peroxidases. However, a Trp radical does not form in BpKatG as in yeast CcP compound I but instead a porphyrin π-cation radical has been demonstrated for both EcKatG (catalase-peroxidase form *Escherichia coli*)[64] and MtKatG (catalase-peroxidase from *M. tuberculosis*).[65]

One of the most surprising results from the crystal structures of the KatGs was the identification of a novel Trp-Tyr-Met covalent cross-link adduct (Trp111-Tyr238-Met264 in BpKatG and Tyr218-Trp95-Met244 in HCMP) in the vicinity of the active site (Figure 3(b)). Although the mechanism leading to the formation of the adduct is unclear, a possible explanation for its formation involves hydrogen peroxide and the heme iron in an oxidative process. What is not clear is whether the adduct provides some functional role. Other unusual adducts have been observed in peroxidases and in monofunctional catalases, including a hydroxy group on the C^{β} of Trp171 in lignin peroxidase,[66] distal Trp51-Tyr52 covalent cross-link in a mutant of CcP,[67] a methionine sulfoxide residue in the catalase from *Proteus mirabilis*,[68] formation of a proximal covalent cross-link between the N^{δ} of His392 and C^{β} of Tyr415 in catalases HPII from *E. coli* concomitant with the cyclization of heme *b* to form oxidized heme *d*[69] in *Penicillium vitale*.[70] One rationale proposed for some of these modifications is that they stabilize the enzyme by reducing the likelihood of other, more damaging oxidations. The Trp-Tyr-Met adduct may impart a similar protective role in that it will prevent further modification of the oxygen-susceptible methionine residue. Another possibility is that the adduct forms a route for electron transfer from the cleft region to the heme.[61] Other metal-based protein modifications are discussed in ***Metal-mediated Protein Modification***.

One of the main goals for the structure determination of the catalase-peroxidases was to determine the INH binding site. The crystal structure of BpKatG revealed a region of undefined electron density in a constricted region in the main channel leading to the distal heme cavity. The location of the density is over 10 Å further away from the heme than is the benzhydroxamic acid bound in HRP.[71] However, the density is in close proximity to Ser324, the equivalent of Ser315 in MtKatG, which is thought to be involved in INH binding. Mutation of this residue to a Thr leads to a loss of INH activation with no loss of either peroxidase or catalase activity.[72] Most of the residues in the pocket surrounding the INH-like electron density are fully conserved between BpKatG and MtKatG, but HMCP and the other catalase-peroxidases of halo-archaebacterial origin have a one residue insertion of Asp269 compared to BpKatG, which is located in a loop adjacent to the pocket. The insertion forces the ring of the adjacent Pro270 into a position that would most interfere with the region of INH-like electron density. This suggests that HMCP should not bind INH in this region, and thus explains why a similar region of electron density was not observed in the HMCP electron density maps.

3 CLASS II PEROXIDASES

3.1 Lignin Peroxidase (LIP)

Lignin is a major component of woody plant cell walls and lignin biodegradation plays a pivotal role in the earth's carbon cycle. Lignin is not only an abundant renewable carbon source but also protects cellulose against enzymatic degradation. The metalloenzymes, LIP and laccase, secreted by filamentous white-rot fungi from *Basidiomycetes*, are the only known sources capable of degrading the recalcitrant lignin. This rather heterogenous and complex biopolymer consists of phenyl propanoid units linked by various nonhydrolyzable C–C and C–O bonds.**[73]** The best studied white-rot fungus, *Phaenerochaete chrysosporium*, secretes two heme peroxidases, LIP and a MnP. Both of these peroxidases appear to be major components of the extracellular degradative system of the fungus.**[74]**

The crystal structures of two fungal LIP isozymes have been characterized**[66,75,76]** and more recently the recombinant enzyme.**[77]** Fungal LIPs are globular and mostly helical glycoproteins of about 40 kDa (including carbohydrate), with 343–344 amino acids depending on the isozyme. LIP also contains the two Ca^{2+} sites found in the class III peroxidases (Figure 4). The overall fold of LIP is that of a typical heme peroxidase, as in CcP,**[18,22]** MnP,**[78]** HRP,**[79]** barley grain peroxidase**[80]** and other nonligninolytic fungal peroxidases like those from ARP**[81]** and *C. cinerius*.**[82]** The heme, which divides the protein into a proximal and a distal heme domain, is buried in the interior of the protein with restricted access via a small channel. This channel, which is similar to substrate access channel found in ARP**[83]** and HRP,**[71]** has a significantly smaller entrance than other peroxidases. Attempts to determine crystal structures of substrate bound form LIP have been unsuccessful.

LIP undergoes the typical peroxidase reaction cycle and forms compounds I and II. However, LIP compound I is not very stable and readily converts to compound II, even in the absence of reducing substrates. In the crystal-structure determination of LIP, a significant residual electron density was visible close to the surface residue Trp171. It was interpreted as a hydroxy group covalently bound to the C^{β} atom of Trp171. Subsequent chemical and EPR spectroscopic analysis by spin trapping proved that Trp171 had, indeed, been hyroxylated (Figure 4(b)).**[84]** In view of the above findings, it was proposed that Trp171 acts as an endogenous electron donor of LIP compound I reduction, which implies the formation of a Trp radical may be part of the catalytic cycle. This assumption was tested by treating LIP with the tryptophan-specific agent *N*-bromosuccinimide (NBS), which led to drastically reduced activity with respect to veratryl alcohol (VA) oxidation.**[85]** Site-directed mutagenesis of Trp171 to Phe or Ser showed no residual activity toward VA.**[86]** These experiments proved the involvement of Trp171 in LIP catalysis. On the basis of this, a catalytic mechanism was proposed for the hydroxylation of Trp171 starting with the formation of Trp cation radical.**[85]** Evidence for a transient Trp171 radical intermediate was obtained by using elegant spin-trapping experiments with methylnitrosopropane (MNPr) in combination with peptide mapping and crystallography.**[84]** In the presence of H_2O_2, MNPr forms a covalent adduct with Trp171 which was confirmed by the crystal structure of MNPr-modified LIP.**[84]**

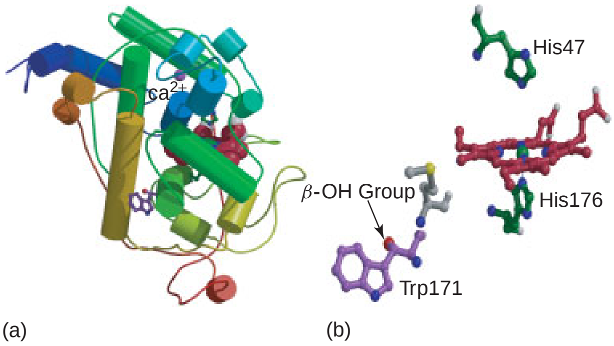

Figure 4 (a) Schematic diagram showing the overall fold of the recombinant pristine lignin peroxidase (LIP) with key residues involved in catalysis. Only one of the $2Ca^{2+}$ ions is shown. The second is hidden in this view. (b) Diagram showing the environment around β-hydroxy-Trp171. (This figure was generated from coordinates of **1LLP** deposited in the *Protein Data Bank*)

In order to complement kinetic work, crystal structures of recombinant LIP isozyme H8 expressed in *E. coli* in the pristine state (lacking hydroxylation at Trp171), of the oxidatively processed enzyme (hydroxylated at Trp171), and a Trp171 Phe mutant,**[77]** were solved. Recombinant enzymes were not glycosylated and had to be refolded *in vitro*.**[87]** The structure of the pristine state was virtually identical to that of C^{β}-hydroxylated form, except for the absence of the –OH group attached to Trp171. A water molecule was found in both structures in a small cavity near the C^{β} atom of Trp171, ideally positioned to attack the C^{β} atom stereospecifically, leading to an *S*-configured C^{β} atom only.**[77]** The Trp171Phe mutation exhibited no structural changes of the helix except in the side chain position of residue 171. Complete lack of activity of this mutant has been attributed to the absence of the redox-active indole side chain. Mutation experiments have not only underlined the importance of Trp171 for the catalytic mechanism but also show that there are two distinct substrate interaction sites in LIP.

3.2 Manganese Peroxidase (MnP)

Like LIP, MnP is produced by *P. chrysosporium* and the structure**[78]** closely resembles LIP. MnP, however, oxidizes Mn(II) to Mn(III). Once formed, Mn(III) is bound to and stabilized by a dicarboxylic acid and the Mn(III)-acid complex serves as a diffusible redox mediator that can oxidize various substrates including lignin model compounds.[88,89] The binding site for Mn(II) is shown in Figure 5 which was correctly predicted by homology modeling.[90] Note that one Mn(II) ligand is a heme propionate leading to the proposal that the heme propionate mediates electron transfer from Mn(II) to the porphyrin radical of compound I. It is also interesting that the specialized site for Mn(II) binding near one heme propionate is also where ascorbate binds in APX. Thus, both APX and MnP use the same region of the protein, near one heme propionate, for selective binding of the physiologically important substrate.

Using crystallographic methods, this binding site was probed by altering the amount of Mn^{2+} bound to the protein. Crystals grown in the absence of Mn(II), or in the presence of EDTA, exhibited diminished electron density at this site. Crystals grown in excess Mn(II) exhibited increased electron density at the proposed binding site but nowhere else in the protein. This suggested that there is only one major Mn(II) binding site in MnP. Crystal structures of a single mutant (D179N) and a double mutant (E35Q-D179N) at this site were determined.[91] The mutant structures lack a cation at the Mn(II) binding site. The structure of the Mn(II) binding site is altered significantly in both mutants, resulting in increased access to the solvent and substrate. Kinetic analyses of the single mutants, E35Q, E39Q, and D179N, yielded K_m values for the substrate Mn(II) that were ∼50-fold greater than the corresponding K_m value for the wild-type enzyme. Similarly, the k_{cat} values for Mn(II) oxidation were ∼300-fold lower than that for the wild-type MNP.

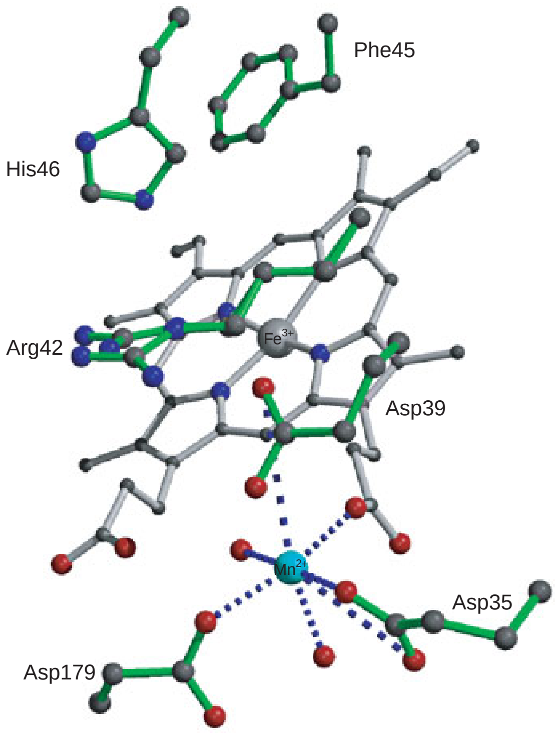

Figure 5 Schematic diagram showing the heme environment and Mn-binding site of manganese peroxidase (MnP)

Despite the presence of this unique Mn(II) binding site, the overall structure of MnP is very similar to all other nonmammalian heme peroxidases. The localized structural alterations near the surface of the protein required to form the Mn(II) site do not induce significant changes in the core peroxidase structure. For example, the structure of *P. chrysosporium* LIP is very similar to that of MnP but lacks the Mn(II) site. LIP has only one of the three acidic residues, Glu39 (Glu40 in LIP). In place of Glu35 and Asp179, LIP has Ala36 and Asn182, respectively.[78] Although it is possible to accommodate an aspartic acid in place of Asn182 in the LIP structure, the space occupied by the side chain of Glu35 in MnP is filled by the backbone structure of the C terminus in LIP. MnP has a longer C terminus, which deviates considerably in its course from that of LIP. In addition, Arg177 pushes the polypeptide chain out and away from the main body of the protein to form the Mn(II) site in MnP. The corresponding residue in LIP is an Ala180. Finally, MnP has an extra disulfide that helps to force the polypeptide chain away from the body of the protein. These differences result in the formation of space for Glu35 near the cation-binding site. These comparisons suggest that constructing a productive Mn(II) binding site in LIP by iterative protein engineering should be possible.

4 CLASS III PEROXIDASE

4.1 Horseradish Peroxidase (HRP) Structure

HRP is prepared from horseradish roots and over 30 isozymes have been identified. Owing to its relative abundance and ease of preparation, HRP is one of the most well-known and thoroughly investigated peroxidases. For reviews see references.[7,92]

HRP consists of a single polypeptide chain of 308 amino acids of M_r 33 890 Da and with one noncovalently bound protoporphyrin IX heme, four disulphide bridges, the two conserved Ca^{2+} binding sites, and contains ∼22% carbohydrate. HRP-C can also be overexpressed in *E. coli* from a synthetic gene comprising 309 amino acids including an N-terminal Met required for translation initiation.[93] The production and refolding of unglycosylated recombinant protein paved the way for the long-awaited determination of the crystal structure to 2.15 Å.[79]

HRP exhibits the typical peroxidase fold and active site structure as shown in Figure 6(b). As with CcP, the native resting form of HRP-C contains a five-coordinate, high-spin Fe^{3+} heme. Compound I of HRP contains two oxidizing equivalents, one as oxyferryl (Fe^{4+}–O) and the other as porphyrin radical.[94] A transient Trp π-cation radical has been detected in the Phe221Trp mutant of HRP-C compound

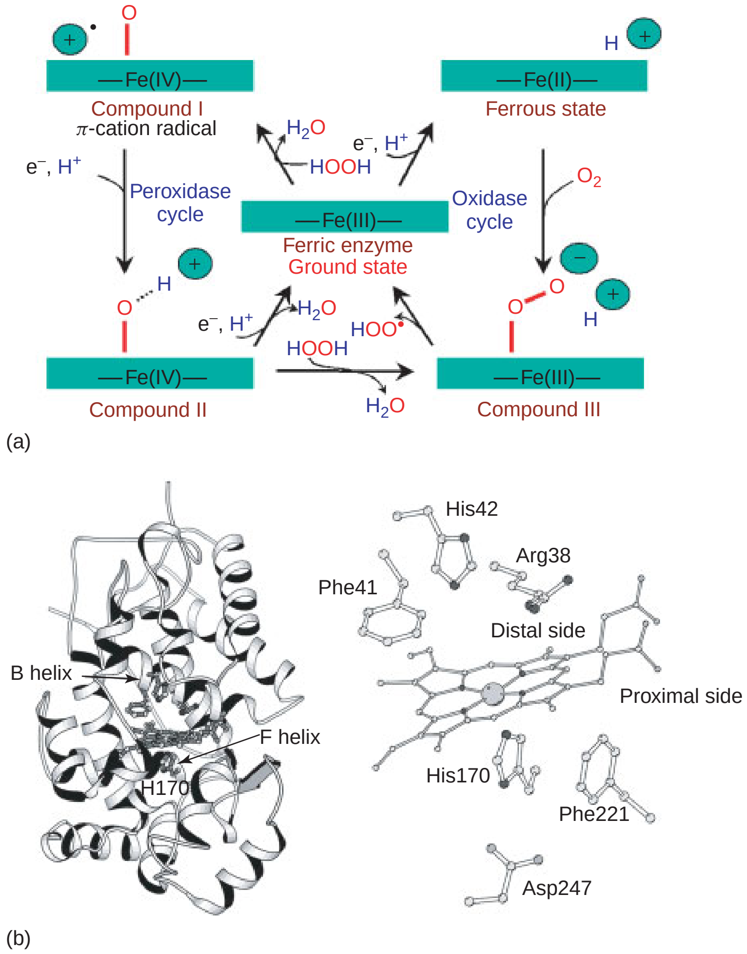
O
+
—Fe(IV)—
Compound I
π-cation radical
H
+
—Fe(II)—
Ferrous state
H2O
HOOH
e−, H+
e−, H+
Peroxidase cycle
—Fe(III)—
Ferric enzyme
Ground state
Oxidase cycle
O2
−
+
H
O
+
H
O
O
e−, H+
H2O
HOO•
HOOH
—Fe(IV)—
Compound II
H2O
—Fe(III)—
Compound III
(a)
B helix
F helix
H170
His42
Arg38
Phe41
Distal side
Proximal side
His170
Phe221
Asp247
(b)

Figure 6 (a) The five redox states of horseradish peroxidase (HRP) as determined from the high-resolution crystal structure of horseradish peroxidase (HRP). (b) Diagram showing the overall fold and active site environment containing key residues in catalysis of horseradish peroxidase (HRP)

I.[95] Recently, Hajdu and coworkers[29] worked out an effective strategy to obtain the 1.57–1.62 Å crystal structures for high-valence redox intermediates and continuous snapshots of the X-ray driven catalytic reduction of a bound dioxygen species. These high-valence intermediates are readily susceptible to reduction by the X-ray beam and as such, the structure of compound I was obtained by merging data from 11 crystals. Despite the problems with deconvoluting a mixture of states, this *tour de force* study has provided the first crystallographic picture of all five HRP redox states as shown in Figure 6(a).

4.2 HRP-substrate Complexes

Crystal structures of HRP-C:substrate/inhibitor complexes have also been solved. Of particular interest is the structure of HRP-C:benzhydroxamic acid (BHA) complex which was solved by Gajhede and coworkers,[71] the HRP-C:ferulic acid (FA) complex,[96] and the HRP-C:FA:cyanide ternary complex.[96] In all three complexes, changes in structure are restricted to the substrate access channel and the heme surroundings. The prevailing view is that enzyme-substrate complexes are relatively nonspecific and weak in peroxidases. One possible reason is that tight binding of an oxidized substrate could lead to enzyme modification. The products of oxidation of substrates are phenoxyl radicals, very similar in structure to their respective substrate molecules, but are chemically reactive species. These products must leave the active site immediately after formation, polymerize or disproportionate. A prolonged retention of the radical in close proximity to the enzyme active site would increase the risk of oxidative damage. Loose association of the reducing substrate with the enzyme, as found in the structure of HRP-C: FA complex,[96] is presumed to be an advantage.

These various structures together with the conserved structures around the δ-edge heme suggests a common pattern of binding between class III peroxidases and aromatic substrates. Such common aromatic contacts have also been observed in the complexes between class II peroxidase ARP and BHA, and salicylhydroxamic acid, respectively.[83,97]

5 BACTERIAL DI-HEME CYTOCHROME *C* PEROXIDASES (BCcP)

5.1 Introduction

Bacterial CcPs have been isolated from a number of organisms: *Pseudomonas aeruginosa*,**[98]** *Nitrosomonas europea*,**[99]** *Paracoccus pantotropus*,**[100]** *Paracoccus denitrificans*,**[101]** *Rhodobacter capsulatus*,**[102]** *Methylococcus capsulatus*,**[103]** *Pseudomonas stutzeri*,**[104]** and *Pseudomonas nautica*.**[105]** The most well-studied and characterized BCcPs are those from *P. aeruginosa* and *Par. denitrificans*. BCcPs are homodimers with about 300 residues per monomer. Each monomer contains two hemes which are covalently tethered to the protein via thioether links between the heme vinyl groups and Cys residues, exactly as in many *c*-type cytochrome. One heme is high-potential (+270 mV), while the other is low-potential (between −190 and −310 mV). Greenwood *et al.***[106]** proposed the following mechanism:

$$\underset{\text{high}}{\mathrm{Fe}^{2+}}\ \underset{\text{low}}{\mathrm{Fe}^{3+}} + \mathrm{H_2O_2} \longrightarrow \underset{\text{Compound I}}{\underset{\text{high}}{\mathrm{Fe}^{3+}}\ \underset{\text{low}}{\mathrm{Fe}^{4+}}}{=}\mathrm{O} + \mathrm{H_2O} \tag{5}$$

$$\underset{\text{Compound I}}{\underset{\text{high}}{\mathrm{Fe}^{3+}}\ \underset{\text{low}}{\mathrm{Fe}^{4+}}}{=}\mathrm{O} + e^- + 2\mathrm{H}^+ \longrightarrow \underset{\text{Compound II}}{\underset{\text{high}}{\mathrm{Fe}^{3+}}\ \underset{\text{low}}{\mathrm{Fe}^{3+}}} + \mathrm{H_2O} \tag{6}$$

$$\underset{\text{Compound II}}{\underset{\text{high}}{\mathrm{Fe}^{3+}}\ \underset{\text{low}}{\mathrm{Fe}^{3+}}} + e^- \longrightarrow \underset{\text{high}}{\mathrm{Fe}^{2+}}\ \underset{\text{low}}{\mathrm{Fe}^{3+}} \tag{7}$$

The high-potential heme accepts an electron from the physiological electron donor, which is then transferred to the low-potential heme where peroxide reacts with the heme to give compound I. In this case, the high-potential heme provides one of the two electrons required to activate peroxide rather than a Trp residue as in yeast CcP.

Most BCcPs require Ca^{2+}. Addition of calcium chloride to the reduced enzyme results in a transition of the low-potential heme from low-spin to high-spin, which indicates a significant change in the heme environment of the enzyme.**[107]** It has been proposed that calcium triggers a conformational change that removes the sixth ligand from the low-potential heme giving a high-spin heme and freeing up one axial coordination position for reaction with peroxide.**[105]**

5.2 Structure and Mechanism

The three-dimensional structure of the completely oxidized di-heme peroxidase (PAP) from *P. aeruginosa* was determined at 2.4 Å resolution.**[108]** More recently, the three-dimensional structure of the completely oxidized di-heme peroxidase from *N. europea* (NEP) was determined at 1.8 Å resolution.**[109]** Preliminary X-ray diffraction analysis of di-heme peroxidases from *R. capsulatus***[110]** and *P. nautica***[111]** also have been reported. Unfortunately, the di-heme peroxidases have proven extremely difficult to overexpress in homologous/heterologous systems except in the case of the purple phototrophic bacterium *R. capsulatus*.**[112]**

Figure 7 shows the overall structure of di-heme peroxidases with key residues involved in catalysis from *P. aeruginosa* and *N. europea*. Each monomer folds into two distinct domains with the fold of each domain closely resembling that found in class I *c*-type cytochromes. Each domain houses one heme which have been designated the high- and the low-potential heme. Electrons enter from a redox partner to the high-potential heme followed by intramolecular electron transfer to the low-potential heme. The closest approach of the 2 hemes is ≈10 Å although the heme propionates are directly bridged by the indole ring of Trp82. This interaction is the same as in Trp94 of PAP which is believed to act as an electron transfer conduit between the two hemes.**[108]** The two domains are related by a quasi two-fold axis, and the domain interface holds a divalent cation, which is now known to be calcium. The likely function of calcium is to maintain structural integrity and/or to modulate electron transfer between two heme domains. In both enzymes, calcium is not coordinated by negatively charged carboxylates but by solvent and peptide carbonyl oxygens. It is also known that calcium plays an important, if as yet ill-defined, role in other peroxidases.

The high-potential heme in both enzymes has Met and His as axial ligands. In the *Pseudomonas* enzyme, the low-potential heme has two His residues as axial heme ligands.**[108]** Since the site of reaction with hydrogen peroxide is the low-potential heme, one His ligand must dissociate. Relevant to this difference, the high-potential heme in PAP must first be reduced in order to activate the enzyme while NEP is fully active in the oxidized state. This implies that reduction of the high-potential heme in PAP leads to dissociation of the His ligand in the PAP low-potential heme. The low-potential heme of the *Nitrosomonas* enzyme is already in an activated state since the low-potential heme has only one His ligand and hence, has an open axial coordination site available for reaction with peroxide.**[109]** A comparison between the two enzymes illustrates the range of conformational changes required to activate the *Pseudomonas* enzyme. This change involves the large repositioning of a loop containing the dissociable His heme ligand from the heme pocket to the molecular surface where the His forms part of the dimer interface. In the *Nitrosomonas* enzyme, the His ligand is already dissociated so activation by reduction of the high-potential heme is not required. The mechanism by which a single electron can induce such a large change remains a fascinating yet unsolved problem. Similar redox induced conformational changes and ligand rearrangements have also been observed in cytochrome cd_1 nitrite reductase.**[113]** This enzyme also has two hemes and upon reduction a Tyr ligand of one heme is displaced, which opens up a distal site for required nitrite reduction chemistry.

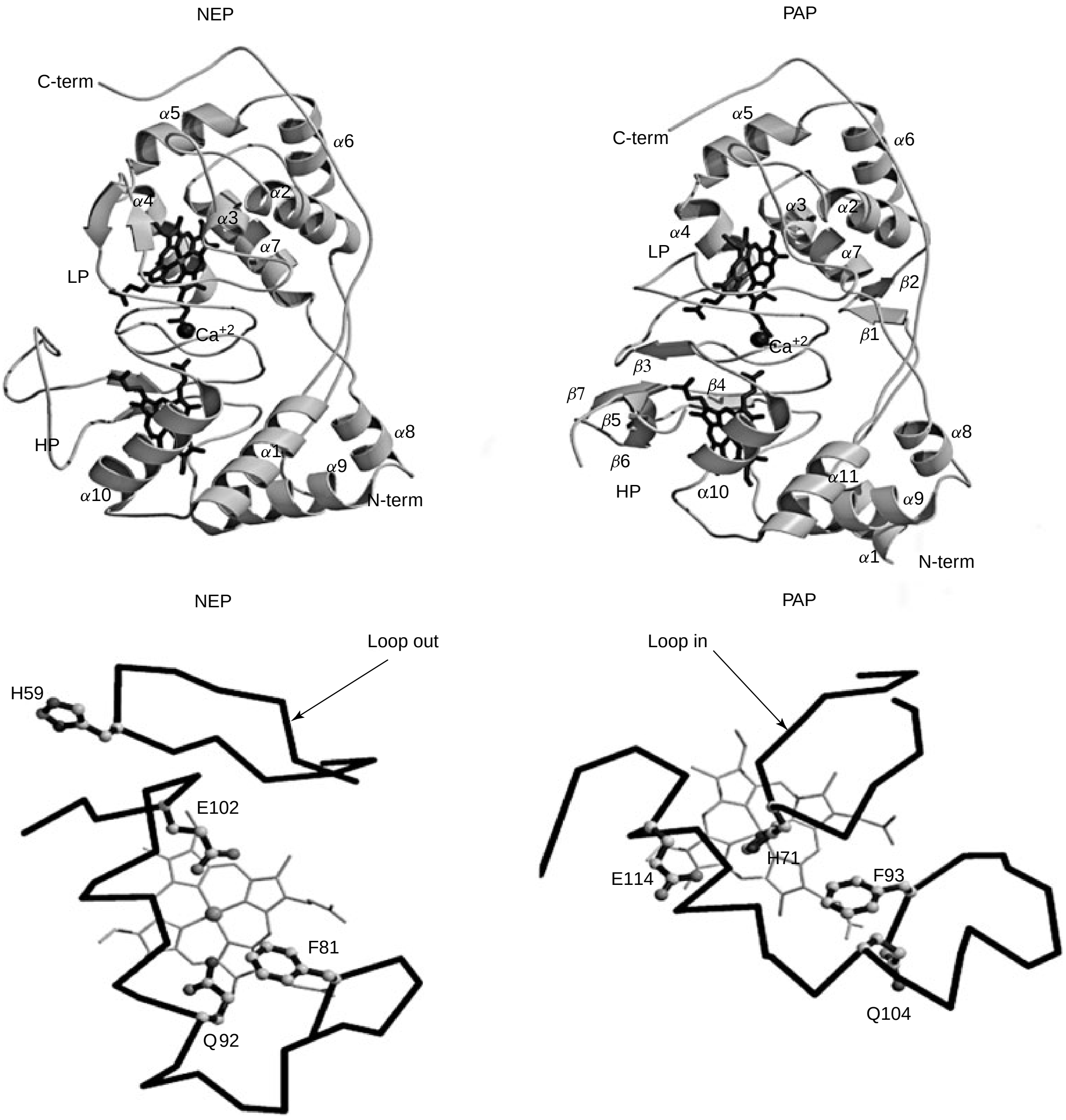
NEP
PAP
C-term
α5
α6
α4
α2
α3
α7
LP
Ca+2
HP
α1
α9
α8
α10
N-term
C-term
α5
α6
α3
α2
α4
LP
α7
β2
β1
Ca+2
β3
β4
β7
β5
β6
HP
α10
α11
α8
α9
α1
N-term
NEP
PAP
Loop out
H59
E102
F81
Q92
Loop in
H71
E114
F93
Q104

Figure 7 Schematic representation of the of di-heme peroxidases from *Pseudomonas aeruginosa* (PAP) and *Nitrosomonas europea* (NEP) showing key residues involved in catalysis. (This figure was generated from coordinates of **1EB7** and **1IQC** deposited in the *Protein Data Bank*)

Little is known about the peroxide activation process in BCcPs. However, the NEP structure revealed a peroxide-binding site quite different from the more traditional peroxidases. BCcPs do not have a distal His that serves as the catalytic acid-base required for heterolytic cleavage of the peroxide O–O bond. The NEP structure has a Glu residue directly adjacent to the peroxide-binding site that most likely operates as the acid-base catalyst. The only other peroxidase known to have a Glu in this position is chloroperoxidase.[114]

6 PROSTAGLANDIN ENDOPEROXIDE H_2 SYNTHASES-1 AND 2 (PGHS)

6.1 Introduction

Prostaglandin endoperoxide H_2 synthase (PGHS) [EC 1.14.99.1] isoenzymes 1 and 2 catalyze the committed step in prostanoid synthesis[115] via two sequential enzymatic reactions

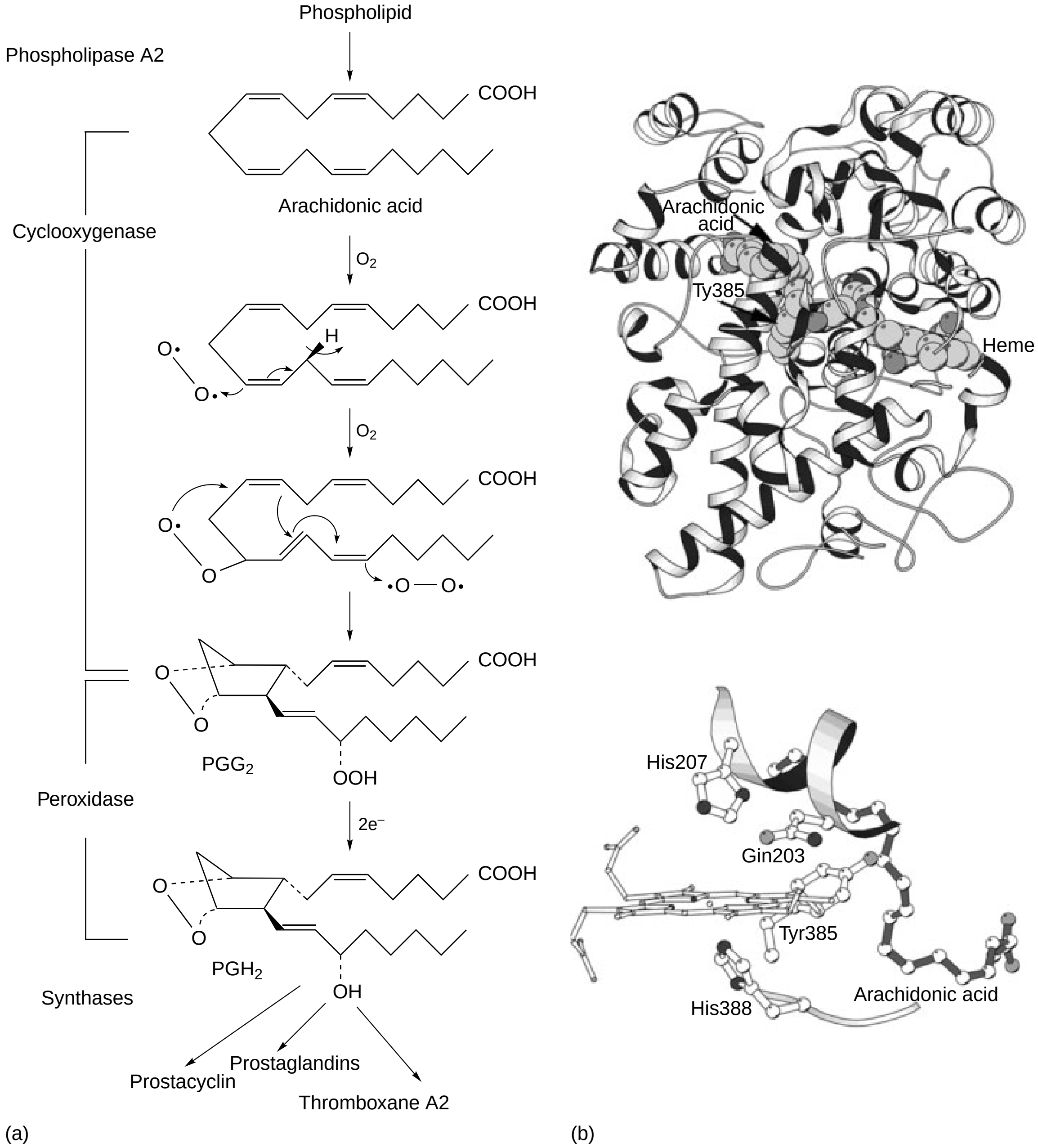
Phospholipid
Phospholipase A2
COOH
Arachidonic acid
Cyclooxygenase
O2
O•
H
O•
O2
O•
O
•O—O•
O
O
PGG2
OOH
Peroxidase
2e−
O
O
PGH2
OH
Synthases
Prostacyclin
Prostaglandins
Thromboxane A2
(a)
Arachidonic acid
Ty385
Heme
His207
Gin203
Tyr385
His388
Arachidonic acid
(b)

Figure 8 (a) Putative reaction scheme of prostaglandin endoperoxide H_2 synthases (PGHS). (b) Structure of PGHS-1 with key residues in catalysis in complex with substrate arachidonic acid (AA). (This figure was generated from coordinates of **1DIY** deposited in the *Protein Data Bank*)

(Figure 8(a)): (1) the bis-oxygenation of arachidonic acid (the cyclooxygenase activity or COX) forms PGG_2; and (2) reduction of 15-hydroperoxide of PGG_2 in the peroxidase (POX) active site to form PGH_2.

PGHS enzymes are targets of nonsteroidal anti-inflammatory (NSAI) drugs, which include over the counter drugs such as aspirin and ibuprofen (Advil®/Motrin®). Moreover, PGHS isozymes play essential roles in pathologies that include, for PGHS-1, thrombosis and for PGHS-2, inflammation, pain, fever, various cancers, and neurological disorders like Alzheimer's and Parkinson's diseases.[116] PGHS-1 (*cox1* gene) is thought to be a housekeeping enzyme present in all tissues. The isolated protein is usually a homodimer of M_r140 kDa, which includes 3.5% carbohydrate. A second more recently discovered PGHS (PGHS-2, *cox2* gene) is induced in a few specific tissues by mitogens, growth factors, and cytokines.[117] Despite the 60% sequence identity between the 2 PGHSs, specific inhibitors of PGHS-1 are available and selective inhibitors of PGHS-2 are already on hand.[118,119] Inhibition of PGHS-1 may be associated with gastric and renal toxicity of the NSAI agents and specific inhibitors of PGHS-2 can alleviate unwanted side effects of anti-inflammatory reagents.

6.2 Structure and Mechanism

Garavito and coworkers solved the first structure of a PGHS at 3.4 Å resolution.[120] Crystal structures of other PGHS isoforms are structurally homologous[121,122] as might be expected from high sequence identity. PGHS is a homodimeric membrane protein with one heme per subunit. Each monomer consists of three structural domains: a N-terminal epidermal growth factor (EGF) domain, a membrane-binding domain of about 48 amino acids in length, and a large C-terminal globular catalytic domain with heme binding site facing the solvent and containing both cyclooxygenase and peroxidase active sites. The structure of the C-terminal segments beyond Pro583 (17 amino acids in PGHS-1 and 35 amino acids in PGHS-2) have not been resolved crystallographically. Nonetheless, this region is of great interest as PGHS-1 and PGHS-2 contain C-terminal Lys-Asp-Glu-Leu (KDEL) like sequences that may target PGHSs to the endoplasmic reticulum and the associated nuclear envelope.[115] The structure supports the proposed model from biochemical studies that cyclooxygenase and peroxidase active sites are distinct but share a common heme cofactor. Despite the low sequence homology between PGHSs and other peroxidases,[123] the secondary and tertiary structure of PGHS is similar to the structure of myeloperoxidase[123] and CcP.[22] However, unlike other systems, the heme in PGHS is more exposed to solvent.

The structure of PGHS-1 in a complex with arachidonic acid is shown in Figure 8(b). The peroxidase active site is very similar to other peroxidases. Histidine serves as an axial heme ligand (Figure 8(b)), while in the distal pocket, His207 serves as the acid-base catalytic group required for heterolytic fission of the peroxide O–O bond. However, PGHS-1 has Gln203 in place of the distal Arg found in other peroxidases. This same type of His/Gln distal site pocket is found in another mammalian peroxidase, myeloperoxidase.

The mechanism shown below requires that Tyr385 first be oxidized to a radical. This reaction is achieved via the traditional peroxidase mechanism.

(1) $\mathrm{Fe^{3+}PTyr385 + ROOH \longrightarrow}$
$\mathrm{Fe^{4+} - OP^{\bullet}Tyr385 + ROH}$
Compound I

(2) $\mathrm{Fe^{4+} - OP^{\bullet}Tyr385 \longrightarrow Fe^{4+} - OPTyr385^{\bullet}}$

(3) $\mathrm{Fe^{4+} - OPTyr385^{\bullet} + AA \longrightarrow Fe^{4+} - OPTyr385}$
Compound II $\mathrm{+ AA^{\bullet}}$

(4) $\mathrm{Fe^{4+} - OPTyr385 + AA^{\bullet} + 2O_2 \longrightarrow}$
$\mathrm{Fe^{4+} - OPTyr385 + O_2AAOO^{\bullet}}$

(5) $\mathrm{Fe^{4+} - OPTyr385 + O_2AAOO^{\bullet} \longrightarrow}$
$\mathrm{Fe^{4+} - OPTyr385^{\bullet} + O_2AAOOH}$

In step 1, the usual compound I is formed via reaction with a hydroperoxide. Tyr385 is less than 5 Å from the heme, so the oxidation of Tyr385 to a radical in step 2 by the porphyrin radical can readily occur. As shown in Figure 8(b), C13 of arachidonic acid (AA) directly contacts Tyr385 thus enabling regio- and stereoselective abstraction of the *pro*-S hydrogen to give the arachidonic acid radical, $\mathrm{AA^{\bullet}}$. After the two oxygenation reactions in steps 4 and 5, the AA peroxy radical in step 5 oxidizes Tyr385 to regenerate the Try385 radical. Details of the cyclooxygenase reaction in steps 4 and 5 are outlined in Figure 8(a). The product dissociates and another arachidonic acid can bind to compound I, without regenerating the resting protein. Thus the oxyferryl center appears to be an innocent bystander. Reduction of $\mathrm{O_2AAOOH}$ to $\mathrm{O_2AAOH}$ proceeds via the traditional peroxidase mechanism to give compound I.

7 MAMMALIAN PEROXIDASES

7.1 Myeloperoxidase (MPO)

MPO (Myeloperoxidase) [EC 1.11.1.7] catalyzes the hydrogen peroxide–dependent two-electron oxidation of halides ($\mathrm{CI^-}$, $\mathrm{I^-}$, $\mathrm{Br^-}$) and thiocyanate to the corresponding hypohalous acids and hypothiocyanate which are cytotoxic to invading pathogens. In addition, MPO is capable of the single-electron oxidation of a wide variety of aromatic alcohols and amines.[124]

MPO occurs in two types of mammalian phagocytic white blood cells: monocytes and neutrophils. MPO is localized in azurophil granules, which comprise 1–5% of dry weight of neutrophils. Following microbial ingestion, degranulation leads to rapid release of MPO into the phagosome.[125] Microbial ingestion or phagocytosis is accompanied by a 'respiratory burst' giving rise to the superoxide anion $\mathrm{O_2}^-$ which, in turn, dismutates to molecular oxygen and hydrogen peroxide. MPO is able to oxidize chloride ions to HOCl, an effective agent in killing bacteria, fungi, and viruses.

MPO is a covalently linked dimeric glycoprotein of M_r 140 kDa comprised of 745 amino acids. MPO consists of three different isoenzyme forms termed a, b, and c.[126] The nature of the chemical differences between these isoforms is not fully understood, and only isoform c has been crystallized.[127] Catalytically active recombinant human MPO has been expressed in Chinese hamster ovary cells. However, incomplete posttranslational processing of the recombinant enzyme yields a monomeric form of the enzyme consisting of a single polypeptide chain of M_r 84 kDa with altered carbohydrate content.[128]

The heme in ferric MPO exhibits a relatively strong absorption band near 680 nm, which is responsible for the characteristic green color. The heme Soret band is considerably red-shifted compared to other heme-containing proteins including its close relatives, EPO (415 nm) and LPO (412 nm).[124] The origin of the red-shift has been attributed to the effects of heme-protein covalent linkages in distorting the planarity of the porphyrin ring and to possible electron-withdrawing effects of the unique sulfonium ion linkage to Met243.[129,130] MPO exhibits a characteristic EPR spectrum of high-spin ferric heme in an environment of rhombic symmetry with $g_x = 6.90$, $g_y = 5.07$.[124] Compound I of MPO exhibits an EPR spectrum characteristic of a hexa-coordinated low-spin heme iron similar to other heme peroxidases.[124] However, complete formation of compound I requires a large excess of peroxide and binding of H_2O_2 to the ferric (Fe^{3+}) enzyme and this appears to be reversible.

7.1.1 Structure of MPO

The crystal structure of MPO was first determined in 1987,[131] and more recently, the data have been extended to 1.8 Å (Figure 9)[132] which has enabled the nature of the heme to be unambiguously established. The heme is covalently attached to the protein via two ester linkages between the carboxyl groups of Glu242 and Asp94 and modified methyl groups on pyrrole rings A and C of the heme as well as a sulfonium ion linkage between the sulfur atom of Met243 and the beta-carbon of the vinyl group on pyrrole ring A.

MPO is a covalently linked dimer which is ellipsoidal in shape with overall dimensions of 110 × 60 × 50 Å^3. The dimer can be cleaved by reduction of a disulfide bond into two identical halves. Each half of the dimer termed *hemi-MPO* has the same optical and catalytic properties of the dimer. Hemi-MPO consists of two polypeptides of 466 and 108 amino acid residues, and a heme prosthetic group covalently bound to the large polypeptide. Like CcP and LIP, MPO is largely a helical bundle protein with very little β-sheet structure. The bulk of the large polypeptide folds into five separate domains and one open loop that surround this core. The small polypeptide wraps around the surface of the molecule with its C-terminal helix penetrating the interior core. There are four intrachain disulfide bonds in the large polypeptide and a single disulfide bridge in the small polypeptide. Four potential asparagine-linked glycosylation sites have been identified in the larger subunit. Sugar residues near the Asn317 glycosylation site close to the dimer interface play a role in dimer–dimer interaction, in addition to the lone disulfide bridge.

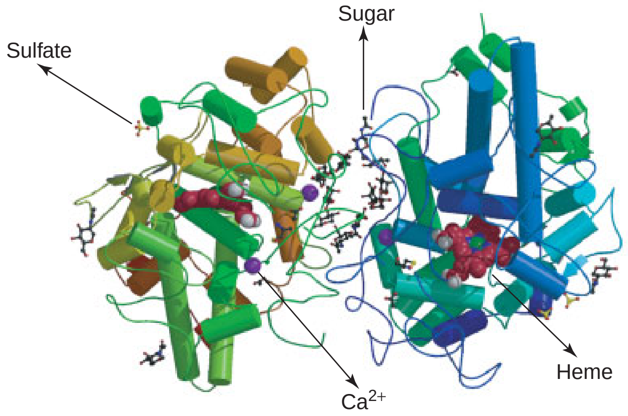

Figure 9 Structure of myeloperoxidase (MPO) along with the heme environment as observed in the high-resolution crystal structure. (This figure was generated from coordinates of **1CXP** deposited in the *Protein Data Bank*)

Crystallography revealed a bound chloride ion at the amino terminus of the helix containing the proximal His336 which can be replaced with bromide.[132] Crystal structures of the human MPO-cyanide, MPO-cyanide-bromide, and MPO-cyanide-thiocyanate have also been determined by Fenna and coworkers to 1.9 Å.[133] These results support a model for a single common binding site for halides and thiocyanate as substrates or as inhibitors near the δ-*meso* carbon of the porphyrin ring in myeloperoxidase.

7.2 Lactoperoxidase (LPO)

The mucosal surfaces of the body provide protection against potential infections. The exocrine glands and their secretions provide both specific immunological and less specific nonimmunological protection to the mucosal surfaces of eye, nose, mouth, trachiobronchial tree, and intestinal tract. The antibacterial system includes lysozyme, lactoferrin, and peroxidase. Peroxidase also provides an antibacterial system in bovine and human milk. LPO (lactoperoxidase) is a heme-containing, calcium-containing glycoprotein of M_r 78 kDa with one heme group per molecule. In bovine milk, LPO is, next to xanthine oxidase (*see* ***Molybdenum: MPT-containing Enzymes***), the most abundant enzyme. Its concentration is around 30 mg/L, constituting 0.5% of whey proteins.[134] Variations in enzyme levels were reported to depend on the sexual cycle of the cow, season, feeding regime, and breed.[135]

The properties and biological function of LPO have recently been reviewed.[7,136] This secretory peroxidase is isolated from cow's milk. Crystalline LPO from bovine milk was obtained in 1943 and shown to be green colored like MPO. Its isolation and purification was simplified by precipitation of casein by rennet. The enzyme with a single polypeptide chain has been known to exist as several isoenzyme forms. The Soret maxima of LPO of 412 nm with molar absorptivity of 112 mM^{-1} cm^{-1} is typical of most peroxidases. It recently has been demonstrated that the heme in LPO is attached to the protein by ester bonds between the heme 1- and 5-methyl groups, and Glu375 and Asp275, respectively.[137]

The heme environment of MPO, both in the proximal and distal heme pockets, is conserved in LPO.[123] As with other peroxidases, LPO reacts with H_2O_2 to give compound I. In the absence of any electron-donor substrate, compound I decomposes to compound I* species which is spectroscopically different from compound I. Compound II is formed spontaneously upon addition of one equivalent of hydrogen peroxide to native LPO and is stable for 20 min. A threefold excess of peroxide can also be used to obtain pure compound II, and addition of 117-fold excess peroxide to the same solution produces pure compound III.[138]

Recent studies have shown that LPO reacts with H_2O_2 to sequentially give two compound I intermediates: the first with an oxyferryl (Fe^{4+}–O) and a porphyrin radical cation, and the second with the same ferryl species and a presumed protein radical.[139,140] Using spin-trapping experiments followed by EPR spectroscopy, LPO was found to react with the spin-trap 3,5-dibromo-4-nitrosobenzenesulfonic acid (DBNBS) to give a protein-bound radical. Furthermore, LPO was shown to undergo H_2O_2-dependent formation of dimers and trimer. The dimer involves a cross-link between Tyr289 in each of two LPO molecules and retains full catalytic activity.[139]

A recent study by Harvey and Bruck followed the oxidation of mitoxantrone, an anthraquinone type anticancer drug, spectrophotometrically under turnover conditions and single turnover conditions using stopped-flow methods. With compound I and compound II, mitoxantrone formed binding complexes that were deactivated with increasing substrate concentration.[141] Under turnover conditions, compound II was the steady state intermediate, but with increasing H_2O_2, compound II reacted with H_2O_2 to form the catalytically inactive intermediate compound III. Nitrite prevented formation of compound III by reducing compound II to the native state.

The physiological role of LPO is to use H_2O_2 to generate $OSCN^-$ which inhibits microbial growth. H_2O_2 is generated endogenously, for example, by polymorphonuclear leukocytes (PMN), in the process of phagocytosis. In addition, under aerobic conditions many lactobacilli, lactococci, and streptococci produce sufficient H_2O_2 to activate LPO. Figure 10 outlines the proposed LPO reaction mechanism.[134] The first step in the enzymatic mechanism is the initiation reaction of the resting ferric (Fe^{3+}) LPO to its ground state, using H_2O_2, according to $Fe^{3+} + H_2O_2 \rightarrow Fe^{2+} + HO_2^{\bullet}$, followed by propagation reactions, as illustrated in Figure 10. The propagation reactions include conversion of LPO from ground state to compound I by reaction with H_2O_2. At low SCN^- (<3 μM) and halide concentrations, compound I reacts with one-electron donors that are present (proteins, peptides) to form compound II that is continuously reduced to ground state at a low rate. At an excess of $[H_2O_2]$ (>0.5 mM), compound II may react to form compound III, leading to a ferrylperoxidase adduct and irreversible inactivation of LPO. The agent that oxidizes SCN^- or halides is compound I. Much of the interest in the LPO system stems from its potential for generating natural biopreservatives in food, feed specialities, cosmetics, and related products. Some of the applications of

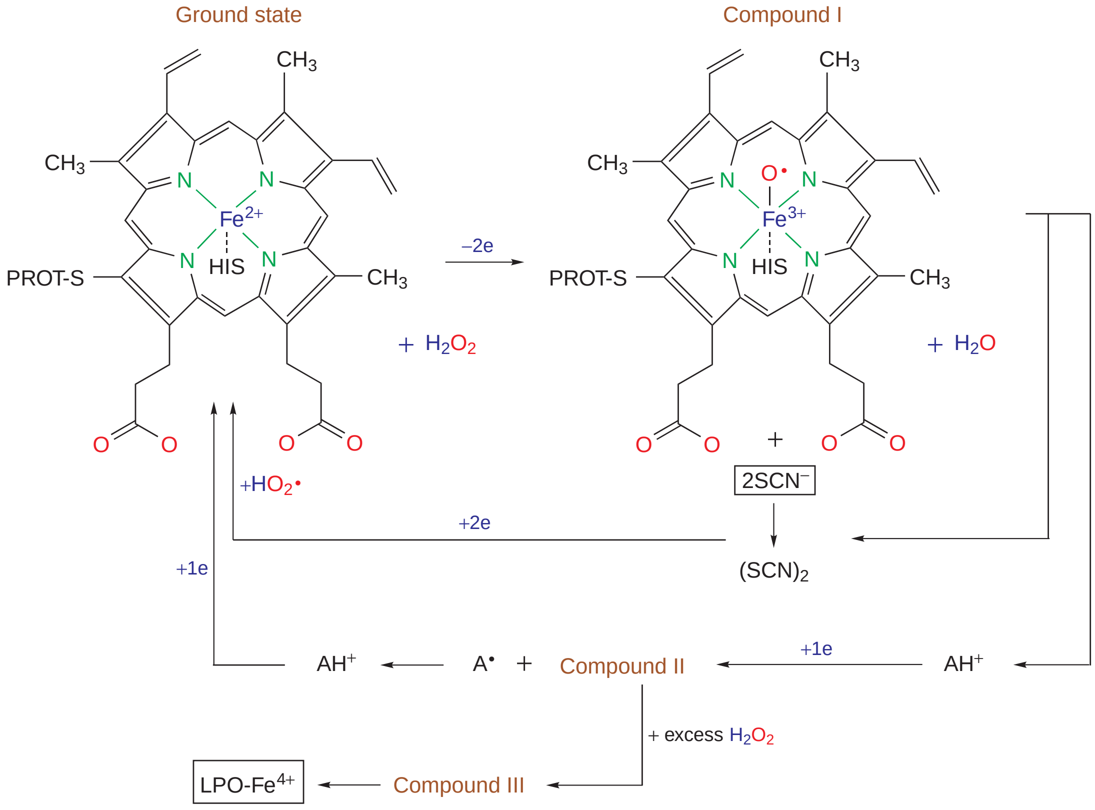

Figure 10 Proposed pathways in the lactoperoxidase-catalyzed reaction mechanism (LPO system)

LPO and their functionality have been reviewed by de Wit and van Hooijdonk.[134]

8 CATALASES

8.1 Introduction

Catalases are ubiquitous metalloenzymes present in almost all aerobic prokaryotic and eukaryotic organisms. Although the full range of biological functions of catalases remains uncertain, the primary role is the removal of hydrogen peroxide from aerobic organisms by catalyzing its dismutation to water and oxygen (equation 8)

$$2H_2O_2 \longrightarrow 2H_2O + O_2 \qquad (8)$$

This type of antioxidant function is essential for all organisms that are exposed to dioxygen, which readily forms H_2O_2 both enzymatically, through the action of oxidases, and nonenzymatically, as a side product of respiration or auto-oxidation of cell components. Hydrogen peroxide exerts its toxic effects in a variety of ways, including transition metal activation of peroxides via Fenton chemistry that generates highly reactive superoxide or hydroxy radicals that can lead to DNA, protein, and lipid damage. Catalase deficient (acatalasemic) cells lead to an accumulation of oxidative agents resulting in increased susceptibility to thermal injury[142] or HIV proliferation,[143] high rates of DNA mutations,[144] and inflammation.[145] Besides this primary protective role, the catalase system is also believed to have physiological significance in various biological oxidations, such as the metabolization of methanol and ethanol.[146,147]

8.2 Functional Classes

Four groups of catalases have been identified. The first, most fully characterized group contains the monofunctional '*classic*' heme-containing catalases, which are homotetramers with one heme per subunit and are present in both prokaryotes and eukaryotes.[69,148] The subunit sizes within this group vary, consisting of approximately 500 residues (small-subunit catalases) or 700 residues (large-subunit catalases). The second group is composed of the nonheme manganese-containing catalases, homohexameric enzymes with two manganese ions in the active site, that have so far only been reported in prokaryotes.[149–151] The third group, heme-containing catalase-peroxidases, were described in Section 2. The final group is composed of miscellaneous heme-containing enzymes with secondary reactions in the form of low levels of catalase activity. Heme-containing enzymes that fall in this group include methemoglobin, metmyoglobin and chloroperoxidase from *Caldariomyces fumago*.

8.3 'Classic' Monofunctional Heme-containing Catalases

Catalases of *Penicillium vitale* (PVC)[152] and beef liver catalase (BLC)[153,154] were the first catalases crystallographically characterized. At present, the crystal structures of seven catalases from this group are known: beef liver,[155] *Penicillium vitale*,[70,156] *Micrococcus lysodeikticus* (MLC),[157] *E. coli* hydroperoxidase (HPII),[158] *Proteus mirabilus* (PMC_PR),[159] *Saccharomyces cerevisiae* (SCC-A),[160] and human erythrocyte (HEC).[161] There is considerable structural similarity among the catalases in this subgroup. The conformation displayed by the homologous molecular regions appears to be exclusive of '*classic*' monofunctional heme catalases, and hence is now typically referred to as the '*catalase fold*'. A typical catalase fold consists of four consecutive regions along the polypeptide chain (Figure 11(a)), which entail an amino

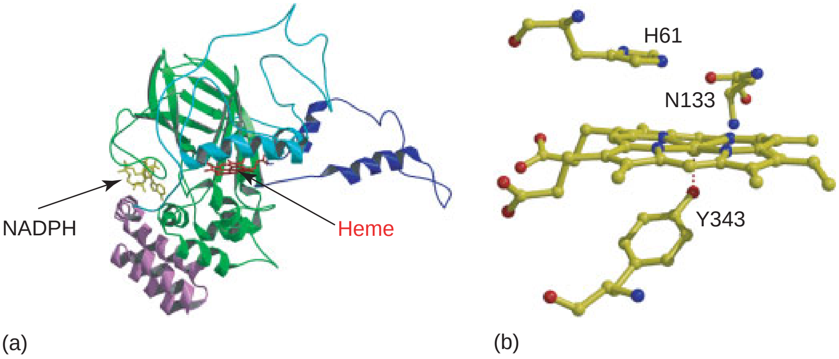

Figure 11 (a) Ribbon drawing of the beef liver catalase structure (PDB code **7CAT**) showing the location of the heme (red) and NADPH (yellow). The four regions of a typical catalase fold are represented with different colors: amino acid terminal arm (purple); anti-parallel eight-stranded β-barrel domain (green); wrapping domain (blue), and α-helical domain (cyan). (b) Diagram showing the heme environment in a monofunctional heme-containing MLC catalase. (This figure was generated from coordinates of **1GWE** deposited in the *Protein Data Bank*)

acid terminal arm, an anti-parallel 8-stranded β-barrel domain, an extended structural part which is referred to as the '*wrapping*' domain, and finally an α-helical domain. Of the various regions in monofunctional heme catalases, the anti-parallel domain appears to be the central feature of a typical catalase fold since the first half of the β-barrel domain contains most of the residues that define the heme distal side, whereas the second half of the β-barrel contributes to the NADPH binding pocket in those catalases that bind this cofactor.[162]

Each subunit of a heme catalase binds a single molecule of heme and some mammalian catalases also possess a second cofactor, NADPH. The binding of NADPH in catalases was at first totally unexpected,[162,163] but has since been a frequent feature of small-subunit catalases from both prokaryotic and eukaryotic organisms. However, the actual biochemical function of NADPH in these catalases is still not fully understood. One possible role is protection of the enzyme against inactivation by its own substrate, especially under conditions of low-peroxide concentrations.[164] The NADPH binding pocket is located on the molecular surface, just above an entrance channel with the nicotinamide active carbon situated approximately 20 Å from the closest heme atom (Figure 11(a)).[162]

The heme group characterized in the active site of various catalases varies from either being a heme *d* (a *cis*-hydroxy γ-spirolactone) as observed in the active site of HPII and PVC[70,165] or the conventional heme *b* as seen in all other catalase structures. Catalase HPII and presumably PVC, initially bind heme *b* and then catalyze its conversion to heme *d* utilizing H_2O_2.[166] This heme conversion is concomitant with formation of a unique covalent bond between C^{β} of the essential Tyr415 and the N^{δ} of His392, and a mechanism relating to its formation to heme modification has been proposed.[69] Although different heme variant groups exist among the catalases, the location and environment of the heme group is very similar among the catalase structures. In general, the heme groups are deeply buried in the catalase tetramer with iron atoms situated approximately 20 Å from the nearest molecular surface. The deep burial of the heme groups results in catalases requiring channels for efficient communication between the active center and the surface molecule. The most significant and best-conserved channel reaches the distal side of the heme pocket, whereas a second, less conserved channel is observed at a location that corresponds to the NADPH binding pocket in catalases that bind the dinucleotide. These channels narrow as the heme is approached and the narrow entrance of these channels is strongly believed to be a 'discrimination gate' between substrates of various sizes and thus accounts for the reduced activity of certain catalases toward larger substrates such as aliphatic alcohols.[167] This is in good agreement with the evidence that MLC, which has one of the narrowest entrances, is slower at catalyzing larger substrates and faster for small substrates relative to other catalases.[168]

The heme pocket in these catalases differs considerably from that of a typical heme peroxidase (Figure 11(b)). The most obvious difference between the two sets of enzymes is the coordination of the proximal iron ligand. In peroxidases, the proximal ligand is a histidine, while in the classic monofunctional heme catalases, the imidazole nitrogen is replaced by an oxygen of the phenolic hydroxy group of a tyrosine. This oxygen, which also hydrogen bonds with a conserved arginine, is most likely deprotonated possessing a localized negative charge that can contribute to the stabilization of the Fe^{4+} oxidation state required in the catalytic cycle.[162] On the distal side of the heme, a His and Asn residue form the peroxide pocket and are considered essential for catalysis. The His is generally considered to operate as an acid-base catalytic group as in peroxidases,[7,21] while the Asn serves the function of the distal side Arg in peroxidases.

8.4 Catalytic Mechanisms

The catalytic mechanism for the formation of compound I in the catalase-peroxidases is believed to occur in a manner very similar to that of the heme peroxidases.[60,61] The main difference in the enzymatic mechanism between catalases and peroxidases is compound I reduction. In the catalase cycle, a second peroxide molecule is also used as a reducing agent for compound I rather than a small organic molecule as in most other peroxidases. Crystal structures of the various catalytic intermediate states (compound I and compound II) have been determined for classic monofunctional heme-containing catalases.[27,160,169] Only minor local rearrangements are observed relative to the native enzyme.[27] In both compounds I and II, the iron appears slightly displaced above the heme ring toward the bound oxygen. In compound I, but not in compound II, the presence of extra electron density, assigned as weakly bound anion, is situated on the heme proximal side ~18 Å from the iron. Interestingly, in the higher resolution compound I structure of PVC at 1.8 Å, no extra density was observed, similar to that reported in PMC_PR.[159] In both the PMC_PR and the PVC compound I structures, the coordinated oxygen is situated between 1.7 and 1.8 Å above the iron atom which is similar to that found in the HRP compound I structure (1.7 Å).[29] In both the PMC_PR and the PVC compound I structures, this coordinated solvent molecule is hydrogen bonded to the N^{ε} and N^{δ} atoms of the essential His and Asn residues.

9 REFERENCES

1. D. Dolphin, A. Forman, D. C. Borg, J. Fajer, and R. H. Felton, *Proc. Natl. Acad. Sci. U.S.A.*, 1971, **68**, 614.
2. A. F. Coulson and T. Yonetani, *Biochem. Biophys. Res. Commun.*, 1972, **49**, 391.

3. M. Sivaraja, D. B. Goodin, M. Smith, and B. M. Hoffman, *Science*, 1989, **245**, 738.
4. H. B. Dunford, Horseradish Peroxidase: Structure and Kinetic Properties, in 'Peroxidases in Chemistry and Biology', eds. J. Everse, E. Everse, and M. B. Grisham, CRC Press, Boca Raton, FL, Vol. 2, 1991, p. 1.
5. B. Chance, *J. Biol. Chem.*, 1943, **151**, 553.
6. K. G. Welinder, *Curr. Opin. Struct. Biol.*, 1992, **2**, 388.
7. H. B. Dunford, 'Heme Peroxidases', John Wiley & Sons, Danvers, MA, 1999.
8. J. E. Erman and L. B. Vitello, *Biochim. Biophys. Acta*, 2002, **1597**, 193.
9. M. Kwon, S. Chong, S. Han, and K. Kim, *Biochim. Biophys. Acta*, 2003, **1623**, 1.
10. C. Charizanis, H. Juhnke, B. Krems, and K. D. Entian, *Mol. Gen. Genet.*, 1999, **262**, 437.
11. D. B. Goodin and D. E. McRee, *Biochemistry*, 1993, **32**, 3313.
12. K. Choudhury, M. Sundaramoorthy, J. M. Mauro, and T. L. Poulos, *J. Biol. Chem.*, 1992, **267**, 25656.
13. J. E. Erman, L. B. Vitello, M. A. Miller, A. Shaw, K. A. Brown, and J. Kraut, *Biochemistry*, 1993, **32**, 9798.
14. S. L. Newmyer and P. R. Ortiz de Montellano, *J. Biol. Chem.*, 1995, **270**, 19430.
15. S. L. Newmyer and P. R. Ortiz de Montellano, *J. Biol. Chem.*, 1996, **271**, 14891.
16. L. B. Vitello, J. E. Erman, M. A. Miller, J. Wang, and J. Kraut, *Biochemistry*, 1993, **32**, 9807.
17. M. A. Miller, R. Q. Liu, S. Hahm, L. Geren, S. Hibdon, J. Kraut, B. Durham, and F. Millett, *Biochemistry*, 1994, **33**, 8686.
18. C. A. Bonagura, B. Bhaskar, H. Shimizu, H. Li, M. Sundaramoorthy, D. E. McRee, D. B. Goodin, and T. L. Poulos, *Biochemistry*, 2003, **42**, 5600.
19. I. Schlichting, J. Berendzen, K. Chu, A. M. Stock, S. A. Maves, D. E. Benson, R. M. Sweet, D. Ringe, G. A. Petsko, and S. G. Sligar, *Science*, 2000, **287**, 1615.
20. W. L. Purcell and J. E. Erman, *J. Am. Chem. Soc.*, 1976, **98**, 7033.
21. T. L. Poulos and J. Kraut, *J. Biol. Chem.*, 1980, **255**, 8199.
22. B. C. Finzel, T. L. Poulos, and J. Kraut, *J. Biol. Chem.*, 1984, **259**, 13027.
23. S. L. Edwards, H. X. Nguyen, R. C. Hamlin, and J. Kraut, *Biochemistry*, 1987, **26**, 1503.
24. V. Fulop, R. P. Phizackerley, S. M. Soltis, I. J. Clifton, S. Wakatsuki, J. Erman, J. Hajdu, and S. L. Edwards, *Structure*, 1994, **2**, 201.
25. S. L. Edwards, T. L. Poulos, and J. Kraut, *J. Biol. Chem.*, 1984, **259**, 12984.
26. H. M. Jouve, P. Andreoletti, P. Gouet, J. Hajdu, and J. Gagnon, *Biochimie*, 1997, **79**, 667.
27. P. Gouet, H. M. Jouve, P. A. Williams, I. Andersson, P. Andreoletti, L. Nussaume, and J. Hajdu, *Nat. Struct. Biol.*, 1996, **3**, 951.
28. H. P. Hersleth, B. Dalhus, C. H. Gorbitz, and K. K. Andersson, *J. Biol. Inorg. Chem.*, 2002, **7**, 299.
29. G. I. Berglund, G. H. Carlsson, A. T. Smith, H. Szoke, A. Henriksen, and J. Hajdu, *Nature*, 2002, **417**, 463.
30. B. Chance, L. Powers, Y. Ching, T. Poulos, G. R. Schonbaum, I. Yamazaki, and K. G. Paul, *Arch. Biochem. Biophys.*, 1984, **235**, 596.
31. J. E. Penner-Hahn, T. J. McMurry, M. Renner, L. Latos-Grazynsky, K. S. Eble, I. M. Davis, A. L. Balch, J. T. Groves, J. H. Dawson, and K. O. Hodgson, *J. Biol. Chem.*, 1983, **258**, 12761.
32. C. M. Reczek, A. J. Sitter, and J. Terner, *J. Mol. Struct.*, 1989, **214**, 27.
33. S. Hashimoto, J. Teraoka, T. Inubushi, T. Yonetani, and T. Kitagawa, *J Biol Chem.*, 1986, **261**, 11110.
34. A. J. Sitter, C. M. Reczek, and J. Terner, *J. Biol. Chem.*, 1985, **260**, 7515.
35. R. Makino, T. Uno, Y. Nishimura, T. Iizuka, M. Tsuboi, and Y. Y. Ishimura, *J. Biol. Chem.*, 1986, **261**, 8376.
36. G. R. Schonbaum and S. Lo, *J. Biol. Chem.*, 1972, **247**, 3353.
37. M. A. Miller, G. W. Han, and J. Kraut, *Proc. Natl. Acad. Sci. U.S.A.*, 1994, **91**, 11118.
38. M. M. Fitzgerald, M. J. Churchill, D. E. McRee, and D. B. Goodin, *Biochemistry*, 1994, **33**, 3807.
39. Y. Cao, R. A. Musah, S. K. Wilcox, D. B. Goodin, and D. E. McRee, *Protein Sci.*, 1998, **7**, 72.
40. C. A. Bonagura, M. Sundaramoorthy, H. S. Pappa, W. R. Patterson, and T. L. Poulos, *Biochemistry*, 1996, **35**, 6107.
41. G. M. Jensen, S. W. Bunte, A. Warshel, and D. B. Goodin, *J. Phys. Chem. B*, 1998, **102**, 8221.
42. T. L. Poulos, T. P. Barrows, B. Bhaskar, C. A. Bonagura, and H. Li, *Int. J. Quantum Chem.*, 2002, **88**, 211.
43. W. R. Patterson and T. L. Poulos, *Biochemistry*, 1995, **34**, 4331.
44. W. R. Patterson, T. L. Poulos, and D. B. Goodin, *Biochemistry*, 1995, **34**, 4342.
45. C. A. Bonagura, M. Sundaramoorthy, B. Bhaskar, and T. L. Poulos, *Biochemistry*, 1999, **38**, 5538.
46. C. A. Bonagura, B. Bhaskar, M. Sundaramoorthy, and T. L. Poulos, *J. Biol. Chem.*, 1999, **274**, 37827.
47. H. Pelletier and J. Kraut, *Science*, 1992, **258**, 1748.
48. H. S. Pappa and T. L. Poulos, *Biochemistry*, 1995, **34**, 6573.
49. S. H. Northrup, J. O. Boles, and J. C. Reynolds, *Science*, 1988, **241**, 67.
50. H. S. Pappa, S. Tajbaksh, A. J. Saunders, G. J. Pielak, and T. L. Poulos, *Biochemistry*, 1996, **35**, 4837.
51. K. H. Sharp, M. Mewies, P. C. Moody, and E. L. Raven, *Nat. Struct. Biol.*, 2003, **10**, 303.

52. K. Wada, T. Tada, Y. Nakamura, T. Ishikawa, Y. Yabuta, K. Yoshimura, S. Shigeoka, and K. Nishimura, *J. Biochem. (Tokyo)*, 2003, **134**, 239.
53. A. N. Hiner, J. I. Martinez, M. B. Arnao, M. Acosta, D. D. Turner, E. Lloyd Raven, and J. N. Rodriguez-Lopez, *Eur. J. Biochem.*, 2001, **268**, 3091.
54. D. Mandelman, J. Jamal, and T. L. Poulos, *Protein Sci.*, 1998, **37**, 17610.
55. E. H. Bursey and T. L. Poulos, *Biochemistry*, 2000, **39**, 7374.
56. C. Dye, S. Scheele, P. Dolin, V. Pathania, and M. C. Raviglione, *JAMA*, 1999, **282**, 677.
57. Y. Zhang, S. Dhandayuthapani, and V. Deretic, *Proc. Natl. Acad. Sci. (USA)*, 1996, **93**, 13212.
58. R. A. Slayden and C. E. Barry III, *Microbes Infect.*, 2000, **2**, 659.
59. Y. Zhang, B. Heym, B. Allen, D. Young, and S. Cole, *Nature*, 1992, **358**, 591.
60. Y. Yamada, T. Fujiwara, T. Sato, N. Igarashi, and N. Tanaka, *Nat. Struc. Biol.*, 2002, **9**, 691.
61. X. Carpena, S. Loprasert, S. Mongkolsuk, J. Switala, P. C. Loewen, and I. Fita, *J. Mol. Biol.*, 2003, **327**, 475.
62. M. Zamocky, G. Regelsberger, C. Jakopitsch, and C. Obinger, *FEBS Lett.*, 2001, **492**, 177.
63. K. G. Welinder, *Biochim. Biophys. Acta*, 1991, **1080**, 215.
64. A. Hillar, B. Peters, R. Pauls, A. Loboda, H. Zhang, A. G. Mauk, and P. C. Loewen, *Biochemistry*, 2000, **39**, 5868.
65. S. Chouchane, I. Lippai, and R. S. Magliozzo, *Biochemistry*, 2000, **39**, 9975.
66. T. Choinowski, W. Blodig, K. H. Winterhalter, and K. Piontek, *J. Mol. Biol.*, 1999, **286**, 809.
67. B. Bhaskar, C. E. Immoos, H. Shimizu, F. Sulc, P. J. Farmer, and T. L. Poulos, *J. Mol. Biol.*, 2003, **328**, 157.
68. A. Buzy, V. Bracchi, R. Sterjiades, J. Chroboczek, P. Thibault, J. Gagnon, H. M. Jouve, and G. Hudry-Clergeon, *J. Protein. Chem.*, 1995, **14**, 59.
69. J. Bravo, I. Fita, J. C. Ferrer, W. Ens, A. Hillar, J. Switala, and P. C. Loewen, *Protein Sci.*, 1997, **6**, 1016.
70. G. N. Murshudov, A. I. Grebenko, V. V. Barynin, Z. Dauter, K. S. Wilson, B. K. Vainshtein, W. R. Melik-Adamyan, J. Bravo, J. M. Ferran, J. C. Ferrer, J. Switala, P. C. Loewen, and I. Fita, *J. Biol. Chem.*, 1996, **271**, 8863.
71. A. Henriksen, D. J. Schuller, K. Meno, K. G. Welinder, A. T. Smith, and M. Gajhede, *Biochemistry*, 1998, **37**, 8054.
72. N. L. Wengenack, J. R. Uhl, A. L. St Amand, A. J. Tomlinson, L. M. Benson, S. Naylor, B. C. Kline, F. Rr. Cockerill, and F. Rusnak, *J. Infect. Dis.*, 1997, **176**, 722.
73. K. Piontek, A. T. Smith, and W. Blodig, *Biochem. Soc. Trans.*, 2001, **29**, 111.
74. P. J. Harvey, R. Floris, T. Lundell, J. M. Palmer, H. E. Schoemaker, and R. Wever, *Biochem. Soc. Trans.*, 1992, **20**, 345.
75. K. Piontek, T. Glumoff, and K. Winterhalter, *FEBS Lett.*, 1993, **315**, 119.
76. T. L. Poulos, S. L. Edwards, H. Wariishi, and M. H. Gold, *J. Biol. Chem.*, 1993, **268**, 4429.
77. W. Blodig, A. T. Smith, W. A. Doyle, and K. Piontek, *J. Mol. Biol.*, 2001, **305**, 851.
78. M. Sundaramoorthy, K. Kishi, M. H. Gold, and T. L. Poulos, *J. Biol. Chem.*, 1994, **269**, 32759.
79. M. Gajhede, D. J. Schuller, A. Henriksen, A. T. Smith, and T. L. Poulos, *Nat. Struct. Biol.*, 1997, **4**, 1032.
80. A. Henriksen, K. G. Welinder, and M. Gajhede, *J. Biol. Chem.*, 1998, **273**, 2241.
81. N. Kunishima, K. Fukuyama, H. Matsubara, H. Hatanaka, Y. Shibano, and T. Amachi, *J. Mol. Biol.*, 1994, **235**, 331.
82. J. F. W. Petersen, A. Kadziola, and S. Larsen, *FEBS Lett.*, 1994, **339**, 291.
83. H. Itakura, Y. Oda, and K. Fukuyama, *FEBS Lett.*, 1997, **412**, 107.
84. W. Blodig, A. T. Smith, K. Winterhalter, and K. Piontek, *Arch. Biochem. Biophys.*, 1999, **370**, 86.
85. W. Blodig, W. A. Doyle, A. T. Smith, K. Winterhalter, T. Choinowski, and K. Piontek, *Biochemistry*, 1998, **37**, 8832.
86. W. A. Doyle, W. Blodig, N. C. Veitch, K. Piontek, and A. T. Smith, *Biochemistry*, 1998, **37**, 15097.
87. W. A. Doyle and A. T. Smith, *Biochem. J.*, 1996, **315**, 15.
88. U. Tuor, H. Wariishi, H. E. Schoemaker, and M. H. Gold, *Biochemistry*, 1992, **31**, 4986.
89. H. Wariishi, K. Valli, and M. H. Gold, *Biochem. Biophys. Res. Commun.*, 1991, **176**, 269.
90. F. Johnson, G. H. Loew, and P. Du, in ‘Plant Peroxidases: Biochemistry and Physiology’, eds. K. G. Welinder, S. K. R., C. Penel, and H. Greppin, Geneva, Switzerland, 1993.
91. M. Sundaramoorthy, K. Kishi, M. H. Gold, and T. L. Poulos, *J. Biol. Chem.*, 1997, **272**, 17574.
92. M. Gajhede, Horseradish Peroxidase, in ‘Handbook of Metalloproteins’, eds. A. Messerschmidt, R. Huber, T. L. Poulos, and K. Wieghardt, John Wiley & Sons, Chichester, 2001, Vols. I, 2, p. 195.
93. A. T. Smith, N. Santama, S. Dacey, M. Edwards, R. C. Bray, R. N. Thorneley, and J. F. Burke, *J. Biol. Chem.*, 1990, **265**, 13335.
94. J. E. Penner-Hahn, K. S. Eble, T. J. McMurry, M. Renner, A. L. Balch, J. T. Groves, J. H. Dawson, and K. O. Hodgson, *J. Am. Chem. Soc.*, 1986, **108**, 7819.
95. A. Morimoto, M. Tanaka, S. Takahashi, K. Ishimori, H. Hori, and I. Morishima, *J. Biol. Chem.*, 1998, **273**, 14753.
96. A. Henriksen, A. T. Smith, and M. Gajhede, *J. Biol. Chem.*, 1999, **274**, 35005.
97. K. Tsukamoto, H. Itakura, K. Sato, K. Fukuyama, S. Miura, S. Takahashi, H. Ikezawa, and T. Hosoya, *Biochemistry*, 1999, **38**, 12558.

98. N. Ellfolk and R. Soininen, *Acta Chem. Scand.*, 1970, **24**, 2126.
99. D. M. Arciero and A. B. Hooper, *J. Biol. Chem.*, 1994, **269**, 11878.
100. C. F. Goodhew, I. B. Wilson, D. J. Hunter, and G. W. Pettigrew, *Biochem J*, 1990, **271**, 707.
101. G. W. Pettigrew, *Biochim. Biophys. Acta*, 1991, **1058**, 25.
102. S. P. Hanlon, R. A. Holt, and A. G. McEwan, *FEMS Microbiol. Lett.*, 1992, **97**, 283.
103. J. A. Zahn, D. M. Arciero, A. B. Hooper, J. R. Coats, and A. A. DiSpirito, *Arch. Microbiol.*, 1997, **168**, 362.
104. J. Villalain, I. Moura, M. C. Liu, W. J. Payne, J. LeGall, A. V. Xavier, and J. J. Moura, *Eur. J. Biochem.*, 1984, **141**, 305.
105. T. Alves, S. Besson, L. C. Duarte, G. W. Pettigrew, F. M. Girio, B. Devreese, I. Vandenberghe, J. Van Beeumen, G. Fauque, and I. Moura, *Biochim. Biophys. Acta*, 1999, **1434**, 248.
106. C. Greenwood, N. Foote, J. Peterson, and A. J. Thomson, *Biochem. J*, 1984, **223**, 379.
107. N. Foote, J. Peterson, P. M. Gadsby, C. Greenwood, and A. J. Thomson, *Biochem. J.*, 1985, **230**, 227.
108. V. Fulop, C. J. Ridout, C. Greenwood, and J. Hajdu, *Structure*, 1995, **3**, 1225.
109. H. Shimizu, D. J. Schuller, W. N. Lanzilotta, M. Sundaramoorthy, D. M. Arciero, A. B. Hooper, and T. L. Poulos, *Biochemistry*, 2001, **40**, 13483.
110. L. De Smet, D. Leys, and J. J. Van Beeumen, *Acta Crystallogr., Sect. D Biol. Crystallogr.*, 2002, **58**, 522.
111. J. M. Diaz, C. Bonifacio, T. Alves, J. J. Moura, I. Moura, and M. J. Romao, *Acta Crystallogr., Sect. D Biol. Crystallogr.*, 2002, **58**, 697.
112. L. De Smet, G. W. Pettigrew, and J. J. Van Beeumen, *Eur. J. Biochem.*, 2001, **268**, 6559.
113. P. A. Williams, V. Fulop, E. F. Garman, N. F. Saunders, S. J. Ferguson, and J. Hajdu, *Nature*, 1997, **389**, 406.
114. M. Sundaramoorthy, J. Terner, and T. L. Poulos, *Chem. Biol.*, 1998, **5**, 461.
115. W. L. Smith, D. L. DeWitt, and R. M. Garavito, *Annu. Rev. Biochem.*, 2000, **69**, 145.
116. R. M. Garavito, Prostaglandin Endoperoxide H_2 Synthases-1 and -2, in ‘Handbook of Metalloproteins’, eds. A. Messerschmidt, R. Huber, T. L. Poulos, and K. Wieghardt, John Wiley & Sons, Chichester, 2001, Vols. 1, 2, p. 245.
117. J. Stubbe and W. A. van der Donk, *Chem. Rev.*, 1998, **98**, 705.
118. W. L. Smith and L. J. Marnett, in ‘Metals in Biological Systems’, eds. H. Sigel and A. Sigel, Marcel Dekker, New York, 1994, Vol. 30.
119. J. Hayllar and I. Bjarnason, *Lancet*, 1995, **346**, 521.
120. D. Picot, P. J. Loll, and R. M. Garavito, *Nature*, 1994, **367**, 243.
121. C. Luong, A. Miller, J. Barnett, J. Chow, C. Ramesha, and M. F. Browner, *Nat. Struct. Biol.*, 1996, **3**, 927.
122. R. G. Kurumbail, A. M. Stevens, J. K. Gierse, J. J. McDonald, R. A. Stegeman, J. Y. Pak, D. Gildehaus, J. M. Miyashiro, T. D. Penning, K. Seibert, P. C. Isakson, and W. C. Stallings, *Nature*, 1996, **384**, 644.
123. J. Zeng and R. E. Fenna, *J. Mol. Biol.*, 1992, **226**, 185.
124. R. E. Fenna, Myeloperoxidase, in ‘Handbook of Metalloproteins’, eds. A. Messerschmidt, R. Huber, T. L. Poulos, and K. Wieghardt, John Wiley & Sons, Chichester, 2001, Vols. 1, 2, p. 211.
125. S. J. Klebanoff, Peroxidases in Chemistry and Biology, in ‘Peroxidases in Chemistry and Biology’, eds. J. Everse, E. Everse, and M. B. Grisham, CRC Press, Boca Raton, FL, 1991, Vol. 1, p. 1.
126. S. O. Pember, R. Shapiro, and J. M. J. Kinkade, *Arch. Biochem. Biophys.*, 1983, **221**, 391.
127. B. J. Sutton, C. Little, R. L. Olsen, and N. P. Willassen, *J. Mol. Biol.*, 1988, **199**, 395.
128. N. Moguilevsky, L. Garcia-Quintana, A. Jacquet, C. Tournay, L. Fabry, L. Pierard, and A. Bollen, *Eur. J. Biochem.*, 1991, **197**, 605.
129. R. E. Fenna, J. Zeng, and C. Davey, *Arch. Biochem. Biophys.*, 1995, **316**, 653.
130. I. M. Kooter, N. Moguilevsky, A. Bollen, L. A. van der Veen, C. Otto, H. L. Dekker, and R. Wever, *J. Biol. Chem.*, 1999, **274**, 26794.
131. R. E. Fenna, *J. Biol. Chem.*, 1987, **196**, 919.
132. T. J. Fiedler, C. A. Davey, and R. E. Fenna, *J. Biol. Chem.*, 2000, **275**, 11964.
133. M. Blair-Johnson, T. Fiedler, and R. E. Fenna, *J. Biol. Chem.*, 2001, **40**, 13990.
134. J. N. de Wit and A. C. M. van Hooijdonk, *Neth. Milk Dairy J.*, 1996, **50**, 227.
135. B. Reiter and J. P. Perraudin, Lactoperoxidase: Biological functions, in ‘Peroxidases in Chemistry and Biology’, eds. J. Everse, E. Everse, and M. B. Grisham, CRC Press, Boca Raton, FL, 1991, Vol. I, p. 143.
136. K. D. Kussendrager and A. C. van Hooijdonk, *Br. J. Nutr.*, 2000, **84**, S19.
137. C. Colas, J. M. Kuo, and P. R. Ortiz de Montellano, *J. Biol. Chem.*, 2001, **277**, 7191.
138. H. Kohler, A. Taurog, and H. B. Dunford, *Arch. Biochem. Biophys.*, 1988, **264**, 438.
139. O. M. Lardinois, K. F. Medzihradszky, and P. R. Ortiz de Montellano, *J. Biol. Chem.*, 1999, **274**, 35441.
140. O. M. Lardinois and P. R. Ortiz de Montellano, *Biochem. Biophys. Res. Commun.*, 2000, **270**, 199.
141. T. B. Bruck and P. J. Harvey, *Biochem. Biophys. Acta*, 2003, **1649**, 154.
142. J. A. Leff, L. K. Burton, E. M. Berger, B. O. Anderson, C. P. Wilke, and J. E. Repine, *Inflammation*, 1993, **17**, 199.

143. J. A. Leff, M. A. Oppegard, T. J. Curiel, K. S. Brown, R. T. Schooley, and J. E. Repine, *Free Radic. Biol. Med.*, 1992, **13**, 143.

144. B. Halliwell and O. I. Aruoma, *FEBS Lett.*, 1991, **281**, 9.

145. B. Halliwell and J. M. Gutteridge, *Methods Enzymol.*, 1990, **186**, 1.

146. C. J. Masters and R. S. Holmes, *TIBS*, 1979, **4**, 233.

147. N. Oshino, R. Oshino, and B. Chance, *Biochem. J.*, 1973, **131**, 555.

148. M. Zamocky and F. Koller, *Prog. Biophys. Mol. Biol.*, 1999, **72**, 19.

149. M. W. Fraaije, H. P. Roubroeks, W. R. Hagen, and W. J. Van Berkel, *Eur. J. Biochem.*, 1996, **235**, 192.

150. S. V. Antonyuk and W. R. Melik-Adamyan, *Crystallogr. Rep.*, 2000, **45**, 105.

151. V. V. Barynin, M. M. Whittaker, S. V. Antonyuk, V. S. Lamzin, P. M. Harrison, P. J. Artymiuk, and J. W. Whittaker, *Structure*, 2001, **9**, 725.

152. B. K. Vainshtein, W. R. Melik-Adamyan, V. V. Barynin, A. A. Vagin, and A. I. Grebenko, *Nature*, 1981, **293**, 411.

153. M. R. N. Murthy, T. J. Reid III, A. Sicignano, N. Tanaka, and M. G. Rossmann, *J. Mol. Biol.*, 1981, **152**, 465.

154. T. J. Reid III, M. R. N. Murthy, A. Sicignano, N. Tanaka, W. D. Musick, and M. G. Rossmann, *Proc. Natl. Acad. Sci. U.S.A.*, 1981, **78**, 4767.

155. I. Fita and A. M. Silva, *Acta Crystallogr.*, 1986, **B42**, 497.

156. B. K. Vainshtein, W. R. Melik-Adamyan, V. V. Barynin, A. A. Vagin, A. I. Grebenko, V. V. Borisov, K. S. Bartels, I. Fita, and M. G. Rossmann, *J. Mol. Biol.*, 1986, **188**, 49.

157. G. N. Murshudov, W. R. Melik-Adamyan, A. I. Grebenko, V. V. Barynin, A. A. Vagin, B. K. Vainshtein, Z. Dauter, and K. S. Wilson, *FEBS Lett.*, 1992, **312**, 127.

158. J. Bravo, N. Verdaguer, J. Tormo, C. Betzel, J. Switala, P. C. Loewen, and I. Fita, *Structure*, 1995, **3**, 491.

159. P. Gouet, H. M. Jouve, and O. Y. Dideberg, *J. Mol. Biol.*, 1995, **249**, 933.

160. M. J. Mate, M. Zamocky, L. M. Nykyri, C. Herzog, P. M. Alzari, C. Betzel, F. Koller, and I. Fita, *J. Mol. Biol.*, 1999, **286**, 135.

161. C. D. Putnam, A. S. Arvai, Y. Bourne, and J. A. Tainer, *J. Mol. Biol.*, 2000, **296**, 295.

162. I. Fita and M. G. Rossmann, *Proc. Natl. Acad. Sci. U.S.A.*, 1985, **82**, 1604.

163. H. N. Kirkman and G. F. Y. Gaetani, *Proc. Natl. Acad. Sci. U.S.A.*, 1984, **81**, 43434.

164. D. C. De Luca, R. Dennis, and W. G. Smith, *Arch. Biochem. Biophys.*, 1995, **320**, 129.

165. J. Bravo, M. J. Mate, T. Schneider, J. Switala, K. Wilson, P. C. Loewen, and I. Fita, *Proteins*, 1999, **34**, 155.

166. P. C. Loewen, J. Switala, I. von Ossowski, A. Hillar, A. Christie, B. Tattrie, and P. Nicholls, *Biochemistry*, 1993, **32**, 10159.

167. P. R. Ortiz de Montellano, *Annu. Rev. Pharmacol. Toxicol.*, 1992, **32**, 89.

168. P. Jones and D. N. Middlemiss, *Biochem. J.*, 1972, **130**, 411.

169. G. N. Murshudov, A. I. Grebenko, J. A. Brannigan, A. A. Antson, V. V. Barynin, G. G. Dodson, Z. Dauter, K. S. Wilson, and W. R. Melik-Adamyan, *Acta Crystallogr., Sect. D Biol. Crystallogr.*, 2002, **58**, 1972.

Iron: Inorganic & Coordination Chemistry

John Burgess[1] **& Martyn V. Twigg**[2]
[1] *University of Leicester, Leicester, UK*
[2] *Johnson Matthey plc, Royston, UK*

Based in part on the article Iron: Inorganic & Coordination Chemistry by Pelham N. Hawker & Martyn V. Twigg which appeared in the Encyclopedia of Inorganic Chemistry, First Edition.

1 Introduction 1
2 The Element 2
3 Binary Compounds 4
4 Simple Salts 7
5 Oxidation States and Coordination Geometries 11
6 Spin States and Spin Crossover 14
7 Cyanide Complexes 16
8 Complexes with Nitrogen Donors 18
9 Ligands with Phosphorus Donors 26
10 Oxygen Donors 28
11 Complexes with Sulfur Donors 32
12 Halide Complexes 36
13 References 36

1 INTRODUCTION

Iron (Anglo-Saxon, isarn; Latin, ferrum), the twenty-sixth element in the periodic table, is the most indispensable of all the metals. ^{56}Fe is the most stable isotope with the highest nuclear binding energy per nucleon. The Earth's dense molten core (diameter ca. 4300 miles) is thought to be largely metallic iron. In the biosphere, it is the most abundant transition element, and the fourth most abundant element (6.2%). Only oxygen (45.5%), silicon (27.2%), and aluminum (8.3%) are more common.[1] Iron became incorporated into biological systems, and is essential in all higher life forms.[2] The human body contains between 4 and 5 g of iron. Iron chemicals have many essential industrial applications, and the metal is of fundamental importance to modern human activities as fabrication and construction material. The period when man began using the metal is known as the Iron Age, but pure iron is too soft for use in implements, and it took a long time to control the carbon content to harden it to an appropriate degree. Some five hundred years ago, considerable quantities of iron were manufactured via reduction with charcoal and the amount increased dramatically through the Industrial Revolution until today large quantities of ores are extracted each year and reduced to iron.

As life evolved on Earth, photosynthetic processes released oxygen into the atmosphere and made it increasingly oxidizing. Iron(II) salts in aqueous solution are readily oxidized by oxygen, and increased oxygen levels led to the formation of insoluble iron(III) hydroxide species in lakes and oceans that became vast oxide ore deposits. The principles underlying the chemistry of iron in natural waters have been presented in Stumm and Morgan's long-established text[3] and in Pankow's more recent book.[4] Chester gives a more geologically oriented treatment.[5] Books on environmental chemistry discuss complexes of iron in general,[6,7] their presence in groundwater in particular,[8] and their kinetic aspects in detail.[9] Today, iron is not a significant contaminant in the sea but it has come to prominence as a result of dumping 'red mud' from the extraction of aluminium from bauxite – this waste material contains between 5 and 40% iron[10] – and acidic iron(II) sulfate from the traditional production of titanium dioxide. In Western Europe, several million tons of acidic iron(II) sulfate solution were discharged each year into the sea directly or via rivers. As Fe(II) becomes oxidized, it is precipitated as complex hydroxo-iron(III) species that drift as a suspension before settling on solid objects. Contamination of shellfish and the gills of fish have been reported, but there does not appear to have been major ecological damage. Nevertheless, the disposal of iron(II) sulfate waste in this way has been markedly reduced. However, it has been suggested[11] $FeSO_4$ be dosed into the ocean at very low concentrations to stimulate plankton growth and encourage them to absorb CO_2, convert it to $CaCO_3$, and hence deposit an excess of greenhouse gases on the ocean floor. Early experiments to test this failed because the high affinity of Fe^{3+} for hydroxide and oxide ligands led to deposition of the added iron on the ocean floor before it could have a significant effect. Alterobactin A, a hydroxycarboxylate-catechol siderophore from an oceanic bacterium, has an extremely high affinity for iron(III) (see Table 9),[12] and its photolysis in the surface ocean produces iron(II), increasing iron availability for plankton.[13] There is a copious literature on iron biominerals in the environment,[14,15] and on the oxidation of iron(II) species[16] and the precipitation of iron(III) in environmental systems.[17] The effects of biological ligands on the precipitation of oxides and hydroxides of iron in marine environments have been considered.[18] A review of model compounds for iron–oxygen aggregation and biomineralization links fairly simple complexes to metalloproteins such as ferritin and hemerythrin; carboxylate bridges support simple oxo bridges throughout the range.[19] Iron(II) salts are generally believed to be toxic to plant life, for example, in the use of iron(II) sulfate as a moss killer, but conversely iron complexes are used to provide essential iron for pin oak and citrus fruit trees in high pH soils and to make hydrangeas blue. Iron toxicity in asbestos chemistry and carcinogenicity has been reviewed.[20]

Included in this article is some information on the distribution of iron and the chemical processes involved in converting its ores into metal, but we are mainly concerned with the chemistry of iron salts and iron coordination complexes. Metallurgical aspects are not considered. Discussion about biologically important systems such as iron porphyrins, iron-containing proteins, iron–sulfur clusters and their model compounds, as well as the chemistry of biological iron storage and transport mechanisms are not discussed in detail, but can be found elsewhere in this Encyclopedia.

2 THE ELEMENT

This section deals with the production of metallic iron, outlines some of its physical properties, and chemical reactivity. Chemically relevant nuclear properties are also discussed.

2.1 Production

Primary reduction of iron oxide ores takes place industrially in a blast furnace (in which many impurities are removed by volatilization) or a direct reduction unit (with synthesis gas – a mixture of H_2, CO, and CO_2) to provide pig iron or iron sponge. Subsequently, this is refined and appropriate elements are added to provide steels of the required composition to achieve a wide spectrum of properties.[21] The chief ores now of commercial importance are hematite (specularite, Fe_2O_3), magnetite (Fe_3O_4), and limonite (FeOOH). The carbonate, siderite, is no longer important, nor are pyrite (disulfide ore) and silicate-containing ores. However, oxidative bacterial action on pyrite gives an acidic solution containing iron(III), which is an important intermediate in the bacterial dissolution of some other metals from their ores, the basis of a method of biological metal extraction.[22]

2.2 Physical Properties

Pure iron is a fairly soft silver/white ductile and malleable metal melting at 1535 °C. It exists in three allotropic forms: body-centered cubic (alpha), face-centered cubic (gamma), and a high-temperature body-centered cubic (delta). In reviewing the literature on the structure of iron, Donohue[23] concluded that the best average value for the lattice constant for α-Fe at 20 °C was 2.86 638(19) Å. Details of the phase transitions and other numerical information are given in Table 1. The physical properties of iron depend on the presence of low levels of impurity, such as carbon or silicon, and the pure metal is of little commercial importance. In contrast the properties of iron containing varying amounts of other components, namely steels, make them commercially very important. Table 1 contains data for some thermal and mechanical properties of technically pure iron (99.5–99.9%). The magnetic properties are also sensitive to impurities; at room temperature, pure iron is ferromagnetic, but above the Curie point (768 °C), it is paramagnetic.

Table 1 Selected properties of iron

Atomic Number	26
Atomic Weight	55.847
Density	7.87 g cm^{-3} (20 °C) 7.08 g cm^{-3} (1550 °C)
Coefficient of Thermal Expansion	1.45×10^{-5} K^{-1} (0–800 °C)
Thermal conductivity	72.44 W m^{-1} K^{-1} (100 °C)
Standard Entropy	27.2 J mol^{-1} K^{-1}
Molar heat capacity	α $Cp = 17.50 + 24.77 \times T$ J mol^{-1} K^{-1} (273–1033 K) γ $Cp = 7.70 + 19.51 \times T$ J mol^{-1} K^{-1} (1183–1673 K) δ $Cp = 43.96 \times T$ (1673–1812 K) liquid $Cp = 41.87 \times T$ (1812–1873 K)
Transition Points	
Curie Point	760 °C (2.76 kJ mol^{-1})
alpha/gamma	910 °C (0.92 kJ mol^{-1})
gamma/delta	1400 °C (1.17 kJ mol^{-1})
delta/melt	1539 °C (15.28 kJ mol^{-1})
melt/vapor	2880 °C (340.4 kJ mol^{-1})
Structures and lattice constants:	
alpha-iron body-centered cubic	$a = 0.2866$ nm
gamma-iron face-centered cubic	$a = 0.3647$ nm
delta-iron body-centered cubic	$a = 0.2932$ nm
Mechanical Properties[a]	
Tensile strength	220–280 N mm^{-1}
Elongation to fracture	40–60%
Modulus of elasticity	10×103 N mm^{-1}
Shear modulus	82×103 N mm^{-2}
Brinell hardness	44–55 HB

[a] Typical data for samples containing 0.005% carbon.

2.3 Nuclear Properties

2.3.1 Isotopes

There are four naturally occurring isotopes of iron. Their abundances and atomic masses are listed in Table 2 together with data for other man-made isotopes of iron whose atomic masses have been determined with precision. The most abundant of the natural isotopes is ^{56}Fe, and this is also the most stable nuclear configuration of all the elements in terms of nuclear binding energy per nucleon. Its stability, viewed in terms of nuclear equilibria established in the last moments of supernovae, perhaps explains its widespread occurrence in the cosmos.[24] The isotope ^{57}Fe has several applications, most notably in Mössbauer spectroscopy, and it has proved to be

Table 2 The isotopes of iron (Z = 26)

Isotope	N	Abundance	Atomic Mass	Half-life
^{51}Fe	25		50.956825	0.25 s
^{52}Fe	26		51.948114	8.28 h
^{53}Fe	27		52.945310	8.51 min
^{54}Fe	28	5.82%	53.939612	
^{55}Fe	29		54.938296	2.7 years
^{56}Fe	30	91.66%	55.934939	
^{57}Fe	31	2.19%	56.935396	
^{58}Fe	32	0.33%	57.933277	
^{59}Fe	33		58.934877	44.5 days
^{60}Fe	34		59.93408	ca. 10^5 years
^{61}Fe	35		60.936748	6.0 min
^{62}Fe	36		61.936773	68 s
^{63}Fe	37		62.94075	4.9 s

Note: Relative atomic mass of natural iron = 55.847.

of some value in studying iron-containing compounds and complexes by EPR spectroscopy;**25** its nuclear properties (low sensitivity, low abundance, and long relaxation times**26**) make the acquisition of serviceable ^{57}Fe NMR spectra difficult.**27** Recently, in the form of single crystals, it has been used in short wavelength neutron monochromators (spin up/down). This isotope has been produced in considerable quantities at the Oak Ridge National Laboratory (Tennessee USA) using electromagnetic separators known as calutrons. The isotope ^{52}Fe has been considered for use in positron emission tomography (PET).**28**

2.3.2 *Mössbauer Spectroscopy*

The ^{57}Fe nucleus is particularly amenable to study by the Mössbauer technique.**29** The effect arises from reabsorption by ^{57}Fe in the sample of γ-rays derived from an excited state of ^{57}Fe at a source formed in the radioactive decay of ^{57}Co, which has a half-life of 270 days. The nuclear transitions involved are shown in Figure 1. The ^{57}Fe nuclide is sufficiently abundant (Table 2) for excellent spectra to be obtained routinely with compounds containing iron of natural isotopic abundance, whilst materials enriched in ^{57}Fe give spectra in less time. However, in some cases (e.g. where samples have a low overall iron content), it may prove essential to use enriched iron. The Döppler shift velocity of the source at which absorption occurs is a measure of absorption frequency, and this is different when the chemical environment of the absorbing nucleus is different. A reference material, usually stainless steel or sodium nitroprusside, is assigned a value of zero and the shift of the sample measured relative to it. This chemical shift (δ) is affected by the electronic environment of the iron and is temperature dependant. It arises from the interaction of s electrons at the nucleus and is a linear function of their density there. With high-spin complexes, δ depends on the oxidation state: from $+1.0$ to $+1.6\,\mathrm{mm\,s^{-1}}$ for iron(II), and from $+0.45$ to $+0.75\,\mathrm{mm\,s^{-1}}$ for iron(III) complexes. The ligand type also influences the value of δ. Large chemical shifts are not observed with low-spin complexes; both iron(II) and iron(III) low-spin complexes have δ in the range 0.0–$+0.3\,\mathrm{mm\,s^{-1}}$.

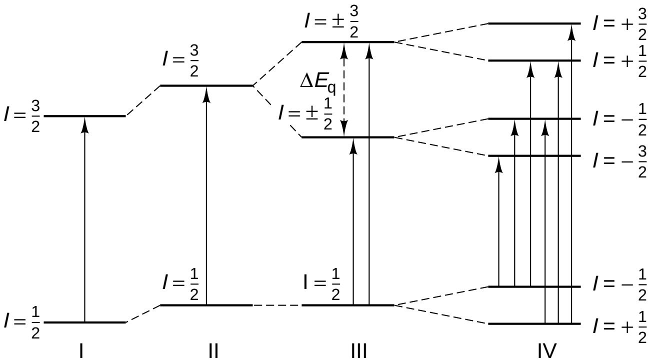

Figure 1 Nuclear energy levels responsible for one-, two-, and six-line iron Mössbauer spectra: I, original energy levels; II, small perturbation via interaction with s-electron density; III, quadrupole interaction splitting; IV, magnetic splitting of the ground and excited states

The $I = 1/2$ to $I = 3/2$ nuclear transition is split by an electric quadrupole to give a two-line Mössbauer spectrum (quadrupole splitting energy ΔE_q), and if the sample is also in a magnetic field, a six-line spectrum results when the nuclear spin degeneracy is removed (Figure 1). An electric field gradient at the iron nucleus can arise from asymmetric occupancy of d orbitals, or from asymmetry of the ligand field. Accordingly, high-spin iron(III) complexes with identical ligands have small ΔE_q values, but similar iron(II) complexes have a two-line Mössbauer spectrum. The symmetrical electronic configuration and ligand environment of low-spin iron(II) complexes with identical ligands, for example, $[Fe(CN)_6]^{4-}$, has a single-line Mössbauer absorbance, while the asymmetric electronic configuration of low-spin iron(III) complexes results in them having a spectrum similar to those of high-spin iron(II). Many low-spin $[FeX_4Y_2]$ and $[FeX_5Y]$ complexes with asymmetric ligand environments have had their two peak Mössbauer spectra recorded.**30** In appropriate situations, iron Mössbauer spectroscopy can be a valuable characterization tool. New Mössbauer techniques using synchrotron radiation, and thus operating in the time domain rather than in the usual energy domain, have been applied to the study of iron porphyrin complexes.**31**

2.4 Chemical Properties

2.4.1 *General Reactivity*

Iron is reactive and, if sufficiently finely divided, is pyrophoric in air. It forms binary compounds by direct reaction with many elements, and some of these are described in more detail later. It reacts with oxygen, sulfur, halogens, phosphorus, and even forms a nitride with dinitrogen. With ammonia, nitride is readily formed above 400 °C, and is the basis of a 'nitriding' process to harden steel surfaces.[32] At elevated temperatures, iron reacts with steam to give hydrogen and one or more iron oxides; Fe_3O_4 is formed below about 570 °C, and FeO at higher temperatures. These oxides are also formed when carbon dioxide is reduced to carbon monoxide by iron. At high pressure, carbon monoxide reacts with the metal to form volatile iron pentacarbonyl ($Fe(CO)_5$, bp 104 °C), a process which is catalyzed by sulfur compounds. Iron dissolves in dilute mineral acids with the evolution of hydrogen and formation of iron(II) salts. However, concentrated nitric acid and other powerful oxidants passivate iron. Iron filings (or turnings) are still used commercially to reduce aromatic nitro compounds, for example, nitrobenzene to aniline, and in one variation of this process, a morphological variant of Fe_3O_4 is produced, which is used as a pigment.

2.4.2 Catalytic Properties

There are many catalytic applications in which metallic iron or its oxides play a vital part; the best known are in the synthesis of ammonia from hydrogen and nitrogen at high pressure (Haber process), and in hydrocarbon synthesis from $CO/CO_2/H_2$ mixtures (Fischer–Tropsch synthesis).[33] Iron oxides also have catalytic activity in mild hydrogenation reactions, for instance, magnetite has long been used to bring water gas (a mixture of hydrogen and carbon monoxide) to equilibrium with excess steam.[34] They were also used to absorb sulfur compounds from town gas, which was obtained by dry distillation of coal.[35]

2.4.3 Rusting

Iron is an electropositive element (−0.44 v) although the massive metal is stable in dry air. However, in the presence of oxygen and water, or even deoxygenated water and carbon dioxide, rusting (formation of hydrated mixed iron oxides) takes place with the formation of the characteristic brown hydrated surface oxides. These flake away permitting the process to continue causing metal loss, and ultimately mechanical failure. Mild steel rusting is essentially electrochemical in nature involving dissolution of iron to give mobile iron(II) salts, subsequent precipitation of insoluble iron(III) oxo species, and recycling of the anions concerned. Thus, chloride (found on many roads in winter), sulfate, and other common anions significantly enhance rusting rates, which are faster in urban environments than in rural ones, and even more rapid in industrial and marine environments.[36] Approaches to rust inhibition include placing a barrier between the metal surface and the environment to slow oxygen transfer, or retardation of iron diffusion near the interface. A variety of coatings are used such as phosphate treatments and paints and these approaches have been used to prevent rusting of automobiles.[37] In well-controlled situations, such as the steam generating systems of power and chemical plants, it is possible to maintain a sufficiently high pH for a coherent film of magnetite to be formed, which prevents further significant corrosion. Under milder conditions, filming amines are used. Since electrochemical dissolution of metal is a key step in rusting, it can be inhibited by cathodic protection: applying a small potential between the steel and an electrode. The latter may be sacrificial (e.g. zinc, specifically as an electrode or as a coating in galvanizing) if it has a higher electrochemical potential than iron, and therefore dissolves preferentially. In contrast to rust formed at ambient conditions, scale formed on steels during hot rolling and other heat treatments comprises all three iron oxides (see Section 3.1.1) in ratios dependent on steel composition, and processing conditions. Removal of scale by dissolution in mineral acid is known as pickling. The most common acids employed with iron and mild steels are sulfuric acid, and increasingly, hydrochloric acid. Phosphoric, nitric, and hydrofluoric acids are used for stainless steels and special purposes. Crystallization of spent pickling solutions is an important source of iron(II) salts, although an electrolysis process has been developed which affords metallic iron, and spray-roasting chloride solutions give iron(III) oxide that is suitable as a raw material for manufacturing ferrites.

Stainless steels do not rust in the same way as mild steel. They contain chromium (typically 18%), and form a thin (tens of Ångstroms) chromium-rich oxide film that inhibits further reaction under normal conditions. Oxidation does however take place at high temperature, but incorporation of nickel (8% or more) gives improved performance alloys, which are widely used in the chemical industry.[38] They are however, considerably more costly than mild steel.

3 BINARY COMPOUNDS

Iron is a reactive element that forms binary compounds with a variety of nonmetallic elements. Oxide and sulfide ores are widely distributed in nature and as such form huge ore reserves. Carbides and phosphides have key roles in steel making. The most common form of iron oxide is probably rust, hydrated iron(III) oxide (see Section 2.4.3). Other oxides are important in corrosion science, and they have a variety of applications based on their physical properties; magnetic (e.g. recording media), light absorption (e.g. inorganic pigments), or hardness (e.g. polishing powders).

3.1 Oxides

3.1.1 Oxides and Hydroxides[39]

The important iron/oxygen system has been extensively studied, and a simplified phase diagram is shown in

Figure 2. Here, the primary concern is the chemistry of the oxides, and for convenience, hydroxides are also included in this section. The mixed oxide ferrites, some of which are manufactured on a large scale, are dealt with in Section 3.1.2.

Several iron oxides and hydroxy oxides exist as minerals, and the more important are listed in Table 3. Three iron oxides are known with ideal compositions: FeO (wüstite), Fe_2O_3 (hematite), and Fe_3O_4 (magnetite). However, all of them tend to be nonstoichiometric. Wüstite is only stable at temperatures above 570 °C, but can be prepared by heating pure $Fe(OH)_2$ under nitrogen at 200 °C. It contains defect clusters related to the magnetite structure (see below), and is an intermediate in the reduction of higher iron oxides. The wide range of stoichiometry of $Fe_{1-x}O$ results from the ease of formation of iron(III) from iron(II). For example, in the omission of one iron(II) center with oxidation of two of those remaining to iron(III), some of the iron(III) atoms are in tetrahedral sites and the resulting defect unit (one tetrahedral iron(III) and two octahedral cation vacancies), can be ordered through the lattice. The main iron ore deposits in the Earth's crust are hematite and magnetite. Bright red hematite has layers of FeO_6 octahedra connected by shared edges and faces and stacked perpendicular to the *c*-axis. Owing to the face sharing, the octahedra are slightly distorted so there is a regular displacement of the iron centers. Mixed-valence magnetite is black due to charge transfer. It is strongly magnetic and has an inverse spinel structure with the tetrahedral positions occupied by Fe(III), and the octahedral sites by equal amounts of Fe(III) and Fe(II). Crystals, formed by chemical transport, are well-formed octahedra with shiny faces and can be up to 5 mm across.[40] Small spheres (~12 nm) of polymers with a hematite surface are being assessed for the removal of arsenic contamination from drinking water in India and Bangladesh.[41]

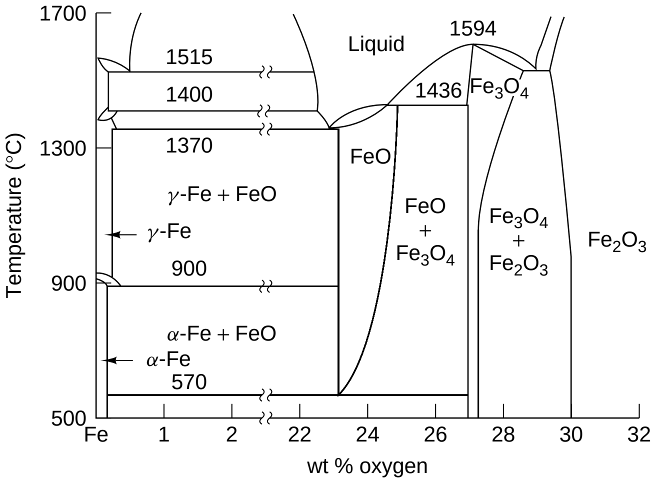

Figure 2 Phase diagram for the iron/oxygen system

Table 3 Iron oxide and oxyhydroxide minerals

Mineral	Formula	Structure	Density[a]	Color[b]
Goethite	α-FeO(OH)	Orthorhombic	4.26	Yellow brown
Akaganeite	β-FeO(OH)	Tetragonal	3.56	Yellow brown
Lepidocrocite	γ-FeO(OH)	Orthorhombic	4.09	Orange
Feroxyhyte	δ'-FeO(OH)	Hexagonal	4.20	Red brown
Ferrihydrite	$Fe_5HO_8 \cdot 4H_2O$	Trigonal	3.96	Red brown
Magnetite	Fe_3O_4	Cubic	5.18	Black
Hematite	α-Fe_2O_3	Trigonal	5.26	Bright red
Maghemite	γ-Fe_2O_3	Cubic/ Tetragonal	4.87	Red brown

[a] g cm^{-3}. [b] Color depends to a significant extent on particle size and morphology.

Slow hydrolysis of iron(III) can be used to prepare hydrated iron(III) oxide;[42] a more convenient preparation involves aerial oxidation of $[FeCl_2(py)_4]$ to the hydrated oxide $Fe_2O_3.H_2O$, which may be dehydrated to ferromagnetic γ-Fe_2O_3 at 250 °C. When heated at 400 °C, this irreversibly gives[43] α-Fe_2O_3 (hematite). Iron(II) hydroxide is obtained as a white precipitate on addition of hydroxide ion to a solution of an iron(II) salt, and when crystalline it has the magnesium hydroxide structure. It is strongly reducing and there is some evidence that it reduces dinitrogen to ammonia.[44] On exposure to air, it turns brown, finally forming hydrated iron(III) oxide. The identification of ores containing similar iron(III) oxides in precambrian deposits has been taken as evidence that the Earth's atmosphere contained oxygen at that time.

The aquated iron(III) cation has a pK_a about 2.5, and readily undergoes hydrolysis; except at low pH it does not exist as $[Fe(H_2O)_6]^{3+}$. Above pH~1, hydrolytic polymerization involving deprotonation takes place to form hydroxo and oxo species leading progressively to increasingly insoluble hydrated iron(III) oxides, similar to rust. When a solution of an iron(III) salt is made alkaline, the nature of the product depends on the final pH, the rate of pH change, temperature, and any other ions present. Equilibria resulting in low-molecular weight hydrolysis products such as $FeOH^{2+}$, $Fe(OH)_2{}^{+}$, and $Fe_2(OH)_2{}^{4+}$ (for simplicity water ligands are omitted) are rapidly established, and are well understood.[45] From these, larger soluble polynuclear species form, and further polymerization gives colloidal red–brown material, with for example, the β-FeO(OH) structure. Low-temperature hydrothermal synthesis can yield β-FeO(OH), in the form of tunnel-type nanorods, and α-Fe_2O_3 nanorods of porous structure.[46] Illustrated in Figure 3 are the three fundamental cationic hydrate cores found in iron(III) polynuclear species: μ-oxo bridged dimers, μ-dihydroxy dimers, and μ-oxo triiron. These basic units are also found in many iron(III) complexes, for example, the basic carboxylates, which contain three iron(III) centers and a central oxygen atom.[47] Layered

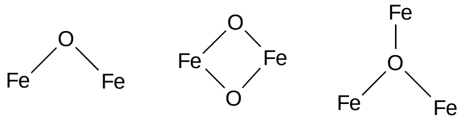

Figure 3 Schematic representation of the fundamental iron–oxygen cores found in many iron(III) polymeric hydroxy/oxide systems

double hydroxides are of current interest; iron-containing versions include Fe^{3+}/Ni^{2+} and Fe^{3+}/Mg^{2+} with carbonate as intercalated counterion and Fe^{3+}/Ni^{2+} with sulfate. Layered double hydroxides such as the $[\mathrm{Fe}^{\mathrm{III}}_x\mathrm{Ni}^{\mathrm{II}}_{1-x}(\mathrm{OH})_2]^{x+}$ cations form a large group of minerals and synthetic materials, capable of intercalating a variety of oxoanions.[48] Complementarily, hexacyanoferrate(II) can act as the intercalating counterion in layered double hydroxides such as $Mg(OH)_2/Cr(OH)_3$, $Mg(OH)_2/Al(OH)_3$, and $Cu(OH)_2/Al(OH)_3$.[49]

3.1.2 Ferrites

'Ferrites' has become a generic term for all magnetoceramic materials widely used in magnetoelectronic applications.[50] True ferrites contain iron(III) and are classified into two main groups: 'cubic ferrites' (MFe_2O_4) with a spinel structure, which are sometimes called ferrospinels, and 'hexagonal ferrites' ($MFe_{12}O_{19}$) with the magnetoplumbite structure ($M =$ divalent cation, e.g. Mn, Fe, Co, Ni, Cu, Mg). These are generally chemically inert materials, which lose oxygen before melting at high temperatures. The former may be obtained by reacting the well-mixed constituent oxides at temperatures above 1000 °C, or more conveniently for the nickel, cobalt, or manganese compounds by decomposition of the appropriate pyridine adduct of the mixed iron acetate.[51] A less controllable, but often used, procedure is coprecipitation of the mixed oxalates followed by thermal decomposition.[52] Lattice constants and magnetic properties of several cubic ferrites are given in Table 4.

3.2 Sulfides

Metallic iron reacts with sulfur when heated to give high-spin iron(II) sulfide. This is also formed when iron(II) is precipitated from solution by addition of sulfide ion, and while it is normally dark gray/brown, when pure it is almost colorless. Rarely is the iron/sulfur ratio unity, and at different times a variety of formulae have been assigned to these nonstoichiometric ferrimagnetic phases.[53] Several minerals contain an approximately octahedral environment of sulfur atoms around iron. Troilite, high-spin stoichiometric FeS, is hexagonal with Fe–S bond lengths ranging from 2.38 Å–2.72 Å. Pyrrhotite ($Fe_{1-x}S$) exists as hexagonal and monoclinic forms, with bond lengths in the range 2.37 Å–2.67 Å. The cubic low-spin iron(II) disulfide FeS_2 has a FeS_6 octahedron with Fe–S bond lengths of 2.26 Å; the tetragonal FeS_2 polymorph, marcasite, has an octahedral geometry distorted by elongation along the c-axis. Iron pyrites, FeS_2, occurs naturally as brass-yellow crystals, sometimes formed in the presence of organic matter such as in coal seams. Iron(III) sulfide may be obtained from aqueous solutions of an Fe^{3+} salt and sodium sulfide at 0 °C. It is unstable, and not easily stored. A tricyclic iron(III) polysulfide anion $[Fe_2S_{12}]^{2-}$ has been characterized.[54]

Table 4 Lattice constants and magnetic properties of some cubic ferrites

Ferrite	Lattice Constant (Å)	Magnetic Transition (°C)	BM/formula(0K)
$MgFe_2O_4$	8.384	440	1.1–1.4
$MnFe_2O_4$	8.512	300	4.5
$CoFe_2O_4$	8.388	520	3.7
$NiFe_2O_4$	8.338	585	2.1
$ZnFe_2O_4$	8.437	264	

3.3 Nitrides

Nitrogen dissolves in iron to form a solid solution and several nitride phases – the phase diagram is complex. Specific nitrides are best obtained via reaction of iron with ammonia. At 400–500 °C, gray orthorhombic Fe_2N is obtained, which when heated at about 500 °C in vacuo, loses nitrogen to give face-centered cubic Fe_4N.

3.4 Carbides

The addition of small amounts of carbon to iron dramatically changes its physical properties. By occupying interstitial sites, carbon can be thought of as locking together the structure, thus reducing ductility and increasing hardness. Thus, physical properties markedly depend on the amount of carbon present. Cast iron contains at least 4% carbon, which is present as graphite, in solid solution, or as cementite (Fe_3C). It is very brittle, whereas mild steel contains less than 1.5% carbon and is much more ductile. Commercially, careful control of carbon content is very important. However, the properties of a particular steel depend not only on carbon content, but also on the amount of other low-level additives, as well as grain size, (which depends on thermal history) and surface treatments. In the irregular structure of cementite, carbon is located in a very distorted trigonal prism of six iron atoms at distances 1.89 Å–2.15 Å, with an additional two iron atoms at 2.31 Å. Other iron carbides are also known. The reaction of cementite with dilute hydrochloric acid has been reported to be complex, forming hydrogen, and a range of liquid and gaseous hydrocarbons. The reasons for this are not clear, for its structure suggests methane would be the major product. This is, however, in accord with the behavior of iron as a Fischer–Tropsch catalyst.[55]

3.5 Phosphides

The iron–phosphorus phase diagram is well established. The phases FeP and FeP_2 are well characterized; Fe_3P is also known, and there are three distinct FeP_4 structures. Hexagonal Fe_2P is formed in the reaction of iron with red phosphorus. It is ferromagnetic (magnetization 2.94 BM/Fe_2P with a Curie temperature of 210K) and contains two iron sites, one in a tetrahedron of P atoms, and the other in a pyramid of five P atoms. Orthorhombic iron monophosphide ($a = 5.19$ Å, $b = 3.099$ Å, $c = 5.79$ Å) may be obtained by electrolysis of iron(III) and sodium metaphosphate at 925 °C in the form of needles with a metallic luster. FeP is antiferromagnetic with a Néel temperature $T_N = 123$ K, and is stable in air, water, and acids at room temperature.[56] FeP is the major constituent of recently characterized nanowires generated by thermal decomposition of (η^4-cyclohexadiene)irontricarbonyl in the presence of tri-*n*-octylphosphine.[57] FeP_2 is orthorhombic.

3.6 Borides

Metal borides have high melting points and considerable hardness, in many ways they resemble nitrides and carbides. Usually, their stoichiometry does not reveal their often-complex structures. Thus, iron boride (FeB, density 7.15 g cm^{-3}) contains infinite zigzag chains of boron atoms (B–B distance 1.77 Å) with each boron atom being surrounded by six iron atoms (Fe–B distances 2.12 to 2.18 Å) located at the apices of a trigonal prism. Fe_2B has a layer structure in which each boron atom has eight iron neighbors with the two near boron atoms, but there are no B–B bonds. The discrete compound FeB_{49} has the iron atom in a rhombohedral boron environment.[58]

4 SIMPLE SALTS

4.1 Halides

4.1.1 Fluorides

Anhydrous iron(II) fluoride, FeF_2 (ferrous fluoride), is an off-white powder obtained by reacting iron with HF, dehydration of the tetrahydrate, displacement of chlorine in $FeCl_2$ by HF, or reduction of FeF_3. It is monomeric in the gas phase, and the solid has the rutile structure in which FeF_6 octahedra are tetragonally distorted with two Fe–F distances of 1.99 Å and four of 2.12 Å. Above 100 K, FeF_2 has a spin-free magnetic moment of 5.56 BM. White iron(II) difluoride tetrahydrate is oxidized in air and becomes brown. It can be made by dissolving iron in warm hydrofluoric acid followed by precipitation with ethanol. Its structure contains discrete $[FeF_2(H_2O)_4]$ octahedra with H_2O and F^- randomly distributed over 12 possible sites, each being occupied by an average of $^1/_3$ O and $^1/_6$ F^-. On standing in air, a saturated aqueous solution of iron(II) fluoride forms a precipitate of yellow $Fe_2F_5{\cdot}7H_2O$, which may be dehydrated at 100 °C under nitrogen to give $Fe_2F_5{\cdot}2H_2O$, and at 180 °C to a gray salt, Fe_2F_5, that has distinct Fe(II) and Fe(III) centers.[59] Iron(III) fluoride, FeF_3 (ferric fluoride), is prepared from the elements, or $FeCl_3$ with ClF_3, or $FeCl_3$ and HF at an elevated temperature. It is antiferromagnetic with a Néel temperature of $T_N = 394$ K. Although only slightly soluble in water, it dissolves in dilute HF. The pale pink trihydrate $FeF_3{\cdot}3H_2O$ may be crystallized from 40% HF in two forms. Low-temperature crystallization favors a form isostructural with α-$AlF_3{\cdot}3H_2O$, while the higher-temperature form has bridging fluorides and one water molecule of hydration in the unit cell.[60] The affinity of iron(III) for fluoride ion is high. Formation constants for aqua fluoride species are several orders of magnitude larger than those for chloride.[61] In the solid state, salts containing $[FeF_6]^{3-}$ are known, but in aqueous solution, only species with less than six fluorides exist.

4.1.2 Chlorides

Iron(II) chloride, $FeCl_2$ (ferrous chloride), occurs as the mineral lawrencite. It is a hygroscopic white/pale green solid, readily soluble in water and ethanol, with a melting point of 677 °C and a boiling point of 1074 °C. When a saturated aqueous solution is cooled to 0 °C, pale green monoclinic crystals of the tetrahydrate are deposited. When this is heated in a partial vacuum above 72.6 °C, a very pale green dihydrate is obtained, and at 120 °C, a monohydrate is obtained.[62] The anhydrous compound is prepared by the action of HCl on iron at red heat (or under milder conditions in THF or methanol, which affords solvates), or by reduction of iron(III) chloride with hydrogen at 200 °C. Anhydrous iron(II) chloride may also be obtained as a tan colored solid by boiling iron(III) chloride in chlorobenzene.[63] When heated at 300 °C in vacuo, $FeCl_3$ decomposes to $FeCl_2$, and this facilitates purification of $FeCl_2$ by vacuum sublimation. Depending on the temperature, the vapor of iron(II) chloride contains monomeric or dimeric species, while the crystalline solid has the $CdCl_2$ structure with the packing of $FeCl_6$ octahedra depending on the method of crystallization; the structure is also pressure sensitive. The anhydrous salt has a magnetic moment of 5.87 BM. Pale green $FeCl_2{\cdot}4H_2O$ is easily oxidized both in the solid and solution forms. In the presence of an excess chloride ion and suitably large cations, salts of tetrahedral $[FeCl_4]^{2-}$ are readily obtained. Thus, mixing ethanolic solutions of $FeCl_2{\cdot}2H_2O$ and NEt_4Cl gives[64] a cream precipitate of $(NEt_4)_2[FeCl_4]$. Recrystallization of iron(II) chloride from pyridine gives yellow *trans*-$[FeCl_2(py)_4]$, which has the advantages of being somewhat less easily oxidized by air than simple iron(II) salts, and soluble in common organic solvents. It is therefore often used in the preparation of other iron(II) compounds.

Anhydrous iron(III) trichloride, $FeCl_3$ (ferric chloride), is soluble in water and organic solvents. It is manufactured by reaction of excess chlorine with iron at 500–700 °C as an almost black crystalline solid with a metallic luster (density $2.89\,g\,cm^{-3}$), which sublimes at about 305 °C, and boils at 332 °C with some decomposition. In the gas phase, it is dimeric up to about 400 °C when increasingly significant amounts of monomer are present; at these temperatures in vacuo, it decomposes to the dichloride. The anhydrous solid has a layer structure, and is very hygroscopic; it forms a series of hydrates when exposed to moist air. The common hydrate is yellow $FeCl_3{\cdot}6H_2O$ (mp about 37 °C), which contains $[FeCl_2(H_2O)_4]^+$. This is very soluble in water, and gives a strongly acidic solution, which when partially neutralized forms a series of polymeric species. The addition of more alkali gives, depending on conditions, brown colloidal β-FeO(OH) or a precipitate of iron(III) hydroxide. With hydrochloric acid, or another source of chloride ion, tetrachloroferrates $[FeCl_4]^-$ and $[FeCl_4(H_2O)_2]^-$ are formed. Salts of the $[FeCl_6]^{3-}$ anion can be obtained in the solid state through the use of large cations such as $[Co(NH_3)_6]^{3+}$ and $[Co(pn)_3]^{3+}$ (pn = 1,2-propanediamine), which provide lattice stabilization.[65] $FeCl_3$ is sometimes used as a catalyst in Friedel–Crafts reactions, and it is also occasionally used as a chlorinating agent. Fe(III) is oxidizing, and many metals dissolve in aqueous $FeCl_3$ solutions (e.g. copper when preparing printed circuit boards, and in the bacterial extraction of ores). When heated strongly in air, chlorine and iron(III) oxides are formed.

The largest consumption of iron(III) chloride is in water treatment where it is used to condition some potable waters. Dilute solutions, adjusted to the appropriate pH, flocculate, and precipitate finely divided solids, colloids, and heavy metals, via adsorption on extremely insoluble iron(III) hydroxide. Very large quantities are employed in sewage plants to coprecipitate, and thus remove from clarified water, oils, polymers, heavy metals, sulfides, and phosphates, which would otherwise be extremely difficult to degrade. Iron(III) chloride was the first inorganic contrast agent in magnetic resonance imaging (MRI) in a human, administered orally for gastrointestinal tract imaging.[66] Iron compounds are now returning (the currently widely used gadolinium complexes are significantly toxic) to favor with iron(III) ammonium citrate (the main ingredient in Geritol, an iron supplement for anemia), iron(II) sulfate, and iron oxide nanoparticles assessed as contrast agents.[67]

4.1.3 Bromides

Iron(II) bromide, $FeBr_2$ (ferrous bromide), is a pale yellow/brown hygroscopic solid soluble in water and donor organic solvents. It may be prepared from iron and bromine at 200 °C, or iron and HBr in methanol, hydrobromination of iron(III) oxide at 200–350 °C, or dehydration of $[FeBr_2(H_2O)_4]$. The anhydrous compound is readily purified from $FeBr_3$ by sublimation under nitrogen or in vacuo. It was used in the early determinations of the atomic weight of iron via quantitative precipitation of silver bromide.[68] It has a layer lattice of the CdI_2 type, and has a magnetic moment of 5.71 BM at 295 K. It readily forms complexes with a wide range of ligands, and a series of hydrates can be crystallized from water. At room temperature, a hexahydrate is obtained, above 49 °C, a tetrahydrate, and above 83 °C, a dihydrate. With excess bromide ion and a suitably large cation, salts of $[FeBr_4]^{2-}$ are readily obtained. Thus, mixing ethanolic solutions of $FeBr_2$ and NEt_4Br precipitates[69] pale brown $(NEt_4)_2[FeBr_4]$. Dark red hygroscopic iron(III) bromide, $FeBr_3$ (ferric bromide) can be obtained from the elements below 200 °C. It dissolves freely in water, and in coordinating organic solvents. Several hydrates are known. Structures have been reported for $Ba[FeBr_4]_2$[70] and for its parent $FeBr_3$, which has the BiI_3 structure with pairs of bromide ligands bridging the Fe^{3+} ions, all of which are octahedrally coordinated.[71]

4.1.4 Iodides

Iron(III) iodide, FeI_3 (ferric iodide), was first isolated in the pure state as recently as 1988 as a black, fairly stable solid, though it is unstable in solution.[72] It reacts with iodide to give the previously characterized complex $[FeI_4]^-$.[73] Iron(II) iodide, FeI_2 (ferrous iodide), is a red–black hygroscopic solid having the CdI_2 structure, and a magnetic moment of 5.75 BM at 295 K. It is readily prepared from finely divided iron and iodine, and is soluble in water, ethanol, and ether. A series of hydrates are known, and at room temperature, a green tetrahydrate crystallizes. Complexes are formed with a range of ligands. There are few applications for FeI_2 although it is used in some discharge lamps.[74]

4.2 Sulfates

Pale green iron(II) sulfate heptahydrate, $FeSO_4{\cdot}7H_2O$ (ferrous sulfate), formerly known as green vitriol (mp 64 °C), is produced by dissolving iron in dilute sulfuric acid, or by the oxidation of moist pyrites (FeS_2) in air. Iron(II) sulfate is a readily available by-product, for example, from steel pickling (see Section 2.4.3), or processes such as traditional titania manufacture, which involves digestion in sulfuric acid. It is readily soluble in water, the heptahydrate crystallizing as green monoclinic crystals. On gentle heating (60–70 °C), water is lost to give a tetrahydrate, and in the absence of oxygen at about 300 °C, a monohydrate is obtained which decomposes at about 480 °C. When heated in air, the monohydrate is oxidized to an iron(III) sulfate. In air, solid $FeSO_4{\cdot}7H_2O$ is gradually oxidized at room temperature; the easily purified Mohr's salt, iron(II) ammonium sulfate $FeSO_4{\cdot}(NH_4)_2SO_4{\cdot}6H_2O$, is more stable, and is preferred in analytical work. Similar double salts are formed with other univalent cations. In acid solution, iron(II) sulfate reduces nitrate and nitrite ions to nitric oxide, which complexes with iron(II) to give the intensely colored cation $[Fe(H_2O)_5NO]^{2+}$, the basis of the Brown Ring Test for these anions (see Section 8.1.1).

Anhydrous iron(III) sulfate, $Fe_2(SO_4)_3$ (ferric sulfate), is a pale yellow solid, which when strongly heated gives iron(III) oxide and sulfur trioxide. It dissolves in water with hydrolysis to give a yellow/brown solution, and when boiled, this forms a precipitate of basic iron(III) sulfate. The related basic complex $K_5[Fe_3O(SO_4)_6(H_2O)_3]$ is structurally similar to basic iron(III) acetate:**[75]** it contains a planar Fe_3O core via which magnetic exchange takes place, and each pair of iron atoms is bridged by two bidentate sulfate groups. Solutions of iron(III) sulfate are prepared by oxidation of iron(II) sulfate in sulfuric acid, or by dissolving iron(III) oxide in warm sulfuric acid. With alkali metal sulfates, alums $MFe(SO_4)_2{\cdot}12H_2O$ (M = alkali metal cation) are formed, which have the violet tinge characteristic of $[Fe(H_2O)_6]^{3+}$ but are otherwise almost colorless. Iron(III) sulfate is used as a sludge coagulant in sewage plants, in tanning, and in the production of iron pigments.

4.3 Nitrates

Green rhombohedral crystals of iron(II) nitrate hexahydrate, $Fe(NO_3)_2{\cdot}6H_2O$ (ferrous nitrate), with a melting point 60.5 °C, are obtained from solutions made by dissolving iron in dilute nitric acid. With more concentrated acid, oxidation takes place, and monoclinic pale violet iron(III) nitrate nonahydrate, $Fe(NO_3)_3{\cdot}9H_2O$ (ferric nitrate), melting point 47 °C, may be crystallized. A colorless hexahydrate can also separate as cubic crystals. Various basic iron(III) nitrates have been described. The eight-coordinate iron(III) anion $[Fe(NO_3)_4]^-$ has an essentially dodecahedral symmetry with four almost symmetrical bidentate nitrate groups.**[76]**

4.4 Phosphates

Insoluble iron(II) orthophosphate, $Fe_3(PO_4)_2$ (ferrous phosphate), occurs as a monoclinic mineral, $Fe_3(PO_4)_2{\cdot}8H_2O$ (Vivianite). When pure it is white, but most samples are greenish-blue due to slight oxidation. Mixing solutions of an iron(III) salt and sodium phosphate gives insoluble yellowish-white iron(III) orthophosphate, $FePO_4{\cdot}2H_2O$ (ferric phosphate), which occurs naturally as various hydrates and from which anhydrous $FePO_4$ may be obtained.**[77]** Both iron(II) and iron(III) salts of hydrogen phosphates are known,**[78]** as well as pyrophosphates. The iron(II) compounds are sensitive toward oxidation. Studies of three-dimensional phosphate networks have been extended to iron arsenate analogues, along with their two- and one-dimensional precursors.**[79]**

4.5 Cyanides

Iron(II) cyanide is obtained as very air-sensitive pale green crystals by carefully heating $(NH_4)_4[Fe(CN)_6]$ to 320 °C in vacuo. Mixing solutions of KCN and iron(II) sulfate (in excess) gives an orange precipitate of uncertain composition. There appears to be no authentic report of iron(III) cyanide; mixing solutions of iron(III) chloride and KCN yields iron(III) hydroxide and HCN. In contrast to the difficulty of obtaining simple iron cyanide salts, the literature on low-spin iron penta and hexacyano complexes is vast (see Section 7).

4.6 Thiocyanates and Azides

Addition of thiocyanate ion to a solution of an iron(III) salt produces a deep bloodred color of $[Fe(H_2O)_5(NCS)]^{2+}$, which is used as a test for iron(III). This reaction has been extensively studied by fast reaction techniques.**[80]** Dark red crystals of $Fe(NCS)_3$ may be obtained by evaporation of ether after extraction of an aqueous solution containing iron(III) and thiocyanate ion; with a large excess of thiocyanate, salts of $[Fe(NCS)_4]^-$ can also be extracted into ether. Recrystallization of $Fe(NCS)_3$ from water affords very soluble red $Fe(NCS)_3{\cdot}3H_2O$. Bright red salts of $[Fe(NCS)_6]^{3-}$ are known, for example, $Na_3[Fe(NCS)_6].12H_2O$, which is soluble in ethanol. Dark red iron(III) azide has a color similar to that of the thiocyanate, and is also a freely soluble salt.

4.7 Formates

Iron(II) formate crystallizes from water as a pale green dihydrate, which loses water in the range 140–150 °C, and undergoes gradual decomposition above 200 °C. It is best prepared by dissolving iron in formic acid, which proceeds smoothly when the mixture is boiled.**[81]**

4.8 Acetates

Anhydrous iron(II) acetate can be obtained by dissolving iron in acetic acid, or in a purer form by reaction of $Fe(CO)_5$ with acetic acid and acetic anhydride in dimethyl formamide. Reaction with pyridine affords**[82]** yellow high-spin $[Fe(O_2CCH_3)_2(py)_2]$. Iron(II) trifluoroacetate can be prepared by photolysis of $Fe(CO)_5$ in $CF_3CO_2H/(CF_3CO_2)_2O$. It presumably contains bridging trifluoroacetate ligands like its manganese analogue.**[83]** Iron(III) forms a series of basic acetates. The complexes $[Fe_3O(O_2CCH_3)_6(L)_3]X$ (L = H_2O, CH_3OH, py, DMF etc, and X = anion) are well characterized, and have a central oxygen atom with a triangular cluster of iron(III) atoms.**[84]** They are easily reduced to $Fe^{II}Fe_2^{III}$ analogs (see Sections 5.5 and 10.3). Commercially, iron(III) acetate is prepared by reacting iron with acetic acid, followed by air oxidation. When boiled, a brown–red basic acetate precipitates, which is used as a mordant in dyeing, for weighting silk and felt, and as a leather colorant.

4.9 Oxalates

Sparingly soluble iron(II) oxalate, $Fe(C_2O_4).2H_2O$ (ferrous oxalate) is precipitated as a yellowish powder on mixing an iron(II) salt solution with one containing an excess of oxalate ion. Its structure is undoubtedly complex, and when heated in the absence of air, pyrophoric iron(II) oxide and/or iron are formed depending on the temperature. Well-characterized iron(II) complexes such as $K_2Fe(C_2O_4)_2{\cdot}2H_2O$ can also be obtained. Pure iron(III) oxalate is difficult to prepare as iron(II) tends to be formed as a result of reduction by oxalate. However, stable iron(III) oxalato complexes are well known – calcium oxalate will dissolve in an iron(III) chloride solution! Green crystals of $K_3[Fe(C_2O_4)_3]{\cdot}3H_2O$ are obtained by hydrogen peroxide oxidation of iron(II) oxalate in the presence of potassium oxalate, or by adding barium oxalate to a solution of potassium oxalate and iron(III) sulfate, followed by filtration to remove barium sulfate, and evaporation.[85] The structure of this six-coordinate anion shows slight trigonal distortion from octahedral symmetry, and as expected, its room temperature–magnetic moment (5.96 BM) is close to the high-spin value. It readily undergoes photochemical reduction with the oxalate ligand being oxidized to carbon dioxide, and is used as a photochemical standard.[86] It loses water to give the anhydrous salt when heated at 120 °C. Fe–O distances in *catena*-$[Fe(\mu\text{-oxalate})(bipy)]_n$ are 2.092(3)–2.162(4) Å,[87] very similar to those in $[Fe(bipy)_3][Fe_2(oxalate)_3]$, where Fe–O = 2.122(2), 2.128(2) Å.[88] Bridging oxalate, and squarate, are particularly effective in transmitting antiferromagnetic coupling between Fe^{3+} ions as much as 5 Å apart. The intramolecular Fe–Fe distance in (**1**) is 7.8 Å, but the nearest intermolecular Fe···Fe distances are 6.6 Å.[89] The bis(ethylenedithio)tetrathiafulvalene compound $[bedt\text{-}ttf][Fe(C_2O_4)_3(H_2O)].PhCN$ was the first molecular superconductor containing a paramagnetic metal ion. It contains alternate layers of bedt-ttf cations and $[Fe(C_2O_4)_3]^{3-}$ anions with associated water and PhCN.[90] The tetrathiafulvalene derivatives $(ttf)_7[Fe(C_2O_4)_3]_2{\cdot}4H_2O$ and $(ttf)_5[Fe(CO_4)_3]{\cdot}2C_6H_5Me{\cdot}2H_2O$ are semiconductors with stacked structures.[91]

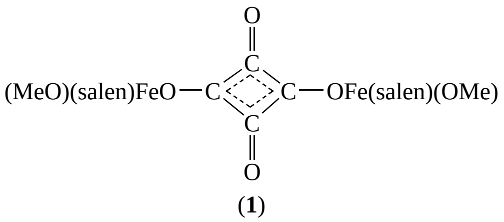

(**1**)

4.10 Citrates

Iron(II) and iron(III) citrates are known but have a poorly defined composition, though octa-iron[92] and nona-iron[93] citrate complexes have been characterized; in solution, complex species exist.[94,95] Brown and green hydrated iron(III) ammonium citrates are commercially available for use as iron supplements in foods. Iron(III) citrate and iron(III) ammonium citrate (Geritol) are used for administering supplementary iron to iron-deficient patients, for inducing iron overload in rats or other creatures prior to testing the efficacy of iron chelators, or for introducing the isotope ^{59}Fe for metabolic tracer studies. There has been a qualitative study of the incorporation of iron into transferrin from iron citrate,[96] which reacts relatively slowly with the aluminium(III)-transferrin complex to give the thermodynamically strongly favored combination of iron(III)-transferrin with aluminium(III) citrate.[97]

4.11 Other Carboxylates

Succinate, fumarate, and gluconate salts and complexes are, like citrates, used in iron supplements.[98] Iron-gluconate complexes are sufficiently stable not to cause iron toxicity (in contrast to Fe^{2+} aq, Fe^{3+} aq, and complexes of low stability) and are safe and effective in hemodialysis;[99] there is information on iron transfer between gluconate and transferrin.[100]

Alkali metal salts of tris-maleato ferrate(III) are high spin; the isomer shifts of their Mössbauer spectra reflect the electronegativity and polarizing power of the cations.[101] Tetraaquabis(hydrogen-maleato)iron(II) is stable to air oxidation as a solid and in aqueous solution.[102] X-Ray diffraction and EXAFS studies of $[Fe^{III}(O_2CCH_2COCH_2CO_2)(H_2O)_2X]$, X = Cl, Br, show the oxodiacetate to be terdentate and planar, giving a *mer* complex with the central ether-O trans to X^-.[103] Humic acid binds Fe^{3+} predominantly or exclusively through carboxylate groups, though there may be a very small amount of ligation by phenolate. Some qualitative observations on stabilities and complex formation and dissociation reactivities are available for humic acid[104] and for fulvic acid.[105] By use of appropriate sterically demanding carboxylates, it is possible to generate four-, five-, and six-coordinated mononuclear iron(III) complexes. Ligand flexibility and electronic properties provide fine-tuning. These complexes are subunits of the models for di-iron(II) sites in metalloproteins.[106]

4.12 Silicates

Iron(II) silicates are widely distributed in nature. Most of the iron in the primary magmatic rocks is in the form of Fe(II) silicates (olivines, pyroxenes, amphiboles, and biotites). When exposed on the Earth's surface, they undergo oxidative hydrolytic weathering to give iron(III) hydroxyoxides such as goethite, the overall stoichiometry being described by equation (1). This form of iron is very insoluble, but subsequent microbial reduction to iron(II) makes it available to the biosphere.

$$Fe_2SiO_4 + \tfrac{1}{2}O_2 + 3H_2O \longrightarrow 2FeO(OH) + H_4SiO_4 \qquad (1)$$

5 OXIDATION STATES AND COORDINATION GEOMETRIES

Compounds of iron in oxidation states from −II (d^{10}) through +VI (d^2) are known though several oxidation states, for example, −I, +I, +V, are rare. This range, and the coordination geometries displayed, are illustrated in Table 5. The most well known are the +II (d^6) and +III (d^5) oxidation states, often referred to as ferrous and ferric iron respectively. The effects of ligand type on the iron(II)/iron(III) redox potential are shown in Figure 4. Although the vast majority of coordination complexes of iron contain the metal in oxidation states two or three, the lower oxidation states of one and zero are not uncommon, especially in areas bordering on organometallic chemistry. Oxidation state four is of relevance to bioinorganic electron transfer systems; oxidation state six is represented by the ferrate(VI) anion, well known but rather little studied. There are many important mixed valence and fractional formal oxidation state compounds (e.g. Fe_3O_4) and complexes of iron.

5.1 Low-oxidation States

Low-oxidation state iron compounds are stabilized by electron acceptor ligands, especially carbon monoxide, isocyanide, and phosphorus donors. The most common coordination geometry encountered in iron compounds is octahedral, but tetrahedral, trigonal bipyramidal, and square pyramidal are also represented. There are only a few compounds with iron in the −II state, although reduction of $[Fe(CO)_5]$ with sodium amalgam in THF affords pale yellow $Na_2[Fe(CO)_4]$, in which the anion is tetrahedral.**[107]** The stabilities of iron(−I) in water and in liquid ammonia have been assessed based on an electrostatic model.**[108]**

Reduction of common iron(II) coordination complexes that have ligands which can accommodate some electron density from the metal can give moderately stable low-oxidation state compounds. For example, reduction of red $[Fe(bipy)_3]^{2+}$ with alkali metal gives black $[Fe(bipy)_3]$, but without full characterization, care is needed when assigning oxidation states in complexes that involve ligands which can exist as coordinated radical species. With extensively delocalized ligands, particularly diimines, and macrocycles like phthalocyanines and porphyrins, reduction at the ligand can take place as well as at the metal center, and thus there is often ambiguity in assigning oxidation states for complexes of ligands with strong π-interactions. Thus, the substitution-inertness of the 1-, 2-, and 3-electron reduction products of $[Fe(diimine)_3]^{2+}$, diimine = bipy (**2**), phen (**3**), or bipym (**4**), and their spectroscopic properties, argue for their representation as iron(II) complexes containing one, two, or three anion radical ligands rather than as complexes of iron(I), iron(0), and iron(−I).**[109]** Similar comments apply to the $[Fe(bmpphen)_2]^+$ and $[Fe(bmpphen)_2]^0$ species from electroreduction of $[Fe(bmpphen)_2]^{2+}$, bmpphen = 2,9-bis(2-methoxyphenyl)-1,10-phenanthroline, (**5**).**[110]** In similar vein, it is now apparent that for the iron complex produced in the long-established ‘Brown Ring Test’, the formulation Fe^{III}-NO^- is to be preferred to Fe^I-NO^+ (see Section 44.3.8).

The iron(0) complex $[Fe(CN)_4]^{4-}$ has been isolated as its Cs^+ salt.**[111]** Iron(0) complexes may also be represented

Table 5 The oxidation states and geometries of iron complexes

Oxidation State	Electronic Configuration	Coordination Number	Complex Geometry	Example
−II	d^{10}	4	Tetrahedral	$[Fe(CO)_4]^{2-}$
0	d^8	5	Trigonal bipyramidal	$[Fe(CO)_3(PPh_3)_2]$
I	d^7	5	Square pyramidal	$[Fe(dppe)_2H]$
II	d^6	4	Tetrahedral	$[FeBr_2(PPh_3)_2]$
		5	Trigonal bipyramidal	$[FeBr(Me_6tren)]^+$
		5	Square pyramidal	$[Fe(ClO_4)(OAsMe_3)_4]^+$
		6	Octahedral	$[Fe(phen)_3]^{2+}$
		7	Pentagonal bipyramidal	$[Fe(HPAP)(H_2O)_2]^{2+}$
		8	Dodecahedral	$[Fe(1,8\text{-}naph)_4]^{2+}$
III	d^5	3	Trigonal	$[Fe\{N(SiMe_3)_2\}_3]$
		4	Tetrahedral	$[FeCl_4]^-$
		5	Square pyramidal	$[FeCl(dtc)_2]^{2-}$
		5	Trigonal bipyramidal	$[Fe(N_3)_5]^{2-}$
		6	Octahedral	$[Fe(phen)_3]^{3+}$
		7	Pentagonal bipyramidal	$[Fe(edta)(H_2O)]^-$
		8	Dodecahedral	$[Fe(NO_3)_4]^-$
IV	d^4	4	Tetrahedral	$[Fe(1\text{-}norbornyl)_4]$
		6	Octahedral	$[Fe(diars)_2Cl_2]^{2+}$
V	d^3	4	Tetrahedral	$FeO_4{}^{3-}$
VI	d^2	4	Tetrahedral	$FeO_4{}^{2-}$

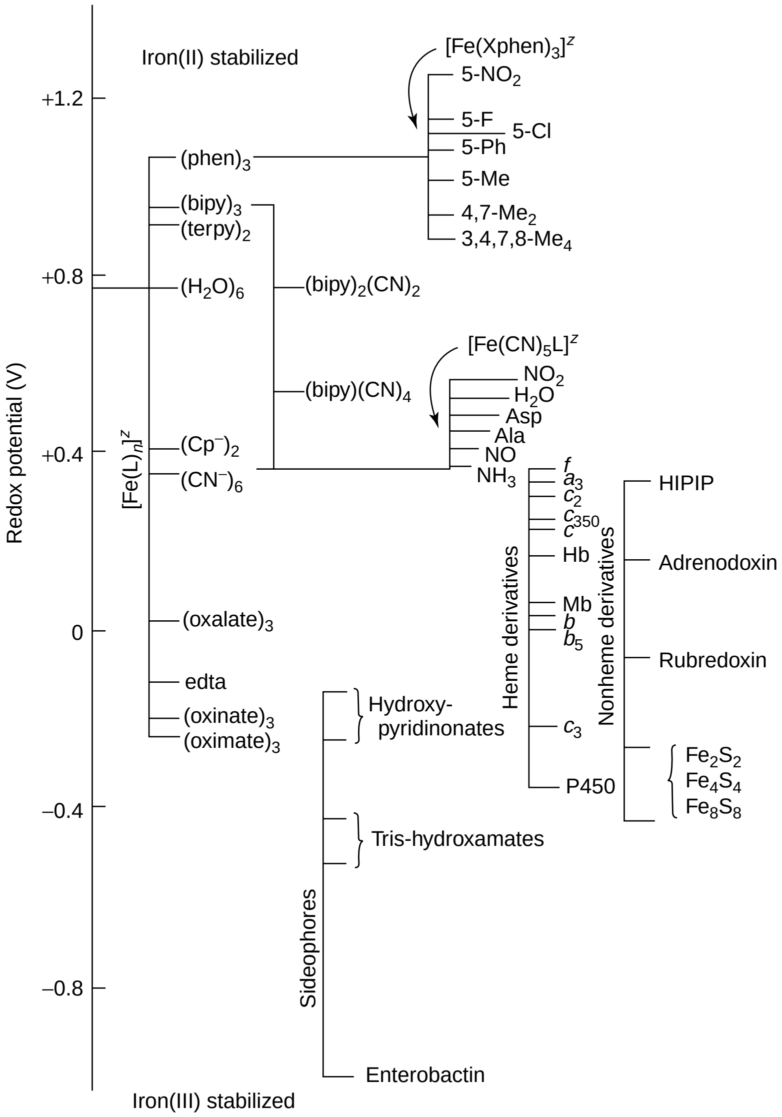

Figure 4 Schematic representation of the range of redox potentials covered by iron(II)/(III) complexes in aqueous media

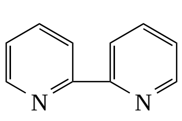
(**2**)

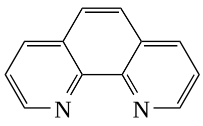
(**3**)

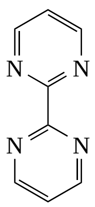
(**4**)

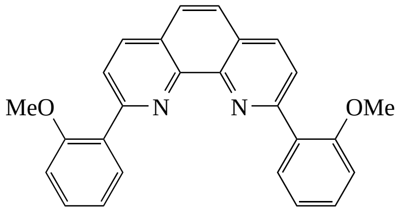
(**5**)

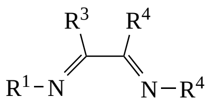
(**6**)

by the diazabutadiene complex [Fe(dab)$_2$], dab = (**6**).[112] Iron(I) complexes are not common, though a number of more or less transient species have been generated by electrochemical or radiolysis techniques, and a small number of stable compounds have been characterized. Thus, an iron(I) catenate has been described,[113] and a series of trigonal bipyramidal [FeCl(dppe)$_2$] (dppe = 1,2-bis(diphenylphosphino)ethane) iron(I) complexes have been reported.

Whereas in many metalloprotein redox systems the oxidation states +II, +III, and +IV are involved, horseradish peroxidase catalysis appears to involve five oxidation states. The interest to coordination chemists of this study goes well beyond bioinorganic systems, for here, as in several cases reported earlier, the X-rays used to obtain the high-resolution structures induced chemical changes during structure determination. The X-rays liberate electrons, which may change the oxidation state of the metal.[114]

5.2 Iron(II) Complexes

The +II oxidation state of iron has a d^6 electronic configuration, and is one of the two most important, iron(III) being the other (d^5). Most iron(II) complexes have an octahedral geometry, although there are examples of four-, five-, and even eight-coordination. The iron(II) $^5D_2$ ground state is split in an octahedral crystal field into $^5T_{2g}$ and ^5E_g states. High-spin octahedral iron(II) complexes have magnetic moments of about 5.2 BM. The one spin-allowed d-d transition is the broad $^5T_{2g}$ to ^5E_g absorption in the visible/near infrared. Thus, $[Fe(H_2O)_6]^{2+}$ is pale green with an absorption at 10 400 cm^{-1} (and a shoulder at about 8300 cm^{-1}, most likely due to a Jahn–Teller effect in the excited state). With high-field ligands such as aromatic nitrogen donors, low-spin iron(II) complexes result, whose spectra are often dominated by an intense metal to ligand charge-transfer band. Their magnetic moments are typically about 1 BM due to a temperature-independent paramagnetic contribution. The magnetism of some six-coordinate complexes, for example, $[Fe(phen)_2X_2]$, is markedly temperature dependent changing sharply from about 1.5 BM to about 5.1 BM. This spin-crossover phenomenon is well documented, and discussed in Section 6.[115]

Tetrahedral iron(II) complexes are high-spin, with magnetic moments rather higher than predicted for four unpaired electrons due to orbital contributions. The ^5E to$^5T_2$ transition normally occurs at about 4000 cm^{-1}, and magnetic moments are usually in the range 5.0–5.2 BM. Iron(II) chloride in the presence of excess chloride ion and a large cation gives salts of the tetrahedral anion $[FeCl_4]^{2-}$. Other tetrahedral complexes include $[Fe(OPPh_3)_4]^{2+}$, $[Fe\{OP(NMe_2)_3\}_4]^{2+}$, and the iron(II) centers in rubredoxins with four sulfur donor ligands. Many tetradentate macrocycles, including phthalocyanines and porphyrins, form square-planar iron(II) complexes, which often have an intermediate spin ($S = 1$) ground state. These complexes readily acquire additional axial ligands to form six-coordinate complexes, which are frequently low spin. The coordination of dioxygen (and carbon monoxide) is of enormous biological importance in respiration, involving heme systems such as hemoglobin and myoglobin. Although once rare, there are now several examples of five-coordinate iron(II) complexes derived from a tetracoordinate macrocycle with the fifth site occupied by a halide ion. Complexes of tripod ligands such as $[Fe(halide)\{N(CH_2CH_2PPh_2)_3\}]^+$ are examples of five-coordinate iron(II) complexes. High- and low-spin complexes are known with such tripod ligands, as well as with some displaying spin-crossover behavior.[116] Coordination numbers higher than six are unusual for iron(II), but seven coordination is known in several macrocyclic complexes, and eight-coordinate red–orange $[Fe(1,8\text{-naphthyridine})_4]^{2+}$ has a distorted dodecahedral geometry.[117]

5.3 Iron(III) Complexes

Most iron(III) complexes are octahedral. In simple complexes, such as red $[Fe(acac)_3]$, the d^5 center is usually high-spin, with magnetic moments close to the expected 5.9 BM (sS). The affinity of iron(III) for amine ligands is not high, but this is not the case for oxygen donors, and often, bridged species are formed, in which there is antiferromagnetic coupling between the iron atoms. In μ-oxo dimers such as $[\{Fe(salen)\}_2O]$ (5-coordinate), $[\{Fe(porphyrin)\}_2O]$ (5-coordinate), and $[(FeCl_3)_2O]^{2-}$ (4-coordinate), it is sufficient for the magnetic susceptibility to be lowered to less than 2 BM/iron atom. This tendency to form bridged complexes extends to sulfur species, many of which are biologically relevant. However, monomeric five-coordinate complexes such as $[Fe(S_2CNR_2)_2X]$ have three unpaired electrons. Little is known about the d-d transitions of iron(III) because their UV/visible spectra are swamped by edges of intense ultraviolet charge-transfer bands, even simple iron(III) salts in water are yellow. Complexes with very high-field ligands are low spin, for example, $[Fe(phen)_3]^{3+}$ and $[Fe(CN)_6]^{3-}$, and they have higher than predicted magnetic moments due to large orbital contributions that decrease at lower temperatures (typically to about 1.9 BM at 77 K). While iron(III) complexes are usually kinetically labile, the low-spin complexes can be quite inert. Several examples of iron(III) species display spin-crossover phenomenon, for instance, a variety of trigonally distorted octahedral dithiocarbamate complex, $[Fe(S_2CNR_2)_3]$, can be high spin or low spin depending on temperature.

5.4 Higher Oxidation States

There are few simple compounds in which iron has an oxidation state higher than three, though a number of species containing iron(IV), iron(V), or iron(VI) have been characterized. There appears to be no example of iron(VII), but iron(VIII) has been claimed[118] as a disproportionation product of ferrate(VI), $FeO_4{}^{2-}$. Oxidizing anions containing the +IV, +V, and +VI oxidation states are known; Fe–O bond distances are 1.889, 1.807, 1.720, and 1.647 Å in the $Fe^{III}O_4{}^{5-}$, $Fe^{IV}O_4{}^{4-}$ $Fe^{V}O_4{}^{3-}$, and $Fe^{VI}O_4{}^{2-}$ anions.[119] Deep red/purple salts containing discrete tetrahedral $Fe^{VI}O_4{}^{2-}$ units are obtained by anodic oxidation of iron, or by hypochlorite oxidation of freshly precipitated iron(III) hydroxide. Potassium ferrate(VI), K_2FeO_4, is water soluble and fairly stable at high pH. It is a more powerful oxidant than permanganate ($E^o \sim 2V$), and has been used in organic oxidations.[120] Strongly heating appropriate hydroxides affords the mixed oxides Sr_2FeO_4 and Ba_2FeO_4, which contain Fe^{IV} but not discrete anions; structural, electronic, and magnetic properties have been established for Ba_2FeO_4 and for Ba_3FeO_5.[121]

Low-spin green/black $[\mathrm{Fe^{IV}(diars)_2X_2}]^{2+}$ is obtained by concentrated nitric acid oxidation of $[\mathrm{Fe^{III}(diars)_2X_2}]^{+}$. It is a rather unstable d^4 complex with a large temperature-independent Mössbauer quadrupole splitting ($\sim$3.2 mms^{-1}), consistent with a *trans*-structure. Intensely colored $[\mathrm{Fe^{IV}(S_2CNEt_2)_3}]^{+}$ is obtained by mild oxidation (with iodine!) of the corresponding iron(III) complex.[122] Mössbauer chemical shifts of 0.1–0.2 mm s^{-1} and quadrupole splittings of 2.0–2.5 mm s^{-1} have been reported for tris-dithiocarbamatoiron(IV) complexes of this type, consistent with a low-spin configuration (3.2–3.4 BM) in a slightly distorted environment. Iron(IV) is also stabilized by, for example, amido-tetraazamacrocyclic[123] and triamidoamine[124] ligands. Both iron(IV) and iron(V) are stabilized by certain porphyrin ligands,[125] for example, octafluoroporphyrin,[126] and by the tetranegative S,N,N,S-donor ligand $(^-\mathrm{S})\mathrm{C_6H_4(N^-)CH_2CH_2(N^-)C_6H_4S^-}$.[127] Intermediates containing $\mathrm{Fe^V=O}$ are believed to be involved in Gif-type hydrocarbon oxidations by O_2 or H_2O_2 catalyzed by iron complexes such as picolinates.[128]

5.5 Mixed Oxidation State Complexes

Mixed oxidation complexes containing iron(II) and iron(III) are fairly common and examples of both localized and delocalized oxidation states are known. Certainly the oldest and perhaps the most extensively studied is $\mathrm{Fe_4{}^{III}[Fe^{II}(CN)_6]_3\cdot 14H_2O}$, Prussian Blue, whose structure has been reported and oxidation state delocalization extensively probed (see Section 7.1). Mixed oxidation state clusters of the type $[\mathrm{Fe_3O(RCO_2)_6L_3}]$, with two iron(III) and one iron(II) centers, have sharp transitions between phases composed of electron localized and delocalized complexes, which are affected by molecules of crystallization. The behavior of these complexes is also complicated by numerous phase transitions. Most phases have localized oxidation states at low temperatures that become delocalized at room temperature. Other solid-state mixed oxidation–state complexes include the oxoferrate $\mathrm{Na_9[Fe^{II}O_3][Fe^{III}O_4]}$;[129] spinel systems $\mathrm{M}_x\mathrm{Fe}_{3-x}\mathrm{O}_4$, which with $x < 0.5$ have magnetite characteristics but those with $x > 0.6$ are semiconductors implying localization of the Fe(II) state.[130] The mixed oxidation state fluoride $\mathrm{Fe_2F_5}$ is referred to in Section 4.1.1. Electrochemical, homogeneous chemical redox reactions, EPR, and Mössbauer spectroscopy established[131] the series Fe(III)Fe(III), Fe(III)Fe(II), and Fe(II)Fe(II) can be derived from the compound $[\mathrm{C_6H_4(CH_2S)_2Fe^{III}(S)_2Fe^{II}(SCH_2)_2C_6H_4}]^{3-}$.

6 SPIN STATES AND SPIN CROSSOVER

For iron(II), the two spin states are high-spin ($^5\mathrm{T}_2$; $S = 2$) and low-spin ($^1\mathrm{A}_1$; $S = 0$), and for iron(III), the common spin states are high-spin ($^6\mathrm{A}_1$; $S = {}^5/_2$) and low-spin ($^2\mathrm{T}_2$; $S = {}^1/_2$). The intermediate spin state of $^3/_2$ is known for a number of iron(III) complexes, for example, of porphyrins. The mixed spin state $S = {}^3/_2, {}^5/_2$ has been observed,[132] and even $S = 2$ ($S = {}^3/_2, {}^5/_2$ coupled) in a peroxo-μ-oxodi-iron(III) complex.[133] Values of S as high as 10 and 11, for $\mathrm{Fe_8}$ and $\mathrm{Fe_{10}}$ complexes, have been reported.[134] Spin-crossover complexes exist both for iron(II) and for iron(III). The spin-crossover phenomenon is of intrinsic interest and potential practical importance. The marked magnetic and optical[135] changes associated with low-spin/high-spin changeover make spin-crossover compounds strong candidates for controlling molecular switching,[136] and thermal hysteresis confers memory possibilities. Applications in temperature sensors, optical switching, information storage and retrieval, and memory devices[137] will be optimized by the use of polymeric species, where interactions and cooperation magnify the desired effects.[138] Density functional calculations for high-spin and low-spin forms of nine iron(II) complexes, including the familiar $[\mathrm{Fe(phen)_2(NCS)_2}]$ and several bis-ligand complexes of terdentate ligands such as tris(2-pyridylmethyl)amine and tris(1-pyrazolyl)methane have been reported.[139] A short general review[141] of crystal structures, magnetic properties, and Mössbauer and vibrational spectroscopy of iron(II) spin-crossover complexes,[140] and a review covering the design and synthesis of such complexes, are available.[142] Spin crossover is determined by temperature, pressure, and by ligand field strengths, which can be tuned by ligand variation. A review of structural changes accompanying spin-state transitions summarizes information on a range of $\mathrm{Fe^{2+}}$ and $\mathrm{Fe^{3+}}$ complexes, after detailing the important case of $[\mathrm{Fe(2\text{-}pic)_3}]\mathrm{Cl_2\cdot CH_3OH}$ (2-pic = 2-(aminomethyl)pyridine).[143]

Spin-crossover kinetics for Fe(II) complexes have been reviewed,[144] and enthalpies, entropies, and rate constants for a range of Fe(II) and Fe(III) spin-crossover complexes documented.[145] Thermodynamic and kinetic parameters, iron-ligand bond distance and volume changes, and calorimetric data relating to the low-spin/high-spin transition in solution and in the solid state obtained prior to 1991 have been fully documented and discussed.[146] A selection of thermodynamic and kinetic parameters for the spin-crossover complexes of 2-(2-pyridyl)imidazole (pyim) and N-(2-pyridylmethyl)picolinamidine (ppa),[147] tetrakis(2-pyridylmethyl)-*trans*-1,2-cyclohexanediamine (tpchxn),[148] 3-(1,10-phenanthrol-2-yl)-5-methyl-1,2,4-oxadiazole (phenmethoxa),[149] and 1,4,7-triazacyclononane (tacn)[150] in various solvents are given in Table 6. Activation parameters are primarily determined by the ease with which the ligands can twist, thus the hexadentate ligands (**7**) cause considerable impediments to the movement required for spin change. The ease of twisting may be determined by solvation effects as much as by intrinsic rigidity of the complex itself.[151] The effect of solvent of crystallization on the ease of spin-state transitions has been explored, by high-resolution deuterium NMR spectroscopy,

Table 6 Thermodynamic and kinetic parameters for low-spin $\rightleftharpoons$ high-spin [$^1A_1 \rightleftharpoons {}^5T_2$] crossover in solution

		ΔV° ($cm^3\,mol^{-1}$)	$\Delta V^\ddagger_{15}$ ($cm^3\,mol^{-1}$)	$\Delta V^\ddagger_{51}$ ($cm^3\,mol^{-1}$)	ΔH° ($kJ\,mol^{-1}$)	$\Delta H^\ddagger_{15}$ ($kJ\,mol^{-1}$)	$\Delta H^\ddagger_{51}$ ($kJ\,mol^{-1}$)	ΔS° ($J\,K^{-1}\,mol^{-1}$)	$\Delta S^\ddagger_{15}$ ($J\,K^{-1}\,mol^{-1}$)	$\Delta S^\ddagger_{51}$ ($J\,K^{-1}\,mol^{-1}$)
$Fe(pyimH)_3{}^{2+}$	MeOH/ 20% MeCN	+5.3	0.0	−5.3	15.5	26.7	11.2	+53	−23	−75
	MeCN	+14.3	+8.9	−5.4	32.3	46.6	14.3	+102	+41	−61
	Me_2CO	+10.3	+4.9	−5.4	15.9	32.0	16.1	+49	−7	−56
$Fe(ppa)_2{}^{2+}$	Me_2CO	+8.7	+2.6	−6.1	20.3	33.7	13.4	+52	−18	−70
$Fe(tpchxn)^{2+}$	MeCN	+11.5	+5.4	−6.1	24.2	26.0	1.8	+75	−27	−102
$Fe(phenmethoxa)^{2+}$	Me_2CO	+12.3	+3.9	−8.4	23.8	32.6	8.8	+94		
$Fe(tacn)_2{}^{2+}$	D_2O				23			+67		
	CD_3CN				21			+66		
	$(CD_3)_2CO$				24			+73		
	$(CD_3)_2SO$				22			+68		

Note: Ligand abbreviations are defined in the text.

for polymeric [Fe(1,2,4-triazole)$_3$](ClO_4)$_2$.$n$$D_2O$ and its 4-amino derivative.[152] An unusual application of isokinetic relationships has been to spin-crossover systems, especially of Fe(II) complexes.[153]

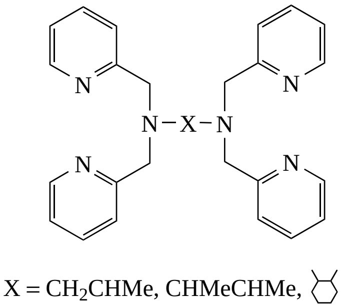

(**7**)

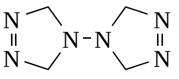

(**8**)

Activation volumes for spin crossover are generally between 0 and $+10\,cm^3\,mol^{-1}$ for low spin → high spin, and close to $+6\,cm^3\,mol^{-1}$ for the reverse, for a range of tris-diimine (e.g. 2-pyridylimidazole), bis-terimine, and hexadentate linked-bis-terimine complexes. The derived volume profiles indicate that transition states are approximately midway between initial and final states.[154] X-ray absorption spectroscopy (XANES) can give useful information on structural changes associated with pressure-induced spin crossover, as was demonstrated for a selection of well-established 'traditional-crossover' systems, such as [Fe(phen)$_2$(NCS)$_2$], and other spin-crossover complexes. Increasing the pressure on a high-spin sample of the hydrate or ethanol solvate of [Fe(pic)$_3$]Cl_2 involves iron-ligand and hydrogen-bonding distance changes. Pressure effects sometimes show that a change in spin state is not a single simple process. Thus, increasing the pressure applied to high-spin [Fe(btrz)$_2$ (NCS)$_2$], where btrz = 4,4′-bis-1,2,4-triazole (**8**), produces a second high-spin modification before the change to the low-spin state.[155] The *cis*-1,2-bis(diphenylphosphino)ethene complexes [Fe($Ph_2PCH{=}CHPPh_2$)$_2$$X_2$], X = Cl or Br, undergo pressure-induced spin-state transitions at about 8 kbar and about 60 kbar respectively.[156] Several iron complexes are mentioned in a review of pressure effects on spin crossover and associated effects on electronic spectra.[157]

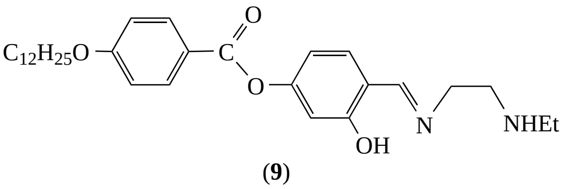

(**9**)

The NO_3^- and PF_6^- salts of the iron(III) complex of the terdentate phenolate anion of the liquid crystal Schiff base (**9**) provide the first example of the coexistence of spin transition and liquid crystal properties in a single compound. The ligand needs to be tuned to increase the spin-crossover transition temperature and decrease the transition temperature to the liquid crystal state.[158]

A unique type of spin-crossover behavior is claimed for the mixed-valence dithiooxalate salt $^nPr_4N[Fe^{II}Fe^{III}\,(dto)_3]$.[159] Here, the spin change is associated with electron transfer, equation (2), with the bridging dithiooxalate favoring Fe^{III}–S bonding at higher temperatures, Fe^{III}–O bonding at lower temperatures:[160]

$$(dto)_2Fe^{II}(S_2C_2O_2)Fe^{III}(dto)_2 \underset{110\,K}{\overset{120\,K}{\rightleftharpoons}} (dto)_2Fe^{III}(S_2C_2O_2)Fe^{II}(dto)_2 \tag{2}$$

7 CYANIDE COMPLEXES

7.1 Hexacyano Complexes

Iron forms exceptionally stable complexes with cyanide ion. Hexacyanoferrate(II), $[Fe(CN)_6]^{4-}$, the ferrocyanide anion, is readily formed[161] ($\Delta H^0 = -358.9\,kJ\,mol^{-1}$) upon the addition of excess cyanide to solutions containing $[Fe(H_2O)_6]^{2+}$. Red hexacyanoferrate(III), $[Fe(CN)_6]^{3-}$, the ferricyanide anion, is readily prepared by oxidation of the corresponding Fe(II) species by chlorine. The iron(III) complex is both more toxic and more labile in terms of ligand substitution than its iron(II) analog. Both $H_4[Fe(CN)_6]$ and $H_3[Fe(CN)_6]$ are known. The Fe–C bond is 0.03 Å shorter in the iron(II) complex (1.92 Å) despite its larger size, due to enhanced π-bonding in the +2 oxidation state ion. The cyanide ion is capable of bridging metal centers, and polymeric transition metal cyanides are well known; many salts of the hexacyanide complexes involve M-N coordination. The Prussian and Turnbull Blues are important examples. Often cited as the first isolated coordination complex,[162] Prussian Blue (PB) is produced (Diesbach, 1704) as a voluminous dark blue precipitate when an excess of an iron(III) salt reacts with $[Fe(CN)_6]^{4-}$. Turnbull's Blue results from the reaction of excess iron(II) with $[Fe(CN)_6]^{3-}$. Only recently was there a claim[163] for the first characterization of authentic Turnbull's Blue, a valence-trapped (Robin and Day Class I[164]) compound. The intense coloration and lightfastness of PB and its family of complexes has led to a long history of exploitation as pigments, the more common examples are listed in Table 7. More recently however, their electrochemical properties in the form of thin films have attracted attention[165] – PB is photoswitchable.[166] The PB family share similar structures in which well-defined octahedral cyanide coordination sites are bridged by cyanide in a cubic array. The individual iron atoms may be iron(II) (low-spin) with Fe–C bonds, or iron(III) (high-spin) with Fe–N bonds, and intense colors arise from electron transfer from the ferrocyanide ground

Table 7 The Prussian Blue family

Trivial Name	Idealized formula	Reference
Soluble Prussian Blue	$KFe^{III}[Fe^{II}(CN)_6]$	*a*
Insoluble Prussian Blue	$Fe_4^{III}[Fe^{II}(CN)_6]_3$	*a*
Prussian Brown and Berlin Green	$Fe^{III}[Fe^{III}(CN)_6]$	*b,c,d*
Prussian Green	$KFe_3{}^{III}[Fe^{II}(CN)_6][Fe^{III}(CN)_6]_2$	*b,c*
Prussian White and Everitt's salt	$K_2Fe^{II}[Fe^{II}(CN)_6]$	*b*

Note: [a]D. Davidson, *J. Chem. Educ.*, 1937, **14**, 277. [b]J. F. De Wet and R. Rolle, *Z. Anorg. Allg. Chem.*, 1965, **336**, 96. [c]P. Ellis, M. Eckhoff and V. D. Neff, *J. Phys. Chem.*, 1981, **85**, 1225. [d]N. V. Sidgwick, ''The Chemical Elements and Their Compounds'', Oxford University Press, London, 1958, 1339.

state. When both iron environments contain only iron(II), the resulting salt is not colored (Prussian White). The oxidation state localization in PB has been studied extensively.**[167]** Structures, electrochemical behavior (electrodes; batteries), and uses in medicine (treatment of ^{137}Cs and of thallium poisoning) of Prussian Blue are mentioned in a review of cyanide complexes.**[168]** In cobalt–iron Prussian Blue analogues, $Na_xCo_yFe(CN)_6{\cdot}zH_2O$ electronic and spin states are controlled by temperature and the ligand field strength around the Co^{2+} ions, which in turn is determined by the Co:Fe ratio.**[169]**

Solubility data (pK_{sp}) for two dozen hexacyanoferrate(II) and hexacyanoferrate(III) salts, and Pourbaix (pe/pH) diagrams for several multicomponent, iron–cyanide-containing systems, are given in a review ostensibly dedicated to hydrometallurgical extraction of gold and silver.**[170]** Kinetics of hexacyanoferrate(II) reductions and hexacyanoferrate(III) oxidations, and of hexacyanoferrate(II)/(III) electron exchange, have been intensively studied for several decades,**[171]** often as a probe of medium effects.**[172]** Pressure effects on the kinetics of the $[Fe(CN)_6]^{3-}/[Fe(CN)_6]^{4-}$ reaction have been studied in solution and at electrodes,**[173]** while factors controlling electron diffusion in electroactive polymer films have been probed by studying the dynamics of incorporated $[Fe(CN)_6]^{3-}/[Fe(CN)_6]^{4-}$.**[174]**

Hexacyanoferrate(II). $K_4[Fe(CN)_6]$ has been used to photosensitize TiO_2.**[175]** The acidity constants for $H_4[Fe(CN)_6]$ are $pK_1 = 2.54$, $pK_2 = 1.08$, $pK_3 = 2.65$, $pK_4 = 4.19$.**[176]** Association constants have been published for alkali metal cations ion pairing with hexacyanoferrate(II).**[177]** Substitution at hexacyanoferrates(II) is very difficult, though it can be catalyzed by metal ions such as Hg^{2+}. Such catalysis can be augmented by surfactants such as sodium dodecyl sulfate (SDS), and indeed SDS-catalysis of Hg^{2+}-catalyzed replacement of cyanides in $[Fe(CN)_6]^{4-}$ by 1,10-phenanthroline has been proposed as an analytical method for the determination of mercury.**[178]**

Hexacyanoferrates(III). These are of particular interest as pigments and in relation to kinetics and mechanisms of intramolecular electron transfer. The structure of $Bi[Fe(CN)_6]{\cdot}4H_2O$ has been elucidated,**[179]** and $Ce[Fe(CN)_6]{\cdot}5H_2O$ and $Gd[Fe(CN)_6]{\cdot}4H_2O$ studied by X-ray crystallography and Mössbauer spectroscopy.**[180]**

7.2 Pentacyano Complexes

A convenient synthesis of the aquapentacyanoferrate(II) ion, $[Fe(CN)_5(H_2O)]^{3-}$, which is a good starting point for many $[Fe(CN)_5L]^{3-}$ complexes, involves reduction of nitroprusside in the presence of ammonia, equation (3), and hydrolysis of the resulting complex at room temperature.**[181]** The iron(II) complex is best formed in the presence of a small amount of ascorbic acid, which prevents oxidation to iron(III).

$$[Fe(CN)_5NO]^{2-} + 2NH_3 + OH^- \longrightarrow [Fe(CN)_5NH_3]^{3-} + N_2 + H_2O \qquad (3)$$

Photolysis of $[Fe(CN)_6]^{4-}$ in aqueous solutions yields some $[Fe(CN)_5(H_2O)]^{3-}$, but both this synthesis and the route via reduction of nitroprusside ions also result in the formation of dimeric species. Two of the observed species are the complex ions $[Fe_2(CN)_{10}]^{6-}$ and $[Fe_2(CN)_{11}]^{7-}$. The former is thought to contain an aqua ligand and a linear cyanide bridge.**[182]** There have been numerous studies of the kinetics of ligand replacement in $[Fe(CN)_5L]^{n-}$ complexes. For the most part, these reactions involve dissociative rate limiting ligand loss, which is accompanied by large positive entropies of activation and volumes of activation. Both the strength of the iron-ligand bond and solvation effects are important in these reactions since they contribute significantly to the volume of activation.**[183]** The electronic spectra of the pentacyano complexes contain a L $\rightarrow$ Fe charge-transfer band, which along with ligand pK_a values has been used to assess the relative contributions of σ- and π-bonding to the linkage. The marked solvatochromism of these charge-transfer bands has been suggested as a probe for selective solvation.**[184]**

7.3 Carbonyl Cyanides

It has been known since the nineteenth century that hexacyanoferrates(II) react with concentrated sulfuric acid to give carbon monoxide; the concurrent formation of $[Fe(CN)_5(CO)]^{3-}$ was reported**[185]** in 1913. Conversion of coordinated –CN into –CO probably proceeds through $–CONH_2$.**[186]** The stereospecific formation of *fac*-$[Fe(CN)_3(CO)_3]^-$ then *cis*-$[Fe(CN)_4(CO)_2]^{2-}$ from $[Fe(CO)_4I_2]$, as well as the stereospecific production of *trans*-$[Fe(CN)_4(CO)_2]^{2-}$ from iron(II) chloride plus cyanide in an atmosphere of CO, appears to be under kinetic control. *cis*-$[Fe(CN)_4(CO)_2]^{2-}$ decomposes rapidly in aqueous solution, whereas the *trans* isomer, first reported in 2001,**[187]** decomposes relatively slowly. *fac*-$[Fe(CN)_3(CO)_3]^-$ and *cis*-$[Fe(CN)_4(CO)_2]^{2-}$ have infrared-spectra characteristics of their C_{3v} and C_{2v} geometries; their carbonyl stretching frequencies are somewhat solvatochromic.**[188]** The presence of both cyanide and carbonyl bonded to iron is a feature of iron–nickel and iron-only hydrogenases.**[189]** The limiting member of the carbonyl cyanide series is the hexacarbonyl anion $[Fe(CO)_6]^{2+}$, long elusive but eventually prepared and characterized as its $[SbF_6]^-$ and $[Sb_2F_{11}]^-$ salts.**[190]**

8 COMPLEXES WITH NITROGEN DONORS

8.1 Monodentate Ligands

Iron(II) and iron(III) form important series of complexes with a variety of nitrogen-donor ligands, ranging from nitric oxide, azide,**[191]** and ammonia, through mono-, bi-, and polydentate amines, diimines (Section 8.2), and a range of tetraaza-macrocycles to phthalocyanines and porphyrins. However, the tendency of iron(III) to complex with ammonia or simple amines is rather low, while many iron(II) complexes are high-spin and susceptible to oxidation. Relative stabilities of the +2 and +3 oxidation states are markedly ligand-dependent (Figure 4). Ligands with two or more nitrogen-donor sites, such as azide,**[192]** pyrazine,**[193]** or 4,4′-bipyridyl can act as bridging ligands, to give binuclear complexes or infinite layers or 3-D structures. Thiocyanate (see Section 4.6) generally prefers to bond to iron through nitrogen, but can bridge pairs of iron atoms, as in the *trans*-1,2-bis(4-pyridyl)ethene complex $[Fe(bpe)_2(NCS)_2]$.MeOH, which is a supramolecular coordination polycatenane consisting of two interpenetrating 2-D networks.**[194]** Dinitrogen itself is reluctant to complex with iron, though diphosphine ligands help to stabilize iron-dinitrogen complexes, of iron(II), iron(I), and iron(0).**[195]** Dinitrogen is end-on (σ; η^1) bonded both in the octahedral $[Fe^{II}Cl(N_2)(depe)_2]^+$ anion**[196]** and in the trigonal bipyramidal $[Fe^0(N_2)(depe)_2]$.**[197]** Dinitrogen can also act as a bridging ligand, as in $[(OC)_2(Et_3P)_2Fe^0(\mu\text{-}N_2)Fe^0(PEt_3)_2(CO)_2]$.**[198]**

8.1.1 Nitric Oxide Complexes

General. Nitric oxide readily forms complexes with transition metals and is in many ways similar to carbon monoxide. It has a single electron in a π^* antibonding electron, which is easily lost. When NO is not bridging, molecular orbital theory would predict a linear M-NO$^+$ moiety and that M-NO$^-$ would be bent. In principal, this would seem to allow a ready indication of the metal oxidation state from an X-ray structure or even examination of the infrared spectrum of the complex. The reality is frequently more complex and it is difficult to assign a formal oxidation state to many iron nitric oxide complexes. A scheme of corrections to the observed NO stretching frequencies has been proposed and, by taking account of the atomic number and coordination number of the metal, the other ligands present in the complex, and its overall charge, it has been possible to predict the geometry of the M-NO group with more accuracy.**[199]**

Binary Nitric Oxide Complexes. A binary iron nitrosyl complex is not known, although described in early reports as $[Fe(NO)_4]$, the compound having that stoichiometry is a dimer with an N_2O_2 bridging ligand (**10**).

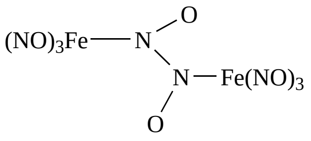

(**10**)

The chloride dimer $[Fe(NO)_2Cl]_2$ also exists, and can be reduced in THF solution to '$Fe(NO)_2$', which is most likely $[Fe(NO)_2(THF)_n]$. The brown color of the familiar, so-called, Brown Ring Test for nitrate in which the sample is treated with ferrous sulfate and sulfuric acid is due to the formation of the nitric oxide complex $[Fe(H_2O)_5NO]^{2+}$.

Nitroprusside. The action of nitric acid or sodium nitrite on $[Fe(CN)_6]^{4-}$ generates sodium nitroprusside, $Na_2[Fe(CN)_5NO]\cdot 2H_2O$, perhaps the best-known transition metal nitrosyl complex. Barium chloride is added to the hot reaction mixture and HCN removed in a stream of carbon dioxide to give the overall reaction shown in equation (4). The red sodium salt dissolves readily in water and alcohol, and aqueous solutions decompose in light. Several of the low-spin salts show a tendency toward high-spin at very high pressures. The X-ray photoelectron spectrum of the nitroprusside ion indicates a positive charge on NO of +0.35; whilst this is consistent with the Mössbauer spectrum and the short Fe–N bond (1.63 Å), one might expect a higher charge considering the N–O bond length (1.13 Å), Fe–N–O angle of 180° and NO stretching frequency (1947 cm^{-1}). $[Fe(CN)_5NO]^{2-}$ can be reduced, for example, by sodium in liquid ammonia, to form $[Fe(CN)_5NO]^{3-}$. Theoretical calculations predict a *cis*-cyanide will be lost to yield a tetragonal pyramid, $[Fe(CN)_4NO]^{2-}$, and this is indeed observed.**[200]**

$$2[Fe(CN)_6]^{4-} + 2NO_2^- + 3Ba^{2+} + 3CO_2 + H_2O \longrightarrow 2[Fe(CN)_5NO]^{2-} + 2HCN + 3BaCO_3 \qquad (4)$$

$Na_2[Fe(CN)_5(NO)]$ reacts in methanol at 2 °C with aqueous NaOH to form the yellow nitro complex $Na_4[Fe(CN)_5NO_2]$. This can be hydrolyzed to $[Fe(CN)_5(H_2O)]^{3-}$, which is also the final product of reactions between nitroprusside and ketones involving highly colored intermediates. The nitroprusside ion is well known for such color reactions, most of which result from a nucleophilic attack on coordinated NO followed either by displacement or the formation of a new ligand. Examples of such reactions abound, for example, the Gmelin test for SH^- (purple/violet) or the identification of mercaptans in mildly basic solution (red/purple) are useful applications. In some cases, these colors develop further and eventually become blue. The chemistry of this color evolution is uncertain but the final color is thought**[201]** to be due to the $[Fe(CN)_5(NCS)]^{3-}$ ion, which can be obtained directly from nitroprusside and thiocyanate ions (e.g. by photolysis). Solutions of salts of this complex ion vary dramatically in color depending on the solvent. The ammonia complex $[Fe(CN)_5(NH_3)]^{3-}$, is formed by the reaction of nitroprusside with ammonia in both stoichiometric and excess quantities, in the latter case nitrogen is evolved, whilst in the former nitrite ion is the coproduct.

$Na_2[Fe(CN)_5(NO)]$ rapidly lowers blood pressure and has been used in both surgical and emergency applications. Caution has been advised because of the possibility that free cyanide is formed in vivo, although it is possible that its detection may have resulted from photodecomposition during colorimetric determinations.**[202]** The April 2002 issue of *Chemical Reviews* contains several references to nitroprusside chemistry.

Nitric Oxide Carbonyl Complexes. Whilst binary iron nitrosyls do not appear to exist as discrete complexes, mixed nitrosyl carbonyls do. $[Fe(CO)_2(NO)_2]$ is readily formed in a number of reactions including the treatment of iron carbonyls with nitric oxide or nitrosyl chloride, and the reaction of $[HFe(CO)_4]^-$ with nitrite ion in acidic solution. The complex is a distorted tetrahedron,**[203]** it forms red, air-sensitive crystals, which melt at 18 °C and can be readily transferred around a vacuum system. In reactions with a variety of ligands, carbon monoxide displacement is observed and both mono and dimeric complexes result. The kinetics of these reactions are second order and the mechanism is thought to be bimolecular with the new ligand forming a five-coordinate transition state.**[204]** The substitution is catalyzed by hard bases, presumably via attack on a CO carbon atom making a more labile leaving group. Many salts of the $[Fe(CO)_3(NO)]^-$ ion are known, for example, bright yellow $[(Ph_3P)_2N][Fe(CO)_3(NO)]$, which is formed in the reaction between $[Fe(CO)_5]$ and $[(Ph_3P)_2N](NO_2)$ in THF. The anion can be isolated as $[Hg\{Fe(CO)_3(NO)\}_2]$ by reaction with mercurous cyanide in methanol; the structure contains a linear Fe-Hg-Fe grouping with trigonal bipyramidal iron. π-Acceptor ligands readily displace carbon monoxide from this complex with no change to the geometry of the metal atoms to form $[Hg\{Fe(CO)_2(NO)L\}_2]$ ($L = R_3P, R_3As, R_3Sb, (RO)_3P$). Reaction with nitrogen bases however leads to disproportionation, for example, in the case of pyridine to form a mixture of $[Fe(py)_6][Fe(CO)_3NO]$ and $[Fe(py)_2(NO)_2]$.

Nitric Oxide Complexes with Sulfur Donors. First reported in 1858, Roussin's red and black salts are formed in a mixture when iron(III) sulphide reacts with nitric oxide and an alkali metal sulfide. Some more convenient routes to the red salt, $K_2[Fe(NO)_2S]_2$ and the dark red diamagnetic so-called esters are shown in Scheme 1. These are dimeric and have a structure with two iron and two sulfur atoms in a plane. The sulfur atoms bridge an Fe–Fe bond and two NO molecules are coordinated to each iron to give a tetrahedral geometry. The black salts $M[Fe_4S_3(NO)_7]$ ($M = Na, K, Cs, AsPh_4$) may be prepared from iron(II) sulfate, $NaNO_2$, and KHS, or by the nitrosylation of iron carbonyl sulfides. The structure is of a trigonal pyramid of iron atoms with triply bridging sulfur atoms and terminal NO groups (**11**). Bonding comparisons with the cluster $[Fe_4(NO)_4(\mu_3\text{-}S)_4]$ reveal close relationships with both the red and black salts, and suggest a common building block. Preparations and properties of $[Fe_2S_2(NO)_4]^{2-}$, $[Fe_4S_4(NO)_4]$, and $[Fe_4S_3(NO)_7]^-$ have been reviewed,**[205]** photolysis of these complexes described,**[206]** and the preparation of $[Fe_5S_4(NO)_8]^-$ and $[Fe_7S_6(NO)_{10}]^-$ reported.**[207]**

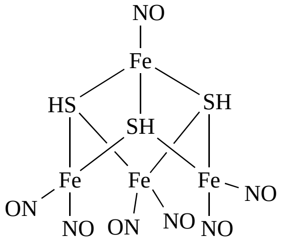

(**11**)

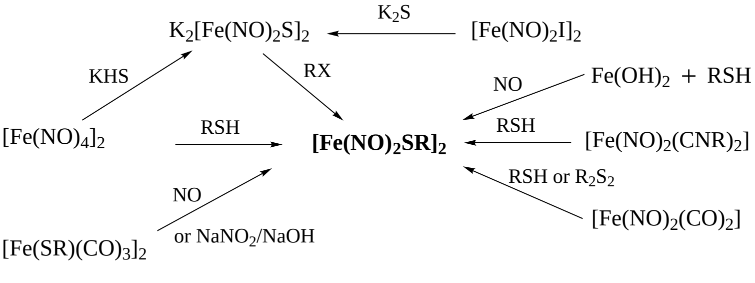

Scheme 1

In methanol, nitric oxide and $Na_2S_2CNR_2$ react with iron(II) salts to form the paramagnetic bis-dithiocarbamato iron nitrosyl complexes $[Fe(NO)(S_2CNR_2)_2]$. The structure is a square pyramid with iron at the apex and the N–O bond is almost linear (Fe–N–O $= 174^\circ$ when R = Et). The EPR and Mössbauer spectra of a number of these complexes support their description as formally d^7 iron(I) complexes, in which the unpaired electron resides in the iron d_{z^2} orbital. The nitrosyl-iron group is also stabilized by dithiolenes and the resulting $[Fe(NO)(S_2C_2R_2)_2]^z$ complexes ($z = 0, -1, -2, -3$) have the same square-pyramidal geometry. These complexes undergo a series of sequential one-electron transfer reactions, which can be demonstrated voltametrically.[208] The ease of electron transfer, as measured by the half-wave potential for each step, correlates strongly with the ligand R groups as a function of their electron-withdrawing ability. When $[Fe(NO)(S_2C_2Ph_2)_2]$ is formed by the reaction between nitric oxide and $[Fe(S_2C_2Ph_2)_2]_n$ in chloroform, purple $[Fe_2(NO)_2(S_2C_2Ph_2)_3].CHCl_3$ may also be isolated and a green monoanionic form can be obtained by reaction of the complex with $NaBH_4$.

Nitric Oxide Halide Complexes. The dimeric diamagnetic halides $[Fe(NO)_2X]_2$ have essentially tetrahedrally coordinated iron atoms with bridging halides. The trinitrosyl halides $[Fe(NO)_3X]$ are comparatively much less stable; they can be prepared by the reaction of $[Fe(CO)_2X]_2$ with iron and nitric oxide. The complexes $[Fe(NO)X_3]$ and $[Fe(NO)_2X_2]$ are known but much more work has been done on the reactivity of the dimeric dinitrosyl, and some of its reactions are illustrated in Scheme 2.

Nitric Oxide Adducts of Other Complexes. Simple nitrosyl complexes containing σ-N donor ligands are rare, as these 'hard' bases do not allow the appreciable d-π interaction required to stabilize the Fe–NO group. As a result, nitric oxide forms adducts with complexes whose ligands can offer a π-acceptor character. In particular planar macrocycles with N-donors such as phthalocyanine, tetraphenylporphyrin and tetraazacyclotetradecane form five-coordinate mono-nitrosyl iron complexes. Nitrosylhemoglobin and nitrosylmyoglobin have been described, as has [Fe(salen)(NO)] [salen = N,N′-ethylenebis(salicylideniminato)]. This black complex exhibits a sharp $S = 3/2$ to $S = 1/2$ spin crossover at 175 K, interestingly when the ligand is 5-Cl-salen, the crossover is not sharp but the complex shows a steady decrease in its magnetic moment from 3.8 to 0.5 BM between 4 and 100 K. These $S = 3/2$ to $S = 1/2$ spin equilibria are a general feature of iron nitrosyl complexes of quadridentate Schiff bases and similar ligands.[209]

8.1.2 Ammonia

Iron(III) ammine complexes appear not to exist in aqueous solution, and when solutions of ammonia and an iron(III) salt are mixed, a highly insoluble hydrated oxide is precipitated. In comparison, iron(II) hydroxide is relatively soluble (solubility product ca. 3×10^{-14}). Initially, when ammonia is added to an iron(II) salt solution, the hydroxide is precipitated but the addition of further ammonia causes it to dissolve, due in part to ammine complex formation. Anhydrous iron(III) halides are reported to form only moderately stable adducts with ammonia ($FeCl_3 \cdot 6\,NH_3$, decomposes at 100 °C) that are unstable in the presence of water, whereas many anhydrous iron(II) salts readily absorb ammonia to form ammine complexes up to the hexammine. Thus, saturating a solution of freshly prepared iron(II) bromide with ammonia in the presence of hydrogen gives a hydroxide precipitate that is converted[210] to light blue–gray crystals of moderately stable $[Fe(NH_3)_6]Br_2$, which has an Fe–N stretching frequency in the infrared at $315\,cm^{-1}$. $[Fe(NCS)_2(NH_3)_2]$ is the product of the evolution of ammonia, at room temperature, from the various ammines of iron(II) thiocyanate, $Fe(NCS)_2 \cdot nNH_3$ ($n = 5, 7$, or 8).[211]

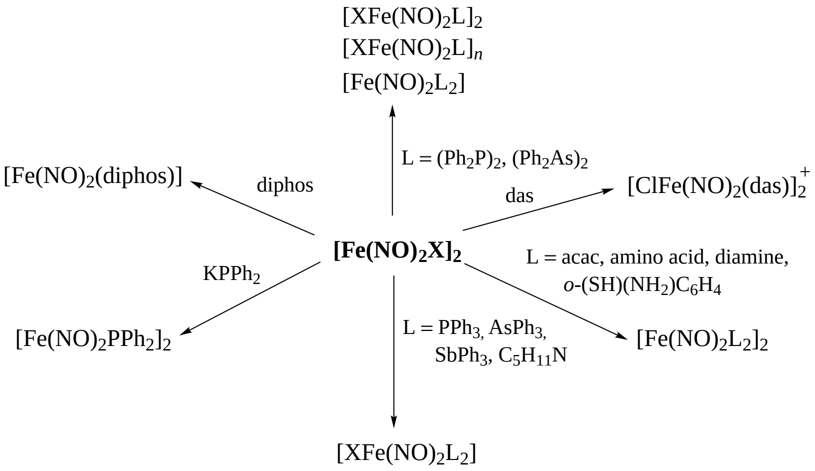

Scheme 2

$[Fe(NH_3)_6]^{2+}$ and $[Fe(en)_3]^{2+}$ have proved useful counterions for crystallization of salts of, for example, the $[AgAsS_4]^{2-}$, $[AgSbS_4]^{2-}$, and $[Sb_2Se_5]^{4-}$ anions.[212]

8.1.3 Aliphatic Amines

Iron(II) chloride reacts directly with excess anhydrous primary amines to give complexes of the type $[Fe(NH_2R)_2Cl_2]$, which are thought to have a distorted tetrahedral geometry. Under similar conditions, iron(III) chloride is reduced and the same product is obtained. Iron pentacarbonyl reacts[213] with anhydrous primary and secondary amines to give an adduct first, which, whilst it can involve two amine molecules, goes on to give $[Fe(CO)_4(amine)]$. Iron(II) forms some interesting complexes with tertiary amines. The monodentate monoprotonated ditertiary ligand dabcoH$^+$ (**12**) in anhydrous ethanol reacts with iron(II) halides to give unusual high-spin (5.1–5.2 BM) trigonal bipyramidal five-coordinate complexes, $[FeX_3(dabcoH^+)_2]X$ (**13**) with X = Cl, Br. Under slightly different conditions, the bridged complex $[FeCl_3(dabco)(dabcoH^+)]$ (**14**), is the product, and when heated, this loses dabco to give tetrahedral $[FeCl_3(dabcoH^+)]$. The less stable complexes $[FeX_3(dabcoMe^+)(L)]$ containing methylated dabco (X = Cl, Br; L = NH_3, H_2O) can be obtained. In contrast with iron(II) iodide, only the tetrahedral complex $[FeI_3(dabcoH^+)]$ is detected. The related monotertiary amine quinuclidine (**15**) in which electrostatic and hydrogen-bonding effects are absent simply forms a four-coordinate (pseudotetrahedral) complex $[FeCl_2(quinuclidine)_2]$.

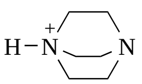

(**12**)

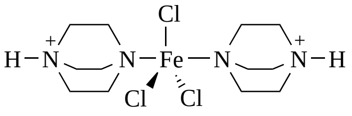

(**13**)

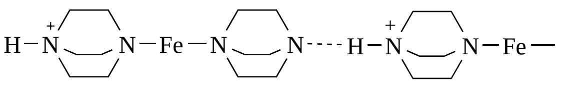

(**14**)

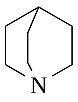

(**15**)

8.1.4 Aromatic Amines

Iron(II) sulfate forms compounds of the type $[Fe(SO_4)(L)_2]$ by direct reaction with aniline and *para*-toluidine. In solution, the affinity of iron(II) for pyridine is very low (log $\beta_2 \sim 0.9$). In the presence of a large excess of pyridine, neutral complexes of the type $[FeX_2(py)_4]$ can be prepared. Yellow *trans*-$[FeCl_2(py)_4]$ (5.34 BM) is precipitated when a saturated solution of $FeCl_2{\cdot}4H_2O$ is added to pyridine. It is more stable toward oxidation than simple iron(II) salts, and has the advantage of being moderately soluble in organic solvents. When heated in the absence of air, successive pyridine molecules are lost with the formation of three polymeric complexes.[214] The related complexes $[FeCl_2(4\text{-}Mepy)_4]$ and $[Fe(NCS)_2(py)_4]$ each form only a single well-defined intermediate with two pyridine ligands when heated. The complexes *trans*-$[FeI_2(py)_4]$.2py (5.64 BM) and *trans*-$[Fe(NCO)_2(py)_4]{\cdot}2py$ (5.13 BM) do not contain $[Fe(py)_6]^{2+}$. They show infrared bands due to free and coordinated pyridine, and have other spectroscopic properties in accordance with the given formulation. The complex $[Fe(NCS)_2(py)_4]$ can be obtained in yellow and black forms, once thought to be *cis* and *trans* isomers. However, X-ray crystallography showed[215] the yellow complex to be *trans*-$[Fe(NCS)_2(py)_4]$, and the black complex has effectively the same Mössbauer and magnetic properties. It appears both forms have the same structure, but the black form contains small amounts of iron(III) and its black color is due to charge transfer. Thus yellow *trans*-$[Fe(NCS)_2(py)_4]$ does not darken under oxygen-free conditions, and the dark violet solutions formed by exposure to air are converted to yellow by sulfur dioxide. The cation $[Fe(py)_6]^{2+}$ can be prepared by reaction of pyridine with iron pentacarbonyl. The product $[Fe(py)_6][Fe_4(CO)_{13}]$ has a high-spin iron(II) center (5.47 BM), and in $[Fe(py)_6]^{2+}$ the ligands are in three mutually perpendicular planes with each pair of *trans* pyridines being coplanar.[216]

8.2 Bidentate Amines

8.2.1 Aliphatic Diamines and Polyamines

The $[Fe(en)_3]^{2+}$ structure[217] was recently redetermined; the average Fe–N bond distance is 2.192 Å. In aqueous solution, ethylenediamine (en) forms mono, bis, and tris complexes with iron(II), having successive enthalpies of formations of 21.1, 43.5, and 66.3 $kJ\,mol^{-1}$ respectively, and data for many other polydentate amines have been reported.[218] Slow addition of en to iron(III) chloride in ethanol affords low-spin $[Fe(en)_3]Cl_3$ (2.45 BM), which has only a small Mössbauer quadrupole splitting ($1.09\,mm\,s^{-1}$) compared with the 1,4-diimine complexes discussed below, consistent with a small distortion from octahedral symmetry. However, the corresponding iron(II) complex can result if reaction conditions are changed. Thus, anhydrous en or propylenediamine react with iron(III) chloride to give tris-ligand iron(II) complexes, while bis(2-dimethylaminoethyl)methylamine reacts with iron(II) chloride to give the very air-sensitive, high-spin, five-coordinate $[Fe\{(Me_2NEt)_2NMe\}Cl_2]$, and the bulky ligand N,N,N',N'-tetramethylethylenediamine gives tetrahedral $[Fe(tmen)I_2]$.[219] Related iron(II) complexes have been isolated with tri- and tetradentate amines. For instance, $[Fe(Me_6tren)Br]Br$ has trigonal bipyramidal geometry, although it appears that in solution, six-coordinate species are present. A problem with these reactions can be precipitation of iron hydroxide rather than complex formation, and with 3,3′,3″-triaminotripropylamine, an iron(II) complex could not be obtained for this reason. An interesting feature of the iron(II) tetraethylenepentamine (tetren) complex is that it forms[220] a mono carbon monoxide adduct, $[Fe(tetren)CO]^+$.

8.2.2 1,4-Diimine Ligands

Historical. Fritz Blau obtained[221] the stable intensely red cation $[Fe(bipy)_3]^{2+}$ in 1888. He used the sensitive color reaction to monitor the presence of 2,2′-bipyridine (bipy) in its synthesis from the pyrolysis of copper(II) picolinate. Ten years later he reported[222] the synthesis of 1,10-phenanthroline (phen) and its red tris-ligand iron(II) complex. In 1912, Werner[223] demonstrated the octahedral geometry of $[Fe(phen)_3]^{2+}$ by resolving its optical isomers. Later, this complex was shown to be a high-potential redox indicator, and it also became much used in the colorimetric determination of iron.[224] Several tris-iron complexes of this type have significant antibacterial activity, but they appear never to have been introduced commercially. Resin-supported $[Fe(bipy)_3]^{2+}$ has recently been proposed as a catalyst for photochemical degradation of organic pollutants by molecular oxygen.[225] A wide variety of 1,4-diimine ligands have been synthesized and properties of their iron complexes investigated. Here, the primary focus is on complexes of the prototype ligands bipy and phen, and a final section outlines the reactivity differences of iron complexes with other 1,4-diimines.

Tris Complexes. In the absence of steric effects, 1,4-diimines in iron complexes are high-field ligands due to back donation of t_{2g} metal electron density into unfilled ligand orbitals. Many octahedral iron(II) tris-diimine complexes are low spin, often with a small temperature-independent paramagnetism of about 1 BM. Strong, metal to ligand charge-transfer bonds cause[226] the complexes to be intensely colored (Table 8). Crystal structures of some iron(II) and iron(III) tris-diimine complexes have been reported: in $[Fe(phen)_3]^{2+}$, the small bite of the ligand results in some compression along the pseudo threefold axis as well as some twist from an exactly octahedral geometry.[227] The mean Fe–N bond distances in the iron(II) and iron(III) complexes are the same, 1.97 Å.[228]

Many tris-(1,4-diimine)iron(II) complexes may be made by adding ligands in acetone, ethanol, or methanol to an aqueous solution of an iron(II) salt. The deeply colored cations are indefinitely stable in neutral solutions and they may be precipitated by addition of large cations such as perchlorate, iodide, thiocyanate, or nitroprusside, followed by recrystallization from an organic solvent (with caution in the case of the potentially explosive perchlorate salts). When the anion concerned is a good ligand, the product obtained on recrystallization is often the neutral bis complex, for instance, $[Fe(bipy)_2Cl_2]$ (see below). Reaction of Fe^{3+} with excess 1,4-diimine gives brown oxo-bridged dinuclear complexes, and not tris complexes.[229] These have an infrared – Fe–O–Fe-stretching vibration at 840–860 cm^{-1}, and temperature-dependent magnetic susceptibilities of about 1.9 BM per iron atom resulting from antiferromagnetic superexchange between the two high-spin centers, via the oxo bridge. Mössbauer spectroscopy confirms this assignment. $[Fe(bipy)_3]^{3+}$ and related complexes are readily obtained by oxidation of the corresponding iron(II) species by, for example, Ce(IV) or PbO_2 in dilute sulfuric acid.[230] These blue cations are less intensely colored than their red iron(II) counterparts and they can also be precipitated as perchlorate salts. They are surprisingly stable in acidic solution, even in concentrated sulfuric acid, probably because the activity of water is so low in this medium.[231] Optically active $[Fe(phen)_3]^{2+}$ is readily obtained via crystallization as the antimony d-tartrate salt. Low-temperature oxidation in acid affords optically active $[Fe(phen)_3]^{3+}$, which racemizes slowly in the solid, whereas in solution, racemization is complete in a few minutes.[232] The corresponding iron(II) complexes racemize relatively slowly in solution and very slowly in the solid. The volume of activation for racemization of crystalline $[Fe(phen)_3](ClO_4)_2$ is $-0.9 \pm 0.1\,cm^{-3}\,mol^{-1}$. In solution, it is $14.2 \pm 0.3\,cm^{-3}\,mol^{-1}$, which is similar to that for dissociative acid aquation. However, the racemization rate is

Table 8 Absorption maxima, extinction coefficients, stability constants, and standard electrode potentials for selected Tris-(1,4-diimine)iron(II) complexes in water

Ligand	λ_{max}/nm	ext coefficient	$\log_{10} \beta_3$	E/V ($[H_2SO_4]$)
Phen	510	1.11×10^4	21.2	1.06 (1.0)
5-Mephen	512	1.22×10^4	21.9	1.02 (1.0)
5-Clphen	512	1.17×10^4	19.7	1.11 (1.0)
5-NO_2phen	510	1.15×10^4	17.8	1.25 (1.0)
5-Phphen	522	1.27×10^4	21.1	1.08 (1.0)
4,7-Me_2phen	512	1.40×10^4	23.1	0.88 (0.1)
5,6-Me_2phen	520	1.26×10^4	23.0	1.00 (0.1)
4,7-Ph_2phen	533	2.24×10^4	21.8	1.13 (4.6)
Bipy	522	8.70×10^3	17.4	1.02 (1.0)
4,4′-Me_2bipy	528	9.30×10^3	–	0.90 (1.0)
4,4′-Ph_2bipy	552	2.11×10^4	–	1.01 (1.0)
4,4′-$(NH_2)_2$bipy	569	1.36×10^4	–	–
Terpy	552	1.25×10^4	–	0.93 (1.0)

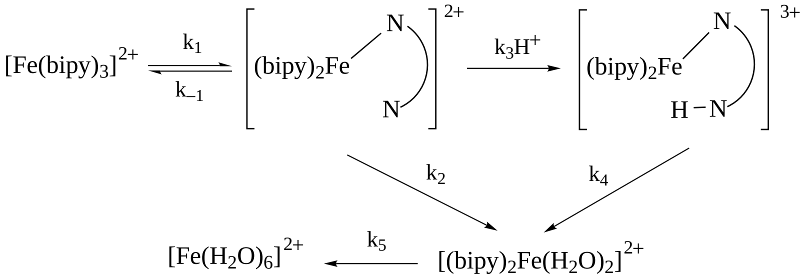

Scheme 3

almost an order of magnitude faster than that for dissociation, suggesting racemization involves an additional intramolecular twist process.[233]

There is a simple dissociative mechanism for $[Fe(phen)_3]^{2+}$ dissociation in acid, which is independent of acid concentration. However, when the ligand is the more flexible bipy, a monodentate protonated intermediate is kinetically significant. Here, the observed rate of dissociation increases with increasing acid concentration up to about $2\,mol\,l^{-1}$, as shown in Scheme 3, and the reaction rate is given by equation (5).

$$\frac{-d[Fe(bipy)_3{}^{2+}]}{dt} = \frac{[Fe(bipy)_3{}^{2+}]k_1(k_2 + k_3[H^+])}{(k_{-1} + k_2 + k_3[H^+])} \qquad (5)$$

Reactions of tris(1,4-diimine)iron(II) complexes with hydroxide and cyanide ions take place via first and second-order processes typified by the rate law, equation (6). With hydroxide, the initial product is iron(II) hydroxide which is oxidized by adventitious oxygen to give very insoluble iron(III) hydroxide, the formation of which is the driving force for the overall reaction, equation (7). With cyanide ion, the product[234] is low-spin $[Fe(phen)_2(CN)_2]$. Over a prolonged period in the presence of sufficient cyanide ion, this goes on to give $[Fe(phen)(CN)_4]^{2-}$ and finally $[Fe(CN)_6]^{4-}$, equation (8). There remains controversy about the mechanistic origin of the second-order reactions of tris(diimine)iron(II) complexes. These have large positive volumes of activation normally considered characteristic of a dissociative rather than an associative mechanism. This dichotomy could have its origin in strong transition state desolvation.[235]

$$\frac{d[Fe(phen)_3{}^{2+}]}{dt} = [Fe(phen)_3{}^{2+}]\{k_1 + k_2[\text{nucleophile}]\} \qquad (6)$$

$$[Fe(phen)_3]^{2+} + \frac{OH^-}{O_2} \longrightarrow Fe(OH)_3 + 3phen \qquad (7)$$

$$[Fe(phen)_3]^{2+} \longrightarrow [Fe(phen)_2(CN)_2] \longrightarrow$$
$$[Fe(phen)(CN)_4]^{2-} \longrightarrow [Fe(CN)_6]^{4-} \qquad (8)$$

Kinetic parameters, including activation volumes, for base hydrolysis of a variety of iron(II)-diimine complexes provide useful indicators of ligand, substituent, and medium effects on reactivity.[236]

The redox potential for tris- 1,4-diimine iron complexes is about 1 V (Table 8), and the iron(III) complexes will oxidize a variety of organic substrates. The addition of a base causes their rapid reduction to iron(II) via an involved process with a hydroxide ion concentration term in the rate equation.[237] Lower oxidation state tris-diimine iron complexes are known. Reduction of $[Fe(bipy)_3]^{2+}$ with Li_2bipy gives black paramagnetic crystalline $[Fe(bipy)_3]$, as in equation (9). This can also be prepared directly from an iron chloride and Li_2bipy in THF, for example, as in equation (10). Solutions in unreactive organic solvents are red–violet but in protic solvents, oxidation to $[Fe(bipy)_3]^{2+}$ takes place and hydrogen gas is evolved. When heated to 145 °C in vacuo, $[Fe(bipy)_3]$ decomposes to metallic iron and the free ligand. In the presence of excess reducing agents, $[Fe(bipy)_3]^{2+}$ affords $[Fe(bipy)_3]^-$ according to equation (11). This complex is best described[238] as an iron(0) complex with a $(bipy)^-$ ligand. The electrochemical reduction of $[Fe(bipy)_3]^{2+}$, and related complexes, to iron(I) and iron(0) species is well characterized. The nature of more highly reduced species is however, not well defined.

$$Li_2bipy + [Fe(bipy)_3]^{2+} \longrightarrow [Fe(bipy)_3] + bipy + 2Li^+ \qquad (9)$$

$$2FeCl_2 + 4bipy + 2Li_2bipy \longrightarrow 2[Fe(bipy)_3] + 4LiCl \qquad (10)$$

$$3Na(bipy) + [Fe(bipy)_3]^{2+} \longrightarrow Na[Fe(bipy)_3] + bipy + 2Na^+ \qquad (11)$$

Bis Complexes. The dicyano complexes $[Fe(CN)_2(diimine)_2]$ are protonated in strong acid to give stable mono and diprotonated species. Protonation is associated with major color changes, typically dark violet to yellow, and these complexes have been used as acid-base indicators in nonaqueous titrations.[239] They also show strong solvatochromatic charge-transfer bands. For example, the absorbance maximum of $[Fe(CN)_2(bipy)_2]$ in water is 515 nm and in pyridine, 629 nm. The solvatochromism of a variety of $[Fe(diimine)_2(CN)_2]$ and $[Fe(diimine)(CN)_4]^{2-}$ complexes has been established,[240] and used to monitor solvation in ranges of single and mixed solvents, and in micelles and microemulsions[241] – indeed a few complexes self-aggregate.[242] Appropriate tailoring of the diimine ligands gives complexes with significant solubility in almost all known solvents.[243] Solubility data[244] and partial molar volumes[245] are available for several diimine-cyanide complexes; transfer chemical potentials (from solubilities) can indicate preferential solvation in mixed solvents.[246] $[Fe(diimine)_2(CN)_2]$ complexes have been used to probe connections between solvatochromism, electronic absorption spectra, and color perception parameters.[247] There are also correspondingly marked changes in extinction coefficient.[248] Oxidation of these complexes gives iron(III) salts, which can be isolated, for example, *cis*-$[Fe(CN)_2(bipy)_2]X$ ($X = ClO_4^-$, NO_3^-). These are low spin, with magnetic and Mössbauer properties similar to the iron(III)-tris-1,4-diimine complexes discussed above. The reaction of iron(III) chloride with 1,10-phenanthroline in acetone gives a compound of empirical formula $Fe(phen)Cl_3$. This is in fact *cis*-$[FeCl_2(phen)_2][FeCl_4]$, in which the cation is high-spin,[249] and the Fe–N bonds are significantly longer than in $[Fe(phen)_3]^{3+}$. Iron(II) complexes of the type $[FeX_2(NN)_2]$ (NN = bipy, phen; X^- not CN^-) are obtained from the corresponding $[Fe(NN)_3]X_2$ salts by extraction with hot organic solvent, or dissociating one diimine ligand at an elevated temperature (140–200 °C) under vacuum over a prolonged period.[250] Most of them are somewhat air sensitive and high spin. For example, $[FeCl_2(bipy)_2]$ has a magnetic susceptibility of 5.3 BM. In the presence of water, the more stable low-spin complex is formed, presumably according to equation (12). With $X^- = NO_2^-$ and NCO^-, the complexes are low spin; when $X^- = 1/2$ oxalate or F^-, the complexes are claimed to have intermediate spin. Of special interest are those complexes with $X^- = NCS^-$ and $NCSe^-$, which display the spin-crossover phenomenon,[251] a change in magnetic and spectral properties over quite a narrow temperature range. Room temperature magnetic moments of $[FeX_2(diimine)_2]$ ($X^- = NCS^-$, $NCSe^-$; diimine = phen, bipy) are in the range 4.9–5.2 BM, but at lower temperatures these abruptly decrease, and at the temperature of liquid nitrogen, become characteristic of low-spin complexes. In some instances, the existence of more than one polymorph is a complication but spectroscopic studies, and in particular, Mössbauer results, confirm a change from the $^5T_2$ to the $^1A_1$ state is involved. Crossover phenomena of this kind have been the subject of several reviews.[252]

$$3[FeCl_2(bipy)_2] \longrightarrow 2[Fe(bipy)_3]^{2+} + Fe^{2+} + 6Cl^- \qquad (12)$$

It has long been known that whereas oxidation of $[Fe(phen)_3]^{2+}$ in solution gives blue $[Fe(phen)_3]^{3+}$, reaction of an iron(III) solution with 1,10-phenanthroline gives a brown solution. In 1936, this was, based on analysis and on conductimetric and magnetic measurements, proposed[253] to be a dihydroxy-bridged species $[(phen)_2Fe(\mu\text{-}OH)_2Fe(phen)_2]^{4+}$. Later X-ray diffraction studies indicated this and related cations contained a bridging oxide rather than a hydroxide, as in $[(phen)_2ClFe(\mu\text{-}O)FeCl(phen)_2]Cl\cdot nH_2O$,[254] $[(H_2O)(phen)_2Fe(\mu\text{-}O)Fe(phen)_2(H_2O)](NO_3)_4\cdot 5H_2O$,[255] and $[(H_2O)_3(phen)Fe(\mu\text{-}O)Fe(phen)(H_2O)_3](NO_3)_4\cdot H_2O$.[256] Simple μ-oxo-di-iron complexes,[257] of which the bis-iron(III) complexes $[Fe_2(\mu\text{-}O)(diimine)_4(H_2O)_2]^{4+}$ provide examples, can act as models for the structure and catalytic activity of di-iron sites in proteins (e.g. in methane monooxygenase), and also as catalysts for oxygen transfer to hydrocarbons or sulfur. $[Fe_2(\mu\text{-}O)(phen)_4(H_2O)_2]^{4+}$ was obtained as a result of an electrochemical study of $[Fe(phen)_3]^{2+/3+}$ in aqueous solution.[258] Subsequently, the other members of the group $[Fe_2(\mu\text{-}O)(diimine)_4L_2]^{n+}$, where diimine = phen, bipy, or 4,4′-bipy and L = H_2O, Cl^-, or $CF_3CO_2^-$, and the slightly different acetate complex $[Fe_2(\mu\text{-}O)(\mu\text{-}O_2CCH_3)(diimine)_4L_2]^{n+}$ (**16**), were synthesized, characterized, and assessed as alkane oxidation catalysts.[259]

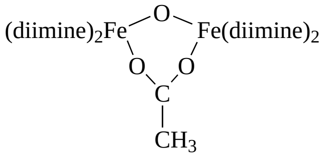

(**16**)

Mono Complexes. The product from the reaction of iron(III) chloride and 1,10-phenanthroline in acetone, originally formulated as $[FeCl_3(phen)]$, is *cis*-$[FeCl_2(phen)_2][FeCl_4]$ (see above). Under the conditions of kinetic experiments, the formation of $[Fe(phen)(H_2O)_4]^{2+}$ from Fe^{2+} and phen is rapid with an unfavorable entropy of activation.[260] It can be produced in significant concentrations when an excess of an iron(II) salt is added to an acid solution of the ligand. The reaction of $[FeF_2(py)_4]$ with 1,10-phenanthroline in pyridine affords polymeric violet $[FeF_2(phen)]$, which has a magnetic susceptibility of 4.4 BM. Other iron(II) dihalide complexes are obtained from extended pyrolysis of the corresponding tris-(1,4-diimine)iron(II) salts. Two isomers of $[FeCl_2(bipy)]$ obtained from $[Fe(bipy)_3]Cl_2$ have been identified.[261] An orange isomer, which was originally thought to be monomeric (and perhaps tetrahedral), is first obtained from $[FeCl_2(bipy)_2]$; on further heating, this is converted into a red polymeric form which is similar to that prepared from iron(II) chloride and 2,2′-bipyridine in hydrochloric acid. The latter form has octahedral iron(II) centers with bridging chloride ligands. It has been proposed that the orange isomer may contain a chain of five-coordinate iron(II) centers with single bridging chlorides. The mono complex with 5,5′-dimethyl-2,2′-bipyridine may also contain the five-coordinate iron(II). The low-spin complexes $[Fe(CN)_4(diimine)]^{2-}$ are obtained after a prolonged reaction of $[Fe(diimine)_3]^{2+}$ with cyanide ion (via the neutral intermediate $[Fe(CN)_2(diimine)_2]$), or better[262] from the reaction of $[Fe(CN)_6]^{4-}$ with free ligands in the presence of a small amount of Hg^{2+}, as illustrated in equation (13).

$$[Fe(CN)_6]^{4-} + \xrightarrow[Hg^{2+}]{bipy} [Fe(CN)_4(bipy)]^{2-} + 2CN^- \qquad (13)$$

Complexes with other Bidentate 1,4-Diimines. The thermodynamic stability of the five-membered iron(II) 1,4-diimine chelate ring in low-spin complexes is illustrated by the facile autoxidation of saturated amine complexes to the corresponding colored 1,4-diimine complexes. The first example**263** of this oxidative dehydrogenation is shown in equation (14), and the more recently studied**264** reaction (15) is known to involve iron(III) species and radical intermediates. Interestingly, the complex $[Fe(CN)_4(HN{=}CHCH{=}NH)]^{2-}$ can be obtained by oxidizing $[Fe(CN)_4(en)]^{2-}$, whereas the tris-ligand complex of this smallest diimine ligand has yet to be prepared.

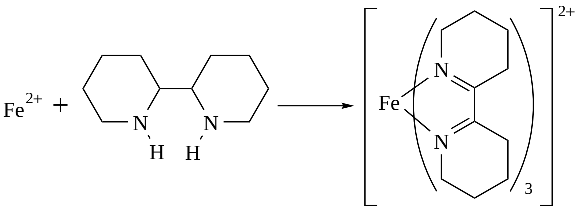

(14)

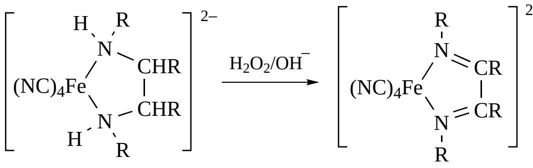

(15)

Similar iron(II) complexes can be formed in template reactions. For example, glyoxal and biacetyl react with amines in the presence of Fe^{2+} to give tris complexes of derivatives of the unsaturated ligand in equation (15). Although such ligands are not particularly stable, the complexes are very stable toward dissociation. Other Schiff bases can be formed in this way, and a wide range of complexes have been prepared from 2-pyridine aldehydes or ketones and amines (**17**). The related tridentate ligands (**18**) as well as the corresponding hydrazones form stable low-spin iron(II) complexes.**265** In some instances, the ligand can be removed, thus forming a convenient metal mediated synthesis.**266**

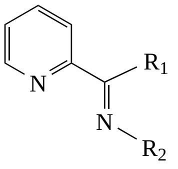

(**17**)

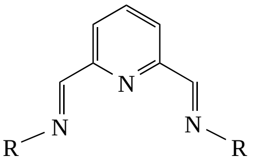

(**18**)

The *cis*- (**19**) and *trans*-isomers (**20**) of the Schiff base from pyridine 2-aldehyde and 2-pyridylhydrazone have been isolated, and both form iron(II) complexes. The tris complex $[Fe(\mathbf{20})_3]^{2+}$ is yellow, and when heated, this is converted to the very stable ($\log \beta_2 = 16.2$) purple colored $[Fe(\mathbf{19})_2]^{2+}$ that can be deprotonated in alkaline solution to give the neutral bis complex.**267**

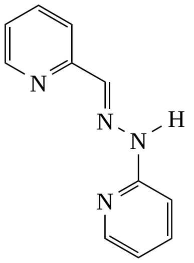

(**19**)

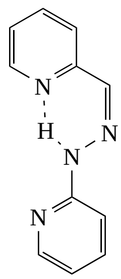

(**20**)

Hexadentate Schiff-base iron(II) complexes have been reported with linear,**268** tripodal,**269** or encapsulating (see below) tris-diimine ligands. Of particular interest are hexadentate ligands which have unsaturated segments and only two 1,4-diimine units (**21**) but still form low-spin complexes. Here, oxidative dehydrogenation does not take place and it appears the additional stability afforded by the chelate effect is significant. This complex, like most of the others described here, behaves in many ways like $[Fe(bipy)_3]^{2+}$. Thus, the rate of acid dissociation of $[Fe(\mathbf{21})]^{2+}$ is slow and depends on acid concentration, while reactions with hydroxide and cyanide are second order. Reaction with cyanide ion gives $[Fe(CN)_4(\mathbf{21})]^{2-}$. Synthesis of suitably designed tripodal ligands containing three bipy moieties can lead to dissteroselective synthesis of the respective iron(II) complexes.**270**

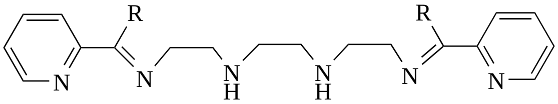

(**21**)

By careful ligand design involving a balance of chelate, electron acceptor, and other effects, it is possible to prepare iron(II) complexes displaying a range of spin-crossover phenomena induced by heat or light, for example, with ligands (**22**) and (**23**) and related derivatives. Even $[Fe(2\text{-}(aminomethyl)pyridine)_3]^{2+}$ displays low-temperature spin crossover, and there is evidence that long-range cooperative interactions are present.**271**

In the absence of a reducing agent, $[Fe(dmg)_2]$ (dmg = dimethylglyoximate) is readily oxidized to iron(III) species. However, in the presence of good axial ligands, stable low-spin complexes result. For example, the structure of $[Fe(dmg)_2(imidazole)_2]$ has two planar dmg ligands with the

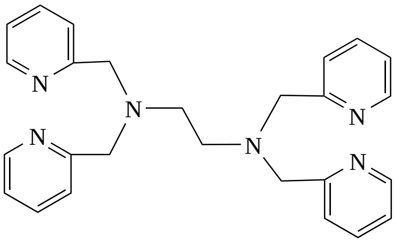

(**22**)

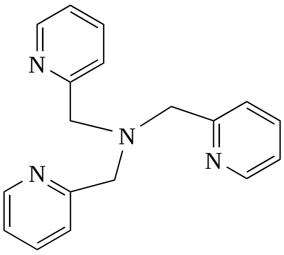

(**23**)

expected tetragonal distortion of the six nitrogen atoms bound to the iron(II) center. A variety of ring closure approaches have been used to provide related macrocyclic systems, which are illustrated in structure (**24**). Encapsulating hexadentate ligands result when three dmg ligands are capped by two species such as ≡BOR. The iron(II) complexes are low spin and have structures approaching trigonal prismatic geometry. Related complexes can be prepared with cyclohexane caps in place of borate.**272**

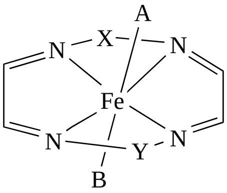

X = Y = O--HO (dmg)
X = $(CH_2)_n$ Y = O--HO
X = Y = $(CH_2)_n$

(**24**)

Ter- and Polydentate Ligands. Low-spin iron(II) complexes of polydentate aromatic nitrogen-donor ligands are significantly more stable than the corresponding iron(III) compounds and this dominates their chemistry in the absence of macrocyclic effects. Thus addition of 2,2′:6′,2″-terpyridine (terpy) to a solution of an iron(III) salt results in formation of $[Fe(terpy)_2]^{2+}$. This can be oxidized (redox potential ca 1.1 V) to the corresponding iron(III) complex and isolated as the perchlorate salt. Under appropriate conditions in the presence of halide or thiocyanate, it appears that high-spin $[FeX_3(terpy)]$ is formed which may have a distorted square-pyramidal structure, and in the presence of nitrate the product is a μ-oxo dimer.**273** The iron(II) complex originally formulated as $[FeCl_2(terpy)]$ is in fact $[Fe(terpy)_2][FeCl_4]$, which is in accord with its magnetic moment of 4.60 BM, that is, below the spin-only value. $[Fe(terpy)_2]^{2+}$ is very stable (log $\beta_2 = 20.4$; $\Delta H = -113\,\text{kJ}\,\text{mol}^{-1}$, $\Delta S = -13\,\text{J}\,\text{K}^{-1}\,\text{mol}^{-1}$). It dissociates only slowly in acid solution, second-order base hydrolysis is faster. It reacts with cyanide ion to form $[Fe(CN)_3(terpy)]^-$ via second-order kinetics and the product is strongly solvatochromic.**274** Controlled reduction of $[Fe(terpy)_2]^{2+}$ gives**275** species with iron in the formal oxidation states of +I and 0. Numerous iron(II) complexes containing other polydentate aromatic, and related nitrogen-donor ligands systems have been reported. Many of these are derivatives of the prototype bipy and phen ligands, while others are based on Schiff bases of pyridines, and so on, as illustrated in structures (**25**), (**26**), (**27**), and (**28**). The chemistry of these iron complexes resembles that described here for terpy, usually modified by their being less stable than those discussed in this and previous sections. However, in some instances, for example complexes of hexadentate ligands, they are surprisingly stable even though they may contain two or more aliphatic nitrogen donors.

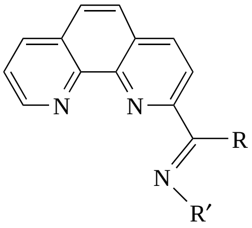

(**25**)

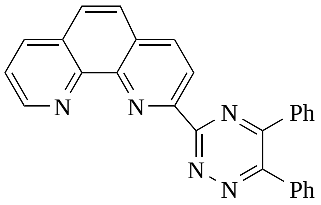

(**26**)

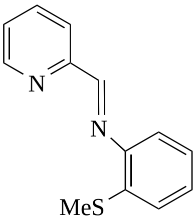

(**27**)

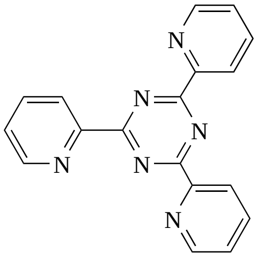

(**28**)

9 LIGANDS WITH PHOSPHORUS DONORS

9.1 Introduction

Phosphorus(III), with its high propensity for accepting π-electron density from coordinated iron, stabilizes complexes in lower oxidation states, but higher oxidation state complexes are also known. For example, $[FeCl_3(PPh_3)]$ is obtained from $Fe_3(CO)_{12}$ and PPh_3 in chloroform. The reaction of iron(III) salts with tertiary phosphines yields an iron(II) bis-phosphine complex. Iron(III) complexes of bidentate phosphines are better known**276** and are typically four coordinate and of the form $[FeX_2(\text{P-P}')]^+$. The lower oxidation state iron complexes containing phosphorus ligands are considered in this Encyclopedia in the sections on the 'organometallic' chemistry of iron. The structure of *cis*-,*mer*-$[Fe(H)_2(\eta^2\text{-}H_2)(PEtPh_2)_3]$ was established by neutron diffraction techniques.[277]

9.2 Iron (II) Complexes

9.2.1 Monodentate Phosphorus Ligands

Many simple iron(II) phosphine complexes are unstable and dissociate in solution, whereas complexes of phosphites are more stable. Anhydrous iron(II) halides react with tertiary phenylphosphines in refluxing benzene to yield $[FeX_2(PR_3)_2]$, which are high-spin and have a tetrahedral structure. With secondary phosphines in anhydrous alcohol, five-coordinate paramagnetic violet/red complexes $[FeX(HPR_2)_4]^+$ are formed, which can be isolated as the BF_4^- or PF_6^- salts. Carbon monoxide displaces a phosphine to form yellow six-coordinate complexes $[FeX(CO)_2(HPR_2)_3]^+$ in which the CO ligands are evidently *trans* in solution. Penta-coordinate complexes $[Fe(HPR_2)_5]^{2+}$ are formed[278] in the reaction between excess secondary phosphine and the iron(II) salts of PF_6^- and BF_4^-. They too react with CO to form a six-coordinate *trans* dicarbonyl complex. Many low-spin complexes of phosphines or phosphites with the stoichiometry $[FeX_2(CO)_2(P)_2]$ are known. Trimethylphosphite, $P(OMe)_3$, is a particularly successful ligand because it has both strong σ-donor and strong π-acceptor capabilities associated with rather small steric hindrances.

9.2.2 Polydentate Phosphorus Ligands

The reaction of metallic iron with *o*-phenylenebis(diethylphosphine) in hydrogen at 200 °C gives a small amount of the complex *trans*-$[FeH_2\{C_6H_4(PEt_2)_2\}_2]$. A monohydride complex *trans*-$[FeHCl(depe)_2]$ is known (depe = 1,2-bis(diethylphosphino)ethane), which reacts with sodium tetraphenylboride under nitrogen to yield *trans*-$[FeH(N_2)(depe)_2]^+$, which can be isolated[279] as the BPh_4^- salt. The bidentate phosphines 1,2-dialkylphosphinoethane (P-P) form octahedral low-spin complexes *trans*-$[FeCl_2(P\text{-}P)_2]$ with ease. Typically, these complexes have Fe–P bond lengths of the order of 2.2 Å. This contrasts with other complexes where a bidentate phosphine ligand forces a high-spin configuration (for example, octahedral $[FeCl_2\{Ph_2PCH_2(CH_2)_2PPh\}_2]$ where the ligand acts in a bidentate fashion and average Fe–P bond lengths of 2.7 Å are observed). The tripod-like ligand $MeC(CH_2PPh_2)_3$ forms, on reaction with iron(II) salts in the presence of borohydride, an unusual diamagnetic dimeric complex having three bridging hydrides (**29**). Tetradentate phosphines can form both five- and six-coordinate complexes of the type $[FeX_2L]$, the complex geometry appears to depend on the flexibility of the hydrocarbon chain, which forms the chelate 'bite', and on the extent of Fe–P overlap. A mixed tridentate P_2N donor ligand (**30**) forms complexes $[Fe(\mathbf{30})XY]$ with iron(II) halides. When X = Y = Cl, Br, the complexes are yellow and display normal high-spin behavior. When X = Y = I or X = I, Y = NCS, however, the complexes are brown and their magnetic moments decrease suddenly[280] at low temperatures although a completely low-spin state is not achieved. This anomalous behavior, which could be due to the existence of a spin equilibrium between a singlet ground state and a low lying triplet state, is found in a number of similar iron(II) phosphine halide complexes.

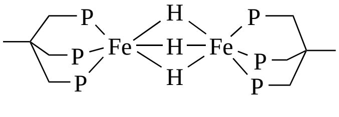

(**29**)

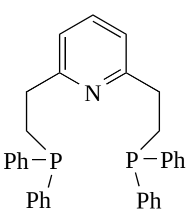

(**30**)

9.3 Iron(I) Complexes

The unusual iron(I) oxidation state is stabilized in some well-characterized phosphorus complexes. In particular, much work has been done on complexes of 1,2-bis(diphenylphosphino)ethane, (dppe). The iron(II) complex $[FeHCl(dppe)_2]$ is reduced[281] by treatment with sodium in benzene under anaerobic conditions to form the iron(I) hydride $[FeH(dppe)_2]$. This deep red complex is paramagnetic, has a sharp EPR signal at $g = 2.085$, and reacts with a large excess of HCl in ethanol at 80 °C to form $[FeCl_2(dppe)_2]$. This can be reduced by sodium in the presence of dppe to yield $[FeCl(dppe)_2]$, which is also red and has a strong EPR signal with some resolvable hyperfine structure at $g = 2.075$. The hydride complex reacts with trityl salts under nitrogen to give $[FeH(N_2)(dppe)_2]^+$. Four-coordinate iron(I) is stabilized by dppe according to equation (16) and the resulting complex $[Fe(dppe)_2]^+$ reacts[282] with a variety of ligands (C_2H_4, CO, N_2, MeCN) to give the corresponding five-coordinate iron(I) species.

$$[Fe^0(dppe)_2] + AlClR_2 \longrightarrow [Fe^I(dppe)_2]^+[AlCl_2R_2]^- \qquad (16)$$

Two quasi-synthetic techniques have been used to investigate the chemistry of iron(I), pulse radiolysis[283] and cyclic voltammetry.[284] In the former, electrons produced by the γ-ray radiolysis of protic solvents have been shown to reduce iron(II) species to iron(I) and a complex set of equilibria are established. Reversible one-electron reductions of a variety of iron(II) phosphine complexes have been shown spectroscopically to generate iron(I). In some instances, the complexes can be useful synthetic precursors, for example, $[Fe(CO)_3(PPh_3)_2]^+$ that can be obtained from *trans*-$[Fe(CO)_3(PPh_3)_2]$. Iron(I) complexes are stabilized by the presence of an imidazolidinylidine ligand, which promotes more effective charge delocalization and a number of monodentate phosphine and phosphite complexes of iron(I) have been generated[285] in association with this ligand.

9.4 Iron(0) Complexes

The thermal or photochemical reaction of $[Fe(CO)_5]$ or other iron carbonyls with PR_3 gives a mixture of $[Fe(CO)_3(PR_3)_2]$ and $[Fe(CO)_4PR_3]$. Where the R groups are bulky, the latter complex tends to be formed. The bisphosphine complexes have a trigonal bipyramidal structure and only the *trans* isomer is known. Bidentate phosphines can yield analogous complexes with either one or both phosphorus atoms coordinated, or dimeric complexes with the phosphine acting as a bridging group. Higher levels of substitution by phosphorus ligands can be obtained in iron(0) complexes by reducing an appropriate carbonyl halide in the presence of a ligand or by metal vapor synthesis.[286] Thus, reduction of $[Fe(P(OMe)_3)_3Cl_2]$ by sodium amalgam in the presence of excess $P(OMe)_3$ gives[287] the air-sensitive complex $[Fe(P(OMe)_3)_5]$. The corresponding reaction with $[Fe(PMe_3)_3Cl_2]$ yields $[Fe(PMe_3)_4]$, however, this is not a four-coordinate but a six-coordinate species, in which oxidative addition has taken place (hydride transfer) to give the iron(II) complex (**31**).[288] The pentakis-phosphite complex reacts with CO to generate members of the series $[Fe(CO)_x(P(OMe)_3)_{5-x}]$, which cannot be obtained by direct substitution from $[Fe(CO)_5]$. The full series of complexes $[Fe(CO)_x(PF_3)_{5-x}]$ can be obtained from $[Fe(CO)_5]$ and PF_3. Direct synthesis from PF_3 and iron atoms[289] is, however, necessary to obtain the unusual dimer $[(PF_3)_3Fe(PF_2)_2Fe(PF_3)_3]$.

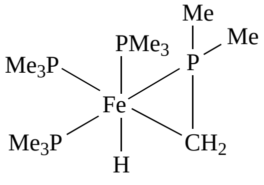

(31)

10 OXYGEN DONORS

10.1 Introduction

In the same way that iron(II) has a particularly strong affinity for nitrogen-donor ligands, so does iron(III) for oxygen donors. Most iron(II) complexes with simple oxygen donor ligands are high-spin and easily oxidized in air to iron(III) species, which are often polynuclear with metallic centers linked by oxygen bridges. Some of the most important and intensively studied species contain mixed nitrogen and oxygen donors and in particular, there is a substantial body of work on complexes of planar nitrogen macrocycles, which bind dioxygen. Because of their biological significance, these are dealt with elsewhere in the Encyclopedia. The numerous mono-, bi-, and polynuclear iron(III) complexes with carbohydrates are also of considerable biochemical importance.[290]

10.2 Water

Metallic iron dissolves in dilute mineral acids to yield $[Fe(H_2O)_6]^{2+}$, which oxidizes slowly in contact with air. In alkaline solutions, iron(II) is strongly reducing and there is some evidence that it will reduce dinitrogen.[291] Solutions of $[Fe(H_2O)_6]^{2+}$ are only mildly acidic such that addition of Na_2CO_3 merely precipitates iron(II) carbonate with no evolution of CO_2. The octahedral cation is pale blue–green in solution and is present in many hydrated iron(II) salts. Iron(II) can become present in surface water due to the reducing effect of decomposing matter, which can make purification a problem. In the removal of iron from drinking water, aeration removes CO_2 and iron is oxidized to iron(III) hydroxide which precipitates. Simple hydrated iron(III) salts are assumed to contain the $[Fe(H_2O)_6]^{3+}$ ion, although in practice many contain coordinated anions. The nitrate is an exception, but even here, iron exists crystallographically in two distinct octahedral environments,[292] the mean Fe^{III}–O distance is 0.14 Å shorter than in the corresponding iron(II) cation. Solutions of the simple $[Fe(H_2O)_6]^{3+}$ are pale violet (as is ferric alum), but aqueous solutions of iron(III) salts are frequently more colored due to charge-transfer bands between the anionic ligand and iron. Iron(III) readily undergoes hydrolytic polymerization in an aqueous solution. Examples of the type of complexes that result include $[(H_2O)_5Fe(\mu\text{-}O)Fe(H_2O)_5]^{4+}$ (Ref. 293) and $[(H_2O)_4Fe(\mu\text{-}OH)_2Fe(H_2O)_4]^{4+}$. The latter is the most abundant species at low pH.[294] Each iron atom is octahedrally coordinated to four water molecules and two bridging hydroxyl groups. The Fe_2O_2 group forms a planar ring with bond angles of 79° at Fe and 101° at oxygen, the Fe–Fe distance is 2.91 Å. All such doubly bridged iron(III) complexes show magnetic moments below the value expected for high-spin iron(III) (spin only, 5.92 BM) and they decrease with decreasing temperature. A number of iron(III) salts react with alcohols (and ethers, aldehydes, ketones etc.) to yield complexes whose precise structure can be difficult to determine.

The properties of the aqua-ions $[Fe(H_2O)_6]^{2+}$ and $[Fe(H_2O)_6]^{3+}$ in solution have been placed in context and reviewed in detail.[295] Their structures, established in the solid state in several X-ray diffraction studies of hydrated iron(II) and iron(III) salts, have been investigated in solution by

X-ray and neutron diffraction and scattering techniques.[296] The equilibrium between Fe^{3+} aq and $FeOH^{2+}$ aq[297] and the kinetics and mechanisms of their reactions with ligands,[298] including environmentally relevant humic and fulvic acids (see Section 4.11) and pharmacologically relevant desferrioxamine,[299] have been reviewed, as have complex formation reactions of $[Fe^{III}(\mu\text{-OH})_2Fe^{II}]^{4+}$ (Ref. 300) and of Fe^{2+}aq,[301] for example, with NO,[302] and electron exchange between Fe^{2+}aq and Fe^{3+}aq/$FeOH^{2+}$ aq.[303]

10.3 Oxo Anions

Iron(III) has a strong affinity for carboxylate ligands (see Sections 4.7–4.10 above), which, together with oxide, hydroxide, alkoxide, or phenoxide, readily act as bridging ligands to give numerous bi-[304] and polynuclear complexes. Magnetic and spectroscopic properties of trinuclear $[Fe_3(\mu^3\text{-}O)(O_2CR)_6L_3]^{n\pm}$ complexes have been intensively studied,[305] especially in relation to electron transfer within mixed-valence species ($n = 0$).[306] Many bi- and polynuclear complexes of this type are biomodels, for example, of nonhaem di-iron enzymes[307] of the active site of purple acid phosphatase,[308] of haemerythrin,[309] or of ferritin,[310] while several large polynuclear complexes, containing up to 19 iron atoms, pave the way for molecular magnets.[311] These large complexes may be planar ('ferric wheels'[312]) or incorporate hexagonal prismatic Fe_6O_6[313] or 'butterfly' Fe_4O_4[314] units.

10.4 Diketones

With complete exclusion of air, *trans*-$[FeCl_2(H_2O)_4]$ reacts with acetylacetone to form hydrated bis(2,4-pentanedionato)iron(II). The complex is coordinatively unsaturated and forms[315] an interesting tetrameric structure $[Fe_4(acac)_8]$ in which two asymmetric triply oxygen bridged dimers (**32**) are linked by rather long Fe–C bonds (2.785 Å, **33**). $[Fe(acac)_2]$ forms simple hexacoordinate adducts in reaction with a variety of bases, for example, heterocyclic diimines such as bipyridines. Complexes formed by iron(II) with other β-diketonates are polymeric and highly air sensitive. Iron(III), however, forms a series of stable highly colored complexes. Neutral $[Fe(acac)_3]$ has a simple, essentially octahedral geometry,[316] it has been reported to have catalytic activity in stereoselective epoxidation reactions. Also neutral and monomeric is the complex $[Fe(acac)_2Cl]$, in which the Fe atom sits slightly above the plane occupied by the four oxygen atoms, the chlorine atom lies above iron at the apex of a square pyramid. A series of corresponding alkoxide complexes exists,[317] although here the structure is dimeric with two OR bridges between the iron atoms in $[Fe(acac)_2OR]_2$.

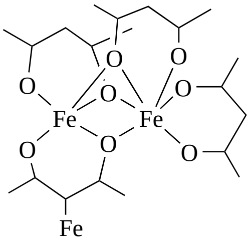

(**32**)

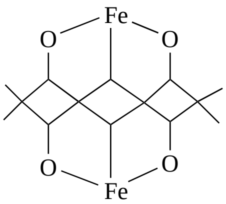

(**33**)

10.5 Other Oxygen Donors

Some *S*-bonded DMSO iron(II) complexes are known, but the explosive pale green complex $[Fe(DMSO)_6](ClO_4)_2$ formed when the hexaqua perchlorate is mixed with dimethylsulfoxide in acetone, appears to be *O*-bonded. Hexaaqua iron(II) reacts with pyridine *N*-oxide to give dark red $[Fe(pyO)_6]^{2+}$, and analogous complexes are formed with a variety of substituted pyridine *N*-oxides.

10.5.1 Phenols, Catechols, and Hydroxamates

Iron(III) reacts with the phenolic moiety to give characteristic colors, which have long been used analytically. Monodentate phenoxide complexes have been relatively elusive, though tetrakis(2,3,5,6-tetramethylphenolato)iron(III) for example, exists[318] as a red–orange tetraethylammonium salt from reaction of $FeCl_3$ with the phenol in anhydrous alcohol. The complex has a distorted FeO_4 unit with rather short Fe–O bonds (1.85 Å) and a reversible one-electron reduction potential at -1.32 v, demonstrating a particularly strong stabilization of the Fe(III) oxidation state, and an electronic spectrum showing three intense charge-transfer bands.

As mentioned above, iron is largely present in the biosphere as insoluble iron(III) oxide, and so a unique complex chemistry has evolved to allow its transport in biological systems. This involves two classes of oxygen donor chelating ligands: catecholates and hydroxamates. Catechol itself ($catH_2 =$ 1,2-dihydroxybenzene) is a poor ligand at low pH, forming a transient complex with iron(III), which decomposes to generate iron(II) and *o*-quinone. In less acid (and anaerobic) conditions, stable tris-catecholate iron(III) complexes are formed. $[Fe(cat)_3]^{3-}$ is a good model for enterobactin (see below).[319] The structure of $K_3[Fe(cat)_3].1.5H_2O$ shows approximate D_3 symmetry with the aromatic rings bent away from the O-M-O plane and an average Fe–O bond distance of 2.015 Å. The weakly acidic hydroxamic acids (LH) form deeply colored complexes[320] with iron(III) at low pH, the colors being characteristic and analytically useful. High-spin $[Fe(L)_3]$ (**34**) is very stable ($\beta_3 \sim 10^{30}$) in contrast to iron(II) derivatives and the reduction of such iron(III) complexes has been postulated as a mechanism for the release of biological iron following its sequestration by siderophores, which also contain hydroxamate groups. The unexpectedly labile neutral iron(III) hydroxamato complexes can be deprotonated in basic solution to yield the corresponding hydroximato complexes according to equation (17). The predominance of the *cis* configuration is common, but not ubiquitous, for tris-hydroxamato iron(III) complexes.[321]

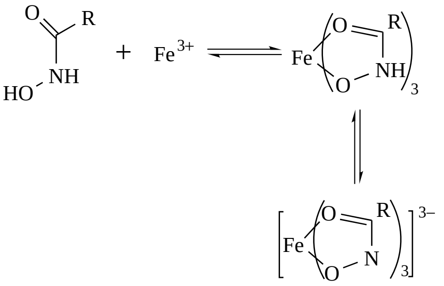

(17)

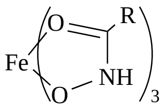

(**34**)

10.5.2 Siderophores and Models

Siderophores,[322] hexadentate tris-catecholate and tris-hydroxamate ligands, are produced by many microorganisms to facilitate iron uptake. Several synthetic models, such as trencam (**35**) and licams (**36**), for the tris-catecholate enterobactin (**37**) do not quite match its affinity for iron(III) (Table 8). Similar tris-hydroxamate ligands model naturally occurring ferrichromes and desferrioxamines (e.g. dfo, (**38**)).

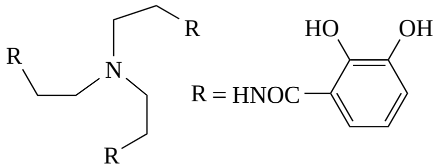

(**35**)

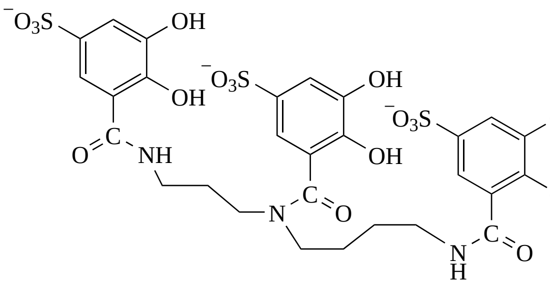

(**36**)

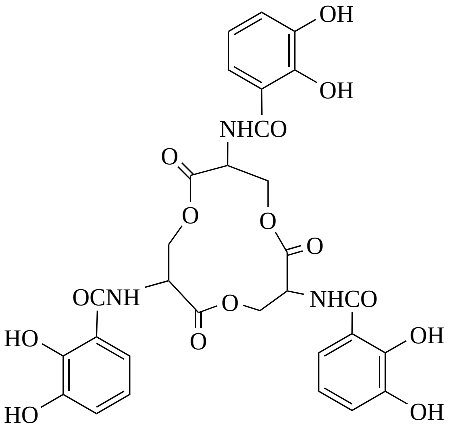

(**37**)

10.5.3 Hydroxypyranones and Hydroxypyridinones

The anionic forms of 3-hydroxypyran-4-ones such as maltol (**39**) or kojic acid (**40**) and of 3-hydroxypyridin-4-ones such as (**41**) – and of their 1-hydroxy-pyridin-2-one isomers – form stable complexes ($\beta_3 \approx 10^{30}$) with iron(III). Several 3-hydroxypyridin-4-ones were originally developed as analytical reagents, for iron and for a number of other metals.[323] In recent years, the main interest[324] in these ligands has been as the most promising potential replacements[325] for desferrioxamine, for many years, the only available but very unsatisfactory agent[326] for the treatment of iron overload in the body, and as agents for the introduction of iron in cases of severe anemia.[327] The facile synthesis[328] of a wide range of hydroxypyridinones, bidentate and hexadentate, with the possibility of tailoring[329] various relevant properties, including solvation[330] to facilitate both administration and trans-membrane transport, has led to their

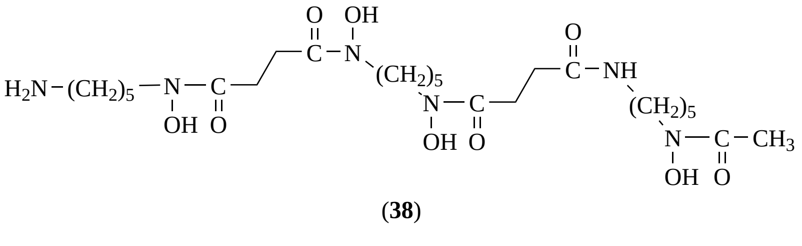

(**38**)

Table 9 Stability constants and redox potentials for iron(III) and iron(II) complexes of hexadentate ligands

	$\log_{10}K_1$ ($Fe^{III}L$)	E°/mV	$\log_{10}K_1$ ($Fe^{II}L$)
Enterobactin	52	−990	22
Alterobactins	49–53		
Synthetic tris-catecholates	43–49		
Desferrioxamine	31	−470	10
Natural and synthetic tris-hydroxamates	29–33		
tren-hopo	27	−177	11
dtpa	28		
edta	25	−120	14
transferrin	20		

intensive investigation. Deferiprone, (**41**), has been studied[331] and clinically assessed,[332] the most though it is claimed that 2-ethyl derivatives might prove preferable.[333] Interestingly, hexadentate analogues[334] have proved to lack the expected (chelate effect) stability advantage over bidentate ligands, presumably due to steric difficulties.[335]

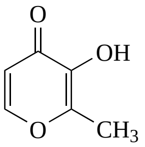

(**39**)

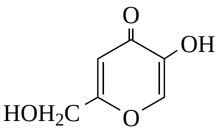

(**40**)

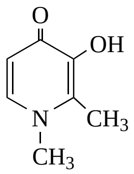

(**41**)

10.5.4 *Stability Constants and Redox Potentials*

The markedly negative redox potentials of tris-catecholate and tris-hydroxamate iron complexes (Figure 4) may be ascribed to the high stabilities of the iron(III) complexes and the rather low stabilities of their iron(II) analogues.[336] Table 9 details the relevant data (interconnected by a thermochemical cycle earlier applied to amino acid pentacyanoferrate complexes[337]), and documents the remarkably higher stabilities of tris-catecholate than of tris-hydroxamate complexes of iron(III).

10.6 Ligands Containing Oxygen and Nitrogen Donors

10.6.1 *Schiff-base complexes*

Condensation of an aldehyde or ketone with a primary amine yields a Schiff base, a class of compounds that have been widely studied as chelating ligands. N,N'-Diimine ligands, resulting from condensation with pyridine-2-aldehyde or 2-pyridyl ketones, are discussed in Section 8.2.2, and N,O-ligands are discussed here. The condensation products of salicylaldehyde are important mixed N,O donor ligands. Those resulting from the condensation of salicylaldehyde and aniline (**42**) form very stable complexes with iron(II). In general, the N-substituted salicylaldimines (**43**) form high-spin complexes $[Fe(salNR)_2X]$ ($X = Cl$ or Br) with iron(III). The X-ray structure[338] ($R = n$-propyl, $X = Cl$) shows five coordination with an intermediate geometry between trigonal bipyramidal and square planar. When R is large, different crystalline modifications can be observed and the magnetic moment can be significantly reduced at lower temperatures. The tridentate base (**44**) forms an iron(III) complex, which is five coordinate and dimeric [Fe(**44**)Cl]$_2$. The iron atoms participate in a four-membered ring, bridged by alkoxide oxygen atoms and the chlorine atoms sit at the apex of a square pyramid (**45**).

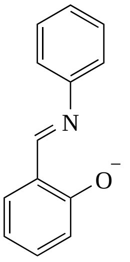

(**42**)

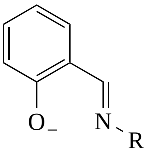

(**43**)

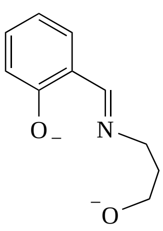

(**44**)

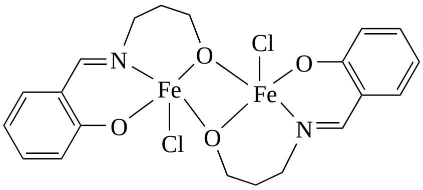

(**45**)

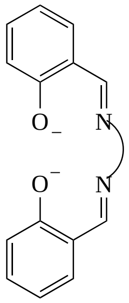

(**46**)

An extremely well-known tetradentate Schiff-base results from the condensation of two molecules of salicylaldehyde with a diprimary amine. Where this is 1,2-diaminoethane, (ethylenediamine, en) the ligand 'salen' results (**46**). [Fe(salen)Cl] may be isolated in both mono- and dimeric forms.[339] The monomer has a distorted square-planar geometry with the iron atom sitting 0.46 Å proud of the plane formed by the salen donor group along the same axis as the apical Cl atom. The dimer has an octahedral geometry at iron, each salen ligand sharing one oxygen atom with two monomer moieties. The *trans*-Fe–O bond in the dimer is 0.26 Å longer than the Fe–O bonds in the salen ligand plane. The isomers, which exist for a wide variety of analogous complexes, can be distinguished by their differing magnetic properties. The monomer exhibits classic behavior with the magnetic moment close to the spin-only value; the dimers, however, have low room temperature moments, which reduce when the temperature is lowered. The differences are emphasized by divergent IR and Mössbauer properties. The air-sensitive neutral iron(II) complex [Fe(salen)] is obtained**340** from [Fe(salen)CH_2Ph]. It can be reduced by sodium in THF to yield the unusual d^7 iron(I) complex Na[Fe(salen)]. Also assigned a d^7 electronic configuration is the NO adduct [Fe(salen)NO]. This complex has a $S = 3/2$ to $S = 1/2$ spin-crossover near 175 K, its geometry is square pyramidal and the N–O bond is bent, both features remain unchanged as the spin-state changes.**341** The Fe(salen) group also forms dimeric complexes with a single oxygen atom bridge, $[(Fe(salen))_2O]$ having square-pyramidal geometry at the iron atoms. The geometry is distorted, however; crystals from different solvents were shown to have Fe–O–Fe angles of 139° and 142°. The bulky isopropyl groups in the Schiff-base ligand derived from salicaldehyde and isopropylamine impose tetrahedral coordination geometry on the iron(II) in its bis-ligand complex; oxidation in air yields an oxo-bridged di-iron(III) product.**342**

10.6.2 Complexes of Other Mixed Oxygen–Nitrogen Donors

A variety of cyclic and acyclic ligands with mixed oxygen and nitrogen-donor atoms form complexes with iron(II) and iron(III), which have five, six, or seven coordination. A series of complexes is also formed**343** in which amino acids act as N and O donors; typically hexacoordinate, these can have extended carboxylate bridged structures. The structure and reactivity of such complexes have been examined as model systems in the search for explanations of the biological activation and transport of oxygen. The oxygen carrying proteins hemerythrins contain active centers**344** in which two iron atoms are linked by both μ-oxo and carboxylate bridges provided by amino acid groups – these are discussed elsewhere in this Encyclopedia.

Polyaminocarboxylate ligands are important in iron(III) chemistry. The classic mixed hexadentate O and N donor ligand edta forms complexes of the type $X[Fe(edta)(H_2O)]\cdot nH_2O$ (X = Li, Rb), in which the coordinated water molecule provides the seventh donor to give a pentagonal bipyramid. Base hydrolysis yields**345** the complex ion $[Fe_2(edta)_2O]^{4-}$, in which a μ-oxo link joins the iron atoms. Related ligands, of which a wide range is now available, assist the buildup of polynuclear μ-oxo-μ-hydroxo-bridged species such as $[Fe_6(\mu\text{-}O)(\mu\text{-}OH)_5(hpdta)_3]^{4-}$.**346** The formation constant for iron(III) edta complexation is high and this ligand is often used to reduce the level of free iron and other metal ions in solution. A wide range of related ligands is now available. The addition of carboxylate-bearing pendant arms to tetraaza-macrocycles, as in dota, (**47**), gives ligands with high affinities for 3+ metal ions, including Fe^{3+} (log $K_1 = 29.4$).**347**

The diimine-hydroxyl ligand poap, (**48**), undergoes self-assembly in the presence of Fe^{3+} to give Fe_5^{III} and Fe_9^{III} species; the latter has a square-grid structure.**348**

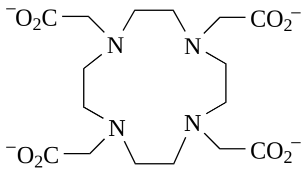

(**47**)

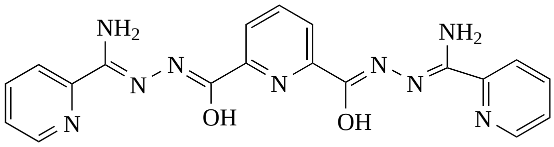

(**48**)

11 COMPLEXES WITH SULFUR DONORS

11.1 Introduction

There is a large body of knowledge**349** on the coordination chemistry of iron–sulfur complexes and iron clusters particularly directed at the modeling and understanding of the action of nonheme proteins whose active sites contain iron–sulfur units. These topics are discussed in detail elsewhere in this Encyclopedia; here, the emphasis is on the basic coordination chemistry.

11.2 Sulfide and Thiolate Complexes

11.2.1 Mononuclear Complexes

Tetrahedral mononuclear iron sulfide units lie at the heart of a number of electron transfer proteins. The active site of the rubredoxins, for example, consists**350** of iron coordinated in a somewhat distorted tetrahedral geometry by the sulfur atoms of four cysteinyl residues. One-electron transfer flips one of the irons between oxidation states II and III. A number of synthetic complexes containing an FeS_4 core have been identified. A simple example is provided by $Ba[Fe(SCH_2CH_2OH)_4]$, whose preparation, structure, and EPR and Mössbauer spectra have been reported.**351** Trimethylarsine sulphide forms both $[Fe(SAsMe_3)_4](ClO_4)_2$ and $[FeX_2(SAsMe_3)_2]$ (X = Cl, Br). The iron(II) complex $[Fe(SPMe_2NPMe_2S)_2]$ (**49**) has Fe–S bond lengths between 2.339 Å and 2.380 Å and S–Fe–S angles of between 100.5° and 114.9°. $[Fe(SPh)_4]^{2-}$ can be prepared from PhS^-. The best example, however, is obtained**352** from the reaction between $[FeCl_4]^{2-}$ and excess *o*-xylyldithiol (*o*-xyl$(SH)_2$) to give the orange complex $[Fe(S_2\text{-}o\text{-}xyl)_2]^{2-}$. Careful aerobic oxididation of this iron(II) species yields the corresponding iron(III) complex, which can be isolated as the Et_4N^+ salt. The Fe(II)–S bond length of 2.356 Å is 0.09 Å longer than that of its iron(III) counterpart. If a lower ligand to metal ratio is used in the synthesis, the dimer $[Fe_2(S_2\text{-}o\text{-}xyl)_3]^{2-}$ results, which can be converted into the monomeric complex with excess thiol. The oxidation state of the iron in the monomer is reversible in cyclic voltammetry experiments in dimethylformide. Sterically hindered sulfur ligands seem to stabilize the FeS_4 unit.

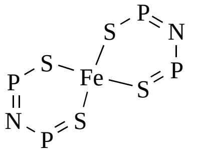

(**49**)

11.2.2 Dinuclear Complexes

The Fe_2S_2 core is most commonly found in biological systems in the two-iron-ferredoxin proteins and several model complexes of the type $[Fe_2S_2(SR)_4]^{2-}$ have been synthesized. Simple reaction of $FeCl_3$ with NaSH and NaOMe is not a viable route since only Fe_4 units are formed. By selecting a dithiolate with a chelate bite approximately equal to the distance between coordination sites in the stable Fe_4 units, a dimeric iron(III) complex is obtained, namely, $[Fe_2S_2(S_2\text{-}o\text{-}xyl)_2]^{2-}$. A successful synthetic route[353] to this and analogous complexes involve the reaction of $FeCl_3$ with elemental sulfur and the thiolate in methanol in the presence of the tetraalkylammonium ion (which appears to prevent the formation of Fe_4S_4 units). These dimeric complexes share many properties with the oxidized forms of the two iron ferredoxin proteins. These include optical spectra and magnetic properties; Mössbauer parameters are also similar. One-electron reduction of the synthetic analogue yields inhomogeneous iron centers on the Mössbauer timescale and the chemical shifts suggest the presence of both high-spin iron(II) and iron(III) that are antiferromagnetically coupled. This behavior is mirrored in the mixed oxidation state form of the protein. The observation in the synthetic analogue confirms that it is not an intrinsic property of the protein but rather an intrinsic property of the Fe_2S_2 system.[354] The stability of the iron–sulfur cores is exemplified in their substitutional chemistry. Thus, aryl thiolate (SAr) readily substitutes S_2-*o*-xyl in the above complexes to yield $[Fe_2S_2(SAr)_4]^{2-}$, which itself reacts with benzoyl chloride to form $[Fe_2S_2Cl_4]^{2-}$. The X-ray structure of $(NEt_4)_2[Fe_2S_2Cl_4]$ shows the transformations have essentially had no effect on the structure of the Fe_2S_2 core. As a result of this inherent stability, ligand substitution can be used as a structural probe for removing the metal core of iron–sulfur proteins (the so-called core extrusion technique).

11.2.3 Trinuclear Complexes

Of more recent discovery[355] are a group of ferredoxins having [3Fe-3S] cores. Structural and spectroscopic investigation suggested structures (**50**), (**51**), and (**52**) as possible core units. There are a number of synthetic cluster complexes with cores containing three iron atoms, notably with two structural types. The first has[356] a pyramidal structure in which a μ^3-sulfur atom caps a ring of three sulfur and three iron atoms (**53**), and is typified by $[Fe_3S(S_2\text{-}o\text{-}xyl)_3]^{3-}$. Once again, there is evidence for magnetic coupling and a reversible one-electron redox process. One further synthetic type of trinuclear iron–sulfur core[357] has three linearly arranged iron atoms with two pairs of sulfide bridges (**54**). Complexes of this type, $[Fe_3S_4(SR)_4]^{3-}$, are prepared by the action of sulfur in acetone on $[Fe(SEt)_4]^{2-}$, a strongly reducing complex that has been very useful in the preparation of a variety of cluster complexes (Scheme 4).

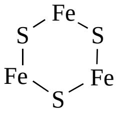

(**50**)

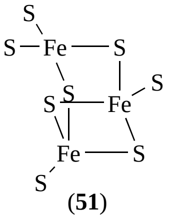

(**51**)

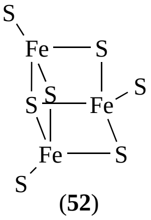

(**52**)

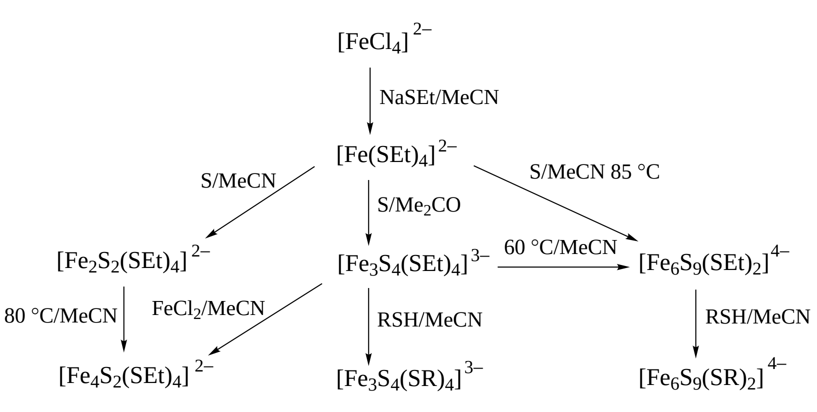

Scheme 4

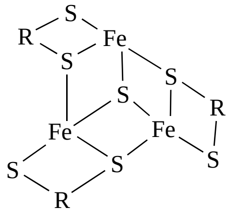

(53)

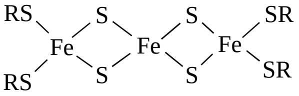

(54)

11.2.4 *Tetranuclear Complexes*

The basic geometry of the important Fe_4S_4 unit found in natural and synthetic systems consists of a tetrahedron of four iron atoms inside a slightly larger tetrahedron of four sulfur atoms forming a distorted cube. Each sulfur atom is coordinated to three iron atoms and each iron atom has a terminal SR ligand. In the case of a protein, this is a cysteinyl residue. In either case, the cube is compressed in the direction of D_{2d} symmetry. The synthetic systems are isoelectronic with their protein analogues, and formally contain two iron(II) and two iron(III) centers, which are antiferromagnetically coupled. $[Fe_4S_4(SR)_4]^{2-}$ complexes undergo reversible one-electron reduction and oxidation reactions in electrochemical studies but the protein-encased natural complexes have slightly different redox potentials. Whilst early explanations of this phenomenon concentrated on the protein, it appears solvent effects are rather crucial. No localized individual atoms in the +2 or +3 oxidation state are observable in these systems.[358]

Preparatively, the synthetic complexes are relatively easy to obtain. $FeCl_3$ reacts with NaSR to give[359] a dark green polymeric sulfide, which, when treated with NaHS and NaOMe gives the corresponding disulfide and the mixed oxidation state cluster $Na_2[Fe_4S_4(SR)_4]$. The reaction is illustrated in equation (18). As with the dimeric complexes, thiolate ligand exchange reactions are facile and have been studied in some detail. Exchange takes place, for example, as in equation (19). Solvent effects can be important from the formation of these complexes as is illustrated in the synthesis of $[Fe_4S_4(SPh)_4]^{2-}$ from $FeCl_3$ and PhS^-. Under appropriate conditions of stoichiometry and solvation in this preparation, $[Fe_4(SPh)_{10}]^{2-}$, $[Fe(SPh)_4]^{2-}$, and $[Fe_2S_2(SPh)_4]^{2-}$ can also be isolated. $FeCl_2$ may also be used as a starting material, in which case rather less thiolate is required since it is not consumed in reducing iron(III) and forming disulfide. If these syntheses are carried out[360] with $MoS_4{}^{2-}$, RS^-, and $FeCl_3$ in methanol containing R_4N^+, a series of novel bridged cluster complexes result. The tungsten analogues[361] are also known. Ligands other than – SR can coordinate to $[Fe_4S_4]$ cores, including dithiocarbamates[362] (see Section 11.4), phosphines,[363] or halides.[364]

$$\begin{aligned}&4FeCl_3 + 6NaSR + 4NaSH + 4NaOMe \longrightarrow \\ &\quad Na_2[Fe_4S_4(SR)_4] + RSSR + 4MeOH + 12NaCl \qquad (18)\end{aligned}$$

$$\begin{aligned}&[Fe_nS_n(SR)_4]^{2-} + mR'SH \longrightarrow [Fe_nS_n(SR)_{4-m}(SR')_m]^{2-} \\ &\quad + mRSH \quad n = 2, 4;\ m = 0-4 \qquad (19)\end{aligned}$$

11.2.5 *Higher Nuclearity Complexes*

Several clusters of the type $[Fe_6S_6L_6]$ are known,[365] as are a few nonbiological complexes with an $[Fe_8S_8]$ core, and at least one with an $[Fe_{16}S_{16}]$ core.[366]

11.3 Complexes with Nitrosyl Ligands

The isolation of $[Fe_2(SMe)_2(NO)_4]$ from certain preserved vegetables[367] and its implication in diet-related carcinogenesis, underlines the similarities between the iron–sulfur nitrosyl systems and the complexes discussed above. The prototypic iron–sulfur nitrosyl complexes are Roussin's salts[368] (Section 'Nitric Oxide Complexes with Sulfur Donors'). $[Fe_2(SR)_2(NO)_4]$ complexes are known with a wide range of R groups. They can be synthesized directly from iron(II) salts, as shown in equation (20), or a variety of other mononuclear iron complex precursors including $[Fe(NO)(S_2CNMe_2)_2]$ (with excess RS^-), $[Fe(CO)_3NO]$, and $[Fe(NO)_2(SR)_2]^-$.

$$\begin{aligned}&4FeSO_4 + 8KOH + 2RSH + 4NO \longrightarrow [Fe_2(SR)_2(NO)_4] \\ &\quad + Fe_2O_3 + 4K_2SO_4 + 5H_2O \qquad (20)\end{aligned}$$

Dinuclear and tetranuclear complexes are also suitable starting materials, and much of the synthetic and substitutional chemistry of these species reflects the ability of the systems to sustain monomeric solvated dinitrosyl species such as $[Fe(NO)_2(solvent)_2]^+$ or $[Fe(NO)_2(SR)(solvent)]$. The latter tend to be formed in solvents having poor and the former in ones having good π-acceptor capabilities. A review[369] of nitrosyl complexes of iron–sulfur complexes is available.

11.4 Dithio Complexes

There are a number of dithio ligands, which readily form complexes with iron, the principal of which are dithiolates (**55**), dithiocarbamates[370] (**56**), dithioacetylacetonates (**57**), xanthates (**58**), and dithiophosphates.

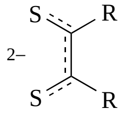

(**55**)

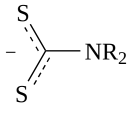

(**56**)

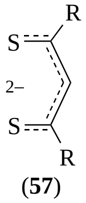

(**57**)

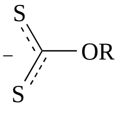

(**58**)

Iron(II) dithiocarbamates $[Fe(R_2dtc)_2]$ have Mössbauer spectra indicating a dimeric structure (**59**) and this is borne out[371] by X-ray investigation. These complexes are air sensitive and are rapidly oxidized to the monomeric tris-dtc species $[Fe(R_2dtc)_3]$, which exhibit spin crossover.[372] The position of the ${}^6A_1 \rightleftharpoons {}^2T_2$ equilibrium is sensitive to the nature of the NR_2 substituent. It has been argued that this effect is largely steric in origin since an increase in the R–N–R angle

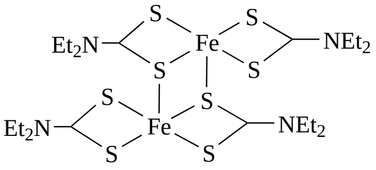

(**59**)

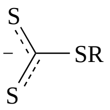

(**60**)

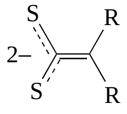

(**61**)

resulting from larger substituents would imply an increasing polarization of charge and therefore an increasing ligand field. This has been disputed, however, and the effect also correlates with the pK_a of the secondary amine. In systems where the CS_2 and NR_2 are coplanar, the electron-releasing ability of the NR_2 group seems to be the important factor. It can be predicted that the transition to the low-spin state would be accompanied by a contraction in the FeS_6 coordination sphere of $[Fe(R_2dtc)_3]$, and that there will therefore be a pressure dependance of the spin equilibrium. This effect has been confirmed experimentally and a typical Fe–S bond contraction of around 0.1 Å observed.[373] The spin transition is also affected by the nature of solvent molecules included in the lattice, solvents capable of hydrogen bonding typically shifting the equilibrium toward the high-spin state. $[Fe(dtc)_3]$ complexes undergo quasi-reversible one-electron redox reactions in polar solvents to yield low-spin d^4 iron(IV) and yellow, air-sensitive, high-spin iron(II) species. $[Fe(S_2CNR_2)_3]^+$ complexes are the most stable iron(IV) species and can be isolated as the BF_4^- salts (R = Me, Et, ^{i}Pr, cyclohexyl) by oxidation of the tris-iron(III) complex. The perchlorate and hexafluorophosphate salts have also been prepared. As would be predicted from the higher charge on the iron and the removal of electron density in an antibonding e_g orbital, the Fe–S bond lengths are observed[374] to be shorter in the iron(IV) complexes than in the iron(III) complexes by ca. 0.11 Å. The corresponding iron(III) xanthate complexes are almost always low spin in the 90–300 K range, whilst the thioxanthates (**60**) exhibit[375] spin-crossover equilibria. Iron(III) xanthates react with pyridine to form high-spin iron(II) $[Fe(S_2COR)_2(py)_2]$. The iron(II) xanthates $[Fe(S_2COEt)_2]$ and $[Fe(S_2COEt)_3]^-$ are known. The iron(II) thioxanthate complex $[Fe(S_2CSEt)_3]^-$ is formed in the reaction of *trans*-$[FeCl_2(H_2O)_4]$ with KS_2CSEt in MeOH or THF. Dithiolate ligands favor oxidation states higher than +2. *n*,*n*-Dithiolates such as $(1{,}1\text{-}S_2CH{=}CH(CN)_2)^{2-}$ (**61**, R = CN) generate a four-membered chelate ring and form high-spin tris-ligand iron(III) complexes. The isomeric *n*,*n*′-dithiolates $(1{,}2\text{-}S_2Et(CN)_2)^{2-}$ (**55**, R = CN) yield five-membered chelate rings and form both bis and tris complexes. $[PPh_4]_3[Fe(1{,}2\text{-}S_2CH{=}CH(CN)_2)_3]$ is six-coordinate low spin but $[NBu_4]_2[Fe(1{,}2\text{-}S_2CH{=}CH(CN)_2)_2]$ is dimeric in the solid state, the iron atom having a square-pyramidal geometry, in which the base consists of four sulfur atoms from the bidentate dithiolene ligands and the apex of a bridging sulfur from a second FeS_4 unit.[376] The PPh_4^+ salt of this dimer forms parallel stacks.[377]

Dithioacetylacetonate (SacSac) forms $[Fe(SacSac)_3]$ by the reaction of iron(II) salts with acac in alcohol at low pH in the presence of H_2S. In this low-spin complex, the metal chelate rings are essentially planar, although one such unit has a larger S–Fe–S angle than the other two leading to a slightly distorted octahedral structure. Attempts to prepare this complex from iron(III) salts result in the formation of the $[FeX_4]^{2-}$ salt of the five-membered cyclic 3,5-dimethyl-1,2-dithiolinium cation. This can be reduced with thiosulfate to give the tris-SacSac complex, but when red–brown crystals of this are shaken further with thiosulfate in chloroform under anaerobic conditions, the bis-SacSac iron(II) complex results. An elegant example of the effect of sulfur as a donor atom on spin-pairing in iron complexes is given by the iron(III) series $[Fe(acac)_3]$, $[Fe(Sacac)_3]$, and $[Fe(SacSac)_3]$ (Sacac = monothioacetylacetonate) in which the first is high-spin, the last low spin and the second either, depending on the ligand substituents.[378]

11.5 Ligands With Sulfur and Other Donor Atoms

Many complexes of iron(II) with ligands having mixed sulfur and nitrogen-donor atoms are known and a wide variety of coordination geometries and magnetic properties have been observed. The familiar Schiff-base condensation reaction can yield mixed-donor atom ligands containing sulfur. Thus, the condensation of 2,6-diacetylpyridine with 4,7-dithiadecane-1,10-diamine gives (**62**) with two sulfur and three nitrogen-donor atoms. Six-coordinate complexes $[Fe(\mathbf{62})X]^+$ are formed, which are high-spin for X = Cl, Br; but low spin for X = I. When X = NCS, $[Fe(\mathbf{62})(NCS)]^+$ is low spin but a complex having the stoichiometry $[Fe(\mathbf{62})(NCS)_2]$ is also known, which appears to exhibit three solid-state modifications, two of which are high and the other low spin.[379] Many iron–sulfur clusters are supported in nature by the thiolate group of cysteinyl residues in proteins. A variety of complex species have been observed in reactions of iron(II) with cysteine, some involving bonding through the carboxylate oxygen and some through bridging thiolate groups. The monothiocarbamates form a series of complexes with iron(III) in a similar way to the dithiocarbamates, these also exhibit the spin-crossover phenomenon.[380] The S_2N_2-donor ligand $(^-S)C_6H_4(N^-)CH_2CH_2(N^-)C_6H_4(S^-)$ stabilizes the +4 and the +5 oxidation states of iron (see Section 5.4).

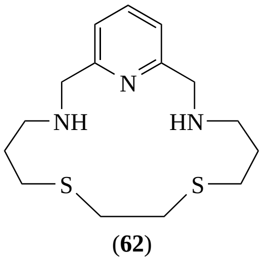

(**62**)

12 HALIDE COMPLEXES

Tetrachloro-, tetrabromo-, and tetraiodo-iron(III) and -iron(II) anions have already been mentioned in Section 4.1 alongside their respective binary halide parents. Metal-halide bond distances for about 300 species of various oxidation states and coordination numbers of iron,**[381]** and solution diffraction structural studies on bromoiron(II) and chloroiron(III), have been documented.**[382]** Tetrachloroiron(III) is a useful counterion for the preparation of salts in a suitable form for X-ray diffraction structural determinations. The redox potential for the $[FeCl_4]^{2-/-}$ couple has ben reported,**[383]** as have the preparation and characterization of salts of $[FeCl_4(H_2O)_2]^-$ and $[FeCl_5(H_2O)]^{2-}$,**[384]** along with EXAFS characterization**[385]** and stability**[386]** of the latter in solution. The crystal structures and magnetic properties of several salts of $[Fe^{II}Cl_6]^{4-}$ and of $[Fe^{III}Cl_6]^{3-}$ have been determined.**[387]** The $[Fe^{II}_2Cl_4(H_2O_6)]^{2-}$ anion contains two octahedral Fe^{2+} centers bridged by two chlorides.**[388]** The $[Fe_2Cl_6]^{2-}$ anion has recently been discovered, in the course of establishing recommended preparations for salts of the well-established $[Fe_2OCl_6]^{2-}$ anion.**[389]** There are many ternary iron(II) and iron(III) halide complexes containing nitrogen-donor ligands – see Sections 8.1.3 and 8.1.4, for examples. Isomerism is possible for complexes FeX_2L_4 and FeX_3L_3; the discussion**[390]** of the fine balance between the relative stabilities of the *mer* and *fac* forms of $[FeCl_3L_3]$ complexes provides an entry into this topic.

13 REFERENCES

1. W. S. Fyfe, ‘Geochemistry’, Oxford University Press, Oxford, 1974; L. H. Ahrens, ‘Distribution of the Elements in Our Planet’, McGraw-Hill, New York, 1965, p. 97.
2. S. J. A. Fatemi, F. H. A. Kadir, D. J. Williamson, and G. R. Moore, *Adv. Inorg. Chem.*, 1991, **26**, 409; R. B. Frankel and R. P. Blakemore eds, ‘Iron Biominerals’, Plenum Press, New York, 1991; Subcommittee on Iron, Division of Medical Sciences Assembly of Life Sciences, National Research Council, ‘Iron’, University Park Press, Baltimore, 1978; E. J. Underwood, ‘Trace Elements in Human and Animal Nutrition’, 2nd edn., Academic Press, New York, 1962; R. Crichton, ‘Inorganic Biochemistry of Iron Metabolism, From Molecular Mechanisms to Clinical Consequences’, 2nd edn., Wiley, New York, 2001.
3. W. Stumm and J. J. Morgan, ‘Aquatic Chemistry’, Wiley-Interscience, New York, 1970.
4. J. F. Pankow, ‘Aquatic Chemistry Concepts’, Lewis Publishers, Chelsea, Michigan, 1991.
5. R. Chester, ‘Marine Geochemistry’, Unwin Hyman, London, 1990.
6. R. M. Harrison ed., ‘Understanding Our Environment’, 2nd edn., Royal Society of Chemistry, Cambridge, 1992.
7. P. O’Neill, ‘Environmental Chemistry’, 2nd edn., Chapman & Hall, London, 1993.
8. C. A. J. Appelo and D. Postma, ‘Geochemistry, Groundwater and Pollution’, Balkema, Rotterdam, 1993.
9. W. Stumm ed., ‘Aquatic Chemical Kinetics’, Wiley-Interscience, New York, 1990.
10. A. S. Wagh and W. R. Pinnock, *Econ. Geol.*, 1987, **82**, 757.
11. R. A. Kerr, *Science*, 1994, **263**, 1089; R. Corfield, *Chem. Brit.*, 2003, **39**, 30.
12. R. T. Reid, D. H. Live, D. J. Faulkner, and A. Butler, *Nature*, 1993, **366**, 455.
13. K. Barbeau, E. L. Rue, K. W. Bruland, and A. Butler, *Nature*, 2001, **413**, 409.
14. J. Webb, D. J. Macey, W. Chua-anusorn, T. G. St. Pierre, L. R. Brooker, I. Rahman, and B. Noller, *Coord. Chem. Rev.*, 1999, **190–192**, 1199.
15. R. B. Frankel and R. P. Blakemore eds, ‘Iron Biominerals’, Plenum, New York, 1991.
16. R. C. Barry, J. L. Schnoor, B. Salzberger, L. Sigg, and W. Stumm, *Water Res.*, 1994, **28**, 323.
17. D. A. Brown, B. L. Sherriff, J. A. Sawicki, and R. Sparling, *Geochim. Cosmochim. Acta*, 1999, **63**, 2163; T. Kasama and T. Murakami, *Chem. Geol.*, 2001, **180**, 117.
18. W. Schneider, *Arzneim. Forsch.*, 1987, **37**, 92; W. Schneider, *Chimia*, 1988, **42**, 9.
19. K. S. Hagen, *Angew. Chem., Int. Ed. Engl.*, 1992, **31**, 1010.
20. J. A. Hardy and A. E. Aust, *Chem. Rev.*, 1995, **95**, 97.
21. E. C. Bain and H. W. Paxton, ‘Alloying Elements in Steel’, Chapman & Hall, London, 1962.
22. D. K. Ewart and M. N. Hughes, *Adv. Inorg. Chem.*, 1991, **36**, 103.
23. J. Donohue, ‘The Structure of the Elements’, Wiley, New York, 1974, p. 202.
24. P. A. Cox, ‘The Elements’, Oxford Science Publications, Oxford, 1989, p. 63.
25. E. Möller, J. Sieler, and R. Kirmse, *Z. Naturforsch.*, 1997, **52B**, 919.
26. R. Benn and A. Rufińska, *Angew. Chem., Int. Ed. Engl.*, 1986, **25**, 861; J. Mason, *Chem. Rev.*, 1987, **87**, 1299.
27. J. J. Dechter, *Prog. Inorg. Chem.*, 1985, **33**, 393 (see p. 441); L. Baltzer and M. Landergren, *J. Chem. Soc., Chem. Commun.*, 1987, 32; M. Bühl, F. T. Mauschick, F. Terstegen, and B. Wrackmeyer, *Angew. Chem., Int. Ed. Engl.*, 2002, **41**, 2312.
28. M. D. Short, in ‘Textbook of Radiopharmacy’, 2nd edn., ed. C. B. Sampson, Gordon and Breach, Yverdon, Switzerland, 1994, p. 6.
29. A. G. Maddock, ‘Mössbauer Spectroscopy: Principles and Applications’, Horwood Publishing, Chichester, 1997, Chaps. 5, 7 and 8.
30. G. J. Long ed., ‘Mössbauer Spectroscopy Applied to Inorganic Chemistry’, Plenum, New York, 1984, and subsequent

volumes in this series; R. H. Herber, ‘Chemical Mössbauer Spectroscopy’, Plenum Press, New York, 1984.

31. A. X. Trautwein, H. Winkler, S. Schwendy, H. Grünsteudel, W. Meyer-Klaucke, O. Leupold, H. D. Rüter, E. Gerdau, M. Haas, E. Realo, D. Mandon, and R. Weiss, *Pure Appl. Chem.*, 1998, **70**, 917.
32. H. E. Knechtel, ‘Encyclopedia of Materials Science and Engineering’, Pergamon Press, Oxford, 1986, Vol. 4, p. 3210; J. M. Cowling, ‘Fatigue Cracking in Nitrided Steels’, Parthenon, London, 1986.
33. J. R. Jennings ed., ‘Catalytic Ammonia Synthesis’, Plenum Press, New York, 1991.
34. M. V. Twigg ed., ‘Catalyst Handbook’, 2nd edn., Manson Publishing Company, London, 1996.
35. J. R. Partington, ‘A Text-Book of Inorganic Chemistry’, 3rd edn., Macmillan, London, 1931, p. 672; T. P. Hilditch, ‘Catalytic Processes in Applied Chemistry’, Chapman & Hall, London, 1929, p. 194.
36. U. R. Evans, ‘An Introduction to Metallic Corrosion’, Arnold, London, 1979; E. Mattson, *Chemtech*, 1988, **15**, 234; H. Leidheister, ‘Metals Handbook’, 9th edn., Corrosion ASM International, Ohio, 1987, Vol. 13; T. E. Graedel and R. P. Frankenthal, *J. Electrochem.*, 1990, **137**, 2385.
37. H. McArthur, ‘Corrosion Prediction and Prevention in Motor Vehicles’, Ellis Horwood, Chichester, 1988.
38. N. Birks and G. H. Meier, ‘Introduction to High Temperature Oxidation of Metals’, Edward Arnold, London, 1983.
39. U. Schwertmann and R. M. Cornell, ‘Iron Oxides in the Laboratory’, 2nd edn., VCH, Weinheim, 2000; R. M. Cornell and U. Schwertmann, ‘The Iron Oxides: Structure, Properties, Reactions, Occurrence and Uses’, VCH, Weinheim, 1996.
40. R. Kershaw and A. Wold, *Inorg. Synth.*, 1968, **11**, 10.
41. A. Apblett, S. I. Kuriyavar, and B. P. Kiran, *J. Mater. Chem.*, 2003, **13**, 983.
42. H. B. Weiser, W. O. Milligan, and E. L. Cook, *Inorg. Synth.*, 1946, **2**, 215.
43. O. Baudisch and W. H. Hartung, *Inorg. Synth.*, 1939, **1**, 185.
44. G. N. Schrauzer and T. D. Guth, *J. Am. Chem. Soc.*, 1977, **99**, 7189.
45. J. A. Thich, C. C. Ou, D. Powers, B. Vasiliou, D. Mastropaolo, J. A. Potenza, and H. J. Schugar, *J. Am. Chem. Soc.*, 1976, **98**, 1425; C. M. Flynn, *Chem. Rev.*, 1984, **84**, 31; W. Schneider, *Comments Inorg. Chem.*, 1984, **5**, 205; *Chimia*, 1988, **42**, 9; W. Schneider and B. Schwyn, in ‘Aquatic Surface Chemistry’, ed. W. Stumm, Wiley, New York, 1987, p. 167.
46. X. Wang, X. Chen, L. Gao, H. Zheng, M. Ji, C. Tang, T. Shen, and Z. Zhang, *J. Mater. Chem.*, 2004, **14**, 905.
47. R. D. Cannon and R. P. White, *Prog. Inorg. Chem.*, 1988, **36**, 195.
48. A. I. Khan and D. O’Hare, *J. Mater. Chem.*, 2002, **12**, 3191; C. Vaysse, L. Guerlou-Demourgues, and C. Delmas, *Inorg. Chem.*, 2002, **41**, 6905.
49. K. A. Carrado, A. Kostapapas, and S. L. Suib, *Solid State Ionics*, 1988, **26**, 77; K. Chibwe and W. Jones, *Chem. Mater.*, 1989, **1**, 489.
50. A. J. Moulson and J. M. Herbert, ‘Electroceramics’, Chapman & Hall, London, 1993, Chap. 9.
51. D. G. Wickham, E. R. Whipple, and E. G. Larson, *J. Inorg. Nucl. Chem.*, 1960, **14**, 217.
52. D. G. Wickham, *Inorg. Synth.*, 1967, **9**, 152.
53. A. H. Stiller, B. J. McCormick, P. Russell, and P. A. Montano, *J. Am. Chem. Soc.*, 1978, **100**, 2553; J. K. Burdett and G. J. Miller, *J. Am. Chem. Soc.*, 1987, **109**, 4081; J. T. Richardson, *Fuel*, 1972, **51**, 150.
54. D. Coucouvanis, D. Swenson, P. Stremple, and N. C. Baenziger, *J. Am. Chem. Soc.*, 1979, **101**, 3392.
55. R. B. Anderson, ‘The Fischer-Tropsch Synthesis’, Academic Press, New York, 1984.
56. D. W. Bellavance and A. Wold, *Inorg. Synth.*, 1973, **14**, 176.
57. J.-H. Chen, M.-F. Tai, and K.-M. Chi, *J. Mater. Chem.*, 2004, **14**, 296.
58. B. Callmer and T. Lundstrom, *J. Solid State Chem.*, 1976, **17**, 165.
59. W. Hall, S. Kim, J. Zubieta, E. G. Walton, and D. B. Brown, *Inorg. Chem.*, 1977, **16**, 1884.
60. R. A. Kent and J. L. Margrave, *J. Am. Chem. Soc.*, 1965, **87**, 4754; W. H. Baur, *Acta Crystallogr.*, 1958, **11**, 488; B. R. Penfold and M. R. Taylor, *Acta Crystallogr.*, 1960, **13**, 953.
61. J. Bjerrum, G. Schwarzenbach, and L. G. Sillén eds, ‘Stability Constants’, Chemical Society Special Publication No. 6, The Chemical Society, London, 1957.
62. K. H. Gayer and L. Woontner, *Inorg. Synth.*, 1957, **5**, 179.
63. P. Kovacic and N. O. Brace, *Inorg. Synth.*, 1960, **6**, 172.
64. N. S. Gill and F. B. Taylor, *Inorg. Synth.*, 1967, **9**, 136.
65. W. E. Hatfield, R. Whyman, R. C. Fay, K. N. Raymond, and F. Basolo, *Inorg. Synth.*, 1968, **11**, 47.
66. I. R. Young, G. J. Clarke, and D. R. Gailes, *Comput. Tomogr.*, 1981, **5**, 534.
67. G. Sosnovsky and N. U. M. Rao, *Eur. J. Med. Chem.*, 1988, **23**, 517; G. E. Wesbey, R. C. Brasch, B. L. Engelstadt, A. A. Moss, L. E. Crooks, and A. C. Brito, *Radiology*, 1983, **149**, 175; P. J. Sadler and Z. Guo, *Angew. Chem., Int. Ed. Engl.*, 1999, **38**, 1512; A. Bjørnerud, L. O. Johansson, K. Briley-Sæbø, and H. K. Ahlström, *Magn. Reson. Med.*, 2002, **47**, 461.
68. G. P. Baxter, T. Thorvaldson, and V. Cobb, *J. Am. Chem. Soc.*, 1911, **33**, 319; G. P. Baxter and T. Thorvaldson, *J. Am. Chem. Soc.*, 1911, **33**, 337.
69. N. S. Gill and F. B. Taylor, *Inorg. Synth.*, 1967, **9**, 136.
70. M. Armbruster, H. W. Rotter, and G. Thiele, *Z. Anorg. Allg. Chem.*, 2000, **626**, 1681.
71. M. Armbruster, T. Ludwig, H. W. Rotter, G. Thiele, and H. Oppermann, *Z. Anorg. Allg. Chem.*, 2000, **626**, 187.

72. K. B. Yoon and J. K. Kochi, *Z. Anorg. Allg. Chem.*, 1988, **561**, 174.
73. S. Pohl and W. Sark, *Z. Naturforsch.*, 1984, **39B**, 1236.
74. S. A. Mucklejohn, N. W. O'Brian, and T. R. Brumleve, *J. Phys. Chem.*, 1985, **89**, 2409.
75. C. Giacovazzo, F. Scordari, and S. Menchetti, *Acta Crystallogr., Sect. B*, 1975, **31**, 2171.
76. T. J. King, N. Logan, A. Morris, and S. C. Wallwork, *J. Chem. Soc., Chem. Commun.*, 1971, 554.
77. Y. Song, P. Y. Zavalij, M. Suzuki, and M. S. Whittingham, *Inorg. Chem.*, 2002, **41**, 5778.
78. A. R. Cowley and A. M. Chippindale, *J. Chem. Soc., Dalton Trans.*, 2000, 3425.
79. S. Chakrabarti and S. Natarajan, *Angew. Chem., Int. Ed. Engl.*, 2002, **41**, 1224.
80. A. Jost, *Ber. Bunsen-Ges. Phys. Chem.*, 1976, **80**, 316.
81. R. N. Rhoda and A. V. Fraioli, *Inorg. Synth.*, 1953, **4**, 159.
82. J. Catterick, P. Thornton, and B. B. Fitzsimmons, *J. Chem. Soc., Dalton Trans.*, 1977, 1420.
83. F. Calderazzo, U. Englert, G. Pampaloni, V. Passarelli, G. Serni, and R. Wang, *Can. J. Chem.*, 2001, **79**, 495.
84. C. T. Dziobkowski, J. T. Wrobleski, and D. B. Brown, *Inorg. Chem.*, 1981, **20**, 671; R. D. Cannon and R. P. White, *Prog. Inorg. Chem.*, 1988, **36**, 195.
85. J. C. Bailar and E. M. Jones, *Inorg. Synth.*, 1939, **1**, 35.
86. A. W. Adamson and P. D. Fleischauer eds, 'Concepts in Inorganic Photochemistry', Wiley, New York, 1975.
87. H.-K. Fun, S. S. S. Raj, X. Fang, L.-M. Zheng, and X.-Q. Xin, *Acta Crystallogr.*, 1999, **55C**, 903.
88. S. Decurtins, H. W. Schmalle, P. Schneuwly, and H. R. Oswald, *Inorg. Chem.*, 1993, **32**, 1888.
89. F. Lloret, M. Julve, J. Faus, X. Solans, Y. Journaux, and I. Morgenstern-Badarau, *Inorg. Chem.*, 1990, **29**, 2232.
90. A. W. Graham, M. Kurmoo, and P. Day, *J. Chem. Soc., Chem. Commun.*, 1995, 2061.
91. E. Coronado, J. R. Galán-Mascaros, and C. J. Gómez-García, *J. Chem. Soc., Dalton Trans.*, 2000, 205.
92. I. Gauthier-Lumeau, C. Fouquard, C. Merie, J.-L. Pierre, and D. Luneau, *J. Chem. Soc., Dalton Trans.*, 2001, 2127.
93. A. Bino, I. Shweky, S. Cohen, E. R. Bauminger, and S. J. Lippard, *Inorg. Chem.*, 1998, **37**, 5168.
94. R. B. Martin, *J. Inorg. Biochem.*, 1986, **28**, 181.
95. X. Ribas, V. Salvadó, and M. Valiente, *J. Chem. Res.*, 1989, [*S*] 332, [*M*] 2533; M.-T. Escot, A.-M. Martre, P. Pouillen, and P. Martinet, *Bull. Soc. Chem. Fr.*, 1989, 316.
96. H. Otsuki, A. Brunetti, E. S. Owens, R. D. Finn, and R. G. Blasberg, *J. Nucl. Med.*, 1989, **30**, 1676.
97. R. B. Martin, J. Savory, S. Brown, R. L. Bertholf, and M. R. Wills, *Clin. Chem.*, 1987, **33**, 405.
98. P. Mason, 'Handbook of Dietary Supplements', Blakewell Science, Oxford, 1995.
99. A. R. Nissenson, R. M. Lindsay, S. Swan, P. A. Seligman, and J. Strobos, *Am. J. Kidney Dis.*, 1999, **33**, 471.
100. P. A. Seligman and R. B. Schleicher, *Clin. Chem.*, 1999, **45**, 898.
101. B. S. Randhawa and K. J. Sweety, *J. Radioanal. Nucl. Chem.*, 1999, **242**, 675.
102. R. K. Barman, R. Chakrabarty, and B. K. Das, *Polyhedron*, 2002, **21**, 1189.
103. A. K. Powell, J. M. Charnock, A. C. Flood, D. C. Garner, M. J. Ware, and W. Clegg, *J. Chem. Soc., Dalton Trans.*, 1992, 203.
104. G. Davies, A. Fataftah, A. Cherkasskiy, E. A. Ghabbour, A. Radwan, S. A. Jansen, S. Kolla, M. D. Paciolla, L. T. Sein, W. Buermann, M. Balasubramanian, J. Budnick, and B. Xing, *J. Chem. Soc., Dalton Trans.*, 1997, 4047.
105. C. H. Langford and T. R. Khan, *Can. J. Chem.*, 1975, **53**, 2979; C. H. Langford, S. M. Wong, and A. W. Underdown, *Can. J. Chem.*, 1981, **59**, 181; J. A. Lavigne, C. H. Langford, and M. K. S. Mak, *Anal. Chem.*, 1987, **59**, 2616.
106. D. Lee and S. J. Lippard, *Inorg. Chim. Acta*, 2002, **341**, 1.
107. R. G. Teller, R. G. Finke, J. P. Collman, H. B. Chin, and R. Bau, *J. Am. Chem. Soc.*, 1977, **99**, 1104; J. P. Collman and R. Winter, U. S. Patent, 1975, 3,872, 218.
108. S. G. Bratsch and J. J. Lagowski, *Polyhedron*, 1986, **5**, 1763.
109. P. S. Braterman, J.-I. Song, and R. D. Peacock, *Inorg. Chem.*, 1992, **31**, 555.
110. M. A. Masood and P. S. Zacharias, *J. Chem. Soc., Chem. Commun.*, 1991, 152.
111. E. Dodsworth, P. J. O'Grady, D. Nicholls, and D. Roberts, *Polyhedron*, 1987, **6**, 1191.
112. H. tom Dieck and H. Bruder, *J. Chem. Soc., Chem. Commun.*, 1977, 24.
113. C. O. Dietrich-Buchecker, J.-P. Sauvage, and J.-M. Lehn, *J. Am. Chem. Soc.*, 1989, **111**, 7791.
114. G. I. Berglund, G. H. Carlsson, A. T. Smith, H. Szöke, A. Henriksen, and J. Hajdu, *Nature*, 2002, **417**, 463.
115. E. König, *Prog. Inorg. Chem.*, 1987, **35**, 527.
116. L. Sacconi and M. Di Vaira, *Inorg. Chem.*, 1978, **17**, 810.
117. P. Singh, A. Clearfield, and I. Bernal, *J. Coord. Chem.*, 1971, **1**, 29.
118. Yu. M. Kiselev, N. S. Kopelev, and V. I. Spitsyn, *Doklady*, 1987, **295**, 882.
119. M. T. Weller and A. L. Hector, *Angew. Chem., Int. Ed. Engl.*, 2000, **39**, 4162.
120. W. Levason and C. A. McAuliffe, *Coord. Chem. Rev.*, 1974, **12**, 15; J. M. Schreyer, G. W. Thompson, and L. T. Ockerman, *Inorg. Synth.*, 1953, **4**, 164.
121. J. L. Delattre, A. M. Stacy, V. G. Young, G. J. Long, R. Hermann, and F. Grandjean, *Inorg. Chem.*, 2002, **41**, 2834.
122. E. A. Pasek and D. K. Staub, *Inorg. Chim. Acta*, 1977, **21**, 23; C. L. Raston, A. H. White, D. Petridis, and D. Taylor, *J. Chem. Soc., Dalton Trans.*, 1980, 1928.

123. T. J. Collins, K. L. Kostka, E. Münck, and E. S. Uffelman, *J. Am. Chem. Soc.*, 1990, **112**, 5637.

124. C. C. Cummins and R. R. Shrock, *Inorg. Chem.*, 1994, **33**, 395.

125. H. Fujii, *Coord. Chem. Rev.*, 2002, **226**, 51; K. Nakamoto, *Coord. Chem. Rev.*, 2002, **226**, 153.

126. A. Nanthakumar and H. M. Goff, *J. Am. Chem. Soc.*, 1990, **112**, 4047.

127. D. Sellmann, S. Emig, F. W. Heinemann, and F. Knoch, *Angew. Chem., Int. Ed. Engl.*, 1997, **36**, 1201; D. Sellmann, S. Emig, and F. W. Heinemann, *Angew. Chem., Int. Ed. Engl.*, 1997, **36**, 1734.

128. D. H. R. Barton and D. Doller, *Acc. Chem. Res.*, 1992, **25**, 504.

129. P. Amann and A. Möller, *Z. Anorg. Allg. Chem.*, 2002, **628**, 917.

130. D. N. Hendrickson, S. M. Oh, T. Y. Dong, and M. F. Moore, *Comments Inorg. Chem.*, 1985, **4**, 329; M. Bhaduri, *J. Chem. Phys.*, 1982, **77**, 1400.

131. P. K. Mascharak, G. C. Papaefthymiou, R. B. Frankel, and R. H. Holm, *J. Am. Chem. Soc.*, 1981, **103**, 6110.

132. C. A. Reed, T. Mashiko, S. P. Bentley, M. E. Kastner, W. R. Scheidt, K. Spartalian, and G. Lang, *J. Am. Chem. Soc.*, 1979, **101**, 2948.

133. H. Hummel, Y. Mekmouche, C. Duboc-Toia, R. Y. N. Ho, L. Que, V. Schünemann, F. Thomas, A. X. Trautwein, C. Lebrun, M. Fontecave, and S. Ménage, *Angew. Chem., Int. Ed. Engl.*, 2002, **41**, 617.

134. A.-L. Barra, P. Debrunner, D. Gatteschi, C. E. Schulz, and R. Sessoli, *Europhys. Lett.*, 1996, **35**, 133; C. Benelli, J. Cano, Y. Journaux, R. Sessoli, G. A. Solan, and R. E. P. Winpenny, *Inorg. Chem.*, 2001, **40**, 188.

135. P. Gütlich and A. Hauser, *Pure Appl. Chem.*, 1989, **61**, 849; P. Gütlich and A. Hauser, *Coord. Chem. Rev.*, 1990, **97**, 1.

136. P. Gütlich, A. Hauser, and H. Spiering, *Angew. Chem., Int. Ed. Engl.*, 1994, **33**, 2024.

137. J. A. Real, E. Andrés, M. C. Muñoz, M. Julve, T. Granier, A. Bousseksou, and F. Varret, *Science*, 1995, **268**, 265.

138. O. Kahn and J. C. Martinez, *Science*, 1998, **279**, 44.

139. H. Paulsen, L. Dueland, H. Winkler, H. Toftlund, and A. X. Trautwein, *Inorg. Chem.*, 2001, **40**, 2201.

140. H. Toftlund, *Coord. Chem. Rev.*, 1989, **94**, 67.

141. P. Gütlich, Y. Garcia, and H. A. Goodwin, *Chem. Soc. Rev.*, 2000, **29**, 419.

142. J. A. Real, *Perspect. Supramol. Chem.*, 1999, **5**, 53.

143. E. König, *Prog. Inorg. Chem.*, 1987, **35**, 527.

144. A. Hauser, J. Jeftić, H. Romstedt, R. Hinek, and H. Spiering, *Coord. Chem. Rev.*, 1999, **190–192**, 471.

145. J. W. Turner and F. A. Schultz, *Coord. Chem.Rev.*, 2001, **219–221**, 81.

146. E. König, *Struct. Bonding*, 1991, **76**, 51.

147. J. J. McGarvey, I. Lawthers, K. Heremans, and H. Toftlund, *J. Chem. Soc., Chem. Commun.*, 1984, 1575.

148. J. J. McGarvey, I. Lawthers, K. Heremans, and H. Toftlund, *Inorg. Chem.*, 1990, **29**, 252.

149. J. DiBenedetto, V. Arkle, H. A. Goodwin, and P. C. Ford, *Inorg. Chem.*, 1985, **24**, 455.

150. J. W. Turner and F. A. Schultz, *Inorg. Chem.*, 2001, **40**, 5296.

151. H. Toftlund, *Monatshefte*, 2001, **132**, 1269.

152. S. Takeda, T. Ueda, A. Watanabe, and G. Maruta, *Polyhedron*, 2001, **20**, 1263.

153. W. Linert and A. B. Kudryavtsev, *Coord. Chem. Rev.*, 1999, **190–192**, 405.

154. J. J. McGarvey, I. Lawthers, K. Heremans, and H. Toftlund, *Inorg. Chem.*, 1990, **29**, 252.

155. M.-L. Boillot, J. Zarembowitch, J.-P. Itié, A. Polian, E. Bourdet, and J. G. Haasnoot, *New J. Chem.*, 2002, **26**, 313.

156. J. K. McCusker, M. Zvagulis, H. G. Drickamer, and D. N. Hendrickson, *Inorg. Chem.*, 1989, **28**, 1380.

157. J. K. Grey and I. S. Butler, *Coord. Chem. Rev.*, 2001, **219–221**, 713.

158. Y. Galyametdinov, V. Ksenofontov, A. Prosvirin, I. Ovchinnikov, G. Ivanova, P. Gütlich, and W. Haase, *Angew. Chem., Int. Ed. Engl.*, 2001, **40**, 4269.

159. N. Kojima, W. Aoki, M. Seto, Y. Kobayashi, and Y. Maeda, *Synth. Met.*, 2001, **121**, 1796.

160. T. Nakamoto, Y. Miyazaki, M. Itoi, Y. Ono, N. Kojima, and M. Sorai, *Angew. Chem., Int. Ed. Engl.*, 2001, **40**, 4716.

161. H. E. Williams, 'Cyanogen Compounds', Edward Arnold, London, 1948.

162. G. B. Kauffman, 'Inorganic Coordination Compounds', Heyden, London, 1981, p. 57, p. 171.

163. V. V. Pavlishchuk, I. A. Koval, E. Goreshnik, A. W. Addison, G. A. van Albada, and J. Reedijk, *Eur. J. Inorg. Chem.*, 2001, 297.

164. M. B. Robin and P. Day, *Adv. Inorg. Chem. Radiochem.*, 1967, **10**, 247; R. J. H. Clark, *Chem. Soc. Rev.*, 1984, **13**, 219.

165. K. Itaya, I. Uchida, and V. D. Neff, *Acc. Chem. Res.*, 1986, **19**, 162.

166. P. Gütlich, Y. Garcia, and T. Woike, *Coord. Chem. Rev.*, 2001, **219–221**, 839.

167. B. Mayoh and P. Day, *J. Chem. Soc., Dalton Trans.*, 1976, 1483.

168. K. R. Dunbar and R. A. Heintz, *Prog. Inorg. Chem.*, 1987, **45**, 283.

169. N. Shimamoto, S. Ohkoshi, O. Sato, and K. Hashimoto, *Inorg. Chem.*, 2002, **41**, 678.

170. X. Wang and K. S. E. Forssberg, *Miner. Process. Extr. Metall. Rev.*, 1990, **6**, 81.

171. B. Sieklucka, *Prog. React. Kinet.*, 1989, **15**, 175.

172. See, e.g., A. Rodriguez, C. Carmona, E. Muñoz, F. Sánchez, and J. Burgess, *Transition Met. Chem.*, 1991, **16**, 535; M. Morillo, C. Denk, P. Pérez, M. López, A. Sánchez, R. Prado, and F. Sánchez, *Coord. Chem. Rev.*, 2000, **204**, 173.
173. T. W. Swaddle and P. A. Tregloan, *Coord. Chem. Rev.*, 1999, **187**, 255; A. Zahl, R. van Eldik, and T. W. Swaddle, *Inorg. Chem.*, 2002, **41**, 757.
174. S. M. Oh and L. R. Faulkner, *J. Electroanal. Chem.*, 1989, **269**, 77.
175. M. Yang, D. W. Thompson, and G. J. Meyer, *Inorg. Chem.*, 2002, **41**, 1254.
176. P. L. Domingo, B. Garcia, and J. M. Leal, *Can. J. Chem.*, 1987, **65**, 583.
177. S. Capone, A. Robertis, and S. Sammartano, *Thermochim. Acta*, 1986, **112**, 1.
178. D. Sicilia, S. Rubio, and D. Perez Bendito, *Talanta*, 1991, **38**, 1147.
179. D. F. Mullica, H. O. Perkins, and E. L. Sappenfield, *Inorg. Chim. Acta*, 1988, **142**, 9; R. E. Marsh, *Inorg. Chim. Acta*, 1989, **157**, 1; D. F. Mullica and E. L. Sappenfield, *Inorg. Chim. Acta*, 1989, **157**, 3.
180. T. Kitazawa, M. Takahashi, and M. Takeda, *Hyperfine Interact.*, 1994, **84**, 527; *Chem. Abstr.*, 1994, **121**, 166327d.
181. D. J. Kenney, T. P. Flynn, and J. B. Gallini, *J. Inorg. Nucl. Chem.*, 1961, **20**, 75; H. Maltz, M. A. Grant, and M. C. Navaroli, *J. Org. Chem.*, 1971, **36**, 363.
182. J. H. Espenson and S. G. Wolenuk, *Inorg. Chem.*, 1972, **11**, 2034.
183. B. Sieklucka, *Prog. React. Kinet.*, 1989, **15**, 175; S. Alshehri, J. Burgess, R. van Eldik, and C. D. Hubbard, *Inorg. Chim. Acta*, 1995, **240**, 305; D. H. Macartney, *Rev. Inorg. Chem.*, 1988, **9**, 101; J. Burgess, in 'Mechanisms of Inorganic and Organometallic Reactions', ed. M. V. Twigg, Plenum Press, New York, 1991, Vol. 7, p. 177, and other volumes in this series.
184. A. Rodriguez, F. Sánchez, M. L. Moyá, J. Burgess, and A. Al-Alousy, *Transition Met. Chem.*, 1991, **16**, 445; S. Alshehri, J. Burgess, G. H. Morgan, B. Patel, and M. S. Patel, *Transition Met. Chem.*, 1993, **18**, 619.
185. S. M. Contakes, S. C. N. Hsu, T. B. Rauchfuss, and S. R. Wilson, *Inorg. Chem.*, 2002, **41**, 1670.
186. J. Jiang, A. Acunzo, and S. A. Koch, *J. Am. Chem. Soc.*, 2001, **123**, 12109.
187. J. Jiang and S. A. Koch, *Angew. Chem., Int. Ed. Engl.*, 2001, **40**, 2629; T. B. Rauchfuss, S. M. Contakes, S. C. N. Hsu, M. A. Reynolds, and S. R. Wilson, *J. Am. Chem. Soc.*, 2001, **123**, 6933.
188. J. Jiang and S. A. Koch, *Inorg. Chem.*, 2002, **41**, 158.
189. A. Volbeda, M.-H. Charon, C. Piras, E. C. Hatchikian, M. Frey, and J. C. Fontecilla-Camps, *Nature*, 1995, **373**, 580; M. Freemantle, *Chem. Eng. News*, 2002, 35.
190. B. Bley, H. Willner, and F. Aubke, *Inorg. Chem.*, 1997, **36**, 158; E. Bernhardt, B. Bley, R. Wartchow, H. Willner, E. Bill, P. Kuhn, I. H. T. Sham, M. Bodenbinder, R. Brochler, and F. Aubke, *J. Am. Chem. Soc.*, 1999, **121**, 7188.
191. J. Drummond and J. S. Wood, *J. Chem. Soc., Chem. Commun.*, 1969, 1373; A. Kornath, *Angew. Chem., Int. Ed. Engl.*, 2001, **40**, 3135.
192. G. De Munno, T. Poerio, G. Viau, M. Julve, F. Lloret, Y. Journaux, and E. Rivière, *J. Chem. Soc., Chem. Commun.*, 1996, 2587; G. De Munno, T. Poerio, G. Viau, M. Julve, and F. Lloret, *Angew. Chem., Int. Ed. Engl.*, 1997, **36**, 1459.
193. X. Hao, Y. Wei, and S. Zhang, *Chem. Commun.*, 2000, 2271; V. Niel, J. M. Martinez-Agudo, M. C. Muñoz, A. B. Gaspar, and J. A. Real, *Inorg. Chem.*, 2001, **40**, 3838; M. James, *Aust. J. Chem.*, 2002, **55**, 219.
194. J. A. Real, E. Andrés, M. C. Muñoz, M. Julve, T. Granier, A. Bousseksou, and F. Varret, *Science*, 1995, **268**, 265.
195. R. A. Cable, M. Green, R. E. Mackenzie, P. L. Timms, and T. W. Turney, *J. Chem. Soc., Chem. Commun.*, 1976, 270.
196. O. Franke, B. E. Wiesler, N. Lehnert, and F. Tuczek, *Z. Anorg. Allg. Chem.*, 2002, **628**, 2395.
197. M. Hirano, M. Akita, T. Morikita, H. Kubo, A. Fukuoka, and S. Komiya, *J. Chem. Soc., Dalton Trans.*, 1997, 3453.
198. H. Kandler, C. Gauss, W. Bidell, S. Rosenberger, T. Bürgi, I. L. Eremenko, D. Veghini, O. Orama, P. Burger, and H. Berke, *Chem. Eur. J.*, 1995, **1**, 541.
199. B. L. Haymore and J. A. Ibers, *Inorg. Chem.*, 1975, **14**, 3060.
200. F. Bottomley and F. Grein, *J. Chem. Soc., Dalton Trans.*, 1980, 1359.
201. J. A. McCleverty, *Chem. Rev.*, 1979, **79**, 53.
202. W. I. K. Bisset, A. R. Butler, C. Glidewell, and J. Reglinski, *Br. J. Anaesth.*, 1981, **53**, 1015.
203. G. Paliani, R. Cataliotti, and A. Poletti, *Can. J. Spectrosc.*, 1976, **21**, 159.
204. D. E. Morris and F. Basolo, *J. Am. Chem. Soc.*, 1968, **90**, 2531, 2536.
205. A. R. Butler, C. Glidewell, and M.-H. Li, *Adv. Inorg. Chem.*, 1989, **32**, 335; P. C. Ford, J. Bourassa, K. Miranda, B. Lee, I. Lorković, S. Boggs, S. Kudo, and L. Laverman, *Coord. Chem. Rev.*, 1998, **171**, 185.
206. J. L. Bourassa and P. C. Ford, *Coord. Chem. Rev.*, 2000, **200–202**, 887.
207. M. Lewin, K. Fisher, and I. Dance, *Chem. Commun.*, 2000, 947.
208. J. A. McCleverty, N. M. Atherton, J. Locke, E. J. Wharton, and C. J. Winscom, *J. Am. Chem. Soc.*, 1967, **89**, 6082.
209. Y. Numata, K. Kubokura, Y. Nonaka, H. Okawa, and S. Kida, *Inorg. Chim. Acta*, 1980, **43**, 193.
210. G. W. Watt and W. A. Jenkins, *Inorg. Synth.*, 1953, **4**, 161.
211. E. Dodsworth, P. J. O'Grady, D. Nicholls, and D. Roberts, *Polyhedron*, 1987, **6**, 1191.

212. G. L. Schimek, J. W. Kolis, and G. J. Long, *Chem. Mater.*, 1997, **9**, 2776.

213. J. R. Miller, B. D. Podd, and M. O. Sanchez, *J. Chem. Soc., Dalton Trans.*, 1980, 1461.

214. O. Baudisch and W. H. Hartung, *Inorg. Synth.*, 1939, **1**, 184; T. Tominaga, M. Takeda, T. Morinoto, and N. Saito, *Bull. Chem. Soc. Jap.*, 1970, **43**, 1093.

215. C. D. Burbridge, M. J. Cleare, and D. M. L. Goodgame, *J. Chem. Soc. (A)*, 1966, 1698; I. Sotofte and S. E. Rasmussen, *Acta Chem. Scand.*, 1967, **21**, 2028.

216. R. J. Dodens and L. F. Dahl, *J. Am. Chem. Soc.*, 1966, **88**, 4847.

217. Z. Chen, R.-J. Wang, X.-Y. Huang, and J. Li, *Acta Crystallogr.*, 2000, **56C**, 1100.

218. M. Ciampolini, P. Paoletti, and L. Sacconi, *J. Chem. Soc.*, 1961, 2994, 5115; 1963, 3589; 1964, 5047; P. Paoletti and A. Vacca, *J. Chem. Soc.*, 1964, 5051.

219. F. Calderazzo, U. Englert, G. Pampaloni, and E. Vanni, *C. R. Acad. Sci., Ser. IIc: Chim.*, 1999, 311.

220. L. R. Melby, *Inorg. Chem.*, 1970, **9**, 2186.

221. F. Blau, *Ber. Dtsch. Chem. Ges.*, 1888, **21**, 1077; *Monatshefte*, 1889, **10**, 375.

222. F. Blau, *Monatshefte*, 1898, **19**, 647.

223. A. Werner, *Ber. Dtsch. Chem. Ges.*, 1912, **45**, 433; see also G. B. Kauffman, 'Inorganic Coordination Compounds', Heyden, London, 1981, p. 49.

224. G. F. Smith and F. P. Richter, 'Phenanthroline and Substituted Phenanthroline Indicators', The G. Fredrick Smith Chemical Company, Columbus, Ohio, 1944; A. A. Schilt, 'Analytical Applications of 1,10-Phenanthroline and Related Compounds', Pergamon Press, Oxford, 1969.

225. J. Li, W. Ma, Y. Huang, X. Tao, J. Zhao, and Y. Xu, *Appl. Catal. B: Environ.*, 2004, **48**, 17.

226. P. Day and N. Sanders, *J. Chem. Soc. (A)*, 1967, 1530, 1536; 1970, 1190.

227. A. Zalkin, D. H. Templeton, and T. Ueki, *Inorg. Chem.*, 1973, **12**, 1641; L. Johansson, M. Molund, and A. Oskarsson, *Inorg. Chim. Acta*, 1978, **31**, 117.

228. J. Baker, L. M. Engelhardt, B. N. Figgis, and A. H. White, *J. Chem. Soc., Dalton Trans.*, 1975, 530; B. S. Brunschwig, C. Creutz, D. H. Macartney, T.-K. Sham, and N. Sutin, *Faraday Discuss. Chem. Soc.*, 1982, **74**, 113.

229. A. V. Khedekar, J. Lewis, F. E. Mabbs, and H. Weigold, *J. Chem. Soc. (A)*, 1967, 1561.

230. E. C. Constable, *Adv. Inorg. Chem.*, 1989, **34**, 1.

231. A. F. Richards, J. H. Ridd, and M. L. Tobe, *Chem. Ind.*, 1963, 1726; R. D. Gillard, L. A. P. Kane-Maguire, and P. A. Williams, *J. Chem. Soc., Dalton Trans.*, 1977, 1792.

232. F. P. Dwyer and E. C. Gyarfas, *J. Am. Chem. Soc.*, 1952, **74**, 4699.

233. P. O'Brien, *Polyhedron*, 1983, **2**, 233.

234. A. A. Schilt, *Inorg. Synth.*, 1970, **12**, 247; *J. Am. Chem. Soc.*, 1960, **82**, 3000.

235. N. Serpone, G. Ponterini, M. A. Jamieson, F. Boletta, and M. Maestri, *Coord. Chem. Rev.*, 1983, **50**, 209; M. J. Blandamer and J. Burgess, *Pure Appl. Chem.*, 1983, **55**, 55; 1982, **54**, 2285.

236. J. Burgess, S. A. Galema, and C. D. Hubbard, *Polyhedron*, 1991, **7**, 703; A. M. Shaker, S. Alshehri, and J. Burgess, *Transition Met. Chem.*, 1998, **23**, 683; J. Burgess and C. D. Hubbard, *Internat. J. Chem. Kinet.*, 2000, **32**, 263; A. Alousy, J. Burgess, D. Elvidge, C. D. Hubbard, and S. Radulović, *Inorg. React. Mech.*, 2000, **2**, 249; E. A. Abu-Gharib, N. Gosal, and J. Burgess, *Croat. Chem. Acta*, 2001, **74**, 545.

237. O. Mønsted and G. Nord, *Adv. Inorg. Chem.*, 1991, **37**, 381.

238. C. Mahon and W. L. Reynolds, *Inorg. Chem.*, 1967, **6**, 1927; S. Herzog and A. Weber, *Z. Chem.*, 1968, **8**, 66.

239. A. A. Schilt, 'Analytical Applications of 1,10-Phenthroline and Related Compounds', Pergamon, Oxford, 1969, p. 132.

240. J. Burgess, S. Radulović, and F. Sánchez, *Transition Met. Chem.*, 1987, **12**, 529; H. E. Toma and M. S. Takasugi, *J. Solution Chem.*, 1989, **18**, 575; A. Alousy, N. J. Blundell, J. Burgess, C. D. Hubbard, and R. van Eldik, *Transition Met. Chem.*, 2002, **27**, 244.

241. M. J. Blandamer, J. Burgess, and B. Shraydeh, *J. Chem. Soc., Faraday Trans.*, 1993, **89**, 531; J. Burgess, M. S. Patel, and C. Tindall, *Spectr. Lett.*, 1993, **26**, 1469; S. Ahmed, J. Burgess, G. Capper, N. C. Fellowes, and M. S. Patel, *Polyhedron*, 1993, **12**, 1145; J. Burgess, R. C. Lane, K. Singh, B. de Castro, and A. P. Gameiro dos Santos, *J. Chem. Soc., Faraday Trans.*, 1994, **90**, 3071.

242. P. Garcia, J. Marques, E. Pereira, P. Gameiro, R. Salema, and B. de Castro, *Chem. Commun.*, 2001, 1298; P. Gameiro, E. Pereira, P. Garcia, S. Breia, J. Burgess, and B. de Castro, *Eur. J. Inorg. Chem.*, 2001, 2755.

243. P. Gameiro, A. Maia, E. Pereira, B. de Castro, and J. Burgess, *Transition Met. Chem.*, 2000, **25**, 283.

244. M. P. Byfield, V. L. Frost, J. L. J. Pemberton, and J. M. Pratt, *J. Chem. Soc., Faraday Trans. I*, 1989, **85**, 2713; J. Burgess, D. N. Drasdo, and K. Singh, *Transition Met. Chem.*, 1994, **19**, 113; J. Burgess, S. Maguire, A. McGranaghan, S. A. Parsons, B. Nowicka, and A. Samotus, *Transition Met. Chem.*, 1998, **23**, 615; T. Tarui, *Bull. Chem. Soc. Jpn.*, 2000, **73**, 2481; J. Benko, J. Burgess, P. López Cornejo, and O. Vollárová, *Croat. Chem. Acta*, 2001, **74**, 607.

245. N. J. Blundell, J. Burgess, P. Guardado, and C. D. Hubbard, *J. Chem. Soc., Dalton Trans.*, 1991, 1743.

246. J. Burgess, S. Radulović, and F. Sánchez, *Transition Met. Chem.*, 1987, **12**, 529; J. Burgess, D. N. Drasdo, and B. Shraydeh, *J. Chem. Res. (S)*, 1992, 288; A. Al-Alousy, S. Alshehri, M. J. Blandamer, N. J. Blundell, J. Burgess, H. J. Cowles, S. Radulović, P. Guardado, and C. D. Hubbard, *J. Chem. Soc., Faraday Trans. 1*, 1993, **89**, 1041.

247. T. Tłaczała and A. Bartecki, *Monatshefte*, 1997, **128**, 225; A. Bartecki and J. Burgess, ‘The Colour of Metal Compounds’, Gordon and Breach, Reading, 2000, p. 91, p. 142.

248. J. Burgess, *Spectrochim. Acta, Part A*, 1970, **26**, 1369.

249. B. N. Figgis, P. A. Reynolds, and R. Mason, *Inorg. Chem.*, 1984, **23**, 1149.

250. K. Madeja, W. Wilke, and S. Schmidt, *Z. Anorg. Chem.*, 1966, **346**, 306; W. A. Baker and H. M. Bobonich, *Inorg. Chem.*, 1963, **2**, 1071; H. Sato and T. Tominaga, *Bull. Chem. Soc. Jap.*, 1976, **49**, 697; W. M. Reiff, B. Bockum, M. A. Weber, and R. B. Frankel, *Inorg. Chem.*, 1975, **14**, 800.

251. H. A. Goodwin, *Coord. Chem. Rev.*, 1976, **18**, 293; E. König, *Coord. Chem. Rev.*, 1968, **3**, 471; P. Ganguli, P. Gütlich, E. W. Muller, and W. Irler, *J. Chem. Soc., Dalton Trans.*, 1981, 441; S. Savage, Z. Jia-Long, and A. G. Maddock, *J. Chem. Soc., Dalton Trans.*, 1985, 991.

252. E. König, *Prog. Inorg. Chem.*, 1987, **35**, 1987; P. Gütlich and A. Hauser, *Coord. Chem. Rev.*, 1990, **97**, 1; H. Toftlund, *Coord. Chem. Rev.*, 1989, **94**, 67.

253. A. Gaines, L. P. Hammett, and G. H. Walden, *J. Am. Chem. Soc.*, 1936, **58**, 1668.

254. P. C. Healy, B. W. Skelton, and A. H. White, *Aust. J. Chem.*, 1983, **36**, 2057.

255. J. E. Plowman, T. M. Loehr, C. K. Schauer, and O. P. Anderson, *Inorg. Chem.*, 1984, **23**, 3553.

256. P. C. Healy, J. M. Patrick, and A. H. White, *Aust. J. Chem.*, 1984, **37**, 1405.

257. D. M. Kurtz, *Chem. Rev.*, 1990, **90**, 585.

258. M. M. Walczack and N. T. Flynn, *J. Electroanal. Chem.*, 1998, **441**, 43.

259. S. Ménage, J.-M. Vincent, C. Lambeaux, G. Chottard, A. Grand, and M. Fontecave, *Inorg. Chem.*, 1993, **32**, 4766.

260. R. S. Bell and N. Sutin, *Inorg. Chem.*, 1962, **1**, 359.

261. J. A. Broomhead and F. P. Dwyer, *Aust. J. Chem.*, 1960, **14**, 250; H. Sato and T. Tominaga, *Bull. Chem. Soc. Jap.*, 1976, **49**, 697.

262. S. Raman, *Indian J. Chem., Sect. A*, 1980, **19**, 907.

263. F. Blau, *Monatshefte*, 1898, **19**, 647; P. Krumholz, *J. Am. Chem. Soc.*, 1953, **75**, 2163.

264. A. M. de Costa Ferreira and H. E. Toma, *J. Chem. Soc., Dalton Trans.*, 1983, 2051.

265. H. Diehl, G. F. Smith, L. McBride, and R. Cryberg, ‘The Iron Reagents: Bathophenanthroline, Bathophenanthroline-disulfonic acid, 2,4,6-Tripyridyl-s-triazine and Phenyl-2-pyridyl Ketoxime’, 2nd edn., The G. Frederick Smith Chemical Company, Columbus, Ohio, 1965; R. C. Stoufer and D. H. Busch, *J. Am. Chem. Soc.*, 1956, **78**, 6016; R. K. Murmann and E. A. Healy, *J. Am. Chem. Soc.*, 1961, **83**, 2092; P. Krumholz, *Inorg. Chem.*, 1965, **4**, 609.

266. D. J. Farrington, J. G. Jones, and M. V. Twigg, *J. Inorg. Nucl. Chem.*, 1975, **37**, 848; D. J. Farrington and J. G. Jones, *Inorg. Chim. Acta*, 1972, **6**, 575.

267. C. F. Bell and D. R. Rose, *J. Chem. Soc. (A)*, 1969, 819; C. Mealli and E. C. Lingafelter, *Chem. Commun.*, 1970, 885.

268. J. Burgess and C. D. Hubbard, *J. Am. Chem. Soc.*, 1984, **106**, 1717; J. Burgess and G. M. Burton, *Rev. Latinoamer. Quim.*, 1980, **11**, 107; M. J. Blandamer, J. Burgess, P. Cookson, D. L. Roberts, P. Wellings, F. M. Mekhail, and P. Askalani, *J. Chem. Soc., Dalton Trans.*, 1978, 996; M. J. Blandamer, J. Burgess, R. I. Haines, F. M. Mekhail, and P. Askalani, *J. Chem. Soc., Dalton Trans.*, 1978, 1001.

269. R. M. Kirchner, C. Mealli, M. Bailey, N. Howe, L. P. Torre, L. J. Wilson, L. C. Andrews, N. J. Rose, and E. C. Lingafelter, *Coord. Chem. Rev.*, 1987, **77**, 89.

270. C. Hamann, A. von Zelewsky, A. Neels, and H. Stoeckli-Evans, *Dalton Trans.*, 2004, 402.

271. H. Toftlund, *Coord. Chem. Rev.*, 1989, **94**, 67; P. Gütlich and A. Hauser, *Coord. Chem. Rev.*, 1990, **97**, 1; E. König, *Prog. Inorg. Chem.*, 1987, **35**, 527.

272. K. Bowman, A. P. Gaughan, and A. Dorf, *J. Am. Chem. Soc.*, 1972, **94**, 727; D. V. Stynes, K. Singh, B. Ng, and S. Wiltshire, *Inorg. Chim. Acta*, 1982, **58**, 179; C. K. Prout and T. J. Wiseman, *J. Chem. Soc. (A)*, 1964, 497; B. W. Dale, R. J. P. Williams, and C. E. Johnson, *Trans. Faraday Soc*, 1968, **64**, 620, 3011; H. C. Rai, A. K. Jena, and B. Sahoo, *Inorg. Chim. Acta*, 1979, **35**, 29; D. R. Boston and N. J. Rose, *J. Am. Chem. Soc.*, 1968, **90**, 6859; S. C. Jackels, J. Zektzer, and N. J. Rose, *Inorg. Synth.*, 1977, **17**, 139; V. L. Goedken, *Inorg. Synth.*, 1980, **22**, 87; S. Grammenudi and F. Vögtle, *Angew. Chem., Int. Ed. Engl.*, 1986, **25**, 1122; Y. Z. Voloshin, V. E. Zavodnik, O. A. Varzatskii, V. K. Belsky, A. V. Palchik, N. G. Strizhakova, I. I. Vorontsov, and M. Yu. Antipin, *J. Chem. Soc., Dalton Trans.*, 2002, 1193.

273. J. S. Judge, W. M. Reiff, G. M. Intille, P. Ballway, and W. A. Baker, *J. Inorg. Nucl. Chem.*, 1967, **29**, 1711; W. M. Reiff, W. A. Baker, and N. E. Erickson, *J. Am. Chem. Soc.*, 1968, **90**, 4794; E. C. Constable, *Adv. Inorg. Chem. Radiochem.*, 1986, **30**, 69.

274. J. Burgess and M. V. Twigg, *J. Chem. Soc., Dalton Trans.*, 1974, 2032.

275. J. M. Rao, M. C. Hughes, and D. J. Macero, *Inorg. Chim. Acta*, 1976, **16**, 231.

276. R. D. Feltham and W. F. Silverthorn, *Inorg. Chem.*, 1970, **9**, 1207.

277. L. S. Van Der Sluys, K. Eckert, O. Eisenstein, J. H. Hall, J. C. Huffman, S. A. Jackson, T. F. Koetzle, G. J. Kubas, P. J. Vergamini, and K. G. Caulton, *J. Am. Chem. Soc.*, 1990, **112**, 4831.

278. M. Bressan and P. Rigo, *Inorg. Chim. Acta*, 1979, **37**, 181.

279. G. M. Bancroft, M. J. Mays, and B. E. Prater, *Chem. Commun.*, 1969, 585.

280. W. S. J. Kelly, G. H. Ford, and S. M. Nelson, *J. Chem. Soc. (A)*, 1971, 388.

281. P. Giannoccaro and A. Sacco, *Inorg. Synth.*, 1977, **17**, 71.

282. V. V. Saraev, K. Smidt, V. A. Gruznukh, T. I. Bakunina, and L. W. Mironova, *Koord. Khim.*, 1979, **5**, 1472.

283. M. T. Nenadović, O. I. Mićić, and A. A. Muk, *J. Chem. Soc., Dalton Trans.*, 1980, 586.

284. R. N. Bagchi, A. M. Bond, C. L. Heggie, T. L. Henderson, E. Mocellin, and R. A. Seikel, *Inorg. Chem.*, 1983, **22**, 3007.

285. M. F. Lappert, J. J. MacQuitty, and P. L. Pye, *J. Chem. Soc., Dalton Trans.*, 1981, 1583.

286. K. J. Klabunde, 'Chemistry of Free Atoms and Particles', Academic Press, New York, 1980.

287. E. L. Muetterties and J. W. Rathke, *J. Chem. Soc., Chem. Commun.*, 1974, 850.

288. T. V. Harris, E. L. Muetterties, and J. W. Rathke, *J. Am. Chem. Soc.*, 1978, **100**, 6966.

289. P. L. Timms, *J. Chem. Soc. (A)*, 1970, 2526.

290. K. Burger ed., 'Biocoordination Chemistry', Ellis Horwood, Chichester, 1990, p. 254 and p. 264.

291. G. N. Schrauzer and T. D. Guth, *J. Am. Chem. Soc.*, 1977, **99**, 7199.

292. N. J. Hair and J. K. Beattie, *Inorg. Chem.*, 1977, **16**, 245.

293. P. C. Junk, B. J. McCool, B. Moubaraki, K. S. Murray, L. Spiccia, J. D. Cashion, and J. W. Steed, *J. Chem. Soc., Dalton Trans.*, 2002, 1024.

294. T. I. Morrison, A. H. Reis, G. S. Knapp, F. Y. Fradin, H. Chen, and E. Klippert, *J. Am. Chem. Soc.*, 1978, **100**, 3262. see also Ref. 45.

295. H. Ohtaki and T. Radnai, *Chem. Rev.*, 1993, **93**, 1157; D. T. Richens, 'The Chemistry of Aqua Ions', Wiley, Chichester, 1997, Chap. 8.

296. G. J. Herdman and G. W. Nielson, *J. Phys. Condens. Matter*, 1992, **4**, 627, 649; Y. Inada and S. Funahashi, *Z. Naturforsch.*, 1999, **54B**, 1518.

297. M. Biruš, N. Kujundžić, and M. Pribanić, *Prog. React. Kinet.*, 1993, **18**, 171; G. Lente and I. Fábián, *Inorg. Chem.*, 2002, **41**, 1306.

298. A. Cusanelli, U. Frey, D. T. Richens, and A. E. Merbach, *J. Am. Chem. Soc.*, 1996, **118**, 5265; M. L. Tobe and J. Burgess, 'Inorganic Reaction Mechanisms', Addison Wesley Longman, Harlow, 1999.

299. M. Biruš, G. Krznarić, N. Kujundžić, and M. Pribanić, *Croat. Chem. Acta*, 1988, **61**, 33.

300. I. Kerezsi, G. Lente, and I. Fábián, *Dalton Trans.*, 2004, 342.

301. K. Micskei and I. Nagypal, *J. Chem. Soc., Dalton Trans.*, 1990, 743.

302. V. Zang, M. Kotowski, and R. van Eldik, *Inorg. Chem.*, 1988, **27**, 3279; V. Zang and R. van Eldik, *Inorg. Chem.*, 1990, **29**, 4462.

303. W. H. Jolley, D. R. Stranks, and T. W. Swaddle, *Inorg. Chem.*, 1990, **29**, 1948.

304. L. Que and W. B. Tolman, *Angew. Chem., Int. Ed. Engl.*, 2002, **41**, 1114; W. B. Tolman and L. Que, *J. Chem. Soc., Dalton Trans.*, 2002, 653.

305. See, e.g., S. M. Oh, D. N. Hendrickson, K. L. Hassett, and R. E. Davis, *J. Am. Chem. Soc.*, 1984, **106**, 7984; S. E. Woehler, R. J. Wittebort, S. M. Oh, T. Kambara, D. N. Hendrickson, D. Inniss, and C. E. Strouse, *J. Am. Chem. Soc.*, 1987, **109**, 1063; R. D. Cannon, U. A. Jayasooriya, R. P. White, and S. K. arapKoske, *Spectrochim. Acta*, 1993, **49A**, 1787; T. Nakamoto, M. Katada, K. Endo, and H. Sano, *Polyhedron*, 1998, **17**, 3507.

306. D. N. Hendrickson, S. M. Oh, T. Y. Dong, T. Kambara, M. J. Cohn, and M. F. Moore, *Comments Inorg. Chem.*, 1985, **4**, 329; R. D. Cannon and R. P. White, *Prog. Inorg. Chem.*, 1988, **36**, 195; F. E. Sowrey, C. Tilford, S. Wocadlo, C. E. Anson, A. K. Powell, S. M. Bennington, W. Montfrooij, U. A. Jayasooriya, and R. D. Cannon, *J. Chem. Soc., Dalton Trans.*, 2001, 862.

307. D. Lee and S. J. Lippard, *J. Am. Chem. Soc.*, 1998, **120**, 12153; D. Lee, J. L. DuBois, B. Pierce, B. Hedman, K. O. Hodgson, M. P. Hendrich, and S. J. Lippard, *Inorg. Chem.*, 2002, **41**, 3172; J. R. Hagadorn, L. Que, and W. B. Tolman, *J. Am. Chem. Soc.*, 1998, **120**, 13531; F. A. Chavez, R. Y. N. Ho, M. Pink, V. G. Young, S. V. Kryatov, E. V. Rybak-Akimova, H. Andres, E. Münck, L. Que, and W. B. Tolman, *Angew. Chem., Int. Ed. Engl.*, 2002, **41**, 149.

308. M. Scarpellini, A. Naves, A. J. Bortoluzzi, I. Vencato, V. Drago, W. A. Ortiz, and C. Zucco, *J. Chem. Soc., Dalton Trans.*, 2001, 2616.

309. J. L. Sessler, J. W. Sibert, and V. Lynch, *Inorg. Chem.*, 1990, **29**, 4143.

310. S. M. Gorun and S. J. Lippard, *Nature*, 1986, **319**, 666; S. M. Gorun, G. C. Papaefthymiou, R. B. Frankel, and S. J. Lippard, *J. Am. Chem. Soc.*, 1987, **109**, 3337; K. L. Taft, G. C. Papefthymiou, and S. J. Lippard, *Science*, 1993, **259**, 1302.

311. D. Gatteschi, A. Caneschi, R. Sessoli, and A. Cornia, *Chem. Soc. Rev.*, 1996, **25**, 101; C. Benelli, J. Cano, Y. Journaux, R. Sessoli, G. A. Solan, and R. E. P. Winpenny, *Inorg. Chem.*, 2001, **40**, 188; J. C. Goodwin, R. Sessoli, D. Gatteschi, W. Wernsdorfer, A. K. Powell, and S. L. Heath, *J. Chem. Soc., Dalton Trans.*, 2000, 1835; L. F. Jones, A. Batsanov, E. K. Brechin, D. Collison, M. Helliwell, T. Mallah, E. J. L. McInnes, and S. Piligkos, *Angew. Chem., Int. Ed. Engl.*, 2002, **41**, 4318.

312. C. Benelli, S. Parsons, G. A. Solan, and R. E. P. Winpenny, *Angew. Chem., Int. Ed. Engl.*, 1996, **35**, 1825; G. L. Abbati, A. Caneschi, A. Cornia, A. C. Fabretti, and D. Gatteschi, *Inorg. Chim. Acta*, 2000, **297**, 291.

313. W. Micklitz and S. J. Lippard, *J. Am. Chem. Soc.*, 1989, **111**, 6856.

314. B. Yan and Z.-D. Chen, *Inorg. Chem. Commun.*, 2001, **4**, 138.

315. F. A. Cotton and G. W. Rice, *Nouv. J. Chim.*, 1977, **1**, 301.

316. M. K. Chaudhuri and S. K. Ghosh, *J. Chem. Soc., Dalton Trans.*, 1983, 839.

317. C. S. Wu, G. R. Rossman, H. B. Gray, G. S. Hammond, and H. J. Schugar, *Inorg. Chem.*, 1972, **11**, 990.

318. S. A. Koch and M. Millar, *J. Am. Chem. Soc.*, 1982, **104**, 5255.

319. K. N. Raymond, S. S. Isied, L. D. Brown, F. R. Fronczek, and J. H. Nibert, *J. Am. Chem. Soc.*, 1976, **98**, 1767; S. Salama, J. D. Strong, J. B. Neilands, and T. G. Spiro, *Biochemistry*, 1978, **17**, 3781.

320. B. Chatterjee, *Coord. Chem. Rev.*, 1978, **26**, 281.

321. T. W. Failes and T. W. Hambly, *Aust. J. Chem.*, 2000, **53**, 879; C. J. Marmion, T. Murphy, Z. Starikova, and K. B. Nolan, *Acta Crystallogr.*, 2000, **56C**, 491.

322. F. Vögtle, 'Supramolecular Chemistry', Wiley, Chichester, 1991, Sect. 2.3; A. M. Albrecht-Gary and A. L. Crumbliss, in 'Metal Ions in Biological Systems', eds. A. Sigel and H. Sigel, Marcel Dekker, New York, 1998, Vol. 35, p. 239.

323. B. Tamhina and M. J. Herak, *Croat. Chem. Acta*, 1973, **45**, 603; K. Jakopčić, B. Tamhina, F. Zorko, and M. J. Herak, *J. Inorg. Nucl. Chem.*, 1977, **39**, 1201.

324. J. B. Porter, E. R. Huehns, and R. C. Hider, *Baillière's Clin. Haematol.*, 1989, **2**, 257; R. J. Bergeron and G. M. Brittenham eds, 'The Development of Iron Chelators for Clinical Use', CRC Press, Boca Raton, 1994; G. Faa and G. Crisponi, *Coord. Chem. Rev.*, 1999, **184**, 291; R. J. Bergeron, D. Badman, and G. M., Brittenham eds, 'Iron Chelators: New Development Strategies', Saratoga Publishers, Ponte Vedra, Florida, 2000; R. R. Crichton, A. Florence, and R. J. Ward, *Coord. Chem. Rev.*, 2002, **228**, 365.

325. A. E. Martell, R. J. Motekaitis, I. Murase, L. F. Sala, R. Stoldt, C. Y. Ng, H. Rosenkrantz, and J. J. Metterville, *Inorg. Chim. Acta*, 1987, **138**, 215; R. C. Hider, S. Singh, J. B. Porter, and E. R. Huehns, *Ann. N. Y. Acad. Sci.*, 1990, **612**, 327; G. S. Tilbrook and R. C. Hider, in 'Metal Ions in Biological Systems', eds. A. Sigel and H. Sigel, Marcel Dekker, New York, 1998, Vol. 35, p. 691.

326. J. B. Dionis, H.-B. Jenny, and H. H. Peter, *J. Org. Chem.*, 1989, **54**, 5623.

327. M. T. Ahmet, C. S. Frampton, and J. Silver, *J. Chem. Soc., Dalton Trans.*, 1988, 1159; see also Section 8.6 of R. C. Hider and S. Singh, in 'Chemistry of Iron', ed. J. Silver, Chapman & Hall, London, 1993.

328. B. E. Fischer and J. E. Hodge, *J. Org. Chem.*, 1964, **29**, 776; R. L. N. Harris, *Aust. J. Chem.*, 1976, **29**, 1329; Z. Zhang, S. J. Rettig, and C. Orvig, *Can. J. Chem.*, 1992, **70**, 763; J. J. Molenda, M. M. Jones, and M. A. Basinger, *J. Med. Chem.*, 1994, **37**, 93; J. Burgess, B. de Castro, C. Oliveira, and M. Rangel, *J. Chem. Res.*, 1996, (*S*) **234**, (*M*) 1338.

329. G. Xiao, D. van der Helm, R. C. Hider, and B. L. Rai, *J. Phys. Chem.*, 1996, **100**, 2345; Z. Hou, T. D. P. Stack, C. J. Sunderland, and K. N. Raymond, *Inorg. Chim. Acta*, 1997, **263**, 341.

330. J. B. Porter, M. Gyparaki, L. C. Burke, E. R. Huehns, P. Sarpong, V. Saez, and R. C. Hider, *Blood*, 1988, **72**, 1497; J. B. Porter, J. Morgan, K. P. Hoyes, L. C. Burke, E. R. Huehns, and R. C. Hider, *Blood*, 1990, **76**, 2389; B. L. Rai, L. S. Dekhordi, H. Khodr, Y. Jin, Z. Liu, and R. C. Hider, *J. Med. Chem.*, 1998, **41**, 3347.

331. G. J. Kontoghiorghes, *Analyst*, 1995, **120**, 845.

332. N. F. Olivieri and G. M. Brittenham, *Ann. N. Y. Acad. Sci.*, 1998, **850**, 217; A. Cohen, R. Galanello, A. Piga, C. Vullo, and F. Tricta, *Ann. N. Y. Acad. Sci.*, 1998, **850**, 223.

333. C. Borgna-Pignatti, S. Rugulotto, P. De Stefano, A. Piga, F. Di Gregorio, M. R. J. B. Porter, K. P. Hoyes, R. Abeysinghe, E. R. Huehns, and R. C. Hider, *Lancet*, 1989, **2**, 156.

334. M. Streater, P. D. Taylor, R. C. Hider, and J. Porter, *J. Med. Chem.*, 1990, **33**, 1749; R. A. Yokel, A. M. Fredenberg, P. W. Durbin, J. Xu, M. K. Rayens, and K. N. Raymond, *J. Pharm. Sci.*, 2000, **89**, 545; J. Xu, B. O'Sullivan, and K. N. Raymond, *Inorg. Chem.*, 2002, **41**, 6731.

335. B. L. Rai, H. Khodr, and R. C. Hider, *Tetrahedron*, 1999, **55**, 1129.

336. S. J. Rodgers, C.-W. Lee, C. Y. Ng, and K. N. Raymond, *Inorg. Chem.*, 1987, **26**, 1622; S. Dhungana, S. Heggemann, P. Gebhardt, U. Möllmann, and A. L. Crumbliss, *Inorg. Chem.*, 2003, **42**, 42.

337. H. E. Toma, A. A. Batista, and H. B. Gray, *J. Am. Chem. Soc.*, 1982, **104**, 7509.

338. J. Davies and B. M. Gatehouse, *Chem. Commun.*, 1970, 1166.

339. M. Gerloch, J. Lewis, F. E. Mabbs, and A. Richards, *J. Chem. Soc. (A)*, 1968, 112.

340. C. Floriani and F. Calderazzo, *J. Chem. Soc. (A)*, 1971, 3665.

341. F. V. Wells, S. W. McCann, H. H. Wickman, S. L. Kessel, D. N. Hendrickson, and R. D. Feltham, *Inorg. Chem.*, 1982, **21**, 2306.

342. M. A. Torzilli, S. Colquhoun, J. Kim, and R. H. Beer, *Polyhedron*, 2002, **21**, 705.

343. B. W. Fitzsimmons, A. Hume, L. F. Larkworthy, M. H. Turnbull, and A. Yavari, *Inorg. Chim. Acta*, 1985, **106**, 109.

344. I. M. Klotz and D. M. Kurtz, *Acc. Chem. Res.*, 1984, **17**, 16.

345. H. J. Schugar, G. R. Rossman, C. G. Barraclough, and H. B. Gray, *J. Am. Chem. Soc.*, 1972, **94**, 2683.

346. W. Schmitt, C. E. Anson, B. Pilawa, and A. K. Powell, *Z. Anorg. Allg. Chem.*, 2002, **628**, 2443.

347. C. A. Chang, L. C. Francesconi, M. F. Malley, K. Kumar, J. Z. Gougoutas, M. F. Tweedle, D. W. Lee, and L. J. Wilson, *Inorg. Chem.*, 1993, **32**, 3501; I. Fábián and H. Diebler, *Inorg. Chem.*, 1987, **26**, 925.

348. L. K. Thompson, L. Zhao, Z. Xu, D. O. Miller, and W. M. Reiff, *Inorg. Chem.*, 2003, **42**, 128.

349. W. Lovenberg ed., 'Iron-sulfur Proteins', Academic Press, New York, Vol. 1, 1973; Vol. 2, 1973; Vol. 3, 1977; Vol. 4, 1982; R. Holm, *Acc. Chem. Res.*, 1977, **10**, 427; H. Ogino, S. Inomata, and H. Tobita, *Chem. Rev.*, 1998, **98**, 2093; J. G. Hughes and P. J. Lawson, *J. Chem. Educ.*, 1987,

64, 973; B. N. S. Manhas, K. Kaur, and S. B. Kalia, *Synth. React. Inorg. Met.-Org. Chem.*, 2000, **30**, 609; S. Singhal, C. L. Sharma, A. N. Garg, and K. Chandra, *Polyhedron*, 2002, **21**, 2489.

350. K. D. Watenpaugh, L. C. Sieker, and L. H. Jensen, *J. Mol. Biol.*, 1979, **131**, 509.
351. M. T. Werth, D. M. Kurtz, B. D. Howes, and B. H. Huynh, *Inorg. Chem.*, 1989, **28**, 1357.
352. R. W. Lane, J. A. Ibers, R. B. Frankel, G. C. Papaefthymiones, and R. H. Holm, *J. Am. Chem. Soc.*, 1977, **99**, 84.
353. J. G. Reynolds and R. H. Holm, *Inorg. Chem.*, 1980, **19**, 3257.
354. P. K. Mascharak, G. C. Papaefthymiones, R. B. Frankel, and R. H. Holm, *J. Am. Chem. Soc.*, 1981, **103**, 6110.
355. D. Ghosh, W. Furey, A. H. Robbins, and C. D. Stout, *J. Mol. Biol.*, 1982, **158**, 73.
356. K. S. Hagan, G. Christou, and R. H. Holm, *Inorg. Chem.*, 1983, **22**, 309.
357. K. S. Hagan, A. D. Watson, and R. H. Holm, *J. Am. Chem. Soc.*, 1983, **105**, 3905.
358. R. H. Holm, B. A. Averill, T. Herskovitz, R. B. Frankel, H. B. Gray, O. Siiman, and J. F. Grunthaner, *J. Am. Chem. Soc.*, 1974, **96**, 2644.
359. K. S. Hagen, J. G. Reynolds, and R. H. Holm, *J. Am. Chem. Soc.*, 1981, **103**, 4054.
360. T. E. Wolff, P. P. Power, R. B. Frankel, and R. H. Holm, *J. Am. Chem. Soc.*, 1980, **102**, 4694.
361. G. Christou and C. D. Garner, *J. Chem. Soc., Dalton Trans.*, 1980, **2354**, 2363.
362. Y. Chen, R. Cai, and Y. Zeng, *Fenxi Huaxue*, 1996, **24**, 1166; *Chem. Abstr.*, 1997, **126**, 54148t.
363. H.-C. Zhou and R. H. Holm, *Inorg. Chem.*, 2003, **42**, 11.
364. S. Rutchik, S. Kim, and M. A. Walters, *Inorg. Chem.*, 1988, **27**, 1513; A. J. Dunford and R. A. Henderson, *Chem. Commun.*, 2002, 360; S. C. Davies, D. J. Evans, R. A. Henderson, D. L. Hughes, and S. Longhurst, *J. Chem. Soc., Dalton Trans.*, 2001, 3470.
365. B. S. Snyder, M. S. Reynolds, G. C. Papaefthymiou, R. B. Frankel, and R. H. Holm, *Polyhedron*, 1991, **10**, 203; M. G. Kanatzidis, A. Salifoglou, and D. Coucouvanis, *Inorg. Chem.*, 1986, **25**, 2460.
366. C. Goh, B. M. Segal, J. Huang, J. R. Long, and R. H. Holm, *J. Am. Chem. Soc.*, 1996, **118**, 11844; H.-C. Zhou and R. H. Holm, *Inorg. Chem.*, 2003, **42**, 11.
367. W. X. Zhang, M. S. Xu, G. H. Wang, and M. Y. Wang, *Cancer Res.*, 1983, **43**, 339.
368. F. Z. Roussin, *Ann. Chim. Phys.*, 1858, **52**, 285.
369. A. R. Butler, C. Glidewell, and M.-H. Li, *Adv. Inorg. Chem.*, 1989, **32**, 335.
370. J. McCormick, R. Bereman, and D. Baird, *Coord. Chem. Rev.*, 1984, **54**, 99.
371. O. A. Ileperuma and R. D. Feltham, *Inorg. Chem.*, 1975, **14**, 3042.
372. J. G. Hughes and P. J. Lawson, *J. Chem. Educ.*, 1987, **64**, 973; B. N. S. Manhas, K. Kaur, and S. B. Kalia, *Synth. React. Inorg. Met.-Org. Chem.*, 2000, **30**, 609; S. Singhal, C. L. Sharma, A. N. Garg, and K. Chandra, *Polyhedron*, 2002, **21**, 2489.
373. P. C. Healy and A. H. White, *J. Chem. Soc., Dalton Trans.*, 1972, 1163.
374. R. L. Martin, N. M. Rhode, G. B. Robertson, and D. Taylor, *J. Am. Chem. Soc.*, 1974, **96**, 3647.
375. A. H. Ewald and E. Sinn, *Aust. J. Chem.*, 1968, **21**, 927.
376. W. C. Hamilton and I. Bernal, *Inorg. Chem.*, 1967, **6**, 2003.
377. G. R. Lewis and I. Dance, *J. Chem. Soc., Dalton Trans.*, 2000, 3176.
378. B. F. Hoskins and C. D. Pannan, *Inorg. Nucl. Chem. Lett.*, 1975, **11**, 409.
379. C. Cairns, S. M. Nelson, and M. G. B. Drew, *J. Chem. Soc., Dalton Trans.*, 1981, 1965.
380. B. J. McCormick, R. Bereman, and D. Baird, *Coord. Chem Rev.*, 1984, **54**, 99.
381. V. N. Serezhkin, L. B. Serezhkina, and N. E. Sidorina, *Russ. J. Coord. Chem.*, 2000, **26**, 500.
382. G. Johansson, *Acta Chem. Scand.*, 1989, **43**, 307.
383. P. Kennepohl and E. I. Solomon, *Inorg. Chem.*, 2003, **42**, 689.
384. K. Murata and D. E. Irish, *Spectrochim. Acta*, 1988, **44A**, 739; M. J. Apted, G. A. Waychunas, and G. E. Brown, *Geochim. Cosmochim. Acta*, 1985, **49**, 2081; B. D. James, M. Bakalova, J. Liesegang, W. M. Reiff, B. W. Skelton, and A. H. White, *Inorg. Chem.*, 2001, **40**, 4617; S. I. Troyanov, M. Feist, and E. Kemnitz, *Z. Anorg. Allg. Chem.*, 1999, **625**, 806.
385. Y. Inada and S. Funahashi, *Z. Naturforsch.*, 1999, **54B**, 1518.
386. R. H. Byrne and D. R. Kester, *J. Solution Chem.*, 1981, **10**, 51; J. Bjerrum and I. Lukeš, *Acta Chem Scand.*, 1986, **40A**, 31; G. R. Brubaker and R. A. Peterson, *Inorg. Chim. Acta*, 1989, **155**, 139.
387. J. K. Beattie and C. J. Moore, *Inorg. Chem.*, 1982, **21**, 1292; M. C. Morón, F. Palacio, R. Navarro, J. Pons, J. Casabó, and R. L. Carlin, *Inorg. Chem.*, 1990, **29**, 842; M. C. Morón, F. Palacio, J. Pons, J. Casabó, X. Solans, K. E. Merabet, D. Huang, X. Shi, B. K. Teo, and R. L. Carlin, *Inorg. Chem.*, 1994, **33**, 746; B. N. Figgis, A. N. Solbolov, E. S. Kucharsk, and V. Broughton, *Acta. Crystallogr.*, 2000, **56C**, e228.
388. S. I. Troyanov, M. Feist, and E. Kemnitz, *Z. Anorg. Allg. Chem.*, 1999, **625**, 806.
389. K. R. Dunbar, J. J. Longridge, J. M. Rawson, and J.-S. Sun, *Inorg. Synth.*, 2002, **33**, 103.
390. S. A. Cotton, V. Franckevicius, and J. Fawcett, *Polyhedron*, 2002, **21**, 2055.

Iron: Models of Proteins with Dinuclear Active Sites

Ferman A. Chavez[1] & Lawrence Que[2]
[1] *Oakland University, Rochester, MI, USA*
[2] *University of Minnesota, Minneapolis, MN, USA*

Based in part on the article Iron: Models of Proteins with Dinuclear Active Sites by Will E. Lynch & Donald M. Kurtz, Jr. which appeared in the Encyclopedia of Inorganic Chemistry, First Edition.

1	Introduction	1
2	Synthesis and Structures	5
3	Spectroscopic Features of Diiron Model Complexes	8
4	Reactivity of Diiron Model Complexes	9
5	Related Articles	10
6	References	10

Glossary

Activated State: form of the enzyme that is capable of effecting substrate turnover
Active site: area in the metalloprotein where catalysis takes place
Diferric: diiron metal binding site in the $Fe^{III}Fe^{III}$ form
Diferrous: diiron metal binding site in the fully reduced $Fe^{II}Fe^{II}$ form
Dinucleating ligand: a ligand that binds two metals
High valent: iron centers in formal oxidation state (IV)
Intermediate: a species that is proposed to be present during the enzymatic catalytic cycle
Mixed valent: containing a diiron site where the oxidation states of the irons are not the same
Resting state: normally the as-isolated form of the enzyme; also a form that is present at the end of the catalytic cycle
Tetrabridged carboxylate: two iron centers that are bonded through four bridging carboxylate groups
Valence delocalized: possessing valence electrons that are exchanged between metal centers
Valence localized: possessing valence electrons that are not exchanged between metal centers

Abbreviations

BBBAN = 2,7-bis-1,8-2-naphthyridine; BEAN = 2,7-bis-(N,N'-diethylaminomethyl)-1,8-naphthyridine; BPMAN = 2,7-bis[bis(2-pyridylmethyl)aminomethyl]-1,8-naphthyridine; BPMCN = N,N'-bis(2-pyridylmethyl)-N,N'-dimethyl-trans-1,2-diaminocyclohexane; dxlCO_2H = 2,6-Bis[(2,6-dimethylphenyl)methyl]-4-*tert*-butylbenzoic acid; ENDOR = electron-nuclear double resonance spectroscopy; EPR = electron paramagnetic resonance spectroscopy; N-Et-HPTB = N,N,N',N'-tetrakis(N'-ethyl-2-benzylimidazolylmethyl)-2-hydroxo-1,3-diaminopropane; 5-Et_3-TPA = tris[(5-ethyl-2-pyridyl)methyl]amine; EXAFS = extended X-ray absorption fine structure spectroscopy; HB(3,5-iPr$_2$pz)$_3$ = hydrotris(3,5-diisipropylpyrazol-1-yl)borate; HBPMP = 2,6-bis[(bis(2-pyridylmethyl)amino)methyl]-4-methylphenol; H-EtOH-HPTB = N,N,N,N-tetrakis(N'(2-hydroxyethyl)-2-hydroxo-1,3-diaminopropane; HMe_2TPD = N,N-bis(6-methyl-2-pyridylmethyl)-N,N-bis(2-pyridylmethyl)-2-hydroxy-1,3-diaminopropane; HO_2CAr^{Mes} = 2,6-bis(mesityl) benzoic acid; HO_2CAr^{Tol} = 2,6-bis(p-tolyl)benzoic acid; HPh-BIMP = 2,6-bis[bis{2-(1-methyl-4,5-diphenylimidaazolyl)methyl}-aminomethyl]-4-methylphenol); H_2Ph_4DBA = dibenzofuran-4,6-bis(diphenylacetic acid); HPh-TIDP = N,N,N',N'-tetrakis(2-(1-methyl-4,5-diphenylimidazolyl)-methyl)-1,3-diaminopropan-2-ol; HPTB = N,N,N',N'-tetrakis (2-benzylimidazolylmethyl)-2-hydroxo-1,3-diaminopropane; Hr = hemerythrin; HTPDP = N,N,N,N-tetrakis(2-pyridylmethyl)-2-hydroxy-1,3-diaminopropane; H_2XDK = m-xylenediamine bis(Kemp's triacid)imide; Me_2HPTB = N,N,N-tetrakis(5,6-dimethyl-2-benzylimidazolylmethyl)-2-hydroxo-1,3-diaminopropane; MMO = methane monooxygenase; MMOH = methane monooxygenase hydroxylase; 6-Me-TPA = [(6-methyl-2-pyridyl)methyl]-bis(2-pyridylmethyl)amine; 5-Me_3-TPA = tris[(5-methyl-2-pyridyl)methyl]amine; 6-Me_3-TPA = tris[(6-methyl-2-pyridyl)methyl] amine; 4,6-Me_6-TPA = tris[(4,6-dimethyl-2-pyridyl)methyl] amine; RNR = ribonucleotide reductase; TPA = tris(2-pyridylmethyl)amine.

1 INTRODUCTION

The goal of diiron model chemistry is to develop small molecule systems that accurately reproduce spectroscopic, structural, and more ambitiously, reactivity aspects of diiron metalloproteins.[1] Despite being structurally similar, diiron enzymes carry out a variety of catalytic processes (*see* ***Iron Proteins with Dinuclear Active Sites***).[2–5] Advancements in the synthesis and characterization of small molecule mimics for nonheme diiron enzymes have been tremendous in the last decade. Biomimetic studies have been carried out in efforts to reproduce the structural and functional aspects of these biocatalysts.[6–10] Although this has been a challenging endeavor, much information regarding the structural and mechanistic aspects of catalytic intermediates has been obtained.

Metalloenzymes with diiron sites where the metal ions are bridged by carboxylates (i.e. glutamate, aspartate) have emerged as an important class of enzyme (*see* ***Iron Proteins with Dinuclear Active Sites***).[3–5] Several members of this

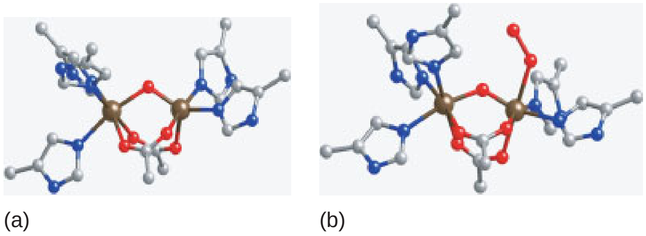

Figure 1 Structure of diferrous Hr (pdb 1HMD) (a), and oxygenated Hr (pdb 1HMO) (b) Key: iron (brown), oxygen (red), nitrogen (blue), and carbon (gray)

class, isolated from mammals, plants, or bacteria, have been characterized by X-ray crystallography. The first structurally characterized protein in this class was hemerythrin (Hr),[11] which is the O_2 carrier protein in marine invertebrates. Shown below is the diferrous iron site of Hr (Figure 1(a)) and the oxygenated form of Hr (Figure 1(b)). In the reduced state, two Fe(II) centers are bridged by a hydroxo ligand along with two 1,3-μ carboxylates. One iron center additionally is bonded by three histidine nitrogens to make it six-coordinate, while the other iron is bonded by two histidine nitrogen ligands rendering it coordinatively unsaturated. This is where dioxygen binds (Figure 1(b)). Upon binding, the dioxygen molecule is reduced to the peroxide level by acceptance of one electron from each iron. The hydrogen from the bridging hydroxo group is transferred to the peroxide to generate a coordinated hydroperoxo ligand. The dioxygen molecule is transported in this manner until it is released to regenerate the deoxy or reduced form of the oxygen carrying site. Like hemoglobin, some Hr enzymes show cooperativity. Model studies of this metalloprotein have advanced the understanding of dioxygen activation and transport in nonheme diiron centers for aerobic organisms.

Other well known examples of diiron centers are those that bind and activate dioxygen for the purpose of carrying out oxidative transformations. These include the plant soluble stearoyl–acyl carrier protein (ACP) delta 9-desaturases (Δ^9D),[12] ribonucleotide reductase (RNR) from *Escherichia coli* and eukaryotes,[13] and methane monooxygenase (MMO)from methanotrophic bacteria.[14] The enzyme Δ^9D introduces a *cis* double bond at the 9,10 position of stearoyl–ACP to form oleyl–ACP. The X-ray structure of the diferrous active site is shown in Figure 2(a). In this structure, two iron sites are bridged by 1,3-μ-carboxylate groups. In addition, each iron has a chelating carboxylate and histidine nitrogen coordinated to it. It is interesting to note that the histidine groups are situated in a *syn* orientation with respect to each other. This may be important in rapid dioxygen binding.

In the small protein of class I RNR, the diiron center found in the R2 subunit serves to oxidize an endogenous tyrosine to a tyrosyl radical.[15,16] This radical is essential for initiating the conversion of ribonucleotides to deoxyribonucleotides in the rate limiting step of the biosynthesis of DNA. The X-ray structure of the diferrous form of RNR[13] is shown in Figure 2(b). This site possesses two bridging glutamates, one chelating glutamate, one chelating aspartate and two terminal histidines. The phenol side chain of a tyrosine residue is

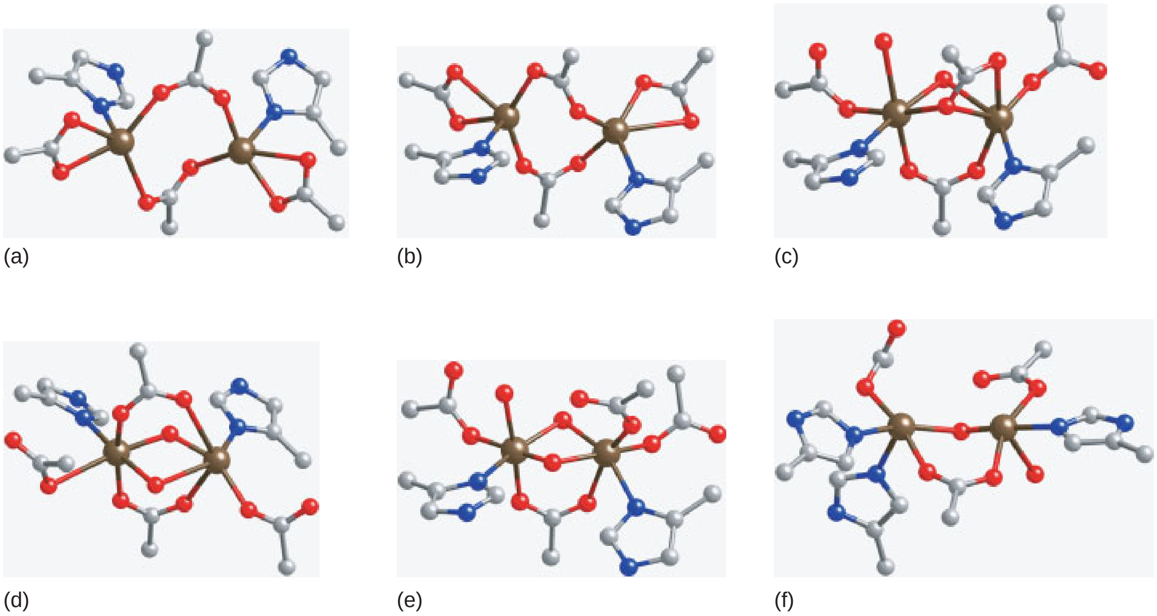

Figure 2 Structures of nonheme diiron active sites: reduced Δ^9D (pdb 1AFR) (a), reduced RNR (pdb 1PFR) (b), reduced MMO (pdb 1FYZ) (c), oxidized RNR (pdb 2R2F) (d), oxidized MMO from (pdb 1MHY) (e), and oxidized ROO (pdb 1E5D) (f) Key: iron (brown), oxygen (red), nitrogen (blue), and carbon (gray)

located nearby (within 5.3 Å). Upon reacting with dioxygen, the enzyme becomes activated through the formation of a tyrosyl radical (Scheme 1), and an oxo ligand bridges the two iron(III) atoms. An intermediate species (Intermediate **X**) is generated prior to oxidation of the tyrosine group. This species is believed to be a mixed valent Fe(III)Fe(IV) center. The oxidized (resting) form of RNR is shown in Figure 2(d). In this structure, the diiron unit contains both bridging and terminal carboxylate ligands as well as terminal histidine ligands. Additional bridging oxo and aqua ligands connecting the iron(III) centers are present.[17]

Methane monooxygenases are widely investigated metalloenzymes that catalyze the oxidation of methane to methanol by dioxygen.[18,19] This unique function achieves the first step in the metabolism of methanotrophic bacteria, which consume methane and dioxygen as their sole source of carbon and energy. The diferrous active site of the hydroxylase component (MMOH) of soluble MMO is shown in Figure 2(c). It features a diiron center containing four glutamate and two histidine residues. There is a hydroxo group bridging the two iron(II) centers (Figure 2(c)). The oxidized form or resting state is shown in Figure 2(e). It consists of a diiron(III) unit that usually contains two bridging hydroxo ligands. Scheme 2 depicts the core transformation that occurs during the MMOH catalytic cycle.

The first spectroscopically characterized intermediate in the reaction of the diferrous state (MMO_{red}) with dioxygen is a peroxo species (Intermediate **P**). This intermediate subsequently converts to a high-valent bis(μ-oxo)diiron(IV) component (Intermediate **Q**). Intermediate **Q** reacts with methane releasing methanol and generating a water molecule. The resting state (MMO_{oxd}) is reduced back to the diferrous form to close the cycle. In addition to methane, many other substrates react with MMO. These include long-chain alkanes, alkenes, halogenated and other substituted alkanes, alkynes, sulfides, and others.[20,21]

A new member of the family of nonheme diiron enzymes recently discovered is called rubrerythrin. This metalloprotein is formally classified as an oxidoreductase (rubredoxin:oxygen oxidoreductase). The diiron(III,III) active site structure is displayed in Figure 2(f). This biomolecule possesses two histidines coordinated to one iron and one histidine coordinated to the second iron. A carboxylate bridges the two irons and there are carboxylate ligands also coordinated to each iron. The purpose of this enzyme in the strict anaerobe is to safely reduce oxygen to water.[22]

It has recently been suggested from sequence analyses that diiron clusters might be present in a larger number of enzymes, thus indicating a much greater role of these clusters in O_2 activation biochemistry than previously appreciated. A number of related membrane-bound enzymes found in plants and animals have not been structurally characterized but are likely to contain a diiron site in their active sites. Bacterial toluene monooxygenase,[23] phenol hydroxylase[24] and alkene epoxidase[25] show significant homology to MMO. Ferroxidase, an enzyme that catalyzes the oxidation and subsequent storage of iron has also been identified as a diiron enzyme.[26]

Juxtaposition of two iron centers bridged by single oxygens or carboxylate oxygens allows for one- and two-electron redox processes to occur. The redox potentials of the iron centers are carefully modulated by ligands. This fine tuning is seen by the fact that removal of a particular donor and possibly changing a geometry has a dramatic influence on

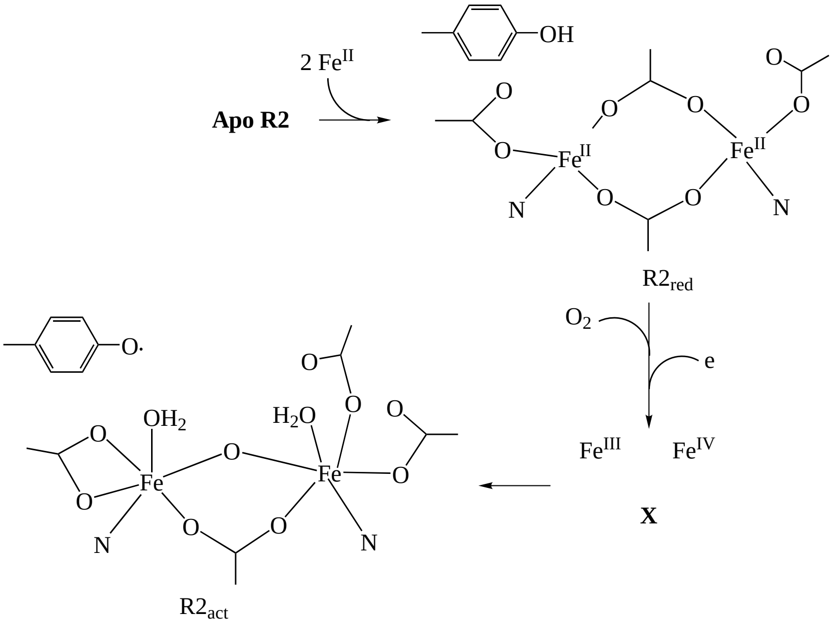

Scheme 1 Reaction cycle for R2 subunit of ribonucleotide reductase

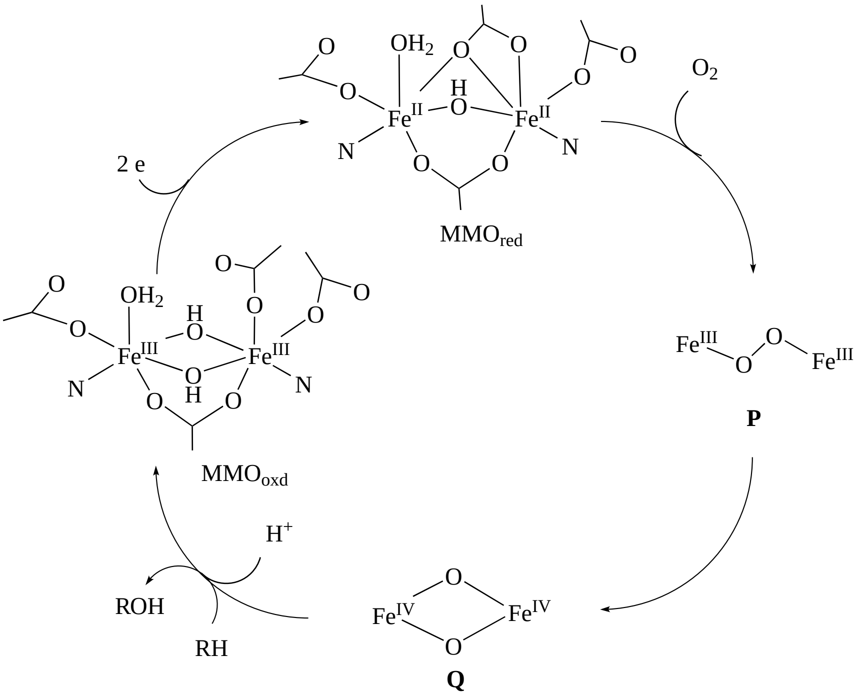

Scheme 2 Reaction cycle for methane monooxygenase hydroxylase

the active site's catalytic ability. Model chemists have the advantage of probing these effects on a much finer level than is currently possible with biological systems. There has been a multitude of crystal structures for diiron enzymes that have been determined both for the native enzymes and for mutants. The delicate balancing act for these enzymes is seen by the fact that subtle alterations in ligand properties and environment can dramatically change the reactivity.[27] A great deal of work has been carried out in the modeling of diiron enzymes and much structural data has been obtained for not only resting and activated states of the enzymes but also for proposed intermediates in various enzyme catalytic cycles. In the recent past, the increased structural information, together with spectroscopic and kinetic data, allowing the detection and characterization of key intermediates of the catalytic cycle, has clarified the mechanism of reductive oxygen activation by RNR and MMO enzymes. In addition, the employment of low-temperature rapid acquisition techniques for X-ray crystallography has allowed, in some cases, for synthetic models of proposed reactive intermediates to be structurally characterized.

The success of understanding the subtle structural, spectroscopic, and mechanistic aspects of these enzymes has been achieved through the use of specially designed supporting ligands. Several ligand types for modeling these active sites have been employed. They include multidentate dinucleating ligands, multidentate mononucleating ligands, preorganized bridging carboxylate ligands and bulky carboxylate ligands.

For many carboxylate-bridged diiron metalloenzymes, the reduced diiron(II,II) state is the most desirable target. Such compounds rarely assemble spontaneously by mixing of an iron(II) salt with carboxylates and other ligands. Designing and synthesizing suitable organic ligand precursors can therefore be a crucial first step, in which the following considerations must be addressed: (a) the ligands should have bridging potential (preferably through carboxylate ligands and/or oxygen(s)). The redox properties of the ligands should be compatible with diiron species in oxidation states II, III, and IV; (b) Steric properties of the ligand are very important. This is how one can control nuclearity and reactivity in the absence of a protein framework. (Inadequate steric bulk can lead to polynuclear complexes, whereas too much steric bulk will lead to mononuclear complexes.) (c) The coordination number of each iron atom in the resulting compound is also important. Since the Fe(II) complex must react with dioxygen, the Fe site must be coordinatively unsaturated or possess labile ligands such as water or other solvent components. Once a target dinuclear compound is in hand and demonstrated to be a reasonable structural and spectroscopic mimic of a diiron metalloprotein active site, the next objective is to explore its chemical reactivity with an oxidant, preferably dioxygen. Generating an intermediate similar to those encountered with the natural systems will help to characterize these species and may also provide a model with functional properties.[9,28] Structural flexibility is important since rearrangement is inevitable in the catalytic cycle.[14] Intraligand hydrogen bonding may assist in the desired chemical transformation. The model compound should be in the diferric state after turnover to allow further cycles to ensue. Achieving substrate turnover in a catalytic manner under mild conditions is an important goal for this research.

The following highlights are in the authors' opinion the most significant advances in the area of model chemistry for diiron enzymes. This article endeavors to review recent developments in nonheme model chemistry with emphasis on well defined structurally characterized synthetic models. Their spectroscopic properties will be discussed along with their relevance to the enzyme active sites and the parallels of their reactivities as they relate to these enzymes.

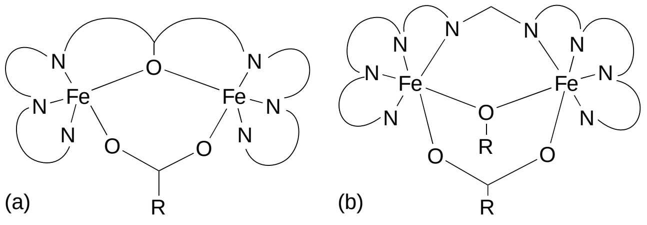

Figure 3 Diiron(II,II) complexes supported by dinucleating ligands

2 SYNTHESIS AND STRUCTURES

2.1 Models Using Multidentate Dinucleating Ligands

Several multidentate dinucleating ligands have been employed to assemble diiron(II) complexes (Scheme 3). The general synthetic strategy for diiron complexes supported by these ligands involves reaction of Fe(II) salts under anaerobic conditions in anhydrous solvent with the ligand in the presence of base and other carboxylate ligand(s).[29–31] Using such an approach, structures such as those shown in Figure 3 can be isolated in crystalline form. These compounds are good models for the diferrous site of hemerythrin since they are nitrogen rich. Recently, diiron compounds supported by naphthyridine-containing dinucleating ligands such as BBBAN (Scheme 3) have been reported. The bridging naphthyridine group is designed to mimic a bridging carboxylate ligand that is almost always present in nonheme diiron enzymes. The advantage of employing this ligand is

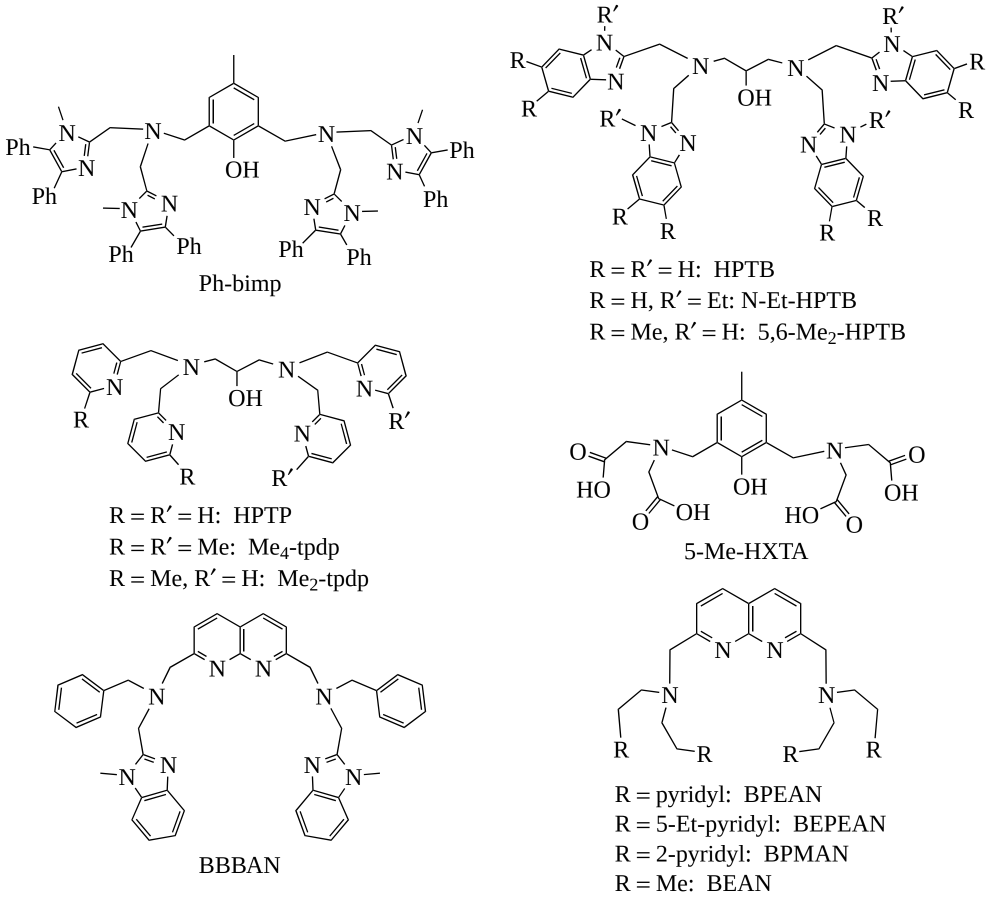

Scheme 3 Multidentate dinucleating ligands

that there is less potential for structural rearrangement in the bridging ligand group.

A great deal of structural diversity is seen with these ligands. A carboxylate ligand can be added to the hydroxo- or alkoxo-bridged diiron(II) compound[32,33] to generate a carboxylato bridged species (Figure 3(b)).[32]

Addition of carboxylate ligands to a non hydroxo-bridged analog leads to multiply bridged carboxylate species (Figure 3(a)).[32,33] Phenoxo-bridged diiron(III,III) compounds with two bridging carboxylate ligands have been synthesized using the dinucleating ligand 5-Me-HXTA (Scheme 3).[34] In this method, iron(III) is mixed with deprotonated 5-Me-HXTA in methanol. Acetate is then added to generate $[Fe_2(HXTA)(OAc)_2]^{2+}$.

2.2 Models Using Multidentate Mononucleating Ligands

Approaches to synthesizing diiron units supported by multidentate mononucleating ligands (Scheme 4) have been investigated using capping nitrogen ligands. With ligands such as TPA and its derivatives, structural diversity for diiron compounds is achieved by variation of the bridging ligand(s) or by introducing steric bulk to the pyridine substituents. For example, double-bridged compounds such as $(6\text{-}Me_3TPA)_2Fe_2(\mu\text{-}OH)_2$,[35] and $(TPA)_2Fe_2(\mu\text{-}Cl)_2$[36] differ primarily by the identity of the bridging ligands with each iron coordinated by three pyridine nitrogens and one central amine nitrogen ligand. The dibridged complex $[L_2Fe_2(\mu\text{-}O)(\mu\text{-}OH)]^{3+}$ can be obtained by reaction of Fe(II) with 6-Me_3-TPA in the presence of *t*-BuOOH and water.[37] A $Fe_2(\mu\text{-}O)(\mu\text{-}HCO_2)$ core was unexpectedly constructed by reaction of TPA with Fe(III) in the presence of base.[38] In efforts to model the resting state of the nonheme enzymes, several diiron(III,III) complexes featuring a bridging oxo group have been synthesized (Figure 4). These structures are noted for complexes where L = TPA.[38]

There have also been several examples of valence-delocalized Fe(II)Fe(III), $S = 9/2$ species generated from diiron complexes supported by terminally chelating ligands $[(Me_3\text{-tacn})_2Fe_2(\mu\text{-}OH)_3]^{2+}$ (Me_3-tacn = 1,4,7-trimethyl-1,4,7-triazacyclononane),[39] and $[(C_{24}H_{26}N_4O_2)Fe_2(\mu\text{-}OAc)_2]^{+}$.[40]

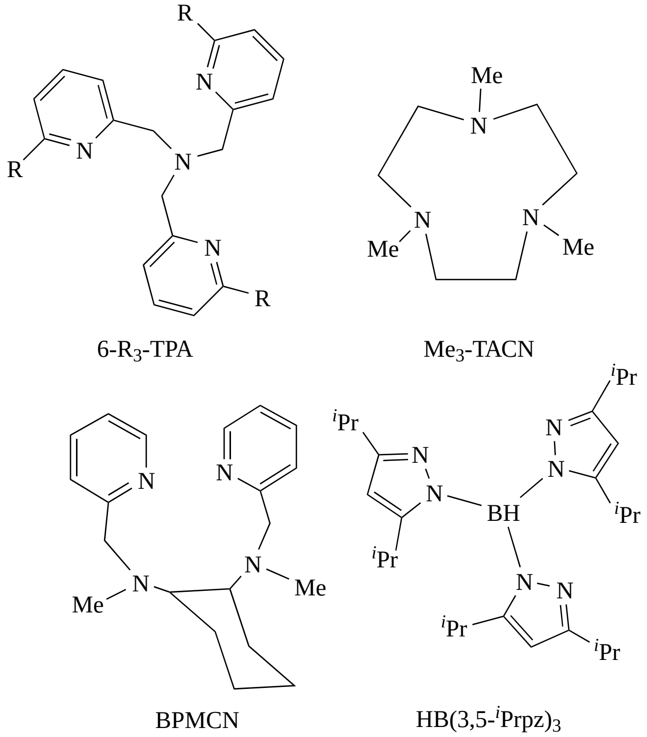

Scheme 4 Multidentate mononucleating ligands

2.3 Models Using Preorganized Bridging Carboxylate Ligands

A recent approach to obtain diiron model compounds involves the employment of preorganized carboxylate-bridged ligands (Scheme 5). Addition of nonchelating N donors and carboxylates completes the coordination.[41] The ligand *m*-xylylenediamine bis(Kemp's triacid)imide (H_2XDK) and related ligands H_2PXDK and H_2BXDK (Scheme 5) provides structures shown in Figure 5(a) when two equivalents of N-donor ligand and two equivalents of carboxylate ligand are added.[42,43] The $Fe_2(\mu\text{-}O)(\mu\text{-}RCO_2)_2$ core can also be synthesized using the preorganized XDK^{2-} ligand.[44] Diiron(II,II) compounds can be constructed with the preorganized dibenzofuran-4,6-bis(diphenyl acetic acid) (H_2Ph_4-DBA) (Scheme 5).

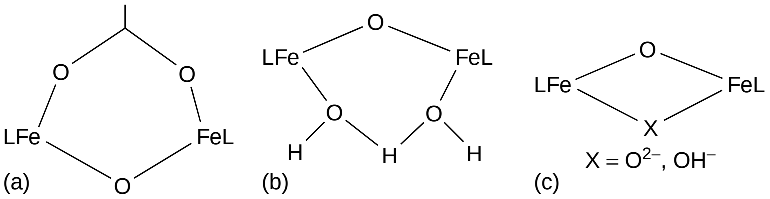

Figure 4 Diiron(III,III) core structures containing multidentate mononuclear ligands

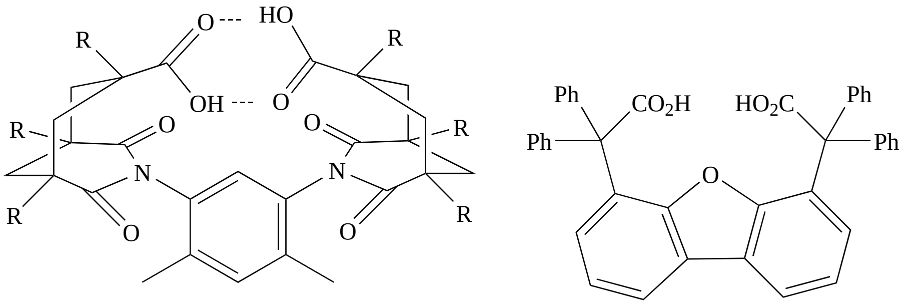

R = Me: H_2XDK
R = Pr: H_2PXDK
R = Bn: H_2BXDK

H_2Ph_4DBA

Scheme 5 Preorganized bridging carboxylate ligands

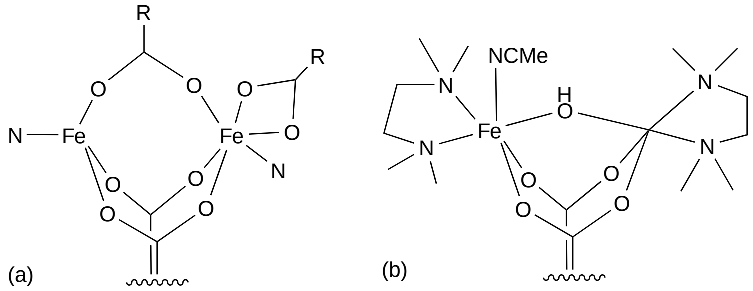

Figure 5 Diiron complexes assembled with XDK^{2-} ligands (a), and Ph_4DBA^{2-} ligand (b)

Using H_2Ph_4-DBA, Lippard and coworkers isolated a diiron(II,II) complex that has a donor set (Figure 5(b)) that is identical to that of diferrous hemerythrin.[45]

2.4 Models Using Bulky Carboxylate Ligands

A method that has recently been introduced to the study of diiron model complexes involves self-assembly reactions using bulky carboxylate ligands (Scheme 6). The steric bulk is employed about the carboxylate group to control nuclearity. In this approach, simple nonchelating N-donor ligands are employed as ancillary ligands. This method allows these complexes to ‘breathe’ structurally thus closely approximating what is seen at the actual nonheme active sites during the catalytic cycles. This approach has been successful in generating several diferrous model complexes that possess the same donor set found in nonheme enzymes (i.e. 4 carboxylates, and two N-donor ligands).[6,9] Utilizing this method, one can obtain di-, tri-, and tetrabridged carboxylate diiron(II,II) compounds with various terminal N-donor ligands.[9,46,47]

The success with this approach is seen by the fact that two groups have successfully synthesized good structural models for the diiron(II,II) centers in reduced RNR (Figure 6(a)).[48,49]

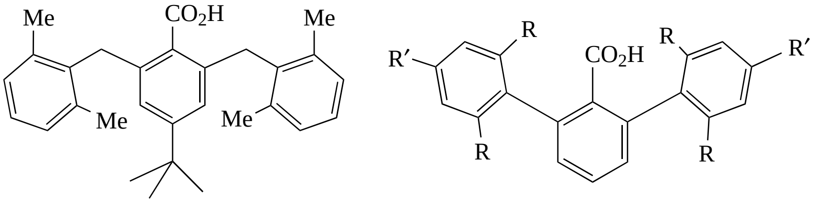

$dxlCO_2H$

R = Me, R′ = Me: Mes_2ArCO_2H
R = H, R′ = Me: $Ar^{Tol}CO_2H$

Scheme 6 Bulky Carboxylate Ligands

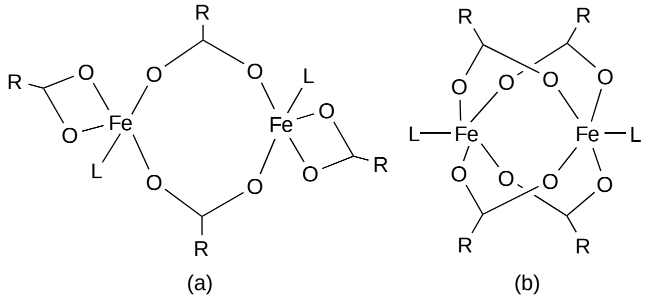

Figure 6 Dibridged (a) and tetrabridged (b) diiron(II,II) carboxylate complexes

The Fe−Fe distances for these complexes are ca. 4.0 Å, which is quite close to the value for RNR. For less sterically hindered carboxylate ligands such as benzoate, pivalate,**[50]** and 2,6-di(*m*-xylyl)benzoate (Scheme 6),**[46]** a tetrabridged carboxylate structure is obtained with Fe−Fe distances of ca. 2.8 Å (Figure 6(b)). Interestingly, this tetrabridged carboxylate structure is also obtained when $Ar^{Tol}CO_2H$ (Scheme 6) and 4-*t*-butylpyridine are used to generate the diiron compound thus demonstrating the low-energy barriers between structures in this case. Because of the lability often encountered with high spin iron(II) complexes, the success of these approaches has been primarily due to the use of intramolecular interactions.

The mixed valent diiron(II,III) species has relevance to nonheme enzymes. Recently, structural information on such compounds with bridging and terminal carboxylate ligands has been obtained.**[51,52]** The structures of one of these compounds is shown in Figure 7. The syntheses for the two species shown are identical. The structural variation in the bridging isopropoxide groups comes about from the conditions for crystallization.**[52]** The structure in Figure 7(a) has an Fe−Fe distance of 2.7485(5) Å while the structure in Figure 7(b) has a Fe−Fe distance of 2.6241(9) Å. This minor conformational difference results in tuning of the electronic state for these two structures. The structure in Figure 7(a) is valence localized with antiferromagnetically coupled iron sites ($S = 1/2$) while the structure in Figure 7(b) is valence delocalized with ferromagnetically coupled iron sites ($S = 9/2$). The compound $(Mes_2ArCO_2)_3Fe_2(OCHMe_2)$**[51,52]** was synthesized by exposing the diferrous starting material $(Mes2_2ArCO_2)_2Fe_2(\mu\text{-}Mes_2ArCO_2)_2$ to dioxygen in the presence of isopropanol. Recently, several valence-delocalized Fe(II,III) complexes have been prepared by Lippard *et al.***[51]** These complexes possess a tetracarboxylate-bridged diiron center (Figure 6(b)) with various axial donor ligands (L = THF, Py, 4-*t*-BuPy). The Fe−Fe distances for the THF, Py, and 4-*t*-BuPy complexes are 2.6633(11), 2.6982(13), and 2.713(3) Å, respectively. For these compounds, it is indicated that direct Fe−Fe interaction may provide the exchange mechanism. $[Fe_2(\mu\text{-}O_2CAr^{Tol})_4(Py)_2]^+$ was synthesized by the stoichiometric addition of one equivalent of oxidizing agent (AgOTf, Cp_2FePF_6) to the diferrous starting material $[Fe_2(\mu\text{-}O_2CAr^{Tol})_4(Py)_2]$.

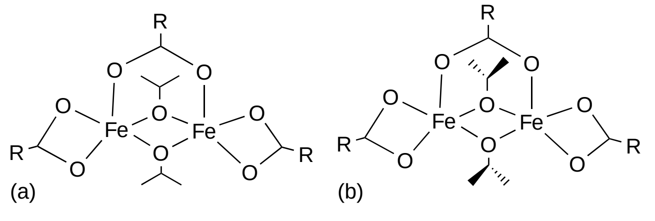

Figure 7 Structure of valence-localized (a), and valence-delocalized Fe(II,III) complex ($R = Mes_2ArCO^{2-}$) (b)

3 SPECTROSCOPIC FEATURES OF DIIRON MODEL COMPLEXES

Carboxylate-rich diiron(II,II) model complexes typically do not have strong absorbances in the visible region. In some cases, charge transfer bands may extend into the visible region leading to compounds that are yellow to beige in color depending on the donor set. These complexes also tend to be high spin and consequently kinetically labile, which is a characteristic found in carboxylate-rich nonheme diiron systems. The d−d transitions of high-spin iron(II) complexes can provide valuable information on the stereochemistry around the iron(II) centers: for six-coordinate complexes of Fe, the electronic transitions from $^5T_2$ to ^5E (in octahedral symmetry) have been shown to split into two bands while for five-coordinate complexes, the splitting is much larger. Diiron(II,II) compounds possessing μ-oxo or μ-hydroxo groups contain visible bands at ∼500 nm and 800 nm ($\varepsilon \sim 70\,M^{-1}\,cm^{-1}$).**[37,53,54]**

The electronic absorption spectra of diiron(III,III) complexes are dominated by ligand-to-metal charge transfer bands. Again, those complexes that accurately mimic the electronic states of nonheme enzymes are high spin. The UV-visible spectra of mixed valent diiron(II,III) complexes are dependent on the electronic characteristics of the complex. For example, in a valence-localized situation ($S = 1/2$), absorption bands in the visible region may correspond to ligand-to-metal charge transfer bands while in a valence-delocalized situation ($S = 9/2$), intervalence charge transfer bands may also be present.

Mössbauer parameters have been instrumental in characterizing diiron sites in model systems. The electronic environment can be assessed by the Mössbauer parameters. At ∼4 K, the isomer shift δ for iron(II) centers typically falls between 1.06 and 1.35 $mm\,s^{-1}$, whereas the quadrupole splitting ΔE_Q varies from 1.95 to 3.28 $mm\,s^{-1}$. The isomer shift for diferric species is characteristically small compared to that for diferrous centers. Typical values fall between 0.40

and 0.52 mm s^{-1}. Quadrupole splittings, however, are less informative regarding the oxidation state of the metal since there is much overlap with ferrous parameters. Mixed valent $Fe^{II}Fe^{III}$ and $Fe^{III}Fe^{IV}$ species have Mössbauer spectra that shed light on the electronic state of the complexes. In a valence-localized state, the absorption bands correspond to the individual iron sites in their oxidation states. In a valence-delocalized situation, the spectra become more complicated.[55] In any event, Mössbauer spectroscopy can be instrumental in determining the spin state and electronic properties of the species under study.

4 REACTIVITY OF DIIRON MODEL COMPLEXES

The reaction of the diferrous form of nonheme enzymes with dioxygen initially leads to several types of intermediates depending on the enzyme. For the oxygen carrier protein hemerythrin, dioxygen reversibly binds to the diferrous form generating a coordinated hydroperoxide complex (vide supra). Model studies for this reaction have successfully reproduced this reaction. Using the preorganized dicarboxylate ligand H_2Ph_4DBA (Scheme 5),[45] the diiron(II,II) complex was synthesized, accurately reproducing the coordination of deoxy hemerythrin. When this diferrous compound is exposed to dioxygen at low temperature, in the presence of three equivalents of 1-methylimidazole, spectroscopic evidence indicates that a diiron(III,III) complex is generated with a putative coordinated hydroperoxide ligand. Evidence for the generation of the hydroperoxide adduct was also obtained for a napthyridine based system. The dinucleating ligands BPEAN and BEPEAN (Scheme 3) were employed to synthesize diiron(III,III) complexes, which possessed the structure shown in Figure 3(b).[56] These complexes were reacted with hydrogen peroxide to generate a diiron(III,III) complex with a coordinated hydroperoxide ligand (verified by resonance Raman spectroscopy). The cryoreduced diiron(II,III) complex was characterized by electron paramagnetic resonance (EPR) and ^1H electron-nuclear double resonance (ENDOR) spectroscopy.[56]

For nonheme enzymes that further activate dioxygen, it is apparent that the diferrous forms also bind O_2 to eventually generate the active species responsible for the oxidative transformations. In the case of MMO, the first intermediate has been labeled compound **P** (Scheme 2), which subsequently converts to compound **Q**; both are kinetically competent to hydroxylate methane. In the case of RNR, compound **X** (Scheme 1) is responsible for the one-electron oxidation of a tyrosine residue to generate a tyrosyl radical. Based on chemical considerations and its Mössbauer properties, it has been proposed that compound **P** is a diferric peroxide species. To date, three model complexes of compound **P**, with comparable spectroscopic properties, have been structurally characterized (Figure 8).[29,57,58] In two of these models O_2 is bound in a *cis* μ-1,2-peroxo fashion while in a third, it is bound in a *trans* μ-1,2-peroxo manner. As in the enzyme, these compounds were all generated during reaction of diiron(II,II) precursors with molecular oxygen. That O_2 binds to the iron center through an oxidative addition is consistent with the fact that MMO can function with hydrogen peroxide as the oxidant in the absence of electrons and oxygen. In this reaction, compound **P** is also likely to be an intermediate. Many other systems that react with dioxygen in the diferrous state to generate diferric peroxide intermediates have been studied.[35,46,59,60]

In MMO, compound **Q** has been identified as a coupled diiron(IV,IV) species, on the basis of its Mössbauer spectrum. While different structures for compound **Q** are possible, there is now some spectroscopic evidence (X-ray absorption fine structure and Mössbauer spectroscopy) that the diiron center in compound **Q** is a high-valent $Fe_2(\mu\text{-}O)_2$ diamond core (Scheme 2). In the proposed mechanism, reaction

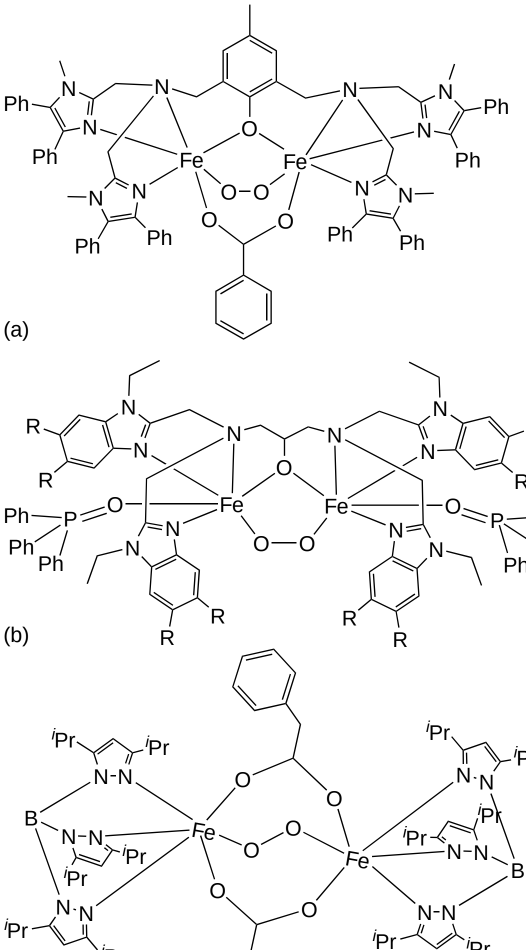

Figure 8 Schematic view of $[Fe_2(Ph\text{-}bimp)(PhCO_2)(\mu\text{-}O_2)]^{2+}$ (a), $[Fe_2(N\text{-}Et\text{-}hptb)(Ph_3PO)_2(O_2)]^{3+}$ (b), and $[Fe_2\{HB(3,5\text{-}iPrpz)_3\}_2\text{-}(PhCH_2CO_2)_2(\mu\text{-}O_2)]^{2+}$ (c)

products are derived from the two-electron oxidation of the substrate by compound **Q**. Recently, a system employed by Que *et al.* was used to generate a complex evidenced to contain a Fe(IV,IV) unit, which is the first example of a model compound for intermediate **Q**.[61] The supporting ligand is BPMCN (Scheme 4), and the compound was synthesized by treatment of the Fe(II) precursor, namely, Fe(BPMCN)(OTf)$_2$ ($Tf^- = CF_3SO_2{}^-$) with 10 equivalents t-BuOOH at −80 °C in dichloromethane. Initially a Fe^{III}-OO-t-Bu species is generated. Upon standing at −80 °C, this species monotonically converts to a species with $S = 1$ spin state. EXAFS measurements support the presence of a Fe$_2$(μ-O)$_2$ core. To explain the spin state, one would have to invoke an exchange coupled low-spin $S_1 = 1/2$, $S_2 = 1/2$ species. This species is capable of alkane oxidation.

Compound **X** from the catalytic cycle of RNR (Scheme 1) is an $S = 1/2$ species, contains only one oxidizing equivalent above the diferric state, and is catalytically competent for oxidizing the tyrosine residue to the tyrosyl radical. While it has first been described as a coupled system consisting of two high-spin Fe(III) plus a ligand radical, recent reanalysis of the ENDOR and Mössbauer experiments now strongly suggests that compound **X** carries a spin-coupled diiron(III,IV) center. A dinuclear $S = 3/2$ diiron(III,IV) complex, containing an Fe$_2$(μ-O)$_2$ core, has been generated during reaction of H_2O_2 with (μ-oxo)diiron(III)(TPA).[62] This complex can carry out oxidation reactions corresponding to those associated with MMO (oxidation of ethylbenzene), desaturase (desaturation of ethylbenzene), or RNR (oxidation of 2,4-di-*tert*-butylphenol to the corresponding phenoxyl radical). In addition, an $S = 1/2$ model containing diiron(III,IV) bridged by a (μ-O)$_2$ core, has also been obtained during reaction of H_2O_2 with a bis-(μ-oxo)diiron(III)(5-R$_3$-TPA) complex (Figure 9; R = Et).[63] This product is dark green and has the formulation for [Fe$_2$(μ-O)2(5-Et-TPA)$_2$]$^{3+}$. Its EPR properties are strikingly similar to those of compound **X**. The fact that no intermediate corresponding to compounds **P** and **Q** could be detected for RNR does not necessarily mean that they are not transiently formed in the enzymatic system. Electron transfer to the metal site may be too fast and prevent accumulation of such species. Nevertheless, two-electron, and not only one-electron, oxidation has been observed in the case of RNR, suggesting the intermediate formation of a compound **Q**-like species, with two oxidizing equivalents above the diiron(III,III) state.

When the precursor to the Fe(III,IV) compound is [Fe^{III}2(μ-O)$_2$(6-Me$_3$-TPA)$_2$]$^{2+}$, one-electron oxidation affords a Fe^{III}-O-Fe^{IV}=O core structure derived from the isomerization of the Fe$_2$(μ-O)$_2$ diamond core, demonstrating the accessibility of a terminal Fe^{IV}=O unit in a nonheme environment.[64] A different approach to achieve the Fe(III,IV) unit has also been carried out by Lippard *et al.*[65] In this method, a tetracarboxylate-bridged diiron(II,II) complex (4-t-BuPy)$_2$Fe$_2$(μ-RCO$_2$)$_4$ where RCO$_2{}^-$ is the bulky carboxylate Ar^{Tol}CO$_2{}^-$ (Scheme 6) is exposed to dioxygen at −79 °C. Among the products identified by Mössbauer and EPR spectroscopy is an Fe(III,IV) species.

Much success has been achieved in the modeling of various states for nonheme enzymes. The shortfall so far has been in reproducing the full reactivity found in these enzymes. Oxidation of substrates using molecular oxygen at moderate temperatures is a goal that has yet to be reached. Only a few examples exist in which a substrate can be oxidized in both a stoichiometric and catalytic manner with molecular oxygen as the oxidant. The substrates in this case tend to be easily oxidizable compounds such as phosphines and thioethers.[66–68] Lippard *et al.* have demonstrated the catalytic oxidation of triphenylphosphine with oxygen as the oxidant. They concluded that in their system, the oxidation was not occurring from an intermediate formed but from transfer of a bridging oxo group to the phosphine.[68] In addition, they also studied the oxidative capabilities of the peroxo species derived from the XDK ligands and found that this intermediate was not capable of oxidizing potent acceptors such as triphenylphosphine and that solvent oxidation occurred via radical autoxidation. In a system employed by Tolman *et al.*, it was demonstrated that a peroxo species derived from a carboxylate-bridged diiron complex was capable of stoichiometrically oxidizing triphenylphosphine.[66] The proposed mechanism involves the direct coordination of the triphenylphosphine substrate to the peroxo species.

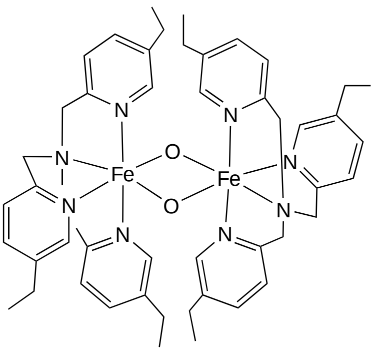

Figure 9 Schematic view of [bis-(μ-oxo)iron(III,IV)(5-Et$_3$-TPA)]$^{3+}$

5 RELATED ARTICLES

Iron Proteins for Storage & Transport & their Synthetic Analogs; Iron Proteins with Dinuclear Active Sites; Iron Proteins with Mononuclear Active Sites.

6 REFERENCES

1. R. H. Holm, P. Kennepohl, and E. I. Solomon, *Chem. Rev.*, 1996, **96**, 2239.

2. E. I. Solomon, T. C. Brunold, M. I. Davis, J. N. Kemsley, S.-K. Lee, N. Lehnert, F. Neese, A. J. Skulan, Y.-S. Yang, and J. Zhou, *Chem. Rev.*, 2000, **100**, 235.
3. P. Nordlund and H. Eklund, *Curr. Opin. Struct. Biol.*, 1995, **5**, 758.
4. B. J. Wallar and J. D. Lipscomb, *Chem. Rev.*, 1996, **96**, 2625.
5. D. M. Kurtz Jr, *J. Biol. Inorg. Chem.*, 1997, **2**, 159.
6. J. DuBois, T. J. Mizoguchi, and S. J. Lippard, *Coord. Chem. Rev.*, 2000, **200–202**, 443.
7. M. Fontecave, S. Ménage, and C. Duboc-Toia, *Coord. Chem. Rev.*, 1998, **178–180**, 1555.
8. A. L. Feig and S. J. Lippard, *Chem. Rev.*, 1994, **94**, 759.
9. W. B. Tolman and L. Que Jr, *J. Chem. Soc. Dalton Trans.*, 2002, 653.
10. D. S. Marlin and P. K. Mascharak, ‘Biomimetic Catalysis by Models of Non-Heme Iron Enzymes in Encyclopedia of Catalysis’, ed. I. T. Horváth, John Wiley and Sons, Inc., New York, 2004.
11. R. E. Stenkamp, *Chem. Rev.*, 1994, **94**, 715.
12. Y. Lindqvist, W. Huang, G. Schneider, and J. Shanklin, *EMBO J.*, 1996, **15**, 4081.
13. D. T. Logan, X.-D. Su, A. Åberg, K. Regnström, J. Hajdu, H. Eklund, and P. Nordlund, *Structure*, 1996, **4**, 1053.
14. D. A. Whittington and S. J. Lippard, *J. Am. Chem. Soc.*, 2001, **123**, 827.
15. A. Jordan and P. Reichard, *Annu. Rev. Biochem.*, 1998, **67**, 71.
16. J. Stubbe, *Curr. Opin. Chem. Biol.*, 2003, **7**, 183.
17. M. Eriksson, A. Jordan, and H. Eklund, *Biochemistry*, 1998, **37**, 13359.
18. M. Merkx, D. A. Kopp, M. H. Sazinsky, J. L. Blazyk, J. Müller, and S. J. Lippard, *Angew. Chem., Int. Ed. Engl.*, 2001, **40**, 4000.
19. L. Westerheide, M. Pascaly, and B. Krebs, *Curr. Opin. Chem. Biol.*, 2000, **4**, 235.
20. E. A. Ambundo, R. A. Friesner, and S. J. Lippard, *J. Am. Chem. Soc.*, 2002, **124**, 8770.
21. H. Fuse, M. Ohta, O. Takimura, K. Murakami, H. Inoue, Y. Yamaoka, J. M. Oclarit, and T. Omori, *Biosci. Biotech. Biochem.*, 1998, **62**, 1925.
22. C. Frazao, G. Silva, C. M. Gomes, P. Matias, R. Coelho, L. Sieker, S. Macedo, M. Y. Liu, S. Oliveira, M. Teixeira, A. V. Xavier, and C. Rodrigues-Pousada, *Nat. Struct. Biol.*, 2000, **7**, 1041.
23. L. M. Newman and L. P. Wackett, *Biochemistry*, 1995, **34**, 14066.
24. J. Powlowski and V. Shingler, *J. Bacteriol.*, 1990, **172**, 6834.
25. T. J. Smith, J. S. Lloyd, S. C. Gallagher, W. L. Fosdike, J. C. Murrell, and H. Dalton, *Eur. J. Biochem.*, 1999, **260**, 446.
26. T. Granier, B. L. d’Estaintot, B. Gallois, J.-M. Chevalier, G. Précigoux, P. Santambrogio, and P. Arosio, *J. Biol. Inorg. Chem.*, 2003, **8**, 105.
27. J. Baldwin, W. C. Voegtli, N. Khidekel, P. Moenne-Loccoz, C. Krebs, A. S. Pereira, B. A. Ley, B. H. Huynh, T. M. Loehr, P. J. Riggs-Gelasco, A. C. Rosenzweig, and J. M. Bollinger Jr, *J. Am. Chem. Soc.*, 2001, **123**, 7017.
28. L. Que Jr, *J. Chem. Soc. Dalton Trans.*, 1997, 3933.
29. T. Ookubo, H. Sugimoto, T. Nagayama, H. Masuda, T. Sato, K. Tanaka, Y. Maeda, H. Okawa, Y. Hayashi, A. Uehara, and M. Suzuki, *J. Am. Chem. Soc.*, 1996, **118**, 701.
30. Y. Dong, S. Ménage, B. A. Brennan, T. E. Elgren, H. G. Jang, L. L. Pearce, and L. Que Jr, *J. Am. Chem. Soc.*, 1993, **115**, 1851.
31. Y. Hayashi, T. Kayatani, H. Sugimoto, M. Suzuki, K. Inomata, A. Uehara, Y. Mizutani, T. Kitagawa, and Y. Maeda, *J. Am. Chem. Soc.*, 1995, **117**, 11220.
32. C. He and S. J. Lippard, *Inorg. Chem.*, 2001, **40**, 1414.
33. J. Kuzelka, S. Mukhopadhyay, B. Spingler, and S. J. Lippard, *Inorg. Chem.*, 2003, **42**, 6447.
34. K. E. Kauffmann, C. V. Popescu, Y. Dong, J. D. Lipscomb, L. Que Jr, and E. Münck, *J. Am. Chem. Soc.*, 1998, **120**, 8739.
35. V. MacMurdo, H. Zheng, and L. Que Jr, *Inorg. Chem.*, 2000, **39**, 2254.
36. Y. Zang, H. G. Jang, Y.-M. Chiou, M. P. Hendrich, and L. Que Jr, *Inorg. Chim. Acta*, 1993, **213**, 41.
37. Y. Zang, G. Pan, and L. Que Jr, *J. Am. Chem. Soc.*, 1994, **116**, 3653.
38. R. E. Norman, R. A. Leising, S. Yan, and L. Que Jr, *Inorg. Chim. Acta*, 1998, **273**, 393.
39. D. R. Gamelin, E. L. Bominaar, M. L. Kirk, K. Wieghardt, and E. I. Solomon, *J. Am. Chem. Soc.*, 1996, **118**, 8085.
40. S. K. Dutta, J. Ensling, R. Werner, U. Flörke, W. Haase, P. Gütlich, and K. Nag, *Angew. Chem., Int. Ed. Engl.*, 1997, **36**, 152.
41. T. J. Mizoguchi, J. Kuzelka, B. Spingler, J. L. D. Bois, R. M. Davydov, B. Hedman, K. O. Hodgson, and S. J. Lippard, *Inorg. Chem.*, 2001, **40**, 4662.
42. S. Herold and S. J. Lippard, *J. Am. Chem. Soc.*, 1997, **119**, 145.
43. D. D. LeCloux, A. M. Barrios, T. J. Mizoguchi, and S. J. Lippard, *J. Am. Chem. Soc.*, 1998, **120**, 9001.
44. S. P. Watton, A. Masschelein, J. Rebek Jr, and S. J. Lippard, *J. Am. Chem. Soc.*, 1994, **116**, 5196.
45. T. J. Mizoguchi and S. J. Lippard, *J. Am. Chem. Soc.*, 1998, **120**, 11022.
46. F. A. Chavez, R. Y. N. Ho, M. Pink, V. G. Young Jr, S. V. Kryatov, E. V. Rybak-Akimova, H. P. Andres, E. Münck, L. Que Jr, and W. B. Tolman, *Angew. Chem. Int. Ed. Engl.*, 2002, **41**, 149.
47. D. Lee and S. J. Lippard, *Inorg. Chem.*, 2002, **41**, 2704.

48. D. Lee and S. J. Lippard, *J. Am. Chem. Soc.*, 1998, **120**, 12153.
49. J. R. Hagadorn, L. Que Jr, and W. B. Tolman, *J. Am. Chem. Soc.*, 1998, **120**, 13531.
50. C. R. Randall, L. Shu, Y.-M. Chiou, K. S. Hagen, M. Ito, N. Kitajima, R. J. Lachicotte, Y. Zang, and L. Que Jr, *Inorg. Chem.*, 1995, **34**, 1036.
51. D. Lee, C. Krebs, B. H. Huynh, M. P. Hendrich, and S. J. Lippard, *J. Am. Chem. Soc.*, 2000, **122**, 5000.
52. J. R. Hagadorn, L. Que Jr, W. B. Tolman, I. Prisecaru, and E. Münck, *J. Am. Chem. Soc.*, 1999, **121**, 9760.
53. H. Zheng, Y. Zang, Y. Dong, V. G. Young Jr, and L. Que Jr, *J. Am. Chem. Soc.*, 1999, **121**, 2226.
54. Y. Zang, Y. Dong, L. Que Jr, K. Kauffmann, and E. Münck, *J. Am. Chem. Soc.*, 1995, **117**, 1169.
55. M. D. Robin and P. Day, *Adv. Inorg. Chem. Radiochem.*, 1967, **10**, 247.
56. C. He, A. M. Barrios, D. Lee, J. Kuzelka, R. M. Davydov, and S. J. Lippard, *J. Am. Chem. Soc.*, 2000, **122**, 12683.
57. K. Kim and S. J. Lippard, *J. Am. Chem. Soc.*, 1996, **118**, 4914.
58. Y. Dong, S. Yan, V. G. Young Jr, and L. Que Jr, *Angew. Chem. Int. Ed. Engl.*, 1996, **35**, 618.
59. J.-J. Girerd, F. Banse, and A. J. Simaan, ‘Characterization and Properties of Non-Heme Iron Peroxo Complexes in Metal-Oxo and Metal-Peroxo Species in Catalytic Oxidations’, ed. B. Meunier, Springer, 2000.
60. S. V. Kryatov, E. V. Rybak-Akimova, V. L. MacMurdo, and L. Que Jr, *Inorg. Chem.*, 2001, **40**, 2220.
61. M. Costas, J.-U. Rohde, A. Stubna, R. Y. N. Ho, L. Quaroni, E. Münck, and L. Que Jr, *J. Am. Chem. Soc.*, 2001, **123**, 12931.
62. H.-F. Hsu, Y. Dong, L. Shu, V. G. Young Jr, and L. Que Jr, *J. Am. Chem. Soc.*, 1999, **121**, 5230.
63. Y. Dong, H. Fujii, M. P. Hendrich, R. A. Leising, G. Pan, C. R. Randall, E. C. Wilkinson, Y. Zang, L. Que Jr, B. G. Fox, K. Kauffman, and E. Münck, *J. Am. Chem. Soc.*, 1995, **117**, 2778.
64. H. Zheng, S. J. Yoo, E. Münck, and L. Que Jr, *J. Am. Chem. Soc.*, 2000, **122**, 3789.
65. D. Lee, J. DuBois, D. Petasis, M. P. Hendrich, C. Krebs, B. H. Huynh, and S. J. Lippard, *J. Am. Chem. Soc.*, 1999, **121**, 9893.
66. S. V. Kryatov, F. A. Chavez, A. M. Reynolds, E. V. Rybak-Akimova, L. Que Jr, and W. B. Tolman, *Inorg. Chem.*, 2004, **43**, 2141.
67. D. LeCloux, A. M. Barrios, and S. J. Lippard, *Bioorg. Med. Chem.*, 1999, **7**, 763.
68. E. Y. Tshuva, D. Lee, W. Bu, and S. J. Lippard, *J. Am. Chem. Soc.*, 2002, **124**, 2416.

Iron: Organometallic Chemistry

Robert S. Paley
Swarthmore College, Swarthmore, PA, USA

Based in part on the article Iron: Organometallic Chemistry by James R. Green which appeared in the Encyclopedia of Inorganic Chemistry, First Edition.

1	Introduction	1
2	Common Synthetic Precursors	1
3	η^1-Ligand Complexes	2
4	η^2-Ligand Complexes	16
5	η^3-Allyl Complexes	28
6	η^4-Ligand Complexes	37
7	η^5-Ligand Complexes	51
8	η^6-Ligand Complexes	72
9	Related Articles	74
10	References	74

Abbreviations

Ac = Acetyl; acac = Acetylacetonate; bda = Benzylideneacetone; BINOL = 1,1′-bi-2-naphthol; Bn = Benzyl; brsm = Yield based on recovered starting material; Bu = Butyl; CAN = Ceric ammonium nitrate; CBS = Corey/Bakshi/Shibata catalyst [(+) or (−)-(S)-2-methyloxazaborolidine]; COD = Cyclo-1,5-octadiene; COT = Cyclooctatetraene; Cp = Cyclopentadienyl; Cp∗ = Pentamethylcyclopentadienyl; Cy = Cyclohexyl; DCC = Dicyclohexylcarbodiimde; DMF = *N*,*N*-dimethylformamide; DMPU = 1,3-dimethyl-3,4,5,6-tetrahydro-2(1H)-pyrimidinone; DMSO = Dimethylsulfoxide; dppe = Diphenylphosphinoethane; dr = Diastereomer ratio; dppm = Diphenylphosphinomethane; E = Electrophile; ee = Enantiomeric excess; EHMO = Extended hückel molecular orbital; Et = Ethyl; ESR = Electron spin resonance; EWG = Electron-withdrawing group; Fp = Dicarbonyl(cyclopentadienyl)iron (II); HMPA = Hexamethylphosphoramide; HPLC = High performance (pressure) liquid chromatography; INDO = Intermediate neglect of differential overlap; IR = Infrared; KHMDS = Potassium bis(trimethylsilyl)amide; L = Ligand; LDA = Lithium diisopropylamide; LiHMDS = Lithium bis(trimethylsilyl)amide; Me = Methyl; Menth = Menthyl; Ms = Methanesulfonyl; NMO = 4-methylmorpholine *N*-oxide; NMR = Nuclear magnetic resonance; Nu = Nucleophile; Ph = Phenyl; PPN$^+$ = $[(Ph_3P)_2N]^+$; Pr = Propyl; RCM = Ring-closing metathesis; S$_N$1 = First-order nucleophilic substitution; S$_N$2 = Second-order nucleophilic substitution; TCNE = Tetracyanoethene; THF = Tetrahydrofuran; Tf = Trifluoromethanesulfonyl; TMEDA = N,N,N',N'-tetramethylethylenediamine; TMM = Trimethylenemethane; TMS = Trimethylsilyl; *p*-Tol = *Para*-tolyl; Ts = *p*-toluenesulfonyl; UV = Ultraviolet; X = Halide.

1 INTRODUCTION

Iron is the most abundant and least expensive of the transition metals, and the level of interest in studying its organometallic chemistry has been, and continues to be, truly staggering. Indeed, the organometallic chemistry of iron has been central to the development of this field of chemistry. In discussing this facet of the chemistry of iron, this article will primarily concentrate on mononuclear species that contain a Fe–C bond. Many of the individual topics covered here have been the subject of reviews, book chapters, and monographs, and the reader will be directed to these for in-depth coverage.

Certain classical coordination complexes (*see Coordination Complexes*) of iron (e.g. Prussian blue) will be dealt with in other articles (*see* ***Iron: Inorganic & Coordination Chemistry*** and ***Cyanide Complexes of the Transition Metals***), as will much of the chemistries of iron carbonyls (*see Metal Carbonyls*) and iron hydrides (*see Hydrides*) (*see* ***Carbonyl Complexes of the Transition Metals***; ***Transition Metal Carbonyls: Infrared Spectra***, and ***Hydride Complexes of the Transition Metals***). The use of organoiron complexes as catalysts (*see Catalysis*) in organic transformations will be mentioned but will primarily be covered elsewhere (*see* ***Asymmetric Synthesis by Homogeneous Catalysis***, and ***Organic Synthesis using Transition Metal Carbonyl Complexes***).

The organometallic chemistry of iron had been frequently reviewed by Kerber between 1984 and 1992,[1] and a thorough review by the same author appeared in *Comprehensive Organometallic Chemistry II*.[2] An extensive review of the application of organoiron complexes to organic synthesis appeared in 1991.[3] A monograph by Pearson was published in 1995, and a more narrowly focused update on recent developments (through 1998) were summarized by Rück-Braun.[4,5] This article will follow a ligand (*see Ligand*)-based classification, depending upon the hapticity (*see Hapticity*) of the ligand of greatest interest.

2 COMMON SYNTHETIC PRECURSORS

By far most of the organometallic chemistry of iron discussed in this article relies on just a handful of commercially available precursors or complexes prepared directly from them. There are three commercially available iron carbonyls: $Fe(CO)_5$ (**1**, iron pentacarbonyl), $Fe_2(CO)_9$ (**2**, iron nonacarbonyl), and $Fe_3(CO)_{12}$ (**3**, iron dodecacarbonyl).**[6]** Though toxic, $Fe(CO)_5$ is by far the least expensive of these, and the latter two complexes may be prepared from it. These are used to gain access to many of the η^2-alkene, η^3-allyl, and η^4-diene iron complexes to be described in subsequent sections of this article; (**1**) is also commonly used as a reagent in a variety of organic functional group transformations. Also, reduction of (**1**) with sodium-benzophenone ketyl affords $Na_2Fe(CO)_4$ (**4**, disodium tetracarbonylferrate or 'Collman's reagent' (*see Collman's Reagent*)), which also has a rich chemistry of its own (see Section 3.1.1) and is commercially available as well (as a 1:1.5 complex with dioxane) (equation 1).

$$(\mathbf{1}) \xrightarrow[\text{or Na(Hg)/THF}]{\text{Na/PhC(O)Ph ketyl, dioxane, reflux}} \underset{\text{Collman's reagent}}{\underset{Na_2Fe(CO)_4}{(\mathbf{4})}} \tag{1}$$

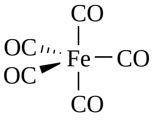

(**1**)
$Fe(CO)_5$
Straw colored liquid
bp 103 °C

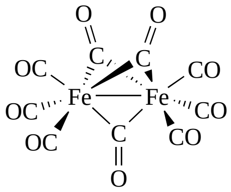

(**2**)
$Fe_2(CO)_9$
Golden orange flakes
mp 100 °C dec

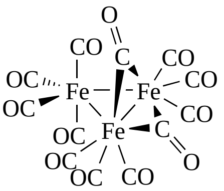

(**3**)
$Fe_3(CO)_{12}$
Black crystals
mp 140 °C dec

Many other iron complexes (η^1-alkyls, η^1-acyls, η^1-alkynyls, cationic η^2-alkenes, and carbenes) are ultimately derived from either sodium dicarbonyl(cyclopentadienyl) ferrate (**5**) (abbreviated as $[Cp(CO)_2Fe]Na$ or simply FpNa) or one of the dicarbonylcyclopentadienylhalo iron species (**6**), $CpFe(CO)_2X$ (where X = Cl, Br, or I). Iodo analog (**6c**) is commercially available. Both (**5**) and (**6**), in fact, are derived from the commercially available dimer $[Cp(CO)_2Fe]_2$ (Scheme 1), and typically (**5**) is prepared and used *in situ* (*see In Situ Reaction*).

The chemistry of ferrocene and its derivatives form a significant subset of iron organometallic chemistry. Ferrocene is commercially available; its chemistry will be discussed in Section 7.

3 η^1-LIGAND COMPLEXES[7]

3.1 Iron σ-Alkyls

3.1.1 Preparation of Anionic Complexes and Use in Functional Group Transformations

Treatment of the d^{10} Fe(−2) Collman's reagent (**4**) with an alkyl halide produces an air-sensitive, coordinatively saturated (*see Coordinative Saturation & Unsaturation*) anionic (*see Anion*) $d^8\sigma$-alkyliron(0) complex (**7**) in situ (Scheme 2) that is readily converted to other organic functionalities.**[8]** Production of this η^1-alkyliron species follows S_N2 (*see Nucleophile*) reactivity (second-order kinetics, stereochemical (*see Stereochemistry*) inversion, sensitivity to steric hindrance). Because (**4**) is quite basic, the reaction is generally limited to simple primary and some secondary halides, as elimination is competitive. Furthermore, transformations that involve an insertion (*see Insertion*) of CO into the alkyl-iron bond (as in the reaction with R'X to form ketones or with iodination/alcoholysis to form esters) fail if R possesses an adjacent electron-withdrawing group. Alternatively, an acyl-iron anion (**8**) may be generated (Scheme 3) by reaction of (**4**) with acid chlorides or by treatment with additional ligand (via CO migratory insertion

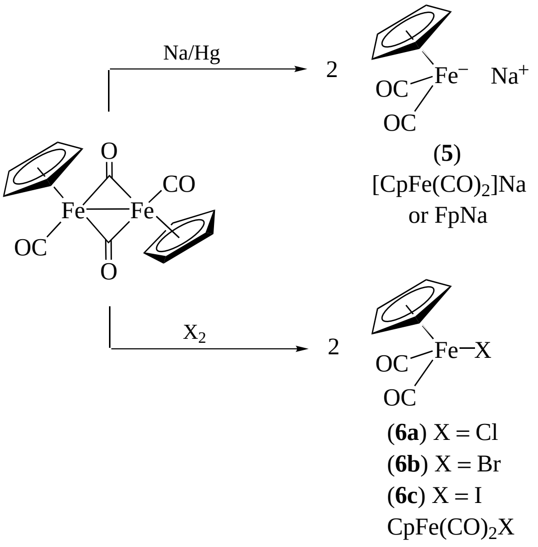

(**5**)
$[CpFe(CO)_2]Na$
or FpNa

(**6a**) X = Cl
(**6b**) X = Br
(**6c**) X = I
$CpFe(CO)_2X$

Scheme 1

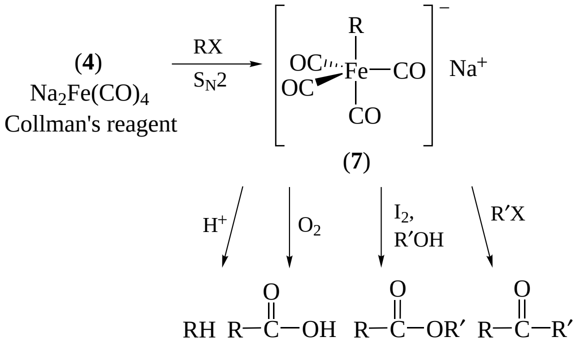

Scheme 2

(*see Migratory Insertion*)). Anion (**8**) may similarly be used to prepare an array of different organic functionality, including aldehydes via protonation (*see Protonation*) with acetic acid. This chemistry has been studied carefully (both (**7**) and (**8**) have been isolated and characterized) and mechanistic details are available.**[9]** Presumably the formation of the organic products occurs by formation of a six-coordinate d^6 species, followed by reductive elimination (*see Reductive Elimination*).

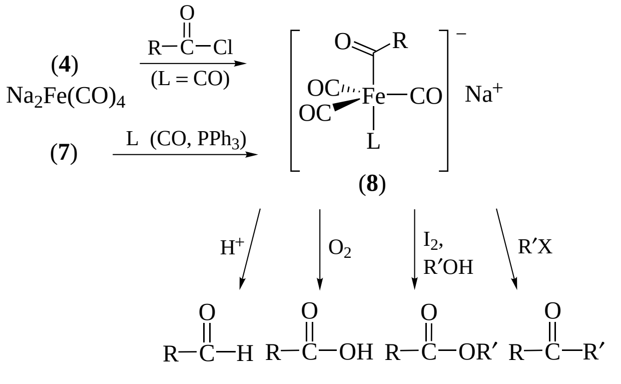
(4)
Na2Fe(CO)4
R–C(=O)–Cl
(L = CO)
(7)
L (CO, PPh3)
O
R
OC
Fe
CO
OC
L
Na+
(8)
H+
O2
I2, R′OH
R′X
R–C(=O)–H
R–C(=O)–OH
R–C(=O)–OR′
R–C(=O)–R′

Scheme 3

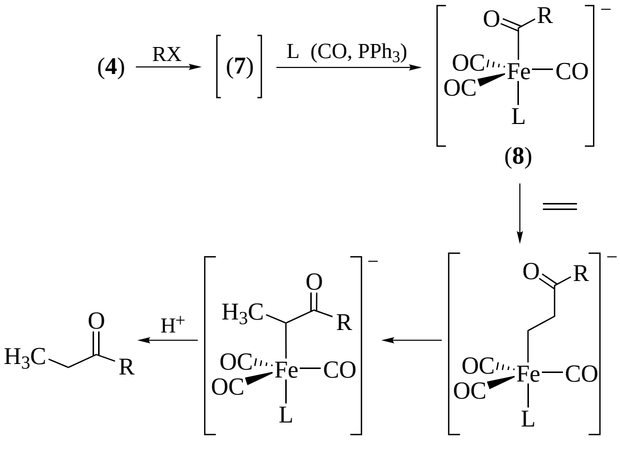
(4)
RX
(7)
L (CO, PPh3)
O
R
OC
Fe
CO
OC
L
(8)
=
H3C
H+
O
R

Scheme 4

Anionic acyl-iron complex (**8**) may be intercepted by ethylene, which inserts into the acyl-iron bond to produce a β-metalloketone that rearranges to an α-metalloketone (Scheme 4). Protonation affords the ethyl ketone. Intramolecular (*see Intramolecular*) versions of this process are known as well, and provide an approach to cyclic ketones. That the cyclization is not always regioselective (*see Regioselectivity*) is shown in an example used in the total synthesis of (±)-aphidicolin (Scheme 5).**[10,11]**

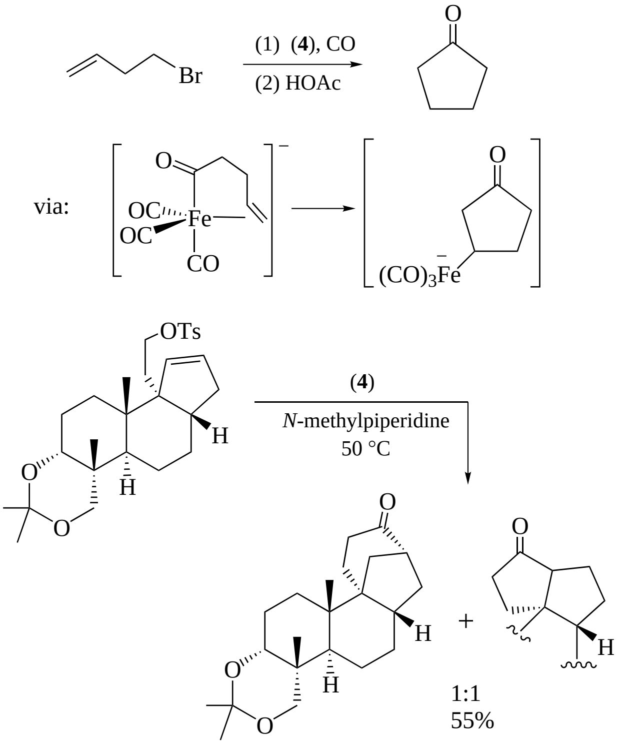
Br
(1) (4), CO
(2) HOAc
O
via:
O
OC
Fe
OC
CO
(CO)3Fe
OTs
(4)
N-methylpiperidine
50 °C
H
O
O
H
+
1:1
55%

(±)-aphidicolin

Scheme 5

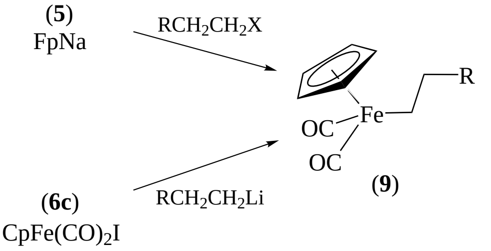
(5)
FpNa
RCH2CH2X
(6c)
CpFe(CO)2I
RCH2CH2Li
R
Fe
OC
OC

(**9**)

Scheme 6

3.1.2 Preparation of Neutral Complexes

Neutral σ-alkyliron complexes are obtained upon reaction of Na[Cp(CO)$_2$Fe] (**5**) with alkyl halides (**9**) (Scheme 6),**[12]** and as with Collman's reagent this occurs in an S_N2 fashion with inversion of configuration at the carbon atom. Epoxides also participate in this reaction,**[4]** but tertiary alkyl halides are poor substrates. Alternatively, complexes (**9**) may be prepared by reaction of an appropriate metal alkyl with Cp(CO)$_2$FeX (**6**). Typically complexes of this type are prepared in order to gain access to the synthetically useful cationic η^2-alkene iron complexes (Section 4.1.2). Also, nucleophilic addition of (**5**) to heteroatom-substituted alkyl halides (such as methoxymethylchloride or chloromethyl methyl sulfide) affords complexes of type (**9**) that can be converted to cationic iron carbenes (Section 3.5.2). These processes can be reversed, as (**9**) can be obtained from nucleophilic addition to either cationic carbene complexes or cationic η^2-alkene complexes (*see Alkene Complexes*). The cyclopropyl analog of (**9**) is best obtained by a decarbonylation of the iron acyl complex via low-temperature photolysis (Section 3.5).

Under ambient conditions σ-alkyl complexes (**9**) are isolable and stable with respect to β-hydride elimination (*see β-Hydride Elimination*), since they are coordinatively saturated. However, it should be noted that related complexes of the type $Cp(CO)(PPh_3)FeCH_2CH_2R$ will thermally decompose in solution (ca. 60 °C) or neat to give the corresponding alkene and an iron hydride $Cp(CO)(PPh_3)FeH$.[13] This is believed to occur via dissociation (*see Dissociation*) of the phosphine ligand to generate a vacant coordination site (*see Vacant Site*), followed by β-hydride elimination to afford an η^2-alkene ironhydride species. Substitution of the alkene ligand by phosphine affords the product hydride. Notably, added phosphine ligand inhibits the decomposition reaction. This mechanism is also believed to be operative in the thermal rearrangement of certain σ-alkyliron complexes (e.g. **10** → **11**) (equation 2).

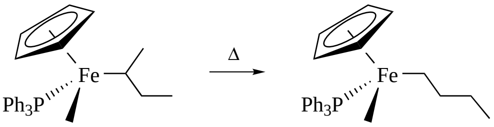

(**10**) (**11**)

(2)

3.1.3 *Cleavage Reactions of Neutral Complexes*

The iron–σ-alkyl bond in (**9**) may be cleaved by reaction with acid, with halogens, or with mercury(II) halides to afford the corresponding alkanes, alkyl halides, or alkyl mercury(II) halides respectively (Scheme 7).[14] This occurs with retention of configuration at the carbon atom for cleavage with acid[15] and mercury(II) chloride,[16] while reaction with halogens gives inversion of configuration at the carbon atom.[16] If the electrophilic cleavage of iron alkyls, chiral (*see Chiral*) at the metal, is not carried to completion, the recovered iron alkyls are partially epimerized.[17] The stereochemistry along with the order of reactivity for electrophilic cleavage of substituted iron alkyls suggests a reversible attack of the electrophile (*see Electrophile*) at iron to give the square-pyramidal (*see Square Pyramidal*) intermediate shown. Stereochemical nonrigidity in this species would explain epimerization at iron. Reductive elimination occurs with retention of configuration for E = H or HgX (path a); however, in the case of E = halogen, then attack by external halide affords the organic product with inversion of configuration (path b).[17]

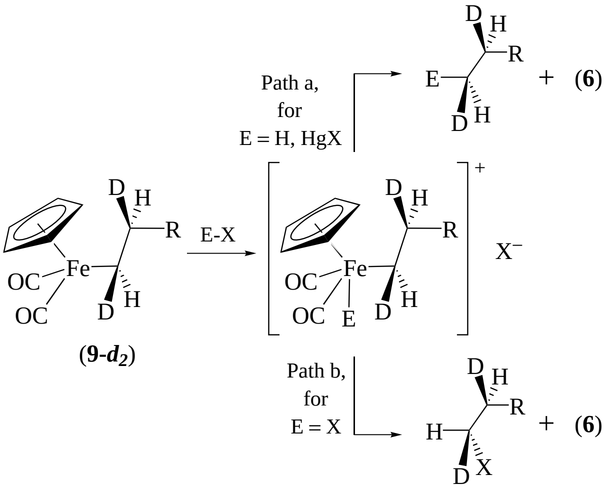

Scheme 7

3.2 η^1-Allyl and Related Complexes[18–20]

3.2.1 *Preparation*

The first reported and still widely used method for the preparation of (η^1-allyl)$(CO)_2$FeCp complexes (**12**; R = H) (η^1-allyl)Fp involves the nucleophilic substitution of allyl halides or pseudohalides (arenesulfonates, phosphinates[21]) with sodium dicarbonylcyclopentadienylferrate (NaFp, **5**) (Scheme 8). The reaction is successful for halides bearing substituents on vinyl carbon atoms, whereas substituents geminal to the halide result in S_N2' products. Cycloalkenyl chlorides have also been successfully employed, giving the (cycloalkenyl)Fp compounds. The analogous reaction on propargyl halides affords the (η^1-propargyl)Fp complexes (**13**) if the acetylenic carbon is substituted; propargyl bromide itself affords the product of S_N2' displacement.

Several alternative methods have been reported for the preparation of (**12**). The addition of $HFe(CO)_2Cp$ to 1,3-dienes results in (η^1-allyl)Fp complexes, although this approach has

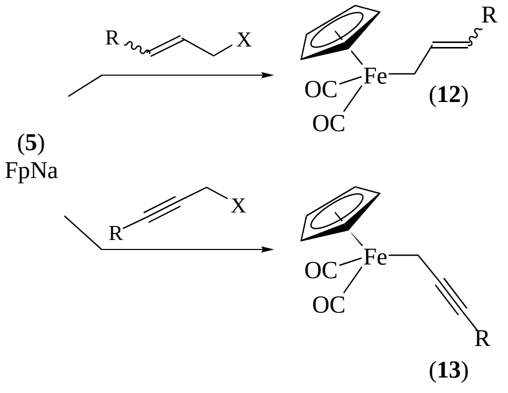

Scheme 8

been employed far less regularly.[22] A much more commonly used route involves proton abstraction of (η^2-alkene)Fp$^+$ cations (Section 4.3.2). In a similar fashion, an alternative approach to propargyl complex (**13**) involves deprotonation of (η^2-allene)Fp$^+$ cations (Section 4.3.2).

(η^1-Allyl)CpFe(CO)(PR$_3$) complexes (**14**) have been prepared from the dicarbonyls, by photolysis in the presence of phosphine or phosphite. The substitution is often aided by a trace of (CpFe(CO)$_2$)$_2$, which is indicative of a radical (*see Radicals*) chain substitution mechanism.[23] Phosphite ligand (as in **15**) has been reported as being a particularly good replacement ligand from the standpoint of thermal stability.[24,25] Nevertheless, neither C-3-substituted (η^1-allyl)Fp complexes (**14b**) nor cyclic allyl complexes (*see Allyl Complexes*) may be made directly by this method; the carbocyclic cases have been prepared by methoxide-induced proton abstraction of alkene cation (**16**) (Section 4.3.2).[24]

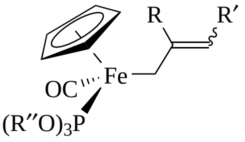

(**14a**) R = H, R′ = H
(**14b**) R = H, R′ = H
(**14c**) R = OMe, R = H

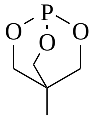

(**15**)

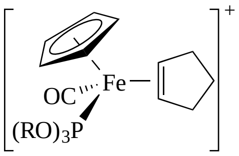

(**16**)

(η^1-Dienyl)Fp (**17**) is known for a limited number of substitution patterns, normally being prepared by the FpNa (**5**) + dienyl chloride route.[26,27] (η^1-Cyclopentadienyl)Fp complex (**18a**) has been prepared by the reaction of NaCp with Cp(CO)$_2$FeI (**6c**). Substituted versions of these complexes can also be made by this method (compounds **18b,c** and **19**) or in the case of (**20**) by reaction of Cp′Fe(CO)$_2$$^+BF_4$$^-$ with the cyclopentadiene, followed by triethylamine-induced proton abstraction of the intermediate alkene complex (**19,20**). It is also possible to replace one CO ligand of (**18**) by carefully selected phosphite ligands by the photolysis method used for (η^1-allyl)Fp complexes.[23] (η^1-Diynyl)Fp (**21**) has been prepared as well.[27]

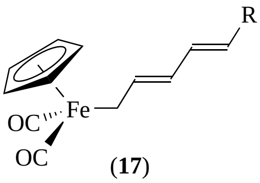

(**17**)

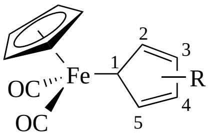

(**18a**), R = H
(**18b**), R = 2-Me
(**18c**), R = 3-Me

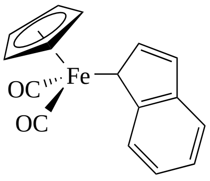

(**19**)

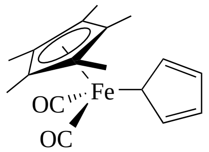

(**20**)

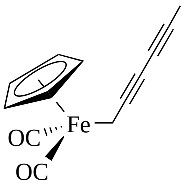

(**21**)

There exist only a few scattered reports of (η^1-allyl)iron complexes lacking a cyclopentadienyl (*see Cyclopentadienyl*) (or related ligand). Treatment of (η^3-allyl)dicarbonylnitrosyliron complexes (*see Nitrosyl Complexes*) with phosphite or phosphine gives five-coordinate (η^1-allyl) complexes (**22**) of limited stability.[28] The reaction of Fe(t-BuNC)$_5$ with both allyl bromide and chloride gives a product formulated as (**23**).[29] Compounds of the general structure (**24**) were prepared by reaction of [(CO)$_4$Fe(SiR$_3$)]$^-$ and HFe(CO)$_4$(SiR$_3$) with allyl bromide and isoprene, respectively.[30]

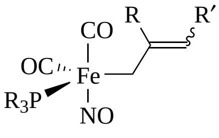

(**22**)

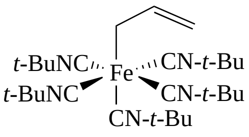

(**23**)

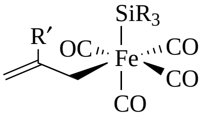

(**24**)

3.2.2 *Properties*

(η^1-Allyl)Fp complexes (**12**) are yellow liquids or low-melting solids that show reasonable air stability when neat, but have greater air sensitivity in solution. The ^{1}H Nuclear magnetic resonance (NMR) spectra show the alkene protons resonate roughly in the normal alkene range, with the protons on C-2 somewhat downfield (5.3–5.95 ppm in acyclic cases, 5.8–6.3 ppm in cyclic cases) from those on C-3 (4.4–5.1 ppm in acyclic cases, 5.35–5.8 ppm in cyclic cases). The protons on the iron-bearing carbon atom (C-1) show a striking difference between acyclic cases (2–2.3 ppm) and cyclic compounds (3.3–3.86 ppm). Coupling constants between the alkene protons are unexceptional. ^{13}C NMR spectra show more distinct differences between the two alkene carbon atoms: C-2 carbon atoms (135–143 ppm in C_6D_6) resonate considerably downfield from the C-3 carbons (116–125 ppm in C_6D_6), while C-1 is very highly shielded (-2 to $+5$ ppm acyclic, $\approx$20 ppm cyclic, C_6D_6).[31,32] The ^{57}Fe NMR spectrum of one (η^1-allyl)Fp complex indicates that the chemical shift (959.1 ppm downfield from $Fe(CO)_5$) is in the midst of known (η^3-allyl)iron complexes.[33]

(η^1-Cyclopentadienyl)Fp (**18**) is one of the classic fluxional molecules (*see Fluxional Molecule*) (*see* ***Stereochemical Nonrigidity of Organometallic Complexes***). At room temperature, all five protons of the (η^1-Cp) ring appear at the same chemical shift (5.7 ppm in CS_2), as do the five ring-carbon atoms in the ^{13}C NMR spectrum (112.0 ppm in CS_2). At ≈ -80 °C the proton spectrum shows sharp peaks at 3.5 (H-1), 6.0 (H-3), and 6.3 ppm (H-2), in a 1:2:2 ratio, and the ^{13}C NMR spectrum shows resonances at 28.2 (C-1), 121.6 (C-3), and 145.3 (C-2) ppm. These changes in spectral characteristics are due to rapid 1,2-shifts of the Fe–C σ-bond, which occur with an activation energy of 44.8–46.5 kJ mol^{-1}.[34] Exchanging the η^5-Cp ligand for the more electron-donating η^5-Cp* (C_5Me_5) ligand results in a lowering of this barrier to 40.2 kJ mol^{-1}; in both cases this activation energy is significantly solvent dependent. Substitution of the η^1-Cp ring with an electron-donating methyl group raises the barrier (56.5 kJ mol^{-1}), while an electron-withdrawing group (CONHTs) lowers the barrier; these effects have been interpreted as evidence for 'some zwitterionic (*see Zwitterion*) character' (Fp$^{\delta+}$ Cp$^{\delta-}$) in the transition state.[35] This is precisely the same character found for the concerted [1,5]-sigmatropic hydrogen rearrangements in cyclopentadiene itself.[36]

3.2.3 Reactions

The overwhelming majority of reported transformations of η^1-allyliron complexes either produce cationic η^2-alkeneiron complexes or proceed through these intermediates to give other products. This chemistry will be discussed later (Section 4.1.2).

(η^1-Allyl)Fp complexes are also subject to attack, at C-3, by radicals. The mechanism of allylic transposition of (η^1-allyl)Fp complexes, as well as the mechanism of phosphite substitution for CO, has been ascribed to attack by Cp(CO)(L)Fe· on the original Fp–allyl. The reaction of (**12**) with CCl_4 proceeds by a radical chain mechanism, ultimately between $\cdot CCl_3$ and the Fp–allyl.[37] The substitution of α-halo ketones and esters most likely proceeds similarly. A radical cation coupling mechanism has been proposed for the dimerization of (η^1-allyl)Fp and (η^1-propargyl)Fp complexes.[38]

Nitrosylcarbonyliron complexes, $[Fe(CO)_3(NO)]^-$ and $Fe(CO)_2(NO)_2$, are capable of catalyzing the substitution of allylic chlorides, formates, acetates, and carbonates by malonate ion. The attack on substituted substrates goes with retention of double bond stereochemistry, with high retention of stereochemistry at the substituted carbon atom, and with only minor amounts of allylic scrambling. A σ-allyliron intermediate, formulated as (**25**), has been implicated in the substitution.[39]

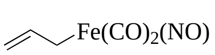

(**25**)

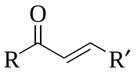

(**26**)

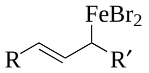

(**27**)

(η^1-Allyl)iron(III) complexes have been implicated in the enzymatic lipoxygenation of polyunsaturated fatty acids. In the proposed model, concerted allylic deprotonation and electrophilic addition (*see Electrophilic Reaction*) of Fe^{III} gives an iron allyl species, which undergoes Fe–C bond insertion by O_2. In model studies, reaction of allyltributyltin compounds with $FeBr_3$, followed by exposure to oxygen, gives oxidation to the carbonyl compounds (**26**) through presumed intermediates (**27**).

(η^1-Cyclopentadienyl)Fp complexes are relatively reactive dienes for cycloaddition reactions with electron-poor (*see Electron Deficient Compound*) alkenes and alkynes. Alkene addition occurs on the face opposite the iron substituent, giving overall retention of alkene stereochemistry but a mixture of *endo* (*see Exo & Endo Substituents*) and *exo* addition products. Available evidence suggests that the reaction is a concerted [2 + 4] cycloaddition. Less reactive dienophiles (methyl acrylate, acrylonitrile) require the presence of a Lewis acid (*see Lewis Acids & Bases*) (Et_2AlCl) for successful reaction. Oxidative removal of the $Cp(CO)_2Fe$ unit from the product (**28**) allows replacement by either an ester or amine function, Fp(η^1-Cp) therefore being the synthetic equivalent of either (**29a**) or (**29b**).[40] Complexes substituted on the η^1-cyclopentadienyl ring give mixtures of regioisomeric products with substitution away from the bridgehead carbon atoms predominating.[35]

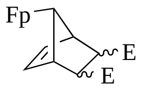

E = CN, Cl, CO_2Me

(**28**)

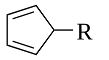

(**29a**) R = CO_2Me
(**29b**) R = NR′$_2$

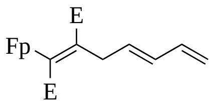

E = CF_3, CO_2Me

(**30**)

Acyclic (η^1-pentadienyl)Fp complexes also behave as Diels–Alder dienes in some cases, although two other reaction pathways compete. With TCNE and maleic anhydride, (**17**; R = H, Me) undergoes cycloaddition in moderate yields. Highly electron-deficient alkynes, on the other hand, undergo Fe–C bond insertion reactions reminiscent of SO_2 reactions with (η^1-allyl)Fp complexes, to give (**30**). Finally, when the pentadiene is disubstituted at C-5, the Diels–Alder route is effectively blocked, and [3 + 2] cycloadditions result with TCNE at the 2,3-double bond.[41]

3.3 σ-Vinyl Iron Complexes

3.3.1 *Preparation and Reactions*

σ-Vinyl iron complexes have been prepared in a number of ways: 1) nucleophilic addition to cationic η^2-alkyne complexes (*see Alkyne Complexes*) (this will be covered in Section 4.5.1), 2) nucleophilic addition to cationic η^2-allenyl complexes (Section 4.3.2), 3) via [3 + 2] cycloaddition of η^1-propargyliron complexes and electron-poor alkenes (Section 4.4), 4) Photolysis of acyliron complexes (Section 3.5), 5) nucleophilic addition to vinylidene complexes (Section 3.7), and 6) the method discussed here, addition-elimination (*see β-Elimination*) of FpNa (**5**) with β-halo-α,β-unsaturated carbonyls.

The synthesis of vinyliron species (**31**) has been described; this has been used to access iron carbenes (Section 3.5) (Scheme 9).[42,43] Analogs of (**31**) are obtained using standard enolate formation with subsequent trapping by an electrophile.[44] Cyclic analogs have also been prepared.[45] More recently related chemistry with acyclic and cyclic enals has been utilized (Scheme 10).[46,47] Kinetically-controlled addition-elimination to (Z)-β-haloenals (*see (E) & (Z) Isomers*) or (Z)-β-(trifluoromethanesulfonyl)enals affords the (Z)-Fp-enals (**32**), and subsequent treatment with primary amines and $TiCl_4$ produces α,β-unsaturated lactams. The key intermediate is believed to be an η^2-alkeneiron hydride complex (**33**) which is formed after intramolecular carbonylation of the amine followed by reductive elimination. Cyclic enals such as (**34a**) behave in an identical manner, and reductions of (**32**) or with (**34a–c**) using $NaBH_4$ provide the α,β-unsaturated lactones or mixtures of these and the saturated analogs. Reduction with K-Selectride gives only the saturated lactones. Using α,β-unsaturated sulfonylimines (N-sulfonyl azadienes) instead of enals provides similar compounds (N-sulfonyl dihydropyrrolones), though in these cases the reaction is triggered by use of a Grignard reagent (*see Grignard Reagents*).[48]

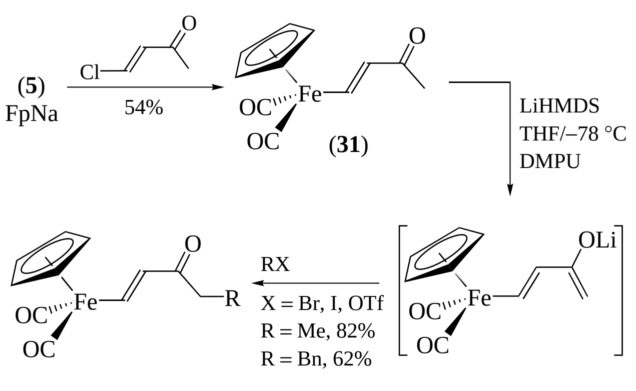

Scheme 9

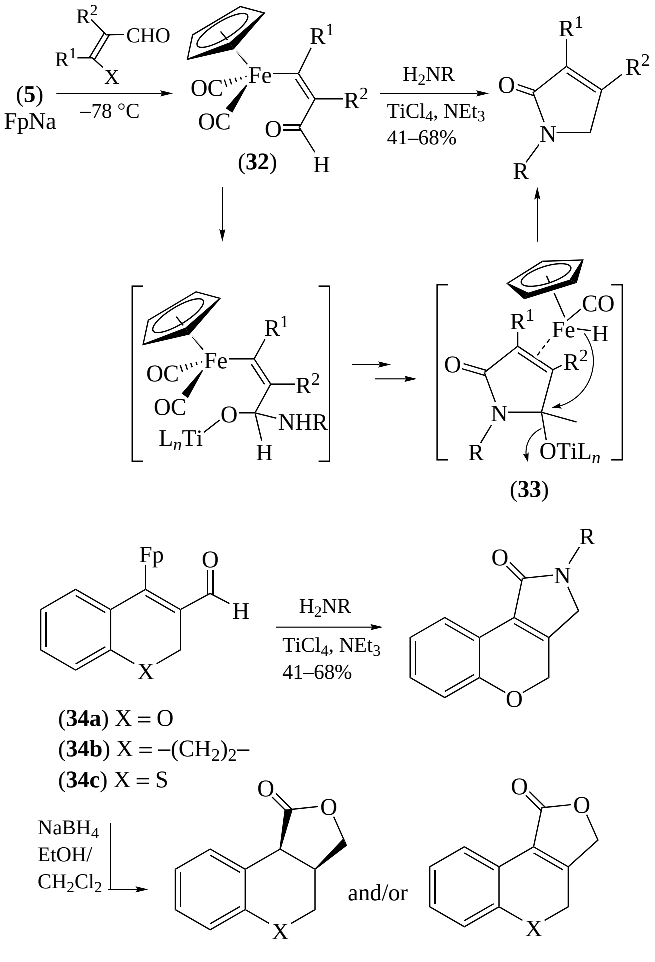

Scheme 10

3.4 σ-Aryl and σ-Heteroaryl Iron Complexes

3.4.1 *Preparation*

Decarbonylation of σ-acyliron complexes by photolysis (Section 3.5) is the primary method for the preparation of σ-aryliron complexes.[2] Alternatively, σ-aryliron complexes can be prepared by the method of Beletskaya from FpNa (**5**).[49] For example, the p-tolyl analog has been recently prepared in order to study the C–H activation of benzene (equation 3).[50]

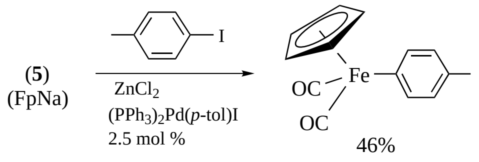

(3)

Aryl-Fp complexes can be prepared from FpNa (**5**) with aryl halides only in cases where the aryl halide is activated toward nucleophilic attack; polyflourinated benzenes and halo-substituted pyridines are examples.[51,52] Heteroaryliron

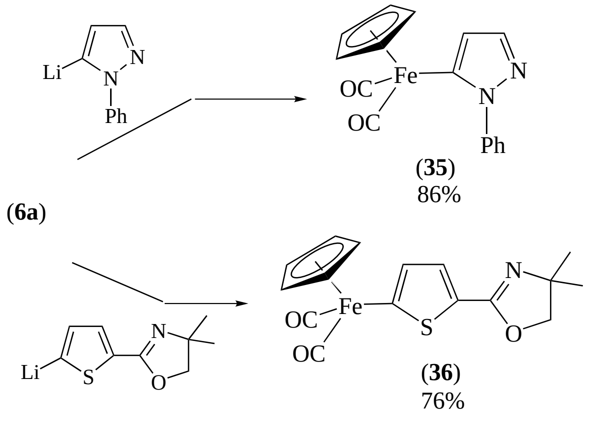

Scheme 11

complexes (**35, 36**) were obtained by Raubenheimer by treatment of $CpFe(CO)_2Cl$ (**6a**) with the appropriate heteroaryllithium species (Scheme 11).[53] Protonation of these complexes led to unusual iron carbene systems.

3.5 Iron Acyls

Iron acyl complexes are among the most widely studied of the organometallic iron species, especially as applied to organic synthesis. As previously mentioned they are prepared to provide access to iron alkyls (via decarbonylation), and because iron acyls can be deprotonated to form enolates much like any carbonyl they have been utilized as chiral auxiliaries in asymmetric synthesis. Also, iron acyls are an important entry point for the preparation of iron carbenes.

There are two primary methods used to prepare ‘simple’ iron acyls (Scheme 12). In analogy to the nucleophilic reaction of FpNa (**5**) and alkyl halides (Scheme 6), FpNa and its analog $[Cp(CO)(PPh_3)Fe]Na$ (occasionally abbreviated Fp′Na) readily react with acyl chlorides to afford the acyl complexes (**37**).[54,55] On the other hand, iron σ-alkyl complexes (**9**) undergo carbonyl insertion in the presence of an external ligand to also produce the acyl complexes (**37**).[56] This may be promoted by the presence of Lewis acids or protic acids, even at 1% of the stoichiometric amount; however, alkoxyalkyl substituents are resistant to carbonylation. Vinyl iron complexes have been converted into the corresponding α,β-unsaturated acyl-iron complexes by $AgBF_4$-promoted CO insertion.[57] For acyl complexes in general, the reverse process – a decarbonylation – occurs upon photolysis; this is the best way to prepare vinyl iron complexes. An example is shown (equation 4).[55]

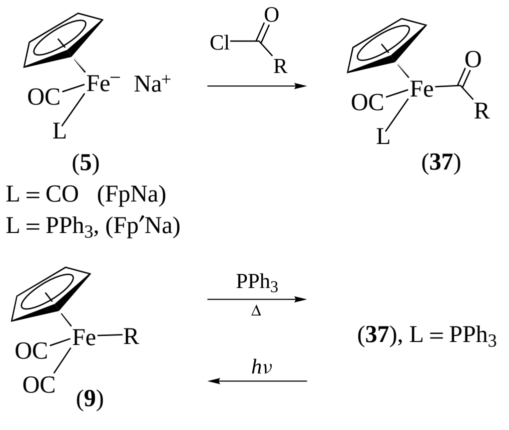

Scheme 12

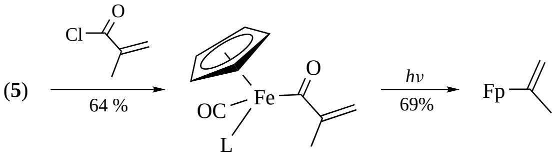

(4)

The acyl carbonyl stretching frequency appears in the range 1580–1700 cm^{-1},[58] and the acyl carbonyl ^{13}C resonance appears at ca. 255–275 ppm.[32] These physical data highlight the highly polar (*see Polar Bonds*) nature of the acyl bond. The positive charge at the carbon is delocalized (*see Delocalized Bonding*) by metal-to-ligand back bonding (*see Back Bonding*) donation into the acyl π^* antibonding (*see Antibonding*) orbital (cf. **38**). This property enables the formation of carbenes (Section 3.5) since these complexes react by alkylation on oxygen.[56] In general, this requires the use of highly reactive alkylation agents.

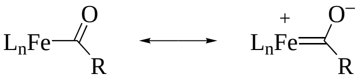

(**38**)

Because the presence of four different ligands about the metal in (**37**) makes complexes of this type chiral at the metal center,[59] the stereochemistry of the CO insertion/decarbonylation process is noteworthy. Thus the chiral complex (*S*)-(**39**)[60] undergoes carbonylation in nitroethane in the presence of carbon monoxide to give the corresponding acyl product (*R*)-(**40**) with greater than 90% enantiomeric excess (*see Enantioselectivity*) (Scheme 13). The stereochemistry of the product is consistent with an ‘alkyl migration’ (*see Alkyl Migration*) to generate the coordinatively unsaturated species (**41**), which is rapidly captured by an external ligand.[60] Photochemical (*see Photochemistry*) decarbonylation of (*R*)-(**40**) has likewise been shown to proceed via an alkyl migration mechanism to afford (*S*)-(**39**).[61] These alkyl migrations proceed with retention of configuration at the carbon atom which migrates. Thus carbonylation of the deuterium-labeled (*see Deuterium*) alkyl (**9**) affords the labeled acyl complex (**42**).[60] Decarbonylation proceeds with retention of configuration at carbon.

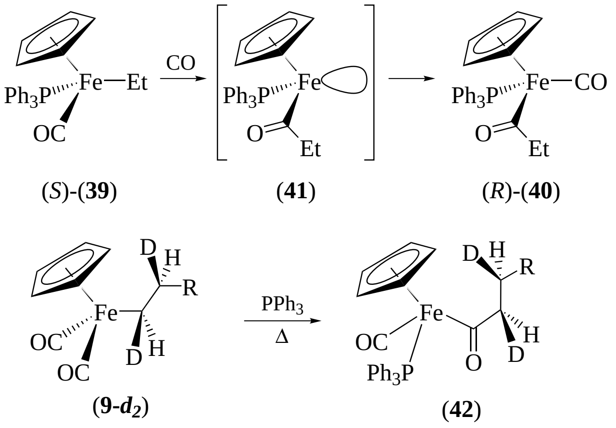
Ph3P
Fe
Et
OC
CO
(S)-(39)
(41)
(R)-(40)
(9-d2)
PPh3
Δ
(42)
D
H
R

Scheme 13

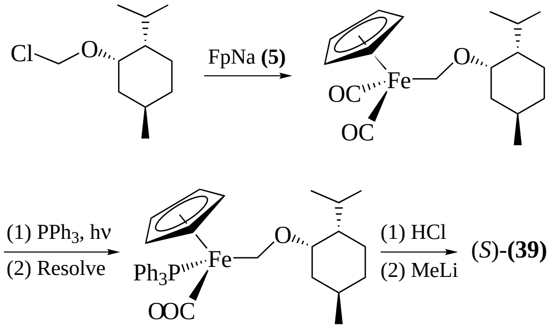
Cl
O
FpNa (5)
OC
Fe
(1) PPh3, hν
(2) Resolve
Ph3P
OOC
(1) HCl
(2) MeLi
(S)-(39)

Scheme 14

To prepare the enantiomerically pure iron acyl complex (*R*)-(**39**), a precursor diastereomeric menthoxyalkyl complex was resolved and then manipulated (Scheme 14). More recently resolution of the chiral-at-metal acyl complexes themselves was achieved, and this has become the basis for a commercial preparation of the iron acyl developed for use as a chiral auxiliary (see below). Cationic iron complex (**43**) was treated with potassium *L*-mentholate to produce diastereomeric esters (**44**) that were not isolated but were reacted with LiBr/MeLi (Scheme 15).**[62]** After chromatography and recrystallization the enantiomerically pure ironacyl complex (*S*)-(**39a**) was obtained. It was suggested that only one diastereomeric ester can react (with inversion of configuration at iron, as shown) with the methyl nucleophile; the unreactive diastereomer suffers from severe steric congestion about the electrophilic CO ligand.

The α-protons of iron acyl complexes are acidic and these can be deprotonated with Lithium diisopropylamide (LDA) or with n-butyllithium. Thus the corresponding enolates are readily functionalized and undergo reaction with alkyl halides, aldehydes, disulfides, trimethylsilyl chloride, and epoxides to afford the corresponding α-derivatized products.**[63–65]** Early work on racemic complexes revealed that these transformations occur in a highly diastereoselective fashion, with respect to the chiral metal center. The later work using enantiomerically pure complexes (described above) will be described here; examples of diastereoselective transformations are shown (Scheme 16). The diastereoselectivity has been rationalized on the basis that the preferred conformer for the enolate (**46**) has the enolate oxygen aligned *anti* to the carbonyl ligand, and that approach of the electrophile is directed toward the face of the enolate which is not blocked by the triphenylphosphine ligand. Since the acyl–iron bond can be cleaved by treatment with one-electron oxidants such as bromine to afford carboxylic acids or esters, the overall transformation has been used for the synthesis of optically pure

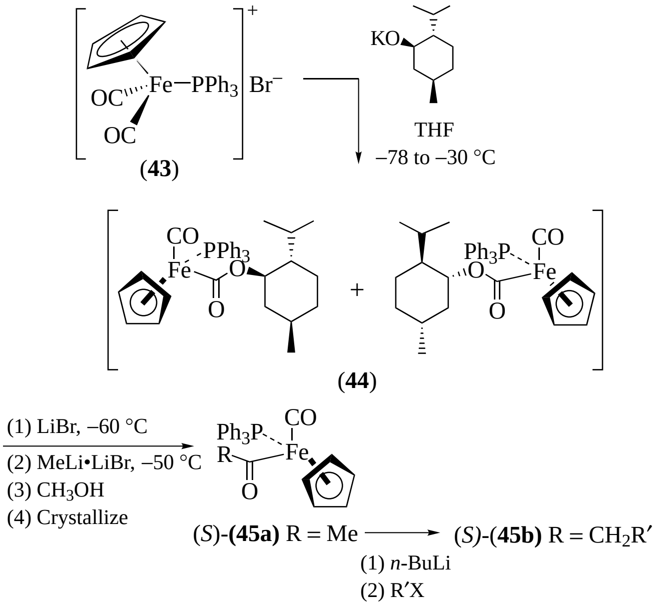
OC
Fe—PPh3
Br−
(43)
KO
THF
−78 to −30 °C
CO
PPh3
Fe
O
Ph3P
+
(44)
(1) LiBr, −60 °C
(2) MeLi•LiBr, −50 °C
(3) CH3OH
(4) Crystallize
R
(S)-(45a) R = Me
(S)-(45b) R = CH2R′
(1) n-BuLi
(2) R′X

Scheme 15

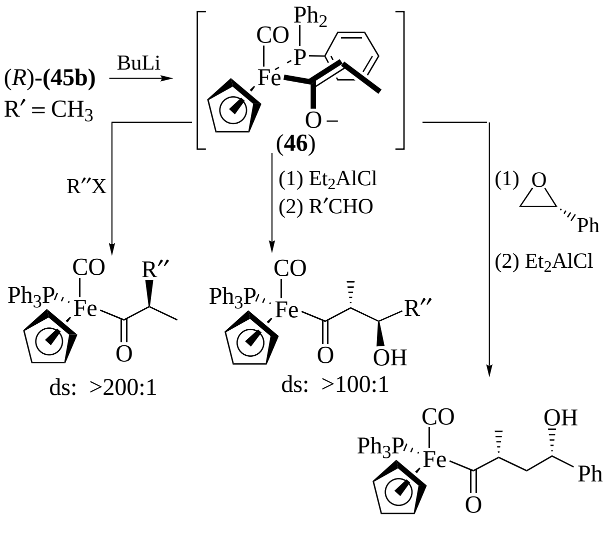
(R)-(45b)
R′ = CH3
BuLi
Ph2
CO
P
Fe
O−
(46)
R″X
(1) Et2AlCl
(2) R′CHO
(1) O
Ph
(2) Et2AlCl
Ph3P
R″
OH
ds: >200:1
ds: >100:1

Scheme 16

organic compounds. α,β-Unsaturated iron acyl complexes have also been prepared, and Michael-type nucleophilic additions, cyclopropanations, and Diels–Alder cycloadditions occur with high diastereoselectivity.[63–65] A review article by Davies that appeared in 1990 described the use of iron acyls as chiral auxiliaries in synthetic organic chemistry and should be consulted for further details; this area was also thoroughly covered in Fatiadi's 1991 review.[3,63] However, with the more recent advent of other nonmetal-containing chiral auxiliaries, this strategy for asymmetric synthesis is currently not in frequent use and only scattered applications have been reported.

3.6 Iron Carbenes

A substantial body of work has been published describing the preparation, properties, and synthetic applications of iron carbenes. These tend to be of the 'Fischer-type' (*see Fischer-type Carbene Complexes*) of carbene species: electrophilic and heteroatom-stabilized. However, electrophilic yet unstabilized iron carbenes can be readily prepared and utilized *in situ*.

3.6.1 Preparation of Neutral Iron Carbene Complexes

While reaction of acyl anion [(**8**), from (**4**) or (**7**) in Scheme 3] with alkyl halides affords the corresponding organic ketone, alkylation of (**8**) with the highly activated ethyl fluorosulfonate generates the Fischer-type carbene complex (**47**) (equation 5).[66] Attempted alkylation of these iron acylates with trimethyloxonium salts, in the general fashion for the preparation of chromium Fischer-type carbene complexes (*see* ***Chromium: Organometallic Chemistry***) is unsuccessful.[67,68] Alternatively, addition of an alkyllithium or Grignard reagent to $Fe(CO)_5$ (**1**) also affords (**8**) by the classic method of Fischer.[68,69]

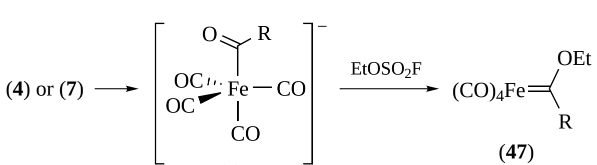

(5)

Exchange of the alkoxy substituent with an amino group can occur by treating (**47**) with an amine. Aminocarbenes can also be prepared by chemistry related to Fischer's method; in this case an alkoxide intermediate is trapped by TMSCl and directly expelled to produce the carbene (equation 6).[70]

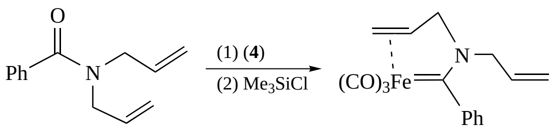

(6)

3.6.2 Preparation of Cationic Iron Carbene Complexes

In comparison to the neutral analogs, there are many cationic iron carbene complexes (**48**) that have been isolated or prepared *in situ*. In general, only those complexes in which one of the carbene substituents is a good electron-donor group (i.e. X or Y = OR, SR, or NHR) are stable enough to be isolated. There are a number of approaches these carbene complexes, and many of the earliest methods – still in current use – are summarized in a 1987 review by Brookhart.[71] (Readers should also consult the 1991 review by Fatiadi).[3]

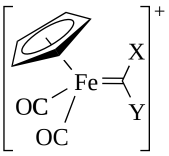

(**48**)

Pettit first described the preparation of these complexes; protonation of the methoxymethyl iron alkyl species (**49**) made by treatment of NaFp (**5**) with CH_3OCH_2Cl (as in Scheme 6) was carried out in the presence of alkenes (Scheme 17). The cyclopropanes that were produced suggested the intermediacy of a carbene complex (**48a**); more highly substituted carbene analogs were isolated and characterized.[72] Trimethylsilyl triflate can also be used to initiate carbene formation; ethylidene, benzylidene, and cyclopropylidene complexes have been generated in this fashion.[71] A milder method has since been developed by utilizing CH_3SCH_2Cl instead of CH_3OCH_2Cl; loss of the heteroatom to provide the carbene was performed by methylation (to give the stable, isolable sulfonium salt (**40**)) followed by thermolysis (100 °C) in the presence of an alkene (Scheme 18).[73] A more functionalized carbene complex (**51**) that has been used in organic syntheses has been prepared via hydride abstraction (equation 7).[74] Finally, the alkoxy carbene precursors can be obtained from the reaction of FpNa (**5**) and acetals in the presence of $BF_3{\cdot}Et_2O$.[75] Alternatively, reaction of (**5**) with an aldehyde affords an

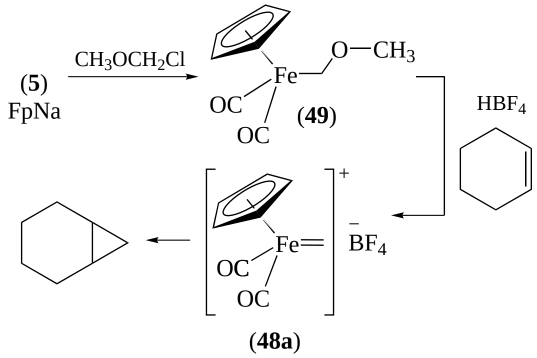

Scheme 17

alkoxy intermediate that is trapped by trimethylsilylchloride.[76] This silyloxy carbene precursor may also be treated by TMSOTf to generate the iron carbene (Scheme 19).

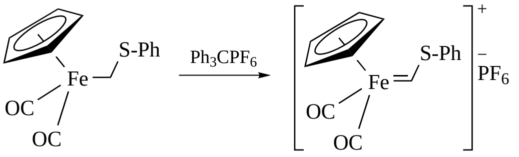
S-Ph
Fe
OC
OC
Ph_3CPF_6
S-Ph
Fe
OC
OC
+
PF_6^-

(51) (7)

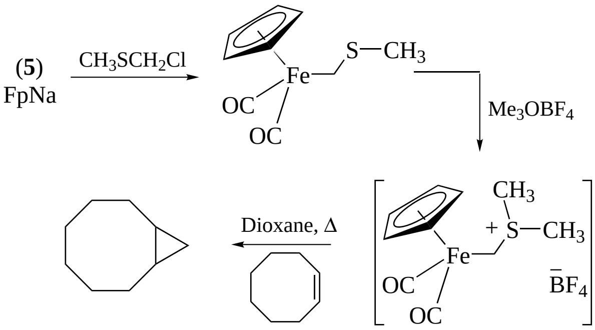
(5)
FpNa
CH_3SCH_2Cl
$S-CH_3$
Fe
OC
OC
Me_3OBF_4
Dioxane, Δ
CH_3
$+ S-CH_3$
Fe
OC
OC
BF_4^-

(50)

Scheme 18

Alkylation of iron acyl complexes also provides access to iron carbenes. Thus, the neutral iron acyl complex will react with acid, with alkylating agents, or with trifluoromethanesulfonic anhydride to afford cationic hydroxy- or alkoxycarbene complexes (**52**) and (**53**) or the cationic vinylidene complex (**54**, L = CO) (Scheme 20).[77] The vinylidene complex can be used to prepare a more substituted analog of (**51**) by treatment with a thiol. The enantiomerically pure iron acyl complex (*R*)-(**45a**) can be converted to the corresponding enantiopure methoxycarbene complex with Me_3OBF_4 as well.[78] Finally, the alkoxycarbene substituent can be exchanged with a primary amine to produce aminocarbenes complexes.[78,79]

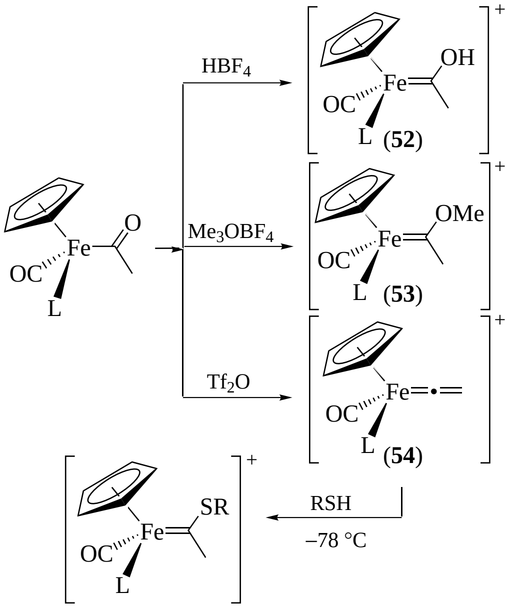
O
Fe
OC
L
HBF_4
OH
Fe
OC
L
(52)
+
Me_3OBF_4
OMe
Fe
OC
L
(53)
+
Tf_2O
Fe
OC
L
(54)
+
RSH
−78 °C
SR
Fe
OC
L
+

Scheme 20

Another tactic that has been used to prepare iron carbene complexes is the protonation of vinyl iron complexes. For example, vinyl iron (**55**) is readily converted to the carbene (equation 8). The acidity of the iron carbene has been demonstrated as well, as treatment of (**56**; L = PPh_3) with pyridine affords (**55**).[55]

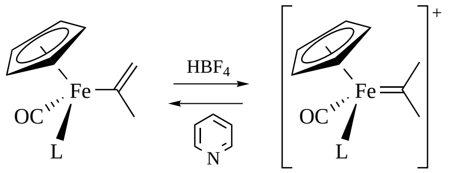
Fe
OC
L
HBF_4
N
Fe
OC
L
+

(**55**)
L = CO, PPh_3

(L = PPh_3)

(**56**)

(8)

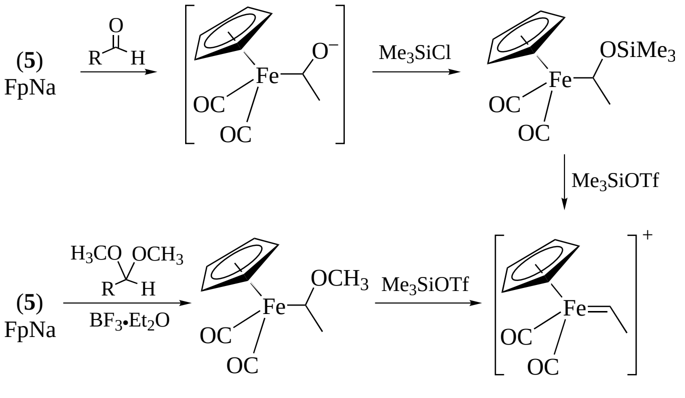
(5)
FpNa
O
R H
Fe
OC
OC
O^-
Me_3SiCl
$OSiMe_3$
Fe
OC
OC
Me_3SiOTf
(5)
FpNa
H_3CO OCH_3
R H
$BF_3{\bullet}Et_2O$
OCH_3
Fe
OC
OC
Me_3SiOTf
Fe
OC
OC
+

Scheme 19

Finally, a heteroatom-substituted carbene can be converted in a two-step process to an analog lacking the electron-donating substituent by hydride addition and subsequent protonation (equation 9).[80–83]

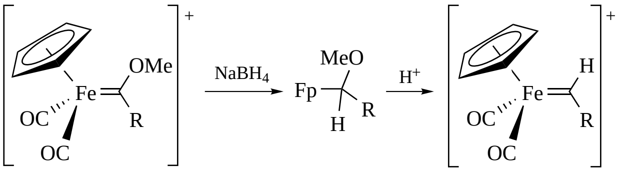

(9)

3.6.3 Structural Characterization

In NMR spectroscopy the carbene proton signals appear at ca. 12–15 ppm, and the carbene carbon resonances appear at ca. 320–420 ppm in NMR spectroscopy.

Thiocarbene complexes have been characterized by X-ray diffraction (*see X-ray Diffraction*) and this data has been tabulated by Kerber.[2,74,84] These structural studies indicate a Fe–C bond length (*see Bond Length*) (ca. 1.90 Å) which is shorter than the typical Fe–C bond length (ca. 2.0–2.2 Å); however, the conformations of the carbene ligand with respect to the remaining ligands are markedly different. In (**51**) the carbene adopts an 'upright' conformation, while in (**57**) the carbene adopts a 'crosswise' conformation. Extended Hückel Molecular Orbital Theory (*see Extended Hückel Molecular Orbital Theory*) calculations predict that the 'upright' conformation is lower in energy by 26 kJ mol^{-1} for methylene analog (**48**, X = Y = H).[85] This conformational preference has been identified for a methoxymethylenecarbene complex by NMR spectroscopy.[86] The solid-state structure of (**57**) has been rationalized on the basis of the steric effects (*see Steric Effect*) of the more substituted carbene ligand. For cationic carbene complexes that lack good electron-donor substituents such as (**48**, X = Y = H), stabilization has been achieved by the presence of the electron-donating bisphosphine ligand Diphenylphosphinoethane (dppe) or the presence of both a Me_5Cp and a PPh_3 ligand.[87,88] In the ^{1}H NMR spectrum of the former complex the methylene protons appear as two distinct signals, at low temperature, that coalesce at higher temperatures (ca. −45 °C). This is consistent with a low-energy 'upright' conformation with the two protons equilibrating by rotation about the Fe–C bond. The activation energy of this bond rotation was determined to be 43.5 kJ mol^{-1}.

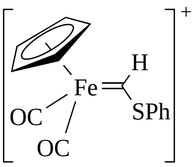

(**51**)

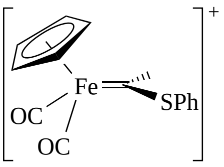

(**57**)

3.6.4 Reactions of Neutral Iron Carbenes

Whereas Fischer-type chromium carbenes react with alkenes, dienes, and alkynes to afford cyclopropanes, vinylcyclopropanes, and aromatic compounds, the iron Fischer-type carbene (**47**, e.g. R = Ph) reacts with alkenes and dienes to afford primarily coupled products (**58**) and (**59**) (Scheme 21).[89] The mechanism proposed involves a [2 + 2] cycloaddition of the alkene the carbene to form a metallacyclobutane (*see Metallacycle*) (**60**). This intermediate undergoes β-hydride elimination followed by reductive elimination to generate the coupled products. Carbenes (**47**) also react with alkynes under CO pressure (ca. 3.7 atm) to afford 6-ethoxy-α-pyrone complexes (**61**).[89] The unstable metallacyclobutene (**62**) is produced by the reaction of (**47**) with 2-butyne in the absence of CO. Complex (**62**) decomposes to the pyrone complex (**61**). It has been suggested that the intermediate (**62**) is transformed into the vinylketene complex (**63**) which undergoes cyclization to form (**61**). On the other hand, the reaction of an aminocarbene complex such as (**64**) with an alkyne gives predominantly the aminofuran as the product.

3.6.5 Reactions of Cationic Iron Carbenes

Owing to their electrophilic character, those cationic iron carbene complexes (**48**) which are isolable undergo reactions with nucleophiles to afford σ-alkyl complexes (Scheme 22).[74,84] The range of nucleophiles which are viable includes borohydrides (equation 9), Grignard reagents, alkyllithiums, organocuprates, enolates, amines, phosphines, and methoxide.[56] For example, the addition of enolates derived from β-alkylcyclohexanone to carbene (**45**) (equation 7) in order to prepare highly functionalized iron alkyl complexes for use in total synthesis has been performed (see below). Where the ligand array about iron is chiral (eg. L = CO, L′ = PPh_3), this nucleophilic addition occurs with excellent diastereoselectivity.[90] As noted previously, cationic carbene complexes which lack electron-donor substituents are unstable. The isopropylidene iron complex (**48**; X = Y = Me) may be generated in solution and spectroscopically characterized at low temperature (−40 °C); however, upon warming (>−10 °C) this complex undergoes rearrangement, via a β-hydride migration, to form the η^2-propene complex (**65**).[43,55,91] In carbene complexes which lack β-hydrogens, for example (**48**; X = H, Y = t-Bu), alkyl migration can occur to afford trisubstituted alkene complexes (**66**). When this involves a polycyclic hydrocarbon, the result is a strained bridgehead alkene complex (**67**).[92]

In contrast to the neutral iron carbene complexes (**47**), cationic methylidene, ethylidene, dimethylallylidene, and benzylidene complexes (**68**) and (**69**) (Y = H, Me, CH=CMe$_2$, Ph) react with alkenes to afford cyclopropanes in good yields (Scheme 23).[71,74,84,93] For the ethylidene and benzylidene complexes of $Fe(CO)_2Cp$ (**68**), *cis* stereoselectivity (*see*

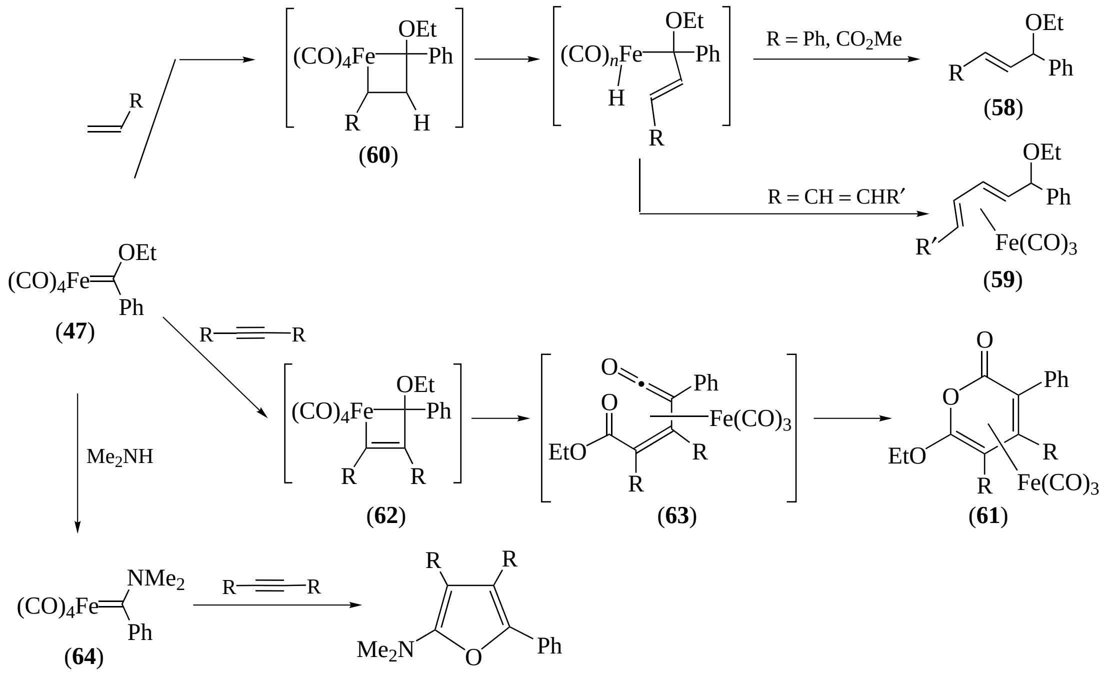

Scheme 21

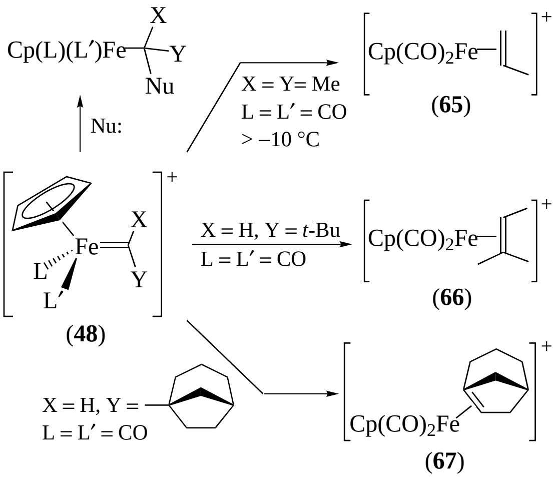

Scheme 22

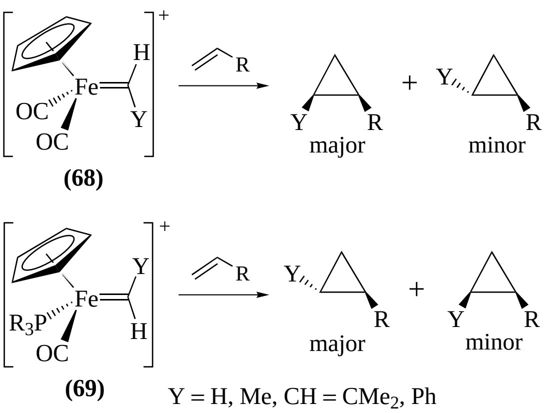

Y = H, Me, CH = CMe$_2$, Ph
R = alkyl, aryl, alkoxy

Scheme 23

Stereoselectivity) is observed; however, for ethylidene complexes of Fe(CO)(PR$_3$)Cp (**69**) the products reflect *trans* selectivity. This difference in stereoselectivity has been suggested to be dependent upon which conformer is more reactive. The reaction of a chiral-at-iron cationic carbene complex (**70**) with styrene or vinyl acetate affords optically active cyclopropane products with high enantioselectivity (Scheme 24).[71,93] Intramolecular cyclopropanation, as in the case of (**71**), proceeds moderately well for the formation of norcarane-type ring systems; however, intramolecular C–H insertion is a competing pathway when the alkene is highly substituted (Scheme 25).[94] In fact, this C–H insertion has also been studied in detail and it has been applied to total synthesis (Scheme 26).[95] Deuterium-labeling experiments have led to a proposal that the process occurs in a one-step, concerted manner.[96] While there have been a number of mechanisms proposed for the cyclopropanation reaction, a complete understanding of this reaction is not yet available.

An intriguing approach to an enantioselective cyclopropanation has recently been reported (Scheme 27).[97] Enantiomerically pure planar chiral η^6-chromium benzaldehydes (**71**) were prepared in the manner described earlier (Scheme 19) and treated with alkenes at low temperature. For some cases

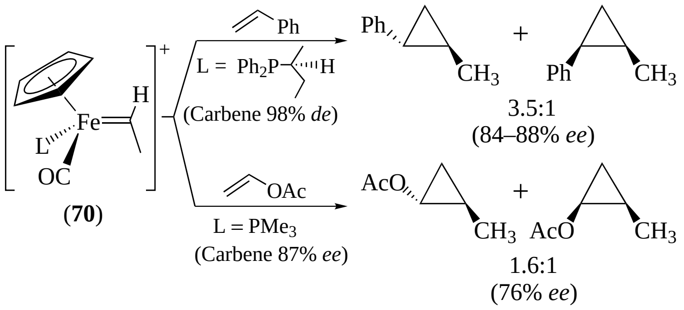

Scheme 24

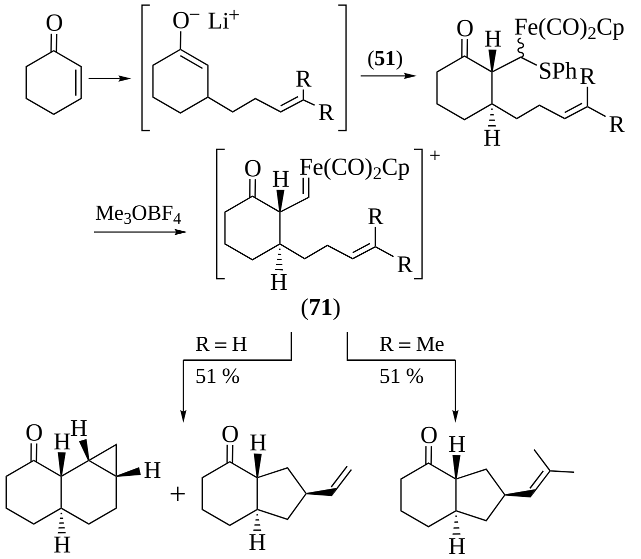

Scheme 25

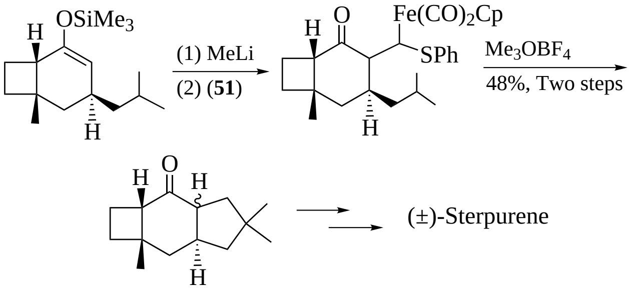

Scheme 26

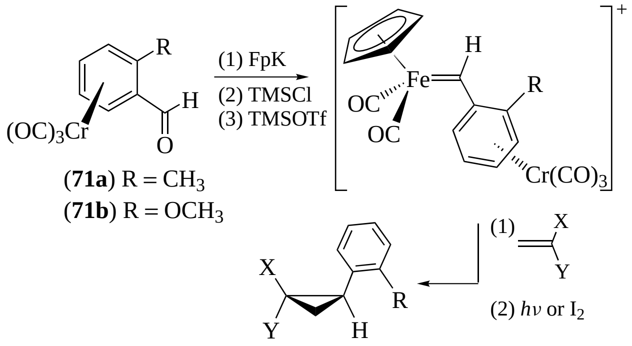

Scheme 27

(especially with (**71a**) and X = Ar, Y = H), *cis*/*trans* selectivity was high and enantiomeric excesses were excellent (>95%). NMR studies revealed that enantioselectivity was dependent on the *syn*/*anti* ratio of the carbene (this refers to rotation of the iron–carbon double bond with respect to the aromatic substituent). The *anti* isomer (*see Isomer, Types of*) that is depicted is the only rotamer present between −90 to +10 °C for R = CH_3 and thus a highly enantioselective cyclopropanation is possible.

Finally, a racemic cyclopropanation process has also been developed that utilizes an iron Lewis acid catalyst (**72**) that presumably proceeds through an iron carbene intermediate (**73**) (Scheme 28). The catalyst is activated by reaction with diazo compounds to produce an intermediate (**74**) that loses dinitrogen (*see Dinitrogen & Dinitrogen Complexes*) to afford the cyclopropane. This chemistry has been extended to the production of epoxides and aziridines and has recently been reviewed.[98]

3.7 σ-Alkynyl Iron Complexes

In the fields of ‘organometallic polymer (*see Polymer*) chemistry’, in which complexes may have particularly interesting physical properties (liquid crystallinity, optical nonlinearity (*see Nonlinear Optical Materials*), etc.), or of ‘molecular electronics’, metal alkynyl complexes play a significant role. These areas have been the subject of recent reviews,[99,100] thus only a brief overview of methods to prepare iron alkynes will be given here. Liu has also recently reviewed the cyclization chemistry of alkynyl organometallics, including those of iron.[101]

Transmetallation of iron halides with lithium acetylides or alkynyl Grignards affords σ-alkynyl complexes in moderate

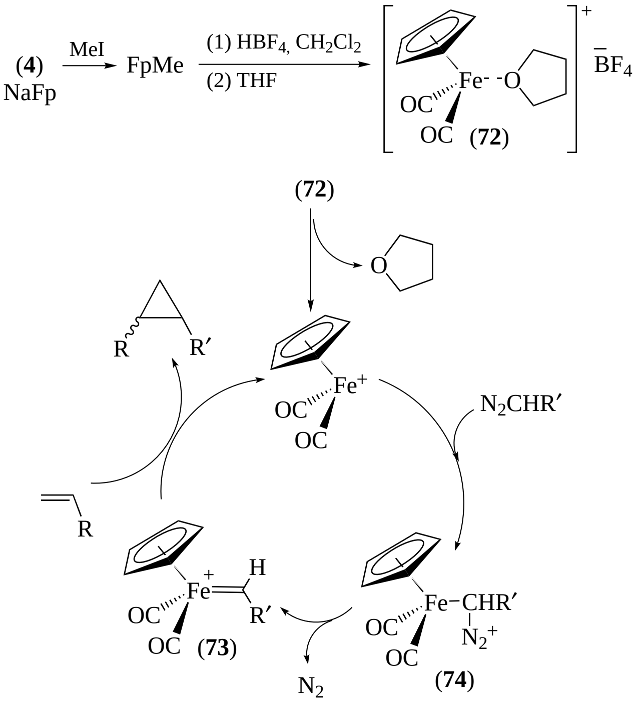
(4)
NaFp
MeI
FpMe
(1) HBF4, CH2Cl2
(2) THF
OC
Fe
O
OC
(72)
BF4
(72)
O
Fe+
OC
OC
N2CHR′
R
R′
R
Fe
H
R′
OC
OC
(73)
N2
Fe
CHR′
N2+
OC
OC
(74)

Scheme 28

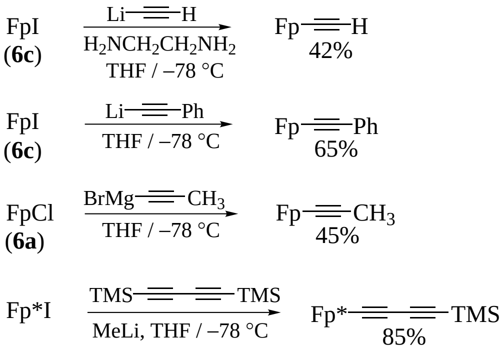
FpI
(6c)
Li—≡—H
H2NCH2CH2NH2
THF / −78 °C
Fp—≡—H
42%
FpI
(6c)
Li—≡—Ph
THF / −78 °C
Fp—≡—Ph
65%
FpCl
(6a)
BrMg—≡—CH3
THF / −78 °C
Fp—≡—CH3
45%
Fp*I
TMS—≡—≡—TMS
MeLi, THF / −78 °C
Fp*—≡—≡—TMS
85%

Scheme 29

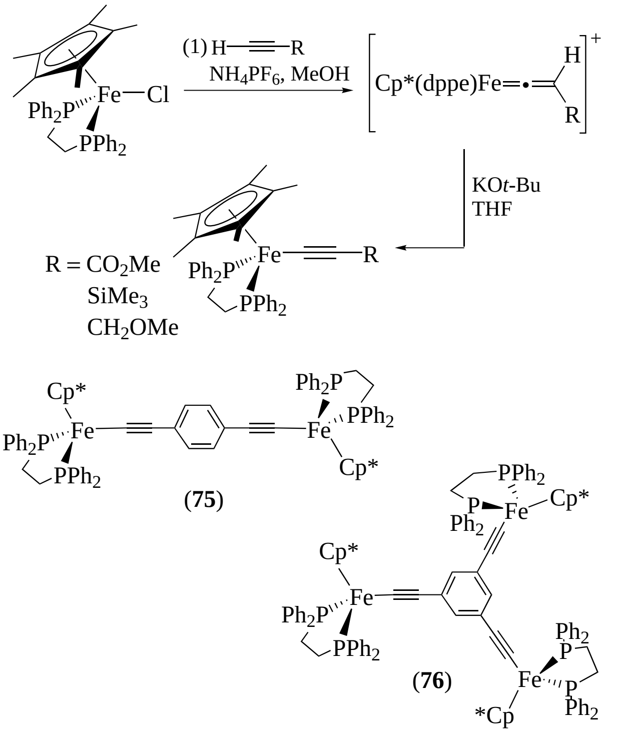
Fe—Cl
Ph2P
PPh2
(1) H—≡—R
NH4PF6, MeOH
Cp*(dppe)Fe=•=
H
R
KOt-Bu
THF
R = CO2Me
SiMe3
CH2OMe
Ph2P
Fe
R
PPh2
Cp*
Ph2P
Fe
PPh2
Ph2P
PPh2
Fe
Cp*
(75)
PPh2
P
Ph2
Fe
Cp*
Cp*
Ph2P
Fe
PPh2
(76)
Ph2
P
Fe
P
Ph2
*Cp

Scheme 30

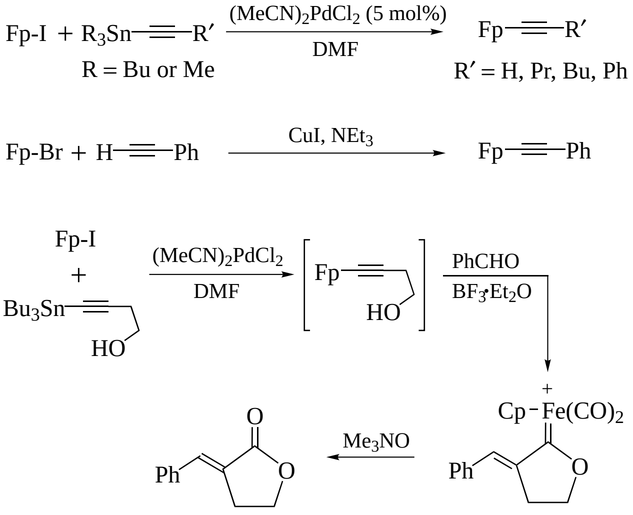
Fp-I + R3Sn—≡—R′
R = Bu or Me
(MeCN)2PdCl2 (5 mol%)
DMF
Fp—≡—R′
R′ = H, Pr, Bu, Ph
Fp-Br + H—≡—Ph
CuI, NEt3
Fp—≡—Ph
Fp-I
+
Bu3Sn—≡
HO
(MeCN)2PdCl2
DMF
Fp—≡
HO
PhCHO
BF3·Et2O
+
Cp-Fe(CO)2
Ph
O
Me3NO
O
Ph
O

Scheme 31

to good yields. Representative examples are depicted (Scheme 29). Indirect conversion of alkynes into alkynylirons is also possible when a halide-ion abstractor is employed; treatment of the resulting isolable vinylidene complex (Section 3.7) with base then affords the alkyne complex (Scheme 30). Complexes (**75**) and (**76**) are examples that bear multiple organometallic units that have been made using this chemistry. Palladium-catalyzed 'metalla-Stille' couplings can also be utilized to produce alkynyliron complexes from iron halides,[102] as can copper-promoted transformations (Scheme 31). The former method was also used to generate an alkynyl iron complex *in situ*; treatment with an electrophile (aldehydes or trimethylorthoformate) in the presence of $BF_3{\cdot}Et_2O$ led to a cyclic iron-oxacarbenium salt. Demetalation led to the α-alkylidene lactones.[101]

3.8 Iron Vinylidene Complexes

As detailed above, alkyne complexes can be prepared from vinylidene complexes by deprotonation. The reverse

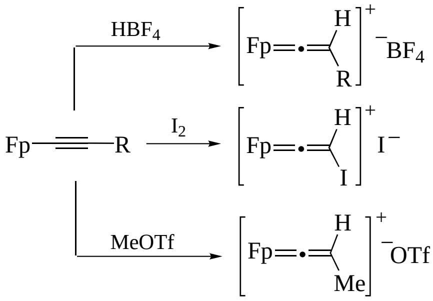

Scheme 32

process is also possible: iron alkynes are readily converted into vinylidenes by treatment with acid or an electrophile (Scheme 32). Vinylidene complexes can also be made by a formal dehydration of iron acyl complexes (equation 10). Furthermore, also as described above, they are available from the reaction of iron halides and alkynes in the presence of a halide-abstractor (Scheme 30).

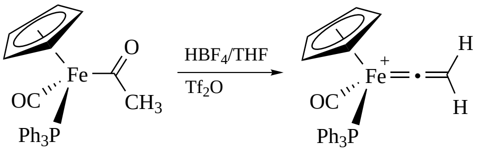

(10)

The chemistry of iron vinylidene complexes is dominated by the electrophilicity of the carbon atom adjacent to the iron organometallic unit. While addition of water leads to an acyl complex (i.e., the reverse of the dehydration shown in equation 10), addition of an alcohol leads to a vinyl ether complex. Similarly, other iron vinyl complexes can be prepared by the addition of thiolate, hydride, or an organocuprate (Scheme 33).[74] The nucleophilic addition of imines gave enaminoiron intermediates that could be further elaborated into cyclic aminocarbenes. This methodology has been used to provide access to β-lactams and ultimately penicillin analogs, and good diastereoselectivities were observed (6:1–15:1) (Scheme 34).[103,104] Also, vinylidene complexes are intermediates in cyclizations of alkynyl irons with substituted ketenes, acid chlorides, and related electrophiles; an example is shown (equation 11).[105] These cyclizations led to the formation of a series of isolable and characterizable cyclic vinyl iron complexes.

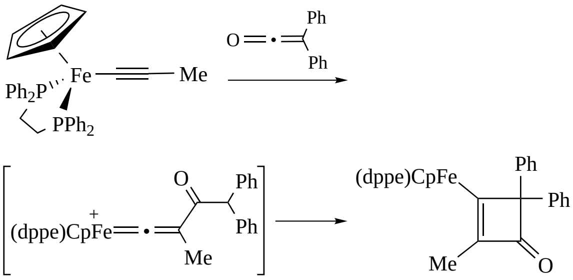

(11)

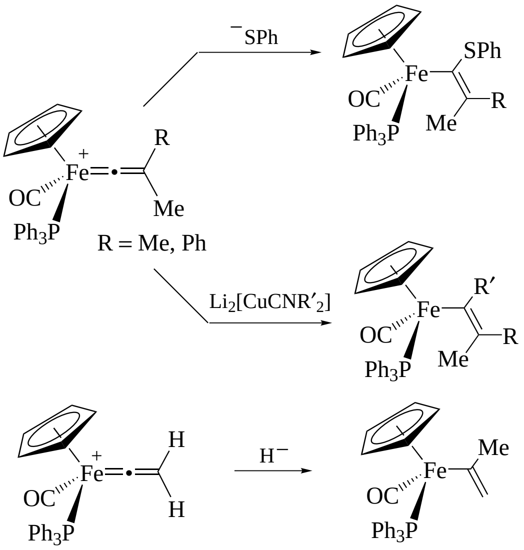

Scheme 33

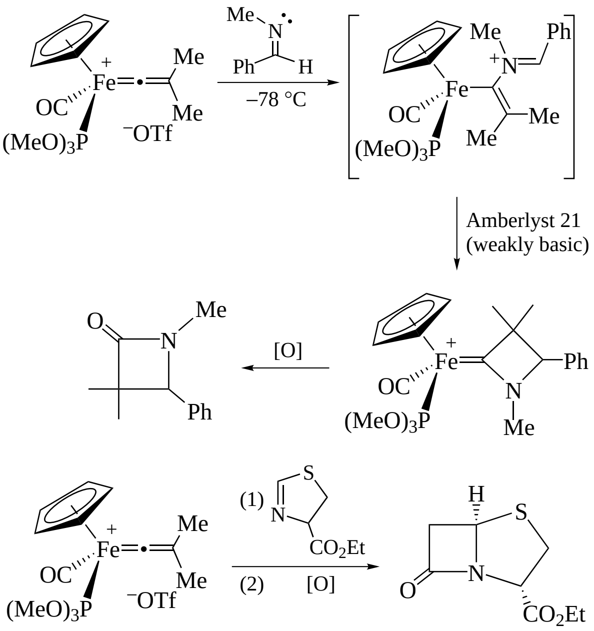

Scheme 34

4 η^2-LIGAND COMPLEXES[106,107]

4.1 Preparation of Alkene Complexes

4.1.1 Neutral Alkene Complexes

The reaction of (**2**) or (**3**) with alkenes in ether or benzene at or slightly above room temperature affords [Fe(CO)$_4$(η^2-alkene)] complexes (**77**) in good yield.[108] Alternatively, (**1**) and Ultraviolet (UV) radiation at or below room temperature is also capable of effecting the same transformation.[109] The stability of the complexes varies with the alkene substrate. In general, alkenes bearing electron-withdrawing groups give more stable complexes than electron-rich (*see Electron Rich Compound*) alkenes; this may be attributed to the slightly electron-releasing nature of the $Fe(CO)_4$ unit.[107] It has, in general, proven possible to complex only one double bond of a conjugated or nonconjugated diene,[110] or solely the C=C double bond of a enone or enal.[111] In the dienes, *trans* double bonds are complexed in preference to *cis* double bonds. Allylic and homoallylic heteroatom substituents direct the complexation to the proximal face of the alkene, often exclusively (e.g. (**78**)), and in some cases may displace CO as a ligand.[112] This 'heteroatom delivery' of the metal fragment is typically a kinetic process. Enantiomerically pure $[Fe(CO)_4(\eta^2\text{-alkene})]$ complexes have been prepared by diastereoselective complexation (Scheme 35). The cyclic example shown relies on heteroatom delivery for selectivity, while for acyclic cases the metal fragment seems likely to complex to the less hindered alkene face.[113–115] The latter complexes have been used to provide access to enantiopure η^3-allyl iron complexes, while nucleophilic replacement of the isopropoxy group in the former examples presumably proceeded via the intermediacy of similar η^3-allyl iron complexes (Section 5.1.1).

Complexation reactions which give alkene complexes with greater than one iron carbonyl unit, or with more than one alkene unit per ion center, have been reported. Use of excess diene relative to the iron carbonyl source allows formation of $(diene)[Fe(CO)_4]_2$ complexes.[7,116] Low-temperature photolysis of alkene and $Fe(CO)_5$ can afford high yields of $(alkene)_2Fe(CO)_3$, and even $(alkene)(alkene)Fe(CO)_3$ or $(alkene)_3Fe(CO)_2$ complexes.[117,118]

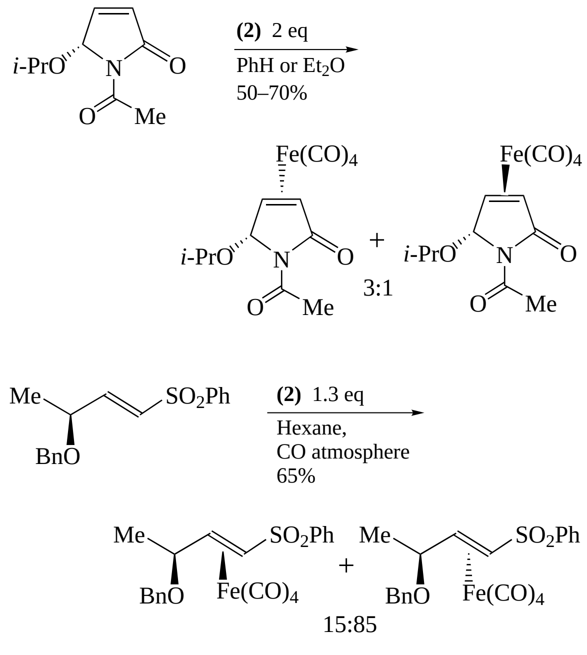

Scheme 35

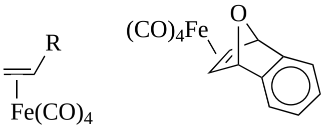

(**77**) (**78**)

Other synthetic routes to $(\eta^2\text{-alkene})Fe(CO)_4$ complexes are much rarer. Nucleophilic attack upon $[(\eta^3\text{-allyl})Fe(CO)_4]^+$ cations results in $(alkene)Fe(CO)_4$ complexes, although they are rarely isolated; this is discussed more fully in Section 5.3.1. There have also been studies on the preparation of simple $(\eta^2\text{-alkene})FeL_4$ complexes with ligands other than CO. η^2-Alkene complexes of iron phosphines have been made in several cases by the reduction of Fe^{II} or Fe^{III} salts in the presence of alkene and phosphine.[119] Complexes with mixed CO and phosphine (or phosphite) ligands have been prepared by the treatment of *vic*-ditriflates with $[(R_3P)Fe(CO)_4]^{2-}$.[120] Complexes with mixed CO and NO ligands, with mixed CO and diazadiene ligands, or with mixed diphosphine and CO ligands may be prepared by photolysis of $Fe(CO)_2(NO)_2$, $(dad)Fe(CO)_3$, or $(diphosphine)Fe(CO)_3$, respectively.[121] In all cases the incoming alkene replaces the CO ligand.

4.1.2 Cationic (See Cation) Complexes

Owing to their relative stability in normal cases, cationic $[Fe(Cp)(CO)_2(\eta^2\text{-alkene})]^+$ complexes (**79** = $(\eta^2\text{-alkene})Fp^+$) are the most widely investigated η^2-alkene complexes of iron (Scheme 36). These complexes may be obtained by hydride abstraction from an iron alkyl complex, by protonation of an allyl iron complex (typically using HBF_4), by treatment of an alkene with a Lewis acid and FpNa (**5**), or by epoxide ring-opening with (**5**) followed by protonation of the alkoxide and subsequent elimination of water. The complex of 2-methylpropene (**79a**, **79b**, or **79c**) has proven particularly effective for alkene exchange reactions with other monosubstituted and *cis*-disubstituted alkenes, and has been used as a double bond protecting group (less hindered alkenes are complexed over more hindered ones, and alkenes are preferred over alkynes). The rate of epoxide opening is greatly enhanced by using FpLi in place of FpNa (**5**); however, other rearrangements are also enhanced in some cases on use of the Li^+ cations.[122] The epoxide ring-opening strategy is particularly effective for preparing the $[Fp{-}alkene]^+$ complexes bearing electron-withdrawing groups. The intermediate alkoxides, and hence the $(alkene)Fp^+$ complexes, may also be formed by aryl/alkyllithium or Grignard attack at the aldehyde function of (β-oxoalkyl)Fp complexes.[123] Finally, hydrogen or alkyl group migration in iron carbene complexes (**48**) gives $(\eta^2\text{-alkene})Fp^+$ complexes (**65,66**), and is particularly good for preparing complexes

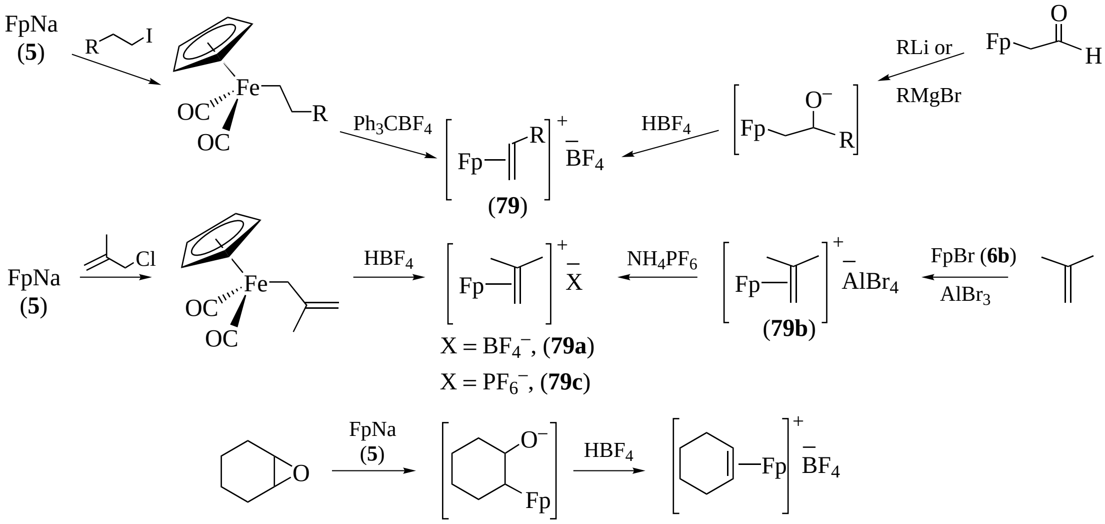

Scheme 36

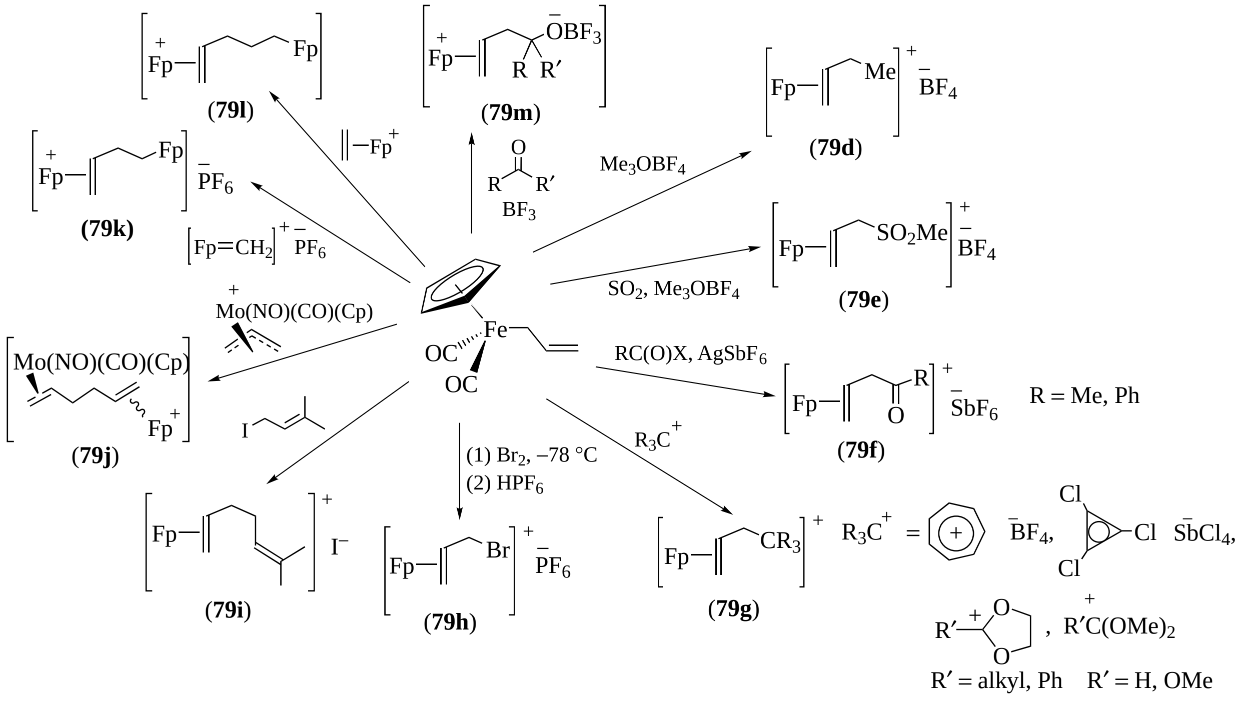

Scheme 37

of bridgehead alkenes (**67**); this has been discussed in Section 3.5.5 (Scheme 22).[87–89]

As a mildly nucleophilic species, (η^1-Allyl)Fp compounds have been shown to react with a fairly wide range of electrophilic species to give substituted (η^2-alkene)Fp^+ cations (**79d–79m**) (Scheme 37).[18,19,124] In general, HBF_4 (as seen in Scheme 36), carbocations, bromine or its equivalents, and sulfur dioxide (provided the zwitterionic intermediate is trapped by $Me_3O^+BF_4^-$) react successfully.[124] More unusual electrophiles include (η^2-alkene)Fp^+ cations themselves, the cationic iron carbene $Fp{=}CH_2^+PF_6^-$, and cationic allylmolybdenum complexes.[125,126] Allyl iodides react very sluggishly, over a period of days; other alkyl halides are not normally reactive enough.[18–20] Although most aldehydes and ketones themselves will not react with (η^1-allyl)Fp complexes, BF_3 etherate induces reaction in

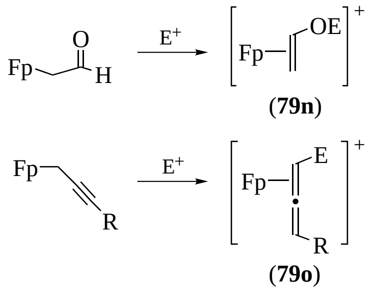

Scheme 38

good yield; this chemistry has been developed further and will be discussed later (Section 4.4).**127** The elaboration of more complex (η^1-allyl)Fp compounds by this reaction in conjunction with subsequent Fp(η^2-alkene) deprotonation will also be described, as will intramolecular attack of (η^1-allyl)Fp complexes with (η^2-alkene)Fp^+ cations (Section 4.3.2).

The analogous reactions on (η^1-propargyl)Fp and (β-oxoalkyl)Fp complexes afford related complexes (**79n**) and (**79o**), respectively (Scheme 38). Cationic allenyl iron complexes related to (**79o**) can also be obtained by protonation of the propargylic species with HBF_4 or by transfer of the Fp cation via reagents (**79a–c**).**18,19**

4.2 Properties of Alkene Complexes

4.2.1 Neutral Alkene Complexes

(η^2-Alkene)$Fe(CO)_4$ complexes are trigonal bipyramidal (*see Trigonal Bipyramidal*), with the alkene ligand occupying an equatorial position and aligned in the equatorial plane (**80**).**128** Fe–C(alkene) bond lengths range between 2.02 and 2.16 Å, with the apparent anomaly of the tetrafluoroethylene complex (1.989 Å) (*see* ***Diffraction Methods in Inorganic Chemistry***). Alkene C–C bond lengths are usually in the 1.39–1.42 Å range. Replacement of a CO ligand by a phosphine results in axial phosphine incorporation, whereas a second alkene ligand is incorporated at another equatorial position. The substituents on alkene carbons are bent back from idealized sp^2 geometry; angles of 10–15° are common. Small rotations of the alkene from the equatorial plane are also often found in crystal structures (*see Crystal Structures*). Temperature-induced changes of the CD spectra of optically active complexes are evidence that this rotation is an intrinsic property.**112** Alkene rotation barriers are in the 45–60 $kJ\,mol^{-1}$ range; this rotation is coupled with Berry pseudorotation (*see Berry Pseudorotation*). For the (diazadiene)$Fe(CO)_2$ complexes the barrier ranges between 40 and 70 $kJ\,mol^{-1}$.**129** Typical ^1H NMR chemical shifts for the coordinated alkene vary significantly. Typical chemical shifts are 2.2–3.0 ppm for unsubstituted alkenes and 3.0–3.5 ppm for monosubstituted alkenes. For alkenes bearing electron-withdrawing groups, the α-protons are significantly downfield (3.7–5.5 ppm), whereas the β-protons are largely unperturbed. Substitution of a phosphine or phosphite for one carbonyl ligand results in shielding of the alkene protons.**130** Typical $^3J(trans)$, $^3J(cis)$, and $^2J(gem)$ are 9–12.5, 6.5–8, and 1–2.5 Hz, respectively. The ^{13}C NMR spectral resonances usually fall in the ranges of 23–35 ppm (unsubstituted) and 44–65 ppm (monosubstituted).**32** ^1J(C–H) coupling constants are approximately the same as the parent alkenes, and limited data give an average value for ^1J(C–C) of 46 Hz.**131**

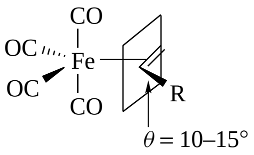

(**80**)

4.2.2 Cationic Alkene Complexes

The average Fe–C bond distance has been determined from crystal structures of (**79**) is considered to be ≈2.20 Å (range of 2.09–2.82 Å), but the alkene carbon atoms are often highly unsymmetrically bonded to the Fe center, with the carbons substituted by electron-donating groups being much further away.**132** This is evidence for contribution of resonance form (**81**) to the bonding description (equation 12), which has been predicted in general terms by Extended Hückel molecular orbital (EHMO) calculations (*see* ***Molecular Orbital Theory***).**133** In the minimum energy conformation the alkene residue is roughly parallel to the plane of the Cp ring, with substituents oriented away from the Cp ring, if possible. Alkene rotation barriers have been shown to vary from ≈33 to >75 $kJ\,mol^{-1}$.**134** Typical ^1H NMR chemical shifts for (η^2-alkene)Fp^+ complexes are 3.5–4.1 ppm (unsubstituted) and 4.7–5.6 ppm (monosubstituted). Electron-donating substituents move the α-proton chemical shifts downfield, and the β-protons upfield, whereas electron-withdrawing groups give the opposite trend.**135,136** The ^{13}C NMR spectral resonances fall in the ranges of 48–61 ppm (unsubstituted) and 80–90 ppm (monosubstituted); the disubstituted alkene carbon of the isobutene complex is even further downfield (118.8 ppm).**17**

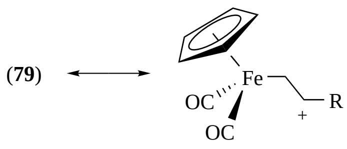

(**81**)

(12)

4.3 Reactions of Alkene Complexes

4.3.1 Neutral Complexes

Alkene–tetracarbonyliron complexes are very susceptible to displacement of the alkene moiety. Reaction of these complexes with reasonably good nucleophiles, such as PPh_3, pyridine, or others, results in formation of free alkene and $LFe(CO)_4$ or $L_2Fe(CO)_3$.**106,107** Photolysis of these complexes in both the gas phase and in low-temperature alkane or Ar matrices results in CO displacement to afford coordinatively unsaturated (η^2-alkene)$Fe(CO)_3$ complexes (**82**). In the presence of H_2 and excess alkene, hydrogenation (*see Hydrogenation*) with high turnover ensues.**137** If the alkene possesses an allylic hydrogen, intramolecular C–H bond insertion occurs to give (**83**), which in turn induces isomerization of 1-pentene.**138** Infrared (IR) (*see Infrared Spectroscopy*) spectroscopic data suggests evidence of two isomers of (**83**).**139**

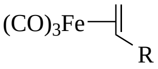
(**82**)

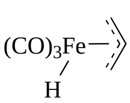
(**83**)

Little synthetic work has been reported on (η^2-alkene)$_2Fe(CO)_3$ complexes, with the exception of $Fe(CO)_3$ (η^2-cyclooctene)$_2$. Grevels has shown this compound to be a versatile source of $Fe(CO)_3$ in solution, and it has been used for that purpose.**117** However, its use is far less common than other mild $Fe(CO)_3$ transfer reagents such as (bda)$Fe(CO)_3$ (Section 6.3.1).

α,β-Unsaturated carbonyl–$Fe(CO)_4$ complexes (**84**) are more stable than most [(η^2-alkene)$Fe(CO)_4$] complexes, and have produced more tractable reactions. Lewis acids react at the carbonyl oxygen to afford intermediate (**85**), which undergoes subsequent reactions with amines at the carbonyl carbon to give (**86**) initially, and often further products.**140** Wittig (*see Wittig Reagent*) and 'phospha-Wittig' reagents react at the aldehyde function of enal complexes; the alkenation is often followed by migration of the iron group.**141,142** Hard nucleophiles, such as organolithiums and Grignard reagents (RLi, RMgBr), give initial metal-bound CO attack, followed by acyl transfer to the β-carbon of the alkene, resulting in 1,4-dicarbonyls (**87**).**143** In some cases, carbonyl carbon attack has been observed. A CO ligand of η^2-enone complexes may be removed selectively using amine N-oxides. In the presence of phosphine or phosphite ligands, the result is ligand substitution (*see Ligand Substitution*) (**88**); in the absence of external ligands, an η^4-enone complex is formed. Since these complexes are chiral, the possibility exists that the enantiomers can be obtained with enantiomerically pure amine N-oxides. In fact, the use of brucine N-oxide has given significant kinetic resolution of both the alkene and enone complexes.**144** An enantiomerically pure vinyl sulfone complex was elaborated to the η^3-allyl complex with loss of the γ-benzyloxy group; this intermediate underwent nucleophilic addition with overall retention of configuration at the γ-position (equation 13).

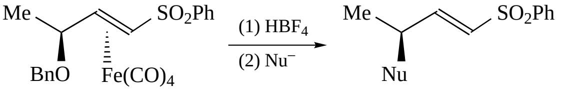

(13)

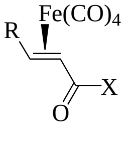

(**84**)

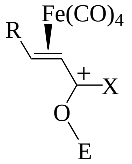

(**85**)

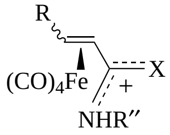

(**86**)

X = H, alkyl, aryl, NR′$_2$, OR′
E^+ = Lewis acid

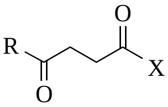
(**87**)

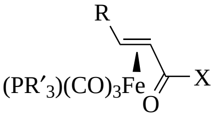

(**88**) X = Ar, Me, H

η^2-Iron carbonyl complexes participate in ring-opening reactions of strained alkenes.**107,145** (Cyclobutene)$Fe(CO)_4$ complexes undergo concerted disrotary ring opening to give (η^4-cyclohexadiene)$Fe(CO)_3$ complexes (**89**) (equation 14). (Methylenecyclopropane)$Fe(CO)_4$ complexes undergo conrotary ring opening to (η^4-trimethylenemethane)$Fe(CO)_3$ complexes (**90**) or, in the case of Feist's ester, to give (η^4-butadiene)$Fe(CO)_3$ complexes (**91**) via C–H insertion and subsequent disrotary concerted ring opening (equation 15). All three rearrangements are preceded by CO loss from iron; detailed studies on the mechanistic aspects of these transformations have been reported.**145**

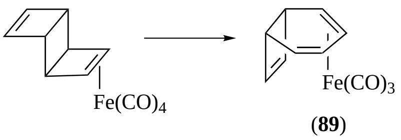

(**89**)
(14)

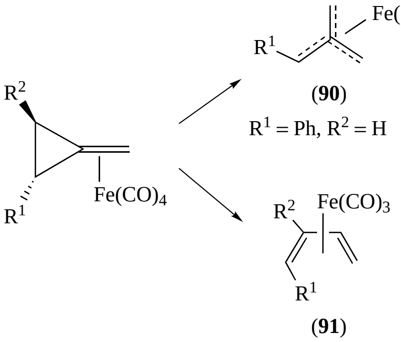

(**90**)
R^1 = Ph, R^2 = H
(**91**)
$R^1 = R^2 = CO_2Me$
(15)

Stable *N*-substituted (azabicyclo[2.2.1]heptadiene)Fe $(CO)_3$ complexes (**92**) undergo nitrene extrusion upon heating, to afford arenes; the analogous iron alkene complexes are almost undoubtedly intermediates in iron carbonyl-mediated deoxygenations of oxabicyclo[2.2.1]heptadienes,that is, (**78**).[146,147] Bicyclo[2.2.1]heptenes lacking a skeletal heteroatom undergo a highly stereoselective cycloaddition, via the η^2-alkene complexes, to give cyclopentanones (equation 16). The stereo- and regiochemical (*see Regiochemistry*) aspects of this reaction have been discussed in detail.[148]

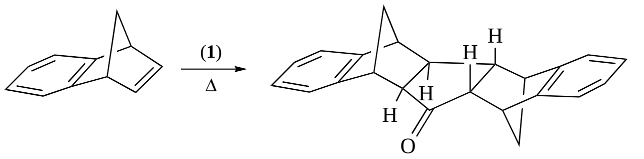

(16)

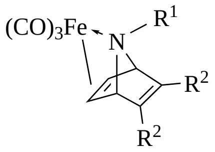

(**92**) $R^1 = CO_2Et, SO_2Me, COMe$; $R^2 = CO_2Me$

4.3.2 Cationic Alkene Complexes

$Fp(\eta^2\text{-alkene})^+$ salts (**79**) are much more electrophilic than $(CO)_4Fe(\eta^2\text{-alkene})$ complexes. The former enter into reaction with a wide range of nucleophiles, and are also therefore susceptible to proton abstraction.

Trialkylamines are capable of deprotonating (**79**), the products being $(\eta^1\text{-allyl})FeCp(CO)_2$ complexes (equation 17). The abstracted proton must be oriented *anti* to the face of the alkene bearing the iron residue; $(\eta^2\text{-cyclopentene})Fp^+$ cations substituted with *trans* acidifying groups (**93**) deprotonate away from the electron-withdrawing group for this reason (equation 18).[136]

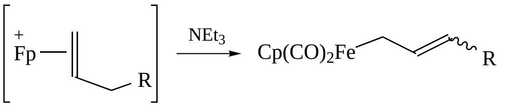

(**79**) (17)

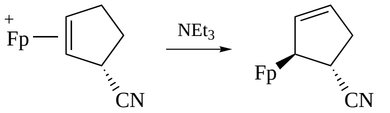

(**93**) (18)

Nucleophilic attack on $(\eta^2\text{-alkene})Fp^+$ cations may be effected by heteroatom nucleophiles including amines, azide ion, cyanate ion (through N), alcohols, and thiols (Scheme 39). Carbon-based nucleophiles, such as the anions of active methylene compounds (malonic esters, β-keto esters, cyanoacetate), enamines, cyanide, cuprates, Grignard reagents, and $(\eta^1\text{-allyl})Fe(Cp)(CO)_2$ complexes react similarly. In addition, several hydride sources, most notably $NaBH_3CN$, deliver hydride ion to $Fp(\eta^2\text{-alkene})^+$ complexes. Subjecting complexes of type (**79**) to NaI or NaBr in acetone, however, does not give nucleophilic attack, but instead results reliably in the displacement of the alkene from the iron residue. Cyclohexanone enolates or silyl enol ethers also may be added, and the iron alkyl complexes thus produced can give Robinson annulation-type products (Scheme 40). Vinyl ether-cationic Fp complexes as the electrophiles are useful as vinyl cation equivalents.[4]

The stereochemistry of nucleophilic attack is consistently *trans* to the metal–alkene bond (Scheme 39, equation 19).[110,149] The regiochemistry of attack is normally at the alkene carbon bearing the most electron-donating (or least electron-withdrawing) group. For weakly electron-donating substituents, such as alkyl, the observed regioselection is modest for carbon-based nucleophiles. For amine and

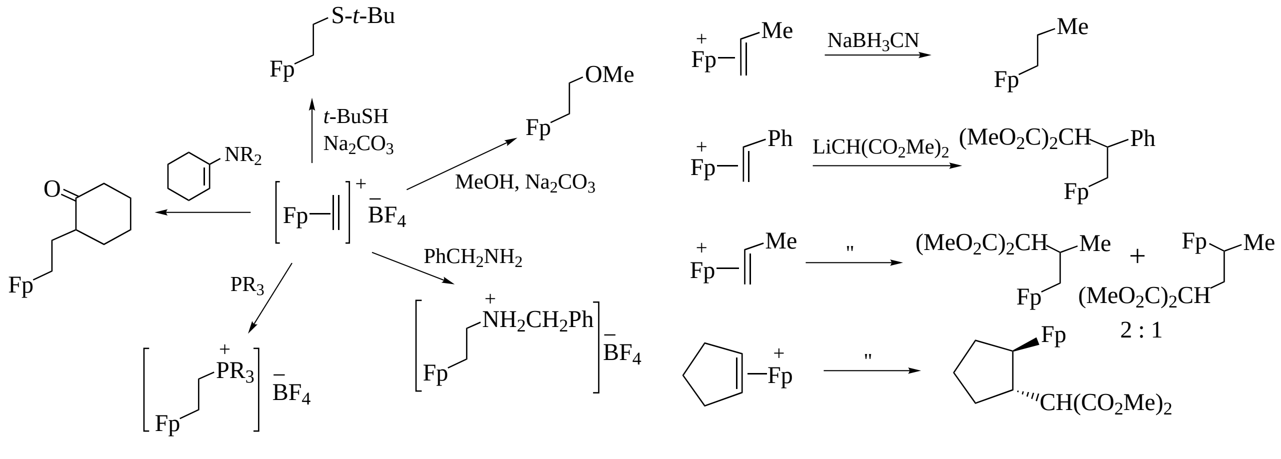

Scheme 39

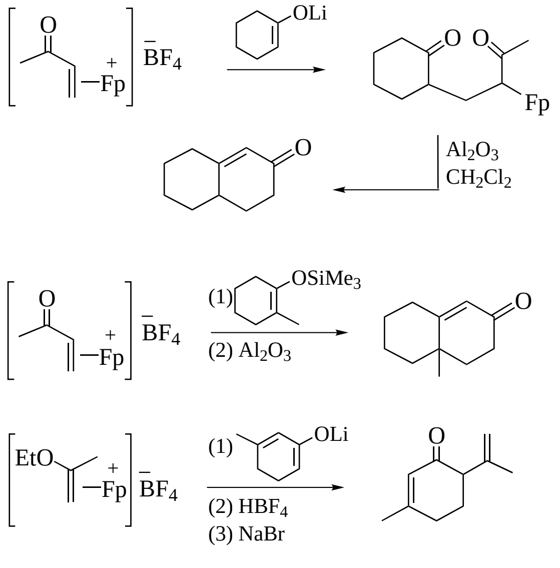

Scheme 40

oxygen-based nucleophiles, however, much better selectivity is realized, presumably due to the reversible nature of the addition of these heteroatom nucleophiles. With more highly electron-donating substituents, such as alkoxy (**94**), or electron-withdrawing ones, such as esters (**95**), the regioselection of attack is excellent.

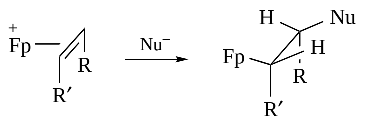

(19)

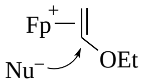

(**94**)

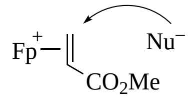

(**95**)

Intramolecular nucleophilic attack has been demonstrated in several cases, particularly with amine and (η^1-allyl)Fp complexes; an example of the former is depicted (equation 20).**4** In such cases, the driving force for formation of five- or six-membered rings overrides the preference for attack at the more substituted alkene center. The ability of trialkylamines to convert (η^2-alkene)Fp$^+$ complexes into (η^1-allyl)Fp complexes via deprotonation allows conversion of alkadiene complexes (*see Diene Complexes*) (**96**) into carbocycles (**97,98**). The reasons for the stereochemical outcome of these cyclization reactions have not been fully delineated. Finally, (η^2-butadiene)Fp$^+$ cations react in two sequential (η^1-allyl)Fp–(η-alkene)Fp$^+$ pairs to give a mixture of cyclic products (Scheme 41).

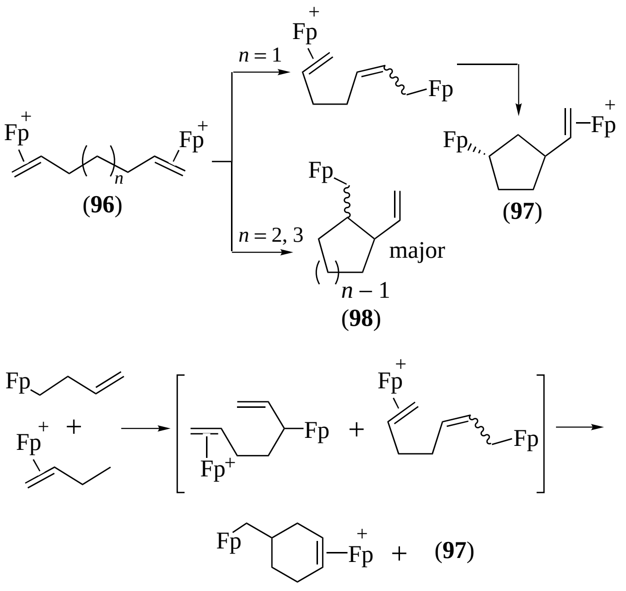

Scheme 41

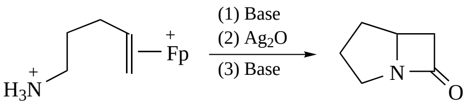

(20)

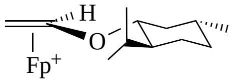

(**99**)

Work in this area has also focused on optically active complexes. Exchange of vinyl ether complex (**94**) with optically active alcohols gives unequal mixtures of diastereomeric vinyl ether complexes; in the best case, (−)-menthol gives a 4:1 mixture enriched in (**99**).**150** Optically active epoxides are capable of affording enantiomerically pure complexes; allylic alcohol substituents allow reversible conversion to the related lactone complexes (**100**) (equation 21).

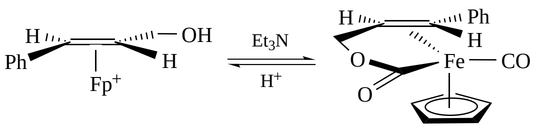

(21)

(**100**)

The reaction of the (*cis*-1,2-dimethoxyethylene)Fp$^+$ complex (**101**) (available from treatment of the alkene with (**79a**)) with (*R*,*R*)-2,3-butanediol gives the optically active Fp$^+$-dioxene complex (**102**). The reaction of (**102**) with nucleophiles proceeds *anti* to the metal fragment; treatment of

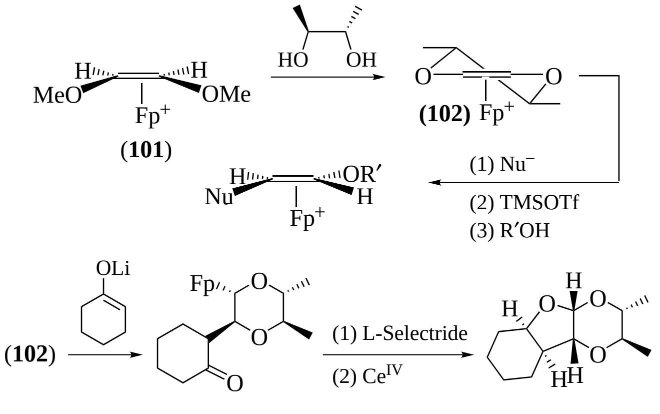

Scheme 42

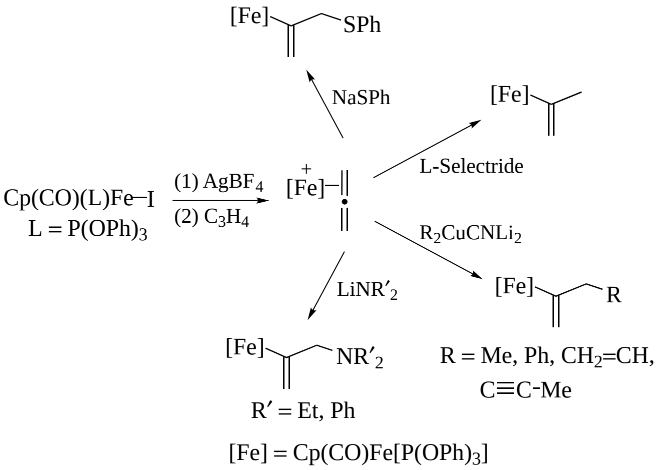

Scheme 43

the iron alkyl thus obtained by with TMSOTf and subsequent exposure to alcohols, gives enantiomerically pure planar chiral vinyl ether complexes (Scheme 42).[4,132] Attack of (**102**) with a cyclohexene enolate, followed by ketone reduction and oxidative removal of the metal fragment gave a tricylic furan.[151]

Nucleophilic addition to the related cationic η^2-allenyl iron complexes is generally a high-yielding process that produces vinylic iron complexes (Scheme 43). Double bond isomerizations to give the internal alkene can be effected by column chromatography or catalytic amounts of acid.[152]

4.4 Alkene Complexes as Reaction Intermediates

Cationic iron alkene complexes are important intermediates in a well-studied series of [3 + 2] cycloaddition reactions between iron allyl complexes and alkenes and related electrophiles. This chemistry has been reviewed by Rosenblum, and was included in subsequent reviews by Welker and Liu.[18,19,101,153] Propargylic iron complexes react in a similar manner, and will be included in this section.

With reactive neutral electrophiles (E=Nu), (η^1-allyl)Fp complexes suffer nucleophilic attack to give zwitterionic intermediate (**103**), which undergoes subsequent intramolecular nucleophilic attack to give the overall product of [3 + 2] cycloaddition (equation 22). (η^1-Propargyl)Fp complexes react similarly. Among electrophilic species suitable in this reaction are α, β-unsaturated nitriles and esters (which must possess at least two geminal electron-withdrawing groups to be sufficiently reactive), isocyanates, hexafluoroacetone, and *N*-sulfonylurethane (Scheme 44). Enones may be induced to react only in the presence of Lewis acids, such as $AlBr_3$. Both allyl and propargyl complexes undergo [3 + 2] cycloaddition with the noncomplexed double bond of tropyliumiron tricarbonyl cationic salts to afford a 7,5-ring system; this chemistry has been used for the synthesis of functionalized hydroazulenes (**104**).[154] Oxidative demetalation of the iron fragment with ceric ammonium nitrate is a typical, though not the only, synthetic strategy employed in this chemistry. Other examples utilizing allyl iron complexes as well as those that employ the propargylic analogs (which presumably proceed via cationic η^2-iron allenyl complexes) are grouped separately (Schemes 45 and 46). It should be noted that the nucleophilicity of (η^1-allyl)Fp complexes may be enhanced by substituting one of the CO ligands with the more electron-donating phosphite ligand. The resulting complexes are $\approx 10^2 - 10^3$ times more reactive than the parent, and will react with alkenes to which the parent is inert.[23]

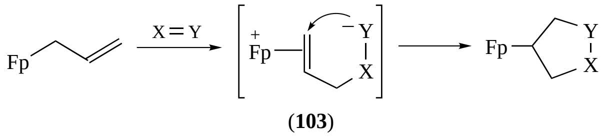

(22)

Other variations of the [3 + 2] cycloaddition chemistry involving either SO_2 or a S_2O equivalent have been explored (Scheme 47).[153,155,156] Iron allenyl complexes undergo reaction with SO_2 to give either vinyl iron (**105**) or (**106**), depending on the substitution pattern. A propargylic iron complex reacts in a similar manner to give (**107**), but reacts with a cyclic thiosulfinate ester to give (**108**).

As previously mentioned, the reaction of allyl iron complexes in the presence of carbonyls and BF_3 has investigated and reviewed (Scheme 37); isolable zwitterionic complexes of the type (**79m**) are obtained.[127,157] Synthetic sequences were developed to utilize these salts; unfortunately, there is only little or modest diastereoselectivity (Scheme 48).[158] Furan formation from the precursor of (**79m**), allylFp, can also be accomplished in a single operation using $ZnCl_2$. Crotyl iron complexes were shown to give the corresponding homoallyl alcohols with modest to good *syn*/*anti* selectivity (3:1 to 14:1).[159] The reaction has also been extended to include imines to provide the homoallyl amines; again, selectivities

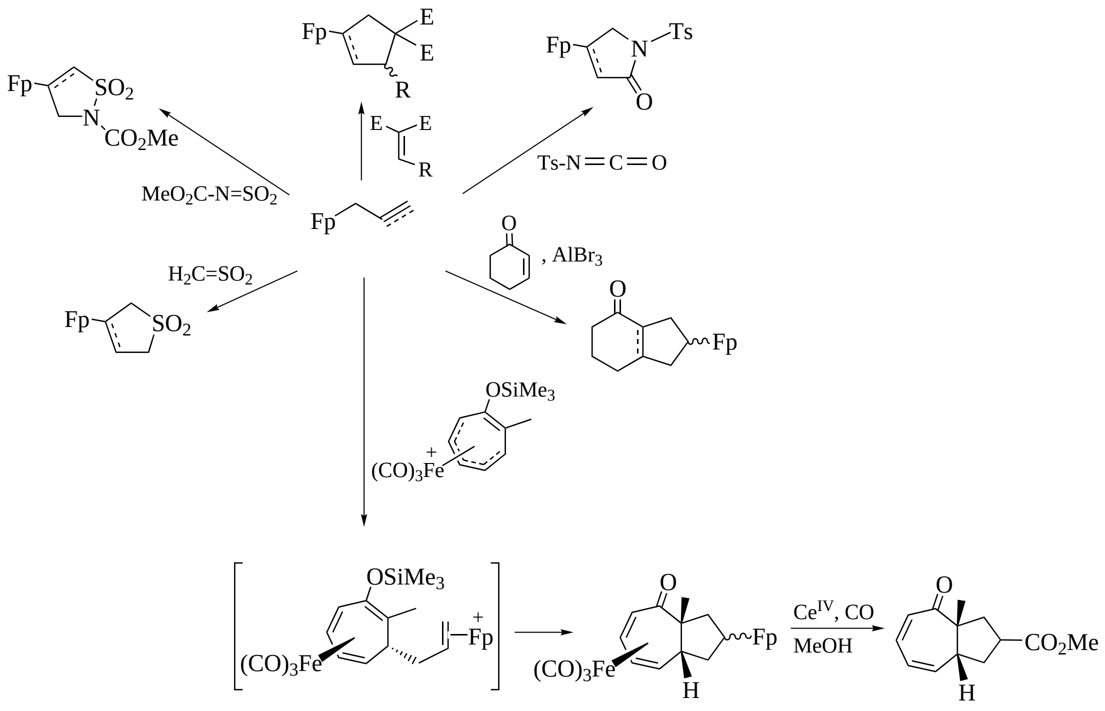
Fp
E
E
R
Ts
N
O
SO2
CO2Me
MeO2C-N=SO2
Ts-N=C=O
, AlBr3
H2C=SO2
OSiMe3
(CO)3Fe
Ce^IV, CO
MeOH
H
CO2Me

(**104**)

Scheme 44

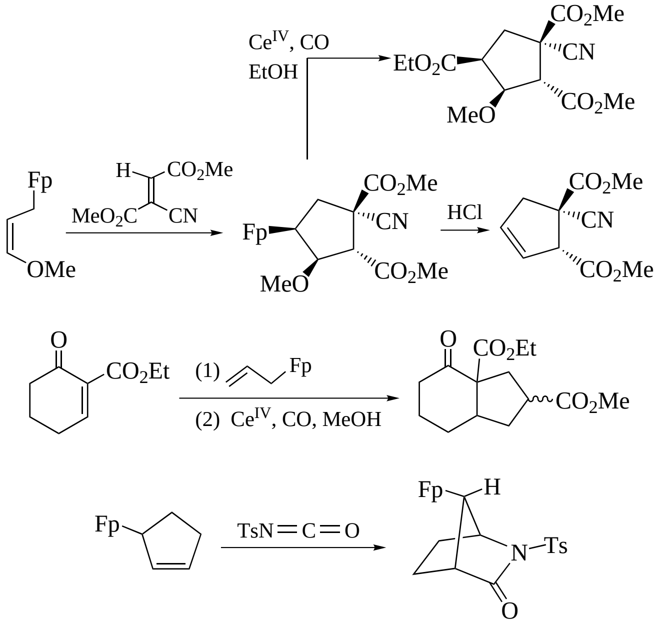
Ce^IV, CO
EtOH
EtO2C
CO2Me
CN
MeO
Fp
OMe
H
MeO2C
HCl
O
CO2Et
(1)
(2) Ce^IV, CO, MeOH
TsN=C=O
N
Ts

Scheme 45

were modest (ca. 2.5:1).[160] Pyrrolidines have been prepared as well. Finally, one intramolecular [3 + 2] cycloaddition was reported, yielding tricylic furan (**109**) in moderate yield and diastereoselectivity (Scheme 49).[158]

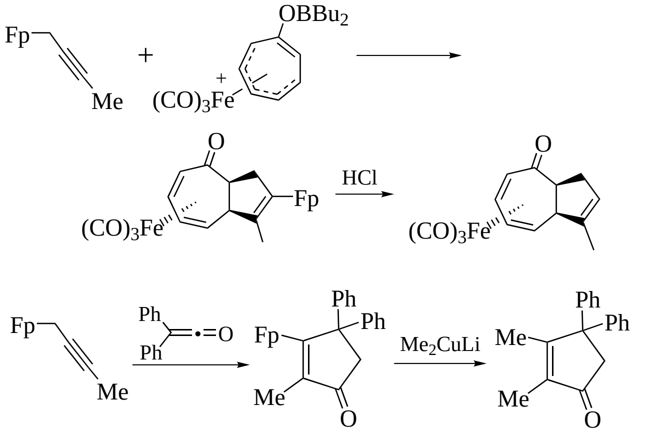
Fp
Me
OBBu2
(CO)3Fe
O
HCl
Ph
Me2CuLi

Scheme 46

4.5 Alkyne Complexes

4.5.1 *Neutral Complexes*

It is typically difficult to isolate [$Fe(CO)_4(\eta^2$-R-CC-R′)] complexes (**110**) without bulky substituents,[161] as they undergo spontaneous alkyne–alkyne coupling reactions, (some of which have tangible synthetic promise).[162] In fact, prior to 1997, only the bistrimethylsilylacetylene complex (**110a**) had been fully characterized. However, a number

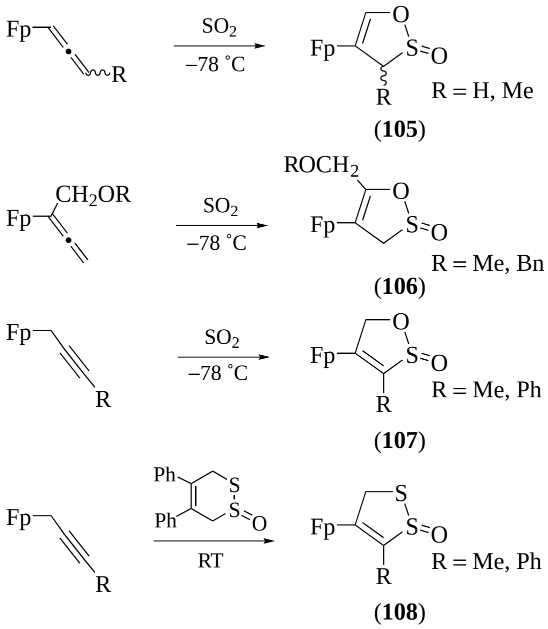

Fp
R
SO_2
−78 °C
Fp
O
S=O
R
R = H, Me
(105)
CH_2OR
$ROCH_2$
R = Me, Bn
(106)
R = Me, Ph
(107)
Ph
S
Ph
RT
R = Me, Ph
(108)

Scheme 47

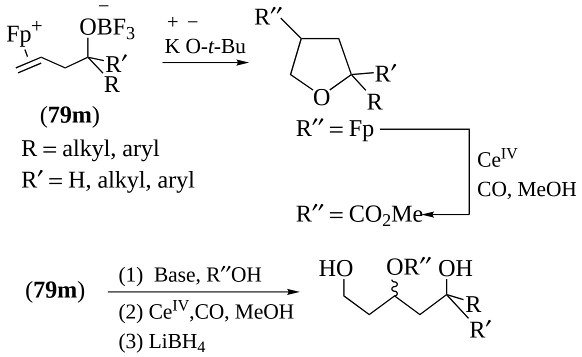

Fp^+
$\overset{-}{O}BF_3$
R′
R
(79m)
R = alkyl, aryl
R′ = H, alkyl, aryl
$\overset{+}{K}\ \overset{-}{O}$-t-Bu
R″
R″ = Fp
Ce^{IV}
CO, MeOH
$R'' = CO_2Me$
(79m)
(1) Base, R″OH
(2) Ce^{IV},CO, MeOH
(3) $LiBH_4$
HO
OR″
OH

Scheme 48

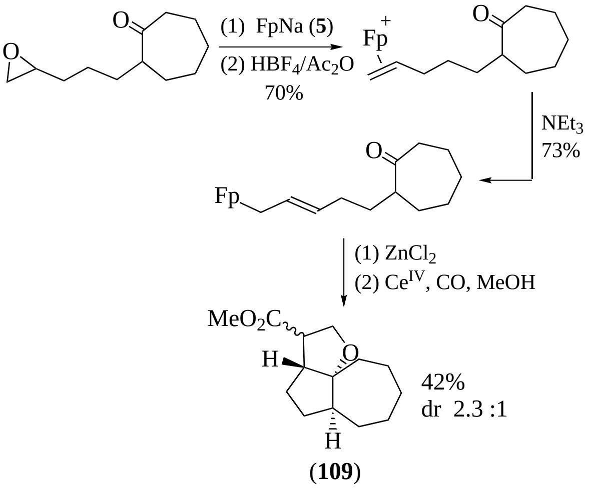

O
(1) FpNa (5)
(2) HBF_4/Ac_2O
70%
$\overset{+}{Fp}$
NEt_3
73%
Fp
(1) $ZnCl_2$
(2) Ce^{IV}, CO, MeOH
MeO_2C
H
42%
dr 2.3 :1
(109)

Scheme 49

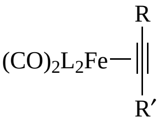

(**110a**) R = R′ = TMS; L = CO
(**110b**) R = R′ = CF_3; L = CO
(**110c**) R = R′ = H; L = CO
(**110d**) R = R′ = CH_3; L = CO
(**110e**) R = H; R′ = CH_3; L = CO
(**110f**) R = H; R′ = CF_3; L = CO
(**110g**) R = H; R′ = Ph; L = $P(OMe)_3$
(**110h**) R = H; R′ = H; L = PEt_3
(**110i**) R = Ph; R′ = Ph; L = $P(OMe)_3$
(**110j**) R = R′ = TMS; L = PEt_3
(**110k**) R = H; R′ = CO_2Me; L = PEt_3
(**110l**) R = R′ = Ph; L = $P(OPh)_3$
(**110m**) R = H; R′ = Ph; L = PEt_3
(**110n**) R = Ph; R′ = Ph; L = PEt_3

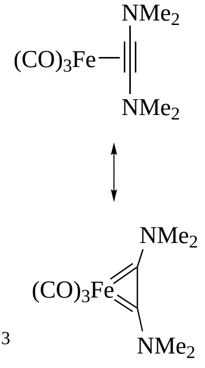

NMe_2
$(CO)_3Fe$
NMe_2
NMe_2
$(CO)_3Fe$
NMe_2

(**111**)

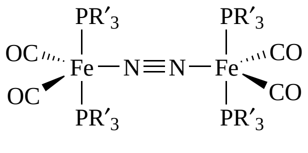

PR′3
PR′3
OC
Fe—N≡N—Fe
CO
OC
CO
PR′3
PR′3

(**112**)

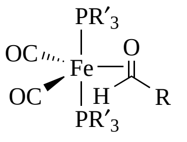

PR′3
O
OC
Fe
OC
H
R
PR′3

R′ = Et, OMe; R = H, Ph

(**113**)

of other complexes (**110b–f**) – all thermally unstable – have now been successfully prepared in fair to good yields by careful photolysis at low temperature, though the reaction scale could not be increased.[163] Dissociation of one of the CO ligands from (**110b**) was reported to be 3 × 10^{13} faster than CO dissociation from $Fe(CO)_5$. Substitution of CO for more electron-rich ligands (such as phosphines or phosphites) leads to more stable alkyne complexes, and a number have been prepared and crystallized (**110g–l**). A remarkably stable iron tricarbonyl-alkyne complex has recently been reported (**111**); there is probably a significant amount of metallacyclic character to this species. Finally, photolysis of (**112**) in the presence of an alkyne also affords alkyne complexes (**110h, m**, and **n**).[164]

4.5.2 Cationic Complexes

$Fp(\eta^2\text{-alkyne})^+$ complexes may been generated by Ag(I)-promoted halide ionization of (**6c**) in the presence of an alkyne or by transfer of the Fp^+ fragment from reagent

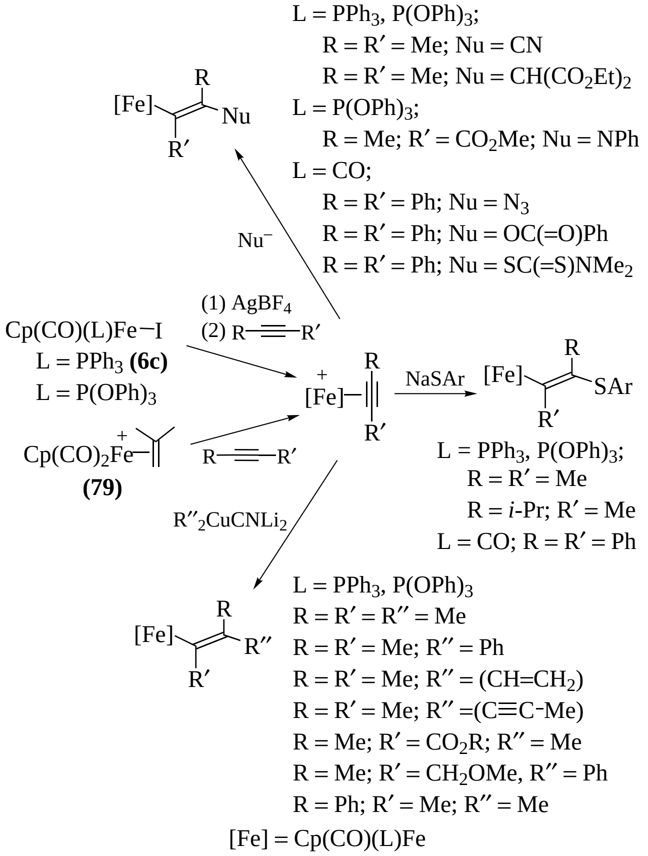
L = PPh3, P(OPh)3;
R = R′ = Me; Nu = CN
R = R′ = Me; Nu = CH(CO2Et)2
L = P(OPh)3;
R = Me; R′ = CO2Me; Nu = NPh
L = CO;
R = R′ = Ph; Nu = N3
R = R′ = Ph; Nu = OC(=O)Ph
R = R′ = Ph; Nu = SC(=S)NMe2
[Fe]
R
R′
Nu
Nu−
(1) AgBF4
(2) R—≡—R′
Cp(CO)(L)Fe—I
L = PPh3 (6c)
L = P(OPh)3
Cp(CO)2Fe
(79)
R—≡—R′
NaSAr
SAr
L = PPh3, P(OPh)3;
R = R′ = Me
R = i-Pr; R′ = Me
L = CO; R = R′ = Ph
R″2CuCNLi2
L = PPh3, P(OPh)3
R = R′ = R″ = Me
R = R′ = Me; R″ = Ph
R = R′ = Me; R″ = (CH=CH2)
R = R′ = Me; R″ =(C≡C-Me)
R = Me; R′ = CO2R; R″ = Me
R = Me; R′ = CH2OMe, R″ = Ph
R = Ph; R′ = Me; R″ = Me
[Fe] = Cp(CO)(L)Fe

Scheme 50

(**79**); these are generally stable complexes except for terminal alkynes, which are in equilibrium with vinylidene complexes. The cationic alkyne complexes are very reactive electrophiles (Scheme 50).[18,19,152,165] Addition of nucleophiles in Scheme 48 proceed in a manner that is *anti* to the iron unit, to give the *trans* product. Other nucleophiles (such as hydride, equation 23) instead react to give the *cis* product, an outcome resulting from initial addition to the Cp ring followed by intramolecular transfer to the alkyne. While a silyl enol ether afforded the *trans* vinyl iron complex, allylation with allyl tributylstannane give a *cis*/*trans* mixture. A study of the addition of nucleophiles to Fp(η^2-alkyne)$^+$ complexes revealed that the product stereochemistry depended on the basicity of the nucleophile.[165]

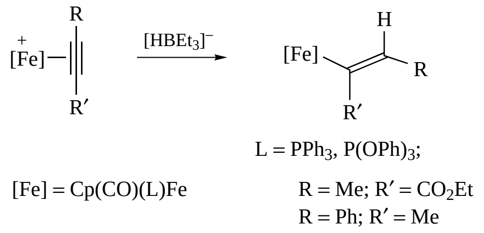
R
[Fe]
R′
[HBEt3]−
H
R
L = PPh3, P(OPh)3;
[Fe] = Cp(CO)(L)Fe
R = Me; R′ = CO2Et
R = Ph; R′ = Me

(23)

4.6 (η^2-C=X) Complexes

4.6.1 Preparation and Reactivity

A number of $(CO)_2(L)_2Fe(\eta^2$-carbonyl) complexes have been isolated (**113**) (η^2-C=O). These have been prepared by replacement of N_2 from μ-dinitrogen complexes (**112**) by the aldehyde in question.[166] Two phosphine or phosphite ligands appear to be necessary for satisfactory stability of these complexes. This is in apparent agreement with the results of both ab initio (*see Ab Initio Calculations*) and EHMO calculations and emphasizes the importance of d–π^* back-donation to the overall bonding in these complexes.[167] The EHMO calculations also emphasize the role of the repulsive four-electron ligand–ligand interactions in determining the likelihood of η^2 coordination.

Very limited reactivity studies have been reported for compounds of type (**113**). Complex (**113**; R = H, R′ = OMe) undergoes attack on electrophiles (E^+X^-) at oxygen to afford octahedral (*see Octahedral*) complexes (**114**), with the electrophile counterion occupying the final coordination site.[168]

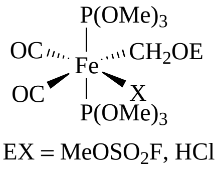
P(OMe)3
OC
CH2OE
Fe
OC
X
P(OMe)3
EX = MeOSO2F, HCl

(114)

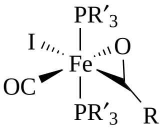
PR′3
I
O
Fe
OC
PR′3
R

(115)

Closely related are the η^2-acyl complexes of iron (**115**). These have been prepared by three methods. Loss of N_2 from (**112**) in the presence of an alkyl halide gives oxidative addition (*see Oxidative Addition*) to yield η^2-acyl complexes for some phosphine ligands.[169] Sodium amalgam reduction of Fe^{II} halide complexes (**116**), and exposure of the resulting (**117**) to an alkyl halide, gives similar complexes (equation 24).[170] Finally, placement of iron alkyl (aryl) complexes (**118**) under a CO atmosphere results in insertion to afford complexes (**119**) (equation 25).[171]

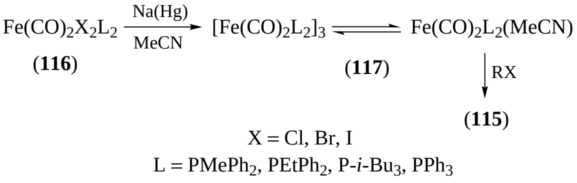
Fe(CO)2X2L2
Na(Hg)
MeCN
[Fe(CO)2L2]3
Fe(CO)2L2(MeCN)
(116)
(117)
RX
(115)
X = Cl, Br, I
L = PMePh2, PEtPh2, P-i-Bu3, PPh3

(24)

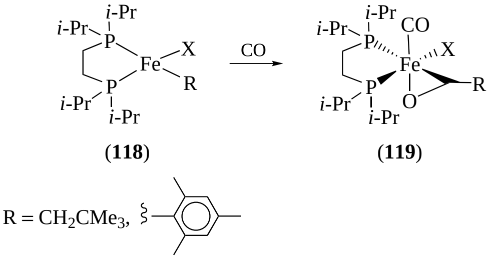
i-Pr
i-Pr
P
Fe
X
R
P
i-Pr
i-Pr
CO
i-Pr
i-Pr
CO
P
X
Fe
R
P
O
i-Pr
i-Pr
(118)
(119)
R = CH2CMe3,

(25)

η^2-Acyl complexes of the type (**115**) are in a closely balanced equilibrium with their isomeric metal alkyl complexes (**120**) (equation 26). The equilibrium between (**115**; R = Me, $R'_3 = Ph_2Me$) and its corresponding (**120**), for example, has a ΔH of $5.4\,kJ\,mol^{-1}$ (favoring **115**), with activation parameters of $\Delta H\ddagger = 41.9\,kJ\,mol^{-1}$ and $\Delta S\ddagger = -28\,J\,mol^{-1}\,K^{-1}$.**172** In fact, η^2-acyl complexes are isolated only with phosphine ligands which have a cone angle (*see Cone Angle*) >135°; less bulky phosphines usually give the alkyl complexes (**120**). The basicity of the phosphine appears to be much less important in the position of this equilibrium.

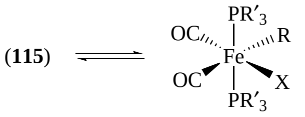

(26)

(**120**)

Reactivity studies of η^2-acyl complexes are limited. Compounds (**115**) react with CO to afford octahedral *cis,trans*-η^1-acyl complexes (**121**), probably via prior conversion to a coordinatively unsaturated monodentate (*see Monodentate Ligand*) acyl (equation 27). The *cis,trans*-(**121**) then isomerizes to *trans,trans*-(**121**). Phenylacetylene reacts with (**115**; R = R′ = Et) to give a mixture of acyl–alkyne coupling products,that is (**122**). Reaction with the R = i-Pr compound proceeds in a different way, by equilibration to the η^1-alkyl, followed by alkyl–alkyne coupling, and finally CO insertion to give η^2-acyl complex (**123**).**173**

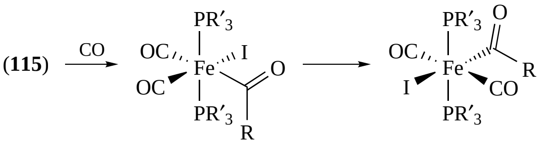

(27)

cis, trans (**121**) *trans, trans*

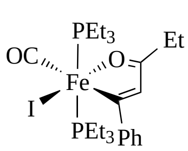

(**122a**)

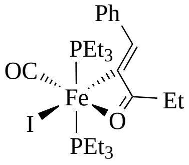

(**122b**)

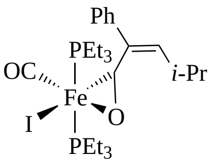

(**123**)

The related η^2-iminoacyl complexes (**124**) are known (η^2-C=N). These may be prepared by reaction of $[Fe(CO)_2(PMe_3)_2(Me)I]$ with t-butyl isocyanide, through an equilibrium with η^1-iminoacyl complex (**125**). The equilibration is catalyzed by halide ion, NO_3^-, and ClO_4^-, but not by BF_4^-, PF_6^-, or BPh_4^-; consequently, the pure compounds are isolated by precipitating the BPh_4^- salt from the mixture. The mechanistic details of the equilibrium have been investigated in detail.**174**

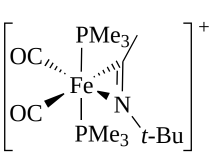

(**124**)

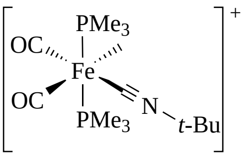

(**125**)

Examples of iron η^2-B=C complexes of a boraalkene are known as well. The $Fe(CO)_4$ complex of 9-fluorenylidene(tetramethylpiperidino)borane (**126**) has recently been prepared by the thermal reaction of the borane and (**2**) or by the photolytic reaction of (**1**) and the borane. The monophosphine/phosphite complexes are prepared from the tetracarbonyl by photolytic CO dissociation, followed by PR_3 addition.**175**

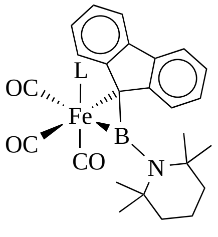

L = CO, PR_3

(**126**)

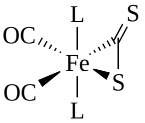

(**127**)

Thiocarbonyl (*see Thiocarbonyl*) compounds react rapidly with iron carbonyls, but only in a few cases are mononuclear η^2-C=S complexes realized. Most of the work in this area has resulted from the discovery that carbon disulfide reacts with iron carbonyl transfer agents, in the presence of phosphines or phosphites, to give complexes (**127**).**176** In several of these cases, it is possible to exchange one or both of the phosphine/phosphite ligands in high yield.

These compounds are nucleophilic at the noncoordinated sulfur, and undergo alkylation there with iodomethane or benzyl bromide to give initially (**128**) (which may be isolated as the PF_6^- salt) and ultimately (**129**) (equation 28). They also react with electron-deficient alkynes, possibly by a dipolar mechanism, to afford cyclized iron carbene complex (**130**).**177** Finally, compounds (**129**) are subject to attack by some nucleophiles; hydride attack occurs initially at the metal, but ultimately gives η^2-dithioester complexes, such as (**131**).**178**

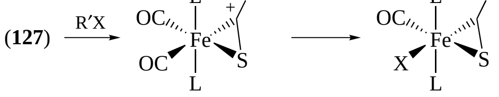

(28)

(**128**) (**129**)

η^2-Complexes of C=P bonds have been reported occasionally. In the majority of cases, the phosphorus atom is coordinated to another transition metal fragment, as the

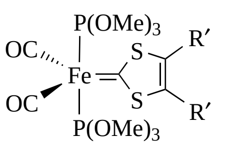

(130)

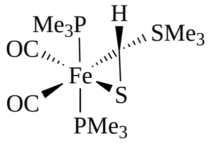

(131)

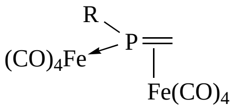

(132)

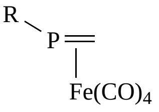

(133)

unpaired electrons on phosphorus make it the most Lewis basic site. Reaction of a bulky *P*-arylphosphaalkene with excess (**2**) gives complex (**132**). If only one equivalent of (**2**) is added, only traces of η^2-complex (**133**) can be detected.[179] Phospha-Wittig reagents react with (η^2-alkenal)Fe(CO)$_4$ complexes, with migration of the iron carbonyl residue, to give complex (**134**) (equation 29).[142] These complexes lose CO to give the η^4-complex upon heating.

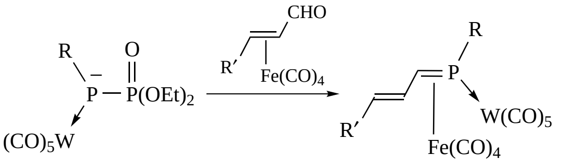

(29)

(134)

4.6.2 *Structure*

X-ray crystallographic (*see X-ray Crystallography*) studies on (η^2-C=X)FeL$_4$ complexes show a distinct structural similarity regardless of the nature of the heteroatom. Almost invariably, these complexes display a trigonal bipyramidal structure, with axial phosphine/phosphite ligands if present and the η^2-C=X ligand in the equatorial plane. For (η^2-carbonyl) complexes (**113**), bond lengths of 1.29 and 1.32 Å for C=O have been observed.[168] Limited spectral data have revealed a weak $\nu_{\mathrm{C=O}}$ of 1215 cm^{-1} in the IR spectrum in one case. The formaldehyde complexes have also given ^{1}H NMR chemical shifts of 3.99 and 4.75 ppm for the H$_2$C=O resonance, and a ^{13}C NMR chemical shift of 73.7 ppm (for the aldehyde carbon) in one case.

Crystallographic studies on (**113**) show the common trigonal bipyramidal structure, with axial phosphine ligands and equatorial η^2-carbonyl ligands; (η^2-acyl) complexes (**115**) show the same properties, with the additional feature that the O-atom of the acyl ligand lies *cis* to the halogen. Complexes (**119**) are somewhat exceptional in that one end of the bidentate (*see Bidentate Ligand*) phosphine is equatorial; the other axial site is occupied by halogen. Acyl C–O bond lengths of 1.23–1.28 Å have been reported for compounds of type (**115/119**). Bonding of iron to the CO unit is not symmetrical: Fe–C and Fe–O bond lengths of 1.8–1.83 and 2.19–2.25 Å, respectively, are typical. IR spectra give a typical $\nu_{\mathrm{C=O}}$ of 1586–1605 cm^{-1}. The acyl carbon resonance appears at 280 ppm in the ^{13}C NMR spectra but is not always observable at room temperature. Structurally, η^2-iminoacyl complexes (**124**) are strictly analogous to η^2-acyl complexes (**115**), with a C–N bond length intermediate between double and triple bond length (1.21–1.30 Å).

The boraalkene complex (**126**) shows many structural properties that parallel the η^2-carbonyl complexes, although the trigonal bipyramid is severely distorted. In the PMe$_3$ complex it is most reasonable to assign both the PMe$_3$ and B=C ligands as axial. Another distinctive feature in (**126**) is that the B atom on the η^2-B=C unit is closer to iron (2.125 Å) than the C atom (2.190 Å); this is indicative of the importance of back bonding from the Fe-centered 2a′ orbital to the boron-centered π^*_{BC} orbital.[175] The η^2-C=S complexes are similar, with the C=S bond length intermediate between single and double bond lengths (1.676 Å).[176]

5 η^3-ALLYL COMPLEXES[106,107]

5.1 Preparation

5.1.1 *(η^3-Allyl)FeL$_4$ Complexes*

The reaction of allyl halides with (**1**) or (**2**) under photolytic or thermal (40 °C) conditions results in oxidative addition of the C–X bond to afford (η^3-allyl)Fe(CO)$_3$X complexes (**135**) (equation 30). This is successful for a wide range of allyl complexes, including η^3-pentadienyl complexes.[180] In some cases, such as the 2-methoxy case, the η^3-allyl complex (for X = Cl, and partially for X = Br) undergoes subsequent HX loss to give a vinylketene complex.[181] Recently, the preparation of (**135**) via Me$_2$SiFe$_2$(CO)$_8$ and allyl halides has been reported.[182] (η^4-Diene)Fe(CO)$_3$ complexes undergo electrophilic attack by HCl (or DCl) to give *anti*-substituted complexes (**135**).[183] Finally, transfer of the allyl unit from other π-allyl transition metal complexes can give complexes of the type (**135**). Specifically, both the reaction of [PdX(η^3-allyl)]$_2$ with (**2**) or the combination of either [Pd(η^3-allyl)$_2$] or the corresponding Ni or Pt bis(allyl) complexes with (**2**), followed by X$_2$, have given (**135**) successfully.[107]

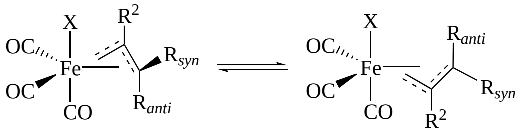

(30)

exo **(135)** *endo*

Reports of complexes of this class bearing phosphorus ligands also exist. The oxidative addition of allyl bromides and iodides to $Fe(PF_3)_5$ gives the analogous η^3-allyl complexes (**136**).**[184]** The reaction of (η^4-diene)$Fe(PMe_3)_3$ with CO_2 under pressure gives chelated π-allyl complex (**137**).**[185]**

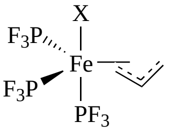

(136)

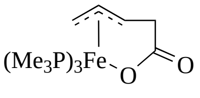

(137)

Closely related to (**135**) are the $[(\eta^3\text{-allyl})Fe(CO)_4]^+$ complexes (**138**). The predominant methods for the preparation of (**138**) include formation of η^2-tetracarbonyliron alkene complexes of allylic alcohols or ethers, followed by ionization of the ether or alcohol function by strong acid (HBF_4, HPF_6) or Lewis acid.**[186]** In fact, the simultaneous addition of allylic alcohol, (**2**), and HBF_4 together results in the formation of (**138**) in variable yields.**[187]** The second common method for the preparation of (**138**) employs previously formed (η^3-allyl)$FeX(CO)_3$ complexes (**135**), silver salts ($AgBF_4$, $AgClO_4$), and a CO atmosphere. Finally, the addition of strong acids (HBF_4, $HClO_4$, $HSbCl_6$) to (η^4-diene)$Fe(CO)_3$ complexes, in the absence or presence (for better yields) of CO, gives (**138**) in excellent yields.**[188]** The carbon atom protonated in this process invariably ends up as an *anti*-oriented substituent in the product allyliron. Performing a similar sequence on the analogous (diene)$Fe(CO)_3(PPh_3)$ complexes gives the allyliron monophosphine complex (**139a**).**[189]** The corresponding (η^2-diene)$Fe(CO)_4$ complex also affords (**138**) upon protonation by HBF_4; in this case the protonated carbon atom ends up predominantly as a *syn* substituent. It has also proved possible to perform a 'one-pot' reaction of this type, with diene, (**2**), and HBF_4 added all at once.**[187]** Numerous papers on the preparation and chemistry of enantiopure cationic (η^3-allyl)$Fe(CO)_4$ complexes have appeared; this work has been reviewed, and is exemplified by complexes (**140**).**[114,115]**

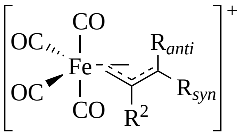

(**138**)

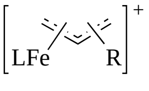

(**139a**) $L = (CO)_3(PPh_3)$
(**139b**) $L = \{P(OMe)_3\}_4$
(**139c**) $L = (CO)_2(PR_3)_2$

Chelated complexes related to (**138**) may be made by closely analogous methods. If the allylic alcohol in question contains a remote, coordinated alkene, protonation can result in (η^3-allyl)$Fe(CO)_3(\text{alkene})^+$ cations (**141**).**[107]** Electrophilic attack on (η^4-cyclooctatetraene)Fe$(CO)_3$ gives reorganization of the carbon framework, to afford a similar type of complex.**[107,190]** In the absence of added CO, addition of electrophiles to acyclic (η^4-diene)$Fe(CO)_3$ may also give chelated complexes. If the electrophile bears an appropriately located oxygen atom, the oxygen atom may occupy the final coordination site of the 18-electron (*see Eighteen Electron Compounds*) complex, to give cations of the type (**142**). Electrophiles that give these types of complexes are acetyl chloride/$AlCl_3$ and SO_2/BF_3 combinations.**[107]**

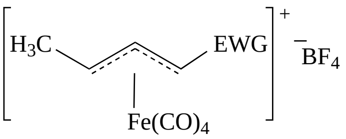

(**140**)
$EWG = CO_2Me, SO_2Ph$

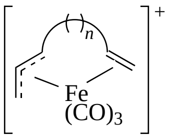

(**141**)

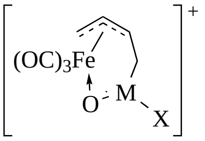

(**142**)
$M = S, X = OBF_3^-, OSbCl_3^-$
$M = C, X = Me$

Cationic phosphine/phosphite η^3-allyliron complexes are more rare. Aside from the previously mentioned report of the preparation of (**139a**), complex (**139b**) has been made from the reaction of allyl halides and $Fe[P(OMe)_3]_5$.**[191]** Additionally, complexes with mixed CO/phosphine ligands (**139c**) have been prepared by the reaction of either (**135**; X = Br) or $[(\eta^3\text{-allyl})Fe(CO)_3]_2$ with two equivalents of phosphine, followed by $NaBPh_4$ addition.**[192]**

5.1.2 *(η^3-Allyl)FeL$_3$ Complexes*

The most thoroughly investigated complexes of this general type are the neutral complexes with mixed nitrosyl and carbonyl ligands, (η^3-allyl)$Fe(CO)_2(NO)$ (**143**), and a review is available.**[193]** These are commonly prepared by the reaction of $Na[Fe(CO)_3(NO)]$ with allylic halides.**[194–197]** A variation employing the potassium salt and a mesylate leaving group (*see Leaving Group*) has been reported,**[198]** and addition of $Na[Fe(CO)_3(NO)]$ to the allyl transmetallation reagent $[(\eta^3\text{-allyl})PdX)]_2$ has been successful as well.**[197]** Also, complexes (**143**, $R^2 = C(O)R$) may be formed by treatment of allenes and alkyl halides with $Bu_4N[Fe(CO)_3(NO)]$ (TBAFe), or from alkenyl epoxides in the presence of acetyl chloride and pyridine (**143**, $R_{anti} = CH_2OC(O)Me$ or $CHPhOC(O)Me$).**[199,200]** A number of enantiomerically pure complexes have been made using TBAFe and either enantiopure allyl tosylates or allyl bromides bearing an amide-based chiral auxiliary.**[195]**

Diastereoselective complexation of the latter cases (**144a**) proceeded with only modest selectivity; for the former cases (**144b**) selectivity varied with solvent and temperature. The best case (dr, 97:3) utilized a 'matched' enantiopure allyl tosylate with a menthyl ester auxiliary. Finally, in a few cases the addition of $HFe(CO)_3(NO)$ across diene has also proved successful in the synthesis of (**143**).[106]

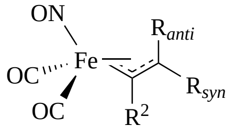

(**143**)

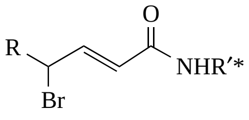

(**144a**) R = H or Me, R′ = chiral aux.

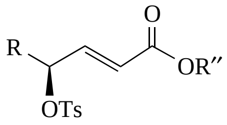

(**144b**) R = Me, R″ = Et or (−)–Menthyl

Substitution of the CO ligand for others in (**143**) has proved to be fairly facile. The mixing of equimolar amounts of (**143**) and a number of phosphines or phosphites results in the formation of complexes (**145**),[28,201] through the intermediacy of (η^1-allyl)$Fe(CO)_2(NO)(PR_3)$ complexes. Selected compounds of type (**145**) have also been prepared by the allyl halide attack method.[202] Even in compound (**145**; $L = P(OMe)_3$) the remaining CO ligand has been shown to be capable of replacement by an NO ligand from $NO^+PF_6^-$ to give cationic complexes (**146**).[203]

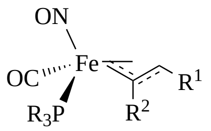

(**145**)

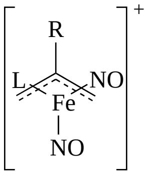

(**146**)

Allyltricarbonyliron anions (**147**) have been prepared by the reduction of the corresponding halides with sodium amalgam.[204] Although little work has been done on substituted analogs of (**148**), two other related anionic species have received attention. Proton abstraction of (η^4-cycloheptatriene)$Fe(CO)_3$ results in an anionic species which was eventually determined to be the (η^3-cycloheptatrienyl)$Fe(CO)_3{}^-$ complex (**148**).[205] Additionally, subjecting the (η^5-indenyl)$Fe(CO)_2{}^-$ anion to an atmosphere of CO results in formation of η^3-indenyl complex (**149**).[206]

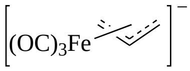

(**147**)

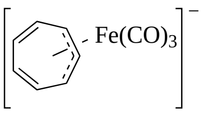

(**148**)

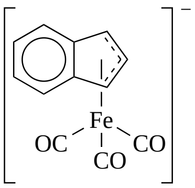

(**149**)

Although protonation of diene complexes with strong acids is one the most common methods for preparation of (η^3-allyl)$FeL_4{}^+$ complexes, it is now clear that the initially formed species are the formally 16-electron (η^3-allyl)$FeL_3{}^+$ complexes (**150**; L = CO, $P(OMe)_3$). These complexes may be observed spectroscopically at low temperatures for the L = CO complexes (Section 5.2.2), but upon warming they convert to (**138**).[207] The L = $P(OMe)_3$ complexes are stable enough to allow isolation at ambient temperatures.[208]

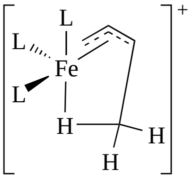

(**150**)

The 17-electron (*see Seventeen Electron Configuration*) (η^3-allyl)FeL_3 radical species (**151**) are also known.[209] These are prepared by the one-electron reduction of allyltricarbonyl halides (**135**; X = CO) or of the (η^3-allyl)$Fe[P(OMe)_3]_3{}^+$ cations ($X = P(OMe)_3$). For the X = CO complexes, the radical species is in equilibrium with dimeric allyl (**152**) (the dimer can be isolated as a solid, whereas (**151**) is increasingly prevalent at higher dilution). Increasing allyl substitution and increasing the number of phosphine substituents increases the relative concentration of (**151**), to the point where the X = $P(OMe)_3$ complexes are paramagnetic (*see Paramagnetism*) monomers even in the solid state.[209]

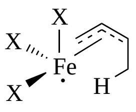

(**151**)

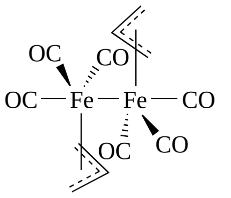

(**152**)

Bis(allyl)iron complexes, (η^3-allyl)$_2FeL_2$ (**153**), are encountered only infrequently. The parent complex (**153a**) has been prepared by allylation of allyltricarbonyliron anion (**147**), but it is an unstable complex, the allyl units spontaneously dimerizing at room temperature. Increased stability in this class of compounds is realized if both allyls are part of a chelating ligand (*see Chelating Ligands*), or if the CO ligands are replaced by phosphine or phosphite ligands. The chelating bis(allyls) have been prepared either by coupling of (η^4-diene)$_2$Fe(CO) complexes (equation 31),[106,210] or in selected cases through nucleophilic attack of aryllithiums on (diene)Fe(CO)$_3$ complexes, which proceeds with ring opening and carbonylation.[211] The phosphine/phosphite complexes (**153a,b,c**) may be prepared in good yields for the allyl, 2-methylallyl, and η^3-pentadienyl complexes by the action of allylmetals (or pentadienylmetals) on Cl$_2$Fe(PR$_3$)$_2$.[212,213] Homoleptic (*see Homoleptic Compound*) bis(allyl)iron complex (**154**) has been recently prepared and characterized by X-ray crystallography; the SiMe$_3$ of each allyl are in a *syn, anti* arrangement in order to minimize their steric bulk.[214] This complex was stable under an inert atmosphere at room temperature, whereas the bis(allyl)Fe(PR$_3$)$_2$ complexes typically decompose above 0 °C. Bis(allyl) complexes can also be prepared from trimethylenemethane (TMM) complexes (Section 6.1).

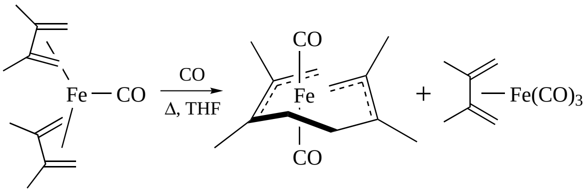

(31)

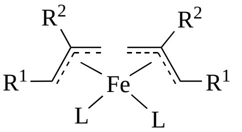

(**153a**) L = CO, R^1 = R^2 = H
(**153b**) L = PR$_3$, R^1 = R^2 = H
(**153c**) L = PR$_3$, R^1 = H, R^2 = Me
(**153d**) L = PMe$_3$, R^1 = vinyl, R^2 = H

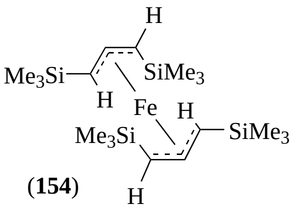

(**154**)

5.1.3 (η^3-Allyl)FeL$_3$R Complexes

The chemistry of this class of complexes is dominated by the π-allyliron tricarbonyl lactone complexes (**155**), which have been studied extensively and reviewed.[215–217] Compounds (**155**) are normally prepared by reaction of vinyl epoxides with a source of ‘Fe(CO)$_4$’, such as (**1**) and photolysis, (**2**) and heat, or (**2**) in Tetrahydrofuran (THF) or with ultrasonication (*see Sonication*); the latter two methods are considered to be superior. It has been reported that butene-1,4-diols, particularly the *cis* isomers, (with or without Lewis acids), 3-butene-1,2-diol sulfites, 3,6-dihydrooxazines, or related compounds also give (**155**) with (**2**).[218] The complexes are isolated as *anti* isomers at C-1. Substituents at C-3 are oriented *syn* when not constrained in a ring, whereas additional substitution at the oxygen-bearing C atom results in a diastereomeric mixture of products (see below).

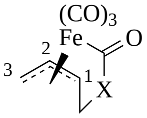

(**155**) X = O
(**156**) X = NR′

A number of enantiomerically pure complexes have been made, and this chemistry has been used in several natural product syntheses.[219] Enantiopure complexes are readily available from the corresponding vinylic epoxides, and in cases where diastereoselective complexation is possible, diastereoselectivities tend to be moderate (typically 3:1–4:1). The rationale for the origin of this diastereoselectivity has been proposed to derive from a preferential complexation of a Fe(CO)$_4$ fragment to the alkene *anti* to the epoxide.[217] Since the initial vinyl epoxide is conformationally flexible, four diastereomeric π-complexes would be produced as a consequence of *anti* or *syn* complexation to the *s-trans* or *s-cis* conformers. Isomerization of these initial π-complexes to alkoxy-π-allyl species would then enable interception of an iron-bound carbonyl ligand by the alkoxide to afford diastereomeric lactone complexes. Fortunately, equilibria between the two possible *trans* π-allyl complexes and their more stable *cis* π-allyl analogs simplifies the outcome significantly. Thus, for *trans* vinyl epoxides, the major diastereomer typically is the one designated as *endo cis* (the C-1 substituent points toward the iron atom); the minor diastereomer corresponds to the *exo cis* isomer (the C-1 substituent points away from the iron atom) (Scheme 51). For *cis* vinyl epoxides, this outcome is reversed – the *exo cis* isomer is the major product.

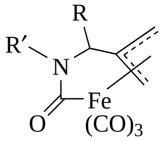

(**157**)

The corresponding ferrilactams (**156**), which have also been the subject of much attention, are available by the nucleophilic substitution of (**155**) by amines in the presence of a Lewis acid, usually ZnCl$_2$. The substitution occurs with allylic transposition,that is, attack at C-3 of (**155**). In selected cases, compounds of the type (**156**) have been prepared by oxidative addition of vinylaziridines or *cis*-4-amino-l-butenols with (**2**). A bridged ferrilactam bonded through C-2 of the allyl (**157**) unit has been reported recently and was prepared by way of oxidative addition of a cyclic allylic

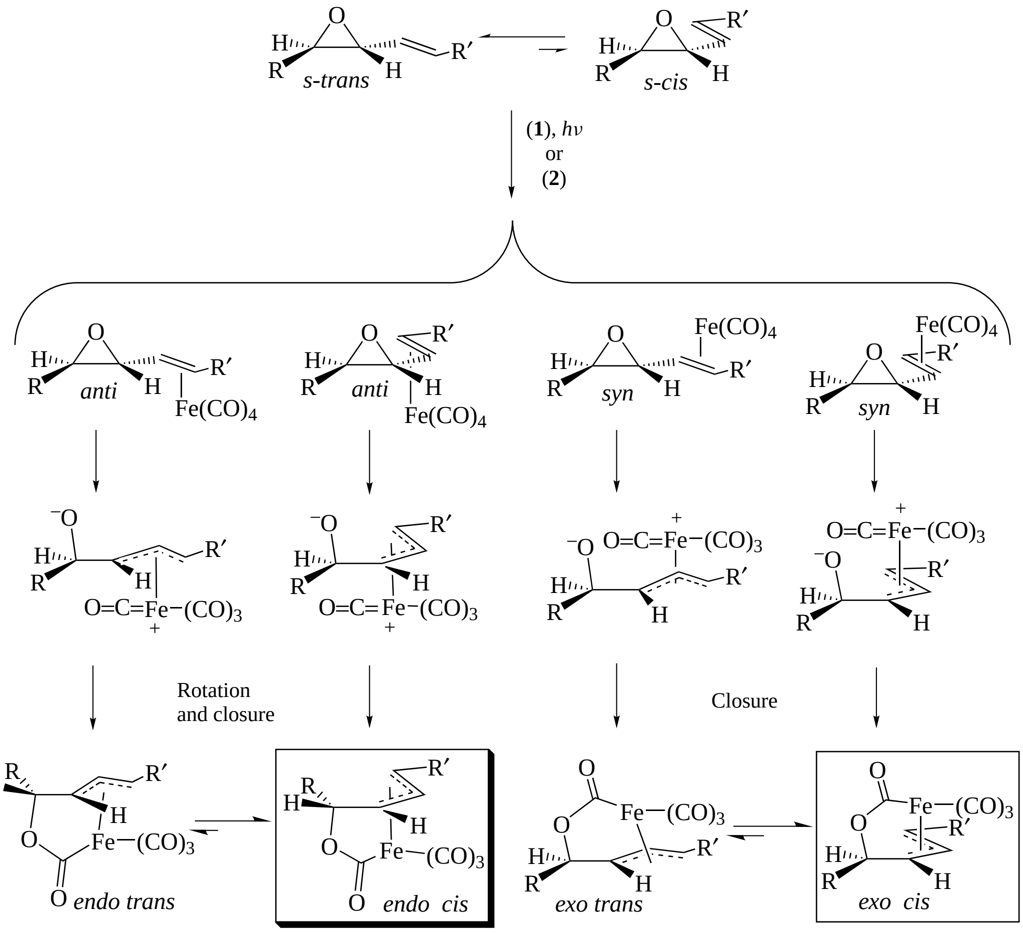

Scheme 51

carbamate; corresponding bridged lactone complexes are also known.[220] Finally, an enantiopure *exo*-π-allyltricarbonyliron lactam has recently been prepared from the corresponding *cis* vinyl aziridine; the complex diastereomer ratio was 18:1 (equation 32).[221]

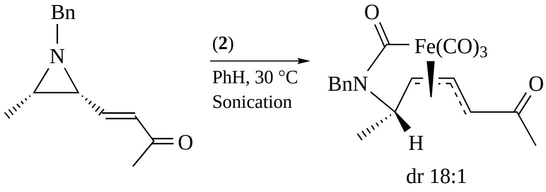

(32)

Other reports of (η^3-allyl)Fe(CO)$_3$R complexes are much more scattered and much less systematic. At least three general types of reactions have been observed in more than one case. First, the reaction of (diene)Fe(CO)$_3$ complexes with electrophilic alkenes gives allyliron complexes in two different ways. If the diene in question is acylic, electrophilic attack at C-1 of the diene gives compounds of type (**158**) (equation 33). In the case of substituted η^4-cycloheptatriene–or azepine–Fe(CO)$_3$ complexes, reaction with TCNE (or less often 4-phenyltriazoline-3,5-dione) gives kinetic [3 + 2] cycloaddition reactions, affording complexes of the type (**159**) (equation 34). These complexes interconvert with other, isomeric σ,π-adducts of this type, as well as (η^4-diene)Fe(CO)$_3$ complexes, by what Goldschmidt has coined [2,2]-, [3,3]-, or [4,4]-sigmahaptotropic rearrangements.[222] Both the cycloaddition and the rearrangements are considered to be concerted, nonsynchronous reactions. In a related transformation, η^4-vinylketene iron tricarbonyl complexes react with alkynes to afford (**160**), a vinylic analog of (**158**) (equation 35). Enantiomerically pure vinylketene complexes undergo this reaction without loss of planar chirality.[223] Second, vinylcyclopropanes undergo, in some cases, oxidative addition with ring opening with iron carbonyls to give (η^3-allyl)(η^1-alkyl)Fe(CO)$_3$ complexes.[107] Although only a minor product in the case of vinylcyclopropane itself, other cases, such as in semibullvalenes, give this reaction in consequential yields of (**161**) (equation 36). (η^3-Allyl)(η^1-alkyl)Fe(CO)$_3$ complexes and/or the corresponding (η^1-Allyl)(η^1-alkyl)Fe(CO)$_3$ complexes are likely intermediates in the thermal conversion of vinylcyclopropanes to η^4-diene Fe(CO)$_3$ complexes using (**1**), or of enantiomerically pure vinylcyclopropanes into alkyl-substituted cyclohexenones of high optical purity.[224,225] Finally, attack of soft nucleophiles (Nu^-) on (η^5-pentadienyl)$Fe(CO)_3{}^+$ cations can occur at C-2 of the pentadienyl unit to afford (**162**) (equation 37) (Section 7.1.2).[226]

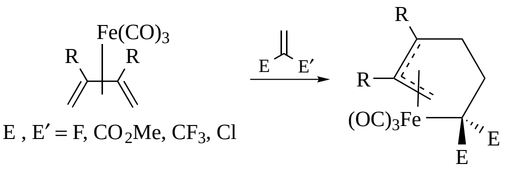

(33)

(**158**)

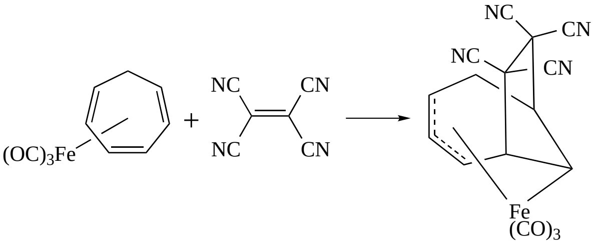

(34)

(**159**)

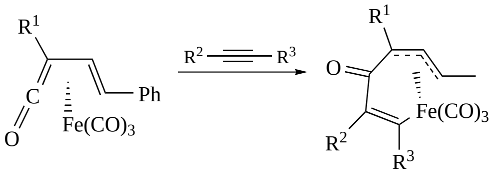

(35)

(**160**)

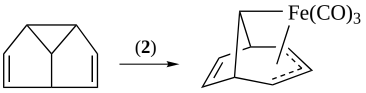

(36)

(**161**)

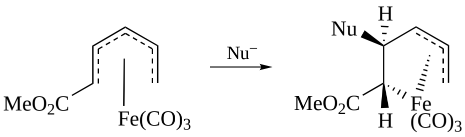

(37)

(**162**)

5.1.4 (η^3-Allyl)FeCp(CO) Complexes

Each of (η^1-allyl)Fp, (η^1-pentadienyl)Fp, and (η^1-cyclopentadienyl)Fp complexes undergo photolytic loss of CO to afford their respective Cp(CO)Fe(η^3) complexes.[26,27,227] In both the cases of allyl and acyclic pentadienyl complexes, the η^3-complexes are stable compounds, isolated as a mixture of *exo* and *endo* complexes, with the *exo* complex being more thermodynamically stable. In the pentadienyl case a significant amount of the (η^5-pentadienyl)FeCp complex is also isolated. In the case of (η^1-cyclopentadienyl)Fp complexes the η^3-complexes are observable (again as an *exo*/*endo* mixture) only at 77 K, by IR spectroscopy. At room temperature, only the (η^5-cyclopentadienyl)FeCp is realized.[228]

Although less common than the related (η^1-allyl)Fp complexes (Section 3.2), (η^3-allyl)FeCp(CO) complexes (**163**) are often encountered. The most common method for preparation of (**163**) involves photolytic ejection of a CO ligand from (**9**). On occasion, CO loss also occurs thermally. This transformation is stereospecific: *trans* (**14**) and *cis* (**14**) afford *syn* and *anti* (**163**), respectively. This approach is successful for a wide range of cases, including alkylidenyl, vinyl, and carboxyl substituents.[26,227,229,230] In the case of (η^1-benzyl)Fp complexes, low-temperature photolysis gives the η^3-benzyl complexes (**164**), which decompose at 25 °C over a period of 1–2 h.[231]

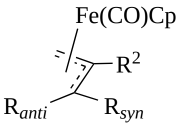

(**163**)

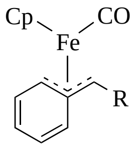

(**164**)

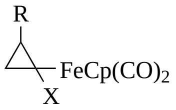

(**165**)

X = OMe, OEt, SPh, Ph
R = H, Me, F

Other syntheses of compounds of the type (**163**) are more specialized. Photolysis of (cyclopropane)Fp complexes (**165**) in several cases ultimately gives cyclopropane ring opening to yield stereoisomeric mixtures of (**163**; $R^2 = X$) when (**165**) possesses β-substituents (the ring opening is not regioselective for R = H in **165**).[232] Nucleophilic attack of alkoxide ion ($R'O^-$) upon (η^2-allene)Fp^+ cations occurs often[27] but not always with CO insertion to give C-2 substituted complexes (**163**; $R = CO_2R', OR'$).[233]

Finally, the coupling reaction of vinyl and alkylidene (*see Alkylidene*) ligands in complexes of the type (**166**) results in the formation of (η^3-allyl)FeCp(CO) complexes (equation 38). The vinyl substituent in these reactions is most often an enolate, whereas the alkylidene unit is formally of the Fischer carbene type.[234] The ultimate product depends upon the starting material and additional reagents. In the case of (ferra-β-diketonato)difluoroboron complexes (**167**), the resulting anion is isolated as tetramethylammonium salt (**168**). In the case of Fp(acyl) complexes as starting materials, benzoylation of the resultant anions gives complexes (**163**; R_{syn} = OBz, R^2 = OBz, OMe, Me).

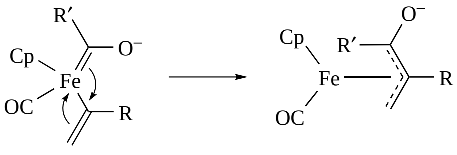

(38)

(**166**) R = O−, Me, OMe

The corresponding phosphine/phosphite complexes (**169**) may be made, in at least selected cases, from (**163**) by photolysis in the presence of the phosphine or phosphite in

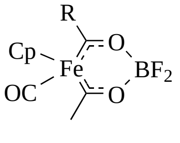
(**167**)

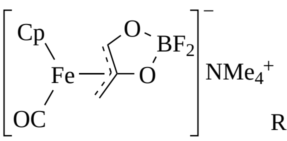
(**168**)

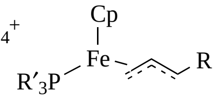
(**169**)

question ($R_{syn} = CO_2Me$).**230** In the case of cyclopropane ring-opening reactions of (**165**), the L = PPh_3 complexes undergo an analogous reaction under thermal conditions to afford (**169**).

5.2 Properties

5.2.1 (η^3-Allyl)FeL_4 Complexes

In (η^3-allyl)$Fe(CO)_3X$ complexes (**135**), the molecules are oriented in what is normally considered an octahedral assembly of ligands around iron (allyl being bidentate) with a *fac* arrangement of the carbonyls. The allyl unit may be oriented in an *endo* or *exo* manner. Spectroscopic studies show that the two isomers are in equilibrium, although the coalescence temperature was above the decomposition temperature of the sample. Furthermore, the *endo* isomer predominates, although the *endo*/*exo* isomer ratios may vary from very large (minor isomer not observable) to 1.3:1.**235**

In the crystallographic structure of compounds of type (**135**), the *endo* isomer is the one observed. In the allyl unit the central carbon is normally found to be closer to Fe than the terminal carbon atoms; for example, the Fe–C bond distances are 2.058 and 2.126 Å, respectively, in (η^3-allyl)$Fe(CO)_3Br$.**236** This trend may be overridden by other effects.**237**

In the case of $[(\eta^3\text{-allyl})Fe(CO)_4]^+$ cations (**138**), there is no possibility for *endo*/*exo* isomerism. Crystal structures of this type of complex have been reported, and are similar to those of (**135**). Noteworthy in the character of these complexes is their geometric stability: the *syn* and *anti* isomers do not interconvert unless heated to 60–70 °C for extended periods of time.**186**

The NMR spectroscopy of (η^3-allyl)iron complexes reveals a consistency across the various types of complexes. The relative shielding of the protons on the allyl unit is invariably $H_{anti} > H_{syn} > H_2$ (see Table 1). The coupling constants are also fairly consistent and extremely useful in isomer determination. The ^{13}C NMR spectra display a similar trend, with resonances of $C_{1,3}$ further upfield than that of C_2. Substitution on any of the atoms of the allyl unit shift both the ^{13}C resonances of the substituted atoms and the resonances for any remaining protons on that atom significantly downfield; the changes in the other ^{13}C and ^1H resonances are far less significant. For complexes of the type (**135**), the ^1H NMR spectroscopy is complicated in some cases by the presence of both *endo* and *exo* isomers, although in a large number of cases the *exo* isomer is so minor as to be barely observable. For those complexes with significant percentages of *exo*, apparent, H_{anti} and H_{syn} protons resonate upfield and H_2 protons resonate downfield relative to the *endo* isomer.**235**

The most noticeable difference between NMR spectra of (**135**) and (**138**) is revealed in the ^{57}Fe NMR.**238** In these spectra the iron allyl cations (**138**) resonate at much higher field (800–1000 ppm) than the halides (**135**) (1235–1700 ppm).

5.2.2 (η^3-Allyl)FeL_3 Complexes

A report of the X-ray crystallographic studies of enantiopure (η^3-allyl)$Fe(CO)_2(NO)$ complex (**170**) has appeared, though little detail was provided.**196** The same report described the CD spectrum of this complex in more detail; the negative band at *ca.* 350 nm and the positive band at *ca.* 450 nm can be used to assign the configuration of the complex. Diastereomeric complexes exhibit the opposite Cotton effect. The crystal structures of corresponding monophosphine complexes (**145**) have been determined.**198,239** It is possible to consider these complexes as either trigonal bipyramidal (bidentate allyl) or tetrahedral (*see Tetrahedral*) (monodentate allyl), with the central carbon of the allyl closer to the iron atom (2.084 Å) than the terminal carbon atoms (2.117 and 2.142 Å). These complexes are chiral at the iron atom, and it has proved possible to separate the diastereomeric complexes formed by enantiomerically pure aminophosphines.

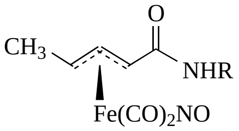
R = (*S*)-CH(CH_3)Ph

(**170**)

Table 1 ^1H, ^{13}C NMR data for η^3-allyl complexes

Complex	H_{anti} (δ, ppm)	H_{syn}	H_2	J_{syn-H_2}	J_{anti-H_2}	$J_{syn-anti}$	C_1	C_2
(**129**), X = Br, *endo*	3.48	4.37	4.92	13–15	7–9	–	65.0	101.7
(**132**)	2.35	4.24	5.26	12–14	6–8	1–3	56.8	99.2
(**137**)	2.12	2.96	5.70	~12	~6	–	–	–
(**155**) *exo*	0.47	2.72	4.33	11	7	2.5	–	–
(η^3-allyl)$Fe(CO)_3Me$	2.18	3.04	3.92	12.2	7.5	2	–	–

It is possible to prepare the *anti* and *syn* isomers of (**143**) stereospecifically from the (Z)- and (E)-mesylates, respectively, and under room temperature conditions they do not interconvert. Replacement of the CO ligand with phosphine (PPh_3, 50 °C) gives only *syn*-(**145**) from either isomer of (**143**); this constitutes evidence for the possible intermediacy of an η^1-allyl in the substitution.**198**

The formally 16-electron (η^3-allyl)$FeL_3{}^+$ complexes (**150**) have been studied crystallographically for the (η^3-cyclooctenyl)$Fe(P(OMe)_3)_3{}^+$ complex and by low-temperature spectroscopy for the $L = P(OMe)_3$ and $L = CO$ complexes.**207,208** Prominent among the structural features of these compounds is an agostic C–H interaction with iron (a 3-center, 2-electron bond). The crystal structure possesses a long C–H bond (1.164 Å) and a Fe–H contact of 1.874 Å. Spectroscopically, both the ^{13}C and ^1H NMR spectra are fairly unexceptional for the allyl portion, whereas the agostic H resonance (−14.59 ppm when frozen out at −86 °C in the parent complex) and C–H coupling constant ($J_{CH} = 106$ Hz for the cyclohexenyl complex) provide strong evidence for this type of bonding. Structures of this type have also been studied calculationally by both EHMO and Intermediate neglect of differential overlap (INDO) methods.**240**

In contrast to the tricarbonyl halide complexes, it is the *exo* conformation of (η^3-allyl)FeCp(CO) complexes (**163**) which is preferred, and at equilibrium only traces of the *endo* isomer can be observed. Existing crystal structures of members of this class are of the *exo* conformation.**26,27,227,229,230** Reasonable percentages of the *endo* conformer are realized upon low-temperature photolyses of their (η^1-allyl)Fp precursors, however, and the activation barrier to *endo*/*exo* conversion has been determined to be $\Delta G\ddagger = 100.8\,\mathrm{kJ\,mol^{-1}}$ for the 2-methallyl complex.**227** In addition, the *anti* isomers, which can be prepared stereospecifically from the (η^1-allyl)Fp complexes, isomerize to the *syn* isomers with brief heating. The ^{57}Fe NMR spectra are known for several of the complexes where CO has been replaced by a phosphine or phosphite (**145**); the chemical shift is highly dependent on the nature of the phosphorus ligand.**241**

In contrast to almost all other iron allyls, the ferrilactone (**155**) and ferrilactam (**156**) allyliron complexes are more stable in their *anti* configuration. Their structures can be considered to be a distorted octahedron with *fac* arrangement of CO ligands. In other respects, the structure is typical of other η^3-allyls, and the NMR spectroscopy is characteristic of an *anti* monosubstituted iron allyl in terms of both chemical shifts and coupling constants.**218,242**

5.3 Reactions

5.3.1 (η^3-Allyl)FeL_4 Complexes

Reactions of (η^3-allyl)$Fe(CO)_3X$ complexes (**135**) have been restricted to silver salt-induced halide replacement, CO replacement by phosphines, or conversion to allyl cations (**138**) (Section 5.1.1). There exists a report of conversion of (**135**; $X = Cl$) to η^1-allyliron complexes by reaction with thioamide ion; the transformation includes CO insertion into the Fe–N bond.**243**

A noteworthy work on complexes of this type has been on the oxyallyl complexes (**171**) and their related dimers (**172**).**237,244** Despite the fact that only electrophilic substitution is observed in the reactions of these complexes and their derived (oxyallyl)$Fe(CO)_4$ cations, these compounds, or structurally very similar ones, have been proposed as intermediates in iron carbonyl mediated [4 + 3] cycloaddition reactions of α,α'-dibromoketones and dienes.**245**

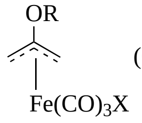

(**171**)
R = H, SiMe3
X = Br, Cl

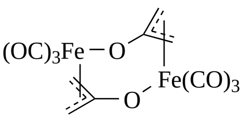

(**172**)

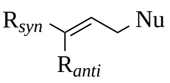

(**173**)

(η^3-Allyl)$Fe(CO)_4{}^+$ cations (**138**) are considerably more electrophilic than (**135**), and are more useful for C–C bond-forming reactions with nucleophiles as a result. Compounds of type (**138**) have been shown to react at the terminal carbon atoms with amines, phosphines, highly stabilized carbanions, electron-rich arenes, allylmetal reagents (silanes, stannanes, (**12**)) and silyl enol ethers, silyl ketene acetals, and ester dienolates. The product iron alkene complexes are often quite unstable, and are not isolated; decomplexation to the alkenes (**173**) is either spontaneous or induced by oxidation. The reactions of (**138**) with organometallics has only seen sporadic attention; organocadmium reagents give fair yields of alkylation, whereas organocopper compounds, RCu(CN)ZnI, give mixtures of alkylation and acylation. Allylic deprotonation to give (η^4-diene)$Fe(CO)_3$ complexes is sometimes a competing reaction. Regiochemistry of attack is predominantly at the least-substituted side of the allyl, and remote to electron-withdrawing or trialkylsilyl groups, whereas stereospecific *anti*-(**138**) to *cis*-alkene and *syn*-(**138**) to *trans*-alkene transformations are observed.**186,246** More recently it has been reported that this nucleophilic attack proceeds with high selectivity for the face *anti* to iron, thus allowing the preparation of highly enantiomerically enriched products from enantiomerically pure allyliron complexes.**113** This reactivity has been utilized with enantiopure complexes of type (**140**), where a number of soft nucleophiles add stereoselectively *anti* to the iron fragment and exclusively γ to the electron-withdrawing group to produce η^2-iron complexes that were subsequently demetalated with ceric ammonium nitrate. This methodology was featured in a number of natural product syntheses.**114**

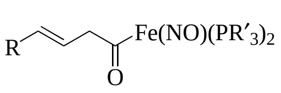

(174)

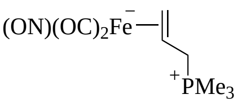

(175)

$(PR'_3)_2 = [P(OMe)_3]_2$, $[P(OEt)_3]_2$, dppe

5.3.2 *(η^3-Allyl)FeL$_3$ Complexes*

Complexes of type (**143**) behave much like (η^3-allyl)Fe(CO)$_4^+$ cations of type (**140**) with respect to the addition of soft nucleophiles (amines, malonate anions,and so on), though regioselectivity appears to be more substrate-dependent.[247] Although the conversion of (η^3-allyl)Fe(CO)$_2$(NO) complexes (**143**) to their monocarbonyl/monosphosphite analogs (**145**) has been described, there is in some cases a side product, acyl-iron complexes (**174**), which arise from CO insertion into the least-substituted terminus of the allyl ligand. This is also the dominant mode of reaction with dppe as added ligand.[175] If more basic trialkylphosphines are reacted with (**143**), nucleophilic attack at the allyl ligand occurs to afford (**175**).[248] Terminal allyl carbon attack has also been observed with highly stabilized carbanions, such as malonate, or with enamines to ultimately give substitution products of the type (**173**).[194,249] Like cations (**138**), stereospecific production of alkene products is possible, and the attack is predominantly at the less-substituted allyl terminus on the allyl face opposite that of the iron residue. Curiously, selected substituted compounds of type (**143**) also undergo reaction with allylic halide electrophiles, the yields of which are enhanced by added P(OPh)$_3$. This transformation is thought to occur by oxidative addition of the allyl halide to the generated (**145**), affording intermediate (**176**), which undergoes subsequent reductive elimination to give (**177**) (equation 39).

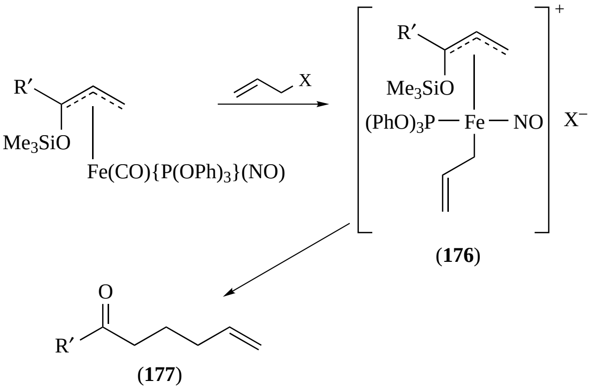

(39)

The cationic dinitrosyl complexes (**146**) are apparently much more electrophilic than (**143**). Studies of the reactivity of (**146**) have been focused on attack of coordinated organic ligands of other transition metal complexes, such as the cyclooctatetraene ligand in L$_3$M(cot) complexes (M = Fe, Ru) and Cp′Co(cot) complexes (Cp′ = Cp, Cp*), the cyclopentadienyl ligand of CpRh(cot) complexes, and the cyanide ligand of (dppm)$_2$Mn(CO)(CN) complexes.[250] Subsequent ligand rearrangements are often observed in these transformations.

As expected, allyltricarbonyliron anions (**147**) possess nucleophilic reactivity. Reaction of these species with alkyl halides (RX) gives initial attack at iron, which is followed by CO insertion and acyl–allyl coupling. Subsequent reorganization of the ligand following PPh$_3$ addition gives an (enone)Fe(CO)$_2$(PPh$_3$) complex (**178**). The use of different trapping ligands (PPh$_3$ or CH$_3$CN) gives different regioselectivities and stereoselectivities.[204,251] Phosphorus-based electrophiles appear to react at iron, without subsequent rearrangement.[252] Work on the (η^3-heptatrienyl)Fe(CO)$_3^-$ anions (**148**) reveals the following reaction dichotomy: C-, Si-, and Ge-based electrophiles give ultimate reaction at allyl carbon (**179**), whereas Sn- and Pb-based electrophiles and transition metal carbonyl halides give ultimate reaction at Fe to give cyclic bimetallic species (**180**).[253]

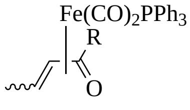

(178)

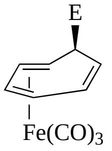

(179)

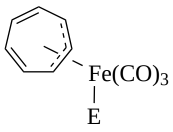

(180)

The facile allyl–allyl coupling of parent bis(allyl) complexes (**153a**) has already been mentioned. Related reactions have been observed in the (η^3-pentadienyl)$_2$Fe(PR$_3$) complexes (**181**). Heating (η^5-pentadienyl)(η^3-pentadienyl)Fe(PR$_3$) complexes (**182**) in the presence of additional phosphine results in transient formation of (**181**), which undergoes interligand coupling to give bis(η^4-diene) complex (**183**) (equation 40).[210] In these type of complexes, removal of the allyl ligand by oxidation or protonation is facile. In one case, cycloaddition of (**153a**) with TCNE has been reported to give, after PPh$_3$ addition, (**184**).[254]

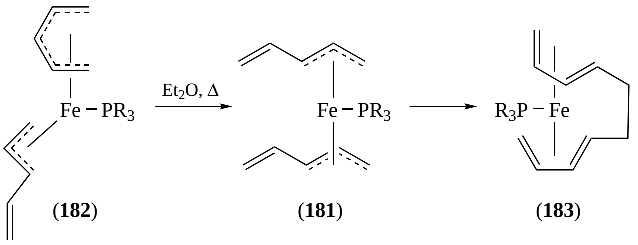

(40)

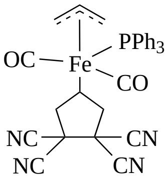

(184)

5.3.3 *(η^3-Allyl)FeL$_3$R Complexes*

As π-allyliron tricarbonyl lactone complexes (**155**) have been the subject of extensive study by Ley, their modes of reactivity are well-established.[215–217] The reaction with nucleophiles, such as amines, to give the corresponding ferrilactams (**156**) has previously been discussed (Section 5.1.3). On the other hand, oxidation of (**155**), normally by Ceric ammonium nitrate (CAN), affords mixtures of α-vinyl-β-lactones (**185**, major) and β, γ-unsaturated-δ-lactones (**186**, minor). However, the δ-lactones are often obtained in much higher yield by subjecting complexes (**155**) to CO under pressure. CAN oxidation of the ferrilactams (**156**) and (**157**) give predominantly α-vinyl-β-lactams (**187**) and β-methylene-γ-lactams (**188**), respectively.[215–218] The oxygen- or nitrogen-bearing carbon atoms in (**155–157**) give (**185–187**) with retention of configuration at the N- or O-bearing carbon atom, so that enantiomerically pure or enriched complexes do not lose their optical activity upon reductive elimination. This methodology has been used extensively in the synthesis of many naturally occurring molecules of biological importance (*see* ***Organic Synthesis using Transition Metal Complexes Containing π-Bonded Ligands***). Another synthetically useful transformation of complexes of type (**155**) involves basic hydrolysis with Ba(OH)$_2$; η^4-iron diene complexes are formed with concomitant decarboxylation of the lactone complex. No loss of enantiomeric purity is observed when enantiopure lactone complexes are employed. Finally, lactone complexes (**155**) can be used as a stereodirecting group in a manner similar to that of η^4-iron diene complexes (Section 6.3). A ketone adjacent to the π-allyliron tricarbonyl lactone complex is subject to nucleophilic addition *anti* to the metal fragment; allyl stannanes (in the presence of BF$_3$Et$_2$O) and organoaluminum reagents have been used to prepare diastereomerically pure alcohols. Decomplexation and simultaneous reduction of the lactone moiety of the complex to afford an alcohol may be effected with sodium triacetoxyborohydride.[255]

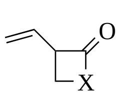

(**185**) X = O
(**187**) X = NR

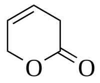

(**186**)

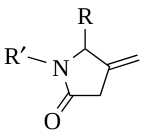

(**188**)

Complexes (**160**) (see equation 35) undergo conversion to phenols upon thermolysis.[223] Alternatively, treatment with AlCl$_3$ under a CO atmosphere gives an η^4-iron cyclohexadienone complex; thermolysis or treatment with CuCl$_2$ affords a phenol as well. Complexes (**162**), derived from nucleophilic addition to (η^5-pentadienyl)Fe(CO)$_3{}^+$ cations (see equation 37), can be converted to vinyl cyclopropanes by using CAN (equation 41).[256]

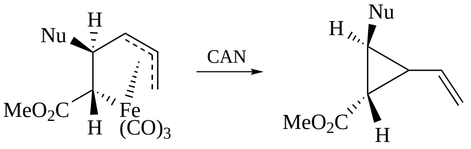

(**162**)

(41)

5.3.4 *(η^3-Allyl)FeCp(CO) Complexes*

Reactivity studies of compounds of this class have received little attention. Aryl-substituted complexes (**161**) (R$_{syn}$ = Ar) are, under heat and photolysis, sources of radical coupling reactions with acrylonitrile to give predominantly (**189**). As the conditions for reaction are also sufficient for conversion of the corresponding (η^1-allyl)Fp complexes (**12**) to (**161**), compounds of type (**12**) may also be used as reagents.[257]

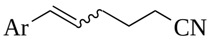

(**189**)

5.4 (η^3-Cyclopropenyl)FeL$_3$Complexes

η^3-Cyclopropenyl iron complexes have been prepared by treatment of cyclopropenyl salts [C$_3$R$_3$][BF$_4$] with [PPN][Fe(CO)$_3$NO], and properties such as the kinetics of their CO substitution reactions have been studied.[258] While treatment of the tri-*t*-butyl complex with phosphine ligand led to a single product, treatment of the triphenyl analog led to a mixture of the η^3-cyclopropenyl and ring-expanded η^3-cyclobutenone complexes. Evidence was presented for a mechanism involving ring-slippage (*see Slip Processes in Ligands*) to the η^1-cyclopropenyl species and subsequent CO insertion (equation 42).

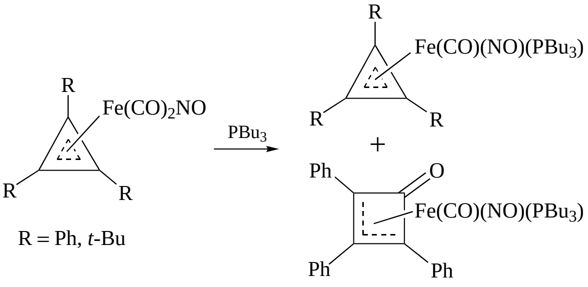

(42)

6 η^4-LIGAND COMPLEXES

6.1 Trimethylenemethane Complexes

6.1.1 *Preparation and Structure*[259]

Trimethylenemethane (TMM) is a highly reactive species that has only been detected by Electron spin resonance (ESR)

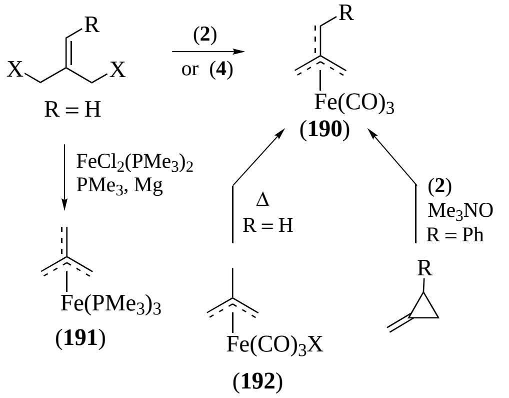

Scheme 52

(*see Electron Paramagnetic Resonance*) spectroscopy at low temperature. It was suggested that this unstable organic species could be stabilized by complexation to a transition metal.[260] Indeed, stable tricarbonyliron complexes of TMM (**190**) have been prepared by the reaction of 2-chloromethyl-3-chloropropene with (**2**) or with (**4**) (Scheme 52).[261] Alkyl, aryl, and methoxycarbonyl substituted derivatives of (**190**) may be prepared in a similar fashion. Reaction of 2-chloromethyl-3-chloropropene and $FeCl_2(PR_3)_2$ with Mg in the presence of additional phosphine gives an electron-rich triphosphine–iron complex (**191**).[262] Thermal dehydrohalogenation of (η^3-2-methallyl)$Fe(CO)_3X$ (**192**; X = Cl, Br) generates the parent TMM complex (**190**), albeit in poor yield.[261] If 1-alkyl-substituted derivatives of (**192**) are used, mixtures of TMM and η^4-diene complexes are generated. The reaction of 2-phenyl-1-methylenecyclopropane with (**2**) affords (**90**) (equation 15).[145] The reaction of (2-acetoxymethyl-1,3-butadiene)$Fe(CO)_3$ (**193**) with weak nucleophiles in the presence of a Lewis acid has been reported to afford substituted TMM complexes (Scheme 53).[263] This reaction is believed to proceed via the intermediacy of a 'cross-conjugated' pentadienyl cation (**194**). The photochemical reaction of aldehydes with allenes in the presence of (**2**) gave π-allyl–σ-acyl complexes (**195**), which undergo decarboxylation to give the substituted TMM complexes, again in poor yield.[264]

The electron and X-ray diffraction structures of a number of TMM complexes have been determined.[259,265,266] The TMM ligand adopts an 'umbrella-like' shape with the central carbon of the TMM ligand displaced out of the plane created by the three terminal carbons (cf. **196**). Even with this ligand puckering, the central atom remains the closest to the metal ($Fe–C_{central} = 1.93$ Å, $Fe–C_{terminal} = 2.12$ Å). The three carbonyl ligands are staggered with respect to the TMM ligand. Substituents on the TMM ligand are tilted away from the metal. Because of its C_{3v} symmetry, the parent (TMM)$Fe(CO)_3$ complex (**190**; R = H) gives only one signal in the ^{1}H NMR spectrum (2.00 ppm, CS_2) and three signals in the ^{13}C NMR spectrum (211.9 ppm, CO; 106.1 ppm, $C_{central}$; 54.9 ppm, $C_{terminal}$; CS_2). For substituted (TMM)$Fe(CO)_3$ complexes the three carbonyl ligands give rise to three distinct signals by ^{13}C NMR spectroscopy, thus indicating restricted rotation about the Fe–TMM bond. The barrier for this rotation is 71–84 kJ mol^{-1}.[267] Extended Hückel calculations, using the solid-state geometry, predict a barrier of 98.6 kJ mol^{-1} for rotation in the parent TMM complex.[268] This barrier to rotation is due to a loss of overlap of the metal fragment orbitals with the ligand orbitals. The protons of a monosubstituted (TMM)$Fe(CO)_3$ complex appear as distinct signals by ^{1}H NMR spectroscopy. Geminal coupling is not observed; however, protons aligned with a 'W' relationship exhibit couplings on the order of 2–4 Hz.[261]

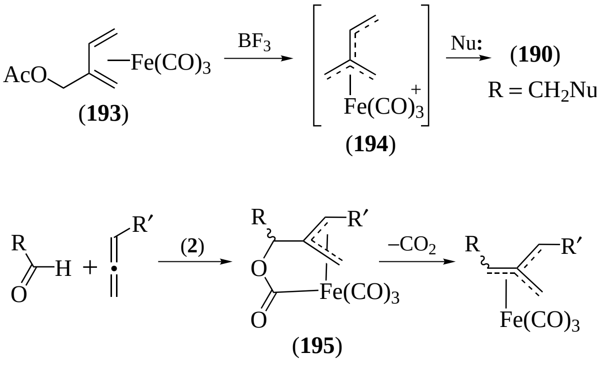

Scheme 53

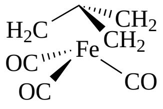

(**196**)

The electronic properties of aryl-substituted analogs of (**190**; R = Ph, *m*-FPh, *p*-FPh, *m*-COOHPh, *p*-COOHPh) have been studied, and Hammett substituent constants were obtained.[269] It was concluded that the TMM$Fe(CO)_3$ group behaves much like a phenyl group – weakly electron-donating via resonance and weakly electron-withdrawing via induction.

6.1.2 Reactions

The parent TMM complex (**190**; R = H) undergoes photochemical ligand substitution with trifluorophosphine or trimethylamine *N*-oxide assisted substitution with tertiary phosphines or *t*-butyl isocyanide (Scheme 54).[266] Trimethylamine *N*-oxide assisted substitution using isoprene as the incoming ligand results in C–C bond formation to afford the bis-π-allyl complex (**197**).[270] An intramolecular version of this reaction is also known.[271] The parent complex (**190**; R = H) reacts with electrophiles. Addition of HCl or Br_2 gives the methallyl complexes (**192**) and (**198**), respectively.[261] Tetrafluoroethylene adds across the Fe–C bond to afford (**199**) under photochemical conditions.[272] Complex (**190**) undergoes Friedel–Crafts-type acylation with

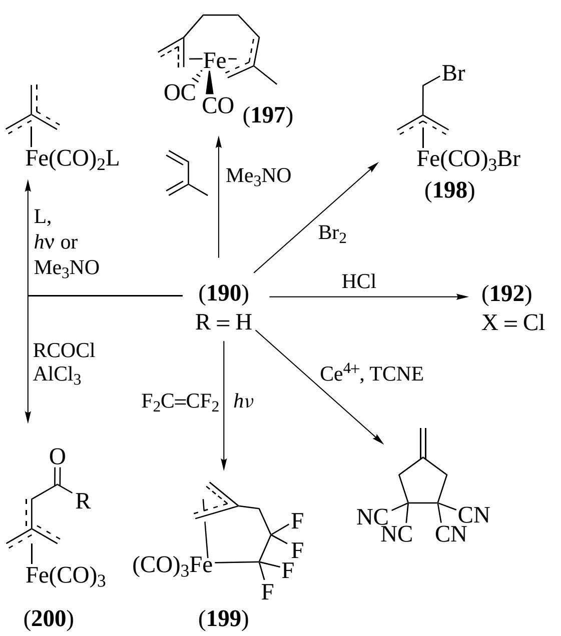
Fe
OC
CO
(197)
Fe(CO)$_2$L
Me$_3$NO
Br
Fe(CO)$_3$Br
(198)
L,
hν or
Me$_3$NO
Br$_2$
(190)
R = H
HCl
(192)
X = Cl
RCOCl
AlCl$_3$
Ce^{4+}, TCNE
F$_2$C=CF$_2$ hν
O
R
Fe(CO)$_3$
(200)
(CO)$_3$Fe
F
F
F
F
(199)
NC
CN
NC
CN

Scheme 54

acetyl or benzoyl chloride to give ketones (**200**) in poor yields (<25%).[261] (Methyltrimethylenemethane)Fe(CO)$_3$ (**190**; R = Me) isomerizes to (η^4-isoprene)Fe(CO)$_3$ in 85% H_2SO_4.[263,272]

Decomplexation of the TMM ligand has been examined. Oxidation of (**190**) in the presence of tetracyanoethylene (Scheme 54) or (**201**) in the presence of diethyl fumarate (equation 43) affords [3 + 2] cycloaddition products in very poor yields (4–19%).[273] This reaction is believed to involve the initial formation of an iron-bound intermediate, which can competitively react with an electron-deficient alkene, or undergo loss of the iron metal to give a triplet (*see Triplet State*) diradical. Photochemical reduction of substituted TMM complexes in acetic acid affords the corresponding alkenes in good yields, but with poor regioselectivity.[274] Reaction of the parent and substituted TMM complexes (**190**; R = H, Me, Ph) with nucleophiles followed by acidic workup affords the corresponding alkenes in which a new C–C bond has been formed (equation 44).[275] This reaction probably occurs via formation of a (π-allyl)Fe(CO)$_3$$^-$ anion. In the case of alkyl- or aryllithium nucleophiles, products incorporating carbon monoxide are observed.

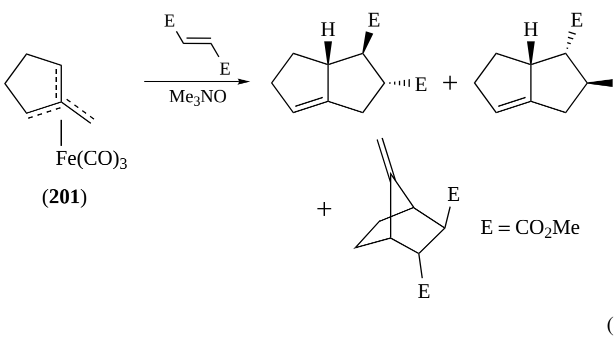
E
E
Me$_3$NO
Fe(CO)$_3$
(201)
H
E
E
+
H
E
E
+
E
E
E = CO$_2$Me

(43)

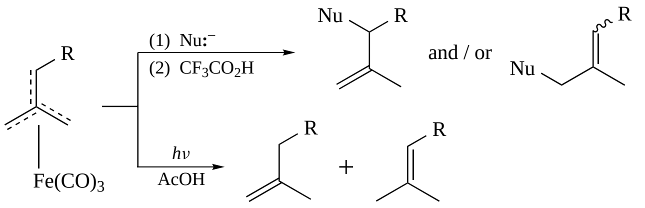
R
Fe(CO)$_3$
(1) Nu:$^-$
(2) CF$_3$CO$_2$H
hν
AcOH
Nu
R
and / or
R
Nu
R
+
R

(44)

Reactions that modify the side chains of TMM complexes have been examined. Nucleophilic addition to a carbonyl adjacent to the TMM ligand occurs with high diastereoselectivity (equation 45).[261,274,276] Likewise, nucleophilic substitution of acetoxymethyl or hydroxymethyl TMM complexes (**202**) with weak carbon nucleophiles proceeds in a stereoselective fashion.[263,277] Similar to the reaction of (**193**), this substitution probably occurs via the intermediacy of a 'cross-conjugated' pentadienyl cation (**194**). Surprisingly, the terminal alkene of this product can be oxidatively cleaved to the aldehyde by ozonolysis without loss of the iron fragment.[271] A hydroxymethyl functionality adjacent to the TMM ligand may be oxidized to the aldehyde by use of MnO_2, without oxidation of the iron.[274] A formyl-TMM complex (**200**, R = H) undergoes hetero-Diels–Alder reaction with Danishefsky's diene to produce a dihydropyrone TMM complex (**203**) with a diastereoselectivity that is greater than the similar reaction with η^4-dienal iron complexes (>25:1 *vs.* <4:1).[278] Complex (**203**) was stable to a number of subsequent transformations (reduction, alkoxymercuration, dihydroxylation). The resolution of a chiral TMM ester complex (**200**, R = O-succinimide) using (*S*)-ethyl lactate or (*R*)-α-methylbenzylamine has also been reported.[279]

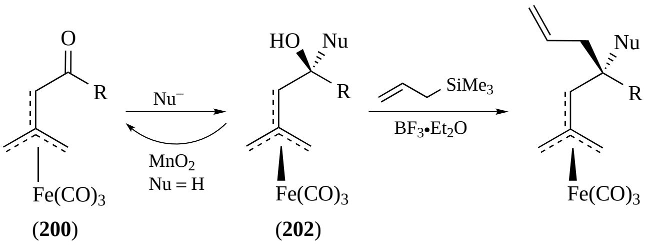
O
R
Fe(CO)$_3$
(200)
Nu$^-$
MnO$_2$
Nu = H
HO
Nu
R
Fe(CO)$_3$
(202)
SiMe$_3$
BF$_3$•Et$_2$O
Nu
R
Fe(CO)$_3$

(45)

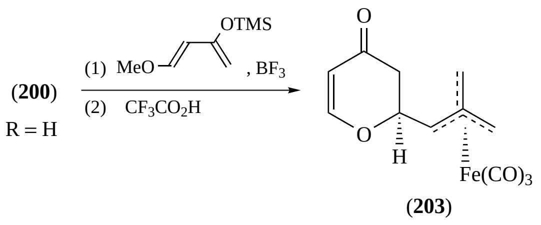
(200)
R = H
OTMS
(1) MeO
, BF$_3$
(2) CF$_3$CO$_2$H
O
O
H
Fe(CO)$_3$
(203)

(46)

6.2 Cyclobutadiene Complexes

6.2.1 Preparation and Structure[280]

Cyclobutadiene, the simplest cyclic polyene, has long intrigued chemists; however, the π-electron molecule has

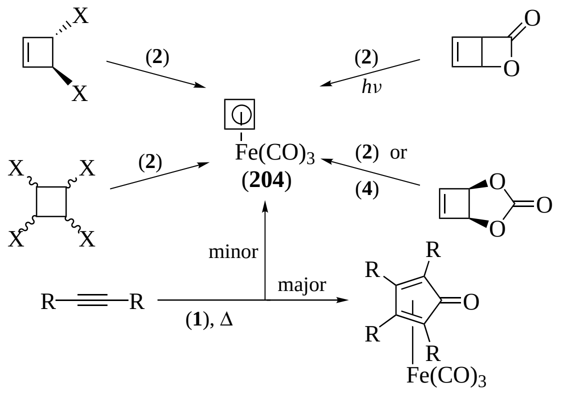

(**204**) (**205**)

Scheme 55

only been isolated at low temperatures in noble gas matrices. Certain highly hindered derivatives of cyclobutadiene have been prepared and their crystal structures determined. Of these, tetra-*t*-butylcyclobutadiene is the only compound to exhibit a 'square', rather than rectangular, geometry.**281** Similar to trimethylenemethane, cyclobutadiene can be stabilized by complexation to a transition metal.**260**

Tricarbonyl(cyclobutadiene)iron (**204**) and substituted derivatives may be prepared in good overall yields by the reaction of 3,4-dihalocyclobutenes or 1,2,3,4-tetrahalocyclobutanes with (**2**), or by the photolysis of photo-α-pyrone with (**1**) (Scheme 55).**282** The reaction of *cis*-3,4-carbonyldioxycyclobutenes with (**2**) or (**4**) generates (cyclobutadiene)Fe(CO)$_3$ complexes, and while this reaction is stereospecific it is not known if it occurs with inversion or retention of configuration.**283** Thermal reaction of alkynes with Fe(CO)$_5$ gives predominantly cyclopentadienone complexes (**205**), but small amounts of cyclobutadiene complexes can be isolated.**280** Thermal reaction of (**1**) with Ni, Pd, or Pt cyclobutadiene complexes results in π-ligand exchange to give the iron cyclobutadiene complexes in high yield.**61** In general, since cyclobutadiene is a highly reactive species, direct complexation of the ligand is not possible; however, a stable highly hindered cyclobutadiene (**206**) may be complexed to iron (equation 47).**284** The photochemical rearrangement of an (η^2-vinylcyclopropene)Fe(CO)$_4$ complex (**207**) has been reported to afford the novel trifluoromethyl substituted cyclobutadiene complex (**208**) (equation 48).**286** Methylation of the iron cyclobutenonyl complex (**209**) affords the cationic methoxycyclobutadiene complex (**210**) (equation 49).**287** Carbomethoxy-substituted complex (**211**) was prepared by pyrone photolysis (equation 50) and has served as the starting point for a number of synthetic applications (Section 6.2.2).

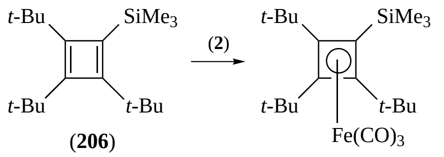

(**206**)

(47)

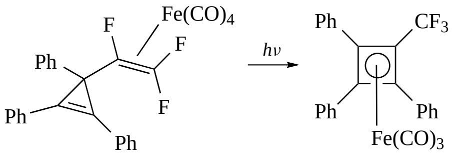

(**207**) (**208**)

(48)

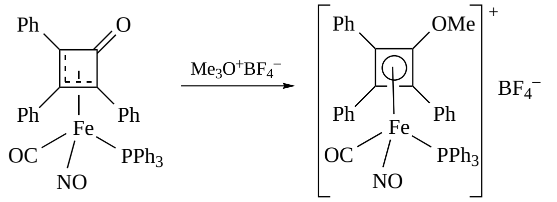

(**209**) (**210**)

(49)

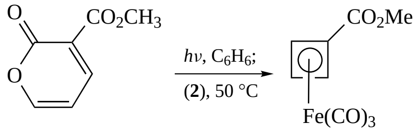

(**211**)

(50)

The X-ray diffraction of several iron cyclobutadiene complexes have been determined.**288** In the majority of these structures, the cyclobutadiene ring is planar with the four C–C ring bonds of nearly equal length (ca. 1.45 Å) and the four carbons equidistant from the iron atom (ca. 2.05 Å). The orientation of the cyclobutadiene ring with respect to the three carbonyl ligands is variable. The parent (cyclobutadiene)Fe(CO)$_3$, at −45 °C, adopts conformation (**212**), whereas other substituted cyclobutadiene complexes adopt conformations between (**212**) and (**213**). On the basis of temperature-dependent proton spin−lattice relaxation times in the solid state, the barrier to rotation about the cyclobutadiene−Fe bond in (**204**) is 22.6 kJ mol^{-1}. Based on calculations, this barrier appears to depend primarily on intermolecular interactions in the crystal.**285** The protons of (**204**) appear as a singlet at 3.91 ppm (CDCl$_3$).**289** The presence of an electron-withdrawing substituent on the cyclobutadiene ligand causes a downfield shift, while the presence of an electron-donor substituent causes an upfield shift of both the α- and β-protons. The ring carbons of (**204**) appear at 63 ppm.**32**

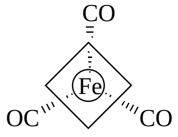

(**212**)

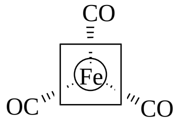

(**213**)

(1,2-Disubstituted-cyclobutadiene)Fe(CO)$_3$ complexes with two different substituents are chiral, and the two enantiomers may be separated by standard resolution techniques.**290** The optically active cyclobutadiene complexes are stable to racemization at 120 °C for 48 h.

6.2.2 Reactions

Neutral (cyclobutadiene)iron complexes undergo thermal and photochemical ligand substitution with phosphines, with alkenes such as dimethyl fumarate and dimethyl maleate, and with the nitrosonium cation. Cationic nitrosyl complexes (e.g. **210**) undergo ligand substitution by treatment with phosphines. Photolysis of (tetraphenylcyclobutadiene)Fe(CO)$_3$ in THF at $-40\,^\circ$C is reported to give the novel bimetallic complex (**214**), which reacts with carbon monoxide (140 atm, 80 °C) to regenerate the starting material.**[291]** An X-ray diffraction analysis of (**214**; R $=$ Ph, R$'$ $=$ t-Bu) reveals a very short Fe–Fe distance of 2.117 Å.

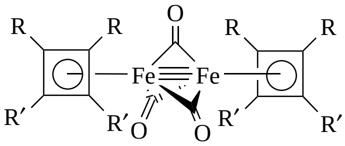
R
R
O
R
R
Fe
Fe
R′
R′
O
O
R′
R′

(**214**)

The organic chemistry of (cyclobutadiene)Fe(CO)$_3$ is much like that of ferrocene (Section 7.2). Protonation in HSO_3F/SO_2 generates a cationic species that exhibits a signal at -11.16 ppm, consistent with a hydride structure, but the proton is coupled to a ring carbon ($J = 91.2$ Hz). A bridging hydride (*see Bridging Ligand*) structure is favored. This protonation occurs on the *endo* face of the ligand.**[292]** Complex (**204**) behaves like an aromatic compound and will undergo electrophilic substitution with a wide variety of reagents; deprotonation and electrophilic trapping of the resulting anion is also possible (Scheme 56).**[293,294]** Notably (**204**), unlike ferrocene, will undergo sulfonation with H_2SO_4. It is not clear whether electrophilic attack occurs on the *exo* or *endo* face of the cyclobutadiene ligand. Acylation of monoalkyl-substituted (cyclobutadiene)Fe(CO)$_3$ complexes generates the 1,3-disubstituted (major) and 1,2-disubstituted (minor) derivatives. The side chains of substituted (cyclobutadiene)Fe(CO)$_3$ complexes may undergo a wide variety of organic transformations. Examples include the conversion of carboxylic acids to acyl halides and the hydroboration (*see Hydroboration*)/oxidation of alkenes. Chemistry of this type has been used to generate the novel cyclobutadiene-cyclophane (**215**).**[295]**

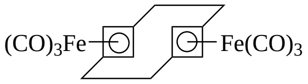
(CO)3Fe
Fe(CO)3

(**215**)

The solvolysis (*see Solvolysis*) of (chloromethylcyclobutadiene)Fe(CO)$_3$ (**216**) in 5% aqueous acetone proceeds at a rate 108 times faster than that of benzyl chloride.**[296]** The rapid rate of this S_N1 solvolysis is attributed to the stability of the α-carbocation (**217**), which can be generated and spectroscopically characterized by treatment of the alcohol (**218**) with CF_3CO_2H or HBF_4 (equation 51). A bis(cyclobutadienyliron tricarbonyl)phenylcarbonium ion has been crystallographically characterized; the data indicate that the cyclobutadiene ligand is planar and that iron is symmetrically bound to the ligand. The α-carbonium center is essentially planar with each cyclobutadiene ligand and is not bent out of the plane as is the case for the α-ferrocenyl carbocation (Section 7.2.3). The p$K_R{}^+$ value has been determined for (cyclobutadiene)Fe(CO)$_3\alpha$-carbocations; these cations are more stable than the corresponding benzyl carbocations, but less stable than the corresponding α-ferrocenyl carbocations.

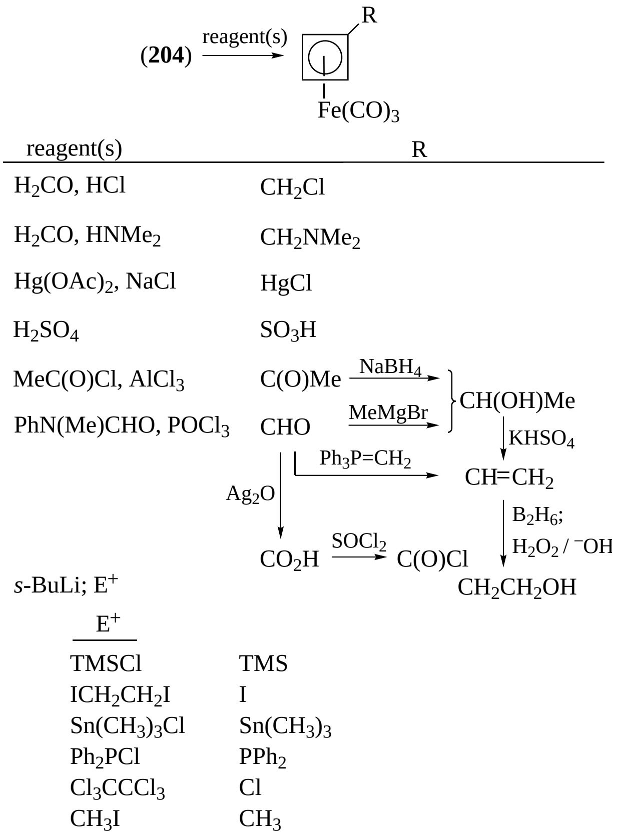
(204)
reagent(s)
R
Fe(CO)3
reagent(s)
R
H2CO, HCl
CH2Cl
H2CO, HNMe2
CH2NMe2
Hg(OAc)2, NaCl
HgCl
H2SO4
SO3H
MeC(O)Cl, AlCl3
C(O)Me
NaBH4
CH(OH)Me
PhN(Me)CHO, POCl3
CHO
MeMgBr
KHSO4
Ph3P=CH2
CH=CH2
Ag2O
B2H6;
H2O2 / −OH
CO2H
SOCl2
C(O)Cl
s-BuLi; E+
CH2CH2OH
E+
TMSCl
TMS
ICH2CH2I
I
Sn(CH3)3Cl
Sn(CH3)3
Ph2PCl
PPh2
Cl3CCCl3
Cl
CH3I
CH3

Scheme 56

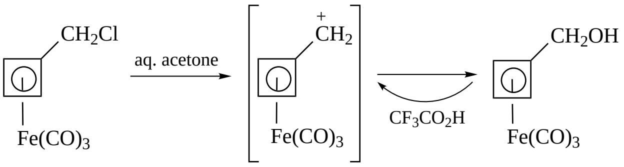
CH2Cl
Fe(CO)3
aq. acetone
+
CH2
Fe(CO)3
CF3CO2H
CH2OH
Fe(CO)3

(**216**) (**217**) (**218**)

(51)

The cyclobutadiene ligand may be liberated by oxidation of the complex with CAN, $Pb(OAc)_4$, or trimethylamine

N-oxide. In the absence of an alkene or acetylene, the cyclobutadiene ligand undergoes dimerization to afford a mixture of *syn*- and *anti*-tricyclo[4.2.0.0^{2,5}]-3,7-octadiene (**219**). In the presence of a dieneophile, cyclobutadiene undergoes Diels–Alder cycloaddition to afford the bicyclo[2.2.0]hexene product (equation 52). A variety of dieneophiles have been used in this reaction, and the products may be carried forward to a series of strained cage compounds.[280] Oxidation of optically active disubstituted (cyclobutadiene)Fe(CO)$_3$ complexes in the presence of a symmetrical alkene generates racemic products.[290] Thus, the chemical oxidation appears to generate 'free' cyclobutadiene. Additional evidence for the presence of the free ligand was provided by the 'three-phase test'. Transfer of the ligand from a polymer-bound (cyclobutadiene)iron complex by oxidation in the presence of a separately polymer-bound dienophile can only be accounted for by the generation of the free ligand, since there is negligible contact between the functionalized sites of the two different polymeric supports.[297] Oxidation of the optically enriched complex (**220**) containing a pendant alkyne dieneophile produces the achiral phthalan (75%) and the optically enriched tricyclic ketone (**221**) (20%) (Scheme 57). The product (**221**) is probably formed via initial coordination of the dienophile to the oxidized complex, followed by alkene insertion, carbonyl insertion, and reductive elimination.[298]

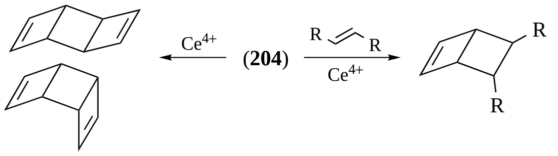

(**219**)

(52)

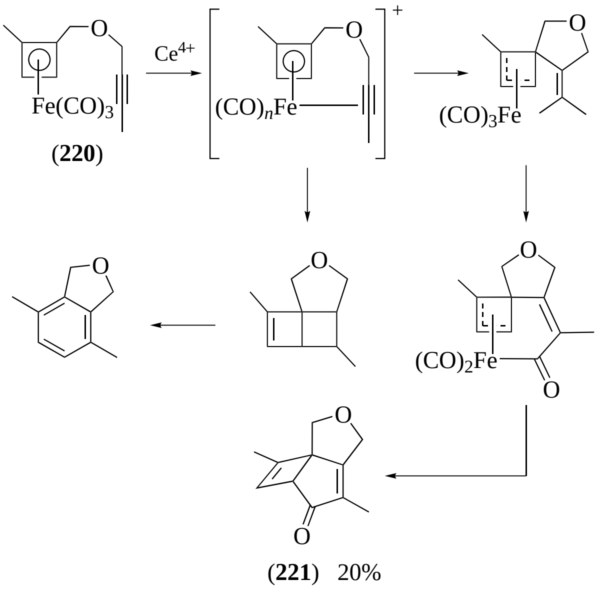

Scheme 57

Intramolecular cycloadditions using (cyclobutadiene)Fe(CO)$_3$ complexes with pendant alkenes have recently been exploited for use in synthetic methodology. The formyl-substituted (cyclobutadiene)Fe(CO)$_3$ complex can be reduced to the corresponding alcohol and then may be etherified by treatment with an allylic alcohol in the presence of an acid catalyst (Scheme 58).[299,300] The intramolecular cycloaddition strategy has been employed in the total synthesis of the natural product (+)-asteriscanolide beginning with carbomethoxy-substituted cyclobutadiene iron complex (**211**) (Scheme 59).[301] The use of a related example using a propargyl alcohol give a Dewar-benzene containing cycloadduct that isomerized to the aromatic benzene system.[298]

Photolysis of substituted (cyclobutadiene)Fe(CO)$_3$ complexes in the presence of alkynes affords substituted benzenes (Scheme 60). From the substituent patterns of the products, it is clear that this reaction cannot be accounted for by generation of the free ligand. The proposed mechanism involves initial loss of a carbon monoxide ligand and coordination of the alkyne. Insertion of the alkyne predominantly into the

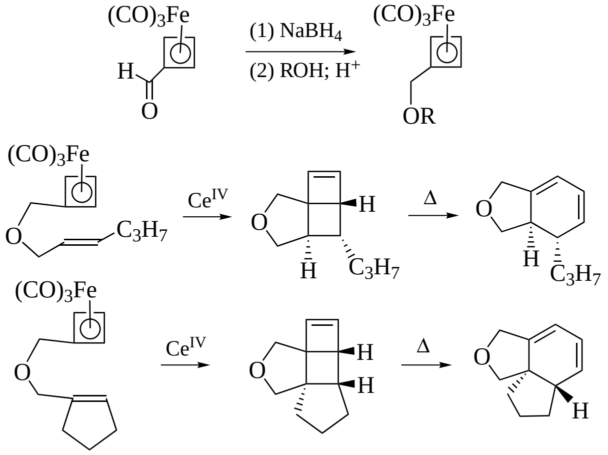

Scheme 58

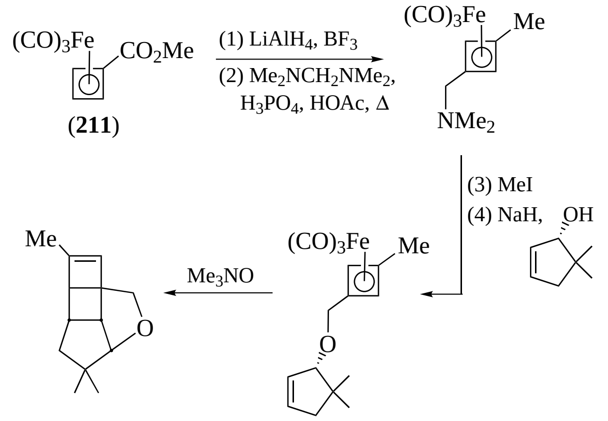

Scheme 59

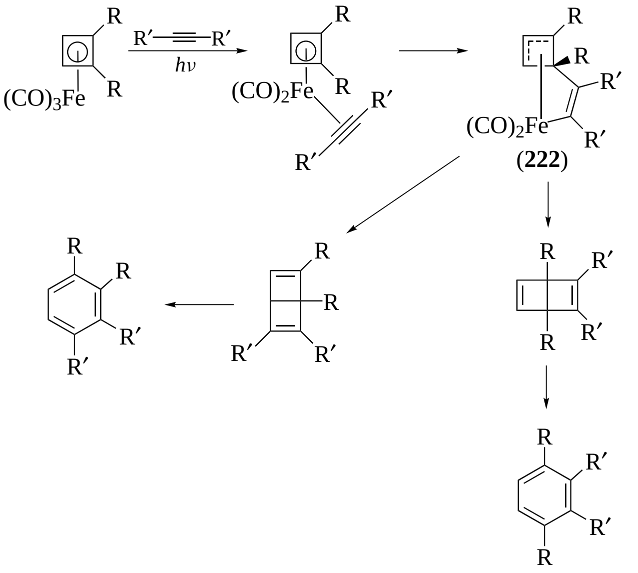
R
R′—≡—R′
hν
(CO)3Fe
(CO)2Fe
(222)
R′

Scheme 60

more substituted cyclobutadiene–iron bond will generate the bridged species (**222**), which undergoes reductive elimination to afford the Dewar-benzene intermediate. Secondary photolysis of this Dewar-benzene gives the observed aromatic product.[302]

Finally, iodo-substituted (cyclobutadiene)$Fe(CO)_3$ complexes can undergo palladium-catalyzed animations as well as Stille reactions using alkynylstannanes (Scheme 61). An iterative process allowed the diiron 'dumbbell' complex to be prepared; alternatively, tetraethynyl complexes could be prepared directly from the tetraiodo(cyclobutadiene)$Fe(CO)_3$ complex.[303–305]

6.3 (Diene)Iron Complexes

Investigations into the synthesis and reactivity of η^4-diene iron tricarbonyl complexes are among the most active areas of research in iron organometallic chemistry. A number of excellent reviews are available for the reader seeking greater detail than can be provided here.[306–313]

6.3.1 Acyclic (Diene)Iron Complexes

Acyclic tricarbonyl(diene)iron complexes may be prepared by reaction of a 1,3-diene with (**1**), (**2**), or (**3**) either thermally, photochemically, or under the influence of ultrasonic stirring (Scheme 62).[106] Ligand transfer species, such as (benzylideneacetone)$Fe(CO)_3$, (1-aza-1,3-diene)$Fe(CO)_3$, or bis(η^2-cyclooctene)$Fe(CO)_3$ are also useful for the complexation of dienes under mild reaction conditions.[117,219,314] The thermal reaction of unconjugated dienes with (**1**) generally results in double bond migration

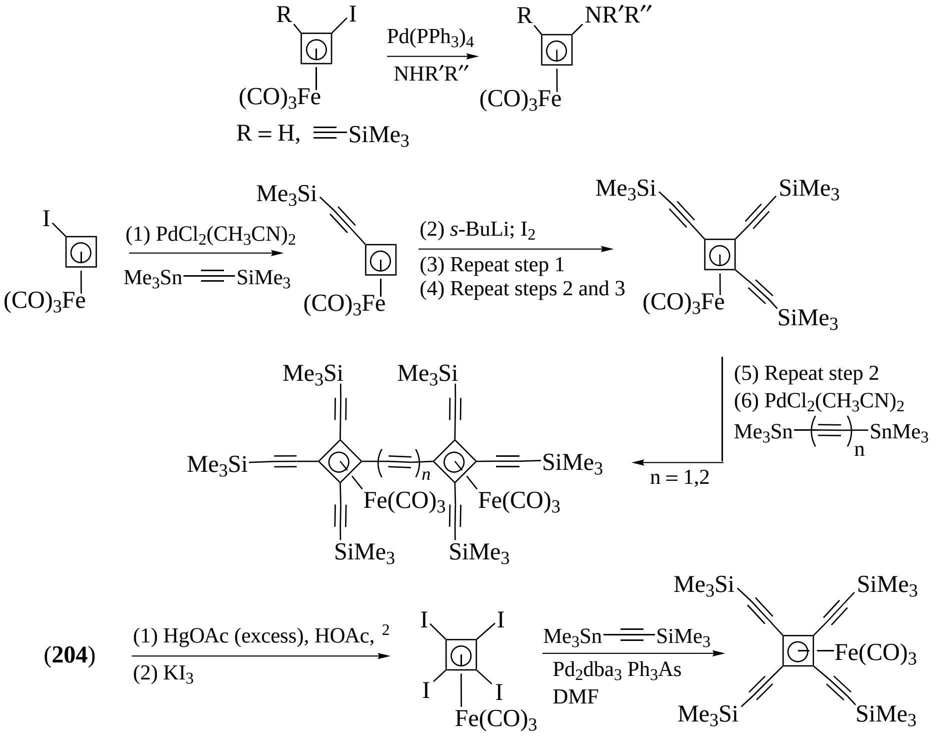
R
I
Pd(PPh3)4
NHR′R″
NR′R″
(CO)3Fe
R = H, ≡—SiMe3
(1) PdCl2(CH3CN)2
Me3Sn—≡—SiMe3
Me3Si
(2) s-BuLi; I2
(3) Repeat step 1
(4) Repeat steps 2 and 3
SiMe3
(5) Repeat step 2
(6) PdCl2(CH3CN)2
Me3Sn—(≡)n—SnMe3
n = 1,2
Fe(CO)3
(204)
(1) HgOAc (excess), HOAc, 2
(2) KI3
Me3Sn—≡—SiMe3
Pd2dba3 Ph3As
DMF

Scheme 61

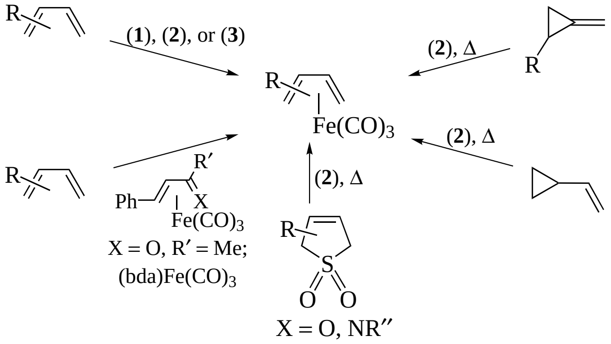

Scheme 62

to afford the 1,3-diene complex, except in cases where this is geometrically impossible. Diene complexes can also be generated by the isomerization of strained organic rings, such as η^2-methylenecyclopropane and η^2-vinylcyclopropane complexes.**136,315** The preparation of 1,3-diene complexes by the thermal extrusion of SO_2 from 2,5-dihydrothiophene 1,1-dioxides or the reduction of 1,2-bis(bromomethyl)benzene with (**4**) is believed to proceed via the formation of the highly reactive free dienes.**316**

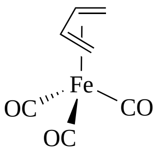

(**223**)

The structures of a wide variety of substituted (1,3-butadiene)$Fe(CO)_3$ complexes have been determined by single-crystal X-ray diffraction.**317** In the parent (1,3-butadiene)$Fe(CO)_3$ complex (**223**) the diene ligand is essentially planar, and all three C–C bond lengths are roughly the same (ca. 1.41 Å). The ligands about iron describe a square-pyramidal geometry, with one carbon monoxide ligand occupying the apical position and the remaining two carbonyls and the diene ligand in the basal plane. The outer diene carbons are slightly further from iron (Fe–C, 2.13 Å) than are the inner carbon atoms (Fe-C, 2.05 Å). The two basal carbonyls eclipse the 1,2- and 3,4-diene bonds, and the apical carbonyl points toward the 'open' end of the diene. Only one ^{13}C NMR signal is observed in the metal carbonyl region, thus indicating a rapid interchange between the two sites. Substituents at C-1 and C-4 are bent out of the plane of the diene ligand, with *exo* substituents displaced towards iron and *endo* substituents displaced away from iron. Complexation of the diene to iron causes distinct changes in the ^1H and ^{13}C NMR spectra of these complexes. Resonance signals for protons on the internal carbons (C-2 and C-3) appear in the region 5–6 ppm, while terminal protons in the *exo* and *endo* positions appear considerably further upfield (ca. 1.9 and 0.3 ppm, respectively). As a consequence of the twisting of the substituents out of the plane of the diene ligand, the *cis* and *trans* couplings are reduced in value to about 7 and 9 Hz, respectively.**318** The resonance signals for the diene carbons appear upfield, with C-2 and C-3 having resonances at 85 ppm and those for C-1 and C-4 at 42 ppm.**32** These spectral features are highly constructive for assigning the relative stereochemistry of substituents on the diene ligand.

The complexation of prochiral dienes to the $Fe(CO)_3$ fragment results in the formation of a racemic mixture of enantiomers. These racemic planar chiral complexes have been resolved and the enantiomerically pure (or enriched) complexes are configurationally stable at 23 °C; however, they undergo a thermal racemization at >100 °C with a $\Delta G\ddagger = 130\,\text{kJ mol}^{-1}$.**319** The resolution of the racemic mixtures has been accomplished by classical formation of diastereomeric derivatives, by chiral chromatography, and by kinetic resolution using optically active reagents or biotransformations.**306,307,320,321** Of particular note was the discovery that dienal complexes underwent kinetic resolution upon reaction with enantiopure allyl boronate, and an analogous transformation of a meso complex proceeded with excellent diastereoselectivity (Scheme 63).**322** This finding led directly to the development of additional diastereoselective transformations along the periphery of the diene unit, as well as to applications in natural product synthesis. The same meso complex has also undergone asymmetric alkylation with alkyl zinc reagents in the presence of chiral ligands.**323**

The complexation of chiral dienes leads to the formation of diastereomeric η^4-diene iron tricarbonyl complexes. An early example was actually carried out for the protection of the diene unit found in the steroid B-ring of ergosteryl acetate (equation 53); neither the stereochemical assignment nor the diastereomer ratio were established.**324,325** Similarly, the tricarbonyl iron complex of calciferol was also prepared.**326**

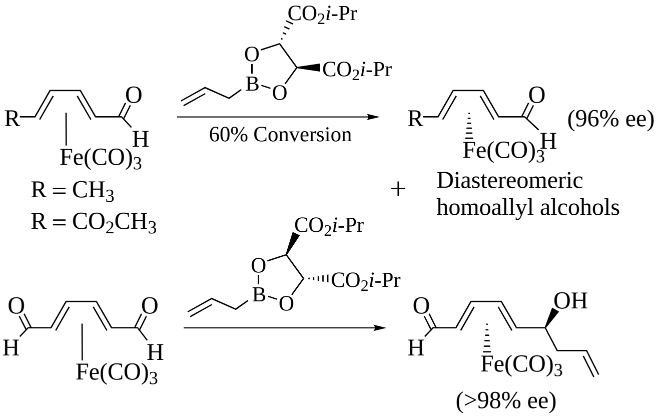

Scheme 63

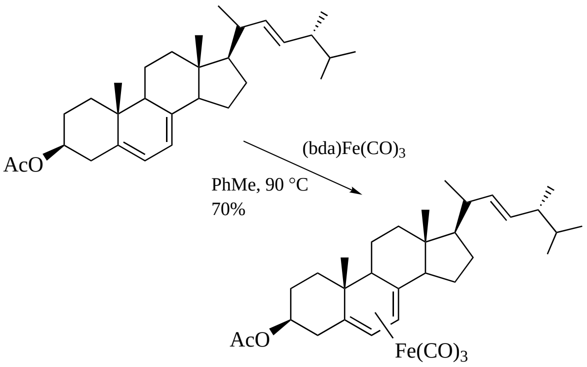

(53)

Complexation of an enantiopure diene derived from ($+$)-*L*-arabinose was a modestly diastereoselective process (equation 54).[327] The major η^4-iron diene complex formed (**224**) was likely the result of heteroatomic delivery and installation of the $Fe(CO)_3$ unit *syn* to the benzyloxy group. The diastereoselectivity of this transformation was solvent dependent; this may be result of conformational differences in different solvents. The diastereomeric iron diene complexes were separable by chromatography and each could be transformed into various derivatives under carefully controlled conditions without loss of optical integrity.[328]

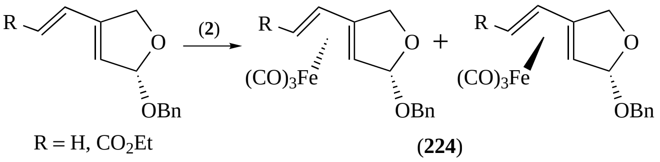

(54)

Chiral auxiliaries may also be used to effect diastereoselective complexations of acyclic dienes. For chiral dienamides (**225a–d**), the best case employed the sterically demanding (*S*)-2-(diphenylhydroxymethyl)pyrrolidine auxiliary. Diene (**225d**) was complexed with excellent diastereoselectivity but in modest yield (Scheme 64).[329] For substrates (**217a–c**), diastereomer ratios of the corresponding complexes were poorer (1.5:1 to 4.6:1), likely a result of the increased distance between the auxiliary's chiral center and the diene.

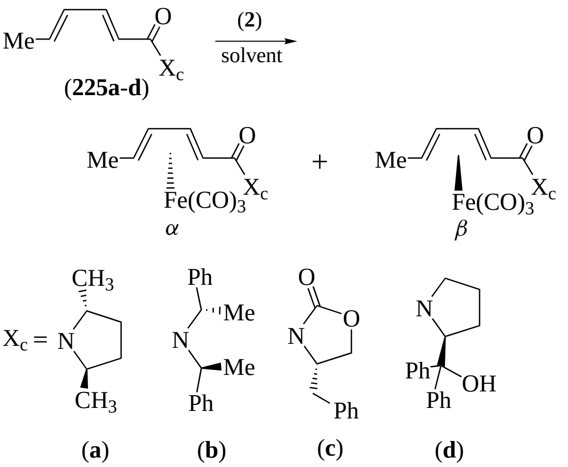

X_c	Solvent / temp	α / β ratio	% Yield
a	Et_2O / Δ	4.6:1	95
b	Et_2O / Δ	1.5:1	46
c	Et_2O / Δ	2:1	78
d	Et_2O-DCM / Δ	>99:1	40 (84, brsm)

Scheme 64

Diastereoselective complexations of an iron tricarbonyl unit to a series of enantiopure sulfinyl dienes has also been reported.[330] (*Z*)-1-Sulfinyl dienes (**226**) (rather than the isomeric (*E*)-1-sulfinyl dienes or 2-sulfinyl dienes) afforded the greatest diastereoselectivities (10:1 to 16:1); 1,3-allylic strain has been cited as the origin of the selectivity, as the favored conformation would place the bulky aromatic group of the sulfoxide group in a position where it blocks one diene face (Scheme 65). While unsubstituted (*Z*)-1-sulfinyldienes (**226**, R, $R' = H$) or their 4-substituted analogs (**226**, $R = CH(OEt)_2$, $R' = H$) can be efficiently complexed using (**1**)/NMO, 3,4-disubstituted-(*Z*)-1-sulfinyldienes (**226**, R, $R' \neq H$) required the use of (bda)$Fe(CO)_3$ as the complexing reagent in order to obtain good (ca. 80%) chemical yields. In virtually all cases, it was demonstrated the complexations with (bda)$Fe(CO)_3$ were under kinetic control. Transformations along the diene periphery have been used to install new chiral centers in a diastereoselective manner. Also, 3-(*o*-dithianylaryl) analogs (**227**) are complexes prepared with simultaneous installation of planar and axial chirality. In the example shown, the iron diene complexes are formed in a ratio for (**228a**:**228b**:**228c**) of 34:2.6:1; the selectivity results from dynamic kinetic resolution (Scheme 65).[331] These complexes are part of a growing class of nonbiaryl atropisomeric complexes.[332]

6.3.2 *Cyclic (Diene)Iron Complexes*

The reaction of 1,3- or 1,4-cyclohexadienes with (**1**), (**2**), or ligand transfer species generates the corresponding (1,3-cyclohexadiene)$Fe(CO)_3$ complexes (**229**).[333] In a similar fashion, reactions of dihydroanisoles, 1,2-dihydrobenzoic acid esters, 1,3-cycloheptadiene, cycloheptatriene, tropone, 1,3-cyclooctadiene, 1,3,5-cyclooctatriene, or cyclooctatetraene with (**1**), (**2**), or (**3**) give the corresponding cyclic (1,3-diene)iron complexes. Monophosphinedicarbonyl or monophosphitedicarbonyl complexes are also available in some cases by treatment of the tricarbonyliron complex with the appropriate phosphine or phosphite. The structures of the cyclic diene complexes are similar to those of the acyclic diene complexes. The cyclooctatetraene complex (**230**) exhibits a single signal in its ^{1}H NMR spectrum (5.39 ppm, $CDCl_3$) at 23 °C, indicating stereochemical nonrigidity. The ^{13}C NMR spectrum of (**230**) is temperature dependent, and

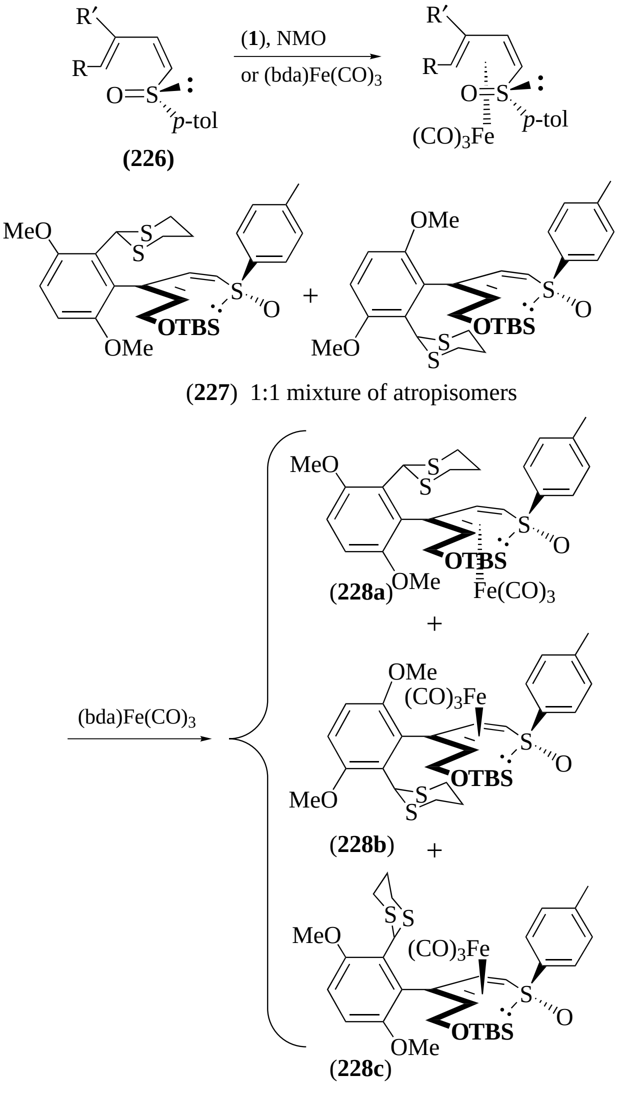
R′
R
O=S
p-tol
(1), NMO
or (bda)Fe(CO)3
(CO)3Fe
(226)
MeO
OMe
OTBS
S
O
(227) 1:1 mixture of atropisomers
(bda)Fe(CO)3
(228a)
Fe(CO)3
(228b)
(228c)

Scheme 65

the single cyclooctatetraene signal at −20 °C splits into four signals at −134 °C. Analysis of the different rates of peak broadening indicates that the fluxional behavior is a 1,2-shift of the $Fe(CO)_3$ (a ‘ring-whizzing’ process (*see Ring Whizzers*)) which has an activation energy of 33.9 kJ mol^{-1}.[334] Compound (**230**) is also fluxional in the solid state. The reaction of perfluorocyclooctatetraene with (**2**) gives the unusual 1,2,3,6 – η-bonded complex (**231**), which has been characterized by X-ray diffraction.[335]

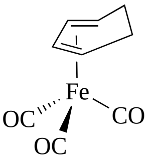

(**229**)

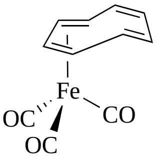

(**230**)

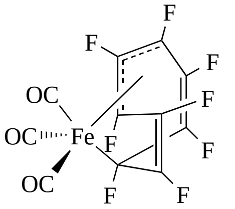

(**231**)

As with acyclic dienes, methods have been developed for enantioselective and diastereoselective complexation of prochiral and chiral cyclic dienes. An approach has been developed for the asymmetric catalytic complexation of prochiral cyclohexa-1,3-dienes using (**1**) in the presence of catalytic amounts of 1-azabuta-1,3-dienes such as (**232**) or (**233**); an enantiomeric excess as high as 86% has been reported.[311–313] By contrast, attempts to effect diastereoselective complexations using cyclic diene systems equipped with chiral auxiliaries have met with limited success.[336–339] On the other hand, direct complexation of chiral cyclic dienes such as (**234**) and (**235**) proceed with a high degree of diastereoselectivity, where the iron tricarbonyl fragment is directed *syn* to alcohols or ethers by transient coordination (‘heteroatom delivery’) (Scheme 66).[340,341]

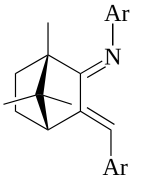

(**232**)

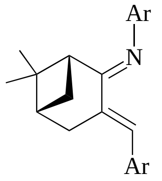

(**233**)

Ar = 4-MeOC_6H_4

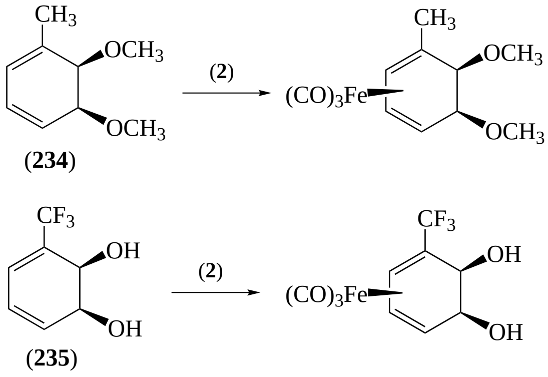
CH3
OCH3
OCH3
(2)
(CO)3Fe
(234)
CF3
OH
OH
(2)
(CO)3Fe
(235)

Scheme 66

6.3.3 *Reaction at the η^4-Diene*

In general, the complexed dienes are not reactive under the same conditions as the free ligand; the (tricarbonyl)iron fragment thus serves as a protecting group for the diene functionality. (Diene)$Fe(CO)_3$ complexes will undergo reaction with electrophiles. Protonation of these complexes generates a cationic η^3-allyl complex (Section 5.1.1). Electrophilic acylation of (butadiene)$Fe(CO)_3$ complexes generates the corresponding dienone complexes. The rate of acylation of (**223**) is 3850 times faster than that of benzene. Acylation occurs on the *endo* face of the diene ligand via initial formation of a cationic η^3-allyl complex (**236**) (equation 55). Deprotonation affords the *cis*-dienone complex (**237**). Complexes (**237**) isomerize to the thermodynamically more stable *trans*-dienone complexes (**238**) in the presence of sodium methoxide or acid.[342] An example of this methodology, used in the synthesis of an enantiomerically pure arachadonic acid metabolite (LTA_4) is shown (equation 56).[343] In general, the electrophilic acylation proceeds at the unsubstituted terminus of 1-substituted diene complexes, and for 2-substituted complexes it occurs with low regioselectivity. The acylation of 1,4-disubstituted diene complexes and diene complexes containing an electron-withdrawing substituent will occur under forcing conditions.[342] Substitution of an acyl group at the internal position of a diene iron complex may be accomplished by palladium-catalyzed coupling of an acyl halide with the 2-stannylated butadiene complex (**239**) to give (**240**) (equation 57).[344] Simple treatment of 1,1,3-trisubstituted diene complexes with $AlCl_3$ results in the formation of substituted cyclopentenones (**241**) (equation 58).[345]

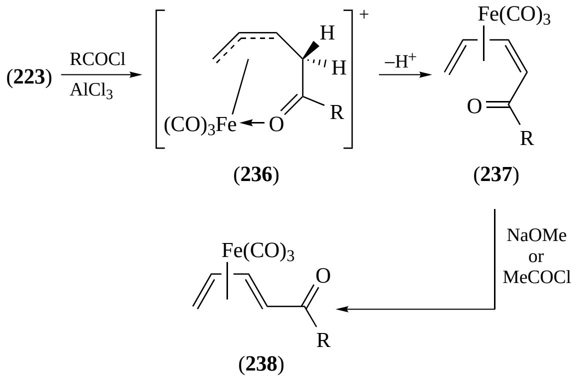

(**236**) (**237**) (**238**)

(55)

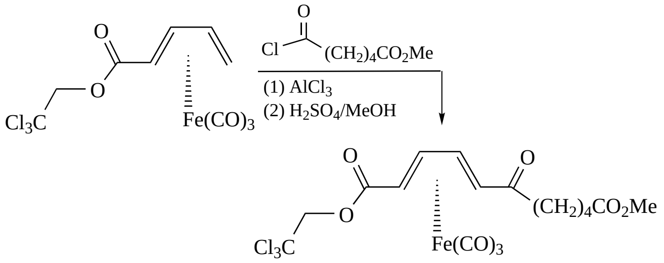

(56)

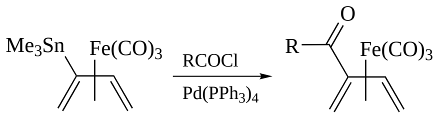

(**239**) (**240**)

(57)

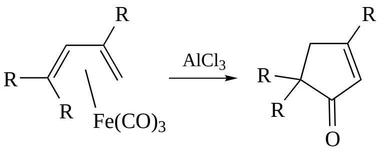

(**241**)

(58)

The η^4-diene ligand will undergo attack by strong nucleophiles (conjugate acid $pK_a >$ ca. 28) (*see Acidity Constants*) in THF/Hexamethylphosphoramide (HMPA) to afford, after protic workup, the products of addition to the diene (Scheme 67).[346] Attack occurs kinetically (−78 °C) at an internal diene position to generate the anion (**242**). This nucleophilic attack is, however, reversible. Allowing the reaction mixture to warm to 23 °C results in irreversible attack at the terminal position to afford the anionic allyl complex (**243**). Protonation of the anionic species gives the organic products shown. The anion (**244**) will undergo carbonyl insertion under an atmosphere of CO, followed by intramolecular alkene insertion to eventually afford cyclopentanone products. An intramolecular version is known as well (equation 59).[347] The alkene insertion step does not occur for cyclic dienes; however, protic workup affords the corresponding aldehydes.

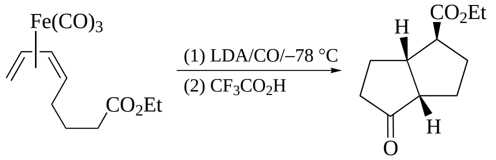

(59)

A number of intramolecular coupling reactions that involve reductive cyclization of a (cyclohexadiene)$Fe(CO)_3$ complex that bears a pendant alkene or diene have been reported.[348,349] Under CO atmosphere, this unusual cyclization presumably produces an intermediate η^3-π-allyl complex that then rearranges via hydride migration. In the case of the pendant diene, a second such process can occur (Scheme 68).

6.3.4 *Reactions Adjacent to the η^4-Diene*

The $Fe(CO)_3$ functionality acts as a sterically bulky substituent attached to the planar diene. Reactions that create a new chiral center adjacent to the diene may occur in a diastereoselective fashion owing to approach of reagents to the complex on the side opposite to the iron center. For example, nucleophilic attack on a carbonyl at C-1 (such as **238**) to afford complexed dienols (**244**) proceeds with high diastereoselectivity for ketones, and with lesser

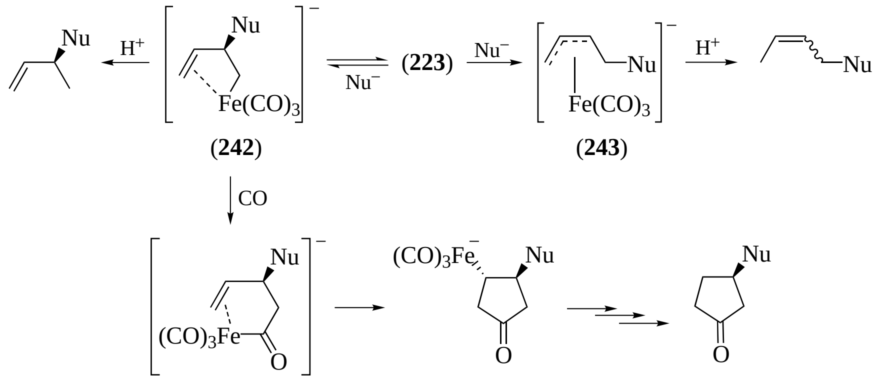
Nu
H+
Nu
Fe(CO)3
Nu−
(223)
Nu−
Nu
Fe(CO)3
H+
Nu
(242)
(243)
CO
Nu
(CO)3Fe
O
(CO)3Fe
Nu
O
Nu
O

Scheme 67

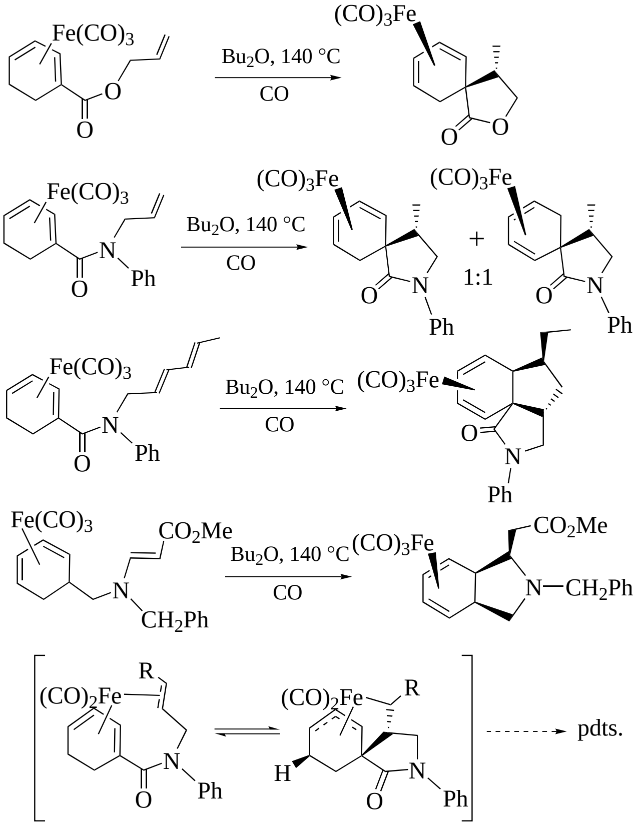
Fe(CO)3
O
O
Bu2O, 140 °C
CO
(CO)3Fe
O
O
Fe(CO)3
N
Ph
O
Bu2O, 140 °C
CO
(CO)3Fe
O
N
Ph
+
1:1
(CO)3Fe
O
N
Ph
Fe(CO)3
N
Ph
O
Bu2O, 140 °C
CO
(CO)3Fe
O
N
Ph
Fe(CO)3
CO2Me
N
CH2Ph
Bu2O, 140 °C
CO
(CO)3Fe
CO2Me
N—CH2Ph
R
(CO)2Fe
N
Ph
O
(CO)2Fe
R
H
O
N
Ph
pdts.

Scheme 68

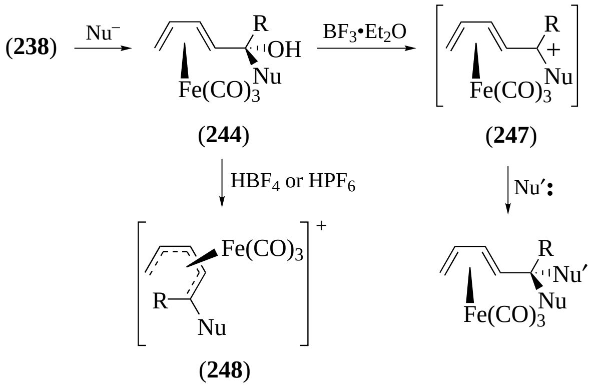
(238)
Nu−
R
OH
Nu
Fe(CO)3
(244)
BF3•Et2O
R
+
Nu
Fe(CO)3
(247)
HBF4 or HPF6
Fe(CO)3
+
R
Nu
(248)
Nu′:
R
Nu′
Nu
Fe(CO)3

Scheme 69

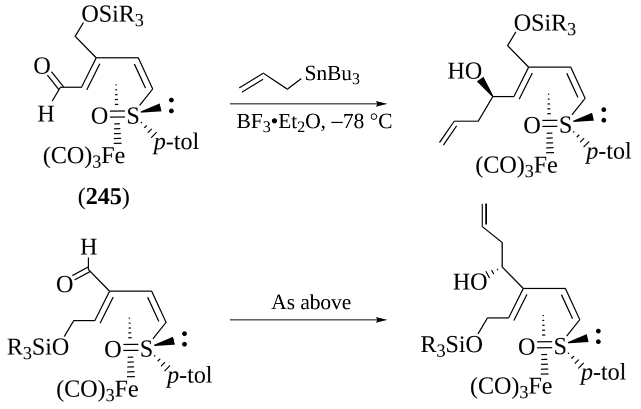
OSiR3
O
H
O=S
p-tol
(CO)3Fe
(245)
SnBu3
BF3•Et2O, −78 °C
OSiR3
HO
O=S
p-tol
(CO)3Fe
H
O
R3SiO
O=S
p-tol
(CO)3Fe
As above
HO
R3SiO
O=S
p-tol
(CO)3Fe

Scheme 70

diastereoselectivity for aldehydes (Scheme 69).[306,307] For those nucleophilic transformations that rely on Lewis acid activation, diastereoselectivity depends on the nature of the Lewis acid.[350] Reaction at a carbonyl at C-2 (such as **240**) can also proceed in a diastereoselective fashion.[263,351] For enantiomerically pure C-2 alkyl, C-1 formyl complexes of type (**245**), nucleophilic addition is diastereoselective (*ca* 7:1) and is favored to proceed through the *s*-trans conformation; for the related C-1 alkyl, C-2 formyl complexes, addition to the *s*-cis conformation is preferred (Scheme 70).[352] Michael additions to α,β-unsaturated diene complexes (**246**) with Grignard reagents or allyl stannane proceed with excellent diastereoselectivity (equation 60).[353,354] Dihydroxylation of alkenes, homo- and hetero-Diels–Alder cycloadditions, dipolar cycloadditions, enolate-Claisen condensations (*see*

Condensation), and enolate alkylations also proceed in highly diastereoselective fashions.[306,307,355–360]

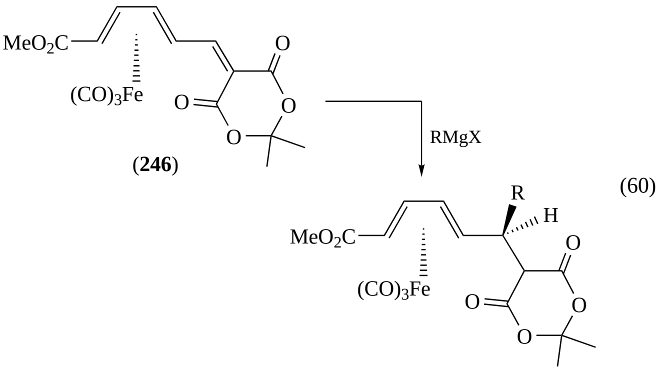

(60)

Substitution of complexed dienols (**244**) or dienol acetates with carbon or heteroatom nucleophiles, in the presence of a Lewis acid, occurs with retention of configuration (Scheme 69). (Alkyl aluminum reagents act as both nucleophile and Lewis acid in this process). This reaction is believed to proceed via stereospecific ionization, with anchimeric assistance from the iron, to generate the transoid pentadienyl cation (**247**) followed by attack of the weak nucleophile on the face opposite to iron.[361,362] The cross-conjugated pentadienyl cation can also be generated; the substitution of (2-acetoxymethyl-1,3-butadiene)Fe(CO)$_3$ (**193**) has previously been discussed (Section 6.1.1).

Protonation of dienol complexes (**244**) with strong acids (e.g. HBF$_4$, HPF$_6$, or HClO$_4$) generates the cisoid (η^5-pentadienyl)iron cations (**248**) (Scheme 69).[363] This reaction is believed to proceed via initial formation of the transoid pentadienyl cation, followed by isomerization to the more stable cisoid form of the cation. Computational methods on the unsubstituted cationic complex (**248**, R = Nu = H) suggest that the cisoid form is 9.2 kcal mol^{-1} more stable.[364] Protonation of an alkene that is adjacent to a diene complex can also lead to the formation of (η^5-pentadienyl)iron cations. Additionally, hydride abstraction using the trityl cation also produces (η^5-pentadienyl)iron cations; the rich chemistry of these species will be described later (Section 7.1).

Deprotonation of tricarbonyl(isoprene)iron generates anion (**249**) which will react with organic electrophiles, such as aldehydes, and alkyl, benzyl, and allyl halides, to give alkylated products (equation 61).[365] The anion is unstable above −30 °C and apparently rearranges to the trimethylenemethane anion (**250**).

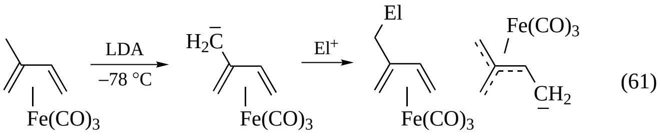

(**249**) (**250**)

(61)

Treatment of α,β-unsaturated complex (**251**) with the basic carbanion LiCH$_2$CN causes a 1,3-migration of the iron tricarbonyl unit rather than deprotonation, with inversion of stereochemistry (Scheme 71).[366] Related 1,5-migrations are also possible using tetraene complexes (**252**), though these proceed with stereochemical retention. Finally, other reactions that can occur adjacent to the iron diene unit include Wittig, Horner-Emmons, or Peterson olefinations, alkene cyclopropanations, and ring-closing metathesis (*see Alkene Metathesis*) catalyzed by Grubbs' ruthenium carbene catalyst.[306,307,354,367]

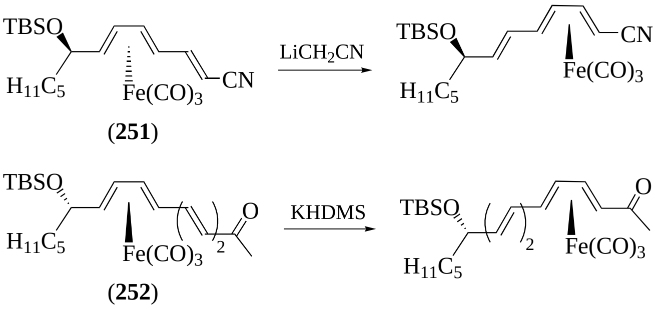

Scheme 71

6.3.5 *Liberation of the Ligand*

The organic ligand of acyclic diene complexes (**223** or derivatives) or cyclohexadiene complexes (**229** or derivatives) may be liberated by oxidation of the metal. Reagents useful for this transformation are CAN/methanol, basic hydrogen peroxide, FeCl$_3$, CuCl$_2$, 3-chloroperbenzoic acid, and trimethylamine *N*-oxide (equation 62).[306,307] Photochemical reduction of (diene)iron complexes in acetic acid gives the corresponding alkene. The regioselectivity for this reaction is good only if the diene is substituted by an electron-withdrawing ligand.[368] Additional reactions that liberate the organic ligand have been discussed (Section 6.3.3). The ease of complexation of the diene, versatile methodology for liberation of the diene ligand, and low cost of the metal, have made the chemistry of diene and dienyl iron complexes of great utility for the synthesis of natural products.

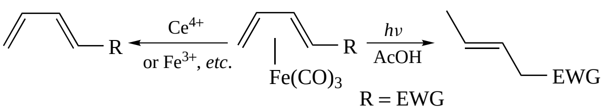

(62)

6.4 Heterodiene Complexes

(Tricarbonyl)iron complexes of α,β-enones (**253**) and vinylimines (**254**) may be prepared by reaction of the organic ligand thermally with (**2**) or photochemically with (**1**). X-ray diffraction analysis of these complexes clearly indicates that the ligand is nearly planar and that iron is bound to all four atoms of the functionality. The heterodiene ligand may be

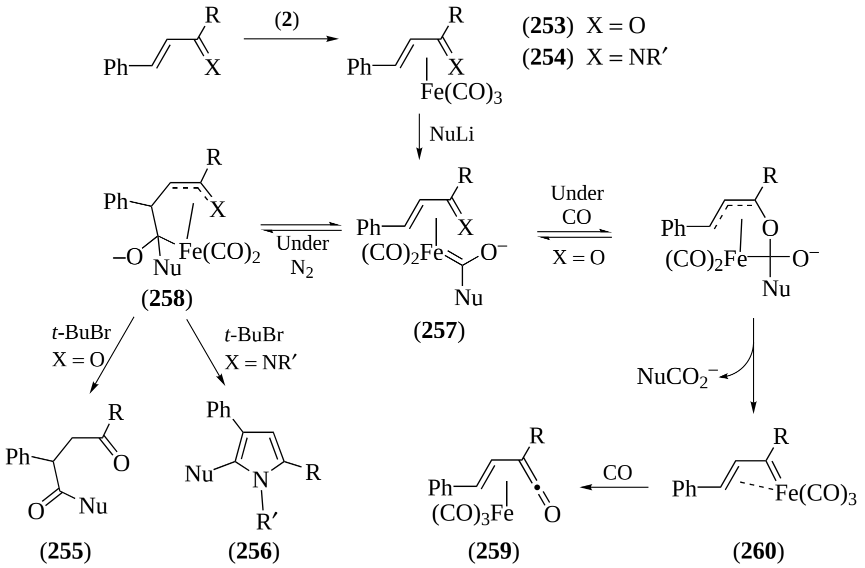

Scheme 72

displaced by treatment of either complex (**253**) or (**254**) with a suitable diene (Section 6.3.1); indeed, benzylidene acetone iron tricarbonyl (**253**, R = CH_3) is a common $Fe(CO)_3$ transfer reagent in organic synthesis. As described in Section 6.3.2, if the heterodiene ligand is chiral, this ligand transfer can occur enantioselectively.[311–313] Vinylimines (**232**) and (**233**) function catalytically in this role.

The reaction of (**253**) or (**254**) with alkyllithium reagents under N_2, followed by workup with *t*-butyl bromide, generates products which have incorporated one of the carbonyl ligands, (**255**) and (**256**), respectively (Scheme 72).[369,370] This reaction probably occurs via initial attack on coordinated carbon monoxide to give the acrylate complex (**257**), followed by coupling to give a heteroallyl anion (**258**), which upon workup gives the products. If the reaction of (**253**; R = H) with alkyllithium reagents is carried out in the presence of an atmosphere of CO, then vinylketene complexes (**259**) are isolated. In this case, the reaction probably proceeds via the acrylate anion (**257**) which couples to the C=O portion of the enone. Under the influence of carbon monoxide as an external ligand, a loss of carboxylate occurs to give the vinylcarbene species (**260**), which inserts a second carbon monoxide to give (**259**) (Scheme 72).[369,370] Vinylketene complexes may also be prepared by the reaction of cyclopropenes with (**2**) (equation 63).[371,372] X-ray diffraction of the vinylketene complexes indicates that the structure may best be represented as a hybrid between an η^4-diene type complex (**259**) and an η^3-allyl-η^1-acyl complex (**261**). The bond distance of (**261**) for C-1–C-2 (ca. 1.45 Å) is longer than for C-2–C-3 or C-3–C-4 (ca. 1.41 Å), the Fe–Cl distance (ca. 1.91 Å) is shorter than the Fe–C-2, Fe–C-3, or Fe–C-4 distances (ca. 2.10 Å), and the ketene C=C=O functionality is nonlinear (bend angle ca. 135°).[372]

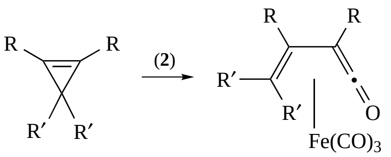

(63)

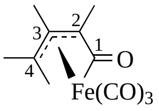

(261)

The vinylketene complexes (**259**) react thermally with isocyanides to afford η^4-vinylketenimine complexes (**262**) (Scheme 73). This reaction proceeds via initial substitution of a carbonyl ligand by the isocyanide. The isocyanide complex then undergoes intramolecular CO deinsertion, and

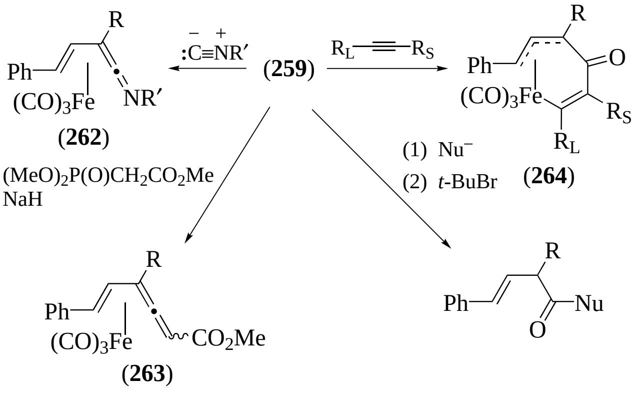

Scheme 73

reinsertion of the isocyanide.[369,370] The vinylketene complexes react with trimethyl phosphonoacetate to afford η^4-vinylallene complexes (**263**). The vinylketene ligand may be liberated by reaction with a variety of carbon and heteroatom nucleophiles, followed by workup with t-butyl bromide, to give products from addition to the ketene carbonyl carbon. As discussed in Section 5.1.3, reaction of alkynes with complexes (**259**) results in the insertion of the alkyne into the Fe–acyl bond to afford the corresponding σ-vinyl–π-allyl complexes (**264**).[373] This insertion is highly regioselective, with the larger alkyne substituent located on the vinyl carbon bound to iron.

Diastereoselective complexations affording chiral heterodiene complexes are also known (Scheme 74).[374–376] The complexation of the enantiomerically pure N-benzyl vinylimines was shown to proceed under kinetic control; equilibration to thermodynamic mixtures possessing poorer diastereomer ratios occurred upon standing. On the other hand, the diastereoselective complexation of an enantiomerically pure enone with a side chain possessing chirality and a chelating phosphite group was shown to proceed under thermodynamic control (Scheme 75).[377] The product (a single diastereomer was formed) could be transformed by nucleophilic addition at the β-position.

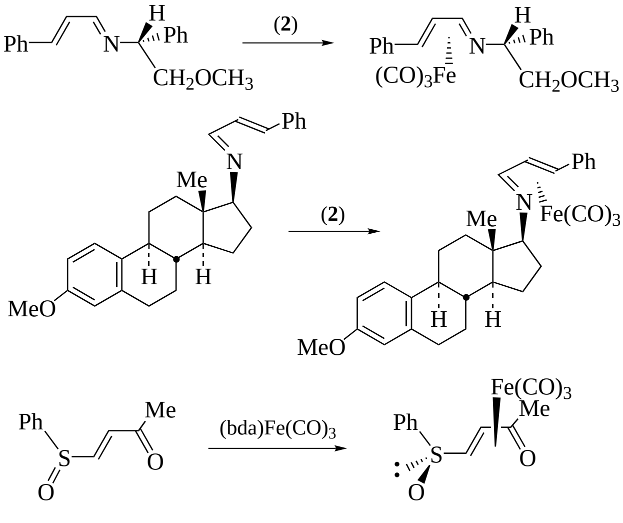

Scheme 74

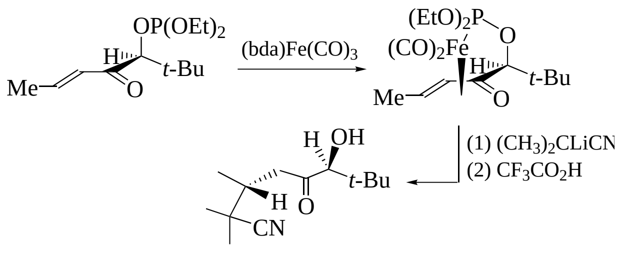

Scheme 75

7 η^5-LIGAND COMPLEXES

7.1 Tricarbonyl(dienyl)Iron Cations[4]

7.1.1 Preparation and Structure

Tricarbonyl(dienyl)iron cations have become an important synthetic intermediate in organic chemistry and have found a significant number of applications in the area of total synthesis. These cations may be prepared and isolated or may be generated transiently and subsequently trapped by nucleophiles. (Cyclohexadiene)iron complexes (**229**) react with the trityl cation to undergo α-hydride abstraction to generate stable and isolable (η^5-cyclohexadienyl)iron cations (**265**) (equation 64).[310,333] This reaction proceeds by removal of a hydride on the cyclic diene face opposite to the iron. For substituted cyclohexadiene complexes, the regioselectivity for the removal of hydride is dictated by the position and nature of the substituents. In many, but not all, cases, the reaction is highly regioselective. (Cycloheptadienyl)iron cations can be generated in an analogous fashion. Alternatively, protonation of (cycloheptatriene)Fe(CO)$_3$ (**266**) or (cyclooctatetraene)Fe(CO)$_3$ (**230**) proceeds on the free alkene, on the face opposite to iron, and results in the formation of cationic (η^5-cycloheptadienyl)Fe(CO)$_3$ complexes (**267**) and (**268**) (Scheme 76).[378] Hydride abstraction to give acyclic (pentadienyl)iron cations is possible for acyclic dienes with a 1-methyl substituent in the *endo* position; however, removal of a hydride from an *exo* 1-methyl substituent does not occur (equation 65).[363]

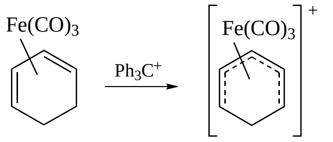

(**229**) (**265**) (64)

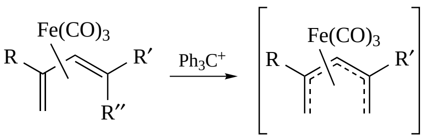

(65)

R″ = Me, R = R′ = H; 50%
R″ = R′ = R = Me; 80%
R = R″ = H, R′ = Me; 0%

The X-ray diffraction analyses of (cyclohexadienyl)iron cations have been reported.[379] These studies reveal that the five carbons of the dienyl portion of ligand are essentially coplanar, the sixth ring carbon is tilted out of this plane away from the iron atom, and one of the carbonyl ligands eclipses the methylene carbon. The ^{13}C NMR spectra of a number of substituted (cyclohexadienyl)iron cations have also been reported.[380] Carbons 2 and 4 appear furthest downfield, and the terminal carbons 1 and 5 appear furthest upfield. A

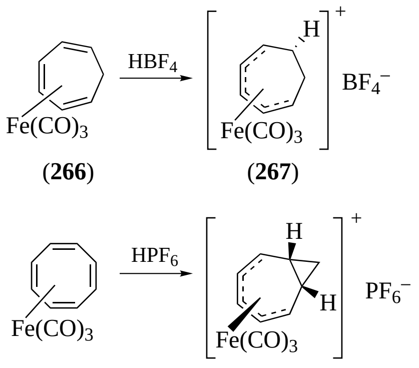

(**266**) (**267**)

(**230**) (**268**)

Scheme 76

methoxy substituent has the greatest effect on the ^{13}C NMR chemical shift.

As described in Section 6.3.4, activation of coordinated dienols (by protonation) or coordinated dienol acetates (by treatment with Lewis acid) affords the corresponding (pentadienyl)iron cations (**248**) (Scheme 69).[363] Since the acyclic pentadienyl cationic complexes do not have the geometrical constraints of their cyclic counterparts, they can potentially adopt either a cisoid (‘U’) or transoid (‘S’, sickle) conformation. Nearly all of the (pentadienyl)iron cations prepared appear to be in the cisoid conformation by ^{1}H NMR spectroscopy. Only a single, sterically biased transoid pentadienyl cation (**269**) has been spectroscopically observed, but not isolated (equation 66).[381] Owing to their potential to undergo ‘U’ to ‘S’ conformational inversion in solution, and owing to the considerably higher reactivity of the less stable ‘S’ conformer, the (pentadienyl)iron cations are considerably more sensitive to moisture than their cyclic counterparts.

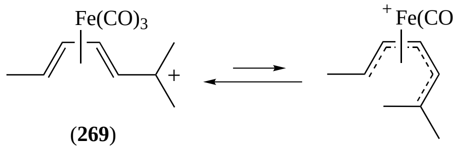

(**269**) (66)

7.1.2 Reactions

The (dienyl)iron cations of type (**248**) and (**265**) are susceptible to reaction with nucleophiles. For the (cyclohexadienyl)iron cations, nucleophilic attack always occurs at a terminal carbon, on the face of the ligand opposite to the metal, to afford η^4-cyclohexadiene products. Typical nucleophiles used are malonate anions, amines, electron-rich aromatics, silyl ketene acetals, enamines, hydrides, and allyl silanes; intramolecular nucleophilic addition is also possible. The addition of highly basic organometallic nucleophiles (Grignard reagents, organolithiums) is often problematic; this may be overcome by replacing one of the iron carbonyl ligands with the poorer π-acceptor triphenylphosphine, where the diminished electron-accepting ability of the unsaturated ligand reduces the electron-transfer process that otherwise interferes with nucleophilic addition. Alternatively, softer organometallic reagents such as organozincs or organocadmiums can be used. While dialkylcuprates are effective nucleophiles with unalkylated (cyclohexadienyl)iron cations, lower order mixed cuprates R(Me_2S)CuLi should be employed with alkyl-substituted analogs. Regarding the regioselectivity of nucleophilic attack, for unsymmetrically substituted (cyclohexadienyl)iron cations this is dependent on the steric and electronic influence of the substituents and on the nature of the nucleophile.[310,333,382] A typical case is that of the (1-alkyl-4-methoxycyclohexadienyl)iron cation (**270**), which undergoes nucleophilic attack at the substituted terminus (equation 67).[383] When R = Me, nucleophilic addition is regioselective (as shown), however, when R is a longer alkyl chain the regioselectivity diminishes and addition to the other end of the η^5-cation system becomes competitive. This loss of regioselectivity is overcome by using the more sterically demanding isopropyl analog of (**270**). Alternatively, selectivity in the formation of the quaternary carbon is enhanced by replacing one of the carbonyl ligands with a triphenylphosphine.[384,385] On the other hand, if R possesses a terminal phosphine or phosphinite group that is capable of forming a bridged chelate complex, the regioselectivity of nucleophilic addition can be reversed (equation 68). Since these reactions (equation 67) generate 2-methoxy-1,3-cyclohexadiene complexes, and since the ligand may be readily liberated by mild oxidation of iron, this reactivity has been utilized in the synthesis of a variety of natural products.[310,333]

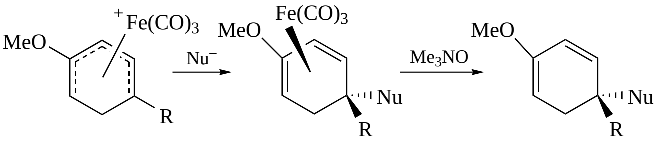

(**270**)

(67)

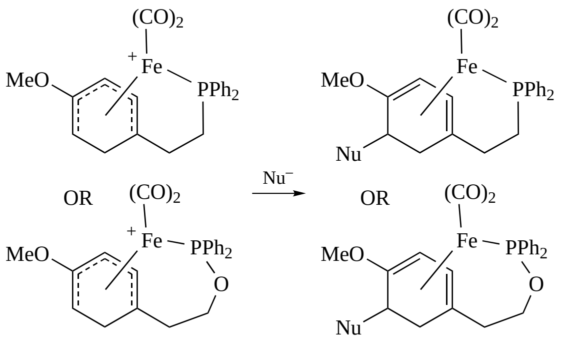

(68)

In comparison, the (cycloheptadienyl)iron cations, for example, (**271**, L = CO), are not well-behaved, tending to undergo nucleophilic attack at the terminal (C-1, C-5) as well as at internal (C-2, C-4) carbon atoms (equation 69).[386,387] However, this limitation can be overcome by replacement of a CO ligand with triphenylphosphite (L = $P(OPh)_3$); nucleophilic addition to the terminal position of the unsaturated ligand is completely regioselective and stereoselective.[4] Treatment of this product with trityl cation selectively produces another (cycloheptadienyl)iron cation, which may undergo a second nucleophilic addition with total regioselectivity and stereoselectivity (equation 70).

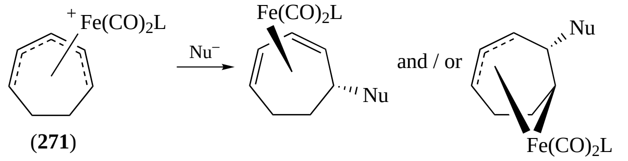
$^+$Fe(CO)$_2$L
Nu$^-$
Fe(CO)$_2$L
Nu
and / or
Nu
Fe(CO)$_2$L

(271)

(69)

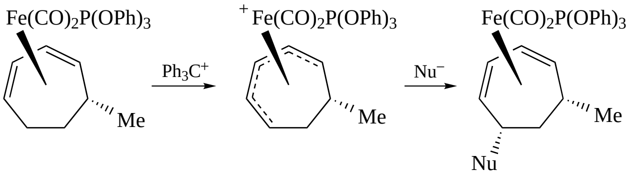
Fe(CO)$_2$P(OPh)$_3$
Me
Ph$_3$C$^+$
$^+$Fe(CO)$_2$P(OPh)$_3$
Me
Nu$^-$
Fe(CO)$_2$P(OPh)$_3$
Me
Nu

(70)

Some progress has been made in performing asymmetric variations of this chemistry. Addition of the anion of sulfoximine ester (**272**) to achiral (cycloheptadienyl)iron cation complex (**271**, L = $P(OPh)_3$), followed by desulfurization, affords enantiomerically enriched (**273**, 50% ee) (Scheme 77).[388] In a similar manner, addition of the enolate derived from a chiral *N*-acyloxazolidinone (**274**) to achiral (cyclohexadienyl)iron cation complex (**275**) and subsequent auxiliary removal affords (**276**, 70% ee).

A number of oxidative cyclizations have been formed that appear to proceed via transiently formed cyclic (cyclohexadienyl)iron cation complexes. Early examples of this methodology focused on oxygen nucleophiles (Scheme 78); more recent applications have employed aryl amines or quinone-imines used to prepare indoles and related heterocycles (Scheme 79).[389–391] This chemistry has found significant application towards the synthesis of carbazole alkaloids. Finally, related iron-mediated spiroannelations (*see Spirocyclic Compound*) have been reported, with either electron-rich aromatics or vinylogous carbamates as the nucleophilic species.[392] Isotopic labeling (*see Isotopes & Isotope Labeling*) evidence suggests that the reactions proceed through an intermediate vinyl-substituted η^5-(cyclohexadienyl) iron cation, (**277**) (Scheme 80).

The reactivity of acyclic (pentadienyl)iron cations with carbon and heteroatom nucleophiles has been examined. Nucleophilic attack may occur on either the cisoid or transoid conformation of the ligand. In general, it has been found that attack by weak nucleophiles (water, alcohols, weakly basic

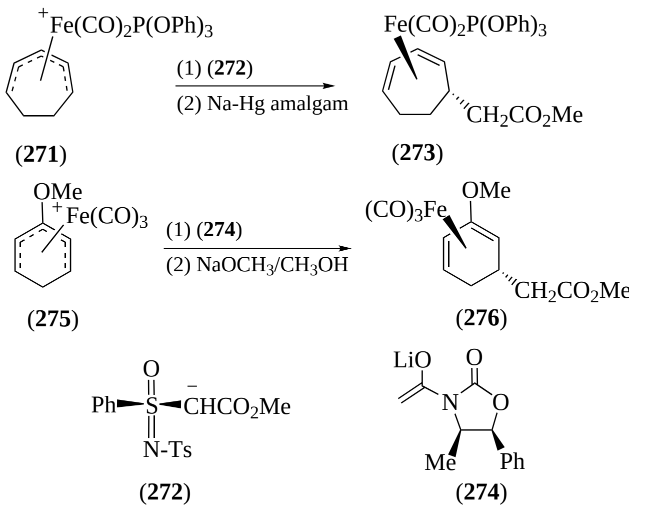
$^+$Fe(CO)$_2$P(OPh)$_3$
(1) (**272**)
(2) Na-Hg amalgam
Fe(CO)$_2$P(OPh)$_3$
CH$_2$CO$_2$Me
(**271**)
(**273**)
OMe
$^+$Fe(CO)$_3$
(1) (**274**)
(2) NaOCH$_3$/CH$_3$OH
(CO)$_3$Fe
OMe
CH$_2$CO$_2$Me
(**275**)
(**276**)
O
Ph
S
CHCO$_2$Me
N-Ts
LiO
O
N
O
Me
Ph
(**272**)
(**274**)

Scheme 77

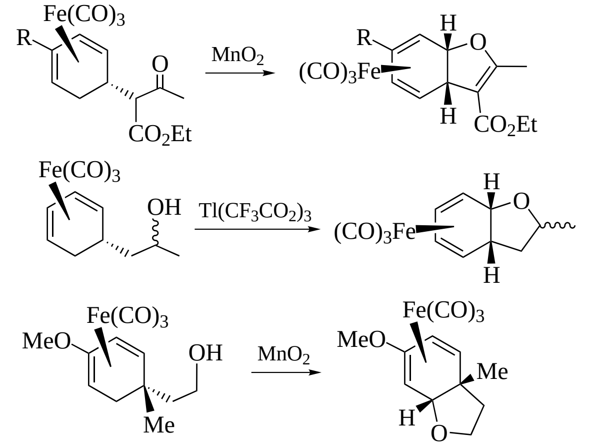
Fe(CO)$_3$
R
O
CO$_2$Et
MnO$_2$
(CO)$_3$Fe
R
H
O
H
CO$_2$Et
Fe(CO)$_3$
OH
Tl(CF$_3$CO$_2$)$_3$
(CO)$_3$Fe
H
O
H
Fe(CO)$_3$
MeO
OH
Me
MnO$_2$
Fe(CO)$_3$
MeO
Me
H
O

Scheme 78

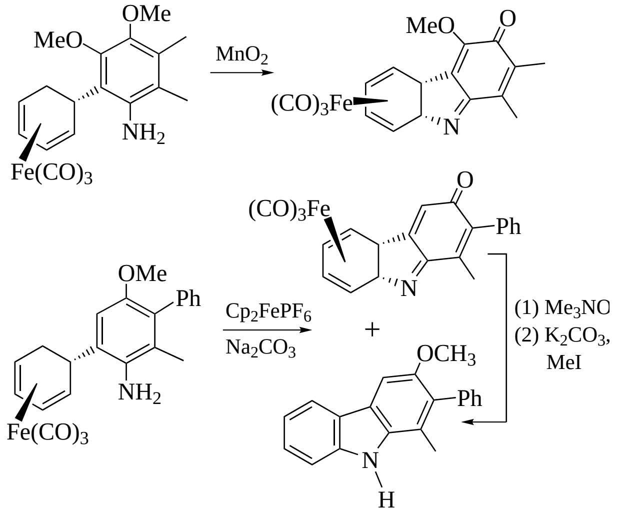
OMe
MeO
NH$_2$
Fe(CO)$_3$
MnO$_2$
MeO
O
(CO)$_3$Fe
N
(CO)$_3$Fe
O
Ph
N
OMe
Ph
NH$_2$
Fe(CO)$_3$
Cp$_2$FePF$_6$
Na$_2$CO$_3$
+
OCH$_3$
Ph
N
H
(1) Me$_3$NO
(2) K$_2$CO$_3$,
MeI

Scheme 79

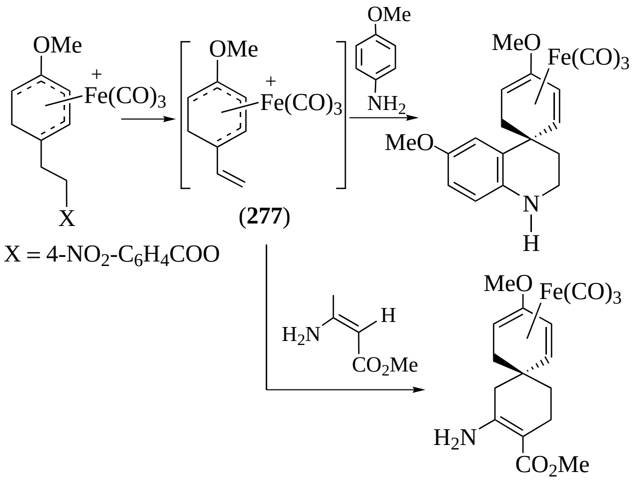
OMe
Fe(CO)3
X
X = 4-NO2-C6H4COO
OMe
Fe(CO)3
(277)
OMe
NH2
MeO
Fe(CO)3
MeO
N
H
H2N
H
CO2Me
MeO
Fe(CO)3
H2N
CO2Me

Scheme 80

amines, electron-rich aromatics, or allylsilanes) occurs on the less stable, and therefore more reactive, transoid conformer of the pentadienyl cation.[393] Conversely, strong nucleophiles (malonate, hydride reagents, and organocuprates) are known to react with the more stable cisoid conformer. In general, attack by the stronger nucleophiles usually occurs at the terminal position (C-1, C-5) of the ligand to afford *cis* diene products;[394] however, several examples of attack at the internal carbons (C-2, C-4) have been noted (equation 71).[395] Attack at the more substituted terminal position of the ligand (to give the less-substituted η^4-iron diene complex) is significantly favored when one of the carbonyl ligands is replaced by triphenylphosphine.[396]

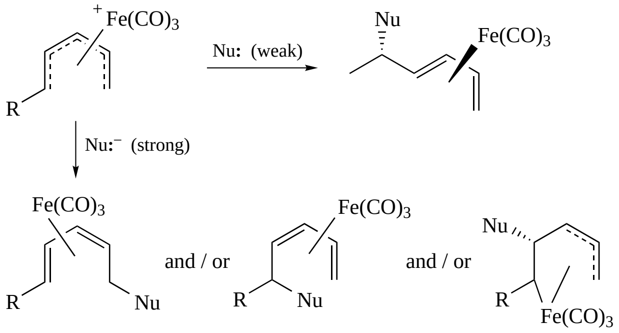
+Fe(CO)3
R
Nu: (weak)
Nu
Fe(CO)3
Nu:⁻ (strong)
Fe(CO)3
R
Nu
and / or
Fe(CO)3
R
Nu
and / or
Nu
R
Fe(CO)3

(71)

As discussed earlier (Section 6.3.4), acyclic (pentadienyl)iron cations are intermediates in reactions involving protonation or Lewis acid activation of iron dienol or dienol acetate complexes. With appropriate functionalization, these cations may also be trapped intramolecularly (Scheme 81). In the case of the formation of tetrahydrofurans (**278**) and (**279**), equilibration of the transoid and cisoid cations is observed.[397] However, this equilibration is not observed in the stereoselective cyclization to provide (racemic) oxocene (**280**).[398] Analogous intramolecular cyclizations of sulfur and nitrogen nucleophiles have also been reported.[399] Cyclizations may also be initiated by protonation of an alkene; thus far either tethered alkenes or an electron-rich aromatic have been shown to participate in this diastereoselective process (Scheme 82).[400]

A variation on the theme of generating an acyclic (pentadienyl)iron cation by activation of a leaving group adjacent to an η^4-iron diene complex has led to the development of a highly diastereoselective 1,5-nucleophilic substitution with concurrent 1,2-migration of the $Fe(CO)_3$ fragment (Scheme 83).[367] Conversion of an iron dienal complex into the unstable *O*-diethylphosphoryl cyanohydrin (**281**) provided the required substrate for the substitution/migration reaction, which occurs stereospecifically depending on the reaction conditions. Since the nitrile of the product can be readily reduced to the corresponding aldehyde, an iterative process is possible and can produce multiple and adjacent chiral centers. The process can also be performed on enantiomerically pure material without any loss of stereochemical fidelity.

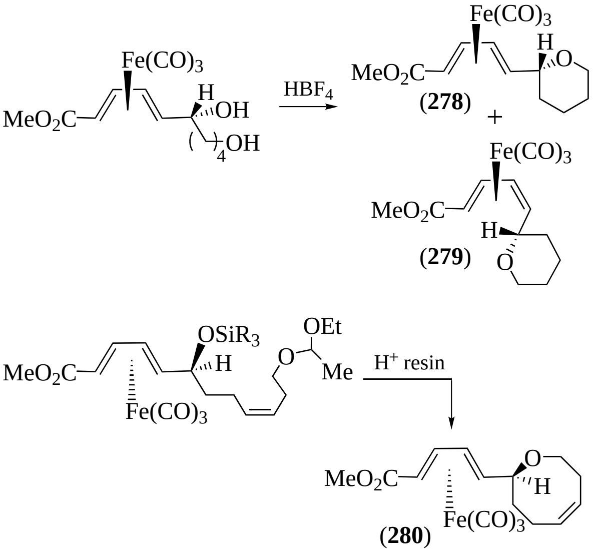
Fe(CO)3
MeO2C
H
OH
( )4 OH
HBF4
Fe(CO)3
MeO2C
H
O
(278)
+
Fe(CO)3
MeO2C
H
O
(279)
OSiR3
H
OEt
O
Me
MeO2C
Fe(CO)3
H+ resin
MeO2C
O
H
Fe(CO)3
(280)

Scheme 81

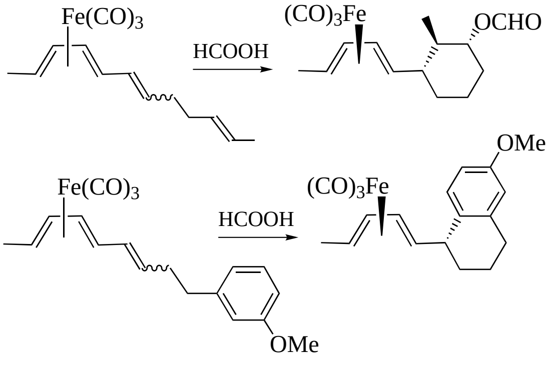
Fe(CO)3
HCOOH
(CO)3Fe
OCHO
Fe(CO)3
HCOOH
(CO)3Fe
OMe
OMe

Scheme 82

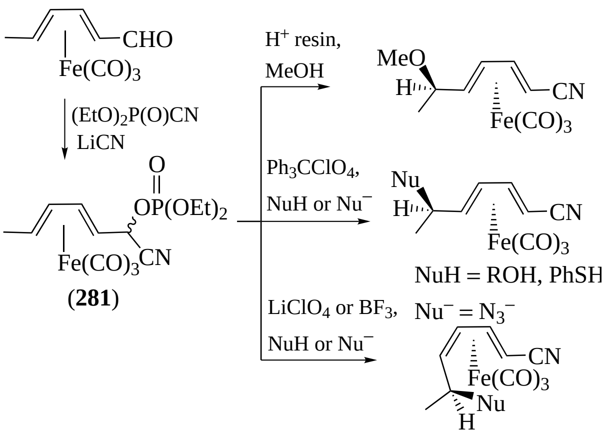

Scheme 83

7.1.3 Cross-conjugated Dienyliron Cations

Dehydration of (2-hydroxymethyl-1,3-butadiene)iron complexes or (hydroxymethyltrimethylenemethane)iron complexes with fluorosulfonic acid/liquid sulfur dioxide generates the corresponding (cross-conjugated dienyl)iron cations (**194**) (equation 72).[276] The ^1H and ^{13}C NMR spectral data for these cations favor an η^4-TMM-methyl cationic structure (**282**) over an η^4-isoprenyl cationic structure (**283**). These cations react with water or alcohols to afford butadiene products via nucleophilic attack at C-5. As indicated earlier (Section 6.1.1), the cross-conjugated dienyl cations are believed to be intermediates in the substitution of (**193**) with weak carbon nucleophiles (Scheme 53). In these cases, nucleophilic attack occurs on C-4 to give predominantly TMM products.[263]

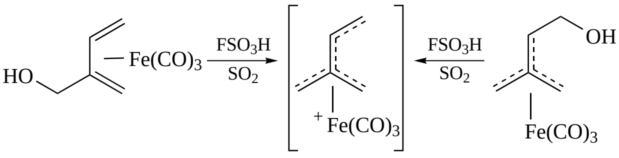

(**194**)

(72)

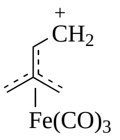

(**282**)

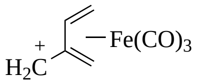

(**283**)

7.2 Ferrocene and its Derivatives

The discovery of ferrocene and the establishment of its structure in the 1950s mark the beginning of modern organometallic chemistry. Today ferrocene chemistry is ubiquitous, and numerous significant applications are to be found in the areas of homogenous catalysis, asymmetric organic synthesis, and materials science. Owing to space limitations, it is not possible here to provide a complete listing of these applications; the reader should seek out more comprehensive sources, such as the 1995 nomograph edited by Togni and Hayashi.[401] There are also a number of more recent review articles available.[402–411]

The reaction of cyclopentadienylmagnesium bromide with $FeCl_3$ was reported by Kealy and Pauson to afford the orange crystalline $Fe(C_5H_5)_2$ (mp 173 °C), which they formulated as a bis-σ-bonded complex.[412] A similar complex was reported by Miller, Tebboth, and Tremaine.[413] This compound was subsequently shown to be the first recognized 'sandwich' complex (*see Sandwich Compound*), and was termed ferrocene (*see Ferrocene*) by Whiting because of its aromatic character.[414] Ferrocene (**284**) has been shown to assume a D_{5h} structure by gas-phase electron diffraction,[415] and is only twisted by 9° from D_{5h} below its Λ-point (164 K) in the solid state. The lengths of the Fe–C bonds and the C–C bonds are 2.064 and 1.440 Å, respectively, and the hydrogen atoms are bent out of the cyclopentadienyl plane towards the iron atom by about 4°. The barrier to rotation of the cyclopentadienyl ligands with respect to each other is an extremely low 3.8 kJ mol^{-1}. Owing to the small energy difference between eclipsed (D_{5h}) and staggered (D_{5d}) conformations, substituted ferrocenes have been found to adopt both conformations.[416] Ferrocene gives a single signal in ^1H (4.04 ppm), ^{13}C (68.2 ppm) and ^{57}Fe (+1535.2 ppm with respect to $Fe(CO)_5$) NMR spectra.[32,318,417] The compound is air and water stable and has a $\Delta H_f°$ of 158 ± 4 kJ mol^{-1}.

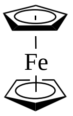

(**284**)

There are numerous methods for the preparation of ferrocene, the most common being the reaction of alkali cyclopentadienyl anions with $FeCl_2$.[418] Ferrocene itself is commercially available and considerably inexpensive. The preparation of substituted ferrocenes will be discussed in subsequent sections.

7.2.1 Electrophilic Attack

Because it is an electron-rich compound, ferrocene reacts with electrophiles. The reaction of (**284**) in strong acid affords the protonated species $[(C_5H_5)_2FeH]^+$ (**285**). The hydrogen is attached to iron, as evidenced by an upfield signal in the ^1H NMR spectrum at ca. −12 ppm.[419] In the case of substituted ferrocenes, the two Cp ligands are tilted with restricted rotation about the Cp–Fe axes.[420] The ring protons of (**284**) undergo exchange, even in weakly acidic solution. Since (**285**) is formed in substantial quantities only in strongly acidic media, it seems unlikely that it is involved in proton exchange, and that the σ-ligand complex (**286**), formed by direct protonation on the cyclopentadienyl ligand, is the intermediate species. In addition, H/D exchange of (**284**) occurs at slower rates in highly acidic solution.[421]

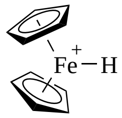

(**285**)

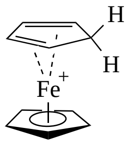

(**286**)

Ferrocene reacts with acetyl chloride and aluminum chloride to afford the acylated product (**287**) (Scheme 84). The Friedel–Crafts acylation of (**284**) is about 3.3×10^6 times faster than that of benzene.[419] Use of these conditions it is difficult to avoid the formation of a disubstituted product unless only a stoichiometric amount of $AlCl_3$ is used. Thus, while the acyl substituent present in (**287**) is somewhat deactivating, the relative rate of acylation of (**287**) is still rapid (1.9×10^2 faster than benzene). Formation of the diacylated product may be avoided by use of acetic anhydride and $BF_3{\cdot}Et_2O$. Electrophilic substitution of (**284**) under Vilsmeyer formylation, Mannich aminomethylation, or acetoxymercuration conditions gives (**288**), (**289**), and (**290**/**291**), respectively, in good yields.[422] Racemic amine (**289**) (also available in two steps from (**287**)) is readily resolved, providing the classic entry to enantiomerically pure ferrocene derivatives that possess central chirality and/or planar chirality. Friedel–Crafts alkylation of (**284**) proceeds with the formation of a mixture of mono- and polyalkyl-substituted ferrocenes. The reaction of (**284**) with other electrophiles (e.g. NO_2^+) is not as successful, owing to facile oxidation of ferrocene to the ferricinium cation (**292**) (also known as the ferricenium or ferrocenium cation).

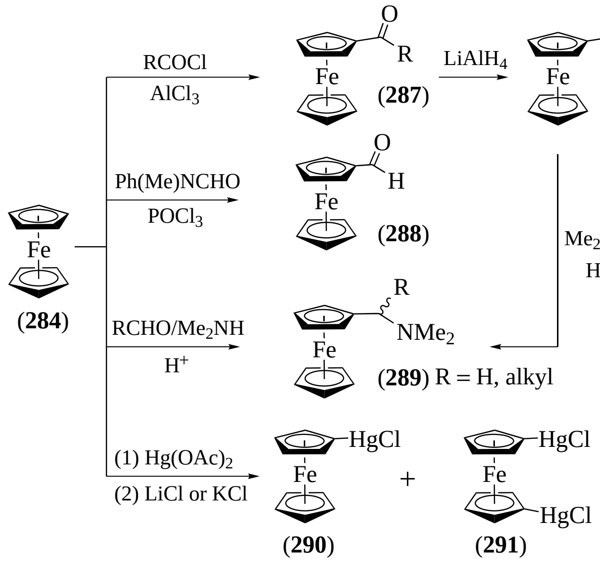

Scheme 84

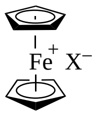

(**292**)

There are a number of pathways possible for the electrophilic substitution of (**284**) (Scheme 85). Pathway (a) involves electrophilic attack at iron to generate (**293**). This pathway is suggested by the results of protonation of ferrocene. Subsequent transfer of the electrophile to the *endo* face of the Cp ligand gives (**294**). Alternatively, direct electrophilic attack on the *endo* face of the ligand, pathway (b), could give (**294**). The fact that facile intramolecular acylation of 3-ferrocenylpropionic acid (**295**), a compound which is constrained to suffer only attack from the *endo* face, gives [3]ferrocenophane (**296**) suggests that the *endo* attack route is feasible.[423] A third possibility, path (c), involves direct electrophilic attack on the less hindered *exo* face of the Cp ligand to give (**297**) followed by loss of a proton.

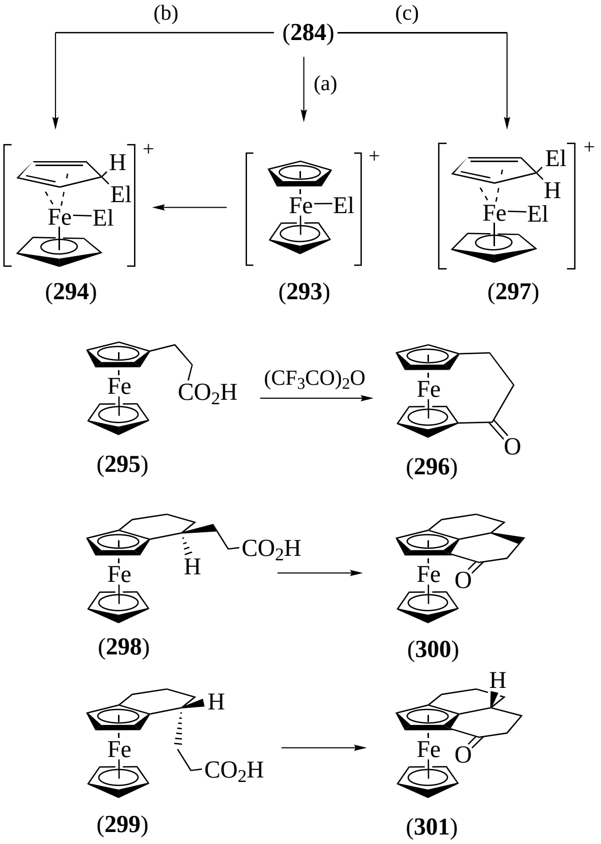

Scheme 85

The relative rates of intramolecular cyclization of the *exo* and *endo* isomeric carboxylic acids (**298**) and (**299**) to give (**300**) and (**301**), respectively, is ca. 4 (k_{exo}/k_{endo}).[424] If it is assumed that electrophilic attack, and not loss of a proton, is the rate limiting step, then these results imply that there may not be a preference for *endo* attack in intermolecular acylation reactions. It has been proposed that the direction of electrophilic attack is dependent on the strength of the electrophile: for strong electrophiles (e.g. RCO^+), the rate-determining step is attack from the *exo* face (pathway c); for weaker electrophiles (e.g. $AcOHg^+$), attack from the *endo* face (pathway b) is followed by slow loss of the proton. In agreement with this analysis, the kinetic isotope effect (*see Isotope Effect*) for acetoxymercuration of (**284**) is $k_H/k_D = 3.2$ while the isotope effect for acylation of (**284**) is $k_H/k_D = 1.0$.[425]

Reaction of (**284**) with an aldehyde, ketone, or enol ether in the presence of acid results in an electrophilic substitution that produces α-ferrocenylalkyl carbocations that may be trapped by nucleophiles (azides, amines, thiols). This chemistry may be used to prepare enantiomerically pure ferrocene derivatives in a manner that avoids resolution procedures (Scheme 86).[401] For example, the enol ether from (-)-menthone affords a kinetic carbocation (**302**) that may be trapped or allowed to rearrange to the more thermodynamically stable cation (**303**) and then trapped, thus offering a means of controlling the configuration of the stereocenter adjacent to the ferrocene unit. Use of an enantiomerically pure aldehyde derived from α-pinene (**304**) affords a 1:1 carbocationic mixture that similarly isomerizes to a single cation.

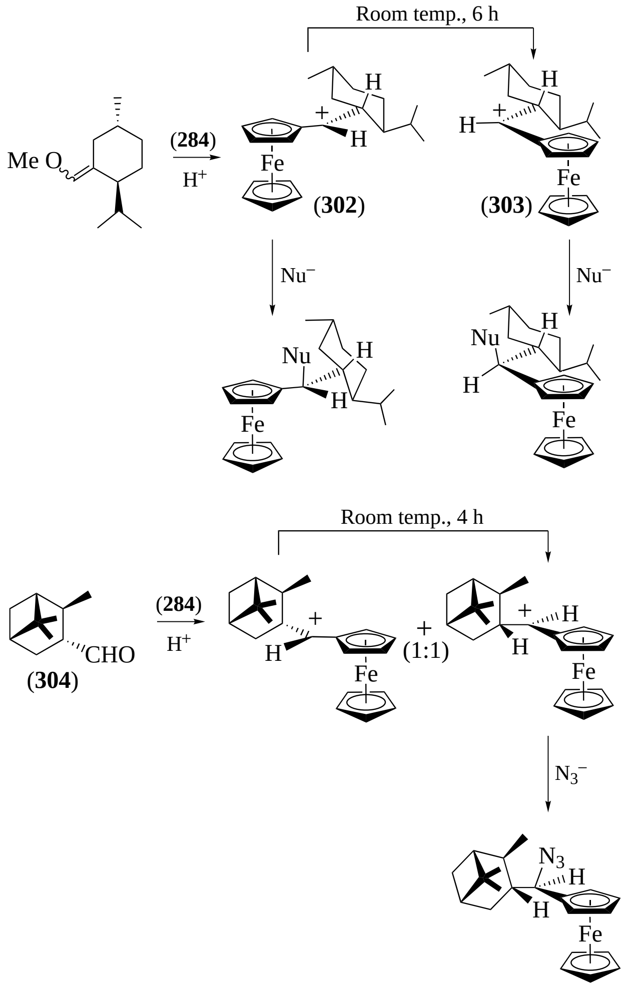

Scheme 86

7.2.2 *Oxidation*

Oxidation of ferrocene gives the 17-electron ferricinium ion (**292**) that is deep red in concentrated solutions. This has been shown electrochemically to be a reversible oxidation with $E_{1/2}$ of 0.34 versus SCE (*see* ***Electrochemistry: Applications in Inorganic Chemistry***). The reaction may be used in the quantitative determination of ferrocene and has been suggested by the IUPAC Commission on Electrochemistry as a standard for measuring redox potentials (*see Redox Potential*) in nonaqueous solutions.[426] Ferrocene (**284**) and the ferricinium cation (**292**) undergo rapid electron exchange which is first order in both with an E_a of $21 \pm 4\,\mathrm{kJ\,mol^{-1}}$. The admixture of ferrocene or substituted ferrocenes with tetracyanoquinodimethane (TCNQ) generates charge-transfer salts. Certain of these salts display semiconductor behavior (*see* ***Semiconductors***).[427]

7.2.3 *Reactions at the Side Chains*

The solvolysis of (1-acetoxyethyl)ferrocene (**305**) in 80% aqueous acetone proceeds at a rate which is ca. 6.5 times faster than the solvolysis of trityl acetate.[428] The rapid rate of this S_N1 solvolysis is attributed to the tremendous stability of the intermediate α-ferrocenylcarbocation (**306**). A review of the relevant literature through 1979 concerning this species has been published.[429] The solvolysis occurs in a stereospecific fashion. Thus, the (*R*)-acetate (**305**) upon solvolysis gives the (*R*)-alcohol (**307**) and acetylation of (*R*)-(**307**) gives (*R*)-(**305**). The acetate (*R*)-(**305**) can be converted into the trimethylammonium salt (*R*)-(**308**) via (*R*)-(**289**), and subsequent solvolysis gives (*R*)-(**305**). Thus, the solvolysis and aminolysis reactions must occur with retention of configuration. It has been suggested that the solvolysis occurs by neighboring group participation of the iron atom, and thus the net inversion is due to preferential ionization of the acetate opposite to iron, followed by rapid nucleophilic attack at the carbocation on the face opposite to the bulky ferrocene substituent. In accord with this proposal, solvolyses of both the *exo* and *endo* acetates (**309**) and (**310**) affords the *exo* alcohol (**311**). However, the solvolysis of (**309**) occurs 2500 times faster than solvolysis of (**310**). The activation entropies for solvolysis of (**309**) and (**310**) are similar, so the difference in rate must not be due to steric hindrance effects on the departure of the *endo* acetate functionality.

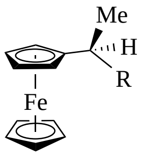

(**305**) R = OAc
(**307**) R = OH
(**308**) R = NMe_3^+

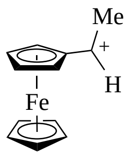

(**306**)

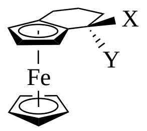

(**309**) X = OAc, Y = H
(**310**) X = H, Y = OAc
(**311**) X = OH, Y = H

The α-ferrocenyl carbocation complexes are also generated by dissolution of the corresponding alcohols or alkenes in acid (e.g. conc. H_2SO_4 or CF_3CO_2H); the cationic species are detectable by NMR. For cation (**306**) in CF_3CO_2H the signals of the substituted Cp ligand appear as a series of four distinct signals (4.49–6.36 ppm). The presence of four signals indicates that there is restricted rotation, on the NMR timescale, about the Cp to α-C bond. The barrier to rotation is $84.0\,kJ\,mol^{-1}$, which is consistent with the stereoselective solvolysis results.

A number of models to explain the stabilizing effect of the α-ferrocenyl substituent have been proposed.[429] The most acceptable model maintains a planar cyclopentadienyl ligand; however, the carbocation substituent is displaced out of the cyclopentadienyl plane toward the iron metal. X-ray diffraction analysis of the α-ferrocenyl carbocation (**312**) is consistent with this model. The diphenylmethyl substituent is bent out of the Cp plane by 20.7° and each of the two Cp rings are planar tilted by 9.3° with respect to being parallel. The α-C–Fe distance (2.715 Å) is considerably longer than normal Fe–C bond distances (ca. 2.1 Å).[430] Extended Hückel calculations of the parent α-ferrocenyl carbocation (**313**) indicate that the carbocation is tilted out of the Cp plane in the lowest energy structure. The positive charge on the iron metal is $+0.5$, with the remainder of the positive charge being distributed on the carbon atoms. The ground state is determined by computation to be a singlet state (*see Singlet State*); however, positioning the carbocation atom in the plane of the cyclopentadienyl ligand (cf. **314**) results in a triplet ground state.[431] Nonamethylferrocenyl carbocations (**315**) may be prepared from the corresponding carbinols. The cation (**315**; R = H) slowly undergoes dimerization in the solid state and more rapidly in solution to afford the bisferricinium cation (**316**). Cations (**315**) with greater steric hindrance (e.g. R = mesityl) give ^1H NMR and Mössbauer spectra which are consistent with the presence of both singlet and triplet species.[432]

Ferrocenyl ketones (**287**) and ferrocenyl aldehyde (**288**) readily undergo a number of classic organic transformations, such as aldol, Knoevenagel, and Wittig reactions. Conversion of (**288**) into the dimethylaminoacetonitrile (**317**)

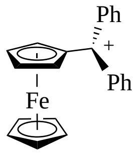

(**312**)

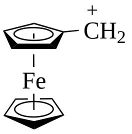

(**313**)

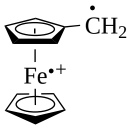

(**314**)

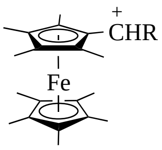

(**315**)

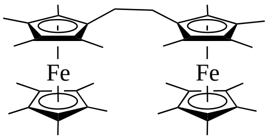

(**316**)

followed by treatment with MeMgI provides another approach to the Ugi-amine (**289**, R = CH_3), which is resolved by using (*R*)-(+)-tartaric acid (equation 73).[4] The preparation and resolution of this compound allowed for the development of chiral ferrocene-based ligands. Another approach involves asymmetric alkylation of (**288**), leading to chiral secondary alcohols with excellent selectivities (up to 99% ee), and is accomplished with dialkylzincs in the presence of a chiral amino alcohol (equation 74).[403] As described above, this can be used as an approach to chiral amines by conversion to the corresponding acetate and subsequent aminolysis in a stereoretentive manner. Alternatively, (**288**) can be converted into an enantiomerically pure hydrazone and then selectively alkylated with an organolithium nucleophile. After hydrogenation of the product hydrazine, acetylation gives *N*-acetylamines in high optical purity (up to 94% ee) (equation 75).[403] Finally, asymmetric reduction (with BH_3 and the Corey/Bakshi/Shibata catalyst (CBS) catalyst) of ferrocenyl ketones and diketones (*see Diketones*) can also be readily accomplished.[433,434]

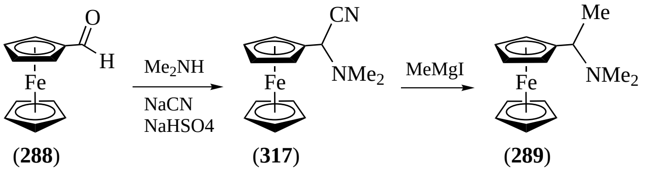

(73)

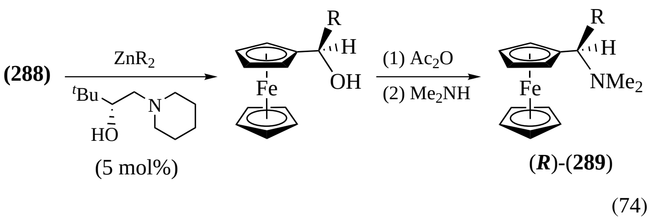

(74)

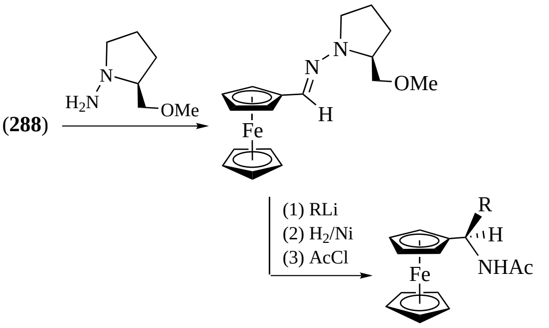
(288)
H_2N
N
OMe
Fe
H
(1) RLi
(2) H_2/Ni
(3) AcCl
R
H
NHAc

(75)

Ferrocenoyl chloride (**318**), ethyl ferrocenecarboxylate (**319**), and cyanoferrocene (**320**) are all used as starting materials for the synthesis of 2-ferrocenyloxazolines (**321**) (Scheme 87). Chirality may be incorporated into the oxazoline ring, and these important chiral compounds have been used to prepare a great number of ferrocene derivatives that are used as catalysts in asymmetric synthesis.[404]

7.2.4 Metalation and Metalation-derived Ferrocenes

Ferrocene is weakly acidic and treatment of (**284**) with *n*-butyllithium affords the lithiated species (**322**) (equation 76). In the presence of *N*,*N*,*N*′,*N*′-tetramethylethylenediamine TMEDA), treatment of (**284**) gives the 1,1′-dilithiated species (**323**).[435] A number of other metalated ferrocene derivatives containing a M–C bond (M = B, Cu, Si, P, Ge, As, Sn) can be prepared from (**322**) and (**323**).[401] Lithiation of alkyl-substituted ferrocenes occurs both homo- and heteroannularly, while the lithiation of *N*,*N*-dimethylaminomethylferrocene (**289**, R = H) is directed to the 2-position by chelation with the nitrogen lone pair (*see Lone Pair*), to give (**324**) (Scheme 88).[435] Anion (**324**) and products generated by the addition of appropriate electrophiles are planar chiral. For analogs bearing a chiral center, such as (*R*)-(1-dimethylaminoethyl)ferrocene (**289**, R = Me), this directed lithiation can occur with high diastereoselectively, and (**289**, R = Me) is preferentially converted to the (*R*, *R*)-lithiated derivative (**325**, 96:4 dr). This is a highly significant transformation, as it created a multitude of opportunities for the development of new chiral catalysts using compounds related to this type of planar chiral ferrocene as bidentate ligands. For example, chiral ferrocenyl bis- and monophosphines (**326**, PPFA) and (**327**, BPPFA) are prepared using this methodology. The diastereomer (**328**) may be prepared by formation of (**325**) and blocking this site toward further lithiation with a removable silyl group. Subsequent lithiation, transmetalation (*see Transmetalation*), and deprotection gives (**328**).[401,405]

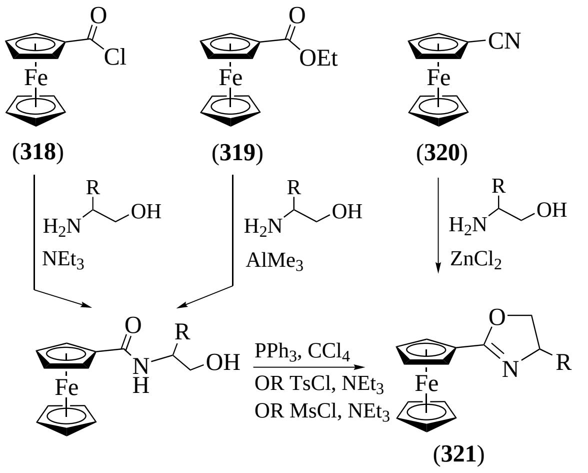
O
Cl
Fe
(318)
O
OEt
Fe
(319)
CN
Fe
(320)
R
H_2N
OH
NEt_3
$AlMe_3$
$ZnCl_2$
O
R
N
H
OH
Fe
PPh_3, CCl_4
OR TsCl, NEt_3
OR MsCl, NEt_3
O
N
R
Fe
(321)

Scheme 87

Additional ligand families can be prepared via further modification of ferrocenes (**326**), (**327**), or (**328**). Retentive S_N1–like displacement of the dimethylamino group with secondary phosphines affords ferrocenyl bisphosphines (**329**, Josiphos), and the use of primary phosphine gives the tridentate (*see Tridentate Ligand*) bisferrocene (**330**, Pigiphos) (Scheme 89).[401] Additionally, pyrazoles of type (**331**) are available, or a two-step process via acetate (**332**) provides ferrocenes with hydroxylated or aminated side chains (**333**) (Scheme 90). Using iodine as an electrophile for anion (**325**) affords iodoferrocene (**334**) that leads to a family of *trans*-chelating diphosphine bisferrocenes by means of a nickel-catalyzed coupling process (**335**, TRAP). Finally, double asymmetric reduction of the ferrocene diketone (**336**)

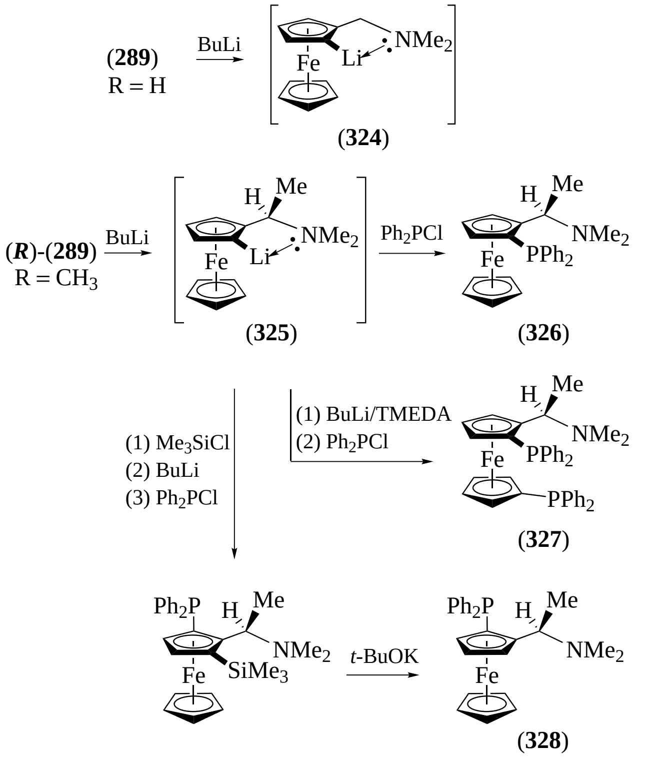
(289)
R = H
BuLi
Fe
Li
NMe_2
(324)
(R)-(289)
R = CH_3
BuLi
H
Me
NMe_2
Fe
Li
(325)
Ph_2PCl
H
Me
NMe_2
Fe
PPh_2
(326)
(1) Me_3SiCl
(2) BuLi
(3) Ph_2PCl
(1) BuLi/TMEDA
(2) Ph_2PCl
H
Me
NMe_2
Fe
PPh_2
PPh_2
(327)
Ph_2P
H
Me
NMe_2
Fe
$SiMe_3$
t-BuOK
Ph_2P
H
Me
NMe_2
Fe
(328)

Scheme 88

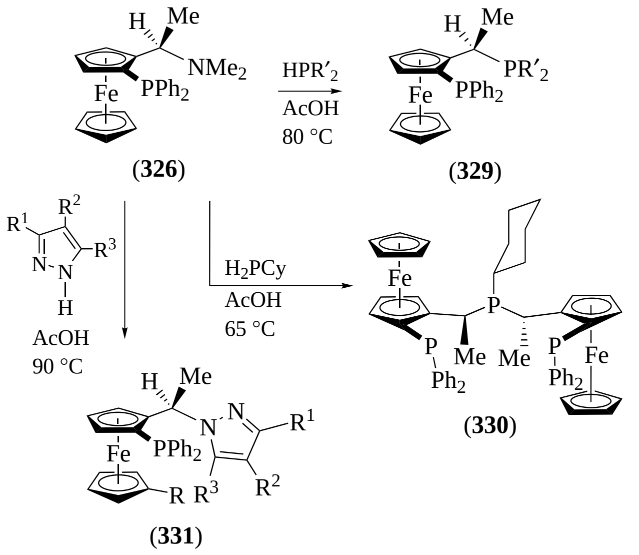
H
Me
NMe$_2$
Fe
PPh$_2$
(326)
HPR′$_2$
AcOH
80 °C
H
Me
PR′$_2$
Fe
PPh$_2$
(329)
R^1
R^2
R^3
N
N
H
AcOH
90 °C
H$_2$PCy
AcOH
65 °C
Fe
P
P
Ph$_2$
Me
Me
P
Ph$_2$
Fe
(330)
H
Me
N
N
R^1
Fe
PPh$_2$
R
R^3
R^2
(331)

Scheme 89

and subsequent manipulation of the product diol produces a family of C_2-symmetric ferrocene bis-aminophosphines (**337**) (equation 77).[436]

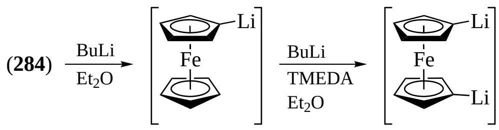
(284)
BuLi
Et$_2$O
Li
Fe
(322)
BuLi
TMEDA
Et$_2$O
Li
Fe
Li
(323)

(76)

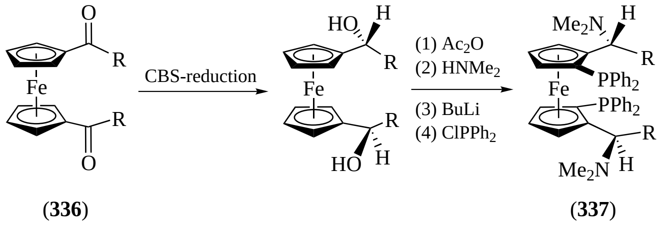
O
R
Fe
R
O
(336)
CBS-reduction
HO
H
R
Fe
R
HO
H
(1) Ac$_2$O
(2) HNMe$_2$
(3) BuLi
(4) ClPPh$_2$
Me$_2$N
H
R
Fe
PPh$_2$
PPh$_2$
R
Me$_2$N
H
(337)

(77)

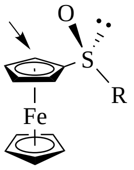

(**338**)

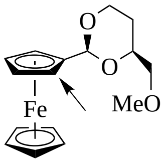

(**339**)

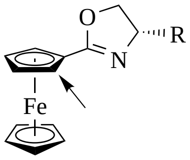

(**321**)

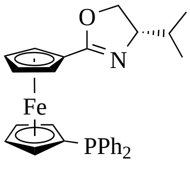

(**340**)

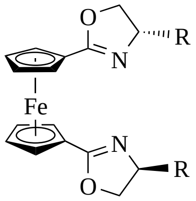

(**341**)

Many of the ferrocene ligand families described above are derived from a resolved chiral precursor (i.e. **289**). Efforts to prepare planar chiral ferrocenes also employ other strategies that rely on a directed metalation (*see Orthometalation*). Sulfoxide (**338**), acetal (**339**), and oxazolines of type (**321**)

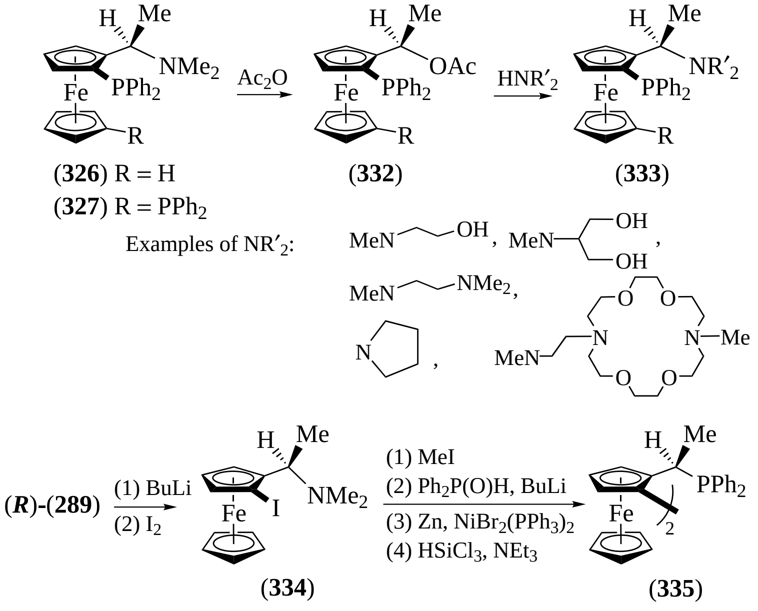
H
Me
NMe$_2$
Fe
PPh$_2$
R
Ac$_2$O
H
Me
OAc
Fe
PPh$_2$
R
HNR′$_2$
H
Me
NR′$_2$
Fe
PPh$_2$
R
(326) R = H
(327) R = PPh$_2$
(332)
(333)
Examples of NR′$_2$:
MeN
OH
MeN
OH
OH
MeN
NMe$_2$
N
O
O
MeN
N
N
Me
O
O
(R)-(289)
(1) BuLi
(2) I$_2$
H
Me
Fe
I
NMe$_2$
(334)
(1) MeI
(2) Ph$_2$P(O)H, BuLi
(3) Zn, NiBr$_2$(PPh$_3$)$_2$
(4) HSiCl$_3$, NEt$_3$
H
Me
PPh$_2$
Fe
2
(335)

Scheme 90

are all selectively metalated at the indicated position and are trapped with electrophiles; for (**340**) and (**341**) good selectivity depends greatly on conditions (lithiating agent, solvent, stoichiometry).[407] The numerous derivatives of oxazoline (**321**) prepared in this manner are also used as ligands in asymmetric synthesis, particularly those that possess phosphorus or sulfur atoms on the ferrocene ring adjacent to the oxazoline.[404] These derivatives are further elaborated into still more variations; an example is bisferrocene (**342**) (equation 78). A direct nonauxiliary based approach is performed by use of (-)-sparteine to mediate enantioselective deprotonation of *N*,*N*-diisopropyl ferrocenecarboxamide (**343**) to produce (**344**) (Scheme 91).[437] Similarly, the C_2-symmetric bisphosphine (**345**) or bissulfide (**346**) can be prepared this way with high enantioselectivity by sequential deprotonations, while a matched chiral-directed metalation of (-)-menthylferrocenesulfonate (**347**) proceeds with a diastereoselectivity of *ca.* 90:10.[438,439]

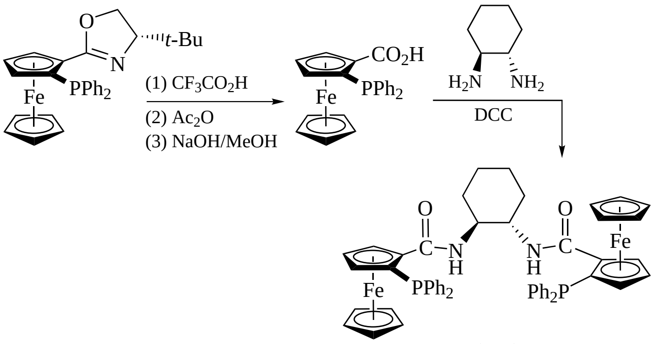
O
t-Bu
N
Fe
PPh2
(1) CF3CO2H
(2) Ac2O
(3) NaOH/MeOH
CO2H
Fe
PPh2
H2N
NH2
DCC
O
O
C
N
H
N
H
C
Fe
Fe
PPh2
Ph2P

(**342**)

(78)

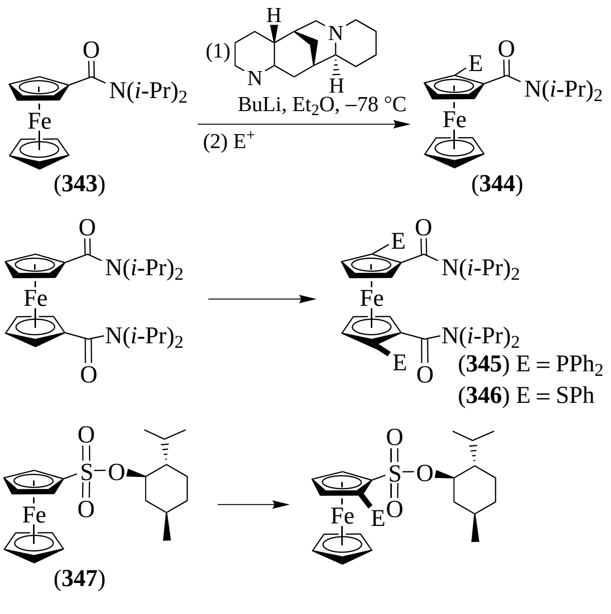
O
N(i-Pr)2
Fe
(1)
H
N
N
H
BuLi, Et2O, –78 °C
(2) E+
E
O
N(i-Pr)2
Fe
O
N(i-Pr)2
Fe
N(i-Pr)2
O
E
O
N(i-Pr)2
Fe
N(i-Pr)2
E
O
O
S
O
O
Fe
O
S
O
Fe
E
O

(**343**)

(**344**)

(**345**) E = PPh$_2$

(**346**) E = SPh

(**347**)

Scheme 91

Metalation of sulfinylferrocene (**338**) to give the lithiated species, followed by transmetalation to give either the isolable boron analog (**348**) or the nonisolable zinc analog (**349**), is an approach used to access yet another class of ferrocene derivatives (equation 79).[440–442] Palladium-catalyzed coupling of (**348**) or (**349**) with aryl iodides affords planar chiral aryl ferrocenes that are converted by standard transformations into planar chiral monophosphine aryl ferrocenes (**350**) that are also useful ligands in asymmetric catalysis. With appropriate *ortho*-substitution on the aryl ring, ferrocenes that possess axial chirality as well as planar chirality are prepared; if the *ortho*-substitutent is a second phosphine unit, access to a bisphosphine aryl ferrocene is achieved.[443]

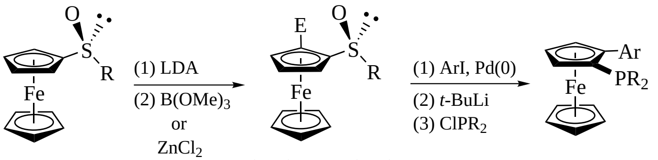
O
S
R
Fe
(1) LDA
(2) B(OMe)3
or
ZnCl2
E
O
S
R
Fe
(1) ArI, Pd(0)
(2) t-BuLi
(3) ClPR2
Ar
PR2
Fe

(**338**)
R = *p*-tol

(**348**) R = B(OH)$_2$
(**349**) R = ZnL$_n$

(**350**)
R = Ph, Cy

(79)

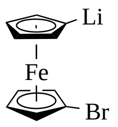

(**351**)

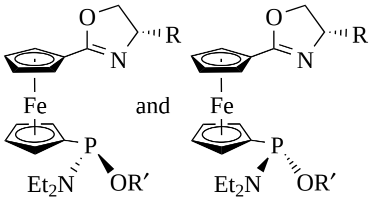
O
R
N
Fe
P
Et2N
OR′
and
O
R
N
Fe
P
Et2N
OR′

(**353**)

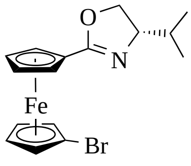

(**352**)

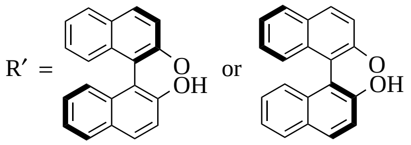

Lithioferrocene (**322**) or dilithioferrocene (**323**) can also be prepared, and then utilized *in situ*, from the corresponding halo- or dihaloferrocenes by halogen-metal exchange with alkyl lithiums. Alternatively, monolithiation of 1,1′-dibromoferrocene gives rise to anion (**351**), which may be reacted with an electrophile in order to afford additional ferrocene derivatives. In this way, monophosphine oxazoline ferrocene (**340**) is prepared from bromo oxazoline ferrocene (**352**), a compound that also is used to prepare chiral-at-phosphorus ferrocenes (**353**).[444,445] Other chiral-at-phosphorus ferrocenes (**354**) are made from (**323**) and a phosphite borane as the electrophile (equation 80).[446,447] The phosphorus atoms may also be contained in a ring that possesses chirality; the sequences used to prepare this family

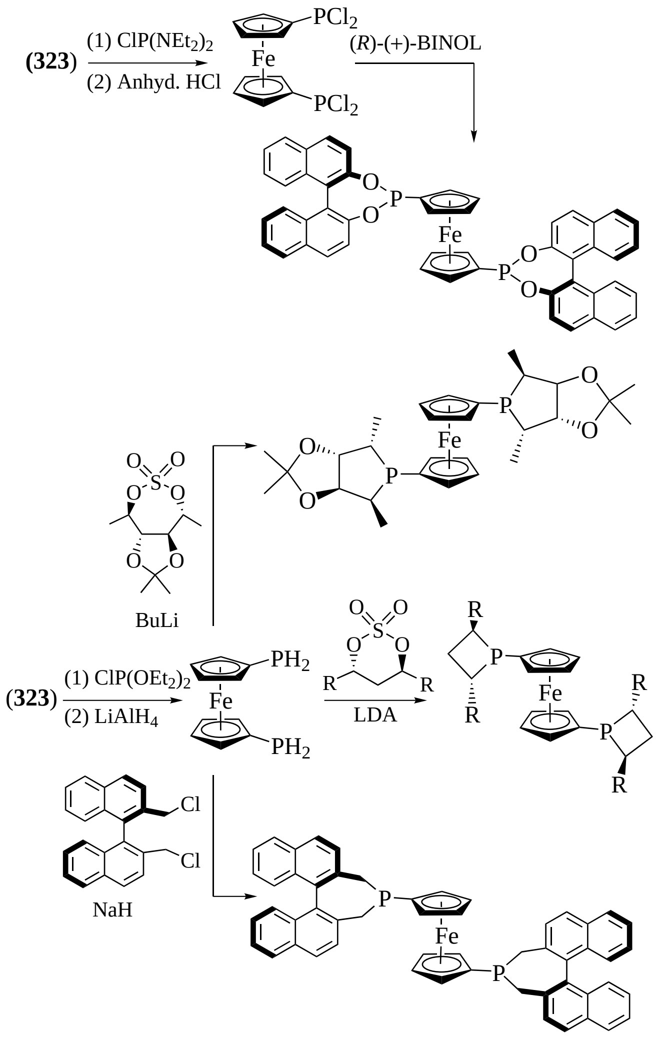
(323)
(1) ClP(NEt2)2
(2) Anhyd. HCl
PCl2
Fe
PCl2
(R)-(+)-BINOL
BuLi
(323)
(1) ClP(OEt2)2
(2) LiAlH4
PH2
Fe
PH2
LDA
R
NaH
Cl
Cl

Scheme 92

of ferrocene ligands also begin with (**323**) (Scheme 92).[448–451]

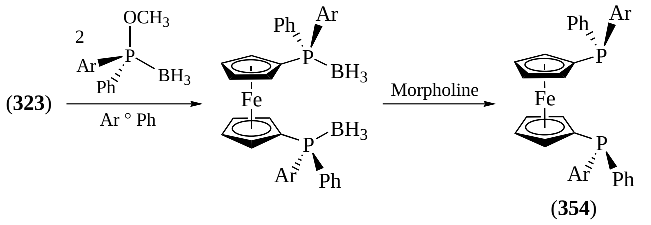
2
OCH3
Ar
Ph
BH3
(323)
Ar ° Ph
Morpholine
Fe
(354)

(80)

7.2.5 Ferrocenes from Chiral Cyclopentadienylides

There are a number of examples of chiral ferrocene derivatives prepared by reaction of substituted cyclopentadiene anions with $FeCl_2$ or a monocyclopentadienyl iron species rather than using the strategy of introduction and modification of a side chain on ferrocene itself. Addition of methyl lithium to chiral fulvene (**355**) produces the chiral cyclopentadienylide which reacts with Cp*Fe(acac) to give the heteroleptic (*see Heteroleptic Compound*) metallocene (*see Metallocene Complexes*); replacement of the chiral auxiliary gives (**356**), the monoCp* analog of Ugi-amine (**289**) in 75% ee (Scheme 93).[452] Similarly, chiral dianion (**357**) is converted into (**358**) or (**359**).[453] Also, mannitol-derived cyclopentadienylide (**360**) and chiral cyclopentadienylide (**361**) produce C_2-symmetric ferrocenes (**362**) and (**363**) (Scheme 94).[454,455] Both heteroleptic ferrocene analogs and C_2-symmetric ferrocenes are available in high optical purity by the use of (-)-sparteine-mediated deprotonation (equation 81).[456]

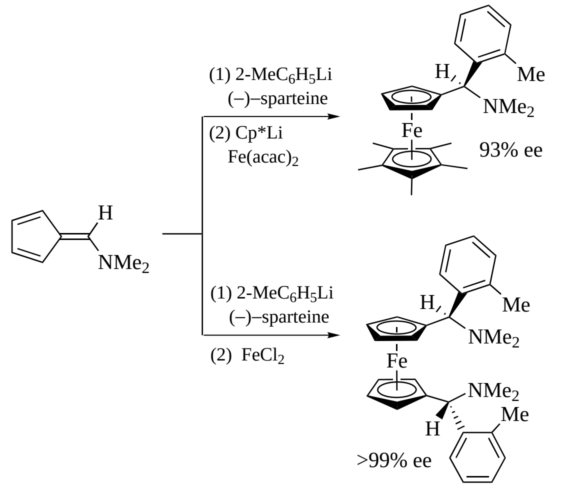
H
NMe2
(1) 2-MeC6H5Li
(–)–sparteine
(2) Cp*Li
Fe(acac)2
H
Me
NMe2
Fe
93% ee
(1) 2-MeC6H5Li
(–)–sparteine
(2) FeCl2
Fe
>99% ee

(81)

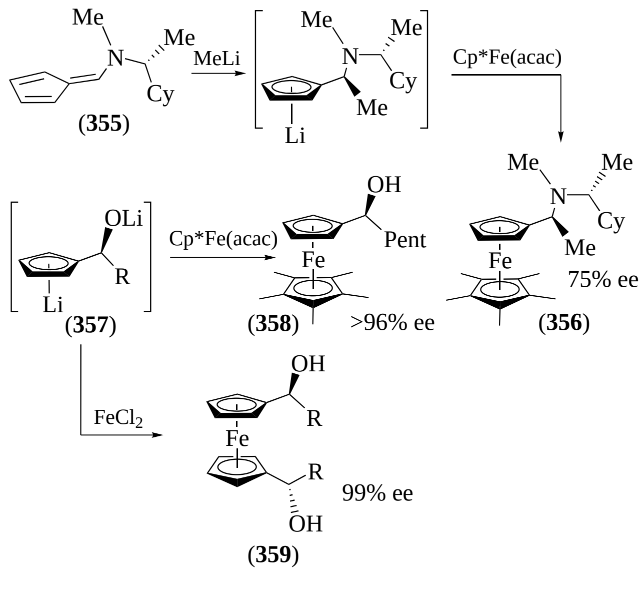
Me
Me
N
Cy
(355)
MeLi
Li
Cp*Fe(acac)
OLi
R
(357)
Cp*Fe(acac)
OH
Pent
Fe
(358)
>96% ee
75% ee
(356)
FeCl2
OH
R
99% ee
(359)

Scheme 93

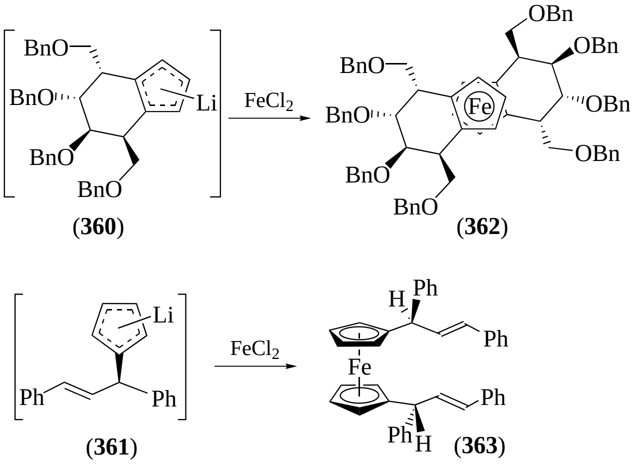
BnO
BnO
BnO
BnO
Li
FeCl$_2$
(360)
OBn
OBn
OBn
OBn
BnO
BnO
BnO
BnO
Fe
(362)
Li
Ph
Ph
FeCl$_2$
(361)
H
Ph
Ph
Fe
Ph
Ph
H
(363)

Scheme 94

7.2.6 *Heteroatom-substituted Ferrocenes*

Some aspects of the preparation of heteroatom-substituted ferrocenes have previously been discussed (Section 7.2.4); a review article that covers this topic through 1994 is available and offers a more complete treatment than can be presented here.[401] Borylation and diborylation of ferrocene is readily accomplished using BBr_3 or BI_3; the haloborylferrocenes provide access to a large number of aminoboryl-, alkylboryl-, thioboryl-, and boronateferrocenes by treatment with amines, alkylstannanes, thiols, and alcohols, respectively (Scheme 95). Methyl- and phenylbromoborylferrocene are available by direct addition of Br_2BMe or Br_2BPh to ferrocene.[457] Ferrocene boronic acid (**364**) and ferrocene diboronic acid (**365**) are both commercially available, and are prepared by treatment of lithio- or dithioferrocene (**322**, **323**) with trialkylborates followed by hydrolysis. These boronic acids can undergo Suzuki couplings to provide aryl-substituted ferrocenes or be converted into the ferrocenyl acetates.[401,458]

Mercurioferrocenes (**290**) and (**291**) are separable by Soxhlet extraction and these may be used to prepare bromoferrocene or dibromoferrocene or the iodo analogs. Alternatively, these halogenated ferrocenes are prepared from the ferrocene boronic acids or from anions (**322**) or (**323**).[401] Bromoferrocene is the starting material for cyanoferrocene, azidoferrocene, or aminoferrocenes, generally in the presence of a copper salt. Aminoferrocene can be acylated to produce an amide, or converted to isocyanoferrocene by a formylation/dehydration sequence (Scheme 96).[459] The 1,1′-diisocyanoferrocene is available from the bis(acyl)azide, itself derived from ferrocene dicarboxylic acid.[460]

Hydroxyferrocene is prepared by hydrolysis of ferrocene acetate, and it undergoes many of the same organic transformations (alkylation, silylation, acylation, acetal formation) that are carried out with phenol. Access to thioferrocene or dithioferrocene is easily accomplished by treatment of anions (**322**) or (**323**) with elemental sulfur, and a number of alkylated and metalated derivatives are known. Finally, a great number of coordination compounds that possess a transition metal center directly bound to the ferrocene unit are known; this topic is beyond the scope of this review.[401]

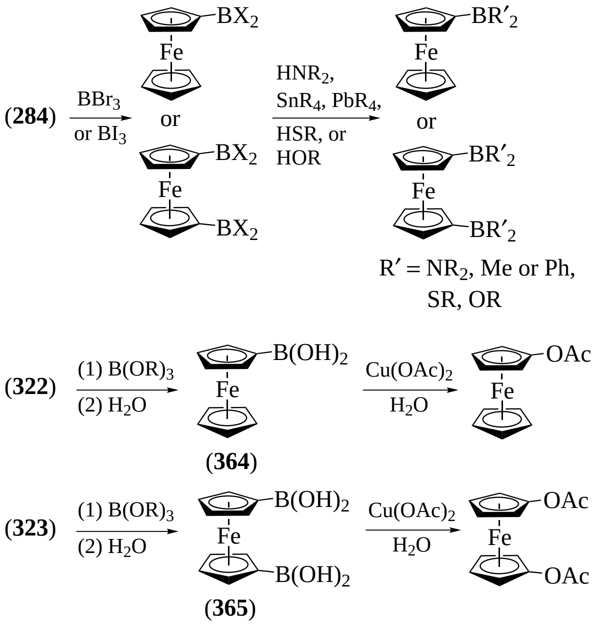
(284)
BBr$_3$
or BI$_3$
BX$_2$
Fe
or
BX$_2$
Fe
BX$_2$
HNR$_2$,
SnR$_4$, PbR$_4$,
HSR, or
HOR
BR′$_2$
Fe
or
BR′$_2$
Fe
BR′$_2$
R′ = NR$_2$, Me or Ph,
SR, OR
(322)
(1) B(OR)$_3$
(2) H$_2$O
B(OH)$_2$
Fe
(364)
Cu(OAc)$_2$
H$_2$O
OAc
Fe
(323)
(1) B(OR)$_3$
(2) H$_2$O
B(OH)$_2$
Fe
B(OH)$_2$
(365)
Cu(OAc)$_2$
H$_2$O
OAc
Fe
OAc

Scheme 95

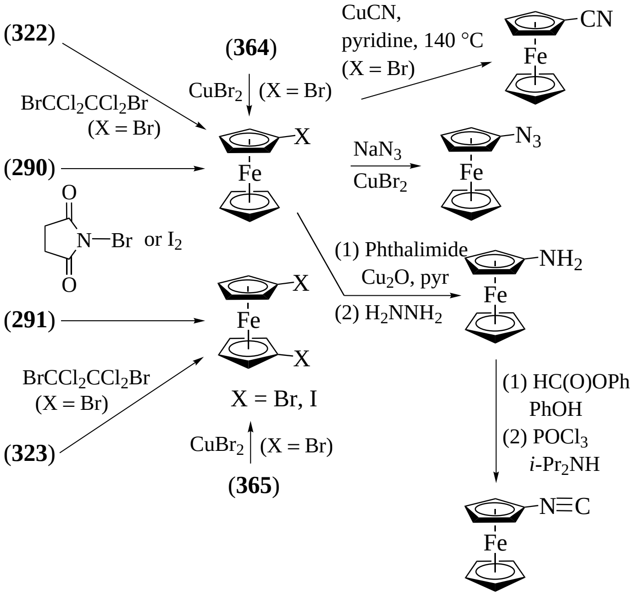
(322)
BrCCl$_2$CCl$_2$Br
(X = Br)
(290)
N—Br or I$_2$
(291)
BrCCl$_2$CCl$_2$Br
(X = Br)
(323)
(364)
CuBr$_2$ (X = Br)
X
Fe
X
Fe
X
X = Br, I
CuBr$_2$ (X = Br)
(365)
CuCN,
pyridine, 140 °C
(X = Br)
CN
Fe
NaN$_3$
CuBr$_2$
N$_3$
Fe
(1) Phthalimide
Cu$_2$O, pyr
(2) H$_2$NNH$_2$
NH$_2$
Fe
(1) HC(O)OPh
PhOH
(2) POCl$_3$
i-Pr$_2$NH
N≡C
Fe

Scheme 96

A series of planar chiral pyridine-fused ferrocene analogs (**366**) have been prepared and the enantiomers are resolved by chiral High performance (pressure) liquid chromatography (HPLC) (*see High Performance Liquid*

Chromatography) (equation 82).[408] These complexes are used as enantioselective nucleophilic catalysts for reactions such as the rearrangements of *O*-acylated azlactones, oxindoles, and benzofuranones, and the kinetic resolution of secondary alcohols via acylation. X-ray crystal structures have been obtained for *N*-acylated derivatives of (**366**), allowing for characterization of a likely intermediate along the catalytic pathway.

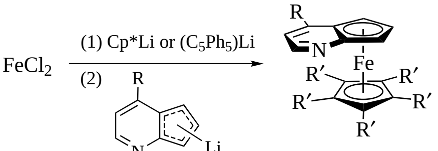

(**366**) (82)

R = H, R′ = Me
R = Me$_2$N, R′ = Me or Ph
R = 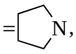, R′ = Me or Ph

7.2.7 *Heteroferrocenes*

Ferrocene analogs that possess a heteroatom in place of one carbon atom have been known for some time. The most common of these heteroferrocenes are the azaferrocenes and the phosphaferrocenes, though complexes having sulfur, boron, arsenic, antimony, bismuth, and nickel atoms are known.[4,461] Review articles that are either comprehensive (in the case of phosphaferrocenes), or cover aspects of this chemistry (in the case of azaferrocenes), are available; space restrictions for this review do not permit complete coverage of these areas.[409,462] Instead, recent developments in the area of planar chiral heteroferrocenes, especially as it relates to asymmetric catalyst design, will be the primary focus here.

The parent azaferrocene is obtained in two steps by the reaction of (**6c**) with pyrrole to give CpFe-NC$_4$H$_4$, followed by photodecarbonylation.[463] Preparation of the Cp* analog (**367**) is carried out by successive treatment of FeCl$_2$ with Cp*Li and potassium pyrrolide.[464] Heteroferrocenes that possess a substituent in the 2- or 3-position are planar chiral, and a racemic mixture of 2-substituted azaferrocene (**368**) is similarly obtained by replacing potassium pyrrolide with the dilithium salt of pyrrole-2-methanol (Scheme 97). Enantiomerically pure (**368**) is obtained by 2-lithiation of (**367**) and conversion to the diastereomer esters that are chromatographically separable. Reduction affords the desired enantiomerically pure azaferrocene, which upon silylation is used as an enantioselective nucleophilic catalyst for the addition of alcohols to ketenes.[464,465] Alcohol (**369**) is used as a ligand in the enantioselective addition of organozinc reagents to aldehydes.[466] A related C_2-symmetric bisazaferrocene is resolved by chiral HPLC and is used as an enantioselective alkene Cu(I)-cyclopropanation catalyst with diazoesters; an X-ray crystal structure is available for this bidentate ligand in a Cu(I) complex (styrene occupies the other positions of this square-planar complex).[467]

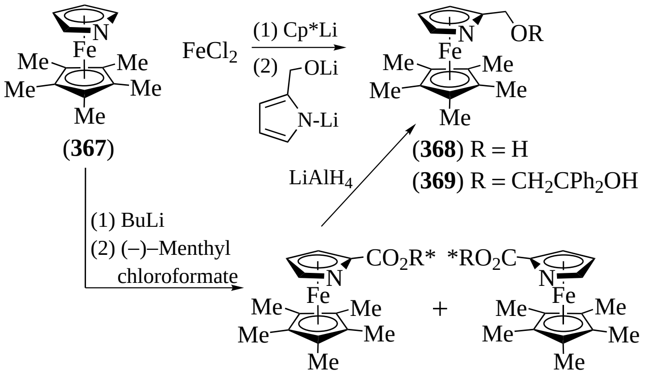

(**367**)
(**368**) R = H
(**369**) R = CH$_2$CPh$_2$OH
R* = (–)–Menthyl

Scheme 97

Another approach to enantiomerically pure planar chiral azaferrocenes involves 2-lithiation of (**367**) followed by addition of (-)-menthyl-(S) – p-toluenesulfinate. The diastereomeric sulfoxides thus obtained are chromatographically separable, and treatment of each diastereomer with t-BuLi produces an enantiomerically pure planar chiral anion that may be trapped with an electrophile (Scheme 98).[468] Finally, in order to obviate the need for performing a resolution or a chromatographic separation, chiral ligand-mediated enantioselective deprotonations have been investigated. Lithiation of (**367**) in the presence of (-)-sparteine followed by addition of an electrophile gives the 2-substituted azaferrocene in good enantioselectivities (Scheme 99).[469] However, lateral lithiation of (**370**) mediated by S-valine-derived bis(oxazoline) (**371**) provides planar chiral products with excellent enantioselectivity.

Unlike the azaferrocenes, direct lithiation of phosphaferrocenes does not occur as the strong nucleophile attacks the

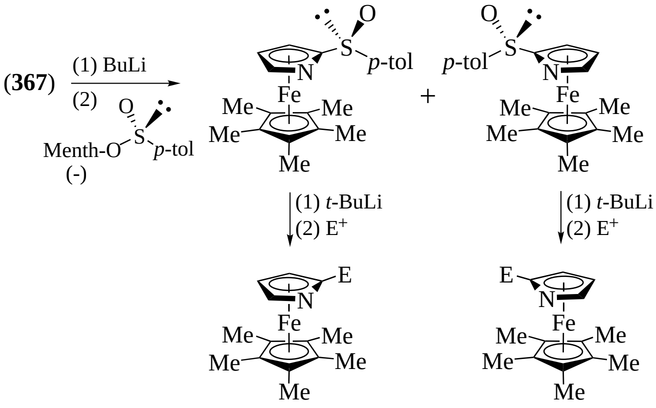

E = I, PPh$_2$, SnBu$_3$, SiMe$_3$, CH$_2$OH, CPh$_2$OH

Scheme 98

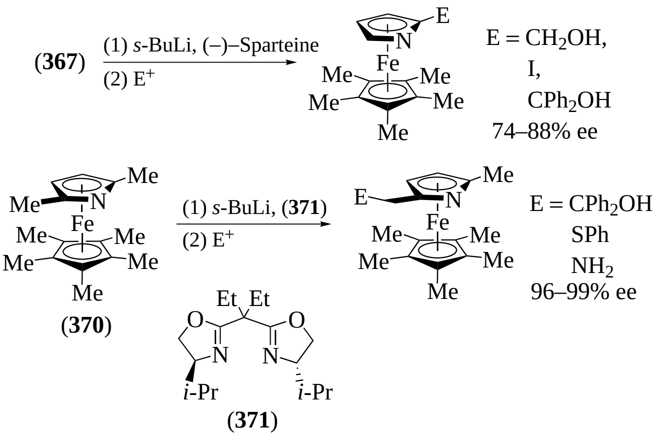
(367)
(1) s-BuLi, (−)-Sparteine
(2) E+
E = CH2OH, I, CPh2OH
74–88% ee
(370)
(1) s-BuLi, (371)
(2) E+
E = CPh2OH, SPh, NH2
96–99% ee
(371)
Et Et
i-Pr
Fe
N
Me

Scheme 99

phosphorus atom. Instead, electrophilic substitution reactions such as acylation and formylation are possible and have been used as an entry into planar chiral systems of this class of heteroferrocenes. The achiral complex (**372**) derived from the anion of 3,4-dimethylphosphole has long been known, and the Cp* analog (**373**) has been recently prepared (equation 83) and was shown to catalyze epoxide ring opening in the presence of trimethylsilyl chloride.[470]

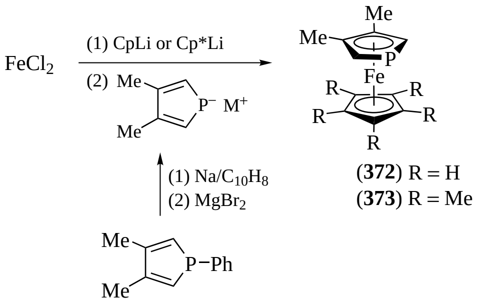
FeCl2
(1) CpLi or Cp*Li
(2) Me, Me, P− M+
(1) Na/C10H8
(2) MgBr2
P–Ph
Fe
P
R
(372) R = H
(373) R = Me

(83)

Vilsmeier formylation of (**372**) and (**373**) proceed smoothly, leading to planar chiral racemic aldehydes (**374**) and (**375**) which can be converted into a number of derivatives by standard methodologies (Scheme 100).[409,471,472] Addition of methyl Grignard to (**374**) is highly diastereoselective, which is in contrast to $LiAlH_4$ reduction which occurs in a stereorandom manner. Acid-promoted nucleophilic substitution of the Grignard-derived secondary alcohol can occur with inversion or retention, depending on the conditions; the intermediate fulvene-like cation slowly undergoes *E*-*Z*-isomerization.[473] Resolution of (**374**) is achieved by chromatographic separation of the diastereomeric aminals, and resolution of the primary alcohol derived from (**375**) is accomplished via chiral HPLC. The latter compound is converted into a bisphosphine (**376**) that is used as a ligand in asymmetric hydrogenations or enantioselective isomerizations of allylic alcohols to β-substituted aldehydes. Condensation of resolved aldehyde (**374**) with cyclopentadiene followed by reduction gives phosphaferrocene cyclopentadienide (**377**) which forms the unique 1,1′-bisphosphaferrocenyl ferrocene (**378**) (equation 84).[474] This complex acts as a bidentate ligand; an X-ray crystal structure of the $Mo(CO)_4$ complex has been obtained, and the ligand has also been used in a palladium-catalyzed asymmetric allylic substitution.

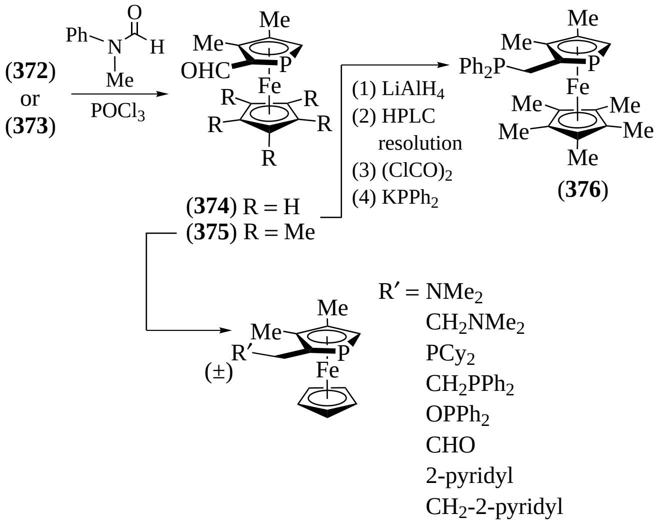
(372) or (373)
Ph–N(Me)–CHO
POCl3
(374) R = H
(375) R = Me
(1) LiAlH4
(2) HPLC resolution
(3) (ClCO)2
(4) KPPh2
Ph2P
(376)
(±)
R′ = NMe2, CH2NMe2, PCy2, CH2PPh2, OPPh2, CHO, 2-pyridyl, CH2-2-pyridyl
OHC
Fe
P
Me

Scheme 100

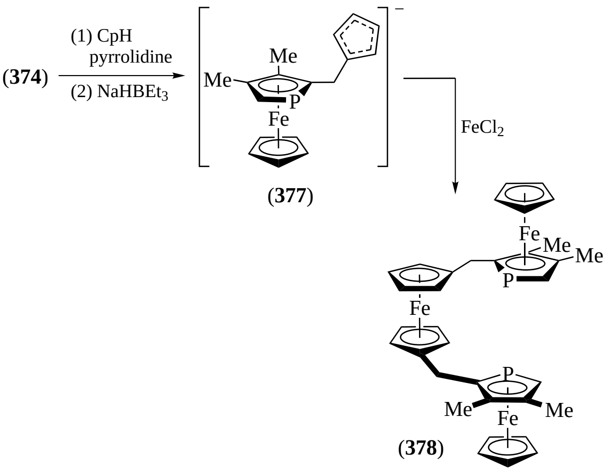
(374)
(1) CpH pyrrolidine
(2) NaHBEt3
(377)
FeCl2
(378)
Fe
P
Me

(84)

Planar chiral phosphaferrocene-oxazolines (**379**) constitute another family of complexes that are useful as ligands in asymmetric catalysis. Preparation of these takes advantage of a modified Friedel–Crafts acylation of (**373**) and an unusual conversion of the resulting trifluoromethyl ketone into an amide that is then cyclized to an oxazoline. The diastereomeric complexes thus formed are chromatographically separable and are used in a palladium-catalyzed asymmetric allylic substitution. Modification of this complex by using the anion derived from 3,4-dimethyl-2-phenylphosphole gives more

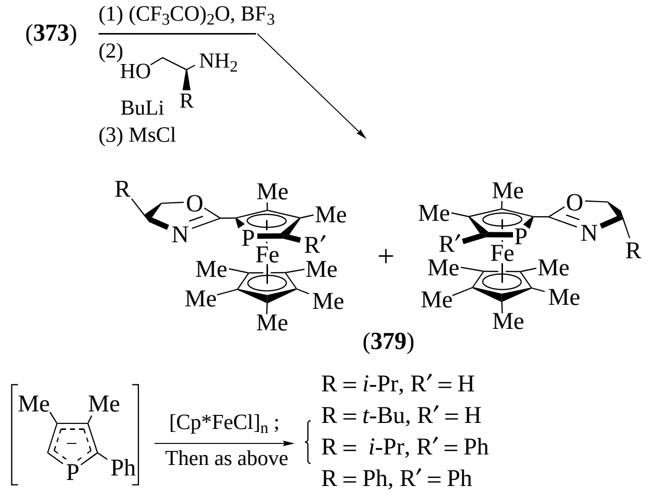

Scheme 101

substituted analogs (**379**, R′ = Ph) that are used in the copper-catalyzed enantioselective conjugate addition of diethyl zinc to acyclic enones (Scheme 101).[475]

7.2.8 Supported Ferrocenyl Phosphine Ligands

The tremendous growth of the use of enantiomerically pure ligands in homogeneous asymmetric catalysis as led to significant efforts to immobilize the active catalysts in order to recycle them or prevent (or minimize) metal leaching into products. Both achiral and chiral ferrocenyl phosphines are among those catalysts that have been utilized in this context, and detailed descriptions of this research have appeared in a number of review articles.[405,476,477]

One approach that is taken is to place the catalytic 1,1′-bisphosphine ferrocene unit in the core of carbosilane dendrimers (**380**). NMR evidence reveals that addition of $PdCl_2$ affords a bidentate palladium complexes with *cis* stereochemistry, and when used in conjunction with catalytic amounts of a palladium source (**380a–c**) acts as ligand and catalysis of allylic alkylation reactions is observed. Product regioselectivity is affected by the size of the dendrimeric system. A similar ferrocenyl dendrimer (**380d**) is used as a ligand in rhodium-catalyzed hydrogenations; catalyst activity, level of leaching, and recyclability all compared favorably to nondendrimeric 1,1′-bisphosphine ferrocene dppf ligand.

A second strategy is to place multiple chiral Josiphos-type (**329**) units along the exterior of dendrimers, and successful applications for rhodium-catalyzed asymmetric hydrogenation utilize cores composed of benzene-1,3,5-tricarboxylic acid esters (**381**), adamantane-1,3,5,7-tetracarboxylic acid esters (**382**), and cyclophosphazenes (*see Phosphazenes*) (**383**).[478] Enantioselectivities are excellent and these dendrimeric materials can be recovered by filtration through a nanofiltration membrane.

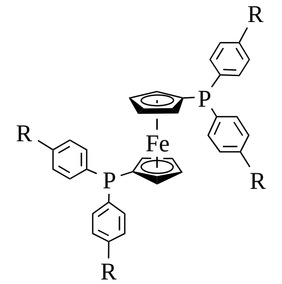

(**380a**) R = $(CH_2{=}CHCH_2)_3SiCH_2CH_2{-}$
(**380b**) R = $[(CH_2{=}CHCH_2)_3Si(CH_2)_3]_3SiCH_2CH_2{-}$
(**380c**) R = $[(R_3SiCH_2CH_2CH_2)_3Si(CH_2)_3]_3SiCH_2CH_2{-}$
(**380d**) R = $(Me_3SiCH_2CH_2CH_2)_3SiCH_2CH_2{-}$

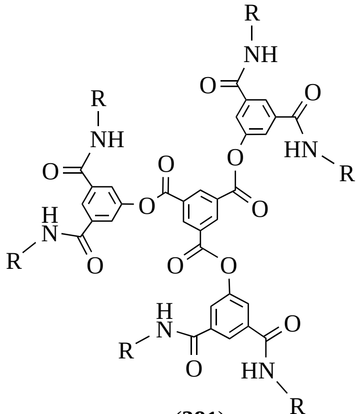

(**381**)

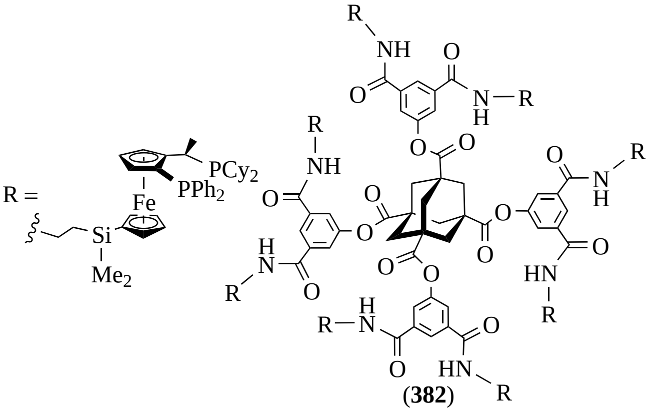

(**382**)

Other means of immobilizing ferrocenyl phosphine ligands include covalent (*see Covalent Bonds*) attachment to either silica gel (*see Silica*) or solid support poly(ethylene glycol) (TantaGel), or confinement within mesoporous MCM-41.[405]

7.2.9 Ferrocene Derivatives as Receptors

As the synthetic community embraced the fields of supramolecular chemistry and molecular recognition, active research areas developed that included the use of ferrocene

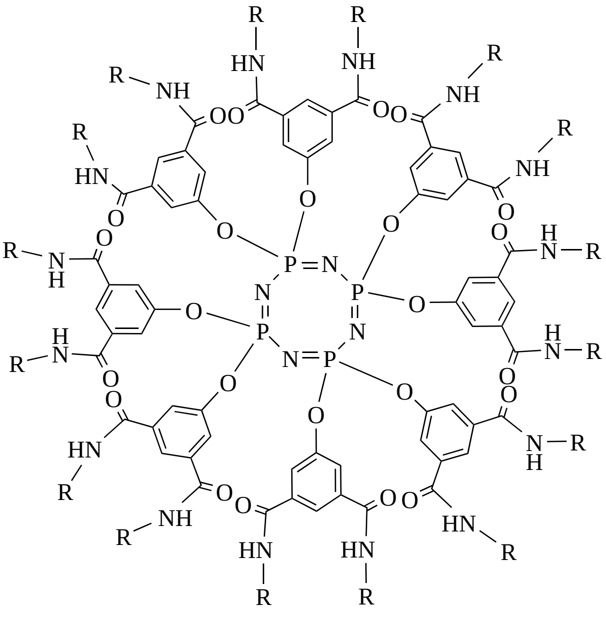

(**383**)

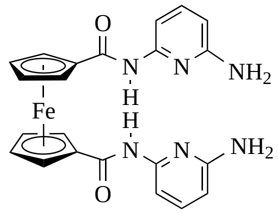

(**384**)

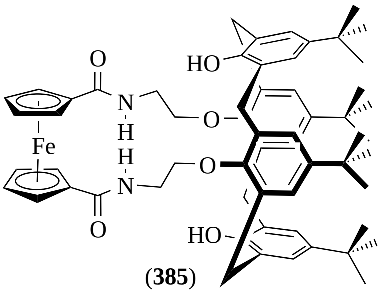

(**385**)

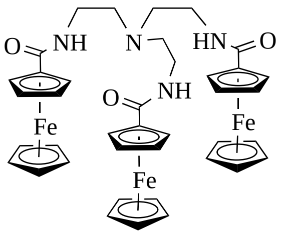

(**386**)

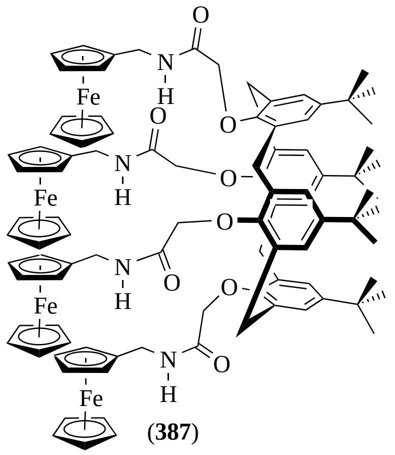

(**387**)

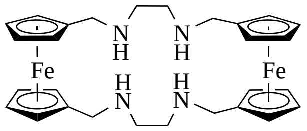

(**388**)

derivatives as receptors and sensors. Though results mostly involve the selective binding for particular anionic species as a result of redox properties (*see Redox Properties & Processes*) of the ferrocene unit, some efforts have studied selective binding of dicarboxylic acids through hydrogen bonding (*see Hydrogen Bonding*). Some recent and thorough reviews that either focus on or simply include the role of ferrocene derivatives in this chemistry are available and should be consulted for a more complete discussion than will be presented here.[479–481]

A number of synthetic receptors based on elaboration of ferrocenecarboxamide or ferrocenyl amines are known; since the ferrocene unit or units are neutral they do not bind with anions. Instead, oxidation to the positively charged ferrocenium ion is induced, and electrostatic binding can occur. Examples include complexes (**384**–**387**) that selectively bind $H_2PO_4^-$, complex (**388**) that discriminates for sulfate over phosphate (pH 4, in aqueous THF), and dendrimeric complex (**389**) that also registers a cathodic shift (and oxidation to ferrocenium) upon addition of $H_2PO_4^-$. Variations on complex (**386**) that utilize a cyclotriveratrylene scaffold bind $H_2PO_4^-$ as well as ATP^{2-}, and a ferrocene-zinc metalloporphyrin (*see Porphyrin*) receptor that is ringed with ferrocenyl amide units is also known.[480] Finally, 1,1′-ferrocenedicarboxamides equipped with carbon chains that terminate with phosphine units are known; complexation of the phosphines to metal centers [$Mo(CO)_4$, $Cr(CO)_4$, Rh(CO)Cl, $Ru(bpy)_2Cl$] strengthens anionic binding.[480] A number of polyferrocene aza- and oxomacrocycles (*see Macrocycle*) exist a well, and ferrocene boronic acid (**364**) exhibits selectivity for fluoride in the presence of a number of other anions.[480]

Urea-substituted ferrocenes are also capable of binding anions. In the case of (**390**), the presence of bulky *t*-butyl groups appears to reverse the selectivity of binding, where chloride is instead favored over $H_2PO_4^-$.[482] Enantiomerically pure (**391**) (prepared by diastereoselective nucleophilic addition to a chiral ferrocene oxime) binds a racemic mixture of the carboxylate anion, tetrabutylammonium 2-phenylbutyrate. While the binding constant of (*R*)-carboxylate is greater than that of its enantiomer, the difference is only moderate but does suggest an opportunity for the design of chiral receptors than can bind enantioselectively.[483]

A series of ferrocene derivatives that bear two dipeptide chains are available from 1,1′-bis(chlorocarbonyl)ferrocene (**336**, R = Cl).[484] The compounds form highly ordered

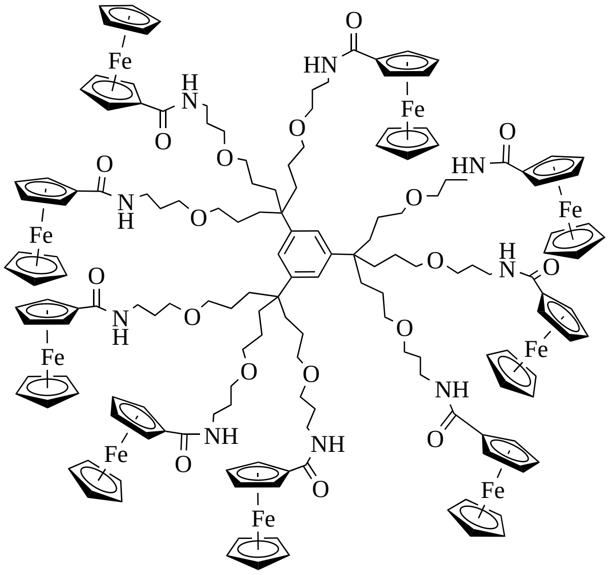

(**389**)

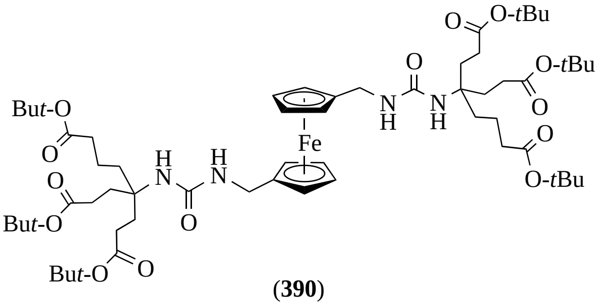

(**390**)

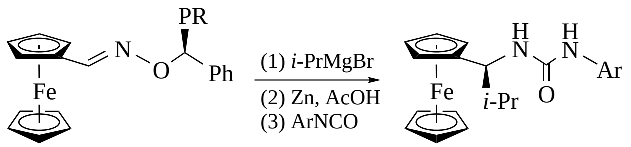

(**391**)

assemblies in the solid state that results from interchain hydrogen bonding. One of these compounds, (**392**), selectively recognizes dicarboxylic acids.[485]

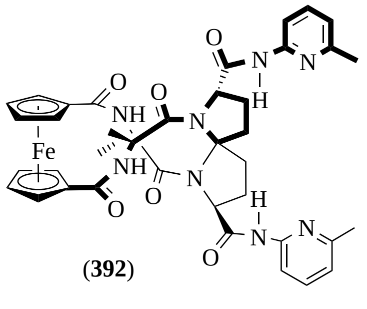

(**392**)

7.2.10 Ligand Displacement

Ferrocene was originally found to be stable to hydrogenation under conditions that effect the reduction of benzene. It was subsequently found that the reductive liberation of the Cp ligand could be effected by use of 10% Pd/C in CF_3CO_2H at 1–2 atm H_2. For 1,2-disubstituted ferrocenes the predominant products are *trans* 1,2-disubstituted cyclopentanes.[486,487] It has been variously suggested, but not proven, that this reaction proceeds via either protonation on Fe or on the Cp ligand. Use of this method for organic synthesis may be limited, since the yields are variable and planar chiral ferrocenes afford racemic cyclopentane products. Indeed, attempted liberation of the Cp ligand of ferrocenes is not commonly encountered. Reductive cleavage of ferrocene itself with lithium/$EtNH_2$ is known, but one report of the analogous transformation on a more substituted ferrocene required lithium di-*tert*-butylbiphenylide but proceeded in poor yield.[488,489] In a unique example of decomplexation, organoborane (**393**) is formed upon treatment of a quinoline-substituted ferrocene with BCl_3 (equation 85).[490] Finally, nitro-2-ferrocenyloxazolines are quite light-sensitive and can be readily photo-decomplexed to give the corresponding nitrofulvalenes.[491]

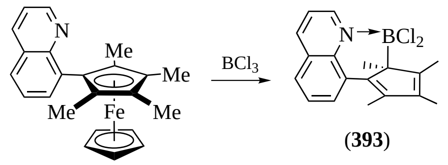

(**393**)

(85)

The $[Cp(CO)_3Fe]^+$ cation (**394**) can be prepared from ferrocene by treatment with carbon monoxide, $AlCl_3$, Al powder, and water.[492] One Cp ligand of ferrocene may also be replaced by an arene to form the (η^6-arene)$FeCp^+$ cations (**395**) by treatment of ferrocene with the arene in the presence of $AlCl_3$, Al powder, and water (ratio of 1:1:3:1:1). The Al powder is present to prevent oxidation of ferrocene to the ferricinium cation (**292**).[493] The chemistry of these (η^6-arene)iron cations will be discussed later (Section 8.1.1). Treatment of ferrocene with $AlCl_3$ in the absence of a good ligand leads to partial decomposition and formation of unusual bridged ferrocenophanes.[493]

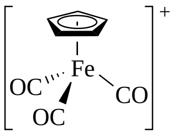

(**394**)

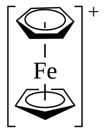

(**395**)

7.3 Ferrocenophanes

Bridged ferrocenes, or ferrocenophanes, have been known for many years. These compounds, in which the two Cp rings are linked by carbon and/or heteroatom chains, are more than merely a scientific curiosity; many provide access to ferrocenyl polymers that have great value in materials science. A recent review of ferrocenophanes that possess only carbon bridges should be consulted for greater detail than can be provided here.[410] Information regarding multinuclear ferrocenes (biferrocenes, etc.) is also incorporated in that review, however that material will not be included here. While a detailed discussion of the synthesis and properties of the ferrocene-based polymers that are often derived from ferrocenophanes is also beyond the scope of this presentation, thorough recent reviews of this topic are available.[100,411]

7.3.1 *Mononuclear [1]Ferrocenophanes*

[1]Ferrocenophanes, that is, ferrocenes with two Cp rings connected by a single carbon atom bridge are unknown. Apparently this system would cause the Cp rings to distort too far from planarity to provide stability. However, there are numerous examples of heteroatom chains of one atom length that are known; larger atomic radii presumably results in less tilting of the Cp rings and therefore increased stability. Silaferrocenophanes may be the most important of this class of complexes, as poly(ferrocenylsilanes) are prepared from them by thermal ring-opening polymerization (equation 86).[411] Also known are [1]ferrocenophanes with boron, oxygen, sulfur, germanium, phosphorus, and tin linkers.[100] Typically these are prepared by treatment of dilithioferrocene (**323**) with the appropriate dihalide (Me_2SiCl_2, $PhPCl_2$, etc.). X-ray structures are available for some of these complexes, and tilt angles vary from *ca.* 27° for the phosphaferrocenophanes to 17° for the germanium analog.

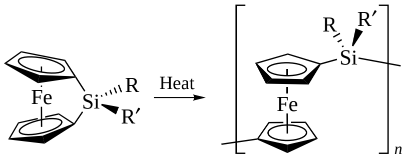

(86)

7.3.2 *Mononuclear [2]Ferrocenophanes*

Though considerably strained, [2]ferrocenophanes (**396**) can be prepared, in modest yield, by condensation of the appropriate biscyclopentadienyl dianion with $FeCl_2$.[423] X-ray analysis of (**396**, R = Me) shows that the strain imposed by short two atom carbon bridge is significant – a tilt angle of 23° and a ring twist angle of 26° are observed. This large tilt angle is manifested in an increased Lewis basicity, and the iron atom more readily forms adducts with Lewis acids and is more readily protonated than less-strained ferrocenophanes. Ring-opening polymerization of these complexes are possible, though initiation requires a higher temperature than the [1]silaferrocenophane analog (300 °C vs. 130–220 °C). The unsaturated analog (**397**, R = H) is prepared by subjecting ferrocene dialdehyde to McMurry coupling conditions ($TiCl_3$, Zn/Cu), and the X-ray structure shows the same 23° tilt angle observed in the saturated analog. Polymerization to give the poorly characterized poly(ferrocenylenevinylene) is accomplished by ring-opening metathesis polymerization (ROMP) (*see Ring Opening Metathesis Polymerization Reactions*). More highly substituted analogs (**397**, R = alkyl) are directly polymerized, and owing to their higher solubility these polymers are better characterized.[100]

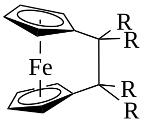

(**396**)

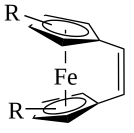

(**397**)

The dianion derived from the monoCp* analog of ferrocene is used with $SiCl_4$ to prepare a sila[2]ferrocenophane (**398**), and similarly treatment of dilithioferrocene (**323**) with $ClMe_2SiSiMe_2Cl$ affords the [2]disilaferrocenophane (**399**) (Scheme 102). However, unlike the [1]silaferrocenophane, (**399**) is resistant to polymerization, and this lack of reactivity may be correlated with the observed tilt angle of only 4°.[494] On the other hand, treatment of [1]silaferrocenophane with $Pt(PEt_3)_3$ results in an oxidative addition to produce a [2]-platinasilaferrocenophane (**400**); an exchange of ligands produces a complex which functions as a catalyst for ring-opening polymerization of [1]silaferrocenophanes.[495,496] It is also possible to prepare a diphospha[2]ferrocenophane; (**401**) is prepared from the diphospholide and $FeCl_2$ in the presence of $AlCl_3$ (equation 87).[497] The tilt angle, 20°, is observed to

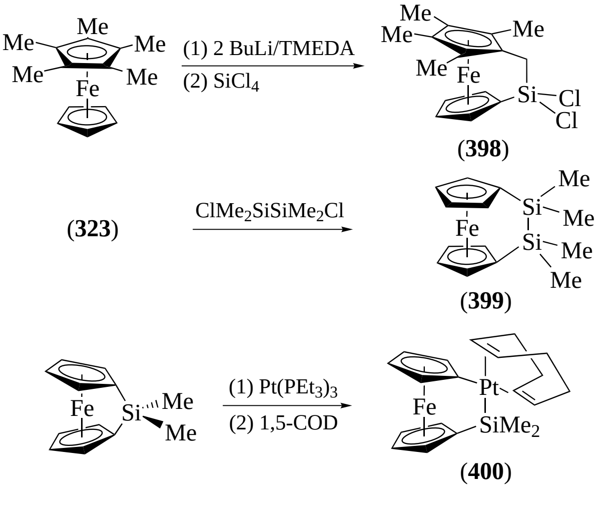

Scheme 102

be similar to (**396**) and (**397**).

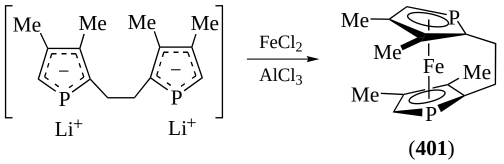

(**401**)

(87)

7.3.3 *Mononuclear [3]Ferrocenophanes*

This class of ferrocenophanes is probably the most-studied, and there are numerous examples that span from the simple mono-bridged [3]-ferrocenophane (prepared from treating the dianion derived from biscyclopentadienyl propane with $FeCl_2$) to the tetra-bridged [3][3][3][3]ferrocenophanes. The pentabridged compound remains unknown.

The facile intramolecular acylation of 3-ferrocenylpropionic acid (**295**) to give keto[3]ferrocenophane (**296**) has already been described (Section 7.2.1), and intramolecular Claisen condensation of (**402**) gives 1,3-diketo[3]ferrocenophane (**403**) (tilt angle, 10°); both of these compounds are used to prepare other [3]ferrocenophanes. An enantiomerically pure C_2-symmetric ferrocenophane (**404**; tilt angle, 6.5°) is made by a sequence that includes a Friedel–Crafts acylation to form a mono-bridged [3]-ferrocenophane and a subsequent intramolecular acylation to install the second bridge (Scheme 103).[498,499]

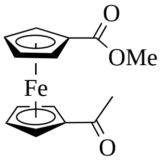

(**402**)

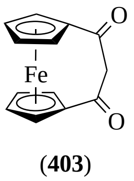

(**403**)

Enantiomerically pure [3]oxaferrocenophanes (**405**) are available as well, from tosyl chloride-induced dehydration of diols (equation 88).[500,501] Tilt angles for these complexes as determined from X-ray structures are in the 11–12° range.

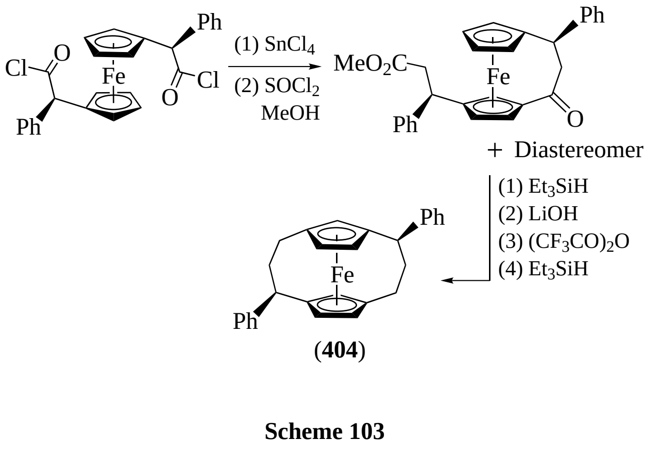

Scheme 103

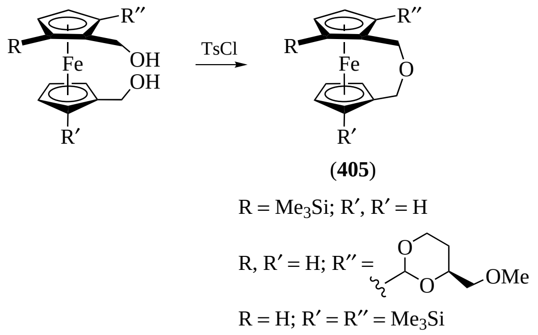

(88)

7.3.4 *Mononuclear [m]Ferrocenophanes (m ≥ 4)*

As in the case of [3]ferrocenophanes, there are numerous examples of [4]- and [5]ferrocenophanes. While the saturated complexes may be prepared from the usual route of treating the corresponding dicyclopentadienide with $FeCl_2$, other approaches may be taken. For example, the reaction of keto[3]ferrocenophane (**296**) with diazomethane results in ring-expanded keto[4]ferrocenophanes (**406a,406b**) (equation 89).

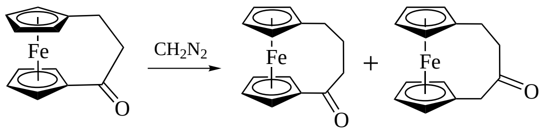

(**296**) (**406a**) (**406b**)

(89)

Unsaturated [4]- and [5]ferrocenophanes, with one or two alkenes in the bridge are readily prepared. Perhaps the most rapid entry to unsaturated [4]ferrocenophanes is via Ring-closing metathesis (RCM) of 1,1′-bispropenylferrocene (Scheme 104).[502] Enantiomerically pure analogs are available if analogs bearing chiral centers are utilized. Similarly, racemic 1,1′-diphospha[4]ferrocenophanes have been prepared.[503] An alternative approach uses the 1,1′-bis(trimethylsilylalkynyl)ferrocene that can be obtained from a Sonogashira-type coupling of 1,1′-diiodoferrocene.[504] Axially chiral (**407**) and helically chiral (**408**) ferrocenophanes are known as well.[489,505] The latter, prepared by reaction of the corresponding helical dianion with $FeCl_2$, has been resolved. X-ray diffraction analysis of (**408**) indicates that the two cyclopentadienyl groups are staggered and tilted by 19.8° with respect to being parallel.

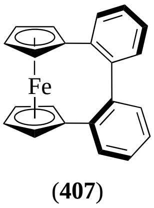

(**407**)

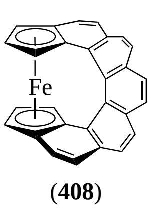

(**408**)

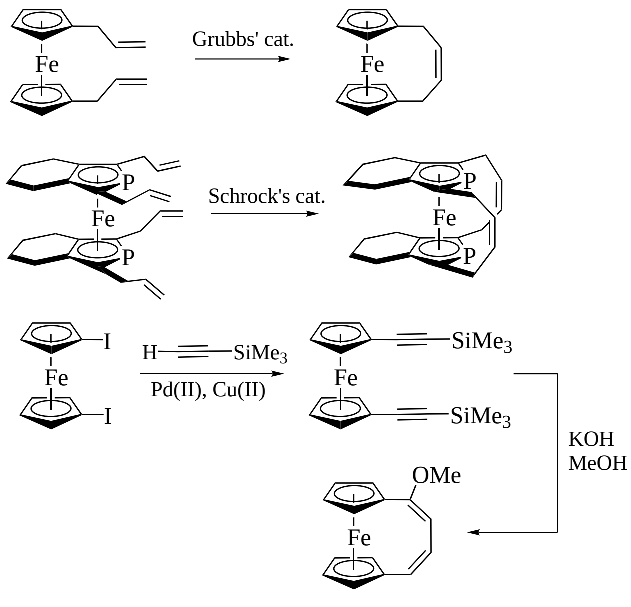

Scheme 104

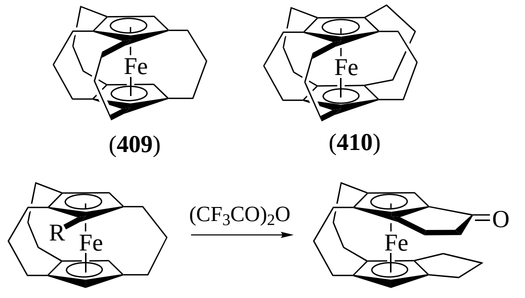

(**409**) (**410**)

(**411**)

R = H

R = $CH_2CH_2CO_2H$

(**412**)

(for R = $CH_2CH_2CO_2H$)

Scheme 105

7.3.5 Multiply-bridged [m]ⁿFerrocenophanes

Numerous di-, tri-, and tetra-bridged ferrocenophanes have been prepared from (**296**) and (**406a**) using acylation or formylation of the ferrocenophane as the first step, and intramolecular acylation to form the bridging chain. An early attempt of the preparation of $[3]^4$- and $[3]^5$-ferrocenophanes (**409**) and (**410**) from (1,2,4)$[3]^3$ferrocenophane (**411**; R = $CH_2CH_2CO_2H$), using this type of intramolecular acylation, failed owing to a novel rearrangement to (**412**) (Scheme 105). It is speculated that the intraring distance – in (**411**; R = H) the average Fe–C_{ring} is 1.99 Å – is too short to allow for *endo* attack of the acylium ion in a heteroannular fashion. Notably, the intramolecular acylation of the one-carbon homolog (**413**; R = $CH_2CH_2CO_2H$) to give (**414**) occurs in reasonable yield.[506] The pentabridged $[4]^5$-, $[5]^5$-, $[4]^4[3]$-, and $[3]^4[4]$ferrocenophanes (**415**), (**416**), (**417**), and (**418**) have been prepared.[506–509] These examples represent a class of compound in which a metal atom is completely surrounded by a hydrocarbon 'cage'. Attempted reduction of the bridged ferrocene (**411**; R = H) results in chain scission to give (**419**).[486]

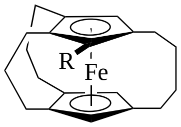

(**413**)

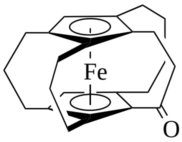

(**414**)

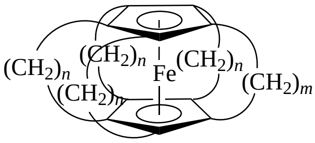

	m	*n*
(**415**)	4	4
(**416**)	5	5
(**417**)	3	4
(**418**)	4	3

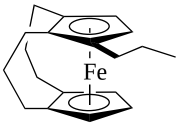

(**419**)

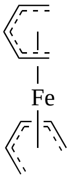

(**420**)

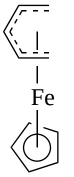

(**421**)

7.4 'Open' and 'Half-open' Ferrocene[510]

Acyclic analogs of ferrocene, (**420**), can be prepared by reaction of the corresponding pentadienyl anion with $FeCl_2$. The mixed-sandwich complexes (**421**), with one cyclopentadienyl ligand and one 'open' pentadienyl ligand (*see Pentadienyl Ligand*), can be prepared by reaction of $FeCl_2$ with a 1:1 mixture of cyclopentadienyl anion and pentadienyl anion. This results in the formation of a nearly statistical, but separable, mixture of (**284**), (**420**), and (**421**) (1:1:2 ratio). X-ray diffraction analysis of (**420**) indicates that it adopts a *gauche*-eclipsed conformation, and that the average Fe–C distance (2.089 Å) is longer than that of ferrocene itself. Rotation of the two ligands with respect to each other is not as facile as for ferrocene. The barrier for rotation in the 'open' ferrocenes is $>35\,\mathrm{kJ\,mol^{-1}}$. The pentadienyl ligand may act as a better σ-acceptor ligand than the cyclopentadienyl ligand, thus resulting in more metal–ligand orbital mixing. Oxidation of (**420**) and (**421**) occurs at lower potential ($E_{1/2} = 0.11$ and 0.29 versus SCE respectively, dimethoxyethane/$Bu_4N^+ClO_4^-$) than that of ferrocene, and these oxidations are not reversible owing to coupling of the pentadienyl ligands.

8 η^6-LIGAND COMPLEXES

This subject has been thoroughly reviewed, and readers should consult these articles for comprehensive information.[4,493,511]

8.1 Cationic η^6-Arene Complexes (*see Arene Complexes*)

8.1.1 Preparation and Structure

As previously indicated, the reaction of ferrocene with arene, $AlCl_3$, Al powder, and water affords (η^6-arene)(η^5-cyclopentadienyl)iron cations (**395**).[493] These cations can also be formed by the reaction of (**6a**) with arenes in the presence of $AlCl_3$,[512] as well as by hydride abstraction from (η^5-cyclohexadienyl)FeCp complexes; however, since these are usually prepared by reduction of cations (**395**), this latter methodology is of little synthetic utility. A wide variety of aromatic compounds can be accommodated in these complexes;[513] however, complexation of polycyclic aromatic hydrocarbons, such as naphthalene, phenanthrene, anthracene, or pyrene, proceeds with partial hydrogenation.[514] Photochemical exchange of a complexed arene ligand by a more basic arene has been effected for the *p*-xylene and chlorobenzene complexes in MeCN as solvent.[515] The labile (*see Labile*) $(MeCN)_3FeCp^+$ cation is believed to be an intermediate in this ligand exchange. The preparation of substituted (arene)$FeCp^+$ by modification reactions will be discussed in the following section.

The crystal structures of a number of (arene)$FeCp^+$ cations have been reported.[516] In general, the planes defined by the arene and cyclopentadienyl ligands are essentially parallel. The Fe–arene centroid distance is in the range 1.52–1.60 Å, while the Fe–Cp centroid distance is 1.62–1.79 Å. The arene C–C bond distance increases upon complexation to 1.39–1.44 Å. An upfield shift is observed for the ^{13}C NMR signals of the complexed arene ring.[32]

8.1.2 Reactions

As might be expected for a polyene metal cation, the arene ligand in complexes (**395**) is unreactive toward normal Friedel–Crafts substitution. In turn, the $FeCp^+$ adjunct acts as a good electron-withdrawing group and facilitates attack by hydride and carbanion nucleophiles on the benzene ligand to form (η^5-cyclohexadienyl)FeCp complexes.[493,513,516] For $LiAlH_4$ as nucleophile and at low temperature this reaction has been shown to proceed via initial electron transfer to afford the 19-electron complex (*see Nineteen Electron Configuration*), which is characterized by ESR (Section 8.2), followed by hydrogen atom transfer.[517] Nucleophilic attack occurs on the *exo* face of the arene ligand. For arenes substituted with electron-withdrawing groups (e.g. **422**, Electron-withdrawing group (EWG) = NO_2, Cl, CO_2R), nucleophilic attack by hydride, cyanide, organometallics, or enolates occurs at the position *ortho* to the substituent to give neutral cyclohexadienyl complexes (**423**) (equation 90).[518] In contrast, reaction of complexes (**422**; EWG = Cl or NO_2) with stabilized nucleophiles, such as amines, alkoxides, thiolates, or β-dicarbonyl anions, results in displacement of chlorine or nitrite to give the substituted arene cations (**424**).[516,519] Sequential substitution of the two chlorines of (*o*-dichlorobenzene)$FeCp^+$ are known,[520] and this methodology is used to prepare polycyclic compounds.

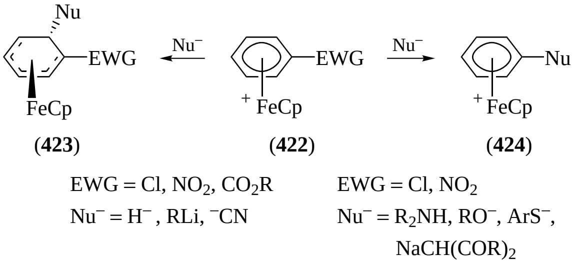

(90)

The (η^6-arene)(η^5-cyclopentadienyl)iron cation is stable to strong oxidants (e.g. conc. H_2SO_4, HNO_3, peroxides (*see Peroxide*), and permanganate); however, toluene and other alkyl-substituted arene cations are oxidized with hot permanganate to give the corresponding benzoic acid complexes.[513] Oxidation of a CH_2Ar side chain (e.g. **425**) gives the corresponding diaryl ketone complex (**426**) (Scheme 106).[521] Nucleophilic addition to ketones of the type (**426**) occurs *exo* to the metal in a highly diastereoselective fashion.

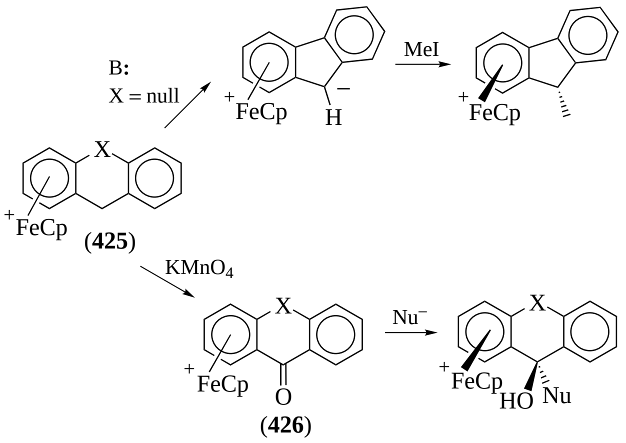

Scheme 106

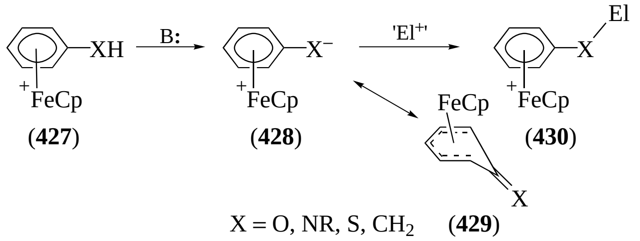

Scheme 107

The protons of OH, NHR, SH, or CH groups attached to a complexed arene exhibit enhanced acidity (e.g. **427**) (Scheme 107). Deprotonation generates the corresponding zwitterionic species (**428**), which might also be drawn as (**429**). The X-ray diffraction structure of the product generated by deprotonation of (η^6-fluorene)FeCp cation indicates that all six carbons of the aryl ring are bonded to iron.**[522]** Reaction of the deprotonated species (**428**) with electrophiles results in the formation of the substituted arene complex (**430**).**[493,516,523,524]** Reaction of the conjugate base of (η^6-fluorene)FeCp$^+$ cation with iodomethane or methyl fluorosulfonate results in formation of a new C–C bond on the face of the ligand opposite to the metal (Scheme 106).**[522]**

Decomplexation of cationic arene iron Cp complexes to afford the functionalized arene may be carried out by heating in a donor solvent (*N*,*N*-dimethylformamide (DMF) or Dimethylsulfoxide (DMSO)). For less robust systems, irradiation by sun or UV lamp is efficient, often in the presence of an exogenous ligand such as triphenylphosphine.**[4,493,525]**

8.2 Nineteen-electron Neutral η^6-arene Complexes

This area has been the subject of several reviews by Astruc.**[526–528]** Electrochemical reduction of (η^6-arene)FeCp$^+$ cations (**395**) generates the corresponding 19-electron neutral η^6-arene complexes (**431**) (Scheme 108). These 19-electron complexes are unstable with respect to dimerization unless the arene ligand is peralkyl substituted. The arene ligand may be electrocatalytically liberated in ethanol solution via the intermediacy of the unstable 19-electron complex (**431b**).**[529]**

The (η^6-hexamethylbenzene)FeCp complex (**431b**) is a green–black sublimable solid. The X-ray diffraction structure of (**431b**) indicates that the arene and Cp rings are planar and parallel; however, the Fe–Cp centroid distance is an extremely long (1.79 Å) and the Fe–arene centroid distance is 1.58 Å.**[530]** The Mössbauer spectrum of (**431b**) indicates that the unpaired electron is in an e_{1g}* orbital which is 65–75% metal-like in character.**[529]** Reaction of (**431b**) with O_2 generates the 18-electron (η^5-cyclohexadienyl) complex (**432**) and the superoxide (*see Superoxide*) radical anion ($O_2{}^{-}\cdot$). The complex (**431b**) thus acts as an excellent 'electron reservoir.' The Fe$^{\text{I}}$/Fe$^{\text{II}}$ redox system can act as a catalyst for electrochemical reduction of nitrate to ammonia.**[526]** Complex (**432**) acts as reducing agent (aldehydes and ketones reduced to alcohols, and alkynes to alkenes), reacts with electrophiles (Ph_2PCl, Me_3SiCl, etc.) to allow modification of one of the arene methyl groups, and also can be peralkylated (KOH, RI).**[528]** Use of 1-(4-iodobutyl)ferrocene as an alkylating agent allows the construction of a heptanuclear complex cation that was prepared as part of a study to identify possible redox catalysts.**[531]**

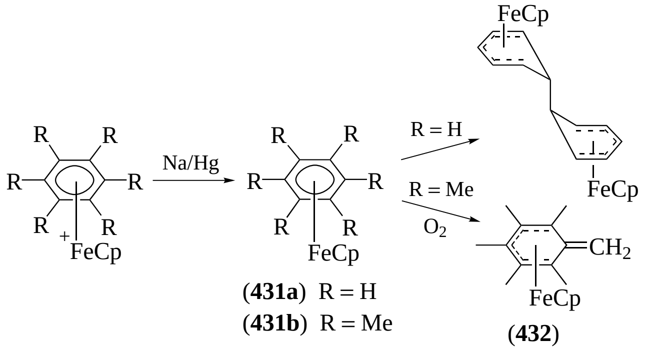

Scheme 108

8.3 Bis(η^6-arene)Iron Dications

The reaction of $FeCl_2$ or $FeCl_3$ with $AlCl_3$ in an arene solvent, at reflux, results in the formation of the corresponding bis(η^6-arene)iron dications (**433**) (Scheme 109).**[4,493,532]** These dications are susceptible to nucleophilic attack to afford the (η^6-arene)(η^5-cyclohexadienyl)iron cations (**434**). For the bis(mesitylene)iron dication, reaction with two equivalents of a nucleophile sequentially occurs on each of the arene rings to afford bis (η^5-cyclohexadienyl)iron complexes (**435**),**[532]** in accord with the prediction of the Davies–Green–Mingos rules (*see Davies–Green–Mingos Rules*) for nucleophilic addition.**[533]** More recently, it has been found that reaction of other cations (**434**) with a variety of nucleophiles, in THF

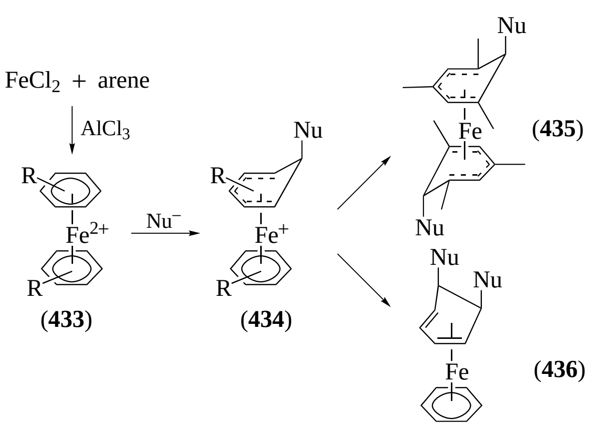

Scheme 109

solution, proceeds via attack at the cyclohexadienyl ligand to afford neutral (η^6-arene)(η^4-cyclohexadiene)iron complexes (**436**).[534] The regioselectivity of this second nucleophilic addition is dependent upon the steric demands of the ligands, the nature of the nucleophile, and the solvent.[535] This methodology may be used for the preparation of *cis*-1,2-disubstituted 2,5-cyclohexadienes.

9 RELATED ARTICLES

Asymmetric Synthesis by Homogeneous Catalysis; Bonding Energetics of Organometallic Compounds; Carbene Complexes; Carbonylation Processes by Homogeneous Catalysis; Coordination & Organometallic Chemistry: Principles; Cyanide Complexes of the Transition Metals; Electron Transfer in Coordination Compounds; Electronic Structure of Organometallic Compounds; Heterogeneous Catalysis by Metals; Hydride Complexes of the Transition Metals; Iron: Inorganic & Coordination Chemistry; Macrocyclic Ligands; Mechanisms of Reaction of Organometallic Complexes; Metathesis Polymerization Processes by Homogeneous Catalysis; Molecular Orbital Theory; Molybdenum: Inorganic & Coordination Chemistry; Oligomerization & Polymerization by Homogeneous Catalysis; Organic Synthesis Using Metal-mediated Coupling Reactions; Organic Synthesis Using Metal-mediated Metathesis Reactions; Organic Synthesis using Transition Metal Carbonyl Complexes; Organic Synthesis using Transition Metal Complexes Containing π-Bonded Ligands; P-donor Ligands; Phosphorus: Organophosphorus Chemistry; Photochemistry of Transition Metal Complexes; S-donor Ligands; Stability Constants & their Determination; Superconductivity; Transition Metal Complexes with Bulky Allyl Ligands.

10 REFERENCES

1. R. C. Kerber, *J. Organomet. Chem.*, 1992, **422**, 209; 1991, **404**, 107; 1989, **380**, 77; 1989, **360**, 319; 1987, **343**, 1; 1987, **318**, 157; 1986, **298**, 77; 1984, **278**, 205.
2. R. C. Kerber, in 'Comprehensive Organometallic Chemistry II', eds. E. W. Abel, F. G. A. Stone, and G. Wilkinson, Pergamon Press, Oxford, 1995, Vol. 7, Chap. 2, p. 101.
3. A. J. Fatiadi, *J. Res. Natl. Inst. Stand. Technol.*, 1991, **96**, 1.
4. A. J. Pearson, 'Iron Compounds in Organic Synthesis', Academic Press, San Diego, 1994.
5. K. Rück-Braun, *Synthesis*, 1999, 727.
6. D. F. Shriver and K. H. Whitmire, in 'Comprehensive Organometallic Chemistry', eds. G. Wilkinson, F. G. A. Stone, and E. W. Abel, Pergamon Press, Oxford, 1982, Vol. 4, Chap. 31.1, p. 243.
7. M. D. Johnson, in 'Comprehensive Organometallic Chemistry', eds. G. Wilkinson, F. G. A. Stone, and E. W. Abel, Pergamon Press, Oxford, 1982, Vol. 4, Chap. 31.2, p. 331.
8. L. S. Hegedus, 'Transition Metals in the Synthesis of Complex Organic Molecules', 2nd edn., University Science Books, Sausalito, CA, 1999, Chap. 5, p. 130.
9. J. P. Collman, R. G. Finke, J. N. Cawse, and J. I. Brauman, *J. Am. Chem. Soc.*, 1977, **99**, 2515; *J. Am. Chem. Soc.*, 1978, **100**, 4766.
10. J. Y. Merour, J. L. Roustan, C. Charrier, J. Collin, and J. J. Benaim, *J. Organomet. Chem.*, 1973, **51**, C24.
11. J. E. McMurry, A. Andrus, G. M. Ksander, and J. H. Musser, *J. Am. Chem. Soc.*, 1979, **101**, 1330.
12. R. B. King, *Acc. Chem. Res.*, 1970, **3**, 417.
13. D. L. Reger and E. C. Culbertson, *J. Am. Chem. Soc.*, 1976, **98**, 2789.
14. M. D. Johnson, *Acc. Chem. Res.*, 1978, **11**, 57.
15. W. N. Rogers and M. C. Baird, *J. Organomet. Chem.*, 1979, **182**, C65.
16. P. L. Bock, D. J. Boschetto, J. R. Rasmussen, J. P. Demers, and G. M. Whitesides, *J. Am. Chem. Soc.*, 1974, **96**, 2814.
17. T. G. Attig, R. G. Teller, S. M. Wu, R. Bau, and A. Wojcicki, *J. Am. Chem. Soc.*, 1979, **101**, 619.
18. M. Rosenblum, *J. Organomet. Chem.*, 1986, **300**, 191.
19. M. Rosenblum, *Acc. Chem. Res.*, 1974, **7**, 122.
20. J. Celebuski and M. Rosenblum, *Tetrahedron*, 1985, **41**, 5741.
21. S. Araki, M. Hatano, and Y. Butsugan, *J. Org. Chem.*, 1986, **51**, 2126.
22. M. Tilset and V. D. Parker, *J. Am. Chem. Soc.*, 1989, **111**, 6711.
23. B. D. Fabian and J. A. Labinger, *Organometallics*, 1983, **2**, 659.
24. M. Rosenblum and P. S. Waterman, *J. Organomet. Chem.*, 1980, **187**, 267.
25. R. Baker, V. B. Rao, and E. Erdik, *J. Organomet. Chem.*, 1983, **243**, 451.
26. S.-F. Lush and R.-S. Liu, *Organometallics*, 1986, **5**, 1908.
27. F. Giulieri and J. Benaim, *J. Organomet. Chem.*, 1984, **276**, 367.
28. G. Cardaci and A. Foffani, *J. Chem. Soc., Dalton Trans.*, 1974, 1808.
29. J.-M. Bassett, M. Green, J. A. K. Howard, and F. G. A. Stone, *J. Chem. Soc., Dalton Trans.*, 1980, 1779.
30. K. C. Brinkman, A. L. Blakeney, W. Krone-Schmidt, and J. A. Gladysz, *Organometallics*, 1984, **3**, 1325.
31. T. A. Shackleton and M. C. Baird, *Organometallics*, 1989, **8**, 2225.

32. B. E. Mann and B. F. Taylor, '^{13}C NMR Data for Organometallic Compounds', Academic Press, New York, 1981.
33. T. Jenny, W. von Philipsborn, J. Kronenbitter, and A. Schwenk, *J. Organomet. Chem.*, 1981, **205**, 211.
34. M. E. Wright, G. O. Nelson, and R. S. Glass, *Organometallics*, 1985, **4**, 245.
35. M. E. Wright, J. F. Hoover, R. S. Glass, and V. W. Day, *J. Organomet. Chem.*, 1989, **364**, 373.
36. S. D. Kahn, W. J. Hehre, N. G. Rondan, and K. N. Houk, *J. Am. Chem. Soc.*, 1985, **107**, 8291.
37. M.-T. Lee, P. S. Waterman, R. H. Magnuson, R. E. Meirowitz, A. Prock, and W. P. Giering, *Organometallics*, 1988, **7**, 2146.
38. P. S. Waterman and W. P. Giering, *J. Organomet. Chem.*, 1978, **155**, C47.
39. B. Zhou and Y. Xu, *J. Org. Chem.*, 1988, **53**, 4419.
40. R. S. Glass, W. W. McConnell, and S. W. Andruski, *J. Org. Chem.*, 1986, **51**, 5123.
41. G.-H. Lee, S.-M. Peng, G.-M. Yang, S.-F. Lush, and R.-S. Liu, *Organometallics*, 1989, **8**, 1106.
42. A. N. Nesmeyanov, L. V. Rubin, M. I. Rybinskaya, and Y. A. Ustynyuk, *J. Gen. Chem. USSR (Engl. Transl.)*, 1967, **37**, 1505.
43. C. P. Casey and W. H. Miles, *Organometallics*, 1984, **3**, 808.
44. M. N. Mattson and P. Helquist, *Organometallics*, 1992, **11**, 4.
45. R. Gompper and E. Z. Kottmair, *Z. Naturforsch.*, 1990, **45b**, 833.
46. M. Mikulás, S. Rust, D. Schollmeyer, and K. Rück-Braun, *Synlett*, 2000, 185.
47. K. Rück-Braun, *Angew. Chem., Int. Ed. Engl.*, 1997, **36**, 509.
48. P. Amrhein, D. Schollmeyer, and K. Rück-Braun, *Organometallics*, 2000, **19**, 3527.
49. G. A. Artamkina, A. Yu. Mil'chenko, N. A. Bunagin, I. P. Beletskaya, and O. A. Reutov, *Izv. Akad. Nauk. SSSR, Ser. Khim.*, 1987, 700.
50. C. E. Webster, Y. Fan, M. B. Hall, D. Kunz, and J. F. Hartwig, *J. Am. Chem. Soc.*, 2003, **125**, 858.
51. R. Chukwu, A. D. Hunter, and B. D. Santarsiero, *Organometallics*, 1991, **10**, 2141.
52. R. Chukwu, A. D. Hunter, B. D. Santarsiero, S. G. Bott, J. L. Atwood, and J. Chassaignac, *Organometallics*, 1992, **11**, 589.
53. H. G. Raubenheimer, M. Desmet, P. Olivier, and G. J. Kruger, *J. Chem. Soc., Dalton Trans.*, 1996, 4431.
54. G. H. Kuo, P. Helquist, and R. C. Kerber, *Organometallics*, 1984, **3**, 806.
55. C. P. Casey, W. H. Miles, and H. Tukada, *J. Amer. Chem. Soc.*, 1985, **107**, 2924.
56. A. R. Cutler, P. K. Hanna, and J. C. Vites, *Chem. Rev.*, 1988, **88**, 1363.
57. D. L. Reger and E. Mintz, *Organometallics*, 1984, **3**, 1759.
58. F. L. Bowden and L. H. Wood, in 'The Organic Chemistry of Iron', eds. E. A. Koerner von Gustorf, F. W. Grevels, and I. Fischler, Academic Press, New York, 1978, Vol. 1, p. 345.
59. H. Brunner, *Adv. Organomet. Chem.*, 1980, **18**, 151.
60. T. C. Flood, K. D. Campbell, H. H. Downs, and S. Nakanishi, *Organometallics*, 1983, **2**, 1590.
61. A. Davidson, *J. Organomet. Chem.*, 1974, **74**, C17.
62. S. J. Cook, J. F. Costello, S. G. Davies, and H. T. Kruk, *J. Chem. Soc., Perkin Trans. I*, 1994, 2369.
63. S. G. Davies, *Aldrichim. Acta*, 1990, **23**, 31.
64. S. G. Davies, *Pure Appl. Chem.*, 1988, **60**, 13.
65. L. S. Liebeskind, M. E. Welker, and R. W. Fengl, *J. Am. Chem. Soc.*, 1986, **108**, 6328.
66. M. F. Semmelhack and R. Tamura, *J. Am. Chem. Soc.*, 1983, **105**, 4099.
67. W. D. Wulff, in 'Advances in Metal-Organic Chemistry', ed. L. S. Liebeskind, JAI Press, Greenwich, CT, 1989, Vol. 1, p. 209.
68. K. H. Dötz, H. Fischer, P. Jofmann, F. R. Kriessl, U. Schubert, and K. Weiss, 'Transition Metal Carbene Complexes', Verlag Chemie, Deerfield Beach, FL, 1984, p. 1.
69. E. O. Fischer, *Adv. Organomet. Chem.*, 1976, **14**, 1.
70. L. Meca, I. Cisarova, and D. Dvorak, *Organometallics*, 2003, **22**, 3703.
71. M. Brookhart and W. B. Studabaker, *Chem. Rev.*, 1987, **87**, 411.
72. P. E. Riley, C. E. Capshew, R. Pettit, and R. E. Davies, *Inorg. Chem.*, 1978, **17**, 408.
73. E. J. O'Connor, S. Brandt, and P. Helquist, *J. Am. Chem. Soc.*, 1987, **109**, 3739.
74. C. Knorrs, G.-H. Kuo, J. W. Lauher, C. Eigenbrot, and P. Helquist, *Organometallics*, 1987, **6**, 988.
75. R. D. Theys and M. M. Hossain, *Tetrahedron Lett.*, 1992, **33**, 3447.
76. R. M. Vargas, R. D. Theys, and M. M. Hossain, *J. Am. Chem. Soc.*, 1992, **114**, 777.
77. B. E. Boland-Lussier, M. R. Churchill, R. P. Hughes, and A. L. Rheingold, *Organometallics*, 1982, **1**, 628.
78. S. G. Davies, A. J. Edwards, S. Jones, M. R. Metzler, K. Yanada, and R. Yanada, *J. Chem. Soc., Dalton Trans.*, 1998, 1587.
79. A. Davison and D. L. Reger, *J. Am. Chem. Soc.*, 1972, **94**, 9237.
80. C. P. Casey and W. H. Miles, *J. Organomet. Chem.*, 1983, **254**, 333.
81. M. Brookhart, J. R. Tucker, and G. R. Husk, *J. Am. Chem. Soc.*, 1983, **105**, 258.
82. C. P. Casey, W. H. Miles, H. Tukada, and J. M. O'Connor, *J. Am. Chem. Soc.*, 1982, **104**, 3761.
83. M. Brookhart, J. R. Tucker, and G. R. Husk, *J. Am. Chem. Soc.*, 1981, **103**, 979.

84. P. Helquist, in ‘Advances in Metal-Organic Chemistry’, ed. L. S. Liebeskind, JAI Press, Greenwich, CT, 1991, Vol. 2, p. 143.
85. B. E. R. Schilling, R. Hoffmann, and D. L. Lichtenberger, *J. Am. Chem. Soc.*, 1979, **101**, 585.
86. V. Guerchais, C. Lapinte, J. Y. Thepot, and L. Toupet, *Organometallics*, 1988, **7**, 604.
87. M. Brookhart, J. R. Tucker, T. C. Flood, and J. Jensen, *J. Am. Chem. Soc.*, 1980, **102**, 1203.
88. V. Guerchais, D. Astruc, C. M. Nunn, and A. Cowley, *Organometallics*, 1990, **9**, 1036.
89. M. F. Semmelhack and J. Park, *J. Am. Chem. Soc.*, 1987, **109**, 935.
90. G. J. Baird, S. G. Davies, and T. R. Maberly, *Organometallics*, 1984, **3**, 1764.
91. K. A. M. Kremer, G. H. Kou, E. J. O’Connor, P. Helquist, and R. C. Kerber, *J. Am. Chem. Soc.*, 1982, **104**, 6119.
92. R. S. Bly, R. K. Bly, M. M. Hossain, L. Lebioda, and M. Raja, *J. Am. Chem. Soc.*, 1988, **110**, 7723.
93. M. Brookhart and Y. Liu, *Organometallics*, 1989, **8**, 1572.
94. S. K. Zhao, C. Knors, and P. Helquist, *J. Am. Chem. Soc.*, 1989, **111**, 8527.
95. S. Ishii, S. Zhao, G. Mehta, C. J. Knors, and P. Helquist, *J. Org. Chem.*, 2001, **66**, 3449.
96. S. Ishii, S. Zhao, and P. Helquist, *J. Am. Chem. Soc.*, 2000, **122**, 5897.
97. Q. Wang, M. F. Mayer, C. Brennan, F. Yang, M. M. Hossain, D. S. Grubisha, and D. Bennett, *Tetrahedron*, 2000, **56**, 4881.
98. M. D. Redlich, M. F. Mayer, and M. M. Hossain, *Aldrichimica Acta*, 2003, **36**, 3.
99. N. J. Long and C. K. Williams, *Angew. Chem., Int. Engl. Ed.*, 2003, **42**, 2586.
100. P. Nguyen, P. Gömez-Elipe, and I. Manners, *Chem. Rev.*, 1999, **99**, 1515.
101. C.-L. Li and R.-S. Liu, *Chem. Rev.*, 2000, **100**, 3127.
102. A. Ricci and C. Lo Sterzo, *J. Organomet. Chem.*, 2003, **653**, 177.
103. A. G. M. Barrett and M. A. Sturgess, *J. Org. Chem.*, 1987, **7**, 3940.
104. A. G. M. Barrett, J. Mortier, M. Sabat, and M. A. Sturgess, *Organometallics*, 1988, **7**, 2553.
105. A. G. M. Barrett, N. E. Carpenter, J. Mortier, and M. Sabat, *Organometallics*, 1990, **9**, 151.
106. R. B. King, in ‘The Organic Chemistry of Iron’, eds. E. A. Koerner von Gustorf, F.-W. Grevels, and I. Fischler, Academic Press, New York, 1978, Vol. 1, p. 397.
107. A. J. Deeming, in ‘Comprehensive Organometallic Chemistry’, eds. G. Wilkinson, F. G. A. Stone, and E. W. Abel, Pergamon Press, Oxford, 1982, Vol. 4, Chap. 31.3, p. 377.
108. E. Weiss, K. Stark, J. E. Lancaster, and H. D. Murdoch, *Helv. Chim. Acta*, 1963, **46**, 288.
109. H. L. Conder and M. Y. Darensbourg, *J. Organomet. Chem.*, 1974, **67**, 93.
110. F. Claret and P. Vogel, *Organometallics*, 1990, **9**, 2785.
111. H. Cherkaoui, J. Martelli, and R. Grée, *Tetrahedron Lett.*, 1991, **32**, 7259.
112. L.-K. Liu, C.-H. Sun, C.-Z. Yang, Y.-S. Wen, C.-F. Wu, S.-Y. Shih, and K.-S. Lin, *Organometallics*, 1992, **11**, 972.
113. W.-J. Koot, H. Hiemstra, and W. N. Speckamp, *J. Chem. Soc., Chem. Commun.*, 1993, 156.
114. D. Enders, B. Jandeleit, and S. von Berg, *Synlett*, 1997, 421.
115. D. Enders, B. Jandeleit, S. von Berg, G. Raabe, and J. Runsink, *Organometallics*, 2001, **20**, 4312.
116. M. I. Rybinskaya, L. V. Rybin, A. A. Pogrebnyak, G. V. Nurtdinova, and Y. P. Yur’ev, *J. Organomet. Chem.*, 1981, **217**, 373.
117. H. Fleckner, F. W. Grevels, and D. Hess, *J. Am. Chem. Soc.*, 1984, **106**, 2027.
118. H. Angermund, A. K. Bandyopadhyay, F.-W. Grevels, and F. Mark, *J. Am. Chem. Soc.*, 1989, **111**, 4656.
119. H. Hoberg, K. Jenni, K. Angermaund, and C. Krüger, *Angew. Chem., Int. Ed. Engl.*, 1987, **26**, 153.
120. E. Lindner, E. Schauβ, W. Hiller, and R. Fawzi, *Chem. Ber.*, 1985, **118**, 3915.
121. M. Brookhart, W. A. Chandler, A. C. Pfister, C. C. Santini, and P. S. White, *Organometallics*, 1992, **11**, 1263.
122. M. Nitay, W. Priester, and M. Rosenblum, *J. Am. Chem. Soc.*, 1978, **100**, 3620.
123. D. F. Marten and M. N. Akbari, *J. Organomet. Chem.*, 1987, **322**, 99.
124. A. Cutler, D. Ehntholt, P. Lennon, K. Nicholas, D. F. Marten, M. Madhavarao, S. Raghu, A. Rosan, and M. Rosenblum, *J. Am. Chem. Soc.*, 1975, **97**, 3149.
125. T. W. Bodnar and A. R. Cutler, *Organometallics*, 1985, **4**, 1558.
126. S. R. Berryhill and J. G. Breitenbucher, *Tetrahedron Lett.*, 1990, **31**, 1671.
127. S. Jiang and E. Turos, *Tetrahedron Lett.*, 1991, **32**, 4639.
128. D. L. Reger, C. J. Coleman, and P. J. McElligott, *J. Organomet. Chem.*, 1979, **171**, 73.
129. H.-W. Frühauf, I. Pein, and F. Seils, *Organometallics*, 1987, **6**, 1613.
130. A. Vessieres, D. Touchard, and P. Dixneuf, *J. Organomet. Chem.*, 1976, **118**, 93.
131. S. Zobl-Ruh and W. von Philipsborn, *Helv. Chim. Acta*, 1981, **64**, 2378.
132. M. M. Turnbull, B. M. Foxman, and M. Rosenblum, *Organometallics*, 1988, **7**, 200.
133. O. Eisenstein and R. Hoffmann, *J. Am. Chem. Soc.*, 1980, **102**, 6148.
134. T. C. T. Chang, B. M. Foxman, M. Rosenblum, and C. Stockman, *J. Am. Chem. Soc.*, 1981, **103**, 7361.

135. D. E. Laycock, J. Hartgerink, and M. C. Baird, *J. Org. Chem.*, 1980, **45**, 291.
136. A. Cutler, D. Ehntholt, W. P. Giering, P. Lennon, S. Raghu, A. Rosan, M. Rosenblum, J. Tancrede, and D. Wells, *J. Am. Chem. Soc.*, 1976, **98**, 3495.
137. M. E. Miller and E. R. Grant, *J. Am. Chem. Soc.*, 1985, **107**, 3386.
138. Y.-M. Wuu, J. G. Bentsen, C. G. Brinkley, and M. S. Wrighton, *Inorg. Chem.*, 1987, **26**, 530.
139. T. M. Barnhart and R. J. McMahon, *J. Am. Chem. Soc.*, 1992, **114**, 5434.
140. M. I. Rybinskaya, *Pure Appl. Chem.*, 1982, **54**, 145.
141. D. Senechal, M.-C. Senechal-Tocquer, J.-Y. Le Bihan, D. Gentric, and B. Caro, *J. Organomet. Chem.*, 1990, **385**, C35.
142. A. Martinetti, L. Richard, and F. Mathey, *Organometallics*, 1990, **9**, 788.
143. T. N. Danks, D. Rakshit, and S. E. Thomas, *J. Chem. Soc., Perkin Trans.*, 1988, **I**, 2091.
144. B. R. Bender, M. Koller, A. Linden, A. Marcuzzi, and W. von Phillipsborn, *Organometallics*, 1992, **11**, 4268.
145. A. R. Pinhas, A. G. Samuelson, R. Risemberg, E. V. Arnold, J. Clardy, and B. K. Carpenter, *J. Am. Chem. Soc.*, 1981, **103**, 1668.
146. C.-H. Sun and T. J. Chow, *J. Chem. Soc., Chem. Commun.*, 1988, 535.
147. R. Rodrigo, *Tetrahedron*, 1988, **44**, 2093.
148. E. Weissberger and P. Laszlo, *Acc. Chem. Res.*, 1976, **9**, 209.
149. H. A. Erlacher, M. M. Turnbull, K.-H. Chu, and M. Rosenblum, *J. Org. Chem.*, 1989, **54**, 3012.
150. M. K. Begum, K.-H. Chu, T. S. Coolbaugh, M. Rosenblum, and X.-Y. Zhu, *J. Am. Chem. Soc.*, 1989, **111**, 5252.
151. M. Rosenblum, B. M. Foxman, and M. M. Turnbull, *Heterocycles*, 1987, **25**, 419.
152. D. L. Reger, *Acc. Chem. Res.*, 1988, **21**, 229.
153. M. E. Welker, *Chem. Rev.*, 1992, **92**, 97.
154. M. Rosenblum and J. C. Watkins, *J. Am. Chem. Soc.*, 1990, **112**, 6316.
155. B. L. Hayes and M. E. Welker, *Organometallics*, 1998, **17**, 5534.
156. A. L. Hurley, M. E. Welker, and C. S. Day, *Organometallics*, 1998, **17**, 2832.
157. S. Jiang, G. E. Agoston, T. Chen, M.-P. Cabal, U. Riaz, K. Ahsan, and E. Turos, *Recent Res. Devel. In Org, Chem.*, 1997, **1**, 229.
158. S. Jiang, T. Chen, and E. Turos, *Organometallics*, 1995, **14**, 4710.
159. S. Jiang, G. E. Agoston, T. Chen, M.-P. Cabal, and E. Turos, *Organometallics*, 1995, **14**, 4697.
160. T. Chen, S. Jiang, and E. Turos, *Tetrahedron Lett.*, 1994, **35**, 8325.
161. K. H. Pannell and G. M. Crawford, *J. Coord. Chem.*, 1973, **2**, 251.
162. H.-J. Knölker, J. Heber, and C. H. Mahler, *Synlett*, 1992, 1002.
163. J. Cooke and J. Takats, *J. Am. Chem. Soc.*, 1997, **119**, 11088.
164. R. Birk, H. Berke, G. Huttner, and L. Zsolnai, *Chem. Ber.*, 1988, **121**, 471.
165. M. Akita, S. Kakuta, S. Sugimoto, M. Terada, M. Tanaka, and Y. Moro-oka, *Organometallics*, 2001, **20**, 2736.
166. R. Birk, H. Berke, H.-U. Hund, K. Evertz, and L. Zsolini, *J. Organomet. Chem.*, 1988, **342**, 67.
167. F. Delbecq and P. Sautet, *J. Am. Chem. Soc.*, 1992, **114**, 2446.
168. H. Berke, G. Huttner, G. Weiler, and L. Zsolnai, *J. Organomet. Chem.*, 1981, **219**, 353.
169. R. Birk, H. Berke, and L. Zsolnai, *Chem. Ber.*, 1988, **121**, 1557.
170. G. Cardaci, G. Bellachioma, and P. Zanazzi, *Organometallics*, 1988, **7**, 172.
171. A. R. Hermes and G. S. Girolami, *Organometallics*, 1988, **7**, 394.
172. C. Jablonski, G. Bellachioma, G. Cardaci, and G. Reichenbach, *J. Am. Chem. Soc.*, 1990, **112**, 1632.
173. P. Kölbener, H.-U. Hund, H. W. Bosch, C. Sontag, and H. Berke, *Helv. Chim. Acta*, 1990, **73**, 2251.
174. G. Bellachioma, G. Cardaci, A. Macchioni, and G. Reichenbach, *Inorg. Chem.*, 1992, **31**, 63.
175. S. W. Helm, G. Linti, H. Nöth, S. Channareddy, and P. Hofmann, *Chem. Ber.*, 1992, **125**, 73.
176. H. Le Bozec, P. H. Dixneuf, A. J. Carty, and N. J. Taylor, *Inorg. Chem.*, 1978, **17**, 2568.
177. H. Le Bozec, J.-L. Fillaut, and P. H. Dixneuf, *J. Chem. Soc., Chem. Commun.*, 1986, 1182.
178. D. Touchard, J.-L. Fillaut, P. H. Dixneuf, R. D. Adams, and B. E. Segmueller, *J. Organomet. Chem.*, 1990, **386**, 95.
179. R. Appel, C. Casser, and F. Knoch, *J. Organomet. Chem.*, 1985, **293**, 213.
180. G. M. Williams and D. E. Rudisill, *Inorg. Chem.*, 1989, **28**, 797.
181. A. E. Hill and H. M. R. Hoffmann, *J. Chem. Soc., Chem. Commun.*, 1972, 574.
182. V. A. Balusov, A. L. Bykova, and I. P. Podol'skaya, *Izv. Vyssh. Uchebn. Zaved., Khim. Khim. Tekhnol.*, 1989, **32**, 18; *Chem. Abstr.*, 1990, **112**, 98752.
183. T. H. Whitesides and R. W. Arhart, *J. Am. Chem. Soc.*, 1971, **93**, 5296.
184. T. Kruck and L. Knoll, *Z. Naturforsch., B*, 1973, **28**, 34.
185. H. Hoberg and K. Jenni, *J. Organomet. Chem.*, 1987, **322**, 193.
186. C. Gajda and J. R. Green, *Synlett*, 1992, s973.
187. V. V. Krivykh, O. V. Gusev, and M. I. Rybinskaya, *J. Organomet. Chem.*, 1989, **362**, 351.
188. A. Salzer and A. Hafner, *Helv. Chim. Acta*, 1983, **66**, 1774.

189. J. A. S. Howell, M.-C. Tirvengadum, and G. Walton, *J. Organomet. Chem.*, 1988, **338**, 217.
190. K. Broadley, N. G. Connelly, J. A. K. Howard, and W. Risse, *J. Organomet. Chem.*, 1981, **221**, C29.
191. E. L. Muetterties and J. W. Rathke, *J. Chem. Soc., Chem. Commun.*, 1974, 850.
192. C. A. Goulin and M. C. Baird, *Inorg. Chim. Acta*, 1990, **168**, 195.
193. S. Nakanishi and T. Takata, *Rev. on Heteroatom Chem*, 1997, **17**, 153.
194. K. Itoh, S. Nakanishi, and Y. Otsuji, *Bull. Chem. Soc. Jpn.*, 1991, **64**, 2965.
195. H. Yamaguchi, S. Nakanishi, and T. Takata, *J. Organomet. Chem.*, 1998, **554**, 167.
196. S. Nakanishi, H. Yamaguchi, K. Okamoto, and T. Takata, *Tetrahedron: Asymmetry*, 1996, **7**, 2219.
197. S. Nakanishi, M. Yasui, N. Kihara, and T. Takata, *Chem. Lett.*, 1999, 843.
198. U. Eberhardt and G. Mattern, *Chem. Ber.*, 1988, **121**, 1531.
199. K. Itoh, S. Nakanishi, and T. Takata, *Chem. Lett.*, 2000, 672.
200. K. Itoh, Y. Otsuji, and S. Nakanishi, *Tetrahedron Lett.*, 1995, **36**, 5211.
201. S. Nakanishi and Y. Shimizu, *Chem. Lett.*, 1994, 1925.
202. J. L. A. Roustan and A. Forgues, *J. Organomet. Chem.*, 1980, **184**, C13.
203. P. K. Baker, S. Clamp, N. G. Connelly, M. Murray, and J. B. Sheridan, *J. Chem. Soc., Dalton Trans.*, 1986, 459.
204. M. Brookhart, J. Yoon, and S. K. Noh, *J. Am. Chem. Soc.*, 1989, **111**, 4117.
205. E. Sepp, A. Pürzer, G. Thiele, and H. Behrens, *Z. Naturforsch., B*, 1978, **33**, 261.
206. T. C. Forschner, A. R. Cutler, and R. K. Kullnig, *Organometallics*, 1987, **6**, 889.
207. M. Brookhart, T. H. Whitesides, and J. M. Crockett, *Inorg. Chem.*, 1976, **15**, 1550.
208. R. K. Brown, J. M. Williams, A. J. Schultz, G. D. Stucky, S. D. Ittel, and R. L. Harlow, *J. Am. Chem. Soc.*, 1980, **102**, 981.
209. N. El Murr and J. D. Payne, *J. Chem. Soc., Chem. Commun.*, 1985, 162.
210. M. L. H. Green, D. O'Hare, and L.-L. Wong, *J. Chem. Soc., Dalton Trans.*, 1987, 2031.
211. J. Chen, J. Yin, W. Xu, L. Lai, Z. Zhang, and M. Shao, *Organometallics*, 1987, **6**, 2607.
212. J. R. Bleeke and R. J. Wittenbrink, *J. Organomet. Chem.*, 1991, **405**, 121.
213. B. Gabor, S. Holle, P. W. Jolly, and R. Mynott, *J. Organomet. Chem.*, 1994, **466**, 201.
214. J. D. Smith, T. P. Hanusa, and V. G. Young, *J. Am. Chem. Soc.*, 2001, **123**, 6455.
215. S. V. Ley, *Pure & Appl. Chem.*, 1994, **66**, 1415.
216. S. V. Ley, L. R. Cox, and G. Meek, *Chem. Rev.*, 1996, **96**, 423.
217. L. R. Cox and S. V. Ley, *Chem. Soc. Rev.*, 1998, **27**, 301.
218. R. W. Bates, D. D´íez-Mart´ín, W. J. Kerr, J. G. Knight, S. V. Ley, and A. Sakellaridis, *Tetrahedron*, 1990, **46**, 4063.
219. R. S. Paley, *Chem. Rev.*, 2002, **102**, 1493.
220. J. G. Knight and S. V. Ley, *Tetrahedron Lett.*, 1991, **32**, 7119.
221. S. V. Ley and B. Middleton, *J. Chem. Soc., Chem. Commun.*, 1998, 1995.
222. Z. Goldschmidt, H. E. Gottleib, and A. Almadhoun, *Tetrahedron Lett.*, 1990, **31**, 6711.
223. S. A. Benyunes, S. E. Gibson (née Thomas), and M. A. Peplow, *Tetrahedron: Asymmetry*, 1997, **8**, 1535.
224. M. M. Schulze and U. Gockel, *Tetrahedron Lett.*, 1996, **37**, 357.
225. D. F. Taber, K. Kanai, Q. Jiang, and G. Bui, *J. Am. Chem. Soc.*, 2000, **122**, 6807.
226. W. A. Donaldson and M. Ramaswamy, *Tetrahedron Lett.*, 1989, **30**, 1339.
227. R. W. Fish, W. P. Giering, D. Marten, and M. Rosenblum, *J. Organomet. Chem.*, 1976, **105**, 101.
228. J. A. Belmont and M. S. Wrighton, *Organometallics*, 1986, **5**, 1421.
229. D. L. Reger and C. A. Swift, *Organometallics*, 1984, **3**, 876.
230. M.-H. Cheng, Y.-J. Wu, S.-L. Wang, and R.-S. Liu, *J. Organomet. Chem.*, 1989, **373**, 119.
231. M. Brookhart, R. C. Buck, and E. Danielson III, *J. Am. Chem. Soc.*, 1989, **111**, 567.
232. N. J. Conti, D. J. Crowther, S. Tivakornpannarai, and W. M. Jones, *Organometallics*, 1990, **9**, 175.
233. F. Giuliéri and J. Bena´ím, *Nouv. J. Chim.*, 1985, **9**, 335.
234. P. G. Lenhert, C. M. Lukehart, and K. Srinivasan, *J. Am. Chem. Soc.*, 1984, **106**, 124.
235. J. W. Faller and M. A. Adams, *J. Organomet. Chem.*, 1979, **170**, 71.
236. F. E. Simon and J. W. Lauher, *Inorg. Chem.*, 1980, **19**, 2338.
237. M. Frey, T. A. Jenny, and H. Stoeckli-Evans, *Organometallics*, 1990, **9**, 1806.
238. W. von Philipsborn, *Pure Appl. Chem.*, 1986, **58**, 513.
239. H. Brunner, H. Weber, I. Bernal, and G. M. Reisner, *Organometallics*, 1984, **3**, 163.
240. N. J. Fitzpatrick and M. A. McGinn, *J. Chem. Soc., Dalton Trans.*, 1985, 1637.
241. R. Benn, H. Brenneke, A. Frings, H. Lehmkuhl, G. Mehler, A. Rufinska, and T. Wildt, *J. Am. Chem. Soc.*, 1988, **110**, 5661.
242. M. R. Churchill and K.-N. Chen, *Inorg. Chem.*, 1976, **15**, 788.
243. K. Dey, D. Koner, P. K. Bhattacharyya, A. Gangopadhyay, K. K. Bhasin, and R. D. Verma, *Polyhedron*, 1986, **5**, 1201.

244. M. Frey and T. A. Jenny, *J. Organomet. Chem.*, 1991, **421**, 257.

245. J. Mann, *Tetrahedron*, 1986, **42**, 4211.

246. M.-C. P. Yeh and S.-I. Tau, *J. Chem. Soc., Chem. Commun.*, 1992, 13.

247. S. Nakanishi, K. Okamoto, H. Yamaguchi, and T. Takata, *Synthesis*, 1998, 1735.

248. G. Cardaci, *J. Organomet. Chem.*, 1980, **202**, C81.

249. J. L. A. Roustan and F. Houlihan, *Can. J. Chem.*, 1979, **57**, 2790.

250. N. G. Connelly, A. G. Orpen, G. M. Rosair, and G. H. Worth, *J. Chem. Soc., Dalton Trans.*, 1991, 1851.

251. S. Chang, J. Yoon, and M. Brookhart, *J. Am. Chem. Soc.*, 1994, **116**, 1869.

252. H. J. Metternich and E. Niecke, *Angew. Chem., Int. Ed. Engl.*, 1991, **30**, 312.

253. J. G. A. Reuvers and J. Takats, *Organometallics*, 1990, **9**, 578.

254. R. Bertani, A. Scrivanti, and G. Carturan, *Inorg. Chim. Acta*, 1985, **98**, L9.

255. S. V. Ley and S. Burckhardt, *J. Chem. Soc., Perkin Trans. I*, 2000, 3028.

256. Y. K. Yun, K. Godula, Y. Cao, and W. A. Donaldson, *J. Org. Chem.*, 2003, **68**, 901.

257. G. Thoma and B. Giese, *Helv. Chim. Acta*, 1992, **75**, 1123.

258. J.-K. Shen, D. S. Tucker, F. Basolo, and R. P. Hughes, *J. Am. Chem. Soc.*, 1993, **115**, 11312.

259. M. D. Jones and R. D. W. Kemmitt, in 'Advances in Organometallic Chemistry', eds. F. G. A. Stone and R. West, Academic Press, New York, 1987, Vol. 27, p. 279.

260. H. C. Lounguet-Higgins and L. E. Orgel, *J. Chem. Soc.*, 1956, 1969.

261. K. Ehrlich and G. F. Emerson, *J. Am. Chem. Soc.*, 1972, **94**, 2464.

262. J. M. Grosselin, H. Le Bozec, C. Moinet, L. Toupet, and P. H. Dixneuf, *J. Am. Chem. Soc.*, 1985, **107**, 2809.

263. W. A. Donaldson and M. A. Hossain, *Tetrahedron Lett.*, 1991, **32**, 7047.

264. R. Aumann, H. D. Melchers, and H. J. Weidenhaupt, *Chem. Ber.*, 1987, **120**, 17.

265. M. R. Churchill and K. Gold, *Inorg. Chem.*, 1969, **8**, 401.

266. L. Girard, J. H. MacNeil, A. Mansour, A. C. Chiverton, J. A. Page, S. Fortier, and M. C. Baird, *Organometallics*, 1991, **10**, 3114.

267. E. S. Magyar and C. P. Lillya, *J. Organomet. Chem.*, 1976, **116**, 99.

268. T. A. Albright, P. Hofmann, and R. Hoffmann, *J. Am. Chem. Soc.*, 1977, **99**, 7546.

269. T. Moore, C. Kiely, and P. C. Reeves, *J. Organomet. Chem.*, 2001, **620**, 308.

270. L. Girard, M. C. Baird, B. S. Haggerty, and A. L. Rheingold, *Organometallics*, 1992, **11**, 2329.

271. M. Franck-Neumann and A. Kastler, *Synlett*, 1995, 61.

272. A. Bond, M. Green, B. Lewis, and S. F. W. Lowrie, *J. Chem. Soc., Chem. Commun.*, 1971, 1230.

273. J. A. Mondo and J. A. Berson, *J. Am. Chem. Soc.*, 1983, **105**, 3340.

274. M. Franck-Neumann, D. Martina, and M. P. Heitz, *Tetrahedron Lett.*, 1989, **30**, 6679.

275. W. A. Donaldson and M. A. Hossain, *Tetrahedron Lett.*, 1992, **33**, 4107.

276. B. R. Bonazza, C. P. Lillya, E. S. Magyar, and G. Scholes, *J. Am. Chem. Soc.*, 1979, **101**, 4100.

277. M. Franck-Neumann, A. Kastler, and P. J. Colson, *Tetrahedron Lett.*, 1991, **32**, 7051.

278. P. J. Kleindl and W. A. Donaldson, *J. Org. Chem.*, 1997, **62**, 4176.

279. M. Franck-Neumann, P. Stöber, and G. Passmore, *Tetrahedron: Asymmetry*, 1996, **7**, 3193.

280. A. Efraty, *Chem. Rev.*, 1977, **77**, 691.

281. H. Irngartinger, N. Riegler, K. D. Malsch, K. A. Schneider, and G. Maier, *Angew. Chem., Int. Ed. Engl.*, 1980, **19**, 211.

282. R. Pettit and J. Henery, *Org. Synth.*, 1970, **50**, 21.

283. F. I. Carroll, H. H. Seltzman, and F. M. Hauser, *Tetrahedron Lett.*, 1976, **17**, 4237.

284. G. Maier and D. Born, *Angew. Chem., Int. Ed. Engl.*, 1989, **28**, 1050.

285. P. D. Harvey, W. P. Schaefer, H. B. Gray, D. F. R. Gilson, and I. S. Butler, *Inorg. Chem.*, 1988, **27**, 57.

286. R. C. Hemond and R. P. Hughes, *J. Chem. Soc., Chem. Comm.*, 1988, 319.

287. U. Behrens, K. J. Jens, J. Kopf, T. Valeri, and E. Weiss, *J. Organomet. Chem.*, 1988, **348**, 379.

288. W. C. Herndon, *J. Organomet. Chem.*, 1982, **232**, 163.

289. P. L. Pruitt, E. R. Biehl, and P. C. Reeves, *J. Chem. Soc., Perkin Trans. 2*, 1977, 907.

290. R. H. Grubbs and R. A. Grey, *J. Am. Chem. Soc.*, 1973, **95**, 5765.

291. W. A. Herrmann, C. E. Barnes, R. Serrano, and B. Koumbouris, *J. Organomet. Chem.*, 1983, **256**, C30.

292. G. A. Olah and G. Liang, *J. Org. Chem.*, 1976, **41**, 2659.

293. J. D. Fitzpatrick, L. Watts, G. F. Emerson, and R. Pettit, *J. Am. Chem. Soc.*, 1965, **87**, 3253.

294. U. Bunz, *Organometallics*, 1993, **12**, 3594.

295. C. M. Adams and E. M. Holt, *Organometallics*, 1990, **9**, 980.

296. P. C. Reeves, *J. Organomet. Chem.*, 1981, **215**, 215.

297. J. Rebek Jr and F. Gavina, *J. Am. Chem. Soc.*, 1975, **97**, 3453.

298. R. H. Grubbs and T. A. Pancoast, *J. Am. Chem. Soc.*, 1977, **99**, 2382.

299. J. Limanto, J. A. Tallarico, J. R. Porter, K. S. Khoung, K. N. Houk, and M. L. Snapper, *J. Am. Chem. Soc.*, 2002, **124**, 14748.

300. J. A. Tallarico, M. L. Randall, and M. L. Snapper, *J. Am. Chem. Soc.*, 1996, **118**, 9196.
301. J. Limanto and M. L. Snapper, *J. Am. Chem. Soc.*, 2000, **122**, 8071.
302. P. C. Reeves, *J. Organomet. Chem.*, 1981, **215**, 221.
303. U. H. F. Bunz and J. E. C. Wiegelmann-Kreiter, *Chem. Ber.*, 1996, **129**, 785.
304. J. E. C. Wiegelmann-Kreiter, V. Enkelmann, and U. H. F. Bunz, *Chem. Ber.*, 1995, **128**, 1055.
305. G. Amiet, K. Nicholas, and R. Pettit, *J. Chem. Soc., Chem. Commun.*, 1970, 161.
306. R. Grée and J. P. Lellouche, in 'Advances in Metal-Organic Chemistry', ed. L. S. Liebeskind, JAI Press, Greenwich, CT, 1995, Vol. 4, p. 129.
307. R. Grée, *Synthesis*, 1989, 341.
308. W. A. Donaldson, *Curr. Org. Chem.*, 2000, **4**, 837.
309. W. A. Donaldson, in 'Comprehensive Organometallic Chemistry II', eds. E. W. Abel, F. G. A. Stone, and G. Wilkinson, Pergamon Press, Oxford, 1995, Vol. 12, Chap. 6.2, p. 623.
310. A. J. Pearson, in 'Comprehensive Organometallic Chemistry II', eds. E. W. Abel, F. G. A. Stone, and G. Wilkinson, Pergamon Press, Oxford, 1995, Vol. 12, Chap. 6.3, p. 637.
311. H.-J. Knölker, A. Braier, D. J. Bröcher, S. Cämmerer, W. Fröhner, P. Gonser, H. Hermann, D. Herzberg, K. R. Reddy, and G. Rhode, *Pure Appl. Chem.*, 2001, **73**, 1075.
312. H.-J. Knölker, *Chem. Rev.*, 2000, **100**, 2941.
313. H.-J. Knölker, *Chem. Soc. Rev.*, 1999, **28**, 151.
314. H.-J. Knölker and P. Gonser, *Synlett*, 1992, 517.
315. R. Aumann, *J. Am. Chem. Soc.*, 1974, **96**, 2631.
316. R. C. Kerber and E. C. Ribakove, *Organometallics*, 1991, **10**, 2848.
317. C. Krueder, B. L. Barnett, and D. Brauer, in 'The Organic Chemistry of Iron', eds. E. A. Koerner von Gustorf, F.-W. Grevels, and I. Fischler, Academic Press, New York, 1978, Vol. 1, p. 1.
318. T. J. Marks, in 'The Organic Chemistry of Iron', eds. E. A. Koerner von Gustorf, F.-W. Grevels, and I. Fischler, Academic Press, New York, 1978, Vol. 1, p. 113.
319. H. W. Whitlock Jr and R. W. Markezich, *J. Am. Chem. Soc.*, 1971, **93**, 5290.
320. M. Xu and C. D. Tran, *J. Chromatogr.*, 1991, **543**, 233.
321. J. A. S. Howell, M. G. Palin, H. El Hafa, S. Top, and G. Jaouen, *Tetrahedron: Asymmetry*, 1992, **3**, 1355.
322. W. R. Roush and J. C. Park, *Tetrahedron Lett.*, 1990, **31**, 4707.
323. Y. Takemoto, Y. Baba, A. Honda, S. Nakao, I. Noguchi, C. Iwata, T. Tanaka, and T. Ibuka, *Tetrahedron*, 1998, **54**, 15567.
324. G. Evans, B. F. G. Johnson, and J. Lewis, *J. Organomet. Chem.*, 1975, **102**, 507.
325. D. H. R. Barton, A. A. L. Gunatilaka, T. Nakanishi, H. Patin, D. A. Widdowson, and B. R. Worth, *J. Chem. Soc., Perkin Trans. I*, 1976, 821.
326. D. H. R. Barton and H. Patin, *J. Chem. Soc., Perkin Trans. I*, 1976, 829.
327. H. G. Schmalz, E. Hessler, J. W. Bats, and G. Dürner, *Tetrahedron Lett.*, 1994, **35**, 4543.
328. E. Hessler, H. G. Schmalz, and G. Dürner, *Tetrahedron Lett.*, 1994, **35**, 4547.
329. A. J. Pearson, K. Chang, D. B. McConville, and W. J. Youngs, *Organometallics*, 1994, **13**, 4.
330. R. S. Paley, A. deDios, L. A. Estroff, J. A. Lafontaine, C. Montero, M. B. Rubio, M. P. Ventura, H. L. Weers, R. Fernández de la Pradilla, S. Castro, R. Dorado, and M. Morente, *J. Org. Chem.*, 1997, **62**, 6326.
331. R. S. Paley, J. M. Liu, B. R. Lichtenstein, V. L. Knoedler, T. T. Sanan, D. J. Adams, J. Fernandez, and P. R. Rablen, *Org. Lett.*, 2003, **5**, 309.
332. J. Clayden, *Angew. Chem., Int. Ed. Engl.*, 1997, **36**, 949.
333. A. J. Pearson, *Synlett*, 1990, 10.
334. F. A. Cotton and D. L. Hunter, *J. Am. Chem. Soc.*, 1976, **98**, 1413.
335. R. P. Hughes, *Adv. Organomet. Chem.*, 1990, **31**, 183.
336. G. A. Potter and R. McGague, *J. Chem. Soc., Chem. Commun.*, 1990, 1172.
337. C.-W. Ong and R. H. Hsu, *Organometallics*, 1994, **13**, 3952.
338. T.-H. Chang, C.-R. Kuo, and C.-W. Ong, *J. Chin. Chem. Soc.*, 1997, **44**, 503.
339. M.-S. Tsai, U. N. Rao, P.-Y. Hsueh, and M. C. P. Yeh, *Organometallics*, 2001, **20**, 289.
340. P. W. Howard, G. R. Stephenson, and S. C. Taylor, *J. Organomet. Chem.*, 1989, **370**, 97.
341. A. J. Pearson, A. M. Gelormini, and A. A. Pinkerton, *Organometallics*, 1992, **11**, 936.
342. M. Franck-Neumann, M. Sedrati, and M. Mokhi, *New J. Chem.*, 1990, **14**, 471.
343. M. Franck-Neumann and J. P. Colson, *Synlett*, 1991, 891.
344. P. J. Colson, M. Franck-Neumann, and M. Sedrati, *Tetrahedron Lett.*, 1989, **30**, 2393.
345. M. Franck-Neumann, E. L. Michelotti, R. Simler, and J.-M. Vernier, *Tetrahedron Lett.*, 1992, **33**, 7361.
346. M. F. Semmelhack, C. M. Bodurow, E. Fewkes, J. W. Herndon, G. Knaus, H. T. M. Le, and M. Sanner, *Chem. Scr.*, 1985, **25**, 131.
347. M.-C. P. Yeh, B.-A. Sheu, H.-W. Fu, S.-I. Tau, and L.-W. Chuang, *J. Am. Chem. Soc.*, 1993, **115**, 5941.
348. A. J. Pearson and X. Wang, *J. Am. Chem. Soc.*, 2003, **125**, 13326.
349. A. J. Pearson and X. Wang, *J. Am. Chem. Soc.*, 2003, **125**, 638.

350. D. F. Harvey and V. B. Selchau, *J. Org. Chem.*, 2000, **65**, 2282.

351. M. Franck-Neumann, D. Martina, and M.-P. Heitz, *J. Organomet. Chem.*, 1986, **301**, 61.

352. R. S. Paley, L. A. Estroff, D. J. McCulley, L. A. Martinez-Cruz, A. J. Sanchez, and F. H. Cano, *Organometallics*, 1998, **17**, 1841.

353. C. K. Wada and W. R. Roush, *Tetrahedron Lett.*, 1994, **35**, 7351.

354. R. S. Paley, L. A. Estroff, J. M. Gauguet, D. K. Hunt, and R. C. Newlin, *Org. Lett.*, 2000, **2**, 365.

355. A. Gigou, J.-P. Lellouche, J.-P. Beaucourt, L. Toupet, and R. Gree, *Angew. Chem., Int. Ed. Engl.*, 1989, **28**, 755.

356. T. Benvegnu, J. Martelli, R. Gree, and L. Toupet, *Tetrahedron Lett.*, 1990, **31**, 3145.

357. W. A. Donaldson, C. Tao, D. W. Bennett, and D. S. Grubisha, *J. Org. Chem.*, 1991, **56**, 4563.

358. W. A. Donaldson, R. Craig, and S. Spanton, *Tetrahedron Lett.*, 1992, **33**, 3967.

359. W. R. Roush and A. B. Works, *Tetrahedron Lett.*, 1997, **38**, 351.

360. W. R. Roush and A. B. Works, *Tetrahedron Lett.*, 1996, **37**, 8065.

361. D. Gree, R. Gree, T. B. Lowinger, J. Martelli, J. T. Negri, and L. A. Paquette, *J. Am. Chem. Soc.*, 1992, **114**, 8841.

362. W. R. Roush and C. K. Wada, *Tetrahedron Lett.*, 1994, **35**, 7347.

363. J. E. Mahler and R. Pettit, *J. Am. Chem. Soc.*, 1963, **85**, 3955.

364. A. Pfletschinger, H. G. Schmalz, and W. Koch, *Eur. J. Inorg. Chem.*, 1999, 1869.

365. M. Semmelhack and E. J. Fewkes, *Tetrahedron Lett.*, 1987, **28**, 1497.

366. Y. Takemoto, K. Ishii, T. Ibuka, Y. Miwa, T. Taga, S. Nakao, T. Tanaka, H. Ohishi, Y. Kai, and N. Kanehisa, *J. Org. Chem.*, 2001, **66**, 6116.

367. Y. Takemoto, N. Yoshikawa, Y. Baba, C. Iwata, T. Tanaka, T. Ibuka, and H. Ohishi, *J. Am. Chem. Soc.*, 1999, **121**, 9143.

368. M. Franck-Neumann, D. Martina, and F. Brion, *Angew. Chem., Int. Ed. Engl.*, 1978, **17**, 690.

369. L. Hill, C. J. Richards, S. P. Saberi, and S. E. Thomas, *Pure Appl. Chem.*, 1992, **64**, 371.

370. L. Hill, C. J. Richards, and S. E. Thomas, *Pure Appl. Chem.*, 1990, **62**, 2057.

371. M. Franck-Neumann, C. Dietrich-Buchecker, and A. K. Khemiss, *J. Organomet. Chem.*, 1981, **220**, 187.

372. M. G. Newton, N. S. Pantaleo, R. B. King, and C.-K. Chu, *J. Chem. Soc., Chem. Commun.*, 1979, 10.

373. K. G. Morris, S. P. Saberi, A. M. Z. Slawin, S. E. Thomas, and D. J. Williams, *J. Chem. Soc., Chem. Commun.*, 1992, 1788.

374. H. J. Knölker, G. Baum, and P. Gonser, *Tetrahedron Lett.*, 1995, **36**, 8191.

375. D. Berger, M. Dubs, A. Göbel, W. Inhof, M. Kötteritzsch, M. Rost, and B. Schönecker, *Tetrahedron: Asymmetry*, 1999, **10**, 2983.

376. A. Ibbotson, A. C. Reduto dos Reis, S. P. Saberi, A. M. Z. Slawin, S. E. Thomas, G. J. Tustin, and D. J. Williams, *J. Chem. Soc., Perkin Trans. I*, 1992, 1251.

377. W.-Y. Zhang, D. J. Jakiela, A. Maul, C. Knors, J. W. Lauher, P. Helquist, and D. Enders, *J. Am. Chem. Soc.*, 1988, **110**, 4652.

378. M. Brookhart, E. R. Davis, and D. L. Harris, *J. Am. Chem. Soc.*, 1972, **94**, 7853.

379. O. Eisenstein, W. M. Butler, and A. J. Pearson, *Organometallics*, 1984, **3**, 1150.

380. A. J. Birch, P. W. Westerman, and A. J. Pearson, *Aust. J. Chem.*, 1976, **29**, 1671.

381. T. S. Sorenson and C. R. Jablonski, *J. Organomet. Chem.*, 1970, **25**, C62.

382. G. R. Stephenson, S. T. Astley, I. M. Palotao, P. W. Howard, D. A. Owen, and S. Williams, in ‘Organic Synthesis via Organometallics’, eds. K. H. Doetz and R. W. Hoffman, Vieweg, Braunschweig, 1991, Vol. 3, p. 169.

383. A. J. Pearson and D. C. Rees, *J. Am. Chem. Soc.*, 1982, **104**, 1118.

384. N. Millot, C. Guillou, and C. Thal, *Tetrahedron Lett.*, 1998, **39**, 2325.

385. N. Millot, C. Guillou, and C. Thal, *Tetrahedron*, 1997, **53**, 12553.

386. A. J. Pearson and M. P. Burello, *Organometallics*, 1992, **11**, 448.

387. A. J. Pearson and K. Srinivasan, *J. Org. Chem.*, 1992, **57**, 3965.

388. A. J. Pearson, S. L. Blystone, H. Nar, A. A. Pinkerton, B. A. Roden, and J. Yoon, *J. Am. Chem. Soc.*, 1989, **111**, 134.

389. A. J. Pearson and C. W. Ong, *J. Org. Chem.*, 1982, **47**, 3780.

390. H. J. Knolker and K. R. Reddy, *Chem. Rev.*, 2002, **102**, 4303.

391. H. J. Knolker, E. Baum, and T. Hopfmann, *Tetrahedron*, 1999, **55**, 10391.

392. H. J. Knolker, E. Baum, H. Goesmann, H. Gossel, K. Hartmann, M. Kosub, U. Locher, and T. Sommer, *Angew. Chem., Int. Ed. Engl.*, 2000, **39**, 781.

393. T. G. Bonner, K. A. Holder, P. Powell, and E. Styles, *J. Organomet. Chem.*, 1977, **131**, 105.

394. W. A. Donaldson, M.-J. Jin, and P. T. Bell, *Organometallics*, 1993, **12**, 1174.

395. G. R. Stephenson, M. Voyle, and S. Williams, *Tetrahedron Lett.*, 1991, **32**, 5265.

396. W. A. Donaldson and L. Shang, *Tetrahedron Lett.*, 1995, **36**, 1575.

397. A. Teniou, L. Toupet, and R. Grée, *Synlett*, 1991, 195.

398. D. M. Grée, J. T. Martelli, R. L. Grée, and L. Toupet, *J. Org. Chem.*, 1995, **60**, 2316.

399. A. Hachem, L. Toupet, and R. Grée, *Tetrahedron Lett.*, 1995, **36**, 1849.

400. A. J. Pearson and V. P. Ghidu, *Org. Lett.*, 2002, **4**, 4069.

401. A. Togni and T. Hayashi eds, 'Ferrocenes: Homogeneous Catalysis, Organic Synthesis, Materials Science', VCH, Weinheim, 1995.

402. A. Togni in 'New Chiral Ferrocenyl Ligands for Asymmetric Catalysis in Metallocenes. Synthesis, Reactivity, Applications', eds. A. Togni and R. L. Halterman, Weinheim, 1998, Vol. 2, p. 685.

403. A. Togni, *Angew. Chem., Int. Ed. Engl.*, 1996, **35**, 1475.

404. O. B. Sutcliffe and M. R. Bryce, *Tetrahedron: Asymmetry*, 2003, **14**, 2297.

405. T. J. Colacot, *Chem. Rev.*, 2003, **103**, 3101.

406. L.-X. Dai, T. Tu, S.-L. You, W.-P. Deng, and X.-L. Hou, *Acc. Chem. Res.*, 2003, **36**, 659.

407. C. J. Richards and A. J. Locke, *Tetrahedron: Asymmetry*, 1998, **9**, 2377.

408. G. C. Fu, *Acc. Chem. Res.*, 2000, **33**, 412.

409. C. Ganter, *J. Chem. Soc., Dalton Trans.*, 2001, 3541.

410. R. W. Heo and T. R. Lee, *J. Organomet. Chem.*, 1999, **578**, 31.

411. I. Manners, *J. Chem. Soc., Chem. Commun.*, 1999, 857.

412. T. J. Kealy and P. L. Pauson, *Nature*, 1951, **168**, 1039.

413. S. A. Miller, J. A. Tebboth, and J. F. Jermaine, *J. Chem. Soc.*, 1952, 632.

414. G. Wilkinson, M. Rosenblum, M. C. Whiting, and R. B. Woodward, *J. Am. Chem. Soc.*, 1952, **74**, 2125.

415. A. Haaland, *Acc. Chem. Res.*, 1979, **12**, 415.

416. C. Kruger, B. L. Barnett, and D. Brauer, in 'The Organic Chemistry of Iron', eds. E. A. Koerner Von Gustorf, F.-W. Grevels, and I. Fischler, Academic Press, New York, 1978, Vol. 1, Chap. 1.IV, p. 23.

417. E. Haslinger, W. Robien, K. Schloegl, and W. Weissensteiner, *J. Organomet. Chem.*, 1981, **218**, C11.

418. J.-J. Brunet, *Chem. Rev.*, 1990, **90**, 1041.

419. M. Rosenblum, 'Chemistry of the Iron Group Metallocenes', Wiley, New York, 1965, Part 1, p. 1.

420. T. E. Bitterwolf and A. C. Ling, *J. Organomet. Chem.*, 1972, **40**, 197.

421. G. Cerichelli, G. Illuminati, G. Ortaggi, and A. M. Giuliani, *J. Organomet. Chem.*, 1977, **127**, 357.

422. D. E. Bublitz and K. L. Rinehart Jr, *Org. React.*, 1969, **17**, 1.

423. I. Omae, *Coord. Chem. Rev.*, 1982, **42**, 31.

424. M. Rosenblum and F. W. Abbate, *J. Am. Chem. Soc.*, 1966, **88**, 4178.

425. J. A. Mangravite and T. G. Traylor, *Tetrahedron Lett.*, 1967, **8**, 4461.

426. IUPAC Commission on Electrochemistry (UK), *Pure Appl. Chem.*, 1984, **56**, 461.

427. M. L. H. Green, J. Qin, and D. O'Hare, *J. Organomet. Chem.*, 1988, **358**, 375.

428. E. A. Hill and J. H. Richards, *J. Am. Chem. Soc.*, 1961, **83**, 3840, 4216.

429. W. E. Watts, *J. Organomet. Chem. Libr.*, 1979, **7**, 399.

430. U. Behrens, *J. Organomet. Chem.*, 1979, **182**, 89.

431. R. Gleiter and R. Seeger, *Helv. Chim. Acta*, 1971, **54**, 1217.

432. M. I. Rybinskaya, A. Z. Kreindlin, and S. S. Fadeeva, *J. Organomet. Chem.*, 1988, **358**, 363.

433. J. Wright, L. Frambes, and P. Reeves, *J. Organomet. Chem.*, 1994, **476**, 215.

434. L. Schwink and P. Knochel, *Tetrahedron Lett.*, 1996, **37**, 25.

435. M. D. Rausch, G. A. Moser, and C. F. Meade, *J. Organomet. Chem.*, 1973, **51**, 1.

436. J. J. Almena Perea, M. Lotz, and P. Knochel, *Tetrahedron: Asymmetry*, 1999, **10**, 375.

437. M. Tsukazaki, M. Tinkl, A. Roglans, B. J. Chapell, N. J. Taylor, and V. Snieckus, *J. Am. Chem. Soc.*, 1996, **118**, 685.

438. R. S. Laufer, U. Veith, N. J. Taylor, and V. Snieckus, *Org. Lett.*, 2000, **2**, 629.

439. C. Metallinos and V. Snieckus, *Org. Lett.*, 2002, **4**, 1935.

440. H. L. Pedersen and M. Johannsen, *J. Org. Chem.*, 2002, **67**, 7982.

441. J. F. Jensen, I. Søtofte, H. O. Sørensen, and M. Johannsen, *J. Org. Chem.*, 2003, **68**, 1258.

442. J. F. Jensen and M. Johannsen, *Org. Lett.*, 2003, **5**, 3025.

443. M. Lotz, G. Kramer, and P. Knochel, *J. Chem. Soc., Chem. Commun.*, 2002, 2546.

444. J. Park, Z. Quan, S. Lee, K. H. Ahn, and C.-W. Cho, *J. Organomet. Chem.*, 1999, **584**, 140.

445. S.-L. You, X.-Z. Zhu, Y.-M. Luo, X.-L. Hou, and L.-X. Dai, *J. Am. Chem. Soc.*, 2001, **123**, 7471.

446. F. Maienza, M. Wörle, P. Steffanut, A. Mezzetti, and F. Spindler, *Organometallics*, 1999, **18**, 1041.

447. U. Nettekoven, P. C. J. Kamer, P. W. N. M. van Leeuwen, M. Widhalm, A. L. Spek, and M. Lutz, *J. Org. Chem.*, 1999, **64**, 3996.

448. M. T. Reetz, A. Gosberg, R. Goddard, and S.-H. Kyung, *J. Chem. Soc., Chem. Commun.*, 1998, 2077.

449. D. Liu, W. Li, and X. Zhang, *Org. Lett.*, 2002, **4**, 4471.

450. U. Berens, M. J. Burk, A. Gerlach, and W. Hems, *Angew. Chem., Int. Ed. Engl.*, 2000, **39**, 1981.

451. D. Xiao and X. Zhang, *Angew. Chem., Int. Ed. Engl.*, 2001, **40**, 3425.

452. H. C. L. Abbenhuis, U. Burckhardt, V. Gramlich, A. Togni, A. Albinati, and B. Müller, *Organometallics*, 1994, **13**, 4481.

453. L. Schwink, S. Vettel, and P. Knochel, *Organometallics*, 1995, **14**, 5000.

454. Z. Li and A. Vasella, *Helv. Chim. Acta*, 1996, **79**, 2201.

455. T. Suzuka, M. Kawatsura, A. Okada, and T. Hayashi, *Tetrahedron: Asymmetry*, 2003, **14**, 511.

456. T. Suzuka, M. Ogasawara, and T. Hayashi, *J. Org. Chem.*, 2002, **67**, 3355.

457. A. Appel, H. Noeth, and M. Schmidt, *Chem. Ber.*, 1995, **128**, 621.

458. D. Braga, M. Polito, M. Bracaccini, D. D'Addario, E. Tagliavini, L. Sturba, and F. Grepioni, *Organometallics*, 2003, **22**, 2142.

459. M. V. Barybin, T. C. Holovics, S. F. Deplazes, G. H. Lushington, D. R. Powell, and M. Toriyama, *J. Am. Chem. Soc.*, 2002, **124**, 13668.

460. D. van Leusen and B. Hessen, *Organometallics*, 2001, **20**, 224.

461. A. J. Ashe III, J. W. Kampf, and S. M. Al-Taweel, *J. Am. Chem. Soc.*, 1992, **114**, 372.

462. C. Janiak and N. Kuhn, *Adv. Nitrogen Heterocycles*, 1996, **2**, 179.

463. J. Zakrzewski and C. Giannotti, *J. Organomet. Chem.*, 1990, **388**, 175.

464. J. C. Ruble and G. C. Fu, *J. Org. Chem.*, 1996, **61**, 7230.

465. B. L. Hodous, J. C. Ruble, and G. C. Fu, *J. Am. Chem. Soc.*, 1999, **121**, 2637.

466. P. I. Dosa, J. C. Ruble, and G. C. Fu, *J. Org. Chem.*, 1997, **62**, 444.

467. M. M. C. Lo and G. C. Fu, *J. Am. Chem. Soc.*, 1998, **120**, 10270.

468. J. G. Hansen and M. Johannsen, *J. Org. Chem.*, 2003, **68**, 1266.

469. T. Fukuda, K. Imazato, and M. Iwao, *Tetrahedron Lett.*, 2003, **44**, 7503.

470. C. E. Garrett and G. C. Fu, *J. Org. Chem.*, 1997, **62**, 4534.

471. G. de Lauzon, B. Deschamps, J. Fischer, F. Mathey, and A. Mitschler, *J. Amer. Chem. Soc.*, 1980, **102**, 994.

472. S. Qiao and G. C. Fu, *J. Org. Chem.*, 1998, **63**, 4168.

473. L. Brassat, B. Ganter, and C. Ganter, *Chem. Eur. J.*, 1998, **4**, 11.

474. C. Ganter, C. Kaulen, and U. Englert, *Organometallics*, 1999, **18**, 5444.

475. R. Shintani and G. C. Fu, *Org. Lett.*, 2002, **4**, 3699.

476. Q.-H. Fan, Y.-M. Li, and A. S. C. Chan, *Chem. Rev.*, 2002, **102**, 3385.

477. R. van Heerbeek, P. C. J. Kamer, P. W. N. M. van Leeuwen, and J. N. H. Reek, *Chem. Rev.*, 2002, **102**, 3717.

478. C. Köllner, B. Pugin, and A. Togni, *J. Amer. Chem. Soc.*, 1998, **120**, 10274.

479. P. D. Beer and P. A. Gale, *Angew. Chem., Int. Ed. Engl.*, 2001, **40**, 486.

480. P. D. Beer and E. J. Hayes, *Coor. Chem. Rev.*, 2003, **240**, 167.

481. P. A. Gale, *Coor. Chem. Rev.*, 2003, **240**, 191.

482. M. D. Pratt and P. D. Beer, *Polyhedron*, 2003, **22**, 649.

483. P. Laurent, H. Miyaji, S. R. Collinson, I. Prokes, C. J. Moody, J. H. R. Tucker, and A. M. Z. Slawin, *Org. Lett*, 2002, **4**, 4037.

484. T. Moriuchi, A. Nomoto, K. Yoshida, A. Ogawa, and T. Hirao, *J. Amer. Chem. Soc.*, 2001, **123**, 68.

485. T. Moriuchi, K. Yoshida, and T. Hirao, *Org. Lett.*, 2003, **5**, 4285.

486. M. Hillman, B. Gordon, N. Dudek, R. Fajer, E. Fujita, J. Gaffney, P. Jones, A. J. Weiss, and S. Takagi, *J. Organomet. Chem.*, 1980, **194**, 229.

487. V. I. Sokolov, T. M. Filippova, N. S. Khrushcheva, and L. L. Troitskaya, *Bull. Acad. Sci. USSR*, 1987, **35**, 2385.

488. D. S. Trifan and L. Nicholas, *J. Am. Chem. Soc.*, 1957, **79**, 2746.

489. M. E. Huttenloch, J. Diebold, U. Rief, H. H. Brintzinger, A. M. Gilbert, and T. J. Katz, *Organometallics*, 1992, **11**, 3600.

490. M. Enders, G. Ludwig, and H. Pritzkow, *Organometallics*, 2002, **21**, 3856.

491. R. Salter, T. E. Pickett, and C. J. Richards, *Tetrahedron: Asymmetry*, 1998, **9**, 4239.

492. E. Roman and D. Astruc, *Inorg. Chem.*, 1979, **18**, 3284.

493. D. Astruc, *Tetrahedron*, 1983, **39**, 4027.

494. W. Finckh, B. Z. Tang, D. A. Foucher, D. B. Zamble, A. Lough, and I. Manners, *Organometallics*, 1993, **12**, 823.

495. J. B. Sheridan, A. J. Lough, and I. Manners, *Organometallics*, 1996, **15**, 2195.

496. J. B. Sheridan, K. Temple, A. J. Lough, and I. Manners, *J. Chem. Soc., Dalton Trans.*, 1997, 711.

497. E. Deschamps, L. Ricard, and F. Mathey, *Organometallics*, 2001, **20**, 1499.

498. A. J. Locke, C. J. Richards, D. E. Hibbs, and M. B. Hursthouse, *Tetrahedron: Asymmetry*, 1997, **8**, 3383.

499. A. J. Locke and C. J. Richards, *Organometallics*, 1999, **18**, 3750.

500. G. Iftime, J.-C. Daran, E. Manoury, and G. G. A. Balavoine, *Organometallics*, 1996, **15**, 4808.

501. G. Iftime, J.-C. Daran, E. Manoury, and G. G. A. Balavoine, *Angew. Chem., Int. Ed. Engl.*, 1998, **37**, 1698.

502. A. J. Locke, C. Jones, and C. J. Richards, *J. Organomet. Chem.*, 2001, **637–639**, 669.

503. M. Ogasawara, T. Nagano, and T. Hayashi, *Organometallics*, 2003, **22**, 1174.

504. J. K. Pudelski and M. R. Callstrom, *Organometallics*, 1992, **11**, 2757.

505. A. Sudhakar and T. J. Katz, *J. Am. Chem. Soc.*, 1986, **108**, 179.

506. J. Watanabe, M. Hisatome, and K. Yamakawa, *Tetrahedron Lett.*, 1987, **28**, 1427.

507. M. Hisatome, J. Watanabe, K. Yamakawa, and Y. Iitaka, *J. Am. Chem. Soc.*, 1986, **108**, 1333.

508. M. Hisatome, R. Yamashita, J. Watanabe, K. Yamakawa, and Y. Iitaka, *Bull. Chem. Soc. Jpn.*, 1988, **61**, 1687.
509. M. Hisatome, Y. Kawajiri, K. Yamakawa, Y. Harada, and Y. Iitaka, *Tetrahedron Lett.*, 1982, **23**, 1713.
510. R. D. Ernst, *Chem. Rev.*, 1988, **88**, 1255.
511. A. S. Abd-El-Aziz and S. Bernardin, *Coor. Chem. Rev.*, 2000, **203**, 219.
512. M. L. H. Green, L. Pratt, and G. Wilkinson, *J. Chem. Soc.*, 1960, 989.
513. R. G. Sutherland, *J. Organomet. Chem. Library*, 1977, **3**, 311.
514. R. G. Sutherland, W. J. Pannekoek, and C. C. Lee, *Ann. N.Y. Acad. Sci.*, 1977, **295**, 192.
515. C. C. Lee, M. Iqbal, U. S. Gill, and R. G. Sutherland, *J. Organomet. Chem.*, 1985, **288**, 89.
516. R. G. Sutherland, M. Iqbal, and A. Piorko, *J. Organomet. Chem.*, 1986, **302**, 307.
517. P. Michaud, D. Astruc, and J. H. Ammeter, *J. Am. Chem. Soc.*, 1982, **104**, 3755.
518. R. G. Sutherland, R. L. Chowdhury, A. Piorko, and C. C. Lee, *J. Organomet. Chem.*, 1987, **319**, 379.
519. R. M. Moriarty and U. S. Gill, *Organometallics*, 1986, **5**, 253.
520. C. C. Lee, A. S. Abd-El-Aziz, R. L. Chowdhury, U. S. Gill, A. Piorko, and R. G. Sutherland, *J. Organomet. Chem.*, 1986, **315**, 79.
521. C. C. Lee, U. S. Gill, and R. G. Sutherland, *J. Organomet. Chem.*, 1984, **267**, 157.
522. J. W. Johnson and P. M. Treichel, *J. Am. Chem. Soc.*, 1977, **99**, 1427.
523. D. Astruc, E. Roman, J. R. Hamon, and P. Batail, *J. Am. Chem. Soc.*, 1979, **101**, 2240.
524. M. Le Rudulier, C. Moinet, and E. Raoult, *J. Organomet. Chem.*, 1986, **310**, 209.
525. A. J. Pearson, J. G. Park, and P. Y. Zhu, *J. Org. Chem.*, 1992, **57**, 3583.
526. D. Astruc, *Chem. Rev.*, 1988, **88**, 1189.
527. D. Astruc, *Acc. Chem. Res.*, 1986, **19**, 377.
528. D. Astruc, *New J. Chem*, 1992, **16**, 305.
529. C. Moinet, E. Roman, and D. Astruc, *J. Organomet. Chem.*, 1977, **128**, C45.
530. D. Astruc, J. R. Hamon, G. Althoff, E. Roman, P. Batail, P. Michaud, J. P. Mariot, F. Varret, and D. Cozak, *J. Am. Chem. Soc.*, 1979, **101**, 5445.
531. J.-L. Fillaut, J. Linares, and D. Astruc, *Angew. Chem., Int. Ed. Engl.*, 1994, **33**, 2460.
532. J. F. Helling and D. M. Braitsch, *J. Am. Chem. Soc.*, 1970, **92**, 7207.
533. S. G. Davies, M. L. H. Green, and D. M. P. Mingos, *Tetrahedron*, 1978, **34**, 3047.
534. D. Astruc, *Synlett*, 1991, 369.
535. K. C. Sturge and M. J. Zaworotko, *J. Chem. Soc., Chem. Commun.*, 1990, 1244.

Iron Porphyrin Chemistry

F. Ann Walker[1] **& Ursula Simonis**[2]
[1] *University of Arizona, Tucson, AZ, USA*
[2] *San Francisco State University, San Francisco, CA, USA*

1 Introduction and Background 1
2 Iron(0) Porphyrins and their Reactions 13
3 Iron(I) Porphyrins and their Reactions 13
4 Iron(II) Porphyrins and their Reactions 14
5 Iron(II) Macrocycle π-Cation Radicals and their Valence Tautomerism with Iron(III) Macrocycles 40
6 Iron(III) Porphyrins and their Reactions 42
7 Iron(III) Porphyrin and Corrole π-Cation Radicals and their Reactions 83
8 Iron(IV) Porphyrins and their Reactions 86
9 Iron(IV) Porphyrin π-Cation Radicals and their Reactions 89
10 Iron(V) Porphyrins 93
11 Related Articles 93
12 References 93

Abbreviations

BNCT = Boron neutron capture therapy; BzNH$_2$ = Benzylamine; 1- or N-BzIm = 1- or N-benzylimidazole; COSY = Homonuclear J-Correlated SpectroscopY (a two-dimensional NMR experiment); CuIM, NiIM = The Cu^{II} and Ni^{II} complexes of the Schiff base condensation product of 5-chloro-2-hydroxybenzophenone, 1,2-diaminobenzene, and imidazole-4-carbaldehyde; DCP, TDCPP, or (2,6-Cl$_2$)$_4$TPP = Tetrakis(2,6-dichlorophenyl)porphyrin; DP or DPIX = deuteroporphyrin IX (see Figure 1); DPDME = Deuteroporphyrin IX dimethyl ester; EDRF = Endothelial-derived relaxing factor; ETIO = Etioporphyrin); EXSY = EXchange SpectroscopY (a two-dimensional NMR experiment that uses the same pulse sequence as NOESY); ImH = Imidazole; MNT^{2-} = *cis*-1,2-dicyano-1,2-ethylenedithiolate; MP or MPIX = Mesoporphyrin IX (see Figure 1); MP8-MP11 = Microperoxidase-8 to -11 (peptide hydrolysis fragments of horse heart cytochrome *c*); MPDME = Mesoporphyrin IX dimethyl ester; NOESY = Nuclear Overhauser and Exchange SpectroscopY (a two-dimensional NMR experiment); N-RIm = *N*-substituted imidazole; OAP = (2,3,7,8,12,13,17,18-octakis(diethylcarboxamide)porphyrin); OEAP = Octaethylazaporphyrin; OEB = Octaethylbiliverdin (see Scheme 3 below); OEC = Octaethylchlorin (see Figure 1); OECorr = Octaethylcorrole; OEiBC = Octaethylisobacteriochlorin (see Figure 1); OEOP = Octaethylverdoheme; OEP = Octaethylporphyrin (2,3,7,8,12,13,17,18-octaethylporphyrin); OEPO = (5-oxo)octaethylporphyrin or octaethylphlorin; OEPOH = (5-hydroxy)octaethylporphyrin; OETPP = Octaethyltetraphenylporphyrin (see Figure 1); OMTPP = Octamethyltetraphenylporphyrin; PP or PPIX = Protoporphyrin IX (see Figure 1); PPDME = Protoporphyrin IX dimethyl ester; Pyz = Pyrazine; RImH = Imidazole with an R substituent on one of the carbon atoms; RNC = Alkyl or aryl isocyanide (isonitrile); RNO = alkyl or aryl nitroso compound; RPy = Substituted pyridine; RTPP = *R*-phenyl substituted tetraphenylporphyrin; TC$_6$TPP = Tetra-β,β'-tetramethylenetetraphenyl-porphyrin; TMINP = Tetrakis(*o*-(methylisonicotinamidophenyl)porphyrin); T(*o*-M)PyP = Tetrakis(methyl-*o*-pyridinium)porphyrin; TMP = Tetramesitylporphyrin; T(*p*-M)PyP = Tetrakis (methyl-*p*-pyridinium)porphyrin; TMTMP = 2,7,12,17-tetramethyl-3,8,13,18-tetramesitylporphyrin; TPC = Tetra − phenylchlorin; TPCorr = Triphenylcorrole; T(*o*-Piv)PP, T$_{\text{Piv}}$PP, or (*o*-Piv)$_4$TPP = Tetrakis(*o*-pivalamidophenyl)porphyrin (the $\alpha,\alpha,\alpha,\alpha$ atropisomer is called the ‘Picket Fence Porphyrin’); TPP = Tetraphenylporphyrin (5,10,15,20-tetraphenylporphyrin); TPPBr$_4$ = Tetraphenylporphyrin brominated on four β-pyrrole positions; TPP(CN)$_3$ and TPP(CN)$_4$ = Tetraphenylporphyrin with three or four β-pyrrole cyano groups, respectively; TPPS = Tetrakis(*m*-sulfophenyl)porphyrin (also called tetraphenylporphine sulfonate); TTMPP = Tetrakis(2,4,6-trimethoxyphenyl)porphyrin; TTP = tetratolylporphyrin; TTPPP = Tetrakis ((2,4,6-triphenyl)phenyl)porphyrin; (X)$_n$(Y)$_{4-n}$TPP = Unsymmetrically phenyl substituted tetraphenylporphyrin, where X and Y are on different phenyl rings.

1 INTRODUCTION AND BACKGROUND

1.1 Occurrence and Roles of Natural Iron Porphyrins (Hemes) and Their Synthetic Analogs

Hemes and heme proteins (*see Polypeptide*; ***Iron: Heme Proteins & Dioxygen Transport & Storage***; ***Iron: Heme Proteins & Electron Transport***; ***Iron: Heme Proteins, Mono- & Dioxygenases***; ***Iron: Heme Proteins, Peroxidases, Catalases & Catalase-peroxidases***) are vital components of essentially every cell of nearly every living organism. They have such diverse roles in vital life processes as the transport and storage of dioxygen in higher animals (hemoglobin and myoglobin, respectively)[1] (*see* ***Iron: Heme Proteins & Dioxygen Transport & Storage***); electron transport in the respiratory chains (*see Electron Transport Chains*) of organisms as diverse as *bacteria, archaea*, yeasts, plants and animals, and in photosynthetic cells from those of the simplest photosynthetic bacteria to those of higher plants (cytochromes *a*, *b*, *c*, *d*, *f*, *o*)[2–23] (*see* ***Iron: Heme Proteins & Electron Transport***; ***Photosynthesis***); synthesis, modification and/or degradation of fatty

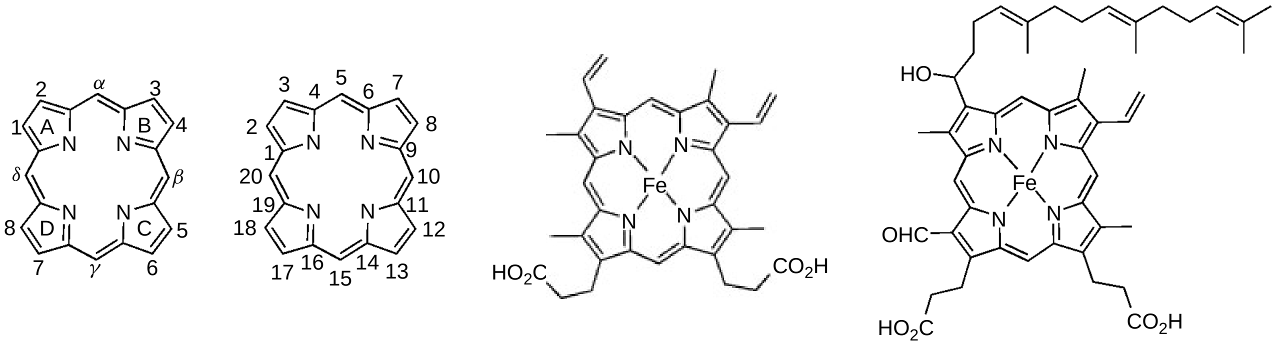

(a) (b) (c) Heme *b* (d) Heme *a*

Iron protoporphyrin IX (PP), Heme (Fe^{II}), Hemin (Fe^{III})
Protoheme IX, Protohemin IX,
Iron (2,4-divinyldeuteroporphyrin IX)

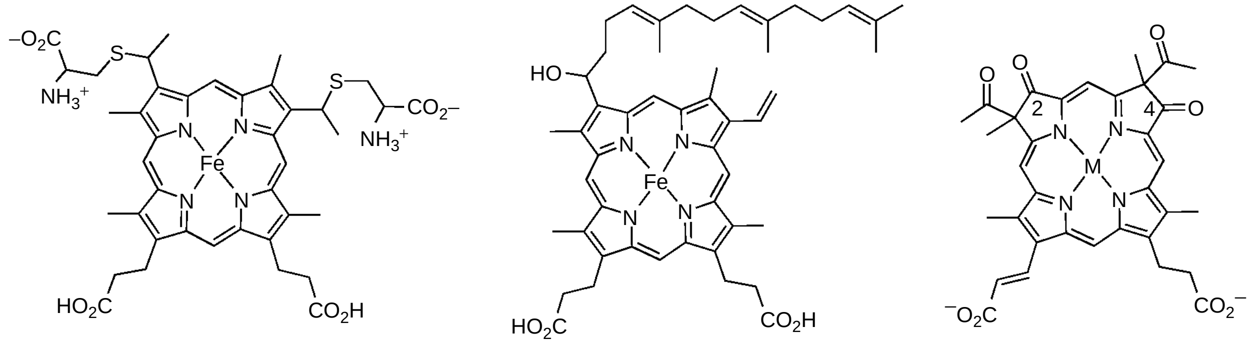

(e) Heme *c* (f) Heme *o* (g) Heme d_1

Figure 1 Structures of iron porphyrins, chlorins, and isobacteriochlorins and examples, with typical nomenclature. (a) Numbering system usually used for natural porphyrins and their derivatives. As will become apparent below, many natural porphyrins and their derivatives are named as 2,4-disubstituted deuteroporphyrin IX derivatives. (b) IUPAC numbering system for porphyrins. Synthetic porphyrins are named by *either* numbering scheme (a) or (b). (c)–(e) Common naturally occurring porphyrins found in heme proteins that are named *a*–*d* and *o* according to the relative positions of the α and β bands of the Fe^{II} form of the heme protein in the presence of excess pyridine (the so-called Pyridine Hemochrome spectrum). (h)–(j) Naturally occurring iron porphyrins. (k) The chlorin ring system. (l) The isobacteriochlorin ring system. (m) An example of an iron chlorin. (n and o) examples of iron isobacteriochlorins (Note also that heme d_1 (g) is the same oxidation level as d_1 an isobacteriochlorin). (p)–(r) Common synthetic porphyrins (note two naming systems). In this article, phenyl-substituted TPP derivatives are abbreviated as either (p-X)$_4$TPP or TpXPP, in line with the usage of the original authors. Common water soluble synthetic porphyrins include (s) and (t). Related macrocycles include (u)–(z)

acids, steroid and adrenal hormones, anesthetics, polycyclic aromatic hydrocarbons and other xenobiotics (cytochromes P450),[24–32] or in general insertion of one or both oxygen atoms of dioxygen into organic substrates (P450, secondary amine monooxygenase (SAMO), heme oxygenase (HO), prostaglandin H synthase (PGHS), indoleamine-2,3-oxygenase (IDO), and tryptophan-2,3-oxygenase (TDO)[32] (*see* ***Iron: Heme Proteins, Mono- & Dioxygenases***); breakdown of heme (HO),[32–34] activation and metabolism of hydrogen peroxide[24–26,35] (peroxidases,[26,35,36] myeloperoxidase, haloperoxidases,[14] lignin peroxidases,[37] catalases, etc.) (*see* ***Iron: Heme Proteins, Peroxidases, Catalases & Catalase-peroxidases***); metabolism of the oxides of nitrogen and sulfur (nitrite reductase,[38–40] sulfite reductase,[41,42] sulfite oxidase,[43,44] etc.); oxygen sensing proteins (FixL,[45–48] DosH[49]) and synthesis (nitric oxide synthase, NOS)[50–54] and transport[55–57] of the so-called endothelial-derived relaxing factor (EDRF), nitric oxide (NO), which has been shown to be an important biochemical effector of such diverse physiological processes as smooth muscle (including blood vessel) relaxation, platelet inhibition, neurotransmission, immune regulation, and penile erection[58] (*see* ***Nitrogen Monoxide (Nitric Oxide): Bioinorganic Chemistry***). Biologically important related molecules that involve modified hemes include the reduced hemes (iron chlorins, bacterio- and isobacteriochlorins, and sulfhemes)[41,59–68] (*see Siroheme*), as well as chlorophylls, pheophytins, and pheophorbides[69–73] vitamin B_{12},[69,74–81] Factor F430,[69,82,83] and some of the luciferins responsible for the diurnal cycles of many species of plants and animals.[84] Breakdown products of heme[33,34]

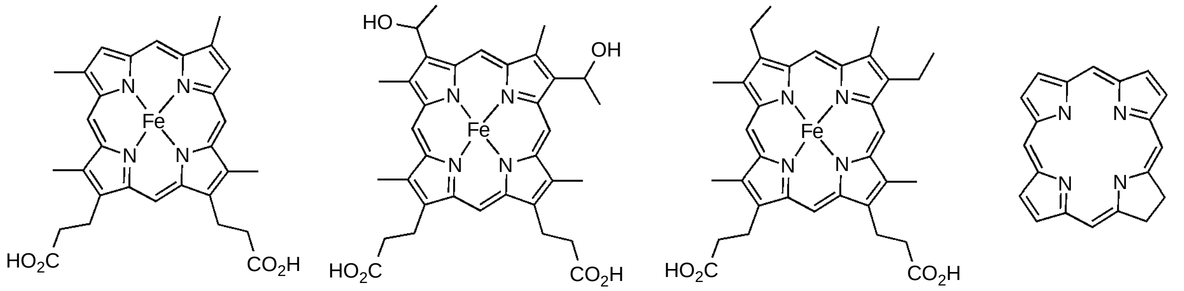

Iron deuteroporphyrin IX (DP)

(h)

Iron hematoporphyrin IX (HP)
Iron(2,4-bis(α-hydroxyethyl)-deuteroporphyrin IX)

(i)

Iron mesoporphyrin IX (MP)
Iron(2,4-diethyldeuteroporphyrin IX)

(j)

Chlorin ring system

(k)

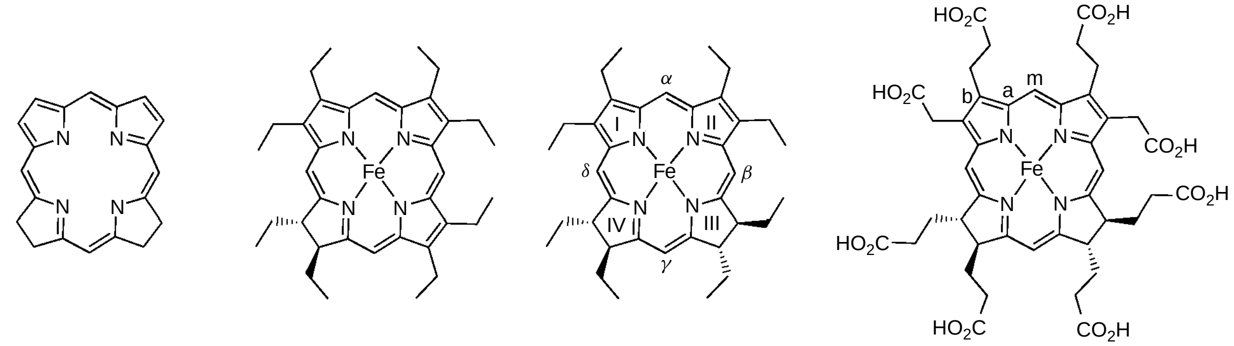

Isobacteriochlorin ring system

(l)

Iron *trans*-octaethylchlorin
(OEC)

(m)

Iron *trans*, *trans*,
trans-octaethylisobacteriochlorin
(OEiBC)

(n)

Siroheme

(o)

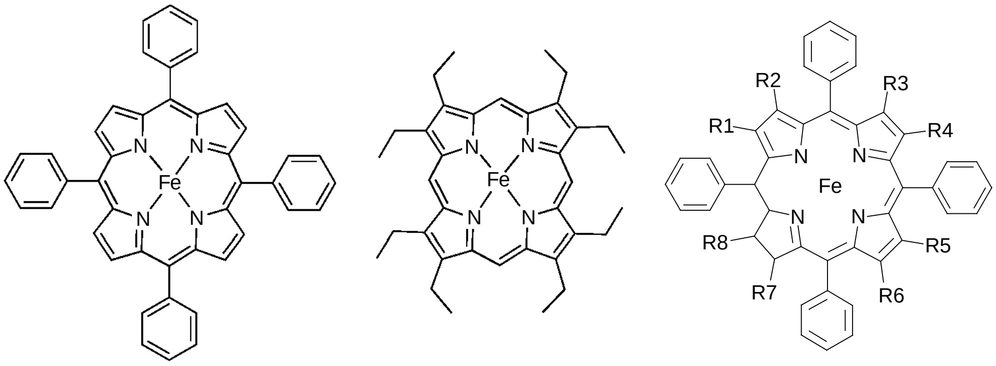

Iron tetraphenylporphyrin (TPP)
(5,10,15,20-tetraphenylporphyrin)
($\alpha,\beta,\gamma,\delta$-tetraphenylporphyrin)

(p)

Iron octaethylporphyrin (OEP)

(q)

Iron octaalkyltetraphenylporphyrin

(r)

Figure 1 cont'd

are harmful to newborn infants and alcoholics,[85] and intermediates in the synthesis of heme cause the genetic diseases called porphyrias.[86–88] Excessive heme breakdown can lead to the accumulation of bilirubin, which, when accumulated in the blood and tissues, leads to a condition called *hyperbilirubinemia* that is seen in neonatal jaundice in infants and the genetic disease *Crigler-Najjar Syndrome*.[89] Genetically modified forms of hemoglobin are responsible for sickle-cell anemia[90,91] and a number of methemoglobinemias.[92] Heme-NO complexes have been detected in cured meats,[93] and synthetic hemes or phthalocyanines can be used in bioremediation of pollutants.[94–99] Since porphyrinic pigments and their metal complexes are known to localize with high affinity in neoplastic tissues,[100–103] synthetically prepared or naturally occurring hemes are investigated with great interest in medical applications. For example, metalated porphyrins are studied as potential contrast agents in magnetic resonance imaging (MRI) techniques.[100,102–104]

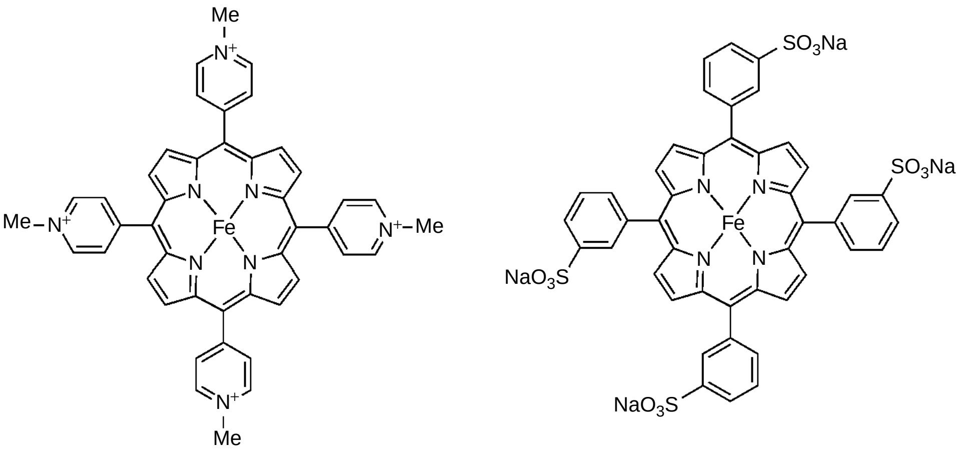

Iron tetra(*p*-methylpyridinium)porphyrin (T(p-M)PyP) (s)

Iron tetrakis(3-sulfonatophenyl)porphyrin (TPPS) (t)

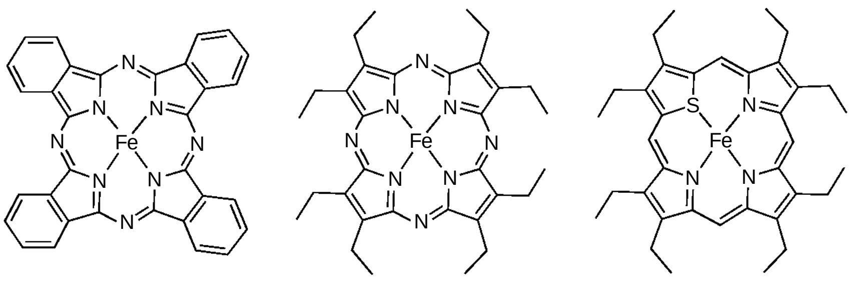

Iron phthalocyanine (u)

Iron octaethyltetraazaporphyrin (v)

Iron octaethylthiaporphyrin (w)

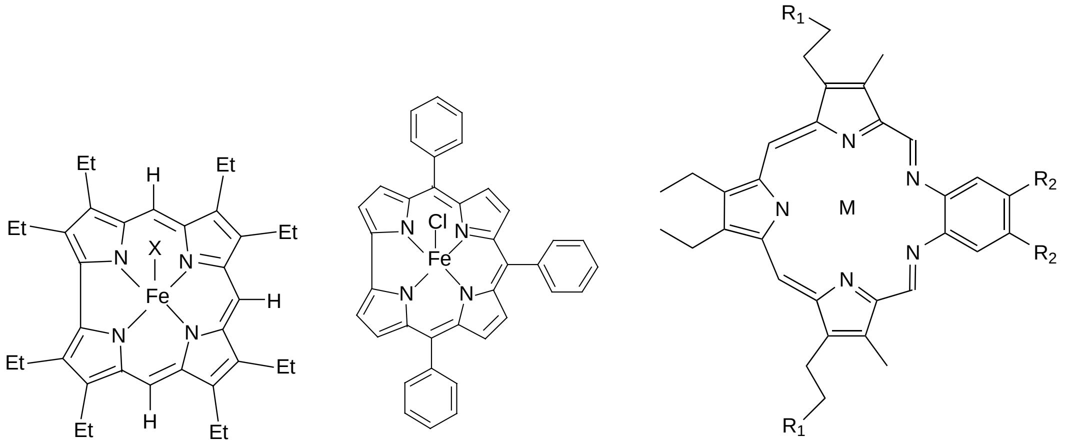

(x) Iron octaethylcorrole

(y) Iron triphenylcorrole

(z) Iron texaphyrin

Figure 1 cont'd

Boronated porphyrins are investigated as agents forboron neutron capture therapy (BNCT),[104–106] whereas metalated and unmetalated porphyrins and other porphyrinic pigments have attracted widespread attention as promising photosensitizers in photodynamic therapy of oncological and non-oncological diseases.[107–122] Artemisinin, chloroquine, and various isonitriles derived from marine organisms form covalent adducts with protohemin and thus prevent the formation of hemozoan by the malaria-causing organism *Plasmodium falciparum*.[123–126] Water-soluble porphyrins and metalloporphyrins are reported to intercalate into DNA,[127–131] and cationic porphyrins have been shown to bind to potassium channel proteins with nanomolar affinities in a reversible fashion[132] to mimic peptide toxins excreted by scorpions, snakes, spiders, and other organisms[133,134] that partially block the electrical conductance of the channels. Metalloporphyrins have been investigated as highly conducting molecular materials,[135] polymers and dendrimers,[136–147] and for preparation of modified electrodes.[148–156] Considering the diverse applications listed above it is not surprising that the isolation, characterization, and spectroscopic investigation of both naturally occurring and synthetic hemes have been active fields of research for many years.

In many cases, synthetic iron porphyrins have been investigated primarily as models of hemes in various proteins, but also as potentially useful magnetic materials, or as metal coordination complexes, since the porphyrin *Macrocycle* often confers upon the metal unique electronic, magnetic, and redox properties (*see Redox Properties & Processes*) and chemical reactivities that are interesting in their own right. The properties and chemical reactivities of iron porphyrins will be summarized in this article. Iron complexes of related macrocycles, including reduced hemes (chlorins, isobacteriochlorins, etc.),[59,61–67,157] N-alkyl- or N-arylporphyrins,[158,159] thiaporphyrins,[160–162] tetraazaporphyrins,[163] phthalocyanines,[164] and corroles[165] have also been investigated and, where appropriate, will be mentioned briefly.

Among the heme proteins, a variety of axial ligations, and oxidation and spin states of the central iron *Active Site* are stabilized by the particular protein environment created within the heme pocket of each of these proteins. Synthetic models of each of these have been prepared and investigated, as will be summarized below. The electronic states of the iron ion are particularly amenable to a wide variety of spectroscopic studies, including electronic (UV−visible−near IR),[166] vibrational (IR, Raman, and especially resonance Raman[167]), NMR,[168–175] EPR (or ESR)[176] (*see Electron Paramagnetic Resonance*), Mössbauer,[177] and MCD[178] spectroscopic techniques. In addition, magnetic susceptibility measurements[179] (*see* ***Magnetism of Transition Metal Ions***) and the investigations of the electrochemistry of heme proteins[180] and model hemes[181] (*see* ***Electrochemistry: Applications in Inorganic Chemistry***) have also been extremely useful in defining the electronic and oxidation states of these compounds. Three-dimensional structure determinations have been carried out for a wide variety of model hemes by single crystal X-ray crystallography,[182–185] and in selected cases by absorption spectroscopy (EXAFS, XANES).[186] In some cases, the arrangement of peripheral substituents has been determined by NMR spectroscopy.[174,175,187–192] Since detailed review of each of these techniques is beyond the scope of this article, the references given above are intended to provide the interested reader with extensive background information.

1.2 Structures and Electron Configurations of Iron Porphyrins

The general structures of iron porphyrins are shown in Figure 1, together with the structures of closely related ring systems, including iron chlorins and isobacteriochlorins, thiaporphyrins, tetraazaporphyrins, phthalocyanines, corroles, and texaphyrin. Examples of substituents present on commonly investigated natural and synthetic iron porphyrins are also included.

The possible coordination states of synthetic and natural iron porphyrins include 4-coordinate (no axial ligands), five-coordinate (one axial ligand), and six-coordinate (two axial ligands) geometries.[182,183] The number of axial ligands and their nature have dramatic influences on the Fe–N_{por} and Fe−axial ligand bond lengths,[182–185] spin states,[179,182–184] EPR g-values,[174,176,193,194] NMR chemical and isotropic shifts,[168,171,174,175,193,195] Mössbauer isomer shifts, quadrupole splittings and hyperfine coupling constants,[177,193,194,196] resonance Raman[167] and MCD[178,193] band positions and shapes, as well as reduction potentials[181] and reactivity towards reagents such as molecular oxygen, carbon monoxide,[197,198] unsaturated hydrocarbons,[24,26,27] and many other substances. The known oxidation states (*see Oxidation Number*) of iron porphyrins range from Fe^0 (d^8) to Fe^{IV} (d^4) and most recently also true Fe^V (d^3). Among these, the possible spin states include high-, intermediate-, and low-spin states (*see High-spin & Low-spin Compounds*) of Fe^{II} (d^6) and Fe^{III} (d^5), and high- and low-spin Fe^I (d^7) and Fe^{IV} (d^4). All of the possible spin states of these *d^n configuration* species have been observed except high-spin d^7, as summarized in Figure 2. It should be noted that the only diamagnetic (*see Diamagnetism*) member of this extensive series of possible oxidation and spin states is low-spin Fe^{II}; all other iron porphyrin complexes are paramagnetic (*see Paramagnetism*).

The valence electrons of iron porphyrins are almost invariably located in the 3d orbitals of the metal, except in the cases of π-cation radicals of Fe^{II} complexes of oxophlorins[199] and reduced hemes bonded to carbon monoxide, isocyanide or PF_3 ligands,[200] or NO,[201,202] and the π-cation radicals of Fe^{III}[203–211] and Fe^{IV}[210,212–219] porphyrins and corroles, where the 3d orbitals (*see d-Orbitals*) of the metal are very similar in energy to the HOMO of the porphyrin. In four-, five-, and six-coordinate metalloporphyrins the d orbitals consist of three general symmetry types (*see* ***Coordination & Organometallic Chemistry: Principles***): (1) the σ-symmetry orbitals that interact with the porphyrin nitrogens and with axial ligands (strictly speaking, in the idealized D_{4h} symmetry of four- and six-coordinate metalloporphyrins; these orbitals are of a_{1g} (d_{z^2}) and b_{1g} ($d_{x^2-y^2}$) symmetry, but in any case, they are engaged in σ-bonding interactions only, unless the iron is 5-coordinate and well out of the plane of the porphyrin[195,220]); (2) the d_π orbitals, d_{xz} and d_{yz}, which may engage in π-bonding with both filled and empty π-symmetry orbitals of the porphyrin ring as well as the axial ligands; and (3) the d_{xy} orbital, which is nonbonding, both in relation to the porphyrin ring if it is planar (see Section 6.3.2 below for the consequences of porphyrin ring nonplanarity), and also in relation to the axial ligands (*see* ***Ligand Field Theory & Spectra***). The splitting patterns of the five d orbitals (*see Crystal Field Theory*; *Splitting, Crystal Field & Molecular Orbital*) are generally expected to be those shown in Figure 2, although individual variations in the relative orbital energies have been observed.[174,175,195]

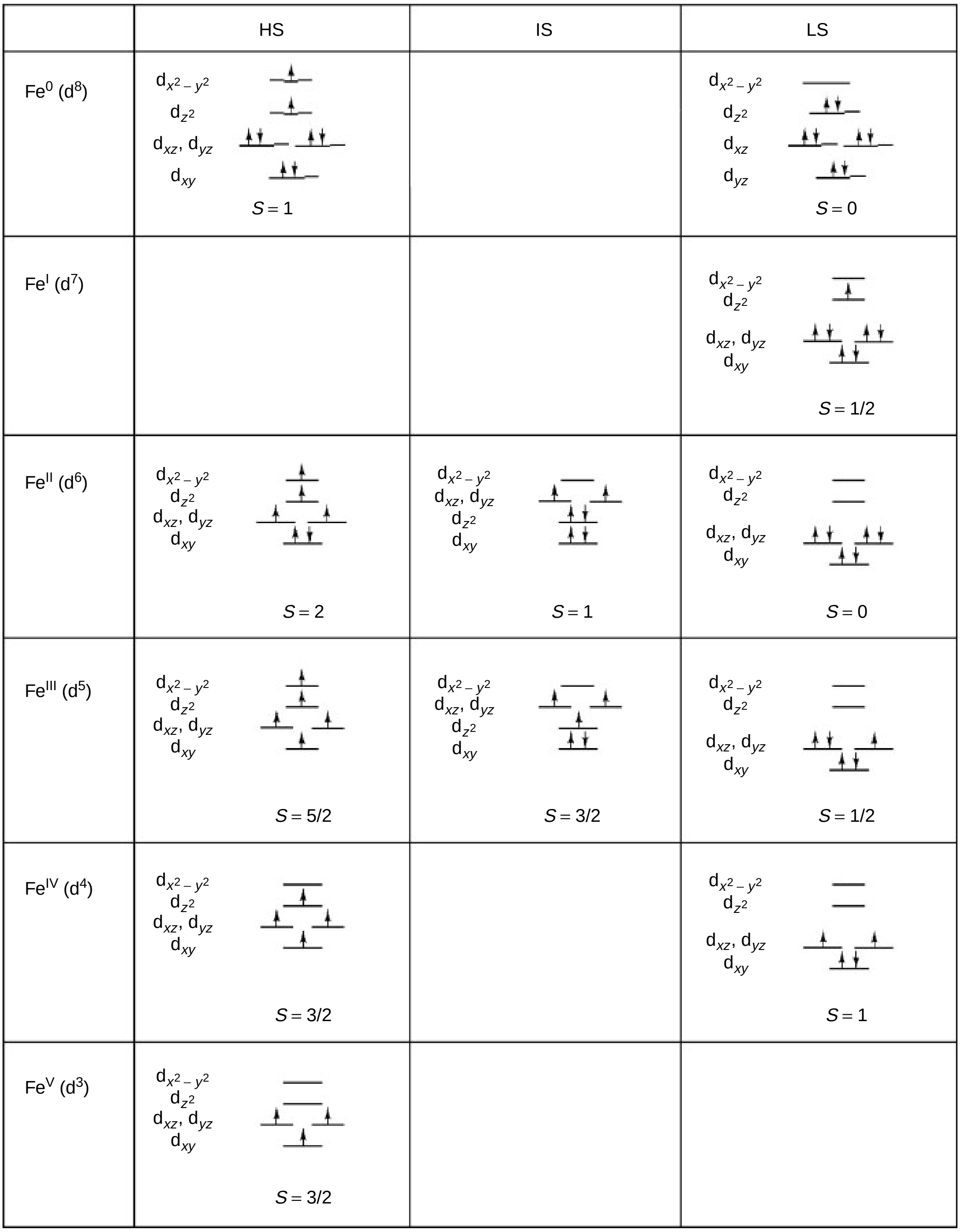
HS
IS
LS
Fe⁰ (d⁸)
dx²−y²
dz²
dxz, dyz
dxy
S = 1
dx²−y²
dz²
dxz
dyz
S = 0
Feᴵ (d⁷)
dx²−y²
dz²
dxz, dyz
dxy
S = 1/2
Feᴵᴵ (d⁶)
dx²−y²
dz²
dxz, dyz
dxy
S = 2
dx²−y²
dxz, dyz
dz²
dxy
S = 1
dx²−y²
dz²
dxz, dyz
dxy
S = 0
Feᴵᴵᴵ (d⁵)
dx²−y²
dz²
dxz, dyz
dxy
S = 5/2
dx²−y²
dxz, dyz
dz²
dxy
S = 3/2
dx²−y²
dz²
dxz, dyz
dxy
S = 1/2
Feᴵⱽ (d⁴)
dx²−y²
dz²
dxz, dyz
dxy
S = 3/2
dx²−y²
dz²
dxz, dyz
dxy
S = 1
Feⱽ (d³)
dx²−y²
dz²
dxz, dyz
dxy
S = 3/2

Figure 2 Possible oxidation and spin states of iron porphyrins and the d orbital configurations expected in each case. All of these states (excluding high-spin d^7, which is not included in the figure) have been observed for iron porphyrins, and are discussed in this article. In addition, the spin-admixed $S = 3/2, 5/2$ state of Fe^{III} and the alternative orbital configuration for low-spin Fe^{III}, with d_{xy} higher in energy than d_{xz},d_{yz}, are also discussed

1.3 π Electron Configuration of the Porphyrin Ring

Both four- and six-coordinate metalloporphyrins have effective D_{4h} symmetry, if the effects of planar axial ligands, unsymmetrically placed porphyrin substituents, and distortions of the porphinato core (ruffling or saddling) are neglected. The bonding interactions between the metal atom and the porphyrin ligand are expected to be those shown in Figure 3, where each porphyrin nitrogen supplies a σ-symmetry lone pair that points directly toward the metal ion either along the x, $-x$, y, or $-y$ axes, and a single π-symmetry p orbital that is perpendicular to the plane of the porphyrin ring. We will call this the p_z orbital of the bonding nitrogen.

Not only does the bonding nitrogen have an available π-symmetry p_z orbital, but so do each of the C_α, C_β, and C_{meso} carbons of the porphyrin skeleton. Researchers in the field[221–226] have developed more-or-less sophisticated molecular orbital treatments of the porphyrin ring and related macrocycles (*see* ***Molecular Orbital Theory***), and recent DFT calculations have been reported,[227] which will be mentioned in this article where appropriate. In the simplest of these treatments, π MOs are constructed based upon the symmetry properties of the idealized D_{4h} symmetry porphyrin ring. The 24 p_z orbitals of the porphine macrocycle are thus combined to produce 24 molecular orbitals (two a_{1u}, four a_{2u}, three b_{1u}, three b_{2u}, and six e_g sets), 13 of which are filled by the 26 p_z electrons of the 24 atoms of the porphyrin macrocycle. Although the theories differ in detail, all agree that the frontier and near-frontier orbitals (*see Frontier Orbitals*) are, in order of increasing energy, $3e(\pi) < 1a_{1u}(\pi) \sim 3a_{2u}(\pi) < 4e(\pi^*)$, using the notation of Longuet-Higgins *et al.*[221] The $3e(\pi)$, $1a_{1u}(\pi)$, and $3a_{2u}(\pi)$ orbitals are filled, while the $4e(\pi^*)$ orbitals are empty. All theories agree further that the $4e(\pi^*)$ set are the LUMO(s) of the porphyrin ring, while the HOMO(s) may be either $1a_{1u}(\pi)$, $3a_{2u}(\pi)$ of the porphyrin ring, or the d_{xy} or d_{xz},$d_{yz} = d_\pi$ orbitals of the metal, depending on the oxidation state of the metal, the porphyrin and degree of reduction of the macrocycle (chlorins and isobacteriochlorins), substituents and the axial ligand(s) present. The symmetry properties and electron distributions of the porphyrin π-symmetry frontier orbitals predicted from the simplest of these treatments are shown in Figure 4.

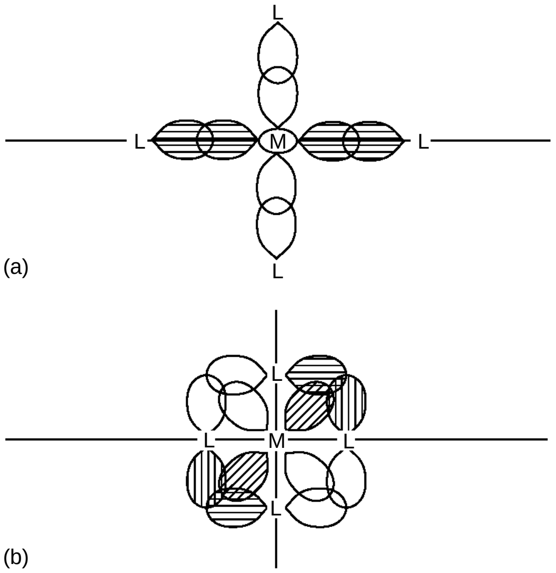

Figure 3 The symmetry-allowed interactions between metal d and porphyrin σ and π orbitals. (a) Interaction of the y-axis portion of the $d_{x^2-y^2}$ orbital with the σ-donor orbitals of two of the porphyrin nitrogens (porphyrin ring represented by the horizontal line) and the d_z^2 orbital interacting with the σ-donors of two axial ligands. (b) Interaction of one of the two d_π orbitals, d_{yz}, with the two porphyrin nitrogen p_π orbitals along the y-axis, and the ligand p_π orbitals of the two axial ligands. Note the nodal plane of this group of orbitals that passes through the axial ligand and metal centers and lies perpendicular to the plane of the figure. It is this nodal plane that ensures that only e-symmetry porphyrin π orbitals can be involved in π-bonding with the metal and π spin delocalization to or from the metal

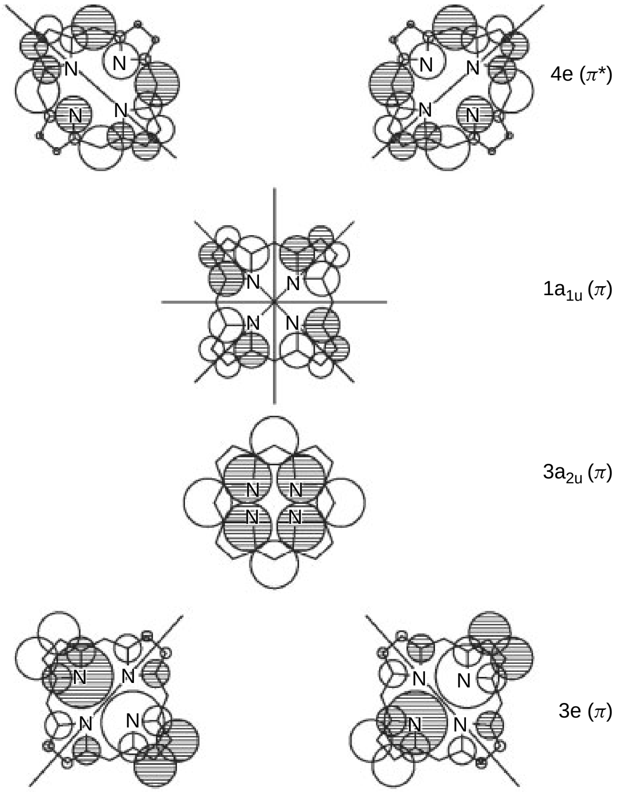

Figure 4 Nodal properties, relative energies, and electron density distributions in the frontier π orbitals of the porphyrin macrocycle.[221] The $3e(\pi)$, $3a_{2u}(\pi)$, and $1a_{1u}(\pi)$ orbitals are filled, and either the $3a_{2u}(\pi)$ or $1a_{1u}(\pi)$ is the HOMO of the porphyrin ring, while the $4e(\pi^*)$ orbitals are empty, and are thus the LUMOs of the porphyrin ring. Note that only the $3e(\pi)$ and $4e(\pi^*)$ orbitals have the proper symmetry (one nodal plane perpendicular to the plane of the porphyrin) for overlap with d_{xz} and d_{yz} (one for each), for planar metalloporphyrins

For electronic absorption spectra, excitations from $1a_{1u}(\pi)$ and $3a_{2u}(\pi)$ to $4e(\pi^*)$ give rise to the so-called α, β, and Soret bands (*see Soret Band*) in the visible spectra.[221–226] The electron configuration of π-cation radicals, $(PM)^{+\bullet}$ or $(P^{-\bullet})$ M, is typically either $(1a_{1u})^1$ or $(3a_{2u})^1$, since one or the other of these orbitals is typically the HOMO of the porphyrin π system.[228] Anion radicals, $(P^{3-\bullet})$ M, typically have the electron configuration $(4e)^1$, and dianions, (P^{4-})M, have the configuration $(4e)^2$.[228]

Although the $1a_{1u}(\pi)$ or $3a_{2u}(\pi)$ orbital is typically the HOMO of the porphyrin ring, neither of these orbitals has the proper symmetry to covalently overlap with the d_π orbitals of the metal if the porphyrin ring is planar. (However, if the porphyrin ring is ruffled, the $3a_{2u}(\pi)$ orbital can interact with the d_{xy} orbital, and if it is saddled it can interact with the $d_{x^2-y^2}$ orbital, as will be discussed in Section 6.3.2; if the porphyrin ring is planar but the metal is 5-coordinate and out of the plane of the porphyrin, then the $3a_{2u}(\pi)$ orbital can interact with the metal d_{z^2} orbital.[220]) Thus, only the 3e(π), which are lower in energy than either $1a_{1u}(\pi)$ or $3a_{2u}(\pi)$, and the $4e(\pi^*)$ orbitals, which are higher in energy than either $1a_{1u}(\pi)$ or $3a_{2u}(\pi)$ (all shown in Figure 4), have the proper symmetry for overlap with the metal d_π orbitals, while under special circumstances the $3a_{2u}(\pi)$ orbital can interact with metal orbitals, and can hence be involved in modification of the properties of the iron porphyrin through π bonding effects. Since the $3e(\pi)$ orbitals are filled, the type of overlap interaction that can occur between them and the metal d_π orbitals is P $\rightarrow$ Fe π bonding (*see π-Bond*). Similarly, since the $4e(\pi^*)$ orbitals of the porphyrin ring are empty, overlap of the metal d_π orbitals with the $4e(\pi^*)$ orbitals can occur via Fe $\rightarrow$ P π *Back-Bonding*. This Fe $\rightarrow$ P π back-bonding can potentially occur to varying degrees when the metal electron configuration is (d_{xz},d_{yz}).[1–3]

For dihydroporphyrins, also known as chlorins, the reduction of one pyrrole ring reduces the symmetry of the molecule, and thus removes the degeneracy of the $3e(\pi)$ and $4e(\pi^*)$ orbitals.[65,221–223] An important feature of this modification of the π orbitals of Figure 4 is that the former $1a_{1u}(\pi)$ orbital, which is denoted A_5 or $a_2(\pi)$ in the case of chlorins, has the proper symmetry at the nitrogens of the two rings adjacent to the reduced ring to allow overlap with one of the d_π orbitals. This has important consequences for the pattern of spin delocalization observed for both high- and low-spin Fe^{III} complexes of chlorins (ring system shown in Figure 1(m)),[65] and also for the reduction potentials of these complexes. Similar modifications of the electron density distribution and symmetry properties of the A,B-tetrahydroporphyrins (ring system shown in Figure 1(n)), better known as isobacteriochlorins, and the A,C-tetrahydroporphyrins, better known as bacteriochlorins, are also expected.

1.4 Synthesis of Metal Free Porphyrins

Because of the continued importance of porphyrin synthesis in biomedical, chemical, and industrial applications many new routes for synthesizing porphyrinic macrocycles have been developed and excellent overview articles have been published on the topic. To highlight the role that porphyrin synthesis plays, the entire volume 1 of the *Porphyrin Handbook* is devoted to the preparation of porphyrinic macrocycles. In this volume, Smith,[229,230] for example, describes strategies for synthesizing octaalkylporphryins by means of monopyrrole tetramerization, di- and tripyrrolic, and open-chain tetrapyrrolic intermediates, by degradation of natural pigments[229] or by means of cyclizations of a,c biladiene salts.[230] In the same volume, Lindsey[231] has reviewed the synthesis of *meso*-substituted porphyrins, Vicente the reactivity and functionalization of β-substituted porphyrins and chlorins,[232] Jaquinod[233] the functionalization of 5,10,15,20-tetra-substituded porphyrins, and Senge[234] the preparation of highly substituted porphyrins. In the following, the main points of some of the methods for synthesizing porphyrins are summarized.

Traditionally, both *meso*-aryl-substituted and β-pyrrole-substituted porphyrins, such as tetraphenylporphyrin (TPP) and octaethylporphyrin (OEP), respectively, as well as their hybrids, the dodecasubstituted porphyrins, such as octaalkyltetraphenylporphyrins and dodecaphenylporphyrins, have been synthesized by condensation of monopyrrolic moieties and the corresponding aromatic aldehydes. This synthetic pathway was described more than 60 years ago by Rothemund for the formation of TPP, which was prepared by reacting pyrrole and benzaldehyde in pyridine in a sealed bomb at 150 °C for 24 h.[235] Because of low product yields and harsh reaction conditions, only a few aromatic aldehydes were successfully used to synthesize the desired tetraphenylporphyrins. Thus, the initial reaction conditions for the synthesis of TPP have been modified. Adler *et al.*[236–240] obtained much higher yields by allowing benzaldehyde and pyrrole to reflux under *aerobic* conditions in propionic acid (141 °C) for about 30 min. By this method, a wider variety of porphyrins, including unsymmetrically substituted TPPs, have been obtained in yields of up to 20–30%. The preparation of the latter including mono-, di-, or trisubstituted tetraphenylporphyrins has been achieved by means of a modified Adler synthesis, the so-called ‘mixed aldehyde approach’. Two different aromatic aldehydes and pyrrole are reacted in propionic or acetic acid to yield a mixture of porphyrins (*see Isomer, Types of*), which are separated by chromatographic techniques.[241–246]

One of the main drawbacks of the Adler method is the formation of large amounts of by-products. Since the separation of these tar-like products from the desired porphyrins by chromatographic techniques is tedious, expensive, and time-consuming, Lindsey[231,247,248] spearheaded the development of a new strategy for synthesizing tetraarylporphyrins by the condensation of dipyrromethanes. The two-step mechanism entails the acid-catalyzed condensation of pyrrole with the desired aromatic aldehyde to yield tetraphenylporphyrinogen, which is subsequently oxidized to the level of the porphyrin using mild oxidizing reagents, as shown in Scheme 1. Conditions for the one-pot, room temperature synthesis of *meso*-tetraphenylporphyrins,[249,250] and for the synthesis of substituted *meso*-tetraphenylporphyrins, such as tetramesitylporphyrin, using an automated microscale multireactor workstation[251] have been developed as well.

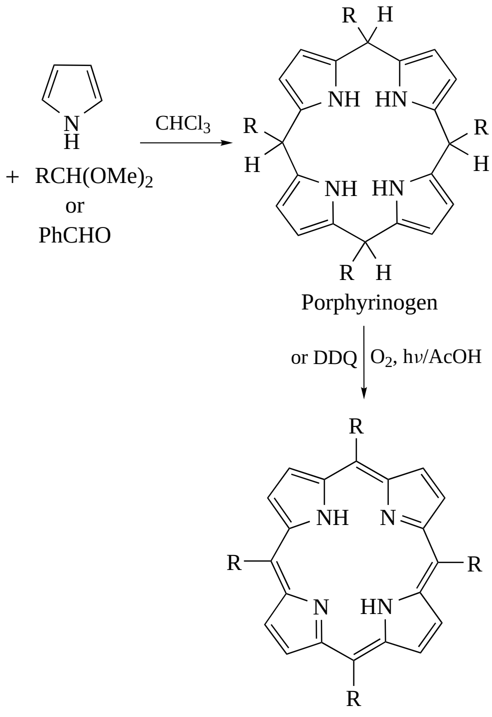

Scheme 1

A variation of this method that removes the water produced in the pyrrole/aldehyde or hydrated aldehyde condensation has been used to produce *meso*-tetrakis(perfluoroalkyl)porphyrins.[252,253] Lindsey's laboratory has also reported a rational synthesis of *meso*-substituted porphyrins bearing one nitrogen heterocyclic group[254] that can readily be used for preparing other mono-functionalized porphyrins, methods for minimizing scrambling in the synthesis of *trans*-porphyrins from dipyrromethanes and aldehydes,[255,256] and a rational synthesis of porphyrins bearing up to four different *meso* substituents.[257]

Van der Made *et al.*[258] and Kihn-Botulinski and Meunier[259] have discussed several factors crucial for the success of the Lindsey reaction and have optimized the conditions necessary to synthesize 'sterically hindered' porphyrins, such as tetramesitylporphyrin and tetrakis(2,6-dichlorophenyl)porphyrin. These compounds can be obtained in fairly high yields if all possible traces of water are removed during the reaction. Rocha-Gonsalves *et al.*[260] showed that porphyrinogens are very efficiently oxidized to porphyrins by nitrobenzene in the presence of acetic or propionic acid. The advantage of this method is that the formation of the porphyrinogen does not have to be maximized before the oxidizing agent is added. When the nitrobenzene/acetic acid or propionic acid oxidation is carried out as a 'one-pot' reaction, a variety of porphyrins have been obtained in crystalline form. The same laboratory has also published a one-step synthesis of dipyrromethanes in water, thereby providing convenient building blocks for the synthesis of a series of porphyrinic macrocycles.[261]

A rather different synthetic method has been developed by Bonar-Law, which involves the synthesis of porphyrins in aqueous micelles derived from sodium dodecylsulfate.[262] This is most appropriate for construction of porphyrins having particular hydrophobic multipoint recognition sites, such as those involving steroid dimers[262] or trans-disubstituted tetraarylporphyrins.[263]

Many investigators, including the authors, have used one or more of the synthetic approaches discussed above for the synthesis of symmetrically and unsymmetrically substituted tetraphenylporphyrins. These include porphyrins containing bulky substituents at one (or both) *ortho* position(s) of one (to four) phenyl ring(s), as well as sterically constrained porphyrins carrying potentially ligating tails. Excellent reviews of the preparation, structures, and reactions of porphyrins with appended peptides, chelated heme models, picket fence porphyrins, and capped and strapped porphyrins are given by Morgan and Dolphin[198] and Collman.[264,265] Since the first of these, many other sterically constrained porphyrins have been synthesized. They include the bis-picket fence porphyrin 5,10,15,20-tetrakis(2,6-dipivalamidophenyl)porphyrin,[266,267] octacarboxy-substituted porphyrins such as the 5,10,15,20-tetrakis(2,6-dicarboxyphenyl)-porphyrins,[268,269] 'picnic-basket' porphyrins,[270] 'arbor' porphyrins,[271] a steroid-capped porphyrin,[272] crown ether and A-frame capped porphyrins,[273] $\alpha,\alpha,\alpha,\alpha$-tetrakis(2-hydroxy-1-naphthyl)porphyrin, which complexes to quinones via multipoint hydrogen-bonding,[274] a picket-fence derivative that acts as a guest in a thermotropic nematic liquid crystalline host phase,[275] a phenol-pendant porphyrin as model of catalase,[276] a 2-hydroxy-5,10,15,20-tetraphenylporphyrin whose iron(III) complex makes a cyclic porphyrin trimer,[277] porphyrin-quinone conjugates for study of their ultrafast charge transfer reactions,[278–280] oxomolybdenum(V)-linked porphyrins,[281] porphyrins having two Kemp's triacid units to create a methane monoxygenase non-heme iron site contiguous with a porphyrin,[282–284] porphyrins having one hydrogen-bonding substituent within reach of an axial ligand,[285–287] porphyrins that self-assemble to form calixarene-porphyrin cages,[288] directly *meso*-*meso*-linked bis(triphenyl)porphyrins,[289] cofacial bisporphyrins[290–301] as models of the photosynthetic reaction center or the light-harvesting complexes, monoporphyrin, mono- or multi-accessory pigment complexes,[302,303] cyclic porphyrin trimers,[304] linear porphyrin dimers,[227,305–322] trimers,[311,321,322] to pentamers,[311,323] including those designed as molecular photonic wires,[324–329] molecular optoelectronic gates,[330–332] and 2,3- and 2,4-dioxoporphyrins as models for heme *d*.[333] Several routes to water-soluble tetraphenylporphyrins having 4-amino or alkylamino groups have been reported.[334–336]

Functionalization of 5,15-dibromo, 10,20-diphenylporphyrins and 2-bromotetraphenyl-porphyrins via metal-mediated cross-coupling methodology has led to a variety of new porphyrins, including those having 2,2′-bipyridyl, vinyl, alkyl, or aryl groups bound to the position(s) originally carrying the bromine substituents.[337,338] As a special class of these reactions, the synthesis of phenylacetylene-linked porphyrins where the acetylene group is directly attached to the porphyrin core[321,322,339] and the related porphyrin-bridged donor-acceptor molecules having large molecular first hyperpolarizabilities[340–346] has been reported. The preparation of Suzuki porphyrins having pinacolborane functions as transmetalation reagents in Pd-catalyzed cross-coupling reactions[347] has provided an additional functionalization approach. Pd-catalyzed cross-coupling of porphyrins carrying aryl iodides to those carrying an aryl ethyne has also been reported.[348,349] Pyrrole-alkyne derivatives have been prepared from the pyrrole-brominated TPPs.[350,351] Mixed 4-substituted derivatives of tetraphenylporphyrin having three carboxy and one OH substituents[352] and other amphiphilic porphyrins that are *Membrane*-soluble[112,113,116,122,353–355] or *Membrane*-spanning[356] have been prepared. Tetraphenylporphyrins having p-carboxy and p-amino functionalities have been polymerized interfacially to produce chemically asymmetric membrane films.[357] Mercaptoporphyrins have also been polymerized to form ultrathin films of a porphyrin homopolymer based upon 5,10,15,20-tetrakis-(α-mercapto-p-tolyl)porphyrin,[358] and thiol-derivatized porphyrins for attachment to electroactive surfaces have been prepared and examined as means of information storage,[359–361] including those having a ferrocenyl moiety appended in several ways.[362] Various means of linking porphyrins to form arrays have been reviewed.[363] Preparation and investigation of the physical properties of cyclic tetra-,[364] hexa-,[365–367] hepta-porphyrin[368] and star-shaped multiporphyrin[325–327,369–372] or star-shaped tetra-[373] or octa-porphyrin, or monophthalocyanine[374] arrays have been described and reviewed.[375] As part of this work, methods of forming porphyrins in the presence of acid-labile metalloporphyrins that provide a new route to mixed-metal multiporphyrin arrays have been reported.[376]

Whereas a large number of model heme complexes are derived from the tetraphenylporphyrin moiety, another very important class of porphyrins bearing substituents only at the β-pyrrole carbon atoms, has been extensively investigated as models of heme proteins. One of the models most studied is octaethylporphyrin (OEP), which was originally synthesized from 2-dimethylaminomethyl-3,4-diethylpyrrole in an acid-catalyzed medium.[377,378] A similar approach is described by Ono *et al.*,[379,380] in which OEP, coproporphyrin or 2,7,12,17-tetraarylporphyrins are prepared in good yields from 2-carboxyethylpyrroles prepared from readily available nitroalkenes, or their equivalents, and aldehydes. A similar approach was used by Konishi *et al.*[381] for the synthesis of chiral strapped porphyrins, which were then resolved by chromatographic means to yield porphyrins with diasterotopic faces. It is also possible to condense 3,4-disubstituted pyrroles with formaldehyde in an acid-catalyzed medium to form octaalkylporphyrins.[382,383] A wide range of pyrroles are conveniently synthesized by reaction of tosylmethyl isocyanide (TosMIC) with a Michael acceptor.[384,385] When the reaction is carried out in the presence of two 3,4-disubstituted pyrroles, such as 3,4-diethylpyrrole and 3,4-bis(N,N-diethylcarboxamide)pyrrole, an isomer mixture containing OEP, the octakis(N,N-diethylcarboxamide)porphyrin, OAP,[383] and four unsymmetrically substituted porphyrins is obtained.[188] *Meso*-amino- and *meso*-amido-substituted OEP metal complexes can be prepared by treatment of the π-cation radical (for example, of Zn(II)) with amines or amides);[386] for primary amines, treatment with NaH to form the amide enhanced the reactivity. Liquid crystalline porphyrins, derived from octakis(β-hydroxyethyl)porphyrin, with long chain hydrocarbons attached at the alcohol functionalities, have also been prepared,[387] as have been porphyrin dimers based upon 5,8-ethanonaphtho-quinone bridging two pyrroles.[388]

Octaalkyltetraphenylporphyrins, which typically have a saddled geometry,[389] have been prepared by different routes.[229] For example, they have been synthesized by first preparing the dialkylpyrrole according to the methods of LeGoff and coworkers,[384,390] followed by reaction with benzaldehyde and oxidation with DDQ.[391] The cyclohexenyl-substituted octaalkyltetraphenylporphyrin, tetra-(β,β'-tetramethylene) tetraphenylporphyrin has been prepared by similar methods,[392,393] by first synthesizing the pyrrole, ethyl 3,4-butanopyrrole-2-carboxylate[394,395] from 1-nitrocyclohexane and ethyl isocyanoacetate in the presence of guanidine base,[396,397] followed by hydrolysis and decarboxylation to yield 3,4-tetramethylenepyrrole.[394] A water-soluble derivative of octaethyltetraphenylporphyrin, the octaacetic acid tetraphenylporphyrin, has also been prepared.[398] A 3,7,13,17-tetramethyl-5,15-diphenylporphyrin,[399] and tetraphenylporphyrins with graded degrees of β-ethyl substitution,[400] as well as octaalkyl-5,15-diphenylporphyrins[401,402] including one having an appended ferrocene derivative,[403] have also been synthesized. Other examples of sterically crowded porphyrins include 2,3,5,7,8,10,12,13,15,17,20-dodecaphenylporphyrin (DPP), which is synthesized according to a method similar to the one described by Lindsey.[247,248] Because of the steric crowding of the phenyl rings the porphyrin macrocycle is forced to adopt a nonplanar conformation in solution and in the solid state. The deviation from planarity is indicated by the red-shifted electronic absorption spectrum.[404] Additional examples include polyhalogenated tetraphenylporphyrins and their iron complexes that have been studied as potential catalysts (*see Catalysis*) for epoxidations and other reactions involving high-valent iron porphyrins.[405] Octafluoro- and octabromotetraphenylporphyrin derivatives have been prepared by the N-bromosuccinimide method described by Callot[406] and Traylor and Tsuchiya[405] or by its modification using CF_3CO_2H described by Battioni *et al.*[407] Another method for synthesizing bromo-substituted derivatives entails the bromination reaction of TPPCu followed by an acid demetalation reaction.[408] It should be noted that the analogous chloro-substituted products cannot be prepared as described above. Facile chlorination is accomplished, when the corresponding porphyrins are reacted with $Cl_2(g)$ in the presence of $FeCl_3$.[409] Mixed β-bromine, cyanide-substituted tetraphenylporphyrins have also been produced.[410]

Multi-ferrocenyl phthalocyanines having up to 16 ferrocene units per molecule have been built with oxyethylene linkers to create aliphatically linked ferrocene units,[411] and ethynyl bridges have been used to create ferrocenyl-linked tetrapyrroles of both phthalocyanine and porphyrin types with unsaturated links;[412] the porphyrins have two ferrocene units, which are placed on opposite *meso* positions. Both the aliphatically linked and the ethynyl-linked compounds were shown to exhibit no electrochemical communication between ferrocene units.[411,412]

Unsymmetrically substituted derivatives of protoporphyrin IX, such as vinylporphyrins, have been successfully synthesized according to the dipyrromethane method originally described by Johnson and Kay.[413,414] This general method has been modified[415] for the preparation of porphyrin-containing receptors for barbiturates as models of barbiturate-induced cytochromes P450.[416] Oxidative cyclization of open-chain tetrapyrrolic compounds, such as 1,19-dimethylbilenes-*b* and 1,19-dimethylbiladienes-*ac*,[417] and oxobilanes-*a* and oxobilanes-*b* (Figure 5), using copper(II) salts in refluxing solvents such as DMF or DMSO/pyridine, results in the formation of the corresponding porphyrins.[418–427] According to this method, in which dipyrrylmethanes were found to be important intermediates in constructing the open-chain tetrapyrrole, biologically relevant macrocycles, such as porphyrin *a* and chlorophylls c_1 and c_2, can be obtained.

Modification of protoporphyrin IX at the propionate positions has been used by Traylor and coworkers[428] and Casella *et al.*[429] to prepare porphyrin complexes with a covalently attached axial ligand or ligands. The latter workers also bonded protohemin-6(7)-L-arginyl-L-alanine and –L-histidine methyl ester modified protohemins to apomyoglobin and investigated the reactivity of these complexes according to peroxidase-type oxidations.[430] Other very useful heme protein models are provided by the microperoxidases, MP8, MP9, MP10 and MP11, also called the heme octa- to undecapeptides, which use a similar approach, where the anchoring of the histidine axial ligand is retained and provided by the peptide chain and one additional axial position is available for various chemical reactions. These compounds, in which bovine cytochrome *c* is hydrolyzed with specific enzymes to leave only short fragments of polypeptide surrounding the Cys-XY-Cys-His sequence that provides the covalent attachment of the heme to the protein and one of the axial ligands can be prepared or purchased. Depending on the enzyme used, different numbers of amino acids are retained. For example, using pepsin and trypsin MP8 is obtained,[431–433] which consists of the fragment Cys-Ala-Gln-Cys-His-Thr-Val-Glu, amino acids 14–21 of the original horse heart cytochrome *c* protein. MP9, which also includes Lys-22, is a product of trypsin cleavage of horse heart cytochrome *c*.[434] MP10 can be made by trypsin-catalyzed peptide bond formation to the C-terminal end of MP9, where the residue added, at the original 23 position of cytochrome *c*, can be any desired amino acid.[435] Gray and coworkers have investigated Tyr-23, Met-23 and His-23 MP10 derivatives and reported that both Tyr-23 and His-23 bind to the Fe^{III} and Fe^{II} states to produce low-spin 6-coordinate heme centers, but that Met-23 does not bind to the iron ion in either oxidation state.[435] MP11 is the fragment that contains three additional N-terminal amino acids, Val-Glu-Lys, and is produced by pepsin cleavage of horse heart cytochrome *c*.[436] The N-terminal amino group is acylated to prevent aggregation.[432–434] Some of the microperoxidases are discussed further in the appropriate sections of this article.

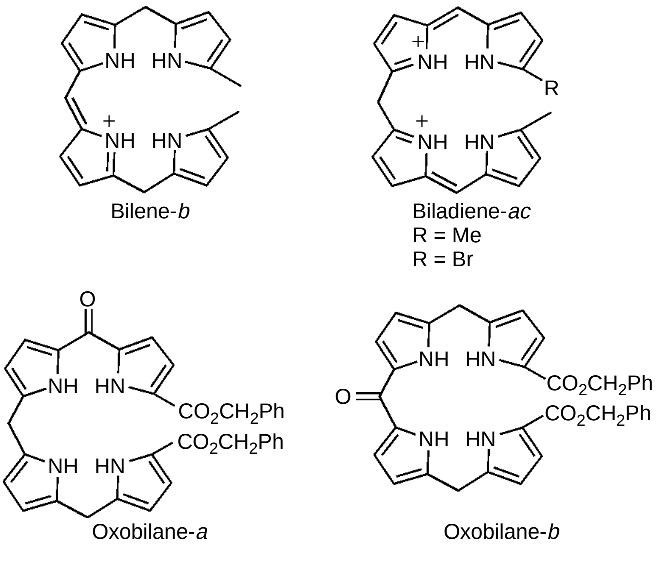

Figure 5 Open-chain tetrapyrroles used in porphyrin synthesis[422]

Synthesis and characterization of other related macrocycles, including chlorins,[59,437–441] isobacteriochlorins,[157,441] bacteriochlorins,[441,442] mono- and dioxoporphyrins,[441,443–447] other more highly saturated hydroporphyrins,[441] *N*-alkyl- or *N*-arylporphyrins,[158,159] some of which are chiral,[448] porphodimethenes,[449,450] thiaporphyrins,[160,451–453] oxaporphyrins,[452,453] N-confused[452,454–456] and carbaporphyrins,[452,457] porphycenes[458–460] and corrphycenes,[461–464] tetraazaporphyrins,[163,465,466] phthalocyanines,[467,468] the ring-expanded sapphyrins,[455,469,470] texaphyrins[471,472] and others,[470] and the ring-contracted corroles[165,473–479] and corrolazines[480] have also been synthesized and are discussed in the indicated references.

1.5 Iron Insertion into Free-base Porphyrins

With a few exceptions, almost all metals and metalloids can be coordinated to the nitrogen atoms of the porphyrin macrocycle according to equation (1):

$$\text{P or H}_2 + \text{M}^{n+} \longrightarrow \text{P or M}^{(n-2)+} + 2\text{H}^+ \qquad (1)$$

For the insertion of the iron ion into the porphyrin a variety of general procedures have been described and reviewed.[481,482] In most cases, these methods lead to the formation of Fe^{III} complexes, which are then used to prepare Fe^{I}, Fe^{II}, Fe^{IV}, and Fe^{V} porphyrins. The most commonly employed methods for synthesizing Fe^{III} porphyrins are described below. The preparation of the Fe^{II} and Fe^{I} complexes from the iron(III) porphyrins by chemical or electrochemical means and the oxidized iron porphyrins (Fe^{III} π-cation radicals, Fe^{IV}, Fe^{IV} π-cation radicals, and Fe^{V}) by chemically or electrochemically oxidizing the iron(III) porphyrins is described in more detail in the sections on the corresponding iron porphyrins below. Whereas Fe^{III} porphyrins can be photochemically reduced to Fe^{II} porphyrins,[483] only a few examples of photooxidations of the iron center are known, which include laser photolysis of the co-condensation products of PFe^{II} at 15 K to produce $PFe^{IV}=O$.[484] Typical photochemical reactions of iron and other metalloporphyrins have been summarized by Suslick and Watson.[483]

1.5.1 *Reaction of the Porphyrin with Iron(II) Sulfate in Acetic Acid*[485]

According to this procedure, which uses mild metalation conditions and has no ill effects on most peripheral porphyrin substituents, the porphyrin is dissolved in a minimum amount of pyridine, diluted with glacial acetic acid, and reacted under an inert gas atmosphere at 90 °C with a freshly prepared saturated aqueous solution of iron(II) sulfate. The reaction mixture is cooled to room temperature while a stream of air is passed through the solution to oxidize Fe^{II} to Fe^{III}. Unreacted porphyrin is removed by column chromatography. This method has also been used with minor modifications for the insertion of ^{57}Fe into a number of porphyrins.[486,487]

1.5.2 *Reaction of the Porphyrin with an Iron(II) Salt in Refluxing DMF*[488–490]

The synthetic procedure for this method, which is a more rapid, but also a more harsh alternative, consists of simply reacting the porphyrin and a stoichiometric amount or a slight excess of an iron(II) salt, such as iron acetate, chloride, bromide, or carbonate, in refluxing DMF. The reaction is quantitative and the porphyrins are usually converted to the metal complex within a few minutes. However, we have found that considerably longer reflux times are required for insertion of iron into the tetrakis(2,6-disubstituted phenyl) porphyrins.[491,492] After cooling, water is added to the solution to crystallize the iron complex. For product isolation on a small scale it is, however, better to add chloroform or dichloromethane to the cooled DMF solution and then pour it through water, separate the organic layer, and then wash it repeatedly with equal volumes of water in a separatory funnel to remove remaining iron salts and DMF before evaporation to dryness.[493] If the reaction is carried out with $FeBr_2$ in 1,2-dimethoxyethane with small amounts of pyridine present, the conversion of the porphyrin to the iron complex is completed in about 4 h; the percent metalation in this solvent is only 50%.[494] If the above-mentioned isolation procedures or those described in method 1 and the methods to follow, are carried out in the presence of air, the iron(III) complex is formed. In the presence of water or hydroxide ion, most Fe^{III} porphyrins readily hydrolyze to form the μ-oxo dimers according to equation (2):

$$2PFe^{III}\text{–}OH \longrightarrow PFe^{III}\text{–}O\text{–}Fe^{III}P + H_2O \qquad (2)$$

To convert the dimer back to the monomeric form, dry gaseous HCl is typically bubbled through a solution (dry benzene, chloroform, or other nonprotic organic solvent) of the sample. Fe^{III} porphyrins containing acid-labile functionalities, including those having appended oxomolybdenum complexes,[281,495] cannot be treated this way, and hence the above-described isolation of the Fe^{III} porphyrin by extraction with water must be carried out using saturated aqueous NaCl, followed by drying over powdered NaCl instead.

1.5.3 *Reaction of the Porphyrin in Chloroform with an Iron(II) Salt in Methanol/Chloroform*[246,496]

Since working with high-boiling DMF is not always convenient, we have shown that iron ion insertion is easily achieved by reacting a chloroform solution containing the porphyrin with an excess of iron(II) salt, preferably anhydrous $FeBr_2$ or iron(II) acetate, dissolved in chloroform containing a minimum amount of methanol.[246,496] The solution is refluxed until no free-base porphyrin is detectable by UV–vis spectroscopy or TLC. Excess iron salt is removed by repeated washings with water,[246,496] as described above, and the solvent is evaporated under vacuum.

1.5.4 *Reaction of the Porphyrin with Fe^{III} Salts*[497]

It has also been shown that iron(III) ion can be directly inserted into the porphyrin ring by reacting it with $FeCl_3 \cdot 6H_2O$ in glacial acetic acid.[497] A trace amount of sodium acetate is added and the solution is allowed to reflux for 90 min. This method, however, is not suitable for protoporphyrin IX derivatives, which are susceptible to acid-catalyzed hydration of the vinyls to yield α-hydroxyethyl groups.

1.5.5 *Reaction of the Porphyrin with Fe^{II} Acetylacetonate in High-boiling Solvents*[498–500]

A less common method involves the reaction of the metal-free porphyrin with a metal(II) acetylacetonate in molten phenol or in refluxing 1,2,4-trichlorobenzene.[498,499] In the case of reduced porphyrins (chlorins, isobacteriochlorins), where metal insertion is more facile, benzene, toluene, and chloroform can be used as refluxing solvents.[500]

1.5.6 Reaction of the Dilithium Salt of the Porphyrin with Ferrous Chloride[501]

In this method, which is appropriate for porphyrins having strongly electron-withdrawing substituents, such as β-tetrakis(trifluoromethyl)-*meso*-tetraphenylporphyrin, the porphyrin free base is reacted with lithium bis(trimethylsilyl)-amide in THF at room temperature under argon or nitrogen for 5 min, and then with a slightly less than stoichiometric amount of ferrous chloride under the inert gas atmosphere at 50 °C for two hours. Following solvent removal, the product is dissolved in CH_2Cl_2/petroleum ether (50/50 v/v) and chromatographed on a neutral alumina column. Solvent evaporation, followed by dissolution of the residue in CH_2Cl_2 and treatment with 6 M HCl, separation from the aqueous layer, drying over Na_2SO_4 and solvent evaporation yields the chloroiron(III) porphyrin complex.[501]

2 IRON(0) PORPHYRINS AND THEIR REACTIONS

As is described in more detail in subsequent sections, it is well established that iron(III) porphyrins can be reduced by photochemical, electrochemical, and radiochemical methods in organic or aqueous solutions to give Fe^{II} and Fe^{I} complexes.[502–510] Recently, it has also been shown that such reactions lead to the formation of complexes with the iron in the zero oxidation state. Such Fe^0 porphyrins are, for example, formed electrochemically when Fe^{III} porphyrins ($[PFe^{III}]^+$) are reduced in three successive steps in DMF in the presence of a weak Brønsted acid as co-catalyst to yield the iron(II) porphyrin ($[PFe^{II}]$), the iron(I) porphyrin ($[PFe^{I}]^-$) and the iron(0) porphyrin ($[PFe^0]^{2-}$).[503–506] Iron(0) porphyrins are described to be effective and persistent molecular catalysts of H^+ and CO_2 reduction to produce H_2 and CO, respectively.[503–506,508] The zero oxidation state complexes are stable in aprotic solvents, such as DMF or DMSO, on the timescale of slow scan cyclic voltammetry, thin-layer spectroelectrochemistry, and even longer periods when water and oxygen are carefully excluded.[506] Electrochemically generated Fe^0 porphyrins undergo metal-centered reactions with alkyl and vicinal mono and dihalides,[506,509,511] and with CO_2[512] leading, for the vicinal dihalides and CO_2, to efficient catalysis of electrochemical reactions.[506] It is noteworthy that the Fe^0 species can be electrochemically generated by reduction of iron(I) porphyrins. However, in the presence of axially coordinated CO this reduction does not take place. Axial CO binding to Fe^{I} yields iron(II) phlorin anion complexes, which may be converted back to iron(II) complexes upon anodic oxidation.[506] For CO_2, the reduction mechanism is suggested to involve a Fe(II)-CO_2 intermediate,[503] whereas the reduction of H^+ is suggested to proceed via the formation of a an iron(II) hydride, which reacts with a second acid molecule with the evolution of H_2.[504] The finding that Fe^0 porphyrins are good reductants of both H^+ and CO_2 was corroborated by studies of Grodkowski *et al.*,[502] who showed that Fe^{I} porphyrins do not directly reduce H^+ or CO_2, but that the Fe^{I} complexes undergo a disproportionation reaction to form PFe^{II} and $[PFe^0]^{2-}$ with the latter acting as reducing agent, in line with the results reported by Lexa and Savéant.[503–505,508–510,512–515]

3 IRON(I) PORPHYRINS AND THEIR REACTIONS

Although highly reduced iron porphyrins have been of interest because of the earlier belief that they might be involved in the catalytic cycles of certain redox proteins,[516–519] their importance for dioxygen activation,[520] and their synthetic value for preparing (σ-alkyl)porphyrin complexes,[513,514] only a few iron porphyrins, in which the metal atom is assigned the +1 oxidation state, have been synthesized and characterized. In these low-valent species, the porphyrin macrocycle is either derived from TPP, OEP, Etioporphyrin (ETIO),[521] 2,7,12,17-tetrabromo-5,10,15,20-tetraphenylporphyrin (Br_4TPP), 2,7,12-tricyano-5,10,15,20-tetraphenylporphyrin ($(CN)_3$TPP), 2,7,12,17-tetracyano-5,10,15,20-tetraphenylporphyrin ($(CN)_4$TPP),[516] dodecaporphyrins (DPP) with varying degrees of fluorination at the peripheral phenyl rings[522] (F_xDPP, with $x = 4$, 8, 12, 20, 28, or 36), or core-modified 5,10,15,20-tetraphenyl-21-oxaporphyrin (OTPP).[523] The TPP, OEP and DPP derivatives can be conveniently synthesized by means of chemical or electrochemical reduction. Both two-electron reduction of the corresponding iron(III) porphyrins by strong reducing reagents[182,518,519,524] or by cathodic electrolysis[515,516,520,525,526] yield the low-spin iron(I) complexes. The oxaporphyrin OTPPFe^{I} has been reported and prepared by two different routes, either by reduction of (OTPP)Fe^{II}Cl with $NaBH_4$ in THF or by the treatment of (OTPP)$Fe^{III}Cl_2$ with 2 equivalents of PhMgBr.[523] As described above, these iron(I) complexes can be further reduced electrochemically[503–505,507–510] or photochemically[502] to yield either ($P^{3-}\cdot$) Fe^{I} or PFe^0 complexes.

A number of spectroscopic techniques and physical measurements have been used to unambiguously describe the electronic structures of the putative iron(I) complexes, and to determine whether the reduced species are best described as d^7 iron(I) porphyrins, $[PFe^{I}]^-$, with the spin of the unpaired electron residing in the d_{z^2} orbital, as porphyrin π anion radicals, or as intermediates between these two limiting cases.[518,522] This distinction is most easily achieved by EPR spectroscopy as was first established by Bocian[516] and was shown recently for the DPP complexes[522] and by DFT calculations of g-tensors of low-spin TPP and OEP iron(I) porphyrins.[527] The Fe^I porphyrin complexes give rise to anisotropic signals with $g_\perp$ around 2.3 and $g_\parallel$ around 1.93, whereas the EPR spectra of iron(II) porphyrin π-anion radicals exhibit isotropic signals with g-values of 2.00. For the $DPPFe^I$ porphyrins, similar values were obtained ($g_\perp = 2.17$ and $g_\parallel = 1.96$).[522] For these complexes it is worth mentioning that the reduction of the non-fluorinated Fe^{II} complexes in benzonitrile leads to the formation of iron(I) porphyrins, whereas the fluorinated complexes, such as $F_{20}DPPFe$, produce iron(II) porphyrin π-anion radicals in the same solvent. By means of an intramolecular electron-transfer reaction, this complex is further reduced to the iron(I) species thereby highlighting the role of non-planar deformations. In pyridine, all DPPFe complexes are converted to porphyrin π-anion radicals upon electrochemical reduction to the Fe^{II} porphyrin independent of the degree of non-planarity of the complexes.[522] For the iron complexes of TPP, OEP, ETIO, the deuteroporphyrin IX dimethyl ester anion,[515] and for the phthalocyanine (Pc) analog,[528] NMR isotropic shifts,[521] EPR g-values ($g_\perp = 2.3$ and $g_\parallel = 1.93$ for $[TPPFe]^-$,[519,529] $g_\perp = 2.24$ and $g_\parallel = 1.92$ for $[OEPFe]^-$,[521] and $g_\perp = 2.119$ and $g_\parallel = 1.956$ for $[PcFe(Py)]^-$,[528] with $g_\perp > g_\parallel$ in each case), resonance Raman spectroscopy,[529,530] Mössbauer data,[518] and magnetic moments ranging from 2.3 to 5.0 μ_B[518,519,524] support the $[PFe^I]^-$ formulation of the complexes. A spin state of $S = 1/2$ is observed, with EPR parameters consistent with the unpaired electron residing in the d_{z^2} orbital,[519,521,528,529] by analogy with Co^{II} porphyrins.[531] Consistent with this electronic structure, five-coordinate complexes of $[PcFe]^-$ exhibit superhyperfine splitting from the N or P donor atom of the axial ligand.[528] The conclusions drawn from the spectroscopic data of four-coordinate porphyrin complexes are consistent with the molecular structure of the $[TPPFe]^-$ complex, which reveals a square planar geometry, with bond lengths fully consistent with the depopulation of the $d_{x^2-y^2}$ orbital.[518] DFT calculations of the g-values using a variational method for handling spin-orbit coupling and applying an average of configuration (AOC) of nearly degenerate states yielded what was considered reasonable comparison between calculated (2.51, 2.01) and experimental (2.3, 1.93) g-values for open-shell complexes,[532] although the difference between the calculated and experimental values seems to the authors to be unacceptably large, and the difference between $g_\parallel > 2$ and $g_\parallel < 2$ suggests that much improvement is still needed in these calculations.

However, based on UV–vis data[515,518,521,533,534] and other crystallographic studies,[535] the description of the reduced species as porphyrin π–anion radicals cannot be excluded in all cases. Electrochemical reduction of $(Br)_4TPPFeCl$, $(CN)_3TPPFeCl$, and $(CN)_4TPPFeCl$ (the Br and CN substituents are on the β-pyrrole positions in these complexes)[516] results also in the formation of low-spin, singly reduced iron(II) complexes, with the spin of the unpaired electron residing either in a metal or porphyrin ring orbital.[516] Optical absorption, EPR, and resonance Raman studies of $[(Br)_4TPPFe]^-$, $[(CN)_3TPPFe]^-$, and $[(CN)_4TPPFe]^-$ indicate that the electron density in singly reduced iron(II) porphyrins can be systematically transferred between the metal ion and the porphyrin ring by altering the electron-withdrawing capability of the porphyrin ligand.[516] Complexes with more negative $[PFe^{II}]/[PFe^I]^-$ redox couple (−0.812 V) ($[TPPFe]^-$ and $[(Br)_4TPPFe]^-$) have the unpaired electron in the d_{z^2} orbital, but reduction results in the transfer of a significant amount of *paired* electron density to the macrocycle through π back-bonding. The ground state for the low-spin Fe^I porphyrin complexes are hence formulated as $^2A_{1g} = (d_{xy})^2(d_{xz},d_{yz})^4(d_{z^2})^1$. For $[(CN)_3TPPFe]^-$ and $[(CN)_4TPPFe]^-$, for which the redox couple is more positive (−0.539 V), the unpaired electron resides on the macrocycle, indicating a $[(P^{3-}\bullet)\ Fe^{II}]\ {}^2E_g$ ground state for these complexes.[516]

The homolytic cleavage decomposition of n-butyliron(II) 5,10,15,20-tetraphenyl-21-oxaporphyrin creates an Fe(I) complex whose EPR spectrum (toluene-d_8) was interpreted as being consistent with a $(d_{xy})^2(d_{xz},d_{yz})^4(d_{z^2})^1(d_{x^2-y^2})^0$ electronic ground state ($g = 2.234, 2.032, 1.990$).[536] However, based on the shape of this EPR spectrum, which is very similar to those of Cu(II) tetragonal complexes, and the ^1H NMR spectral shifts, the authors suggest instead a $(d_{xy})^2(d_{xz},d_{yz})^4(d_{x^2-y^2})^1(d_{z^2})^0$ electron configuration. The ^1H NMR spectra, with large positive pyrrole-H shifts of 156.2, 129.5, and 76.3 ppm and furan-H shift of 161.4 ppm, is totally consistent with a low-spin d^7 electron configuration in which the unpaired electron is in the $d_{x^2-y^2}$ orbital.[536]

As already mentioned above, iron(I) porphyrins can undergo various reactions. They are of synthetic value for preparation of σ-alkyl iron porphyrins, which can be obtained by direct alkylation of the corresponding electrochemically generated iron(I) porphyrins with alkyl halides.[513,537] The highly reduced species can also be oxidized by molecular oxygen or hydrogen peroxide to yield the iron oxyporphyrin (oxophlorin), which is further oxidized to verdoheme by molecular oxygen,[538–540] as discussed in Section 6.1.5.

As potential models for the assimilatory nitrite reductases, electrochemical reduction of nitrosyliron(II) porphyrins (*see Nitrosyl Complexes*), PFeNO, yields first the Fe^I–NO complex, followed by two additional one-electron reductions. In the presence of phenols, the product of electrolysis is hydroxylamine.[541]

4 IRON(II) PORPHYRINS AND THEIR REACTIONS

Iron in the oxidation state +2 plays an important role in model heme and heme protein chemistry because of dioxygen binding, activation, and transfer. Depending on the coordination and environment of the metal ion, iron porphyrins are either four-, five-, or six-coordinate, with intermediate spin states ($S = 1$) for the four-coordinate complexes, [PFe^{II}], high-spin ($S = 2$) states for the five- or six-coordinate complexes, [$PFe^{II}L$] or [$PFe^{II}L_2$], and low-spin ($S = 0$) states for the five- or six-coordinate complexes, [$PFe^{II}L$] and [$PFe^{II}L_2$]. Unlike iron(II) phthalocyanine, [$PcFe^{II}$], iron(II) porphyrins are typically very reactive toward dioxygen, not only in solution, but also in the solid state,[542] and thus have been extensively studied to elucidate, for example, the mechanisms of reversible dioxygen binding by hemoglobin (Hb) and myoglobin (Mb) (*see* ***Iron: Heme Proteins & Dioxygen Transport & Storage***), and the modes of action of the P450 monooxygenases and other heme-containing oxygenases (*see* ***Iron: Heme Proteins, Mono- & Dioxygenases***).[32] The +2 oxidation state has also been identified for the ferrous and ferrous-CO forms of cytochrome P460, which belongs to the group of mono-heme cytochromes of ∼18 kDa molecular weight. It is one of the monomers of the enzyme hydroxylamine oxidoreductase (HAO), which is a very complex homotrimer with a molecular weight of 64 kDa per monomer. Each monomer contains seven *c*-type hemes and a so-called P460 as the eighth heme.[543,544] Many of these proteins employ a five-coordinate iron center in their native deoxy state and are high-spin, $S = 2$ species. The sixth coordination site is vacant for binding of dioxygen or other small molecules, such as carbon monoxide, nitric oxide, or isocyanides and phosphines. Upon small molecule binding, either five- or six-coordinate iron porphyrin complexes may be formed, and, depending on the field strength of the coordinating ligand, a spin-state change occurs from the paramagnetic to the diamagnetic, low-spin ($S = 0$) state. Comprehensive overviews of the interactions of iron porphyrins with small ligands have been published. Momenteau and Reed[545] have summarized the chemistry of synthetic heme dioxygen complexes, covering the literature up to early 1993. To assess the factors that influence heme conformations, the late Momenteau also reviewed the literature on supramolecular control of structure and reactivity.[546] The binding and activation of nitric oxide by metalloporphyrins and hemes have been reviewed by Cheng and Richter-Addo,[547] and the solid state structures of metalloporphyrin NO_x compounds by Wyllie and Scheidt,[185] who also summarized the systematics of the stereochemistry of porphyrin and metalloporphyrin structures.[548] The mechanistic aspects of the reactions of nitric oxide with transition metal complexes have been discussed by Ford *et al.*,[549–551] the axial coordination chemistry of iron(II) by Sanders *et al.*,[552] and the binding of isocyanides and phosphines as axial ligands in heme proteins and iron porphyrin models by Simonneaux and Bondon.[553] We will begin our discussion of Fe^{II} porphyrins with the four-coordinate *Square Planar*, $S = 1$ state, then turn to the five-coordinate, $S = 2$ state, and finally to the six-coordinate, diamagnetic, $S = 0$ state.

Theoretical calculations of the energies of the electronic states of iron porphyrinates of coordination numbers 4, 5 and 6 have developed significantly in recent years. For example, the performance of density functional theory (DFT) calculations of the low-lying excited states of iron(II) porphyrinates using the B3LYP density functional in combination with ab initio effective core potentials (ECPs) that are derived from either Hartree-Fock or Dirac-Fock calculations was investigated.[554] Five low-lying spin states, $^1A_{1g}$, $^3A_{1g}$, $^3B_{2g}$, $^5A_{2g}$, and $^5B_{1g}$ and their properties were calculated. It was found that the effects of replacing the core electrons with ECPs are less significant than the choice of basis functions, and that ab initio ECPs can be combined with the B3LYP density functional theory to provide consistent and accurate results.[554] Other nonlocal DFT calculations using the 6-31G-(d) basis set for H, N, O, and the VTZ basis of Ahlrichs[555] have identified 8[556] or 10[557] low lying states ($^5A_{1g}$, ^5E_g, $^5B_{2g}$, $^3A_{2g}$, $^3B_{2g}$, $^3E_g(A)$, $^3E_g(B)$, $^1A_{1g}$). A relationship between the electronic state and the size of the porphyrin core was found, with the singlet and triplet states exhibiting the smaller, and the quintet states the larger, core sizes. From this it was concluded that for low-spin Fe^{II} porphyrins the metal-N_{por} bond lengths are determined mainly by the electronic state and the occupancy of the antibonding $d_{x^2-y^2}$ orbital,[556] and to a lesser extent by the nonbonding interactions between the axial-ligand atom and the porphyrin N atoms. The results of these calculations of particular model systems will be presented in the appropriate section below.

4.1 Four-coordinate Intermediate Spin ($S = 1$) Iron(II) Porphyrin Complexes

Structural Aspects. Four-coordinate iron(II) porphyrins are of intermediate spin state ($S = 1$) and are in general square planar, with the iron placed in the center of the porphyrin core. However, the porphyrin ring is not always planar, as is observed for the $OEPFe^{II}$ species. It can be ruffled as was found for $TPPFe^{II}$ or $OECFe^{II}$ derivatives,[548] or saddled as was reported for a second crystalline form of $TPPFe^{II}$.[558] All complexes are characterized by relatively short Fe-N_{por} bond lengths (1.95–1.97 Å), which are indicative of the depopulation of the $d_{x^2-y^2}$ orbital, as is required for the $S = 1$ spin state.

Synthesis. The [PFe^{II}] complexes are most conveniently prepared by reduction of the corresponding Fe^{III} porphyrins in the absence of potential axial ligands using either chromium(II) complexes, aqueous dithionite under vacuum,[559–561] sodium amalgam,[562,563] borohydride salts,[564] or zinc amalgam in aprotic organic solvents.[565–575] Using aqueous sodium dithionite or Zn/Hg an Fe(II) porphycene complex, namely the Fe(II) complex of 2,7,12,17-tetra-*n*-propylporphycene [$(TprPc)Fe^{II}$] has also been synthesized by the reduction of the respective Fe(III) complex.[576] Whereas superstructured or picket fence iron(II) porphyrins are often prepared by reduction with dithionite under vacuum,[559–561] an additional method of preparation involves the reaction of the four-coordinate porphyrin with anhydrous potassium carbonate and ferrous bromide under strictly anaerobic conditions.[577,578] Another strategy entails the demetalation of zinc(II) complexes with CF_3SO_3H followed by treatment with $FeBr_2$ in absolute ethanol.[579] Highly fluorinated [F_xTPPFe^{II}] complexes have been synthesized using mercury activated zinc powder in the reduction of the Fe^{III} species,[580,581] whereas the corresponding [Br_xTPPFe^{II}] complexes with $x = 0-8$ are generated by electroreduction of the high-spin Fe^{III} porphyrins.[582] This reaction also allowed the Fe^{I} and Fe^{I} π-cation radical to be electrochemically formed.[582] Other methods include the photoreduction of, for example, protoporphyrin dimethyl ester Fe^{III}, which in DMSO at 150 K leads to the formation of the unligated $S = 1$ Fe^{II} complex.[583] TMPFe^{II} complexes have been prepared by reduction of [TMPFe^{III}OH] solution in an aprotic solvent with ethanethiol or with a chloroform solution of zinc amalgam.[575] Ethanethiol has also been used to synthesize 4-coordinate perfluoroalkyltetraphenylporphyrinatoiron(II) complexes[584,585] or to synthesize TPPFe^{II} complexes[586] by reduction of the μ-oxo dimer $[FeTPP]_2O$ according to a method developed by Stolzenberg.[59] Two polymorphs of octaethyltetraazaporphyriniron(II) (α- and β-OETAPFe^{II}) have also been synthesized by reacting the unmetallated porphyrins with FeI_2 in THF/toluene with added 2,6-lutidine to give the air-sensitive unligated Fe(II) complexes.[587,588] These complexes have interesting magnetic properties, an extraordinarily large internal hyperfine field (62.4 T), and represent a rare case of true ferromagnetically ordered molecular solids.

Electronic Ground-state Configuration. While researchers agree that the ground state of four-coordinate Fe^{II} porphyrins is of intermediate spin, $S = 1$,[589] the electronic ground-state configuration remains controversial.[590] Among the ten low-lying possible ground states for four-coordinate iron(II) porphyrins ($^5A_{1g}$, ^5E_g, $^5B_{2g}$, $^3A_{2g}$, $^3B_{2g}$, ^3E_g(A), ^3E_g(B), $^1A_{1g}$, $^1B_{2g}$, and ^1E_g),[557] the one that is favored by most spectroscopic studies including magnetic, Mössbauer, NMR, and optical spectra of [TPPFe^{II}] and [OEPFe^{II}],[589] and DFT calculations,[556,590] is the $^3A_{2g}$ state arising from the electron configuration $(d_{xy})^2(d_{z^2})^2(d_{xz},d_{yz})^2$. However, the $^3A_{2g}$ assignment is not supported by the early literature. Resonance Raman data of [OEPFe^{II}] and Mössbauer and magnetic measurements of the Fe^{II} complex of octamethylbenzoporphine were in this literature interpreted in terms of the ^3E_g $(d_{xy})^2(d_{z^2})^1(d_{xz},d_{yz})^3$,[589,590] which does not rule out the $^3A_{2g}$ state, or the $^5B_{2g}$ states, respectively.[590] Whereas most workers have settled on the triplet $^3A_{2g}$ state, they differ in opinion on the details of the relative energies of the excited states. Susceptibility and magnetic anisotropy studies of single crystals of [TPPFe^{II}] at 4–300 K support the $^3A_{2g}$ ground state, but consider the ^3E and ^3B excited states as being close in energy (1425 and 2425 cm^{-1}, respectively) to the $^3A_2$ ground state.[544] Optical spectra have been explained in terms of the $^3A_{2g}$ ground state with the ^3E_g state being only 240 cm^{-1} higher in energy.[591] Mössbauer[592] and NMR[565–569,589] data pinpoint the $^3A_{2g}$ ground state as arising from the $(d_{xy})^2(d_{z^2})^2(d_{xz},d_{yz})^2$ configuration. Analyzing the isotropic shifts of the TPPFe^{II}, RTPPFe^{II}, and OEPFe^{II}, Goff and La Mar[565] found that with the exception of the pyrrole-H signals all other proton resonances are significantly shifted to lower shielding, which implies that at least a major portion of the isotropic shifts originates in the dipolar interaction. This is an expected result for four-coordinated Fe^{II} porphyrins, since they are highly magnetically anisotropic.[565] The negative pyrrole-H isotropic shifts indicate that electron spin is absent from the $d_{x^2-y^2}$ orbital and that the d_{xz} or d_{yz} orbital(s) are occupied by at least one unpaired electron.[168,174] These reflect extensive π spin delocalization via P $\rightarrow$ Fe π electron transfer, with no evidence for Fe $\rightarrow$ P π back-bonding, which requires unpaired spin in d_{xz} and d_{yz} thereby strongly supporting the $^3A_{2g}$ ground-state with the $(d_{xy})^2(d_{z^2})^2(d_{xz},d_{yz})^2$ electronic configuration.[565] In agreement with this configuration are most recent DFT calculations of TPP, OEP and octamethylbenzoporphyrin iron(II) complexes, and Fe porphine, which identified four-coordinate unligated complexes to have a $^3A_{2g}$ ground state.[556,590] These findings are also in agreement with McGarvey's theory[589] that was developed for interpreting NMR dipolar and contact shifts of four-coordinated Fe^{II} complexes. When applied to temperature studies of TPPFe^{II}, OEPFe^{II}, and OECFe^{II}, the $^3A_{2g}$ ground state is predicted for intermediate-spin Fe^{II} porphyrins with spin–orbit coupling to the ^3E_g state at energies of 600 cm^{-1} for [OECFe] and [OEPFe], and 1000 cm^{-1} for [TPPFe]. The theory also explains the temperature dependence of the dipolar shifts, but is less satisfactory in analyzing the contact shifts, particularly at the β-pyrrole positions, when the macrocycle is ruffled, as in the case of the chlorin complex.[548,589]

In contrast to the RTPPFe^{II} complexes, the ^{1}H NMR shifts of OEPFe^{II} and other naturally occurring porphyrin Fe(II) complexes have been found to be concentration dependent. The isotropic shifts for most resonances of functional groups close to the porphyrin ring are affected substantially by concentration changes with all signals broadened and shifted to lower frequency.[565,566] These spectral changes are reported to arise from intermolecular ring currents, dipolar shifts, and dipolar relaxation caused by aggregation, with the formation of face-to-face dimers favored at low concentrations and parallel stacking of the porphyrin planes at higher concentrations.[566]

The ^{1}H NMR spectra of the iron(II) porphycene complex of 2,7,12,17-tetra-*n*-propylporphycene [(TprPc)Fe^{II}], with an $S = 1$ ground state have also been reported.[576] The chemical shifts of all the proton resonances (pyrrole-H at −37.52 ppm; *meso*-H at 71.56 ppm, α-CH_2 at 27.47 ppm, β-CH_2 at 8.92 ppm, γ-CH_2 at 5.55 ppm) are consistent with a planar unligated $S = 1$ iron(II) porphyrin. The complex is not very stable and upon exposure to dioxygen a (μ-peroxo)diiron(III) porphycene complex is formed.[576]

4.2 Six-coordinate Low-spin ($S = 0$) Iron(II) Porphyrin Complexes

4.2.1 *Bis-ligand Complexes: Addition of Ligands to Four-coordinate Iron(II) Porphyrins*

The four-coordinate square planar iron(II) porphyrins discussed above are not only of great value in heme protein model chemistry, but also in chemical applications, since they undergo a wealth of ligand addition reactions. For example it has been shown that $TPPFe^{II}$ complexes are active catalysts for important carbon transfer reactions in organic chemistry and are found to catalyze the stereoselective cyclopropanation of alkenes,[593] olefin formation from diazoalkanes,[593] and the efficient and selective olefination of aldehydes[594] and other carbonyl compounds.[595] The active species in these carbon transfer reactions are presumably iron porphyrin carbene complexes.[593–596] It was also found that ferrous hemin anchored to TiO_2 thin films reduce organic halides, which can pose serious health problems and are of considerable environmental concern because of their prevalence in groundwater.[597]

As already mentioned above, the $S = 1$ complexes undergo a wealth of ligand addition reactions to form in general either high-spin ($S = 2$) five- or six-coordinate complexes or five- or six-coordinate low-spin ($S = 0$) iron(II) complexes. However, it is important to recognize that it is synthetically not easy to control ligand addition to form selectively the five-coordinated species.[548] Very often six-coordinate species are unwanted by-products, which can be explained by the fact that the binding constant K_2 for the second ligand addition is in many cases more than 10 times, sometimes 15 times larger than the equilibrium constant K_1 for the binding of the first ligand.[548,552,598,599] Ligands that have been bonded to the square planar Fe(II) porphyrins in the solid and non-aqueous liquid state include anions[580,581,600] (acetate, bromide, chloride, cyanide, fluoride, hydroxide, imidazolate, isocyanide, mercaptide, methoxide, perchlorate, phenoxide), alkanes (*n*-heptane,[577,578] nitrosoalkanes[601]); amines (butyl-, benzyl-, and phenylethylamine),[602] carbon monosulfide (CS),[562] diazo compounds N≡N–C(Ph)R (R = –Ph, $–CO_2Et$, $–CO_2CH_2CH{=}CH_2$); nitrogen bases (imidazoles, pyridines, piperidines);[559–561,603–613] and small molecules (O_2, CO, CS, NO, RCN).[185,545,547,549,550,553] Each of these iron porphyrins is treated in their separate sections below.

4.2.2 *Addition of Aromatic Nitrogen-donor Ligands*

Because of their relevance in heme protein model chemistry, many studies have focused on the addition of nitrogen bases, such as hindered and non-hindered imidazoles or pyridines (*see* ***Ammonia & N-donor Ligands***), to four-coordinate PFe^{II} complexes to obtain a better understanding of the factors that affects the redox potentials and axial-ligand binding behavior of proteins such as the cytochromes *b*. In general, addition of imidazole or pyridine ligands to the four-coordinate complexes leads to the formation of the corresponding six-coordinate, diamagnetic, low-spin Fe^{II} complexes due to the large driving force for the binding of the second ligand.[548,552,575,599] Extensive investigations of the stepwise formation of the 1:1 and 2:1 axial-ligand complexes (see Section 6.3.6 and *see* ***Stability Constants & their Determination***) has shown that in the case of L = nonhindered imidazoles and pyridines, $K_1 < K_2$ (equations 3–7).[603–605]

$$PFe^{II} + L \rightleftharpoons PFe^{II}(L) \tag{3}$$

$$K_1 = \frac{[PFe^{II}(L)]}{[PFe^{II}][L]} \tag{4}$$

$$PFe^{II}(L) + L \rightleftharpoons PFe^{II}(L)_2 \tag{5}$$

$$K_2 = \frac{[PFe^{II}(L)_2]}{[PFe^{II}(L)][L]} \tag{6}$$

$$\beta_2 = K_1K_2 = \frac{[PFe^{II}L_2]}{[PFe^{II}][L]^2} \tag{7}$$

When the addition of the base is controlled, that is, when only one equivalent of base is added to one equivalent of PFe^{II}, typically only the four- and six-coordinate, and essentially none of the five-coordinate, species are detected; the five-coordinate complex usually disproportionates into the four- and six-coordinate iron(II) porphyrins. Only when L is a hindered ligand, such as a 2-substituted imidazole or pyridine, is K_1 sufficiently greater than K_2 that the five-coordinate complex is observed in solution. This has relevance for the stabilization of five-coordinate Fe^{II} porphyrins in solution, discussed in Sections 4.2 and 4.3.

Representative formation constants, K_1, K_2, and/or β_2, are summarized in Table 1, where it can be seen that the overall formation constants, β_2, are quite sensitive to solvent effects. For DMSO and DMF as solvents, it is known that the starting Fe^{II} porphyrin is six-coordinate[606,607] and high-spin.[491,599] The structure of the axial ligand and the magnitude of the equilibrium constants also have profound effects on the reactions observed. As mentioned above, 'hindered' ligands such as 2-methylimidazole and 1,2-dimethylimidazole tend to form only 1:1 complexes with Fe^{II} porphyrins, while they much more readily form 2:1 complexes with Fe^{III} porphyrins.[599,608] For example, for 2-MeImH addition to $TPPFe^{III}Cl$ in $CHCl_3$, $K_1 \leq 16\,M^{-1}$ and $\beta_2 = 3.3 \times 10^3\,M^{-2}$, while for addition of the same ligand to $TPPFe^{II}$ in benzene, $K_1 = 2.4 \times 10^4\,M^{-1}$ and K_2 is too small to be measured.[604,609] The reasons for this behavior of Fe^{II} porphyrins is not entirely clear, although a number of possibilities have been considered.[610] $Fe–N_{ax}$ bond lengths (*see Bond Length*) of six-coordinate low-spin Fe^{II} and Fe^{III} porphyrins are very similar

Table 1 Equilibrium constants for addition of imidazoles and pyridines to Fe^{II} porphyrins

Porphyrin	Ligand	Solvent	T (°C)	Method	log K_1	log K_2	log β_2
TPP	ImH	Benzene	25	UV−vis[604]	3.94	4.89	8.83
		DMF	25	e-chem[524]	–	–	7.29
	2-MeImH	Benzene	25	UV−vis[604]	4.38	–	–
		DMF	25	e-chem[491,599]	3.42	–	–
	1,2-Me$_2$Im	Benzene	25	UV−vis[609]	4.43	0.39	4.82
	N-MeIm	Benzene	25	UV−vis/kinet[610]	≈4.0	4.89	≈8.9
		DMF	25	e-chem[491,599]	–	–	6.5
	4-NMe$_2$Py	CH$_2$Cl$_2$	25	e-chem[614]	–	–	9.7
		DMF	25	e-chem[491,599]	–	–	6.7
	Py	Benzene	25	UV−vis[604]	3.18	4.28	7.46
		Benzene	25	UV−vis[604]	–	–	7.45
		CH$_2$Cl$_2$	25	e-chem[614]	–	–	7.8
		DMSO	25	e-chem[607]	2.44	0.78	3.22
		DMF	25	e-chem[574]	–	–	5.64
		DMF	25	e-chem[491,599]	–	–	5.3
	4-CNPy	CH$_2$Cl$_2$	25	e-chem[614]	–	–	4.2
		DMF	25	e-chem[491,599]	–	–	5.7
TMP	2-MeImH	DMF	25	e-chem[491,599]	–	–	5.5
	1,2-Me$_2$Im	Toluene	25	UV−vis[610]	4.15	2.92	7.07
	N-MeIm	Toluene	25	UV−vis/kinet[610]	≈4.0	4.95	≈9.0
		DMF	25	e-chem[491,599]	–	–	7.3
	4-NMe$_2$Py	DMF	25	e-chem[491,599]	–	–	7.9
	Py	DMF	25	e-chem[491,599]	–	–	7.4
	4-CNPy	DMF	25	e-chem[491,599]	–	–	7.5
(2,6-(OMe)$_2$)$_4$TPP	2-MeImH	DMF	25	e-chem[491,599]	3.2	–	–
	N-MeIm	DMF	25	e-chem[491,599]	–	–	4.9
	4-NMe$_2$Py	DMF	25	e-chem[491,599]	–	–	5.8
	Py	DMF	25	e-chem[491,599]	–	–	5.8
	4-CNPy	DMF	25	e-chem[491,599]	–	–	6.6
(2,6-Cl$_2$)$_4$TPP	2-MeImH	DMF	25	e-chem[491,599]	–	–	5.6
	N-MeIm	DMF	25	e-chem[491,599]	–	–	7.4
	4-NMe$_2$Py	DMF	25	e-chem[491,599]	–	–	8.4
	Py	DMF	25	e-chem[491,599]	–	–	8.2
	4-CNPy	DMF	25	e-chem[491,599]	–	–	8.0
(2,6-Br$_2$)$_4$TPP	2-MeImH	DMF	25	e-chem[491,599]	–	–	5.2
	N-MeIm	DMF	25	e-chem[491,599]	–	–	7.7
	4-NMe$_2$Py	DMF	25	e-chem[491,599]	–	–	>9.0
	Py	DMF	25	e-chem[491,599]	–	–	9.4
	4-CNPy	DMF	25	e-chem[491,599]	–	–	9.1
PPIX	ImH	H$_2$O	25	UV−vis[615]	–	–	4.0
	Py	H$_2$O	25	UV−vis[615]	–	–	5.4
DPDME	ImH	Benzene	25	UV−vis/kinet[616]	3.65	4.83	8.48
		DMF	25	e-chem[524]	–	–	6.72
	2-MeImH	Benzene	25	UV−vis/kinet[616]	4.11	–	–
MPDME	2-MeImH	2% CTAB, pH 9.5	25	UV−vis/kinet[616]	1.53	1.52	3.05
	N-MeIm	2% CTAB, pH 9.5	25	UV−vis/kinet[616]	1.93	–	–
TpivPP	1,2-Me$_2$Im	Toluene	25	UV−vis[617]	4.5	–	–
C$_2$Cap	N-MeIm	Toluene	23	UV−vis[570,609]	2.90	–	–
	1,5-DCIm	Toluene	23	UV−vis[570,609]	3.17	–	–
	1,2-Me$_2$Im	Toluene	23	UV−vis[570,609]	3.06	–	–
	Py	Toluene	23	UV−vis[570]	1.88	–	–
	s-BuNH$_2$	Toluene	23	UV−vis[570,609]	2.15	–	–
	t-BuNH$_2$	Toluene	23	UV−vis[570,609]	2.50	–	–
C$_3$Cap	N-MeIm	Toluene	23	UV−vis[570,609]	3.31	0.77	4.08
	1,5-DCIm	Toluene	23	UV−vis[570,609]	3.00	–	–
	1,2-Me$_2$Im	Toluene	23	UV−vis[570,609]	3.61	–	–

Table 1 cont'd

Porphyrin	Ligand	Solvent	T (°C)	Method	log K_1	log K_2	log β_2
	Py	Toluene	23	UV–vis[570]	2.17	–	–
	s-BuNH$_2$	Toluene	23	UV–vis[570,609]	2.79	2.85	5.64
	t-BuNH$_2$	Toluene	23	UV–vis[570,609]	2.23	–	–
NapC$_2$Cap	N-MeIm	Toluene	23	UV–vis[609]	2.87	–	–
	1,5-DCIm	Toluene	23	UV–vis[609]	3.22	–	–
	1,2-Me$_2$Im	Toluene	23	UV–vis[609]	2.32	–	–
	s-BuNH$_2$	Toluene	23	UV–vis[609]	1.18	–	–
	t-BuNH$_2$	Toluene	23	UV–vis[609]	0.90	–	–

(2.004–2.014 Å[611] and 1.964–1.977 Å,[612] respectively), with the Fe^{III}–N$_{ax}$ bond lengths being only very slightly shorter, and the Fe^{III}–N$_{ax}$ bond lengths of [TPPFe(2-MeImH)$_2$]$^+$ (2.015 Å[618]) being much longer than those of [TPPFe(ImH)$_2$]$^+$ (1.997 and 1.957 Å,[619] 1.964 or 1.977 Å, depending on ligand orientation[612]), and are almost identical in length to those of Fe^{II} porphyrin complexes with unhindered imidazoles, listed above. The possible effect of the low-spin d^6 electron configuration of the product is not of itself the reason, since the isoelectronic [TMPCo(2-MeImH)$_2$]$^+$ complex is stable and diamagnetic, with ligands in perpendicular planes at ambient temperatures,[620] and the Co–N$_{ax}$ bond lengths of the related complex, [TPPCo(ImH)$_2$]$^+$ (1.945 and 1.909 Å[613]), are only slightly shorter than those of [TPPFe(ImH)$_2$]ClO$_4$ quoted above. Thus, while it appears that axial bond lengths tend to decrease in the order Fe^{II} > Fe^{III} > Co^{III}, the existence of bis(2-MeImH) complexes of both Fe^{III} and Co^{III} makes it all the more curious that such complexes of Fe^{II} are relatively unstable. The reported log K_1, log K_2 and log β_2 values for 2-MeImH binding to TMPFe^{II} in toluene,[610] and those for the same ligand binding to TMPFe^{II}, (2,6-Cl$_2$)$_4$TPPFe^{II} and (2,6-Br$_2$)$_4$TPPFe^{II} in DMF,[491,599] reveals the need for further theoretical studies of these systems.

It should be noted that the crystal structures of all low-spin Fe^{II} model hemes investigated thus far, except for tetra-(*meso*-n-C$_3$H$_7$)porphyrinatoiron(II)-*bis*-pyridine[621] and [Br$_8$TFPPFe(Py)$_2$],[598] have been found to have their axial ligands lying over the *meso* positions ($\phi \sim 45°$) if those ligands are pyridines,[575,611] and at any angle, including over or near the porphyrin nitrogens ($\phi \sim 0$–$10°$), if the ligands are non-hindered imidazoles,[611] in parallel planes in both cases. Both π-donor and π-acceptor ligand complexes have these ligands in parallel planes,[575,611] which seems to be the preferred geometry for Fe^{II} porphyrinates that do not have bulky *meso*-substituents.[621] For cross-*trans*-linked iron(II) basket-handle porphyrin complexes, it is suggested that imidazoles or pyridines are bound in perpendicular planes, but no structures have been determined. In these cases the perpendicular orientation, if present, and the ruffling of the porphyrin core, are caused by the distortion due to short basket handles.[559] Unfortunately, no binding constants for the imidazoles or pyridines were reported. But it is mentioned that up to 1 M concentrations of the axial ligands were required to insure complete coordination, and the complexes showed particularly low affinity for pyridine.[559] With porphyrins having no such superstructures, there is evidence (Mössbauer[622] and NMR[188,620] spectroscopy) that only for the bis-(1,2-dimethylimidazole) complex of TMPFe^{II} at very low temperatures (200 to 4.2 K) can the axial ligands be stabilized in perpendicular planes. Hence, for complexes in which the axial ligands lie over the *meso* positions of the porphyrin ring, there appears to be an energy barrier to having the axial ligands in perpendicular planes *for Fe*^{II}, while Fe^{III} *prefers* having axial ligands in perpendicular planes if there is any steric interference between porphyrin substituents and axial ligands. It should be noted, however, that if there is no steric interference, Fe^{III} also prefers to have axial ligands in parallel planes. It has been hypothesized that the energy barrier in the case of Fe^{II} complexes might be because of the required ruffling of the porphyrin for the axial ligands to lie in perpendicular planes over the *meso* positions.[194] However, mammalian cytochromes c have very ruffled porphyrin rings with the histidine imidazole plane lying over the α,γ-*meso* positions,[623–625] yet ligand binding in the Fe^{II} state is very strong, stronger than in the Fe^{III} state, as evidenced by the positive reduction potentials of many cytochromes c.[626,627] Thus, theoretical investigations of the importance of ruffling in (de)stabilizing Fe^{II} heme centers are certainly needed.

Porphyrin substituents also have large effects on log β_2. In particular, the presence of *meso*-2,6-phenyl substituents greatly enhances the stability of the six-coordinate complexes, except when these substituents are methoxy groups.[491,599] In fact, for TMPFe^{II}, (2,6-Cl$_2$)$_4$TPPFe^{II}, and (2,6-Br$_2$)$_4$TPPFe^{II} in DMF, the bis-2-methylimidazole complexes are stable, with log $\beta_2 = 5.1$–5.8 (Table 1).[491,599] However, it should be noted that bis-axially coordinated TMPFe^{II}(2-MeImH)$_2$ is stable at ambient temperatures, but that 2-MeImH does not form complexes with TPPFe^{II}, (2,6-F$_2$)TMPFe^{II}, and 2,6 (2,6-(OCH$_3$)$_2$)TPPFe^{II}.[599] The increased stability of all TMPFe^{II} complexes over their TPP counterparts has been discussed by Traylor and coworkers,[610] and attributed to the perceived greater tendency of TMP to resist doming. However, in the absence of molecular structures of five-coordinate TMPFe^{II} complexes with nitrogen donor ligands it is not possible at present to verify this suggestion. Comparison of the values of log β_2 for tetraphenylporphyrin derivatives in DMF reveals that there is both an electronic effect ($2,6\text{-}(OMe)_2 \ll 2,6\text{-}H_2 \ll 2,4,6\text{-}Me_3 \sim 2,6\text{-}Cl_2 \sim 2,6\text{-}Br_2$ for N-MeIm complexes) and a steric effect ($2,6\text{-}(OMe)_2 \ll 2,4,6\text{-}Me_3 < 2,6\text{-}Cl_2 < 2,6\text{-}Br_2$) involved, the latter evidenced by the 'levelling effect' of bis(substituted pyridine) complex formation constants for pyridines ranging in basicity from 4-NMe_2Py ($pK_a(PyH^+) = 9.7$) to 4-CNPy ($pK_a(PyH^+) = 1.1$) for each of the larger 2,6-phenyl substituents.[491,599] For axially N- and 2-methylimidazole, and pyridine ligated $FeTPP^{II}$ complexes with *ortho*-phenyl substituents of varying bulkiness, it was shown that the log β_2 values decrease in the order of Br > Cl > CH_3 > F > OCH_3 > H. This trend was described to be mainly due to the steric size of the substituent(s) rather than its electronegativity or the electron-donating/withdrawing characteristics of the substituent(s); it was found that the complexes with the sterically most bulky substituents have the largest equilibrium constants.[599]

One-side-hindered $TPPFe^{II}$ derivatives will in some cases bind two Lewis base axial ligands, especially if they are small and the porphyrin is a 'picket fence' type porphyrin, $(o\text{-Piv})_4TPP$ ($T_{Piv}PP$), or the larger 'cap' porphyrin, C_3cap (Table 1). The structure of one such complex, $[T_{Piv}PPFe(Im)(ImH)]^-$, has been reported,[628] but it was not possible to distinguish the neutral and anionic ligands crystallographically. Other *bis*-base sterically protected complexes were also studied. For example, the *bis*-base ligated pivalamido and the cross-trans-linked basket-handle iron(II) porphyrins mentioned above were studied by absorption and resonance Raman spectroscopy.[559,561] The visible absorption spectra of *bis* *N*-methylimidazole, 1,5-dicyclohexylimidazole, and pyridine coordinated complexes of atropisomers of Fe(II)-tetrakis(*o*-pivalamidophenyl)porphyrins [$\alpha\beta\alpha\beta\text{-}T_{Piv}PPFe^{II}$] revealed redshifts of the B and Q absorption bands by about 4–5 nm, and a shift by $+5\,cm^{-1}$ of the low frequency ν_8 resonance Raman mode, but no shifts of the skeletal high frequency modes. These data were interpreted in terms of the change in relative position of the axial imidazole rings from nearly parallel in the *bis*-*N*-methylimidazole complex to nearly perpendicular in the *bis*-dicyclohexylimidazole complex and the change from a planar to a saddled porphyrin ring structure.[559] Studies of the *bis*-imidazole and *bis* pyridine-ligated 'basket-handle' porphyrin complexes[561] complement these findings and allowed the spectroscopic properties of ruffled complexes to be characterized. As for the [$\alpha\beta\alpha\beta\text{-}T_{Piv}PPFe^{II}L_2$] complexes, a gradual red shift was observed for the Q and B bands, which was accompanied by both a downshift of the resonance Raman frequency ν_2 mode and an increased upshift of the ν_8 mode when the handles were shortened and/or when the steric hindrance of the axial ligands was increased. The spectroscopic data were attributed to the degree of ruffling in these complexes, which increases from *N*-methylimidazole to pyridine axial substitution, presumably due to steric interaction constraints between the axial-ligand rings, the porphyrin macrocycle, and the porphyrin handles.[561] The crystal structure of the *bis*-pyridine-ligated iron(II) complex of the highly brominated pentafluorophenyl TPP, [$(TFPPBr_8)(Py)_2$] mentioned above[598] revealed a highly deformed porphyrin core, which had a twisted S_4 saddle-shape structure with an average $Fe\text{-}N_{por}$ bond of 1.963 Å that is shorter than in other bis-pyridine-ligated iron(II) porphyrins.[548] The complex reacts very slowly with dioxygen, but is readily oxidized by *tert*-butyl hydroperoxide.

Bis-pyridine-coordinated low-spin iron(II) complexes of the octaethylporphyrin dianion (OEP^{2-}) were found to undergo interesting chemistry, which is discussed in greater detail in Section 6.1.5: Treatment of a series of *meso*-substituted [$OEPFe^{II}(Py)_2$] complexes including [*meso*-NO_2-$OEPFe^{II}(Py)_2$], [*meso*-CN-$OEPFe^{II}(Py)_2$], [*meso*-HC(O)-$OEPFe^{II}(Py)_2$], [*meso*-Cl-$OEPFe^{II}(Py)_2$], [*meso*-OMe-$OEPFe^{II}(Py)_2$, [*meso*-Ph-$OEPFe^{II}(Py)_2$], and [*meso*-*n*-Bu-$OEPFe^{II}(Py)_2$] with hydrogen peroxide in pyridine–d_5 at low temperature under strict exclusion of dioxygen led to the formation of stable oxophlorin ($OEPOFe^{II}$) complexes, where OEPO is the monoanion of octaethyl-5-oxaporphyrin.[629] As revealed by ^1H NMR spectroscopy, the reaction produced a mixture of three oxygenation products, [*cis*-*meso*-R-$OEPOFe^{II}(Py)_2$], [*trans*-*meso*-R-$OEPOFe^{II}(Py)_2$], and [$OEPOFe^{II}(Py)_2$]. The isotropic shift patterns for these oxophlorins showed negatively-shifted *meso*-H resonances ranging from −41 ppm in the cis isomer of [*meso*-HC(O)-$OEPOFe^{II}(Py)_2$] to −152 ppm for the same isomer of [*meso*-OMe-$OEPOFe^{II}(Py)_2$], and positively- and negatively-shifted methylene signals. The methyl protons resonated in the spectral region of 0–5 ppm. For the *trans* isomers even greater variations in the *meso*-H shifts were observed. For [*meso*-HC(O)-$OEPOFe^{II}(Py)_2$] the single resonance of the *meso*-H is found at −17 ppm and for the [*meso*-OMe-$OEPOFe^{II}(Py)_2$] it is observed at −168 ppm. For all resonances non-Curie behavior was observed.[629] Further steps of oxidation can take place, leading to verdoheme and biliverdin, the breakdown products of heme. The topics of coupled oxidation of both Fe^{II} and Fe^{III} porphyrins, and the relationship of these reactions to those of the enzyme heme oxygenase, are discussed in more detail in Section 6.1.5 below.

4.2.3 *Photodissociation of Six-coordinate Low-spin Iron(II) Porphyrins, $PFeL_2$*

Not only has binding of imidazoles and pyridines to Fe^{II} protoporphyrin IX been studied,[615] as discussed in Section 4.1.2, but also photodissociation of axial ligands such as pyridines, imidazoles, or piperidines from six-coordinate, low-spin Fe^{II} porphyrins, in which the porphyrin is derived from protoporphyrin IX, or proto- or deuteroporphyrin IX dimethyl ester, has been investigated in nonaqueous solvents using picosecond transient absorption spectroscopy[630] (*see* ***Photochemistry of Transition Metal Complexes***). It has been shown that photodissociation leads to the formation of five-coordinate complexes, that is, only one ligand appears to be released upon excitation of the six-coordinate complex.[630]

Recombination rates range from 10^8 to $10^9\,M^{-1}\,s^{-1}$, with similar values obtained by nanosecond measurements, whereas photodissociation yields are low and range from 0.03–0.08. These low yields have been interpreted in terms of rapid relaxation of the photoexcited six-coordinate complex competing with ligand release.**[630]** Other five-coordinate complexes are also formed on picosecond photolysis; for example, a protoheme dimethyl ester bis(*t*-butyl isocyanide) in pure *t*-butyl isocyanide or in toluene. This photolysis results in the loss of one isocyanide ligand to produce an electronically excited five-coordinate complex, which decays to the ground state within 40 ps.**[631]** The recombination rate for the formation of the bis(isocyanide) complex is $2.5 \times 10^8\,M^{-1}\,s^{-1}$.**[631]** It has been further shown that when the photolyzed ligand is derived from other isocyanides or *N*-methylimidazole, a concentration-independent relaxation is observed, with a 40 to 95% return to the starting compound.**[631,632]** For CO, geminate recombination is only observed at high viscosity.**[633]**

4.2.4 Addition of Aliphatic Amine Ligands

Complexes with unprecedented structural data for the coordination of primary amines by iron(II) porphyrins are found in low-spin ($S = 0$), bis(primary amine)-ligated iron(II) porphyrins [Fe(TPP)(RNH_2)$_2$] with RNH_2 = 1-butylamine, benzylamine, and phenethylamine.**[602]** The complexes were prepared by reduction of the TPPFe^{III}Cl with silver triflate followed by the addition of the amines in a nitrogen inert gas atmosphere, and were found to be structurally and spectroscopically similar to [Fe(TPP)(Py)$_2$] derivatives.**[602]** The Fe-N$_{por}$ distances of the three complexes average 1.990(2) Å and the axial Fe-N$_{amine}$ distances range from 2.028 Å in the [Fe(TPP)($PhCH_2CH_2NH_2$)$_2$] complex to 2.043 Å in the [Fe(TPP)($BzNH_2$)$_2$] complex. Consistent with an $S = 0$ iron(II) spin state, the zero-field Mössbauer spectra (5–300 K) show comparable isomer shifts (0.393(1)-0.493(1) mm/s) and quadrupole splittings (1.144(6)-1.204(3) mm/s. Molecular mechanics (MM) calculations with a force field parameterized for iron(II) porphyrin amine complexes show that stable conformations arise when the α-CH_2 and NH_2 protons of the coordinated ligands are staggered relative to the Fe-N$_p$ bonds of the porphyrin core. The lowest energy conformations of the [Fe(TPP)(RNH_2)$_2$] complexes have the ligand α-carbons positioned directly over the Fe-N$_p$ bonds of the porphyrin core.**[602]**

4.2.5 Addition of Phosphine Ligands

Trimethylphosphine and mixed phenyl, methyl phosphines readily bind to both Fe^{II} and Fe^{III} porphyrins to form low-spin complexes. The (p-OCH_3)$_4$TPPFe^{II}(PMe_3)$_2$ and OEPFe^{II}(PMe_3)$_2$ complexes have been characterized structurally,**[634]** as well as by ^{57}Fe NMR ($\delta_{Fe} = 7670$ and 7873 ppm, respectively)**[487,634]** and Mössbauer (for the OEP complex, $\delta = 0.36\,mm\,s^{-1}$, $\Delta E_Q = 0.35\,mm\,s^{-1}$)**[635]** spectroscopies. Mixed-ligand complexes of the types PFe^{II}(PMe_3)$_2$, PFe^{II}(PMe_3)(L), PFe^{II}(L)(L') and PFe^{II}(L)$_2$ have also been investigated by the two spectroscopic techniques, and a correlation was found between the ^{57}Fe chemical shift, δ_{Fe}, and the Mössbauer quadrupole splitting, ΔE_Q.**[635]** This correlation helped to correct the unusual ^{57}Fe chemical shifts of the bis-pyrrolidine and bis-pyridine-d$_5$ complexes of TPPFe^{II} that were reported earlier.**[636]**

4.2.6 Binding of Anionic Ligands

Certain anionic ligands can also bind to iron(II) porphyrins to yield low-spin complexes. Mandon *et al.* showed that binding of imidazolate to a picket fence porphinatoiron(II) imidazole complex forms the corresponding ImH, Im$^-$ low-spin complex ($S = 0$).**[628]** The low-spin nitrite complex has also been well characterized,**[637]** as discussed near the beginning of Section 4.3. Evidence for binding of Br$^-$, OAc$^-$, Cl$^-$, and F$^-$ to TPPFe^{II} complexes has been obtained by spectroelectrochemical techniques. For binding of F$^-$, the [TPPFeF]$^-$ complex is formed, with a formation constant of approximately $600\,M^{-1}$.**[600]** For binding of Cl$^-$ this constant, measured in DMF at 20 °C, is much smaller ($56\,M^{-1}$).**[638]** The formation constants for Cl$^-$ complexes of a series of basket-handle porphyrins in DMF at 20 °C are much larger for amide linked handles (1.8×10^3 to $1.1 \times 10^2\,M^{-1}$)**[638]** and much smaller for ether-linked handles (3.6–$9.6 \times 10^{-2}\,M^{-1}$),**[638]** suggesting a 'local solvation effect' of the amide groups. It has also been shown that the addition of cyanide to the hydroxo complex of high-spin [(TMP)Fe^{III}OH] leads to the formation of the low-spin *bis*-cyanide ligated complex [(TMP)Fe^{II}(CN)$_2$]$^{2-}$. This complex has been crystallized with the cation *bis*-triphenylphospine nitrogen (PPN$^+$) acting as counterion. The average Fe-N$_{por}$ bond is 2.003 Å, which is a typical value for $S = 0$ iron(II) complexes, and the Fe-CN bond length is 1.990 Å, slightly larger than that of the [(TPP)Fe(CN)$_2$]K complex.**[639]**

4.3 Five-coordinate $S = 2$ Iron(II) Porphyrin Complexes

Five-coordinate, high-spin Fe^{II} porphyrin complexes with imidazoles or pyridines as axial ligands are of specific interest, since they represent not only direct models of the oxygen transport and storage proteins deoxyhemoglobin and deoxymyoglobin (*see* ***Iron: Heme Proteins & Dioxygen Transport & Storage***), but they are also excellent models of the reduced states of cytochromes P450 and chloroperoxidase, as well as peroxidases (*see* ***Iron: Heme Proteins, Mono- & Dioxygenases***; ***Iron: Heme Proteins, Peroxidases, Catalases & Catalase-peroxidases***). Axially imidazole coordinated iron(II) porphyrins may also serve as models for characterizing the active site of prostaglandin H synthase (PGHS) that is also known as cyclooygensae or COX, a member of the peroxidase family. This enzyme has two isoforms (PGHS-1, PGHS-2), but consists in its ferrous state as a single species with histidine coordinating as the proximal axial ligand.[640]

Synthetic Aspects. Because of the much greater stability of many bis-ligated complexes of Fe^{II} porphyrins, discussed in Section 4.2, the synthesis of five-coordinate HS Fe^{II} complexes is challenging, and special methods must be used to prepare five-coordinate $PFe^{II}L$ complexes. The simplest method is the addition of sterically hindered bases, such as 2-substituted imidazoles or pyridines, to four-coordinate, nonhindered intermediate spin PFe^{II} complexes (see Section 4.1). The addition of one ligand decreases the binding constant for the second ligand without affecting the equilibrium constant of the binding of the first ligand.[548] This strategy was for example used to synthesize the [TPPFe(2-MeImH)] complex, which is produced by reacting $TPPFe^{II}$ with an excess of 2-methylimidazole.[548] In a similar fashion, other complexes are obtained, including complexes derived from synthetic and natural porphyrins. In these five-coordinate complexes the iron atom is displaced from the mean porphyrin plane by 0.3–0.6 Å,[641] which ensures that only a single sterically hindered base such as 2-methyl- or 1,2-dimethylimidazole coordinates to the metal ion. For many, but not all, porphyrinate iron(II) complexes, the energetics for bringing the Fe^{II} atom into the porphyrin plane to form a six-coordinate complex are quite unfavorable in the presence of these sterically bulky ligands as is evidenced by the fact that the binding constant for the second ligand addition is usually extremely small,[548,552,575,608,609] as is discussed above in Section 4.2.

The other approach that ensures five-coordination is to block one face of the porphyrin by the covalent attachment of an axial ligand, as was done for some of the models of deoxyhemoglobin and deoxymyoglobin, involving tailed picket fence porphyrins,[642] pocket porphyrins,[643] 'tailed basket-handle' porphyrins, or biphenyl-strapped porphyrins,[644] and other superstructured porphyrins.[645] These models are discussed in more detail under O_2/CO binding (Sections 4.5.1 and 4.5.2). NMR studies of the pocket porphyrin complexes, which form stable and reversible dioxygen adducts, revealed that these complexes remain predominantly five coordinate in the absence of gaseous ligands.[642,643,645] However, as the temperature is lowered to −25 °C, new sets of resonances between 10 and −10 ppm appear that are attributed to the disproportionation of the five-coordinate, high-spin Fe^{II} complex to yield one four-coordinate, intermediate-spin Fe^{II} complex and one diamagnetic, six-coordinate low-spin Fe^{II} complex by intermolecular sharing of axial ligands (equation 8).[642]

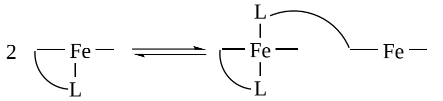

(8)

Other superstructured Fe(II) porphyrin complexes, in which the axial ligand is provided by 'straps, arms, or tethers' attached to the porphyrin macrocycle, have been prepared in many laboratories, including our laboratories. This strategy was also used to synthesize high-spin Fe^{II} complexes of peptide-sandwiched mesohemes, which were formed by attaching 13-residue peptides to the propionate groups of the mesoporphyrin IX iron(II) complex (MPIXFe) via amide linkages.[646] In these complexes, the imidazolyl ring of a histidine (His) residue in the peptide chain coordinates to the mesohemin iron.[646] The superstructured strategy was also employed to prepare synthetic analogs for the oxygen binding site in cytochrome c oxidase (*see* ***Cytochrome Oxidase***).

A third approach for synthesizing high-spin iron(II) porphyrins includes the binding of anions, such as imidazolate, thiolate, or acetate, to form complexes with an overall negative charge.[548]

Crystal Structures. Only a few crystal structures of high-spin Fe^{II} five-coordinate porphyrin complexes have been reported,[548,586] and these have been reviewed by Scheidt.[548] These include complexes of TPP, picket fence and hybrid porphyrins, and (*p*-chlorophenyl)porphyrin.[548] Because of the population of the $d_{x^2-y^2}$ orbital, these complexes are characterized by an expanded porphyrin core, long Fe-N_{por} bond lengths, and substantial displacement of the iron ion from the porphyrin core. Typical Fe–N_{ax} bond lengths are 2.13 Å (Fe 0.31 Å out of plane) in a *N*-methylimidazole complex[647] and 2.095 Å (Fe 0.40 Å out of plane) and 2.161 Å (Fe 0.42 Å out of plane) in the 2-MeImH complexes of the picket fence porphyrin[648] and an earlier $TPPFe^{II}$ structure,[641] respectively, but 2.127 Å (Fe 0.32 Å out of plane) in a more recent structure that is more highly ordered.[586] This structure demonstrates porphyrin core distortions and an asymmetry in the Fe–N_P bond distances, and emphasizes that high-spin iron(II) porphyrinate derivatives display substantial structural pliability with significant variations in iron atom displacements, porphyrin core hole size and axial and equatorial Fe–N bond lengths.[586] For the thiocarbonyl ligated complex [$OEPFe^{II}$(CS)], the average Fe–N bond length is 1.982 Å and the Fe–C(CS) bond distance is 1.662 Å with a fairly small 0.23 Å displacement of the iron ion from the mean plane of the porphyrin core.[649]

Typical geometries observed for anionic complexes relevant to biological systems include the 2-methylimidazolate (2.002 Å (Fe–N_{ax}), 0.65 Å out of the mean plane of the porphyrin core),[628] phenolate (1.937 Å, 0.56 Å out of plane),[650] thiolate (2.36–2.37 Å, 0.4–0.5 Å out of plane)[651,652] and acetate (2.03 Å, 0.64 Å out of plane)[653] complexes. Note that in cases where the picket fence porphyrin was used, the anionic ligand (imidazolate,[628] thiolate,[651,652,654] and acetate[653]) is on the same side of the porphyrin plane as the pivalamide 'pickets'.

Mössbauer Spectroscopy. Mössbauer spectra of high-spin Fe^{II} porphyrins are unique and vary greatly in their quadrupole splitting parameters ΔE_Q. With nitrogen bases such as 2-MeImH, quadrupole splittings $\Delta E_Q \sim 2.3–2.4\,mm\,s^{-1}$ and isomer shifts $\delta \sim 0.90–0.94\,mm\,s^{-1}$ are observed.[177,586,655] However, if anionic oxygen or nitrogen donors or chloride ion replaces the neutral base, then the Mössbauer spectrum changes characteristically. Extremely large quadrupole splittings are observed,[650,651,656,657] for example $\Delta E_Q = 3.51\,mm\,s^{-1}$ at 77 K for the imidazolate complex[628] or 4.01 or 4.25 $mm\,s^{-1}$ for anionic oxygen donors PhO^- or $MeCO_2{}^-$,[653] respectively.

Vibrational Spectroscopy. It was also shown that water can coordinate to the iron center to form an unusual monoaqua adduct of tetrakis [(*N*-*t*-butylcarbamoyl)phenyl]porphinatoiron(II).[658] The stabilization of this complex is ascribed to the formation of an internal hydrogen bond between the coordinated water molecule and one (or two) of the four carbamoyl carbonyl groups of the porphyrin. Resonance Raman spectra of the four-coordinate precursor complex show the ν_2 and ν_4 porphyrin modes at 1561 and 1362 cm^{-1}, indicating an increased degree of ruffling when compared to the picket fence analog $TpivPPFe^{II}$ ($\nu_2 = 1566\,cm^{-1}$ and $\nu_4 = 1370\,cm^{-1}$). For the high-spin monoaqua five-coordinate complexes the skeletal porphyrin modes are observed at 1542 and 1346 cm^{-1}.[658] Depolarized resonance Raman bands sensitive to spin-, coordination-, and oxidation-state of iron porphyrins are observed at $\nu_{10} > 1600\,cm^{-1}$, while for iron chlorins the same band is strong and polarized, and is also observed in the IR spectrum. For iron isobacteriochlorins there is a strong polarized ν_{29}-equivalent band at $\approx 1400\,cm^{-1}$.[659] Recently resonance Raman spectroscopy was also used to study the iron out-of-plane mode in the proximal cavity mutant of deoxymyoglobin H93G.[660] In this mutant histidine is replaced by glycine to create a cavity for binding of numerous ligands, including, imidazoles (ImH, 1-, 2-, 4-MeIm, 1,2- and 1,4-Me_2Im, 2-ethyl-ImH, 4-CH_2OH-ImH, 4-BrImH, 4-Br-2-MeImH) and pyridines (3-FPy, 3-MePy, 3-BrPy, and 4-MePy). It was found that several RR modes in the low frequency region show axial-ligand dependencies. The largest effect was observed for the iron-ligand out-of-plane mode ranging from 180 cm^{-1} in the 4-BrImH and 2 Me-ImH mutants to 228 cm^{-1} in the 4-CH_2OH-ImH-ligated mutant, which in contrast to model hemes increased with the basicity of the axial ligand. Theoretical calculations revealed that this mode contained significant contributions from the Fe-ligand stretching and from the iron-heme doming.[660]

NMR Spectroscopy. The NMR spectra of five-coordinate complexes of iron(II) porphyrins are distinctive: the isotropic shifts of the pyrrole-H in the TPP complexes are positive, and those of the phenyl protons are negative, with typical isotropic shifts of 43.5 ppm for the pyrrole-H and −1.0 to −1.5 ppm for the *o*-, *m*-, and *p*-phenyl protons.[565] For five-coordinate $OEPFe^{II}$ complexes, isotropic shifts of −7.0 ppm for the *meso*-H and +8.5 ppm for the pyrrole-α-CH_2 protons have been reported.[565] The *meso*-H protons in the natural porphyrins appear in the spectral region of 0 to +6 ppm.[565]

The isotropic shifts in these complexes, especially the shifts for the pyrrole-H and pyrrole α-CH_2 protons, serve as convenient probes for both oxidation and spin state of the metal ion.[168,565] The positive pyrrole-H and α-CH_2 isotropic shifts are indicative of primarily σ spin delocalization to the pyrrole positions. Such positive isotropic shifts at the β-pyrrole positions are characteristic of an unpaired electron in the $d_{x^2-y^2}$ orbital, leading to a ground-state assignment of $(d_{xy})^2(d_{xz},d_{yz})^2(d_{z^2})^1(d_{x^2-y^2})^1$ for the high-spin Fe^{II} ion.[218] Moderate π delocalization to the *meso* position is indicative of partially filled d_π orbitals, also consistent with the ground state proposed.[168,174]

The ^1H NMR spectrum of the high-spin Fe(II) complex of oxaporphyrin $(OTPP)Fe^{II}Cl$ that is formed when the high-spin six-coordinate iron(III) complex $(OTPP)Fe^{III}Cl_2$ is reduced by means of moderate reducing agents, such as aqueous sodium dithionite or zinc amalgam, is characterized by unpaired electron spin density delocalization into both σ and filled and vacant π molecular orbitals.[536] This unpaired electron spin delocalization pattern explains that two of the pyrrole proton resonances are downfield shifted (39.3 and 29.5 ppm) and one is upfield shifted (−6.4 ppm), whereas the furan protons give rise to a downfield-shifted signal (33.2 ppm).[536] A similar upfield shift for one of the pyrrole resonances was also observed for iron(II) N-methylporphyrin ($N-CH_3$-TPP)FeCl and iron(II) 21-thiaporphyrin (STPP)FeCl.[523]

4.4 Six-coordinate $S = 2$ Fe(II) Porphyrin Complexes

Although high-spin iron(II) porphyrins are in general five-coordinate with large out-of-plane iron ion displacements, there are exceptions to this rule. In rare cases six-coordinate complexes are formed with the iron in the plane of the porphyrin macrocycle. Examples of such complexes include the bis (N-alkyl)porphyrin with two axial metallocycles reported by Battioni *et al.*,[661] the $[TPPFe^{II}(THF)_2]$ complex described by Reed[662] and reexamined by Lecomte,[663] the THF adduct of $[(F_8TPP)Fe^{II}(THF)_2]$ described by Karlin and Meyer,[664] and the *bis*-alcohol or aqua-coordinated adducts of *meso*-tetrakis(*o*-dichlorophenyl)-ß-octanitroporphyriniron(II).[579] $[TPPFe^{II}(THF)_2]$ is an example of a high-spin complex that is six coordinate.[662] The iron is in the plane of the macrocycle. Magnetic susceptibility measurements ($\mu_{corr} = 5.5\,\mu_B$) and Mössbauer data ($\Delta E_Q = 2.65\,mm\,s^{-1}$ and $\delta = 0.95\,mm\,s^{-1}$ at 77 K; $\Delta E_Q = 2.42\,mm\,s^{-1}$ and $\delta = 0.89\,mm\,s^{-1}$ at 195 K, ΔE_Q of 2.76 $mm\,s^{-1}$ and an isomer shift $\delta = 0.98\,mm\,s^{-1}$ at 4.2 K) confirm the spin state ($S = 2$) of the complex. The quadrupole doublet exhibits narrow lines with ΔE_Q of 2.76 $mm\,s^{-1}$ and an isomer shift $\delta = 0.98\,mm\,s^{-1}$ at

4.2 K. Upon increasing the temperature the isomer shift decreases, consistent with expectations based on the second-order Doppler effect.[662,663] Electron density maps of the complex support the $^5E_{2g}$ ground state with an electronic configuration of $\{(d_{xy})^1(d_{xz},d_{yz})^3(d_{z^2})^1(d_{x^2-y^2})^1\}$.[663] Another high-spin, *bis*-ligated adduct of THF has also been characterized. The structure of $[(F_8TPP)Fe^{II}(THF)_2]$ is characterized by an average Fe–N_{por} bond distance of 2.07 Å with the ferrous iron in the plane of the porphyrin macrocycle. The ^1H NMR spectrum of the complex is that characteristic of a high-spin species. The pyrrole protons give rise to a single signal at 56.7 ppm, the *para*- and *meta*-phenyl protons give rise to the signals in the diamagnetic region at 8.38 and 7.15 ppm, respectively.[664] The electron-deficient *bis*-ethanol, *bis*-propanol, and *bis*-aqua-coordinated adducts of *meso*-tetrakis(*o*-dichlorophenyl)-ß-octanitroporphyriniron(II) complexes are air-stable and extraordinarily difficult to oxidize ($E_{1/2} = +1030$ mV).[579] Consistent with the $S = 2$ spin state are the Mössbauer data of the $(EtOH)_2$-coordinated complex with a quadrupole splitting of 2.136 mm s^{-1} and isomer shift of 0.921 mm s^{-1} at 77 K that decrease to $\Delta E_Q = 2.064$ mm s^{-1} and $\delta = 0.844$ mm s^{-1} at ambient temperature, and Fe–N bond distances of 2.088 Å and 2.095 Å that are slightly longer than those in the THF ligated complex. The porphyrin macrocycle is essentially planar, in contrast to the *bis*-aqua complex, which is ruffled at 100 K and has Fe–N_{por} (1.945 Å) and Fe–O (1.976 Å) bond distances that are atypically short for $S = 2$ Fe(II) porphyrin complexes. Several quintet ground-state configurations are theoretically possible for the electron-deficient complexes, $^5B_{2g}$, $^5A_{1g}$, $^5B_{1g}$, and $^5E_{2g}$. Whether they have the same ground state as the THF-ligated complex ($^5E_{2g}$) remains to be researched.[579]

4.5 Addition of Small Molecules to 5-Coordinate High-spin Iron(II) Porphyrins; Binding of O_2, CO, NO, HNO and Others to Heme Proteins and Their Models

Six-coordinate, diamagnetic Fe^{II} porphyrins have been studied for a variety of reasons; the most relevant ones include the understanding of the mechanism of reversible dioxygen binding to hemoglobin (Hb) and myoglobin (Mb) (*see* ***Iron: Heme Proteins & Dioxygen Transport & Storage***), dioxygen sensors (FixL,[45–48] DosH[49]) or oxidases including cytochrome *c* oxidase (*see* ***Cytochrome Oxidase***). These proteins employ a five-coordinate iron center in their native deoxy states and are high-spin, $S = 2$ species. The sixth coordination site is vacant for binding of dioxygen, carbon monoxide, or other small ligands, such as nitric oxide or isocyanides. Upon dioxygen binding, six-coordinate species are formed, which are diamagnetic and low-spin; that is the spin state changes from $S = 2$ Fe^{II} and $S = 1$ O_2 to $S = 0$ for the complex. Within the proteins, little oxidation occurs to form heme complexes with iron in its +3 oxidation state. As is discussed in the comprehensive review by Momenteau and Reed,[545] the FeO_2 moiety in hemoglobin and myoglobin has been the subject of many reviews and debates. For many years it was discussed whether an iron(II) dioxygen or an iron(III) superoxide formalism was the best description for the FeO_2 moiety. However, in recent years consensus seem to have developed that the best formalism to describe the polar $Fe^{\delta+}$–$O_2^{\delta-}$ bond is as iron(III) superoxo species with the understanding of the limitations of such a description.[545]

Whereas carbonmonoxymyoglobin, MbCO, has been shown to be a diamagnetic species, there has been controversy for some time as to whether oxymyoglobin and oxyhemoglobin indeed exist solely in their diamagnetic states.[665] The existence of a paramagnetic component in oxyhemoglobin has been supported by magnetic susceptibility investigations,[666] the temperature dependence of the Mössbauer quadrupole splitting,[667] and by single crystal Mössbauer studies.[668] $Hb(O_2)_4$ and MbO_2 have been discussed in terms of various possible spin-coupled systems: low-spin ($S = 1/2$) $Fe^{III}/O_2{}^{-}\cdot$, low-spin ($S = 0$) Fe^{II}/singlet O_2, or intermediate spin ($S = 1$) Fe^{II}/triplet O_2.[665] Theoretical studies performed on oxyhemoglobin predict a low-lying triplet state, which can be in thermal equilibrium with the singlet ground state.[669] To investigate whether the thermally populated paramagnetic state can be accommodated, Waleh and Loew have calculated the low-energy triplet states of HbCO and found that the energy of the lowest triplet state is too high to accommodate thermal population of the paramagnetic state.[670] However, it should be noted that the dioxygen complex is obtained when PFe^{III} is reacted with superoxide salts in weakly coordinating solvents (equation 9).[671,672] This suggests a facile valence tautomerism between the two species in equation (9), as discussed again in Section 6.1.

$$PFe^{III} + O_2{}^{-}\cdot \longrightarrow PFe^{II}O_2 \qquad (9)$$

To model the binding of dioxygen to heme proteins is a major task, since reversible oxygen binding without competing autoxidation is very difficult to accomplish in synthetic iron(II) porphyrins,[197,545,673] which are easily oxidized. Hence, proper care is needed in handling the compounds. Simple iron(II) porphyrins bind dioxygen reversibly only at low temperatures (−60 °C), whereas at room temperature, reaction with dioxygen in solution leads to autoxidation and μ-oxo Fe^{III}–O–Fe^{III} dimer formation, as already discussed earlier (Section 1.5). Scheme 2, adapted from the review article of Morgan and Dolphin,[198] highlights the process.

Another problem in mimicking the oxygen uptake by heme proteins is the preference of iron(II) for forming low-spin, six-coordinate Fe^{II} complexes. Nitrogen donor ligands such as pyridines and imidazoles normally coordinate readily to the iron to form complexes of the general type $PFe^{II}B_2$, as discussed above in Section 4.2. While formation of these six-coordinate Fe^{II} complexes impedes irreversible oxidation to the μ-oxo dimer, it also impedes formation of the

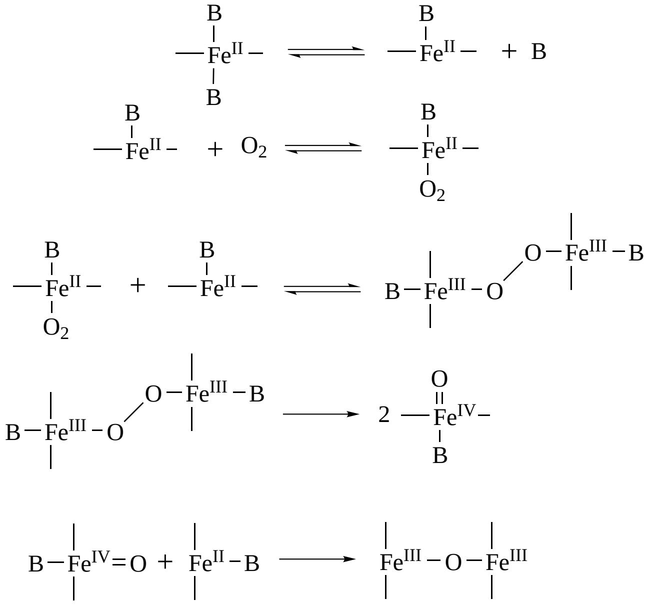

Scheme 2

desired dioxygen complex. Approaches for controlling the coordination of axial ligands in heme models, and for preventing the irreversible oxidation and subsequent formation of the μ-oxo dimers, include use of a hindered ligand, addition of excess ligand (in some cases), metal substitution, immobilization, covalent attachment of one ligand,[642,674,675] or steric blockage or protection of one or both coordination sites of the porphyrin. The approaches that have been developed for designing models that bind dioxygen reversibly are described in more detail elsewhere.[545,546] The wide variety of sterically protected systems include the following porphyrins: 'picket-fence[676,677]', 'picket pocket[676,678,679]', 'tailed picket fence[642]', 'capped[609,680–684]', 'cyclophane[685–687]', 'durene-capped[688]', 'crowned[689]', 'strapped[690–692]', biphenyl strapped,[644] 'gyroscope[693]', 'basket-handle[694,695]', picnic basket handle,[696] cross-trans-linked basket handle,[559] 'chiral '*ansa*' handle[697]', twin coronet,[698] and 'hybrid[647,655]' porphyrins, in which one or both faces of the porphyrin ring are protected by covalently attaching side chains to the macrocycle. (Examples of each of the above and several 'tailed', 'chelated' or 'pendant' hemes are shown in Figure 6). This approach ensures the formation of five-coordinate complexes by allowing the base to bind only to the open face. In addition, the steric blockage of at least one side helps to minimize or prevent μ-oxo dimer formation. Extensive coverage of such approaches is given by Morgan and Dolphin,[198] Momenteau and Reed,[545] and Momenteau.[546]

The mechanisms of binding of small ligands, such as O_2, CO, NO, and isocyanides (*see* ***Dioxygen & Related Ligands***) to model hemes and to heme proteins have been the subject of many investigations (*see* ***Iron: Heme Proteins & Dioxygen Transport & Storage***). It has been suggested that ligand binding to heme proteins may be envisioned in terms of at least the following three steps: (1) diffusion up to and penetration of the ligand into the protein surface, (2) diffusion through the macromolecular structure to reach the sixth coordination site of the iron, and (3) covalent bond formation with concomitant orbital rearrangements and changes in the coordination geometry of the proximal ligand.[701] To assess the significance of such processes and to understand the factors that influence ligand binding in heme proteins, the following approaches have been undertaken: (1) measurement of the rates of rebinding of ligand molecules trapped within various parts of the protein after laser flash photolysis at low temperatures and high viscosities;[702] (2) structure determination of a variety of model heme complexes by X-ray crystallography;[183,548] (3) investigation of the ligand binding properties of five-coordinate ferrous porphyrins;[197,198,676,703–712] and (4) assessment of the influence of ligand size and stereochemistry on the rates and equilibrium constants for ligand binding to hemoglobin by using alkyl isocyanides as the sixth axial ligand.[545,713]

Reversible O_2 binding to synthetic iron(II) porphyrins was first reported by Wang.[714] Since then a variety of porphyrin complexes have been synthesized that reversibly bind dioxygen. In the following section we will address ligand binding to hemoglobin, myoglobin, and cytochrome P450 model complexes and focus on the literature that has not been covered by review articles on binding of O_2, CO, and other ligands to iron(II) porphyrins by Scheidt and Reed,[183] Traylor,[197] Morgan and Dolphin,[198] Collman,[676] Jones *et al.*,[703] Smith and James,[704] Bogatskii and Zhilina,[705] Collman *et al.*,[706,707] Jameson and Ibers,[708] David *et al.*,[709] Baldwin and Perlmutter,[710] Suslick and Reinert,[711] Momenteau and Reed,[545] and Momenteau.[546]

4.5.1 O_2/CO Binding to Models of Hemoglobin and Myoglobin

Investigations of the binding of dioxygen and carbon monoxide to iron(II) porphyrin complexes have provided valuable insights into the structure–function relationships of the dioxygen binding proteins hemoglobin and myoglobin, especially the concepts of cooperative ligand binding by hemoglobin and the factors that influence such binding (*see* ***Iron: Heme Proteins & Dioxygen Transport & Storage***).[708,711] Large differences in the binding constants for dioxygen and carbon monoxide to hemoglobin have been observed. O_2 and CO affinities in heme proteins can vary over a wide range, and a 100- to 600-fold difference in the affinities of the R- and T-states of hemoglobin are observed,[712] with the T-state having lower affinity. For binding of O_2, typical values of $P_{1/2}$(human R-state Hb) $= 1.7 \times 10^{-1}$ mm and $P_{1/2}$(human T-state Hb) $\sim$26 mm Hg,[609,681,715,716] while those of $P_{1/2}$(CO) for human R- and T-state Hb have been found to be $\approx 1-4 \times 10^{-3}$ mm and $1-2.8 \times 10^{-1}$ mm, respectively,[609,681,715,716] where $P_{1/2}$ is the pressure of the

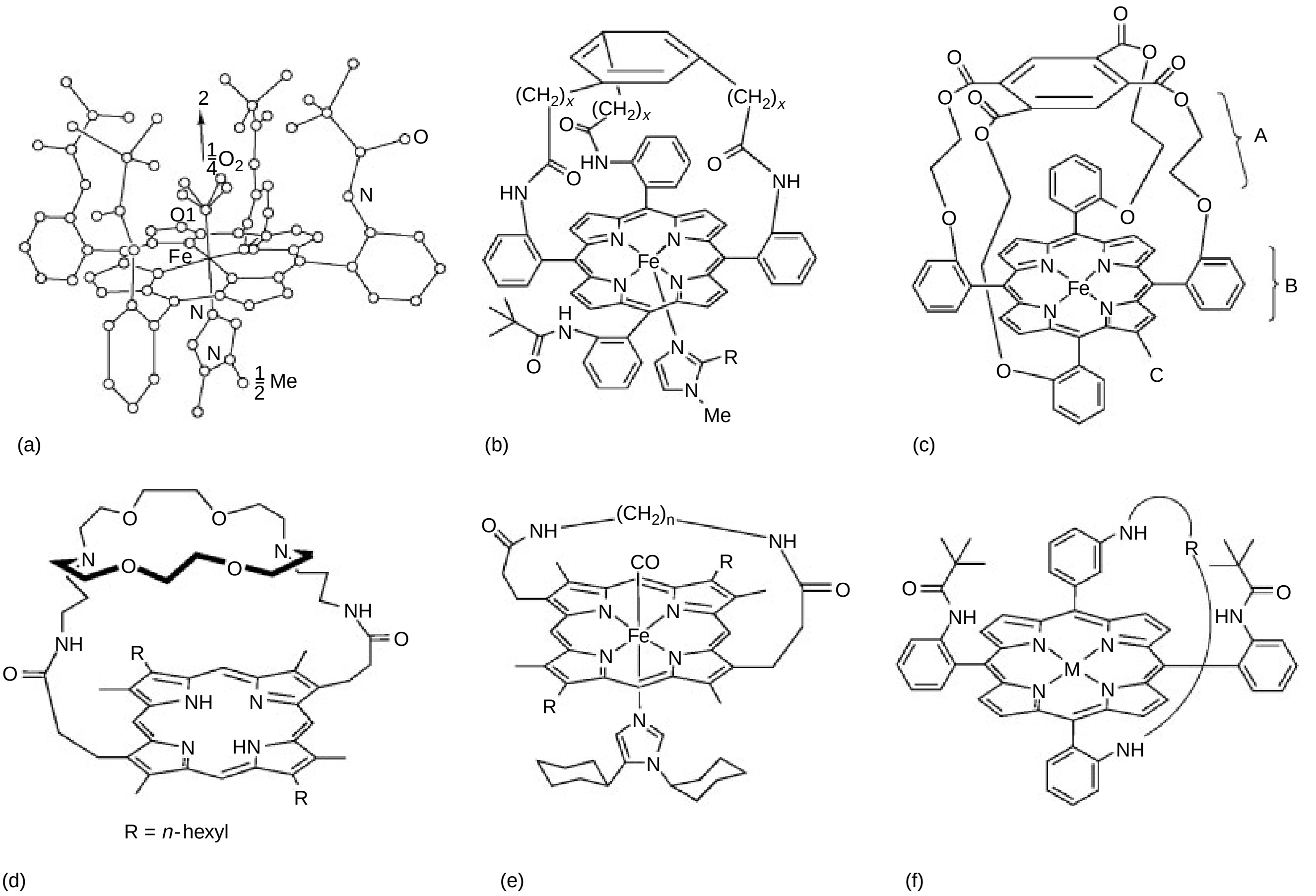

Figure 6 'Superstructured' and 'tailed' iron porphyrins used as models of myoglobin and hemoglobin for the investigation of dioxygen and CO binding to Fe^{II}. (a) The 'picket fence porphyrin' complexed to 2-methylimidazole and dioxygen[699] (b) The 'picket-pocket porphyrin[678]'; (c) 'capped' porphyrins, where the length of the attaching chain (A) (C_2Cap and C_3Cap) and nature of the aryl substituent (B) (phenyl, as in C_2Cap and C_3Cap or naphthyl as in $NapC_2Cap$) have been varied;[609,680,681] (d) 'crowned' porphyrin;[689] (e) 'cyclophane' porphyrins;[685–687] (f) 'hybrid' porphyrins;[586,647,648,650–655] (g) 'strapped' porphyrins;[691] (h) 'tailed picket fence' porphyrins;[642] (i) 'pendant base basket-handle' porphyrins;[700] and (j) 'chelated hemes'[674,675]

corresponding gas necessary to bind to one-half of all hemes in solution. ($P_{1/2}$ is the inverse of the binding constant for the gas, $P_{1/2} = 1/K_f$.). Additional values are given by Momenteau and Reed[545] and Collman.[717]

Equilibrium and Rate Constants. Under physiological conditions, hemoglobin reacts with O_2, CO, and NO to form oxyhemoglobin, $Hb(O_2)_4$, carbonmonoxyhemoglobin, $Hb(CO)_4$, and nitrosylhemoglobin, $Hb(NO)_4$. Comparison of the relative equilibrium constants, $K_{f,rel}$, for formation of the fully loaded complexes:[716,718]

$K_f(O_2)$	$K_f(CO)$	$K_f(NO)$
1.0	4×10^2	5×10^{15}

indicated that CO and NO complexes are much more stable than the O_2 complex. Similar trends are observed for other five-coordinate heme proteins containing iron(II). The reaction with O_2 is reversible, and the dissociation rate is rapid, whereas CO and NO dissociate much more slowly,[719] and typically laser flash photolysis is required to effect dissociation. The relative binding of O_2 and CO to Fe^{II} porphyrins and heme proteins is typically characterized in terms of the ratio $P_{1/2}(O_2)/P_{1/2}(CO)$. The ratio of $P_{1/2}(O_2)/P_{1/2}(CO)$, which is the same as $K_f(CO)/K_f(O_2)$, and is also referred to as the partition coefficient, in heme proteins ranges from 6000 for glycera Hb[720] to 0.075 in Ascaris Hb[721] (i.e. Ascaris Hb is the only heme protein that binds O_2 with greater affinity than CO), whereas those for model compounds range from ≈ 5 in polar environments to $\approx 50\,000$ in toluene or benzene.[686]

The differences in O_2/CO affinities have been the focus of many studies and debates[722] and were for years related to the proposed bent or tilted binding of CO to iron(II) heme proteins. This hypothesis was based on earlier, less well-resolved protein crystal structures, which were interpreted to show that the oxygen atom of the bound CO ligand deviates considerably

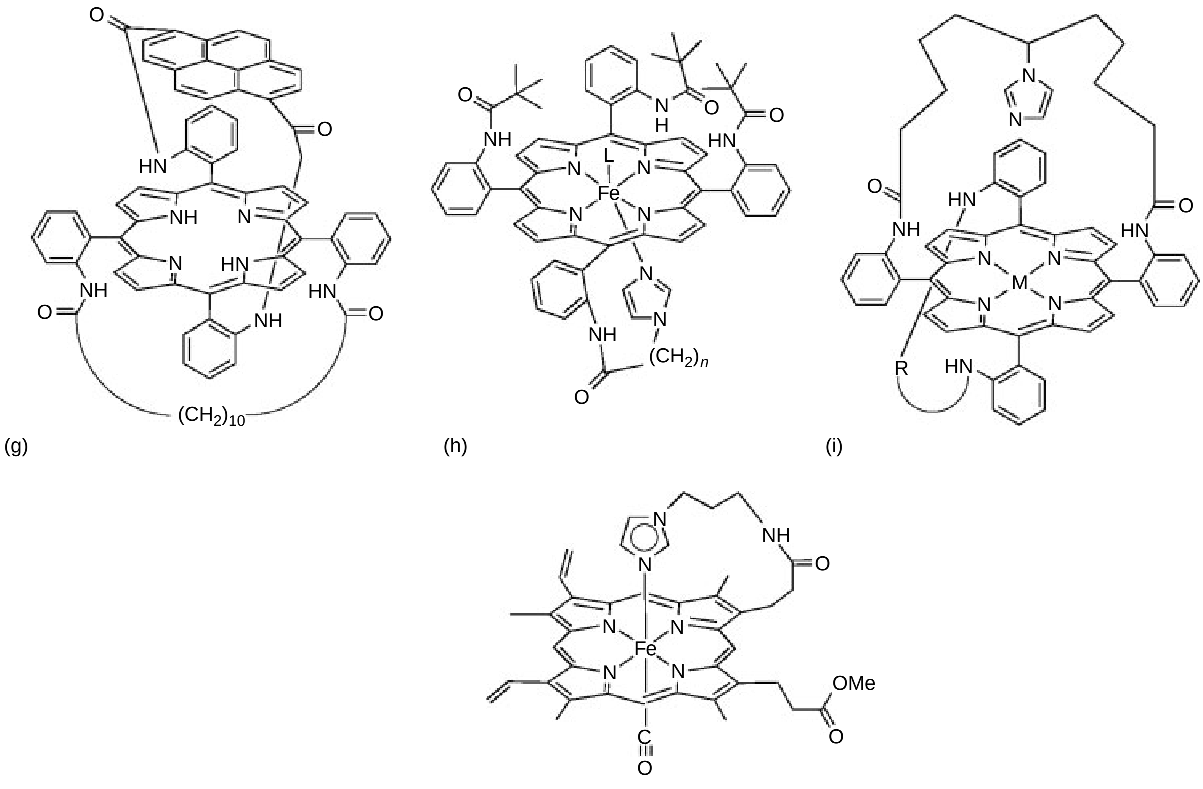

(g) (h) (i)

(j)

Figure 6 cont’d

from the normal to the heme plane.[723–730] This distortion was consequently attributed to nonbonding interactions of nearby distal protein residues with the CO ligand, which were believed to force the CO moiety to adopt the strained/bent or slanted geometry, whereas dioxygen does not experience such strains since it binds naturally in a bent fashion.[617,647,731–735] These steric interferences to ligation, referred to as distal steric effects, were hypothesized to decrease the affinity ratio of CO versus O_2,[692] resulting in discrimination between O_2 and CO binding. The knowledge of such factors that control O_2 or CO binding are believed to play an important role in preventing poisoning of O_2-carrying heme proteins by endogenously or exogenously produced CO.[530,709,733,734,736]

However, the idea of a bent CO adduct has come under increasing scrutiny over the past years.[737] More recent crystal structures of myoglobin do not show the large deviations from linearity that were reported earlier,[737] which is in agreement with most model heme crystal structures that also do not show large deviation from linearity, and with spectroscopic studies.[737] For example, a very recent crystal structure of myoglobin shows displacement of the O atom of the CO bond from linearity by only about 0.3 to 0.6 Å, as is also shown for most model heme complex structures. Thus, the Fe-CO unit seems to prefer a linear geometry to maximize Fe d_π – CO π^* back-bonding. For model hemes, the X-ray structures of various iron(II) porphyrins show that dioxygen adopts the end-on bent geometry,[648,699,736] as in the protein, with an average O–O separation of 1.22 Å and an Fe–O–O angle of 129°,[738] whereas carbon monoxide is shown to bind in a linear fashion to the metal.[641,739,740] Recent crystal structures of protected pocket and capped iron(II) porphyrin complexes demonstrate that the CO moiety is essentially linear. Fe-C-O angles around 178° are quite typical for CO-ligated complexes.[684] However, there is an example of a crystal structure of a sterically encumbered Fe^{II} porphyrin CO complex, [(β-PocPivP)Fe(1,2-Me_2Im)(CO)], which shows that the CO ligand does not necessarily adopt the linear geometry in model hemes.[741] In that structure the bound carbonyl ligand deviates slightly from linearity with the CO moiety being bent and tilted off the axis normal to the porphyrin plane, the Fe–C–O angle being 172.5°,[741] and the off-axis displacement for the C and O atoms are 0.18 and 0.38 Å, respectively. Nevertheless, it should be noted that no structure is available at present that models the large distortions of the Fe–CO unit that were predicted earlier for the proteins.[742,743]

The main distortions that can occur upon CO binding are distortion of the porphyrin ring, such as ruffling, and/or expansion of the porphyrin core, but no significant tilting or bending of the Fe-CO bond.[684] This finding is also supported by ^{13}C CP/MAS studies of heme protein models with axially coordinated N-methylimidazole or 1,2-dimethylimidazole,[744] which showed that 1,2-MeIm coordination has no or little effect on the CO chemical shift and thus presumably the local CO geometry, and thus does not appear to result in a significant increase in bending of the Fe-CO unit. Similar conclusions were also drawn for [(OEP)Fe^{II}(CO)(N-MeIm)]. Solid state NMR spectroscopy coupled with DFT calculations revealed that the Fe-CO bond is close to linear.[745] Thus, at the current state of knowledge it can be at least assumed for myoglobin that the differences in O_2/CO ligand affinities are related to the polarity of the binding pocket and that H-bonding by the distal histidine ligand accounts for about 85% of the O_2/CO discrimination, whereas steric hindrance accounts for the remaining 15%.[737] It remains to be investigated whether this conclusion will also apply to other heme proteins.

Since the idea of the distal effect, that is, the steric interaction between bound CO and distal protein residues that result in a tilt or bend of the Fe-CO bond,[712,716,732,741,746] in altering the binding affinity of small ligands such as CO or O_2, has come under scrutiny,[737] other factors have been considered to explain the differences in O_2 and CO binding. These other factors that have been discussed at length elsewhere[545] include:

1. steric effects on the proximal axial ligand (axial-ligand strain),[732,747]
2. solvent effects,[748,749]
3. ligand stabilization through distal side effects,[750–755]
4. electronic effects associated with the porphyrin (*cis* effect),[609,756–764] and
5. electronic effects associated with the axial ligand (*trans* effect).[604,758,764–769]
6. hydrogen bonding[545]
7. polar interactions in the binding pocket.[744]

Among steric effects, two have been postulated to be of significance for heme proteins and their model complexes:[685] (1) heme deformation that moves the iron atom either toward (proximal push) or away from the incoming ligand (proximal pull) and (2) nonbonding groups that interfere with the approaching or bound ligand. It is believed that the proximal deformation of the heme macrocycle could preferentially stabilize either the five- or the six-coordinate state, resulting in decreased or increased ligand affinity.[685] The proximal pull effect is thought to be responsible for the R- to T-state change in hemoglobin.[685]

To evaluate the importance of the factors discussed above for the discrimination of CO and O_2 binding, a variety of five-coordinate model heme complexes have been synthesized.[198,369,545,546,645,648,653,686] Since addition of ligands such as imidazoles or pyridines to four-coordinate PFe^{II} complexes favors the formation of six-coordinate, diamagnetic complexes, as discussed in Section 4.1.2 (i.e. the open coordination site at the iron, essential to mimic reversible O_2 binding in model hemes, is blocked by the second ligand), it is often necessary to control the addition of ligand or use sterically bulky ligands.

Rate and equilibrium constants for O_2 and CO binding to Fe^{II} hemes have been measured in various solvents and at various temperatures. Dioxygen binding to Fe^{II} porphyrins can be studied at low temperatures by a variety of spectroscopic techniques,[545,708] where reactions that lead to irreversible autoxidation are suppressed. However, at higher temperatures (above ~0 °C) fast *Kinetic Methods*[570,631,633,675,710,770–774] must be employed to measure either the equilibria of dioxygen binding before oxidation takes place, or the kinetics of both O_2 and CO binding. The rates of O_2 and CO association, as well as O_2 dissociation, are conveniently measured by employing photochemical (*see Photochemistry*) techniques, namely nano-[775,776] or picosecond[630,653,685,687,692,701,748,774,777,778] laser flash photolysis techniques (*see* ***Photochemistry of Transition Metal Complexes***). The typical reaction scheme is shown in equation (10).

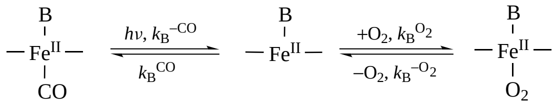

$$\underset{\mathrm{CO}}{\overset{\mathrm{B}}{-\mathrm{Fe}^{II}-}} \underset{k_B^{CO}}{\overset{h\nu,\ k_B^{-CO}}{\rightleftharpoons}} \overset{\mathrm{B}}{-\mathrm{Fe}^{II}-} \underset{-O_2,\ k_B^{-O_2}}{\overset{+O_2,\ k_B^{O_2}}{\rightleftharpoons}} \underset{O_2}{\overset{\mathrm{B}}{-\mathrm{Fe}^{II}-}} \qquad (10)$$

If the observed rate constant, k_{obs}, is defined as k_{return}, that for the return to the CO-ligated complex before O_2 is added, the kinetics are then described by equation (11):

$$\frac{1}{k_{\mathrm{return}}} = \frac{1}{k_B^{O_2}} + \frac{K_B^{O_2}[O_2]}{k_B^{CO}[CO]} \qquad (11)$$

and $k_B^{O_2}$ and $k_B^{-O_2}$ can be calculated from a plot of $1/k_{return}$ versus $[O_2]$.

Thermodynamic and kinetic data obtained by flash photolysis methods have indeed increased the understanding of O_2 and CO binding in heme proteins and have revealed that two factors, namely distal steric[197,198,686,687,706,708,711,779] and polarity effects,[197,545,686,694,709,711,749,780–785] appear to be important for the discrimination of O_2 and CO binding to simple Fe^{II} porphyrins. The '*ansa*' hanging basket porphyrin bridged by – CH_2–C_6H_4–CH_2 – appears to have the closest match of $P_{1/2}(O_2)/P_{1/2}(CO)$[779] to those reported for hemoglobins,[708,786] of models investigated thus far. The importance of the distal steric effect has been discussed by Tetreau *et al.*,[778] who showed for so-called 'hybrid' model complexes that increasing distal steric hindrance, by changing the length of the carbon chain, results in a reduction by a factor of 2500 of the affinity constant of CO, while dioxygen binding is reduced by less than a factor of 5. It was further shown that change in the carbon chain length affects only the CO association rate, whereas for O_2 binding, both association and dissociation rates are unchanged. Hence it was concluded that constraining the handle in such compounds results in increased sensitivity of both the rate and equilibrium constants upon changing the length of the distal chain.

To understand these effects, the profile of the energy barriers was also investigated. The compounds were found to react according to a double-energy barrier scheme, where the ligand must first overcome a free energy barrier due to steric hindrance on the distal side. This external barrier and the height of the top of the internal barrier are associated with bond formation and found to increase with encumbered hemes. Changes in $\Delta G^{\ddagger}$ are almost identical for CO and O_2 binding, confirming that steric discrimination against CO does not occur in the transition state.[785] Steric effects were also named as reasons for discriminating against CO binding in ether-linked capped systems.[683] It was shown that four-atom capped porphyrin systems discriminate against CO binding to an extent unknown in other models. Whereas the amide linked systems did not bind O_2 or CO even at very high partial pressures, the ether-linked systems had exceptionally high values of $P_{1/2}(CO)$ (100 torr at 25 °C), which was ascribed to steric effects induced by the attachment of the benzene cap.[683] Tang and Dolphin,[682] however, showed for other capped complexes that the introduction of the amide functionality to the distal cage increases the O_2 affinity of these systems and suggested that hydrogen-bonding plays an important role in stabilizing O_2 binding and differentiating between O_2 and CO binding. Traylor[780] argued that the differentiation between O_2 and CO binding may be accomplished by solvent or local polarity effects, and not by steric effects, a conclusion that has been subject to some controversy, but seems to be generally accepted.[780,784,785] Studies performed for 3,5-pyridine-5,5-cyclophane heme[687] and other systems[780] confirmed that the differentiation of O_2 and CO binding, that is, the value of $P_{1/2}(O_2)/P_{1/2}(CO)$, is strongly determined by polarity effects. Steric differentiation, observed in the association rates, was found to be controlled by the shape and size of the ligand, but not by the geometry of the bound state.[780]

In an earlier study, Stanford *et al.*[758] showed, by measuring the rates of CO binding to Fe^{II} porphyrins, that electronic control through π donor/acceptor interactions with the macrocycle is not an important consideration in controlling the reactivity of heme proteins toward O_2 and CO. Their study, however, confirmed that control through changes in the electronic properties of the metal-bound imidazole can have a large influence on the heme reactivity. Effects of electronic and steric changes in the equatorial plane of the porphyrin on the addition of axial ligands, such as oxygen and carbon monoxide, have also been examined by investigation of modified cap porphyrin complexes.[609] It was found that placing electron-withdrawing groups on the porphyrin ring, that is, transferring electron density away from the porphyrin macrocycle, stabilizes ligation by nitrogen bases, but destabilizes the dioxygen complex. Similar conclusions were reached earlier concerning the binding of nitrogen bases and dioxygen to cobalt(II) porphyrins.[766,787–792] It was further observed that the solvent effect on O_2 binding by the capped complexes is small, suggesting that the environment of the dioxygen bound inside the cap is protected from changes in solvent effects.[609]

Lopez and Kollman applied molecular dynamics and free energy perturbation computational techniques to simulate O_2 and CO binding to cyclophane, picket fence, and monochelated hemes.[793] These calculations showed that in 5,5-pyridinecyclophane heme and in the picket fence heme complex, O_2 binding is favored over CO binding, whereas in the monochelated heme and in 7,7-durenecyclophane heme, binding of CO is favored over O_2,[793] consistent with a distal steric effect playing an important role in discrimination.

The rates and equilibrium constants for dioxygen and carbon monoxide binding to model hemes have been reviewed by several authors, and selected kinetic and thermodynamic data for O_2 and CO binding are summarized in Table 2. Analysis of the data listed in Table 2 suggests that, in addition to distal steric and polarity effects, other factors need to be considered for the differentiation in O_2 and CO binding to Fe^{II} model complexes. These include other steric effects, such as proximal effects (i.e. it has been shown that the overall rates of ligand binding decrease if the fifth ligand is bulky and presents steric strain to the polar heme structure),[616,617,678] strain and blocking effects,[794] and effects such as molecular reorganization, solvation energy effects, solvent polarity, hydrogen-bonding, dipole–dipole interactions, intramolecular solvating of coordinated ligands, intrinsic affinity, and electron donation to the porphyrin or fifth ligand.[708,709,711,780,795–800] The suggestion that a combination of factors must be considered to understand O_2/CO binding is corroborated by studies of picnic basket porphyrin iron(II) complexes.[696] For these and those of other sterically encumbered picket fence, pocket, and basket-handle porphyrin complexes it was concluded that the dramatic variations in the observed O_2 affinities may be due to the combined effects of the electronic and structural nature of the porphyrin, solvation, and particularly the polarity of the dioxygen binding site and dipole–dipole or H-bonding interactions between bound dioxygen and protons of neighboring functional groups.

For a ferrous complex of hemiporphycene incorporated into the pocket of sperm whale apomyoglobin to form a functionally active Fe(II) myoglobin, it was shown that the system was able to bind O_2 and CO reversibly.[802] The O_2 affinity was 12-fold higher than that of the native myoglobin, while CO affinity was slightly lower, suggesting a decreased discrimination between O_2 and CO in the pocket. This functional anomaly was interpreted to reflect increased σ-bonding character in the Fe^{II}–O_2 bond. Similar observations were made by Hayashi *et al.* for ‘blue myoglobin’, reconstituted with an iron porphycene. The association rate of the ferrous rMb was 5 fold faster than that of the native protein.[803]

Although many interesting iron(II) porphyrin complexes have been synthesized that bind dioxygen reversibly, they are not suitable for achieving the cooperative O_2 binding profile of hemoglobin or myoglobin. However, entirely synthetic

Table 2 Kinetic and equilibrium parameters for O_2 and CO binding in model heme complexes

Compound	$k_{\mathrm{on}}(O_2)$ ($M^{-1}\,s^{-1}$)	$k_{\mathrm{on}}(CO)$ ($M^{-1}\,s^{-1}$)	$k_{\mathrm{off}}(O_2)$ (s^{-1})	$k_{\mathrm{off}}(CO)$ (s^{-1})	$P_{1/2}(O_2)$ (Torr)	$P_{1/2}(CO)$ (Torr)	$P_{1/2}(O_2)$/ $P_{1/2}(CO)$	Solvent
Myoglobin[678,716]	$(1-2)\cdot 10^{7}$	$(3-5)\cdot 10^{5}$	10–30	0.0015–0.04	0.37–1	0.014–0.025	20–40	H_2O
Hemoglobin								
R-state[708]	$3\cdot 10^{7}$	$4.6\cdot 10^{6}$	13	0.009	0.15–1.5	$(1-4)\cdot 10^{-3}$	200–250	H_2O
T-state[795]	$7\cdot 10^{6}$	$2.2\cdot 10^{5}$	1340	0.09	9–160	$(1-2.8)\cdot 10^{-1}$	32–1600	H_2O
Tetramesitylporphyrin[610]								
$TMPFe^{II}$ + N-MeIm	–	$3.29\cdot 10^{6}$	–	0.0109	–	$3.36\cdot 10^{-4}$	–	Toluene
$TMPFe^{II}$ + 1,2-Me_2Im	–	$8.43\cdot 10^{5}$	–	0.06	–	$7.23\cdot 10^{-3}$	–	Toluene
Tetraphenylporphyrin[610]								
$TPPFe^{II}$ + N-MeIm	–	$2.52\cdot 10^{6}$	–	0.0171	–	$6.9\cdot 10^{-4}$	–	Toluene
$TPPFe^{II}$ + 1,2-Me_2Im	–	$8.2\cdot 10^{4}$	–	0.09	–	$1.11\cdot 10^{-1}$	–	Toluene
Picket-fence porphyrins[678]								
R-state	$4.3\cdot 10^{3}$	$3.6\cdot 10^{7}$	2900	0.0078	0.58	$2.2\cdot 10^{-5}$	26600	Toluene
T-state	$1.1\cdot 10^{8}$	$1.4\cdot 10^{6}$	46000	0.14	38	$8.9\cdot 10^{-3}$	4300	Toluene
Picket-pocket porphyrin[678]								
FePocPiv(1-MeIm)	$2.2\cdot 10^{6}$	$5.8\cdot 10^{5}$	9	0.0086	0.36	$1.5\cdot 10^{-3}$	270	Toluene
FePocPiv(1,2-Me_2Im)	$1.9\cdot 10^{6}$	$9.8\cdot 10^{4}$	280	$5.5\cdot 10^{-2}$	12.6	$6.7\cdot 10^{-2}$	216	Toluene
FeMedPoc(1-MeIm)	$1.7\cdot 10^{7}$	$1.5\cdot 10^{6}$	71	$9.4\cdot 10^{-3}$	0.36	$6.5\cdot 10^{-4}$	550	Toluene
FeAmPoc(1,2-Me_2Im)	–	–	–	$5.0\cdot 10^{-2}$	–	–	–	Toluene
Bis-pocket porphyrin[783]	–	–	–	–	640	$8.0\cdot 10^{-3}$	80000	Mesitylene
					473	$9.2\cdot 10^{-3}$	51000	Benzene
					227	$1.6\cdot 10^{-2}$	14000	*o*-Cl_2benzene
Chelated hemes								
Short tail[732]	$4.9\cdot 10^{7}$	–	160	–	1.8	–	–	Toluene
Medium tail[732]	$2.2\cdot 10^{7}$	$1.1\cdot 10^{7}$	23	0.015	0.57	$1.0\cdot 10^{-3}$	600	Toluene
Long tail[678]	$2.9\cdot 10^{7}$	–	24	–	0.45	–	–	Toluene
Chelated TP heme[678]	$2.9\cdot 10^{7}$	$4.2\cdot 10^{6}$	30000	∼ 0.04$	83	$\sim 1\cdot 10^{-3}$	∼8000	Toluene
Chelated protoheme[796,797]	$2.6\cdot 10^{7}$	$3.6\cdot 10^{6}$	47	0.009	1.0	0.0018	560	H_2O/MTAB
	$6.2\cdot 10^{7}$	$1.1\cdot 10^{7}$	4000	0.025	5.6	0.00025	22400	Benzene
Chelated mesoheme[686,687]	$5.3\cdot 10^{7}$	$8\cdot 10^{6}$	1700	0.05	2.8	0.0005	5600	Toluene/ 10% CH_2Cl_2
	$8.4\cdot 10^{7}$	$1.1\cdot 10^{7}$	4800	∼0.05	4.9	–	–	Toluene
Strapped heme								
Tight strap[692]	$3\cdot 10^{5}$	$8\cdot 10^{3}$	–	0.04	–	0.5	–	–
Loose strap[711]	$1.7\cdot 10^{6}$	$9.1\cdot 10^{4}$	250	0.04	15	0.05	300	–
Capped porphyrins								
Fe(C_2-Cap)(1-MeIm)[609]	–	$9.5\cdot 10^{-5}$	–	0.05	23	$5.4\cdot 10^{-3}$	4300	Toluene
Fe(C_2-Cap)(1,2-Me_2Im)[609]	–	–	–	–	4000	$2.0\cdot 10^{-1}$	200	Toluene
Fe(C_3-Cap)(1,5-DCI)[609]	–	$4.1\cdot 10^{6}$	–	0.17	54	$4.1\cdot 10^{-3}$	13170	Toluene
Fe(C_4-Cap)(1,2-Me_2Im)[798]	–	–	–	–	–	4.1	–	Toluene
Fe(C_4-Cap)(1,5-DcIm)[798]	–	–	–	–	–	$2.1\cdot 10^{-2}$	–	Toluene
‘Hybrid’ Hemes								
Short strap[655,799]	$2.2\cdot 10^{6}$	$8\cdot 10^{4}$	2.0	$8.3\cdot 10^{-3}$	$1.0\cdot 10-1$	$1.1\cdot 10^{-2}$	7	Toluene
Long strap[655,799]	$6.2\cdot 10^{8}$	$6.3\cdot 10^{7}$	$1.3\cdot 10^{2}$	$2.7\cdot 10^{-3}$	$3.0\cdot 10^{-2}$	$4.4\cdot 10^{-6}$	4960	Toluene
‘Jellyfish Porphyrins’								
Fe(AzP)(1,2-Me_2Im)[800]	–	–	–	–	27	0.083	325	Toluene
Fe(Azvalbb)(1,2-Me_2Im)[800]	–	–	–	–	12	0.029	414	Toluene
Fe(Azpivbb)(1,2-Me_2Im)[800]	–	–	–	–	269	0.27	996	Toluene
Cyclophane Porphyrins								
7,7-Anthracene[797]	$6.5\cdot 10^{7}$	$6.0\cdot 10^{6}$	1000	0.05	1.4	0.0009	1500	Benzene
6,6-Anthracene[797]	$1.0\cdot 10^{5}$	$3.0\cdot 10^{4}$	800	0.05	700	0.17	4000	Benzene
6,6-Adamantane[686,687]	$1.5\cdot 10^{5}$	$9.2\cdot 10^{3}$	690 (540)	0.05	300	0.59	530	Toluene
6,6,6 Cyclophane[686,687]	$1.7\cdot 10^{7}$	$1.5\cdot 10^{6}$	71	0.0093	0.36	$6.5\cdot 10^{-4}$	550	Toluene
5,5,5 Cyclophane[678]	$2.2\cdot 10^{6}$	$5.8\cdot 10^{5}$	9	0.0086	0.36	$1.5\cdot 10^{-3}$	270	Toluene
7,7,7 Cyclophane[678]	–	$9.5\cdot 10^{5}$	–	0.05	23	$5.0\cdot 10^{-3}$	4300	Toluene
Chel. 18-cyclophane[678]	$1.8\cdot 10^{8}$	$4\cdot 10^{7}$	620	0.0067	0.29	$1.7\cdot 10^{-5}$	17000	Toluene

Table 2 cont'd

Compound	$k_{on}(O_2)$ ($M^{-1}\,s^{-1}$)	$k_{on}(CO)$ ($M^{-1}\,s^{-1}$)	$k_{off}(O_2)$ (s^{-1})	$k_{off}(CO)$ (s^{-1})	$P_{1/2}(O_2)$ (Torr)	$P_{1/2}(CO)$ (Torr)	$P_{1/2}(O_2)/P_{1/2}(CO)$	Solvent
5,5-Pyridine[686]	$1.1 \cdot 10^4$	$6 \cdot 10^2$	68	0.24	540	37	14	Toluene
	–	–	–	–	290	62	5	o-Cl_2benzene
13-Cyclophane[692]	–	$6 \cdot 10^2$	–	0.07	–	12	–	Benzene
15-Cyclophane[692]	$1.7 \cdot 10^6$	$9.1 \cdot 10^4$	250	0.04	15	0.05	300	Benzene
Hanging-base porphyrins								
'Amide' hanging[801]	$3.6 \cdot 10^8$	$3.5 \cdot 10^7$	5000	–	2	–	–	Toluene
'Ether' hanging[801]	$3.0 \cdot 10^8$	$6.8 \cdot 10^7$	40000	–	18.6	–	–	Toluene
Amide 'ansa' short hanging[779]	–	$7.0 \cdot 10^4$	–	3.5	–	5.5	–	Toluene
Amide 'ansa' long hanging[779]	–	–	–	–	21	0.2	105	Toluene

O_2-carrying heme proteins have recently been synthesized by incorporating hydrophobic pivalamido porphyrin iron(II) complexes ($T_{Piv}PFe^{II}(ImH)$ bearing a covalently linked axial imidazole into recombinant human serum albumin (HSA).[804–810] In these red-blood substitutes the iron(II) porphyrin is present as five-coordinate high-spin Fe(II) complexes that are non-covalently bonded to HSA. Up to an average of eight $Fe^{II}P$ are bonded per HSA molecule with stepwise equilibrium constants ranging from 1.2×10^6 to 1.3×10^4.[809] These so-called human serum albumin-heme hybrids are remarkable, since they reversibly bind and release dioxygen under physiological conditions (pH = 7.4, 37 °C), thereby closely mimicking the behavior of Hb and Mb.[805–809] The red-colored solution is stable for up to three months at 4 °C and satisfies the physiological requirements for dioxygen infusion.[809] The dioxygen affinity $P_{1/2}(O_2)$ and O_2 transporting efficiency of HSA-Fe(II)P are 30 torr and 22%, respectively.[810] The kinetics of CO binding were suggested to occur in three phases (fast axial-ligand elimination, and slower recombination of the CO to the five-coordinate HS Fe^{II} ion). The rate constants ranged from $4.9 \times 10^6\,M^{-1}\,s^{-1}$ to $6.7 \times 10^5\,M^{-1}\,s^{-1}$.[804] In addition the oxygen binding and dissociation constants are extremely high in comparison to those of Hb.[810] However, the half-life of the dioxygen adduct with imidazole as axial ligand is short, 1 h at 37 °C[810] and 2 h under a 100% oxygen atmosphere.[804] The lifetime of the O_2 adduct, however, was lengthened by modifying the nature of the Fe^{II} porphyrin. When the substituents on the pickets were changed and histidine was coordinated as the axial ligand, the O_2 binding was significantly increased as was the lifetime of the O_2 adduct. Histidine coordination led to a lifetime of 25 h at 37 °C, which is 13 times longer than that of the unmodified $T_{Piv}PPFe(Im)$ systems.[804] From these observations it was concluded that rather than chemical modifications of the pickets being responsible for the improved oxygen binding, axial histidine coordination, that is, the molecular environment of the coordination site, is a major factor in modulating O_2 binding affinities. Tsuchida's laboratory also showed that self-assembled lipid porphyrin bilayer vesicles can act as totally synthetic O_2 carriers under physiological conditions. These systems also bind dioxygen reversibly.[811]

Heme-ligand model systems, such as $PFe^{II}BL$ with PFe^{II} = a picket fence porphyrin Fe(II) complex, B = methyl- or dimethylimidazole, and L = O_2 or CO, also proved useful for exploring the detailed kinetics of photodissociation-geminate recombination within the solvent cage.[679] It was shown that cage recombination efficiency in toluene after photolysis with 314 nm laser light is about 43%, when methylimidazole is used as base, but only 20% when dimethylimidazole is used. Geminate rebinding of CO was shown to be only 10% efficient. The addition of CO to deoxy heme proteins was shown to be a two-step process: diffusion of CO into the heme pocket and geminate recombination with the iron ion, which is typically the rate-determining step. The kinetics are complex, with a distribution of barriers centered around 2.5 kcal mol^{-1} in the case of the low-temperature reaction of photolyzed Mb-CO. Upon warming the distribution shifts to reach a value of 5 kcal mol^{-1} at temperature > 170 K.[812] DFT calculations were recently used to characterize the intrinsic barrier to the CO recombination reaction.[812] The ground state of deoxyheme was found to be a $^5A'$ state in C_s symmetry, with the excited $^5A''$, $^3A'$, and $^3A''$ lying 1–2 kcal mol^{-1} higher in energy, which revealed that the computed energies and geometries are in good agreement with experimental data.[812]

To lay the foundation for applying CO flash photolysis fast time-scale studies to cytochrome *c* model heme chemistry, flash photolysis studies were used to resolve the CO rebinding kinetics for the low-spin ($S = 0$) cytochrome *c* model heme $[(F_8TPP)Fe^{II}(CO)(THF)]$ in both THF and cyclohexane. In CO-saturated THF, the conversion of $[(F_8TPP)Fe^{II}(THF)_2]$ to $[(F_8TPP)Fe^{II}(CO)(THF)]$ was monoexponential, with $k_{obs} = 1.6\,(\pm 0.2) \times 10^4\,s^{-1}$. Reduction in the concentration of CO by vigorous Ar purging gave a $k_{obs} = 10^3\,s^{-1}$ in cyclohexane.[664]

As mentioned above, only a few Fe^{II} porphyrins do not undergo reversible oxygenation. In addition to the sterically protected complexes, discussed above, the reaction of *N*-methylporphyrin with $FeCl_3$ in the presence of Fe^0 leads to the formation of the air-stable chloro(*N*-methylporphinato)iron(II).[158] $TPPFe^{II}$ synthesized by laser photolysis of $\mathrm{TPPFe^{III}Cl}$ in methanol reacts with dioxygen to give the $\mathrm{TPPFe^{II}O_2}$ adduct, which dissociates to regenerate $[\mathrm{TPPFe^{III}}]^+$ and form the $\mathrm{O_2}^-$ radical.[813] Due to the presence of the coordinatively restrictive *N*-methylporphyrin ligand the $\mathrm{Fe^{II}}$ oxidation state is stabilized in this complex. Oxidation and the well-established phenomenon of dimerization of $\mathrm{Fe^{II}}$ porphyrins can also be prevented if six-coordinate low-spin $\mathrm{Fe^{II}}$ porphyrins are produced and embedded in a micellar environment.[801]

UV-visible Spectra. Some synthetic diamagnetic $\mathrm{Fe^{II}}$ porphyrin complexes with various axial ligands have spectroscopic properties similar to the heme proteins. UV-visible spectra of the six-coordinate CO and $\mathrm{O_2}$ complexes are characterized by three bands, the Soret band and the $\mathrm{Q}(0,0) = \beta$ and $\mathrm{Q}(1,0) = \alpha$ bands.[223] The CO complex of Traylor's chelated protoheme has Soret, β, and α bands at very similar wavelengths (420, 540, 569 nm) to those of carbonmonoxyhemoglobin (419, 540, 569 nm),[197] while the spectra of CO complexes of TPP-based models with imidazole ligands are slightly shifted and often do not have separate α and β bands, but rather a broad combined α,β band (Soret at 422–427 nm, α,β at 540–542 nm).[641,653,677,700,814] Myoglobin-CO derivatives typically have absorptions at around 420, 540 nm, and 570 nm.[815,816] Often there is a shoulder observed near 580 nm for both the models and the proteins.[700,814–816] For the CS complex of $\mathrm{TPPFe^{II}}$(N-MeIm), the $\lambda_{\max}$ values are 425, 547, 583 nm,[817] and for the CSe complex they are nearly identical (426, 547, 583 nm).[818] For the corresponding $\mathrm{O_2}$ complexes, again the chelated protoheme and oxyhemoglobin have similar $\lambda_{\max}$ values (414, 575, 543 nm and 415, 577, 541 nm, respectively),[197] while $\mathrm{TPPFe^{II}O_2}$ derivatives with imidazole ligands have slightly shifted spectra (Soret at 425–429, α,β at 546–549 nm,[641,653,677,700] occasionally with a shoulder near 582 nm[700]). Hindered imidazoles as the 'proximal' base cause slight shifts of the $\lambda_{\max}$ values for both CO (424, 542 nm) and $\mathrm{O_2}$ (421, 544 nm) complexes of TPP derivatives,[677] and for the CO complex of the chelated protoheme (420, 540, 569 nm).[769] Providing a 'congested' binding site for CO complexes, with strapped porphyrins, decreases the intensity of the Soret band and shifts the α,β band to lower wavelength, as in the series of $[\mathrm{(Piv)_2(C}_n\mathrm{)TPPFe^{II}(N\text{-}MeIm)(CO)}]$ complexes having $n = 12$ (541 nm), 10 (537 nm), 9 (520 nm), and 8 (514 nm).[653] Similarly, the diamidopyrene strapped TPP derivative of Weiss and coworkers has the Soret maximum at 432 nm and the α,β band at 526 nm.[691] Much smaller shifts from the $\lambda_{\max}$ values quoted above are observed in the band maxima of the dioxygen complexes.[653,691] MCD spectra of five-coordinate high-spin and six-coordinate low-spin complexes of $\mathrm{Fe^{II}}$ porphyrin and chlorin models have been reported.[819]

Vibrational Spectra. The IR spectra of the hexacoordinate carbonyl complexes of model hemes and the proteins show characteristic ν_{CO} stretching frequencies. Those of the α and β subunit CO moieties of carbonmonoxyhemoglobin are $\nu_{\mathrm{CO}} = 1951$ and $1952\ \mathrm{cm^{-1}}$,[764] while for TPP-derived model compounds, $\nu_{\mathrm{CO}} = 1965\ \mathrm{cm^{-1}}$ for $[\mathrm{(Piv)_4TPPFe^{II}(N\text{-}MeIm)(CO)}]$.[677] For the four $[\mathrm{(Piv)_2(C}_n\mathrm{)TPPFe^{II}(N\text{-}MeIm)(CO)}]$ complexes mentioned above, the ν_{CO} band shifts $10\ \mathrm{cm^{-1}}$ to lower frequency as the chain is shortened from 12 to 8 carbons ($1958 \rightarrow 1948\ \mathrm{cm^{-1}}$),[653] but for the diamidopyrene strapped TPP derivative, $\nu_{\mathrm{CO}} = 1980\ \mathrm{cm^{-1}}$.[691] For the CS and CSe complexes of $\mathrm{TPPFe^{II}}$(N-MeIm), $\nu_{\mathrm{CS}} = 1278\ \mathrm{cm^{-1}}$,[817] and $\nu_{\mathrm{CSe}} = 1140\ \mathrm{cm^{-1}}$.[818] For $\mathrm{Fe^{II}}$ $\mathrm{Hb(NO)_4}$ and MbNO, $\nu_{\mathrm{NO}} \sim 1623\ \mathrm{cm^{-1}}$, and $\nu_{\mathrm{Fe\text{–}NO}} \sim 551\ \mathrm{cm^{-1}}$.[820] To find the FeCO bending fundamental, resonance Raman spectra in the range of $200–600\ \mathrm{cm^{-1}}$ were acquired for CO-coordinated hemoglobin, and myoglobin, and also cytochromes *c* and P450. A new CO-isotope sensitive band near $365\ \mathrm{cm^{-1}}$ was found for all proteins except MbCO where the band was found at $575\ \mathrm{cm^{-1}}$. These results were interpreted to suggest that the $365\ \mathrm{cm^{-1}}$ mode is due to the FeCO fundamental, whereas the $575\ \mathrm{cm^{-1}}$ mode is a result of its combination with a porphyrin vibration and/or Fe-C deformation mode.[821] For ferrous chlorin complexes the Fe-C-O mode was found at around $500–530\ \mathrm{cm^{-1}}$.[822] More recently, the Fe–NO stretching frequencies of $\mathrm{Fe^{II}}$–NO and $\mathrm{Fe^{III}}$–NO complexes have been reported. For $\mathrm{PFe^{II}NO}$, $\nu_{\mathrm{Fe\text{–}NO}} \sim 527\ \mathrm{cm^{-1}}$; upon oxidation to $\mathrm{PFe^{III}NO}$, $\nu_{\mathrm{Fe\text{–}NO}}$ shifts to $602\ \mathrm{cm^{-1}}$.[823] Addition of a pyridine or imidazole ligand to the sixth coordination site has very little effect on $\nu_{\mathrm{Fe\text{–}NO}}$ for either oxidation state.[823] A detailed study of the vibrational spectra of a large number of PFeCO model hemes has appeared.[824]

Mössbauer Spectra. Debrunner has summarized the Mössbauer data of a variety of model heme complexes, including CO and $\mathrm{O_2}$ complexes of pentacoordinate $\mathrm{Fe^{II}}$ porphyrins with nitrogen bases as fifth ligands. For [PFe(L)(CO)] complexes, values of $0.21\ \mathrm{mm\,s^{-1}} < \delta\mathrm{Fe} \leq 0.32\ \mathrm{mm\,s}-1$ and $0 \leq \Delta E_Q \leq 0.94\ \mathrm{mm\,s^{-1}}$, typical of diamagnetic FeII, are reported,[177] whereas for the dioxygen complexes $[\mathrm{PFe(L)(O_2)}]$, although the isomer shift is also small ($0.23 \leq \delta_{\mathrm{Fe}}(4.2\ \mathrm{K}) \leq 0.32\ \mathrm{mm\,s^{-1}}$), the quadrupole splitting is relatively large ($\Delta E_Q = (-2.23 \pm 0.15)\ \mathrm{mm\,s^{-1}}$).[177] For some complexes, substantial temperature dependence of the quadrupole splitting has been observed. Some of these values agree well with those obtained for hemoglobin and myoglobin: for $\mathrm{Hb(O_2)_4}$, $\delta_{\mathrm{Fe}}(4.2\ \mathrm{K}) = 0.27\ \mathrm{mm\,s^{-1}}$, $\Delta E_Q = -2.25\ \mathrm{mm\,s^{-1}}$; for $\mathrm{Hb(CO)_4}$, $\delta_{\mathrm{Fe}}(4.2\ \mathrm{K}) = 0.26\ \mathrm{mm\,s^{-1}}$, $\Delta E_Q = 0.36\ \mathrm{mm\,s^{-1}}$;[825] for $\mathrm{MbO_2}$, $\delta_{\mathrm{Fe}}(4.2\ \mathrm{K}) = 0.27\ \mathrm{mm\,s^{-1}}$, $\Delta E_Q = -2.31\ \mathrm{mm\,s^{-1}}$;[826] and for MbCO, $\delta_{\mathrm{Fe}}(4.2\ \mathrm{K}) = 0.27\ \mathrm{mm\,s^{-1}}$, $\Delta E_Q = +0.35\ \mathrm{mm\,s^{-1}}$.[827] Both the large size of the ΔE_Q of the dioxygen complexes and the temperature dependence of some of them have been considered incompatible with a low-spin $\mathrm{d^6}$ ($S = 0$) ground state until 1991, when it was shown that the five-coordinate, low-spin, anionic complex $[\mathrm{(Piv)_4TPPFe^{II}(NO_2)}]^-$ also has a large quadrupole splitting ($\Delta E_Q = 2.28\,\mathrm{mm\,s^{-1}}$, $\delta = 0.41\,\mathrm{mm\,s^{-1}}$, neither with appreciable temperature dependence).**637** It thus appears that the large quadrupole splitting arises from a significant difference in the energies of the d_{xz} and d_{yz} orbitals due to the binding of the planar nitrite ion. It was concluded that 'the origin of the large ΔE_Q for the nitro- and oxyheme derivatives is the same, namely, a large rhombicity in the heme plane'.**637** For bis-ligated $\mathrm{Fe^{II}}$ porphyrins, $\mathrm{PFe^{II}LL'}$, where L and L′ are either nitrogen or phosphorus donors, the following values of δ_{Fe} and ΔE_Q are characteristic: $0.33\,\mathrm{mm\,s^{-1}} \leq \delta_{\mathrm{Fe}}(4.2\,\mathrm{K}) \leq 0.51\,\mathrm{mm\,s^{-1}}$ and $0.5\,\mathrm{mm\,s^{-1}} \leq \Delta E_Q \leq 1.5\,\mathrm{mm\,s^{-1}}$.**177** The only exception to this is the case of $\mathrm{L} = \mathrm{L'} = 2-\mathrm{MeImH}$ and 1,2-$\mathrm{Me_2Im}$, where for $\mathrm{TMPFe^{II}}$ the quadrupole splittings are 1.67 and $1.73\,\mathrm{mm\,s^{-1}}$, respectively.**635** DFT calculations have shown that these values are only consistent with a highly ruffled porphyrinate core.**622**

^{13}C NMR Spectra. The ^{13}C resonance signal for the CO moiety has been observed at around 205 ppm for model complexes,**664,690** whereas for the proteins this resonance is slightly downfield shifted and observed at 206–207 ppm.**828** Providing steric encumbrance to the CO binding site using chiral '*ansa* handle' porphyrins with $-\mathrm{C_6H_4}-$ or $-\mathrm{CH_2}-\mathrm{C_6H_4}-\mathrm{CH_2}-$ bridging groups causes a shift to lower frequency (199.4 and 202.7 ppm, respectively).**829** The ^{57}Fe NMR shifts of a number of CO complexes of myoglobin**830,831** and model hemes**487,830,832–834** have been reported in a variety of solvents. The shifts (vs. external $\mathrm{Fe(CO)_5}$) range from 8110 to 8219 ppm for the models and 8227 ppm for MbCO.**830,832** Three basket-handle porphyrin complexes of $\mathrm{Fe^{II}}$(N-BuIm)(CO) show a decrease in the ^{57}Fe chemical shift from 8036 to 7728 to 7500 ppm as the basket-handle chain is shortened from twelve to ten to nine $\mathrm{CH_2}$ units, probably due to bending of the Fe–CO bond,**834** discussed in greater detail above. For a series of superstuctured iron(II) complexes with ruffled porphyrin ring conformation, the ^{57}Fe signal was observed at around 8000 ppm.**835** An excellent correlation was found between the ^{57}Fe chemical shift and the degree of ruffling in these complexes. The correlation between the chemical shifts of ^{57}Fe and the *meso*-porphyrin ring carbons suggests that the two nuclear probes reflect similar types of electronic and structural perturbation, which are primarily due to porphyrin ruffling.**835** For comparison, the ^{57}Fe signal of a *bis*-pyridine-ligated $\mathrm{TMPFe^{II}}$ complex was observed at 11 715 ppm and falls within its predicted range based on the correlation of the Fe chemical shifts with the Mössbauer quadrupole splittings.**635** Experimental measurements**836** and DFT calculations**836–839** of ^{57}Fe chemical shifts and Mössbauer quadrupole splittings in metalloporphyrins and heme proteins have been reported. DFT calculations of ^{17}O NMR chemical shifts and nuclear quadrupole coupling tensors of oxyheme model complexes have also been reported.**840**

4.5.2 $\mathrm{O_2}$/CO Binding to Cytochrome P450 Model Complexes

Up to this point we have only discussed carbon monoxide and dioxygen binding to pentacoordinate $\mathrm{Fe^{II}}$ porphyrins that employ a nitrogen base, such as imidazole or pyridine, at the fifth coordination site, a feature important for understanding dioxygen transport and storage in hemoglobin and myoglobin. However, high-spin $\mathrm{Fe^{II}}$ complexes in which one of the axial coordination sites is occupied by a thiolate moiety are also capable of binding small ligands, such as carbon monoxide,**651,652,698,777,841–849** dioxygen,**651,846,849–852** and superoxide.**533** Pentacoordinate high-spin iron(II) thiolate complexes**777,841–853** and their ligand-binding properties (*see* ***S-donor Ligands***) have been investigated to obtain a better understanding of the structure–function relationships of cytochromes P450 (*see* ***Iron: Heme Proteins, Mono- & Dioxygenases***), especially to understand which factors control ligand binding in this family of enzymes. The diversity of reactions catalyzed by heme-thiolate proteins was recently reviewed by Mansuy.**854**

When CO is bound to cytochrome P450, the visible spectrum exhibits a typical hyperporphyrin spectrum with a very characteristic and unique feature: the Soret band is split, giving peaks at ∼380 and ∼450 nm (hence the name of this family of enzymes). The split Soret band is attributed to the presence of the thiolate ligand, with its strong σ and π donating capabilities.**845,855** To reproduce this feature, a variety of $\mathrm{PFe^{II}(RS^-)(CO)}$ complexes have been synthesized. To force coordination of the thiolate ligand to the iron center and to prevent oxidation of the thiolate moiety to the disulfide, either a large excess of the thiolate has been used**856,857** or a tail has been attached covalently to one**846,847,858** or two**844,845,849,859** points on the porphyrin ring to successfully synthesize P450 models. Examples of such tailed complexes are shown in Figure 7.

Some of the carbon monoxide complexes of the P450 models have optical spectra that are very similar to those of the proteins; for example, the CO adduct of alkanethiolate complexes give typical hyperporphyrin spectra with absorption bands at 380 and 456 nm,**848** whereas a picket fence tetrafluorophenylthiolate complex gives rise to split Soret bands at 387 and 451 nm and a visible band at 559 nm.**651** The IR band associated with the carbonyl stretch is observed at $1956\,\mathrm{cm^{-1}}$, and shifts to $1942\,\mathrm{cm^{-1}}$ in the solid state.**651** Mössbauer data of $\Delta E_{\mathrm{Q}} = 0.56\,\mathrm{mm\,s^{-1}}$ at 4.2 K are also characteristic for the CO complex. The analogous $\mathrm{O_2}$ adduct has $\Delta E_Q = 2.17\,\mathrm{mm\,s^{-1}}$ at 4.2 K, very close to those reported for oxy $\mathrm{P450_{cam}}$.**654** The IR frequencies of ν ($^{16}\mathrm{O_2}$) at $1141\,\mathrm{cm^{-1}}$ and ν ($^{18}\mathrm{O_2}$) at $1075\,\mathrm{cm^{-1}}$ indicate a bent end-on geometry for the Fe–$\mathrm{O_2}$ moiety.**651,654** The structure of this dioxygen adduct of $[\mathrm{T_{Piv}PPFe^{II}(C_6HF_4S^-)}]$ has also been reported, confirming the bent end-on geometry.**654** ^{13}C NMR spectroscopy is also a very valuable tool to investigate CO coordination in thiolate heme models. For example, the CO complex of a strapped porphyrin**844** has a ^{13}CO NMR

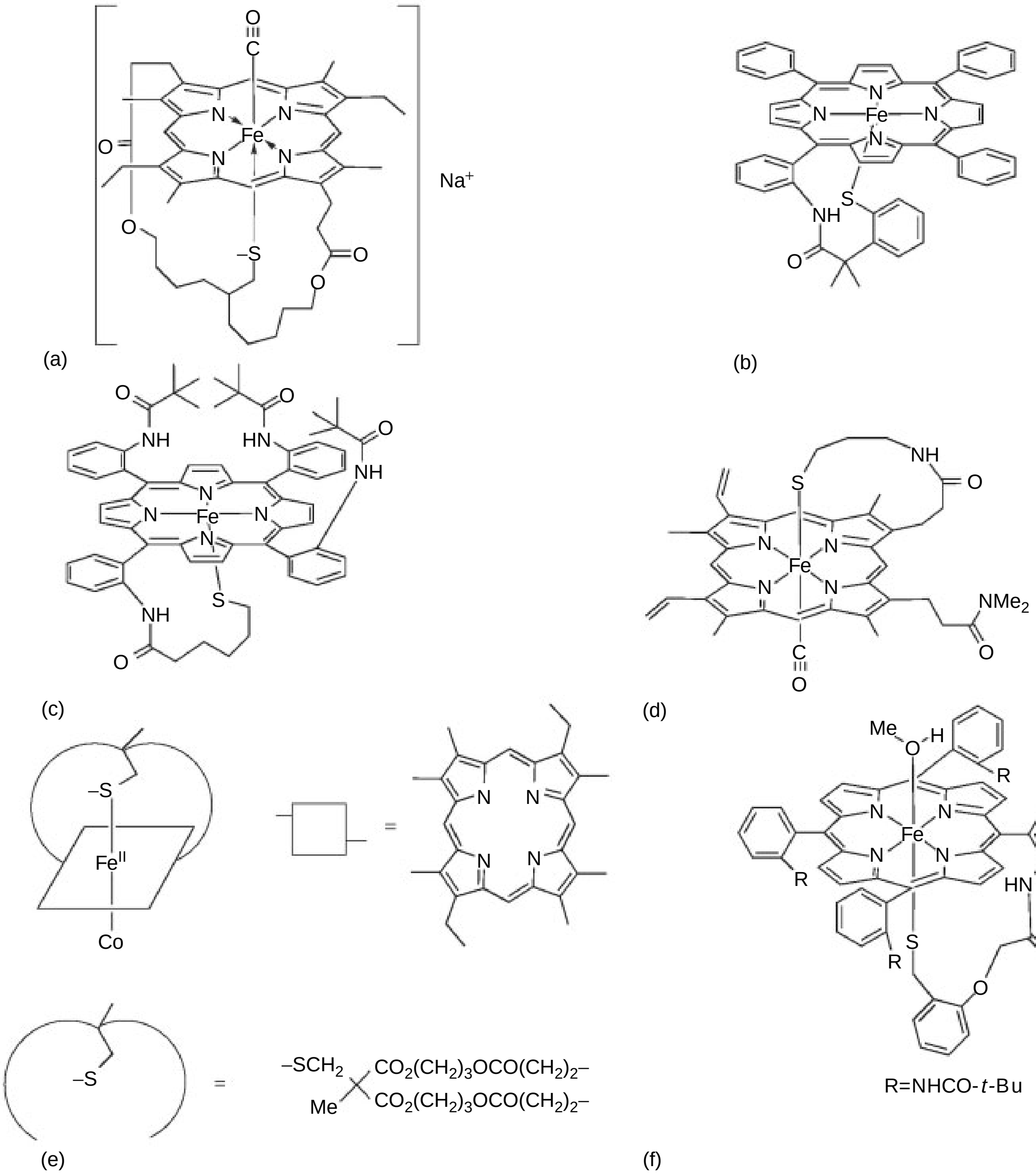

Figure 7 ‘Tailed’ iron porphyrins used as models of cytochrome P450. (a) model designed by Battersby and coworkers, attached at two points;[844] (b) TPP derivative with a pendant aryl thiol capable of bonding to the metal;[847] (c) a ‘picket fence’ derivative with a pendant alkyl thiol;[847] (d) a ‘chelated heme’ with a thiolate ligand;[858] (e) precursor of a model designed by Tatsuno *et al*., attached to the porphyrin at two points;[859] (f) another TPP derivative with a pendant aryl thiolate[846]

resonance frequency of 196.8 ppm, in good comparison to the natural P450$_{\mathrm{cam}}$ ^{13}CO complex (200.3 ppm).[860]

Significant differences in the equilibrium constants for carbon monoxide binding to cytochromes P450 from bacterial, liver microsomal, and adrenal cortex microsomal sources, different isozymes of the liver microsomal proteins, and for substrate-free and substrate-bound enzymes, have been observed and have been related to similar factors that affect O_2 and CO binding in oxygen transport and storage heme proteins. The importance of the *cis* and *trans* effects, that is electronic effects associated with the porphyrin or the axial ligand, respectively, have been investigated by Gaul and Kassner.[777] CO affinities were also determined for *n*-butanethiolate Fe$^{\mathrm{II}}$ complexes. CO affinities follow the order diacetyldeuteroporphyrin > spirographisporphyrin > 2-acetyl-4*H*-DP > PP > MP, coproporphyrin > diacetyldeuteroporphyrin > dicyanodeuteroporphyrin, which corresponds to the order of decreasing porphyrin basicity. It was concluded that the direction and magnitude of the *cis* effects on CO binding is dependent on the *trans* axial-ligand basicity; the magnitude of the *Trans Effect* on CO binding appears to be related to the (*cis*) porphyrin basicity.[777] Using laser flash photolysis, the O_2

and CO association and dissociation rates of strapped and basket-handle thiolate-coordinated Fe(II) complexes have also been studied.[849] It was found that the increase in pK_a of the proximal ligand is accompanied by a decrease in O_2 and CO association rates, while the dissociation rates increase for CO, but decrease for O_2.

Since it has been shown that the structures of cytochromes P450 have at least one NH···S hydrogen bond at the active site,[861–866] the factors that affect the reduction potentials of the heme-thiolate center of these enzymes have been probed. P450 model complexes with single and double NH···S hydrogen bonds (provided by amides) at the thiolate site have been synthesized and characterized by X-ray crystallography, electrochemistry and infrared spectroscopy.[848,867,868] The reduction potentials of the Fe^{III}/Fe^{II} couples of these complexes show a positive shift of 0.10–0.33 V as compared to model complexes that do not have hydrogen bonds to the thiolate sulfur,[867] indicating greater ease in forming the reduced state that can bind dioxygen. However, there are complexes that have a NH···S hydrogen bond, which include one of the alkanethiolate complexes reported by Suzuki *et al*.[848] In this complex the hydrogen atom of the amide group is directed toward the thiolate sulfur atom to form a N–H···S hydrogen bond with a distance of 2.800 Å and an angle of 130.73°. The H-bond is described to shorten the Fe–S bond length, which is 2.18 Å. To confirm the shortening of the Fe–S bond, resonance Raman experiments were carried. The ν_{Fe-S} mode shifted to 394 cm^{-1} compared to the complex lacking the hydrogen bond. This result was interpreted as confirming that H-bonding induced Fe–S bond shortening, which was suggested to occur when the HOMO involves antibonding metal-S interaction. In support of the N–H···S hydrogen bond is the positive shift of the Fe^{III}/Fe^{II} redox couple by 0.1 V. Both the Fe–S and average Fe–N bond lengths (1.98 or 1.99 Å, depending on the nature of the thiolate ligand) are in good agreement with the structural data of $P450_{cam}$ and $P450_{terp}$.[848]

4.5.3 NO Binding to Iron(II) Porphyrins

Traylor and coworkers[869,870] showed that addition of NO to a carbonmonoxy chelated heme model complex leads to the formation of a five-coordinate PFe^{II}–NO complex. The same reaction occurs when NO is added to the *N*-methylimidazole–protoheme–CO complex at low base concentrations, that is CO is readily replaced by NO, with loss of the imidazole ligand. It has been suggested[869,870] that this loss of proximal ligand may have relevance to the EDRF (Endothelial-Derived Relaxing Factor) activity of nitric oxide in biological systems (*see* ***Nitrogen Monoxide (Nitric Oxide): Bioinorganic Chemistry***).[51,58] Since this report, NO binding to iron(II) porphyrins has become of great interest because of its physiological importance. As discussed earlier, NO plays key roles in many biological processes, and is involved in blood pressure control, vasodilation, and platelet aggregation, acts as neurotransmitter, and is able to kill intracellular parasites.[871,872] In 1992, NO was declared *molecule of the year*,[873] and in 1997 a journal (*Nitric Oxide: Biology and Chemistry*) was established with sole focus on NO chemistry and biology.[871] NO is important in processed nitrite-cured meats, since it is contained in the pentacoordinate nitrosylheme pigment that gives cured meat its color.[93] Nitric oxide is known to bind to many heme proteins, and thus it should not come as a surprise that five- and six-coordinate NO-ligated iron(II) porphyrins are extensively investigated to model the interactions of NO with these proteins. With three exceptions, all $Fe(NO_x)$-containing heme proteins contain a nitrosyl-bound iron porphyrin.[185,547] Some of the best known of the Fe^{II}-NO complexes include the nitrosyl adducts of hemoglobin and myoglobin, $P450_{nor}$, and cytochromes *c* and *c*′, to name only those proteins that are structurally characterized.[185] (see Section 6.3.4 for discussion of the Fe^{III}-NO models and proteins.) In recent years many reviews on NO model heme chemistry have been published. Ferrous nitrosyl hemes are covered by Scheidt and Wyllie,[185] Scheidt and Ellison,[874] and Scheidt[548] who addressed structural aspects of NO porphyrin chemistry; the laboratory of Ford, Laverman, and Lorkovic,[549,550] who summarized aspects of NO model chemistry, and Cheng and Richter-Addo,[547] who reviewed binding and activation of nitric oxide by metalloporphyrins and hemes. Because of the amount of information available, this section will highlight only certain structural and spectroscopic properties that pertain solely to ferrous NO porphyrins and that have received considerable attention as models of the heme proteins. Iron(III) NO systems are discussed in Section 6.3.4.

Both five and six-coordinate NO-ligated ferrous porphyrins are known, and in the Enemark and Feltham formalism[875] are described as $\{FeNO\}^7$, where the superscript 7 indicates the sum of the six d-electrons of the iron and the π^* electron of the NO ligand. Although all complexes are low-spin, they are paramagnetic because of the unpaired electron derived from the NO ligand.[876,877] These complexes are frequently synthesized by the reduction of the high-spin Fe^{III} porphyrins in an inert gas atmosphere followed by purging with purified NO gas. Techniques and pitfalls in working with NO are summarized in the review by Ford and Lorkovic.[550]

Structural Aspects. Five-coordinate Fe^{II} complexes that have been characterized by single crystal X-ray crystallography include the TPP complex, (TPP)FeNO,[878] the octabromopyrrole substituted TPP complex (Br_8TPP)FeNO, the tetrabromopyrrole substituted TPP complex (Br_4TPP)FeNO, the dichlorophenyl substituted TPP (2,6-Cl_2TPP)FeNO, the pivalamido TPP (T_{Piv}PP)FeNO, the octaethylporphyrin (OEP)FeNO, the ocatethyltetraazaporphyrin complex (OETAP)FeNO, the octaethylchlorin complex (oxo-OEC)FeNO,[185] and the deuteroporphyrin complex (DP) FeNO.[879] These Fe^{II} porphyrins and chlorins are characterized by $Fe-N_{por}$ bond lengths typically observed in low-spin complexes, which range from 1.931 Å in the (OETAP)FeNO complex to 2.010 Å in the (OEP)FeNO complex.[185] The

NO ligand binds in a bent fashion with an Fe-N-O bond angle ranging from 138.9° in (2,6-Cl_2TPP)FeNO to 149.2° in (TPP)FeNO.[878] With this value, the angle lies between that for the strongly bent NO metal systems and the essentially linear complexes.[875] The nitrosyl ferrous proteins show a much larger range for this angle, which may be related to the lower resolutions of the heme protein crystal structures. As they become more refined, the angles may narrow. A summary of the NO geometry is given by Wyllie and Scheidt.[879] The iron is on average displaced by about 0.3 Å from the 24-atom porphyrin core and is tilted toward the NO ligand.[185,548,880] This tilt seems to be a general feature of five-coordinate ferrous-NO porphyrins and has been rationalized by DFT calculations in terms of three important interactions: σ-antibonding d_{z^2}(metal)$-\pi^*$(NO) interaction; d_{z^2}(metal)$-\pi^*$(NO) interaction; and d_{z^2}(metal)$-\pi$ (porphyrin) interaction.[881] The Fe–N_{NO} bond lengths show larger variations than the Fe–N_{por} distances and range from 1.691 Å in (Br_4TPP)FeNO to 1.74 Å in (T_{Piv}PP)FeNO, which reflects the difference in axial bonding and the loss of π interaction when transitioning from the linear to the bent geometry.[185,548]

The six-coordinate Fe^{II} complexes have very similar structural features to those of the five-coordinate complexes, indicating that the increase in coordination number does not affect the structural properties.[185,548,871] To date the structures of a number of complexes with imidazoles, piperidines, pyridines, or nitrites as second axial-ligand bonded to the iron have been solved. Most of these are TPP derivatives. These complexes include (TPP)Fe(NO)(N-MeIm),[185,882,883] (TPP)Fe(NO)(4-MePip),[185,871] (TPP)Fe(NO)(4-MePy),[871] (TPP)Fe(NO)(4-NMe_2Py),[871] (TPP)Fe(NO)(NO_2),[871] and [(T_{Piv}PP)Fe(NO)(NO_2)].[877] These six-coordinate Fe^{II} porphyrins are characterized by Fe–N_{por} bond lengths that are similar to those of the five-coordinate complexes and range from 1.988 Å in the (TPP)Fe(NO)(NO_2) complex to 2.008 Å in (TPP)Fe(NO)(N-MeIm).[185,871] The NO ligand binds in a bent fashion with an Fe-N-O bond angle that ranges from 137.4 Å in the (TPP)Fe(NO)(NO_2) complex to 143.7° in (TPP)Fe(NO)(4-MePip).[185,871] The largest displacement of the iron from the 24-atom porphyrin core is 0.11 Å, which is small compared to the 5-coordinate complexes. The Fe–N_{NO} bond lengths range from 1.72 Å in (TPP)Fe(NO)(4-MePip) to 1.84 Å in (TPP)Fe(NO)(NO_2).[871] An important feature in all complexes is the trans effect exhibited by the NO moiety, that is, the effect associated with the sixth ligand coordinating trans to NO. Related to the trans effect is the relatively long Fe-L bond,[185,548] which ranges from 2.463 Å in one of the two (TPP)Fe(NO)(4-MePip) forms to 2.060 Å in (TPP)Fe(NO)(NO_2).[871] The structural trans effect, which has been explained in terms of the partial population of the d_{z^2} orbital by an unpaired electron derived from the NO ligand,[185] has important implications. The binding constant of the sixth ligand is very low (estimated at 1–10 M^{-1}), thereby explaining why the formation of the of six-coordinate [PFe^{II}(NO)L] species is not favored.[185,869] The lengthening and weakening of the trans bond, which has been discussed recently by Scheidt's laboratory more thoroughly,[871] also has important physiological consequences. Bond breakage of the trans bond upon NO coordination is described as one of the means by which NO is believed to activate guanylate cyclase,[884] which then begins the process of vasodilation.

UV–vis Spectroscopy. The UV–vis spectra of five-coordinate ferrous nitrosyl complexes have been reported to reveal three bands with quite often a shoulder of the Soret band. The Soret band of tetraphenylporphyrin complexes is centered at around 405–412 nm, while that of the OEP complex is blue-shifted (TPPFeNO: 405 nm;[878] T_{piv}PPFeNO: 412 nm;[885] OEPFeNO: 387 nm[874]) and quite often has a shoulder at 475–477 nm (TPPFeNO: 475 nm; T_{Piv}PPFeNO: 476 nm; OEPFeNO: 480 nm). The β band is observed at 537–539 nm (TPPFeNO: 537 nm; T_{Piv}PPFeNO: 539 nm; OEPFeNO: 530 nm), whereas for TPP complexes the α band is found at 604–611 nm (TPPFeNO: 606 nm; OEPFeNO: 570 nm). For the six-coordinate complexes, the absorption band maxima of all bands are shifted to higher wavelength. For the representative example of [TPPFe(NO)(N-MeIm)] the following values were obtained: Soret band at 415 nm, shoulder at 460 nm, β band at 545 nm with a shoulder at 580 nm, α band at 643 nm,[883] while for [OEPFe(NO)(N-MeIm)] the same bands are found at 402, 480(sh), 535 and 565 nm.[874]

Vibrational Spectroscopy. For purposes of product identification, both the NO and the Fe-NO stretching frequencies are sensitive reporters on the nature of the bond between the iron(II) and the NO ligand, and reflect the bent geometry observed for the Fe-NO moiety in these complexes. The values for the NO stretching frequency are distinctively different in five- and six-coordinate complexes.[550,871] In five-coordinate complexes, the ν_{NO} band is observed in the narrow range of 1666 cm^{-1} to 1673 cm^{-1}. Representative examples are: ν_{NO} (TPPFeNO) = 1670 cm^{-1}, ν_{NO}(OEPFeNO) = 1666, 1673 cm^{-1}, ν_{NO}((oxoOEC)FeNO)) = 1673 cm^{-1}, and ((T_{Piv}PP)FeN) = 1665 cm^{-1}).[550,871] The nitrosyl stretching frequency in six-coordinate ferrous NO complexes shifts by about 10–30 cm^{-1} to lower frequency, which is associated with an increased electronic population of the π^* NO orbitals. The NO stretch is quite sensitive to the trans effect; ν_{NO} increases with decreasing interaction with the trans ligand. Representative examples of ν_{NO} values are found in [(TPP)Fe(NO)(NO_2)] – ν_{NO} 1625 cm^{-1}; [(TPP)Fe(NO)(N-MeIm)] – ν_{NO} 1628 cm^{-1}; [(TPP)Fe(NO)(4-MePip)] – ν_{NO} 1653–1656 cm^{-1}, and [(TPP)Fe(NO)(4-NMe_2Py)] – ν_{NO} 1653 cm^{-1}.[550,871] Whereas there is a distinctive difference in the nitrosyl stretching frequencies of five- and six-coordinate complexes, this difference is not reflected in the ν(Fe–N(NO)) stretching frequencies of penta- and hexa-coordinated complexes. Resonance Raman bands associated with the ν(Fe–N(NO)) stretching frequency are in both types of complexes very similar in value. For the five-coordinate complex TPPFeNO, the ν(Fe–N(NO)) was observed at 525 cm^{-1},[886] whereas the corresponding band in the six-coordinate (TPP)Fe(NO)(Py) complex is found at 527 cm^{-1}.[887] Using Soret-excitation resonance Raman spectroscopy, it was also shown that the Fe^{II}–NO bond strength in six-coordinate complexes is not affected by steric or electronic properties of the sixth axial base ligand. However, solvent effects are found to be substantial.[887]

IR spectroscopy was also shown to provide an important tool for investigating the interactions of nitric oxide gas with thin layers of Fe^{II}(TPP).[888] The addition of NO to Fe^{II}(TPP) yields Fe(TPP)(NO) layers, which are inert to further reaction with excess NO. However, the nitrosyl-nitro complex, (TPP)Fe(NO)(NO_2), is readily formed when traces of dioxygen are added to the NO atmosphere. At high NO_2 concentrations in the NO/NO_2 mixture, the nitrato complex (TPP)Fe(NO_3) is also formed. Moderate shifts in the nitrosyl stretching frequency of (TPP)Fe(NO) were related to crystal packing effects, rather than to H-bonding of coordinated NO to protic contaminants. Removal of NO from layers containing (TPP)Fe(NO)(NO_2) led to the formation of Fe(TPP)(NO) and (TPP)Fe(NO_3).[888] Synchrotron far-IR spectroscopy has recently been used to investigate heme doming modes of model heme-CO complexes.[889]

A relatively new type of vibrational spectroscopy is that made available by synchrotron radiation at the Mössbauer γ-ray energy of ^{57}Fe (14.4 keV) or other probe nucleus, which is called Nuclear Resonance Vibrational Spectroscopy (NRVS) or Nuclear Inelastic Scattering (NIS).[890–899] This technique allows the measurement of the complete set of probe (iron for our interest) vibrational modes. Thus, all modes involving significant Fe motion will contribute to the measured spectrum. For hemes and heme proteins, these motions include heme doming, Fe–N_P symmetric and asymmetric stretches, Fe–N_{ax} and Fe–L stretches,[891,893,894,896–899] where L may be NO, CO or any number of other possible axial ligands. For TPPFeL complexes it has been found that there is significant mode coupling of the phenyl groups with the Fe-active modes, and DFT calculations are very helpful in understanding these couplings.[898,899] For (TPP)Fe(CO)(N-MeIm), it was possible to identify the iron-imidazole stretching mode for the first time, at 226 cm^{-1}.[898] For (TPP)Fe(CO)(N-MeIm)[898] and (TPP)Fe(NO),[899] quantitative comparison of calculated and measured Fe dynamics on an absolute scale reveals good overall agreement, suggesting that DFT calculations provide a reliable guide to the character of observed Fe vibrational modes. These include a series of modes involving Fe motion in the plane of the porphyrin, which are rarely identified using infrared and Raman spectroscopies, because these modes are generally weak in comparison to macrocycle vibrational modes. The NO binding geometry breaks the four-fold symmetry of the Fe environment, and the resulting frequency splittings of the in-plane modes predicted for (TPP)Fe(NO) agree with those observed. In contrast to expectations of a simple three-body model, mode energy remains localized on the FeNO fragment for only two modes, an N-O stretch and a mode with mixed Fe-NO stretch and FeNO bend character. Bending of the FeNO unit also contributes to several of the in-plane modes, but no primary FeNO bending mode is identified for (TPP)Fe(NO). Vibrations associated with hindered rotation of the NO and heme doming are predicted at low frequencies, where Fe motion perpendicular to the heme is identified experimentally at 73 and 128 cm^{-1}.[899] Identification of the latter two modes is a crucial first step toward quantifying the reactive energetics of Fe porphyrins and heme proteins.

EPR Spectroscopy. EPR spectroscopy provides insights into the electronic nature of the paramagnetic species, and allows determining whether ferrous nitrosyl iron^{II} porphyrins are formed during a reaction, and to distinguish five- and six-coordinated Fe^{II} complexes. The EPR spectra of both types of Fe^{II} porphyrins have been studied and give rhombic EPR spectra owing to the π^* electron of the NO ligand[550,871,877,879–883,900] The spectra of five-coordinate Fe^{II} porphyrins show similar features in the solid and liquid state, and reveal hyperfine splittings that are consistent with the coupling to the nitrogen atom of the axially coordinated NO moiety.[877] EPR g-values for representative five-coordinate ferrous complexes are: TPPFeNO (toluene at 120 K): g_{max}2.102, a_{max}(^{14}N) 12.6 G, g_{mid}2.064, a_{mid}(^{14}N)17.2 G, g_{min}2.010, a_{min}(^{14}N)17.3 G;[876] (CH_2Cl_2 at 77 K): g_{max}2.098, g_{mid}2.031, g_{min}2.001;[879] and OEPFeNO (doped single crystal): g_{max}2.110, g_{mid}2.040, g_{min}2.012.[900] The EPR spectrum of the pigment contained in nitrite-cured red meat reveals similar features (g_{max}2.112, g_{mid}2.070, g_{min}2.009) that clearly can be attributed to a pentacoordinate nitrosyl heme present in the pigment.[93]

Depending on the nature of the sixth axial ligand, the spectra of six-coordinate Fe^{II} porphyrins reveal two different hyperfine splitting patterns. A nine-line hyperfine pattern arising from the interaction of the unpaired electron with both the nitrogen atom of NO and the N atom of the coordinating ligand was observed first for [(TPP)Fe(NO)(pip)][876] and more recently for [(TPP)Fe(NO)(N-MeIm)].[871] A less resolved three line pattern was obtained for [(T_{Piv}PP)Fe(NO)(NO_2)].[877] EPR g-values for representative six-coordinate complexes are: [(TPP)Fe(NO)(pip)] (toluene at 77 K): g_{max}2.08, g_{mid}2.04, g_{min}2.003;[871,876] [(TPP)Fe(NO)(N-MeIm)] (toluene at 77 K): g_{max}2.072, g_{mid}2.004, g_{min}1.966;[871] and [(TPP)Fe(NO)(4-NMePy)] (toluene at 77 K): g_{max}2.069, g_{mid}2.002, g_{min}1.973.[871] The hyperfine splitting patterns observed are consistent with the interpretation that the unpaired electron density in both five- and six-coordinated low-spin Fe^{II} complexes is localized in the d_{z^2} iron orbital. The three g-values reflect the non-axial symmetry of the complexes and the bent Fe-NO moiety. DFT calculation of the g-tensors[901] of $\{FeNO\}^7$ complexes as a function of their structures have been reported.

Mössbauer Spectroscopy. Mössbauer spectroscopy has been used as a powerful technique to probe the electronic structure of the five- and six-coordinate ferrous nitrosyl porphyrins.[871,877] The isomer shifts of both types of complexes ($\delta \approx 0.35\,\mathrm{mm\,s^{-1}}$) are similar and show temperature dependences that are consistent with a second-order Doppler effect, but are slightly smaller than those of most other iron(II) porphyrin complexes ($\delta \approx 0.45\,\mathrm{mm\,s^{-1}}$).[871] Unlike the isomer shifts, the quadrupole splittings change upon coordination of a sixth ligand. As the environment changes from five- to six-coordination, the values of ΔE_Q decrease from, for example $1.22\,\mathrm{mm\,s^{-1}}$ in the pentacoordinate TPPFeNO complex to $0.75\,\mathrm{mm\,s^{-1}}$ in the corresponding 1-methylimidazole ligated porphyrin [(TPP)Fe(NO)(N-MeIm)] or $0.91\,\mathrm{mm\,s^{-1}}$ in the [(TPP)Fe(NO)(4-MePy)] complex.[871] To obtain reasonable spectral fits, rotation of the Mössbauer electric field gradients is required for the six-coordinate ferrous nitrosyl complexes, but not for the five-coordinate species. This result was interpreted as reflecting differing g-tensor orientations in five- and six-coordinate complexes.[871] DFT calculation of the Mössbauer parameters[902] of $\{FeNO\}^7$ complexes as a function of their structures have been reported.

X-ray Absorption Spectroscopy – EXAFS and XANES. To develop additional tools for characterizing electronic and structural properties of nitrosyl complexes, NO adducts of ferrous porphyrins and phthalocyanines were attached to the surface of high area carbon electrodes in an acidic aqueous solution and subjected to EXAFS and XANES investigations.[903,904] EXAFS spectra of a tetramethoxyphenyl substituted TPPFe complex were recorded in situ, that is, under potential control, in which the Fe^{II} center was constrained to reside in the center of the porphyrin macrocycle. Under these constraints, analysis of the iron K-edge data showed that the Fe-NO moiety is bent, which is in excellent agreement with single crystal X-ray data, as are the $Fe\text{-}N_{por}$ and Fe-NO bond distances and angles.[903] The analysis of the Fe K-edge data of the nitrosyl complex of the phthalocyanine analog demonstrated that the geometry around the iron center is very similar to that of the better-characterized iron(II) porphyrin NO adducts. The Fe center in the phthalocyanine complex shows a five-coordinate square planar arrangement, with the axially coordinated NO forming an angle of about 40° with respect to the normal to the phthalocyanine plane.[904]

Mechanistic Aspects. To elucidate the controversial chemistry relating to the reactions of NO with (TPP)Fe(NO), a series of reactions were carried out in several laboratories, including that of Ford.[905] With highly pure NO the sole species, only observable at low temperature, was the diamagnetic *trans* dinitrosyl adduct $Fe(TPP)(NO)_2$.[906] This reaction was also observed for the more stable tetra-*m*-tolylporphyrinatoiron(II) complex, which reacted with NO at low temperature to form the *bis*-NO adduct $(T\mathit{m}TP)Fe(NO)_2$.[906] Wayland and Olson had originally detected the formation of this complex using (TPP)Fe(NO) by the disappearance of the EPR signal in the presence of high pressures of NO gas (400 torr).[876] Experimental evidence for the formation of the $TPPFe(NO)_2$, $(T\mathit{m}TP)Fe(NO)_2$ or also $(OEP)Fe(NO)_2$ complexes was obtained by IR spectroscopy.[907] Although the observation of a single NO stretching band in the IR spectrum of each complex first suggested a centrosymmetric D_{4h} or C_{2h} structure, DFT geometry optimizations and frequency calculations indicate that the trans-syn C_{2v} conformation should be more stable.[907] It should be noted that TPPFeNO does not react with NO to form $(TPP)Fe(NO_2)(NO)$ at room temperature in aprotic solvents,[908] but it readily reacts reversibly with N_2O_3 in the presence of excess NO to give the nitro nitrosyl complex $(TPP)Fe(NO_2)(NO)$.[905] This observation indicates that claims that Fe(TPP)(NO) promotes NO disproportionation to give $Fe(TPP)(NO_2)(NO)$[909] are most likely compromised by traces of air present in the nitric oxide sources.[905] $(TPP)Fe(NO_2)(NO)$ also undergoes reversible loss of NO to give the nitro species $(TPP)Fe(NO_2)$, which has been implicated as a powerful oxygen atom transfer agent in reactions with various substrates.[910]

The NO_2 complex can be synthesized from the 5-coordinate NO complex by controlled reaction of $(T_{Piv}PP)Fe(NO)$ with air in the presence of pyridine, and reconverted to the starting nitrosyl complex using triphenylphosphine as reductant.[911] In the presence of excess NO_2, $(TPP)Fe(NO_2)$ undergoes oxidation to the stable nitrato analog $(TPP)Fe(NO_3)$.[905] Owing to the reactivity of $(TPP)Fe(NO_2)$, flash photolysis and stopped-flow kinetics has been used to measure accurately the dissociation equilibria of $Fe(TPP)(NO_2)(NO)$ in toluene at 298 K.[905] Flash photolysis of $Fe(TPP)(NO_2)(NO)$ resulted in competitive NO_2 and NO dissociation to give Fe(TPP)(NO) and $Fe(TPP)(NO_2)$, respectively. The rate constant for the reaction of Fe(TPP)(NO) with N_2O_3 to generate $Fe(TPP)(NO_2)(NO)$ was determined to be $1.8 \times 10^6\,\mathrm{M^{-1}\,s^{-1}}$, and that for the NO reaction with $Fe(TPP)(NO_2)$ was similarly determined to be $4.2 \times 10^5\,\mathrm{M^{-1}\,s^{-1}}$.[905] Stopped-flow rapid dilution techniques were used to determine a rate constant of $2.6\,\mathrm{s^{-1}}$ for NO dissociation from $(TPP)Fe(NO_2)(NO)$. Rapid dilution experiments also demonstrated that $Fe(TPP)(NO_2)$ readily undergoes further oxidation to give $(TPP)Fe(NO_3)$.[905] Hoshino *et al.* also reported that $TPP\text{-}Fe^{II}NO$ undergoes facile photodenitrosylation to give NO and TPPFe. The photodissociation yield was determined to be 0.55.[912] Laser flash photolysis in the presence of low concentrations of pyridine led to the formation of the five-coordinate complex $TPPFe^{II}Py$, which is in equilibrium with $(TPP)Fe^{II}(Py)_2$ and recombines with NO to reform $TPPFe^{II}NO$.[912] Analogously, it was also shown by laser-photolysis studies of nitrosyl protoporphyrin IX iron(II), that the $(PPIX)Fe^{II}NO$ complex readily photodissociates NO to leave the (PPIX)Fe complex in the micellar solution. The quantum yield was 0.15 for (PPIX)Fe^{II}(NO).[913] The (PPIX)Fe complex produced in the micelles recombines with NO to regenerate the parent nitrosyl porphyrin. The decay of (PPIX)Fe in the absence of excess NO follows second-order kinetics. In the presence of excess NO, the decay of (PPIX)Fe is pseudo-first-order.

As part of the work on model heme $\{FeNO\}^7$ complexes, mechanistic studies on the reversible binding of nitric oxide to metmyoglobin[914] and water soluble Fe^{II}, Co^{II} and Fe^{III} porphyrin complexes[915] in aqueous solution, ligand-promoted rapid NO or NO_2 dissociation from Fe^{II} porphyrins,[916] reductive nitrosylation of water-soluble iron porphyrins,[917,918] activation of nitrite ions to carry out O-atom transfer by Fe^{III} porphyrins,[910,919–921] demonstration of the role of scission of the proximal histidine-iron bond in the activation of soluble guanylyl cyclase through metalloporphyrin substitution studies,[922] reactions of peroxynitrite with iron porphyrins,[923,924] and the first observation of photoinduced nitrosyl linkage isomers of $\{FeNO\}^7$ heme complexes[925] have been reported.

Reactions of NO were also studied with the synthetic heme protein discussed earlier, namely the recombinant human serum albumin (rHSA) with eight incorporated $TPPFe^{II}$ derivatives bearing a covalently linked axial base, were also investigated.[926] The UV−vis absorption spectrum of the phosphate buffer solution at physiological pH showed absorption band maxima at 425 and 546 nm upon the addition of NO to form the nitrosyl species, which was also formed when the six-coordinate CO-adducts were reacted with NO gas. EPR spectroscopy revealed that the albumin-incorporated iron(II) porphyrin formed six-coordinate nitrosyl complexes. It was observed that the proximal imidazole moiety does not dissociate from the central iron when NO binds to the trans position. The NO-binding affinity $P1/2_{NO}$ was 1.7×10^{-6} torr at pH 7.3 and 298 K, significantly lower than that of the porphyrin complex itself, and was interpreted as arising from the decreased association rate constant (k_{on}(NO), $8.9 \times 10^8\,M^{-1}\,s^{-1}$–$1.5 \times 10^7\,M^{-1}\,s^{-1}$). Since NO-association is diffusion controlled, incorporation of the synthetic heme into the albumin matrix appears to restrict NO access to the central iron(II).[926]

4.5.4 *HNO Binding to Iron(II) Porphyrins*

The protonated 1-electron reduction product of NO, HNO, also known as nitroxyl, also binds to heme centers;[927] Farmer and coworkers have characterized the reaction of myoglobin(Fe^{II})-NO with Cr^{II} in the presence of H^+ to produce myoglobin(Fe^{II})–HNO and Cr^{III}:[928]

$$\mathrm{Mb(Fe^{II}) - NO + Cr^{II} + H^+ \longrightarrow Mb(Fe^{II}) - HNO + Cr^{III}} \quad (12)$$

The same complex can also be produced by decomposition of Angeli's salt, $Na_2N_2O_3$, in neutral solution:[928]

$$\mathrm{N_2O_3{}^{2-} + H^+ \longrightarrow HNO + NO_2{}^-} \quad (13)$$

$$\mathrm{HNO + Mb(Fe^{II}) \longrightarrow Mb(Fe^{II}) - HNO} \quad (14)$$

The HNO adduct is characterized by a proton NMR resonance at 14.8 ppm that is due to the proton of coordinated HNO, a strictly diamagnetic species[927–929] (although it could also be thought of as a strongly antiferromagnetically-coupled Mb(Fe^{III})–($HNO^{-}\cdot$) electron configuration), and the solution structure of the Mb(Fe^{II})–HNO heme pocket has been determined by 2D NMR techniques.[929] HNO is an interesting small molecule, in that it is a singlet (spin-paired) species, while the ground state of its conjugate base, NO^-, is a triplet (isoelectronic with O_2).[930,931] Therefore, the deprotonation of HNO is spin forbidden, and the pK_a has been estimated as 11,[932,933] which is quite different from the earlier reported value of 4.7.[934] HNO reacts with itself to produce N_2O and H_2O, and is thought to be an intermediate in the enzymatic reduction of NO to N_2O, the reaction that is carried out by nitric oxide reductases (discussed in Section 6.1.4). An Fe-bound nitroxyl intermediate has been spectroscopically identified during turnover of $P450_{nor}$,[935,936] a fungal nitric oxide reductase (see also Section 6.1.4).

4.5.5 *Isocyanide Binding to Iron(II) Porphyrins*

Although isocyanides are not natural substrates, their interactions with heme proteins have been extensively investigated to obtain a better understanding of the importance of the distal steric effect.[716] Even though this effect has been addressed in a wide variety of studies, as discussed above, isocyanide binding has provided an understanding of the importance of the distal side steric effect.[709] Not unexpectedly, heme proteins generally bind alkyl and aryl isocyanides with reduced affinities as compared to simple model compounds.[428,685,687,703,713,937–940] A recent review has discussed in detail axial isocyanide and phosphine binding in heme proteins and model hemes.[553] Thus, in this section only certain aspects of isocyanide binding are highlighted.

Although isocyanide-ligated complexes are quite stable in de-gassed solutions, they react rapidly with traces of air. Thus, care must be taken when preparing such complexes.[553] Both mono- and *bis*-isocyanide ligated complexes are known, which most frequently are synthesized by the reduction of the corresponding Fe(III) porphyrins followed by the addition of excess alkyl or aryl isocyanide in the presence or absence of other potential ligands, including imidazoles or pyridines.[553] In this way, ferrous isocyanide complexes have been prepared from sterically unencumbered porphyrins (TPP, OEP, methylesters of 3,8 diacetyl deuteroporphyrin and protoporphyrin IX) and encumbered porphyrins (capped and anthracene porphyrins, as well as basket-handle porphyrins).[553]

Mono-axially coordinated species are most conveniently formed by the reaction of single face-hindered Fe(II) porphyrins with isocyanide in a non-coordinating solvent, such as toluene or benzene,**[553]** or when four-coordinate PFe^{II} are reacted under an inert atmosphere with nitrogen bases, such as imidazoles and pyridines in the presence of isocyanide.**[745]** This is consistent with equilibrium constant studies, which show that, for example, benzyl isocyanide binds more strongly to ferrous porphyrins than 1-methylimidazole, pyridine, or triphenylphosphine.**[553]** For isocyanide binding, correlations have been established among ligand basicity and binding affinity. But it should be noted that isocyanides bind Fe(II) ion more strongly than one would expect based on their ligand basicities.**[553]** It has been shown that addition of sterically bulky isocyanides, such as tosylmethyl isocyanide for example, affects only the ligand association rates, suggesting that steric effects are primarily manifested in the association and not the dissociation rates.**[685]**

Six-coordinate mono-isocyanide ligated ferrous complexes of TPP were investigated recently in the laboratory of Oldfield.**[745]** Both the pyridine and imidazole mixed isocyanide-ligated complexes $TPPFe^{II}(i\mathrm{PrNC})(\mathrm{N\text{-}MeIm})$ and $TPPFe^{II}(i\mathrm{PrNC})(\mathrm{Py})$ were prepared by reacting the reduced *bis*-pyridine and imidazole complexes with isopropylisocyanide (iPrNC). The crystal structure of $TPPFe^{II}(i\mathrm{PrNC})(\mathrm{N\text{-}MeIm})$ showed that the porphyrin ring was planar in the complex, but that the isocyanide moiety was considerably tilted. The average $Fe–N_{por}$ bond distance of 1.998 Å was consistent with the $S = 0$ spin state.**[745]** These features are consistent with an earlier crystal structure of $TPPFe^{II}((CH_3)_3CNC)_2$.**[938]** Solid state ^{13}C and ^{15}N NMR studies showed that the ^{13}C chemical shift of the isocyanide carbon ($\delta_{iso} = 151$ ppm) is about 18 ppm shielded from that in sperm whale Mb ($\delta_{iso} = 173.4$ ppm) and in adult human Hb ($\delta_{iso} = 173.3$ ppm). The chemical shifts and shift tensor were also calculated by DFT methods, which showed good agreement with the experimentally observed values.**[745]**

Bis-isocyanide-ligated ferrous porphyrins were synthesized by Le Plouzennec *et al.***[941]** who showed that reaction of $TPPFe^{II}$ with two equivalents of N-benzoyl isocyanide results in the formation of the six-coordinate, low-spin bis(isocyanide) complex. The UV–visible bands are found at 428, 553, and 593 nm, and NMR shifts and Mössbauer quadrupole splittings are consistent with the hexacoordinate complex. If N-pivaloyl isocyanide is used, then both the mono and bis adducts are formed. The IR absorption band associated with the C≡N stretch of the mono adduct is observed at 1970 cm^{-1}, whereas the corresponding band in the bis adduct is shifted to higher frequency (2045 cm^{-1}). Reaction of the bis adduct with pyridine results in the replacement of one isocyanide ligand.**[941]** ^{57}Fe NMR shifts of Mb(RNC), where R = Et, i-Pr and n-Bu, range from 9223 to 9257 ppm versus external $Fe(CO)_5$,**[942]** and the model heme complex $TPPFe^{II}(PMe_3)(n\text{-}BuNC)$ in C_6D_6 has a shift of 8100 ppm versus external 90% $Fe(CO)_5$ in C_6D_6.**[487]**

4.5.6 *Binding of Other Ligands to Iron(II) Porphyrins*

Nitrosoalkanes as Ligands. Nitrosoalkane ligands are also capable of binding to Fe^{II} porphyrins with high affinities.**[601]** These complexes are conveniently obtained by reaction of the corresponding PFe^{II} complexes with the nitrosoalkane, RNO, or by reaction of the corresponding high-spin $PFe^{III}Cl$ complex with the hydroxylamino alkane, RNHOH, in the presence of excess ligand. It is found that hexacoordinate complexes are in fast exchange with the corresponding pentacoordinate PFe(RNO) complexes, and are low-spin species, with N=O stretching frequencies in the range 1400–1445 cm^{-1}.

Thiocarbonyl (CS) as Ligand. Both five- and six-coordinate low-spin iron complexes with a thiocarbonyl ligand have been structurally characterized.**[548,562]** An example of a five-coordinate low-spin thiocarbonyl ligated complex is exhibited by $[OEPFe^{II}(CS)]$. In this complex the average Fe–N bond length is 1.982 Å and the Fe–C(CS) bond distance is 1.662 Å with a fairly small displacement (0.23 Å) of the iron ion from the mean plane of the porphyrin core.**[649]** For low-spin Fe^{II} complexes, large quadrupole splittings (1.95 mm s^{-1} at 293 K, 1.93 mm s^{-1} at 4.2 K) have been observed for the thiocarbonyl ligated $OEPFe^{II}CS$ complex, which has an isomer shift (-0.03 mm s^{-1} at 293 K, +0.08 mm s^{-1} at 4.2 K) that is among the smallest reported for formally iron(II) porphyrins. This isomer shift is comparable to iron porphyrins with formal oxidation states of +3 and +4.**[548,562]** Six-coordinate complexes are also formed when the thiocarbonyl-ligated complex $OEPFe^{II}(CS)$ mentioned above is reacted with Py, N-MeIm, Pip, 4-CNPy, or 4-NMe_2Py.**[562]** The [OEPFe(CS)(Py)] and [OEPFe(CS)(N-MeIm)] complexes have been structurally characterized and have Fe–C bond distances ranging from 1.703 to 1.706 Å. These are significantly longer than those in the [OEPFe(CS)] complex and the $Fe–N_{por}$ bond lengths range from 2.112 to 2.155 Å.

Carbenes as Ligands. As mentioned above, $TPPFe^{II}$ complexes have been reported to be active catalysts in carbon transfer reactions, in which the active species are assumed to be iron porphy-rin carbene complexes.**[593–596]** Since carbene complexes are typically synthesized as models of cytochrome P450 enzymes, they are discussed in the corresponding section on P450 models, Section 8.2.

5 IRON(II) MACROCYCLE π-CATION RADICALS AND THEIR VALENCE TAUTOMERISM WITH IRON(III) MACROCYCLES

Although there has not yet been a report of the preparation and full characterization of a bona fide Fe^{II} porphyrin π-cation radical, the $[OETPPFe(4\text{-}CNPy)_2]ClO_4$ complex has overall spin state $S = 3/2$, but with very large and negative phenyl-H shift differences, $\delta_m - \delta_p$ and $\delta_m - \delta_o$, may indicate the presence of negative spin density at the *meso*-carbons.**[195,943]** Careful analysis of the pyrrole-CH_2 shifts also shows that they are much larger**[943]** than expected for either of the proposed**[944]** electronic configurations of intermediate spin Fe^{III}, $S = 3/2$, but rather indicate that the $d_{x^2-y^2}$ orbital of iron is at least partially occupied.**[943]** Thus, the combination of negative phenyl-H shift differences and the larger-than-expected pyrrole-CH_2 shifts indicates at least partial electron transfer from the porphyrin to the metal, yielding an electron configuration of $(d_{xy})^2(d_{xz},d_{yz})^2(d_{z^2})^1(d_{x^2-y^2})^{(1-x)}$ for the iron, and $(OETPP)^{(2-x)-}$ for the porphyrinate ring.**[943]** Thus, this is at least one possible example of a Fe^{II} porphyrin π-cation radical.

In addition, there have been several reports of reduced porphyrin or oxophlorin π-cation radicals of Fe^{II}.**[199–202]** Since it has been suggested that Fe^{III} isobacteriochlorin π-cation radicals are viable species for at least two reaction states of the hemoprotein subunit of *E. coli* sulfite reductase**[945]** and assimilatory nitrite reductases from several organisms,**[38]** and at least one state of the heme d_1 (chlorin) center of the dissimilatory nitrite reductases from several microorganisms,**[38]** the investigation of the one-electron reduced states of these proposed intermediates has also been undertaken.

The one-electron electrochemical oxidation of $(MAC)Fe^{II}$ NO complexes, where MAC are the porphyrin, chlorin, and isobacteriochlorin macrocycles, has been reported.**[201]** In all three cases the oxidations are reversible: $E_{1/2} = 0.63$ (OEP), 0.48 (OEC), and 0.22 V (OEiBC) in butyronitrile.**[201]** Controlled potential electrolysis in vacuo of each of these complexes yielded species whose optical spectra correspond to those of $[(OEP^{2-})Fe^{III}(NO)]ClO_4$, but in the cases of the reduced macrocycles the spectra were indicative of the valence isomer, $[(OEC^{-}\bullet)\ Fe^{II}(NO)]ClO_4$, the π-cation radical of the OEC macrocycle, and $[(OEiBC^{-}\bullet)Fe^{II}(NO)]ClO_4$, the π-cation radical of the OEiBC macrocycle. The typical $[Fe^{II}NO]$ EPR spectrum of each complex disappeared upon oxidation as a result of the production of even-electron species in each case. The presence of the NO ligand in each case was confirmed by re-reduction to yield the original $[Fe^{II}NO]$ optical and EPR spectra. The IR spectra of the oxidized compounds also confirmed the presence of NO: $\nu_{NO} = 1830$ (OEP), 1705 (OEC), and 1680 (OEiBC) cm^{-1}.**[201]**

Chemical oxidation of iron(II) nitrosyl complexes of deuterium-substituted octaethylchlorin and octaethylisobacteriochlorin with silver hexafluoroantimonate ($AgSbF_6$) in dichloromethane has been reported.**[202]** Although no EPR spectra are observed, electron spin relaxation due to the unpaired electron on the NO moiety allows these radical species to have well-resolved hyperfine-shifted ^2H NMR spectra. The pattern of isotropic shifts observed in each case is characteristic of an $a_2(\pi)$ -type unpaired electron (the analog of the $1a_{1u}$ (π) orbital of the porphyrin ring, Figure 4), having large spin density at the α-C positions of the reduced pyrrole rings of the macrocycles.**[202]** From the temperature dependence of the NMR spectra it appears that the two unpaired electrons are weakly antiferromagnetically coupled, with $J \sim -46\,cm^{-1}$, and about 35% triplet content at 296 K. Addition of ligands (L) such as imidazole, pyridine, THF, and acetonitrile at low temperatures appears to change the electron configuration to $[Fe^{III}NO]$ in both cases, as evidenced by changes in the optical spectra, and upon warming to room temperature the optical spectra convert to those of $OECFe^{III}L_2{}^{+}$ and $OE\mathit{i}BCFe^{III}L_2{}^{+}$, respectively. Thus for the reduced hemes there appears to be a facile valence tautomerism (equation 15):**[202]**

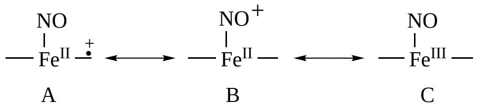

$$\underset{A}{-\overset{\overset{NO}{|}}{Fe^{II}}\overset{+}{\underset{\bullet}{-}}} \longleftrightarrow \underset{B}{-\overset{\overset{NO^{+}}{|}}{Fe^{II}}-} \longleftrightarrow \underset{C}{-\overset{\overset{NO}{|}}{Fe^{III}}-} \qquad (15)$$

For five-coordinate complexes, A is the electron configuration, while for six-coordinate complexes the electron configuration could be represented by either B or C, but in the presence of Lewis bases, NO is labile, suggesting the configuration shown in C.**[202]** (Interestingly, the binding constants of NO to the Fe^{III} state of hemoglobins and myoglobins are of the order of $10^3 - 10^5\ M^{-1}$ and the kinetics of NO dissociation are fast,**[946]** while the binding constants for NO to the Fe^{II} state of the same proteins are in the order of $10^{11}\ M^{-1}$ and the kinetics of NO dissociation are very slow.**[947]** This lability of NO from Fe^{III} heme proteins may be used as a means of delivery of this biological effector from the saliva of a blood-sucking insect from the Amazon basin (*Rhodnius prolixus*) to the blood stream of its victim.**[55–57]**)

Deprotonation of *meso*-hydroxyoctaethylporphyrinato-iron(III) $(OEPOH)Fe^{III}$, discussed in Section 6.1.5 below, and simultaneous coordination of two pyridine ligands in pyridine-d_5, produces a species whose optical and NMR spectra suggested that it should be characterized as an Fe^{II} oxophlorin π-cation radical.**[948]** This would be another example of valence tautomerism, that is of $(OEPO^{-})Fe^{III}(Py)_2 \rightleftarrows (OEPO^{+}\bullet)\ Fe^{II}(Py)_2$. The NMR spectra of the complex are characterized by large π delocalization to the *meso* positions and relatively small σ delocalization to all but one of the β-pyrrole positions, suggesting that the electron has been removed from the $b_2(\pi)$ orbital, the analog of the $3a_{2u}(\pi)$ orbital of the porphyrin ring (Figure 4). The curvature observed in the temperature dependence of the NMR spectra suggests that the $a_2(\pi)$ orbital (the analog of the $1a_{1u}(\pi)$ orbital of the porphyrin ring (Figure 4)) is nearly degenerate with the $b_2(\pi)$ orbital and that these two π orbitals are populated to different extents as the temperature is changed.**[948]** However, the EPR spectra of the bis-pyridine and – imidazole complexes showed that the unpaired electron was located on the iron, rather than on the macrocycle, and thus the complexes contain Fe^{III}–$OEPO^{2-}$ rather than Fe^{II}–$OEPO^{-}\bullet$; the g-values change from 2.64, 2.20, 1.64 (N-MeIm)**[199,948]** to 2.20, 2.20, 1.90 (4-AcPy)**[948]** in a manner consistent with a change in electronic ground state of the low-spin $\mathrm{Fe^{III}}$ complexes from $(\mathrm{d}_{xy})^2(\mathrm{d}_{xz},\mathrm{d}_{yz})^3$ to $(\mathrm{d}_{xz},\mathrm{d}_{yz})^4(\mathrm{d}_{xy})^1$ as the basicity of the axial ligands is lowered.[948] However, when 2,6-xylylisocyanide ligands are bound to FeOEPO, a true free radical EPR signal is observed, indicating that with π-acceptor axial ligands the $\mathrm{Fe^{II}}$–$\mathrm{OEPO^{-}\cdot}$ electron configuration is stabilized.[199] It was also found that the bis-N-MeIm complex, although low-spin at 4.2 K, becomes high-spin ($S = 5/2$) or spin-admixed ($S = 3/2{-}5/2$) $\mathrm{Fe^{III}}$ at ambient temperatures, as shown by a study of the temperature dependence of the magnetic susceptibility and the Fe–$\mathrm{N_{ax}}$ bond lengths determined by X-ray crystallography.[199]

The reversible reaction of chloroiron(III) octaethylisobacteriochlorin (or the $\mathrm{Br^-}$, $\mathrm{NCS^-}$, or $\mathrm{PhS^-}$ analog) with π-acid ligands such as carbon monoxide, t-butyl isocyanide or $\mathrm{PF_3}$ in toluene solution produces EPR spectra at 77 K that are indicative of a π-cation radical (equation 16):[200]

$$(\mathrm{OE}i\mathrm{BC}^{2-})\mathrm{Fe^{III}X} + \mathrm{L} \rightleftharpoons (\mathrm{OE}i\mathrm{BC}^{-}\cdot)\mathrm{Fe^{II}(L)X} \tag{16}$$

In contrast to the iron(III) isobacteriochlorins, iron(III) porphyrins do not react with CO.[200]

6 IRON(III) PORPHYRINS AND THEIR REACTIONS

Since the porphyrin ring neutralizes only two of the positive charges of the metal, $\mathrm{Fe^{III}}$ porphyrins must have an associated counterion. This counterion may be directly bound to the metal, as in five-coordinate high-, intermediate-, and low-spin $\mathrm{Fe^{III}}$ porphyrins, or may exist as a separate species that forms an ion-pair with the iron porphyrin complex, as in all six-coordinate complexes of $\mathrm{Fe^{III}}$ porphyrins with neutral ligands. We will survey the structures, properties, and reactions of $\mathrm{Fe^{III}}$ porphyrins of each of the possible spin states.

6.1 High-spin ($S = 5/2$) Iron(III) Porphyrins

6.1.1 Five-coordinate, Monomeric High-spin Iron(III) Complexes

These complexes have the metal significantly (≈0.5 Å) out of the plane, as is evidenced by the 3D structures of five-coordinate porphyrin complexes determined by X-ray crystallography[182,183] and the existence of two o-H and m-H NMR resonances for TPP derivatives and two α-$\mathrm{CH_2}$ resonances for OEP, OETPP and *meso*-alkyl porphyrin complexes.[174,175] In addition to halides as counterions,[174,182,183] a number of other monomeric, five-coordinate, high-spin $\mathrm{Fe^{III}}$ porphyrins have been reported, including those having $\mathrm{X^-} = \mathrm{OH^-}$,[949–951] $\mathrm{OR^-}$,[215,952–956] $\mathrm{RS^-}$,[956–959] $\mathrm{OO^{2-}}$,[960,961] $\mathrm{OOR^-}$,[215] $\mathrm{N_3}^-$,[962,963] $\mathrm{NCS^-}$,[964,965] $\mathrm{C{\equiv}CR^-}$,[966] $\mathrm{RCO_2}^-$,[967] $\mathrm{NO_3}^-$,[968] $\mathrm{OTeF_5}^-$,[447] $\mathrm{SO_4}^{2-}$,[968,969] $\mathrm{HSO_4}^-$,[969,970] $\mathrm{RSO_3}^-$,[968,969] $\mathrm{RSO_2}^-$,[971] $\mathrm{WS_4}^{2-}$,[972] 2-methylimidazole,[962] (triazolate)$^-$,[973] (tetrazolate)$^-$,[973] and the microperoxidases, MP8[432] and MP11,[974] at pH 7.0, where the imidazole ring of histidine serves as the ligand. Of these, the $\mathrm{NO_3}^-$ complex is known to have the anion binding in a bidentate fashion to $\mathrm{Fe^{III}}$ in the solid state,[968] and both it and the $\mathrm{RSO_3}^-$ complexes are believed to behave as bidentate anions in solution.[968] However, a recent structure of $\mathrm{TC_6TPPFcONO_2}$ shows the nitrate ion to be monodentate, and NMR data are consistent with monodentate coordination of this anion in solution.[975] The electron configuration of high-spin $\mathrm{Fe^{III}}$ ($S = 5/2$) gives rise to a ^6A ground state, with relatively large splittings of the zero-field Kramers' doublets, $\pm 1/2$, $\pm 3/2$, $\pm 5/2$.[976] In addition to the halides,[976] zero-field splitting constants, D, have been estimated for some of these anions: $\mathrm{OTeF_5}^-$ appears to be similar to $\mathrm{Cl^-}$,[977] $\mathrm{N_3}^- < \mathrm{Cl^-} \sim \mathrm{N_4C(Me)^-} < \mathrm{N_4C(Ph)^-}$.[973] For the complexes [TPPFeX] having anions $\mathrm{X^-} = \mathrm{NCS^-}$, $\mathrm{Cl^-}$, $\mathrm{Br^-}$, and $\mathrm{I^-}$, $D = 5.1$, 6.0, 12.5, and 13.5 $\mathrm{cm^{-1}}$, respectively,[964,965] and for $\mathrm{OH^-}$ in TMPFeOH, $D = 8.9\ \mathrm{cm^{-1}}$.[951]

At 300 K the ^{1}H NMR spectra of 5-coordinate high-spin $\mathrm{Fe^{III}}$ porphyrinates have β-pyrrole–H resonances (of TPP-type porphyrins) at 82 ppm for the chloride and hydroxide complexes (and for a series of 2-substituted TPPFeCl complexes, the 3-H ranges from 33.4 to 104 ppm, with the other six pyrrole-H resonances giving a spread from 89 to 71 ppm[978]) and +82–70 ppm or so for other anionic complexes, and the pyrrole-H of the very domed and ruffled tetramethylchiroporphyriniron(III) chloride resonate between 80 and 100 ppm,[979] while the pyrrole $\mathrm{CH_2}$ or $\mathrm{CH_3}$ ^{1}H resonances (of OEP-type or natural porphyrins) occur at about 40–50 ppm for α-$\mathrm{CH_2}$ and +50–80 ppm for α-$\mathrm{CH_3}$ at 298 K.[168,174,175] A unique feature of the ^{1}H NMR spectra of 5-coordinate high-spin $\mathrm{Fe^{III}}$ complexes of OEP-type or natural porphyrins is that the *meso*-H resonances occur at about −57 ppm at 294 K for the 5-coordinate chloride complex,[168,174,175] yet at +42 ppm at 294 K for the 6-coordinate high-spin bis-DMSO complex discussed in Section 6.1.2. The reason for the very negative chemical shifts of the *meso*-H resonances of 5-coordinate high-spin $\mathrm{Fe^{III}}$ porphyrinates was earlier explained as being indicative of the involvement of the $4e(\pi)$ orbitals (Figure 4) in Fe → porphyrin π spin delocalization,[168,174] but no adequate explanation was provided for the approximately 100 ppm shift of the *meso*-H resonances upon change of coordination number from 5 to 6.[175] Recently, however, the chemical shifts of the *meso*-H resonances of 5-coordinate high-spin $\mathrm{Fe^{III}}$ porphyrinates have been explained via DFT calculations, which show the importance of the d_{z^2} orbital of high-spin $\mathrm{Fe^{III}}$ in allowing spin delocalization by porphyrin → Fe π spin delocalization via the filled $3a_{2u}(\pi)$ orbital (Figure 4), which is made possible by the strongly out-of-plane position of the iron(III) when it is 5-coordinate.[220] For symmetry reasons, this mechanism of spin delocalization is not available to 6-coordinate high-spin

Fe^{III} porphyrinates,[220] and hence the *meso*-H resonances of these complexes are shifted into the positive chemical shift region. The positive shifts of the *meso*-H resonances of 6-coordinate high-spin Fe^{III} porphyrinates are thus undoubtedly characteristic of σ spin delocalization, largely from the $d_{x^2-y^2}$ unpaired electron, and there is probably thus little, if any, spin delocalization to the $4e(\pi)$ orbitals of the porphyrin ring in any high-spin Fe^{III} porphyrinates or reduced hemes.

Five-coordinate Fe^{III} complexes of tetra-(*meso*-heptafluoro-*n*-propyl)porphyrin have pyrrole-H peaks at 101.5 and 86.4 ppm as a result of S_4-distortion of the porphyrin ring, probably a ruffling distortion, since the structure of the bis-pyridine Fe^{II} complex is highly ruffled.[621] Five-coordinate Fe^{III} complexes of reduced porphyrins have also been reported: ^1H NMR spectra of high-spin Fe^{III} complexes of *trans*-octaethylchlorin (OEC) ($X^- = Cl^-$, $OTeF_5^-$, NCS^-) and tetraphenylchlorin (TPC) ($X^- = Cl^-$, $OTeF_5^-$) have been compared to those of the corresponding OEP and TPP complexes.[980] The pattern of spin delocalization to the *meso* positions is most consistent with that expected for the filled orbital, A_5, which is derived from the $a_{1u}(\pi)$ orbital of the porphyrin.[980] More recently, the resonances of OECFeCl and TPCFeCl have been assigned by saturation transfer from the low-spin complexes.[981,982] The protons on the *meso* positions on either side of the reduced pyrrole ring are those that exchange more rapidly with deuterium under acid conditions,[983] and these *meso* positions are thus most electron-rich. Five-coordinate HS Fe^{III} complexes of both *trans,trans,trans* (*ttt*) and *trans,cis,trans* (*tct*) octaethylisobacteriochlorin, OE*i*BC, have also been investigated by NMR spectroscopy[983] and by electrochemistry.[984]

Particularly notable among the five-coordinate, monomeric, high-spin Fe^{III} complexes is the hydroxo complex, because of the difficulty of preventing its well-known hydrolysis to form the μ-oxo dimer (equation 17), which was discussed earlier (Section 4.3, Scheme 2):

$$2[PFeOH] \rightleftharpoons [PFeOFeP] + H_2O \qquad (17)$$

This problem was solved by using tetraphenylporphyrin ligands having *o,o′*-substituents on the phenyl rings, such as Me (TMP),[247,248] OMe ($[2,4,6\text{-}(OMe)_3]_4TPP$),[973] or halogens (F or Cl),[950] very bulky *m,m′*-substituents such as *t*-butyl,[949] or by use of superstructured porphyrins such as ‘basket-handle[985]’, ‘picket fence[986]’, or related water-soluble ‘picket fence’ derivatives[987] (see Section 4.3). $Fe^{III}TPPS_4$, the tetrasulfonate of TPP, was shown to aggregate on cationic reversed micelles as a function of pH, in part probably due to formation of μ-oxo dimers.[988] $Fe^{III}TPPS_4$ also has been found to bind to cyclodextrins, which reduces the rotational correlation time of the porphyrin and thereby increases the magnetic relaxation efficiency of the complex and also inhibits dimer formation, making it a better water relaxation agent for MRI purposes.[989]

The reaction of superoxide, $O_2^-\bullet$, with TPPFeCl in nonaqueous solvents generates $TPPFe^{II}$ and O_2 in strongly coordinating solvents (pyridine, DMSO),[671,672] and $TPPFe^{II}O_2$ in weakly coordinating solvents (DMF).[672] The formation of the dioxygen complex of an Fe^{II} porphyrin in this way is strong evidence for the valence tautomerism of this complex (equation 18):

$$[PFe^{II}O_2] \rightleftharpoons [PFe^{III}O_2^-\cdot] \qquad (18)$$

Reaction of superoxide with water-soluble Fe^{III} porphyrins results in dismutation of superoxide to O_2 and H_2O_2 (equation 19)[990] (*see* ***Oxygen: Inorganic Chemistry***):

$$HO_2\bullet + O_2^-\bullet + H_2O \longrightarrow O_2 + H_2O_2 + OH^- \qquad (19)$$

The peroxo complex $[TPPFeO_2]^-$ was prepared from $[TPPFe^{II}]$ and superoxide,[672,960] and is another example of the facile, reversible redox reaction that takes place between Fe^{II} and dioxygen and its redox-active reduced derivatives, superoxide and peroxide. The OEP and TPP complexes can also be prepared by treatment of PFeCl with 2 mols of superoxide in acetonitrile.[961] The NMR spectrum is clearly diagnostic of a high-spin Fe^{III} porphyrin.[960] However, the crystal structure of the Mn^{III} analog, $[TPPMn^{III}O_2^-]$, shows that the peroxide ion is bound in a symmetrical, η^2 fashion.[991] By analogy, the Fe^{III} complex is believed to have the same structure.[961] The Fe^{III} complex has been shown to be very nucleophilic in its reactions with olefins.[992,993] More recent work related to the peroxo intermediates of cytochromes P450,[32] peroxidases,[32] and heme oxygenase[994] indicates that if a strong-field nitrogen- or sulfur-donor ligand is bound to the iron, the structure is that of an unsymmetrical Fe-O-O unit[995,996] whose further reaction depends upon which oxygen atom is protonated, as discussed in Section 9 below. Based upon its reactivity, the hydroperoxo complex of heme oxygenase is believed to be electrophilic.[33]

Formation and spectroscopic properties of peroxoiron(III) chlorin complexes of tetraphenylchlorin (TPC), tetramesitylchlorin (TMC) and octaethylchlorin (OEC) have also been reported and shown to be high-spin Fe(III) complexes with EPR g-values of 8.5–8.8, 4.2 and 2.0.[997] These complexes have red-shifted Soret and α,β visible bands and an O–O stretching frequency of 806 cm^{-1}, the latter implying that the peroxo ligand is bound in an η^2 fashion.[997] The ^1H and ^2H NMR spectra of these complexes are also consistent with their formulation as HS Fe^{III} complexes, with pyrrole-H or – D shifts of 66, 61, and 57 ppm and pyrroline-H or – D shifts of 7 and -50 ppm at 293 K, as compared to those of the chloroiron(III) complex (87, 79, 69 ppm and -6 ppm, respectively);[997] for $[OECFeO_2]^-$ the *meso*-H or – D signals are found at −29 and −54 ppm and the pyrroline-H or – D are found at 29 and −38 ppm at 273 K in these 5-coordinate complexes.[997] Alkylperoxo complexes, $PFe^{III}OO$-*t*-Bu, formed from PFe^{II} and *t*-BuOOH, have been studied at very low temperatures

($-70\,°$C)[215,998] to prevent thermal decomposition to $\mathrm{PFe^{IV}O}$ and t-BuO· (equations 20 and 21):

$$[\mathrm{TMPFe^{II}}] + t\text{-Bu-OOH} \longrightarrow [\mathrm{TMPFe^{III}}\text{-OO-}t\text{-Bu}] + \text{side products} \tag{20}$$

$$[\mathrm{TMPFe^{III}}\text{-OO-}t\text{-Bu}] \longrightarrow [\mathrm{TMPFe^{IV}{=}O}] + t\text{-BuO}\cdot \tag{21}$$

(followed by further reactions). Decomposition is catalyzed by bases, such as N-methylimidazole.[215] The chemical properties and reactions of the $(\mathrm{Fe^{IV}} = \mathrm{O})^{2+}$ unit will be discussed in Section 8.

While both 5-coordinate alkylperoxide and methoxide complexes of $\mathrm{TPPFe^{III}}$ are high-spin, the combination of a methoxide and an alkylperoxide ligand, or two of either one, creates low-spin $\mathrm{Fe^{III}}$ complexes,[999–1002] as is discussed further in Section 6.3.1.

Model hemes coordinated to phenoxides and aryl thiolates have been investigated as models of catalase and hemoglobins M (which have tyrosine substituted for either the proximal or distal histidine)[952,956] and cytochromes P450 (which have the thiolate of cysteine coordinated to $\mathrm{Fe^{III}}$).[533,956]

6.1.2 *Six-coordinate, Monomeric High-spin Iron(III) Porphyrin Complexes*

In the presence of ligands of medium coordinative ability, with weakly binding counterions, $\mathrm{Fe^{III}}$ porphyrins form high-spin, six-coordinate complexes. Such is the case of [TPPFeI] in 1:3 mixed $\mathrm{CDCl_3/CD_2Cl_2}$ solutions with added DMSO.[1003] Varying the concentrations of both [TPPFeI] and DMSO confirmed that the stoichiometry of the complex was 2 DMSO:1 $\mathrm{Fe^{III}}$. The crystal structure of $\mathrm{[TPPFe(tetramethylene\ sulfoxide)_2]ClO_4}$ shows that the porphyrin core is expanded, with $\mathrm{Fe{-}N_P} = 2.045$ Å, and long $\mathrm{Fe{-}O_{sulfoxide}}$ bonds (2.069, 2.087 Å).[1004] The phosphine oxide complex was also prepared and characterized.[1004] The crystal structure of $\mathrm{[TPPFe(phenylphosphinic\ methyl\ ester)_2]ClO_4}$ has also been reported, and shows similar porphyrin core expansion ($\mathrm{Fe{-}N_P} = 2.034$, 2.038 Å) and long $\mathrm{Fe{-}O_{PO}}$ bonds (2.102 Å).[1005] Several naturally occurring iron(III) chlorins have been investigated by ^{1}H NMR spectroscopy, including the bis(DMSO) complex of the stable green sulfhemin prosthetic group extracted from sulfmyoglobin[64,65] and that of (pyropheophorbide a)iron(III).[1006,1007] The positive NMR ^{1}H chemical shifts of the *meso*-H suggest six-coordinate, bis(DMSO) complexes in each case. The shift patterns observed are consistent with those observed earlier for complexes of $\mathrm{OECFe^{III}}$.[980] A similar positive *meso*-H chemical shift is also observed for the corresponding OEP complex.[175]

DMF also appears to coordinate to [TPPFeI] to form six-coordinate complexes,[1003,1008] and the structures and magnetic susceptibilities of two bis(ethanol) complexes of $\mathrm{TPPFe^{III}}$ salts[1009] and one $\mathrm{OEPFe^{III}}$ salt[1010] have been reported. The structure of $\mathrm{[TPPFe(H_2O)_2]ClO_4}$ has also been reported;[1011] the $\mathrm{Fe{-}N_P}$ bond distances are 2.041 Å and the Fe–O(aqua) bond distances are quite long, at 2.097 Å, with the metal in the plane of the porphyrin ring. A different type of six-coordinate high-spin $\mathrm{Fe^{III}}$ porphyrin complex is produced if [TPPFeF] is reacted with hydrated tetrabutylammonium fluoride ($\mathrm{Bu_4NF{\cdot}3H_2O}$) in dichloromethane:[1012] The bis-fluoride anionic complex $\mathrm{[TPPFeF_2]^-}$ is stable ($K_\mathrm{f} = 4 \times 10^3\,\mathrm{M^{-1}}$ at 25 °C). Lack of splitting of the ^{1}H NMR signals of o- and m-phenyl protons of $\mathrm{[TPPFeF_2]^-}$ supports the assumption of diaxial fluoride coordination with the metal in the plane of the porphyrin.[217,1012] In aqueous solution at high pH, water-soluble iron(III) porphyrins such as tetrakis(o-methylpyridinium)porphyrin, T(o-MPy)$\mathrm{PFe^{III}}$, bind two hydroxide ions and give rise to a characteristic $\nu_{\mathrm{HO{-}Fe{-}OH}}$ resonance Raman band at 447 cm^{-1}.[1013]

The high-spin dichloroiron(III) complex of 5,10,15,20-tetraphenyl-21-oxaporphyrin has been prepared and characterized.[536] Its ^{1}H NMR spectra show pyrrole-H shifts of 86.2, 67.9, and 66.3, highly characteristic of the pyrrole-H shifts of high-spin $\mathrm{Fe^{III}}$ porphyrins, and furan-H shift of 47.7 ppm. The Fe–Cl bonds (2.302 Å) are much longer than that of TPPFeCl,[1014] as might be expected for a dichloride complex of $\mathrm{Fe^{III}}$.

Six-coordinate complexes of several $\mathrm{Fe^{III}}$ porphyrins, having one pyridine and one isothiocyanate ligand, have been reported.[1015,1016] Interestingly, the pyridine/N-bound thiocyanate anion combination appears to lie close to the $S = 1/2 \rightleftharpoons 5/2$ spin crossover point for the $\mathrm{TPPFe^{III}}$ complex and, depending on the crystal lattice, exists as either a low-spin[1015] or a thermal equilibrium between a low-spin and a high-spin complex,[1016] while the $\mathrm{OEPFe^{III}}$ complex is high-spin at all temperatures.[1015]

Finally, an unusual six-coordinate, mononuclear $\mathrm{Fe^{III}}$ complex is formed in the solid state by *meso*-$\alpha,\alpha,\alpha,\alpha$-tetrakis($o$-nicotinamidophenyl)porphyrinatoiron(III) chloride, which consists of polymeric chains in which the Fe atom of one molecule is coordinated to a pyridine nitrogen of the nicotinamide unit of a second molecule. The chloride ion occupies the sixth coordination site, inside the ‘pocket’ of the four nicotinamide groups. Magnetic susceptibility, EPR, and Mössbauer data on solid samples indicated a mixture of high-spin monomer (70%) and high-spin Heisenberg chain (30%), with $D = 10\,\mathrm{cm^{-1}}$, $E = 2.25\,\mathrm{cm^{-1}}$, and $J = -5\,\mathrm{cm^{-1}}$ contributions from spin crossover.[986] The solution behavior of the complex resembles that of other monomeric five-coordinate $\mathrm{Fe^{III}}$ porphyrins.

6.1.3 *Bridged Dimeric Complexes of High-spin Iron(III) Porphyrins and Chlorins*

A number of the properties of μ-oxo dimers of $\mathrm{Fe^{III}}$ porphyrins, formed by hydrolysis of the hydroxo complex (equation 17)[1017] or by reaction of molecular oxygen with $\mathrm{Fe^{II}}$ porphyrins (see below), have been investigated, including ^{1}H and ^{13}C NMR, IR and Raman, and Mössbauer spectra, magnetic susceptibilities, and crystal and molecular structures.

The structure of [(TPPFe)$_2$O] was reported by Hoard.[1018] Structures of two crystalline forms of [(OEPFe)$_2$O] have been solved and in this case show nearly eclipsed porphyrin ring orientation.[1019] The eight Fe–N$_\mathrm{P}$ bond distances have average values of 2.077 and 2.080 Å, the average Fe–O bond lengths are 1.756 and 1.755 Å, and the average displacement of the iron(III) from the mean porphinato plane are 0.50 and 0.54 Å, respectively, in the triclinic and monoclinic forms.[1019] The linear PFe–O–FeP units are antiferromagnetically coupled dimers of high-spin Fe$^{\mathrm{III}}$. Attempts to measure the coupling constant, $-2J$, from the temperature dependence of the magnetic susceptibility or NMR isotropic shifts have yielded a range of values.[168,183] Magnetic susceptibility results for [(TPPFe)$_2$O] in the solid state give $-2J = 271\,\mathrm{cm}^{-1}$,[1020] while values of $258\,\mathrm{cm}^{-1}$ and $312\,\mathrm{cm}^{-1}$ have been obtained from ^{1}H[1021] and ^{13}C[179] NMR results, respectively. Calculation of $-2J$ from the temperature dependence of the NMR spectra of these complexes is complicated by the possibility of dipolar, ZFS, and contact contributions to the isotropic shifts.[168] In any case, the isotropic shifts of the protons of these PFe–O–FeP dimers are significantly different from those of the high-spin Fe$^{\mathrm{III}}$ monomers,[168] with all resonances occurring between 7 and 14 ppm at 320 K. Similar NMR spectra are observed for the reduced porphyrin analog [(TPCFe)$_2$O], with the addition of two signals from the two types of protons in the pyrroline ring.[1021] The tetraphenylchlorin complex has a similar derived value of $-2J$ ($265\,\mathrm{cm}^{-1}$).

As mentioned in Section 1.5.2, the μ-oxo dimers PFeOFeP are readily cleaved by dry HCl in nonaqueous solvents (equation 22):

$$\mathrm{PFe{-}O{-}FeP} + 2\mathrm{HCl} \longrightarrow 2\mathrm{PFeCl} + \mathrm{H_2O} \qquad (22)$$

In nonaqueous solvents, such treatment with dry hydrohalic acids is the only way to cleave the μ-oxo dimer nonoxidatively. However, the μ-oxo dimers of water-soluble porphyrins are readily cleaved by Lewis bases such as hydroxide, imidazole, histidine, and pyridine.[1022–1024] Both the equilibria[1022] and kinetics[1023] of such reactions have been reported. In addition, μ-oxo dimers of water-insoluble Fe$^{\mathrm{III}}$ porphyrins in dichloromethane can be oxidatively cleaved to yield PFe$^{\mathrm{III}}$F$_2^-$ and (probably) an Fe$^{\mathrm{IV}}$ species.[1025] Studies of the picosecond decay of the excited state of (TPPFe)$_2$O in benzene following a 532- or 355-nm 25-ps pulse suggest that the intermediate state is a photodissociated pair, (TPP$^-\cdot$)Fe$^{\mathrm{II}}$ + TPPFe$^{\mathrm{III}}$ − (O$^-\cdot$), and a small amount of disproportionation reaction products, TPPFe$^{\mathrm{II}}$ + TPPFe$^{\mathrm{IV}}$ = O.[1026]

It has been shown that the μ-oxo dimer (OEPFe)$_2$O can be monoprotonated to yield the μ-hydroxo species [(OEPFe)$_2$OH]ClO$_4$, via a mixed-phase reaction.[1027] The formulation of the complex has been confirmed by an X-ray diffraction study, which reveals a single bridging group and a single perchlorate counterion per dimer unit. The Fe–O(H)–Fe bond, with an angle of 146.2°, is considerably bent from the linear Fe–O–Fe geometry typically observed for μ-oxo dimers of Fe$^{\mathrm{III}}$ porphyrins,[1027] while the Mn(III) analog is nearly linear.[1028] The UV–vis spectrum of [(OEPFe)$_2$OH]ClO$_4$ shows a large blue shift (Soret band at 362 nm) compared to (OEPFe)$_2$O (389 nm); the Mössbauer parameters are typical of high-spin Fe$^{\mathrm{III}}$. Consistent with the magnetic susceptibility, which shows strong antiferromagnetic coupling, no EPR spectrum is observed.[1027]

Iron(III) porphycenes readily form μ-oxo dimers, and a complex having tetra-CF$_3$ etioporphycene was investigated by X-ray crystallography, electrochemistry and solution reactivity.[1029] The structure displays a severe saddled distortion of the porphycene framework as a result of the steric and electronic effects of the CF$_3$ substituents. The oxidation and reduction potentials for the μ-oxo dimer are significantly more positive compared to those observed for non-CF$_3$-containing iron porphycenes.[1030] Further study of the redox chemistry of μ-oxo dimers of iron(III) porphycenes shows that oxidation states of these dimers can range from −4 to +4.[1031,1032] The μ-oxo dimer is readily converted into the monomeric ferrous complex in pyridine-d$_5$ through autoreduction for one day.[1029]

A series of mixed metal μ-oxo dimers of the type PFe–O–CrP′ have been prepared from PFe$^{\mathrm{II}}$ and P′Cr$^{\mathrm{IV}}$ = O.[1033] Their ^{1}H NMR spectra are characterized by resonances due to the PFe$^{\mathrm{III}}$ in the positions found for the symmetrical PFe–O–FeP dimer, and a resonance at 38 ppm that is due to the pyrrole-H of the chromium porphyrin unit. The temperature dependence of the magnetic susceptibility of the mixed-metal dimer leads to its formulation as antiferromagnetically coupled Fe$^{\mathrm{III}}$ ($S = 5/2$) and Cr$^{\mathrm{III}}$ ($S = 3/2$), yielding $S' = 1$, with $-2J \sim 260{-}300\,\mathrm{cm}^{-1}$ and D_{Fe} and g_{Fe} ranging from $3.8{-}4.9\,\mathrm{cm}^{-1}$ and 1.98–2.05, respectively, assuming $D_{\mathrm{Cr}} \sim -1\,\mathrm{cm}^{-1}$.[1033] Similar mixed-metal dinuclear μ-oxo dimers can be synthesized in which the iron complex is the phthalocyanine, PcFe$^{\mathrm{III}}$.[1033]

The μ-peroxo dimer intermediate, C, in the oxidation of four-coordinate Fe$^{\mathrm{II}}$ porphyrins to the PFe–O–FeP μ-oxo dimer via equations (23A–C) (cf. Scheme 2) of tetrakis(m-tolyl)porphinatoiron(III), has been detected by NMR spectroscopy at low temperatures.[1034] The μ-peroxo complex has a larger isotropic shift (16 vs. 13 ppm for the μ-oxo dimer at −50 °C) for the pyrrole-H at all temperatures, and has an antiferromagnetic coupling constant, $-2J$, that is about 30% smaller than that for the μ-oxo dimer, E; the magnetic moment decreases from $2.6\,\mu_\mathrm{B}$ at −50 °C to about $2.2\,\mu_\mathrm{B}$ at −80 °C, both consistent with weaker antiferromagnetic coupling in the μ-peroxo complex.[1034]

$$\begin{tikzcd}
\underset{\mathrm{A}}{\mathrm{PFe^{II}}} + \mathrm{O_2} \arrow[r] & \underset{\mathrm{B}}{\mathrm{PFeO_2}} & \\
\mathrm{PFeO_2} + \mathrm{PFe^{II}} \arrow[r] & \underset{\mathrm{C}}{\mathrm{PFe^{III}{-}OO{-}Fe^{III}P}} \arrow[r] \arrow[d] & \underset{\mathrm{D}}{2\mathrm{PFe^{IV}O}} \\
\mathrm{PFe^{IV}O} + \mathrm{PFe^{II}} \arrow[r] & \underset{\mathrm{E}}{\mathrm{PFe^{III}{-}O{-}Fe^{III}P}} &
\end{tikzcd} \qquad (23)$$

Dimeric complexes of the oxoanions SO_4^{2-} and CrO_4^{2-}, $[(PFe)_2XO_4]$, have been shown to have both ^1H and ^{13}C NMR resonances that are sharp and at very similar isotropic shifts as those of monomeric, high-spin Fe^{III} complexes,[968,1035] suggesting that antiferromagnetic coupling is very weak or nonexistent in these dimeric complexes. Consistent with this, the Fe–Fe separation in $[TPPFe]_2SO_4$ is 6.049 Å.[1036] The geometry of the sulfato ion results in a canting of the porphinato cores at an angle of 24°.

There has been a report of bridged dinitrogen complexes of iron(III) and chromium(III) complexes, formed by reaction of the metallo(III)porphyrinate triflate with $[Re(N_2)(PMe_2Ph)_4Cl]$ to make the Fe-N-N-Re or Cr-N-N-Re bridged complexes.[1037] The Fe^{III} complex has a magnetic moment of about 4.4 μ_B at room temperature, consistent with a $S = 3/2,5/2$ admixed spin state for the iron(III), and a pyrrole-H shift of -3.23 ppm, consistent with the expected weak-field nature of the N_2 ligand.[1037] The structure shows a linear Fe–N–N–Re unit (Fe–N1–N2 = 170°, N1–N2–Re = 177°) with Fe–N bond length of 1.93 Å,[1037] similar to that of the TPPFe^{III}-azide complex (1.953 Å).

An intermolecular type of dimer formation has been observed for the unsymmetrically substituted 5-(2-hydroxyphenyl)-10,15,20-tritolylporphyrin complex of Fe^{III}, in which the *o*-OH functions of one molecule are deprotonated and bind as RO^- ligands to the Fe^{III} of a second molecule, which in turn binds its deprotonated *o*–OH function to the Fe^{III} of the first. Despite this intramolecular dimeric structure, the proton NMR spectra reveal pyrrole-H signals in the 80 ppm region at 25 °C, diagnostic of a high-spin Fe^{III} center, and the magnetic moments in solution ($6.0 \pm 0.2\,\mu_B$) and solid-state ($5.91 \pm 0.05\,\mu_B$) match the spin-only value for high-spin Fe^{III}, thus indicating that antiferromagnetic coupling is extremely weak.[953]

A novel intermolecular type of trimer formation occurs with 2-hydroxy-5,10,15,20-tetraphenylporphyrinatoiron(III). Deprotonation of the 2-hydroxy group creates an anionic aryloxo ligand for another Fe^{III} center, and the cyclic trimer thus forms.[277] The metal ions are weakly coupled high-spin Fe^{III} centers ($\mu_{eff} = 5.4 \pm 0.2\,\mu_B$), and the 3-H NMR resonances of this low-symmetry trimer are uniquely found at very negative chemical shifts (-89.8, -94.7 and -99.3 ppm at 291 K) and are very broad (670−690 Hz), while all other β-pyrrole protons resonate in the $+82$ to $+62$ ppm region[277] typical of high-spin Fe^{III} in monomeric complexes.[174,175] The structure of the trimeric complex has also been reported.[1038]

6.1.4 *Bridged or Through-space Magnetically Coupled Complexes of High-spin Iron(III) Porphyrins with Other Types of Metal Complexes; Possible Models for Cytochrome Oxidase, Assimilatory Sulfite Reductases, and Sulfite Oxidase*

Cytochrome *c* oxidase (CcO) in mitochondria and in bacterial cells catalyzes the four-electron reduction of O_2 to H_2O by cytochrome *c*, and is the terminal electron acceptor of the electron transport chains of animals and many other organisms (*see* ***Cytochrome Oxidase***). Structures of four different CcO enzymes have been reported.[2–6] Four electrons and four protons are needed to reduce O_2 to $2\,H_2O$, and there are four redox-active metal centers (Fe_a, Cu_A, Fe_{a3}, and Cu_B) that participate in this reduction, in which O_2 is believed to bind to the Fe_{a3} heme, which is in close proximity to Cu_B.[1039,1040] The two iron centers are heme *a* prosthetic groups (*see Prosthetic Group*), Figure 1(d), which will hereafter be referred to as heme *a* and heme a_3. The heme a_3-Cu_B (sometimes called Cu_{a3}) center of the resting oxidized form of the enzyme has been a subject of considerable interest for some years, since it is EPR silent; the same is true of *E. coli* cytochrome bo_3,[1041] which is also called a quinol oxidase because it uses a quinol in place of the Cu_A, the diamond-shaped dicopper center, $[Cu(SR)_2Cu]^{+/0}$, and the spectroscopic investigation of the quinol oxidases is simpler because of the absence of this cofactor. The most widely accepted explanation for this EPR silence is that there is strong ligand-mediated antiferromagnetic (*see Antiferromagnetism*) coupling ($J = 200\,cm^{-1}$ or larger in magnitude) between the Cu^{II} and Fe^{III} centers.[1042–1047] However, it has recently been shown for one form of *Thermus thermophilus* cytochrome c_1aa_3 (another member of the CcO family that has a heme c_1 in place of the Cu_A center) that the Mössbauer spectra could be fit to either strong or weak ($|J| \sim 1\,cm^{-1}$) coupling schemes,[1048–1050] and by a combination of parallel and perpendicular mode EPR and MCD spectroscopies that cytochrome bo_3 (yet another member of the CcO family), which has the same Fe–Cu interacting system in the same structural arrangement, has very weak antiferromagnetic coupling ($J = 1\,cm^{-1}$) for the fluoride,[1041] chloride, azide, and formate-bound complexes.[1051] In contrast to the apparent antiferromagnetic coupling (*see* ***Magnetism of Transition Metal Ions***) of the resting state of CcO,[1042] the cyanide-inactivated form has been interpreted in terms of ferromagnetic (*see Ferromagnetism*) coupling ($J > 100\,cm^{-1}$) between Fe^{III} and Cu^{II}, on the basis of both MCD[1052] and Mössbauer[1053] spectroscopic data. A σ/π orthogonality of the magnetic orbitals of Cu^{II} $((d_{x^2-y^2})^1)$ and low-spin Fe^{III} $((d_{xz},d_{yz})^3)$ with respect to a proposed Fe–CN–Cu bridge provides an appealing rationale for the ferromagnetic interaction.[1054,1055]

In addition to cytochrome *c* oxidase, a protein complex having a very similar fold and arrangement of metal centers is that of the heme-containing nitric oxide reductase (NOR).[1056–1059] This protein complex is found in a number of anaerobic bacteria and archaea, including *Paracoccus denitrificans*,[1060,1061] *Bacillus azotoformans*,[1062] and *Pyrobaculum aerophilum*,[1063,1064] and carries out the enzymatic reaction $2NO + 2e^- + 2H^+ = N_2O + H_2O$. (Although this is only a 2-electron reduction, NORs can also reduce O_2 to $2H_2O$, a 4-electron reduction,[1065–1067] and at least several CcOs can reduce 2NO to $N_2O + H_2O$,[1067–1069] a

2-electron reduction.) There are actually three types of NORs that belong to the heme-copper oxidase superfamily: cNOR (cytochrome *c* dependent), qNOR (quinol-dependent), and qCu$_A$NOR (qNOR that contains Cu$_A$ at the electron entry site).**[1063]** Because copper is absent from the heme-containing subunit of these NORs, the binuclear metal center is believed to contain a non-heme iron instead of copper; all of the histidines present in CcO subunit I are conserved in these NORs.**[1056,1070,1071]** The hemes present are two hemes *b* in the protein called norB (the analog of subunit I of CcO), and, in cNORs, a membrane-bound *c* heme protein (called norC) that apparently takes the place of the Cu$_A$ subunit. These proteins are believed to be extremely ancient, with the menaquinone-containing qNORs possibly being the oldest, the so-called Urenzymes, possibly the precursors to others, including the CcOs.**[1063]** There is another kind of heme-containing NOR, that being cytochrome P450$_{nor}$ from the denitrifying fungi, *Fusarium oxysporum***[1072]** and *Cylindrocarpon tonkinese*.**[1073]** The structure of the enzyme from *F. oxysporum* has been determined, and shows it to be similar to other cytochromes P450 except for the openness of the heme distal pocket to solvent.**[1074]** The mechanism of NO reduction to N_2O by this enzyme is believed to involve the intermediate HNO, which can react with itself to produce N_2O and H_2O; a heme-bound HNO complex has been detected.**[935,936]**

Several types of models of the spin-coupled Fe–Cu centers of CcO were reported between 1980 and 1992,**[1075–1083]** with the work from 1993 to present having been reported by the groups of Holm,**[1084–1091]** Karlin**[1092–1106]** and Collman.**[707,1107–1116]** The first of the earlier models was the Cu^{II} complex of $\alpha, \alpha, \alpha, \alpha$-tetrakis(*o*-nicotinamidophenyl)porphyrinatoiron(III) chloride, shown in Figure 8(a).**[1075]** The long Fe–Cl and Cu–Cl distances determined at room temperatures, as well as the temperature dependence of the magnetic susceptibility, and the Mössbauer spectra, suggest that there may be either a temperature-dependent spin equilibrium between $S = 5/2$ and 3/2, or a quantum-admixed $S = 5/2, 3/2$ state, or that some molecules have the chloride ion outside the pocket and thus do not contain chloride-bridged metals.**[1075]** At low temperatures (4.2–30 K) this complex showed EPR signals from both Fe^{III} and Cu^{II}, indicating little or no antiferromagnetic coupling, because of the σ, π mismatch in orbital symmetry. The existence of these EPR signals at low temperatures, and their loss as a result of dipolar spin relaxation above 40 K, suggested that purely dipolar spin relaxation cannot account for the EPR silence of the oxidized resting state of CcO.**[1075]** The cyanide-bridged analog of this model compound showed weak ferromagnetic coupling ($J = +0.25\,\text{cm}^{-1}$), and EPR spectra that are not superpositions of the low-spin Fe^{III} and Cu^{II} spectra as a result of a combination of isotropic, anisotropic and asymmetric exchange, dipole–dipole, and Zeeman terms.**[986]**

A second model of the resting oxidized form of CcO from the same research group, in which the geometry of the Cu^{II} complex was changed to allow orbital overlap between the $d_{x^2-y^2}$ orbital of Cu and the d_{z^2} orbital of high-spin Fe^{III}, has been reported. In this model, also shown in Figure 8(b), a strapped porphyrin having S–N$_{Py}$–S ligands for the Cu, and a bridging hydroxide (*see Bridging Ligand*) ion between the two metals, produced an $S = 3/2$ spin state at the iron center with weak antiferromagnetic coupling between metal spins.**[1076]** Another strapped porphyrin, in this case supplying N–S–N ligands for the Cu, and having a μ-oxo bridge between high-spin Fe^{III} and Cu^{II}, showed weak HS Fe^{III} and Cu^{II} EPR signals, and the temperature dependence of the magnetic susceptibility was consistent with antiferromagnetic coupling ($J = -44\,\text{cm}^{-1}$),**[1077]** Figure 8(c).

Cu^{II} chelates that incorporate potentially bridging ligands have been used to form μ-imidazolato,**[1081,1082]** μ-carboxylato,**[1080]** or μ-thiolato**[1085,1117]** bridged complexes with Fe^{III} porphyrins. In one case, two moles of TPPFe^{III} bind to one Cu(MNT)$_2{}^{2-}$ to form a bridged trimeric complex in which one sulfur of each MNT^{2-} ligand bridges Cu^{II} and Fe^{III}.**[1083]** In another case, two moles of the Cu^{II} chelate, CuIM, or its Ni^{II} analog, NiIM, bind to TPPFeCl,**[1079]** OEPFeCl,**[1080]** or TPPFeB$_{11}$CH$_{12}$**[1081,1082]** to form the μ-imidazolato-bridged complex shown in Figure 8(d). The binding constants, β_2, for addition of CuIM to TPPFeCl and OEPFeCl in DMSO are more than a factor of 10^3 larger that those of N-MeIm for the same porphyrins in the same solvent.**[1079]** Although the enthalpies of formation of the bis(imidazole) complexes are similar, the entropies are much less negative for formation of the CuIM complex, possibly due to intermolecular dimerization of this complex in solution.**[1079]** The TPPFe(CuIM)$_2{}^+$ has been characterized by X-ray crystallography, and it and its Fe^{II} and Fe^{III} (NiIM)$_2$ analogs have been characterized by detailed magnetic susceptibility and Mössbauer spectroscopic studies.**[1081,1082]** The effective magnetic moment of the PFe^{II}(CuIM)$_2$ system at temperatures above 20 K is 2.60 μ_B, corresponding to two Cu ions with $S = 1/2$ and $g_{Cu} = 2.12$, while the magnetic moment below 20 K decreases significantly and can be fitted with pairwise antiferromagnetic coupling with $J_{CuCu} = -1.52\,\text{cm}^{-1}$. All parameters for the Fe^{III}(NiIM)$_2$ system are consistent with the $S = 1/2$ state of this system, while the effective magnetic moment of 3.4 μ_B for the Fe^{III}(CuIM)$_2$ system at 300 K corresponds to a susceptibility that is the sum of those of the two analogs. However, as the temperature is decreased, the effective moment rises to a maximum at 8 K, indicating ferromagnetic Fe–Cu coupling ($J = 22.2\,\text{cm}^{-1}$) and an antiferromagnetic, chainlike through-space coupling of Cu^{II} on adjacent units ($J_{CuCu} = -1.87\,\text{cm}^{-1}$). This can be understood in terms of a σ/π orthogonality of the magnetic orbitals of Cu^{II} and low-spin Fe^{III}.**[1081,1082]**

Three 1:1 Fe:Cu model compounds have been reported, each of which contains a dinuclear anion in which an iron(III) porphyrin and a copper(II) maleonitrile dithiolate are bridged by one of the thiolate anions. The other ligand to Fe^{III} in each case is THF. The cations of the three compounds are either [TPPFe(THF)$_2$]$^+$, [TPPGa(THF)$_2$]$^+$, or [TPPAl(THF)(H$_2$O)]$^+$**[1117]** (Figure 8(e)). The structural results and the Mössbauer parameters suggest that the Fe^{III} center in

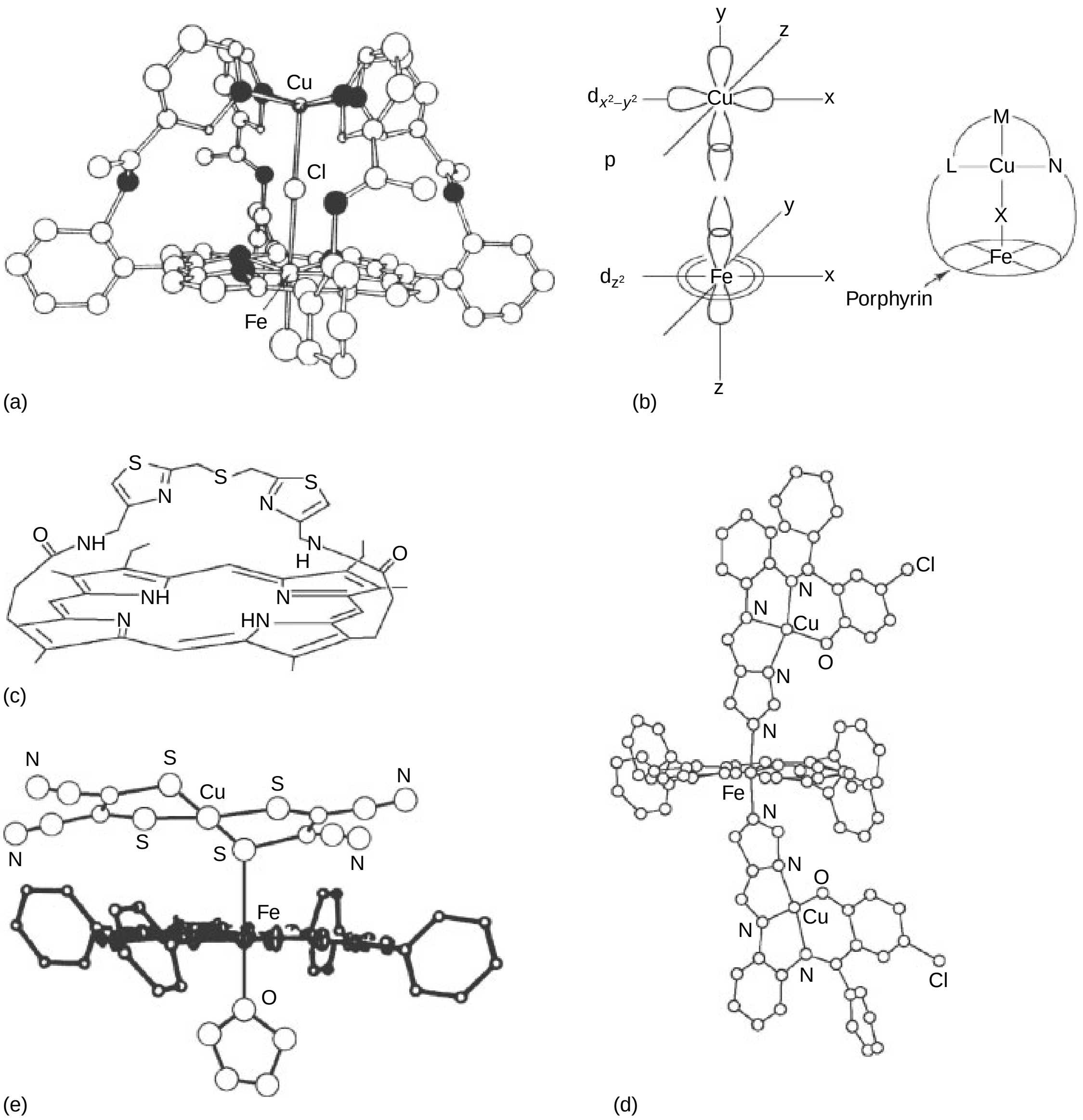

Figure 8 Cytochrome *c* oxidase (CcO) models. (a) The complex formed from iron $\alpha, \alpha, \alpha, \alpha$-tetrakis(*o*-nicotinamidophenyl)porphyrin and Cu^{II}, bridged by a chloride ion;**1075** (b) (left) schematic representation of the orientation of metal atomic orbitals predicted for significant exchange interaction between a single unpaired electron in the d_{z^2} orbital of a high-spin Fe^{III} ion in a porphyrin with an electron in the singly occupied $d_{x^2-y^2}$ orbital of a Cu^{II} ion in a square planar ligand field, via the p orbitals of a single bridging ligand X, and (right) a general ligand system that could maximize such orbital overlap, which was tested by creation of a 'strapped' porphyrin designed to complex a Cu^{II} in the S–N–S ligand strap created by two aliphatic thioethers (L, N) and a pyridine (M), bridged to an Fe^{III} porphyrin through bridging ligand X;**1076** (c) a 'strapped porphyrin designed to complex a Cu^{II} in a similar geometry as that of (b), using the N–S–N ligand strap shown;**1077** (d) a bis(CuIM) complex of $TPPFe^{III}$;**1082** (e) the anionic 1:1 complex of $Cu^{II}(MNT)_2$ with $TPPFe^{III}$;**1117** (f) the cyanide-bridged Cu(Me_6tren) and Cu(Me_5dien) complexes of OEPFe(Py);**1086** (g) the (tris-imidazole)-Cu^{II} model of Collman,**1114** and (h) two views of the oxo-bridged complex of (F_8-$TPPFe^{III}$ with Cu^{II}(TMPA)**1093**

each of the dinuclear anions is intermediate spin ($S = 3/2$). The $Fe^{III}-Cu^{II}$ dimers give rise to no EPR signal. The metal ions are weakly antiferromagnetically coupled in each of the anions; the exchange coupling constants calculated from the magnetic susceptibility data for the compounds having $TPPGa^{III}$ or $TPPAl^{III}$ cations are $J = -17.94$ and $-15.18\,\text{cm}^{-1}$, respectively. The absence of EPR signals for the Ga^{III} and Al^{III} compounds is consistent with calculations showing that the values of J and D for these complexes are sufficiently large and that the energies required for allowed transitions are greater than the X-band EPR quantum at the magnetic fields used. The investigators concluded that 'given the existence of a series of 'EPR silent' Fe^{III}/Cu^{II} systems that are not strongly antiferromagnetically coupled, it

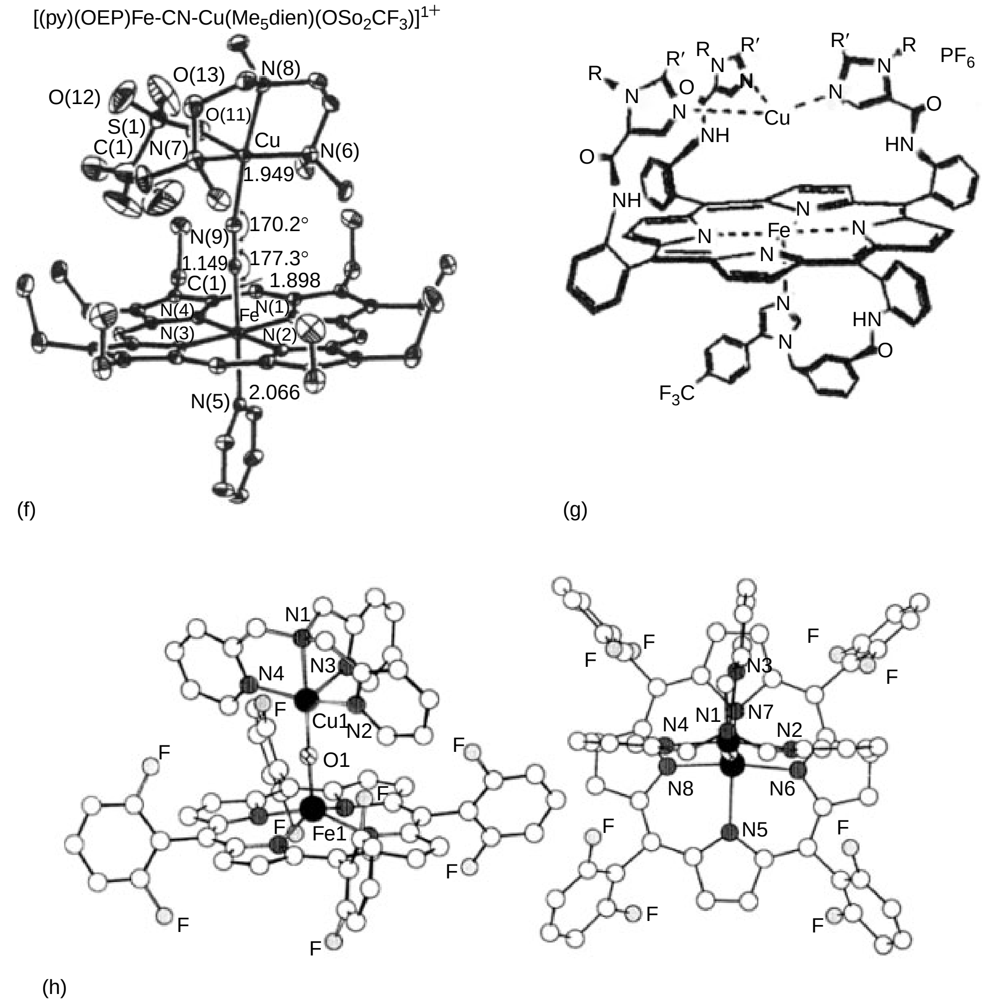

(f) (g)

(h)

Figure 8 cont’d

seems necessary to carefully reexamine the basis for the EPR silence of the active site of the resting form of cytochrome *c* oxidase’.[1117]

Holm’s group has prepared monomeric 1:1 model complexes consisting of OEPFe^{III} and Me$_6$trenCu^{II}, where tren = triethylenetetramine, or Me$_5$dienCu^{II}, where dien = diethylenetriamine, Figure 8(f), with a weak-field anion present in each case.[1084,1085] Structures of cyanide-bridged complexes have also been reported.[1087] Further characterization of these complexes by multiple-edge XAS,[1088,1091] vibrational spectroscopies,[1090] Mössbauer spectroscopy[1089] and magnetization studies[1089] has been reported. The structures of all fully oxidized cyanide-bridged complexes show linear Fe^{III}-CN fragments (bond angle 176–180°), and any deviations therefrom occur in the Cu^{II}-CN fragment (nearly linear for trigonal bipyramidal-axial and distorted square pyramidal-equatorial complexes (170–174°), and bent in other square pyramidal-equatorial (163°) and square pyramidal-axial (147–159°) and doubly bridged tetragonal octahedral (140°) complexes).[1087] In the bridges of the fully oxidized complexes, decreasing Cu–N–C bond angles correlate with increasing Cu–NC bond distances. Increasing υ_{CN} values correlate with decreasing Cu–N–C angles and increasing Cu–N bond distances, and the values encompass those for cyanide-inhibited oxidized CcO enzymes (2152–2146 cm^{-1}).[1087] The infrared data, together with magnetic and Mössbauer spectroscopic results, which show coupled Fe^{III} and Cu^{II} spins, lead to the conclusion that these enzymes possess a tight [Fe^{III}–CN–Cu^{II}] bridge, rather than a binuclear site in which cyanide is bridged exclusively to one subsite, or interacts weakly with another subsite or is hydrogen-bonded at the uncoordinated end. The existence of the [Fe^{III}–NC–Cu^{I}] bridge in the one-electron-reduced complex, [OEPFe–NC–Cu(Me$_5$dien)]ClO$_4$, raises the question of whether a similar atom sequence may occur in biological bridges of the same oxidation state.[1087] The cyanide moiety of this complexes contains two bent M-cyanide bonds, with Fe–N–C = 165.3° and Cu–C–N = 168.9°; this complex has no sixth ligand to the iron.

Multiple-edge XAS studies of the μ-oxo, μ-hydroxo and η^2-cyano complexes that have been characterized crystallographically have provided important benchmarks that can be used to analyze the data from various forms of CcO enzymes,**1088,1091** because the structures of CcO that have been reported**2–6** do not exhibit the discrete bridges anticipated on the basis of exchange coupling between Fe^{III} and Cu^{II} in the fully oxidized enzymes, possibly because one or both metal centers become reduced over the course of X-ray crystallographic data collection or perhaps the microscopic pH around the binuclear center was not consistent with formation of the bridge. For the model complexes it is found that there is a dramatic increase in the amplitude of the Fe–X–Cu long-range multiple scattering pathway as the bridge unit approaches linearity.**1088,1091** The oxo and hydroxo ligated bridges can be differentiated by features in the Fe absorption preedge. Significantly, no EXAFS spectrum of a heme-copper oxidase yet displays the intervening atom effect consistent with a linear Fe–O–Cu bridge.**1088** For the cyanide-bridged model complexes, a strong long range Fe· · ·Cu interaction (4.94 Å) is observed from both the Fe and Cu K-edge data of the linearly bridged complex studied, and this strong interaction is not observed in the K-edge data for either metal for the complex in which the angle deviates significantly from linearity.**1091** These data will be useful for examining cyanide-inhibited CcO.

Resonance Raman ($\lambda_{excit} = 647$ nm) and mid-infrared spectra of the cyanide-bridged model compounds display three isotope-dependent vibrational modes. Two vibrations (2182 and 535 cm^{-1}) show monotonic decreases with increasing mass of the cyanide ligand and could thus be assigned to the C-N stretch and Fe-CN-Cu stretch, respectively.**1089** The C-N stretch was also observed by resonance Raman for the first time. The third vibration, detected with resonance Raman, showed a zigzag-type behavior (495, 487, 493, 485 cm^{-1}) with the $^{12}C–^{14}N$, $^{13}C–^{14}N$, $^{12}C–^{15}N$, $^{13}C–^{15}N$ isotopomers that is characteristic of a bending vibration. The measurements strengthen the proposal that cyanide bridges the two metal atoms in the cyanide-ligated, oxidized binuclear center of CcO. A quantitative consideration of the vibrational characteristics of cyanide bound to the resting enzyme, in light of the model compound results,**1089** strongly suggests that the binuclear center of the enzyme is flexible and can undergo structural rearrangement to accommodate exogenous ligands.

Mössbauer and magnetization studies of oxo-, hydroxo- and formate-bridged complexes of $[OEPFe–X–Cu(Me_5dien)(OClO_3)]^+$ were interpeted in terms of strong antiferromagnetic coupling between a high-spin Fe^{III} ($S = 5/2$) and Cu^{II} ($S = 1/2$) resulting in an $S = 2$ ground state. The exchange coupling of the hydroxo-bridged complex is substantial ($J = 170\,cm^{-1}$), but is smaller than that of the oxo-bridged complex ($J \geq 200\,cm^{-1}$). The formate-bridged complex maintains an *anti–anti* carboxylate bridged conformation and has $J = +18\,cm^{-1}$.**1090** In light of the recent findings that the antiferromagnetic coupling of the Fe^{III} and Cu^{II} of fully oxidized, resting state CcO is weak,**1048,1051** carboxylate bridging of the model complex metal centers should be considered more carefully.

Karlin's group's work has been reviewed recently;**1106** they have prepared a model complex consisting of *meso*-tetrakis(2,6-difluorophenyl)porphyrinatoiron(III/II) ($F_8TPPFe^{III/II}$) and tris-2-pyridylmethylaminecopper(II/I) ($(TMPA)Cu^{II/I}$).**1092,1093,1105** The structure of the μ-oxo-bridged complex in which both metals are in their oxidized states has been reported,**1093** and is shown in Figure 8(h); the spin state of this complex is $S = 2$. The μ-hydroxo complex has also been characterized structurally.**1093–1095** The μ-peroxo complex has also been prepared by reaction of the Fe^{II} and Cu^I precursors with O_2 at low temperatures, and characterized by UV-visible, resonance Raman, Mössbauer and ^1H NMR spectroscopies.**1103** The Mössbauer data indicate that the Fe^{III} center is high-spin ($\delta = 0.57$ mm/s, $\Delta E_Q = 1.14\,mm\,s^{-1}$) and bound to an electron-rich ligand such as a peroxide; the magnetic field dependence is consistent with the complex being an integer spin system. Stopped-flow UV-visible spectroscopy at -94 to $-75\,°C$ revealed the presence of a heme-superoxo intermediate, formed within the mixing time, prior to formation of the heme-peroxo-Cu complex. The overall kinetics are complicated by several side reactions.**1103**

A covalently linked version of this complex, linked via an ether bond from one *ortho*-phenyl position of the porphyrin to an *ortho*- or *meta*-pyridyl group of the TMPA has also been characterized structurally and by ^1H NMR and resonance Raman spectroscopies and EXAFS.**1096** The *ortho*-pyridyl linkage yields a nearly linear Fe-O-Fe bridge (171°),**1096,1098** while the *meta*-pyridyl linkage yields a very bent bridge (141°).**1096** Protonation of the two complexes led to the formation of the hydroxo-bridged complex for the *ortho*-pyridyl-linked complex, but a broken bridge for the *meta*-pyridyl-linked complex.**1096** ^1H NMR spectra of the Fe^{II}/Cu^I forms of the *ortho*-pyridyl complex before addition of O_2 show the Fe^{II} center of the complexes to be high-spin in THF-d_8, intermediate-spin in CD_2Cl_2, and low-spin in toluene-d_8.**1098** An additional series of complexes having amide-linked TMPA groups with variable-length links and an amide-linked pyridine ligand for the iron have also been prepared and characterized, and their reactivity with dioxygen investigated in solution.**1100**

Stopped-flow kinetics studies of the O_2 reaction with a 1:1 mixture of the Fe^{II} and Cu^I starting materials of another system, $[F_8TPPFe^{II}]$ and $[MePY2Cu^I]$ (MePY2 = N,N-bis[2-(2-pyridyl)ethyl]methylamine), show the formation of at least two intermediates (i.e. a superoxo species, $[F_8TPPFe\text{-}O_2]$ first, and then a presumed peroxo-bridged Fe-O_2-Cu species) prior to the formation of the final μ-oxo complex $[F_8TPPFe^{III}\text{-}O\text{-}Cu^{II}(MePY2)]^+$.**1099** The ^1H NMR spectrum of the latter complex in CD_2Cl_2 exhibits a pyrrole-H resonance at 67.7 ppm, while downfield (23.4 and 18.9 ppm) and dramatically upfield-shifted resonances (-87.7, -155.4 and -189.4 ppm) have been assigned to the pyridyl protons. Protonation of the μ-oxo complex with CF_3SO_3H shifts the pyrrole-H resonance to 70.3 ppm. The protonation is slow on the NMR timescale.[1099] The ^{1}H NMR spectral properties are consistent with antiferromagnetically coupled high-spin Fe^{III} and Cu^{II} ions ($S = 2$) for the oxo-bridged complex ($\mu_{eff} = 5.05\,\mu_B$). The coupling is weaker for the hydroxo-bridged complex ($\mu_{eff} = 5.60\,\mu_B$).[1099]

The structures of both mono- and bis-cyanide-bridged complexes, having one or two $TMPACu^{II}$ units per F_8TPPFe^{III}, have also been reported.[1097] The 1:1 complex has a low-spin Fe^{III} center bridged to Cu^{II}. The Fe^{III}–CN vector is nearly linear (174.5°) while the 5-coordinate Cu^{II} center has a Cu–N–C angle of 163.8°. The 2:1 complex has a low-spin Fe^{III} center axially coordinated to two cyanide ligands capped on either side by trigonally coordinated [Cu(TMPA)] moieties. The Cu-N-C angle of one of these is 168° while that of the other is nearly linear (175°). The solution magnetic moments ($\mu_{eff} = 2.7\,\mu_B$ for the 1:1 complex and $\mu_{eff} = 3.4\,\mu_B$ for the 2:1 complex) suggest ferromagnetic coupling between the paramagnetic metal ions. This coupling gives rise to an enhancement of the electron spin relaxation rate for Cu^{II} in both complexes, which allows for the observation of the sharp and downfield-shifted TMPA ligand proton signals.[1097]

Both oxo- and hydroxo-bridged complexes containing two $TMPACu^{II}$ covalently linked to the porphyrinate phenyls[1100] or a tridentate derivative containing two 2-ethylpyridine links have been prepared[1099] and characterized by NMR spectroscopy.[1099] Peroxo-bridged complexes of $TMPACu^{II}$ and porphyrin-tethered variants have also been reported.[1101–1103,1105] Investigation of the rates of O_2 binding to $TMPACu^{I}$ has shown that these rates are of the order $k_{O_2} = 1.3 \times 10^9\ M^{-1}s^{-1}$, faster than to 5-coordinate hemes (10^5–$10^8\ M^{-1}s^{-1}$).[1104]

Collman's group has prepared several cytochrome oxidase models since 1994,[1107–1116] the latest of which have three covalently attached imidazoles for binding the $Cu^{II/I}$ on the α face and one on the β face to bind the Fe^{III}, as shown in Figure 8(g).[1114] This complex, as well as the Zn^{II} porphyrin analog, have been characterized by IR, NMR and EPR spectroscopy.[1114] Collman and coworkers have also done extensive studies of the electrocatalysis of O_2 reduction by simple iron porphyrins and iron porphyrin/Cu_B models;[1108,1112] this important work is reviewed in reference.[707] The diamagnetism of many oxygenated heme/Cu complexes, attributed to formation of Cu^{II} antiferromagnetically coupled to the Fe^{III} center via a bridging peroxide unit, does not simulate the O_2-bound binuclear site of CcO (i.e. 2-electron-reduced CcO), which is known to consist of a $Fe^{III}_{a3}O_2{}^{-\bullet}/Cu^{I}_{B}$ complex.[1118] Recently, Collman, Solomon and coworkers have shown that the Co^{II} porphyrin complex with the tris-imidazole-bound copper attached to three pickets above the porphyrin (Figure 8(h)) binds O_2 to form a Co–O_2 complex whose EPR spectra show that the complex can be formulated as Co^{III}–$O_2{}^{-\bullet}$, and that the rotation of the $O_2{}^{-\bullet}$ is hindered when Cu_I or Zn^{II} are bound to the three imidazole pickets,[1115] due to hydrogen-bonding from the picket amide N–H to the superoxide, in direct analogy to earlier studies of the O_2 complex of a mono-*ortho*-acetamido derivative of CoTPP.[285] The Fe^{II} porphyrin analog is paramagnetic in the absence of O_2 but diamagnetic in its presence, with non-shifted ^{1}H NMR spectra indicative of a diamagnetic complex.[1116] The O_2 complexes of both metal porphyrins have resonance Raman spectra that are indicative of non-bridged M^{III}–$O_2{}^{-\bullet}/Cu^{I}$ centers that are direct spectroscopic models of the dioxygen-bound binuclear metal center of CcO.[1115,1116]

The mechanism proposed for the 4-electron reduction of dioxygen to water by cytochrome *c* oxidase may be similar to that proposed for the monoxygenase enzymes, the cytochromes P450, as well as the peroxidases and catalase, all of which are discussed in Section 9 below. DFT calculations of the mechanism of the O–O bond cleavage step, specifically addressing CcO, have been reported[1119] and an excellent overview provided.[1120]

Attempted synthesis of another type of bridged mixed metal system, which involves an iron–sulfur cluster, either $Fe_2S_2(SPh)_4{}^{2-}$ or $Fe_4S_4(SPh)_4{}^{2-}$, bound to a Fe^{III} porphyrin, has been reported.[1121] Such bridged complexes, if they could be formed, would be models of the active site of assimilatory sulfite reductases, which have a siroheme and an Fe_4S_4 cluster that are chemically linked.[41] However, at present, preparation of such bridged heme–Fe_nS_n clusters has not yet been achieved: depending on solvent, the reaction of OEPFeX ($X^- = ClO_4{}^-$ or $CF_3SO_3{}^-$) with either $[Et_4N]_2[Fe_4S_4(SPh)_4]$ (acetonitrile) or $[PPh_4][Fe_2S_2(SPh)_4]$ (acetonitrile or DMF) resulted in ligand substitution, yielding OEPFe(SPh), while reaction of the same Fe_4S_4 complex in DMF or DMSO resulted in a redox reaction, yielding $OEPFe^{II}$.[1121] Thus a successful synthetic approach to model the active site of assimilatory sulfite reductases must eliminate the problems that (1) the affinity of simple Fe^{III} porphyrins for simple thiolates is significantly greater than is that of the iron–sulfur cluster, and (2) that weak or labile Fe^{III} heme axial ligands must be avoided. Presence of an inert axial ligand capable of stabilizing the Fe^{III} oxidation state must be sought.[1121]

Finally, two potential models for the Mo and Fe sites of sulfite oxidase have been prepared in which a hydrotris(3,5-dimethylpyrazolyl)borate complex of oxomolybdenum(V) is covalently attached to one of the phenyl rings of a tetraphenylporphinatoiron(III) derivative in which three phenyl rings carry *p*-Me groups and the other is either a 2,3- or 3,4-catecholate.[281,1122] Although the metals are not directly bridged in these complexes, they are held at fixed Mo···Fe distances. EPR spectroscopy at 4 K shows distance-dependent static dipolar coupling between the Mo^{V} and Fe^{III} centers. At 77 K the dipolar coupling is modulated by rapid relaxation of the Fe^{III} center.[1122] Coordination of two *N*-methylimidazoles to the Fe^{III} centers produce $(S = 1/2)_{Fe}$–$(S = 1/2)_{Mo}$ coupled systems that are not only sensitive to distance, but also to the orientation of the *g*-tensor of the low-spin Fe^{III}.[281] The ^1H NMR spectra of the bis-N-methylimidazole complexes of the 2,3- and 3,4-catecholatoMo(V) derivatives have been investigated in detail and shown to have a preferred orientation of at least one N-methylimidazole for the 2,3-catecholatoMo(V) derivative,[1123] but two freely rotating N-methylimidazole ligands for the 3,4-catecholatoMo(V) derivative.[1124] The pyrrole-H resonances of the former were assigned on the basis of Homonuclear *J*-Correlated SpectroscopY (COSY) and T_1 relaxation times.[1123]

6.1.5 *Coupled Oxidation of Hemes by H_2O_2 or Its Equivalent, and Relationship to the Reactions of Heme Oxygenase*

In reactions related to those discussed in Sections 8 and 9 that involve peroxidases and cytochromes P450 and their models, it has also been shown that hydroperoxides will oxidize iron(III) porphyrins at one *meso* position to create isoporphyrins.[1125] If the hydroperoxide is H_2O_2, and if the *meso* substituent is H, the first product is a *meso*-hydroxyporphyrin,[1126] also called an oxyporphyrin or oxophlorin, because of the possible tautomeric forms of the free base.[539] Iron oxophlorins are believed to be intermediates in the conversion of heme to biliverdin in both the in vivo process that is catalyzed by heme oxygenase[34] and the in vitro model system that is known as 'coupled oxidation'.[539,1127] Rivera and coworkers have investigated the mechanism and product formation for a heme protein via the coupled oxidation reaction with H_2O_2 as compared to heme oxygenation with O_2 and a reducing agent, and shown that the product distribution is different in the two reactions.[1128] (Octaethyl- and etiooxophlorins can also be synthesized[1129,1130] and iron can be inserted into the free ligand.[539]) The reducing agent can be ascorbic acid or hydrazine, and if hydrazine, it has been shown that in pyridine solution in the presence of O_2, (OEPO)Fe(Py)$_2$, (OEPO)Fe(Py)(N_2H_4) and (OEPO)Fe(N_2H_4)$_2$ are present transiently, although the two hydrazine-containing complexes are eventually converted to (OEPO)Fe(Py)$_2$ before (OEOP)Fe^{II}(Py)$_2$ and (OEB)Fe^{III}(Py)$_2$ are formed.[1131] Treatment of iron(II) porphyrins, (OEP)Fe^{II}(Py)$_2$, (EtioP)Fe^{II}(Py)$_2$, (DeuteroP)Fe^{II}(Py)$_2$, (MesoP)Fe^{II}(Py)$_2$ and (ProtoP)Fe^{II}(Py)$_2$ with H_2O_2 in the strict absence of dioxygen also gave the corresponding oxophlorin complexes,[1132] as mentioned in Section 4.2.2. For the unsymmetrically substituted porphyrins, the four isomeric oxophlorin products are formed in a nonrandom fashion. Solvent effects can produce a significant alteration in the regiospecificity of heme oxygenation.[1132] In the absence of pyridine, the structure of the first stable product, (OEOPFe)$_2$, is dimeric, with the deprotonated hydroxo group of one molecule acting as the anion and fifth ligand to Fe^{III} for the other molecule, and vice versa.[539] Magnetic susceptibility measurements indicate that the *meso*-oxo-bridged dimer is antiferromagnetically coupled, but that the coupling is weak ($J = -12\,cm^{-1}$),[1126] compared to porphyrin μ-oxo dimers. The NMR spectrum confirms this finding, with the methylene protons of (OEPOFe)$_2$ having resonances in the 18–40 ppm region, compared to 24–42 ppm for (OEPOH)FeBr.[539] (OEPO)Fe^{III}(Py)$_2$, is formed upon addition of pyridine, which both deprotonates the *meso*-OH group and also coordinates to the metal.[1133] (OEPOFe)$_2$ can be oxidized chemically by silver perchlorate or silver tetrafluoroborate.[1134] NMR spectra indicate that the oxidation is ligand-based.[1134] (OEPO)Fe(Py)$_2$ can also be reacted with NO to produce a *meso*-linked dimer that has one NO and one Py ligand bound to each heme.[1135] Treatment of (OEPO)Fe(Py)$_2$ with HCl in air produces (OEOP)$FeCl_2$.[540]

Upon further treatment of (OEPO)Fe(Py)$_2$ with O_2 and a reducing agent such as ascorbic acid, CO is lost from the partially oxidized *meso* position to produce the Fe^{II} or Fe^{III} verdoheme analog $[(OEOP)Fe^{II}(Py)_2]^+\ Cl^-$. Verdoheme is the green iron complex of the 5-oxaporphyrin macrocycle and can be obtained by reaction of iron porphyrin with dioxygen in the presence of axial pyridine or cyanide, as detailed in Scheme 3 for the analogous natural (protoheme) reactions.[540,1136–1138] Octaethylverdoheme was structurally characterized and was shown to contain the 5-oxaporphyrin macrocycle.[1139] This iron verdoheme complex can be treated with phenylmagnesium bromide to yield the paramagnetic (bromo)(phenyl)iron(III) and diphenyliron(III) OEOP complexes.[1140] Treatment instead with hydroxide or methoxide leads to several different ring-opened biliverdin complexes.[1141] These species are (OEB)Fe^{III}(OH), (OEBOMe)Fe(Py), (OEBOMe)Fe(Py)$_2$ and (OEBOMe)Fe(OMe).[1142] If the $[(OEOP)Fe^{II}(Py)_2]^+Cl^-$ is instead treated with hydrogen peroxide, the bridged dimeric biliverdin complex $[(OEB)Fe^{III}]_2$ is obtained;[1143] use of unsymmetrical hemins such as 3-demethyl-3-(trifluoromethyl)mesohemin IX leads to the four biliverdin isomers.[1144] Treatment of OEBFe(Py)$_2$ with O_2 in the presence of pyridine yields a tripyrrole complex of iron(III).[1145] The *meso*-NH_2-substituted OEPFe^{II}(Py)$_2$ complex reacts with O_2 to form what appears to be an intermediate in this type of 'de-pyrrolization' of biliverdin-type derivatives, in that it yields a crystalline product that has one dangling pyrrole group in which the amino group is present as a nitrile.[1146,1147] If the $[(OEOP)Fe^{II}(Py)_2]^+\ Cl^-$ is treated with ammonia followed by acid, the octaethylazaporphyrin macrocycle complex $[(OEAP)Fe^{III}Cl]$ is formed,[1148] as also detailed in Scheme 3 for the analogous protoheme system. If the *meso*-CO of OEOP is not lost, then formylbiliverdin is formed.[1149] Its metal complexes have also been investigated, although it was not possible to obtain the iron complex because of its instability.[1149]

At least one example of each of these species has been characterized by X-ray crystallography and ^1H NMR spectroscopy.[539,540,1133–1149] Thus structures of compounds involved in most of the steps leading to the production of biliverdin by the in vitro process of coupled oxidation have been elucidated. Presumably similar species are involved in the in vivo reactions of the enzyme heme oxygenase, a P450- or peroxidase-like enzyme that, as isolated, contains no heme yet binds heme and then follows a P450-like reaction scheme with electrons and dioxygen, but instead of the Fe^{III} peroxide species forming Compound I (see also Section 9), one oxygen of this group attacks a *meso*-position of the heme and (in several steps) destroys it, forming first *meso*-hydroxyheme and finally biliverdin,[33,34] which, in humans, is then reduced to bilirubin, conjugated with sugars, and excreted in the feces.[33] Heme oxygenases have a histidine that serves as axial ligand to the heme that they destroy.

6.1.6 Iron(III) Porphyrins as Reduction Catalysts

The [TPPFeCl]–$NaBH_4$ system in diglyme has been shown to perform remarkably efficiently as a catalyst for the reduction of nitrobenzenes to anilines.[1150] Although both TPPCo and TPPMnCl also catalyze the reduction of *p*-chloronitrobenzene to *p*-chloroaniline, their catalytic activities are much lower than that of TPPFeCl.[1150] Another type of reduction catalyst, in this case of dioxygen to water, begins with carbon-supported chloroiron(III) tetramethoxyphenylporphyrin, which is then heat-treated at 900 °C for one h.[1151] This causes decomposition of the porphyrin to produce metallic, carbidic and oxidic iron, as detected by Mössbauer spectroscopy. The active

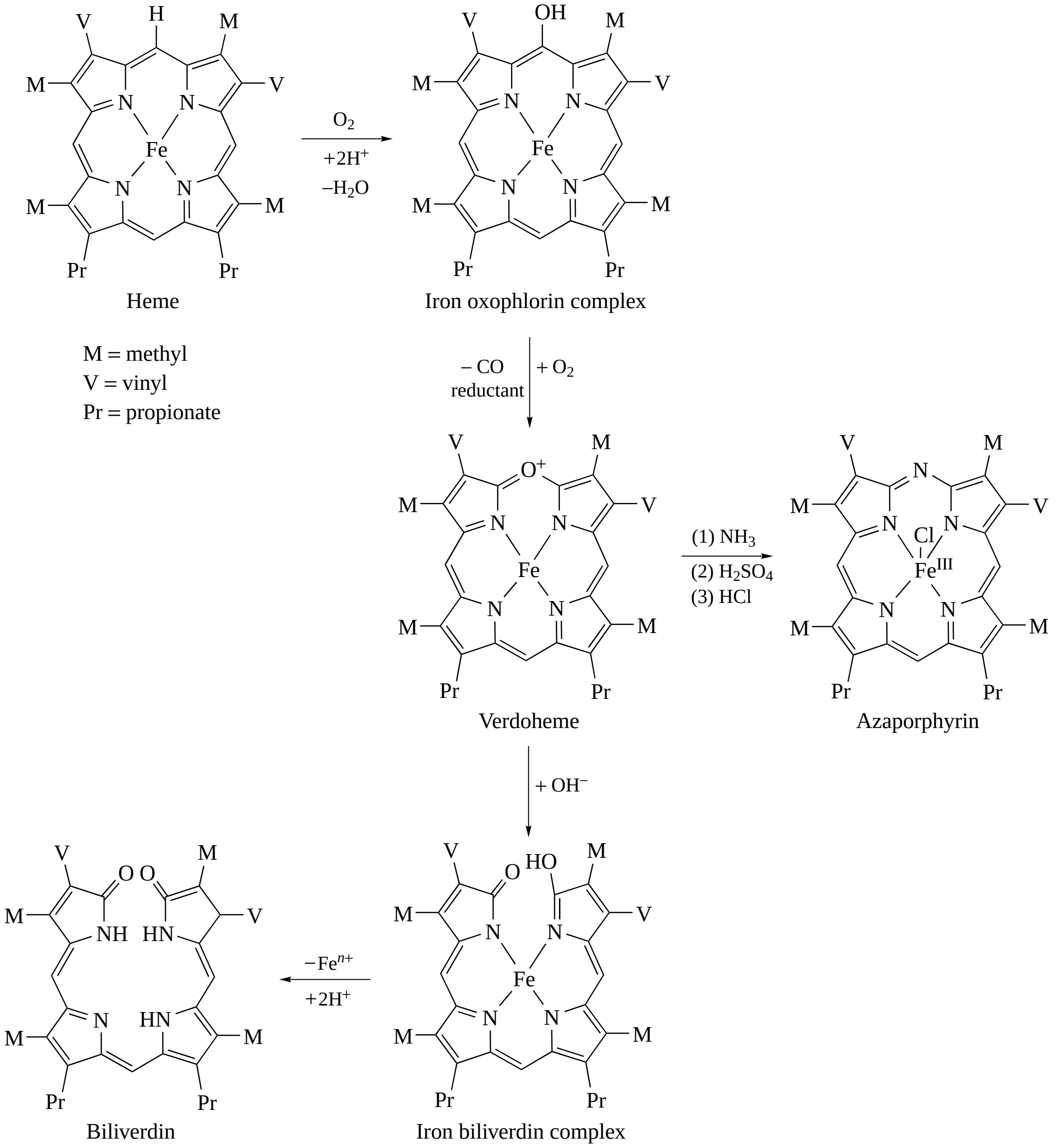
Heme
Iron oxophlorin complex
O_2
$+2H^+$
$-H_2O$
M = methyl
V = vinyl
Pr = propionate
− CO
reductant
+ O_2
Verdoheme
(1) NH_3
(2) H_2SO_4
(3) HCl
Azaporphyrin
Fe^{III}
+ OH^-
$-Fe^{n+}$
$+2H^+$
Biliverdin
Iron biliverdin complex

Scheme 3

catalytic form seems to be a 6-coordinate Fe^{III} center, which comprises about 8% of the iron content. H_2O_2 is a side product of the reduction reaction, and it causes degradation of the active iron sites. However, an earlier study, in which the samples were heat-treated at increasing temperatures (10 °C per hour) up to the highest temperature (325, 700, 800 °C), and held there for a dwell time of 2 h, found that the $Fe–N_4$ moiety seemed to be persistent.[1152]

6.1.7 Photochemistry of High-spin Iron(III) Porphyrins

Several investigations of photochemical reactions of high-spin Fe^{III} porphyrins have been reported,[1153–1155] and the subject has been reviewed[483] (*see* ***Photochemistry of Transition Metal Complexes***). When bound to anions such as Cl^- or OH^-, Fe^{III} porphyrins are photochemically reduced to Fe^{II}, with production of a radical ($Cl\bullet$ or $HO\bullet$).[1154,1155] In the case of a cofacial $Fe^{III}-Zn^{II}$ diporphyrin, however, the photochemical reaction produced $[P^{-}\bullet Zn^{II\cdots}\ PFe^{II}]Cl$ by electron transfer from the Zn^{II} porphyrin to the Fe^{III} porphyrin.[1153] The kinetics and thermodynamics of the back reaction were investigated ($k \sim 10^{10}\ s^{-1}$).[1153]

6.1.8 Complexes of Iron(III) Porphyrins with Fullerenes

Cocrystallization of binuclear iron(III) porphyrins, either the μ-oxo dimer, $[(OEPFe)_2O]$, or the oxophlorin, $[(FeOEPO)_2]$, dissolved in benzene solution, with C_{60}, yields solids of formula $C_{60}\cdot\mu\text{-}O(OEPFe)_2\cdot C_6H_6$ and $2C_{60}\cdot(FeOEPO)_2\cdot 4C_6H_6$.[1156] For the former, each independent molecule of μ-$O(OEPFe)_2$ makes close contact with two fullerene molecules. The Fe-O-Fe angles (150.18 and 151.89°) are markedly bent, with a benzene molecule wedged into the opening between the two porphyrins. Another crystalline form, however, has Fe-O-Fe angles that are more linear (172.16 and 176.2°). The structure of $2C_{60}\bullet\ (FeOEPO)_2\cdot 4C_6H_6$ consists of a centrosymmetric $(FeOEPO)_2$ molecule in which the two macrocycles are connected to one another through axial coordination of the *meso*-oxygen atoms to iron ions in the neighboring porphyrin. Each molecule of $(FeOEPO)_2$ engages a fullerene on its two exposed faces. The distances of the iron from the fullerene in both types of crystalline solids is too far for any bonding interaction, but the work shows that C_{60} can cocrystallize with dimeric metalloporphyrins to yield new solids with interesting supramolecular architectures. A review of earlier work on the reactions of transition metal complexes with fullerenes has been published.[1157]

6.2 Intermediate Spin ($S = 3/2$) Iron(III) Porphyrins

The bacterial cytochromes c' are known to contain five-coordinate heme c, with no distal residues present capable of hydrogen-bonding to endogenous ligands.[1158,1159] Moss and Maltempo have proposed the existence of an intermediate-spin ($S = 3/2$) state with a quantum mechanical admixture of the more common high-spin ($S = 5/2$) state for the protein.[1160–1162] This differs from a simple $S = 3/2 \rightleftharpoons S = 5/2$ equilibrium, in that the EPR and Mössbauer features are unique, rather than simply a superposition of the expected spectra of the two spin states, and the ground state is composed of contributions from each state.[1163] Models for the cytochromes c' have been prepared with Fe^{III} porphyrins bound to weakly coordinating anionic axial ligands such as $ClO_4{}^-$,[179,492,1164–1167] $SO_3CF_3{}^-$,[1168] $SbF_6{}^-$,[1165,1166,1169,1170] $C(CN)_3{}^-$,[1168,1171] and $B_{11}CH_{12}{}^-$,[1172] or two weakly basic neutral ligands such as tetrahydrofuran,[1173] 3-chloropyridine,[1174,1175] dimethylformamide + $N_3{}^-$,[1176] and 3,5-dichloropyridine (in the case of β-pyrrole alkyl-substituted porphyrins such as OEP and etioporphyrin).[1165,1166,1177] These Fe^{III} porphyrins exhibit a broad derivative-shaped EPR feature near $g = 4$[492,1165,1166,1168,1177] and ^1H NMR spectra that show anti-Curie behavior.[171,492,965,1178] Many of these spectral features are similar to those of the cytochromes c', including the EPR,[492,1161,1165,1166,1179,1180] near-IR MCD,[1163] Mössbauer,[1162,1170,1177] and resonance Raman[1181,1182] spectra, and the NMR spectra of *Chromatium vinosum* cytochrome c', but not those of *Rhodospirillum rubrum*, *Rhodospirillum molischianum*, and *Rhodopseudomonas palustris*.[1183]

The dramatic anti-Curie dependence (*see* ***Magnetism of Transition Metal Ions***) of the pyrrole-H resonance of $[TPPFeOClO_3]$ from about −20 ppm at −45 °C to +20 ppm at +54 °C[1184] is a now-familiar hallmark of the ^1H NMR spectra of spin-admixed $S = 3/2,5/2$ model heme species. At low temperatures the $S = 3/2$ contribution to the spin-admixed state usually increases, leading to depopulation of the $d_{x^2-y^2}$ orbital of the $S = 5/2$ state, thus decreasing the large σ contact shift contribution characteristic of simple high-spin five- and six-coordinate Fe^{III} porphyrins.[174,175] However, a study of the temperature dependence of the pyrrole-H shifts of a series of 2,6-phenyl substituted derivatives of $[TPPFeOClO_3]$ showed that either the $S = 3/2$ or the $S = 5/2$ state can be of lower energy, and thus the pyrrole-H resonance can in fact shift in either direction as the temperature is lowered,[492] as shown in Figure 9, where the temperature dependence has been fit with a 2-level expansion of the Curie law appropriate for systems having a thermally accessible excited state.[492,1185] The tendency of the 2,6- or 2,4,6-substituents to stabilize the $S = 3/2$ level decreases in the order $(OMe)_3 \gg (Me)_3 > (H)_5 > (Cl)_2 > (Br)_2$, while $(F)_2$ and $(OMe)_2$ have the tendency to stabilize the $S = 5/2$ level in increasing order, respectively.[492] The tetrakis-(2,4,6-trimethoxyphenyl)porphyrinatoiron(III) perchlorate complex is thus the purest $S = 3/2$ ground-state complex known thus far.[492,1165,1166] The fact that many of the temperature dependences cross each other at temperatures within or near the range of the NMR investigations (Figure 9) suggests the need for caution in using single-temperature measurements to define relative tendencies for spin state stabilization; in spite of this cautionary note, all of the work discussed below has used a single temperature NMR shift measurement to define relative spin state stabilization.

The tendency of weak-field anions to stabilize the $S = 3/2$ ground state of the spin-admixed 3/2,5/2 systems has been defined in terms of the pyrrole-H shift of the $\mathrm{TPPFe^{III}}$ complex at a given temperature, and increases (in reverse order of the actual shifts) in the order $\mathrm{ReO_4}^-$ ($\delta_{\mathrm{pyrrole}} = +62$ ppm) $<$ $\mathrm{ONC(CN)_2}^-$ $<$ $\mathrm{BF_4}^-$ $<$ $\mathrm{CF_3CO_2}^-$ $<$ $\mathrm{CF_3SO_3}^-$ $<$ $\mathrm{C(CN)_3}^-$ $<$ $\mathrm{ClO_4}^-$ $<$ $\mathrm{AsF_6}^-$ $<$ $\mathrm{Co(CB_{11}H_{12})_2}^-$ $<$ $\mathrm{SbF_6}^-$ $<$ $\mathrm{Ag(CB_{11}H_6Br_6)_2}^-$ ($\delta_{\mathrm{pyrrole}} = -62$ ppm)[1168,1172,1186] for $\mathrm{TPPFe^{III}}$, and $\mathrm{CF_3SO_3}^-$ $<$ $\mathrm{C(CN)_3}^-$ $\ll$ $\mathrm{ClO_4}^-$ $<$ $\mathrm{SbF_6}^-$ for $\mathrm{OEPFe^{III}}$.[1165,1166,1168] These have been called a 'magnetochemical series' of ligand field strengths.[1186] However, as noted above, this assumes that the temperature dependences of the complexes in the series do not cross (see Figure 9). The perrhenate anion, $\mathrm{ReO_4}^-$, bound to $\mathrm{TPPFe^{III}}$ has been shown to favor the $S = 5/2$ component to a much greater extent than $\mathrm{ClO_4}^-$,[1187] and H_2O and $\mathrm{OH^-}$ have reversed orders of ligand field strength on the magnetochemical series relative to the spectrochemical series (*see Spectrochemical Series*), with H_2O producing a $S = 3/2,5/2$ spin admixed state ($\delta_{\mathrm{pyrrole}} = -43$ ppm) and $\mathrm{OH^-}$ producing a $S = 5/2$ spin state ($\delta_{\mathrm{pyrrole}} = +82$ ppm).[1188] A low-basicity ligand, 3,5-dichloropyridine, appears to stabilize the $S = 3/2$ ground state in $\mathrm{[OEPFe(3,5\text{-}Cl_2Py)_2]^+}$ about as well as $\mathrm{ClO_4}^-$ or $\mathrm{SbF_6}^-$.[1165,1166] A study of the dependence of the solution magnetic moment (ranging from 2.0 to $4.4\,\mu_B$) of a large number of $\mathrm{PFe(3\text{-}ClPy)_2ClO_4}$ complexes indicated that species with more basic porphyrinate ligands have higher-spin multiplicity.[1189] As a possible explanation, it was suggested that the more basic porphyrins donate more electron density to the $\mathrm{Fe^{III}}$ atom and thus decrease its charge attraction for the axial ligands, which results in a decrease of the axial-ligand field, leading to higher-spin multiplicity.[1189] For *para*-substituted derivatives of $\mathrm{[TPPFeOClO_3]}$ the $S = 5/2$ contribution, as judged by the pyrrole-H chemical shift at 29 °C, increases in the order *p*-OMe $<$ *p*-H $<$ *p*-Cl $<$ *p*-$\mathrm{CF_3}$,[1165,1166] so electron-donating substituents on the phenyl rings favor the $S = 3/2$ ground state, where the $d_{x^2-y^2}$ orbital is depopulated. Consistent with this, as mentioned above, the 2,4,6-trimethoxy derivative, $\mathrm{[(2,4,6\text{-}(OMe)_3)_4TPPFeOClO_3]}$, has the lowest-frequency chemical shift reported for the pyrrole-H (−31 ppm at 29 °C),[492,1165,1166] and thus appears to be the 'purest' $S = 3/2$ complex among tetraphenylporphyrin derivatives. However, comparison of the temperature dependence of the 2,6-$\mathrm{(OMe)_2}$ and (2,4,6-$\mathrm{OMe)_3}$-substituted TPP complexes (Figure 9) indicates that *p*-OMe and *o*-OMe have opposite effects on the spin state,[492] and comparison with the *p*-OMe-only complex[1165,1166] (the temperature dependence of whose pyrrole-H shift has not been reported) suggests that substituent effects in this system of methoxy-TPPs are dramatically non-additive.

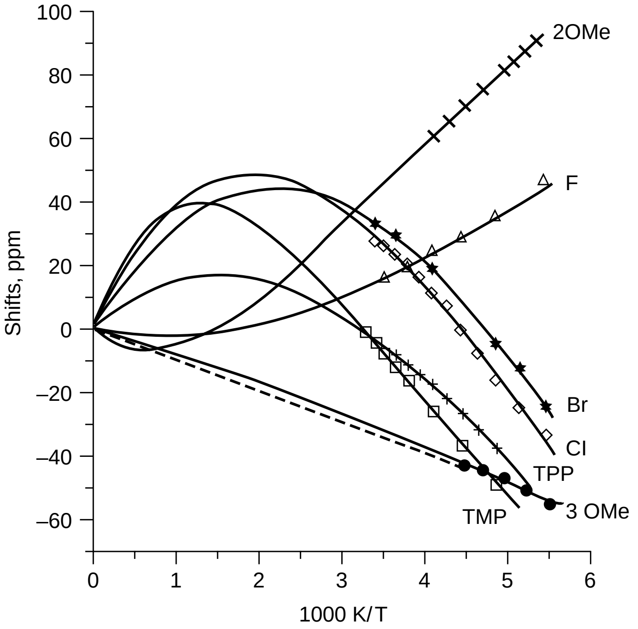

Figure 9 Isotropic shifts of the listed complexes as a function of inverse temperature and fits to equation x (——) or to a 1-level linear fit (- - -): *, $\mathrm{(2,6\text{-}Br_2)_4TPPFeOClO_3}$; □, $\mathrm{(2,6\text{-}Cl_2)_4TPPFeOClO_3}$; ×, $\mathrm{TPPFeOClO_3}$; ◊, $\mathrm{TMPFeOClO_3}$; △, $\mathrm{(2,6\text{-}F_2)_4TPPFeOClO_3}$; +, $\mathrm{(2,6\text{-}(OMe)_2)_4TPPOClO_3}$; •, $\mathrm{(2,4,6\text{-}(OMe)_3)_4TPPOClO_3}$. (Reprinted with permission from Ref. 492. © 2000 American Chemical Society)

The highly saddled octaethytetraphenylporphyrinatoiron(III) chloride complex has been shown to be spin-admixed, with largely $S = 5/2$ but with some $S = 3/2$ character.[1190,1191] In comparison, both tetraazaporphyrin[163] and phthalocyanine[1192] complexes of chloroiron(III) are pure $S = 3/2$ compounds. $\mathrm{XFe^{III}}$ complexes of etioporphycene and etiocorrphycene, where X = F, Cl, Br and I, have been prepared and their structures determined via X-ray crystallography; they have also been investigated by Mössbauer, ^{1}H NMR, and EPR spectroscopy as well as SQUID magnetometry.[1193] The iodide complex of etioporphycene was found to have a quite pure $S = 3/2$ spin state with only a small amount of $S = 5/2$ spin admixture. In contrast, all of the other complexes, of both etioporphycene and etiocorrphycene, show the $S = 5/2$ spin state with a small amount of $S = 3/2$ spin admixture.[1193]

Crystalline complexes of iron(III) tetramethylchiroporphyrin having two ethanol or one ethanol and one water axial ligands have been structurally characterized and their magnetic moments, Mössbauer, EPR and NMR spectra reported.[1194] The magnetic moment of $3.8\,\mu_B$ and quadrupole splitting ΔE_Q of 3.79 mm/s for the mixed ethanol-water-ligated samples strongly supports a $S = 3/2$ state; the pyrrole-H signal is at about −30 ppm at ambient temperature, indicating no population of the $d_{x^2-y^2}$ orbital.[1194] Bis-THF complexes of iron porphyrinates also yield the $S = 3/2$ spin state, and Nakamura and coworkers have proposed that there are two possible electron configurations for these complexes:

$(d_{xz},d_{yz})^3(d_{xy})^1(d_{z^2})^1$ and $(d_{xy})^2(d_{xz},d_{yz})^2(d_{z^2})^1$.[944] The latter, which has two d_π unpaired electrons, should have more negative pyrrole-H chemical shifts than the former. Based upon the typical ambient temperature pyrrole-H shift of ~ -30 ppm of most of these $S = 3/2$ complexes, the latter electron configuration is by far more common. The [OETPPFe(4-CNPy)$_2$]ClO$_4$ complex has been investigated by EPR and NMR spectroscopy[943,1195,1196] and X-ray crystallography.[943] The solution magnetic moments, measured by the Evans method,[1197,1198] are reported to be $\sim 3.3\,\mu_B$[943] and $4.3\,\mu_B$[1196] at ambient temperatures, both of which depart from the expected spin-only moment of $3.87\,\mu_B$. The reasons for the departure from the spin-only moment are largely the experimental errors inherent in the Evans method (knowledge of the molecular weight of the complex being studied, which depends on whether there are solvent molecules in the crystal lattice, weighing errors, solvent evaporation, relatively few Hz difference in the frequencies of the reference signal in the two compartments of the NMR sample cell). The temperature dependence of the ^{1}H NMR spectra of [OETPPFe(4-CNPy)$_2$]ClO$_4$ shows no evidence of a thermally accessible excited state over the range of the measurements (303–180 K),[943] and thus the complex appears to be a pure $S = 3/2$ system, as also concluded by Nakamura and coworkers.[1196] However, the phenyl-H shift differences, $\delta_m - \delta_p$ and $\delta_m - \delta_o$, are both large and negative, indicating the presence of negative spin density at the *meso*-carbons.[195,943] Careful analysis of the pyrrole-CH$_2$ shifts also shows that they are much larger[943] than expected for either of the proposed[944] electronic configurations of intermediate spin Fe^{III}, $S = 3/2$, but rather indicate that the $d_{x^2-y^2}$ orbital of iron is at least partially occupied.[943] Thus, the combination of negative phenyl-H shift differences and the larger-than-expected pyrrole-CH$_2$ shifts indicates at least partial electron transfer from the porphyrin to the metal, yielding an electron configuration of $(d_{xy})^2(d_{xz},d_{yz})^2(d_{z^2})^1(d_{x^2-y^2})^{(1-x)}$ for the iron, and (OETPP)$^{(2-x)-}$ for the porphyrinate ring.[943]

Five-coordinate iron(III) 2,7,12,17-tetrapropylporphycenes with anions $C_6H_5O^-$, Cl^-, Br^-, I^- and $ClO_4{}^-$ have been investigated by ^{1}H NMR spectroscopy and found to have spin-admixed $S = 3/2,5/2$ electron configurations.[1199] The pyrrole-H chemical shifts are 65.3, 28.5, −7.8, −49.4, and −77.1 ppm, respectively. This wide chemical shift range suggests that these porphycene complexes are particularly useful for determining the ligand strength in the magnetochemical series.[1199] The chloroiron(III) complex could be reduced in three one-electron steps (Fe^{III}/Fe^{II} and Fe^{II}/π-mono and -dianion radicals) and oxidized in two one-electron steps.[1030] The bis-THF adduct of the same Fe^{III} porphycene yields a pure $S = 3/2$ complex.[1200]

A triclinic crystalline form of [TPPFeOSO$_2$CF$_3$] has been reported to have two crystallographically and magnetically distinct crystal lattice sites, one of which (1) is unique in that its structure is temperature dependent, whereas the second spin-admixed site (2) has a structure that is essentially independent of temperature.[1201] These results suggest different spin ground states for molecules 1 and 2. It was found that molecule 1 pairs form π–π dimers, whereas molecule 2 pairs do not.

Iron(III) tetraphenylporphyrin, in the presence of the most weakly binding anion known, $CB_{11}H_6Br_6{}^-$, binds weakly to benzene, toluene, *p*-xylene and C$_{60}$ ([60]fullerene), yielding complexes with distinctively short Fe···C contacts in the range of 2.65–2.95 Å.[1202] Dihedral angles of 13–16° between the arene and metalloporphyrin planes are also diagnostic of ligand versus solvate roles. The essential features of the arene coordination can be faithfully reproduced using density functional theory.[1202] In contrast to these structures, as well as those of a number of divalent first-row transition metal OEP complexes co-crystallized with C$_{60}$, C$_{60}$O, C$_{70}$ and C$_{120}$O, OEPFeCl does not have close spacing of metal and fullerene.[1203]

6.3 Low-spin ($S = 1/2$) Iron(III) Porphyrins

Low-spin Fe^{III} porphyrins continue to be of major interest to many investigators, both because of the large number of different low-spin complexes that can be prepared, and because of the relevance of this spin state to a variety of heme proteins. Ligands that give rise to low-spin complexes of Fe^{III} porphyrins include: two imidazoles,[168,174,175,183,194,486,612,618,619,1204–1207] two imidazolates,[1208] two pyridines (for TPPs but not OEP and natural porphyrins for lower-basicity pyridines),[168,174,175,1204,1205,1209–1212] two thioethers,[1213] two thiolates,[1214–1216] two isocyanides,[1217–1219] two phosphines,[1220] two ammonia molecules,[1221] two primary amines (as amino acid esters),[1222] two cyanides,[851,1223–1225] two nitrite ions,[1226,1227] two methoxide ions,[1001] two alkyl peroxide ions,[1001] two dialkylnitrosamines,[1228–1230] two N-hydroxylamines,[1231] two nitrosohydroxylamines,[1230,1232] two N-hydroxyguanidines,[1233] one imidazole and one hydroxide,[432] one imidazole and one cyanide or other strong field anion,[637,1223,1225,1234] one pyridine and one cyanide[1224,1235,1236] or other strong field anion,[1015,1237,1238] one thiolate and one nitrite ion,[1239] one imidazolate and one alkylperoxide ion,[1000] one methoxide and one alkylperoxide ion,[999,1001,1002] one hydroxide and one peroxide ion,[1001] one imidazole and one phosphine,[1220] one pyridine and one phosphine,[1220] one imidazole and one thioether,[1213,1240] one imidazole and one thiolate,[1241] one imidazole and one phenolate,[955] one imidazole and one pyridine,[1236] two different pyridines,[1236] one nonhindered imidazole and one hindered imidazole,[1242,1243] one imidazole and one imidazolate,[1234] one imidazole or pyridine and one carbanion (aryl, alkyl or alkynyl).[966,1244] In addition, five-coordinate Fe^{III} porphyrins having one nitrite[1227] or hydrosulfide[1245] or a σ-alkyl or -aryl ligand[1246,1247] bound to the metal are also low spin. An extensive review of the NMR spectroscopy and a summary of the EPR data of these complexes has appeared,[175] and the reader is referred to this article for more detailed information and complete references to the primary literature.

Axial-ligand combinations found among the low-spin ferricytochromes that are involved in electron transport in a wide variety of cells include two histidine imidazoles (cytochromes b_5,[1248] the *b* cytochrome of sulfite oxidase,[43] the bc_1 mitochondrial protein complex[2–9] and cytochrome b_6 of chloroplasts,[1249] cytochrome *a* of mitochondrial cytochrome *c* oxidase,[2–6] and the bacterial tetraheme proteins called the cytochromes c_3,[1250,1251] as well as other bacterial multiheme cytochromes *c*[1252] (*see* ***Multi-Heme Cytochromes & Enzymes***)) and one histidine imidazole and one methionine thioether (mitochondrial cytochromes *c* and their bacterial counterparts[626,627] (*see* ***Iron: Heme Proteins & Electron Transport***), cytochrome c_1 of the mitochondrial bc_1 protein complex,[7–9] and *E. coli* cytochrome b_{562}[1253]). The axial ligands of chloroplast cytochrome *f* are one histidine imidazole and the N-terminal aliphatic amino group,[1254] those of the heme center of bacterioferritin are two methionine thioethers,[1255,1256] and those of bacterial cytochrome *o* are believed to be two histidine imidazoles.[1257] These axial-ligand combinations (as well as heme substituents) lead to different reduction potentials for each of the above-mentioned cytochromes, as well as different EPR, NMR, Mössbauer, magnetic circular dichroism (MCD), and resonance Raman spectra for each of the cytochromes mentioned. For each of the aforementioned, magnetic spectroscopies have been valuable in establishing the axial-ligand combinations present in these and other heme proteins containing low-spin Fe$^{\text{III}}$. Of these, near-IR MCD spectroscopy at very low temperatures appears to provide the most unique spectra for each axial-ligand combination.[1255] The MCD spectra of several alkylamine and imidazole-ligated Fe$^{\text{III}}$ chlorin complexes have also been reported.[819]

The resting state, the low-spin Fe$^{\text{III}}$ complexes of the family of monooxygenase and oxidase enzymes known as the cytochromes P450 (*see* ***Iron: Heme Proteins, Mono- & Dioxygenases***), have one cysteine thiolate as the proximal ligand[24–31,1241,1258] and a water molecule[1216,1259] as the distal ligand, though the distal ligand may be replaced by a phosphine, imidazole or other strong-field ligand.[1241,1260] The spectral changes that usually accompany the transition from low-spin to high-spin upon binding of substrate are typical of the spin state change itself.[1261] This spin transition is accompanied by loss of the water molecule, and probably a lengthening of the Fe-thiolate bond.[1262,1263] Similarly, the five-coordinate mono-histidine ferriheme forms of a number of proteins, including small molecule (O_2, CO, NO) carriers such as hemoglobin and myoglobin (*see* ***Iron: Heme Proteins & Dioxygen Transport & Storage***) and enzymes such as the large family of peroxidases (including horseradish and other plant peroxidases, cytochrome *c* peroxidase, myeloperoxidase, and lignin peroxidases) (*see* ***Iron: Heme Proteins, Peroxidases, Catalases & Catalase-peroxidases***) and the heme a_3 of mitochondrial cytochrome oxidase (*see* ***Cytochrome Oxidase***) readily bind cyanide and other strong-field ligands to produce low-spin Fe$^{\text{III}}$ complexes having the common axial ligation of one cyanide and one histidine imidazole.

As might be expected, the preparation and investigation of a wide variety of low-spin Fe$^{\text{III}}$ porphyrins with various axial ligands have provided a wealth of valuable information about the electronic, magnetic, and redox properties of the heme proteins. We will first briefly review the possible electron configurations of low-spin Fe$^{\text{III}}$ porphyrins, then discuss the phenomenon of ruffling of the porphyrin macrocycle and its consequences, and the preferred orientation of planar axial ligands for the low-spin d^5 electronic configuration. We will then discuss the redox chemistry of, the formation of, and factors that affect, the stability of low-spin complexes and the rates of ligand addition and exchange in low-spin d^5 Fe$^{\text{III}}$ complexes, and the preparation of 'synthetic heme proteins' that utilize this information. Other reactions of low-spin Fe$^{\text{III}}$ porphyrins, including the very important one of electron self-exchange, as well as autoreduction, will also be addressed. Finally, the preparation of synthetic 'proteins' that bind hemes in a way that models specific naturally occurring heme proteins will be discussed.

6.3.1 *Possible Electron Configurations of Low-spin Iron(III) Porphyrins*

From the Griffith theory for the *g*-values of low-spin Fe$^{\text{III}}$,[1265,1266] using the formulation of Taylor[1267] (see also Section 6.3.3 below), and NMR spectroscopic data, it has been accepted for a number of years that low-spin Fe$^{\text{III}}$ porphyrins always have a $(d_{xy})^2(d_{xz},d_{yz})^3$ ground state.[168] This ground state gives rise in many cases to rhombic EPR spectra, for which the relative energies of the d_{xy}, d_{xz}, and d_{yz} orbitals can be calculated,[1267] if the orientation of the three g-values with respect to the molecular axes of the heme center are known: if the largest g-value is aligned along the normal to the heme plane, then indeed, the electron configuration is $(d_{xy})^2(d_{xz},d_{yz})^3$, but if instead the smallest g-value is aligned along the normal, then the electron configuration is $(d_{xz},d_{yz})^4(d_{xy})^1$. Determining the orientation of the largest (or smallest) g-value with respect to the heme normal can be achieved by single crystal EPR[1224,1268,1269] or pulsed EPR spectroscopy.[1002,1270–1275] In the pulsed EPR studies it has been found that the criteria originally used by Taylor[1267] to determine the orientation of the g-values with respect to the molecular axis, the so-called Rhombicity (V/Δ) being less than or equal to 2/3, a purely geometric definition, is actually often violated, as in the cases of $[\text{TPPFe(PzH)}_2]^+$,[1270] $[\text{TPPFe(3-NH}_2\text{PzH)}_2]^+$,[1273] $[\text{TPCFe(ImH)}_2]^+$,[1274] $[\text{OECFe(ImH)}_2]^+$,[1276] $[\text{oxo-OECFe(ImH)}_2]^+$,[1276] $[\text{OECFe(4-NMe}_2\text{Py)}_2]^+$[982] and $[\text{TPPFe(OCH}_3)(\text{OO}t\text{-Bu)}]^-$,[1002] all of which have the more common $(d_{xy})^2(d_{xz},d_{yz})^3$ ground state in spite of the fact that the Rhombicity is significantly larger than 2/3 in each case (see also Section 6.3.3 below). There are undoubtedly additional cases where knowing the orientation of the largest g-value with respect to the normal to the heme plane would lead to an unambiguous assignment of the orbital occupation of low-spin iron(III) porphyrins.

The $(d_{xy})^2(d_{xz},d_{yz})^3$ electron configuration gives rise to ^{1}H NMR spin delocalization to protons on the β-pyrrole substituents of the molecule via the filled $3e(\pi)$ porphyrin orbitals, that is P → Fe π bonding, which is symmetry-allowed.[168,174,175] The interpretation of the NMR spectra in terms of MO theory is based upon the fact that for bis-imidazole complexes, π contact shifts are observed at the β-pyrrole positions, while there are negligible π contact shifts at the *meso* positions.[168,174,175] 2D NMR (COSY) studies of unsymmetrically phenyl-substituted derivatives of $[\mathrm{TPPFe(N\text{-}MeIm)_2}]^+$ conclusively show that the pattern of spin delocalization to the β-pyrrole positions is exactly that expected for the $3e(\pi)$ orbitals, as modified by the electron-donating/withdrawing characteristics of the substituent,[1264,1277] as shown in Figure 10. However, while the COSY crosspeaks are genuine, Nuclear Overhauser and Exchange SpectroscopY (NOESY) crosspeaks observed in the later study[1277] were subsequently shown to be artifacts, probably arising from overlap of ridges in the 2D spectra; calculations show conclusively that protons on adjacent pyrrole rings are too far apart to yield measurable NOEs in these model heme complexes.[1278] Heteronuclear multiple bond correlation spectra (HMBC) have been shown to be valuable for assigning the α- and *meso*-carbon resonances of these model hemes.[1279]

It has also been shown that with certain kinds of axial ligands (isocyanides,[1217–1219,1275] low-basicity pyridines[621,1280,1281]) or certain modifications of the porphyrin π orbitals (such as occurs in the highly reduced hemes), the relative energies of the d_{xy} and d_π orbitals (d_{xz},d_{yz}) can be reversed, leading to an electron configuration that is $(d_{xz},d_{yz})^4(d_{xy})^1$. This electron configuration results in axial (with $g_\perp > 2 > g_\parallel$),[174,175,621,1217–1219,1280,1281] as shown in Figure 11, or near-axial EPR spectra,[59] and ^{1}H NMR[174,175,1217–1219,1281] and/or pulsed EPR[1275] spectra that show just the reverse types of π spin delocalization patterns: negligible π spin delocalization to the β-pyrrole positions, but large π spin delocalization to the *meso* positions. (It must be noted that because of the temperatures at which EPR and NMR spectra are recorded, 4–77 K that is 180–340 K, respectively, there is not necessarily a direct correspondence between the electron configuration observed by EPR spectroscopy and that observed by NMR spectroscopy.[174,175] This appears to be particularly true of some of the low-spin $\mathrm{Fe^{III}}$ complexes of the reduced hemes[1282] (but not for $[\mathrm{TPCFe(ImH)_2}]^{+}$[1274]) and models of the peroxide complex of heme oxygenase.[1002]) However, for this electronic ground state the d_{xz},d_{yz} orbital set, which has proper symmetry for π spin delocalization to the e-symmetry porphyrin orbitals, is filled, and the d_{xy} orbital does not have proper symmetry for overlap with any of the π orbitals of the porphyrin ring if it is flat (Figure 4).

Hence the large π spin delocalization to the *meso* positions suggested at least partial porphyrin π radical character to the electron configurations of these complexes,[174,175,1283] even though the EPR g-values deviate considerably from 2.00 and thus indicate a metal-based unpaired electron rather than a carbon-based free radical. The limit of this π radical character is to convert the electron configuration to that of $(\mathrm{P^{-}\cdot})\mathrm{Fe^{II}}$,[199,200] as discussed above in Section 5. It appears that $\mathrm{Fe^{III}}$ porphyrins that have a $(d_{xz},d_{yz})^4(d_{xy})^1$ ground state invariably appear to be pushed toward having partial porphyrin π-cation radical character (in terms of both their EPR and NMR spectra), even though the d_{xy} orbital is orthogonal to the π orbitals of a flat porphyrin ring. The reasons for this behavior are related, at least in part, to the almost invariably observed strong S_4 ruffling of the porphinato core[1218,1219,1280,1281] in systems having a predominantly $(d_{xz},d_{yz})^4(d_{xy})^1$ ground state, as is discussed in detail in Section 6.3.2.

In spite of this, however, not all highly ruffled iron(III) porphyrinates have their unpaired electron in the d_{xy} orbital. The 'large $g_{\max}$' EPR signal-producing bis-hindered imidazole complexes discussed in Sections 6.3.2 and 6.3.3 are good examples of highly ruffled heme centers that have the more common $(d_{xy})^2(d_{xz},d_{yz})^3$ electron configuration.

6.3.2 *The Phenomenon and Possible Electronic Consequences of Ruffling of the Porphinato Core in Iron(III) Porphyrins*

There have been a number of investigations of the tendency of metal complexes of the reduced hemes (chlorins and isobacteriochlorins) and Factor F430 to deform from planarity in a manner that is described in terms of the group theory of a symmetrical porphyrin ring as either S_4 saddled (sad), a B_{2u}-symmetry distortion, or S_4 ruffled (ruf), a B_{1u}-symmetry distortion, although other deformations are possible as well.[623–625] In S_4 saddled structures, opposite pyrrole rings, and hence, metal–porphyrin nitrogen bonds, are displaced from planarity, creating a pseudo-tetrahedral distortion in the metal coordination. In S_4 ruffled structures, opposite pyrrole rings are counter-rotated about the metal–nitrogen bonds, such that the metal and the four porphyrin nitrogens are in a plane, but the *meso*-carbons and the β-pyrrole carbons are displaced from this plane in an up–down alternating fashion.[1284] It is fairly well accepted that the facility of ruffling generally increases in the order porphyrins < chlorins < isobacteriochlorins < F430.[68,1285,1286] However, it is now clear that porphyrins may deform from planarity much more easily than assumed heretofore. Crystal and molecular structure determinations for a series of $[\mathrm{TMPFe(L)_2}]^+\mathrm{ClO_4}^-$ complexes in which L is a pyridine (4-$\mathrm{NMe_2Py}$,[1204] 3-EtPy,[1280] 3-ClPy,[1280] 4-CNPy,[1280] and 3-CNPy[1280]) or a hindered imidazole (1,2-$\mathrm{Me_2Im}$)[1287] show that, as expected from their EPR spectra[1204,1280] discussed more fully in Section 6.3.3, both pyridine and hindered imidazole ligands

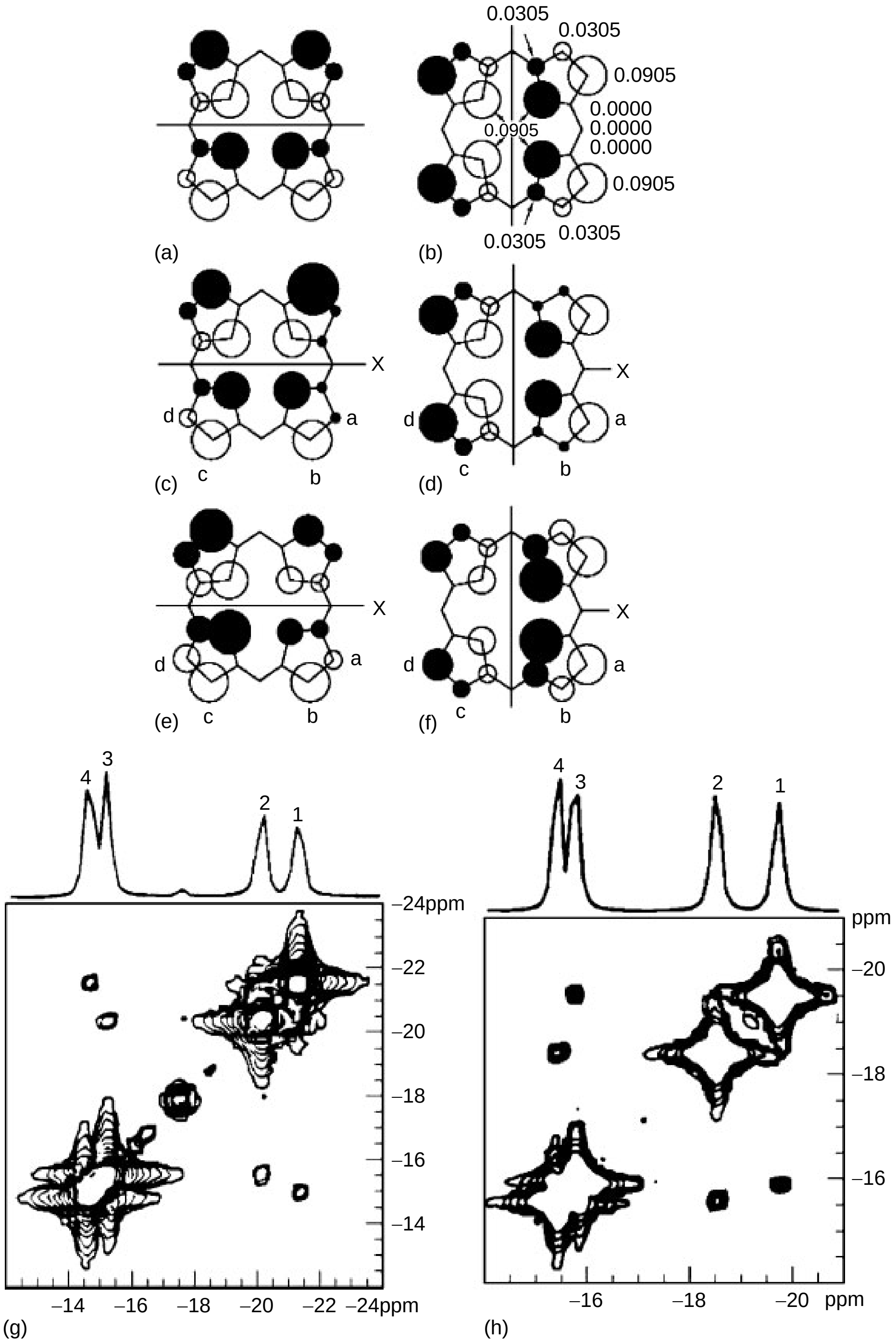

Figure 10 Symmetry properties of and electron density distribution in the filled $3e(\pi)$ porphyrin orbitals[221] that have proper symmetry for overlap with the d_{xz} and d_{yz} orbitals of low-spin Fe^{III}. (a, b) Linear combinations of the $3e(\pi)$ orbitals that are appropriate for *meso*-substituted porphyrins; (c, d) exaggerated modifications of these orbitals due to the presence of one uniquely substituted phenyl ring, X, if the effect of the substituent is felt only as far as the adjacent pyrrole positions a and b; (e, f) exaggerated modifications of these orbitals if the effect of the unique substituent is felt over all four pyrrole positions a–d. Since we expect the proton attached to the carbon with largest spin density to have the largest hyperfine shift, the coupling pattern predicted by these simple modifications is a,b and c,d or pyrrole-H peaks 1,4 and 2,3 in the case of (c) and (d), or peaks 1,3 and 2,4 in the case of (e) and (f). (g) One- and two-dimensional COSY spectra of the pyrrole-H region of $[(o\text{-OEt})_1\text{TPPFe(N-MeIm)}_2]^+\text{Cl}^-$ in CD_2Cl_2 recorded at room temperature. The small peak at −17.5 ppm is due to the presence of a small amount of $[\text{TPPFe(N-MeIm)}_2]^+\text{Cl}^-$ in the sample. The COSY spectrum exhibits the 1,4 and 2,3 coupling pattern. (h) One- and two-dimensional NMR spectra of the pyrrole-H region of $[(o\text{-Cl})_1(p\text{-OMe})_3\text{TPPFe(N-MeIm)}_2]^+\text{Cl}^-$ recorded at room temperature in CD_2Cl_2. The COSY spectrum exhibits the 1,3 and 2,4 coupling pattern. (Reprinted with permission from Ref. 1264. © 1992 American Chemical Society)

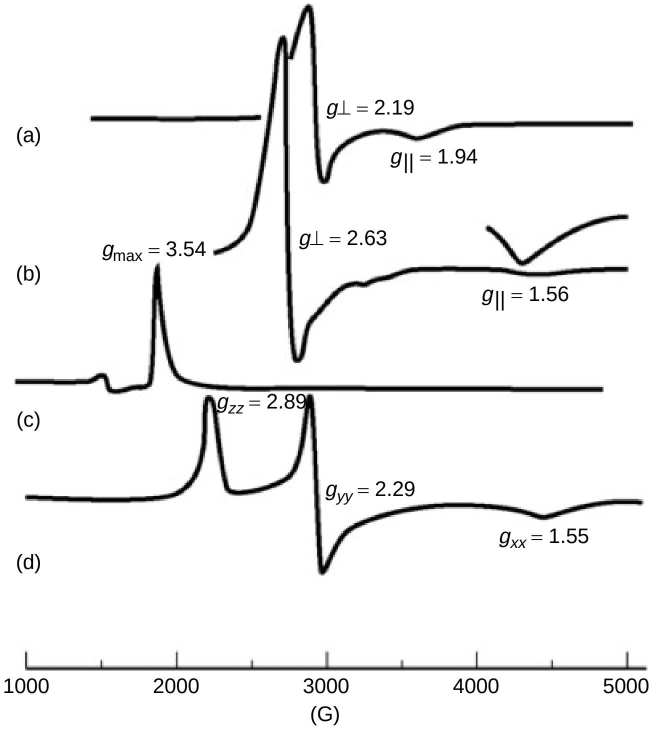

Figure 11 Typical types of EPR spectra exhibited by low-spin Fe^{III} porphyrins. (a) Axial, with small difference between $g_{\perp}$ and $g_{\parallel}$, as in the case of $[TPPFe(n\text{-}BuNC)_2]^+ ClO_4^-$;[1218] (b) axial, with large difference between $g_{\perp}$ and $g_{\parallel}$, as in the case of $[TPPFe(4\text{-}CNPy)_2]^+ ClO_4^-$;[1281] (c) 'large g_{max}', as in the case of $[OEPFe(PMe_3)_2]^+ClO_4^-$ (C. T. Watson, unpublished); and (d) a 'normal' rhombic 'B Hemichrome' EPR spectrum, as in the case of $[TPPFe(N\text{–}MeIm)_2]^+ClO_4^-$[486]

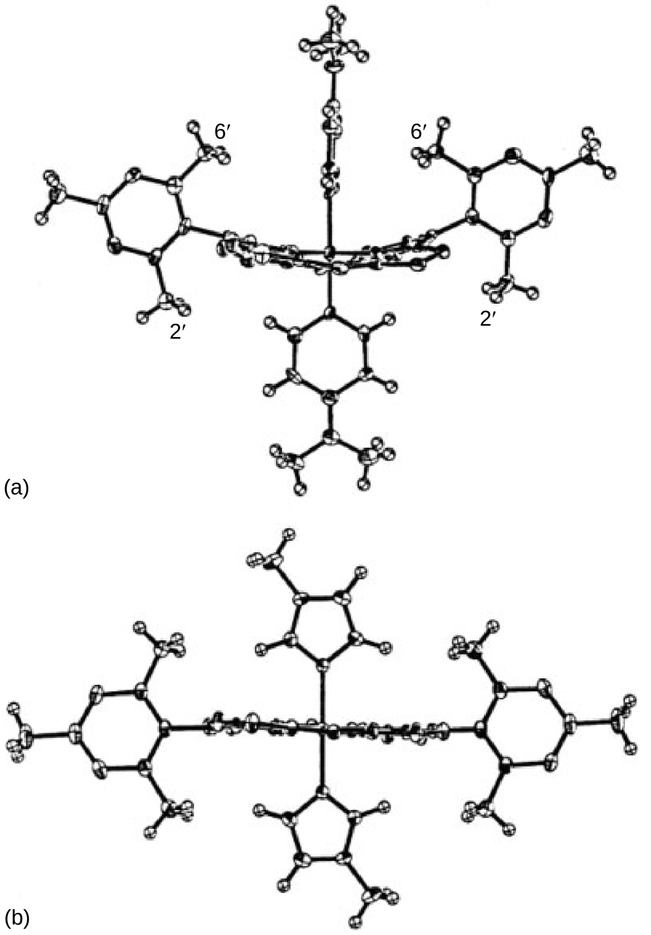

Figure 12 Comparison of ruffled (a) and planar (b) porphyrin complexes of low-spin Fe^{III}: (a) $[TMPFe(4\text{-}NMe_2Py)_2]^+ClO_4^-$; and (b) $[TMPFe(N\text{-}MeIm)_2]^+ClO_4^-$[1204]

are aligned in perpendicular planes whose projections on the porphinato core approximately bisect the $N_1{-}N_3$ and $N_2{-}N_4$ porphinato axes. The nonbonded interactions between the *ortho*-H of the pyridine ligands or the 2-Me of the hindered imidazole ligands and the methyl groups of the porphyrin mesityl rings for this orientation of the axial ligands are believed to produce a strongly ruffled porphyrin core having two oblong 'cavities' at right angles to each other, one above and one below the plane of the porphyrin, which hold the axial ligands in perpendicular planes over the *meso* positions, as shown in Figure 12.

The average displacements of the *meso* carbons from the mean plane of the porphinato core are ±0.36–0.51 Å for the bis-pyridine complexes,[1204,1280] and ±0.71 Å for the bis-1,2-Me_2Im complex.[1287] However, the same ruffling, to an even greater extent among pyridine complexes, is observed for $[TPPFe(4\text{-}CNPy)_2]^+ClO_4^-$, with an average displacement of the *meso* carbons of ±0.55 Å,[1281] even though no *ortho*-methyl groups are present on the phenyl rings. Even more striking is the fact that the structure of $[OEPFe(t\text{-}BuNC)_2]^+ClO_4^-$ also shows severe ruffling, with average displacements of the *meso* carbons of ±0.38 Å,[1218] even though the porphinato plane is totally uncongested. In the last two examples, $[TPPFe(4\text{-}CNPy)_2]^+ClO_4^-$ and $[OEPFe(t\text{-}BuNC)_2]^+ClO_4^-$, it becomes clear that there must be an *electronic* reason for the strong S_4 ruffling. It should be noted that in each of these cases the electron configuration is at least largely $(d_{xz},d_{yz})^4(d_{xy})^1$.[1218,1281]

A molecular mechanics (MM) study of the ruffling of metal complexes of porphine in the absence of axial ligands has shown that MM techniques can be used to simulate the structure of metalloporphyrins containing a wide range of sizes of metal ions and hence a wide range of porphyrin core ruffling.[1284] For the ions Ni^{II}, Fe^{II}, and Zn^{II}, the extent of core ruffling could be satisfactorily reproduced by varying the $M\text{–}N_P$ bond-stretching parameters. For the very small P^V ion, specific torsional parameters involving the central ion had to be adjusted to induce the observed ruffling of the porphyrin core. For the very large Pb^{II} ion, it was necessary to reduce the $N_P\text{–}M\text{–}N_P$ equilibrium bond angle from 90° to 60° to accommodate the observed square-pyramidal coordination geometry about the metal ion.[1284] For low-spin Ni^{II}, which is known to exist in both planar and ruffled structures, the calculated difference in energy between the two is very small ($<1.5\,\text{kcal mol}^{-1}$), and thus for a very modest expense of $1.3\,\text{kcal mol}^{-1}$ the porphyrin ring can undergo a core expansion of 0.15 Å to accommodate a change in spin state of Fe^{II} from $S = 0$ to $S = 2$.[1284] It was also found that for Fe^{III} porphyrins a planar core is always more stable than a ruffled core, although the calculated differences are small, and hence metalloporphyrins are therefore capable of adopting a variety of conformations in response to such factors as the orientation of axial ligands and the interaction with their environment.[1284] Thus, it does not seem to be possible at present to predict what conformation the porphyrin ring of a given metalloporphyrin will adopt on the basis of MM calculations.

The hemes of cytochromes *c* are generally quite ruffled, and this is believed to be due to the tight 5-amino acid turn of the Cys-X-Y-Cys-His peptide in which the two cysteines bind covalently to the vinyl groups of the heme and the histidine is an axial ligand to the iron.[623–625] Even in the microperoxidases, for example MP8-Fe^{III}, resonance Raman investigations show clearly that upon displacement of the histidine ligand by an exogenous imidazole molecule, the ν_{10} mode is upshifted in frequency, indicating that the porphyrin skeleton is less distorted when the internal coordination of the proximal histidine to iron is broken; likewise, the out-of-plane distortion mode ν_8 is also shifted to higher frequency.[1288] In contrast to this behavior, bis-(N-acetylated) MP11 shows no tendency to bind more than one exogenous ligand, so the histidine ligand cannot be displaced.[1289]

An additional electronic factor that may favor the ruffled conformation for six-coordinate low-spin Fe^{III} porphyrins having the $(d_{xz},d_{yz})^4(d_{xy})^1$ ground state has been suggested.[1281] The d_{xy} orbital is orthogonal to the π orbitals of the porphyrin ring when it is planar; however, when the porphyrin ring is strongly S_4 ruffled the p_z orbitals of the four nitrogen atoms are tilted away from the normal to the mean plane of the porphyrin ring to create a small projection of the p_z orbitals (as partial p_x or p_y character) on the *xy* plane that have proper symmetry to interact with the d_{xy} orbital of the metal. Although the amount of nitrogen p_x or p_y character thus created is small, the overlap with the d_{xy} orbital of the metal should be quite efficient. The remaining nitrogen p_z orbital projections normal to the mean plane of the porphyrin have the symmetry of the near-valence $3a_{2u}(\pi)$ orbital of the porphyrin ring (Figure 4).[1281] This would allow $P \rightarrow Fe$ π back-bonding to occur, producing the observed tendency (in terms of both NMR shifts and EPR *g*-values) toward π-cation radical character of the bis(*t*-butyl isocyanide)[1218] complexes of $OEPFe^{III}$, $TPPFe^{III}$, and $TMPFe^{III}$ and of the bis-pyridine complex of tetra-(*meso*-*n*-C_3F_7)porphyriniron(III)[621] mentioned in Section 6.3.1, and would tend to reinforce the tendency toward S_4 ruffling. However, investigations of the highly saddled octaalkyltetraphenylporphyrin complexes of Fe^{III} bound to two 4-cyanopyridine[943] or *t*-butylisocyanide[1290] axial ligands have shown that although the porphyrinate ring shows no ruffling for [OMTPPFe(*t*-BuNC)$_2$]ClO$_4$,[1290] the g-values of that complex and the related ones, [OETPPFe(*t*-BuNC)$_2$]ClO$_4$ and [TC$_6$TPPFe(*t*-BuNC)$_2$]ClO$_4$,[1290] are the same ($g_\perp = 2.19 - 2.20$, $g_\parallel = 1.94 - 1.96$) as those of [OEPFe(*t*-BuNC)$_2$]ClO$_4$,[1218] [TPPFe(*t*-BuNC)$_2$]ClO$_4$[1218] and [TTPFe(2,6-XylylNC)$_2$]ClO$_4$.[1219] Similarly, the [OMTPPFe(4-CNPy)$_2$]ClO$_4$ and [TC$_6$TPPFe(4-CNPy)$_2$]ClO$_4$ complexes[943] have very similar axial EPR spectra ($g_\perp = 2.49$, $g_\parallel = 1.6$) to those of [TMPFe(4-CNPy)$_2$]ClO$_4$[1280] and [TPPFe(4-CNPy)$_2$]ClO$_4$,[1281] although in the 4-CNPy case it was not possible to obtain structures of the low-spin form, since the crystals were grown at ambient temperatures, where [OMTPPFe(4-CNPy)$_2$]ClO$_4$ is intermediate spin, $S = 3/2$.[943] However, although the EPR values are the same, indicating the same metal orbital for the unpaired electron (d_{xy}), ^1H NMR studies showed significantly less spin delocalization to the $3a_{2u}(\pi)$ orbital of the porphyrinate ring for these saddled porphyrinates.[943,1290] Thus, it must be concluded that a ruffled geometry may well stabilize the $(d_{xz},d_{yz})^4(d_{xy})^1$ ground state, but is not necessary for its existence.[1290]

Bis-cyanide complexes of iron(III) synthetic and natural porphyrins have been studied for many years, and were assumed to have the more common $(d_{xy})^2(d_{xz},d_{yz})^3$ electron configuration,[168,1223] but within recent years there have been increasing numbers of reports of the stabilization of the less common $(d_{xz},d_{yz})^4(d_{xy})^1$ electron configuration, often by bulky *meso*-substituents, including in increasing tendency the series H, Me, Et, *i*-Pr,[1291] for which the pyrrole-H NMR resonance is found at −21.7, 8.7, 8.3, 12.8 ppm, respectively, at 248 K in CD_2Cl_2-CD_3OD,[1291] the (1R)-*cis*-caronaldehyde acid methyl ester,[1292] for which the pyrrole-H NMR resonance is found at 11.1, 10.6 ppm,[1292] and the cyclohexyl group,[1293] for which it is found at 12.0 ppm[1293] at 293 K in CD_3OD, respectively, both compounds with very small temperature dependence.[1292,1293] Of all of these listed compounds, only the H-substituted (porphine) complex[1291] clearly has the more common electron configuration, while all of the *meso*-alkyl substituted complexes have the unpaired electron in the d_{xy} orbital, as is also shown by the g-values ($g_{max} = 3.65$ for the porphine complex, $g_\perp = 2.43$, $g_\parallel = 1.73$ for the *meso*-*i*-Pr complex[1291]). The d_{xy} ground state appears to be stabilized by hydrogen-bonding solvents,[1291–1294] and even the original work on the bis-cyanide complexes of $OEPFe^{III}$ and $TPPFe^{III}$ by La Mar, Del Gaudio and Frye showed that there was an overall positive bias of the chemical shifts of the porphyrin as the solvent hydrogen-bonding donor strength increased.[1223] All complexes mentioned above show negative pyrrole-H shifts when non-hindered imidazole ligands are bound to iron instead of cyanide.[1291–1293] Bulky *meso*-aryl substituents also produce what appears to be a $(d_{xz},d_{yz})^4(d_{xy})^1$ electron configuration for the bis-cyanide complex, with $g_\perp = 2.47 - 2.45$ and $g_\parallel = 1.5$ for Me, Et or *i*-Pr groups at the 2,4,6-R-phenyl positions of $TPPFe^{III}$; the pyrrole-H resonance shifts from −11.7 to −5.7 to +4.4 to +6.0 for the series R = H, Me, Et, *i*-Pr, respectively.[1295] Nakamura and coworkers have shown the large variation in ^{13}C shifts, for example of the *meso*-carbons of the porphyrin ring, as the electron configuration of the metal changes from $(d_{xy})^2(d_{xz},d_{yz})^3$ to $(d_{xz},d_{yz})^4(d_{xy})^1$ upon change of axial ligand or porphyrin or phenyl substituent,[1291,1295–1297] and this large variation makes it all the more challenging to attempt to calculate the NMR shifts of various nuclei using DFT methods, although two first attempts have been reported.[1298,1299]

Introducing only one *meso*-substituent into $[\mathrm{OEPFe(CN)_2}]^-$ yields a shift in the *trans*-*meso*-H resonance from +5.5 ppm to −10.5 ppm at 298 K in the order –CN > –C(O)H > $-\mathrm{NO_2}$ > –H > $-\mathrm{C_6H_5}$ > –Cl > $-\mathrm{OCH_3}$ > −*n*-Bu, and in the *cis*-*meso*-H resonance from 3.3 ppm to −17.2 ppm in the order –H > –CN > –C(O)H > $-\mathrm{NO_2}$ > $-\mathrm{C_6H_5}$ > –Cl > $-\mathrm{OCH_3}$ > –*n*-Bu.[1300] The bis-cyanide complex of the -H substituted complex (OEP itself) was shown to have the $(d_{xy})^2(d_{xz},d_{yz})^3$ electron configuration many years ago,[1223] so it appears that electron-donating (or bulky) substituents relative to – H shift the electron configuration toward that of $(d_{xz},d_{yz})^4(d_{xy})^1$. Variations in the methylene-H resonances through the series are also observed.[1300] The high-spin chloroiron(III) complexes of these *mono-meso*-substituted OEPs also show quite altered NMR spectra, as well as structures that are no longer domed, as seen for OEPFeCl.[1300] And finally, modification of a pyrrole ring, as in quinoxalineotetraphenylporphyrin (quinoxaline = the N–C–C–N atoms of pyrazine fused to the β,β' positions of one pyrrole ring), also creates a $(d_{xz},d_{yz})^4(d_{xy})^1$ electron configuration for the bis-cyanide and -pyridine complexes (with the exception of the high-basicity pyridine, 4-$\mathrm{NH_2}$Py, which, along with ImH, produce the more common electron configuration).[1301] The deviation of the temperature dependence of the ^{1}H NMR shifts of the bis-cyanide complex from Curie behavior has been suggested to be due to Boltzmann population of four electron configurations:

$$\begin{aligned}(d_{xz})^2(d_{yz})^2(d_{xy})^2(a_{2u})^1 &\rightleftharpoons (d_{xz})^2(d_{yz})^2(d_{xy})^1(a_{2u})^2\\ &\rightleftharpoons (d_{xz})^1(d_{yz})^2(d_{xy})^2(a_{2u})^2\\ &\rightleftharpoons (d_{xz})^2(d_{yz})^1(d_{xy})^2(a_{2u})^2\end{aligned}\tag{24}$$

In comparison to these cases, the mono-pyrrole-substituted derivatives of $[\mathrm{TPPFe(CN)_2}]^-$ show 3-H resonances (the adjacent pyrrole position to that of the substituent) that shift from −44 to −1.5 ppm at 293 K in $\mathrm{CD_3OD}$ in the order $-\mathrm{O^-}$ > $-\mathrm{NH_2}$ > $-\mathrm{NHCH_3}$ > –OH > $-\mathrm{OCH_3}$ > $-\mathrm{CH_3}$ > OBz > –Cl > –Br > –CN > $-\mathrm{NO_2}$ > $-\mathrm{Py^+}$ > $\mathrm{PPh_3}^+$.[978] Although not recognized at the time of publication of this work, there is likely an increase in the contribution of the $(d_{xz},d_{yz})^4(d_{xy})^1$ electron configuration through this series, for the substituents to the right of $-\mathrm{OCH_3}$ in this list show increased alternation in the phenyl-H shifts to produce shift differences $\delta_\mathrm{m}-\delta_\mathrm{p}$ and $\delta_\mathrm{m}-\delta_\mathrm{o}$ that are increasingly positive,[978] indicating increasing spin density at the *meso*-carbons that is characteristic of contribution from the less common electron configuration.[195] The bis-cyano complex of 5,10,15,20-tetraphenyl-21-oxaporphyriniron(III), however, shows pyrrole-H shifts that are totally consistent with the more common $(d_{xy})^2(d_{xz},d_{yz})^3$ electron configuration.[536] Interestingly, to the knowledge of the authors, there have been no reports of molecular structure determination of $(d_{xz},d_{yz})^4(d_{xy})^1$ electron configuration bis-cyanide complexes, which would be expected to have highly ruffled porphyrinate rings.

Iron(III) complexes of reduced hemes have been claimed to stabilize the $(d_{xz},d_{yz})^4(d_{xy})^1$ ground state much more readily than iron porphyrinates.[1285,1286] However, in some cases this may be more a result of the choice of axial ligands than to the electronic nature of the reduced heme ligand. It is now clear that iron(III) chlorins, when bound to imidazole,[1274] dimethylphenylphosphine[1302] or aliphatic amine ligands,[1303] have the same electronic ground state as iron(III) porphyrins, that is, $(d_{xy})^2(d_{xz},d_{yz})^3$, whereas when bound to cyanide ions,[61–65,1282,1304] a somewhat different pattern of spin delocalization and thus electron configuration seem to be present. In the case of the bis-cyano complex of siroheme this appears to be a fairly pure $(d_{xz},d_{yz})^4(d_{xy})^1$ electron configuration, and even the mono-cyano complex of the sulfite reductase heme domain (SiR-HP) has shifts that are indicative of this electron configuration,[1304] whereas the mono-cyano complexes of other histidine-bound heme proteins, including met-myoglobin, peroxidase and heme oxygenase, have totally different heme resonance shifts that are indicative of the $(d_{xy})^2(d_{xz},d_{yz})^3$ electron configuration.[1305] However, when bound to the sulfite anion (the substrate) the SiR–HP–$\mathrm{SO_3}^{2-}$ shifts are more typical of the $(d_{xy})^2(d_{xz},d_{yz})^3$ electron configuration.[1304]

An interesting case of orbital ground state, one in which the ground state is different from the electronic state that is stable at ambient and physiological temperatures, is the case of the heme oxygenase model developed first by Tajima and coworkers,[999–1001] $[\mathrm{TPPFe(OCH_3)(OO}\text{-}t\text{-}\mathrm{Bu)}]^-$, which has more recently been examined in detail by pulsed EPR and ^{13}C NMR spectroscopy by Rivera and coworkers.[1002] As mentioned in Section 6.1.1, either a single methoxide or alkyl peroxide ligand alone bound to $\mathrm{TPPFe^{III}}$ creates a high-spin complex, $S = 5/2$. However, two of either one or the combination of one of each of the two ligands were shown to yield EPR spectra of an $S = 1/2$ center with very compressed g-values (2.311, 2.150, 1.953 for the mixed-ligand complex).[999–1002] Because these g-values were in between those shown by bis-4-CNPy and bis-*t*-BuNC complexes, both of which have $(d_{xz},d_{yz})^4(d_{xy})^1$ ground states, it was postulated that the methoxide-alkyl peroxide complex, as well as the imidazole-peroxide complex that would be a more direct model of the active form of heme oxygenase,[33,34] might also have a $(d_{xz},d_{yz})^4(d_{xy})^1$ ground state, which, in the natural protohemin, should lead to large ruffling of the porphyrin ring.[1002] This ruffling would bring the terminal oxygen of the peroxo-bound complex much closer to the *meso*-carbon to be attacked, and the large spin density at that *meso*-carbon in a $(d_{xz},d_{yz})^4(d_{xy})^1$ ground-state heme center could contribute to a possible radical attack by the terminal oxygen of $O_2{}^{2-}$ or OOH^- on the *meso*-carbon to begin the breakdown of heme.[1002] However, pulsed EPR studies conclusively showed that at 4.2 K the ground state of this model heme complex, $[TPPFe(OCH_3)(OO\text{-}t\text{-}Bu)]^-$, has the more common $(d_{xy})^2(d_{xz},d_{yz})^3$ electron configuration, which should favor a more planar heme.[1002] In spite of this finding, ^{13}C NMR investigations of the *meso*-^{13}C-labeled version of this model heme complex showed that over the temperatures of the NMR investigations (183–303 K) there is a thermodynamic equilibrium between the heme complexes with $(d_{xy})^2(d_{xz},d_{yz})^3$ and $(d_{xz},d_{yz})^4(d_{xy})^1$ electron configurations (and thus also likely between planar and ruffled heme rings) that makes the latter the most stable at physiological temperatures, where heme oxygenation takes place;[1002] hence the hypothesis of a role for the $(d_{xz},d_{yz})^4(d_{xy})^1$ electron configuration in the mechanism of action of heme oxygenase is supported by the data obtained,[1002] and further investigations of this and related systems should be carried out.

A different type of nonplanarity, which is called saddling, the S_4 saddle (sad) deformation, is enforced by β-substituted tetraphenylporphyrins, including octa-(β-alkyl)TPP derivatives[391] (except for one[1306]) or β-Cl_8- or β-Br_8TPP derivatives and β-substituted TPPs having 2,6-phenyl substituents such as 2,4,6-trimethylphenyl (mesityl),[1307] 2,6-dichlorophenyl,[405] and pentafluorophenyl[1308] groups. Structures of Br_8TMPH_2, Br_8TMPNi^{II}, and $Br_8(F_5)_4TPPNi^{II}$ reveal that these complexes are extremely saddled, with the porphyrin nitrogens alternating above and below the plane, and the phenyl rings canted at some angle less than 90° to the porphyrin plane, in order to accommodate the eight large β substituents.[1309] This canting of the phenyl rings in turn enforces the saddle ruffling of the porphyrin ring. The Soret peak of tetraarylporphyrins is strongly red-shifted upon substitution of the eight β-pyrrole positions by alkyl, chloro, or bromo groups.[391,1307–1309] AM1 molecular orbital calculations have shown that the saddle conformation of Br_8TPPH_2 is 59 $kJ\,mol^{-1}$ more stable than the corresponding planar conformation.[1310] The difference in energy of planar and saddle conformations of Cl_8TPPH_2, however, is less (12 $kJ\,mol^{-1}$).[1310] These calculations also show that the energy gap between the HOMO and the LUMO is very little modified by the nature (H, Cl, or Br) of the β substituents, while there is a large shift to lower energy of both the HOMO and LUMO when going from H_8TPPH_2 to Br_8TPPH_2.[1310] However, these calculations also suggest that the *meso* carbons should be in the mean plane of the porphyrin, while X-ray data clearly indicate that the *meso* carbons are 0.1–0.5 Å out of the mean plane.[391,1309] For the Zn^{II} analogs the order of energies of a_{1u} and a_{2u} is reversed for the β-halogenated TPP complexes, making a_{2u} the HOMO in each case.[1310] β-Octafluoro TPP complexes of several first-row transition metal complexes have also been prepared and their molecular structures and ^{19}F NMR spectra investigated.[1311]

The first structures of the chloroiron(III) complex of a β-chlorinated porphyrin, $[Cl_8TMPFeCl]$, and its β-brominated analog have been reported,[1312] and similar complexes with perfluorinated phenyl rings have also been synthesized and characterized structurally.[598,1311] In each case the metal is 0.55 Å above the (distorted) mean plane of the porphyrin, with the C_β atoms being displaced from the mean plane by 0.87 and 0.91 Å, respectively,[598] slightly less than in the metal-free analogs (0.90 and 0.95 Å, respectively).[1309] It would be interesting to see what the conformation of low-spin six-coordinate Fe^{III} complexes would be, if they could be stabilized against the autoreduction that is typically observed when Lewis bases are added to these β-halogenated $TPPFe^{III}$ complexes.[598]

6.3.3 *The Preferred Orientation of Planar Axial Ligands Bound to Low-spin Iron(III) Porphyrins*

During the past few years there have been a number of investigations of the factors that affect the relative orientations of planar axial ligands in Fe^{III} and Fe^{II} porphyrins.[193,194,486,575,586,613,615–1207,1224,1268,1269,1280,1313–1316] One of the main reasons for interest in this question is that among the bis(imidazole)heme-containing cytochromes with known molecular structures that are involved in electron transfer (cytochromes b_5[1248] and c_3[1250,1251]), two types of limiting structures and two types of EPR spectra have been observed. Cytochrome b_5[1248] and three of the four hemes of cytochromes c_3[1250,1251] have the imidazole rings of the two coordinated histidines in nearly parallel planes, while one heme in each of the cytochromes c_3 for which structures are available has the imidazole rings in nearly perpendicular planes.[1250,1251] The EPR spectra of cytochromes b_5[1317–1319] and three of the hemes of the cytochromes c_3[1320–1324] are rhombic, with $g_z \sim 2.9–3.0$, $g_y \sim 2.25–2.35$, and $g_x \sim 1.4–1.6$, typical of the class of heme proteins called ‘B Hemichromes’ by Blumberg and Peisach.[1325] The fourth has a single feature EPR signal at $g = 3.3–3.7$[1320] that others have called a HALS (highly anisotropic low-spin[1326–1328]) signal and that we have called the ‘strong g_{max}[1329]’ or ‘large g_{max}[486]’ signal. The ‘large g_{max}’ name is now preferred, because the only spectral feature observed generally has a g-value of 3.3 or larger, and the signals are extremely weak compared to normal rhombic signals, as a result of the fact that the transition probability at that maximum g-value depends upon the sum of the squares of the other two g-values divided by the ‘large g_{max}’ value.[1330,1331] In the case of ‘large g_{max}’ species, g_x and g_y are much smaller than for normal rhombic signals, while g_z is much larger, and thus all factors lead to much lower signal intensity for the ‘large g_{max}’ species. An example of this type of EPR spectrum, and a typical rhombic ‘B Hemichrome’ EPR spectrum, are included in Figure 11. In addition, there are a number of membrane-bound cytochromes *b*, including the two *b* cytochromes of mitochondrial 'Complex III' (also known as ubiquinone-cytochrome *c* oxidoreductase), as well as chloroplast cytochrome b_6, which also have bis-histidine coordination to the hemes in each case.[1332,1333] These cytochromes *b* also have 'large $g_{\max}$' EPR spectra[1334–1336] and a wider range of reduction potentials than observed for the cytochromes b_5, b_2, and the *b* heme of sulfite oxidase, all of which have rhombic, typical 'B Hemichrome', EPR spectra. The reduction potentials of the four hemes of cytochromes c_3 vary over a range of ~200–300 mV,[1320,1337] raising the question as to whether there is a relationship between the axial-ligand plane orientations and their reduction potentials. Zarić and coworkers have surveyed the Protein Data Bank for structures of heme proteins that have at least one histidine ligand, and have interpreted the data obtained with molecular force field computations.[1338] It was found that the imidazole ring of histidine makes important interactions with the propionic acid side chains of the heme and with the histidine backbone. The hydrogen-bonding pattern is obviously not decisive, though it is probably used by nature to fine-tune the orientation of imidazole axially ligated to heme. The imidazole adopts a preferred orientation with respect to its histidine backbone such that the plane of the imidazole ring is practically never parallel to the C_α–C_β bond of its histidine backbone. The interaction of the imidazole with the backbone also influences the orientation of the imidazole with respect to the heme. It was shown that there is an energy minimum when the N-H group of the imidazole is oriented toward the propionic acid groups, and there are energy minima for orientations where the imidazole ring is orthogonal to the plane defined by the C_α–C_β and C_β–C_γ bonds of the histidine, and that these interactions are mainly of electrostatic origin.[1338]

Investigation of the molecular structures, EPR spectra and in some cases Mössbauer spectra of well-defined low-spin Fe^{III} heme model compounds has provided conclusive proof that the 'large $g_{\max}$' EPR signal is correlated with near-axial symmetry,[193,194,486,1224] and in the case of planar axial ligands, with perpendicular alignment of these ligands.[486,1204–1207,1339] The first investigation of this type[486] was of $[TPPFe(ImH)_2]^+$ Cl^-,[612] in which the axial ligands are in parallel planes, and $[TPPFe(2\text{-}MeImH)_2]^+$ ClO_4^-,[618] in which the axial ligands are in perpendicular planes. EPR spectra of crystals from the same batches as those from which the structures were determined showed two overlapping rhombic EPR signals for $[TPPFe(ImH)_2]^+$ Cl^-,[486] consistent with the fact that the crystals contained molecules with two different projections of the parallel imidazole planes on the porphinato core, one molecule having an angle of 6° and the other an angle of 41° to the N_1–N_3 axis.[612] In contrast, the EPR spectrum of crystals of $[TPPFe(2\text{-}MeImH)_2]^+ClO_4^-$ gave a 'large $g_{\max}$' feature at $g = 3.41$;[486] in this case the 2-methylimidazole ligand planes are aligned at 89° to each other, with angles of 32° and −58° to the N_1–N_3 axis of the porphinato core.[618] Mössbauer spectra at 4.2 K in an applied magnetic field (500 G to 6 Tesla) allowed estimation of the two unresolved g-values.[486] In fact, magnetic Mössbauer spectra measured at 4.2 K in a large applied magnetic field (6–7 Tesla) have been very helpful in estimating the two unresolved g-values in a number of model heme systems.[193,194,486,1204,1340,1341] Mössbauer isomer shifts and quadrupole splittings have been calculated using DFT methods for low-spin Fe^{III} as well as other spin states from $S = 0$ to 5/2.[1342,1343]

From the Griffith theory[1265,1266] for the g-values of low-spin Fe^{III}, using the formulation of Taylor,[1267] *Ligand Field Theory* calculations of the relative energies of the d_{xy}, d_{xz}, and d_{yz} orbitals for the two complexes and the idealized parallel and perpendicular orientations of the axial imidazoles were carried out.[486] The crystal field parameters ('Rhombic splitting,' V/λ 'Tetragonality,' Δ/λ, and 'Rhombicity,' V/Δ) can be obtained from the three g-values of the rhombic spectra. The energy separation of the three formerly t_{2g} orbitals of strictly octahedral symmetry, split by the lower-symmetry field of the ferriheme center, in units of the spin-orbit coupling constant λ, can be estimated from the following expressions:[1267]

$$\frac{V}{\lambda} = E_{yz} - E_{xz} = \frac{g_{xx}}{g_{zz} + g_{yy}} + \frac{g_{yy}}{g_{zz} - g_{xx}} \tag{25}$$

$$\frac{\Delta}{\lambda} = E_{yz} - E_{xy} - \frac{1/2V}{\lambda} = \frac{g_{xx}}{g_{zz} + g_{yy}} + \frac{g_{zz}}{g_{yy} - g_{xx}} - \frac{1/2V}{\lambda} \tag{26}$$

The results confirmed that parallel alignment gives the more stable structure. In that work[486] it was also concluded that perpendicular alignment of planar axial ligands could lead to a positive shift in reduction potential of up to about 50 mV over that observed for parallel alignment, all other structural and environmental factors being equal.[486] However, that conclusion relied upon the assumption that parallel and perpendicular ligand plane orientations would be of equal energy for the Fe^{II} complexes, which is now known not to be the case,[575] as discussed in Section 4.1.2 above.

Following that first study of the relationship between EPR spectral type and axial-ligand plane orientation,[486] Strouse and coworkers showed by single-crystal EPR spectroscopy that in cases of parallel alignment of imidazoles bound to low-spin Fe^{III} porphyrins, 'pseudo-Jahn–Teller' distortion (*see Jahn–Teller Effect*) of the porphyrin ligand, particularly in cases where the projection of the imidazole plane on the porphyrin ring makes a small angle with the N_1–N_3 axis, can contribute significantly to the rhombic splitting;[1268,1269] an extension of this has been published recently.[1344] Strouse and coworkers also found that while crystal field stabilization of the parallel orientation is significant for axial ligands such as imidazoles that are strong π donors, for weak π donors, such as pyridine, and nonplanar ligands, such as cyanide, spin–orbit stabilization of the complexes results in equal or nearly equal population of the d_{xz} and d_{yz} orbitals.[1224] Even strong π donor pyridine ligands, such as 4-dimethylaminopyridine, can be forced to bind in perpendicular planes if bulky groups are placed on the 2,6-phenyl positions of TPP, as in TMPFe^{III}, Figure 10 top, and again, a 'large g_{max}' EPR signal is observed, in this case at $g = 3.48$.[1204] Lower-basicity pyridines (decreasing pK_a(BH$^+$) in the order 4-NH$_2$Py, 3-EtPy, 3-ClPy, 3-CNPy, and 4-CNPy) have also been shown to bind to TMPFe^{III} in perpendicular planes, but the g-values of the 'large g$_{max}$' signals shift to progressively smaller values as the basicity of the pyridine decreases (from 3.48 for 4-NMe$_2$Py to 2.53 for 4-CNPy (but see below)).[1280] The Mössbauer quadrupole splittings of the less-basic pyridine ligand complexes of TMPFe^{III} also become smaller as the basicity decreases (1.75–0.97 mm s^{-1} for the same series of pyridines).[1280] The ^{1}H NMR spectra also change in a linear manner with the pK_a of the ligand (the pyrrole-H resonance shifts from −30.9 to +2.21 ppm at – 80 °C for the series 4-NMe$_2$Py to 4-CNPy).[1280] Nevertheless, all of these complexes have extremely similar molecular structures, with ruffled porphyrinate rings ($|\Delta C_m| = 0.36–0.43$ Å), large ϕ angles of 29 to 44° and $\Delta\phi$ angles of 90, 87, and 77° for the 3-EtPy, 4-CNPy and 3-ClPy complexes, respectively.[1280] The Fe–N$_P$ bond lengths in all cases are again shorter (1.961–1.966 Å)[1280] than expected for iron porphyrinates having planar porphyrin cores (∼1.988–2.002 Å). Axial ligand-Fe bond lengths vary slightly (1.989, 2.002; 2.001, 2.002; 2.018, 2.006 Å, respectively) but non-systematically for the three complexes.[1280] Because the type of EPR signal of the bis-(4-cyanopyridine) complex is not 'large g$_{max}$' but rather axial, with $g_\perp = 2.53$, $g_\parallel = 1.56$, and the pyrrole-H chemical shift at – 80 °C is not negative, but rather +2.1 ppm, the results for the entire series of complexes were interpreted as being indicative of a smooth change in the electron configuration of the low-spin Fe(III) porphyrinates from $(d_{xy})^2(d_{xz},d_{yz})^3$, with small energy difference between d_{xz} and d_{yz}, toward $(d_{xz},d_{yz})^4(d_{xy})^1$ as the basicity of the pyridine ligand decreases from pK_a of the conjugate acid = 9.7 to 1.1.[1280] Study of the low temperature MCD spectra of [TMPFe(4-CNPy)$_2$]$^+$[1345] and of the corresponding [TPPFe(4-CNPy)$_2$]$^+$ complex by X-ray crystallography,[1281] EPR,[1281] Mössbauer,[1281] and NMR[1346] spectroscopies confirmed that the electronic ground state of both of these complexes at low temperatures is the less common $(d_{xz},d_{yz})^4(d_{xy})^1$ electron configuration discussed above in Section 6.3.1. Separately it was shown that for the Fe^{III} complexes of TPP, TMP and its larger alkyl analogs having 2,4,6-ethyl or isopropyl substituents on the phenyl rings, the g$_{max}$ values for the bis-2-MeImH and -benzimidazole complexes shift from 3.40 to 3.13, 3.17, 3.08 and 3.43 to 2.89, 2.91 and 3.01, respectively;[1296,1297] there thus appears to be a tendency for highly ruffled iron(III) porphyrinates with bulky planar ligands in perpendicular planes to move from a pure $(d_{xy})^2(d_{xz},d_{yz})^3$ state toward a $(d_{xz},d_{yz})^4(d_{xy})^1$ state as the degree of ruffling distortion increases, even when the axial ligands are strong σ and π donors.

The isolation of two crystalline forms of [TMPFe(5-MeImH)$_2$]ClO$_4$ showed that one form had the axial ligands in approximately parallel planes ('*paral*', $\Delta\phi = 26$ and 30° for the two molecules in the unit cell), while the other had the axial ligands in approximately perpendicular planes ('*perp*', $\Delta\phi = 76°$),[1205] but in fact both of these observed dihedral angles are markedly different from the ideal values of 90° for perpendicular and 0° for parallel.[1205] The planes of the axial imidazoles of *perp*-[TMPFe(5-MeImH)$_2$]$^+$ are tilted (by 12.5° and 7.6°) from the heme normal. It is probable that crystal packing effects and/or hydrogen-bonding of the non-coordinated 5-MeImH molecules in the lattice to the N-H proton of the coordinated imidazoles may influence whether the ligands bind in an off-axis manner, since not all mono- and bis-imidazole complexes show this type of distortion. Off-axis binding of imidazole (histidine) ligands has also been seen in a number of heme proteins. *Perp*-[TMPFe(5-MeImH)$_2$]$^+$ has a small Mössbauer quadrupole splitting ($\Delta E_Q = 1.78$ mm s^{-1} at 120 K) and a 'large g$_{max}$' EPR signal at g = 3.43, while *paral*-[TMPFe(5-MeImH)$_2$]$^+$ has a larger quadrupole splitting ($\Delta E_Q = 2.56$ mm s^{-1} at 120 K) and a rhombic EPR signal (g = 2.69, 2.34–2.43, 1.75) in the crystalline state.[1205] These values are similar to those observed for ferriheme centers bound to one imidazolate anion and one neutral imidazole,[1347] and it is interesting to note that one of the 5-MeImH ligands is hydrogen-bound to a 5-MeImH molecule in the lattice in this structure, thus probably imparting partial imidazolate character to that ligand in each of the molecules in the unit cell.[1205]

Molecular mechanics calculations on *paral*- and *perp*-[TMPFe(5-MeImH)$_2$]$^+$ provided information about the relative stability of these two non-ideal axial-ligand plane orientations: it was found that to have two ligands in parallel planes with $\phi_1, \phi_2 = 45°$ and a planar porphyrin core is the maximum energy conformation, while having the two ligands in perpendicular planes with $\phi_1 = -45°$, $\phi_2 = 45°$ with a ruffled core is the minimum energy.[1205] The observed ligand orientation in *perp*-[TMPFe(5-MeImH)$_2$]$^+$ ($\phi_1 = -46°$, $\phi_2 = 30°$, $\Delta\phi = 76°$) has an energy only 0.4 kcal/mol higher than the minimum. Having the conformation exhibited by *paral*- [TMPFe(5-MeImH)$_2$]$^+$ yields a calculated energy of ∼2.6 kcal mol^{-1} above the global minimum, and this conformation is close to the local maximum with ligands over a pair of trans Fe–N$_P$ vectors (ϕ_1, $\phi_2 = 0°$).[1205] Thus, the orientation of axial ligands in *paral*- and *perp*-[TMPFe(5-MeImH)$_2$]$^+$ are within ∼2–3 kcal mol^{-1} of each other according to the molecular mechanics calculations, with the 'parallel' being slightly higher in energy. However, for low-spin d^5 systems the 'parallel' axial-ligand orientation is stabilized by the Jahn-Teller effect by the rhombic splitting of d_{xz} and d_{yz}, $V = 2–3\lambda$, where λ is the spin-orbit coupling constant for low-spin Fe^{III}. With $\lambda = 400$ cm^{-1}, or 1.14 kcal mol^{-1}, this stabilization is 2.3–3.4 kcal mol^{-1}, a stabilization for which molecular mechanics calculations do not account. In this work[1205] it was concluded that relative parallel orientation of axial-ligands is the apparently preferred orientation for most characterized low-spin Fe^{III} porphyrinates having two planar high-basicity axial ligands, with relative perpendicular orientations being observed only in special circumstances, primarily those of introduced steric effects. The appearance, in the solid state, of ligand orientations approaching the two limiting forms speaks to a near energetic equivalence of conformational isomers. The energy balance between the two forms is the result of crystal field stabilization effects that favor the parallel form, and steric strain effects that favor the perpendicular form.**[1205]**

Because *meso*-only substituted ferriheme complexes (TPP, TMP, etc.) having perpendicularly arranged axial ligands lying over the *meso*-carbons tend to be highly ruffled (see also Section 6.3.2), it was hypothesized that synthetic iron porphyrinates that were designed to orient the axial ligands close to the N_P–Fe–N_P axes might be better models of the membrane-bound cytochromes,**[194]** which must carry out reversible redox between Fe^{III} and Fe^{II}, the latter of which strongly prefers non-ruffled porphyrin rings (see below and also Section 4.1.2). To accomplish this, a detailed study of the bis-imidazole- or bis-pyridine-ligated ferriheme complexes of the octaalkyltetraphenylporphyrins, where the alkyl substituents are methyl (OMTPP), ethyl (OETPP) and β,β'-tetramethylene (TC_6TPP), has been carried out.**[1348]** These dodecasubstituted porphyrin ligands all have saddled porphyrin rings, with two opposite pyrrole rings tilted above, while the other two are tilted below the mean plane of the porphyrin, thus creating two cavities that should help to encourage the axial ligands to bind in perpendicular orientation with the ligand planes lying over or close to the N_P–Fe–N_P axes; the degree of saddling increases in the order TC_6TPP < OMTPP < OETPP, as observed in approximately twenty crystal structures of bis-ligand Fe^{III} complexes.**[1348]** It was found that such synthetic heme complexes are rich in structural diversity, which allowed crystallization of bis-ligated iron(III) complexes having many different axial-ligand orientations and differing amounts of ruffling admixture to the largely saddled porphyrin cores.**[943,1206,1207]** For example, with the common non-hindered ligand, N-methylimidazole (N-MeIm), four molecular structures have been obtained, including that of $[OETPPFe(N\text{-}MeIm)_2]Cl$, which has an axial-ligand plane dihedral angle of 73.1° and a 'large g_{max}' EPR feature at $g = 3.27$; that of $[TC_6TPPFe(N\text{-}MeIm)_2]Cl$, which has an axial-ligand plane dihedral angle of 90°, small N_P–Fe–N_P angles (15.3°) yet a large ruffling component to the porphyrin core, and in frozen solution shows both a g_{max} value of 3.14 and a rhombic EPR signal with $g = 1.45$, 2.39, 2.86; that of *perp*-$[OMTPPFe(N\text{-}MeIm)_2]Cl$, which has an axial-ligand plane dihedral angle of 90° yet very large displacement from the N_P–Fe–N_P axes (29°) and has $g_{max} = 3.61$; and that of *paral*-$[OMTPPFe(N\text{-}MeIm)_2]Cl$, which has an axial-ligand plane dihedral angle of 19.5° and a normal rhombic EPR spectrum with $g = 1.54$, 2.51, and 2.71.**[1207]** The ORTEP and formal core diagrams of the two OMTPP and the OETPP molecules are shown in Figure 13. It is quite surprising to see that such a small dihedral angle as 19.5° can be obtained in these saddled porphyrinates, especially because the ligand in 'wrong' orientation has a very small displacement from the N_P–Fe–N_P axis (5.9°).**[1207]**

Among the tetramesitylporphyrin and octaalkyltetraphenylporphyrin complexes of iron(III) whose structures have been determined to date, the largest axial-ligand plane dihedral angle that has been observed for which the EPR spectral type is normal rhombic is 30°, for *paral*-$[TMPFe(5\text{-}MeImH)_2]ClO_4$;**[1205]** the smallest axial-ligand plane dihedral angle that has been observed for which the EPR spectral type is 'large g_{max}' is 70°, for $[OETPPFe(4\text{-}NMe_2Py)_2]Cl$,**[1206]** with another, $[OETPPFe(N\text{-}MeIm)_2]Cl$, at 73.1°.**[1207]** Thus, the switch in EPR spectral type from normal rhombic to 'large g_{max}' must occur somewhere between 30 and 70° axial-ligand plane dihedral angles.**[194]** For comparison to the membrane-bound cytochromes, further investigation of model systems designed to produce perpendicular alignment of axial ligands in low-spin Fe^{II} porphyrins, for example, the iron(II) analogs of the OETPP and OMTPP complexes shown in Figure 13, is needed to better understand the spectroscopic and redox properties of the mitochondrial cytochromes *b* and chloroplast cytochrome b_6, for which all ferriheme EPR signals are of the 'large g_{max}' type, strongly suggesting perpendicular orientation of the two histidines. Since it seems unlikely that axial-ligand plane orientation within the protein matrix changes upon redox (since it is expected to be stabilized by hydrogen-bonding of the histidine N–H to protein main or side chain atoms and to the typically observed close packing of protein residues around the coordinated histidine), these membrane-bound cytochromes,**[7–9]** and the one heme of cytochrome c_3,**[1250,1251]** each in their reduced state, may be some of the only examples of Fe^{II} hemes having perpendicularly aligned axial imidazole planes. Or, expressed in another way, whatever the dihedral angles are for the histidine imidazole planes of these proteins, their EPR spectra are typical of those in which the axial-ligand plane dihedral angles are 90° – 70°**[1207,1348]** – ~58°.**[1349]**

Calculation of the g-tensors of several low-spin iron(III) porphyrins that have been discussed above via DFT methods, where spin-orbit coupling has been handled by the zeroth order regular approximation to the Dirac equation, has been reported.**[532]** Although the g-values obtained are not in numerical agreement with those measured by EPR spectroscopy, some interesting trends are observed: (1) the relative orientation of the N-H group of the two imidazoles (or pyrazoles) affects the calculated g-values rather significantly if the ligands lie in parallel planes over two of the *meso*-carbons, but very little if they are in parallel planes over one of the N_P–Fe–N_P axes; (2) two imidazoles in perpendicular orientation lying over the porphyrin nitrogens yield much larger g-anisotropy and more nearly degenerate d_{xz} and d_{yz} orbitals than do two imidazoles in perpendicular planes lying over the *meso*-carbons; (3) the product of the three g-values, $g_x g_y g_z$, is positive for complexes having parallel, but negative for those having perpendicular axial-ligand planes; (4) pyridine ligands in parallel planes lying over one of the

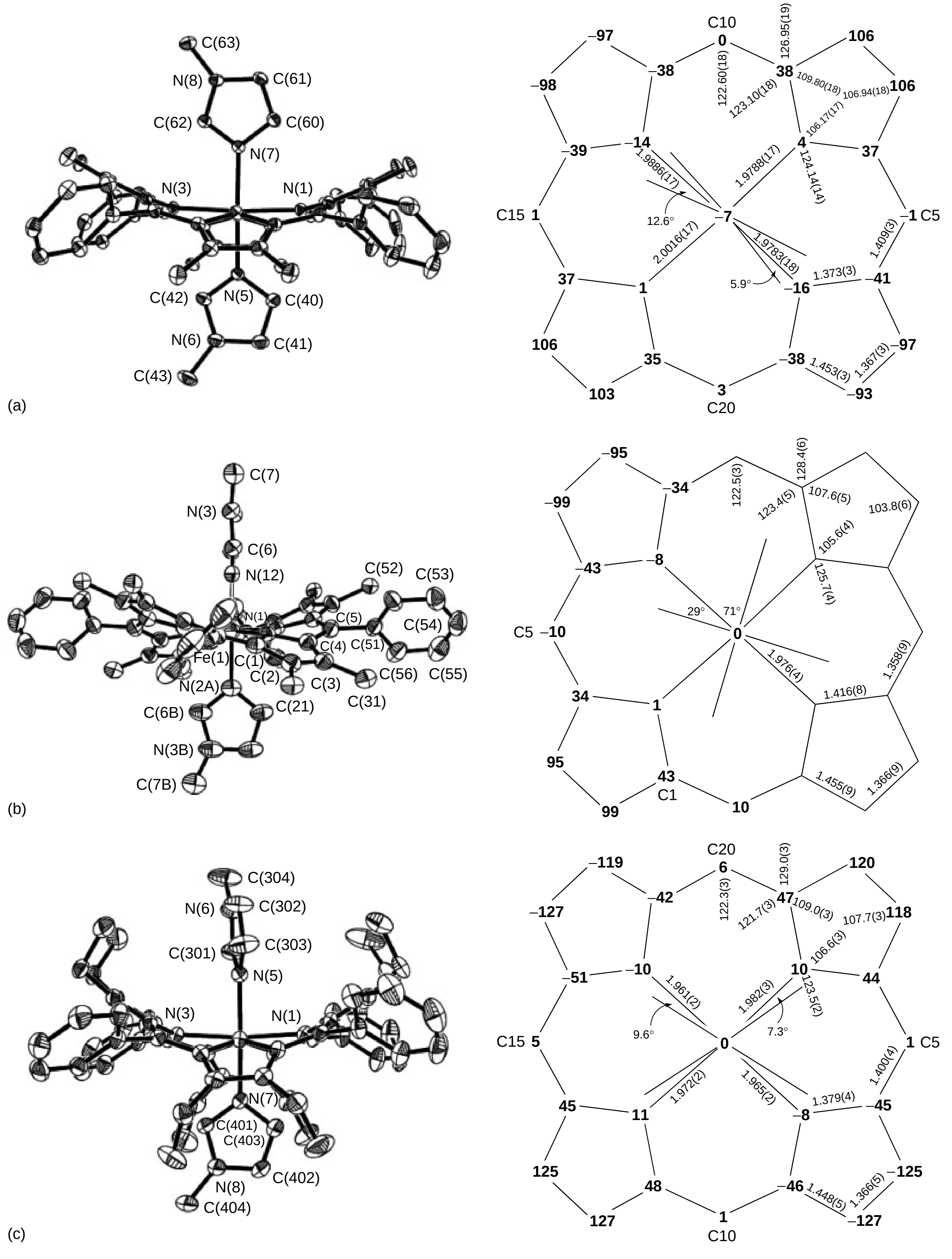
C(63)
N(8)
C(61)
C(62)
C(60)
N(7)
N(3)
N(1)
C(42)
N(5)
C(40)
N(6)
C(41)
C(43)
(a)
C10
0
126.95(19)
106
−97
−38
38
−98
122.60(18)
123.10(18)
109.80(18)
106.94(18)
106
106.17(17)
−14
4
−39
1.9886(17)
1.9788(17)
124.14(14)
37
C15 1
12.6°
−7
−1 C5
2.0016(17)
1.9783(18)
1.409(3)
37
1
5.9°
−16
1.373(3)
−41
106
35
−38
1.367(3)
−97
1.453(3)
103
3
−93
C20
C(7)
N(3)
C(6)
N(12)
C(52)
C(53)
N(1)
C(5)
C(54)
Fe(1)
C(1)
C(4)
C(51)
C(2)
C(3)
C(56)
C(55)
N(2A)
C(21)
C(31)
C(6B)
N(3B)
C(7B)
(b)
−95
128.4(6)
−34
122.5(3)
107.6(5)
−99
123.4(5)
103.8(6)
105.6(4)
−43
−8
125.7(4)
29°
71°
C5 −10
0
1.976(4)
1.358(9)
1.416(8)
34
1
95
43
C1
1.455(9)
1.366(9)
99
10
C(304)
N(6)
C(302)
C(301)
C(303)
N(5)
N(3)
N(1)
N(7)
C(401)
C(403)
C(402)
N(8)
C(404)
(c)
C20
6
129.0(3)
−119
120
−42
47
−127
122.3(3)
121.7(3)
109.0(3)
107.7(3)
118
106.6(3)
−10
10
−51
1.961(2)
1.982(3)
123.5(2)
44
9.6°
7.3°
C15 5
0
1 C5
1.400(4)
45
1.972(2)
1.965(2)
1.379(4)
11
−8
−45
125
48
−46
1.448(5)
1.366(5)
−125
127
1
−127
C10

Figure 13 ORTEP and formal core diagrams of (a) *paral*-[OMTPPFe(N-MeIm)$_2$]$^+$, (b) *perp*-[OMTPPFe(N-MeIm)$_2$]$^+$, and (c) [OETPPFe(N-MeIm)$_2$]$^+$[1207]

N_P–Fe–N_P axes yield a normal rhombic set of g-values, while if they lie over two opposite *meso*-carbons a 'large g_{max}' EPR signal is predicted; and (5) pyridine ligands in perpendicular planes over the N_P–Fe–N_P axes yield a predicted perfectly axial g-tensor with $g_z \gg g_x, g_y$, while pyridine ligands in perpendicular planes over the *meso*-carbons are predicted to have a perfectly axial g-tensor with $g_x, g_y \gg g_z$ and all g-values less than 2.0.[532] (These predictions do not take into account spin-orbit mixing of the three occupied d orbitals.) The sensitivity (in that case in terms of spin density) to the relative orientation of the N-H vectors of the imidazoles in parallel planes (point 1) was also shown by spin density calculations on low-spin bis-imidazole ferrihemes via DFT methods,[1350] but this should be further checked. Point 2 is interesting from the point of view of using the octaalkyltetraphenylporphyrins to investigate experimentally the effect of holding axial ligands in perpendicular planes near the N_P–Fe–N_P axes to avoid the ruffling that occurs when axial ligands in perpendicular planes lie near the *meso*-carbons.[194,1207] Point 3 is interesting because it is not possible to determine the signs of the g-values from EPR spectroscopy; Mössbauer should in principle give the relative signs and allow determining the sign of the product, as was shown some time ago by Huynh and coworkers.[1351] Points 4 and 5 suggest that additional parameters need to be introduced into the calculations involving pyridine ligands, for there are no structures known for either ferro- or ferriheme systems in which the ligands lie in parallel planes over one of the N_P–Fe–N_P axes, while if the ligands are high-basicity pyridines and they lie over opposite *meso*-carbons, a normal rhombic EPR spectrum is observed in the absence of bulky *meso*-substituents, and 'large g_{max}' EPR spectra are observed when pyridine ligands (again, high-basicity) lie either over the *meso*-carbons in the presence of bulky *meso*-substituents in perpendicular planes,[194,575,613,615,618–620,943,1193–1205,1280] or close to the N_P–Fe–N_P axes in ferric octaalkyltetraphenylporphyrins in perpendicular planes.[194,1206,1207] Recent DFT calculations have suggested that parallel and perpendicular axial-ligand orientations should be of essentially equal energy for both Fe^{III} and Fe^{II},[1352] but these findings do not explain the near absence of structures of Fe^{II} porphyrinates with perpendicular ligand orientation (see also Section 4.1.2). Other DFT calculations on ferriheme complexes have also been reported.[1353]

NMR studies of several types of low-spin Fe^{III} model hemes having restricted rotation of one or both axial ligands have demonstrated that the pattern of spin delocalization is strongly influenced by the preferred orientation of axial ligands.[175,187,193,796,1123,1124,1242,1243,1354–1360] These results are consistent with the observed patterns of heme methyl resonances of a number of ferriheme proteins,[1360] including cytochromes *c*[1361–1363] and b_5[1364] and metmyoglobin cyanide.[1365] This angular dependence of heme methyl (and *meso*-H) shifts on the orientation of the planar axial ligand(s) (or methionine π-symmetry lone pair) is caused by the preferential spin delocalization to one of the $3e(\pi)$ orbitals (Figure 4) of low-spin Fe^{III} complexes having the $(d_{xy})^2(d_{xz},d_{yz})^3$ electronic ground state, where the orientation of the nodal planes of these *e*-symmetry metal d and porphyrin π orbitals can be shifted to any angle (as long as the two orbitals have nodal planes oriented at 90° to each other), particularly that dictated by the orientation of the nodal plane of the axial ligand(s) (usually π donors). This concept and the plot shown in Figure 14, top left, have proven very valuable in predicting the orientations of heme ligands from the pattern of assigned methyl resonances of heme proteins;[1360] the program is available on the worldwide web.[1366] Besides the major contribution from the contact interaction, there is a smaller, yet important contribution from the dipolar or pseudocontact interaction, and in order to estimate the magnitude and sign of this term, the concept of counter-rotation of the magnetic axes with rotation of the planar axial ligand(s) bound to the ferriheme becomes very important.[1367] Several variants of the angular dependence shown in Figure 14, top left, have been published more recently,[1368–1371] but this simple plot remains a useful, simple means of predicting the approximate orientation of heme ligands, both in proteins[1372] and in model hemes.[1123,1359] In particular, the ^1H NMR spectra of the dichelated protohemin cyanide complexes reported by Traylor and Berzinis in 1980,[673] which show eight methyl resonances ranging from 20.4 to 4.8 ppm at 35 °C in DMSO-d_6, or from 30.2 to 3.7 ppm at – 57 °C in DMF-d_7, have been assigned by NOESY/EXSY, COSY, ROESY and DQF-COSY techniques and the nodal planes of the single imidazole ligand in the two isomers have been shown to lie at 100° and 170° counterclockwise of the x-axis of the hemes shown in Figure 14, bottom.[1359] Isomer **I**, with imidazole ligand plane lying at 100° to the x-axis, has heme methyl shifts in the order $3 > 8 \gg 5 > 1$, while isomer **II**, with imidazole ligand plane lying at 170° to the x-axis, has heme methyl shifts in the order $5 > 1 \gg 3 > 8$,[1359] as predicted by Figure 14, top.[1360] The $8 > 5 > 1 > 3$ heme methyl order observed for microperoxidase-8 cyanide[1373] indicates that this fragment of cytochrome *c* has an almost identical histidine ligand plane orientation to that of the cyanide complex of M80A cytochrome *c*,[1374] both with histidine imidazole plane orientation of slightly greater than 45°, whereas wild type cytochrome *c* cyanide has the order $5 > 8 > 1 > 3$,[1375] indicating a histidine imidazole plane orientation of slightly less than 45°.

DFT calculations of spin densities in low-spin ferric porphyrins have been reported, and in some cases they agree quite well with the predictions of Figure 14, but in others exactly the opposite pattern of large and small spin densities are predicted.[1350] Probably the counterintuitive cases are a result of small differences between positive and negative contributions, and additional calculations will need to be done to refine the methods and functionals so that useful predictions of the relationship between axial-ligand plane orientation and spin density distribution can be made.

The possibility that axial-ligand plane orientation might affect the reduction potentials of bis-histidine-coordinated

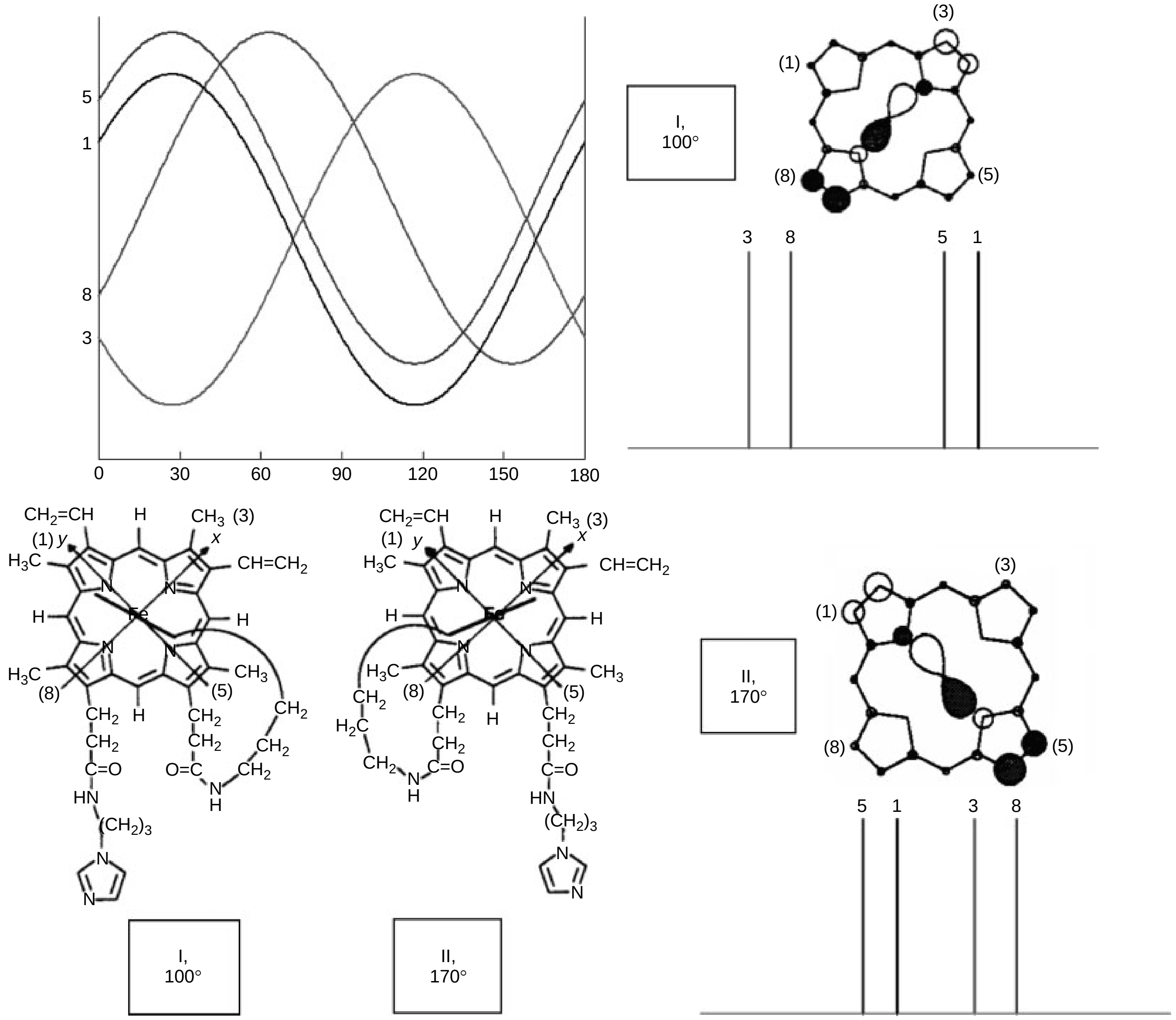

Figure 14 (a): Angular dependence of the heme methyl shifts on axial-ligand plane orientation, as measured from the x-axis of the heme, shown in (c), where the two geometrical isomers of Traylor and Berzinis,[673] here called I and II, are shown. Dihedral angles of axial-ligand planes are measured counterclockwise from the x-axis. (b): Predicted heme methyl shift patterns for isomers I (b) and II (d). Colors: Green – 5-Me, black – 1-Me, blue – 8-Me, red – 3-Me. Angular and spectral plots created with Heme Methyl Shift Patterns, a program available on the web[1359,1360,1366]

cytochromes would have to rely on the fact that the relative energies of the d orbitals of the product, Fe^{II}, remain the same as those of the reactant, Fe^{III}. While it has become clear that low-spin Fe^{III} prefers parallel alignment of planar axial ligands, one might have expected that low-spin Fe^{II} would prefer perpendicular alignment, since for low-spin d^6 there should be no obvious crystal field stabilization associated with removal of the degeneracy of d_{xz} and d_{yz}. As mentioned above in Section 4.1.2, however, of the many molecular structures of porphinatoiron(II) complexes with planar axial ligands that have been published, the vast majority have the axial ligands in parallel planes,[183,575,621] yet the structure of only one isoelectronic Co^{III} complex, $[TMPCo(N\text{-}MeIm)_2]ClO_4$, has its axial ligands in perpendicular planes.[1376] Charge iterative extended Hückel theory calculations on electronic effects for a broad selection of representative systems (HS and LS d^5, HS and LS d^6, LS d^7) indicate no preference for parallel rather than perpendicular orientation of the axial ligands, except in the case of low-spin d^5.[1316] However, they do indicate a previously unrecognized orientational preference in the M–N(imidazole) π bond, which favors eclipsed orientations.[1316] This π-bonding interaction was found to be dominated by the metal–imidazole p_π interaction,[1316] thus providing an explanation of why axial imidazole ligands in metalloporphyrins tend to prefer sterically unfavorable orientations that eclipse equatorial M–N_p bonds.[183] DFT calculations of the energies of both Fe^{III} and Fe^{II} porphyrins with parallel versus perpendicular axial-ligand planes indicated that there is practically no difference in the energies of either oxidation state porphyrin with relative orientation of axial ligands, but the geometries were optimized, which probably means that the porphyrinate ring of the Fe^{II} complexes was planar for both parallel and perpendicular ligand planes (although the Fe^{III} complex with perpendicular ligand planes had a ruffled porphyrin plane), and again, these studies did not take into account the Jahn-Teller effect for low-spin Fe^{III}.[1377] Thus, additional calculations on low-spin Fe^{II} porphyrinates that take into account all of the factors that affect axial-ligand plane orientation must be carried out.

6.3.4 Nitric Oxide Complexes of Iron(III)Porphyrins

As discussed in Section 4.5.3, the first $\{FeNO\}^7$ structures were reported in the mid-1970s.[878,882,883] In contrast, it was some ten years later when the first structure of an $\{FeNO\}^6$ complex was reported: the structures of a five- and a six-coordinate nitrosyl complex of Fe^{III} porphyrinates ($[OEPFeNO]ClO_4$ and $[TPPFeNO(H_2O)]ClO_4$), in which the FeNO moieties have electron configuration $\{FeNO\}^6$, and are thus diamagnetic in each case, were reported in 1984.[1378] (The $\{MNO\}^n$ notation was created in 1974 by Enemark and Feltham,[875] to describe these very covalent triatomic fragments where n denotes the number of d electrons on the metal M plus the number of π^* electrons on NO, normally 1, since NO is usually considered a neutral fragment in this notation.) Since then, the structures of a number of 5- and 6-coordinate $\{FeNO\}^6$[1313,1314,1379–1382] complexes, including those of three of the NO-carrying proteins, the nitrophorins from the saliva of the blood-sucking insect, *Rhodnius prolixus*,[1383–1386] have been reported and the topic of the structures and properties of the enzymes has been reviewed.[56,57]

The nitrophorins of the kissing bug, *Rhodnius prolixus*, are unique NO-binding heme proteins, in that they are stable as Fe^{III} heme centers and are not autoreduced by excess NO in the solution as are other heme proteins such as met-myoglobin;[1387] consistent with this property, their reduction potentials are about 300 mV more negative than that of met-myoglobin ($E^\circ \sim 0$ mV vs. SHE at pH = 7.5),[1383,1388] which is easily autoreduced by NO. The function of nitrophorins in the salivary glands of at least two blood-sucking insects[56,57,1389] is to keep NO stable for long periods of time, so that whenever the insect has the opportunity to suck the blood of a mammal or bird, the NO-bound proteins can be injected into the tissues of the victim, which causes the NO to be released by dilution and increased pH to diffuse through the tissues to the capillaries, where it causes vasodilation, thus bringing more blood to the region of the bite. At the same time, in the case of the *Rhodnius* insect, the histamine released from mast cells and platelets of the victim, whose function is to cause itching and swelling and to begin the immune response, is bound by the nitrophorins, called NP1-NP4, thus preventing the detection of the biting insect for a longer period of time and thereby allowing the insect to obtain a more sufficient meal.[56] The structures of the *R. prolixus* nitrophorins show clearly that there is sufficient space in the distal cavity to allow histamine, as well as NO, to bind.[56,1390]

The molecular structures of both insect nitrophorins are unique for heme proteins; the *R. prolixus* nitrophorins have eight-stranded beta-barrel structures, as do other members of the lipocalin protein fold,[1391] closed at one end, with the heme propionates protruding from the open end of the barrel.[56,1384,1385] The heme is quite ruffled, especially when bound to NO,[1384,1385] while in model heme complexes having the same $\{FeNO\}^6$ electron configuration as NP2-NO and NP4-NO and bound to a neutral nitrogen-donor sixth ligand, the heme is planar or slightly domed, with Fe slightly displaced (0.01–0.06 Å) from the plane of the four porphyrin nitrogens in the direction of the axial NO ligand.[1378,1380] The Fe-N-O angle in the models, as well as the proteins, is near linear (but in the proteins is affected by the degree of photoreduction of the heme center by the X-rays); $\{FeNO\}^6$ centers are normally linear or near linear, while $\{FeNO\}^7$ centers are typically quite bent, with angles in the 120–145° range.[185] The NO stretching frequency of $\{FeNO\}^6$ complexes ranges from 1899 to 1921 cm^{-1} in the models[185] and is at 1917 and 1904 cm^{-1} for two populations of NP1-NO.[1383] UV-visible spectra of 5-coordinate $[OEPFeNO]^+$ show the Soret band at 359 nm with a shoulder at 410 nm, and α, β band at 557 nm,[1381] while those of a variety of 6-coordinate complexes (N-MeIm, pyrazole, indazole, pyrazine)[1380] have their Soret bands at 408–410 nm (414, 415 nm for 2-MeImH[1382] and NO_2^-[1379] complexes, respectively), α bands at 524–525 nm (529, 528 nm for 2-MeImH and NO_2^- complexes, respectively), and β bands at 556–558 nm (561, 560 nm for 2-MeImH and NO_2^- complexes, respectively). DFT calculations on model heme-NO complexes have been reported.[1392,1393] Some of these indicate that the HOMO consists of mainly porphyrin contributions, with no p_x,p_y contribution from NO, and thus the electron configuration is Fe^{II}–NO^+.[1393] The strongly ruffled heme ring, a property of the NP-NO $\{FeNO\}^6$ complexes only, is believed to result from steric interaction with the two leucine residues in the distal pocket, that push down on two of the *meso*-carbons of the heme of NP2.[1384,1385] Mutation of either L132 or L122/L132 of NP2 to valine leads to positive shifts of the reduction potential of 88 and 90 mV, respectively at pH 7.5, that is, the heme becomes easier to reduce by about 90 mV when the steric interaction between the leucines and the heme is reduced;[1394] the structures, determined by X-ray crystallography, show less ruffling for the mutants, although perhaps not as much decrease as was expected.[1395]

The structure of the bedbug (*Cimexlectularius*) nitrophorin, called cNP, is also unique for a heme protein; it consists of a beta-sandwich with the heme on the outside of the sandwich, covered only by a single alpha-helix that carries the cysteine that acts as axial ligand.**[1396]** The structure of the bis-NO-bound complex that includes the cysteine-SNO, mentioned above, is included in that publication.**[1396]** The protein fold is very similar to that of a myo-inositol 1,4,5-triphosphate 5-phosphatase enzyme.**[1397]** Unlike the *Rhodnius* nitrophorins, in the case of the bedbug salivary nitrophorin, histamine does not bind,**[1389]** and the structure shows that there is not sufficient room in the distal cavity for such a large ligand.**[1396]** To make up for this, perhaps, the *C. lectularius* protein binds (and releases) *two* molecules of NO at the heme center, one to iron (as a $\{FeNO\}^7$ center) and the other to the cysteine thiolate (as a thionitrosyl group, RSNO) that is the heme proximal ligand in the absence of NO.**[1396]** To our knowledge, this is the first example of the formation of a thionitrosyl group from a cysteine thiolate that was the heme ligand in the absence of NO. But this reaction does not occur for at least one cytochrome P450, the bacterial P450BM3 from *Bacillus megaterium*.**[1398]**

A model for the NO-heme-thiolate complex of nitric oxide synthase (NOS)**[54]** and cytochrome $P450_{nor}$ (nitric oxide reductase)**[1074]** (as well as the NO-carrying protein, the nitrophorin from the bedbug, *Cimex lectularius***[1396]**) has been synthesized and characterized by optical, resonance Raman and EPR spectroscopy and electrochemistry.**[1399]**

6.3.5 Reduction Potentials of Iron(III) Porphyrins

The redox reactions of iron porphyrins, as for any other metal complexes, provide important insights into the relative stabilities of various oxidation states, and how these stabilities are related to ligation reactions. Because there has been a tendency for inorganic chemists to equate reduction potentials with orbital energies of one of the oxidation states involved in the redox couple, or to talk about the so-called 'HOMO-LUMO gap' (the electrochemical potential difference between the reversible $E_{1/2}$ values for formation of a porphyrin π-cation and π-anion radical)**[1400]** as though it measures something approaching orbital energies, this section has been included to attempt to clarify this misconception. Reduction potentials, in fact, measure the relative thermodynamic stability of the two oxidation states involved in the redox couple (*see* ***Electrochemistry: Applications in Inorganic Chemistry***). For example, in the case of a Fe^{III} porphyrin, a 1-electron reduction to yield the Fe^{II} porphyrin may be written as

$$PFe^{III} + e^- \rightleftharpoons PFe^{II} \tag{27}$$

In fact, this equation is incomplete, because no solvent for the system or anion for the PFe^{III} have been specified. Since electrochemical measurements are not done in the gas phase, but rather in homogeneous solution (or in solid matrices, but that is not the subject of this discussion), the conditions must be carefully specified, because the measured reduction potential will quite likely depend on those chosen conditions to a very great extent. In the case of the reaction specified in equation (27), the use of a potentially coordinating solvent such as dimethylformamide (DMF) or dimethylsulfoxide (DMSO) will yield a very different reduction potential than if a weakly- or non-coordinating solvents such as acetonitrile, benzonitrile, CH_2Cl_2 or $CHCl_3$ were used. This is because, according to the Nernst equation, the measured reduction potential is given by

$$E_c^\circ - E^\circ = -\frac{RT}{nF}\ln\left(\frac{K_{eq}^{III}}{K_{eq}^{II}}\right) \tag{28}$$

where E_c° is the measured potential for the metal ion fully complexed to the porphyrin and solvent molecules of a coordinating solvent (and, depending on the solvent, possibly the anion associated with the Fe^{III} state) in both oxidation states in the presence of a particular anion, probably the same anion as that of the electrolyte, and ideally one that does not bind strongly to Fe^{III}, E° is the measured potential for the metal ion in the absence of the porphyrin and coordinating solvent molecules but with the same anion, and K_{eq}^{III} and K_{eq}^{II} are the products of the binding constants for the porphyrin and solvent molecules to the Fe^{III} and Fe^{II} states, respectively. Since we are not really interested in the free metal ion, we typically take the metal porphyrin itself as our standard state and define E° as being the measured potential for the reduction reaction for that metal porphyrin in a given solvent. Then solvent effects can be evaluated by measuring E° in various solvents – if the junction potential of the reference electrode solution/sample solution interface either remains constant as the solvent is changed, or if it is carefully estimated in each solvent. The problem begins when researchers wish to compare the reduction potentials of two different Fe^{III} porphyrins, for example, $TPPFeOClO_3$ and $(p\text{-}NO_2)_4TPPFeOClO_3$. Now, what is the standard state? By comparing the reduction potentials for two different porphyrins we are really looking at a ratio of ratios of equilibrium constants. We must really go back to the initial reaction, equation (27), and consider how to evaluate the equilibrium constants of equation (28) for the binding of each of the porphyrins to both Fe^{III} and Fe^{II} and the solvent molecules, for buried in the two different reduction potentials measured are their individual $\ln(K_{eq}^{III}/K_{eq}^{II})$ values, and there is no simple way to determine whether the potential shifted in the observed direction as a result of a major effect of the substituents on either K_{eq}^{III} or on K_{eq}^{II}, or on opposite effects on the two, or on some other combination of possibilities. Hence, because reduction potentials measure the *ratio* of the equilibrium constants of the two oxidation states, one cannot extract the effects of one of the oxidation states, and assume that one knows something about orbital energies. Nevertheless, the measurement of reduction potentials and the comparison of those of one complex to those of another is a worthwhile and valid pursuit, as long as one does not attempt to draw conclusions as to what the potentials mean with regard to the properties of *one* of the two oxidation states involved in the redox couple. Excellent articles on the electrochemistry of porphyrins and metalloporphyrins have been published,[1400,1401] and a large compilation of electrochemical data for these systems is available.[1402]

Electrochemical studies of iron porphyrins have provided valuable information about the stabilities of various oxidation states, and the stabilities of various axial-ligand complexes, as well as the reversibility of a given redox reaction. One of the most widely used methods is cyclic voltammetry, where the potential is scanned linearly at a chosen rate in one direction and then back again, over the chosen potential range. The voltammograms thus obtained are rich in information, not only about the half-wave potentials, $E_{1/2}$, but also, from the shape of the wave, the kinetics of the redox reaction at the electrode. In this section only the potentials are considered, and the reader is referred to useful reference books[1403,1404] and research papers[1405–1408] for detailed information on the kinetics aspects, including electron-transfer kinetics of generation of organoiron(IV) porphyrins and their π-cation radicals.[1409]

For metalloporphyrins, there are quite a number of reversible redox reactions that involve changes in the number of electrons on both the metal and the porphyrin ring. In the case of iron porphyrins, the most frequently studied redox reactions are those involving Fe^{IV}/Fe^{III}, Fe^{III}/Fe^{II}, and Fe^{II}/Fe^{I}, although various investigators have also concentrated on Fe^{I}/Fe^{0} and the reactions of higher oxidation states than Fe^{IV}, as well as porphyrin ring oxidations and/or reductions. The effects of porphyrin ring distortion on the reduction potentials of β-brominated tetraphenylporphyrin complexes of iron have been studied,[1410–1412] as have OETPPFeCl and OETPPFe(R), where R is C_6H_5, C_6F_4H and C_6F_5,[1413] a series of fluorinated dodecaphenylporphyrins,[1414] and the tetrakis(perfluoroalkyl)porphyrinatoiron complexes.[621] Etioporphycene complexes of sigma-bonded metal complexes, either phenyl or chloro as the ligand, have also been studied by cyclic voltammetry.[1415] With regard to the site of the redox reaction (metal-centered or macrocyclic ligand-centered), rules of thumb have developed for metalloporphyrins that suggest that the difference in the potential of the first porphyrin ring oxidation and the first ring reduction is approximately constant for all metalloporphyrins (the so-called ‘HOMO-LUMO gap’), but Kadish and coauthors have pointed out that this is not always the case.[1400] Thus, for metals like iron, for which a number of metal oxidation states exist, it is not always possible to define the site of removal or addition of an electron simply by invoking the ‘HOMO-LUMO gap’, and other methods, often spectroscopic (NMR, EPR, UV–vis, IR, etc.) must be used to determine the electron configuration of the product of the redox reaction of interest. Added to this is the fact that for other macrocycles even less is known about the existence or lack thereof of something like the ‘HOMO-LUMO gap’, and thus it is very risky to try to conclude the site of electron addition or removal based upon the observed reduction potential alone, when the observed reduction potential is determined by the relative stabilities of the two oxidation states involved in the redox couple, as discussed above and represented by equation (28). Hence, it is dangerous to decide the site of electron removal from chloroiron corrolates, their μ-oxo dimers, for various corrole ring substituents, on the basis of observed potential[1416,1417] in the absence of confirmatory spectroscopic data. Nevertheless, the ‘redox gap’ or ‘HOMO-LUMO gap’, $\Delta E_{1/2} = E_{1/2}^{Ox1} - E_{1/2}^{Red1}$ has been reported to be 2.25 ± 0.1 V for porphyrins, 1.85 ± 0.15 V for porphycenes and 2.15 ± 0.08 V for corrphycenes and their metal complexes;[1418] Kadish and coauthors have, however, stated that the value for porphyrins, at least, is not a constant.[1400]

Axial-ligand binding constants, for example to Fe^{III} and Fe^{II} porphyrins, can be measured in favorable cases by measuring the $E_{1/2}$ values for the Fe^{III}/Fe^{II} and Fe^{II}/Fe^{I} waves by cyclic voltammetry as a function of the concentration of axial ligand and then fitting the ligand concentration dependence of the reduction potential observed for each half-reaction to the full Nernst equation,[491,599]

$$(E_{1/2})_c = (E_{1/2})_s - \frac{RT}{nF} \ln \left\{ \frac{1 + \beta_1^{III}[L] + \beta_2^{III}[L]^2}{1 + \beta_1^{II}[L] + \beta_2^{II}[L]^2} \right\} \qquad (29)$$

where $(E_{1/2})_c$ is the reduction potential measured for the complex at each concentration of axial ligand, $(E_{1/2})_s$ is the reduction potential measured for the iron porphyrinate in the absence of added ligand, [L] is the equilibrium concentration of axial ligand, and the β_n are the overall equilibrium constants for the binding of 1 ($n = 1$) or 2 ($n = 2$) axial ligands to Fe^{III} and Fe^{II} (for the Fe^{III}/Fe^{II} wave) or Fe^{II} and Fe^{I} (for the Fe^{II}/Fe^{I} wave). Thus, for example, $\beta_1^{II} = K_1^{II} = [PFe^{II}L]/[PFe^{II}][L]$ and $\beta_2^{II} = K_1^{II}K_2^{II} = [PFe^{II}L_2]/[PFe^{II}][L]^2$, where all concentrations are those at equilibrium. (Overall charges on the complex have been omitted for simplicity.) In many cases $\beta_1^{III}[L] \ll \beta_2^{III}[L]^2 \gg 1$, and the analogous situation holds for $\beta_1^{II}[L]$ and $\beta_2^{II}[L]^2$, so that equation (29) can be simplified to:[491,599]

$$(E_{1/2})_c = (E_{1/2})_s - \frac{2.303RT}{nF} \log \left\{ \frac{\beta_2^{III}}{\beta_2^{II}} \right\} \qquad (30)$$

for the Fe^{III}/Fe^{II} wave, as given above for the general case where the solvent is the ligand, in equation (28). Likewise, for the Fe^{II}/Fe^{I} wave, in many cases the binding of axial ligands to the Fe^{I} oxidation state over the concentration ranges utilized for these studies could not be detected, and $Fe^{II}L_2$ is the dominant form of the Fe^{II} state, equation (29) in that case reduces to:

$$(E_{1/2})_c = (E_{1/2})_s - \frac{2.303RT}{nF} \log \beta_2^{II} - \frac{2.303RT}{nF} \log[L]^2 \qquad (31)$$

In such cases, log β_2^{II} can be directly determined from the concentration dependence of the Fe^{II}/Fe^{I} potential using equation (31), and then this value can be utilized in equation (30) with reduction potential data for the Fe^{III}/Fe^{II} couple, where log β_2^{III} is then the only unknown. In many cases, however, it is necessary to use the full equation (29).[491,599]

The observed reduction potentials for the Fe^{III}/Fe^{II} couple in the presence of a large concentration of the axial ligand that is sufficient to fully complex both oxidation states measure the relative stability of the bis-axial ligand complexes of the two oxidation states, in terms of log $\beta_2^{III}/\beta_2^{II}$. The results of some of these measurements of equilibrium constants are discussed in the following section.

6.3.6 *Thermodynamics of Ligand Addition to Iron(III) Porphyrins*

Numerous studies of the thermodynamics of ligand addition to Fe^{III} porphyrins have been reported. Three main methods have been utilized for measurement of binding constants: (1) UV–visible spectroscopic techniques based on Beer's law;[608,1419] (2) electrochemical techniques based on the Nernst equation (equations 26–28);[491,599,607,1420] and (3) NMR techniques based on the relative intensity of peaks that are due to known proton types within the starting material, PFeX, and product, PFe(X)(L) or $PFeL_2^+$ X^-[174,175,1421] (*see* ***Stability Constants & their Determination***). In nonaqueous solvents the reaction of ligands with iron(III) porphyrins is found to proceed as in equations (32) and (33):

$$\mathrm{PFeX} + \mathrm{L} \rightleftharpoons \mathrm{PFe(X)(L)} \qquad K_1 \tag{32}$$

$$\mathrm{PFe(X)(L)} + \mathrm{L} \rightleftharpoons \mathrm{PFeL_2}^+\mathrm{X}^- \qquad K_2 \tag{33}$$

for an overall reaction as in equation (34):

$$\mathrm{PFeX} + 2\mathrm{L} \rightleftharpoons \mathrm{PFeL_2}^+\mathrm{X}^- \qquad \beta_2 = K_1K_2 \tag{34}$$

The equilibrium constant for equation (34), β_2, is given by equation (35):[608]

$$\beta_2 = \frac{[\mathrm{PFeL_2}^+\mathrm{X}^-]}{[\mathrm{PFeX}][\mathrm{L}]^2} \tag{35}$$

Note that the units of β_2 are M^{-2}. The intermediate complex, [PFe(X)(L)], can be either six-coordinate, as implied by the parentheses and brackets, or five-coordinate, as a tight ion pair, $[(PFeL)^+\ X^-]$, and is often not detected by UV–visible spectroscopy.[608,1419] However, both NMR spectroscopic investigations[168,1346,1421] and electrochemical measurements[491,599,607] indicate conclusively that the mono-ligand complex is present in measurable concentrations in many cases. Furthermore, kinetic data clearly show that the mono-imidazole complex not only forms, but they also suggest that it is high-spin, six-coordinate, that is, both halide and imidazole ligand are bound to the metal center, at least in low dielectric solvents.[1422] Only the overall binding constant, β_2, could be measured by NMR spectroscopy at 25 °C and below,[1421] while UV–visible techniques sometimes allow estimation of the stepwise constants.[608] As discussed in Section 6.3.5 above, electrochemical techniques allow measurement of the stepwise constants under favorable conditions.[491,599] Ligands for which binding constants to either tetraarylporphinatoiron(III) or protohemin have been measured include imidazoles,[608,1339,1419,1421,1423–1426] pyridines,[491,599,614] cyanide,[1423] and pyridine/water.[1427] Representative values of log β_2 are summarized in Table 3.[1428–1432]

It should also be noted that the product of equations (33) and (34), as written, is an ion pair, and it behaves as a single species. This is the situation for Fe^{III} porphyrins in chloroform, dichloromethane, acetone, and DMF at concentrations of 10^{-5} M and greater.[608] However, at lower concentrations (7×10^{-7} M and below) the constant can only be calculated by assuming that the cation and anion are separate species.[608] The reaction under these conditions is as in equation (36):

$$\mathrm{PFeX} + 2\mathrm{L} \rightleftharpoons \mathrm{PFeL_2}^+ + \mathrm{X}^- \tag{36}$$

and the equilibrium constant for this reaction, which we will call β_{2D}, is as in equation (37):

$$\beta_{2\mathrm{D}} = \frac{[\mathrm{PFeL_2}^+][\mathrm{X}^-]}{[\mathrm{PFeX}][\mathrm{L}]^2} \tag{37}$$

Note that the units of β_{2D} are M^{-1}, and hence, the sizes of β_2 (equations 34 and 35) and β_{2D} (equations 36 and 37) cannot be directly compared.[608]

Hydrogen-bonding between a coordinated N–H imidazole and the ion-paired anion greatly enhances the binding of the axial ligands in low-polarity solvents, as is evidenced by the approximately 10^3 increase in size of β_2 when L is changed from N-MeIm to ImH in $CHCl_3$.[608] This effect decreases as the polarity of the solvent increases. It has also been reported that under conditions where equations (34) and (35) are obeyed, the binding of *N*-methylimidazole is greatly enhanced by the presence of a hydrogen-bond donating substituent on at least one phenyl ring of the TPP derivative that can stabilize the anion of the ion-paired product.[1428] If the hydrogen-bonding group is acetamido (NHCOMe), the enhancement in log β_2 increases in the order H ∼*ortho* ≪ *para* ≪ *meta*, as a result of the favorable structure of the ion-paired product when the H-bonding group is in the meta position of the phenyl ring.[1434] Hydrogen bonding of coordinated ImH to other additives, such as *ortho*-phenanthroline, not only stabilizes the complex, but also shifts the Fe^{III}/Fe^{II} reduction potential cathodically by over 100 mV,[1435] thus indicating a significant stabilization (≈ 2.4 kcal mol^{-1}) of the Fe^{III} oxidation state when strong H-bond acceptors are present. Hydrogen bonding of an imidazole N–H to a polar or anionic group is thus an important way to modulate the reduction potentials of heme proteins.

The effect of porphyrin substituents on the size of the binding constants β_2 has been investigated in detail.[608,1419,1421]

Table 3 Equilibrium constants for addition of imidazoles and pyridines to Fe^{III} porphyrins

Porphyrin	Anion	Ligand	Solvent	T (°C)	Method	log β_2
TPP	Cl^-	ImH	$CHCl_3$	25	UV–vis[608]	6.18
			CH_2Cl_2	25	UV–vis[1428]	5.68
			Benzene	25	UV–vis[608]	4.66 sq rt
			Acetone	25	UV–vis[1428]	5.82
			DMF	25	UV–vis[524]	5.99
			DMF	25	e-chem[524]	5.93
			DMF	25	UV–vis[608]	5.49
		2-MeImH	$CHCl_3$	25	UV–vis[608]	3.52
			$CDCl_3$	−35	NMR[1425,1426]	7.66
			DMF	25	e-chem[244]	3.48
		5,6-Me_2Bzim	$CHCl_3$	25	UV–vis[608]	3.18
		N-MeIm	$CHCl_3$	25	UV–vis[608]	3.32
			$CDCl_3$	25	NMR[1421]	3.13
			$CHCl_3$	25	UV–vis[1422]	3.13
			$CDCl_3$	25^{ext}	NMR[1426]	3.04
			$CDCl_3$	−35	NMR[1426]	7.98
			CH_2Cl_2	25	UV–vis[608]	4.00
			Benzene	25	UV–vis[608]	0.76
			DMF	25	UV–vis[608]	4.79
			DMF	25	e-chem[244]	4.38
			DMSO	25	UV–vis[1429]	4.11
			DMSO	25	UV–vis[1079]	4.08
		CuIM	DMSO	25	UV–vis[1079]	7.64
		1,2-Me_2Im	$CHCl_3$	25	UV–vis[608]	0.97
			$CDCl_3$	25^{ext}	NMR[1426]	0.85
			$CDCl_3$	−35	NMR[1426]	2.93
		4-NMe_2Py	$CHCl_3$	25	UV–vis[608]	3.42
		3,4-Me_2Py	$CHCl_3$	25	UV–vis[608]	1.40
		Py	$CHCl_3$	25	UV–vis[608]	−0.3
TPP	OAc^-	ImH	DMF	25	e-chem[524]	5.30
	SCN^-	ImH	DMF	25	e-chem[524]	5.83
	ClO_4^-	2-MeImH	DMF	25	e-chem[491,599]	5.2
		N-MeIm	DMF	25	e-chem[491,599]	7.2
		4-NMe_2Py	DMF	25	e-chem[491,599]	6.8(est)
			CH_2Cl_2	25	e-chem[614]	16.3
		Py	DMF	25	e-chem[491,599]	1.7
			CH_2Cl_2	25	e-chem[614]	10.2
		4-CNPy	DMF	25	e-chem[491,599]	−1.4
			CH_2Cl_2	25	e-chem[614]	2.6
TMP	Cl^-	2-MeImH	$CDCl_3$	−35	NMR[1425,1426]	10.31
		N-MeIm	$CDCl_3$	25^{ext}	NMR[1426]	3.92
				−35	NMR[1426]	9.08
		1,2-Me_2Im	$CDCl_3$	25^{ext}	NMR[1426]	1.59
				−35	NMR[1426]	6.69
	ClO_4^-	2-MeImH	DMF	25	e-chem[491,599]	7.4
		N-MeIm	DMF	25	e-chem[491,599]	7.9
		4-NMe_2Py	DMF	25	e-chem[491,599]	8.3(est)
		Py	DMF	25	e-chem[491,599]	3.3
		4-CNPy	DMF	25	e-chem[491,599]	0.2
$(2,6\text{-}Cl_2)_4$TPP	ClO_4^-	2-MeImH	CH_2Cl_2	25	UV–vis[1339]	7.11
			DMF	25	e-chem[491,599]	7.3
		N-MeIm	CH_2Cl_2	25	UV–vis[1339]	5.15
			DMF	25	e-chem[491,599]	7.1
		4-NMe_2Py	DMF	25	e-chem[491,599]	8.4(est)
		Py	DMF	25	e-chem[491,599]	3.8
		4-CNPy	DMF	25	e-chem[491,599]	−0.2

Table 3 cont'd

Porphyrin	Anion	Ligand	Solvent	T (°C)	Method	log β_2
$(2,6\text{-}Br_2)_4$TPP	ClO_4^-	2-MeImH	DMF	25	e-chem[491,599]	6.7
		N-MeIm	DMF	25	e-chem[491,599]	7.7
		4-NMe_2Py	DMF	25	e-chem[491,599]	>9.0
		Py	DMF	25	e-chem[491,599]	5.0
		4-CNPy	DMF	25	e-chem[491,599]	~0.8
$(2,6\text{-}(OCH_3)_2)_4$TPP	ClO_4^-	2-MeImH	DMF	25	e-chem[491,599]	6.7
		N-MeIm	DMF	25	e-chem[491,599]	6.4
		4-NMe_2Py	DMF	25	e-chem[491,599]	6.9
		Py	DMF	25	e-chem[491,599]	2.4
		4-CNPy	DMF	25	e-chem[491,599]	−0.3
OEP	Cl^-	ImH	$CHCl_3$	25	UV–vis[608]	6.02
		N-MeIm	$CHCl_3$	25	UV–vis[608]	3.83
		1,2-Me_2Im	$CHCl_3$	25	UV–vis[608]	0.90
DPDME	Cl^-	ImH	$CHCl_3$	25	UV–vis[1430]	6.45
PPDME	Cl^-	ImH	$CHCl_3$	25	UV–vis[1431]	6.72
		N-MeIm	$CHCl_3$	25	UV–vis[1431]	3.77
PP	Cl^-	ImH	DMF	25	UV–vis[524]	5.74
			DMF	25	e-chem[524]	5.79
			DMSO-d_6	20	NMR[1423]	4.77
		N-MeIm	DMSO	25	UV–vis[1079]	3.40
		CuIM	DMSO	25	UV–vis[1079]	7.94
		CN^-	DMSO-d_6	20	NMR[1423]	7.32
TPPS	–	ImH	H_2O	25	UV–vis[1432]	6.23
		Py	H_2O	25	UV–vis[1432]	3.18
$(2,6\text{-}Me_2,3\text{-}SO_3^-)_4$TPP	–	ImH	H_2O	25	UV–vis[1433]	8.81
		NH_3	H_2O	25	UV–vis[1433]	4.81

Note: Deuteroporphyrin IX dimethyl ester (DPDME).

It has been found that in noncoordinating solvents, electron-donating substituents on the phenyl rings of substituted tetraphenylporphyrin complexes of Fe^{III} stabilize the complex, that is the Hammett ρ value is negative.[608,1419,1421] This behavior is opposite to that typically expected for Lewis base reactions with Lewis acids, and in particular other metallotetraphenylporphyrins, including V^{IV},[1436] Co^{II},[787] Ni^{II},[1436] and Zn^{II},[1437] and also opposite to that observed for the reaction of N-methylimidazole with TPPFeCl in DMSO, where the starting material is $[TPPFe(DMSO)_2{}^+]Cl^-$.[1079] The reason for this opposite behavior has been explained in terms of the oxidation state of the metal (+3 rather than +2, with VO^{2+} behaving as a +2 unit). Hence, the product of equations (33), (34), or (36) has a formal positive charge at the metal center, whereas the reactant does not, and the reaction is favored by electron-donating substituents, which can help to stabilize the positive charge on the metal center of the product.[608,1419]

More detailed investigations of the binding of N-methylimidazole to a series of unsymmetrically substituted tetraphenylporphyrins have revealed that both tetra-*para*- and mono-*para*-phenyl substituted derivatives of TPPFeCl should be viewed as behaving 'anomalously', compared to either tetra-*meta*-substituted derivatives or unsymmetrically *para*-substituted derivatives of the type $[(p\text{-X})_x(p\text{-Y})_{4-x}TPPFeCl]$.[1419] The reason for this 'anomalous' behavior in the symmetric tetra-*para*-substituted compounds is believed to be nonadditivity of the substituent effects, that is due to the direct conjugation of the fourth phenyl ring in the product, $[(p\text{-X})_4TPPFe(N\text{-MeIm})_2]^+\ Cl^-$, which is necessary to remove the formal positive charge from the Fe^{III} center. The unsymmetrical multiply *para*-substituted TPP derivatives are also believed to engage in direct conjugation between phenyl and porphyrin ring, but they appear to choose to utilize the 'least willing' substituent in this conjugation. For the series of six complexes $[(p\text{-Cl})_x(p\text{-NEt}_2)_{4-x}TPPFe(N\text{-MeIm})_2]^+\ Cl^-$ it was also found that variation in the energy of the Q_o electronic band with the intensity ratio of the Q_o to Q_v transitions is consistent with an important role for direct conjugation in these low-spin complexes, but not in the high-spin chloroiron(III) starting materials.[1419] Evidence for direct conjugation between phenyl rings and the porphyrin ring has also been supplied by Traylor and coworkers[1438] and Milgrom,[1439] who showed that tetrakis(p-hydroxyphenyl)porphyrins and their metal complexes can be oxidized by two electrons to a diquinone form that requires direct conjugation between two phenyl rings and the porphyrin, and by Worthington *et al*.[1440] The latter workers found electrochemical evidence (an additional reduction wave) for direct conjugation of 4-methylpyridinium groups when these replace one or more phenyl rings of $TPPH_2$.[1440] The sequential protonation of the tetra-(p-dimethylaminophenyl)porphyrin free base has been studied by optical and NMR spectroscopy, and shown to yield charge transfer excited states that produce hyperporphyrin spectra[1441] and unique ^{1}H NMR shifts.[1442]

The equilibrium constants for binding various nitrogen-donor ligands to iron(III) complexes of tetrakis(2,6-disubstituted phenyl)porphyrins (where the 2- and 6-substituents are F, Cl, Br, OMe) and the tetrakis(2,4,6-trimethylphenyl)porphyrin, also known as tetramesitylporphyrin, TMP, have been measured by several workers[491,599,614,1339,1346,1421–1429] (Table 3). It is interesting to note that rather than hindering the binding of axial ligands, most of the above substituents appear to aid this binding, in the approximate order of the sizes of the substituents ($\mathrm{H} < \mathrm{OMe} < \mathrm{Me} < \mathrm{Cl} < \mathrm{Br}$).[491,599] This appears to be due in part to electron donation (field effects) from the *ortho*-substituents,[245] as well as from a stabilization that is due to ruffling of the porphyrin core.[1204,1280,1339] Note that the order is different from that observed for the binding of the same series of ligands to the same series of 2,6-disubstituted TPP complexes of Fe$^{\mathrm{II}}$ ($\mathrm{OMe} \ll \mathrm{H} \ll \mathrm{Me} \sim \mathrm{Cl} \sim \mathrm{Br}$) discussed in Section 4.1.2.

Further investigations, by NMR spectroscopy, of the steric effects involved in the binding of imidazoles to a series of alkylated phenyl analogs of TMPFeCl, where all methyl groups are replaced by either ethyl or isopropyl groups, have been reported.[1426] At −35 °C the stabilities of the N-MeIm complexes of the 2,4,6-substituted TPPFe$^{\mathrm{III}}$ derivatives increase in the order $\mathrm{H} \ll i\text{-Pr} \sim \mathrm{Me} < \mathrm{Et}$, and for the 1,2-Me$_2$Im complexes $\mathrm{H} \ll \mathrm{Me} \sim i\text{-Pr} \sim \mathrm{Et}$. In all cases, $\beta_2(\text{N-MeIm}) > \beta_2(\text{1,2-Me}_2\text{Im})$, but by very different factors: H ($\approx 10^5$), Me (240), Et (10^3), i-Pr (160). Clearly, increasing the bulkiness of the *ortho*-phenyl substituents both increases the stability of axial-ligand complexes and also greatly enhances the stability of complexes of hindered axial ligands over those of TPPFe$^{\mathrm{III}}$. While the formation of the TPPFe$^{\mathrm{III}}$ complex suffers a large loss in bond strength when N-MeIm is replaced by 1,2-Me$_2$Im ($\Delta H^\circ = -26.5$ vs. $-20.6\,\mathrm{kcal\,mol^{-1}}$), the same is not true for the TMP and related complexes ($\Delta\mathrm{H}^\circ$ ranging from -27.2 to -28.0 (N-MeIm) and -27.8 to $-29.1\,\mathrm{kcal\,mol^{-1}}$ (1,2-Me$_2$Im)). However, while the entropies of complex formation of the two TPP complexes are very similar, those for the TMP and related complexes are much more negative for the hindered than the nonhindered imidazole ($\Delta S^\circ = -69$ to $-76\,\mathrm{J\,mol^{-1}\,K^{-1}}$ (N-MeIm) and -86 to $-91\,\mathrm{J\,mol^{-1}\,K^{-1}}$ (1,2-Me$_2$Im)), indicating the loss of internal rotation of the 1,2-Me$_2$Im ligands upon binding to the TMP and related porphyrin complexes, but not TPPFe$^{\mathrm{III}}$, at low temperatures.[1426] Competitive binding of 1- and 2-methylimidazole to TMPFe$^{\mathrm{III}}$ revealed that formation of the sterically more hindered complex, TMPFe(2-MeImH)$_2$]$^+$Cl$^-$, is favored over either the mixed-ligand complex, TMPFe(2-MeImH)(N-MeIm)$^+$Cl$^-$, or the nonhindered TMPFe(N-MeIm)$_2{}^+$Cl$^-$.[1424,1425] The increased stability of the sterically hindered porphyrin complexes was explained in terms of attractive, rather than repulsive, interactions between the *ortho*-methyl groups of the mesityl rings and the π system and/or the 2-alkyl substituent of the coordinated imidazoles.[1424] The existence of such attractive forces appears to be borne out by molecular mechanics calculations.[1281,1287] However, another important contributing factor must be that an N–H imidazole was used for the 'hindered' ligand while a N–Me imidazole was used for the 'non-hindered' ligand. There is a difference in the size of β_2 of N′10−1000 for these two classes of imidazole ligands.[608]

In contrast to the case of imidazoles binding to tetraphenylporphyrins, Wang *et al.*[1423] have demonstrated that binding of cyanide to high-spin protoporphyrin IX iron(III) chloride in DMSO-d_6 is a two-step process as shown in equations (38) and (39), and whether DMSO acts as a sixth ligand for the mono-cyano complex is not known:

$$\mathrm{PPFe(DMSO)_2{}^+ + CN^- \rightleftharpoons PPFe(CN)(DMSO)_{1/0}} \quad (K_1) \tag{38}$$

$$\mathrm{PPFe(CN)(DMSO)_{1/0} + CN^- \rightleftharpoons PPFe(CN)_2{}^-} \quad (K_2) \tag{39}$$

The binding constants K_1 and K_2 were found to be 1.9×10^4 and $1.1 \times 10^3\,\mathrm{M^{-1}}$ at 20 °C, respectively. Imidazole binding, however, is an overall two-step process, and only the formation of the bis-imidazole complex can be observed. The overall binding constant is $6 \times 10^4\ \mathrm{M^{-2}}$ at 20 °C.[1423] It should be noted that since the starting material already has the chloride ion dissociated, the overall $\beta_2 (= K_1K_2)$ is not directly comparable to the β_2 values for the addition of imidazoles to synthetic hemins in CDCl$_3$.[1421] In fact, it should be stressed that solvent plays an important role in determining not only the coordination state of the high-spin starting material, but also the degree of ion pairing of the product.[608]

For water-soluble porphyrins, including T(p-M)PyPFe$^{\mathrm{III}}$ and (*meso*-$\alpha,\alpha,\alpha,\alpha$-tetrakis[$o$-($N$-methylnicotinamido) phenyl]porphinato)iron(III), α^4-(TMINP)Fe$^{\mathrm{III}}$, however, the addition of cyanide in basic aqueous solution again appears to be an overall two-step at one time process, with log $\beta_2 = 13.56$ at pH 10.4 (T(p-M)PyP) and 14.7 at pH 10.2 (α_4-(TMINP)).[1024] At lower pH, however, T(p-M)PyPFe$^{\mathrm{III}}$ can bind CN$^-$ in a stepwise fashion: at pH 6.5, a maximum of about 72% of the porphyrin is in the 1:1 cyano complex, while at pH 9.6, less than 8% is in the form of the 1:1 complex.[1024]

6.3.7 *Kinetics of Axial Ligand Addition to Iron(III) Porphyrins*

The reaction of N-methylimidazole with TPPFeCl proceeds rapidly according to the overall equation (34) to give the low-spin complex TPPFe(N-MeIm)$_2{}^+$ Cl$^-$, but the stepwise kinetics could be studied in various solvents by stopped-flow kinetics.[1422] The rate law is consistent with the steps shown in equations (40–42):

$$\text{TPPFeCl} + \text{N-MeIm} \underset{\text{fast}}{\overset{K_1}{\rightleftharpoons}} \text{TPPFe(N-MeIm)Cl} \tag{40}$$

$$\text{TPPFe(N-MeIm)Cl} \underset{k_2}{\overset{k_1}{\rightleftharpoons}} \text{TPPFe(N-MeIm)}^+\text{Cl}^- \tag{41}$$

$$\text{TPPFe(N-MeIm)}^+\text{Cl}^- + \text{N-MeIm} \underset{k_4}{\overset{k_3}{\rightleftharpoons}} \text{TPPFe(N-MeIm)}_2{}^+\text{Cl}^- \tag{42}$$

For the case where $k_3[\mathrm{L}] \gg k_2$, this mechanism gives rise to a predicted equation (equation 43) for the observed rate constant:

$$k_{\text{obs}} = \frac{k_1 K_1[\mathrm{L}]}{1 + K_1[\mathrm{L}]} \tag{43}$$

Analysis of the kinetic data in terms of equation (43) shows that the equilibrium constant for formation of the mono-*N*-methylimidazole complex (equation 35) shows a small solvent dependence ranging from 22 to 0.3 M^{-1} (acetonitrile and $\mathrm{CHCl_3}$, respectively), but the rate constant k_1, for dissociation of the high-spin six-coordinate complex, shows a larger solvent dependence, ranging from 360 to 0.7 s^{-1} ($\mathrm{CHCl_3}$ and *n*-chloropropane, respectively). The size of k_1 is strongly dependent on the ability of the solvent to hydrogen bond to the departing chloride in the transition state, and low concentrations of potential hydrogen-bonding additives such as trifluoroethanol and phenol have a large accelerating effect on k_1.[1422] Similar effects were found for the reaction of *N*-methylimidazole with the corresponding protoporphyrin IX and protoporphyrin IX dimethyl ester complexes of chloroiron(III)[1443] and for the reaction of imidazole (HIm) with TPPFeF and (PPDME)FeF.[1444] In the latter case, the first intermediate to form is, as before (equation 40), the six-coordinate high-spin PFe(HIm)F, and the second is PFe(HIm)F$\cdots$HIm in which an external imidazole is hydrogen bonded to the fluoride.[1444] It has also been shown that reaction of hindered imidazoles such as 2-MeImH and 1,2-$\mathrm{Me_2Im}$ with TPPFeCl introduces a steric strain with the porphyrin ring that causes about a factor of ten decrease in the formation constant, K_1 (equation 40), and a factor of ten or more increase in the rate of chloride ion dissociation (equation 41).[1445]

The binding of apomyoglobin to hemin can also be thought of as an axial ligation reaction of a $\mathrm{Fe^{III}}$ porphyrin, for indeed, all heme proteins except the cytochromes *c* have non-covalently attached heme groups. The equilibrium constant for binding hemin to apomyoglobin has been estimated as $10^{14}\,\mathrm{M}^{-1}$ at neutral pH.[1446] This value is determined by a complex set of nonspecific hydrophobic (10^5–10^7), specific, mainly ionic (10^3–10^4) and covalent (His-Fe, 10^3–10^4) interactions.[1446] Olson and coworkers have investigated some of the factors that affect the equilibrium constants and rates of hemin dissociation in some 100 different metmyoglobin mutants.[1447] It was found that mutations of the proximal histidine (His-93 (F8)) and the nearby leucine (Leu-89 (F4)) can result in >100 fold increases in the rates of hemin loss at pH 5 and 7. Some replacements of the contact residues His-64 (E7), Val-68 (E-11), His-97 (FG3), Ile-99 (FG5), Thr-39 (C4), and Tyr-103 (G4) cause >10-fold changes in the rate of hemin dissociation. Substitutions of the noncontact residues Leu-29 (B10), Phe-46 (CD4), and Gly-65 (E8) can also increase the rate of hemin loss >10-fold. The key structural factors stabilizing bound hemin in myoglobin are (1) hydrophobic interactions between apolar residues in the heme pocket and the porphyrin ring, (2) the coordinate bond between His-93 (F8) and the $\mathrm{Fe^{III}}$ atom, and (3) hydrogen bonding between distal residues and coordinated water.[1447] It has also been shown that many heme proteins, including bovine microsomal cytochrome b_5,[1448] will release their heme to apomyoglobin at pH 7.0, indicating that the binding constant of hemin to the bovine b_5 is less than $10^{14}\,\mathrm{M}^{-1}$.

'Heme rotation' is another aspect of the binding and dissociation of hemin from a number of heme proteins. Protohemin is an unsymmetrical molecule (Figure 1(c)), and if one of the two heme orientations is significantly more thermodynamically stable than the other in a given protein pocket, then the initial 50–50 mixture of the two heme orientations that exists upon mixing the apoprotein with hemin and random binding of this hemin to the protein will change over time until the equilibrium ratio of the two is reached.[1449] For cytochromes b_5, that ratio is ~90:10 for the rabbit and bovine microsomal proteins,[1449–1451] ~95:5 for the chicken microsomal protein,[1452] 62:38 for the rat microsomal protein,[1453] and 47:53 for the rat outer mitochondrial protein.[1454] While the half-lives of heme rotation are on the order of 12 hr for the bovine microsomal cytochromes b_5,[1450,1455] it has been shown that the half-life is much longer for the rat outer mitochondrial protein, in that it requires heating the protein to 65 °C for several hours to reach the equilibrium mixture of heme orientations.[1454] Thus rat outer mitochondrial cytochrome b_5 represents the first documented example of a cytochrome b_5 exhibiting a thermodynamic preference for hemin isomer B and in which hemin is kinetically trapped under physiologically relevant conditions.[1454,1456] The hemin is tightly bound to the protein, and is not released to apomyoglobin at pH values as low as 5.2.[1454,1456] Two hydrophobic patches that are largely responsible for the relative kinetic inertness of outer mitochondrial cytochrome b_5 have been identified and studied, and two point mutations were identified that make the protein strongly favor hemin orientational isomer B (I32L, A:B = 1:4.0) or isomer A (L71S, A:B = 5.2:1).[1457] Hemin release from isomers A and B can be kinetically resolved in some of the rat outer mitochondrial cytochrome b_5 mutants.[1457]

6.3.8 *Kinetics of Axial-ligand Exchange on Low-spin Iron(III) Porphyrins*

La Mar and Walker[1458] first reported investigations of the dynamics of axial-ligand exchange in the low-spin Fe^{III} complex $[TPPFe(N\text{-}MeIm)_2]^+Cl^-$ in $CDCl_3$ by observing line broadening of the coordinated N-methyl peak of N-MeIm as a function of temperature. It was established that, even in the presence of excess ligand, ligand exchange proceeds by a dissociative mechanism involving a five-coordinate $PFeL^+$ X^- transition state (equations 44 and 45):

$$[PFeL_2]^+X^- \rightleftharpoons [[PFeL]^+X^-]^{\ddagger} + L \qquad k_1 \qquad (44)$$

$$[[PFeL]^+X^-]^{\ddagger} + L^* \longrightarrow [PFeLL^*]^+X^- \quad \text{rapid} \qquad (45)$$

Satterlee *et al.*[1346] extended these studies to characterize the axial lability of various imidazoles and pyridines in bis-ligated low-spin Fe^{III} complexes of synthetic porphyrins, including tetraphenyl-, octaethyl-, and tetra-n-propylporphyrins. For $L = N$-methylimidazole, typical rate constants k_1 are $35-100\,s^{-1}$ for TPPFeCl and T-n-PrPFeCl, and $950\,s^{-1}$ for OEPFeCl; typical activation parameters determined in this study are $\Delta H^{\ddagger} = 17-20\,kcal\,mol^{-1}$, $\Delta S^{\ddagger} = 15-19\,J\,mol^{-1}\,K^{-1}$.[1346] More recently it has been shown by a combination of saturation transfer, linewidth analysis and lineshape analysis in the intermediate exchange rate region that, as for the TPP complexes, ligand exchange in sterically more hindered tetramesitylporphinatoiron(III) complexes is also dissociative.[1424,1425] In both the TPP and TMP complexes the axial lability of coordinated imidazoles increases with increasing steric bulk of the base; that is, 2-methylimidazole complexes have larger dissociation rate constants ($k_1 = 8.9 \times 10^3\,s^{-1}$ for $[TPPFe(2\text{-}MeImH)_2]^+$ and $1.1 \times 10^5\,s^{-1}$ for $[TPPFe(1,2\text{-}Me_2Im)_2]^+$; $18\,s^{-1}$ for $[TMPFe(2\text{-}MeImH)_2]^+$ and $100\,s^{-1}$ for $[TMPFe(1,2\text{-}Me_2Im)_2]^+$) than the corresponding N-methylimidazole species ($k_1 = 120$ and $7\,s^{-1}$ for the TPP and TMP complexes, respectively).[1425] The increased lability is believed to be due to the steric repulsion between the alkyl substituent in the 2-position of the imidazole ring and the porphyrin macrocycle. Overall, TPP complexes are more labile than their TMP counterparts. However, the stability of the TMP complexes is invariably greater than their TPP counterparts, as discussed in Section 6.3.6 above. In fact, the rate constants are inversely proportional to the equilibrium constants, β_2,[1425] suggesting that this reaction indeed proceeds as described by equations (41) and (42), and that $\beta_2 \propto K_2 = k_f/k_r$, where $k_r = k_1$.

For a number of mono-*ortho*-substituted derivatives of $[TPPFe(N\text{-}MeIm)_2]^+$, including a series of $[(o\text{-}CONR_2)_1TPPFe(N\text{-}MeIm)_2]^+$ complexes having amide R groups of varying sizes, large effects are observed in the rate constants for exchange of one of the two unique N-methylimidazole ligands, with the rate constants being determined partly by the electronic effect and partly by the size of the *ortho* substituent.[246] However, the NMR spectra themselves, in combination with kinetics data obtained from analysis of the line broadening of the N-methyl peaks of the two coordinated N-MeIm ligands, indicate that for these and selected other *ortho*-substituted complexes, the N-methylimidazole ligand that dissociates most rapidly is the one on the *opposite* side of the porphyrin plane from the *ortho*-substituent, probably due to buckling of the macrocycle to accommodate the substituent. Such buckling is expected to have the effect of strengthening the Fe–N bond of the ligand on the same side of the porphyrin plane as the substituent and weakening that of the ligand on the opposite side of the plane.[246] Similar results have been reported for ligand exchange on Ru^{II} 'picnic basket' porphyrins.[270]

The rate of axial water exchange on the water-soluble porphyrins $TMPyPFe^{III}$ and $TPPSFe^{III}$ have been investigated by ^{17}O NMR.[1459] For the former at 25 °C, $k_1 = 7.8 \times 10^5\,s^{-1}$, $\Delta H^{\ddagger} = 13.8\,kcal\,mol^{-1}$ and $\Delta S^{\ddagger} = 14.7\,J\,mol^{-1}\,K^{-1}$, and for the latter at 25 °C, $k_1 = 1.4 \times 10^7\,s^{-1}$, $\Delta H^{\ddagger} = 13.7\,kcal\,mol^{-1}$ and $\Delta S^{\ddagger} = 20.2\,J\,mol^{-1}\,K^{-1}$.[1459] Note that although the rate of dissociation of water from the pentapositive complex, T(p-M)PyPFe^{III}, is a factor of a hundred slower than from the trinegative complex, $TPPSFe^{III}$, the activation parameters are nearly identical.

Photodissociation of a N-methylimidazole ligand from $[OEPFe(N\text{-}MeIm)_2]^+$ has been studied using resonance Raman detection.[1460] The rate constants for ligand dissociation and association are $k^- = 5.3 \times 10^3\,s^{-1}$ (as compared to $950\,s^{-1}$ for the non-photoactivated dissociation[1346]) and $k^+ = 3.7 \times 10^7\,s^{-1}$, respectively.[1460]

6.3.9 *Kinetics of Iron(III) Porphyrin Axial-ligand Rotation and Porphyrin Ring Inversion*

Nakamura and Groves[1354] first reported the coalescence behavior observed in the proton NMR spectra of the pyrrole-H, o-Me, p-Me, and m-H resonances of $TMPFe(2\text{-}MeImH)_2{}^+$ as the temperature is lowered from room temperature to −48 °C. They correctly ascribed this behavior to a slowing of axial-ligand rotation as the temperature is lowered, and calculated activation parameters from complete lineshape analysis of the two p-Me signals of the TMP ligand. For the rotation of 2-MeImH ($\Delta H^{\ddagger} = 54 \pm 1.7\,kcal\,mol^{-1}$; $\Delta S^{\ddagger} = 3.7 \pm 1.6\,J\,mol^{-1}\,K^{-1}$) and $1,2\text{-}Me_2Im$ ($\Delta H^{\ddagger} = 52.7 \pm 3.3\,kcal\,mol^{-1}$; $\Delta S^{\ddagger} = 5.2 \pm 3.6\,J\,mol^{-1}\,K^{-1}$).[1354] Although their proposed structure of the low-temperature complex, in which ligand rotation is hindered, was later modified on the basis of NOESY investigations of this system,[187] the activation parameters clearly describe the barriers to rotation of the two 2-substituted imidazoles. These barriers are considerably lower than those for axial-ligand exchange,[1346] and clearly represent a totally different kinetic process. The rates of simultaneous 2-MeImH rotation and porphyrin ring inversion of $TMPFe^{III}$, $2,6\text{-}Cl_2TPPFe^{III}$ and $2,6\text{-}Br_2TPPFe^{III}$ bound to two 2-MeImH, and of TMPCo^{III} bound to two 2-MeImH and 1,2-Me$_2$Im axial ligands were measured over a wide temperature range by 2D NOESY/EXSY methods,**1461** and yielded somewhat different activation parameters for the two metals: While the $\Delta H^{\ddagger}$ values were similar in all cases, ranging from 46 to 51 kJ mol^{-1}, the $\Delta S^{\ddagger}$ values were quite small in magnitude for Fe^{III}, but much larger and negative for Co^{III} (-63, -84 J mol^{-1}K^{-1}, respectively).**1461** Different solvation effects, due to the anion used in each case (ClO$_4^-$ vs. BF$_4^-$, respectively),**1461** may have led to the different entropies of activation. Saturation transfer**1462** and ^{1}H transverse relaxation rate**1463** methods yielded quite similar rates and activation parameters to those obtained by NOESY/EXSY techniques.**1461** Additional measurements of the rates of ligand rotation/porphyrin inversion have been reported for TMPFe^{III}-related systems with 2-MeImH and other hindered axial ligands, measured by DNMR (line-broadening) techniques, have also been reported;**1464,1465** in these studies, the authors believed that the axial ligands were 'fixed' at just below the lowest temperatures they used for their measurements, but the NOESY/EXSY measurements**1461** make it quite clear that chemical exchange continues until some 50–75 degrees lower in temperature than can be detected from 1D measurements, and that at even lower temperatures than that, chemical exchange is simply too slow to be detected by NMR techniques. Thus, axial ligands in these iron porphyrin complexes should not be thought of as 'fixed'.

Similarly, for the octaalkyltetraphenylporphyrinatoiron(III) complexes, the rates and activation parameters for the five-coordinate complexes OETPPFeCl, F$_{20}$OETPPFeCl, OMTPPFeCl and TC$_6$TPPFeCl,**1466** and for bis-ligated complexes of OETPPFe^{III}, where the axial ligands are 4-NMe$_2$Py,**1466** N-MeIm,**1466** and 4-CNPy**943** could be measured by NOESY/EXSY and/or DNMR techniques. The results show that the rate constants for ring inversion of the porphyrin cores of PFeCl, extrapolated to 298 K, decrease in the order TC$_6$TPP > OMTPP > F$_{20}$OETPP > OETPP (k$_{298}$ $\sim 4.4 \times 10^7$, 2×10^5, 73 and 16 s^{-1}, respectively); $\Delta H^{\ddagger}$ increases in the order TC$_6$TPP < OMTPP < F$_{20}$OETPP < OETPP (34, 46, 47, 54, with errors of ± 1–2 kJ mol^{-1}, respectively), and the $\Delta S\ddagger$ changed from small positive to larger negative (16, 11, – 52, – 42, with errors of ± 4–7 J mol^{-1} K^{-1}, respectively).**1466** For bis-ligand complexes of OETPPFe^{III}, the rates of ring inversion were fastest for the cylindrical ligands (t-BuNC, CN$^-$; k$_{298}$ $\sim 2.6 \times 10^6$ s^{-1} for both) and slowest for 4-CNPy (overall $S = 3/2$; PFe$^{II}\pi$-cation radical) (k$_{298}$ $\sim$ 59 s^{-1}); among $S = 1/2$ complexes, the extrapolated rate constant at 298 K is larger for the bis-4-NMe$_2$Py complex (970 s^{-1}) than for the bis-N-MeIm complex (174 s^{-1}). The $\Delta H^{\ddagger}$ values for these bis-ligand complexes are 40, 58, 32, 49, and 59 kJ mol^{-1}, respectively, and the $\Delta S^{\ddagger}$ values are 13, 73, -104, -22, and -3 J mol^{-1} K^{-1}, respectively, for the series of ligands listed.**1466** The $\Delta S^{\ddagger}$ values are probably dominated by solvation effects (DMF for the bis-cyanide complex, CD$_2$Cl$_2$ for the others), but the reason for the very negative value for the bis-4-CNPy complex is not clear.

The free energy barrier to inversion of the chloroiron porphyrin π-cation radicals of OMTPP and OETPP have been reported and compared to those of the starting materials.**1467** For [OMTPPFeCl]SbCl$_6$ the barrier to ring inversion was found to be 4 kcal mol^{-1} (16.8 kJ $^{-1}$ mol) higher than for the neutral complex, while that for [OETPPFeCl]SbCl$_6$ is about 2 kcal mol^{-1} (8.4 kJ mol^{-1}) higher than that of the neutral complex. Because these are single point measurements, the enthalpy and entropy contributions cannot be deconvoluted.

6.3.10 Kinetics of Reduction of Low-spin Iron(III) Porphyrins

The kinetics of reduction of low-spin water-soluble Fe^{III} porphyrins by superoxide,**1024,1468,1469** CO$_2^-$•,**1024** dithionite,**1470** ascorbic acid,**1471** and phenols in the presence of hydrogen peroxide**1472** have also been reported. For T(p-M)PyPFe^{III} and α^4-TMINPFe^{III}, reduction by CO$_2^-$• is close to diffusion controlled ($k = 1.4 \times 10^{10}$ and 6.1×10^9 M^{-1} s^{-1}, respectively, at pH 5.6),**1024** while rate constants for O$_2^-$· reduction are about two orders of magnitude slower (1.2×10^8 and 8.1×10^8 M^{-1} s^{-1}, respectively, also at pH 5.6).**1024** The reader is referred to the original literature for further details of these investigations.

6.3.11 Autoreduction of Iron(III) Porphyrins

Several investigators have shown that Fe^{III} porphyrins in solution are autoreduced by certain ligands. Examples of such cases are the autoreduction of tetraphenylporphinatoiron(III) chloride in the presence of piperidine,**1473** primary amines,**1474** cyanide,**1024,1475** thiols and phosphines,**1475,1476** or hydroxide or alkoxide ions or solid sodium hydride.**1477** Magnetic resonance techniques (NMR and EPR) have been successfully employed to probe the mechanism of the autoreduction and to characterize reaction intermediates and final products.**1473–1482** It is believed that the autoreductions proceed by similar pathways for a variety of ligands and involve an intramolecular electron transfer to give Fe^{II} species and ligand radicals. The mechanisms of such reactions are relevant to the understanding of both the activation of coordinated ligands in certain hemoproteins and modes of intramolecular electron transfer in cytochromes.**1473**

Detailed ^{1}H NMR and EPR spectroscopic studies performed in DMSO solution demonstrated that the autoreduction of tetraphenylporphinatoiron(III) chloride in the presence of piperidine or potassium cyanide leads to the formation of the corresponding six-coordinate, diamagnetic dicyano or bis(piperidine) Fe^{II} complexes, [TPPFe^{II}(CN)$_2$]$^{2-}$ or [TPPFe^{II}(Pip)$_2$], which are identified by their characteristic pyrrole-H shifts at 8.8–9.0 ppm.**1473–1482** In addition to the Fe^{II} complexes, a cyanide or a piperidine radical is formed, indicating that the iron reduction is accompanied by one-electron oxidation of the ligand molecules. The generation of the cyanide radical during the reduction of $\mathrm{Fe^{III}}$ suggests that the mechanisms for the autoreduction of the dicyano complex involves homolytic bond cleavage according to the overall reaction in equation (46):

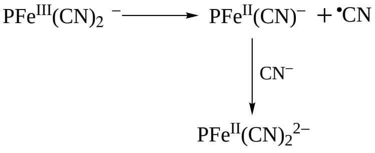

$$\begin{tikzcd}
\mathrm{PFe^{III}(CN)_2{}^-} \arrow[r] & \mathrm{PFe^{II}(CN)^-} + {}^{\bullet}\mathrm{CN} \arrow[d, "\mathrm{CN^-}"] \\
& \mathrm{PFe^{II}(CN)_2{}^{2-}}
\end{tikzcd} \qquad (46)$$

(The ·CN radicals appear to dimerize rapidly to produce dicyanogen, NCCN.[1475]) The reduction rate of $[\mathrm{TPPFe^{III}(CN)_2}]^-$ depends on a variety of factors. Light and increased cyanide concentrations accelerate the reduction, while small amounts of water inhibit the reaction. Reoxidation of the dicyano $\mathrm{Fe^{II}}$ complex by molecular oxygen leads directly to the formation of the low-spin complex, as opposed to μ-oxo dimer formation, because of the presence of excess strong-field ligand (i.e. the reaction with $\mathrm{O_2}$ is probably outer-sphere). Autoreduction of a series of dicyanoiron(III) porphyrins studied by White-Dixon *et al.*[1476] showed that the rate of autoreduction depends on porphyrin structure. TPP complexes autoreduce faster than protoporphyrin IX species and much faster than deuteroporphyrin derivatives, for which no autoreduction was observed.[1008] For water-soluble porphyrins, T(p-M)PyP$\mathrm{Fe^{III}(CN)_2}$ (charges omitted) is autoreduced by excess cyanide, while α^4-TMINP$\mathrm{Fe^{III}(CN)_2}$ is not.[1024]

In benzene or DMF solution, primary and secondary amines having an α-CH react with $\mathrm{Fe^{III}}$ porphyrins to give bis(amine) adducts of $\mathrm{Fe^{II}}$ porphyrins, plus one mole of the corresponding imine (equation 47):[1474]

$$\mathrm{2PFeCl + 5RNH_2 \longrightarrow 2PFe^{II}(RNH_2)_2 + R'CH{=}NH + 2RNH_3{}^+Cl^-} \qquad (47)$$

The reaction path entails two successive reversible ligation steps, followed by two one-electron reductions of the bis(amine)-ligated low-spin $\mathrm{Fe^{III}}$ adduct. In benzene the kinetics are biphasic. The second ligation is rate limiting [k_1(ligation) > k(reduction) > k_2(ligation)]. In DMF the first reduction step is rate limiting. The influence of nonreducing amines, porphyrin substituents (proto > TPP > meso > OEP > deutero), axial ligands, and deuteration of the substrate upon the kinetics leads to the formulation of the first reduction step as a reversible outer-sphere electron transfer to the porphyrin periphery. This is followed by a rapid conversion of the generated aminium cation radical to an α-aminocarbinyl radical. The latter completes the reduction in an irreversible second step. The authors pointed out the relevance of this system to the monoamine oxidase reaction of cytochrome P450.[1474]

Shin *et al.*[1477] have shown that $\mathrm{Fe^{III}}$ complexes of tetraphenylporphyrins and etioporphyrin undergo autoreduction in DMSO solution by addition of hydroxide or alkoxide ions or solid sodium hydride. The autoreduction leads to the formation of the corresponding five-coordinate hydroxoiron(II) ($S = 2$) complexes. This reduction can be followed easily by NMR spectroscopy.

6.3.12 Electron Self-exchange between Low-spin Iron(III) and Iron(II) Porphyrins

To understand the pathway of electron transfer in proteins such as the cytochromes, it is essential to determine the role of the protein in controlling the rate of electron transfer between two cytochrome molecules[1478–1481] (*see* ***Long-range Electron Transfer in Biology***; ***Iron: Heme Proteins & Electron Transport***). Accurate assessment of the role of the protein requires knowledge of the factors that control electron transfer in hemes themselves. Hence, the electron self-exchange rate constants between two hemes free in solution have been determined by NMR spectroscopy using ^{1}H line-broadening techniques. White-Dixon and coworkers have employed this method to determine electron self-exchange rate constants in a variety of heme model compounds with the goal of establishing how changes in porphyrin or axial-ligand structure and in macrocycle saturation affect the exchange rates.[1476,1482–1484] Saturation transfer and 2D EXchange SpectroscopY (EXSY) experiments are now additional NMR methods for measuring the rates of electron exchange in model hemes (equation 48), if the reactions are in the slow exchange region of the NMR timescale.[491]

$$\mathrm{PFe^{III}L_2}^{(n)} + \mathrm{PFe^{II}L_2}^{(n-1)} \rightleftharpoons \mathrm{PFe^{II}L_2}^{(n-1)} + \mathrm{PFe^{III}L_2}^{(n)} \qquad (48)$$

The electron self-exchange rates for various N-methylimidazole complexes determined at −21 °C in $\mathrm{CD_2Cl_2}$ are found to be in the range of $5{-}8 \times 10^7\ \mathrm{M^{-1}\,s^{-1}}$ for various phenyl-substituted TPP complexes and do not vary in a regular fashion with increase of steric crowding on the periphery of the porphyrin macrocycle.[1008,1482,1483] Similar rate constants were measured for systems with sterically bulky imidazole ligands, such as N-butylimidazole. Hence it was concluded that increasing the steric bulk at either the heme site or on the axial ligand has almost no effect on the rate of electron exchange. However, complexes with axial imidazoles bearing NH groups have self-exchange rate constants that are a factor of 2−3 smaller than those with N-alkylimidazole substituents.[1008] This suggests that hydrogen bonding or complete deprotonation of the axial imidazole nitrogen atom may play a role in controlling electron-transfer rates.[1476] However, this is a complex system, and the role of anions that hydrogen-bond to the axial imidazole N-H group needs to be elucidated, for such anions could serve as bridges between the N-H groups of two molecules, one having $\mathrm{Fe^{III}}$ and the other $\mathrm{Fe^{II}}$ oxidation states, or on the other hand, the anions might serve to organize the solvent to a greater extent for the N-H imidazoles, and thus create bulkier species that cannot approach each other as closely as the non-H-bonding imidazole case.

Changes in the degree of saturation of the macrocycle affect the rate constants in a minor way. Similar rate constant values are obtained for both the porphyrin and the octaethylisobacteriochlorin (OE*i*BC) complexes, thus indicating little effect of the macrocycle on the electron-transfer rate, perhaps as a result of counterbalancing effects in either the inner or outer sphere reorganization and orbital occupation.[1484]

The value of the rate constant obtained for the heme undecapeptide, MP11 ($1.3 \times 10^7\,M^{-1}\,s^{-1}$), is comparable to those of other model compounds.[1485] The rate constants for model hemes and the heme *c* undecapeptide are approximately a factor of 10 larger than those found in cytochromes with 80–90 amino acids. This argues further that the heme exposure to the solvent seems not to be a major factor controlling the rate constants for electron self-exchange in cytochromes.[1485]

MP11 has been reacted with a peptide containing a photoactive ruthenium(II) tris-bipyridyl moiety at one end and a histidine that coordinates to the heme at the other end.[1486] Photoexcitation of the Ru^{II} results in rapid ($k_{ET} > 10^7\,s^{-1}$), reversible ET to the ferric heme. Clear evidence for reversible photoinduced ET was observed in time-resolved luminescence and transient resonance Raman studies of the MP11-RuProHis samples.[1486] In a separate study a photoreactive RuII tris-bipyridyl donor was covalently attached to MP11.[1487] This arrangement eliminates complications arising from the equilibrium complexation of ruthenium donor and heme acceptor required for the model systems just described, and leaves an axial position in the octahedral geometry of the heme iron open for ligation. Various optical spectroscopies and molecular modeling calculations were employed to characterize the equilibrium properties and interchromophore interactions of RuMP11. Preliminary luminescence quenching, transient absorption, and transient resonance Raman studies demonstrated that rapid reversible electron transfer can be photoinduced in this system.[1487]

6.3.13 *Synthetic Ferriheme Proteins*

There have been a number of reports of the preparation of synthetic peptides that are designed to bind to hemes in similar fashions to how they are bound in various heme proteins.[1488–1521] The types of peptide systems designed include (1) four-helix bundles in which each peptide is covalently attached to a ‘corner’ of a porphyrin scaffold and in which the bundle is oriented perpendicular to the porphyrin plane,[1488–1490] (2) preformed four-helix bundles that bind one,[1491–1494] or more[1496–1505] metalloporphyrins via bis-His coordination, usually with the heme plane oriented parallel to the helices, (3) disulfide-dimerized peptides that bind a single metalloporphyrin via bis-His coordination,[1504,1507] (4) reversible complexes formed between a water-soluble Fe^{III} porphyrin and amphiphilic peptides bearing centrally located His residues,[1508,1509] (5) porphyrin-spanning peptides either covalently attached to *meso*-phenyl rings[1510] or bound via metal-to-ligand coordination[1511] and (6) bis-peptide adducts of metalloporphyrins in which His ligands within each peptide coordinate to the porphyrin-bound metal ion.[1512–1518] There have been three recent reviews of this subject.[1519–1521]

The main reasons for the preparation of these synthetic heme proteins are to allow probing the effects of individual amino acid side chains on the properties of the heme centers, notably their reduction potentials and the stability of the Fe-histidine bonds in the two oxidation states (see Sections 6.3.5 and 6.3.6), and the stability of the 3- or 4-helix bundles with heme bound that are often used for creation of these synthetic proteins. Some of the 4-helix bundle maquettes, designed to bind only one hemin molecule per peptide, bind hemin to one peptide with dissociation constants of as low as 65 nM; addition of a second equivalent of hemin results in binding a second heme molecule to the other peptide of the 4-helix bundle with dissociation constants in the range of 35–800 nM.[1503] (In comparison, the K_d for hemin dissociation from myoglobin is ~10 fM,[1446] meaning that it forms a factor of 10^5–10^6 more stable complex, as discussed in Section 6.3.6.) The equilibrium reduction midpoint potentials, $E_{m7.5}$, determined in the monoheme state range from −156 to −210 mV versus SHE and in the diheme state range from −144 to −288 mV. An observed heme–heme electrostatic interaction (>70 mV) in the diheme state indicates a syn global topology of the di-α-helical monomers, as shown in Figure 15. The results of this study illustrate that conservative hydrophobic amino acid changes near the heme-binding site can modulate the E_m by up to ±50 mV and the K_d by an order of magnitude. Furthermore, the effects of multiple

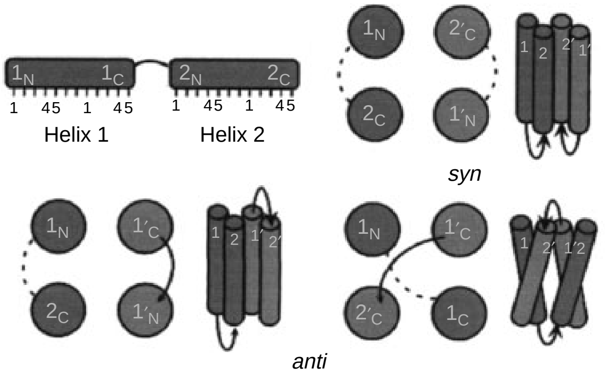

Figure 15 A dimeric, four-helix bundle can adopt six distinct topologies. The topology diagrams shown are for the three possible clockwise-turning helical bundles. Counterclockwise-turning helical bundles are also possible and have interfacial interactions different from their clockwise-turning correlates. (Reprinted with permission from Ref. 1519. © 2000 American Chemical Society)

single amino acid changes on E_m and K_d do not appear to be additive.[1503] Another study showed that the contribution of His-Fe coordination to the difference in reduction potentials of two hemoprotein models was of the order of 90 mV, which is comparable to effects due to local electrostatic interactions (50–80 mV) and proton coupling (>100 mV) in other systems, but pales in comparison to heme solvent exposure effects (∼500 mV, based upon investigations of MP8 and comparison to cytochrome *c*[1522]) and ligand changes (>150 mV).[1516] It was pointed out that there are two limiting situations, one for the synthetic heme proteins, in which reduction potential differences are dominated by the relative affinities of the ligands for Fe^{II} and Fe^{III}, and the other, for the case of the electron-transfer hemoproteins, in which reduction potential differences are dominated by structural changes that alter heme solvent exposure; a decrease in solvent exposure results in positively shifted reduction potentials.[1516] Investigations of the electrochemistry of cytochromes *c* and b_5 have led to the conclusion that the protein matrix mimics the behavior of a low dielectric solvent and shields the heme from the solvent;[1523] it appears that naturally occurring heme proteins are much better in shielding the heme than are the synthetic heme proteins.[1516]

The 4-helix bundles typically have up to 124 amino acids, and thus have molecular weights of over 15 000 Daltons, at least as large as some naturally-occurring heme proteins. NMR studies indicate that the synthetic proteins in general show more dynamics of the polypeptides than do naturally occurring 4-helix bundle proteins.[1503,1504] One crystal structure of such a maquette scaffold, with 1-letter amino acid sequence {[CGGG EIWKL HEEFLKK FEELLKL HEERLKKM]$_2$}$_2$, not bound to heme, has been solved using MAD phasing and refined to 2.8 Å resolution.[1524] The structure shows that the maquette scaffold is an antiparallel four-helix bundle with 'up-up-down-down' topology. No pre-formed heme-binding pocket exists in the protein scaffold. Unexpected inter-helical crossing angles, residue positions and translations between the helices were found. The crossing angles between the parallel helices are – 5° rather than the expected +20° for typical left-handed coiled-coils. Deviation of the scaffold from the design is likely due to the distribution and size of hydrophobic residues – the maquette scaffold did not exhibit knob-in-hole packing. This structure points out that four identical helices may interact differently in a bundle, and heptad repeats with an alternating [HPPHHPP]/[HPPHHPH] (H = hydrophobic, P = polar) pattern are not a sufficient design criterion to generate left-hand coiled-coils.[1524] A 4-helix bundle modeled after the heme-binding core of the cytochrome *b* portion of the cytochrome bc_1 protein complex of mitochondria[7–9] binds two ferrihemes to yield a complex that has a broad 'large g_{max}' EPR signal at g = 3.35. In this model, histidine imidazole planes were held in approximate perpendicular orientations via inclusion of residues designed to be hydrogen-bond acceptors from the imidazole N-H groups.[1504]

6.3.14 *Synthesis and Properties of Five-coordinate Low-spin Iron(III) Porphyrins Having σ-Alkyl or σ-Aryl Groups*

Reports of the synthesis of a number of low-spin Fe^{III} complexes bound to one alkyl, aryl, or silyl axial ligand have appeared.[998,1244,1246,1525–1529] The three major synthetic methods are (1) the reaction of the chloroiron(III) porphyrin with the Grignard reagent (*see Grignard Reagents*) of the desired alkyl or aryl group,[1525,1527] (2) the reaction of the chloroiron(III) porphyrin with a lithium alkyl,[1529] and (3) the reaction of the four-coordinate Fe^{II} porphyrin with an alkyl halide.[998] The group 14 anions are expected to be extremely strong σ-donors, and indeed, they are able to stabilize both low-spin Fe^{II}[1530] and low-spin Fe^{III} in the five-coordinate state, except when four or five electronegative fluorine atoms are present on the aryl ring, in which case the five-coordinate complexes are high spin.[1527,1531] It has been shown that σ-alkynyl complexes of $TPPFe^{III}$ can be prepared from lithium acetylides.[966] However, in this case the five-coordinate PFe^{III} complex is high spin, although it becomes low spin upon addition of a nitrogen base to the sixth coordination site.[966]

^1H NMR studies have shown that for the low-spin five-coordinate σ-alkyl and σ-aryl Fe^{III} complexes, porphyrin β-pyrrole–H and $–CH_2$ shifts are indicative of the 'normal' $(d_{xy})^2(d_{xz},d_{yz})^3$ ground state, with spin delocalization via $P \rightarrow Fe$ π bonding.[1244] The NMR resonances of α-H of alkyl groups have been detected by Li and Goff, who reported the ^2H NMR spectra of [d_8-$TPPFeCD_3$] and [d_8-$TPPFeC_2D_5$] in toluene at 25 °C, recorded over a very large spectral width at 55 MHz.[1532] For the CD_3 group, $\delta_{obs} = 532$ ppm; for the C_2D_5 group, δ_{obs} for the CD_2 is 562 ppm, with the CD_3 signal at −117 ppm. These are the largest chemical shifts reported thus far for iron porphyrins; the low frequency of the ^2H nucleus makes possible the use of spectral bandwidths that correspond to such a large chemical shift range. Widths of the α-CD_3 and -CD_2 resonances are reasonably narrow, 80 and 115 Hz, respectively, in both THF and toluene.[1532] In light of the expected narrowing of deuterium resonances of up to a factor of 42 over those of protons[1532] at the same molecule positions, it is not surprising that α-CH_3 and $–CH_2$ signals have not been detected. Both high- and low-spin σ-bonded aryl-, alkyl-, and perfluoroaryliron(III) porphyrins have been characterized, including not only NMR and EPR spectra but also Mössbauer spectra.[1533] For low-spin alkyl and aryl complexes, isomer shifts were found to vary over the range $0.28 < \delta$ Fe(80–95 K) $<0.34\ \text{mm s}^{-1}$ and quadrupole splittings $2.6 < \Delta E_Q < 3.57\ \text{mm s}^{-1}$, while for the high-spin complexes $TPPFe(C_6F_4H)$ and $OEPFe(C_6F_5)$, δ Fe(80–85 K) = 0.53 and $0.23\ \text{mm s}^{-1}$ and $\Delta E_Q = 0.48\ \text{mm s}^{-1}$ and unresolved, respectively.[1533]

The σ-alkyl complexes of $TPPFe^{III}$ can be reduced with $LiHBEt_3$ or $KHB(i\text{-}Bu)_3$ in benzene/THF to yield diamagnetic $[TPPFe^{II}R]^-$ (R = *n*-propyl or ethyl).[1530]

These complexes are easily reoxidized by dioxygen to TPPFe^{III}R.[1530] Alkyliron(III) porphyrins will undergo CO and CO_2 insertion into the Fe–C bond, forming acyliron(III) (PFeC(O)R) and alkyl carboxylate (PFeOC(O)R) complexes, respectively.[1529]

Addition of *N*-methylimidazole or pyridine to either five-coordinate low-spin or high-spin σ-alkyl, σ-aryl, or σ-alkynyl Fe^{III} porphyrins produces low-spin mixed-ligand complexes.[966,1244] NMR results indicate that upon adding a sixth ligand the aryl anion acts as a π donor, rather than a π acceptor, toward low-spin Fe^{III}, in that the electron configuration is $(d_{xy})^2(d_{xz},d_{yz})^3$. Interestingly, however, the planar nature and potential π donor character of the aryl ligand is not sufficient to produce a resolved rhombic EPR spectrum for [TTPFe(C_6H_5)]; instead, a 'large g_{max}' signal at $g = 3.54$ is observed, with a broad feature at about $g \sim 1.7$,[1534] indicating near-degeneracy of d_{xz} and d_{yz}, probably due to the strong σ-donor nature of the aryl ligand. Addition of pyridine shifts this signal to $g = 3.86$ and the broad feature to higher field (lower g-value).[1534]

Exposure of σ-alkyl complexes to dioxygen leads to insertion of O_2 into the Fe–C bond, with the formation of the corresponding alkyl peroxide (equation 49):[998,1535]

$$\mathrm{PFe^{III}CHR_2} + \mathrm{O_2} \longrightarrow \mathrm{PFe^{III}OOCHR_2} \qquad (49)$$

The alkyl peroxide then can decompose to give PFe^{III}OH and O=CR_2, or, if a tertiary alkyl group, σ-$CR'R_2$, is involved, PFe^{IV}O, HOR$'$, and OCR_2, as discussed in Section 8.1 below. Acyl complexes such as PFe^{III}C(O)C_4H_9 react with dioxygen to yield only PFe^{III} carboxylate complexes and the μ-oxo dimer, PFe^{III}-O-Fe^{III}-P, with no evidence of ferryl complexes being formed.[1536]

A series of iron(III) σ-bonded porphycenes have been characterized by electrochemistry, EPR, NMR and optical spectroscopy and in one case X-ray crystallography.[1537] The macrocyclic ligand was etioporphycene, and the aryl group R was C_6H_5, 3,5-$C_6F_2H_3$, 3,4,5-$C_6F_3H_2$, or 2,3,5,6-C_6F_4H. All of the complexes appear to have the less common $(d_{xz},d_{yz})^4(d_{xy})^1$ electron configuration, based upon their EPR spectra, which have g-values ranging from 2.34–2.29 and 1.94–1.92.[1537]

The methyliron(III) corrphycene complex has been prepared and is stable in the absence of dioxygen; the methylcobalt(III) complex is stable even in the presence of dioxygen.[1538] Radiolytic reduction occurs at the metal center to produce Fe(II) and Co(I) corrphycenes, which are also stable; upon further radiolytic reduction in neutral solutions they yield species with chlorin-like spectral signatures. In alkaline solutions, species with phlorin-anion-like characteristics are produced.[1538]

7 IRON(III) PORPHYRIN AND CORROLE π-CATION RADICALS AND THEIR REACTIONS

7.1 Iron(III) Porphyrin Radicals

One-electron oxidation of Fe^{III} porphyrins may lead to either Fe^{III} porphyrin π-cation radicals or Fe^{IV} porphyrins, depending upon the axial ligation of the metal ion and the reaction conditions. In this section we will consider the systems that have been formulated as Fe^{III} porphyrin π-cation radicals, and in the next section those that have been formulated as Fe^{IV} porphyrins.

Only a few Fe^{III} porphyrin π-cation radicals have been characterized structurally,[1539–1541] since they are quite reactive species. They have been characterized mainly by NMR spectroscopy, magnetic susceptibility measurements, and a diagnostic band in the IR spectrum in the region of 1270–1295 cm^{-1}.[1542] Their main use has been as chemical oxidants of porphyrins, metalloporphyrins, and so on.[206]

In view of the three different spin states observed for Fe^{III} porphyrins, it is not surprising to find that all three have been observed for the one-electron ring-oxidized complexes. Some high-spin, monomeric Fe^{III} porphyrin radicals, including [TPPFeCl]$^+$, give rise to antiferromagnetically coupled $S = 2$ species,[203–205,1539] while others, including [TPPFe($OClO_3$)$_2$], give rise to noninteracting $S = 5/2$, $S = 1/2$ species;[205,1539,1540] spin-admixed $S = 3/2,5/2$ Fe^{III} complexes give rise to spin-admixed π-cation radical species of either $S = 5/2,3/2$[208,1540] or $S = 3/2,5/2$[209] ground ($S = 1$) states; and low-spin Fe^{III} porphyrins give rise to low-spin ferromagnetically coupled Fe^{III} π-cation radical species.[207]

Chemical or electrochemical oxidation of [TPPFeCl] in the presence of perchlorate or hexafluoroantimonate salts, or chemical oxidation with a Fe^{III} porphyrin π-cation radical of higher oxidation potential, produces a $S = 5/2$, $S = 1/2$ antiferromagnetically coupled (effectively $S_{tot} = 2$) five-coordinate [TPPFeCl]$^+$ $(3a_{2u})^1\pi$-cation radical.[205,1539] The same is true of the chlorin complex [TMCFeCl]$^+$.[1543] The X-ray crystal structure of [TTPFeCl]SbF_6 consists of isolated five-coordinate [TPPFeCl]$^+$ units, in which the porphyrin macrocycle is strongly S_4 ruffled.[205,1539] In comparison, in the solid state, [OEPFeCl]ClO_4 exists as a tight cofacial $\pi-\pi$ dimer with an interplanar separation of 3.24 Å, a lateral shift of 0.2 Å, a twist angle between the two rings of 31.2°, an Fe–Fe distance of 4.112 Å, and has strong coupling of the $S = 1/2$ radical spins on the two porphyrin rings, with Fe^{III} in the high-spin state.[1541] In solution, there are no near IR absorption bands caused by dimer formation, as seen with the π-cation radicals of a number of other OEPM complexes discussed in the next paragraph.[1541] The NMR spectra of these [PFeCl]$^+$ complexes suggest that in the case of β-pyrrole-substituted porphyrins the electron is removed from the $1a_{1u}(\pi)$ orbital (Figure 4), as evidenced by the small isotropic shifts of the *meso*-H resonances.[206]

Several metallooctaethylporphyrin π-cation radicals have been examined in methylene chloride solution. For [OEPM]Y, where $M = Cu$, Ni, Zn, Pd, or VO and $Y = ClO_4^-$ or $SbCl_6^-$, are found to dimerize to form $[OEPM]_2^{2+}$.[1544] These dimeric species are characterized by the appearance of a new, strongly concentration-dependent near-infrared absorption band, found in the region of 900–960 nm for all compounds except the vanadyl complex, whose band was found at 1375 nm. Equimolar solutions of these π-cation radicals and their analogous neutral OEPM derivatives react to form new binuclear species, $[OEPM]_2^+$, in which the single radical electron is delocalized over both porphyrin rings.[1544] These mixed-valence π-cation radicals bear a formal relationship to the oxidized special pair of photosynthetic reaction centers, and also display a near-infrared absorption band that is distinctly different from the π-cation radical dimers. The equilibrium constants and ΔH and ΔS values for both equilibrium processes have been determined, and the differences interpreted in terms of the much stronger solvation of the π-cation radical compared to the neutral porphyrin.[1544]

The β-oxochlorin derivative [3,3,7,8,12,13,17,18-octaethyl-(3H)-porphin-2-onato(2-)] iron(III) chloride, [Fe(oxoOEC)Cl], and its π-cation radical derivative [Fe(oxoOEC)Cl]$SbCl_6$ have been prepared and studied by X-ray crystallography, IR, UV–vis/NIR and Mössbauer spectroscopies and by temperature-dependent magnetic susceptibility measurements.[1545] The macrocycles of both [Fe(oxoOEC)Cl] and [Fe(oxoOEC)Cl]$SbCl_6$ are saddled, and the latter is also slightly ruffled. The inter-ring mean plane separation and the lateral shift of the rings are both larger for the π-cation radical (4.82 and 8.79 Å, respectively). A broad near-IR absorption band appears at 1415 nm for the π-cation radical in solution.[1545] Solid-state magnetic susceptibility measurements for the π-cation radical resulted in a large temperature dependence of the magnetic moment that is best fit with a model that includes a zero-field splitting parameter D of 6 cm^{-1}, antiferromagnetic intermolecular iron–iron coupling ($2J_{Fe–Fe} = -0.14\ cm^{-1}$), and antiferromagnetic radical–radical coupling ($2J_{r-r} = -13\ cm^{-1}$).[1545]

The π-cation radicals of PFe–O–FeP species, the μ-oxo dimers of Fe^{III} porphyrins, are convenient chemical oxidants of the chloroiron porphyrins,[206] and they are interesting species in their own right. Those in which $P = TPP$ or one of its derivatives have NMR shifts that suggest the same $(a_{2u})^1$ ground state for the porphyrin π-cation radical, this time delocalized over the two porphyrin rings.[206]

The neutrally charged μ-nitrido dimer of TPPFe, $[(TPPFe)_2N]$ and its phthalocyanine[1546,1547] and mixed-macrocycle[1548] counterparts, are isoelectronic with the π-cation radical of the μ-oxo dimers discussed above, but they have a different electron configuration.[1549] NMR shifts are more consistent with their description as delocalized system having two $Fe^{3.5+}$ rather than a delocalized porphyrin π-cation radical. This complex readily reacts reversibly with dioxygen to produce an EPR-active species that has $g_\parallel = 2.07$, $g_\perp = 2.01$.[1550] Although the EPR parameters are very similar to those of the superoxide ion,[1551] and the spectral change did not occur when the complex was dissolved in a nonpolar solvent such as toluene,[1550] the authors preferred to consider the reaction to involve weak binding between O_2 and $[(TPPFe)_2N]$. One-electron oxidation with I_2/Ag^+ produces a complex that is believed to consist of $Fe^{IV}-N^{-3}-Fe^{IV}$,[1549] with the metals strongly antiferromagnetically coupled. This complex has a magnetic moment less than 1.8 μ_B at room temperature. Unlike $[(TPPFe)_2O]^+$ or $[(TPPFe)_2O]^{2+}$, both of which autoreduce in the presence of pyridine, $[(TPPFe)_2N]^+$ readily coordinates one or two pyridine ligands; stepwise addition can be observed by monitoring the pyridine o-H resonances at −1.26 ppm (1:1) and −1.46 ppm (2:1).[1549] Structures of two six-coordinate complexes of this oxidation level, $[(THF)(TPP)Fe\text{-}N\text{-}Fe(Pc)(H_2O)]^+$[1552] and [(THF)(TPP)Fe-N-Fe(Pc)(THF)][1553] have been reported. The structure of $[(TTPFe)_2N]SbCl_6$ has also been reported,[1554] and shows shorter Fe-N distances and porphyrin plane separations than does $[(TPPFe)_2N]$, consistent with the higher charge on the metal. Structures of $[(TPPFe)_2C]$[1555] and $[(OEPFe)_2C]$[1556] have also been reported. $[(TPPFe)_2N]^+$ can be further oxidized by one electron to produce $[(TPPFe)_2N]^{2+}$ in good yield.[1557] This complex is formulated as a Fe^{IV}–$Fe^{IV}\pi$-cation radical (one electron removed from one of the porphyrin rings).[1557]

One-electron electrochemical oxidation of $[TPPFe(ROH)_2]ClO_4$, where ROH is water or ethanol, in the presence of perchlorate salts produces $[TPPFe(OClO_3)_2]$, a six-coordinate complex, described as a $S = 5/2$, $S = 1/2$, noninteracting high-spin species because of its room-temperature magnetic moment in the solid state ($\mu_{eff} = 6.5 \pm 0.2\ \mu_B$).[205] Its NMR spectrum at 25 °C in CD_2Cl_2 suggests a π-cation radical of a_{2u} type.[205] Non-Curie dependence of the ^1H NMR shifts has indicated that in this spin-admixed state the ground state is largely $S = 5/2$.[208] The magnetic moment in solution, $4.8 \pm 0.4\ \mu_B$, is much lower than that observed in the solid state,[205] suggesting antiferromagnetic coupling between the a_{2u} (π) electron (Figure 4) and the spin-admixed Fe^{III}.[208]

The complexity of the behavior of Fe^{III} porphyrin radicals, and those of tetramesitylporphyrin in particular, is demonstrated by the properties of $[TMPFe(OClO_3)_2]$ in various solvents.[209] This π-cation radical of Fe^{III} was prepared by oxidation of $[TMPFeOClO_3]$ with iron(III) perchlorate and isolated before dissolution in CD_2Cl_2. ^1H NMR investigations indicate that, in the case of the TMP complex, the $S = 3/2$ ground state is greatly favored over the spin-admixed 3/2,5/2 or 5/2,3/2 ground states. Treatment of the latter Fe^{III} porphyrin π-cation radical complex with two equivalents of sodium methoxide produced the electron configuration isomer, the d^4 Fe^{IV} porphyrin complex,[209] as discussed in Section 8.

Although complexes of the type $[PFe(ImH)_2]^+$ could not be electrochemically oxidized to π-cation radicals, titration of high-spin $[(p\text{-}OMe)_4TPPFeCl]ClO_4$ in CD_2Cl_2 with imidazole at −38 °C produced a transient complex whose NMR spectrum was consistent with transient formation of the radical species $[(p\text{-OMe})_4\text{TPPFe(ImH)}_2]^{2+}$.[207] Warming to room temperature causes immediate reduction to the Fe^{III} porphyrin. ^{1}H NMR shifts (large and negative at the *meso* positions) are indicative of an $a_{2u}(\pi)$ ground state for the radical.[207] The magnitudes of the shift differences, $\delta_\text{m}-\delta_\text{p}$ and $\delta_\text{m}-\delta_\text{o}$, are very large and positive at 235 K, +52.5 and +62.1, indicating ferromagnetic coupling between the iron and porphyrin unpaired electrons,[195] as suggested by Reed and coworkers,[1558] and not the Fe^{IV} configuration suggested from DFT calculations.[1559] In a planar porphyrin ring, a low-spin Fe^{III} center with $(\text{d}_{xy})^2(\text{d}_{xz},\text{d}_{yz})^3$ electron configuration would not have the proper symmetry to interact with the $a_{2u}(\pi)$ porphyrin orbital, yet the proximity of the spin density on the four porphyrin nitrogens would strongly favor ferromagnetic coupling. The large phenyl-H shift differences are not at all consistent with metal-centered unpaired electrons.

As an illustration of the chemical reactivity of these $\text{Fe}^{\text{III}}\pi$-cation radicals, $[\text{TPPFe(ClO}_4)_2]$ reacts with nucleophiles such as nitrite ion or triphenylphosphine to produce the mono-β-substituted Fe^{III} porphyrins.[1560–1562] The products were isolated as the six-coordinate dichloride complexes, $[(2\text{-NO}_2)\text{TPPFeCl}_2]$ and $[(2\text{-PPh}_3)\text{TPPFeCl}_2]$, respectively; the latter was characterized by X-ray crystallography and ^{1}H NMR spectroscopy in CD_2Cl_2 as the bis-imidazole complex.[1560]

7.2 Chloroiron(III) and Other Iron Corrole Radicals

The corrole macrocycle lacks one of the *meso*-carbons of the corresponding porphyrin ring (Figure 1(x),1(y)), and produces a trinegative ligand that is said to stabilize higher oxidation states of transition metals,[165] although it is now clear that this is not necessarily the case. A number of different chloroiron corrolates have been synthesized,[479,1563–1567] and these complexes were first believed to consist of Fe^{IV} bound to chloride and the trinegative macrocycle,[1563,1564] and in fact, there have been recent claims that this is the case.[1568,1569] However, these claims ignore the ^{1}H NMR data,[1563,1565–1567] as well as other magnetic data[211] and DFT calculations.[211,1570] All of these chloroiron corrolates exhibit magnetic moments consistent with $S=1$ systems.[1563,1565–1567] However, the NMR spectra of octaalkylcorrolatoiron(III) chloride complexes at room temperature exhibit *meso*-H resonances at +172−177 ppm for the 5,15-H and +183 −189 ppm for the 10-H,[1563,1565] indicating, in analogy to the 5-coordinate ClFe^{III} porphyrinate π-cation radicals discussed above,[203–205,1539] the presence of large negative spin density at the *meso*-carbons that is consistent with the presence of corrolate π-cation radicals. At the same time, *meso*-triphenylcorrolatoiron(III) chloride and its *p*-phenyl substituted analogs have large alternating sign phenyl-H isotropic shifts, such that the phenyl-H shift differences, $\delta_\text{m}-\delta_\text{o}$ and $\delta_\text{m}-\delta_\text{p}$, are large and negative,[195,1566,1567] a clear sign of large negative spin density at the *meso*-carbons in these triphenylcorrolates. Magnetic susceptibility measurements are only consistent with the formulation $S=3/2$ Fe^{III} antiferromagnetically coupled to a $S=1/2$ π-cation radical corrolate$^{2-}\bullet$, while magnetic Mössbauer spectra could be interpreted either as $S=1$ Fe^{IV} or as $S=3/2$ Fe^{III} antiferromagnetically coupled to a $S=1/2$ π-cation radical corrolate$^{2-}\bullet$, although the isomer shift (+0.21 mm s^{-1}) is indicative of iron(III).[211] DFT calculations were extremely informative in showing that the chloroiron corrolates have −0.22 to −0.26 spin density at each *meso*-carbon, as well as smaller negative spin densities (−0.07 to −0.12) at each nitrogen, and alternating positive and negative spin density around the corrole ring.[211] The net spin density on the entire corrolate ring is −0.7 to −0.8, or nearly one unpaired electron with spin opposite to the sign of the spin on the metal.[211] The d_{z^2} unpaired electron on the out-of-plane Fe^{III} was found to be important in mediating the antiferromagnetic coupling to the unpaired electron in the $a_{2u}(\pi)$-type orbital of the corrolate ring; as in the porphyrinate ring (Figure 4), this orbital has very large amplitude at the *meso*-carbons and the nitrogens, but essentially no amplitude at the β-pyrrole carbons.[211] The DFT calculations, showing approximately 1/4 of an unpaired electron with negative spin at each *meso*-carbon,[211] were thus quite consistent with the NMR shifts of the chloroiron octaalkylcorrolate *meso*-H of +170−190 ppm.[1563,1565]

In contrast to the results for the chloroiron corrolates, the phenyliron 7,13-dimethylhexaethyl-corrolate had much smaller *meso*-H shifts of 53.4 and 49.4 ppm at 303 K, the magnetic susceptibility and magnetic Mössbauer spectra could be interpreted as either $S=1$ Fe^{IV} bound to a simple corrolate^{3-} or $S=3/2$ Fe^{III} antiferromagnetically coupled to a $S=1/2\pi$-cation radical corrolate$^{2-}\bullet$, although the isomer shift (−0.10 mm/s) was much more consistent with Fe^{IV}.[211] Thus DFT calculations were required to fully interpret the experimental data; they showed that while the corrolate ring had overall spin density of nearly zero, there was negative spin density (−0.04 each) at the *meso*-carbons and the nitrogens (−0.03 each), and alternating spin density at the other carbons of the ring.[211] Thus it could be concluded that while the net spin density on the corrolate ring was nearly zero, the corrolate ligand is certainly not 'innocent', in that it has non-negative spin densities of alternating sign on adjacent atoms of the ring that add up to nearly zero. The excellent correlation between ^{1}H NMR chemical shifts[195,211,1563,1565–1567] and DFT-calculated spin densities[195,211] provides confidence that ^{1}H NMR shifts can be used in the future to predict the existence of radical character on the macrocycle. In fact, a record NMR study of $[\text{OECFe}(t\text{-BuNC})_2]^+$ showed a pyrroline-H chemical shift of +132 ppm,[982] while $[\text{TPCFe}(t\text{-BuNC})_2]^+$ has a pyrroline-H chemical shift of −36 ppm,[1315] both at 298 K. DFT calculations showed that a ruffled chlorin ring has negative spin density at the C_∞, thus producing a negative chemical shift for the pyrroline-H, while a planner chlorin ring has large positive spin density at the C_∞ positions, thus yielding a positive chemical shift for the pyrroline-H.[982]

Both the chloroiron and phenyliron octaalkylcorrolates can be oxidized electrochemically by two or three one-electron processes, and reduced by two one-electron processes.[1571] One-electron reduction of each produces the simple $[\mathrm{XFe^{III}Corr}]^-$, while one-electron oxidation of each produces the $[\mathrm{XFe^{IV}Corr^{2-}}\bullet]^+$ π-cation radicals. The nitrosyl complex of iron(III) octaethylcorrolate has been formed and both it and its 1-electron oxidized product have been characterized structurally and electrochemically.[1572]

If the chloroiron octaalkylcorrolates are reacted with Lewis bases such as imidazole[1565] or cyanide,[1573] the complexes retain overall spin $S = 1$, but from the NMR shifts (bis-imidazole complex at 203 K: 7,13-CH_3 at -9.7 ppm, CH_2 at 37.1, 11.9, -11.1 ppm, *meso*-H at $-188.5(1)$ and $-161.3(2)$ ppm;[1565] bis-cyanide complex at 303 K: 7,13-CH_3 at -18.7 ppm, CH_2 at 81.5, 23.3 and -17.2 ppm, *meso*-H at $-450(1)$ and $-364(2)$ ppm[1573]) it is clear that the complexes consist of $S = 1/2$ $\mathrm{Fe^{III}}$ either uncoupled or weakly ferromagnetically coupled to a $S = 1/2$ π-cation radical corrolate$^{2-}\bullet$; clearly the degree of coupling differs for the two bis-ligand complexes. Notably, the *meso*-H signals moved ~536 and ~633 ppm upfield upon cyanide addition, which indicates a reversal in the spin of the macrocycle unpaired electron.[1573] The bis-cyanide complex is not stable, and over an hour's time it autoreduces to a simple $S = 1/2$ $\mathrm{Fe^{III}}$ corrolate^{3-} complex that loses one cyanide ligand to prevent having a total 2− charge on the complex.[1573] Thus, this is a case where an axial ligand serves as a reducing agent of the macrocycle and not of the metal.

A number of other metallocorroles also appear to have radical character on the macrocycle. These include the 4-coordinate Mn complex of 7,13-dimethyl-2,3,8,12,17,18-hexaethylcorrolate, which is nominally $\mathrm{Mn^{III}}$ but in terms of ^{1}H NMR shifts appears to be $\mathrm{Mn^{II}}$ bound antiferromagnetically to a corrolate radical (*meso*-H resonances at 70.5(2) and 25.0(1) ppm), overall $S = 1$,[1574] as in the $\mathrm{ClFe^{III}}$ case.[1565,1566] The phenylcobalt octaethylcorrolate has g-values that suggest a largely metal-based electron (1.967, 2.004, 2.112), but also has large ^{1}H ENDOR couplings for the ethyl protons; DFT calculations indicate that there is significant spin density on both the macrocycle and in the cobalt d_{yz} orbital.[1575] Copper *meso*-triarylcorrolates, both *meso*-triphenylcorrolate[1576] and β-octafluoro-*meso*-triphenylcorrolate,[479] have been shown to have a diamagnetic $S = 0$ $\mathrm{Cu^{III}}$ ground state but an excited state that is $S = 1/2$ $\mathrm{Cu^{II}}$ coupled antiferromagnetically to an $S = 1/2$ π-cation radical corrolate$^{2-}\bullet$. The excited state is much more highly populated over the temperature range of the NMR measurements for the non-fluorinated triphenylcorrolates.[1576] The structure of CuTPCorr shows the molecule to be highly saddled.[1576] The corresponding silver complex, AgTPCorr, is slightly saddled, but shows no evidence of paramagnetism; thus the metal is $\mathrm{Ag^{III}}$ bound to an 'innocent' corrolate^{3-} anion.[1577] The As, Sb and Bi octaethylcorrolates are also simple $\mathrm{M^{III}}$ complexes of 'innocent' corrolate^{3-} anions; the electrochemical oxidation of these and their methyl complexes have also been reported.[1578]

Iron,[1579,1580] manganese,[1581,1582] rhodium[1580] and chromium[1583] tri-(pentafluorophenyl)corrolates have been shown to be potent catalysts for aerobic oxidation of organic molecules, and reduced iron and cobalt corrolates have been shown to be active in CO_2 reduction.[1584]

8 IRON(IV) PORPHYRINS AND THEIR REACTIONS

Five types of $\mathrm{Fe^{IV}}$ porphyrin complexes have been reported, all of which have spin state $S = 1$: (1) the deep red, five-coordinate ferryl, $(\mathrm{Fe^{IV}{=}O})^{2+}$, complexes[1585] and the six-coordinate adducts of these ferryl complexes, the $(\mathrm{B})(\mathrm{Fe^{IV}} = \mathrm{O})^{2+}$ complexes;[213,1585,1586] (2) the $\mathrm{Fe^{IV}}$–phenyl complex;[1587] (3) iron(IV) carbene complexes;[593–596,1588–1595] (4) iron(IV) hydrazine complexes; and (5) the six-coordinate d^4 complex $[\mathrm{TPPFe(OMe)_2}]$[209] mentioned briefly in Section 7 above. The ferryl and $\mathrm{Fe^{IV}}$–phenyl cases have direct application to active states of heme proteins, particularly the cytochromes P450, peroxidases, catalases, and related enzymes.

8.1 Five- and Six-coordinate Ferryl, $(\mathrm{FeO})^{2+}$, Porphyrin Complexes

Ferryl complexes have been implicated in the reaction mechanisms of peroxidases and cytochromes P450.[24–32,36,38,1596] For horseradish peroxidase, two intermediates are spectroscopically detectable.[13] Compound I, formed upon addition of peroxide to the resting $\mathrm{Fe^{III}}$ form of the enzyme, is a green species that is formally two oxidation levels higher than the resting state, and is widely believed to consist of an $(\mathrm{Fe^{IV}{=}O})^{2+}$ unit complexed by a porphyrin π-cation radical. The $[(\mathrm{P}^-\bullet)\ \mathrm{Fe^{IV}{=}O}]^+$ complexes are discussed in Section 9. Compound II, which is red, and is obtained upon one-electron reduction of Compound I, also possesses a $(\mathrm{Fe^{IV}{=}O})^{2+}$ unit, in this case complexed by a normal porphyrin dianion, $\mathrm{PFe^{IV}{=}O}$. The fifth ligand, provided by the protein in the various enzymes, is a cysteine thiolate for the cytochromes P450,[24,25,1597] nitric oxide synthases (NOS)[1598] and chloroperoxidase (CPO),[1599,1600] a histidine for horseradish peroxidase (HRP),[1601] heme oxygenase (HO)[32,34] and cytochrome *c* peroxidase (CCP),[1602,1603] and a tyrosine for catalase.[1604]

As in the case of horseradish peroxidase, several synthetic metalloporphyrins in the presence of H_2O_2 have been found to be potent catalysts for the chemiluminescent oxidation of luminol or isoluminol.[1605] The microperoxidases, mainly MP8 and MP11, have been shown to act as functional peroxidase enzyme models.[1606–1612] However, they are readily inactivated within one min of catalytic turnover,[1612,1613] and incorporation into a molecular sieve

(MCM-41) does not afford protection from inactivation.[1611] Cytochrome P450-type enzymes not only include those that carry out hydroxylation and epoxidation reactions, but also aromatizations, such as estrogen synthetase,[29,30,1614] and oxidations of heteroatoms. Nitric oxide synthases,[50,1615] which have very similar heme-thiolate active sites, oxidize a nitrogen atom of the guanidine group of arginine to nitric oxide. Since detailed discussion of the chemistry of peroxidases and catalases is given in the article entitled (*see* ***Iron: Heme Proteins, Peroxidases, Catalases & Catalase-peroxidases***) and of mono- and dioxygenases in the article entitled (*see* ***Iron: Heme Proteins, Mono- & Dioxygenases***), the presentation in the present article has been abbreviated.

Model heme complexes containing the ferryl unit and a nonoxidized porphyrin ring have been prepared and investigated by ^{1}H NMR spectroscopy at low temperatures by Balch and La Mar and coworkers[213,215,1585,1616] and by resonance Raman spectroscopy by Nakamoto and coworkers.[1617] The ferryl species have been produced by several means, including

(1) thermal decomposition (at −30 °C) of the μ-peroxo dimer of PFe^{III}, formed from reaction of 2 PFe^{II} with molecular oxygen at −70 °C (equations 23a, b above),[1585,1618]

(2) by base-catalyzed cleavage of the μ-peroxo dimer at similar low temperatures (equation 50):[213,1585,1586,1618]

$$\underset{\mathrm{Fe^{III}(O_2{}^{2-})Fe^{III}}}{\mathrm{PFe{-}OO{-}FeP}} + 2\mathrm{B} \longrightarrow \underset{\mathrm{(B)(Fe^{IV}O)}}{2\mathrm{(B)PFeO}} \qquad (50)$$

(3) by base-catalyzed cleavage of PFeOOCR$'$R$_2$ complexes (equation 51):[215,1618–1620]

$$\mathrm{PFe{-}OO{-}CR'R_2 + B \longrightarrow (B)PFe^{IV}O + \cdot OCR'R_2} \qquad (51)$$

(a) In the absence of a radical trap (equation 52):

$$\mathrm{(B)PFe^{IV}O + \cdot OCR'R_2 \xrightarrow{H^+} PFe^{III} + \underset{>50\%}{HOR'} + \underset{90\%}{O{=}CR_2} + B} \qquad (52)$$

(b) In the presence of radical trap (equation 53):

$$\mathrm{(B)PFe^{IV}O + \cdot OCR'R_2 \xrightarrow{H^+} PFe^{III} + \underset{10-20\%}{O{=}CR_2} + \underset{80-90\%}{HOCR'R_2}} \qquad (53)$$

(yields given for R$'$ = R = Me);[1620]

(4) by oxidation of PFe^{III} with hydrogen peroxide[1619,1621] or hypochlorite[1622] under basic conditions (equations 54 and 55)

$$\mathrm{2PFe^{III}(H_2O)_2 + H_2O_2 \longrightarrow PFe^{IV}O + 5H_2O} \qquad (54)$$

$$\mathrm{2PFe^{III} + OCl^- \longrightarrow 2PFe^{IV}O + Cl^-} \qquad (55)$$

(5) by oxidation of PFe^{III}OH with organic peracids (equation 56):[218,1619]

$$\mathrm{PFe^{III}OH + \mathit{m}\text{-}ClC_6H_4C(O)OOH \longrightarrow PFe^{IV}O + H_2O + \mathit{m}\text{-}ClC_6H_4CO_2H} \qquad (56)$$

or (6) by electrochemical oxidation of hydroxide or methoxide complexes of ‘protected’ (from μ-oxo dimer formation) Fe^{III} porphyrins such as TMPFe^{III}, (2,6-Cl$_2$)$_4$TPPFe^{III}, (2,6-Br$_2$)$_4$TPPFe^{III},[1619,1623,1624] or (2,4,6-Ph$_3$)$_4$TPPFe^{III}, also called TTPPPFe^{III}.[1625] In cases (3)–(5) above, the Compound I state, [PFe=O]$^+$, may be formed initially, but the Compound II state, [PFe=O], is the only product detected spectroscopically. The kinetics of equations (50–56), including the formation of the Compound I precursor, have been studied in detail by several groups.[1619,1626–1630] The Compound I state is readily reached by reaction of an iron(III) porphyrin with iodosylbenzene,[29,1631–1635] potassium monopersulfate,[1636] or an amine *N*-oxide,[1637] and these reagents are frequently used for generation of the hydroxylation catalysts of the Compound I level that are discussed in Section 9.

Bruice and coworkers have investigated the electrochemical oxidation of hydroxide- and methoxide-ligated Fe^{III} 2,6-disubstituted tetraphenylporphyrins and report that one-electron oxidation produces the Fe^{IV}–oxo porphyrins, analogous to Compound II of peroxidases; removal of another electron produces the Fe^{IV}–oxo porphyrin radicals analogous to Compound I.[1623,1624,1638] However, in the corresponding Mn porphyrin case, the two-electron oxidized species is believed to be P^{2-}Mn^{V} = O, rather than P$^{-}\cdot$ Mn^{IV} = O.[1638] The first and second one-electron oxidation potentials are separated by about 100 mV in dry CH$_2$Cl$_2$ and overlap in wet CH$_2$Cl$_2$.[1624] A third one-electron oxidation, presumably to the Fe^{IV}–oxo porphyrin dication, one-electron more oxidized than Compound I, has a potential in wet or dry CH$_2$Cl$_2$ between 300 and 460 mV more positive than the second oxidation, depending on the porphyrin substituents.[1624]

Both the five- and six-coordinate ferryl porphyrin complexes have very small ^{1}H NMR isotropic shifts of all resonances. The Curie plots for all resonances are strictly linear, and the observed shifts extrapolate to nearly to the diamagnetic positions for each type of proton.[1585] NMR results for the six-coordinate adducts indicate that the axial ligand, which is located *trans* to the strongly π-donating oxo ligand, has very characteristic proton shifts. Investigation of imidazole and pyridine adducts of synthetic ferryl porphyrins and ferryl myoglobin led to detection of broad, weak axial histidine resonances at −11 and −16 ppm in ferryl myoglobin at 35 °C.[1616] There is significant spin delocalization from the d$_{xz}$,d$_{yz}$ orbitals of the metal to the p$_x$ and p$_y$ orbitals of oxygen in both the model compounds and ferryl myoglobin.[1616] The small observed shifts are entirely consistent with theoretical calculations,[1639–1642] which indicate substantial π interaction between iron and oxygen orbitals and effective localization of unpaired spin density within the $(Fe^{IV}{=}O)^{2+}$ unit, a significant amount of which may be localized on the oxygen, in line with the reactivity of this group.**[24,1596]** $TMPFe^{IV}{=}O$ reacts with substituted styrenes with a reactivity that is very unlike that of the 1-electron oxidized complex $[TMPFe^{IV}{=}O]^+$.**[1643]**

The *N*-methylimidazole complex of $(2,6\text{-}Cl_2)_4TPPFe^{IV} = O$ has been characterized by ^{1}H NMR, UV–visible, resonance Raman, and Mössbauer spectroscopies.**[218]** The Fe=O stretching frequency varies inversely with the donor strength of the sixth ligand: THF ($841\,cm^{-1}$) < DMF ($829\,cm^{-1}$) < N-MeIm ($818\,cm^{-1}$). Likewise, although the Mössbauer isomer shifts are essentially constant ($0.07–0.09\,mm\,s^{-1}$), quadrupole splittings vary inversely with axial-ligand donor strength: THF ($2.08\,mm\,s^{-1}$) < DMF ($1.81\,mm\,s^{-1}$) < N-MeIm ($1.35\,mm\,s^{-1}$).**[218]**

Oxoiron(IV) tetraphenylchlorin complexes have been prepared as the first models of a reaction intermediate in the catalytic cycle of cytochrome *d*.**[1644]** Optical absorption spectra show a characteristic red-shifted band at 630 nm as observed in the oxoferryl intermediate of cytochrome *d*, and the proton NMR spectra of the N-MeIm complex exhibit very small hyperfine shifts of the pyrrole protons, as is true for oxoferryl porphyrin complexes. The pyrroline protons of the saturated pyrrole ring show unusual splitting into upfield and downfield resonances. The N-MeIm complex also shows normal $Fe^{IV}{=}O$ stretching frequencies as compared to the corresponding oxoferryl porphyrin complexes.**[1644]** And finally, for iron porphycenes, both peroxo and ferryl intermediates have been detected by ^{1}H NMR spectroscopy during the oxygenation of the Fe^{II} complexes.**[1645]**

8.2 Five-coordinate Iron(IV) Phenyl Porphyrins and Related Cytochrome P450-inactivating Complexes

One-electron oxidation of phenyl iron(III) tetraarylporphyrin complexes with bromine in chloroform at −60 °C produces deep red solutions whose ^{1}H and ^{2}H NMR spectra indicate that they are the corresponding iron(IV) complexes.**[1587]** For the low-spin aryl Fe^{III} porphyrins the electron configuration is $(d_{xy})^2(d_{xz},d_{yz})^3$, with one π-symmetry unpaired electron, and for the low-spin aryl Fe^{IV} porphyrins the electron configuration is $(d_{xy})^2(d_{xz},d_{yz})^2$, with two π-symmetry unpaired electrons.**[1587]** The aryl Fe^{IV} porphyrins are thermally unstable, and upon warming convert cleanly to *N*-phenylporphyrin complexes of Fe^{II} by reductive elimination.**[1244]** This process has been investigated by electrochemical techniques,**[1646,1647]** by which it was shown that the reversible (at fast scan rates) one-electron oxidation of σ-aryl complexes of PFe^{III} was followed by an irreversible chemical reaction that yielded the Fe^{II} complex of the *N*-phenylporphyrin, which could then be oxidized reversibly by one electron to yield the Fe^{III} complex of the *N*-phenylporphyrin. (If the Fe^{II} complex of the *N*-phenylporphyrin is instead reduced by one electron, the Fe^{I} complex of the *N*-phenylporphyrin is formed reversibly at fast scan rates.**[1646]** However, it slowly converts back to the σ-phenyl complex of the Fe^{III} porphyrin by phenyl migration from nitrogen to iron. This $PFe^{III}(\sigma\text{-Ph})$ can be reduced reversibly to the corresponding $[PFe^{II}(\sigma\text{-Ph})]^-$ complex,**[1646]** as mentioned in Section 6.3.14.) Phenyl migration from Fe^{IV} to a porphyrin nitrogen, which produces a green pigment, is known to occur under aerobic conditions in protein systems such as cytochrome P450, catalase, hemoglobin, or myoglobin.**[1648,1649]** The phenyl heme is also produced by attack of aryl hydrazines in the presence of oxygen,**[1650,1651]** and probably goes through a phenyl Fe^{IV} intermediate. These *N*-arylporphyrin complexes of iron, and their *N*-alkyl counterparts, are readily demetallated, leading to destruction of function of the heme protein.**[1651]**

Reactions of high-valent iron porphyrins with a number of other reagents besides aryl hydrazines lead to so-called ‘suicide inactivation’ of the catalyst, and similar reactions are known to inactivate cytochromes P450. One example is the suicide inactivation by terminal alkenes, which can either react with the Compound I-level ferryl species to produce epoxides, or can react with one of the porphyrin nitrogens to produce *N*-alkyl–O–Fe (N–C–C–O–Fe) metallacyclic hemins.**[1652,1653]** Loss of iron yields *N*-hydroxyethylporphyrins.**[1652,1654]** *N*-Alkyl metalloporphyrins can be dealkylated by nucleophiles, such as di-*n*-butylamine.**[1655]** An antibody specific for *N*-methylmesoporphyrin IX binds iron(III) mesoporphyrin IX and the resulting complex has peroxidase activity toward typical HRP substrates (pyrogallol, hydroquinone, *o*-dianisidine and 2,2′-azinobis(3-ethylbenzothiazoline-6-sulfonic acid), ABTS) in the presence of H_2O_2.**[1656]**

8.3 Iron(IV) Carbene Complexes

Porphyrinatoiron(IV) carbenes, including that resulting from the reaction of 1,1-bis(*p*-chlorophenyl)-2,2,2-trichloroethane (DDT),**[1588]** are produced by reaction of polyhalogenated hydrocarbons with PFe^{II} (equation 57):**[1588,1589]**

$$PFe^{II} + RR'CX_2 \xrightarrow[-2X^-]{+2e^-} PFe^{II}(CRR') \qquad (57)$$

It has been shown that these carbenes can insert into $Fe–N_{por}$ bonds to form vinylidine (*N*-alkyl–iron porphyrin metallacycle (N–C–C–Fe)) complexes,**[1590–1593]** which can then go on to form *cis*-bridged vinylidines of the porphyrin,**[1594]** with loss of iron. Carbene equivalents of iodosylbenzene can also react with iron porphyrins to give five-membered Fe–O–C–C–N metallocycles.**[661]** Iron porphyrin carbenes can also react with amines to produce the isocyanide complexes (equation 58):**[1595]**

$$PFeCCl_2 + 2RNH_2 \longrightarrow PFe(CNR)(RNH_2) + 2HCl \qquad (58)$$

As mentioned above, $TPPFe^{II}$ complexes have been reported to be active catalysts for the cyclopropanation of alkenes with ethyldiazoacetate. The active species in such carbon transfer reactions are assumed to be iron porphyrin carbene complexes of the general formula TPPFe=CHR.[593–596] Species such as TPPFe($CHCO_2Et$) have been proposed, but thus far have not been observed directly because of their high reactivity. However, remarkably stable arylcarbene or (alkoxycarbonyl)carbene porphyrin complexes are formed when the electron-deficient iron complex of *meso*-tetrakis(pentafluoro)porphyrinato dianion [Fe(TPFPP)C(Ph)R] is reacted with diazo compounds N≡N–C(Ph)R with R = Ph, CO_2Et, and $CO_2CH_2CH=CH_2$.[596] In contrast to the carbene complex [TPPFe(CCl_2)],[1588] only one of these complexes, namely the [Fe(TPFPP)(CPh_2)] porphyrin, reacted with N-methylimidazole to form the six-coordinate diamagnetic complex [Fe(TPFPP)(CPh_2)(N-MeIm)], which is unstable in moist air, suggesting that the addition of the imidazole ligand destabilizes the Fe=CPh_2 bond. The other two complexes did not add N-MeIm or pyridine. Pyridine could also not be added to the [Fe(TPFPP)(CPh_2)] compound. Prolonged reaction with pyridine led to the formation of the [TPFPPFe$(Py)_2$] complex reported originally by Therien.[621] The crystal structures for [Fe(TPFPP)(CPh_2)] and the N-methylimidazole complex were obtained and reveal Fe=CPh_2 bond lengths of 1.767 and 1.827 Å, respectively and Fe–N_{por} bond lengths ranging from 1.96 to 1.98 Å with very large ruffling of the porphyrin core.[596] Of the four carbene complexes synthesized two, [Fe(TPFPP)(CPh_2)CO_2Et] and [Fe(TPFPP)(CPh_2)(N-MeIm)], reacted with styrenes to form cyclopropanes, and with cyclohexene and cumene to form benzylic C-H insertion products. Kano *et al.*[1657] have also shown that reduction of alkenes and alkynes by the BH_4^- anion are mediated by iron porphyrins. It was assumed that as intermediates in these reactions (σ-alkyl) iron^{II} and iron^{III} porphyrins were formed. It was also shown that the addition of thiophenol or other thiols to styrenes or other alkenes was catalyzed by iron(II) porphyrins, for example the complex of protoporphyrin IX dianion. The reaction mechanisms were proposed to proceed via (σ-alkyl)iron(II) porphyrins, which may act as nucleophiles.[1657]

8.4 Iron(IV) Hydrazine Complexes

Hydrazines, such as 1-amino-2,2,6,6-tetramethylpiperidine or phenylhydrazine, in the presence of either dioxygen or one equivalent of iodosylbenzene react with PFe^{III} to give the corresponding nitrene complexes, PFe(NNR_2),[1658,1659] which, in the presence of limited amounts of O_2, react to give σ-alkyl or σ-aryl Fe^{III} complexes.[1659] Similarly, activated nitrogen atoms, such as the imide analogs of iodosylbenzene, PhI=NNR_2, react to form the corresponding nitrenes,[1660] which can insert into a Fe–N_{por} bond to give a Fe−porphyrin−N-aziridine.[1661] Likewise, a side reaction of m-chloroperbenzoic acid with TMPFe^{III} is to insert oxygen into a Fe−N_{por} bond, producing an iron(III) porphyrin N-oxide.[1662]

8.5 Six-coordinate, Bis-methoxide Iron(IV) Porphyrins

As mentioned in Section 7 above, Groves and coworkers[209] have reported the valence isomerization of the Fe^{III} porphyrin π-cation radical in the presence of methoxide (equation 59):

$$\underset{(P^{-}\bullet)Fe^{III}}{[TMPFe(ClO_4)_2]} + 2OMe^- \longrightarrow \underset{(P^{2-})Fe^{IV}}{[TMPFe(OMe)_2]} + 2ClO_4^- \qquad (59)$$

8.6 Comparison of Iron(IV) Porphyrins and Iron(III) Porphyrin π-Cation Radicals

As concluded by Balch and Renner,[1587] axial ligands play a major role in determining the electronic distribution within highly oxidized iron porphyrins. It has been found that an oxo ligand, a phenyl ligand, or two methoxy ligands favor the Fe^{IV} porphyrin dianion structure, while halide ions, imidazole, or perchlorate ligands produce the Fe^{III} porphyrin π-cation radical monoanion electronic structure. The ability of the iron π electron to interact with the axial ligand(s) appears to make a major contribution to these differences. Density function calculation studies of one-electron oxidized mono- and difluoroiron(III) porphyrins have corroborated this conclusion by showing that for the six-coordinate difluoro complex, the Fe^{IV} ($S = 1$) state is stabilized relative to the Fe^{III} a_{2u} π-cation radical ($S = 3$) state, while for the monofluoro complex this ordering of states is reversed.[1663] A possible relationship between Fe^{III} spin state and the site of one-electron oxidation in iron(III) porphyrins is rationalized in terms of exchange energy stabilization and the σ- and π-donor properties of the axial ligand(s),[1663] in agreement with conclusions reached from experimental investigations.[1587]

9 IRON(IV) PORPHYRIN π-CATION RADICALS AND THEIR REACTIONS

As mentioned in Section 8, the green Compound I species observed in peroxidase enzymes, which contains a heme that is two oxidation levels above PFe^{III}, is believed to consist of a ferryl porphyrin radical, $[(P^-\cdot)\ (Fe^{IV}{=}O)]^+$; the Mössbauer spectrum of this species is consistent with a $S = 1$ ferryl center bound antiferromatically to the porphyrin radical,[1664] although in some cases (notably the cytochrome c peroxidases) it has been shown that the radical is located on a tryptophan residue near the heme center (W191), which gives rise to an intense axial[1665] radical signal at g = 2[1666] that is unlike the broadened radical signal reported for the porphyrin π-cation radical form of HRP Compound I (*see* ***Iron: Heme Proteins, Peroxidases, Catalases & Catalase-peroxidases***).[1664] The crystal structures of the resting state and Compound I forms of CCP have recently been reported,[1666] and although W191 is π-stacked with the

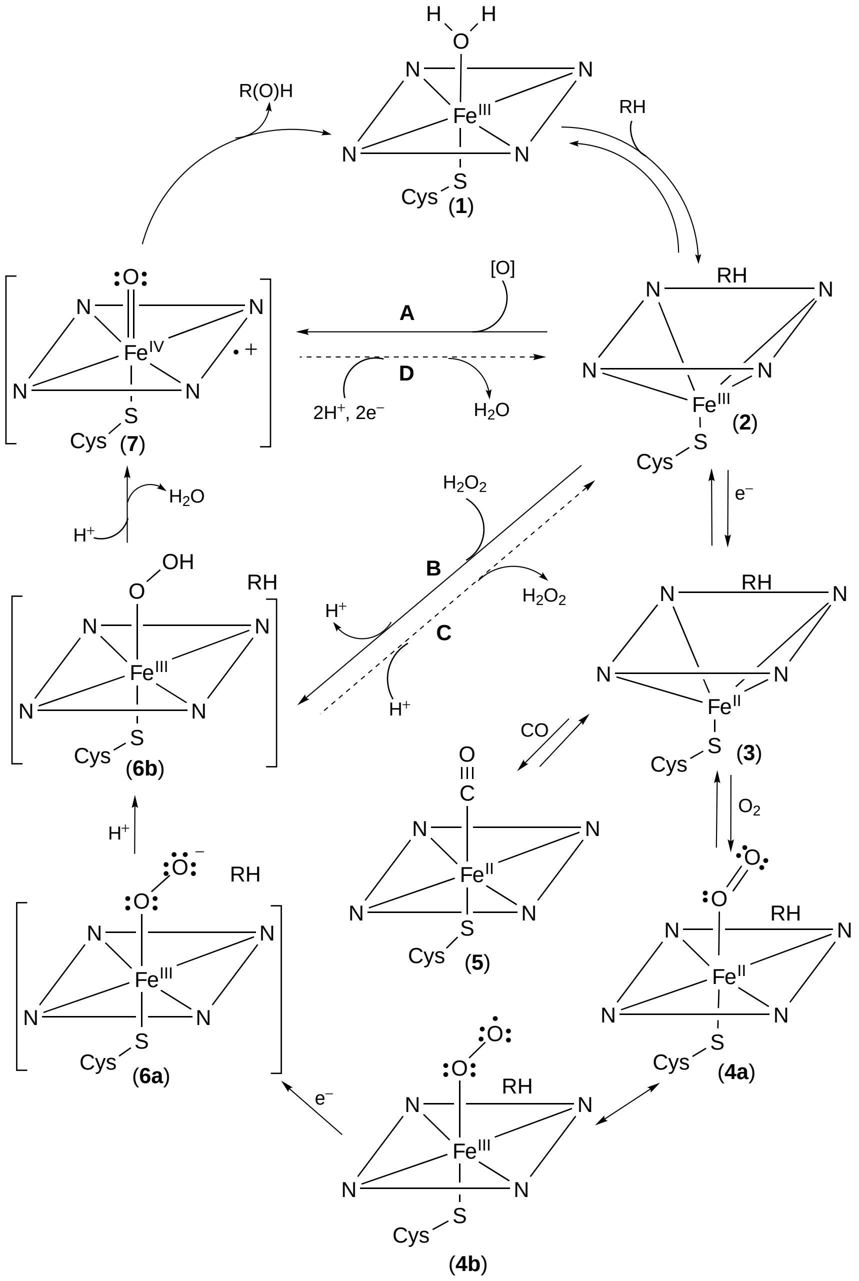

Figure 16 Intermediates involved in alkane oxidation by cytochrome P450.[27] Catalytic cycles involving either O_2 and electrons (from NADPH), or a single oxygen atom donor (AO) are shown. Model reactions often use single oxygen atom donors AO such as iodosylbenzene, amine *N*-oxides and organic or inorganic hydroperoxides or peroxy acids[32]

proximal histidine, H175,[1666] there is much less magnetic coupling between the tryptophan radical and the Fe(IV) center in CCP.[1665]

The same ferryl porphyrin radical, $[(P^{-}\cdot)\ (Fe^{IV}{=}O)]^{+}$, electronic structure is believed to exist for the activated oxygen-inserting species of cytochromes P450, although attempts to trap this species by freeze-quench experiments utilizing peroxyacetic acid on the timescale of 8 ms have invariably led to the observation of a tyrosyl radical of a nearby tyrosine side chain rather than the porphyrin radical.[1667,1668] Thus, the porphyrin π radical part of the ferryl porphyrin radical state of cytochromes P450, is a transient and very reactive species (either in the enzymes or in model hemes) and can readily insert the ferryl oxygen atom into many C–H bonds, epoxidize olefins, and carry out many other monooxygenase, epoxidase and dehalogenase reactions.[24–32,1596] The mechanism proposed for cytochrome P450 hydroxylations is shown in Figure 16. The same general mechanism is believed to be involved in the reactions of peroxidases, except that H_2O_2 reacts with PFe^{III}, rather than one-electron reduction of PFe^{III}, followed by O_2 binding, followed by one more one-electron reduction.

A number of theoretical calculations related to Compound I and II states and stereoselectivity of oxo-transfer reactions have been reported,[225,1669–1678] and the role of the heme active site and protein environment in structure, spectra, and function of the cytochromes P450 from a theoretical point of view has been reviewed more recently.[1679] Theoretical calculations of the electron configuration of the compound I state have suggested that instead of being porphyrin-based, the radical is thiolate-based,[1680–1684] and possible roles for a higher-spin state ($S = 3/2$)[1680,1682–1684] and either a saddle[1685] or ruffle[1686] distortion of the porphyrin ring have been proposed, especially with regard to the oxygen rebound mechanism of Groves and coworkers,[1687–1693] but not in the case of benzene hydroxylation.[1694] Alternatively, other recent work suggests the possibility of two different electrophilic pathways.[1695–1697] The role of protonation of the peroxide species in producing Compound I of both P450s and peroxidases has also been studied theoretically; it has been shown that for P450s, single protonation of the distal (terminal) oxygen of the bent Fe^{III}–O–O^- unit results in significant weakening of the O–O bond, and that addition of a second proton to the same oxygen leads directly to Compound I and water as products,[1698,1699] while a series of events involving deprotonation of the proximal oxygen of hydrogen peroxide and then donation of the proton back to the other (distal) oxygen atom, then leading to the same products as for P450s are involved for peroxidases.[1700–1702] The multiplicity of reaction pathways of the Fe^{III}-hydroperoxo species is shown by DFT calculations that indicate there are four low-energy epoxidation pathways for the Fe^{III}-hydroperoxo complex, in which the species transfers oxygen to olefins either from the proximal or the distal oxygen atoms, in both concerted and stepwise manners.[1703] However, the barriers of these four pathways, $37-53\,\text{kcal mol}^{-1}$, are too high in comparison with the $14\,\text{kcal mol}^{-1}$ observed for epoxidation by Compound I. Therefore, Fe^{III}-hydroperoxo, as such, cannot be the second oxidant in epoxidation reactions, in line with its significant basicity and poor electron-accepting capability.[1703] Further work on this system has resulted in the conclusion that ‘Compound I is a chameleon oxidant that tunes its reactivity and selectivity patterns in response to the protein environment in which it is accommodated’.[1704,1705] This appears to be true for both cytochromes P450 and horseradish peroxidase.[1706] Calculations have also suggested that the radical of catalase Compound I is not located on the proximal tyrosine.[1707] Experimental evidence of alternative pathways of reactivity of these Compound I species has been reported.[1708–1711]

A number of research groups have investigated the NMR, EPR, Mössbauer, and resonance Raman spectra of model complexes of this reactive species.[212,214–217,1618–1656,1588–1595,1657–1713] Resonance Raman spectra have diagnostic bands for Fe=O ($828\,\text{cm}^{-}1$) in the Compound I species.[1714,1715] Weiss, Gold, and coworkers[218,219,1716] have also generated oxoferrylporphyrin radicals by m-chloroperoxybenzoic acid oxidation of the chloro- and trifluoromethanesulfonato complexes of [$TMPFe^{III}$] and the trifluoromethanesulfonato complex of tetrakis(2,6-dichlorophenyl)porphinatoiron(III), [$(2,6\text{-}Cl_2)_4TPPFe^{III}$] or [$DCPFe^{III}$], and tetrakis(2,4,6-trimethoxyphenyl)porphinatoiron(III), [$TTMPPFe^{III}$], and have characterized them by EPR, Mössbauer, resonance Raman, and UV–visible spectroscopy. In all but three cases,[213,1717] ‘hindered’ or ‘protected’ porphyrins, such as those mentioned above plus 2,7,12,17-tetramethyl-3,8,13,18-tetramesityl-porphyrin (TMTMP)[216] and tetrakis(2,6-difluorophenyl)porphyrin ($(2,6\text{-}F_2)_4TPP$),[210] were used to elucidate the spectroscopic properties of the π-cation radicals of PFe^{IV}=O. In the case of the TMP complexes it was found that the porphyrin radical is of the $3a_{2u}(\pi)$ type (Figure 4), since large π spin delocalization is detected at the *meso*-phenyl-H and –CH_3 positions, as well as a smaller amount of π spin delocalization at the β-pyrrole positions.[214,228] However, the TMTMP complex has an unpaired $a_{1u}(\pi)$ electron, since the very large pyrrole CH_3 isotropic shift indicates large spin delocalization to the pyrrole positions in this case.[216,228] In comparison, pyrrole-CH_3 and *meso*-H shifts for the ferryl complex of protohemin are 4 and 16 ppm, respectively.[213] The $[TMPFe^{IV}{=}O]^+$ complex has been characterized by MCD spectroscopy.[1718] Horseradish peroxidase Compound I has been assigned as an $a_{2u}(\pi)$ radical, while catalase Compound I is believed to be an $a_{1u}(\pi)$ radical,[1719,1720] and cytochrome c peroxidase Compound I is believed to have a tryptophan rather than a porphyrin π-cation radical,[1665] as mentioned above. Compound I and II analogs have also been created from iron(III) porpholactones.[1721]

The most important property of the model hemes of Compound I oxidation level is their ability to act as catalysts for the hydroxylation of unactivated hydrocarbons,[1630,1631,1722–1726,1717,1727–1733] epoxidation of alkenes,[212,1631,1734–1760] and aromatization of partially unsaturated rings.[1761] Not only iron porphyrins, but also cobalt, manganese, and chromium porphyrins will carry out these reactions.[26,1596,1729,1759,1760,1762,1763] Porphyrin substituents play a role in determining the reactivities of these high-valent species, and it has been shown that oxo-iron porphyrins having electron-withdrawing substituents rapidly epoxidize olefins, that high-valent iron oxo complexes of electron-deficient porphyrin ligands are more powerful oxidizing species than are those of electron-rich porphyrin ligands in alkane hydroxylation reactions, and the presence of electron-donating substituents on a porphyrin ligand gives a relatively high ^{18}O incorporation from labeled $H_2\ {}^{18}O$ into an oxygenated product when a mixture of olefin and $H_2\ {}^{18}O$ is added to a reaction solution containing a high-valent iron oxo intermediate, whereas only a small amount of ^{18}O incorporation is observed with iron porphyrin complexes containing electron-withdrawing substituents.[1764] Structure-reactivity studies of olefin epoxidation indicate that the oxene is formed exclusively via a heterolytic mechanism, and provide evidence for continual changes in transition-state structure rather than a change of mechanism from heterolysis with peracids to homolysis with hydroperoxides, as had previously been proposed.[1765] A highly electron-deficient iron porphyrinate, having four CF_3 groups on two opposite pyrrole rings, was found to be unstable with respect to decomposition, and hence not suitable for use as an oxidation catalyst.[501] Highly halogenated porphyrins[405–409,1766,1767] produce quite robust catalysts that allow many catalytic turnovers before degradation. High degrees of regio- and enantioselectivity can be obtained,[1762,1766] and the adsorption,[1759] intercalation,[1759] or covalent attachment[1760] of these catalysts to various mineral supports offers the possibility of yet more robust and selective catalysts.

A study of isobutane oxidation using O_2 as the sole oxidant by three highly halogenated porphyrin complexes, $(C_6F_5)_4PFe$, $Br_8(C_6F_5)_4PFe$, and $(C_3F_7)_4PFe$, has produced interesting findings that relate to the mechanism of this reaction.[1768,1769] It was found that the nature and distribution of hydrocarbon oxidation products show that an autoxidation reaction pathway dominates the reaction kinetics, consistent with a radical chain process. For each catalytic system examined, PFe^{II} species were shown not to be stable under moderate O_2 pressure at 80 °C; in every case, the PFe^{II} catalyst precursor was converted quantitatively to high-spin PFe^{III} complexes prior to the observation of any hydrocarbon oxidation products.[1769] Once catalytic isobutane oxidation is initiated, all reactions are marked by concomitant decomposition of the porphyrin-based catalyst, even including $Br_8(C_6F_5)_4PFe$-based catalysts, which lack macrocycle C-H bonds, do not exhibit augmented stability with respect to analogous catalysts based on $(C_6F_5)_4PFe$ and $(C_3F_7)_4PFe$ species.[1769] The data presented are consistent with a hydrocarbon oxidation process in which PFe complexes play dual roles of radical chain initiator and the species responsible for the catalytic decomposition of organic peroxides. This modified Haber-Weiss reaction scheme provides for the decomposition of *tert*-butyl hydroperoxide intermediates via reaction with PFe-OH complexes: the PFe^{III} species responsible for hydroperoxide decomposition are regenerated by reaction of PFe^{II} with dioxygen under these experimental conditions.[1769]

Photoactivation of polyhalogenated porphyriniron(III)–hydroxo complexes with light of wavelengths between 350 and 450 nm has been shown to allow oxidation by O_2 without consumption of a reducing agent.[1770] MP8 can also generate ferryl and π-cation radical species upon photoinduced oxidation.[1771]

Other related reactions of these high-valent species include cyclopropanation of alkenes,[1772–1776] oxidation of benzyltrialkylstannanes,[1777] dehydration of aldoximes,[1778] and olefination of aldehydes and ketones.[1779–1781] Mechanisms of reaction of the $[PM{=}O]^+$ species are believed to involve the intermediates proposed in Figure 16.[32,1679] The manganese complexes are the most active catalysts.[1782,1783]

Usually, Lewis bases that might act as sixth ligands for the $(P^{-}\bullet)\ Fe^{IV}{=}O$ active species have not been explicitly provided in these catalytic reactions. However, the nature and possible role of the sixth ligand is finally becoming recognized as being important in the activity of the oxotransferase model catalysts, as it has been for some time for the proteins.[36,1784,1785] As suggested in Figure 17 the thiolate ligand of cytochromes P450 is believed to aid in cleavage of the O–O bond by 'pushing' electron density on to the metal, while the histidine ligand of horseradish peroxidase is believed to need assistance from a distal hydrogen-bonding framework to cleave the O–O bond by 'pulling' on the terminal oxygen.[36] In view of these considerations, catalysis of hydroxylation and epoxidation reactions of model hemes by peroxide-containing oxidants might be expected to have enhanced rates of reaction in the presence of suitable Lewis bases. Anionic axial ligands of $TMPFe^{III}$ have a marked influence on the formation of oxoiron(IV) porphyrin intermediates in their reactions with PhIO and *m*-CPBA; anions of good electron-donating ability (Cl^-, F^-, $CH_3CO_2{}^-$ and OH^-) increased the tendency to form the high-valent oxoiron(IV) porphyrin intermediates over those of poor electron-donating ability ($CF_3SO_3{}^-$, $ClO_4{}^-$, and $NO_3{}^-$).[1786,1787]

In line with the above hypothesis, Momenteau and coworkers[1788] showed that with a proximal imidazole ligand, Fe and Mn hanging-base porphyrins, in the presence of H_2O_2, will carry out both epoxidation and dismutation (of H_2O_2) reactions, while with a phenolate proximal ligand, dismutation of H_2O_2 is favored by the Mn porphyrin, and is the exclusive reaction of the Fe porphyrin. Furthermore, Bruice and coworkers have shown that addition of small concentrations of NH_3 or $CF_3CH_2NH_2$ enhances

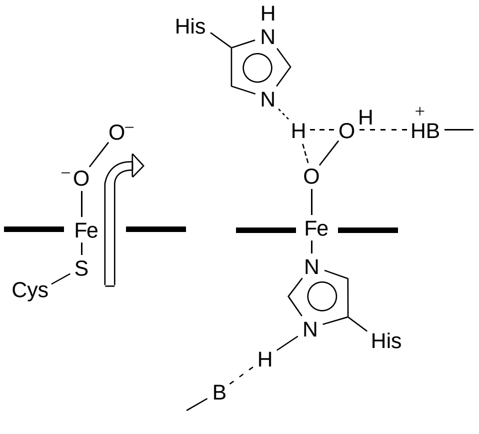

Figure 17 A schematic view of the involvement of axial ligands and distal residues in the 'push–pull' mechanism for O–O bond cleavage of an iron-bound peroxide in thiolate-ligated (left) and histidine-ligated (right) systems such as cytochrome P450 and horseradish peroxidase, respectively[36]

the reaction of water-soluble Fe^{III} porphyrins with *t*-BuOOH by a factor of about 100 over that observed in water, while addition of imidazole did not produce a rate enhancement.**1433** (However, reaction of water-soluble Mn^{III} porphyrins with methyl diphenylhydroperoxyacetate showed 100-fold rate inhancements in the presence of imidazole.**1789**) The proposed kinetic scheme for the *t*-BuOOH reactions depends upon the ability to form mono-nitrogen base complexes, $PFe^{III}(H_2O)(L)$ or $PFe^{III}(OH)(L)$, since the bis-ligand complexes, $PFe^{III}(L)_2$, were shown to be unreactive with *t*-BuOOH.**1433** The observed lack of rate enhancement for the reaction in the presence of small concentrations of ImH is thus undoubtedly due to the overwhelming stability of the bis-imidazole complex over the mono-imidazole complex ($K_1 = (1–5) \times 10^3\,M^{-1}$; $\beta_2 = (5–8) \times 10^8\,M^{-2}$) compared to the bis-ammonia complex over the mono-ammonia complex ($K_1 = (0.1–1.5) \times 10^2\,M^{-1}$; $\beta_2 = (4.4–8.4) \times 10^4\,M^{-2}$).**1433** Morishima and coworkers have also shown that addition of one equivalent of imidazole to an acylperoxoiron(III) porphyrin in methylene chloride at −80 °C produces heterolytic cleavage to the corresponding oxoferryl porphyrin π-cation radical, $(P^{-}\bullet)Fe^{IV}{=}O$, while the same reaction in toluene solution shows little or no heterolysis; however, at higher temperatures (−40 to −6 °C), homolytic cleavage occurs to form the oxoferryl porphyrin ($PFe^{IV}{=}O$) and some iron(III) porphyrin *N*-oxide.**1790** Presumably the apparent change in mechanism is due to the suppression of formation of ionic species (the oxoferryl porphyrin π-cation radical) in toluene, leaving homolytic cleavage as the only (but less favorable) reaction. In the absence of imidazole, both reactions, but especially that in methylene chloride, are slowed.**1790** Dimethyldioxirane is also an effective oxidant.**1791**

10 IRON(V) PORPHYRINS

True high-valent iron porphyrins with the formal iron oxidation state +5 are rare, although complexes have been reported as Compound I intermediates of the heme proteins catalases and peroxidases and their model complexes.**1792** However, as suggested by Dey and Ghosh,**1792** some of these complexes are not true Fe(V) complexes, but are better described as oxoiron(IV) π-cation radical species with the radical either residing on the porphyrin or the axial ligand or being delocalized into porphyrin or ligand orbitals. For example, the perferryl complex $PFe(O)(OCH_3)$ described by Morishima *et al.***1793,1794** is, according to theoretical calculations, not a true Fe(V) species, but rather contains a ferryl unit coordinated to a methoxy radical.**1795** Spectroscopic studies of heme-peroxidases agree with this finding and show that the catalytically relevant species is not an (oxo)iron(V) complex, but that both the metal and the porphyrin ligand are oxidized, resulting in an (oxo)iron(IV) and a porphyrin π-cation radical. Among the true Fe(V) porphyrins with a $S = 3/2$ ground state and an assumed electron configuration of $(d_{xy})^1(d_{yz})^1(d_{xz})^1$ are the nitrido iron species reported by Wagner and Nakamoto**1796,1797** and the complex described by Nanthakumar and Goff.**1717** The Fe(V) nitrido complexes, which were synthesized at 30 K by laser irradiation of the azide coordinated TPPFe(III) or OEPFe(III) compounds, are very unstable, exhibit a Resonance Raman band at 876 cm^{-1} for the Fe–N stretching frequency, and according to DFT calculations**1792** have a Fe–N bond length of 1.722 Å that is slightly longer than the $Fe^{IV}{=}O$ ferryl bond in oxo porphyrin π-cation radical species. The Fe^{V} porphyrin described by Nanthakumar and Goff**1717** bears electronegative fluorine substituents on the phenyl rings and was obtained by using strong oxidizing agent *m*-chloroperbenzoic acid. A red complex was produced with a Soret band at 430 nm and visible band at 550 nm, similar to those of $PFe^{IV}O$ complexes,**97,218** but with different NMR and EPR spectra. The pyrrole-^{2}H signal was observed at +1.3 ppm at 210 K. The EPR spectrum at moderate temperatures ($g = 4.38$, 3.11, and 2.70, plus a $g = 2$ radical signal from decomposition products) is described to be indicative of a $S = 3/2$ species, rather than a $S = 1\ Fe^{IV}/S = 1/2$ porphyrin radical species, which is expected to be EPR silent above ≈5 K.**1717**

11 RELATED ARTICLES

Ammonia & N-donor Ligands; Coordination & Organometallic Chemistry: Principles; Cytochrome Oxidase; Dioxygen & Related Ligands; Electrochemistry: Applications in Inorganic Chemistry; Electron Transfer in Coordination Compounds; Electron Transfer Reactions: Theory; Iron: Heme Proteins & Dioxygen Transport & Storage; Iron: Heme Proteins & Electron Transport; Iron: Heme Proteins, Mono- & Dioxygenases; Iron: Heme Proteins, Peroxidases, Catalases & Catalase-peroxidases; Ligand Field Theory & Spectra; Long-range Electron Transfer in Biology; Magnetism of Transition Metal Ions; Molecular Orbital Theory; Nitrogen Monoxide (Nitric Oxide): Bioinorganic Chemistry; Oxygen: Inorganic Chemistry; Photochemistry of Transition Metal Complexes; Photosynthesis; S-donor Ligands; Stability Constants & their Determination.

12 REFERENCES

1. M. F. Perutz, G. Fermi, B. Luisi, B. Shaanan, and R. C. Liddington, *Acc. Chem. Res.*, 1987, **20**, 309.
2. S. Iwata, C. Ostermeier, B. Ludwig, and H. Michel, *Nature*, 1995, **376**, 660.

3. T. Tsukihara, H. Aoyama, E. Yamashita, T. Tomizaki, H. Yamaguchi, K. Shinzawa-Itoh, R. Nakashima, R. Yaono, and S. Yoshikawa, *Science*, 1995, **269**, 1069.
4. R. Gennis and S. Ferguson-Miller, *Science*, 1995, **269**, 1063.
5. T. Tsukihara, H. Aoyama, E. Yamashita, T. Tomizaki, H. Yamaguchi, K. Shinzawa-Itoh, R. Nakashima, R. Yaono, and S. Yoshikawa, *Science*, 1996, **272**, 1136.
6. E. Wallin, T. Tsukihara, S. Yoshikawa, G. Heijne, and A. Elofsson, *Protein Sci.*, 1997, **6**, 808.
7. D. Xia, C.-A. Yu, H. Kim, J.-Z. Xia, A. M. Kachurin, L. Zhang, L. Yu, and J. Deisenhofer, *Science*, 1997, **277**, 60.
8. S. Iwata, J. W. Lee, K. Okada, J. K. Lee, M. Iwata, B. Rasmussen, T. A. Link, S. Ramaswamy, and B. K. Jap, *Science*, 1998, **281**, 64.
9. Z. Zhang, L. Huang, V. M. Shulmeister, Y.-I. Chi, K. K. Kim, L.-W. Hung, A. R. Crofts, E. A. Berry, and S.-H. Kim, *Nature*, 1998, **392**, 677.
10. H. Sigel and A. Sigel eds, 'Metal Ions in Biological Systems', Vol. 27, Electron Transfer Reactions in Metalloproteins, Marcel Dekker, New York, 1991.
11. W. A. Cramer, M. T. Black, W. R. Widger, and M. E. Girvin, in 'The Light Reactions', ed. J. Barber, Elsevier, Amsterdam, 1987, p. 447.
12. S. de Vries and C. A. M. Marres, *Biochim. Biophys. Acta*, 1987, **895**, 205.
13. P. N. Furbacher, M. E. Girvin, and W. A. Cramer, *Biochemistry*, 1989, **28**, 8990.
14. J. C. Salerno, B. Bolgiano, R. K. Poole, R. B. Gennis, and W. J. Ingledew, *J. Biol. Chem.*, 1990, **265**, 4364.
15. C. Breyton, *Biochim. Biophys. Acta*, 2000, **1459**, 467.
16. D. Zannoni, *Biochim. Biophys. Acta*, 1989, **975**, 299.
17. H. Michel and J. Deisenhofer, *Biochemistry*, 1988, **27**, 1.
18. R. Huber, *Eur. J. Biochem.*, 1990, **187**, 283.
19. C. R. D. Lancaster, A. Kröger, M. Auer, and H. Michel, *Nature*, 1999, **402**, 377.
20. C. R. D. Lancaster, *Biochim. Biophys. Acta*, 2002, **1553**, 1.
21. R. S. Lemos, A. S. Fernandes, M. M. Pereira, C. M. Gomes, and M. Teixeira, *Biochim. Biophys. Acta*, 2002, **1553**, 158.
22. M. Jormakka, S. Törnroth, B. Byrne, and S. Iwata, *Science*, 2002, **295**, 1863.
23. V. Yankovskaya, R. Horsefield, S. Törnroth, C. Luna-Chavez, H. Miyoshi, C. Léger, B. Byrne, G. Cecchini, and S. Iwata, *Science*, 2003, **299**, 700.
24. P. R. Ortiz de Montellano ed., 'Cytochrome P-450, Structure, Mechanism and Biochemistry', Plenum Press, New York, 1986.
25. P. R. Ortiz de Montellano, *Acc. Chem. Res.*, 1987, **20**, 289.
26. M. J. Gunter and P. Turner, *Coord. Chem. Rev.*, 1991, **108**, 115.
27. D. Mansuy and P. Battioni, in 'Bioinorganic Catalysis', ed. J. Reedijk, Marcel Dekker, New York, 1993, p. 395.
28. G. T. Miwa and A. Y. H. Lu, in 'Cytochrome P-450, Structure, Mechanism and Biochemistry', ed. P. R. Ortiz de Montellano, Plenum Press, New York, 1986, p. 77.
29. P. R. Ortiz de Montellano, in 'Cytochrome P-450, Structure, Mechanism and Biochemistry', ed. P. R. Ortiz de Montellano, Plenum Press, New York, 1986, p. 217.
30. M. R. Waterman, M. E. John, and E. R. Simpson, in 'Cytochrome P-450, Structure, Mechanism and Biochemistry', ed. P. R. Ortiz de Montellano, Plenum Press, New York, 1986, p. 345.
31. P. R. Ortiz de Montellano ed., 'Cytochrome P450: Structure, Mechanism and Biochemistry', 2nd edn., Plenum, New York, 1995.
32. M. Sono, M. P. Roach, E. D. Coulter, and J. H. Dawson, *Chem. Rev.*, 1996, **96**, 2841.
33. P. R. Ortiz de Montellano, *Acc. Chem. Res.*, 1998, **31**, 543.
34. P. R. Ortiz de Montellano and A. Wilks, *Adv. Inorg. Chem.*, 2000, **51**, 359.
35. L. J. Marnett, P. Weller, and J. R. Battista, in 'Cytochrome P-450, Structure, Mechanism and Biochemistry', ed. P. R. Ortiz de Montellano, Plenum Press, New York, 1986, p. 29.
36. J. H. Dawson, *Science*, 1988, **240**, 433.
37. F. Cui, D. Dolphin, T. Wijesekera, R. Farrell, and P. Skerker, in 'Biotechnology in Pulp and Paper Manufacture', eds. T. K. Kirk and H.-M. Chang, Butterworth-Heinmann, Boston, MA, 1990.
38. L. P. Solomonson and M. J. Barber, *Annu. Rev. Plant Physiol. Plant Mol. Biol.*, 1990, **41**, 225.
39. O. Einsle, A. Messerschmidt, P. Stach, G. P. Bourenkov, H. D. Bartunik, R. Huber, and P. M. H. Kroneck, *Nature*, 1999, **400**, 476.
40. O. Einsle, P. Stach, A. Messerschmidt, J. Simon, A. Kröger, R. Huber, and P. M. H. Kroneck, *J. Biol. Chem.*, 2000, **275**, 39608.
41. D. E. McRee, D. C. Richardson, J. S. Richardson, and L. M. Siegel, *J. Biol. Chem.*, 1986, **261**, 10277.
42. B. R. Crane, L. M. Siegel, and E. D. Getzoff, *Science*, 1995, **270**, 59.
43. J. H. Enemark and C. G. Young, *Adv. Inorg. Chem.*, 1993, **40**, 1.
44. C. Kisker, H. Schindelin, A. Pacheco, W. Wehbi, R. M. Garrett, K. V. Rajagopalan, J. H. Enemark, and D. C. Rees, *Cell*, 1997, **91**, 973.
45. M. A. Gilles-Gonzalez, G. Ditta, and D. R. Helinski, *Nature*, 1991, **350**, 170.
46. M. A. Gilles-Gonzalez and G. Gonzalez, *J. Biol. Chem.*, 1993, **268**, 16293.
47. M. A. Gilles-Gonzalez, G. Gonzalez, M. F. Perutz, L. Kiger, M. Marden, and C. Poyart, *Biochemistry*, 1994, **33**, 8067.
48. W. Gong, B. Hao, and M. K. Chan, *Biochemistry*, 2000, **39**, 3955.

49. H. Park, C. Suquet, J. D. Satterlee, and C. Kang, *Biochemistry*, 2004, **43**, 2738.
50. K. A. White and M. A. Marletta, *Biochemistry*, 1992, **31**, 6627.
51. J.-P. Renaud, J.-L. Boucher, S. Vadon, M. Delaforge, and D. Mansuy, *Biochem. Biophys. Res. Commun.*, 1993, **192**, 53.
52. W. K. Alderton, C. E. Cooper, and R. G. Knowles, *Biochem. J.*, 2001, **357**, 593.
53. B. R. Crane, A. S. Arvai, D. K. Ghosh, C. Wu, E. D. Getzoff, D. J. Stuehr, and J. A. Tainer, *Science*, 1998, **279**, 2121.
54. C. S. Raman, H. Li, P. Martásek, V. Král, B. S. S. Masters, and T. L. Poulos, *Cell*, 1998, **95**, 939.
55. J. M. C. Ribeiro, J. M. H. Hazzard, R. Nussenzveig, D. E. Champagne, and F. A. Walker, *Science*, 1993, **260**, 539.
56. F. A. Walker and W. R. Montfort, The Nitric Oxide-Releasing Heme Proteins from the Saliva of the Blood-Sucking Insect *Rhodnius prolixus*, in 'Advances in Inorganic Chemistry', eds. A. G. Mauk and A. G. Sykes, Academic Press, San Diego, CA, 2001, Vol. 51, Chap. 5, p. 295.
57. F. A. Walker, *J. Inorg. Biochem.*, 2005, **99**, 216.
58. J. S. Stamler, D. J. Singel, and J. Loscalzo, *Science*, 1992, **258**, 1898; S. H. Snyder, *Science*, 1993, **257**, 494.
59. A. M. Stolzenberg, S. H. Strauss, and R. H. Holm, *J. Am. Chem. Soc.*, 1981, **103**, 4763.
60. J. A. Berzofsky, J. Peisach, and W. E. Blumberg, *J. Biol. Chem.*, 1971, **246**, 3367.
61. M. J. Chatfield, G. N. La Mar, A. L. Balch, and J. T. J. Lecomte, *Biochem. Biophys. Res. Commun.*, 1986, **135**, 309.
62. M. M. Chatfield, G. N. La Mar, J. T. J. Lecomte, A. L. Balch, K. M. Smith, and K. C. Langry, *J. Am. Chem. Soc.*, 1986, **108**, 7108.
63. M. J. Chatfield, G. N. La Mar, and R. J. Kauten, *Biochemistry*, 1987, **26**, 6939.
64. M. J. Chatfield, G. N. La Mar, K. M. Smith, H.-K. Leung, and R. K. Pandey, *Biochemistry*, 1988, **27**, 1500.
65. M. J. Chatfield, G. N. La Mar, W. O. Parker, K. M. Smith, H.-K. Leung, and I. K. Morris, *J. Am. Chem. Soc.*, 1988, **110**, 6352.
66. L. L. Bondoc, M.-H. Chau, M. A. Price, and R. Timkovich, *Biochemistry*, 1986, **25**, 8458.
67. S. Licoccia, M. J. Chatfield, G. N. La Mar, K. M. Smith, K. E. Mansfield, and R. R. Anderson, *J. Am. Chem. Soc.*, 1989, **111**, 6087.
68. K. M. Barkigia, C. K. Chang, J. Fajer, and M. W. Renner, *J. Am. Chem. Soc.*, 1992, **114**, 1701.
69. B. Kräutler, *Chimia*, 1987, **41**, 277; B. Kräutler and S. Ostermann, 'Structure, Reactions and Function of B_{12} and B_{12}-Proteins, in The Porphyrin Handbook', eds. K. M. Kadish, K. M. Smith, and R. Guilard, Academic Press, San Diego, CA, 2003, Vol. 11, p. 229.
70. K. Kadono, K. Hori, K. Fukuda, H. Inoue, T. Shirai, and E. Fluck, *Inorg. Chim. Acta*, 1992, **201**, 213.
71. Y. Nakamura, A. Murakami, K. Koshimizu, and H. Ohigashi, *Biosci. Biotechnol. Biochem.*, 1996, **60**, 1028.
72. S. Hortensteiner, *Cell. Mol. Life Sci.*, 1999, **56**, 330.
73. P. Wongsinkongman, A. Brossi, H. K. Wang, K. F. Bastow, and K. H. Lee, *Bioorg. Med. Chem.*, 2002, **10**, 583.
74. A. Eschenmoser, *Angew. Chem., Int. Ed. Engl.*, 1988, **27**, 6.
75. J. R. Roth, J. G. Lawrence, and T. A. Bobik, *Annu. Rev. Microbiol.*, 1996, **50**, 137.
76. R. Banergee, 'Chemistry and Biochemistry of B_{12}', Wiley, New York, 1999.
77. E. N. G. Marsh, *Essays Biochem.*, 1999, **34**, 139.
78. A. R. Battersby, *Nat. Prod. Rep.*, 2000, **17**(6), 507.
79. R. Banergee and S. W. Ragsdale, *Annu. Rev. Biochem.*, 2003, **124**, 8974.
80. T. Toraya, *Chem. Rev.*, 2003, **103**, 2095.
81. D. P. Chimento, A. K. Mohanty, R. J. Kadner, and M. C. Weiner, *Nat. Struct. Biol.*, 2003, **10**, 394.
82. A. Pfaltz, B. Jaun, A. Fässler, A. Eschenmoser, R. Jaenchen, H. H. Gilles, G. Diekert, and R. K. Thauer, *Helv. Chim. Acta*, 1982, **65**, 828.
83. S. Ragsdale, Biochemistry of Methyl-CoM Reductase and Coenzyme F430, in 'The Porphyrin Handbook', eds. K. M. Kadish, K. M. Smith, and R. Guilard, Academic Press, San Diego, CA, 2003, Vol. 11, p. 205.
84. D. S. Morse, L. Fritz, and J. W. Hastings, *Trends Biochem. Sci.*, 1990, **15**, 262.
85. Z. J. Petryka and R. B. Howe, Historic and Clinical Aspects of Bile Pigments, in 'The Porphyrins', ed. D. Dolphin, Academic Press, New York, 1979, Vol. VI, p. 805.
86. L. Eales, Clinical Chemistry of the Porphyrins, in 'The Porphyrins', ed. D. Dolphin, Academic Press, New York, 1979, Vol. VI, p. 663.
87. J. B. Stanbury, J. B. Wyngarden, D. S. Fredrickson, J. L. Goldstein, and M. S. Brown eds, 'The Metabolic Basis of Inherited Disease', 5th edn., McGraw-Hill, New York, 1983.
88. N. A. McCarroll, *Anal. Chem.*, 1995, **67**, 425R.
89. A. Y. Louie and T. J. Maede, *Chem. Rev.*, 1999, **99**, 2711.
90. R. E. Dickerson and I. Geis, 'Hemoglobin: Structure, Function, Evolution, and Pathology', Benjamin/Cummings, Menlo Park, CA, 1982.
91. C. T. Noguchi and A. N. Schechter, *Annu. Rev. Biophys. Biophys. Chem.*, 1985, **14**, 239.
92. G. Stamatoyannopoulos, A. W. Niehaus, P. Leder, and P. W. Majerus eds, 'Molecular Basis of Blood Diseases', Saunders, New York, 1986.
93. R. B. Pegg, F. Shahidi, N. J. Gogan, and S. I. DeSilva, *J. Agric. Food Chem.*, 1996, **44**, 416.
94. B. Kurek, I. Artaud, B. Pollet, C. Lapierre, and B. Monties, *J. Agric. Food Chem.*, 1996, **44**, 1953.

95. B. Meunier and A. Sorokin, *Acc. Chem. Res.*, 1997, **30**, 470.
96. J. A. Perlinger, J. Buschmann, W. Angst, and R. P. Schwarzenbach, *Environ. Sci. Technol.*, 1998, **32**, 2431.
97. G. M. Keserü, G. Balogh, I. Czudor, T. Karancsi, A. Fehér, and B. Bertók, *J. Agric. Food Chem.*, 1999, **47**, 762.
98. J. Buschmann, W. Angst, and R. P. Schwarzenbach, *Environ. Sci. Technol.*, 1999, **33**, 1015.
99. M. Fukushima, A. Sawada, M. Kawasaki, H. Ichikawa, K. Morimoto, K. Tatsumi, and M. Aoyama, *Environ. Sci. Technol.*, 2003, **37**, 1031.
100. R. Lipson, E. Baldes, and A. Olson, *J. Natl. Cancer Inst.*, 1961, **26**, 1.
101. J. Winkelman, G. Slater, and J. Grossman, *Cancer Res.*, 1967, **27**, 2060.
102. M. D. Ogan, D. Revel, and R. C. Brasch, *Invest. Radiol.*, 1987, **22**, 822.
103. C. W. Chen, J. S. Cohen, C. E. Myers, and M. Sohn, *FEBS Lett.*, 1984, **168**, 70.
104. L. R. Huang, R. M. Straubinger, S. B. Kahl, M.-S. Koo, J. J. Alletto, R. Mazurchuk, R. I. Chau, S. L. Thamer, and R. J. Fiel, *J. Magn. Reson. Imaging*, 1993, **3**, 351.
105. J. Tibbitts, N. C. Sambol, J. R. Fike, W. F. Bauer, and S. B. Kahl, *J. Pharm. Sci.*, 2000, **89**, 469.
106. M. F. Hawthorne and M. W. Lee, *J. Neurol. Oncol.*, 2003, **62**, 33.
107. J. J. Schuitmaker, P. Baas, H. L. L. M. van Leengoed, F. W. van der Meulen, W. M. Star, and N. van Zandwijk, *J. Photochem. Photobiol. B, Biol.*, 1996, **34**, 3.
108. T. J. Dougherty, B. W. Henderson, S. Schuartz, J. W. Winkelman, and R. L. Lipson, in ‘Photodynamic Therapy: Basic Principles and Clinical Applications’, ed. B. W. Henderson, Marcel Dekker, New York, 1998, Vol. 3247, p. 145.
109. E. D. Sternberg and D. Dolphin, *Tetrahedron*, 1998, **54**, 4151.
110. R. Bonnett, *Rev. Contemp. Pharmacol.*, 1999, **10**, 1.
111. A. R. Oseroff, B. W. Henderson, and T. J. Dougherty, *Photochem. Photobiol.*, 1999, **69**, 50S.
112. R. K. Pandey and G. Zheng, in ‘The Porphyrin Handbook’, eds. K. M. Kadish, K. M. Smith, and R. Guilard, Academic Press, San Diego, CA, 2000, Vol. 6, p. 158.
113. R. K. Pandey, *J. Porphyrins Phthalocyanines*, 2000, **4**, 368.
114. R. M. Ion and M.-L. Pascu, *Proc. SPIE-Int. Soc. Opt. Eng.*, 2000, **4430**, 642.
115. A. A. Rosenkranz, D. A. Jans, and A. S. Sobolev, *Immunol. Cell Biol.*, 2000, **78**, 452.
116. I. J. MacDonald and T. J. Dougherty, *J. Porphyrins Phthalocyanines*, 2001, **5**, 105.
117. R. Ackroyd, C. Kelty, N. Brown, and M. Reed, *Photochem. Photobiol.*, 2001, **74**, 656.
118. M. R. Detty, *Expert Opin. Ther. Patents*, 2001, **11**, 1849.
119. L. Della Via and S. M. Magno, *Curr. Opin. Med. Chem.*, 2001, **8**, 1405.
120. C. M. Allen, W. M. Sharman, and J. E. van Lier, *J. Porphyrins Phthalocyanines*, 2001, **5**, 161.
121. Y. H. Chen, A. Graham, W. Potter, J. Morgan, L. Vaughan, D. A. Bellnier, B. W. Henderson, A. Oseroff, T. J. Dougherty, and R. K. Pandey, *J. Med. Chem.*, 2002, **45**, 255.
122. J. Osterloh and M. H. G. Vicente, *J. Porphyrins Phthalocyanines*, 2002, **6**, 305.
123. A. Robert and B. Meunier, *J. Am. Chem. Soc.*, 1997, **119**, 5968.
124. D. Monti, B. Vodopivec, N. Basilico, P. Olliaro, and D. Taramelli, *Biochemistry*, 1999, **38**, 8858.
125. A. D. Wright, H. Wang, M. Gurrath, G. M. König, G. Kocak, G. Neumann, P. Loria, M. Foley, and L. Tilley, *J. Med. Chem.*, 2001, **44**, 873.
126. A. Robert, O. Dechy-Cabaret, J. Cazelles, and B. Meunier, *Acc. Chem. Res.*, 2002, **35**, 167.
127. R. F. Pasternack, A. Giannetto, P. Pagano, and E. J. Gibbs, *J. Am. Chem. Soc.*, 1991, **113**, 7799.
128. R. F. Pasternack, M. Caccam, B. Keogh, T. A. Stephenson, A. P. Williams, and E. J. Gibbs, *J. Am. Chem. Soc.*, 1991, **113**, 6835.
129. J. A. Strickland, L. G. Marzilli, W. D. Wilson, and G. Zon, *Inorg. Chem.*, 1989, **28**, 4191.
130. L. G. Marzilli, *New J. Chem.*, 1990, **14**, 409.
131. H. Ogoshi, H. Hatakeyama, J. Kotani, A. Kawashima, and Y. Kuroda, *J. Am. Chem. Soc.*, 1991, **113**, 8181.
132. S. N. Gradl, J. P. Felix, E. Y. Isacoff, M. L. Garcia, and D. Trauner, *J. Am. Chem. Soc.*, 2003, **125**, 12668.
133. M. L. Garcia, M. Hanner, and G. J. Kaczorowski, *Toxicon*, 1998, **36**, 1641.
134. M. L. Garcia, Y. D. Gao, O. B. McManus, and G. J. Kaczorowski, *Toxicon*, 2001, **39**, 739.
135. B. M. Hoffman and J. A. Ibers, *Acc. Chem. Res.*, 1983, **16**, 15.
136. E. Tsuchida, T. Komatsu, K. Arai, K. Yamada, H. Nishide, and J.-H. Fuhrhop, *Langmuir*, 1995, **11**, 1877.
137. A. Ivanisevic and A. B. Ellis, *J. Phys. Chem. B*, 1999, **103**, 1914.
138. D. L. Pilloud, F. Rabanal, B. R. Gibney, R. S. Farid, P. L. Dutton, and C. C. Moser, *J. Phys. Chem. B*, 1998, **102**, 1926.
139. G. R. Newkome, E. He, and C. N. Moorefield, *Chem. Rev.*, 1999, **99**, 1689.
140. T. Komatsu, T. Yanagimoto, Y. Furubayashi, J. Wzu, and E. Tsuchida, *Langmuir*, 1999, **15**, 4427.
141. R. Paolesse, C. Di Natale, A. Macagnano, F. Sagone, M. A. Scarselli, P. Chiaradia, V. I. Troitsky, T. S. Berzina, and A. D’Amico, *Langmuir*, 1999, **15**, 1268.

142. G. Kalyuzhny, A. Vaskevich, G. Ashkenasy, A. Shanzer, and I. Rubinstein, *J. Phys. Chem. B*, 2000, **104**, 8238.
143. G. Ashkenasy, A. Ivanisevic, R. Cohen, C. E. Felder, D. Cahen, A. B. Ellis, and A. Shanzer, *J. Am. Chem. Soc.*, 2000, **122**, 1116.
144. O. Nestler and K. Severin, *Org. Lett.*, 2001, **3**, 3907.
145. M. Kimura, T. Shiba, M. Yamazaki, K. Hanabusa, H. Shirai, and N. Kobayashi, *J. Am. Chem. Soc.*, 2001, **123**, 5636.
146. S. O. Obare, T. Ito, M. H. Balfour, and G. J. Meyer, *Nano Lett.*, 2003, **3**, 1151.
147. T. Yamaguchi, N. Ishii, K. Tashiro, and T. Aida, *J. Am. Chem. Soc.*, 2003, **125**, 13934.
148. T. Malinski and Z. Taha, *Nature*, 1992, **358**, 676.
149. D. Gao, J.-Z. Li, R.-Q. Yu, and G.-D. Zheng, *Anal. Chem.*, 1994, **66**, 2245.
150. S. R. Snyder and H. S. White, *J. Phys. Chem.*, 1995, **99**, 5626.
151. C. Shi and F. C. Anson, *Anal. Chem.*, 1998, **70**, 3114.
152. J. W. Long and R. W. Murray, *Anal. Chem.*, 1998, **70**, 3355.
153. K. Di Gleria, D. P. Nickerson, H. A. O. Hill, L.-L. Wong, and V. Fülöp, *J. Am. Chem. Soc.*, 1998, **120**, 46.
154. D. L. Pilloud, X. Chen, P. L. Dutton, and C. C. Moser, *J. Phys. Chem. B*, 2000, **104**, 2868.
155. S. Rywkin, C. M. Hosten, J. R. Lombardi, and R. L. Birke, *Langmuir*, 2000, **18**, 5869.
156. I. M. Shiryaeva, J. P. Collman, R. Boulatov, and C. J. Sunderland, *Anal. Chem.*, 2003, **75**, 494.
157. A. M. Stolzenberg, L. O. Spreer, and R. H. Holm, *J. Am. Chem. Soc.*, 1980, **102**, 364.
158. O. P. Anderson, A. B. Kopelove, and D. K. Lavallee, *Inorg. Chem.*, 1980, **10**, 2101.
159. A. L. Balch, C. R. Cornman, L. Latos-Grażyński, and M. M. Olmstead, *J. Am. Chem. Soc.*, 1990, **112**, 7522.
160. L. Latos-Grażyński, J. Lisowski, M. M. Olmstead, and A. L. Balch, *J. Am. Chem. Soc.*, 1987, **109**, 4428.
161. R. D. Arasasingham, A. L. Balch, and M. M. Olmstead, *Heterocycles*, 1988, **27**, 2111.
162. L. Latos-Grażyński, J. Lisowski, M. M. Olmstead, and A. L. Balch, *Inorg. Chem.*, 1989, **28**, 1183.
163. J. P. Fitzgerald, B. S. Haggerty, A. L. Rheingold, L. May, and G. A. Brewer, *Inorg. Chem.*, 1992, **31**, 2006.
164. C. C. Leznoff and A. B. P. Lever eds, 'Phthalocyanines: Properties and Applications', VCH, New York, 1989.
165. S. Licoccia and R. Paolesse, *Struct. Bonding*, 1995, **84**, 71.
166. M. W. Makinen and A. K. Churg, in 'Iron Porphyrins', eds. A. B. P. Lever and H. B. Gray, Addison-Wesley, Reading, MA, 1983, Part I, p. 141.
167. T. G. Spiro, in 'Iron Porphyrins', eds. A. B. P. Lever and H. B. Gray, Addison-Wesley, Reading, MA, 1983, Part II, p. 89.
168. G. N. La Mar and F. A. Walker, in 'The Porphyrins', ed. D. Dolphin, Academic Press, New York, 1979, Vol. IVB, p. 57.
169. G. N. La Mar, in 'Biological Applications of Magnetic Resonance', ed. R. G. Shulman, Academic Press, New York, 1979, p. 305.
170. R. M. Keller and K. Wüthrich, in 'Biological Magnetic Resonance', eds. L. J. Berliner and J. Reuben, Plenum Press, New York, 1981, Vol. 3.
171. H. M. Goff, in 'Iron Porphyrins', eds. A. B. P. Lever and H. B. Gray, Addison-Wesley, Reading, MA, 1983, Part I, p. 237.
172. J. D. Satterlee, *Annu. Rep. NMR Spectrosc.*, 1986, **17**, 79.
173. J. D. Satterlee, in 'Metal Ions in Biological Systems', ed. H. Sigel, Marcel Dekker, New York, 1987, Vol. 21, p. 121.
174. F. A. Walker and U. Simonis, in 'Biological Magnetic Resonance, Volume 12: NMR of Paramagnetic Molecules', eds. L. J. Berliner and J. Ruben, Plenum Press, New York, 1992, p. 133.
175. F. A. Walker, in 'The Porphyrin Handbook', eds. K. M. Kadish, K. M. Smith, and R. Guilard, Academic Press, San Diego, 2000, Chap. 36, Vol. 5, p. 81.
176. G. Palmer, in 'Iron Porphyrins', eds. A. B. P. Lever and H. B. Gray, Addison-Wesley, Reading, MA, 1983, Part II, p. 43.
177. P. G. Debrunner, in 'Iron Porphyrins', eds. A. B. P. Lever and H. B. Gray, Addison-Wesley, Reading, MA, 1989, Part III, p. 137.
178. J. H. Dawson and D. M. Dooley, in 'Iron Porphyrins', eds. A. B. P. Lever and H. B. Gray, Addison-Wesley, Reading, MA, 1989, Part III, p. 1.
179. S. Mitra, in 'Iron Porphyrins', eds. A. B. P. Lever and H. B. Gray, Addison-Wesley, Reading, MA, 1983, Part II, p. 1.
180. F. A. Armstrong, H. A. O. Hill, and N. J. Walton, *Acc. Chem. Res.*, 1988, **21**, 407.
181. K. M. Kadish, in 'Iron Porphyrins', eds. A. B. P. Lever and H. B. Gray, Addison-Wesley, Reading, MA, 1983, Part II, p. 161.
182. W. R. Scheidt and M. Gouterman, in 'Iron Porphyrins', eds. A. B. P. Lever and H. B. Gray, Addison-Wesley, Reading, MA, 1983, Part I, p. 89.
183. W. R. Scheidt and C. A. Reed, *Chem. Rev.*, 1981, **81**, 543.
184. W. R. Scheidt and Y. J. Lee, *Struct. Bonding*, 1987, **64**, 1.
185. G. R. A. Wyllie and W. R. Scheidt, *Chem. Rev.*, 2002, **102**, 1067.
186. J. E. Penner-Hahn and K. O. Hodgson, in 'Iron Porphyrins', eds. A. B. P. Lever and H. B. Gray, Addison-Wesley, Reading, MA, 1989, Part III, p. 235.
187. F. A. Walker and U. Simonis, *J. Am. Chem. Soc.*, 1991, **113**, 8652.
188. T. Kh. Shokhireva, M. J. M. Nesset, and F. A. Walker, *Inorg. Chim. Acta*, 1998, **272**, 204.

189. M. F. Isaac, U. Simonis, Q. Lin, D. J. Suffian, D. L. Wilson, and F. A. Walker, *Inorg. Chem.*, 1993, **32**, 4030.

190. C. K. Chang, *J. Biol. Chem.*, 1985, **260**, 9520.

191. C. K. Chang and W. Wu, *J. Biol. Chem.*, 1986, **261**, 8593.

192. P. M. Iovine, G. Veglia, G. Furst, and M. J. Therien, *J. Am. Chem. Soc.*, 2001, **123**, 5668.

193. F. A. Walker, *Coord. Chem. Rev.*, 1999, **185–186**, 471.

194. F. A. Walker, *Chem. Rev.*, 2004, **104**, 589.

195. F. A. Walker, *Inorg. Chem.*, 2003, **42**, 4526.

196. R. Benda, V. Schünemann, A. X. Trautwein, S. Cai, J. R. Polam, C. T. Watson, T. Kh. Shokhireva, and F. A. Walker, *J. Biol. Inorg. Chem.*, 2003, **8**, 787.

197. T. G. Traylor, *Acc. Chem. Res.*, 1981, **14**, 102.

198. B. Morgan and D. Dolphin, *Struct. Bonding*, 1987, **61**, 115.

199. S. P. Rath, M. M. Olmstead, and A. L. Balch, *J. Am. Chem. Soc.*, 2004, **126**, 6379.

200. E. P. Sullivan and S. H. Strauss, *Inorg. Chem.*, 1989, **28**, 3093.

201. E. Fujita and J. Fajer, *J. Am. Chem. Soc.*, 1983, **105**, 6743.

202. S. Ozawa, H. Fujii, and I. Morishima, *J. Am. Chem. Soc.*, 1992, **114**, 1548.

203. M. A. Phillippi, E. T. Shimomura, and H. M. Goff, *Inorg. Chem.*, 1981, **20**, 1322.

204. W. F. Scholz, C. A. Reed, Y. J. Lee, W. R. Scheidt, and G. Lang, *J. Am. Chem. Soc.*, 1982, **104**, 6791.

205. G. Buisson, A. Deronzier, E. Duee, P. Gans, J.-C. Marchon, and J.-R. Regnard, *J. Am. Chem. Soc.*, 1982, **104**, 6793.

206. M. A. Phillippi and H. M. Goff, *J. Am. Chem. Soc.*, 1982, **104**, 6026.

207. H. M. Goff and M. A. Phillippi, *J. Am. Chem. Soc.*, 1983, **105**, 7567.

208. A. D. Boersma and H. M. Goff, *Inorg. Chem.*, 1984, **23**, 1671.

209. J. T. Groves, R. Quinn, T. J. McMurry, M. Nakamura, G. Lang, and B. Boso, *J. Am. Chem. Soc.*, 1985, **107**, 354.

210. A. Nanthakumar and H. M. Goff, *Inorg. Chem.*, 1992, **31**, 4460.

211. O. Zakharieva, V. Schünemann, M. Gerdan, S. Licoccia, S. Cai, F. A. Walker, and A. X. Trautwein, *J. Am. Chem. Soc.*, 2002, **124**, 6636.

212. J. T. Groves, R. C. Haushalter, M. Nakamura, T. E. Nemo, and B. Evans, *J. Am. Chem. Soc.*, 1981, **103**, 2884.

213. G. N. La Mar, J. S. de Ropp, L. Latos-Grażyński, A. L. Balch, R. B. Johnson, K. W. Smith, D. W. Parish, and R. J. Cheng, *J. Am. Chem. Soc.*, 1983, **105**, 782.

214. A. L. Balch, L. Latos-Grażyński, and M. W. Renner, *J. Am. Chem. Soc.*, 1985, **107**, 2983.

215. R. D. Arasasingham, C. R. Cornman, and A. L. Balch, *J. Am. Chem. Soc.*, 1989, **111**, 7800.

216. H. Fujii and K. Ichikawa, *Inorg. Chem.*, 1992, **31**, 1110.

217. D. L. Hickman, A. Nanthakumar, and H. M. Goff, *J. Am. Chem. Soc.*, 1988, **110**, 6384.

218. A. Gold, K. Jayaraj, P. Doppelt, R. Weiss, G. Chottard, E. Bill, X. Ding, and A. X. Trautwein, *J. Am. Chem. Soc.*, 1988, **110**, 5756.

219. E. Bill, X.-Q. Ding, E. L. Bominaar, A. Trautwein, H. Winkler, D. Mandon, R. Weiss, A. Gold, K. Jayaraj, W. E. Hatfield, and M. L. Kirk, *Eur. J. Biochem.*, 1990, **188**, 665.

220. R.-J. Cheng, P.-Y. Chen, T. Lovell, T. Liu, L. Noodleman, and D. L. Case, *J. Am. Chem. Soc.*, 2003, **125**, 6774.

221. H. C. Longuet-Higgins, C. W. Rector, and J. R. Platt, *J. Chem. Phys.*, 1950, **18**, 1174.

222. M. Zerner, M. Gouterman, and H. Kobayashi, *Theor. Chim. Acta*, 1966, **6**, 363.

223. M. Gouterman, in ‘The Porphyrins’, ed. D. Dolphin, Academic Press, New York, 1978, Vol. III, p. 1.

224. A. Antipas, J. W. Buchler, M. Gouterman, and P. D. Smith, *J. Am. Chem. Soc.*, 1978, **100**, 3015.

225. G. H. Loew, in ‘Iron Porphyrins’, eds. A. B. P. Lever and H. B. Gray, Addison-Wesley, Reading, MA, 1983, Part I, p. 1.

226. R. A. Binstead, M. J. Crossley, and N. S. Hush, *Inorg. Chem.*, 1991, **30**, 1259.

227. R. Shediac, M. H. B. Gray, H. T. Uyeda, R. C. Johnson, J. T. Hupp, P. J. Angiolillo, and M. J. Therien, *J. Am. Chem. Soc.*, 2000, **122**, 7017.

228. J. Fajer and M. S. Davis, in ‘The Porphyrins’, ed. D. Dolphin, Academic Press, New York, 1979, Vol. IV, p. 197.

229. K. M. Smith, in ‘The Porphyrin Handbook’, eds. K. M. Kadish, K. M. Smith, and R. Guilard, Academic Press, San Diego, CA, 2000, Vol. 1, p. 1.

230. K. M. Smith, in ‘The Porphyrin Handbook’, eds. K. M. Kadish, K. M. Smith, and R. Guilard, Academic Press, San Diego, CA, 2000, Vol. 1, p. 119.

231. J. S. Lindsey, in ‘The Porphyrin Handbook’, eds. K. M. Kadish, K. M. Smith, and R. Guilard, Academic Press, San Diego, CA, 2000, Vol. 1, p. 158.

232. M. D. G. H. Vicente, in ‘The Porphyrin Handbook’, eds. K. M. Kadish, K. M. Smith, and R. Guilard, Academic Press, San Diego, CA, 2000, Vol. 1, p. 149.

233. L. Jaquinod, in ‘The Porphyrin Handbook’, eds. K. M. Kadish, K. M. Smith, and R. Guilard, Academic Press, San Diego, CA, 2000, Vol. 1, p. 210.

234. M. O. Senge, in ‘The Porphyrin Handbook’, eds. K. M. Kadish, K. M. Smith, and R. Guilard, Academic Press, San Diego, CA, 2000, Vol. 1, p. 239.

235. P. Rothemund, *J. Am. Chem. Soc.*, 1936, **58**, 625; *J. Am. Chem. Soc.*, 1939, **61**, 2912.

236. A. D. Adler, F. R. Longo, and W. Shergalis, *J. Am. Chem. Soc.*, 1964, **86**, 3145.

237. A. D. Adler and J. L. Harris, *Anal. Biochem.*, 1966, **14**, 472.

238. A. D. Adler, F. R. Longo, J. D. Finarelli, J. Goldmacher, J. Assour, and L. Korsakoff, *J. Org. Chem.*, 1967, **32**, 476.

239. A. D. Adler, L. Sklar, F. R. Longo, J. D. Finarelli, and M. C. Finarelli, *J. Heterocycl. Chem.*, 1968, **5**, 669.

240. J. B. Kim, A. D. Adler, and F. R. Longo, in 'The Porphyrins', ed. D. Dolphin, Academic Press, New York, 1978, Vol. 1, p. 85.

241. R. G. Little, J. A. Anton, and J. A. Ibers, *J. Heterocycl. Chem.*, 1975, **12**, 343.

242. R. G. Little, *J. Heterocycl. Chem.*, 1981, **18**, 129.

243. J. A. Anton and P. A. Loach, *J. Heterocycl. Chem.*, 1975, **12**, 573.

244. F. A. Walker, V. L. Balke, and G. A. McDermott, *Inorg. Chem.*, 1982, **21**, 3342.

245. R. Koerner, J. L. Wright, M. J. M. Nesset, X. D. Ding, K. Aubrecht, R. Watson, R. A. Barber, A. R. Tipton, C. J. Norvell, L. M. Mink, U. Simonis, and F. A. Walker, *Inorg. Chem.*, 1998, **37**, 733.

246. F. A. Walker, U. Simonis, H. Zhang, J. M. Walker, T. M. Ruscitti, C. Kipp, M. A. Amputch, B. V. Castillo, S. H. Cody, D. L. Wilson, R. E. Graul, G. J. Yong, K. Tobin, J. T. West, and B. A. Barichievich, *New J. Chem.*, 1992, **16**, 609.

247. J. S. Lindsey, I. C. Schreiman, and H. C. Hsu, *Tetrahedron Lett.*, 1986, **27**, 4969.

248. J. S. Lindsey, I. C. Schreiman, H. C. Hsu, P. C. Kearney, and A. M. Marguerettaz, *J. Org. Chem.*, 1987, **5**, 827.

249. J. S. Lindsey, K. A. MacCrum, J. S. Tyhonas, and Y.-Y. Chuang, *J. Org. Chem.*, 1994, **59**, 579.

250. G. R. Geier III, Y. Ciringh, F. Li, D. M. Haynes, and J. S. Lindsey, *Org. Lett.*, 2000, **2**, 1745.

251. R. W. Wagner, F. Li, H. Du, and J. S. Lindsey, *Org. Process Res. Dev.*, 1999, **3**, 28.

252. S. G. DiMagno, R. A. Williams, and M. J. Therien, *J. Org. Chem.*, 1994, **59**, 6943.

253. J. F. Foll, K. R. Moore, A. Ghosh, and M. J. Therien, *J. Am. Chem. Soc.*, 1996, **118**, 8344.

254. D. Gryko and J. S. Lindsey, *J. Org. Chem.*, 2000, **65**, 2249.

255. B. J. Littler, Y. Ciringh, and J. H. Lindsey, *J. Org. Chem.*, 1999, **64**, 2864.

256. P. D. Rao, B. J. Littler, G. R. Geier III, and J. S. Lindsey, *J. Org. Chem.*, 2000, **65**, 1084.

257. P. D. Rao, S. Dhanalekshimi, B. J. Littler, and J. S. Lindsey, *J. Org. Chem.*, 2000, **65**, 7323.

258. A. W. van der Made, E. J. H. Hoppenbrouwer, R. J. M. Nolte, and W. Drenth, *Recl. Trav. Chim. Pays-Bas*, 1988, **107**, 15.

259. M. Kihn-Botulinski and B. Meunier, *Inorg. Chem.*, 1988, **27**, 209.

260. A. Md. A. Rocha-Gonsalves, J. M. T. B. Varejao, and M. M. Pereira, *J. Heterocycl. Chem.*, 1991, **28**, 635.

261. A. J. F. N. Sobral, N. G. C. L. Rebanda, M. da Silva, S. H. Lampreia, M. R. Silva, A. M. Beja, J. A. Paixão, and A. M. D. A. Rocha Gonsalves, *Tetrahedron Lett.*, 2003, **44**, 3971.

262. R. P. Bonar-Law, *J. Am. Chem. Soc.*, 1995, **117**, 12397.

263. H. Ogura and F. A. Walker, *Inorg. Chem.*, 2001, **40**, 5729.

264. J. P. Collman, *Inorg. Chem.*, 1997, **36**, 5145.

265. J. P. Collman, B. Boitrel, L. Fu, J. Galanter, A. Straumanis, and M. Rapta, *J. Org. Chem.*, 1997, **62**, 2308.

266. C. M. Drain and B. B. Corden, *Inorg. Chem.*, 1989, **28**, 4374.

267. E. Rose, M. Soleihavoup, L. Christ-Tommasino, G. Moreau, J. P. Collman, M. Quelquejeu, and A. Straumanis, *J. Org. Chem.*, 1998, **63**, 2042.

268. Z. Gross and I. Toledano, *J. Org. Chem.*, 1994, **59**, 8312.

269. H. Nakagawa, T. Nagano, and T. Higuchi, *Org. Lett.*, 2001, **3**, 1805.

270. J. P. Collman, J. I. Brauman, J. P. Fitzgerald, P. H. Hampton, Y. Naruta, J. W. Sarapany, and J. A. Ibers, *J. Am. Chem. Soc.*, 1988, **110**, 3477.

271. B. Andrioletti, B. Boitrel, and R. Guilard, *J. Org. Chem.*, 1998, **63**, 1312.

272. R. P. Bonar-Law and J. K. M. Sanders, *J. Chem. Soc. Chem. Commun.*, 1991, 574.

273. J. P. Collman, X. Zhang, P. C. Herrmann, E. S. Uffelman, B. Boitrel, A. Straumanis, and J. I. Brauman, *J. Am. Chem. Soc.*, 1994, **116**, 2681.

274. T. Hayashi, T. Miyahara, N. Hashizume, and H. Ogoshi, *J. Am. Chem. Soc.*, 1993, **175**, 2049.

275. S. Michaeli, M. Hugerat, H. Levanon, M. Bernitz, A. Natt, and R. Neumann, *J. Am. Chem. Soc.*, 1992, **114**, 3612.

276. B. Garcia, C. H. Lee, A. Blasko, and T. C. Bruice, *J. Am. Chem. Soc.*, 1991, **113**, 8118.

277. J. Wojaczynski and L. Latos-Grażyński, *Inorg. Chem.*, 1995, **34**, 1044.

278. K. Wynne, S. M. LeCours, C. Galli, M. J. Therien, and R. M. Hochstrasser, *J. Am. Chem. Soc.*, 1995, **117**, 3749.

279. P. M. Iovine, M. A. Kellett, N. P. Redmore, and M. J. Therien, *J. Am. Chem. Soc.*, 2000, **122**, 8717.

280. Y. K. Kang, I. V. Rubtsov, P. M. Iovine, J. Chem, and M. J. Therien, *J. Am. Chem. Soc.*, 2002, **124**, 8275.

281. P. Basu, A. M. Raitsimring, M. J. LaBarre, I. K. Dhawan, J. L. Weibrecht, and J. H. Enemark, *J. Am. Chem. Soc.*, 1994, **116**, 7166.

282. X.-X. Zhang, P. Fuhrmann, and S. J. Lippard, *J. Am. Chem. Soc.*, 1998, **120**, 10260.

283. X.-X. Zhang and S. J. Lippard, *Inorg. Chem.*, 2000, **39**, 4388.

284. X.-X. Zhang and S. J. Lippard, *J. Org. Chem.*, 2000, **65**, 5298.

285. F. A. Walker and J. H. Bowen, *J. Am. Chem. Soc.*, 1985, **107**, 7632.

286. F. A. Walker, V. L. Balke, and J. T. West, in ‘Frontiers in Bioinorganic Chemistry’, ed. A. V. Xavier, VCH, Weinheim, 1985, p. 183.
287. C.-Y. Yeh, C. J. Chang, and D. G. Nocera, *J. Am. Chem. Soc.*, 2001, **123**, 1513.
288. L. Baldini, P. Ballester, A. Casnati, R. M. Gomila, C. A. Hunter, F. Sansone, and R. Ungaro, *J. Am. Chem. Soc.*, 2003, **125**, 14181.
289. J. Wojaczynski, L. Latos-Grażyński, P. J. Chmielewski, P. Van Calcar, and A. L. Balch, *Inorg. Chem.*, 1999, **38**, 3040.
290. S. Wolowiec and L. Latos-Grażyński, *Inorg. Chem.*, 1994, **33**, 3576.
291. M. O. Senge, M. G. H. Vicente, K. R. Gerzevske, T. P. Forsyth, and K. M. Smith, *Inorg. Chem.*, 1994, **33**, 5625.
292. M. Lachkar, A. Tabard, S. Brandès, R. Guilard, A. Atmani, A. De Cian, J. Fischer, and R. Weiss, *Inorg. Chem.*, 1997, **36**, 4141.
293. S. Tsuchiya, *J. Am. Chem. Soc.*, 1999, **121**, 48.
294. Y. Deng, C. J. Chang, and D. G. Nocera, *J. Am. Chem. Soc.*, 2000, **122**, 410.
295. J. T. Fletcher and M. J. Therien, *J. Am. Chem. Soc.*, 2000, **122**, 12393.
296. J. T. Fletcher and M. J. Therien, *Inorg. Chem.*, 2002, **41**, 331.
297. C. J. Chang, C.-Y. Yeh, and D. G. Nocera, *J. Org. Chem.*, 2002, **67**, 1403.
298. C. J. Chang, E. A. Baker, B. J. Pistorio, Y. Deng, Z.-H. Loh, S. E. Miller, S. D. Carpenter, and D. G. Nocera, *Inorg. Chem.*, 2002, **41**, 3102.
299. B. J. Pistorio, C. J. Chang, and D. G. Nocera, *J. Am. Chem. Soc.*, 2002, **124**, 7884.
300. L. Yu, K. Muthukumaran, I. V. Sazanovich, C. Kirmaier, E. Hindin, J. R. Diers, P. D. Boyle, D. F. Bocian, D. Holten, and J. S. Lindsey, *Inorg. Chem.*, 2003, **42**, 6229.
301. M. Taniguchi, D. Ra, C. Kirmaier, E. Hindin, J. K. Schwartz, J. R. Diers, R. S. Knox, D. F. Bocian, J. S. Lindsey, and D. Holten, *J. Am. Chem. Soc.*, 2003, **125**, 13461.
302. F. Li, S. I. Yang, Y. Ciringh, J. Seth, C. H. Martin III, D. L. Singh, D. Kim, R. R. Birge, D. F. Bocian, D. Holten, and J. S. Lindsey, *J. Am. Chem. Soc.*, 1998, **120**, 10001.
303. K. Tomizaki, R. S. Loewe, C. Kirmaier, J. K. Schwartz, J. L. Retsek, D. F. Bocian, D. Holten, and J. S. Lindsey, *J. Org. Chem.*, 2002, **67**, 6519.
304. L. G. Mackay, R. S. Wylie, and J. K. M. Sanders, *J. Am. Chem. Soc.*, 1994, **116**, 3141.
305. A. Giraudeau, L. Ruhimann, L. El Kahef, and M. Gross, *J. Am. Chem. Soc.*, 1996, **118**, 2969.
306. J.-P. Strachan, S. Gentemann, J. Seth, W. A. Kalsbeck, J. S. Lindsey, D. Holten, and D. F. Bocian, *J. Am. Chem. Soc.*, 1997, **119**, 11191.
307. J.-P. Strachan, S. Gentemann, J. Seth, W. A. Kalsbeck, J. S. Lindsey, D. Holten, and D. F. Bocian, *Inorg. Chem.*, 1998, **37**, 1191.
308. P. Hascoat, S. I. Yang, R. K. Lammi, J. Alley, D. F. Bocian, J. S. Lindsey, and D. Holten, *Inorg. Chem.*, 1999, **38**, 4849.
309. S. I. Yang, R. K. Lammi, J. Seth, J. A. Riggs, T. Arai, D. Kim, D. F. Bocian, D. Holten, and J. S. Lindsey, *J. Phys. Chem. B*, 1998, **102**, 9426.
310. L. X. Chen, P. L. Lee, D. Gosztola, W. A. Svec, P. A. Montano, and M. R. Wasielewski, *J. Phys. Chem. B*, 1999, **103**, 3270.
311. M. A. Miller, R. K. Lammi, S. Prathapan, D. Holten, and J. S. Lindsey, *J. Org. Chem.*, 2000, **65**, 6634.
312. C. Clausen, D. T. Gryko, A. A. Yasseri, J. R. Diers, D. F. Bocian, W. G. Kuhr, and J. S. Lindsey, *J. Org. Chem.*, 2000, **65**, 7371.
313. S. Prathapan, S. I. Yang, J. Seth, M. A. Miller, D. F. Bocian, D. Holten, and J. S. Lindsey, *J. Phys. Chem. B*, 2001, **105**, 8237.
314. S. I. Yang, S. Prathapan, M. A. Miller, J. Seth, D. F. Bocian, J. S. Lindsey, and D. Holten, *J. Phys. Chem. B*, 2001, **105**, 8249.
315. W. J. Youngblood, D. T. Gryko, R. K. Lammi, D. F. Bocian, D. Holten, and J. S. Lindsey, *J. Org. Chem.*, 2002, **67**, 2111.
316. J. T. Fletcher and M. J. Therien, *J. Am. Chem. Soc.*, 2002, **124**, 4298.
317. K. Susumu and M. J. Therien, *J. Am. Chem. Soc.*, 2002, **124**, 8550.
318. I. V. Rubtsov, K. Susumu, G. I. Rubtsov, and M. J. Therien, *J. Am. Chem. Soc.*, 2003, **125**, 2687.
319. I. V. Sazanovich, A. Balakumar, K. Muthukumaran, E. Hindin, C. Kirmaier, J. R. Diers, J. S. Lindsey, D. F. Bocian, and D. Holten, *Inorg. Chem.*, 2003, **42**, 6616.
320. L. Yu, K. Muthukumaran, I. V. Sazanovich, C. Kirmaier, E. Hindin, J. R. Diers, P. D. Boyle, D. F. Bocian, D. Holten, and J. S. Lindsey, *Inorg. Chem.*, 2003, **42**, 6629.
321. P. J. Angiolillo, V. S.-Y. Lin, J. M. Vanderkooi, and M. J. Therien, *J. Am. Chem. Soc.*, 1995, **117**, 12514.
322. R. Kumble, S. Palese, V. S.-Y. Lin, M. J. Therien, and R. M. Hochstrasser, *J. Am. Chem. Soc.*, 1998, **120**, 11489.
323. J. Seth, V. Palaniappan, T. E. Johnson, S. Prathapan, J. S. Lindsey, and D. F. Bocian, *J. Am. Chem. Soc.*, 1994, **116**, 10578.
324. R. W. Wagner and J. S. Lindsey, *J. Am. Chem. Soc.*, 1994, **116**, 9759.
325. R. W. Wagner, T. E. Johnson, and J. S. Lindsey, *J. Am. Chem. Soc.*, 1996, **118**, 11166.
326. J.-S. Hsiao, B. P. Krueger, R. W. Wagner, T. E. Johnson, J. K. Delaney, D. K. Mauzerall, G. R. Fleming, J. S. Lindsey, D. F. Bocian, and R. J. Donohoe, *J. Am. Chem. Soc.*, 1996, **118**, 11181.

327. J. Seth, V. Palaniappan, R. W. Wagner, T. E. Johnson, J. S. Lindsey, and D. F. Bocian, *J. Am. Chem. Soc.*, 1996, **118**, 11194.
328. R. K. Lammi, R. W. Wagner, A. Ambroise, J. R. Diers, D. F. Bocian, D. Holten, and J. S. Lindsey, *J. Phys. Chem. B*, 2001, **105**, 5341.
329. A. Ambroise, C. Kirmaier, R. W. Wagner, R. S. Loewe, D. F. Bocian, D. Holten, and J. S. Lindsey, *J. Org. Chem.*, 2002, **67**, 3811.
330. R. W. Wagner, J. S. Lindsey, J. Seth, V. Palaniappan, and D. F. Bocian, *J. Am. Chem. Soc.*, 1996, **118**, 3996.
331. R. K. Lammi, A. Ambroise, T. Balasubramanian, R. W. Wagner, D. F. Bocian, D. Holten, and J. S. Lindsey, *J. Am. Chem. Soc.*, 2000, **122**, 7579.
332. A. Ambroise, R. W. Wagner, P. D. Rao, J. A. Riggs, P. Hascoat, J. R. Diers, J. Seth, R. K. Lammi, D. F. Bocian, D. Holten, and J. S. Lindsey, *Chem. Mater.*, 2001, **13**, 1023.
333. M. Mylrajan, L. A. Andersson, T. M. Loehr, W. Wu, and C. K. Chang, *J. Am. Chem. Soc.*, 1991, **113**, 5000.
334. T. La, R. Richards, and G. M. Miskelly, *Inorg. Chem.*, 1994, **33**, 3159.
335. A. Jakobs, J. Bernadou, and B. Meunier, *J. Org. Chem.*, 1997, **62**, 3505.
336. T. La, G. M. Miskelly, and R. Bau, *Inorg. Chem.*, 1997, **36**, 5321.
337. S. G. DiMagno, V. S.-Y. Lin, and M. J. Therien, *J. Am. Chem. Soc.*, 1993, **115**, 2513.
338. S. G. DiMagno, V. S.-Y. Lin, and M. J. Therien, *J. Org. Chem.*, 1993, **58**, 5983.
339. S. M. LeCours, S. G. DiMagno, and M. J. Therien, *J. Am. Chem. Soc.*, 1996, **118**, 11854.
340. S. M. LeCours, H.-W. Guan, S. G. DiMagno, C. H. Wang, and M. J. Therien, *J. Am. Chem. Soc.*, 1996, **118**, 1497.
341. S. Priyadarshy, M. J. Therien, and D. N. Beretan, *J. Am. Chem. Soc.*, 1996, **118**, 1504.
342. S. M. LeCours, C. M. Philips, J. C. de Paula, and M. J. Therien, *J. Am. Chem. Soc.*, 1997, **119**, 12578.
343. L. Karki, F. W. Vance, J. T. Hupp, S. M. LeCours, and M. J. Therien, *J. Am. Chem. Soc.*, 1998, **120**, 2606.
344. H. T. Uyeda, Y. Zhao, K. Wostyn, I. Asselberghs, K. Clays, A. Persoons, and M. J. Therien, *J. Am. Chem. Soc.*, 2002, **124**, 13806.
345. N. P. Redmore, I. V. Rubtsov, and M. J. Therien, *Inorg. Chem.*, 2002, **41**, 566.
346. N. P. Redmore, I. V. Rubtsov, and M. J. Therien, *J. Am. Chem. Soc.*, 2003, **125**, 8769.
347. A. G. Hyslop, M. A. Kellett, P. M. Iovine, and M. J. Therien, *J. Am. Chem. Soc.*, 1998, **120**, 12676.
348. R. S. Wagner, T. E. Johnson, F. Li, and J. S. Lindsey, *J. Org. Chem.*, 1995, **60**, 5266.
349. R. S. Wagner, Y. Ciringh, C. Clausen, and J. S. Lindsey, *Chem. Mater.*, 1999, **11**, 2974.
350. T. Chandra, B. J. Craft, J. C. Huffman, and J. M. Zaleski, *Inorg. Chem.*, 2003, **42**, 5158.
351. M. Nath, J. C. Huffman, and J. M. Zaleski, *J. Am. Chem. Soc.*, 2003, **125**, 11484.
352. J. Lahiri, G. Xu, D. M. Dabba, N. Yao, I. A. Aksay, and J. T. Groves, *J. Am. Chem. Soc.*, 1997, **119**, 5449.
353. J. T. Groves and R. Neumann, *J. Am. Chem. Soc.*, 1987, **109**, 5045; *J. Am. Chem. Soc.* 1989, **111**, 2900.
354. E. Tsuchida, T. Komatsu, T. Babe, T. Nakata, H. Nishide, and H. Inoue, *Bull. Chem. Soc. Jpn.*, 1990, **63**, 2323.
355. T. Komatsu, K. Nakao, H. Nishide, and E. Tsuchida, *J. Chem. Soc., Chem. Commun.*, 1993, 728.
356. N. Nishino, R. W. Wagner, and J. S. Lindsey, *J. Org. Chem.*, 1996, **61**, 7534.
357. C. C. Wamser, R. R. Bard, V. Senthilathipan, V. C. Anderson, J. A. Yates, H. K. Lonsdale, G. W. Rayfield, D. T. Friesen, D. A. Lorenz, G. C. Stangle, P. van Eikeren, D. R. Baer, R. A. Ransdell, J. H. Golbeck, W. C. Babcock, J. J. Sandberg, and S. E. Clarke, *J. Am. Chem. Soc.*, 1989, **111**, 8485.
358. L. Wen, M. Li, and J. B. Schlenoff, *J. Am. Chem. Soc.*, 1997, **119**, 7726.
359. D. T. Gryko, C. Clausen, and J. S. Lindsey, *J. Org. Chem.*, 1999, **64**, 8635.
360. D. T. Gryko, C. Clausen, K. M. Roth, N. Dontha, D. F. Bocian, W. G. Kuhr, and J. S. Lindsey, *J. Org. Chem.*, 2000, **65**, 7345.
361. C. Clausen, D. T. Gryko, R. B. Dabke, N. Dontha, D. F. Bocian, W. G. Kuhr, and J. S. Lindsey, *J. Org. Chem.*, 2000, **65**, 7363.
362. D. T. Gryko, F. Zhao, A. A. Yasseri, K. M. Roth, D. F. Bocian, W. G. Kuhr, and J. S. Lindsey, *J. Org. Chem.*, 2000, **65**, 7356.
363. A. K. Burrell, D. L. Officer, P. G. Plieger, and D. C. W. Reid, *Chem. Rev.*, 2001, **101**, 2751.
364. R. W. Wagner, J. Seth, S. I. Yang, D. Kim, D. F. Bocian, D. Holten, and J. S. Lindsey, *J. Org. Chem.*, 1998, **63**, 5042.
365. J. Li, A. Ambroise, S. I. Yang, J. R. Diers, J. Seth, C. R. Wack, D. F. Bocian, D. Holten, and J. S. Lindsey, *J. Am. Chem. Soc.*, 1999, **121**, 8927.
366. L. Yu and J. S. Lindsey, *J. Org. Chem.*, 2001, **66**, 7402.
367. K. Tomizaki, L. Yu, L. Wei, D. F. Bocian, and J. S. Lindsey, *J. Org. Chem.*, 2003, **68**, 8199.
368. A. Ambroise, J. Li, L. Yu, and J. S. Lindsey, *Org. Lett.*, 2000, **2**, 2563.
369. S. Prathapan, T. E. Johnson, and J. S. Lindsey, *J. Am. Chem. Soc.*, 1993, **115**, 7519.
370. J. Seth, V. Palaniappan, T. E. Johnson, S. Prathapan, J. S. Lindsey, and D. F. Bocian, *J. Am. Chem. Soc.*, 1994, **116**, 10578.

371. D. Kuciauskas, P. A. Liddell, S. Lin, T. E. Johnson, S. J. Weghorn, J. S. Lindsey, A. L. Moore, T. A. Moore, and D. Gust, *J. Am. Chem. Soc.*, 1999, **121**, 8604.
372. G. Kodis, P. A. Liddell, L. de la Garza, P. C. Clausen, J. S. Lindsey, A. L. Moore, T. A. Moore, and D. Gust, *J. Phys. Chem. A*, 2002, **106**, 2036.
373. J. Li, J. R. Diers, J. Seth, S. I. Yang, D. F. Bocian, D. Holten, and J. S. Lindsey, *J. Org. Chem.*, 1999, **64**, 9090.
374. J. Li and J. S. Lindsey, *J. Org. Chem.*, 1999, **64**, 9101.
375. D. Holten, D. F. Bocian, and J. S. Lindsey, *Acc. Chem. Res.*, 2002, **35**, 57.
376. M. Speckbacher, L. Yu, and J. S. Lindsey, *Inorg. Chem.*, 2003, **42**, 4322.
377. H. W. Whitlock and R. J. Hanauer, *J. Org. Chem.*, 1968, **33**, 2169.
378. J. B. Paine, W. Kirshner, and D. Maskowitz, *J. Org. Chem.*, 1976, **41**, 3857.
379. N. Ono, H. Kawamura, M. Bougauchi, and K. Maruyama, *J. Chem. Soc., Chem. Commun.*, 1989, 1580.
380. N. Ono, H. Kawamura, M. Bougauchi, and K. Maruyama, *Tetrahedron*, 1990, **46**, 7483.
381. K. Konishi, K. Oda, K. Nishida, T. Aida, and S. Inoue, *J. Am. Chem. Soc.*, 1992, **114**, 1313.
382. A. M. Van Leusen, H. Siderius, B. E. Hoogenboom, and D. Van Leusen, *Tetrahedron Lett.*, 1972, **52**, 5337.
383. A. Shirazi, R. Marianelli, and G. Sturgeon, *Inorg. Chim. Acta*, 1983, **72**, 5.
384. K. S. Chamberlin and E. LeGoff, *Synth. Commun.*, 1978, **8**, 579.
385. K. S. Chamberlin and E. LeGoff, *Heterocycles*, 1979, **12**, 1567.
386. K. Jayaraj, A. Gold, and P. S. White, *Inorg. Chem.*, 2000, **39**, 3652.
387. B. A. Gregg, M. A. Fox, and A. J. Bard, *J. Am. Chem. Soc.*, 1989, **111**, 3024.
388. H. Uno, A. Matsumoto, and N. Ono, *J. Am. Chem. Soc.*, 2003, **125**, 12082.
389. L. D. Sparks, C. J. Medforth, M.-S. Park, J. R. Chamberlain, M. R. Ondrias, M. O. Senge, K. M. Smith, and J. A. Shelnutt, *J. Am. Chem. Soc.*, 1993, **115**, 581.
390. D. O. Cheng, T. L. Bowman, and E. LeGoff, *Tetrahedron Lett.*, 1976, **13**, 1145.
391. K. M. Barkigia, M. D. Berber, J. Fajer, C. J. Medforth, M. W. Renner, and K. M. Smith, *J. Am. Chem. Soc.*, 1990, **112**, 8851.
392. C. J. Medforth, M. D. Berber, and K. M. Smith, *Tetrahedron Lett.*, 1990, **31**, 3719.
393. C. J. Medforth, M. O. Senge, K. M. Smith, L. D. Sparks, and J. A. Shelnutt, *J. Am. Chem. Soc.*, 1992, **114**, 9859.
394. D. H. R. Barton, J. Kervagoret, and S. Z. Zard, *Tetrahedron*, 1990, **26**, 7587.
395. S. Chen and T. D. Lash, *J. Heterocycl. Chem.*, 1997, **34**, 273.
396. D. H. R. Barton, J. D. Elliot, and S. D. Gero, *J. Chem. Soc., Chem. Commun.*, 1981, 1136.
397. D. H. R. Barton, J. D. Elliot, and S. D. Gero, *J. Chem. Soc., Perkin Trans. 1*, 1982, 2085.
398. M. Miura, S. A. Majumder, J. D. Hobbs, M. W. Renner, L. R. Furenlid, and J. A. Shelnutt, *Inorg. Chem.*, 1994, **33**, 6078.
399. A. Valasinas, J. Hurst, and B. Frydman, *J. Org. Chem.*, 1998, **63**, 1239.
400. M. O. Senge and W. W. Kalisch, *Inorg. Chem.*, 1997, **36**, 6103.
401. M. J. Gunter and L. N. Mander, *J. Org. Chem.*, 1981, **46**, 4792.
402. M. R. Wasielewski, M. P. Neimczyk, W. A. Svec, and E. B. Pewitt, *J. Am. Chem. Soc.*, 1985, **107**, 5562.
403. R. Giasson, E. J. Lee, X. Zhao, and M. S. Wrighton, *J. Phys. Chem.*, 1993, **97**, 2596.
404. C. J. Medforth and K. M. Smith, *Tetrahedron Lett.*, 1990, **31**, 5583.
405. T. G. Traylor and S. Tsuchiya, *Inorg. Chem.*, 1987, **26**, 1338.
406. H. J. Callot, *Bull. Soc. Chim. Fr.*, 1974, 1492.
407. P. Battioni, O. Brigaud, H. Desvaux, D. Mansuy, and T. G. Traylor, *Tetrahedron Lett.*, 1991, **32**, 2893.
408. P. Bhyrappa and V. Krishnan, *Inorg. Chem.*, 1991, **30**, 239.
409. T. Wijesekera, A. Matsumoto, D. Dolphin, and D. Lexa, *Angew. Chem., Int. Ed. Engl.*, 1990, **9**, 1028.
410. H. Duval, V. Bulach, J. Fischer, and R. Weiss, *Inorg. Chem.*, 1999, **38**, 5495.
411. K.-W. Poon, Y. Yan, X.-y. Li, and D. K. P. Ng, *Organometallics*, 1999, **18**, 3528.
412. K.-W. Poon, W. Liu, P.-K. Chan, Q. Yang, F.-W. D. Chan, T. C. W. Mak, and D. K. P. Ng, *J. Org. Chem.*, 2001, **66**, 1553.
413. A. W. Johnson and I. T. Kay, *J. Chem. Soc.*, 1966, 22.
414. J. B. Paine III, in ‘The Porphyrins’, ed. D. Dolphin, Academic Press, New York, 1978, p. 101.
415. G. M. Dubowchik and A. D. Hamilton, *J. Chem. Soc., Chem. Commun.*, 1986, 665.
416. G. Slobodkin, E. Fan, and A. D. Hamilton, *New J. Chem.*, 1992, **16**, 643.
417. A. W. Johnson, in ‘The Porphyrins’, ed. D. Dolphin, Academic Press, New York, 1978, Vol 1, p. 235.
418. A. R. Battersby, E. McDonald, M. Thompson, I. A. Chaudhry, P. S. Clezy, C. J. R. Fookes, and T. T. Hai, *J. Chem. Soc., Perkin Trans. 1*, 1985, 135.
419. P. S. Clezy and C. J. R. Fookes, *Aust. J. Chem.*, 1980, **33**, 557.
420. P. S. Clezy and C. J. R. Fookes, *Aust. J. Chem.*, 1981, **34**, 871.
421. P. S. Clezy, L. V. Phuc, and J. K. Prashar, *Aust. J. Chem.*, 1991, **44**, 1061.

422. P. S. Clezy, *Aust. J. Chem.*, 1991, **44**, 1163.

423. P. Yon-Hin, T. Wijesekera, and D. Dolphin, *Can. J. Chem.*, 1990, **68**, 1867.

424. K. M. Smith and D. A. Goff, *J. Org. Chem.*, 1986, **51**, 657.

425. K. M. Smith, D. W. Parish, and W. S. Inouye, *J. Org. Chem.*, 1986, **51**, 666.

426. K. M. Smith, M. Miura, and I. K. Morris, *J. Org. Chem.*, 1986, **51**, 4660.

427. K. M. Snow and K. M. Smith, *J. Org. Chem.*, 1989, **54**, 3270.

428. T. G. Traylor, C. K. Chang, J. Geibel, A. Berzinis, T. Mincey, and J. Cannon, *J. Am. Chem. Soc.*, 1979, **101**, 6716.

429. L. Casella, E. Monzani, P. Fantucci, M. Gullotti, L. De Gioia, A. Strini, and F. Chillemi, *Inorg. Chem.*, 1996, **35**, 439.

430. E. Monzani, G. Alzuet, L. Casella, C. Redaelli, C. Bassani, A. M. Sanangelantoni, M. Gullotti, L. De Gioia, L. Santagostini, and F. Chillemi, *Biochemistry*, 2000, **39**, 9571.

431. J. Aron, D. A. Baldwin, H. M. Marques, J. M. Pratt, and P. A. Adams, *J. Inorg. Biochem.*, 1986, **27**, 227.

432. O. Q. Munro and H. M. Marques, *Inorg. Chem.*, 1996, **35**, 3752.

433. O. Q. Munro and H. M. Marques, *Inorg. Chem.*, 1996, **35**, 3768.

434. J. Peterson, M. M. M. Saleem, J. Silver, M. T. Wilson, and I. E. G. Morrison, *J. Inorg. Biochem.*, 1983, **19**, 165.

435. D. W. Low, G. Yang, J. R. Winkler, and H. B. Gray, *J. Am. Chem. Soc.*, 1997, **119**, 4094.

436. J. Peterson, J. Silver, M. T. Wilson, and I. E. G. Morrison, *J. Inorg. Biochem.*, 1980, **13**, 75.

437. J.-P. Strachan, D. F. O'Shea, T. Balasubramanian, and J. S. Lindsey, *J. Org. Chem.*, 2000, **65**, 3160.

438. T. Balasubramanian, J.-P. Strachan, P. D. Boyle, and J. S. Lindsey, *J. Org. Chem.*, 2000, **65**, 7919.

439. M. Taniguchi, D. Ra, G. Mo, T. Balasubramanian, and J. S. Lindsey, *J. Org. Chem.*, 2001, **66**, 7342.

440. D. H. Burns, Y. H. Li, D. C. Shi, and T. M. Caldwell, *J. Org. Chem.*, 2002, **67**, 4536.

441. F.-P. Montforts, B. Gerlach, and F. Höper, *Chem. Rev.*, 1994, **94**, 327.

442. P. Yon-Hin, T. P. Wijesekera, and D. Dolphin, *Tetrahedron Lett.*, 1991, **32**, 2875.

443. A. M. Stolzenberg, P. A. Glazer, and B. M. Foxman, *Inorg. Chem.*, 1986, **261**, 8593.

444. P. A. Connick, K. J. Haller, and K. A. Macor, *Inorg. Chem.*, 1993, **32**, 3256.

445. M. Taniguchi, H.-J. Kim, D. Ra, J. K. Schwartz, C. Kirmaier, E. Hindin, J. R. Diers, S. Prathapan, D. F. Bocian, D. Holten, and J. S. Lindsey, *J. Org. Chem.*, 2002, **67**, 7329.

446. K. Muthukumaran, R. S. Loewe, C. Kirmaier, E. Hindin, J. K. Schwartz, I. V. Sazanovich, J. R. Diers, D. F. Bocian, D. Holten, and J. S. Lindsey, *J. Phys. Chem. B*, 2003, **107**, 3431.

447. C. Kirmaier, E. Hindin, J. K. Schwartz, I. V. Sazanovich, J. R. Diers, J. S. Lindsey, and D. Holten, *J. Phys. Chem. B*, 2003, **107**, 3443.

448. K. Konishi, Y. Takahata, T. Aida, and S. Inoue, *J. Am. Chem. Soc.*, 1993, **115**, 1169.

449. J. W. Buchler and K. L. Lay, *Z. Naturforsch. B*, 1975, **30B**, 385.

450. A. Botulinski, J. W. Buchler, Y. J. Lee, W. R. Scheidt, and M. Wicholas, *Inorg. Chem.*, 1988, **27**, 927.

451. L. Latos-Grażyński, J. Lisowski, L. Szterenberg, M. M. Olmstead, and A. L. Balch, *J. Org. Chem.*, 1991, **56**, 4043.

452. L. Latos-Grażyński, Core Modified Heteroanalogues of Porphyrins and Metalloporphyrins, in 'The Porphyrin Handbook', eds. K. M. Kadish, K. M. Smith, and R. Guilard, Academic Press, New York, 2000, Vol. 2, p. 361.

453. W.-S. Cho, H.-J. Kim, B. J. Littler, M. A. Miller, C.-H. Lee, and J. S. Lindsey, *J. Org. Chem.*, 1999, **64**, 7890.

454. W.-C. Chen and C.-H. Hung, *Inorg. Chem.*, 2001, **40**, 5070.

455. G. R. Geier III and J. S. Lindsey, *J. Org. Chem.*, 1999, **64**, 1596.

456. G. R. Geier III, D. M. Haynes, and J. S. Lindsey, *Org. Lett.*, 1999, **1**, 1455.

457. M. Stepien and L. Latos-Grażyński, *J. Am. Chem. Soc.*, 2002, **124**, 3838.

458. E. Vogel, M. Köcher, H. Schmickler, and J. Lex, *Angew. Chem., Int. Ed. Engl.*, 1986, **25**, 257.

459. E. Vogel, M. Balci, K. Pramod, P. Koch, J. Lex, and O. Ermer, *Angew. Chem., Int. Ed. Engl.*, 1987, **26**, 928.

460. M. P. Donzello, D. Dini, G. D'Arcangelo, C. Ercolani, R. Zhan, Z. Ou, P. A. Stuzhin, and K. M. Kadish, *J. Am. Chem. Soc.*, 2003, **125**, 14190.

461. M. A. Aukauloo and R. Guilard, *New J. Chem.*, 1994, **18**, 1205.

462. J. L. Sessler, E. A. Grucker, S. J. Weghorn, M. Kosters, M. Schäfer, J. Lex, and E. Vogel, *Angew. Chem., Int. Ed. Engl.*, 1994, **33**, 2308.

463. H. Falk and Q. Q. Chen, *Monatsh. Chem.*, 1996, **127**, 69.

464. A. Heger, Ph.D. dissertation, University of Cologne, 1997.

465. P. A. Stuzhin, S. I. Vagin, and M. Hanack, *Inorg. Chem.*, 1998, **37**, 2655.

466. S. Vagin, M. Barthel, D. Dini, and M. Hanack, *Inorg. Chem.*, 2003, **42**, 2683.

467. C. C. Leznoff, in 'Phthalocyanines: Properties and Applications', eds. C. C. Leznoff and A. B. P. Lever, VCH, New York, 1989, p. 1.

468. M. Kimura, T. Hamakawa, K. Hanabusa, H. Shirai, and N. Kobayashi, *Inorg. Chem.*, 2001, **40**, 4775.

469. B. L. Iverson, K. Shreder, T. Morishima, M. Rosingana, and J. L. Sessler, *J. Org. Chem.*, 1995, **60**, 6616.

470. A. Jasat and D. Dolphin, *Chem. Rev.*, 1997, **97**, 2267.

471. J. L. Sessler, G. Hemmi, T. D. Mody, T. Murai, A. Burrell, and S. W. Young, *Acc. Chem. Res.*, 1994, **27**, 43.

472. T. D. Mody, L. Fu, and J. L. Sessler, *Prog. Inorg. Chem.*, 2001, **49**, 551.
473. M. Fujiki, H. Tabei, and K. Isa, *J. Am. Chem. Soc.*, 1986, **108**, 1532.
474. R. Paolesse, S. Liococcia, and T. Boschi, *Inorg. Chim. Acta*, 1990, **178**, 9.
475. R. Paolesse, S. Licoccia, G. Bandoli, A. Dolmella, and T. Boschi, *Inorg. Chem.*, 1994, **33**, 1171.
476. T. Boschi, S. Licoccia, R. Paolesse, M. A. Tehran, G. Pelizzi, and F. Vitali, *J. Chem. Soc., Dalton Trans.*, 1990, 463.
477. R. Paolesse, L. Jaquinod, M. O. Senge, and K. M. Smith, *J. Org. Chem.*, 1997, **62**, 6193.
478. Z. Gross, N. Galili, and I. Saltsman, *Angew. Chem., Int. Ed. Engl.*, 1999, **38**, 1427.
479. E. Steene, A. Dey, and A. Ghosh, *J. Am. Chem. Soc.*, 2003, **125**, 16300.
480. B. Ramdhanie, C. L. Stern, and D. P. Goldberg, *J. Am. Chem. Soc.*, 2001, **123**, 9447.
481. J. E. Falk, 'Porphyrins and Metalloporphyrins', Elsevier, Amsterdam, 1964, p. 129.
482. K. M. Smith, in 'Porphyrins and Metalloporphyrins', ed. K. M. Smith, Elsevier, Amsterdam, 1975, p. 757.
483. K. S. Suslick and R. A. Watson, *New J. Chem.*, 1992, **16**, 633.
484. L. M. Proniewicz, K. Bajdor, and K. Nakamoto, *J. Phys. Chem.*, 1986, **90**, 1760.
485. D. B. Morell, J. Barrett, and P. S. Clezy, *Biochem. J.*, 1961, **78**, 793.
486. F. A. Walker, B. H. Huynh, W. R. Scheidt, and S. R. Osvath, *J. Am. Chem. Soc.*, 1986, **108**, 5288.
487. L. M. Mink, K. A. Christensen, and F. A. Walker, *J. Am. Chem. Soc.*, 1992, **114**, 6930.
488. A. D. Adler, F. R. Longo, F. Kampas, and J. Kim, *J. Inorg. Nucl. Chem.*, 1970, **32**, 2443.
489. A. D. Adler, F. R. Longo, and V. Varadi, *Inorg. Synth.*, 1976, **16**, 213.
490. L. D. Sparks, C. J. Medforth, M.-S. Park, J. R. Chamberlain, M. R. Ondrias, M. O. Senge, K. M. Smith, and J. A. Shelnutt, *J. Am. Chem. Soc.*, 1993, **115**, 581.
491. M. J. M. Nesset, Ph.D. Dissertation, The Effect of Axial Ligands and Porphyrin Substituents on the Dynamic and Electronic Properties of Model Hemes, University of Arizona, 1993.
492. M. J. M. Nesset, S. Cai, T. Kh. Shokhireva, N. V. Shokhirev, S. E. Jacobson, K. Jayaraj, A. Gold, and F. A. Walker, *Inorg. Chem.*, 2000, **39**, 532.
493. F. A. Walker, V. L. Balke, and G. A. McDermott, *J. Am. Chem. Soc.*, 1982, **104**, 1569.
494. T. N. Sorrell, *Inorg. Synth.*, 1980, **20**, 161.
495. M. LaBarre, Ph.D. Dissertation, Investigation of the Catalytic Cycle of the Molybdoenzyme Sulfite Oxidase: Synthesis and Spectroscopic Study of Model Systems, University of Arizona, 1992.
496. U. Simonis, F. A. Walker, P. L. Lee, B. J. Hanquet, D. J. Meyerhoff, and W. R. Scheidt, *J. Am. Chem. Soc.*, 1987, **109**, 2659.
497. C. K. Chang, R. K. Dinello, and D. Dolphin, *Inorg. Synth.*, 1980, **20**, 143.
498. J. W. Buchler, G. Eikelmann, L. Puppe, K. Rohbock, H. H. Schneehage, and D. Weck, *Liebigs Ann. Chem.*, 1971, **745**, 135.
499. J. W. Buchler, M. Folz, H. Habets, J. van Kaam, and K. Rohbock, *Chem. Ber.*, 1976, **109**, 1477.
500. G. K. Lahiri, J. S. Summers, and A. M. Stolzenberg, *Inorg. Chem.*, 1991, **30**, 5049.
501. Y. Terazono and D. Dolphin, *Inorg. Chim. Acta*, 2003, **346**, 261.
502. J. Grodkowski, D. Behar, P. Neta, and P. Hambright, *J. Phys. Chem. A*, 1997, **101**, 248.
503. I. Bhugun, D. Lexa, and J.-M. Savéant, *J. Am. Chem. Soc.*, 1994, **116**, 5015.
504. I. Bhugun, D. Lexa, and J.-M. Savéant, *J. Am. Chem. Soc.*, 1996, **118**, 3982.
505. E. Anoxolabéhère, G. Chottard, and D. Lexa, *New J. Chem.*, 1994, **18**, 889.
506. G. Balducci, C. Geneviève, C. Gueutin, D. Lexa, and J.-M. Savéant, *Inorg. Chem.*, 1994, **33**, 1972.
507. D. Lexa and J. M. Savéant, *J. Am. Chem. Soc.*, 1982, **104**, 3504.
508. I. Bhugun, D. Lexa, and J.-M. Savéant, *Inorg. Chem.*, 1994, **33**, 1972.
509. D. Lexa, J.-M. Savéant, H. J. Schafer, K. B. Su, B. Vering, and D. L. Wang, *J. Am. Chem. Soc.*, 1990, **112**, 6162.
510. I. Bhugun, D. Lexa, and J.-M. Savéant, *J. Phys. Chem.*, 1996, **100**, 19981.
511. C. Gueutin, D. Lexa, D. L. Wang, and J. M. Savéant, *Organometallics*, 1989, **8**, 1607.
512. M. Hammouche, D. Lexa, M. Momenteau, and J. M. Savéant, *J. Am. Chem. Soc.*, 1991, **113**, 8455.
513. D. Lexa, J. Mispelter, and J. M. Savéant, *J. Am. Chem. Soc.*, 1981, **103**, 6806.
514. C. Gueutin, D. Lexa, M. Momenteau, and J. M. Savéant, *J. Am. Chem. Soc.*, 1990, **112**, 1874.
515. D. Lexa, M. Momenteau, and J. Mispelter, *Biochim. Biophys. Acta*, 1974, **338**, 151.
516. R. J. Donohoe, M. Atamian, and D. F. Bocian, *J. Am. Chem. Soc.*, 1987, **109**, 5593.
517. J. P. Collman, T. N. Sorell, J. H. Dawson, J. R. Trudell, E. Bunnenberg, and C. Djerassi, *Proc. Natl. Acad. Sci. U.S.A.*, 1976, **73**, 6.
518. C. A. Reed, *Adv. Chem. Ser.*, 1982, **201**, 333.
519. I. A. Cohen, D. Ostfeld, and B. Lichtenstein, *J. Am. Chem. Soc.*, 1972, **94**, 4522.

520. C. H. Welborn, D. Dolphin, and B. R. James, *J. Am. Chem. Soc.*, 1981, **103**, 2869.

521. D. L. Hickman, A. Shirazi, and H. M. Goff, *Inorg. Chem.*, 1985, **24**, 563.

522. K. M. Kadish, E. Van Caemelbecke, F. D'Souza, M. Lin, D. J. Nurco, C. J. Medforth, T. P. Forsyth, B. Kattinger, K. M. Smith, S. Fukuzumi, and J. A. Shelnutt, *Inorg. Chem.*, 1998, **38**, 2188.

523. M. Pawlicki and L. Latos-Grażyński, *Inorg. Chem.*, 2002, **41**, 5866.

524. J. P. Collman, J. I. Brauman, T. R. Halbert, and K. S. Suslick, *Proc. Natl. Acad. Sci. U.S.A.*, 1976, **73**, 333.

525. K. M. Kadish, G. Larson, D. Lexa, and M. Momenteau, *J. Am. Chem. Soc.*, 1975, **97**, 282.

526. K. M. Kadish and G. Larson, *Bioinorg. Chem.*, 1977, **7**, 95.

527. E. Van Lenthe, A. van der Avoird, W. R. Hagen, and E. J. Rejerse, *J. Phys. Chem. A*, 2000, **104**, 2070.

528. A. B. P. Lever and J. P. Wilshire, *Inorg. Chem.*, 1978, **17**, 1145.

529. G. S. Srivatsa, D. T. Sawyer, N. J. Boldt, and D. F. Bocian, *Inorg. Chem.*, 1985, **24**, 2133.

530. J. Teraoka, S. Hashimoto, H. Sugimoto, M. Mori, and T. Kitagawa, *J. Am. Chem. Soc.*, 1987, **109**, 180.

531. F. A. Walker, *J. Am. Chem. Soc.*, 1970, **92**, 4235.

532. E. van Lenthe, A. van der Avoird, W. R. Hagen, and E. J. Reijerse, *J. Phys. Chem. A*, 2000, **104**, 2070.

533. S. E. Jones, G. S. Srivatsa, D. T. Sawyer, T. G. Traylor, and T. C. Mincey, *Inorg. Chem.*, 1983, **22**, 3903.

534. D. Brault, R. Santus, E. J. Land, and A. J. Swallow, *J. Phys. Chem.*, 1984, **88**, 5836.

535. T. Mashiko, C. A. Reed, K. J. Haller, and W. R. Scheidt, *Inorg. Chem.*, 1984, **23**, 3192.

536. M. Pawlicki and L. Latos-Grażyński, *Inorg. Chem.*, 2002, **41**, 5866.

537. C. Gueutin, D. Lexa, J. M. Savéant, and M. Momenteau, *J. Electroanal. Chem. Interfacial Electrochem.*, 1988, **256**, 219.

538. S. Sano, Y. Maeda, S. Ogawa, and I. Morishima, *J. Am. Chem. Soc.*, 1981, **103**, 2888.

539. A. L. Balch, L. Latos-Grażyński, B. C. Noll, M. M. Olmstead, and E. P. Zovinka, *Inorg. Chem.*, 1992, **31**, 2248.

540. A. L. Balch, L. Latos-Grażyński, B. C. Noll, M. M. Olmstead, L. Szterenberg, and N. Safari, *J. Am. Chem. Soc.*, 1993, **115**, 1422.

541. I.-K. Choi, Y. Liu, D. W. Feng, K.-J. Paeng, and M. D. Ryan, *Inorg. Chem.*, 1991, **30**, 1832.

542. P. D. Boyd, D. A. Buckingham, R. E. McMeeking, and S. Mitra, *Inorg. Chem.*, 1979, **18**, 3585.

543. D. J. Bergman and A. B. Hooper, *Eur. J. Biochem.*, 2003, **270**, 1935.

544. M. Z. Cabail and A. A. Pacheco, *Inorg. Chem.*, 2003, **42**, 270.

545. M. Momenteau and C. A. Reed, *Chem. Rev.*, 1994, **94**, 659.

546. M. Momenteau, in 'Supramolecular Control of Structure and Reactivity', ed. A. D. Hamilton, Wiley, Chichester, 1996, p. 155.

547. L. Cheng and G. B. Richter-Addo, The Binding and Activation of Nitric Oxide by Metalloporphyrins and Hemes, in 'The Porphyrin Handbook', eds. K. M. Kadish, K. M. Smith, and R. Guilard, Academic Press, New York, 2000, Vol. 4, p. 219.

548. W. R. Scheidt, Systematics of the Stereochemistry of Porphyrins and Metalloporphyrins, in 'The Porphyrin Handbook', eds. K. M. Kadish, K. M. Smith, and R. Guilard, Academic Press, New York, 2000, Vol. 3, p. 79.

549. P. C. Ford, L. E. Laverman, and I. M. Lorkovic, *Adv. Inorg. Chem.*, 2003, **54**, 203.

550. P. C. Ford and I. M. Lorkovic, *Chem. Rev.*, 2002, **102**, 993.

551. M. Hoshino, L. Laverman, and P. C. Ford, *Coord. Chem. Rev.*, 1999, **187**, 75.

552. J. K. M. Sanders, N. Bampos, Z. Clyde-Watson, S. L. Darling, J. C. Hawley, H.-J. Kim, C. C. Mak, and S. J. Webb, Axial Coordination Chemistry of Metalloporphyrins, in 'The Porphyrin Handbook', eds. K. M. Kadish, K. M. Smith, and R. Guilard, Academic Press, New York, 2000, Vol. 3, p. 15.

553. G. Simonneaux and A. Bondon, Isocyanides and Phosphines as Axial Ligands in Heme Proteins and Iron Porphyrin Models, in 'The Porphyrin Handbook', eds. K. M. Kadish, K. M. Smith, and R. Guilard, Academic Press, New York, 2000, Vol. 5, p. 300.

554. Y.-P. Liu, *J. Chem. Inf. Comput. Sci.*, 2001, **41**, 22.

555. A. Schäfer, H. Horn, and R. Ahlrichs, *J. Phys. Chem.*, 1992, **97**, 2571.

556. P. M. Kozlowski, T. G. Spiro, A. Bérces, and M. Z. Zgierski, *J. Phys. Chem. B*, 1998, **102**, 2603.

557. Y.-K. Choe, T. Nakajima, K. Hirao, and R. Lindh, *J. Phys. Chem.*, 1999, **111**(9), 3837.

558. B. Song, S. Namgoong, and B. Yu, *Korean Chem. Soc.*, 1997, **41**, 420.

559. T. Picaud, C. Le Moigne, B. Loock, M. Momenteau, and A. Desbois, *J. Am. Chem. Soc.*, 2003, **125**, 11616.

560. S. Othman, A. Le Lirzin, and A. Desbois, *Biochemistry*, 1993, **32**, 9781.

561. C. Le Moigne, T. Picaud, A. Boussac, B. Loock, M. Momenteau, and A. Desbois, *Inorg. Chem.*, 2003, **42**, 6081.

562. C. Cao, S. Dahal, M. Shang, A. M. Beatty, W. Hibbs, C. E. Schulz, and W. R. Scheidt, *Inorg. Chem.*, 2003, **42**, 5202.

563. C. J. Chang, E. A. Baker, B. J. Pistorio, Y. Deng, Z.-H. Loh, S. E. Miller, S. D. Carpenter, and D. G. Nocera, *Inorg. Chem.*, 2002, **41**, 3102.

564. A. Robert and B. Meunier, *J. Am. Chem. Soc.*, 1997, **119**, 5968.

565. H. M. Goff and G. N. La Mar, *J. Am. Chem. Soc.*, 1977, **99**, 6599.
566. K. Migita and G. N. La Mar, *J. Phys. Chem.*, 1980, **84**, 2953.
567. L. Latos-Grazynski, R. J. Cheng, G. N. La Mar, and A. L. Balch, *J. Am. Chem. Soc.*, 1982, **104**, 5922.
568. S. H. Strauss, M. E. Silver, K. M. Long, R. G. Thompson, R. A. Hudgens, K. Spartalian, and J. A. Ibers, *J. Am. Chem. Soc.*, 1985, **107**, 4207.
569. J. Mispelter, M. Momenteau, and J. M. Lhoste, *Mol. Phys.*, 1977, **33**, 1715.
570. P. E. Ellis, T. Linard, T. Symanski, R. D. Jones, J. R. Budge, and F. Basolo, *J. Am. Chem. Soc.*, 1980, **102**, 1889; J. E. Linard, P. E. Ellis, J. R. Budge, R. D. Jones, and F. Basolo, *J. Am. Chem. Soc.*, 1980, **102**, 1896.
571. J. Mispelter, M. Momenteau, and J. M. Lhoste, *J. Chem. Phys.*, 1980, **72**, 1003.
572. H. M. Goff, G. N. La Mar, and C. A. Reed, *J. Am. Chem. Soc.*, 1977, **99**, 3641.
573. G. A. Tondreau and R. G. Wilkins, *Inorg. Chem.*, 1986, **25**, 2745.
574. K. M. Kadish and D. Schaefer, *J. Chem. Soc., Chem. Commun.*, 1980, 1273.
575. M. K. Safo, M. J. M. Nesset, F. A. Walker, P. G. Debrunner, and W. R. Scheidt, *J. Am. Chem. Soc.*, 1997, **119**, 9438.
576. K. Rachlewicz, L. Latos-Grażyński, and E. Vogel, *Inorg. Chem.*, 2000, **39**, 3247.
577. G. E. Wuenschell, C. Tetreau, D. Lavalette, and C. R. Reed, *J. Am. Chem. Soc.*, 1992, **115**, 3635.
578. D. R. Evans, T. Drovetskaya, R. Bau, C. R. Reed, and P. D. W. Boyd, *J. Am. Chem. Soc.*, 1997, **119**, 3633.
579. K. M. Barkigia, M. Palacio, Y. Sun, M. Nogues, M. W. Renner, F. Varret, P. Battioni, D. Mansuy, and J. Fajer, *Inorg. Chem.*, 2002, **41**, 5647.
580. B. Song, B. Park, and C. Han, *Bull. Korean Chem. Soc.*, 2002, **23**, 119.
581. B. Song, B. Park, and B. Yu, *Bull. Korean Chem. Soc.*, 2003, **24**, 981.
582. P. Tagliatesta, J. Li, A. Autret, E. Van Caemelbecke, A. Villard, F. D-Souza, and K. M. Kadish, *Inorg. Chem.*, 1996, **35**, 5570.
583. N. K. Chaudhury, G. S. S. Saini, and A. L. Verma, *Inorg. Chem.*, 1995, **34**, 346.
584. K. T. Moore, J. T. Fletcher, and M. J. Therien, *J. Am. Chem. Soc.*, 1999, **121**, 5196.
585. K. T. Moore, I. T. Horváth, and M. J. Therien, *Inorg. Chem.*, 2000, **121**, 5196.
586. M. K. Ellison, C. E. Schulz, and W. R. Scheidt, *Inorg. Chem.*, 2002, **41**, 2173.
587. W. M. Reiff, C. M. Frommen, G. T. Yee, and S. P. Sellers, *Inorg. Chem.*, 2000, **39**, 2076.
588. S. P. Sellers, B. J. Korte, J. P. Fitzgerald, W. M. Reiff, and G. T. Yee, *J. Am. Chem. Soc.*, 1998, **120**, 4662.
589. B. R. McGarvey, *Inorg. Chem.*, 1988, **27**, 4691.
590. M.-S. Liao and S. Scheiner, *J. Phys. Chem.*, 2002, **116**(9), 3635.
591. W. D. Edwards, B. Weiner, and M. C. Zerner, *J. Am. Chem. Soc.*, 1986, **108**, 2196.
592. G. Lang, K. Spartalian, C. A. Redd, and J. P. Collman, *J. Phys. Chem.*, 1978, **69**, 5242.
593. J. Robbins Wolf, C. G. Hamaker, J.-P. Djukic, T. Kodadek, and L. K. Woo, *J. Am. Chem. Soc.*, 1995, **117**, 9194.
594. G. A. Mirafzai, G. Cheng, and K. L. Woo, *J. Am. Chem. Soc.*, 2002, **124**, 176.
595. G. Cheng, G. A. Mirafzal, and K. L. Woo, *Organometallics*, 2003, **22**, 1468.
596. Y. Li, J.-S. Huang, Z.-Y. Zhou, C.-M. Che, and X.-Z. You, *J. Am. Chem. Soc.*, 2002, **124**, 13185.
597. S. O. Obare, T. Ito, M. H. Balfour, and G. J. Meyer, *Nano Lett.*, 2003, **3**(8), 1151.
598. M. W. Grinstaff, M. G. Hill, E. R. Birnbaum, W. P. Schaefer, J. A. Labinger, and H. B. Gray, *Inorg. Chem.*, 1995, **34**, 4896.
599. M. J. M. Nesset, N. V. Shokhirev, P. D. Enemark, S. E. Jacobson, and F. A. Walker, *Inorg. Chem.*, 1996, **35**, 5188.
600. K. M. Kadish and R. K. Rhodes, *Inorg. Chem.*, 1983, **22**, 1090.
601. D. Mansuy, P. Battioni, J. C. Chottard, C. Riche, and A. Chiaroni, *J. Am. Chem. Soc.*, 1983, **105**, 455.
602. O. Q. Munro, P. S. Madlala, R. A. F. Warby, T. B. Seda, and G. Hearne, *Inorg. Chem.*, 1999, **38**, 4724.
603. G. C. Wagner and R. Kassner, *Biochim. Biophys. Acta*, 1975, **392**, 319.
604. D. Brault and M. Rougee, *Biochemistry*, 1974, **13**, 4591.
605. M. Rougee and D. Brault, *Biophys. Chem.*, 1975, **14**, 4100.
606. K. M. Kadish and L. A. Bottomley, *J. Am. Chem. Soc.*, 1977, **99**, 2380.
607. K. M. Kadish, L. A. Bottomley, and D. Beroiz, *Inorg. Chem.*, 1978, **17**, 1124.
608. F. A. Walker, M.-W. Lo, and M. T. Ree, *J. Am. Chem. Soc.*, 1976, **98**, 5552.
609. T. Hashimoto, R. L. Dyer, M. L. Crossley, J. E. Baldwin, and F. Basolo, *J. Am. Chem. Soc.*, 1982, **104**, 2101.
610. C. F. Portela, D. Magde, and T. G. Traylor, *Inorg. Chem.*, 1993, **32**, 1313.
611. M. K. Safo, G. P. Gupta, and W. R. Scheidt, *Inorg. Chem.*, 1990, **29**, 626.
612. W. R. Scheidt, S. R. Osvath, and Y. J. Lee, *J. Am. Chem. Soc.*, 1987, **109**, 1958.
613. J. W. Lauher and J. A. Ibers, *J. Am. Chem. Soc.*, 1974, **96**, 4447.

614. K. M. Kadish and L. A. Bottomley, *Inorg. Chem.*, 1980, **19**, 832.

615. G. Al-Jaff, J. Silver, and M. T. Wilson, *Inorg. Chim. Acta*, 1990, **176**, 307.

616. D. K. White, J. B. Cannon, and T. G. Traylor, *J. Am. Chem. Soc.*, 1979, **101**, 2443.

617. J. P. Collman, J. I. Brauman, K. M. Doxsee, T. R. Halbert, and K. S. Suslick, *Proc. Natl. Acad. Sci. U.S.A.*, 1978, **75**, 564.

618. W. R. Scheidt, J. F. Kirner, J. L. Hoard, and C. A. Reed, *J. Am. Chem. Soc.*, 1987, **109**, 1963.

619. D. M. Collins, R. Countryman, and J. L. Hoard, *J. Am. Chem. Soc.*, 1972, **94**, 2066.

620. J. R. Polam, T. Kh. Shokhireva, K. Raffii, U. Simonis, and F. A. Walker, *Inorg. Chim. Acta*, 1977, **263**, 109.

621. K. T. Moore, J. T. Fletcher, and M. J. Therien, *J. Am. Chem. Soc.*, 1999, **121**, 5196.

622. M. Grodzicki, H. Flint, H. Winkler, F. A. Walker, and A. X. Trautwein, *J. Phys. Chem. A*, 1997, **101**, 4202.

623. W. Jentzen, X.-Z. Song, and J. A. Shelnutt, *J. Phys. Chem. B*, 1996, **101**, 1684.

624. W. Jentzen, J.-G. Ma, and J. A. Shelnutt, *Biophys. J.*, 1998, **74**, 753.

625. J.-G. Ma, J. Zhang, R. Franco, S.-L. Jia, I. Moura, J. J. G. Moura, P. M. H. Kroneck, and J. A. Shelnutt, *Biochemistry*, 1998, **37**, 12431.

626. G. W. Pettigrew and G. R. Moore, ‘Cytochromes c: Biological Aspects’, Springer-Verlag, Berlin, 1987.

627. G. R. Moore and G. W. Pettigrew, ‘Cytochromes c: Evolutionary, Structural and Physicochemical Aspects’, Springer-Verlag, Berlin, 1990.

628. D. Mandon, F. Ott-Woelfel, J. Fischer, R. Weiss, E. Bill, and A. X. Trautwein, *Inorg. Chem.*, 1990, **29**, 2442.

629. H. Kalish, J. E. Camp, M. Stępién, L. Latos-Grażyński, and A. L. Balch, *J. Am. Chem. Soc.*, 2001, **123**, 11719.

630. D. White-Dixon, C. Kirmaier, and D. Holten, *J. Am. Chem. Soc.*, 1985, **107**, 808.

631. D. Taube, T. G. Traylor, D. Magde, K. Walde, and J. Luo, *J. Am. Chem. Soc.*, 1992, **114**, 9182.

632. T. G. Traylor, K. W. Hill, W.-P. Fann, S. Tsuchiya, and B. E. Dunlap, *J. Am. Chem. Soc.*, 1992, **114**, 1308.

633. T. G. Traylor, D. Magde, J. Luo, K. N. Walda, D. Bandyopadhyay, G.-Z. Wu, and V. S. Sharma, *J. Am. Chem. Soc.*, 1992, **114**, 9011.

634. L. M. Mink, J. R. Polam, K. A. Christensen, M. A. Bruck, and F. A. Walker, *J. Am. Chem. Soc.*, 1995, **117**, 9329.

635. J. R. Polam, J. L. Wright, K. A. Christensen, F. A. Walker, H. Flint, H. Winkler, M. Grodzicki, and A. X. Trautwein, *J. Am. Chem. Soc.*, 1996, **118**, 5272.

636. T. Nozawa, M. Sato, M. Hatano, N. Kobayashi, and T. Osa, *Chem. Lett.*, 1983, 1289.

637. H. Nasri, Y. Wang, B. H. Huynh, and W. R. Scheidt, *J. Am. Chem. Soc.*, 1991, **113**, 717.

638. D. Lexa and J. M. Savéant, Supramolecular Effects in the Redox and Coordination Chemistry of Superstructured Iron Porphyrins, in ‘Redox Chemistry and Interfacial Behaviour of Biological Molecules’, eds. G. Dryhurst and K. Niki, Plenum, New York, 1988, p. 1.

639. T. J. Bartczak, S. Wolowiec, and L. Latos-Grażyński, *Inorg. Chim. Acta*, 1998, **277**, 242.

640. B. S. Lou, J. K. Snyder, P. Marshall, J. S. Wang, G. Wu, R. J. Kulmacz, A. L. Tsai, and J. Wang, *Biochemistry*, 2000, **39**, 12424.

641. J. L. Hoard, in ‘Porphyrins and Metalloporphyrins’, ed. K. M. Smith, Elsevier, Amsterdam, 1975, p. 317.

642. J. P. Collman, J. I. Brauman, K. M. Doxsee, T. R. Halbert, E. Bunnenberg, R. E. Linder, G. N. La Mar, J. Del Gaudio, G. Lang, and K. Spartalian, *J. Am. Chem. Soc.*, 1980, **102**, 4182.

643. J. P. Collman, J. I. Brauman, T. J. Collins, B. L. Iverson, G. Lang, R. B. Pettman, J. L. Sessler, and M. A. Walters, *J. Am. Chem. Soc.*, 1983, **105**, 3038.

644. L. Jaquinod, L. Prevot, J. Fischer, and R. Weiss, *Inorg. Chem.*, 1998, **37**, 1142.

645. J. Mispelter, M. Momenteau, and J. M. Lhoste, *Biochimie*, 1981, **63**, 911.

646. P. A. Arnold, D. R. Benson, D. J. Brink, M. P. Hendrich, G. S. Jas, M. L. Kennedy, D. T. Petasis, and M. Wang, *Inorg. Chem.*, 1997, **36**, 5306.

647. M. Momenteau, W. R. Scheidt, C. W. Eigenbrot, and C. A. Reed, *J. Am. Chem. Soc.*, 1988, **110**, 1207.

648. G. B. Jameson, F. S. Molinari, J. A. Ibers, J. P. Collman, J. I. Brauman, E. Rose, and K. S. Suslick, *J. Am. Chem. Soc.*, 1978, **100**, 6769; G. B. Jameson, F. S. Molinari, J. A. Ibers, J. P. Collman, J. I. Brauman, E. Rose, and K. S. Suslick, *J. Am. Chem. Soc.*, 1978, **100**, 3224.

649. W. R. Scheidt and D. K. Geiger, *Inorg. Chem.*, 1982, **21**, 1208.

650. H. Nasri, J. Fischer, R. Weiss, E. Bill, and A. Trautwein, *J. Am. Chem. Soc.*, 1987, **109**, 2549.

651. M. Schappacher, L. Ricard, R. Weiss, R. Montiel-Montoya, U. Gonser, E. Bill, and A. Trautwein, *Inorg. Chim. Acta*, 1983, **78**, L9.

652. C. Caron, A. Mitschler, G. Rivière, L. Ricard, M. Schappacher, and R. Weiss, *J. Am. Chem. Soc.*, 1979, **101**, 7401; M. Schappacher, L. Ricard, J. Fischer, R. Weiss, R. Montiel-Montoya, E. Bill, and A. X. Trautwein, *Inorg. Chem.*, 1989, **28**, 4639.

653. E. L. Bominaar, X. D. Ding, A. Gismelseed, E. Bill, H. Winkler, A. X. Trautwein, H. Nasri, J. Fischer, and R. Weiss, *Inorg. Chem.*, 1992, **31**, 1845.

654. M. Schappacher, L. Ricard, J. Fischer, R. Weiss, E. Bill, R. Montiel-Montoya, H. Winkler, and A. X. Trautwein, *Eur. J. Biochem.*, 1987, **168**, 419.

655. M. Momenteau, B. Loock, C. Tetreau, D. Lavalette, A. Croisy, C. Schaeffer, C. Huel, and J. M. Lhoste, *J. Chem. Soc., Perkin Trans. 2*, 1987, 249.

656. J. Silver and B. Luckas, *Inorg. Chim. Acta*, 1983, **80**, 107; *Inorg. Chim. Acta*, 1984, **91**, 125.

657. B. A. Shaevitz, G. Lang, and C. A. Reed, *Inorg. Chem.*, 1988, **27**, 4607.

658. L. Leondiadis, M. Momenteau, and A. Desbois, *Inorg. Chem.*, 1992, **31**, 4691.

659. L. A. Andersson, M. Mylrajan, T. M. Loehr, E. P. Sullivan, and S. H. Strauss, *New J. Chem.*, 1992, **16**, 569.

660. S. Franzen, S. G. Boxer, R. B. Dyer, and W. H. Woodruff, *J. Phys. Chem. B*, 2000, **104**, 10359.

661. J.-P. Battioni, I. Artaud, D. Dupre, P. Leduc, I. Akhrem, D. Mansuy, J. Fischer, R. Weiss, and I. Morgenstern-Badarau, *J. Am. Chem. Soc.*, 1986, **108**, 5598.

662. C. A. Reed, T. Mashiko, W. R. Scheidt, K. Spartalian, and G. Lang, *J. Am. Chem. Soc.*, 1980, **102**, 2302.

663. C. Lecomte, R. H. Blessing, P. Coppens, and A. Tabard, *J. Am. Chem. Soc.*, 1986, **108**, 9942.

664. D. W. Thompson, R. M. Kretzer, E. L. Lebeau, D. V. Scaltrito, R. A. Ghiladi, K.-C. Lam, A. L. Rheingold, K. D. Karlin, and G. J. Meyer, *Inorg. Chem.*, 2003, **42**(17), 5211.

665. J. E. Newton and M. B. Hall, *Inorg. Chem.*, 1984, **23**, 4627, and references therein.

666. M. Cerdonio, A. Congui-Castellano, L. Calabrese, S. Morante, B. Pipisa, and S. Vitale, *Proc. Natl. Acad. Sci. U.S.A.*, 1978, **75**, 4916.

667. M. Bacci, M. Cerdonio, and S. Vitale, *Biophys. Chem.*, 1979, **10**, 113.

668. Y. Maeda, T. Harami, Y. Morita, A. Trautwein, and U. Gonser, *J. Chem. Phys.*, 1981, **75**, 36.

669. Z. S. Herman, G. H. Loew, and M. M. Rohmer, *Int. J. Quantum Chem., Quantum Biol. Symp.*, 1980, **7**, 137.

670. A. Waleh and G. H. Loew, *J. Am. Chem. Soc.*, 1982, **104**, 3513.

671. J. S. Valentine and A. B. Curtis, *J. Am. Chem. Soc.*, 1975, **97**, 224.

672. E. McCandlish, A. R. Miksztal, M. Nappa, A. Q. Sprenger, J. S. Valentine, J. D. Strong, and T. G. Spiro, *J. Am. Chem. Soc.*, 1980, **102**, 4268.

673. T. G. Traylor and A. P. Berzinis, *J. Am. Chem. Soc.*, 1980, **102**, 2844.

674. J. Cannon, J. Geibel, M. Whipple, and T. G. Traylor, *J. Am. Chem. Soc.*, 1976, **98**, 3395.

675. C. K. Chang and T. G. Traylor, *J. Am. Chem. Soc.*, 1973, **95**, 5810; *Proc. Natl. Acad. Sci. U.S.A.*, 1973, **70**, 2647.

676. J. P. Collman, *Acc. Chem. Res.*, 1977, **10**, 265.

677. J. P. Collman, R. R. Gagne, C. A. Reed, T. R. Halbert, G. Lang, and W. T. Robinson, *J. Am. Chem. Soc.*, 1975, **97**, 1427.

678. J. P. Collman, J. I. Brauman, B. L. Iverson, J. L. Sessler, R. M. Morris, and Q. H. Gibson, *J. Am. Chem. Soc.*, 1983, **105**, 3052.

679. T. C. Grogan, N. Bag, T. G. Traylor, and D. Magde, *J. Phys. Chem.*, 1994, **98**, 13791.

680. J. Almog, J. E. Baldwin, and J. Huff, *J. Am. Chem. Soc.*, 1975, **97**, 227.

681. E. Rose, F. Basolo, P. N. Venkatasubramanian, J. C. Swartz, R. D. Jones, and B. M. Hoffman, *Proc. Natl. Acad. Sci. U.S.A.*, 1982, **79**, 5742.

682. H. Tang and D. Dolphin, *Inorg. Chem.*, 1996, **35**, 6539.

683. N. Bag, T. M. Grogan, D. Magde, C. Slebodnick, M. R. Johnson, and J. A. Ibers, *J. Am. Chem. Soc.*, 1994, **116**, 11833.

684. C. Slebodnick, J. C. Fettinger, H. B. Peterson, and J. A. Ibers, *J. Am. Chem. Soc.*, 1996, **118**, 3216.

685. T. G. Traylor, S. Tsuchiya, D. Campbell, M. Mitchell, D. Stynes, and N. Koga, *J. Am. Chem. Soc.*, 1985, **107**, 604.

686. T. G. Traylor, N. Koga, and L. A. Deardruff, *J. Am. Chem. Soc.*, 1985, **107**, 6504, and references therein.

687. T. G. Traylor, N. Koga, L. A. Deardruff, P. N. Swepston, and J. A. Ibers, *J. Am. Chem. Soc.*, 1984, **106**, 5132.

688. S. David, B. R. James, D. Dolphin, T. G. Traylor, and M. A. Lopez, *J. Am. Chem. Soc.*, 1994, **116**, 6.

689. C. K. Chang, *J. Am. Chem. Soc.*, 1977, **99**, 2819.

690. A. R. Battersby, S. A. J. Bartholomew, and T. Nitta, *J. Chem. Soc., Chem. Commun.*, 1983, 1291.

691. P. Schmitt, D. Mandon, J. Fischer, and R. Weiss, *New J. Chem.*, 1992, **16**, 763.

692. B. Ward, C. B. Wang, and C. K. Chang, *J. Am. Chem. Soc.*, 1981, **103**, 5236.

693. A. Lecas, Z. Renko, and E. Rose, *Tetrahedron Lett.*, 1985, **26**, 1019; B. Boitrel, A. Lecas, Z. Renko, and E. Rose, *J. Chem. Soc., Chem. Commun.*, 1985, 1820; *New J. Chem.*, 1989, **13**, 73.

694. M. Momenteau, J. Mispelter, B. Loock, and E. Bisagni, *J. Chem. Soc., Perkin Trans. 1*, 1983, 189.

695. J. P. Collman, J. I. Brauman, J. P. Fitzgerald, J. W. Sarapany, and J. A. Ibers, *J. Am. Chem. Soc.*, 1988, **110**, 3486.

696. J. P. Collman, X. Zhang, K. Wang, and J. I. Brauman, *J. Am. Chem. Soc.*, 1994, **116**, 6245.

697. B. Boitrel, A. Lecas, and E. Rose, *J. Chem. Soc., Chem. Commun.*, 1989, 349; B. Boitrel, A. Lecas-Nawrocka, and E. Rose, *Tetrahedron Lett.*, 1992, **33**, 227.

698. M. Matsu-ura, F. Tani, and Y. Naruta, *J. Am. Chem. Soc.*, 2002, **124**, 1941.

699. J. P. Collman, R. R. Gagne, C. A. Reed, W. T. Robinson, and G. A. Rodley, *Proc. Natl. Acad. Sci. U.S.A.*, 1974, **71**, 1326; G. B. Jameson, G. A. Rodley, W. T. Robinson, R. R. Gagne, C. A. Reed, and J. P. Collman, *Inorg. Chem.*, 1978, **17**, 850.

700. M. Momenteau, J. Mispelter, B. Loock, and J.-M. Lhoste, *J. Chem. Soc., Perkin Trans. 1*, 1985, 221.

701. J. S. Olson, R. E. McKinnie, M. P. Mims, and D. K. White, *J. Am. Chem. Soc.*, 1983, **105**, 1522.

702. R. H. Austin, K. W. Beesen, L. Eisenstein, H. Frauenfelder, and I. C. Gunsalus, *Biochemistry*, 1975, **14**, 5355; P. Beece, L. Eisenstein, H. Frauenfelder, G. Good, M. C. Marden, L. Reinisch, A. H. Reynolds, L. B. Sorensen, and K. T. Yu, *Biochemistry*, 1980, **19**, 5147.

703. R. D. Jones, D. A. Summerville, and F. Basolo, *Chem. Rev.*, 1979, **79**, 139.

704. K. M. Smith and B. R. James, *Coord. Chem. Rev.*, 1981, **39**, 31.

705. A. V. Bogatskii and Z. I. Zhilina, *Russ. Chem. Rev.*, 1982, **51**, 592.

706. J. P. Collman, T. R. Halpert, and K. S. Suslick, in ‘Metal Activation of Dioxygen’, ed. T. G. Spiro, Wiley, New York, 1980, p. 1.

707. J. P. Collman, R. Boulatov, C. J. Sunderland, and L. Fu, *Chem. Rev.*, 2004, **104**, 561.

708. G. B. Jameson and J. A. Ibers, *Comments Inorg. Chem.*, 1983, **2**, 97.

709. S. David, D. Dolphin, and B. R. James, in ‘Frontiers in Bioinorganic Chemistry’, ed. A. V. Xavier, VCH, Weinheim, 1985, p. 163.

710. J. E. Baldwin and P. Perlmutter, *Top. Curr. Chem.*, 1984, **121**, 181.

711. K. S. Suslick and T. J. Reinert, *J. Chem. Educ.*, 1985, **11**, 974.

712. T. G. Traylor, D. H. Campbell, S. Tsuchiya, D. V. Stynes, and M. J. Mitchell, in ‘Hemoglobin and Dioxygen Binding’, ed. C. Ho, Elsevier, Amsterdam, 1982, p. 426.

713. P. I. Reisberg and J. S. Olson, *J. Biol. Chem.*, 1980, **255**, 4144; P. I. Reisberg and J. S. Olson, *J. Biol. Chem.*, 1980, **255**, 4151.

714. J. H. Wang, in ‘Oxygenases’, ed. O. Hayashi, Academic Press, New York, 1962, p. 502.

715. R. MacQuarrie and Q. H. Gibson, *J. Biol. Chem.*, 1971, **246**, 5832; V. S. Sharma, M. R. Schmidt, and H. M. Ranny, *J. Biol. Chem.*, 1976, **251**, 4267; W. H. Huestis and H. M. Raftery, *Biochemistry*, 1975, **14**, 1886.

716. E. Antonini and M. Brunori, ‘Hemoglobin and Myoglobin and their Reactions with Ligands’, North Holland, Amsterdam, 1971.

717. J. P. Collman, *Inorg. Chem.*, 1997, **36**, 5145.

718. J. W. Buchler, *Angew. Chem., Int. Ed. Engl.*, 1978, **17**, 407.

719. Q. H. Gibson and F. J. W. Roughton, *J. Physiol.*, 1957, **136**, 507.

720. L. J. Parkhurst, P. Sima, and D. J. Goss, *Biochemistry*, 1980, **19**, 2688.

721. Q. H. Gibson and M. H. Smith, *Proc. R. Soc. London, Ser. B*, 1965, **163**, 206.

722. S. A. Bornman, *Chem. Eng. News*, 1999, **77**, 31.

723. R. Huber, O. Epp, and H. Formanek, *J. Mol. Biol.*, 1970, **52**, 349.

724. E. A. Padlan and W. E. Love, *J. Biol. Chem.*, 1974, **249**, 4067.

725. J. C. Norvell, A. C. Nunes, and B. P. Schoenborn, *Science*, 1975, **190**, 568; J. C. Hanson and B. P. Schoenborn, *J. Mol. Biol.*, 1981, **153**, 117.

726. E. J. Heidner, R. C. Ladner, and M. F. Perutz, *J. Mol. Biol.*, 1976, **104**, 707.

727. P. W. Tucker, S. E. V. Phillips, M. F. Perutz, R. Houtchens, and W. S. Caughey, *Proc. Natl. Acad. Sci. U.S.A.*, 1978, **75**, 1076.

728. W. Steigeman and E. Weber, *J. Mol. Biol.*, 1979, **127**, 309.

729. J. M. Baldwin, *J. Mol. Biol.*, 1980, **136**, 103.

730. J. Kuriyan, S. Wilz, M. Karplus, and G. A. Petsko, *J. Mol. Biol.*, 1986, **192**, 133.

731. J. P. Collman, J. I. Brauman, T. J. Collins, B. Iverson, and J. L. Sessler, *J. Am. Chem. Soc.*, 1981, **103**, 2450.

732. J. Geibel, J. Cannon, D. Campbell, and T. G. Traylor, *J. Am. Chem. Soc.*, 1978, **100**, 3575.

733. W. S. Caughey, *Ann. N.Y. Acad. Sci.*, 1970, **174**, 148.

734. J. P. Collman, J. I. Brauman, and K. M. Doxsee, *Proc. Natl. Acad. Sci. U.S.A.*, 1979, **76**, 6035.

735. M. W. Makinen, R. A. Houtchens, and W. S. Caughey, *Proc. Natl. Acad. Sci. U.S.A.*, 1979, **76**, 6042.

736. M. F. Perutz, *Br. Med. Bull.*, 1976, **32**, 195.

737. T. G. Spiro and P. M. Kozlowski, *Acc. Chem. Res.*, 2001, **34**, 137.

738. G. B. Jameson, F. S. Molinari, J. A. Ibers, J. P. Collman, J. I. Brauman, E. Rose, and K. S. Suslick, *J. Am. Chem. Soc.*, 1980, **102**, 3224.

739. S. M. Peng and J. A. Ibers, *J. Am. Chem. Soc.*, 1976, **98**, 8032.

740. W. R. Scheidt, K. J. Haller, M. Fons, T. Mashiko, and C. A. Reed, *Biochemistry*, 1981, **20**, 3653.

741. K. Kim, J. Fettinger, J. L. Sessler, M. Cyr, J. Hugdahl, J. P. Collman, and J. A. Ibers, *J. Am. Chem. Soc.*, 1989, **111**, 403.

742. M. R. Johnson, W. K. Seok, and J. A. Ibers, *J. Am. Chem. Soc.*, 1991, **113**, 3998.

743. K. Kim and J. A. Ibers, *J. Am. Chem. Soc.*, 1991, **113**, 6077.

744. I. P. Geronthanassis, M. Momenteau, P. J. Barrie, C. G. Kalodimos, and G. E. Hawkes, *Inorg. Chem.*, 1996, **35**, 2674.

745. R. Salzmann, M. T. McMahon, N. Godbout, L. K. Sanders, M. Wojdelski, and E. Oldfield, *J. Am. Chem. Soc.*, 1999, **121**, 3818.

746. W. J. Wallace, J. A. Volpe, J. C. Maxwell, W. S. Caughey, and S. Charache, *Biochem. Biophys. Res. Commun.*, 1976, **68**, 1379.

747. M. F. Perutz, *Nature (London)*, 1970, **228**, 726.

748. C. K. Chang and T. G. Traylor, *Proc. Natl. Acad. Sci. U.S.A.*, 1975, **72**, 1166.
749. K. S. Suslick and M. M. Fox, *J. Am. Chem. Soc.*, 1983, **105**, 3507.
750. S. E. V. Phillips and B. P. Schoenborn, *Nature (London)*, 1981, **292**, 81.
751. B. Shaanan, *Nature (London)*, 1982, **296**, 683.
752. T. Kitagawa, M. R. Ondrias, D. L. Rousseau, M. Ikeda-Saito, and T. Yonetani, *Nature (London)*, 1982, **296**, 869.
753. J. C. Maxwell and W. S. Caughey, *Biochemistry*, 1976, **15**, 368.
754. J. D. Satterlee, M. Teintze, and J. H. Richards, *Biochemistry*, 1978, **17**, 1456.
755. W. H. Fuchsman and C. A. Appleby, *Biochemistry*, 1979, **18**, 1309.
756. W. S. Caughey, E. Eberspaecher, W. H. Fuchsman, S. McCoy, and J. O. Alben, *Ann. N.Y. Acad. Sci.*, 1969, **153**, 722.
757. E. H. Abbott and P. A. Rafson, *J. Am. Chem. Soc.*, 1974, **96**, 7378.
758. M. A. Stanford, J. C. Swartz, T. E. Phillips, and B. M. Hoffman, *J. Am. Chem. Soc.*, 1980, **102**, 4492.
759. J. E. Falk, J. N. Phillips, and E. A. Magnusson, *Nature (London)*, 1966, **212**, 1531.
760. J. A. McGray, M. Sono, and T. Asakura, *Porphyrin Chem. Adv.*, 1979, **189**, 205.
761. I. Yamazaki, T. Araiso, H. Yamada, and R. Makino, *Adv. Biophys.*, 1978, **11**, 249.
762. D. Dolphin, B. R. James, and H. C. Welborn, *J. Mol. Catal.*, 1980, **7**, 201.
763. T. G. Traylor, D. K. White, D. H. Campbell, and A. B. Berzinis, *J. Am. Chem. Soc.*, 1981, **103**, 4932.
764. J. O. Alben and W. S. Caughey, *Biochemistry*, 1968, **7**, 175.
765. M. Chevion, J. M. Salhany, J. Peisach, C. L. Castillo, and W. E. Blumberg, *Isr. J. Chem.*, 1977, **15**, 311.
766. F. A. Walker, *J. Am. Chem. Soc.*, 1973, **95**, 1154.
767. J. C. Swartz, M. A. Stanford, J. N. Moy, B. M. Hoffman, and J. S. Valentine, *J. Am. Chem. Soc.*, 1979, **101**, 3396.
768. T. G. Traylor, A. Berzinis, D. Cambell, J. Cannon, W. Lee, T. Mincey, and D. K. White, in ‘Biochemical and Clinical Aspects of Oxygen’, ed. W. S. Caughey, Academic Press, New York, 1979, p. 455.
769. T. Mincey and T. G. Traylor, *J. Am. Chem. Soc.*, 1979, **101**, 455.
770. H. Diekmann, C. K. Chang, and T. G. Traylor, *J. Am. Chem. Soc.*, 1971, **93**, 4068.
771. J. E. Baldwin and J. Huff, *J. Am. Chem. Soc.*, 1973, **95**, 5757.
772. D. H. Busch, L. L. Zimmer, J. J. Grzybowski, D. J. Olszanski, S. C. Jackels, R. C. Callahan, and G. C. Christoph, *Proc. Natl. Acad. Sci. U.S.A.*, 1981, **78**, 5919.
773. M. Momenteau, *Pure Appl. Chem.*, 1986, **58**, 1493.
774. J. A. Hutchinson, T. G. Traylor, and L. J. Noe, *J. Am. Chem. Soc.*, 1982, **104**, 3221.
775. M. Momenteau and D. Lavalette, *J. Am. Chem. Soc.*, 1978, **100**, 4322.
776. D. Lavalette, C. Tetreau, and M. Momenteau, *J. Am. Chem. Soc.*, 1979, **101**, 5395.
777. E. M. Gaul and R. Kassner, *Inorg. Chem.*, 1986, **25**, 3734.
778. C. Tetreau, M. Momenteau, and D. Lavalette, *Inorg. Chem.*, 1990, **29**, 1727.
779. C. Tetreau, B. Boitrel, E. Rose, and D. Lavalette, *J. Chem. Soc., Chem. Commun.*, 1989, 1805.
780. T. G. Traylor, *Pure Appl. Chem.*, 1991, **63**, 265, and references therein.
781. J. Mispelter, M. Momenteau, D. Lavalette, and J. H. Lhoste, *J. Am. Chem. Soc.*, 1983, **105**, 5165.
782. D. Lavalette, C. Tetreau, J. Mispelter, M. Momenteau, and J. Lhoste, *Eur. J. Biochem.*, 1984, **145**, 155.
783. K. S. Suslick, M. M. Fox, and T. Reinert, *J. Am. Chem. Soc.*, 1984, **106**, 4522.
784. S. H. Lin, N. T. Yu, J. Tame, D. Shih, P. Renaud, J. Pagnier, and K. Nagai, *J. Biochem.*, 1990, **29**, 5562.
785. C. Tetreau, D. Lavalette, M. Momenteau, and J. M. Lhoste, *Proc. Natl. Acad. Sci. U.S.A.*, 1987, **84**, 2267.
786. O. K. Medhi, S. Mazumdar, and S. Mitra, *Inorg. Chem.*, 1989, **28**, 3243; S. Mazumdar, O. K. Medhi, and S. Mitra, *Inorg. Chem.*, 1991, **30**, 700; S. Mazumdar and O. K. Medhi, *J. Chem. Soc., Dalton Trans.*, 1990, 2633; S. Mazumdar, O. K. Medhi, and S. Mitra, *Inorg. Chem.*, 1988, **27**, 2541.
787. F. A. Walker, *J. Am. Chem. Soc.*, 1973, **95**, 1150.
788. H. C. Stynes and J. A. Ibers, *J. Am. Chem. Soc.*, 1972, **94**, 1559.
789. H. C. Stynes and J. A. Ibers, *J. Am. Chem. Soc.*, 1972, **94**, 5125.
790. D. V. Stynes, H. C. Stynes, B. R. James, and J. A. Ibers, *J. Am. Chem. Soc.*, 1973, **95**, 1142.
791. D. V. Stynes, H. C. Stynes, B. R. James, and J. A. Ibers, *J. Am. Chem. Soc.*, 1973, **95**, 1796.
792. F. Basolo, B. M. Hoffman, and J. A. Ibers, *Acc. Chem. Res.*, 1975, **8**, 384.
793. M. A. Lopez and P. A. Kollman, *J. Am. Chem. Soc.*, 1989, **111**, 6212.
794. T. G. Traylor, D. J. Taube, K. A. Jongeward, and D. Magde, *J. Am. Chem. Soc.*, 1990, **112**, 6875.
795. C. A. Sawicki and Q. H. Gibson, *J. Mol. Biol.*, 1977, **252**, 7538.
796. T. G. Traylor and A. P. Berzinis, *Proc. Natl. Acad. Sci. U.S.A.*, 1980, **77**, 3171.
797. T. G. Traylor, M. G. Mitchell, S. Tsuchiya, D. H. Campbell, D. V. Stynes, and N. Koga, *J. Am. Chem. Soc.*, 1981, **103**, 5234.
798. M. Shimizu and F. Basolo, *Inorg. Chim. Acta*, 1984, **91**, 247.

799. D. Lavalette and M. Momenteau, *J. Chem. Soc., Perkin Trans. 2*, 1983, 962.

800. Y. Uemori and E. Kyono, *Inorg. Chem.*, 1989, **28**, 1690.

801. M. Momenteau and D. Lavalette, *J. Chem. Soc., Chem. Commun.*, 1982, 341.

802. S. Neya, K. Imai, H. Hori, H. Ishikawa, K. Ishimori, D. Okuno, S. Nagatomo, M. Hata, and N. Funasaki, *Inorg. Chem.*, 2003, **42**, 1456.

803. T. Hayashi, H. Dejima, T. Matsuo, H. Sato, D. Murata, and Y. Hisaeda, *J. Am. Chem. Soc.*, 2002, **124**, 11226.

804. T. Komatsu, Y. Matsukawa, and E. Tsuchida, *Bioconjugate Chem.*, 2002, **13**, 397.

805. A. Nakagawa, T. Komatsu, and E. Tsuchida, *Bioconjugate Chem.*, 2001, **12**, 648.

806. A. Nakagawa, T. Komatsu, and E. Tsuchida, *Bioconjugate Chem.*, 2000, **11**, 772.

807. E. Tsuchida, T. Komatsu, and T. Yanagimoto, *J. Porphyr. Phthalocyan.*, 2000, **4**, 81.

808. E. Tsuchida, T. Komatsu, Y. Matsukawa, K. Hamamatsu, and J. Wu, *Bioconjugate Chem.*, 1999, **10**, 797.

809. T. Komatsu, K. Hamamatsu, J. Wu, and E. Tsuchida, *Bioconjugate Chem.*, 1999, **10**, 82.

810. E. Tsuchida, K. Ando, H. Maejima, N. Kawai, T. Komatsu, S. Takeoka, and H. Nishide, *Bioconjugate Chem.*, 1997, **8**, 534.

811. E. Tsuchida, K. T. Komatsu, K. Arai, K. Yamada, H. Nishide, and H.-J. Fuhrhop, *Langmuir*, 1995, **11**, 1877.

812. J. N. Harvey, *J. Am. Chem. Soc.*, 2000, **122**, 12401.

813. M. Hoshino and T. Baba, *J. Am. Chem. Soc.*, 1998, **120**, 6820.

814. J. E. Baldwin, J. H. Cameron, M. J. Crossley, I. J. Dagley, S. R. Hall, and T. Klose, *J. Chem. Soc., Dalton Trans.*, 1984, 1739.

815. E. Monzami, G. Alzuet, L. Casella, C. Redaelli, C. Bassani, A. M. Sanangelantoni, M. Gullotti, L. De Gioia, L. Santagostini, and F. Chillemi, *Biochemistry*, 2000, **39**, 9571.

816. D. Barrick, *Biochemistry*, 1994, **33**, 6554.

817. J.-P. Battioni, J.-C. Chottard, and D. Mansuy, *Inorg. Chem.*, 1982, **21**, 2056.

818. J.-P. Battioni, D. Mansuy, and J.-C. Chottard, *Inorg. Chem.*, 1980, **19**, 791.

819. A. M. Huff, C. K. Chang, D. K. Cooper, K. M. Smith, and J. H. Dawson, *Inorg. Chem.*, 1993, **32**, 1460.

820. M. Tsubaki and N.-T. Yu, *Biochemistry*, 1982, **21**, 1140.

821. S. Hirota, T. Ogura, K. Shinzawa_itoh, S. Yoshikawa, M. Nagai, and T. Kitagawa, *J. Phys. Chem.*, 1994, **98**, 6652.

822. J. Sun, C. K. Chang, and T. M. Loehr, *J. Phys. Chem. B*, 1997, **101**, 1476.

823. L. A. Lipscomb, B.-S. Lee, and N.-T. Yu, *Inorg. Chem.*, 1993, **32**, 281.

824. G. B. Ray, X.-Y. Li, J. A. Ibers, J. L. Sessler, and T. G. Spiro, *J. Am. Chem. Soc.*, 1994, **116**, 162.

825. G. Lang and W. Marshall, *Proc. Phys. Soc.*, 1966, **87**, 3.

826. K. Spartalian and G. Lang, *J. Phys.*, 1976, **37**, C6.

827. Y. Maeda, T. Harami, Y. Morita, A. Trautwein, and U. Gonser, *J. Chem. Phys.*, 1981, **75**, 36.

828. R. B. Moon and J. H. Richards, *Biochemistry*, 1974, **13**, 3437.

829. B. Boitrel, A. Lecas-Nawrocka, and E. Rose, *Tetrahedron Lett.*, 1991, **32**, 2129.

830. G. N. La Mar, D. B. Viscio, D. L. Budd, and K. Gersonde, *Biochem. Biophys. Res. Commun.*, 1978, **82**, 19; G. N. La Mar, C. M. Dellinger, and S. S. Sankar, *Biochem Biophys. Res. Commun.*, 1985, **128**, 628.

831. H. C. Lee, J. K. Gard, T. L. Brown, and E. Oldfield, *J. Am. Chem. Soc.*, 1985, **107**, 4087.

832. L. Baltzer, E. D. Becker, B. A. Averill, J. M. Hutchinson, and O. Gansow, *J. Am. Chem. Soc.*, 1984, **106**, 2444.

833. L. Baltzer and M. Landergren, *J. Chem. Soc., Chem. Commun.*, 1987, 32.

834. L. Baltzer and M. Landergren, *J. Am. Chem. Soc.*, 1990, **112**, 2804.

835. C. G. Kalodimos, I. P. Geronthanassis, E. Rose, G. E. Hawkes, and R. Pieratelli, *J. Am. Chem. Soc.*, 1999, **121**, 2903.

836. R. H. Havlin, N. Godbout, R. Salzmann, M. Wojdelski, W. Arnold, C. E. Shulz, and E. Oldfield, *J. Am. Chem. Soc.*, 1998, **120**, 3144.

837. N. Godbout, R. Havlin, R. Salzmann, P. G. Debrunner, and E. Oldfield, *J. Phys. Chem. A*, 1998, **102**, 2342.

838. M. T. McMahon, A. C. deDios, N. Godbout, R. Salzmann, D. D. Laws, H. Le, R. H. Havlin, and E. Oldfield, *J. Am. Chem. Soc.*, 1998, **120**, 4784.

839. R. Salzmann, M. T. McMahon, N. Godbout, R. K. Sanders, M. Wojdelski, and E. Oldfield, *J. Am. Chem. Soc.*, 1999, **121**, 3818.

840. M. Kaupp, C. Rovira, and M. Parrinello, *J. Phys. Chem. B*, 2000, **104**, 5200.

841. J. O. Stern and J. Peisach, *J. Biol. Chem.*, 1974, **249**, 7495.

842. J. P. Collman and T. N. Sorell, *J. Am. Chem. Soc.*, 1975, **97**, 4133.

843. C. K. Chang and D. Dolphin, *Proc. Natl. Acad. Sci. U.S.A.*, 1976, **73**, 3338.

844. A. R. Battersby, W. Howson, and A. D. Hamilton, *J. Chem. Soc., Chem. Commun.*, 1982, 1266.

845. F. Niedercorn, H. Ledon, and I. Tkatchenko, *J. Organomet. Chem.*, 1987, **328**, C7.

846. T. Higuchi, S. Uzu, and M. Hirobe, *J. Am. Chem. Soc.*, 1990, **112**, 7051.

847. J. P. Collman and S. E. Groh, *J. Am. Chem. Soc.*, 1982, **104**, 1391.

848. N. Suzuki, T. Higuchi, Y. Urano, K. Kikuchi, H. Uekusa, Y. Ohashi, T. Uchida, T. Kitagawa, and T. Nigano, *J. Am. Chem. Soc.*, 1999, **121**, 11571.

849. D. El-Kasmi, C. Tetreau, D. Lavalette, and M. Momenteau, *J. Am. Chem. Soc.*, 1995, **117**, 6041.

850. C. K. Chang and D. Dolphin, *J. Am. Chem. Soc.*, 1976, **98**, 1607.

851. M. Schappacher, L. Ricard, R. Weiss, R. Montiel-Montoya, E. Bill, U. Gonser, and A. Trautwein, *J. Am. Chem. Soc.*, 1981, **103**, 7646.

852. F. Tani, M. Matsu-ura, S. Nakayama, M. Ichimura, N. Nakamura, and Y. Naruta, *J. Am. Chem. Soc.*, 2001, **123**, 1133.

853. M. Schappacher, L. Ricard, J. Fischer, R. Weiss, R. Monteil-Montoya, E. Bill, and A. X. Trautwein, *Inorg. Chem.*, 1989, **28**, 4639.

854. D. Mansuy and P. Battioni, Isocyanides and Phosphines as Axial Ligands in Heme Proteins and Iron Porphyrin Models, in 'The Porphyrin Handbook', eds. K. M. Kadish, K. M. Smith, and R. Guilard, Academic Press, New York, 2000, Vol. 4, p. 1.

855. G. Loew and M. M. Rohmer, *J. Am. Chem. Soc.*, 1980, **102**, 3655.

856. C. K. Chang and D. Dolphin, *Bioorg. Chem.*, 1978, **4**, 37.

857. L. Ricard, M. Schappacher, J. Fischer, R. Weiss, R. Monteil-Montoya, E. Bill, U. Gonser, and A. Trautwein, *Nouv. J. Chim.*, 1983, **7**, 405.

858. T. G. Traylor, T. C. Mincey, and A. P. Berzinis, *J. Am. Chem. Soc.*, 1981, **103**, 7084.

859. Y. Tatsuno, K. Tomita, and K. Tani, *Inorg. Chim. Acta*, 1988, **152**, 5.

860. A. P. Berzinis and T. G. Traylor, *Biochem. Biophys. Res. Commun.*, 1979, **87**, 229.

861. C. A. Hasemann, K. G. Ravichandran, J. A. Peterson, and J. Deisenhofer, *J. Mol. Biol.*, 1994, **236**, 1169.

862. H. Li and T. L. Poulos, *Acta Crystallogr.*, 1995, **D51**, 21.

863. J. R. Cupp-Vickery and T. L. Poulos, *Nat. Struct. Biol.*, 1995, **2**, 144.

864. M. Sundaramoorthy, J. Terner, and T. L. Poulos, *Structure*, 1995, **3**, 1367.

865. T. L. Poulos, B. C. Finzel, and A. J. Howard, *J. Mol. Biol.*, 1987, **195**, 687.

866. B. R. Crane, A. S. Arvai, R. Gachhui, C. Wu, D. K. Ghosh, E. D. Getzoff, D. J. Stuehr, and J. A. Tainer, *Science*, 1997, **278**, 425.

867. N. Ueyama, N. Nishikawa, Y. Yamada, T. Okamura, and A. Nakamura, *J. Am. Chem. Soc.*, 1996, **118**, 12826.

868. N. Ueyama, N. Nishikawa, Y. Yamada, T. Okamura, S. Oka, H. Sakurai, and A. Nakamura, *Inorg. Chem.*, 1998, **37**, 2415.

869. T. G. Traylor and V. S. Sharma, *Biochemistry*, 1992, **31**, 2847.

870. T. G. Traylor, A. F. Duprat, and V. S. Sharma, *J. Am. Chem. Soc.*, 1993, **114**, 810.

871. G. R. A. Wyllie, C. E. Schulz, and W. R. Scheidt, *Inorg. Chem.*, 2003, **42**, 5722.

872. E. A. Morlina and M. A. J. Rodgers, *J. Am. Chem. Soc.*, 1996, **118**, 11798.

873. D. E. Koshland, *Science*, 1992, **258**, 1861.

874. W. R. Scheidt and M. K. Ellison, *Acc. Chem. Res.*, 1999, **32**, 350.

875. J. H. Enemark and R. D. Feltham, *Coord. Chem. Rev.*, 1974, **13**, 339.

876. B. B. Wayland and L. W. Olson, *J. Am. Chem. Soc.*, 1974, **96**, 6037.

877. H. Nasri, M. K. Ellison, S. Chen, B. H. Huynh, and W. R. Scheidt, *J. Am. Chem. Soc.*, 1997, **119**, 6274.

878. W. R. Scheidt and M. E. Frisse, *J. Am. Chem. Soc.*, 1975, **97**, 17.

879. G. R. A. Wyllie and W. R. Scheidt, *Inorg. Chem.*, 2003, **42**, 4259.

880. M. K. Ellison and W. R. Scheidt, *J. Am. Chem. Soc.*, 1997, **119**, 7404.

881. A. Ghosh and T. Wondimagegn, *J. Am. Chem. Soc.*, 2000, **122**, 8101.

882. P. G. Piciulo, G. Rupprecht, and W. R. Scheidt, *J. Am. Chem. Soc.*, 1974, **96**, 5293.

883. W. R. Scheidt and P. G. Piciulo, *J. Am. Chem. Soc.*, 1976, **98**, 1913.

884. D. P. Ballou, Y. Zhao, P. E. Brandish, and M. A. Marletta, *Proc. Natl. Acad. Sci. U.S.A.*, 2002, **99**, 12097.

885. H. Nasri, K. J. Haller, Y. Wang, B. H. Huynh, and W. R. Scheidt, *Inorg. Chem.*, 1992, **31**, 3459.

886. I.-K. Choi, Y. Liu, D. W. Feng, K.-J. Paeng, and M. R. Ryan, *Inorg. Chem.*, 1991, **30**, 1832.

887. L. A. Lipscomb, B.-S. Lee, and N.-T. Yu, *Inorg. Chem.*, 1993, **32**, 281.

888. T. S. Kurtikyan, G. G. Martirosyan, I. M. Lorkovic, and P. C. Ford, *Inorg. Chem.*, 2002, **124**, 10124.

889. D. D. Klug, M. Z. Zgierski, J. S. Tse, Z. Liu, J. R. Kincaid, K. Czarnecki, and R. J. Hemley, *Proc. Natl. Acad. Sci. U.S.A.*, 2002, **99**, 12526.

890. M. Seto, Y. Yoda, S. Kikuta, X. W. Zhang, and M. Ando, *Phys. Rev. Lett.*, 1995, **74**, 3828.

891. C. Keppler, K. Achterhold, A. Ostermann, U. van Bürck, W. Potzel, A. I. Chumakov, A. Q. Baron, R. Rüffer, and F. Parak, *Eur. Biophys. J.*, 1997, **25**, 221.

892. H. Paulsen, H. Winkler, A. X. Trautwein, H. Grünsteudel, V. Rusanov, and H. Toftlund, *Phys. Rev. B*, 1999, **59**, 975.

893. J. T. Sage, S. M. Durbin, W. Sturhahn, D. C. Wharton, P. M. Champion, P. Hession, J. Sutter, and E. E. Alp, *Phys. Rev. Lett.*, 2001, **86**, 4966.

894. J. T. Sage, C. Paxson, G. R. A. Wyllie, W. Sturhahn, S. M. Durbin, P. M. Champion, E. E. Alp, and W. R. Scheidt, *J. Phys.: Condens. Matter*, 2001, **13**, 7707.

895. H. Paulsen, V. Rusanov, R. Benda, C. Herta, V. Schünemann, C. Janiak, T. Dorn, A. I. Chumakov, H. Winkler, and A. X. Trautwein, *J. Am. Chem. Soc.*, 2002, **124**, 3007.

896. B. K. Rai, S. M. Durbin, E. W. Prohofsky, J. T. Sage, G. R. A. Wyllie, W. R. Scheidt, W. Sturhahn, and E. E. Alp, *Biophys. J.*, 2002, **82**, 2951.

897. B. K. Rai, S. M. Durbin, E. W. Prohofsky, J. T. Sage, M. K. Ellison, W. R. Scheidt, W. Sturhahn, and E. E. Alp, *Phys. Rev. E*, 2002, **66**, 051904.

898. B. K. Rai, S. M. Durbin, E. W. Prohofsky, J. T. Sage, M. K. Ellison, A. Roth, W. R. Scheidt, W. Sturhahn, and E. E. Alp, *J. Am. Chem. Soc.*, 2003, **125**, 6927.

899. B. M. Leu, M. Z. Zgierski, G. R. A. Wyllie, W. R. Scheidt, W. Sturhahn, E. E. Alp, S. M. Durbin, and J. T. Sage, *J. Am. Chem. Soc.*, 2004, **126**, 4211.

900. R. G. Hayes, M. E. Ellison, and W. R. Scheidt, *Inorg. Chem.*, 2000, **39**, 3665.

901. S. Patchkovskii and T. Ziegler, *Inorg. Chem.*, 2000, **39**, 5354.

902. Y. Zhang, W. Gossman, and E. Oldfield, *J. Am. Chem. Soc.*, 2003, **125**, 16387.

903. I. T. Bae, Y. Tolmachev, Y. Mo, D. Scherson, W. R. Schiedt, M. K. Ellison, M.-C. Cheng, R. S. Armstrong, and P. A. Lay, *Inorg. Chem.*, 2001, **40**, 3256.

904. I. C. Stefan, Y. Mo, S. Y. Ha, S. Kim, and D. A. Scherson, *Inorg. Chem.*, 2003, **42**, 4316.

905. M. D. Lim, I. M. Lorkovic, K. Wedeking, A. W. Zanella, C. F. Works, S. M. Massick, and P. C. Ford, *J. Am. Chem. Soc.*, 2002, **124**, 9737.

906. I. Lorković and P. C. Ford, *J. Am. Chem. Soc.*, 2000, **122**, 6516.

907. J. C. Patterson, I. M. Lorković, and P. C. Ford, *Inorg. Chem.*, 2003, **42**, 4902.

908. I. M. Lorković and P. C. Ford, *Inorg. Chem.*, 2000, **39**, 632.

909. R. Lin and P. J. Farmer, *J. Am. Chem. Soc.*, 2001, **123**, 1143.

910. M. Frangione, J. Port, M. Baldiwala, A. Judd, J. Galley, M. DeVega, K. Linna, L. Caron, E. Anderson, and J. A. Goodwin, *Inorg. Chem.*, 1997, **36**, 1904.

911. L. Cheng, D. R. Powell, M. A. Khan, and G. B. Richter-Addo, *Chem. Commun.*, 2000, 2301.

912. M. Hoshino and M. Kogure, *J. Phys. Chem.*, 1989, **93**, 5478.

913. H. Adachi, H. Sonoki, M. Hoshino, M. Wakasa, H. Hayashi, and Y. Miyazaki, *J. Phys. Chem. A*, 2001, **105**, 392.

914. L. E. Laverman, A. Wanat, J. Oszajca, G. Stochel, P. C. Ford, and R. van Eldik, *J. Am. Chem. Soc.*, 2001, **123**, 285.

915. L. E. Laverman and P. C. Ford, *J. Am. Chem. Soc.*, 2001, **123**, 11614.

916. D. S. Bohle and C.-H. Hung, *J. Am. Chem. Soc.*, 1995, **117**, 9584.

917. B. O. Fernandez, I. M. Lorcovic, and P. C. Ford, *Inorg. Chem.*, 2003, **42**, 2.

918. N. S. Trofimova, A. Y. Safronov, and O. Ikeda, *Inorg. Chem.*, 2003, **42**, 1945.

919. C. E. Castro and S. K. O'Shea, *J. Org. Chem.*, 1995, **60**, 1922.

920. C. E. Castro, *J. Am. Chem. Soc.*, 1996, **118**, 3984.

921. S. K. O'Shea, W. Wang, R. S. Wade, and C. E. Castro, *J. Org. Chem.*, 1996, **61**, 6388.

922. E. A. Dierks, S. Hu, K. M. Vogel, A. E. Yu, T. G. Spiro, and J. N. Burstyn, *J. Am. Chem. Soc.*, 1997, **119**, 7316.

923. J. Lee, J. A. Hunt, and J. T. Groves, *J. Am. Chem. Soc.*, 1998, **120**, 7493.

924. M. P. Jensen and D. P. Riley, *Inorg. Chem.*, 2002, **41**, 4788.

925. L. Cheng, I. Novozhilova, C. Kim, A. Kovalevsky, K. A. Bagley, P. Coppens, and G. B. Richter-Addo, *J. Am. Chem. Soc.*, 2000, **122**, 7142.

926. T. Komatsu, Y. Matsukawa, and E. Tsuchida, *Bioconjugate Chem.*, 2001, **12**, 71.

927. R. Lin and P. J. Farmer, *J. Am. Chem. Soc.*, 2000, **122**, 2393.

928. F. Sulc, C. E. Immoos, D. Pervitsky, and P. J. Farmer, *J. Am. Chem. Soc.*, 2004, **126**, 1096.

929. F. Sulc, D. Ma, E. Fleisher, P. J. Farmer, and G. N. La Mar, *J. Biol. Inorg. Chem.*, 2003, **8**, 348.

930. V. Shafirovich and S. Lymar, *Proc. Natl. Acad. Sci. U.S.A.*, 2002, **99**, 7342.

931. V. Shafirovich and S. Lymar, *J. Am. Chem. Soc.*, 2003, **125**, 6547.

932. M. D. Bartberger, J. M. Fukuto, and K. N. Houk, *Proc. Natl. Acad. Sci. U.S.A.*, 2001, **98**, 2194.

933. M. D. Bartberger, W. Liu, E. Ford, K. M. Miranda, C. Switzer, J. M. Fukuto, P. J. Farmer, D. A. Wink, and K. N. Houk, *Proc. Natl. Acad. Sci. U.S.A.*, 2002, **99**, 10958.

934. M. Grätzel, S. Taniguchi, and A. Henglein, *Ber. Bunsen-Ges. Phys. Chem.*, 1970, **74**, 1003.

935. Y. Shiro, M. Fujii, T. Iizuka, S. I. Adachi, K. Tsukamoto, K. Nakahara, and H. Shoun, *J. Biol. Chem.*, 1995, **270**, 1617.

936. A. Daiber, T. Nauser, N. Takaya, T. Kudo, P. Weber, C. Hultschig, H. Shoun, and V. Ullrich, *J. Inorg. Biochem.*, 2002, **88**, 343.

937. W. S. Caughey, C. H. Barlow, D. H. O'Keeffe, and M. C. O'Toole, *Ann. N.Y. Acad. Sci.*, 1973, **206**, 296.

938. G. B. Jameson and J. A. Ibers, *Inorg. Chem.*, 1979, **18**, 1200.

939. T. G. Traylor and D. V. Stynes, *J. Am. Chem. Soc.*, 1980, **102**, 5938.

940. T. G. Traylor, D. Campbell, S. Tsuchiya, M. Mitchell, and D. V. Stynes, *J. Am. Chem. Soc.*, 1980, **102**, 5941.

941. M. Le Plouzennec, A. Bondon, and G. Simonneaux, *Inorg. Chem.*, 1984, **23**, 4398.

942. J. Chung, H. C. Lee, and E. Oldfield, *J. Magn. Reson.*, 1990, **90**, 148.

943. L. A. Yatsunyk and F. A. Walker, *Inorg. Chem.*, 2004, **43**, 757.

944. T. Sakai, Y. Ohgo, T. Ikeue, M. Takahashi, M. Takeda, and M. Nakamura, *J. Am. Chem. Soc.*, 2003, **125**, 13028.

945. L. J. Young and L. M. Siegel, *Biochemistry*, 1988, **27**, 4990.

946. V. S. Sharma, T. G. Traylor, R. Gardiner, and H. Mizukami, *Biochemistry*, 1985, **26**, 3837.

947. E. Antonini, M. Brunori, J. Wyman, and R. W. Noble, *J. Biol. Chem.*, 1966, **241**, 3236; R. Cassoly and Q. H. Gibson, *J. Mol. Biol.*, 1975, **91**, 301.

948. I. Morishima, H. Fujii, Y. Shiro, and S. Sano, *J. Am. Chem. Soc.*, 1986, **108**, 3858.

949. T. K. Miyamoto, S. Tsuzuki, T. Hasegawa, and Y. Sasaki, *Chem. Lett. (Jpn.)*, 1983, 1587.

950. T. C. Woon, A. Shirazi, and T. C. Bruice, *Inorg. Chem.*, 1986, **25**, 3845.

951. R.-J. Cheng, L. Latos-Grażyński, and A. L. Balch, *Inorg. Chem.*, 1982, **21**, 2412.

952. E. W. Ainscough, A. W. Addison, D. Dolphin, and B. R. James, *J. Am. Chem. Soc.*, 1978, **100**, 7585.

953. H. M. Goff, E. T. Shimomura, Y. J. Lee, and W. R. Scheidt, *Inorg. Chem.*, 1984, **23**, 315.

954. D. V. Behere and H. M. Goff, *J. Am. Chem. Soc.*, 1984, **106**, 4945.

955. R. D. Arasasingham, A. L. Balch, C. R. Cornman, J. S. de Ropp, K. Eguchi, and G. N. La Mar, *Inorg. Chem.*, 1990, **29**, 1847.

956. T. Uno, K. Hatano, Y. Nishimura, and Y. Arata, *Inorg. Chem.*, 1990, **29**, 2803.

957. S. Koch, S. C. Tang, R. H. Holm, R. B. Frankel, and J. A. Ibers, *J. Am. Chem. Soc.*, 1975, **97**, 916.

958. S. P. Cramer, J. H. Dawson, K. O. Hodgson, and L. P. Hager, *J. Am. Chem. Soc.*, 1978, **100**, 7282.

959. K. M. Miller and C. E. Strouse, *Inorg. Chem.*, 1984, **23**, 2395.

960. A. Shirazi and H. M. Goff, *J. Am. Chem. Soc.*, 1982, **104**, 6318.

961. J. N. Burstyn, J. A. Roe, A. R. Miksztal, B. A. Shaevitz, G. Lang, and J. S. Valentine, *J. Am. Chem. Soc.*, 1988, **110**, 1382.

962. W. R. Scheidt, D. K. Geiger, Y. J. Lee, C. A. Reed, and G. Lang, *J. Am. Chem. Soc.*, 1985, **107**, 5693.

963. Y. Zhang, W. A. Hallows, W. J. Ryan, J. G. Jones, G. B. Carpenter, and D. A. Sweigert, *Inorg. Chem.*, 1994, **33**, 3306.

964. D. V. Behere, R. Birdy, and S. Mitra, *Inorg. Chem.*, 1981, **21**, 386.

965. L. B. Dugad and S. Mitra, *Proc. Indian Acad. Sci.*, 1984, **93**, 295.

966. A. L. Balch, L. Latos-Grażyński, B. C. Noll, and S. L. Phillips, *Inorg. Chem.*, 1993, **32**, 1124.

967. H. Oumous, C. Lecomte, J. Protas, P. Cocolios, and R. Guilard, *Polyhedron*, 1984, **3**, 651.

968. M. A. Phillippi, N. Baenziger, and H. M. Goff, *Inorg. Chem.*, 1981, **20**, 3904.

969. P. W. Crawford and M. D. Ryan, *Inorg. Chim. Acta*, 1991, **179**, 25.

970. W. R. Scheidt, Y. J. Lee, and M. G. Finnegan, *Inorg. Chem.*, 1988, **27**, 4725.

971. P. Cocolios, G. Lagrange, R. Guilard, H. Oumous, and C. Lecomte, *J. Chem. Soc., Dalton Trans.*, 1984, 567.

972. Y. O. Kim, B. Song, and H. M. Goff, *Inorg. Chem.*, 1993, **32**, 1304.

973. R. Guilard, I. Perrot, A. Tabard, P. Richard, C. Lecomte, Y. H. Liu, and K. M. Kadish, *Inorg. Chem.*, 1991, **30**, 27.

974. A. D. Carraway, G. T. Miller, L. L. Pearce, and J. Peterson, *Inorg. Chem.*, 1998, **37**, 4654.

975. L. A. Yatsunyk and F. A. Walker, *J. Porphyrins Phthalocyanines*, 2005, in press.

976. G. D. Brackett, P. L. Richards, and W. S. Caughey, *J. Chem. Phys.*, 1971, **54**, 4383.

977. P. J. Kellett, M. J. Pawlik, L. F. Taylor, R. G. Thompson, M. A. Levstik, O. P. Anderson, and S. H. Strauss, *Inorg. Chem.*, 1989, **28**, 440.

978. J. Wojaczynski, L. Latos-Grażyński, W. Hrycyk, E. Pacholska, K. Rachlewicz, and L. Szterenberg, *Inorg. Chem.*, 1996, **35**, 6861.

979. M. Mazzanti, J.-C. Marchon, J. Wajaczynski, S. Wolowiec, L. Latos-Grażyński, M. Shang, and W. R. Scheidt, *Inorg. Chem.*, 1998, **37**, 2476.

980. M. J. Pawlik, P. K. Miller, E. P. Sullivan, M. A. Levstik, D. A. Almond, and S. H. Strauss, *J. Am. Chem. Soc.*, 1988, **110**, 3007.

981. S. Cai, Ph.D. dissertation, Magnetic Resonance Investigations of Iron Tetrapyrrolic Macrocycles, University of Arizona, 2001.

982. S. Cai, D. L. Lichtenberger, and F. A. Walker, *Inorg. Chem.*, 2004, **43**, 1890.

983. E. P. Sullivan, J. D. Grantham, C. S. Thomas, and S. H. Strauss, *J. Am. Chem. Soc.*, 1991, **113**, 5264.

984. I.-K. Choi and M. D. Ryan, *New J. Chem.*, 1992, **16**, 591.

985. D. Lexa, M. Momenteau, J.-M. Saveant, and F. Xu, *Inorg. Chem.*, 1985, **24**, 122.

986. M. J. Gunter, G. M. McLaughlin, K. J. Berry, K. S. Murray, M. Irving, and P. E. Clark, *Inorg. Chem.*, 1984, **23**, 283.

987. P. Hambright, A. Turner, J. S. Cohen, R. C. Lyon, A. Katz, P. Neta, and A. Adeyemo, *Inorg. Chim. Acta*, 1987, **128**, L11.

988. V. E. Yushmanov, *Inorg. Chem.*, 1999, **38**, 1713.

989. S. K. Sur and R. G. Bryant, *J. Phys. Chem.*, 1995, **99**, 7172.

990. R. F. Pasternack and B. Halliwell, *J. Am. Chem. Soc.*, 1979, **101**, 1026.

991. R. B. VanAtta, C. E. Strouse, L. K. Hanson, and J. S. Valentine, *J. Am. Chem. Soc.*, 1987, **109**, 1425.
992. M. Selke, M. F. Sisemore, and J. S. Valentine, *J. Am. Chem. Soc.*, 1996, **118**, 2008.
993. M. F. Sisemore, M. Selke, J. N. Burstyn, and J. S. Valentine, *Inorg. Chem.*, 1997, **36**, 979.
994. S. Takahashi, K. Ishikawa, N. Takeuchi, M. Ikeda-Saito, T. Yoshida, and D. L. Rousseau, *J. Am. Chem. Soc.*, 1995, **117**, 6002.
995. G. Loew and M. Dupuis, *J. Am. Chem. Soc.*, 1996, **118**, 10584.
996. D. Harris, G. Loew, and L. Waskell, *J. Am. Chem. Soc.*, 1998, **120**, 4308.
997. S. Ozawa, Y. Watanabe, and I. Morishima, *Inorg. Chem.*, 1994, **33**, 306.
998. R. D. Arasasingham, A. L. Balch, C. R. Cornman, and L. Latos-Grażyński, *J. Am. Chem. Soc.*, 1989, **111**, 4357.
999. K. Tajima, J. Jinno, K. Ishizu, H. Sakurai, and H. Nishiguchi-Ohya, *Inorg. Chem.*, 1989, **28**, 709.
1000. K. Tajima, S. Oka, T. Edo, S. Miyake, H. Mano, K. Mukai, H. Sakurai, and K. Ishizu, *Chem. Commun.*, 1995, 1507.
1001. K. Tajima, K. Tada, J. Jinno, T. Eddo, H. Mano, N. Azuma, and K. Makino, *Inorg. Chim. Acta*, 1997, **254**, 29.
1002. M. Rivera, G. A. Caignan, A. V. Astashkin, A. M. Raitsimring, T. Kh. Shokhireva, and F. A. Walker, *J. Am. Chem. Soc.*, 2002, **124**, 6077.
1003. M. Zobrist and G. N. La Mar, *J. Am. Chem. Soc.*, 1978, **100**, 1944.
1004. T. Mashiko, M. E. Kastner, K. Spartalian, W. R. Scheidt, and C. A. Reed, *J. Am. Chem. Soc.*, 1978, **100**, 6354.
1005. M. Guillemot, L. Toupet, and G. Simonneaux, *Inorg. Chem.*, 1996, **35**, 6334.
1006. A. L. Balch, R. J. Cheng, G. N. La Mar, and L. Latos-Grażyński, *Inorg. Chem.*, 1985, **24**, 2651.
1007. K. A. Keating, J. S. de Ropp, G. N. La Mar, A. L. Balch, F.-Y. Shiau, and K. M. Smith, *Inorg. Chem.*, 1991, **30**, 3258.
1008. D. White-Dixon, M. Barbush, and A. Shirazi, *Inorg. Chem.*, 1985, **24**, 1081.
1009. W. R. Scheidt, D. K. Geiger, Y. J. Lee, P. Gans, and J.-C. Marchon, *Inorg. Chem.*, 1992, **31**, 2660.
1010. F. W. B. Einstein and A. C. Willis, *Inorg. Chem.*, 1978, **17**, 3040.
1011. M. E. Kastner, W. R. Scheidt, T. Mashiko, and C. A. Reed, *J. Am. Chem. Soc.*, 1978, **100**, 666.
1012. D. L. Hickman and H. M. Goff, *Inorg. Chem.*, 1983, **22**, 2787.
1013. K. R. Rodgers, R. A. Reed, T. G. Spiro, and Y. O. Su, *New J. Chem.*, 1992, **16**, 533.
1014. J. L. Hoard, G. H. Cohen, and M. D. Glick, *J. Am. Chem. Soc.*, 1967, **89**, 1992.
1015. W. R. Scheidt, Y. J. Lee, D. K. Geiger, K. Taylor, and K. Hatano, *J. Am. Chem. Soc.*, 1982, **104**, 3367.
1016. D. K. Geiger, V. Chunplang, and W. R. Scheidt, *Inorg. Chem.*, 1985, **24**, 4736.
1017. A. A. El-Awady, P. C. Wilkins, and R. G. Wilkins, *Inorg. Chem.*, 1985, **24**, 2053.
1018. A. B. Hoffman, D. M. Collins, V. W. Day, E. B. Fleischer, T. S. Srivastava, and J. L. Hoard, *J. Am. Chem. Soc.*, 1972, **94**, 3620.
1019. B. Cheng, J. D. Hobbs, P. G. Debrunner, J. Erlebacher, J. A. Shelnutt, and W. R. Scheidt, *Inorg. Chem.*, 1995, **34**, 102.
1020. J. H. Helms, L. W. ter Haar, W. E. Hatfield, D. L. Harris, K. Jayaraj, G. E. Toney, A. Gold, T. D. Mewborn, and J. R. Pemberton, *Inorg. Chem.*, 1986, **25**, 2334.
1021. S. H. Strauss, M. J. Pawlik, J. Skowyra, J. R. Kennedy, O. P. Anderson, K. Spartalian, and J. L. Dye, *Inorg. Chem.*, 1987, **26**, 724.
1022. E. B. Fleischer and D. A. Fine, *Inorg. Chim. Acta*, 1978, **29**, 267.
1023. A. N. Thompson and M. Krishnamurthy, *Inorg. Chim. Acta*, 1979, **34**, 145.
1024. V. B. McLaughlin, M. Faraggi, and D. L. Leussing, *Inorg. Chem.*, 1993, **32**, 941.
1025. A. Nanthakumar and H. M. Goff, *Inorg. Chem.*, 1989, **28**, 4561.
1026. C. R. Guest, K. D. Straub, J. A. Hutchinson, and P. M. Rentzepis, *J. Am. Chem. Soc.*, 1988, **110**, 5276.
1027. W. R. Scheidt, B. Cheng, M. K. Safo, F. Cukiernik, J.-C. Marchon, and P. G. Debrunner, *J. Am. Chem. Soc.*, 1992, **114**, 4420.
1028. B. Cheng, P. H. Fries, J.-C. Marchon, and W. R. Scheidt, *Inorg. Chem.*, 1996, **35**, 1024.
1029. T. Hayashi, Y. Nakashima, K. Ito, T. Ikegami, I. Aritome, K. Aoyagi, T. Ando, and Y. Hisaeda, *Inorg. Chem.*, 2003, **42**, 7345.
1030. C. Bernard, J. P. Gisselbrecht, M. Gross, E. Vogel, and M. Lausmann, *Inorg. Chem.*, 1994, **33**, 2393.
1031. K. M. Kadish, P. Boulas, F. D'Souza, M. A. Aukauloo, R. Guilard, M. Lausmann, and E. Vogel, *Inorg. Chem.*, 1994, **33**, 471.
1032. C. Bernard, Y. Le Mest, and J. P. Gisselbrecht, *Inorg. Chem.*, 1998, **37**, 181.
1033. D. J. Liston, B. J. Kennedy, K. S. Murray, and B. O. West, *Inorg. Chem.*, 1985, **24**, 1561.
1034. D.-H. Chin, J. Del Gaudio, G. N. La Mar, and A. L. Balch, *J. Am. Chem. Soc.*, 1977, **99**, 5486.
1035. G. M. Godziela, L. A. Ridnour, and H. M. Goff, *Inorg. Chem.*, 1985, **24**, 1610.
1036. W. R. Scheidt, Y. J. Lee, T. Bartzcak, and K. Hatano, *Inorg. Chem.*, 1984, **23**, 2552.
1037. Q.-F. Zhang, J. L. C. Chim, W. Lai, W.-T. Wong, and W.-H. Leung, *Inorg. Chem.*, 2001, **40**, 2470.

1038. J. Wojaczynski, L. Latos-Grażyński, M. N. Olmstead, and A. L. Balch, *Inorg. Chem.*, 1997, **36**, 4548.

1039. B. G. Malmström, in ‘Metal Ion Activation of Dioxygen’, ed. T. G. Spiro, Wiley, New York, 1980, Chap. 5.

1040. D. E. Metzler, ‘Biochemistry’, 2nd edn., Elsevier Academic Press, New York, 2003, Vol. 2, Chap. 18.

1041. V. S. Oganesyan, C. S. Butler, N. J. Watmough, C. Greenwood, A. J. Thomson, and M. R. Cheesman, *J. Am. Chem. Soc.*, 1998, **120**, 4232.

1042. G. Palmer, G. T. Babcock, and L. E. Vickery, *Proc. Natl. Acad. Sci. U.S.A.*, 1976, **73**, 2206.

1043. M. F. Tweedle, L. J. Wilson, L. Garcia-Iñiguez, G. T. Babcock, and G. Palmer, *J. Biol. Chem.*, 1978, **253**, 8065.

1044. W. R. Hagen, *Biochim. Biophys. Acta*, 1982, **708**, 82.

1045. Z. K. Barnes, G. T. Babcock, and J. L. Dye, *Biochemistry*, 1991, **30**, 7597.

1046. E. D. Day, J. Peterson, M. S. Sendova, J. R. Schoonover, and G. Palmer, *Biochemistry*, 1993, **32**, 7855.

1047. K. E. Falk, T. Vänngård, and J. ångström, *FEBS Lett.*, 1997, **75**, 23.

1048. T. A. Kent, E. Münck, W. R. Dunham, W. F. Filter, K. L. Findling, T. Yoshida, and J. A. Fee, *J. Biol. Chem.*, 1982, **257**, 12489.

1049. F. M. Rusnak, E. Münck, C. I. Nitsche, B. H. Zimmerman, and J. A. Fee, *J. Biol. Chem.*, 1987, **262**, 16328.

1050. J. A. Fee, M. G. Choc, K. L. Findling, R. Lorence, and T. Yoshida, *Proc. Natl. Acad. Sci. U.S.A.*, 1980, **77**, 147.

1051. M. R. Cheesman, V. S. Oganesyan, N. J. Watmough, C. S. Butler, and A. J. Thomson, *J. Am. Chem. Soc.*, 2004, **126**, 0000.

1052. A. J. Thomson, M. K. Johnson, C. Greenwood, and P. E. Gooding, *Biochem. J.*, 1980, **193**, 687.

1053. T. A. Kent, E. Münck, W. R. Dunham, W. F. Filter, K. L. Findling, T. Yoshida, and J. A. Fee, *J. Biol. Chem.*, 1982, **257**, 12489.

1054. O. Kahn, *Struct. Bonding*, 1987, **68**, 89.

1055. A. J. Thomson, C. Greenwood, P. M. A. Gadsby, J. Peterson, D. G. Eglinton, B. C. Hill, and P. Nicholls, *J. Inorg. Biochem.*, 1985, **23**, 187.

1056. M. Saraste, *Q. Rev. Biophys.*, 1990, **23**, 331.

1057. M. Saraste and J. Castresana, *FEBS Lett.*, 1994, **341**, 1.

1058. J. Sastresana, M. Lubben, M. Saraste, and D. G. Higgins, *EMBO J.*, 1994, **13**, 2516.

1059. J. Hendriks, A. Oubrie, J. Castresana, A. Urbani, S. Gemeinhardt, and M. Saraste, *Biochim. Biophys. Acta*, 2000, **1459**, 266.

1060. P. Moënne-Loccoz and S. de Vries, *J. Am. Chem. Soc.*, 1998, **120**, 5147.

1061. P. Moënne-Loccoz, O.-M. H. Richter, H. Huang, I. M. Wasser, R. A. Ghiladi, K. D. Karlin, and S. de Vries, *J. Am. Chem. Soc.*, 2000, **122**, 9344.

1062. Suharti, M. J. F. Strampraad, I. Schröder, and S. de Vries, *Biochemistry*, 2001, **40**, 2632.

1063. S. de Vries and I. Schröder, *Biochem. Soc. Trans.*, 2002, **30**, 662.

1064. S. de Vries, M. J. F. Strampraad, S. Lu, P. Moënne-Loccoz, and I. Schröder, *J. Biol. Chem.*, 2003, **278**, 35861.

1065. T. Fujiwara and Y. Fukumori, *J. Bacteriol.*, 1996, **178**, 1866.

1066. G. Butland, S. Spiro, N. J. Watmough, and D. J. Richardson, *J. Bacteriol.*, 2001, **183**, 189.

1067. I. M. Wasser, S. de Vries, P. Moënne-Loccoz, I. Schröder, and K. D. Karlin, *Chem. Rev.*, 2002, **102**, 1201.

1068. A. Giuffre, G. Stubauer, P. Sarti, M. Brunori, W. G. Zumft, G. Buse, and T. Soulimane, *Proc. Natl. Acad. Sci. U.S.A.*, 1999, **96**, 14718.

1069. L. L. Pearce, E. L. Bominaar, B. C. Hill, and J. Peterson, *J. Biol. Chem.*, 2003, **278**, 52139.

1070. W. G. Zumft, C. Braun, and H. Cuypers, *Eur. J. Biochem.*, 1994, **219**, 481.

1071. J. van der Oost, A. P. de Boer, J. W. de Gier, W. G. Zumft, A. H. Stouthamer, and R. J. van Spanning, *FEMS Microbiol. Lett.*, 1994, **121**, 1.

1072. H. Shoun and T. Tanimoto, *J. Biol. Chem.*, 1991, **266**, 11078.

1073. T. Kudo, D. Tomura, D. L. Liu, X. Q. Dai, and H. Shoun, *Biochimie*, 1996, **78**, 792.

1074. S.-Y. Park, H. Shimizu, S. Adachi, A. Nakagawa, I. Tanaka, K. Nakahara, H. Shoun, E. Obayashi, H. Nakamura, T. Iizuka, and Y. Shiro, *Nat. Struct. Biol.*, 1997, **4**, 827.

1075. M. J. Gunter, L. N. Mander, G. M. McLaughlin, K. S. Murray, K. J. Berry, P. E. Clark, and D. A. Buckingham, *J. Am. Chem. Soc.*, 1980, **102**, 1470.

1076. M. J. Gunter, L. N. Mander, K. S. Murray, and P. E. Clark, *J. Am. Chem. Soc.*, 1981, **103**, 6784.

1077. C. K. Chang, M. S. Koo, and B. Ward, *J. Chem. Soc., Chem. Commun.*, 1982, 716.

1078. M. J. Gunter, K. J. Berry, and K. S. Murray, *J. Am. Chem. Soc.*, 1984, **106**, 4227.

1079. C. T. Brewer and G. A. Brewer, *Inorg. Chem.*, 1987, **26**, 3420.

1080. C. M. Elliott, N. C. Jain, B. K. Cranmer, and A. W. Hamburg, *Inorg. Chem.*, 1987, **26**, 3655.

1081. C. A. Koch, C. A. Reed, G. A. Brewer, N. P. Rath, W. R. Scheidt, G. Gupta, and G. Lang, *J. Am. Chem. Soc.*, 1989, **111**, 7645.

1082. G. P. Gupta, G. Lang, C. A. Koch, B. Wang, W. R. Scheidt, and C. A. Reed, *Inorg. Chem.*, 1990, **29**, 4234.

1083. C. K. Schauer, K. Akabori, C. M. Elliott, and O. P. Anderson, *J. Am. Chem. Soc.*, 1984, **106**, 1127.

1084. S. C. Lee and R. H. Holm, *J. Am. Chem. Soc.*, 1993, **115**, 5833.

1085. S. C. Lee, M. J. Scott, K. Kauffmann, E. Münck, and R. H. Holm, *J. Am. Chem. Soc.*, 1994, **116**, 401.

1086. M. J. Scott, S. C. Lee, and R. H. Holm, *Inorg. Chem.*, 1994, **33**, 4651.

1087. M. J. Scott and R. H. Holm, *J. Am. Chem. Soc.*, 1994, **116**, 11357.

1088. H. H. Zhang, A. Filipponi, A. Di Cicco, S. C. Lee, M. J. Scott, R. H. Holm, B. Hedman, and K. O. Hodgson, *Inorg. Chem.*, 1996, **35**, 4819.

1089. M. T. Gardner, G. Deinum, Y. Kim, G. T. Babcock, M. J. Scott, and R. H. Holm, *Inorg. Chem.*, 1996, **35**, 6878.

1090. K. E. Kauffmann, C. A. Goddard, Y. Zang, R. H. Holm, and E. Münck, *Inorg. Chem.*, 1997, **36**, 985.

1091. H. H. Zhang, A. Filipponi, A. Di Cicco, M. J. Scott, R. H. Holm, B. Hedman, and K. O. Hodgson, *J. Am. Chem. Soc.*, 1997, **119**, 2470.

1092. A. Nanthakumar, S. Fox, N. N. Murthy, K. D. Karlin, N. Ravi, B. H. Huynh, R. D. Orosz, E. P. Day, K. S. Hagen, and N. J. Blackburn, *J. Am. Chem. Soc.*, 1993, **115**, 8513.

1093. K. D. Karlin, A. Nanthakumar, S. Fox, N. N. Murthy, N. Ravi, B. H. Huynh, R. D. Orosz, and E. P. Day, *J. Am. Chem. Soc.*, 1994, **116**, 4753.

1094. S. Fox, A. Nanthakumar, M. Wikström, K. D. Karlin, and N. J. Blackburn, *J. Am. Chem. Soc.*, 1996, **118**, 24.

1095. A. Nanthakumar, S. Fox, N. N. Murthy, and K. D. Karlin, *J. Am. Chem. Soc.*, 1997, **119**, 3898.

1096. H. V. Obias, G. P. F. van Strijdonck, D.-H. Lee, M. Ralle, N. J. Blackburn, and K. D. Karlin, *J. Am. Chem. Soc.*, 1998, **120**, 9696.

1097. D. M. Corsi, N. N. Murthy, V. G. Young Jr, and K. D. Karlin, *Inorg. Chem.*, 1999, **38**, 848.

1098. T. D. Ju, R. A. Ghiladi, D.-H. Lee, G. P. F. Strijdonck, A. S. Woods, R. J. Cotter, V. G. Young Jr, and K. D. Karlin, *Inorg. Chem.*, 1999, **38**, 2244.

1099. M.-A. Kopf, Y.-M. Neuhold, A. D. Zuberbühler, and K. D. Karlin, *Inorg. Chem.*, 1999, **38**, 3093.

1100. M.-A. Kopf and K. D. Karlin, *Inorg. Chem.*, 1999, **38**, 4922.

1101. R. A. Ghiladi, T. D. Ju, D.-H. Lee, P. Moënne-Loccoz, S. Kaderli, Y.-M. Neuhold, A. D. Zuberbühler, A. S. Woods, R. J. Cotter, and K. D. Karlin, *J. Am. Chem. Soc.*, 1999, **121**, 9885.

1102. R. A. Ghiladi and K. D. Karlin, *Inorg. Chem.*, 2002, **41**, 2400.

1103. R. A. Ghiladi, K. R. Hatwell, K. D. Karlin, H. Huang, P. Moënne-Loccoz, C. Krebs, B. H. Huynh, L. A. Marzilli, R. J. Cotter, S. Kaderli, and A. D. Zuberbühler, *J. Am. Chem. Soc.*, 2001, **123**, 6183.

1104. H. C. Fry, D. V. Scaltrito, K. D. Karlin, and G. J. Meyer, *J. Am. Chem. Soc.*, 2003, **125**, 11866.

1105. E. E. Chufán and K. D. Karlin, *J. Am. Chem. Soc.*, 2003, **125**, 16160.

1106. E. Kim, E. E. Chufán, K. Kamaraj, and K. D. Karlin, *Chem. Rev.*, 2004, **104**, 1077.

1107. J. P. Collman, P. C. Herrmann, B. Boitrel, X. Zhang, T. A. Eberspacher, and L. Fu, *J. Am. Chem. Soc.*, 1994, **116**, 9783.

1108. J. P. Collman, L. Fu, P. C. Herrmann, and X. Zhang, *Science*, 1997, **275**, 949.

1109. J. P. Collman, M. Bröring, L. Fu, M. Rapta, R. Schwenninger, and A. Straumanis, *J. Org. Chem.*, 1998, **63**, 8082.

1110. J. P. Collman, M. Bröring, L. Fu, M. Rapta, and R. Schwenninger, *J. Org. Chem.*, 1998, **63**, 8084.

1111. J. P. Collman, R. Schwenninger, M. Rapta, M. Bröring, and L. Fu, *Chem. Commun.*, 1999, 137.

1112. J. P. Collman, M. Rapta, M. Bröring, L. Raptova, R. Schwenninger, B. Boitrel, L. Fu, and M. L'Her, *J. Am. Chem. Soc.*, 1999, **121**, 1387.

1113. J. P. Collman, M. Zhong, S. Costanzo, and C. Zhang, *J. Org. Chem.*, 2001, **66**, 8252.

1114. J. P. Collman, C. J. Sunderland, and R. Boulatov, *Inorg. Chem.*, 2002, **41**, 2282.

1115. J. P. Collman, K. E. Berg, C. J. Sunderland, A. Aukauloo, M. A. Vance, and E. I. Solomon, *Inorg. Chem.*, 2002, **41**, 6583.

1116. J. P. Collman, C. J. Sunderland, K. E. Berg, M. A. Vance, and E. I. Solomon, *J. Am. Chem. Soc.*, 2003, **125**, 6648.

1117. B. R. Serr, C. E. L. Headford, O. P. Anderson, C. M. Elliot, K. Spartalian, V. E. Fainzilberg, W. E. Hatfield, B. R. Rohrs, S. S. Eaton, and G. R. Eaton, *Inorg. Chem.*, 1992, **31**, 5450.

1118. S. Ferguson-Miller and G. T. Babcock, *Chem. Rev.*, 1996, **96**, 2889.

1119. M. R. A. Blomberg, P. E. M. Siegbahn, G. T. Babcock, and M. Wickström, *J. Am. Chem. Soc.*, 2000, **122**, 12848.

1120. M. R. A. Blomberg and P. E. M. Siegbahn, *J. Phys. Chem. B*, 2001, **105**, 9375.

1121. A. M. Stolzenberg and M. T. Stershic, *Inorg. Chem.*, 1985, **24**, 3095.

1122. M. J. LaBarre, A. M. Raitsimring, and J. H. Enemark, in 'Molybdenum Enzymes, Cofactors and Model Systems', ACS Symposium Series, eds. E. I. Stiefel, D. Coucouvanis, and W. E. Newton, 1993, Chap. 9.

1123. P. Basu, N. V. Shokhirev, J. H. Enemark, and F. A. Walker, *J. Am. Chem. Soc.*, 1995, **117**, 9042.

1124. P. Basu, A. M. Raitsimring, J. H. Enemark, and F. A. Walker, *Inorg. Chem.*, 1997, **36**, 1088.

1125. A. Gold, W. Ivey, G. E. Toney, and R. Sangaiah, *Inorg. Chem.*, 1984, **23**, 2932.

1126. N. Masuoka and H. A. Itano, *Biochemistry*, 1987, **26**, 3672.

1127. R. Bonnett and M. J. Dimsdale, *J. Chem. Soc., Perkin Trans. 1*, 1972, 2540.

1128. L. Avila, H. Huang, C. O. Damaso, S. Lu, P. Moënne-Loccoz, and M. Rivera, *J. Am. Chem. Soc.*, 2003, **125**, 4103.

1129. G. H. Barnett, M. F. Hudson, S. W. McCombie, and K. M. Smith, *J. Chem. Soc., Perkin Trans. 1*, 1973, 691.

1130. J.-H. Fuhrhop, S. Besecke, J. Subramanian, C. Mengersen, and D. Ricones, *J. Am. Chem. Soc.*, 1975, **97**, 7141.

1131. T. N. St. Claire and A. L. Balch, *Inorg. Chem.*, 1999, **38**, 684.

1132. H. R. Kalish, L. Latos-Grażyński, and A. L. Balch, *J. Am. Chem. Soc.*, 2000, **122**, 12478.

1133. A. L. Balch, B. C. Noll, S. M. Reid, and E. P. Zovinka, *Inorg. Chem.*, 1993, **32**, 2610.

1134. A. L. Balch, L. Latos-Grażyński, and T. N. St. Claire, *Inorg. Chem.*, 1995, **34**, 1395.

1135. S. P. Rath, R. Koerner, M. M. Olmstead, and A. L. Balch, *J. Am. Chem. Soc.*, 2003, **125**, 11798.

1136. R. Koerner, L. Latos-Grażyński, and A. L. Balch, *J. Am. Chem. Soc.*, 1998, **120**, 9246.

1137. A. L. Balch, R. Koerner, L. Latos-Grażyński, J. E. Lewis, T. N. St. Claire, and E. P. Zovinka, *Inorg. Chem.*, 1997, **36**, 3892.

1138. L. Latos-Grażyński, J. Wojaczyński, R. Koerner, J. J. Johnson, and A. L. Balch, *Inorg. Chem.*, 2001, **40**, 4971.

1139. A. L. Balch, L. Latos-Grażyński, B. C. Noll, M. M. Olmstead, L. Szterenberg, and N. Safari, *Inorg. Chem.*, 1999, **38**, 684.

1140. P. A. Lord, L. Latos-Grażyński, and A. L. Balch, *Inorg. Chem.*, 2002, **41**, 1011.

1141. L. Latos-Grażyński, J. Wojaczyński, R. Koerner, J. J. Johnson, and A. L. Balch, *Inorg. Chem.*, 2001, **40**, 4971.

1142. R. Koerner, L. Latos-Grażyński, and A. L. Balch, *J. Am. Chem. Soc.*, 1998, **120**, 9246.

1143. A. L. Balch, L. Latos-Grażyński, B. C. Noll, M. M. Olmstead, and N. Safari, *J. Am. Chem. Soc.*, 1993, **115**, 9056.

1144. J. Crusats, A. Suzuki, T. Mizutani, and H. Ogoshi, *J. Org. Chem.*, 1998, **63**, 602.

1145. S. P. Rath, M. M. Olmstead, L. Latos-Grażyński, and A. L. Balch, *J. Am. Chem. Soc.*, 2003, **125**, 12678.

1146. H. Kalish, H. M. Lee, M. M. Olmstead, L. Latos-Grażyński, S. P. Rath, and A. L. Balch, *J. Am. Chem. Soc.*, 2003, **125**, 4674.

1147. S. P. Rath, H. Kalish, L. Latos-Grażyński, M. M. Olmstead, and A. L. Balch, *J. Am. Chem. Soc.*, 2004, **126**, 646.

1148. A. L. Balch, M. M. Olmstead, and N. Safari, *Inorg. Chem.*, 1993, **32**, 291.

1149. R. Koerner, M. M. Olmstead, A. Ozarowski, S. L. Phillips, P. M. Van Calcar, K. Winkler, and A. L. Balch, *J. Am. Chem. Soc.*, 1998, **120**, 1274.

1150. S. Sakaki, S. Mitarai, and K. Ohkubo, *Chem. Lett. (Japan)*, 1991, 195.

1151. H. Schulenburg, S. Stankov, V. Schünemann, J. Radnik, I. Dorbandt, S. Fiechter, P. Bogdanoff, and H. Tributsch, *J. Phys. Chem. B*, 2003, **107**, 9034.

1152. A. L. Bouwkamp-Wijnoltz, W. Visscher, J. A. R. van Veen, E. Boellaard, A. M. van der Kraan, and S. C. Tang, *J. Phys. Chem. B*, 2002, **106**, 12993.

1153. I. Fujita, T. L. Netzel, C. K. Chang, and C.-B. Wang, *Proc. Natl. Acad. Sci. U.S.A.*, 1982, **79**, 413.

1154. T. Imamura, T. Jin, T. Suzuki, and M. Fujimoto, *Chem. Lett. (Japan)*, 1985, 847.

1155. D. N. Hendrickson, M. G. Kinnaird, and K. S. Suslick, *J. Am. Chem. Soc.*, 1987, **109**, 1243.

1156. H. M. Lee, M. M. Olmstead, G. G. Gross, and A. L. Balch, *Cryst. Growth Design*, 2003, **3**, 691.

1157. A. L. Balch and M. M. Olmstead, *Chem. Rev.*, 1998, **98**, 2123.

1158. P. C. Weber, A. Howard, N. H. Xuong, and F. R. Salemme, *J. Mol. Biol.*, 1981, **153**, 399.

1159. B. C. Finzel, P. C. Weber, K. D. Hardman, and F. R. Salemme, *J. Mol. Biol.*, 1985, **186**, 627.

1160. M. M. Maltempo and T. H. Moss, *Q. Rev. Biophys.*, 1976, **9**, 181.

1161. M. M. Maltempo, *J. Chem. Phys.*, 1974, **61**, 2540.

1162. T. H. Moss, A. J. Bearden, R. G. Bartsch, and M. A. Cusanovich, *Biochemistry*, 1968, **7**, 1583.

1163. J. Rawlings, P. J. Stephens, L. A. Nafie, and M. D. Kamen, *Biochemistry*, 1977, **16**, 1725.

1164. C. A. Reed, T. Mashiko, S. P. Bentley, M. E. Kastner, W. R. Scheidt, K. Spartalian, and G. Lang, *J. Am. Chem. Soc.*, 1979, **101**, 2948.

1165. G. E. Toney, L. W. ter Haar, J. E. Savrin, A. Gold, W. E. Hatfield, and R. Sangaiah, *Inorg. Chem.*, 1984, **23**, 2561.

1166. G. E. Toney, A. Gold, J. Savrin, L. W. ter Haar, R. Sangaiah, and W. E. Hatfield, *Inorg. Chem.*, 1984, **23**, 4350.

1167. E. T. Kintner and J. H. Dawson, *Inorg. Chem.*, 1991, **30**, 4892.

1168. A. D. Boersma and H. M. Goff, *Inorg. Chem.*, 1982, **21**, 581.

1169. K. Shelly, T. Bartczak, W. R. Scheidt, and C. A. Reed, *Inorg. Chem.*, 1985, **24**, 4325.

1170. G. P. Gupta, G. Lang, C. A. Reed, K. Shelly, and W. R. Scheidt, *J. Chem. Phys.*, 1987, **86**, 5288.

1171. D. A. Summerville, I. A. Cohen, K. Hatano, and W. R. Scheidt, *Inorg. Chem.*, 1978, **17**, 2906.

1172. G. P. Gupta, G. Lang, Y. J. Lee, W. R. Scheidt, K. Shelly, and C. A. Reed, *Inorg. Chem.*, 1987, **26**, 3022.

1173. H. Masuda, T. Taga, K. Osaki, H. Sugimoto, Z. Yoshida, and H. Ogoshi, *Bull. Chem. Soc. Jpn.*, 1982, **55**, 3891.

1174. W. R. Scheidt, D. K. Geiger, and K. J. Haller, *J. Am. Chem. Soc.*, 1982, **104**, 495.

1175. W. R. Scheidt, D. K. Geiger, R. G. Hayes, and G. Lang, *J. Am. Chem. Soc.*, 1983, **105**, 2625.

1176. J. W. Owens, J. Robinson, and C. J. O'Connor, *Inorg. Chim. Acta*, 1993, **206**, 141.

1177. W. R. Scheidt, S. R. Osvath, Y. J. Lee, C. A. Reed, B. Shavez, and G. P. Gupta, *Inorg. Chem.*, 1989, **28**, 1591.

1178. L. B. Dugad, V. R. Marathe, and S. Mitra, *Proc. Indian Acad. Sci.*, 1985, **95**, 189.

1179. M. M. Maltempo, T. H. Moss, and M. A. Cusanovich, *Biochim. Biophys. Acta*, 1974, **342**, 290.

1180. M. M. Maltempo, *Biochim. Biophys. Acta*, 1975, **379**, 95.

1181. J. Teraoka and T. Kitagawa, *J. Phys. Chem.*, 1980, **84**, 1928.

1182. J. D. Hobbs, R. W. Larsen, T. E. Meyer, J. H. Hazzard, M. A. Cusanovich, and M. R. Ondrias, *Biochemistry*, 1990, **29**, 4166.

1183. G. N. La Mar, J. T. Jackson, L. B. Dugad, M. A. Cusanovich, and R. G. Bartsch, *J. Biol. Chem.*, 1990, **265**, 16173.

1184. H. M. Goff and E. Shimomura, *J. Am. Chem. Soc.*, 1980, **102**, 31.

1185. N. V. Shokhirev and F. A. Walker, *J. Phys. Chem.*, 1995, **99**, 17795.

1186. C. A. Reed and F. Guiset, *J. Am. Chem. Soc.*, 1996, **118**, 3281.

1187. L. N. Ohlhausen, D. Cockrum, J. Register, K. Roberts, G. J. Long, G. L. Powell, and B. B. Hutchinson, *Inorg. Chem.*, 1990, **29**, 4886.

1188. D. R. Evans and C. A. Reed, *J. Am. Chem. Soc.*, 2000, **122**, 4660.

1189. D. K. Geiger and W. R. Scheidt, *Inorg. Chem.*, 1984, **23**, 1970.

1190. R. J. Cheng, P. Y. Chen, P. R. Gau, C. C. Chen, and S. M. Peng, *J. Am. Chem. Soc.*, 1997, **119**, 2563.

1191. V. Schünemann, M. Gerdan, A. X. Trautwein, N. Haoudi, D. Mandon, J. Fischer, R. Weiss, A. Tabard, and R. Guilard, *Angew. Chem., Int. Ed. Engl.*, 1999, **38**, 3181.

1192. B. Kennedy, K. Murray, P. Zweck, H. Homborg and W. Kalz, *Inorg. Chem.*, 1986, **25**, 2539.

1193. Y. Ohgo, S. Neya, T. Ikeue, M. Takahashi, M. Takeda, N. Funasaki, and M. Nakamura, *Inorg. Chem.*, 2002, **41**, 4627.

1194. J.-P. Simonato, J. Pécaut, L. Le Pape, J.-L. Oddou, C. Jeandey, M. Shang, W. R. Scheidt, J. Wojaczynski, S. Wolowiec, L. Latos-Grażyński, and J.-C. Marchon, *Inorg. Chem.*, 2000, **39**, 3978.

1195. T. Ikeue, Y. Ohgo, T. Yamaguchi, M. Takahashi, M. Takeda, and M. Nakamura, *Angew. Chem., Int. Ed. Engl.*, 2001, **40**, 2617.

1196. T. Ikeue, Y. Ohgo, O. Ongayi, M. G. H. Vicente, and M. Nakamura, *Inorg. Chem.*, 2003, **42**, 5560.

1197. D. F. Evans, *J. Chem. Soc.*, 1959, 2003.

1198. S. K. Sur, *J. Magn. Reson.*, 1989, **82**, 169.

1199. K. Rachlewicz, L. Latos-Grażyński, E. Vogel, Z. Ciunik, and L. B. Zerzykiewicz, *Inorg. Chem.*, 2002, **41**, 1979.

1200. T. Ikeue, Y. Ohgo, M. Takahashi, M. Takeda, S. Neya, N. Funasaki, and M. Nakamura, *Inorg. Chem.*, 2001, **40**, 3650.

1201. J. A. Gonzalez and L. J. Wilson, *Inorg. Chem.*, 1994, **33**, 1543.

1202. D. R. Evans, N. L. P. Fackler, Z. Xie, C. E. F. Rickard, P. D. W. Boyd, and C. A. Reed, *J. Am. Chem. Soc.*, 1999, **121**, 8466.

1203. M. M. Olmstead, D. A. Costa, K. Maitra, B. C. Noll, S. L. Phillips, P. M. Van Calear, and A. L. Balch, *J. Am. Chem. Soc.*, 1999, **121**, 7090.

1204. M. K. Safo, G. P. Gupta, F. A. Walker, and W. R. Scheidt, *J. Am. Chem. Soc.*, 1991, **113**, 5497.

1205. O. Q. Munro, J. A. Serth-Guzzo, I. Turowska-Tyrk, K. Mohanrao, F. A. Walker, P. G. Debrunner, and W. R. Scheidt, *J. Am. Chem. Soc.*, 1999, **121**, 11144.

1206. H. Ogura, L. Yatsunyk, C. J. Medforth, K. M. Smith, K. M. Barkigia, M. W. Renner, D. Melamed, and F. A. Walker, *J. Am. Chem. Soc.*, 2001, **123**, 6564.

1207. L. A. Yatsunyk, M. D. Carducci, and F. A. Walker, *J. Am. Chem. Soc.*, 2003, **125**, 15986.

1208. R. Quinn, C. E. Strouse, and J. S. Valentine, *Inorg. Chem.*, 1983, **22**, 3934.

1209. H. A. O. Hill and K. G. Morallee, *J. Am. Chem. Soc.*, 1972, **94**, 731.

1210. L. B. Dugad, O. K. Medhi, and S. Mitra, *Inorg. Chem.*, 1987, **26**, 1741.

1211. V. P. Shedbalkar, L. B. Dugad, S. Mazumdar, and S. Mitra, *Inorg. Chim. Acta*, 1988, **148**, 17.

1212. A. K. Gregson, *Inorg. Chem.*, 1981, **20**, 81.

1213. T. Mashiko, C. A. Reed, K. J. Haller, M. E. Kastner, and W. R. Scheidt, *J. Am. Chem. Soc.*, 1981, **103**, 5758.

1214. M. P. Byrn and C. E. Strouse, *J. Am. Chem. Soc.*, 1981, **103**, 2633.

1215. M. P. Byrn, B. A. Katz, N. L. Keder, K. R. Levan, C. J. Magurany, K. M. Miller, J. W. Pritt, and C. E. Strouse, *J. Am. Chem. Soc.*, 1983, **105**, 4916.

1216. H. Sakurai and T. Yoshimura, *J. Inorg. Biochem.*, 1985, **24**, 75.

1217. G. Simonneaux, F. Hindre, and M. Le Plouzennec, *Inorg. Chem.*, 1989, **28**, 823.

1218. F. A. Walker, H. Nasri, I. Turowska-Tyrk, K. Mohanrao, C. T. Watson, N. V. Shokhirev, P. G. Debrunner, and W. R. Scheidt, *J. Am. Chem. Soc.*, 1996, **118**, 12109.

1219. G. Simonneaux, V. Schünemann, C. Morice, L. Carel, L. Toupet, H. Winkler, A. X. Trautwein, and F. A. Walker, *J. Am. Chem. Soc.*, 2000, **122**, 4366.

1220. G. Simonneaux and P. Sodano, *Inorg. Chem.*, 1988, **27**, 3636.

1221. Y. O. Kim and H. M. Goff, *Inorg. Chem.*, 1990, **29**, 3907.

1222. C. Morice, P. Le Maux, and G. Simonneaux, *Inorg. Chem.*, 1998, **37**, 6100.

1223. G. N. La Mar, J. Del Gaudio, and J. S. Frye, *Biochim. Biophys. Acta*, 1977, **498**, 422.

1224. D. Inniss, S. M. Soltis, and C. E. Strouse, *J. Am. Chem. Soc.*, 1988, **110**, 5644.

1225. H. Fujii, *J. Am. Chem. Soc.*, 2002, **124**, 5936.

1226. H. Nasri, J. A. Goodwin, and W. R. Scheidt, *Inorg. Chem.*, 1990, **29**, 185.

1227. O. Q. Munro and W. R. Scheidt, *Inorg. Chem.*, 1998, **37**, 2308.

1228. G.-B. Yi, M. A. Khan, and G. B. Richter-Addo, *J. Am. Chem. Soc.*, 1995, **117**, 7850.

1229. L. Chen, G.-B. Yi, L.-S. Wang, U. R. Dharmawardana, A. C. Dart, M. A. Khan, and G. B. Richter-Addo, *Inorg. Chem.*, 1998, **37**, 4677.

1230. G. B. Richter-Addo, *Acc. Chem. Res.*, 1999, **32**, 529.

1231. I.-K. Choi, Y. Liu, Z. Wei, and M. D. Ryan, *Inorg. Chem.*, 1997, **36**, 3113.

1232. G.-B. Yi, M. A. Khan, and B. B. Richter-Addo, *Inorg. Chem.*, 1995, **34**, 5703.

1233. D. Lefevre-Groboillot, S. Dijols, J.-L. Boucher, J.-P. Mahy, R. Ricoux, A. Desbois, J.-L. Zimmermann, and D. Mansuy, *Biochemistry*, 2001, **40**, 9909.

1234. V. P. Chacko and G. N. La Mar, *J. Am. Chem. Soc.*, 1982, **104**, 7002.

1235. W. R. Scheidt, Y. J. Lee, W. Luangdilok, K. J. Haller, K. Anzai, and K. Hatano, *Inorg. Chem.*, 1983, **22**, 1516.

1236. T. J. Bold, Ph.D. thesis, University of California, Davis, 1978.

1237. H. Nasri, Y. Wang, B. H. Huynh, F. A. Walker, and W. R. Scheidt, *Inorg. Chem.*, 1991, **30**, 1483.

1238. K. M. Adams, P. G. Rasmussen, W. R. Scheidt, and K. Hatano, *Inorg. Chem.*, 1979, **18**, 1892.

1239. H. Nasri, K. J. Haller, Y. Wang, B. H. Huynh, and W. R. Scheidt, *Inorg. Chem.*, 1992, **31**, 3459.

1240. T. Mashiko, J.-C. Marchon, D. T. Musser, C. A. Reed, M. E. Kastner, and W. R. Scheidt, *J. Am. Chem. Soc.*, 1979, **101**, 3653.

1241. M. Chevion, J. Peisach, and W. E. Blumberg, *J. Biol. Chem.*, 1977, **252**, 3637.

1242. H. M. Goff, *J. Am. Chem. Soc.*, 1980, **102**, 3252.

1243. F. A. Walker, *J. Am. Chem. Soc.*, 1980, **102**, 3254.

1244. A. L. Balch and M. W. Renner, *Inorg. Chem.*, 1986, **25**, 303.

1245. D. R. English, D. N. Hendrickson, K. S. Suslick, C. W. Eigenbrot, and W. R. Scheidt, *J. Am. Chem. Soc.*, 1984, **106**, 7258.

1246. A. L. Balch, R. L. Hart, L. Latos-Grażyński, and T. G. Traylor, *J. Am. Chem. Soc.*, 1990, **112**, 7552.

1247. P. Doppelt, *Inorg. Chem.*, 1984, **23**, 4009.

1248. F. S. Mathews, E. W. Czerwinski, and P. Argos, in 'The Porphyrins', ed. D. Dolphin, Academic Press, New York, 1979, Vol. VII, p. 108.

1249. W. A. Cramer, M. T. Black, W. R. Widger, and M. E. Girvin, in 'The Light Reactions', ed. J. Barber, Elsevier, Amsterdam, 1987, p. 447.

1250. M. Pierrot, R. Haser, M. Frey, F. Payan, and J.-P. Astier, *J. Biol. Chem.*, 1982, **257**, 14341.

1251. Y. Higuchi, M. Kusunoki, Y. Matsuura, N. Yasuoka, and M. Kakudo, *J. Mol. Biol.*, 1984, **172**, 109.

1252. M. Bruschi, M. Woudstra, B. Guigliarelli, M. Asso, E. Lojou, Y. Petillot, and C. Abergel, *Biochemistry*, 1997, **36**, 10601.

1253. F. Lederer, A. Glatigny, P. H. Bethge, H. D. Bellamy, and F. S. Mathews, *J. Mol. Biol.*, 1981, **148**, 427.

1254. S. E. Martinez, D. Huang, A. Szczepaniak, W. A. Cramer, and J. L. Smith, *Structure*, 1994, **2**, 95.

1255. M. R. Cheesman, A. J. Thomson, C. Greenwood, G. R. Moore, and F. Kadir, *Nature*, 1990, **346**, 771.

1256. F. Frolow, A. J. Kalb (Gilboa), and J. Yariv, *Nat. Struct. Biol.*, 1994, **1**, 453.

1257. J. C. Salerno, B. Bolgiano, R. K. Poole, R. B. Gennis, and W. J. Ingledew, *J. Biol. Chem.*, 1990, **265**, 4364.

1258. T. Shimizu, T. Iizuka, H. Shimada, Y. Ishimura, T. Nozawa, and M. Hatano, *Biochim. Biophys. Acta*, 1981, **670**, 341.

1259. J. H. Dawson, L. A. Anderson, M. Sono, and L. P. Hager, *New J. Chem.*, 1992, **16**, 577.

1260. M. Sono, J. H. Dawson, and L. P. Hager, *Inorg. Chem.*, 1985, **24**, 4339.

1261. D. Harris and G. Loew, *J. Am. Chem. Soc.*, 1993, **115**, 5799.

1262. G. Loew and M. Dupuis, *J. Am. Chem. Soc.*, 1997, **119**, 9848.

1263. M. D. Segall, M. C. Payne, W. Ellis, G. T. Tucker, and N. Boyes, *Chem. Res. Toxicol.*, 1998, **11**, 962.

1264. Q. Lin, U. Simonis, A. R. Tipton, C. J. Norvell, and F. A. Walker, *Inorg. Chem.*, 1992, **31**, 4216.

1265. J. S. Griffith, *Nature*, 1957, **180**, 30.

1266. J. S. Griffith, *Mol. Phys.*, 1971, **21**, 135.

1267. C. P. S. Taylor, *Biochim. Biophys. Acta*, 1977, **491**, 137.

1268. R. Quinn, J. S. Valentine, M. P. Byrn, and C. E. Strouse, *J. Am. Chem. Soc.*, 1987, **109**, 3301.

1269. S. M. Soltis and C. E. Strouse, *J. Am. Chem. Soc.*, 1988, **110**, 2824.

1270. A. M. Raitsimring, P. Borbat, T. Kh. Shokhireva, and F. A. Walker, *J. Phys. Chem.*, 1996, **106**, 5235.

1271. A. M. Raitsimring and F. A. Walker, *J. Am. Chem. Soc.*, 1998, **120**, 991.

1272. A. V. Astashkin, A. M. Raitsimring, and F. A. Walker, *Chem. Phys. Lett.*, 1999, **306**, 9.

1273. V. Schünemann, A. M. Raitsimring, R. Benda, A. X. Trautwein, T. Kh. Shokhireva, and F. A. Walker, *J. Biol. Inorg. Chem.*, 1999, **4**, 708.

1274. A. V. Astashkin, A. M. Raitsimring, and F. A. Walker, *J. Am. Chem. Soc.*, 2001, **123**, 1905.

1275. A. V. Astashkin, A. M. Raitsimring, A. R. Kennedy, T. Kh. Shokhireva, and F. A. Walker, *J. Phys. Chem. A*, 2002, **106**, 74.

1276. S. Cai, E. Belikova, L. A. Yatsunyk, A. M. Stolzenberg, and F. A. Walker, *Inorg. Chem.*, 2004, **43**, 0000.

1277. H. Tan, U. Simonis, N. V. Shokhirev, and F. A. Walker, *J. Am. Chem. Soc.*, 1994, **116**, 5784.

1278. K. I. Momot and F. A. Walker, *J. Phys. Chem. A*, 1997, **101**, 9207.

1279. K. Skidmore and U. Simonis, *Inorg. Chem.*, 1996, **35**, 7470.

1280. M. K. Safo, G. P. Gupta, C. T. Watson, U. Simonis, F. A. Walker, and W. R. Scheidt, *J. Am. Chem. Soc.*, 1992, **114**, 7066.

1281. M. K. Safo, F. A. Walker, A. M. Raitsimring, W. P. Walters, D. P. Dolata, P. G. Debrunner, and W. R. Scheidt, *J. Am. Chem. Soc.*, 1994, **116**, 7760.

1282. K. A. Keating, G. N. La Mar, F.-Y. Shiau, and K. M. Smith, *J. Am. Chem. Soc.*, 1992, **114**, 6513.

1283. A. Ghosh, E. Gonzalez, and T. Vangberg, *J. Phys. Chem. B*, 1999, **103**, 1363.

1284. O. Q. Munro, J. C. Bradley, R. D. Hancock, H. M. Marques, F. Marsicano, and P. W. Wade, *J. Am. Chem. Soc.*, 1992, **114**, 7218.

1285. K. M. Barkigia, M. A. Thompson, J. Fajer, R. K. Pandey, K. M. Smith, and M. G. H. Vincente, *New J. Chem.*, 1992, **16**, 599.

1286. L. D. Sparks, C. J. Medforth, M.-S. Park, J. R. Chamberlain, M. R. Ondrias, M. O. Senge, K. M. Smith, and J. A. Shelnutt, *J. Am. Chem. Soc.*, 1993, **115**, 581.

1287. O. Q. Munro, H. M. Marques, P. G. Debrunner, K. Mohanrao, and W. R. Scheidt, *J. Am. Chem. Soc.*, 1995, **117**, 935.

1288. S. Othman, A. Le Lirzin, and A. Desbois, *Biochemistry*, 1994, **33**, 15437.

1289. A. D. Carraway, M. G. McCollum, and J. Peterson, *Inorg. Chem.*, 1996, **35**, 6885.

1290. L. A. Yatsunyk and F. A. Walker, *Inorg. Chem.*, 2004, **43**, 4341.

1291. M. Nakamura, T. Ikeue, H. Fujii, and T. Yoshimura, *J. Am. Chem. Soc.*, 1997, **119**, 6284.

1292. S. Wolowiec, L. Latos-Grażyński, M. Mazzanti, and J.-C. Marchon, *Inorg. Chem.*, 1997, **36**, 5761.

1293. S. Wolowiec, L. Latos-Grażyński, D. Toronto, and J.-C. Marchon, *Inorg. Chem.*, 1998, **37**, 724.

1294. A. Ikezaki and M. Nakamura, *Inorg. Chem.*, 2002, **41**, 2761.

1295. M. Nakamura, T. Ikeue, A. Ikezaki, Y. Ohgo, and H. Fujii, *Inorg. Chem.*, 1999, **38**, 3857.

1296. M. Nakamura, K. Tajima, K. Tada, K. Ishizu, and N. Nakamura, *Inorg. Chim. Acta*, 1994, **224**, 113.

1297. M. Nakamura, T. Ikeue, H. Fujii, T. Yoshimura, and K. Tajima, *Inorg. Chem.*, 1998, **37**, 2405.

1298. J. Mao, Y. Zhang, and E. Oldfield, *J. Am. Chem. Soc.*, 2002, **124**, 13911.

1299. M. Hada, *J. Am. Chem. Soc.*, 2004, **126**, 486.

1300. H. Kalish, J. E. Camp, M. Stepien, L. Latos-Grażyński, M. M. Olmstead, and A. L. Balch, *Inorg. Chem.*, 2002, **41**, 909.

1301. J. Wolowiec, L. Latos-Grażyński, and T. Glowiak, *Inorg. Chem.*, 1997, **36**, 6299.

1302. M. Kobeissi, L. Toupet, and G. Simonneaux, *Inorg. Chem.*, 2001, **40**, 4494.

1303. G. Simonneaux, M. Kobeissi, and L. Toupet, *Inorg. Chem.*, 2003, **42**, 1644.

1304. J. Kaufman, L. M. Siegel, and L. D. Spicer, *Biochemistry*, 1993, **32**, 8782.

1305. G. N. La Mar, J. D. Satterlee, and J. S. de Ropp, Nuclear Magnetic Resonance of Hemoproteins, in 'The Porphyrin Handbook', eds. K. M. Kadish, K. M. Smith, and R. Guilard, Academic Press, San Diego, CA, 2000, Vol. 5, p. 185.

1306. M. O. Senge, C. J. Medforth, L. D. Sparks, J. A. Shelnutt, and K. M. Smith, *Inorg. Chem.*, 1993, **32**, 1716.

1307. P. Hoffman, G. Labat, A. Robert, and B. Meunier, *Tetrahedron Lett.*, 1990, **31**, 1991.

1308. J. F. Bartoli, O. Brigaud, P. Battioni, D. Mansuy, and T. G. Traylor, *Chem. Commun.*, 1991, 440.

1309. D. Mandon, P. Ochsenbein, J. Fischer, R. Weiss, K. Jayaraj, R. N. Austin, A. Gold, P. S. White, O. Brigaud, P. Battioni, and D. Mansuy, *Inorg. Chem.*, 1992, **31**, 2044.

1310. O. Brigaud, P. Battioni, and D. Mansuy, *New J. Chem.*, 1992, **16**, 1031.

1311. E. R. Birnbaum, J. A. Hodge, M. W. Grinstaff, W. P. Schaefer, L. Henling, J. A. Labinger, J. E. Bercaw, and H. B. Gray, *Inorg. Chem.*, 1995, **34**, 3625.

1312. P. Ochsenbein, D. Mandon, J. Fischer, R. Weiss, R. Austin, K. Jayaraj, A. Gold, J. Terner, E. Bill, M. Müther, and A. X. Trautwein, *Angew. Chem., Int. Ed. Engl.*, 1993, **32**, 1437.

1313. W. R. Scheidt, H. F. Duval, T. J. Neal, and M. K. Ellison, *J. Am. Chem. Soc.*, 2000, **122**, 4651.

1314. G. B. Richter-Addo, R. A. Wheelker, C. A. Hixson, L. Chen, M. A. Khan, M. K. Ellison, C. E. Schulz, and W. R. Scheidt, *J. Am. Chem. Soc.*, 2001, **123**, 6314.

1315. G. Simonneaux and M. Kobeissi, *J. Chem. Soc., Dalton Trans.*, 2001, 1587.

1316. W. R. Scheidt and D. M. Chipman, *J. Am. Chem. Soc.*, 1986, **108**, 1163.

1317. R. Bois-Poltoratsky and A. Ehrenberg, *Eur. J. Biochem.*, 1967, **2**, 361.

1318. P. G. Passon, D. W. Reed, and D. E. Hultquist, *Biochim. Biophys. Acta*, 1972, **275**, 51.

1319. M. Rivera, C. Barillas-Mury, K. A. Christensen, J. W. Little, M. A. Wells, and F. A. Walker, *Biochemistry*, 1992, **31**, 12233.

1320. R. Cammack, D. Fauque, J. J. G. Moura, and J. LeGall, *Biochim. Biophys. Acta*, 1984, **784**, 68.

1321. J. P. Gayda, P. Bertrand, C. More, F. Guerlesquin, and M. Bruschi, *Biochim. Biophys. Acta*, 1985, **829**, 262.

1322. J. P. Gayda, T. Yagi, H. Benosman and P. Bertrand, *FEBS Lett.*, 1987, **217**, 57.

1323. J. P. Gayda, H. Benosman, P. Bertrand, C. More, and M. Asso, *Eur. J. Biochem.*, 1988, **177**, 199.

1324. I. Moura, M. Teixeira, B. H. Huynh, J. LeGall, and J. J. Moura, *Eur. J. Biochem.*, 1988, **176**, 365.

1325. W. E. Blumberg and J. Peisach, *Adv. Chem. Ser.*, 1971, **100**, 271.

1326. C. T. Migita and M. Iwaizumi, *J. Am. Chem. Soc.*, 1981, **103**, 4378.

1327. K. R. Carter, A.-L. T'sai, and G. Palmer, *FEBS Lett.*, 1981, **132**, 243.

1328. M. Fahnenschmidt, H. K. Rau, R. Bittl, W. Haehnel, and W. Lubitz, *Chem. Eur. J.*, 1999, **5**, 2327.

1329. F. A. Walker, D. Reis, and V. L. Balke, *J. Am. Chem. Soc.*, 1984, **106**, 6888.

1330. R. Aasa and T. Vänngård, *J. Magn. Reson.*, 1975, **19**, 308.

1331. S. De Vries and S. P. J. Albracht, *Biochim. Biophys. Acta*, 1979, **546**, 334.

1332. W. R. Widger, W. A. Cramer, R. G. Herrmann, and A. Trebst, *Proc. Natl. Acad. Sci. U.S.A.*, 1984, **81**, 674.

1333. G. T. Babcock, W. R. Widger, W. A. Cramer, W. A. Oertling, and J. Metz, *Biochemistry*, 1985, **24**, 3638.

1334. K. R. Carter, A.-L. Tsai, and G. Palmer, *FEBS Lett.*, 1981, **132**, 243.

1335. J. C. Salerno, *J. Biol. Chem.*, 1984, **259**, 2331.

1336. J. Bergström, *FEBS Lett.*, 1985, **183**, 87.

1337. K. Niki, Y. Kawasaki, N. Nishimura, Y. Higuchi, N. Yasuoka, and M. Kakudo, *J. Electroanal. Chem.*, 1984, **168**, 275.

1338. S. D. Zarić, D. M. Popović, and E.-W. Knapp, *Biochemistry*, 2001, **40**, 7914.

1339. K. Hatano, M. K. Safo, F. A. Walker, and W. R. Scheidt, *Inorg. Chem.*, 1991, **30**, 1643.

1340. R. Benda, V. Schünemann, A. X. Trautwein, S. Cai, J. R. Polam, C. T. Watson, T. Kh. Shokhireva, and F. A. Walker, *J. Biol. Inorg. Chem.*, 2003, **8**, 787.

1341. T. Teschner, L. A. Yatsunyk, P. Wegner, V. Schünemann, C. Hu, W. R. Scheidt, F. A. Walker, and A. X. Trautwein, submitted to *J. Am. Chem. Soc.*

1342. Y. Zhang, J. Mao, and E. Oldfield, *J. Am. Chem. Soc.*, 2002, **124**, 7829.

1343. Y. Zhang, J. Mao, N. Godbout, and E. Oldfield, *J. Am. Chem. Soc.*, 2002, **124**, 13921.

1344. J. Silver, P. J. Marsh, M. C. R. Symons, D. A. Svistunenko, C. S. Frampton, and G. R. Fern, *Inorg. Chem.*, 2000, **39**, 2874.

1345. M. R. Cheesman and F. A. Walker, *J. Am. Chem. Soc.*, 1996, **118**, 7373.

1346. J. D. Satterlee, G. N. La Mar, and T. J. Bold, *J. Am. Chem. Soc.*, 1977, **99**, 1088.

1347. R. Quinn, M. Nappa, and J. S. Valentine, *J. Am. Chem. Soc.*, 1982, **104**, 2588.

1348. L. A. Yatsunyk, Ph.D. dissertation, Synthesis, Structures, Redox and Magnetic Resonance Spectroscopy of Saddle-Distorted Porphyrin Complexes of Iron, University of Arizona, 2003.

1349. L. A. Yatsunyk, A. Dawson, M. D. Carducci, and F. A. Walker, submitted to *J. Am. Chem. Soc*.

1350. M. P. Johansson, D. Sundholm, G. Gerfen, and M. Wikström, *J. Am. Chem. Soc.*, 2002, **124**, 11771.

1351. B. H. Huynh, M. H. Emptage, and E. Münck, *Biochim. Biophys. Acta*, 1978, **534**, 295.

1352. V. Medaković and S. D. Zarić, *Inorg. Chim. Acta*, 2003, **349**, 1.

1353. D. M. A. Smith, M. Dupuis, E. R. Vorpagel, and T. P. Straatsma, *J. Am. Chem. Soc.*, 2003, **125**, 2711.

1354. M. Nakamura and J. T. Groves, *Tetrahedron*, 1988, **44**, 3225.

1355. F. A. Walker, J. Buehler, J. T. West, and J. L. Hinds, *J. Am. Chem. Soc.*, 1983, **105**, 6923.

1356. H. Zhang, U. Simonis, and F. A. Walker, *J. Am. Chem. Soc.*, 1990, **112**, 6124.

1357. U. Simonis, J. L. Dallas, and F. A. Walker, *Inorg. Chem.*, 1992, **31**, 5349.

1358. N. V. Shokhirev, T. Kh. Shokhireva, J. R. Polam, C. T. Watson, K. Raffii, U. Simonis, and F. A. Walker, *J. Phys. Chem. A*, 1997, **101**, 2778.

1359. A. B. Minniear, T. Kh. Shokhireva, and F. A. Walker, *Inorg. Chem.*, 1999, **38**, 5856.

1360. N. V. Shokhirev and F. A. Walker, *J. Biol. Inorg. Chem.*, 1998, **3**, 581.

1361. R. M. Keller, A. Schejter, and K. Wüthrich, *Biochim. Biophys. Acta*, 1980, **626**, 15.

1362. H. Senn and K. Wüthrich, *Biochim. Biophys. Acta*, 1983, **747**, 16.

1363. H. Senn, H. Böhme, and K. Wüthrich, *Biochim. Biophys. Acta*, 1984, **789**, 311.

1364. S. J. McLachlan, G. N. La Mar, and K. B. Lee, *Biochim. Biophys. Acta*, 1988, **957**, 430.

1365. S. D. Emerson and G. N. La Mar, *Biochemistry*, 1990, **29**, 1556.

1366. 2002, http://www.chem.arizona.edu/∼shokhirn/nikolai/programs/prog/ShiftPatterns.zip.

1367. N. V. Shokhirev and F. A. Walker, *J. Am. Chem. Soc.*, 1998, **120**, 981.

1368. R. O. Louro, I. J. Correia, L. Brennan, I. B. Coutinho, A. V. Xavier, and D. L. Turner, *J. Am. Chem. Soc.*, 1998, **120**, 13240.

1369. I. Bertini, C. Luchinat, G. Parigi, and F. A. Walker, *J. Biol. Inorg. Chem.*, 1999, **4**, 515, 846.

1370. D. L. Turner, *J. Biol. Inorg. Chem.*, 2000, **5**, 328.

1371. L. Banci, I. Bertini, G. Cavallaro, and C. Luchinat, *J. Biol. Inorg. Chem.*, 2002, **7**, 416.

1372. G. A. Caignan, R. Deshmukh, A. Wilks, Y. Zeng, H. Huang, P. Moënne-Loccoz, R. A. Bunce, M. A. Eastman, and M. Rivera, *J. Am. Chem. Soc.*, 2002, **124**, 14879.

1373. D. W. Low, H. B. Gray, and J. Ø. Duus, *J. Am. Chem. Soc.*, 1997, **119**, 1.

1374. L. Banci, I. Bertini, K. L. Bren, M. A. Cremoni, H. B. Gray, C. Luchinat, and P. Turano, *J. Biol. Inorg. Chem.*, 1996, **1**, 117.

1375. L. Brennan and D. L. Turner, *Biochim. Biophys. Acta*, 1997, **1342**, 1.

1376. H. Bang, J. O. Edwards, J. Kim, R. G. Lawler, K. Reynolds, W. J. Ryan, and D. A. Sweigert, *J. Am. Chem. Soc.*, 1992, **114**, 2843.

1377. V. Medakovic and S. D. Zaric, *Inorg. Chim. Acta*, 2003, **349**, 1.

1378. W. R. Scheidt, Y. J. Lee, and K. Hatano, *J. Am. Chem. Soc.*, 1984, **106**, 3191.

1379. M. K. Ellison, C. E. Schulz, and W. R. Scheidt, *Inorg. Chem.*, 1999, **38**, 100.

1380. M. K. Ellison and W. R. Scheidt, *J. Am. Chem. Soc.*, 1999, **121**, 5210.

1381. M. K. Ellison, C. E. Schulz, and W. R. Scheidt, *Inorg. Chem.*, 2000, **39**, 5102.

1382. M. K. Ellison, C. E. Schulz, and W. R. Scheidt, *J. Am. Chem. Soc.*, 2002, **124**, 13833.

1383. X. D. Ding, A. Weichsel, C. Balfour, T. Kh. Shokhireva, A. Pierik, B. A. Averill, W. R. Montfort, and F. A. Walker, *J. Am. Chem. Soc.*, 1999, **121**, 128.

1384. A. Weichsel, J. F. Andersen, S. A. Roberts, and W. R. Montfort, *Nat. Struct. Biol.*, 2000, **7**, 551.

1385. S. A. Roberts, A. Weichsel, Y. Qiu, J. A. Shelnutt, F. A. Walker, and W. R. Montfort, *Biochemistry*, 2001, **40**, 11327.

1386. A. Weichsel, R. E. Berry, F. A. Walker and W. R. Montfort, to be submitted.

1387. M. Hoshino, M. Maeda, R. Konishi, H. Seki, and P. C. Ford, *J. Am. Chem. Soc.*, 1996, **118**, 5702.

1388. J. F. Andersen, X. D. Ding, C. Balfour, D. E. Champagne, F. A. Walker, and W. R. Montfort, *Biochemistry*, 2000, **39**, 10118.

1389. J. G. Valenzuela, F. A. Walker, and J. M. C. Ribeiro, *J. Exp. Biol.*, 1995, **198**, 1519.

1390. A. Weichsel, J. F. Andersen, D. E. Champagne, F. A. Walker, and W. R. Montfort, *Nat. Struct. Biol.*, 1998, **5**, 304.

1391. D. R. Flower, *Biochem. J.*, 1996, **318**, 1.

1392. Y. Zhang, W. Gossman, and E. Oldfield, *J. Am. Chem. Soc.*, 2003, **125**, 16387.

1393. P. Wegner, R. Benda, V. Schünemann, F. Averseng, A. X. Trautwein, R. E. Berry, C. A. Balfour, D. Wert, and F. A. Walker, to be submitted.

1394. T. Kh. Shokhireva, R. E. Berry, E. Uno, C. A. Balfour, H. Zhang, and F. A. Walker, *Proc. Natl. Acad. Sci. U.S.A.*, 2003, **100**, 3778.

1395. A. Weichsel *et al.*, to be submitted.

1396. A. Weichsel, E. M. Maes, J. F. Andersen, J. G. Valenzuela, T. Kh. Shokhireva, F. A. Walker and W. R. Montfort, *Proc. Natl. Acad. Sci. U.S.A.*, 2005, **102**, 594.

1397. T. Tsujishita, S. Guo, L. E. Stolz, J. D. York, and J. H. Hurley, *Cell*, 2001, **105**, 379.

1398. M. B. Murataliev, A. V. Astashkin, and A. M. Raitsimring, unpublished results.

1399. N. Suzuki, T. Higuchi, U. Urano, K. Kikuchi, T. Uchida, M. Mukai, T. Kitagawa, and T. Nagano, *J. Am. Chem. Soc.*, 2000, **122**, 12059.

1400. K. M. Kadish, E. van Caemelbecke, and G. Royal, Electrochemistry of Metalloporphyrins in Nonaqueous Media, in 'The Porphyrin Handbook', eds. K. M. Kadish, K. M. Smith, and R. Guilard, Academic Press, San Diego, CA, 2000, Vol. 8, Chap. 55.

1401. K. M. Kadish, *Prog. Inorg. Chem.*, 1986, **34**, 435.

1402. K. M. Kadish, G. Royal, E. van Caemelbecke, and L. Gueletti, Metalloporphyrins in Nonaqueous Media: Database of Redox Potentials, in 'The Porphyrin Handbook', eds. K. M. Kadish, K. M. Smith, and R. Guilard, Academic Press, San Diego, CA, 2000, Vol. 9, Chap. 59.

1403. A. J. Bard and L. R. Faulkner, 'Electrochemical Methods Fundamentals and Applications', John Wiley & Sons, New York, 1980.

1404. P. H. Rieger, 'Electrochemistry', Chapman and Hall, New York, 1994.

1405. V. D. Parker, G. Zheng, and H. Wang, *Acta Chem. Scand.*, 1995, **49**, 351.

1406. R. Seetharaman, S. P. White, and M. Rivera, *Biochemistry*, 1996, **35**, 12455.

1407. M. Wirtz, J. Klucik, and M. Rivera, *J. Am. Chem. Soc.*, 2000, **122**, 1047.

1408. V. Proux-Delrouyre, C. Demaille, W. Leibl, P. Setif, H. Bottin, and C. Bourdillon, *J. Am. Chem. Soc.*, 2003, **125**, 13686.

1409. S. Fukuzumi, I. Nakanishi, K. Tanaka, T. Suenobu, A. Tabard, R. Guilard, E. Van Caemelbecke, and K. M. Kadish, *J. Am. Chem. Soc.*, 1999, **121**, 785.

1410. K. M. Kadish, F. D'Souza, A. Villard, M. Autret, E. Van Caemelbecke, P. Blanco, A. Antonini, and P. Tagliatesta, *Inorg. Chem.*, 1994, **33**, 5169.

1411. A. Ghosh, *J. Phys. Chem.*, 1994, **98**, 11004.

1412. P. Tagliatesta, J. Li, M. Autret, E. Van Caemelbecke, A. Villard, F. D'Souza, and K. M. Kadish, *Inorg. Chem.*, 1996, **35**, 5570.

1413. K. M. Kadish, E. Van Caemelbecke, F. D'Souza, C. J. Medforth, K. M. Smith, A. Tabard, and R. Guilard, *Inorg. Chem.*, 1995, **34**, 2984.

1414. K. M. Kadish, E. Van Caemelbecke, F. D'Souza, M. Lin, D. J. Nurco, C. J. Medforth, T. P. Forsyth, B. Krattinger, K. M. Smith, S. Fukuzumi, I. Nakanishi, and J. A. Shelnutt, *Inorg. Chem.*, 1999, **38**, 2188.

1415. K. M. Kadish, F. D'Souza, E. Van Caemelbecke, P. Boulas, E. Vogel, A. M. Aukauloo, and R. Guilard, *Inorg. Chem.*, 1994, **33**, 4474.

1416. E. Steene, T. Wondimagegn, and A. Ghosh, *J. Phys. Chem. B*, 2001, **105**, 11406.

1417. A. Ghosh and E. Steene, *J. Inorg. Biochem.*, 2002, **91**, 423.

1418. J.-P. Gisselbrecht, M. Gross, E. Vogel, and J. L. Sessler, *Inorg. Chem.*, 2000, **39**, 2850.

1419. F. A. Walker, V. L. Balke, and J. T. West, *J. Am. Chem. Soc.*, 1985, **107**, 1226.

1420. F. A. Walker, J. A. Barry, V. L. Balke, G. A. McDermott, M. Z. Wu, and P. F. Linde, *Adv. Chem. Ser.*, 1982, **201**, 377.

1421. J. D. Satterlee, G. N. La Mar, and J. S. Frye, *J. Am. Chem. Soc.*, 1976, **98**, 7275.

1422. M. M. Doeff and D. A. Sweigert, *Inorg. Chem.*, 1982, **21**, 3699.

1423. J.-T. Wang, H. J. C. Yeh, and O. F. Johnson, *J. Am. Chem. Soc.*, 1978, **100**, 2400.

1424. M. Nakamura, *Chem. Lett. (Japan)*, 1988, 453.

1425. M. Nakamura, *Inorg. Chim. Acta*, 1989, **161**, 73.

1426. M. Nakamura and N. Nakamura, *Chem. Lett. (Japan)*, 1990, 181.

1427. S. Mazumdar, O. K. Medhi, and S. Mitra, *Inorg. Chem.*, 1988, **27**, 2541.

1428. C. L. Coyle, P. A. Rafson, and E. H. Abbott, *Inorg. Chem.*, 1973, **12**, 2007.

1429. R. F. Pasternack, B. S. Gillies, and J. R. Stahlbush, *J. Am. Chem. Soc.*, 1978, **100**, 2613.

1430. M. Momenteau, *Biochim. Biophys. Acta*, 1973, **304**, 814.

1431. T. Yoshimura and T. Ozaki, *Bull. Chem. Soc. Jpn.*, 1979, **52**, 2268.

1432. E. B. Fleischer and D. A. Fine, *Inorg. Chim. Acta*, 1978, **29**, 267.

1433. M. J. Beck, E. Gopinath, and T. C. Bruice, *J. Am. Chem. Soc.*, 1993, **115**, 21.

1434. F. A. Walker, V. L. Balke, and J. T. West, in 'Frontiers in Bioinorganic Chemistry', ed. A. V. Xavier, VCH, Weinheim, 1985, p. 183.

1435. M. M. Doeff, D. A. Sweigert, and P. O'Brien, *Inorg. Chem.*, 1983, **22**, 851.

1436. F. A. Walker, E. Hui, and J. M. Walker, *J. Am. Chem. Soc.*, 1975, **97**, 2390.

1437. G. A. McDermott and F. A. Walker, *Inorg. Chim. Acta*, 1984, **91**, 95.

1438. T. G. Traylor, K. B. Nolan, and R. Hildreth, *J. Am. Chem. Soc.*, 1983, **105**, 6149.

1439. L. R. Milgrom, *Tetrahedron*, 1983, **39**, 3895.

1440. P. Worthington, P. Hambright, R. F. X. Williams, M. R. Feldman, K. M. Smith, and K. C. Langry, *Inorg. Nucl. Chem. Lett.*, 1980, **46**, 441.

1441. E. C. A. Ojadi, H. Linschitz, M. Gouterman, R. I. Walter, J. S. Lindsey, R. W. Wagner, P. R. Droupadi, and W. Wang, *J. Phys. Chem.*, 1993, **97**, 13192.

1442. R. I. Walter, E. C. A. Ojadi, and H. Linschitz, *J. Phys. Chem.*, 1993, **97**, 13308.

1443. Q.-J. Meng, G. A. Tondreau, J. O. Edwards, and D. A. Sweigert, *J. Chem. Soc., Dalton Trans.*, 1985, 2269.

1444. J. G. Jones, G. A. Tondreau, J. O. Edwards, and D. A. Sweigert, *Inorg. Chem.*, 1985, **24**, 296.

1445. Y. Zhang, J. G. Jones, and D. A. Sweigert, *Inorg. Chim. Acta*, 1989, **166**, 85.

1446. M. S. Hargrove, D. Barrick, and J. S. Olson, *Biochemistry*, 1996, **35**, 11293.

1447. M. S. Hargrove, A. J. Wilkinson, and J. S. Olson, *Biochemistry*, 1996, **35**, 11300.

1448. C. L. Hunter, E. Lloyd, L. D. Eltis, S. P. Rafferty, H. Lee, M. Smith, and A. G. Mauk, *Biochemistry*, 1997, **36**, 1010.

1449. G. N. La Mar, P. D. Burns, J. T. Jackson, K. M. Smith, K. C. Langry, and P. Strittmatter, *J. Biol. Chem.*, 1981, **256**, 6075.

1450. S. J. McLachlan, G. N. La Mar, P. D. Burns, K. M. Smith, and K. C. Langry, *Biochim. Biophys. Acta*, 1986, **874**, 274.

1451. K.-B. Lee, E. Jun, G. N. La Mar, I. N. Rezzano, R. K. Pandey, K. M. Smith, F. A. Walker, and D. H. Buttlaire, *J. Am. Chem. Soc.*, 1991, **113**, 3576.

1452. K.-B. Lee, G. N. La Mar, L. A. Kehres, E. M. Fujinari, K. M. Smith, T. C. Pochapsky, and S. G. Sligar, *Biochemistry*, 1990, **29**, 9623.

1453. K.-B. Lee, G. N. La Mar, R. K. Pandey, I. N. Rezzano, K. E. Mansfield, K. M. Smith, T. C. Pochapsky, and S. G. Sligar, *Biochemistry*, 1991, **30**, 1878.

1454. S. Silchenko, M. L. Sippel, O. Kuchment, D. R. Benson, A. G. Mauk, A. Altuve, and M. Rivera, *Biochem. Biophys. Res. Commun.*, 2000, **271**, 467.

1455. F. A. Walker, D. Emrick, J. E. Rivera, B. J. Hanquet, and D. H. Buttlaire, *J. Am. Chem. Soc.*, 1988, **110**, 6234.

1456. A. Altuve, S. Silchenko, K.-H. Lee, K. Kuczera, S. Terzyan, X. Zhang, D. R. Benson, and M. Rivera, *Biochemistry*, 2001, **40**, 9469.

1457. A. B. Cowley, A. Altuve, O. Kuchment, S. Terzyan, X. Zhang, M. Rivera, and D. R. Benson, *Biochemistry*, 2002, **41**, 11566.

1458. G. N. La Mar and F. A. Walker, *J. Am. Chem. Soc.*, 1972, **94**, 8607.

1459. I. J. Ostrich, G. Liu, H. W. Dodgen, and J. P. Hunt, *Inorg. Chem.*, 1980, **19**, 619.

1460. J. Teraoka and M. Nakamoto, *J. Am. Chem. Soc.*, 2000, **122**, 6301.

1461. N. V. Shokhirev, T. Kh. Shokhireva, J. R. Polam, C. T. Watson, K. Raffii, U. Simonis, and F. A. Walker, *J. Phys. Chem. A*, 1997, **101**, 2778.

1462. K. I. Momot and F. A. Walker, *J. Phys. Chem. A*, 1997, **101**, 2787.

1463. K. I. Momot and F. A. Walker, *J. Phys. Chem. A*, 1998, **102**, 10682.

1464. M. Nakamura, K. Tajima, K. Tada, K. Ishizu, and N. Nakamura, *Inorg. Chim. Acta*, 1994, **224**, 113.

1465. M. Nakamura, T. Ikeue, S. Neya, N. Funasaki, and N. Nakamura, *Inorg. Chem.*, 1996, **35**, 3731.

1466. L. A. Yatsunyk, H. Ogura, and F. A. Walker, *Inorg. Chem.*, 2004, **43**, 0000.

1467. M. Nakamura, T. Yamaguchi, and Y. Ohgo, *Inorg. Chem.*, 1999, **38**, 3126.

1468. R. F. Pasternack and W. R. Showronek, *J. Inorg. Biochem.*, 1979, **11**, 261.

1469. D. Solomon, P. Peretz, and M. Faraggi, *J. Phys. Chem.*, 1982, **86**, 1842.

1470. P. Worthington and P. Hambright, *J. Inorg. Nucl. Chem.*, 1980, **42**, 1651.

1471. J. C. Oxley and D. L. Toppen, *Inorg. Chem.*, 1978, **17**, 3119.

1472. P. Jones, D. Mantle, and I. Wilson, *J. Inorg. Biochem.*, 1982, **17**, 293.

1473. J. Del Gaudio and G. N. La Mar, *J. Am. Chem. Soc.*, 1978, **100**, 1112.

1474. C. E. Castro, M. Jamin, W. Yokoyama, and R. Wade, *J. Am. Chem. Soc.*, 1986, **108**, 4179.

1475. G. N. La Mar and J. Del Gaudio, *Adv. Chem. Ser.*, 1977, **162**, 207.

1476. D. White-Dixon, M. Barbush, and A. Shirazi, *J. Am. Chem. Soc.*, 1985, **106**, 4638.

1477. K. Shin, K. Kramer, and H. Goff, *Inorg. Chem.*, 1987, **26**, 4103.

1478. G. McLendon, *Struct. Bonding*, 1991, **75**, 159.

1479. A. G. Mauk, *Struct. Bonding*, 1991, **75**, 131.

1480. M. J. Therien, J. Chang, A. L. Raphael, B. E. Bowler, and H. B. Gray, *Struct. Bonding*, 1991, **75**, 109.

1481. B. M. Hoffman, M. J. Natan, J. M. Nocek, and S. A. Wallin, *Struct. Bonding*, 1991, **75**, 85.

1482. D. White-Dixon, M. Barbush, and A. Shirazi, *J. Am. Chem. Soc.*, 1984, **103**, 2869.

1483. A. Shirazi, M. Barbush, S. Ghosh, and D. White-Dixon, *Inorg. Chem.*, 1985, **24**, 2495.

1484. D. White-Dixon, S. Woejler, X. Hong, and A. Stolzenberg, *Inorg. Chem.*, 1988, **27**, 3682.

1485. K. Kimura, J. Peterson, M. Wilson, D. J. Cookson, and R. J. P. Williams, *J. Inorg. Biochem.*, 1981, **15**, 11.

1486. B. Fan, D. L. Fontenot, R. W. Larsen, M. C. Simpson, J. A. Shelnutt, R. Falcon, L. Martinez, S. Niu, S. Zhang, T. Niemczyk, and M. R. Ondrias, *Inorg. Chem.*, 1997, **36**, 3839.

1487. B. Fan, M. C. Simpson, J. A. Shelnutt, L. Martinez, R. Falcon, T. Buranda, A. J. Pastuszyn, and M. R. Ondrias, *Inorg. Chem.*, 1997, **36**, 3847.

1488. T. Sasaki and E. T. Kaiser, *J. Am. Chem. Soc.*, 1989, **111**, 380.

1489. K. S. Akerfeldt, R. M. Kim, D. Camac, J. T. Groves, J. D. Lear, and W. F. DeGrado, *J. Am. Chem. Soc.*, 1992, **114**, 9656.

1490. H. Mihara, K.-Y. Tomizaki, T. Fujimoto, S. Sakamoto, H. Aoyagi, and N. Nishino, *Chem. Lett. (Japan)*, 1996, 187.

1491. C. T. Choma, J. D. Lear, M. J. Nelson, P. L. Dutton, D. E. Robertson, and W. F. DeGrado, *J. Am. Chem. Soc.*, 1994, **116**, 856.

1492. H. K. Rau and W. Haehnel, *J. Am. Chem. Soc.*, 1998, **120**, 468.

1493. R. E. Sharp, J. R. Diers, D. F. Bocian, and P. L. Dutton, *J. Am. Chem. Soc.*, 1998, **120**, 7103.

1494. H. K. Privett, C. J. Reedy, M. L. Kennedy, and B. R. Gibney, *J. Am. Chem. Soc.*, 2002, **124**, 6828.

1495. L. Cristian, P. Piotrowiak, and R. S. Farid, *J. Am. Chem. Soc.*, 2003, **125**, 11814.

1496. D. E. Robertson, R. S. Farid, C. C. Moser, J. L. Urbauer, S. E. Mulholland, R. Pidikiti, J. D. Lear, A. J. Wand, W. F. DeGrado, and P. L. Dutton, *Nature*, 1994, **368**, 425.

1497. F. Rabanal, W. F. DeGrado, and P. L. Dutton, *J. Am. Chem. Soc.*, 1996, **118**, 473.

1498. B. R. Gibney, F. Rabanal, K. S. Reddy, and P. L. Dutton, *Biochemistry*, 1998, **37**, 4635.

1499. W. A. Kalsbeck, D. E. Robertson, R. K. Pandey, K. M. Smith, P. L. Dutton, and D. F. Bocian, *Biochemistry*, 1996, **35**, 3429.

1500. J. M. Shifman, B. R. Gibney, R. E. Sharp, and P. L. Dutton, *Biochemistry*, 2000, **39**, 14813.

1501. J. M. Shifman, C. C. Moser, W. A. Kalsbeck, D. F. Bocian, and P. L. Dutton, *Biochemistry*, 1998, **37**, 16815.

1502. B. R. Gibney, Y. Isogai, F. Rabanal, K. S. Reddy, A. M. Grosset, C. C. Moser, and P. L. Dutton, *Biochemistry*, 2000, **39**, 11041.

1503. B. R. Gibney, S. S. Huang, J. J. Skalicky, E. J. Fuentes, A. J. Wand, and P. L. Dutton, *Biochemistry*, 2001, **40**, 10550.

1504. C. J. Reedy, M. L. Kennedy, and B. R. Gibney, *Chem. Commun.*, 2003, 570.

1505. G. Ghirlanda, A. Osyczka, W. Liu, M. Antolovich, K. M. Smith, P. L. Dutton, A. J. Wand, and W. F. DeGrado, *J. Am. Chem. Soc.*, 2004, **126**, 8141.

1506. P. A. Arnold, W. R. Shelton, and D. R. Benson, *J. Am. Chem. Soc.*, 1997, **119**, 3181.

1507. S. Sakamoto, A. Ueno, and H. Mihara, *J. Chem. Soc., Perkin Trans. 2*, 1998, 2395.

1508. D. L. Huffman, M. M. Rosenblatt, and K. S. Suslick, *J. Am. Chem. Soc.*, 1998, **120**, 6183.

1509. M. M. Rosenblatt, D. L. Huffman, X. Wang, H. A. Remmer, and K. S. Suslick, *J. Am. Chem. Soc.*, 2002, **124**, 12394.

1510. G. R. Geier III and T. Sasaki, *Tetrahedron Lett.*, 1997, **38**, 3821.

1511. T. B. Karpishin, T. A. Vannelli, and K. J. Glover, *J. Am. Chem. Soc.*, 1997, **119**, 9063.

1512. D. R. Benson, B. R. Hart, X. Zhu, and M. B. Doughty, *J. Am. Chem. Soc.*, 1995, **117**, 8502.

1513. P. A. Arnold, D. R. Benson, D. J. Brink, M. P. Hendrich, G. S. Jas, M. L. Kennedy, D. T. Petasis, and M. Wang, *Inorg. Chem.*, 1997, **36**, 5306.

1514. D. Liu, K.-H. Lee, and D. Benson, *Chem. Commun.*, 1999, 1205.

1515. D. Liu, D. A. Williamson, M. L. Kennedy, T. D. Williams, M. M. Morton, and D. R. Benson, *J. Am. Chem. Soc.*, 1999, **121**, 11798.

1516. M. L. Kennedy, S. Silchenko, N. Houndonougbo, B. R. Gibney, P. L. Dutton, K. R. Rodgers, and D. R. Benson, *J. Am. Chem. Soc.*, 2001, **123**, 4635.

1517. F. Nastri, A. Lombardi, G. Morelli, O. Maglio, G. D'Auria, C. Pedone, and V. Pavone, *Chem. Eur. J.*, 1997, **3**, 340.

1518. G. D'Auria, O. Maglio, F. Nastri, A. Lombardi, M. Mazzeo, G. Morelli, L. Paolillo, C. Pedone, and V. Pavone, *Chem. Eur. J.*, 1997, **3**, 350.

1519. R. B. Hill, D. P. Raleigh, A. Lombardi, and W. F. DeGrado, *Acc. Chem. Res.*, 2000, **33**, 745.

1520. A. Lombardi, F. Nastri, and V. Pavone, *Chem. Rev.*, 2001, **101**, 3165.

1521. C. J. Reedy and B. R. Gibney, *Chem. Rev.*, 2004, **104**, 617.

1522. F. A. Tezcan, J. R. Winkler, and H. B. Gray, *J. Am. Chem. Soc.*, 1998, **120**, 13383.

1523. J. I. Blankman, N. Shahzad, B. Dangi, C. J. Miller, and R. D. Guiles, *Biochemistry*, 2000, **39**, 14799.

1524. S. S. Huang, B. R. Gibney, S. E. Stayrook, P. L. Dutton, and M. Lewis, *J. Mol. Biol.*, 2003, **326**, 1219.

1525. P. Cocolios, G. Lagrange, and R. Guilard, *J. Organomet. Chem.*, 1983, **253**, 65.

1526. D. Lançon, P. Cocolios, R. Guilard, and K. M. Kadish, *Organometallics*, 1984, **3**, 1164.

1527. R. Guilard, B. Boisselier-Cocolios, A. Tabard, P. Cocolios, B. Simonet, and K. M. Kadish, *Inorg. Chem.*, 1985, **24**, 2509.

1528. Y. O. Kim and H. M. Goff, *J. Am. Chem. Soc.*, 1988, **110**, 8706.

1529. I. M. Arafa, K. Shin, and H. M. Goff, *J. Am. Chem. Soc.*, 1988, **110**, 5228.

1530. A. L. Balch, C. R. Cornman, N. Safari, and L. Latos-Grażyński, *Organometallics*, 1990, **9**, 2420.

1531. K. M. Kadish, A. Tabard, W. Lee, Y. H. Liu, C. Ratti, and R. Guilard, *Inorg. Chem.*, 1991, **30**, 1542.

1532. Z. Li and H. M. Goff, *Inorg. Chem.*, 1992, **31**, 1547.

1533. A. Tabard, P. Cocolios, G. Lagrange, R. Gerardin, J. Hubsch, C. Lecomte, J. Zarembowitch, and R. Guilard, *Inorg. Chem.*, 1988, **27**, 110.

1534. R. D. Arasasingham, A. L. Balch, R. L. Hart, and L. Latos-Grażyński, *J. Am. Chem. Soc.*, 1990, **112**, 7566.

1535. R. D. Arasasingham, A. L. Balch, and L. Latos-Grażyński, *J. Am. Chem. Soc.*, 1987, **109**, 5846.

1536. A. L. Balch, M. M. Olmstead, N. Safari, and T. N. St. Claire, *Inorg. Chem.*, 1994, **33**, 2815.

1537. K. M. Kadish, A. Tabard, E. Van Caemelbecke, A. M. Aukauloo, P. Richard, and R. Guilard, *Inorg. Chem.*, 1998, **37**, 6168.

1538. D. M. Guldi, P. Neta, A. Heger, E. Vogel, and J. L. Sessler, *J. Phys. Chem. A*, 1998, **102**, 960.

1539. P. Gans, G. Buisson, E. Duee, J.-C. Marchon, B. S. Erler, W. F. Scholz, and C. A. Reed, *J. Am. Chem. Soc.*, 1986, **108**, 1223.

1540. W. R. Scheidt, H. Song, K. J. Haller, M. K. Safo, R. D. Orosz, C. A. Reed, P. G. Debrunner, and C. E. Schulz, *Inorg. Chem.*, 1992, **31**, 941.

1541. C. E. Schulz, H. Song, A. Mislankar, R. D. Orosz, C. A. Reed, P. G. Debrunner, and W. R. Scheidt, *Inorg. Chem.*, 1997, **36**, 406.

1542. E. T. Shimomura, M. A. Phillippi, and H. M. Goff, *J. Am. Chem. Soc.*, 1981, **103**, 6778.

1543. S. Ozawa, Y. Watanabe, and I. Morishima, *J. Am. Chem. Soc.*, 1994, **116**, 5832.

1544. K. E. Brancato-Buentello, S.-J. Kang, and W. R. Scheidt, *J. Am. Chem. Soc.*, 1997, **119**, 2839.

1545. T. J. Neal, S.-J. Kang, I. Turowska-Tyrk, C. E. Schulz, and W. R. Scheidt, *Inorg. Chem.*, 2000, **39**, 872.

1546. V. L. Goedken and C. Ercolani, *J. Chem. Soc., Chem. Commun.*, 1984, 378.

1547. B. J. Kennedy, K. S. Murray, H. Homborg, and W. Kalz, *Inorg. Chim. Acta*, 1987, **134**, 19.

1548. C. Ercolani, S. Hewage, R. Heucher, and G. Rossi, *Inorg. Chem.*, 1993, **32**, 2975.

1549. K. M. Kadish, R. K. Rhodes, L. A. Bottomley, and H. M. Goff, *Inorg. Chem.*, 1981, **20**, 3195.

1550. D. F. Bocian, E. W. Findsen, J. A. Hofmann, G. A. Schick, D. R. English, D. N. Hendrickson, and K. S. Suslick, *Inorg. Chem.*, 1984, **23**, 800.

1551. P. Knowles, J. Gibson, F. Pick, and R. Bray, *Biochem. J.*, 1969, **111**, 53.

1552. C. Ercolani, J. Jubb, G. Pennesi, U. Russo, and G. Trigiante, *Inorg. Chem.*, 1995, **34**, 2535.

1553. L. Galich, A. Kienast, H. Huckstadt, and H. Homborg, *Z. Anorg. Allg. Chem.*, 1998, **624**, 1235.

1554. M. Li, M. Shang, N. Ehlinger, C. E. Schulz, and W. R. Scheidt, *Inorg. Chem.*, 2000, **39**, 580.

1555. V. L. Goedken, M. D. Deakin, and L. A. Bottomley, *Chem. Commun.*, 1982, 607.

1556. A. Kienast, L. Galich, K. S. Murray, B. Moubaraki, G. Lazarev, J. Cashion, and H. Homborg, *J. Porphyr. Phthalocy.*, 1997, **1**, 141.

1557. D. R. English, D. N. Hendrickson, and K. S. Suslik, *Inorg. Chem.*, 1985, **24**, 121.

1558. P. Gans, G. Buisson, E. Duée, J.-C. Marchon, B. S. Erler, W. F. Scholz, and C. A. Reed, *J. Am. Chem. Soc.*, 1986, **108**, 1223.

1559. J. Conradie and A. Ghosh, *J. Phys. Chem. B*, 2003, **107**, 6486.

1560. A. Malek, L. Latos-Grażyński, T. J. Bartczak, and A. Zadlo, *Inorg. Chem.*, 1991, **30**, 3222.

1561. K. Rachlewicz and L. Latos-Grażyński, *Inorg. Chem.*, 1995, **34**, 718.

1562. K. Rachlewicz and L. Latos-Grażyński, *Inorg. Chem.*, 1996, **35**, 1136.

1563. E. Vogel, S. Will, A. S. Tilling, L. Neumann, J. Lex, E. Bill, A. X. Trautwein, and K. Wieghardt, *Angew. Chem., Int. Ed. Engl.*, 1994, **33**, 731.

1564. L. Simkhovich, N. Galili, I. Saltsman, I. Goldberg, and Z. Gross, *Inorg. Chem.*, 2000, **39**, 2704.

1565. S. Cai, F. A. Walker, and S. Licoccia, *Inorg. Chem.*, 2000, **39**, 3466.

1566. S. Cai, S. Licoccia, C. D'Ottavi, R. Paolesse, S. Nardis, V. Bulach, B. Zimmer, T. Kh. Shokhireva, and F. A. Walker, *Inorg. Chim. Acta*, 2002, **339**, 171.

1567. E. Steene, T. Wondimagegn, and A. Ghosh, *J. Phys. Chem. B*, 2001, **105**, 11406; 2002, **106**, 5312.

1568. Z. Gross, *J. Biol. Inorg. Chem.*, 2001, **6**, 733.

1569. L. Simkhovich, I. Goldberg, and Z. Gross, *Inorg. Chem.*, 2002, **41**, 5433.

1570. A. Ghosh, T. Wandemagegn, and A. B. J. Parusel, *J. Am. Chem. Soc.*, 2000, **122**, 5100.

1571. E. Van Caemelbecke, S. Will, M. Autret, V. A. Adamian, J. Lex, J.-P. Gisselbrecht, M. Gross, E. Vogel, and K. M. Kadish, *Inorg. Chem.*, 1996, **35**, 184.

1572. M. Autret, S. Will, E. Van Caemelbecke, J. Lex, J.-P. Gisselbrecht, M. Gross, E. Vogel, and K. M. Kadish, *J. Am. Chem. Soc.*, 1994, **116**, 9141.

1573. S. Cai, S. Licoccia, and F. A. Walker, *Inorg. Chem.*, 2001, **40**, 5795.

1574. S. Licoccia, E. Morgante, R. Paolesse, F. Polizio, M. O. Senge, E. Tondello, and T. Boschi, *Inorg. Chem.*, 1997, **36**, 1564.

1575. J. Harmer, S. Van Doorslaer, I. Gromov, M. Bröring, G. Jeschke, and A. Schweiger, *J. Phys. Chem. B*, 2002, **106**, 2801.

1576. C. Brückner, R. P. Priñas, and J. A. Krause Bauer, *Inorg. Chem.*, 2003, **42**, 4495.

1577. C. Brückner, C. A. Barta, R. P. Priñas, and J. A. Krause Bauer, *Inorg. Chem.*, 2003, **42**, 1673.

1578. K. M. Kadish, C. Erben, Z. Ou, V. A. Adamian, S. Will, and E. Vogel, *Inorg. Chem.*, 2000, **39**, 3312.

1579. Z. Gross, L. Simkhovich and N. Galili, *J. Chem. Soc., Chem. Commun.*, 1999, 599.

1580. L. Simkhovich, A. Mahammed, I. Goldberg, and Z. Gross, *Chem. Eur. J.*, 2001, **7**, 1041.

1581. Z. Gross, G. Golubkov, and L. Simkhovich, *Angew. Chem., Int. Ed. Engl.*, 2000, **39**, 4045.

1582. G. Golubkov, J. Bendix, H. B. Gray, A. Mahammed, I. Goldberg, A. J. DiBilio, and Z. Gross, *Angew. Chem., Int. Ed. Engl.*, 2001, **40**, 2132.

1583. A. Mahammed, H. B. Gray, A. E. Meier-Callahan, and Z. Gross, *J. Am. Chem. Soc.*, 2003, **125**, 1162.

1584. J. Grodkowski, P. Neta, E. Fujita, A. Mahammed, L. Simkhovich, and Z. Gross, *J. Phys. Chem. A*, 2002, **106**, 4772.

1585. A. L. Balch, Y.-W. Chan, R.-J. Cheng, G. N. La Mar, L. Latos-Grażyński, and M. W. Renner, *J. Am. Chem. Soc.*, 1984, **106**, 7779.

1586. D. H. Chin, A. L. Balch, and G. N. La Mar, *J. Am. Chem. Soc.*, 1980, **102**, 1446.

1587. A. L. Balch and M. W. Renner, *J. Am. Chem. Soc.*, 1986, **108**, 2603.

1588. D. Mansuy, J.-P. Battioni, D. K. Lavallee, J. Fischer, and R. Weiss, *Inorg. Chem.*, 1988, **27**, 1052.

1589. D. Mansuy, J.-P. Battioni, J.-C. Chottard, and V. Ullrich, *J. Am. Chem. Soc.*, 1979, **101**, 3971.

1590. B. Chevrier, R. Weiss, M. Lange, J.-C. Chottard, and D. Mansuy, *J. Am. Chem. Soc.*, 1981, **103**, 2899.

1591. M. M. Olmstead, R.-J. Cheng, and A. L. Balch, *Inorg. Chem.*, 1982, **21**, 4143.

1592. I. Artaud, N. Gregoire, J.-P. Battioni, D. Dupre, and D. Mansuy, *J. Am. Chem. Soc.*, 1988, **110**, 8714.

1593. P. R. Ortiz de Montellano and L. A. Grab, *J. Am. Chem. Soc.*, 1986, **108**, 5584.

1594. T. J. Wisnieff, A. Gold, and S. A. Evans, *J. Am. Chem. Soc.*, 1981, **103**, 5616.

1595. T. C. Bruice, P. G. Furter, and S. S. Ball, *J. Am. Chem. Soc.*, 1981, **103**, 4578.

1596. T. J. McMurry and J. T. Groves, in 'Cytochrome P-450, Structure, Mechanism and Biochemistry', ed. P. R. Ortiz de Montellano, Plenum Press, New York, 1986, p. 1.

1597. P. M. Champion, B. R. Stallard, G. C. Wagner, and I. C. Gunsalus, *J. Am. Chem. Soc.*, 1982, **104**, 5469.

1598. W. K. Alderton, C. E. Cooper, and R. G. Knowles, *Biochem. J.*, 2001, **357**, 593.

1599. J. H. Dawson, J. R. Trudell, G. Barth, R. E. Linder, E. Bunnenberg, C. Djerassi, R. Chiang, and L. P. Hager, *J. Am. Chem. Soc.*, 1976, **98**, 3709.

1600. M. Sono, J. H. Dawson, and L. P. Hager, *Inorg. Chem.*, 1985, **24**, 4339.

1601. H. B. Dunford and J. S. Stillman, *Coord. Chem. Rev.*, 1976, **19**, 187.

1602. T. L. Poulos, S. T. Freer, R. A. Alden, S. L. Edwards, U. Skogland, K. Tokio, B. Ericksson, N. Xuong, T. Yonetani, and J. Kraut, *J. Biol. Chem.*, 1980, **255**, 575.

1603. M. Ronnberg, A.-M. Lambeir, N. Ellfolk, and H. B. Dunford, *Arch. Biochem. Biophys.*, 1985, **236**, 714.

1604. M. R. N. Murthy, T. J. Reid, A. Sicignano, N. Tanaka, and M. G. Rossmann, *J. Mol. Biol.*, 1981, **152**, 465.

1605. Y. Adam, J. Bernadou, and B. Meunier, *New J. Chem.*, 1992, **16**, 525.

1606. J. Arnon, D. A. Baldwin, H. M. Marques, J. M. Pratt, and P. A. Adams, *J. Inorg. Biochem.*, 1986, **27**, 227.

1607. J.-S. Wang and H. E. van Wart, *J. Phys. Chem.*, 1989, **93**, 7925.

1608. J.-S. Wang, H. K. Baek, and H. E. van Wart, *Biochem. Biophys. Res. Commun.*, 1991, **179**, 1320.

1609. J.-S. Wang, A.-L. Tsai, J. Heldt, G. Palmer, and H. E. van Wart, *J. Biol. Chem.*, 1992, **267**, 15310.

1610. A. M. Osman, M. A. Posthumus, C. Veeger, P. J. van Bladeren, C. Laane, and I. M. C. M. Rietjens, *Chem. Res. Toxicol.*, 1998, **11**, 1319.

1611. V. Schünemann, A. X. Trautwein, I. M. C. M. Rietjens, M. G. Boersma, C. Veeger, D. Mandon, R. Weiss, K. Bahl, C. Colapietro, M. Piech, and R. N. Austin, *Inorg. Chem.*, 1999, **38**, 4901.

1612. C. Dallacosta, E. Monzani, and L. Casella, *J. Biol. Inorg. Chem.*, 2003, **8**, 770.

1613. A. M. Osman, J. Koerts, M. B. Boersma, S. Boeren, C. Veeger, and I. M. C. M. Rietjens, *Eur. J. Biochem.*, 1996, **240**, 232.

1614. P. A. Cole and C. H. Robinson, *J. Am. Chem. Soc.*, 1991, **113**, 8130.

1615. R. C. Prince and D. E. Gunson, *TIBS*, 1993, **18**, 35.

1616. A. L. Balch, G. N. La Mar, L. Latos-Grażyński, M. W. Renner, and V. Thanabal, *J. Am. Chem. Soc.*, 1985, **107**, 3003.

1617. I. R. Paeng, H. Shiwaku, and K. Nakamoto, *J. Am. Chem. Soc.*, 1988, **110**, 1995.

1618. A. L. Balch, *Inorg. Chim. Acta*, 1992, **108–200**, 297.

1619. T. C. Bruice, *Acc. Chem. Res.*, 1991, **24**, 243, and references therein.

1620. K. Murata, R. Panicucci, E. Gopinath, and T. C. Bruice, *J. Am. Chem. Soc.*, 1990, **112**, 6072.

1621. M. F. Zipplies, W. A. Lee, and T. C. Bruice, *J. Am. Chem. Soc.*, 1986, **108**, 4433.

1622. R. E. Rodriguez and H. C. Kelly, *Inorg. Chem.*, 1989, **28**, 589.

1623. W. A. Lee, T. S. Calderwood, and T. C. Bruice, *Proc. Natl. Acad. Sci. U.S.A.*, 1985, **82**, 4301.

1624. T. S. Calderwood and T. C. Bruice, *Inorg. Chem.*, 1986, **25**, 3722.

1625. J. T. Groves and Y. Watanabe, *Inorg. Chem.*, 1987, **26**, 785.

1626. T. G. Traylor and F. Xu, *J. Am. Chem. Soc.*, 1990, **112**, 178.

1627. T. G. Traylor and J. P. Ciccone, *J. Am. Chem. Soc.*, 1989, **111**, 8413.

1628. T. G. Traylor, W. A. Lee, and D. V. Stynes, *J. Am. Chem. Soc.*, 1984, **106**, 755.

1629. R. E. Rodriguez, F. S. Woo, D. A. Huckaby, and H. C. Kelly, *Inorg. Chem.*, 1990, **29**, 1434.

1630. H. Sugimoto, H.-C. Tung, and D. T. Sawyer, *J. Am. Chem. Soc.*, 1988, **110**, 2465.

1631. J. T. Groves, T. E. Nemo, and R. S. Myers, *J. Am. Chem. Soc.*, 1979, **101**, 1032.

1632. C. K. Chang and M. S. Kuo, *J. Am. Chem. Soc.*, 1979, **101**, 3413.

1633. C. L. Hill and B. C. Schardt, *J. Am. Chem. Soc.*, 1980, **102**, 6374.

1634. H. C. Kelly and S. C. Yasui, *Inorg. Chem.*, 1984, **23**, 3559.

1635. T. G. Traylor, W.-P. Fann, and D. Bandyopadhyay, *J. Am. Chem. Soc.*, 1989, **111**, 8009.

1636. B. Meunier, *New J. Chem.*, 1992, **16**, 203.

1637. C. M. Dicken, F.-L. Lu, M. W. Nee, and T. C. Bruice, *J. Am. Chem. Soc.*, 1985, **107**, 5776.

1638. T. W. Kaaret, G. H. Zhang, and T. C. Bruice, *J. Am. Chem. Soc.*, 1991, **113**, 4652.

1639. G. H. Loew and Z. S. Herman, *J. Am. Chem. Soc.*, 1980, **102**, 6114.

1640. L. K. Hanson, C. K. Chang, M. S. Davis, and J. Fajer, *J. Am. Chem. Soc.*, 1981, **103**, 663.

1641. A. Ghosh, J. Almlöf, and L. Que Jr, *J. Phys. Chem.*, 1994, **98**, 5576.

1642. J. Antony, M. Grodzicki, and A. X. Trautwein, *J. Phys. Chem. A*, 1997, **101**, 2692.

1643. J. T. Groves, Z. Gross, and M. K. Stern, *Inorg. Chem.*, 1994, **33**, 5065.

1644. S. Ozawa, Y. Watanabe, S. Nakashima, T. Kitagawa, and I. Morishima, *J. Am. Chem. Soc.*, 1994, **116**, 634.

1645. K. Rachlewicz, L. Latos-Grażyński, and E. Vogel, *Inorg. Chem.*, 2000, **39**, 3247.

1646. D. Lançon, P. Cocolios, R. Guilard, and K. M. Kadish, *J. Am. Chem. Soc.*, 1984, **106**, 4472.

1647. S. Fukuzumi, I. Nakanishi, K. Tanaka, A. Tabard, R. Guilard, E. Van Caemelbecke, and K. M. Kadish, *Inorg. Chem.*, 1999, **38**, 5000.

1648. D. Mansuy, P. Battioni, J.-F. Bartoli, and J.-P. Mahy, *Biochem. Pharmacol.*, 1985, **34**, 431.

1649. P. R. Ortiz de Montellano and K. L. Kunze, *J. Am. Chem. Soc.*, 1981, **103**, 581.

1650. K. L. Kunze and P. R. Ortiz de Montellano, *J. Am. Chem. Soc.*, 1983, **105**, 1380.

1651. P. R. Ortiz de Montellano and N. O. Reich, in ‘Cytochrome P-450, Structure, Mechanism and Biochemistry’, ed. P. R. Ortiz de Montellano, Plenum Press, New York, 1986, p. 273.

1652. J. P. Collman, P. D. Hampton, and J. I. Brauman, *J. Am. Chem. Soc.*, 1990, **112**, 2977.

1653. J. P. Collman, P. D. Hampton, and J. I. Brauman, *J. Am. Chem. Soc.*, 1990, **112**, 2986.

1654. T. Mashiko, D. Dolphin, T. Nakano, and T. G. Traylor, *J. Am. Chem. Soc.*, 1985, **107**, 3735.

1655. D. K. Lavallee and D. Kuila, *Inorg. Chem.*, 1984, **23**, 3987.

1656. A. G. Cochran and P. G. Schultz, *J. Am. Chem. Soc.*, 1990, **112**, 9414.

1657. M. Takeuchi, H. Shimakoshi, and K. Kano, *Organometallics*, 1994, **13**, 1208.

1658. J.-P. Mahy, P. Battioni, D. Mansuy, J. Fisher, R. Weiss, J. Mispelter, I. Morgenstern- Badarau, and P. Gans, *J. Am. Chem. Soc.*, 1984, **106**, 1699.

1659. P. Battioni, J. P. Mahy, G. Gillet, and D. Mansuy, *J. Am. Chem. Soc.*, 1983, **105**, 1399.

1660. E. W. Svastits, J. H. Dawson, R. Breslow, and S. H. Gellman, *J. Am. Chem. Soc.*, 1985, **107**, 6427.

1661. J.-P. Mahy, P. Battioni, and D. Mansuy, *J. Am. Chem. Soc.*, 1986, **108**, 1079.

1662. J. T. Groves and Y. Watanabe, *J. Am. Chem. Soc.*, 1986, **108**, 7836.

1663. D. H. Jones, A. S. Hinman, and T. Ziegler, *Inorg. Chem.*, 1993, **32**, 2092.

1664. R. Rutter, M. Valentine, M. P. Hendrich, L. P. Hager, and P. G. Debrunner, *Biochemistry*, 1983, **22**, 4769.

1665. G. Lang, K. Spartalian, and T. Yonetani, *Biochim. Biophys. Acta*, 1976, **451**, 250.

1666. C. A. Bonagura, B. Bhaskar, H. Shimizu, H. Li, M. Sundaramoorthy, D. E. McRee, D. B. Goodin, and T. L. Poulos, *Biochemistry*, 2003, **42**, 5600.

1667. V. Schünemann, C. Jung, A. X. Trautwein, C. Mandon, and R. Weiss, *FEBS Lett.*, 2000, **179**, 149.

1668. V. Schünemann, F. Lendzian, C. Jung, J. Contzen, A.-L. Barra, S. G. Sligar, and A. X. Trautwein, *J. Biol. Chem.*, 2004, **279**, 10919.

1669. G. H. Loew, D. Spangler, and A. Pudzianowski, *NATO Adv. Study Inst. Ser., Ser. C*, 1982, **89**, 295.

1670. A. Goldblum and G. H. Loew, *J. Am. Chem. Soc.*, 1985, **107**, 4265.

1671. K. Korzekwa, W. Trager, M. Gouterman, D. Spangler, and G. H. Loew, *J. Am. Chem. Soc.*, 1985, **107**, 4273.

1672. G. H. Loew, F. U. Axe, J. R. Collins, and P. Du, *Inorg. Chem.*, 1991, **30**, 2291.

1673. P. Du, F. U. Axe, G. H. Loew, S. Canuto, and M. C. Zerner, *J. Am. Chem. Soc.*, 1991, **113**, 8614.

1674. J. R. Collins, D. L. Camper, and G. H. Loew, *J. Am. Chem. Soc.*, 1991, **113**, 2736.

1675. L. K. Hanson, in ‘Chlorophylls’, ed. H. Scheer, CRC Press, Boca Raton, FL, 1991, p. 1015.

1676. K. A. Jørgensen, *J. Am. Chem. Soc.*, 1987, **109**, 698.

1677. K. R. Korzekwa, J. P. Jones, and J. R. Gillette, *J. Am. Chem. Soc.*, 1990, **112**, 7042.

1678. J. P. Jones, W. F. Trager, and T. J. Carlson, *J. Am. Chem. Soc.*, 1993, **115**, 381.

1679. G. H. Loew and D. L. Harris, *Chem. Rev.*, 2000, **100**, 407.

1680. I. M. C. M. Reitjens, A. M. Osman, C. Veeger, O. Zakharieva, J. Antony, M. Grodzicki, and A. X. Trautwein, *J. Biol. Inorg. Chem.*, 1996, **1**, 372.

1681. M. T. Green, *J. Am. Chem. Soc.*, 1999, **121**, 7939.

1682. D. Harris, G. Loew, and L. Waskell, *J. Biol. Inorg. Chem.*, 2001, **83**, 309.

1683. J. C. Schöneboom, H. Lin, N. Reuter, W. Thiel, S. Cohen, F. Ogliaro, and S. Shaik, *J. Am. Chem. Soc.*, 2002, **124**, 8142.

1684. S. Shaik, S. P. de Visser, F. Ogliaro, H. Schwarz, and D. Schröder, *Curr. Opin. Chem. Biol.*, 2002, **6**, 556.

1685. R. J. Deeth, *J. Am. Chem. Soc.*, 1999, **121**, 6074.

1686. T. Vangberg and A. Ghosh, *J. Am. Chem. Soc.*, 1999, **121**, 12154.

1687. F. P. Guengerich, *Chem. Res. Toxicol.*, 2001, **14**, 611.

1688. J. T. Groves and G. A. McClusky, *J. Am. Chem. Soc.*, 1976, **98**, 859.

1689. J. T. Groves, G. A. McClusky, R. E. White, and M. J. Coon, *Biochem. Biophys. Res. Commun.*, 1978, **81**, 154.

1690. J. T. Groves and Y.-Z. Han, in ‘Cytochrome P450. Structure, Mechanism, and Biochemistry’, 2nd edn., ed. P. R. Ortiz de Montellano, Plenum, New York, 1995, p. 3.

1691. F. P. Guengerich, *Arch. Biochem. Biophys.*, 2003, **409**, 59.

1692. M. Newcomb, P. F. Hollenberg, and M. J. Coon, *Arch. Biohem. Biophys.*, 2003, **409**, 72.

1693. T. Kamachi and K. Yoshizawa, *J. Am. Chem. Soc.*, 2003, **125**, 4652.

1694. S. P. De Visser and S. Shaik, *J. Am. Chem. Soc.*, 2003, **125**, 7413.

1695. T. J. Volz, D. A. Rock, and J. P. Jones, *J. Am. Chem. Soc.*, 2002, **124**, 9724.

1696. M. Newcomb, D. Aebisher, R. Shen, R. E. P. Chandrasena, P. F. Hollenberg and M. J. Coon, *J. Am. Chem. Soc.*, 2003, **125**, 6064.

1697. R. E. P. Chandrasena, K. P. Vatsis, M. J. Coon, P. F. Hollenberg, and M. Newcomb, *J. Am. Chem. Soc.*, 2004, **126**, 115.

1698. D. L. Harris and G. H. Loew, *J. Am. Chem. Soc.*, 1998, **120**, 8941.

1699. F. Ogliaro, S. Cohen, S. P. de Visser, and S. Shaik, *J. Am. Chem. Soc.*, 2000, **122**, 12892.

1700. D. L. Harris and G. H. Loew, *J. Am. Chem. Soc.*, 1996, **118**, 10588.

1701. D. E. Woon and G. H. Loew, *J. Phys. Chem. A*, 1998, **102**, 10380.

1702. M. Wirstam, M. R. A. Blomberg, and P. E. M. Siegbahn, *J. Am. Chem. Soc.*, 1999, **121**, 10178.

1703. F. Ogliaro, S. P. de Visser, S. Cohen, P. K. Sharma, and S. Shaik, *J. Am. Chem. Soc.*, 2002, **124**, 2806.

1704. S. P. de Visser, F. Ogliaro, P. K. Sharma, and S. Shaik, *J. Am. Chem. Soc.*, 2002, **124**, 11809.

1705. P. K. Sharma, S. P. de Visser, and S. Shaik, *J. Am. Chem. Soc.*, 2003, **125**, 8698.

1706. S. P. de Visser, S. Shaik, P. K. Sharma, D. Kumar, and W. Thiel, *J. Am. Chem. Soc.*, 2003, **125**, 15779.

1707. M. T. Green, *J. Am. Chem. Soc.*, 2001, **123**, 9218.

1708. J. P. Collman, A. S. Chien, T. A. Eberspacher, and J. I. Brauman, *J. Am. Chem. Soc.*, 1998, **120**, 425.

1709. W. Nam, M. H. Lim, H. J. Lee, and C. Kim, *J. Am. Chem. Soc.*, 2000, **122**, 6641.

1710. W. Nam, H. J. Han, S.-Y. Oh, Y. J. Lee, M.-H. Choi, S.-Y. Han, C. Kim, S. K. Woo, and W. Shin, *J. Am. Chem. Soc.*, 2000, **122**, 8677.

1711. J. P. Collman, A. S. Chien, T. A. Eberspacher, and J. I. Brauman, *J. Am. Chem. Soc.*, 2000, **122**, 11098.

1712. K. Jayaraj, A. Gold, R. N. Austin, D. Mandon, R. Weiss, J. Terner, E. Bill, M. Müther, and A. X. Trautwein, *J. Am. Chem. Soc.*, 1995, **117**, 9079.

1713. K. Jayaraj, J. Terner, A. Gold, D. A. Roberts, R. N. Austin, D. Mandon, R. Weiss, E. Bill, M. Müther, and A. X. Trautwein, *Inorg. Chem.*, 1996, **35**, 1632.

1714. S. Hashimoto, Y. Tatsuno, and T. Kitagawa, *J. Am. Chem. Soc.*, 1987, **109**, 8096.

1715. K. Czarnecki, L. M. Proniewicz, H. Fujii, and J. R. Kincaid, *J. Am. Chem. Soc.*, 1996, **118**, 4680.

1716. D. Mandon, R. Weiss, K. Jayaraj, A. Gold, J. Terner, E. Bill, and A. X. Trautwein, *Inorg. Chem.*, 1992, **31**, 4404.

1717. A. Nanthakumar and H. M. Goff, *J. Am. Chem. Soc.*, 1990, **112**, 4047.

1718. R. Jones, K. Jayaraj, A. Gold, and M. L. Kirk, *Inorg. Chem.*, 1998, **37**, 2842.

1719. D. Dolphin, A. Forman, D. C. Borg, J. Fajer, and R. H. Felton, *Proc. Natl. Acad. Sci. U.S.A.*, 1971, **3**, 614.

1720. D. Dolphin and R. H. Felton, *Acc. Chem. Res.*, 1974, **7**, 26.

1721. K. Jayaraj, A. Gold, R. N. Austin, L. M. Ball, J. Terner, D. Mandon, R. Weiss, J. Fischer, and A. DeCian, *Inorg. Chem.*, 1997, **36**, 4555.

1722. J. T. Groves and T. E. Nemo, *J. Am. Chem. Soc.*, 1983, **105**, 6243.

1723. B. R. Cook, T. J. Reinert, and K. S. Suslick, *J. Am. Chem. Soc.*, 1986, **108**, 7281.

1724. M. J. Nappa and C. A. Tolman, *Inorg. Chem.*, 1985, **24**, 4711.

1725. J. T. Groves and P. Viski, *J. Am. Chem. Soc.*, 1989, **111**, 8537.

1726. P. A. Grieco and T. L. Stuk, *J. Am. Chem. Soc.*, 1990, **112**, 7799.

1727. P. E. Ellis and J. E. Lyons, *Coord. Chem. Rev.*, 1990, **105**, 181.

1728. T. G. Traylor, K. W. Hill, W.-P. Fann, S. Tsuchiya, and B. E. Dunlap, *J. Am. Chem. Soc.*, 1992, **114**, 1308.

1729. W. Y. Lu, J. F. Bartoli, P. Battioni, and D. Mansuy, *New J. Chem.*, 1992, **16**, 621.

1730. W. Nam, Y. M. Goh, Y. J. Lee, M. H. Lim, and C. Kim, *Inorg. Chem.*, 1999, **38**, 3238.

1731. R. Song, A. Sorokin, J. Bernadou, and B. Meunier, *J. Org. Chem.*, 1997, **62**, 673.

1732. K. A. Lee and W. Nam, *J. Am. Chem. Soc.*, 1997, **119**, 1916.

1733. K. T. Moore, I. T. Horvath, and M. J. Therien, *Inorg. Chem.*, 2000, **39**, 3125.

1734. J. T. Groves and R. S. Myers, *J. Am. Chem. Soc.*, 1983, **105**, 5791.

1735. K. Machii, Y. Watanabe, and I. Morishima, *J. Am. Chem. Soc.*, 1995, **117**, 6691.

1736. J. P. Collman, T. Kodadek, S. A. Raybuck, J. I. Brauman, and L. M. Papazian, *J. Am. Chem. Soc.*, 1985, **107**, 4343.

1737. J. T. Groves and Y. Watanabe, *J. Am. Chem. Soc.*, 1986, **108**, 507.

1738. T. G. Traylor and F. Xu, *J. Am. Chem. Soc.*, 1987, **109**, 6201.

1739. A. J. Castellino and T. C. Bruice, *J. Am. Chem. Soc.*, 1988, **110**, 1313.

1740. D. Ostovic and T. C. Bruice, *J. Am. Chem. Soc.*, 1988, **110**, 6906.

1741. D. Ostovic and T. C. Bruice, *J. Am. Chem. Soc.*, 1989, **111**, 6511.

1742. D. Ostovic and T. C. Bruice, *Acc. Chem. Res.*, 1992, **25**, 314.

1743. D. Dolphin, A. Matsumoto, and C. Shortman, *J. Am. Chem. Soc.*, 1989, **111**, 411.

1744. R. Panicucci and T. C. Bruice, *J. Am. Chem. Soc.*, 1990, **112**, 6063.

1745. J. P. Collman, P. D. Hampton, and J. I. Brauman, *J. Am. Chem. Soc.*, 1990, **112**, 2986.

1746. E. Gopinath and T. C. Bruice, *J. Am. Chem. Soc.*, 1991, **113**, 4657 and 6090.

1747. A. Weselucha-Birczynska, I. R. Paeng, A. A. Shabana, and K. Nakamoto, *New J. Chem.*, 1992, **16**, 563.

1748. M. Palucki, P. J. Pospisil, W. Zhang, and E. N. Jacobsen, *J. Am. Chem. Soc.*, 1994, **116**, 9333.

1749. J. Bernadou, A.-S. Fabiano, A. Robert, and B. Meunier, *J. Am. Chem. Soc.*, 1994, **116**, 9375.

1750. Z.-Q. Tian, J. L. Richards, and T. G. Traylor, *J. Am. Chem. Soc.*, 1995, **117**, 21.

1751. Z. Gross and S. Nimri, *J. Am. Chem. Soc.*, 1995, **117**, 8021.

1752. W. Nam, H. H. Kim, S. H. Kim, R. Y. N. Ho, and J. S. Valentine, *Inorg. Chem.*, 1996, **35**, 1045.

1753. A. Maldotti, C. Bartocci, G. Varani, A. Molinari, P. Battioni, and D. Mansuy, *Inorg. Chem.*, 1996, **35**, 1126.

1754. Z. Gross and S. Ini, *J. Org. Chem.*, 1997, **62**, 5514.

1755. C. Kim, T. G. Traylor, and C. L. Perrin, *J. Am. Chem. Soc.*, 1998, **120**, 9513.

1756. S. J. Yang and W. Nam, *Inorg. Chem.*, 1998, **37**, 606.

1757. R. Zhang, W.-Y. Yu, K.-Y. Wong, and C.-M. Che, *J. Org. Chem.*, 2001, **66**, 8145.

1758. W. Nam, S.-Y. Oh, Y. J. Sun, J. Kim, W.-K. Kim, S. K. Woo, and W. Shin, *J. Org. Chem.*, 2003, **68**, 7903.

1759. L. Barloy, J. P. Lallier, P. Battioni, D. Mansuy, Y. Piffard, M. Tournoux, J. B. Valim, and W. Jones, *New J. Chem.*, 1992, **16**, 71.

1760. P. Battioni, J. F. Bartoli, D. Mansuy, Y. S. Byun, and T. G. Traylor, *J. Chem. Soc., Chem. Commun.*, 1992, 1054.

1761. Y. Watanabe and Y. Ishimura, *J. Am. Chem. Soc.*, 1989, **111**, 410.

1762. J. P. Collman, V. J. Lee, X. Zhang, J. A. Ibers, and J. I. Brauman, *J. Am. Chem. Soc.*, 1993, **115**, 3834.

1763. G.-X. He, R. D. Arasasingham, G.-H. Zhang, and T. C. Bruice, *J. Am. Chem. Soc.*, 1991, **113**, 9828.

1764. Y. M. Goh and W. Nam, *Inorg. Chem.*, 1999, **38**, 914.

1765. T. G. Traylor, C. Kim, J. L. Richards, F. Xu, and C. L. Perrin, *J. Am. Chem. Soc.*, 1995, **117**, 3468.

1766. J. F. Bartoli, O. Brigaud, P. Battioni, and D. Mansuy, *J. Chem. Soc., Chem. Commun.*, 1991, 440.

1767. H. L. Chen, P. E. Ellis Jr, T. Wijesekera, T. E. Hagan, S. E. Groh, J. E. Lyons, and D. P. Ridge, *J. Am. Chem. Soc.*, 1994, **116**, 1086.

1768. K. T. Moore, I. T. Horváth, and M. J. Therien, *J. Am. Chem. Soc.*, 1997, **119**, 1791.

1769. K. T. Moore, I. T. Horváth, and M. J. Therien, *Inorg. Chem.*, 2000, **39**, 3125.

1770. A. Maldotti, C. Bartocci, R. Amadelli, E. Polo, P. Battioni, and D. Mansuy, *J. Chem. Soc., Chem. Commun.*, 1991, 1487.

1771. D. W. Low, J. R. Winkler, and H. B. Gray, *J. Am. Chem. Soc.*, 1996, **118**, 117.

1772. J. R. Wolf, C. G. Hamaker, J.-P. Djukic, T. Kodadek, and L. K. Woo, *J. Am. Chem. Soc.*, 1995, **117**, 9194.

1773. Y. Chen, L. Huang, and X. P. Zhang, *Org. Lett.*, 2003, **5**, 2493.

1774. C.-M. Che, J.-S. Huang, F.-W. Lee, Y. Li, T.-S. Lai, H.-L. Kwong, P. F. Teng, W.-S. Lee, W.-C. Lo, X.-M. Peng, and Z.-Y. Zhou, *J. Am. Chem. Soc.*, 2001, **123**, 4119.

1775. C. G. Hamaker, G. A. Mirafzal, and L. K. Woo, *Organometallics*, 2001, **20**, 5171.

1776. C. G. Hamaker, J.-P. Djukic, D. A. Smith, and L. K. Woo, *Organometallics*, 2001, **20**, 5189.

1777. E. Baciocchi and M. Ioele, *J. Org. Chem.*, 1995, **60**, 5504.

1778. J. Hart-Davis, P. Battioni, J.-L. Boucher, and D. Mansuy, *J. Am. Chem. Soc.*, 1998, **120**, 12524.

1779. G. A. Mirafzal, G. Cheng, and L. K. Woo, *J. Am. Chem. Soc.*, 2001, **124**, 176.

1780. G. Cheng, G. A. Mirafzal, and L. K. Woo, *Organometallics*, 2003, **22**, 1468.

1781. Y. Chen, L. Huang, and X. P. Zhang, *J. Org. Chem.*, 2003, **68**, 7903.

1782. J. T. Groves, W. J. Kruper, and R. C. Haushalter, *J. Am. Chem. Soc.*, 1980, **102**, 6375.

1783. C. L. Hill and B. C. Schardt, *J. Am. Chem. Soc.*, 1983, **105**, 6374.

1784. Z. Gross and S. Nimri, *Inorg. Chem.*, 1994, **33**, 1731.

1785. H. Fujii, T. Yoshimura, and H. Kamada, *Inorg. Chem.*, 1997, **36**, 6142.

1786. W. Nam, M. H. Lim, and S.-Y. Oh, *Inorg. Chem.*, 2000, **39**, 5572.

1787. W. Nam, S. W. Jin, M. H. Lim, J. Y. Ryu, and C. Kim, *Inorg. Chem.*, 2002, **41**, 3647.

1788. A. Robert, B. Loock, M. Momenteau, and B. Meunier, *Inorg. Chem.*, 1991, **30**, 706.

1789. R. D. Arasasingham and T. C. Bruice, *J. Am. Chem. Soc.*, 1991, **113**, 6095.

1790. K. Yamaguchi, Y. Watanabe, and I. Morishima, *J. Am. Chem. Soc.*, 1993, **115**, 4058.

1791. S. Wolowiec and L. Latos-Grażyński, *Inorg. Chem.*, 1998, **37**, 2984.

1792. A. Dey and A. Ghosh, *J. Am. Chem. Soc.*, 2002, **124**, 3206.

1793. K. Yamaguchi, Y. Watanabe, and I. Morishima, *J. Chem. Soc. Chem. Commun.*, 1992, 1721.

1794. T. Murakami, K. Yamaguchi, Y. Watanabe, and I. Morishima, *Bull. Chem. Soc. Jpn.*, 1998, **71**, 1343.

1795. A. Ghosh, in 'The Porphyrin Handbook', eds. K. M. Kadish, K. M. Smith, and R. Guillard, Academic Press, New York, 2000, Vol. 7, p. 1.

1796. W.-D. Wagner and K. Nakamoto, *J. Am. Chem. Soc.*, 1989, **110**, 4044.

1797. W.-D. Wagner and K. Nakamoto, *J. Am. Chem. Soc.*, 1988, **111**, 1590.

Acknowledgments

The support of NIH grant DK 31038 during the writing of the original and revised article and of F. Ann Walker's research on iron porphyrins over the past 22 years is gratefully acknowledged. Professor Dennis Evans H. Evans provided very helpful comments on the electrochemistry and thermodynamics sections. This revised article was prepared while both authors were on Sabbatical, Professor Simonis at the University of California, San Francisco, and Professor Walker at the University of Lübeck, Physics Institute, with support from an Alexander von Humboldt Senior Research Award.

This article is dedicated to the memory of Dr. Teddy G. Traylor (1925–1993), who was Distinguished Professor of Chemistry at the University of California, San Diego, and an active contributor to our understanding of iron porphyrin chemistry, as detailed in the sections on Fe^{II}, Fe^{III}, and Fe^{IV}

porphyrins and Fe^{IV} porphyrin π -cation radicals. Teddy's iron porphyrin research spanned the design of models for the active sites of hemoglobin and myoglobin and the investigation of their reactions with O_2 and CO, the design of low-spin Fe^{III} model hemes, the design and detailed investigation of the reactions of high-valent iron porphyrin models of the cytochromes P450 with organic substrates, and the utilization of these high-valent iron porphyrins for the development of useful catalytic systems. His scientific creativity, insight, and enthusiasm for discussing and solving chemical problems are sorely missed, as is his vitality, wonderful sense of humor, fun, and adventure, and his great success at enjoying life to the fullest.

Iron Proteins with Dinuclear Active Sites

Donald M. Kurtz, Jr
University of Georgia, Athens, GA, USA

1 Introduction 1
2 Purple Acid Phosphatases 2
3 Flavo-diiron Enzymes 2
4 Hemerythrin 3
5 O_2-Activating Enzymes 5
6 Related Articles 14
7 References 14

Abbreviations

ACP = acyl carrier protein; ACPΔ^9D = ACPΔ^9 desaturase; AlkB = octane 1-monooxygenase; AOX = alternative oxidase; DMQ hydroxylase = 5-demethoxyquinone hydroxylase; EXAFS = extended X-ray absorption fine structure spectroscopy; FMN = flavin mononucleotide; FprA = flavoprotein A (flavo-diiron enzyme homologue); Hr = hemerythrin; MCD = magnetic circular dichroism; MME hydroxylase = Mg-protophorphyrin IX monomethyl ester hydroxylase; MMO = methane monooxygenase; MMOH = hydroxylase component of MMO; NADH = reduced nicotinamide adenine dinucleotide; PAPs = purple acid phosphatases; PCET = proton-coupled electron transfer, PTOX = plastid terminal oxidase; R2 = ribonucleotide reductase R2 subunit; Rbr = rubrerythrin; RFQ = rapid freeze-quench; RNR = ribonucleotide reductase; ROO = rubredoxin:oxygen oxidoreductase; XylM = xylene monooxygenase.

1 INTRODUCTION

1.1 Scope and Brief History

The class of proteins referred to in the title includes only those containing nonheme, non-sulfur diiron sites. Several reviews of various members of this class of proteins are available,**[1–4]** although none are simultaneously comprehensive and completely up-to-date. This state of affairs signals neither neglect nor lack of interest, but rather the rapid expansion and development of knowledge in this area. Though still dwarfed by the numbers of heme or iron–sulfur proteins, the list of proteins known to contain nonheme, non-sulfur diiron sites has steadily expanded over the past thirty years. Until 1973, the O_2-carrying protein, hemerythrin (Hr), was the only known member of this class, whereas at least a dozen proteins with distinct activities containing nonheme, non-sulfur diiron sites have been characterized as of 2003. While Hr for many years served as the prototype, its structure and function have turned out to be distinct from those of the O_2-activating proteins, which now form the largest subclass: at least seven distinct types of such O_2-activating enzymes containing nonheme, non-sulfur diiron sites have been identified.

Some respiratory nitric oxide (NO) reductases, which contain a mixed dinuclear heme, nonheme iron site (*see* ***Cytochrome Oxidase***), and [2Fe-2S] ferredoxins (*see* ***Iron–Sulfur Proteins***), are covered in separate chapters of this encyclopedia. Ferritins and bacterioferritins, which contain a metastable nonheme diiron site are also covered elsewhere in this Encyclopedia (*see* ***Iron Proteins for Storage & Transport & their Synthetic Analogs***). Another chapter in this encyclopedia, ***Iron: Models of Proteins with Dinuclear Active Sites***, provides a synthetic perspective on the properties of nonheme, non-sulfur diiron sites in proteins. Recent reports of synthetic polypeptides that contain nonheme, non-sulfur diiron sites**[5]** should also be noted.

1.2 General Similarities and Differences

Nonheme, non-sulfur diiron active sites in proteins share the following properties: (1) two iron atoms separated by 4 Å or less; (2) stable high spin ferrous and ferric oxidation states; (3) terminal histidinyl imidazole, carboxylate, and solvent ligands; (4) at least one ligand that bridges the two irons; and (5) magnetic superexchange coupling of the unpaired spins on the two irons mediated by the bridging ligand atom(s). With one possible exception, the bridging ligands are either known or are strongly suspected to include one or two carboxylates, and for this reason these proteins have also been aptly referred to as 'diiron-carboxylate proteins'.**[6]** The observed superexchange coupling at these sites, however, occurs predominantly via a bridging, solvent-exchangeable oxo or hydroxo ligand. This coupling is typically antiferromagnetic in the diferric and mixed-valent Fe^{II}, Fe^{III} oxidation levels, resulting in ground $S = 0$ and $S = 1/2$ spin states, respectively. The latter mixed-valent ground spin state gives rise to a characteristic axial or rhombic EPR signal with $g_{ave} < 2$, which is observable only below about 30 K. This characteristic signal has proven useful for initial verification of the presence of these nonheme diiron sites in newly isolated proteins. For those diiron proteins where the mixed-valent form is not sufficiently stable, the presence of an antiferromagnetically coupled diferric site can be verified by ^{57}Fe Mössbauer spectroscopy in strong applied magnetic fields. X-ray crystallography, however, has become increasingly important in verifying the diiron nature as well as the structural details of these proteins. The diferrous oxidation

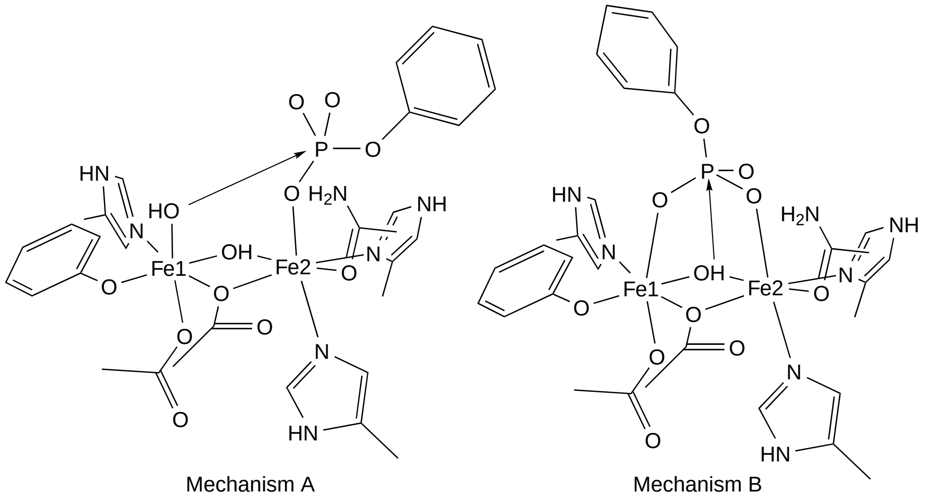

Figure 1 Active site structure of PAPs and proposed mechanisms for their catalytic hydrolysis of a phosphate monoester, involving either a terminal (Mechanism A) or bridging (Mechanism B) hydroxide. The Fe1, containing the tyrosine ligand, is in the Fe(III) oxidation state. (Reprinted with permission from Ref. 9. © 2002 American Chemical Society)

level of these proteins is typically stable under anaerobic conditions, but spontaneously oxidizes (albeit with varying rates) to the diferric level upon exposure to dioxygen.

The active site similarities listed above belie a remarkable functional diversity, which includes phosphate ester hydrolysis, dioxygen and NO reduction, reversible O_2 binding, and O_2 activation, the last of which includes enzymes involved in ribonucleotide reduction, hydrocarbon monooxygenation, and fatty acyl desaturation. At the overall protein level, the purple acid phosphatases (PAPs) seem to be completely unrelated, both structurally and functionally, to any of the others in this class. Similarly, the flavo-diiron enzymes form a structurally and probably functionally distinct family of proteins, catalyzing both dioxygen and NO reduction. These last two examples illustrate that attempts to ‘shoehorn’ all of these enzymes into a single class can sometimes provide a simplistic and misleading view of their chemistry and biochemistry.

2 PURPLE ACID PHOSPHATASES

PAPs are glycoenzymes of M_r 35–40 kDa characterized by their intense purple color due to a tyrosine ligand-to-iron(III) charge transfer transition near 600 nm.[7] The best studied PAPs are those from bovine spleen, porcine uterine fluids, and rat bone, which have been proposed to be involved in iron transport, the immune response, and bone resorption respectively. However, the biological relevance of the phosphatase activity of PAPs has not been unequivocally established. Recently, a bacterial phospholipase with active site properties resembling those of PAPs has also been reported.[8] All PAPs contain a conserved dimetal binding amino acid sequence motif in which an iron(III) is ligated to tyrosine, histidine, and aspartate side chains and a divalent metal ion (Fe, Zn, or Mn) is ligated by an asparagine and two histidine side chains. The two metal ions are bridged by a hydroxide and an aspartate side chain. The generic active site structure of PAPs, which has been confirmed by X-ray crystallography, is shown in Figure 1. The identification of the solvent bridge as hydroxo, rather than oxo or aqua, has been inferred from the magnitude of the magnetic coupling between the irons.[9] PAPS are enzymatically active only at low pH (pH optimum ∼5), hence their classification as acid phosphatases. Most proposed mechanisms for the phosphatase activity invoke an attack of a coordinated hydroxide, either bridging the metal ions[9] or terminally coordinating to iron(III),[10] on the coordinated phosphate ester substrate (cf. Figure 1). For those PAPS containing a diiron site, only the mixed-valent Fe^{II},Fe^{III} oxidation level, which is air stable, is enzymatically active.

3 FLAVO-DIIRON ENZYMES

Flavo-diiron enzymes, also referred to as flavoproteins A (FprAs) or A-type flavoproteins, are the most recently recognized of the nonheme diiron proteins. FprA homologues are widely distributed among anaerobic bacteria and archaea,[11–13] as well as some facultative anaerobes, including *Escherichia coli*. The discovery that at least some FprAs contain a diiron site came from a 2.5-Å resolution X-ray crystal structure of an enzyme dubbed rubredoxin:oxygen oxidoreductase (ROO), an FprA homologue that had been isolated from an anaerobic sulfate-reducing bacteria.[14] The diiron site in ROO was completely unanticipated because the amino acid sequence showed no homology to other known diiron proteins. The protein domain surrounding the diiron site also exhibited a folding motif that was completely unrelated to the four-helix bundle motif found in Hr or in the O_2-activating diiron enzymes (discussed below). Each subunit of the ROO homodimer is folded into two distinct domains, one containing flavin mononucleotide (FMN) and the other containing the diiron site, the structure of which is shown in Figure 2. The folding motif of the diiron domain in ROO resembles that of metallo-β-lactamases (*see* ***Zinc Enzymes***).[12] The two subunits of the homodimer are associated in a head-to-tail fashion, which brings the FMN moiety of one subunit into close proximity of the diiron site in the other subunit. This close juxtaposition to a flavin cofactor and the β-lactamase-like diiron domain constitute the unique and defining structural feature of this subclass of nonheme diiron proteins. Since the ROO was crystallized and maintained under aerobic conditions, it was assumed that the diiron site and FMN in the ROO crystal structure are fully oxidized. As with all other known nonheme diiron proteins, the ligands are provided by a combination of histidine, glutamate, and aspartate. The two irons are 3.4 Å apart and bridged by a bidentate aspartate and a solvent ligand, suggested to be either oxo or hydroxo. The carboxylate oxygen of the Glu81 terminal ligand is ~3.5 Å from the C8-methyl group of the FMN across the subunit interface, and this Glu presumably participates in an electron-transfer pathway between FMN and the diiron site. A region of electron density positioned in a pocket just above the diiron site (OXY in Figure 2) was interpreted as a dioxygen molecule. Given the relatively low resolution of the crystal structure, this assignment must be considered inconclusive. The distance from this putative dioxygen molecule and the nearest iron is longer than would be expected for direct coordination, but the proximity is consistent with an O_2-binding pocket near the diiron site of ROO. One reason for assigning a dioxygen molecule to the electron density above the diiron site was the previous report that in vitro, ROO, when combined with a reductase and the small electron-transfer protein, rubredoxin (*see* ***Iron–Sulfur Proteins***), could catalyze the NADH oxidase reaction: $2NADH + 2H^+ + O_2 \longrightarrow 2H_2O + 2NAD^+$, in which it was proposed that the diiron site binds dioxygen during its four-electron reduction by the fully reduced ROO.[14] Two of the four electrons would be donated by the two ferrous irons of the diiron site and two more by the fully reduced proximal FMN. A function for this ‘dioxygen reductase’ activity in anaerobic microorganisms is not obvious; energy conservation and oxidative stress protection during periods of exposure to air have been suggested.[14] More recently, however, evidence has accumulated that, at least in some bacteria, FprA homologues function not as dioxygen reductases but rather as NO reductases, catalyzing the two-electron reduction: $2NO + 2H^+ + 2e^- \longrightarrow N_2O + H_2O$.[15,16] This latter catalysis apparently serves a protective function against exposure to NO, micromolar levels of which are toxic to bacteria even under anaerobic growth conditions. A mechanism for catalysis of NO reduction by FprAs involving a diferrous dinitrosyl intermediate can be readily envisioned, but observation of such a species has not been reported. Whether all flavo-diiron enzymes function as NO reductases in vivo also remains to be established.

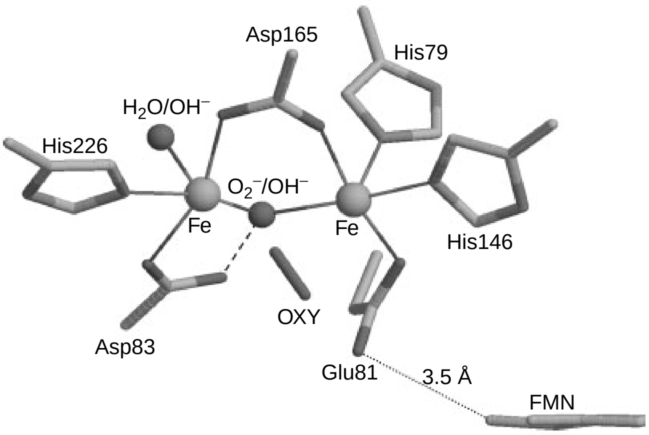

Figure 2 Structure of the diiron site in the flavo-diiron enzyme, ROO from *Desulfovibrio gigas*.[14] Drawing was generated using RASMOL[17] and coordinates from 1ESD in the Protein Data Bank. Iron atoms and solvent ligands are shown as larger and smaller spheres respectively, and protein side chains providing ligands are shown in wireframe representation. The dashed line indicates hydrogen bonding between an aspartate carboxylate and bridging solvent ligands. A portion of the FMN ring is shown approximately edge-on at the lower right. The dotted line indicates the shortest distance between the Glu81 carboxylate ligand and an FMN carbon

4 HEMERYTHRIN

4.1 Background

Hemerythrin (Hr) is an O_2-carrying protein found in a few phyla of marine invertebrates where it is thought to function as an O_2 storage reservoir.[18,19] The diiron active site reversibly binds the O_2. Several reviews that discuss various aspects of Hr structure and function are available.[2,4,20–22] Hr most often occurs as an octamer of essentially identical O_2-binding subunits, although tetrameric, trimeric, and dimeric Hrs are also known.[21] A monomeric counterpart, myoHr, is confined to muscle tissues of the same marine invertebrates. The structure of the myoHr subunit and active site are both very similar to those of Hr.[21] The following discussion, therefore, applies, with very few exceptions, equally well to both Hr and myoHr.

4.2 Structure and Spectroscopy

The characteristic structure of the Hr polypeptide consists of a ‘four-helix bundle’ surrounding the diiron site, as shown in Figure 3(a).[21,23]

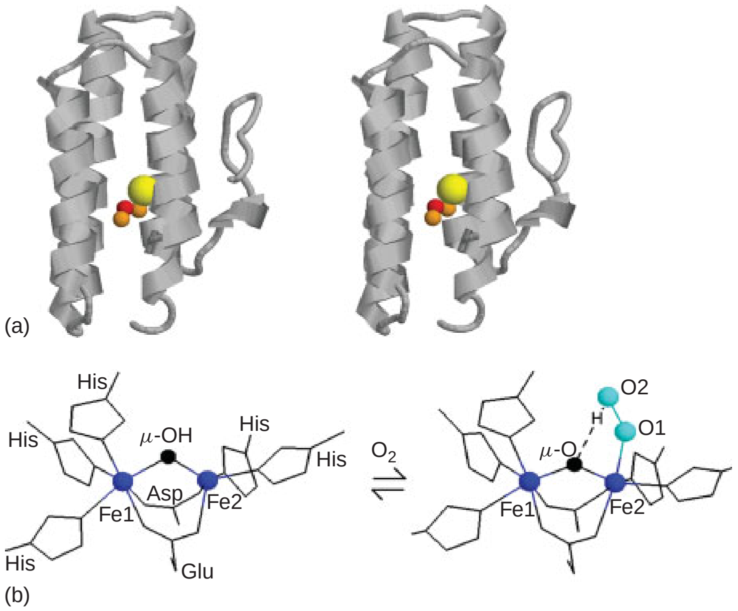

Figure 3 (a) Stereo view of the tertiary structure of a metchloroHr subunit. Protein backbone is traced in ribbon representation, iron atoms (orange), oxo bridge (red), and Cl^- (yellow) are shown as spheres. Drawing was generated using RASMOL[17] and coordinates from 1I4Y in the Protein Data Bank;[23] (b) The diiron site structures of deoxy- (left) and oxy- (right) Hrs. O_2 (cyan) and iron (dark blue) are shown as spheres, and iron ligands are shown in wireframe representation. The hydrogen bond between the oxo bridge and bound O_2 is indicated as a dashed line. Drawing was generated using coordinates from 1HMO[21] in the Protein Data bank

As shown in Figure 3(b), the two iron atoms at the active site are bound directly to protein side chains: five histidines, one aspartate, and one glutamate. The carboxylate side chains of the latter two residues bridge the two irons in a bidentate fashion in both the oxy and deoxy forms. The diiron site structures shown in Figure 3(b) were derived from X-ray crystal structures of both oxy- and deoxyHr.[21] The Hr oxygenation reaction has the well-established formulation: $[Fe^{II}(\mu\text{-OH})Fe^{II}](deoxy) + O_2 \rightleftharpoons [Fe^{III}(\mu\text{-O})Fe^{III}O_2H^-](oxy)$, in which O_2 binds to the five-coordinate iron in deoxyHr, and the hydroxo-bridged diferrous site is converted to an oxo-bridged diferric-hydroperoxo site in oxyHr. It is apparent from the crystal structures that the binding of O_2 to Hr occurs with little structural change or movement of the iron atoms and protein ligands. The only significant structural change upon oxygenation (other than addition of dioxygen) is a shortening of the Fe–O distances of the solvent-derived bridging ligand by $\sim$0.2 Å, consistent with the formal oxidation of the iron atoms and proton transfer from the hydroxo bridge to the dioxygen.

From a bioinorganic perspective, the most celebrated structural feature of Hr has traditionally been the diferric oxo-bridged unit. The spectroscopic feature most readily identified with the diferric oxo-bridged unit having a bent geometry is the presence of two electronic absorptions between 300 and 400 nm with $\varepsilon \sim 6000\,M^{-1}\ cm^{-1}$ per diiron site. While initially controversial, the assignment of these transitions as oxo → Fe^{III} charge transfer in oxyHr has withstood the scrutiny of single-crystal electronic absorption, magnetic circular dichroism (MCD), and resonance Raman spectroscopies.[2] The met form, which results from autoxidation of oxyHr, also shows these characteristic oxo-bridged diferric charge transfer absorptions. ^{57}Fe Mössbauer spectroscopy clearly established that the best description of the irons in both oxy- and metHrs is high-spin Fe^{III}, but with ground-state diamagnetism, due to antiferromagnetic coupling of the two high-spin ($S = 5/2$) Fe^{III}.[24] From the temperature dependence of the magnetic susceptibility, the strength of this coupling, J, (expressed in the $-2J\mathbf{S}_1\cdot\mathbf{S}_2$ Heisenberg–Dirac–Van Vleck formalism) was reported as $-77\,cm^{-1}$ for oxyHr and $-134\,cm^{-1}$ for metHr. Couplings of the latter magnitude are characteristic of the diferric-oxo bridged unit.[24] The hydrogen bonding interaction between the hydroperoxo ligand and the oxo bridge of oxyHr (cf. Figure 3(b)) could be responsible for the lower $-J$ reported for oxyHr. On the basis of paramagnetic NMR shifts of the His ligand Nδ protons, however, the ΔJ between oxy- and metHrs was judged to be smaller than the magnetic susceptibility measurements had indicated, and to support the oxo-bridged formulation for oxyHr.

The assignment of a less intense electronic absorption of oxyHr near 500 nm ($\varepsilon \sim 2000\,M^{-1}\ cm^{-1}$ per diiron site) as a peroxo $\pi^* \rightarrow Fe^{III}$ charge transfer transition has also withstood rigorous scrutiny.[2] Resonance Raman excitation within this absorption band led to the discovery of an O–O stretching frequency at $844\,cm^{-1}$.[25] Isotope labeling studies showed unequivocally that this frequency was due to the bound O_2 and also identified the corresponding Fe–O_2 stretching frequency near 500 cm^{-1}. Comparison to the O–O stretching frequencies of synthetic complexes clearly classifies the bound O_2 in Hr as a peroxo ligand rather than dioxygen or superoxo. Finally, resonance Raman excitation into the μ-oxo $\rightarrow$ $\mathrm{Fe^{III}}$ charge transfer band of oxyHr enhanced a vibrational mode at 486 cm^{-1}, which shifted downward in $H_2{}^{18}O$ but not with $^{18}O_2$.[26] This frequency was assigned to the symmetric Fe–O–Fe stretch of the oxo bridge, and is close to (but distinct from) the corresponding $H_2{}^{18}O$-sensitive Fe–O–Fe stretch of metHr at 510 cm^{-1}, which can be unambiguously assigned to the oxo bridge.[27] That is, oxyHr contains an oxo bridge similar to that of the met form.

Temperature and field-dependent MCD and paramagnetic ^{1}H NMR measurements showed that the ground state of deoxyHr is also diamagnetic due to antiferromagnetic coupling between the two high spin ($S = 2$) $\mathrm{Fe^{II}}$.[20] The magnitude of this coupling, $J = -15\,\mathrm{cm}^{-1}$,[28] closely matches that of a synthetic (μ-hydroxo)bis(μ-carboxylato)diiron(II) complex, but is significantly stronger than that of a corresponding μ-aqua bridged core (in which the irons may actually be weakly ferromagnetically coupled).[2] The X-ray crystal structure of the deoxyHr active site was, therefore, interpreted as containing a hydroxo rather than an aqua bridge (oxo-bridged diferrous complexes being unknown). The energies and intensities of the near-infrared (near-IR) d-d electronic transitions of deoxyHr support the crystallographically determined result of one six- and one five-coordinate ferrous iron.[2]

4.3 Mechanism of Dioxygen Binding

A striking feature of the oxygenation reaction of Hr is that, although both iron atoms formally undergo oxidation, O_2 appears to have direct, inner-sphere access to only the five-coordinate iron atom of deoxyHr. The relatively small structural changes and open coordination site on Fe2 in deoxyHr (cf. Figure 3b) seem designed for a facile O_2 association reaction, and this impression is borne out by the rapid rates of oxygenation, 10^7–$10^8\,\mathrm{M^{-1}s^{-1}}$, and low activation enthalpies (a few kcal/mole or less) for O_2 association.[20,27,29] On the basis of computational studies, a concerted proton/electron transfer mechanism following the initial contact of O_2 with the diiron site has been proposed.[2] Since no solvent deuterium isotope effect was detected for O_2 association, this concerted proton/electron transfer would have to occur after the rate-determining step, which may be diffusion of O_2 through the protein matrix.[20] A more recent computational study has suggested that the stability of the O_2 adduct is due to van der Waal's interactions of the bound O_2 with protein side chains and an increase in the hydrogen bond strength between one of the histidine ligand side chains and a second coordination sphere glutamate carboxylate.[30] The O_2 binding pocket of Hr is lined with hydrophobic amino acid residues.[20] These hydrophobic side chains and accompanying steric restrictions favor the localized hydrogen bonding interaction of the bound O_2 with the oxo bridge. The hydrophobic, sterically restricted O_2-binding pocket also kinetically inhibits autoxidation, in which oxyHr spontaneously converts to the met form with release of hydrogen peroxide.[20,27,29] Finally, the very stable oxo bridge in oxyHr, together with the lack of simultaneously accessible coordination positions on both irons probably inhibits further activation of the peroxo ligand,[2] in contrast to its behavior in the monooxygenases and desaturases (discussed below). Such subtle protein design features may be the reason that this deceptively simple reversible binding of O_2 in an end-on fashion to one iron of the diiron site depicted in Figure 3(b) has yet to be duplicated by any synthetic nonheme diiron complex.

4.4 Bacterial and Archaeal Hr-like Proteins

Perhaps the most interesting recent development in the area of Hrs is the discovery that Hr-like proteins are present in bacteria and archaea, where they may function as O_2 sensors.[31] This discovery potentially opens an entire new chapter in Hr biochemistry.

5 O_2-ACTIVATING ENZYMES

5.1 General Properties

In 1993, when a similar article was written for the previous version of this encyclopedia, only three O_2-activating diiron enzymes were known: ribonucleotide reductase (RNR), methane monooxygenase (MMO), and stearoyl-acyl carrier protein Δ^9 desaturase (Δ^9D), and these three remain the best characterized within this subclass. As of 2003, however, at least seven additional types of O_2-activating diiron enzymes have been discovered. The majority of these enzymes are monooxygenases, catalyzing insertion of one atom of dioxygen into an alkyl or aryl C–H bond. Other reactions catalyzed by this subclass include formation of a protein tyrosyl radical by RNR, desaturation of a fatty acyl C–C bond by the desaturases, and reduction of dioxygen to water by so-called alternative oxidases. Another feature of some members of this subclass to emerge in recent years is their tight, sometimes integral association with cell membranes, in contrast to the first three enzymes listed above, which are categorized as ‘soluble’. As a subclass, the O_2-activating enzymes are in general larger per diiron site than Hr, perhaps reflecting their more complicated functions and the need for regulation of their activities. Nevertheless, as for Hr, the available X-ray crystal structures show four-helix bundle protein folds surrounding the diiron sites in the O_2-activating enzymes. In all of the known O_2-activating enzymes, dioxygen activation occurs upon reaction of the diferrous site with dioxygen. These apparent similarities to Hr, however, belie some key structural differences. A distinct amino acid sequence motif, consisting of a pair of (D)$EX_{29-37}EX_2H$ sequences (where D = aspartate, E = glutamate, H = histidine and X = an intervening residue), provides protein ligands to the diiron sites in nearly all of the known O_2-activating enzymes. This sequence motif makes the diiron coordination spheres much more carboxylate rich and histidine poor than that of Hr (cf. Figure 3). An exception to this pattern may be the membrane alkane monooxygenases, which appear to have a much more histidine-rich diiron coordination sphere.[22] The coordination spheres of both irons of the diferrous sites in the O_2-activating enzymes contain open or labile (i.e. solvent occupied) coordination sites, which would seem to promote a bridging coordination geometry for dioxygen unlike the diiron site of Hr, where only terminal coordination of dioxygen has been observed. Finally, redox-dependent coordinative flexibility, particularly for the carboxylate ligands, seems to be a characteristic feature of the diiron sites in O_2-activating enzymes.[22]

An organizing reaction scheme for all of the O_2-activating diiron enzymes is shown in Figure 4. A key mechanistic feature of this scheme is hydrogen abstraction from the substrate by a highly oxidizing, formally diiron(IV) species created upon reaction of the diferrous site with dioxygen. The extent to which every O_2-activating diiron enzyme follows this reaction scheme is currently unclear. In fact, with the exception of RNR, the participation of organic radicals in the catalytic mechanisms of these enzymes is controversial. Nevertheless, this scheme or its variants have provided a useful mechanistic framework for investigation of these enzymes.[22] From a bioinorganic perspective, these mechanistic investigations, particularly the trapping and identification of the intermediates along the vertical pathway shown in Figure 4, have been a focal point of study for all of these enzymes.

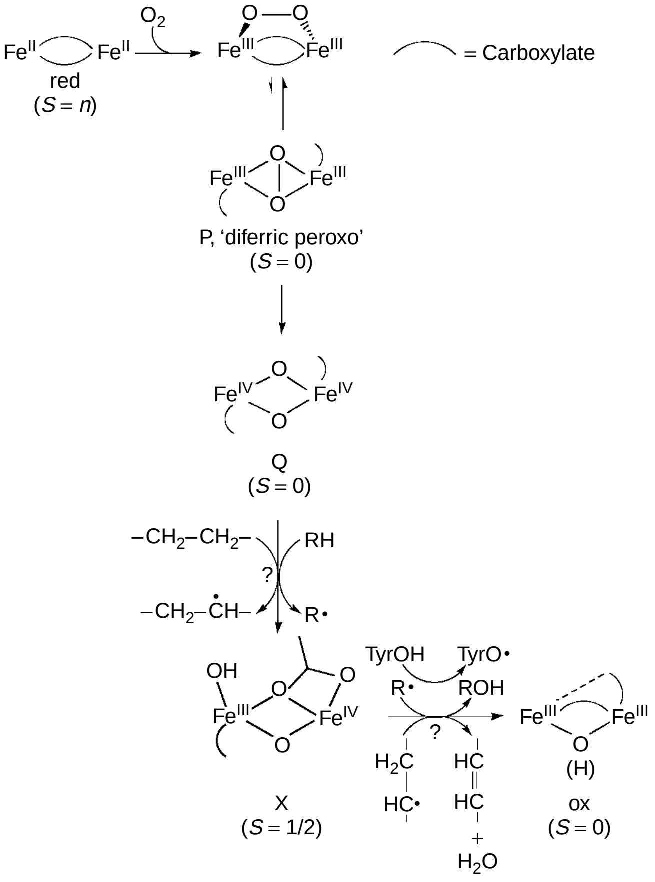

Figure 4 A possible scheme for the catalytic reactions of diiron sites in the O_2-activating enzymes. Formal oxidation states, ground spin states, and shorthand letter designations are listed below each diiron species. Except for tyrosyl (in RNR), the depiction of organic radicals is hypothetical (Ref. 22, © 1997 Springer Verlag)

5.2 Ribonucleotide Reductase

RNRs catalyze the reduction of ribonucleotides to deoxyribonucleotides, which represents the first committed step in DNA biosynthesis and repair.[32] These enzymes are therefore required for all known life forms. Three classes of RNRs have been identified, all of which turn out to be metalloenzymes. The so-called class I RNRs contain a diiron site (*see* ***Cobalt: B_{12} Enzymes & Coenzymes*** and ***Iron–Sulfur Proteins*** for the other two types of RNRs). As diagrammed in Figure 5, these enzymes generate first a tyrosyl radical proximal to the diiron site in the protein subunit labeled R2, and then a thiyl radical in an adjacent subunit (R1) that ultimately abstracts a hydrogen atom from the ribonucleotide substrate. This controlled tyrosine/thiol radical transfer must occur over an estimated distance of ~35 Å, and a highly choreographed proton-coupled electron transfer (PCET) mechanism across intervening aromatic residues has been proposed.[33] Perhaps, even more remarkably, evidence has been presented suggesting that the tyrosyl radical is regenerated by reverse PCET during every turnover cycle.[34]

The most thoroughly studied class I RNR is that from *E. coli*, and the remaining discussion focuses on the diiron site in the R2 homodimer of that enzyme, hereafter referred to simply as R2. R2 can be isolated separately from the R1 subunit. The crystal structures of R2 in both the diferrous and diferric (nonradical) forms revealed the diiron site structures shown in Figure 6.[32] The phenol hydroxyl of tyrosine 122 that forms the radical is hydrogen bonded to an aspartate carboxylate ligand of the diferrous site.

An unusual feature that has been recognized earlier is that the as-isolated R2 contained a stable tyrosyl radical along with an oxo-bridged diferric site. The latter oxo-bridged diferric structure was apparent even before X-ray crystal structures were available from the strong absorption features between 300 and 400 nm, reminiscent of oxy- and metHrs.[2] Superimposed on this diferric site absorption is a sharp absorption feature at 410 nm due to the tyrosyl radical.

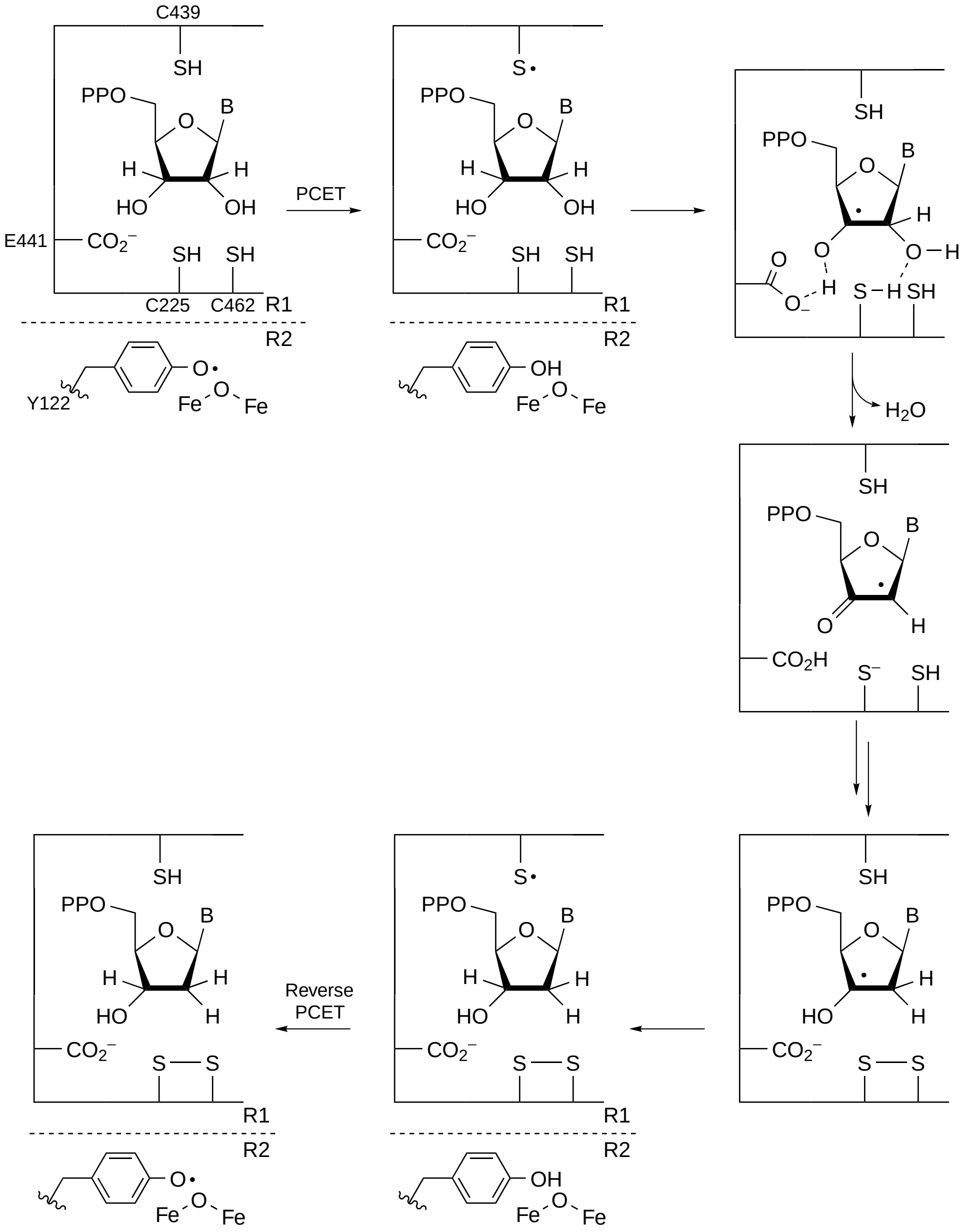

Figure 5 Proposed catalytic mechanism of ribonucleotide reductase. (Reprinted with permission from Ref. 34. © 2003 American Chemical Society)

Stopped-flow UV-vis absorption and rapid freeze-quench (RFQ) EPR and Mössbauer studies have shown that the reaction pathway diagrammed in Figure 4 for formation of the tyrosyl radical is essentially accurate except that the diiron(IV) species labeled Q in Figure 4 has never been detected in R2. Instead, an intermediate labeled U (not shown in Figure 4), occurring prior to X, has properties consistent with a protonated tryptophan cation radical. This radical may shuttle an electron from an external donor to the diiron site in order to reach intermediate X.[2,3,32] In any case, these rapid kinetic studies have established that intermediate X is kinetically competent to oxidize Tyr122, and that X is an antiferromagnetically coupled ($S = 1/2$) $Fe^{III}Fe^{IV}$ species (cf. Figure 4).[2] The diferric-peroxo species, P (cf. Figure 4) has been detected only in an engineered variant of R2 in which Asp84 (cf. Figure 6) was replaced with a glutamate residue.[35] The bridging ligands in X have been a matter of some controversy. Current evidence favors a mono-oxo-bridged structure, as shown in Figure 4, in which the other atom of the reduced dioxygen is a terminal solvent ligand to the Fe^{III} rather than a second bridging ligand.[2,36]

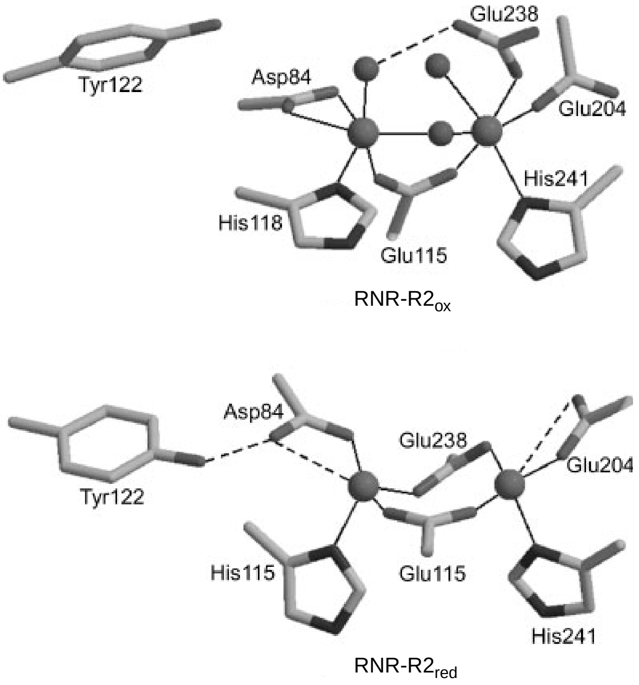

Figure 6 Diferric (RNR-R2$_{ox}$) and diferrous (RNR-R2$_{red}$) site structures in *E. coli* R2. Iron atoms and solvent ligands are shown as larger and smaller spheres respectively, and amino acid side chains are shown in wireframe representation (with β-carbons of glutamate residues omitted for clarity). Dashed lines indicate hydrogen bonds. Structures were drawn using RASMOL[17] and coordinates from 1RIB and 1XIK in the Protein Data Bank[32]

5.3 Methane Monooxygenase

Methanotrophic bacteria can grow on methane as their sole carbon and energy source, which they achieve via its oxidation to carbon dioxide. The first catalytic step in this pathway is the oxidation of methane to methanol catalyzed by methane monooxygenase (MMO). From an energetic point of view, this room temperature oxidation of methane is arguably the most impressive catalytic reaction in all of biology. MMO catalyzes the insertion of one atom of O_2 into the very inert C–H bond of methane upon its conversion to methanol. Two types of MMO have been identified, namely, soluble and membrane-bound. The hydroxylase component of the soluble MMO (MMOH) is an ~250 kDa protein with an $(\alpha\beta\gamma)_2$ subunit composition. The membrane-bound MMOH contains copper at its active site (*see* ***Copper Proteins: Oxidases***). Hereafter, the MMOH from the soluble MMO is simply referred to as MMOH. Beginning in 1986, EPR, Mössbauer, and other spectroscopic evidence began to accumulate for a nonheme, non-sulfur diiron active site in MMOH.[3] Subsequent X-ray crystal structures of the soluble MMOH confirmed and extended these earlier observations.[2,37] The diferrous and diferric site structures of MMOH revealed by X-ray crystallography are shown in Figure 7. Even before these structures became available, it was clear from the UV-vis absorption spectrum, particularly the lack of any intense absorption features between 300 and 400 nm, that, unlike hemerythrin and RNR-R2, the diferric MMOH site does not contain an oxo bridge. Rather the solvent bridges in Figure 7 are either hydroxo or aqua.

Analogously to the RNR studies discussed above, the key question occupying bio-inorganic investigations on MMOH has been: how does the diferrous site activate dioxygen for insertion into methane, or more specifically, to what extent is the generic reaction pathway in Figure 4 followed? Single turnover experiments established that MMOH could effect hydroxylation of hydrocarbons starting from the diferrous form, MMOH$_{red}$, and adding dioxygen. Starting in 1993, a series of elegant stopped-flow UV-vis absorption, RFQ EPR, and Mössbauer experiments provided evidence for at least two consecutive intermediates, labeled P and Q, which formed upon reaction of MMOH$_{red}$ with dioxygen.[3] (The intermediate analogous to X in RNR has not been unequivocally detected in MMOH.[38]) In the presence of hydrocarbon substrates, the lifetime of P was unaffected, whereas the decay (but not buildup) of Q was substantially accelerated with methane showing the largest such effect. The decay rate of Q also showed a large deuterium isotope for perdeuterated methane:

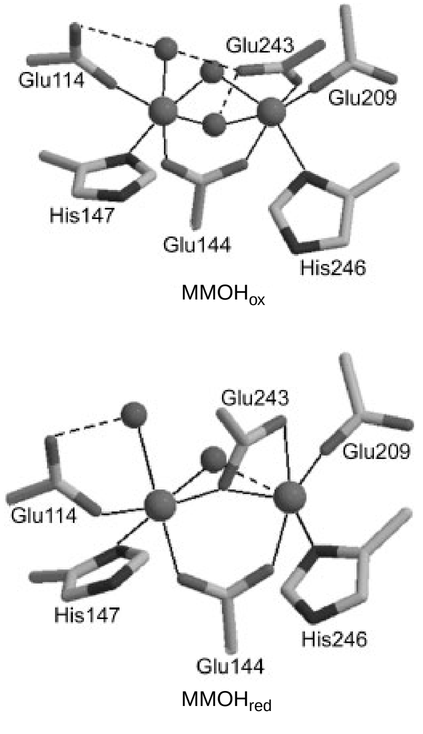

Figure 7 Diferric (MMOH$_{ox}$) and diferrous (MMOH$_{red}$) site structures in MMOH. Iron atoms and solvent ligands are shown as larger and smaller spheres respectively, and amino acid side chains are shown in wireframe representation (with β-carbons of glutamate residues omitted for clarity). Dashed lines indicate hydrogen bonds. Structures were drawn using RASMOL[17] coordinates from 1MTY and 1FYZ in the Protein Data Bank[37]

$k(CH_4)/k(CD_4)$ of 20–50.[37] All of these results pointed to Q as the intermediate that reacts directly with methane in the committed step leading to its hydroxylation. Q was found to be EPR silent; ^{57}Fe Mössbauer spectra of Q were most consistent with a $Fe^{IV}Fe^{IV}$ oxidation level and a diamagnetic ground state due to antiferromagnetic coupling between the two high- or intermediate-spin d^4 Fe^{IV} centers.[3,39] Extended X-ray absorption fine structure (EXAFS) studies of the diiron center obtained from RFQ experiments led to two unusually short interatomic distances in Q: Fe–O = 1.77 Å and Fe–Fe = 2.46 Å.[40] This Fe–Fe distance for Q is much shorter than those determined by X-ray crystallography for either the diferrous (3.28 Å) or diferric (3.1 Å) oxidation levels of MMOH (cf. Figure 7). Analysis of the EXAFS and pre-edge spectra also indicated a coordination number no greater than five for the irons in Q. These structural parameters together with the previous spectroscopic results led to the proposed 'diamond core' structure for Q shown in Figure 4.

The hydrogen abstraction mechanism for methane hydroxylation by intermediate Q originated by analogy to the 'oxygen-rebound' mechanism proposed for hydrocarbon hydroxylation catalyzed by cytochrome P450, which invokes a high-valent heme iron-oxo intermediate (*see* ***Iron: Heme Proteins, Mono- & Dioxygenases***). The question of whether or not a discrete hydrocarbon radical species actually forms upon reaction of methane with Q in MMOH has been the subject of lively experimental investigations and debates. Some experiments, particularly the elegant 'chiral ethane' experiments first carried out by Lipscomb and coworkers,[3] seem to indicate at least some degree of hydrocarbon radical formation, whereas, experiments with so-called 'radical clock' substrates seem to argue against this possibility.[2,39] Unfortunately, experiments addressing this issue with methane itself are difficult to design. The results of computational studies on the mechanism by several groups, while tending to agree on hydrogen abstraction from methane by a bis(μ-oxo)diiron(IV) species, have generally not favored discrete hydrocarbon radical formation. On the other hand, these various studies have not converged on any single alternative mechanism. In-depth discussions of various alternative mechanisms for methane hydroxylation by Q based on these computational studies are available.[2,39,41,42]

5.4 Butane Monooxygenase

A soluble butane monooxygenase has been isolated from an aerobic bacteria capable of growing on butane as carbon and an energy source.[43] The first step in the degradation of butane is its hydroxylation to 1-butanol catalyzed by a butane monooxygenase. The hydroxylase component of this enzyme shows very high amino acid sequence and subunit homology to the diiron MMOH discussed above. The strain does not grow on methane, however, suggesting that the butane monooxygenase cannot function as an MMO. No studies of the putative diiron site in the butane monooxygenase have been reported as of mid-2003.

5.5 Toluene and Phenol Monooxygenases

Following the discovery of a diiron site in MMOH, the same iron-ligating amino acid sequence motif (i.e. a pair of $EX_{29-37}EX_2H$ sequences) was recognized in the toluene and phenol monooxygenases (TMO and PMO respectively).[3,22,44,45] The hydroxylase components of these enzymes also have the $(\alpha\beta\gamma)_2$ subunit composition homologous to that of MMOH. Thus, although no X-ray crystal structures are yet available for any TMO or PMO, their diiron site structures are expected to closely resemble those of MMOH shown in Figure 7. Mössbauer and EPR studies have confirmed the presence of a diiron site in PMO and in at least one TMO.[3,22,44,46] Three distinct TMOs, T2MO, T3MO, and T4MO catalyze conversion of toluene to *o*-, *m*-, and *p*-cresol respectively. Surprisingly, none of the TMOs catalyze significant oxygenation of the toluyl methyl group, as might be expected by analogy to MMO. PMO catalyzes the oxygenation of phenol and substituted phenols to the corresponding catechols, but shows little or no activity toward toluene. Conversely, TMOs show little activity toward phenol. Finally, while MMOH shows some reactivity toward a variety of aromatic substrates, TMOs and PMOs show no catalysis of methane hydroxylation. The fact that this apparently similar set of monooxygenases can catalyze such substrate specific and regiospecific reactions implies that the surrounding protein environments subtly tune the reactivity of the diiron site in ways that are largely unclear at present. The most systematic mechanistic studies among enzymes in this subclass have been carried out on T4MO. On the basis of product analyses of various specifically deuterated toluenes and xylenes, a mechanism for toluene hydroxylation by TMOs was proposed that invoked formation of an epoxide intermediate (cf. Figure 8) rather than H-atom abstraction upon reaction with the high-valent diiron site.[47] Steric restrictions within the toluene binding pocket of the TMOs may position the substrate for predominant 2-, 3-, or 4-hydroxlation.

5.6 Alkene Monooxygenases

A few species of aerobic bacteria are able to metabolize small alkenes, such as ethylene and vinyl chloride as

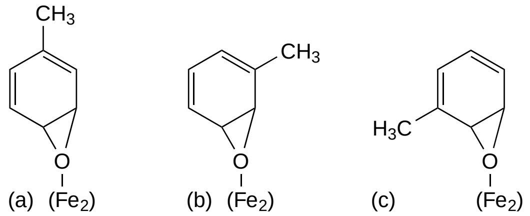

Figure 8 Proposed epoxide intermediates at the diiron sites of TMOs leading to predominantly 4- (a), 3- (b), or 2- (c) hydroxylation of toluene (Ref. 47, © 2003 National Academy of Sciences, USA)

their sole carbon and energy source.[48,49] The first step in the metabolism of these alkenes is oxidation to the corresponding epoxides. These epoxidations are catalyzed by alkene monooxygenases, which have amino acid sequence and subunit structural homologies to the MMOH-diiron type of monooxygenases.[44] Only limited structural and spectroscopic characterizations of these enzymes have been reported up to now. One alkene monooxygenase has been reported to exhibit EPR spectra consistent with antiferromagnetically coupled mixed-valent and diferrous diiron sites.[50]

5.7 Fatty Acyl–Acyl Carrier Protein Desaturases

Fatty acyl−acyl carrier protein desaturases are soluble plant enzymes that catalyze insertion of cis double bonds into specific methylene positions of fatty acids.[44] A distinct group of membrane fatty acyl desaturases are discussed in Section 5.10. The substrate for the soluble plant enzymes is a fatty acyl chain covalently linked to a phoshopantetheine group of an acyl carrier protein (ACP). These desaturases contain the diiron-binding amino acid sequence motif common to the other O_2-activating enzymes discussed above. The best characterized of these enzymes is the ACP Δ^9 desaturase (ACP Δ^9D) from castor bean. Spectroscopic studies established that the diferric site in the castor bean ACP Δ^9D contains an oxo bridge, although a minor proportion of a hydroxo-bridged diferric site may also be present.[2,44] An X-ray crystal structure of this ACP Δ^9D was obtained on an X-ray photoreduced enzyme, that is, containing a diferrous site. The diiron site structure (cf. Figure 9) is highly symmetrical with two five-coordinate irons bridged by two carboxylate ligands. The Fe–Fe separation of 4.1 Å is too long for a single atom solvent bridge.

A more recent X-ray crystal structure[52] of the same enzyme has shown that the open coordination sites on the ferrous irons can be occupied by a 1,3-bridging azide, perhaps mimicking an initial 1,2-bridging mode of dioxygen. A deep hydrophobic channel leading from the surface of the protein likely binds and orients the fatty acyl substrate for a specific reaction of the 9,10-carbons with the diiron site. Spectroscopic studies indicate that one of the ferrous centers switches to four-coordinate upon substrate binding, perhaps triggering its reaction with dioxygen. A diferric-peroxo intermediate was trapped upon rapid mixing of the artificially reduced enzyme-substrate complex with dioxygen, but this intermediate did not break down to form the desaturated product.[53,54] A ferredoxin (*see* ***Iron–Sulfur Proteins***) is apparently required as the catalytically competent electron donor to the desaturase-substrate complex.[53,55] Events in addition to the fatty acyl C–H bond breakage may contribute to the rate-limiting step, which has likely hindered trapping of catalytically competent diiron intermediates.[55,56] Deuterium labeling of the substrate has shown that the desaturation is both regio- and stereospecific and is consistent with hydrogen abstraction from a diiron(IV) intermediate, as shown in Figure 10.

5.8 Rubrerythrin

Rubrerythrin (Rbr) appears to be an ‘oddball’ among the O_2-activating diiron proteins. The name, rubrerythrin, is a contraction of rubredoxin (*see* ***Iron–Sulfur Proteins***) and hemerythrin, which reflects its two types of iron sites as well as the fact that Rbr was isolated before a function was described for it.[57] Rbr containing these two distinct types of iron sites has been reported so far only in anaerobic bacteria and archaea. Pyrophosphatase,[58] ferroxidase[59] and, most recently, peroxidase[60–62] activities have all been ascribed to this protein. In vivo studies suggest a role for Rbr in oxidative stress protection during periods when these anaerobic microorganisms are transiently exposed to air.[63,64] Amino acid sequence homologies to the MMOH diiron-ligating motif initially suggested an O_2-activation function for Rbr.[22] In fact, sequence analyses have tended to group Rbrs together on one branch of the same phylogenetic dendrogram that contains all the known diiron proteins

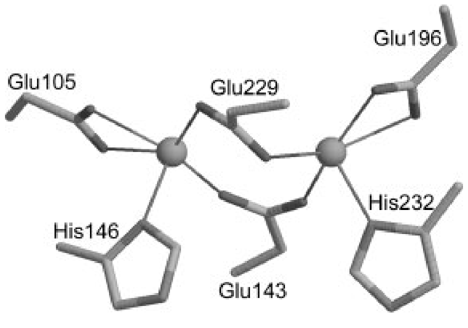

Figure 9 Diferrous site structure of castor bean ACP Δ^9D. Iron atoms are shown as spheres; iron ligands are shown in wireframe representation. Structure was drawn using RASMOL[17] and coordinates from 1AFR in the Protein Data Bank[51]

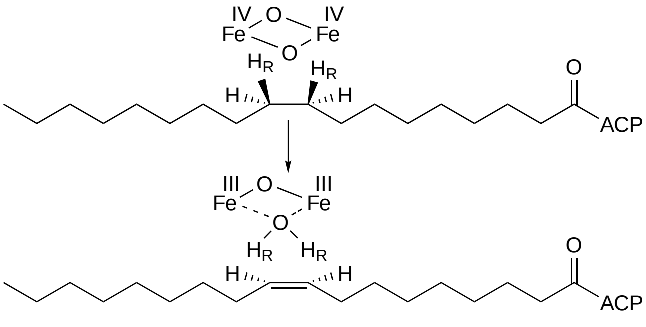

Figure 10 A schematic diagram of stereospecific H-atom abstraction from stearoyl-ACP by a putative diiron(IV) intermediate of castor bean ACP Δ^9D. (Reprinted with permission from Ref. 56. © 2003 American Chemical Society)

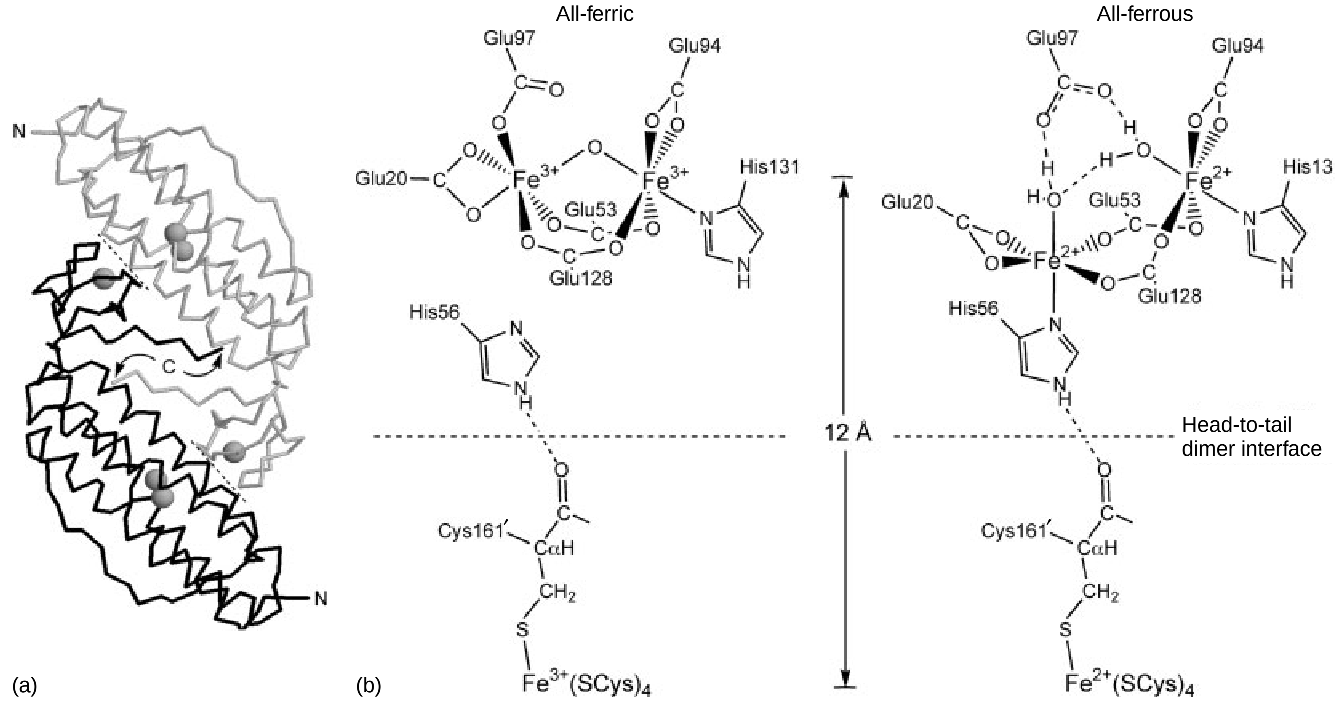

Figure 11 (a) Protein backbone tracing of the *D. vulgaris* Rbr 'head-to-tail' homodimer viewed along its twofold rotation axis drawn using RASMOL[17] and coordinates from 1RYT in the Protein Data Bank.[67] Amino (N) and carboxyl (C) termini are labeled, iron atoms are represented as spheres, and dashed lines indicate subunit interface regions between the [Fe(SCys)$_4$] and diiron sites. (b) Schematic structures of the diiron sites and subunit interfaces from the all-ferric and all-ferrous Rbr X-ray crystal structures.[68] (Reprinted with permission from Refs. 68 & 69. © 2002 & 2003 American Chemical Society)

having the characteristic pair of (D)EX$_{29-37}$EX$_2$H sequence motifs.[65] Genome sequence analyses have indicated that some microorganisms contain multiple Rbrs.[60] The best characterized Rbr is that from the sulfate-reducing bacteria, *Desulfovibrio vulgaris*, and the remaining discussion focuses on that Rbr. *D. vulgaris* also contains a second Rbr-like protein called nigerythrin.[66] The X-ray crystal structure of *D. vulgaris* Rbr showed that the functional unit in solution is the 'head-to-tail' homodimer, in which the rubredoxin-type Fe(SCys)$_4$ site is ∼12 Å from the diiron site across the subunit interface, as shown schematically in Figure 11.

No monooxygenation chemistry catalyzed by Rbr has been reported, nor does Rbr associate with other nonidentical subunits, as do the soluble diiron monooxygenases. While the ferroxidase activity of *D. vulgaris* Rbr is consistent with the close structural resemblance of both its subunit structure and diiron site to those of bacterioferritin (*see* ***Iron Proteins for Storage & Transport & their Synthetic Analogs***),[67,68] there is no evidence that Rbr forms a large aggregate of subunits that could store the resulting oxidized exogenous iron, as does bacterioferritin. The physiological relevance of the ferroxidase activity of *D. vulgaris* Rbr, if any, is thus unclear. Two independent laboratories have been unable to reproduce the reported pyrophosphatase activity.[57] Hydrogen peroxide oxidizes the diferrous site of Rbr rapidly compared to dioxygen,[60–62] which is the opposite trend to that shown by diferrous sites in the O$_2$-activating enzymes. The diferric Rbr site shows little or no reactivity with hydrogen peroxide, a behavior that is also in contrast to the O$_2$-activating diiron enzymes.[44] One possible source of these differences in reactivity may lie in some unique structural features of the Rbr diiron site, which are illustrated in Figure 11. The X-ray crystal structure of the oxidized (all-ferric) Rbr showed the expected oxo-bridged diferric site with two bridging carboxylates, but also revealed an extra terminal carboxylate ligand, Glu97 in Figure 11, to one of the irons. This extra glutamate carboxylate, which has no counterpart in the O$_2$-activating diiron proteins, is conserved in all known Rbrs.[60,67] This extra carboxylate ligand appeared to displace an expected histidine ligand (His56 in Figure 11) located in an approximately trans coordination position. However, in the X-ray crystal structure of the all-ferrous Rbr, the iron atom ligated to this extra glutamate in the diferric site had moved approximately 1.8 Å such that it was now ligated to the histidine and not to the extra glutamate.[68] The Fe–Fe distance also increased from 3.3 Å in the oxo-bridged diferric site to 4.0 Å in the diferrous site, and the oxo bridge was replaced by two terminal solvent ligands. This redox-dependent Glu ↔ His ligand switching and the extensive movement of one iron are unique among the diiron proteins and presumably contribute to the facile hydrogen peroxide reductase activity of Rbr. Another contributing factor may be the relatively greater solvent exposure of the Rbr diiron site compared to those in the O_2-activating enzymes.[68] Kinetics studies on engineered site-directed Rbr variants are consistent with a mechanism, in which the diferrous site of Rbr rapidly reduces hydrogen peroxide to water and the $Fe(SCys)_4$ site funnels electrons from exogenous donors to the diiron site.[60] The His56 side chain that exchanges with the Glu97 ligand is hydrogen-bonded to a carbonyl of one of the cysteine residues that provides a ligand to the $Fe(SCys)_4$ site across the subunit interface (C161′; cf. Figure 11). This hydrogen bond is presumably part of the inter-iron site electron-transfer pathway. An X-ray crystal structure of a μ-1,3-azide adduct of the diferrous Rbr site[68] suggests a μ-1,2-H_2O_2 intermediate, as shown in Figure 12. The mixed-valent diiron site structure shown in the lower left corner of Figure 12 is based on recent ENDOR studies.[69]

A mixed-metal Zn,Fe site rather than a diiron site has been reported in Rbr 'as-isolated' from *D. vulgaris*,[70,71] despite the fact that earlier spectroscopic characterizations of the same Rbr isolated directly from the same organism by the same lab,[72] and also by a second independent lab,[66] clearly demonstrated the presence of antiferromagnetically coupled diiron sites and no magnetically isolated iron other than the $Fe(SCys)_4$ site. The Rbr-like protein, nigerythrin, 'as-isolated' from *D. vulgaris* also clearly contained a diiron site,[66] as did an Rbr from another sulfate-reducing bacteria.[65,73,74] The Zn,Fe site in the 'as-isolated' *D. vulgaris* Rbr could be an artifact of either the isolation or crystallization procedure.[70] More recently, the structure of an Rbr homologue, called sulerythrin, which lacks the $Fe(SCys)_4$ domain, was reported.[75] The sulerythrin structure was also reported to contain Zn,Fe sites. The electronic absorption spectrum of sulerythrin, however, clearly showed the intense features between 300 and 400 nm characteristic of an oxo-bridged diferric site,[76] suggesting that the crystallized protein may not reflect the metal occupancy of the as-isolated protein in solution. The crystal structure also

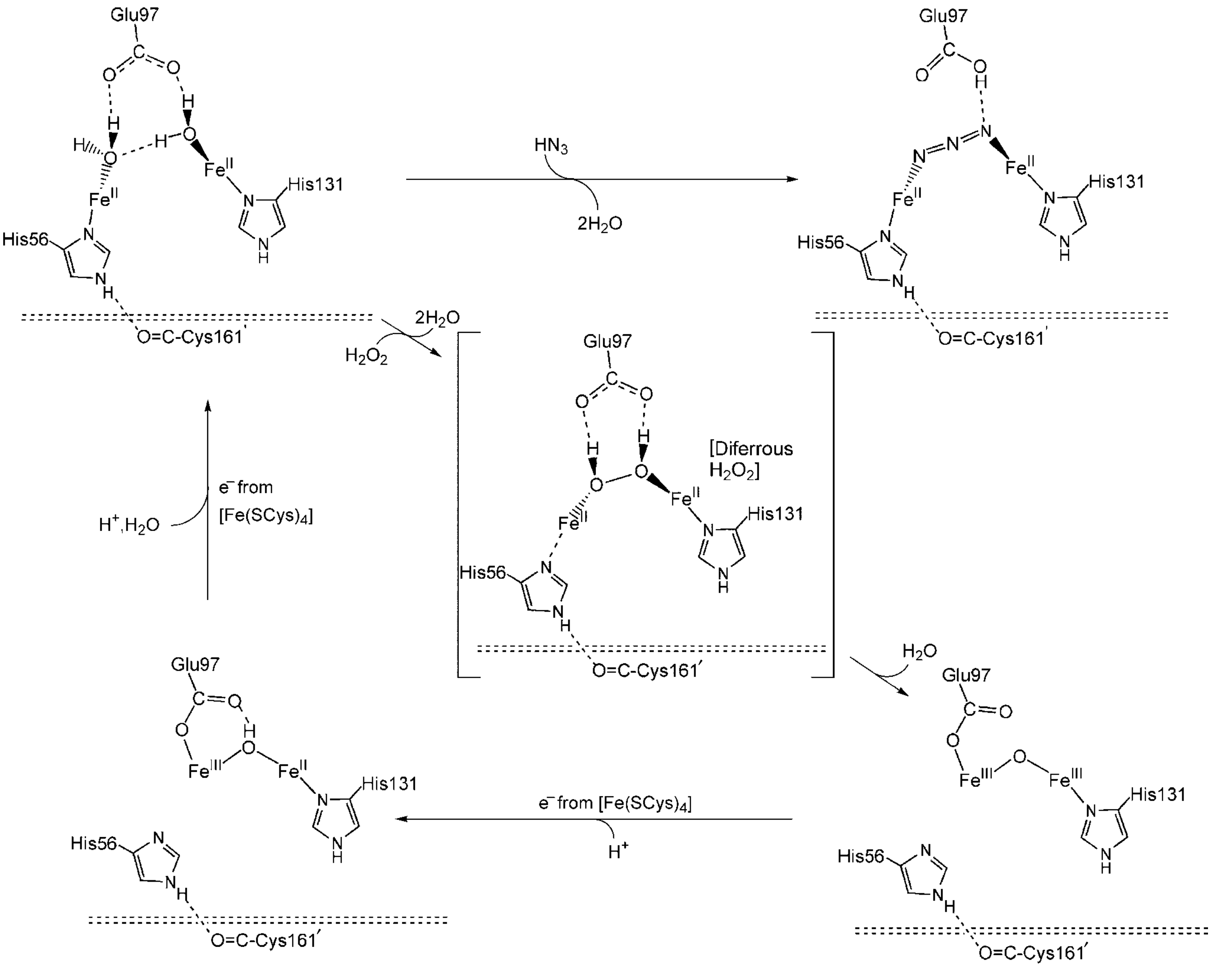

Figure 12 Proposed mechanism for hydrogen peroxide reduction catalyzed by *D. vulgaris* Rbr. (Reprinted with permission from Ref. 68. © 2003 American Chemical Society)

showed that sulerythrin was ‘domain swapped’ compared to that of *D. vulgaris* Rbr, such that the metal ligands to each of the two Zn,Fe sites were contributed by both subunits of the homodimer. The function of sulerythrin, which is found in an aerobic archaeon, is unknown.

5.9 Membrane Oxidases/Hydroxylases

Membrane oxidases/hydroxylases were first recognized as belonging to the nonheme diiron protein class via their amino acid sequence homologies to the soluble O_2-activating diiron enzymes discussed above.[77] On the basis of these sequence homologies and several site-directed mutagenesis studies, the diiron sites are likely to contain the same mixture of histidine and carboxylate ligands as do those of the O_2-activating diiron enzymes of the soluble MMO type. The sequence homologies and molecular modeling studies also indicate that the diiron sites in these enzymes are surrounded by four-helix protein bundles, once again reminiscent of the soluble O_2-activating diiron enzymes.[1,78] However, the membrane oxidases/hydroxylases contain additional protein domains, which are tightly associated with and possibly embedded within cell or organelle membranes, hence their designation as membrane oxidases/hydroxylases. While reports of homology modeled structures are available,[1,78] no X-ray crystal structure is yet available for any enzyme in this subclass.

Four functionally distinct enzymes in this subclass have so far been identified: alternative oxidase (AOX), plastid terminal oxidase (PTOX), Mg-protoporphyrin IX monomethyl ester hydroxylase (MME hydroxylase), and 5-demethoxyquinone hydroxylase (DMQ hydroxylase).[1] AOX, PTOX, and MME hydroxylases have been found in green plants, algae, fungi, and protists, and recently a bacterial AOX homologue has been reported.[79] AOX is a quinol oxidase, apparently functioning as a nonenergy conserving ‘alternative’ oxidase under conditions where the normal respiratory membrane oxidases are nonfunctional (*see* ***Cytochrome Oxidase***). PTOX is a plastoquinol oxidase, which is functional during chloroplast development. However, the exact physiological roles of AOX and PTOX are matters of some contention.[1,80,81] DMQ hydroxylase and its homologues have been found in organisms ranging from bacteria to humans, where it functions as a quinol hydroxylase required for ubiquinone biosynthesis. MME hydroxylase catalyzes one or more steps, including an alkyl carbon hydroxylation, in the formation of the exocyclic ring of chlorophyll.

The plant AOX was the first of this class to be recognized and is the most thoroughly studied to date. The most direct evidence for a diiron site in this subclass is a mixed-valent Fe^{II}, $Fe^{III} = 1/2$ EPR signal that was observed from a plant AOX.[82] This signal is reminiscent of that arising from the mixed-valent diiron sites in Hr and the O_2-activating enzymes discussed above. The relatively weak magnetic coupling between the irons in this mixed-valent site and lack of strong electronic absorption between 300 and 400 nm in the diferric form argue for a hydroxo rather than an oxo solvent bridge between the irons at these oxidation levels. Little or no mechanistic information is available for the enzymes in this subclass. Dioxygen is presumably a substrate in all cases.

5.10 Membrane Eight-His Desaturases/Monooxygenases

The membrane ‘eight-His’ enzymes constitute a structurally distinct subclass from the other O_2-activating enzymes: they have been recognized to contain a conserved eight-histidine amino acid sequence motif, $HX_{3-4}HX_{20-50}HX_{2-3}HHX_{100-200}HX_{2-3}HH$, that putatively binds a nonheme, non-sulfur diiron site.[2,44] Conserved residues that could conceivably supply carboxylate ligands have not been unequivocally identified in the eight-His enzymes,[83] which may, therefore, represent an exception to the ‘diiron-carboxylate proteins’.[6] These eight-His motif enzymes are found in plants, animals, and bacteria where they perform a diverse range of functions that include not only fatty acyl desaturation, long-chain alkane omega hydroxylation, and xylene methyl monooxygenation but also decarbonylation, epoxidation, and acetylenation. Because they are all integral membrane proteins, these eight-His enzymes have proven difficult to isolate and characterize. Only one member of this subclass, a bacterial octane 1-monooxygenase called AlkB, has been proven by Mössbauer spectroscopy to contain a diiron site; the magnitude of the antiferromagnetic coupling between the irons in AlkB implies a bridging solvent ligand, at least at the diferric oxidation level.[84] Although site-directed mutagenesis studies have shown that all eight residues of the histidine motif are required for activity of at least one fatty acyl desaturase and for AlkB,[83] it is unclear whether all eight histidines actually supply iron ligands. Both molecular biological and molecular modeling evidence[44,83,85] indicate that the portions of the polypeptide chain that contain the eight conserved histidine residues and, therefore, the diiron site, protrude from the membrane surface towards the inside of the cell. A speculative model for the xylene monooxygenase (XylM) diiron

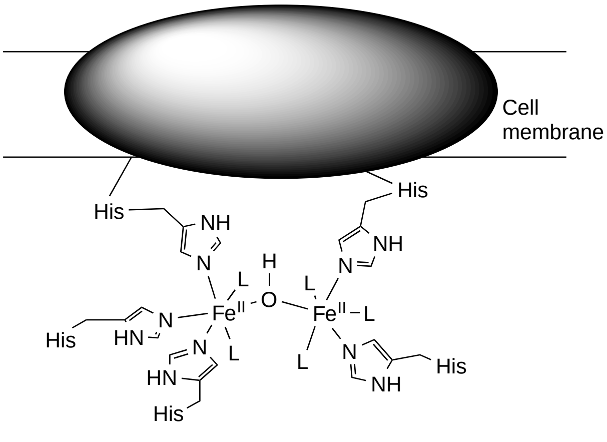

Figure 13 Speculative model for the diferrous site in XylM (Ref. 87, © 2003 Springer Verlag)

site is shown in Figure 13. XylM catalyzes the methyl group monooxygenation of toluene and xylene.[86] Experiments with alternative substrates have suggested a radical mechanism for XylM.[87] These membrane eight-His enzymes are among the most mysterious and intriguing of the nonheme, non-sulfur diiron class.

6 RELATED ARTICLES

Iron: Models of Proteins with Dinuclear Active Sites; Iron Proteins for Storage & Transport & their Synthetic Analogs; Iron–Sulfur Proteins.

7 REFERENCES

1. D. A. Berthold and P. Stenmark, *Annu. Rev. Plant. Biol.*, 2003, **54**, 497.
2. E. I. Solomon, T. C. Brunold, M. I. Davis, J. N. Kemsley, S.-K. Lee, N. Lehnert, F. Neese, A. J. Skulan, Y.-S. Yang, and J. Zhou, *Chem. Rev.*, 2000, **100**, 235.
3. B. J. Wallar and J. D. Lipscomb, *Chem. Rev.*, 1996, **96**, 2625.
4. A. L. Feig and S. J. Lippard, *Chem. Rev.*, 1994, **94**, 759.
5. E. N. Marsh and W. F. DeGrado, *Proc. Natl. Acad. Sci. U.S.A.*, 2002, **99**, 5150.
6. P. Nordlund and H. Eklund, *Curr. Opin. Struct. Biol.*, 1995, **5**, 758.
7. A. Vogel, F. Spener, and B. Krebs, in ‘Handbook of Metalloproteins’, eds. A. Messerschmidt, R. Huber, T. Poulos, and K. Weighardt, John Wiley & Sons, Chichester, 2001, Vol. 2, p. 752.
8. C. Zambonelli and M. F. Roberts, *J. Biol. Chem.*, 2003, **278**, 13706.
9. S. K. Smoukov, L. Quaroni, X. Wang, P. E. Doan, B. M. Hoffman, and L. Que Jr, *J. Am. Chem. Soc.*, 2002, **124**, 2595.
10. M. Merkx, M. W. Pinkse, and B. A. Averill, *Biochemistry*, 1999, **38**, 9914.
11. A. Wasserfallen, S. Ragettli, Y. Jouanneau, and T. Leisinger, *Eur. J. Biochem.*, 1998, **254**, 325.
12. C. M. Gomes, C. Frazao, A. V. Xavier, J. Legall, and M. Teixeira, *Protein Sci.*, 2002, **11**, 707.
13. J. B. Vicente, C. M. Gomes, A. Wasserfallen, and M. Teixeira, *Biochem. Biophys. Res. Commun.*, 2002, **294**, 82.
14. C. Frazão, G. Silva, C. M. Gomes, P. Matias, R. Coelho, L. Sieker, S. Macedo, M. Y. Liu, S. Oliveira, M. Teixeira, A. V. Xavier, C. Rodrigues-Pousada, M. A. Carrondo, and J. Le Gall, *Nat. Struct. Biol.*, 2000, **7**, 1041.
15. A. M. Gardner, R. A. Helmick, and P. R. Gardner, *J. Biol. Chem.*, 2002, **277**, 8172.
16. R. Silaghi-Dumitrescu, E. D. Coulter, A. Das, L. G. Ljungdahl, G. N. Jameson, B. H. Huynh, and D. M. Kurtz Jr, *Biochemistry*, 2003 **42**, 2806.
17. R. Sayle and E. J. Milner-White, *Trends Biochem. Sci.*, 1995, **20**, 374.
18. C. P. Mangum, in ‘Advances in Comparative and Environmental Physiology 13. Blood and Tissue Oxygen Carriers’, ed. C. P. Mangum, Springer-Verlag, New York, 1992, Vol. 13, p. 173.
19. N. B. Terwilliger, *J. Exp. Biol.*, 1998, **201**, 1085.
20. D. M. Kurtz Jr, in ‘Comprehensive Coordination Chemistry – II: From Biology to Nanotechnology’, eds. L. Que Jr and W. B. Tolman, Elsevier Science, Oxford, 2003, Vol. 8, Chap. 10, p. 229.
21. R. E. Stenkamp, *Chem. Rev.*, 1994, **94**, 715.
22. D. M. Kurtz Jr, *J. Biol. Inorg. Chem.*, 1997, **2**, 159.
23. C. S. Farmer, D. M. Kurtz Jr, Z. J. Liu, B. C. Wang, J. Rose, J. Ai, and J. Sanders-Loehr, *J. Biol. Inorg. Chem.*, 2001, **6**, 418.
24. D. M. Kurtz Jr, *Chem. Rev.*, 1990, **90**, 585.
25. I. M. Klotz and D. M. Kurtz Jr, *Acc. Chem. Res.*, 1984, **17**, 16.
26. A. K. Shiemke, T. M. Loehr, and J. Sanders-Loehr, *J. Am. Chem. Soc.*, 1984, **106**, 4951.
27. J. Xiong, R. S. Phillips, D. M. Kurtz Jr, S. Jin, J. Ai, and J. Sanders-Loehr, *Biochemistry*, 2000, **39**, 8526.
28. E. I. Solomon and Y. Zhang, *Acc. Chem. Res.*, 1992, **25**, 343.
29. C. S. Farmer, D. M. Kurtz Jr, R. S. Phillips, J. Ai, and J. Sanders-Loehr, *J. Biol. Chem.*, 2000, **275**, 17043.
30. M. Wirstam, S. J. Lippard, and R. A. Friesner, *J. Am. Chem. Soc.*, 2003, **125**, 3980.
31. J. Xiong, D. M. Kurtz Jr, J. Ai, and J. Sanders-Loehr, *Biochemistry*, 2000, **39**, 5117.
32. H. Eklund, U. Uhlin, M. Färnegårdh, D. T. Logan, and P. Nordlund, *Prog. Biophys. Mol. Biol.*, 2001, **77**, 177.
33. J. Stubbe, D. G. Nocera, C. S. Yee, and M. C. Chang, *Chem. Rev.*, 2003, **103**, 2167.
34. J. Ge, G. Yu, M. A. Ator, and J. Stubbe, *Biochemistry*, 2003, **42**, 10071.
35. J. Baldwin, C. Krebs, L. Saleh, M. Stellinng, B. H. Huynh, J. M. Bollinger Jr, and P. Riggs-Gelasco, *Biochemistry*, 2003, **42**, 13269.
36. N. Mitic, L. Saleh, G. Schenk, J. M. Bollinger, and E. I. Solomon, *J. Am. Chem. Soc.*, 2003, **125**, 11200.
37. M. Merkx, D. A. Kopp, M. H. Sazinsky, J. L. Blazyk, J. Müller, and S. J. Lippard, *Angew. Chem., Int. Ed. Engl.*, 2001, **40**, 2782.
38. A. M. Valentine, P. Tavares, A. S. Pereira, R. Davydov, C. Krebs, B. M. Koffman, D. E. Edmondson, B. H. Huynh, and S. J. Lippard, *J. Am. Chem. Soc.*, 1998, **120**, 2190.
39. M. H. Baik, M. Newcomb, R. A. Friesner, and S. J. Lippard, *Chem. Rev.*, 2003, **103**, 2385.
40. L. Shu, J. Nesheim, K. Kauffman, E. Munck, J. D. Lipscomb, and L. Que Jr, *Science*, 1997, **275**, 515.

41. P. E. M. Siegbahn and R. H. Crabtree, *Struct. Bond. (Berlin)*, 2000, **97**, 125.
42. R. A. Friesner, M. H. Baik, B. F. Gherman, V. Guallar, M. Wirstam, R. B. Murphy, and S. J. Lippard, *Coord. Chem. Rev.*, 2003, **238**, 267.
43. M. K. Sluis, L. A. Sayavedra-Soto, and D. J. Arp, *Microbiology*, 2002, **148**, 3617.
44. B. G. Fox, in ‘Comprehensive Biological Catalysis’, ed. M. Sinnott, Academic Press, San Diego, CA, 1998, Vol. 3, p. 261.
45. S. Divari, F. Valetti, P. Caposio, E. Pessione, M. Cavaletto, E. Griva, G. Gribaudo, G. Gilardi, and C. Giunta, *Eur. J. Biochem.*, 2003, **270**, 2244.
46. E. Cadieux, V. Vrajmasu, C. Achim, J. Powlowski, and E. Münck, *Biochemistry*, 2002, **41**, 10680.
47. K. H. Mitchell, C. E. Rogge, T. Gierahn, and B. G. Fox, *Proc. Natl. Acad. Sci. U.S.A.*, 2003, **100**, 3784.
48. N. V. Coleman, T. E. Mattes, J. M. Gossett, and J. C. Spain, *Appl. Environ. Microbiol.*, 2002, **68**, 6162.
49. N. V. Coleman and J. C. Spain, *J. Bacteriol.*, 2003, **185**, 5536.
50. S. C. Gallagher, R. Cammack, and H. Dalton, *Eur. J. Biochem.*, 1997, **247**, 635.
51. Y. Lindqvist, W. Huang, G. Schneider, and J. Shanklin, *EMBO J.*, 1996, **15**, 4081.
52. M. Moche, J. Shanklin, A. Ghoshal, and Y. Lindqvist, *J. Biol. Chem.*, 2003, **278**, 25072.
53. J. A. Broadwater, J. Ai, T. M. Loehr, J. Sanders-Loehr, and B. G. Fox, *Biochemistry*, 1998, **37**, 14664.
54. J. A. Broadwater, C. Achim, E. Münck, and B. G. Fox, *Biochemistry*, 1999, **38**, 12197.
55. K. S. Lyle, J. A. Haas, and B. G. Fox, *Biochemistry*, 2003, **42**, 5857.
56. B. Behrouzian, C. K. Savile, B. Dawson, P. H. Buist, and J. Shanklin, *J. Am. Chem. Soc.*, 2002, **124**, 3277.
57. D. M. Kurtz Jr and E. D. Coulter, *Chemtracts, Inorg. Chem.*, 2001, **14**, 407.
58. M.-Y. Liu and J. LeGall, *Biochem. Biophys. Res. Commun.*, 1990, **171**, 316.
59. F. Bonomi, D. M. Kurtz Jr, and X. Cui, *J. Biol. Inorg. Chem.*, 1996, **1**, 67.
60. E. D. Coulter, N. V. Shenvi, Z. Beharry, J. J. Smith, B. C. Prickril, and D. M. Kurtz Jr, *Inorg. Chim. Acta*, 2000, **297**, 231.
61. E. D. Coulter and D. M. Kurtz Jr, *Arch. Biochem. Biophys.*, 2001, **394**, 76.
62. E. D. Coulter, N. V. Shenvi, and D. M. Kurtz Jr, *Biochem. Biophys. Res. Commun.*, 1999, **255**, 317.
63. H. L. Lumppio, N. V. Shenvi, A. O. Summers, G. Voordouw, and D. M. Kurtz Jr, *J. Bacteriol.*, 2001, **183**, 101.
64. M. Sztukowska, M. Bugno, J. Potempa, J. Travis, and D. M. Kurtz Jr, *Mol. Microbiol.*, 2002, **44**, 479.
65. C. M. Gomes, J. Le Gall, A. V. Xavier, and M. Teixeira, *Chembiochem*, 2001, **2**, 583.
66. A. J. Pierik, R. B. G. Wolbert, G. L. Portier, M. F. J. M. Verhagen, and W. R. Hagen, *Eur. J. Biochem.*, 1993, **212**, 237.
67. F. deMaré, D. M. Kurtz Jr, and P. Nordlund, *Nature Struct. Biol.*, 1996, **3**, 539.
68. S. Jin, D. M. Kurtz Jr, Z.-J. Liu, J. Rose, and B.-C. Wang, *J. Am. Chem. Soc.*, 2002, **124**, 9845.
69. S. K. Smoukov, R. M. Davydov, P. E. Doan, B. Sturgeon, I. Y. Kung, B. M. Hoffman, and D. M. Kurtz Jr, *Biochemistry*, 2003, **42**, 6201.
70. M. Li, M.-Y. Liu, J. LeGall, L. L. Gui, J. Liao, T. Jiang, J.-P. Zhang, D.-C. Liang, and W.-R. Chang, *J. Biol. Inorg. Chem.*, 2003, **8**, 149.
71. L. C. Sieker, M. Holmes, I. Le Trong, S. Turley, M.-Y. Liu, J. LeGall, and R. E. Stenkamp, *J. Biol. Inorg. Chem.*, 2000, **5**, 505.
72. J. LeGall, B. C. Prickril, I. Moura, A. V. Xavier, J. J. G. Moura, and B. M. Huynh, *Biochemistry*, 1988, **27**, 1636.
73. I. Moura, P. Tavares, and N. Ravi, *Meth. Enzymol.*, 1994, **243**, 216.
74. C. V. Romao, M. Regalla, A. V. Xavier, M. Teixeira, M. Y. Liu, and J. Le Gall, *Biochemistry*, 2000, **39**, 6841.
75. S. Fushinobu, H. Shoun, and T. Wakagi, *Biochemistry*, 2003, **42**, 11707.
76. T. Wakagi, *FEMS Microbiol. Lett.*, 2003, **222**, 33.
77. J. N. Siedow, A. L. Umbach, and A. L. Moore, *FEBS Lett.*, 1995, **362**, 10.
78. M. S. Albury, C. Affourtit, P. G. Crichton, and A. L. Moore, *J. Biol. Chem.*, 2002, **277**, 1190.
79. P. Stenmark and P. Nordlund, *FEBS Lett.*, 2003, **552**, 189.
80. X. Huang, U. von Rad, and J. Durner, *Planta*, 2002, **215**, 914.
81. A. L. Moore, M. S. Albury, P. G. Crichton, and C. Affourtit, *Trends Plant. Sci.*, 2002, **7**, 478.
82. D. A. Berthold, N. Voevodskaya, P. Stenmark, A. Grèaslund, and P. Nordlund, *J. Biol. Chem.*, 2002, **277**, 43608.
83. J. Shanklin and E. Whittle, *FEBS Lett.*, 2003, **545**, 188.
84. J. Shanklin, C. Achim, H. Schmidt, B. G. Fox, and E. Münck, *Proc. Natl. Acad. Sci. U.S.A.*, 1997, **94**, 2981.
85. A. R. Diaz, M. C. Mansilla, A. J. Vila, and D. de Mendoza, *J. Biol. Chem.*, 2002, **277**, 48099.
86. B. Bühler, A. Schmid, B. Hauer, and B. Witholt, *J. Biol. Chem.*, 2000, **275**, 10085.
87. R. N. Austin, K. Buzzi, E. Kim, G. J. Zylstra, and J. T. Groves, *J. Biol. Inorg. Chem.*, 2003, **8**, 733.

Iron Proteins with Mononuclear Active Sites

Joseph P. Emerson, Mark P. Mehn & Lawrence Que Jr
University of Minnesota, Minneapolis, MN, USA

1 Introduction 1
2 Iron Superoxide Dismutase and Superoxide Reductase 1
3 Lipoxygenase 2
4 Catechol Dioxygenases 4
5 α-Keto Acid Dependent Enzymes 7
6 Isopenicillin N Synthase 10
7 Pterin-dependent Hydroxylases 12
8 Rieske Dioxygenases 14
9 Perspective 17
10 Related Articles 17
11 References 17

Abbreviations

α-KG = α-ketoglutarate; ACmC = δ-(L-α-aminoadipoyl)-L-cysteinyl-L-S-methyl-cysteine; ACOV = δ-(L-α-aminoadipoyl)-L-cysteinyl-D-α-hydroxyisovaleryl ester; ACV = δ-(L-α-aminoadipoyl)-L-cysteinyl-D-valine; BF = Benzoylformic acid; BH$_2$ = Quinoid dihydropterin; BH$_3$OH = 4a-hydroxypterin; BH$_4$ = Tetrahydrobiopterin; Bn-TPEN = N-benzyl-N,N',N'-*tris*(2-pyridylmethyl)ethane-1,2-diamine; BphC = 2,3-dihydroxybiphenyl 1,2-dioxygenase; 2,3-DHBP = 2,3-dihydroxybiphenyl; DFT = Density functional theory; ENDOR = Electron-nuclear double resonance spectroscopy; EPR = Electron paramagnetic resonance; EXAFS = Extended X-ray absorption fine structure; HIF = Hypoxia inducible factor; HPP = 4-hydroxyphenylpyruvate; HtxA = Hypophosphite dioxygenase; IPNS = Isopenicillin N synthase; LO = Lipoxygenase; MCD = Magnetic circular dichroism; MhpB = 3-(2′,3′-dihydroxyphenyl)propionate 1′,2′-dioxygenase; NADH = Reduced nicotinamide adenine dinucleotide; NADPH = Reduced nicotinamide adenine dinucleotide phosphate; NDO = Naphthalene 1,2-dioxygenase; NHE = Normal hydrogen electrode; NMR = Nuclear magnetic resonance; N4Py = N,N-*bis*(2-pyridylmethyl)-N-*bis*(2-pyridyl)methylamine; 2-OG = 2-oxoglutarate; PCD = Protocatechuate 3,4-dioxygenase; PCD = Protocatechuate; PDO = Phthalate dioxygenases; PheH = Phenylalanine hydroxylase; SOD = Superoxide dismutase; SOR = Superoxide reductase; TauD = Taurine dioxygenase; TfdA = Dichlorophenoxyacetate hydroxylase; TMC = Tetramethylcyclam; Tp = Trispyrazolylborate; TPA = *Tris*(2-pyridylmethyl)amine; TrpH = Tryptophan hydroxylase; TyrH = Tyrosine hydroxylase; XAS = X-ray absorption spectroscopy.

1 INTRODUCTION

In the 10 years since the first edition of this Encyclopedia was published,**[1]** there has been an explosion of information on the coordination chemistry of mononuclear nonheme iron centers in metalloenzymes. Almost all of these enzymes are involved in some aspect of dioxygen metabolism. While superoxide dismutase and superoxide reductase are involved in superoxide processing, the rest activate dioxygen to carry out substrate transformations. Electron sources for the latter reactions include NADH (delivered via a reductase), cofactors such as tetrahydrobiopterin and α-keto acids, and the substrates themselves. In this section, we focus on the present state of knowledge regarding their active site structures and the role of the metal center in the catalytic mechanisms. Absent from this section are the metalloproteins rubredoxin and transferrin. Rubredoxin is the simplest iron-sulfur protein, having an iron center tetrahedrally coordinated by four cysteine residues; it is discussed in (*see* ***Iron–Sulfur Proteins***) together with other proteins in its class. Transferrin, an iron transport protein, is discussed in (*see* ***Iron Proteins for Storage & Transport & their Synthetic Analogs***) together with ferritin, the iron storage protein. Transferrin has an iron center that is coordinated to two tyrosines, an aspartate, a histidine, and an exogenous bicarbonate.

2 IRON SUPEROXIDE DISMUTASE AND SUPEROXIDE REDUCTASE

Superoxide dismutases (SODs) catalyze the disproportionation of superoxide into O$_2$ and H$_2$O$_2$ and are proposed to defend the cell against the deleterious effects of exposure to dioxygen (*see* ***Dioxygen & Related Ligands***).**[2]** In general, SODs react with superoxide at nearly diffusion-controlled rate constants, $\sim 3 \times 10^8$ to $1 \times 10^9\ \mathrm{M^{-1}\,sec^{-1}}$. SODs are available in four varieties, a CuZn form found primarily in eukaryotes (*see* ***Copper Proteins with Type 2 Sites***), manganese (*see* ***Manganese Proteins with Mono- & Dinuclear Sites***) and iron forms found in certain fungi, prokaryotes, mitochondria, and some blue-green algae, and most recently a nickel form originally found in several *Streptomyces* species (*see* ***Nickel Enzymes & Cofactors***). All four have been structurally characterized revealing rather distinct active sites. The diversity of metal active sites that nature has evolved to carry out this function is fascinating. The metal centers must all have a redox potential that allows them in their oxidized states to accept an electron from superoxide forming O_2 and in their reduced states to donate an electron to superoxide forming H_2O_2. In practical terms, this requirement constrains the reduction (or redox) potential values to $+200\,\mathrm{mV} \pm 100\,\mathrm{mV}$ versus NHE. The iron enzyme is in a sense the prototype of mononuclear nonheme iron enzymes involved in oxygen metabolism as it was the first of this group to have a crystal structure solved.**[3]** The active site consists of four endogenous ligands arranged in a trigonal pyramid (Figure 1a), with an axial His perpendicular to a trigonal plane defined by two His and an Asp. The iron is 0.5 Å below this plane and displaced towards the axial His. A solvent molecule bound to the available coordination site trans to the axial histidine could be displaced by superoxide allowing an inner-sphere reaction. There is a conserved tyrosine (Tyr34) about 5 Å away from the iron center and bordering the open coordination site. It is proposed that the tyrosine may serve as an acid/base center in the catalytic mechanism. The redox potential of the metal center is $+260\,\mathrm{mV}$ versus NHE,**[4]** a value that permits it to shuttle readily between Fe^{III} and Fe^{II} oxidation states to facilitate the disproportionation of superoxide under physiological conditions.

Interestingly, there is substantial structural homology between the Fe and Mn enzymes; the two metal coordination sites are nearly congruent.**[5]** However these two metal ions have distinct redox properties; Mn tends to have potentials half a volt higher than Fe in the same ligand environment. The best explanation to date derives from the efforts of A.-F. Miller and coworkers, who have proposed that the second sphere residues tune the redox potentials of the metal centers by controlling the ionization state of the bound water.**[6]** Thus the Fe and Mn potentials are brought into the same range by having a water ligand on the Fe and a hydroxide ion coordinated to the Mn. This simple yet elegant hypothesis has been supported by experimental evidence that shows the Mn potential to be too high in the Mn-substituted Fe enzyme, and the Fe potential to be too low in the Fe-substituted Mn enzyme.**[6]**

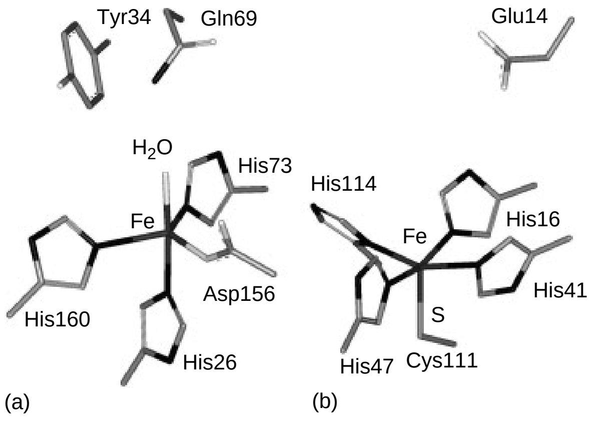

Figure 1 Active sites of (a) iron superoxide dismutase from *Pseudomonas ovalis* (1DTO.pdb) and (b) superoxide reductase from *Pyrococcus furiosus* (1DQK.pdb)

More recently, several iron proteins characterized to have superoxide reductase activity have been identified in several microaerophilic and anaerobic bacteria and archaea.**[7–10]** In these systems, transient exposure to dioxygen produces reactive (reduced) dioxygen species, one of which is superoxide. These enzymes are proposed to serve a protective function by lowering the overall steady-state concentration of superoxide in *vivo*, similar to the role of superoxide dismutases in aerotolerant organisms. However, these superoxide reductases (SORs) directly reduce superoxide to hydrogen peroxide, without producing dioxygen. Interestingly, X-ray crystal structures of SORs show a very different iron active site representative for this new class of enzymes (Figure 1b) consisting of a square pyramidal iron(II) center with four basal histidines and an apical cysteine.**[11,12]** The open coordination site (trans to the cysteine) allows diffusion-controlled ($\sim 1 \times 10^9\,\mathrm{M^{-1}\,sec^{-1}}$) direct ligation of superoxide to the iron(II) center, producing a violet ($\lambda_{\max} \sim 600\,\mathrm{nm}$, $\varepsilon_{600} \sim 3500\,\mathrm{M^{-1}\,cm^{-1}}$) intermediate proposed to be an Fe^{III}–OO(H) species.**[13]** A nearby glutamate residue (Glu14 in Figure 1b) then displaces this peroxo moiety, leaving a blue ($\lambda_{\max} \sim 650\,\mathrm{nm}$, $\varepsilon_{650} \sim 1900\,\mathrm{M^{-1}\,cm^{-1}}$) pseudo-octahedral iron(III) center.**[14]** Recently an iron(III)-peroxo intermediate was trapped in the active site of a mutant SOR,**[15,16]** when the coordinating Glu was mutated to an Ala, and then reacted with H_2O_2. This transient iron(III)-peroxo species has been characterized using EPR, resonance Raman, and Mössbauer spectroscopy.

Similar to their SOD counterparts, the iron centers of SORs have reduction potentials typically ranging between + 200 mV to 300 mV versus NHE.**[14,17]** In SORs, however, little catalytic disproportionation of superoxide is measurable, even in Glu14-variant SORs. This implies that superoxide is unable to reduce the SOR active center, as it does with SODs, a result which remains quite perplexing.

3 LIPOXYGENASE

Lipoxygenases (LOs) are nonheme, mononuclear iron enzymes that catalyze the regio- and stereoselective conversion of polyunsaturated fatty acids with a *cis,cis*-1,4-diene functionality into products having a 1-hydroperoxy-*trans,cis*-2,4-diene functionality.**[18,19]** The mammalian LOs typically act on arachidonic acid and produce alkyl hydroperoxides that are converted into leukotrienes and lipoxins, which are involved as messengers in the inflammatory response. Plant enzymes act on linoleic acid, but the role of the product alkyl hydroperoxide is less well understood.

Owing to its relative availability, the soybean LO has been the focus of most efforts to characterize the iron active site. As isolated, the enzyme is colorless and the iron is in the high-spin Fe^{II} state. This form appears to be inactive, as full enzyme activity is elicited only after an extended lag period. This lag is eliminated when the iron center is oxidized to the high-spin Fe^{III} state, which is yellow in color ($\lambda_{max} \sim 350$ nm, $\varepsilon_{350} \sim 2000\,M^{-1}\,cm^{-1}$) arising from a hydroxo-to-iron(III) charge-transfer transition.[20] The presence of this hydroxide has been unequivocally established by the observation of a short Fe–O distance (1.9 Å) from EXAFS analysis, which is highly consistent with an Fe^{III}–OH bond.[21] This Fe^{III} state has been further characterized as having an $S = 5/2$ EPR signal, which is axial ($g \sim 6$) for the soybean enzyme but rhombic ($g \sim 4.3$) in the rabbit enzyme.[20,22] Interestingly, the only known oxidant to afford active enzyme is the product hydroperoxide.[23] Presumably the inactive iron(II) enzyme is slowly activated by trace amounts of the product hydroperoxide derived from autoxidation of linoleic acid.

The iron active site for soybean LO as determined by several crystal structures of the Fe^{II} form[24–28] has a distorted octahedral geometry. The six coordinating ligands are derived from three histidines, the carbonyl oxygen of an asparagine side chain, a carboxylate of the C-terminal isoleucine, and a solvent molecule (Figure 2a). The X-ray crystal structure of rabbit lipoxygenase has a slightly modified iron center, where the asparagine residue is replaced by a fourth more strongly binding histidine residue.[29]

When the Fe^{III} enzyme is treated with an excess of the product hydroperoxide or a combination of linoleic acid and O_2, a transient purple intermediate having a chromophore at 585 nm ($\varepsilon_{585} \sim 1300\,M^{-1}\,cm^{-1}$) is formed.[18] The structure of this species has been determined by X-ray crystallography on soybean lipoxygenase-3. This structure shows the known product hydroperoxide bound to the iron center, in place of the solvent molecule (Figure 2b).[30]

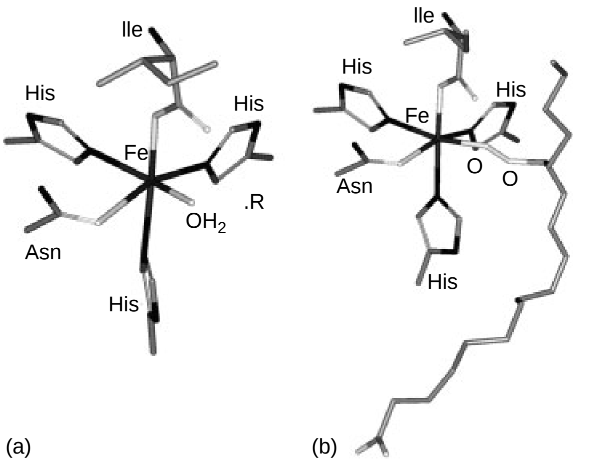

Figure 2 Iron centers of (a) as-isolated soybean Lipoxygenase (1F8N.pdb) and (b) the Fe^{III}–OOR intermediate (1IK3.pdb)

The role of the iron(III) center in the catalytic reaction has been the subject of some speculation. A plausible mechanism for lipoxygenase is shown in Figure 3. The Fe^{III}–OH unit is proposed to abstract a hydrogen atom from the fatty acid, producing an organic radical. Kinetic studies of this step have revealed a large kinetic isotope effect of greater than 50, indicating the C–H bond cleavage step is rate determining.[31,32] Dioxygen enters and reacts with the organic radical and then binds the metal center, affording the Fe^{III}-(product

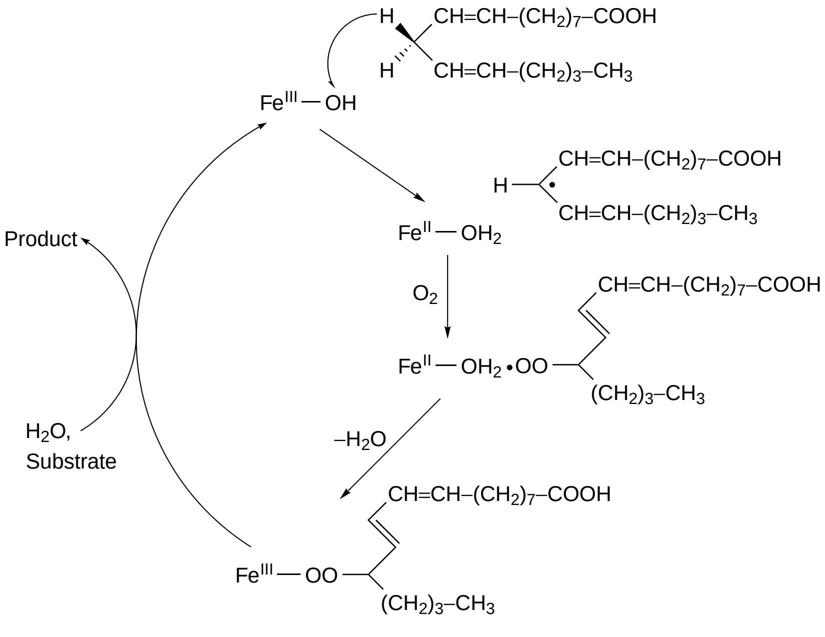

Figure 3 Proposed mechanism for lipoxygenase

alkylperoxo) species. The proposed role of the Fe^{III}–OH center is analogous to that of Fe^{IV}=O centers in other iron enzymes (see below). The relatively high redox potential of the metal center ($\geq +600$ mV vs. NHE)[33] and the rather weak C–H bond to be cleaved allows this chemistry to proceed without requiring the iron(IV) state. A high potential Fe^{III}–OCH_3 complex described by Stack and coworkers mimics the C–H cleavage step in LO chemistry and has provided further insights into the energetic considerations of this key step in the mechanism.[34]

4 CATECHOL DIOXYGENASES

Nonheme iron enzymes of the catechol dioxygenase family catalyze the last step in Nature's strategy for converting aromatic molecules into aliphatic products.[35] These bacterial enzymes transform dihydroxylated aromatic molecules into acyclic aliphatic products. The catechol substrates can be oxidatively cleaved in two distinct modes: intradiol cleavage breaks the C–C bond between the two hydroxyl functions, while extradiol cleavage breaks the C–C bond adjacent to the enediol function. In the process, the elements of dioxygen are incorporated into the product, therefore the name dioxygenases (*see* ***Iron: Heme Proteins, Mono- & Dioxygenases***).

4.1 Intradiol-cleaving Enzymes

The intradiol-cleaving enzymes represented by catechol 1,2-dioxygenase and protocatechuate 3,4-dioxygenase (PCD) catalyze the reactions shown in Figure 4. Both enzymes have iron(III) active sites and are spectroscopically well characterized.[35,36] The enzymes exhibit a distinct burgundy red color ($\lambda_{max} \sim 460$ nm, $\varepsilon_{460} \sim 3500\ M^{-1}\ cm^{-1}$) that is associated with ligand-to-metal charge-transfer transitions from two distinct tyrosine ligands as deduced from resonance Raman data. The participation of solvent water is evidenced by the line broadening found in the EPR spectrum of the native enzyme from *Brevibacterium fuscum* dissolved in $H_2{}^{17}O$.[37] Analysis of the first-shell EXAFS data required the solvent water to be bound as hydroxide,[38] thereby providing a charge-neutral active site.

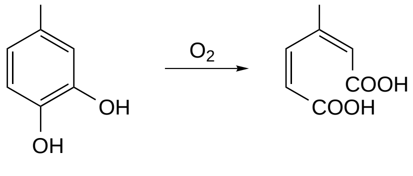

Figure 4 Reaction catalyzed by catechol 1,2-dioxygenase (R = H) and protochatechuate 3,4-dioxygenase (R = COOH)

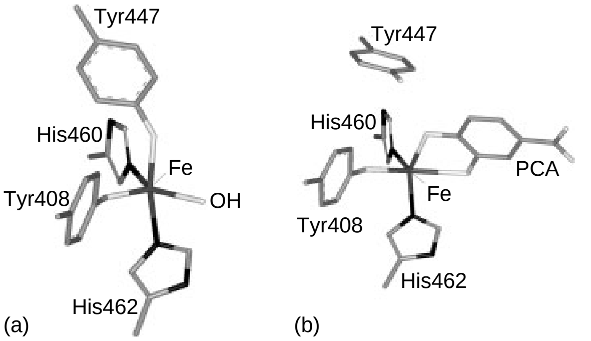

Figure 5 Active sites of (a) *P. putida* 3,4-PCD (2PCA.pdb) and (b) the 3,4-PCD-substrate complex (2PCD.pdb)

In agreement with spectroscopic studies, the crystal structure of as-isolated PCD from *Pseudomonas putida* (formally known as *Pseudomonas aeruginosa*) displays a trigonal bipyramidal geometry about the iron center with four endogenous protein ligands, namely, His460, His462, Tyr408, and Tyr447, as shown in Figure 5(a), and a solvent-derived ligand in the fifth position.[39] Structures of several enzyme-substrate complexes,[40,41] and many enzyme complexes with inhibitors[42] are also available, providing many details on how the PCD active site interacts with exogenous aromatic ligands. In particular, the structure of the PCD-substrate complex shows that the axial Tyr447 residue and the hydroxide ligand are displaced upon substrate binding.[40,41] The catechol donates both enediol protons to the displaced ligands and chelates to the metal center as a dianionic ligand (Figure 5b) trans to His460 and Tyr408. The Fe–$O_{catecholate}$ bonds differ by 0.2 Å in length, presumably due to the distinct trans effects exerted by the histidines and the tyrosinates.

When the structural data of *P. putida* PCD are combined with the wealth of spectroscopic data, a clear picture of the enzyme active center during catalysis emerges,[35,43] validating the substrate activation mechanism proposed ~ 30 years ago (Figure 6).[44] This novel mechanism has the metal center retaining its iron(III) character throughout the catalytic cycle. The lack of spectroscopic evidence for the participation of the iron(II) oxidation state[45,46] strongly suggested that O_2 does not first bind to the metal center but instead attacks a different site. This notion is supported by the lack of reactivity of the enzyme-substrate complex with the O_2 surrogate NO, unless the metal center was first reduced by added reductant.[47,48]

The first step in the proposed mechanism (Figure 6) is the binding of the catecholate substrate to the iron(III) center, displacing the hydroxide and the axial Tyr447 residue to generate a square pyramidal $[Fe(His)_2(Tyr)(catecholate)]$ complex. The covalency of the iron(III)-catecholate interaction introduces semiquinonate radical character to bound substrate and makes it susceptible to O_2 attack, generating a transient alkylperoxoiron(III) intermediate. This alkylperoxo intermediate then undergoes a Criegee-type rearrangement to form muconic anhydride and a Fe^{III}–OH species. The

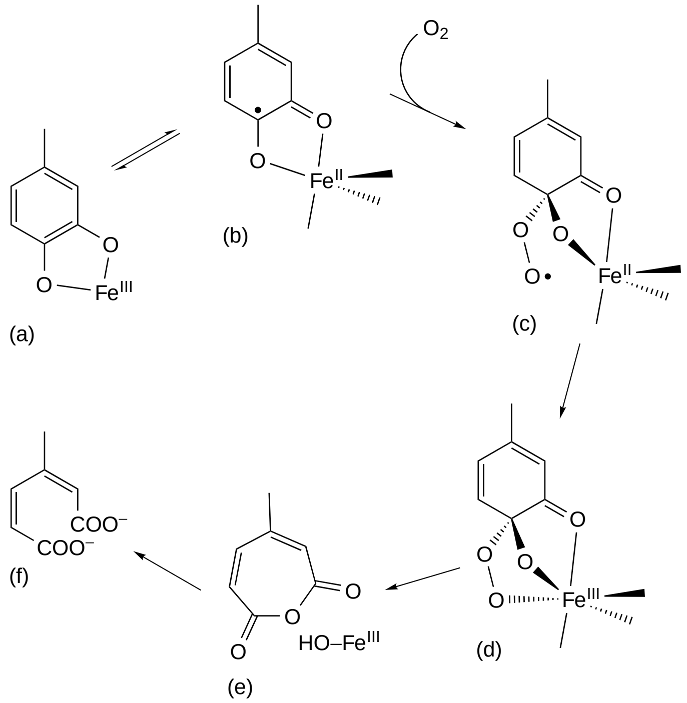

Figure 6 Proposed substrate activation mechanism for intradiol-cleaving catechol dioxygenases. Substrate activation is proposed to occur via an iron(II)-semiquinone prior to O_2 binding

hydroxoiron(III) species then acts as the nucleophile converting the anhydride into the ring-opened product.

Model studies support the mechanism proposed in Figure 6. A large number of [Fe^{III}(L)(catecholate)] complexes (L = tetradentate ligands) have been synthesized by various groups and found to react with O_2 and afford intradiol cleavage products.[49] In a systematic study,[50–53] Que and coworkers found that, as the iron became more Lewis acidic, the yield of intradiol cleavage product increased to approach quantitative conversion and the rate of reaction accelerated significantly. These results are rationalized by the argument that the increased Lewis acidity of the iron center enhances the covalency of the iron-catecholate bond and increases the semiquinone character of the bound catecholate, which renders it more reactive toward O_2.

4.2 Extradiol-cleaving Dioxygenases

Extradiol cleavage of dihydroxybenzenes represents the more common pathway for biodegradation of aromatic molecules in soil.[35] While the intradiol-cleaving enzymes utilize an iron(III) active site, the extradiol-cleaving enzymes typically use iron(II) (or manganese(II) in a few examples). A representative reaction of this subgroup is shown in Figure 7(a). This class of dioxygenases has been shown to cleave a variety of substrates including catechol (2,3), protocatechuate (2,3 or 4,5), and 3,4-dihydroxyphenylacetate (2,3). Also included in this class are the enzymes that cleave gentisate and homogentisate (Figure 7b). Although these substrates are not catechols but substituted benzene-1,4-diols, these enzymes also require Fe^{II} for activity and have similar properties as the catechol-cleaving enzymes.

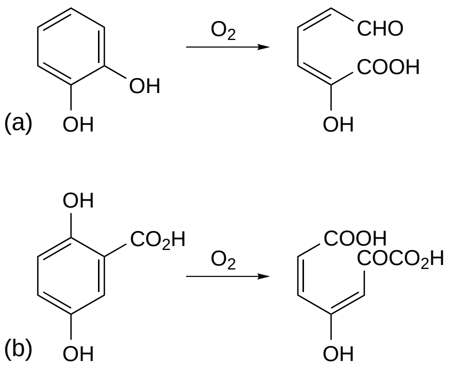

Figure 7 Reactions catalyzed by (a) catechol 2,3-dioxygenase and (b) gentisate 1,2-dioxygenase

The extradiol-cleaving enzymes are more challenging to study than their intradiol-cleaving counterparts because of the lability of the Fe^{II} centers and the difficulty of probing such sites by spectroscopy. Sequence comparisons classify the enzymes in this category into three subclasses,[54] but crystallographic data for representative proteins of each subclass show a common active site with the metal center bound to two His residues and an Asp or a Glu residue, which

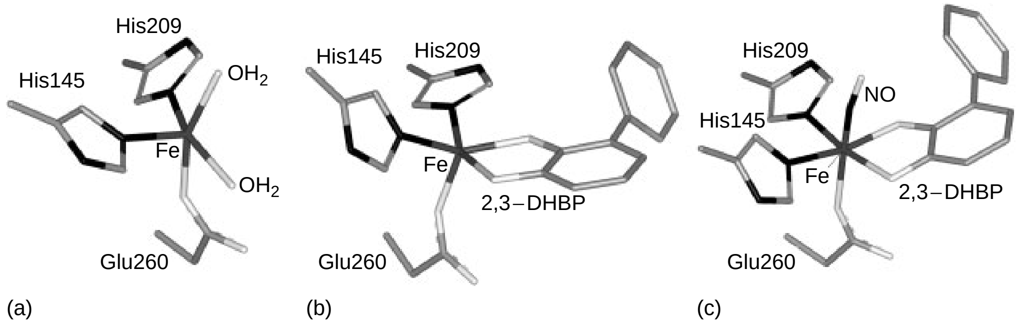

Figure 8 Active sites of BphC in (a) the as-isolated form (1KW3.pdb), (b) the enzyme-substrate complex (1KW6.pdb), and (c) the ternary enzyme-substrate-NO adduct (1 KW8.pdb)

together occupy one face of an octahedron (Figure 8a).[55–59] This metal-binding arrangement has been termed the 2-His-1-carboxylate facial triad[60,61] and is emerging as a recurring motif for dioxygen activating nonheme iron(II) enzymes.

Steady-state kinetic studies have revealed that extradiol-cleaving enzymes utilize an ordered mechanism with substrate binding prior to O_2 activation.[35] The coordination of the substrate appears to serve as a trigger to significantly increase the affinity of the metal center for O_2, as inferred from NO binding studies.[62] Crystallographic studies on 2,3-dihydroxybiphenyl 1,2-dioxygenase (BphC),[55,57] 3,4-dihydroxyphenylacetate 2,3-dioxygenase,[59] and protocatechuate 4,5-dioxygenase[56,58] demonstrate that substrate binding results in the displacement of the water ligands found in the active sites of the as-isolated enzymes to form a square pyramidal metal center poised to bind O_2. In the BphC structure, the site trans to Glu260 is vacant (Figure 8b) and has been shown to bind the O_2 surrogate NO (Figure 8c).

EXAFS studies[63] and the aforementioned high-resolution crystallography[55–59] indicate that the catechol substrate binds in an asymmetric fashion to the iron(II) center with Fe–$O_{catecholate}$ bond lengths that differ by 0.2–0.4 Å. These structural parameters are in excellent agreement with those reported for synthetic iron(II)-monoanionic catecholate complexes,[64,65] and, on the basis of this comparison, it was proposed that the catechol binds to the iron(II) center as a monoanion. This notion was supported by subsequent UV-resonance Raman[66] and UV-vis studies.[67–69] The monoanionic nature of the catechol substrate in extradiol dioxygenases is in sharp contrast with the dianionic catecholate character commonly found in iron(III) complexes.[35,43] This difference can be rationalized by the differing Lewis acidities of the metal centers in their divalent and trivalent oxidation states.

The structural and spectroscopic data accumulated so far have led to the proposed mechanism in Figure 9.[49] The first step of the reaction involves the displacement of water

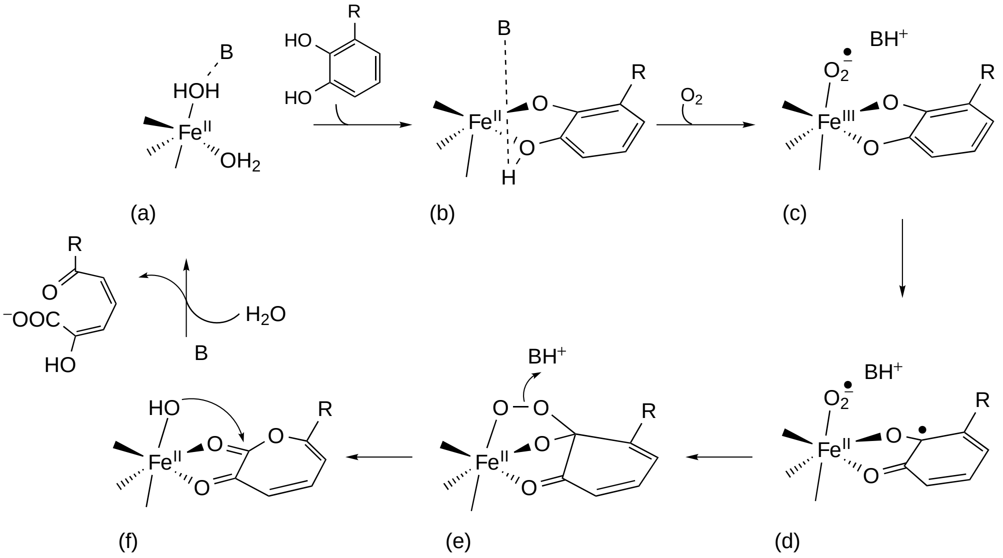

Figure 9 Proposed mechanism for the extradiol-cleaving catechol dioxygenases

molecules from the enzyme resting state (Figure 9a) by substrate to form typically a five-coordinate iron(II) species with a chelated monoanionic catecholate (Figure 9b). This change in ligation would be expected to lower the redox potential of the metal center, readying it to react with O_2. The ternary enzyme·substrate·O_2 complex is formed as O_2 binds to the iron(II) center, resulting in a one-electron transfer from metal to O_2 forming an iron(III)-superoxide complex, analogous to the formation of the Fe–NO adduct, as shown in Figure 9(c). This arrangement poises the two substrate molecules into the proper orientation for reaction.

Another one-electron transfer from substrate to metal gives rise to a semiquinonatoiron(II)-superoxide species (Figure 9d). Evidence for the development of a radical species on the catecholate substrate in the mechanism is provided by experiments on the enzyme 3-(2′,3′-dihydroxyphenyl)propionate 1′,2′-dioxygenase.[70] Bugg and co-workers used a substrate analogue containing a cyclopropyl side chain as a radical probe and found that the substituents on the cyclopropyl group underwent substantial epimerization in the course of enzyme-catalyzed extradiol cleavage. The formation of a semiquinonate radical (Figure 9d) during the catalytic cycle would promote reversible cyclopropyl ring opening that rationalizes the observed epimerization.

The next step of the mechanism is the nucleophilic attack of the aromatic ring by the incipient superoxide generating an alkylperoxo intermediate (Figure 9e) similar to that proposed for the intradiol-cleaving enzymes (Figure 6d). This species undergoes a Criegee rearrangement to generate a seven-membered α-oxolactone ring (Figure 9f) that is hydrolyzed to afford product. The structural similarity between intermediates 9E and 6D raises the question of how the regiospecificity of ring cleavage can be so exquisitely controlled. Bugg has proposed that the regiospecificity of the cleavage may derive from the different orientations of the peroxo group.[71] Rearrangement of the alkylperoxo intermediate (Figure 9e) by acyl migration would afford the intradiol product, while alkenyl migration would give rise to the extradiol product. There are precedents for both alkenyl and acyl migration in organic hydroperoxo species, and the choice of mechanism may be dictated by stereoelectronic factors.[72] An axial orientation for the peroxo group favors alkenyl migration, while an equatorial orientation favors acyl migration. Bugg and coworkers tested this model by preparing a series of substrate analogues where the putative hydroperoxo function was replaced by a CH_2OH, and the 1-hydroxocyclohexadien-2-one moiety was replaced by a 1-hydroxocyclohexan-2-one ring.[73] Only substrate analogues with the proximal hydroxymethyl group placed in an axial orientation relative to the cyclohexanone ring exhibited competitive inhibition of the MhpB enzyme. A recent DFT study provides yet another view of what determines the regiospecifity of cleavage.[74]

To date the few structurally characterized biomimetic extradiol-cleaving systems are all five-coordinate iron(III) complexes.[49] The facts that oxidative cleavage is regiospecific in many cases and quantitative in some strongly suggest that a divalent metal oxidation is not absolutely required for this chemistry. There are also examples of iron(II) complexes that catalyze extradiol cleavage, but these systems are less well characterized.[75–77] The observation that iron(II) centers may be better effectors of extradiol cleavage should serve as a compelling rationale for future work aimed at obtaining structurally characterized functional models with iron(II) centers.

5 α-KETO ACID DEPENDENT ENZYMES

α-Keto acid-dependent enzymes, which are found in microorganisms, plants, and animals, play vital roles in environmental, pharmaceutical, and biological pathways. Enzymes that require an α-keto acid, typically 2-oxoglutarate (2-OG), as a co-substrate constitute the largest and most diverse family of mononuclear nonheme iron enzymes, catalyzing many pivotal metabolic transformations that require dioxygen activation.[78–80] The function of the α-keto acid is to provide the two electrons required to reduce O_2 and generate an oxidant capable of functionalizing a C–H bond on the substrate. For example, the bacterial enzyme TfdA hydroxylates the broadleaf herbicide 2,4-dichlorophenoxyacetate in the first step in its biodegradation;[81,82] AlkB demethylates 1-methyladenine and 3-methylcytosine residues in the repair of single-stranded DNA and RNA;[83–85] clavaminic acid synthase catalyzes three distinct steps in the synthesis of the β-lactamase inhibitor clavulanic acid;[86] deacetoxycephalosporin C synthase (DAOCS) catalyzes the ring expansion of the thiazolidine ring of the penicillin *N* nucleus to afford deacetoxycephalosporin C;[87,88] and carbapenam synthase (CarC) catalyzes the epimerization/desaturation of carbapenam in the formation of carbapenam-related antibiotics.[89] These enzymes also appear in microbes that can utilize alternative nutrient sources such as sulfonates and hypophosphites. For example, taurine dioxygenase (TauD) enables *E. coli* to use the aliphatic sulfonate taurine as a sulfur source during periods of sulfate starvation,[90] and hypophosphite dioxygenase (HtxA) allows microbes to oxidize phosphite and hypophosphite.[91]

α-Keto acid-dependent oxygenases are also found in higher organisms and enzyme mutations are linked to a variety of diseases. Prolyl 3-hydroxylase, prolyl 4-hydroxylase and lysyl hydroxylase are responsible for the post-translational modification of procollagen, which is crucial to the formation of fibrous tissues.[80] Recent reports show prolyl and asparaginyl hydroxylases are linked to oxygen sensing in cells.[92–94] Under conditions of low oxygen tension (hypoxia), hypoxia inducible factor (HIF) promotes increased expression of: erythropoietin, a precursor to red blood cells; vascular endothelial growth factor, a vasodilator and key component in the growth of new blood vessels; certain glycolytic enzymes, leading to the liberation of energy rich compounds; and tyrosine hydroxylase (vide infra), which catalyzes the rate determining step in the synthesis of adrenaline. At normal oxygen concentrations, proline hydroxylation leads to ubiquitination and degradation of HIF, while asparagine hydroxylation inhibits interaction of HIF with transcriptional co-activators, thereby exerting a second level of control over gene expression. Disruption of the signaling cascade in which prolyl and asparaginyl hydroxylases participate can affect the onset and development of cancerous tumors and ischemia.[95,96] This, coupled with observation of an α-keto acid-dependent enzyme in a virus that initiates DNA replication,[97] has led to a proliferation of interest in the relationship of structure to function in α-keto acid-dependent dioxygenases not only on therapeutic grounds but also for etiological reasons.

Several enzymes in this class have substrates with a built-in α-keto acid functionality and thus do not require 2-oxoglutarate as a co-substrate. These enzymes appear to have different topologies from enzymes utilizing 2-oxoglutarate and include 4-hydroxyphenylpyruvate (HPP) dioxygenase and 4-hydroxymandelate synthase, which utilize the same substrate but catalyze different transformations. Nonfunctional mammalian HPP dioxygenase has been linked to conditions of tyrosinaemia type III and hawksinuria related to the build up of metabolites of tyrosine.[79,98] 4-Hydroxymandelate synthase and HPP dioxygenase exhibit 43% sequence similarity and 34% identity.[99] A third member of this subset is α-ketoisocaproate dioxygenase, which is involved in leucine metabolism.[100]

Figure 10 illustrates the range of the reactions catalyzed by α-keto acid-dependent iron enzymes. In many cases, the substrate is hydroxylated as shown in Figures 10(a) and 10(b), respectively for prolyl hydroxylase where the requisite α-keto acid is 2-OG and HPP dioxygenase where the α-keto acid function is built into the substrate. For these reactions, one atom of dioxygen is incorporated as the hydroxyl oxygen of the product, while the other ends up on the carboxylate derived from the oxidized keto acid, so both these enzymes are technically considered dioxygenases. As shown in the transformations of Figures 10(c) and 10(d), this class of enzymes can also catalyze heterocyclic ring expansion, heterocyclic ring formation, and desaturation. In these cases,

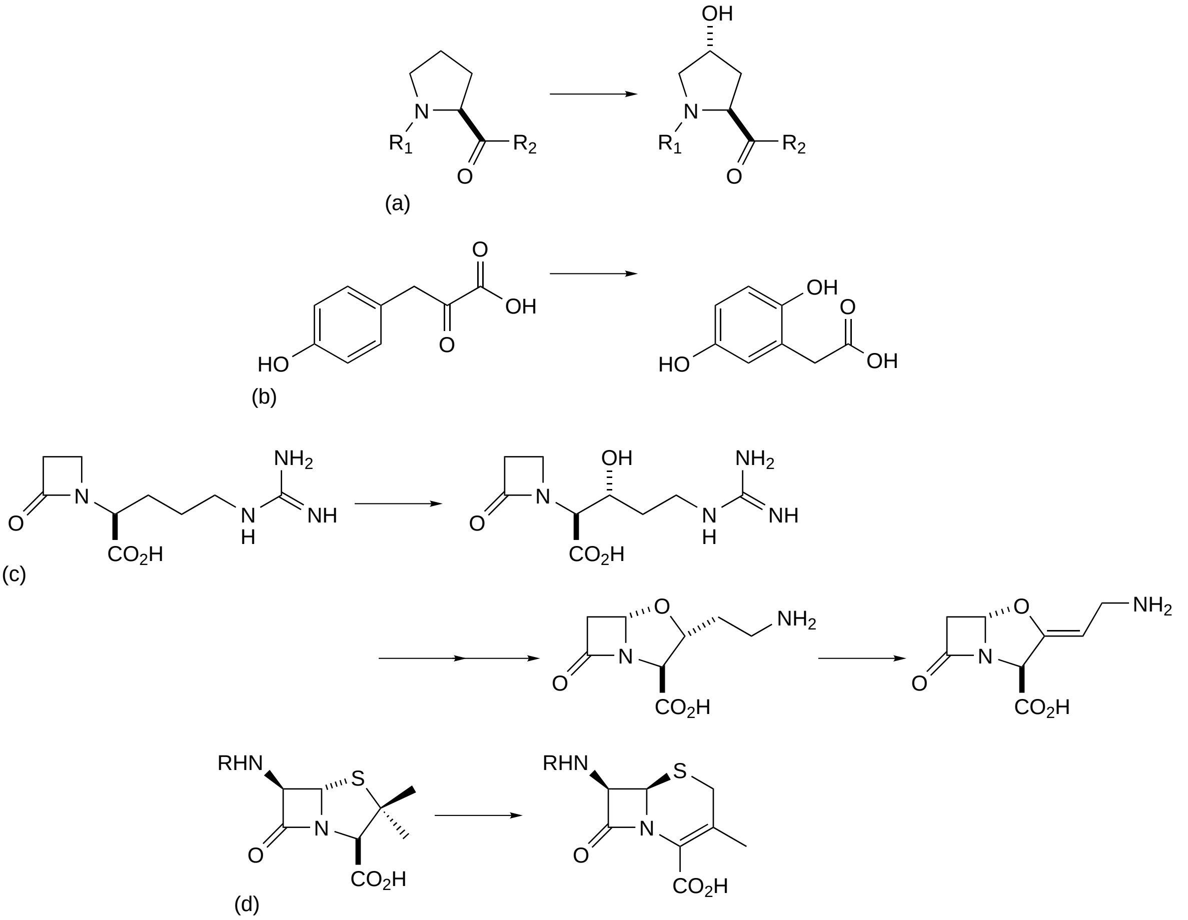

Figure 10 Several reactions catalyzed by α-keto acid-dependent iron enzymes, (a) prolyl 4-hydroxylase, (b) deacetoxycephalosporin C synthase (DAOCS), (c) 4-hydroxyphenylpyruvate (HPP) dioxygenase and (d) clavaminate synthase 2 (CAS)

dioxygen is incorporated only into the succinate byproduct and the other oxygen atom is reduced to water.

Crystal structures for a number of enzymes in this family are now available.[49,78] Despite the fact that many of these enzymes exhibit minimal sequence identity, they have a conserved Hx(D/E)x$_n$H sequence that provides the three endogenous protein ligands of the recurring 2-His-1-carboxylate facial triad motif that binds the high-spin iron(II) center. Three solvent molecules on the opposite face complete the iron coordination sphere.

Steady-state kinetic studies on a number of enzymes support an ordered mechanism in which the α-keto acid binds first.[101–107] This observation suggests the formation of an iron-α-keto acid adduct to initiate the activation of O_2. Consistent with this notion, crystallographic and spectroscopic studies show that the α-keto acid acts as a bidentate ligand displacing two of the solvent water molecules on the six-coordinate iron(II) center (Figure 11a). Upon substrate binding, the third water molecule is displaced to afford a five-coordinate iron(II) center poised to bind O_2 (Figure 11b),[108,109] which is confirmed by the crystal structure of an NO adduct (Figure 11c) with NO serving as an O_2 surrogate.[110]

Figure 12 shows a generally accepted reaction sequence for these enzymes. O_2 can bind trans to any of the facial triad residues forming an adduct that may be described as an iron(III)-superoxide complex as shown in Figure 12d. This superoxide then attacks the electrophilic carbonyl carbon of 2-OG to form iron(IV)-peroxo adduct Figure 12e, which in turn undergoes C–C bond cleavage and subsequent O–O bond

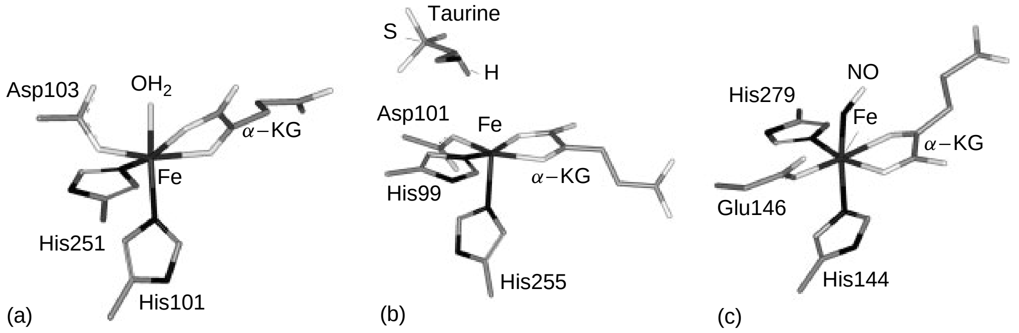
Asp103
OH2
α−KG
Fe
His251
His101
(a)
Taurine
S
H
Asp101
Fe
His99
α−KG
His255
(b)
NO
His279
Fe
α−KG
Glu146
His144
(c)

Figure 11 Crystal structures of stages in the catalytic cycle of α-keto acid-dependent enzymes: (a) the binary complex of CarC (1NX4.pdb), (b) the ternary complex of TauD (1GQW.pdb), and (c) the NO adduct of the ternary complex of CAS (1GVG.pdb)

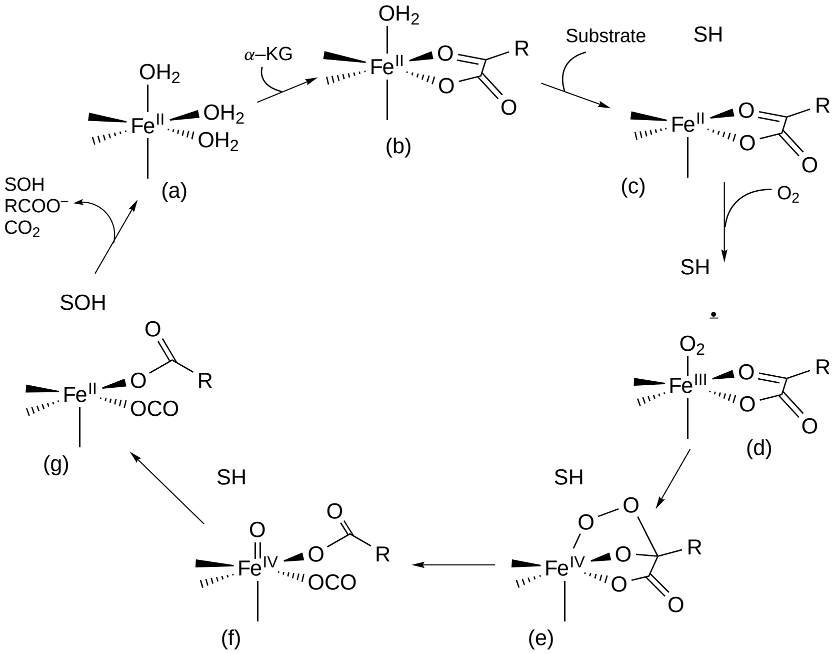
OH2
Fe^II
OH2
OH2
(a)
α−KG
OH2
Fe^II
O
R
O
O
(b)
Substrate
SH
Fe^II
O
R
O
O
(c)
O2
SH
O2
Fe^III
O
R
O
O
(d)
SH
O
O
Fe^IV
O
R
O
O
(e)
SH
O
Fe^IV
O
O
R
OCO
(f)
SOH
O
Fe^II
O
R
OCO
(g)
SOH
RCOO−
CO2

Figure 12 Proposed mechanism for the α-keto acid-dependent iron enzymes, where substrate is indicated as SH

heterolysis to form an iron(IV)-oxo intermediate Figure 12f that is responsible for the oxidation of the substrate. The oxidized product, the carboxylate byproduct, and carbon dioxide (Figure 12g) subsequently leave the active site to prepare for another turnover.

Experimental evidence has thus far been obtained for only one intermediate after O_2 binding. An iron(IV)-oxo moiety of TauD has been observed by stopped flow kinetics and trapped by rapid-freeze-quench experiments.[111] This species has an absorption feature near 320 nm ($\varepsilon_{320} \sim 1500\,M^{-1}\,cm^{-1}$) whose rate of decay is dependent on whether the target C–H bond on taurine is hydrogen or deuterium.[112] (A kinetic isotope effect of about 30 is observed.) Mössbauer spectroscopy of the intermediate reveals an iron center with an isomer shift of $0.31\,mm\,s^{-1}$, whose high field behavior corresponds to that of a high-spin iron(IV) ($S = 2$) center. The presence of an $Fe^{IV}{=}O$ unit is indicated by an oxygen-isotope-sensitive feature at $821\,cm^{-1}$ from flow resonance Raman studies,[113] and a short (1.62 Å) Fe–O distance determined from an EXAFS study.[114] Taken together, these results provide evidence for intermediate shown in Figure 12f.

Synthetic complexes modeling α-keto carboxylate-dependent enzymes have played a key role in furthering our understanding of these enzymes. Several $[Fe^{II}(L)(\alpha\text{-keto acid})]$ complexes have been reported as functional models using tetradentate and tridentate ligands.[49] All of the model complexes that react with O_2 afford quantitative yields of the decarboxylated α-keto acid, but in only two cases was the active oxidant trapped. Intermolecular olefin epoxidation has been observed in the case of $[Fe^{II}(Tp^{Me2})(BF)]$ complex.[115] This complex reacts with O_2 to form a species capable of stereospecific oxidation of *cis*-stilbene to its oxide as the product. However *trans*-stilbene is not epoxidized, suggesting that the active oxidant is capable of steric discrimination.

The other example is an intramolecular hydroxylation of a ligand phenyl ring of $[Fe(Tp^{Ph2})(BF)]$ upon exposure to O_2.[116,117] The hydroxylated product is obtained within an hour in 70% yield. In contrast, the corresponding $[Fe(Tp^{Ph2})(benzoate)]$ complex also reacts with O_2 to give the same product in 55% yield, but this reaction requires 2–3 days, clearly demonstrating the key role the α-keto group plays in activating O_2. The use of $^{18}O_2$ resulted in the incorporation of one labeled oxygen into the benzoate product and the other into the hydroxylated phenyl ring of the Tp ligand. The absence of ^{18}O incorporation when the reaction is carried out in the presence of $H_2{}^{18}O$ suggests that an iron(IV)-oxo species, if involved in the mechanism, has too short a lifetime relative to $H_2{}^{18}O$ exchange in the biomimetic transformation.

A significant recent development has been the generation of high-yield synthetic oxoiron(IV) complexes in a nonheme ligand environment.[118–123] The $Fe^{IV}{=}O$ unit is stabilized by coordination to polydentate nitrogen ligands such as the macrocyclic TMC, the tetradentate tripodal TPA, and the pentadentate N4Py and Bn-TPEN. A crystal structure of $[Fe^{IV}(O)TMC]^{2+}$ has been reported revealing a Fe–O bond distance of 1.646 Å, the first high-resolution determination of this unit. Unlike the TauD intermediate, these complexes are low-spin ($S = 1$) iron(IV) complexes. Nevertheless these first examples of synthetic nonheme oxoiron(IV) complexes serve as excellent starting points to obtain detailed information about the electronic structure and reactivity properties of this intriguing, high-valent oxidant in iron biochemistry.

6 ISOPENICILLIN *N* SYNTHASE

Isopenicillin *N* synthase (IPNS) is a nonheme iron enzyme found in *Cephalosporium*, *Penicillium*, and *Streptomyces* strains. It activates O_2 and catalyzes the formation of isopenicillin *N* from δ-(L-α-aminoadipoyl)-L-cysteinyl-D-valine (ACV) (Figure 13). Interestingly, it has the conserved $HX(D/E)X_mHX_nRXS$ sequence motif, similar to those found in many 2-oxoglutarate-dependent enzymes but does not require 2-oxoglutarate for activity.[78,124]

Crystallographic studies have established IPNS as another member of the superfamily of nonheme iron enzymes with active sites containing a 2-His-1-carboxylate facial triad. The extensive crystallographic information available provides a wealth of mechanistic insight. The Mn(II)-substituted IPNS from *Aspergillus nidulans* has been crystallized in the absence of substrate to reveal a six-coordinate metal center with four endogenous protein ligands (His214, Asp216, His270, and Gln330) and two H_2O molecules occupying the remaining cis ligand sites (Figure 14a).[125] As shown by the crystal structure of the $Fe^{II}{\cdot}IPNS{\cdot}ACV$ complex, substrate binding results in the displacement of the Gln ligand by the ACV thiolate sulfur (Figure 14b),[126] confirming earlier EXAFS results that showed a sulfur scatterer at 2.3 Å.[127]

O_2 can interact with the metal center only at this stage. This suggests that the coordination of the ACV thiolate primes the iron(II) center for its reaction with O_2, presumably by shifting the Fe^{III}/Fe^{II} redox potential to a

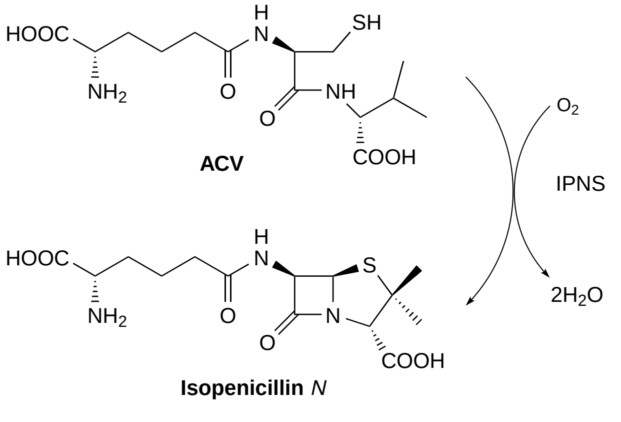

Figure 13 Reaction catalyzed by isopenicillin *N* synthase

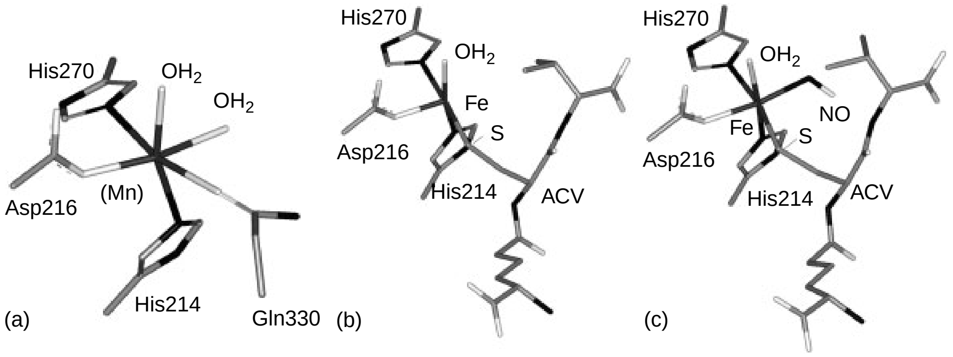
His270
OH2
OH2
Asp216
(Mn)
His214
Gln330
(a)
His270
OH2
Fe
S
Asp216
His214
ACV
(b)
His270
OH2
NO
Fe
S
Asp216
His214
ACV
(c)

Figure 14 Crystal structures of IPNS complexes (a) Mn·IPNS (1IPS.pdb), (b) Fe·IPNS·ACV (1BKO.pdb), and (c) Fe·IPNS·ACV·NO (1BLZ.pdb)

less positive value, similar to the mechanisms proposed for the extradiol-cleaving dioxygenases and the α-keto acid-dependent enzymes. To date there is no spectroscopic evidence for a Fe^{II}·IPNS·ACV·O_2 adduct, as such an intermediate appears to be too reactive to be trapped. However the corresponding Fe^{III}IPNS·ACV·NO adduct has been studied. Exposure of NO to the substrate-bound iron(II) center engenders an $S = 3/2$ EPR signal characteristic of high-spin iron(II)-nitrosyl adducts[128] and gives rise to a short (1.7 Å) Fe–NO bond observed by EXAFS.[127] The crystal structure of the ternary enzyme·substrate·NO complex (Figure 14c) confirms many aspects of the active site earlier deduced from spectroscopic experiments and shows that NO binds trans to Asp216, with its oxygen atom equidistant from both the valine nitrogen and the cysteinyl β-carbon.[129] Assuming that NO serves as an O_2 surrogate, these are the atoms from which a hydrogen atom must be abstracted to close the β-lactam ring in the first stage of isopenicillin formation.

The elegant and comprehensive work of Baldwin and coworkers[130] using a number of ACV analogues has provided insight into the steps subsequent to O_2 binding and led to the mechanism for IPNS action shown in Figure 15. The reduction of O_2 occurs in two stages with the sequential formation of the β-lactam and the thiazolidine rings corresponding to

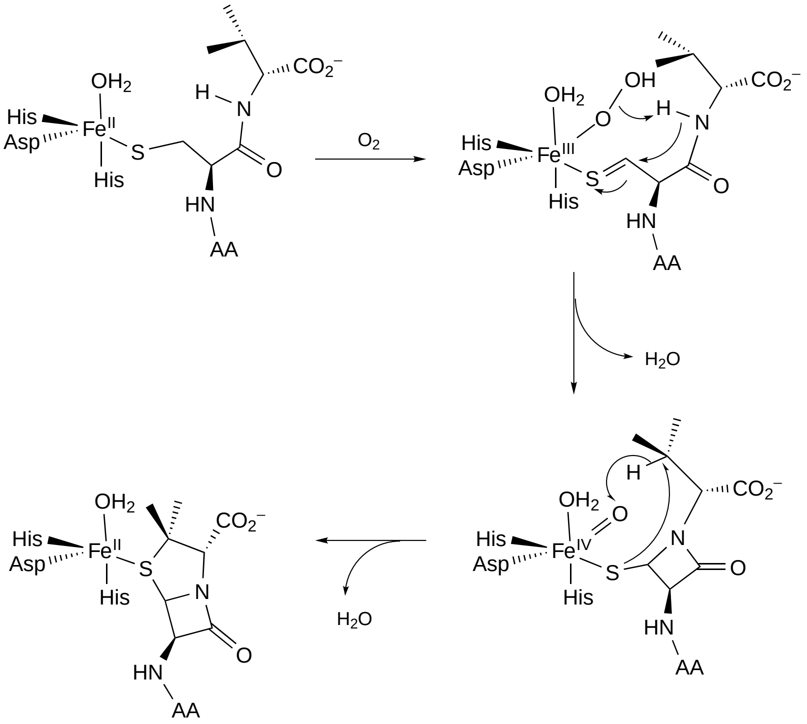
OH2
His
Fe^II
Asp
His
S
H
N
CO2−
O
HN
AA
O2
OH2
OH
O
H
N
CO2−
His
Fe^III
Asp
S
His
O
HN
AA
H2O
OH2
H
O
CO2−
His
Fe^IV
Asp
S
N
O
His
HN
AA
H2O
OH2
CO2−
His
Fe^II
Asp
S
N
His
O
HN
AA

Figure 15 Proposed mechanism for the reaction catalyzed by isopenicillin *N* synthase

two distinct two-electron reduction steps. In the first stage, O_2 is reduced to the peroxide oxidation level concomitant with the oxidation of the Cys thiolate to a thioaldehyde (or some equivalent moiety). O–O bond heterolysis leads to the abstraction of the proton from the valinyl peptide nitrogen, generating an $\mathrm{Fe^{IV}{=}O}$ intermediate and the amidate anion. The latter then nucleophilically attacks the thiocarbonyl carbon to form the β-lactam ring and regenerates the thiolate. The $\mathrm{Fe^{IV}{=}O}$ moiety then initiates the second stage of the reaction by abstraction of the valinyl C3-H hydrogen atom, followed by C3-S bond formation to generate the thiazolidine ring. A crystal structure of the $\mathrm{Fe^{II}}$·IPNS·IPN product complex shows the thiazolidine sulfur atom bound to the metal center (Figure 16a).

Much of the recent crystallographic work on IPNS has involved brief exposure of crystalline enzyme-substrate complexes to hyperbaric O_2 followed by cryo-crystallography.[131,132] With AC*O*V, the substrate analogue wherein the valine peptide bond is converted to an ester linkage, β-lactam ring formation is not possible and the thiolate of the ACV substrate is instead oxidized to a thiocarboxylate, with one atom of O_2 incorporated into the thiocarboxylate (Figure 16b). On the other hand, ACmC, the substrate analogue where the valine residue is replaced by S-methylcysteine, affords a product wherein the reaction cycle is interrupted after the formation of the β-lactam ring; the $\mathrm{Fe^{IV}{=}O}$ moiety is instead trapped by the S-methylcysteine to form a sulfoxide that is coordinated to the iron center trans to the Asp residue (Figure 16c). This result corroborates the proposal that O_2 binds trans to the Asp residue, as indicated by the NO complex, and is converted to an oxo group in the latter part of the reaction cycle. Besides oxo transfer to sulfide, the $\mathrm{Fe^{IV}{=}O}$ moiety can also epoxidize double bonds, as demonstrated by the substrate analogue with the valine replaced by allylglycine,[133] and can carry out hydrogen-atom abstraction, as shown by a ring opening isomerization of the product derived from the cyclopropylalanine analogue.[134] Thus there is strong experimental evidence for the various steps of the proposed IPNS mechanism (Figure 15). This scheme is also strongly supported by DFT calculations.[135]

7 PTERIN-DEPENDENT HYDROXYLASES

The pterin-dependent oxygenases, typified by the aryl amino acid hydroxylases, are a small family of closely related enzymes, which are essential to mammalian physiology.[136,137] This class of metalloenzymes employs tetrahydrobiopterin (BH_4) as a two-electron donating cofactor for the activation of O_2. Members of this class include phenylalanine (PheH), tyrosine (TyrH) and tryptophan (TrpH) hydroxylases, which effect regiospecific aromatic hydroxylations of the namesake amino acids.

Phenylalanine hydroxylase is located primarily in the liver and affords the major pathway for phenylalanine catabolism. In contrast, the other two enzymes function primarily within the central and peripheral nervous system, providing the rate-limiting initial steps in biosynthetic pathways for a range of neurotransmitters including dopamine, norepinephrine, and epinephrine for TyrH and serotonin and melatonin for TrpH. Dysfunctions of these essential enzymatic activities have been implicated in several severe neurological and psychological diseases, and this has stimulated the significant body of biochemical and biomedical research to date.[137]

High-resolution crystal structures have now been solved for PheH, TyrH, and TrpH.[49,138] Most of these structures have been obtained from enzymes with truncated catalytic domains in an inactive, oxidized form with iron(III) and BH_2 bound. Very recently, structures have become available for the active human PheH catalytic domain as the iron(II) complex, the binary BH_4 complex (Figure 17a), and ternary complexes with BH_4 and the substrate analogues *l*-thienylalanine (Figure 17b) or *l*-norleucine.[139–141]

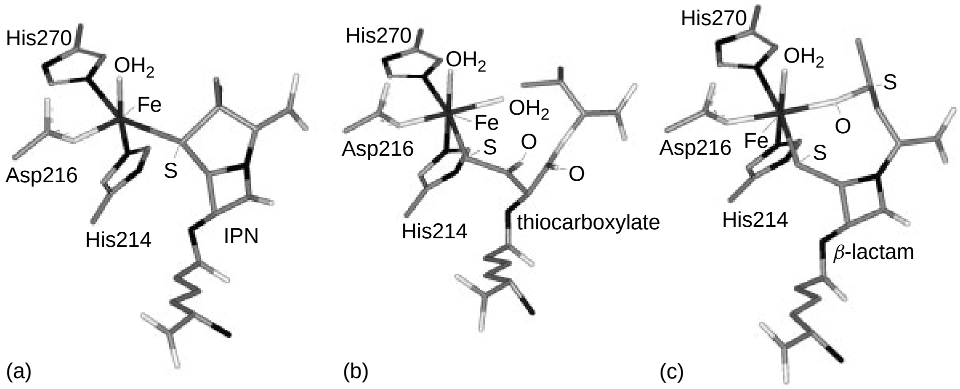

Figure 16 IPNS-product complex crystal structures with varying substrates: (a) IPN (1QJE.pdb), (b) AC*O*V (1HB4.pdb), and (c) ACmC (1QJF.pdb)

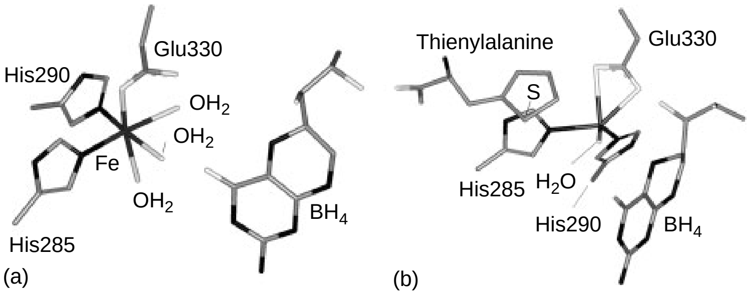

Figure 17 Crystal structures of phenylalanine hydroxylase: (a) the binary enzyme·BH_4 complex (1J8U.pdb) and (b) the ternary complex with *l*-thienylalanine (1KWO.pdb)

The iron active site can be found in a deep central cleft some 10 Å beneath the enzyme surface.[138] The six-coordinate iron center is ligated to a 2-His-1-carboxylate facial triad (consisting of His285, His290, and Glu330 in *H. sapiens* PheH) and three water molecules (Figure 17a). The pterin binds to a site located just beyond the iron center at the very base of the cleft, and is π-stacked against a conserved phenylalanine (Phe254). The pterin also hydrogen bonds to a number of residues, particularly to a conserved glutamate (Glu286) via the hydroxypropyl sidechain. The stereochemistry of the pterin cofactor oxidation product has been determined, and only a single diastereomer corresponding to hydroxylation of the structurally exposed face of the pterin is formed.[142] The distance from the metal to the reactive pterin C4a is on the order of 6 Å in both the iron(II) and iron(III) structures.

Large changes are observed upon binding of substrate to form the ternary enzyme-pterin-substrate complex. As shown by the crystal structure of the ternary PheH·BH_4·*l*-thienylalanine complex, the iron center becomes 5-coordinate and adopts a square pyramidal geometry (Figure 17b).[140] Two water ligands are lost and the monodentate Glu330 becomes bidentate. Moreover, the pterin is significantly displaced towards the iron center, as indicated by a decrease in the distance between Fe and C4a from 5.9 to 4.5 Å. These changes in principle facilitate dioxygen binding at the metal as well as attack of the nearby pterin. However, the single water ligand retained in the ternary complex occupies the apical position of the square pyramid proximal to the BH_4 moiety, so formation of an Fe–O–O–pterin adduct would require the loss or shift of this water ligand. Near IR, MCD, and XAS studies of the PheH·tetrahydrobiopterin·phenylalanine complex in frozen solution are in accord with the crystallographic results, showing that the iron(II) center is 6-coordinate in the resting iron(II) form and the binary complexes with either phenylalanine or a pterin cofactor analogue, but attains a 5-coordinate square pyramidal geometry upon formation of the ternary complex.[143,144]

The structural and spectroscopic studies provide a firm foundation upon which to postulate a catalytic mechanism, but unfortunately give little insight into the activation of dioxygen within the reactive quaternary complex. Two key intermediates are presented in Figure 18. The first is an adduct of the coordinatively unsaturated iron(II) center, O_2 and the nearby C4a of the BH_4 cofactor, which is best described as an iron(II)-peroxypterin complex (Figure 18a).[145,146] Since no intermediate has been directly observed to date, formation of this adduct may be rate-limiting. The putative Fe^{II}–O–O–pterin intermediate is then proposed to cleave heterolytically to form 4a-hydroxypterin (BH_3OH) and a reactive oxoiron(IV) species that carries out

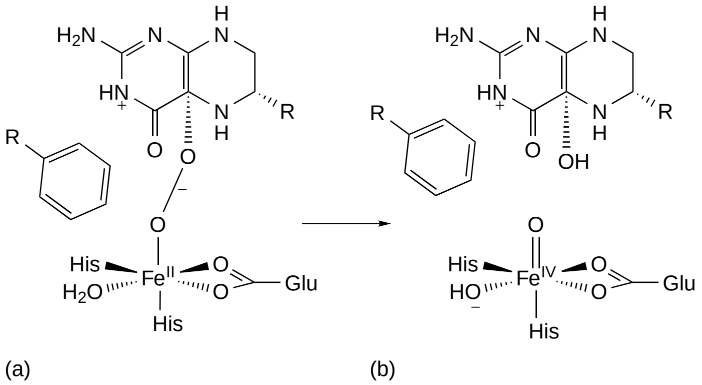

Figure 18 Key intermediates in the proposed mechanism for pterin-dependent hydroxylases

the electrophilic attack of the aromatic substrate (Figure 18b). This step is supported by the observation of the nearly quantitative incorporation of isotope from $^{18}O_2$ into both the amino acid and BH_3OH products.[142,147] Pterin-dependent enzymes are thus proposed to utilize an $Fe^{II}/Fe^{IV}=O$ couple, distinct from the formal $Fe^{III}/Fe^{V}=O$ couple associated with heme enzymes such as cytochrome P450 (*see* ***Iron: Heme Proteins, Mono- & Dioxygenases***).[148]

There is currently no consensus with respect to the mechanism of Fe–O–O–pterin adduct formation. Observation of an ^{18}O kinetic isotope effect for TyrH, $\Delta V/K = 1.017(2)$, coupled with the lack of solvent (H_2O, D_2O) isotope effects, indicates a significant O–O bond order change in the rate determining step.[149] Stepwise O_2 binding may occur initially at Fe^{II} to form an $Fe^{III}–O_2^-$ species that subsequently couples to BH_4, as favored by recent DFT calculations.[150] In this case, the metal ion plays a role in stabilizing incipient charge on the O_2 unit and mitigating the spin barrier, and a metal-independent reaction trajectory could not be found. Alternatively, O_2 attacks initially at BH_4 to form a pterin hydroperoxide,[149,151] paralleling the chemistry of metal-free flavin-dependent oxygenases,[152] with the metal center subsequently required for activation of the peroxo species. Experiments on the Glu280Lys mutant of PheH favor the latter option.[153] Despite the fact that the iron(II) center of this mutant enzyme remains 6-coordinate in the ternary complex, pterin oxidation activity is nevertheless retained and in fact is enhanced twofold. A third option may be the concerted addition of O_2 to both the metal center and pterin.

The next step in the mechanism is O–O bond heterolysis of the Fe^{II}–O–O–pterin intermediate to form an $Fe^{IV}=O$ species. Heterolysis is predicted by DFT calculations to be quite difficult for a tetrahedral iron(II) model,[154] but relatively facile for six-coordinate iron(II),[150] especially when assisted by protonation at the departing β-oxygen. Consistent with the weak ligand field, DFT calculations suggest a reactive oxoiron(IV) intermediate in a high-spin, $S = 2$ ground state.[150] This intermediate is postulated to attack a single carbon atom on aromatic substrates to form a 2,4-dienone intermediate, which subsequently tautomerizes to phenolic product. While this oxoiron(IV) species has not been experimentally observed, there is indirect evidence implicating such an electrophilic hydroxylating agent. Besides arene hydroxylation, the pterin-dependent enzymes can accommodate a number of substrate analogues and carry out sulfoxidation, epoxidation, and benzylic hydroxylation,[146] a reactivity pattern closely related to that associated with the $Fe^{IV}=O$ porphyrin radical intermediate of cytochrome P450 (*see* ***Iron: Heme Proteins, Mono- & Dioxygenases***).[148] Secondly, TyrH can hydroxylate a series of *para*-substituted phenylalanines with consistent rates of pterin oxidation, but with increasing degrees of uncoupling as substrate analogues become electron-poor.[155,156] Correlation of arene hydroxylation against the consistent pterin oxidation rate was observed using the standard Hammett σ parameter, yielding $\rho = -4.3(7)$ for tetrahydrobiopterin and $-5.6(8)$ for the 6-methyltetrahydrobiopterin cofactor analog; these values are consistent with an electron-deficient transition state produced by an electrophilic oxidant.[155] Thirdly, the hydroxylation of deuterated substrate by TrpH exhibits an inverse isotope effect that suggests a partially rate-limiting electrophilic substitution step in this specific instance.[157] Lastly, arene hydroxylation is often accompanied by a 1,2-hydrogen shift commonly referred to as an 'NIH shift', by which substrates labeled with hydrogen isotopes at the site of attack are converted to metabolites with isotope retention on an adjacent carbon (*see* ***Iron: Heme Proteins, Mono- & Dioxygenases***).[158] Such a shift is usually indicative of cationic intermediates associated with oxo atom transfer, forming epoxides or 2,4-dieneones.[150,157–159] An appropriate model system that mimics the step involving attack of an $Fe^{IV}=O$ moiety on an aromatic ring has been investigated in some detail,[160] and supports mechanistic notions discussed above.

8 RIESKE DIOXYGENASES

The *cis*-dihydroxylation of arenes catalyzed by Rieske (*see* ***Iron–Sulfur Proteins***) dioxygenases constitutes the first step in the biodegradation of aromatic molecules by soil bacteria and leads in two subsequent steps to the formation of catechols,[161–163] which are in turn degraded by the intradiol and extradiol-cleaving catechol dioxygenases discussed in Section 4. Furthermore, there is strong interest in these enzymes as biotechnological tools since the enzyme-catalyzed reactions are both stereo- and enantiospecific and arene *cis*-dihydroxylation is a novel transformation not observed thus far in synthetic organic chemistry.[164–167] Rieske dioxygenases are multi-component enzymes with an oxygenase component where O_2 activation and substrate dihydroxylation occur and a reductase component that mediates electron transfer between NAD(P)H and the oxygenase component. In the course of catalysis, both atoms of O_2 are incorporated into the *cis*-diol product (Figure 19).[161,167–170] Aside from *cis*-dihydroxylation, Rieske dioxygenases also catalyze a number of oxidations such as benzylic hydroxylation, desaturation, sulfoxidation, O- and N-dealkylation.[168,171] This large range of oxidative transformations indicates that Rieske dioxygenases may even be more versatile than the cytochromes P450 (*see* ***Iron: Heme Proteins, Mono- & Dioxygenases***).

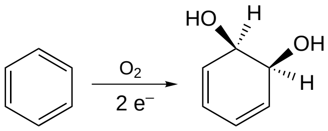

Figure 19 Rieske dioxygenase-catalyzed arene *cis*-dihydroxylation reaction

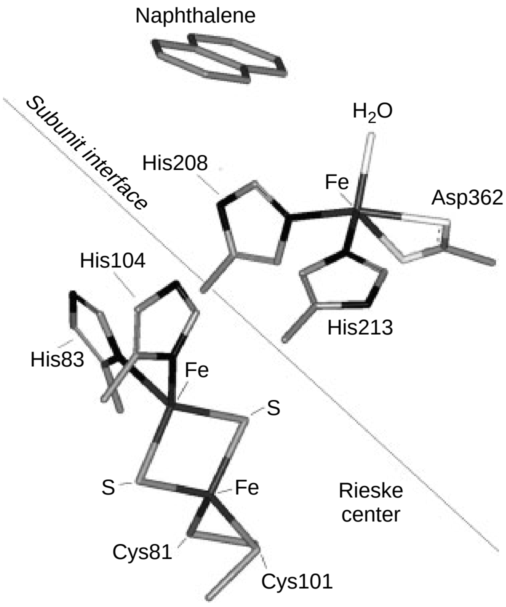

Figure 20 Crystal structure of the enzyme-substrate complex of naphthalene dioxygenase Fe·NDO·napthalene (1O7G.pdb)

There is thus far only one Rieske dioxygenase that is crystallographically characterized (Figure 20).[172–174] The structure of the oxygenase component of naphthalene 1,2-dioxygenase (NDO) from *P. putida*, the enzyme that catalyzes the formation of *cis*-(1R,2S)-1,2-dihydroxy-1,2-dihydronaphthalene from naphthalene[172] shows two metal centers, a mononuclear iron center where O_2 binding and activation takes place and a nearby Rieske-type Fe_2S_2 cluster (*see* ***Iron–Sulfur Proteins***), which delivers electrons to the mononuclear center in a controlled fashion during catalysis. These results confirm earlier notions derived from spectroscopic studies mainly on phthalate dioxygenase (PDO).[175,176] The mononuclear iron center of NDO is coordinated to two histidine residues (His208 and His213) and a bidentate aspartate (Asp362) (Figure 20),[172–174] occupying four sites of the metal center, again, in a variation of the 2-His-1-carboxylate facial triad.[60,61] A water molecule occupies a fifth coordination site, and there is an asparagine residue 3.7 Å from the iron in the vicinity of the sixth coordination site. The Rieske cluster with its characteristic $Fe_2S_2(Cys)_2(His)_2$ core is 12 Å away with His104 on the cluster connected to His208 on the monoiron center by hydrogen bonding to Asp205. Structures of the oxygenase component with bound naphthalene (Figure 20) or the substrate analogue indole are also available and show a substrate binding pocket nearby that orients the double bond to be attacked in position for substrate oxidation 4 Å away from the monoiron center.

Spectroscopic studies also provide insight into the coupling of substrate binding and the redox state of the Rieske cluster to changes at the mononuclear iron center in preparation for oxygen activation. MCD studies on PDO show that the iron(II) center is six-coordinate and becomes five-coordinate upon substrate binding.[176] This substrate-triggered change follows the general mechanistic paradigm for oxygen activation by iron(II) enzymes with 2-His-1-carboxylate active sites.[177] NO, an O_2 analogue, binds to the mononuclear iron(II) site of NDO and converts the EPR-silent high-spin iron(II) center into an EPR-active $S = 3/2\{\text{Fe-NO}\}^7$ center.[178] ENDOR studies of the NO adduct show that protons on the naphthalene substrate are dipolarly coupled to the paramagnetic center, indicating that the substrate remains in the crystallographically characterized binding pocket even after NO binding.[179,180] Furthermore the substrate is sensitive to the redox state of the Rieske cluster and undergoes an allosteric shift towards the mononuclear nonheme iron center upon reduction of the Rieske cluster.

An exciting recent development is the crystallographic characterization of O_2 adducts of NDO in the absence and in the presence of substrate, the first example for a nonheme iron enzyme.[173,174] The crystal structure of the reduced enzyme exposed to O_2 in the absence of substrate shows a side-on bound dioxygen moiety with Fe–O distances of 2.2 and 2.3 Å. The observed O–O distance of 1.4 Å suggests the reduction of O_2 to the peroxide level. The same experiment performed with crystals previously soaked in solutions of the substrate analogue indole and then exposed to O_2 shows an even more tightly bound side-on peroxo species with Fe–O distances of 1.8 and 2.0 Å and an O–O bond distance of 1.4 Å (Figure 21a). The Fe–O bond distances of the latter are in good agreement with Fe–O$_{\text{peroxo}}$ bond lengths obtained from the EXAFS analysis for $[\text{Fe(N4Py)}(\eta^2\text{-O}_2)]^+$ (1.93 Å)[181] and from the crystal structure of a heme/copper complex with a μ-$\eta^1 : \eta^2$-peroxo bridge (1.89 and 2.03 Å).[182] The asymmetry of the bound dioxygen moiety in the enzyme structures on the measured Fe–O bonds suggests the strong possibility that it may be a side-on bound hydroperoxide. The observation of these side-on bound dioxygen intermediates in two crystal forms differs from an earlier observation by the same group of a dioxygen adduct in which one oxygen atom is bound to the metal center and the other to the C3 carbon atom of the substrate analogue indole.[173] This structure may be construed to be an intermediate subsequent to the initially formed side-on

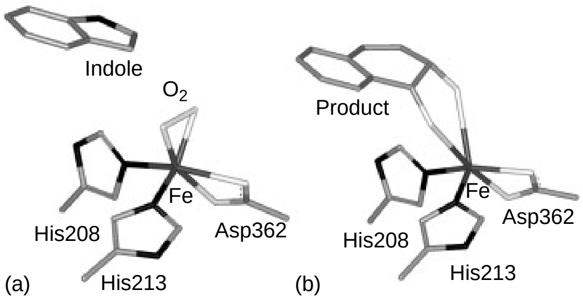

Figure 21 Structurally characterized intermediate species of NDO: (a) Fe·NDO·indole·O_2 (1O7N.pdb), and (b) Fe·NDO·product (1O7P.pdb)

bound dioxygen complex, demonstrating dioxygen attack on substrate. Lastly, the crystal structure of an enzyme-product complex demonstrates that the *cis*-dihydroxylated product coordinates the iron center as a bidentate ligand to the metal center (Figure 21b).[174] Product release occurs only after the two redox active iron sites (the mononuclear and Rieske centers) are reduced, allowing the enzyme to initiate another round of catalysis.

Although early studies on PDO have shown that the oxygenase and the reductase components form an essential complex for catalytic turnover,[183,184] recent studies on NDO[178] and benzoate 1,2-dioxygenase (BzDO)[185] demonstrate that the fully reduced oxygenase component alone is competent to activate O_2. In the absence of substrate, the fully reduced oxygenase reacts slowly with O_2 resulting in the autoxidation of the enzyme. The addition of substrate accelerates this reaction, producing nearly a single turnover of product *cis*-dihydrodiol. The rate of this reaction is in fact more than one order of magnitude faster than the overall catalytic turnover rate, suggesting that other steps control the overall kinetics. At this stage, both the monoiron center and the Rieske cluster are oxidized and the product can only be recovered from the enzyme via a procedure involving thermal denaturation and chemical extraction.[178,185] The tighter binding of the product diol at this stage is not surprising, given the expectation that the Lewis acidic iron(III) center should have a strong affinity for the diol oxygens. Product release could then be triggered by reduction of the oxygenase by the reductase and probably constitutes the rate determining step during catalysis.

The above observations can be considered together to assemble the following mechanistic sequence. The fully reduced enzyme binds the arene substrate to initiate the reaction. O_2 binding followed by electron transfer from the reduced Rieske cluster generates the side-on bound O_2 adduct shown. Studies on NDO with benzene as a substrate analogue[186] show that, the reduction of O_2 can be uncoupled from substrate dihydroxylation, and H_2O_2 is released with no benzene oxidation, presumably the result of protonation of a putative Fe^{III}–OOH intermediate. The fully oxidized NDO has also been shown to undergo a peroxide shunt (*see* ***Iron: Heme Proteins, Mono- & Dioxygenases***), catalyzing the single turnover oxidation of naphthalene with H_2O_2 to afford the corresponding *cis*-(1*R*,2*S*)-1,2-dihydroxy-1,2-dihydronaphthalene product.[187] Isotope labeling studies show almost full incorporation of the two oxygen atoms of the peroxide into the *cis*-diol product. Thus substrate oxidation can be brought about by an iron(III)-peroxo moiety or derivatives thereof.

From the above results, a mechanism for arene dihydroxylation can be formulated (Figure 22). Upon coordination of the substrate, dioxygen binds the iron(II) center in a side-on fashion. This Fe^{III}-η^2-O_2^- species is reduced and protonated to a side-on bound hydroperoxo iron(III) species. The Fe^{III}-η^2-OOH intermediate could then attack the substrate directly to form the (η^1-alkylperoxo)iron species found in an NDO crystal structure,[173] but the chemistry underlying this transformation is difficult to envision. The fact that the O–O bond remains intact suggests a nucleophilic attack of the substrate by the bound peroxide, but how this should come about is not clear. Alternatively, the Fe^{III}-η^2-OOH intermediate may undergo O–O bond cleavage and convert to an electrophilic HO–Fe^V=O species prior to substrate attack. Such a species may be akin to the high-valent *cis*-dioxometal species such as OsO_4, RuO_4 or MnO_4^- well known to effect *cis*-dihydroxylation of olefins.[188,189] The involvement of an

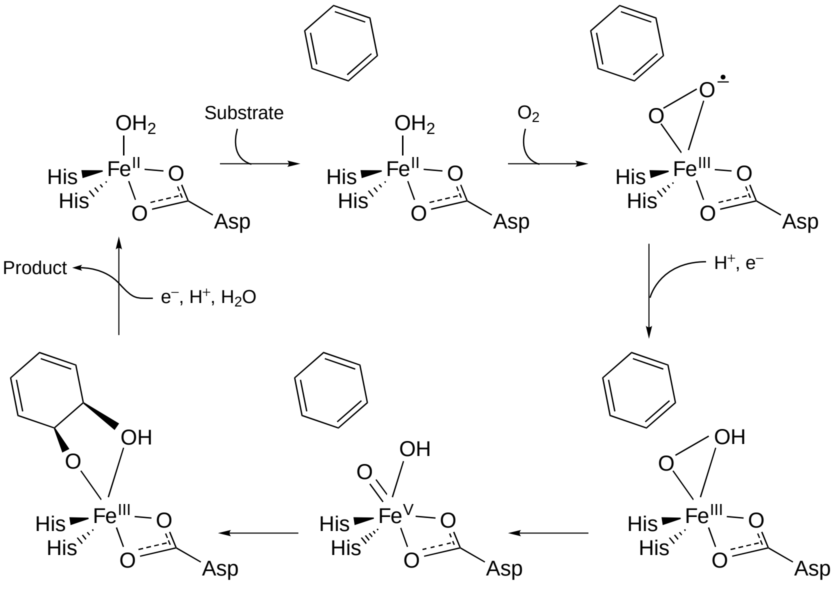

Figure 22 Proposed mechanism for Rieske dioxygenases

iron-oxo species in the catalytic mechanism may be implicated by the incorporation of $H_2{}^{18}O$ into the product. Indeed a small amount of oxygen from water (3–10%) is incorporated into the naphthalene *cis*-diol product in the peroxide shunt studies of Wolfe *et al*.[187] Furthermore Wackett *et al*. have found significant label incorporation from $H_2{}^{18}O$ (70%) in the oxidation of the substrate analogue indane by toluene dioxygenase to 1-indanol.[190] These results argue for the involvement of an intermediate that allows solvent to be incorporated into the product.

Insights have also been provided by the first examples of biomimetic iron complexes that catalyze olefin *cis*-dihydroxylation.[191,192] Using H_2O_2 as an oxidant, complexes exemplified by $[Fe^{II}(TPA)(CH_3CN)_2]^{2+}$ convert olefins stereospecifically to *cis*-diols (and epoxides). A Fe^{III}–OOH intermediate is observed at low temperature and an $HO–Fe^{V}{=}O$ oxidant is implicated by ^{18}O labeling experiments. These results support the mechanism proposed in Figure 22. Interestingly, introduction of 6-methyl substituents on TPA affords a catalyst that incorporates both oxygen atoms of H_2O_2 into the *cis*-diol product. These results reveal a rich reaction landscape that requires further exploration.

9 PERSPECTIVE

In the decade since the publication of the first edition of this encyclopedia, there has been a virtual explosion of X-ray crystallographic information on mononuclear nonheme iron enzymes involved in dioxygen metabolism. In many cases structures are now available for various states of the enzymes, providing a detailed picture of the interactions leading to oxygen binding. Significant progress has also been made in spectroscopic, kinetic, and biomimetic studies leading to the characterization of plausible reaction intermediates. Taken together, this body of information has furthered our understanding of how mononuclear nonheme iron centers activate dioxygen (or process superoxide). Prominent among these developments is the emergence of the 2-His-1-carboxylate facial triad as a recurring structural motif for the active sites of different classes of iron enzymes, demonstrating the versatility of this motif for dioxygen activation. Also significant is the recent characterization of the elusive nonheme $Fe^{IV}=O$ species common to the mechanisms of many of these iron enzymes. The crystallization and spectroscopic investigation of corresponding biomimetic oxoiron(IV) complexes are also providing new opportunities to gain insight into the nature of this key oxidant and how it reacts with substrates. Great strides have been made in the past decade, but a great deal more remains to be learned of how dioxygen is activated by this novel family of mononuclear, nonheme iron enzymes.

10 RELATED ARTICLES

Iron: Heme Proteins, Mono- & Dioxygenases; Iron–Sulfur Proteins; Manganese Proteins with Mono- & Dinuclear Sites.

11 REFERENCES

1. L. Que Jr, in ‘Encyclopedia of Inorganic Chemistry’, eds. R. B. King, J. K. Burdett, R. H. Crabtree, C. M. Lukehart, R. A. Scott, and R. L. Wells, John Wiley & Sons, New York, 1994, p. 1859.
2. A.-F. Miller, in ‘Comprehensive Coordination Chemistry II’, eds. J. A. McCleverty, T. J. Meyer, L. Que Jr, and W. B. Tolman, Elsevier, San Diego, CA, 2004, Vol. 8, p. 479.
3. B. L. Stoddard, P. L. Howell, D. Ringe, and G. N. Petsko, *Biochemistry*, 1990, **29**, 8885.
4. C. K. Vance and A.-F. Miller, *Biochemistry*, 2001, **40**, 13079.
5. M. S. Lah, M. M. Dixon, K. A. Pattridge, W. C. Stallings, J. A. Fee, and M. L. Ludwig, *Biochemistry*, 1995, **34**, 1646.
6. C. K. Vance and A.-F. Miller, *J. Am. Chem. Soc.*, 1998, **120**, 461.
7. F. Rusnak, C. Ascenso, I. Moura, and J. J. Moura, *Methods Enzymol.*, 2002, **349**, 243.
8. D. M. Kurtz Jr and E. D. Coulter, *J. Biol. Inorg. Chem.*, 2002, **7**, 653.
9. I. A. Abreu, A. V. Xavier, J. Le Gall, D. E. Cabelli, and M. J. Teixeira, *J. Biol. Inorg. Chem.*, 2002, **7**, 668.
10. M. W. Adams, F. E. Jenney Jr, M. D. Clay, and M. K. Johnson, *J. Biol. Inorg. Chem.*, 2002, **7**, 647.
11. A. V. Coehlo, P. Matias, V. Fülop, A. Thomson, A. Gonzalez, and M. A. Carrondo, *J. Biol. Inorg. Chem.*, 1997, **2**, 680.
12. A. P. Yeh, Y. Hu, F. E. Jenney Jr, M. W. W. Adams, and D. C. Rees, *Biochemistry*, 2000, **39**, 2499.
13. E. D. Coulter, J. P. Emerson, D. M. Kurtz Jr, and D. E. Cabelli, *J. Am. Chem. Soc.*, 2000, **122**, 11555.
14. M. D. Clay, F. E. Jenney Jr, P. L. Hagedoorn, G. N. George, M. W. W. Adams, and M. K. Johnson, *J. Am. Chem. Soc.*, 2002, **124**, 788.
15. C. Mathé, T. A. Mattioli, O. Horner, M. Lombard, J.-M. Latour, M. Fontecave, and V. Nivière, *J. Am. Chem. Soc.*, 2002, **124**, 4966.
16. O. Horner, J.-M. Mouseca, J.-L. Oddou, C. Jeandey, V. Nivière, T. A. Mattioli, C. Mathé, M. Fontecave, P. Maldivi, P. Bonville, J. A. Halfen, and J.-M. Latour, *Biochemistry*, 2004, **43**, 8815.
17. M. F. Verhagen, W. G. Voorhost, J. A. Kockman, R. B. Wolbert, and W. R. Hagen, *FEBS Lett.*, 1993, **336**, 13.
18. M. J. Nelson and S. P. Seitz, in ‘Active Oxygen in Biochemistry’, eds. J. S. Valentine, C. S. Foote, A. Greenberg, and J. F. Liebman, Chapman & Hall, London, 1995, p. 276.

19. E. H. Oliw, *Prostaglandins Other Lipid Mediat.*, 2002, **68–69**, 313.
20. Y. Zhang, M. S. Gebhard, and E. I. Solomon, *J. Am. Chem. Soc.*, 1991, **113**, 5162.
21. R. C. Scarrow, M. G. Trimitsis, C. P. Buck, G. N. Grove, R. A. Cowling, and M. J. Nelson, *Biochemistry*, 1994, **33**, 15023.
22. T. R. Holman, J. Zhou, and E. I. Solomon, *J. Am. Chem. Soc.*, 1998, **120**, 12564.
23. S. Slappendel, G. A. Velkink, J. F. G. Vleigenthart, R. Aasa, and B. G. Malmstrom, *Biochim. Biophys. Acta*, 1981, **667**, 77.
24. W. Minor, J. Steczko, J. T. Bolin, Z. Otwinowski, and B. Axelrod, *Biochemistry*, 1993, **32**, 6320.
25. J. C. Boyington, B. J. Gaffney, and L. M. Amzel, *Science*, 1993, **260**, 1482.
26. W. Minor, J. Steczko, R. Stec, Z. Otwinowski, J. T. Bolin, R. Walter, and B. Axelrod, *Biochemistry*, 1996, **35**, 10687.
27. E. Skrzypczak-Jankun, L. M. Amzel, B. A. Kroa, and M. O. Funk Jr, *Proteins: Struct., Funct., Genet.*, 1997, **29**, 15.
28. D. R. Tomchick, P. Phan, M. Cymborowski, W. Minor, and T. R. Holman, *Biochemistry*, 2001, **40**, 7509.
29. S. A. Gillmor, A. Villaseñor, R. Fletterick, E. Sigal, and M. F. Browner, *Nat. Struct. Biol.*, 1997, **4**, 1003.
30. E. Skrzypczak-Jankun, R. A. Bross, R. T. Carroll, W. R. Dunham, and M. O. Funk Jr, *J. Am. Chem. Soc.*, 2001, **123**, 10814.
31. M. H. Glickman, S. Cliff, M. Thiemens, and J. P. Klinman, *J. Am. Chem. Soc.*, 1997, **119**, 11357.
32. E. R. Lewis, E. Johansen, and T. R. Holman, *J. Am. Chem. Soc.*, 1999, **121**, 1395.
33. M. J. Nelson, *Biochemistry*, 1988, **27**, 4273.
34. C. R. Goldsmith, R. T. Jonas, and T. D. P. Stack, *J. Am. Chem. Soc.*, 2002, **124**, 83.
35. J. D. Lipscomb and A. M. Orville, in 'Metal Ions in Biological Systems', eds. H. Sigel and A. Sigel, Marcel Dekker, New York, 1992, Vol. 28, p. 243.
36. L. Que Jr, *J. Chem. Educ.*, 1985, **62**, 938.
37. J. W. Whittaker and J. D. Lipscomb, *J. Biol. Chem.*, 1984, **259**, 4487.
38. A. E. True, A. M. Orville, L. L. Pearce, J. D. Lipscomb, and L. Que Jr, *Biochemistry*, 1990, **29**, 10847.
39. D. H. Ohlendorf, A. M. Orville, and J. D. Lipscomb, *J. Mol. Biol.*, 1994, **244**, 586.
40. A. M. Orville, J. D. Lipscomb, and D. H. Ohlendorf, *Biochemistry*, 1997, **36**, 10052.
41. T. E. Elgren, A. M. Orville, K. A. Kelly, J. D. Lipscomb, D. H. Ohlendorf, and L. Que Jr, *Biochemistry*, 1997, **36**, 11504.
42. A. M. Orville, N. Elango, J. D. Lipscomb, and D. H. Ohlendorf, *Biochemistry*, 1997, **36**, 10039.
43. L. Que Jr and R. Y. N. Ho, *Chem. Rev.*, 1996, **96**, 2607.
44. L. Que Jr, J. D. Lipscomb, E. Münck, and J. M. Wood, *Biochim. Biophys. Acta*, 1977, **485**, 60.
45. C. Bull, D. P. Ballou, and S. Otsuka, *J. Biol. Chem.*, 1981, **256**, 12681.
46. T. A. Walsh, D. P. Ballou, R. Mayer, and L. Que Jr, *J. Biol. Chem.*, 1983, **258**, 14422.
47. A. M. Orville and J. D. Lipscomb, *J. Biol. Chem.*, 1993, **268**, 8596.
48. E. C. Wasinger, M. I. Davis, M. Y. M. Pau, A. M. Orville, J. M. Zaleski, B. Hedman, J. D. Lipscomb, K. O. Hodgson, and E. I. Solomon, *Inorg. Chem.*, 2002, **42**, 365.
49. M. Costas, M. P. Mehn, M. P. Jensen, and L. Que Jr, *Chem. Rev.*, 2004, **104**, 939.
50. L. S. White, P. V. Nilsson, L. H. Pignolet, and L. Que Jr, *J. Am. Chem. Soc.*, 1984, **106**, 8312.
51. L. Que Jr, R. C. Kolanczyk, and L. S. White, *J. Am. Chem. Soc.*, 1987, **109**, 5373.
52. D. D. Cox and L. Que Jr, *J. Am. Chem. Soc.*, 1988, **110**, 8085.
53. H. G. Jang, D. D. Cox, and L. Que Jr, *J. Am. Chem. Soc.*, 1991, **113**, 9200.
54. L. D. Eltis and J. T. Bolin, *J. Bacteriol.*, 1996, **178**, 5930.
55. F. H. Vaillancourt, S. Han, P. D. Fortin, J. T. Bolin, and L. D. Eltis, *J. Biol. Chem.*, 1998, **273**, 34887.
56. K. Sugimoto, T. Senda, H. Aoshima, E. Masai, M. Fukuda, and Y. Mitsui, *Structure*, 1999, **7**, 953.
57. Y. Uragami, T. Senda, K. Sugimoto, N. Sato, V. Nagarajan, E. Masai, M. Fukuda, and Y. Mitsui, *J. Inorg. Biochem.*, 2001, **83**, 269.
58. N. Sato, Y. Uragami, T. Nishizaki, Y. Takahashi, G. Sazaki, K. Sugimoto, T. Nonaka, E. Masai, M. Fukuda, and T. Senda, *J. Mol. Biol.*, 2002, **321**, 621.
59. M. W. Vetting, L. P. Wackett, L. Que Jr, J. D. Lipscomb, and D. H. Ohlendorf, *J. Bacteriol.*, 2004, **186**, 1945.
60. E. L. Hegg and L. Que Jr, *Eur. J. Biochem.*, 1997, **250**, 625.
61. L. Que Jr, *Nat. Struct. Biol.*, 2000, **7**, 182.
62. D. M. Arciero, A. M. Orville, and J. D. Lipscomb, *J. Biol. Chem.*, 1985, **260**, 14035.
63. L. Shu, Y.-M. Chiou, A. M. Orville, M. A. Miller, J. D. Lipscomb, and L. Que Jr, *Biochemistry*, 1995, **34**, 6649.
64. Y.-M. Chiou and L. Que Jr, *Inorg. Chem.*, 1995, **34**, 3577.
65. D.-H. Jo, Y.-M. Chiou, and L. Que Jr, *Inorg. Chem.*, 2001, **40**, 3181.
66. F. H. Vaillancourt, C. J. Barbosa, T. G. Spiro, J. T. Bolin, M. W. Blades, R. F. Turner, and L. D. Eltis, *J. Am. Chem. Soc.*, 2002, **124**, 2485.
67. C. A. Tyson, *J. Biol. Chem.*, 1975, **250**, 1765.
68. M. A. Miller and J. D. Lipscomb, *J. Biol. Chem.*, 1996, **271**, 5524.
69. M. F. Reynolds, M. Costas, M. Ito, D.-H. Jo, A. A. Tipton, A. K. Whiting, and L. Que Jr, *J. Biol. Inorg. Chem.*, 2003, **8**, 263.

70. E. L. Spence, M. Kawamukai, J. Sanvoisin, H. Braven, and T. D. H. Bugg, *J. Bacteriol.*, 1996, **178**, 5249.

71. T. D. H. Bugg and G. Lin, *Chem. Commun.*, 2001, **11**, 941.

72. K. L. Eley, P. J. Crowley, and T. D. H. Bugg, *J. Org. Chem.*, 2001, **66**, 2091.

73. D. J. Winfield, Z. Al-Maahrizy, M. Gravestock, and T. D. H. Bugg, *J. Chem. Soc., Perkin Trans.*, 2000, **1**, 3277.

74. P. Siegbahn and F. Haeffner, *J. Am. Chem. Soc.*, 2004, **126**, 8919.

75. T. Funabiki, A. Mizoguchi, T. Sugimoto, S. Tada, M. Tsuji, H. Sakamoto, and S. J. Yoshida, *J. Am. Chem. Soc.*, 1986, **108**, 2921.

76. G. Lin, G. Reid, and T. H. D. Bugg, *Chem. Commun.*, 2000, **13**, 1119.

77. G. Lin, G. Reid, and T. H. D. Bugg, *J. Am. Chem. Soc.*, 2001, **123**, 5030.

78. C. J. Schofield and Z. Zhang, *Curr. Opin. Struct. Biol.*, 1999, **9**, 722.

79. A. G. Prescott and M. D. Lloyd, *Nat. Prod. Rep.*, 2000, **17**, 367.

80. H. M. Hanauske-Abel and A. M. Popowicz, *Curr. Med. Chem.*, 2003, **10**, 1005.

81. F. Fukumori and R. P. Hausinger, *J. Biol. Chem.*, 1993, **268**, 24311.

82. E. L. Hegg, A. K. Whiting, R. E. Saari, J. McCracken, R. P. Hausinger, and L. Que Jr, *Biochemistry*, 1999, **38**, 16714.

83. P. Ø. Falnes, R. F. Johansen, and E. Seeberg, *Nature*, 2002, **419**, 178.

84. S. C. Trewick, T. F. Henshaw, R. P. Hausinger, T. Lindahl, and B. Sedgwick, *Nature*, 2002, **419**, 174.

85. P. A. Aas, M. Otterlei, P. Ø. Falnes, C. B. Vågbø, F. Skorpen, M. Akbari, O. Sundheim, M. Bjørås, G. Slupphaug, E. Seeberg, and H. E. Krokan, *Nature*, 2003, **421**, 859.

86. S. P. Salowe, E. N. Marsh, and C. A. Townsend, *Biochemistry*, 1990, **29**, 6499.

87. J. E. Baldwin, R. M. Adlington, N. P. Crouch, C. J. Schofield, N. J. Turner, and R. T. Aplin, *Tetrahedron*, 1991, **47**, 9881.

88. J. E. Baldwin and E. Abraham, *Nat. Prod. Rep.*, 1988, **5**, 129.

89. I. J. Clifton, L. X. Doan, M. C. Sleeman, M. Topf, H. Suzuki, R. C. Wilmouth, and C. J. Schofield, *J. Biol. Chem.*, 2003, **278**, 20843.

90. J. R. van der Ploeg, M. A. Weiss, E. Saller, H. Nashimoto, N. Saito, M. Kertesz, and T. Leisinger, *J. Bacteriol.*, 1996, **178**, 5438.

91. A. K. White and W. W. Metcalf, *J. Biol. Chem.*, 2002, **277**, 38262.

92. M. Ivan, K. Kondo, H. Yang, W. Kim, J. Valiando, M. Ohh, A. Salic, J. M. Asara, W. S. Lane, and W. G. Kaelin Jr, *Science*, 2001, **292**, 449.

93. P. Jaakkola, D. R. Mole, Y. M. Tian, M. I. Wilson, J. Gielbert, S. J. Gaskell, A. von Kriegsheim, H. F. Hebestreit, M. Mukherji, C. J. Schofield, P. H. Maxwell, C. W. Pugh, and P. J. Ratcliffe, *Science*, 2001, **292**, 468.

94. D. Lando, D. J. Peet, J. J. Gorman, D. A. Whelan, M. L. Whitelaw, and R. K. Bruick, *Genes Dev.*, 2002, **16**, 1466.

95. G. L. Semenza, *Annu. Rev. Cell Dev. Biol.*, 1999, **15**, 551.

96. A. L. Kung, S. Wang, J. M. Klco, W. G. Kaelin Jr, and D. M. Livingston, *Nat. Med.*, 2000, **6**, 1335.

97. P. M. J. Clement, H. M. Hanauske-Abel, E. C. Wolff, H. K. Kleinman, and M. H. Park, *Int. J. Cancer*, 2002, **100**, 491.

98. B. Lindblad, G. Lindstedt, and S. Lindstedt, *J. Am. Chem. Soc.*, 1970, **92**, 7446.

99. O. W. Choroba, D. H. Williams, and J. B. Spencer, *J. Am. Chem. Soc.*, 2000, **122**, 5389.

100. P. J. Sabourin and L. L. Bieber, *J. Biol. Chem.*, 1982, **257**, 7468.

101. E. Holme, *Biochemistry*, 1975, **14**, 4999.

102. R. Myllylä, L. Tuderman, and K. I. Kivirikko, *Eur. J. Biochem.*, 1977, **80**, 349.

103. L. Tuderman, R. Myllylä, and K. I. Kivirikko, *Eur. J. Biochem.*, 1977, **80**, 341.

104. M. Rundgren, *J. Biol. Chem.*, 1977, **252**, 5094.

105. U. Puistola, T. M. Turpeenniemi-Hujanen, R. Myllylä, and K. I. Kivirikko, *Biochim. Biophys. Acta*, 1980, **611**, 51.

106. E. De Carolis and V. De Luca, *J. Biol. Chem.*, 1993, **268**, 5504.

107. K. Johnson-Winters, V. M. Purpero, M. Kavana, T. Nelson, and G. R. Moran, *Biochemistry*, 2003, **42**, 2072.

108. J. M. Elkins, M. J. Ryle, I. J. Clifton, J. C. D. Hotopp, J. S. Lloyd, N. L. Burzlaff, J. E. Baldwin, R. P. Hausinger, and P. L. Roach, *Biochemistry*, 2002, **41**, 5185.

109. Z. Zhang, J. Ren, D. K. Stammers, J. E. Baldwin, K. Harlos, and C. J. Schofield, *Nat. Struct. Biol.*, 2000, **7**, 127.

110. Z. Zhang, J.-S. Ren, K. Harlos, C. H. McKinnon, I. J. Clifton, and C. J. Schofield, *FEBS Lett.*, 2002, **517**, 7.

111. J. C. Price, E. W. Barr, B. Tirupati, J. M. Bollinger Jr, and C. Krebs, *Biochemistry*, 2003, **42**, 7497.

112. J. C. Price, E. W. Barr, T. E. Glass, C. Krebs, and J. M. Bollinger Jr, *J. Am. Chem. Soc.*, 2003, **125**, 13008.

113. D. A. Proshlyakov, T. F. Henshaw, G. R. Monterosso, M. J. Ryle, and R. P. Hausinger, *J. Am. Chem. Soc.*, 2004, **136**, 1022.

114. P. Riggs-Gelasco, J. C. Price, R. B. Guyer, J. H. Brehm, E. W. Barr, J. M. Bollinger Jr, and C. Krebs, *J. Am. Chem. Soc.*, 2004, **126**, 8108.

115. E. H. Ha, R. Y. N. Ho, J. F. Kisiel, and J. S. Valentine, *Inorg. Chem.*, 1995, **34**, 226.

116. E. L. Hegg, R. Y. N. Ho, and L. Que Jr, *J. Am. Chem. Soc.*, 1999, **121**, 1972.

117. M. P. Mehn, K. Fujisawa, E. L. Hegg, and L. Que Jr, *J. Am. Chem. Soc.*, 2003, **125**, 7828.

118. J.-U. Rohde, J. H. In, M. H. Lim, W. W. Brennessel, M. R. Bukowski, A. Stubna, E. Münck, W. Nam, and L. Que Jr, *Science*, 2003, **299**, 1037.
119. M. H. Lim, J.-U. Rohde, A. Stubna, M. R. Bukowski, M. Costas, R. Y. N. Ho, E. Münck, W. Nam, and L. Que Jr, *Proc. Natl. Acad. Sci. U.S.A.*, 2003, **100**, 3665.
120. J. Kaizer, M. Costas, and L. Que Jr, *Angew. Chem., Int. Ed. Engl.*, 2003, **42**, 3671.
121. J. Kaizer, E. J. Klinker, N. Y. Oh, J.-U. Rodhe, W. J. Song, A. Stubna, J. Kim, W. Nam, E. Münck, and L. Que Jr, *J. Am. Chem. Soc.*, 2004, **126**, 472.
122. A. Decker, J.-U. Rohde, L. Que Jr, and E. I. Solomon, *J. Am. Chem. Soc.*, 2004, **126**, 5378.
123. M. S. Seo, J.-H. In, S. O. Kim, N. Y. Oh, J. Hong, J. Kim, L. Que Jr, and W. Nam, *Angew. Chem., Int. Ed. Engl.*, 2004, **43**, 2417.
124. W. A. Schenk, *Angew. Chem., Int. Ed. Engl.*, 2000, **39**, 3409.
125. P. L. Roach, I. J. Clifton, V. Fülöp, K. Harlos, G. J. Barton, J. Hajdu, I. Andersson, C. J. Schofield, and J. E. Baldwin, *Nature*, 1995, **375**, 700.
126. P. L. Roach, I. J. Clifton, C. M. H. Hensgens, N. Shibata, A. J. Long, R. W. Strange, S. S. Hasnain, C. J. Schofield, J. E. Baldwin, and J. Hajdu, *Eur. J. Biochem.*, 1996, **242**, 736.
127. C. R. Randall, Y. Zang, A. E. True, L. Que Jr, J. M. Charnock, C. D. Garner, Y. Fujishima, C. J. Schofield, and J. E. Baldwin, *Biochemistry*, 1993, **32**, 6664.
128. A. M. Orville, V. J. Chen, A. Kriauciunas, M. R. Harpel, B. G. Fox, E. Münck, and J. D. Lipscomb, *Biochemistry*, 1992, **31**, 4602.
129. P. L. Roach, I. J. Clifton, C. M. Hensgen, N. Shibata, C. J. Schofield, J. Hajdu, and J. E. Baldwin, *Nature*, 1997, **387**, 827.
130. J. E. Baldwin and M. Bradley, *Chem. Rev.*, 1990, **90**, 1079.
131. N. I. Burzlaff, P. J. Rutledge, I. J. Clifton, C. M. H. Hensgens, M. Pickford, R. M. Adlington, P. L. Roach, and J. E. Baldwin, *Nature*, 1999, **401**, 721.
132. J. M. Ogle, I. J. Clifton, P. J. Rutledge, J. M. Elkins, N. I. Burzlaff, R. M. Adlington, P. L. Roach, and J. E. Baldwin, *Chem. Biol.*, 2001, **8**, 1231.
133. J. E. Baldwin, in 'Recent Advances in the Chemistry of beta-Lactam Antibiotics', eds. P. H. Bentley and R. Southgate, Royal Society of Chemistry, London, 1989, p. 1.
134. J. E. Baldwin, R. M. Adlington, C. J. Schofield, N. P. Crouch, and H.-H. Ting, *J. Chem. Soc., Chem. Commun.*, 1987, **20**, 1556.
135. M. Wirstam and P. E. M. Siegbahn, *J. Am. Chem. Soc.*, 2000, **122**, 8539.
136. T. J. Kappock and J. P. Caradonna, *Chem. Rev.*, 1996, **96**, 2659.
137. P. F. Fitzpatrick, *Biochemistry*, 2003, **42**, 14083.
138. T. Flatmark and R. C. Stevens, *Chem. Rev.*, 1999, **99**, 2137.
139. O. A. Andersen, T. Flatmark, and E. Hough, *J. Mol. Biol.*, 2001, **314**, 279.
140. D. A. Andersen, T. Flatmark, and E. Hough, *J. Mol. Biol.*, 2002, **320**, 1095.
141. O. A. Andersen, A. J. Stokka, T. Flatmark, and E. Hough, *J. Mol. Biol.*, 2003, **333**, 747.
142. T. A. Dix, G. E. Bollag, P. L. Domanico, and S. J. Benkovic, *Biochemistry*, 1985, **24**, 2955.
143. K. E. Loeb, T. E. Westre, J. J. Kappock, N. Mitié, E. Glasfeld, J. P. Caradonna, B. Hedman, K. O. Hodgson, and E. I. Solomon, *J. Am. Chem. Soc.*, 1997, **119**, 1901.
144. J. N. Kemsley, N. Mitic, K. L. Zaleski, J. P. Caradonna, and E. I. Solomon, *J. Am. Chem. Soc.*, 1999, **121**, 1528.
145. E. I. Solomon, T. C. Brunold, M. I. Davis, J. N. Kemsley, S.-K. Lee, N. Lehnert, F. Neese, A. J. Skulan, Y.-S. Yang, and J. Zhou, *Chem. Rev.*, 2000, **100**, 235.
146. P. F. Fitzpatrick, *Annu. Rev. Biochem.*, 1999, **68**, 355.
147. H. U. Siegmund and S. Kauffman, *J. Biol. Chem.*, 1991, **266**, 2903.
148. M. Sono, M. P. Roach, E. D. Coulter, and J. H. Dawson, *Chem. Rev.*, 1996, **96**, 2841.
149. W. A. Francisco, G. Tian, P. F. Fitzpatrick, and J. P. Klinman, *J. Am. Chem. Soc.*, 1998, **120**, 4057.
150. A. Bassan, M. R. A. Blomberg, and P. E. M. Siegbahn, *Eur. Chem. J.*, 2003, **9**, 106.
151. J. P. Klinman, *J. Biol. Inorg. Chem.*, 2001, **6**, 1.
152. V. Massey, *J. Biol. Chem.*, 1994, **269**, 22459.
153. J. N. Kemsley, E. C. Wasinger, S. Datta, N. Mitic, T. Acharya, B. Hedman, J. P. Caradonna, K. O. Hodgson, and E. I. Solomon, *J. Am. Chem. Soc.*, 2003, **125**, 5677.
154. N. Lehnert, K. Fujisawa, and E. I. Solomon, *Inorg. Chem.*, 2003, **42**, 469.
155. P. J. Hillas and P. F. Fitzpatrick, *Biochemistry*, 1996, **35**, 6969.
156. P. F. Fitzpatrick, *Biochemistry*, 1991, **30**, 3658.
157. G. R. Moran, A. Derecskei-Kovacs, P. J. Hillas, and P. F. Fitzpatrick, *J. Am. Chem. Soc.*, 2000, **122**, 4535.
158. G. Guroff, J. W. Daly, D. M. Jerina, J. Renson, B. Witkop, and S. Udenfriend, *Science*, 1967, **157**, 1524.
159. P. F. Fitzpatrick, *J. Am. Chem. Soc.*, 1994, **116**, 1133.
160. M. P. Jensen, S. J. Lange, M. P. Mehn, E. L. Que, and L. Que Jr, *J. Am. Chem. Soc.*, 2003, **125**, 2113.
161. D. T. Gibson ed., 'Microbial Degradation of Organic Compounds', Marcel Dekker, New York, 1984.
162. D. T. Gibson and R. E. Parales, *Curr. Opin. Biotechnol.*, 2000, **11**, 236.
163. K. N. Timmins and D. H. Pieper, *Trends Biotechnol.*, 1999, **17**, 201.
164. B. D. Ensley, B. J. Ratzkin, T. D. Osslund, M. J. Simon, L. P. Wackett, and D. T. Gibson, *Science*, 1983, **222**, 167.

165. T. Huclicky, X. Tian, K. Königsberger, R. Maurya, J. Rouden, and B. Fan, *J. Am. Chem. Soc.*, 1996, **118**, 10752.
166. T. Hudlicky, D. Gonzalez, and D. T. Gibson, *Aldrichimica Acta*, 1999, **32**, 35.
167. D. R. Boyd and G. N. Sheldrake, *Nat. Prod. Rep.*, 1998, **15**, 309.
168. S. M. Resnick and D. T. Gibson, *J. Ind. Microbiol.*, 1996, **17**, 438.
169. K. Lee and D. T. Gibson, *J. Bacteriol.*, 1996, **289**, 3353.
170. C. C. Lange and L. P. Wackett, *J. Bacteriol.*, 1997, **179**, 3858.
171. D. T. Gibson, S. M. Resnick, K. Lee, J. M. Brand, D. S. Torok, L. P. Wackett, M. J. Schocken, and B. E. Haigler, *J. Bacteriol.*, 1995, **177**, 2615.
172. B. Kauppi, K. Lee, E. Carredano, R. E. Parales, D. T. Gibson, H. Eklund, and S. Ramaswamy, *Structure*, 1998, **6**, 571.
173. E. Carredano, A. Karlsson, B. Kauppi, D. Choudhury, R. E. Parales, J. V. Parales, K. Lee, D. T. Gibson, H. Eklund, and S. Ramaswamy, *J. Mol. Biol.*, 2000, **296**, 701.
174. A. Karlsson, J. V. Parales, R. E. Parales, D. T. Gibson, H. Eklund, and S. Ramaswamy, *Science*, 2003, **299**, 1039.
175. D. Kuila, J. R. Schoonover, R. B. Dyer, C. J. Batie, D. P. Ballou, J. A. Fee, and W. H. Woodruff, *Biochim. Biophys. Acta*, 1992, **1140**, 175.
176. E. G. Pavel, L. J. Martins, W. R. Ellis Jr, and E. I. Solomon, *Chem. Biol.*, 1994, **1**, 173.
177. E. I. Solomon, A. Decker, and N. Lehnert, *Proc. Natl. Acad. Sci. U.S.A.*, 2003, **100**, 3589.
178. M. D. Wolfe, J. V. Parales, D. T. Gibson, and J. D. Lipscomb, *J. Biol. Chem.*, 2001, **276**, 1945.
179. T.-C. Yang, M. D. Wolfe, M. B. Neibergall, Y. Mekmouche, J. D. Lipscomb, and B. M. Hoffman, *J. Am. Chem. Soc.*, 2003, **125**, 2034.
180. T.-C. Yang, M. D. Wolfe, M. B. Neibergall, Y. Mekmouche, J. D. Lipscomb, and B. M. Hoffman, *J. Am. Chem. Soc.*, 2003, **125**, 7056.
181. G. Roelfes, V. Vrajmisu, K. Chen, R. Y. N. Ho, J.-U. Rohde, C. Zondervan, R. M. la Crois, E. P. Schudde, M. Lutz, A. L. Spek, R. Hage, B. L. Feringa, E. Münck, and L. Que Jr, *Inorg. Chem.*, 2003, **42**, 2639.
182. T. Chishiro, Y. Shimazaki, F. Tani, Y. Tachi, Y. Naruta, S. Karasawa, S. Hayami, and Y. Maeda, *Angew. Chem., Int. Ed. Engl.*, 2003, **42**, 2788.
183. C. J. Batie, E. LaHai, and D. P. Ballou, *J. Biol. Chem.*, 1987, **262**, 1510.
184. D. Ballou and C. Batie, *Prog. Clin. Biol. Res.*, 1988, **274**, 211.
185. M. D. Wolfe, D. J. Altier, A. Stubna, C. V. Popescu, E. Münck, and J. D. Lipscomb, *Biochemistry*, 2002, **41**, 9611.
186. S.-K. Lee and J. D. Lipscomb, *Biochemistry*, 1999, **38**, 4423.
187. M. D. Wolfe and J. D. Lipscomb, *J. Biol. Chem.*, 2003, **278**, 829.
188. M. Schröder, *Chem. Rev.*, 1980, **80**, 187.
189. D. G. Lee and T. Chen, *J. Am. Chem. Soc.*, 1989, **111**, 7534.
190. L. P. Wackett, L. D. Kwart, and D. T. Gibson, *Biochemistry*, 1988, **27**, 1360.
191. K. Chen, M. Costas, J. Kim, A. K. Tipton, and L. Que Jr, *J. Am. Chem. Soc.*, 2002, **124**, 3026.
192. K. Chen, M. Costas, and L. Que Jr, *J. Chem. Soc., Dalton Trans.*, 2002, **5**, 672.

Acknowledgments

Lawrence Que’s research program on mononuclear nonheme iron enzymes has been generously supported by the National Institutes of Health (GM-33162). Joseph P. Emerson Mark P. Mehn were respectively supported by a National Institute of Health postdoctoral fellowship (GM-72287) and predoctoral traineeship (GM-08700).

Iron Proteins for Storage & Transport & their Synthetic Analogs

Allison Lewin, Nick E. Le Brun & Geoffrey R. Moore
University of East Anglia, Norwich, UK

1 Introduction 1
2 Ferric-siderophore Receptors 1
3 Animal Transferrins 3
4 Microbial Transferrin-like Proteins 5
5 Protein-mediated Absorption of Dietary Iron 7
6 Other Iron Transport Systems 7
7 Ferritins 7
8 Dps 14
9 Hemosiderin 15
10 Frataxin 15
11 Hemopexin 16
12 Hemophores 17
13 Related Articles 18
14 References 18

1 INTRODUCTION

Iron is an essential micronutrient (*see* ***Nutritional Aspects of Metals & Trace Elements***) but in order to obtain sufficient iron and then to handle it in a safe way, biological organisms have evolved complex transport proteins for iron. A major reason for this is that iron bound to low molecular weight ligands can be highly toxic owing to its ability to catalyze Fenton-type reactions, which produce free radicals, as in reactions (1) and (2) below.

$$Fe^{2+} + O_2 \longrightarrow Fe^{3+} + O_2^{\bullet -} \qquad (1)$$

$$Fe^{2+} + H_2O_2 \longrightarrow Fe^{3+} + OH^{\bullet} + OH^{-} \qquad (2)$$

These free radicals can cause DNA damage and eventually lead to cell death. Another problem is that although iron is abundant in the environment, it is usually present in insoluble forms. Microorganisms and plants overcome this obstacle by a variety of iron uptake systems, which actively recruit iron and transport it back to the organism. Multicellular animals acquire iron through their diet, but still need mechanisms to absorb the iron from their digestive systems and transport it to its place of use. Proteins for iron storage are another common necessity, not only as a means of conserving a hard-won resource, but also to prevent oxidative damage; the latter is particularly important in organisms that lack a pathway for iron excretion, such as humans.

All iron transport and storage proteins share a common requirement: they need to keep the iron in a soluble and safe form to prevent Fenton chemistry as described by equations (1) and (2). Both types of proteins also need to bind iron tightly, and the transport proteins in particular need to be able to release the metal when required. In the present article we will concentrate on chemically well-characterized iron transport and storage proteins with a focus on their structural and mechanistic features. We shall consider proteins that transport heme as well as proteins that transport nonheme iron, recognizing, as Baker *et al.*[1] have noted, that there are common structural and mechanistic principles operating in such proteins. There are many other proteins involved in iron metabolism other than those we describe however. Many of the systems we discuss are controlled at the transcriptional or translational level by iron-responsive proteins, such as the ferric uptake regulatory protein (FUR) in bacteria and the iron-responsive element binding protein in eukaryotes (*see* ***Metalloregulation***). Iron trafficking with cells must also involve molecules apart from the proteins we have discussed, but despite chaperone proteins for other transition metal ions having been identified and well-characterized (*see* ***Metallochaperones & Metal Ion Homeostasis***), unambiguous identification of similar chaperone proteins for iron has not been reported.

2 FERRIC-SIDEROPHORE RECEPTORS

In times of iron deficiency, many bacteria and fungi release low molecular weight chelators called siderophores (*see* ***Iron Transport: Siderophores***). These molecules bind ferric iron tightly and the ferric-siderophore complexes are then transported into the cell by a system of uptake proteins. The first stage in the uptake process involves an outer membrane receptor specific to each siderophore. One of the best characterized of these receptors is FhuA,[2] the ferrichrome uptake receptor of *E. coli*, and we will describe this in detail. However, though other ferric-siderophore complexes are taken up by cells, and their iron released by systems similar to those of ferrichrome, their mechanisms may vary from those of ferrichrome in some respects. FepA[3] and FecA[4] are two of the outer membrane ferric-siderophore receptors that have recently been structurally characterized.

2.1 Structure of Fhua

FhuA has two domains that fold independently of one another[2] (Figure 1). The C-terminal domain has 22 antiparallel β-strands, which form a β-barrel that spans the outer

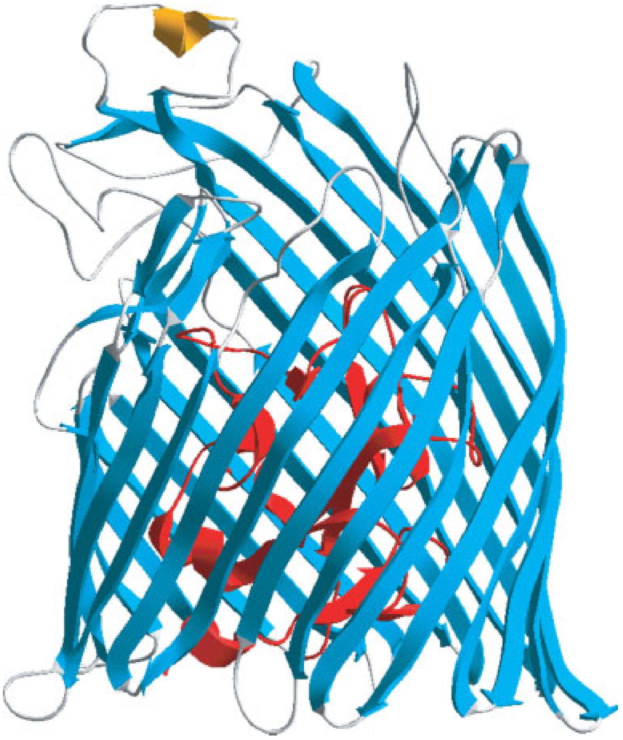

Figure 1 Crystal structure of apo FhuA from *E. coli*. The plug domain is shown in red. Figure created using pdb coordinates 1by3[2]

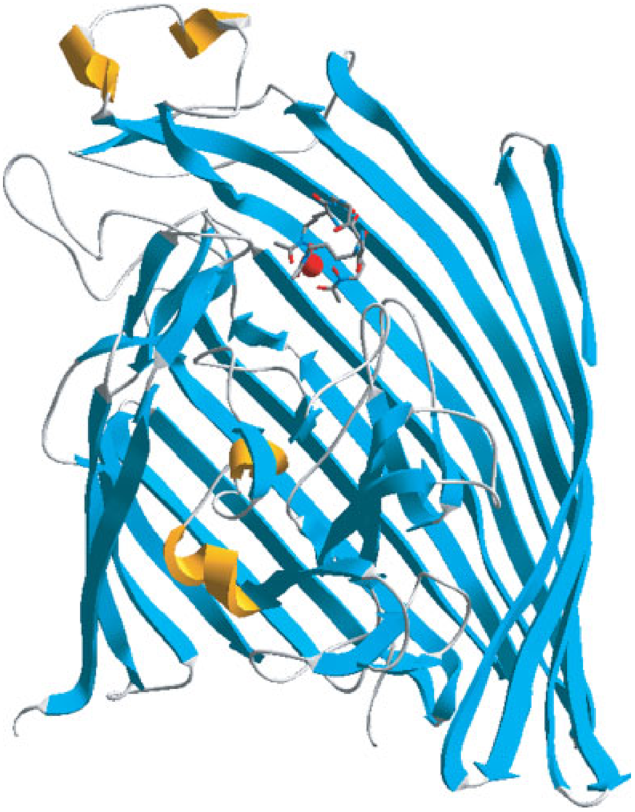

Figure 2 Ferrichrome bound to FhuA. The iron atom is shown as a red sphere, and part of the β-barrel has been removed for clarity. Figure created using pdb coordinates 1by5[2]

membrane. The N-terminal domain of the protein forms a plug, which is positioned within the β-barrel on the periplasmic side of the membrane. This plug domain consists of a mixed 4-stranded β-sheet interspersed with four α-helices. The outer membrane receptors for ferric citrate and ferric enterobactin, FepA, and FecA, respectively, have similar structures to that of FhuA,[3,4] and a β-barrel structure is present in all bacterial outer membrane proteins characterized to date.[5]

The crystal structure of FhuA bound to the iron ligand ferrichrome has also been determined.[2] This shows that the ferric-siderophore complex binds inside the barrel above the plug, forming hydrogen bonds and van der Waals interactions with residues within the plug domain and with the β-strands of the barrel (Figure 2).

2.2 Iron Transport Into the Cell

The N-terminus of the plug domain appears to be disordered.[2] This region contains the TonB box, a stretch of 7 residues that interact with the C-terminal domain of the periplasmic protein TonB. The TonB box has the consensus sequence (Asp or Glu)-Thr-(hydrophobic residue)$_2$-Val-(Ser or Thr)-Ala. The disorder in this region of FhuA means that the TonB box does not appear in the crystal structure, and it is likely to extend into the periplasm to allow binding of TonB, as seen for FepA.[3] TonB interacts with the ExbB-ExbD system, which allows the transfer of chemiosmotic energy from the cytoplasmic membrane to the TonB-dependent outer membrane receptor, driving transport of the ferric siderophore across the outer membrane. The ExbB-ExbD complex charges TonB with conformational energy and promotes its binding to the TonB binding epitope in the plug domain of FhuA. The stored energy is then transduced to FhuA, which drives a conformational change that reduces the ligand binding affinity and leads to the Fe(III)-siderophore complex passing through the outer membrane and into the periplasm. Chemical details of this passage are unclear and several possibilities have been discussed, including that the complex diffuses through an aqueous channel in the outer membrane formed by the β-barrel.[6] Recently, evidence has been provided from studies of amonabactin-mediated iron transport in *Aeromonas hydrophila* for a ‘shuttle’ mechanism in which free ferric siderophores interact with apo siderophores bound to their receptors and transfer iron to the receptor-bound molecule.[7] This attractive proposal may be the route by which other outer membrane receptors operate.

Once in the periplasm the Fe(III)-siderophore complex is bound by a specific protein, which in the case of ferrichrome is FhuD. FhuD has a fold different from other periplasmic binding proteins, and although it is bilobal, the two lobes are connected by an α-helix rather than a flexible linker.[8] The reduced flexibility caused by this, coupled with hydrophobic contacts between the two lobes, appears to result in a smaller conformational change than that seen in the binding mechanisms of other periplasmic binding proteins.[8] The Fe(III)-siderophore complex binds in a negatively charged cleft between the lobes that has a localized positive region that interacts with carbonyls of the hydroxamate. There are fewer hydrogen bonds and hydrophobic contacts between FhuD and the siderophore than seen for FhuA, and this may contribute to the lower specificity of FhuD, which is able to transport other ferric hydroxamates in addition to ferrichrome, including coprogen and aerobactin.[8] Note that in both the FhuA and FhuD structures, ferrichrome binds to the protein through contacts with its organic component and not through coordination to the Fe(III) ion.

FhuD delivers the ferric-siderophore complex to the FhuBC complex in the cytoplasmic membrane.[8] FhuB is an intrinsic cytoplasmic membrane protein through which the iron complex can pass, driven by energy supplied by ATP hydrolysis catalyzed by the ATPase FhuC. Ferrous iron may be released from the hydroxamate via reduction by the reductase FhuF, which is loosely associated with the cytoplasmic membrane and, like FhuD, appears to have a lower specificity than FhuA and is active with coprogen and ferrichrome.[9]

3 ANIMAL TRANSFERRINS

Transferrins are Fe(III)-carrying proteins found in the bodily fluids of vertebrates and some invertebrates. The group includes serum transferrin and ovotransferrin, found in blood and avian egg white respectively, and lactoferrin, which is found in milk.[10] The transferrin family have a general bacteriostatic role in that iron is safely sequestered by the protein and is therefore unavailable to invading pathogenic bacteria. Pathogens have of course evolved methods to try and circumvent this problem; transferrin receptors have been identified on the outer membranes of bacteria such as *Neisseria meningitidis* and *Hemophilus influenzae*, thus allowing them to use host transferrins as an iron source.[11,12] Not only do *N. meningitidis* and *H. influenzae* scavenge iron from host transferrin but they also have transferrin-like iron transport proteins in their periplasms; which have been named Ferric Binding Proteins (Fbps).[13,14] We shall consider animal transferrins separately from Fbps because despite their evident similarities, there are distinct chemical differences between them.

Serum transferrin has a more specialized function than simply iron sequestration, transporting iron from sources of iron in the body (e.g. after absorption through the gut or degradation of redundant iron-containing molecules) to its point of use or storage.[15] There are numerous cell types with a high requirement for iron, such as immature erythroid cells, which synthesize hemoglobin in bone marrow, placental tissue, and rapidly dividing cells. All of these express particularly high levels of the transferrin receptor.[16] Transferrins are also able to bind other metal ions,[17] some of which (e.g. Al(III) and Ga(III)) may be physiologically important.

3.1 Structure

All the transferrins crystallized to date share a common structure,[18] an example of which is shown in Figure 3. The protein has two structurally homologous lobes of roughly 330 residues each, with a high sequence identity between them. Each lobe comprises two domains with a central mixed β-sheet surrounded by α-helices. Between the domains is a cleft in which the metal ion binding site contained in each lobe is situated. One ferric ion binds to each site, with a carbonate ion binding concomitantly with each metal.

The fold of the transferrin protein resembles those of microbial periplasmic binding proteins that transport small solute molecules (such as sugars, amino acids, and other metabolites) and Fbp.[18,20] These structural studies indicate an intriguing combination of divergent and convergent evolutionary relationships between animal transferrins and Fbps,[20,21] though these are beyond the scope of this article. They also suggest common features to their mechanisms of action; in particular, that a ‘Venus fly trap’ mechanism is in operation, whereby the apo protein adopts an open conformation that hinges closed upon binding iron. However, the observation of a closed conformation for some apo-lactoferrins suggests that in solution the apo protein is in equilibrium between its open and closed forms.[22] In this case, Fe(III) binding may then displace the equilibrium to the closed form.

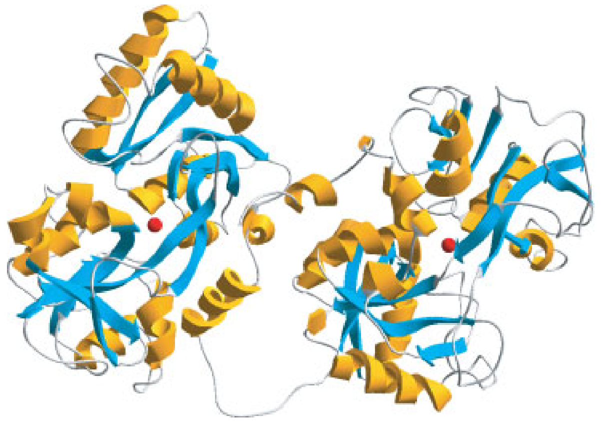

Figure 3 Crystal structure of rabbit transferrin. Bound iron atoms are shown as red spheres. Figure created using pdb coordinates 1jnf[19]

3.2 Iron Binding

The two iron-binding sites in most transferrins are similar to each other, with each consisting of two tyrosines, one aspartic acid and one histidine. In some transferrins, however, conservation of the binding site residues is reduced; for example, cockroach transferrin lacks the histidine in the N-lobe binding site, while several other invertebrate transferrins lack conserved binding site residues in the C-lobe. This may contribute to a lack of binding in the C-lobe of invertebrate transferrins.[23]

The charge on the bound ferric ion is balanced by the deprotonated tyrosine and aspartic acid residues, while the charge on the carbonate ion is balanced by binding to the positively charged arginine and the N-terminus of an α-helix.[24] This results in an overall charge-balanced complex in which the iron is ligated by two oxygens from the carbonate ion in addition to the protein ligands, leaving the metal in an octahedral environment. Though carbonate is the physiological anion, in vitro others, such as oxalate and nitrilotriacetic acid, can replace it.[25,26]

Using iron chelated to small ligands it has been shown that the carbonate ion binds to the protein first, attracted to a positively charged arginine residue close to the metal binding site, followed by the binding of the Fe(III)-chelate complex to the two tyrosine residues. A conformational change then takes place to close the protein over the bound iron, leading to loss of the chelator and completion of the interactions between the Fe(III) and its remaining amino acid ligands.[27] The carbonate anion forms a hydrogen bond network to the protein backbone (Figure 4), which helps stabilize the closed conformation of the iron-loaded protein.

Reported stability constants (*see* ***Stability Constants & their Determination***) for metal ion binding to transferrins are generally conditional association constants under specified conditions as there are many factors affecting their magnitudes: temperature, pH, bicarbonate concentration, and ionic strength among them.[17,28,29] A further complication with determining stability constants is that the properties of the metal ion donors are important and their association equilibria need to be considered in the analysis. Aisen *et al*.[28] showed that the two iron-binding sites on human serum transferrin had slightly different binding affinities for Fe(III), consistent with a small degree of negative cooperativity in iron binding. At 25 °C, pH 7.4 and 2×10^{-4} M $NaHCO_3$, the macroscopic association constants for Fe(III) binding to transferrin are $\geq 10^{20}\,M^{-1}$. The binding affinities of the two sites change their relative order under some conditions and kinetic factors are important, so that site loading varies greatly depending upon conditions.[28–30] For example, some iron donors preferentially load the N-lobe site and some the C-lobe site. Once loaded to produce monoferric transferrin, kinetic barriers inhibit the equilibrium distribution expected from consideration of the intrinsic site association constants.

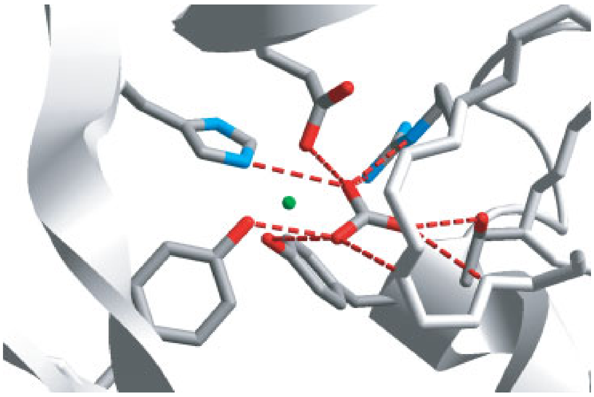

Figure 4 The iron-binding site of the transferrin N-lobe showing hydrogen bonds to the carbonate ion. The iron atom is shown as a small green sphere; and for clarity bonds involving the iron atom are not shown. Figure created using pdb coordinates 1jnf[19]

The $Fe^{3+/2+}$ reduction potentials for holo-transferrin have been difficult to determine because of their low values and the need to take account of the dissociation of Fe(II) from diferrous-transferrin. This has been estimated[31] from the association constant for Fe(II) binding to transferrin at pH 7.4, $\sim 10^6\,M^{-1}$, which yields reduction potentials < -500 mV at pH 7.4 for the C-terminal and N-terminal sites of human serum transferrin, and probably more negative potentials at the lower pH present in the endosome where iron is released.[32,33]

It is not known whether other proteins are involved in loading transferrin with iron in vivo, though in vitro apo transferrin on its own can bind and oxidize ferrous iron rapidly.[34] A role for the copper-containing protein ceruloplasmin (*see* ***Copper Proteins: Oxidases***) has been suggested for iron loading of transferrin in vivo[35] as ceruloplasmin is known from studies of patients with aceruloplasminemia[36,37] and genetic disruption studies[38] to be involved in iron metabolism, catalyzes the oxidation of Fe(II), and no other function has been convincingly demonstrated for it.[39] However, there is no unambiguous physiological evidence pointing to such a role, though ceruloplasmin does form a complex with lactoferrin.[40]

3.3 Iron Transport Into the Cell and Release From Transferrin

As noted above, iron-loaded serum transferrin has the role of transporting Fe(III) to cells requiring it. Once it reaches a target cell, it binds to the transferrin receptor (TfR) on the cell outer surface. TfR is a disulfide-linked dimer that binds two transferrin molecules.[29] At neutral pH, apo transferrin does not bind to the transferrin receptor.[41] Once formed, the transferrin receptor complex becomes detached from the cell membrane and enters the cell enclosed in a clathrin-coated vesicle.[29] Uncoating of the vesicle generates an endosome in which the pH is lowered to 5.5, promoting release of iron. At this pH, the transferrin remains bound to its receptor,[41] and is then returned to the outer surface of the cell. The external pH around the cell is slightly alkaline, generally around pH 7.4, and this greatly reduces the affinity of the complex and so the apo transferrin is released ready to pick up more iron in serum.

The transferrin receptor TfR may have a role in reduction of the transferrin-bound Fe(III) within the endosome. Iron leaves the endosome to enter the cytoplasm via the divalent metal ion transporter DMT1,[42] which only transports Fe(II), not Fe(III) (see Section 5). As noted above, the reduction potential of Fe(III) bound to transferrin not associated with TfR is less than $-500\,\mathrm{mV}$, which is too low for reduction of the bound Fe(III) by physiological systems such as reduced pyridine nucleotides. However, as Dhungana *et al*. have shown,[43] the reduction potential of Fe(III)-transferrin bound to TfR is considerably higher at around $-300\,\mathrm{mV}$, which puts it in the range for reaction with physiological reductants.

Protonation of the carbonate ion and its removal as a ligand from the bound Fe(III) occurs at an early stage in iron release from Fe(III)-Tf-TfR.[44] This is followed by protonation of the histidine residue, which further weakens iron binding. At this point in the mechanism, iron release from the N-lobe may be facilitated by a dilysine trigger.[45] Two lysine residues in the N-lobe lie very close to one another, such that charge repulsion ensures there is not enough room for both to be protonated without a change in their relative dispositions. One of the residues is thought to have a particularly low $\mathrm{p}K_\mathrm{a}$, and so would only become protonated when the pH is decreased to 5.5 within the endosome. The two positive charges then repel each other, opening the cleft in the N-lobe of the protein. The C-lobe of transferrin does not have these lysine residues and requires a lower pH to release bound iron in vitro.[46] Recently, mutagenesis experiments have helped to identify three residues in the transferrin C-lobe (K534, R632 and D634) that are implicated in iron release. These residues may act by destabilizing the iron bound conformation of the C-lobe; alternatively they could provide a binding site for iron chelators.[15] As with Fe(III) loading, however, the rates of Fe(III) release are influenced by the properties of any Fe(III) acceptor molecules present in addition to the intrinsic characteristics of the protein.[47] In vitro, polyphosphates promote Fe(III) release[48] but it is not known whether this is physiologically relevant. The possibility that iron is released from transferrin as Fe(II), discussed above, obviates the need for an Fe(III)-chelator within the endosome.

3.4 Spectroscopy

Studies of ferric transferrins with a wide range of spectroscopic methods have been reported but here we focus on their optical and EPR properties. Ferric transferrins are a salmon pink color, resulting from a weak Fe(III)-phenolate charge transfer absorption at 470 nm (for lactoferrin $\varepsilon = 2,070\,\mathrm{L\,mol^{-1}\,cm^{-1}}$ per Fe),[30] which has been used to monitor iron binding to transferrins. Diamagnetic metals, such as Ga(III), Al(III) and Zn(II), do not produce an absorption band in the visible region of the spectrum on binding to apo transferrin, but, like Fe(III), they do perturb the spectrum in the region 220–290 nm as a result of the metal ions binding to tyrosines and perturbing their $\pi-\pi^*$ transitions. UV difference spectroscopy over this range has been a productive method for investigating metal binding.[17,49]

EPR spectra of the diferric species have been thoroughly investigated.[50] The two high-spin Fe(III) ions have an absorption at $g \sim 9.7$ and a three-line signal centered at $g \sim 4.3$. The complexity of these signals is a result of zero-field splitting of the electronic energy levels. In most high-spin Fe(III) systems, zero-field splitting is not understood in a quantitative way but this is not so for diferric transferrin, which is now routinely used as an EPR standard for quantitating $g \sim 4.3$ signals of nonheme iron systems.[50,51]

3.5 Synthetic Analogs

The search for synthetic analogs of ferric-containing transferrins has concentrated on reproducing spectroscopic properties of the protein. Prior to the X-ray structure determinations, various compounds were synthesized based on sporting interpretations of the spectroscopic data for diferric transferrin. Powell[52] has reviewed these noting that none reproduced the coordination sphere of Fe(III) in transferrin and all left 2 trans sites open for coordination by the synergistic anion while transferrin provides two cis sites for this. Subsequent to the X-ray structure determinations, a compound has been described[53] in which the Fe(III) is octahedrally coordinated by O and N ligands, including phenolate and monodentate carboxylate, and in ethanol has a similar visible absorption spectrum to that of transferrin ($\lambda_\mathrm{max} = 494\,\mathrm{nm}$, $\varepsilon = 1340\,\mathrm{M^{-1}\,cm^{-1}}$ per Fe) suggesting that the electronic environment of the Fe(III) resembled that of transferrin.

4 MICROBIAL TRANSFERRIN-LIKE PROTEINS

As noted in Section 3, some pathogenic bacteria have transferrin receptors on their outer membranes to acquire diferric transferrin from their host. These outer membrane receptors extract the iron from the transferrin and transport it into the periplasm where it is picked up by the periplasmic ferric binding proteins (Fbp), which carry the iron to a transmembrane protein in the inner membrane that conveys it into the cytoplasm.[54] A considerable amount of chemical and structural information has been gathered for Fbp, which is sometimes referred to as bacterial transferrin in recognition of its similarities with animal transferrin.[55]

4.1 Structure of Fbp and Its Fe^{3+} Binding Site

Fbp is about half the size of transferrin and has the appearance of a single lobed transferrin-like protein: not only does the polypeptide fold into a bidomain $\alpha\beta$-structure similar to that of transferrin (Figure 3), with a central mixed β-sheet surrounded by α-helices, but also the fold creates a single iron-binding site between the two domains. The amino acid ligand set for the bound Fe(III) of *N. gonorrhoeae* and *H. influenzae* Fbp is the same as provided by transferrin; namely, two tyrosinates, a carboxylate and a histidine. However, despite the similarity in overall fold and Fe(III) binding site, the sequence positions of the metal ion ligands are very different suggesting that the Fe(III) binding sites have evolved in a convergent fashion.**[21]** As with animal transferrin, Fe(III) binding to *N. gonorrhoeae* and *H. influenzae* apo-Fbp causes a switch from an open to a closed structure. In the apoprotein, the two domains are rotated relative to their positions in the closed Fe(III)-Fbp structure and some of the Fe(III) ligand residues are too far apart to make an effective metal ion binding site.

Tight binding of Fe(III) to Fbp requires a synergistic anion, which is likely to be phosphate in vivo for *N. gonorrhoeae* and *H. influenzae* Fbp, as their iron-containing Fbp's are isolated with bound phosphate.**[55]** A bound H_2O completes the octahedral coordination of Fe(III). Other anions, including citrate and oxalate, can bind to the Fbp-bound iron,**[55]** and in the H9Q mutant of *H. influenza* Fbp the bound Fe(III) is coordinated by tetradentate EDTA located at the site normally occupied by phosphate.**[56]** Thus, it is possible that multiple forms of Fbp differing in the identity of the bound anion occur under physiological conditions. Dhungana *et al.***[55]** propose that variable anion binding may play a role in iron release in vivo. An indication of the scope for this is provided by a comparison of citrate and phosphate binding to Neisserial Fe(III)-Fbp. These have effective association constants (for reaction 3) at pH 6.5 of 1.4×10^{17} for citrate and $4.2 \times 10^{18}\,\mathrm{M}^{-1}$ for phosphate, but significantly different $Fe^{3+/2+}$ redox potentials of −191 and −300 mV, respectively. Dhungana *et al.***[55]** suggest that the exchange of bound anions modulates the redox potential and may lead to the reduction of the bound iron to Fe(II), which is readily lost from Fbp.

$$Fe^{3+}{}_{aq} + \mathrm{Fbp} + X^{n-} \longrightarrow Fe^{3+}\text{-Fbp}(X^{n-}) \qquad (3)$$

A comparison of Fe(III) binding characteristics of animal transferrins and Fbp is revealing about structural influences on their iron chemistries. Though Fe(III)-Fbp binds many anions, binding of carbonate at pH 6.5 has not been detected in vitro.**[55]** Presumably this is because the anion binding site adjacent to the Fe(III) binding sites is configured for phosphate rather carbonate. Partly as a consequence of the anion exchange, the redox potential of Fe(III)-Fbp(phosphate) is ∼200 mV more positive than that of Fe(III)-Tf(carbonate), though the greater solvent exposure of the Fbp site as compared to the transferrin site has also been suggested to be an important contributing factor to this difference.**[55]**

P. haemolytica Fbp has significantly different spectroscopic properties from other Fbp's, with bound Fe(III) having an absorbance of 419 nm, blue-shifted from the ∼480 nm usually observed for Fbp.**[57]** The X-ray structure of apo-Fbp from *P. haemolytica* suggests an explanation for this.**[58]** Although the protein did not contain bound Fe(III) it did contain two bound formate ions and was in a closed rather than open conformation. This led Shouldice *et al.***[58]** to propose that the Fe(III) binding site in this Fbp consists of three tyrosines, the two formate ions and a glutamine.

4.2 Multinuclear Oxo-metal Clusters and Fbp

X-ray structures of wild-type *N. gonorrhoeae* Fbp**[59,60]** and mutant forms of *H. influenzae* Fbp**[61]** have been described in which multinuclear oxo-metal clusters are bound to the protein. These surprising results are informative about aspects of the Fbp structure and formation of oxo-metal clusters on a protein surface, but it is not clear whether they have any physiological relevance. Sadler and coworkers present a case for this,**[59,60]** noting that the outer membrane transport protein FecA passes diferric dicitrate into the periplasm**[4]** and so at least one dinuclear iron complex is available to Fbp.

The polynuclear Fe(III) clusters are bound to the two tyrosines in the conventional mononuclear Fe(III) site, Y195 and Y196, but are not bound to other amino acid residues. Trinuclear and tetranuclear clusters were observed for the H9A and N175L mutants of *H. influenzae* Fbp, respectively, and with *N. gonorrhoeae* Fbp, trinuclear clusters were seen though the structural details of these clusters varied over the different molecules in the unit cell. The crystals of *N. gonorrhoeae* Fbp containing polynuclear iron were obtained using crystals of apo-Fbp to seed iron-containing solutions. Since the apo-Fbp crystallizes in an open conformation, the question remains as to whether the formation of the polynuclear iron cluster is a consequence of crystal packing forces constraining the molecule into the open form. Shouldice *et al.***[61]** note that the *H. influenzae* mutant Fbp's in which the iron-binding site residues were systematically substituted appear to be locked into the open conformation, suggesting that this is the preferred conformation for Fbp with the Fe(III) ligating residues playing a key role in closure of the structure. They then suggest that the open structure of Fbp provides a surface on which the formation of polynuclear clusters takes place. This is similar to the proposal of Malone *et al.***[62]** regarding protein-template-assisted formation of polynuclear iron clusters on the surface of mutant bacterioferritins (see Section 7.8).

5 PROTEIN-MEDIATED ABSORPTION OF DIETARY IRON

Iron absorption from the mammalian gut takes place mainly in the duodenum and upper ileum. The inside of the intestine is lined with villi, the tips of which are coated with mucosal cells that provide the pathway for iron to gain access to the bloodstream. Heme iron is more readily absorbed than nonheme iron,[63] because heme does not bind most of the dietary chelators that interfere with absorption of nonheme iron. However, the mechanisms for heme absorption have not yet been fully established. Once inside the cell, the porphyrin ring is degraded and the ferrous iron produced is released into the intracellular iron pool. Nonheme iron appears to be transported to the labile iron pool within the mucosal cell via reduction by a membrane-bound ferric reductase, the diheme duodenal cytochrome *b* (Dcytb),[64] and transfer of ferrous iron to DMT1, previously called Nramp2 and DCT1.[65] This is an integral membrane protein that facilitates the proton-coupled transport of divalent cations across the cell membrane. Evidence for the involvement of DMT1 in iron acquisition comes from a natural mutation in DMT1 in some rodents, which causes microcytic anemia associated with defective iron absorption from the intestine.[65] This mutation (G195R) does not directly affect iron binding, but three negatively charged residues (D86, D192, and E299) that are highly conserved within the Nramp family have been identified by mutagenesis as being essential for cation transport.[66] Two further conserved residues, H267 and H272, are also involved in cation transport but appear to mediate a pH-dependent conformational change in the protein rather than directly binding metals.[66]

Once inside the mucosal cell, iron then has to be transported across the membrane to serum transferrin. This appears to take place via the Ireg1 transporter protein (also known as ferroportin 1 or MTP1).[67] Ireg1 is a transmembrane protein located at the basolateral membrane of the cell that has been shown to be involved in iron uptake. Oxidation of Ireg1-bound ferrous iron and its release to transferrin is likely to be enhanced by the membrane-bound multicopper ferroxidase hephaestin. This protein is 50% identical to ceruloplasmin, a soluble protein identified as having a possible role in iron loading of transferrin (*see* ***Copper Proteins: Oxidases***).[35] Mutation of hephaestin in mice leads to a build up of iron in duodenal cells and overall iron deficiency in the body.[68]

6 OTHER IRON TRANSPORT SYSTEMS

6.1 FeoABC

In conditions where a lack of oxygen stabilizes ferrous iron, the metal can be directly transported into some bacterial cells, in contrast with aerobic environments where iron is mostly present as insoluble ferric species. *E. coli* uses the FeoABC system, which comprises FeoB in the cytoplasmic membrane and two smaller proteins, FeoA and FeoC, with unknown functions. The system can use both ferrous and ferric iron as a source, although ferric ions need to be reduced before they can be transported. FeoB is also used by *Helicobacter pylori*[69] and *feo* genes are present in *Salmonella typhimurium*.[70] Both *E. coli* and *S. typhimurium* can also transport ferrous iron using the CorA protein,[71] which is a transporter of various divalent metal ions including Co(II), Mg(II), Mn(II) and Ni(II) in addition to Fe(II).

6.2 Iron Transport in Yeast

There are two main iron transport systems in *Saccharomyces cerevisiae*, one predominant under aerobic conditions and a lower affinity system utilized under anaerobic conditions.[29] In the high affinity system, which is more selective and more tightly regulated, ferric iron is first reduced to ferrous by outer membrane ferric reductases, and is then bound by the Fet3p-Ftr1p complex. Fet3p is a multicopper ferroxidase with structural and functional similarities to ceruloplasmin, although it has a higher level of ferroxidase activity (*see* ***Copper Proteins: Oxidases***).[29] Ftr1p is a permease with 6 transmembrane domains, possesses residues that suggest a potential iron-binding site, and is believed to allow iron to pass through it into the cell.[29] The low affinity pathway involves the integral membrane protein Fet4p, which appears to be another plasma membrane permease.[29] This protein can also transport other divalent transition metal ions including Cu(II), Mn(II) and Cd(II).

7 FERRITINS

The majority of organisms need a method for iron storage that protects against metal toxicity but retains bioavailability. A widespread solution to this problem is ferritin, found in almost all bacteria, plants and animals.[72] These proteins have a high capacity for storing iron, with space for up to 4,500 ferric ions per protein molecule as the mineral ferrihydrite.[73] The potential capacity for storing Fe(III) is even greater if the mineral form is different[74] though there is no compelling evidence for naturally occurring mineral cores other than ferrihydrite or amorphous phases.

7.1 Structure

The structures of several members of the ferritin family have been solved, and show a high level of conservation. Ferritin subunits, with a molecular weight of $\sim$20kDa, are four-helix bundles with a fifth short helix at the C-terminal end of the protein chain. These subunits assemble to form a 24-meric, roughly spherical hollow shell with an outer diameter of ∼120Å and an inner diameter of ∼80Å (Figure 5). *Listeria innocua* ferritin, which is dodecameric, was thought to be an exception to the normal 24-meric ferritin structure but this protein is now recognized to be a member of the Dps family and will be discussed further below.

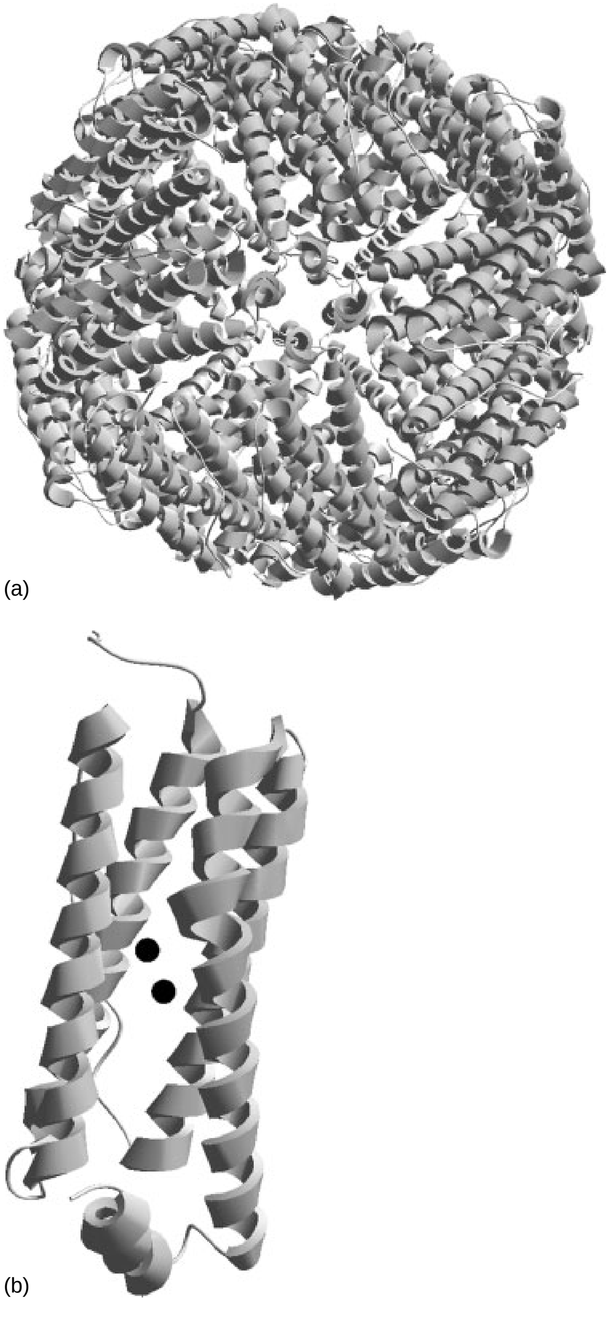

Figure 5 (a) Crystal structure of bacterioferritin from *E. coli* showing the 24-meric structure characteristic of the ferritin family. Figure created using pdb coordinates 1bfr.[75] (b) shows subunit monomer of human H-chain ferritin, with iron-binding site marked with black spheres. Figure created using pdb coordinates 2fha[76]

Mammalian ferritins are heteropolymers of H- and L-chains. These subunits are very closely related, with an α-carbon rmsd of 0.5 Å and ∼55% sequence identity;[76] conservation of primary sequence rises to 79% when considering those residues responsible for intersubunit interactions.[77] Subunit assembly appears to take place via partially structured monomers associating to form fully structured homodimers, which then aggregate further. Upon chemical denaturation and refolding, heterodimers are rarely observed.[72,78]

Ferritins have eight channels located at the threefold symmetry axes and six channels at the fourfold axes. The threefold channels are often hydrophilic and the sixfold channels hydrophobic, though this polarity difference is not conserved. This may have important mechanistic consequences that are still being explored, as it appears that iron accesses the protein cavity via the hydrophilic channels.[72] The hydrophobic channels could act as the pathway for protons to be released from the protein cavity, possibly with water molecules in the channel acting as a proton wire.[79] Bacterioferritin and nonheme bacterial ferritin have extra channels located between the three- and fourfold axes. These B channels have clusters of negative charge and are large enough to allow iron atoms into the protein cavity.[80]

7.2 Oxidation of Ferrous Iron by H-chain Ferritins

Each ferritin H-chain subunit possesses a conserved dinuclear iron site known as the ferroxidase center, which catalyzes iron oxidation. Residues E27, E61, E62, H65, and E107 act as metal ligands while residues Y34 and Q144 form hydrogen bonds (the numbering refers to the human H-chain sequence) (see Figure 6).

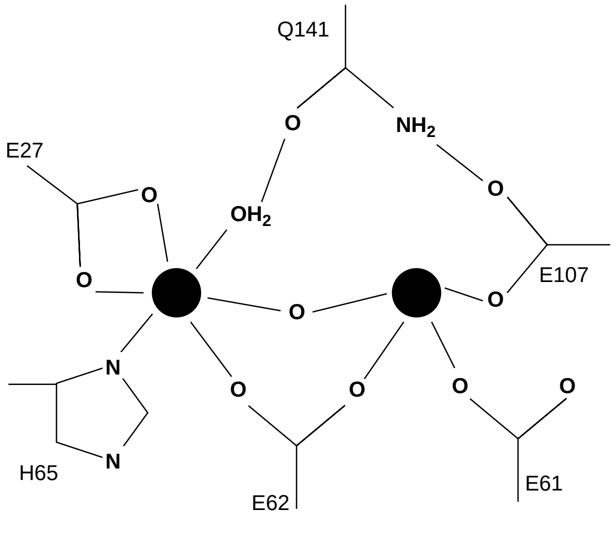

Figure 6 Schematic model of the human H-chain ferroxidase center based on the X-ray structure of Tb(III)-containing ferritin[81]

Ferrous iron binds to H-chain ferritin with the release of $\sim 0.25\mathrm{H}^+$ per Fe(II) ion.[82] Iron oxidation then takes place via a combination of three pathways, with the proportions of each dependent on the amount of iron added. At low iron loading (<50 Fe per H-chain homopolymer, that is, less than required to saturate the ferroxidase centers) the dominant reaction is at the ferroxidase center (equation 4):

$$2\mathrm{Fe}^{2+} + \mathrm{O}_2 + 4\mathrm{H}_2\mathrm{O} \longrightarrow 2\mathrm{FeOOH}_{(\mathrm{core})} + \mathrm{H}_2\mathrm{O}_2 + 4\mathrm{H}^+ \qquad (4)$$

The oxidized iron travels from the ferroxidase center to the core, thus regenerating the ferroxidase center for further reactions. When large amounts of iron are added (>800 Fe per protein), following oxidation of the first two ferrous ions per subunit an autooxidation reaction catalyzed by the core surface takes over and becomes the predominant mechanism (equation 5):

$$4\mathrm{Fe}^{2+} + \mathrm{O}_2 + 6\mathrm{H}_2\mathrm{O} \longrightarrow 4\mathrm{FeOOH}_{(\mathrm{core})} + 8\mathrm{H}^+ \qquad (5)$$

When intermediate-sized additions are made (100–500 Fe per molecule), some of the hydrogen peroxide produced in reaction (4) is used to oxidize ferrous iron in a hydrogen peroxide/iron detoxification reaction (equation 6):

$$2\mathrm{Fe}^{2+} + \mathrm{H}_2\mathrm{O}_2 + 2\mathrm{H}_2\mathrm{O} \longrightarrow 2\mathrm{FeOOH}_{(\mathrm{core})} + 4\mathrm{H}^+ \qquad (6)$$

The result of this is that the majority of the hydrogen peroxide produced by reaction (4) goes undetected.[83]

During the ferroxidation reaction, a blue color with an absorption maximum of 650 nm appears. This persists in oxygen-limited conditions and decays as iron oxidation proceeds.[84] In frog H-chain ferritin, resonance Raman studies indicate a similar absorption is associated with an Fe(III)-tyrosinate.[85] Harrison and Treffry[86] have considered these and other studies and attribute the transient color to formation of a μ-1,2-peroxodiferric intermediate, which decays to a more stable μ-oxodiferric species as occurs in methane monooxygenase, ribonucleotide reductase, and model compounds.[87] Protein radicals distinct from reactive oxygen species have been observed that have been attributed to damage caused by Fenton chemistry.[88]

The two iron-binding sites at the dinuclear ferroxidase center are not identical. Mutagenesis of residues E27 (in site A) and E107 (site B) shows that site A can bind iron independently but requires site B for iron oxidation. In contrast, iron binding in site B is greatly decreased in the absence of site A, whereas oxidation is unaffected.[89]

7.3 L-chain Ferritin

In L-chain subunits, the ferroxidase center present in the H-chain is absent; the space occupied by it in H-chain ferritin has a salt bridge between K62 and E107 that stabilizes the protein. Nevertheless, L-chain homopolymers can accumulate Fe(III) particles through oxidation of Fe(II) at sites different from the intra-subunit ferroxidase centers of H-chain ferritins. These sites involve glutamic acid residues 53, 56, 57 and 60, and face the inner cavity of the molecule.[90,91] Because ferritins rich in L-chains oxidize iron more slowly than H-chain ferritins, they form iron particles of greater average size, crystallinity, and magnetic ordering.[77]

H- and L-chains have complementary roles in iron uptake, with heteropolymers having a higher ferroxidase activity per H subunit than H-chain homopolymers. This is because L-chain subunits bind ferric iron with a higher affinity than H-chains, thus promoting the regeneration of the ferroxidase center.[92] The rate of iron oxidation increases with increasing H-chain content up to a maximum of $\sim 35\%$, above which the rate-limiting step changes from ferroxidation to nucleation.[78] Heteropolymer composition varies according to the tissue of origin: organs which accumulate iron, such as the liver and spleen, have a high L content (up to 90%) to maximize storage capacity, while organs with a greater requirement for rapid iron detoxification such as the heart and brain can be two thirds H-chain.[77]

7.4 Nonheme Bacterial Ferritins

Bacterial H-chain ferritins are similar to their animal ferritin counterparts, though they are usually considered separately from these.[72] It is not clear whether the native proteins are heteropolymers or not as most of the chemical and structural studies have been carried out with recombinant protein. As-isolated proteins tend to have high levels of phosphate associated with the iron, resulting in an amorphous core structure.[93] Ferritin from *E. coli*, EcFtnA, has a dinuclear ferroxidase site that corresponds to that of H-chain ferritin, with one difference: residue E61 in human H-chain ferritin is replaced as a metal ligand by E130. EcFtnA also has a third iron-binding site, site C, on the inner surface of the protein cavity. This site shares residue E130 with site B and has E49 and E126 as additional metal ligands (Figure 7).[94] It is not essential for ferroxidase activity, as mutagenesis of site C residues results in only a slight reduction in oxidation rate. Although a third metal binding site has been suggested for human H-chain ferritin following crystallization using Tb(III), this is in a different position from the EcFtnA site C and has not been shown to bind iron.[81]

Oxidation of iron by EcFtnA produces a blue-colored intermediate with an absorption maximum at 650 nm and a shoulder at 370 nm.[86] This intermediate in human H-chain ferritin corresponds to a diferric peroxo species and is likely to be the same for EcFtnA, as mutation of Y24 has indicated that it cannot be an iron-tyrosinate.[95]

7.5 Bacterioferritins

Another member of the ferritin family found in bacteria is bacterioferritin (BFR). BFR has the same 24-meric

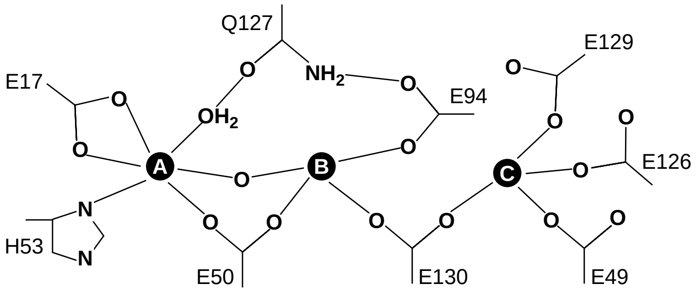

Figure 7 Schematic model of EcFtnA ferroxidase center including site C based on crystal structure[94]

three-dimensional structure as the mammalian ferritins described above, but it differs from other ferritins in containing up to 12 heme groups per molecule[96,97] bound at the interface between pairs of monomers (Figure 8), with each heme iron ligated by a methionine residue from each subunit (Met52).[75,98,99] In most characterized BFR proteins the heme macrocycle is protoporphyrin IX but in *Desulfovibrio desulfuricans* BFR it is coproporhyrin III.[100] The heme groups of *E. coli* and *A. vinelandii* BFR have been shown not to play a part in oxidative aerobic iron uptake, and their function may be in iron release or electron storage.[96,99,101]

As with H-chain ferritins, the three-dimensional structure of BFR results in channels through the protein at the symmetry axes. However, while the hydrophilic threefold channels in bacterioferritin are similar to those in ferritin, the BFR fourfold channels are hydrophilic rather than hydrophobic in character.[72,80]

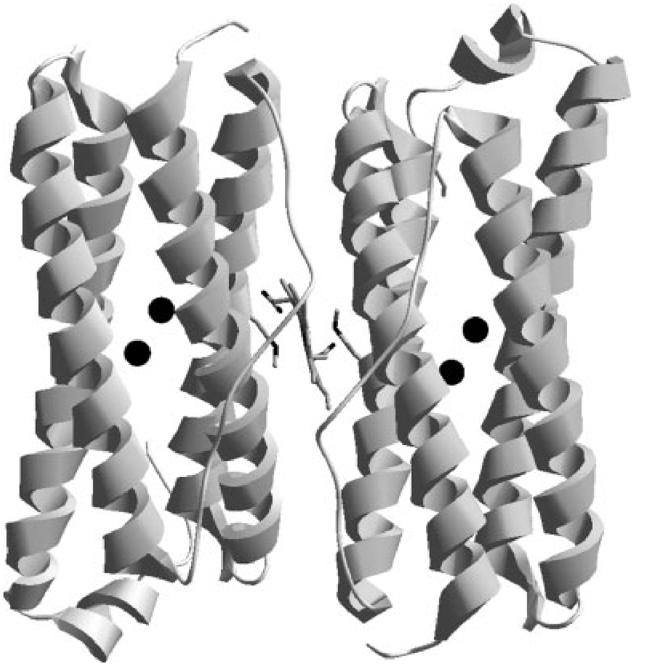

Figure 8 The structure of the BFR subunit dimer showing heme bound at monomer interface by M52 residues. The iron atoms in the ferroxidase centers are shown as black spheres. Figure created using pdb coordinates 1bcf[75]

The residues that make up the bacterioferritin ferroxidase center also differ from those seen in H-chain ferritins. Although there are differences between mammalian and nonheme bacterial ferritins in the individual residues used to ligate the iron, H-chain ferroxidase centers have four glutamate residues, one histidine, and a bridging glutamine that interacts with metal ions indirectly via a hydrogen bonded water molecule. The BFR ferroxidase center, in contrast, more closely resembles the di-iron sites of proteins such as methane monooxygenase and ribonucleotide reductase (*see* ***Iron Proteins with Dinuclear Active Sites***). It has four glutamate residues, one of which replaces the bridging glutamine, and Glu130 in EcFtnA is replaced by an additional histidine (Figure 9). Although the bacterioferritin ferroxidase center is more symmetrical than those in H-chain ferritins, the surrounding residues induce an element of asymmetry in the BFR center. This leads to nonequivalence in the two iron sites. Mutagenesis of E18 in site A abolishes iron uptake, giving iron oxidation rates similar to those of autooxidation, while mutagenesis of E94 (the corresponding residue in site B) results in a much less dramatic reduction in activity.[102] Similar effects are seen for the histidines. A third iron site similar to site C of EcFtnA has not been described for BFR.

A significant difference between BFR and H-chain ferritins is the mechanism of iron uptake and core formation. In H-chain ferritins, initial iron uptake takes place by ferrous iron being oxidized at the ferroxidase center and moving into the core, and once a sizeable core has been established, autooxidation at the core surface takes over from the ferroxidase center reaction (see Section 7.2). In BFR, iron uptake takes place in three distinct phases.[103] Phase 1 is the binding of two ferrous ions per ferroxidase center (48 per protein). Phase 2 corresponds to rapid oxidation at the ferroxidase center according to reactions (7) and (8), where z represents the charge on the protein.[51,102–104]

$$[\mathrm{Fe^{II}}_2\text{-P}]^z + \mathrm{O_2} + \mathrm{H_2O} \longrightarrow [\mathrm{Fe^{III}}_2\mathrm{O}\text{-P}]^z + \mathrm{H_2O_2} \qquad (7)$$

$$[\mathrm{Fe^{II}}_2\text{-P}]^z + \mathrm{H_2O_2} \longrightarrow [\mathrm{Fe^{III}}_2\mathrm{O}\text{-P}]^z + \mathrm{H_2O} \qquad (8)$$

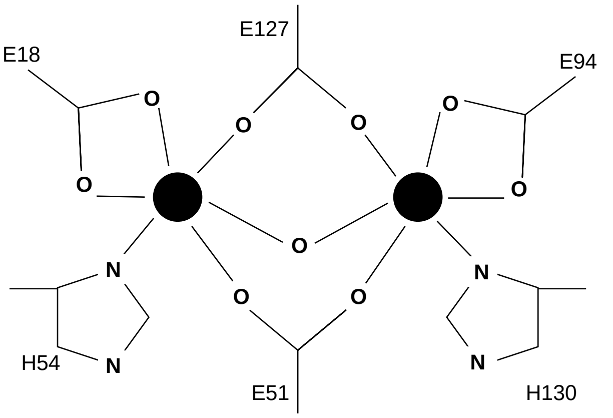

Figure 9 Schematic model of BFR ferroxidase center based on the crystal structure of iron-bound BFR from *D. desulfuricans* (EcBFR numbering). The bridging ligand, shown here as a μ-oxo group, cannot be determined in the structure but there is sufficient electron density for a μ-oxo, μ-hydroxo, H_2O and even peroxo group[100]

The overall ferroxidase reaction is therefore reaction (9) below:

$$2[\mathrm{Fe^{II}}_2\text{-P}]^z + O_2 \longrightarrow 2[\mathrm{Fe^{III}}_2\mathrm{O}\text{-P}]^z \qquad (9)$$

Note that reaction (9) indicates a pairwise reaction within subunit dimers rather than individual ferroxidase centers reacting separately. Although reaction (7) indicates the formation of hydrogen peroxide, no diferric peroxo intermediate has been observed for BFR. This may be because such a species is not formed, or, more likely, because such an intermediate is too short lived or has too low an extinction coefficient to be detected.[86]

Following reaction (9), the ferric iron remains at the ferroxidase center as a μ-oxo bridged species instead of moving into the core and thus regenerating the ferroxidase center. The addition of more than 48 ferrous ions per protein saturates the ferroxidase reaction and any further iron is oxidized within the core (phase 3). This process is significantly slower than phase 2. Core formation occurs according to reaction (10) below.

$$4\mathrm{Fe}^{2+} + O_2 + 6H_2O \longrightarrow 4[\mathrm{FeOOH}] + 8H^+ \qquad (10)$$

Although reaction (10) takes place after the ferroxidase center has been filled, experiments involving blockage of the BFR ferroxidase centers with zinc in BFR containing a significant ferric core show that the ferroxidase center is required throughout core formation.[102,105] However, the rate of core formation is linked to the core surface area, indicating a role for the core surface in the phase 3 reaction. This has led to the proposal that in phase 3 ferrous iron binds at the growing mineral surface, or to acidic residues on the inner surface of the protein, becoming oxidized to Fe(III) with the electrons from this oxidation passing through the core to the ferroxidase center, which becomes reduced. The ferroxidase center iron is then reoxidized by molecular oxygen according to reaction (9) above. Thus the core surface is the site of iron oxidation but not oxygen reduction.[105] This reaction mechanism is illustrated in Figure 10.

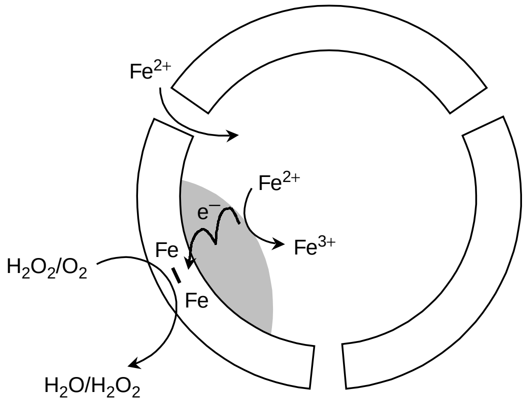

Figure 10 Schematic model of BFR core formation mechanism

7.6 Iron Release from Ferritins

Iron can be removed from ferritin containing Fe(III) by Fe(III) chelators or, following reduction, by Fe(II) chelators.[106–108] Rapid iron release results from reduction of the core in the presence of a ligand; reduction alone does not lead to iron release. For example, at pH 7 thioglycollic acid removed ~5% of the core iron after a 10 min incubation, and reduced flavin mononucleotide removed ~25% after only a 2.5 min incubation. Moreover, Fe(III) chelators, such as EDTA, 1,10-phenanthroline and desferrioxamine B, removed only a small fraction ($\leq$10%) of the iron of horse spleen ferritin after 24 hr at pH 7 and this, coupled with calculations of iron turnover in cells synthesizing heme, is generally taken to indicate that the release of Fe(III) is not physiologically significant.[106,108] This suggests that the core contains Fe(II) in vivo or that iron release involves the prior reduction of core iron. The physiological significance of such experiments is open to question however, as the iron acceptor molecules and any reductants employed are rarely physiologically relevant. Proteins involved with intracellular trafficking of iron in bacteria have been reported, such as YggX in *Salmonella enterica*[109,110] and Bfd in *E. coli*,[111,112] making this a topic ripe for revisiting with these proteins in place of the normal iron acceptors.

The mechanism of the reductive iron release has not been fully characterized but several lines of evidence point to small reductants and chelators remaining outside the protein shell during reaction[107,113,114] with the rate-limiting step for Fe(II) release being long-range electron transfer (*see* ***Long-range Electron Transfer in Biology***) into the core across the protein shell.[101,111] If correct, this implies that Fe(II) migrates through the protein shell faster than electrons. Nevertheless, iron passage through the shell is relatively slow with a rate that is influenced by the structural dynamics of the channels though the protein shell by which iron enters and leaves the cavity.[115]

7.7 Redox Properties of Ferritins

Rapid iron uptake or release by ferritins to form, or breakdown, a Fe(III) core involves redox reactions, as discussed in previous sections. The present section summarizes data regarding measurement of redox properties not involving iron release or uptake.

The reduction potentials of the core iron of *A. vinelandii* and horse spleen ferritins have been determined electrochemically to be $-420 \pm 20\,\mathrm{mV}$ and $-190\,\mathrm{mV}$, respectively, at pH 7.[116,117] The former potential was invariant over the pH range 7.0–9.0 while the latter potential decreased with increasing pH. The $\mathrm{Fe}^{3+/2+}$ reduction potential at pH 8 of the heme of *A. vinelandii* ferritin is $-475\,\mathrm{mV}$ in the presence of the core and $-225\,\mathrm{mV}$ in its absence.[116] Since magneto-optical spectroscopic properties of the heme are not affected by the core this shift in potential has been ascribed to a core electrostatic field effect.[118]

Horse spleen apoferritin undergoes additional redox reactions with an overall stoichiometry of 4.0–7.1 electrons/24-mer at a midpoint reduction potential of $-310\,\mathrm{mV}$.[119] This potential was invariant over the pH range 6–9 showing that H^+ uptake or release does not accompany the redox process. The identity of the group(s) giving rise to these processes has not been established but studies with recombinant H- and L-chain ferritins suggest that the formation of protein-bound organic redox centers involves the H-chain, but only when it is associated with L-chain in heteropolymers.[120] Since this study found that the W93F H-chain mutant was redox-inactive, it appears as if W93 is required for this activity.

The polynuclear iron cores of reduced horse spleen ferritin and *A. vinelandii* ferritin can be oxidized by a variety of proteins via long-range electron transfer across the protein shell.[113,121] The rates for horse spleen ferritin varied from $<0.2\,\mathrm{M}^{-1}\,\mathrm{s}^{-1}$ for metmyoglobin to $1.1 \times 10^3\,\mathrm{M}^{-1}\,\mathrm{s}^{-1}$ for horse ferricytochrome *c*. None of the reported interprotein electron transfer studies with ferritins are physiologically significant because nonphysiological partner proteins were used, and it will be interesting to see this kind of study extended to bacterioferritin reacting with proteins like YggX[109,110] and Bfd.[111,112]

7.8 Physicochemical Characteristics of the Nonheme Iron Cores of Ferritins

There are a variety of types of ferritin nonheme iron core, ranging from the highly ordered cores of horse spleen ferritin to the amorphous cores of bacterioferritins.[72] As noted earlier, the central cavity of ferritin has a sufficient volume to accommodate 4,500 iron atoms as $\mathrm{Fe_2O_3 \cdot 9H_2O}$, though ferritins are rarely isolated fully loaded.[73] Mature horse spleen ferritin generally has 1,000–3,000 iron ions per molecule and bacterioferritins are usually isolated with only 800–1,500 iron ions per molecule,[122] even though their mean core sizes determined by electron microscopy are not too different from those of animal ferritin.[123,124] This is one indication that the density of ferritin cores differ markedly. This difference in core morphology is often associated with the phosphate content of the core, a high phosphate content being correlated with an amorphous core,[124] and indeed, the phosphate content of ferritin is generally low, with the phosphate located at the surface of the core,[125] while native bacterioferritins have a greater phosphate content, suggesting that bacterioferritin may have a role as a phosphate store.[107,126]

There is a lack of precise structural information for ferritin cores because while preparations of iron-containing ferritins may be monodisperse with regards to their protein components they are polydisperse in their core components as a result of the high symmetry of the inner surfaces bordering their central cavities. A consequence of the polydisperse nature of the cores is that in crystals of ferritin, though the protein shell is ordered the iron-containing core is not.[72,73] Consequently, the structure of the core mineral has not been determined by X-ray crystallography, and complete structural characterization of intact ferritins may not be possible. For this reason, stabilized subunit dimer forms of ferritins have been made by site-directed mutagenesis. Fe(III)-binding properties of two of these engineered proteins, the E128R/E135R mutant bacterioferritins from *E. coli* and *Rhodobacter capsulatus*, have been described.[62] They both acquire polynuclear Fe(III)-containing particles on their surfaces that are resistant to rapid removal by chelating agents, and thus they may represent a way forward for determining structural features of the core iron.

EXAFS studies of *A. vinelandii* bacterioferritin have shown that there are fewer Fe–Fe contacts in the mineral core than occur with native horse ferritin, and those that do occur are at a greater interatomic distance.[127] Moreover, the EXAFS data showed that the core iron of bacterioferritin had 5 to 6 phosphorus atoms no more than 3.17 Å distant, thus supporting a model for the core of an amorphous Fe(III)-phosphate complex in which some of the phosphate bridges Fe(III) ions and some of it is nonbridging.

The generally accepted structure for the crystalline iron core of ferritin is the ferrihydrite structure proposed by Towe & Bradley.[128] This consists of oxygen layers with iron in octahedral sites between the layers. Ford *et al*.[73] and Powell[74] have summarized the evidence in support of this model for ferritin, which includes electronic spectroscopic data and EXAFS measurements confirming the presence of six-coordinate Fe(III) and indicating that four-coordinate Fe(III) is present, if at all, at low levels only. This latter point is important because the X-ray powder diffraction patterns of air-dried ferritin cores can be adequately fitted with both the Towe & Bradley model and with a model containing both tetrahedrally and octahedrally coordinated Fe(III);**[73]** and because the Towe & Bradley model itself is not accepted by all workers for the structure of ferrihydrite.**[129]** Moreover, as Powell notes,**[74]** even in the crystalline native ferritin cores there is disorder which makes their characterization difficult. This is one of the reasons so much effort has been expended on synthetic analog studies of ferritin cores (see Section 7.9).

Reconstitution experiments with apoferritins from animal and bacterial sources, whose native iron-loaded ferritins had crystalline and amorphous cores respectively, have been informative in showing that the core morphology is not determined by the protein shell. For example, Baaghil *et al.***[105]** and Mann *et al.***[130]** were able to form crystalline cores in bacterioferritins, and Rohrer *et al.***[127]** formed cores of iron-phosphate in horse spleen ferritin with fewer short range Fe–Fe distances than in the native cores. Thus it appears that the composition of the medium within which the ferritin cores are laid down, particularly the phosphate content, influences strongly the nature of the core. This is consistent with the role of phosphate as an iron oxide chain terminator.**[126]**

^{57}Fe Mössbauer spectroscopy has been widely employed to study ferritins.**[116,124,130]** The spectra of the ferric cores are temperature dependent and consist of a quadrupole-split doublet at high temperature and a magnetically split sextet at low temperature. Two general cases have been observed. In the first, the magnetic ordering temperature (T_{ord}) is greater than the blocking temperature (T_B), and in the second, $T_B > T_{ord}$. Proteins in the former class, exemplified by horse ferritin with a T_B of $\sim$40 K, exhibit superparamagnetic behavior. The latter class of ferritins, illustrated by *Pseudomonas aeruginosa* bacterioferritin,**[131]** with a $T_B > 3$ K and a $T_{ord} < 3$ K, does not show superparamagnetic behavior. The presence of superparamagnetism appears to be correlated with both the size and degree of crystallinity of cores; the higher the magnetic anisotropy barrier the greater T_B is. Hence at constant K, a higher T_B indicates a greater particle volume, and hence a greater crystallinity. Thus ^{57}Fe Mössbauer spectra are consistent with electron microscopic data indicating that the cores of bacterioferritin are largely amorphous while those of mammalian ferritins are largely crystalline. Magnetic circular dichroism spectra of amorphous bacterioferritin and crystalline ferritin cores are also consistent with this.**[132]**

EPR data also reveal a difference between the ferritin and bacterioferritin cores. At high temperatures the latter yield a broad signal with $g \sim 2$ and at 4 K are EPR silent,**[118,133]** while the former give signals at high temperatures at $g \sim 6$ and $g \sim 2.2$ that are lost at 4 K.**[134,135]** The origin of the bacterioferritin signal is not certain but since bacterioferritin cores of 800 iron atoms per 24-mer and 24–68 iron atoms per 24-mer have similar EPR characteristics which are absent from core-free protein, the signal must arise from the core particle.**[118]** The signal appears to be reporting the relaxation characteristics of the core and may arise either from uncompensated spins or, more likely, from uncoupled spins since the exchange coupling temperature is below 4 K. It has been assumed that the ferritin EPR signals originate from the uncompensated electron spins of the antiferromagnetically ordered cores**[135]** and if this is so there should be a correlation between the EPR and Mössbauer data. This appears to be the case for animal ferritin, which Mössbauer indicates is magnetically ordered at 4 K.

7.9 Synthetic Analogs of the Polynuclear Clusters of Ferritins

A variety of approaches have been adopted in attempts to obtain analogs of crystalline ferritin cores but, as Powell has pointed out,**[74]** uncertainty over the structure of the ferritin core itself complicates this field. The earliest synthetic approach was that of Spiro *et al.*,**[136]** who obtained citrate-coated spheres of polymeric iron hydroxide by hydrolysis of ferric citrate. Though the early characterization of these spheres indicated they might be good models for ferritin,**[137]** the difficulty in obtaining reproducible samples, and the lack of structural information, has led to greater efforts being put into other approaches.

One of these approaches is the formation of polysaccharide iron complexes**[138–140]** (PIC), such as Niferex, a compound used in the treatment of iron deficiency anemia. PICs are formed by neutralization of $FeCl_3$-containing carbohydrate solutions with base. Mineral particles of roughly the same size as ferritin cores can be made. These contain iron in an octahedral environment coordinated to oxygen. However, the long-range order of the polynuclear iron core is closer to that of akaganéite rather than ferrihydrite.**[140]**

Addition of base to aqueous solutions of Fe(III) in the presence of the ligand $N(CH_2COOH)_2(CH_2CH_2OH)$ (‘heidi’), produced 19-iron and 17-iron species, neither of which have a 3-D framework of Fe(III) ions. These species contain close-packed iron hydroxide cores bound, via oxide and hydroxide bridges, to Fe(III) located on the inner surface of the heidi coat.**[74,141]** The inner core, which is common to both Fe_{17} and Fe_{19} compounds and consists of an $[Fe_7(\mu_3\text{-}OH)_6(\mu_2\text{-}OH)_4\{(\mu_3\text{-}O)Fe\}_2]^{13+}$ unit, derives from a portion of an infinite 2-D $[Fe(OH)_2{}^+]_n$ framework. This suggests that the ligand shell, $[Fe_{10}(heidi)_{10}(H_2O)_{12}(\mu_3\text{-}O)_4(\mu_2\text{-}OH)_4]^{12-}$, traps the iron in an unusual, for Fe(III), hydroxide mineral structure, and poses the question of whether the core of ferritin is a similarly ‘trapped’ structure.**[74]**

An alternative approach is to use nonaqueous synthetic routes to achieve tight control of any hydrolytic processes taking place. Many species have been prepared this way including Fe_3, Fe_4, Fe_6, Fe_8, Fe_{10}, Fe_{11} and Fe_{16} iron-oxo compounds.**[52,142–145]** Though the compounds produced via this route have an intriguing set of structures and properties, it is not clear that they are good models for the ferritin core since most are not close-packed structures. However, they may be relevant to the early stages of nucleation and core formation. The most relevant compound produced from nonaqueous solutions, and the only characterized poly iron-oxo complex with a 3-D close-packed structure, is $[\mathrm{Fe(III)_4Fe(II)_8(O)_2(OCH_3)_{18}(O_2CCH_3)_6(CH_3OH)_{4.67}}]$. This compound was prepared by Taft *et al.*[146] by controlled oxidation of a methanol solution of Fe(II) and $\mathrm{LiOCH_3}$. The central distinction between this compound and that of the heidi complexes is that the former only contain μ_3-oxo ligands and μ_4, or greater, are needed to form a 3D lattice. The $\mathrm{Fe_{12}}$ compound of Taft *et al.* contains μ_6-oxo ligands.

8 Dps

Another protein able to sequester iron in a mineral core is Dps, a member of the ferritin superfamily. The name Dps comes from DNA-binding protein from starved cells,[147] but although some Dps (for example, those from *E. coli* and *Synechoccus* sp.[147,148]) do bind DNA nonspecifically, others such as those from *Campylobacter jejuni* and *Agrobacterium tumefaciens* have no DNA-binding activity.[149,150] These proteins retain the ability to protect DNA from damage via reactions with hydrogen peroxide.

Those Dps proteins that bind DNA do so nonspecifically via positive residues at the N-terminus of the protein. When a cell is under prolonged stress, Dps cocrystallizes with DNA in vivo.[147] This process is favored because it occurs spontaneously and does not deplete the cell's ATP levels. The formation of a multilayered complex provides a physical barrier around the DNA in addition to the hydrogen peroxide detoxification that accompanies iron oxidation.[147]

In addition to the ferritin from *L. innocua* already mentioned, a variety of proteins show structures and iron assimilation activities similar to Dps, although they do not bind DNA. These include the Dpr (Dps-like peroxide resistance) protein from *Streptococcus mutans*,[151] Dlp from *Bacillus anthracis*[152] and the neutrophil-activating protein from *Helicobacter pylori*, HP-NAP.[153]

8.1 Structure

Dps subunits have a molecular weight of ∼17kDa and a four-helix bundle structure very similar to that of ferritin. The subunits are assembled into dodecamers (Figure 11), again giving a roughly spherical shell surrounding a central cavity with an internal diameter of 45 Å (compared to the 80 Å internal diameter of ferritin).[154] This means that the Dps cavity has a volume approximately one fifth to one sixth the size of ferritin. The protein has tetrahedral symmetry, resulting in two different pores associated with each of four threefold axes. Four of these pores are hydrophobic and, by analogy with ferritin, may provide a route for exiting protons. The remaining four acidic pores correspond to the threefold channels in ferritin and so could be the point of entry for ferrous iron.[154]

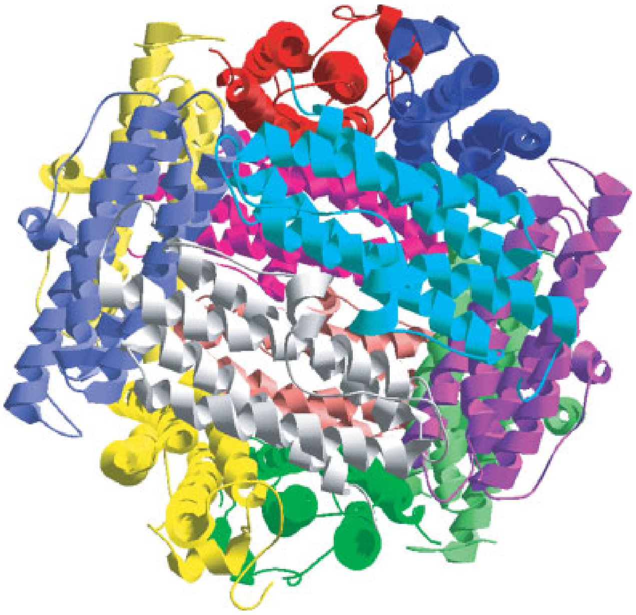

Figure 11 The X-ray structure of Dps from *E. coli* showing its 12-meric structure. Figure created using pdb coordinates 1dps[154]

8.2 Iron Uptake

Dps has ferroxidase activity and has 12 ferroxidase centers, two situated at each subunit dimer interface. The iron ligands are donated from both subunits; H31, H43 and E47 from one subunit and D58 and E62 from the other. The iron-bound ferroxidase center of the Dps from *Bacillus brevis* is shown in Figure 12.

Two ferrous ions bind per Dps subunit with the release of one proton per iron. The oxidation reaction takes place according to reaction (11) below:

$$\mathrm{Fe^{II}\text{-}P + H_2O_2 + H_2O \longrightarrow Fe^{III}{}_2O(OH)\text{-}P + 3H^+} \qquad (11)$$

Hydrogen peroxide is the preferred oxidant, which accounts for the ability of Dps to protect DNA from the effects of hydrogen peroxide; the rate of oxidation using molecular oxygen is little different from that of autooxidation.[156]

At higher iron concentrations, a ferrihydrite core is deposited, up to a maximum of 500 ferric ions per protein. This mineralization reaction occurs via reaction (12) below.

$$\mathrm{2Fe^{2+} + H_2O_2 + 2H_2O \longrightarrow 2FeOOH_{core} + 4H^+} \qquad (12)$$

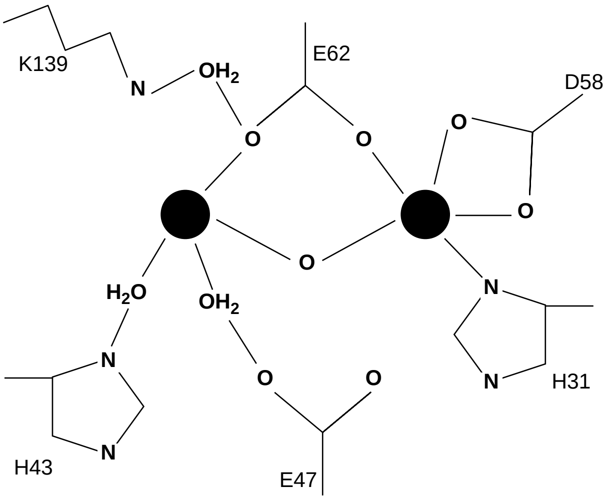

Figure 12 Schematic model of Dps binding site based on the X-ray structure of iron-bound Dps from *B. brevis*[155]

The mechanism of iron oxidation and core formation in Dps differs from that of ferritin and bacterioferritin in that the rate of mineralization is faster than oxidation at the ferroxidase center; in *L. innocua* ferritin and *E. coli* Dps core formation is 60% faster than the ferroxidation reaction.[156]

Fe(III) at the ferroxidase center of Dps has a very high extinction coefficient (~30 000 $M^{-1}\,cm^{-1}$, as contrasted with ~2000 $M^{-1}\,cm^{-1}$ for ferric iron in the bacterioferritin ferroxidase center). This high value, which shows a gradual decrease as the ferroxidase center empties, may be due to the presence of more than one bridging group between the ferric ions.[156] The Dps from *B. brevis* has been crystallized with some iron remaining at the ferroxidase centers, although the two binding sites are not equally occupied. This crystal structure shows the two metal ions linked by a μ-oxo bridge and a water molecule (Figure 12).[155]

9 HEMOSIDERIN

Hemosiderin was the first form of iron storage protein to be identified. It is the chief form of stored iron in animals suffering from iron overload but is also a nonpathological form of storage in many birds and animal species. The protein content of hemosiderin varies, but it appears to be composed of degradation products of ferritins. It is water-insoluble and has a molecular mass greater than 4,000 kDa. It has a high iron-to-protein ratio with the iron in a mineral form, although mineralization varies depending on the pathology of the source. In nonpathological hemosiderin, the iron is mainly in the form of ferrihydrite, as seen for ferritins and frataxin, whereas in genetic hemochromatosis and thalassemia (*see* ***Metal-related Diseases of Genetic Origin***) it is present mainly as amorphous ferric oxide and goethite, respectively. It is not clear how these different cores are formed, although hemosiderin from sources with genetic hemochromatosis often has high levels of phosphate associated with the iron, which may contribute to the amorphous nature of the core.[157] In overloaded liver tissue, studies have shown that hemosiderin is composed mainly of denatured H-chain ferritin. This is possibly due to L-chain ferritin having greater stability, as discussed earlier.[158]

10 FRATAXIN

Although a ferritin has been identified in some mammalian mitochondria, the role of the mitochondrion in the synthesis of heme and iron–sulfur clusters means that this organelle requires a more widespread way of controlling iron homeostasis, and this is where frataxin, a 14 kDa protein found in most eukaryotes, plays a role. A reduction in frataxin levels in humans causes the recessive neurodegenerative and cardiodegenerative disease Friedreich's ataxia. The wide-ranging effects of the disease are due to the broad distribution of the protein, with particularly high expression in the heart, cerebellum, and spinal cord.[159] Patients with the condition have been found to have increased iron deposits, with a resulting hypersensitivity to oxidative stress, as well as reduced synthesis of iron–sulfur cluster proteins. Deletion of the protein in yeast causes similar biochemical effects.[159]

The structure of the human frataxin monomer is an $\alpha\beta$ sandwich with a 7-stranded antiparallel β-sheet and 2 α-helices (Figure 13). A cluster of conserved acidic residues on the protein surface forms a large anionic patch that is likely to provide a site for iron nucleation. Frataxins from

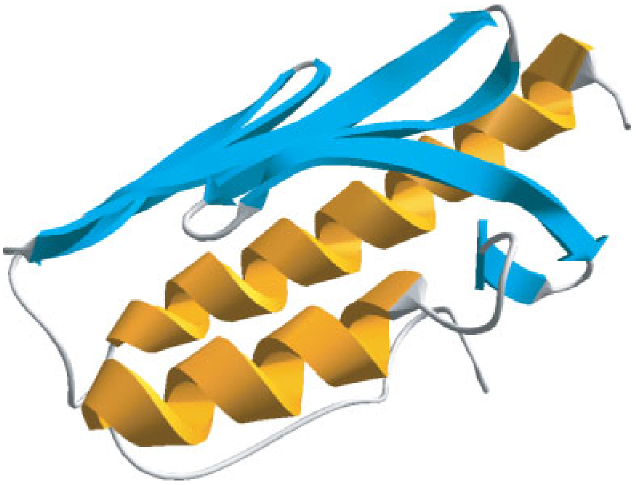

Figure 13 The X-ray structure of human frataxin. The figure was created using pdb coordinates 1ekg[160]

other organisms, including yeast, are predicted to have similar structures.[160]

The coupling between assembly of monomers and Fe(II) oxidation is complex and may be different for frataxin from different sources. A further complication is that the aerobic oxidation of Fe(II) in yeast frataxin is sufficiently slow that in vitro it stabilizes Fe(II) against autooxidation, and under some conditions a 40:60 mixture of Fe(II) and Fe(III) is retained by the protein.[161] Iron binding by human frataxin is faster than with yeast frataxin but the resulting mineral cores are identical; and when human frataxin is expressed in yeast cells grown under iron-rich conditions, roughly 50% of the mitochondrial iron is retained as a complex with frataxin (with iron levels of 5 per monomer).[159] We consider further aspects of yeast and human frataxins separately as they appear to have significantly different properties.

10.1 Yeast Frataxin

At low iron concentrations of Fe(II) (up to 0.5 per monomer), monomers of yeast frataxin are activated to assemble by a combination of ferrous iron and molecular oxygen. Iron oxidation occurs according to reaction (13) below:

$$2Fe^{2+} + O_2 + 2H^+ \longrightarrow 2Fe^{3+} + H_2O_2 \qquad (13)$$

Although this reaction produces hydrogen peroxide, less than 2% of the expected amount can be detected, because most of the peroxide goes on to react with the protein in reactions separate from iron oxidation.[162] At higher concentrations of Fe(II) (up to 1.5 ferrous iron per monomer), autooxidation begins to take over as in reaction (14):

$$4Fe^{2+} + O_2 + 4H^+ \longrightarrow 4Fe^{3+} + 2H_2O \qquad (14)$$

During reactions (13) and (14), the frataxin monomers link to form trimers.[162] These trimers have negatively charged inner surfaces that promote nucleation of the polynuclear iron mineral. As iron concentrations increase further and iron crystallites at the nucleation centers grow, the mineral components of the protein bind to each other, linking the protein trimers pairwise. These ultimately form 48-mers with a molecular weight of 840 kDa, although 96-mers have been observed. These protein aggregates contain up to 50 iron ions per monomer that X-ray absorption spectroscopy indicates is in a ferrihydrite core similar to those found in ferritins, although they are less ordered and much smaller than mammalian ferritin cores.[162–164]

Iron oxidation and trimer formation appear to be linked, as no iron-containing monomers have been observed for yeast frataxin. Trimers do not form under anaerobic conditions in the presence of Fe(II)[162] or following the addition of other divalent metal ions or Fe(III),[161] and the removal of the tightly bound Fe(III) using EDTA causes the protein to disassemble into monomers. Given the stoichiometry of the ferroxidation reaction and the low concentrations required to saturate ferroxidation, it has been suggested that a dinuclear iron site is formed between three monomers.[162]

10.2 Human Frataxin

Expression of human frataxin in *E. coli* gives a mixture of preassembled aggregates of ~1MDa and rod-shaped polymers of these, which can accommodate roughly 7–10 Fe per monomer.[159] The same protein expressed in *S. cerevisiae* forms a mixture of monomers and higher molecular weight (>600 kDa) aggregates. In contrast to yeast frataxin, treatment of these monomers with Fe(II) in an aerobic environment results in minimal aggregation (less than 10%). Although the observed preassembly may be an artifact due to overexpression, the aggregates formed are soluble and remain active in accumulating iron. They are also less prone to degradation than monomers. A similar distribution of monomers and higher molecular weight aggregates are also observed in native samples taken from mouse heart.[159]

11 HEMOPEXIN

Following degradation of heme-containing proteins, free heme is released into the extracellular environment. Although the iron is bound in the porphyrin ring, this is not enough to protect the organism from the potentially toxic effects of iron catalyzed Fenton-type reactions and, in addition, free heme provides a good source of iron to pathogenic bacteria. Mammals minimize these problems by the production of hemopexin, a serum protein that binds one heme per molecule with high affinity (K_d <1pM) as a low-spin bis-histidyl complex.[165] This process of heme recycling therefore not only protects the organism from the deleterious effects of free iron but has the additional benefit of enabling the iron within the heme to be reused.

Hemopexin is a 40 kDa protein divided into two domains with a high level of homology between them (25% amino acid sequence identity). Both domains are four-bladed β-propellers linked by a 20-residue hinge region (see Figure 14), with the bound heme in a pocket between the domains that is formed by the linker region. H213 from the linker and H266 from the C-terminal domain bind the heme. Although the N-terminal domain does not bind heme in the intact protein, the separated domain prepared by proteolytic cleavage of the intact protein does bind heme and in this case too, the heme binds as a low-spin bis-histidyl complex, though the identity of the heme ligands have not been determined.[165–167] Probably because the heme binding site involves the flexible linker peptide, heme binding to intact hemopexin induces a conformational change in the protein that apparently facilitates receptor binding.[165,168]

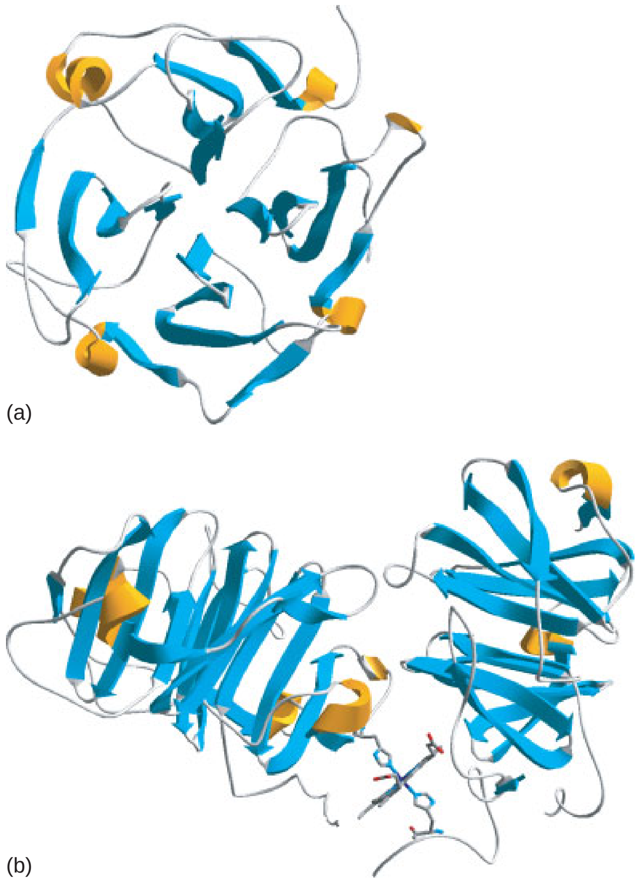

Figure 14 (a) The X-ray structure of heme-bound rabbit hemopexin. (b) shows the β-propeller structure of individual domains. The figure was created using pdb coordinates 1qhu[168]

Hemopexin delivers heme to specific cells, chiefly in the liver, by a mechanism involving receptor-mediated endocytosis similar to that employed by diferric transferrin.[165] Heme-loaded hemopexin binds to a specific receptor on the cell surface, with the hemopexin C-terminal domain promoting interactions between the two proteins. Following endocytosis, the heme is released from hemopexin in the low-pH environment of the endosome. At this point, the heme is released and the porphyrin ring degraded via heme oxygenase. At the same time, downregulation of transferrin receptors and induction of ferritin synthesis occurs as a protective mechanism to prevent cell damage from the released iron.[169]

12 HEMOPHORES

In addition to siderophores, pathogenic bacteria possess a range of other mechanisms to acquire iron from their host. Specific transferrin or lactoferrin receptors on the outer membrane allow iron to be removed from the host protein and transported into the cell, although the mechanism for this process is as yet unclear. Proteases and cytolysins may be released into the host by bacteria, and these enzymes then release hemoglobin from erythrocytes. This hemoglobin, or the free heme, can be transported into the bacterial cells by heme uptake systems with specific outer membrane receptors. Also, some pathogens secrete extracellular proteins called hemophores, which bind free heme and return it to the bacteria in a similar kind of uptake pathway to siderophore-mediated acquisition of nonheme iron. A well-characterized example of a hemophore is the HasA protein.

HasA has been identified in *P. aeruginosa*,[170] *P. fluorescens*,[171] *Yersinia pestis*[172] and *Serratia marcescens*.[173] It is a 19 kDa protein with no sequence homology to other known heme proteins. It binds free heme tightly and can remove it from hemoglobin, a property it shares with hemopexin. The mechanism by which HasA removes heme from hemoglobin is unclear; it does not form a stable complex with hemoglobin so there may be formation of a transient protein complex or alternatively binding may be due to a higher affinity of HasA for heme following diffusion of heme out of hemoglobin.[174]

The crystal structure of heme-loaded HasA has been determined, and reveals an $\alpha\beta$ protein that does not resemble any known structure (see Figure 15). The heme molecule is located between the α and β regions of the protein and is exposed to the bulk solvent. The heme iron is ligated by His32 and Tyr75, although His32 is not essential for in vitro heme binding. Numerous hydrophobic and stacking interactions with the porphyrin ring provided by surrounding residues in the heme pocket help contribute to the high binding affinity

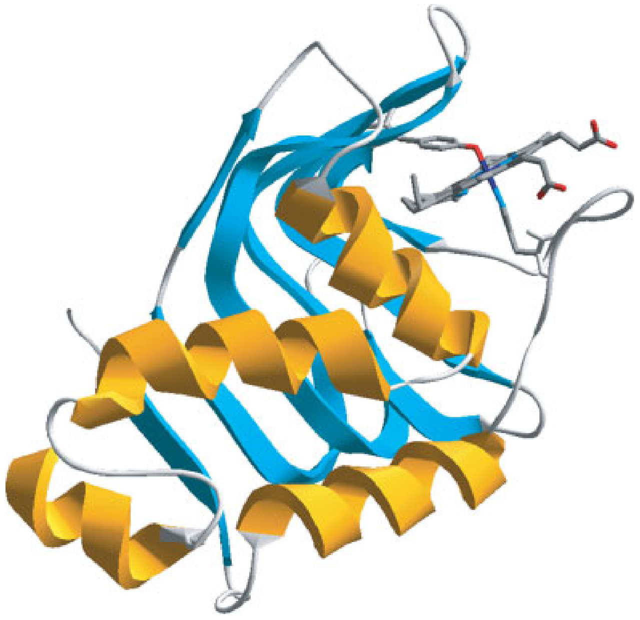

Figure 15 The X-ray structure of HasA from *S. marcescens* showing heme ligated by Y75 and H32. The figure was created using pdb coordinates 1b2v[176]

of the protein for heme. Another histidine residue, His83, stabilizes the iron-phenolate bond via hydrogen bonding and holds the tyrosine residue in an optimal orientation for heme binding. When Tyr75 is removed, His83 appears to be able to act as a replacement iron ligand.[175]

Once loaded with heme, HasA delivers it to its outer membrane receptor, HasR. This is able to take up heme directly, but the addition of HasA greatly increases its efficiency. Like uptake of many ferric-siderophore complexes, entry of heme into the cell via HasR requires the TonB-ExbB-ExbD system, although formation of the HasA-HasR complex is independent of TonB. Two regions of HasA (residues 51–60 and 95–107) bind HasR independently of each other, with a high enough affinity that the deletion of one region does not prevent complex formation. This has led to a suggested scheme in which the two regions, which fall either side of the ligating tyrosine, bind to HasR and then move apart, opening the heme pocket and destabilizing the heme-protein contacts.[177] Another factor affecting heme uptake by the cell is that apo and heme-loaded HasA bind the HasR receptor with apparently similar affinities; experiments using a mixture of radiolabelled and unlabelled HasA indicate that the proteins do not exchange. This raises the question of why the receptors do not become saturated with apo HasA once the heme has been delivered. One possibility is that heme-loaded HasA transfers heme to receptor-bound apo HasA, a mechanism we have already encountered in this article for some siderophore-receptor systems.[174]

13 RELATED ARTICLES

Biomineralization; Iron: Heme Proteins & Dioxygen Transport & Storage; Iron: Heme Proteins & Electron Transport; Iron: Heme Proteins, Mono- & Dioxygenases; Iron: Heme Proteins, Peroxidases, Catalases & Catalase-peroxidases; Iron: Inorganic & Coordination Chemistry; Iron Proteins with Dinuclear Active Sites; Iron Proteins with Mononuclear Active Sites; Iron–Sulfur Proteins; Iron Transport: Siderophores; Metal Ion Toxicity.

14 REFERENCES

1. H. M. Baker, B. F. Anderson, and E. N. Baker, *Proc. Natl. Acad. Sci. U.S.A.*, 2003, **100**, 3579.
2. K. P. Locher, B. Rees, R. Koebnik, A. Mitschler, L. Moulinier, J. P. Rosenbusch, and D. Moras, *Cell*, 1998, **95**, 771.
3. S. K. Buchanan, B. S. Smith, L. Venkatramani, D. Xia, L. Esser, M. Palnitkar, R. Chakraborty, D. van der Helm, and J. Deisenhofer, *Nat. Struct. Biol.*, 1999, **6**, 56.
4. W. W. Yue, S. Grizot, and S. K. Buchanan, *J. Mol. Biol.*, 2003, **332**, 353.
5. R. Koebnik, K. P. Locher, and P. van Gelder, *Mol. Microbiol.*, 2000, **37**, 239.
6. F. Endriß, M. Braun, H. Killman, and V. Braun, *J. Bacteriol.*, 2003, **185**, 4683.
7. A. Stintzi, C. Barnes, and K. Raymond, *Proc. Natl. Acad. Sci. U.S.A.*, 2000, **97**, 10691.
8. T. E. Clarke, S.-Y. Ku, D. R. Dougan, H. J. Vogel, and L. W. Tari, *Nat. Struct. Biol.*, 2000, **7**, 287.
9. B. F. Matzanke, S. Anemüller, V. Schünemann, A. X. Trautwein, and K. Hantke, *Biochemistry*, 2004, **43**, 1386.
10. B. Lonnerdal and S. Iyer, *Annu. Rev. Nutr.*, 1995, **15**, 93.
11. M. Legrain, V. Mazarin, S. W. Irwin, B. Bouchon, M. J. Quentin-Millet, E. Jacobs, and A. B. Schryvers, *Gene*, 1993, **130**, 73.
12. S. M. Loosmore, Y. P. Yang, D. C. Coleman, J. M. Shortreed, D. M. England, R. E. Harkness, P. S. Chong, and M. H. Klein, *Mol. Microbiol.*, 1996, **19**, 575.
13. C. Ferreiros, M. T. Criado, and J. A. Gomez, *Comp. Biochem. Physiol., B*, 1999, **123**, 1.
14. R. E. Harkness, P. Chong, and M. H. Klein, *J. Bacteriol.*, 1992, **174**, 2425.
15. P. J. Halbrooks, Q.-Y. He, S. K. Briggs, S. J. Everse, V. C. Smith, R. T. A. MacGillivray, and A. B. Mason, *Biochemistry*, 2003, **42**, 3701.
16. P. Ponka and C. N. Lok, *Int. J. Biochem. Cell Biol.*, 1999, **31**, 1111.
17. H. Sun, M. C. Cox, H. Li, and P. J. Sadler, *Struct. Bonding*, 1997, **88**, 71.
18. E. N. Baker and P. F. Lindley, *J. Inorg. Biochem.*, 1992, **47**, 147.
19. D. R. Hall, J. M. Hadden, G. A. Leonard, S. Bailey, M. Neu, M. Winn, and P. F. Lindley, *Acta Crystallogr.*, 2002, **58**, 70.
20. E. N. Baker, *Nat. Struct. Biol.*, 1997, **4**, 869.
21. C. M. Bruns, A. J. Nowalk, A. S. Arvai, M. A. McTigue, K. G. Vaughn, T. A. Mietzner, and C. E. McRee, *Nat. Struct. Biol.*, 1997, **4**, 919.
22. A. Sharma, K. R. Rajashankar, M. P. Yadav, and T. P. Singh, *Acta Crystallogr.*, 1999, **D55**, 1152.
23. T. Yoshiga, T. Georgieva, B. C. Dunkov, N. Harizanova, K. Ralchev, and J. H. Law, *Eur. J. Biochem.*, 1999, **260**, 414.
24. E. N. Baker, *Adv. Inorg. Chem.*, 1994, **41**, 389.
25. O. Zak, K. Ikuta, and P. Aisen, *Biochemistry*, 2002, **41**, 7416.
26. H. M. Baker, B. F. Anderson, A. M. Brodie, M. S. Shongwe, C. A. Smith, and E. N. Baker, *Biochemistry*, 1996, **35**, 9007.
27. L.-N. Lin, A. B. Mason, R. C. Woodworth, and J. F. Brandts, *Biochemistry*, 1994, **33**, 1881.
28. P. Aisen, A. Leibman, and J. Zweier, *J. Biol. Chem.*, 1978, **253**, 1930.

29. P. Aisen, C. Enns, and M. Wessling-Resnick, *Int. J. Biochem. Cell Biol.*, 2001, **33**, 940.
30. P. Aisen, R. Aasa, and A. G. Redfield, *J. Biol. Chem.*, 1969, **244**, 4628.
31. W. R. Harris, *J. Inorg. Biochem.*, 1986, **27**, 41.
32. S. A. Kretchmar, Z. E. Reyes, and K. N. Raymond, *Biochim. Biophys. Acta*, 1988, **956**, 85.
33. D. C. Kraiter, O. Zak, P. Aisen, and A. L. Crumbliss, *Inorg. Chem.*, 1998, **37**, 964.
34. G. W. Bates, E. F. Workman Jr, and M. R. Schlabach, *Biochem. Biophys. Res. Commun.*, 1973, **50**, 84.
35. P. F. Lindley, *Rep. Prog. Phys.*, 1996, **59**, 867.
36. Z. L. Harris, Y. Takahashi, H. Miyajima, M. Serizawa, R. T. A. MacGillivray, and J. D. Gitlin, *Proc. Natl. Acad. Sci. U.S.A.*, 1995, **92**, 2539.
37. H. Miyajima, *Neuropathology*, 2003, **23**, 345.
38. Z. L. Harris, A. P. Durley, T. K. Man, and J. D. Gitlin, *Proc. Natl. Acad. Sci. U.S.A.*, 1999, **96**, 10812.
39. P. Lindley, G. Card, I. Zaitseva, and V. Zaitsev, *Perspect. Bioinorg. Chem.*, 1999, **4**, 51.
40. M. O. Pulina, E. T. Zakharova, A. V. Sokolov, M. M. Shavlovski, M. G. Bass, K. V. Solovyov, V. N. Kokryakov, and V. B. Vasilyev, *Biochem. Cell Biol.*, 2002, **80**, 35.
41. M. Hémadi, P. H. Kahn, G. Miquel, and J.-M. El Hage Chahine, *Biochemistry*, 2004, **43**, 1736.
42. N. C. Andrews, M. D. Fleming, and H. Gunshin, *Nutr. Rev.*, 1999, **57**, 114.
43. S. Dhungana, C. H. Taboy, O. Zax, M. Larvie, A. L. Crumbliss, and P. Aisen, *Biochemistry*, 2004, **43**, 205.
44. O. Zak, P. Aisen, J. B. Crawley, C. L. Joannou, K. J. Patel, M. Rafiq, and R. W. Evans, *Biochemistry*, 1995, **34**, 14428.
45. J. C. Dewan, B. Mikami, M. Hirose, and J. C. Sacchettini, *Biochemistry*, 1993, **32**, 11963.
46. Q.-Y. He, A. B. Mason, B. M. Tam, R. T. A. MacGillivray, and R. C. Woodworth, *Biochemistry*, 1999, **38**, 9704.
47. P. Aisen, *Met. Ions in Biol. Syst.*, 1998, **35**, 563.
48. H. M. Marques, *J. Inorg. Biochem.*, 1991, **41**, 187.
49. Y. Tomimatsu and J. W. Donovan, *FEBS Lett.*, 1976, **71**, 299.
50. S. Sun and N. D. Chasteen, *Biochemistry*, 1994, **33**, 15095.
51. X. Yang, N. E. Le Brun, A. J. Thomson, G. R. Moore, and N. D. Chasteen, *Biochemistry*, 2000, **39**, 4915.
52. A. K. Powell, in 'Chemistry of Iron', ed. J. Silver, Blackie, Glasgow, 1993, p. 244.
53. M. R. McDevitt, A. W. Addison, E. Sinn, and L. K. Thompson, *Inorg. Chem.*, 1990, **29**, 3425.
54. S. D. Gray-Owen and A. B. Schryvers, *Trends Microbiol.*, 1996, **4**, 185.
55. S. Dhungana, C. H. Taboy, D. S. Anderson, K. G. Vaughn, P. Aisen, T. A. Mietzner, and A. L. Crumbliss, *Proc. Natl. Acad. Sci. U.S.A.*, 2003, **100**, 3659.
56. S. R. Shouldice, D. R. Dougan, R. J. Skene, L. W. Tari, D. E. McRee, R.-H. Yu, and A. B. Schryvers, *J. Biol. Chem.*, 2003, **278**, 11513.
57. S. D. Kirby, F. A. Lainson, W. Donachie, A. Okabe, M. Tokuda, O. Hatase, and A. B. Schryvers, *Microbiol.*, 1998, **144**, 3425.
58. S. R. Shouldice, D. R. Dougan, P. A. Williams, R. J. Skene, G. Snell, D. Scheibe, S. Kirby, D. J. Hosfield, D. E. McRee, A. B. Schryvers, and L. W. Tari, *J. Biol. Chem.*, 2003, **278**, 41093.
59. D. Alexeev, H. Zhu, M. Guo, W. Zhong, D. J. B. Hunter, W. Yang, D. J. Campopiano, and P. J. Sadler, *Nat. Struct. Biol.*, 2003, **10**, 297.
60. H. Zhu, D. Alexeev, D. J. B. Hunter, D. J. Campopiano, and P. J. Sadler, *Biochem. J.*, 2003, **376**, 35.
61. S. R. Shouldice, R. J. Skene, D. R. Dougan, D. E. McRee, L. W. Tari, and A. B. Schryvers, *Biochemistry*, 2003, **42**, 11908.
62. S. A. Malone, A. Lewin, M. A. Kilic, D. Svistunenko, R. Boetzel, C. Cooper, M. T. Wilson, N. E. Le Brun, S. Spiro, and G. R. Moore, *J. Am. Chem. Soc.*, 2003, **126**, 496.
63. M. E. Conrad and J. N. Umbreit, *Blood Cell. Mol. Dis.*, 2002, **29**, 336.
64. A. T. McKie, D. Barrow, G. O. Latunde-Dada, A. Rolfs, G. Sager, E. Mudaly, M. Mudaly, C. Richardson, D. Barlow, A. Bomford, T. J. Peters, K. B. Raja, S. Shirali, M. A. Hediger, F. Farzaneh, and R. J. Simpson, *Science*, 2001, **291**, 1755.
65. V. Picard, G. Govoni, N. Jabado, and P. Gros, *J. Biol. Chem.*, 2000, **275**, 35738.
66. S. Lam-Yuk-Tseung, G. Govoni, J. Forbes, and P. Gros, *Blood*, 2003, **101**, 3699.
67. N. T. V. Le and D. R. Richardson, *Int. J. Biochem., Cell Biol.*, 2002, **34**, 103.
68. H. Chen, T. Su, Z. K. Attieh, T. C. Fox, A. T. McKie, G. J. Anderson, and C. D. Vulpe, *Blood*, 2003, **102**, 1893.
69. J. Velayudhan, N. J. Hughes, A. A. McColm, J. Bagshaw, C. L. Clayton, S. C. Andrews, and D. J. Kelly, *Mol. Microbiol.*, 2000, **37**, 274.
70. R. M. Tsolis, A. J. Bäumler, F. Heffron, and I. Stojiljkovic, *Infect. Immun.*, 1996, **64**, 4549.
71. K. Hantke, *J. Bact.*, 1997, **178**, 6201.
72. P. M. Harrison and P. Arosio, *Biochim. Biophys. Acta*, 1996, **1275**, 161.
73. G. C. Ford, P. M. Harrison, D. W. Rice, J. M. A. Smith, A. Treffry, J. L. White, and J. Yariv, *Philos Trans. R. Soc. London. B.*, 1984, **304**, 551.
74. A. K. Powell, *Met. Ions Biol. Syst.*, 1998, **35**, 515.
75. F. Frolow, A. J. Kalb, and J. Yariv, *Nat. Struct. Biol.*, 1994, **1**, 453.
76. P. D. Hempstead, S. J. Yewdall, A. R. Fernie, D. M. Lawson, P. J. Artymiuk, D. W. Rice, G. C. Ford, and P. M. Harrison, *J. Mol. Biol.*, 1997, **268**, 424.

77. N. D. Chasteen and P. M. Harrison, *J. Struct. Biol.*, 1999, **126**, 182.
78. P. Santambrogio, S. Levi, A. Cozzi, E. Rovida, A. Albertini, and P. Arosio, *J. Biol. Chem.*, 1993, **268**, 12744.
79. T. Takahashi and S. Kuyucak, *Biophys. J.*, 2003, **84**, 2256.
80. M. A. Carrondo, *EMBO J.*, 2003, **9**, 1959.
81. D. M. Lawson, P. J. Artymiuk, S. J. Yewdall, J. M. Smith, J. C. Livingstone, A. Treffry, A. Luzzago, S. Levi, P. Arosio, G. Cesareni, C. D. Thomas, W. V. Shaw, and P. M. Harrison, *Nature*, 1991, **349**, 541.
82. X. Yang, Y. Chen-Barrett, P. Arosio, and N. D. Chasteen, *Biochemistry*, 1998, **37**, 9743.
83. G. Zhao, F. Bou-Abdallah, X. Yang, P. Arosio, and N. D. Chasteen, *Biochemistry*, 2001, **40**, 10832.
84. A. Treffry, Z. Zhao, M. A. Quail, J. R. Guest, and P. M. Harrison, *Biochemistry*, 1995, **34**, 15204.
85. J. Fetter, J. Cohen, D. Danger, J. Sanders-Loehr, and E. C. Theil, *J. Biol., Inorg. Chem.*, 1992, **2**, 652.
86. P. M. Harrison and A. Treffry, in ‘Iron Metabolism: Inorganic Biochemistry and Regulatory Mechanisms’, eds. G. C. Ferreira, J. J. G. Moura and R. Franco, Wiley-VCH, Weinham, 1999, p. 227.
87. E. Y. Tshuva and S. J. Lippard, *Chem. Rev.*, 2004, **104**, 987.
88. Y. Chen-Barrett, P. M. Harrison, A. Treffry, M. A. Quail, P. Arosio, P. Santambrogio, and N. D. Chasteen, *Biochemistry*, 1995, **34**, 7847.
89. A. Treffry, Z. Zhao, M. A. Quail, J. R. Guest, and P. M. Harrison, *Biochemistry*, 1997, **36**, 432.
90. R. R. Crichton, A. Herbas, O. Chavez-Alba, and F. Roland, *J. Biol. Inorg. Chem.*, 1996, **1**, 567.
91. B. Gallois, B. L. d’Estaintot, M.-A. Michaux, A. Dautant, T. Granier, G. Précigoux, J.-A. Soruco, F. Roland, O. Chavez-Alba, A. Herbas, and R. R. Crichton, *J. Biol. Inorg. Chem.*, 1997, **2**, 360.
92. S. Levi, P. Santambrogio, A. Cozzi, E. Rovida, B. Corsi, E. Tamborini, S. Spada, A. Albertini, and P. Arosio, *J. Mol. Biol.*, 1994, **238**, 649.
93. A. J. Hudson, S. C. Andrews, C. Hawkins, J. M. Williams, M. Izuhara, F. C. Meldrum, S. Mann, P. M. Harrison, and J. R. Guest, *Eur. J. Biochem.*, 1993, **218**, 985.
94. P. D. Hempstead, A. J. Hudson, P. J. Artymiuk, S. C. Andrews, M. J. Banfield, J. R. Guest, and P. M. Harrison, *FEBS Lett.*, 1994, **350**, 258.
95. Z. Zhao, A. Treffry, M. A. Quail, J. R. Guest, and P. M. Harrison, *J. Chem. Soc. Dalton Trans.*, 1997, 3977.
96. E. I. Stiefel and G. D. Watt, *Nature*, 1979, **279**, 81.
97. G. R. Moore, F. H. Kadir, F. K. al-Massad, N. E. Le Brun, A. J. Thomson, C. Greenwood, J. N. Keen, and J. B. Findlay, *Biochem. J.*, 1994, **304**, 493.
98. M. R. Cheesman, A. J. Thomson, C. Greenwood, G. R. Moore, and F. Kadir, *Nature*, 1990, **346**, 771.
99. S. C. Andrews, N. E. Le Brun, V. Barynin, A. J. Thomson, G. R. Moore, J. R. Guest, and P. M. Harrison, *J. Biol. Chem.*, 1995, **270**, 23266.
100. S. Macedo, C. V. Romão, E. Mitchell, P. M. Matias, M. Y. Liu, A. V. Xavier, J. LeGall, M. Teixeira, P. Lindley, and M. A. Carrondo, *Nat. Struct. Biol.*, 2003, **10**, 285.
101. G. R. Moore, F. H. A. Kadir, and F. Al-Massad, *J. Inorg. Biochem.*, 1992, **47**, 175.
102. N. E. Le Brun, S. C. Andrews, J. R. Guest, P. M. Harrison, G. R. Moore, and A. J. Thomson, *Biochem. J.*, 1995, **312**, 385.
103. N. E. Le Brun, M. T. Wilson, S. C. Andrews, P. M. Harrison, J. R. Guest, A. J. Thomson, and G. R. Moore, *FEBS Lett.*, 1993, **333**, 197.
104. F. Bou-Abdallah, A. C. Lewin, N. E. Le Brun, G. R. Moore, and N. D. Chasteen, *J. Biol. Chem.*, 2002, **277**, 37064.
105. S. Baaghil, A. Lewin, G. R. Moore, and N. E. Le Brun, *Biochemistry*, 2003, **42**, 14047.
106. P. M. Harrison, S. C. Andrews, P. J. Artymiuk, G. C. Ford, J. R. Guest, J. Hirsmann, D. M. Lawson, J. C. Livingstone, J. M. A. Smith, A. Treffry, and S. J. Yewdall, *Adv. Inorg. Chem.*, 1991, **36**, 449.
107. S. J. A. Fatemi, F. H. A. Kadir, D. J. Williamson, and G. R. Moore, *Adv. Inorg. Chem.*, 1991, **36**, 409.
108. R. R. Crichton and R. J. Ward, in ‘Iron and Human Disease’, ed. R. B. Lauffer, CRC Press, 1992, p. 23.
109. J. Gralnick and D. Downs, *Proc. Natl. Acad. Sci. U.S.A.*, 2001, **98**, 8030.
110. J. A. Gralnick and D. Downs, *J. Biol. Chem.*, 2003, **278**, 20708.
111. R. P. Garg, C. J. Vargo, X. Cui, and D. M. Kurtz, Jr *Biochemistry*, 1996, **35**, 6297.
112. M. A. Quail, P. Jordan, J. M. Grogan, J. N. Butt, M. Lutz, A. J. Thomson, S. C. Andrews, and J. R. Guest, *Biochem. Biophys. Res. Commun.*, 1996, **229**, 635.
113. G. D. Watt, D. Jacobs, and R. B. Frankel, *Proc. Natl. Acad. Sci. U.S.A.*, 1988, **85**, 7457.
114. D. L. Jacobs, G. D. Watt, R. B. Frankel, and G. C. Papaefthymiou, *Biochemistry*, 1989, **28**, 1650.
115. X. Lie, W. Jin, and E. C. Theil, *Proc. Natl. Acad. Sci. U.S.A.*, 2003, **100**, 3653.
116. G. D. Watt, R. B. Frankel, G. C. Papaefthymiou, K. Spartalian, and E. I. Stiefel, *Biochemistry*, 1986, **25**, 4330.
117. G. D. Watt, R. B. Frankel, and G. C. Papaefthymiou, *Proc. Natl. Acad. Sci. U.S.A.*, 1985, **82**, 3640.
118. M. R. Cheesman, F. H. A. Kadir, J. Al-Basseet, F. Al-Massad, J. Farrar, C. Greenwood, A. J. Thomson, and G. R. Moore, *Biochem. J.*, 1992, **286**, 361.
119. R. K. Watt, R. B. Frankel, and G. D. Watt, *Biochemistry*, 1992, **31**, 9673.
120. J. L. Johnson, D. C. Norcross, P. Arosio, R. B. Frankel, and G. D. Watt, *Biochemistry*, 1999, **38**, 4089.

121. F. H. Kadir, F. K. al-Massad, S. J. Fatemi, H. K. Singh, M. T. Wilson, and G. R. Moore, *Biochem. J.*, 1991, **278**, 817.

122. N. E. Le Brun, A. J. Thomson, and G. R. Moore, *Structure and Bonding*, 1997, **88**, 103.

123. G. R. Moore, S. Mann, and J. V. Bannister, *J. Inorg. Biochem.*, 1986, **28**, 329.

124. T. G. St Pierre and S. Mann, in ‘Biomineralization: Chemical & Biochemical Perspectives’, eds. S. Mann, J. Webb, and R. J. P. Williams, VCH, Weinheim, 1989, p. 295.

125. J. L. Johnson, M. Cannon, R. K. Watt, R. B. Frankel, and G. D. Watt, *Biochemistry*, 1999, **38**, 6706.

126. E. C. Theil and T. Hase, in ‘Iron Chelation in Plants and Soil Microorganisms’, Academic Press, 1993, p. 133.

127. J. S. Rohrer, Q. T. Islam, G. D. Watt, D. E. Sayers, and E. C. Theil, *Biochemistry*, 1990, **29**, 259.

128. K. M. Towe and W. F. Bradley, *J. Colloid Interface Sci.*, 1967, **24**, 384.

129. R. A. Eggleton and R. W. Fitzpatrick, *Clays and Clay Miner.*, 1990, **38**, 335.

130. S. Mann, J. M. Williams, A. Treffry, and P. M. Harrison, *J. Mol. Biol.*, 1987, **198**, 405.

131. T. G. St Pierre, S. H. Bell, D. P. E. Dickson, S. Mann, J. Webb, G. R. Moore, and R. J. P. Williams, *Biochim. Biophys. Acta*, 1986, **870**, 127.

132. N. E. Le Brun, G. R. Moore, and A. J. Thomson, *Mol. Phys.*, 1995, **85**, 1061.

133. M. R. Cheesman, N. E. Le Brun, F. H. A. Kadir, A. J. Thomson, G. R. Moore, S. C. Andrews, J. R. Guest, P. M. Harrison, J. M. A. Smith, and S. J. Yewdall, *Biochem. J.*, 1993, **292**, 47.

134. M. P. Weir, J. F. Gibson, and T. J. Peters, *Cell Biochem. and Funct.*, 1984, **2**, 186.

135. N. Deighton, A. Abu-Raqabah, I. J. Rowland, M. C. R. Symons, T. J. Peters, and R. J. Ward, *J. Chem. Soc., Faraday Trans.*, 1991, **87**, 3193.

136. T. G. Spiro, S. E. Allerton, J. Renner, A. Terzis, R. Bils, and P. Saltman, *J. Am. Chem. Soc.*, 1966, **88**, 2721.

137. T. G. Spiro, L. Pape, and P. Saltman, *J. Am. Chem. Soc.*, 1967, **89**, 5555.

138. E. C. Theil, D. E. Sayers, and M. A. Brown, *J. Biol. Chem.*, 1979, **254**, 8132.

139. C. Y. Yang, A. M. Bryan, E. C. Theil, D. E. Sayers, and L. H. Bowen, *J. Inorg. Biochem.*, 1986, **28**, 393.

140. E. M. Coe, L. H. Bowen, A. Speer, Z. Wang, D. E. Sayers, and R. D. Bereman, *J. Inorg. Biochem.*, 1995, **58**, 269.

141. S. L. Heath and A. K. Powell, *Angew. Chem., Int. Ed. Engl.*, 1992, **31**, 191.

142. S. J. Lippard, *Angew. Chem., Int. Ed. Engl.*, 1988, **27**, 344.

143. K. S. Hagen, *Angew. Chem., Int. Ed. Engl.*, 1992, **31**, 1010.

144. A. Caneschi, A. Cornia, A. C. Fabretti, and D. Gatteschi, *Angew. Chem., Int. Ed. Engl.*, 1995, **34**, 2716.

145. C. Benelli, S. Parsons, G. A. Solan, and R. E. P. Winpenny, *Angew. Chem., Int. Ed. Engl.*, 1996, **35**, 1825.

146. K. L. Taft, G. C. Papaefthymiou, and S. J. Lippard, *Science*, 1993, **259**, 1302.

147. A. Martinez and R. Kolter, *J. Bacteriol*, 1997, **179**, 5188.

148. M. M. O. Peña and G. S. Bullerjahn, *J. Biol. Chem.*, 1995, **270**, 22478.

149. T. Ishikawa, Y. Mizunoe, S.-i. Kawabata, A. Takade, M. Harada, S. N. Wai, and S.-i. Yoshida, *J. Bacteriol*, 2003, **185**, 1010.

150. P. Ceci, A. Ilari, E. Falvo, and E. Chiancone, *J. Biol. Chem.*, 2003, **278**, 20319.

151. Y. Yamamoto, M. Higuchi, L. B. Poole, and Y. Kamio, *J. Bacteriol*, 2000, **182**, 3740.

152. E. Papinutto, W. G. Dundon, N. Pitulis, R. Battistutta, C. Montecucco, and G. Zanotti, *J. Biol. Chem.*, 2002, **277**, 15093.

153. F. Tonello, W. G. Dundon, B. Satin, M. Molinari, G. Tognon, G. Grandi, G. Del Giudice, R. Rappuoli, and C. Montecucco, *Mol. Microbiol.*, 1999, **34**, 238.

154. R. A. Grant, D. J. Filman, S. E. Finkel, R. Kolter, and J. M. Hogle, *Nat. Struct. Biol.*, 1998, **5**, 294.

155. B. Ren, G. Tibbelin, T. Kajino, O. Asami, and R. Ladenstein, *J. Mol. Biol.*, 2003, **329**, 467.

156. G. Zhao, P. Ceci, A. Ilari, L. Giangiacomo, T. M. Laue, E. Chiancone, and N. D. Chasteen, *J. Biol. Chem.*, 2002, **277**, 27689.

157. E. Miyazaki, J. Kato, M. Kobune, K. Okomura, K. Sasaki, N. Shintani, P. Arosio, and Y. Niitsu, *Gut*, 2002, **50**, 413.

158. R. J. Ward, R. Legssyer, C. Henry, and R. R. Crichton, *J. Inorg. Biochem.*, 2000, **79**, 311.

159. P. Cavadini, H. A. O’Neill, O. Benada, and G. Isaya, *Hum. Mol. Genet.*, 2002, **11**, 217.

160. S. Dhe-Paganon, R. Shigeta, Y. I. Chi, M. Ristow, and S. E. Shoelson, *J. Biol. Chem.*, 2000, **275**, 30753.

161. J. Adamec, F. Rusnak, W. G. Owen, S. Naylor, L. M. Benson, A. M. Gacy, and G. Isaya, *Am. J. Hum. Genet.*, 2000, **67**, 549.

162. S. Park, O. Gakh, S. M. Mooney, and G. Isaya, *J. Biol. Chem.*, 2002, **277**, 38589.

163. S. Park, O. Gakh, H. A. O’Neill, A. Mangravita, H. Nichol, G. C. Ferreira, and G. Isaya, *J. Biol. Chem.*, 2003, **278**, 31340.

164. H. Nichol, O. Gakh, H. A. O’Neill, I. J. Pickering, G. Isaya, and G. N. George, *Biochemistry*, 2003, **42**, 5971.

165. W. T. Morgan and A. Smith, *Adv. Inorg. Chem.*, 2001, **51**, 205.

166. T. Satoh, H. Satoh, S.-I. Iwahara, Z. Hrkal, D. H. Peyton, and U. Muller-Eberhard, *Proc. Natl. Acad. Sci. U.S.A.*, 1994, **91**, 8423.

167. M. C. Cox, N. Le Brun, A. J. Thomson, A. Smith, W. T. Morgan, and G. R. Moore, *Biochim. Biophys. Acta*, 1995, **1253**, 215.

168. M. Paoli, B. F. Anderson, H. M. Baker, W. T. Morgan, A. Smith, and E. N. Baker, *Nat. Struct. Biol.*, 1999, **6**, 926.
169. J. R. Delanghe and M. R. Langlois, *Clin. Chim. Acta*, 2001, **312**, 13.
170. S. Létoffé, V. Redeker, and C. Wandersman, *Mol. Microbiol.*, 1998, **28**, 1223.
171. A. Idei, E. Kawai, H. Akatsuka, and K. Omori, *J. Bacteriol*, 1999, **181**, 7545.
172. M. S. Rossi, J. D. Fetherston, S. Létoffé, E. Carniel, R. D. Perry, and J. M. Ghigo, *Infect. Immun.*, 2001, **69**, 6707.
173. S. Létoffé, J. M. Ghigo, and C. Wandersman, *J. Bacteriol*, 1994, **176**, 5372.
174. S. Létoffé, C. Deniau, N. Wolff, E. Dassa, P. Delepelaire, A. Lecroisey, and C. Wandersman, *Mol. Microbiol.*, 2001, **41**, 439.
175. C. Deniau, R. Gilli, N. Izadi-Pruneyre, S. Létoffé, M. Delepierre, C. Wandersman, C. Briand, and A. Lecroisey, *Biochemistry*, 2003, **42**, 10627.
176. P. Arnoux, R. Haser, N. Izadi, A. Lecroisey, C. Wandersman, and M. Czjzek, *Nat. Struct. Biol.*, 1999, **6**, 516.
177. S. Létoffé, L. Debarbieux, N. Izadi, P. Delepelaire, and C. Wandersman, *Mol. Microbiol.*, 2003, **50**, 77.

Iron–Sulfur Models of Protein Active Sites

David J. Collins & Hong-Cai Zhou
Miami University, Oxford, OH, USA

Based in part on the article Iron–Sulfur Models of Protein Active Sites by Akira Nakamura & Norikazu Ueyama which appeared in the Encyclopedia of Inorganic Chemistry, First Edition.

1	Introduction	1
2	Rubredoxin Model Complexes	1
3	[Fe_2S_2] Model Complexes	3
4	[Fe_3S_4] Model Complexes	4
5	[Fe_4S_4] Model Complexes	6
6	[Fe_8S_7] Nitrogenase P-cluster Model Complexes	9
7	Perspective	10
8	Related Articles	10
9	References	10

Abbreviations

CV = cyclic voltammetry; Fd = ferredoxin; HP = high potential iron–sulfur protein; IRP = iron regulatory protein; LS_3 = 1,3,5-tris((4,6-dimethyl-3-mercaptophenyl)thio)-2,4,6-tris(*p*-tolylthio)benzene (3-); Rd = rubredoxin; SCE = standard calomel electrode; tibt = 2,4,6-triisopropylphenyl; Tp = tris(pyrazolyl)hydroborate (1-).

1 INTRODUCTION

Iron–sulfur clusters appear in a great many proteins as both electron-transport and enzymatic sites (*see* ***Iron–Sulfur Proteins***); for this reason there has been great interest for 30 years in the development and understanding of iron–sulfur model complexes. Both structure and properties of synthetic analogs of 1-, 2-, 3-, and 4-iron protein active sites have been studied extensively.[1] This article will address the structural and chemical properties, synthesis, and catalytic activity of these synthetic analogs, as compared to the native protein-bound iron–sulfur cores.

In general, iron–sulfur clusters are coordinated to native proteins via cysteine thiolate bonding, often in a Cys-X-Y-Cys motif (X, Y = nonsulfur containing amino acids). In clusters with more than one iron atom, μ_2- or μ_3-sulfur linkages connect the iron atoms within the cluster. At the active site of proteins, iron–sulfur clusters perform a variety of functions, including electron transport and enzymatic activity.

2 RUBREDOXIN MODEL COMPLEXES

The active site of rubredoxin (Rd), (**1**) (Figure 1), consists of one Fe ion tetrahedrally coordinated by four cysteine thiolate ligands. The iron core serves as the electron-transport site of rubredoxin proteins.

2.1 Synthesis

The common synthetic route for Fe^{II} simple model complexes is shown in reaction (1).

$$FeCl_2 + 4RS^- \longrightarrow [Fe(SR)_4]^{2-} + 2Cl^- \tag{1}$$

Controlled oxidation by dioxygen or other means can provide the oxidized Fe^{III} complex. However, the $[Fe(SR_4)]^-$ complexes are often not stable. A ligand exchange reaction, (2), provides an elegant solution to the problem,[2] presumably because the phenolate stabilizes the Fe^{III} ion through the course of the synthesis. These methods have been widely used to create a large set of oxidized and reduced Rd model complexes for study.

$$[Fe(OC_6H_3\text{-}2,6\text{-}Me_2)_4]^- + 4RSH \longrightarrow [Fe(SR)_4]^- + 4\ 2,6\text{-}Me_2C_6H_3OH \tag{2}$$

2.2 Structures

The structure of the $[Fe(RS)_4]$ core is shown in Figure 1. Bond lengths and angles for both typical rubredoxin and rubredoxin analogs are consistent, with typical ranges of Fe^{III}–S = 2.25–2.31 Å and Fe^{II}–S = 2.29–2.39 Å for both protein-bound [1Fe] clusters and synthetic analogs, as shown in Table 1. The iron sites in these proteins and model compounds exhibit distorted tetrahedral symmetry, generally following a D_{2d} symmetry tetragonally compressed along the S_4 axis. The sum of structural data indicate that distortions within the enzyme core are imposed by the surrounding protein, and are not unlike crystal packing forces in the synthetic model compounds.

2.3 Properties and Biochemical Activity

The essential redox reaction in both protein active sites and in the model complexes is the reduction of the Fe^{III} ion, as shown in reaction (3).

$$[Fe(SR)_4]^- + e^- \longrightarrow [Fe(SR)_4]^{2-} \tag{3}$$

Within the natural clusters, the redox potential is highly dependent on protein environment and on solvent effects, including electrostatic interactions (such as hydrogen bonding), pH, and ionic strength. The potentials for this

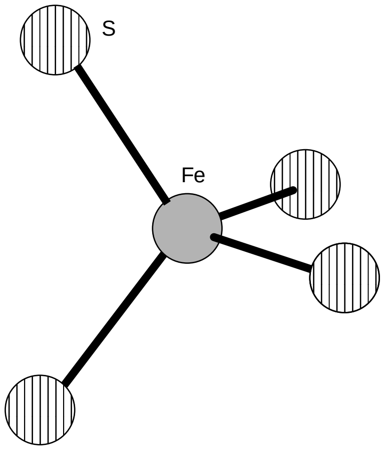

(**1**)

Figure 1 The Rd active site

couple in synthetic analogs also exhibit expected shifts owing to chemical environment. Most native rubredoxin proteins exhibit a reduction potential of 0.10 to −0.10 V versus SCE, while model complexes exhibit a considerably more negative range, in most cases −0.11 to −1.11 V versus SCE. Table 2 shows reduction potential and Mössbauer shift of selected rubredoxin analogs. Of course, deviations between protein properties and synthetic analog properties imply the influence of the protein environment and may provide direction for the elucidation of protein effects.

Table 1 Comparison of bond lengths (Å) and angles (deg) in (**1**) of oxidized and reduced rubredoxins and synthetic analogs

Species	Fe–S	S–Fe–S	References
Clostridium pasteurianum $\mathrm{Rd_{ox}}$	2.270 2.249 2.302 2.250	101.6–114.7	3
$[Fe(SPh)_4]^{1-}$	2.296 2.296 2.289 2.307	103.7–115.2	2
$[Fe(S_2\text{-}o\text{-xyl})_2]^{1-}$	2.268 2.255 2.266 2.278	106.2–112.3	4
Clostridium pasteurianum $\mathrm{Rd_{red}}$	2.394 2.306 2.369 2.384	103.9–112.8	3
$[Fe(SPh)_4]^{2-}$	2.355 2.338 2.360 2.359	97.9–119.0	2
$[Fe(S_2\text{-}o\text{-xyl})_2]^{2-}$	2.378 2.324 2.347 2.376	103.5–114.9	4

Other properties of synthetic rubredoxin analogs approach those of protein sites with the same oxidation state.

Table 2 CV and Mössbauer data of selected $[Fe(SR)_4]^{1-,2-}$ complexes

			Mössbauer data		
	R	$E_{1/2}$, $[Fe(SR)_4]^{1-/2-}$ (V vs. SCE)	δ (mm/s)	ΔE_Q (mm/s)	References
Fe(III)	Me	−0.98			2
	Et	−1.07			2
	^{i}Pr	−1.11			2
	o-xyl (bidentate ligand)	−1.02[b]	0.61	3.34	4
	Ph	−0.50	0.64	3.24	2
	2,3,5,6-Me_4C_6H	−0.85			2
	2,4,6-$^iPr_3C_6H_2$	−1.10			2
Fe(II)	Et	−1.10			5
	CH_2CH_2OH	−0.35	0.73	3.48	6
	CH_2CONMe_2	−0.71			5
	o-xyl (bidentate ligand)	−1.06	0.13[a]	0.57[a]	4, 5
	Ph	−0.51			7
	2-$NH_2C_6H_4$	−0.48			7
	4-$NMe_2C_6H_4$	−0.72			7
	2-$(MeCONH)C_6H_4$	−0.28			8
	2-$(CF_3CONH)C_6H_4$	−0.13			8
	2-$(^tBuCONH)C_6H_4$	−0.29			8
	2-$(Ph_3CCONH)C_6H_4$	−0.32			8
	2,6-$(MeCONH)_2C_6H_3$	+0.03			8
	4-$(MeCONH)C_6H_4$	−0.57			8

All voltammetry data in CH_3CN, unless otherwise noted. All Mössbauer data (δ vs. Fe metal) at 4.4 K, unless otherwise noted. [a] 77 K. [b] in DMF.

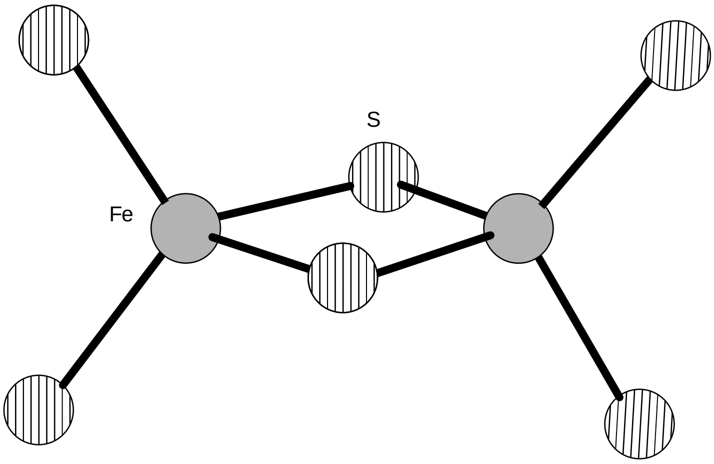

(**2**)

Figure 2 The [2Fe-2S] cluster

These include atomic spectral patterns, vibrational modes, bond covalency, and ground- and excited-state assignments consistent with the spin state and bonding structure.

Simple [1Fe] model complexes have been shown to catalyze the oxidation of mandelate to methylbenzoylformate, benzhydrol to benzophenone, and benzoin to benzil.

3 [Fe_2S_2] MODEL COMPLEXES

The $[Fe_2S_2]^{2+}$ core, (**2**) (Figure 2), appears in plant-type (chloroplast) ferredoxins (Fd) and in Rieske proteins.[9] In ferredoxins, the $[Fe_2S_2]^{2+}$ core is ligated with thiolate from Cys residues, while in Rieske proteins, the thiolates ligating one of the iron atoms are substituted with imidazole ligands from His residues.

3.1 Synthesis

The four reactions shown below are the principal methods of synthesizing [Fe_2S_2] complexes.[1,10,11]

$$2FeCl_3 + 4RS^- + 2HS^- + 2MeO^- \longrightarrow [Fe_2S_2(SR)_4]^{2-} + 6Cl^- + 2MeOH \quad (4)$$

$$2FeCl_3 + 8RS^- + 2S \longrightarrow [Fe_2S_2(SR)_4]^{2-} + 2RSSR + 6Cl^- \quad (5)$$

$$2[Fe(SR)_4]^{2-} + 2S \longrightarrow [Fe_2S_2(SR)_4]^{2-} + RSSR + 2RS^- \quad (6)$$

$$2[Fe(SR)_4]^{-} + 2S \longrightarrow [Fe_2S_2(SR)_4]^{2-} + 2RSSR \quad (7)$$

Typical ligand substitution reactions are as follows:[1]

$$[Fe_2S_2(SR)_4]^{2-} + 4R'SH \rightleftharpoons [Fe_2S_2(SR')_4]^{2-} + 4RSH \quad (8)$$

$$[Fe_2S_2X_4]^{2-} + 4RS^- \longrightarrow [Fe_2S_2(SR)_4]^{2-} + 4X^- \quad (9)$$

3.2 Structures

Figure 2 shows the structure of the [Fe_2S_2] core. All clusters of this type contain an Fe_2S_2 rhomb which is planar or with small nonplanar deviations from D_{2h} symmetry.[12–14] Protein clusters tend toward longer Fe–Fe distances, while most model complexes fall within a small range of Fe–Fe = 2.69–2.71 Å. The trend in Fe–S distances is not as clear-cut; overall, however, the synthetic analogs accurately reflect the important structural features of the active sites of native oxidized ferredoxin proteins, as shown in Table 3.

3.3 Properties and Biochemical Activity

Ferredoxins and Rieske proteins employ a $(Fe^{III})_2/Fe^{III}Fe^{II}$ redox couple for biological electron transfer reactions. Within the protein, the two iron atoms are rendered inequivalent, even in the fully oxidized $(Fe^{III})_2$ state, by the surrounding protein environment. Within a synthetic cluster, however, both iron atoms are typically equivalent, as may be expected from the symmetry of the overall complex. Table 4 shows reduction potentials for selected analog clusters.

In proteins, the redox couple operates at $E_0' \approx -0.42\,\text{V}$ versus SHE.[17] As with Rd-analog clusters, the redox couple in the synthetic analogs operates at a considerably more negative potential, but again can be significantly positively shifted by intramolecular N–H···S hydrogen bonding.[12] It is interesting to note that a 20-peptide artificial miniprotein has been designed and synthesized which exhibits a potential similar to that of native spinach Fd.[18]

Synthetic [Fe_2S_2] clusters have also shown catalytic activity. During redox, the cluster is particularly labile, and facile ligand swapping occurs under these conditions. It has

Table 3 Comparison of interatomic distances (Å) and angles (deg) in (**2**) of oxidized ferredoxins and synthetic analogs

Species	Fe–μS	Fe–S	Fe–μS–Fe	μS–Fe–μS	S–Fe–S	Fe$\cdots$Fe	References
Anabena PCC7119 Fd_{ox}	2.227 2.278 2.184 2.234	2.335 2.276 2.287 2.288	76.0	103.9	106.3	2.746	13
Spinacia oleracea Fd_{ox}	2.28 2.27 2.22 2.31	2.28 2.32 2.36 2.27	75.0	104.9	107.2	2.76	15
$[Fe_2S_2(S_2\text{-}o\text{-xyl})_2]^{2-}$	2.185 2.232	2.306 2.303	75.3	104.7	106.4	2.698	16

Table 4 Redox potentials of selected ferredoxins and $[Fe_2S_2(SR)_4]^{2-,3-}$ analogs

	R	$E_{1/2}$, $[Fe_2S_2]^{2+/1+}$ (V vs. SCE)	References
$[Fe_2S_2]^{2+}$	*o*-xyl (bidentate ligand)	−1.49	16
	4-ClC_6H_4	−0.95	16
	4-MeC_6H_4	−1.15	16
	4-$NMe_3C_6H_4$	−0.83	16

All voltammetry data in DMF.

also been found that these clusters can stabilize radicals in processes that occur via free-radical pathways. Redox reactions with the synthetic cluster have been used to oxidize alcohols and keto alcohols, and to reduce ketones, alkenes, alkynes, and CO_2.

4 $[Fe_3S_4]$ MODEL COMPLEXES

The trinuclear $[Fe_3S_4]$ site has been described as either a linear cluster, (**3a**) (shown in Figure 3), or cuboidal cluster, (**3b**) (shown in Figure 4), and models of each have been prepared and studied. It is unclear whether the linear cluster is present in functioning proteins in vivo, but it has been claimed in vitro in various sources, including a number of bacterial proteins and in human iron regulatory protein 1 (IRP-1) (*see* ***Metalloregulation***).[19–23] Only one cuboidal cluster has been successfully synthesized and studied.[24,25]

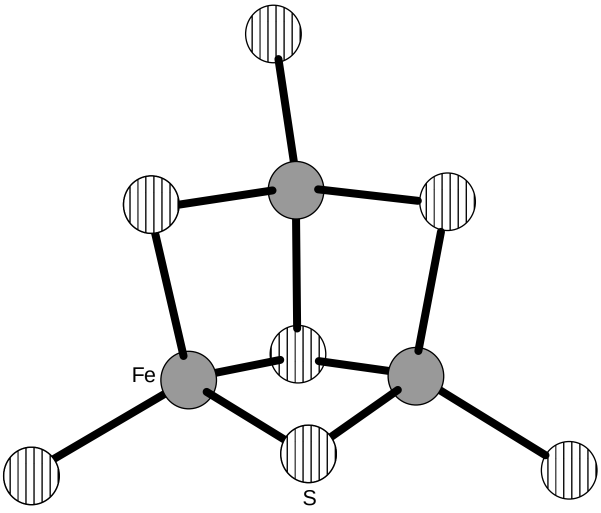

(**3b**)

Figure 4 The cuboidal $[Fe_3S_4]$ cluster

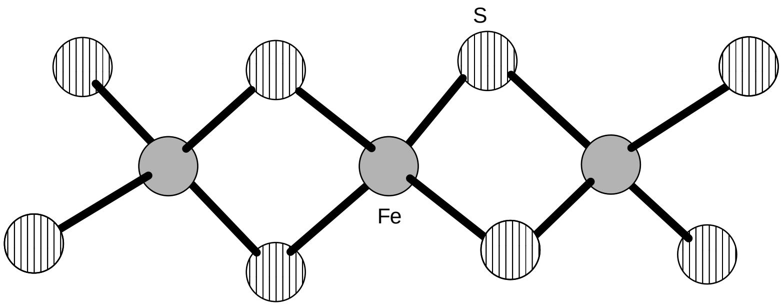

(**3a**)

Figure 3 The linear $[Fe_3S_4]$ cluster

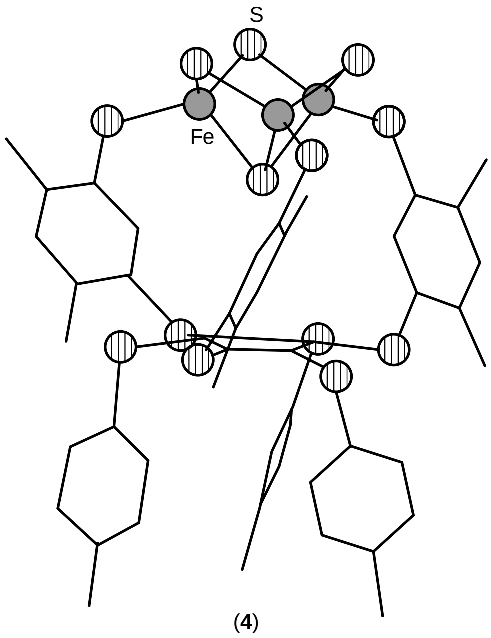

(**4**)

Figure 5 $[Fe_3S_4(LS_3)]^{3-}$

4.1 Synthesis

With careful control of stoichiometry and scale, the linear $[Fe_3S_4(SEt)_4]^{3-}$ complex can be generated from $[Fe(SEt)_4]^{2-}$ by reaction (10).**26**

$$3[Fe(SEt)_4]^{2-} + 4S \longrightarrow [Fe_3S_4(SEt)_4]^{3-} + 2.5\ EtSSEt + 3EtS^- \quad (10)$$

The other forms of the linear three-iron core shown in Table 6 can be generated by reaction (11) utilizing ligand substitution.**10,26**

$$[Fe_3S_4(SEt)_4]^{3-} + 4RSH \longrightarrow [Fe_3S_4(SR)_4]^{3-} + 4EtSH \quad (11)$$

The cuboidal form is closely related to the cubane structure, addressed in Section 5. To form the $[Fe_3S_4]$ cuboidal structure, Holm's group first used the semirigid trifunctional cavitand 1,3,5-*tris*((4,6-dimethyl-3-mercaptophenyl)thio)-2,4,6-*tris*(*p*-tolylthio)benzene (3-) (LS_3) to ligate a $[Fe_4S_4]$ cubane at three of the four iron corners, thereby forming a 3:1 site-differentiated cluster. The unique iron was then removed by reaction with *N*-methylimidodiacetate.**24,25** The $[Fe_3S_4(LS_3)]^{3-}$ structure, (**4**), is shown in Figure 5.

4.2 Structures

As shown in Tables 5 and 6, average Fe–S distances, Fe···Fe distances, and angles are in excellent agreement between synthetic models and protein clusters. The linear cluster consists of two rhombs of the $[Fe_2S_2]$ core, joined at one of the iron atoms, with bond lengths and angles quite similar to those found in that structure.

Structural data of the cuboidal model compound and of protein sites indicate that the cuboidal cluster is structurally closely related to the cubane cluster and shares many of the same structural properties.

4.3 Properties and Biochemical Activity

The $[Fe_3S_4]$ complex occurs naturally in a completely oxidized ($3Fe^{III}$) and mixed Fe^{III}/Fe^{II} oxidation states. Fully reduced forms of the three-iron clusters in either synthetic or natural systems have not been isolated. In mixed-valence clusters, electron delocalization and antiferromagnetic pairing

Table 5 Comparisons of interatomic distances (Å) and angles (deg) in the $[Fe_3S_4]$ units, (**3a**), of the linear cores of IRP1 and an analog

Species	Fe–μS	Fe–S	Fe–μS–Fe	μS–Fe–μS	S–Fe–S	Fe···Fe	References
IRP1	2.25					2.70 5.40	23
$[Fe_3S_4(SPh)_4]^{3-}$	2.235 2.196	2.335	75.6	105.6 102.9	110.0 102.5	2.714 5.42	10

Table 6 Comparison of bond lengths (Å) and angles (deg) in (**3b**) of *Azotobacter vinelandii* Fd_{ox} and $[Fe_3S_4(LS_3)]^{3-}$

Species	Fe–S	Fe–μ_2S	Fe–μ_3S	Fe–μ_2S–Fe	Fe–μ_3S–Fe	μ_2S–Fe–μ_2S	References
A. vinelandii	2.29 2.31 2.32	2.25	2.31	73.2	71.1	113.3	27
$[Fe_3S_4(LS_3)]^{3-}$	2.310 2.327 2.316	2.26	2.31	73.5	71.8	112.6	25

Table 7 CV and Mössbauer data of selected protein $[Fe_3S_4]$ clusters and analogs

	R	$E_{1/2}$, $[Fe_3S_4]^{1+/0}$ (V vs. SCE)	Mössbauer data δ (mm/s)	Mössbauer data ΔE_Q (mm/s)	References
Linear $[Fe_3S_4]^+$	Et	-1.66			10
	Ph	-1.35			10
Cuboidal $[Fe_3S_4]^0$	LS_3	-0.79	0.49,0.49,0.35	1.5,1.2,0.5	25
		$[Fe_3S_4]^{0/1-}$			
		-1.72			25

All voltammetry data in CH_3CN. All Mössbauer data (δ vs. Fe metal) at 4.4 K.

occur within a Fe^{III}–Fe^{II} pair, effectively rendering each as an $Fe^{2.5+}$ ion.

These compounds, both the model complexes and in nature, engage in electron transfer, reducing to successively more ferrous oxidation states. Reduction of the oxidized forms of the model complexes occur at negative potentials (~ -1.5 V).[10] The electrochemical properties and Mössbauer data of these clusters are shown in Table 7.

The linear and cuboidal clusters also demonstrate reactivity to produce four-iron $[Fe_4S_4]$ and heterometal $[MFe_3S_4]$ cubane clusters.[28–33] It has not been established whether the linear cluster remains intact in the reaction to form a cubane cluster.[33] The cuboidal cluster, however, readily bonds iron and many other metals at the voided site to form a cubane cluster with minimal structural change.[24,31,34] Biologically, this assembly of the $[Fe_4S_4]$ cluster by addition of iron to a cuboidal $[Fe_3S_4]$ core has been shown to be the regulatory step in the action of IRP-1 (*see* ***Metalloregulation***).

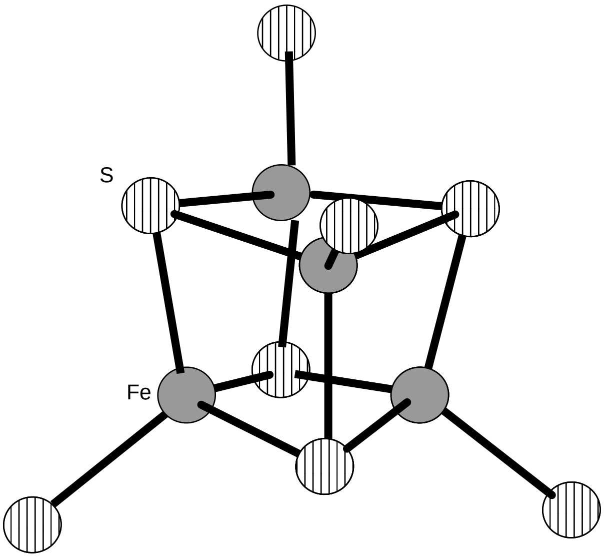

(**5**)

Figure 6 The cubane $[Fe_4S_4]$ cluster

5 $[Fe_4S_4]$ MODEL COMPLEXES

The $[Fe_4S_4]$ cluster, (**5**), appears in ferredoxins, in high-potential ferredoxin proteins (HP or HiPiP), and in a variety of enzymes. As shown in Table 8, the cluster itself is of mixed-valency (Fe^{III} and Fe^{II}) for all forms except the most reduced, $[Fe_4S_4]^0$.

5.1 Structures

All $[Fe_4S_4]$ cores have a 'cubane-type' structure consisting of six edge-shared nonplanar Fe_2S_2 rhombs, as seen in Figure 6. None have perfect T_d symmetry. A D_{2d}-compressed distortion is often encountered, producing four 'short' and eight 'long' Fe–S bonds, parallel and perpendicular, respectively, to an idealized fourfold axis. One-electron reduction of this form often produces a D_{2d}-elongated form, with the previously 'short' bonds lengthening significantly and the eight previous 'long' bonds shortening slightly.

As the oxidation state drops, Fe–SR bond lengths increase because of the increasing ferrous character of the core. Close agreement in bond lengths, angles, and core volume

Table 8 The electron-transfer series of $[Fe_4S_4]$ protein sites and analogs showing core oxidation states and iron valences

Core oxidation state	$[Fe_4S_4]^{3+}$ $Fe^{II} + 3Fe^{III}$ $(2Fe^{2.5} + 2Fe^{III})$	$[Fe_4S_4]^{2+}$ $2Fe^{II} + 2Fe^{III}$ $(4Fe^{2.5})$	$[Fe_4S_4]^{+}$ $3Fe^{II} + Fe^{III}$ $(2Fe^{2.5} + Fe^{II})$	$[Fe_4S_4]^0$ $4Fe^{II}$
Proteins:	HP_{ox}	HP_{red}, Fd_{ox}	Fd_{red}	Fe protein of *A. vinelandii* nitrogenase
Analogs	$[Fe_4S_4(SR)_4]^-$	$[Fe_4S_4(SR)_4]^{2-}$	$[Fe_4S_4(SR)_4]^{3-}$	$[Fe_4S_4(SR)_4]^{4-}$

Table 9 Comparisons of interatomic distances (Å) of selected $[Fe_4S_4]$ protein cores and analogs

	Species	Fe–μ_3S	Fe–S	Fe···Fe	References
$[Fe_4S_4]^{3+}$	$(Bu_4N)_2[Fe_4S_4(Stibt)_4]$	2.269 2.236	2.208	2.74	35
$[Fe_4S_4]^{2+}$	*T. tepidum* HP_{red}	2.302 2.231	2.261	2.713	36
	C. acidi-urici Fd_{ox}	2.301 2.252	2.272	2.72	18
	$[Fe_4S_4(SCH_2Ph)_4]$	2.310 2.239	2.251	2.732	37
$[Fe_4S_4]^{1+}$	$[Fe_4S_4(SPh)_4]$	2.354 2.286	2.295	2.743	38

is found both among the protein clusters themselves and with isoelectronic synthetic analogs. Structural parameters of a number of clusters are shown in Table 9.

Like the $[Fe_3S_4]$ cluster, the $[Fe_4S_4]$ exhibits electron delocalization across iron atoms in mixed-valence oxidation states. Within the $[Fe_4S_4]^{3+}$ state $[(Fe^{III})_3/Fe^{II}]$ and the $[Fe_4S_4]^+$ state $[Fe^{III}/(Fe^{II})_3]$, this pairing occurs within an Fe^{III}–Fe^{II} pair, while in the $[Fe_4S_4]^{2+}$ state $[(Fe^{III})_2/(Fe^{II})_2]$, electrons are delocalized across all four iron atoms, rendering all four electronically equivalent. Generally speaking, electron transfer energies and rates for these clusters reflect the interplay between electronic exchange, spin-dependent delocalization, and vibronic trapping of electrons on the Fe atoms.

The $[Fe_4S_4]$ cluster, like the $[Fe_2S_2]$ cluster, has been found to be very labile under reduced conditions. Catalytically, it has also been used to oxidize and/or reduce a number of alcohols, ketones, alkenes, and alkynes. Of particular interest, the $[Fe_4S_4(SCH_2Ph)_4]^{2-}$ cluster has been shown to catalyze the carboxylation of thioesters with CO_2, mimicking the fixation of CO_2 by coenzyme A in biological systems.

5.2 Synthesis and Properties

A summary of the CV and Mössbauer data of a variety of clusters is shown in Table 10.

5.2.1 $[Fe_4S_4]^{3+}$ Clusters

The $[Fe_4S_4]^{3+}$ state is isoelectronic with HP_{ox} cores. EPR and Mössbauer studies of the sole isolated synthetic cluster, $[Fe_4S_4(Stibt)_4]^{2-}$, indicate that it closely resembles HP_{ox} in electronic structure.[35,39] The redox couple exhibited by this and other model compounds, however, show significantly more negative potentials than the protein-bound cluster.

5.2.2 $[Fe_4S_4]^{2+}$ Clusters

The $[Fe_4S_4]^{2+}$ state is isoelectronic with HP_{red} and Fd_{ox} cores. A number of synthetic methods have been devised, including assembly reactions, (12) and (13), and ligand substitutions, (14) (X = halide) and (15) (n = 1 to 4).

$$4FeCl_2 + 10RS^- + 4S \longrightarrow [Fe_4S_4(SR)_4]^{2-} + 3RSSR + 8Cl^- \qquad (12)$$

$$4FeCl_3 + 14RS^- + 4S \longrightarrow [Fe_4S_4(SR)_4]^{2-} + 5RSSR + 12Cl^- \qquad (13)$$

$$[Fe_4S_4X_4]^{2-} + nRS^- \rightleftharpoons [Fe_4S_4X_{4-n}(SR)_n]^{2-} + nX^- \qquad (14)$$

$$[Fe_4S_4(SR)_4]^{2-} + nR'S^- \rightleftharpoons [Fe_4S_4(SR)_{4-n}(SR')_n]^{2-} + nRSH \qquad (15)$$

A very large set of clusters have been produced, only some of which are listed in Table 4; extensive study with a variety of methods have been performed on a number of these. Absorption spectra studies of alkylthiolate clusters have shown absorption bands very similar to those of HP_{red} and Fd_{ox}. As typical with other Fe–S cluster analogs, synthetic models have more negative reduction potentials than the native protein cluster: $E = -1.04$ to -1.42 V (in DMF) for the synthetic analogs, $E = -0.3$ to -0.8 V for most typical Fd_{ox}. Less negative values can be produced by suitable variation of ligand substituents. Additionally, the reduction potential of these clusters increases dramatically when in aqueous solution. Study of synthetic Cys-ligated $[Fe_4S_4]^{2+}$ clusters and of native Fd and HP proteins have shown similar shifts in redox potential due to variable N–H···S hydrogen bonding, solvent dielectric effects, pH, and ionic strength.[51]

5.2.3 $[Fe_4S_4]^+$ Clusters

The $[Fe_4S_4]^+$ state is isoelectronic with the Fd_{red} core. Compounds are typically prepared by reduction of $[Fe_4S_4(SR)_4]^{2-}$ with reducing agents of potential -1.5 V, as shown in reaction (16).

$$[Fe_4S_4(SR)_4]^{2-} + NaC_{12}H_8 \longrightarrow [Fe_4S_4(SR)_4]^{3-} + C_{12}H_8 + Na^+ \qquad (16)$$

Spectra and spin states are generally similar between synthetic analogs and protein-bound clusters; however, both exhibit considerable variability from species to species.

Table 10 CV and Mössbauer data of selected $[Fe_4S_4(SR)_4]$ protein cores and synthetic analogs

	R	$E_{1/2}$, $[Fe_4S_4]^{2+/1+}$ (V vs. SCE)	Mössbauer data δ (mm/s)	 ΔE_Q (mm/s)	References
$[Fe_4S_4]^{3+}$	2,4,6-^{i}$Pr_3C_6H_2$		0.40,0.34	−1.05, −0.90	39
$[Fe_4S_4]^{2+}$	Me	−1.294^c			40
	Et	−1.32			41
	Pr	−1.341^c			40
	^{i}Pr	−1.385^c			40
	CH_2CH_2OH		0.43^a	1.17^a	42
	$(CH_2)_3OH$		0.43^a	1.25^a	42
	$(CH_2)_4OH$		0.43^a	1.17^a	42
	$(CH_2)_6OH$		0.43^a	1.24^a	42
	$(LS_3)Et$	−1.12	0.46	1.16	43
	$(LS_3)Ph$	−1.04	0.46	1.12	43
	^{t}Bu	−1.424^c	0.44^a	0.97^a	40,44
	$CH_2CO_2C_2H_5$		0.43^a	0.81^a	44
	2-$NH_2C_6H_4$		0.33	0.88	45
	2-$SMeC_6H_4$		0.32,0.54	0.85,1.87	45
	2-OHC_6H_4		0.31,0.36,0.51	0.75,1.22,1.84	45
	2-MeC_6H_4		0.36,0.40	1.06,1.50	45
	$CH_2C_6H_{11}$	−1.404^c			40
	3-$C_6H_4(CH_2)_2$	−1.391^c			40
	C_6F_5	−0.787			40
	C_6Cl_5	−0.776			40
	Ph	−1.00			41
	4-MeC_6H_4	−1.086^c			40
	4-$NMe_2C_6H_4$	−1.140^c			40
	cyclodextrin dithiolate	−0.93^c			46
	CH_2CONBu_2	−1.65^c			47
	CH_2CO-monoaza-18-crown-6	−1.58^c			47
	2-$C_6H_4CONBu_2$	−1.52^c			47
	2-C_6H_4CO-monoaza-18-crown-6	−1.50^c			47
	3-C_6H_4-monoaza-18-crown-6	−1.74^c			47
	$CH_2CH_2NMe_3$	−0.79			41
	4-$NO_2C_6H_4$	−0.65^c			41
	4-$(NMe_3)C_6H_4$	−0.73^c			41
	4-$(NBu_2Me)C_6H_4$	−0.85^d			41
	$(LS_3)CH_2CH_2NMe_3$	−1.00			41
	(LS_3)4-$NO_2C_6H_4$	−0.97			41
	(LS_3)4-$NMe_3C_6H_4$	−0.98			41
	(LS_3)4-$NEt_3C_6H_4$	−1.06^d			41
	(LS_3)4-$NBu_3C_6H_4$	−1.07^d			41
	$(LS_3)C_6F_5$	−0.99			41
$[Fe_4S_4]^{+}$	CH_2Ph		0.60,0.60	1.41,0.93	38
	2-MeC_6H_4		0.50,0.43	1.93,1.09	48
	3-MeC_6H_4		0.45	1.01	48
	4-MeC_6H_4		0.43	1.06	48
	4-^{i}PrC_6H_4		0.44	1.01	48
	$CH_2C_6H_4$-4-OMe		0.43	0.86	48
		$E_{1/2}$, $[Fe_4S_4]^{1+/0}$			
	Ph	−1.73	0.44,0.48	1.01,1.78	41,49
	2-S^tBuC_6H_4		0.48,0.48	1.35,1.15	49
	^{t}Bu		0.45,0.48	0.93,1.74	49
	Et		0.44	1.12	49
	$LS_3(SEt)$		0.50^b	0.99^b	43
	$LS_3(SPh)$		0.55,0.63	2.33,1.37	43
	C_6H_{11}		0.44	0.96	50
	4-BrC_6H_4		0.40,0.48	0.94,2.07	50

All voltammetry data in CH_3CN unless otherwise noted. All Mössbauer data (δ vs. Fe metal) at 4 K, unless otherwise noted. [a]77 K. [b]200 K. [c]In DMF. [d]In DMSO.

5.2.4 *$[Fe_4S_4]^0$ Clusters*

The $[Fe_4S_4]^0$ state has been demonstrated in the fully reduced iron protein of *A. vinelandii* nitrogenase. The analog complex $[Fe_4S_4(SPh)_4]^{4-}$ has been detected electrochemically from the reversible reduction of $[Fe_4S_4(SPh)_4]^{3-}$ at -1.73 V, but neither this species nor any other has been isolated and fully characterized. Work continues in Holm's lab with $[Fe_4S_4(SPh)_4]^{3-/4-}$, $[Fe_4S_4(SCH_2CH_2CO_2)_4]^{7-/8-}$, phosphine-ligated clusters, and other pathways to construct and isolate this complex and to characterize it further.[52]

5.3 Peptide Clusters

To better simulate the behavior of Fe-S clusters in the protein environment, a logical step is to ligate the clusters to actual cysteinyl peptides. Peptide-ligated clusters can be prepared via ligand exchange reaction (17) or cluster reconstitution using $FeCl_3$, Na_2S, a reductant, and the peptide in aqueous buffer.

$$[Fe_4S_4(SR)_4]^{2-} + n(\mathrm{Cys})_x\mathrm{peptide} \longrightarrow [Fe_4S_4\{(\mathrm{Cys})_x\mathrm{peptide}\}_n]^{2-} + 4\mathrm{RSH} \qquad (17)$$

These procedures have been used to create a number of peptide clusters with over 65 amino acid residues. A common motif for forming these clusters is the ferredoxin consensus sequence (**6**) (Figure 7) incorporated into a longer chain or even peptide sequences with additional secondary structure.

The clusters thus generated have been found to have properties closely matching those of native proteins.[51] Further studies have shown that N–H···S hydrogen bonding to sulfur atoms within the cluster creates a small positive shift in redox potentials. The sequence Cys-(X)$_3$-Cys-(X)$_2$-Cys-(X)$_2$-Cys, which includes sequence (**6**) and is often found in ferredoxins, has been shown to support efficient cluster reconstitution.[53]

The following conclusions can be drawn from the various peptide-ligated clusters studied. First, the ligation of the cluster by the Cys residue is more stabilizing than any other residue. Secondly, three Cys residues in the sequence Cys-(X)$_2$-Cys-(X)$_2$-Cys are critical for ligation; the fourth iron site may be occupied by an exogenous ligand. Finally, nonligating residues have important roles in stabilizing $[Fe_4S_4]$ clusters.

5.4 Site-differentiated $[Fe_4S_4]$ Clusters

Enzyme activity has been recognized in protein-bound 3:1 site-differentiated clusters, in which the cubane $[Fe_4S_4]$ is bound to a ligand other than a Cys residue at one of the iron sites. This differentiated iron atom is unique and becomes the site of substrate binding and catalysis. The first recognized example of this was in the enzyme aconitase. In this enzyme, the inactive form actually contains the cuboidal $[Fe_3S_4]$ cluster, which is activated by the reversible insertion of a fourth iron atom, with little change in structure.

$\underline{\text{Cys}}$-Ile-Ala-$\underline{\text{Cys}}$-Gly-Ala-$\underline{\text{Cys}}$

(**6**)

Figure 7 The ferredoxin consensus peptide sequence (**6**)

Synthetically, similar clusters have been produced using deprotonated trithiols, which ligate three of the cubane iron sites at once. One example is the LS_3 ligand discussed earlier (Figure 5); steric factors force the ligand into a shape which is ready to capture the cluster in its cavity.[54] Additionally, an $[Fe_4S_4]$ cluster has been encapsulated in diphenylglycoluril and cyclotriveratrylene cavitands in a way that also created a 3:1 site-differentiation; this encapsulation modified the electrochemical properties of the cluster in ways analogous to the effects of encapsulation of the cluster by proteins.[55]

This unique iron site proves to be exceptionally labile, and supports a wide variety of ligand exchange and reactivity. Bridging to additional iron–sulfur clusters via a sulfide-containing bridge can also be supported at this site, allowing the construction of more complex clusters. Additionally, the unique iron atom can be removed altogether and replaced with other metals (as discussed in Section 4.3).

The $[Fe_4S_4(LS_3)(SR')]^{3-}$ cluster has been shown to engage in an electrophilic attack of the sulfonium ion, while causing reductive cleavage of the cofactor S-adenosylmethionine. This behavior is analogous to the enzymatic action of biotin synthase and other enzymes in the S-adenosylmethionine family (*see* ***Iron–Sulfur Proteins***).[43]

6 $[Fe_8S_7]$ NITROGENASE P-CLUSTER MODEL COMPLEXES

The $[Fe_8S_7]$ core of the P-cluster of nitrogenase (*see* ***Nitrogenase: Metal Cluster Models*** and ***Nitrogenase***

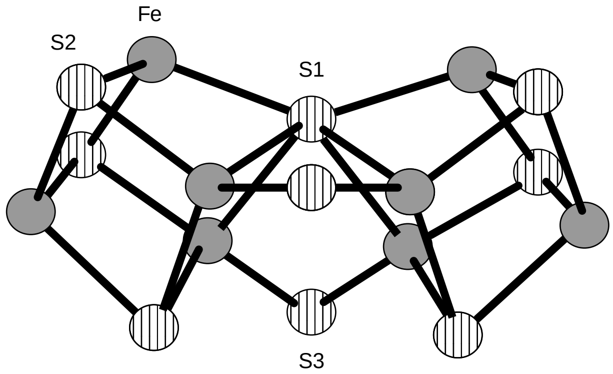

(**7**)

Figure 8 The P-cluster of nitrogenase

Catalysis & Assembly), (**7**) (Figure 8), consists of two $[Fe_4S_3]$ cubane structures linked by a hexa-coordinated sulfur atom (μ_6-S) and two bridging sulfur atoms of Cys residues (μ_2-S_{Cys}). The cluster is attached at the terminus by four additional thiolates of Cys residues. Some have speculated that the core itself is unstable and cannot exist outside the protein environment in a sulfur-ligated state. To this date, there have been attempts by several laboratories to synthesize a model of this complex with varying degrees of incomplete success.

The first synthetic analog is the $[(Tp)_2M_2Fe_6S_9(SH)_2]^{n-}$ cluster (M = Mo, V; $n = 3, 4$). This cluster maintains the μ_2-S bridges (as S rather than S_{Cys}) and the hexa-coordinated sulfur, but replaces the outermost two iron atoms with Mo or V, two of the terminal cysteinyl ligands with the Tp ligand, and the other two terminal ligands with S–H. The most notable characteristic of this cluster is its near congruence structurally (bond lengths and angles) with the native P^N-cluster.[56]

Another cluster that has been prepared with the same topology as the native P-cluster is $[N(SiMe_3)_2(SC(NMe_2)_2)Fe_4S_3]_2$-($\mu_6$-S)($\mu_2$-$N(SiMe_3)_2$). The primary difference exists in bridging μ_2-$N(SiMe_3)_2$ groups rather than S_{cys}, and terminal ligation by two $N(SiMe_3)_2$ groups and two $SC(NMe_2)_2$ groups. The electronic properties of this cluster in some ways resemble those of the P^N-cluster, although the oxidation state of the model is that of the P^{2+} oxidized form.[57]

7 PERSPECTIVE

The research on iron–sulfur models has played a historical role in the elucidation of the topology and electronic structure of the active sites of iron–sulfur proteins. The development of iron–sulfur cluster chemistry paralleled the evolution of the field of bioinorganic chemistry. As protein crystallography and other structure determination techniques become more and more routine and accurate, it seems that building analogs of protein active sites would become less desirable. On the contrary, it turns out that the determination of a protein structure is often just a new starting point for the study of its function, mechanism, and biosynthesis. The existence and function of iron–sulfur proteins have inspired and propelled the development of synthetic iron–sulfur cluster chemistry, which now features the most structural types in any binary metal–nonmetal combination.[1] On one hand, most of these structural types have yet to be found in biological systems. On the other hand, building analog systems for the all-ferrous Fe_4S_4 center, P-cluster, and the FeMoco center of nitrogenase have posed a formidable challenge no less daunting than the total synthesis of natural products. Future breakthroughs in this endeavor will undoubtedly be beneficial to our further understanding of the biological systems.

8 RELATED ARTICLES

Iron–Sulfur Proteins; Nitrogenase: Metal Cluster Models.

9 REFERENCES

1. P. Venkateswara Rao and R. H. Holm, *Chem. Rev.*, 2004, **104**, 527.
2. L. E. Maelia, M. Millar, and S. A. Koch, *Inorg. Chem.*, 1992, **31**, 4594.
3. T. Min, C. E. Ergenekan, M. K. Eidsness, T. Ichiye, and C. Kang, *Protein Sci.*, 2001, **10**, 613.
4. R. W. Lane, J. A. Ibers, R. B. Frankel, G. C. Papaefthymiou, and R. H. Holm, *J. Am. Chem. Soc.*, 1977, **99**, 84.
5. K. Bose, J. Huang, B. S. Haggerty, A. L. Rheingold, R. J. Salm, and M. A. Walters, *Inorg. Chem.*, 1997, **36**, 4596.
6. M. T. Werth, D. M. Kurtz Jr, B. D. Howes, and B. H. Huynh, *Inorg. Chem.*, 1989, **28**, 1357.
7. J. Huang, J. C. Dewan, and M. A. Walters, *Inorg. Chim. Acta.*, 1995, **228**, 199.
8. T. Okamura, S. Takamizawa, N. Ueyama, and A. Nakamura, *Inorg. Chem.*, 1998, **37**, 18.
9. T. A. Link, *Adv. Inorg. Chem.*, 1999, **47**, 83.
10. K. S. Hagen, A. D. Watson, and R. H. Holm, *J. Am. Chem. Soc.*, 1983, **105**, 3905.
11. R. H. Holm, in 'Comprehensive Coordination Chemistry Vol. 8', eds. L. Que Jr and W. B. Tolman, Elsevier, New York, 2004, p. 61.
12. N. Ueyama, Y. Yamada, T. Okamura, S. Kimura, and A. Nakamura, *Inorg. Chem.*, 1996, **35**, 6473.
13. R. Morales, M.-H. Chron, G. Hudry-Clergeon, Y. Pétillot, S. Norager, M. Medina, and M. Frey, *Biochemistry*, 1999, **38**, 15764.
14. A. Müller, J. J. Müller, Y. A. Müller, H. Uhlmann, R. Bernhardt, and U. Heinemann, *Structure*, 1998, **6**, 269.
15. C. Binda, A. Coda, A. Aliverti, G. Zanetti, and A. Mattevi, *Acta. Crystallogr.*, 1998, **D54**, 1353.
16. J. J. Mayerle, S. E. Denmark, B. V. DePamphilis, J. A. Ibers, and R. H. Holm, *J. Am. Chem. Soc.*, 1975, **97**, 1032.
17. H. Matsubara and K. Saeki, *Adv. Inorg. Chem.*, 1992, **38**, 223.
18. Z. Dauter, K. S. Wilson, L. C. Sieker, J. Meyer, and J.-M. Moulis, *Biochemistry*, 1997, **36**, 16065.
19. D. H. Flint, M. H. Emptage, M. G. Finnegan, W. Fu, and M. K. Johnson, *J. Biol. Chem.*, 1993, **268**, 14732.
20. C. Krebs, T. F. Henshaw, J. Cheek, B. H. Huynh, and J. B. Broderick, *J. Am. Chem. Soc.*, 2000, **122**, 12497.
21. P. Wittung-Stafshede, C. M. Gomes, and M. Teixeira, *J. Inorg. Biochem.*, 2000, **78**, 35.
22. K. Jones, C. M. Gomes, M. Teixeira, and P. Wittung-Stafshede, *J. Biol. Inorg. Chem.*, 2002, **7**, 357.

23. J. Gailer, G. N. George, I. J. Pickering, R. C. Prince, P. Kohlhepp, D. Zhang, F. A. Walker, and J. J. Winzerling, *J. Am. Chem. Soc.*, 2001, **123**, 10121.
24. J. Zhou and R. H. Holm, *J. Am. Chem. Soc.*, 1995, **117**, 11353.
25. J. Zhou, Z. Hu, E. Münck, and R. H. Holm, *J. Am. Chem. Soc.*, 1996, **118**, 1966.
26. K. S. Hagen and R. H. Holm, *J. Am. Chem. Soc.*, 1982, **104**, 5496.
27. C. D. Stout, *J. Mol. Biol.*, 1989, **205**, 545.
28. D. Coucouvanis, S. A. Al-Ahmad, A. Salifoglou, V. Papaefthymiou, A. Kostikas, and A. Simopoulos, *J. Am. Chem. Soc.*, 1992, **114**, 2472.
29. J. Zhou, M. J. Scott, Z. Hu, G. Peng, E. Münck, and R. H. Holm, *J. Am. Chem. Soc.*, 1992, **114**, 10843.
30. D. Coucouvanis, S. A. Al-Ahmad, A. Salifoglou, W. R. Dunham, and R. H. Sands, *Angew. Chem., Int. Ed. Engl.*, 1988, **27**, 1353.
31. J. W. Raebiger, C. A. Crawford, J. Zhou, and R. H. Holm, *Inorg. Chem.*, 1997, **36**, 994.
32. S. Ciurli, S.-B. Yu, R. H. Holm, K. K. P. Srivastava, and E. Münck, *J. Am. Chem. Soc.*, 1990, **112**, 8169.
33. S. Ciurli, P. K. Ross, M. J. Scott, S.-B. Yu, and R. H. Holm, *J. Am. Chem. Soc.*, 1992, **114**, 5415.
34. J. Zhou, J. W. Raebiger, C. A. Crawford, and R. H. Holm, *J. Am. Chem. Soc.*, 1997, **119**, 6242.
35. T. O'Sullivan and M. M. Millar, *J. Am. Chem. Soc.*, 1985, **107**, 4096.
36. L. Liu, T. Nogi, M. Kobayashi, T. Nozawa, and K. Miki, *Acta Crystallogr.*, 2002, **D58**, 1085.
37. B. A. Averill, T. Herskovitz, R. H. Holm, and J. A. Ibers, *J. Am. Chem. Soc.*, 1973, **95**, 3523.
38. E. J. Laskowski, R. B. Frankel, W. O. Gillum, G. C. Papaefthymiou, J. Renaud, J. A. Ibers, and R. H. Holm, *J. Am. Chem. Soc.*, 1978, **100**, 5322.
39. V. Papaefthymiou, M. M. Millar, and E. Münck, *Inorg. Chem.*, 1986, **25**, 3010.
40. B. V. DePamphilis, B. A. Averill, T. Herskovitz, L. Que Jr, and R. H. Holm, *J. Am. Chem. Soc.*, 1974, **96**, 4159.
41. C. Zhou, J. W. Raebiger, B. M. Segal, and R. H. Holm, *Inorg. Chim. Acta*, 2000, **300–302**, 892.
42. J. E. Barclay, S. C. Davies, D. J. Evans, D. L. Hughes, and S. Longhurst, *Inorg. Chim. Acta*, 1999, **291**, 101.
43. C. J. A. Daley and R. H. Holm, *J. Inorg. Biochem.*, 2003, **97**, 287.
44. J. Silver, G. R. Fern, G. R. Miller, J. R. McCammon, D. J. Evans, and G. J. Leigh, *Inorg. Chem.*, 1999, **38**, 4256.
45. R. E. Johnson, G. C. Papaefthymiou, R. B. Frankel, and R. H. Holm, *J. Am. Chem. Soc.*, 1983, **105**, 7280.
46. Y. Kuroda, Y. Sasaki, Y. Shiroiwa, and I. Tabushi, *J. Am. Chem. Soc.*, 1988, **110**, 4049.
47. R. J. M. Klein Gebbink, S. I. Klink, M. C. Feiters, and R. J. M. Nolte, *Eur. J. Inorg. Chem.*, 2000 253.
48. E. J. Laskowski, J. G. Reynolds, R. B. Frankel, S. Foner, G. C. Papaefthymiou, and R. H. Holm, *J. Am. Chem. Soc.*, 1979, **101**, 6562.
49. M. J. Carney, G. C. Papaefthymiou, R. B. Frankel, and R. H. Holm, *Inorg. Chem*, 1989, **28**, 1497.
50. M. J. Carney, G. C. Papaefthymiou, K. Spartalian, R. B. Frankel, and R. H. Holm, *J. Am. Chem. Soc.*, 1988, **110**, 6084.
51. M. L. Kennedy and B. R. Gibney, *J. Am. Chem. Soc.*, 2002, **124**, 6826.
52. H.-C. Zhou and R. H. Holm, *Inorg. Chem.*, 2003, **42**, 11.
53. S. E. Mulholland, B. R. Gibney, F. Rabanal, and P. L. Dutton, *J. Am. Chem. Soc.*, 1998, **120**, 10296.
54. R. H. Holm, *Pure Appl. Chem.*, 1998, **70**(4), 931.
55. M. C. Feiters, R. J. M. Klein Gebbink, A. P. H. J. Schenning, G. P. F. Strijdonck, C. F. Martens, and R. J. M. Nolte, *Pure Appl. Chem.*, 1996, **68**, 2163.
56. Y. Zhang, J.-L. Zuo, H.-C. Zhou, and R. H. Holm, *J. Am. Chem. Soc.*, 2002, **124**, 14292.
57. Y. Ohki, Y. Sunada, M. Honda, M. Katada, and K. Tatsumi, *J. Am. Chem. Soc.*, 2003, **125**, 4052.

Iron–Sulfur Proteins

Michael K. Johnson & Archer D. Smith
University of Georgia, Athens, GA, USA

1 Introduction 1
2 Structures and Properties of Iron–Sulfur Centers 5
3 Functions of Biological Iron–Sulfur Centers 13
4 Related Articles 25
5 References 25

Abbreviations

5′-GTP = 5′-guanosine triphosphate; AE = Activating enzyme; BAN = Backbone amide nitrogen; BioB = Biotin synthase; CD = Circular dichroism; cyt = Cytochrome; DFT = Density functional theory; DMSO = Dimethylsulfoxide; Dx = Desulforedoxin; ENDOR = Electron-nuclear double resonance; EPR = Electron paramagnetic resonance; ESEEM = Electron-spin echo envelop modulation; ETF = Electron transferring flavoprotein; EXAFS = Extended x-ray absorption fine structure; FAD = Flavin adenine dinucleotide; Fd = Ferredoxin; FMN = Flavin mononucleotide; FNR = Fumarate–nitrate reduction; FTIR = Fourier-transform infrared; FTR = Ferredoxin–thioredoxin reductase; HDR = Heterodisulfide reductase; HemN = An oxygen-independent coproporphyrinogen III oxidase; HiPIP = High potential iron–sulfur protein; IRE = Iron-responsive element; IRP = Iron-regulatory protein; J = Magnetic coupling constant based on a Heisenberg spin Hamiltonian, $H = J\mathbf{S_1}\bullet\mathbf{S_2}$; LipA = Lipoyl synthase; MiaB = A tRNA–methylthiotransferase; Moco = Molybdenum cofactor; NHE = Normal hydrogen electrode; NMR = Nuclear magnetic resonance; PFL = Pyruvate formate-lyase; PRPP = Phosphoribosylpyrophosphate; QFR = Quinol–fumarate oxidoreductases; Rd = Rubredoxin; SAM = S-adenosylmethionine; SOR = Superoxide reductase; SQR = succinate–quinone oxidoreductase; TPP = Thiamine pyrophosphate; VTMCD = Variable-temperature magnetic circular dichroism; Wco = Tungsten cofactor; XAS = X-ray absorption spectroscopy.

1 INTRODUCTION

Iron–sulfur proteins are broadly defined as proteins containing Fe with at least partial S coordination. This definition, therefore, includes proteins containing mononuclear Fe centers coordinated by cysteinyl-S, in addition to the large group of proteins containing clusters of Fe bridged by inorganic S^{2-} and attached to the protein via amino acid side-chain coordination of Fe. Following the International Union of Biochemistry (IUB) recommendation,[1] they can be further classified into simple and complex Fe–S proteins. Simple Fe–S proteins have Fe–S centers as their sole prosthetic group, whereas complex Fe–S proteins have additional prosthetic groups, such as flavin, Mo/W cofactors, siroheme, or another type of metal center.

Since the discovery of ferredoxins in the early 1960s, the number and diversity of Fe–S proteins has greatly proliferated. There are now well in excess of 160 enzymes and proteins that contain Fe–S centers, and the list continues to grow rapidly. They are found ubiquitously in nature and are intimately involved in all membrane-bound electron transport systems in addition to the metabolism of carbon, oxygen, hydrogen, sulfur, and nitrogen. Not surprisingly, they have been the subject of recent books[2] and review articles.[3–8] The widespread occurrence of Fe–S proteins and the chemical versatility of iron and sulfur[4,5,9] are also of interest from an evolutionary standpoint. For example, they lend credence to the proposal for the exergonic formation of pyrite, FeS_2, from H_2S and Fe^{2+}, as the driving force for a chemoautotrophic theory for the origin of life under hyperthermophilic conditions. Further support for such a theory has come from the laboratory demonstration of C–C bond formation on Ni/Fe–S or Fe–S surfaces under primordial conditions.[10–12] Indeed it is conceivable that the first Fe–S proteins may have formed at a pyrite surface by replacement of SH-groups in inorganic Fe–S clusters by cysteinyl groups of surface-bonded peptides rather than polypetides folding around preformed Fe–S clusters in solution.

X-ray crystallography as well as other biophysical techniques, that is, X-ray absorption (XAS), electron paramagnetic resonance (EPR), electron-nuclear double resonance (ENDOR), electron-spin echo envelop modulation (ESEEM), Mössbauer, optical absorption, circular dichroism (CD), variable-temperature magnetic circular dichroism (VTMCD), resonance Raman, nuclear magnetic resonance (NMR), and saturation magnetization, have all been important in characterizing biological Fe–S centers. No one technique is a panacea. Rather they each provide unique and often complementary information that *taken together* provides a detailed picture of electronic, magnetic, structural, and functional properties. Parallel studies of structurally defined analog complexes have also played a crucial role in developing our current understanding of Fe–S biochemistry[13] (*see* ***Iron–Sulfur Models of Protein Active Sites***). In many instances, for example, [2Fe–2S] and linear [3Fe–4S] clusters, this approach has led to structural predictions for biological Fe–S centers prior to X-ray crystallographic studies.

With the improvements in diagnostic tools for identification and characterization, the structural and functional diversity of biological Fe–S centers is now becoming apparent. In the 1970s, the structural types were confined to mononuclear Fe centers, binuclear [2Fe–2S] clusters and cubane-type

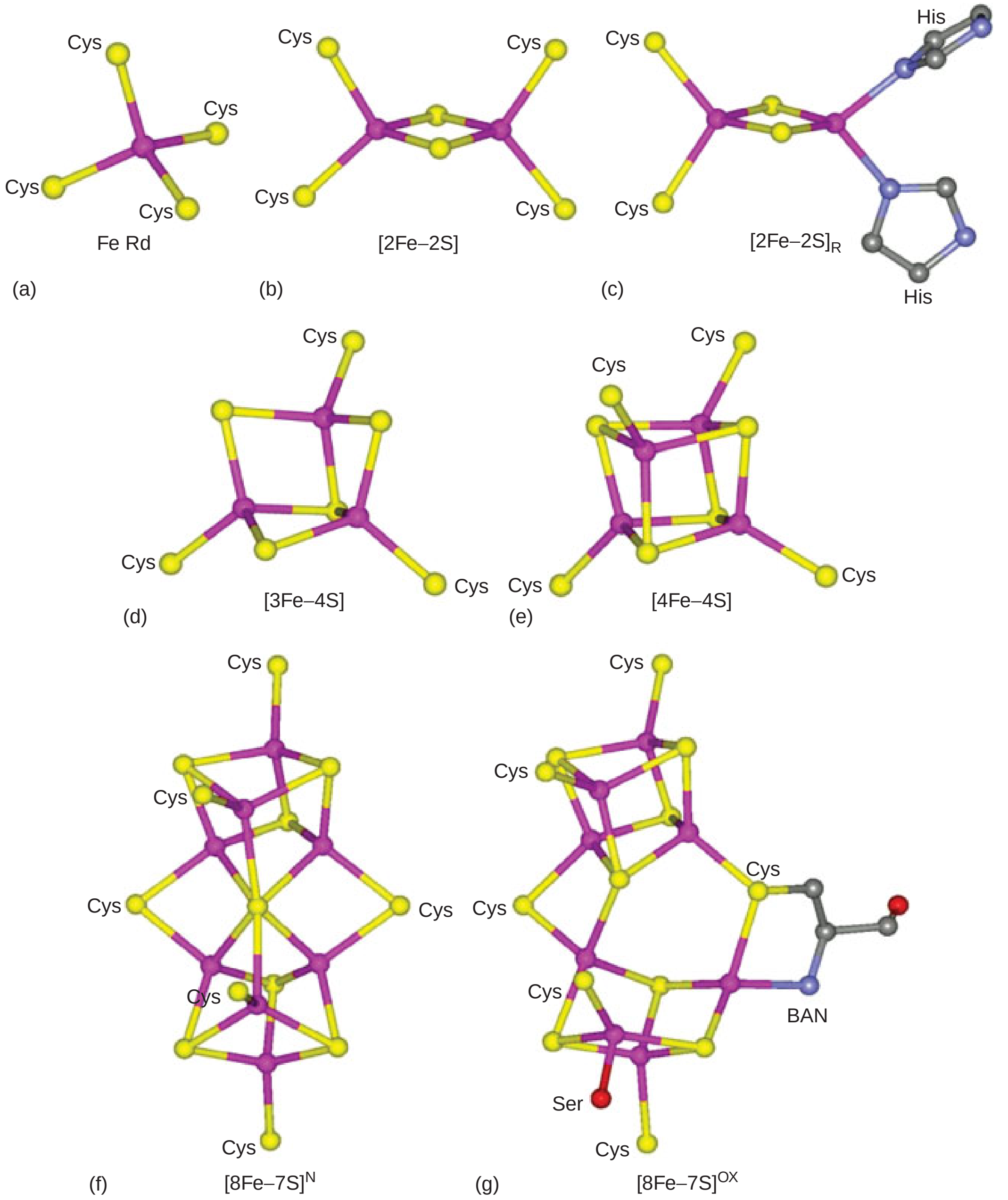
Cys
Cys
Cys
Cys
Fe Rd
(a)
Cys
Cys
Cys
Cys
[2Fe–2S]
(b)
Cys
Cys
His
His
$[2Fe–2S]_R$
(c)
Cys
Cys
Cys
[3Fe–4S]
(d)
Cys
Cys
Cys
Cys
[4Fe–4S]
(e)
Cys
Cys
Cys
Cys
Cys
Cys
$[8Fe–7S]^N$
(f)
Cys
Cys
Cys
Cys
Cys
Cys
BAN
Ser
$[8Fe–7S]^{OX}$
(g)

Figure 1 Crystallographically defined structures for Fe–S centers that function in biological electron transfer. Structures are taken from coordinates deposited in the Protein Data Bank: (a) Fe Rd, PDB ID# 8RXN, rubredoxin from *Desulfovibrio vulgaris*;[16] (b) [2Fe–2S], PDB ID# 1FRD, *Anabaena* pcc7120 Fd;[17] (c) $[2Fe–2S]_R$, PDB ID# 1JM1, *Sulfolobus acidocaldarius* Rieske protein;[18] (d) [3Fe–4S], PDB ID# 6FDR, *Azotobacter vinelandii* FdI;[19] (e) [4Fe–4S], PDB ID# 6FDR, *A. vinelandii* FdI;[19] (f) $[8Fe–7S]^N$, PDB ID# 1M1N, dithionite-reduced *A. vinelandii* MoFe protein;[20] (g) $[8Fe–7S]^{OX}$, PDB ID# 2 MIN, thionine-oxidized *A. vinelandii* MoFe protein.[15] Color code: purple, Fe; yellow, S; gray, C; red, O. Unlabeled S atoms correspond to bridging sulfides. BAN = backbone amide nitrogen

[4Fe–4S] clusters, all with cysteinyl-S completing tetrahedral Fe coordination (Figure 1) and the function was exclusively electron transport. New types of electron transfer Fe–S clusters involving cubane-type [3Fe–4S] clusters[14] and double-cubane-type [8Fe–7S] clusters[15] have subsequently been characterized (Figure 1). Moreover, the known functions of Fe–S centers have now expanded to include coupling electron and proton transfer, substrate binding and activation, storage of Fe, electrons or clusters, purely structural roles, regulation of gene expression and enzyme activity, disulfide reduction, and sulfur donation (see Table 1). The crystallographically defined structures of Fe–S centers involved with substrate binding and activation are shown in Figure 2.

Table 1 Functions of biological Fe–S centers

Function	Examples	Center or cluster type[a]
Electron transfer	Ferredoxins; soluble and membrane-bound redox enzymes[3,5,21]	Fe Rd; [2Fe–2S]; [2Fe–2S]$_{\mathrm{R}}$; [3Fe–4S]; [4Fe–4S]
Coupled electron and proton transfer	Rieske protein[22,23]	[2Fe–2S]$_{\mathrm{R}}$
	Nitrogenase[15,24]	[8Fe–7S]
Substrate binding and activation	Nitrile hydratase[25,26]	Fe NHase
	Fe–S cluster (de)hydratases[27,28]	[4Fe–4S]; [2Fe–2S]
	Superoxide reductase[29–31]	Fe SOR
	Radical-SAM enzymes[32–34]	[4Fe–4S]
	NiFe-hydrogenase[35,36]	Ni–Fe H_2ase
	Nitrogenase[20,37]	[Mo–7Fe–9S–X]
	Sulfite and nitrite reductase[38,39]	siroheme–[4Fe–4S]
	Fe-hydrogenase[40,41]	Fe–Fe–[4Fe–4S]
	CO dehydrogenase[42,43]	[Ni–4Fe–5S]
	Acetyl-CoA synthase[44–46]	Ni–Ni–[4Fe–4S], [Ni–4Fe–5S]
Fe/electron/cluster storage	Ferredoxins[47]	[4Fe–4S]
	Polyferredoxins[48,49]	[4Fe–4S]
Structural	Endonuclease III[50,51]	[4Fe–4S]
	MutY[52,53]	[4Fe–4S]
Regulation of gene expression	SoxR[54,55]	[2Fe–2S]
	FNR[56,57]	[4Fe–4S]/[2Fe–2S]
	IRP[27,58]	[4Fe–4S]
	IscR[59]	[2Fe–2S]
Regulation of enzyme activity	Glutamine PRPP amidotransferase[60,61]	[4Fe–4S]
	Ferrochelatase[62,63]	[2Fe–2S]
Disulfide reduction	Ferredoxin:thioredoxin reductase[64,65]	[4Fe–4S]
	Heterodisulfide reductase[65,66]	[4Fe–4S]
Sulfur donor	Biotin synthase[67,68]	[2Fe–2S]

[a] Structures shown in Figures 1 and 2.
PRPP = Phosphoribosylpyrophosphate.

The structures shown in Figures 1 and 2 illustrate several general structural themes that facilitate rationalization of functional diversity. Exclusive cysteinyl ligation is generally observed in centers that function purely in electron transfer roles. Histidine, aspartate, serine, or backbone amide N ligation at a unique Fe site are occasionally encountered in clusters that function in electron transport and serve to modify redox potential[22] and gate electron transport,[72] or facilitate coupling of proton and electron transport.[15,22–24] While Fe(SCys)$_4$, [2Fe–2S], [3Fe–4S] and [4Fe–4S] clusters all function as one-electron donors or acceptors, the more complex double-cubane [8Fe–7S] cluster that is found only in nitrogenases (*see* ***Nitrogenase Catalysis & Assembly***) has the potential to mediate two-electron transfer processes.[15,24] Three methods have been employed to functionalize Fe–S centers for substrate binding and activation. The first involves having an accessible Fe coordination site as in the mononuclear Fe centers of nitrile hydratase[25,26] and SOR,[31,73] and the [4Fe–4S] clusters at the active sites of hydratases/dehydratases[27,28] and radical-*S*-adenosylmethionine (SAM) enzymes.[33,74] Indeed the recent recognition of the importance of the superfamily of radical-SAM enzymes in initiating radical reactions, via cluster–mediated reductive cleavage of SAM to yield a transient $5'$-deoxyadenosyl radical, has established Fe–S clusters as the dominant method of radical generation in biology.[32,34,75] The second involves incorporation of a heterometal site as in the case of the [M–7Fe–9S–X] cluster (M = Mo or V; X = N, O, or C) at the active site of nitrogenase[20,37] and the [Ni–4Fe–5S] active site of CO dehydrogenases[42,43] (*see* ***Nickel Enzymes & Cofactors***). The third involves attaching a substrate-binding metal site to an Fe site of a [4Fe–4S] cluster via a bridging cysteinyl residue as in the case of the Ni–Ni–[4Fe–4S] active site of acetyl-CoA synthase,[44–46] the Fe–Fe–[4Fe–4S] active site of Fe-hydrogenase,[40,41] and the siroheme–[4Fe–4S] active site of sulfite and nitrite reductases.[38]

The ability of designed and unstructured minimal synthetic peptides (maquettes) to correctly assemble Fe–S clusters,[76] coupled with examples of Fe–S cluster driven protein reorganization in response to medium effects[77] and cysteine substitutions,[78] demonstrate that Fe–S clusters control protein structure in the vicinity of the cluster. Hence, it not surprising that Fe–S clusters have important structural roles in DNA repair enzymes such as endonuclease III[50,51] and MutY,[52,79] as well as sensing and regulatory roles in controlling gene expression and enzyme activity[58] (*see* ***Metalloregulation***).

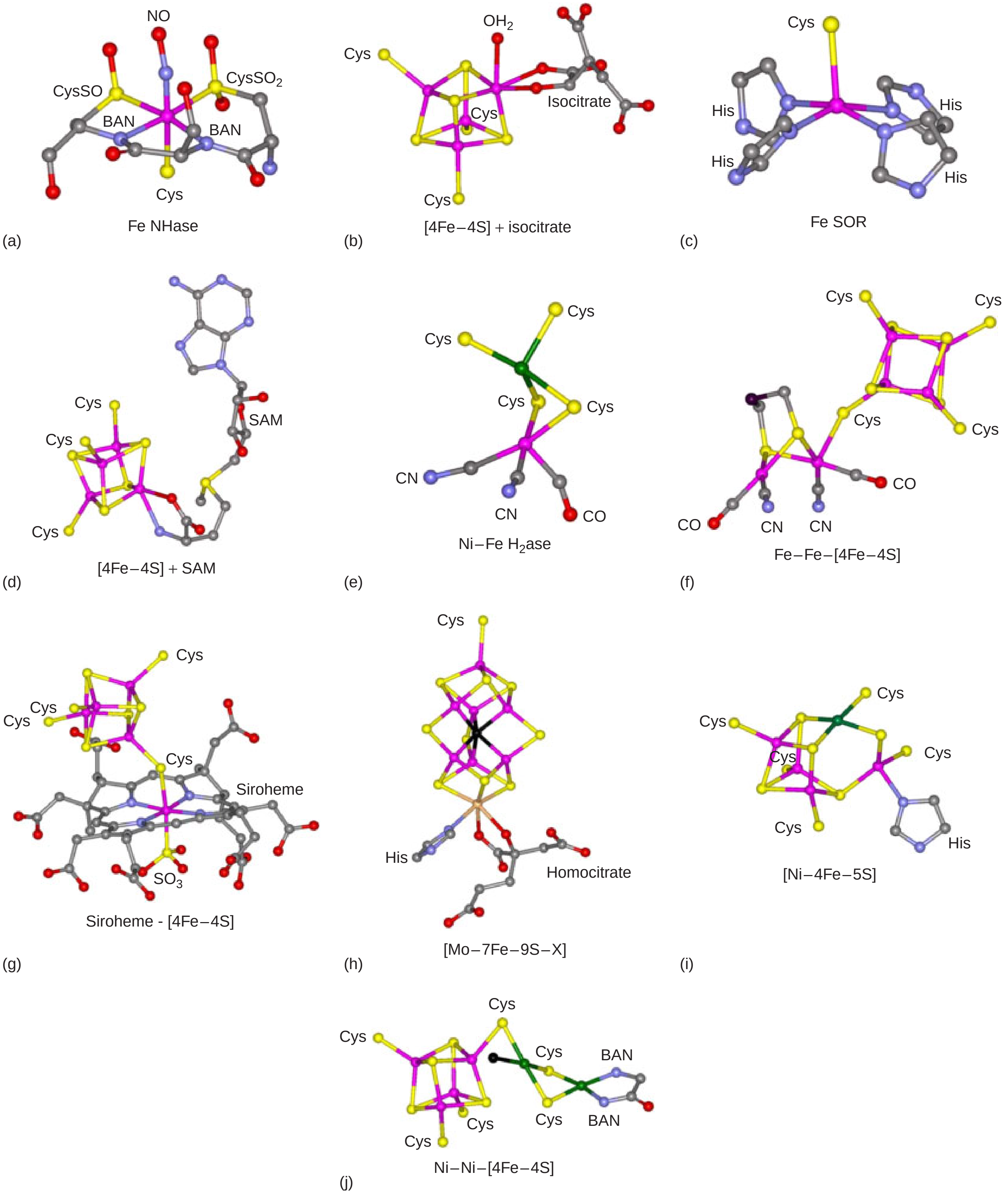
NO
CysSO
$CysSO_2$
BAN
BAN
Cys
OH_2
Cys
Cys
Isocitrate
Cys
Cys
His
His
His
His
Cys
SAM
Cys
Cys
Cys
Cys
Cys
Cys
CN
CN
CO
Cys
Cys
Cys
Cys
Cys
CO
CO
CN
CN
Cys
Cys
Cys
Cys
Siroheme
SO_3
Cys
His
Homocitrate
Cys
Cys
Cys
Cys
Cys
His
Cys
Cys
Cys
BAN
Cys
Cys
Cys
BAN

(a) Fe NHase

(b) [4Fe–4S] + isocitrate

(c) Fe SOR

(d) [4Fe–4S] + SAM

(e) Ni–Fe H_2ase

(f) Fe–Fe–[4Fe–4S]

(g) Siroheme - [4Fe–4S]

(h) [Mo–7Fe–9S–X]

(i) [Ni–4Fe–5S]

(j) Ni–Ni–[4Fe–4S]

In fact, one of the most interesting discoveries of the past decade is that Fe–S clusters are used as sensors for a variety of different types of environmental stimuli and use a wide range of sensing mechanisms involving cluster assembly, transfer, conversion, or redox chemistry to perturb protein structure.

New roles have recently emerged for Fe–S clusters in disulfide reduction and sulfur donation. At least two classes of disulfide reductase, ferredoxin-thioredoxin reductase (FTR) in chloroplasts[64,65] and heterodisulfide reductase (HDR) in methanogenic archaea,[65,66] have been shown to use an active-site [4Fe–4S] cluster to cleave disulfides in two sequential one-electron steps, using novel site-specific cluster chemistry, involving an intermediate with two thiolate ligands at a unique Fe site. The radical-SAM enzyme biotin synthase contains a [2Fe–2S] cluster that degrades and provides the sulfur for the conversion of dethiobiotin to biotin during a single catalytic turnover.[67,68,80,81] This raises the possibility that Fe–S clusters can function as sulfur donors and that Fe–S cluster degradation and assembly can be part of a catalytic cycle. Understanding the structure/function relationships that have evolved for Fe–S clusters offers a fascinating challenge to inorganic biochemists and bioinorganic chemists and this review should be read as a progress report on this dynamic and rapidly advancing area of research.

The revitalization of interest in the diverse roles and properties of biological Fe–S centers and the realization that cluster degradation and assembly or repair may be important in regulatory and catalytic functions has occurred as major progress is being made in understanding the biogenesis of Fe–S clusters.[82,83] Although [2Fe–2S] and [4Fe–4S] clusters can be assembled in many simple Fe–S proteins by incubation of apo–protein with $Fe^{3+,2+}$ and S^{2-} ions under anaerobic conditions, the toxicity of free $Fe^{3+,2+}$ and S^{2-} ions indicates that this type of spontaneous self-assembly is unlikely to be a viable general mechanism for cluster biosynthesis. Rather Fe–S clusters or cluster fragments are delivered intact to apo Fe–S proteins by specific scaffold proteins that sequester Fe and S in non-toxic forms. Three distinct biological systems, termed the NIF, ISC, and SUF systems, have emerged for Fe–S biogenesis. However, the central theme of cysteine desulfurase-mediated assembly of transient Fe–S clusters on scaffold proteins appears to be remarkably conserved in almost all forms of life. The mechanism of assembly of Fe–S centers in proteins is a rapidly advancing area of research and is discussed in more detail elsewhere (*see* ***Metallocenter Biosynthesis & Assembly***).

2 STRUCTURES AND PROPERTIES OF IRON–SULFUR CENTERS

The accessible redox states and properties of the fundamental types of biological Fe–S centers involving $Fe(SCys)_4$, $Fe_2(\mu_2{-}S)_2(SCys)_4$, $Fe_3(\mu_2{-}S)_3(\mu_3{-}S)(SCys)_3$, and $Fe_4(\mu_3{-}S)_4(SCys)_4$ units are summarized in Figure 3. It is customary and convenient to refer to Fe–S clusters by the stoichiometry of Fe and inorganic-S in square brackets with the formal charge of the Fe inorganic-S core indicated as a superscript, that is, $[2Fe–2S]^{2+,+}$, $[3Fe–4S]^{+,0,2-}$, and $[4Fe–4S]^{3+,2+,+,0}$. The number of unpaired electrons in the electronic ground state, as determined by magnetic or spectroscopic studies at cryogenic temperatures, is indicated by the spin state, S. Figure 3 also indicates the extent of valence localization/delocalization as determined by Mössbauer spectroscopy for each type of cluster in each accessible redox state, with formal Fe^{3+} in red, Fe^{2+} in blue, and $Fe^{2.5+}$ in green. As discussed below for each type of cluster, the extent of valence delocalization is essential for understanding the redox and electronic properties. At this stage, it is sufficient to note that valence-delocalized $Fe_2(\mu_2{-}S)_2$ rhombs are an important building block of all higher nuclearity clusters. Such delocalization facilitates efficient electron transfer by minimizing reorganization energy[84,85] and hence is likely to be an important determinant of the use of Fe–S clusters in mediating biological electron transfer. In addition, Fe–S bonds are highly covalent as evidenced by sulfur K-edge XAS studies[86–88] and this approach coupled with density function theory (DFT) calculations have demonstrated that *both* Fe and S (inorganic and cysteinyl) are redox active.[89,90] Hence electron delocalization involves both Fe and S and the assignment of formal Fe oxidation states within a cluster should not be taken too literally.

Figure 2 Crystallographically defined active-site structures for Fe–S centers involved with substrate binding and activation. Structures are taken from coordinates deposited in the Protein Data Bank: (a) Fe NHase, PDB ID# 2AHJ, NO-bound form of *Rhodococcus erythropolis* nitrile hydratase;[25] (b) [4Fe–4S] + isocitrate, PDB ID# 7ACN, isocitrate-bound form of porcine heart aconitase;[69] (c) Fe SOR, PDB ID# 1DQK, reduced *Pyrococcus furiosus* SOR;[31] (d) [4Fe–4S] + SAM, PDB ID# 1OLT, SAM-bound *Escherichia coli* HemN;[33] (e) Ni–Fe H_2ase, PDB ID# 1H2R, reduced *D. vulgaris* NiFe-hydrogenase;[70] (f) Fe–Fe–[4Fe–4S], PDB ID# 1HFE, *Desulfovibrio desulfuricans* Fe-hydrogenase;[71] (g) siroheme–[4Fe–4S], PDB ID# 2GEP, sulfite–bound *E. coli* sulfite reductase;[39] (h) [Mo–7Fe–9S–X], PDB ID#1M1M, *A. vinelandii* MoFe protein;[20] (i) [Ni–4Fe–5S], PDB ID# 1SU8, reduced *Carboxydothermus hydrogenoformans* CO dehydrogenase II;[43] (j) Ni–Ni–[4Fe–4S], PDB ID# 1RU3, *C. hydrogenoformans* acetyl-CoA synthase.[46] Color code: purple, Fe; yellow, S; gray, C; red, O; green, Ni; gold, Mo; black, unknown low-Z atom (O/C/N). Unlabeled S atoms correspond to bridging sulfides and BAN indicates backbone amide N. BAN = backbone amide nitrogen

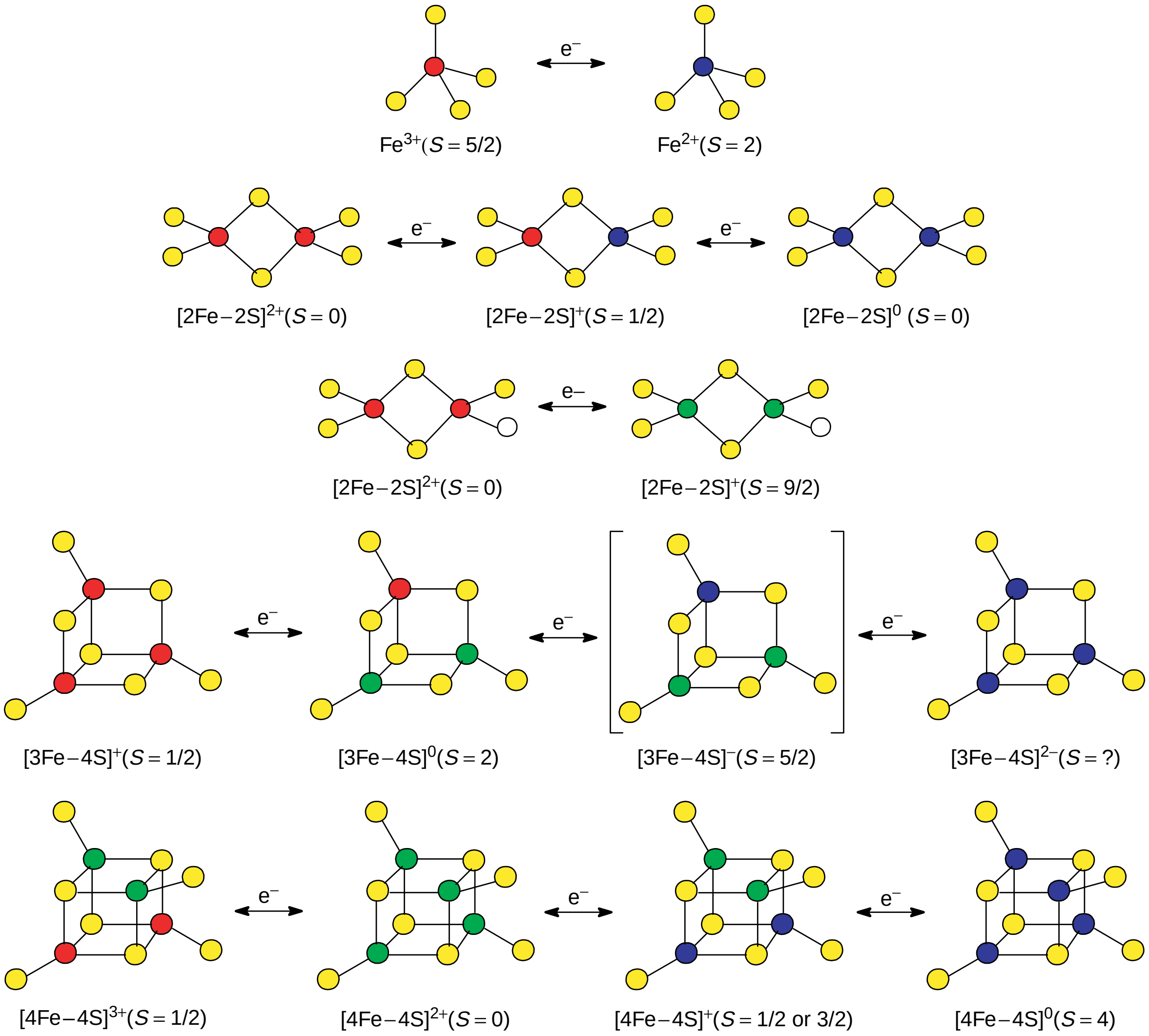

Figure 3 Ground-state spin (S) and valence-delocalization schemes for the fundamental types of Fe–S centers. Discrete $[3Fe–4S]^-$ clusters are shown in parenthesis since they have not been observed in any protein, but have been identified as fragments of heterometallic cubane clusters.[91] Reduction of the $[3Fe–4S]^+$ clusters by three electrons to yield the $[3Fe–4S]^{2-}$ cluster occurs with the concomitant addition of three protons.[92] Valence-delocalized $[2Fe–2S]^+$ clusters have only been observed in the C56S and C60S variants of *C. pasteurianum* 2Fe Fd.[93–95] Color code: Fe^{3+}, red; Fe^{2+}, blue; $Fe^{2.5+}$, green; S, yellow; O, white

The range of midpoint potentials that have been reported for redox cycling between the most common redox states of each of these fundamental types of Fe–S center in both complex and simple Fe–S proteins are summarized in Figure 4. Clearly the type of center, the specific redox couple, and the cluster ligands are all major determinants of the redox potential. For example, Rd-type centers, Rieske-type $[2Fe–2S]^{2+,+}$ clusters that have two histidyl ligands at the reducible Fe site, and $[4Fe–4S]^{3+,2+}$ clusters all can be viewed as high potential centers ($E_m > -100$ mV), whereas all-cysteinyl-ligated $[2Fe–2S]^{2+,+}$, $[3Fe–4S]^{+,0}$, and $[4Fe–4S]^{2+,+}$ clusters are low-potential centers ($E_m < +100$ mV). However, the potentials can span 350 to 800 mV even for a specific type of center, indicating that the protein environment plays a crucial role in determining the redox potential. Both theoretical and experimental approaches indicate that solvent exposure, the proximity and orientation of backbone and side-chain dipoles, the location of changed residues, and the extent of NH–S hydrogen-bonding interactions all need to be considered in rationalizing the observed potential of a specific center.[96,97]

2.1 Rubredoxin-type Centers

Mononuclear Fe centers in an approximately tetrahedral environment of cysteinyl-S (Rd-type centers) (see Figure 1) mediate electron transfer in a variety of different bacterial proteins and their structures and properties have recently

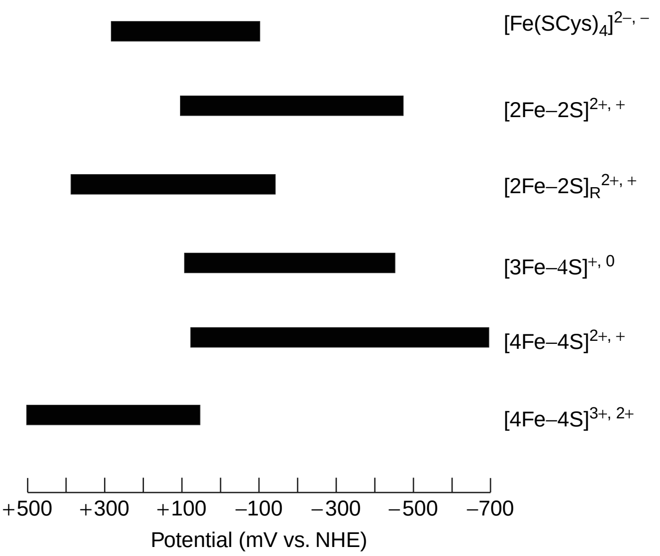

Figure 4 Ranges of midpoint potentials (mV vs. NHE) for biological Fe–S centers. $[2Fe–2S]_R^{2+,+}$, Rieske-type Fe–S center

been reviewed.[98] They constitute the sole prosthetic groups of rubredoxin (Rd) and desulforedoxin (Dx) and are found together with an oxo–bridged dinuclear Fe center in a class of nonheme peroxidases, formally known by the trivial names rubrerythrin and nigerythrin (*see* ***Iron Proteins with Dinuclear Active Sites***), and a novel mononuclear Fe active site in 2Fe SORs, formally known by the trivial name desulfoferredoxin (*see* ***Iron Proteins with Mononuclear Active Sites***).[99] Rd-type centers undergo redox cycling between high-spin Fe^{III} and high-spin Fe^{II} with reported midpoint potentials between +20 to −87 mV in the case of Rds, Dxs, and 2Fe SORs, and significantly higher potentials in the peroxidases, +281 mV for rubrerythrin and +213 mV for nigerythrin (Figure 4). X-ray crystallographic studies of Rds (0.95–1.8 Å resolution) indicate approximate D_{2d} symmetry for the FeS_4 unit (two opposite S–Fe–S angles in the range 102–104° with the remaining four S–Fe–S angles between 110° and 115°), with average Fe–S bond lengths of 2.28 Å for oxidized and 2.32 Å for the reduced. The structures are in accord with ground-state vibrational and electronic properties of oxidized Rds ($S = 5/2$ ground state, with $E/D \sim 0.25$, $D \sim -0.6\,\mathrm{cm}^{-1}$)[100,101] and the intense thiolate-to-iron charge transfer transitions that dominate the UV-visible absorption spectra of oxidized Rds have been assigned under effective D_{2d} symmetry on the basis of single crystal polarization studies and VTMCD studies.[101]

The arrangement of coordinating cysteine residues is highly conserved in all Rds including the Rd-type centers in nonheme peroxidases, and involves Cys–X_2–Cys motifs near the C- and N-termini. Desulforedoxin and the Dx-type centers in 2Fe SORs provide an interesting variant with Cys–X_2–Cys and Cys–Cys motifs for the coordinating cysteine residues; the stereochemical constraint imposed by the adjacent cysteines results in a more distorted tetrahedral structure. The crystal structure of desulforedoxin (1.8 Å resolution) shows that the S–Fe–S angle involving the adjacent cysteines increases to between 120° and 126°, compared to the range of 102–110° for the other five angles, with the Fe–S bond lengths all very similar and in the range 2.25–2.38 Å.[29] This structural difference is also manifest in the ground-state vibrational and electronic properties of the oxidized Dx-type centers ($S = 5/2$ ground state with $E/D \sim 0.08$ and $D \sim +2.2\,\mathrm{cm}^{-1}$),[102,103] and in the ground-state properties of the reduced centers as deduced by Mössbauer spectroscopy ($S = 2$, with $E/D \sim 0.28$ and $D \sim +7.5\,\mathrm{cm}^{-1}$ for Rd, compared to $E/D \sim 0.19$ and $D \sim -6\,\mathrm{cm}^{-1}$ for Dx).[103]

Site-directed mutagenesis studies of Rd in which the coordinating Cys residues were individually mutated to Ala/Gly or Ser residues have yielded interesting and in some cases surprising results. Rd-type centers are assembled in each of the Cys-to-Ser variants with reduction potentials for the $Fe^{III/II}$ couple decreased by 100–200 mV.[104] Moreover, the midpoint potentials are pH dependent, indicating protonation of the oxygenic ligand on reduction with pK_a values in the range 7–9. Crystallographic and/or spectroscopic evidence indicates serinate ligation at the Fe^{III} site in three of the Cys-to-Ser variants and hydroxide ligation in one of the two interior Cys-to-Ser variants.[104,105] Mutation of either of the two surface Cys residues to Ala or Gly resulted in unstable proteins which can assemble a mononuclear Fe^{III} site with three Cys and one hydroxide or noncysteinyl protein ligand.[106] However, in one case, spectroscopic studies of the as-purified recombinant protein have provided definitive evidence for a $[2Fe–2S]^{2+}$ cluster.[107] Although the location and ligation of the [2Fe–2S] cluster have yet to be fully defined, this is currently the first and only example of a polypeptide incorporating a binuclear cluster rather than a mononuclear Fe site as a result of a single point mutation.

2.2 [2Fe–2S] Clusters

[2Fe–2S] clusters generally have complete cysteinyl ligation and undergo redox cycling between the 2+ and 1+ core oxidation states (Figures 1 and 3). However, there is large group, termed Rieske-type centers $[2Fe–2S]_R$, with two histidyl ligands at one Fe site[22] (see Figure 1), and a few examples of [2Fe–2S] clusters with one noncysteinyl ligand, for example, aspartate in some succinate dehydrogenases[108] and a sulfide dehydrogenase,[109] and arginine in biotin synthase.[68] $[2Fe–2S]^{2+,+}$ centers mediate electron transfer in a wide range of Fds and complex metalloenzymes, as well as being intrinsic components in the photosynthetic and respiratory electron transport chains. Redox potentials for the $[2Fe–2S]^{2+,+}$ couple span a range from +380 to −460 mV, with Rieske-type centers generally having higher potentials (+380 to −150 mV) than all-cysteinyl-ligated centers (+100 to −460 mV) owing to the presence of the more electropositive histidine ligands at the reducible Fe site

(Figure 4). While their role is predominantly electron transfer, there is one example of a [2Fe–2S]-containing dehydratase, several examples of [2Fe–2S] clusters that have regulatory roles and one example of a [2Fe–2S] cluster acting as a sulfur donor (see Table 1).

Structures are available for [2Fe–2S] centers in several Fds[21,110–114] and Rieske-type proteins,[22,23] as well as in more complex enzyme systems such as mammalian ferrochelatase,[62] succinate dehydrogenase and fumarate reductase,[108,115] members of the xanthine oxidase family of molybdoenzymes,[116,117] Fe-hydrogenase,[40] and biotin synthase.[68] In all cases, coordination at each Fe is approximately tetrahedral, and the $Fe_2(\mu_2-S)_2$ core is approximately planar with Fe–Fe distances in the range 2.7−2.8 Å, and Fe–S distances generally between 2.2−2.3 Å. In addition, high-resolution structures of the oxidized and reduced forms of a plant-type [2Fe–2S] Fd (1.3 and 1.17 Å resolution, respectively) show that reduction occurs with no major structural reorganization and slight lengthening of the Fe–S bonds (maximally 0.01 to 0.02 Å).[118] Several different types of protein folds are apparent in [2Fe–2S]-cluster proteins or domains. The Fd-fold is common to plant-type, hydroxylase- or mammalian-type, and Isc-type [2Fe–2S] Fds, in addition to several complex [2Fe–2S]-containing Fe–S enzymes, and contains a Cys–$X_{4/5}$–Cys–X_2–Cys–X_{29-37}–Cys motif of coordinating cysteines.[110] A thioredoxin-fold is utilized by a distinct class of [2Fe–2S] Fds and uses a Cys–$X_{10/12}$–Cys–X_{29-34}–Cys–X_3–Cys arrangement of coordinating cysteines.[114] Homologous subunits or domains in complex Fe–S enzymes such as NADH dehydrogenase and hydrogenases also appear to contain thioredoxin-type [2Fe–2S] centers, albeit with a different cysteine motif, Cys–X_4–Cys–X_{30-35}–Cys–X_3–Cys.[114] The Rieske-fold is common to all Rieske-type centers and coordinates the [2Fe–2S] cluster via the Cys and His residues in a Cys–X–His–X_{15-47}–Cys–X_2–His motif.[22] Unique folds are also associated with [2Fe–2S] centers in biotin synthase[68] and members of the xanthine oxidase family of molybdoenzymes.[116]

The electronic, magnetic, and vibrational properties of $[2Fe–2S]^{2+,+}$ clusters have been extensively characterized using the combination of absorption, CD, VTMCD, EPR, ENDOR, Mössbauer, NMR and resonance Raman spectroscopies, and the ground-state electronic properties are summarized in Figure 3. In the oxidized state, the two $S = 5/2$ Fe^{III} ions in the $[2Fe–2S]^{2+}$ cluster are antiferromagnetically coupled ($J \approx 360\ cm^{-1}$ for plant-type Fds and $>550\ cm^{-1}$ for hydroxylase-type Fds) to give a diamagnetic $S = 0$ ground state (Figure 3). In the reduced $[2Fe–2S]^+$ form, Mössbauer has shown that the valences are localized and the $S = 2$ Fe^{II} and $S = 5/2$ Fe^{III} sites are antiferromagnetically coupled ($J \approx 200, 330$, and $130\ cm^{-1}$ for plant-type Fds, hydroxylase-type Fds, and Rieske proteins, respectively) to give an $S = 1/2$ ground state with a rhombic or axial g-tensor (Figure 3). NMR has been used to assess the cysteine residues that coordinate the reducible Fe site in simple Fds.[119] Such information, coupled with the available structural data, suggests that the nature of the coordinating residues, solvent exposure, and the asymmetry in hydrogen-bonding interactions involving coordinated cysteinyl-S and backbone amide NH are primarily responsible for determining the site of reduction. The g-value anisotropy and average g-values of the $S = 1/2$ EPR signal of $[2Fe–2S]^+$ centers have been successfully rationalized in terms of distortion at the Fe^{II} site using a ligand field model[120] and more recently in terms of the Fe–Fe–S–C dihedral angles at the Fe^{II} site using DFT calculations.[121] However, antisymmetric exchange interactions are required to explain the anomalous EPR properties of the $[2Fe–2S]^+$ centers in Rieske-type centers at pH 14 and in members of the xanthine oxidase family of enzymes.[122] Rieske-type centers have also recently been shown to have an accessible all-ferrous $[2Fe–2S]^0$ redox state that is stabilized by protonation on one of the μ_2−sulfides.[123] The $[2Fe–2S]^0$ cluster was found to have an $S = 0$ ground state as a result of antiferromagnetic interaction between the two $S = 2$ Fe^{II} sites ($J = 60\ cm^{-1}$) (see Figure 3). However, since the $[2Fe–2S]^{+,0}$ couple is ∼1.0 V lower than the $[2Fe–2S]^{2+,+}$ couple,[123] it seems unlikely that the all-ferrous redox state is physiologically relevant.

Site-directed mutagenesis studies involving coordinating cysteines and histidines have shown that individual cysteinates can be replaced as cluster ligands by serinate or aspartate in all-cysteine-ligated [2Fe–2S] clusters[124,125] and that an individual histidine can be replaced by a cysteinate ligand in a Rieske−type center.[126] All three types of substitutions decrease the redox potential, provided the substituted residue ligates the reducible Fe site, indicating that the $[2Fe–2S]^{2+,+}$ redox potentials decrease with increasing ligand nucleophilicity, that is, histidine > cysteinate > serinate ∼ aspartate. Mutagenesis studies also led to the discovery of the only known examples of valence-delocalized $[2Fe–2S]^+$ clusters. EPR and Mössbauer studies of the C56S and C60S variants of *Clostridium pasteurianum* [2Fe–2S] Fd revealed the presence of valance-delocalized $[2Fe–2S]^+$ clusters with $S = 9/2$ ground states[93–95,127] (Figure 3). Ferromagnetic coupling facilitates valence delocalization since the electron with antiparallel spin can visit both Fe sites without undergoing a spin flip. These high-spin states are stabilized via spin-dependent resonance delocalization (double exchange) and theoretical studies indicate that the ground and excited properties of $[2Fe–2S]^+$ centers are critically dependent on the interplay of Heisenberg exchange, double exchange, and vibronic interactions.[85] As indicated in Figure 3, valence-delocalized $[2Fe–2S]^+$ units are integral components of all higher nuclearity clusters and the ability to investigate such clusters in isolation has facilitated characterization of the ground and excited state electronic properties as well as the vibrational properties using the combination of EPR, Mössbauer, VTMCD, and resonance Raman spectroscopies.[95,127]

2.3 [3Fe–4S] Clusters

Both cubane-type and linear [3Fe–4S] clusters have been reported in biological systems, but only the cubane-type appears to be physiologically relevant. Cubane-type clusters have a $Fe_3(\mu_3{-}S)(\mu_2{-}S)_3$ core that is best visualized as a cubane $Fe_4(\mu_3{-}S)_4$ core minus one Fe, with cysteinyl-S invariably completing the tetrahedral coordination at each Fe site (Figure 1). Indeed, the early discovery that cubane-type [3Fe–4S] clusters can be formed via oxidative loss of one Fe from [4Fe–4S] clusters led to speculation that all clusters of this type may be artifacts of aerobic protein isolation procedures.[128] While this is clearly the case in (de)hydratase enzymes such as aconitase and several Fds, particularly those containing [4Fe–4S] clusters with noncysteinyl ligation at a unique Fe site, there is now overwhelming evidence, based on X-ray structures, primary sequences, and *in vivo* detection, that cubane-type [3Fe–4S] clusters are also intrinsic components of numerous redox enzymes and proteins.[14] Electron transfer is the only known biological function and they have been established as intrinsic redox-active centers in numerous 3Fe and 7Fe Fds, succinate dehydrogenase, fumarate reductase, nitrate reductase, NiFe-hydrogenase, arsenite oxidase, and Fd- and NAD(P)H-dependent glutamate synthases.[14,129] In contrast, linear [3Fe–4S] clusters have only been rigorously identified in the 1+ oxidation state in alkaline (pH > 9.5) or denatured forms of [3Fe–4S] aconitase,[130,131] by virtue its unique electronic and magnetic properties, via comparative spectroscopic studies (absorption, Mössbauer, EPR, and VTMCD) of crystallographically defined synthetic analog complexes such as $[Fe_3S_4(SEt)_4]^{3-}$ (*see* ***Iron–Sulfur Models of Protein Active Sites***). Although no direct structural information is available for protein-bound linear $[3Fe–4S]^{+}$ clusters, the close correspondence in spectroscopic properties to those of synthetic $[3Fe–4S]^{+}$ complexes provides compelling evidence for a linear $Fe_3(\mu_2{-}S)_4$ core with cysteinyl-S completing tetrahedral coordination at the two terminal Fe sites. Thus far there is no evidence for the presence of a linear $[3Fe–4S]^{+}$ cluster as a functional component of any Fe–S protein.

Electrochemical studies indicate that biological cubane-type [3Fe–4S] clusters have accessible 1+, 0, and 2− redox states.[14] However, only the $[3Fe–4S]^{+,0}$ couple appears to be used to mediate biological electron transport and redox potentials for this couple span a range from +90 to −460 mV[14] (Figure 4). The midpoint potential for the two-electron $[3Fe–4S]^{0,2-}$ couple is ∼ −700 mV at pH 7, and is strongly pH dependent with reduction to the $[3Fe–4S]^{2-}$ state involving the net uptake of three protons.[132] Protonation of the $[3Fe–4S]^{0}$ clusters in some 7Fe Fds has also been observed with a $pK_a \sim 7.5$.[14] Although the protonation sites of reduced clusters have yet to be definitively established, the three $\mu_2{-}S$ atoms are the most likely candidates.[133]

X-ray crystal structures are available for cubane-type [3Fe–4S] centers in 3Fe and 7Fe Fds, aconitase, NiFe-hydrogenases, succinate dehydrogenase, fumarate reductase, arsenite oxidase, and nitrate reductase, and formate dehydrogenase.[14,21,108,115,129,134,135] In all cases, coordination at each Fe is approximately tetrahedral and the $Fe_3(\mu_3{-}S)(\mu_2{-}S)_3$ core has approximate C_{3v} symmetry. High-resolution structures are available for both the $[3Fe–4S]^{+}$ and $[3Fe–4S]^{0}$ centers in *Azotobacter vinelandii* FdI (1.4 Å resolution).[19,136] The core structures in both oxidation states are the same within experimental error and both exhibit a splayed configuration with respect to the three μ_2S atoms in the absence of the fourth Fe. However, the structure of the $[3Fe–4S]^{0}$ center displays significant distortions compared to a well-characterized analog complex,[137] suggesting that the protein–bound structure may represent an entatic state in order to facilitate electron transfer.[19] The average Fe–μ_2S bonds lengths (2.24 Å for $[3Fe–4S]^{+}$ and 2.26 Å for $[3Fe–4S]^{0}$) are generally shorter than the average Fe–μ_3S bond lengths (2.29 Å for $[3Fe–4S]^{+}$ and 2.28 Å for $[3Fe–4S]^{0}$) and the average Fe–S(Cys) bond lengths (2.28 Å for $[3Fe–4S]^{+}$ and 2.29 Å for $[3Fe–4S]^{0}$), and the Fe–Fe distances are significantly distributed with two short (2.64–2.67 Å) and one long (2.70–2.73 Å). A variety of arrangements of cysteine residues can coordinate cubane-type [3Fe–4S] clusters. However, in structurally characterized centers, the arrangement involves two closely spaced cysteines, Cys–X_2–Cys (aconitase), Cys–X_5–Cys (e.g. some 3Fe and 7Fe Fds, succinate dehydrogenase, fumarate reductase, nitrate reductase), or Cys–X_7–Cys (some 3Fe and 7Fe Fds), and one other remote cysteine.[21] Facile interconversion between [3Fe–4S] and [4Fe–4S] clusters is possible in aconitase and many ferredoxins (see Section 2.5). With this in mind, it is important to note that the consensus sequence for coordination of a [4Fe–4S] cluster in bacterial Fds is Cys–X_2–Cys(or Asp)–X_2–Cys with a more remote cysteine supplying the fourth ligand. Indeed, in ferredoxins where it is possible to effect facile [3Fe–4S] ↔ [4Fe–4S] interconversions, a coordinating residue, either cysteine or aspartic acid, is located between two closely spaced cysteines that coordinate the [3Fe–4S] clusters in a Cys–X_2–Cys/Asp–X_2–Cys arrangement.

The electronic, magnetic, and vibrational properties of [3Fe–4S] centers in each accessible redox state have been characterized in detail using the combination of absorption, VTMCD, EPR, ENDOR, Mössbauer, saturation magnetization, NMR, and resonance Raman. The results have recently been reviewed[14] and the ground-state properties and valence-delocalization schemes for cubane-type [3Fe–4S] centers are summarized in Figure 3. In cubane-type $[3Fe–4S]^{+}$ clusters, the three $S = 5/2$ Fe^{III} ions are antiferromagnetically coupled to give an $S = 1/2$ ground state. This gives rise to an isotropic or axial EPR signal centered with g_{av} between 2.02 and 1.96 with a well-defined low-field g-value close to 2.02. Saturation magnetization studies and NMR measurements have been interpreted in terms of three nearly equivalent exchange interactions with $J_{12} \sim J_{13} \sim J_{23} \sim 300\,cm^{-1}$, and recent studies have demonstrated that antisymmetric exchange coupling with slightly distributed J values are required to explain the broad high-field EPR spectra that are observed for many [3Fe–4S]$^+$ clusters.[138] In contrast, linear [3Fe–4S]$^+$ clusters exhibit a rhombic $S = 5/2$ ground state ($E/D \sim 0.31$) that results from highly asymmetric coupling among the three Fe atoms, $J_{12} \sim J_{23} > 2J_{13}$, reflecting the linear rather than triangular arrangement of Fe atoms.[130] One-electron reduction of cubane-type [3Fe–4S]$^+$ centers results in a [3Fe–4S]^0 cluster with a $S = 2$ ground state ($D \sim -2.5\,\mathrm{cm}^{-1}$ and $E/D = 0.20-0.25$) that arises from antiferromagnetic interaction between a valence-delocalized Fe$^{\mathrm{II}}$/Fe$^{\mathrm{III}}$ pair ($S = 9/2$) and a valence trapped Fe$^{\mathrm{III}}$ site ($S = 5/2$). Although there is no spectroscopic or electrochemical evidence for discrete [3Fe–4S]$^-$ clusters in biological samples, the properties of center have been deduced from studies of protein-bound heterometallic cubanes [M–3Fe–4S]$^+$ (see Section 2.5), in which M is a redox-inert diamagnetic d^{10} transition metal ion such as Zn^{2+} or Cd^{2+}. The [3Fe–4S]$^-$ cluster fragment has an $S = 5/2$ ground state ($D \sim -2.5\,\mathrm{cm}^{-1}$ and E/D in the range $0.18-0.33$) that arises from antiferromagnetic interaction between a valence-delocalized Fe$^{\mathrm{II}}$/Fe$^{\mathrm{III}}$ pair ($S = 9/2$) and a valence trapped Fe$^{\mathrm{II}}$ site ($S = 2$). The electronic properties of the all-ferrous cubane-type [3Fe–4S]$^{2-}$ center have yet to be established.

2.4 [4Fe–4S] Clusters

Cubane-type clusters involving a $\mathrm{Fe_4(\mu_3{-}S)_4}$ core are one of the most pervasive electron transfer centers in biology (Figure 1). Almost all have complete cysteinyl-S ligation. However, there are a few well-characterized examples of electron transfer [4Fe–4S] clusters with noncysteinyl ligation at one Fe site: aspartate in some ferredoxins[139] and histidine in both NiFe- and Fe-hydrogenases[35,40] and nitrate reductase.[134] Mutagenesis studies have also demonstrated that [4Fe–4S] clusters can be assembled with one cysteinate ligand replaced by serinate,[140,141] aspartate[142] or histidine.[143] In addition to their ubiquitous role in mediating biological electron transport, [4Fe–4S] clusters also have catalytic roles in substrate binding and disulfide reduction, as well as regulatory, structural, and storage roles (Table 1). In both (de)hydratases[27,28] and radical-SAM enzymes,[34,144] the absence of an amino acid residue ligand at a unique Fe site of a [4Fe–4S] cluster creates a site for binding and activating the substrate (Figure 2).

Biological [4Fe–4S] clusters have been characterized in the 3+, 2+, 1+, and 0 core oxidations states. However, with the notable exception of the nitrogenase Fe-protein, all electron transfer [4Fe–4S] clusters only undergo one-electron redox cycling between either the [4Fe–4S]$^{3+,2+}$ or [4Fe–4S]$^{2+,+}$ couples under physiological conditions. Fd-type centers cycle between the [4Fe–4S]$^{2+,+}$ states with midpoint potentials between +80 and −715 mV, whereas high potential iron–sulfur protein, HiPIP-type centers cycle between the [4Fe–4S]$^{3+,2+}$ states at higher potentials, +50 to +500 mV (Figure 4). Despite the existence of several ultrahigh–resolution (≤ 1.0 Å) crystal structures for HiPIP-type and Fd-type [4Fe–4S]$^{2+}$ centers,[145–148] the factors that determine the choice of redox couple are not yet clearly defined. One important factor is the number of amide NH–S hydrogen bonds to the [4Fe–4S] center (∼5 in HiPIPs compared to 8–10 in Fds). However, other factors such as hydrophobic interactions, solvent exposure, and the electrostatic interaction of the charged cluster with its protein environment also play an important role in determining both the redox couple and the redox potential within a particular class.[149] The nitrogenase Fe-protein is unique in containing a subunit-bridging [4Fe–4S] cluster that can be stabilized in three core oxidation states, 2+, 1+, and 0, and hence has the capability to act as a two-electron donor. Following the pioneering work of Watt and coworkers,[150] the all-ferrous [4Fe–4S]^0 center was prepared by reduction with Ti(III) citrate and characterized spectroscopically and structurally.[151,152] Structural data and calculations suggest that increased solvent exposure and NH–S H-bonding interactions (∼14 in Fe-protein) are responsible for stabilizing the [4Fe–4S]^0 center in the Fe-protein.[149] However, the most recent estimates for the redox potential of the [4Fe–4S]$^{+,0}$ couple, ∼−790 mV, indicate that it is substantially more negative than the [4Fe–4S]$^{2+,+}$ couple, ∼−350 mV, and consequently raise doubts concerning the physiological relevance of the all-ferrous form of the nitrogenase Fe-protein.[153]

X-ray crystal structures are available for [4Fe–4S] centers in a large number of simple and complex Fe–S proteins (see Table 1 for examples), and atomic resolution structures are available for [4Fe–4S]$^{2+}$ centers in HiPIP,[145,146] 4Fe Fd,[148] 7Fe Fd,[136] and 8Fe Fd.[147] In accord with the structures of analog complexes[13] and resonance Raman studies of protein-bound [4Fe–4S]$^{2+}$ centers,[154] a tetragonal compression resulting in approximate D_{2d} symmetry is generally observed within the [4Fe–4S] core, resulting in four parallel short bonds (average Fe–S distances between 2.24 and 2.28 Å) and eight long bonds (average Fe–S distances between 2.29 and 2.31 Å), with the average Fe–S(Cys) and Fe–Fe distances in the range 2.26–2.28 Å and 2.71–2.75 Å, respectively. The tetragonal compression appears to be more pronounced in HiPIP- than Fd-type [4Fe–4S]$^{2+}$ clusters, with average long Fe–S minus average short Fe–S distances in the range 0.06–0.07 Å for HiPIPs and 0.02–0.05 Å for Fds. Although no high-resolution X-ray crystal structures are currently available for protein-bound [4Fe–4S]$^{3+}$ and [4Fe–4S]$^+$ clusters, crystallographic studies of analog complexes[13] suggest that oxidation will primarily involve contraction of the eight long Fe–S bonds and that reduction will primarily involve elongation of the four short Fe–S bonds, yielding clusters with decreased tetragonal compressions. An alternative and useful method of analyzing distortions in [4Fe–4S] centers has recently been proposed based on the radii and circumcenters of the circumspheres defined by the Fe, inorganic-S, and cysteinyl-S atoms.[155] The circumcenters are generally non-coincident by 0.01–0.06 Å and the Fe radius (1.66–1.69 Å) appears to be relatively insensitive to the core oxidation state, whereas the inorganic-S and cysteinyl-S radii (2.18–2.24 Å and 3.87–3.94 Å, respectively) both increase by ∼3% on reduction from the 3+ to 1+ core oxidation states. The X-ray crystal structure of the $[4Fe–4S]^0$ in the nitrogenase Fe-protein has been reported at 2.25 Å resolution.[152] However, this resolution may not be adequate for defining cluster distortion and it is significant that the metrical parameters are not in accord with those derived from extended x-ray absorption fine structure (EXAFS) analysis.[156] For example, the best fit to the EXAFS data gives a 4:2 short-to-long pattern of Fe–Fe distances with average Fe–Fe distances of 2.52 and 2.77 Å, whereas the X-ray structure gives a 2:4 short-to-long pattern with Fe–Fe distances in the ranges 2.54–2.57 Å and 2.66–2.79 Å. Nevertheless, comparison with other Fe-protein X-ray crystal structures clearly demonstrates that reduction to the all-ferrous state occurs without major conformational changes in the protein environment and that the [4Fe–4S] core stays intact.[152]

The magnetic and electronic properties of [4Fe–4S] centers are less well understood than for [2Fe–2S] and [3Fe–4S] centers. Phenomenologically, the Mössbauer and EPR data have been rationalized in terms of antiferromagnetic exchange interaction between valence-delocalized, ferromagnetically coupled [2Fe–2S] units (Figure 3): $[4Fe–4S]^{3+}$ ($S = 1/2$) results from Fe^{III}/Fe^{III} ($S = 5$) coupled to Fe^{II}/Fe^{III} ($S = 9/2$); $[4Fe–4S]^{2+}$ ($S = 0$) results from Fe^{II}/Fe^{III} ($S = 9/2$) coupled to Fe^{II}/Fe^{III} ($S = 9/2$); $[4Fe–4S]^{+}$ ($S = 1/2$) results from Fe^{II}/Fe^{II} ($S = 4$) coupled to Fe^{II}/Fe^{III} ($S = 9/2$). However, this is likely to be an oversimplification, since analyses of hyperfine coupling constants and/or NMR studies of $S = 1/2$ $[4Fe–4S]^{3+}$ and $[4Fe–4S]^{+}$ clusters suggests that $S = 7/2$ or $S = 7/2$, 9/2 mixed spin are likely to be more appropriate formal spin states for the valence-delocalized $[2Fe–2S]^{+}$ fragments in these clusters.[157,158] Moreover, NMR studies of protein-bound $[4Fe–4S]^{3+}$ centers indicate that the location of the valence-delocalized pair is dynamic on the NMR timescale, such that the cluster exists in rapid equilibrium between different forms. Both $[4Fe–4S]^{3+}$ and $[4Fe–4S]^{+}$ centers have $S = 1/2$ ground states, but they are readily distinguished by EPR. $[4Fe–4S]^{3+}$ centers give rise to axial EPR signals (typically $g_{\parallel} = 2.12$ and $g_{\perp} = 2.04$) with $g_{av} > 2$, whereas $[4Fe–4S]^{+}$ centers give rise to rhombic EPR signals (typically $g = 2.06, 1.92, 1.88$) with $g_{av} < 2$. The EPR signals from $S = 1/2$ $[4Fe–4S]^{+}$ centers are similar to those exhibited by $[2Fe–2S]^{+}$ centers in plant-type Fds, but can usually be distinguished, since they are faster relaxing and not generally observable above 30 K. Although the majority of biological $[4Fe–4S]^{+}$ centers exhibit $S = 1/2$ ground states, there are many that exist as a mixture of species with $S = 1/2$ and 3/2 ground states,[3] as well as a few examples of pure $S = 3/2$ ground states[159,160] and quantum mechanically admixed $S = 1/2$, 3/2 ground states.[161] The implication is that $S = 1/2$ and 3/2 states of $[4Fe–4S]^{+}$ centers are close in energy and the structural, electronic, or environmental factors that determine which is lower in energy are subtle and have yet to be fully elucidated.[162] EPR and Mössbauer studies have determined an $S = 4$ ground state for the $[4Fe–4S]^0$ center in the nitrogenase Fe-protein.[151] Moreover, the coupling scheme appears to be quite distinct from that characterized in the three higher oxidation states, with four high-spin Fe(II) sites coupled in a 3:1 alignment of up:down spin vectors.[163] This would predict a 3:3 pattern of short-to-long bonds reflecting the three ferromagnetic and three antiferromagnetic Fe–Fe interactions, rather that the 2:4 or 4:2 short-to-long patterns that have been reported based on EXAFS and crystallographic data, respectively.[152,156] A higher resolution crystal structure will clearly be required in order to provide a structural framework for the observed coupling scheme.

Numerous different arrangements of cysteine residues and protein folds are able to accommodate [4Fe–4S] clusters. By far the most common among electron transfer [4Fe–4S] centers are the Fd-type fold which involves ligation by three closely spaced Cys residues, typically Cys–X_2–Cys–X_2–Cys plus a more remote Cys, and the HiPIP-type fold which involves ligation by four Cys residues in a Cys–X_2–Cys–X_{8-16}–Cys–X_{11-15}–Cys arrangement.[21] In addition, electron transfer [4Fe–4S] clusters can also bridge subunits in homodimeric proteins using two cysteines from each monomer. The best-characterized examples are nitrogenase Fe-protein,[164] the F_X cluster in photosystem I (*see* ***Photosynthesis***),[165,166] and cluster D in CO dehydrogenase and acetyl-CoA synthase.[42,44] The protein folds and arrangements of coordinating cysteine residues in [4Fe–4S] clusters whose function is not solely electron transfer (Table 1) are described in Section 3.

2.5 Cluster Conversions

Biological Fe–S clusters can frequently be degraded or converted into other structural types in response to exposure to O_2 or NO, chemical oxidation or reduction, changes in pH, denaturants, or site-directed mutagenesis of specific residues. Moreover, since Fe–S clusters control a local region of protein structure, cluster transformations, or degradation can provide a sensory mechanism for regulating gene expression or enzyme activity in response to external stimuli.[58] Figure 5 provides a summary of the well-characterized types of cluster transformation that have been observed in Fe–S proteins.

Aconitase has been a particularly fertile protein for investigating and establishing cluster transformations.[27] Aerobic isolation of aconitase or air-exposure of the active $[4Fe–4S]^{2+,+}$ form results in an inactive enzyme containing a $[3Fe–4S]^{+}$ cluster. However, under reducing conditions the $[3Fe–4S]^0$ cluster avidly takes up Fe to reform the catalytically active $[4Fe–4S]^{2+,+}$ cluster. The [4Fe–4S] clusters in (de)hydratases such as aconitase and ferredoxins which have noncysteinyl ligation at a specific Fe atom are particularly susceptible to this type of reversible cluster

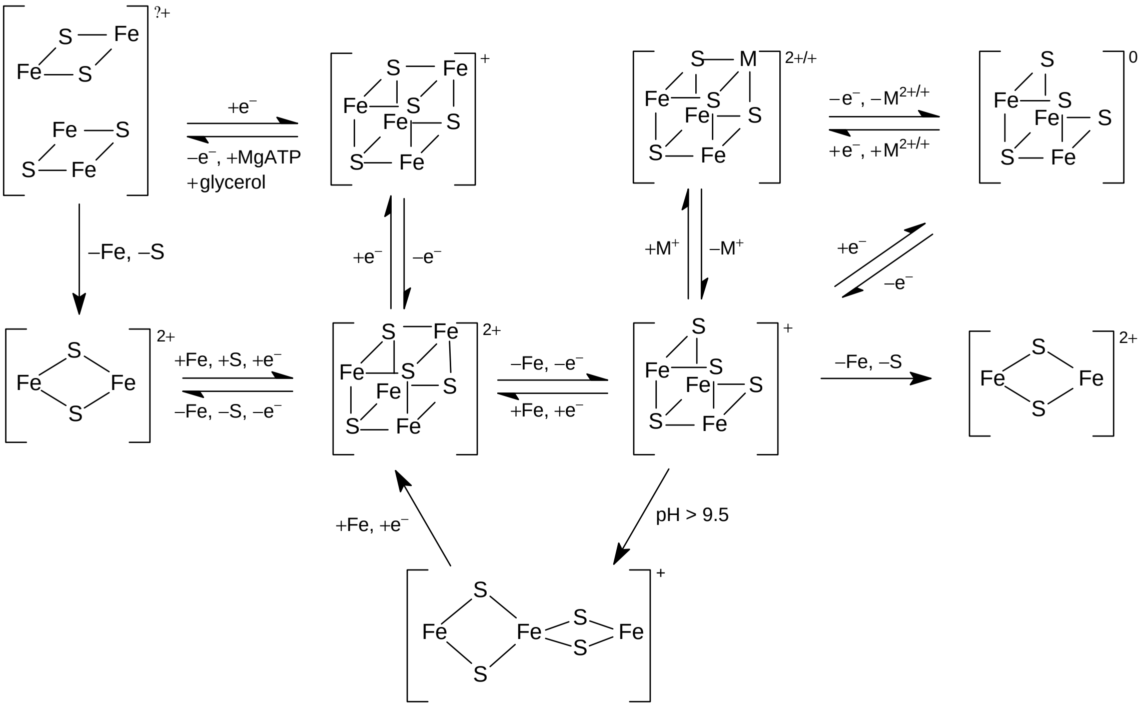

Figure 5 Summary of the types of cluster transformations that have been observed in Fe–S proteins. $M^{+} = Cu^{+}$ and Tl^{+}; $M^{2+} = Cr^{2+}$, Mn^{2+}, Co^{2+}, Ni^{2+}, Zn^{2+}, Cd^{2+}

transformation. Indeed this has been used to great effect for the assembly and characterization of mixed-metal cubane clusters of the type [M–3Fe–4S]$^{2+,+}$ (M = Zn, Co, Ni, Cr, Mn, Cu, Cd, Ga, Tl) in bacterial ferredoxins.[14] Many [4Fe–4S] clusters with complete cysteinyl ligation are also susceptible to partial oxidative degradation to [3Fe–4S]$^{+}$ clusters, although the conditions required are usually more extreme, that is, prolonged exposure to air and/or large excesses of ferricyanide. [3Fe–4S] $\leftrightarrow$ [4Fe–4S] and [4Fe–4S] $\leftrightarrow$ [3Fe–4S] cluster conversions have also been accomplished by site-directed mutagenesis for clusters containing Fd-like arrangements of cysteine residues. In enzymes such as fumarate reductase[167] and NiFe-hydrogenase[168] containing an endogenous [3Fe–4S] cluster ligated by a Fd-type Cys–X_2–Y–X_2–Cys grouping of cysteines, conversion to a [4Fe–4S] cluster is effected upon replacement of the Y residue by Cys. Conversely, mutagenesis of the middle Cys in the Fd-type Cys–X_2–Cys–X_2–Cys grouping of cysteines in dimethylsulfoxide (DMSO) reductase[169] and NiFe-hydrogenase[170] result in [4Fe–4S] to [3Fe–4S] cluster conversions.

Aconitase is currently the only well-characterized example of a cubane-type [3Fe–4S]$^{+}$ to linear [3Fe–4S]$^{+}$ cluster conversion.[130,131] This remarkable transformation occurs at pH > 9.5 or under conditions of partial denaturation, despite requiring a major protein rearrangement. Only two of the cysteine ligands to the cubane-type [3Fe–4S]$^{+}$ cluster are retained and two more remote cysteines are recruited as cluster ligands.[77] On the basis of absorption data alone, linear [3Fe–4S]$^{+}$ clusters have also been reported under alkaline conditions or during denaturation of 7Fe and [2Fe–2S] Fds.[171–173] However, definitive evidence for linear [3Fe–4S]$^{+}$ clusters in these proteins requires the application of more discriminating spectroscopic techniques, as soluble polymeric iron-sulfides exhibit similar absorption characteristics. Reduction of the linear [3Fe–4S]$^{+}$ center in aconitase in the presence of Fe leads to the formation of [4Fe–4S]$^{2+,+}$ clusters. Similar cluster transformations have been observed with synthetic clusters and have been utilized to synthesize a variety of mixed-metal cubane clusters of the type [M–3Fe–4S]$^{2+,+}$.[13]

There are also several examples of [4Fe–4S]$^{2+}$ and cubane-type [3Fe–4S]$^{+}$ clusters that undergo degradation to [2Fe–2S]$^{2+}$ clusters under oxidative or denaturing conditions. For example, some [2Fe–2S]$^{2+}$ clusters are formed, in addition to linear [3Fe–4S]$^{+}$ clusters, during denaturation of aconitase.[130] The SAM-binding [4Fe–4S]$^{2+}$ clusters in radical-SAM enzymes also undergo facile aerial oxidative conversion to yield a semistable [2Fe–2S]$^{2+}$ cluster,[174] and in some cases this conversion appears to proceed via a [3Fe–4S]$^{+}$ cluster intermediate. Oxygen-induced [4Fe–4S]$^{2+}$ to [2Fe–2S]$^{2+}$ cluster conversion in the FNR (fumarate–nitrate reduction) regulatory protein constitutes the O_2-sensing mechanism that triggers the switch from anaerobic to aerobic growth of *E. coli*,[57,58] and recent spectroscopic studies indicate that this conversion involves a $[3Fe–4S]^{+}$ intermediate.[175] Another intriguing example of $[4Fe–4S]^{2+}$ to $[2Fe–2S]^{2+}$ cluster conversion is provided by nitrogenase Fe-protein.[176] MgATP binding to the oxidized protein in the presence of iron chelators such as α, α'-dipyridyl results in conversion of the endogenous $[4Fe–4S]^{2+}$ cluster to a $[2Fe–2S]^{2+}$ cluster. Moreover, recent crystallographic and spectroscopic studies of a mimic of the nucleotide-bound form of the nitrogenase Fe-protein have revealed a novel transformation in which the reduced [4Fe–4S] cluster is reversibly cleaved into two [2Fe–2S] fragments separated by ∼5Å under oxidizing conditions in the presence of glycerol.[177] Each [2Fe–2S] fragment has one cysteinyl ligand at each Fe site and glycerol appears to be bound as a bidentate bridging ligand. This is likely to correspond to stabilized intermediate in the oxidative $[4Fe–4S]^{2+}$ to $[2Fe–2S]^{2+}$ conversion and provides a model system for investigating reductive coupling of $[2Fe–2S]^{2+}$ clusters at a subunit interface to yield $[4Fe–4S]^{2+}$, a process that may be of fundamental importance in the biosynthesis of $[4Fe–4S]^{2+}$ clusters.[83,178] All of these oxidatively induced $[4Fe–4S]^{2+}$ to $[2Fe–2S]^{2+}$ cluster conversions are reversible under reducing conditions in the presence of ferrous ions and sulfide.

Iron–sulfur clusters are frequently sensitive targets for NO cytotoxicity and are generally degraded to yield dinitrosyl-iron-dithiol species, as judged by the appearance of the characteristic EPR signal ($g_{\perp} = 2.03$, $g_{\parallel} = 2.01$).[179] Recent studies of the nitrosylated form of a 2Fe Fd have shown that the dinitrosyl-iron-dithiol species can be converted back to a [2Fe–2S] cluster by cysteine desulfurases.[180] Although it remains to be established if this constitutes a general method of repair of nitrosylated Fe–S centers, it does provide a plausible mechanism for NO sensing by Fe–S centers.

3 FUNCTIONS OF BIOLOGICAL IRON–SULFUR CENTERS

3.1 Electron Transport

Biological electron transfer chains containing one or more Fe–S centers are present in numerous membrane-bound and soluble oxidoreductases and play important roles in both respiratory and photosynthetic energy conversion. In addition, Fds, Rds, and HiPIPs constitute one of the largest groups of mobile electron carriers that serve as electron donors or acceptors. The recent proliferation of oxidoreductase structures has revealed that Fe–S centers are generally arranged in chains connecting the sites of catalysis and interprotein electron transfer. Moreover, their proximity (edge-to-edge distances between 4 to 14 Å) is sufficient to allow for tunneling of electrons at rates far faster than the substrate redox reactions, thereby obviating the need for specific through-bond electron transfer pathways.[181] In accord with this hypothesis, the redox potentials of Fe–S centers in many chains are frequently not ordered in increasing sequence, and up-and-down variations spanning up to 300 mV still allow thermal electron tunneling through the chains much faster than typical msec–sec catalytic turnovers. Other oxidoreductases modulate Fe–S cluster redox potential and/or conformation with external affecters, for example, MgATP in nitrogenase[182] and benzoyl-CoA reductase,[183] in order to change intracluster distances and bring thermally activated tunneling into the range of measured catalytic rates. Fe–S clusters are also implicated in coupled electron/proton transfer reactions in NADH-quinone oxidoreductase, quinol-cytochrome *c* oxidoreductases and nitrogenases, and many Fe–S enzymes contain active sites at which proton-coupled redox reactions occur. The combination of spectroscopic and crystallographic studies has also revealed three examples of metalloenzyme active sites with [4Fe–4S] clusters that are directly attached to the substrate-binding site via a bridging cysteinate in order the facilitate rapid electron transfer to or from the substrate: the siroheme–[4Fe–4S] active site of sulfite and nitrite reductases[38,39] (Figure 2(g)); the Fe–Fe–[4Fe–4S] active site of Fe-hydrogenases[40,41] (Figure 2(f)); the Ni–Ni–[4Fe–4S] active site of acetyl-CoA synthases[44–46] (Figure 2(j)).

3.1.1 Mobile Electron Transport Proteins

As indicated above, much of our current understanding of biological Fe–S centers comes from studies of low-molecular weight (6–12 kDa) simple Fe–S proteins containing $[Fe(Cys)_4]^{2-,-}$, $[2Fe–2S]^{2+,+}$, $[3Fe–4S]^{+,0}$, $[4Fe–4S]^{3+,2+,+}$ centers, that is, Rds, Dxs, 2Fe-, 3Fe-, 4Fe-, 7Fe-, and 8Fe-Fds, and HiPIPs. The 7Fe- and 8Fe-Fds contain one $[3Fe–4S]^{+,0}$ and $[4Fe–4S]^{2+,+}$ center and two $[4Fe–4S]^{2+,+}$ centers, respectively, with the clusters separated by approximately 12 Å. Ferredoxins function as electron donors/acceptors for a wide variety of prokaryotic and eukaryotic oxidoreductases, for example, hydrogenase, nitrogenase, cytochrome P-450, nitrite reductase, nitrate reductase, sulfite reductase, formate dehydrogenase, aldehyde oxidoreductase, glutamate synthase, and dioxygenases. However, in many cases, their lack of specificity prevents assignment of a specific electron transport function, and many appear to function as electron donors/acceptors for several different enzymes. For example, the chloroplast 2Fe Fds which accept electrons from photosystem I can act as the electron donor to nitrite reductase, sulfite reductase, glutamate synthase, thioredoxin reductase, or $NADP^{+}$ reductase.[21] Homologs of the hydroxylase–type of 2Fe Fds that function as electron donors to cytochrome P-450s, also have a role as an electron acceptors or donors in Fe–S cluster biosynthesis.[83] HiPIPs are found in purple phototrophic bacteria and halophilic denitrifying bacteria, and suggested roles include electron transport in photosynthesis, anaerobic metabolism, thiosulfate oxidation, and iron oxidation. Rubredoxins have been shown or proposed to function as electron donors to nitrate reductase, hydrogenase, alkane hydroxylase, and bacterioferritin, and an electron acceptor for pyruvate-ferredoxin oxidoreductase.**98** In addition, Rds appear to play an important role as the electron donors to 1Fe and 2Fe SORs, the nonheme Fe peroxidase rubrerythrin, and rubredoxin:oxygen oxidoreductase, three key enzymes involved in oxidative stress protection in anaerobic organisms.**184**

3.1.2 Membrane-bound Electron Transport Chain Enzymes and Proteins

The [2Fe–2S], [3Fe–4S], and [4Fe–4S] clusters that are found in simple Fe–S proteins are also constituents of respiratory and photosynthetic electron transport chains. Multicluster Fe–S enzymes such as hydrogenase, formate dehydrogenase, NADH dehydrogenase, and succinate dehydrogenase feed electrons into respiratory chains, while others such as nitrate reductase, fumarate reductase, DMSO reductase, and HDR catalyze the terminal step in anaerobic electron transport chains that utilize nitrate, fumarate, DMSO, and the CoB–S–S–CoM heterodisulfide as the respiratory oxidant. All comprise membrane anchor polypeptide(s) and soluble subunits on the membrane surface that mediate electron transfer to or from Mo cofactor (Moco), NiFe, Fe–S cluster or flavin active sites. Multiple Fe–S clusters define electron transport pathways between the active site and the electron donor or acceptors associated with the membrane anchor subunits. For example, *E. coli* nitrate reductase (NarGHI) and formate dehydrogenase (FdnGHI) each contain linear electron transport chains comprising four $[4Fe–4S]^{2+,+}$ and one $[3Fe–4S]^{+,0}$ cluster (NarGHI) or five $[4Fe–4S]^{2+,+}$ clusters (FdnGHI) in the soluble GH subunits, and two *b*-type cytochromes in the membrane anchor I subunits, that mediate transfer of electrons from menaquinol to the Moco active site (NarGHI) or from the Moco active site to menaquinone (FdnGHI).**134,185** Positioning the soluble subunits on the periplasmic (FdnGHI) and cytoplasmic (NarGHI) side of the membrane facilitates proton motive force generation via a redox loop involving menaquinol/menaquinone redox cycling in the membrane associated quinone pool.**134,185** This mechanism for proton motive force generation is common to a wide range of bacterial respiratory enzymes.

The mitochondrial respiratory chain, which contains at least 13 Fe–S clusters (Figure 6), perhaps best illustrates the importance of Fe–S clusters in membrane-bound electron transport. Electrons enter via three principal pathways, from the oxidation of NADH to NAD^+ (NADH-ubiquinone oxidoreductase or Complex I) and succinate to fumarate (succinate:ubiquinone oxidoreductase or Complex II), and from the β-oxidation of fatty acids via the electron transferring flavoprotein (ETF-ubiquinone oxidoreductase). All three pathways involve a complex Fe–S flavoprotein dehydrogenase, that is, NADH dehydrogenase, succinate dehydrogenase, and ETF dehydrogenase, and in each case the Fe–S clusters mediate electron transfer from the flavin active site to the ubiquinone pool via protein-associated ubiquinone.

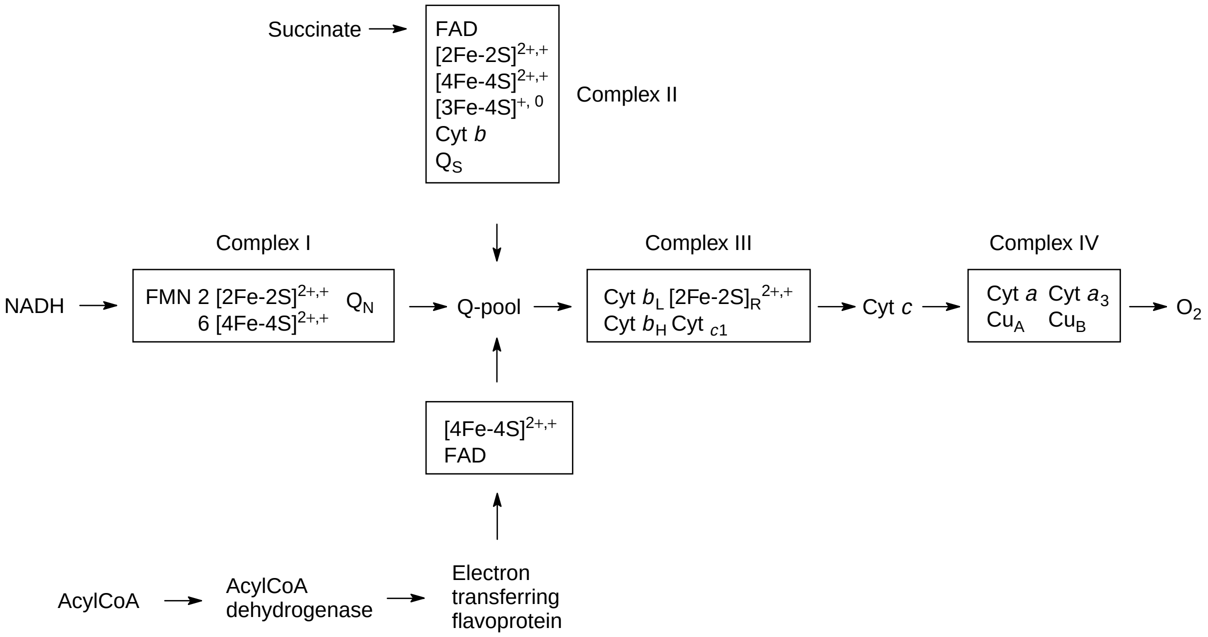

Figure 6 Mitochondrial respiratory chain. Q_S and Q_N are protein-associated pools of ubiquinone that can be distinguished from the bulk ubiquinone pool

Ubihydroquinone is then used to reduced cytochrome *c* via ubihydroquinone-cytochrome *c* reductase (Complex III) which contains two *b*-type and one c_1-type cytochrome in addition to a Rieske-type [2Fe–2S] center (*see* ***Iron: Heme Proteins & Electron Transport***). Cytochrome *c* is the electron donor for cytochrome *c* oxidase where the terminal electron acceptor O_2 is reduced to H_2O (*see* ***Cytochrome Oxidase***). Electron transfer along the respiratory chain is coupled to ATP synthesis via the generation of a proton electrochemical gradient across the inner mitochondrial membrane, in the process known as oxidative phosphorylation. The coupling sites are in Complexes I, III, and IV. Understanding the detailed molecular mechanisms of redox-linked proton translocation remains one of the major goals of bioenergetics research and the recent crystal structures of Complex II, III, and IV, represent important landmarks in this endeavor.

Complex I catalyzes electron transfer from NADH to quinone (Q) coupled with the translocation of four protons (see equation 1)

$$\mathrm{NADH} + \mathrm{Q} + 5\mathrm{H}_{\mathrm{N}}^{+} \longrightarrow \mathrm{NAD}^{+} + \mathrm{QH}_2 + 4\mathrm{H}_{\mathrm{P}}^{+} \qquad (1)$$

where H_N^+ and H_P^+ indicate proteins on the negative inner side and the positive outer side of the membrane, respectively. It is the most elaborate of all Fe–S proteins and has yet to be structurally defined by crystallography. Mitochondrial complex I comprises at least 46 subunits (~1 MDa). However, characterization of Complex I from bacteria has revealed a conserved catalytic core comprising 14 subunits (~535 kDa) that appears to correspond to the minimal functional unit for a proton-pumping NADH:ubiquinone oxidoreductase.[186,187] The extra eukaryotic subunits are all encoded by nuclear genes and may be necessary for regulating assembly or insulating Complex I to prevent the escape of high-energy electrons. Of the 14 core subunits, seven are peripheral proteins on a hydrophilic arm that protrudes out from the membrane and contains all known redox cofactors, and seven are intrinsic membrane-spanning proteins, with the overall structure approximately L-shaped. On the basis of sequence analysis, Complex I is proposed to have evolved from three major modules for electron transport and proton translocation.[187] The soluble NADH dehydrogenase module is for electron input and is found in many nonenergy converting NAD(P)H-dependent hydrogenases and dehydrogenases. The hydrogenase module is involved with redox-coupled proton translocation, comprises hydrophilic and hydrophobic subunits, and is also found in membrane-bound NiFe-hydrogenases. The membrane transporter module is composed entirely of hydrophobic subunits, some which are homologous with H^+/Na^+ or H^+/K^+ antiporter subunits, suggesting a role in conformationally driven ion translocation. Extensive spectroscopic studies of purified Complex I samples have provided evidence for two $[2Fe–2S]^{2+,+}$ clusters and approximately six $[4Fe–4S]^{2+,+}$ clusters, although there is still an ongoing debate concerning the number and subunit location of some of the $[4Fe–4S]^{2+,+}$.[186–188] The NADH dehydrogenase module contains the NADH and flavin mononucleotide (FMN) binding sites in addition to two $[2Fe–2S]^{2+,+}$ and three or four $[4Fe–4S]^{2+,+}$ clusters, and the hydrogenase module contains the ubiquinone binding site and two or three $[4Fe–4S]^{2+,+}$ clusters, one of which has a pH-dependent midpoint potential and is likely to be directly involved with redox-linked proton coupling.[186,187,189,190] Crystallographic refinement of Complex I is anticipated in the near future and is awaited with great interest by both the bioenergetics and bioinorganic communities.

A clearer picture has emerged for Complex II and crystal structures are available for the *E. coli* succinate–quinone oxidoreductase (SQR) and closely related bacterial quinol–fumarate oxidoreductases (QFR) that catalyze the reverse reaction in order to use fumarate as a terminal electron donor in anaerobic respiration.[108,115] The structure of the SQR monomer showing the location of the redox cofactors is shown in Figure 7.[108] The $[2Fe–2S]^{2+,+}$ ($E_m = +10$ mV), $[4Fe–4S]^{2+,+}$ ($E_m = -175$ mV) and $[3Fe–4S]^{+,0}$ ($E_m = +65$ mV) clusters in the SdhB subunit provide a linear electron transport chain for transferring electrons from the flavin adenine dinucleotide (FAD) active site ($E_m = -79$ mV) in the SdhA subunit to ubiquinone ($E_m = +113$ mV) in the SdhC membrane anchor subunit. The edge-to-edge distances

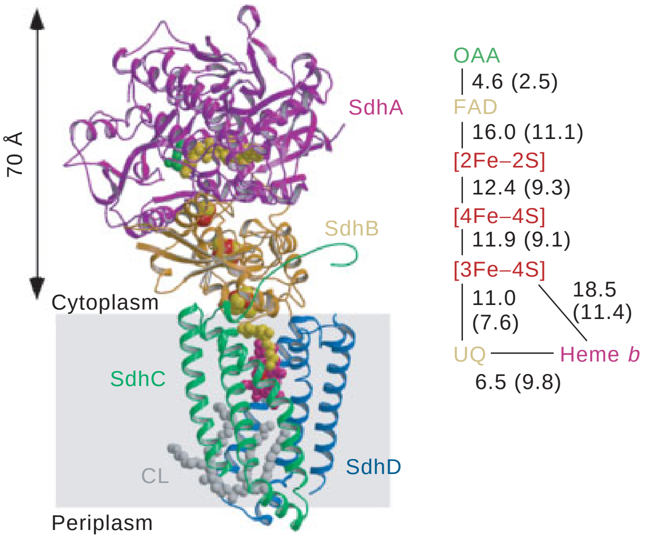

Figure 7 Structure of *E. coli* succinate-ubiquinone oxioreductase monomer. SdhA, SdhB, SdhC, and SdhD subunits are shown in purple, orange, green, and blue, respectively. FAD is shown gold, oxaloacetate (OAA) in green, heme *b* in magenta, ubiquinone (UQ) in yellow, Fe in red, inorganic-S in yellow, and cardiolipin (CL) in gray. Gray shading indicates the position of the membrane. The center-to-center distances (Å) between the cofactors are shown to the right, with edge-to-edge distances in parenthesis. (Reprinted with permission from V. Yankovskaya, R. Horsefield, S. Törnroth, C. Luna-Chavez, H. Miyoshi, C. Léger, B. Byrne, G. Cecchini, and S. Iwata, *Science*, 2003, **299**, 700. © 2003 AAAS)

are in the range established for efficient tunneling (4–14 Å),[181] which means that the low potential of the central $[4Fe–4S]^{2+,+}$ cluster is not a thermodynamic barrier to efficient electron transfer. Very similar arrangements of redox cofactors in the A and B subunits are found in the structurally characterized QFRs from *E. coli*[191] and *Wolinella succinogenes*.[192] The only major differences are that the [2Fe–2S] cluster in the SQR has a monodentate aspartate in place of a cysteine ligand (the majority of SQRs and QFRs have complete cysteinyl ligation for all Fe–S clusters) and that the [4Fe–4S] cluster in the SQR has an additional H-bond involving the thiol group of a fifth cysteine residue and the S of a coordinated cysteine. These differences are likely to relate to the differences in the redox potentials, for example, the $[4Fe–4S]^{2+,+}$ couple is 100–150 mV higher in SQRs than QFRs in accord with increased H-bonding in SQRs. The major differences in the structurally characterized SQR and QFRs reside in the membrane anchor subunits. *E. coli* SQR has a ubiquinone binding site and a bis-histidine ligated cytochrome $b(E_m = +35\,\mathrm{mV})$ that bridges the SdhC and SdhD subunits.[108] In contrast, *E. coli* QFR has no cyt *b* and two menaquinone binding sites that are both different from the SQR quinone binding sites[191] and *W. succinogenes* QFR has a single membrane anchor subunit with two *b*-type cytochromes and lacks a SQR quinone binding site.[192] The implication is that cyt *b* is not an essential component of the electron transfer chain, and the closer proximity of the [3Fe–4S] cluster to ubiquinone compared to cyt *b* in SQR supports this conclusion (Figure 7). An alternative role for the cyt *b* is as an electron sink to prevent electron leakage and build–up of reactive oxygen species has been proposed.[108]

ETF-ubiquinone reductase is one of the simplest quinone oxidoreductases comprising a single subunit (64 kDa) Fe–S flavoprotein with one $[4Fe–4S]^{2+,+}$ cluster ($E_m = +47\,\mathrm{mV}$) and one FAD ($E_m = +28$ and $-6\,\mathrm{mV}$) separated by ∼12 Å.[193,194] It accepts electrons from ETF, which oxidizes 11 primary flavoprotein dehydrogenases in the mitochondrial matrix, thereby providing a link for electrons derived from a variety of oxidative processes into the respiratory chain. While it was generally assumed that electrons from ETF enter ETF-ubiquinone oxidoreductase through FAD and are transferred to ubiquinone via the $[4Fe–4S]^{2+,+}$ cluster, the spatial proximity of FAD and ubiquinone (minimum separation 8.5 Å, compared to 19 Å between the [4Fe–4S] cluster and ubiquinone), suggests that ubiquinone accepts electrons directly from FAD.[193] Both the role of the cluster and the origin of the anomalously high redox potential for a $[4Fe–4S]^{2+,+}$ center in a Fd-like domain remain to be elucidated.

Complex III (cytochrome bc_1 complex or quinol-cytochrome *c* oxidoreductase) has been structurally characterized[195–197] and is one of the best understood of the Fe–S containing mitochondrial respiratory complexes.[198,199] The mammalian complex consists of 11 subunits, three of which contain redox centers: a hydrophobic cytochrome *b*, which contains the high and low-potential *b*-type hemes (cyt b_L, $E_m = -50\,\mathrm{mV}$; cyt b_H, $E_m = +50\,\mathrm{mV}$); cytochrome c_1, which contains covalently bound heme c_1 ($E_m = +250\,\mathrm{mV}$); and Rieske protein, which contains a high potential Rieske-type $[2Fe–2S]^{2+,+}$ center ($E_m = +280\,\mathrm{mV}$ at pH 7) (*see* ***Iron: Heme Proteins & Electron Transport***). Analogous centers with similar redox potentials are also present in the homologous bc_1 complex of respiratory and photosynthetic bacteria. In all cases, the electron transfer from quinol to cyt *c* is coupled to proton translocation by the Q-cycle mechanism first proposed by Mitchell.[200] The essential reaction of the Q-cycle mechanism is the bifurcation of the pathway for the electron transport pathway upon oxidation of quinol. One electron is transferred to the Rieske center and then to cyt c_1 and cyt *c*, while the other is transferred to cyt b_L and from there across the membrane to cyt b_H, where it is used to reduce quinone. Thus half of the electrons from the oxidation of quinol are cycled back to quinone, thereby doubling the protonmotive efficiency of the bc_1 complex.[198,199] The crystallographic data indicate that the bifurcation of the electron pathways is facilitated by mobility of the catalytic domain of the Rieske protein, such that the Rieske center shuttles between positions close to the quinol binding site and the propionate group of cytochrome c_1, which are some 22 Å apart.[195,196] Moreover, both spectroscopic and crystallographic evidence point to a direct H-bonding interaction between the quinol OH and the Nε of one of the Rieske center histidine ligands.[195,198] Taken together with the electrochemical and structural evidence for redox-linked protonation of the Rieske center histidine ligands,[23,201] the implication is that the Rieske center couples proton and electron transfer from quinol, by using a histidine ligand to shuttle a proton out of the quinol binding site.

Spectroscopic and crystallographic studies have identified four Fe–S clusters in the membrane-bound photosynthetic electron transport chain of plant and cyanobacterial chloroplasts. One is the Rieske-type $[2Fe–2S]^{2+,+}$ center in the cyt b_6f complex, which catalyzes electron transfer from plastoquinol to plastocyanin with concomitant proton translocation, and is functionally analogous to the cyt bc_1 complex, with cyt *f* in place of cyt c_1.[202] The remainder are low-potential $[4Fe–4S]^{2+,+}$ centers in Photosystem I which constitute the terminal part of the electron transfer chain that is initiated by the primary donor chlorophyll.[165,166] One is a very low-potential $[4Fe–4S]^{2+,+}$ center, F_X ($E_m = -705\,\mathrm{mV}$), that bridges two similar subunits (PsaA and PsaB) and is coordinated by two cysteines from each subunit in a $C–X_8–C$ arrangement. This cluster transfers electrons to the 2Fe-Fd acceptor via an electron transfer chain composed of F_A, a $[4Fe–4S]^{2+,+}$ cluster with $E_m = -530\,\mathrm{mV}$, and F_B, a $[4Fe–4S]^{2+,+}$ clusters with $E_m = -580\,\mathrm{mV}$. F_A and F_B are in a low-molecular weight subunit (PsaC, 9 kDa) that shows strong sequence and structural homology with bacterial 8Fe-Fds. The center-to-center distance between F_X and F_A and between F_A and F_B are 14.9 Å and 12.3 Å, respectively, well within the limits for efficient electron tunneling, and a putative 2Fe Fd docking site has been identified.

3.1.3 Soluble Redox Enzymes

A wide range of soluble redox enzymes contain one or more intrinsic $[2Fe–2S]^{2+,+}$, $[3Fe–4S]^{+,0}$, or $[4Fe–4S]^{2+,+}$ clusters that function in electron transport chains to transfer electrons to or from nonheme Fe, Moco/Wco, corrinoid, flavin, thiamine pyrophosphate (TPP), Fe–S cluster containing, or NiFe active sites. Many have been structurally and spectroscopically characterized and only a few of the most recent examples of each type are summarized here. Dioxygenases that function in the dihydroxylation of aromatics such as benzene, toluene, benzoate, naphthalene, and phthalate contain a Rieske-type $[2Fe–2S]^{2+,+}$ cluster that serves as the immediate electron donor to the monomeric nonheme Fe active site (*see* ***Iron Proteins with Mononuclear Active Sites***).[203] The xanthine oxidase family of molybdoenzymes (*see* ***Molybdenum: MPT-containing Enzymes***) contain two $[2Fe–2S]^{2+,+}$ clusters that mediate electron transfer between the Moco active site and the FAD.[116,117,204] Other soluble molybdoenzymes and tungstoenzymes (*see* ***Tungsten Proteins***) have electron transfer chains involving a single $[4Fe–4S]^{2+,+}$ cluster (e.g. dissimilatory nitrate reductase,[205] W-containing aldehyde oxidoreductases,[206,207] and W- and Mo-containing formate dehydrogenases[208,209]), three $[4Fe–4S]^{2+,+}$ clusters (e.g. pyrogallol-phloroglucinol transhydroxylase[210]), and one $[3Fe–4S]^{+,0}$ and one Rieske-type $[2Fe–2S]^{2+,+}$ cluster (e.g. arsenite oxidase[129]). Currently there is only one example of a corrinoid-containing Fe–S protein, the corrinoid iron–sulfur protein that functions as a methyl transferase in acetyl-CoA synthase (*see* ***Cobalt: B_{12} Enzymes & Coenzymes***).[211] The protein contains a $[4Fe–4S]^{2+,+}$ cluster that does not participate directly in the methyl transfer step, but appears to provide a conduit for electron flow to the Co center from physiological reductants to effect reductive activation.[211] Soluble iron–sulfur enzymes with flavin active sites include Fd-dependent glutamate synthase (FMN and one $[3Fe–4S]^{+,0}$ cluster[212]) and NADPH-dependent glutamate synthase (FMN, FAD, one $[3Fe–4S]^{+,0}$ and two $[4Fe–4S]^{2+,+}$ clusters[212]), trimethylamine dehydrogenase (FMN and one $[4Fe–4S]^{2+,+}$ cluster[213]), 2,4-dienyl-CoA reductase (FMN, FAD, and one $[4Fe–4S]^{2+,+}$ cluster[214]), adenylylsulfate reductase (FAD and two $[4Fe–4S]^{2+,+}$ clusters[215]), and dihydroorotate dehydrogenase (FMN, FAD and one $[2Fe–2S]^{2+,+}$ cluster[216]). Oxoacid-ferredoxin oxidoreductases such as pyruvate-ferredoxin oxidoreductase and 2-oxoglutarate-ferredoxin oxidoreductase are radical enzymes with a TPP active site and an electron transfer chain involving one or three $[4Fe–4S]^{2+,+}$ clusters.[217,218]

All structurally characterized NiFe- and Fe-hydrogenases contain redox chains involving 2–4 Fe–S clusters that deliver electrons to or take electrons from the NiFe (Figure 2(e)) or Fe–Fe–[4Fe–4S] (Figure 2(f)) active sites. Soluble NiFe-hydrogenases generally catalyze H_2 uptake and comprise a large subunit that houses the NiFe active site and a small subunit containing three linearly arranged and evenly spaced Fe–S clusters: two low-potential $[4Fe–4S]^{2+,+}$ clusters that are proximal and distal with respect to the active site and a middle cluster that can be either a high potential $[3Fe–4S]^{+,0}$ cluster or a low-potential $[4Fe–4S]^{2+,+}$ cluster.[35] Mutagenesis-induced conversion of the $[3Fe–4S]^{+,0}$ cluster to a $[4Fe–4S]^{2+,+}$ cluster in *Desulfovibrio fructosovorans* NiFe-hydrogenase results in a ∼300-mV decrease in the potential of the middle cluster, making it approximately isopotential with the proximal and distal clusters.[168] However, in accord with the electron tunneling theory for electron transport, this did not result in a significant change in catalytic activity using natural and artificial electron acceptors. In contrast, the reverse cluster transformation in the F_{420}-reducing NiFe–hydrogenase from *Methanococcus voltae* raises the potential of the middle cluster to ∼400 mV higher than that of the proximal and distal clusters and results in a 10-fold decrease in activity using the physiological electron acceptor F_{420}.[170] The implication is that the increase in potential is too large to permit efficient tunneling, such that electron transfer has become the rate-limiting step in the mutant protein. Fe-hydrogenases catalyze H_2 uptake or H_2 evolution, and both contain an 8Fe–Fd-like domain containing two low-potential $[4Fe–4S]^{2+,+}$ clusters that mediates electron transfer to or from the Fe–Fe–[4Fe–4S] active site.[41,219] Some H_2-evolving enzymes, such as hydrogenase I from *Clostridium pasteurianum*, have extended electron transfer chains involving additional domains containing one $[4Fe–4S]^{2+,+}$ and one $[2Fe–2S]^{2+,+}$ cluster.[40]

Ni-containing CO dehydrogenases catalyze the oxidation of CO to CO_2 and are homodimeric proteins containing two buried [Ni–4Fe–5S] active sites (C-cluster, see Figure 2(i)), two $[4Fe–4S]^{2+,+}$ centers (B-cluster), and a solvent-exposed subunit-bridging $[4Fe–4S]^{2+,+}$ cluster (D-cluster).[42,43] In each monomer, the electron transfer pathway is from $C \rightarrow B \rightarrow D$ and the edge-to-edge distances are 11 Å and 10 Å, respectively, well within the range for efficient tunneling. Acetyl-CoA synthases build on this core by adding two identical subunits containing the Ni–Ni–[4Fe–4S] active site (A-cluster, see Figure 2(j)) that is responsible for the synthesis of acetyl-CoA using CO that is derived from CO_2 reduction at the C-cluster.[44–46] The different active sites of this bifunctional enzyme complex are connected via a channel, 138 Å long, which provides a conduit for transfer of CO generated at the C-cluster to the A-cluster.

Nitrogenase catalyzes the ATP-driven eight-electron and eight-proton reduction of N_2 to $2\,NH_3$ and H_2 and offers the most complex and fascinating example of Fe–S cluster mediated electron transfer. The electron transport chain involves transfer of electrons from the subunit-bridging [4Fe–4S] center on the homodimeric Fe-protein,[182] to the subunit-bridging double-cubane [8Fe–7S] P-cluster (see

Figure 1(f) and 1(g)) and then to the [Mo–7Fe–9S–X] FeMoco active site (see Figure 2(h)), both of which are located in the MoFe protein.[20,220] Electron transfer is facilitated by MgATP hydrolysis[221] and the Fe-protein has two nucleotide binding sites, one in each subunit. Moreover structures of the Fe-protein in its native, MgATP- and MgADP-bound conformations and of the Fe-protein-MoFe protein complex in an MgATP-bound conformation indicate that the Fe-protein undergoes major conformational changes on complex formation and nucleotide binding.[164,177,182] This conformational change appears to facilitate electron transfer by decreasing the distance between the [4Fe–4S] and [8Fe–7S] clusters.[182]

Numerous questions remain concerning the MgATP control of complex formation and the redox properties of the [4Fe–4S] cluster, whether the electrons are transferred in eight one–electron or four two-electron steps, and the mechanism of coupling of proton and electron transfer. Both the all-ferrous $[4Fe–4S]^0$ and $[4Fe–4S]^+$ forms of the Fe-protein bind MgATP, undergo a MgATP-induced conformational change, form a productive complex with the MoFe protein, and transfer electrons to the MoFe protein, leaving the cluster in the $[4Fe–4S]^{2+}$ redox state, indicating that it has the potential to act as a one- or two-electron donor.[222] Indeed, the concept of a two-electron donor is particularly appealing for nitrogenase as the intermediate electron carrier, the [8Fe–7S] P-cluster, is a two-electron acceptor, all known substrates are reduced by multiples of two electrons, and it would cut the ATP requirement in half. Nevertheless, potential physiological electron donors are not able to reduce Fe-protein to the $[4Fe–4S]^0$ state and the midpoint potential for the $[4Fe–4S]^{+,0}$ couple is highly negative, $\sim -790\,\text{mV}$, implying that this redox state is unlikely to be attainable in vivo.[153] The double-cubane [8Fe–7S] P-cluster is stable in the all-ferrous $[8Fe–7S]^{2+}$ redox state (P^N) and the two-electron oxidized $[8Fe–7S]^{4+}$ redox state (P^{OX}) and a transient one-electron oxidized $[8Fe–7S]^{3+}$ state has been observed during redox titrations.[223] Moreover, a dramatic structural change accompanies two-electron oxidation from the P^N to the P^{OX} states (cf. see Figures 1(f) and 1(g)) involving the cleavage of two Fe–μ_6S bonds and coordination by serine and a backbone amide nitrogen (BAN) to maintain tetracoordinated Fe sites.[15] Hence oxidation by two electrons has the potential to occur with the release of two protons, since both recruited ligands will be protonated in their free state and may be deprotonated in their bound states. In accord with the proposal that the [8Fe–7S] P-cluster couples proton and electron transfer, the P-cluster has been shown to have a pH-dependent redox potential.[24] Although the $[8Fe–7S]^{+,0}$ couple ($E_m = -310\,\text{mV}$) is independent of pH over the range 6.0–8.5, the $[8Fe–7S]^{2+,+}$ couple decreases from $E_m = -224$ to $-338\,\text{mV}$ over the same range, indicating that oxidation occurs with release of one proton. The BAN is currently the best candidate for the protonation/deprotonation site as the pH-dependent redox potential is retained on mutation of the coordinating serine residue.[24]

3.2 Substrate Binding and Activation

Several redox and nonredox enzymes have Fe–S centers that constitute the active site, in whole or in part. As illustrated by the active-site structures shown in Figure 2, the clusters are functionalized for binding and activating substrates by having unique ligation at a specific Fe site, incorporating a heterometal into the cluster, or attachment of a metal site at a unique Fe site.

3.2.1 Nonredox Enzymes

Nitrile Hydratase (see ***Iron Proteins with Mononuclear Active Sites****).* Nitrile hydratase catalyzes the hydrolysis of organic nitriles to the corresponding amide (see equation 2) and plays an important role in the assimilation of nitriles by microorganisms.

$$\text{R–C}\equiv\text{N} + \text{H}_2\text{O} \longrightarrow \text{R–CONH}_2 \qquad (2)$$

The structure of the NO-inhibited form of Fe nitrile hydratase revealed a remarkable active site comprising a monomeric octahedral Fe^{III} site with two BANs and the sulfur atoms of postranslationally modified cysteine sulfinic and sulfenic groups providing the equatorial ligands and a cysteinate trans to a bound NO providing the axial ligands (Figure 2(a)).[25] In the functional form of the enzyme, NO is replaced by hydroxide. However, the mechanism of catalysis, that is, Lewis acid activation of the bound hydroxyl or a bound nitrile, and the role of the novel set of sulfur ligands remains largely unresolved.[224]

Fe–S Cluster Containing (de)hydratases. The pioneering spectroscopic and crystallographic studies of aconitase by Beinert and coworkers[27] led to the characterization of a large class of Fe–S cluster containing hydratases and dehydratases that includes phosphogluconate dehydratase, maleate hydratase, lactyl-coenzyme A dehydratase, 2-hydroxyglutaryl-coenzyme A dehydratase, tartarate dehydratase, serine dehydratase, isopropylmalate isomerase, fumarase, and bacterial dihydroxy acid dehydratase.[28] With the exception of the putative $[2Fe–2S]^{2+}$-containing plant dihydroxy acid dehydratase that has yet to be structurally or mechanistically characterized,[225] all contain a $[4Fe–4S]^{2+}$ cluster with a unique, non-cysteine-ligated Fe site that acts a Lewis acid to facilitate reversible abstraction of the hydroxyl and a proton from adjacent carbon atoms on the substrate. By far the best-characterized example is the citric acid cycle enzyme aconitase, which catalyzes both the dehydration and rehydration steps in the stereospecific isomerization of citrate to isocitrate via a *cis*-aconitate intermediate (see equation 3).

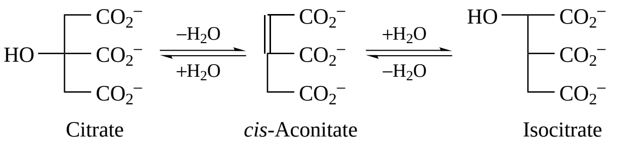

(3)

The ligation at the unique Fe site in the absence and presence of the hydrated substrates was initially deduced from a series of elegant Mössbauer, EPR, and ENDOR studies and subsequently confirmed by crystallography for the isocitrate-bound form (Figure 2(b)). In the absence of substrate, the unique Fe site is four-coordinate with the fourth ligand a solvent hydroxyl. Substrate binding occurs with protonation of the bound hydroxyl, and involves coordination via the hydroxyl and the β-carboxyl (for citrate) or the α-carboxyl (for isocitrate) resulting in a six-coordinate unique Fe site (Figure 2(b)). The dehydrated intermediate, *cis*-aconitate, can be bound by either the α- or β-carboxyl groups via a bridging and exchangeable hydroxyl at the α or β carbon and must rotate by 180° between these modes during catalysis.

3.2.2 Redox Enzymes

Superoxide Reductase (see ***Iron Proteins with Mononuclear Active Sites****).* Detoxification of reactive oxygen species in anaerobic microorganisms has recently been shown to center around SOR, a novel mononuclear iron enzyme that reduces superoxide to hydrogen peroxide (see equation 4),[30] rather than dismuting superoxide to oxygen and hydrogen peroxide as is the case for the superoxide dismutases found in aerobic organisms.

$$O_2^- + 2H^+ + e^- \longrightarrow H_2O_2 \qquad (4)$$

Spectroscopic and crystallographic studies indicate that the active site is six-coordinate in the Fe^{III} state, with four equatorial histidine ligands and axial cysteinate and monodentate glutamate ligands, and five-coordinate with a vacant coordination site as a result of loss of the glutamate ligand on reduction to the Fe^{II} state (Figure 2(c)).[31,73] Optically monitored pulse radiolysis have revealed one or two transient catalytic intermediates that are proposed to correspond to a ferric-peroxo and ferric-hydroperoxo species[226,227] and a transient ferric-peroxo species with a side-on peroxo has been spectroscopically characterized in samples frozen rapidly in the presence of H_2O_2.[228,229] The proposed mechanistic scheme therefore involves superoxide binding at the vacant coordination site of reduced SOR, coupled with electron transfer from Fe to superoxide, to yield a side-on ferric-peroxo intermediate. Protonation yields a transient end-on ferric-hydroperoxo that rapidly dissociates yielding hydrogen peroxide. Since electronic studies indicate strong $(Cys)S(p_\pi)-Fe(d_\pi)$ bonding in both the oxidized and reduced states,[73] the presence of a cysteine ligand trans to the binding site has been proposed as the major determinant of SOR rather than superoxide dismutase activity.[230] This would facilitate reduction of O_2^- on binding at the ferrous site and promote dissociation of the hydroperoxide product from the ferric site.

Radical-SAM Enzymes. The initial characterization of a diverse group of SAM-dependent Fe–S enzymes catalyzing radical reactions,[75,231] led to the discovery of a radical-SAM superfamily that may contain over 600 distinct enzymes based on bioinformatics analysis.[32] These enzymes catalyze diverse reactions involving radical mechanisms, including unusual methylations, isomerization, sulfur insertion, ring formation, anaerobic oxidation, and protein radical formation and they function in DNA precursor, vitamin, cofactor, antibiotic and herbicide biosynthesis, and in biodegradation pathways. For example, radical-SAM enzymes are now known to catalyze previously unresolved steps in the biosynthesis of biotin (vitamin H), lipoic acid, thiamine, heme, bacteriochlorophyll, molybdopterin, nitrogenase FeMo-cofactor, and the diiron active site of Fe–hydrogenases. Radical-SAM enzymes have attracted intense recent interest from both the bioinorganic and bioorganic communities and constitute arguably the most rapidly expanding area of Fe–S protein research, as evidenced by a proliferation of recent publications and reviews.[8,34,232,233]

Radical-SAM enzymes share a common $C–X_3–C–X_2–C$ motif that coordinates an oxidatively labile $[4Fe–4S]^{2+,+}$ cluster in an incomplete triosephosphate isomerase barrel domain.[33,68,144] The role of the cluster is to initiate the radical reaction by binding SAM at the unique Fe site in order to facilitate reductive cleavage to yield a 5′-deoxyadenosyl radical. This highly reactive radical then generates a substrate radical in enzymes such as lysine 2,3-aminomutase, lipoyl synthase (LipA), biotin synthase (BioB), spore photoproduct lyase, an oxygen-independent coproporphyrinogen III oxidase (HemN), and a tRNA–methylthiotransferase (MiaB), or a catalytic glycyl radical in enzymes such as in anaerobic ribonucleotide reductase, pyruvate formate-lyase (PFL), benzylsuccinate synthase, and glycerol dehydratase, that utilize a radical-SAM activating enzyme (AE).[34,232,233] The mode of attachment of SAM at the [4Fe–4S] cluster was originally determined by an elegant series of ENDOR studies on PFL-AE[74] and subsequently confirmed in the crystal structures of HemN,[33] BioB,[68] and MoaA, the enzyme that catalyzes the first step in molybdopterin biosynthesis involving the formation of precursor Z from 5′-guanosine triphosphate (5′-GTP).[144] SAM is anchored to the cluster via coordination of the amino nitrogen (Fe–N distance ~2.6 Å) and carboxyl oxygen (Fe–O distance 1.9–2.3 Å) of the methionine, with the sulfonium sulfur 3.3–3.5 Å from the same Fe and 3.6–3.7 Å from a μ_3–S (Figure 2(d)). The detailed mechanism of the reductive cleavage of SAM has still to be elucidated, but the available evidence points to a concerted reaction involving transfer of an electron from the cluster to the sulfonium sulfur coupled with homolytic cleavage of the S–C bond.[34,232]

The recent discovery that several radical-SAM enzymes contain an Fe–S cluster in addition to the [4Fe–4S] cluster that is responsible for binding and cleaving SAM has led to proposals for new roles for Fe–S clusters. Spectroscopic and crystallographic studies of BioB have revealed the presence of an additional $[2Fe–2S]^{2+}$ cluster[68,174] that has been shown to act as the immediate sulfur donor for biotin formation from dethiobiotin in a single turnover reaction[80] (equation 5).

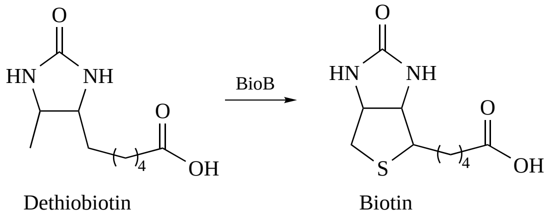

(5)

Since the $[2Fe–2S]^{2+}$ cluster is degraded during a single turnover,[67,81] this suggests that BioB is either a suicide enzyme or that cluster reassembly occurs after each turnover. An alternative possibility is that the $[2Fe–2S]^{2+}$ cluster is an artifact of overexpression of recombinant BioB and that degradation leads to formation of a cysteine persulfide which acts as the immediate sulfur donor.[67] LipA catalyzes a similar sulfur insertion reaction involving the incorporation of two sulfur atoms and spectroscopic and analytical studies have recently demonstrated the presence of an additional $[4Fe–4S]^{2+,+}$ cluster that is coordinated by cysteine residues in a C–X_4–C–X_5–C motif.[234] However, the role of the additional [4Fe–4S] cluster in LipA has still to be determined. MoaA and its human counterpart, MOCS1A, do not catalyze a sulfur insertion reaction, but spectroscopic and crystallographic studies have demonstrated the presence of a second $[4Fe–4S]^{2+,+}$ cluster that is coordinated by only three cysteines in a C–X_2–C–X_{13}–C motif and located 17 Å from the SAM-binding [4Fe–4S] cluster.[144,235] On the basis of the crystal structure, the second [4Fe–4S] cluster is proposed to bind the 5′-GTP substrate at a unique Fe site, in order to position and/or activate the substrate for radical attack by the 5′-deoxyadenosyl radical.

NiFe- and Fe-hydrogenases. Hydrogenases catalyze the simplest of all reactions in microorganisms, the reversible two-electron reduction of two protons to yield hydrogen gas, and have been the subject of several recent reviews.[236–238] Hydrogen cleavage is invariably heterolytic, requiring the active sites to contain proton and hydride acceptor sites as well as a H_2 binding site. The two main classes of hydrogenases are termed NiFe and Fe (also known as Fe–Fe or Fe-only) based on the metal composition of the active-site cluster or subcluster, both of which contain the diatomic π-acceptor ligands, CO and CN^-, in order to stabilize low metal oxidation states. Consequently active-site structures have largely been determined using the novel combination of crystallography and Fourier-transform infrared (FTIR) spectroscopy, with EPR playing a crucial role in defining paramagnetic species in the catalytic cycles.

NiFe-hydrogenases generally catalyze H_2 uptake under physiological conditions. The functional active site comprises a binuclear NiFe center bridged by two cysteinyl-S ligands, with two terminal cysteinyl-S ligands (in NiFeSe hydrogenases one is substituted by selenocysteine) completing distorted tetrahedral coordination at the Ni center, and two CN^- and one CO completing approximate square pyramidal coordination at the Fe center (Figure 2(e)).[239] Oxidized inactive forms (termed Ni-A and Ni-B) have an additional oxo or hydroxo bridging ligand, and there is growing consensus that this is replaced by a bridging hydride in one of the reduced active forms (Ni-C).[238,239] There is also a general consensus from both spectroscopic studies and DFT calculations that the Ni center cycles between formal Ni^{II} and Ni^{III} oxidation states during catalysis, while the Fe site remains low spin Fe^{II}.[238,239] However, the H_2 and H^+ binding sites have still to be determined, with the Fe site and the terminal cysteinyl ligands, respectively, as the most likely candidates. A more detailed discussion of the catalytic cycle of NiFe-hydrogenases is presented elsewhere.

Fe-hydrogenases catalyze either H_2 uptake or evolution under physiological conditions and are unrelated to NiFe-hydrogenase in terms of protein sequence and structure.[41] Hence the striking similarities in the active sites (cf Figures 2(e) and 2(f)) appear to reflect convergent evolution.[41,219] The Fe-hydrogenase active site (also known as the H-cluster) comprises a [4Fe–4S] cluster that is directly attached via a bridging cysteinyl-S to a 2Fe subcluster, which is the site for H_2 activation (Figure 2(f)). The Fe atoms in the 2Fe subcluster (termed distal and proximal with respect to the [4Fe–4S] cluster) each have a terminal CO and CN^- ligand and are bridged by a nonprotein ligand that was first modeled as a 1,3-propane dithiolate[71] (Figure 2(f)). However, a di-(thiomethyl)-amine in which the central nitrogen could serve a catalytic base is a viable and attractive alternative.[41] A bridging CO (not shown in the structure depicted in Figure 2(f)) that becomes terminal on the distal Fe on reduction, and a weakly bound solvent molecule on the distal Fe (not shown in Figure 2(f)) that is lost during reductive activation, completes the ligation. Indeed, the variability in the published crystal structures concerning the bridging CO ligand[40,71] is likely to reflect the redox–induced conformational flexibility of the center. The current consensus is that the three oxidation states of the 2Fe subcluster formally correspond to $Fe^{II}Fe^{II}$ (oxidized, inactive, and EPR silent), $Fe^{II}Fe^{I}$ (oxidized, active, and EPR active, $S = 1/2$), and $Fe^{I}Fe^{I}$ (reduced, active, and EPR silent), with each having the [4Fe–4S] cluster in the 2+ redox state.[238] However, defining a detailed structure-based catalytic mechanism has been complicated by the FTIR and theoretical evidence for facile conversion between forms containing terminal and bridging CO ligands in the $Fe^{II}Fe^{I}$ redox state and the H_2, H^+ and H^- binding sites have yet to be definitively determined.[238] By analogy with NiFe-hydrogenases, it is tempting to speculate on the existence of a bridging hydride intermediate, but there is as yet no direct experimental evidence for this mode of ligation. The mechanism of this fascinating 'organometallic' active site is a subject of intense current interest and has been greatly enhanced by the study of organometallic analog complexes[237,240] and DFT calculations.[241,242]

Sulfite and Nitrite Reductase. Sulfite and nitrite reductases are found in plants and bacteria and catalyze similar reactions involving the six-electron reduction of $SO_3{}^{2-}$ and $NO_2{}^-$ to yield S^{2-} and $NH_4{}^+$, respectively (equations 6 and 7).[243,244]

$$SO_3{}^{2-} + 6H^+ + 6e^- \longrightarrow S^{2-} + 3H_2O \qquad (6)$$

$$NO_2{}^- + 8H^+ + 6e^- \longrightarrow NH_4{}^+ + 2H_2O \qquad (7)$$

Both contain active sites comprising a $[4Fe–4S]^{2+,+}$ cluster attached to siroheme (iron isobacteriochlorin) via a bridging cysteinyl-S. These active sites are exquisitely designed to catalyze multielectron reduction of $SO_3{}^{2-}$ or $NO_2{}^-$ bound at the vacant coordination site of the siroheme (Figure 2(g)). A series of elegant crystallographic studies of the hemoprotein subunit of *E*. coli sulfite reductase in different redox states and complexed with substrates, inhibitors, intermediates, and products have provided a detailed picture of the catalytic mechanism.[38,39,245] Sequential two-electron transfers from the coupled [4Fe–4S]–siroheme prosthetic groups to the bound anions result in successive cleavage of S-O and N-O bonds, leaving the oxygen atom as part of a water molecule. Hydrogen bonds supplied by basic residues in the substrate-binding pocket facilitate the charge transfer and reductive cleavage.

Nitrogenase (see ***Nitrogenase Catalysis & Assembly****).* Nitrogenase catalyzes the MgATP-dependent reduction of nitrogen gas to ammonia according the reaction shown in equation (8).[246]

$$N_2 + 8e^- + 16MgATP + 8H^+ \longrightarrow 2NH_3 + H_2 + 16MgADP + 16P_i \qquad (8)$$

The MgATP requirement would be cut in half if the Fe-protein functions as a two-electron donor (see discussion in Section 3.1.3). In addition to N_2, nitrogenase will also catalyze the reduction of a variety of triple-bonded substrates including alkynes and cyanide.[246] The substrate-binding site is a unique heterometallic Mo–Fe–S cluster, [Mo–7Fe–9S–X] (termed the FeMo-cofactor), that is attached to the protein by a single cysteinyl–S–Fe and histidyl–N–Mo linkage with homocitrate, coordinated by its 2-hydroxy and 2-carboxy groups, completing octahedral coordination at the Mo center (Figure 2(h)). The discovery of a low-Z central atom (μ_6N/O/C) resulted from a recent high-resolution (1.16 Å) crystal structure[20] and dramatically changes the predicted reactivity and properties,[247] since the cluster no longer has a central cavity surrounded by six three-coordinate Fe atoms, as indicated in the original crystal structure.[248] The nature of the central atom has yet to be determined, although it is generally assumed to be N. However, the available evidence indicates a purely structural role for the central atom, since ENDOR and ESEEM studies indicate that none of the N atoms associated with the cluster exchange with $^{15}N_2$ or $^{14}N_2$ during catalytic turnover.[249] The available evidence strongly suggests a similar structure for the FeV-cofactor in V nitrogenases, with Mo replaced by V,[250] although this has yet to be confirmed by crystallography (*see* ***Vanadium in Biology***).

One of the major unresolved questions in nitrogenase research concerns where and how substrates bind to the FeMo-cofactor during catalysis. Indeed, the question of whether substrates bind to Mo or Fe has been the subject of a recent comprehensive review that does not arrive at any definitive conclusion.[251] This issue has been difficult to address experimentally as the FeMo-cofactor only binds substrates when it is further reduced from the well characterized and EPR-detectable resting state ($S = 3/2$ ground state). Such reduction requires turnover conditions and generally leads to transient EPR-silent species. However, EPR signals from more reduced states have been observed in samples frozen during turnover with C_2H_2 and CS_2 as substrates and in the presence of the inhibitor CO, and in all cases ENDOR studies implicate binding through C to one or more Fe atoms.[251] In addition, evidence has recently been obtained for the binding of acetylene, the physiological substrate dinitrogen, and its semireduced form hydrazine, to a specific FeS face of the FeMo-cofactor.[252] The activity with each of these three substrates was dramatically modulated by mutating the valine residue that controls access to this face, to a smaller (alanine) or larger (isoleucine) residue. Furthermore, the binding of a non–physiological substrate (propargyl alcohol, $HC{=}C–CH_2OH$) to the Val-to-Ala variant enzyme has been localized to a specific Fe site via EPR and ENDOR studies of a freeze-trapped intermediate.[253] Intriguingly, it is proposed that the intermediate involves an organometallic iron-cyclopropane ring.[253] These very recent studies provide compelling mutagenesis and spectroscopic evidence for substrate binding to Fe rather than Mo. Moreover, they are consistent with the existence of Fe-only nitrogenases that appear to have a similar active site with Mo or V replaced by Fe.[254] Hence the role of the heterometal in the Mo and V nitrogenase active sites remains an enigma.

CO dehydrogenase/Acetyl-CoA Synthase. Both CO dehydrogenases and acetyl-CoA synthases contain novel Ni–Fe–S actives sites and a more detailed discussion of their active-site structures and catalytic mechanism is presented elsewhere. CO dehydrogenases catalyze the reversible oxidation of CO to CO_2 (see equation 9).

$$CO + H_2O \rightleftharpoons CO_2 + 2H^+ + 2e^- \qquad (9)$$

The structure of the functional form of the [Ni–4Fe–5S] active site[42,43] (Figure 2(i)) is best considered in terms of a [3Fe–4S] fragment that is covalently attached via bridging S atoms to a μ_2–S–bridged NiFe fragment. The NiFe center comprises a Ni(μ_2–S)(μ_3–S)$_2$(SCys) site with approximate square-planar geometry for the NiS_4 unit and a Fe(μ_2–S)(μ_3–S)(SCys)(NHis) site with distorted tetrahedral geometry for the FeS_3N unit. Crystallographically defined active-site structures corresponding to a [Ni–4Fe–4S] cluster that lacks the μ_2–S, have also been reported at lower resolution.[44,45,255] However, this form has recently been shown to correspond to an inactive decomposition product.[43] Oxidation of CO is proposed to occur by CO binding at the square-planar Ni center because of the direct accessibility of this site via a substrate channel. The Fe site of μ_2-S-bridged NiFe fragment is presumed to be the hydroxyl donor ligand for CO_2 formation.[256] However, the mechanistic details have yet to be fully worked out.

The acetyl-CoA synthase active site catalyzes formation of acetyl-CoA from CO, CoA, and a methyl group supplied by the corrinoid-containing iron–sulfur protein (equation 10).

$$\begin{aligned} CO + CH_3\text{–}Co^{III}FeSP + CoASH &\rightleftharpoons CH_3\text{–}C(O)\text{–}SCoA \\ &+ Co^{I}FeSP + H^+ \qquad (10) \end{aligned}$$

The structure of the functional Ni–Ni–[4Fe–4S] active site (Figure 2(j)) consists of a novel dinickel center bridged by two cysteinyl-S ligands, that is attached to a [4Fe–4S] cluster via another bridging cysteinyl-S. The distal Ni has approximate square-planar geometry with two BANs as the terminal ligands and the proximal Ni is ligated by the three bridging cysteinyl-S ligands with another small molecular ligand that has been modeled as acetate and water in different structures.[45,46] Controversy has arisen over the identity of the proximal metal center. Although this site can also accommodate Cu or Zn,[44,45] it is now clear that only the Ni form is catalytically active. However, it is currently unclear if acetyl formation occurs via a mononuclear mechanism involving binding of CO and CH_3 to only the proximal Ni center or via a dinuclear mechanism with CO and CH_3 binding to different Ni sites. In addition, the role of the [4Fe–4S] cluster in the catalytic mechanism is still unresolved. Rapid progress in elucidating the details of the catalytic mechanism is anticipated now that the active-site structures are known and the ambiguities concerning the metal content have been resolved. An excellent series of commentaries that discuss these issues has recently appeared in the *Journal of Biological Inorganic Chemistry*.[257–262]

3.3 Structural

Two classes of DNA repair enzymes contain $[4Fe\text{–}4S]^{2+}$ clusters that are not involved in catalysis and appear to have purely structural roles. Several members of the superfamily of helix-hairpin-helix DNA repair enzymes contain a redox-inert $[4Fe\text{–}4S]^{2+}$ cluster coordinated by a C–X_6–C–X_2–C–X_5–C cysteine motif, for example, endonuclease III,[50,51,263] MutY,[52,79,264,265] and thymine-DNA glycosylase.[266] These enzymes target specific base lesions and function in DNA repair either as pure glycosylases or combined glycosylases/apurinic-apyrimidinic lyases. The structurally distinct family 4 uracil-DNA glycosylase is specific for the excision of uracil bases from DNA and contain a $[4Fe\text{–}4S]^{3+,2+}$ cluster coordinated by N-terminal C–X_2–S and central C–X_{14-17}–C arrangements of cysteine residues.[267,268] The crystallographic, spectroscopic, and mutagenesis studies of members of both classes (cited above) clearly demonstrate that the [4Fe–4S] clusters are not directly involved in substrate binding or catalysis. Rather the $[4Fe\text{–}4S]^{2+}$ clusters function as structural cross-links, analogous to disulfide bonds or zinc fingers (*see* ***Zinc: DNA-binding Proteins***), and thereby contribute to enzyme stability and reactivity by maintaining conformation in regions associated with DNA interactions.

3.4 Regulation

The ability of an Fe–S center to control a local region of protein structure by cluster assembly/disassembly, cluster transformation, or changes in cluster redox state, means that Fe–S centers can function as sensors for a variety of different types of environmental stimuli.[58] Indeed there are now four well-documented examples of Fe–S proteins that are involved in regulating gene expression and several examples in which Fe–S centers have been proposed to regulate enzymatic activity (*see* ***Metalloregulation***).

3.4.1 Gene Expression

SoxR. SoxR is a dimeric protein containing one all-cysteine-ligated $[2Fe\text{–}2S]^{2+,+}$ cluster ($E_m = -285$ mV) in each subunit, that functions as a redox-responsive genetic switch for monitoring cellular oxidative stress in bacteria.[55] When oxidative stress increases in *E. coli*, SoxR mediates transcriptional regulation of the *soxRS* regulon that leads to the activation of ~45 genes whose products (e.g. superoxide dismutase) facilitate removal of superoxide and the repair of oxidative damage.[55] The SoxR protein remains tightly bound to its target SoxS promoter in the absence or presence of oxidative stress,[269] and both in vitro and in vivo EPR studies indicate that SoxR is activated by oxidation or nitrosylation of the $[2Fe\text{–}2S]^{2+,+}$ cluster in order to stimulate transcription of the *soxS* gene.[270,271] However, it is currently unclear if the cluster is oxidized by superoxide directly or if superoxide acts on the recently identified reductase system that maintains

SoxR in the reduced state in the cell.[272] Detailed understanding of molecular mechanism of transcription activation by SoxR awaits structural refinement.

FNR. The *E. coli* FNR regulatory protein is an oxygen-sensing protein that controls the switch between aerobic and anaerobic respiration by controlling the expression of >100 genes.[56] In contrast to SoxR, the FNR protein belongs to the family of helix-turn-helix transcription factors whose activity is dictated by site-specific binding to DNA. The active, DNA-binding form of FNR is a homodimer containing one $[4Fe–4S]^{2+}$ cluster per subunit.[273] Mössbauer studies of the purified protein and in whole cells have shown that O_2 exposure results in rapid conversion to a monomeric form containing one $[2Fe–2S]^{2+}$ cluster per subunit.[57] Hence the O_2-sensing mechanism involves oxidative $[4Fe–4S]^{2+}$ to $[2Fe–2S]^{2+}$ cluster conversion which destabilizes the active dimeric form. Recent spectroscopic studies indicate that this cluster conversion involves a $[3Fe–4S]^{+}$ intermediate (Figure 5) and is accompanied by the production of H_2O_2.[175] The proposed O_2 sensing mechanism predicts that the $[2Fe–2S]^{2+}$-containing from of FNR would be present under aerobic conditions. However, FNR isolated from aerobically grown cells is predominantly in the apo form.[56] This dilemma appears to have been resolved by recent spectroscopic studies which demonstrate that the $[2Fe–2S]^{2+}$ cluster in FNR is labile to superoxide both *in vitro* and *in vivo*.[274] The mechanism of assembly of the $[4Fe–4S]^{2+}$ cluster in apo FNR under anaerobic conditions and the molecular details of the O_2 sensing mechanism remain to be established. NO has also been shown to be effective for inactivating FNR via the formation of monomeric and dimeric dinitrosyl-iron-dithiol species.[275] However, the physiological relevance of NO-induced inactivation remains to be established and it has yet to be determined if the nitrosylated form of FNR can be repaired *in vivo*.

IscR/SufR. IscR is a transcriptional regulator of the iron–sulfur cluster biosynthesis operon (*iscRSUAhscBAfdx*) and contains a DNA-binding region as well as an Fe–S cluster-binding region comprising three conserved cysteine residues.[59] Spectroscopic studies have shown that IscR can accommodate a $[2Fe–2S]^{2+,+}$ cluster and the cluster-bound form has been shown to act as a transcriptional repressor of the *isc* operon by binding to a promoter upstream of *iscR*.[59] In the current model of IscR-directed regulation, apo Fe–S proteins compete with apo IscR for $[2Fe–2S]^{2+}$ clusters assembled on the IscU or IscA scaffold proteins. Hence IscR appears to be an Fe–S cluster sensor that provides feedback regulation to control the supply of clusters generated by the ISC cluster assembly machinery when supply exceeds demand. A similar mechanism has recently been suggested for the SufR protein in cyanobacteria.[276] SufR is proposed to act as a transcriptional repressor of the *sufBCDS* operon, which encodes for SUF iron–sulfur cluster assembly proteins. However, the arrangement of the four conserved cysteines in the Fe–S binding domain of SufR is completely different to IscR and preliminary EPR studies indicate that SufR binds a $[4Fe–4S]^{2+,+}$ cluster rather than a $[2Fe–2S]^{2+,+}$ cluster.[276] Much has still to be learned concerning the role and mechanism of both IscR and SufR. For example, it has yet to established if they are specific for regulating the *isc* and *suf* operons, the processes by which the Fe–S clusters are acquired and removed have still to be addressed, and the molecular mechanisms by which cluster binding induces DNA binding are currently unknown.

IRP. Iron-regulatory proteins (IRPs) corresponding to apo and holo forms of aconitase are responsible for translational regulation in response to iron availability and/or oxidative stress in both eukaryotic and prokaryotic cells.[27,58] Under conditions of iron starvation in eukaryotic cells, apo IRP stabilizes the transferrin receptor and inhibits the translation of ferritin mRNAs by binding to iron-responsive elements (IREs) within their untranslated regions. Under Fe-replete conditions, IRP assembles a [4Fe–4S] cluster with three cysteine ligands and this prevents IRE binding. Hence the ability to assemble an Fe–S cluster is used as the sensor of iron availability. However, it is becoming increasing apparent that the [4Fe–4S] clusters in the holo forms of both eukaryotic and prokaryotic IRPs respond in diverse ways to other stimuli associated with reactive oxygen and nitrogen species, such as H_2O_2, NO, superoxide, and peroxynitrite. This suggests a complex interplay of the iron sensing and oxidative stress responses and the involvement of IRPs in the latter are still being characterized.[58,277]

3.4.2 Enzyme Activity

There are several examples of enzymes containing Fe–S clusters that are essential for activity, but are not required for substrate activation or electron transfer, implying a structural or regulatory role. However, direct evidence for a regulatory role is often difficult to obtain. The best-documented example of an enzyme containing a regulatory Fe–S cluster is the *Bacillus subtilis* glutamine phosphoribosylpyrophosphate amidotransferase that catalyzes the first step in purine nucleotide biosynthesis. The combination of biochemical and crystallographic evidence strongly suggest that the [4Fe–4S] cluster is selectively destroyed by O_2 with concomitant proteolysis.[60,61] The cluster therefore appears to act as an O_2 sensor in order to regulate purine biosynthesis. Another proposed example is mammalian ferrochelatase, the enzyme responsible for the iron-insertion step in heme biosynthesis. In contrast to almost all bacterial ferrochelatases, mammalian ferrochelatases contain a [2Fe–2S] cluster that is essential for activity and is very sensitive to NO-induced degradation.[62,63] Since bacterial infections can be viewed as a ‘fight over iron’ and some pathogenic microorganisms can directly use heme made by host, local inactivation of ferrochelatase in the region of infection, in response to NO produced by macrophages, may be desirable. Hence the notion of the [2Fe–2S] cluster in mammalian ferrochelatases acting as a NO sensor is an attractive, albeit unproven, possibility.

3.5 Disulfide Reduction

Biological disulfide reduction is generally catalyzed by a large family of pyridine nucleotide-disulfide oxidoreductase flavoenzymes that use NADPH as a two-electron donor to effect FAD-mediated two-electron reduction of an active-site disulfide. The reduced active-site dithiol then reduces substrate disulfides via dithiol-disulfide exchange. However, the FTRs found in chloroplasts and the HDRs found in methanogenic archaea have emerged as unique types of disulfide reductase that catalyze disulfide reduction using one-electron donors and an active site comprising a [4Fe–4S] cluster. The combination of spectroscopic and crystallographic approaches has recently yielded major insights concerning the role of [4Fe–4S] clusters in cleaving disulfides in two sequential one-electron steps.[65]

3.5.1 Ferredoxin–Thioredoxin Reductase

FTR plays the central role in light regulation of the activity of enzymes involved in oxygenic photosynthesis. The light signal is converted into reducing equivalents in the form of reduced 2Fe Fd by photosystem I and FTR catalyzes the reduction of disulfides in thioredoxin (Trx) f and m using the reduced 2Fe Fd as the one-electron donor (see equation 11).

$$2Fd_{red} + Trx_{ox} + 2H^+ \longrightarrow 2Fd_{ox} + Trx_{red} \qquad (11)$$

The reduced thioredoxins activate or inactive numerous target enzymes involved with oxygenic photosynthesis by reduction of regulatory disulfides. FTR is a disc-shaped $\alpha\beta$-heterodimer, 40–50 Å in diameter and ~10Å thick, comprising a highly conserved catalytic β-subunit that contains a [4Fe–4S] cluster with nearby asymmetrically disposed cysteine disulfide (Figure 8) and a variable α-subunit with low sequence homology between species.[64] Detailed spectroscopic characterization of FTR and a modified form in which one of the cysteines of the active site has been alkylated, indicate that the one-electron reduced catalytic intermediate involves two-electron disulfide reduction coupled with one-electron cluster oxidation of a $[4Fe–4S]^{2+}$ cluster to yield a unique type of $S = 1/2$ $[4Fe–4S]^{3+}$ cluster with two cysteine residues ligated at a specific Fe site.[278,279] The results provide the basis for a novel mechanism for disulfide cleavage in two one-electron steps involving site-specific [4Fe–4S] cluster chemistry and distinct roles for each of the cysteines of the active-site disulfide[65] (Figure 8).

3.5.2 Heterodisulfide Reductase

In the final step of methanogenesis, methyl coenzyme M reductase catalyzes the reaction of methyl coenzyme M (CH_3–S–CoM) with coenzyme B (CoB–SH) to form methane and the CoM–S–S–CoB heterodisulfide.[280] The heterodisulfide functions as the terminal electron acceptor of

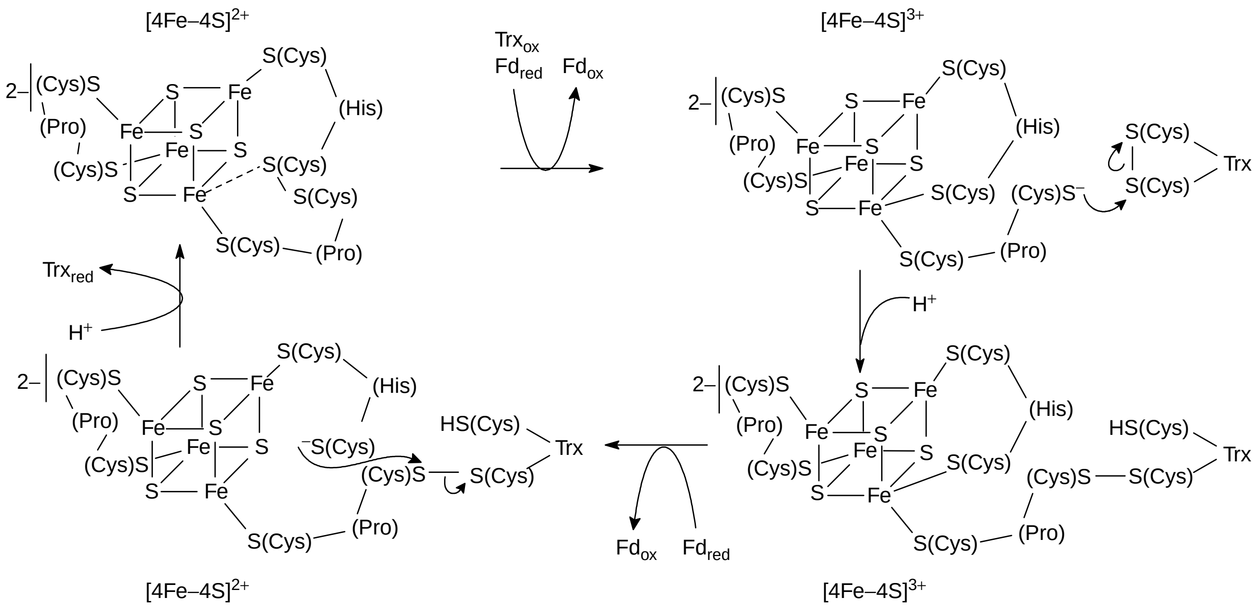

Figure 8 Proposed catalytic mechanism for ferredoxin–thioredoxin reductase

an energy-conserving electron transport chain, in a process called disulfide respiration.[281] HDR is the terminal enzyme in the disulfide respiratory chain and catalyzes the reversible reduction of the CoM–S–S–CoB heterodisulfide to yield coenzyme M (CoM–SH) and CoB–SH (equation 12).

$$\text{CoM–S–S–CoB} + 2\text{H}^+ + 2\text{e}^- \longrightarrow \text{CoM–SH} + \text{CoB–SH} \quad (12)$$

Spectroscopic studies indicate a [4Fe–4S] cluster active site that interacts directly with the substrate disulfide, rather than via an active–site disulfide as in FTR.[66] Moreover, they have provided compelling evidence for a one-electron reduced intermediate, similar to that characterized in FTR, involving a $[4\text{Fe–4S}]^{3+}$ cluster with both cysteinate and the CoM thiolate bound at a unique Fe site.[66,282] Hence a similar mechanism to that shown in Figure 8 for FTR is also proposed for the direct [4Fe–4S]-mediated cleavage of the CoM–S–S–CoB heterodisulfide in methanogenic archaea by HDR.[65]

3.6 Iron, Electron, or Cluster Storage

A convincing case has been made for an iron storage role for 8Fe Fds containing two $[4\text{Fe–4S}]^{2+,+}$ clusters in *Clostridia*[47] and similar arguments can be made for many anaerobic bacteria and archaea. This is further supported by the presence of polyferredoxins containing up to 14 [4Fe–4S] clusters in seven repeated 8Fe Fd-like domains in methanogenic archaea.[48,49,283] Genes encoding polyferredoxins are found in operons encoding enzymes such as hydrogenase and formylmethanofuran dehydrogenase, which contain multiple [4Fe–4S] clusters. Hence it has been proposed that polyferredoxins and 8Fe Fds function in iron and/or electron storage.[48] However, an attractive alternative proposal that arises from the realization that Fe–S clusters are assembled on scaffold proteins prior to insertion into apoproteins,[82,83] is that 8Fe Fds and polyferredoxins provide storage sites for [4Fe–4S] clusters that are used in the maturation of Fe–S proteins.

4 RELATED ARTICLES

Cobalt: B_{12} Enzymes & Coenzymes; Cytochrome Oxidase; Iron: Heme Proteins & Electron Transport; Iron Proteins with Dinuclear Active Sites; Iron Proteins with Mononuclear Active Sites; Iron–Sulfur Models of Protein Active Sites; Metallocenter Biosynthesis & Assembly.; Metalloregulation; Molybdenum: MPT-containing Enzymes; Nickel Enzymes & Cofactors; Nitrogenase Catalysis & Assembly; Photosynthesis; Tungsten Proteins; Vanadium in Biology; Zinc: DNA-binding Proteins.

5 REFERENCES

1. M. W. G. de Bolster, *Pure Appl. Chem.*, 1997, **69**, 1251.
2. A. G. Sykes and R. Cammack eds, 'Iron–Sulfur Proteins', Academic Press, San Diego, CA, 1999.
3. M. K. Johnson, Iron–Sulfur Proteins, in 'Encyclopedia of Inorganic Chemistry', ed. R. B. King, John Wiley & Sons, Chichester, 1994, p. 1896.
4. H. Beinert, R. H. Holm, and E. Münck, *Science*, 1997, **277**, 653.
5. H. Beinert, *J. Biol. Inorg. Chem.*, 2000, **5**, 2.
6. D. C. Rees, *Annu. Rev. Biochem.*, 2002, **71**, 221.
7. H. Beinert, Iron-Sulfur Proteins: Properties and Functions, in 'Cellular Implications of Redox Signalling', eds. C. Gitler and A. Danon, Imperial College Press, London, 2003, p. 47.
8. J. B. Broderick, Iron-Sulfur Clusters in Enzyme Catalysis, in 'Comprehensive Coordination Chemistry II', eds. J. A. McCleverty and T. J. Meyer, Elsevier, Oxford, 2004, Vol. 8, p. 739.
9. H. Beinert, *Eur. J. Biochem.*, 2000, **267**, 5657.
10. C. Huber and G. Wächtershäuser, *Science*, 1997, **276**, 245.
11. C. Huber and G. Wächtershäuser, *Science*, 1998, **281**, 670.
12. G. C. Cody, N. Z. Boctor, T. R. Filley, R. M. Hazen, J. H. Scott, A. Sharma, and J. S. Yoder, *Science*, 2000, **289**, 1337.
13. P. V. Rao and R. H. Holm, *Chem. Rev.*, 2004, **104**, 527.
14. M. K. Johnson, R. E. Duderstadt, and E. C. Duin, *Adv. Inorg. Chem.*, 1999, **47**, 1.
15. J. W. Peters, M. H. B. Stowell, S. M. Soltis, M. G. Finnegan, M. K. Johnson, and D. C. Rees, *Biochemistry*, 1997, **36**, 1181.
16. Z. Dauter, L. C. Sieker, and K. S. Wilson, *Acta Crystallogr.*, 1992, **48**, 42.
17. B. L. Jacobson, Y. K. Chae, J. L. Markley, I. Rayment, and H. M. Holden, *Biochemistry*, 1993, **32**, 6788.
18. H. Bonisch, C. L. Schmidt, G. Schafer, and R. Ladenstein, *J. Mol. Biol.*, 2002, **319**, 791.
19. C. G. Schipke, D. B. Goodin, D. E. McRee, and C. D. Stout, *Biochemistry*, 1999, **38**, 8228.
20. O. Einsle, F. A. Tezcan, S. L. A. Andrade, B. Schmid, M. Yoshida, J. B. Howard, and D. C. Rees, *Science*, 2002, **297**, 1696.
21. H. Sticht and P. Rösch, *Prog. Biophys. Mol. Biol.*, 1998, **70**, 95.
22. T. A. Link, *Adv. Inorg. Chem.*, 1999, **47**, 83.
23. L. M. Hunsicker-Wang, A. Heine, Y. Chen, E. P. Luna, T. Todaro, Y. M. Zhang, P. A. Williams, D. E. McRee, J. Hirst, C. D. Stout, and J. A. Fee, *Biochemistry*, 2003, **42**, 7303.
24. W. N. Lanzilotta, J. Christiansen, D. R. Dean, and L. C. Seefeldt, *Biochemistry*, 1998, **37**, 11376.

25. S. Nagashima, M. Nakasako, N. Dohmae, M. Tsujimura, K. Takio, M. Odaka, M. Yohda, N. Kamiya, and I. Endo, *Nat. Struct. Biol.*, 1998, **5**, 347.
26. P. E. Doan, M. J. Nelson, H. Jin, and B. M. Hoffman, *J. Am. Chem. Soc.*, 1996, **118**, 7014.
27. H. Beinert, M. C. Kennedy, and C. D. Stout, *Chem. Rev.*, 1996, **96**, 2335.
28. D. H. Flint and R. M. Allen, *Chem. Rev.*, 1996, **96**, 2315.
29. M. Archer, C. Huber, P. Tavares, J. J. G. Moura, M. A. Carrondo, L. C. Sicker, J. LeGall, and M. J. Romao, *J. Mol. Biol.*, 1995, **251**, 690.
30. F. E. Jenney, M. F. J. M. Verhagen, X. Cui, and M. W. W. Adams, *Science*, 1999, **286**, 306.
31. A. P. Yeh, Y. Hu, F. E. Jenney, M. W. W. Adams, and D. C. Rees, *Biochemistry*, 2000, **39**, 2499.
32. H. J. Sofia, G. Chen, B. G. Hetzler, J. F. Reyes-Spindola, and N. E. Miller, *Nucleic Acids Res.*, 2001, **29**, 1097.
33. G. Layer, J. Moser, D. W. Heinz, D. Jahn, and W.-D. Schubert, *EMBO J.*, 2003, **22**, 6214.
34. J. T. Jarrett, *Curr. Opin. Chem. Biol.*, 2003, **7**, 174.
35. A. Volbeda, M.-H. Charon, C. Piras, E. C. Hatchikian, M. Frey, and J. C. Fontecilla-Camps, *Nature*, 1995, **373**, 580.
36. A. Volbeda, E. Garcin, C. Piras, A. L. de Lacey, V. M. Fernandez, E. C. Hatchikian, M. Frey, and J. C. Fontecilla-Camps, *J. Am. Chem. Soc.*, 1996, **118**, 12989.
37. J. Kim and D. C. Rees, *Science*, 1992, **257**, 1677.
38. B. R. Crane, L. M. Siegel, and E. D. Getzoff, *Science*, 1995, **270**, 59.
39. B. R. Crane, L. M. Seigel, and E. D. Getzoff, *Biochemistry*, 1997, **36**, 12120.
40. J. W. Peters, W. N. Lanzilotta, B. J. Lemon, and L. C. Seefeldt, *Science*, 1998, **282**, 1853.
41. Y. Nicolet, C. Cavazza, and J. C. Fontecilla-Camps, *J. Inorg. Biochem.*, 2002, **91**, 1.
42. H. Dobbek, V. Svetlitchnyi, L. Gremer, R. Huber, and O. Meyer, *Science*, 2001, **293**, 1281.
43. H. Dobbek, V. Svetlitchnyi, J. Liss, and O. Meyer, *J. Am. Chem. Soc.*, 2004, **126**, 5382.
44. T. I. Doukov, T. M. Iverson, J. Seravalli, S. W. Ragsdale, and C. L. Drennan, *Science*, 2002, **298**, 567.
45. C. Darnault, A. Volbeda, E. J. Kim, P. Legrand, X. Vernède, P. A. Lindahl, and J. C. Fontecilla-Camps, *Nat. Struct. Biol.*, 2003, **10**, 271.
46. V. Svetlitchnyi, H. Dobbek, W. Meyer-Klaucke, T. Meins, T. Thiele, P. Rõmer, R. Huber, and O. Meyer, *Proc. Natl. Acad. Sci. U.S.A.*, 2004, **101**, 446.
47. R. K. Thauer and P. Schönheit, Iron–Sulfur Complexes of Ferredoxin as a Storage Form of Iron in *Clostridium pasteurianum*, in ‘Iron–Sulfur Proteins’, ed. T. G. Spiro, Wiley, New York, 1982, p. 329.
48. J. N. Reeve, G. S. Beckler, D. S. Cram, P. T. Hamilton, J. W. Brown, J. A. Krzycki, A. F. Kolodziej, L. A. Alex, W. H. Orme–Johnson, and C. T. Walsh, *Proc. Natl. Acad. Sci. U.S.A.*, 1989, **86**, 3031.
49. R. Hedderich, S. P. J. Albracht, D. Linder, J. Koch, and R. K. Thauer, *FEBS Lett.*, 1992, **298**, 65.
50. R. P. Cunningham, H. Asahara, J. F. Bank, C. P. Scholes, J. C. Salerno, K. K. Surerus, E. Münck, J. McCracken, J. Peisach, and M. H. Emptage, *Biochemistry*, 1989, **28**, 4450.
51. C.-F. Kuo, D. E. McRee, C. L. Fisher, S. F. O’Handley, R. P. Cunningham, and J. A. Tainer, *Science*, 1992, **258**, 434.
52. S. L. Porello, M. J. Cannon, and S. S. David, *Biochemistry*, 1998, **37**, 6465.
53. Y. Guan, R. C. Manuel, A. S. Arvai, S. S. Parikh, C. D. Mol, J. H. Miller, R. S. Lloyd, and J. A. Tainer, *Nat. Struct. Biol.*, 1998, **5**, 1058.
54. E. Hidalgo and B. Demple, *EMBO J.*, 1994, **13**, 138.
55. B. Demple, H. Ding, and M. Jorgensen, *Methods Enzymol.*, 2002, **348**, 355.
56. P. J. Kiley and H. Beinert, *FEMS Microbiol. Rev.*, 1998, **22**, 341.
57. C. Popescu, D. M. Bates, H. Beinert, E. Münck, and P. J. Kiley, *Proc. Natl. Acad. Sci. U.S.A.*, 1998, **95**, 13431.
58. P. J. Kiley and H. Beinert, *Curr. Opin. Microbiol.*, 2003, **6**, 181.
59. C. J. Schwartz, J. L. Giel, T. Patschkowski, C. Luther, F. J. Ruzicka, H. Beinert, and P. J. Kiley, *Proc. Natl. Acad. Sci. U.S.A.*, 2001, **98**, 14895.
60. J. A. Grandoni, R. L. Switzer, C. A. Marakoff, and H. Zalkin, *J. Biol. Chem.*, 1989, **264**, 6058.
61. J. L. Smith, E. J. Zaluzec, J.-P. Wery, L. Niu, R. L. Switzer, H. Zalkin, and Y. Satow, *Science*, 1994, **264**, 1427.
62. C.-K. Wu, H. A. Dailey, J. P. Rose, A. Burden, V. M. Sellers, and B.-C. Wang, *Nat. Struct. Biol.*, 2001, **8**, 156.
63. V. M. Sellers, M. K. Johnson, and H. A. Dailey, *Biochemistry*, 1996, **35**, 2699.
64. S. Dai, C. Schwendtmayer, K. Johansson, S. Ramaswamy, P. Schürmann, and H. Eklund, *Q. Rev. Biophys.*, 2000, **33**, 67.
65. E. M. Walters and M. K. Johnson, *Photosynth. Res.*, 2004, **79**, 249.
66. E. C. Duin, S. Madadi–Kahkesh, R. Hedderich, M. D. Clay, and M. K. Johnson, *FEBS Lett.*, 2002, **512**, 263.
67. G. N. L. Jameson, M. M. Cosper, H. L. Hernández, M. K. Johnson, and B. H. Huynh, *Biochemistry*, 2004, **43**, 2022.
68. F. Berkovitch, Y. Nicolet, J. T. Wan, J. T. Jarrett, and C. L. Drennan, *Science*, 2004, **303**, 76.
69. H. Lauble, M. C. Kennedy, H. Beinert, and C. D. Stout, *Biochemistry*, 1992, **31**, 2735.
70. Y. Higuchi, H. Ogata, K. Miki, N. Yasuoka, and T. Yagi, *Structure Fold. Des.*, 1999, **5**, 549.
71. Y. Nicolet, C. Piras, P. Legrand, C. E. Hatchikian, and J. C. Fontecilla-Camps, *Structure Fold. Des.*, 1999, **7**, 13.

72. L. Calzolai, Z.-H. Zhou, M. W. W. Adams, and G. N. La Mar, *J. Am. Chem. Soc.*, 1996, **118**, 2513.
73. M. D. Clay, F. E. Jenney, P. L. Hagedoorn, G. N. George, M. W. W. Adams, and M. K. Johnson, *J. Am. Chem. Soc.*, 2002, **124**, 788.
74. C. J. Walsby, W. Hong, W. E. Broderick, J. Cheek, D. Ortillo, J. B. Broderick, and B. M. Hoffman, *J. Am. Chem. Soc.*, 2002, **124**, 3143.
75. J. Cheek and J. B. Broderick, *J. Biol. Inorg. Chem.*, 2001, **6**, 209.
76. S. E. Mulholland, B. R. Gibney, F. Rabanal, and P. L. Dutton, *J. Am. Chem. Soc.*, 1998, **120**, 10296.
77. D. W. Plank, M. C. Kennedy, H. Beinert, and J. B. Howard, *J. Biol. Chem.*, 1989, **264**, 20385.
78. M.-P. Golinelli, C. Chatelet, E. C. Duin, M. K. Johnson, and J. Meyer, *Biochemistry*, 1998, **37**, 10429.
79. Y. Guan, R. C. Manuel, A. S. Arvai, S. S. Parikh, C. D. Mol, J. H. Miller, R. S. Lloyd, and J. A. Tainer, *Nat. Struct. Biol.*, 1998, **5**, 1058.
80. B. Tse Sum Bui, D. Florentin, F. Fournier, O. Ploux, A. Méjean, and A. Marquet, *FEBS Lett.*, 1998, **440**, 226.
81. N. B. Ugulava, C. J. Sacanell, and J. T. Jarrett, *Biochemistry*, 2001, **40**, 8352.
82. S. S. Mansy and J. A. Cowan, *Acc. Chem. Res.*, 2004, **37**, 719.
83. D. Johnson, D. R. Dean, A. D. Smith, and M. K. Johnson, *Annu. Rev. Biochem.*, 2005, in press.
84. E. L. Bominaar, Z. Hu, E. Münck, J.-J. Girerd, and S. A. Borshch, *J. Am. Chem. Soc.*, 1995, **117**, 6976.
85. L. Noodleman, T. Lovell, T. Liu, F. Himo, and R. A. Torres, *Curr. Opin. Chem. Biol.*, 2002, **6**, 259.
86. T. Glaser, B. Hedman, K. O. Hodgson, and E. I. Solomon, *Acc. Chem. Res.*, 2000, **33**, 859.
87. E. Anxolabéhère-Mallart, T. Glaser, P. Frank, A. Aliverti, G. Zanetti, B. Hedman, K. O. Hodgson, and E. I. Solomon, *J. Am. Chem. Soc.*, 2001, **123**, 5444.
88. T. Glaser, K. Rose, S. E. Shadle, B. Hedman, K. O. Hodgson, and E. I. Solomon, *J. Am. Chem. Soc.*, 2001, **123**, 442.
89. L. Noodleman and D. A. Case, *Adv. Inorg. Chem.*, 1992, **38**, 423.
90. A. Dey, T. Glaser, M. M. J. Couture, L. D. Eltis, R. H. Holm, B. Hedman, K. O. Hodgson, and E. I. Solomon, *J. Am. Chem. Soc.*, 2004, **126**, 8320.
91. K. K. Surerus, E. Münck, I. Moura, J. J. G. Moura, and J. LeGall, *J. Am. Chem. Soc.*, 1987, **109**, 3805.
92. J. L. Breton, J. L. C. Duff, J. N. Butt, F. A. Armstrong, S. J. George, Y. Petillot, E. Forest, G. Schafer, and A. J. Thomson, *Eur. J. Biochem.*, 1995, **233**, 937.
93. B. R. Crouse, J. Meyer, and M. K. Johnson, *J. Am. Chem. Soc.*, 1995, **117**, 9612.
94. C. Achim, M.-P. Golinelli, E. L. Bominaar, J. Meyer, and E. Münck, *J. Am. Chem. Soc.*, 1996, **118**, 8168.
95. M. K. Johnson, E. C. Duin, B. R. Crouse, M.-P. Golinelli, and J. Meyer, Valence–Delocalized $[Fe_2S_2]^+$ Clusters, in ‘Spectroscopic Methods in Bioinorganic Chemistry’, eds. E. I. Solomon and K. O. Hodgson, American Chemical Society, Washington, DC, 1998, p. 286.
96. P. J. Stephens, D. R. Jolie, and A. Warshel, *Chem. Rev.*, 1996, **96**, 2491.
97. K. Chen, C. A. Bonagura, G. J. Tilley, J. P. McEvoy, Y.-S. Jung, F. A. Armstrong, C. D. Stout, and B. K. Burgess, *Nat. Struct. Biol.*, 2002, **9**, 188.
98. M. J. Romao and M. Archer, Structural Versatility of Proteins Containing Rubredoxin–Type Centers, in ‘Iron Metabolism’, eds. G. C. Ferreira, J. J. G. Moura, and R. Franco, Wiley–VCH Verlag, Weinheim, 1999, p. 341.
99. D. M. Kurtz Jr and E. D. Coulter, *Chemtracts. Inorg. Chem.*, 2001, **14**, 407.
100. R. S. Czernuszewicz, J. LeGall, I. Moura, and T. G. Spiro, *Inorg. Chem.*, 1986, **25**, 696.
101. V. S. Oganesyan, S. J. George, M. R. Cheesman, and A. J. Thomson, *J. Chem. Phys.*, 1999, **110**, 762.
102. P. Tavares, N. Ravi, J. J. G. Moura, J. LeGall, Y. H. Huang, B. R. Crouse, M. K. Johnson, B. H. Huynh, and I. Moura, *J. Biol. Chem.*, 1994, **269**, 10504.
103. I. Moura, B. H. Huynh, R. P. Hausinger, J. LeGall, A. V. Xavier, and E. Münck, *J. Biol. Chem.*, 1980, **255**, 2493.
104. Z. Xiao, M. L. Lavery, M. Ayhan, S. D. B. Scrofani, M. C. J. Wilce, J. M. Guss, P. A. Tregloan, G. N. George, and A. G. Wedd, *J. Am. Chem. Soc.*, 1998, **120**, 4135.
105. Z. Xiao, A. R. Gardner, M. Cross, E. M. Maes, R. S. Czernuszewicz, M. Sola, and A. G. Wedd, *J. Biol. Inorg. Chem.*, 2001, **6**, 638.
106. M. Cross, Z. Xiao, E. M. Maes, R. S. Czernuszewicz, S. C. Drew, J. R. Pilbrow, G. N. George, and A. G. Wedd, *J. Biol. Inorg. Chem.*, 2002, **7**, 781.
107. J. Meyer, J. Gagnon, J. Gaillard, M. Lutz, C. Achim, E. Münck, Y. Pétillot, C. M. Colangelo, and R. A. Scott, *Biochemistry*, 1997, **36**, 13374.
108. V. Yankovskaya, R. Horsefield, S. Törnroth, C. Luna-Chavez, H. Miyoshi, C. Léger, B. Byrne, G. Cecchini, and S. Iwata, *Science*, 2003, **299**, 700.
109. W. R. Hagen, P. J. Silva, M. A. Amorim, P. L. Hagedoorn, H. Wassink, H. Haaker, and F. T. Robb, *J. Biol. Inorg. Chem.*, 2000, **5**, 527.
110. K. Fukuyama, *Photosynth. Res.*, 2004, **81**, 289.
111. A. V. Grinberg, F. Hannemann, B. Schiffler, J. Müller, U. Heinemann, and R. Bernhardt, *Proteins*, 2000, **40**, 590.
112. Y. Kakuta, T. Horio, Y. Takahashi, and K. Fukuyama, *Biochemistry*, 2001, **40**, 11007.
113. I. F. Sevrioukova, C. Garcia, H. Li, B. Bhaskar, and T. L. Poulos, *J. Mol. Biol.*, 2003, **333**, 377.
114. J. Meyer, *FEBS Lett.*, 2001, **509**, 1.
115. G. Cecchini, I. Schröder, R. P. Gunsalus, and E. Maklashina, *Biochim. Biophys. Acta*, 2002, **1553**, 140.

116. M. J. Romao, M. Archer, I. Moura, J. J. G. Moura, J. LeGall, R. Engh, M. Schneider, P. Hof, and R. Huber, *Science*, 1995, **270**, 1170.

117. C. Enroth, B. T. Eger, K. Okamoto, N. Tomoko, T. Nishino, and E. F. Pai, *Proc. Natl. Acad. Sci. U.S.A.*, 2000, **97**, 10723.

118. R. Morales, M.-H. Chron, G. Hudry-Clergeon, Y. Pétillot, S. Norager, M. Medina, and M. Frey, *Biochemistry*, 1999, **38**, 15764.

119. L. B. Dugad, G. N. La Mar, L. Banci, and I. Bertini, *Biochemistry*, 1990, **29**, 2263.

120. B. Guigliarelli and P. Bertrand, *Adv. Inorg. Chem.*, 1999, **47**, 421.

121. S. Gambarelli and J.-M. Mouesca, *Inorg. Chem.*, 2004, **43**, 1441.

122. F. Tiago de Oliveira, E. L. Bominaar, J. Hirst, J. A. Fee, and E. Münck, *J. Am. Chem. Soc.*, 2004, **126**, 5338.

123. E. J. Leggate, E. Bill, T. Essigke, G. M. Ullmann, and J. Hirst, *Proc. Natl. Acad. Sci. U.S.A.*, 2004, **101**, 10913.

124. J.-M. Moulis, V. Davasse, M. P. Golinelli, J. Meyer, and I. Quinkal, *J. Biol. Inorg. Chem.*, 1996, **1**, 2.

125. A. P. Yeh, X. I. Ambroggio, S. L. A. Andrade, O. Einsle, C. Chatelet, J. Meyer, and D. C. Rees, *J. Biol. Chem.*, 2002, **277**, 34499.

126. A. Kounosu, Z. Li, J. E. Shokes, R. A. Scott, T. Imai, A. Urushiyama, and T. Iwasaki, *J. Biol. Chem.*, 2004, **279**, 12519.

127. C. Achim, E. L. Bominaar, J. Meyer, J. Peterson, and E. Münck, *J. Am. Chem. Soc.*, 1999, **121**, 3704.

128. H. Beinert and A. J. Thomson, *Arch. Biochem. Biophys.*, 1983, **222**, 333.

129. P. J. Ellis, T. Conrads, R. Hille, and P. Kuhn, *Structure*, 2001, **9**, 125.

130. M. C. Kennedy, T. A. Kent, M. H. Emptage, H. Merkle, H. Beinert, and E. Münck, *J. Biol. Chem.*, 1984, **259**, 14463.

131. A. J. M. Richards, A. J. Thomson, R. H. Holm, and K. S. Hagen, *Spectrochim. Acta*, 1990, **46A**, 987.

132. J. L. C. Duff, J. L. Breton, J. N. Butt, F. A. Armstrong, and A. J. Thomson, *J. Am. Chem. Soc.*, 1996, **118**, 8593.

133. K. K. Surerus, M. Chen, J. W. van der Zwaan, F. M. Rusnak, M. Kolk, E. C. Duin, S. P. J. Albracht, and E. Münck, *Biochemistry*, 1994, **33**, 4980.

134. M. G. Bertero, R. A. Rothery, M. Palak, C. Hou, D. Lim, F. Blasco, J. H. Weiner, and N. C. Strynadka, *Nat. Struct. Biol.*, 2003, **10**, 681.

135. M. S. Nielsen, P. Harris, B. L. Ooi, and H. E. M. Christensen, *Biochemistry*, 2004, **43**, 5188.

136. C. D. Stout, E. A. Stura, and D. E. McRee, *J. Mol. Biol.*, 1998, **278**, 629.

137. J. Zhou, Z. Hu, E. Münck, and R. H. Holm, *J. Am. Chem. Soc.*, 1996, **118**, 1966.

138. Y. Sanakis, A. L. Macedo, I. Moura, J. J. G. Moura, V. Papaefthymiou, and E. Münck, *J. Am. Chem. Soc.*, 2000, **122**, 11855.

139. L. Calzolai, C. M. Gorst, Z.-H. Zhou, Q. Teng, M. W. W. Adams, and G. N. La Mar, *Biochemistry*, 1995, **34**, 11373.

140. P. S. Brereton, R. E. Duderstadt, C. R. Staples, M. K. Johnson, and M. W. W. Adams, *Biochemistry*, 1999, **38**, 10594.

141. S. S. Mansy, Y. Xiong, C. Hemann, R. Hille, M. Sundaralingam, and J. A. Cowan, *Biochemistry*, 2002, **41**, 1195.

142. Y. S. Jung, C. A. Bonagura, G. J. Tilley, H. S. Gao-Sheridan, F. A. Armstrong, C. D. Stout, and B. K. Burgess, *J. Biol. Chem.*, 2000, **275**, 36974.

143. T. E. Messick, N. H. Chmiel, M.-P. Golinelli, M. R. Langer, L. Joshua–Tor, and S. S. David, *Biochemistry*, 2002, **41**, 3931.

144. P. Hänzelmann and H. Schindelin, *Proc. Natl. Acad. Sci. U.S.A.*, 2004, **101**, 12870.

145. E. Parisini, F. Capozzi, P. Lubini, V. Lamzin, C. Luchinat, and G. M. Sheldrick, *Acta Crystallogr., Sect. D*, 1999, **55**, 1773.

146. L. Liu, T. Nogi, M. Kobayashi, T. Nozawa, and T. Miki, *Acta Crystallogr., Sect. D*, 2002, **58**, 1085.

147. Z. Dauter, K. S. Wilson, L. C. Sieker, J. Meyer, and J.-M. Moulis, *Biochemistry*, 1997, **36**, 16065.

148. K. Fukuyama, T. Okada, Y. Kakuta, and Y. Takahashi, *J. Mol. Biol.*, 2002, **315**, 1155.

149. R. A. Torres, T. Lovell, L. Noodleman, and D. A. Case, *J. Am. Chem. Soc.*, 2003, **125**, 1923.

150. G. D. Watt and K. R. N. Reddy, *J. Inorg. Biochem.*, 1994, **53**, 281.

151. H. C. Angove, S. J. Yoo, B. K. Burgess, and E. Münck, *J. Am. Chem. Soc.*, 1997, **119**, 8730.

152. P. Strop, P. M. Takahara, H.-J. Chiu, H. C. Angove, B. K. Burgess, and D. C. Rees, *Biochemistry*, 2001, **40**, 651.

153. M. Guo, F. Sulc, M. W. Ribbe, P. J. Farmer, and B. K. Burgess, *J. Am. Chem. Soc.*, 2002, **124**, 12100.

154. R. S. Czernuszewicz, K. A. Macor, M. K. Johnson, A. Gewirth, and T. G. Spiro, *J. Am. Chem. Soc.*, 1987, **109**, 7178.

155. J. A. Fee, J. M. Castagnetto, D. A. Case, L. Noodleman, C. D. Stout, and R. A. Torres, *J. Biol. Inorg. Chem.*, 2003, **8**, 519.

156. K. B. Musgrave, H. C. Angove, B. K. Burgess, B. Hedman, and K. O. Hodgson, *J. Am. Chem. Soc.*, 1998, **120**, 5325.

157. L. Noodleman, D. A. Case, and J.-M. Mouesca, *J. Biol. Inorg. Chem.*, 1996, **1**, 177.

158. M. I. Belinsky, I. Bertini, O. Galas, and C. Luchinat, *Inorg. Chim. Acta*, 1996, **243**, 91.

159. R. E. Duderstadt, P. S. Brereton, M. W. W. Adams, and M. K. Johnson, *FEBS Lett.*, 1999, **454**, 21.

160. B. P. Koehler, S. Mukund, R. C. Conover, I. K. Dhawan, R. Roy, M. W. W. Adams, and M. K. Johnson, *J. Am. Chem. Soc.*, 1996, **118**, 12391.

161. A. F. Arendsen, J. Hadden, G. Card, A. S. McAlpine, S. Bailey, V. Zaitsev, E. H. M. Duke, P. F. Lindley, M. Kröckel, A. X. Trautwein, M. C. Feiters, J. M. Charnock, C. D. Garner, S. J. Marritt, A. J. Thomson, I. M. Kooter, M. K. Johnson, W. A. M. van den Berg, W. M. A. M. van Dongen, and W. R. Hagen, *J. Biol. Inorg. Chem.*, 1998, **3**, 81.

162. M. J. Carney, G. C. Papaefthymiou, M. A. Whitener, K. Spartalian, R. B. Frankel, and R. H. Holm, *Inorg. Chem.*, 1988, **27**, 346.

163. S. J. Yoo, H. C. Angove, B. K. Burgess, M. P. Hendrich, and E. Münck, *J. Am. Chem. Soc.*, 1999, **121**, 2534.

164. M. M. Georgiadis, H. Komiya, P. Chakrabarti, D. Woo, J. J. Kornuc, and D. C. Rees, *Science*, 1992, **257**, 1653.

165. I. R. Vassiliev, M. L. Antonkine, and J. H. Golbeck, *Biochim. Biophys. Acta*, 2001, **1507**, 139.

166. P. Jordan, P. Fromme, H. T. Witt, O. Klukas, W. Saenger, and N. Krauss, *Nature*, 2001, **411**, 909.

167. A. Manodori, G. Cecchini, I. Schröder, R. P. Gunsalus, M. T. Werth, and M. K. Johnson, *Biochemistry*, 1992, **31**, 2703.

168. M. Rousset, Y. Montet, B. Guigliarelli, N. Forget, M. Asso, P. Bertrand, J. C. Fontecilla-Camps, and E. C. Hatchikian, *Proc. Natl. Acad. Sci. U.S.A.*, 1998, **95**, 11625.

169. R. A. Rothery and J. H. Weiner, *Biochemistry*, 1991, **30**, 8296.

170. R. Bingemann and A. Klein, *Eur. J. Biochem.*, 2000, **267**, 6612.

171. K. Jones, C. M. Gomes, H. Huber, M. Teixeira, and P. Wittung-Stafshede, *J. Biol. Inorg. Chem.*, 2002, **7**, 357.

172. S. Griffin, C. L. Higgins, T. Soulimane, and P. Wittung-Stafshede, *Eur. J. Biochem.*, 2003, **270**, 4736.

173. C. L. Higgins and P. Wittung-Stafshede, *Arch. Biochem. Biophys.*, 2004, **427**, 154.

174. M. M. Cosper, B. Krebs, H. Hernandez, G. Jameson, M. K. Eidsness, B. H. Huynh, and M. K. Johnson, *Biochemistry*, 2004, **43**, 2007.

175. J. Crack, J. Green, and A. J. Thomson, *J. Biol. Chem.*, 2004, **279**, 9278.

176. G. L. Anderson and J. B. Howard, *Biochemistry*, 1984, **23**, 2118.

177. S. Sen, R. Igarashi, A. D. Smith, M. K. Johnson, L. C. Seefeldt, and J. W. Peters, *Biochemistry*, 2004, **43**, 1787.

178. J. N. Agar, B. Krebs, J. Frazzon, B. H. Huynh, D. R. Dean, and M. K. Johnson, *Biochemistry*, 2000, **39**, 7856.

179. M. C. Kennedy, W. E. Antholine, and H. Beinert, *J. Biol. Chem.*, 1997, **272**, 20340.

180. W. Yang, P. A. Rogers, and H. Ding, *J. Biol. Chem.*, 2002, **277**, 12868.

181. C. C. Page, C. C. Moser, X. Chen, and P. L. Dutton, *Nature*, 1999, **402**, 47.

182. H. Schindelin, C. Kisker, J. L. Schlessman, J. B. Howard, and D. C. Rees, *Nature*, 1997, **387**, 370.

183. H. Möbitz, T. Friedrich, and M. Boll, *Biochemistry*, 2004, **43**, 1376.

184. E. D. Coulter and D. M. Kurtz Jr, *Arch. Biochem. Biophys.*, 2001, **394**, 76.

185. M. Jormakka, S. Törnroth, B. Byrne, and S. Iwata, *Science*, 2002, **295**, 1863.

186. T. Yagi and A. Matsuno-Yagi, *Biochemistry*, 2003, **42**, 2266.

187. T. Friedrich and B. Böttcher, *Biochim. Biophys. Acta*, 2004, **1608**, 1.

188. M. Chevallet, A. Dupuis, J.-P. Issartel, J. Lunardi, R. van Belzen, and S. P. J. Albracht, *Biochim. Biophys. Acta*, 2003, **1557**, 51.

189. S. P. J. Albracht and R. Hedderich, *FEBS Lett.*, 2000, **485**, 1.

190. J. Hirst, *Proc. Natl. Acad. Sci. U.S.A.*, 2003, **100**, 773.

191. T. M. Iverson, C. Luna-Chavez, G. Cecchini, and D. C. Rees, *Science*, 1999, **284**, 1961.

192. C. R. D. Lancaster, A. Kröger, M. Auer, and H. Michel, *Nature*, 1999, **402**, 377.

193. J.-J. P. Kim, J. Zhang, and F. E. Frerman, Three-Dimensional Structure of Pocine Electron Transfer Flavoprotein-Ubiquinone Oxidoreductase, in ‘Flavins and Flavoproteins 2002’, eds. S. K. Chapman, R. N. Perham, and N. S. Scrutton, Rudolf Weber, Berlin, 2002, p. 77.

194. M. Šimkovic and F. E. Frerman, *Biochem. J.*, 2004, **378**, 633.

195. Z. Zhang, L. Huang, V. M. Shulmeister, Y.-I. Chi, K. K. Kim, L.-W. Hung, A. R. Crofts, E. A. Berry, and S.-H. Kim, *Nature*, 1998, **392**, 677.

196. S. Iwata, J. W. Lee, K. Okada, J. K. Lee, M. Iwata, B. Rasmussen, T. A. Link, S. Ramaswamy, and B. M. Jap, *Science*, 1998, **281**, 64.

197. C. Hunte, J. Koepke, C. Lange, T. Rossmanith, and H. Michel, *Structure*, 2000, **8**, 669.

198. E. A. Berry, M. Guergova-Kuras, L.-S. Huang, and A. R. Crofts, *Annu. Rev. Biochem.*, 2000, **69**, 1005.

199. C. Hunte, H. Palsdottir, and B. L. Trumpower, *FEBS Lett.*, 2003, **545**, 39.

200. P. Mitchell, *J. Theor. Biol.*, 1976, **62**, 327.

201. Y. Zu, M. M. J. Couture, D. R. J. Kolling, A. R. Crofts, L. D. Eltis, J. A. Fee, and J. Hirst, *Biochemistry*, 2003, **42**, 12400.

202. W. A. Cramer, H. Zhang, J. Yan, G. Kurisu, and J. L. Smith, *Biochemistry*, 2004, **43**, 5921.

203. A. Karlsson, J. V. Parales, R. E. Parales, D. T. Gibson, H. Eklund, and S. Ramaswamy, *Science*, 2003, **299**, 1039.

204. H. Dobbek, L. Gremer, R. Kiefersauer, R. Huber, and O. Meyer, *Proc. Natl. Acad. Sci. U.S.A.*, 2002, **99**, 15971.

205. J. M. Dias, M. E. Than, A. Humm, R. Huber, G. P. Bourenkov, H. D. Bartunik, S. Bursakov, J. Calvete, J. Caldeira, C. Carneiro, I. Moura, J. J. G. Moura, and M. J. Romao, *Structure Fold. Des.*, 1999, **7**, 65.

206. M. K. Chan, S. Mukund, A. Kletzin, M. W. W. Adams, and D. C. Rees, *Science*, 1995, **267**, 1463.

207. Y. Hu, S. Faham, R. Roy, M. W. W. Adams, and D. C. Rees, *J. Mol. Biol.*, 1999, **286**, 899.

208. J. C. Boyington, V. N. Gladyshev, S. V. Khangulov, T. Stadtman, and P. D. Sun, *Science*, 1997, **275**, 1305.

209. H. Raaijmakers, S. Macieira, J. M. Dias, S. Teixeira, S. Bursakov, R. Huber, J. J. G. Moura, I. Moura, and M. J. Romão, *Structure*, 2002, **10**, 1261.

210. A. Messerschmidt, H. Niessen, D. Abt, O. Einsle, B. Schink, and P. M. H. Kroneck, *Proc. Natl. Acad. Sci. U.S.A.*, 2004, **101**, 11571.

211. S. Menon and S. W. Ragsdale, *J. Biol. Chem.*, 1999, **274**, 11513.

212. R. H. H. van den Heuvel, B. Curti, M. A. Vanoni, and A. Mattevi, *Cell. Mol. Life Sci.*, 2004, **61**, 669.

213. L. W. Lim, N. Shamala, F. S. Matthews, D. J. Steenkamp, R. Hamlin, and N. H. Xuong, *J. Biol. Chem.*, 1986, **261**, 15140.

214. P. A. Hubbard, X. Liang, H. Schulz, and J.-J. P. Kim, *J. Biol. Chem.*, 2003, **278**, 37553.

215. G. Fritz, A. Roth, A. Schiffer, T. Büchert, G. Bourenkov, H. D. Bartunik, H. Huber, K. O. Stetter, P. M. H. Kroneck, and U. Ermler, *Proc. Natl. Acad. Sci. U.S.A.*, 2002, **99**, 1836.

216. P. Rowland, S. Nørager, K. F. Jensen, and S. Larsen, *Structure*, 2000, **8**, 1227.

217. E. Dorner and M. Boll, *J. Bacteriol.*, 2002, **184**, 3975.

218. S. W. Ragsdale, *Chem. Rev.*, 2003, **103**, 2333.

219. Y. Nicolet, B. J. Lemon, J. C. Fontecilla-Camps, and J. W. Peters, *Trends Biochem. Sci.*, 2000, **25**, 138.

220. D. C. Rees and J. B. Howard, *Curr. Opin. Chem. Biol.*, 2000, **4**, 260.

221. L. C. Seefeldt and D. R. Dean, *Acc. Chem. Res.*, 1997, **30**, 260.

222. H. C. Angove, S. J. Yoo, E. Münck, and B. K. Burgess, *J. Biol. Chem.*, 1998, **273**, 26330.

223. W. N. Lanzilotta and L. C. Seefeldt, *Biochemistry*, 1997, **35**, 16770.

224. P. K. Mascharak, *Coord. Chem. Rev.*, 2002, **225**, 201.

225. D. H. Flint and M. H. Emptage, *J. Biol. Chem.*, 1988, **263**, 3558.

226. J. P. Emerson, E. D. Coulter, D. E. Cabelli, R. S. Phillips, and D. M. Kurtz Jr, *Biochemistry*, 2002, **41**, 4348.

227. M. Lombard, C. Houée-Levin, D. Touati, M. Fontecave, and V. Nivière, *Biochemistry*, 2001, **40**, 5032.

228. C. Mathé, T. A. Mattioli, O. Horner, M. Lombard, J. M. Latour, M. Fontecave, and V. Nivière, *J. Am. Chem. Soc.*, 2002, **124**, 4966.

229. O. Horner, J.-M. Mouesca, J.-L. Oddou, C. Jeandey, V. Nivière, T. A. Mattioli, C. Mathé, M. Fontecave, P. Maldivi, P. Bonville, J. A. Halfen, and J.-M. Latour, *Biochemistry*, 2004, **43**, 8815.

230. M. W. W. Adams, F. E. Jenney Jr, M. D. Clay, and M. K. Johnson, *J. Biol. Inorg. Chem.*, 2002, **7**, 647.

231. P. A. Frey, *Annu. Rev. Biochem.*, 2001, **70**, 121.

232. E. N. G. Marsh, A. Patwardhan, and M. S. Huhta, *Bioorg. Chem.*, 2004, **32**, 326.

233. G. Layer, D. W. Heinz, D. Jahn, and W.-D. Schubert, *Curr. Opin. Chem. Biol.*, 2004, **8**, 468.

234. R. M. Cicchillo, K.-H. Lee, C. Baleanu-Gogonea, N. M. Nesbitt, C. Krebs, and S. J. Booker, *Biochemistry*, 2004, **43**, 11770.

235. P. Hänzelmann, H. Hernández, C. Menzel, R. García-Serres, B. H. Huynh, M. K. Johnson, R. R. Mendel, and H. Schindelin, *J. Biol. Chem.*, 2004, **279**, 34721.

236. R. Cammack, M. Frey, and R. L. Robson, 'Hydrogen as a Fuel: Learning from Nature', Taylor & Francis, London and NewYork, 2001.

237. D. J. Evan and C. J. Pickett, *Chem. Soc. Rev.*, 2003, **32**, 268.

238. F. A. Armstrong, *Curr. Opin. Chem. Biol.*, 2004, **8**, 133.

239. A. Volbeda and J. C. Fontecilla-Camps, *Dalton Trans.*, 2003, 4030.

240. M. Y. Darensbourg, E. J. Lyon, X. Zhao, and I. P. Georgakaki, *Proc. Natl. Acad. Sci. U.S.A.*, 2003, **100**, 3683.

241. Z.-P. Liu and P. Hu, *J. Am. Chem. Soc.*, 2002, **124**, 5175.

242. T. Zhou, Y. Mo, A. Liu, Z. Zhou, and K. R. Tsai, *Inorg. Chem.*, 2004, **43**, 923.

243. B. R. Crane and E. D. Getzoff, *Curr. Opin. Chem. Biol.*, 1996, **6**, 744.

244. M. Nakayama, T. Akashi, and T. Hase, *J. Inorg. Biochem.*, 2000, **82**, 27.

245. B. R. Crane, L. M. Siegel, and E. D. Getzoff, *Biochemistry*, 1997, **36**, 12101.

246. B. K. Burgess and D. J. Lowe, *Chem. Rev.*, 1996, **96**, 2983.

247. T. Lovell, T. Liu, D. A. Case, and L. Noodleman, *J. Am. Chem. Soc.*, 2003, **125**, 8377.

248. J. Kim and D. C. Rees, *Nature*, 1992, **360**, 553.

249. H.-I. Lee, P. M. C. Benton, M. Laryukhin, R. Y. Igarashi, D. R. Dean, L. C. Seefeldt, and B. M. Hoffman, *J. Am. Chem. Soc.*, 2003, **125**, 5604.

250. R. R. Eady, *Coord. Chem. Rev.*, 2003, **237**, 23.

251. L. C. Seefeldt, I. G. Dance, and D. R. Dean, *Biochemistry*, 2004, **43**, 1401.

252. B. M. Barney, R. Y. Igarashi, P. C. Dos Santos, D. R. Dean, and L. C. Seefeldt, *J. Biol. Chem.*, 2004, **279**, 53621.

253. H.-I. Lee, R. Y. Igarashi, M. Laryukhin, P. E. Doan, P. C. Dos Santos, D. R. Dean, L. C. Seefeldt, and B. M. Hoffman, *J. Am. Chem. Soc.*, 2004, **126**, 9563.

254. E. Krahn, B. J. R. Weiss, M. Kröckel, J. Groppe, G. Henkel, S. P. Cramer, A. X. Trautwein, K. Schneider, and A. Müller, *J. Biol. Inorg. Chem.*, 2004, **7**, 37.

255. C. L. Drennan, J. Heo, M. D. Sintchak, E. Schreiter, and P. W. Ludden, *Proc. Natl. Acad. Sci. U.S.A.*, 2001, **98**, 11973.

256. V. J. DeRose, J. Telser, M. E. Anderson, P. A. Lindahl, and B. M. Hoffman, *J. Am. Chem. Soc.*, 1998, **120**, 8767.

257. C. G. Riordan, *J. Biol. Inorg. Chem.*, 2004, **9**, 509.

258. C. L. Drennan, T. I. Doukov, and S. W. Ragsdale, *J. Biol. Inorg. Chem.*, 2004, **9**, 511.

259. P. A. Lindahl, *J. Biol. Inorg. Chem.*, 2004, **9**, 516.

260. A. Volbeda and J. C. Fontecilla-Camps, *J. Biol. Inorg. Chem.*, 2004, **9**, 525.

261. T. C. Brunold, *J. Biol. Inorg. Chem.*, 2004, **9**, 533.

262. C. G. Riordan, *J. Biol. Inorg. Chem.*, 2004, **9**, 542.

263. W. Fu, S. F. O'Handley, R. P. Cunningham, and M. K. Johnson, *J. Biol. Chem.*, 1992, **267**, 16135.

264. M.-P. Golinelli, N. H. Chmiel, and S. S. David, *Biochemistry*, 1999, **38**, 6997.

265. A.-L. Lu and P. M. Wright, *Biochemistry*, 2003, **42**, 3742.

266. C. D. Mol, A. S. Arvai, T. J. Begley, R. P. Cunningham, and J. A. Tainer, *J. Mol. Biol.*, 2002, **315**, 373.

267. J. A. Hinks, M. C. W. Evans, Y. de Miguel, A. A. Sartori, J. Jiricny, and L. H. Pearl, *J. Biol. Chem.*, 2002, **277**, 16936.

268. J. Hoseki, A. Okamoto, R. Masui, T. Shibata, Y. Inoue, S. Yokoyama, and S. Kuramitsu, *J. Mol. Biol.*, 2003, **333**, 515.

269. P. Gaudu and B. Weiss, *Proc. Natl. Acad. Sci. U.S.A.*, 1996, **93**, 10094.

270. H. Ding and B. Demple, *Proc. Natl. Acad. Sci. U.S.A.*, 1997, **94**, 8445.

271. H. Ding and B. Demple, *Proc. Natl. Acad. Sci. U.S.A.*, 2000, **97**, 5146.

272. M.-S. Koo, J.-H. Lee, S.-Y. Rah, W.-S. Yeo, J.-W. Lee, K.-L. Lee, Y.-S. Koh, S.-O. Kang, and J.-H. Roe, *EMBO J.*, 2003, **22**, 2614.

273. D. M. Bates, C. Popescu, N. Khoroshilova, K. Vogt, H. Beinert, E. Münck, and P. J. Kiley, *J. Biol. Chem.*, 2000, **275**, 6234.

274. V. R. Sutton, A. Stubna, T. Patschkowski, E. Münck, H. Beinert, and P. J. Kiley, *Biochemistry*, 2004, **43**, 791.

275. H. Cruz-Ramos, J. Crack, G. Wu, M. N. Hughes, C. Scott, A. J. Thomson, J. Green, and R. K. Poole, *EMBO J.*, 2002, **21**, 3235.

276. T. Wang, G. Shen, R. Balasubramanian, L. McIntosh, D. A. Bryant, and J. H. Golbeck, *J. Bacteriol.*, 2004, **186**, 956.

277. K. Pantopoulos, *Ann. N.Y. Acad. Sci.*, 2004, **1012**, 1.

278. C. R. Staples, E. Gaymard, A.-L. Stritt-Etter, J. Telser, B. M. Hoffman, P. Schürmann, D. B. Knaff, and M. K. Johnson, *Biochemistry*, 1998, **37**, 4612.

279. G. N. L. Jameson, E. M. Walters, W. Manieri, P. Schürmann, M. K. Johnson, and B. H. Huynh, *J. Am. Chem. Soc.*, 2003, **125**, 1146.

280. R. K. Thauer, *Microbiology*, 1998, **144**, 2377.

281. R. Hedderich, O. Klimmek, A. Kröger, R. Dirmeier, M. Keller, and K. O. Stetter, *FEMS Microbiol. Rev.*, 1998, **22**, 353.

282. E. C. Duin, C. Bauer, B. Jaun, and R. Hedderich, *FEBS Lett.*, 2003, **538**, 81.

283. A. Tersteegen and R. Hedderich, *Eur. J. Biochem.*, 1999, **264**, 930.

Acknowledgments

Research on iron–sulfur proteins in the Johnson laboratory is supported by grants from the National Institutes of Health (GM60329 and GM62524).

Iron Transport: Siderophores

Berthold F. Matzanke
University of Lübeck, Lübeck, Germany

1	Introduction	1
2	Structures of Siderophores	2
3	Coordination Geometry of Siderophores	6
4	Equilibrium Thermodynamics of Siderophore-iron Binding	11
5	Siderophore Transport in Microorganisms	15
6	Additional Functions of Siderophores	21
7	Related Articles	22
8	References	23

Abbreviations

AL = alcaligin; BC = bisucaberin; DHBS = dihydroxybenzoylserine; DMB = N,N-dimethyl-2,3-dihydroxybenzamide; Fe-ent = ferric enterobactin; LICAMS = N,N',N''-tris (2,3-dihydroxy-5-sulfobenzoyl)-1,5,10-triazadecane; MEC AM = N,N',N''-tris(2,3-dihydroxy-5-benzoyl)-1,3,5-tris (aminomethyl)benzene; MECAMS = N,N',N''-tris(2,3-dihydroxy-5-sulfobenzoyl)-1,3,5-tris(aminomethyl)benzene; men = N-methyl-l-menthoxyacet-hydroxamato; OMR = outer membrane receptor; RA = rhodotorulic acid; Sid = siderophore; TREN = tris(2-aminomethyl)amine; TRIMCAM = N,N',N''-tris(2,3-dihydroxy-5-benzoyl)-1,3,5-tricar-bamoylbenzene; TRIMCAMS = N,N',N''-tris(2,3-dihydroxy-5-sulfobenzoyl)-1,3,5-tricarbamoylbenzene.

1 INTRODUCTION

For all plants and animals, and for virtually all microbes, with the exception of some *Lactobacilli* and a *Borrelia* species,[1] life without iron is impossible. A multitude of essential enzymes bind iron in their active centers. Therefore, up to 10^5 Fe-ions are typically required in key metabolic processes of a single bacterial cell. Why iron has gained such an eminent role in the course of biological evolution remains open to speculation.[2] Though iron is the fourth most abundant element in the Earth's crust, it is present under aerobic conditions at nearly neutral pH in the form of extremely insoluble minerals like hematite, goethite, and pyrite, or as polymeric oxidehydrates, carbonates, and silicates, which severely restricts the bioavailability of this metal. In response to this, microorganisms secrete high-affinity iron-binding compounds called siderophores (from the Greek, 'iron carrier').[3–10] In any natural environment of microbial activity, siderophores are present. Significant amounts of siderophores can be extracted from soil and from fresh or salt water. Even some foods contain siderophores.[8] Biosynthesis of siderophores is executed on a cellular level by a set of enzymes specific for the respective siderophore. The corresponding genes are located on the chromosome or on a plasmid.[11] Expression of these genes is controlled by the amount of cellularly available iron (Section 5).[11–14] Therefore, microbial metabolic products (mainly secondary metabolites) can be classified as siderophores, if (1) they exhibit iron chelating capability, (2) they participate in active transport across the cell membrane(s), and (3) their biosynthesis is regulated by the intracellular iron level.

During the last decade we witnessed exceptional progress in the field of iron-transport research (*see also* ***Iron Proteins for Storage & Transport & their Synthetic Analogs***).[3–6] Almost 500 naturally occurring siderophores have been isolated and characterized (Section 2),[3,4] and the discovery of new siderophores is continuing at a good rate. The physical properties of siderophores yield important information on biological mechanisms involving siderophore-iron complexes. Fundamental data on solution thermodynamics (Section 4.1), electrochemistry (Section 4.3), and kinetic studies (Section 4.2) have been used in the search for likely intracellular iron-release mechanisms (Section 5). Moreover, sufficient thermodynamic and kinetic data facilitate an estimation of the advantages of certain siderophores over others in their competition for iron. Siderophore uptake in microorganisms is, in general, a receptor-dependent process (Section 5.1). A diversity of high-affinity receptors has evolved either to recover iron-loaded endogenous siderophores that have been excreted to scavenge iron from the environment, or to utilize xenosiderophores or iron-sequestering agents of a host. Crystal structures have been solved of a variety of siderophore receptors and of other components of the high-affinity, energy-dependent siderophore-transport systems as well (Section 5.1). Nevertheless, siderophores may exhibit both optical and geometrical isomers (Section 3). Synthesis of Cr^{3+} or Rh^{3+} siderophores enables isolation and characterization of these isomers (Section 3.3). Stereochemically well-characterized isomers are an indispensible prerequisite for studying the specificity of siderophore-mediated iron uptake in microorganisms (Section 5.2). A variety of cellular iron-release mechanisms from siderophores have been characterized, the majority of which involve reduction of ferric iron either on the membrane level or in the cytoplasm (Section 5.4). The molecular nature of the overall transport process is complex (Section 5.3) and strictly regulated (Section 5.5).

In vivo Mössbauer spectroscopic investigations on the time course of iron assimilation revealed that siderophores function as iron-storage compounds in various fungi (Section 6.1). Siderophores are also employed clinically for removal of iron and aluminum from the body (Section 6.2). Siderophores may serve as magnetic resonance imaging (MRI) agents and as templates for novel classes of antibiotics. Invading microorganisms exposed to circulating blood produce siderophores to compete for iron with the human transport protein transferrin (*see* ***Iron Proteins for Storage & Transport & their Synthetic Analogs***, ***Metalloregulation***), thus constituting one aspect of virulence and pathogenicity (Section 6.3).

2 STRUCTURES OF SIDEROPHORES

As with secondary metabolites, various and complex chemical structures are typical within the siderophores, preventing their unequivocal and universal classification. Since the biosyntheses and structural features of siderophores are diverse, a classification scheme will be to some extent arbitrary. Criteria may include the producing organisms (bacteria, fungi, plants), the nature of the backbone (peptidic or nonpeptidic, cyclic or open chain), or the nature of the chelating group. Despite the considerable structural variation found in the siderophores, their common feature is to form six-coordinate complexes with iron (III) of great thermodynamic stability. The ligating groups contain the oxygen atoms of hydroxamate, catecholate, α-hydroxy-carboxylic acids, and α-keto-carboxylic acids. In addition, siderophores with diverse Fe^{III} ion binding groups were isolated, like salicylic acid, oxazoline and thiazoline nitrogen, and even negatively charged nitrogen (in the case of maduraferrin). Comprehensive reviews on the structural variety of siderophores are available.[3,7–9,15] Therefore we shall focus on salient structural features of siderophores. NMR studies of most siderophores have been part of the general chemical and structural characterization. The metal is generally removed from the complex prior to NMR spectroscopy, because Fe^{III} causes severe line broadening of the NMR signals. To obtain spectra of the siderophore in the metal-chelated form, usually the diamagnetic Ga^{3+} or Al^{3+} siderophore analogs are employed.[15–18] ^{1}H and ^{13}C NMR data of a variety of hydroxamate-type siderophores have been tabulated.[19]

Investigations on the biosynthesis of siderophores represent a major activity in the field.[11] Considerable effort has been devoted to the chemical synthesis of natural siderophores, enantiomeric siderophores, and completely synthetic siderophore analogs. This topic will not be covered here and the reader is referred to the corresponding literature.[8,10,20–23]

2.1 Hydroxamate-type Siderophores

Hydroxamate group-bearing siderophores are mainly synthesized by fungi and Gram-positive filament-forming bacteria (streptomycetes). In fungal systems the hydroxamic acid chelating group is commonly derived from acylated N^{δ}-acyl-N^{δ}-hydroxy-L-ornithine.

The ferrichromes comprise one large family of hydroxamate siderophores (Figure 1(a)) and were isolated from low-iron cultures of many fungi.[24] With few exceptions, ferrichromes possess cyclic hexapeptide backbones in which one tripeptide is linked to a second tripeptide of N^{δ}-acyl-N^{δ}-hydroxy-L-ornithine. Linear derivatives of the latter tripeptide form backbones of various antibiotics, termed albomycines.

Crystal structures have been determined of several ferrichromes. Most of this work was performed by van der Helm and coworkers.[25,26] The crystal structures of the members of this siderophore family can be superposed and a root-mean-square deviation of the 49 atoms, which are common to all members, is obtained of approximately 0.30 Å. A comparison of the conformational angles around the cyclic hexapeptide ring shows differences of not more than 25°. This indicates that the structures and conformations are not the same but that they are similar with some conformational freedom. In all structures, the iron coordination site is on one side of the molecule, the coordination of the metal is Λ-*cis*, and the conformation of the amino acids is L. A β (II) bend and a β (I) bend of the cyclic peptide skeleton is found. In addition, extensive conformational analyses of siderophores in solution were performed by Llinas and coworkers employing ^{1}H and ^{13}C NMR.[9]

Building blocks composed of N^{δ}-hydroxyornithine acylated with *cis*-5-hydroxy-3-methyl-2-pentoic acid are found in fusarinens (fusigens) isolated from *Aspergillus, Penicillium*, and *Fusarium* species. These building blocks are esterified head-to-tail to build the various linear and cyclic fusarinines (Figure 1(b)). The crystal structure of N',N'',N'''-triacetylfusarinine C shows a disk-like shape with the metal being located in the center of the molecule.[27,28]

Ferrioxamines, typical constituents of culture broths of *Actinomycetes*, occur as both linear and cyclic compounds containing 1-amino-5-hydroxyaminopentane (N-hydroxycadaverine) and succinic acid as building blocks (Figure 1(c)). A cyclic trimer of succinyl-(N-hydroxycadaverine), is named ferrioxamine E. In some cases the pentane moiety is replaced by a butane carbon skeleton (putrescine). The most prominent representative of this siderophore family, desferrioxamine B (Figure 1), has become the drug of choice for the treatment of transfusional iron overload (Section 6.2).[29] The crystal structure of ferric ferrioxamine B has been published recently.[30] Certain derivatives of the ferrioxamines display antibiotic activity and therefore have been designated as ferrimycins.[31]

Coprogen is a linear trihydroxamate composed of three units of N^{δ}-acyl-N^{δ}-hydroxy-L-ornithine, the acyl groups of which are represented by anhydromevalonic acid

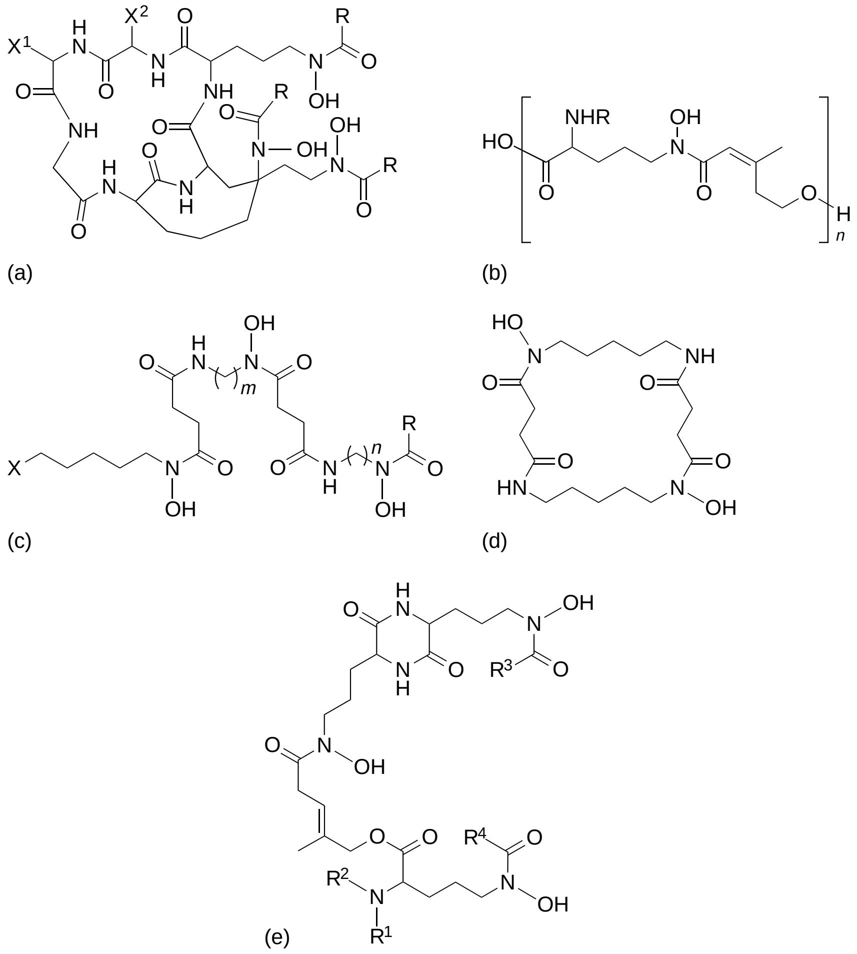

Figure 1 Structures of representative hydroxamate siderophores: (a) ferrichromes (R = Me, $X^1 = X^2 = H$, ferrichrome; R = Me, $X^1 = CH_2OH$, $X^2 = H$, ferricrocin); (b) fusarinines ($n = 1$, fusarinine; $n = 3$, R = acetyl, cyclic, triacetylfusarinine); (c) ferrioxamines ($X = NH_2$, $m = n = 5$, R = Me, ferrioxamine B; X = NH (cyclic), $m = n = 5$, $R = (CH_2)_2CO$-[X], ferrioxamine E); (d) bisucaberin; (e) coprogens ($R^1 = H$, $R^2 = COMe$, $R^3 = R^4$ = isopentenol, coprogen; $R^1 = H$, $R^2 = COMe$, $R^3 = R^4 = Me$, neocoprogen II)

(Figure 1(e)).[19] Two of these building blocks are cyclized to form a diketopiperazine ring. This unit, named dimerum acid, is typical of all coprogens. Coprogens are produced by *Penicillium* species, *Neurospora crassa*, *Curvularia subulata*, *Alternaria longipes*, *Epicoccum purpurascens*, and *Fusarium dimerum*.[19] The crystal structure of one member of this family has been determined, namely of neocoprogen I.[32] Like in ferrichromes, the metal coordination site is not located in the center of the molecule and not sheltered by the carbon skeleton. The metal appears to be rather accessible. Typical tetradentate representatives of the hydroxamate-siderophore family include rhodotorulic acid,[32] dimerum acid,[19] bisucaberin,[33] alcaligin[34] and putrebactin.[35] Bisucaberin (Figure 1(d)), a cyclic dimer of succinyl-(*N*-hydroxycadaverine), which sensitizes tumor cells to macrophage-mediated cytolysis, was isolated from the supernatant of cultures of the marine bacterium *Alteromonas haloplanktis*.[33] Putrebactin is a cyclic dimer of succinyl-(N-hydroxyputrescine) whereas rhodotorulic acid is a linear tetradentate chelator assembled of two N^δ-(res)-N^δ-hydroxyornithine units which are cyclized to form a diketopiperazine ring.[32] The crystal structure of the Fe-alcaligin complex disclosed a monobridged topology and a Fe_2L_3 stoichiometry at near neutral pH.[36]

2.2 Siderophores with Catecholate Ligands

Under conditions of iron deficiency, many bacteria excrete siderophores exhibiting phenolate or 2,3-dihydroxybenzoate (DHB) iron-binding groups. In 1970, enterobactin (also known as enterochelin), the first tricatechol siderophore, was isolated from culture fluids of *Escherichia coli*, *Aerobacter aerogenes*, and *Salmonella typhimurium* (Figure 2(a)).[37] Enterobactin is the cyclic triester of DHBS (2,3-dihydroxybenzoylserine) exhibiting extraordinary features: (1) an extremely high complex formation constant; (2) a redox potential too low

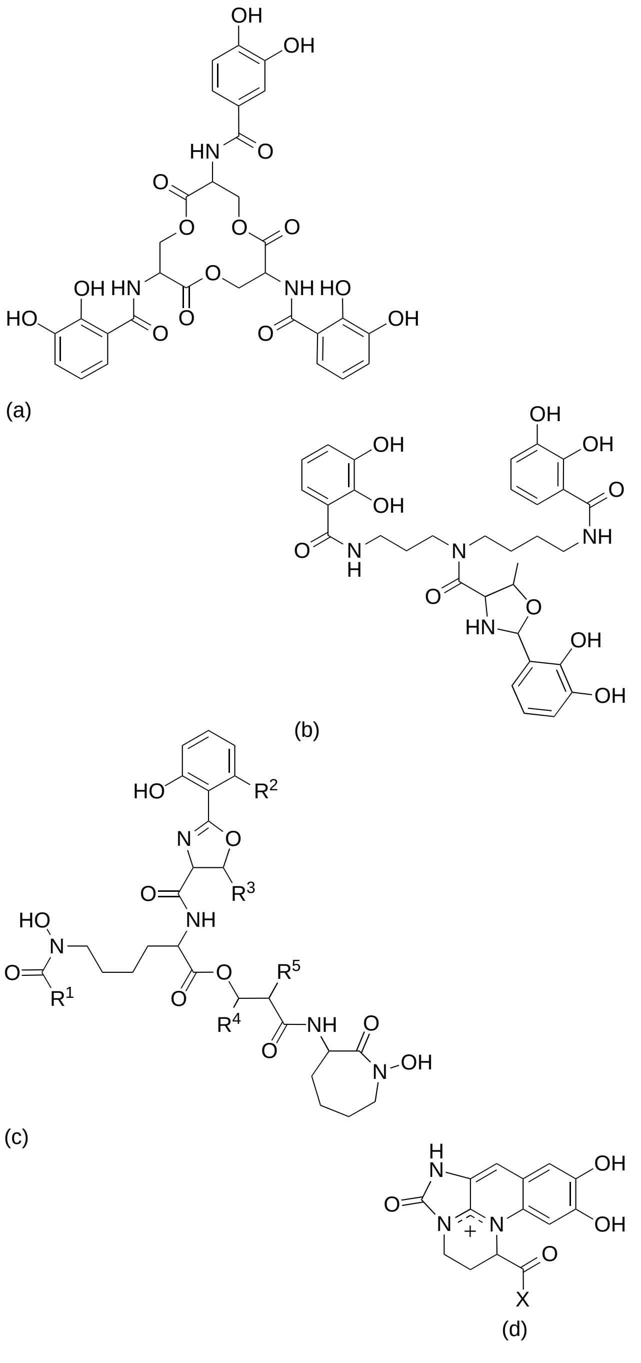

Figure 2 Structures of representative catecholate and mixed-ligand siderophores: (a) enterobactin; (b) parabactin; (c) mycobacins (R^1 = various alkyl chains, $R^2 = R^3 = R^5$ = Me or H, R^4 = alkyl chains or H;[3]) (d) fluorescent chromophore of pseudobactins and pyoverdins

for physiological reductants; (3) a strong pH-dependence of (1) and (2); and (4) a trilactone backbone, the cleavage of which lowers the redox potential. Due to these exceptional properties relevant to its physiological reactions, enterobactin is one of the most intensively analyzed siderophores. Recently, enterobactin was also isolated from Gram-positive bacteria[38] as well as the enterobactin homolog corynebactin from *Corynebacterium glutamicum* and *Bacillus subtilis*[39,40] Corynebactin incorporates threonine trilactone and glycine spacers, which elongate the three chelating arms as compared with enterobactin. All other known tris-catecholate siderophores exhibit a linear backbone based on spermidine or norspermidine. Parabactin, N^4-(2,3-dihydroxybenzene-3-methyloxazoline-2-carboxamidyl)-N^1, N^8-bis(2,3-dihydroxybenzoyl) spermidine, is produced by *Paracoccus denitrificans* (Figure 2(b)). Exposure to acid destroys the oxazoline ring, producing a threonyl moiety.[41] Other members of the linear tris-bidentate catecholate-type siderophores include Vibriobactin,[7] Vulnibactin,[7] Fluvibactin,[7] Protochelin,[7] and Salmochelin-2.[42] Salmochelin is unique, because the backbone of the DHBS-chelating units is made up by glucose. Azotochelin, Myxochelin, Serratiochelin, and Amonabactin belong to the bis-bidentate catecholates, whereas aminochelin, chrysobactin, and DHBS form the mono-bidentate group of catecholate siderophores.[3,7]

2.3 Carboxylate-type Siderophores

A great variety of siderophores exhibit carboxylate and hydroxy donor groups. Many of these siderophores belong to the mixed-ligand group (see next section). In the nineties of the last century, however, a completely novel class of siderophores was detected whose members neither possess hydroxamate nor phenolate ligands. Rather, Fe^{III} binding is achieved exclusively by α-hydroxycarboxylates and carboxylates. The late discovery of these compounds is mainly based on the fact that they are colorless, therefore requiring novel methods for screening and isolation (chromazurole test and iron nutrition bioassays).[43] These siderophores are found in the kingdom of bacteria as well as in the realm of fungi. A very hydrophilic complex, termed staphyloferrin A, was isolated from *Staphylococcus hyicus* (Figure 3(b)).[44] The molecule is composed of two moles of citrate linked by ornithine. Besides Staphyloferrin A,[44] also staphyloferrin B,[45] vibrioferrin,[46] and rhizoferrin[47] contain citric acid building blocks. Rhizoferrin has been isolated from culture filtrates of *Rhizopus* and other members of the class of Zygomycetes (Figure 3(c)).[47] In this compound, two citric acid residues are linked to diaminobutane, resulting in N^1, N^4-bis(1-oxo-3-hydroxy-3,4-dicarboxybutyl)diaminobutane. Although citrate is an intracellular primary metabolite, it may be regarded – from an evolutionary view – as the simplest siderophore from which the above-mentioned siderophores, as well as the mixed-ligand compounds schizokinen, arthrobactin, and aerobactin (Section 2.4), have evolved. Under acidic conditions, rhizoferrin undergoes dehydration and cyclization to imidorhizoferrin and bisimidorhizoferrin. Moreover, this type of siderophore might be photolabile, given that light-mediated decarboxylation reactions of α-hydroxy carboxylic acids complexed to transition metals are well known. In fact,

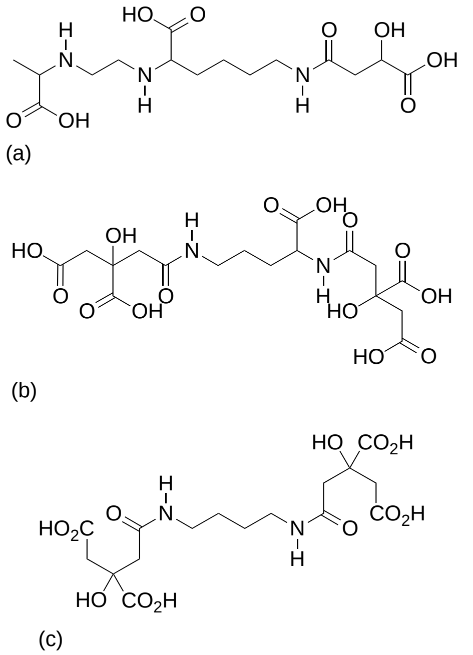

Figure 3 Structures of carboxylate siderophores: (a) rhizobactin; (b) staphyloferrin; (c) rhizoferrin

photolability was demonstrated in a novel siderophore, named petrobactin from *Marinobacter hydrocarbonoclasticus*. The ferric complex of petrobactin undergoes a ligand-to-metal charge-transfer reaction resulting in decarboxylation and oxidation of the citryl moiety forming 3-ketoglutarate.[48]

Rhizobium meliloti, capable of fixing atmospheric nitrogen when symbiotically associated with certain legumes, excretes and utilizes rhizobactin DM4 (Figure 3(a)), N^2-[2-{(1-carboxymethyl)amino}ethyl]-N^6-(3-carboxy-3-hydroxy-1-oxopropyl)lysine. Iron binding is achieved via ethylenediaminedicarboxyl- and α-hydroxycarboxyl-ligands.[49] Phytosiderophores, detected in root washings of gramineous plants, represent a separate subclass of the carboxylate-type of siderophores. For example, the phytosiderophores nicotianamin, mugineic, avenic and distichonic acid are produced and utilized by cereals, like barley, wheat, rye, oat, and so on.[3]

2.4 Siderophores with mixed ligands and heterocyclic chelating groups

Fifty-six years ago the very first siderophore, mycobactin, was isolated by the crystallization of the aluminum complex.[50] Mycobactins from Gram-positive *Mycobacteria* and the closely related nocobactins from *Nocardia* embody a series of lipid-soluble siderophores located in the lipid-rich boundary layers of these bacteria (Figure 2(c)).[51] The X-ray structure revealed that iron binding in mycobactins is accomplished by two hydroxamates, a phenolate group, and oxazoline nitrogen.

It is generally assumed that in oxazoline- and thiazoline-containing donor-deficient siderophores, the imine-N will participate in ferric ion complexation. These heterocycles result physiologically from an enzymatic cyclization of cysteinyl, seryl, or threonyl side chains. The imine-type of Fe-coordination is a common feature of the siderophores pyochelin, yersiniabactin, anguibactin, and acinetobactin (Figure 4).[3,7] In the case of anguibactin (ab), the crystal structure of the Ga-complex, $[Ga(ab)_2(CH_3O)_2]$, established the imine nitrogens as part of the iron coordination.[52] Another heterocyclic binding group, β-hydroxyhistidine, participates in Fe^{3+} complex formation of exochelin MN from *Mycobacterium neoaurum*.[53]

A variety of fluorescent chromopeptide siderophores, termed pseudobactins and pyoverdins, are synthesized by *Pseudomonas* species.[54] The chromophores, derived from 2,3-diamino-6,7-dihydroxyquinoline (Figure 2(d)), are linked to a peptide chain exhibiting either two hydroxamate groups or one hydroxamate and one α-hydroxycarboxylate group.

Another major group within the mixed-ligand siderophores combines carboxylate and hydroxamate ligands. Representatives are, for example, the ornibactins.[55] In one subgroup, citric acid constitutes the central building block. Members of this group include schizokinen, rhizobactin 1021, acinetoferrin, arthrobactin, aerobactin and nannochelins.[7]

Recently, a suite of amphiphilic peptide siderophores, named amphibactins, containing a unique peptidic headgroup that coordinates Fe^{3+} and one of a series of fatty acid appendices, was discovered.[56] The compounds were isolated from *Halomonas aquamarina* (aquachelins), and *Marinobacter* sp. (marinobactins) and characterized.[57] Iron

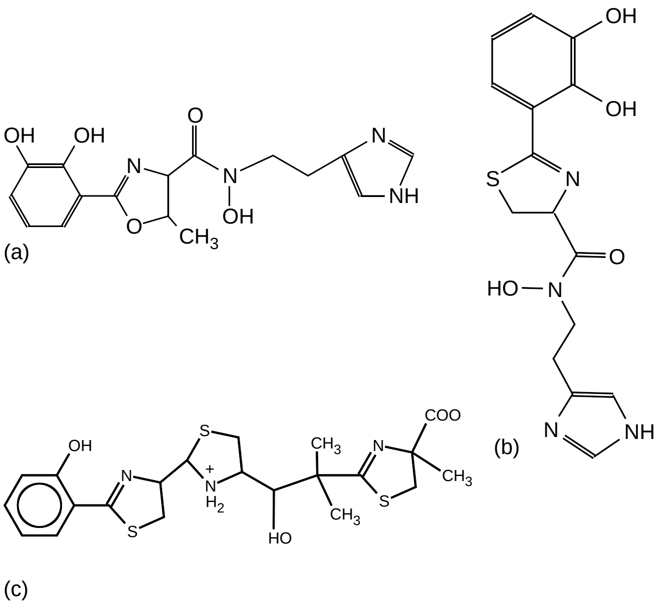

Figure 4 Structures of siderophores with heterocyclic ligands: (a) acinetobactin, (b) anguibactin, and (c) yersiniabactin

binding occurs via hydroxamates and β-hydroxy-aspartate residues.[57] Finally, in another group, ferric ion is encapsulated employing hydroxamate and catecholate/phenolate ligands, observed in a recently characterized antibiotic from *Nocardia asteroides*, named asterobactin, and in the heterobactins from *Rhodococcus erythropolis*.[58,59]

3 COORDINATION GEOMETRY OF SIDEROPHORES

The stereochemistry of siderophores is a very important aspect of their role in mediated iron uptake, since it has been shown that very subtle discrimination by microbial iron transport systems takes place between siderophore isomers. In fact, uptake of siderophores by microorganisms shows – at least in part – stereospecific preferences (Section 5.2).

3.1 Geometrical and Optical Isomers

Upon metal chelation, a tris complex with a bidentate ligand forms a more or less distorted coordination octahedron via three five-membered chelate rings. According to IUPAC rules,[60] the planes of these five-membered rings may form a right-handed (Δ) propellor or a left-handed (Λ) propellor (Figure 5). If the ligand is not optically active, one will find a racemic mixture of Δ and Λ optical isomers. If the ligand is chiral (e.g. D), two complexes are again possible, DΛ and DΔ. However, they are not formed in equal amounts because they have different standard free energies of formation. Exclusively, one optical isomer may be formed if there is a large thermodynamic advantage for this isomer (as, for instance, in the case of ferrichromes where LΛ is exclusively observed).

Many siderophores are hexadentate ligands with three asymmetrical bidentate functional units attached to an asymmetrical backbone. These complexes reveal a rather complicated stereochemistry. The bidentates are not equivalent and there will be $2^3 = 8$ cis and trans isomers. Each can have a Λ and Δ metal environment and when the siderophore is made from chiral residues there are 16 diastereomers, none of which is enantiomeric to one another. A selection of such diastereomers is shown in Figure 5. Nomenclature for the geometrical isomers of hydroxamate tris-bidentates was outlined by Leong and Raymond.[10,61] No general rule can be applied for an absolute assignment of the chelate ring sequence. However, if the structure exhibits a unique functional group, this group can be utilized to define the chelate ring sequence. In the case of ferrioxamine B or D1, the unique functional group is the N-terminus. (1) In the case of the coprogens, this group is a diketopiperazine ring placed between rings 1 and 2. (2) Looking down the $C3$ axis the sequence of the chelate rings 1, 2, and 3 corresponds to the rotation direction, that is, clockwise for Λ-isomers and counterclockwise for Δ-isomers. (3) If the ring 1 has the carbon atom of the hydroxamate group below the nitrogen, it is denoted 'C'; if the reverse is true, it is called 'N'. (4) For rings 2 and 3, each is called *cis* or *trans* depending upon whether it has the same or opposite relative orientation with respect to the coordination axis as does ring 1.

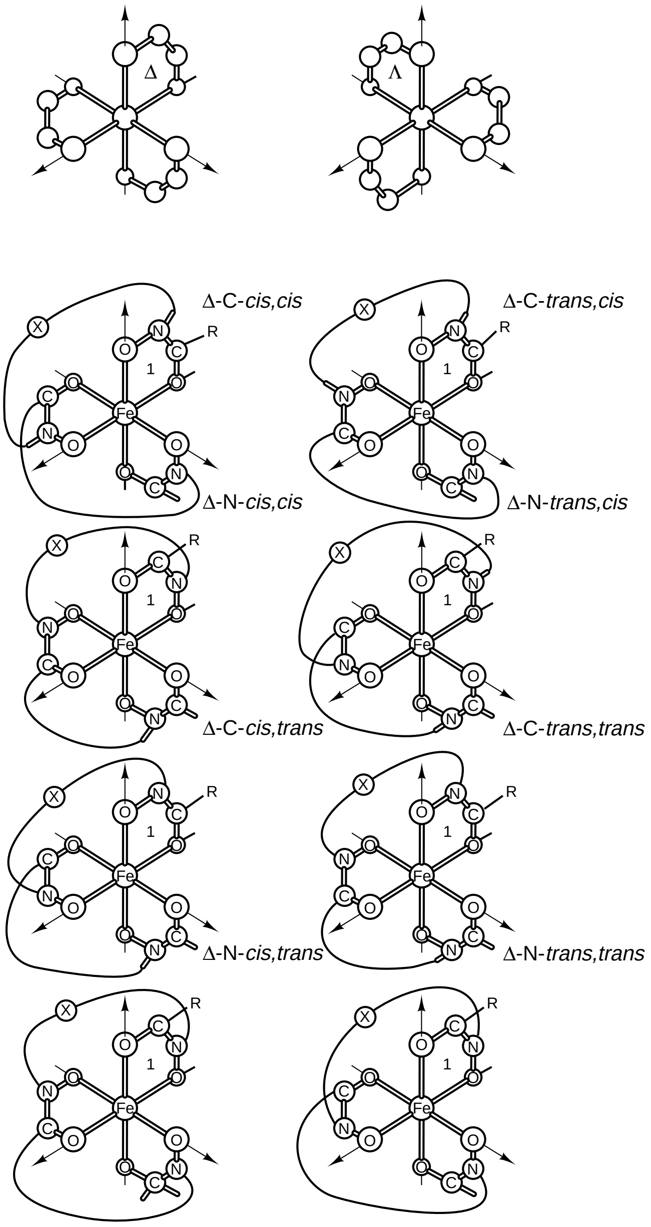

Figure 5 Λ and Δ optical configuration at the metal center (top) and eight geometrical isomers of a Fe^{III} Δ-trichelate complex, involving three unsymmetrical bidentate ligands attached to an asymmetric backbone. Not shown is the set of eight Λ diastereomers. R, X correspond to unique functional groups, for example, amino terminus of ferrioxamine B (R) or diketopiperazine ring of coprogen (X)[25]

The X-ray crystallographic analysis of all ferrichrome siderophores yielded Λ-C-*cis,cis* configurations of the coordination octahedron.[62] Neocoprogen I adopts a Δ-C-*trans,trans* configuration in the crystal structure.[61] N,N',N''-Triacetylfusarinine crystallizes as either the Δ or Λ isomer, depending on the solvent system used.[63] Achiral siderophores such as ferrioxamine E and ferrioxamine D_1 crystallize as racemic mixtures of Δ and Λ isomers.[64,65] Similarly, the crystal structure of Ferrioxamine B displays a racemic mixture of Λ-N-*cis, cis* and Δ-N-*cis,cis*,[30] although various geometrical isomers of the inert Cr-complex are present in solution (see Section 3.3).

A multitude of siderophores achieve iron chelation via catecholates. Unlike hydroxamate, catecholate is a symmetric, bidentate ligand. Thus, there are no geometrical isomers of simple tris(catecholate) metal complexes. The chirality at the metal center of (bis(catecholato)-siderophores) was determined in amonobactins, where a slight Δ preference in Fe_2L_3 stoichiometry was observed whereas the corresponding $FeL(H_2O)_2$−complexes in the low-pH region are achiral.[66] Enterobactin displays a Δ-*cis* configuration, dictated by the asymmetric centers (L) of the trilactone ring.[67] Synthetic enterobactin analogs composed of tris(2-aminomethyl)amine (TREN) as anchors and amino acids linking the anchor to catechol units also form Fe^{3+} complexes of preferential Δ-*cis* configuration when L-amino acids are used. These complexes are stabilized by intramolecular H-bonds from the catechoylamides CONH to the catecholate oxygens, as in enterobactin. When the possibility of this type of H-bond is eliminated by replacing the amide proton CONH by an amide N-methyl (CONMe), the chiral preference of the complex is inverted from the Δ-*cis* to the Λ-*cis* configuration.[68] Surprisingly, the recently detected trilactone siderophore corynebactin forms a Λ-ferric complex. The addition of a glycine spacer and the methylation of the trilactone ring as compared with enterobactin are sufficient to favor the opposite chirality.[69,70]

3.2 UV/vis and CD Spectra of Ferric Siderophores

The d^5 electronic configuration of Fe^{3+} rules out any crystal field stabilization energy (CFSE) and makes the complexes relatively labile with respect to isomerization and ligand exchange in aqueous solution. Furthermore, high-spin Fe^{3+} has no spin-allowed d–d transitions. Therefore the UV/vis and CD spectra of iron(III) microbial iron chelates arise from the coulombic interaction between the positively charged metal ion and the negatively charged oxygen atoms (charge-transfer transition), which is not as readily interpreted as are ligand-field (d–d) transitions.

Although transitions in high-spin iron(III) complexes are extremely weak, the determination of the metal-center chirality of Fe^{3+} complexes in solution is possible through comparison of the solution and solid-state CD spectra. However, the correlation of the rotary power with left-handed or right-handed helical stereochemistry requires an absolute assignment based on crystal structure data that are usually determined employing the Bijvoet method for anomalous dispersion of Cu-K_α radiation by the Fe^{3+} ion in the crystalline solids. This correlation could be established for triacetylfusarinine and neurosporin.[63,71] The correspondence extends into the other Fe^{3+} complexes and shows that the CD spectra of the iron(III) complexes in solution can be used for determinations of the metal-center chirality. Fe^{3+} complexes will have the Λ configuration (at least predominantly) if the CD

Table 1 Visible and CD spectral characteristics of aqueous ferric siderophores and of a model complex

Siderophore	λ_{max} (nm) (ε (M^{-1} cm^{-1}))	λ_{max} (nm) ($\Delta\varepsilon$ (M^{-1} cm^{-1})) Δ-configuration	λ_{max} (nm) ($\Delta\varepsilon$ (M^{-1} cm^{-1})) Λ-configuration
Ferrichrome	425 (2895)		360 (−3.7), 465 (2.4)
Ferricrocin	434 (2460)		290 (−3.78), 360 (−1.62), 450 (+2.47)
Ferrioxamine B	428 (2800)		
Coprogen	434 (2820)	375 (+2.1), 474 (−1.26)	
N,N',N''-Triacetylfusarinine		370 (+3.25), 467 (−2.04)	
Fe_2RA_3	425 (2700)^b	372 (+2.73), 464 (−1.41)	
$Fe(benz)_3{}^a$	435 (4910)	350 (+2.3), 452 (−1.5)	350 (−2.8), 455 (+1.1)
Enterobactin	495 (5600)^b	553(−2.2)Δ-*cis*	
Corynebactin			545(+1.7)
Agrobactin	505 (4100)		Λ-*cis*
Parabactin	512 (3300)		Λ-*cis*
Pseudobactin	400 (15 000)		400 (+2.0), 436 (−0.8), 502 (+0.3)
Pseudobactin A	400 (2000)		
Neurosporin		360 (−4.8), 465 (+4.5)	

[a] In acetone solution. [b] At pH 7.

band in the region of the absorption maximum (400–500 nm for hydroxamates) has a positive sign. The visible and CD spectral parameters of siderophores in aqueous solution are summarized in Table 1.

3.3 UV/vis and CD Band Assignments of Chromic Siderophores

An alternative method that enables the classification of geometrical and optical isomers is accomplished by substituting the Fe^{3+} ion with kinetically more inert d^3 Cr^{3+} or d^6 Rh^{3+} ions.[72] Since the substituted ions have almost the same ionic radii and the same charge as Fe^{3+}, their complexes show a high degree of structural similarity with the corresponding Fe^{3+} complexes, as demonstrated by the crystal structures of model compounds.[73,74] The d-electron configurations of Cr^{3+} and Rh^{3+} grant significant CFSE for kinetic inertness and provide well-characterized d–d transitions with distinct UV/vis and CD spectra.

For bidentate ligands with nonequivalent ligating groups, four isomers are possible, Δ-*cis*, Λ-*cis*, Δ-*trans*, Λ-*trans*. Raymond and coworkers have synthesized and separated optical and geometrical isomers of simple hydroxamate and phenolate Cr^{3+} complexes and assigned the absolute configuration of these isomers.[72] Tris(benzhydroxamate)chromium(III), $[Cr(benz)_3]$, was separated into cis and trans geometrical isomers, as confirmed by X-ray structural analyses.[73] Three fractions of optically active tris(*N*-methyl-1-methoxyacetohydroxamato)chromium(III), $[Cr(men)_3]$, were separated by silica gel column chromatography. These were assigned to be a Λ-*cis* fraction, a Δ-*cis* fraction, and a mixture of Λ, Δ-*trans* isomers (Table 2). The cis isomers exhibit a higher dipole moment than the trans isomers. Therefore they bind more strongly to sorbents (e.g. silica gel, ion-exchange resin), yielding bands with lower R_f values compared to trans isomers. This parallels the results obtained for the geometrical isomers of a number of similar compounds.[74–76]

The visible spectra of the Cr^{3+} geometrical isomers exhibit two spin-allowed d–d transitions for octahedral symmetry, namely, ${}^4A_{2g} \rightarrow {}^4T_{1g}$ at higher energy and ${}^4A_{2g} \rightarrow {}^4T_{2g}$ at lower energy. The absorption maximum of the trans isomers is considerably lower at the high-energy transition manifold, and in addition the peak maxima are shifted to higher and lower energy compared to the cis isomers (Table 2). The CD spectrum for *cis*-tris-hydroxamate complexes consists of three bands, due to E_a, A_2, and E_b transitions. The Λ configuration in the model compounds was found to have a positive CD band for the dominant energy transition at 500–600 nm (E_a); the Δ isomer had a negative CD band in this region. For the trans isomer, which has no symmetry (C_1), the E_b transition at high energy is split, providing an additional criterion for differentiating between cis and trans isomers (Table 2). The electronic features are discussed in more detail elsewhere.[9]

Based on these assignments, the absolute configuration of chromium(III) complexes of various siderophores could be determined. The corresponding UV/vis spectral data and CD spectroscopic parameters are shown in Table 2. Whereas chromic desferriferrichromes exclusively show Λ chirality at the metal center, Δ chirality of the coordination octahedron is observed for chromic desferrienterobactin. Chromic complexes of linear chiral ligands such as chromic desferricoprogen and chromic rhodotorulate represent mixtures of Λ and Δ isomers with an overall preference for delta chirality at the metal site, as demonstrated by separation of various geometrical and optical isomers of chromic linear siderophores. Geometrical cis and trans isomers could be separated for linear chromic hydroxamate siderophores, including ferrioxamine B, coprogen, and rhodotorulic acid (Table 2).[9,14,77–80] For the cyclic siderophores, the existence of trans isomers has not been detected. Apparently much larger macrocycle ring dimensions or longer side chains bearing hydroxamate groups are required to allow sufficient flexibility for trans isomer formation.

3.4 Metal-center Symmetry

Derived from X-ray structures, two different models have been presented for the detailed analysis of tris-chelate geometries, and both reach substantially the same conclusion.[81,82] One model describes how close the coordination geometry is to either the trigonally elongated octahedron (trigonal antiprism, D_{3d}) or the trigonal prism (D_{3h}), using shape parameters (which are dihedral angles between trigonal faces sharing common edges of the polyhedron).[83] In the second model, a twist angle is defined as the average of the projection angles of the top and bottom triangular faces spanned by the oxygens and perpendicular to the C_3 or pseudo-C_3 axis. The angle is 60° for an octahedron and 0° for the trigonal prism. The twist angle is a linear function of the ligand bite (the ratio of ring $O\cdots O$ to M–O distance) for a wide range of tris-chelate complexes.

Most structural data are available on the metal centers of hydroxamate siderophores (Figure 6).[26] The observed twist angles range between 36° and 45°. Thus the relative orientations of the octahedral faces formed by the three O(N) and the three O(C) atoms, as described by the twist angle, reflect intermediate structures between the trigonal prism and octahedron. The $O\cdots O$ distance in the bidentate hydroxamate ligand remains constant at 2.55 Å. The (N)–O–Fe–O–(C) angle for hydroxamates is 78°, reflecting the trigonal distortion from the perfect octahedral symmetry (90°). There is not an equal distribution of charges over the two oxygen atoms. The Fe–O–(C) distance is found to be 0.06–0.10 Å longer than the Fe–O–(N) distance in all hydroxamate structures, indicating that the charge on (N)–O is larger than on (C)–O.

The structures of several $[M(catechol)_3]$ complexes are known, including $[Fe(cat)_3]^{3-}$, and all have been found to be pseudo-octahedral. There exists only one crystal structure of an iron(III) tris(catechoylamide), namely of a synthetic compound trivially named bicapped TRENCAM (Figure 7).[84] The

Table 2 UV/vis and CD spectra in solution of various geometrical and optical isomers of chromium(III) siderophores and of model compounds: rhodoturulic acid (A), men (B), coprogen (C), enterobactin (D), catechol (E), and ferrioxamine B (F).**[8]** UV/vis values are for λ_{max} (nm) and ε (M^{-1} cm^{-1}); CD values are for λ_{max} (nm) and θ (M^{-1} cm^{-1})

Cr-RA	Δ-*cis*	Δ-*trans*	Λ-*trans*
CD	415 (+1.05)	425, −445 (+1.24)	405−440 (−0.4)
CD		576 (−4.35)	572 (+1.92)
CD	668 (0.95)	665 (+1.05)	637−677 (−0.3)
UV/vis	418 (67)	416 (49.01)	414 (50.03)
UV/vis (A)	582 (68.1)	588 (66.6)	584 (67.5)

$Cr(men)_3$	Δ-*cis*	Δ-*trans*	Λ-*cis*
CD		395 (+0.21)	
CD	425 (+2.95)	461 (+0.21)	429 (−2.82)
CD	574 (−8.26)	574 (−0.62)	573 (+7.83)
CD	671 (+1.91)	678 (+0.17)	670 (−1.85)
UV/vis	424 (66.7)	416 (49.6)	425 (65.5)
UV/vis (B)	593 (70.2)	596 (69.6)	591 (70.3)

Coprogen	Δ-*trans*	Λ-*cis*
CD	414 (+0.05)	418 (−0.73)
CD	567 (−1.77)	561 (+1.61)
CD	666 (+0.47)	654 (−1.01)
UV/vis	406 (82.7)	406 (88.2)
UV/vis (C)	588 (85.3)	584 (82.1)

$[NH_4]_3[Cr(ent)]$	Δ-*trans*
CD	420 (+1.6)
CD	574 (−7.0)
UV/vis	425 (60)
UV/vis (D)	586 (80)

$K_3[Cr(cat)_3]$	Δ-*cis*	Δ-*trans*	Λ-*cis*
CD		435 (+0.93)	435 (−0.91)
CD		582 (−2.0)	582 (+2.3)
CD		663 (0.43)	663 (−0.49)
UV/vis	425 (104)		
UV/vis (E)	592 (78)		

Cr-ferrioxamine B	N-*cis,cis* racemic	C-*cis,cis* racemic	*Trans* racemic
UV/vis	420 (67.6)	420 (74.7)	412 (50.4)
UV/vis (F)	586 (70.2)	582 (71.1)	592 (71.8)

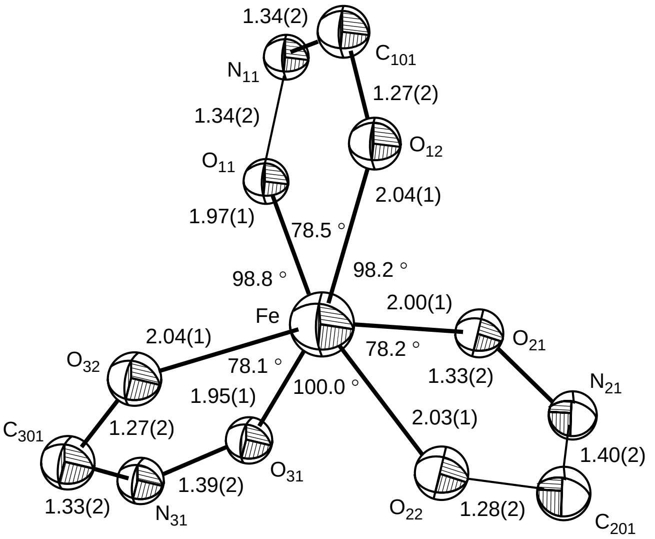

Figure 6 The geometry and dimensions of the iron-coordination octahedron in a natural tris(hydroxamate) complex, triacetylfusarinine. (Reprinted with permission from Ref. 71. © 1980 American Chemical Society)

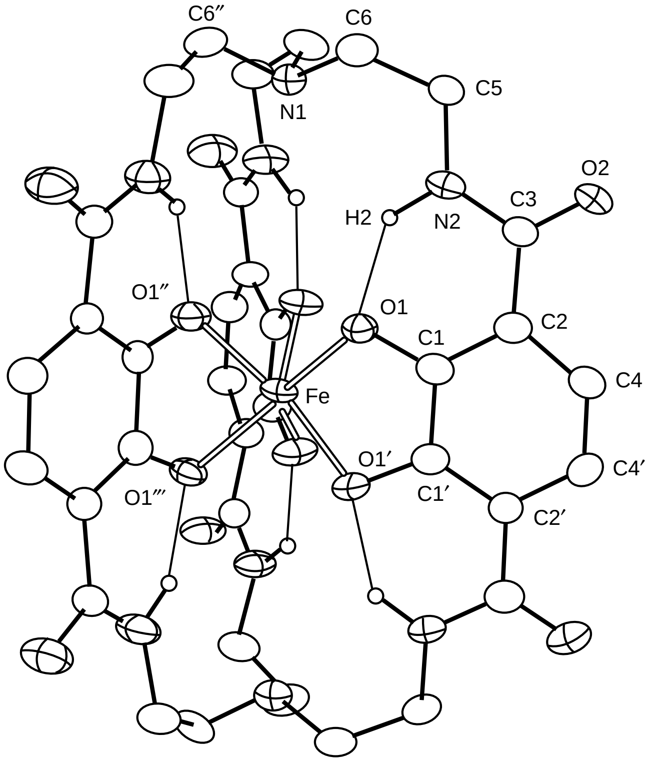

Figure 7 Structure of $\mathrm{Fe^{III}}$ (bicapped TRENCAM). The ellipsoids are scaled to represent the 50% probability surface. Selected bond distances (Å) and angles (deg): Fe–O1, 2.012; C1–O1, 1.333; C3–N2, 1.332; N2–H2, 0.89; O1···O1″, 2.713; O1···N2, 2.620; O1···H2, 1.89; O1–Fe–O1′, 77.75; O1–Fe–O1″, 84.78; O1–Fe–O‴, 134.18; O1···H2–N2, 138. (Reprinted with permission from Ref. 40. © 1987 American Chemical Society)

structure analysis shows the coordination geometry around the metal center to be trigonal prismatic, a structure previously unknown for $\mathrm{Fe^{3+}}$. In the structure, shown in Figure 7, the entire catechoylamide group is planar, and the trans configuration of the amide allows a strong hydrogen bond between the amide proton and the coordinated catechol oxygen. The result is a highly stable ligand structure which incorporates three planar catechoylamide groups and six strong amide hydrogen bonds. To accommodate this ligand geometry, the metal ion lies 0.81 Å out of the catechol plane. The molecular and crystallographic site symmetry of the complex is C_{3h}.[84]

3.5 Ligand Denticity and Metal-center Binding Mode

The structure of the metal center is also dependent on the denticity of the ligand. Tetradentate ligands are of particular interest because they are not able to achieve the octahedral coordination geometry in a 1:1 stoichiometry. The dihydroxamate siderophores rhodotorulic acid (RA), bisucaberin (BC) and alcaligin (AL) were analyzed in some detail.[85,86] The binding mode of these complexes is pH-dependent. At low pH (<5) a cationic species of the type $\mathrm{[FeL(H_2O)_2]^+}$ was observed. In order to completely encapsulate the metal, a binuclear complex of $\mathrm{Fe_2L_3}$ stoichiometry, which was shown to be formed at near neutral pH, is required. This complex may exhibit either a monobridged or a tribridged binding mode of the bis-hydroxamate ligands.[85,86] At high pH a μ-oxo-bridged alcaligin-complex $\mathrm{[Fe_2L_2O_2]}$ is present.[86] Like the bis-hydroxamates, amonabactins, a series of four bis-catecholate siderophores form 2:3 metal:ligand complexes at high pH and in excess of ligand. At lower pH, a 1:1 $\mathrm{Fe^{3+}}$:ligand stoichiometry is found, again like in the corresponding hydroxamate complexes.[87]

3.6 Metal-center Symmetries Based on EPR and Mössbauer Spectroscopy

In $\mathrm{Fe^{3+}}$ ions, d–d transitions are both multiplicity- and Laporte-forbidden. Splitting of $^6\mathrm{S}$ is possible due to a second-order spin–orbit coupling of the $^6\mathrm{S}$ manifold with excited quartet spin states or due to higher order effects of the crystal field.[88]

According to Kramers theorem, half-integer spin states like $^6\mathrm{S}_{5/2}$ will always be doubly degenerate as long as no strong external magnetic fields are applied. The $^6\mathrm{S}_{5/2}$ state splits into three Kramers doublets if the crystal field exhibits a symmetry lower than cubic.

The most common approach to the interpretation of EPR and Mössbauer spectra of siderophores is the spin Hamiltonian formalism. The wavefunctions are parameterized in terms of a few coupling constants that arise in the spin Hamiltonian description of the electronic states. In this approach, the crystal field potential is generally described by a series of spherical harmonics. The corresponding operators are tabulated.[89]

The spin Hamiltonian usually employed for the analysis of siderophores can be represented by equation (1):

$$H = D\left[S_x^2 - \tfrac{1}{3}S(S+1)\right] + E(S_x^2 - S_y^2) + \mu_B \vec{S} \cdot \overleftrightarrow{g} \cdot \vec{B}\,\vec{S} \cdot \overleftrightarrow{A} \cdot I + \frac{1}{4I}(2I-1)QV_{zz}[3I_z^2 - I(I+1)] - g_N\mu_N \vec{B} \cdot \vec{I} \qquad (1)$$

$\vec{S}$ and $\vec{I}$ are the electron spin vector operators, respectively, and their projections on the principal axis, $\overleftrightarrow{g}$ and $\overleftrightarrow{A}$ are second rank tensors, $\vec{B}$ is the applied magnetic field, g_N is the nuclear g-factor of the ground and of the excited state, respectively. Q is the quadrupole moment of the excited state; μ_B and μ_N are the Bohr and the nuclear magneton, respectively; D is the zero-field splitting of the Kramers doublets. In trigonal fields the crystal field splitting is given by $\Delta_{CF} = 6D$, separating the Kramers-doublets at a ratio 4:2. E represents the rhombicity and affects the separation of the Kramers doublets. For $D = 3E$ the three Kramers doublets are separated symmetrically by 3.53D which corresponds to a maximal rhombic distortion (symmetries lower than C_3). The ratio E/D is also called the rhombicity parameter λ with $0 \leq \lambda \leq 1/3$.[90] A simulation based on the formalism described in equation (1) is shown in Figure 8.

Based on the spin Hamiltonian of equation (1), EPR and Mössbauer spectra of various siderophores have been analyzed. The parameters obtained are listed in Table 3.[90] All siderophores have some features in common. Isomer shifts and quadrupole splittings are typical for high-spin Fe^{3+}. The internal field is on the order of −55 T. For comparison, the internal field of the isolated Fe^{3+} ion is −63 T, FeF_3 exhibits a value of −62 T, and $FeCl_3$ of −48.6 T. The internal field of siderophores indicates a high degree of ionicity and is typical for an isolated FeO_6 octahedral configuration. The λ-values near 0.333 listed in Table 3 reflect a nearly complete rhombic distortion of the FeO_6 octahedron arising from crystal fields at the nucleus with symmetries lower than C_3. Similarly, ^{13}C NMR spectra of alumichromes show that the hydroxamate carbonyl functionalities are inequivalent, since two carbonyl resonances (161.57 ppm and 161.96 ppm) with a ratio of 2:1 are found.[91,92] These observations are not consistent with a cis geometrical configuration of the metal hydroxamate propellor derived from UV/vis and CD spectroscopy and from crystal structures.

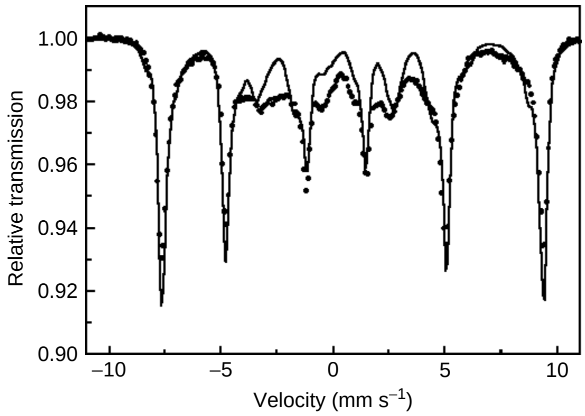

Figure 8 Mössbauer spectrum of a frozen aqueous solution of [$^{57}Fe^{3+}$]-ferrioxamine B (12 mM) employing BSA (100 mM) as a dilutant to minimize spin-spin relaxation. The solid line represents a simulation based on a spin Hamiltonian: line width = 0.35 mm s^{-1}; zero-field splitting, $D = 1.2\,\mathrm{cm}^{-1}$; rhombicity parameter, $E/D = 0.33$; $\delta = 0.52\,\mathrm{mm\,s}^{-1}$; $\Delta E_Q = -0.84\,\mathrm{mm\,s}^{-1}$; asymmetry parameter, $\eta = 1$; and isotropic hyperfine coupling tensor: $A_{xx}/g_N\mu_N = A_{yy}/g_N\mu_N = A_{zz}/g_N\mu_N = -22.1$ T. The simulation does not completely fit the experimental data. This discrepancy is caused by relaxation effects that are not dealt with in the spin Hamiltonian simulation

4 EQUILIBRIUM THERMODYNAMICS OF SIDEROPHORE-IRON BINDING

The formation constants of siderophore complexes define the thermodynamic limits for the conditions in which

Table 3 Mössbauer and EPR parameters of siderophores[a]

Siderophore	δ (mm s^{-1})	ΔE_Q (mm s^{-1})	H_{int} (T)	D	λ
Enterobactin (methanol)	0.28	−0.38	55.5	0.48	0.46
	0.51	–	53.6	–	–
Enterobactin	0.51	–	53.6	–	–
Mycobactin	–	–	–	0.34	0.27
Ferrichrome A	–	0.64	−53.75	−0.29	0.25
	–	0.94	−55.0	1.0	0.25
Ferrirubin	–	–	–	0.44	0.3
Ferrichrysin	–	–	–	0.42	0.267
Ferricrocin	0.65	−0.60	−56.0	0.46	0.31
Coprogen	0.65	−0.60	−55.0	0.47	0.32
RA analog ($n = 10$)	0.5	−0.63	−55.0	−0.8	0.33

[a] Mössbauer analyses have been performed of spectra measured at 4.2 K.

siderophores can compete for iron and extract it from a weaker substrate. Superior propagation conditions will be provided for that organism from which the superior complexing agent was secreted. In addition, these constants are a measure of the siderophore ligand's selectivity for aqueous Fe^{3+} in the presence of competing metal ions and its ability to solubilize Fe and prevent precipitation by hydrolysis. The tenacity of Fe^{3+} binding may determine the mechanism of metabolic turnover of the metal in microorganisms by means of ligand exchange, reductive removal, or ligand destruction.

4.1 Ligand Protonation and Complex Formation Constants

Hydroxamate- or catecholate-containing siderophores are strongly absorbing species with characteristic spectra (see Table 1) which can be utilized for spectrophotometric determination of the complex formation constant. Iron(III) hydroxamates absorb in the visible region, producing a broad absorption band in the 420–440 nm region. Iron(III) catecholates exhibit pH-dependent absorption maxima. Unfortunately, the overall Fe^{3+} ion complex formation constants cannot be determined directly at neutral pH, because the extremely high stability of siderophore complexes precludes direct measurements of the equilibrium of interest, which would yield the desired formation constant for a tris-bidentate siderophore complex, β_{110} (equation (2)).[10,15]

$$\mathrm{Fe}^{3+} + \mathrm{L}^{n-} \rightleftharpoons \mathrm{FeL}^{3-n} \qquad \beta_{110} = \frac{[\mathrm{FeL}^{3-n}]}{[\mathrm{Fe}^{3+}][\mathrm{L}^{n-}]} \tag{2}$$

One method of circumventing this problem is the spectrophotometric measurement of competition for the metal by another thermodynamically well-characterized ligand, typically EDTA. To convert the resultant proton-dependent equilibrium constant into the conventional formation constant, it is necessary to know the ligand protonation constants.[10]

Ligand protonation constants (pK) of the iron-binding groups of siderophores were determined by spectrophotometric and potentiometric titration. Hydroxamic acid-containing siderophores are fairly weak acids with pK_a values ranging from 7.6 to 9.9.[10] Catechols are very weak diprotic acids with widely separated protonation constants (pK_1 between 7.3 and 9.2, pK_2 between 11.5 and 13).[10] In general, the greater the basicity of a chelator, the greater its affinity for $\mathrm{Fe}^{\mathrm{III}}$. However, when the p$K_\mathrm{a}$ of the ligand is substantially greater than the physiological pH (7.4), proton competition will considerably decrease the concentration of the basic form of the ligand, thus reducing iron binding.

Although the conventional form of tabulation, formation constants are not meaningful alone in judging the relative ability of ligands to compete with one another for $\mathrm{Fe}^{\mathrm{III}}$ at a given pH. This is due to differences in ligand protonation constants (their number and absolute value), which define the amount of free, uncomplexed, and unprotonated ligand L in aqueous solution. To have a more direct ranking of the ligands under physiologically relevant conditions, so-called pM values have been used. Here pM is defined as $-\log[\mathrm{M(H_2O)}_n]^{m+}$, calculated from the constant at pH 7.4, an assumed ligand concentration of 10 μM, and metal concentration 1 μM.[10] Stability constants and pM values of selected siderophores are listed in Table 4. The constants indicate unusually high specificity of the ligands for Fe^{3+}. The reason for this is the high charge and small size of the $\mathrm{Fe}^{\mathrm{III}}$ ion, which makes it a hard acid (*see* ***Hard & Soft Acids and Bases***). This, in turn, requires the ligand to be a hard base and charged oxygen atoms as occur in catecholates and hydroxamates behave as hard basic ligands.

A comparison of the stability constants of the naturally occurring siderophores uncovers a difference of 17 orders of magnitude between enterobactin ($K \sim 10^{49}$)[93,94] and the most stable hydroxamate complex, ferrioxamine E.[9,10] Using the more comparable pM values, enterobactin remains still eight orders of magnitude more effective than ferrioxamine E. Enterobactin has the highest affinity for $\mathrm{Fe}^{\mathrm{III}}$ ion of any biological iron chelator tested so far.

The protonation constants K_{MHL} of iron(III) trihydroxamate siderophore complexes are in the range of 1, indicating that these complexes are stable even under very acidic conditions. In contrast, tricatecholate complex structures are strongly pH-dependent. The pH-dependence reflects changes of the iron environment. In enterobactin, the metal is coordinated by three catecholate dianions at pH 7. Raymond and coworkers proposed that with decreasing pH the catecholate oxygens are protonated stepwise concomitant with a bonding shift from catecholate to a salicylate mode of binding, resulting eventually in the neutral complex $[\mathrm{Fe}^{3+}\,(\mathrm{H_3ent})]^0$ (path 1 in Figure 9).[94] For enterobactin and the synthetic analog MECAM, the following complex protonation constants have been evaluated: $K_{\mathrm{MHL}} = 4.89$ and 7.08, respectively, $K_{\mathrm{MHL}} = 3.15$ and 5.6, respectively.[94,95] Raymond and coworkers corroborated their initial proposal, employing

Table 4 Stability constants and redox potentials of natural $\mathrm{Fe}^{\mathrm{III}}$ siderophore complexes[a]

Siderophore	log β_{110}[b]	pM[c]	log K_{MHL}[d]	$E_{1/2}$ (mV vs. NHE)
Ferrioxamine E	32.5	27.7	–	–
Coprogen	30.2	27.5	0.5	−447
Ferrioxamine B	30.5	26.6	1.0	−468
Aerobactin	22.5	23.3	–	−336
Enterobactin	49	35.5	4.80	−750
DHBS	–	–	–	−350
Parabactin	–	–	–	−673
Parabactin A	–	–	–	−400

[a] All solutions are aqueous. [b] See text. [c] $\mathrm{p}M = -\log[\mathrm{Fe(H_2O)_6}^{3-}]$ when $[\mathrm{Fe}]_\mathrm{T} = 10^{-6}$ M, $[\mathrm{L}] = 10^{-5}$ M, pH 7.4. [d] $K_{\mathrm{MHL}} = [\mathrm{FEHL}^{4-n}]/[\mathrm{H}^+][\mathrm{FeL}^{3-n}]$.

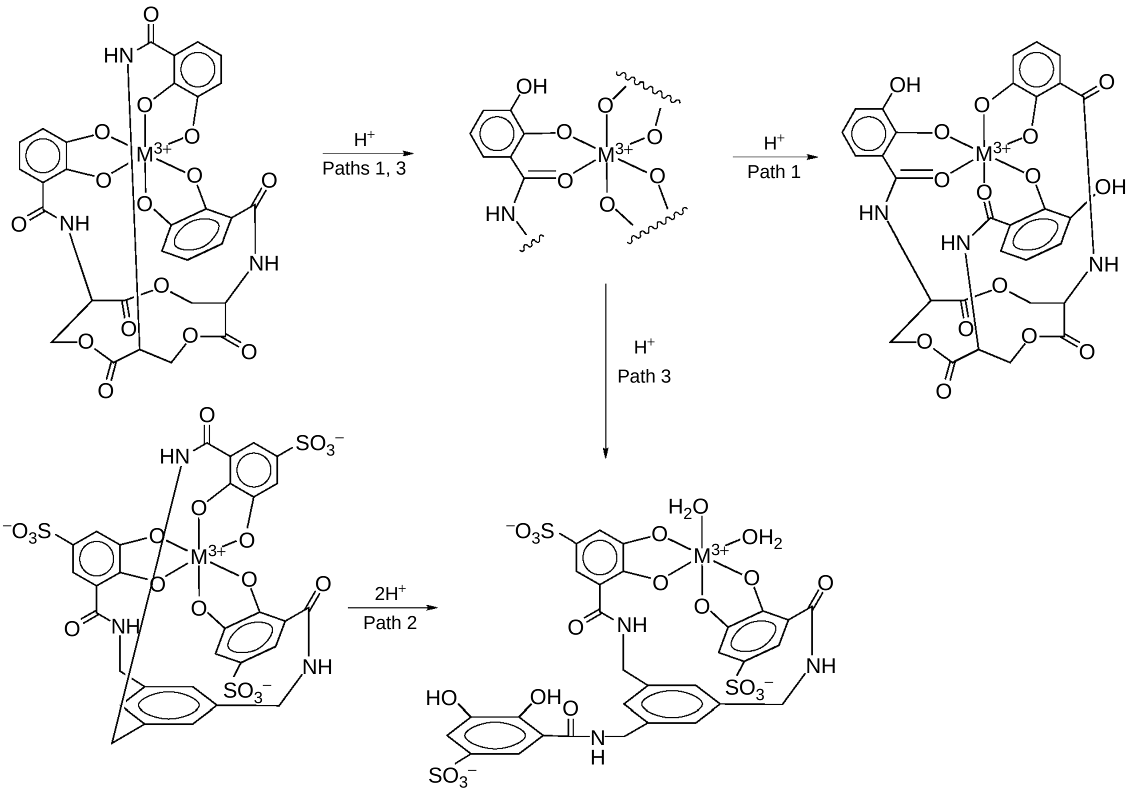

Figure 9 Possible protonation schemes of tris(catecholate) metal complexes. In path 1, the metal complex undergoes a series of two overlapping one-proton steps to generate a mixed salicylate–catecholate coordination. Further protonation results in the precipitation of a tris(salicylate) complex (e.g. enterobactin, MECAM). This differs from path 2, in which a single two-proton step dissociates one arm of the ligand to form a bis(catecholate) chelate. Path 3 incorporates features of paths 1 and 2. In this model, the metal again undergoes a series of two overlapping one-proton reactions. However, unlike the case of path 1, the second proton displaces a catecholate arm, which results in a bis(catecholate) metal complex

spectrophotometric titrations,[94] pH-dependent Mössbauer spectra,[96] an IR study,[97] and a ^{2}H NMR investigation.[98]

4.2 Iron-exchange Kinetics

In early papers on chelate exchange of iron(III) siderophore complexes, it was assumed that the Fe^{III} ion is readily exchanged, due to the known kinetic lability of high-spin Fe^{III}-ion binding. More recent investigations disclosed, however, that ligand exchange reactions are slow and involve stepwise ligand dissociation and protonation, and ternary complex formation.[10,99] From exchange kinetics of the form shown in equation (3)

$$^{55}FeL + L' \rightleftharpoons {}^{55}FeL' + L \qquad (3)$$

an approximate linear-free-energy relationship between the equilibrium competition constant and the second-order rate constant for iron removal from ferrichrome, ferricrocin, and coprogen to ferrioxamine B has been derived.[10] Taking triacetylfusarine C as competing ligand, 63% ^{59}Fe was removed from iron(III) citrate after 0.5 h, and even 82% from iron(III) rhodotorulate but only 4% from ferrichrome A.[100] In addition, it was shown that backbone sequence changes in siderophore structures can influence Fe^{3+} lability, but the largest effect is observed on going from a cyclic to an open-chain structure.[101] ^{55}Fe exchange kinetics of the form of equation (4)

$$^{55}FeL + FeL' \rightleftharpoons FeL + {}^{55}FeL' \qquad (4)$$

between ferrioxamine B and ferrichrome A were measured at equimolar concentrations (4.0 mM) and 5% excess of desferriferrioxamine B at pH 7.4. The $t_{1/2}$ for exchange is very slow (220 h).[10] In contrast, the exchange reaction between ferrioxamine B and a synthetic tris-catecholate complex exhibits a half-life of approximately 10 hours for equimolar concentrations (1.0 mM) of the competing complexes with no excess free ligand. From a mechanistic point of view, the characteristic feature of siderophore iron-exchange processes is the unraveling of one ligand from the inner coordination sphere, concomitant with complexation by the incoming ligand. This occurs via the formation of a ternary complex between metal ion and entering and leaving ligands. The general features of these exchange processes conform to ideas formulated in earlier studies of multidentate ligand exchange.[102]

Dissociation of iron from its siderophore complex is a proton driven process and its first step is relatively fast at low pH ($t_{1/2} \cong$ 2-5 ms)[103,104] This step normally involves the dissociation of a bidentate moiety from the fully formed complex ($k_1 = 3.8 \times 10^2\,M^{-1}\,s^{-1}$). Further dissociation is much slower (second-order rate constant $k_3 = 2.3 \times 10^{-2}\,M^{-1}\,s^{-1}$).[105] Proton driven ligand dissociation from tetradentate siderophore complexes (Fe_2L_3) exhibit relatively fast rate constants ($k_3 = 1.5 \times 10^2\,M^{-1}\,s^{-1}$ for alcaligin and $k_3 = 6.8 \times 10^2\,M^{-1}\,s^{-1}$ for rhodoturulic acid).[104] The resulting tetracoordinated complex is relatively stable and requires a drop in pH below 1 for further dissociation. In the case of the hexadentate siderophore ferrioxamine B, dissociation kinetics disclosed an extreme kinetic and thermodynamic stability at physiological pH.[105] In contrast to hexadentate siderophores, tetradentate siderophores can undergo ligand dissociation by multiple pathways. Intermediates of different structures, depending on environmental conditions (pH, Fe:L ratio), have been identified by electrospray ionization mass spectrometry (ESI-MS). The multiplicity of interconvertible species may play a role in cellular recognition, and in the formation of ternary complexes representing a likely prerequisite for biological reduction.[104,106]

Both $\Lambda \rightleftharpoons \Delta$ and cis $\rightleftharpoons$ trans equilibria of siderophore complexes can exist in solution. The chirality of the ligand can impose a preferred metal-center chirality. In addition, the degree of this preference depends on the stereochemical rigidity of the ligand. In principle, the magnitude of the molar circular dichroism can be used as a measure for diastereoisomeric equilibria based on a comparison of the solid-state and solution ellipticity. Nevertheless, predictions of metal-center chiralities require theoretical calculations. For example, empirical-force-field calculations of iron(III) enterobactin show that the Δ orientation at the metal center is more stable than the Λ by 0.5 kcal mol^{-1}, which is consistent with the CD spectra.[107]

In linear siderophores, increasing the chain lengths will obviously cause greater flexibility, resulting in smaller energy differences between both optical and geometrical isomers. These small energy differences allow intramolecular rearrangement reactions of tris-chelate complexes of labile metal ions, such as Mn^{2+}, Fe^{3+}, Al^{3+}, and Ga^{3+}.[108–110] For ferrioxamine B the kinetics of isomerization has been analyzed in detail by NMR spectroscopy.[111] In these experiments, Fe^{III} was substituted by Ga^{III} and Al^{III} to circumvent the problems associated with paramagnetic line broadening. The isomerization reactions were slow enough to allow detection of two geometrical isomers and to measure the rearrangement kinetics by NMR spectroscopy, employing the hydroxamate carbonyls as sensitive probes for metal-center symmetries. The enthalpies of activation ($\Delta H = 53.3\,kJ\,mol^{-1}$ in D_2O and $69.7\,kJ\,mol^{-1}$ in methanol-d_4) are indicative of small activation barriers. The observations favored an intramolecular rearrangement process that involves neither explicit solvent association nor metal–hydroxamate dissociation in the transition state.[111]

4.3 Redox Chemistry of Siderophores

In microbial iron assimilation, one mechanism for the release of iron from siderophores is the enzymatic reduction to the Fe^{II} state. Siderophore stability constants are much lower for Fe^{2+}, which has a lower charge-to-radius ratio. Moreover, ligand exchange reactions for the high-spin Fe^{II} ion are much faster than for the Fe^{III} ion. Stability constants of ferrous siderophores are experimentally difficult to obtain. Limiting pH-independent redox potentials can be utilized, however, to describe the electrochemical and chemical equilibria between fully coordinated Fe^{3+} and Fe^{2+}-siderophore complexes and the uncomplexed $Fe(H_2O)_6{}^{3+}$ and $Fe(H_2O)_6{}^{2+}$, respectively, in a simple model as described in equation (5)[112]

$$E^0_{\mathrm{Fe(III)Sid/Fe(II)Sid}} = E^0_{\mathrm{aq}} - 59.15 \log\left(\frac{\beta^{\mathrm{FeIII}}_{110}}{\beta^{\mathrm{FeII}}_{110}}\right) \qquad (5)$$

where E^0_{aq} is the redox potential of hexaaquated iron ($E^0_{\mathrm{aq}} = +770$ mV/NHE).[113] Given the redox potential of the siderophore, and the stability constant of the ferric siderophore complex, the stability constant of the ferrous siderophore complex can be calculated. Based on these considerations Fe^{2+}-siderophore stability constants were determined. Fe^{2+}-siderophores are some 20 orders of magnitude less stable than their Fe^{3+} counterparts.

Table 4 illustrates the redox potentials of various siderophores obtained by cyclic voltammetry. The values of most of the hydroxamates are within the range of typical biological reductants such as NADH-dehydrogenase [−320 mV (NHE)] (Section 5.4). However, the redox potential of tris-catecholate siderophores such as enterobactin and parabactin are considerably more negative than those of hydroxamates. Raymond and coworkers have also measured the redox potentials of Fe^{3+} complexes of synthetic tricatechols and found them to be in the range −0.8 to −1.1 V (NHE).[9,99,114,115] In the case of enterobactin the enormous stability of the Fe^{III} complex, its high specificity for Fe^{3+}, and low affinity for Fe^{2+} result in the Fe^{3+}/Fe^{2+} formal potential being highly negative. The full coordination of Fe^{3+} by all three catechol groups requires the loss of six protons. Thus there is a strong dependence of the stability of the iron(III) enterobactin complex and its reduction potential on pH. The formal electrochemical potentials for $Fe^{III/II}$ enterobactin are (at pH noted) −0.99 (>10.4), −0.79 (7.4), −0.57 (6.0), +0.17 (4.0) V (vs. NHE).[96,116] The redox equilibria have been discussed controversially for some years but there now seems to be agreement on the formulation of the redox chemistry. Below pH 6, protonation of the Fe^{III} complex and dissociation of the Fe^{II} become significant and the electrochemical reaction is not well defined. Therefore, at pH 4 the potential has been estimated assuming no complexation of the $\mathrm{Fe}^{\mathrm{II}}$ ion by enterobactin.[96] Mössbauer spectra revealed that, in a methanolic solution, $\mathrm{Fe}^{\mathrm{III}}$ enterobactin undergoes protonation and a ligand-based redox reaction with the formation of a semiquinone/$\mathrm{Fe}^{\mathrm{II}}$ couple under acidic conditions.[117] The reaction becomes irreversible if the solution is allowed to stand under aerobic conditions. The mechanism is described as shown in equations (6) and (7)

$$[\mathrm{Fe}^{3+}(\mathrm{ent})]^{3-} + n\mathrm{H}^{+} \longrightarrow \mathrm{Fe}^{3+}[\mathrm{H}_n(\mathrm{ent})]^{n-3}(\text{methanol}) \quad (6)$$

$$\mathrm{Fe}^{3+}[\mathrm{H}_n\mathrm{ent}]^{n-3} \xrightarrow{\mathrm{H}^{+}} \mathrm{Fe}^{2+}[\mathrm{H}_n\mathrm{ent}]^{n-3} \xrightarrow{\mathrm{O}_2} \text{polymeric quinones} + \mathrm{Fe}^{2+} \quad (7)$$

5 SIDEROPHORE TRANSPORT IN MICROORGANISMS

Siderophore-mediated iron uptake in microorganisms is both a receptor- and an energy-dependent process.[4,5] Moreover, many receptor–siderophore interactions are very specific.[118–122] Therefore, unraveling the molecular basis of siderophore recognition by the cell continues to represent a major topic of siderophore research. Both the transport mechanisms and the closely related processes of metal release from the complex are of comparable importance. Various excellent books and review articles have been published on iron transport and iron transport agents in microorganisms.[4–6,8,9,123–125] At this point it should be mentioned that recently a series of specific microbial iron transport systems have been discovered which do not require siderophores in order to fulfill their central task of solving the iron-supply problem. These systems include various heme transporters,[126,127] lactoferrin transport[128] and microbial transferrin[129] (*see also* ***Iron Proteins for Storage & Transport & their Synthetic Analogs***). In addition, direct mobilization of metals from a mineral surface by membrane proteins might be another strategy of iron acquisition in microbes.[130] Merely salient features of siderophore transport will be presented in the following sections. Within the past two decades our knowledge on bacterial iron transport systems exploded. In particular, the Gram-negative bacterium *E. coli* has been analyzed in great

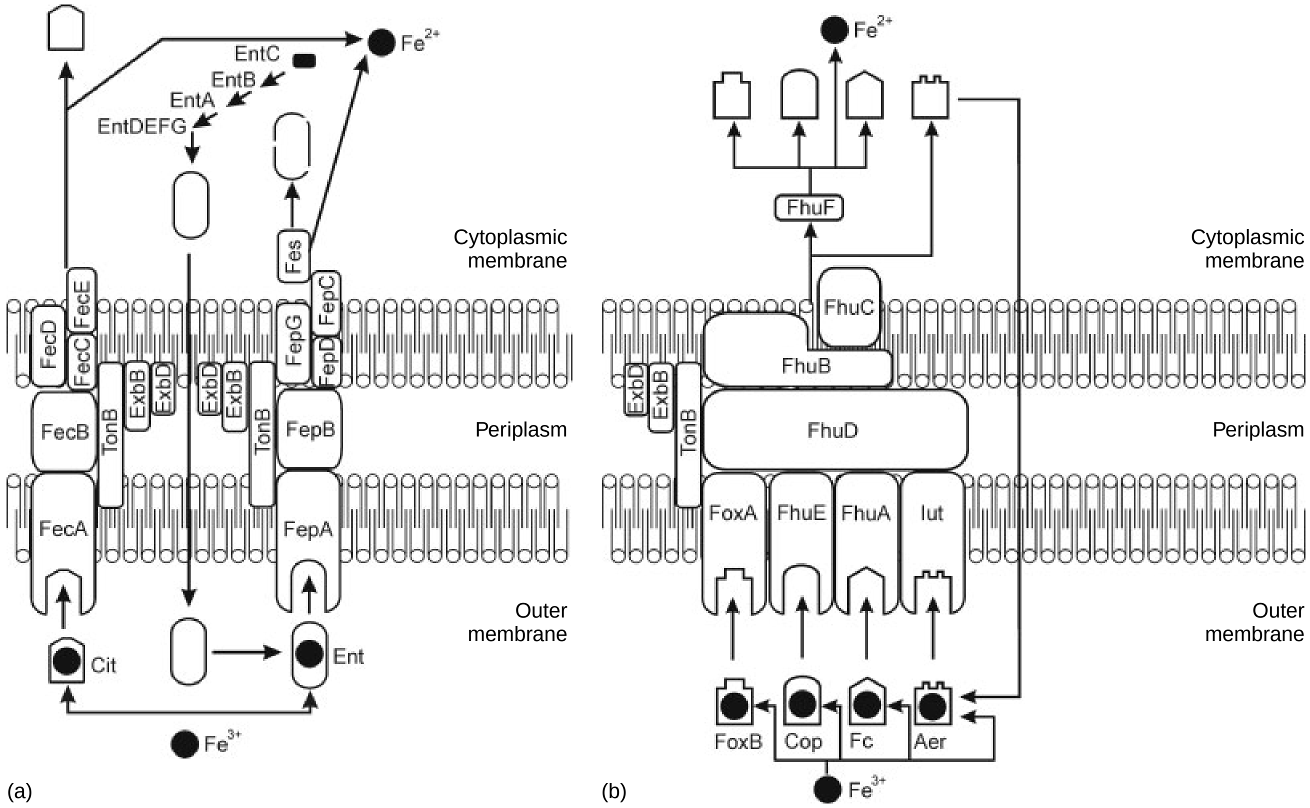

Figure 10 A schematic drawing of the cell envelope of *E. coli* consisting of the cytoplasmic membrane, the periplasm, and the outer membrane. Various proteins are shown, sets of which represent specific siderophore-transport systems. Outer-membrane receptors (OMR) shown here are FepA (enterobactin), IutA (aerobactin), Fec A ($\mathrm{Fe}^{\mathrm{III}}$ dicitrate), FhuA (ferrichrome), and FhuE (coprogen, $\mathrm{Fe}^{\mathrm{III}}$ rhodotorulate, and ferrioxamine B). FoxA (ferrioxamine B), is not a receptor of *E.coli*, but of the closely related *Salmonella*. Not shown here are the receptors Fiu and Cir ($\mathrm{Fe}^{\mathrm{III}}$ $(\mathrm{DHBS})_n$; n indicates 3 possible linear degradation products of enterobactin) and FeO, a transport system for $\mathrm{Fe}^{\mathrm{II}}$. Details are discussed in Section 5.1

detail by means of genetic methods. Therefore we shall mainly focus on the model organism, *E. coli*.

Gram-negative bacteria like *E. coli* are surrounded by two membranes, the outer membrane and the cytoplasmic membrane (Figure 10).[131] Between these two layers is the compartment known as the periplasmic space, which may make up 10−40% of the total cell volume, depending on the osmotic strength of the external medium. Solutes from the medium have to diffuse, or be transported, across these three regions to reach the cytoplasm. Pores large enough to allow diffusion of siderophores through the outer membrane pose a threat to the organism, because they would also allow entry of noxious substances like detergents and antibiotics. Therefore, receptor proteins arose parallel to siderophores during the course of evolution exhibiting extraordinary specificities for individual siderophores or a small group thereof. Figure 10 depicts the proteins involved in siderophore transport in *E. coli*. These proteins are essential constituents of the different transport systems.

5.1 Siderophore Receptors

For *E. coli*, seven Fe^{3+} transport systems have been characterized.[5,132] At the level of the outer membrane, these seven transport systems are determined by specific receptors (the corresponding gene products are mentioned in parentheses) which selectively recognize the siderophores enterobactin (FepA), Fe^{III} $(DHBS)_n$ (Fiu and Cir; n indicates 3 possible linear degradation products of enterobactin),[42] aerobactin (IutA), Fe^{III} dicitrate (FecA), ferrichrome and closely related ferricrocin and ferrichrysin (FhuA), and coprogen, Fe^{III} rhodotorulate, and ferrioxamine B (FhuE). In addition, a transport system for Fe^{II} iron has been detected (Feo).[133] Only enterobactin and, in some *E. coli* strains, aerobactin are synthesized by the organism itself. The residual siderophores transported in *E. coli* are xenosiderophores produced by different microorganisms. The enormous metabolic activity aimed at iron acquisition underscores the central role that this metal plays for survival. In general, similar transport systems were identified in other Gram-negative bacteria.[134] In Gram-positive bacteria, which lack an outer membrane, the receptor protein is anchored by a covalently linked lipid. The receptor proteins are synthesized in response to iron limitation in such amounts that they become major outer-membrane proteins with copy numbers between 10 000 and 100 000 per cell.

In the past few years, crystal structures have been published of three of the seven outer-membrane-siderophore receptors from *E.coli*, namely of FepA,[134,135] FhuA,[136–138] and FecA.[139,140] FepA and FhuA represent similar monomeric transmembrane proteins that are composed of 22 antiparallel ß-strands of approximately 70 Å height (Figure 11).[140] The right-handed twist of the β-strands produces an elliptical-shaped barrel with a diameter of 35×47 Å constituting a transmembrane pore.[140] Large extracellular loops extend approx 35 Å (in the case of FepA) above the surface of the outer membrane.[141] These loops are predominantly hydrophilic but contain in addition a large number of aromatic amino acids (Tyr,Phe) and are believed to represent the region of initial siderophore contact. The globular, N-terminal domain of the receptor protein inserts from the periplasmic side into the β-barrel functioning as a plug/cork (Figure 11).

Fortunately, X-ray structures of various FhuA-substrate complexes have been determined recently allowing a more detailed analysis.[142,143] Surprisingly, siderophore binding does not trigger big changes at the extracellular side of the receptor. Some alterations are detectable in the periplasmic loops and very few in the barrel and extracellular loops. Transition from the unliganded to siderophore-liganded conformation induces local and allosteric transitions illustrating an induced-fit binding mechanism. Changes occur primarily in the N-terminal domain. The most visible change is the unwinding of the first helix ($\alpha 1$) in the N-terminal domain.[141] The mode of receptor-binding to ferrichrome and to other ferrichrome analogs discloses that it is the iron chelating hydroxamic acid portion and key groups on the peptide backbone of the siderophore that are preferentially recognized (‘binding pocket’). It is noteworthy that this mode of

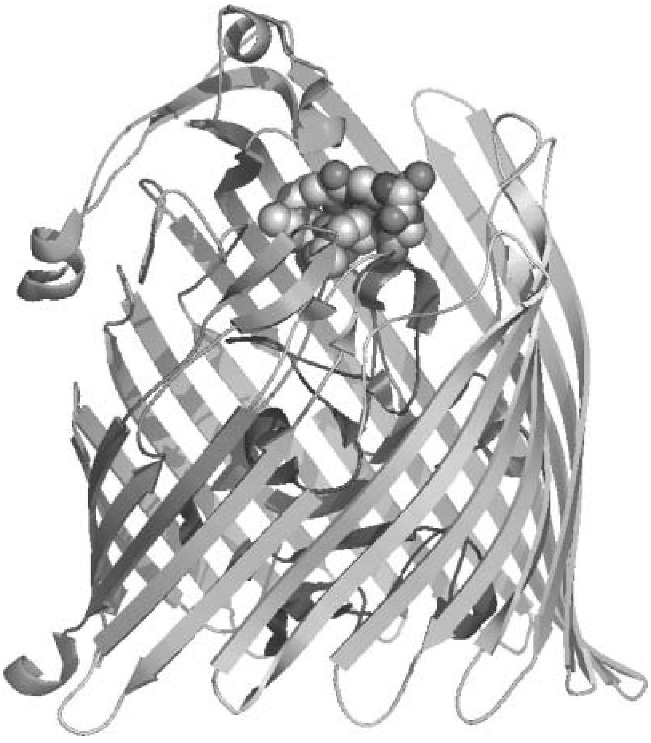

Figure 11 Crystal structure of the OM-siderophore receptor FhuA[136] with the bound siderophore ferrichrome (emphasized by a space filling atom presentation). The plot is based on PDB file 1QFF, taken from the NCBI database using the program PYMOL. Resolution of the structure is 2.70 Å, and the space group is $P6_1$. The upper side of the figure corresponds to the extracellular side of the outer membrane. See Section 5.2 for a detailed discussion

recognition was predicted already 15 years earlier based on siderophore-transport and -inhibition studies employing modified siderophores, siderophore analogs and Fe, Ga, Cr, and Rh complexes thereof (see Section 5.2). Unfortunately, a crystal structure of Fe-ent and of the Fe-ent-FepA complex is still missing. However, a recently published structure of a Fe-ent complex with the human serum protein lipocalin NGAL allows us to imagine what kind of interaction can be expected for the FepA-Fe-ent receptor complex.[144] The crystal structure disclosed a novel type of substrate binding consisting of simple ionic and concomitantly of cation-π interactions. The ionic interaction is achieved by intercalation of positively charged side chains (lysine, arginine) of the NGAL-protein between the ligand catecholates.[144]

The outer-membrane receptors exhibit two functional states. In an unenergized conformation the siderophore binds to the receptor, but is not transported through the membrane. The energized state of the receptors requires a periplasmic protein, named TonB, which serves as a coupling device between the cytoplasmic membrane and the outer-membrane receptors.[145–148] It is assumed that the above mentioned unwinding of helix $\alpha 1$ of the N-terminal domain facilitates the interaction of the outer-membrane siderophore-receptor complexes with TonB. All TonB-dependent siderophore membrane receptors exhibit a pentapeptide consensus sequence, termed the TonB box indicating its involvement in coupling to the TonB protein.[149,150] TonB is anchored in the cytoplasmic membrane, with the rest bridging the periplasmic space.[151] A current model proposes that TonB forms a complex of unknown stoichiometry together with two additional proteins, ExbB and ExbD, stabilizing TonB and increasing TonB activity.[152] In total, the interaction between TonB and TonB-dependent outer-membrane siderophore receptors remains enigmatic. Further intensive research will be required to fully understand the complete process of siderophore outer-membrane transport on a molecular level.[153–157]

5.2 Specificity and Stereospecificity of Siderophore Recognition Probed by Metal and Ligand Substitution

Recognition of siderophores may be dependent on different parts and structural features of the molecule: (a) the molecule as an entity; (b) the geometry and chirality of the backbone; (c) chirality or geometry at the metal center; (d) peripheral groups. As described in Section 5.1, crystal structures of siderophore-receptor proteins are now available. However, the molecular nature of the siderophore-receptor interactions is still not fully understood. In an early approach, the structural elements responsible for specific recognition were traced out by using compounds that are related to the natural siderophore, that is, by employing homologous siderophores, synthetic enantiomers, or synthetic analogs.[118–122] Moreover, diastereoisomers or geometrical isomers might affect such discriminations. Substitution of Fe^{III} iron with kinetically inert ions such as Cr^{3+} or Rh^{3+} enables separation of isomers and studies of their receptor specificity in vivo employing transport and inhibition studies. Based on metal-substituted siderophores and separated geometrical isomers, the Stereospecificity and mechanisms of uptake were studied in *E. coli*,[118,119] *Rhodotorula minuta*,[122] *Streptomyces pilosus*,[77,120] and *Neurospora crassa*.[78,121]

In *E. coli*, the Fe^{III} complexes of some synthetic analogs of enterobactin can act as iron sources and detailed kinetic and inhibition studies enabled a more precise description of the molecular groups essential for recognition by Fep A (Figures 12 and 13).[118,119] Fe-ent carries a Δ absolute configuration at the metal center, and although the synthetic Fe^{III} enantio-enterobactin does not promote growth in *E. coli*,[79] subsequent studies revealed that both enantiomers are transported.[158] Therefore, chirality is not required for receptor-binding. On the other hand, enterobactin uptake is effectively inhibited by the structural analog Fe–MECAM (Figure 12) and Rh–MECAM,[119] indicating that the trilactone backbone is also not required for recognition.

In addition, substrates which are modified at the aromatic rings (MECAMS, LICAMS) or at the amide bond connecting the 2,3-hydroxybenzoyl groups with the backbone

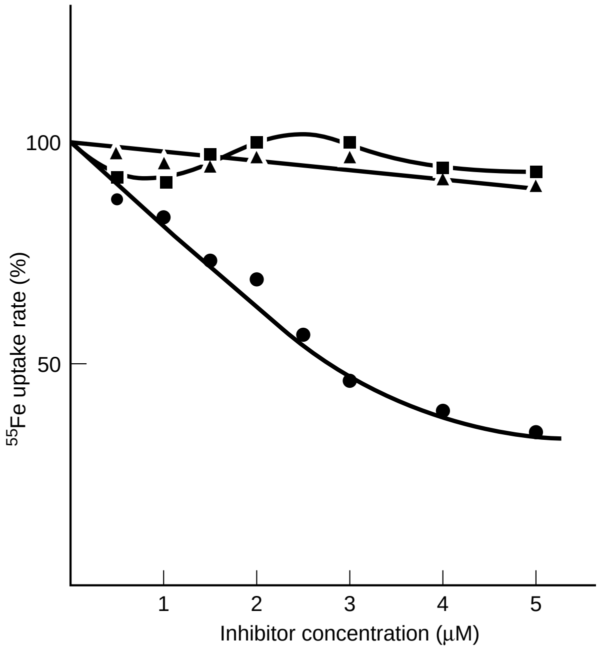

Figure 12 Inhibition of [^{55}Fe]enterobactin uptake in *E. coli* by structural analogs. The initial uptake rate (five minute interval) of [^{55}Fe]enterobactin was determined with and without inhibitor. The synthetic analogs of enterobactin, Fe–MECAM (circles), Fe–TRIMCAM (squares) and Fe–3,4-LICAMS (triangles) were added at various concentrations as potential inhibitors to the transport assay. The [^{55}Fe]enterobactin uptake rate (36 pmol mg^{-1} min^{-1} at 0.5 μM complex concentration) without any inhibitor is defined as 100%. Only Fe MECAM is an efficient inhibitor of Fe-enterobactin uptake. See text for discussion[118]

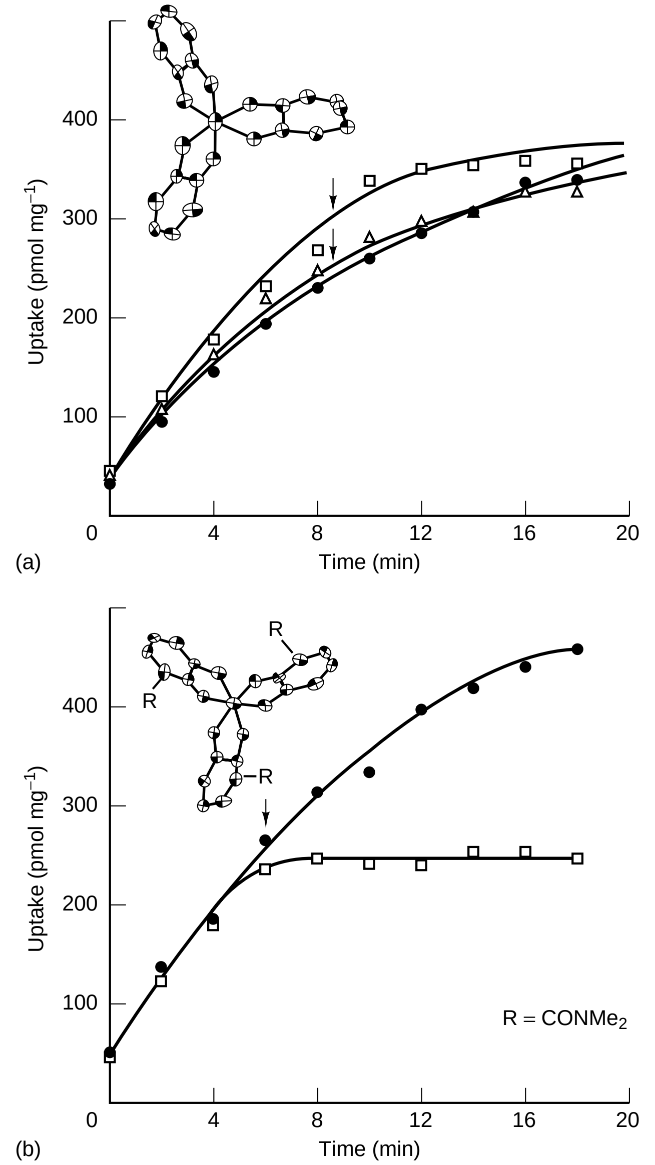

Figure 13 (a) Inhibition of 2 µM [^{59}Fe]enterobactin by [Rh(cat)$_3$]$^{3-}$. Control (closed circles) represents uptake of 1 µM label with no inhibitor added. Inhibition experiments: K$_3$[Rh(cat)$_3$]$^{3-}$ added at $t = 6$ min in 10-fold excess (open squares) or 100-fold excess (open triangles). (b) Inhibition of 2 µM [^{59}Fe]enterobactin by [Rh(DMB)$_3$]$^{3-}$. Control (closed circles) represents uptake of 1 µM label with no inhibitor added. K$_3$[Rh(DMB)$_3$]$^{3-}$ added at $t = 6$ min in 50-fold excess (open squares). (Reprinted with permission from Ref. 120. © 1988 American Chemical Society)

(TRIMCAM) are ineffective inhibitors (Figures 12 and 13).[118] From these experiments, it was concluded that the part of the molecule recognized by the receptor is the metal-binding end, but the ligand to which these functionalities are attached is not important in receptor recognition. Actually, an unsubstituted triscatechol iron center and the amide linkage is essential for recognition. These studies clearly show that modified siderophores and synthetic models are excellent tools in determining specificity of siderophore uptake at the molecular level.

Stereospecific recognition in *R. minuta* was probed with separate Λ-*trans*, Δ-*trans*, and Δ-*cis* chromium(III) RA as well as with synthetic enantio-RA.[80] The RA uptake system discriminates between RA and its enantiomeric form. It also discriminates between Λ-*trans* and Δ-*trans* isomers of Cr$_2$(RA)$_3$, as shown by inhibition of Fe^{III} RA uptake[80] and, finally, changes in the backbone have only little effect on uptake rates.[122] In *S. pilosus* the racemic C-*cis,cis*, N-*cis,cis*, and trans isomers of Cr^{3+} desferriferrioxamine B (see Table 2) inhibited equally well the ^{55}Fe-ferrioxamine B uptake, suggesting that no differentiation between cis and trans geometrical isomers occurs in this system.[77] Coprogen is the species-specific siderophore synthesized by *Neurospora crassa*. For Cr^{3+} desferricoprogen, two fractions were separated by HPLC, a cis complex (20% excess Λ) and a mixture of trans complexes (20% excess Δ) (see Table 2).[78] Although this separation of optical and geometrical isomers was not complete, inhibition studies suggest a predominant recognition of the Δ-*trans* isomers. In summary, these investigations revealed that the metal-center chirality and the shape of the metal-center portions of siderophores are of central importance for molecular recognition by receptors in the cell envelope.

5.3 Transport Mechanisms

After Fe^{3+} siderophores have docked at the binding pocket of the outer-membrane receptors of *E. coli*, translocation into the periplasmic space is mediated by the TonB complex. Once released into the periplasm, siderophores are rapidly bound by the specific periplasmic binding proteins FhuD (hydroxamate siderophores),[159] FepB (enterobactin),[160] and FecB (ferric dicitrate).[161] FhuD, for example, exhibits a broad substrate specificity for a variety of hydroxamate siderophores including ferrichrome, coprogen, aerobactin, ferrioxamine B, shizokinen, rhodotorulic acid, and the antibiotic albomycin. The dissociation constants of FhuD with these siderophores range from 0.3 to 5.4 µM.[162,163] X-ray structures of FhuD and FhuD-siderophore complexes[164–166] explain this broad substrate specificity. Ferrichrome bound to FhuD is exposed at the protein surface thus enabling fewer constraints to ligands than a deep cavity does.

The siderophore-loaded periplasmic siderophore-carrier proteins eventually transfer the siderophores to so-called ABC-Transporter systems (from ATP-binding cassette)[167–169] consisting of two proteins, one to span the membrane acting as a permease and a second one which can hydrolyze ATP to provide the energy for transport. The transmembrane permeases are FhuB for hydroxamates, FepDG for enterobactin, and FecCD for ferric dicitrate. The corresponding ATP-hydrolyzing proteins at the cytoplasmic side of the cytoplasmic membrane are named FhuC, FepC, and FecE. Ferric siderophores are released from the transport system at the cytoplasmic side of the cytoplasmic membrane. Eventually, iron is rapidly released from the siderophore complex via reduction (details in Section 5.4) The molecular mechanism of siderophore transport across the cytoplasmic membrane is not yet fully understood.[170] A completely different iron transport mechanism has been suggested for an OM-transport of pyoverdin via the FpvA receptor in *Pseudomonas aeruginosa*.[171] The ligand exchange step occurs at the cell surface and involves the exchange of iron from a ferric pyoverdin to an iron-free pyoverdin strongly bound to the receptor FpvA. This mechanism suggests an increase of the iron uptake rate, with increasing concentration of iron-free siderophore. A similar transport system has been identified in the fresh water bacterium *Aeromonas hydrophila*.[172] However, in contrast to *Pseudomanas aeruginosa*, the *Aeromonas* receptor recognizes and transports an extremely broad range of siderophores, with chelating groups as varied as catecholate, hydroxamate, or hydroxopyridoxinate.

In fungal systems, only little is known about the number and spatial organization of the proteins of the siderophore-transport systems. Employing the modern methods of molecular biology some information is now available on yeasts and Ascomycetes.[173–176] Most is known on the siderophore transporters from *Saccharomyces cerevisiae* because it is the only fungus the whole genome of which is known. The yeast transporter family–as far as it is known–includes Taf1 (triacetylfusarinine C), Arn1 (ferrichromes), Enb1 (enterobactin), and Sit1 (ferrioxamine and ferrichrome transporter).[177]

In general, two different types of siderophore-transport mechanisms are operative in fungi.[8–10,178] One major path comprises transport across cell membrane(s) into the cytoplasm. In the cytoplasm, Fe^{III} is removed from the complex by a specific or unspecific ferrireductase and Fe^{II} is transferred to an intracellular Fe^{II} carrier, the structure of which has not yet been determined. Finally the metal-free siderophore is resecreted for additional solubilization–assimilation cycles. Coprogen transport into the ascomycete *Neurospora crassa* and ferrichrome transport into the yeast *Ustilago sphaerogena* are typical representatives of this mechanism. The most prominent feature of the second transport mechanism is the lack of membrane permeation by the iron complex. The extracellular siderophore complex releases the metal to a membrane-associated iron shuttle system either by ligand exchange or by reduction. A ligand exchange mechanism was found for Fe^{III} rhodotorulate transport in *Rhodotorula pilimanae*[122] (Figure 14) and a reductive removal is typical of the ferrichrome A transport in *U. sphaerogena*.

In principle, redox-relevant aspects of transport mechanisms can be determined employing Ga^{III}, Rh^{III} and Cr^{III} desferrisiderophores. The redox potentials of these metal-substituted siderophores are outside the range observed for

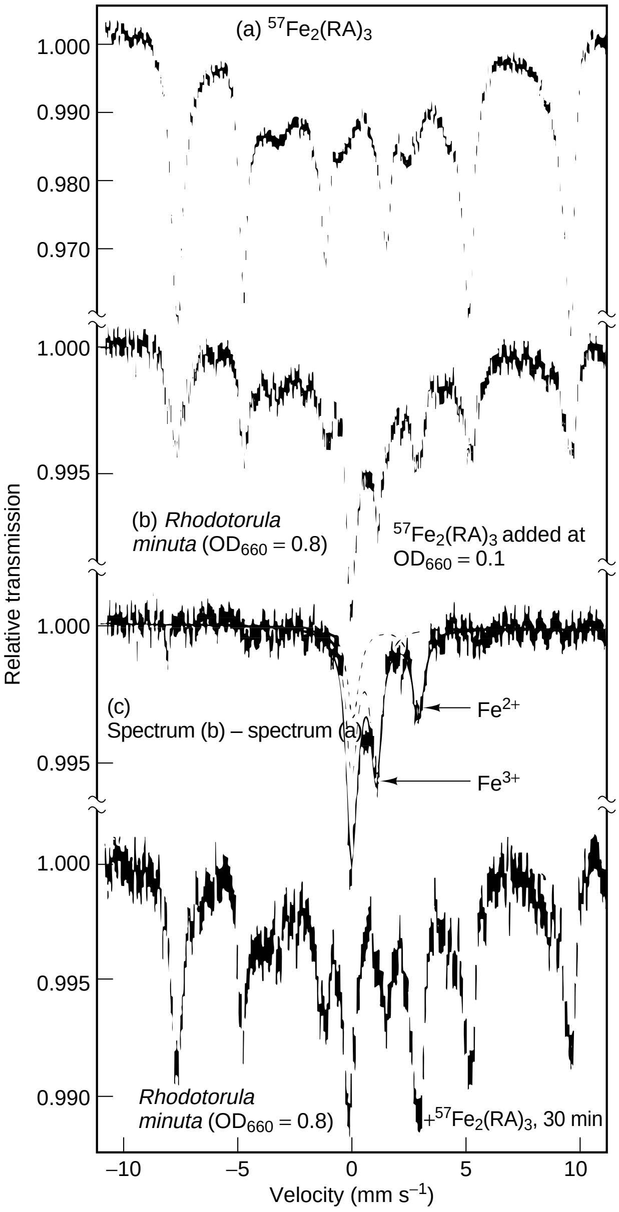

Figure 14 Mössbauer spectra of the frozen aqueous siderophore solution of [^{57}Fe]rhodotorulate, $Fe_2(RA)_3$, (a), and of the yeast *R. minuta* (b–d) at 4.2 K in a magnetic field $H_{app} = 20$ mT perpendicular to the γ-rays. Spectrum (b) corresponds to frozen *R. minuta* cells, grown in a salt medium supplied with 15 µM $^{57}Fe_2(RA)_3$ and harvested at $OD_{660} = 0.85$. The spectrum exhibits various components. The magnetically split subspectrum is due to $Fe_2(RA)_3$ (a), as can be demonstrated by subtraction (c). This indicates that $Fe_2(RA)_3$ is present in the cell. However, the metal is exchanged at the membrane level as shown by uptake studies with Cr- and Ga-substituted RA. (c) shows the residual spectrum (b) after stripping. Only two species can be observed. This metabolic pattern is similar to those found in Gram-negative bacteria.[177,179] Part (d) represents the Mössbauer spectrum of *R. minuta* at $OD_{660} = 0.8$ grown in iron-depleted medium. $^{57}Fe_2(RA)_3$ (15 µM) was added for 30 min. The $^{57}Fe_2(RA)_3$ contribution is 68% of the absorption area; the residual contribution is solely due to an Fe^{2+} high-spin species which seems to be the first iron metabolite after uptake

biological reductants. If these complexes show lack of intracellular accumulation, this could imply a reductive step during uptake. If Ga is transported and Cr is not, the uptake process should involve a ligand exchange step because Ga^{III} complexes are kinetically labile.[77,80] Detailed information on transport mechanisms and steps of iron metabolization have also been derived from in vivo Mössbauer spectroscopy (Figure 14).[179–182,183]

5.4 Reductive Removal of Iron from Siderophores In Vivo

Siderophores exhibit an affinity for Fe^{2+} that is some 20 orders of magnitude lower than for Fe^{3+}.[103] The kinetics of ligand exchange of high-spin Fe^{2+} are much faster than for high-spin Fe^{3+}.[184] Therefore, reduction of ferric siderophores accompanied by ligand exchange is an excellent mechanism for intracellular iron release. In fact, one main route of bacterial iron acquisition includes active transport of ferric siderophores across cell membranes, followed by intracellular iron removal from the siderophore carrier via reduction.[180,182,185,186] The deferrated siderophore is rapidly excreted.[186] Many flavin reductases show the property of reducing a broad spectrum of $[Fe^{3+}]$-siderophores in vitro. However, surprisingly it is not known which enzymes reduce the $[Fe^{3+}]$-siderophore in the cell.[185] Moreover, a substantial number of trihydroxamate-siderophores possess very negative redox potentials well below −320 mV at neutral pH precluding reduction via NADH or NADPH. In a very recent investigation, the Fe_2S_2-protein, FhuF, of *E. coli* has been identified as a siderophore reductase exhibiting a redox potential $E_{1/2}$ of -310 ± 25 mV vs NHE.[187]

Although the redox potential of FhuF is in the same range as NADH, FhuF is capable of reducing ferrioxamine B (see Table 4) in vitro and in vivo.[187] In fact, it has been postulated that it is the redox potential of the ternary reductase-ferric-siderophore complex rather than the redox potential of the free ferric siderophore that is important when considering reduction as a process involved in iron release.[188] In general, one has to bear in mind that a thermodynamically unfavorable process can nevertheless be driven if steady-state conditions are applied. In addition, the pH could influence the redox potential of a siderophore. For example, the midpoint potential of ferrioxamine B is −468 mV at pH 7.4, but increases to −180 mV at pH 4.5.[189]

A different strategy of intracellular iron release was found for the catechol siderophores enterobactin and parabactin. The pH 7 redox potential values for these siderophores are beyond the range of normal physiological reducing agents (see Table 4). This suggests that cellular iron release may occur by a reductive mechanism only after chemical transformation of the Fe^{III} siderophore to a form with an appropriate redox potential; an alternative process would be a significant drop in pH (e.g. in the acidic periplasm) to bring about an increase in Fe^{III} siderophore redox potential. In fact, an esterase was found in the cell extracts of *E. coli* that cleaves the ester backbone of Fe^{III} enterobactin.[190] In addition, it was demonstrated that the redox potential of the hydrolysis product $Fe(DHBS)_3$ (dihydroxybenzoylserine = DHBS) is −350 mV and within the range available from biological reductants (Table 4). Therefore, a mechanism of enterobactin-mediated iron uptake was proposed which involved an initial ester cleavage to metabolize iron. However, uptake studies with synthetic analogs which lack ester units and which are not susceptible to hydrolysis showed growth response of *B. subtilis* and of *E. coli* (see Figure 9).[191] Thus the esterase mechanism for in vivo iron release from Fe^{III} enterobactin became uncertain. An in vivo Mössbauer study of ^{57}Fe(ent) and ^{57}Fe(MECAM) uptake in the *aro*⁻ mutant *E. coli* K12 RW193 has helped to address this problem.[192] Whereas both Fe(ent) and Fe(MECAM) are taken up as the intact complex, the rates of metabolic utilization are drastically different (70% of enterobactin-bound iron within 140 min, but only traces after two hours of Fe(MECAM) uptake). This is clear evidence for a merely slow, that is, nonspecific, utilization of MECAM-bound iron. Above all, this finding substantiates the esterase mechanism of iron removal from enterobactin. Since no appreciable amounts of $Fe(DHBS)_3$ could be detected in the enterobactin experiments, any esterase activity and reductive ligand exchange must be closely correlated. The positive growth promotion with Fe(MECAM) uptake must be interpreted as being due to a small amount of nonspecifically metabolized complex which is still sufficient for normal growth rates of *E. coli*.[192] Although the existing data provide a consistent model, there continues to be confusion on this subject. Even a recent major microbiolical review[193] incorrectly assigned the major route of iron release from enterobactin.

Another illustration of a ligand-degradation process may be seen in the case of parabactin. Parabactin also has too negative a redox potential for iron removal via a reductive mechanism. However, upon hydrolysis of the oxazoline group of parabactin to produce parabactin A the redox potential is shifted to a more positive value that is within the physiological range for Fe^{III} reduction (Table 4). Therefore, in vivo oxazoline ring cleavage followed by Fe^{III} reduction may be involved in metabolic iron removal in *Paracoccus denitrificans*.

Finally, it has to be pointed out that the formation of bulk ‘free’ $Fe_{aq}{}^{2+}$ in the cytoplasm of microorganisms is not to be expected in vivo under ‘healthy’ conditions. $Fe_{aq}{}^{2+}$ is Fenton-active and thus deleterious to cells. Therefore, it is likely that the ferrous iron is bound by a chaperone-like structure or other novel structural elements to enable sheltered intracellular transfer of this ion. In fact, an oligomeric sugar phosphate was detected in *E. coli*[194] that binds ferrous iron (cytoplasmic concentration: approximately 500 μM) intracellularly released from ferrichrome (*E. coli*[182]) or ferrioxamine E (*Pantoea agglomerans*[180]). This compound was named ferrochelatin.[195]

5.5 Siderophore Uptake Regulation

The genes coding the proteins of siderophore-transport systems and the enzymes of siderophore biosynthesis and a variety of additional genes scattered through the chromosome are regulated by the iron requirement of the organism. A protein, named Fur (*f*erric *u*ptake *r*egulation) has been identified which is responsible for the transcriptional regulation of these genes (*see* ***Metalloregulation***). The *fur* gene product acts as a classical repressor requiring Fe^{2+} as an activator.[196–198] When the internal iron concentration is high, Fur forms a complex with Fe^{II} iron, exhibiting a strong binding affinity to DNA sequences (fur boxes) in the promoter regions of all genes which are negatively regulated by iron.[199] The Fur binding prevents transcription of these genes. The crystal structure of Fur from *P. aeruginosa* uncovered a functional dimer, each subunit exhibiting an N-terminal DNA-binding domain and a C-terminal dimerization domain.[199] Two metal centers were found, a Zn^{2+}-, and a Zn^{2+}/Fe^{2+}-binding site.[199,200] The Zn-binding site probably plays an important role in maintaining the integrity of the structure. At the second site Zn is exchangeable with Fe^{2+} and hence represents the regulatory site. Binding of ferrous iron leads to local conformational changes, which in turn probably alter the DNA-binding of the DNA-binding domain. Under conditions of iron deficiency, Fe^{II} iron is removed from Fur, the binding affinity to the DNA recognition sequences is lost, and Fur-dependent genes are transcribed. In addition, it has been demonstrated by in vivo Mössbauer spectroscopy that very high intracellular levels of Fe^{II} iron are maintained even under extreme growth conditions in *fur*$^{-}$ mutants, whereas wild-type strains show high levels of Fe^{III} iron.[182,201] Therefore it has been concluded that *fur* also regulates the oxidation state of the main components of iron metabolism in *E. coli*. It is now well established that a major subclass of Fur-like proteins is mainly involved in cellular iron homeostasis (*see****Metalloregulation***). But in addition, it can function in acid tolerance and protection against oxidative stress.[202–205]

6 ADDITIONAL FUNCTIONS OF SIDEROPHORES

6.1 Siderophores as Iron-storage Compounds

The predominant class of intracellular iron-storage compounds is represented by ferritin in eukaryotes and bacterioferritin in prokaryotes (*see* ***Iron Proteins for Storage & Transport & their Synthetic Analogs***). In various in vivo Mössbauer spectroscopic studies on siderophore uptake in fungi, it was realized that siderophores can also function as intracellular iron-storage compounds.[179,181,206] In the ascomycete *Neurospora crassa*, the transport siderophore coprogen represents an intracellular transient iron pool. A major part of coprogen-bound iron is transferred to a second siderophore, ferricrocin, which represents the long-term iron-storage form in this fungus.[206] Spores of *N. crassa* and of *Aspergillus ochraceus* are also lacking in ferritin-like iron-storage proteins. Rather, ferricrocin constituted 47% of the total iron content in *N. crassa*. In spores of *A. ochraceus*, 74% of the iron content was bound by ferrichrome-type siderophores.[181] It is safe to conclude that these siderophores are iron-storage peptides in spores. In view of the large siderophore iron-storage pools in spores, the intracellular accumulation of ferricrocin in mycelia seems to warrant an iron pool sufficiently large for sporulation. In the heterobasidiomycetous yeast *R. minuta*, the major intracellular iron pool is Fe^{III} rhodotorulate, and in the smut fungus *U. sphaerogena*, ferrichrome is found.[207] Again, no ferritins or bacterioferritins could be detected. From this the conclusion was drawn that, in various Ascomycetes and Heterobasidiomycetes, intracellular siderophores replace ferritins as iron-storage compounds. This further extends the biological role of siderophores. Whether genes for ferritin or bacterioferritin are present in these organisms remains an open question. However, ferritins definitely do not play a significant role in iron storage of these fungi.

6.2 Siderophores in Medicine

In the treatment of β-thalassemia and certain other anemias, periodic whole blood transfusions are required.[208–211] Since there is no specific physiological mechanism for the excretion of iron in man, continued transfusion therapy leads to a steady buildup of iron in the body and to deposition of iron in a number of organs, resulting in tissue damage and premature death. These iron excesses, as well as the primary iron overload diseases such as hemochromatosis and hemosiderosis, and accidental iron poisoning, require the removal of iron from the body, especially from the liver. The current drug of choice for the treatment of transfusional iron overload is the trihydroxamate siderophore desferrioxamine B. The long-term treatment with desferrioxamine B is generally well tolerated but it has two major drawbacks: lack of oral efficacy and short lifetime in the serum. Because of these limitations, there has been a wide search for new drugs with increased efficacy. Ideally, such an agent should be orally active and resistant to degradation or metabolism in the gastrointestinal tract, the bloodstream, the liver, and the kidneys. Furthermore, the drug should be effective at concentrations much lower than the gram amounts per day presently used for desferrioxamine B, should show a relatively long retention time in the body, and should have no adverse side effects. The design of such drugs continues to use siderophores as a principal model.[210–212]

Desferrioxamine B has also found therapeutic application for various pathological conditions due to aluminum overload.[213–215] Accumulation of this toxic metal is frequently observed in chronically dialyzed patients who have lost the ability to clear via renal excretion. Desferrioxamine B has also been recommended for the diagnosis of such an overload state.

For improved contrast enhancement for magnetic resonance imaging, different paramagnetic ions like Mn^{2+}, Fe^{3+}, and Gd^{3+} have been used. Gd^{3+} is particularly well suited as a contrast agent in diagnostic medical MRI due to its high magnetic moment and favorable electronic relaxation rate, However, Gd^{3+} is highly toxic at concentrations required for MRI. Therefore, chelators are required that prevent release of the free cation in vivo. Again, siderophores and their synthetic analogs serve as principal models for such chelators.[216]

As with almost any organism, iron is an essential nutrient for *Plasmodium falciparum*, the parasite causing malaria. In a series of investigations the antimalarial activities of various iron chelators were scrutinized. Some of these iron chelators exhibit activity in vitro and in animals with experimental plasmodial infections.[217] In particular, desferrioxamine B, the only chelator that is widely available for use in humans, has clinical antimalarial activity. The same siderophore was shown to inhibit growth of *Trypanosoma brucei*, another protozoic parasite causing sleeping sickness in human bloodstream.[218] However, in order to assess a siderophore or iron-chelator based therapy, extensive further investigations are required in this field. There might also be some therapeutic potential for siderophores and synthetic iron chelators in the treatment of cancers.[219,220] One strategy is aimed at the antineoplastic activity of siderophores.[221] A second strategy is focused on chelators for the clearance of non-transferrin-bound iron in serum which occurs in cancer therapy as a result of some chemotherapies.[222]

It has been shown in early inhibition studies as well as in recent crystal structures (see Sections 5.1 and 5.2) that the backbone portion of siderophores is not predominantly involved in receptor interactions; the carbon skeleton is partially solvent exposed instead. To this portion of the molecule, antibiotics may be attached. The resulting mixed compounds would be actively taken up into the cell, where the antibiotic portion of the molecule can kill the cell.[223] Indeed, the naturally occurring antibiotics albomycin and ferrimycin utilize this route for action. This ‘Trojan horse’ concept led to the synthesis of a series of siderophore-antibiotics.[224–226] Given the growing resistance, for example, of *Mycobacterium tuberculosis* and certain strains of *Pseudomonas* against antibiotic drugs currently at hand, there is an urgent need for completely new classes of antibiotics. The above mentioned approach might turn out to be of importance in the battle against pathogenic microbes and deserves therefore further intensive investigations.

6.3 Siderophore-transport Systems and Virulence

The relationship between siderophore production and bacterial growth rates has led to the belief that siderophore production contributes to bacterial virulence.[227,228] Reduced virulence of mutants deficient in siderophore production have been reported for *Yersinia pestis*, the causative agent of bubonic plague[229] and *Vibrio vulnificus*, a cholera-related pathogen associated with septicaemia arising from eating infected shell fish. It has frequently been noted that one of the host’s responses to infection is a reduction in serum iron levels, termed hypoferemia of infection. Under these conditions, the iron transport systems of the invading microorganism are expressed.[230,231] Indeed, antibodies against enterobactin and the enterobactin receptor have been detected in vertebrate serum. Very recently, it was discovered that a member of the human lipocalin-protein family, NGAL, binds Fe-enterobactin tightly (see Section 5.1).[144] NGAL is a potent bacteriostatic agent under iron-limiting conditions. Therefore, NGAL very likely participates in the antibacterial iron depletion strategy of the innate immune system. Also very important was the finding that certain invasive strains of *E. coli*, responsible for infections in vertebrates, harbor plasmids that enhance their virulence. One set of proteins encoded by these plasmids was identified as the transport system for the mixed-ligand siderophore aerobactin. It has been demonstrated in various studies that the ability to synthesize and transport aerobactin enhances virulence of bacteremic strains. Iron is not only an essential nutrient for invading microorganisms but may also serve as a regulatory signal influencing the expression of a variety of virulence factors. It is likely that iron, like calcium and constant temperature, is one of the environmental signals which serve to regulate the expression of genes required for survival and virulence in the host. There are several bacterial toxins that are derepressed under the conditions of low-iron stress typically found in a host. These include exotoxin A in *Pseudomonas aeruginosa*, the phage-mediated diphtheria toxin in *Corynebacterium diphtheriae*, the tetanus toxin of *Clostridium tetani*, and the shiga toxin of *Shigella dysentheriae*.

6.4 Other Applications of Siderophores

Siderophores have been found to bind effectively to actinides, such as Th, U, Np, and Pu.[232–234] Siderophores and other naturally occurring ligands may therefore affect actinide mobility in waste repositories and in the environment and may also be used to treat radioactive waste prior to storage or to decontaminate soils and water[234–236] Siderophores and siderophore analogs have also been investigated for possible medical use in the decorporation of actinides from the body,[232] while simple hydoxamates may have uses in the reprocessing of nuclear fuel.

7 RELATED ARTICLES

Iron: Inorganic & Coordination Chemistry; Iron Proteins for Storage & Transport & their Synthetic Analogs; Iron–Sulfur Proteins; Ligand Field Theory & Spectra; Metal Ion Toxicity; Metalloregulation.

8 REFERENCES

1. J. E. Posey and F. C. Gheradini, *Science*, 2000, **288**, 1651.
2. G. Wächtershäuser, *Microbiol. Rev.*, 1988, **52**, 452.
3. G. Winkelmann and H. Drechsel, Microbial Siderophores, in ‘Biotechnology’, 2nd edn., eds. H.-J. Rehm and G. Reed, VCH, Weinheim, 1997, Vol. 7, p. 199..
4. A. Sigel and G. Sigel, ‘Iron Transport and Storage in Microorganisms, Plants, and Animals’, Metal Ions in Biological Systems Vol. 35, Marcel Dekker, Basel, 1998.
5. G. Winkelmann ed., ‘Microbial Ttransport Systems’, Wiley-VCH, Weinheim, 2001.
6. D. M. Templeton and R. F. Barron eds, ‘Molecular and Cellular Iron Transport’, Marcel Dekker, New York, 2002.
7. H. Drechsel and G. Winkelmann, Iron Chelation and Siderophores, in ‘Transition Metals in Microbial Metabolism’, eds. G. Winkelmann and C. J. Carrano, Harwood Academic Publishers, Amsterdam, NY, 1997, p. 1.
8. G. Winkelmann, ‘Handbook of Microbial Iron Chelates’, CRC Press, Boca Raton, FL, 1991.
9. B. F. Matzanke, G. Müller-Matzanke, and K. N. Raymond, Siderophore-Mediated Iron Transport, in ‘Iron Carriers and Iron Proteins’, ed. T. M. Loehr, VCH, New York, 1989, p. 1.
10. K. N. Raymond, G. Müller, and B. F. Matzanke, *Top. Curr. Chem.*, 1984, **123**, 49.
11. J. H. Crosa and C. T. Walsh, *Microbiol. Mol. Biol. Rev.*, 2002, **66**, 223.
12. K. Hantke, *J. Mol. Microbiol. Biotechnol.*, 2002, **4**, 217.
13. N. Baichoo, T. Wang, R. Ye, and J. D. Helmann, *Mol. Biol.*, 2002, **45**, 1613.
14. J. H. Crosa, *Microbiol. Mol. Biol. Rev.*, 1997, **61**, 319.
15. B. F. Matzanke, Structures, Coordination Chemistry and Functions of Microbial Iron Chelates, in ‘Handbook of Microbial Iron Chelates’, ed. G. Winkelmann, CRC Press, Boca Raton, FL, 1991, p. 15.
16. E. Wasielwski, R. A. Atkinson, M. A. Abdallah, and B. Kieffer, *Biochemistry*, 2002, **41**, 12488.
17. R. A. Atkinson, A. L. M. Salah El Din, B. Kieffer, J.-F. Lefèvre, and M. A. Abdallah, *Biochemistry*, 1998, **37**, 15965.
18. H. Stephan, S. Freund, J.-M. Meyer, G. Winkelmann, and G. Jung, *Liebigs Ann. Chem.*, 1993, 43.
19. M. A. F. Jalal and D. van der Helm, Isolation and Spectroscopic Identification of Fungal Siderophores, in ‘Handbook of Microbial Iron Chelates’, ed. G. Winkelmann, CRC Press, Boca Raton, FL, 1991, p. 235.
20. J. M. Roosenberg, Y. M. Lin, Y. Lu, and M. J. Miller, *Curr. Med. Chem.*, 2000, **7**, 159.
21. S. Dhungana, S. Heggemann, M. S. Gebhard, U. Möllman, and A. L. Crumbliss, *Inorg. Chem.*, 2003, **42**, 42.
22. L. Dong, J. M. Roosenberg II, and M. J. Miller, *J. Am. Chem. Soc.*, 2002, **124**, 15001.
23. A. Shanzer and J. Libman, Biomimetic Siderophores; from Structural Probes to Diagnostic Tools, in ‘Iron Transport and Storage in Microorganisms, Plants, and Animals’, Vol. 35 of Series Metal Ions in Biological Systems, eds. A. Sigel and H. Sigel, Marcel Dekker, Basel, 1998, p. 329.
24. T. F. Emery and J. B. Neilands, *J. Am. Chem. Soc.*, 1961, **83**, 1626.
25. M. A. F. Jalal, M. B. Hossain, and D. van der Helm, *Biol. Met.*, 1988, **1**, 77.
26. D. van der Helm and G. Winkelmann, Hydroxamates and Polycarboxylates as iron Transport Agents (Siderophores) in Fungi, in ‘Metal Ions in Fungi’, eds. G. Winkelmann and G. Winge, Dekker, New York, 1994, p. 39.
27. H. Diekmann, *Arch. Microbiol.*, 1967, **58**, 1.
28. R. E. Moore and T. Emery, *Biochemistry*, 1976, **15**, 2719.
29. H. Bickel, G. Hall, W. Keller-Schierlein, V. Prelog, E. Vischer, and A. Wettstein, *Helv. Chim. Acta*, 1960, **43**, 2129.
30. S. Dhungana, P. S. White, and A. L. Crumbliss, *J. Biol. Inorg. Chem.*, 2001, **6**, 810.
31. H. Bickel, E. Gäumann, G. Nussberger, P. Reusser, E. Vischer, W. Voser, A. Wettstein, and H. Zähner, *Helv. Chim. Acta*, 1960, **43**, 2105.
32. M. B. Hossain, M. A. F. Jalal, B. A. Benson, C. L. Barnes, and D. van der Helm, *J. Am. Chem. Soc.*, 1987, **109**, 4948.
33. A. Takahashi, H. Nakamura, T. Kameyama, S. Kurasawa, H. Naganawa, Y. Okami, S. Takeuchi, and H. Umezawa, *J. Antibiot.*, 1987, **40**, 1671.
34. T. Nishio, N. Tanaka, J. Hiratake, Y. Katsube, Y. Ishida, and J. Oda, *J. Am. Chem. Soc.*, 1988, **110**, 8733.
35. K. M. Ledyard and A. Butler, *J. Biol. Inorg. Chem.*, 1997, **2**, 93.
36. Z. Hou, K. N. Raymond, B. O’Sullivan, T. W. Esker, and T. Nishio, *Inorg. Chem.*, 1998, **37**, 6630.
37. J. R. Pollack and J. B. Neilands, *Biochem. Biophys. Res. Commun.*, 1970, **38**, 989.
38. H.-P. Fiedler, P. Krastel, J. Müller, K. Gebhardt, and A. Zeeck, *FEMS Microbiol. Lett.*, 2001, **196**, 147.
39. H. Budzikiewicz, A. Boessenkamp, K. Taraz, A. Pandey, and J. M. Meyer, *Z. Naturforsch*, 1997, **52**, 551.
40. J. J. May, T. M. Wendrich, and M. A. Marahiel, *J. Biol. Chem.*, 2001, **276**, 7209.
41. G. H. Tait, *Biochem. J.*, 1975, **146**, 191.
42. K. Hantke, G. Nicholson, W. Rabsch, and G. Winkelmann, *Proc. Natl. Acad. Sci. U.S.A.*, 2003, **100**, 3677.
43. B. Schwyn and J. B. Neilands, *Anal. Biochem.*, 1987, **160**, 47.
44. J. Meiwes, H.-P. Fiedler, H. Haag, S. Konetschny-Rapp, and G. Jung, *FEMS Microbiol. Lett.*, 1990, **67**, 201.
45. H. Drechsel, S. Freund, G. Nicolson, H. Haag, O. Jung, H. Zähner, and G. Jung, *Biometals*, 1993, **6**, 185.
46. S. Yamamoto, N. Okujo, T. Yoshida, S. Matsuura, and S. Shinoda, *J. Biochem.*, 1994, **115**, 868.

47. A. Thieken and G. Winkelmann, *FEMS Microbiol. Lett.*, 1992, **94**, 37.
48. K. Barbeau, G. Zhang, D. H. Live, and A. Butler, *J. Am. Chem. Soc.*, 2002, **124**, 378.
49. M. J. Smith, J. N. Shoolery, B. Schwyn, I. Holden, and J. B. Neilands, *J. Am. Chem. Soc.*, 1985, **107**, 1739.
50. J. Francis, J. Madinaveitia, H. M. Macturk, and G. A. Snow, *Nature*, 1949, **163**, 365.
51. C. Ratledge, Mycobactins and Nocobactins, in 'Handbook of Microbiology', 2nd edn., eds. A. I. Laskin and H. A. Lechevalier, CRC Press, Boca Raton, FL, 1982, Vol. 4, p. 575.
52. M. A. F. Jalal, M. B. Houssain, D. van der Helm, J. Sanders-Loehr, L. A. Actis, J. H. Crosa, *J. Chem. Soc.*, 1989, **111**, 292.
53. G. J. Sharman, D. H. Williams, D. F. Ewing, and C. Ratledge, *Chem. Biol.*, 1995, **2**, 553.
54. M. Abdallah, Pyoverdins and Pseudobactins, in 'Handbook of Microbial Iron Chelates', ed. G. Winkelmann, CRC Press, Boca Raton, FL, 1991, p. 139.
55. H. Stephan, S. Freund, J.-M. Meyer, G. Winkelmann, and G. Jung, *Liebigs Ann. Chem.*, 1993, 43.
56. J. S. Martinez, N. J. Carter-Franklin, E. L. Mann, J. D. Martin, M. G. Haygood, and A. Butler, *Proc. Natl. Acad. Sci. U.S.A.*, 2003, **100**, 3754.
57. J. S. Martinez, G. P. Zhang, P. D. Holt, H.-T. Jung, C. J. Carrano, M. G. Haygood, and A. Butler, *Science*, 2000, **287**, 1245.
58. A. Nemoto, Y. Hoshino, K. Yazawa, A. Ando, Y. Mikami, H. Komaki, Y. Tanaka, and U. Gräfe, *J. Antibiot.*, 2002, **55**, 593.
59. C. J. Carrano, M. Jordan, H. Drechsel, D. G. Schmid, and G. Winkelmann, *Biometals*, 2001, **14**, 119..
60. K. A. Jensen, *Inorg. Chem.*, 1970, **9**, 1.
61. M. B. Hossain, M. A. F. Jalal, B. A. Benson, C. L. Barnes, and D. van der Helm, *J. Am. Chem. Soc.*, 1987, **109**, 4948.
62. C. L. Barnes, D. L. Eng-Wilmot, and D. van der Helm, *Acta Crystallogr.*, 1984, **C40**, 922.
63. M. B. Hossain, D. L. Eng-Wilmot, R. A. Loghry, and D. van der Helm, *J. Am. Chem. Soc.*, 1980, **102**, 5766.
64. M. B. Hossain, M. A. F. Jalal, and D. van der Helm, *Acta Crystallogr.*, 1986, **C42**, 1305.
65. M. B. Hossain and D. van der Helm, *Acta Crystallogr.*, 1983, **B39**, 258.
66. J. R. Telford and K. N. Raymond, *Inorg. Chem.*, 1998, **37**, 4578.
67. S. Isied and K. N. Raymond, *J. Am. Chem. Soc.*, 1976, **98**, 1763.
68. Y. Tor, J. Libman, A. Shanzer, C. E. Felder, and S. Lifson, *J. Am. Chem. Soc.*, 1992, **114**, 6661.
69. M. E. Bluhm, S. S. Kim, E. A. Dertz, and K. N. Raymond, *J. Am. Chem. Soc.*, 2002, **124**, 2436.
70. M. E. Bluhm, B. P. Hay, S. S. Kim, E. A. Dertz, and K. N. Raymond, *Inorg. Chem.*, 2002, **41**, 5475.
71. D. L. Eng-Wilmot, A. Rhaman, J. V. Mendenhall, S. L. Grayson, and D. van der Helm, *J. Am. Chem. Soc.*, 1984, **106**, 1285.
72. J. Leong and K. N. Raymond, *J. Am. Chem. Soc.*, 1974, **96**, 1757.
73. K. Abu-Dari and K. N. Raymond, *Inorg. Chem.*, 1980, **19**, 2034.
74. K. N. Raymond, K. Abu-Dari, and S. R. Sofen, Stereochemistry of Microbial Iron Transport Compounds, in 'Stereochemistry of Optically Active Transition Metal Compounds', Vol. 119, ACS Symposium Series, eds. B. E. Douglas and Y. Saito, 1980, p. 7.
75. K. N. Raymond, in 'Bioinorganic Chemistry II', ed. K. N. Raymond, American Chemical Society; *Adv. Chem. Ser. C*, 1977, **162**, 33.
76. A. J. McCaffery, S. F. Mason, and R. E. Ballard, *J. Chem. Soc.*, 1965, 2883.
77. G. Müller and K. N. Raymond, *J. Bacteriol.*, 1984, **160**, 304.
78. T. D. Y. Chung, B. F. Matzanke, G. Winkelmann, and K. N. Raymond, *J. Bacteriol.*, 1986, **165**, 283.
79. J. B. Neilands, T. J. Erickson, and W. H. Rastetter, *J. Biol. Chem.*, 1981, **256**, 3831.
80. G. Müller, Y. Isowa, and K. N. Raymond, *J. Biol. Chem.*, 1985, **260**, 13921.
81. D. L. Kepert, *Inorg. Chem.*, 1972, **11**, 1561.
82. A. Avdeef and J. P. Fackler, *Inorg. Chem.*, 1975, **14**, 2002.
83. E. L. Muetterties and L. J. Guggenberger, *J. Am. Chem. Soc.*, 1974, **96**, 1748.
84. T. J. McMurry, M. W. Hosseini, T. M. Garrett, F. E. Hahn, Z. E. Reyes, and K. N. Raymond, *J. Am. Chem. Soc.*, 1987, **109**, 7196.
85. C. J. Carrano, S. R. Cooper, and K. N. Raymond, *J. Am. Chem. Soc.*, 1979, **101**, 599.
86. Z. Hou, K. N. Raymond, B. O'Sullivan, T. W. Esker, and T. Nishio, *Inorg. Chem.*, 1998, **37**, 6630.
87. J. R. Telford and K. N. Raymond, *Inorg. Chem.*, 1998, **37**, 4578.
88. P. Gütlich, R. Link, and A. X. Trautwein, 'Mössbauer Spectroscopy and Transition Metal Chemistry', Springer Verlag, Berlin, 1978.
89. A. Abragam and B. Bleany, 'Electron Paramagnetic Resonance of Transition Ions', Clarendon Press, Oxford, 1970.
90. B. F. Matzanke, Mössbauer Spectroscopy of Microbial Iron Uptake and Metabolism, in 'Iron Transport in Microbes, Plants and Animals', eds. G. Winkelmann, D. van der Helm, and J. B. Neilands, VCH, Weinheim, 1987, p. 251.
91. M. Llinas, D. M. Wilson, and M. P. Klein, *J. Am. Chem. Soc.*, 1977, **99**, 6846.
92. M. Llinas and K. Wüthrich, *Biochim. Biophys. Acta*, 1978, **532**, 29.

93. L. D. Loomis and K. N. Raymond, *Inorg. Chem.*, 1991, **30**, 906.
94. W. R. Harris, C. J. Carrano, S. R. Cooper, S. R. Sofen, A. E. Avdeef, J. V. McArdle, and K. N. Raymond, *J. Am. Chem. Soc.*, 1979, **101**, 6097.
95. W. R. Harris and K. N. Raymond, *J. Am. Chem. Soc.*, 1979, **101**, 6534.
96. V. L. Pecoraro, G. B. Wong, T. A. Kent, and K. N. Raymond, *J. Am. Chem. Soc.*, 1983, **105**, 4617.
97. V. L. Pecoraro, W. R. Harris, G. B. Wong, C. J. Carrano, and K. N. Raymond, *J. Am. Chem. Soc.*, 1983, **105**, 4623.
98. M. E. Cass, T. M. Garrett, and K. N. Raymond, *J. Am. Chem. Soc.*, 1989, **111**, 1677.
99. A. L. Crumbliss, Aqueous Solution Equilibrium and Kinetic Studies of Iron Siderophore and Model Siderophore Complexes, in ‘Handbook of Microbial Iron Chelates’, ed. G. Winkelmann, CRC Press, Boca Raton, FL, 1991, p. 177.
100. J. P. Adjimani and T. Emery, *J. Bacteriol.*, 1987, **169**, 3664.
101. M. Akiyama, A. Katoh, and T. Mutoh, *J. Org. Chem.*, 1988, **53**, 6089.
102. D. C. Olson and D. W. Margerum, *J. Am. Chem. Soc.*, 1963, **85**, 297.
103. H. Boukhalfa and A. L. Crumbliss, *Biometals*, 2002, **15**, 325.
104. H. Boukhalfa, T. J. Brickmann, S. K. Armstrong, and A. L. Crumbliss, *Inorg. Chem.*, 2000, **39**, 5591.
105. M. Birus, Z. Bradic, G. Krznaric, N. Kujundzic, M. Pribanic, P. C. Wilkins, and R. G. Wilkins, *Inorg. Chem.*, 1987, **26**, 1000.
106. I. Spasojevic, H. Boukhalfa, R. D. Stevens, and A. L. Crumbliss, *Inorg. Chem.*, 2001, **40**, 49.
107. A. Shanzer, J. Libman, S. Lifson, and C. E. Felder, *J. Am. Chem. Soc.*, 1986, **108**, 7609.
108. S. S. Eaton, J. R. Hutchinson, R. H. Holm, and E. L. Muetterties, *J. Am. Chem. Soc.*, 1972, **94**, 6411.
109. E. L. Muetterties, *Acc. Chem. Res.*, 1970, **3**, 266.
110. D. B. Rorabacher and D. W. Margerum, *Inorg. Chem.*, 1964, **3**, 382.
111. B. Borgias, A. D. Hugi, and K. N. Raymond, *Inorg. Chem.*, 1989, **28**, 3538.
112. I. Spasojevic, S. K. Armstrong, T. J. Brickmann, and A. L. Crumbliss, *Inorg. Chem.*, 1999, **38**, 449.
113. E. H. Swift and E. A. Butler, ‘Quantitative Measurements and Chemical Equilibria’, Freeman, San Francisco, CA, 1972.
114. T. M. Garrett and K. N. Raymond, *Pure Appl. Chem.*, 1988, **60**, 1807.
115. S. J. Rodgers, C.-W. Lee, C. Y. Ng, and K. N. Raymond, *Inorg. Chem.*, 1987, **26**, 1622.
116. C.-W. Lee, D. J. Ecker, and K. N. Raymond, *J. Am. Chem. Soc.*, 1985, **107**, 6920.
117. V. L. Pecoraro, G. B. Wong, T. A. Kent, B. H. Huynh, and K. N. Raymond, *J. Am. Chem. Soc.*, 1983, **105**, 4617.
118. D. J. Ecker, B. F. Matzanke, and K. N. Raymond, *J. Bacteriol.*, 1986, **167**, 666.
119. D. J. Ecker, L. D. Loomis, M. E. Cass, and K. N. Raymond, *J. Am. Chem. Soc.*, 1988, **110**, 2457.
120. G. Müller, B. F. Matzanke, and K. N. Raymond, *J. Bacteriol.*, 1984, **160**, 313.
121. H. Huschka, H.-U. Naegeli, H. Leuenberger-Ryf, K. Keller-Schierlein, and G. Winkelmann, *J. Bacteriol.*, 1985, **162**, 715.
122. G. Müller, S. J. Barclay, and K. N. Raymond, *J. Biol. Chem.*, 1985, **280**, 13916.
123. K. Poole and G. A. McKay, *Front. Biosci.*, 2003, **8**, d661.
124. V. Braun and M. Braun, *Curr. Opin. Microbiol.*, 2002, **5**, 194.
125. K. N. Raymond, E. A. Dertz, and S. S. Kim, *Proc. Natl. Acad. Sci. U.S.A.*, 2003, **100**, 3584.
126. C. A. Genco and D. W. Dixon, *Mol. Biol.*, 2001, **39**, 1.
127. P. Arnoux, R. Haser, N. Izadi, A. Lecroisey, M. Delepierre, C. Wandersmann, and M. Czjzek, *Nat. Struct. Biol.*, 1999, **6**, 516.
128. C. N. Cornelissen, *Front. Biosci.*, 2003, **8**, d836.
129. C. H. Taboy, K. G. Vaughan, T. A. Mietzner, P. Aisen, and A. L. Crumbliss, *J. Biol. Chem.*, 2001, **276**, 2719.
130. D. Alexeev, H. Zhu, M. Guo, W. Zhong, D. J. Hunter, W. Yang, D. J. Campopiano, and P. J. Sadler, *Nat. Struct Biol.*, 2003, **4**, 297.
131. H. Nikaido and M. Vaara, Outer Membrane, in ‘*Escherichia Coli* and *Salmonella Typhimurium* – Cellular and Molecular Biology’, ed. F. C. Neidhard, American Society for Microbiology, Washington, DC, 1987, p. 7.
132. V. Braun, K. Hantke, and W. Köster, Bacterial Iron Transport: Mechanisms, Genetics, and Regulation, in ‘Iron Transport and Storage in Micoorganisms, Plants, and Animals’, Vol. 35 of Series, Metal Ions in Biological Systems, eds. A. Sigel and H. Sigel, Marcel Dekker, Basel, 1998, p. 67.
133. M. Kammler, C. Schön, and K. Hantke, *J. Bacteriol.*, 1993, **175**, 6212.
134. S. K. Buchanan, B. S. Smith, L. Venkatramani, D. Xia, L. Esser, M. Palnitkar, R. Chakraborty, D. van der Helm, and J. Deisenhofer, *Nat. Struct. Biol.*, 1999, **6**, 56.
135. K. C. Usher, E. Özkan, K. H. Gardner, and J. Deisenhofer, *Proc. Natl. Acad. Sci. U.S.A.*, 2001, **98**, 10676.
136. D. Ferguson, E. Hofmann, J. W. Coulton, K. Diederichs, and W. Welte, *Science*, 1998, **282**, 2215.
137. A. D. Ferguson, V. Braun, H.-P. Fiedler, J. W. Coulton, K. Diederichs, and W. Welte, *Protein Sci.*, 2000, **9**, 956.
138. P. Locher, B. Rees, R. Koebnik, A. Mitschler, L. Moulinier, J. P. Rosenbusch, and D. Moras, *Cell*, 1998, **95**, 771.
139. W. Yue, S. Grizot, and S. K. Buchanan, *J. Mol. Biol.*, 2003, **332**, 353..
140. A. D. Ferguson and J. Deisenhofer, *Biochim. Biophys. Acta*, 2002, **1565**, 318.

141. D. van der Helm and R. Chakraborty, Structures of Siderophore Receptors, in ‘Microbial Transport Systems’, ed. G. Winkelmann, Wiley-VCH, Weinheim, 2001, p. 261.

142. A. D. Ferguson, J. Ködding, J. W. Coulton, K. Diederichs, V. Braun, and W. Welte, *Structure*, 2001, **9**, 707.

143. A. D. Ferguson, R. Chakraborty, B. S. Smith, L. Esser, D. van der Helm, and J. Deisenhofer, *Science*, 2002, **295**, 1715.

144. D. H. Goetz, M. A. Holms, N. Borregaard, M. E. Bluhm, K. N. Raymond, and R. K. Strong, *Mol. Cells*, 2002, **10**, 1033.

145. H. Schöffler and V. Braun, *Mol. Gen. Genet.*, 1989, **217**, 378.

146. U. Roos, R. E. Harkness, and V. Braun, *Mol. Microbiol.*, 1989, **3**, 891.

147. E. Fischer, K. Günter, and V. Braun, *J. Bacteriol.*, 1989, **171**, 5127.

148. K. Eick-Helmerich and V. Braun, *J. Bacteriol.*, 1989, **171**, 5117.

149. V. Braun, *FEMS Microbiol. Rev.*, 1995, **16**, 295.

150. V. Braun, S. I. Patzer, and K. Hantke, *Biochimie*, 2002, **84**, 365.

151. R. A. Larsen, M. G. Thomas, and K. Postle, *Mol. Microbiol.*, 1999, **31**, 1809..

152. A. Sauter, S. P. Howard, and V. Braun, *J. Bacteriol.*, 2003, **185**, 5747.

153. J. D. Faraldo-Gomez, G. R. Smith, and M. S. P. Sansom, *Biophys. J.*, 2003, **85**, 1406.

154. M. Braun, F. Endriss, H. Killmann, and V. Braun, *J. Bacteriol.*, 2003, **185**, 5508.

155. C. S. Klug, S. S. Eaton, G. R. Eaton, and J. B. Feix, *Biochemistry*, 1998, **37**, 9016.

156. T. J. Barnard, M. E. Watson Jr, and M. A. McIntosh, *Mol. Microbiol.*, 2001, **41**, 527.

157. P. E. Klebba, *Front. Biosci.*, 2003, **8**, s1422.

158. P. Thulasiraman, S. M. Newton, J. Xu, K. N. Raymond, C. Mai, A. Hall, M. A. Montague, and P. E. Klebba, *J. Bacteriol.*, 1998, **180**, 6689.

159. J. W. Coulton, P. Mason, D. R. Cameron, G. Carmel, R. Jean, and H. N. Rode, *J. Bacteriol*, 1986, **165**, 181.

160. M. L. Lundrigan and R. J. Kadner, *J. Biol. Chem.*, 1986, **261**, 10797.

161. U. Pressler, H. Staudenmaier, L. Zimmermann, and V. Braun, *J. Bacteriol.*, 1988, **170**, 2716.

162. W. Köster and V. Braun, *J. Biol. Chem.*, 1990, **265**, 21407.

163. M. R. Rohrbach, V. Braun, and W. Köster, *J. Bacteriol.*, 1995, **177**, 7186.

164. T. E. Clarke, V. Braun, G. Winkelmann, L. W. Tari, and H. J. Vogel, *J. Biol. Chem.*, 2002, **277**, 13966.

165. T. E. Clarke, M. R. Rohrbach, L. W. Tari, H. J. Vogel, and W. Köster, *Biometals*, 2002, **15**, 121.

166. T. E. Clarke, S.-Y. Ku, D. R. Dougan, H. J. Vogel, and L. W. Tari, *Nat. Struct. Biol.*, 2000, **7**, 287.

167. A. L. Davidson and H. Nikaido, *J. Biol. Chem.*, 1991, **266**, 8946.

168. P.-Q. Liu and G. F.-L. Ames, *Proc. Natl Acad. Sci. U.S.A.*, 1998, **95**, 3495.

169. W. Boos and T. Eppler, Prokaryotic Binding Protein-Dependent ABC Transporters, in ‘Microbial Transport Systems’, ed. G. Winkelmann, Wiley-VCH, Weinheim, 2001, p. 77.

170. V. Braun and K. Hantke, Mechanisms of Bacterial Iron Transport, in ‘Microbial Transport Systems’, ed. G. Winkelmann, Wiley-VCH, Weinheim, 2001, p. 289.

171. I. J. Schalk, C. Hennard, C. Dugave, K. Poole, M. A. Abdallah, and F. Pattus, *Mol. Microbiol.*, 2001, **39**, 351.

172. A. Stintzi, C. Barnes, J. Xu, and K. N. Raymond, *Proc. Natl. Acad. Sci. U.S.A.*, 2000, **97**, 10691.

173. H. Haas, M. Schoeser, E. Lesuisse, J. F. Ernst, W. Parson, B. Abt, G. Winkelmann, and H. Oberegger, *Biochem. J.*, 2003, **371**, 505.

174. K. Haselwandter and G. Winkelmann, *Biometals*, 2002, **15**, 73.

175. H. Haas, *Appl. Microbiol. Biotechnol.*, 2003, **62**, 316.

176. P. Heymann, M. Gerads, M. Schaller, F. Dromer, G. Winkelmann, and J. F. Ernst, *Infect. Immun.*, 2002, **70**, 5246.

177. G. Winkelmann, Siderophore Transport in Fungi, in ‘Microbial Transport Systems’, ed. G. Winkelmann, VCH, Weinheim, 2001, p. 463.

178. G. Winkelmann, D. van der Helm, and J. B. Neilands, ‘Iron Transport in Microbes, Plants and Animals’, VCH, Weinheim, 1987.

179. B. F. Matzanke, E. Bill, G. I. Müller, G. Winkelmann, and A. X. Trautwein, *Eur. J. Biochem.*, 1987, **162**, 643.

180. B. F. Matzanke, I. Berner, E. Bill, A. X. Trautwein, and G. Winkelmann, *Biometals*, 1991, **4**, 181.

181. B. F. Matzanke, E. Bill, A. X. Trautwein, and G. Winkelmann, *J. Bacteriol.*, 1987, **169**, 5873.

182. B. F. Matzanke, G. Müller, E. Bill, and A. X. Trautwein, *Eur. J. Biochem.*, 1989, **183**, 371.

183. L. Rauscher, D. Expert, B. F. Matzanke, and A. Trautwein, *J. Biol. Chem.*, 2002, **277**, 2385.

184. S. N. Lincoln and A. E. Merbach, *Adv. Inorg. Chem.*, 1995, **42**, 1.

185. M. Fontecave, J. Coves, and J. L. Pierre, *Biometals*, 1994, **7**, 3.

186. A. Hartmann, H. P. Fiedler, and V. Braun, *Eur. J. Biochem.*, 1979, **99**, 517.

187. B. F. Matzanke, S. Anemüller, V. Schünemann, A. X. Trautwein, and K. Hantke, *Biochemistry*, 2004, **43**, 1386.

188. J. B. Neilands, *J. Biol. Chem.*, 1995, **270**, 26723..

189. R. Helman and G. D. Lawrence, *J. Electroanal. Chem.*, 1989, **22**, 276.

190. T. J. Brickman and M. A. McIntosh, *J. Biol. Chem.*, 1992, **267**, 12350.

191. S. Heidinger, V. Braun, V. L. Pecoraro, and K. N. Raymond, *J. Bacteriol.*, 1983, **153**, 109.

192. B. F. Matzanke, D. J. Ecker, T.-S. Yang, B. H. Huynh, and K. N. Raymond, *J. Bacteriol.*, 1986, **167**, 674.

193. C. Ratledge and L. G. Dover, *Annu. Rev. Microbiol.*, 2000, **54**, 881.

194. R. Böhnke and B. F. Matzanke, *Biometals*, 1995, **8**, 223.

195. B. F. Matzanke, Iron Storage in Microorganisms, in 'Transition Metals in Microbial Metabolism', eds. G. Winkelmann and C. Carrano, Harwood Academic Publishers, 1997, p. 117.

196. K. Hantke, *Mol. Gen. Genet.*, 1984, **197**, 337.

197. S. Schäffer, K. Hantke, and V. Braun, *Mol. Gen. Genet.*, 1985, **200**, 110.

198. D. W. Griggs and J. Konisky, *J. Bacteriol.*, 1989, **171**, 1048.

199. E. Pohl, J. C. Haller, A. Mijovilovich, W. Meyer-Klauke, E. Garman, and M. L. Vasil, *Mol. Microbiol.*, 2003, **47**, 903.

200. A. Gonzalez de Peredo, C. Saint-Pierre, A. Adrait, L. Jacquemet, J. M. Latour, I. Michaud-Soret, and E. Forest, *Biochemistry*, 1999, **38**, 8582.

201. B. F. Matzanke, E. Bill, and A. X. Trautwein, *Hyperfine Interact.*, 1992, **71**, 1259.

202. K. Hantke, *Curr. Opin. Microbiol.*, 2001, **4**, 172.

203. H. K. Hall and J. W. Foster, *J. Bacteriol*, 1996, **178**, 5683.

204. N. Bsat, A. Herbig, L. Cassillas-Martinez, P. Setlow, and J. D. Helmann, *Mol. Biol.*, 1998, **29**, 189.

205. S. Dubrac and D. Touati, *Microbiology*, 2002, **148**, 147.

206. B. F. Matzanke, E. Bill, A. X. Trautwein, and G. Winkelmann, *Biometals*, 1988, **1**, 18.

207. B. F. Matzanke, E. Bill, A. X. Trautwein, and G. Winkelmann, *Hyperfine Interact.*, 1990, **58**, 2359.

208. C. Hershko, G. Link, and A. M. Konijn, Cardioprotective Effect of Iron Chelators, in 'Iron Chelation Therapy', 1st edn., ed. C. Hershko, Kluwer Academic/Plenum Publishers, New York, 2002, Vol. 509, p. 77.

209. B. Modell, E. A. Letsky, E. A. Flynn, R. Peto, and D. J. Weatherall, *Br. Med. J.*, 1982, **284**, 1081.

210. A. Pietrangelo, Mechanism of Iron Toxicity, in 'Iron Chelation Therapy', 1st edn., ed. C. Hershko, Kluwer Academic/Plenum Publishers, New York, 2002, Vol. 509, p. 19.

211. T. B. Chaston and D. R. Richardson, *Am. J. Hematol.*, 2003, **73**, 200.

212. A. N. Martonosi ed., 'Membranes', Plenum Press, New York, 1985, Vol. 3.

213. P. Ackrill, A. J. Ralston, J. P. Day, and K. C. Hodge, *Lancet*, 1980, **2**, 692.

214. R. A. Romero and J. P. Day, *Trace Elem. Med.*, 1985, **2**, 1.

215. H. G. Nebeker and J. W. Coburn, *Annu. Rev. Med.*, 1986, **37**, 79.

216. D. M. J. Doble, M. Melchior, B. O'Sullivan, C. Siering, J. Xu, V. C. Pierre, and K. N. Raymond, *Inorg. Chem.*, 2003, **42**, 4930.

217. V. R. Gordeuk and M. Loyevsky, Antimalarial Effect of Iron Chelators, in 'Iron Chelation Therapy', 1st edn., ed. C. Hershko, Kluwer Academic/Plenum Publishers, New York, 2002, Vol. 509, p. 251.

218. T. Breidbach, S. Scory, R. L. Krauth-Siegel, and D. Steverding, *Int. J. Parasitol.*, 2002, **32**, 473.

219. D. R. Richardson, Therapeutic Potential of Iron Chelators in Cancer Therapy, in 'Iron Chelation Therapy', 1st edn., ed. C. Hershko, Kluwer Academic/Plenum Publishers, New York, 2002, Vol. 509, p. 231.

220. J. D. Kemp, *Histol. Histopathol.*, 1997, **12**, 291.

221. A. Kicic, A. C. G. Chua, and E. Baker, *Br. J. Pharmacol.*, 2002, **135**, 1393.

222. A. C. A. Chua, H. A. Ingram, K. N. Raymond, and E. Baker, *Eur. J. Biochem.*, 2003, **270**, 1689.

223. B. F. Matzanke, U. Möllmann, R. Reissbrodt, V. Schünemann, and A. X. Trautwein, *Hyperfine Interact.*, 1998, **112**, 123.

224. J. M. Rosenberg, Y. M. Lin, Y. Lu, and M. J. Miller, *Curr. Med. Chem.*, 2000, **7**, 159.

225. C. Hennard, Q. C. Truong, J.-F. Desnottes, J.-M. Paris, N. J. Moreau, and M. A. Abdallah, *J. Med. Chem.*, 2001, **44**, 2139.

226. L. Heinisch, S. Wittmann, T. Stoiber, A. Berg, D. Ankel-Fuchs, and U. Mollmann, *J. Med. Chem.*, 2002, **45**, 3032.

227. J. J. Bullen and E. Griffith, 'Iron and Infection', John Wiley, Chichester, 1999.

228. M. Stork, M. Di Lorenzo, T. J. Welch, L. M. Crosa, and J. H. Crosa, *Plasmid*, 2002, **48**, 222.

229. R. D. Perry, J. Abney, I. Mier Jr, Y. Lee, S. W. Bearden, and J. D. Fetherston, *Adv. Exper. Med. Biol.*, 2003, **529**, 275.

230. E. D. Weinberg, *Clin. Physiol. Biochem.*, 1986, **4**, 50.

231. S. M. Payne, *CRC Crit. Rev. Microbiol.*, 1988, **16**, 81.

232. P. W. Durbin, N. Jeung, S. J. Rodgers, P. N. Turowski, F. L. Weitl, D. L. White, and K. N. Raymond, *Radiat. Prot. Dosim.*, 1989, **26**, 351.

233. G. N. Stradling, *J. Alloys Compd.*, 1998, **271–273**, 72.

234. J. C. Renshaw, V. Halliday, G. D. Robson, A. P. J. Trinci, M. G. Wiebe, F. R. Livens, D. Collison, and R. J. Taylor, *Appl. Environ. Microbiol.*, 2003, **69**, 3600.

235. C. E. Ruggiero, M. P. Neu, J. H. Matonic, and S. D. Reilly, *Actinide Res. Q.*, 2000, 16.

236. H. R. von Gunten and P. Benes, *Radiochim. Acta*, 1995, **69**, 1.

Lead: Inorganic Chemistry

Mohan S. Bharara & David A. Atwood
University of Kentucky, Lexington, KY, USA

Based in part on the article Lead: Inorganic Chemistry by Philip G. Harrison which appeared in the Encyclopedia of Inorganic Chemistry, First Edition.

1	Introduction	1
2	General Trends	2
3	Coordination Geometries	2
4	Lead Halides and Complex Halides	3
5	Lead Pseudohalides	4
6	Oxides and Other Chalcogenides	4
7	Carboxylates and Oxyacid Derivatives	6
8	Solution Studies	7
9	Lead(II) Alkoxides	8
10	Lead Thiolates, Dithiophosphates, Dithioxanthates, and Dithiocarbamates	9
11	Compounds Containing Bonds to Nitrogen or Phosphorus	9
12	Compounds with Lead–Transition Metal Bonds	10
13	Metallic Clusters	11
14	Related Articles	11
15	References	11

1 INTRODUCTION

Lead has been known to man since antiquity, and must have been of not inconsiderable value by the second millennium BC, since the earliest known reference to it is as part of a tribute brought back to Pharaoh Thutmosis III (ca. 1500 BC) when his victorious army returned from Mesopotamia. However, its use in pottery glazes predates this by several thousand years. The use of lead in water piping and plumbing was extensive in ancient times, giving rise to the terminology used today. Unfortunately, in present times lead is associated most strongly with its toxic effects. Initially these arose from the use of lead piping for supplies of potable water, or, in ancient times, from the use of lead acetate ('sugar of lead') to sweeten food! In the past few decades, the major origin of lead toxicity has been from motor vehicle exhaust emissions resulting from the use of tetraethyllead as an 'anti-knock' agent. Other sources include the use of 'surma' (a preparation made from lead sulfide) in certain ethnic communities.

The extreme toxicity of lead results from the manifold modes of activity. In the stable state, $\geq$90% of total body lead is stored in the skeleton. Lead appears to have the capacity to seek out areas of active bone formation, where it occupies lattice interstices or exchanges with calcium in the bone apatite structure, although only ca. 0.65% of bone calcium is exchangeable. Lead in this form can be slowly released back into the bloodstream with the obvious consequences of chronic damage to major organs and soft tissue. At the chemical level, lead is capable of interrupting most of the steps in heme synthesis and porphyrin metabolism. In addition, it can inhibit the activity of many enzymes including ATPase, carbonic anhydrase, acetylcholine-esterase, and acid phosphatase, and also interfere with protein synthesis by interaction with transfer-RNA. Acute lead poisoning, which usually arises from the accidental ingestion of a soluble lead salt, is characterized by an intense thirst and metallic taste in the mouth, a burning abdominal pain, vomiting, diarrhea, hemolysis, renal damage with ologuria, shock, and coma. Chronic poisoning, due usually to accumulation of small quantities of lead in the body by either inhalation, ingestion, or skin absorption, has somewhat different symptoms. Early symptoms can be anorexia, constipation, headache, weakness, development of a black or blue line on the gums, and anemia. There may be accompanying vomiting, irritability with paralysis in more advanced cases, and renal damage. Encephalopathy with visual disturbance, persistent vomiting, ataxia, delirium, and convulsions may develop, especially in children. Organolead(IV) compounds have a specific action on the nervous tissues, leading to mental disturbance and convulsions. Treatment is usually by sequestering the lead using a strongly chelating agent such as D-penicillamine, EDTA and its salts (known usually as edetates), or BAL (British anti-Lewisite, dimercaptopropanol). Initial treatment commonly involves disodium calcium edetate in order to prevent hypocalcemia in conjunction with dimercaptopropanol, followed by longer-term treatment with D-penicillamine. Dimercaptopropanol functions by successfully competing for lead associated with the SH groups of proteins, forming stable complexes. Both edetate salts and D-penicillamine chelate lead, forming stable complexes, which are excreted in the urine.

At 13 ppm, lead is by far the most abundant of the heavier metals. This is due in large part because ^{206}Pb, ^{207}Pb, and ^{208}Pb arise as the stable end products of natural radioactive decay sequences. The most important ore is galena (PbS), but several other ores are known [cerussite ($PbCO_3$), anglesite ($PbSO_4$), pyromorphite ($Pb_5(PO_4)_3Cl$), and mimesite ($Pb_5(AsO_4)_3Cl$)]. The extraction of lead from galena involves roasting to give PbO, which is then reduced using coke and limestone or using fresh galena. The initial product contains many impurities (Cu, Ag, Au, Zn, Sn, As, and Sb), all of which can be removed prior to final purification by electrolytic methods. Most of the lead produced is used in batteries with the remainder used for solders, sheeting and tubing, cable sheathing, pigments and chemicals, and tetraethyl- and tetramethyllead. Lead compounds are widely used as pigments, as ceramic glazes ($PbSi_2O_5$), in lead crystal glass, and as stabilizers in poly(vinyl chloride) plastics for nonfood use (lead soaps). Red lead (Pb_3O_4) and Ca_2PbO_4 are used as primers for iron and steel. Lead chromate ($PbCrO_4$) is the yellow pigment used in paints for road markings and, in conjunction with iron, blue pigments in green paints. Other lead-based pigments include red–orange $PbMoO_4$, yellow PbO, and white $2PbCO_3{\cdot}Pb(OH)_2$. Increasingly important are electroactive lead ceramic materials.

2 GENERAL TRENDS

Lead metal is soft, malleable, and ductile, and low melting (mp 327 °C, bp 1751 °C). It is very dense ($11.342\,g\,cm^{-3}$ at 20 °C) with a typically metallic face-centered cubic structure. The electrical resistivity is very low ($20 \times 10^{-6}\,\Omega\,cm$ at 20 °C). Finely divided lead is pyrophoric but the reactivity is greatly reduced by the formation of a thin coherent protective layer of oxide, oxocarbonate, sulfate or chloride, depending upon the ambient atmosphere. Such coatings render the metal quite inert; hence the use of lead in the handling of hot concentrated sulfuric acid. Reactivity with mineral acids is generally very slow, although lead reacts with concentrated nitric acid, giving lead(II) nitrate and oxides of nitrogen. Lead metal and lead-containing solders react with organic acids such as acetic acid, which precludes storage of acidic foodstuffs such as citrus fruits and tomatoes in cans with solder seams. Direct reaction of lead metal with other elements at room temperature is restricted to fluorine (giving PbF_2), although chlorine, and the chalcogenides oxygen, sulfur, selenium, and tellurium, react on heating.

Inorganic compounds of lead are far more abundant in the $+2$ oxidation state than in the $+4$ state. This is a manifestation of the greater stability of the $+2$ state with respect to the $+4$ state, and is related to the *Inert Pair Effect* seen quite generally for the heavier posttransition metal p-block elements. The effect is not so much a result of low ionization energies [for lead: 715.4 (1st), 1450.0 (2nd), 3080.7 (3rd), and 4082.3 (4th) $kJ\,mol^{-1}$], rather than that the energy required to involve the s electrons is not compensated by the energy released by the formation of additional bonds. Obviously this is a rather simple view, and in practice many other factors (structure, bonding type, enthalpies of solvation, entropy effects) are also involved. It is notable, however, that in the organometallic chemistry of lead, the abundance of compounds is the converse, that is, many more organolead(IV) compounds are known.

The electronegativity of lead differs little from germanium and tin [Pauling 1.9 (cf. tin and germanium 1.8)], being somewhat lower than for carbon (2.5). Elemental radii are rather large [r(IV)(covalent) 146 pm, r(IV)('ionic' six-coordinate) 78 pm, r(II)('ionic' six-coordinate) 119 pm]. These data are only approximate guidelines, and actual values will depend upon the particular structure and bonding present in the compound under study. Nevertheless, it is to be expected that in lead(IV) compounds the bonding will be covalent in character with well-defined geometries. In contrast, in bivalent lead compounds the much larger size of the ion will make the metal center much softer and the metal–ligand bonding will be more electrostatic in character. This coupled with the large size of the metal will lead to higher coordination numbers and a greater variety of coordination geometries.

Table 1 Bond energy data

Bond	Compound	Bond energy ($kJ\,mol^{-1}$)
Pb–F	PbF_4	331
Pb–F	PbF_2	394
Pb–Cl	$PbCl_4$	243
Pb–Cl	$PbCl_2$	303
Pb–Br	$PbBr_2$	260
Pb–C	$PbMe_4$	205
Pb–C	$PbEt_4$	130
Pb–H	Me_3PbH	259
Pb–Pb	Me_6Pb_2	230

Few bond energy data are available for lead (Table 1), and are rather subjective. They do, however, follow expected trends, for example, bonds to halogen are strongest with fluorine and decrease with increasing size of the halogen; bonds to carbon, hydrogen, and lead are quite weak.

3 COORDINATION GEOMETRIES

The variety of coordination geometries exhibited by lead is illustrated in Table 2, which contains examples of the principal types found. The list is extensive with coordination numbers ranging from one to twelve, but is by no means comprehensive. Many irregular coordination geometries of high coordination number are observed. The only example of multiple bonding between lead and an electronegative element are the matrix-isolated species PbO and PbO_2.

In contrast to the lighter congeners of group 14, the stability of the $+$II oxidation state[1] is greater than of the $+$IV state. Compounds in the $+$III state, that is, the radical species $R_3Pb\bullet$, are normally only transiently stable intermediates except when the R group is bulky, as in $\bullet Pb[CH(SiMe_3)_2]_3$. Such radicals can have extremely long lifetimes.[2]

Few compounds of the type PbX_4 (X $=$ electronegative ligand) are stable with respect to reductive elimination to the corresponding PbX_2 compound (hence the utility of some lead(IV) compounds as synthetic reagents for oxidation reactions; see Section 7). Lead compounds with oxidation state $+$IV are much more common when lead–carbon bonds are present. Tetrahedral four-coordination is only observed for lead in R_4Pb (R $=$ organic group) and R_nPbX_{4-n} derivatives which are either sterically crowded or in which the ligand X is weakly electronegative and a poor donor. Coordination

Table 2 Coordination geometries of lead compounds

Coordination number	Geometry	Examples
1	Diatomic	PbO[a]
2	Linear	PbO_2,[d] $(C_5H_5)(CO)_2MnPbMn(CO)_2(C_5H_5)$
2	Bent	Lead(II) halides[a,c] $Pb[OC_6H_2Me(t\text{-}Bu_2)]_2$ $Pb[N(SiMe_3)_2]_2$
3	Trigonal planar	$Pb(EPh)_3^-$ (E = S, Se)
3	Pyramidal	PbX_3, $PbX_2{\cdot}L$, $Pb(SPh_3)$, plumbyl radicals, R_3Pb[b]
4	Tetrahedral	R_4Pb, Ph_3Pb SAr, R_6Pb_2
4	Square pyramidal	PbO, phthalocyaninatolead(II)
4	Pseudotrigonal bipyramidal[e]	$[Pb_4(OSiPh_3)_6]O$, $Pb[(Ph_2P)_2(SiMe_3)_2]_2$
5	Trigonal bipyramidal	$Me_3Pb(O_2CMe)$, Me_3PbN_3, Ph_3PbOH, Ph_3PbCl, R_3PbX_2
6	Octahedral	Ph_2PbCl_2, $Me_2Pb(OMe)_2$, $Ph_2PbX_4^{2-}$, $Ph_2PbX_2.2L$, $[Pb(antipyrine)_6]^{2+}$, PbS, PbSe
7	Pentagonal bipyramidal	$[Ph_2Pb(O_2CMe)_2]_2{\cdot}H_2O$
8	Hexagonal bipyramidal	$[Ph_2Pb(O_2CMe)_3]^-$, $Pb(SCN)_2(C_{12}H_{26}N_2O_4)$
8	Dodecahedral	$Pb(O_2CMe)_4$
8	Square antiprismatic	$Pb(O_2CC_6F_5)_2{\cdot}2MeOH$, 34 $Pb(O_2CH)_2{\cdot}4SC(NH_2)_2$
9	Trifacially capped trigonal prismatic	$PbCl_2$, $PbBr_2$
10	Various	$Pb(SCN)_2(C_{18}H_{36}N_2O_6)$ $Pb_3(PO_4)_2$
12	Various	$Pb(NO_3)_2$, $PbSO_4$

[a] Matrix-isolated species. [b] Unstable intermediates. [c] In the gas phase. [d] In solution. [e] One equatorial coordination site occupied by the metal(II) lone pair.

numbers higher than four are achieved wherever possible. When the lead atom is bonded to three organic groups, coordination saturation is invariably reached at five as a trigonal bipyramid. For compounds with one or two bonds to carbon, coordination saturation is usually achieved at six in an octahedral or distorted octahedral geometry, but some examples with coordination numbers of seven or eight have been characterized.

Two factors combine to lend a greater diversity in the stereochemistry for bivalent lead compounds: the increased radius of lead(II) compared with that of lead(IV) and the presence of a nonbonding pair of electrons.[3] When the nonbonding pair of electrons occupies the isotropic 6s orbital as in, for example, the complex cations $[Pb\{SC(NH_2)_2\}_6]^{2+}$,[4] $[Pb(antipyrine)_6]^{2+}$,[5] and various trispyrazolylmethane derivatives,[6] or when they are donated to conductance band levels as in the binary lead selenide and telluride or the perovskite ternary phases $CsPbX_3$ (X = Cl, Br, I),[7,8] the metal coordination is regular. However, in the majority of compounds an apparent vacancy in the coordination sphere is observed, which is usually ascribed to the presence of the nonbonding pair of electrons in a hybrid orbital and cited as evidence for a stereochemically-active lone pair. Being large and soft, metal–ligand bonding is electrostatic in nature and the demands of the ligands determine in large part the particular stereochemistry adopted in any particular case.

Examples of compounds exhibiting the two-coordinate 'bent' or 'V'-shaped geometry are relatively uncommon, and only when the two ligands are very bulky do they occur under ordinary conditions. The preferred coordination geometries for lead(II) are pyramidal three-coordination (**1**) and four-coordination based upon a distorted pseudotrigonal bipyramid (**2**), where the stereochemically-active lone pair occupies an equatorial coordination site. Much higher coordination numbers in a variety of geometries are also abundant. Square-antiprismatic eight coordination (**3**) is quite common. Several other types of coordination numbers from 7 to 12 are also observed, many of which are irregular.

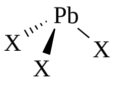

(**1**)

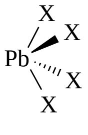

(**2**)

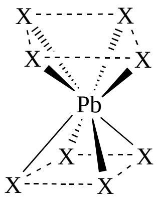

(**3**)

4 LEAD HALIDES AND COMPLEX HALIDES

Lead forms binary halides in both oxidation states, although the tetrahalides, PbX_4, are generally much less stable than their bivalent analogs, PbX_2. Lead(IV) fluoride is the only halide of lead which is stable under ordinary conditions. It is a crystalline solid with a melting point >600 °C and obviously has a fluorine-bridged polymeric structure. Lead(IV) chloride is described as a yellow oil and can be obtained by the action of concentrated sulfuric acid on pyridinium hexachloroplumbate. Like tin(IV) chloride it is covalent and tetrahedral, soluble in solvents such as chloroform and carbon tetrachlorade, and fumes in air. However, it is reported to decompose explosively to give $PbCl_2$ and chlorine. Much more stable are salts of the complex anions $[PbX_6]^{2-}$ (X = halide), many of which have been characterized. The two lower congeners, $PbBr_4$ and PbI_4, are of very low stability or do not exist at all. In contrast, the bivalent lead halides, PbX_2, are stable crystalline solids which can be obtained by treating any soluble lead(II) salt with halide anions, whereby the insoluble halide is precipitated. Many mixed halides, for example, PbFX (X = Cl, Br, I), and a wide range of ternary halides, for example, $CsPbX_3$,[9] Cs_4PbX_6 (X = Cl, Br, I)[10] and $[CuPbBrIL_2]_2$ (L = 2-dimethylaminoethanol),[11] have also been isolated. Many of the lead(II) halides exhibit photo and electrical properties.

Structurally, lead(II) halides only adopt monomeric molecular structures under special circumstances. Isolated molecules of the lead(II) halides (C_{2v} geometry) are only found in the vapor phase or in low-temperature rare gas matrices.[12] In the solid, variants of close-packed lattices are formed with distortions arising because of the metal nonbonding pair of electrons. The basic structural unit is usually recognizable as a trigonal bipyramid, where the metal forms three quite short bonds with angles of ca. 90°, but additional bonds or contacts are often present leading to distorted pseudotrigonal bipyramidal, octahedral (**4**), or facially capped trigonal prismatic (**5**) coordination geometries.[13]

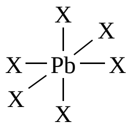

(**4**)

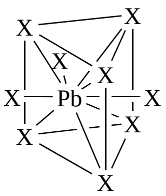

(**5**)

The prototype lattice adopted by most lead(II) halides is the $PbCl_2$ lattice, which is also found for $PbBr_2$. In this layer-type lattice, the metal is surrounded by nine halogen atoms as in (**5**) from three different layers, six at the apices of a trigonal prism and three in facially capping positions. The coordination is, however, far from regular, and the metal forms three short bonds (the typical $\{MX_3\}$ structural unit) together with four additional close contacts. A further two halogen atoms are at even longer distances. However, PbF_2 crystallizes with a cubic fluorite lattice at normal temperatures, but also forms an orthorhombic modification with the $PbCl_2$ lattice structure. Lead(II) iodide crystallizes with the hexagonal anti-CdI_2 lattice in which the metal atom is surrounded octahedrally by six iodine neighbors, although a large number of modifications are known which differ in the layer sequence.[14–16]

The structure of the hydrate $3PbBr_2{\cdot}2H_2O$ is also based upon the $PbCl_2$-type structure. The lead atom is surrounded by a trigonal prism of bromine atoms, with bromine atoms, water molecules, or vacancies in the facially capping sites.[17] In the basic lead chloride, Pb(OH)Cl, the lead atom is surrounded by five chlorine atoms and three hydroxyl groups in a polyhedron best described as a strongly distorted square antiprism.[18] ^{207}Pb NMR can be used to distinguish the halide from the oxyhalide.[19]

The cesium salts $Cs[PbX_3]$ (X = Cl, Br, I) exhibit two crystal modifications, one in which the coordination at the lead atom is distorted octahedral and a second perovskite phase in which the lead has ideal octahedral coordination.[7–10] Similarly, the tetramethylammonium salts $[MeNH_3][PbX_3]$ and $[MeNH_3][Pb_nSn_{1-n}X_3]$ (X = Cl, Br, I) also have the cubic perovskite lattice.[20] All three series with the perovskite structure are intensely colored and exhibit electrical conductivity because of the population of lattice conduction bands by the lead nonbonding electrons.[21] Regular octahedral coordination is very common with the iodides, presumably largely due to steric reasons, there being little room for lone pair stereoactivity, and is found in orthorhombic $RbPbI_3$ and the hydrates $KPbI_3{\cdot}2H_2O$, $NH_4PbI_3{\cdot}2H_2O$, and $RbPbI_3{\cdot}2H_2O$, which all comprise double chains of edge-sharing $[PbI_6]$ octahedra held together by the cations and all, in the case of the hydrates, water molecules.[22,23] Lead(II) chloride iodide has a distorted trigonal bipyramidal geometry.[24]

Of current interest because of their potential as electronic materials are layered perovskite-type lead iodide compounds of general composition $(RNH_3)_2(MeNH_3)_{n-1}Pb_nI_{3n+1}$, of which representative examples are $(Ph(CH_2)_2NH_3)_2PbI_4$ and $(Me(CH_2)_8NH_3)_2(MeNH_3)Pb_2I_7$.[25]

5 LEAD PSEUDOHALIDES

Lead(II) cyanide, $Pb(CN)_2$, a yellowish white powder, lead(II) cyanate, $Pb(NCO)_2$, as white needles, and lead(II) thiocyanate, $Pb(NCS)_2$, also as white needles, have all been known for a long time. Like the lead halides, the pseudohalides also form complexes with donor molecules (e.g. $Pb(NCS)_2{\cdot}L_2$, L = phen, terpy)[26,27] and complex anions (e.g. $[Bu_4N][Pb(N_3)_6]$).[28] In general, the coordination of the lead(II) pseudohalides and their complexes is irregular with a high coordination number for lead.

6 OXIDES AND OTHER CHALCOGENIDES

Lead forms several binary oxides and a large number of ternary oxides, several of which have important electronic and other technological applications. Lead monoxide, PbO, forms two modifications, a red, tetragonal modification (litharge) stable at room temperature and a yellow, orthorhombic modification (massicot) stable at temperatures above ca. 490 °C. These oxides are of considerable interest because they exhibit photoactivity over a wide range of electromagnetic radiation wavelengths and are used in the manufacture of ceramic silicate glasses and porous electrodes in lead acid batteries. Tetragonal lead(II) oxide forms a layer-lattice structure with square pyramidal coordination and equal lead–oxygen distances. The metastable orthorhombic modification has a similar, but more loosely bound layer structure with two short and two longer lead–oxygen distances. The structure of both modifications can be visualized as a face-centered cubic array of lead atoms, as in lead metal, swelled and distorted by the introduction of double layers of oxygen atoms between each second layer of lead atoms. However, whereas the lead and oxygen layers in litharge are flat, the [100] sheets in massicot are strongly corrugated, producing significant differences in both the thickness and separation of the layers.[29]

Like SnO_2, maroon-colored PbO_2 exhibits the rutile structure with the lead atom in almost ideal octahedral coordination.[30] A second black, orthorhombic modification of PbO_2 is formed at high pressures.[31] PbO_2 is a good oxidizing agent, and in air decomposes on heating to give, via intermediate compositions of $Pb_{12}O_{19}$, $Pb_{12}O_{17}$, and Pb_3O_4, ultimately PbO. The black, vitreous monoclinic sesquioxide, Pb_2O_3, can also be obtained by decomposing PbO_2 or PbO at 580–620 °C under a pressure of oxygen (1.4 kbar). The mixed valence oxide Pb_3O_4, made by heating PbO at 450–500 °C, consists of chains of edge-sharing $(Pb^{IV}O_6)$ octahedra linked by pyramidal $[Pb^{II}O_3]$ units, and finds commercial application as a pigment and a primer. The two intermediate oxides, $Pb_{12}O_{19}$ and $Pb_{12}O_{17}$, both form defect fluorite structures with ordered anion vacancies. Materials with nonstoichiometric intermediate compositions can also be formed in which the anion defects are quasi-random in nature.[32,33]

Many ternary and mixed oxides of lead with both lead(II) and lead(IV) are known. These are usually obtained by heating stoichiometric mixtures of PbO or PbO_2 with the appropriate metal oxide, hydroxide, or carbonate. A variety of structural types are observed and some examples are given here. Potassium, rubidium, and cesium orthoplumbates, M_4PbO_4 (M = K, Rb, Cs), all contain isolated $[PbO_4]$ tetrahedra, as does Rb_3NaPbO_4.[34–36] The structure of the 'metaplumbate', Li_2PbO_3, is a variant of the NaCl-type lattice, with octahedrally coordinated lead,[37] whilst the diplumbate, $K_2Li_2[Pb_2O_8]$,[38] and the triplumbates, $M_2Li_{14}[Pb_3O_{14}]$ (M = K, Rb, Cs),[39] contain the discrete $[Pb_2O_8]$ and $[Pb_3O_{14}]$ units, respectively. Sodium plumbate(II), Na_2PbO_2, has a layer lattice, although the analogous silver salt contains infinite $[PbO_2]_{2\infty}{}^{\infty-}$ chains.[40]

Several ternary oxides are electroactive.[41] The mixed ion lead oxides $PbFe_{2n}O_{3n+1}$ ($n = 6$, 5, 2.5, 1, 0.5) are ferrimagnetic but not as commercially attractive as $BaFe_{12}O_{19}$. Structurally characterized Ce_5Pb_3O orders ferrimagnetically at Tc = 46 K.[42] However, several ternary oxides with the perovskite structure have become extremely important. The most important of these are lead titanate, $PbTiO_3$ (PT) (ferroelectric below 490 °C),[43] lead zirconate, $PbZrO_3$ (PZ) (ferroelectric below 230 °C),[44] lead hafnate, $PbHfO_3$ (antiferroelectric below 215 °C),[45,46] mixed lead titanate zirconate (PZT),[47] $PbTi_xZr_{1-x}O_3$, lanthanide-doped PZT,[48,49] $Pb(Fe_{1/2}Nb_{1/2})O_3$ (PFN),[50,51] and $Pb(Mg_{2/3}Nb_{1/3})O_3$ (PFN). These materials are characterized by large dielectric constants, PFN having a magnitude of 2000 at 60 Hz. Related materials such as the tungsten bronze-type lead niobate, $PbNb_2O_6$ (ferroelectric up to 560 °C), the perovskite lead magnesium niobate, $Pb(Mg_{1/3}Nb_{2/3})O_3$, and lead zinc niobate, $Pb(Zn_{1/3}Nb_{2/3})O_3$, also find important applications.

Mixed-metal oxide halides such as $Pb_3Te_2O_6X_2$ and $Pb_3Te_2O_4X_2$ (X = Cl or Br) are interesting structurally as well as having potential utility as ion exchange and optical materials.[52] However, no simple hydroxide of lead exists. Hydrolysis of lead(II) salts yields oxolead ions of which many types, depending on the conditions, particularly the pH,[53] have been isolated and characterized crystallographically. The $[Pb_4(OH)_4]^{4+}$ cation, in which the lead atoms occupy the corners of a slightly distorted tetrahedron with the hydroxyl groups capping each face, is present in crystals of $[Pb_4(OH)_4]_3(CO_3)(ClO_4)_{10}\cdot 6H_2O$,[54] $[Pb_4(OH)_4](ClO_4)_4$,[55] and $[Pb_4(OH)_4][O_2C_6H(NO_2)_3$-2,4,6].[56] The homologous $[Pb_6O(OH)_6]^{4+}$ cation is present in the α- and β-modifications of $[Pb_6O(OH)_6](ClO_4)_4\cdot H_2O$[57,58] and in $[Pb_6O(OH)_6](ReO_4)_4\cdot H_2O$,[59] the latter being obtained by heating ReO_3, PbO, and water at 523 K. This cation is made up of three $[Pb_4]$ tetrahedra sharing common faces, with the unique oxygen atom located at the center of the central tetrahedron rather like in the structure of the neutral molecule $Pb_4O(OSiPh_3)_6$.[60] The six hydroxyl groups are located above each of the six unshared faces of the two terminal tetrahedra. From neutral solutions the hydrated oxide formulated variously as $3PbO\cdot H_2O$ or $Pb_3O_2(OH)_2$ but actually $Pb_6O_4(OH)_4$ can be isolated.[61] This contains the adamantane-like $[Pb_6O_8]$ cluster as the central feature in which the eight faces of a slightly distorted octahedron of lead atoms are capped by oxygen atoms. Adjacent $\{Pb_6O_4(OH)_4\}$ units are linked by a network of hydrogen bonds. Like the thallium compound $TlPb_8O_4Br_9$, the mixed lead oxide bromide $Pb_9O_4Br_{10}$ contains the $\{Pb_8O_4\}$ core.[62] While the nucleus of this structural unit is a $\{Pb_4O_4\}$ cube similar to that found in $[Pb_4(OH)_4](ClO_4)_4$, the overall structure may be considered as four $\{Pb_4O\}$ tetrahedra similar to that in $Pb_4O(OSiPh_3)_6$ fused together. The bromine atoms are located around the periphery of the $\{Pb_8O_4\}$ cluster. In bis[hydroxylead(II)] 5,5′-azotetrazolediide the hydroxylead cation has an infinite one-dimensional structure in which the lead atoms have the three-coordinated pyramidal structure, although there are two additional weak interactions with nitrogen atoms from the anions.[63]

Lead(II) sulfide (black), selenide (gray), and telluride (white) all adopt the cubic NaCl-type structure. PbS is an intrinsic semiconductor which can develop either n-type or p-type properties depending upon the level of impurities or stoichiometric imbalance. All three compounds are photoconductors, and are widely used in photoelectric cells and as IR detectors.[64] Many ternary and even more complex sulfides are known, many as minerals, for example, $PbSnS_2$ (teallite), $AgPbAsS_3$ (marrite), $PbAgSbS_3$ (freislebenite), $Pb_2Bi_2S_5$ (cosalite), and the plagionite series, $Pb_{3+2n}Sb_8S_{15+2n}$ ($n = 0-3$).[13] Binary lead(IV) chalcogenides do not exist.

7 CARBOXYLATES AND OXYACID DERIVATIVES

Apart from lead(IV) acetate, $Pb(O_2CMe)_4$, and lead(IV) trifluoroacetate, $Pb(O_2CCF_3)_4$, both of which have found extensive use as selective oxidizing agents in organic synthesis, lead(IV) sulfate, $Pb(SO_4)_2$, essentially all lead derivatives of oxyacids and organic acids contain bivalent lead. The lead nitrate oxalate hydrate, $Pb_2(NO_3)_2(C_2O_4).2H_2O$, provides another example.[65] Many are well known, for example, lead(II) acetate, $Pb(O_2CMe)_2$, $Pb(NO_3)_2$, $PbSO_4$ (used for the gravimetric determination of sulfate), $PbSeO_4$, $PbCO_3$ (the mineral cerussite), and a multitude of phosphates, phosphites, and hypophosphites. Many basic salts, for example, the basic carbonate $2PbCO_3{\cdot}Pb(OH)_2$ once widely used as a white pigment, and basic phosphates of which many have been reported, and mixed halide carbonates, $PbX_2{\cdot}PbCO_3$ (X = Cl, Br), and halide phosphates (lead apatites), $3[Pb_3(PO_4)_2]{\cdot}PbX_2$ (X = F, Cl, Br, I, OH), are known. The nitrate and acetate are very soluble in water, in which they can be made from PbO and the appropriate acid, and are used widely for the preparation of other lead compounds. The nitrate has a highly symmetric structure in which the arrangement of lead ions is face-centered cubic with the nitrate anions in between. In contrast, lead(II) nitrite monohydrate, $Pb(NO_2)_2{\cdot}H_2O$, has a very irregular structure with two lead atoms in two types of coordination. Both have contacts to seven nitrite oxygen atoms and one water oxygen atom, but they differ in the number of contacts to nitrogen atoms: in one case there are contacts to two and in the other only to one nitrogen.

A number of lead salts of the halogen oxyacids are known including the chlorite, $Pb(ClO_2)_2$, chlorate, $Pb(ClO_3)_2$, bromate, $Pb(BrO_3)_2$, iodate, $Pb(IO_3)_2$, and perchlorate, $Pb(ClO_4)_2{\cdot}3H_2O$. The latter, like the nitrate, is extremely soluble in water and so serves as a useful source of soluble Pb^{2+} cations. One note of caution, however, concerns the bromate. If preparation is attempted using lead(II) acetate, the highly dangerous double salt $Pb(BrO_3)_2{\cdot}Pb(O_2CMe)_2$, may be formed which *explodes violently at 165 °C* but can also *detonate at room temperature on impact.*

Lead(IV) acetate is obtained from Pb_3O_4 and glacial acetic acid as an air-sensitive crystalline solid. The mode of action of lead(IV) acetate as a synthetic reagent has been well documented.[66] Many types of substrate (alcohols, diols, phenols, oximes, alkenes, amines, diamines, carboxylic acids, cyclopropanes, etc.) can undergo reaction. The initial step is invariably the formation of a tris(acetato)lead(IV) derivative of the substrate. Further reaction usually involves homolysis of the intermediate Pb–O bond although heterolysis may occur depending on the reaction conditions and the substrate. Two examples are shown here: oxidation of a carboxylic acid (Scheme 1) and the cyclization of an alcohol (Scheme 2). The former follows a free-radical chain process forming radicals, R•, or carbocations, R^+. Products can be formed from either. Primary R• radicals abstract hydrogen from solvent, giving the corresponding RH. The carbocations can react in a variety of ways, losing H^+ to form an alkene, reacting with acetic acid to form an ester, reacting with the solvent or another functional group within the molecule, or undergo rearrangement.

The structures of lead(II) carboxylates and their complexes are quite varied and are characterized by intermolecular association and high coordination numbers at lead.[67,68] Both bridging and chelating carboxylate groups are found. A few illustrative examples are described here. The simplest, lead(II) formate, $Pb(O_2CH)_2$, has a three-dimensional polymeric structure in which adjacent lead atoms are bridged by formate groups. Both oxygen atoms of each ligand form bonds to two different lead atoms, and therefore each formate group links four neighboring lead atoms. The resulting stereochemistry at lead is that of a distorted dodecahedron, with the lead forming three short bonds and five longer bonds to oxygen. No vacancy in the coordination polyhedron is apparent, and hence the bivalent lead lone pair in this case is not stereochemically active and is confined to the 6s orbital.

$$\begin{array}{lcl}
\mathrm{Pb(OAc)_4 + RCO_2H} & \longrightarrow & \mathrm{Pb(OAc)_3OCOR\ \ (or\ Pb(OAc)_2(OCOR)_2} \\
\mathrm{Pb(OAc)_3OCOR} & \longrightarrow & \mathrm{{\bullet}Pb(OAc)_3 + R{\bullet} + CO_2} \\
\mathrm{R{\bullet} + Pb(OAc)_3OCOR} & \longrightarrow & \mathrm{R^+ + {\bullet}Pb(OAc)_2OCOR + OAc^-} \\
\mathrm{{\bullet}Pb(OAc)_2OCOR} & \longrightarrow & \mathrm{Pb(OAc)_2 + R{\bullet} + CO_2}
\end{array}$$

Scheme 1

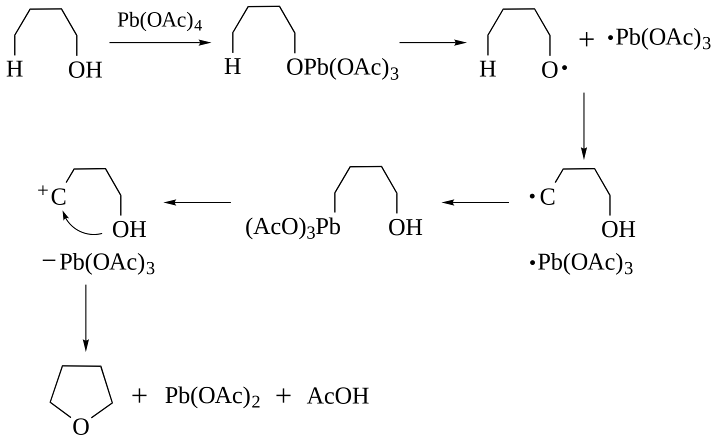

Scheme 2

The other common type of eight coordination, square antiprismatic, is exhibited by lead(II) bis(pentafluorophenylbenzoate bis(methanol) solvate. Each lead atom is coordinated by two symmetrically chelating carboxylate groups and the two methanol solvate molecules. One oxygen atom of each carboxylate group is also bonded to an adjacent lead atom, thus forming a one-dimensional chain. The resulting square-antiprismatic stereochemistry is distorted in such a way that the four upper oxygen atoms are more opened out than the lower four, suggesting stereochemical activity for the lead lone pair.

Both lead(II) acetate trihydrate**[67,69]** and the pyridine complex of lead(II) benzoate have one-dimensional chain structures, but are quite different in nature. The lead atoms in the former again have a distorted square-antiprismatic coordination, but in this case only one acetate group participates in bridging, symmetrically chelating the lead atom and forming longer bonds to both of the adjacent lead atoms in the chain. The other acetate group exhibits anisobidentate coordination. The coordination polyhedron is completed by three water molecules at rather long Pb–O distances.

The lead(II) benzoate–pyridine complex is only seven coordinate. Nevertheless, the relationship of the coordination polyhedron to square antiprismatic is quite apparent, with one site unoccupied. The square base of the antiprism is formed by contacts to adjacent lead atoms by the bridging carbonyl oxygen atoms of the benzoate groups, and is nearly planar. The three upper sites are occupied by the two nonbridging oxygen atoms of the benzoate groups and the pyridine nitrogen atom. The bridging in the chain is thus similar to that in $Pb(O_2CC_6F_5)_2 \cdot 2MeOH$, with each carboxylate group chelating one lead whilst bridging to an adjacent lead atom. The two types of bridging do, however, differ in that in the pentafluorobenzoate complex, each of the two carboxylate groups bridges to different adjacent lead atoms in the chain, whilst in $Pb(O_2CPh)_2 \cdot py$, both groups bridge to the same lead. The question of possible stereochemical activity for the lead lone pair in this case is quite interesting. The four oxygen atoms of the square base of the antiprism are significantly opened out such that the lead is almost coplanar with the four oxygen atoms, suggesting lone pair–bond pair repulsion. However, if the stereochemistry is examined more closely, it can be seen that the pyridine ring is oriented in such a way as to largely occupy the vacant site, although at a large enough distance from lead so as to preclude both Pb···N and Pb···ring interactions.

The stereochemistry exhibited by (phenanthroline)lead(II) acetate dihydrate is very unusual. Each lead atom is chelated by the phenanthroline and the two acetate groups, giving a $[(phen)Pb(O_2CCH_3)_2]$ unit, the geometry of which is highly distorted. The origin of the distortion appears to be due to the formation of weakly bound dimers, of which there are two different types in the crystal and which are interlinked by a system of hydrogen bonds involving the water molecules. The two halves of each dimer unit are held together by very weak carboxyl bridging and possibly a weak Pb–Pb interaction. The Pb–Pb distances in the two dimers are 4.05 and 3.73 Å (cf. Pb–Pb distance in lead metal, 3.50 Å). Quite notably, of all the structures described here, this complex exhibits the weakest carboxyl bridging yet has the shortest Pb–Pb distance.

8 SOLUTION STUDIES

In solution, lead compounds invariably participate in equilibria involving a variety of species. Two methods have been employed for investigations in this area, potentiometry**[53]** and ^{207}Pb NMR.**[70]** The latter is quite convenient, and with $I = 1/2$, abundance = 21.1%, and sensitivity = 9.13×10^{-3} (cf. ^{13}C, sensitivity = 1.59×10^{-2}), ^{207}Pb is relatively easy to observe. Since the chemical shift range is very large (ca. 4000 ppm), very subtle changes in the electronic distribution about lead may be detected. The simplest parameters to vary in solution are the concentration of the solute and the pH. Advantages of the NMR method are that solutions of solvents other than water may be investigated and at solute concentrations much higher than those customary for potentiometry. Typical results are illustrated here.

Lead-207 NMR spectra invariably exhibit a single line indicative of the presence of equilibria which are rapid on the NMR timescale.**[70]** More recently, the first two-dimensional ^{207}Pb-^{1}H heteronuclear multiple-quantum correction (HMQC) NMR spectra have been reported for Pb(II)-EDTA complexes in solution.**[71]** The chemical shift observed for aqueous solutions of lead(II) perchlorate occurs at extremely high field (-2880 ppm at infinite dilution) and corresponds to the hydrated lead(II) cation, $[Pb(H_2O)_n]^{2+}$. The efficient shielding of the lead nucleus is most probably a result of the localization of the lead(II) lone pair in the isotropic 6s orbital, and that the shift is essentially invariant with concentration indicates that this is the only species present at all concentrations. The chemical shifts of aqueous lead(II) nitrate solutions are also at very high field, but in this case exhibit concentration dependence varying from -2961 ppm at 1 mol dm^{-3} to -2854 ppm at 0.01 mol dm^{-3}. At low concentrations the predominant species is again the hydrated lead(II) cation, but at higher concentrations the equilibrium (shown in equation 1) occurs with an association constant, K, of 1.23 dm^{-3} mol^{-1} at 25 °C. Large changes in chemical shift are observed for aqueous solutions of lead(II) acetate. In the concentration range 0.25–1.0 mol dm^{-3}, the variation in chemical shift is relatively small (-1429 to -1370 ppm), but at concentrations of less than 0.1 mol dm^{-3}, the chemical shift moves rapidly to higher field, reaching a value of -1956 ppm at a concentration of 0.01 mol dm^{-3}. In this case, the equilibrium involves the dissociation of an acetate ligand from the neutral hydrated bis(acetato)lead(II) (equation 2)

$$[Pb(H_2O)_n]^{2+} + NO_3^{-} \rightleftharpoons [Pb(NO_3^{-})(H_2O)_m]^{+} \qquad (1)$$

$$[Pb(O_2CMe)_2(H_2O)_p] \rightleftharpoons [Pb(O_2CMe)(H_2O)_q]^{+} + {}^{-}O_2CMe \qquad (2)$$

with a dissociation constant of 0.014 mol dm^{-3} at 25 °C. By varying the temperature, thermodynamic quantities for the equilibrium, $\Delta H_{298} = -14.2$ kJ mol^{-1}, $\Delta G_{298} = 10.5$ kJ mol^{-1}, and $\Delta S_{298} = -82.9$ J K^{-1} mol^{-1}, may also be accessed. Unlike potentiometry, NMR can be used to study equilibria in nonaqueous media. Lead(II) pentafluorobenzoate is insoluble in water but freely soluble in THF, and in this solvent the chemical shift change from -1258 ppm at 0.3 mol dm^{-3} to -959 ppm at 0.06 mol dm^{-3} corresponds to an equilibrium between monomer and dimer solution species with an association constant of 0.14 mol dm^{-3} at 25 °C.

Using potentiometry,**[53]** several oxolead species have been shown to be present in aqueous solutions of lead(II) nitrate, depending on the pH and the concentration of solute. At low pH (<6) the principal species is the $[Pb(OH)]^{+}$ cation, but as the pH increases more associated species including $[Pb_3(OH)_4]^{2+}$, $[Pb_3(OH)_5]^{+}$, $[Pb_4(OH)_4]^{4+}$, and $[Pb_6(OH)_8]^{4+}$ are present, the more associated species being more abundant at higher pH levels. In general, solutions involve a complex series of equilibria, the positions of which are dependent on a number of variables.

9 LEAD(II) ALKOXIDES

Poorly characterized insoluble, polymeric lead(II) alkoxides of formula $[Pb(OR)_2]_n$ have been reported to form via the decomposition of trimethyllead methoxide (R = Me) or by substitution of dicyclopentadienyllead(II) or lead(II) salts such as the iodide or nitrate (R = Me or t-Bu).**[72,73]** The most general method for the synthesis of lead(II) alkoxides is by the protolysis of $Pb[N(SiMe_3)_2]_2$ by the appropriate alcohol, and two well-defined lead(II) alkoxide polymers have been characterized, lead(II) isopropoxide and lead(II) 2-methoxyethoxide.**[74]** Both are isostructural in the solid, and comprise one-dimensional chains with bridging alkoxide groups and pseudotrigonal bipyramidal coordination at lead. However, by increasing the steric bulk of the organic group the aggregation can be broken down completely, and red monomeric, ‘V’-shaped lead(II) 2,6-di-t-butylphenoxide has been obtained by substitution of $PbCl_2$ and also by protolysis of $Pb[N(SiMe_3)_2]_2$ using the corresponding phenol. In between these two extremes, a variety of aggregation numbers are found.**[75]** Stirring PbO with Me_3SiOH in THF affords $Pb(OSiMe_3)_2$ which is dimeric in benzene**[76]** (cf. the adamantane-like cluster $Pb_4O(OSiPh_3)_6$ which is obtained by the reaction of $Pb(C_5H_5)_2$ and Ph_3SiOH).**[60]** Dimeric $[Pb(O\text{-}t\text{-}Bu)_2]_2$ is formed together with the cluster $Pb_4O(O\text{-}t\text{-}Bu)_6$ by the reaction between $Pb[N(SiMe_3)_2]_2$ and t-BuOH in dilute pentane at -70 °C, but $Pb_4O(O\text{-}t\text{-}Bu)_6$ is the only product when the reaction is carried out at higher concentrations or temperatures.**[77]** Similar oxoalkoxide clusters are obtained by metathesis between lead(II) acetate and NaO-i-Pr or NaO-t-Bu. By contrast, the reaction of $PbCl_2$ with three equivalents of NaO-t-Bu affords the sodium plumbate $Na_2Pb_2(O\text{-}t\text{-}Bu)_6$, which reacts with $PbCl_2$ to give trimeric $Pb_3(O\text{-}t\text{-}Bu)_6$.**[78]** This compound, which has also been obtained by the alcoholysis of $Pb[N(SiMe_3)_2]_2$,**[74]** has an unusual structure with nonequivalent lead atoms, with the central six-coordinated lead being bridged to the two three-coordinated lead atoms by alkoxide groups. Many variations of this structural type have been synthesized starting either from $Pb_3(O\text{-}t\text{-}Bu)_6$, $Na_2Pb_2(O\text{-}t\text{-}Bu)_6$, or $PbI_2{\cdot}$dioxane.**[78,79]** For example:

$$\frac{2}{3}Pb_3(O\text{-}t\text{-}Bu)_6 + M(O\text{-}t\text{-}Bu)_2 \xrightarrow[M\,=\,Ca,\,Sr,\,Ba]{} Pb(O\text{-}t\text{-}Bu)_3M(O\text{-}t\text{-}Bu)_3Pb \qquad (3)$$

$$2PbI_2{\cdot}\text{dioxane} + 3Ca(O\text{-}t\text{-}Bu)_2 \longrightarrow Pb(O\text{-}t\text{-}Bu)_3Ca(O\text{-}t\text{-}Bu)_3Pb + 2CaI_2 \qquad (4)$$

$$\mathrm{Na_2Pb_2(O\text{-}\mathit{t}\text{-}Bu)_6 + MCl_2 \xrightarrow[\text{M = Cd, Mn, Zn}]{} 2NaCl + Pb(O\text{-}\mathit{t}\text{-}Bu)_3M(O\text{-}\mathit{t}\text{-}Bu)_3Pb} \quad (5)$$

$$\mathrm{\frac{2}{3}Pb_3(O\text{-}\mathit{t}\text{-}Bu)_6 + \frac{1}{2}[Ge(O\text{-}\mathit{t}\text{-}Bu)_2]_2 \longrightarrow Pb(O\text{-}\mathit{t}\text{-}Bu)_3Pb(O\text{-}\mathit{t}\text{-}Bu)_3Ge} \quad (6)$$

$$\mathrm{Pb_3(O\text{-}\mathit{t}\text{-}Bu)_6 + [Sn(O\text{-}\mathit{t}\text{-}Bu)_2]_2 \longrightarrow Sn(O\text{-}\mathit{t}\text{-}Bu)_3Pb(O\text{-}\mathit{t}\text{-}Bu)_3Sn} \quad (7)$$

All are structurally similar, and lead can occupy either the central or terminal position depending on the composition and the method of synthesis. These mixed alkoxides form complexes with $Fe_2(CO)_9$, for example, $[(CO)_4Fe–Sn(O\text{-}t\text{-}Bu)_3Pb(O\text{-}t\text{-}Bu)_3Sn–Fe(CO)_4]$ in which the stannylene behaves as the donor towards iron, and (**6**) where the $[Fe(CO)_4]$ unit bridges the lead and germanium atoms.[80] Many of these compounds, $Pb_2Zn_2(C_2H_3O_2)_4(C_3H_7O_2)_4$[81] and $Pb_4Zr_2(O^iPr)_{16}$,[82] for example, are being explored as precursors to ceramic materials.

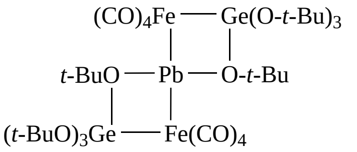

(**6**)

10 LEAD THIOLATES, DITHIOPHOSPHATES, DITHIOXANTHATES, AND DITHIOCARBAMATES

Lead(II) thiolates, $Pb(SR)_2$, are crystalline compounds readily obtained by the addition of the appropriate thiol to lead(II) acetate in ethanol.[83] Their particular use is as thiol transfer reagents[84] (equation 8).

$$\mathrm{2Me_2GeX_2 + Pb(SR)_2 \xrightarrow[\text{X = Cl, Br}]{} Me_2(RS)GeX + PbX_2} \quad (8)$$

With excess thiolate anion, complex tris(thiolate) anionic species such as $[Pb(SPh)_3]^-$ can be formed.[85]

The $\{S_2E\}$ group in lead(II) dithiophosphates, $Pb[S_2P(OR)_2]_2$, dithioxanthates, $Pb[S_2COR]_2$, and dithiocarbamates, $Pb[S_2CNR_2]_2$, all function as chelating ligands towards lead.[13,86] The distorted pseudotrigonal bipyramidal geometry is common, but other geometries occur as the nature of the organic group changes and additional intermolecular Pb – S contacts are formed. Tetraethylammonium tris(ethylxanthato)lead(II), lead(II) bis(*O,O′*-diisopropyldithiophosphate) D-penicillaminatolead(II), and lead(II) ethanedithiolate have structures based on a pseudopentagonal bipyramidal geometry at lead.[13,85] However, in the first the apparent vacant coordination site (presumably occupied by the lead lone pair) is one of the axial sites, whereas in the others the coordination vacancy is one of the equatorial sites. The lead(II) dithiophosphates and xanthates readily form complexes with nitrogen donor ligands, for example, $Pb(S_2COPr)_2{\cdot}py$, $Pb[S_2P(OEt)_2]_2{\cdot}en$, $Pb[S_2P(OEt)_2]_2{\cdot}bipy$, and $[Pb\{S_2P(OEt)_2\}_2]_2{\cdot}en$, the structures of which are often complex and involve intermolecular Pb – S interactions.[87] One example exemplifying this observation is the oxygen-centered cluster $Pb_5O(SR_F)_8{\cdot}2C_7H_8$ [R_F = 2,4,6-Tris(trifluoromethyl)phenyl].[88] It contains a central Pb_3O unit with Pb–O distance averaging 2.205 Å.

11 COMPOUNDS CONTAINING BONDS TO NITROGEN OR PHOSPHORUS

Lead(II) compounds of the general composition $Pb(NR_2)_2$ may adopt monomeric or dimeric structures depending on the nature of the organic group. Synthesis is usually by substitution of lead(II) chloride using the appropriate lithium amide. The simplest amido derivative, lead(II) dimethylamide, most probably has the dimeric structure (**7**) like the tin analog.[89] It is soluble in aprotic organic solvents and may be recrystallized from n-hexane at low temperature. However, it is very thermally unstable and even at −20 °C it slowly turns black and deposits a metallic mirror. The more bulky amide $Pb[NCMe_2(CH_2)_3CMe_2]_2$ still decomposes below 0 °C, but the monomeric amides, $Pb[N(CMe_3)(SiMe_3)]_2$ and $Pb[N(SiMe_3)_2]_2$ and the cyclic compound $Pb(N\text{-}t\text{-}Bu)_2)SiMe_2$ are stable under ambient conditions.[90–92] $Pb[N(SiMe_3)_2]_2$ has the monomeric ‘V’-shaped structure in both the crystal and the gas phase, although the NPbN bond angle is different (91(2)° in the gas phase and 103.6(7)° in the solid). The monomeric amidoplumbylenes are colored ($Pb[N(CMe_3)(SiMe_3)]_2$ (red), $Pb[N(SiMe_3)_2]_2$ (deep yellow), $Pb(N\text{-}t\text{-}Bu)_2)SiMe_2$ (yellow) and thermochromic, becoming very pale colored at −196 °C. Unlike the tin and germanium analogs (which afford very long-lived metal-centered $\cdot MR_3$ radicals), photolysis of the lead amides only results in the formation of a lead mirror. Reaction of $Pb[N(SiMe_3)_2]_2$ with transition metal complexes leads to either insertion or complexation.[93] Thus with $[\{Pd(\eta\text{-}C_3H_5)Cl\}_2]$ the lead(II) amide functions as a two-electron donor, cleaving the chloride bridge and forming the complex $[\{Pd(\eta\text{-}C_3H_5)Cl\}\{Pb[N(SiMe_3)_2]_2\}]$. With *trans*-$[\{Pt(\mu\text{-}Cl)Cl(PEt_3)\}_2]$, however, the product is *trans*-$[\{Pt(\mu\text{-}Cl)\{PbCl[N(SiMe_3)_2]_2\}(PEt_3)\}_2]$. Treatment of the monomeric amidoplumbylenes $Pb[N(SiMe_3)_2]_2$ and $Pb(N\text{-}t\text{-}Bu)_2SiMe_2$ with primary amines results in the formation of $\{Pb_4N_4\}$ cubane structures, for example, (**8**).[94] Reaction of $Pb(N\text{-}t\text{-}Bu)_2SiMe_2$ with $Me_2Si(NMeH)_2$ gives polymeric (**9**), and with $Sn_3(N\text{-}t\text{-}Bu)_4H_2$ a mixture of the mixed cubane cages (**10**)−(**12**).[95]

The most stable type of compounds with Pb–N bonds are those with pyrazolylborate ligands.[96] This type of complex

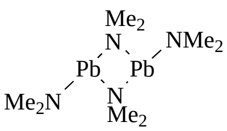

(7)

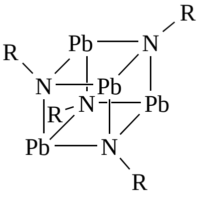

(8)

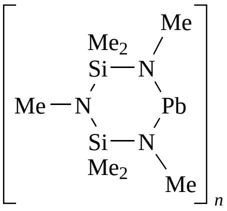

(9)

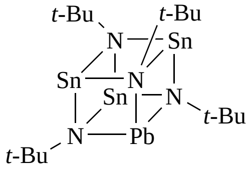

(10)

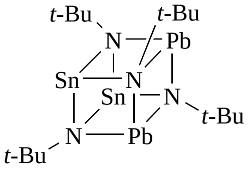

(11)

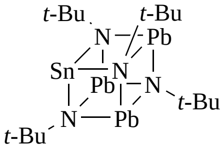

(12)

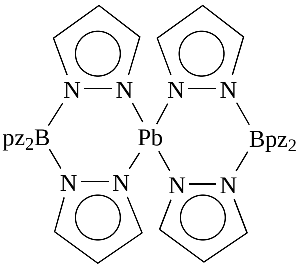

(13)

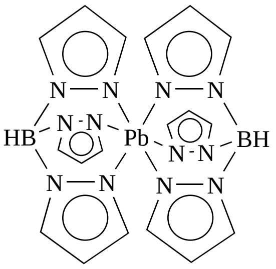

(14)

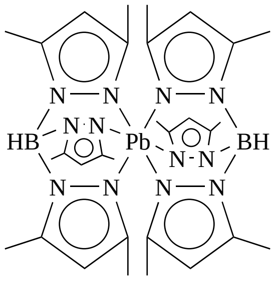

(15)

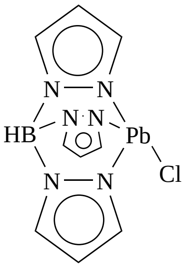

(16)

with two bis-, tris-, or tetrakis(pyrazolyl)borate ligands coordinated to lead(II) are readily prepared by the addition of aqueous solutions of $PbCl_2$ to solutions of the ligand salt (equation 9).

$$2K[H_nB(pz)_{4-n}] + PbCl_2 \xrightarrow[n\,=\,0-2]{} [H_nB(pz)_{4-n}]_2Pb + KCl \qquad (9)$$

Similarly, the mixed compounds are obtained by addition of one equivalent of the ligand salt to solutions of $PbCl_2$. Unlike the Pb–N bonded complexes described above, the pyrazolylborate complexes are all air stable, high-melting solids. The stability is most probably derived from the chelating nature of the ligands. Typical structures are illustrated in (**13**)–(**15**). The coordination geometry at lead in $(Bpz_4)_2Pb$ is that of a distorted pseudotrigonal bipyramid with the lead lone pair occupying an equatorial site (**13**). In $(HBpz_3)_2Pb$ both ligands are terdentate, forming a six-coordinate monomeric structure (**14**). The geometry about lead is best described as based on a capped octahedron with the lone pair located in the capping position of a triangular face. The lead is again six coordinate in $[HB(3,5\text{-}Me_2pz)_3]_2Pb$ (**15**). However, in this case the geometry about lead is a trigonally distorted octahedron in which the lone pair is clearly stereochemically inactive. The difference in structure between (**13**) and (**15**) can be attributed to steric effects. The mixed $(HBpz_3)PbCl$ compound (**16**) adopts the pseudotrigonal bipyramidal geometry.

The only compounds containing lead–phosphorus bonds are $Pb[(Ph_2P)_2CH]_2$ and $Pb[(Ph_2P)_2C(SiMe_3)_2]_2$, formed as orange crystals from $PbCl_2$ and the appropriate lithium salt in THF. $Pb[(Ph_2P)_2CH]_2$ is highly unusual in that each of the two ligands has a different mode of coordination to the lead. One has the expected unidentate *C*-coordination while the other functions as a chelating diphosphino ligand, resulting in pyramidal coordination at lead as in (**17**). $Pb[(Ph_2P)_2C(SiMe_3)_2]_2$ has the distorted pseudotrigonal bipyramidal structure (**18**) with a stereochemically-active lone pair. In solution both compounds are fluxional.**[97,98]**

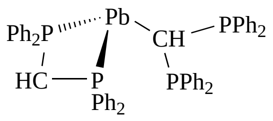

(17)

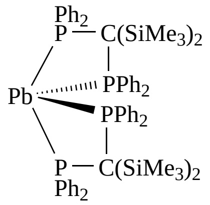

(18)

12 COMPOUNDS WITH LEAD–TRANSITION METAL BONDS

Lead forms a number of organolead compounds containing Pb–TM bonds similar to those formed by its group 4 congeners, although the range is less extensive. Examples include $Ph_2Pb\{Mn(CO)_5\}_2$, $Ph_3PbRe(CO)_5$, $Ph_2Pb\{Co(CO)_4\}_2$, $(PPh_3)_2Pt(PbPh_3)_2$, $Fe(CO)_3(PbEt_3)_2$, and $[(CO)_4FePbEt_2]_2$. Reaction of these compounds with elemental halogens results in cleavage of the Pb–M bonds.**[99]**

There are several nonorganometallic examples of neutral or anionic compounds in which the lead is bonded to transition metal atoms. The simplest of these are the complexes $(C_5H_4R)(CO)_2Mn{=}Pb{=}Mn(CO)_2$ (R = H, Me) (**19**) which are obtained from $(C_5H_4R)(CO)_3Mn$ and $PbCl_2$ and contain essentially linearly coordinated lead. The Pb–Mn bond distances are significantly shortened (20–25 pm) compared to typical Pb–Mn bond distances and are consistent with truly Pb=Mn double bond character.[100] A similar linear arrangement is found[101] in the anion $[Pb\{Pt(C_6F_5)_4\}_2]^{2-}$ and also probably in $[Pb\{Fe(CO)_4\}_2]^{2-}$.[102] Treatment of $Pb[N(SiMe_3)_2]_2$ with the molybdenum hydrides $Mo(R)(CO)_3H$ (R = C_5H_5, C_5Me_5, $C_5H_3(SiMe_3)_2$) in THF affords the THF adducts $Pb\{Mo(R)(CO)_3\}_2{\cdot}THF$.[103] Solvent free complexes result from evacuation. Both types have three-coordinated lead, the solvate via THF coordination but in $Pb\{Mo(C_5Me_5)(CO)_3\}_2$ by dimer formation and carbonyl oxygen-to-lead coordination.

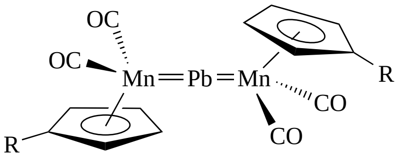

(**19**)

Examples of lead in three-coordinated trigonal planar and four-coordinated tetrahedral environments have also been characterized. Reaction of $(C_5H_4R)(CO)_2Mn{=}Pb{=}Mn(CO)_2(C_5H_4R)$ with excess $(C_5H_4R)(CO)_2(THF)Mn$ gives (**20**),[104,105] while a number of Pb–Fe bonded complexes including anionic $[Pb\{Fe(CO)_4\}_2]^{2-}$ and $[Pb\{Fe(CO)_4\}_3]^{2-}$ (**21**) and neutral (**22**) result from the reaction of simple lead salts with $Fe(CO)_5$ under various conditions.[102,106,107]

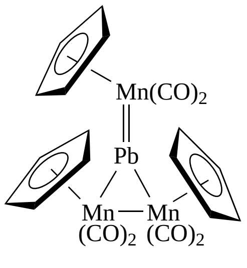

(**20**)

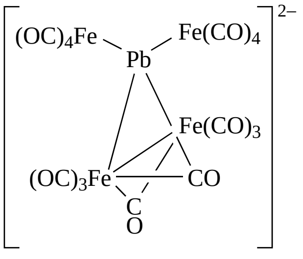

(**21**)

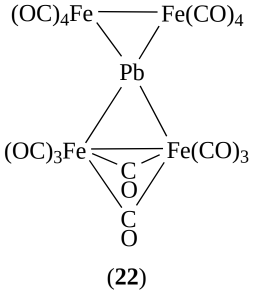

(**22**)

13 METALLIC CLUSTERS

Reduction of lead or lead alloys in liquid ammonia or amines gives polyatomic metal anions. Thus dissolution of the lead alloy $NaPb_{1.7-2}$ in ethylenediamine in the presence of a polydentate crypt ligand such as $[N\{(C_2H_4)O(C_2H_4)O(C_2H_4)\}_3N]$ affords the red crystalline compound $[Na(crypt)]_2{}^+[Pb_5]^{2-}$, which contains the trigonal bipyramidal $[Pb_5]^{2-}$ anion.[108] The emerald green species $[Pb_9]^{2-}$, which is stable in liquid ammonia solution, has not so far proved amenable to isolation via crypt-complexed cations. The mixed *nido*-$[Sn_{9-x}Pb_x]^{4-}$ ($x = 0{-}9$), $[Sn_{8-x}Pb_xTl]^{5-}$ ($x = 1{-}4$), and $[Pt(PPh_3)_zPb_9]^{4-}$ anionic species have been identified by NMR in solution.[109,110] Other anions prepared similarly include tetrahedral $[Pb_2Sb_2]^{2-}$[111] and trigonal bipyramidal $[Pb_2Se_3]^{2-}$ and $[Pb_2Te_3]^{2-}$.[112] Direct fusion of various elemental combinations at 700 °C leads to the formation, and in most cases production of single crystal of the cluster anions $[M_3M'][Pb_4]$ (where M = Cs, Rb, K; M′ = Na, Li). The structures are either noncapped square antiprism or tricapped trigonal prism.[113] A wide range of binary metal-lead cluster anions can be detected after laser ablation of the metals (Ti, Cr, Mn, Fe, Co, Ni, Zn,[114] Cu, Ag, Au[115]) and Pb. It is proposed that the units $[MPb_4]^-$ and $[MPb_5]^-$ are the building blocks to the $[M_xPb_y]$ cluster (albeit with M no greater than four).

14 RELATED ARTICLES

Cluster Compounds: Inorganometallic Compounds Containing Transition Metal & Main Group Elements; Coordination Numbers & Geometries; Electronic Structure of Main-group Compounds; Lead: Organometallic Chemistry; Mixed Valence Compounds; Tin: Inorganic Chemistry.

15 REFERENCES

1. P. Jonathan, *Polyhedron*, 1997, **16**, 551.
2. S. Mosseri, A. Henglein, and E. Janata, *J. Phys. Chem.*, 1990, **94**, 2722.
3. L. Shimoni-Livny, J. P. Glusker, and C. W. Bock, *Inorg. Chem.*, 1998, **37**, 1853.
4. I. Goldberg and F. H. Herbstein, *Acta Crystallogr.*, 1972, **B28**, 400.
5. M. Vijayan and M. A. Viswamitra, *Acta Crystallogr.*, 1966, **21**, 522.
6. D. L. Reger, J. E. Collins, A. L. Rheingold, L. M. Sand, and G. P. A. Yap, *Inorg. Chem.*, 1997, **36**, 345.
7. J. D. Donaldson, D. Laughlin, S. D. Ross, and J. Silver, *J. Chem. Soc., Dalton Trans.*, 1973, 1985.

8. J. D. Donaldson and J. Silver, *J. Chem. Soc., Dalton Trans.*, 1972, 666.
9. Y. H. Chang, C. H. Park, and K. Matsuishi, *J. Korean Phys. Soc.*, 2004, **44**, 889.
10. Shin.-Ichi. Kondo, K. Amaya, and T. Saito, *J. Phys. Soc. Jpn.*, 2001, **70**, 3751.
11. L. A. Kovbasyuk, O. Y. Vassilyeva, V. N. Kokozay, W. Linert, and P. R. Raithby, *J. Chem. Res., Synop.*, 1999, **11**, 670.
12. I. Hargittai, J. Tremmel, E. Vadja, A. A. Ishchenko, A. A. Ivanov, L. S. Ivashkevich, and V. P. Spiridonov, *J. Mol. Struct.*, 1977, **42**, 147.
13. P. G. Harrison, *Coord. Chem. Rev.*, 1976, **20**, 1.
14. A. Bystrom, *Ark. Kemi, Miner. Geol.*, 1945, **19A**, 9.
15. J. Andersson, *Acta Chem. Scand.*, 1975, **A29**, 956.
16. M. Chand and G. C. Trigunayat, *Acta Crystallogr.*, 1975, **B31**, 1222.
17. J. Andersson and G. Lundgren, *Acta Chem. Scand.*, 1970, **24**, 2670.
18. C. C. Venetopoulos and P. J. Rentzeperis, *Z. Kristallogr.*, 1975, **141**, 246.
19. C. Dybowski, M. L. Smith, M. A. Heep, E. D. Gaffney, G. Neue, and D. L. Perry, *Appl. Spectrosc.*, 1998, **52**, 426.
20. D. Weber, *Z. Naturforsch., Teil B*, 1978, **33**, 862, 1443; 1979, **34**, 939.
21. K. Matsuishi, T. Suzuki, S. Onari, E. Gregoryanz, R. J. Hemley, and H. K. Mao, *Phys. Status Solidi B*, 2001, **223**, 177.
22. H. J. Haupt, F. Huber, and H. Preut, *Z. Anorg. Allg. Chem.*, 1974, **408**, 209.
23. D. Bedlivy and K. Mereiter, *Acta Crystallogr.*, 1980, **B36**, 782.
24. S. Vilminot, W. Gramer, Z. Al Oraibi, and L. Cot, *Acta Crystallogr.*, 1980, **B36**, 1537.
25. J. Calabrese, N. L. Jones, R. L. Harlow, N. Herron, D. L. Thorn, and Y. Wang, *J. Am. Chem. Soc.*, 1991, **113**, 2328.
26. L. M. Engelhardt, B. M. Furphy, J. McB. Harrowfield, J. M. Patrick, B. W. Skelton, and A. H. White, *J. Chem. Soc., Dalton Trans.*, 1989, 595.
27. L. M. Engelhardt, B. M. Furphy, J. McB. Harrowfield, J. M. Patrick, and A. H. White, *Inorg. Chem.*, 1989, **28**, 1410.
28. A. Vogler, C. Quett, A. Paukner, and H. Kunkely, *J. Am. Chem. Soc.*, 1986, **108**, 8263.
29. W. J. Moore and L. Pauling, *J. Am. Chem. Soc.*, 1941, **63**, 1392; R. J. Hill, *Acta Crystallogr.*, 1985, **C41**, 1281.
30. P. D'Antonio and A. Santoro, *Acta Crystallogr.*, 1980, **B36**, 2394.
31. T. I. Dyuzheva, L. M. Lityagina, and N. A. Bendeliani, *J. Alloys Compd.*, 2004, **377**, 17.
32. W. B. White and R. Ray, *J. Am. Ceram. Soc.*, 1964, **47**, 247.
33. J. S. Anderson and M. Sterns, *J. Inorg. Nucl. Chem.*, 1959, **11**, 272.
34. B. Brazel and R. Hoppe, *Z. Anorg. Allg. Chem.*, 1983, **499**, 161; 1983, **505**, 99.
35. B. Nowitzki and R. Hoppe, *Z. Anorg. Allg. Chem.*, 1983, **505**, 111.
36. K. P. Martens and R. Hoppe, *Z. Anorg. Allg. Chem.*, 1980, **471**, 64.
37. B. Brazel and R. Hoppe, *Z. Naturforsch., Teil B*, 1983, **38**, 661.
38. B. Brazel and R. Hoppe, *Z. Anorg. Allg. Chem.*, 1983, **497**, 176.
39. B. Brazel and R. Hoppe, *Z. Anorg. Allg. Chem.*, 1982, **493**, 93; 1983, **498**, 167.
40. P. Panek and R. Hoppe, *Z. Anorg. Allg. Chem.*, 1973, **400**, 219.
41. L. L. Hench and J. K. West, 'Principles of Electronic Ceramics', Wiley, New York, 1990; N. W. Thomas, *Acta Crystallogr.*, 1989, **B45**, 337.
42. R. T. Macaluso, N. O. Moreno, Z. Fisk, J. D. Thompson, and J. Y. Chan, *Chem. Mater.*, 2004, **16**, 1560.
43. J. S. Forrester, J. S. Zobec, D. Phelan, and E. H. Kisi, *J. Solid State Chem.*, 2004, **177**, 3553.
44. Y. G. Lee and S. Y. Woo, *J. Mater. Sci. Lett.*, 2003, **22**, 1677.
45. V. Madigou, J. L. Baudour, F. Bouree, C. L. Favotto, M. Roubin, and G. Nihoul, *Philos. Mag. A*, 1999, **79**, 847.
46. E. R. Carmago and M. Kakihana, *J. Am. Ceram. Soc.*, 2002, **85**, 2107.
47. T. Tanase, Y. Kobayashi, and M. Konno, *Thin Solid Films*, 2004, **457**, 264.
48. S. A. Olafa, *Indian Ceram.*, 1997, **40**, 40115.
49. T. J. Boyle, P. G. Clem, B. A. Tuttle, G. L. Brennecka, J. T. Dawley, M. A. Rodriguez, T. D. Dunbar, and W. F. Hammetter, *J. Mater. Res.*, 2002, **17**, 871.
50. J. T. Wang and C. Zhang, *Ferroelectrics*, 2004, **301**, 214.
51. K. Wojcik, K. Zieleniec and M. Milata, *Ferroelectric*, 2003, **289**, 107.
52. Y. Porter and P. S. Halasyamani, *Inorg. Chem.*, 2003, **42**, 205.
53. R. N. Sylva and P. L. Brown, *J. Chem. Soc., Dalton Trans.*, 1980, 1577.
54. S. H. Hong and A. Olin, *Acta Chem. Scand.*, 1973, **27**, 2304.
55. S. H. Hong and A. Olin, *Acta Chem. Scand.*, 1974, **28**, 233.
56. M. A. Pierce-Butler, *Acta Crystallogr.*, 1984, **C40**, 1364.
57. T. G. Spiro, D. H. Templeton, and A. Zalkin, *Inorg. Chem.*, 1969, **4**, 865.
58. A. Olin and R. Sonderquist, *Acta Chem. Scand.*, 1972, **26**, 3505.
59. C. Haag-Bruhl, H. Fuess, P. Lightfoot, and A. K. Cheetham, *Acta Crystallogr.*, 1988, **C44**, 8.
60. C. Gaffney, P. G. Harrison, and T. J. King, *J. Chem. Soc., Chem. Commun.*, 1980, 1251.

61. R. J. Hill, *Acta Crystallogr.*, 1985, **C41**, 998.
62. H.-L. Keller, *Angew. Chem., Int. Ed. Engl.*, 1983, **22**, 324.
63. M. A. Pierce-Butler, *Acta Crystallogr.*, 1984, **B38**, 2681.
64. M. Lach-hab, D. A. Papaconstantopoulos, and M. J. Mehl, *J. Phys. Chem. Solids*, 2002, **63**, 833.
65. C. Boudaren, J. Auffredic, P. Bernard-Rocherulle, and D. Louer, *Solid State Sci.*, 2001, **3**, 847.
66. R. N. Butler, 'Synthetic Reagents', Wiley, Chichester, 1977, Vol. 3, p. 278.
67. P. G. Harrison and A. T. Steel, *J. Organomet. Chem.*, 1982, **239**, 105.
68. C. D. Chandler, M. J. Hampden-Smith, and E. N. Duesler, *Inorg. Chem.*, 1992, **31**, 4891.
69. R. G. Bryant, V. P. Chacko, and M. C. Etter, *Inorg. Chem.*, 1984, **23**, 3580.
70. P. G. Harrison and A. T. Steel, *J. Chem. Soc., Dalton Trans.*, 1983, 1845.
71. E. S. Claudio, M. A. Horst, C. E. Forde, C. L. Stern, M. K. Zart, and H. A. Godwin, *Inorg. Chem.*, 2000, **39**, 1391.
72. A. K. Holliday, P. H. Makin, and R. J. Puddephatt, *J. Chem. Soc., Dalton Trans.*, 1976, 435; 1979, 228.
73. E. Amberger and R. Honnigschmid-Grossich, *Chem. Ber.*, 1965, **98**, 3795.
74. S. C. Goel, M. Y. Chiang, and W. E. Buhro, *Inorg. Chem.*, 1990, **29**, 4640.
75. B. Cetinskaya, I. Gunrukcu, M. F. Lappert, J. L. Atwood, R. D. Rogers, and H. J. Zaworotko, *J. Am. Chem. Soc.*, 1980, **102**, 2088.
76. W. W. Du Mont, *Chem. Ber.*, 1981, **114**, 1180.
77. R. Papiernik, L. G. Hubert-Pfalzgraf, and M.-C. Massiani, *Inorg. Chim. Acta*, 1989, **165**, 1.
78. M. Veith, J. Hens, L. Stahl, P. May, V. Huch, and A. Senald, *Z. Naturforsch., Teil B*, 1991, **46**, 403.
79. M. Veith, D. Kafer, J. Kuch, P. May, L. Stahl, and V. Huch, *Chem. Ber.*, 1992, **125**, 1033.
80. M. Veith and J. Hans, *Angew. Chem., Int. Ed. Engl.*, 1991, **30**, 878.
81. L. F. Francis and D. A. Payne, *Chem. Mater.*, 1990, **2**, 645.
82. D. J. Teff, J. C. Huffman, and K. G. Caulton, *Inorg. Chem.*, 1996, **35**, 2981.
83. P. Bergstrom, L. M. Ellis, and E. E. Reid, *J. Am. Chem. Soc.*, 1929, **51**, 3649.
84. G. G. Hoffmann, *Z. Naturforsch., Teil B*, 1985, **40**, 335.
85. P. A. W. Dean, J. J. Vittal, and N. C. Payne, *Inorg. Chem.*, 1985, **24**, 3594.
86. P. G. Harrison, A. T. Steel, G. Pelizzi, and C. Pelizzi, *Main Group Chem.*, 1988, **11**, 181.
87. P. G. Harrison, M. G. Begley, T. Kikabhai, and A. T. Steel, *J. Chem. Soc., Dalton Trans.*, 1989, 2443.
88. F. T. Edelmann, J. F. Buijink, S. A. Brooker, R. H. Irmer, U. Kilimann, and F. A. Bonen, *Inorg. Chem.*, 2000, **39**, 6134.
89. M. M. Olmstead and P. P. Power, *Inorg. Chem.*, 1984, **23**, 413.
90. M. J. S. Gynane, D. H. Harris, M. F. Lappert, P. P. Power, P. Riviere, and M. Riviere-Baudet, *J. Chem. Soc., Dalton Trans.*, 1977, 2004.
91. M. F. Lappert, P. P. Power, M. J. Slade, L. Hedberg, K. Hedberg, and V. Schomaker, *J. Chem. Soc., Chem. Commun.*, 1979, 369.
92. T. Fjeldberg, H. Hope, M. F. Lappert, P. P. Power, and A. J. Thorne, *J. Chem. Soc., Chem. Commun.*, 1983, 639.
93. M. F. Lappert and P. P. Power, *J. Chem. Soc., Dalton Trans.*, 1985, 51.
94. H. Chen, R. A. Bartlett, H. V. Rasika Dias, M. M. Olmstead, and P. P. Power, *Inorg. Chem.*, 1991, **30**, 3390.
95. M. Veith and M. Grosser, *Z. Naturforsch., Teil B*, 1982, **37**, 1375.
96. D. L. Reger, M. F. Huff, A. L. Rheingold, and B. S. Haggerty, *J. Am. Chem. Soc.*, 1992, **114**, 579.
97. A. L. Balch and D. E. Oram, *Organometallics*, 1986, **5**, 2159.
98. A. L. Balch and D. E. Oram, *Inorg. Chem.*, 1987, **26**, 1906.
99. P. G. Harrison, in 'Comprehensive Coordination Chemistry', eds. G. Wilkinson, R. D. Gillard, and J. A. McCleverty, Pergamon Press, Oxford, Vol. 2, p. 183.
100. W. A. Herrmann, H.-J. Kneuper, and E. Herdtweck, *Angew. Chem., Int. Ed. Engl.*, 1985, **24**, 1062.
101. R. Uson, J. Fornies, L. R. Falvello, M. A. Uson, and I. Uson, *Inorg. Chem.*, 1992, **31**, 3697.
102. K. H. Whitmire, C. B. Lagrone, M. R. Churchill, J. C. Fettinger, and B. H. Robinson, *Inorg. Chem.*, 1987, **26**, 3491.
103. P. B. Hitchcock, M. F. Lappert, and M. J. Michalczyk, *J. Chem. Soc., Dalton Trans.*, 1987, 2635.
104. H.-J. Kneuper, E. Herdtweck, and H.-J. Kneuper, *J. Am. Chem. Soc.*, 1987, **109**, 2508.
105. W. A. Herrmann, H.-J. Kneuper, and E. Herdtweck, *Chem. Ber.*, 1989, **122**, 445.
106. C. B. Lagrone, K. H. Whitmire, M. R. Churchill, and J. C. Fettinger, *Inorg. Chem.*, 1986, **25**, 2080.
107. J. M. Cassidy and K. H. Whitmire, *Inorg. Chem.*, 1989, **28**, 2494.
108. P. A. Edwards and J. D. Corbett, *Inorg. Chem.*, 1977, **16**, 903.
109. F. Teixidor, M. L. Luetkins Jr, and R. W. Rudolph, *J. Am. Chem. Soc.*, 1983, **105**, 149.
110. W. L. Wilson, R. W. Rudolph, L. L. Lohr, R. C. Taylor, and P. Pyykko, *Inorg. Chem.*, 1986, **25**, 1535.

111. S. S. Critchlow and J. D. Corbett, *Inorg. Chem.*, 1985, **24**, 979.

112. M. Bjorvinsson, J. F. Sawyer, and G. J. Schrobilgen, *Inorg. Chem.*, 1987, **26**, 741; 1991, **30**, 1231.

113. S. Bobev and S. C. Sevov, *Polyhedron*, 2002, **21**, 641.

114. X. Zhang, Z. Tang, and Z. Gao, *Rapid Commun. Mass Spectrom.*, 2003, **17**, 621.

115. X. Xing, Z. Tian, H. Liu, and Z. Tang, *Rapid Commun. Mass Spectrom.*, 2003, **17**, 1411.

Lead: Organometallic Chemistry

Hemant K. Sharma & Keith H. Pannell
University of Texas at El Paso, El Paso, TX, USA

Based in part on the article Lead: Organometallic Chemistry by R. Bruce King which appeared in the Encyclopedia of Inorganic Chemistry, First Edition.

1 Introduction 1
2 Divalent Lead 1
3 Tetravalent Lead 6
4 References 7

1 INTRODUCTION

Organometallic chemistry of lead is less developed in comparison with that of lighter group 14 elements, owing to low thermal and photochemical stability of organoplumbanes. In the early 1920s, tetraalkyl lead chemistry led to two major discoveries: thermal generation of free radicals and antiknock additives for gasoline;[1,2] however, the development of lead chemistry is clearly hampered by the environmental hazard associated with lead.

A number of reviews dealing with organoplumbanes have been published,[3–12] however, and the purpose of this contribution is to overview the advances in organometallic chemistry of lead in the last decade for both divalent lead, R_2Pb, and tetravalent lead, $R_{4-n}PbX_n$.

2 DIVALENT LEAD

2.1 Plumbylenes

Simple dialkyl/diphenyl lead compounds, R_2Pb, are postulated as reactive intermediates in the synthesis of R_4Pb and $R_3Pb{-}PbR_3$ compounds. These R_2Pb species are usually unstable and highly reactive and undergo disportionation/oligomerization in the absence of stabilizing substituents on the lead atom. In general, low-valent R_2E compounds are kinetically stabilized by introducing sterically demanding substituents onto group 14 element (E = Si, Ge, Sn, Pb) and the synthetic methods for plumbylenes are restricted mainly to nucleophilic substitution of divalent lead halides and amides with organolithium or Grignard reagents[13–29] (equation 1), and the first dialkylplumbylene, $:Pb[CH(SiMe_3)_2]_2$, was obtained by Lappert in 1973,[13] from the reaction of $PbCl_2$ with $[(Me_3Si)_2CH]_2Li$ in low yield according to equation (2).

$$PbCl_2 + 2ArMgBr \longrightarrow :PbAr_2 + 2MgBrCl \qquad (1)$$

$$PbCl_2 + 2[(Me_3Si)_2CH]_2Li \longrightarrow :Pb[CH(SiMe_3)_2]_2 + 2LiCl \qquad (2)$$

Other synthetic methods are less known. For example, an aryl (arylthio)plumbylene has been obtained by unusual 1,2-aryl migration from cyclic five-membered tetrathiaplumbane by desulfurization with a triphenylphosphine[30] along with other products at high temperature according to equation (3). Presumably, the reaction occurs through the plumbathione $Ar_2Pb{=}S$ intermediate.

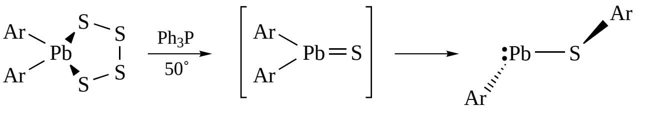

(3)

Another interesting dialkylplumbylene in which the lead atom is a central part of a seven-membered ring[22] with a C–Pb–C angle of 117.2° has been synthesized by nucleophilic substitution of $PbCl_2$ (Figure 1).

An unusual spectroscopic feature of the cyclic plumbylene is ^{207}Pb NMR chemical shift at $\delta 10\,050$ ppm in C_6D_6, the largest downfield shift reported for a lead compound. In general, the strong downfield chemical shift values for plumbylenes are consistent with low-coordination numbers and are in the range of (4000 – 10 500 ppm).

Significant developments have been made in the low-valent lead chemistry in the last decade and a number of thermally stable heteroleptic plumbylenes including those in which one of the organic group is replaced either by halide or sulfur have been synthesized and structurally characterized.[28–30] Plumbylenes containing heteroatoms F, N, S, and O as pendent groups are stabilized by intramolecular Pb–heteroatom interactions.[23–29] The plumbylenes, RPbX, exist as halogen-bridged dimers and trimers in the solid state (Figure 2) and provide useful reagents for the transfer of 'PbR' moiety. The X-ray diffraction studies show that the plumbylenes exist as a V-shaped monomer in the solid state and show little tendency of dimerization.

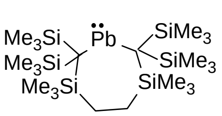

Figure 1 Cyclic plumbylene

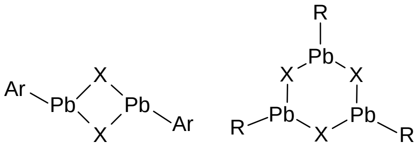

Figure 2 Halogen-bridged plumbylenes

2.2 Plumbylene Dimers and Diplumbenes

Theoretical calculations on the possibility of forming the parent diplumbene $H_2Pb{=}PbH_2$ suggested it was stable and would exhibit a bond length of 2.95–3.00 Å.[31] Several groups have attempted to synthesize such species with a series of surprising results that are very dependent upon the substituents on lead. For example, the dimerization of the heteroleptic plumbylenes R_fRPb, R = $SiMe_3$ and R_f = 2,4,6-trifluoromethylphenyl or 2-*t*-butyl-4,5,6 trimethylphenyl (equation 4),

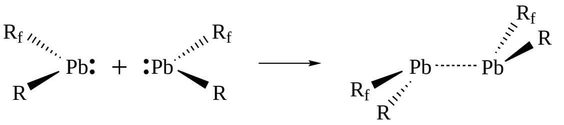

(4)

led to interesting species with very long Pb· · ·Pb internuclear distances.[32,33] The Pb–Pb distances of 3.370(1) Å and 3.537(1) Å were much longer than predicted for the parent diplumbene but the observed *trans*-bent configuration, with angles of 40.8° and 46.5°, respectively was in the expected range continuing the progressively nonplanar trend noted for the species from Si=Si to Ge=Ge to Sn=Sn. Dimerization of the corresponding divalent species can be thought to occur through donor–acceptor interaction between electron pair in 6s orbitals and empty 6p orbitals of two singlet plumbylenes (Figure 3).

The question whether or not these compounds are truly diplumbenes is complicated, since other systems with much shorter Pb–Pb bonds have been isolated. Indeed the first thermally stable diplumbene was obtained from the low-temperature reaction of $PbCl_2$ with the bulkier aryl Grignard reagent TipMgBr (Tip = 2,4,6-triisopropylphenyl).[34] The resulting compound had a short Pb–Pb separation of 3.0515(3) Å, only marginally longer than the calculated bond distance for $H_2Pb{=}PbH_2$, and *trans*-bent angles of 43.9° and 51.2°. The material was obtained as light and air-sensitive red crystals, and whereas in the solid state a diplumbene formulation is appropriate, in solution it readily dissociates into plumbylenes (equation 5).

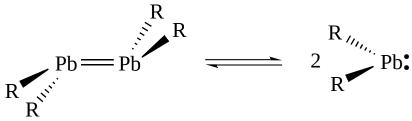

(5)

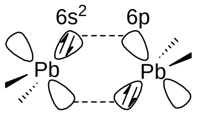

Figure 3 Donor–acceptor interactions of two singlet plumbylenes showing the formation of Pb=Pb bond

Further studies on the system showed that the size of the lead substituents is crucial. For example the reaction of the less bulky 2,4,6-triethylphenyl Grignard reagent with $PbCl_2$ in THF gave an unusual product in which two plumbylenes were stabilized by the weak interactions with Br atoms of a bridging $MgBr_2$ species[35] (Figure 4).

With the even less bulky mesityl Grignard reagent, the reaction with $PbCl_2$ produced another Pb–Pb dimeric species stabilized by two terminal $MgBr_2$ molecules (Figure 5). The Pb–Pb separation in the dimer was found to be 3.3549(6) Å.[36]

The above substituent effects fail to address the question about the steric requirements for the dimerization of plumbylenes, and the reaction conditions such as solvent and temperature play a dominant role in the outcome of the reactions.

Heteroleptic diplumbenes even shorter Pb–Pb bond lengths from 2.903–2.9899(5) Å can be obtained by the substituent exchange between two homoleptic plumbylenes,[12,36] equation (6), Sisyl = $(Me_3Si)_3Si$, presumably formed by initial formation of the symmetrical diplumbene.

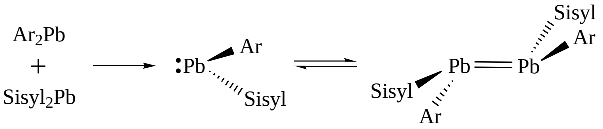

(6)

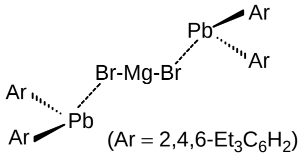

Figure 4 Interactions of bromine atoms of $MgBr_2$ with two plumbylenes

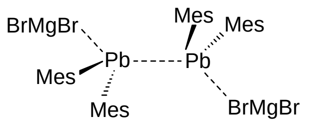

Figure 5 Plumbylene dimer stabilized by two molecules of $MgBr_2$

2.3 Cycloplumbanes

To further complicate the chemistry, the reaction between 2,4,6-triethylphenyl magnesium bromide and $PbBr_2$, which in THF gave the product illustrated in Figure 4, in dioxane at low temperature yielded the first thermally stable triplumbacyclopropane,[37] equation (7).

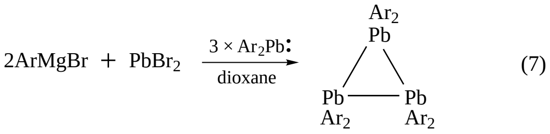

(7)

The average Pb–Pb bond length of 3.184 Å in this cyclotriplumbane is significantly longer than the single Pb–Pb bond of $Ph_3Pb–PbPh_3$, 2.844(4) Å,[38] and the aryl lead substituents are twisted by about 37° from their ideal positions. The long Pb–Pb bonds suggests that the three-membered ring is held together by weak Pb–Pb interactions in contrast to other homonuclear ring systems of group 14 elements in which the bond distances between E–E bonds indicate normal single bonds.

2.4 Diplumbyne

The first example of a species that could be thought of as a diplumbyne[39] was synthesized by the reduction of ArPbBr with $LiAlH_4$; presumably the dimerization occurs through transient ArPbH, equation (8).

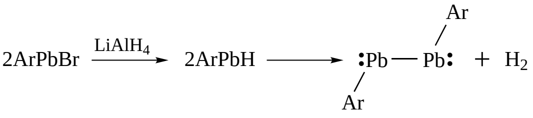

$$2ArPbBr \xrightarrow{LiAlH_4} 2ArPbH \longrightarrow :\underset{Ar}{Pb}—\overset{Ar}{Pb}: + H_2 \quad (8)$$

(Ar = 2,6-Trip$_2$-C_6H_3)

However, close examination suggests it is better thought of as a diplumbylene. For example, the Pb–Pb bond of 3.1881(1) Å, which is significantly longer than the single Pb–Pb bond $Ph_3Pb–PbPh_3$,[38] and a *trans*-bent geometry with a Pb–Pb–C angle of ~90° indicate the lone pairs essentially remain in the 6s orbitals of each lead atom. However, stable germanium and tin analogs of alkynes have also been isolated. They also exhibit a *trans*-bent geometry and possess much shorter E–E distances, and both experimental and theoretical studies suggested an E–E bond order of approximately two.

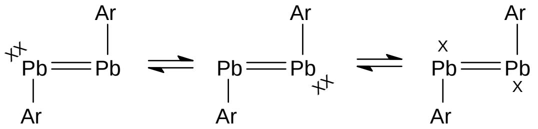

Figure 6 Bonding representations for $(ArPb)_2$

More recent studies have suggested that a more appropriate formulation of the $(ArPb)_2$ compounds may be envisaged in terms of a ''diradicaloid'' species:[40] (Figure 6)

2.5 Plumbathiones

Plumbathiones, the compounds containing Pb=S, have not been isolated yet, but as noted above, they were synthesized in situ, equation (3), and were trapped with mesitylisocyanates and phenylisothiocyanates to give [3 + 2] and [2 + 2] cycloaddition products,[41] equation (9).

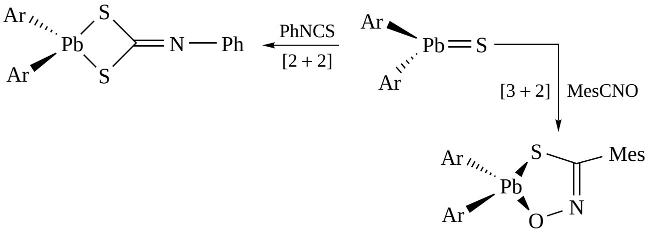

(9)

2.6 Low-valent Lead Cations

The study of carbocations analogs of group 14 elements (Si, Ge, Sn, Pb) have received attention owing to their intermediacy in number of chemical transformations. The cations of group 14 have been isolated by inter- or intramolecular stabilization of the cationic center through donor ligands or by coordination through the solvent. Donor-free cations of Si, Ge, and Sn have recently been isolated and characterized.[42] The reaction of decamethyl plumbocene $(C_5Me_5)_2Pb$ with tetrafluroboric acid led to the isolation the η^5-bonded lead cation, $[Me_5C_5Pb]^+$, equation (10).[43]

$$(C_5Me_5)_2Pb + HBF_4 \longrightarrow [Me_5C_5Pb]^+[BF_4]^- + C_5Me_5H \quad (10)$$

The X-ray analysis of the salt displays the dimeric nature of the cation bridged by the fluorine atoms of the tetrafluroborate anion. Recently, Power *et al.* synthesized a one-coordinated lead cation by abstracting methyl group from an arylmethyl plumbylene with tris(pentafluorophenyl)boron in toluene at room temperature,[44] equation (11).

$$\text{Ar-Pb-Me} + (C_6F_5)_3B \longrightarrow [\text{Ar-Pb}]^+[(C_6F_5)_3MeB]^- \quad (11)$$

The X-ray analysis of the cation shows a weak interaction with the solvent but no close interactions between the lead and the anion. In general, the Lewis acidity of the cations is displayed by ready adduct formation with pyridine and bipyridine and the ^{207}Pb NMR resonance at 8974 ppm is consistent with low coordination of lead.

2.7 Reactivity of Plumbylenes

The reactivity of plumbylenes shows them to be useful precursors for the synthesis of various tetravalent organolead compounds. A limited number of reports show that the diarylplumbylenes inserts into MeI, CBr_4, $(PhX)_2$, X = S, Se to give corresponding tetravalent lead derivatives[8,18–20] (Scheme 1).

The reaction of less hindered diarylplumbylenes with elemental sulfur, S_8, gives three different types of Pb-S heterocycles, whereas the reaction of highly crowded diaryl plumbylenes gives only the aryl substituted polysulfides[20] (Scheme 2).

An interesting plumbylene stabilized by intramolecular Pb···S interactions is obtained by the double insertion of carbon disulfide into Pb–S bonds of bis(arylthio) plumbylene[45] according to equation (12).

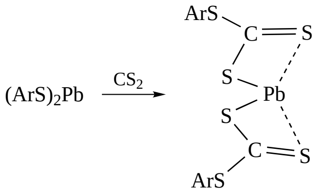

(12)

Thermally stable cyclic carbenes can act as electron donors to plumbylenes to form Zwitterionic adducts,[46,47] equation (13).

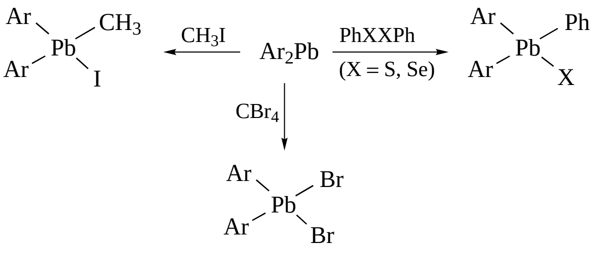

Scheme 1 Formation of tetravalent lead compounds from plumbylenes

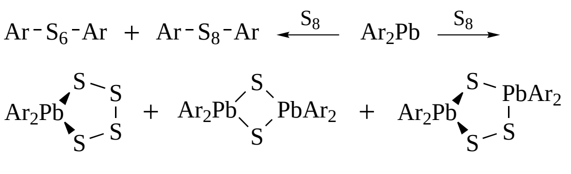

Scheme 2 Reactions of diaryl plumbylenes with S_8 showing the formation of plumbathione hetrocycles and aryl polysulfides

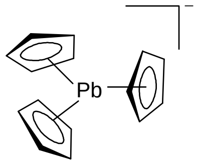

Figure 7 Structure of paddle-wheel η^5-Cp_3Pb anion

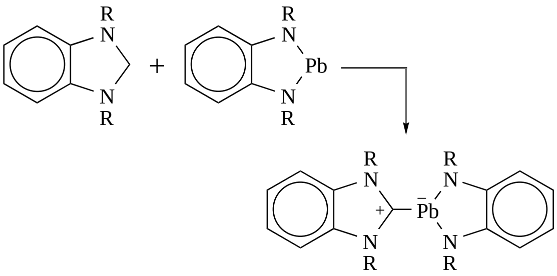

(13)

In the solid state, the adducts are monomeric and the three-coordinate carbene C atom is essentially planar and the Pb atom is pyramidalized with a relatively long carbene C–Pb bond, 2.586(7) Å. In solution, the adducts dissociate to free carbenes and plumbylenes.

Plumbylenes also form stable 1:1 adducts with alkylisonitriles, phosphines, and amines.[12] In an attempt to synthesize a lead imine, the reactions of bis (sisyl)plumbylene with arylazide provided an unusual four-membered heterocyclic plumbylene as shown in equation (14).

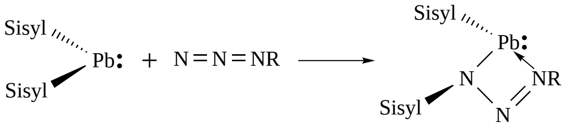

(14)

(Sisyl = $(Me_3Si)_3Si$, R = Ad)

The crystal structure revealed the pyramidal geometry around lead atom with two unequal Pb–N bonds of 2.344(7) Å and 2.372(6) Å. Similar chemistry was observed with aryl isocyanates.

2.8 Plumbocene

Plumbocene, $(\eta^5\text{-}C_5H_5)_2Pb$, (Cp = η^5-C_5H_5), was first reported by Fischer and Grubert from the reaction between Cp^-Na^+ and $Pb(NO_3)_2$ in 2:1 molar ratio in DME.[48] It is thermally unstable and monomeric in gas phase and has different structural motifs in the solid state because of flexibility of the metal-Cp bonding. The known polymorphs of plumbocene are cyclic hexamer, helical, sinusoidal, and zigzag chains bridged by the cyclopendienyl ring.[49]

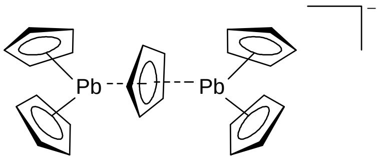

Figure 8 Structure of $[Cp_5Pb_2]^-$ anion showing bridging Cp

Plumbocenes exhibit rich reaction chemistry.[49–54] They undergo nucleophilic addition of Cp^- anions to produce $(\eta^5\text{-}Cp_3Pb)^-$ paddle-wheel anions containing trigonal-planar Cp_3Pb units.[50,51] The structure of the $(\eta^5\text{-}Cp_3Pb)^-$ is shown in Figure 7.

Multidecker anions are obtained if the nucleophilic addition of Cp^- anion is carried in the presence of crown ethers. For example, the oligomeric mixed salt $\{[Cp_5Pb_2]^-[Cp_9Pb_4]^-[Li(12\text{-crown-}4)_2{}^+]_2\}$ was obtained from the reaction between Cp_2Pb and CpLi in the presence of 12-crown-4.[53] The $[Cp_5Pb_2]^-$ anion, Figure 8 is formed predominantly under a broad range of different reaction conditions.

There are no close interactions between cations and anions in multinuclear complexes and this factor, along with the solvation of cations by crown ethers or cryptands, is responsible for the formation of multidecker anions in which the Cp_2Pb units are linked through bridging $\mu\text{-}\eta^5$-Cp ligand. The multidecker anion $[Cp_9Pb_4]^-$ could be thought of as the $[Cp_5Pb_2]^-$ anion bridged by two additional Cp_2Pb units, as shown in Figure 9.

2.9 Transition Metal Plumbylene Complexes

Compounds that contain bonds between lead (II) and transition metals are rare. Dimeric group 14 bridged complexes $[R_2EM(CO)_4]_2$ (M = Mn and Fe) were obtained from the reaction of $[M(CO)_4]^{2-}$ $2Na^+$ with R_2PbX_2 in THF.[55–58] In the presence of donor solvents like pyridine, THF, DMF, and acetonitrile, these complexes undergo reversible cleavage of the metal-group 14-element bond to yield base-stabilized plumbylene metal complexes,[58] equation (15).

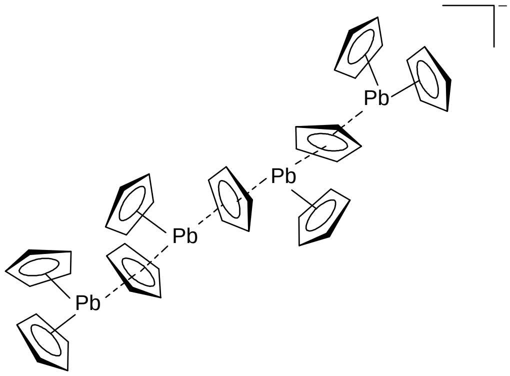

Figure 9 Structure of multidecker $[Cp_9Pb_4]^-$ anion

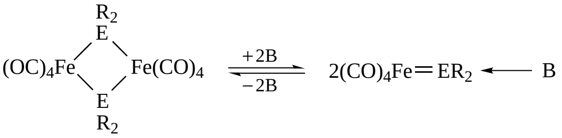

$$(OC)_4Fe(\mu\text{-}ER_2)_2Fe(CO)_4 \underset{-2B}{\overset{+2B}{\rightleftharpoons}} 2(CO)_4Fe{=}ER_2 \longleftarrow B \qquad (15)$$

Two spectroscopically characterized examples of base-free plumbylene complexes are $(CO)_5MoPb\{N(SiMe_3)_2\}_2$ and $[Pd(\eta^3\text{-}C_3H_5)(\mu\text{-}Cl)Pb\{N(SiMe_3)_2\}_2]_2$.[59] A simple route to obtain Mo-Pb(II) complexes involves the amine elimination reaction shown in equation (16).[60]

$$2[Cp^*Mo(CO)_3H] + Pb[N(SiMe_3)_2]_2 \longrightarrow [Cp^*Mo(CO)_3]_2Pb + 2HN(SiMe_3)_2 \qquad (16)$$

Bis-metallaplumbylenes containing three-coordinate lead complexes $[\{Cp^*Mo(CO)_3\}_2Pb(THF)]$ and an unusual bridging carbonyl dimeric complex $\{(Cp^*Mo(CO)_3)PbCp^*Mo(CO)_2(\mu\text{-}CO)\}_2$ were structurally characterized.[60] Plumbylene complexes of group 6 metals (M = Cr, Mo, W) were synthesized by reacting $(FcN)_2Pb$ (Fc = $(\eta^5\text{-}C_5H_5)Fe(\eta^5\text{-}C_5H_4)$, N = CH_2NMe_2) with metal carbonyls.[61] The M–Pb bond distances of 2.7157(4) Å, Cr; 2.8531(13) Å, Mo; and 2.8497(3) Å for W indicate some degree of π-bonding in these complexes. The geometry around Pb is distorted trigonal bipyramidal owing to Pb-N close interactions, whereas the transition metal is in a distorted octahedral environment.

In an attempt to synthesize M≡Pb triple bond complexes, Power *et al.* obtained metallaplumbylenes of the type L_nM-Pb-Ar (M = Cr, Mo, W and Ar = 2,6 $Trip_2C_6H_3$) of group 6 metals by salt elimination, as shown in equation (17).[62]

$$[(\eta^5\text{-}C_5H_5)M(CO)_3]^-Na^+ + ArPbBr \longrightarrow (\eta^5\text{-}C_5H_5)(CO)_3M\text{-}Pb\text{-}Ar + NaCl \qquad (17)$$

The M≡Pb triple bond complexes were not obtained because of the inert pair effect of $6s^2$ electrons and the larger size of the lead atom, which decreased the steric protection, thus preventing the CO elimination. The special feature of these metallaplumbylene complexes is the relatively long M–Pb bonds: 2.9092(9) Å Cr; 2.9845(7) Å, Mo; 3.0055(6) Å for W, and bent geometry at lead with M–Pb–C angles is in the range of 108.6(2)–113.58(9)°. These complexes can be best described as having primarily M–Pb single bond character with lone pair of electrons localized at the lead atom.

A lead allene analog of Mn, $CpMn(CO)_2{=}Pb{=}Mn(CO)_2Cp$, was prepared from the reaction of the thermally labile Mn complex $CpMn(CO)_2(THF)$ with $PbCl_2$ as a reddish-brown air- and light-sensitive complex.[63,64]

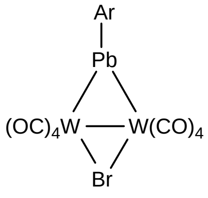

(Ar = 2,6-$Trip_2$-C_6H_3)

Figure 10 Bridging plumbylene tungsten complex

2.10 Transition Metal Plumbylyne Complexes

An unusual bridging plumbylyne complex was obtained in poor yield from the reaction of $W(CO)_5{\cdot}THF$ with bromoplumbylene, ArPbBr. Since the Pb atom is a three-electron donor to the metals, it may be regarded as a plumbylyne ligand, Figure 10.[28]

The structure of the complex exhibits two Pb–W bonds at 2.7517(3) Å and 2.7423(3) Å which are markedly shorter than Pb–W single bonds. The geometry around lead is distorted trigonal with acute W–Pb–W angle of 70.177(8)°. These features demonstrate some degree of double bond character between Pb–W bonds.

Recently, a first complex containing a M≡Pb triple bond has been reported and this was obtained by the reaction Mo dinitrogen complex with aryl lead bromide in toluene at ambient temperature according to equation (18).[65]

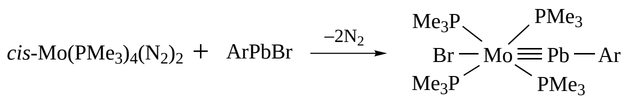

$$cis\text{-}Mo(PMe_3)_4(N_2)_2 + ArPbBr \xrightarrow{-2N_2} Br{-}Mo(PMe_3)_4{\equiv}Pb{-}Ar$$

(Ar = 2,6-$Trip_2$-C_6H_3)

(18)

The complex is air sensitive but thermally stable. The Mo–Pb bond of 2.55 Å is very short and the almost linear geometry, Mo–Pb–C bond angle 177.8(2)°, clearly indicates the formation of a Mo≡Pb triple bond.

3 TETRAVALENT LEAD

3.1 Lead Oligomers

A well known reaction in lead chemistry is the synthesis of $Ph_3Pb{-}PbPh_3$ from phenyl Grignard reagent and lead (II) halides. The mechanism for this reaction is presumed to involve the formation of diphenylplumbylene, which then oligomerizes and disproportionates to hexaphenyldilead and metallic lead. However, repeating the above reaction at low temperature led to the isolation of unexpected oligomeric lead anion, $:[Pb(PbPh_3)_3]^-$.[66] The four Pb atoms in the anion form trigonal pyramid with Pb–Pb bonds of about 2.98A, which are significantly longer than the Pb–Pb bond in hexaphenyldilead, and the Pb–Pb–Pb angles are compressed to an average value of 93°.

3.2 Acylplumbanes

Thermally stable acylplumbanes were isolated by using bulky mesityl substituents on the lead using the simple reaction of Mes_3PbLi with acyl chlorides (R = Me, Ph), equation (19).[67]

$$Mes_3PbLi + RCOCl \longrightarrow Mes_3PbCOR \qquad (19)$$

The photochemistry of the acylplumbanes, which involves cleavage of both the Pb-acyl and Pb-mesityl bonds, is less developed in comparison with acylsilanes, which exhibit a rich vein in photochemistry.

3.3 Intra Group 14 Bonds

Attempts to synthesize lead derivatives of E = Si, Ge, and Sn with direct Pb–E bonds are unsuccessful owing to the low stability of the Pb–E bond, which is prone to undergo decomposition because of 1,2-alkyl/aryl migrations from the lead atom.[68,69] By using aryl groups on lead and the bulky substituents $E(SiMe_3)_3$ (E = Si, Ge), the migration of aryl groups from lead to group 14 element can be suppressed, thereby stabilizing the Pb–E bond and facilitating the isolation of intra group 14 derivatives. Both symmetrical and unsymmetrical aryl lead-aryl/sisyl (sisyl = $(SiMe_3)_3$) group 14 compounds were obtained by salt-elimination reactions, equation (20).[70–73]

$$Ar_3PbLi + Ar'_3EX \longrightarrow Ar_3Pb{-}EAr'_3 + LiX \qquad (20)$$

$$(E = Si, Ge, Sn)$$

3.4 Transition Metal-lead Complexes

The first transition metal-lead compounds were reported in 1941;[74] in general they are prone to decompose thermally, and this process is accelerated in the presence of light. A recent comprehensive review is available.[75]

The salt-elimination reaction involving the use of a transition metallate and organo-lead halides has been widely used to form metal-lead complexes, equation (21), and a range of such derivatives has been prepared for many metals: Cr,[76–78] Mo,[76–78] W,[76–78] Mn,[55,56,79] Re,[79] Fe,[57,78,80,81] Os,[82] Co,[83] Rh,[84] and Ir.[84]

$$[(CO)_5Mn]^-Na^+ + Me_3PbCl \longrightarrow [(CO)_5Mn]PbMe_3 + NaCl \qquad (21)$$

Highly reduced metal anions $[M(CO)_n]^{3-}$ (M = Mn, Re; $n = 4$; M = Co, $n = 3$) react with two equivalents of Ph_3PbCl

to provide anionic complexes that were isolated as crystalline tetraammonium salts, equation (22).[85,86]

$$[Co(CO)_3]^{3-}3Na^+ + 2Ph_3PbCl + NH_4Cl \longrightarrow (NH_4)[Co(CO)_3(PbPh_3)_2] \quad (22)$$

Complexes of Pd and Pt were synthesized by the reaction of *cis* or *trans*-$[ML_2Cl_2]$ (M = Pd or Pt; L = PEt_3 or $AsEt_3$) with triphenyllead lithium, equation (23). The red solution produced yellow crystalline solids of *trans*-$[ML_2(PbPh_3)_2]$ complexes.[87] These complexes are thermally stable.

$$[Pt(PEt_3)_2Cl_2] + [Ph_3Pb]^-Li^+ \longrightarrow \textit{trans}\text{-}[Pt(PEt_3)_2(PbPh_3)_2] + 2LiCl \quad (23)$$

Oxidative addition of the relatively weak Pb–Pb, Pb–C, and Pb–Cl bonds to metal-centers is a useful reaction for the formation of Pb–M bonds, equations (24 and 25).[88–90]

$$(Ph_3P)_4Pt + Ph_3Pb\text{–}PbPh_3 \longrightarrow [(Ph_3P)_2Pt(PbPh_3)_2] + 2Ph_3P \quad (24)$$

$$(Ph_3P)_4Pt + Ph_4Pb \longrightarrow [(Ph_3P)_2Pt(PbPh_3)(Ph)] + 2Ph_3P \quad (25)$$

Addition of PbR_2 to a benzene solution of the iron complexes $CpFe(CO)_2X$ (X = I, Br or Cl) resulted in the formation of four-coordinated functionalized Fe-Pb complexes, via insertion chemistry, that is, $[CpFe(CO)_2(PbR_2X)]$.[91]

Another interesting approach for the synthesis of transition metal-lead bonds is the reaction of metal hydrides with R_3Pb–X.[92]

3.5 Reactivity of Transition Metal-lead Complexes

Metal-lead complexes can undergo the cleavage of Pt–Pb bond with halogens and halogen acids[88,93] (Scheme 3).

On the other hand, halogenation of the binuclear Mn complex $[Mn(CO)_5]_2PbPh_2$ with Cl_2 or Br_2 cleaves the Pb–C bond rather than the Mn–Pb bond to produce halogenated Mn-Pb derivatives, equation (26), X = Cl, Br.[56]

$$[(CO)_5Mn]_2PbPh_2 + 2X_2 \longrightarrow [(CO)_5Mn]_2PbX_2 + 2PhX \quad (26)$$

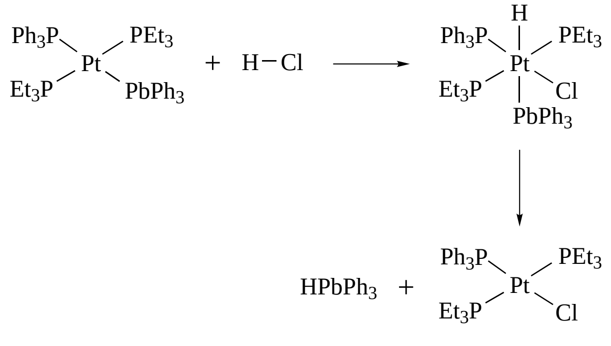

Scheme 3 M–Pb bond cleavage with halogen acid

There are several reports concerning the thermal and photochemical reactivity of triorganolead metal complexes. In general, they eliminate plumbylenes, R_2Pb, with a concurrent transfer of the organic radical to the metal center. Such chemistry is reported for platinum, iron, and molybdenum *inter alia*. A typical reaction is outlined in equation (27).[77,81,88,90]

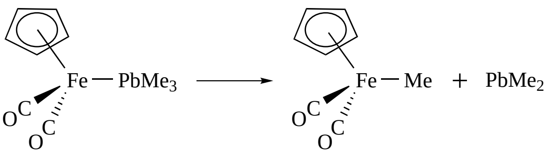

(27)

Related disproportionations were also observed in Mn[55] and Fe[94] complexes; for example, the $Mn(CO)_5$-$PbEt_3$ complex in THF gave the *bis*-Mn complex $[Mn(CO)_5]_2PbEt_2$, equation (28).

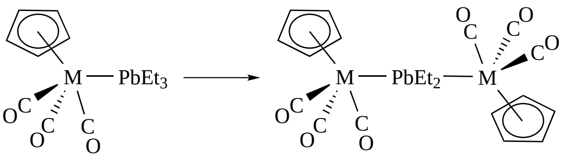

(28)

3.6 ^{207}Pb NMR Spectroscopy of Transition Metal-lead Complexes

^{207}Pb NMR spectroscopy is a valuable method for studying transition metal-lead bond in solution. It is evident that the variations in chemical shift values with respect to the transition metal are large, for example, ^{207}Pb NMR of $[Fe(CO)_4]_4Pb$ exhibits a resonance at 3587 ppm.[57] The trends in chemical shift values are consistent with the trends observed in ^{29}Si and ^{119}Sn NMR spectra of the corresponding transition metal complexes where a comparison is possible.

Since this article was written, several notable developments in organolead chemistry have been reported. New diplumbenes,[95] a W-Pb triple bond,[96] a tri(trisbiphenylplumbyl)lead anion,[97] and new lead clusters[98] have been obtained.

4 REFERENCES

1. (a) F. Paneth and W. Hofeditz, *Chem. Ber.*, 1929, **62**, 1335; (b) F. Paneth and W. Lautsch, *Chem. Ber.*, 1931, **64**, 2702.
2. T. Midgley Jr, C. A. Hochwalt, and G. Calingaert, *J. Am. Chem. Soc.*, 1923, **45**, 1821.
3. Z. Rappoport ed., 'The Chemistry of Organic Germanium, Tin and Lead Compounds', John Wiley, Interscience, 2002, Vol. 2.
4. R. B. King, *Encycl. Inorg. Chem.*, 1995, **4**, 1955.
5. P. G. Harrison, in 'Comprehensive Organometallic Chemistry II', eds. G. Wilkinson, F. G. A. Stone, and E. A. Abel, Pergmon, New York, 1995, Vol. 2, p. 305.
6. P. P. Power, *Chem. Rev.*, 1999, **99**, 3463.

7. M. Widenbruch, *Chem. Rev.*, 1995, **95**, 1479.
8. T. Norihio and O. Renji, *Coord. Chem. Rev.*, 2002, **210**, 251.
9. M. Driess and H. Grützmann, *Angew. Chem., Int. Ed. Engl.*, 1996, **35**, 827.
10. M. Widenbruch, *Organometallics*, 2003, **22**, 4348.
11. (a) M. Widenbruch, *Eur. J. Inorg. Chem.*, 1999, 373; (b) M. Widenbruch, *J. Organomet. Chem.*, 2002, **646**, 39.
12. K. Klinkhammer, *Polyhedron*, 2002, **21**, 587.
13. D. J. Davidson and M. F. Lappert, *J. Chem. Soc., Chem. Commun.*, 1973, 317.
14. M. Driess, R. Januschek, H. Pritzkow, S. Rell, and U. Winkler, *Angew. Chem., Int. Ed. Engl.*, 1995, **34**, 1614.
15. K. W. Klinkhammer and W. Schwarz, *Angew. Chem., Int. Ed. Engl.*, 1995, **34**, 1334.
16. J. Klett, K. W. Klinkhammer, and M. Niemeyer, *Chem. – Eur. J.*, 1999, **5**, 2531.
17. B. Gehrhus, P. B. Hitchcock, and M. F. Lappert, *Angew. Chem., Int. Ed. Engl.*, 1997, **36**, 2514.
18. (a) K. Shibata, N. Tokitoh and R. Okazaki, *Tetrahedron Lett.*, 1993, **34**, 1495; (b) N. Tokitoh, N. Kano, K. Shibata, and R. Okazaki, *Phosphorus, Sulfur Silicon Relat. Elem.*, 1994, **189**, 93; (c) N. Tokitoh, N. Kano, K. Shibata, and R. Okazaki, *Organometallics*, 1995, **14**, 3121.
19. N. Kano, N. Tokitoh, and R. Okazaki, *Organometallics*, 1997, **16**, 2748.
20. N. Kano, K. Shibata, N. Tokitoh, and R. Okazaki, *Organometallics*, 1999, **18**, 2999.
21. R. S. Simons, L. Pu, M. M. Olmstead, and P. P. Power, *Organometallics*, 1997, **16**, 1920.
22. C. Eaborn, T. Ganicz, P. B. Hitchcock, J. D. Smith, and S. E. Sözerli, *Organometallics*, 1997, **16**, 5621.
23. J. Barrau, G. Rima, and T. El Amraoui, *Organometallics*, 1998, **17**, 607.
24. K. Hübler and U. Hübler, *Z. Anorg. Allg. Chem.*, 2000, **626**, 1224.
25. N. Seidel, K. Jacob, A. A. H. van der Zeijden, H. Menge, K. Merzweiler, and C. Wagner, *Organometallics*, 2000, **19**, 1438.
26. S. Brooker, J. K. Buijink, and F. T. Edelman, *Organometallics*, 1991, **10**, 25.
27. S. Wingerter, H. Gornitzka, R. Bertermann, S. K. Pandey, J. Rocha, and D. Stalke, *Organometallics*, 2002, **19**, 3890.
28. L. Pu, B. Twamley, and P. P. Power, *Organometallics*, 2002, **19**, 2874.
29. C. Eaborn, P. B. Hitchcock, J. D. Smith, and S. E. Sözerli, *Organometallics*, 1997, **16**, 5653.
30. (a) N. Kano, N. Tokitoh, and R. Okazaki, *Organometallics*, 1997, **16**, 4237; (b) N. Kano, N. Tokitoh, and R. Okazaki, *Phosphorus, Sulfur and Silicon*, 1997, **517**, 124.
31. (a) G. Trinquier, *J. Am. Chem. Soc.*, 1990, **112**, 2130; (b) H. Jacobson and T. Ziegler, *J. Am. Chem. Soc.*, 1994, **116**, 3667.
32. K. W. Klinkhammer, T. F. Fässler, and H. Grützmacher, *Angew. Chem., Int. Ed. Engl.*, 1998, **37**, 124.
33. M. Stürmann, M. Weidenbruch, K. W. Klinkhammer, F. Lissner, and H. Marsmann, *Organometallics*, 1998, **17**, 4425.
34. M. Stürmann, W. Saak, H. Marsmann, and M. Weidenbruch, *Angew. Chem., Int. Ed. Engl.*, 1999, **38**, 187.
35. M. Stürmann, W. Saak, and M. Weidenbruch, *Z. Anorg. Allg. Chem.*, 1999, **625**, 705.
36. M. Stürmann, W. Saak, M. Weidenbruch, and K. W. Klinkhammer, *Eur. J. Inorg. Chem.*, 1999, 579.
37. F. Stabenow, W. Saak, H. Marsmann, and M. Widenbruch, *J. Am. Chem. Soc.*, 2003, **125**, 10172.
38. H. Preut and F. Huber, *Z. Anorg. Allg. Chem.*, 1976, **419**, 92.
39. L. Pu, B. Twamley, and P. P. Power, *J. Am. Chem. Soc.*, 2000, **122**, 3524.
40. P. P. Power, *Chem. Commun.*, 2003, 2091.
41. (a) N. Kano, N. Tokitoh, and R. Okazaki, *Chem. Lett.*, 1997, 277; (b) N. Kano, N. Tokitoh, and R. Okazaki, *J. Synth. Org. Chem. Jpn.*, 1998, **56**, 919.
42. (a) J. B. Lambert, L. Kania, and S. Zhang, *Chem. Rev.*, 1995, **95**, 1191; (b) C. A. Reed, *Acc. Chem. Res.*, 1998, **31**, 325; (c) I. Zharov and J. Michl, in ‘The Chemistry of Organic Germanium, Tin and Lead Compounds’, ed. Z. Rappoport, John Wiley, Interscience, 2002, Vol. 2, p. 633.
43. P. Jutzi, R. Dickbreder, and H. Nöth, *Chem. Ber.*, 1989, **122**, 865.
44. S. Hino, M. Brynda, A. D. Phillips, and P. P. Power, *Angew. Chem., Int. Ed. Engl.*, 2004, **43**, 2655.
45. N. Kano, N. Tokitoh, and R. Okazaki, *Organometallics*, 1998, **17**, 1241.
46. B. Gehrhus, P. B. Hitchcock, and M. F. Lappert, *J. Chem. Soc., Dalton Trans.*, 2000, 3094.
47. F. Stabenow, W. Saak, and M. Weidenbruch, *Chem. Commun.*, 1999, 1131.
48. E. O. Fischer and H. Grubert, *Z. Anorg. Allg. Chem.*, 1956, **286**, 237.
49. P. Jutzi and N. Burford, *Chem. Rev.*, 1999, **99**, 969.
50. M. A. Beswick, J. S. Palmer, and D. S. Wright, *Chem. Soc. Rev.*, 1998, **27**, 225.
51. D. R. Armstrong, M. J. Duer, M. G. Davidson, D. Moncrieff, C. A. Russell, C. Stourton, A. Steiner, D. Stalke, and D. S. Wright, *Organometallics*, 1997, **16**, 3340.
52. D. R. Armstrong, M. A. Beswick, N. L. Cromhout, C. N. Harmer, D. Moncrieff, C. A. Russell, P. R. Raithby, A. Steiner, A. E. H. Wheatley, and D. S. Wright, *Organometallics*, 1997, **16**, 3176.
53. M. A. Beswick, H. Gornitzka, J. Kärcher, M. E. G. Mosquera, J. S. Palmer, P. R. Raithby, C. A. Russell, D. Stalke, A. Steiner, and D. S. Wright, *Organometallics*, 1999, **18**, 1148.
54. R. A. Layfield, M. McPartlin, and D. S. Wright, *Organometallics*, 2003, **22**, 2528.
55. R. D. Gorsich, *J. Am. Chem. Soc.*, 1962, **84**, 2486.

56. H. J. Haupt, W. Schubert, and F. Huber, *J. Organomet. Chem.*, 1973, **54**, 231.
57. M. Herberhold, V. Tröbs, W. Milius, and B. Wrackmeyer, *Z. Naturforsch., Teil B*, 1994, **49**, 1781.
58. T. J. Marks and A. R. Neuman, *J. Am. Chem. Soc.*, 1973, **95**, 769.
59. M. F. Lappert, S. J. Miles, and P. P. Power, *J. Chem. Soc., Chem. Commun.*, 1977, 458.
60. P. B. Hitchcock, M. F. Lappert, and M. J. Michalczyk, *J. Chem. Soc., Dalton Trans.*, 1987, 2635.
61. N. Seidel, K. Jacob, and A. K. Fischer, *Organometallics*, 2001, **20**, 578.
62. L. Pu, P. P. Power, I. Boltes, and R. Herbst-Irmer, *Organometallics*, 2000, **19**, 352.
63. W. A. Hermann, H. J. Kneuper, and E. Herdtweck, *Angew. Chem., Int. Ed. Engl.*, 1985, **24**, 1062.
64. W. A. Hermann, *Angew. Chem., Int. Ed. Engl.*, 1986, **25**, 56.
65. A. C. Filippou, H. Rohde, and G. Schnakenburg, *Angew. Chem., Int. Ed. Engl.*, 2004, **43**, 2243.
66. F. Stabenow, W. Saak, and M. Weidenbruch, *Chem. Commun.*, 1999, 2342.
67. R. Villazana, H. Sharma, F. Cervantes-Lee, and K. H. Pannell, *Organometallics*, 1993, **12**, 4278.
68. H. K. Sharma, R. J. Villazana, F. Cervantes-Lee, L. Parkanyi, and K. H. Pannell, *Phosphorus, Sulfur and Silicon*, 1994, **87**, 25.
69. S. M. Whittaker, F. Cervantes-Lee, and K. H. Pannell, *Inorg. Chem.*, 1994, **33**, 6406.
70. C. Schneider-Koglin, K. Behrends, and M. Dräger, *J. Organomet. Chem.*, 1993, **448**, 29.
71. H.-J. Koglin, K. Behrends, and M. Dräger, *Organometallics*, 1994, **13**, 2733.
72. (a) S. P. Mallela and R. A. Geanangel, *Inorg. Chem.*, 1993, **32**, 602; (b) S. P. Mallela, J. Myrczek, I. Bernal, and R. A. Geanangel, *J. Chem. Soc., Dalton Trans.* 1993, 2891.
73. S. P. Mallela and R. A. Geanangel, *Inorg. Chem.*, 1994, **33**, 6357.
74. F. Hein, H. Poblath, and E. Heuser, *Z. Anorg. Allg. Chem.*, 1941, **248**, 84.
75. H. K. Sharma, I. Haiduc, and K. H. Pannell, in ‘The Chemistry of Organic Germanium, Tin and Lead Compounds’, ed. Z. Rappoport, John Wiley, Interscience, 2002, Vol. 2, p. 1241.
76. H. R. H. Patil and W. A. G. Graham, *Inorg. Chem.*, 1966, **5**, 1401.
77. K. H. Pannell and R. N. Kapoor, *J. Organomet. Chem.*, 1981, **214**, 47.
78. K. H. Pannell and R. N. Kapoor, *J. Organomet. Chem.*, 1984, **269**, 59.
79. W. Jetz, P. B. Simons, J. A. J. Thompson, and W. A. G. Graham, *Inorg. Chem.*, 1966, **5**, 2217.
80. F. Hein and E. Heuser, *Z. Anorg. Allg. Chem.*, 1947, **254**, 138.
81. K. H. Pannell, *J. Organomet. Chem.*, 1980, **198**, 37.
82. R. D. George, S. A. R. Knox, and F. G. A. Stone, *J. Chem. Soc., Dalton Trans.*, 1973, 972.
83. D. J. Patmore and W. A. G. Graham, *Inorg. Chem.*, 1967, **6**, 981.
84. M. A. Bennett and D. J. Patmore, *Inorg. Chem.*, 1971, **10**, 2387.
85. J. E. Ellis and R. A. Faltynek, *J. Am. Chem. Soc.*, 1977, **99**, 1801.
86. J. E. Ellis, P. T. Barger, M. L. Winzenburg, and G. F. Warnock, *J. Organomet. Chem.*, 1990, **383**, 521.
87. G. Deganello, G. Carturan, and U. Belluco, *J. Chem. Soc. A*, 1968, 2873.
88. B. Crociani, M. Nicolini, D. A. Clemente, and G. Bandoli, *J. Organomet. Chem.*, 1973, **49**, 249.
89. S. Carr, R. Colton, and D. Dakternieks, *J. Organomet. Chem.*, 1982, **240**, 143.
90. M. C. Baird, *J. Inorg. Nucl. Chem.*, 1967, **29**, 367.
91. M. F. Lappert, M. J. McGeary, and R. V. Parish, *J. Organomet. Chem.*, 1989, **373**, 107.
92. G. I. Nikonov, E. V. Avtomonov, and W. Massa, *Chem. Ber.*, 1997, **130**, 1629.
93. V. G. Albano, C. Castellari, M. Monari, V. D. Felice, M. L. Ferrara, and F. Ruffo, *Organometallics*, 1995, **14**, 4213.
94. F. Hein and W. Jehn, *Justus Leibigs Ann. Chem.*, 1965, **684**, 4.
95. M. Shirley, M. Olmstead, A. D. Phillips, R. J. Wright, and P. P. Power, *Inorg. Chem.*, 2004, **43**, 7346.
96. A. C. Filippou, N. Weidemann, G. Schnakenburg, H. Rohde, and A. I. Philippopoulos, *Angew. Chem., Int. Ed. Engl.*, 2004, **43**, 6512.
97. Y. Wang, B. Quillian, P. Wei, X.-J. Yang, and G. H. Robinson, *Chem. Commun.*, 2004, 2224.
98. K. W. Klinkhammer, Y. Xiong, and S. Yao, *Angew. Chem., Int. Ed. Engl.*, 2004, **43**, 6202.

Acknowledgments

We thank NSF, NIH (MARC program grant # 08048), and Welch Foundation (grant # AH-0546) for support of this research.

Ligand Field Theory & Spectra

Derek W. Smith
University of Waikato, Hamilton, New Zealand

1 Introduction 1
2 Crystal Field (CF) Approach 1
3 Deficiencies of the Crystal Field Model 5
4 Ligand Field (LF) Spectroscopy 7
5 Quantitative Determination of LF Energy-level Diagrams 13
6 Ligand Field Spectra of Noncubic Complexes 14
7 Other Applications of Ligand Field Theory 16
8 Related Articles 18
9 References 18

Glossary

Chromophore: central atom and coordination sphere responsible for d–d and charge–transfer transitions in complex or crystal
Perturbation theory: mathematical technique for determining the effect on state energies and wavefunctions of small perturbations, for example, electric or magnetic fields

1 INTRODUCTION

The transition elements are characterized by the occurrence of stable oxidation states in which the *n*d subshell is partly filled. For example, the most familiar compounds of iron can be classified as containing Fe^{II} or Fe^{III}. These are deemed to contain Fe^{2+} and Fe^{3+} ions, whose ground states (*see Ground State*) are $3d^6$ and $3d^5$ respectively (*see d^n Configuration*). In contrast, stable oxidation states exhibited by the main group elements nearly always correspond to empty or filled subshells. The consequences of partly filled *n*d subshells largely determine the physical and chemical properties that characterize the transition elements. Ligand field theory (LFT) is a valuable tool for analyzing these properties, by focusing attention on the partly filled subshell. In particular, LFT recognizes that the subshell will lose its fivefold degeneracy when the atom or ion is placed in any chemical environment, that is, the five *n*d orbitals will no longer all have the same energy and their precise occupancies have to be scrutinized.

LFT has an important place in the historical development of inorganic chemistry. Its elegance attracted a large proportion of the 'new wave' of inorganic chemists who revolutionized the subject in the 1950s and 1960s. Inorganic chemistry texts[1–14] give elementary accounts; advanced general treatments are found in monographs.[15–32] References to more specialized reviews and articles are made in the text.

LFT has been applied to the splitting of the 4f and 5f orbitals in compounds of the lanthanides and actinides respectively.[33] This article deals only with applications to d-block chemistry.

2 CRYSTAL FIELD (CF) APPROACH

The term *Crystal Field Theory* (CFT) is often used almost interchangeably with LFT. Strictly speaking, CFT refers to an early version of what most inorganic chemists now understand to be LFT. The name is derived from the title of a classic 1929 paper by Bethe,[34] 'The Splitting of Terms in Crystals'. This shows how the methods of group theory can be used to determine what happens to the degeneracy of a spectroscopic state (term) when a free atom or ion is placed in a chemical environment having less than spherical symmetry. Bethe's approach was quickly taken up by physicists who were interested in the quantum mechanical theory of *Paramagnetism* in compounds of the transition elements. CFT was 'rediscovered' in the early 1950s by inorganic and physical chemists who extended its applications to spectroscopic, structural, thermodynamic, and kinetic properties of transition-element complexes. As discussed in Section 3, it was clear by the late 1950s that CFT, in its purest form, was untenable. However, it remains useful to this day for qualitative purposes, and, with some adjustments, can be applied to quantitative treatments of spectroscopic and magnetic observations. Thus, LFT encompasses a broader approach, which acknowledges the shortcomings of CFT while recognizing its value.

2.1 The Five d Orbitals in a Free Atom or Ion

Here, we look at the atomic orbitals (AOs) that constitute the partly filled subshell; we are dealing for the moment with free atoms/ions, as observed in the gas phase. An AO is a function of the coordinates of just one electron, and is the product of two parts: the radial part is a function of r, the distance of the electron from the nucleus and thus has spherical symmetry; the angular part is a function of the x, y, and z axes and conveys the directional properties of the orbital. The notation *n*d indicates an AO whose l quantum number is 2; we have five *n*d orbitals corresponding to $m_l = 2, 1, 0, -1$, and -2. Solving the Schrödinger equation, we obtain the angular wavefunctions as equations (1–5).

$$d_2 = (x + iy)^2 \tag{1}$$

$$d_1 = z(x + iy) \tag{2}$$

$$d_0 = \left(\tfrac{1}{2}\right)(2z^2 - x^2 - y^2) \tag{3}$$

$$d_{-1} = z(x - iy) \tag{4}$$

$$d_{-2} = (x - iy)^2 \tag{5}$$

These are acceptable for many purposes, but the complex number $\sqrt{i}$ $(= -1)$ makes them difficult to visualize. Given a set of solutions to the wave equation, which we find inconvenient, it is always permissible to transform these into an equal number of new functions obtained by taking linear combinations of the original ones, provided that orthogonality is upheld, that is, the overlap integral $\int \psi_i \psi_j \, d\tau \;\; (i \neq j)$ is always zero. (This procedure is utilized in other familiar situations, for example, in the construction of hybrid orbitals, and of MOs as linear combinations of AOs; *see* ***Molecular Orbital Theory***.) Eliminating i from equations (1–5) by equations (6–9),

$$\left(\frac{1}{2}\right)(d_2 + d_{-2}) = x^2 - y^2 \tag{6}$$

$$\left(\frac{1}{2i}\right)(d_2 - d_{-2}) = 2xy \tag{7}$$

$$\left(\frac{1}{2}\right)(d_1 + d_{-1}) = 2xz \tag{8}$$

$$\left(\frac{1}{2i}\right)(d_1 - d_{-1}) = 2yz \tag{9}$$

we have a set of mutually orthogonal functions labeled in terms of angular functions $d_{x^2-y^2}$, d_{xy}, d_{xz}, and d_{yz}; d_0 is retained as in equation (3) and relabeled as d_{z^2}. These are the familiar d orbitals, although other formulations are possible. In a free atom/ion, they are of equal energy (fivefold degenerate). As discussed in Section 4.2, the spectroscopic states of a d^n atom/ion differ in energy by amounts expressible as interelectron repulsion parameters.

2.2 CF Splitting of d Orbitals in Cubic Systems

Here we examine the d orbitals of an atom/ion in an octahedral or tetrahedral environment; these symmetries are called *cubic* because of their relationship to the cube, having three equivalent spatial directions. Symmetry arguments show that the fivefold degeneracy of an nd subshell cannot persist if the atom is in chemical combination. Even in cubic molecules and crystals, there can be no orbital degeneracy greater than three. Where the three axes are nonequivalent, there can be no orbital degeneracies at all.

2.2.1 Octahedral ML$_6$

Octahedral six-coordination is the most common chemical environment for the transition elements (*see* ***Coordination Numbers & Geometries***). Apart from the great number of octahedral complexes, the formally ionic oxides and halides usually adopt structures in which the cation is in an octahedral site. LFT is equally applicable to a complex species such as $CrF_6{}^{3-}$ and to the binary halide CrF_3. For spectroscopic purposes, we say that CrF_3 and complex fluorides such as $KCrF_4$, K_2CrF_5, and K_3CrF_6 all contain the octahedral $Cr^{III}F_6$ chromophore (i.e. ‘color-bearer’). Likewise, $[Cr(NH_3)_5OH]Cl_2$ contains the $Cr^{III}N_5O$ chromophore.

In the simplest CF approach, the ligands are represented by negative point charges. No covalency is explicitly considered, so that the bonding is deemed to be ionic; this may seem unduly simplistic, but CFT does not purport to be a theory of bonding in compounds of the transition elements. In a quantitative treatment, the array of point charges around the central ion is formulated as an electrostatic potential, the crystal field, whose effect on the nd subshell can be calculated by means of perturbation theory. Here we give only a qualitative treatment.

The energy of an orbital is a nebulous concept, having meaning only when an electron is in it. The effect of a negative potential field, whatever its symmetry, upon a d orbital must be to raise its energy relative to that in the free atom/ion. In quantitative treatments, the potential is divided into a spherically symmetric part (whose effect is to raise equally the energies of all five d orbitals) and a symmetry-dependent part; the latter will determine the splitting of the fivefold degeneracy. Let us place the six-point charges representing the ligands on the x, y, and z axes as shown in Figure 1. An orbital whose electron density is concentrated along the axes will be destabilized more than one that avoids the ligands/point charges. Thus, in Figure 2, we see that an electron in $d_{x^2-y^2}$ will experience a stronger field than one in d_{xy}. It should be obvious from the equivalence of the x, y, and z axes that d_{xy}, d_{xz}, and d_{yz} are equally affected and are triply (or threefold) degenerate; less obviously, $d_{x^2-y^2}$ and d_{z^2}, higher in energy than $d_{xy,xz,yz}$, are doubly (twofold) degenerate. This is best shown by symmetry arguments (there are several texts that deal with symmetry/*Group Theory*).**[35–47]** The effect of any symmetry operation upon a nondegenerate function is either to leave the function unchanged, or to change its sign everywhere. The effect of a symmetry operation upon any member of a degenerate set of functions may be:

a) to leave the function unchanged
b) to change its sign everywhere
c) to transform the function into one of its degenerate partners
d) to transform the function into a linear combination of two or more members of the degenerate set.

To say that the x, y, and z axes are equivalent in the O_h point group (which denotes octahedral symmetry; *see* ***Symmetry Point Groups***) is to assert that there exist symmetry operations that interchange these axes. Thus, if we rotate the octahedron in Figure 1 and 2 by 120° about the axis that joins the centroids of the triangular faces defined by ligands 125 and 346, we are performing the symmetry operation C_3 which transforms $x \rightarrow z$, $z \rightarrow y$ and $y \rightarrow x$. Thus, the function $(x^2 - y^2)$ becomes $(z^2 - x^2)$ and $(2z^2 - x^2 - y^2)$

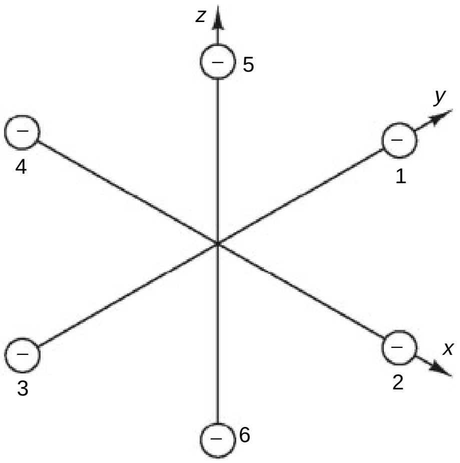

Figure 1 Six negative point charges located at ligand positions for an octahedral complex, providing the crystal/ligand field

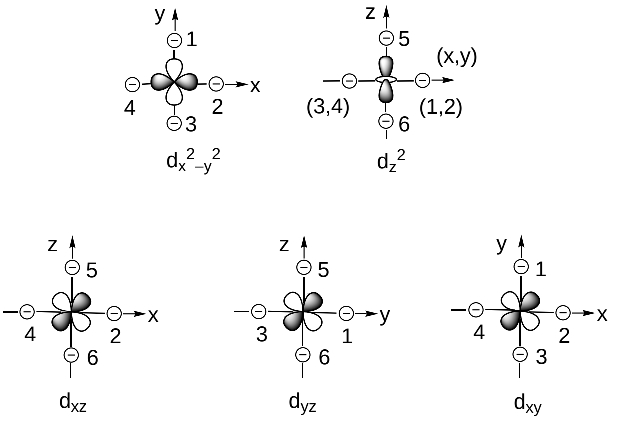

Figure 2 The five d orbitals in octahedral symmetry, with point charges as in Figure 1. Shaded areas indicate positive amplitude

becomes $(2y^2 - z^2 - x^2)$. From equations (10) and (11), we see that the $d_{x^2-y^2}$ and d_{z^2} orbitals are equivalent since under C_3, each is transformed into a linear combination of itself with its partner. We thus arrive at the CF splitting diagram shown in Figure 3.

$$(z^2 - x^2) = \left(\frac{1}{2}\right)(2z^2 - x^2 - y^2) - \left(\frac{1}{2}\right)(x^2 - y^2) \tag{10}$$

$$(2y^2 - z^2 - x^2) = -\left(\frac{3}{2}\right)(x^2 - y^2) - \left(\frac{3}{2}\right)(2z^2 - x^2 - y^2) \tag{11}$$

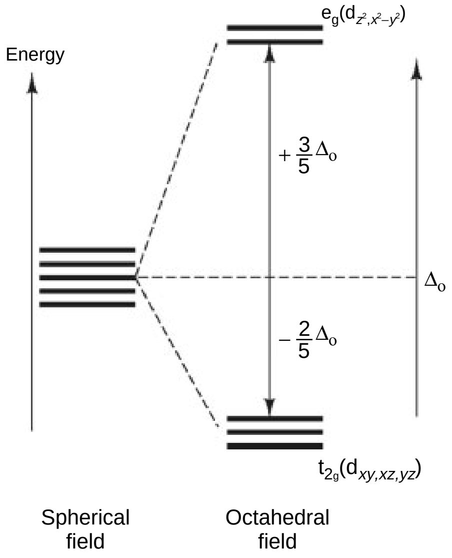

Figure 3 Splitting of d orbitals in octahedral symmetry

It is conventional to depict only the splitting owing to the nonspherical component of the field; the orbital energies are shown relative to the situation in a spherical field. Perturbation theory requires that the sum of the energies of the orbitals in an octahedral field must be equal to the orbital energy in the spherical field, so that a 'center-of-gravity' rule applies. The splitting Δ_o is thus shown so that the twofold-degenerate d_{z^2} and $d_{x^2-y^2}$ are destabilized by $(3/5)\Delta_o$, while the threefold-degenerate $d_{xy,xz,yz}$ are stabilized by $(2/5)\Delta_o$, both relative to a spherical field. The labels e_g and t_{2g} are group-theoretical symbols, which specify the symmetry properties of the functions (more precisely, they designate irreducible representations of the O_h point group).

This diagram makes it possible to specify the occupancies of the d orbitals more precisely than would be the case if fivefold degeneracy remained, or if the orbitals were split unpredictably. For example, an octahedral complex of Cr^{III} is deemed to contain Cr^{3+} ions having the ground-state configuration $[Ar]3d^3$. We can predict from Figure 3 that the three electrons will occupy the t_{2g} orbitals; we can further assert that, to minimize interelectron repulsion energy, each of the t_{2g} orbitals is singly occupied with the electrons all having the same spin. Thus, the ground state of an octahedral Cr^{III} complex has the configuration $(t_{2g})^3$; the allocation of the three electrons to different t_{2g} orbitals, with spins parallel, specifies the ground state. In the case of an octahedral Mn^{III} complex (Mn^{3+} has the ground-state configuration $[Ar]3d^4$), the situation is less straightforward. Briefly, the ground state might be derived from $(t_{2g})^4$ (minimizing the orbital energy) or from $(t_{2g})^3(e_g)^1$ (which minimizes the interelectron repulsion). This issue is discussed in more detail in Section 4.3.4.

2.2.2 *Tetrahedral ML_4*

Tetrahedral coordination geometry is far less common than octahedral, except where the central cation is d^0 or d^{10} (of little interest in LFT).

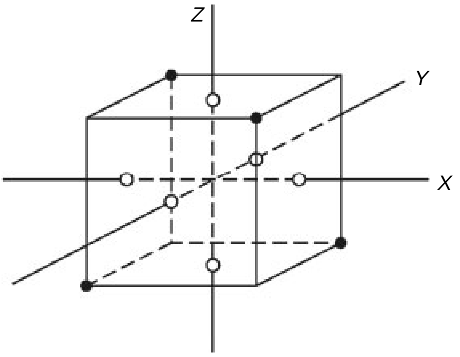

Figure 4 Relationship between octahedral and tetrahedral arrangements of point charges in the Cartesian axis system

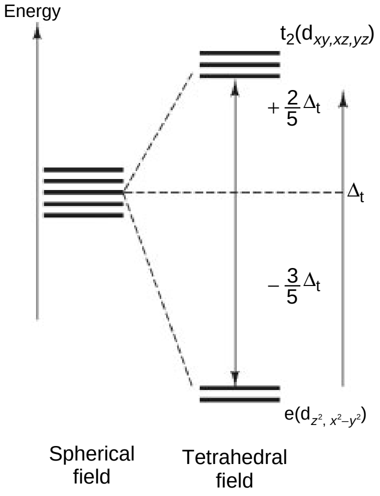

Figure 5 Splitting of d orbitals in tetrahedral symmetry

The most convenient coordinate system for a tetrahedral species is that shown in Figure 4. Qualitative inspection shows that, as in the octahedron, $d_{xy,xz,yz}$ are a threefold-degenerate set, given the equivalence of x, y, and z. The d_{z^2} and $d_{x^2-y^2}$ orbitals are likewise twofold-degenerate. However, inspection will show that the d_{z^2,x^2-y^2} pair (labeled 'e' in the notation appropriate to the tetrahedral point group T_d) interact less with the applied field than the $d_{xy,xz,yz}$ orbitals (labeled t_2; the subscripts g and u in O_h signify, respectively, symmetry or antisymmetry with respect to a center of symmetry but are inappropriate for T_d; a tetrahedron has no center of symmetry). Thus, we arrive at the splitting diagram shown in Figure 5. The splitting is smaller than that for the octahedron: the tetrahedral t_2 orbitals obviously point less directly at the ligands than do the octahedral e_g. Electrostatic calculations give $\Delta_t = (4/9)\Delta_o$, which agrees with the experimental data (Section 2.3).

2.3 The Magnitudes of Cubic CF/LF Splitting Parameters

The splitting parameters are usually found experimentally from d–d spectra, that is, the electronic transitions between the states arising from the d^n configuration, perturbed by the ligand field (Sections 4 and 5). Meanwhile, we consider the magnitudes of LF splittings.

The splitting parameters obtained from d–d spectra are usually expressed in cm^{-1}, or sometimes kK (kilokaysers, $1\,kK = 1000\,cm^{-1}$). Most Δ_o values are in the range $7000–40\,000\,cm^{-1}$, that is, in the near-IR, visible, and near-UV. A selection of experimental values is collected in Table 1. A number of generalizations can be made.

Table 1 LF splittings Δ_o and Δ_t for selected octahedral and tetrahedral systems

Central ion	Ligands	Δ (cm^{-1})
Ti^{3+} (d^1)	$6H_2O$	20 100
	$6F^-$	18 900
	$6Cl^-$	13 000
	$4Cl^-$	6 000
V^{4+} (d^1)	$6F^-$	20 100
	$6Cl^-$	15 400
	$4Cl^-$	9 000
Ti^{2+} (d^2)	$6Cl^-$	8 400
V^{3+} (d^2)	$6H_2O$	19 000
	$6F^-$	16 100
	$6Cl^-$	12 000
	$6CN^-$	23 900
V^{2+} (d^3)	$6H_2O$	12 300
	$6Cl^-$	7 200
	3bipy	15 900
Cr^{3+} (d^3)	$6H_2O$	17 400
	$6\,NH_3$	21 600
	3en	21 900
	$6F^-$	14 900
	$6Cl^-$	13 200
	$6Br^-$	12 700
	$6CN^-$	26 700
Mo^{3+} (d^3)	$6Cl^-$	19 200
	$6Br^-$	18 300
	$6I^-$	16 600
Mn^{4+} (d^3)	$6F^-$	21 800
	$6Cl^-$	17 900
Cr^{2+} (d^4)	$6H_2O$	14 000
	$6Cl^-$	10 200
Mn^{3+} (d^4)	$6H_2O$	21 000
	$6F^-$	21 700
	$6Cl^-$	17 500
	$6CN^-$	31 000
Mn^{2+} (d^5)	$6H_2O$	7 300
	3en	10 000
	$6Cl^-$	6 700
Fe^{3+} (d^5)	$6H_2O$	13 700
	$6Cl^-$	11 600
	$4Cl^-$	5 200

Table 1 cont'd

Central ion	Ligands	Δ (cm^{-1})
Fe^{2+} (d^6)	6H$_2$O	10 400
	3phen	13 100
	4Cl$^-$	4 100
	4Br$^-$	3 100
Ru^{2+} (d^6)	6H$_2$O	19 800
	3en	28 100
Co^{3+} (d^6)	6H$_2$O	20 800
	6 NH$_3$	22 900
	3en	23 200
	6F$^-$	14 500
	6CN$^-$	32 200
Rh^{3+} (d^6)	6 NH$_3$	34 000
	6F$^-$	23 300
	6Cl$^-$	20 400
	6Br$^-$	19 000
	6CN$^-$	45 500
Ir^{3+} (d^6)	6 NH$_3$	41 200
	3en	41 400
	6Cl$^-$	25 000
Pt^{4+} (d^6)	6F$^-$	33 000
	6Cl$^-$	29 000
	6Br$^-$	25 000
Co^{2+} (d^7)	6H$_2$O	9 200
	6 NH$_3$	10 200
	4Cl$^-$	3 300
	4Br$^-$	2 900
	4I$^-$	2 700
Ni^{2+} (d^8)	6H$_2$O	8 500
	6 NH$_3$	10 800
	3en	11 500
	3bipy	12 700
	6F$^-$	7 300
	6Cl$^-$	7 000
	6Br$^-$	6 800
	4Cl$^-$	4 100
	4Br$^-$	3 800
	4I$^-$	3 700

1. The splitting increases with increasing oxidation number of the central atom. This can be explained in electrostatic terms by noting that the ionic radius of (say) Co^{3+} is smaller than that of Co^{2+}; according to the CF model, Δ_o and Δ_t are proportional to r^{-5}, where r is the distance between the central atom and the donor atom/point charge. Since r is typically about 7–8% shorter for an M^{III} complex compared to M^{II} with the same ligands, we expect Δ to be 40–50% greater for M^{III}.
2. Splittings for complexes of the 4d and 5d elements are much greater than for those of the 3d elements. This is not easily explained by the CF model.
3. For a given set of ligands, the variation of Δ for M^{II} and M^{III} across each series is irregular and has no simple explanation.
4. The dependence of Δ_o or Δ_t on the ligands follows a fairly constant sequence for all central atoms, viz. $I^- < Br^- < Cl^- < F^- < H_2O < NH_3 < NO_2{}^- < CN^- < CO$. This is the *Spectrochemical Series*. There is a clear correlation between the position of a ligand in the spectrochemical series and the position of the donor atom in the Periodic Table, thus $C > N > O > F > Cl > Br > I$. No simple electrostatic interpretation is available.

3 DEFICIENCIES OF THE CRYSTAL FIELD MODEL

While there is abundant evidence from magnetic and ESR data, as well as from electronic spectroscopy (Section 4), to support qualitatively the d-orbital splittings predicted by the simple CF model for cubic complexes, the model is clearly inadequate. Electrostatic calculations of Δ_o fail to account for the experimental order of magnitude, and sometimes even the sign! An even more serious objection is raised by experimental evidence suggesting that a purely ionic description of the bonding in transition-element compounds is inappropriate.

3.1 Evidence for Covalency in d-Block Chemistry

Here we set out some of the experimental evidence, which forces us to reexamine the electrostatic, ionic approach inherent in CFT.

1. ESR measurements suggest that unpaired electrons, which (in CF language) are in pure d orbitals on the central atom/ion, are appreciably delocalized over the ligands. This can be explained in terms of MO theory (*see* ***Molecular Orbital Theory***); the 'd electrons' are now in MOs, which have considerable ligand character.
2. NMR measurements likewise reveal the delocalization of unpaired electrons over the ligands.
3. The *Nephelauxetic Effect* (Section 5) provides evidence for the donation of electron density from ligand to central atom/ion (as suggested by the usual theories of covalent bonding in complexes) and for the delocalization of electrons which, in the CF approach, should be localized in central atom d orbitals.
4. Quantitative measurements of the paramagnetism of compounds of the d elements (*see* ***Magnetism of Transition Metal Ions***) also imply delocalization of the unpaired electrons in 'd orbitals'.

Such observations did not necessarily mean that CFT had to be discarded. After all, there is evidence that the bonding in three-dimensional solids involves considerable covalency, yet the ionic description of solids like NaCl remains firmly rooted in the thinking of most chemists. These deficiencies were becoming apparent within a few years of the 'rediscovery' of CFT by inorganic chemists in the early 1950s, when magnetochemistry, electronic spectroscopy, ESR, and NMR were arousing great interest. Some chemists took the view that simple CFT was still useful even if we had to take its basic assumptions with a grain of salt. Others insisted that the theory needed a thorough overhaul and refurbishment, and some were inclined to abandon it altogether.

While these issues were being debated (1955–1960), MO theory was rapidly gaining ground. In the 1960s, there was much enthusiasm for semiempirical MO calculations (*see* ***Molecular Orbital Theory*** and *Extended Hückel Molecular Orbital Theory*) on complexes. These could be performed by the rudimentary computers then available, and purported to provide everything CFT could furnish, and more. Their weakness lay in the criterion used for their calibration, that is, the precision with which they reproduced spectroscopically measured d-orbital splittings. By the late 1960s, it was agreed that such methods were inappropriate for the calculation of spectroscopic quantities, although they have served inorganic chemists well in other areas.

More successful approaches tried to preserve the simplicity of the original 'five-orbital' CF model. At the same time, it was necessary (especially for the interpretation of magnetic and spectroscopic measurements) to make allowance, albeit implicitly, for the effects of orbital overlap and covalency. For d–d spectra, further details are given in Section 5; for magnetic and ESR properties, (*see* ***Magnetism of Transition Metal Ions***). Some writers use the term Ligand Field Theory (LFT) as opposed to Crystal Field Theory to describe an approach, which retains the language and spirit of the old CFT. Others use LFT to encompass all approaches, including CFT, which focus on the five orbitals of the partly filled subshell.

3.2 Angular Overlap Model (AOM)

The *Angular Overlap Model* (AOM) first appeared in a paper[48] entitled 'The Angular Overlap Model: an Attempt to Revive the Ligand Field Approaches', during the heyday of the semiempirical MO treatments when CF/LFT was in danger of obsolescence. Even the simplest MO calculation for an octahedral complex leads to 15 MOs of which 6 to 11 are occupied (qualitative discussions exist on this topic[1–18]). It is easy to reconcile the CF and MO approaches and to identify the MOs that correspond to the d orbitals of CFT. A t_{2g} set of MOs lies higher in energy than the filled and mainly ligand bonding and nonbonding MOs. Where the donor atoms are incapable of π overlap, these t_{2g} orbitals are pure, nonbonding $d_{xy,zx,yz}$. If the ligands have filled orbitals, capable of π overlap with $d_{xy,xz,yz}$, and lower in energy than the central atom d orbitals, the t_{2g} level now becomes π antibonding, but its constitution is mainly d. If the ligand has empty π orbitals, these (e.g. the π^* antibonding MOs of CO or an aromatic ligand) will lie higher in energy than the d subshell, and we obtain a predominantly-d bonding t_{2g} level corresponding to the t_{2g} level of CFT. Above this is an e_g σ-antibonding level, comprising mainly the d_{z^2} and $d_{x^2-y^2}$ orbitals; this is the MO counterpart of the CF e_g level. These situations are shown in Figure 6. The number of electrons to be allocated to these MOs is equal to the number of d electrons in a CF description; hence, we can retain much of the language and spirit of CF theory within an MO framework. Ligands that function according to Figure 6(b) are π donors, because the effect is to transfer electron density from ligand to central atom. Figure 6(c) specifies a π-acceptor ligand; the electrons in the t_{2g} level are 'd electrons', which are now delocalized over the ligands. All ligands are, of course, σ donors.

In most expositions, the AOM is developed from semiempirical MO considerations[18,49] (although a reformulation, the cellular ligand field (CLF) approach (see Section 6.3),[50–53] avoids any such derivation). The AOM retained the five-orbital concept by regarding the LF splitting as a consequence of overlap between AOs on the central atom and on the ligands. A simple perturbation treatment, assuming that the overlap is small, shows that the effect on a d orbital is proportional to the square of the overlap integral. A d orbital will have nonzero overlap with any linear combination of ligand orbitals having the same symmetry. The effect on the energy of a d orbital can be written as $n_\lambda e_\lambda$, where n_λ is a constant determined by the coordination geometry and e_λ is a parameter having units

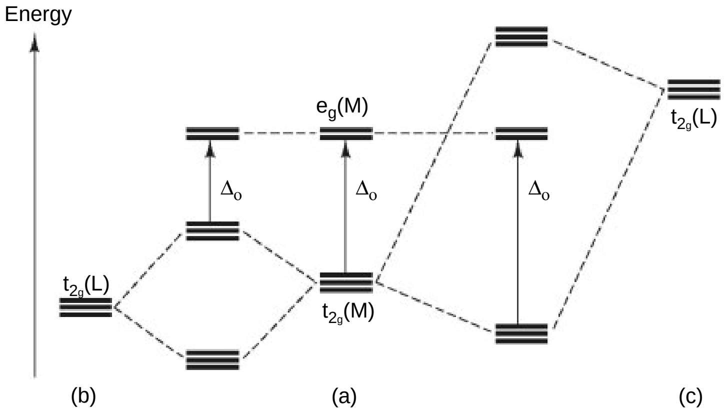

Figure 6 Effect of π-bonding on LF orbitals in an octahedral complex ML_6, showing interaction between ligand (L) and central atom (M) t_{2g} orbitals where the ligands are (a) pure σ-donors, (b) π-donors, and (c) π-acceptors

of energy; the subscript λ specifies the overlap as $\sigma, \pi, \delta, \ldots$, and so on. In an octahedral complex where each ligand has two equivalent π orbitals, the relative energies of the d orbitals are given by equations (12) and (13), and the LF splitting by equation (14).

$$E(z^2) = E(x^2 - y^2) = E(e_g) = 3e_\sigma \tag{12}$$

$$E(xy) = E(xz) = E(yz) = E(t_{2g}) = 4e_\pi \tag{13}$$

$$\Delta_o = 3e_\sigma - 4e_\pi \tag{14}$$

Now e_σ must be positive, because the e_g orbitals are unequivocally σ antibonding; their energies are higher than the free atom/ion values. e_π will be positive if the ligands are π donors, and negative if they are π acceptors. Because π overlap is usually weaker than σ overlap, we may infer that $|e_\pi| < e_\sigma$. Thus, the AOM predicts a positive Δ_o.

For tetrahedral complexes, we obtain equations (15) to (17). Note that (Δ_t/Δ_o) is (4/9), as obtained by CFT.

$$E(xy) = E(xz) = E(yz) = \left(\frac{4}{3}\right)e_\sigma + \left(\frac{8}{9}\right)e_\pi \tag{15}$$

$$E(z^2) = E(x^2 - y^2) = \left(\frac{8}{3}\right)e_\pi \tag{16}$$

$$\Delta_t = \left(\frac{4}{3}\right)e_\sigma - \left(\frac{16}{9}\right)e_\pi \tag{17}$$

The AOM helps to rationalize the spectrochemical series. The ligands towards the left-hand side (e.g. halide ions) are π donors, having filled orbitals capable of π overlap with, in the octahedral case, $d_{xy,xz,yz}$. Ligands at the right-hand side, giving large values of Δ, are π acceptors (CO, CN^-, phen, etc.). Amines, having no orbitals available for π overlap, are pure σ donors and occur in the middle of the spectrochemical series. From spectroscopic studies of noncubic complexes (which require more than one splitting parameter, Section 6), we can obtain separate e_σ and e_π values for ligands, and thus determine a two-dimensional spectrochemical series:

$$e_\sigma\text{: } I^- < Br^- < Cl^- < H_2O \approx NH_3 \approx F^- < {NO_2}^- < CN^- < CO$$

$$e_\pi\text{: } CO < CN^- < {NO_2}^- < NH_3 < H_2O < I^- < Br^- < Cl^- < F^-$$

For NH_3, e_π is assumed to be zero, so that the ligands to its left are π acceptors (negative e_π), while those to its right are π donors (positive e_π). Further aspects of the AOM will be discussed in Section 6. A more recent development, the CLF approach,[50–53] is described in Section 6.3.

4 LIGAND FIELD (LF) SPECTROSCOPY[23,26,31,54]

The colors associated with many compounds of the transition elements arise from electronic transitions, that is, the ground state and excited state have different electronic wavefunctions. Electronic spectra are mostly observed in the UV; colored species absorb in the visible region (12 000–25 000 cm^{-1}), implying relatively low-lying electronic transitions. Indeed, many d-block species have electronic transitions in the near IR. These are attributed to transitions involving the partly filled subshell; in atomic spectroscopy, transitions in which electrons are excited to higher shells or subshells usually occur in the UV. Electronic transitions within the d subshell are called *d–d Transitions* or bands. These are not always responsible for familiar colors; in purple ${MnO_4}^-$ and yellow ${CrO_4}^{2-}$, the central atoms are formally d^0, and many d^{10} species are colored (e.g. yellow AgI). These colors arise from *Charge Transfer* (CT) bands, where an electron jumps from a ligand lone pair orbital into an empty d orbital on the central atom. This is a ligand-to-metal transition; a metal-to-ligand transition is from a d orbital to an empty ligand orbital, and may occur at low energy if the central atom is easily oxidized (*see Ligand-to-Metal Charge Transfer*).

4.1 d–d Transitions: Intensities and Selection Rules

The d–d bands are usually relatively low in intensity compared to CT bands; contrast the palish hues of familiar salts of Cr, Mn, Fe, Co, Ni, and Cu with the intense purple of ${MnO_4}^-$. This can be explained within the CF model. The probability of a transition is governed by selection rules (*see Group Theory*). In atomic spectra, transitions between states having the same l quantum number are forbidden; if this rule were strictly obeyed, d–d transitions should not be observable. Moreover, if there is a center of symmetry, as in an octahedral or square coplanar complex, d–d transitions are forbidden although they can be observed, albeit relatively weakly. Molecular vibration can disturb the center of symmetry, and *Vibronic Coupling* lends intensity to d–d absorption. A tetrahedral complex has no center of symmetry and the $nd_{xy,xz,yz}$ orbitals have the same symmetry as the $(n+1)p_{x,y,z}$ orbitals; these subshells can therefore mix and the selection rules forbidding d–d transitions are accordingly relaxed. CT bands, as already noted, are often fully allowed and very intense. A d–d excited state, where allowed by symmetry and/or other perturbations, may mix with a CT state and a ‘forbidden’ d–d transition can ‘borrow’ intensity from a CT state.

Another selection rule allows only transitions between states having the same spin. This is relaxed somewhat through spin–orbit (SO) coupling (*see Coupling*). In a free atom/ion, this means that the spin and orbital angular momenta (represented respectively by S and L for a state labeled ${}^{2S+1}L$) are combined so that the state is split into $2S+1$ levels, classified according to their total angular momentum quantum number $J = L+S, L+S-1, \ldots, L-S$. For example, the ${}^3P$ (spoken as ‘triplet pee’) ground state of the carbon atom ($L = 1, S = 1$) is split into three states with $J = 2$, 1, and 0. The magnitude of SO coupling increases rapidly with increasing atomic number. Thus, for the heaviest atoms, the quantum numbers L and S have largely lost their integrity and are no longer appropriate for the classification of states. The significance of SO coupling for LF spectroscopy lies mainly in its importance for the heavy transition elements, where it is less meaningful to classify states as singlets, triplets, and so on according to the superscript $2S + 1$, which appears in such designations as ^{1}D and ^{3}F. The need to include SO coupling in quantitative calculations of d–d states complicates matters. The greater LF splittings for complexes of the 4d and 5d elements mean that d–d transitions appear further into the UV than for complexes of the 3d elements; they are often obscured by, and/or mixed with, CT bands. Hence, most of our discussion relates to the LF spectra of 3d complexes; here, SO splitting may appear in high-resolution spectra, and is allowed for in the most elaborate calculations.

4.2 States and Configurations[55]

LF spectroscopy is concerned with transitions between electronic states (the lower of which is nearly always the ground state) arising from the various configurations, which, in turn, arise from the splitting of the nd subshell in a chemical environment. We have already spoken of d–d states and, for both free atoms/ions and cubic environments, electron configurations. It is now necessary to distinguish carefully between 'state' and 'configuration'.

The state of any system is represented by a many-electron wavefunction, which can be factorized as an antisymmetrized product of one-electron functions, that is, orbitals. A configuration (*see Electron Configuration*) is a statement of how many electrons are present in each subshell (for an atom or ion) or in each degenerate level (for a molecule or complex ion). Where a degenerate set is partly filled, a configuration does not specify the occupancy of each orbital, or the electron spins; such a precise description denotes a state. Orbitals are denoted by lower-case letters, s, p, d, f, ... for atoms and by group-theoretical symbols such as a_1, t_{2g} for molecules and polyatomic ions. States are denoted by capitals. For atoms, we use S, P, D, F, ... which correspond to the state L quantum numbers of 0, 1, 2, 3, ... and which convey degeneracies of $(2L + 1)$, that is, M_L values of $L, L-1, L-2, \ldots, -L$. For molecules and polyatomic ions, we use symmetry symbols such as A_1, T_{2g}. A given configuration may give rise to more than one state. Moreover, two or more states of the same symmetry become mixed, especially if they are close together in energy. Where such *Configuration Interaction* is strong, the ground state is not associated with a unique configuration, although in most cases, one configuration dominates.

Consider the carbon atom, as a simple example. To say that 'the ground-state configuration is $1s^22s^22p^2$' is a rather loose way of saying that the ground state (among others) arises principally from this configuration. There are $3 \times 3 = 9$ ways of allocating two electrons to the three 2p orbitals. If the electrons have the same spin, they must have different m_l values. Representing a 'microstate' by the notation $\{m_l(1)m_l(2)\}$ to denote the m numbers for electrons (1) and (2), we can thus have $\{1, 0\}$, $\{1, -1\}$, and $\{0, -1\}$. These correspond, respectively, to the M_L values ($M_L = m_l(1) + m_l(2)$) of 1, 0, and -1, which arise from a ^{3}P state. If the electrons have opposite spins, there are six possible microstates $\{1, 1\}$, $\{1, 0\}$, $\{1, -1\}$, $\{0, 0\}$, $\{0, -1\}$, and $\{-1, -1\}$, having M_L values of 2, 1, 0, 0, -1, and -2, respectively. Thus, we can infer a ^{1}D state ($L = 2$; $M_L = 2, 1, 0, -1, -2$) and a ^{1}S state ($L = 0$, $M_L = 0$); the latter can be represented as a mixture of $\{1, -1\}$ and $\{0, 0\}$.

The energy of a state may be expressed as the sum of its total orbital energy and its interelectron repulsion energy. All states arising from a given configuration have the same orbital energy, and interelectron repulsion is minimized by placing the electrons in separate orbitals, with spins parallel. Hence, ^{3}P is unequivocally the ground state for the C atom; ^{1}D and ^{1}S are excited states. There are other ^{3}P states of the C atom arising, for example, from $1s^22s^22p3p$ or $1s^22s^23d^2$, but these lie very high in energy and configuration interaction, mixing these into the ground state, need not be considered for most purposes.

4.3 d–d States of Cubic d^n Systems

We now consider the electronic states that arise when a d^n ion is perturbed by a cubic field. Methods for working out the symmetry species of the states arising from a given configuration $t_{2g}^m\ e_g^n$ (or $e^mt_2^n$ for a tetrahedral complex) are given in detail in monographs;[15,19,21–32] a 'user-friendly' introduction for beginners in group theory is available.[56] For quantitative calculations, there are two extreme viewpoints. The weak field model considers the effect of the ligand field to be small compared to interelectron repulsion. Hence, we work out how the free-ion states are perturbed by a weak cubic field. The energies of the resulting LF states are the eigenvalues of determinants whose off-diagonal terms are multiples of LF splitting parameters. In the strong-field model, the effect of the ligand field is deemed to be much stronger than the interelectron repulsion terms that split states arising from the same d^n configuration. Here the off-diagonal terms are interelectron repulsion parameters. In either case, the diagonal terms are expressed as the sums of orbital splitting parameters and interelectron repulsion terms. The 'truth' generally lies somewhere between these extremes.

4.3.1 Octahedral and Tetrahedral d^1 and d^9

For octahedral d^1, the possible configurations are $(t_{2g})^1$ and $(e_g)^1$ (Figure 3). With $(t_{2g})^1$, the electron can be in any of d_{xy}, d_{xz}, or d_{yz}. Each of these situations corresponds to the same energy, because the three t_{2g} orbitals are degenerate and there is no interelectron repulsion. Thus, we have a threefold degenerate state $^2T_{2g}$, where the superscript $(2S + 1)$ denotes a total spin S of (1/2). This is the ground state, and the electron spends equal amounts of time in each of the t_{2g} orbitals. Likewise, the $(e_g)^1$ configuration gives rise to a twofold-degenerate state ^2E_g where the electron spends equal amounts of time in $d_{x^2-y^2}$ and d_{z^2}. This is the only d–d excited state; there is only one d–d transition, $^2T_{2g} \rightarrow {}^2E_g$. Any electronic transition energy ΔE can be expressed as equation (18), where ΔE_{orb} and ΔE_{int} are respectively the changes in orbital and interelectron repulsion energy.

$$\Delta E = \Delta E_{\text{orb}} + \Delta E_{\text{int}} \tag{18}$$

For octahedral d^1, ΔE is equal to $\Delta E_{\text{orb}} (= \Delta_o)$ since ΔE_{int} is zero. Octahedral d^1 complexes do indeed exhibit a single, relatively weak absorption in the visible or near-UV. The historically important example of $[Ti(H_2O)_6]^{3+}$ is shown in Figure 7. The broadness of the band is a normal feature for d–d transitions where ΔE_{orb} is nonzero, for example, where an electron jumps between t_{2g} and e_g; there are (in other d^n systems) d–d transitions involving no change in orbital energy.

For tetrahedral d^1 (referring to Figure 5), we can have two configurations, $(e)^1$ and $(t_2)^1$. The former gives rise to a ^2E ground state and the latter to a $^2T_2$ excited state, so that we expect one d–d transition, $^2E \rightarrow {}^2T_2$.

Prima facie, it might be thought that for the d^9 case we will have to consider interelectron repulsion, but the situation is actually much simpler. We can view a d^9 subshell as a 'one-hole' or one-positron system; the interaction of a positron (i.e. a positive electron) with the ligand field is equal in magnitude but opposite in sign to that of an electron. Thus, the splitting parameter defined in Figure 3 is now negative; a 'one-positron' octahedral complex has in its ground state a positron in e_g. Thus, we have the d–d states $^2T_{2g}$ and ^2E_g, but the ground state is now ^2E_g and we predict a single d–d transition $^2E_g \rightarrow {}^2T_{2g}$; the transition energy is equal to $-\Delta_o$. It is difficult to verify this prediction experimentally, because (for reasons discussed in Section 7.2) regularly octahedral d^9 complexes rarely (if ever) occur and the d–d spectra of, for example, six-coordinate copper(II) systems show at least two d–d transitions.

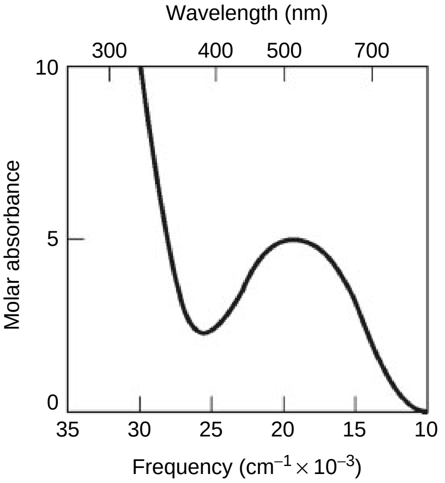

Figure 7 Electronic spectrum of $[Ti(H_2O)_6]^{3+}$ in water

Similarly, for tetrahedral d^9 systems, we predict a $^2T_2$ ground state and one d–d transition to a ^2E excited state; but, as in the octahedral case, 'tetrahedral' d^9 systems are not so simple. An added complication is that SO coupling can split the ground state.

In either a d^1 or d^9 free atom/ion, there can be only one d–d state ^2D (split by SO coupling into $^2D_{5/2}$ and $^2D_{3/2}$). The effect on ^2D of an octahedral or tetrahedral field is shown in Figure 8. The energy zero represents the ion in a spherical field. Where Δ is positive, we have the d–d states for octahedral d^1 or tetrahedral d^9 (to accommodate both, the g and u subscripts appropriate to the octahedral case are omitted); for negative values, we have the states for octahedral d^9 and tetrahedral d^1. For the d^1 case, Δ is defined as $E(e) - E(t_2)$, which is positive for octahedral and negative for tetrahedral symmetry. For d^9, Δ is defined for a one-positron system and is therefore negative for octahedral and positive for tetrahedral symmetry. Thus, four distinct types of cubic complex can be treated in a single energy-level diagram. In fact, four more situations have the same diagram (Sections 4.3.4 and 4.3.6). Figure 8 is of limited practical value, but it illustrates how d–d spectra of other d^n systems can be tackled.

4.3.2 *Octahedral and Tetrahedral d^2 and d^8*

Since a d^8 complex can be described as a two-positron system, the d–d energy levels obtained for d^2 will be applicable, with the necessary changes, to d^8 as well. Consider first a free d^2 atom/ion; d^2 gives rise to singlet and triplet states, but the ground state must be a triplet. If the electrons have the same spin, occupying different d orbitals, we can have the microstates {2, 1}, {2, 0}, {2, −1}, {2, −2}, {1, 0}, {1, −1}, {1, −2}, {0, −1}, {0, −2}, and {−1, −2}, with M_L values of 3, 2, 1, 0, 1, 0, −1, −1, −2, and −3, respectively. These can

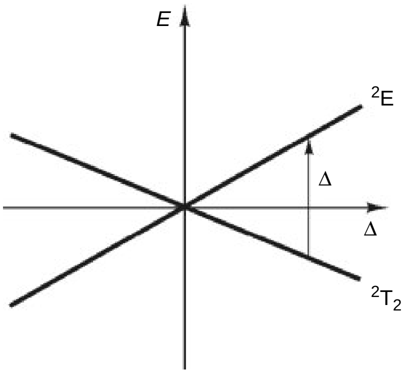

Figure 8 Energies E of d–d states for cubic d^1 and d^9 systems plotted against splitting parameter Δ

only arise from the atomic states ^{3}F and ^{3}P, of which the former (with the greater L) is the ground state. The difference in interelectron repulsion energy between ^{3}P and ^{3}F is commonly expressed in multiples of the Racah parameters B and C (*see Racah Parameter*). Here we find $E(^3\mathrm{P} - {}^3\mathrm{F}) = 15B$. The numerical values of B and C are obtained from atomic spectra; for example, in V^{3+} (g), the $^3\mathrm{F} \rightarrow {}^3\mathrm{P}$ transition is observed at 13 344 cm^{-1} so that $B = 890\,\mathrm{cm}^{-1}$. In the d^8 case, the results are the same; the ground state is ^{3}F, with ^{3}P lying higher by $15B$.

For octahedral d^2, three configurations are possible: $(\mathrm{t_{2g}})^2$, $(\mathrm{t_{2g}})^1(\mathrm{e_g})^1$, and $(\mathrm{e_g})^2$, whose orbital energies (relative to the spherical field) are, respectively, $-(4/5)\Delta_\mathrm{o}$, $(1/5)\Delta_\mathrm{o}$, and $(6/5)\Delta_\mathrm{o}$. The ground state will be a spin triplet arising from $(\mathrm{t_{2g}})^2$, with the electrons in two separate d orbitals having parallel spins. There are three ways of thus allocating two electrons to three orbitals, and the equivalence of d_{xy}, d_{xz}, and d_{yz} means that each will have the same interelectron repulsion energy. Thus, the ground state is $^3\mathrm{T_{1g}}$ (not $\mathrm{T_{2g}}$, for group-theoretical reasons not discussed here). The singlet excited states $^1\mathrm{T_{2g}}$, $^1\mathrm{E_g}$, and $^1\mathrm{A_{1g}}$ also arise from $(\mathrm{t_{2g}})^2$; transitions to these may appear weakly as spin-forbidden bands, if they are not obscured by nearby spin-allowed d–d bands, or by CT transitions.

For the configuration $(\mathrm{t_{2g}})^1(\mathrm{e_g})^1$, there are six ways of allocating the electrons with parallel spins. However, we cannot have a sixfold orbital degeneracy. By group-theoretical methods, we obtain two threefold degenerate states, $^3\mathrm{T_{1g}}$ and $^3\mathrm{T_{2g}}$ (plus the corresponding singlet states $^1\mathrm{T_{1g}}$ and $^1\mathrm{T_{2g}}$). The two distinct $^3\mathrm{T_{1g}}$ states require further labeling to avoid confusion. Moreover, two states of the same symmetry become mixed; this is expressed by a 2 × 2 determinant (equation 19).

$$\begin{vmatrix} -\left(\frac{4}{5}\right)\Delta_\mathrm{o} + 3B - E & 6B \\ 6B & \left(\frac{1}{5}\right)\Delta_\mathrm{o} + 12B - E \end{vmatrix} = 0 \qquad (19)$$

The diagonal terms are the calculated energies of the 'pure' (unmixed) states, and each is expressed as the sum of an orbital energy (a multiple of Δ_o) and an interelectron repulsion energy (a multiple of B), relative to the free-ion ground state ^{3}F. The determination of the orbital energy term is obvious; the calculation of the repulsion terms in both diagonal and off-diagonal elements is explained in standard monographs.**[19–28]** The $(\mathrm{t_{2g}})^2$ configuration has the orbital energy $2(-2\Delta_\mathrm{o}/5) = -4\Delta_\mathrm{o}/5$, while $(\mathrm{t_{2g}})^1(\mathrm{e_g})^1$ has $(-2\Delta_\mathrm{o}/5 + 3\Delta_\mathrm{o}/5) = \Delta_\mathrm{o}/5$. The *Noncrossing Rule* requires that states of the same symmetry cannot coincide in energy, so that in the limit, where $\Delta_\mathrm{o} \rightarrow 0$, the two $^3\mathrm{T_{1g}}$ states must converge to different triplet free-ion states. The lower of the two, arising from $(\mathrm{t_{2g}})^2$, is labeled $^3\mathrm{T_{1g}}$(F) since it becomes ^{3}F in the free-ion limit, while the higher is designated $^3\mathrm{T_{1g}}$(P). In the strong-field limit, where interelectron repulsion is negligible compared to orbital energy, the energies of $^3\mathrm{T_{1g}}$(F) and $^3\mathrm{T_{1g}}$(P) are equal to $-(4\Delta_\mathrm{o}/5)$ and $\Delta_\mathrm{o}/5$, respectively. Note that (except in the strong-field limit) the ground state cannot be described exactly in terms of the configuration $(\mathrm{t_{2g}})^2$; mixing of the two $^3\mathrm{T_{1g}}$ states means that each can claim parentage from both $(\mathrm{t_{2g}})^2$ and $(\mathrm{t_{2g}})^1(\mathrm{e_g})^1$, an example of configuration interaction.

The $(\mathrm{e_g})^2$ configuration can give rise to only one, nondegenerate triplet state, there being only one way of assigning two electrons to two separate orbitals with parallel spins. This is labeled $^3\mathrm{A_{2g}}$ (in cubic symmetry, A, E, and T mean nondegenerate, twofold, and threefold degenerate, respectively); there are also the singlet states $^1\mathrm{E_g}$ and $^1\mathrm{A_{1g}}$. Since $^3\mathrm{T_{1g}}$(P) becomes ^{3}P at the weak-field limit, and we have to account for the sevenfold degeneracy of the ^{3}F free-ion state, it follows that $^3\mathrm{A_{2g}}$, together with $^3\mathrm{T_{2g}}$ and $^3\mathrm{T_{1g}}$(F), are derived from ^{3}F. The energy of $^3\mathrm{A_{2g}}$ (relative to ^{3}F) is found to be $(6/5)\Delta_\mathrm{o}$; at the weak-field limit, this is lower than $^3\mathrm{T_{1g}}$(P), but with large values of Δ_o, $^3\mathrm{A_{2g}}$ is the highest d–d triplet state. We can now construct an energy-level diagram for octahedral d^2, which (cf. Figure 8) can be extended to tetrahedral d^2 and to both octahedral and tetrahedral d^8. This exercise will be deferred, however, until we have dealt with d^{3,7}.

4.3.3 *Octahedral d^3 and Tetrahedral d^7*

The free-ion states arising from d^3 bear close similarities to the d^2 case. The ground state is bound to be a quartet, with three singly occupied d orbitals (this might be viewed as a two-positron problem, with two vacancies in a half-filled d subshell). The microstates for a quartet are $\{2, 1, 0\}$, $\{2, 1, -1\}$, $\{2, 1, -2\}$, $\{2, 0, -1\}$, $\{2, 0, -2\}$, $\{1, 0, -1\}$, $\{1, 0, -2\}$, $\{1, -1, -2\}$, and $\{0, -1, -2\}$, whose M_L values are respectively 3, 2, 1, 1, 0, 0, −1, −2, and −3. Analogous to the d^2 case, these are derived from the free-ion states ^{4}F and ^{4}P, the former being the ground state, separated from the latter by $15B$. It is therefore not surprising that the pattern of LF states is similar to that for d^2. We will concentrate on quartet states, since the ground state for octahedral d^3 is a quartet, with spin-allowed d–d transitions to quartet excited states.

As for d^2, three configurations can lead to a quartet ground state for octahedral d^3: $(\mathrm{t_{2g}})^3$, $(\mathrm{t_{2g}})^2(\mathrm{e_g})^1$, and $(\mathrm{t_{2g}})^1(\mathrm{e_g})^2$. For $(\mathrm{t_{2g}})^3$, $(\mathrm{d}_{xy})^1(\mathrm{d}_{xz})^1(\mathrm{d}_{yz})^1$ with parallel spins describes a unique state having the same symmetry as $(\mathrm{d}_{z^2})^1(\mathrm{d}_{x^2-y^2})^1$; thus the ground state for octahedral d^3 is $^4\mathrm{A_{2g}}$. The $(\mathrm{t_{2g}})^2(\mathrm{e_g})^1$ configuration, analogous to $(\mathrm{t_{2g}})^1(\mathrm{e_g})^1$, produces the quartet states $^4\mathrm{T_{1g}}$ and $^4\mathrm{T_{2g}}$, while $(\mathrm{t_{2g}})^1(\mathrm{e_g})^2$ leads to $^4\mathrm{T_{1g}}$; this latter is clearly to be distinguished as $^4\mathrm{T_{1g}}$(P), while $^4\mathrm{T_{1g}}$(F) is derived from $(\mathrm{t_{2g}})^2(\mathrm{e_g})^1$. The situation resembles octahedral d^2, except that the relative energies are inverted, that is, we have for octahedral d^3 a ground state $^4\mathrm{A_{2g}}$ with excited states $^4\mathrm{T_{2g}}$, $^4\mathrm{T_{1g}}$(F), and $^4\mathrm{T_{1g}}$(P). Transitions to the doublet states $^2\mathrm{E_g}$ and $^2\mathrm{A_{1g}}$, derived from $(\mathrm{t_{2g}})^3$, can be observed as weak, sharp bands in absorption (the sharpness of such transitions is discussed in Section 4.3.5); however, the emission $^2\mathrm{E_g}, {}^2\mathrm{A_{1g}} \rightarrow {}^4\mathrm{A_{2g}}$ is of more importance. Under certain conditions, a Cr^{3+} ion in an octahedral environment can absorb a photon and jump to ${}^4T_{2g}$, which then undergoes a radiationless transition to ${}^2E_g$ or ${}^2A_{1g}$; this decays back to the ground state with emission of laser light. The first laser (1960) employed crystals of ruby, that is, Cr^{3+}-doped Al_2O_3.

It may be inferred that tetrahedral d^7 has the same energy-level diagram as octahedral d^3 (omitting the g and u subscripts). Moreover, the energy levels for octahedral d^2 and tetrahedral d^8 are, with the appropriate adjustments, applicable to octahedral d^7. Hence, a single energy-level diagram can cover octahedral and tetrahedral d^2, d^3, d^7, and d^8. In Figure 9, the energies of the states of highest multiplicity (triplets for $d^{2,8}$, quartets for $d^{3,7}$) are plotted as y against the cubic splitting parameter x. A positive x is appropriate for octahedral $d^{2,7}$ or tetrahedral $d^{3,8}$ and corresponds to a positive Δ_o or Δ_t as appropriate, while the negative x axis corresponds to the cubic splitting for octahedral $d^{3,8}$ or tetrahedral $d^{2,7}$.

4.3.4 *Octahedral d^4 and Tetrahedral d^6*

In the cases discussed so far, the configuration from which the ground state is derived can be unequivocally identified. In each case, the ground state has the lowest possible orbital energy, and also the maximum number of unpaired spins that minimizes the interelectron repulsion energy. For octahedral d^4 the situation is more difficult. The configuration $(t_{2g})^4$ (which requires one t_{2g} orbital to be doubly occupied) has minimum orbital energy, but $(t_{2g})^3(e_g)^1$ allows four singly occupied d orbitals, and a total spin S of 2, compared with a maximum of $S = 1$ for states arising from $(t_{2g})^4$, giving rise to the state of minimum interelectron repulsion. Which of these will be the ground state will depend on the relative importance of orbital energy and interelectron repulsion. Assuming that the interelectron repulsion parameters are approximately the same as in the free ions (but see Section 5), the magnitude of Δ_o will be critical. The $(t_{2g})^4$ configuration gives rise to a triplet state ${}^3T_{1g}$ plus singlets ${}^1T_{2g}$, ${}^1E_g$, and ${}^1A_{1g}$ (cf. d^2; $(t_{2g})^4$ is related to $(t_{2g})^2$ in the same way as d^8 is to d^2). Its rival $(t_{2g})^3(e_g)^1$ gives rise to a quintet ${}^5E_g$ (twofold degenerate since there is only one way of allocating the three t_{2g} electrons but two ways of allocating one electron to e_g) plus triplets and singlets. The transition ${}^3T_{1g} \rightarrow {}^5E_g$ involves the excitation of one electron from t_{2g} to e_g but produces two additional unpaired spins. A large value of Δ_o will favor the low-spin ground state ${}^3T_{1g}$ while a small splitting will favor the high-spin ground state ${}^5E_g$ (*see High-spin & Low-spin Compounds*). Thus, ligands towards the right-hand side of the spectrochemical series (Section 2.3) will enforce a ground state having minimum orbital energy, while ligands lower in the series will favor a ground state having the minimum interelectron repulsion, that is, the maximum number of unpaired spins. Both types of ground state are found for octahedral d^4. The most direct evidence comes from magnetic measurements (*see* ***Magnetism of Transition Metal Ions***). Thus, $[Cr(CN)_6]^{4-}$ and $[Mn(CN)_6]^{3-}$ have magnetic moments consistent with only two unpaired electrons, indicating a ${}^3T_{1g}$ ground state; $[Cr(NH_3)_6]^{2+}$ and $[MnF_6]^{3-}$ apparently have four unpaired electrons, consistent with ${}^5E_g$. Thus, complexes of Cr^{II} and Mn^{III} are classified as high-spin or low-spin. ESR is also useful for the experimental determination of the ground state.

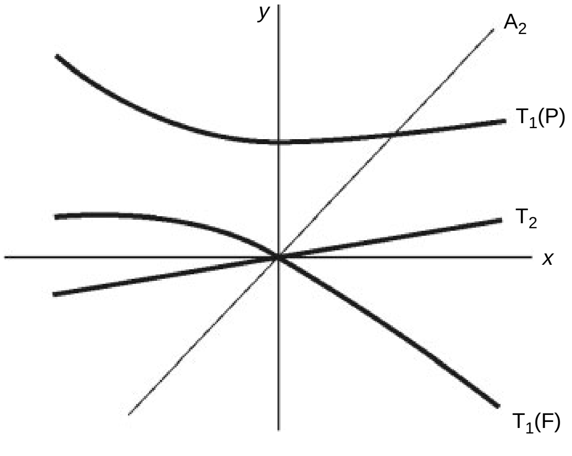

Figure 9 Energies of d–d states of highest spin (y) for cubic d^2, d^3, d^7, d^8 plotted against splitting parameter (x)

We can plot the d–d states on an energy-level diagram, showing the changeover of the ground state at a critical value of Δ_o. There is a simpler way, however. In the high-spin case, there is only one quintet excited state ${}^5T_{2g}$ (derived from $(t_{2g})^2(e_g)^2$), so there can be only one spin-allowed d–d transition, ${}^5E_g \rightarrow {}^5T_{2g}$. The transition energy is exactly equal to Δ_o; there is no change in interelectron repulsion. High-spin d^4 can be regarded as a one-positron system, one electron short of a half-filled subshell, and is thus related to d^1 but with the relative energies of the states reversed. Hence, Figure 8 will serve for octahedral high-spin d^4, treated as for d^9. For tetrahedral high-spin d^4, that part of Figure 8 appropriate for tetrahedral d^9 may be used. For octahedral low-spin d^4, with a ${}^3T_{1g}$ ground state, the energy-level diagram for octahedral d^2 (Figure 9) will serve, as long as we are interested only in triplet–triplet transitions. What of low-spin tetrahedral d^4? The splitting Δ_t appears never to be large enough for orbital energy considerations to dominate over interelectron repulsion. Tetrahedral d^3, d^4, d^5, and d^6 complexes could all, in principle, have either a high-spin or a low-spin ground state, but the latter is never found in practice.

Our deliberations for d^4 complexes will have some relevance for d^6 systems. But we will first look at the d^5 situation.

4.3.5 *Octahedral and Tetrahedral d^5*

In identifying the ground state for octahedral d^5, we are again faced with a conflict between considerations of orbital energy and of interelectron repulsion energy. The latter is minimized by placing the electrons separately in the five d orbitals with parallel spins, while the minimum orbital energy is obtained with the $(t_{2g})^5$ configuration. We look first at the high-spin case. The unique allocation $(t_{2g})^3(e_g)^2$ with all spins parallel gives rise to a sextet state $^6A_{1g}$. There being no other sextet state, there are no spin-allowed d–d transitions for high-spin d^5. The $(t_{2g})^3(e_g)^2$ configuration also gives quartet and doublet states, and weak transitions to the former are observed. Quartet states also arise from other configurations.

A typical spectrum is shown in Figure 10. The intensity of a band is measured by the molar absorbance (or extinction coefficient) ε, usually of the order of 10^3–10^6 L mol^{-1} cm^{-1} for fully allowed transitions and 1–100 for spin-allowed d–d transitions in octahedral complexes. For octahedral high-spin Mn^{II} complexes, ε is around 10^{-2} L mol^{-1} cm^{-1}, typical for spin-forbidden d–d bands in 3d complexes. Some of the bands are broad but others are sharp. Most d–d transitions are broad because of vibrational structure; the rapid changing of the central atom–ligand distances, and distortion from octahedral symmetry, mean that the LF splitting fluctuates rapidly with time, and in a solution or crystal, we observe a complex band envelope. Any change in configuration, with electron jumps between different energy levels, gives a broad band, except at low temperatures. However, a transition between states arising from the same configuration, with no change in orbital energy, may be very sharp. The first two transitions in the spectrum shown in Figure 10 at 18 900 and 23 100 cm^{-1} are, respectively, $^6A_{1g} \rightarrow {}^4T_{1g}$ and $^6A_{1g} \rightarrow {}^4T_{2g}$, both excited states arising from $(t_{2g})^4(e_g)^1$. Each is thus accompanied by a negative change in orbital energy, and of course by a larger positive change in interelectron repulsion energy with the pairing of two electrons in one t_{2g} orbital. The next two bands are to quartet states ^4E_g and $^4A_{1g}$ derived from the same configuration, $(t_{2g})^3(e_g)^2$, as the ground state. These involve only an increase in interelectron repulsion and are narrow. The energy-level diagrams for high-spin tetrahedral and octahedral d^5 are the same; d^5 is its own ‘hole equivalent’.

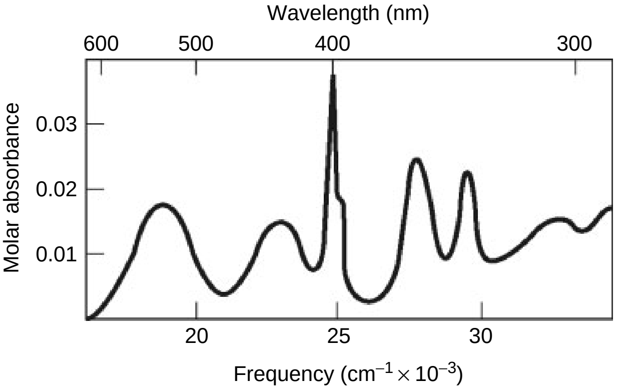

Figure 10 d–d spectrum of $[Mn(H_2O)_6]^{2+}$

For low-spin octahedral d^5, the ground state is $^2T_{2g}$, that is, $(t_{2g})^5$. One hole in t_{2g} is analogous to octahedral d^1 or tetrahedral d^9. Thus Figure 8 is applicable, with one spin-allowed d–d transition, $^2T_{2g} \rightarrow {}^2E_g$, whose energy is equal to Δ_o. There are quartet excited states, plus the unique sextet state $^6A_{1g}$. The vast majority of octahedral Mn^{II} compounds are high-spin; iron(III) complexes have larger Δ_o values and low-spin ground states are more common, for example, in $[Fe(CN)_6]^{3-}$ and $[Fe(bipy)_3]^{3+}$.

4.3.6 *Octahedral d^6*

High-spin octahedral d^6 complexes have the ground state $^5T_{2g}$, derived from $(t_{2g})^4(e_g)^2$ with four orbitals singly occupied and one t_{2g} orbital filled. As already noted, the energy-level diagram for the quintet states is covered by Figure 8 along with d^1, d^4, and d^9. Only one spin-allowed d–d transition, $^5T_{2g} \rightarrow {}^5E_g$, is possible for octahedral high-spin d^6.

The configuration $(t_{2g})^6$, with the t_{2g} orbitals filled and no unpaired electrons, minimizes the orbital energy and produces the unique state $^1A_{1g}$. This is the low-spin ground state; a very high proportion of all known octahedral complexes are low-spin d^6. The octahedral complexes of M^0 (M = Cr, Mo, and W) and M^I (M = Mn, Tc, and Re) are of little interest here, being associated with π-acceptor ligands (CO, PR_3, etc.) which produce very large LF splittings; the d–d bands are obscured by CT transitions (metal-to-ligand). This is true to a lesser degree for M^{II} (M = Fe, Ru, and Os). Many high-spin octahedral Fe^{II} complexes are known but octahedral Ru^{II} and Os^{II} complexes are invariably low-spin. Most d–d spectra of low-spin d^6 complexes have been recorded for octahedral M^{III} (M = Co, Rh, and Ir), and to a lesser extent Pt^{IV}.

The configuration $(t_{2g})^5(e_g)^1$ gives rise to two singlet states, $^1T_{1g}$ and $^1T_{2g}$; transitions to these, and little else, are commonly observed in the d–d spectra of low-spin octahedral d^6 complexes.

4.3.7 *Octahedral d^7*

Here we can have a high-spin ground state $^4T_{1g}$, arising from $(t_{2g})^5(e_g)^2$ with three unpaired electrons, or a low-spin ground state ^2E_g, arising from $(t_{2g})^6(e_g)^1$. The quartet states are related to tetrahedral d^3 as shown in Figure 9. Most octahedral Co^{II} complexes are high-spin. Low-spin octahedral d^7 is represented by a relatively small number of Co^{II}, Ni^{III}, and Cu^{IV} systems. Among the 4d and 5d series, oxidation states corresponding to d^7 are rare: the $(t_{2g})^6(e_g)^1$ configuration is unstable with respect to oxidation, with loss of the e_g electron (which in MO language is σ-antibonding). This configuration gives rise to the ground state ^2E_g, and there can be only one doublet excited state $^2T_{2g}$ resulting from excitation from t_{2g} to e_g. Thus, low-spin octahedral d^7 is analogous to octahedral d^9, as depicted in Figure 8.

5 QUANTITATIVE DETERMINATION OF LF ENERGY-LEVEL DIAGRAMS

Figures 8 and 9 are presented as qualitative plots of the energies of LF states versus the cubic splitting parameter. For any cubic complex, the energy of a symmetrically unique LF state, that is, one that does not mix with any other state of the same symmetry, can be simply expressed as the sum of an orbital energy (a multiple of the splitting parameter Δ_o) and an interelectron repulsion term, usually written in terms of the Racah parameters as $mB + nC$. Where two or more states have the same symmetry and spin, we have to set up determinants like equation (19) (SO coupling will not be dealt with here). Thus, the energy of a d–d state is a function of Δ and the Racah parameters; the state energies are plotted as functions of Δ. This requires numerical values for the Racah parameters; free-ion values are obtained from atomic spectra, but there is evidence that these are inappropriate for real crystals and complexes. This became apparent from studies of high-spin octahedral $\mathrm{Mn^{II}}$ systems. As noted in Section 4.3.5, the sharp $^6A_{1g} \rightarrow {}^4E_g, {}^4A_{1g}$ transitions involve only changes in interelectron repulsion; hence their energies should be the same as in the free ion. Experimentally, these transition energies are around 75–90% of the free-ion values. Detailed studies for other d^n species reveal this *Nephelauxetic Effect*; the adjective is derived from the Greek, meaning 'cloud-expanding'. This is deemed to be a manifestation of covalency; the formation of coordinate bonds with donation from ligands to the central ion lowers the charge on the cation, so that its orbitals expand outwards, reducing the repulsion among the d electrons. Ligands can be arranged in a nephelauxetic series of increasing cloud-expansion: $F^- < H_2O < NH_3 \sim Cl^- < Br^- < CN^- < I^-$. This follows the decreasing electronegativities of donor atoms, so that the nephelauxetic series reflects the extent of covalency in the central atom–ligand bond.

The discovery of the nephelauxetic effect and series in the mid-1950s did not necessarily discredit CFT. Overlap involving $(n + 1)$s and $(n + 1)$p could be entirely responsible for covalency and the nephelauxetic effect, so that the CF/LF orbitals remain pure nd orbitals, albeit with some adjustments to their radial wavefunctions. However, there is evidence that the nephelauxetic effect is more marked for e_g than for t_{2g} orbitals. This is consistent with the view (Section 2.3) that the e_g orbitals are σ-antibonding, while the t_{2g} orbitals may be (relatively weakly) π-bonding or π-antibonding and are often effectively nonbonding. We can distinguish between 'central-field' covalence, involving $(n + 1)$s and $(n + 1)$p and affecting all nd orbitals equally, and 'symmetry-restricted covalence', which affects an nd orbital to the extent of its involvement in covalent bonding.

Recognition of the nephelauxetic effect means that the free-ion values of Racah parameters are no longer appropriate in the quantitative interpretation of LF spectra and in the construction of energy-level diagrams. The simplest solution is to assume that B and C are reduced by a fixed amount (say 15%) from the free-ion values (C is often set equal to $4B$). The d–d states can then be calculated as functions of Δ and plotted accordingly; this is an Orgel diagram (*see Tanabe–Sugano Diagram*). Allowance for the nephelauxetic effect means that the d–d states do not converge exactly to the free-ion state energies when $\Delta = 0$. We seek a value for Δ that gives the best fit to the observed transition energies; the diagram enables us both to assign the bands and to determine the magnitude of the d-orbital splitting.

An alternative procedure is to leave both Δ and B (assuming $C = 4B$) as parameters to be determined by fitting the experimental transition energies. For any assumed value of the ratio Δ/B (Δ may refer to either the octahedral or tetrahedral splitting parameter), we can write the energy of a d–d state relative to the ground state as a multiple of B. Hence, we can plot E/B against Δ/B for all the d–d states. An example is given in Figure 11 (drawn for octahedral d^8 but also applicable to octahedral d^3 and tetrahedral $d^{2,7}$). The $^3A_{2g} \rightarrow {}^3T_{2g}$ transition energy is equal to Δ_o, but is in the near IR where it may escape observation. For tetrahedral d^7, the analogous $^4A_2 \rightarrow {}^4T_2$ transition is even more difficult to measure (ca. 3000 $\mathrm{cm^{-1}}$). However, if the other two spin-allowed bands can be observed, we can find the appropriate value of (Δ/B) from the ratio of their transition energies. Hence, we can obtain (E/B) for the two transitions and, since the absolute values of E are known, we have an experimental value for B, and Δ will follow from the measured value of (Δ/B). This is a *Tanabe–Sugano Diagram*. The spectrochemical and nephelauxetic series have been largely established by such determinations of Δ and B. König and Kremer[57] have published very detailed LF energy-level diagrams.

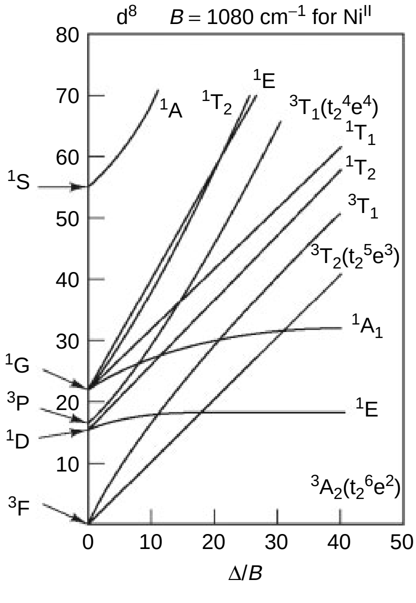

Figure 11 Tanabe–Sugano diagram for octahedral d^8

The quantitative treatment of the nephelauxetic effect – especially the treatment of differential covalence in the d subshell – has been the subject of recent developments;[58] of particular interest has been the use of density functional theory to calculate the interelectron repulsion terms with the LF model.[59,60]

At very low temperatures, high resolution is possible, and vibrational structure may be observed. SO coupling will split cubic T states as well as mixing components of different d–d states, and will mix d–d with CT states; for 3d species, SO splittings are comparable in magnitude to vibrational structure, but they are much more important among the 4d and 5d elements; there are several texts that provide more detail.[15,21,24–26]

6 LIGAND FIELD SPECTRA OF NONCUBIC COMPLEXES

These have aroused interest for two main reasons. First, they may be useful for characterization if we can identify the coordination geometry about the central atom from the d–d spectrum; this is important in situations (e.g. in bioinorganic chemistry) where standard structural methods are much more time-consuming than visible/UV spectroscopy. The second reason rests in their promise to yield information about the M–L bond if the AOM can extract values of e_σ and e_π. We will illustrate the value of such studies by looking at results for chlorocuprates(II), and at tetragonal $\mathrm{Cr^{III}}$ systems such as $[\mathrm{Cr(NH_3)_4X_2}]^+$ (X = F, Cl, Br, I, etc.). The remarkable stereochemical variety of chlorocuprates(II)[61] has made them ideal subjects for both experimental and theoretical studies, while the two-dimensional spectrochemical series (Section 2.3) was largely established by studies of $\mathrm{Cr^{III}N_4X_2}$ systems.[62]

6.1 Chlorocuprates(II)

For a noncubic complex, we need at least two parameters to describe the LF splitting. In the case of a homoleptic complex ML_n (*see Homoleptic Compound*), where all M–L distances r are equal, the simple CF description[63–65] requires two parameters, a_2 and a_4, which are proportional to r^{-3} and r^{-5}, respectively. A less regular complex requires more than two parameters. For example, the d-orbital splitting in regular square planar $\mathrm{CuCl_4}^{2-}$ can be written in terms of just two parameters. For trigonal bipyramidal $\mathrm{CuCl_5}^{3-}$, where the axial and equatorial Cu–Cl distances are unequal, we still need just two parameters, because a_2(eq) and a_2(ax), and a_4(eq) and a_4(ax), are related by their respective r^{-3} and r^{-5} dependence. Thus, the CF model suggests that the d-orbital splittings for all chlorocuprates(II) should be capable of analysis in terms of just two parameters. For a d^9 system (cf. Section 4.3.1), d–d transition energies can be equated to differences in orbital energies. (This is valid only if all the d orbitals have the same radial wavefunction; if we admit to some symmetry-restricted covalence, interelectron repulsion terms have to be considered.[66,67])

Some early studies[63–65] suggested that the d–d spectra of several chlorocuprates(II), including square coplanar, flattened tetrahedral, trigonal bipyramidal, and elongated octahedral geometries, could be fitted to the two parameters a_2 and a_4, scaled according to the observed internuclear distances. However, it is now agreed that this was fortuitous; much of the structural and spectroscopic data upon which these studies were based are now superseded and it is apparent that the simple CF treatment fails to explain the d–d spectra of chlorocuprates(II). The earliest application of the AOM[68] to chlorocuprates(II) appeared to be equally successful, even with neglect of π overlap; this, too, appears to have been fortuitous. The incorporation of both σ and π overlap within the AOM, plus a CF perturbation, was more successful.[69] Since the e_λ are deemed to be proportional to the squares of the appropriate overlap integrals, this proportionality constant is the only parameter needed in the analysis for all the chlorocuprates(II). However, in common with other CF/LF approaches, this model failed to account for the spectrum of square-planar $\mathrm{CuCl_4}^{2-}$ (which, to be carefully distinguished from the tetragonally elongated $\mathrm{CuCl_6}$ octahedron, was not established until 1974.[70]) Here, group theory shows that the d orbitals are split into four levels, $\mathrm{d}_{x^2-y^2}(\mathrm{b_{1g}})$, $\mathrm{d}_{xy}(\mathrm{b_{2g}})$, $\mathrm{d}_{z^2}(\mathrm{a_{1g}})$, and $\mathrm{d}_{xz,yz}(\mathrm{e_g})$. The d–d states are labeled $^2\mathrm{B_{1g}}$, $^2\mathrm{B_{2g}}$, $^2\mathrm{A_{1g}}$, and $^2\mathrm{E_g}$ according to the symmetry of the singly occupied orbital that accommodates the 'hole'. All approaches agree that $\mathrm{d}_{x^2-y^2}$ is highest in energy, and ESR measurements confirm that the ground state is $^2\mathrm{B_{1g}}$. Likewise, all models agree on the relative energies $\mathrm{d}_{x^2-y^2} > \mathrm{d}_{xy} > \mathrm{d}_{xz,yz}$, but the position of d_{z^2} is uncertain. The AOM gives the orbital energies as equations (20–23), and the d–d transition energies as equations (24–26).

$$E(x^2-y^2) = 3e_\sigma \tag{20}$$

$$E(xy) = 4e_\pi \tag{21}$$

$$E(xz, yz) = 2e_\pi \tag{22}$$

$$E(z^2) = e_\sigma \tag{23}$$

$$E(^2\mathrm{B_{1g}} \longrightarrow {}^2\mathrm{B_{2g}}) = 3e_\sigma - 4e_\pi \tag{24}$$

$$E(^2\mathrm{B_{1g}} \longrightarrow {}^2\mathrm{E_g}) = 3e_\sigma - 2e_\pi \tag{25}$$

$$E(^2\mathrm{B_{1g}} \longrightarrow {}^2\mathrm{A_{1g}}) = 2e_\sigma \tag{26}$$

Since Cl^- is a π donor, e_π should be positive and, on the basis of overlap integral calculations, equal to about $0.25e_\sigma$. This would place d_{z^2} close in energy to d_{xy}, and $^2\mathrm{A_{1g}}$ close to $^2\mathrm{B_{2g}}$. However, the spectroscopic evidence[71] indicates the energy sequence $^2\mathrm{B_{1g}} < {}^2\mathrm{B_{2g}} < {}^2\mathrm{E_g} < {}^2\mathrm{A_{1g}}$, that is, $\mathrm{d}_{x^2-y^2} > \mathrm{d}_{xy} > \mathrm{d}_{xz,yz} > \mathrm{d}_{z^2}$. The same orbital sequence had earlier been established for square $\mathrm{PtCl_4}^{2-}$, using the same technique of measuring the spectra of oriented single crystals with plane-polarized radiation. The selection rules insist that the $^2B_{1g} \rightarrow {}^2B_{2g}$ (or $d_{xy} \rightarrow d_{x^2-y^2}$) transition can have nonzero intensity only if the incident polarized beam has a nonzero component in the *xy* plane, so that this transition is readily identified.

It must be noted that in the appropriate point group (D_{4h}) $n\mathrm{d}_{z^2}$ and $(n+1)$s have the same symmetry, a_{1g}, and therefore can mix; in MO language, the LF a_{1g} orbital is mostly $n\mathrm{d}_{z^2}$, and is σ-antibonding with respect to overlap between d_{z^2} and the ligand σ orbitals; however, there is a contribution from $(n+1)$s, and the MO is necessarily bonding with respect to its overlap. Thus, the effect of d–s mixing is to depress the energy of the LF a_{1g} orbital. This can be taken into account[72] by introducing an additional parameter e_{ds}. This, together with e_{dp}, where there is d–p mixing (e.g. T_{d}), helps to rationalize other anomalies in copper(II) d–d spectra. The LF splitting in the gaseous, linear $CuCl_2$ molecule has aroused much discussion. Simple CF or AOM arguments place the d_{z^2} orbital highest, so that the ground state should be $^2\Sigma_g^+$.[61,69] However, laser-induced fluorescence studies,[73] supported by elaborate theoretical calculations,[74–76] show that the ground state is $^2\Pi_g$, that is, the $\mathrm{d}_{xz,yz}$ pair is highest in energy. This suggests a substantial depression of d_{z^2} by d-s mixing. In the analogous linear d^9 anion $[NiO_2]^{3-}$, the ground state is $^2\Sigma_g^+$, which might indicate less d–s mixing in Ni(I) compared with Cu(II), and/or less π donation to Ni(I) compared with Cu(II).[77]

It might be felt that refinements implicating s and p orbitals violate the spirit of LF theory, with its focus on just five orbitals. Moreover, the introduction of e_{ds} and so on, means that in many cases we have too many theoretical parameters to fit the spectroscopic data. In complexes of relatively high symmetry, local e_σ and e_π parameters assigned to each donor atom make additive contributions to the ligand field; but e_{ds} and e_{dp} are global, rather than local parameters except in special cases.[78] Notwithstanding these disadvantages, the d-s mixing model has undergone further refinement.[79,80]

6.2 Tetragonal Chromium(III) Complexes

Cations $[Cr(NH_3)_4X_2]^+$ have *cis* and *trans* geometrical isomers (*see* ***Coordination & Organometallic Chemistry: Principles***). The higher symmetry of the *trans* form makes its d–d spectrum easier to analyze. We assume NH_3 to be a pure σ donor (*see* ***Ammonia & N-donor Ligands***). Hence e_π (NH_3) is zero. The axial ligands are π donors ($e_\pi > 0$). The AOM orbital energies E are given in equations (27–30).

$$E(x^2-y^2) = 2e_\sigma(\mathrm{N}) + e_\sigma(\mathrm{X}) \quad (27)$$

$$E(z^2) = e_\sigma(\mathrm{N}) + 2e_\sigma(\mathrm{X}) \quad (28)$$

$$E(xz, yz) = 2e_\pi(\mathrm{X}) \quad (29)$$

$$E(xy) = 0 \quad (30)$$

The d–d spectra yield three empirical splitting parameters so that $e_\sigma(NH_3)$, e_σ(X), and e_π(X) were obtained, and the two-dimensional spectrochemical series established.[62,81] The planar ligand py (C_5H_5N) has potentially both π donor and π-acceptor orbitals with lobes perpendicular to the molecular plane; thus e_π(py) could be positive or negative, and must be added to equations (27–30) with trigonometric factors determined by the orientations of the py rings with respect to the *xy* (CrN_4) plane. Assuming the transferability of e_σ(X) and e_π(X) from $[Cr(NH_3)_4X_2]^+$ to $[Cr(py)_4X_2]^+$, it was possible to determine e_σ(py) and e_π(py), together with the angle of orientation of the py plane.[81] The value for e_π(py) turned out to be negative, implying that py is a π acceptor. This finding was challenged,[82] partly on the grounds that the transferability of AOM parameters was questionable and partly because the implied acceptor function of py towards Cr^{III} seemed incompatible with the positive e_π found[83] for py bonded to Ni^{II} and Co^{II}. Further work[53,84,85] has clarified matters, although the transferability of AOM parameters remains controversial. Some authors ascribe a quantitative significance to the relative magnitudes of AOM parameters as measures of σ donor and π donor or -acceptor function. Others reject this view, noting (among other things) that in Cr^{III} systems, $e_\sigma(F^-)$ is comparable with $e_\sigma(NH_3)$ although ammonia is surely a better σ donor than fluoride. It must be understood that the effect of a ligand on d orbital energies is not necessarily related to the extent of electron donation or acceptance. It has been noted[85] that cyanide produces large values of Δ_o, suggesting a negative e_π, even in complexes where the oxidation number of the metal is +3 or greater and CN^- is unlikely to be a net π acceptor. Ligands such as cyanide and pyridine can function in principle both as π donors and π acceptors; e_π is therefore a composite parameter, the algebraic sum of a positive and a negative term. It is possible that a small amount of π acceptance might have energetic consequences which outweigh the effects of π donation, leading to a negative e_π even where there is net π donation. Thus, even the sign of e_π is not necessarily reliable as a qualitative indicator of a ligand's π function. However, useful comparisons can be made from data for a range of related systems.

6.3 The Cellular LF (CLF) Model[50–53]

Gerloch and Woolley[50,51] reformulated the AOM in a way that resolves some of the difficulties encountered with, for example, square planar $CuCl_4{}^{2-}$, but rejects parameter transferability. The LF parameters are determined from both optical and magnetic data, with SO coupling taken fully into account. The 'five-orbital' model, which lies at the heart of LF theory is retained; the d orbitals, it is argued, are not significantly involved in covalency and remain 'pure', albeit with expanded radial functions as a consequence of central-field covalence.

Although certainly inspired by the AOM, the CLF approach parts company from its parent in some important respects. The d-orbital splitting is deemed to arise from 'spatially local' interactions between the d orbitals and 'bond orbitals'; the bonding involves mainly the central atom $(n+1)$s and $(n+1)$p orbitals. However, some of the notation of AOM is retained, and, for the simplest situations, the results are the same. The CLF approach explains such anomalies as the position of d_{z^2} in square $CuCl_4{}^{2-}$ without the need to introduce d–s mixing. Thus, the absence of axial ligands in a square-planar complex creates 'voids' whose effect can be shown to depress the energy of the d_{z^2} orbital. These developments have brought LFT round almost in a full circle in the last 40 years. However, other formulations of the AOM continue to be used, and the concept of voids has been harshly criticized.**[78]** Computer programs for both CLF and conventional AOM analyses of spectroscopic and/or magnetic data have been described.**[86]**

7 OTHER APPLICATIONS OF LIGAND FIELD THEORY

7.1 Crystal Field/Ligand Field Stabilization Energy

This useful concept has been the butt of much criticism. The basic idea is that the total orbital energy of the d^n configuration in the ground state of a complex is always less than or equal to the orbital energy in the spherical field. Thus, from Figure 3, the orbital energy associated with the configuration $(t_{2g})^m(e_g)^n$ for an octahedral complex is equal to $(3n-2m)\Delta_o/5$. The crystal (or ligand) field stabilization energy (CFSE or LFSE, *see Crystal Field Stabilization Energy*) is the lowering in orbital energy of the d^n configuration in a specified coordination geometry relative to that in an equivalent spherical field: for octahedral geometry, this is equal to $(2m-3n)\Delta_o/5$. For the tetrahedral configuration $(e)^n(t_2)^m$, the CFSE is equal to $(3n-2m)\Delta_t/5$. In both cases, the CFSE is zero for d^0, d^{10}, and high-spin d^5. For high-spin systems, remembering that the low-spin option is never exercised in the tetrahedral case, we obtain a maximum CFSE of $(6/5)\Delta$ for octahedral d^3/d^8, and for tetrahedral d^2/d^7. Higher CFSEs are obtained for low-spin octahedral d^n $(n = 4–7)$, with a maximum at d^6. These maxima are alleged to be related to the prevalence of these configurations, which are marked by both thermodynamic stability and kinetic inertness. The following observations are noteworthy.

1. Octahedral complexes of Cr^{III} (d^3), and of the low-spin d^6 species Co^{III}, Rh^{III}, Ir^{III}, and Pt^{IV}, are numerous and well studied. They are kinetically inert, that is, they undergo ligand-substitution reactions relatively slowly, and the bulk of kinetic and mechanistic studies on transition element complexes have been performed on them; this implies high activation barriers. Most substitution reactions of octahedral complexes appear to have dissociative mechanisms, with five-coordinate intermediates; both CF and AOM calculations lead to large losses of CFSE for d^3 and low-spin d^6 systems in going from octahedral ML_6 to ML_5 (*see Coordinatively Inert & Labile Complexes*).
2. Tetrahedral complexes are particularly common for d^7, which is well represented by cobalt(II). Although tetrahedral d^2 is less common, this configuration seems to stabilize otherwise unusual oxidation states (e.g. isoelectronic $CrO_4{}^{4-}$, $MnO_4{}^{3-}$, and $FeO_4{}^{2-}$).
3. The 'ionic' species MX_2 (X = halogen) and MO (where M is a 3d element other than Zn) have octahedrally coordinated M^{II}. If their lattice energies (as positive ΔH quantities) are plotted against the atomic number of M, there are maxima at M = V and Ni, corresponding to d^3 and d^8. Likewise, maxima are observed in a plot of the hydration enthalpy of M^{2+} against atomic number at V^{2+} and Ni^{2+}. This is attributed to the extra CFSE of $[M(H_2O)_6]^{2+}$ where M^{2+} is d^3 or d^8.

Burdett**[87]** has examined the CFSE concept in terms of the AOM. Essentially similar conclusions can be reached concerning the relative stabilities of configurations. The case of Ni^{II} (d^8) is particularly interesting. This has maximum CFSE for octahedral coordination, but other geometries are competitive; for example, Cr^{III} is rarely found in any coordination other than octahedral, but four- and five-coordinate Ni^{II} complexes are abundant, and octahedral Ni^{II} is not conspicuously inert. The removal of two ligands to convert octahedral to square planar will stabilize d_{z^2} (see also Section 7.2) and it can be seen that the change from $(d_{xy})^2(d_{xz})^2(d_{yz})^2(d_{z^2})^1(d_{x^2-y^2})^1$ to $(d_{xy})^2(d_{xz})^2(d_{yz})^2(d_{z^2})^2$ will lower the orbital energy and enhance CFSE. Octahedral to square equilibria of the type

$$Ni^{II}(L-L)_2L'_2 \rightleftharpoons Ni(L-L)_2 + 2L'$$

are common where (L–L) is a bidentate ligand and $Ni^{II}(L–L)_2$ is square planar. Such equilibria and distortions will be mentioned again in Section 7.2.

Finally in this section, we note the remarkable prevalence of tetrahedral four-coordination in zinc(II) chemistry (*see* ***Zinc: Inorganic & Coordination Chemistry***), to an extent comparable with cobalt(II), although d^{10} enjoys no advantage from CFSE. Tetrahedrally bonded zinc(II) is found in many metalloenzymes (*see* ***Zinc Enzymes***) and can often be replaced by cobalt without loss of enzymatic activity. This can be attributed to d–p mixing.**[88]** In tetrahedral symmetry (T_d), the $nd_{xy,xz,yz}$ and $(n+1)p_{x,y,z}$ orbitals each constitute a threefold-degenerate t_2 set and become mixed. The LF t_2 orbitals are thus lowered in energy, and the d^{10} configuration (where t_2 is filled) is consequently stabilized.

7.2 The Jahn–Teller (J–T) Effect

The *Jahn–Teller Effect* is something of a totem or icon among inorganic chemists. The original paper[89] showed how interactions between vibrational and electronic states caused a nonlinear molecule or complex ion in an orbitally degenerate state (e.g. E_g, T_{1g}) to be unstable with respect to a distortion that relieves the degeneracy (the J–T theorem). The ground state of any system will be orbitally degenerate if any degenerate set of orbitals is unevenly occupied, that is, if the degenerate orbitals are other than all empty, filled or half-filled. The J–T effect is the observation of such distortions where they are predicted by the theorem. Thus, regularly octahedral complexes ML_6 where M is d^9 or high-spin d^4 are rarely, if ever, found: here, an E_g ground state is predicted but the observed structures of six-coordinate Cr^{II} and Cu^{II} species can always be described as distorted octahedra with nondegenerate ground states. Distortions that relieve a threefold degeneracy, for example, for octahedral d^2, are less pronounced.

Most of the structural features that have been blamed on the J–T effect are to be found in Cu^{II} chemistry.[90] In six-coordinate Cu^{II} systems, the structure is usually a tetragonally elongated octahedron. Two trans axial ligands are at much longer (ca. 20%) distances from the Cu atom than expected for an octahedron, while the four equatorial ligands are at slightly shorter distances than expected. This is shown in Figure 12, where we compare the bond lengths of $[Ni(NH_3)_4(NO_2)_2]$ and $[Cu(NH_3)_4(NO_2)_2]$.

Notwithstanding the vibronic origins of the J–T theorem, attempts have been made to find simple explanations based on orbital energy considerations for those structural features described as J–T distortions. A simple CF analysis considers the effect on the d orbitals of an octahedral d^9 complex of withdrawing two axial ligands away from the central atom, while allowing (on account of the consequent relief of interligand repulsion) the four equatorial ligands to move a little closer to the center. The axis of elongation is conventionally labeled z. The axial elongation will stabilize d_{z^2}, which experiences a weaker field, and to a lesser extent $d_{xz,yz}$. The equatorial contraction will destabilize $d_{x^2-y^2}$ and to a lesser extent d_{xy}. The further d-orbital splitting, as octahedral ML_6 is distorted towards square planar ML_4, is shown in Figure 13. There will be a lowering in orbital energy, that is, a gain in CFSE, and this provides the driving force for the J–T distortion. In Section 7.1, we looked at a similar distortion in the case of octahedral Ni^{II}; although this does not have an orbitally degenerate ground state, we can interpret the tendency for the removal of two opposite ligands by arguments similar to those advanced for the so-called J–T distortion of octahedral Cu^{II}! Burdett[91–94] has applied the AOM to the discussion of these points.

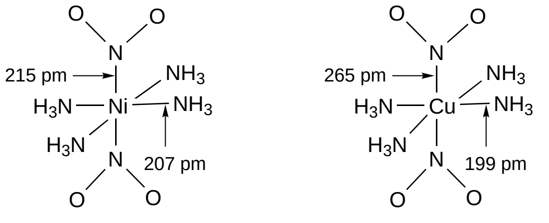

Figure 12 Bond lengths in $[Cu(NH_3)_4(NO_2)_2]$ and $[Ni(NH_3)_4(NO_2)_2]$, an illustration of the Jahn–Teller effect

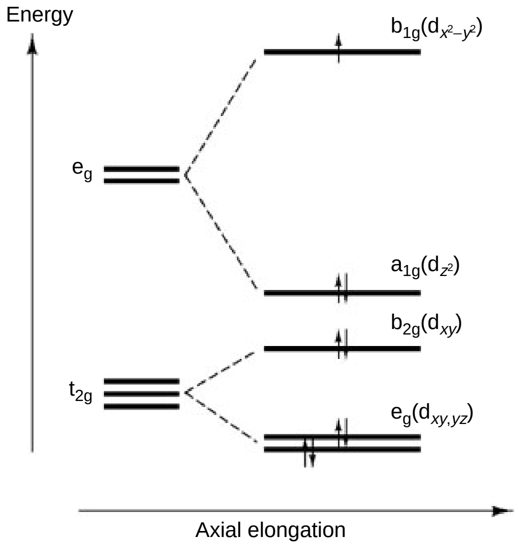

Figure 13 Effect on d-orbital energies for an octahedral d^9 system of an axial elongation

The point is often made that the original proof of the J–T theorem provides no guidance as the nature of the predicted distortion, except that it must remove the orbital degeneracy. In the case of octahedral Cu^{II}, we can envisage many distortions that would satisfy the theorem. For example, an equatorial compression, leading to two short and four long bonds ($2 + 4$ coordination, as opposed to $4 + 2$ already described) would relieve the degeneracy, giving an $^2A_{1g}$ ground state with the odd electron in d_{z^2}. However, such a distortion is rarely observed except in an environment that imposes a flattened configuration. The frequently cited example of K_2CuF_4 actually contains axially elongated CuF_6 octahedra,[95] although extended X-ray absorption fine structure (EXAFS) studies show that in $KAlCuF_6$, the coordination about Cu(II) is definitely compressed octahedral.[96] Several cases of compressed octahedra inferred from X-ray measurements have been shown by EXAFS to contain the usual elongation.[97] There is often a dynamic equilibrium among three conformers, differing in the orientation of the long axis. Where these are all of equal (or nearly equal) energy, as in $[Cu(H_2O)_6][SiF_6]$, a room temperature X-ray analysis leads to a regularly octahedral configuration, with averaged bond lengths, and the ESR signal is isotropic. However, an axial elongation is apparent from EXAFS measurements.[98] In some cases, two of the three conformers are much lower in energy than the third; the X-ray analysis then gives one short axis and two longer axes, intermediate between short and long.[97] As an example of this behavior, $(NH_4)_2[Cu(H_2O)_6](SO_4)_2$ appears to be tetragonally compressed at high temperatures, but low temperature X-ray and neutron diffraction studies show an elongation with a rhombic distortion. On deuteration, the directions of the long and intermediate axes are interchanged.[99] The dynamics of the Jahn–Teller effect has also been thoroughly studied in copper(II) complexes containing two tridentate N-donor ligands.[100] The preference for axial elongation can be explained if we recall (Section 6.1) that in D_{4h} symmetry (which holds for both types of tetragonal distortion, as well as square planar), $3d_{z^2}$ mixes with 4s, and the LF d_{z^2} orbital is further stabilized. This enhances the CFSE more in the case of an axial elongation (where d_{z^2} is doubly occupied) than for an equatorial compression (where d_{z^2} is singly occupied). Such mixing will also assist the octahedral–square transformation for Ni^{II}.[100,101]

8 RELATED ARTICLES

Ammonia & N-donor Ligands; Chromium: Inorganic & Coordination Chemistry; Coordination Numbers & Geometries; Copper: Inorganic & Coordination Chemistry; Magnetism of Transition Metal Ions; Molecular Orbital Theory; Nickel: Inorganic & Coordination Chemistry; Zinc Enzymes; Zinc: Inorganic & Coordination Chemistry.

9 REFERENCES

1. G. Wulfsberg, ‘Inorganic Chemistry’, University Science Books, Sausalito, CA, 2000.
2. G. L. Miessler and D. A. Tarr, ‘Inorganic Chemistry’, 3rd edn., Prentice Hall, New York, 2003.
3. K. F. Purcell and J. C. Kotz, ‘Introduction to Inorganic Chemistry’, Harcourt, New York, 1997.
4. K. F. Purcell and J. C. Kotz, ‘Inorganic Chemistry’, Saunders, Philadelphia, PA, 1977.
5. T. Moeller, ‘Inorganic Chemistry: a Modern Introduction’, John Wiley & Sons, New York, 1982.
6. J. E. Huheey, E. A. Keiter, and R. L. Keiter, ‘Inorganic Chemistry: Principles of Structure and Reactivity’, 4th edn., Addison-Wesley, New York, 1993.
7. N. N. Greenwood and A. Earnshaw, ‘The Chemistry of the Elements’, 2nd edn., Butterworth-Heinemann, Oxford, 1997.
8. W. L. Jolly, ‘Modern Inorganic Chemistry’, McGraw-Hill, New York, 1984.
9. F. A. Cotton, G. Wilkinson, C. A. Murillo, and M. Bochmann, ‘Advanced Inorganic Chemistry’, 6th edn., John Wiley & Sons, New York, 1999.
10. K. M. Mackay, R. A. Mackay, and W. Henderson, ‘Introduction to Modern Inorganic Chemistry’, 6th edn., Nelson Thorne, Cheltenham, 2002.
11. D. F. Shriver and P. W. Atkins, ‘Inorganic Chemistry’, 3rd edn., Freeman, New York, 1999.
12. C. E. Housecroft and A. G. Sharpe, ‘Inorganic Chemistry’, Pearson Publishing, New York, 2001.
13. I. S. Butler and J. F. Harrod, ‘Inorganic Chemistry: Principles and Applications’, Benjamin, Redwood City, CA, 1989.
14. R. B. Heslop and K. Jones, ‘Inorganic Chemistry: A Guide to Advanced Study’, Elsevier, Amsterdam, 1976.
15. S. F. A. Kettle, ‘Coordination Compounds’, Nelson, London, 1969.
16. M. Gerloch and R. C. Slade, ‘Ligand Field Parameters’, Cambridge University Press, Cambridge, UK, 1973.
17. L. E. Orgel, ‘Introduction to Transition Metal Chemistry’, John Wiley & Sons, New York, 1966.
18. J. K. Burdett, ‘Molecular Shapes’, John Wiley & Sons, New York, 1980.
19. C. K. Jørgensen, ‘Absorption Spectra and Bonding in Complexes’, Pergamon Press, Oxford, 1962.
20. C. K. Jørgensen, ‘Modern Aspects of Ligand Field Theory’, North Holland, Amsterdam, 1971.
21. C. J. Ballhausen, ‘Ligand Field Theory’, McGraw-Hill, New York, 1962.
22. C. J. Ballhausen, ‘Molecular Electronic Structures of Transition Metal Complexes’, McGraw-Hill, New York, 1979.
23. D. Sutton, ‘Electronic Spectra of Transition Metal Complexes’, McGraw-Hill, New York, 1968.
24. B. N. Figgis, ‘Introduction to Ligand Fields’, John Wiley & Sons, New York, 1966.
25. M. Gerloch, ‘Magnetism and Ligand Field Analysis’, Cambridge University Press, Cambridge, UK, 1983.
26. A. B. P. Lever, ‘Inorganic Electronic Spectroscopy’, 2nd edn., Elsevier, Amsterdam, 1984.
27. F. E. Mabbs and D. J. Machin, ‘Magnetism and Transition Metal Complexes’, Chapman & Hall, London, 1973.
28. H. L. Schläfer and G. Gliemann, ‘Basic Principles of Ligand Field Theory’, John Wiley & Sons, New York, 1969.
29. B. N. Figgis and M. A. Hitchman, ‘Ligand Field Theory and its Applications’, Wiley-VCH, New York, 2000.
30. I. B. Bersuker, ‘Electronic Structure and Properties of Transition Metal Complexes. Introduction to the Theory’, John Wiley & Sons, New York, 1996.
31. E. I. Solomon and A. B. P. Lever eds, ‘Inorganic Electronic Structure and Spectroscopy’, John Wiley & Sons, New York, 1999 Vol. 1.
32. S. F. A. Kettle, ‘Physical Inorganic Chemistry’, University Science Books, Sausalito, CA, 1996.

33. D. J. Newman and B. Ng eds, ‘Crystal Field Handbook’, Cambridge University Press, Cambridge, 2001.
34. H. Bethe, *Ann. Phys.*, 1929, **3**, 133.
35. J. M. Hollas, ‘Symmetry in Chemistry’, Chapman & Hall, London, 1972.
36. P. B. Dorain, ‘Symmetry in Inorganic Chemistry’, Addison-Wesley, Reading, MA, 1965.
37. W. E. Hatfield and W. E. Parker, ‘Symmetry in Chemical Bonding and Structure’, Merrill, Columbus, OH, 1974.
38. A. Vincent, ‘Molecular Symmetry and Group Theory’, 2nd edn., John Wiley & Sons, Chichester, 2000.
39. D. S. Urch, ‘Orbitals and Symmetry’, Penguin, Harmondsworth, 1970.
40. F. A. Cotton, ‘Chemical Applications of Group Theory’, 3rd edn., John Wiley & Sons, New York, 1990.
41. G. Davidson, ‘Group Theory for Chemists’, Macmillan Publishing, Basingstoke, 1991.
42. S. F. A. Kettle, ‘Symmetry and Structure’, John Wiley & Sons, Chichester, 1985.
43. D. M. Bishop, ‘Group Theory and Chemistry’, Oxford University Press, Oxford, 1990.
44. J. R. Ferraro and J. S. Ziomek, ‘Introduction to Group Theory and its Application to Molecular Structure’, 2nd edn., Plenum Publishing, New York, 1975.
45. R. L. Carter, ‘Molecular Symmetry and Group Theory’, John Wiley & Sons, New York, 1997.
46. P. H. Walton, ‘Beginning Group Theory for Chemistry’, Oxford University Press, Oxford, 1998.
47. J. N. Murrell and S. F. A. Kettle, ‘The Chemical Bond’, 2nd edn., John Wiley & Sons, Chichester, 1985.
48. C. E. Schäffer and C. K. Jørgensen, *Mol. Phys.*, 1965, **9**, 401.
49. D. W. Smith, *Struct. Bonding*, 1978, **35**, 87.
50. M. Gerloch, J. H. Harding, and R. G. Woolley, *Struct. Bonding*, 1981, **46**, 1.
51. M. Gerloch and R. G. Woolley, *Prog. Inorg. Chem.*, 1984, **31**, 371.
52. M. Gerloch, *Coord. Chem. Rev.*, 1990, **99**, 117.
53. A. J. Bridgeman and M. Gerloch, *Prog. Inorg. Chem.*, 1997, **45**, 179.
54. J. Ferguson, *Prog. Inorg. Chem.*, 1970, **12**, 159.
55. M. Gerloch, ‘Orbitals, Terms and States’, John Wiley & Sons, Chichester, 1986.
56. D. W. Smith, *J. Chem. Educ.*, 1996, **73**, 504.
57. E. König and S. Kremer, ‘Ligand Field Energy Level Diagrams’, Plenum Publishing, New York, 1977.
58. R. Stranger, K. L. McMahon, L. R. Gahan, J. I. Bruce, and T. W. Hambley, *Inorg. Chem.*, 1997, **36**, 3466.
59. C. Anthon and C. E. Schäffer, *Coord. Chem. Rev.*, 2002, **226**, 17.
60. C. Anthon, J. Bendix, and C. E. Schäffer, *Inorg. Chem.*, 2003, **42**, 4088.
61. D. W. Smith, *Coord. Chem. Rev.*, 1976, **17**, 89.
62. C. E. Schäffer, *Pure Appl. Chem.*, 1970, **24**, 361.
63. A. L. Companion and M. R. Komarynsky, *J. Chem. Educ.*, 1964, **41**, 257.
64. P. Day, *Proc. Chem. Soc.*, 1964, 18.
65. W. E. Hatfield and T. S. Piper, *Inorg. Chem.*, 1964, **3**, 841.
66. D. W. Smith, *J. Chem. Soc., Dalton Trans.*, 1973, 1853.
67. R. J. Deeth, *Faraday Discuss.*, 2003, **124**, 379.
68. P. Day and C. K. Jørgensen, *J. Chem. Soc.*, 1964, 6226.
69. D. W. Smith, *Struct. Bonding*, 1972, **12**, 49.
70. R. L. Harlow, W. J. Wells, G. W. Watt, and S. H. Simonsen, *Inorg. Chem.*, 1974, **13**, 2106.
71. M. A. Hitchman and P. J. Cassidy, *Inorg. Chem.*, 1979, **18**, 1745.
72. D. W. Smith, *Inorg. Chim. Acta*, 1977, **22**, 107.
73. I. R. Beattie, J. M. Brown, P. Crozet, A. J. Ross, and A. Yiannopoulu, *Inorg. Chem.*, 1997, **36**, 3207.
74. C. W. Bauschlicher and B. O. Roos, *J. Chem. Phys.*, 1989, **91**, 4785.
75. R. J. Deeth, *J. Chem. Soc., Dalton Trans.*, 1993, 1061.
76. A. J. Bridgeman, *J. Chem. Soc., Dalton Trans.*, 1996, 2601.
77. A. Möller, M. A. Hitchman, E. Krausz, and R. Hoppe, *Inorg. Chem.*, 1995, **34**, 2684.
78. C. E. Schäffer, *Inorg. Chim. Acta*, 1995, **240**, 581.
79. M. J. Riley, *Inorg. Chim. Acta*, 1998, **268**, 55.
80. C. Lepadatu, H. Adamsky, and H.-H. Schmidtke, *J. Mol. Struct. (THEOCHEM)*, 1999, **488**, 241.
81. J. Glerup, O. Mønsted, and C. E. Schäffer, *Inorg. Chem.*, 1976, **15**, 1399.
82. D. W. Smith, *Inorg. Chem.*, 1978, **17**, 3153.
83. A. B. P. Lever, *Coord. Chem. Rev.*, 1968, **3**, 119.
84. J. Glerup, O. Mønsted, and C. E. Schäffer, *Inorg. Chem.*, 1980, **19**, 2855.
85. C. E. Schäffer and H. Yamatera, *Inorg. Chem.*, 1991, **30**, 2840.
86. B. N. Figgis and M. A. Hitchman, ‘Ligand Field Theory and its Applications’, Wiley-VCH, New York, 2000, p. 80.
87. J. K. Burdett, *J. Chem. Soc., Dalton Trans.*, 1976, 1725.
88. D. W. Smith, ‘Inorganic Substances’, Cambridge University Press, Cambridge, UK, 1990, p. 289.
89. H. A. Jahn and E. Teller, *Proc. Roy. Soc.*, 1937, **A161**, 220.
90. B. J. Hathaway, *Struct. Bonding*, 1984, **57**, 55.
91. J. K. Burdett, *Inorg. Chem.*, 1975, **14**, 375.
92. J. K. Burdett, *Inorg. Chem.*, 1975, **14**, 931.
93. J. K. Burdett, *Inorg. Chem.*, 1976, **15**, 212.

94. J. K. Burdett, *Adv. Inorg. Chem. Radiochem.*, 1978, **21**, 113.

95. C. Friebel and D. Reinen, *Z. Anorg. Allg. Chem.*, 1974, **407**, 193.

96. V. M. Masters, M. J. Riley, and M. A. Hitchman, *J. Synchrotron Radiat.*, 1999, **6**, 242.

97. V. M. Masters, M. J. Riley, M. A. Hitchman, and C. Simmons, *Inorg. Chem.*, 2001, **40**, 4478.

98. I. Persson, P. Persson, M. Sandström, and A.-S. Ullström, *J. Chem. Soc., Dalton Trans.*, 2002, 1256.

99. M. A. Hitchman, Y. V. Yablokov, V. E. Petrashen, M. A. Augustyniak-Jabłokov, H. Stratemeier, M. J. Riley, K. Łukaszewicz, P. E. Tomaszewski, and A. Pietraszko, *Inorg. Chem.*, 2002, **41**, 229.

100. G. S. Beddard, M. A. Halcrow, M. A. Hitchman, M. P. de Miranda, C. J. Simmons, and H. Stratemeier, *J. Chem. Soc., Dalton Trans.*, 2003, 1028.

101. R. J. Deeth and M. A. Hitchman, *Inorg. Chem.*, 1986, **25**, 1225.

Luminescence

C. Fouassier
Institut de Chimie de la Matière Condensée (ICMCB-CNRS), Pessac cedex, France

1 Introduction 1
2 Luminescence Processes 1
3 Main Families of Luminescent Ions 7
4 Donor–Acceptor Transitions 14
5 Excitation through the Host Lattice 15
6 Electroluminescence 16
7 References 17

Glossary

Activator: luminescent center
AX: B means that the luminescent-ion B is substituted for the A cation of the host lattice AX
Excitation spectrum: variation of the luminescence intensity at a given wavelength as a function of the wavelength of the excitation radiation
Phosphor: luminescent material, usually in powder form
VUV (vacuum ultraviolet): ultraviolet radiation with wavelength below 190 nm

1 INTRODUCTION

Luminescence is the emission of light from a nonthermal excitation. The use of the term has been extended to the emission of UV or IR radiation. A luminescence is obtained under a variety of excitation sources, for example:

- electromagnetic radiation: Vacuum ultraviolet (VUV), UV (photoluminescence), X rays, γ rays
- particles: electron beam (cathodoluminescence), neutrons, and so on
- electric field (electroluminescence).

The luminescence yield depends on the probabilities of excitation and radiative decay of luminescent centers. Photon emission competes with phonon emission, the latter resulting in temperature rise.

In most luminescent materials, emission is the result of an electronic transition within an ion. The luminescent ion, called the activator, is generally substituted for ions with comparable size in a compound termed host lattice, transparent to the emitted radiation. The emitting level must lie below the conduction band in order to avoid ionization. The luminescence characteristics are strongly dependent on the nature of the host. For instance, depending on the covalency and crystal field, the position of the emission band of Eu^{2+} in oxide lattices can vary from the UV (maximum at 367 nm in SrB_4O_7) to the red (733 nm in CaO). The luminescence spectra of most efficient materials have been collected in Ref. 1.

Luminescence can also arise from a trapped exciton or from a transition between two centers (donor–acceptor transitions).

2 LUMINESCENCE PROCESSES

2.1 Electronic Transitions within Ions

Transitions occur mainly by an electric dipole mechanism. Such transitions are allowed if the initial and final states are made up of orbitals of opposite parity ($\Delta l = 1, 3, \ldots$; l: orbital angular momentum quantum number) and if the spin remains unchanged ($\Delta S = 0$) (Laporte rules, *see* ***Ligand Field Theory & Spectra***). However parity-forbidden transitions can occur as a result of mixing with states of opposite parity. Mixing of states by the crystal field requires that the cationic site lacks an inversion center. If the site is centrosymmetric, transitions can nevertheless be observed owing to vibronic coupling. Their probability is low and increases with temperature.

In absorption spectra, the probability of a transition is expressed by its oscillator strength, f. While f is close to unity for allowed transitions, it is of the order of 10^{-5}–10^{-4} and 10^{-6}–10^{-5} respectively for spin-allowed transitions within the $3d^N$ and $4f^N$ configurations. Efficient conversion of a UV radiation to light (as needed in fluorescent lamps) requires strong absorption properties at the wavelength of incident photons. Figure 1 shows a comparison of the luminescence intensity for 4f → 5d ($\Delta l = 1$) and 4f → 4f ($\Delta l = 0$) excitations in the case of a terbium compound.

When isolated ions in a lattice have been promoted to the excited state, the population of emitting ions decreases exponentially:

$$I(\mathrm{t}) = I_0 \exp(-Wt) \tag{1}$$

where I_0 is the initial luminescence intensity and W the sum of radiative and nonradiative rates expressed in s^{-1}: $W = W_\mathrm{r} + W_\mathrm{nr}$. The radiative rate is given by:

$$W_\mathrm{r} = \frac{64\pi^4 \chi e^2}{3hg_i\lambda^3}\mathrm{S} \tag{2}$$

where g_i is the degeneracy of the initial state, λ the peak emission wavelength, and S the line strength: $S = |\langle\psi_\mathrm{a}|P|\psi_\mathrm{b}\rangle|^2$ where P is the electric dipole operator; χ is the local field correction:

$$\chi = \frac{n(n^2+2)^2}{9} \tag{3}$$

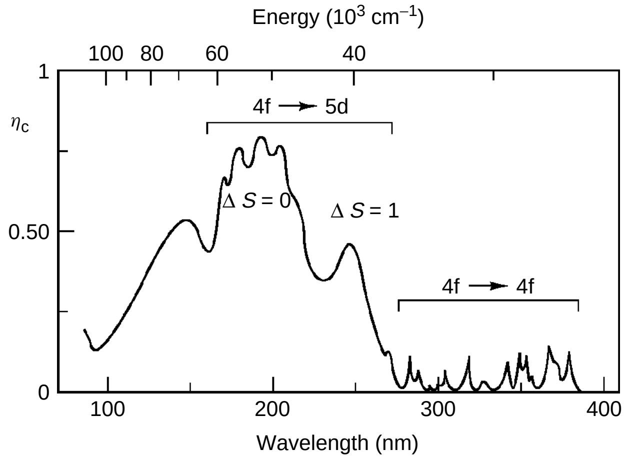

Figure 1 Variation of the conversion yield, η_c (ratio of the number of photons emitted to the number of incident photons), as a function of the excitation wavelength for $Tb_{0.70}La_{0.30}MgB_5O_{10}$ [2]

where n is the refractive index. For allowed transitions such as the 5d → 4f transitions of Eu^{2+} or Ce^{3+} S is little influenced by the host.[3,4] Thus the radiative rate depends essentially on the emission wavelength and refractive index.

$\tau_r = 1/W_r$ is the radiative lifetime. τ_r varies from 10^{-8} to 10^{-7} s for allowed transitions to 10^{-4}–10^{-2} s for forbidden transitions.

Magnetic dipole transitions play a role in the luminescence of some lanthanide ions, specially Eu^{3+}, when the local symmetry deviates little from inversion symmetry. They are parity-allowed between states of the $3d^N$ or $4f^N$ configurations but have a low probability. They are subject to selection rules: $\Delta L = \Delta S = 0$ and $\Delta J = 0, \pm 1$ ($0 \leftrightarrow 0$ forbidden).

2.2 Shape of Emission Bands – The Single-configurational-coordinate Diagram Model

Figure 2 shows configuration curves for the ground state and an excited state. They represent the energy dependence on the cation-anion distance: $E = 1/2\,kr^2$, where r is the cation–anion distance and k the force constant, and the equilibrium distance of the ground state is taken as the origin. Equidistant lines inside the parabolas represent vibrational energy levels whose population corresponds to a Bolztmann distribution. The amplitude of the vibrational wavefunction is maximum for $r = 0$ for the first vibrational level and at the end of the segments (at the turning points), on the parabola, for higher levels. Electronic transitions are represented by vertical lines because they occur in a very short time compared to that of atomic displacements.

If the transition involves only inner orbitals, the equilibrium distance is not modified (Figure 2a); the parabola of the excited state has the same shape than that of the ground state. Since the two parabolas are parallel, all transitions have nearly the same energy. The corresponding spectrum consists of a narrow line at the same position in absorption and emission. Because the 4f levels are internal, the bonding is not significantly modified when electronic transitions occur between these levels. 4f–4f transitions give rise to sharp lines in absorption and emission spectra.

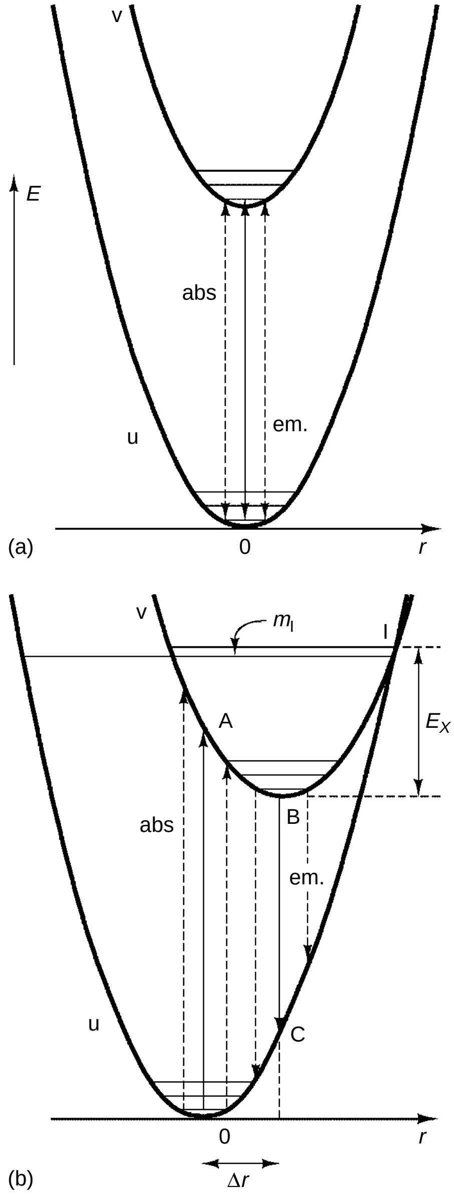

Figure 2 Configurational-coordinate diagrams for (a) negligible and (b) strong offset Δr

If the transition involves an external orbital, the equilibrium distance is changed (Figure 2b). Transitions from a vibrational level of the ground state end on different vibrational levels of the excited state. The absorption spectrum consists of a band which broadens with increasing temperature as a result of the population of higher vibrational levels of the initial state. After excitation the ion returns to the ground state by the following processes:

1. relaxation to the bottom of the excited-state parabola (transitions A → B, Figure 2b) by emitting phonons (i.e. by giving up heat to the lattice), in a time of the order of 10^{-13} s;
2. radiative emission (transitions B → C);
3. relaxation to the minimum of the ground-state parabola with phonon emission (transitions C → 0).

The emission band lies at lower energy than the absorption band. The energy difference between the maxima is called the Stokes shift. The energetic distribution of transitions in absorption or emission has approximately a Gaussian shape. Because of the weakening of the bonding, the excited-state parabola is wider than the ground state one. Consequently the emission band is broader than the corresponding absorption band. The width increases with increasing offset Δr and phonon energies.

Examples of band emissions are the 3d → 3d transitions of transition metal ions such as Mn^{2+}, the 5d → 4f transitions of lanthanide ions such as Ce^{3+} and Eu^{2+} and the np → ns transitions of ions with s^2 configuration such as Pb^{2+}, Sb^{3+}, and Bi^{3+}.

2.3 Luminescence Quantum Efficiency – Nonradiative Transitions

The luminescence quantum yield is the result of the competition between radiative and nonradiative transitions:

$$\eta_r = \frac{W_r}{W_r + W_{nr}} \tag{4}$$

Nonradiative transitions between the 4f levels of lanthanide ions are caused by multiphonon processes. In the case of band emissions, the quantum efficiency is commonly interpreted by the Mott's model. It should be noted that Struck and Fonger have shown that in fact an unified model can be used for these two types of emission.[5]

2.3.1 *Narrow Line Emission – Multiphonon Processes*

Nonradiative relaxation between the 4f states of lanthanide ions can occur by the simultaneous emission of several phonons.[6,7] The multiphonon emission rate decreases exponentially with the energy gap ΔE to the next-lower level:

$$W_{nr} = C\exp(-\alpha\Delta E) \tag{5}$$

C and α are constants characteristic of the host and, with rare exceptions, independent of the nature of the lanthanide ion or electronic state involved. The validity of the exponential dependence on the energy gap has been well experimentally established.[8] A modified exponential energy gap has been derived by van Dijk and Schuurmans:[9]

$$W_{nr} = \beta_{el}\exp[-\alpha(\Delta E - 2\hbar\omega)] \tag{6}$$

Unlike C, β_{el} varies little with the host lattice.

The nonradiative transition rate increases with rising temperature. The effect of T increases with the number of phonons involved in the process:

$$W_{nr}(T) = W(0)(n+1)^p \tag{7}$$

where $W(T)$ is the transition rate at temperature T, p is the number of phonons of equal energy emitted, $p = \Delta E/\hbar\omega$, and n the average occupation number of vibrational levels,

$$n = \left[\exp\left(\frac{\hbar\omega}{kT}\right) - 1\right]^{-1} \tag{8}$$

Since the transition rate decreases exponentially with the number of phonons required to bridge the energy gap, the highest-energy phonons make the largest contribution to the process. Vibrational frequencies increase with increasing bond strength and decreasing atomic mass, following the trend

oxides > fluorides > sulfides > chlorides > bromides

Figure 3 shows the nonradiative rate dependence on the energy gap to next-lower level for some halide and oxide host lattices. The nonradiative rate amounts to $10^4\,s^{-1}$ (a value of the order of the radiative rate of spin-allowed 4f → 4f

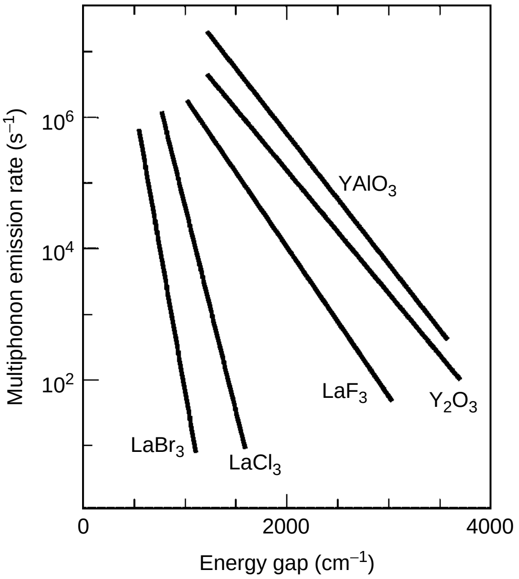

Figure 3 Multiphonon emission rates from excited states of trivalent rare earths as a function of energy gap to the next lower level. (Reproduced by permission of Ref. 5)

transitions) for an energy gap of 1000 cm^{-1} in chlorides and 2500–3000 cm^{-1} in oxides such as Y_2O_3 or $YAlO_3$.[8]

2.3.2 Quantum Efficiency of Band Emissions

In the Mott's model, nonradiative transitions are pictured as taking place at the intersection of the configuration coordinate curves, I (Figure 2b). The stability of the emission depends on the energy difference, E_X, between the minimum of the excited-state parabola and the intersection. When with rising temperature the m_I vibrational level becomes populated, the luminescence center can return to the ground state by giving up phonons to the lattice. The rate is described by Mott's activation-energy formula:

$$W_{nr} = A_M \exp\left(\frac{-E_X}{kT}\right) \tag{9}$$

where A_M is a rate constant of the order of 10^{13} s^{-1}.

Hence the thermal stability increases with increasing energy of the excited state and decreasing value of the offset, Δr.

The effect of the excited-state energy can be illustrated by the charge transfer (CT) luminescence of tetrahedral groups $MO_4{}^{2-}$ where M is a transition metal: Cr, Mo, W. These groups exhibit an absorption band corresponding to a transition from a predominantly anionic molecular orbital to a predominantly cationic molecular orbital.[10] Its position lowers in energy with increasing oxidizing character of the cation: W > Mo > Cr. The luminescence of chromates has been observed only at very low temperature and for all molybdates quenching starts below room temperature. In contrast, the emission of various tungstates, $MgWO_4$, $CaWO_4$, $CdWO_4$, exhibits high efficiency at 300 K.[11]

Quenching curves actually often deviate from the shape expected from a single activation energy. The reason is that the probability of nonradiative transitions from vibrational levels below the intersection I is not negligible. Struck and Fonger proposed a method of calculation of nonradiative rates.[5] For the ground state u and excited state v, the vibrational wavefunctions and phonon energies are called u_n, $\hbar\omega_u$ and v_m, $\hbar\omega_v$ respectively. The rate of a transition between the vibrational levels m and n is proportional to the product of the population of the initial level according to a Boltzmann distribution and the square overlap integral $\langle u_n | v_m\rangle^2$. The multiple activation energies $m\hbar\omega_v$ to the initial vibrational states produce an increase in the nonradiative rate poorly described, in general, by a single activation energy. This model shows that in addition to the energy of the excited state and the offset Δr, phonon energies are an important parameter governing the probability of nonradiative transitions. For a hypothetical red phosphor exhibiting an excitation band in the UV at about 310 nm, the temperature at which the intensity is reduced to half of its value at low temperature falls from 560 K for $\hbar\omega = 400$ cm^{-1} to 325 K for $\hbar\omega = 600$ cm^{-1}.[12] In the latter case, at low temperature the quantum efficiency remains far below unity.

Configurational-coordinate diagrams can be established from the shape of absorption and emission bands. It must be stressed that the validity of the model is limited by the assumption of a single vibrational mode.

2.4 Energy Transfer

An ion in an excited state can transfer part or whole of its energy to a neighbor ion (Figure 4) by a radiative or nonradiative process. The acceptor ion can be in the ground state or in an excited state *(upconversion)*. Energy transfer is responsible for the drop in luminescence efficiency usually observed at high activator concentration (*concentration quenching*) and is used for increasing the probability of excitation of luminescent ions (*sensitization*).

2.4.1 Energy Transfer Mechanisms

Radiative transfer plays a role essentially when the absorption band of the acceptor ion is allowed. A photon emitted by an ion is absorbed by an other ion before escaping from the material. This requires overlap of the emission spectrum of the donor with the absorption spectrum of the acceptor. Radiative transfer between identical ions causes a modification of the spectral distribution. This is the case for the Ce^{3+} emission when the Stokes shift is small. The cerium emission originates from the lowest 5d state and consists of two bands because the ground state $4f^1$ is split by spin-orbit coupling into the states $^2F_{5/2}$ and $^2F_{7/2}$ (Figure 5), the shorter-wavelength component 5d → $4f(^2F_{5/2})$ having the

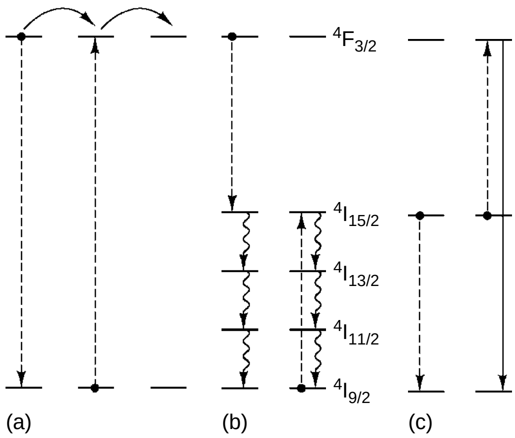

Figure 4 Schematic representation of energy transfers: (a) energy migration; (b) cross-relaxation; (c) upconversion. Vertical arrows in broken lines correspond to energy transfer and in solid lines to radiative transition. The energy diagram that illustrates the cross-relaxation mechanism is the Nd^{3+} one

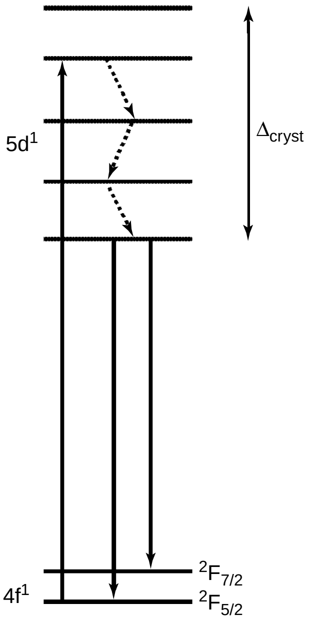

Figure 5 Luminescent processes of Ce^{3+}

strongest intensity. Owing to the overlap with the lower-energy 4f($^2F_{5/2}$) → 5d absorption band, with increasing Ce concentration the relative intensity of the shorter-wavelength emission band decreases with respect to that of the longer-wavelength component.

Nonradiative energy transfer is due to electric or magnetic multipolar interactions or to exchange interactions.[10,13–15]

For electric multipolar interactions, the transfer rate W_{DA} is proportional to the probability of the donor and acceptor transitions, to the overlap between the emission and absorption bands of the donor and acceptor, and to an inverse power of the donor–acceptor separation, R^{-s} with $s = 6, 8, 10$ for dipole–dipole, dipole-quadrupole, or quadrupole–quadrupole interaction. For electric dipole–dipole interaction, the transfer rate is proportional to

$$\frac{Q_A}{R^6 \tau_r} \int \frac{F_D(E) F_A(E)}{E^4} \tag{10}$$

where Q_{A} is the area under the absorption band of the acceptor: $Q_{\mathrm{A}} = \int \sigma(E)\, dE$, σ absorption coefficient; τ_r is the luminescence lifetime of the donor and $F_{\mathrm{D}}(E)$ and $F_{\mathrm{A}}(E)$ are normalized functions such as $\int F(E)\, dE = 1$.[16] If the activator is dilute in the lattice, transfer occurs mainly by dipole–dipole interaction.[6]

For exchange interaction, the transfer rate decreases exponentially with the donor–acceptor distance. It depends on wavefunction overlap and is not influenced by the probability of transitions.[16]

The critical distance is the distance at which the probability of energy transfer is equal to the probability of intrinsic decay rate $W = 1/\tau_{\mathrm{D}}$, where τ_{D} is the excited-state lifetime of the donor. The critical distance may reach 30 Å if the optical transitions of the donor and acceptor ions are electric dipole allowed transitions; it is of the order of 4–6 Å for overlap between an allowed emission band and the 4f → 4f absorption lines of lanthanide ions (oscillator strength f ≈ 10^{-6}).[12]

When acceptor ions are present, the decay of donor ions does not exhibit an exponential behavior. In the absence of energy transfer between donor ions and assuming a random distribution of acceptor ions, for multipolar interactions the decay is given by

$$I = I_0 \exp\left(\frac{-t}{\tau_{\mathrm{D}}} - \alpha \left(\frac{t}{\tau_{\mathrm{D}}}\right)^{3/s}\right) \tag{11}$$

where α is a parameter which depends on the acceptor concentration and critical distance.[17] The presence of acceptor ions results in a faster initial decay. With time the luminescence originates increasingly from excited ions which are far from acceptor ions and relax at a rate governed by the intrinsic decay rate.

If energy transfer between donor ions is possible, excitation may migrate until it comes into the vicinity of an acceptor ion. When the rate of energy diffusion is slow and the acceptor concentration is low, the donor decay is governed by intrinsic relaxation and by diffusion-limited relaxation to acceptors. The decay at long times after the excitation pulse is exponential with a decay time given by $1/\tau = 1/\tau_{\mathrm{D}} + 1/\tau_{\mathrm{dif}}$ where $1/\tau_{\mathrm{dif}}$ is the decay rate due to diffusion. When the probability of energy transfer between donor ions is large, energy diffusion can be very rapid. The rate limiting step in the energy transfer process is the donor–acceptor transfer rate. Because the diffusion occurs on a much shorter timescale, the emission of donor ions exhibits an exponential decay.

2.4.2 Concentration Quenching

Interactions between luminescent ions cause nonradiative losses by two mechanisms: *energy migration* and *cross-relaxation.*

1. By a sequence of energy transfers between identical ions, the excitation can migrate in the lattice (Figure 4a). When there is no intermediate level between the emitting and ground states, concentration quenching is the consequence of *energy migration* to defects or impurities where the excitation is lost nonradiatively. Because of the broadening of emission and absorption bands, losses due to concentration quenching increase with rising temperature.

   For strong spectral overlap and high oscillator strengths, energy transfer can occur between distant ions. For Bi^{3+} in LaMgB$_5$O$_{10}$ (6s–6p transitions) the critical distance has been estimated to be 25 Å and concentration quenching starts at low Bi^{3+} concentrations, that is, above about

2%.[18] The arrangement of ions in the lattice in this case does not influence the migration. For ions like Eu^{3+} or Tb^{3+}, owing to the small oscillator strengths of the 4f–4f transitions involved in the transfer ($^7F_0$,$^7F_1$–$^5D_0$ for Eu^{3+} and $^7F_6$–$^5D_4$ for Tb^{3+}, Figure 9), transfer occurs mainly between nearest neighbors. The shape of the decay curves shows that the migration has the dimensionality of the assembly of coordination polyhedra with common corners.[12] In $EuMgB_5O_{10}$, the rare earth ions form a monodimensional assembly. The probability of energy transfer between the Eu^{3+} ions at 300 K has been estimated to be $10^7\,s^{-1}$ within the chains and $10\,s^{-1}$ between the chains.[19] A small amount of rare earth ions R^{3+} like Y^{3+}, La^{3+}, or Gd^{3+} in the chains is sufficient to inhibit energy migration to impurities. In solid solutions such as $Li_6\ Eu_xR_{1-x}(BO_3)_3$ or $MgEu_xR_{1-x}B_5O_{10}$, quenching appears only for x values close to unity.

2. *Cross-relaxation* is the main cause of concentration quenching for the lanthanide ions having a great number of 4f levels like Pr^{3+}, Nd^{3+}, Ho^{3+}, Er^{3+}, or Tm^{3+} (Figure 9). Some emission lines originating from an excited level are close in energy to absorption lines, hence part of the energy of the excited ion can be transferred to a neighbor ion. This is illustrated in Figure 4(b) by neodymium. When two Nd^{3+} ions occupy neighbor sites, an ion in the excited state $^4F_{3/2}$ can decay nonradiatively to the intermediate state $^4I_{15/2}$ by giving the corresponding energy to the second ion which is excited to the level $^4I_{15/2}$. Both ions then decay nonradiatively. The transfer is often phonon-assisted, that is, phonon absorption or emission compensates for small differences in energy between emission and absorption lines. The probability for energy transfer decreases with decreasing crystal field splitting of 4f levels. The effect of cross-relaxation is very pronounced. For instance about 50% of the ions excited in the levels $^3H_4$, $^1G_4$, or $^1I_6$ of Tm^{3+} in Y_2O_3 are depopulated nonradiatively for a concentration of 1%.[21]

2.4.3 Sensitization

Energy transfer is used for increasing luminescence efficiency. In photoluminescence, a high conversion yield requires a strong absorption of the excitation radiation. When the absorption properties of the activator at the excitation wavelength are insufficient, the luminescence yield can be improved by adding an ion, called sensitizer, which absorbs the excitation radiation more efficiently and transfers the energy to the activator. For instance, in green-emitting phosphors for low-pressure mercury-vapor lamps ($\lambda_{exc.} = 254\,nm$), Tb^{3+} is excited through the intense 4f → 5d absorption bands of Ce^{3+} and in YVO_4:Eu, the red phosphor for high-pressure mercury-vapor lamps ($\lambda_{exc.} = 365\,nm$), Eu^{3+} is excited via the CT transition of ${VO_4}^{3-}$ groups.[12]

2.4.4 Upconversion

If an ion possesses two excited states with approximately same energy separation, energy transfer can occur between two ions in the first excited state (Figure 4c). One ion returns nonradiatively to the ground state while the second is promoted to the second excited state, then decays with emission of a photon whose energy is about twice that of incident photons. There are other upconversion processes: two-step absorption, cooperative sensitization, cooperative luminescence.[22] Upconversion by energy transfer is the most efficient process.

2.5 Influence of the Host Lattice on the Position of the Emitting Level

The energy of the emitting level depends on the *nephelauxetic effect* and the *crystal field* at the luminescent-ion site.

The nephelauxetic effect is a reduction of the electrostatic interaction of the luminescent-ion electrons when the covalency of the bonds increases, resulting in a lowering of the position of the energy levels. This effect therefore increases with decreasing ligand electronegativity:

$$F < O < Cl < Br < S$$

The crystal field splitting increases with increasing charge and decreasing size of ligands:

$$O > S > F > Cl > Br > I$$

For the same ligand, the nephelauxetic effect and the crystal field depend on the following factors:

1. The ionic radius of the substituted cation M: the higher the size of M, the smaller the overlap of cationic and anionic orbitals and therefore the lower the nephelauxetic effect and the ligand field.
2. The coordination. Transition element ions are in general tetrahedrally or octahedrally coordinated. The ligand field is about twice lower for the fourfold coordination than for the sixfold one (*see* ***Ligand Field Theory & Spectra***). The coordination number of lanthanide ions varies from 6 to 12. The nephelauxetic effect and crystal field decrease with increasing coordination number.
3. The nature and number of other cations (M′) in the lattice: if the ligands form strongly covalent bonds with other atoms in the lattice, the bonds with the luminescent ion weaken, resulting in a decrease in nephelauxetic effect and ligand field interaction (inductive effect).[23] The higher the number of bonds formed by the ligand with M′ atoms, the stronger this effect. If the ligand–M′ bonds have a marked ionic character, the charge of the M cations reduces the field generated by the ligands.

Table 1 influence of the host lattice on the nature of the luminescence of Eu^{2+} in alkaline earth fluorides. A 4f → 4f emission is observed when the first $4f^6 5d$ states are above the first excited level of the $4f^7$ configuration at 27 800 cm^{-1}

Host	Coordination number	Lowest limit of the 4f → 5d absorption band (cm^{-1})	Nature of radiative transitions
CaF_2	8	24 200	5d → 4f
SrF_2	8	25 000	
BaF_2	8	25 500	
$BaMgF_4$	8	26 500	
$CaBeF_4$	8	26 600	
α-$SrBeF_4$	9	28 000	5d → 4f and 4f → 4f
$BaBeF_4$	10	29 000	
$BaLiF_3$	12	29 500	
BaY_2F_8	12	30 000	4f → 4f
$SrSiF_6$	12	31 000	
$BaSiF_6$	12	32 000	

The influence of these three factors is illustrated in Table 1 by the energy of the first 4f → 5d transitions in the excitation spectra of Eu^{2+}-doped alkaline earth fluorides. A smaller nephelauxetic effect and lower ligand field with increasing coordination number shift the lower 5d level to high energies. The splitting is particularly reduced for BaY_2F_8, $SrSiF_6$, and $BaSiF_6$ owing to the presence in the lattice of atoms with high oxidation state. This results in a change of the nature of the Eu^{2+} emission. In most host lattices, the nephelauxetic effect and crystal field splitting lowers the bottom of the 5d band well below the first excited level of the $4f^7$ configuration $^6P_{7/2}$, located at about 27 800 cm^{-1}, and similarly to Ce^{3+} (Figure 5), Eu^{2+} exhibits a 5d → 4f emission. This is not the case for BaY_2F_8 and the fluorosilicates. Excitation into a 5d state is followed by nonradiative deexcitation to the $^6P_{7/2}$ state which gives rise to a UV line emission. For fluoroberyllates and $BaLiF_3$, because of the proximity of the lowest 5d states with $^6P_{7/2}$, both the 5d → 4f band and the 4f → 4f lines are present in the emission spectra at 300 K.

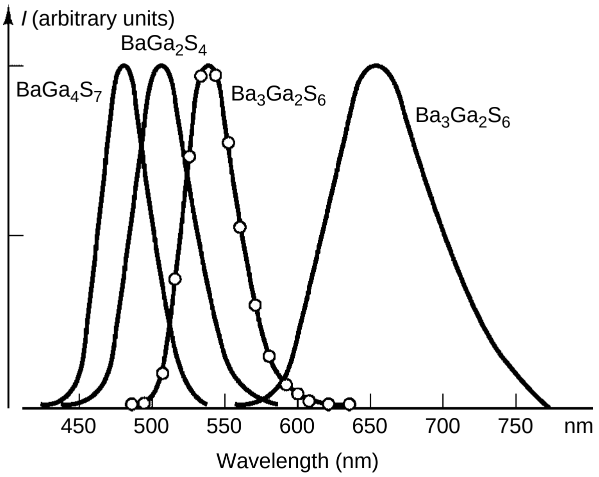

Figure 6 Spectral distribution of the Eu^{2+} emission in barium thiogallates.[24] The points on the $Ba_3 Ga_2S_6$:Eu band correspond to the calculation of the shape from the single-configurational-coordinate model. (Reproduced by permission of Ref. 4)

The effect of the number of covalent bonds formed by the ligand (point (3) above) is illustrated in Figure 6 by the shift of the emission band of Eu^{2+} in barium thiogallates. When phases with various MO/M'_xO_y or MS/M'_xS_y ratios exist (M = alkaline earth, M′ = B, Al, Ga, Si, etc.), the first 5d level of Eu^{2+} substituted for M tends to lower with increasing value of the ratio. This results in the case of barium thiogallates in a shift of the emission maximum from 480 nm, in the blue, for the Ga_2S_3-richest phase, to 655 nm, in the red, for the BaS-richest one.

3 MAIN FAMILIES OF LUMINESCENT IONS

Table 2 lists the main families of luminescent ions with representative lifetimes.

3.1 Transition Metal Ions

3.1.1 Ions with a Partly Filled nd Subshell

The number of states for the nd^N ($n = 3, 4, 5$) electronic configurations of transition metal ions is equal to the number of combinations $C_{10}{}^N$. Interelectronic repulsions partially remove the degeneracy, leading to the spectroscopic terms ^{2S+1}L with $(2S+1)(2L+1)$ degeneracy. In a lattice, the degeneracy of the ^{2S+1}L terms is partially removed by interaction with the crystal field. Figure 7 shows the effect of an octahedral field for the $3d^3$ and $3d^5$ configurations. For the d^3 ions, spin-allowed transitions can occur from the ground state, $^4A_{2g}$, to three excited states, $^4T_{2g}$, $^4T_{1g}(^4F)$, $^4T_{1g}(^4P)$. Chromium compounds are strongly colored as a result of absorption of light by the two lower-energy spin-allowed transitions. For d^5 ions like Mn^{2+}, all transitions are spin-forbidden since the subshell is half-filled, and light absorption is often too small to give rise to a discernible color.

A high probability of radiative deexcitation requires a large gap between a level and the next-lowest level (2.3). Excitation of transition element ions in a high-energy state is followed by nonradiative transitions between the different states down to the lowest excited state from which emission can occur if the energy separation with the ground state is high enough. This condition is fulfilled for Ti^{3+} (d^1), Cr^{3+}, Mn^{4+} (d^3), and Mn^{2+}, Fe^{3+} (d^5), which emit in the visible range.[15] Also Ni^{2+} can give an emission at 300 K, located in the IR.[25] At low temperature, V^{2+} (d^3) and Co^{2+} (d^7) show an infrared emission when incorporated in lattices with low phonon energies like halides and chalcogenides. For most ions,

Table 2 Main families of luminescent ions, nature of transitions, and order of magnitude of radiative lifetimes (values at 300 K, except for the charge transfer (CT) emission of Ce^{4+} and Yb^{3+} whose emission is affected by thermal quenching at room temperature)

Nature of ions	Transition	Δ l	τ (s)
Ti^{3+}, V^{2+}, Cr^{3+}, Mn^{2+}, Mn^{4+}, Fe^{3+}, Co^{2+}, Ni^{2+}	3d $\rightarrow$ 3d	0	10^{-5}–10^{-4} ($\Delta S = 0$) 10^{-3}–10^{-1} ($\Delta S = 1$)
Cu^+	4s $\rightarrow$ 3d	2 ($\Delta S = 1$)	10^{-5}–10^{-4}
Ag^+	5s $\rightarrow$ 4d	2 ($\Delta S = 1$)	10^{-6}–10^{-5}
In^+, Sn^{2+}, Sb^{3+}	5p $\rightarrow$ 5s	1 ($\Delta S = 1$)	
Tl^+, Pb^{2+}, Bi^{3+}	6p $\rightarrow$ 6s	1 ($\Delta S = 1$)	Bi^{3+} 10^{-6}–10^{-5}
Pr^{3+}, Nd^{3+}, Sm^{3+}, Eu^{3+}, Gd^{3+}, Tb^{3+}, Dy^{3+}, Ho^{3+}, Er^{3+}, Tm^{3+}, Yb^{3+}	4f $\rightarrow$ 4f	0	10^{-4}–10^{-2}
Ce^{3+}	5d $\rightarrow$ 4f	1	2–4.10^{-8}
Eu^{2+}			5.10^{-7}–10^{-6}
Oxyanions $MO_p{}^{q-}$ M = nd^0 transition metal ion, p: coordination number (4, 5, or 6)	O $\rightarrow$ M CT	($\Delta S = 1$)	
n = 3 titanate, vanadate			VO_4
n = 4 zirconate, niobate			VO_4^{3-} 10^{-3}
n = 5 hafnate, tantalate, tungstate			WO_4 $WO_4{}^{2-}$ 5.10^{-6}
Oxyanions of a lanthanide: Ln = Ce^{4+}, Yb^{3+}	O $\rightarrow$ Ln CT	(CeΔS = 1) (YbΔS = 0)	Ln = Ce 3–6.10^{-5} Ln = Yb 1–2.10^{-7}
Oxyanions of U^{6+}	O $\rightarrow$ U CT		

the first excited state corresponds to an electronic transition between orbitals of different symmetry, for instance, from a t_{2g} to e_g orbital in octahedral coordination. This causes a change in the equilibrium interatomic distances and the spectrum consists of a band (or at low temperature of a zero-phonon line corresponding to transitions between the m = 0 and n = 0 levels, accompanied by a broad vibronic band). The first excited states of d^3 ions in a strong crystal field, ^2E_g and $^2T_{1g}$ (Figure 7), like the ground state, arise from the t_{2g3} configuration. The change in equilibrium distance in this case is very small. Mn^{4+} ions exhibit a line emission in the deep red around 650 nm.[1] Depending on the strength of the crystal field, Cr^{3+} gives a band emission originating from $^4T_{2g}$ or a line emission from ^2E_g. The $^2E_g \rightarrow {}^4A_{2g}$ emission line of Cr^{3+} in the red is responsible for the laser emission of ruby (694 nm).[26] The luminescence band of crystals of Al_2O_3:Ti^{3+}, $BeAl_2O_4$:Cr^{3+}, $LiSrAlF_6$:Cr^{3+}, and V^{2+}, Co^{2+} or Ni^{2+}-doped fluorides such as MgF_2 permits tunable laser operation.[27]

For a d^5 ion, the energy of the luminescence transition, $^4T_1 \rightarrow {}^6A_1$, decreases with increasing crystal field (Figure 7). In oxide lattices, the emission of Mn^{2+} lies in the green for tetrahedral coordination (e.g. Zn_2SiO_4:Mn^{2+}, a phosphor for lamp, plasma display panel (PDP) or cathode ray tube (CRT) display, or $MgAl_2O_4$:Mn^{2+}) and in the red for octahedral coordination ($LaMgB_5O_{10}$:Mn^{2+} or $Cd_2B_2O_5$:Mn^{2+}).[1] Because of the low oscillator strengths of the f–f absorption bands, the luminescence is weak for excitation into these transitions. Mn^{2+} can be excited efficiently in the UV range by energy transfer from sensitizing ions such as Sb^{3+}, Bi^{3+}, Ce^{3+}, or Eu^{2+}, which have allowed transitions. In Zn_2SiO_4, Mn^{2+} possesses an intense absorption band below 300 nm allowing efficient direct excitation.[1] This band has been ascribed to a CT in which Mn^{2+} is involved. The luminescence transition being parity- and spin-forbidden, at low concentration the manganese emission exhibits long decay times, of the order of 10 ms in oxide hosts for tetrahedral coordination. In some host lattices such as Zn_2SiO_4, the decay becomes faster with increasing Mn concentration owing to the contribution of Mn^{2+} pairs to the luminescence. In pairs the oscillator strengths are increased by exchange interactions.[28] The decay time is one order of magnitude shorter than for isolated ions: 1.7 ms instead of 15 ms in Zn_2SiO_4 at 300 K.[29]

3.1.2 *d^{10} Ions*

The luminescence of the monovalent ions Cu^+ and Ag^+ is usually ascribed to $3d^94s \rightarrow 3d^{10}$ and $4d^95s \rightarrow 4d^{10}$ transitions, respectively.[15,30] In octahedral coordination the excited configuration d^9s is split into the levels ^3E_g, ^1E_g, $^3T_{2g}$, and $^1T_{2g}$. The emission originates from the lower state ^3E_g. The luminescence of isolated Cu^+ and Ag^+ ions lies in the UV in fluorides and in the blue or blue-green regions in alkaline earth sulfides.[31,32]

3.1.3 *Complexes of d^0 Ions – Charge Transfer Luminescence*

Oxides containing a nd^0 ion ($n = 3, 4, 5$) (titanates, vanadates, molybdates…) show an intense absorption band in the UV due to a CT transition, whose energy varies linearly with the corresponding ionization potential.[33] The first excited states are triplets ($S = 1$: the spin of the electron transferred

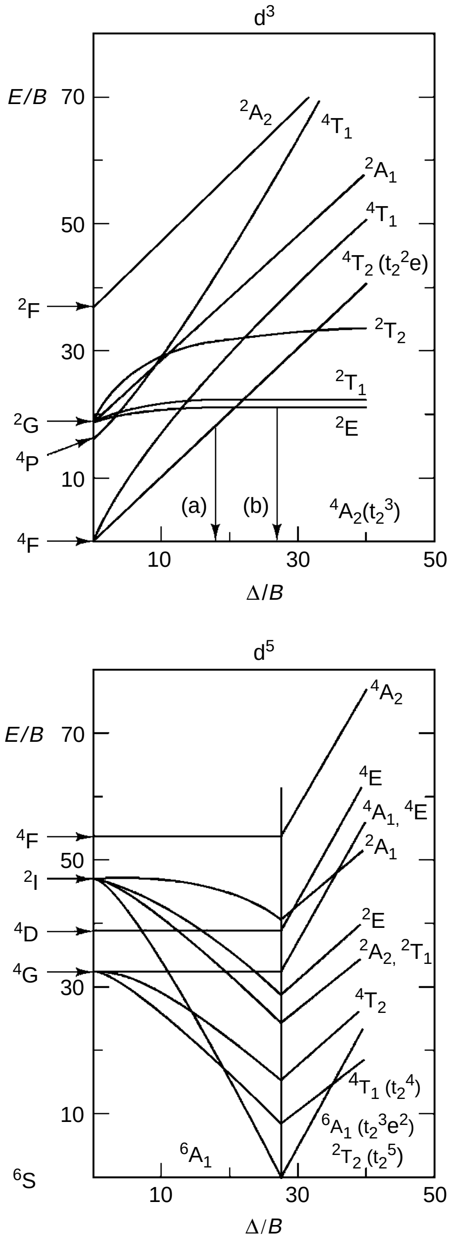

Figure 7 Crystal field splitting of the lower spectroscopic terms of d^3 and d^5 ions for octahedral coordination (Tanabe-Sugano diagrams): Δ, ligand field parameter; B, Racah parameter (for Cr^{3+} substituted for Al^{3+} in Al_2O_3, $\Delta = 17\,800\,cm^{-1}$ and $B = 665\,cm^{-1}$). Vertical arrows in the d^3 ion diagram represent radiative transitions: (a) band emission exhibited by V^{2+} and Cr^{3+} for low crystal field; (b) line emission shown by Cr^{3+} for high crystal field and by Mn^{4+}

onto a predominantly cationic molecular orbital is parallel to that of the unpaired electron on ligand MOs).[10] Transitions from the ground state $^1A_1$ to these levels are therefore spin-forbidden. The intense absorption bands correspond to transitions to higher-energy singlet states ($\Delta S = 0$). They lie at lower energy for octahedral groups than for the tetrahedral ones.[10]

Because of the strong variation of the equilibrium distance Δr, a radiative decay requires a high position of the emitting level (2.3.2). A high efficiency cannot be expected if the absorption bands extend to the visible. The emission of titanate, zirconate, vanadate, niobate, tantalate, tungstate groups can show high thermal stability. Emission occurs from the lower excited states ($\Delta S = 1$). Because of the large offset Δr, the Stokes shift is very high, 12 000 to 20 000 cm^{-1}, and the emission bands very broad, typically 4000–5000 cm^{-1}. The thermal stability and the Stokes shift depend strongly on composition and structure.[10] The presence in the lattice of cations forming relatively strong bonds like Mg^{2+}, Zn^{2+}, Ca^{2+}, and Y^{3+} is favorable, since they hinder displacements caused by the CT.[11] The Stokes shift is in general lower for octahedral than for tetrahedral coordination. Because of the absence of overlap between absorption and emission, often no concentration quenching occurs. An example is $CaWO_4$ which was used for many years in radiology.[34]

The selection rule $\Delta S = 1$ is partially relaxed by the spin-orbit coupling. The latter increases with the principal quantum number n. The lifetime is of the order of 10^{-3} s for tetrahedral vanadate groups and lowers to 15×10^{-6} s and 5×10^{-6} s (at 77 K) for $YNbO_4$ and $YTaO_4$, respectively.

3.2 Lanthanide ions

3.2.1 *Nature of Transitions*

Three types of transitions are responsible for the luminescence of lanthanide ions:

1. 4f–4f transitions. Trivalent lanthanide ions from Pr^{3+} ($4f^2$) to Yb^{3+} ($4f^{13}$) show a luminescence corresponding to transitions between levels of the $4f^N$ configurations. The number of states, $C_{14}{}^N$, can be very high. Interelectronic repulsions partially remove the degeneracy, leading to the spectroscopic terms ^{2S+1}L. Because of the shielding effect of the 5s and 5p electrons, the crystal field interaction with the 4f electrons is weak. The influence of spin-orbit coupling on the position of levels is much more pronounced (Figure 8). The splitting of the ^{2S+1}L levels into $^{2S+1}L_J$ levels ($(L-S) \leq J \leq (L+S)$) ranges from 2×10^3 to 5×10^3 cm^{-1} for the first elements of the series to more than 10^4 cm^{-1} for the last ones. Maximum values of the crystal field splitting of the $^{2S+1}L_J$ levels in oxides are of the order of 10^3 cm^{-1}. Spin-orbit coupling mixes states with the same J value. The wavefunctions are linear combinations of Russell–Saunders wavefunctions; S and L in the symbol $^{2S+1}L_J$ refer to orbitals providing the most important contribution. For a large admixture of states having different S values, the requirement $\Delta S = 0$ is relaxed. This is not, however, the case for the Eu^{3+} and Tb^{3+} transitions in the visible region, whose probability is reduced by a factor of about 10 (unlike other lanthanide

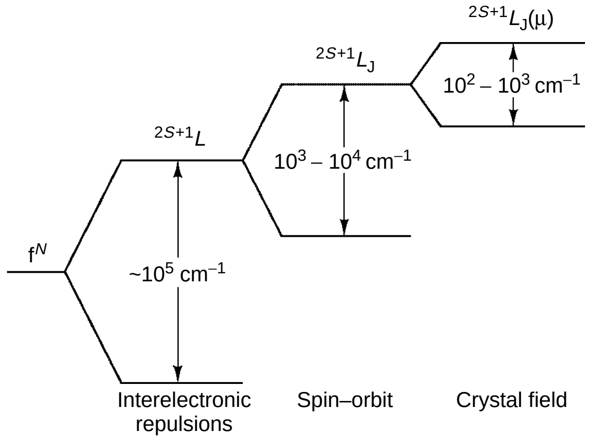

Figure 8 Splitting of rare earth energy levels owing to the interelectronic, spin-orbit, and crystal field interactions

ions having f–f transitions in this wavelength range, Eu^{3+} and Tb^{3+} are nearly colorless).

Figure 9 shows the energy level diagrams of trivalent lanthanide ions in LaF_3. Since the crystal field is a minor perturbation, the sequence of most $^{2S+1}L_J$ levels does not depend on the host.

2. 4f–5d transitions. The first excited configuration of rare earth ions is $4f^{N-1}5d$. The 4f → 5d absorption bands are very intense ($\Delta l = 1$). Figure 10 shows the energy difference between the lowest levels of the $4f^N$ and $4f^{N-1}5d$ configurations for the trivalent ions incorporated in CaF_2. The plot consists of two zig-zag curves having their maximum at $N = 7$ and 14 with slightly higher energy for $N + 7$ than for N. The variation reflects the influence of the spin-pairing energy. Only Ce^{3+} ($4f^1$), Pr^{3+} ($4f^2$), and Tb^{3+} ($4f^8$) exhibit absorption bands above 200 nm.[35] For the other cations, the 4f → 5d transitions

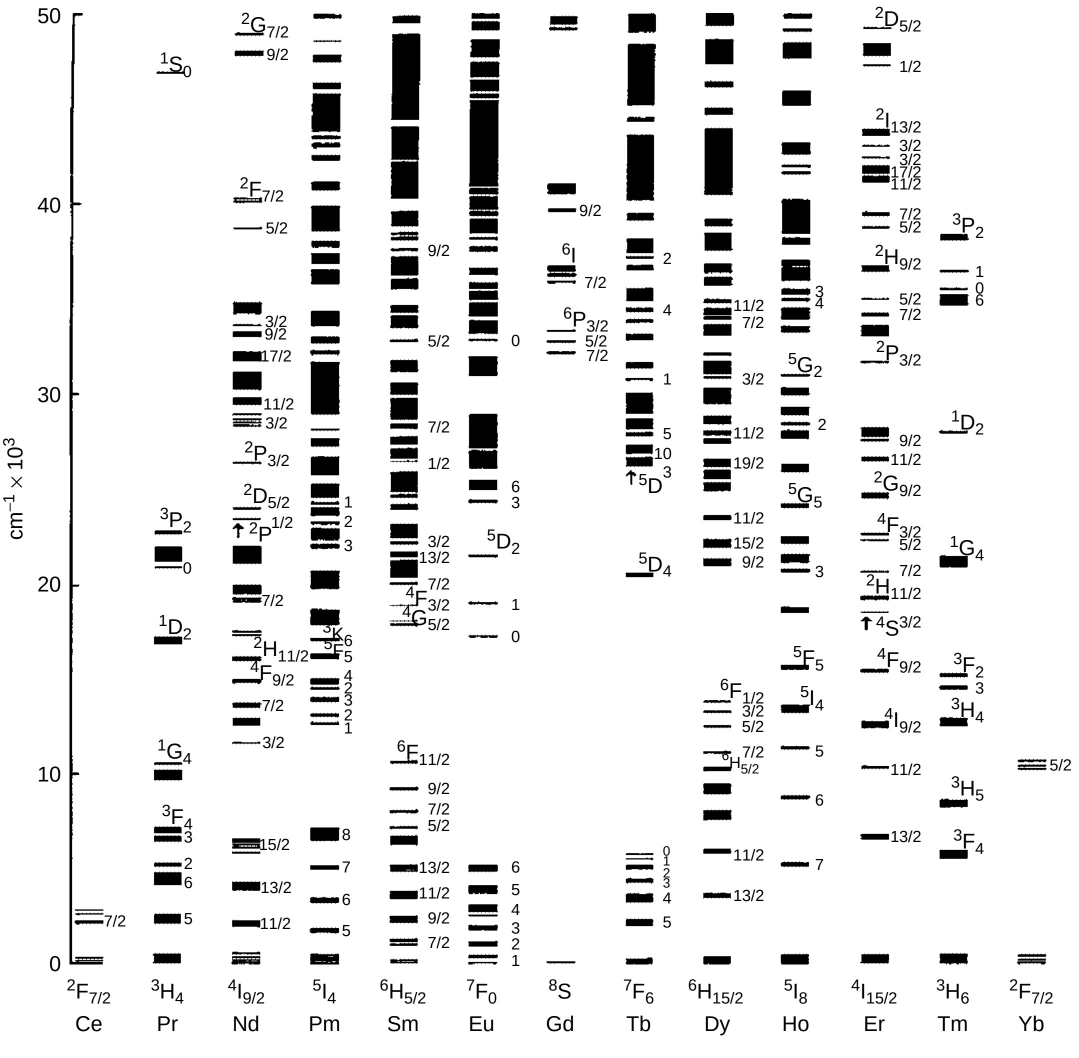

Figure 9 Energy level diagrams of lanthanide ions in LaF_3. (Reprinted with permission from W.T. Carnall, G.L. Goodman, K. Rajnak, and R.S. Rana, *J. Chem. Phys.*, 1989, **90**, 3443. © 1989 American Institute of Physics)

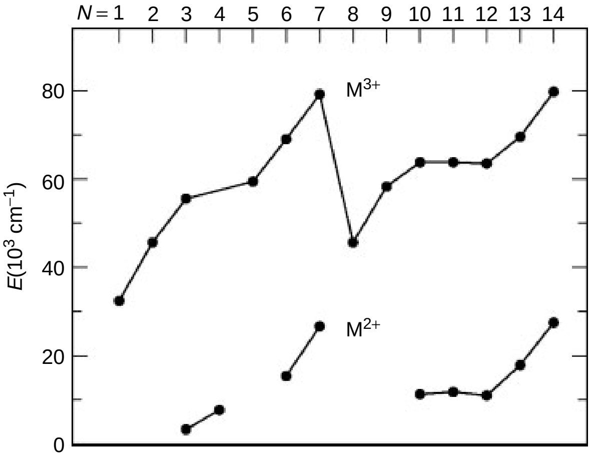

Figure 10 Energy difference between the lowest levels of the $4f^N$ and $4f^{N-1}5d$ configurations for divalent and trivalent lanthanide ions in fluorite. (Reproduced by permission of Ref. 37)

are located in the VUV and hence can be observed essentially in fluorides.[35,36]

The energy of 4f → 5d transitions is much lower for divalent ions (Figure 10). For the most stable ions, Eu^{2+} ($4f^7$) and Yb^{2+} ($4f^{14}$), the corresponding absorption bands in oxide or fluoride hosts most often lie in the UV range.

3. CT transitions: electron transfer can occur from the highest filled ligand MOs to the partly filled 4f shell. As a consequence of the gain in spin-pairing energy, ions with a nearly half-filled or filled 4f shell have the higher oxidizing character. In the case of trivalent ions, the energy of the CT transition increases according to the sequence.

$$Eu^{3+}(4f^6) < Yb^{3+}(4f^{13}) < Sm^{3+}(4f^5) < Tm^{3+}(4f^{12})$$

The position of the CT band shifts to longer wavelengths with decreasing electronegativity of the ligand. Typical values of the energy of the absorption band maximum of Eu^{3+} are: 30 000–34 000 cm^{-1} in oxysulfides and oxybromides, 33 000–35 000 cm^{-1} in oxychlorides, 37 000–45 000 cm^{-1} in oxides, and around 65 000 cm^{-1} in fluorides.[38]

3.2.2 4f → 4f Emission

Relaxation from a high-energy level of the $4f^N$ configuration occurs by multiphonon transitions between closely spaced levels down to a level whose energy gap to the next-lower level is wide enough to allow radiative decay (Section 2.3).

The radiative rate is increased by covalency, which causes admixing of states of opposite parity. The excited-state lifetime becomes shorter with decreasing ligand electronegativity, as shown below for the $^4F_{3/2}$ emission of neodymium:

Host	LaF_3	Y_2O_3	$LaCl_3$	γ-La_2S_3
τ(μs)	700	260	220	60

The wavelength range of luminescence transitions within the $4f^N$ configurations extends from the infrared to the ultraviolet.

UV and Visible Emisssions. A large energy gap exists for ions in the middle of the series of trivalent lanthanide ions (Figure 9). In oxides, the probability for radiative decay is nearly unity for Eu^{3+} ($^5D_0$) (red emission), Gd^{3+} ($^6P_{7/2}$) (UV) and Tb^{3+} ($^5D_4$) (green). It is also very high for Pr^{3+} ($^1D_2$) (red), Sm^{3+} ($^4G_{5/2}$) (orange), Dy^{3+} ($^4F_{9/2}$) (whitish or yellow), and Tm^{3+} ($^1I_6$) (UV) and ($^1D_2$, $^1G_4$) (predominantly blue). Water molecules are particularly detrimental for luminescence owing to the high vibrational frequencies (3500 cm^{-1}). However, because of the large energy gap, Gd^{3+} and to a lesser extent Tb^{3+} show high efficiency, even in aqueous solution or in hydrates:[38]

Ion:	Gd^{3+} ($^6P_{7/2}$)	Tb^{3+} ($^5D_4$)	Eu^{3+} ($^5D_0$)	Sm^{3+} ($^4G_{5/2}$)	Dy^{3+} ($^4F_{9/2}$)
Energy gap (cm^{-1}):	32 000	14 500	12 000	7000	7000
Efficiency (%):	100	70	10	≈1	≈1

Concentration quenching of the $Eu^{3+5}D_0$ and $Tb^{3+5}D_4$ emissions occur by energy migration to defects. This process starts at relatively high activator concentrations, for instance, for $x = 0.07$ and 0.15 respectively in the solid solutions $Y_{2(1-x)}Eu_{2x}O_3$ and $Y_{1-x}Eu_xBO_3$.[39] Because of the possibility of high dopant concentration, high luminescence efficiencies can be achieved under UV, VUV, or electron beam excitation. Short-wavelength UV radiation can be wholly absorbed by the CT band of Eu^{3+}. The CT induces a large offset Δr (Figure 2b). Hence a high position of the CT state is necessary for avoiding nonradiative transitions to the fundamental multiplet ^7F_J ($J = 0$–6). The position of the CT absorption band tends to lower with increasing coordination of the Eu^{3+} ion and for a same coordination number with increasing radius of the substituted cation.[40] The CT band lies at markedly longer wavelength in lanthanum compounds than in gadolinium or yttrium compounds. The energy of the transition depends also on the nature of the bonds formed by the ligand with other elements of the matrix. In oxides, the highest energies are observed when the oxygen atoms surrounding europium belong to covalent groups such as $(BO_4)^{5-}$ or $(PO_4)^{3-}$. The quantum efficiency of the luminescence of Eu^{3+} is near unity for excitation in the CT band of YBO_3: Eu and YPO_4: Eu, located in these lattices at very short wavelength (maximum at 220 nm). At longer wavelengths, Eu^{3+} can be efficiently excited by energy transfer from oxidizing groups such as the titanate, vanadate, tungstate groups, possessing CT bands. Tb^{3+} can be efficiently excited into its parity-allowed $4f \rightarrow 5d$ transitions below 250 nm (Figure 1) or by energy transfer from Ce^{3+}, as in the case of the lamp phosphors $CeMgAl_{11}O_{19}$:Tb, $LaPO_4$:Ce,Tb, and $GdMgB_5O_{10}$:Ce,Tb.[1,12]

The spectral distribution of the Eu^{3+} emission is very sensitive to the site symmetry. An example of interest for lighting or display application is that of the influence of a center of symmetry. Figure 11 shows the emission spectra of this ion in two oxides with crystal structures related to NaCl:$NaInO_2$, and $NaGdO_2$. The $^5D_0 \rightarrow {}^7F_1$ transitions around 590 nm have magnetic dipole character; the $^5D_0 \rightarrow {}^7F_2$ transitions in the 610–630 nm range have electric dipole character and are allowed only if the site lacks a center of symmetry. Minor differences in the structural characteristics induce large differences in emission spectra. The site of the trivalent ion in $NaInO_2$, of α-$NaFeO_2$ structure type, is centrosymmetric; the spectrum consists essentially of the $^5D_0 \rightarrow {}^7F_1$ transitions in the orange region of the visible spectrum; weak broad lines in the range of the $^5D_0 \rightarrow {}^7F_2$ transitions are due to vibronic transitions. The site of the rare earth ion in $NaGdO_2$, of α-$LiFeO_2$ structure type, lacks an inversion center. Since the radiative rate of electric dipole transitions is much higher than that of magnetic dipole transitions, the $^5D_0 \rightarrow {}^7F_2$ emission is predominant. Such is the case for the red-emitting phosphors YVO_4: Eu, Y_2O_3: Eu, and Y_2O_2S:Eu.[1]

The luminescence of other luminescent ions emitting in the visible, Pr^3, Sm^{3+}, Dy^{3+}, Tm^{3+} is most often affected by cross-relaxation processes at low activator concentration (2.4.2).

Two visible photons per UV photon can be obtained by a cascade process with Pr^{3+}. In lattices generating a low crystal field, the lowest 5d states lie above the highest level of the configuration $4f^2$, $^1S_0$ (Figure 9), which decays radiatively by the transition $^1S_0 \rightarrow {}^1I_6$, followed by a nonradiative transition to $^3P_0$ from which a second photon is emitted when the phonon energies are sufficiently low.[42] Two photons per UV photon absorbed can also be obtained in Eu-doped Gd fluorides. Excitation of Gd^{3+} into the ^6G_J levels around 50 000 cm^{-1} is followed by two successive energy transfers to Eu^{3+} ions which are promoted to the $^5D_0$ state.[43]

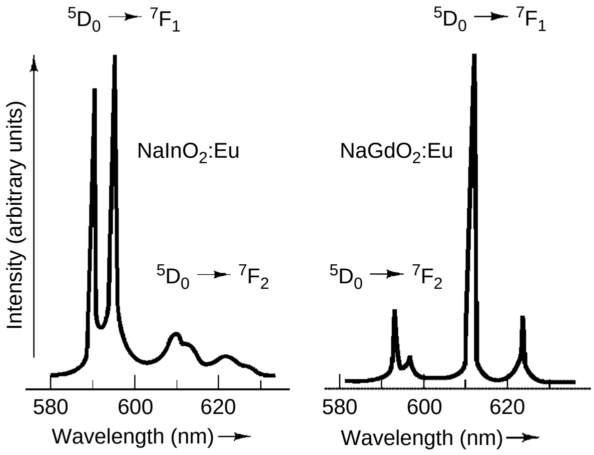

Figure 11 Emission spectrum of Eu^{3+} substituted for the trivalent ion in $NaInO_2$ and $NaGdO_2$. (Reproduced by permission of Ref. 41)

Ions such as Ho^{3+} or Er^{3+} can decay radiatively from levels in the visible range in halide or sulfide hosts. This is the case, for instance, for the green-emitting level $^4S_{3/2}$ of Er^{3+} in fluorides.[44,45] With Ho^{3+}, Er^{3+}, and Tm^{3+} IR radiation can be converted to visible by upconversion (2.4.4). Only a small amount of doping ions can be introduced without concentration quenching. The absorption in the IR around 0.98 nm is increased by codoping with ytterbium which can be incorporated in large quantity since its excited state, $^2F_{5/2}$, is not affected by cross-relaxation processes. The proximity of the position of the $Yb^{3+2}F_{5/2}$, and $Er^{3+4}I_{11/2}$ levels allows energy transfer.[22,45]

IR emission. The $^4F_{3/2}$ level of Nd^{3+} (Figure 4) is separated from the lower-lying level by 5000 cm^{-1}, a gap generally large enough for inhibiting nonradiative processes, except in borate glasses where vibrational frequencies exceed 1300 cm^{-1}. The most intense transition from this level is $^4F_{3/2} \rightarrow {}^4I_{11/2}$ at about 1.06 µm. Laser radiation can be obtained by pumping into the numerous absorption transitions in the visible. In most lattices with increasing Nd concentration, the luminescence is strongly affected by cross-relaxation processes (Figure 4) and disappears nearly completely at high concentrations. The overlap between emission and absorption lines decreases with decreasing crystal field splitting of the J levels. For a few neodymium compounds, as shown by the comparison of the lifetimes of the emitting state $^4F_{3/2}$ (Table 3), the quantum efficiency is only reduced by a factor of about 2.5 in the nondilute material. For such lattices the crystal field is particularly low, as indicated by the splitting of the ground state, $\Delta E(^4I_{9/2})$ (Table 3). A criterion for low quenching is that ΔE must be lower than 470 cm^{-1}.[46] This is observed in phosphates or borates rich in covalent groups. In addition, the neodymium coordination polyhedra must have no common apices. Owing to the high

Table 3 Minimum Nd–Nd distance, splitting of the ground state $^4I_{9/2}$, and ratio of the luminescence lifetimes for $x = 1$ (τ) and $x = 0.01$ (τ_0) for (a) Low or (b) High concentration quenching neodymium materials ($1/\tau = 1/\tau_0 + W_{nr}$ where W_{nr} is the rate of nonradiative decay due to concentration quenching)[46]

	Composition	Nd–Nd distance (Å)	$\Delta E(^4I_{9/2})$ (cm^{-1})	τ/τ_0
(a)	$LiLa_{1-x}Nd_xP_4O_{12}$	5.94	375	0.42
	$La_{1-x}Nd_xAl_3B_4O_{12}$	5.91	410	0.40
	$La_{1-x}Nd_xP_5O_{14}$	5.19	320	0.36
(b)	$NaLa_{1-x}Nd_xO_2$	3.59	619	<0.03
	$Y_{3(1-x)}Nd_{3x}Al_5O_{12}$	–	857	–

neodymium concentration, with crystals of phosphates like NdP_5O_{14}, laser emission can be achieved for a low pumping threshold.[47]

The large gap between the levels $^4F_{5/2}$ and $^4F_{7/2}$ of Yb^{3+} ($10\,000\,cm^{-1}$) prevents nonradiative decay. Because of the absence of intermediate levels the concentration of Yb^{3+} can be very high. Hence powerful compact lasers can be obtained with diode-pumped Yb^{3+}-doped materials.[48,49]

Laser emissions over the 1–5 μm wavelength range are obtained with Dy^{3+}, Ho^{3+}, Er^{3+}, Tm^{3+}.[50,51]

3.2.3 5d → 4f Emission

After excitation into one of the 5d states the lanthanide ion relaxes by nonradiative transitions to the lowest-energy one from which emission can occur if there is a large energy gap with the ground or excited 4f levels. This condition is fulfilled by Ce^{3+} ($4f^1$), Yb^{2+} ($4f^{14}$) and generally Eu^{2+} ($4f^7$) (Section 2.5). Also Pr^{3+} ($4f^2$) exhibits a 5d → 4f emission, located mainly in the UV, when the nephelauxetic effect and crystal field splitting lower the first 5d state below the $^1S_0$ ($4f^2$) level at $47\,000\,cm^{-1}$.[52] 5d → 4f emissions in the VUV are observed for Nd^{3+}, Er^{3+} and Tm^{3+} in fluorides.[36,53]

A second requirement for luminescence is that the lowest 5d state is located under the conduction band. Ce^{3+}, Eu^{2+}, Yb^{2+} can easily take the upper oxidation state. The 4f ground state of Ce^{3+} lies well above the valence band, $20\,000\,cm^{-1}$ in $Y_3Al_5O_{12}$.[54] In this lattice, Ce^{3+} exhibits an intense emission for excitation in the first 5d level. Excitation in the higher 5d levels is much less efficient because these levels can be depopulated by electron transfer to the conduction band (photoionization process). The absence of luminescence in La_2O_3, Y_2O_3, and Lu_2O_3 is ascribed to the fact that all 5d levels, as shown by photoconductivity measurements, lie in the conduction band.[55] In oxide lattices, Ce^{3+} exhibits high efficiency for band gaps exceeding $50\,000\,cm^{-1}$ ($\lambda = 200\,nm$). Likewise the luminescence of Eu^{2+} has been observed in borates, aluminates, silicates, phosphates, and not in gallates and germanates, which have smaller band gap. In the fluorides CaF_2 and SrF_2, Eu^{2+} exhibits a 5d → 4f blue emission. This is not the case in BaF_2. All the 5d states being in the conduction band, irradiation in the 4f → 5d absorption bands causes ionization with the formation of an exciton-like state: the electron is held on neighbor barium ions in the Coulomb field of the Eu^{3+} ion.[56] At low temperature, the electron-Eu^{3+} recombination yields a yellow emission.

Because of their interest for applications, the luminescence of Ce^{3+} and Eu^{2+} has been investigated in a great number of compounds.

1. Ce^{3+}: The energy of the emitting 5d level lowers with increasing nephelauxetic effect and crystal field splitting Δ_{cryst} (Figure 5). The positions of the shorter-energy 4f → 5d absorption band and the emission band published for Ce^{3+} in inorganic compounds have been collected in Ref. 57. The Stokes shift of the Ce^{3+} emission is usually moderate, of the order of $2000–4000\,cm^{-1}$. In fluorides, the Ce^{3+} emission is generally located in the UV around 300 nm. In most oxides, the emission peaks in the UV, between 300 and 400 nm. The shorter wavelengths are observed for B-rich borates ($LaMgB_5O_{10}$, GdB_3O_6) and P-rich phosphates (LaP_3O_9, $LiLaP_4O_{12}$). In these lattices, the ionicity of the Ce–O bond is enhanced and the crystal field reduced by the covalent bonds formed by the ligands with B or P. In the garnets such as $Y_3Al_5O_{12}$:Ce^{3+}, the lower 5d state lies exceptionally in the visible, leading to a yellow emission. In sulfides, the nephelauxetic effect shifts the emission to the visible. In most hosts, concentration quenching starts for a cerium content of a few percents. However, in a few host lattices, owing to a strong Stokes shift (ΔE_{St}) nearly no concentration quenching occurs up to complete substitution of Ce for the host cation. This is the case in $LaMgAl_{11}O_{19}$ ($\Delta E_{St} = 7000\,cm^{-1}$) and LaF_3 ($\Delta E_{St} = 5000\,cm^{-1}$).
   The radiative lifetime varies between 15 and 60 ns. For comparable refractive indices, the lifetime increases with increasing wavelength of the peak emission (Section 2.1): $\tau = 18\,ns$ for $YAlO_3$:Ce with $\lambda_{em.} = 362\,nm$, $\tau = 62\,ns$ for $Y_3Al_5O_{12}$:Ce with $\lambda_{em.} = 550\,nm$.[4] For emission in the same wavelength range, τ varies according to: sulfides < oxides < fluorides.
2. Eu^{2+}: The emission of Eu^{2+} is shifted to the red compared with that of Ce^{3+}. For the same host lattice, the position of the emitting level is lowered by about $3000\,cm^{-1}$.[58] In oxide lattices, the position of the emission band shows considerable variations. For instance, in the Sr-rich borate $Sr_3(BO_3)_2$ the band peaks in the orange (585 nm) while in SrB_4O_7 because of the weak nephelauxetic effect and low crystal field the emission lies in the UV (367 nm).[59] Eu^{2+} is usually substituted for an alkaline earth ion M. The larger the size of M, the smaller the ligand field splitting of the 5d states and hence the higher the position of the emitting level. Higher energy of the 5d emitting state and often smaller offset Δr result in a higher thermal stability of the 5d → 4f emission when the size of M increases as shown, for instance, by the thermal quenching of structurally related silicates or borophosphates.[3,60,61] Phonon energies also appear to influence the stability: while in various aluminates or silicates Eu^{2+} exhibits a blue or green emission whose quenching starts above 300 K (e.g. the blue phosphor $BaMgAl_{10}O_{17}$: Eu),[62] in borates the luminescence is generally strongly affected by nonradiative losses at this temperature when the emission lies in the visible.[59,63]

When the lanthanide ion is surrounded by voluminous polarizable anions like chloride, bromide, or sulfide ions, the Stokes shift is generally small. At low temperature, a zero-phonon line is present in absorption and emission spectra, in addition to the band corresponding to transitions involving absorption or emission of phonons (vibronic transitions). Low phonon energies and small offset Δr result in high thermal stability. For example, in the sulfides CaS and SrS, despite the low position of the emitting state (the lowest-energy absorption band, $4f \rightarrow 5d(t_{2g})$, covers most of the blue and green regions of the visible spectrum, inducing a red or orange color, respectively), quenching starts above room temperature.[64]

The fluorescence lifetimes are around 1 µs.[3] Because the $4f^6 5d$ emitting level contains octets and sextets, the radiative rate of transitions to the ground state $^8S_{7/2}(4f^7)$ is reduced compared with the $5d \rightarrow 4f$ transitions of Ce^{3+}.

3.2.4 *Charge Transfer Emission*

1. Yb^{3+}: When excited in its CT band, located around 200 nm in oxide lattices, Yb^{3+} exhibits an emission consisting of two bands corresponding to transitions from the CT state to the $^2F_{7/2}$ and $^2F_{5/2}$ $(4f^{13})$ states, separated by $10\,000\ \mathrm{cm^{-1}}$.[65] The Stokes shift is very high, of the order of $15\,000\ \mathrm{cm^{-1}}$.
2. Ce^{4+}: A CT luminescence has been observed for tetravalent cerium in Sr_2CeO_4. This compound shows a blue-white luminescence partially quenched at 300 K.[66]

3.3 Ions with s^2 Configuration

The A elements of the last rows of the periodic table give rise to stable ions having a pair of s electrons (e.g. Tl^+, Pb^{2+}, Bi^{3+}). The excited energy levels corresponding to the transfer of an electron onto a p orbital are indicated in Figure 12. The spin-allowed $^1S_0 \rightarrow {}^1P_1$ transition is the most intense (f close to 1). As a result of strong spin-orbit coupling, the spin selection rule for the $^1S_0 \rightarrow {}^3P_1$ transition is considerably relaxed ($f = 0.1$). This is illustrated in Figure 12 by the excitation spectrum of the Tl^+ emission in KF.[67]

At low temperature, the emission originates from the lowest excited level, $^3P_0$, and is therefore characterized by a long lifetime, of the order of 1 ms. As the temperature is increased, the $^3P_1$ level becomes populated, emission from this level becomes dominant, and the lifetime drops to values of a few µs.

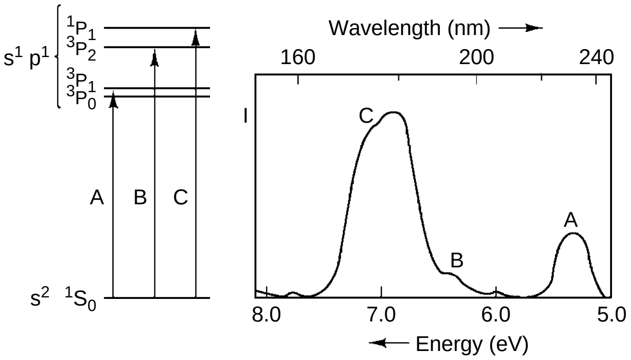

Figure 12 Excitation spectrum of the luminescence of Tl^+ in KF (variation of the emission intensity as a function of the excitation wavelength). (Reproduced by permission of Ref. 67)

Table 4 Influence of the size of the site occupied by the Sb^{3+} or Bi^{3+} ion on the Stokes shift of the $np \rightarrow ns$ emission[68,69]

Host	Substituted cation radius (Å)	Coordination number	Stokes shift ($\mathrm{cm^{-1}}$) Sb^{3+}	Stokes shift ($\mathrm{cm^{-1}}$) Bi^{3+}
$ScBO_3$	0.745	6	7 900	1800
$LuBO_3$	0.861	6	10 700	2300
YBO_3	0.900	8	14 000	5200
		8	16 300	7700
$GdBO_3$	0.938	8	14 500	–
		8	16 400	–
$LaBO_3$	1.216	9	19 500	9300

The Stokes shift of the $np \rightarrow ns$ emission is strongly host-dependent with variations from 1000 to $20\,000\ \mathrm{cm^{-1}}$.[12] Table 4 lists the values observed for Sb^{3+} and Bi^{3+} in trivalent orthoborates. The Stokes shift increases with the size of the substituted cation, M. This has been ascribed to the trend of s^2 ions to occupy an off-center position. When an electron is transferred onto a p orbital, the ion moves to a more central position. A voluminous site allows large displacements, resulting in high Stokes shift values. The lower the size of the s^2 ion, the larger the atomic shift. Table 4 shows that the Stokes shift is considerably higher for Sb^{3+} (radius $r = 0.76$ Å in VI coordination) than for Bi^{3+} ($r = 1.03$ Å). A larger offset Δr with increasing M size causes stronger thermal quenching.[68,69]

4 DONOR–ACCEPTOR TRANSITIONS

This type of transition has been extensively investigated in ZnS doped with a monovalent d^{10} cation (Cu^+, Ag^+, Au^+) (usually called the activator) and a trivalent ion such as Al^{3+} (coactivator) substituted for divalent zinc. The coactivator can also be Cl^- substituted for S^{2-}. The monovalent cations create deep acceptor states, Al^{3+} or Cl^- form shallow donor levels (0.1 eV for Al) (Figure 13). When electrons are transferred from the valence to the conduction band, for instance, under electron beam irradiation, they are trapped by the coactivator while holes formed in the valence band are captured by Cu^+ or Ag^+, which are oxidized to the divalent state. The energy of the photons emitted depends on the energy difference between the donor and acceptor levels and on the acceptor–donor distance:[70]

$$E = E_g - (E_A + E_D) + \frac{e^2}{K r_{D-A}} \qquad (12)$$

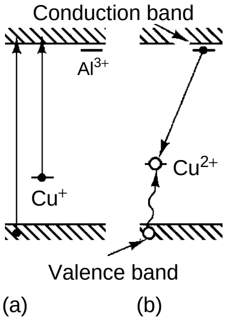

Figure 13 Schematic representation of the mechanism of the green luminescence of ZnS:Cu,Al

where E_g is the band gap of the lattice (3.8 eV for the hexagonal form of ZnS), E_D and E_A are the depths of the donor and acceptor levels, respectively; e the electronic charge, r_{D-A} the intrapair separation, and K the static dielectric constant. The emission band is composed of the emissions produced by the different pairs. The Ag^{2+} and Cu^{2+} levels lie at 1 and 1.4 eV above the top of the valence band respectively. If the monovalent and trivalent ions are incorporated in equal concentration, the donor–acceptor transitions give rise to a band emission in the blue with Ag^+ and in the green with Cu^+. The emission can be displaced to longer wavelengths by decreasing the band gap by substitution of cadmium for zinc. Because the average distance between the trapped electrons and the Ag^{2+} or Cu^{2+} ions decreases, the peak of the emission band shifts toward higher energies with increasing excitation intensity.

The probability of the donor–acceptor transition decreases with increasing intrapair separation:**[70]**

$$W(r_{D-A}) = W_0 \exp\left(\frac{-(r_{D-A})}{R_B/2}\right) \tag{13}$$

where W_0 is a constant and R_B is the Bohr radius of the shallower state. Consequently since the emission band is composed of the emission bands of donor-acceptor pairs with different separations, a donor–acceptor type emission shows the following characteristics:

- the decay rate becomes faster with increasing photon energy in the emission band;
- the emission band shifts to lower energies during the decay (t-shift).

5 EXCITATION THROUGH THE HOST LATTICE

5.1 Excitation in the UV or VUV

The excitation mechanism consists of electron transitions from the valence to conduction band of the lattice followed by transfer of the electron–hole (e–h) recombination energy to luminescent ions. The electron transferred into the conduction band can be bound to the hole formed in the valence band by coulombic interaction, forming an exciton which can propagate in the lattice up to luminescent ions. The quantum efficiency is generally maximum when the wavelength of incident photons corresponds to energies close to the band gap.**[71]** The efficiency decrease at shorter wavelengths has been ascribed to two causes: (i) the dissociation of e–h pairs, (ii) the decrease of the penetration depth with increasing absorption coefficient, resulting in surface losses. In plasma display panels, phosphors are excited by a Xe-discharge. The Xe spectrum consists of a line at 147 nm and a band centered at 172 nm. Under these excitation conditions, the most efficient materials are $BaMgAl_{10}O_{17}$:Eu^{2+} for the blue, Zn_2SiO_4:Mn^{2+} for the green, Y_2O_3:Eu^{3+} or (Y,Gd)BO_3: Eu^{3+} for the red.**[1,71]**

5.2 Cathodoluminescence

Within the material, the incident electron loses its energy by generating e–h pairs or optical phonons.**[72]**

The efficiency of the process can be written as

$$\eta_{cr} = (1 - r_b).\left(\frac{h\nu_m}{\varepsilon}\right).\eta_t.\eta_r \tag{14}$$

where r_b is the primary back-scattering coefficient, $h\nu_m$ the mean energy of luminescent photons, ε the average energy required to generate one e–h pair, η_t the efficiency for transfer of the e–h recombination energy to luminescent ions, and η_r the quantum efficiency of the activator emission. The back-scattering coefficient increases with the average atomic number of the material atoms.

In efficient materials, η_t and η_r are close to unity. ε depends on the host band gap and phonon energies:

1. ε increases with increasing band gap. For high efficiency, the band gap must be slightly larger than the energy of the photons emitted (with, however, large enough energy separation between the excited state of the luminescent ion and the bottom of the conduction band to prevent ionization). ZnS with a band gap of 3.8 eV is most appropriate for emission in the visible. On the contrary, a high efficiency in this spectral region cannot be expected from fluorides since these materials are characterized by wide band gaps.
2. ε increases with increasing energy of the phonons created. Sulfides are more favorable than oxides regarding this characteristic.

Table 5 indicates the order of magnitude of energy efficiencies, η_{cr}, of various phosphors for accelerating voltages of 20–30 kV.**[71,73,74]** With sulfides, energy yields of 20% can be achieved; with oxides the highest value is

Table 5 Energy efficiencies, η_{cr}, of cathodoluminescent materials

6–9%	Zn_2SiO_4:Mn, YVO_4:Eu, Y_2O_3:Eu, $Y_3(Al,Ga)_5O_{12}$:Tb, $InBO_3$:Tb, Y_2SiO_5:Tb, $Y_3Al_5O_{12}$:Ce
11–14%	Y_2O_2S:Eu, Gd_2O_2S:Tb, LaOBr:Tb
15–20%	ZnS:Cu,Al, ZnS:Ag,Cl, CaS:Pb, CaS:Ce

9%. Intermediate values are obtained with oxysulfides and oxybromides.

The luminescence can be of the donor–acceptor type. This is the case for ZnS:Ag,Cl and ZnS:Cu,Al used for the blue and green components of TV screens. At low electron beam current density, the intensity of the green phosphor is maximum for Cu concentrations of about 10^{-2} mole %.[74]

For other efficient materials, the luminescence is due to intraatomic transitions. After trapping of a charge carrier by the doping ion, a carrier with opposite charge is attracted, so that electron–hole recombination occurs at the activator site. It has been shown that ions that can change their oxidation state are favorable for high η_t values.[75] Among trivalent lanthanide ions, Ce^{3+} ($4f^1$) and Tb^{3+} ($4f^8$) are hole-trapping centers, whereas Eu^{3+} ($4f^6$) preferentially binds an electron to achieve the half-filled shell structure. In contrast, Gd^{3+} ($4f^7$) forms no stable bound state.

It must be stressed that the criterion for display application is the value of the luminous efficiency, which takes into account eye response. For instance, in the red spectral region (above about 600 nm), eye sensitivity decreases rapidly with increasing wavelength.[12] Despite lower-energy yield, Y_2O_2S:Eu, the red-emitting phosphor used in television screens, has higher luminous efficiency than the copper-doped solid-solution $Zn_{1-x}Cd_xS$ giving similar color, because the major part of the emission is concentrated near the lower limit of the red region.

To obtain high luminance (for instance, for projection television), a high current density of the incident electron beam is necessary.[12,73] Under these conditions, the luminous efficiency of the oxysulfides Y_2O_2S:Eu, Gd_2O_2S:Tb and the sulfides ZnS:Ag,Cl, ZnS:Cu,Al drops. For the oxysulfides, this is due to thermal quenching caused by the temperature rise of the screen.[1] For the ZnS phosphors, this has been ascribed in part to activator depletion, especially at very low activator concentration, and to excited-state absorption and Auger processes.[12,74] In contrast, the current density dependence of the luminescence intensity is close to linearity up to very high values for various oxides such as Zn_2SiO_4:Mn, $InBO_3$:Tb or $Y_3(Al,Ga)_5O_{12}$:Tb for the green and Y_2O_3:Eu for the red. Higher luminous efficiencies can therefore be obtained with these materials than with sulfides.

High current densities are also required in low-voltage field emission displays (300 V to a few kV). The phosphors must have low threshold voltage and some electrical conductivity. Efficient materials under these excitation conditions are $SrGa_2S_4$:Ce for the blue, $SrGa_2S_4$:Eu, Gd_2O_2S:Tb and $Y_3Al_5O_{12}$:Tb for the green, and Y_2O_2S:Eu for the red.[76,77]

5.3 X-ray-excited Luminescence

The mechanisms of X-ray-excited luminescence are similar to those of cathodoluminescence. Conventional radiographs are produced by combination of a photographic film and an intensifying screen, which converts X rays to photons whose wavelength is located in the high-sensitivity region of the film. The luminescent powders used in intensifying screens must show high absorption at the energy of the X rays used (typically in radiology of the order of 50 keV). $CaWO_4$ has long been used. Since 1970, new X-ray phosphors with higher luminescence efficiency and stronger absorption properties have been developed, for example, Gd_2O_2S:Tb, LaOBr:Tm, and $YTaO_4$:Nb.[1,12,34]

Superior images can be obtained using computerized radiography based on photostimulated luminescence.[78] Under X-ray irradiation, electrons are trapped in anionic vacancies, forming color centers (F centers). A scanning of the screen with a laser radiation whose wavelength lies in the absorption bands appearing after X-ray exposure, releases the trapped electrons; the electron–hole recombination energy is then transferred to a luminescent ion. An efficient photostimulable material is BaFBr:Eu^{2+} whose stimulation can be performed with a helium–neon laser ($\lambda = 633$ nm).[1,12]

5.4 γ-Ray-excited Luminescence

Scintillator crystals are luminescent crystals used for the detection of ionizing radiation (γ, neutrons, etc.). Depending on the nature of the radiation and the type of measure, they have to meet various requirements such as an appropriate composition allowing strong absorption of the radiation, fast decay, and stability under irradiation.[1,12,79,80] The highest efficiencies under γ-ray irradiation are achieved with halides such as NaI:Tl (40 000 photons/MeV). The scintillators $Bi_4Ge_3O_{12}$, $CdWO_4$, and $PbWO_4$ have high densities, 7.1, 8, and 8.2 g cm^{-3} respectively. Fast decays can be obtained with BaF_2 and cerium materials such as $YAlO_3$:Ce, $Y_3Al_5O_{12}$:Ce, or CeF_3.

6 ELECTROLUMINESCENCE

Electroluminescent materials are used in the form of powders or thin films. Owing to their high brightness and stability, ac thin film devices are the most appropriate electroluminescent systems for display.[81,82] The main criterion for an electroluminescent material is its ability to have its electrons accelerated loss-freely in electric fields. Chalcogenides fulfill this requirement. The higher luminous efficiency is obtained with ZnS:Mn, which gives an orange color. The blue can be obtained with $CaGa_2S_4$:Ce, $BaAl_2S_4$:Eu, SrS:Cu,Ag, and SrS:Ce filtered (blue-green emission), the green with ZnS:Tb, and the red with CaS:Eu.[77]

7 REFERENCES

1. S. Shionoya and W. M. Yen eds, ‘Phosphor Handbook’, CRC Press, New York, 1999.
2. B. Saubat, C. Fouassier, P. Hagenmuller, and J.-C. Bourcet, *Mater. Res. Bull.*, 1981, **16**, 193.
3. S. H. m. Poort, A. Meyerink, and G. Blasse, *J. Phys. Chem. Sol.*, 1997, **58**, 1451.
4. L.-J. Lyu and D. S. Hamilton, *J. Lumin.*, 1991, **48–49**, 251.
5. C. W. Struck and W. H. Fonger, ‘Understanding Luminescence Spectra and Efficiency Using W_p and Related Functions’, Springer, 1991.
6. L. A. Riseberg and M. J. Weber, Relaxation Phenomena in Rare-earth Luminescence, in ‘Prog. in Optics XIV’, North-Holland, Amsterdam, 1976, p. 91.
7. B. Di Bartolo ed., ‘Advances in Nonradiative Processes in Solids’, Plenum, New York, 1991.
8. M. J. Weber, *Phys. Rev. B*, 1973, **8**, 54.
9. J. M. van Dijk and M. F. Schuurmans, *J. Chem. Phys.*, 1983, **78**, 5317.
10. G. Blasse, *Struct. Bonding (Berlin)*, 1980, **42**, 1.
11. F. A. Kröger, ‘Some Aspects of the Luminescence of Solids’, Elsevier, 1948.
12. G. Blasse and B. C. Grabmaier, ‘Luminescent Materials’, Springer-Verlag, Berlin, 1994.
13. R. Reisfeld, *Struct. Bonding (Berlin)*, 1976, **30**, 65.
14. B. Di Bartolo ed., ‘Energy Transfer Processes in Condensed Matter’, Plenum, New York, 1984.
15. B. Henderson and G. F. Imbusch, ‘Optical Spectroscopy of Inorganic Solids’, Clarendon, Oxford, 1989.
16. D. L. Dexter, *J. Chem. Phys.*, 1953, **21**, 836.
17. M. Inokuti and F. Hirayama, *J. Chem. Phys.*, 1965, **43**, 1978.
18. M. Saakes, M. Leskelä, and G. Blasse, *Mater. Res. Bull.*, 1984, **19**, 83.
19. M. Buijs and G. Blasse, *J. Lumin.*, 1986, **34**, 263.
20. W. T. Carnall, G. L. Goodman, K. Rajnak, and R. S. Rana, *J. Chem. Phys.*, 1989, **90**, 3443.
21. M. J. Weber, *Phys. Rev.*, 1968, **171**, 283.
22. F. Auzel, Up-Conversion by Energy Transfer, in ‘Rare Earths Spectroscopy’, eds. B. Jezowska-Trzebiatowska, J. Legendziewicz, and W. Strek, World Scientific, Singapore, 1985, p. 502.
23. J. Etourneau, J. Portier, and F. Mesnil, *J. Alloys Compd.*, 1992, **188**, 1.
24. M. R. Davolos, A. Garcia, C. Fouassier, and P. Hagenmuller, *J. Solid State Chem.*, 1989, **83**, 316.
25. R. Moncorgé, J. Théry, and D. Vivien, *J. Lumin.*, 1989, **43**, 167.
26. G. F. Imbusch, in ‘Lasers, Spectroscopy and New Ideas’, eds. W. M. Yen and M. V. Levenson, Springer, Berlin, 1988.
27. A. B. Budgor and A. Pinto, ‘Tunable Solid State Lasers’, Springer, Berlin, 1985.
28. C. R. Ronda and T. Amrein, *J. Lumin.*, 1996, **69**, 245.
29. C. Barthou, J. Benoit, P. Benalloul, and A. Morell, *J. Electrochem. Soc.*, 1994, **141**, 524.
30. G. Blasse, *Struct. Bonding (Berlin)*, 1991, **76**, 153.
31. P. Boutinaud and H. Bill, *J. Phys. Chem. Solids*, 1996, **57**, 55.
32. N. Yamashita, *Jpn. J. Appl. Phys.*, 1991, **30**, 3335.
33. G. Blasse, *J. Inorg. Nucl. Chem.*, 1971, **33**, 4356.
34. L. H. Brixner, *Mater. Chem. Phys.*, 1987, **16**, 253.
35. P. Dorenbos, *J. Lumin.*, 2000, **91**, 91.
36. R. T. Wegh and A. Meijerink, *Phys. Rev. B*, 1999, **60**, 10820.
37. C. K. Jørgensen, *Struct. Bonding (Berlin)*, 1975, **22**, 49.
38. G. Blasse, Luminescence of Inorganic Solids: From Isolated Centres to Concentrated Systems, in ‘Progress in Solid State Chemistry’, Pergamon, 1988, Vol. 18, p. 79.
39. V. Jubera, J. P. Chaminade, A. Garcia, F. Guillen, and C. Fouassier, *J. Lumin.*, 2003, **101**, 1.
40. H. E. Hoefdraad, *J. Solid State Chem.*, 1975, **15**, 175.
41. G. Blasse and A. Bril, *J. Chem. Phys.*, 1966, **45**, 3327.
42. A. M. Srivastava, D. A. Doughty, and W. W. Beers, *J. Electrochem. Soc.*, 1997, **144**, L190.
43. R. T. Wegh, H. Donker, K. D. Oskam, and A. Meijerink, *J. Lumin.*, 1999, **82**, 93.
44. M. J. Weber, *Phys. Rev.*, 1967, **157**, 262.
45. J. L. Adam, Optical Properties and Applications of Fluoride Glasses, in ‘Advanced Inorganic Fluorides’, eds. T. Nakajima, B. Zemva, and A. Tressaud, Elsevier, New York, 2000, p. 235.
46. F. Auzel, *Mater. Res. Bull.*, 1979, **14**, 223.
47. H. G. Danielmayer and H. P. Weber, *IEEE J. Quantum Electron.*, 1972, **8**, 805.
48. P. H. Haumesser, R. Gaumé, J. M. Benitez, B. Viana, B. Ferrand, G. Aka, and D. Vivien, *J. Cryst. Growth*, 2001, **233**, 233.
49. A. Brenier, *J. Lumin.*, 2001, **92**, 199.
50. M. J. Weber, ‘Handbook of Laser Wavelengths’, CRC Press, New York, 1998.
51. C. Fouassier, Luminescent Properties of Fluorides, in ‘Advanced Inorganic Fluorides’, eds. T. Nakajima, B. Zemva, and A. Tressaud, Elsevier, New York, 2000, p. 315.

52. C. Pedrini, D. Bouttet, C. Dujardin, B. Moine, and H. Bill, *Chem. Phys. Lett.*, 1994, **220**, 433.
53. J. Becker, J. Y. Gesland, N. Y. Kirikova, J. C. Krupa, V. N. Makhov, M. Runne, M. Queffelec, T. V. Uvarova, and G. Zimmerer, *J. Alloys Compd.*, 1998, **275–277**, 205.
54. D. S. Hamilton, S. K. Gayen, G. J. Pogatshnik, R. D. Ghen, and W. J. Miniscalco, *Phys. Rev. B*, 1989, **39**, 8807.
55. W. M. Yen, M. Raukas, S. A. Basun, W. van Schaik, and U. Happek, *J. Lumin.*, 1996, **69**, 287.
56. B. Moine, C. Pedrini, and B. Courtois, *J. Lumin.*, 1991, **50**, 31.
57. P. Dorenbos, *J. Lumin.*, 2000, **91**, 155.
58. T. E. Peters and J. A. Baglio, *J. Electrochem. Soc.*, 1972, **119**, 230.
59. A. Diaz and D. A. Keszler, *Chem. Mater.*, 1997, **9**, 2071.
60. G. Blasse, W. L. Wanmaker, J. W. ter Vrugt, and A. Bril, *Philips Res. Rep.*, 1968, **23**, 189.
61. G. Blasse, A. Bril, and J. de Vries, *J. inorg. nucl. Chem.*, 1969, **31**, 568.
62. A. L. Stevels and A. D. Schrama-de Pauw, *J. Electrochem. Soc.*, 1976, **123**, 691.
63. S. H. Poort, J. W. van Krevel, R. Stomphorst, A. P. Vink, and G. Blasse, *J. Solid State Chem.*, 1996, **122**, 432.
64. C. Fouassier, Luminescence of Rare-Earth-doped Alkaline-Earth-Sulfides, in ‘Inorganic and Organic Electroluminescence’, eds. R. H. Mauch and H. E. Gumlich, W&T, Berlin, 1996, p. 313.
65. L. van Pieterson, M. Heeroma, E. de Heer, and A. Meijerink, *J. Lumin.*, 2000, **91**, 177.
66. L. van Pieterson, S. Soverna, and A. Meijerink, *J. Electrochem. Soc.*, 2000, **147**, 4688.
67. U. Mayer, D. Schmid, and H. Seidel, *Phys. Status Solidi. (B)*, 1975, **70**, 269.
68. E. W. Oomen, L. C. van Gorkom, W. M. Smit, and G. Blasse, *J. Solid State Chem.*, 1986, **65**, 156.
69. A. Wolfert, E. W. Oomen, and G. Blasse, *J. Solid State Chem.*, 1985, **59**, 280.
70. K. Era, S. Shionoya, and Y. Washizawa, *J. Phys. Chem. Solids*, 1968, **29**, 1827.
71. C. R. Ronda, *J. Lumin.*, 1997, **72–74**, 49.
72. D. J. Robbins, *J. Electrochem. Soc.*, 1980, **127**, 2694.
73. T. Welker, *J. Lumin.*, 1991, **48–49**, 49.
74. M. Bredol, Chemistry and Physics of Cathodoluminescent Materials, in ‘Handbook of Luminescence, Display Materials and Devices’, eds. H. S. Nalwa and L. S. Rohwer, ASP, 2003, Vol. 2, p. 457.
75. D. J. Robbins, B. Cockayne, J. L. Glasper, and B. Lent, *J. Electrochem. Soc.*, 1979, **126**, 1221.
76. F. L. Zhang, S. Yang, C. Stoffers, J. Penczek, P. N. Yocom, D. Zaremba, B. K. Wagner, and C. J. Summers, *Appl. Phys. Lett.*, 1998, **72**, 2226.
77. M. Leskelä, *J. Alloys. Compd.*, 1998, **275–277**, 702.
78. W. Chen, Luminescence, Storage Mechanisms, and Applications of R-ray Storage Phosphors, in ‘Handbook of Luminescence, Display Materials and Devices’, eds. H. S. Nalwa and L. S. Rohwer, ASP, 2003, Vol. 2, p. 1.
79. E. Zych, Luminescence and Scintillation of Inorganic Phosphor Materials, in ‘Handbook of Luminescence, Display Materials and Devices’, eds. H. S. Nalwa and L. S. Rohwer, ASP, 2003, Vol. 2, p. 251.
80. M. J. Weber, *J. Lumin.*, 2002, **100**, 35.
81. G. O. Mueller, Thin Film Electroluminescence, in ‘Solid State Luminescence’, ed. A. H. Kitai, Chapman & Hall, 1993, p. 133.
82. G. O. Mueller ed., ‘Semiconductors and Metals’, Electroluminescence II, Academic Press, 2000, Vol. 65.

Macrocyclic Ligands

Kristin Bowman-James
University of Kansas, Lawrence, KS, USA

1 Introduction 1
2 Classification of Ligands 1
3 Synthesis 5
4 Thermodynamics and Structural Aspects 9
5 Applications 17
6 Related Articles 18
7 References 18

Glossary

Bis-macrocycles: two macrocycles joined together
Calixarenes: basket-shaped macrocycles with phenyl backbones
Catenands: two interlocked macrocycles
Compartmental ligands: macrocycles with ‘compartments’ for housing more than one substrate
Crown ethers: polyoxa macrocycles
Cryptands: bicyclic macrocycles with aza bridgeheads
Cyclidenes: lacunar tetraaza macrocycles
Expanded porphyrins: macrocycles based on pyrrolic frameworks
Lariat ethers: crown ethers with pendant chains
Sepulchrates: bicyclic caged macrocycles
Spherands: macrocycles with phenyl backbones

Abbreviations

Polyaza macrocycles: $[n]$aneN$_m$: $n =$ Number of ring atoms; N$_m =$ Number of nitrogen atoms; Polyoxa macrocycles: n-crown-m: $n =$ Number of ring atoms; $m =$ Number of oxygen atoms; TRI = Tribenzo[b,f,j][1,5,9]triazacyclododecine; TAAB = Tetrabenzo[b,f,j,n][1,5,9,13]tetraazacyclohexadecine.

1 INTRODUCTION

Macrocyclic ligands are defined as cyclic molecules generally consisting of organic frames into which heteroatoms, capable of binding to substrates, have been interspersed. Some reports of ‘synthetic’ macrocycles (as opposed to the naturally occurring species such as porphyrins, corrins, and chlorins) appeared as early as 1936, when the first synthesis of 1,4,8,11-tetraazacyclotetradecane was reported.[1] Nonetheless, the field only began to blossom in the early 1960s with the pioneering work of Busch[2] and Curtis’ discovery of the nickel-mediated condensation of $[\mathrm{Ni(en)_3}]^{2+}$ with acetone.[3] The early macrocycles were synthesized with an eye to mimicking biologically occurring macrocycles such as the porphyrins, corrins, chlorins, and, more recently, the corphins.

Another area of macrocyclic development began in the late 1960s and initial applications were focused toward modeling biological processes such as ion transport. These macrocycles initially included the oxygen-based crown ethers of Pedersen,[4] and the mixed oxygen–nitrogen bicyclic cryptands of Lehn,[5] both of which exhibit high selectivity toward alkali and alkaline earth metal ions. Several years later, the concept of ‘preorganized’ cavities resulted in the synthesis of the cavitands by Cram.[6]

Since its birth, the development of macrocyclic chemistry has proceeded along two lines:

1. as models of the naturally occurring macrocyclic systems, containing predominantly nitrogen donor atoms; and
2. as receptors designed for recognition and supramolecular chemistry, with a variety of donor atoms and recognition capabilities.

Macrocyclic chemistry has expanded phenomenally since the 1960s to provide exciting and novel chemistry. The award of the 1987 Nobel Prize in Chemistry to Pedersen, Lehn, and Cram is testimony to the importance of this rapidly expanding field.

In such a large subject, this article can only focus on certain aspects, namely those that involve complexation with inorganic substrates. We only consider the synthetic macrocycles, with emphasis on transition metal complexation. Aza, oxa, and, to a lesser extent, thia and phospha macrocycles are also covered. The naturally occurring porphyrins, corrins, corphins, chlorins, and phthalocyanins,[7] as well as the cyclodextrins,[8] are not included. Because of the general complexity of macrocyclic systems and the resulting complicated systematic names, commonly used abbreviations or simplified names will be employed. This review will encompass the synthesis, thermodynamics, structure, and applications of macrocyclic ligands.

2 CLASSIFICATION OF LIGANDS

Two major areas of complexation have developed over the years with regard to synthetic macrocycles. Those with nitrogen, sulfur, phosphorus, and arsenic tend predominantly to form traditional covalent coordination complexes with transition metal ions. A notable exception to this tendency, however, is the rapidly expanding chemistry of the polyammonium macrocycles, which are capable of forming a variety of complexes with anionic substrates. Oxygen-derived macrocycles are noted for complexation with alkali and alkaline earth metal ions, as well as with organic cations and molecular substrates. In this latter situation, associations tend to be electrostatic in nature, and in many instances hydrogen-bonding interactions are vital to complex formation.

Macrocyclic ligands will be classified, for the purposes of this article, as rings with at least nine members and three or more donor atoms. In a number of cases of unique structural units, elegant descriptive names have developed, which more appropriately describe the macrocyclic shape. Macrocycles will be classified as to donor types and, within the donor types, specific classifications of macrocycles will be noted where applicable.

2.1 Polyaza Macrocycles (1)–(10)[9–18]

2.1.1 *Simple Polyaza Macrocycles*

Until recently, the tetraaza macrocycles, such as (**1**) (cyclam) and related ligands with extensive varieties of modifications including differing degrees of saturation and ring size (**2**), had been the most studied, primarily because of the relationship of these molecules to naturally occurring tetraaza macrocycles, such as the porphyrins and corrins. Currently, with interest in metal–metal interactions, increased activity has occurred in the area of larger macrocycles capable of incorporating more than one metal ion, such as (**3**) ([24]aneN_8).[18] Interest in the smaller triaza macrocycles, such as (**4**) ([9]aneN_3) and its variations, has also accelerated in recent years.[14] Added to the simple polyaza macrocycles has been the effort to achieve functionalized macrocycles in order to expand the chemistry of these ligands by combining the rigid structural aspects of the macrocyclic ring with the more flexible and kinetically labile properties of pendant chains, as in (**5**).[11]

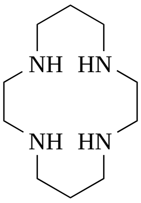
(**1**)

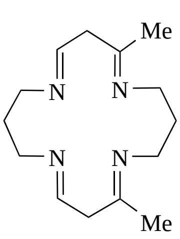

(**2**)

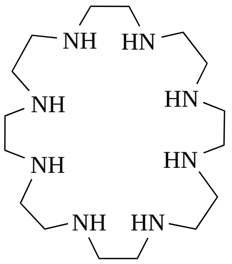
(**3**)

2.1.2 *Cyclidenes*

Cyclidenes (**6**) are a subset of the polyaza macrocycles and are the lacunar ligands first synthesized and extensively studied by Busch.[19] They coordinate a single metal ion and maintain a 'persistent void' which allows access to small molecules within the vaulted cavity.

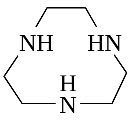
(**4**)

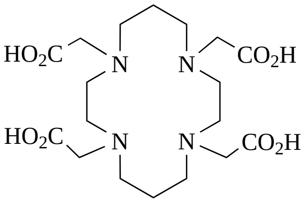

(**5**)

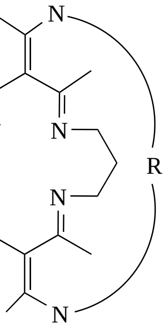

(**6**)

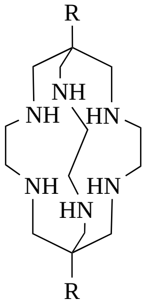

(**7**)

2.1.3 *Sepulchrates*

Sepulchrates (**7**) are polyaza cage macrocycles. They are noted for their exceptionally strong hold on encapsulated metal ions.[20]

2.1.4 *Expanded Porphyrins*

Expanded porphyrins are macrocycles based on the pyrrolic backbone of porphyrins, but are expanded in size to achieve a larger cavity (**8**)[21] or binucleating capabilities (**9**).[22]

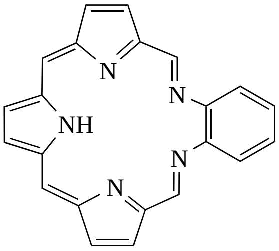
(**8**)

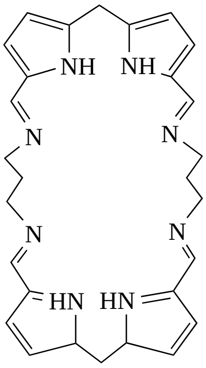
(**9**)

2.1.5 Bis-Macrocycles

Bis-macrocycles (**10**) provide another mechanism for achieving complexation of more than one metal ion. They are joined by a bridge linking two simple macrocycles.[13,23]

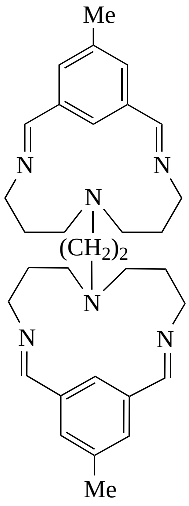

(**10**)

2.2 Polythia, Polyphospha, and Polyarsa Macrocycles

Polythia macrocycles (**11**), the thioether analogs of the crown ethers, have been known since the 1930s.[24] These are the most extensively studied macrocycles in line after the polyoxa and polyaza macrocycles.

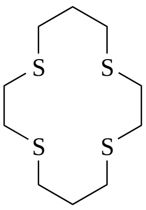

(**11**)

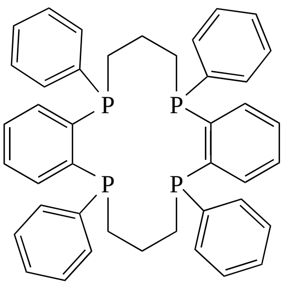

(**12**)

The 'pure' polyphospha macrocycles (**12**) (as opposed to the mixed donor phospha macrocycles) were first reported in 1975.[25] These macrocycles have been found to complex a variety of transition metals, but have not received the same attention as the more readily accessible polyaza and polyoxa macrocycles.

The polyarsa macrocycles (**13**) comprise one of the least common type of macrocycles.[26]

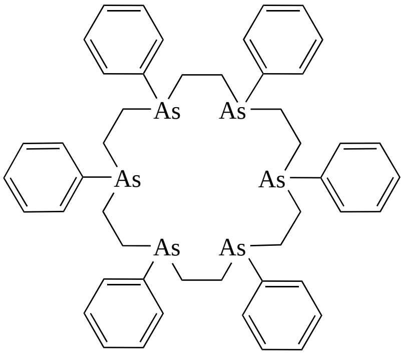

(**13**)

2.3 Mixed Donor Macrocycles

2.3.1 Simple Mixed Donor Macrocycles

The simple mixed donor macrocycles (**14**) at one time were the major source of study of the influence of the incorporation of 'soft' phosphorus and arsenic donors into macrocycles.[27] Mixed oxygen–nitrogen macrocycles have been studied quite extensively, since they serve as bridges for examining the coordination tendencies of the aza macrocycles and the oxa crown ethers.[13]

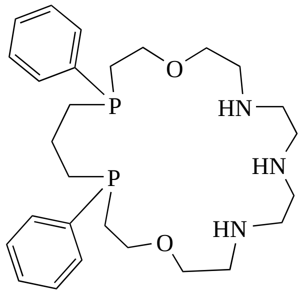

(**14**)

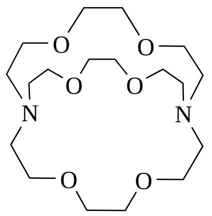

(**15**)

2.3.2 Cryptands

Cryptands (**15**) are bicyclic macrocycles which can contain a variety of donor atoms with bridgehead nitrogen atoms.[5] They are highly selective for alkali and alkaline earth metal ions.

2.3.3 Compartmental Ligands

Compartmental ligands (**16**) are macrocyclic ligands (as well as nonmacrocyclic ligands) which contain 'compartments' for housing more than one metal ion.[28] Only the macrocyclic counterparts will be treated here.

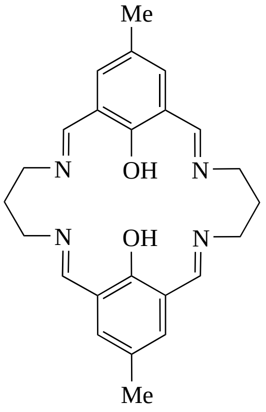

(**16**)

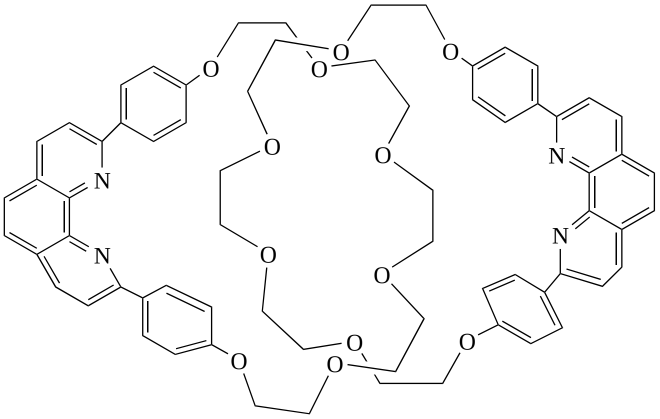

(**17**)

2.3.4 *Catenands*

Catenands (**17**) are interlocked macrocyclic ligands, which complex a variety of metal ions.[29]

2.4 Polyoxa Macrocycles

Polyoxa macrocycles, known more commonly as the crown ethers, comprise an extensive area of research, with a repertoire of types and variations.[30] Some of these macrocycles have been utilized predominantly for purposes other than metal ion complexation, and these will not be discussed in depth in this review. Included in this latter category are the polycarbonyls,[31] polylactones,[32] polylactams[33] and carcerands.[34]

2.4.1 *Polyether Macrocycles*

Polyether macrocycles (**18**) are the simplest of the polyoxa macrocycles. The commonly used name for these macrocycles is the crown ethers, due to their crown-like structure in the solid state. These molecules have been extensively studied as complexing agents for the alkali and alkaline earth metal ions.[30]

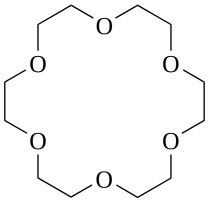

(**18**)

2.4.2 *Lariat Ethers*

The lariat ethers comprise a subset of the polyether macrocycles, and are identified by their pendant chains.[35] They can be categorized as either N-pivot (**19**) or C-pivot (**20**), depending on which type of atom the chain is attached. As for their polyether parents, much of the focus on these macrocycles has been on complexation of alkali and alkaline earth metal ions.

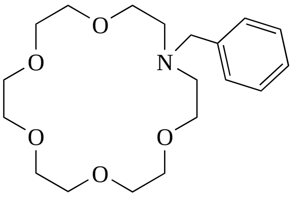

(**19**)

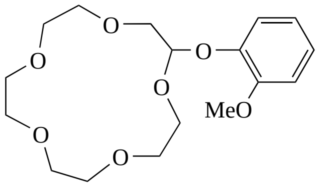

(**20**)

2.4.3 *Spherands and Hemispherands*

These consist of an arrangement of phenyl groups which provide a preorganized cavity for complexation,[36] e.g. (**21**) and (**22**).

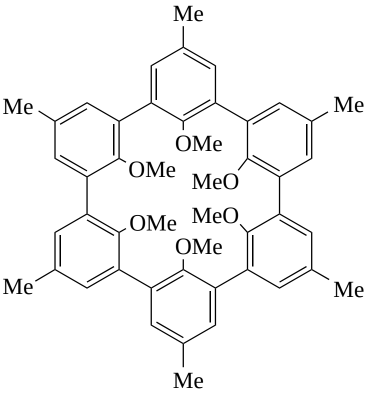

(**21**)

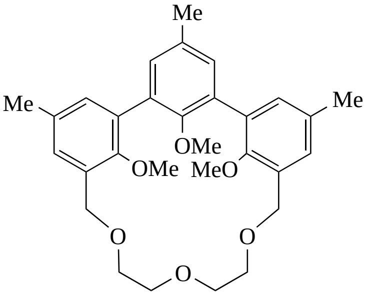

(**22**)

2.4.4 *Calixarenes*

Calixarenes (**23**) are the macrocyclic result of condensations between phenols and formaldehyde[37] and have been referred to as the most easily accessible molecular basket.[38]

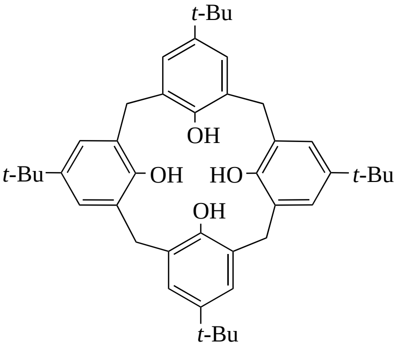

(**23**)

3 SYNTHESIS

3.1 Polyaza Macrocycles

3.1.1 *Conventional (Nontemplate) Syntheses*

Reviews of synthetic procedures can be found for tridentate and pentadentate macrocyclic ligands with nitrogen donors, mixed nitrogen donors, and sulfur donor macrocycles,[39] the techniques of which can be expanded to other ring sizes. The general procedures will be summarized below.

Cyclic secondary amines, [*n*]aneN$_m$, are generally prepared by macrocyclization reactions known as the Richman–Atkins procedure.[40] These reactions involve ring closure by condensation of two precursor fragments of the cyclic molecule. In general, one fragment consists of a salt of a sulfonamide, while the other contains two terminal leaving groups, which can vary in identity and include chloride, bromide, hydroxide, or, more often, a sulfonate ester (Scheme 1). The reaction is performed in polar aprotic solvents and may involve high dilution techniques. Simplified routes to tri-, tetra-, and pentaaza systems have been described.[41] A handy synthetic technique for the smaller triaza ring has been described by Alder, where the macrocycle is built by using a single carbon as template.[42] Treatises on the synthesis of pyridine-containing macrocycles[43] and imidazole-containing macrocycles[44] have also been reported.

Functionalized macrocycles (**5**) with additional ligating components attached as pendant arms have been an area of focus in efforts to expand the chemistry of macrocyclic receptors by incorporating additional recognition sites. Synthetic techniques for N-functionalized, C-functionalized,

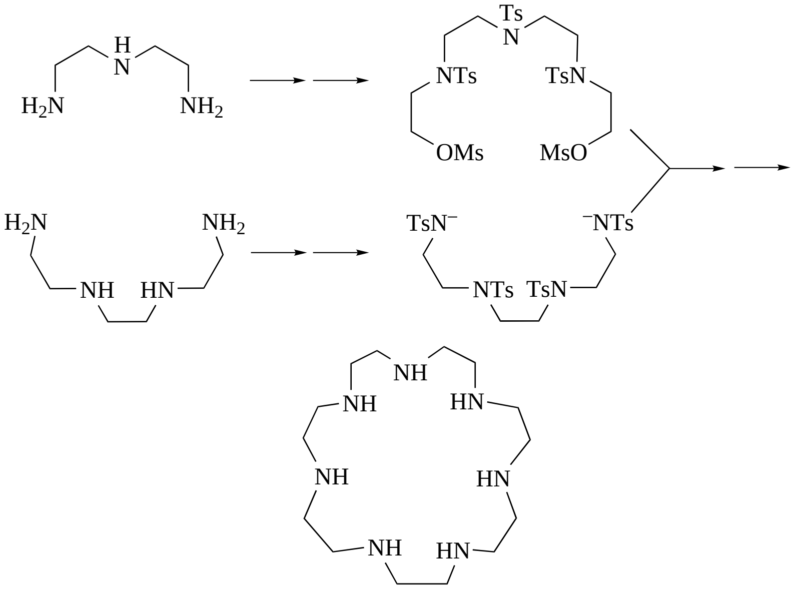

Scheme 1

and bis-macrocycles are known.[11] *N*-Alkylation, the more common of the functionalization routes, is usually achieved by alkylation or acylation of the amino nitrogens using a variety of agents such as chloroacetic acid, ethylene oxide, acrylonitrile, and formaldehyde.[11] Routes for selective alkylations are known, including the use of selective protection and deprotection techniques.[45]

Bis-macrocycles (**10**), another extension of the concept of functionalized macrocycles, can be made by several different methods. One of the more commonly used is the condensation of two precursor chains already joined by the linker.[23] Bis-macrocycles also can be formed from cyclam (**1**) as a by-product bis-macrocycle in low yield (**24**).[46]

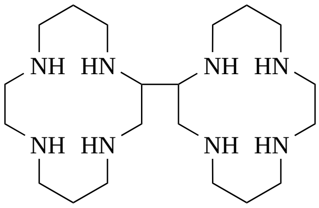

(**24**)

3.1.2 *Template-Mediated Syntheses*

Metal ion template mediation in macrocyclic synthesis has been a part of the field since its inception, its importance having been realized early in the development of this area. Two specific roles for the metal ion in template reactions have been proposed. These are, in turn, kinetic and thermodynamic in origin.[47] In the kinetic template effect, the arrangement of ligands already coordinated to the metal ion provides control in a subsequent condensation during which the macrocycle is formed. The thermodynamic effect serves to promote stabilization of a structure which would not be favored in the absence of a metal ion. Schiff base condensations tend to be dependent on this latter type of template effect. Some of the more routine and general synthetic procedures will be described here. A more in-depth treatment can be found in a review by Curtis, with particular emphasis on general methods as well as modifications of preformed macrocycles.[48]

Carbonyl compounds are commonly used precursors for the polyaza macrocycles, as in the classic synthesis of the Curtis ligand from the condensation of acetone with $Ni(en)_3$ (Scheme 2).[3] 2,6-Diacetylpyridine has provided the precursor for a number of pyridine-derived imine macrocycles (Scheme 3), where smaller metal ions as templates tend to implement the formation of 1:1 condensates, while larger metal ions allow for 2:2 stoichiometries.[49] Schiff base condensations can be considered as another variation of the carbonyl condensations (Scheme 4).[50] The expanded porphyrins (**8**) and (**9**)[21,22] and the compartmental ligands (**16**)[28] are usually synthesized by Schiff base condensations. In some instances the macrocyclic analog cannot be obtained via other methods. This is true for the self-condensation of *o*-aminobenzaldehyde, which can yield both tridentate (TRI) and tetradentate (TAAB) macrocycles (**25**) and (**26**).[51]

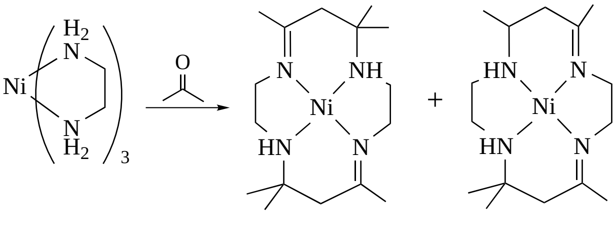

Scheme 2

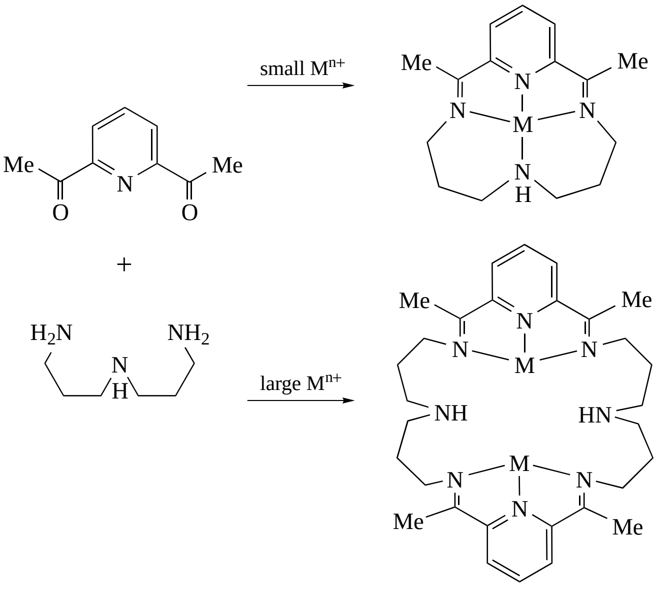

Scheme 3

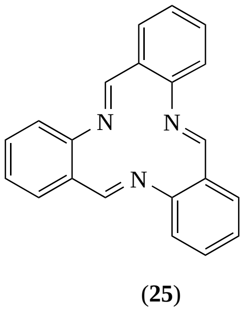

(**25**)

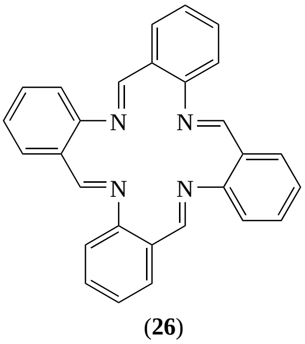

(**26**)

Template-assisted condensations of amines with formaldehyde yield a wide variety of macrocyclic products. Sepulchrates (**7**) can be synthesized from the template-assisted condensation of $[Co(en)_3]^{3+}$ with formaldehyde and ammonia under basic conditions.[20] Primary aldehydes other than formaldehyde have also been used.[52] Caged metal ion complexes in which the metal ion is used as a template are normally

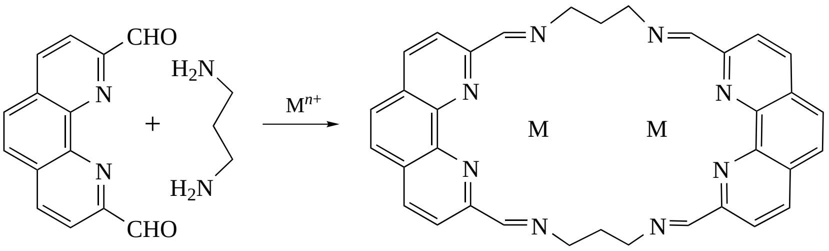

Scheme 4

extremely inert, so much so that removal of the metal is often impossible. Nonmetal template syntheses of polyaza cages have also been reported.[53] A number of interesting variations utilizing the template-assisted condensation of formaldehyde and amines have also resulted in structurally new macrocycles such as (**27**).[54]

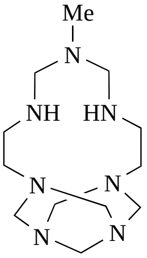

(**27**)

3.2 Polythia, Polyphospha, and Polyarsa Macrocycles

One of the reasons for the relative 'late-blooming' of the thioether macrocycles can be found in synthetic difficulties. While the polyaza and polyoxa macrocycles can often utilize template effects in controlling the critical condensations, polythia condensations are more limited in this area. In general, these macrocycles are made from condensation of the appropriate polythiane with a dibromoalkane (Scheme 5).[55] Synthetic procedures and yields have been greatly enhanced by the addition of high dilution techniques.[56,57] A cage-like sulfur macrocycle has been reported as an analog of the nitrogen-containing sepulchrates (**28**).[58] Mixed nitrogen–sulfur cages can also be obtained.[58]

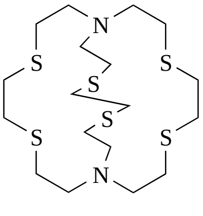

(**28**)

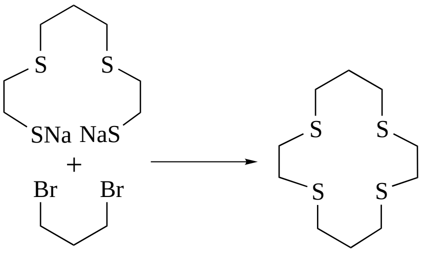

Scheme 5

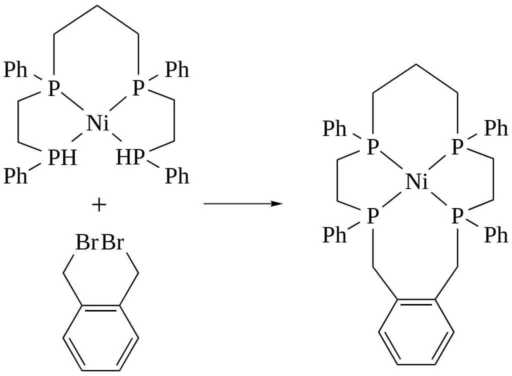

Scheme 6

Polyphospha macrocycles can be made via template condensations of coordinated polyphosphine ligands and dibromoalkanes (Scheme 6).[59,60]

Polyarsa macrocycles can be made by the reaction of lithiated polyarsanes with a dichloroalkane (Scheme 7).[26,60]

3.3 Mixed Donor Macrocycles

Simple mixed donor macrocycles, such as aza–oxa, aza–thia, oxa–thia, and analogous phospha and arsa analogs are generally achieved via combinations of the routes used for synthesis of the 'pure' donor analogs. Since the possibilities are so extensive they will not be treated here, but are found elsewhere.[16,60] New mixed donor phosphorus techniques have been devised for phospha–thia and phospha–aza macrocycles.[61,62]

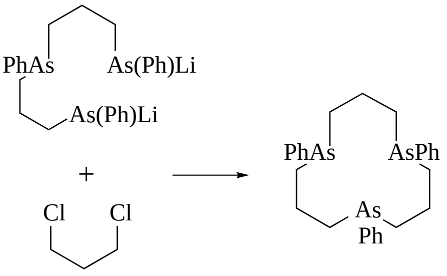

Scheme 7

Cryptands are usually synthesized via sequential condensations between a diamine and an acid chloride, which yields a diamide, followed by reduction with $LiAlH_4$ to give the macromonocycle. Condensation with another equivalent of acyl chloride will yield the bicyclic precursor, which can be reduced by B_2H_6 to give the bicycle (Scheme 8).[5]

Compartmental ligands (**16**) are derived from diketonates and triketonates and are usually synthesized from Schiff base reactions of the ketone with a diamine.[28]

Catenands (**17**) are also made using the metal ion template effect. A bis-complex is formed from an *α*,*α*′-disubstituted *o*-phenanthroline. Then the initial product is treated with a diiodoalkane to accomplish the ring closure.[29]

3.4 Polyoxa Macrocycles

Polyethers were originally synthesized by template assistance from an oligo(ethylene glycol), monoglyme, and potassium *t*-butoxide (Scheme 9).[4]

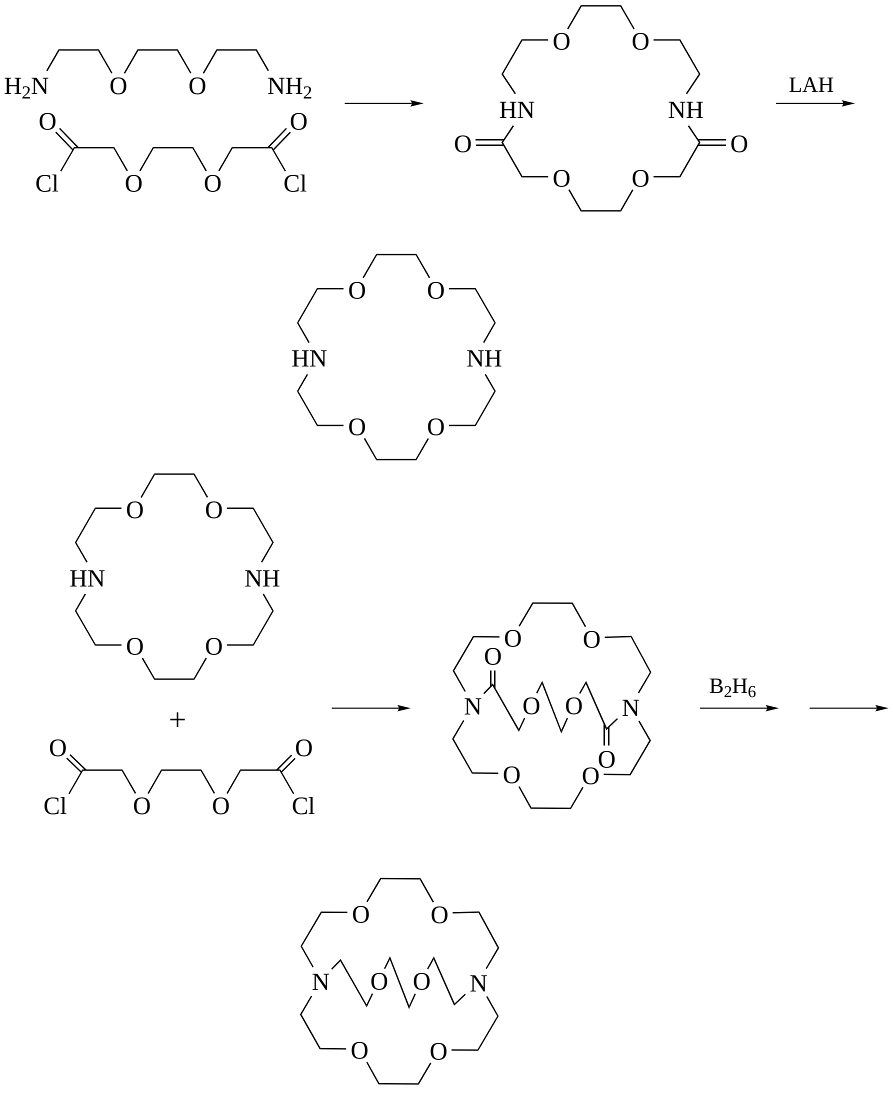

Scheme 8

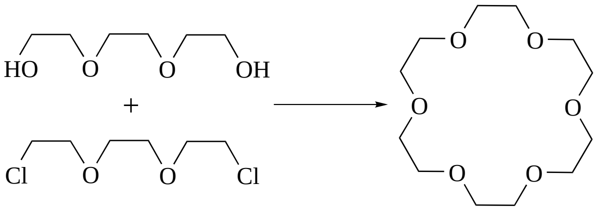

Scheme 9

Spherands and hemispherands (**21**) and (**22**) are synthesized by ring closure reactions of aryllithium with Fe(acac)$_3$, often using high dilution techniques.[36]

Calixarenes (**23**) are obtained from base-catalyzed condensations of p-substituted phenols with formaldehyde.[37]

4 THERMODYNAMICS AND STRUCTURAL ASPECTS

4.1 Introduction

4.1.1 The Macrocyclic Effect

This term refers to the amazing stability of macrocyclic ligands. It was initially described in studies of tetraaza macrocycles with copper(II).[63] For polyaza macrocycles this effect has been attributed to both entropic and enthalpic considerations and considerable controversy raged for a number of years as to which was the predominant factor.[64,65] The conflicting reports are now realized to be extremely dependent on the experimental methods used for the determination of the thermodynamic parameters. Two main types of technique have been employed, each of which has its strengths and weaknesses: the calorimetric titration method and the use of the temperature variation of the stability constants. The controversy has been largely settled by more recent studies.[66,67] Important contributions to the enthalpic term are now attributed to a number of factors, including solvation and conformation changes upon bond formation. Likewise, the entropic considerations include the number of species present and particularly solvation effects. Detailed discussions of the historical development can be found.[13,17]

Related to the macrocyclic effect are the decreased rates of dissociation observed for macrocyclic complexes. Busch and co-workers have coined a term to describe these long-term stabilities incurred by synthetic macrocycles: multiple juxtapositional fixedness. The premise is that straight-chain ligands can undergo dissociative displacements in consecutive steps starting at one end of the ligand and finishing with the opposite end. This is not the case for macrocyclic ligands, for which each dissociated donor is still held in proximity to the metal ion by the rest of the ligand framework.[68]

The macrocyclic effect has been observed for polyaza, polythia, and polyoxa, as well as mixed donor atom, macrocycles.[69]

4.1.2 Selectivity

The selectivity of a macrocycle for either a metal ion or another substrate is critically dependent on the structure of the macrocycle and electronic effects, i.e. the types of donor atoms. Some of the important aspects are described below.

1. The number of binding sites is perhaps one of the most crucial influences on the binding properties of the substrate. Electronic effects of the binding of macrocycles with substrates are charge, polarity, and polarizability of the binding sites. For metal ion binding, this means ion pair interactions for negatively charged ligands, ion–dipole and ion–induced dipole interactions for neutral ligands, and the hard–soft acid–base criteria. Nitrogen, phosphorus, and sulfur donors are noted for their complexation of transition metal ions. Oxygen is more likely to complex alkali or alkaline earth metal ions.
2. The arrangement of the binding sites should be such as to maximize the potential ligand–metal ion interactions. In this regard the selection of spacers between donor atoms to allow for the formation of five- and six-member chelate rings has been the most utilized.
3. The preferred conformations of the macrocycles dictate its propensity to bind a metal ion internally or externally to the cavity. The propensity of the lone pair to point in or out of the cavity is also a deciding factor. Hence, it is not always a foregone conclusion that the metal ion will be bound within the macrocyclic cavity.
4. The identity of the macrocyclic framework also plays a major role in structure. For example, saturated hydrocarbon chains provide considerably more flexibility than incorporated aromatic units. Likewise the presence of other functional groups, such as amides or esters, serve to stiffen the macrocyclic framework. Decreasing the flexibility of the macrocycle by adding selected ‘shaping groups’ is the theory behind preorganization, so important in the cavitands. Another method of creating rigidity is to increase the dimensionality of the macrocycle, inherent in cryptand selectivities.
5. The size of the macrocyclic cavity also plays a large role in governing the flexibility of the ligand, and its propensity for metal ion binding.

Since the focus of this article is primarily on transition metal chemistry, the structural aspects related to complexation of transition metals will be emphasized, and other aspects of complexation will only be briefly treated.

In addition to the traditional measurement of thermochemical properties, molecular mechanics calculations are now available to supplement and correlate with experimental findings. An extensive review which links the large data base of thermodynamic and kinetic data with items such as ring size, number and arrangement of ligand binding sites, and solvent effects, for all types of donor atoms including coronands, cryptands, spherands, and nitrogen donors can be found.[69] A more recent series of molecular mechanics calculations have added to this base of thermochemical data and point to structural factors affecting complex stabilities from the viewpoint of steric strain.[70]

4.2 Polyaza Macrocycles

An extensive review of the thermodynamic aspects of polyaza macrocycles has been reported.[17] Other reviews include the chemistry of tridentate and pentadentate aza macrocycles,[16] 1,4,7-triazacyclononane and derivatives,[14] and polyaza macrocycles with pendant chains.[11] In general, the polyaza macrocycles form extremely stable complexes with transition metals of the later transition series, but show reduced affinity for alkali and alkaline earth metal ions compared to the oxa macrocycles.

4.2.1 Triaza Macrocycles

One of the simplest and smallest of the polyaza macrocycles according to definition is 1,4,7-triazacyclononane (**4**). The geometrical constraints of the triaza macrocycles are such that they do not allow for the incorporation of the metal ion within the macrocyclic ring. Hence, these macrocycles are facially coordinated in either a mono- or bis-ligand complex with a variety of metal ions.[14] The macrocyclic effect is observed, and the stability constants of the complexes follow the *Irving–Williams Series*.[17] Both microcalorimetric[71] and stability constant determinations at different temperatures[72] indicate that the effect is most probably enthalpic in origin. The triaza macrocycles also form extremely stable complexes with the heavier main group metals (such as $\mathrm{Ga^{III}}$, $\mathrm{In^{III}}$, $\mathrm{Tl^{I}}$, and $\mathrm{Tl^{III}}$) as well as transition metals. The chemistry of this macrocycle and its derivatives is wide in scope and is treated extensively in a review which includes the base compound and its N-functionalized derivatives.[14] Depending on the appendages employed in N-functionalization, three more coordination sites are potentially available, rounding out the coordination to pseudooctahedral.

The formation of dinuclear and higher nuclearity species is common for the mono-coordinated triazacyclononane, with bridging acetates, hydroxides, and oxides being very common. Extensive studies of the chemistry of the variety of bridged species have been made using the relatively substitutionally inert chromium(III) ion. Different dimers and trimers have been isolated and structurally characterized, as in (**29**) and (**30**).[73,74] Higher nuclear clusters such as an octanuclear iron system are relevant as a model for the iron storage protein ferritin (*see* ***Iron Proteins for Storage & Transport & their Synthetic Analogs***).[75]

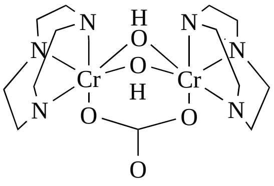

(**29**)

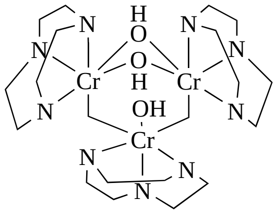

(**30**)

A more ‘preorganized’ ligand system is derived from the self-condensation of *o*-aminobenzaldehyde.[51] The tridentate form of the ligand (**25**) (TRI) imparts considerable inertness toward substitution. For example, the salts of the $[\mathrm{Ni(TRI)(H_2O)_3}]^{2+}$ ion can be resolved into optical isomers.[76] A copper(II) complex of the methyl-substituted tetradentate macrocycle $\mathrm{Me_4TAAB}$, in which bis-coordination occurs, displays a dynamic Jahn–Teller distortion based on crystallographic evidence.[77]

4.2.2 Tetraaza Macrocycles

Because of the potential relationship to the naturally occurring porphyrins and porphyrin-analog macrocycles, the tetraaza macrocycles have been the focus of much attention.

Tetraaza macrocycles often, but not always, form a coplanar arrangement of the four nitrogen donors. Empirical force field calculations of free macrocycles from 12- to 16-membered rings indicate that cyclam (**1**) exhibits the least strain with the best planarity. A straightforward assessment of the relationship of hole size to selectivity is complicated by the conformational flexibility of the ligands. Results of studies for the tetraaza macrocycles show that hole size does not appear to be the predominant factor in metal ion discrimination. Rather, the selectivity of these macrocycles is governed by the relative stability of the conformers of the macrocycle which have different metal ion size preferences. An interesting observation regarding the relationship of the tetraaza macrocycles with regard to hole size and metal ion selectivity can be found for the most studied of the simple tetraaza macrocycles, cyclam. Cyclam is proposed to have five configurational isomers, based on the orientation of the amine hydrogens. From molecular mechanics calculations, where the best M–N distance is calculated as that giving the minimum energy, the trans-III analog of $[12]\mathrm{aneN_4}$ (**31**) is found to have an extremely high strain energy of $19.7\,\mathrm{kcal\,mol^{-1}}$ with a best-fit M–N distance of 1.81 Å, compared to the trans-I form (**32**) ($10.8\,\mathrm{kcal\,mol^{-1}}$ and 2.11 Å, respectively).[70,78] In general, the larger, more flexible, planar coordination is provided by the trans-I conformer, and often if a metal is too large for the macrocyclic cavity, it will coordinate lying out of the plane of the donor atoms. When the metal ion is not incorporated into the macrocyclic plane, the factors influencing stability are the same as for the acyclic aza analogs, namely that for larger metal ions, as the size of the chelate ring increases from five to six, the complex stability decreases. A detailed discussion of the thermodynamics of changing chelate sizes for tetraaza macrocycles can be found.[17,78]

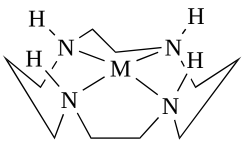

(**31**)

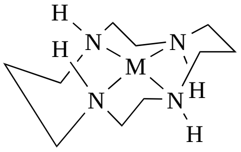

(**32**)

An elegant example of the importance of conformational changes in tetradentate macrocycles is the blue to yellow conversion observed for nickel(II) complexes. The yellow form is the low-spin square planar complex NiL^{2+}, while the blue form is high-spin pseudooctahedral $[NiL(H_2O)_2]^{2+}$. In the blue to yellow conversion the Ni–N bonds contract, which compensates for the breaking of the axial $Ni–OH_2$ bonds. The reaction is controlled by entropy, and the addition of an inert salt is such as to favor the dissociation of the water molecules. At equilibrium in aqueous solution, both [12]aneN_4 (cyclam) (**1**) and the 15-membered analog, [15]aneN_4, have 99% of the high-spin form present, while the 13- and 14-membered macrocycles exist in predominantly the low-spin square planar form (87 and 71%, respectively).[79]

For the nonplanar octahedral *cis*-coordinated macrocycles [*n*]aneN_4, changes in the ligand field correlate well with the analogous ligand field strengths for nonmacrocyclic analogs, specifically as related to the chelate ring size. A general rule of thumb is that increasing the chelate ring size from five to six increases the stability of complexes of smaller metals compared to larger metal ions. The origin of this effect can be attributed to increases in ring strain energy when metal ions larger than tetrahedral carbon are part of the ring.[78] For the planar-coordinated macrocycles, the equatorial ligand field, as anticipated, is dependent on the ring size. These findings have been related to the calculation of the optimum hole size permitting the macrocycle to adopt its most preferable *endo* configuration. Thus, it has been found that the macrocyclic hole size increases by 10–15 pm for each increment in *n* for [*n*]aneN_4.[79]

In order to introduce a greater rigidity into the flexible polyaza macrocycles and to implement greater hole size–metal ion size match correlations, reinforced macrocycles such as (**33**) have been created, which contain fused diaza rings.[80] Crystallographic results for the nickel(II) complex indicate that the Ni–N bonds are shortened from the strain-free value of 1.91 Å for diamagnetic nickel to 1.86 Å. Ligand field strength is also found to increase, and this has been suggested as being due to the compression of the bond lengths[80] as well as the presence of tertiary nitrogen donors.[78] In a more recent comparative study of nickel macrocycles with two fused 1,3-diazacyclohexane rings (**35**) compared to two fused 1,3-diazacyclopentane rings (**34**), structural results revealed weaker ligand field strengths for the 1,3-diazacyclohexane compared to 1,3-diazacyclopentane.[54]

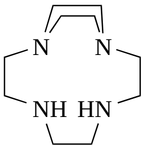

(**33**)

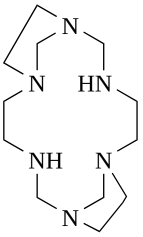

(**34**)

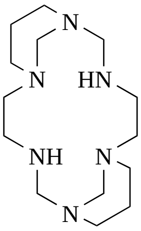

(**35**)

Attempts to achieve macrocycles that are capable of stabilizing highly oxidized transition metal complexes has led to the design of ‘noninnocent’ ligands.[81] The structures of high-valent chromium(V) oxo species with the two tetraamido N ligands (**36**) and (**37**) were determined. Both structures were found to contain distinctly nonplanar amide groups, and in (**36**) all four amides are nonplanar.

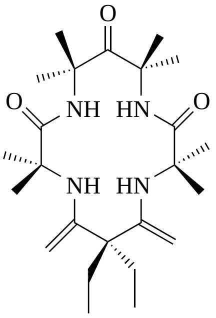

(**36**)

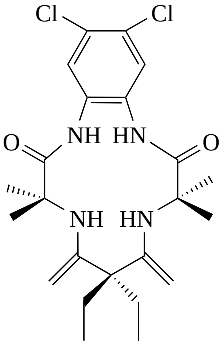

(**37**)

Polyaza macrocycles with pendant arms have been studied extensively, in particular with respect to protonation and complexation as well as to the kinetics of metal complex formation. These aspects are treated in a review by Kaden.[11] Of particular interest is the fact that metal complex formation constants of macrocycles with pendant carboxylates can be 10^3 to 10^4 times higher than for the unsubstituted analogs.

4.2.3 Higher Polyaza Macrocycles

Transition metal complexes of the larger polyaza macrocyclic ligands have been less extensively studied than for the smaller ring systems. For the pentaaza macrocycles, [15]aneN_5 with ethylene bridges appears to form the most stable complexes with most metal ions.[17] Structural data for a variety of pentaaza macrocyclic complexes have been reviewed.[16] The N–H bonds as well as the different sized chelate rings must be considered in calculating the number of possible isomers. For each of the complexes, three configurations of the in-plane N–H bonds are possible: (**38**), (**39**), and (**40**). Crystallographic data indicate that most of the complexes with pentadentate macrocycles have pseudooctahedral geometries. Pentadentate macrocycles also tend to stabilize unusual oxidation states. For example, the nickel(II) complexes of [15]aneN_5 (**41**), [16]aneN_5 (**42**), and one of the isomers of [17]aneN_5 (**43**), are readily oxidized to the Ni^{III} analogs. Also, there is little dependence of $E_{1/2}$ values on the macrocyclic ring size, which has been attributed to the absence of in-plane ring size effects.[16]

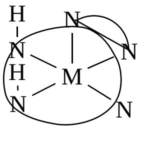

(**38**) *meso–syn*

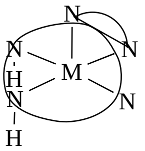

(**39**) *meso–anti*

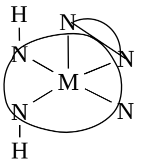

(**40**) racemic

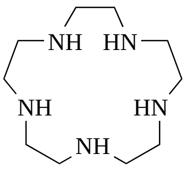

(**41**)

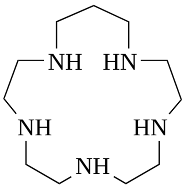

(**42**)

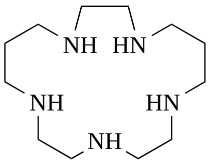

(**43**)

The hexaaza [18]aneN_6 forms complexes with transition metal ions and with certain alkali and alkaline earth and lanthanide ions.[82] For the higher aza macrocycles with seven or more donor atoms, dinuclear complexes become possible. A systematic investigation of both the structural and thermodynamic aspects of copper complexes formed with the larger polyaza macrocycles from heptaaza to dodecaaza has been published.[18] All of the macrocycles were found to form hydroxo species as well as polynuclear complexes. A number of structures have been determined for the higher polyaza macrocycles, both in complexed and noncomplexed forms, and structures range from highly boat shaped to nearly planar.[18,50,83,84]

A review of macrocycles possessing subheterocyclic rings has appeared, which includes pyridine, furan, and thiophene.[85] In a study of formation constants for transition metal ions with pyridine- and furan-containing macrocycles, (**44**) and (**45**), it was found that the pyridine macrocycles follow the Irving–Williams series and bind even more effectively than their saturated analogs (i.e. [18]aneN_6 and [18]aneN_4O_2). The furan analogs showed little tendency to bind, which has been attributed to the increased rigidity of the furan ring.[86]

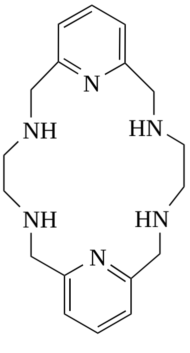

(**44**)

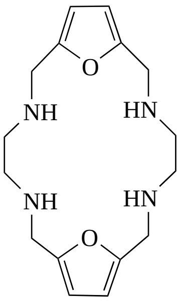

(**45**)

4.2.4 *Anion Coordination*

While the initial interest in polyaza macrocycles involved metal ion coordination, the finding in 1968 by Simmons[87] that diaza bicyclic catapinands can incorporate halide ions into their cavity opened the door on a vast new area of chemistry, that of anion complexation. The thermodynamics of anion binding can be divided into several different areas: that of simple inorganic anions; more complex carboxylate and polycarboxylates; corresponding phosphates, polyphosphates, and nucleotides; and culminating in anionic metal complexes.[17,88–90] Binding is accomplished via both electrostatic and hydrogen-bonding interactions between the protonated macrocyclic amines and the anionic substrates. The general trend appears to be that the increased flexibility of larger polyammonium macrocycles tends to facilitate complexation of more complex anionic substrates.

The results of studies for complexes formed between polyammonium macrocycles and transition metal complex anions indicate that cation–anion electrostatic attraction is a crucial factor in complexation reactions and serves to regulate the stoichiometry of the complexes formed. Hydrogen-bonding, size, and conformational factors also play major roles.[89] Anions can be incorporated in or out of the ring. Two illustrative examples are metal ion complexes with the octaprotonated macrocycle H_8[30]aneN_{10} (**46**). In the complex with $Co(CN)_6^{3-}$, the anion lies outside the macrocycle. The $PdCl_4^{2-}$ complex is a true ‘inclusion’ situation, however, in which the $PdCl_4^{2-}$ is situated along the minor axis of the macrocyclic cavity, and the Cl atoms are out of the frame, forming strong hydrogen bonds with the polyammonium sites.[90]

4.2.5 *Cyclidenes*

Crystallographic results for the cyclidenes (**6**) show that a wide variety of structural ranges can result from designed modifications of the lacunar cavity (or void).[91] The affinity of the cobalt(II) complexes of the cyclidenes for molecular oxygen was found to be very dependent on the identity of the overhead bridge and was found to increase with increasing bridge length. Further design has also allowed for expanding

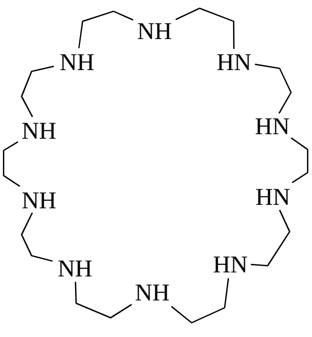

(**46**)

the capability of these macrocycles beyond simple oxygen binding to oxygenase activity observed for the cytochrome P-450s. This has been achieved by adding piperazine 'risers' to increase the cavity size (9 Å high) as well as increasing the hydrophobicity of the molecules, and by adding anthracene and durene 'roofs'. The crystal structure of the anthracene-bridged derivative shows that the macrocycle is indeed capable of hosting an acetonitrile molecule.

4.2.6 *Sepulchrates*

Sepulchrates (**7**) are the most noted of the caged macrocyclic ligands and are the nitrogen analogs of the cryptands. The Co–N distances are 1.99 Å for Co^{III} and 2.16 Å for Co^{II} from crystallographic data, and do not vary greatly from other cobalt amines.[20]

4.2.7 *Expanded Porphyrins*

A review of expanded porphyrin ligands can be found.[92] The texaphyrins (**8**) can be considered as 22-π-electron benzannulene systems with an 18-π-electron delocalization path, based on crystal structure data as well as NMR. The cadmium complex of the macrocycle is found to be planar with pentadentate coordination of the macrocycle to cadmium, which becomes seven-coordinate as a result of axial coordination to two pyridine molecules. The cavity is nearly circular with a center-to-nitrogen distance of 2.39 Å. Because of the larger size of this macrocycle, metal ion coordination is generally seen with the larger transition metals and lanthanides.

A more flexible expanded porphyrin is the 'accordion' porphyrin (**9**).[22] The structural aspects of this macrocycle illustrate the importance of flexibility in achieving unanticipated structures. The free-base macrocycle is elliptical with the inclusion of two water molecules (**47**), while the dicopper(II) complex is highly distorted by means of *exo* and *endo* orientations of the imine groups (**48**).

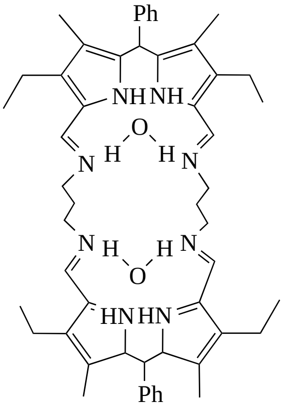

(**47**)

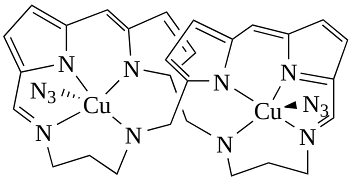

(**48**)

4.3 Polythia and Polyphospha Macrocycles

4.3.1 *Polythia Macrocycles*

The coordination chemistry of thioether macrocycles has expanded greatly only since the mid-1980s, as seen by a number of reviews.[55,93–95] The macrocyclic effect is also noted for thioethers, but to a lesser extent than some of the other macrocyclic ligands. This is due primarily to the reorganizational energy requirements, since a number of the free-ligand thia macrocycles have a tendency to adopt 'exodentate' conformations in the uncomplexed form, where the sulfurs are pointed out of the macrocycle (**49**). Macrocyclic thioethers must then undergo a reorganization of their *exo* lone pairs in order to incorporate metal ions within the cavity. It was found in a study of the complexation of a number of open-chain thia ligands and thia macrocycles that the enthalpy changes were essentially identical for both macrocyclic and nonmacrocyclic ligands. Hence, the favorable macrocyclic effect is more attributable to the entropy changes in the sulfur macrocycles.[96] The smaller trithia analog of the extensively studied nitrogen donor triazacyclononane does not require such organization and, as such, has been extensively studied itself.[55] Because of the preference for exodentate sulfurs, metal ion coordination in many cases is external to the cavity (**50**).[97] A comprehensive review of the structural aspects of thia macrocycles can be found.[55]

Considerable effort has been made with regard to conformation analysis of crown thioethers. It has been found that ligand strain is most evident in torsion angles, whereby an examination of the deviations from the optimum values of

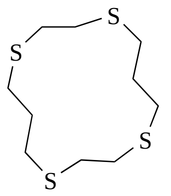

(49)

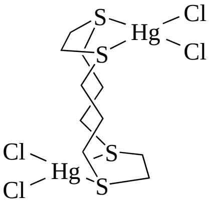

(50)

60° for *gauche* or 180° for *anti* configurations can lead to an assessment of the overall strain in the molecules.[93]

Examination of the influence of ring size has been reported for the 12- to 16-membered tetrathia systems with copper(II).[96,98] The results indicate a marked interrelationship between ring size and stability. The stability peaks at 14-membered rings, and the rings are large enough to incorporate the copper only for the 14- to 16-membered systems.

Results from the correlation of stability constants in conjunction with redox data have led to insights regarding the coordination chemistry of thia macrocycles. For example, the electrochemical behavior of a number of copper(II)/(I) redox couples has been investigated,[99] and redox potentials as well as protonation and stability constants of Cu^I species were determined for a number of tetradentate and pentadentate thia-derived macrocycles with thia- and mixed thia–aza rings with the basic backbones (**51**) and (**52**). Results of the examination of the stability constants in conjunction with the $Cu^{II/I}$ redox potentials indicate that the stability constants for the Cu^I oxidation state are relatively constant regardless of the mixing in of nitrogen donor atoms. Hence, the dramatic increase in the $Cu^{II/I}$ redox potential which is observed in the presence of the sulfur macrocycles can be attributed to a destabilization of the Cu^{II} state rather than stabilization of the Cu^I state, contrary to popular belief from the hard–soft acid–base system.

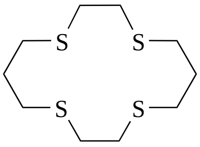

(**51**)

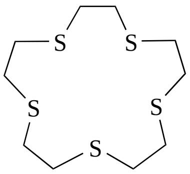

(**52**)

In order to force binding of trithia structural units into an endodentate conformation, one strategy has been to add rigid xylyl groups into the ring to limit the flexibility (**53**).[100] While the conformation of the free ligands is exodentate, a number of transition metal complexes of this ligand have been found to exhibit endodentate coordination, including Mo, Cu, Ag, Pd, and Rh. Results for the bis-macrocyclic silver complex with a variety of noncoordinating anions, indicate that the conformational interconversions of the ligand are low in energy.

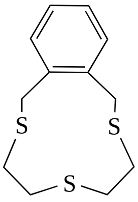

(**53**)

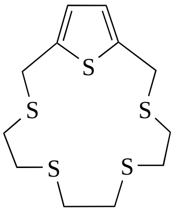

(**54**)

Thiophene units have also been incorporated into the thia crowns (**54**).[101]

4.3.2 Polyphospha Macrocycles

Phosphorus macrocycles can exist in a variety of conformations, a number of which are stable. The barrier for inversion of phosphate is 146.4 kJ mol^{-1}.[102] Hence there are five conformations possible for the tetraphosphorus macrocycle (**12**). Two are preferred: the one in which the macrocyclic benzo groups are *trans* (**55**) and that in which they are *cis* (**56**).[60,103]

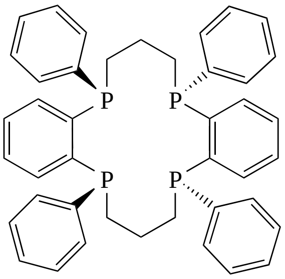

(**55**)

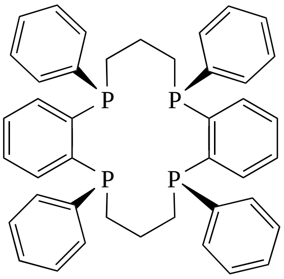

(**56**)

4.4 Mixed Donor Macrocycles

4.4.1 Simple Mixed Donors

Much of the work in this area has been reported by Lindoy and co-workers, who have performed extensive studies on the role of hole size in complex stability and rates of complex formation.[13,27,104] Bradshaw, Krakowiak, and Izatt have published an extensive text on the synthesis of aza crowns.[105] A review of tri- and pentadentate macrocyclic ligands also includes mixed donor results as well as the influence of pendant arms.[16] Due to the numerous ramifications of this area, a few key findings will be cited for the simplest systems.

A major focus in the study of mixed metal ion systems has been to examine metal ion discrimination. In particular, two specific mechanisms can be attributed to metal ion discrimination: macrocyclic hole size and what Lindoy has termed as a 'dislocation' mechanism. The key to this mechanism is the assumption that coordination geometry preferences can be suddenly changed at some point along a series of ligands where gradual changes in the ligand framework are made. Because these changes can occur at different points for different metal ions, discrimination can be achieved. A particularly appealing aspect of the mixed donor aza–oxa systems is the lower ligand field which they provide, which then tends to minimize spin state changes. These systems are treated in a comprehensive review of O_3N_2, O_2N_3, and other pentadentate macrocycles with N, O, S heteroatoms.[104]

Examples of the use of synthetic mixed donor macrocycles in heavy metal ion separations are found in the discrimination of silver from lead. A number of studies indicate that the inclusion of sulfur in macrocyclic sequestering agents shifts the discrimination to silver.[104] An example of this is seen with (**57**) and (**58**). For the aza–oxa macrocycle (**57**) the log K is 5.9 for both silver and lead ions, while the thia-incorporated ligand (**58**) complexes silver more efficiently (log $K = 9.9$) compared to lead (log $K = 5.7$).[106,107]

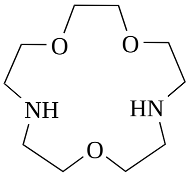
(**57**)

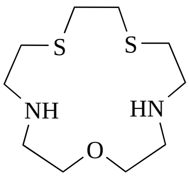
(**58**)

The larger mixed aza–oxa, aza–thia, and aza–and oxa–phospha macrocycles are noted for their ability to complex more than one metal ion and to alter the magnetic properties of bimetallic complexes.[108–110] An example of tri-metal coordination is the tricopper complex of a 27-member ring system (**59**).[108] A classic series of dicopper complexes which illustrates the influence of donor atoms on magnetism are the dicopper structures (**60**)–(**62**).[110] The magnetic properties were found to be extremely dependent on the mode of azide coordination, which is thought to be influenced by the orientation of the orbitals on the metal ions. In complex (**60**), the two copper ions are ferromagnetically coupled with a triplet ground state; in (**61**), the metal ions are antiferromagnetically coupled; and in (**62**), the two copper ions are not coupled.

4.4.2 *Cryptands*

Cryptands (**15**) are noted for their highly selective complexation of alkaline earth metal ions, and for their ring size–metal ion match ability.[5] The thermodynamic properties of these macrocycles have been extensively investigated, and results indicate that the high stability of the bicyclic macrocycles compared to their monocyclic analogs is enthalpic in origin.[88]

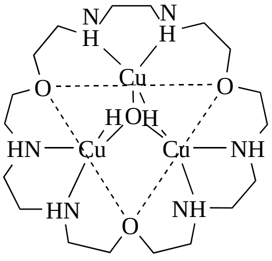
(**59**)

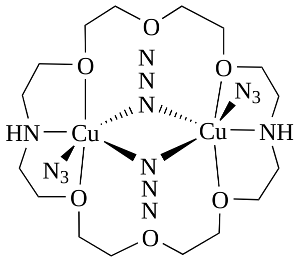
(**60**)

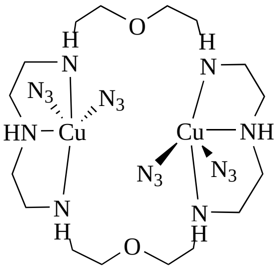
(**61**)

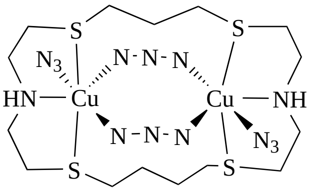
(**62**)

4.4.3 *Compartmental Ligands*

Compartmental ligands (**16**) provide extensive opportunities for multiple metal ion complexation. An example of a mixed donor ligand incorporating different metal ions is the macrocyclic trinucleating ligand (**63**), which is capable of complexing two 'soft' donor metal centers in addition to a 'hard' alkali or alkaline earth metal.[111]

4.5 Oxa Macrocycles

4.5.1 *Crown Ethers*

In the crown ethers (**18**) the interactions between the ligand and metal ion are considered to be more electrostatic in nature, rather than the covalent binding observed for the transition metal complexes of the aza, thia, and phospha macrocycles. The thermodynamic properties of these macrocycles have been extensively studied, with numerous reviews covering complexation, selectivity, and structural aspects, some with extensive tables of thermodynamic data.[69,70,112–119] Considerable efforts have been made to correlate the interrelationship between cavity size of the macrocycles and stability of alkali and alkaline earth metal complexes. From X-ray and CPK models, cavity radii are determined as 0.86–0.92 Å for 15-crown-5 (**64**), 1.34–1.43 Å for 18-crown-6 (**65**), and about 1.7 Å for 21-crown-7 (**66**).[69] For complex formation between the alkali metal ions and 18-crown-6, the maximum stability

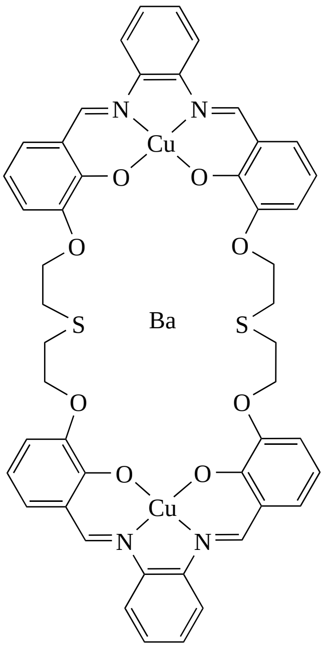

(**63**)

occurs for the potassium ion, which has a radius of 1.38 Å, thus correlating well with the cavity radius. However, 18-crown-6 forms extremely stable complexes with all of the alkali and alkaline earth metal ions. Hence, Gokel argues that the data indicate that the hole size concept is inapplicable, since the binding constants for sodium, potassium, ammonium, and calcium ions are the largest for the 18-crown-6 compared to almost all of the other simple crown ethers.[119] Hancock has proposed that chelate ring size is the critical factor, and that the high stabilities observed for the crown ethers with large metal ions is a result of the presence of five-membered chelate rings. Thus the high affinity of these macrocycles for the potassium ion is explained by the fact that potassium is the right size for the five-membered chelate rings of the crown ethers.[78]

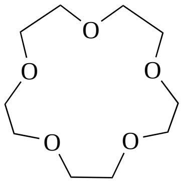

(**64**)

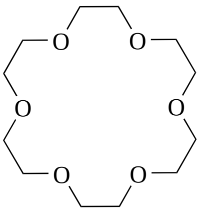

(**65**)

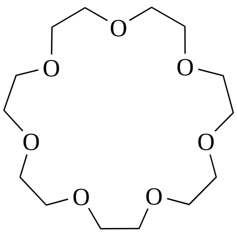

(**66**)

A number of reviews of the structural aspects of crown ethers can be found.[115–117] These structures vary considerably in complexity. An example of the flexibility of the crown ethers can be seen in the variation in the structures as a result of ring size of three different benzo crowns. When the cavity of the crown matches the radius of the metal ion, the metal ion can be readily incorporated in the cavity, such as in the structure of the rubidium thiocyanate complex with the dibenzo-18-crown-6 (**67**). In cases where the cavity of the crown is too large to surround the metal ion snugly, a folded structure can result, as with the dibenzo-30-crown-10 (**68**) and the potassium ion. For very large metal ions incapable of fitting into smaller macrocyclic cavities, sandwich-type structures can occur, as in the benzo-15-crown-5 (**69**) with the potassium ion.[115]

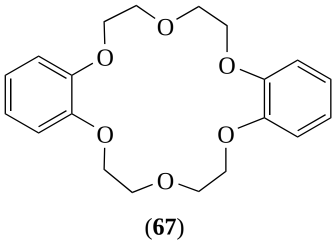

(**67**)

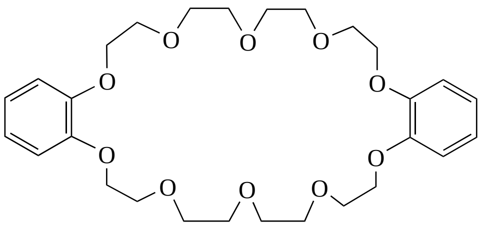

(**68**)

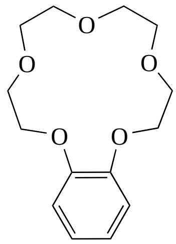

(**69**)

Molecular mechanics studies indicate that the lowest energy conformer of the uncomplexed ligand is not necessarily that required for complexation, i.e. oxygen donors may be exodentate as in the thia macrocycles. This means that in order for complex formation to occur, the ligand must undergo both reorganization as well as desolvation. A general rule of thumb with respect to size, however, is that the larger macrocycles are more flexible and subject to adaptability, while the smaller macrocycles are more rigid and, in that sense, 'preorganized'. Cram has provided an excellent treatise on preorganization.[118] His principle of preorganization is that 'the more highly hosts and guests are organized for binding and low solvation prior to their complexation, the more stable will be their complexes.'[118] ΔG values for a variety of macrocyclic oxygen donors indicate that the 'prearranged' ligands in general bind their guests more strongly and are, in sequence, the spherands $>$ cryptaspherands $\approx$ cryptands $>$ hemispherands $>$ crown ethers.[116]

A useful correlation of enthalpy–entropy considerations for complexation has been shown by Inoue, Liu, and Hakushi.[113] The treatment reflects enthalpy–entropy relationships for given types of ligands. The general concept is that as the enthalpic contributions become strong, a higher level of organization is obtained, which will result in unfavorable entropy changes. For a given type of system with similar entropic versus enthalpic considerations, the $T\Delta S$ and ΔH values determined for a series of ligands should thus exhibit a linear relationship. This is found for the macrocyclic crown ethers, the cryptands, lariat ethers, and bis-crown ethers, as well as the acyclic polyethers known as podands. The slopes are all positive with high correlation coefficients. Gokel has suggested that these slopes can be used to assess the ligand flexibility: glymes and podands (0.86) $>$ crown ethers (0.76) $>$ cryptands (0.51).[119]

4.5.2 Lariat Ethers

The lariat ethers (**19**) and (**20**) known to date consist of macrocycles with many different types of podand groups, and much of their complexation chemistry involves electrostatic binding of guests. Reviews of both structural and thermodynamic aspects of the lariat ethers can be found.[120–122] The trends are noted to be relatively similar for both the carbon-pivot and nitrogen-pivot types of lariat ethers. Binding strengths and selectivities are dependent on ring size and in general increase as ligand size increases. Strong selectivities are noted for the potassium ion, as in the crown ethers.

4.5.3 Spherands and Hemispherands

The spherands (**21**) were specifically designed using the concept of 'preorganization' wherein the oxygen donors are arranged in an enforced spherical cavity. Totally prearranged (spherand) and partially arranged (hemispherand, (**22**)) complexes are possible.[118] Due to the structural restraints imposed by the rigidly joined phenyl rings, the spherands are considered to be highly 'preorganized' binding sites. In these macrocycles the lone pair of electrons will always be pointed toward the center of the macrocyclic cavity.

4.5.4 Calixarenes

The calixarenes (**23**) are also highly preorganized molecules which are capable of forming different conformational isomers. The conformational flexibility is determined by the size of the ring, with the preferred conformation becoming more planar as the ring size increases.[37]

5 APPLICATIONS

As macrocyclic chemistry has developed, the variety and scope of the applications of these molecules have continued to multiply. This concluding section is an attempt to provide an overview of only three of the applications of synthetic macrocycles. A particularly insightful treatment can be found in the Nobel Lecture of Jean-Marie Lehn,[123] which describes the concept of supramolecular chemistry from simple recognition, to cation and anion receptors, multiple recognition, catalysis, transport, and molecular devices.

5.1 Ion Transport

Ion transport, especially cation transport, was one of the early focal points in macrocyclic chemistry, revolving primarily around the crown ethers and cryptands. Later efforts have been to provide switches to control the rates of cation transport. Two examples of the types of switches that have been developed include photo switches using cryptands,[124] and electrochemical switches using anthraquinone-derived lariat ethers.[125]

Related to transport capabilities is the use of synthetic macrocycles in analytical chemistry. Because of their selective complexation of a variety of cations, the crown ethers and related macrocycles have been widely used for separations and analyses.[126]

While transport efforts have largely involved metal cations, more recent developments have led to the use of macrocycles for transport of more complex molecules such as nucleosides.[127]

5.2 Catalysis

Catalysis can be broken down into a number of areas, depending on the substrate and the catalytic reaction. One of the prime areas of the initial effort in catalysis has been small molecule activation, such as oxygen with a number of transition metal ion macrocycles[128,129] and carbon dioxide, the latter particularly with cobalt(I) and nickel(I) macrocycles.[130,131] Once the polyammonium macrocycles were found to be able to recognize substrates other than metal ions, other catalysis applications evolved. For example, phosphoryl transfer catalysis with simple polyammonium macrocycles has become quite accessible.[132]

5.3 Magnetic Resonance Imaging

Macrocyclic complexes have gained recognition in magnetic resonance imaging.[133,134] In order to be effective imaging agents, complexes must provide a significant enhancement in the proton relaxation rates of water, as well as be nontoxic, and thermodynamically stable. Hence, macrocyclic ligands with pendant carboxylates, such as (**5**), have been examined primarily because of their thermodynamic stability.

6 RELATED ARTICLES

Ammonia & N-donor Ligands; Mixed Donor Ligands P-donor Ligands; S-donor Ligands; Water & O-donor Ligands.

7 REFERENCES

1. J. Van Alphen, *Recl. Trav. Chim. Pays-Bas*, 1936, **55**, 835.
2. M. C. Thompson and D. H. Busch, *Chem. Eng. News*, 1962, 57.
3. N. F. Curtis, *J. Chem. Soc.*, 1960, 4409.
4. C. J. Pedersen, *J. Am. Chem. Soc.*, 1967, **89**, 7017.
5. B. Dietrich, J.-M. Lehn, and J.-P. Sauvage, *Tetrahedron Lett.*, 1969, 2889.
6. J. Almy, D. C. Garwood, and D. J. Cram, *J. Am. Chem. Soc.*, 1973, **95**, 2961.
7. T. Mashiko and D. Dolphin, in 'Comprehensive Coordination Chemistry', eds. G. Wilkinson, R. D. Gillard, and J. A. McCleverty, Pergamon, Oxford, 1982, Vol. 2, p. 813.
8. V. T. Souza and M. L. Bender, *Acc. Chem. Res.*, 1987, **20**, 146.
9. G. A. Melson ed., 'Coordination Chemistry of Macrocyclic Compounds', Plenum, New York, 1979.
10. D. H. Busch, *Acc. Chem. Res.*, 1978, **11**, 393.
11. T. A. Kaden, *Top. Curr. Chem.*, 1984, **121**, 157.
12. E. Kimura, *Top. Curr. Chem.*, 1985, **128**, 113.
13. L. F. Lindoy, 'The Chemistry of Macrocyclic Ligand Complexes', Cambridge University Press, Cambridge, MA, 1989.
14. P. Chaudhuri and K. Wieghardt, *Prog. Inorg. Chem.*, 1987, **35**, 329.
15. D. Parker, *Chem. Soc. Rev.*, 1990, **19**, 271.
16. R. Bhula, P. Osvath, and D. C. Weatherburn, *Coord. Chem. Rev.*, 1988, **91**, 89.
17. A. Bianchi, M. Micheloni, and P. Paoletti, *Coord. Chem. Rev.*, 1991, **110**, 17.
18. A. Bianchi, M. Micheloni, and P. Paoletti, *Pure Appl. Chem.*, 1988, **60**, 525.
19. D. H. Busch and C. Cairns, in 'Progress in Macrocyclic Chemistry', eds. R. M. Izatt and J. J. Christensen, Wiley, New York, 1987, Vol. 3, Chap. 1, p. 1.
20. A. M. Sargeson, *Pure Appl. Chem.*, 1984, **56**, 1603.
21. J. L. Sessler, T. Murai, and V. Lynch, *Inorg. Chem.*, 1989, **28**, 1333.
22. F. V. Acholla, F. Takusagawa, and K. B. Mertes, *J. Am. Chem. Soc.*, 1985, **107**, 6902.
23. I. Murase, K. Hamada, and S. Kida, *Inorg. Chim. Acta*, 1981, **54**, L171.
24. N. B. Tucker and E. E. Reid, *J. Am. Chem. Soc.*, 1933, **55**, 775.
25. L. Horner, H. Kunz, and P. Walach, *Phosphorus Relat. Group B Elem.*, 1975, **6**, 63.
26. J. Ennen and T. Kauffmann, *Angew. Chem., Int. Ed. Engl.*, 1981, **28**, 118.
27. L. Lindoy, in 'Cation Binding by Macrocycles', eds. Y. Inoue and G. W. Gokel, Dekker, New York, 1990, Chap. 16, p. 599.
28. D. E. Fenton, U. Casellato, P. A. Vigato, and M. Vidali, *Inorg. Chim. Acta*, 1982, **62**, 57.
29. C. O. Dietrich-Buchecker, J.-M. Kern, and J.-P. Sauvage, *J. Am. Chem. Soc.*, 1984, **106**, 3043.
30. Y. Inoue and G. W. Gokel eds, 'Cation Binding by Macrocycles', Dekker, New York, 1990.
31. I. Tabushi, Y. Kobuki, and T. Nishiya, *Tetrahedron Lett.*, 1979, **20**, 3515.
32. A. Shanzer, J. Libman, and F. Frolow, *J. Am. Chem. Soc.*, 1981, **103**, 7339.
33. E. Schwartz and A. Shanzer, *J. Chem. Soc., Chem. Commun.*, 1981, 634.
34. D. J. Cram, S. Karbach, Y. H. Kim, L. Baczynskyj, and W. Kalleymeyn, *J. Am. Chem. Soc.*, 1985, **107**, 2575.
35. G. W. Gokel, D. M. Dishong, and C. J. Diamond, *J. Chem. Soc., Chem. Commun.*, 1980, 1053.
36. D. J. Cram, *Angew. Chem., Int. Ed. Engl.*, 1986, **25**, 1039.
37. C. D. Gutsche, in 'Calixarenes', ed. G. F. Stoddart, Royal Society Chemistry, Cambridge, MA, 1989.
38. C. D. Gutsche, I. Alam, M. Iqbal, T. Mangiafico, K. C. Nam, J. Rogers, and K. A. See, *J. Inclusion Phenom.*, 1989 **7**, 61.
39. R. Bhula, P. Osvath, and D. C. Weatherburn, *Coord. Chem. Rev.*, 1988, **91**, 89.
40. J. E. Richman and T. J. Atkins, *J. Am. Chem. Soc.*, 1974, **96**, 2268.
41. F. Chavez and A. D. Sherry, *J. Org. Chem.*, 1989, **54**, 2990.
42. R. W. Alder, R. W. Mowlam, D. J. Vachon, and G. R. Weisman, *J. Chem. Soc., Chem. Commun.*, 1992, 507.
43. M. W. Hosseini, J. Comarmond, and J.-M. Lehn, *Helv. Chim. Acta*, 1989, **72**, 1066.
44. Y.-D. Choi and J. P. Street, *J. Org. Chem.*, 1992, **57**, 1258.
45. L. Qian, Z. Sun, M. P. Mertes, and K. B. Mertes, *J. Org. Chem.*, 1991, **56**, 4904.
46. E. K. Barefield, D. Chueng, D. vanDerveer, and F. Wagner, *J. Chem. Soc., Chem. Commun.*, 1981, 302.
47. M. C. Thompson and D. H. Busch, *J. Am. Chem. Soc.*, 1964, **86**, 3651.

48. N. F. Curtis, in 'Comprehensive Coordination Chemistry', eds. G. Wilkinson, R. D. Gillard, and J. A. McCleverty, Pergamon, Oxford, 1982, Vol. 2, Chap. 21.1, p. 899.
49. S. M. Nelson, *Pure Appl. Chem.*, 1980, **52**, 461.
50. K. Krakowiak, J. S. Bradshaw, W. Jiang, N. K. Dalley, G. Wu, and R. M. Izatt, *J. Org. Chem.*, 1991, **56**, 2675.
51. G. A. Melson and D. H. Busch, *J. Am. Chem. Soc.*, 1964, **86**, 4834.
52. A. Hohn, R. J. Geue, and A. M. Sargeson, *J. Chem. Soc., Chem. Commun.*, 1990, 1473.
53. A. Bencini, A. Bianchi, A. Borselli, M. Ciampolini, P. Dapporto, E. Garcia-España, M. Micheloni, P. Paoli, J. A. Ramirez, and B. Valtancoli, *J. Chem. Soc., Perkin Trans. 2*, 1989, 1131.
54. M. P. Suh, S.-G. Kang, V. L. Goedken, and S.-J. Park, *Inorg. Chem.*, 1991, **30**, 365.
55. A. J. Blake and M. Schröder, *Adv. Inorg. Chem.*, 1990, **35**, 1.
56. D. P. Riley and J. D. Oliver, *Inorg. Chem.*, 1983, **22**, 3361.
57. R. E. Wolf, J. R. Hartman, J. M. E. Storey, B. M. Foxman, and S. R. Cooper, *J. Am. Chem. Soc.*, 1987, **109**, 4328.
58. P. Osvath, A. M. Sargeson, B. W. Skelton, and A. H. White, *J. Chem. Soc., Chem. Commun.*, 1991, 1036.
59. T. A. DelDonno and W. Rosen, *J. Am. Chem. Soc.*, 1977, **99**, 8051.
60. C. A. McAuliffe, in 'Comprehensive Coordination Chemistry', eds. G. Wilkinson, R. D. Gillard, and J. A. McCleverty, Pergamon, Oxford, 1982, Vol. 2, Chap. 14, p. 989.
61. T. L. Jones, A. C. Willis, and S. B. Wild, *Inorg. Chem.*, 1992, **31**, 1411.
62. F. Gonce, A.-M. Caminade, F. Boutonnet, and J.-P. Majoral, *J. Org. Chem.*, 1992, **57**, 970.
63. D. K. Cabbiness and D. W. Margerum, *J. Am. Chem. Soc.*, 1969, **91**, 6540.
64. M. Kodama and E. J. Kimura, *J. Chem. Soc., Dalton Trans.*, 1976, 2341.
65. F. P. Hinz and D. W. Margerum, *Inorg. Chem.*, 1974, **13**, 2941.
66. A. Bianchi, L. Bologni, P. Dapporto, M. Micheloni, and P. Paoletti, *Inorg. Chem.*, 1984, **23**, 1201.
67. M. Micheloni, P. Paoletti, and A. Sabatini, *J. Chem. Soc., Dalton Trans.*, 1985, 1169.
68. D. H. Busch, K. Farmery, V. Goedken, V. Katovic, A. C. Melnyk, C. R. Sperati, and N. Tokel, *Adv. Chem. Ser.*, 1971, **100**, 44.
69. R. M. Izatt, J. S. Bradshaw, S. A. Nielsen, J. D. Lamb, J. J. Christensen, and D. Sen, *Chem. Rev.*, 1985, **85**, 271.
70. R. D. Hancock and A. E. Martell, *Chem. Rev.*, 1989, **89**, 1875.
71. M. Nonoyama and K. Nonoyama, *Inorg. Chim. Acta*, 1979, **35**, 231.
72. L. Fabrizzi and L. J. Zompa, *Inorg. Nucl. Chem. Lett.*, 1977, **13**, 28.
73. K. Wieghardt, W. Schmidt, R. van Eldik, B. Nuber, and J. Weiss, *Inorg. Chem.*, 1980, **19**, 2922.
74. K. Wieghardt, W. Schmidt, H. Endres, and C. R. Wolfe, *Chem. Ber.*, 1979, **112**, 2837.
75. K. Wieghardt, K. Pohl, I. Jibril, and G. Huttner, *Angew. Chem., Int. Ed. Engl.*, 1984, **23**, 77.
76. L. T. Taylor and D. H. Busch, *J. Am. Chem. Soc.*, 1967, **89**, 5372.
77. R. I. Sheldon, A. J. Jircitano, M. A. Beno, J. M. Williams, and K. B. Mertes, *J. Am. Chem. Soc.*, 1983, **105**, 3028.
78. R. D. Hancock, *Acc. Chem. Res.*, 1990, **23**, 257.
79. L. Fabrizzi, M. Micheloni, and P. Paoletti, *Inorg. Chem.*, 1982, **19**, 535.
80. K. P. Wainwright and A. J. Ramasubbu, *J. Chem. Soc., Chem. Commun.*, 1982, 277.
81. T. J. Collins, C. Slebodnick, and E. S. Uffelman, *Inorg. Chem.*, 1990, **29**, 3433.
82. M. Kodama and E. Kimura, *J. Chem. Soc., Dalton Trans.*, 1978, 1081.
83. L. Qian, Z. Sun, J. Gao, B. Movassagh, L. Morales, and K. B. Mertes, *J. Coord. Chem.*, 1991, **23**, 155.
84. A. Bencini, A. Bianchi, E. Garcia-España, E. C. Scott, L. Morales, B. Wang, M. P. Mertes, and K. B. Mertes, *Bioorg. Chem.*, 1992, **20**, 8.
85. G. R. Newkome, J. D. Sauer, J. M. Roper, and D. C. Hager, *Chem. Rev.*, 1977, **77**, 513.
86. G. L. Rothermel, L. Miao, A. L. Hill, and S. C. Jackels, *Inorg. Chem.*, 1992, **31**, 4854.
87. E. Simmons and C. H. Park, *J. Am. Chem. Soc.*, 1968, **90**, 2428.
88. K. B. Mertes and J.-M. Lehn, in 'Comprehensive Coordination Chemistry', eds. G. Wilkinson, R. D. Gillard, and J. A. McCleverty, Pergamon, Oxford, 1982, Vol. 2, Chap. 21.3, p. 915.
89. A. Bencini, A. Bianchi, P. Dapporto, E. Garcia-España, M. Micheloni, J. A. Ramirez, P. Paoletti, and P. Paoli, *Inorg. Chem.*, 1992, **31**, 1902.
90. A. Bencini, A. Bianchi, M. Micheloni, P. Paoletti, P. Dapporto, P. Paoli, and E. Garcia-España, *J. Inclusion Phenom.*, 1992, **12**, 291.
91. D. H. Busch, *Acc. Chem. Res.*, 1978, **11**, 392.
92. J. L. Sessler and A. K. Burrell, *Top. Curr. Chem.*, 1991, **161**, 177.
93. S. R. Cooper and S. C. Rawle, *Struct. Bonding*, 1990, **72**, 1.
94. S. R. Cooper, *Acc. Chem. Res.*, 1988, **21**, 141.
95. M. Schröder, *Pure Appl. Chem.*, 1988, **60**, 517.
96. S. Lucia, W. L. Sokol, L. A. Ochrymowycz, and D. B. Rorabacher, *Inorg. Chem.*, 1981, **20**, 3189.

97. N. W. Alcock, H. Heron, and P. Moore, *J. Chem. Soc., Chem. Commun.*, 1976, 886.
98. V. B. Pett, L. L. Diaddario, E. R. Dockal, P. W. Corfield, C. Ceccarelli, and M. D. Glick, *Inorg. Chem.*, 1983, **22**, 661.
99. M. M. Bernardo, M. J. Heeg, R. R. Schroeder, L. A. Ochrymowycz, and D. B. Rorabacher, *Inorg. Chem.*, 1992, **31**, 191.
100. B. de Groot, H. A. Jenkins, and S. J. Loeb, *Inorg. Chem.*, 1992, **31**, 203.
101. C. M. Lucas, L. Shuang, M. J. Newlands, J.-P. Charland, and E. J. Gabe, *Can. J. Chem.*, 1989, **66**, 639.
102. K. Mislow and R. Baechler, *J. Am. Chem. Soc.*, 1970, **92**, 3090.
103. E. P. Kyba, R. E. Davis, C. W. Hudson, A. M. John, S. B. Brown, M. J. McPhaul, L. K. Liu, and A. C. Glover, *J. Am. Chem. Soc.*, 1981, **103**, 3868.
104. L. F. Lindoy, in ‘Progress in Macrocyclic Chemistry’, eds. R. M. Izatt and J. J. Christensen, Wiley, New York, 1987, Vol. 3, Chap. 2, p. 53.
105. J. S. Bradshaw, K. Krakowiak, and R. M. Izatt, ‘Aza Crown Macrocycles’, Wiley, New York, 1993.
106. F. Arnaud-Neu, M. J. Schwing-Weill, R. Louis, and R. Weiss, *Inorg. Chem.*, 1979, **18**, 2956.
107. F. Arnaud-Neu, B. Spiess, and M. J. Schwing-Weill, *Helv. Chim. Acta*, 1977, **60**, 2633.
108. J. Comarmond, B. Dietrich, J.-M. Lehn, and D. Parker, *J. Chem. Soc., Chem. Commun.*, 1985, 75.
109. A. Bencini, A. Bianchi, E. Garcia-España, M. Micheloni, and P. Paoletti, *Inorg. Chem.*, 1987, **26**, 1243.
110. J. Comarmond, P. Plumeré, J.-M. Lehn, Y. Agnus, R. Louis, R. Weiss, O. Kahn, and I. Morgenstern-Badaru, *J. Am. Chem. Soc.*, 1982, **104**, 6330.
111. F. C. J. M. van Veggel, M. Bos, S. Harkema, H. van de Bovenkamp, W. Verboom, J. Reedijk, and D. N. Reinhoudt, *J. Org. Chem.*, 1991, **56**, 225.
112. A. I. Popov and J.-M. Lehn, in ‘Coordination Chemistry of Macrocyclic Compounds’, ed. G. A. Melson, Plenum, New York, 1979.
113. Y. Inoue and T. Hakushi, in ‘Cation Binding by Macrocycles’, eds. Y. Inoue and G. W. Gokel, Dekker, New York, 1990, Chap. 1, p. 1.
114. R. L. Brueining, R. M. Izatt, and J. S. Bradshaw, in ‘Cation Binding by Macrocycles’, eds. Y. Inoue and G. W. Gokel, Dekker, New York, 1990, Chap. 2, p. 111.
115. M. R. Truter, *Struct. Bonding*, 1973, **16**, 71.
116. I. Goldberg, in ‘The Chemistry of Functional Groups’, ed. S. Patai, Wiley, New York, 1980, p. 175.
117. R. Hilgenfeld and W. Saenger, *Top. Curr. Chem.*, 1982, **101**, 1.
118. D. J. Cram, *Science*, 1988, **242**, 760.
119. G. W. Gokel and J. E. Trafton, in ‘Cation Binding by Macrocycles’, eds. Y. Inoue and G. W. Gokel, Dekker, New York, 1990, Chap. 6, p. 253.
120. F. R. Fronczek and R. D. Gandour, in ‘Cation Binding by Macrocycles’, eds. Y. Inoue and G. W. Gokel, Dekker, New York, 1990, Chap. 7, p. 311.
121. J. Tsukube, *J. Coord. Chem.*, 1987, **16**, 101.
122. K. E. Krakowiak, J. S. Bradshaw, and D.-J. Zamecka-Krakowiak, *Chem. Rev.*, 1989, **89**, 929.
123. J.-M. Lehn, *Angew. Chem., Int. Ed. Engl.*, 1988, **27**, 89.
124. S. Shinkai and O. Manabe, ‘Host Guest Complex Chemistry III’, Springer-Verlag, Berlin, 1984, p. 67.
125. L. E. Echegoyen, H. K. Yoo, V. J. Gatto, G. W. Gokel, and L. Echegoyen, *J. Am. Chem. Soc.*, 1989, **111**, 2440.
126. K. Kimura and T. Shono, in ‘Cation Binding by Macrocycles’, eds. Y. Inoue and G. W. Gokel, Dekker, New York, 1990, Chap. 10, p. 429.
127. H. Furuta, K. Furuta, and J. L. Sessler, *J. Am. Chem. Soc.*, 1991, **113**, 4706.
128. C. J. Burrows, in ‘Inclusion Phenomena and Molecular Recognition’, ed. J. L. Atwood, Plenum, New York, 1990, p. 199.
129. L. D. Margerum, K. I. Liao, and J. S. Valentine, in ‘Metal Clusters in Proteins’, ed. L. Que Jr, American Chemical Society, Washington, DC, 1988, Chap. 6, p. 105.
130. M. H. Schmidt, G. M. Miskelly, and N. S. Lewis, *J. Am. Chem. Soc.*, 1990, **112**, 3420.
131. E. Fujita, C. Creutz, N. Sutin, and D. J. Szalda, *J. Am. Chem. Soc.*, 1991, **113**, 343.
132. M. P. Mertes and K. B. Mertes, *Acc. Chem. Res.*, 1990, **23**, 413.
133. D. Parker, *Chem. Soc. Rev.*, 1990, **19**, 271.
134. J. F. Carvalho, S.-H. Kim, and C. A. Chang, *Inorg. Chem.*, 1992, **31**, 4065.

Magnetic Oxides

John E. Greedan
The Brockhouse Institute for Materials Research, McMaster University, Hamilton, Canada

1	Introduction	1
2	Basic Principles of Magnetism	1
3	The Origin of Spin–Spin Coupling in Oxides – Superexchange and Double Exchange	4
4	Key Experimental Probes of Magnetic Oxides	5
5	Survey of Selected Recent Results for Magnetic Oxides	10
6	Concluding Remarks	32
7	References	32

1 INTRODUCTION

Materials that can be classified as 'Magnetic Oxides' have continued to attract interest and the result is a remarkably high level of research activity over the past decade or so. In this chapter, an attempt will be made to describe some of the major results in this area within the time window from about 1993 to the present. There are a number of ways in which such a discussion could be organized. One approach involves a framework based on the phenomenon or effect exhibited by specific magnetic oxides that have received the preponderance of attention in the literature. Among these are, for example, 'colossal magneto-resistance', low-dimensional magnetism, geometrically frustrated magnetism, and 'half-metallic' ferromagnetism. An alternative is to organize by structure type and chemical periodicity, which has the advantage of being more systematic. While the latter approach will be adopted here, an attempt will be made to cross connect with phenomena of current interest. Before commencing with this survey, we introduce some basic principles of magnetism and magnetic materials.

2 BASIC PRINCIPLES OF MAGNETISM

A brief review of some of the basic principles of magnetism relevant to understanding the detailed behavior of the specific magnetic oxides discussed later in this chapter will be presented. A more expanded discussion is available in Volume I of this series.[1]

2.1 Varieties of Magnetic Ordering

Nearly all of the examples to be discussed later in this chapter involve oxide materials that exhibit some form of cooperative magnetism, that is, correlations between the spins residing on magnetic ions in a lattice of some symmetry. These correlations can exist on length scales ranging from one or only a few neighbors, called short range correlations, to essentially infinity, called long-range order. It may be most instructive to begin with the case in which there is no correlation between the spins, that is, the random state known as paramagnetism.

2.1.1 *Paramagnetism*

Paramagnetism can be regarded as the analog of the ideal, gaseous state of matter for magnetic systems. Here we assume the spins to be noninteracting and thus, there are no correlations even between spins on nearest neighbors. The mean magnetic moment for noninteracting spins can be calculated by standard statistical methods.[2] The general result for the magnetic moment, M, is $M = N_o\langle\mu\rangle = N_o g\mu_B S B_s(\eta)$, where N_o is Avogadro's number, g the Lande splitting factor, μ_B the Bohr magneton, S is the spin of the electronic system in question (the total angular momentum, $J = L + S$, is appropriate for the f-group elements where the orbital angular momentum is not quenched), η is the ratio of the magnetic to the thermal energies, $\eta = g\mu_B H_z/k_B T$, where k_B is Boltzmann's constant, T is the temperature in Kelvins, and H_z is the relevant component of the magnetic field. The function, $B_{S(J)}(\eta)$ is known as the Brillouin function and is given by equation (1):

$$B_{S(J)}(\eta) = \frac{(S(J) + 1/2)\cosh(S(J) + 1/2)\eta - 1/2\cosh\eta/2}{\sinh S(J) + 1/2\eta\sinh\eta/2} \qquad (1)$$

In the limit of $\eta \ll 1$, that is, high temperatures or very low fields, $B_{S(J)}$ reduces to $H_z g\mu_B S(S + 1)/3kBT$ or the corresponding expression with J. Defining the magnetic susceptibility as $\chi = M/H_z$ gives equation (2), which is known as the Curie law,

$$\chi = \frac{N_o g^2\mu_B^2 S(S + 1)}{3k_B T} = \frac{C}{T} \qquad (2)$$

where the Curie constant, C, is defined. This quantity is clearly diagnostic of the spin or total angular momentum. Another quantity in common use is the effective magnetic moment, $\mu_{eff} = [g^2\mu_B^2 S(S + 1)]^{1/2}$. The two are related by $\mu_{eff} = [8C]^{1/2}$. While (2) is the equation for a hyperbola, it can be linearized by plotting χ^{-1} versus T and $C = (\text{slope})^{-1}$ of such a plot. The effective moment (or Curie constant) is thus obtained from analysis of data in the high-temperature limit.

In the other extreme, $\eta \gg 1$, the low-temperature or high-field limit, $B_{S(J)}(\eta) \rightarrow 1$ and $M_S = N_o g\mu_B S(J)$, which is called the saturation moment and is obtained from analysis of data at very low temperatures. These two moments are often confused.

2.1.2 *Spin-spin Coupling, Long-range Ordered States, and Phase Transitions*

In the discussion of paramagnetism above, the possibility of correlations between the spins has been ignored. Spin–spin correlations are described in terms of a basic pair-wise exchange Hamiltonian of the form (equation 3) (sometimes called the Heisenberg-Dirac-VanVleck Hamiltonian, HDVV)

$$\mathbf{H}_{\mathrm{ex}} = -2J\mathbf{S}_{\mathrm{A}} \cdot \mathbf{S}_{\mathrm{B}} \tag{3}$$

where J is a scalar known as the exchange constant and $\mathbf{S}_{\mathrm{A}}$ and $\mathbf{S}_{\mathrm{B}}$ are spin operators on two sites. Note the presence of negative sign and the factor of 2. This is more or less the standard form but one can encounter other forms which omit the factor and reverse the sign. The reader should be aware of this and check the exact form of the Hamiltonian for any reported result. Note that the scalar product demands that the spins be either exactly parallel or antiparallel and that if $J > 0$ the former is found and with $J < 0$, the latter. The origin of the sign and magnitude of J will be discussed in a following section.

Now, when spin–spin correlations are not neglected, there should exist a temperature below which a phase transition to a more organized state will occur. If this state is characterized by order on an infinite length scale (i.e. the length scale of the correlations is essentially the dimension of the sample) this is known as long-range order (LRO). The transition that occurs is analogous to the condensation of a gas to form a crystalline solid. We are not concerned here with a detailed discussion of the voluminous literature on phase transitions of this type (also known as critical phenomena).

The temperature at which the phase transition occurs is called the ‘critical’ temperature or T_c. Most, but not all, magnetic phase transitions are ‘continuous’, sometimes called ‘second order’. From a microscopic point of view, such phase transitions follow a scenario in which, upon cooling from high temperature, finite size, spin-correlated, fractal like, clusters develop from the random, paramagnetic state at temperatures above T_c, the so-called ‘critical regime’. As $T \rightarrow T_c$ from above, the clusters grow in size until at least one cluster becomes infinite (i.e. it extends, uninterrupted, throughout the sample) in size at T_c.[3] As the temperature decreases more clusters become associated with the infinite cluster until at $T = 0\,\mathrm{K}$ all spins are completely correlated.

Continuous phase transitions show anomalies in the specific heat and magnetic susceptibility (or magnetization) at or very near T_c. There is, however, no latent heat as in so-called first-order transitions but of course there is a decrease in spin entropy.

There are three basic types of long-range magnetic order: ferromagnetism, antiferromagnetism, and ferrimagnetism. These are illustrated, along with more complex cases, in Figure 1.

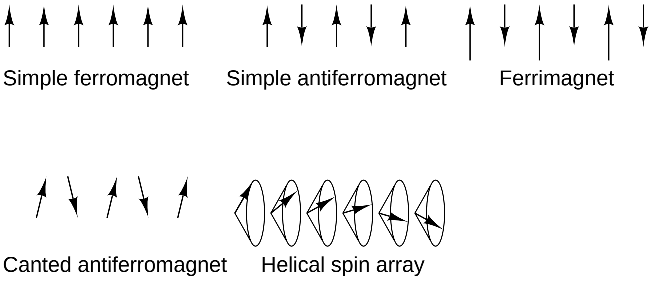

Figure 1 Schematic diagrams representative of various types of magnetic LRO

2.1.3 *Ferromagnetism*

This is the simplest case of magnetic LRO, albeit that most rarely found in nature. All of the spins are parallel, from Figure 1. This corresponds to $J > 0$ in equation (3). There is clearly only one possible ferromagnetic spin configuration, no matter how complex the sublattice of the magnetic atoms, although of course the spins will tend to orientate along some preferred direction in the crystal. For historical reasons, the critical temperature for ferromagnets, T_c, is often called the Curie temperature, which has, confusingly, the same symbol, T_c. Ferromagnets possess a net magnetization below T_c, $M = N_o g|\mathbf{S}|$.

2.1.4 *Antiferromagnetism*

As seen from Figure 1, in this case the spins are coupled antiparallel, corresponding to the case of $J < 0$ in equation (3). Real antiferromagnetic materials are of course three dimensional and more complex than the one-dimensional situation presented in the figure. In three dimensions, it is convenient to subdivide the magnetic sublattice. The minimum number of sublattices is two, say A and B, with equal numbers of spins on each and with equal spin magnitudes, $|\mathbf{S}_{\mathrm{A}}| = |\mathbf{S}_{\mathrm{B}}|$.

As the spins on A are antiparallel to those on B, the ground state of the entire ensemble is a singlet with $\Sigma_{\mathrm{I}}\,\mathbf{S}_{\mathrm{I}} = 0$, where I represents the sublattice index. For any given magnetic sublattice symmetry, there are clearly several ways to achieve this condition. Take the simplest case of a primitive sublattice, Figure 2, where three distinct antiferromagnetic spin configurations are shown, the open and closed circles representing antiparallel spins. The nomenclature, A, C, and G, has historical roots as will be described in a later section on perovskite manganates. Note that in each case the periodicity of the ‘magnetic’ unit cell is greater than the

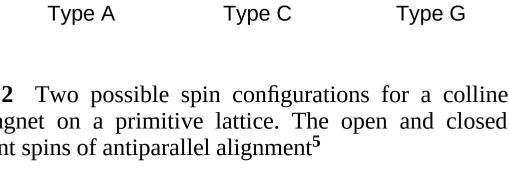

Figure 2 Two possible spin configurations for a collinear antiferromagnet on a primitive lattice. The open and closed circles represent spins of antiparallel alignment[5]

primitive, 'chemical' cell. For type G, the magnetic cell is doubled in all three directions: $\mathbf{a}_{\mathrm{mag}} = 2\mathbf{a}_{\mathrm{chem}}$, $\mathbf{b}_{\mathrm{mag}} = 2\mathbf{b}_{\mathrm{chem}}$, and $\mathbf{c}_{\mathrm{mag}} = 2\mathbf{c}_{\mathrm{chem}}$. Type A requires doubling of **c** only and type C, doubling of both **a** and **b**. As will be described later, neutron diffraction can be used to distinguish among the possibilities. Also, for historical reasons, the critical temperature for and antiferromagnet is often denoted the Néel temperature, T_N, after Louis Néel, who first postulated the existence of antiferromagnetism.

2.1.5 Ferrimagnetism

This type of magnetic LRO arises also when there exist at least two magnetic sublattices but for which the magnetizations are unequal. Defining the sublattice magnetization as $M_l = N_l g_l |\mathbf{S}_l|$ where N is the population of spins of magnitude $|\mathbf{S}|$ on sublattice I, ferrimagnetism can arise for the two sublattice case, for example, when $N_A \neq N_B$ or $|\mathbf{S}_A| \neq |\mathbf{S}_B|$ or both. Normally, the spin correlations are such that the inter sublattice coupling is antiparallel, so a net magnetization arises, $M_{\mathrm{net}} = |\mathbf{M}_A - \mathbf{M}_B|$. As one might imagine, there exist a large variety of ways to achieve ferrimagnetism by manipulating the crystal chemistry and composition of magnetic oxides.

2.1.6 Canted Antiferromagnetism, Helimagnetism, and Other Noncollinear Orderings

Only LRO schemes that involve collinear spin arrangements have been considered so far. Figure 1 also shows two examples of noncollinear spin orderings, the canted antiferromagnet and the helimagnet.[4] The simpler case is the canted antiferromagnet, where $|\mathbf{M}_A| = |\mathbf{M}_B|$ but for which the angle between the sublattice moments is not precisely 180° but deviates by a small 'canting' angle, usually no more than 1° or 2°, and thus the sublattice magnetizations do not exactly cancel. This gives rise to a small, net magnetization of order $\sim 10^{-2}\,\mu_B$ or so, hence the alternative nomenclature of 'weak ferromagnetism' for this phenomenon. The physical origin of the spin-canting is the anisotropic exchange interaction or D-M interaction (Dzialoshansky-Moriya), which involves the expression $\mathbf{D} \cdot \mathbf{S}_A \times \mathbf{S}_B$, where $\mathbf{D}$ is a vector (rather than the scalar J in equation 3) and the vector product is taken rather than the scalar.[6] The D-M interaction is allowed only when there does not exist a center of inversion symmetry at the midpoint of a vector connecting $\mathbf{S}_A$ and $\mathbf{S}_B$, so canted antiferromagnetism is fairly common in low symmetry materials.

In other more complex cases, the spins can take on a configuration that is not well approximated as a perturbed collinear configuration and such is the case for the spiral or helimagnetic ordering depicted in Figure 1. Noncollinear configurations are also observed in the family of so-called geometrically frustrated materials to be discussed later.

2.1.7 Short Range Order (SRO) and Low-dimensional Magnetic Correlations

Normally, the conditions of a high concentration of magnetic centers and strong exchange coupling between them is sufficient to guarantee the occurrence of magnetic LRO at finite temperatures. This is generally true only when the magnetic sublattice is clearly three dimensional, that is, when the anisotropy of the exchange interactions is small.

For cases in which the magnetic lattice dimensionality is one (chains) or two (planes), magnetic *Short Range Order* (SRO) can develop and persist over a wide temperature range, often many tens of kelvins. Effectively, this is an expansion of the critical regime discussed above, which is normally only a few degrees at best for three-dimensional systems. As well as lattice dimensionality, the spin dimensionality must be considered to provide a complete picture. Spin dimensionality is a somewhat more subtle concept that can be best introduced by considering an expansion of the HDVV Hamiltonian into its components as in equation (4)

$$\mathbf{H}_{\mathrm{ex}} = -2[J_{xx} S_{xA} S_{xB} + J_{yy} S_{yA} S_{yB} + J_{zz} S_{zA} S_{zB}] \qquad (4)$$

Three cases are identified, (1) $J_{xx} \sim J_{yy} \sim J_{zz}$, with spin dimensionality three, called the Heisenberg model, (2) $J_{zz} \gg J_{xx} \sim J_{yy}$, with spin dimensionality one, called the Ising model and (3) $J_{zz} \ll J_{xx} \sim J_{yy}$, with spin dimensionality of two, the XY model. There are thus nine possible space/spin dimensionality categories and in Table 1 are shown the correlations with LRO and SRO. Thus, only four combinations permit LRO and three spatial dimensions are normally required, the one exception being the two dimensional Ising case.[7]

There exist many examples, some of which will be discussed in later sections, of metal oxides with crystal structures that enable low-dimensional magnetic correlations and whose magnetic properties are thus dominated by SRO. One canonical structure is the so-called K_2NiF_4 type, adopted by many magnetic oxides, shown in Figure 3. Here layers of corner-sharing NiF_6 are separated by KF layers resulting in a considerably more facile intraplanar exchange pathway than between planes. Note that the magnetic sublattice has body-centered tetragonal symmetry, which also contributes to the magnetic two dimensionality. If the Ni^{2+} spins within a layer are coupled antiferromagnetically, the spins in the next

Table 1 Space and spin dimensionalities and consequences for magnetic LRO

	Spatial dimension		
Spin dimension	1	2	3
1	SRO	LRO	LRO
2	SRO	SRO	LRO
3	SRO	SRO	LRO

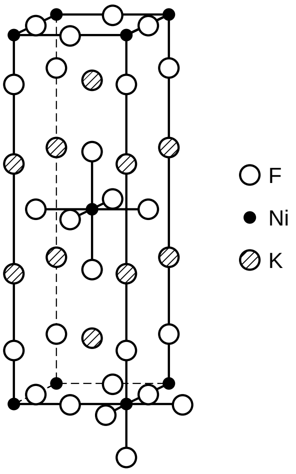

Figure 3 The chemical unit cell of the K_2NiF_4 structure

layer will see four ↑ and four ↓ moments and the interplanar coupling will be 'cancelled' by symmetry. The result of both the distance and symmetry effects can result in ratios $J_{\mathrm{intra}}/J_{\mathrm{inter}} \sim 10^3-10^4$, which ensures the observation of SRO over a wide thermal range.

As all crystalline materials are three dimensional, ultimately one expects to see a 'cross-over' to LRO at some temperature for all nominally low-dimensional magnetic materials. This will occur even if the exchange that couples the chains or planes is very weak. For example, for a planar magnetic material, the critical temperature for the cross-over depends most strongly on the length scale of the correlated region (called, not surprisingly, the 'correlation length') in the planes and is estimated as $T_c \sim \zeta^2_{\mathrm{intra}} J_{\mathrm{inter}} S^2/k_B$, where ζ is the correlation length and J_{inter} is the interplanar exchange constant.[8]

While the spatial dimensionality is generally obvious from the crystal structure (although interesting exceptions exist), engineering various spin dimensionalities can be more subtle. This is normally done by taking advantage of the presence or lack of anisotropy in the g-tensor of magnetic ions. For example, the second two terms in equation (4) will nearly vanish with respect to the first, if $g_z \gg g_x$, g_y, thus giving an Ising model, and the opposite situation provides XY like behavior. When the three components are comparable, the Heisenberg model emerges. Good Heisenberg candidates are ions with orbital singlet ground states, such as half-filled shell d^5 or f^7 ions, examples being Mn^{2+}, Fe^{3+}, Gd^{3+}, or Eu^{2+} and half-filled crystal field states, t^3_{2g} (Cr^{3+}, Mn^{4+}) or $t^6_{2g}e^2_g$ (Ni^{2+}) or even $t^6_{2g}e^3_g$ (Cu^{2+}). Anisotropic spin dimensionalities come from ions with unquenched orbital angular momentum such as high-spin Co^{2+} ($t^5_{2g}e^2_g$) or Fe^{2+} ($t^4_{2g}e^2_g$) for d-group ions or Dy^{3+}, Ho^{3+}, and others in the f-group series. Depending on the details of the crystal field interaction, these ions can be either Ising or XY.

3 THE ORIGIN OF SPIN–SPIN COUPLING IN OXIDES – SUPEREXCHANGE AND DOUBLE EXCHANGE

As most magnetic oxides are electrical insulators, the dominant exchange mechanism is superexchange. The basis of this interaction was described more than 50 years ago by Anderson.[9] Several versions of the theory accessible to inorganic chemists or solid-state chemists exist.[5] Qualitatively, the fundamental idea is illustrated with the aid of Figure 4. Consider a linear array M_A–O–M_B with half-filled d^2_z orbitals on the M's overlapping a p_z orbital on the oxide ion. The ground-state spin–spin correlations can be predicted by recourse to the Pauli principle. If the d^2_z orbital on M_A mixes with the left hand lobe of the p_z orbital and electron transfer p_z to d^2_z occurs, then the antiparallel spin–spin correlations are dictated by the Pauli principle. The same applies to the interaction of M_B with the right hand lobe of p_z and the overall spin-spin correlation between M_A and M_B is antiferromagnetic. Anderson has shown using a perturbation theory treatment that the exchange constant J (equation 3) for the above example is given by

$$J = \frac{-2b^2_{AB}}{U} \tag{5}$$

where b_{AB} is the electron transfer integral ($p_z \rightarrow d^2_z$) that is proportional to the overlap between the two orbitals and U is the correlation energy, that is, the additional electron–electron repulsion due to having two electrons in the same orbital (after the transfer). This interaction involving two half-filled orbitals is always antiferromagnetic.

Consider another case in which the d^2_z orbital on M_A is still half-filled but that on M_B is empty. Assume also that unpaired electrons reside on M_B but in an orbital that is orthogonal to d^2_z, say d_{xz}. The electron transfer from $p_z \rightarrow d^2_z$ (M_B) now must be such that the spin is parallel to the spin in the d_{xz} orbital and the overall spin–spin correlation between M_A and M_B is now ferromagnetic. An attempt to illustrate this situation is shown below:

$M_Ad_z{}^2$(↑) p_z(↑↓) ( ) $M_Bd_z{}^2$ $M_Ad_z{}^2$(↑) p_z(↓) (↑) $M_Bd_z{}^2$
(↑) M_Bd_{xz} (↑) M_Bd_{xz}
(before transfer) (after transfer)

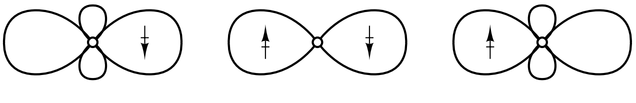

Figure 4 Orbital overlaps and spin correlations in a linear M_A–O–M_B array involving $d^2_z - p_z - d^2_z$ orbitals

Table 2 Net sign and relative magnitude for selected M_A–O–M_B superexchange interactions[5,10]

Interaction	180°	90°
d^3/d^3 (t_{2g}^3/t_{2g}^3) [Cr^{3+}, V^{2+}, Mn^{4+}]	AF (weak)	AF or F (weak)
d^5/d^5 ($t_{2g}^3e_g^2/t_{2g}^3e_g^2$) [$Mn^{2+}$, Fe^{3+} high spin]	AF (strong)	AF (weak)
d^3/d^5 ($t_{2g}^3/t_{2g}^3e_g^2$) [Cr^{3+} /Fe^{3+}]	F(weak)	AF(weak)
d^3/d^8 ($t_{2g}^3/t_{2g}^6e_g^2$) [Cr^{3+} /Ni^{2+}]	F(moderate)	?
d^8/d^8 ($t_{2g}^6e_g^2/t_{2g}^6e_g^2$) [$Ni^{2+}$ /Ni^{2+}]	F(strong)	AF or F(weak)

The value of J is now

$$J = \frac{2b_{AB}^2}{U \times J_{\text{intra}}/U} \tag{6}$$

where J_{intra} is the Hund's rule intra-atomic exchange constant. In general, for this case the overall interaction will be smaller in magnitude than that in (5) by the factor J_{intra}/U, which means a factor of 10 or so.

From the brief account above, it is clear that both the sign and magnitude of J depend strongly on orbital overlaps, orbital symmetry, and orbital filling. Goodenough and Kanamori have developed a well-known set of rules for qualitative prediction of the sign of J and its relative magnitude for two limiting M_A–O–M_B geometries, 180° and 90°.[5,10] Selected examples are shown in Table 2.

These rules should be treated as a rough guide and it should be borne in mind that in real oxides, the M_A–O–M_B angle is rarely exactly 180° or 90°. Also, the net exchange coupling for any real case is an algebraic sum of J for each of many pathways of varying sign and magnitude. As a result of the fact that most superexchange pathways tend to favor antiferromagnetic spin configurations, in the vast majority of magnetic oxides, antiferromagnetic correlations predominate. There are still not more than a handful of insulating oxides that are ferromagnetic.

The problem of calculating superexchange J's from first principles is still formidable and while progress has been made, especially with the development of modern computer codes, a discussion of this topic lies outside of the scope of this chapter.

A second exchange mechanism is found in some oxides, especially the manganates to be described later, called double exchange. Double exchange was first proposed by Zener, again some 50 years ago.[11,12] This mechanism assumes that a subset of the d electrons is highly mobile, hopping rapidly between two ions of the same element and coupling more localized spins in a ferromagnetic manner. The best examples are the mixed valence manganate perovskites containing Mn^{3+} ($t_{2g}^3e_g^1$) and Mn^{4+} (t_{2g}^3), formally. Here the localized electrons are in the t_{2g}^3 sublevels and the itinerant electron occupies the e_g^* levels, which are broadened into bands in the solid. Since the hopping of the electron from site to site occurs without change of spin, Hund's rule again requires that the local moments in the t_{2g}^3 levels be parallel, that is, ferromagnetically coupled.

4 KEY EXPERIMENTAL PROBES OF MAGNETIC OXIDES

4.1 Magnetic Susceptibility and Magnetization

The most important and basic technique is the measurement of the dc magnetic susceptibility or magnetization. The widespread availability of modern magnetometers based on Superconducting Quantum Interference Device (SQUID) sensors has rendered such measurements more or less routine in a large region of H−T space from 2 K to 700 K and applied fields from 0 to >6T. The quantity actually measured is the magnetic moment or magnetization, M, which is converted to susceptibility by dividing by the applied field, $\chi = M/H$. For the oxides of interest here, one expects strong spin−spin correlations that will be manifested as deviations from the Curie law, equation (2). These deviations can usually be accommodated by the Curie-Weiss law,

$$\chi = \frac{C}{T - \theta} \tag{7}$$

where θ is known as the Weiss constant which has the dimensions of temperature and therefore, of energy as $k_B\theta$.

The significance of θ is most easily demonstrated by application of the mean or molecular field theory (MFT).[2,13] The central idea here is that magnetic moments on neighboring atoms give rise to an internal or exchange or 'molecular' field, H_i, in addition to any applied field as in (8)

$$H_i = H_{\text{appl}} + \sum_{j=1}^{n} \gamma_{ij} M_j \tag{8}$$

where H_i is the molecular field at atom i from n sets of equivalent neighboring atoms, j, and γ_{ij} is the coupling constant, which can be expressed as $\gamma_{ij} = n(2Z_{ij}J_{ij})/N_o g^2 \mu_B^2$.

Z_{ij} is the number of neighbors on a given sublattice and n is the number of sublattices needed to describe the magnetic lattice. It is clear that γ_{ij} depends directly on J_{ij}, the HDVV exchange constant. Returning to the definition of the susceptibility and substituting H_i for H we get $M_i = C/nT \times H_i$ and substituting equation (8) for H_i a set of linear equation results, which can be manipulated to give

$$M = \frac{CH_{\text{appl}}}{T\left(1 - \dfrac{C}{nT}\displaystyle\sum_{j=1}^{n}\gamma_{ij}\right)} \text{ or } \chi = \frac{C}{T - \dfrac{C}{n}\displaystyle\sum_{j=1}^{n}\gamma_{ij}} \tag{9}$$

which has the form of the Curie-Weiss law, where

$$\theta = \frac{C}{n}\sum_{j=1}^{n}\gamma_{ij} = \frac{2S(S+1)}{3k_B}\sum_{j=1}^{n}Z_{ij}J_{ij} \qquad (10)$$

Thus, θ is equal to the algebraic sum of all of the exchange interactions acting on a given atom. It follows that the sign of θ is diagnostic of the net exchange, and $\theta > 0$ for net ferromagnetic exchange and $\theta < 0$ for net antiferromagnetic exchange. As well, $k_B\theta$ sets the energy scale for the magnetic exchange and one expects to see deviations from the simple Curie law at temperatures near θ.

Two caveats should be raised here. First, the identification of the sign and magnitude of θ with exchange forces must be treated with caution. Single ion effects can also result in a Curie-Weiss susceptibility showing fairly large, negative θ values. Famous cases are Ti^{3+} in a cubic crystal field and many 4f group ions.[14] Secondly, the MFT is too simple a model to describe magnetic systems in detail, especially near T_c and at low temperatures. The theory is the exact analog of the van der Waals model for the imperfect gas and (while not obvious from the above) assumes an interaction of infinite range. As the superexchange interaction is very short range, depending on orbital overlaps, corrections are needed but a discussion of these lies outside the scope of this chapter.

4.1.1 *Susceptibility and Magnetization of Ferromagnets and Antiferromagnets*

The magnetic susceptibility of a paramagnet, a ferromagnet, and an antiferromagnet are contrasted in Figure 5 in terms of the Curie-Weiss law, plotted in the usual linearized form, χ^{-1} versus T. Note that the temperature intercept at $\chi^{-1} = 0$, which is θ, is zero for the paramagnet, >0 for the ferromagnet and <0 for the antiferromagnet. In performing such an analysis it is important to use data at 'high' temperatures, relative to any critical temperature, T_c, which might be present. In general, the minimum temperature to begin fitting should be at least $2T_c$. A useful check of whether the Curie-Weiss paramagnetic regime has been reached is to compare the derived Curie constant with the expected value. Good agreement is usually a sign that the data are well into the paramagnetic regime for systems which show LRO.

The susceptibility for both ferromagnets and antiferromagnets show strong deviations from the C-W law near and below T_c. For a ferromagnet, χ diverges to very large values, reflecting the onset of parallel spin correlations and becomes strongly dependent on the magnitude of the applied field, owing to the presence of microscopic 'domains'. It is thus better to talk about the magnetization. The MFT can be used again to give a prediction for the expected behavior by substituting Hi (equation 8) into the Brillouin function (equation 1) and plotting in reduced units, $\sigma = M(T)/M(0)$ versus $\tau = T/T_c$, which gives the results of Figure 6. So, one expects a sharp rise just below T_c and an approach to saturation, $\sigma \rightarrow 1$ as $\tau \rightarrow 0$. At saturation, $M_s = M(0) = g\mu_B SN_o$. The problem of determining T_c experimentally for a ferromagnet from magnetization data is nontrivial owing to the aforementioned critical regime. The most reliable methods are to use either heat capacity data (later section) or to measure the magnetization in zero applied field (to eliminate domain effects). The latter is best done using neutron scattering (later section).

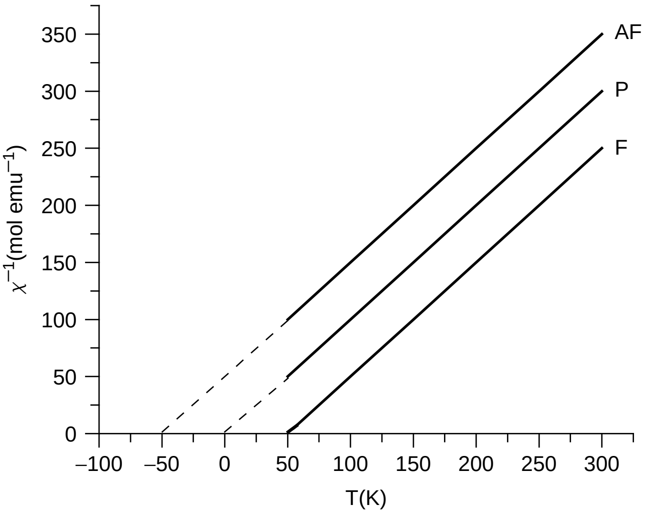

Figure 5 Idealized Curie-Weiss law behavior for a paramagnet, P, an antiferromagnet, AF, and a ferromagnet, F. The simulation has been done assuming C = 1.0 and $|\theta| = 50$ K

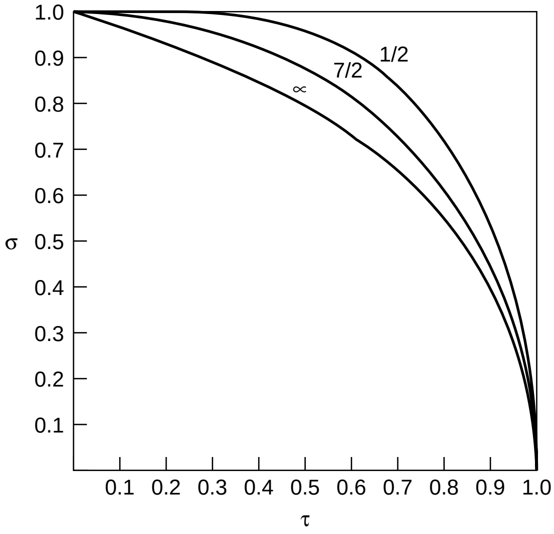

Figure 6 Brillouin functions describing the behavior of the magnetization of a ferromagnet or a single sublattice of an antiferromagnet in the range $T < T_c$. $\sigma = M(T)/M(0)$ and $\tau = T/Tc$. The curves are labeled for different S. (Reprinted from Ref. 13, © 1966, with permission from Elsevier)

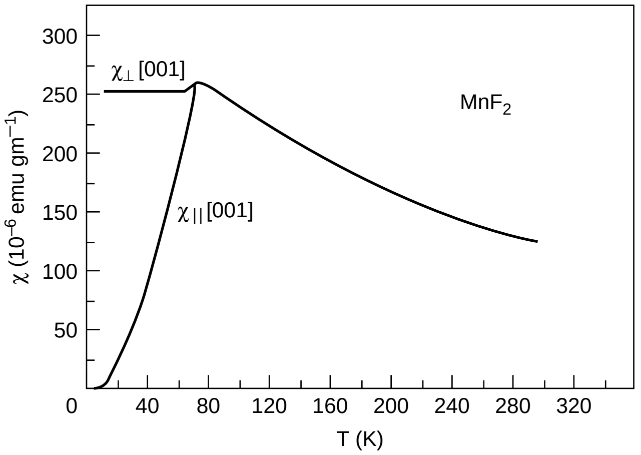

Figure 7 Magnetic susceptibility for a single crystal of MnF_2. The preferred direction is [001][5]

For an antiferromagnet there is a sharp cusp in χ near T_c (T_N) as illustrated by data for MnF_2 Figure 7, below which the susceptibility decreases owing to the build up of antiparallel spin correlations. An initially surprising fact about antiferromagnets is that the total susceptibility does not fall to 0 as $T \to 0$ as illustrated in Figure 7. This is due to magnetocrystalline anisotropy, that is the spins will always find a preferred direction in the crystal. Data taken with the applied field normal to the preferred direction will show temperature independence. This arises because the field induces a small net misalignment of the nominally antiparallel spins (Figure 8). In a polycrystalline sample, one measures the random, powder average $\langle\chi\rangle = 1/3\chi_{\|} + 2/3\chi_{\perp}$ which decreases only to a value of $\sim 2/3\chi_{max}$ at $T = 0$.

The canted antiferromagnet shows ferromagnetic like behavior for the susceptibility and magnetization but can be distinguished from a true ferromagnet by the observation of $\theta < 0$ and a $M_s \sim 10^{-2}$ or $10^{-3}\,\mu_B$.

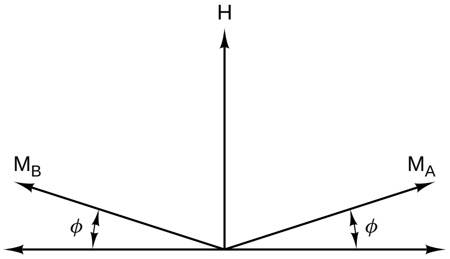

Figure 8 The result of applying a magnetic field normal to the preferred spin direction for an antiferromagnet. The spins are misaligned by a small angle ϕ, giving rise to a small, net moment

The ferrimagnet shows very complex susceptibility and magnetization behavior, which have been described in texts.[5] The ferrimagnet can be distinguished from a true ferromagnet again by the observation of $\theta < 0$ and that $M_s = |MA - MB|$.

4.1.2 Susceptibility and Magnetization for Materials Exhibiting SRO

The most common case is for antiferromagnetic SRO correlations. SRO usually results from the nature of the spatial dimensionality, which limits the spin–spin interactions to dimensions of 0 (isolated oligomers, dimers, trimers, etc.), 1 (chains), or 2 (planes). The common feature of the susceptibility of such systems is (usually) the presence of a very broad maximum, quite distinct from the rather sharp feature seen near T_c for an LRO antiferromagnet. The finite-sized oligomers can usually be solved exactly and analytic solutions are available.[2,14,15] SRO in extended systems, spatial dimensionality 1 or 2, have also been

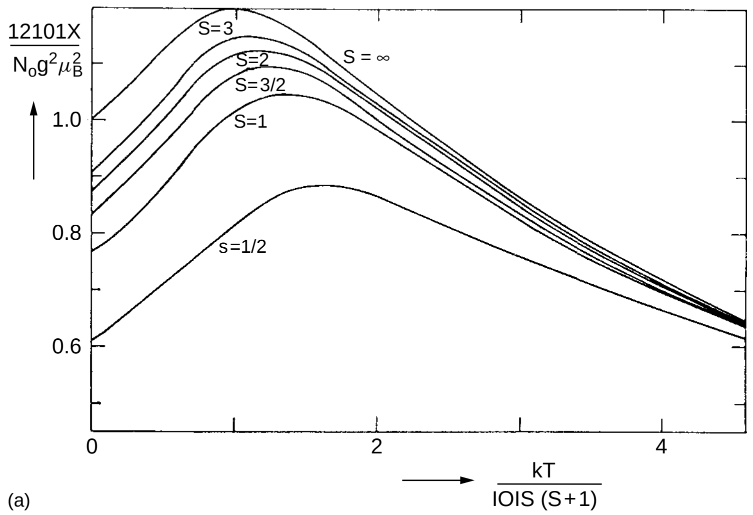

Figure 9 Calculated reduced susceptibility curves for the one-dimensional Heisenberg model for various S. (Reprinted from Ref. 2 with permission from Springer Verlag)

studied intensively. In general, only numerical solutions exist but these are considered to be of an accuracy sufficient for comparison with experiment.[2,8] Typical calculations are shown in Figure 9, where reduced χ is plotted versus reduced T for one-dimensional Heisenberg systems of various spins. The precise details of the curves depend on S and the space and spin dimensionalities. Fitting the data to the models allows extraction of J values.

For systems exhibiting ferromagnetic SRO, no maximum occurs in χ versus T. The best way to detect ferromagnetic SRO is to plot χT versus T. As χT is proportional to $[\mu_{\mathrm{eff}}]^{1/2}$ or C, such a curve will deviate from the horizontal in a positive sense as T is decreased. An example is shown for $PbMnBO_4$, which is a good approximation to a ferromagnetic chain (it also shows ferromagnetic LRO below 31 K) (Figure 10).[17] The data can be compared to a model due to Fisher and J_{chain} can be estimated.[18]

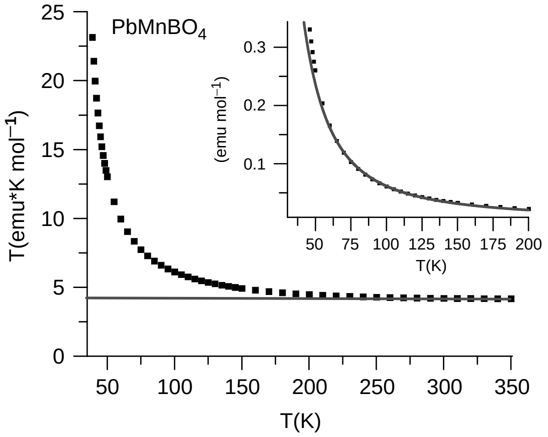

Figure 10 Evidence for one-dimensional ferromagnetic correlations in $PbMnBO_4$. Note the positive deviation from the horizontal $\chi T = C$ line with decreasing temperature. The inset shows a fit to Fisher's model for a linear ferromagnet with $S = 2\,J/k_B = +11\,K$ is found for the intrachain coupling constant. (Reprinted with permission from Ref. 17, © 2003 American Chemical Society)

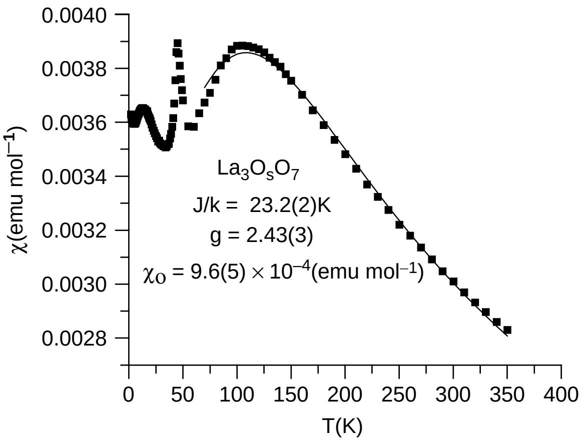

Figure 11 The temperature dependence of the susceptibility for $La_3O_sO_7$, a quasi-linear antiferromagnet showing both SRO (broad maximum near ~125 K) and the cross-over to LRO (sharp peak at ~50 K). (Reprinted from Ref. 19, © 2002, with permission from Elsevier)

It is important to reiterate that there is no true phase transition involved in SRO (refer to Table 1). As already mentioned, for most materials showing SRO there will be a cross-over to LRO at some temperature. A clear example is the oxide $La_3O_sO_7$, which is quasi-one dimensional and from the data (Figure 11), the broad maximum at ~125 K, the SRO signature, is easily distinguished from the sharp maximum, the LRO signature, at ~50 K.[19] It is not uncommon to find, even today, authors claiming the presence of an 'antiferromagnetic' transition from observation of a broad susceptibility maximum.

4.2 Heat Capacity

Heat capacity measurements give information complementary to magnetic susceptibility and magnetization. This complementarity arises naturally from thermodynamics.[2] This technique has also become much more available as instrumentation based on the relaxation method has been marketed widely in the past few years. The heat capacity diverges at T_c and thus provides a very precise measure of T_c, as seen in Figure 12. The shape of the anomaly resembles the Greek

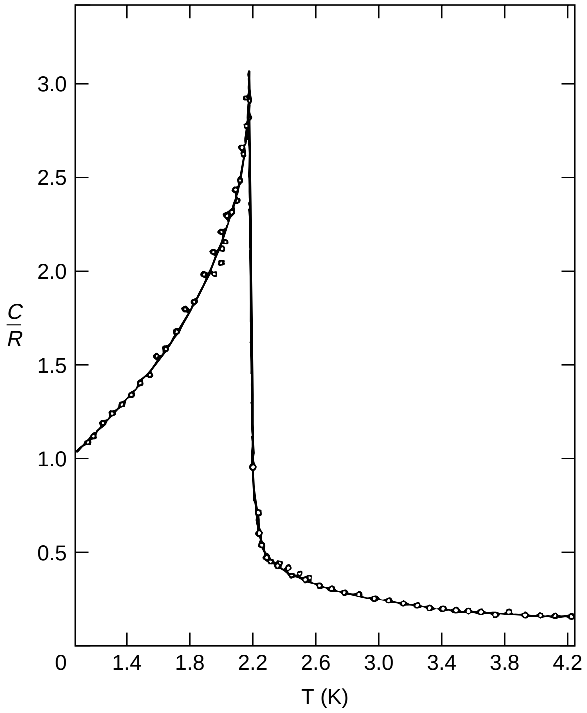

Figure 12 Divergence of the heat capacity at T_c for ferromagnetic $GdCl_3$. (Reprinted from Ref. 13, © 1966, with permission from Elsevier)

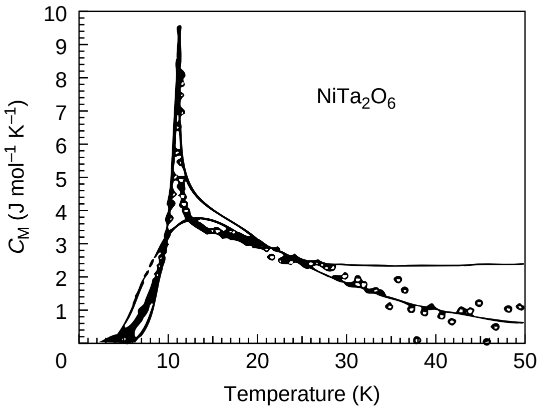

Figure 13 Heat capacity for the tri-rutile oxide NiTa$_2$O$_5$ showing features due to SRO (broad maximum near 20 K) and LRO (sharp λ – peak near 10 K). (Ref. 20. Reproduced by permission from EDP Sciences)

letter lambda and it is often known as the λ–anomaly. As with the susceptibility, heat capacity data are also sensitive to SRO, giving broad maxima instead of the sharp λ-like feature. This is illustrated in Figure 13 for NiTa$_2$O$_6$, which shows both broad SRO and sharp LRO features. Finally, a quantity known as the magnetic entropy can usually be isolated, although this requires a means of estimating and subtracting the heat capacity of the lattice. From the standard relationship between entropy, S, and the heat capacity, C,

$$\Delta S_{\mathrm{mag}} = \int \frac{C_{\mathrm{mag}}}{T} \qquad (11)$$

it is possible to measure the magnetic contribution to the entropy and compare with the theoretical prediction that $\Delta S_{\mathrm{mag}} = R\ln(2S + 1)$.

4.3 Neutron Scattering

Neutron scattering remains the single most useful technique to probe the magnetic properties of matter. Through the de Broglie relationship, neutrons with a velocity appropriate to a kinetic energy equivalent to $k_B T$ where $T \sim 300$ K have a distribution of wavelengths with a maximum slightly greater than 1 Å, comparable to wavelengths used in X-ray diffraction. Such ‘thermal’ neutrons are the principal product of fission reactors and are also produced by particle accelerators at facilities called spallation sources.

Neutron diffraction is complementary to X-ray diffraction and is used widely as a tool for structure refinement in oxide chemistry. For example, the expressions for the structure factor F_{hkl} are compared for both radiation types below:

$$\begin{aligned} F_{hkl} &= \Sigma f_i \exp 2\pi i(hx_i + ky_i + lz_i) \quad (\text{X} - \text{rays}) \\ F_{hkl} &= \Sigma b_i \exp 2\pi i(hx_i + ky_i + lz_i) \quad (\text{Neutrons}) \qquad (12) \end{aligned}$$

where the atomic scattering factor for x-rays, f_i, is replaced by the scattering length for neutrons, b_i. As well, the neutron, by virtue of its spin, has a magnetic moment and thus will be sensitive to magnetic fields owing to unpaired electron density. One can define a magnetic scattering length, p, given by:

$$p = \frac{e^2\gamma}{2mc^2} gSf \quad (\text{for d electrons}) \qquad (13)$$

where e and m are the electronic charge and mass, c is the velocity of light, γ the nuclear magneton, and f is a ‘form factor’, which is a strong function of scattering angle. As it turns out, p is of the same order of magnitude as b for most elements and therefore the magnetic scattering will be of the same order of magnitude as the ‘chemical’ scattering and contributions from the two sources will be superimposed in the same experiment and can be scaled conveniently. One can define a magnetic structure factor in an analogous manner

$$F_{hkl}(\text{mag}) = \Sigma p_i \exp 2\pi i(hx_i + ky_i + lz_i) \qquad (14)$$

It can be shown that what is actually measured in a neutron diffraction experiment is the component of S (or J), which is normal to the scattering vector (which is in turn normal to the scattering plane, hkl), and the total diffracted intensity is then proportional to

$$F^2_{hkl}(\text{total}) = F^2_{hkl}(\text{chem.}) + q^2 F^2_{hkl}(\text{mag}) \qquad (15)$$

where $q^2 = \sin^2\alpha$ and α is the angle between the scattering and magnetic moment vectors. Thus, from a neutron diffraction experiment one can, in principle, determine the dimensions and symmetry of the magnetic sublattice and the magnitude and spatial orientation of the magnetic moments, that is, the magnetic structure. An example is shown in Figure 14 for CoSb$_2$O$_6$, a tri-rutile structure oxide with $T_c = 12.6$ K. Data sets at 298 K and 7.5 K are compared and the latter shows many more reflections, which can be ascribed to LRO. Two possible magnetic structures are shown.

It should be noted that magnetic scattering can also be observed in X-ray diffraction but the intensities of the magnetic reflections are only 10^{-4} at best relative to the normal scattering and these experiments are usually done at synchrotron sources. There is no method of determining a magnetic moment from X-ray scattering. There does exist a technique called resonant magnetic X-ray scattering in which the magnetic intensities can be enhanced by factors of $\sim 10^4$ but this works for only a few elements and there is no detailed theory for scaling the magnetic intensity to extract magnetic moments.

Neutron diffraction/scattering can also probe SRO and low-lying excited states called spin waves, but this discussion lies again outside the scope of this article.

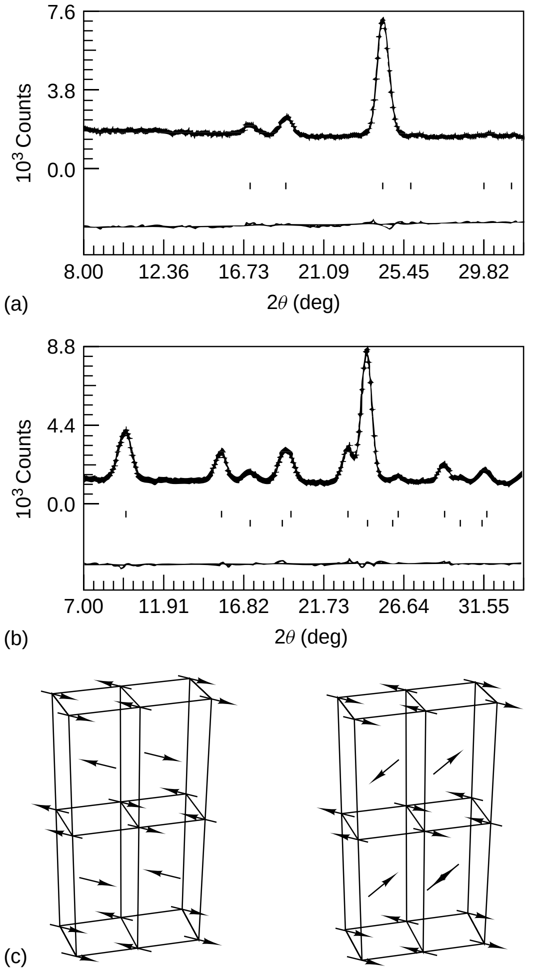

Figure 14 Neutron diffraction data for $CoSb_2O_5$, an antiferromagnet with $T_c = 12.6$ K. (a) Data at 298 K. (b) Data at 7 K, showing the presence of many new reflections due to the AF LRO. (c) Two possible magnetic structures consistent with the data. (Reprinted from Ref. 21, © 1989, with permission from Elsevier)

5 SURVEY OF SELECTED RECENT RESULTS FOR MAGNETIC OXIDES

5.1 Perovskites and Ruddlesden–Popper Phases

It is not surprising that perovskite oxides continue to attract unusual levels of attention. In this category, we include the Ruddlesden–Popper phases of compositions $(AO)(ATO_3)_n$ where A is a large cation, either a divalent alkaline earth or a trivalent lanthanide, and T is a transition element. The index, n, enumerates the number of perovskite ATO_3 units intergrown with rock salt AO layers.

Idealizations of the crystal structures of both the Ruddlesden–Popper phases from $n = 1$, 2, 3, and ∞ (the parent perovskite) are shown in Figure 15.

We begin with the first-row transition elements.

5.1.1 ATO_3, T = Ti

The rare earth titanates crystallize in an orthorhombically distorted form of the perovskite structure, commonly known as the $GdFeO_3$ type, found widely for other $LnTO_3$ materials and described in Pnma (Pbnm in earlier literature) (Figure 16). As the Ln^{3+} ions are too small for 12-fold coordination, the TO_6 octahedral tilt to accommodate a lower coordination number, which is near 9-fold.

As a result the T–O–T angles are significantly less than the ideal 180° in cubic perovskite and vary directly with the radius of the Ln^{3+}, which permits the angles to be tuned by changing the Ln^{3+} radius. The rare earth titanates are unique among $LnTO_3$ materials in that the sign of the Ti–Ti coupling changes from antiferromagnetic for Ln = La, Ce, Pr, Nd, and Sm to ferromagnetic for Gd to Lu.[22] $NdTiO_3$ and $SmTiO_3$ have been reinvestigated. Earlier reports had suggested that $NdTiO_3$ failed to show long-range magnetic order, in spite of the fact that order is observed in all other $LnTiO_3$ perovskites. More recent data indicated an antiferromagnetic transition near 100 K.[23] This was finally confirmed by a neutron diffraction study in which a G-type(G_zF_x) magnetic structure was found on the Ti sublattice, $T_N = 100$ K, while the Nd sublattice was polarized in a F_xC_y structure. Ti(3+) and Nd(3+) ordered moments were 0.99(5) and 1.11(5) μ_B, respectively.[24] The various types of magnetic structure exhibited by perovskites G,A,C, and CE are depicted in Figure 17. $SmTiO_3$ with $T_N = 52$ K had not been investigated in much detail owing in part to the obstacle of an extremely high absorption for thermal neutrons by Sm. This problem was solved using short wavelength neutrons from a 'hot' source and a single-crystal sample. The use of a single crystal allowed the unambiguous determination of the magnetic structure as G_{xy} on Ti^{3+} ($0.72\mu_B$) and C_z ($0.43\mu_B$) on Sm^{3+}.[25] Much attention has also been paid to unraveling the origin of the unprecedented change in the sign of the Ti^{3+}–Ti^{3+} exchange coupling from antiferromagnetic to ferromagnetic as the radius of the Ln^{3+} ion is decreased by sweeping through the lanthanide series.

To this end, much attention has been directed to detailed experimental and theoretical studies of antiferromagnetic $LaTiO_3$ and ferromagnetic $YTiO_3$. While there may not yet be a consensus, a very interesting explanation has been offered by Mochizuki and Imada.[16] Here the key is the orbital ordering of the t_{2g} electrons due to crystal field splitting. The term 'orbital ordering' will also arise in the discussions of many other magnetic oxides, especially T = Mn, but the origin in that case has more to do with Jahn–Teller ordering. There is some confusion in the literature regarding which case is anomalous but it is now generally thought that it is the G-type AF order on $LaTiO_3$. Mochizuki pointed out that the often ignored crystal field of nearly D_{3d} symmetry due to the Ln^{3+} sublattice

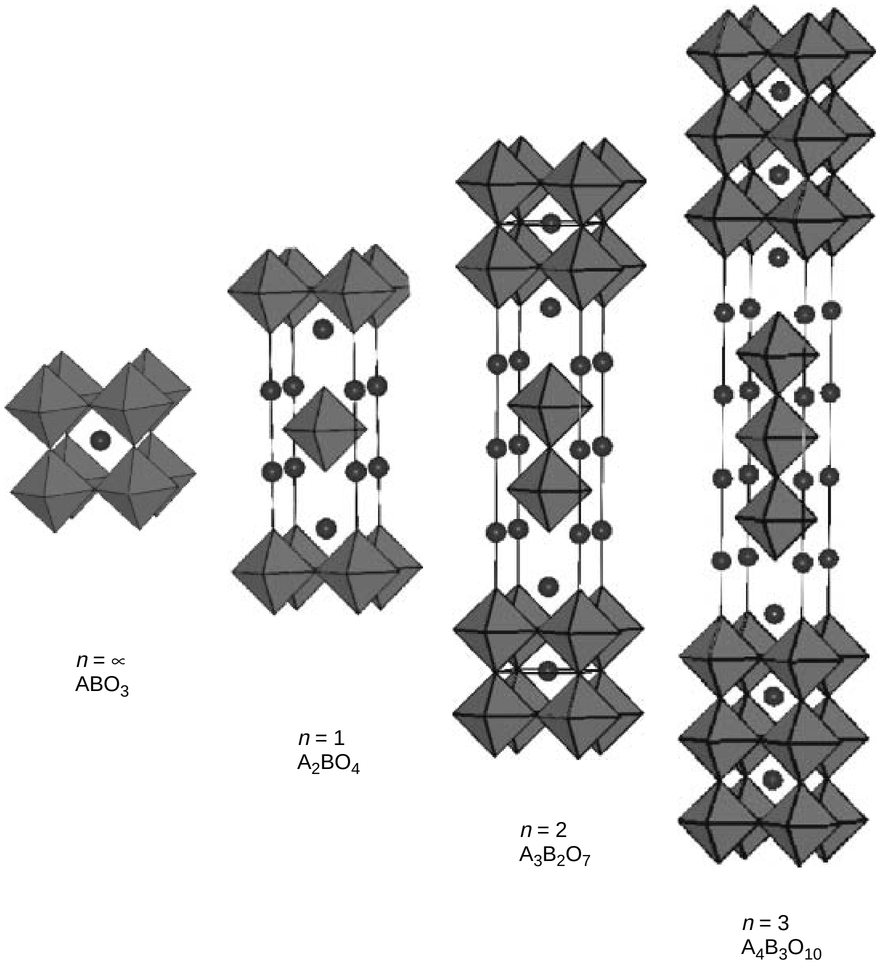

Figure 15 Idealized crystal structures of the Ruddlesden–Popper phases, $(AO)(ABO_3)_n$, $n = \infty$, ABO_3; $n = 1$, A_2BO_4; $n = 2$, $A_3B_2O_7$; $n = 3$, $A_4B_3O_{10}$. The corner-sharing BO_3 octahedrals are shown in polyhedral representation while the A atoms are shown as spheres

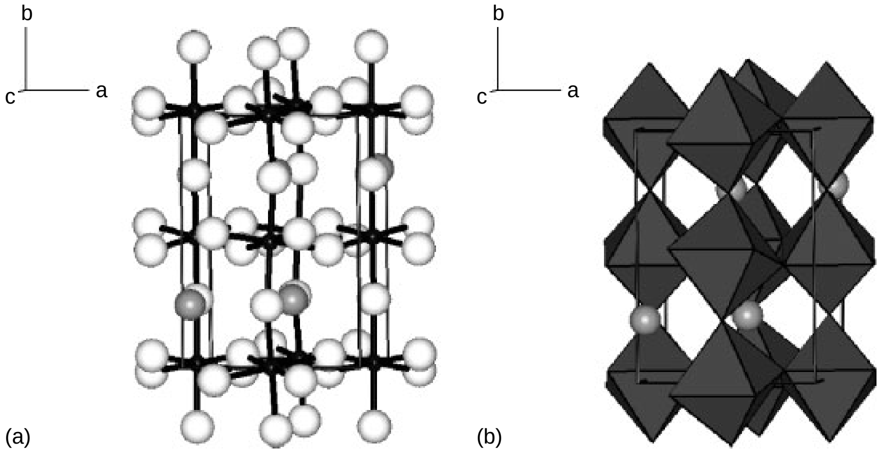

Figure 16 The $GdFeO_3$ structure type, Pnma. (a) Atoms/bond representation. The small black spheres are the Fe ions, the white spheres are O^{2-} and the grey spheres are the Gd ions. (b) Polyhedral representation. The corner-sharing FeO_3 octahedra are shown in black and the Gd ions are represented by grey spheres

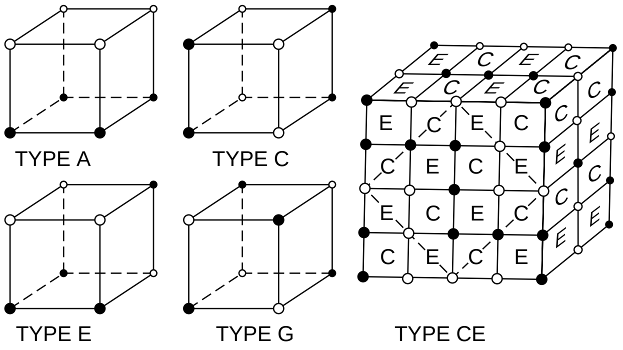

Figure 17 Magnetic structures for antiferromagnetic perovskites. The open and solid black spheres represent sublattices of opposing spin

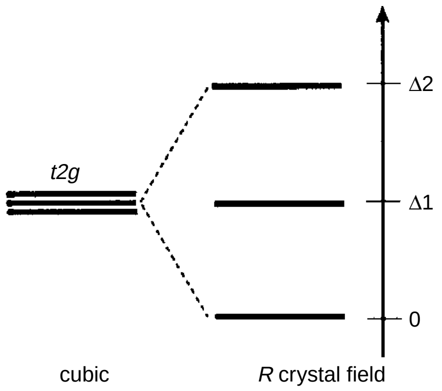

Figure 18 Crystal field splitting of the t_{2g} manifold by the quasi-trigonal crystal field in $LnTiO_3$ perovskites. (Ref. 16. Reproduced by permission of Physical Society of Japan)

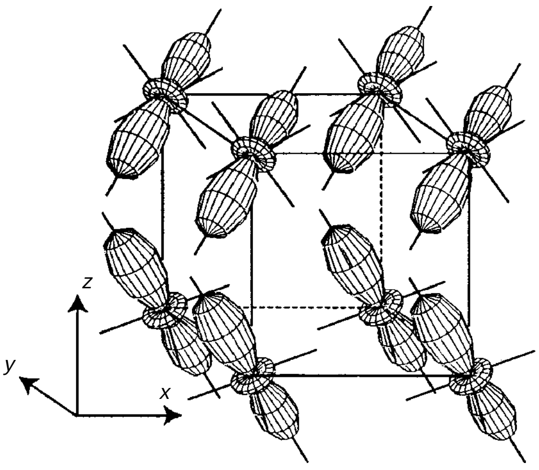

Figure 19 Orbital ordering within the t_{2g}^1 ground state due to the trigonal field in $LnTiO_3$ perovskites. (Ref. 16. Reproduced by permission of Physical Society of Japan)

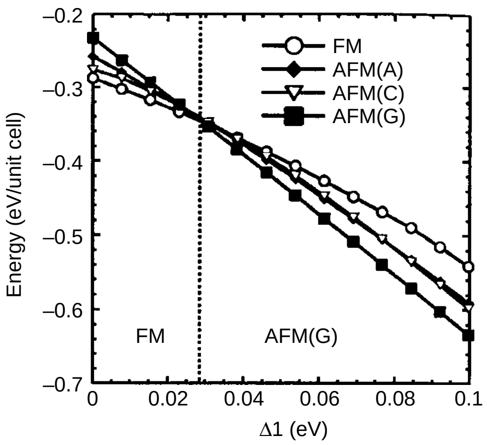

Figure 20 Dependence of the magnetic structure on the crystal field splitting, Δ (see Figure 4), in $LnTiO_3$ perovskites.[16] (Ref. 16. Reproduced by permission of Physical Society of Japan.) Note that for $\Delta > 0.03$ eV, the antiferromagnetic type G (see Figure 17) structure is favored

splits the t_{2g} set into three orbital singlets (Figure 18). In the lowest lying state, the orbitals point along the diagonals of the TiO_6 octahedra (Figure 19). Finally (Figure 20), detailed calculations show that the magnetic ground state is a strong function of the crystal field splitting separating the lowest level from the next highest, Δ in Figure 18. Note the cross-over from G-type AF to ferro F as Δ increases and it is generally regarded that Δ increases as the Ln^{3+} radius decreases (La^{3+} to Y^{3+}). Evidence for a splitting of the t_{2g} levels in $LaTiO_3$ has been inferred recently from a structural study at low temperatures.[27]

5.1.2 ATO_3, $T = Mn$

Excluding the cuprate superconductors, manganese perovskite oxides that exhibit the so-called ‘colossal’ magnetoresistance (CMR) effect constitute, probably, the most extensively studied set of materials over the past decade or so. Several review articles exist.[28–32]

Most attention has been focused on manganates with the perovskite or a related Ruddlesden–Popper type structure, that is, $AMnO_3$ or $A_3Mn_2O_7$. These structures are illustrated in Figure 15, where they are described in the conventional manner in terms of the intergrowth of layers of AO and $AMnO_3$ composition of general formula $(AO)(AMnO_3)_n$. In this notation, the parent perovskite is $n = \infty$ and the various Ruddlesden–Popper variants are labeled in terms of the number of perovskite ($AMnO_3$) layers intergrown with rock salt (AO) layers. Thus, all of the attention has been directed toward the $n = \infty$ and $n = 2$ structure types.

What is ‘colossal’ magneto-resistance (CMR) (or even magneto-resistance)? Magneto-resistance is any change in the resistivity of a material induced by an applied magnetic field and is usually expressed as $(\rho_0 - \rho_H)/\rho_0$ where ρ_0 is

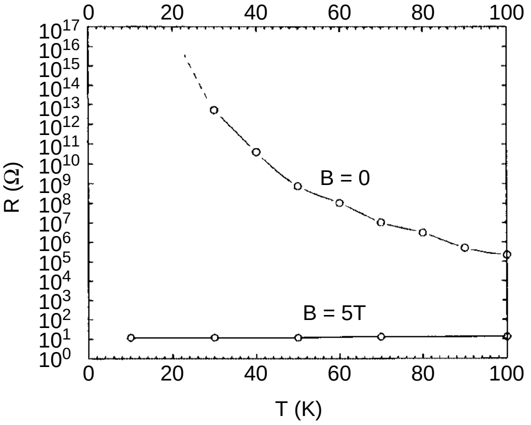

Figure 21 The colossal magneto-resistance (CMR) effect exemplified in $Pr_{0.7}Ca_{0.3}MnO_3$. (Reprinted with permission from Ref. 33, © 1998 American Chemical Society)

the resistivity in zero field and ρ_H is the resistance in a field. The effect is normally seen only in metallic conductors, although there are exceptions, and is a very weak effect in normal metals of the order of a few percent. A larger effect, termed 'giant' magneto-resistance, is exhibited by artificially produced magnetic multilayers in which very thin films (a few nanometers) of a ferromagnetic metal alternate with nonmagnetic layers. Here the effect is due to the so-called spin valve phenomenon and is of a few tenths of a percent. Colossal magneto-resistance (CMR) is illustrated in Figure 21,[33] where the change in resistance can be several orders of magnitude.

CMR occurs for very specific compositions of the type $A_{1-x}A'_xMnO_3$ where $A = Ln^{3+}$ (a lanthanide) and $A' =$ a group 2 ion such as Ca^{2+} or Sr^{2+} and $x \sim 1/3$. Nonetheless, the entire 'solid solution' series, $x = 0$ to 1, has been extensively investigated. In general, an extraordinarily rich 'phase diagram' is found as a function of the ratio of Mn^{3+}/Mn^{4+} and this is presented in Figure 22.[34] In fact, the evolution of magnetic structures had been known since the pioneering work of Wollan and Koehler in the 1950s.[35] The details of the phase diagram depend very strongly on the identity of the Ln^{3+} and A^{2+} species, which will be discussed in a following section. Thus, not all of the magnetic ground states shown in Figure 22 will be realized in every case. Nonetheless, the succession of phases is, beginning with Ln^{3+} Mn^{3+} O_3, A ($x = 0.0$ to ~ 0.10), F ($x = 0.10$ to ~ 0.50), CE ($x \sim 0.50$), C ($x > 0.5$ to ~ 0.80) and G ($x > 0.85$ to 1.00), A^{2+} Mn^{4+} O_3. The magnetic structures represented by the symbols A, F, CE, C, and G are shown in Figure 3. That the CE ground state requires charge and orbital ordering such that Mn^{4+} ions have only Mn^{3+} ions as nearest neighbors (Figure 23) has been known for some time.[26] The phenomenon known as 'charge ordering' is thought to result at least in part from Coulomb repulsion, which acts to avoid (4+) – (4+) nearest neighbors and the local requirements of the Jahn–Teller Mn^{3+} ion. Charge ordering implies a structural phase transition indicated in Figure 22 as T_{CO}.

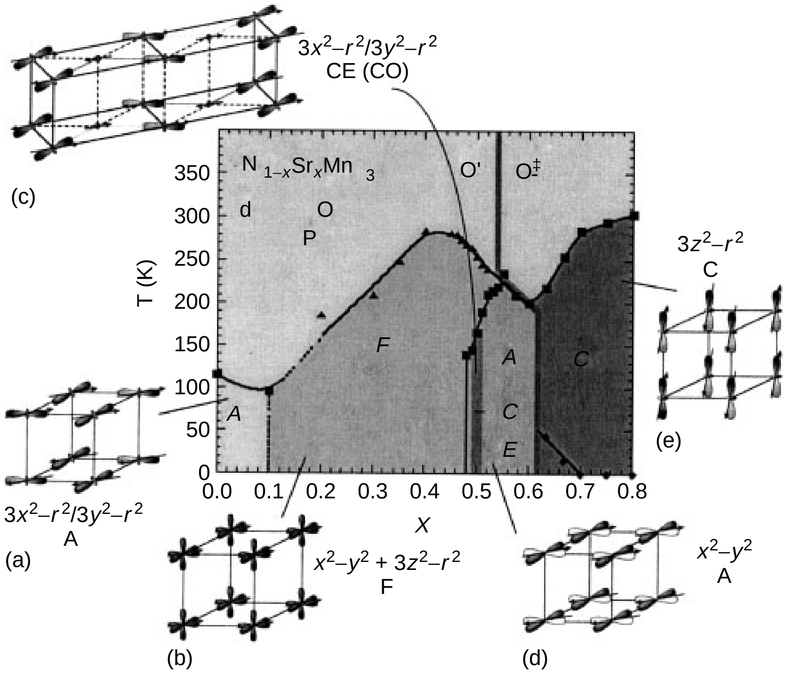

Figure 22 The extraordinarily rich 'phase diagram' of perovskite $Ln_{1-x}{}^{3+}A_x{}^{2+}MnO_3$, illustrated by $Nd_{1-x}Sr_xMnO_3$. (Reprinted from Ref. 34, © 1999, with permission from Elsevier)

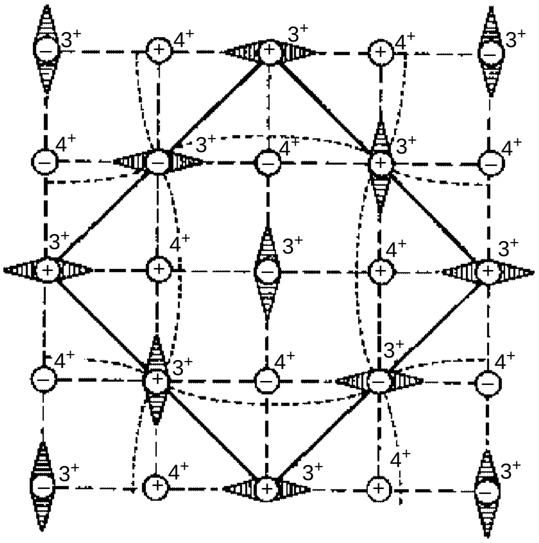

Figure 23 One layer of the CE magnetic structure, illustrating charge ordering between Mn^{3+} and Mn^{4+}

Charge and Orbital Ordering. Again, essentially all of the above had been known since roughly the 1950s. What is relatively new is the realization and experimental verification that in addition to magnetic and charge ordering, the spatial ordering of the e_g orbitals on the Jahn–Teller Mn^{3+} ions must be involved. This connection is shown in Figure 22 for $Nd_{1-x}Sr_xMnO_3$.[34] These orbital orderings have been deduced from synchrotron X-ray scattering studies, which have become possible within the last few years.

Also new is the apparent observation of charge ordering for x values away from 0.50, particularly $x \sim 2/3$, although the precise form of the ordering is somewhat controversial.

Two competing models are the so-called ‘bistripe’ model and the Wigner crystal, both of which involve ordered regions with F, AF, and frustrated near neighbor links as seen in Figure 24.[36]

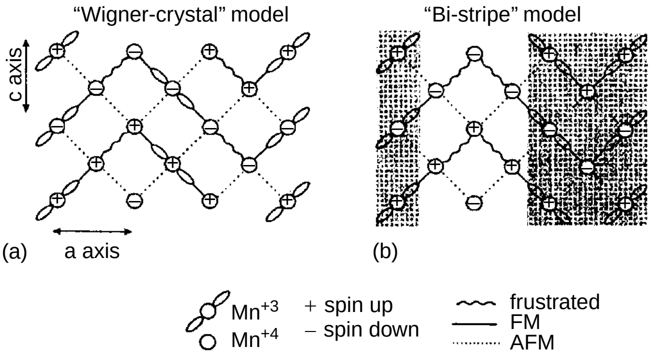

Figure 24 Possible models for charge ordering near $x \sim 2/3$ in $Ln_{1-x}A_xMnO_3$, the Wigner crystal versus the bistripe model. (Reprinted with permission from P.G. Radaelli, D.E. Cox, L. Capogna, S.-W. Cheong, M. Marezio, *Phys. Rev.*, 1999, **B59**, 14440. © 1999 by the American Physical Society)

In addition to the perovskites of the type $A^{2+}_{1-x}Ln^{3+}_xMnO_3$, other dopings have been investigated, for example, the introduction of the tetravalent cations Ce^{4+} and Th^{4+} in place of the trivalent lanthanides. In principle, for each tetravalent dopant ion, two Mn^{4+} ions are reduced to Mn^{3+} and one expects the phase diagram to reflect this and for the most part this is the case.[37] Another approach is to dope with oxide vacancies, for example, $CaMnO_{3-x}$, which also introduces two Mn^{3+} ions per introduced O^{2-} vacancy. In fact, a modest MR effect is seen for $x = 0.06$ and 0.11.[38] As well, a usual charge ordering is reported for the $x = 0.11$ phase, which is required to explain the neutron diffraction data in the magnetically ordered state. Here layers of Mn^{3+} ions order in every fourth layer in the G-type magnetic structure known for $CaMnO_3$ (see Figure 25).[39]

Effect of A-site Disorder and Cation Radius on $T_c(T_{mi})$ and T_{CO}. The effect of changing the contents of the A-site on the various transition temperatures of interest, T_c (Curie temperature for ferromagnetism), which is generally the same as T_{MI} (the metal/insulator transition temperature) and T_{CO} (the charge ordering transition temperature), can be quite large as in Figure 26[40] Attfield was able to show that $T_c(T_{MI})$ correlated very well with the statistical variance, σ, of the A-site ions, that is, $\sigma = \Sigma y_i r_i^2 - \langle rA \rangle^2$. Here the r_i are the standard Shannon radii for 9-fold[41] coordination, y_i

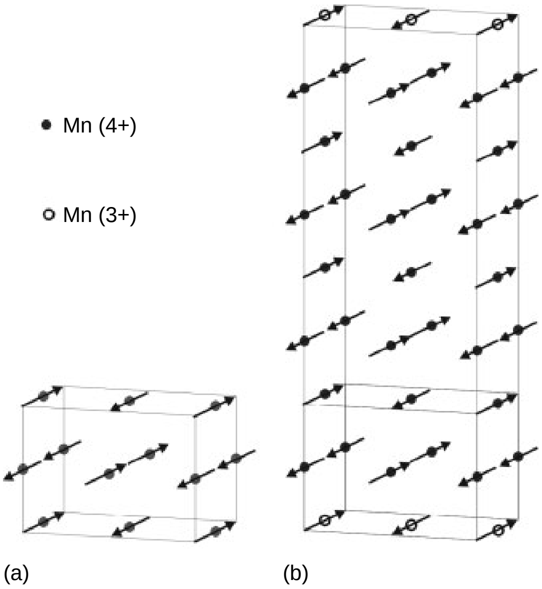

Figure 25 Charge and magnetic ordering in $CaMnO_{2.89}$.[39] The structure (a) shows the type G structure of $CaMnO_3$ and (b) the charge ordered $k = (\,0 \quad 0 \quad 1/4\,)$ found for $CaMnO_{2.89}$. (Reprinted with permission from C.R. Wiebe, J.E. Greedan, J.S. Gardner, Z. Zeng, M. Greenblatt, *Phys. Rev.*, 2001, **B64**, 064421. © 2001 by the American Physical Society)

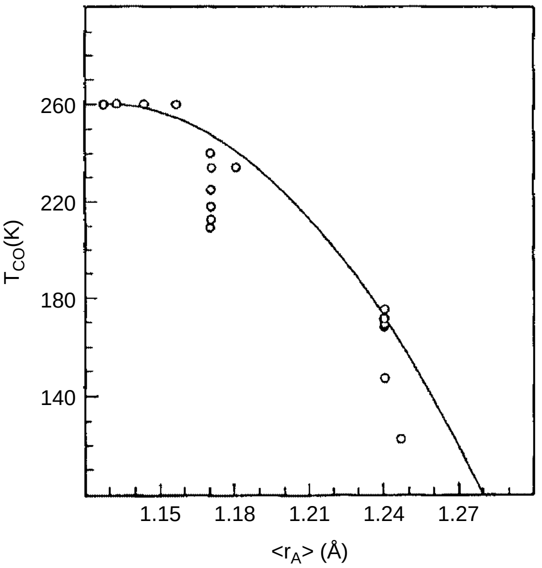

Figure 26 Strong dependence of the charge ordering transition temperature, T_{CO}, on the variance of the radii of the A-site ions in perovskite manganates. (Reprinted with permission from P.V. Vanitha, P.N. Santosh, R.S. Singh, C.N.R. Rao, J.P. Attfield, *Phys.Rev.*, 1999, **B59**, 13539. © 1999 by the American Physical Society)

the concentration of the ith ion on the A-site, and ⟨rA⟩ is the mean A-site radius. An example is shown in Figure 27.[42] Ultimately, these effects were traced to systematic changes in the MnO_3 framework, which work to bend the Mn–O–Mn angles to smaller values, leading to more narrow bands and localization with increasing σ_A^2.[43]

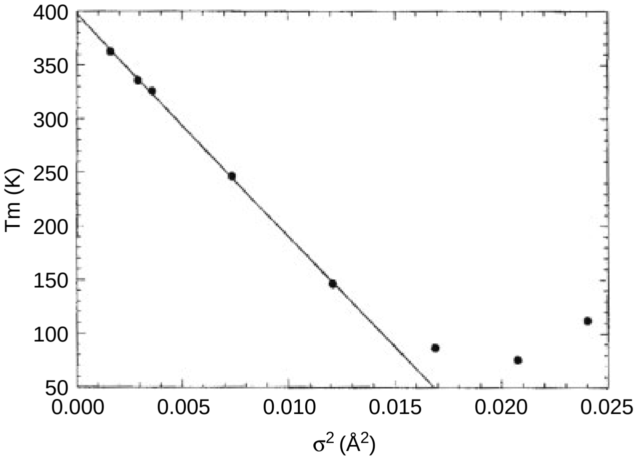

Figure 27 Strong dependence of the metal/insulator transition temperature, T_m, on the variance of the radii of the A-site ions in perovskite manganates. (Reprinted with permission from L.M. Rodriguez, J.P. Attfield, *Phys.Rev.*, 1996, **B54**, R15622. © 1996 by the American Physical Society)

Manganates with $n = 1$ and 2 Ruddlesden–Popper Phases. The $n = 1$ manganates are less studied, primarily because the CMR effect is generally not found. A moderate effect, ∼60%, has been demonstrated for $Ca_{1.92}Pr_{0.08}MnO_4$ at 7T.[44] Charge, orbital, and magnetic order are reported for $La_{0.5}Sr_{1.5}MnO_4$, which has the 1:1 Mn^{3+}/Mn^{4+} composition.[45,46]

The all Mn^{4+} materials, A_2MnO_4, A = Ca, Sr, show strong two dimensional AF correlations and, eventually, long-range AF order.[47] A^{2+} $LaMnO_4$ materials, with all Mn^{3+}, are also two dimensional AF materials with three-dimensional AF order at lower temperatures with one notable exception, $BaLaMnO_4$. In spite of a paramagnetic moment equal to the spin only value for Mn^{3+}, this compound does not order to 1.5 K.[48] In fact, addition of only ∼30% Ba to $SrLaMnO_4$ (which orders at 130 K in the standard AF structure for materials with the $n = 1$ structure) quenches completely the long-range AF order.

The $n = 2$ RP phases do show the CMR effect and have attracted much attention.[49] A recent review surveys the field.[50] A phase diagram for $La_{2-2x}Sr_{1-2x}Mn_2O_7$ is shown in Figure 28.[51] Note that the ferromagnetic Curie temperatures are low, ∼126 K, relative to the perovskite manganates, and that the magnetic structures found are different. Both of these effects result from the layered crystal structure. The types of magnetic structure are illustrated in Figure 29.[51] A singular feature of some of the $n = 2$ materials is the occurrence of phase separation in the CMR regime. That is, the materials Nd_{2-2x} Sr_{1+2x} Mn_2O_7, $x = 0$ and 0.10, actually comprise two phases with very similar lattice constants and compositions. This was discovered in high-resolution neutron diffraction experiments.[52] Also, these Nd-based phases are never either metallic nor ferromagnetic, yet show a moderate MR, >10%. This also illustrates an important feature of the $n = 2$ RP

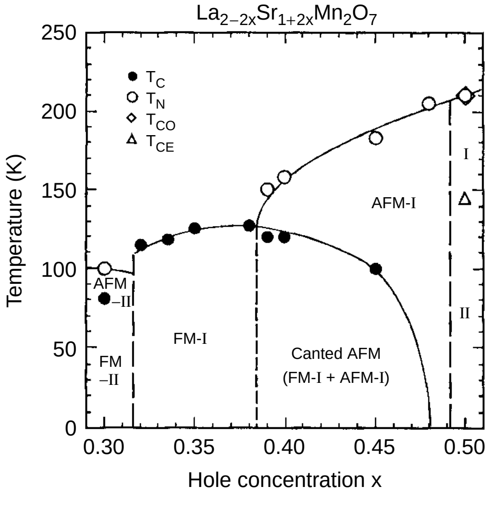

Figure 28 Phase diagram for $n = 2$ Ruddlesden–Popper phases illustrated by $Sr_{2-x}La_{1+x}Mn_2O_7$. (Reprinted from Ref. 51, © 1999, with permission from Elsevier)

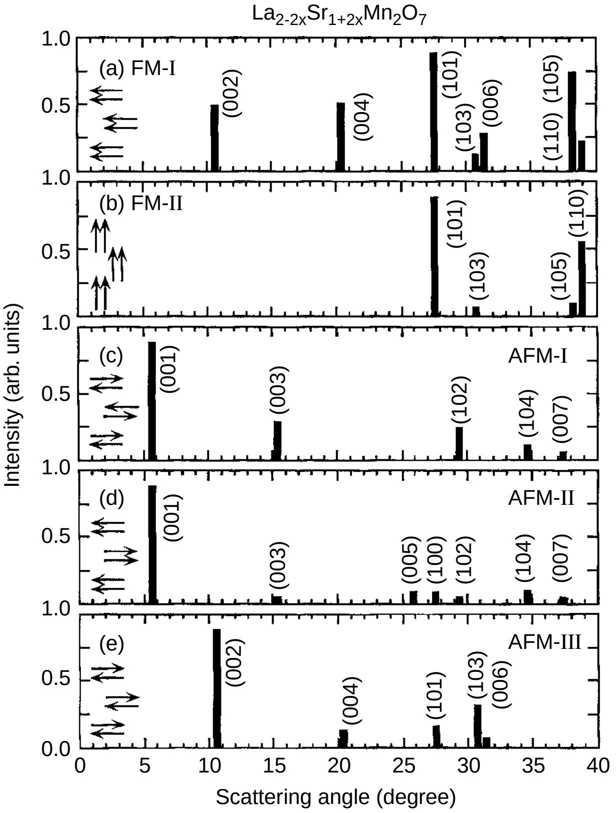

Figure 29 Magnetic structures exhibited by the $n = 2$ RP manganates. (Reprinted from Ref. 51, © 1999, with permission from Elsevier)

phases, namely, the fragility of the ferromagnetic regime as the size of the Ln^{3+} ion is decreased.

5.1.3 ATO_3, $T = Fe$

SrFeO₃. The synthesis of oxygen stoichiometric $SrFeO_{3-\delta}$ with $\delta \sim 0$ generally requires high O_2 pressures of at least 6 GPa to stabilize the Fe^{4+} state.[53] The crystal structure is cubic Pm3m. The material is an unusual metallic antiferromagnet with $T_N = 134$ K and a spiral spin structure that has been interpreted as arising from competition between nearest neighbor ferromagnetic exchange interactions and further neighbor antiferromagnetic interactions.[54] Fe^{4+} is in either the HS state ($t_{2g}^3e_g^1$) or a hybrid (d^5L), where L is a ligand hole.[55] Either doping with Co, $SrFe_{1-x}Co_xO_3$, or oxygen vacancies, $SrFeO_{3-\delta}$, induces ferromagnetism as seen in Figure 30 for the Co-doped materials.[34] In the Co-doped system, the ferromagnetism is thought to result from exchange between LS Co^{4+} (t_{2g}^5) and HS Fe^{4+} ($t_{2g}^3e_g^1$). A small MR effect (few %) is seen in the Co-doped compounds.[56]

Vacancy-doped $SrFeO_{2.81}$ shows MR of ~90% at low temperature, ~70 K. This is proposed to result from Fe^{4+}/Fe^{3+} CO at this temperature.[57]

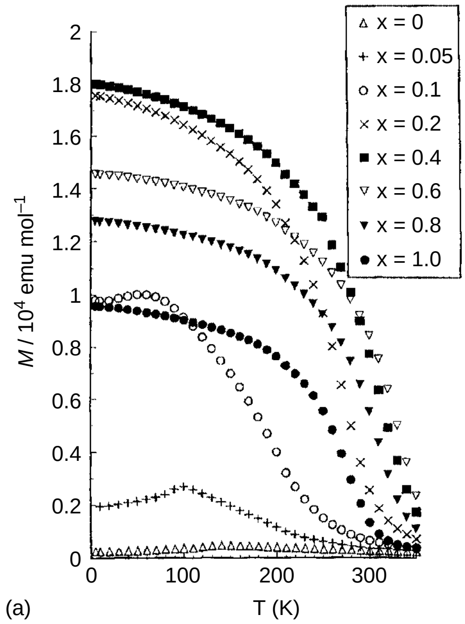

Figure 30 Induction of ferromagnetism in $SrFe_{1-x}Co_xO_3$ for $x \geq 0.20$. (Reprinted from Ref. 53, © 1996, with permission from Elsevier)

5.1.4 ATO_3, $T = Co$

LaCoO₃. This perovskite contains Co^{3+} and the crystal structure is rhombohedral. While the basic properties have been studied since the 1960s,[58] a consensus interpretation has emerged only recently. Typically, the magnetic susceptibility shows a behavior similar to that in Figure 31.[59] The susceptibility is essentially zero at low temperatures (after allowance for a low concentration of paramagnetic impurities, which give a Curie tail) and rises sharply near 90 K–100 K and then falls with increasing temperature. It is natural to assume that the ground state is nonmagnetic LS Co^{3+} ($t_{2g}^6\,e_g^0$, $S = 0$) and that the susceptibility rise is due to a spin state transition. The question remaining is whether the lowest lying excited spin state is HS ($t_{2g}^4e_g^2$, $S = 2$) or intermediate spin, IS, ($t_{2g}^5e_g^1$, $S = 1$). For some time, the HS state was implicated but much evidence, experimental in the direct measurement of the paramagnetic scattering from polarized neutron diffraction,[60] detailed fitting of the susceptibility and the observation of a Jahn–Teller lattice distortion,[61] and theoretical calculations of the relative energies of the three possible spin states[62] seem to indicate the IS state.

SrCoO₃. High pressures are required to stabilize the rare Co^{4+} state and produce a reasonably stoichiometric $SrCoO_{3-x}$. Post annealing of melt grown single crystals in 1.0 to 1.6 kbar O_2 can achieve $x = 0.03$.[63] At this stoichiometry, the structure is reported to be cubic. It has been known for sometime that $SrCoO_3$ is ferromagnetic with T_c reported from 190 K to 220 K and a saturation moment of 1.5 μ_B/F.U.[63] In the paramagnetic

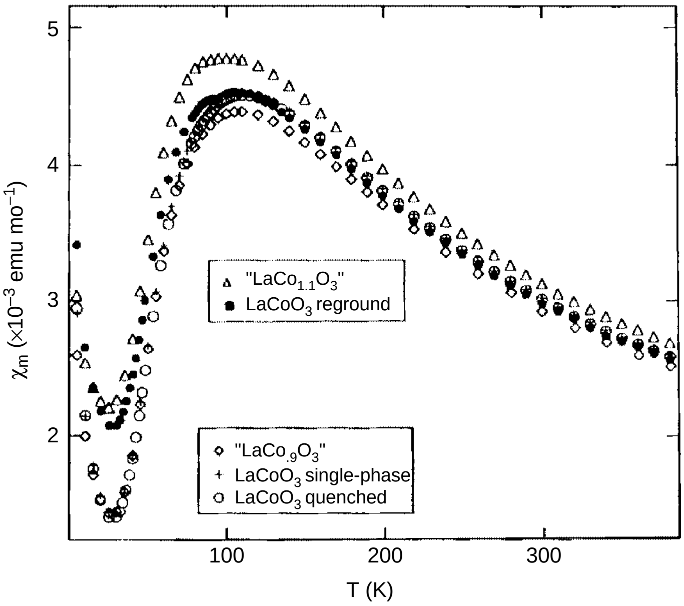

Figure 31 Typical magnetic susceptibility of $LaCoO_3$. (Reprinted from Ref. 59, © 1995, with permission from Elsevier)

regime, a $\mu_{\text{eff}} = 3\mu_B$ is found. Again, until recently the ground state was thought to be LS Co^{4+} ($t_{2g}^5e_g^0$). However, discrepancies with the Co 2p X-ray absorption spectra have led to a new interpretation. It has been proposed that strong hybridization with the ligand p states can actually result in an IS (intermediate spin), $S = 3/2$ ground state rather than the LS, $S = 1/2$.[64] The IS state can be thought of as an HS d^6 configuration with a ligand hole antiferromagnetically coupled to the e_g levels giving $S = 1.5$. The IS state is also consistent with the observed ferromagnetism through a Zener double exchange.[11,12]

$La_{1-x}Sr_xCoO_3$. Substitution of Sr^{2+} for La^{3+} induces both ferromagnetism and metallic behavior, which parallels observations in the related manganates. Indeed, a large magneto-resistance was reported for thin films with $0.15 < x < 0.20$.[65] A possible phase diagram of remarkable complexity is shown in Figure 32.[66] Compositions up to $x = 0.5$ have been studied in detail. While a detailed discussion of the phase diagram is beyond the scope of this article, salient facts are that an insulator to metal transition occurs near $x = 0.3$ and strong ferromagnetic correlations appear even at $x = 0.1$. Originally, it was not clear that true long-range ferromagnetic order was present in these materials but neutron scattering seems to show its existence for substitution levels in the range $0.10 < x < 0.30$[67] and possibly to 0.50[68] but this is somewhat controversial at present. There is evidence for a highly inhomogeneous microstructure involving hole-rich metallic, ferromagnetic domains formed about the substituted Sr^{2+} ions and hole-poor regions with properties more like $LaCoO_3$.[67]

5.1.5 ATO_3, $T = Ru$

In addition to the more commonly investigated 3d transition elements, there has been much interest in perovskite oxides involving 4d and 5d elements. The most intensely studied materials have been the 'ruthenates' and the story is quite complex. $SrRuO_3$ was identified as a ferromagnetic, metallic oxide as early as 1968 with $T_c = 160$ K.[69] At that time, $CaRuO_3$ was characterized as an antiferromagnetic metal with $T_N \sim 110$ K. With the report of superconductivity in Sr_2RuO_4 ($n = 1$RP phase) at ~1 K,[70] many laboratories began systematic explorations of the properties of the RP ruthenates. Brief reviews focusing on the magnetic and transport properties have been published, which provide a convenient summary of work up to ~1999[71] and for more recent results.[72] However, owing to difficulties in crystal growth and control of intergrowth between the structurally similar RP phases, the facts regarding the true properties of the various materials have only recently been established. Beginning with the $n = \infty$ phases, $CaRuO_3$ is now regarded as a paramagnetic metal that is highly susceptible to doping induced magnetic anomalies.[73] For $n > 1$, the Ca-based materials show a variety of behaviors. Ca_2RuO_4 is an antiferromagnetic insulator (AFI), $T_N = 110$ K. $Ca_3Ru_2O_7$ is metallic and AF with $T_N = 56$ K but undergoes a MI transition at 48 K. On the other hand, the Sr-based ruthenates are all metallic. Sr_2RuO_4 is metallic and superconducting below 1 K as mentioned and $Sr_3Ru_2O_7$ is metallic and paramagnetic. It has been argued very recently that the ferromagnetism once ascribed to this compound is due in fact to the $n = 3$ phase, $Sr_4Ru_3O_{10}$, which is a ferromagnetic metal with $T_c = 105$ K[74] and of course the $n = \infty$ member, $SrRuO_3$, is a metallic ferromagnet, as mentioned. The difference in the degree of

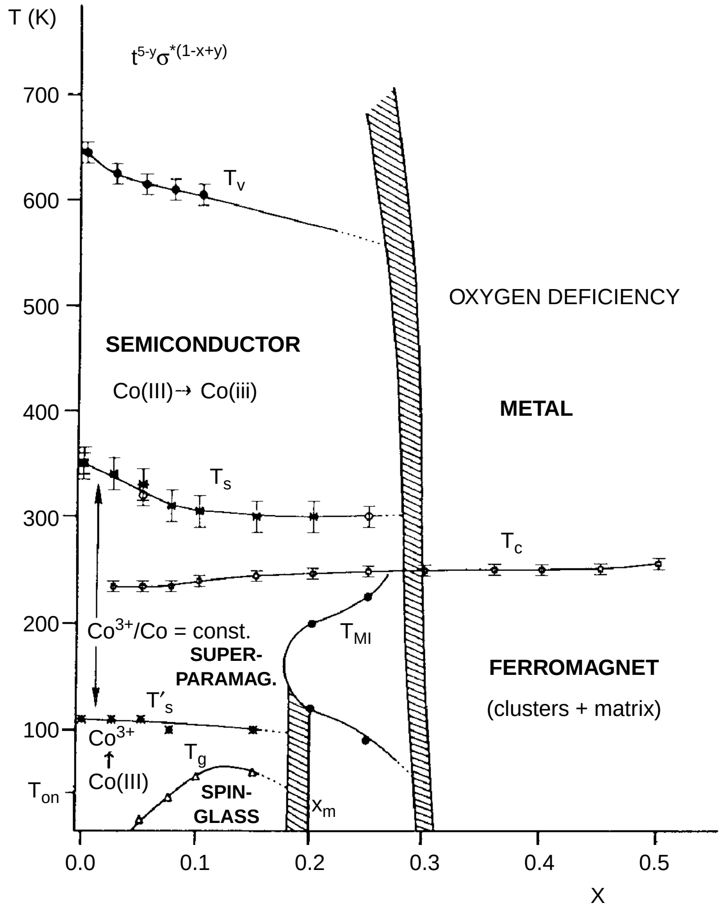

Figure 32 Phase diagram of the $La_{1-x}Sr_xCoO_3$ system. (Reprinted from Ref. 66, © 1995, with permission from Elsevier)

electron localization can be attributed to the difference in Ru–O–Ru bond angles, which are more acute for the Ca-based materials. For example, while Sr_2RuO_4 crystallizes in the ideal I4/mmm structure for which the Ru–O–Ru angles connecting corner-sharing octahedra are rigorously 180°, Ca_2RuO_4 is described in orthorhombic Pbca wherein the corresponding angles are significantly more acute, ~151°.[75] The structures of $Ca_3Ru_2O_7$ and $Sr_3Ru_2O_7$ are both distorted from I4/mmm.[76] In the case of $Ca_3Ru_2O_7$, the AFI state can be destroyed by application of a very large field, 28T, giving rise to a CMR effect.[77]

5.2 Other Perovskite – Based Magnetic Oxides

5.2.1 B-site Ordered Double Perovskites

In perovskites of the type $AA'BB'O_6$, ordering of the B-site ions may occur if the differences between ionic size and formal charge is sufficiently large. The crystal chemistry of these complex perovskites has been reviewed recently.[78] More than 300 materials can be identified as 'double perovskites' so only a few compounds will be described here. Attention will be focused on perovskites for which there is significant crystallographic order between the B and B′ ions. For 1:1 B-site order, the idealized, cubic structure can be described as a 'rock salt' type, since the B and B′ ions form a NaCl supercell (Figure 33). Factors that determine B-site ordering are the differences in ionic radius and formal charge as seen in Figure 34.[78] Guidelines that can be deduced are that Δ(IR) ≥ 0.2 Å and Δ(FC) ≥ 2 for 'rock salt' order although a few exceptions exist. The use of the 'rock salt' label in Figure 34 does not imply always Fm3m symmetry. The true symmetry is a function of the A-site/B-site size ratio. Twelve possible symmetries have been identified from group theory analysis,[79] with the most common cases being tetragonal, I4/m, and monoclinic, $P2_1/n$, with the ideal Fm3m being somewhat rare. As well, the observation of superlattice reflections does not imply that the B-site ordering is complete. In many important cases. it has been shown that partial ordering occurs and that the extent of ordering is a strong function of preparation details.

Magnetic B-site ordered perovskites are of interest in at least two contexts, 'half-metallic ferromagnets', which show a large MR due to intergrain effects, and geometric magnetic

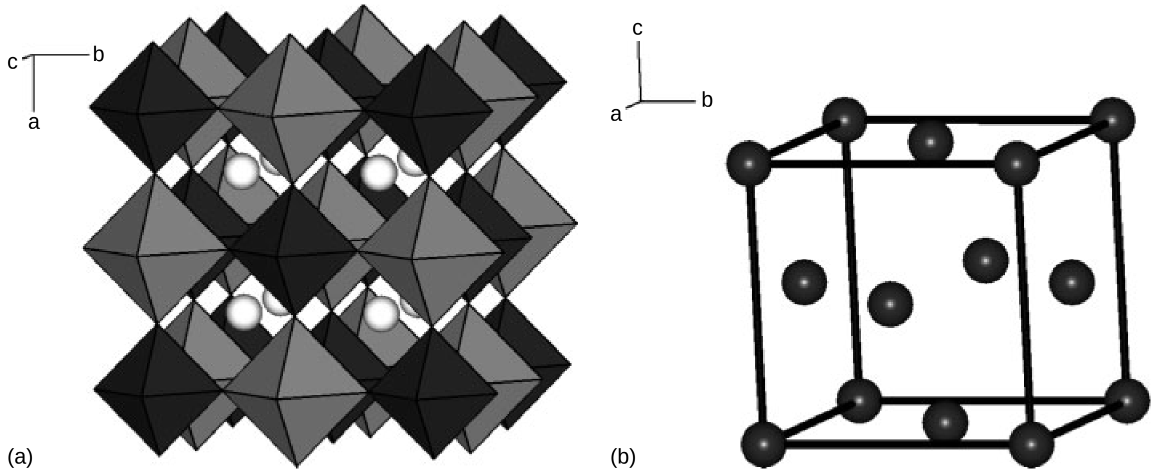

Figure 33 Unit cell of the B-site ordered double perovskite, $A_2B'B''O_6$.(Fm3m). (a) The light grey octahedral represent the B″ sublattice, the dark grey octahedra the B′ sublattice, and the white spheres the A_2 sublattice. (b) The fcc sublattice for either the B′ or B″ sublattice

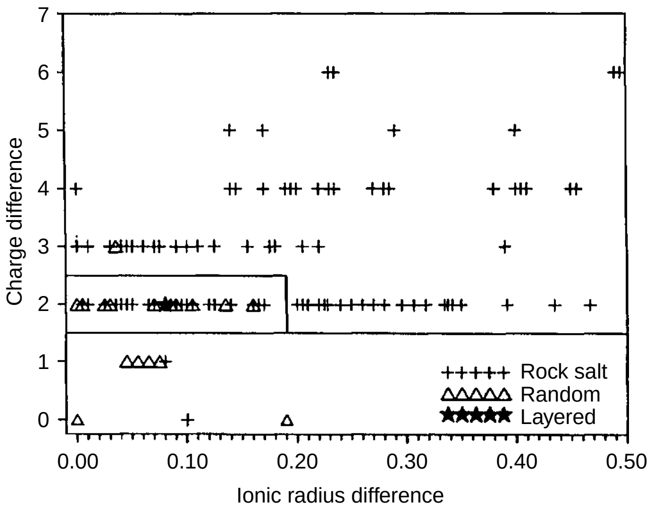

Figure 34 Phase diagram showing the dependence of B-site ordering on the differences in formal charge and ionic radii in $A_2B'B''O_6$ perovskites. (Reprinted from Ref. 78, © 1993, with permission from Elsevier)

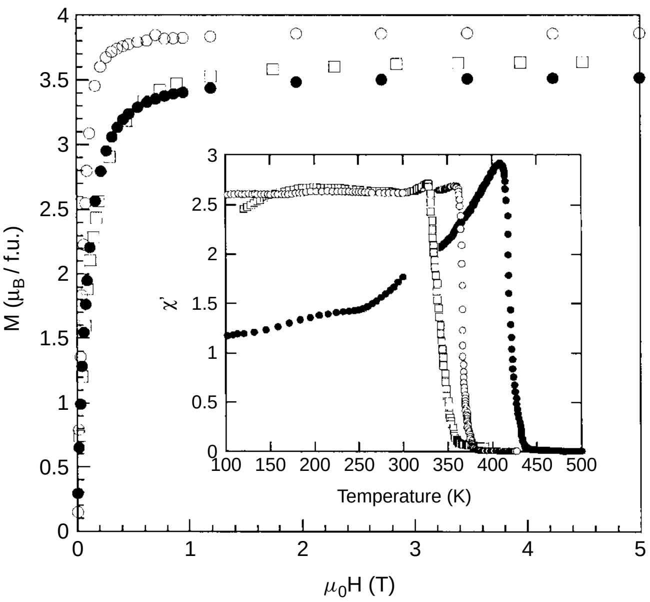

Figure 35 Ferromagnetism in Sr_2FeMoO_6 with $T_c > 400$ K. (Ref. 82. Reproduced by permission of IOP Publishing Ltd)

frustration. Materials in the latter category will be discussed in a following section. The most intensively studied perovskite in the former class is Sr_2FeMoO_6 while many variants $A_2BB'O_6$ where $A = $ Ca, Sr, or Ba, $B = $ Cr, Mn, Fe, Co, and $B' = $ Mo, Re have also received attention.

Sr_2FeMoO_6. While this material has been known since 1963,[80] intense interest was sparked by the announcement of room temperature MR in 1998.[81] The material is ferro or ferrimagnetic with $T_c > 400$ K and a metallic conductor, Figure 35.[82] This unusual combination of properties can be explained in terms of the 'half-metallic ferromagnetic' electronic structure model, Figure 36.[83] Note that the Fermi level lies in a gap with respect to the spin-up polarized DOS but within the t_{2g} spin-down band which has contributions from both Fe 3d and Mo 4d states, that is, the material is insulating with respect to the spin-up states but metallic with respect to spin-down and the unequal population of the spin states gives rise to a spontaneous ferromagnetic moment, hence the nomenclature 'half-metallic ferromagnet'.

The crystal structure is clearly tetragonal, most likely I4/m, at room temperature although a transition from cubic Fm3m to I4/m accompanies the magnetic phase transition near 400 K in the samples studied (Figure 37).[84] The issue

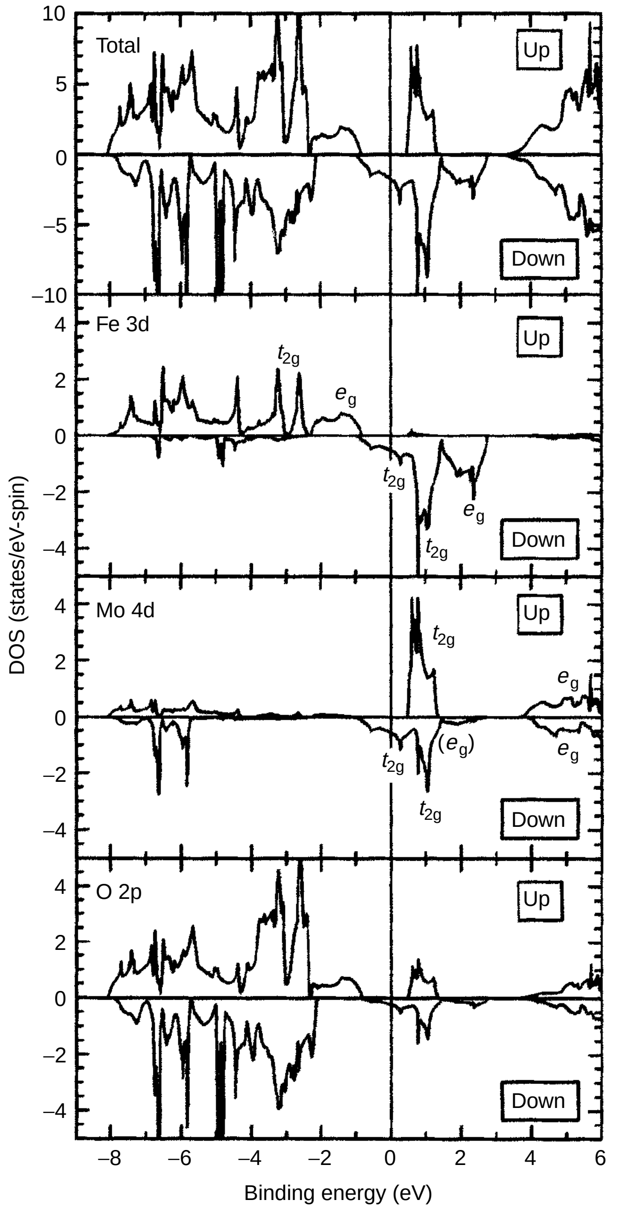

Figure 36 Band structure calculations for Sr_2FeMoO_6 showing 'half-metallic' ferromagnetic character. (Reprinted with permission from T. Saitoh, M. Nakatake, A. Kakizaki, H. Nakajima, O. Morimoto, Sh. Xu,Y. Moritomo, N. Hamada, Y. Aiura, *Phys.Rev.*, 2002, **B66**, 035112. © 2002 by the American Physical Society)

of the extent of B-site order has been debated. This is quantified in terms of antisite disorder (ASD), that is, the fraction of Fe and Mo site interchanged. In single-crystal samples prepared by float zone melting, ASD levels of less than 5% are reported but for powder samples prepared at lower temperatures it is claimed that the antisite disorder level (ASD) can be tuned with annealing temperature with values up to 80%.[85] Not surprisingly, sample properties such as T_c and saturation magnetization are a strong function of ASD.

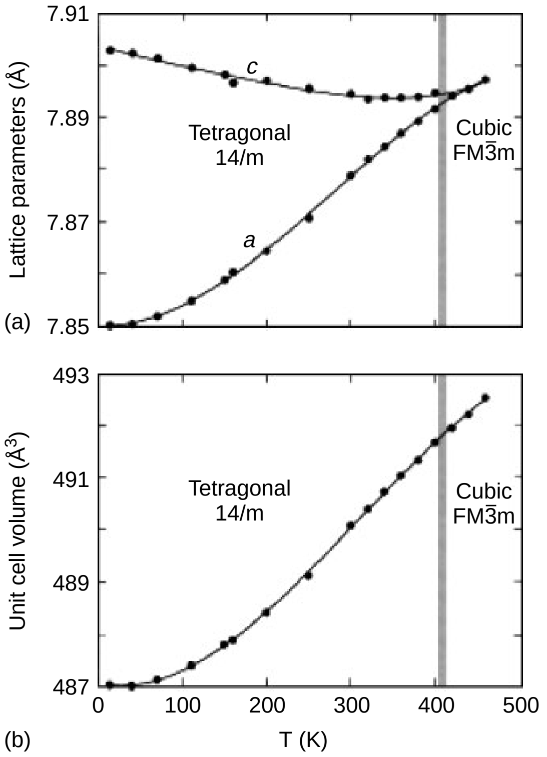

Figure 37 Cubic to tetragonal structural transition in Sr_2FeMoO_6 at T_c. (Reprinted with permission from O. Chmaissem, R. Kruk, B. Dabrowski, D.E. Brown, X. Xiong, S. Kolesnik, J.D. Jorgensen, C.W. Kimball, *Phys.Rev.*, 2000, **B62**, 14197. © 2000 by the American Physical Society)

As well, the issues of the oxidation states of Fe, Mo and the magnetic structure have been debated. A mixed valency according to the equilibrium

$$Fe^{3+} + Mo^{5+} = Fe^{2+} + Mo^{6+} \tag{16}$$

has been proposed. Various relevant techniques such as ^{57}Fe Mössbauer and core-level X-ray spectroscopies seem to support such a formulation although it seems clear that the picture $Fe^{3+} + Mo^{5+}$ is a good first approximation.[86,87] Neutron diffraction results seem consistent with HS Fe^{3+} ($\mu_{\text{spinonly}} = 5\,\mu_B$, $\mu_{\text{obs}} = 4.3\,\mu_B$) and a moment of $\sim 1\,\mu_B$ on Mo^{5+}, which is also consistent with the measured bulk saturation moment on the best ordered samples of $\sim 3.6\,\mu_B$.[83,88]

Finally, the MR effect in this and related double perovskites is not of the same origin as the bulk effect seen in perovskite manganates but is due to spin dependent scattering at grain boundaries via a charge carrier tunneling mechanism.[81] The advantage and promise of the double perovskites is that the MR effect of several percent occurs at room temperature and at quite low fields in the mT range.

5.2.2 *A-site Ordered Double and Triple Perovskites*

In addition to B-site ordering, A-site order can occur although its observation is much more rare. A-site ordering is seen only when the large Ba^{2+} ion is present in company with a Ln^{3+} ion. Both double, $LnBaT_2O_{5+\delta}$, where T = Fe or Mn, and triple, $LnBa_2T_3O_{8+\delta}$, where T = Fe, perovskites of this type have been reported recently.[89–91]

In these cases, A-site ordering results in a doubling or tripling of one of the perovskite unit cell axes, hence the nomenclature. Note also that the oxygen content is always less than the fully stoichiometric level, $5 + \delta$ instead of 6, and $8 + \delta$ instead of 9, for the double and triple perovskites, respectively. A consequence of this is that the coordination environment of at least one set of T ions is 5-fold pyramidal rather than 6-fold octahedral.

Figure 38 shows both structures. The $LnBaT_2O_5$ phases are compositionally similar to the well-known brownmillerites, such as $Ca_2Fe_2O_5$, but the structure is very different. In the brownmillerites, the B-site coordination geometries are distorted octahedral and tetrahedral, not 5-fold square pyramidal. The $LnBa_2Fe_3O_8$ materials are of course directly related to $YBa_2Cu_3O_7$! Another consequence of the oxygen stoichiometry in the $LnBaT_2O_5$ materials is that the T element is present in a mixed valence state, T^{2+}/T^{3+} as found in magnetite, Fe_3O_4.

$LnBaFe_2O_{5+\delta}$. These exist for Ln = Nd – Y(Ho), spanning a reasonable range of Ln^{3+} radii from relatively large (Nd^{3+}) to relatively small(Ho^{3+}) The materials must be prepared within a narrow range of pO_2 (oxygen partial pressure) between 10^{-15} and 10^{-16} and δ is a strong function of pO_2.[89] The crystal symmetry varies with δ, being Pmmm for $\delta < 0.04$ and transforming to P4/mmm for $\delta > 0.1$. All materials in the series order antiferromagnetically at high temperatures with $T_N = 435$ K (Nd) and 432 K(Ho), with essentially no size dependence. The antiferromagnetic order seems odd at first as both Fe^{2+} and Fe^{3+} are formally present. This is explained as resulting from a situation in which the Fe ions are electronically equivalent (at higher temperatures) and are considered as $Fe^{+2.5}$. However, for all materials in this series, a CO transition (analogous Verwey transition in Fe_3O_4) occurs at lower temperature, ~200 K (Ho) or ~300 K(Nd), into a HS Fe^{3+} and a Fe^{2+} state, which can be seen in neutron diffraction, calorimetry,, and magnetic susceptibility.[92] A change in magnetic structure accompanies the Verwey transition. This is shown for $TbBaFe_2O_5$ in Figure 39.[93]

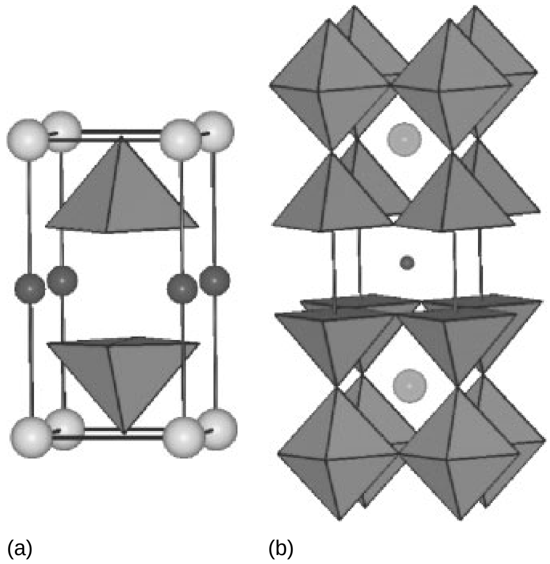

Figure 38 Crystal structures of the A-site ordered double (a), $LnBaT_2O_5$, and triple (b) perovskites. Of particular interest is the occurrence of fivefold square-planar sites

YBa_2MnO_5. Only the Ln = Y phase has been studied in much detail for the T = Mn materials. In sharp contrast to the T = Fe phases, evidence for short range CO is

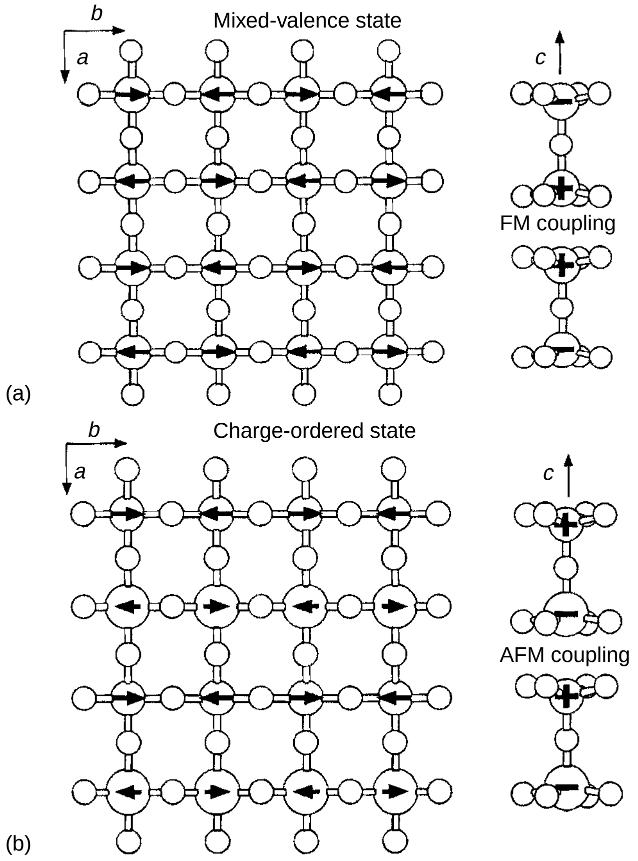

Figure 39 Change in the magnetic structure for $TbBaFe_2O_5$ at the charge ordering or Verwey transition. (a) Mixed valence state. (b) Charge ordered state. (Reprinted with permission from P. Karen, P.M. Woodward, J. Linden, T. Vogt, A. Studer, P. Fischer. *Phys. Rev.*, 2001, **B64**, 214405. © 2001 by the American Physical Society)

found even at 300 K, well above the transition to long-range ferrimagnetic order below 167 K.[94] Figure 40 shows the valence and magnetic ordering model for this material.

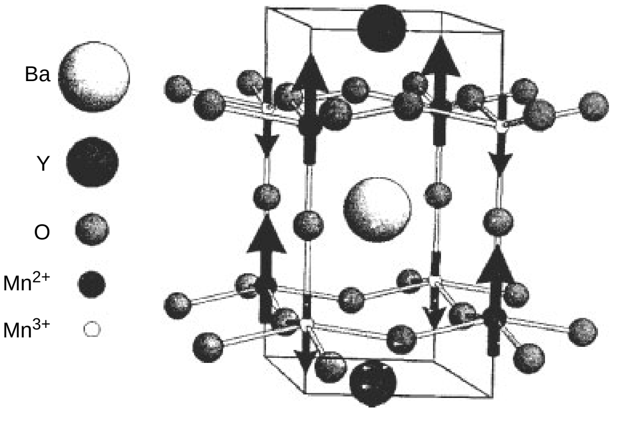

Figure 40 Charge and magnetic order in YBa_2MnO_5. (Ref. 94. Reproduced by permission of Royal Society of Chemistry)

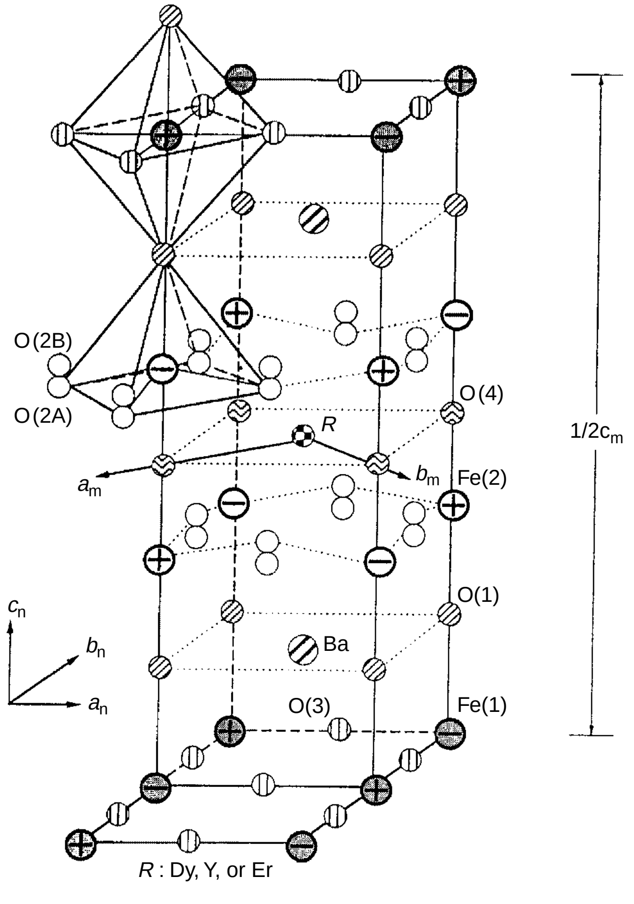

Figure 41 Magnetic structure of $YBa_2Fe_3O_8$. Only one-half of the magnetic cell is shown. (Reprinted from Ref. 91, © 1998, with permission from Elsevier)

$LnBa_2Fe_3O_8$. Only the small Ln^{3+} ions, Dy, Y, Er, give the triple perovskite structure, described in P4/mmm. Larger ions show only a disordered cubic Pm3m cell and no perovskite phase forms for ions smaller than Er.[91] These materials all order magnetically well above room temperature, $T_N \sim 650$ K. The magnetic unit cell is related to the chemical cell as $a_{\text{mag}} = b_{\text{mag}} = \sqrt{2}a_{\text{chem}}$, $c_{\text{mag}} = 2c_{\text{chem}}$ and the magnetic structure is shown in Figure 41.

5.2.3 *Pillared Perovskites*

Recently, an unusual series of perovskite related materials has been reported with the composition $La_5T_3T'O_{16}$, where $T = Mo^{4+}$ or Re^{5+} and $T' = Mo^{4+/5+}$, Mg^{2+}, Mn^{2+}, Fe^{2+}, Co^{2+}, and Ni^{2+}.[95,96] The structure can be visualized as a 'pillaring' of corner-shared octahedral layers of $TT'O_6$ by dimeric edge-sharing T_2O_{10} units as in Figure 42. For the Re^{5+} based series, the Re_2O_{10} dimer is diamagnetic and involves a Re=Re double bond. The Re^{5+} and T'^{2+} ions order crystallographically in the perovskite layers as expected given the +3 difference in formal charge. As Re^{5+} ($5d^2$, S = 1) is magnetic in these compounds, the perovskite layers are in principle 2D ferrimagnets. Evidence for this is shown in Figure 43 for $La_5Re_3CoO_{16}$ where a plot of χT versus T displays first decreasing values of the effective moment with decreasing temperature indicating antiparallel correlations between Co^{2+} (S = 3/2) and Re^{5+} (S = 1) followed by a sharp increase at lower temperatures when finite ferrimagnetic clusters form. The strong decrease at still lower temperatures is due to long-range antiferromagnetic order between the ferrimagnetic layers. In spite of the rather large interlayer separation of >10 Å, ordering temperatures as high as 161 K ($La_5Re_3MnO_{16}$) or even 200 K ($La_5Mo_4O_{16}$) are seen (Figure 44).[97,98] The long-range ordered AF ground state

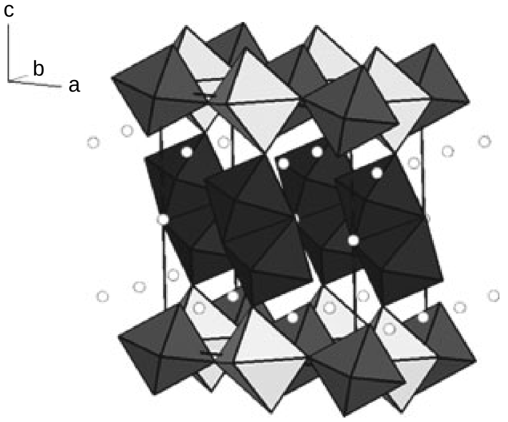

Figure 42 Crystal structure of a pillared perovskite material, $La_5Re_3MnO_{16}$. The grey and white octahedra represent the $MnReO_6$ site-ordered perovskite like layers and the black octahedra, the Re_2O_{10} edge-sharing dimers. The white spheres show the La ion positions

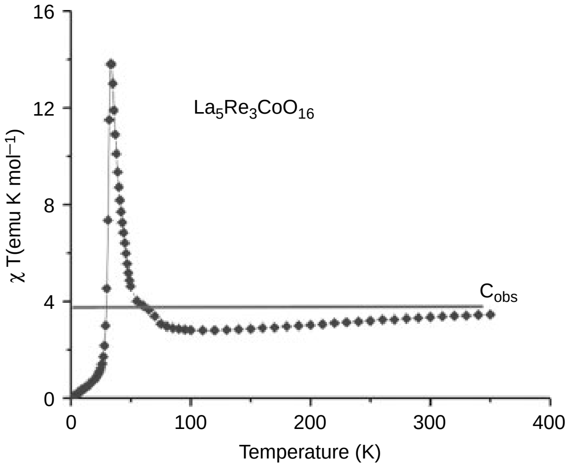

Figure 43 Evidence for short range ferrimagnetic correlations in $La_5Re_3CoO_{16}$. Note the negative deviation from the horizontal $\chi T = C$ line at high temperatures and the strong positive deviation at low temperatures. (Reprinted from Ref. 99, © 2003, with permission from Elsevier)

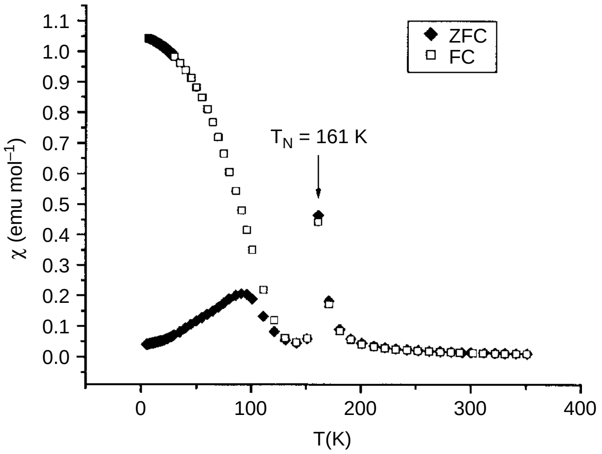

Figure 44 Evidence for long-range magnetic order in $La_5Re_3MnO_{16}$ at $T_c = 161$ K. (Reprinted from Ref. 98, © 2002, with permission from Elsevier)

has been confirmed from neutron diffraction for $La_5Re_3FeO_{16}$ ($T_N = 155$ K), which consists of AF order of the ferrimagnetic layers with ordered moments of $3.0\,\mu_B$ on Fe^{2+} ($S = 2$) and $1.5\mu_B$ on Re^{5+} ($S = 1$) (Figure 45).[99] The AF structure can be destroyed by relatively weak applied fields(0.5T), where meta-magnetic or spin flop transitions are observed.

5.3 Low-Dimensional Oxides, Materials with 2H-Perovskite Related Structures

5.3.1 Sr_4PtO_6 Structure Compounds

Other oxides with composition analogous to perovskite, that is, ABO_3, exist but with a very different condensation scheme for the BO octahedra. In the so-called 2H-perovskite structure, the octahedra share opposite faces forming linear chains. Many other structures share this motif and the crystal chemistry has been reviewed.[100] In particular there has been considerable interest in materials that are isostructural with Sr_4PtO_6, the structure of which is shown in Figure 46.[100] Here the linear chains feature alternating face-sharing sites of octahedral and trigonal prismatic geometry, the latter being rather rare in oxide crystal chemistry.

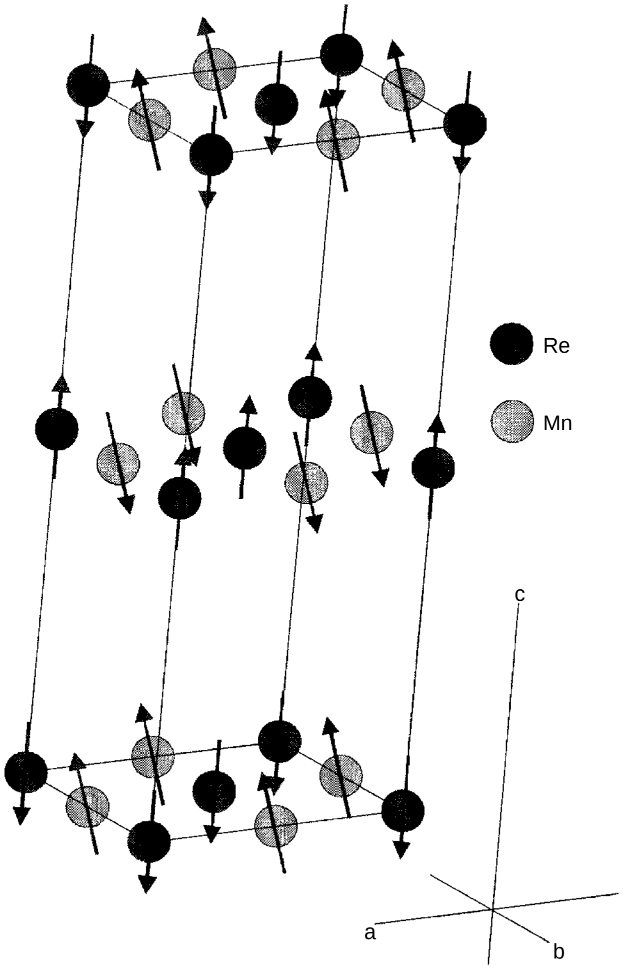

Figure 45 The magnetic structure of $La_5Re_3MnO_{16}$ in which ferromagnetic layers couple antiferromagnetically. (Reprinted from Ref. 98, © 2002, with permission from Elsevier)

The Sr_4PtO_6 structure type is highly versatile to substitution on the in-chain Sr site and the Pt site and perhaps is better formulated as $A_3A'BO_6$, where A' and B can be magnetic or nonmagnetic transition metal ions from the 3d, 4d, and 5d series. There is, thus, considerable scope for tuning the sign (F or AF) of the intra and interchain exchange and the spin dimensionality (Heisenberg, Ising, or XY) as well and these opportunities have been exploited.

In principle, one would expect 1D magnetic correlations to dominate but the interchain separation is not sufficiently great

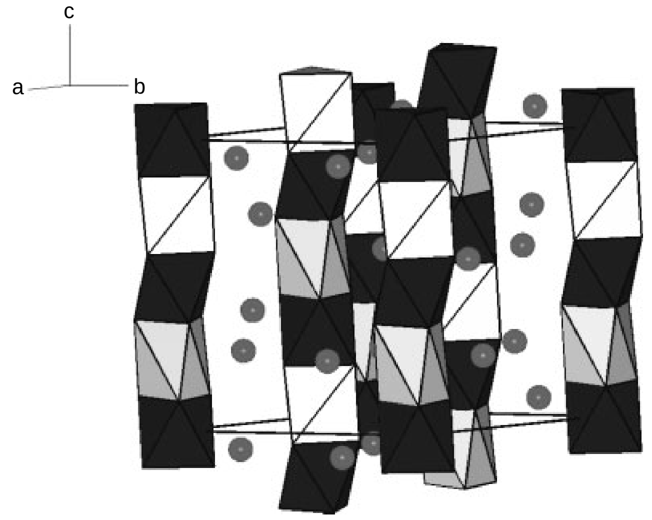

Figure 46 Crystal structure of Sr_4PtO_6 materials, which can also be written $Sr_3(SrPtO_6)$. Infinite chains of alternating face-sharing PtO_3 octahedra(dark grey) and SrO_3 trigonal prisms(light grey) are formed. The remaining Sr^{2+} ions are represented by grey spheres

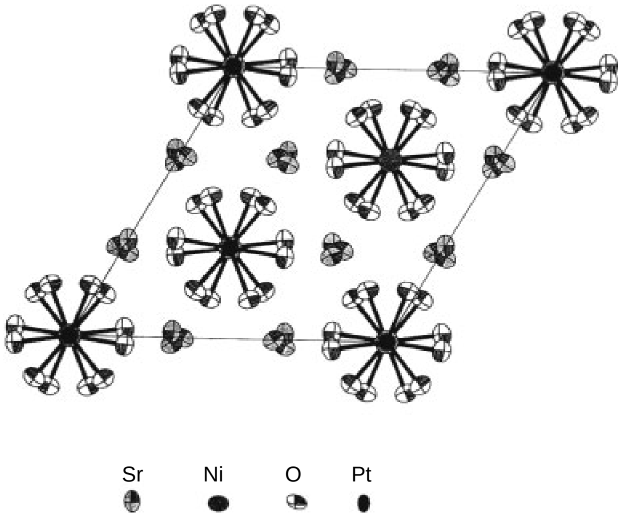

Figure 47 The crystal structure of Sr_3NiPtO_6 along the chain direction showing the trigonal lattice of chains. Note also the relatively close interchain separation. (Reprinted with permission from Ref. 101, © 1999 American Chemical Society)

to isolate the chains completely as seen in the projection of the structure parallel to the chain direction (Figure 47).[101] As well, the chains themselves form a trigonal lattice, introducing an element of geometric frustration (to be discussed in more detail in the following section) into the mix.

Sr_3ABO_6, B^{4+} = Ir,Pt; A^{2+} = Co,Ni,Cu,Zn. Systematic studies on the above series illustrate the variety of magnetic phenomena that can be obtained by chemical tuning.[101–103] The Pt-based materials have LS Pt^{4+} (t_{2g}^6) in the octahedral sites and the divalent TM ions in the unusual trigonal prismatic sites, thus only that site is magnetic. Data for single crystals of the A = Ni^{2+} (S = 1) material show no obvious short range magnetic correlations but can be fitted to a paramagnetic model with large zero field splitting, D/k = 94 K, which implies a single ion ground state singlet.[101] Apparently, magnetic order can be induced by application of a field >4T. The A = Cu^{2+} compound behaves as a Heisenberg S = 1/2 linear chain system (Figure 48),[101] but with a significant ratio of $J_{\mathrm{inter}}/J_{\mathrm{intra}} \sim 1/3$. Evidence for long-range AF order is also evident from the ZFC/FC divergence near 10 K.

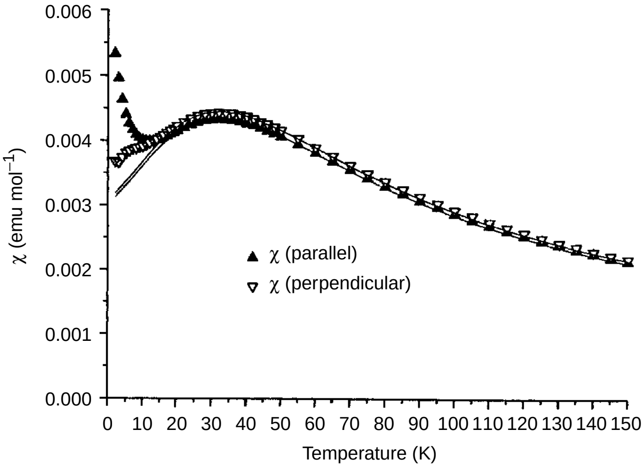

Figure 48 Magnetic susceptibility of Sr_3CuPtO_6 showing linear chain, S = 1/2, AF Heisenberg behavior. The ZFC/FC divergence near 10 K is likely a sign of long-range AF order due to inter chain coupling. (Reprinted with permission from Ref. 101, © 1999 American Chemical Society)

When B = Ir^{4+} (t_{2g}^5, S = 1/2), there are obvious changes. For A = Ni, deviations from the Curie-Weiss law set in below 150 K and show a strong dependence on applied field, suggesting intrachain F interactions but a nearly singlet ground state at low temperatures suggesting AF interchain coupling, but a conclusive judgment cannot be deduced from the available data. The Sr_3CuIrO_6 phase, where both sites are S = 1/2, shows unequivocal intrachain F correlations (Figure 49)[103] while Sr_3ZnIrO_6, where only the Ir site is S = 1/2, is a Heisenberg alternating chain AF. Finally, by exploiting the fact that for A = Cu^{2+}, the B = Pt phase is AF and the B = Ir phase is F with respect to intrachain correlations, a random quantum (S = 1/2) spin chain material can be realized for $Sr_3CuPt_{0.5}Ir_{0.5}O_6$ and the experimental susceptibility curves are in excellent agreement with detailed theory.[104]

$Sr_3A^{1+}Ru^{5+}O_6$ and $Ca_3A^{1+}Ru^{5+}O_6$, A = Li, Na. This series features the Ru^{5+} ion (t_{2g}^3, S = 3/2) as the only magnetic species. In general, these materials show only weak evidence

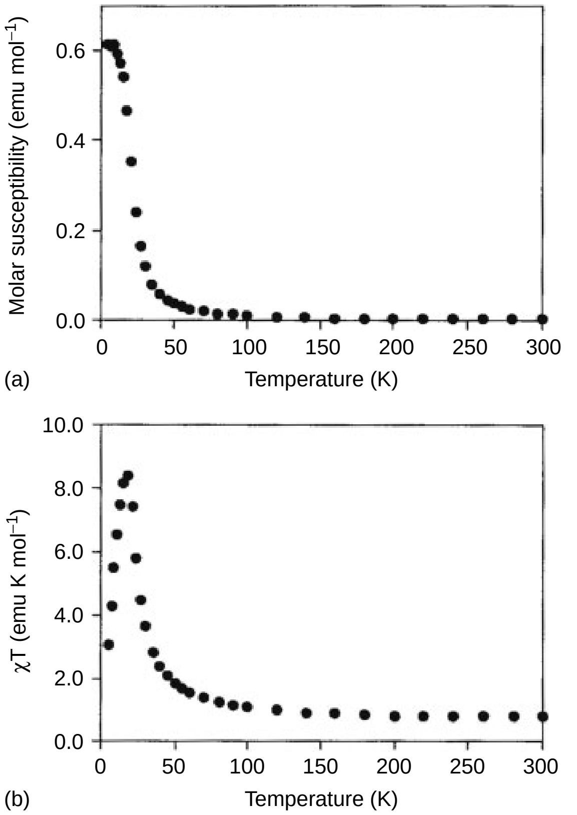

Figure 49 Magnetic susceptibility (a) for Sr_3CuIrO_6 and χT versus T (b), giving clear evidence for intrachain ferromagnetic correlations. (Reprinted from Ref. 103, © 1995, with permission from Elsevier)

for intrachain magnetic correlations and all show large, negative Weiss temperatures and long-range AF magnetic order at rather high temperatures, $T_N = 120$ K(Ca,Li) to 70 K (Sr,Na) (Figure 50).[105] Thus, in this set of compounds the interchain correlations seem to be dominant, exactly opposite to the case just discussed above. Similar observations are reported for other B = Ru compounds such as Ca_3CoRuO_6, which exhibits long-range 3D order at relatively high temperatures with little evidence for intrachain correlations.[106]

$Ca_3B^{2+}Mn^{4+}O_6$, B = Ni, Zn. Examples in which both the A(trigonal prismatic) and B(octahedral) sites are occupied solely by 3d transition elements also exist. Cases in which Mn^{4+} (t^3_{2g}, $S = 3/2$) occupy the octahedral sites have been studied.[107] Ca_3NiMnO_6 gives indications of significant intrachain SRO in the form of a broad susceptibility maximum near 100 K, whereas AF long-range order, albeit of a complex spiral type, sets in only below 20 K according to neutron diffraction results. Not surprisingly, the corresponding Zn phase shows no evident intrachain coupling and $T_N = 25$ K.

$Ca_3Co_2O_6$. This interesting material with the same ion, Co^{3+}, on the octahedral and trigonal prismatic sites is perhaps the best studied material in this structure class. While it seems reasonably clear that Co^{3+} is LS, $S = 0$ on the octahedral site, the spin state for the A site Co^{3+} appears to be an effective $S' = 1$, brought about by a highly anisotropic g-tensor, wherein $g_z \sim 4.5$.[108] The intrachain exchange coupling is unequivocally F with $\Theta_c = 28(3)$ K.[109] Long-range order appears to set in below 25 K but the ground state is complex and highly sensitive to applied fields (Figure 51), which shows a large number of meta-magnetic type transitions.[110]

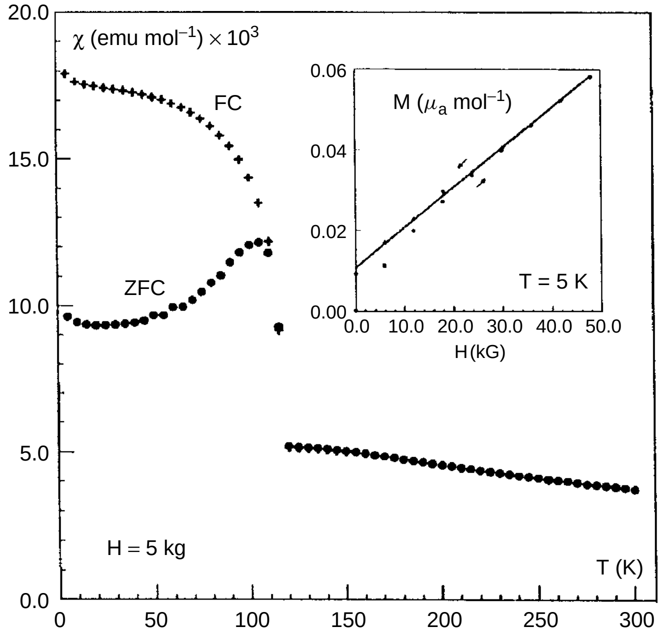

Figure 50 Long-range, three-dimensional magnetic order for Ca_3LiRuO_6 near 120 K. (Reprinted from Ref. 105, © 1997, with permission from Elsevier)

5.4 Geometrically Frustrated Magnetic Materials

The final broad category of magnetic oxides to be discussed in this chapter are those that are subject to what is known as geometric magnetic frustration (GFM). Most of the key materials in this class are either rare earth or d group transition metal oxides or both. What is meant by geometric frustration? In principle, the Third Law of Thermodynamics dictates that $S \rightarrow 0$ as $T \rightarrow 0$. For magnetic systems at high temperatures, spin disorder makes a significant contribution to the total entropy. As the temperature decreases, the magnetic entropy can be quenched by formation of long-range ordered states of the type that have been discussed in the preceding sections. In nature, most such ordered states are AF. However, for particular lattice geometries or topologies, an impediment can arise to entropy removal, as illustrated in Figure 52, which shows possible AF spin orderings on 'plaquettes' of various simple geometries such as the square (c,d,e), the equilateral triangle (a), and the tetrahedron (b).[110] For a square

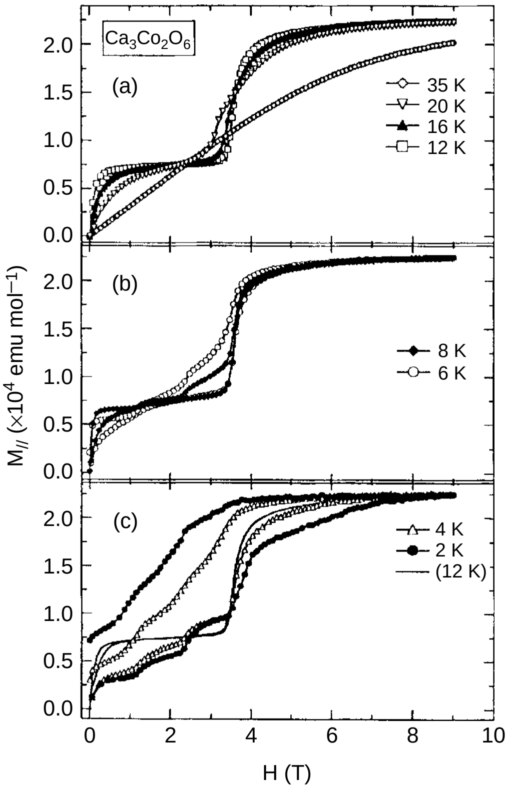

Figure 51 Complex behavior in applied magnetic fields of $Ca_3Co_2O_6$. (Ref. 108. Reproduced by permission of Physical Society of Japan)

plaquette with the condition $J_{nn} \gg J_{nnn}$ or $J_{nnn} > J_{nn}$ (J is the magnitude of the exchange coupling interaction between either nearest neighbor, nn, or next nearest neighbor, nnn, spins), there is no difficulty in finding an AF ordering but for the triangular case it is clear that only two of the three spins can be rigorously antiparallel, one corner is always unsatisfied or ‘frustrated’. The situation is worse for the tetrahedron wherein two of the four nn interactions are frustrated. Even the square lattice can be frustrated if $J_{nn} \sim J_{nnn}$, although this situation may be difficult to realize experimentally. In general, the combination of a triangular plaquette motif and $J_{nn} < 0$ (i.e. an AF constraint) are necessary conditions for geometric magnetic frustration. In general, systems with $J_{nn} > 0$ (F constraint) are not frustrated with one notable exception to be discussed later.

In real materials, the spins reside on the sites of infinite lattices, which can be considered to arise from the condensation of plaquettes. Figure 53 shows a representative but not exhaustive set of frustrating lattices, which involve the condensation by either corner or edge-sharing of triangles or tetrahedra.[110] Such lattices are quite common in nature, especially the edge-sharing triangular and face-centered cubic lattices and even the pyrochlore lattice, so geometric frustration is not a rare condition.

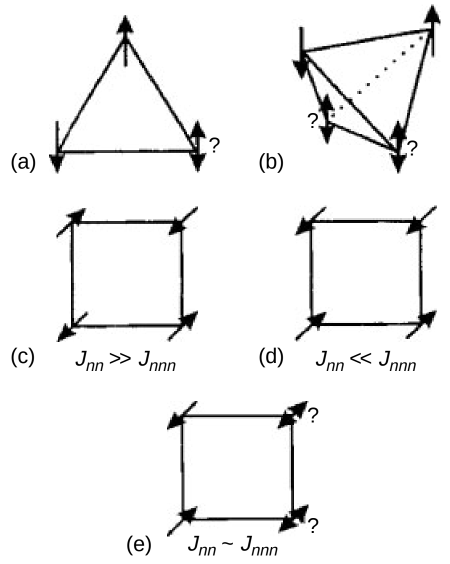

Figure 52 AF spin correlations on ‘plaquettes’ of square-planar, triangular, and tetrahedral geometries. (Ref. 110. Reproduced by permission of Royal Society of Chemistry.) Plaquettea a, b, and e picture geometrically frustrated situations

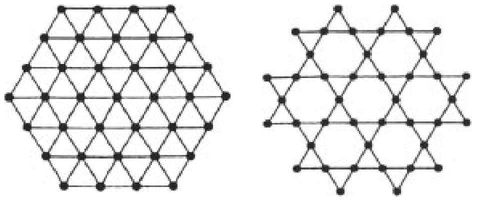

(a) Triangular (b) Kagome

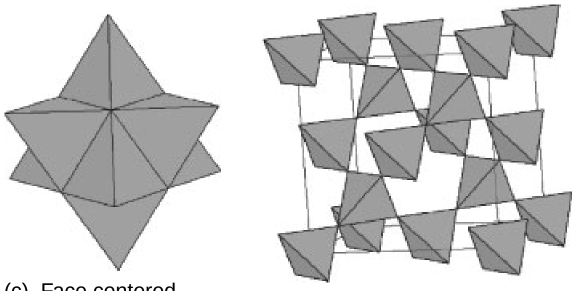

(c) Face centered cubic (d) Pyrochlore

Figure 53 Representative ‘frustrated’ lattices in two and three dimensions. (Ref. 110. Reproduced by permission of Royal Society of Chemistry)

5.4.1 *Experimental Signs of the Presence of Geometric Frustration*

A commonly used criterion is the so-called frustration index, which is simply the ratio of the modulus of the Weiss temperature to the ‘ordering’ temperature, $|\Theta_c|/T_O$, where ordering can be of the usual long-range type or a more exotic variety such as spin-glass freezing.[111] The idea here is that the quantity $k_B\Theta_c$, where k_B is Boltzmann's constant, sets the mean field energy scale for magnetic exchange coupling. Therefore, some form of magnetic order is expected at a temperature near Θ_c/n where n is number ranging from 1 → ∼4 for nonfrustrating lattices. For many geometrically frustrated materials, one finds $|\Theta_c|/T_O > 10$, although there can be exceptions. Another fairly reliable sign is the absence of evidence of a long-range ordered ground state from neutron diffraction or specific heat measurements at the lowest temperatures, often $T < 1\,\mathrm{K}$ as discussed in the following section.

5.4.2 Ground States in Geometrically Frustrated Magnets (GFM's)

Noncollinear 120° or 109° States: Chirality. Some frustrated materials find a truly long-range ordered state but one in which the spin arrangement is not collinear, such as those depicted in Figure 54, the 120° and 109° structures, which can arise on the triangular and pyrochlore lattices, respectively.[110] These are clearly AF ground states as the vector sum of the spins = 0 for each plaquette. The 120° structure is commonly found for oxides with triangular magnetic sublattices but the 109° case is known for only one material, the metastable pyrochlore form of FeF_3. Note that these noncollinear structures possess chirality, a concept familiar to chemists (Figure 55), and, thus, the ground state is degenerate.

Spin Glasses, Spin Liquids, and Spin Ices Macroscopic Degeneracy. Another ground state commonly found in GFM materials is the spin glass (SG) state, although its occurrence is not understood in detail. Here the spins literally freeze into a random, static array below a characteristic temperature, T_f, which is akin to the glass transition temperature, T_g, in positional glasses or polymeric materials (Figure 56(a)). Normally, both positional disorder and frustration are considered to be twin necessary conditions for the formation of the spin glass state but many GFM's exhibit something like a canonical SG state in the apparent absence of detectable positional disorder, as will be discussed later. A striking feature of the SG state is that it is essentially infinitely degenerate. That is, there exists a nearly infinite set of random spin orientations with essentially the same energy.

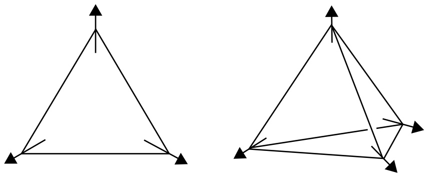

Figure 54 Noncollinear AF magnetic structures, 120° for the triangular lattice and 109° for the tetrahedral lattice. (Ref. 110. Reproduced by permission of Royal Society of Chemistry)

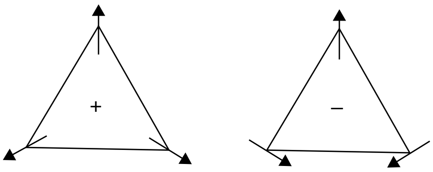

Figure 55 Chirality in the 120° triangular lattice

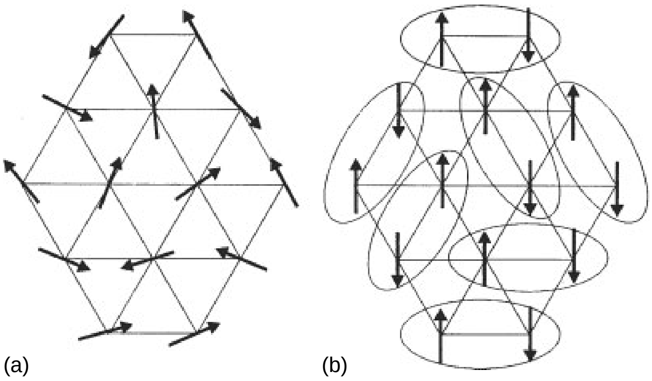

Figure 56 Representations of the spin glass (a) and spin liquid (b) ground states

An even more exotic possibility is the spin liquid (SL) as first proposed by Anderson (with apologies to Linus Pauling) for quantum, $S = 1/2$, spins. Here (Figure 56(b)), the spins form singlet dimers, as in Pauling's valence bond theory, but the state remains dynamic and fluctuating to $T = 0\,\mathrm{K}$. The SL state is quite remarkable in that long-range static order is never realized in spite of strong spin−spin correlations. The SL state is rare. Equally exotic is the spin ice state, which will be discussed in more detail in the context of some pyrochlore structure oxides in a following section.

Most of the key GFM materials are oxides and a brief description of some of these follows. There exist a number of fairly recent reviews including References.[110–115]

5.4.3 Rare Earth Transition Metal Pyrochlores

The Pyrochlore Structure. This structure is described in Fd3m and contains 88 atoms per unit cell, so figures of the full structure can be confusing. There are some similarities with the perovskite structure in that two ions of very different size are involved, the larger is usually a Ln^{3+} ion and the smaller a T^{4+} ion. A network of corner-sharing octahedra forms of composition TO_3 but the network is very rigid relative to perovskite. A partial view of the network is shown in Figure 57. The T−O−T angle is constrained near a value of ∼130°, and is not a strong function of the size of the

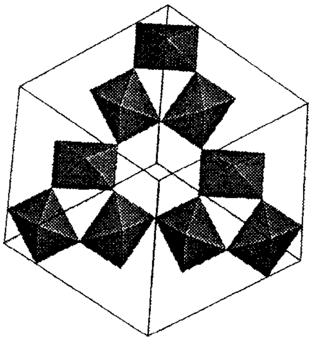

Figure 57 Part of the corner-sharing B_2O_6 network in the pyrochlore structure. The A^{3+} ions reside in the hexagonal channels

Ln^{3+} partner. The Ln^{3+} ions occupy the large hexagonal channels and are 8-fold coordinated in a highly distorted site with two very different Ln–O distances and pronounced axial symmetry (Figure 58). The axis of symmetry is along the various $\langle 111 \rangle$ directions of the cubic pyrochlore cell, a fact that will be of great importance in the so-called 'spin ice' materials. The Ln^{3+} ions and the T^{4+} ions occupy the 16d and 16c sites, respectively, in Fd3m. In both cases, the site topology consists of a corner-sharing network of tetrahedral, one of the canonical frustrated lattices of Figure 53.

$Ln_2Ti_2O_7$.Ln = Gd, Tb, Dy, Ho. The rare earth titanates that crystallize in the so-called pyrochlore structure have received much attention. Here only the Ln^{3+} site is magnetic as Ti^{4+} is a $3d^0$ ion. These four materials exemplify the variety of exotic magnetic phenomena that can be found in frustrated pyrochlores.

$Gd_2Ti_2O_7$ represents the case where the Ln single ion magnetism should be simplest as Gd^{3+}, $4f^7$ ($^8S_{7/2}$), has no orbital contribution to first order and will be least affected by the axial crystal field. The compound obeys the Curie-Weiss law down to ~10 K, giving

$\mu_{\text{eff}} = 7.9\,\mu_B$, as expected for $S = 7/2$ and $\Theta_c = -9.6$ K. Measurements on $(Gd_{0.02}Y_{0.98})_2Ti_2O_7$ show that $\Theta_c \rightarrow 0$ K, indicating that Gd–Gd interactions determine Θ_c for the

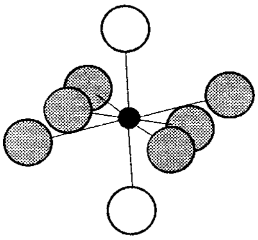

Figure 58 Coordination of the A-site in the pyrochlore structure. The axial oxygens (open circles) are at ~2.2 Å and the equatorial oxygens (grey circles) are at ~2.6 Å. (Ref. 110. Reproduced by permission of Royal Society of Chemistry)

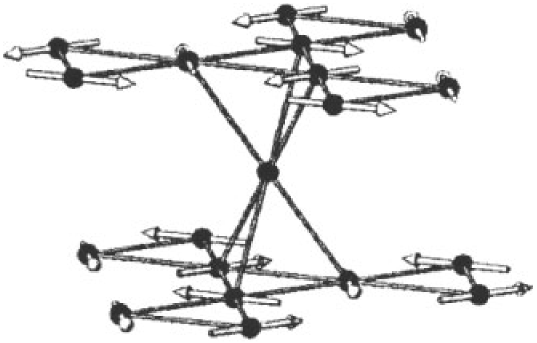

Figure 59 The magnetic structure of $Gd_2Ti_2O_7$ at 50 mK showing the Kagome type planes separated by paramagnetic Gd^{3+} ions on a planar triangular lattice. (Reprinted with permission from J.M.D. Champion, A.S. Wills, T. Fennell, S.T. Bramwell, J.S. Gardner, M.A. Green, *Phys.Rev.*, 2001, **B64**, R140407. © 2001 by the American Physical Society)

undiluted material. A phase transition occurs at 0.97 K and another at about 0.75 K, as detected by specific heat and susceptibility.[116,117] Thus, $|\Theta_c|/T_c \sim 10$ and one criterion for the presence of frustration is satisfied. Theoretical considerations suggest that Gd–Gd exchange makes the largest contribution to Θ_c with a secondary contribution from magnetic dipole–dipole interactions. The magnetic structure was determined using neutron diffraction on an isotopically substituted ^{160}Gd sample and the result is remarkable (Figure 59).[118] The experiment shows only partial order with the spins aligned in a noncollinear manner in the Kagome planes (the pyrochlore lattice can be constructed by stacking Kagome layers in an ...ABCABC... manner, see Ref. 110) but with uncoupled spins in alternating layers. Thus, $Gd_2Ti_2O_7$ finds a partially ordered ground state but with significant dynamics even at temperatures as low as 50 mK (well below the two-phase transitions seen in specific heat).

$Tb_2Ti_2O_7$ presents a sharp contrast to $Gd_2Ti_2O_7$. Tb^{3+} ($^7F_6$) will be strongly influenced by the crystal field. The Curie-Weiss law is also obeyed but with $\Theta_c = -18.9$ K. Experiments on a diluted sample with 2% Tb in $Y_2Ti_2O_7$ indicate a residual $\Theta_c = -6$ K, demonstrating a substantial 'crystal field' contribution. The effects of the crystal field have been investigated via calculations and neutron inelastic scattering with the result that the ground state is a doublet with the nearest excited state (doublet) at only 18 K above and other levels at 115 and 168 K.[119] Thus, $Tb_2Ti_2O_7$ can be regarded as an Ising system with a effective spin ground state, $S' = 1/2$. Extensive searches with neutron scattering, specific heat, muon spin relaxation and other probes have failed to find any evidence for long-range order down to 50 mK.[120] Yet, neutron scattering shows significant short range magnetic correlations even up to 50 K (Figure 60),[121] suggesting strongly that this material is an example of the rare and elusive spin liquid ground state. Finally, it has recently

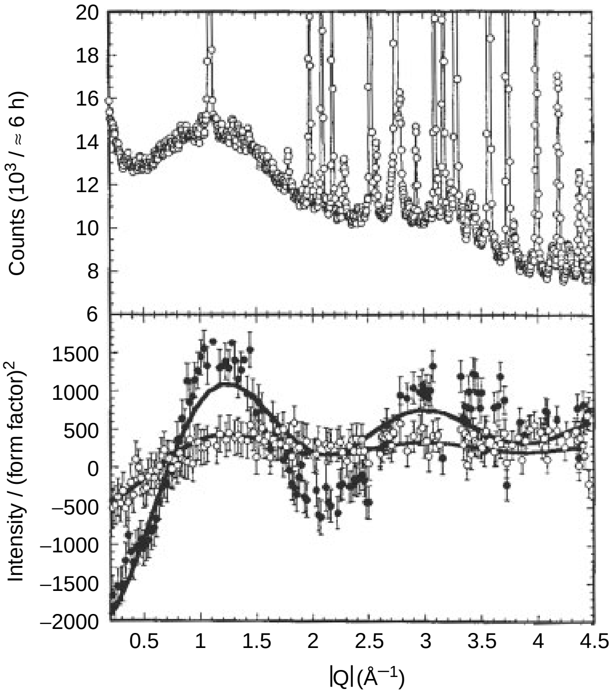

Figure 60 Short range magnetic correlations in $Tb_2Ti_2O_7$ at various temperatures up to 50 K. The x-axis is $Q = 4\pi \sin\theta/\lambda$. (Reprinted with permission from J.S. Gardner, S.R. Dunsiger, B.D. Gaulin, M.J.P. Gingras, J.E. Greedan, R.F. Kiefl, M.D. Lumsden, W.A. MacFarlane, N.P. Raju, J.E. Sonier, I. Swainson, Z. Tun, *Phys.Rev.Lett.*, 1999, **82**, 1012. © 1999 by the American Physical Society)

been shown that long-range order can be induced in applied fields of ∼9 GPa.[122]

$Dy_2Ti_2O_7$ and $Ho_2Ti_2O_7$ are widely regarded as examples of 'spin ice' ground-state materials and a very nice summary of this phenomenon is available.[115] The spin ice state depends on two conditions: one, that the magnetic moments be constrained by anisotropy to lie parallel to the ⟨111⟩ directions and two, that the correlations be ferromagnetic. The first condition results from the strong axial crystal field at the Ln^{3+} site which creates a well-isolated ground state Ising like doublet with a ground-state wave function composed primarily of components with +/− M_J(max) where $M_J(\max)> = J$, the total angular momentum ($J = 8$ for Ho and 15/2 for Dy). The unusual ferromagnetism in these two materials is traceable to long-range magnetic dipole–dipole interactions. With these constraints, the spin configuration in a given tetrahedron must be of the 'two in, two out' type as shown in Figure 61(b). Within a single tetrahedron, the ⟨111⟩ directions are vectors that point from the corners to the midpoint of the opposite face. The connection to water ice arises in considering the environment of any given oxygen atom. There must be two short bonds to hydrogen (covalent) and two long bonds (hydrogen bonds) (Figure 61(a)), and these are known as the 'ice rules'. As the ice rules are a local constraint, there are a macroscopic number of ways to satisfy them over the entire lattice, which leads to a degeneracy shown by Linus Pauling to be $\sim(3/2)^{N/2}$, where N is the number of oxygen atoms in the lattice, that is, a macroscopic degeneracy as $N \sim 10^{23}$.[123] There is, thus, a residual entropy due to this macroscopic disorder, which is $S = (R/2)\ln(3/2)$ where R is the gas constant. The observation of a residual entropy is the determining criterion of the spin ice state and such evidence is shown for $Dy_2Ti_2O_7$ (Figure 62).[115,124]

It is remarkable that the nature of the ground state in these pyrochlores can be modified so strongly from a mixed long-range/short-range order (Gd) to a completely dynamic spin liquid (Tb) to a spin ice (Dy,Ho) simply by substituting one rare earth ion for another.

Other Pyrochlores, $Y_2Mo_2O_7$ and $Tl_2Mn_2O_7$. $Y_2Mo_2O_7$ is one of the most extensively investigated GFM materials.[110] It behaves as a canonical spin glass with a very well defined $T_f = 22$ K but diffraction studies indicate a crystallographically well-ordered material. Normally, both positional disorder and frustration are requirements to stabilize the spin glass ground state. Some evidence for a type of short

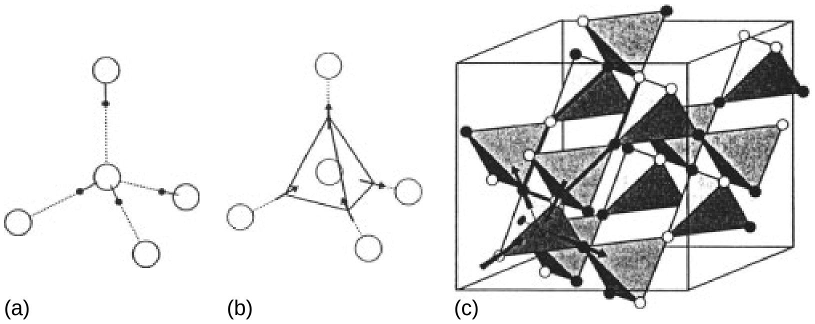

Figure 61 The connection between 'spin ice' and water ice. (a) The two short, two long O–H bonds about a single O atom in water ice. (b) The two in, two out configuration (obeying the 'ice rules') in any tetrahedron for a F Ising model. (c) One possible ground state of an infinitely degenerate set for a 'spin ice'. The open circles are spin in and the solid circles, spin out. (Reprinted with permission from S.T. Bramwell, M.J.P. Gingras, *Science*, 2001, **294**, 1495. © 2001 American Association for the Advancement of Science. www.sciencemag.org)

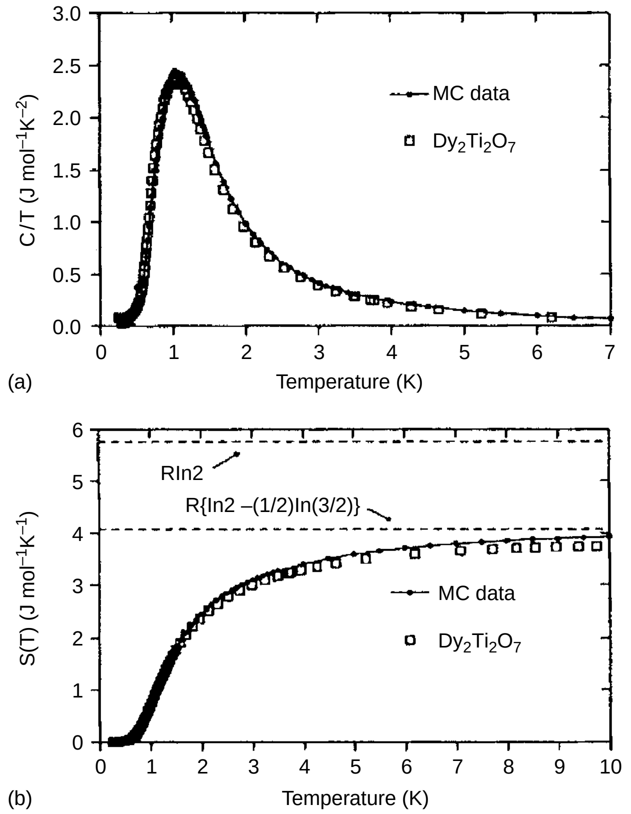

Figure 62 Heat capacity and entropy for $Dy_2Ti_2O_7$ showing the excess entropy, experimental evidence for the spin ice state.[115,124] (Reprinted by permission from Nature Ref. 124, © 1999 Macmillan Publishers Ltd. www.nature.com)

range disorder has been claimed from EXAFS studies.[125] Unfortunately, no attempt has been made to reconcile this observation with the diffraction studies and the disorder level is not easy to quantify but it appears to be inadequate to explain, quantitatively, such a large T_f.

$Tl_2Mn_2O_7$, while not a GFM, is remarkable in that it shows a transition from an insulating to a ferromagnetic, metallic state at 121 K.[126] Shortly after this report, CMR was discovered in this material, which was shown to contain only Mn^{4+} and, thus, the mechanism must be very different from that causing CMR in the perovskite manganates.[127,128] This mechanism is still not well understood.

Spinel Structure Oxides. Oxides with the spinel structure have composition AB_2O_4 and are also described in the cubic space group Fd3m. For a so-called 'normal' spinel, A^{2+} ions occupy tetrahedral sites but the B^{3+} ions occupy the 16d positions. Thus, the B ions form a pyrochlore sublattice and are potential GFM materials, a possibility noted as long ago as 1956![129] Several B-site magnetic spinels have been investigated recently but brief accounts will be given for two materials, $ZnCr_2O_4$ and the system $Li_{1+/-x}Mn_2O_4$.

$ZnCr_2O_4$ shows typical signs of GFM behavior with $\Theta_c = -330$ K but no sign of magnetic order until $T_N = 12.5$ K, a frustration index ~26.[130,131] The magnetic phase transition is remarkable in that it is first order rather than continuous as is usually found and there is a simultaneous crystallographic phase transition and a large dielectric anomaly. There is evidence for short range AF clustering at temperatures >100 K. These facts have led to speculation that the crystallographic phase transition is driven by a need to relieve the geometric frustration and arguments in terms of strain energies and magnetic energies.[130] Interestingly, as of yet the details of the low-temperature crystal and magnetic structure have not been determined. Arguments for both tetragonal and orthorhombic symmetry for the crystal structure have been advanced.[132] Finally, this material is extremely sensitive to positional disorder; only 3% substitution of Ga^{3+} for Cr^{3+} and 5% Cd^{2+} for Zn^{2+} can induce a spin glass ground state.[133]

For $Li_{1+/-x}Mn_2O_4$, x can vary from -1 to $+1$ and three compositions have been studied in detail, $x = -1$ (λ-MnO_2), $x = 0$ ($LiMn_2O_4$), and $x = +1$ ($Li_2Mn_2O_4$). The crystal structures are shown in Figure 63.[110]

$LiMn_2O_4$ is a normal spinel, with mixed Mn^{3+}/Mn^{4+} valence. There is a structural CO phase transition near 280 K to an orthorhombic form, Fddd, with a unit cell of nine times the volume of the Fd3m cell, but the CO appears to be partial.[134] Magnetic order does not occur until $T_c = 60$ K and the ground state is remarkable.[135] Approximately half of the magnetic scattering, measured by polarized neutron methods, is involved in long-range order of a very complex structure yet to be determined (the magnetic cell may involve 1152 spins!) and half is involved in a very short range order with correlation length of about 2 Mn nearest neighbors.

λ-MnO_2 is a spinel with empty A-sites and only Mn^{4+}. This compound orders with $T_N = 32$ K in a very complex magnetic structure with 128 spins per cell, indicative of a high level of frustration. A possible magnetic structure is shown in Figure 64.[136]

The all Mn^{3+} phase, $Li_2Mn_2O_4$, which is tetragonal ($I4_1$/amd) due to a static Jahn–Teller distortion, is perhaps the most remarkable of all. Θ_c is at least -600 K and yet no long-range order occurs down to 1.5 K. Instead a strange two dimensional order sets in at ~60 K, which can be understood as ordering in completely uncoupled Kagome planes, related to the situation in $Gd_2Ti_2O_7$.[137]

Other Pyrochlore Related Materials, Kagome Lattices, Jarosites, and SCGO. In contrast to the three-dimensional GFM pyrochlores and spinels, real examples of the Kagome lattice are very rare. The best examples are the Fe^{3+} based jarosite structure materials of composition $AFe_3(SO_4)_2(OH)_6$, where A is a group I ion or H_3O^+. The Kagome nets (see Figure 53) are stacked . . . ABCABC. . . and are well separated. The case of $A = H_3O^+$ is the most unusual. Θ_c for this material is ~ -700 K but no long-range order occurs down to 1.5 K; instead, evidence for two dimensional correlations in the form

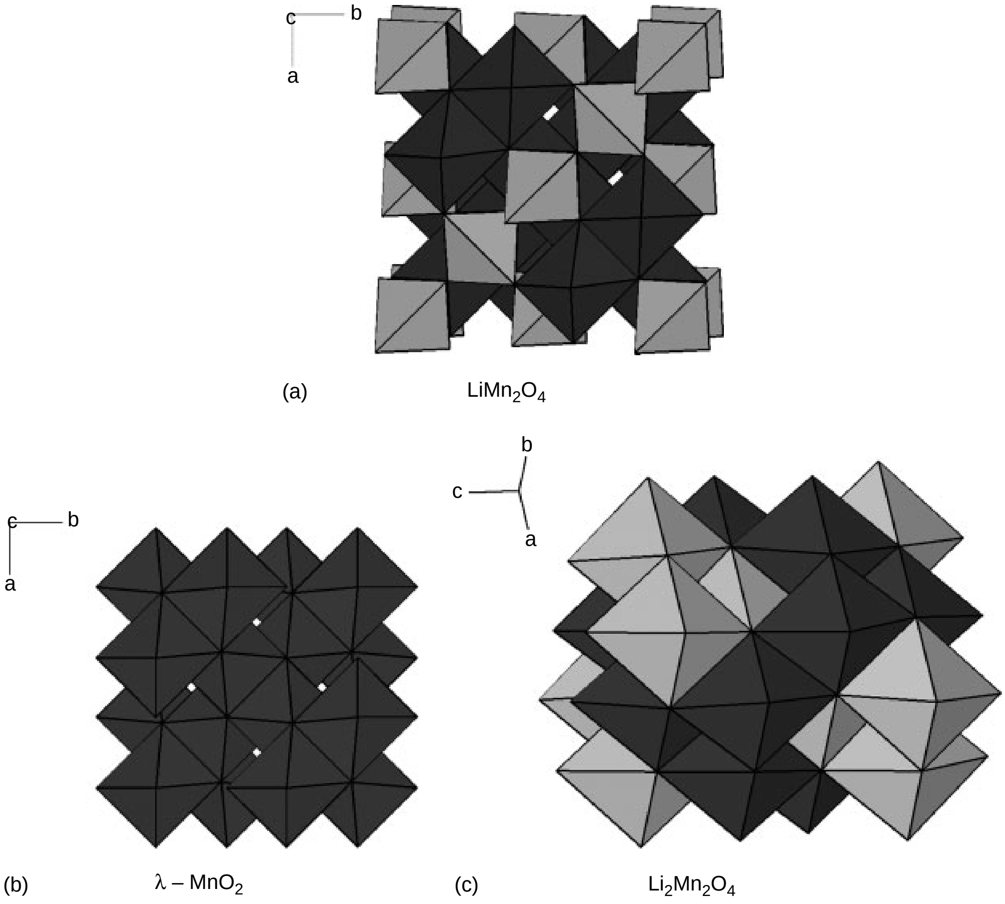

Figure 63 Crystal structures of the spinel structure materials, λ-MnO_2, $LiMn_2O_4$, and $Li_2Mn_2O_4$, in a polyhedral representation. The light colored polyhedra are the Li ions and the dark polyhedra the Mn ions. (Ref. 110. Reproduced by permission of Royal Society of Chemistry)

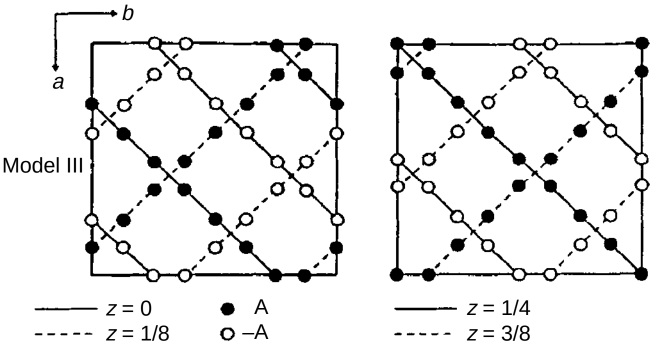

Figure 64 A possible magnetic structure for λ-MnO_2 with 128 spins per magnetic unit cell. The open and closed circles represent spins of opposite direction. (Reprinted with permission from Ref. 136, © 1998 American Chemical Society)

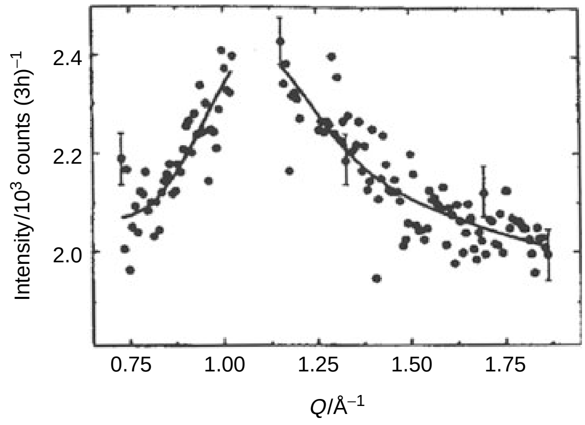

Figure 65 Evidence for short range, two dimensional order from neutron scattering for the jarosite, $D_3OFe_3(SO_4)_2(OH)_6$. Note the asymmetric 'Warren' line shape. (Ref. 138. Reproduced by permission from EDP Sciences)

of an asymmetric Warren peak is seen Figure 65.[138] A phase transition at 13.8 K is thus ascribed to a spin glass freezing.

SCGO, $SrCr_{12-x}Ga_xO_{19}$, has been studied extensively and is covered in many of the earlier reviews.[93] Although often labeled a Kagome system, in fact the structure is better described in terms of a 'pyrochlore slab' motif (Figure 66).[139]

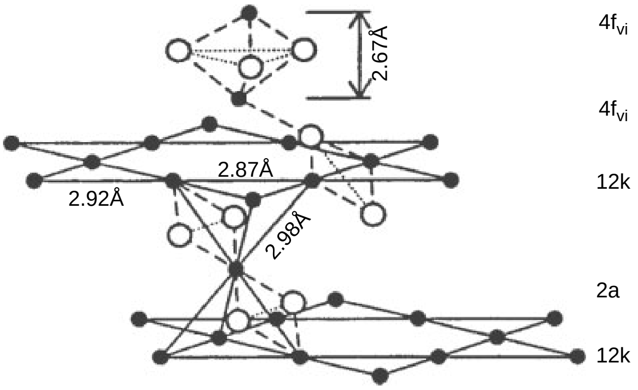

Figure 66 A 'pyrochlore slab' in $SrCr_{12-x}Ga_xO_{19}$. (Reprinted with permission from S.-H Lee, C. Broholm, G. Aeppli, T.G. Perring, B. Hessen, A. Taylor, *Phys. Rev .Lett.*, 1996, **76**, 4424. © 1996 by the American Physical Society)

It shows a huge frustration index of ∼150 with a spin freezing $T_f = 3.4$ K for a sample with 90% coverage of the pyrochlore slabs by Cr^{3+}. Several anomalous properties appear in the specific heat that are still not understood in detail but point to the possible involvement of spin singlets in the ground state.

B-site Ordered Double Perovskites. As mentioned in a preceding section, the B and B′ sites of B-site ordered double perovskites each form a f.c.c. lattice and are therefore potentially frustrated. This connection had not always been realized in earlier work and, indeed, there was often little experimental evidence for frustration. For compounds involving the first-row elements $A_2B'B''O_6$ where A = Ca, Sr, and Ba and B″ = Mo or W, the frustration indices were often in the range of 2–3 with only a few notable exceptions, in particular Ba_2FeBiO_6, f = 17 or Ba_2FeSbO_6, f = 18.[140] With 4d elements, for example, Ba_2LaRuO_6, which contains Ru^{5+} ($4d^3$, S = 3/2), a large f = 10 was noted.[141] Nonetheless, all of these materials with well established B-site order (materials with significant B′ – B″ site mixing are spin glasses) and magnetic B' sites having $S \geq 3/2$ with nonmagnetic B″ ions show long range magnetic order at low temperatures and not the more exotic ground states found for the pyrochlores and spinels.[142] This situation changes when S = 1/2 and possibly S = 1. For the first-row double perovskites, none of the $B' = Cu^{2+}$ materials, such as Sr_2CuWO_6 and Ba_2CuWO_6, show long-range order in spite of very large, negative Θ_c's, −230 K and −180 K, respectively. The absence of LRO in these cases has been discussed in terms of orbital ordering and low dimensionality, as the local symmetry at the Cu^{2+} site is highly distorted from octahedral, but geometric frustration may also play a major role.[143] The role of the spin quantum number is perhaps clearer in another set of perovskites, Sr_2CaReO_6 and Sr_2MgReO_6, both involving Re^{6+} ($5d^1$, S = 1/2), where no strong Jahn–Teller distortion is present to cloud the issue.[144,145] The Ca phase is $P2_1/n$ and the Mg compound I4/m. Despite what is nearly complete B-site ordering, both materials behave as spin-glass like, although the Ca phase shows many anomalous properties, especially in the heat capacity, including an unprecedented T^3 dependence at low temperatures and a robustness of the heat capacity anomaly to fields as large as 6T. It is not yet clear whether the absence of LRO in these materials is related to quantum spin fluctuations, orbital ordering within the t_{2g} manifold, both, or neither.

6 CONCLUDING REMARKS

Magnetic oxides have continued to provide a focus for intensive research over the past 10 years or so and this is unlikely to change for the foreseeable future as many interesting challenges clearly remain. The contents of this article represent a very selective and necessarily somewhat superficial overview of the major themes. The interested reader is urged to consult the numerous references provided for more details. As well, owing to limitations of time and space, topics that have received much attention have been omitted. Such areas include oxides that exhibit low-dimensional phenomena such as the spin-Peierls, spin ladder, and related effects, seen in certain Cu^{2+} and V^{4+} oxides. There is also no mention of the increasing use of ab initio computational methods in the understanding of magnetic structures.

7 REFERENCES

1. J. E. Greedan, Magnetic Oxides, in 'Encyclopedia of Inorganic Chemistry', ed. R. B. King Jr, Wiley, 1994.
2. R. L. Carlin and A. J. van Duyneveldt, 'Magnetic Properties of Transition Metal Compounds', Springer-Verlag, New York, 1977, p. 7.
3. H. E. Stanley, 'Introduction to PhaseTransitions and Critical Phenomena', Oxford University Press, Oxford, 1971, p. 7.
4. C. Kittel, 'Introduction to Solid State Physics', 3rd edn., Wiley, New York, 1967.
5. J. B. Goodenough, 'Magnetism and the Chemical Bond', Interscience, New York, 1963.
6. T. Moriya, in 'Magnetism', eds. G. T. Rado and H. Suhl, Academic Press, New York, 1963, Vol. I, p. 85.
7. M. F. Collins, 'Magnetic Critical Scattering', Oxford University Press, 1989, p. 16.
8. L. J. de Jongh, in 'Magnetic Properties of Layered Transition Metal Compounds', ed. L. J. de Jongh, Kluwer Academic Publishers, 1990, p. 19.

9. P. W. Anderson, *Phys. Rev.*, 1950, **79**, 350; **115**, 1959, 2; G. T. Rado and H. Suhl, eds, ‘Magnetism’, Academic Press, New York, 1963, Vol I, p. 25.

10. J. Kanamori and J. Phys, *Chem. Solids*, 1959, **10**, 87.

11. C. Zener, *Phys. Rev.*, 1951, **81**, 440.

12. P. G. de Gennes, *Phys. Rev.*, 1960, **118**, 141.

13. J. S. Smart, ‘Effective Field Theories of Magnetism’, Saunders, Philadelphia, PA, 1966, p. 74.

14. F. E. Mabbs and D. J. Machin, ‘Magnetism and Transition Metal Complexes’, Chapman & Hall, 1973, p. 79.

15. R. L. Martin, in ‘New Pathways in Inorganic Chemistry’, ed. H. J. Emeleus, Cambridge University Press, 1968, p. 175.

16. M. Mochizuki and M. Imada, *J. Phys. Soc. Jpn.*, 2004, **73**, 1833.

17. H. Park, R. Lam, J. E. Greedan, and J. Barbier, *Chem. Mater.*, 2003, **15**, 1703.

18. M. E. Fisher, *Am. J. Phys.*, 1964, **32**, 343.

19. R. Lam, F. Wiss, and J. E. Greedan, *J. Solid State Chem.*, 2002, **167**, 182.

20. R. K. Kremer, J. E. Greedan, E. Gmelin, W. Dai, M. A. White, S. M. Eicher, K. J. Lushington, and *J. Phys. Colloq. C8*, 1988, **49**,(Suppl. 12), 1495.

21. J. N. Reimers, J. E. Greedan, C. V. Stager, and R. K. Kremer, *J. Solid State Chem.*, 1989, **83**, 20.

22. J. E. Greedan, *J. Less-Common. Met.*, 1986, **111**, 335.

23. C. Eylem, H. L. Ju, B. W. Eichhorn, and R. L. Greene, *J. Solid State Chem.*, 1995, **114**, 164.

24. G. Amow and J. E. Greedan, *J. Solid State Chem.*, 1996, **121**, 443.

25. G. Amow and J. E. Greedan, *J. Solid State Chem.*, 1998, **141**, 262.

26. J. B. Goodenough, ‘Magnetism and the Chemical Bond’, Interscience, 1963, p. 230.

27. M. Cwik, T. Lorenz, J. Baier, R. Muller, G. Andre, F. Bouree, F. Lichtenberg, A. Freimuth, R. Schmitz, E. Muller-Hartmann, and M. Braden, *Phys. Rev.*, 2003, **B68**, 060401R.

28. A. P. Ramirez, *J. Phys.: Condens. Matter*, 1997, **9**, 8171.

29. J. M. D. Coey, M. Viret, and S. von Molnar, *Adv. Phys.*, 1999, **48**, 167.

30. Y. Tokura and Y. Tomioka, *J. Magn. Magn. Matter.*, 1999, **200**, 1.

31. C. N. R. Rao, A. Arulraj, A. Cheetham, and B. Raveau, *J. Phys.: Condens. Matter*, 2000, **12**, 83.

32. M. B. Salamon and M. Jaime, *Rev. Mod. Phys.*, 2001, **73**, 583.

33. B. Raveau, A. Maignan, C. Martin, and M. Hervieu, *Chem. Mater.*, 1998, **10**, 2641.

34. T. Okuda, T. Kimura, H. Kuwahara, Y. Tomioka, A. Asamitsu, Y. Okimoto, E. Saitoh, and Y. Tokura, *Mater. Sci. Eng.*, 1999, **B63**, 163.

35. E. O. Wollan and W. C. Koehler, *Phys. Rev.*, 1955, **100**, 545.

36. P. G. Radaelli, D. E. Cox, L. Capogna, S.-W. Cheong, and M. Marezio, *Phys. Rev.*, 1999, **B59**, 14440.

37. A. Maignan, C. Martin, F. Damay, and B. Raveau, *Chem. Mater.*, 1998, **10**, 950.

38. Z. Zeng, M. Greenblatt, and M. Croft, *Phys. Rev.*, 1999, **B59**, 8784.

39. C. R. Wiebe, J. E. Greedan, J. S. Gardner, Z. Zeng, and M. Greenblatt, *Phys. Rev.*, 2001, **B64**, 064421.

40. P. V. Vanitha, P. N. Santosh, R. S. Singh, C. N. R. Rao, and J. P. Attfield, *Phys. Rev.*, 1999, **B59**, 13539.

41. R. D. Shannon, *Acta Crystallogr.*, 1976, **A32**, 751.

42. L. M. Rodriguez and J. P. Attfield, *Phys. Rev.*, 1996, **B54**, R15622.

43. L. M. Rodriguez-Martinez and J. P. Attfield, *Chem. Mater.*, 1999, **11**, 1504.

44. A. Maignan, C. Martin, G. van Tendeloo, M. Hervieu, and B. Raveau, *J. Mater. Chem.*, 1998, **8**, 2411.

45. Y. Moritomo, Y. Tomioka, A. Asamitsu, Y. Tokura, and Y. Matsui, *Phys. Rev.*, 1995, **B51**, 3297.

46. B. J. Sternlieb, J. P. Hill, U. C. Wildgruber, G. M. Luke, B. Nachumi, Y. Moritomo, and Y. Tokura, *Phys. Rev. Lett.*, 1996, **76**, 2169.

47. G. LeFlem, P. Courbin, C. Delmas, and J. L. Soubeyroux, *Z. Anorg. Allg. Chem.*, 1981, **476**, 69.

48. M. Bieringer and J. E. Greedan, *J. Mater. Chem.*, 2002, **12**, 279.

49. Y. Moritomo, Y. Tomioka, A. Asamitsu, Y. Tokura, and Y. Matsui, *Nature*, 1996, **380**, 141.

50. P. D. Battle and M. J. Rosseinsky, *Curr. Opin. Sol. State Mat. Sci.*, 1999, **4**, 163.

51. M. Kubota, H. Fujioka, K. Ohoyama, K. Hirota, Y. Moritomo, H. Yoshizawa, and Y. Endoh, *J. Phys.: Chem. Solids*, 1999, **60**, 1161.

52. P. D. Battle, M. A. Green, N. S. Laskey, J. E. Millburn, P. G. Radaelli, M. J. Rosseinsky, S. P. Sullivan, and J. F. Vente, *Phys. Rev.*, 1996, **B54**, 15967.

53. S. Kawasaki, M. Takano, and Y. Takeda, *J. Solid State Chem.*, 1996, **121**, 174.

54. T. Takeda and H. Watanabe, *J. Phys. Soc. Jpn.*, 1972, **33**, 967.

55. M. Abbate, F. M. F. de Groot, J. C. Fuggle, A. Fujimori, Q. Strebel, F. Lopez, M. Domke, G. Kaindl, G. A. Sawatzky, M. Takano, H. Elsaki, S. Uchida, and Y. Takeda, *Phys. Rev.*, 1992, **B46**, 4511.

56. A. Maignan, C. Martin, N. Nguyen, and B. Raveau, *Solid State Sci.*, 2001, **3**, 57.

57. A. Lebon, P. Adler, C. Bernhard, A. V. Boris, A. V. Pimenov, A. Maljuk, C. T. Lin, C. Ulrich, and B. Keimer, *Phys. Rev. Lett.*, 2004, **92**, 037202.

58. G. H. Jonker *J. Appl. Phys.*, 1966, **37**, 1424; P. M. Raccah and J. B. Goodenough, *Phys. Rev.*, 1967, **155**, 932.

59. M. A. Senaris-Rodriguez and J. B. Goodenough, *J. Solid StateChem.*, 1995, **116**, 224.

60. K. Asai, O. Yokokura, N. Nishimori, H. Chou, J. M. Tranquada, G. Shirane, S. Higuchi, Y. Okajima, and K. Kohn, *Phys. Rev.*, 1994, **B50**, 3025.
61. Y. Yamaguchi, Y. Okimoto, and Y. Tokura, *Phys. Rev.*, 1997, **B55**, R8666.
62. M. A. Korotin, S. Yu Ezhov, I. V. Solovyev, V. I. Anisimov, D. I. Khomskii, and G. A. Sawatzky, *Phys. Rev.*, 1996, **B54**, 5309.
63. H. Watanabe, Y. Yamaguchi, H. Oda, and H. Takei, *J. Magn. Magn. Mater.*, 1980, **15–18**, 521.
64. R. H. Potze, G. A. Sawatzky, and M. Abbate, *Phys. Rev.*, 1995, **B51**, 11501.
65. G. Briceno, H. Chang, X. Sun, P. G. Schultz, and X. D. Xiang, *Science*, 1995, **270**, 273.
66. M. A. Senaris-Rodriguez and J. B. Goodenough, *J. Solid StateChem.*, 1995, **118**, 323.
67. R. Caciuffo, D. Rinaldi, G. Barucca, J. Mira, J. Rivas, M. A. Senaris-Rodriguez, P. G. Radaelli, D. Fiorani, and J. B. Goodenough, *Phys. Rev.*, 1999, **B59**, 1068.
68. V. G. Sathe, A. V. Pimpale, V. Siruguri, S. K. Paranjpe, *J. Phys.: Condens. Matter*, 1996, **8**, 3889.
69. J. M. Longo, P. M. Raccah, and J. B. Goodenough, *J. Appl. Phys.*, 1968, **39**, 1327.
70. Y. Maeno, H. Hashimoto, K. Yoshida, S. Nishizaki, T. Fujita, and J. G. Bednorz, *Nature*, 1994, **372**, 6506.
71. G. Cao, C. S. Alexander, S. McCall, J. E. Crow, R. P. Guertin, *Mater. Sci. Eng.*, 1999, **B63**, 76.
72. C. S. Alexander, G. Cao, J. E. Crow, and S. McCall, *J. Alloys Compd.*, 2004, **369**, 2.
73. G. L. Catchen, T. M. Rearick, and D. G. Schlom, *Phys. Rev.*, 1994, **B49**, 318.
74. K. Crawford, R. L. Harlow, W. Marshall, Z. Li, G. Cao, R. L. Lidstrom, Q. Huang, and J. W. Lynn, *Phys. Rev.*, 2002, **B65**, 214412.
75. M. Braden, G. Andre, S. Nakatsuji, and Y. Maeno, *Phys. Rev.*, 1998, **B58**, 847.
76. H. Shaked, O. Chmaissem, S. Ikeda, and Y. Maeno, *J. Solid StateChem.*, 2000, **154**, 361; G. Cao, K. Abboud, S. McCall, J. E. Crow, and R. P. Guertin, *Phys. Rev.*, 2000, **B62**, 998.
77. G. Cao, L. Balicas, X. N. Lin, S. Chikara, E. Elhami, V. Duairaj, J. W. Brill, R. C. Cai, and J. E. Crow, *Phys. Rev.*, 2004, **B69**, 014404.
78. M. T. Anderson, K. B. Greenwood, G. A. Taylor, and K. R. Poeppelmeier, *Prog. Solid State Chem.*, 1993, **22**, 197.
79. C. J. Howard, B. J. Kennedy, and P. M. Woodward, *Acta Crystallogr.*, 2003, **B59**, 463.
80. F. K. Patterson, C. W. Moeller, and R. Ward, *Inorg. Chem.*, 1963, **2**, 196.
81. K.-I. Kobayashi, T. Kimura, H. Sawada, and K. Terakura, *Nature*, 1998, **395**, 677.
82. R. P. Borges, R. M. Thomas, J. M. D. Coey, R. Suryanarayanan, L. Ben-Dor, L. Pinsard-Gaudart, and A. Revcolevschi, *J. Phys.: Condens. Matter*, 1999, **11**, L445.
83. T. Saitoh, M. Nakatake, A. Kakizaki, H. Nakajima, O. Morimoto, Sh. Xu, Y. Moritomo, N. Hamada, and Y. Aiura, *Phys. Rev.*, 2002, **B66**, 035112.
84. O. Chmaissem, R. Kruk, B. Dabrowski, D. E. Brown, X. Xiong, S. Kolesnik, J. D. Jorgensen, and C. W. Kimball, *Phys. Rev.*, 2000, **B62**, 14197.
85. D. Sanchez, J. A. Alonso, M. Garcia-Hernandez, M. J. Martinez-Lope, J. L. Martinez, and A. Mellergård, *J. Magn. Magn. Mater.*, 2002, **242–245**, 729.
86. M. S. Moreno, J. E. Gayone, M. Abbate, A. Caneiro, D. Niebieskikwiat, R. D. Sanchez, A. de Siervo, R. Landers, and G. Zampieri, *Solid State Commun.*, 2001, **120**, 161.
87. M. Karppinen, H. Yamauchi, Y. Yasukawa, J. Linden, T. S. Chan, R. S. Liu, and J. M. Chen, *Chem. Mater.*, 2003, **15**, 4118.
88. Y. Moritomo, S. Xu, A. Machida, T. Akimoto, E. Nishibori, M. Takata, M. Sakata, and K. Ohoyama, *J. Phys. Soc. Jpn.*, 2000, **69**, 1723.
89. P. Karen and P. M. Woodward, *J. Mater. Chem.*, 1999, **9**, 789.
90. J. P. Chapman, J. P. Attfield, M. Molgg, C. M. Friend, and T. P. Beales, *Angew. Chem. Int. Ed.*, 1996, **35**, 2482.
91. P. Karen, A. Kjekshus, Q. Huang, J. W. Lynn, N. Rosov, I. Natali Sora, V. L. Karen, A. D. Mighell, and A. Santoro, *J. Solid State Chem.*, 1998, **136**, 21.
92. P. M. Woodward, E. Suard, and P. Karen, *J. Am. Chem. Soc.*, 2003, **125**, 8889.
93. P. Karen, P. M. Woodward, J. Linden, T. Vogt, A. Studer, and P. Fischer, *Phys. Rev.*, 2001, **B64**, 214405.
94. J. A. McAllister and J. P. Attfield, *J. Mater. Chem.*, 1998, **8**, 1291.
95. M. Ledesert, Ph. Labbe, W. H. McCarroll, H. Leligny, and B. Raveau, *J. Solid State Chem.*, 1993, **105**, 143.
96. C. R. Wiebe, A. Gourrier, T. Langet, J. F. Britten, and J. E. Greedan, *J. Solid State Chem.*, 2000, **151**, 31.
97. K. V. Ramanujachari, M. Greenblatt, W. H. McCarroll, and J. B. Goodenough, *Mater. Res. Bull.*, 1993, **28**, 1256; K. V. Ramanujachari, S. E. Lofland, W. H. McCarroll, T. J. Emge, M. Greenblatt, and M. Croft, *J. Solid State Chem.* 2002, **164**, 60.
98. A. E. C. Green, C. R. Wiebe, and J. E. Greedan, *Solid State Sci.*, 2002, **4**, 305.
99. L. Chi, A. E. C. Green, R. Hammond, C. R. Wiebe, and J. E. Greedan, *J. Solid State Chem.*, 2003, **170**, 165; L. Chi and I. Swainson, *J.E. Greedan*, 2004, **177**, 3086.
100. J. Darriet and M. A. Subramanian, *J. Mater. Chem.*, 1995, **5**, 543.
101. J. B. Claridge, R. C. Layland, W. H. Henley, and H.-C. zur Loye, *Chem. Mater.*, 1999, **11**, 1376.
102. T. N. Nguyen, D. M. Giaquinta, and H.-C. zur Loye, *Chem. Mater.*, 1994, **6**, 1642.

103. T. N. Nguyen and H.-C. zur Loye, *J. Solid State Chem.*, 1995, **117**, 300.
104. T. N. Nyugen, P. A. Lee, and H.-C. zur Loye, *Science*, 1996, **271**, 489.
105. J. Darriet, F. Grasset, and P. D. Battle, *Mater. Res. Bull.*, 1997, **32**, 139.
106. H. Kageyama, K. Yoshimura, and K. Kosuge, *J. Solid State Chem.*, 1998, **140**, 14.
107. S. Kawasaki, M. Takano, and T. Inami, *J. Solid State Chem.*, 1999, **145**, 302.
108. H. Kageyama, K. Yoshimura, K. Kosuge, M. Azuma, M. Takano, H. Mitamura, and T. Goto, *J. Phys. Soc. Jpn.*, 1997, **66**, 3996.
109. S. Aasland, H. Fjellvåg, and B. Hauback, *Solid State Commun.*, 1997, **101**, 187.
110. J. E. Greedan, *J. Mater. Chem.*, 2001, **11**, 37.
111. P. Schiffer and A. P. Ramirez, *Comm. Cond. Mat. Phys.*, 1996, **10**, 21.
112. A. P. Ramirez, *Annu. Rev. Mater. Sci.*, 1994, **24**, 453.
113. B. D. Gaulin, *Hyperfine Interact.*, 1994, **85**, 159.
114. A. P. Ramirez, *Handbook Magn. Mater.*, 2001, **13**, 423.
115. S. T. Bramwell and M. J. P. Gingras, *Science*, 2001, **294**, 1495.
116. N. P. Raju, M. Dion, M. J. P. Gingras, T. E. Mason, and J. E. Greedan, *Phys. Rev.*, 1999, **B59**, 14489.
117. A. P. Ramirez, B. S. Shastry, A. Hayashi, J. J. Krajewski, D. A. Huse, and R. J. Cava, *Phys. Rev. Lett.*, 2002, **89**, 067202.
118. J. M. D. Champion, A. S. Wills, T. Fennell, S. T. Bramwell, J. S. Gardner, and M. A. Green, *Phys. Rev.*, 2001, **B64**, R140407.
119. M. J. P. Gingras, B. C. den Hertog, M. Faucher, J. S. Gardner, S. R. Dunsiger, L. J. Chang, B. D. Gaulin, N. P. Raju, and J. E. Greedan, *Phys. Rev.*, 2000, **B62**, 6469.
120. J. S. Gardner, A. Keren, G. Ehlers, C. Stock, E. Segal, J. M. Roper, B. Fåk, M. B. Stone, P. R. Hammar, D. H. Reich, and B. D. Gaulin, *Phys. Rev.*, 2003, **B68**, 180401.
121. J. S. Gardner, S. R. Dunsiger, B. D. Gaulin, M. J. P. Gingras, J. E. Greedan, R. F. Kiefl, M. D. Lumsden, W. A. MacFarlane, N. P. Raju, J. E. Sonier, I. Swainson, and Z. Tun, *Phys. Rev. Lett.*, 1999, **82**, 1012.
122. I. Mirebeau, I. N. Goncharenko, P. Cadavez-Peres, S. T. Bramwell, M. J. P. Gingras, and J. S. Gardner, *Nature*, 2003, **420**, 54.
123. L. Pauling, *J. Am. Chem. Soc.*, 1935, **57**, 2680.
124. A. P. Ramirez, A. Hayashi, R. J. Cava, R. Siddharthan, and B. S. Shastry, *Nature*, 1999, **399**, 333.
125. C. H. Booth, J. S. Gardner, and G. Kwei, *Phys. Rev.*, 2000, **B62**, R755.
126. N. P. Raju, J. E. Greedan, and M. A. Subramanian, *Phys. Rev.*, 1994, **B49**, 108.
127. Y. Shimakawa, Y. Kubo, and T. Manako, *Nature*, 1996, **379**, 53.
128. M. A. Subramanian, B. H. Toby, A. P. Ramirez, W. J. Marshall, A. W. Sleight, and G. H. Kwei, *Science*, 1996, **273**, 81.
129. P. W. Anderson, *Phys. Rev.*, 1956, **102**, 1008.
130. S.-H. Lee, C. Broholm, T. H. Kim, W. Ratcliff II, and S.-W. Cheong, *Phys. Rev. Lett.*, 2000, **84**, 3718.
131. I. Kogamiya, K. Kohn, M. Toki, Y. Hata, and E. Kita, *J. Phys. Soc. Jpn.*, 2002, **71**, 916.
132. I. Kagomiya, K. Kohn, M. Toki, Y. Hata, and E. Kita, *Ferroelectrics*, 2002, **268**, 327.
133. H. Martinho, N. O. Moreno, J. A. Sanjurjo, C. Rettori, A. J. Garcia-Adeva, D. L. Huber, S. B. Oseroff, W. Ratcliff II, S.-W. Cheong, P. G. Pagliuso, J. L. Sarrao, and G. B. Martins, *Phys. Rev.*, 2001, **B64**, 024408.
134. J. Rodriguez-Carvajal, G. Rousse, C. Masquelier, and M. Hervieu, *Phys. Rev. Lett.*, 1998, **81**, 4660.
135. J. E. Greedan, C. R. Wiebe, A. S. Wills, and J. R. Stewart, *Phys. Rev.*, 2002, **B65**, 184424.
136. J. E. Greedan, N. P. Raju, A. S. Wills, C. Morin, and S. M. Shaw, *Chem. Mater.*, 1998, **10**, 3058.
137. A. S. Wills, N. P. Raju, C. Morin, and J. E. Greedan, *Chem. Mater.*, 1999, **11**, 1936.
138. A. S. Wills, A. Harrison, S. A. M. Mentink, T. E. Mason, and Z. Tun, *Euro. Phys. Lett.*, 1998, **42**, 325.
139. S.-H. Lee, C. Broholm, G. Aeppli, T. G. Perring, B. Hessen, and A. Taylor, *Phys. Rev. Lett.*, 1996, **76**, 4424.
140. M. Itoh, I. Ohta, and Y. Inaguma, *Mat. Sci. Eng.*, 1996, **B41**, 58.
141. S. A. Almaer, P. D. Battle, P. Lightfoot, R. S. Mellen, and A. V. Powell, *J. Solid StateChem.*, 1993, **102**, 375.
142. A. Munoz, J. A. Alonso, M. T. Casais, M. J. Martilnez-Lope, and M. T. Fernandez-Diaz, *J. Phys.: Condens. Matter*, 2002, **14**, 817.
143. D. Iwanaga, Y. Inaguma, and M. Itoh, *J. Solid StateChem.*, 1999, **147**, 291.
144. C. R. Wiebe, J. E. Greedan, G. M. Luke, and J. S. Gardner, *Phys. Rev.*, 2002, **B65**, 144413.
145. C. R. Wiebe, J. E. Greedan, P. P. Kyriakou, G. M. Luke, J. S. Gardner, A. Fukaya, I. M. Gat-Malureanu, P. L. Russo, A. T. Savici, and Y. J. Uemura, *Phys. Rev.*, 2003, **B68**, 134410.

Magnetism of Extended Arrays in Inorganic Solids

Christopher P. Landee & Mark M. Turnbull
Clark University, Worcester, MA, USA

1 Introduction 1
2 Fundamentals 2
3 Exchange Coupling in One-dimensional Lattices 13
4 Concluding Remarks 22
5 Related Articles 22
6 References 22

Glossary

Anisotropic exchange: exchange coupling between electrons that is dependent on direction; that is, exchange along the x coordinate, for example, differs from exchange along the y or z coordinates
Antiferromagnet: an ordered magnet in which the individual moments point antiparallel to their neighbors owing to antiferromagnetic exchange
Antiferromagnetic exchange: an exchange interaction that couples adjacent moments antiparallel
Antisymmetric exchange: an exchange coupling process that tends to align the electrons perpendicular to one another; there cannot be a center of inversion between the two sites on which the electrons reside, and the g values must be different
Direct exchange: exchange coupling between electrons on centers that are close enough to one another that there can be direct overlap of the atomic wavefunctions
Dzialoshinski-Moriya exchange: an exchange coupling mechanism that is antisymmetric in nature and tends to align moments perpendicular to each other
Exchange interaction: a process that is responsible for short-range magnetic interactions; it may be thought of as the exchange of coordinates of pairs of electrons
Ferrimagnet: an ordered antiferromagnet formed by antiferromagnetic exchange between inequivalent moments
Ferromagnet: an ordered magnet in which all moments are parallel
Ferromagnetic exchange: an exchange interaction that couples adjacent moments parallel
Indirect exchange: exchange coupling between electrons on centers that require the orbitals of an intermediate group or groups for the process to occur
Ordered Magnet: a magnetic state in which moments have spontaneously aligned themselves owing to the action of short-range or long-range interactions; can be destroyed by sufficient thermal energy
Superexchange: see Indirect Exchange

Abbreviations

C = Curie constant; T_C = Curie temperature; T_N = Néel temperature; Θ = Weiss constant; χ_v = Magnetic susceptibility per unit volume; χ_M = Magnetic susceptibility per mole.

1 INTRODUCTION

The magnetic properties of extended array systems have received considerable attention from both chemists and physicists over the past decades.[1–8] The novel magnetic properties of these materials arise from interactions between paramagnetic sites. The origin of these interactions, known as exchange, is electrostatic and quantum mechanical in nature, as first realized by Heisenberg and Dirac in 1926.[1,2] As described in Section 2, it is possible to interpret exchange as formally equivalent to the vector coupling of spins. This equivalence permits the use of a vector-coupling scheme to model the quantitative behavior of coupled spins with the Heisenberg-Dirac-Van Vleck (HDVV) Hamiltonian[3]

$$H = -2JS_i \cdot S_j \tag{1}$$

where the subscripts i and j correspond to the two different spins and J is the exchange coupling constant. This Hamiltonian may be expanded to encompass many different geometries and to account for anisotropic properties, the latter being especially useful in the application of these materials. In the scientific literature, the HDVV Hamiltonian is used in a variety of forms (with or without the factor of 2, with or without the minus sign) and care must be used to avoid the misinterpretation of a given exchange strength. The exchange constant has units of energy, but is frequently reported in units of temperature (K), or in cm^{-1} where $J = k_B T$ and $1\,\mathrm{cm}^{-1} = 1.431\,\mathrm{K}$. In this article, a negative exchange coupling constant corresponds to antiparallel alignment of the electron spins, or an antiferromagnetic exchange interaction, while a positive exchange coupling constant denotes parallel alignment of the electrons, or a ferromagnetic exchange interaction.

Basic theoretical concepts of exchange will be developed in this article. Useful theoretical models invented for the rationalization of the results will be described and their use illustrated by descriptions of extended arrays, principally one-dimensional for simplicity. The development of molecular-based magnetism over the past 15 years has been particularly rapid,[9] so emphasis is given to the use of molecular units in connecting the paramagnetic centers in this article. Surveys of the magnetic properties of extended arrays of a variety of geometries, metal oxidation states, and other diverse chemical features are available.**[10–15,]**

2 FUNDAMENTALS

It is convenient to classify extended arrays in terms of a scheme based on the specific nature of the exchange coupling between the magnetic units plus the structural dimensionality of the array. (This article will only concern interactions between nearest neighbors.) In this scheme, the magnetic units in the arrays may be either radicals or transition metal ions; the ions themselves may be of mixed valence and there may be more than one type of metal ion.

The magnetic properties of individual transition metal ions in compounds and complexes are considered in (*see* ***Magnetism of Transition Metal Ions***). There, the properties of a given ion are assumed to be independent of the presence of any other ions. However, the possibility of *minor* interactions between ions is taken into account in those cases in which the temperature dependence of the inverse magnetic susceptibility deviates from the Curie law.**[11]** This was accomplished by inclusion of the Weiss constant Θ and the generation of the Curie–Weiss law. The properties of extended arrays of this type may be primarily understood in terms of single ions, and they will not be discussed here.

Many interesting problems arise when significant interactions between magnetic moments exist in extended arrays of magnetic moments. When the array consists of two dimensions or more, transitions to a state of long-range magnetic order can occur, giving rise to a host of theoretically and technologically important properties. (If the magnetic system contains a finite number of interacting moments, no long-range order is possible but the magnetic behavior can nevertheless be complex (*see* ***Electronic Structure of Clusters***).)

2.1 Origins of Magnetic Exchange

As mentioned in the Introduction, magnetic exchange is both electrostatic and quantum mechanical in nature. It is electrostatic because the relevant energies are related to the energy costs of overlapping electron densities. It is quantum mechanical because of the fundamental requirement that the total wavefunction Ψ of two electrons must be antisymmetric to the exchange of both the spin and spatial coordinates of the two electrons. The wavefunction Ψ is separable into a product of spatial wavefunction $\psi(r_1, r_2)$ that is a function of the positions r_1 and r_2 of the two electrons, and a spin coordinate wavefunction $\chi(\sigma_1, \sigma_2)$, where σ_i is the Pauli matrix for the spin operator: $S_i = \hbar\sigma_i/2$. Both $\psi(r_1, r_2)$ and $\chi(\sigma_1, \sigma_2)$ can be symmetric or antisymmetric individually but the fundamental requirement permits only two combinations, that is,

$$\Psi_T = \psi_A(r_1, r_2)\chi_S(\sigma_1, \sigma_2) \tag{2a}$$

$$\Psi_A = \psi_S(r_1, r_2)\chi_A(\sigma_1, \sigma_2) \tag{2b}$$

The state with the symmetric spin part is labeled the triplet state while the state with the antisymmetric spin part is the singlet state. As seen below in the context of the hydrogen molecule, there is an electrostatic energy difference $\Delta E_{S,T}$ between the singlet and triplet states. By definition this energy difference equals the exchange energy,

$$\Delta E_{S,T} \equiv 2J \tag{3}$$

Consider a two-electron system in which there are two hydrogen nuclei, a and b, each with a positive charge. The Schrödinger equation for this system may be written as

$$(T + V)\psi = E\psi \tag{4}$$

where the kinetic energy term is

$$T = -\frac{\hbar^2}{2m}(\nabla_1^2 + \nabla_2^2) \tag{5}$$

and the potential energy term is

$$V = e^2\left(\frac{1}{r_{1,2}} - \left(\frac{1}{r_{a,1}} + \frac{1}{r_{b,1}}\right) - \left(\frac{1}{r_{a,2}} + \frac{1}{r_{b,2}}\right)\right) \tag{6}$$

The solution to the full Hamiltonian is rendered difficult by the electron–electron repulsion term that depends on $r_{1,2}$. The full solution can be approximated by initially ignoring this term, solving the remaining simplified Hamiltonian, and then reintroducing the term as a perturbation.

In the Heitler-London approach, the full Hamiltonian of equation (4) can be subdivided as follows

$$H = H_1 + H_2 + H_{1,2} \tag{7}$$

$$H_1 = -\frac{\hbar^2}{2m}\nabla_1^2 - \frac{e^2}{r_{a,1}},\ H_2 = -\frac{\hbar^2}{2m}\nabla_2^2 - \frac{e^2}{r_{b,2}},$$

$$H_{1,2} = \frac{e^2}{r_{1,2}} - \left(\frac{e^2}{r_{a,2}} + \frac{e^2}{r_{b,1}}\right)$$

with H_1 depending only on the coordinates of the first electron and H_2 depending only on the coordinates of the second. The Schrödinger equations involving only H_1 or H_2 correspond to that of the isolated hydrogen atom, yielding atomic wavefunctions $U_n(r_1)$, $U_m(r_2)$, and corresponding energies E_n, E_m.

The first approximation to the two-electron solution for the hydrogen molecule can be formed as a linear combination of the two atomic wavefunctions. The combination wavefunction $\psi(r_1,r_2)$ must be indistinguishable under interchange of the labels of the two electrons so $\psi(r_1,r_2)$ must be either the symmetric or antisymmetric linear combination

$$\Psi_+(r_1, r_2) = N_+ [U_n(r_1)U_m(r_2) + U_m(r_1)U_n(r_2)] \tag{7a}$$

$$\Psi_-(r_1, r_2) = N_- [U_n(r_1)U_m(r_2) - U_m(r_1)U_n(r_2)] \tag{7b}$$

as solutions to the approximate two-electron Schrödinger equation

$$(H_1 + H_2)\psi = E\psi \tag{8}$$

($N+$ and $N-$ are the normalization constants for the symmetric and antisymmetric wavefunctions.) The energies for the molecule can now be calculated to the first order in the perturbation by evaluating the following integral using the approximate wavefunctions of equation (7) and the full Hamiltonian of equation (9).

$$E = \iint \psi^* H \psi dv_1 dv_2 \tag{9}$$

Four separate integrals result from the above equation with the result

$$E_\pm = E_n + E_m + 2N_\pm^2(Q \pm J) \tag{10}$$

where

$$\begin{aligned} E_n &= \int U_n^*(r_1)H_1U_n(r_1)dv_1,\ E_m = \int U_m^*(r_2)H_2U_m(r_2)dv_2 \\ Q &= \iint U_n^*(r_1)U_m^*(r_2)H_{1,2}U_n(r_1)U_m(r_2)dv_1dv_2 \\ J &= \iint U_n^*(r_1)U_m^*(r_2)H_{1,2}U_m(r_1)U_n(r_2)dv_1dv_2 \end{aligned} \tag{11}$$

The plus and minus signs for the energies in equation (10) correspond to the energy of the triplet and singlet states, respectively. The difference between these two energies follows from equation (9) as

$$\begin{aligned} \Delta E_{S,T} &= E_+ - E_- = 2N_+^2(Q + J) - 2N_-^2(Q - J) \\ &= 2Q(N_+^2 - N_-^2) + 2J(N_+^2 + N_-^2) \end{aligned} \tag{12}$$

When the one-electron wavefunctions are orthogonal, both $N+$ and $N-$ equal $1/\sqrt{2}$, and we have regained the equivalence of the singlet-triplet energy gap with twice the exchange integral, as described in equation (3). The difference in energy between the symmetric and antisymmetric states is due to the difference in the correlation of the two electrons in their orbits.[7] In one wavefunction, they are more likely to be found close together and in the other, more likely to be further apart. This energy difference has nothing to do with the relative orientation of the electron's moments. However, the fundamental requirement that the total wavefunction be antisymmetric means that the antisymmetric spatial wavefunction is partnered with the symmetric two-electron spin function and visa versa. The spin singlet and triplet state therefore correspond to different energy levels.

Use of the Heisenberg spin Hamiltonian (equation 1) to represent the energy difference of the singlet and triplet spin states is easily demonstrated. Two spins, S_i and S_j, can be added to produce a maximum spin of $S_{\max} = S_i + S_j$, and lower values $S_{\max} - 1$, $S_{\max} - 2$ down to a minimum of $S_i - S_j$. When the two spins are both one-half, the two possible values for the total spin are $S_{\text{tot}} = 1$ and $S_{\text{tot}} = 0$, the spin triplet and singlet, respectively. To evaluate the energies of these states from equation 1, it is necessary to know the value of $S_i \cdot S_j$ for the two states. This can be found by evaluating the vector sum of the spins and employing the basic quantum rule

$$S^2 = S(S + 1) \tag{13}$$

$$S_{\text{tot}}^2 = S_{\text{tot}}(S_{\text{tot}} + 1) = (S_i + S_J)^2 = S_i^2 + S_j^2 + 2S_i \cdot S_j \tag{14}$$

Therefore

$$\begin{aligned} 2S_i \cdot S_j &= S_{\text{tot}}(S_{\text{tot}} + 1) - S_i^2 + S_j^2 = S_{\text{tot}}(S_{\text{tot}} + 1) - \frac{3}{4} - \frac{3}{4} \\ &= S_{\text{tot}}(S_{\text{tot}} + 1) - \frac{3}{2} \end{aligned} \tag{15}$$

where we have used $S^2 = (1/2)(3/2) = 3/4$ for a spin one-half.

$$\begin{aligned} S_{\text{tot}} &= 1 : 2S_i \cdot S_j = 1(1 + 1) - \frac{3}{2} = \frac{1}{2} \\ S_{\text{tot}} &= 0 : 2S_i \cdot S_j = 0(0 + 1) - \frac{3}{2} = -\frac{3}{2} \end{aligned} \tag{16}$$

From equation (1), the energy eigenvalues for the two spin states can be evaluated as

$$\begin{aligned} E_{S=1} &= -J_{i,j}\left(\frac{1}{2}\right) = -\frac{J_{i,j}}{2} \\ E_{S=0} &= -J_{i,j}\left(-\frac{3}{2}\right) = +\frac{3J_{i,j}}{2} \end{aligned} \tag{17}$$

leading to the expected result for the singlet-triplet energy gap

$$\Delta E_{S,T} = E_{S=0} - E_{S=1} = +\frac{3J_{i,j}}{2} - \left(-\frac{J_{i,j}}{2}\right) = 2J_{i,j} \tag{18}$$

In the antiferromagnetic case in which the exchange constant is negative, the singlet state lies an energy $2J$ below the triplet state.

The argument above establishes the formal equivalence between the HDVV Hamiltonian and the singlet-triplet energy gap, but such a formal definition is of little use. Calculating energy levels from first principles requires extensive basis sets and much computing effort. The uncertainties in any energy level can easily be as large as the small differences between adjacent singlet and triplets states, typically a few hundreds of wavenumbers or less. What is needed in practice is an approach that can describe trends in exchange strength as a function of observable parameters such as bond distances or angles. This approach permits a conversation between the theoretical modeling and experimental discoveries, as described in the following section.

2.2 Superexchange Models and Magnetostructural Correlations

An important advance in magnetochemistry was the discovery by Hatfield and coworkers[16] that the exchange strength in a family of planar hydroxo-bridged copper dimers (Figure 1) varied linearly with the Cu–O–Cu bridging angle Φ over a range of $2J$ from $+170\,\mathrm{cm}^{-1}$ ($\Phi = 95.5°$) to $-510\,\mathrm{cm}^{-1}$ ($\Phi = 104.1°$) with ferromagnetic exchange occurring for bridging angles of less than 98°. Their data were well described by the empirical equation

$$2J(cm^{-1}) = 7270\,\mathrm{cm}^{-1} - 74(\mathrm{cm}^{-1}/°)\Phi \tag{19}$$

This correlation demonstrated that exchange strength was not strictly bipolar, strictly ferro- or antiferromagnetic in sign, but was rather a *tunable* quantity subject to modification by chemical/structural means. Its discovery led to a renewed interest[17–19] in superexchange theory with emphasis on the use of molecular orbital models (see Ref. 11 for a lucid description). A similar correlation was found[20] for dichlorobridged copper dimers with ferromagnetic exchange occurring for angles less than 90°.

Kahn and coworkers introduced the useful concept of natural magnetic orbitals.[18] For two paramagnetic centers A, B bridged by a ligand X, the natural magnetic orbital a in AXB is defined as the singly occupied molecular orbital for the AX fragment in its local ground state, while b is defined the same way for the XB fragment. The interaction between A and B leads to two molecular states, a singlet and triplet separated by $2J$. If the interaction is weak enough for the spin states to be described by Heitler-London wave functions built up of a and b, and if the metal–metal charge-transfer configuration is too high in energy to couple significantly with the ground-state configuration, then it is possible to express the exchange as the sum of two components: a positive ferromagnetic component J_F and a negative antiferromagnetic component J_AF:

$$2J = 2J_\mathrm{F} + 2J_\mathrm{AF} \tag{20}$$

where

$$J_\mathrm{F} = 2j \tag{21}$$

$$J_\mathrm{AF} = -2S(\Delta^2 - \delta^2)^{1/2} \tag{22}$$

S is the overlap integral between the magnetic orbitals, and j is the two-electron exchange integral.

$$S = \int \Phi_A^*(1)\Phi_B(2)\,\mathrm{d}v_1 \tag{23}$$

$$j = \int \Phi_A^*(1)\Phi_B^*(2)\frac{1}{r_{1,2}}\Phi_A(2)\Phi_B(1)\,\mathrm{d}v_1\,\mathrm{d}v_2 \tag{24}$$

Δ is the energy gap between the two molecular orbitals in the A–B dimer constructed from the magnetic orbitals for the triplet state and δ is the energy gap between Φ_A and Φ_B (Figure 2). When the two paramagnetic centers are identical, $\delta = 0$ and J_AF is simplified to

$$J_\mathrm{AF} = -2S\Delta \tag{25}$$

The net interaction then depends on two distinct and competing terms: the two-electron exchange integral that favors the triplet state, and the product of the overlap integral and the energy gap that favors the singlet state. To first order the energy gap is proportional to the overlap integral so J_AF varies as $-S^2$. The smooth variation in exchange strength with bridging angle observed by Hatfield for the hydroxy-bridged copper dimers can now be understood in terms of different angular dependencies for the exchange integral j and the overlap integral S. (Including the interaction between the ground-state configuration and the charge-transfer configuration adds additional terms to J_AF that are also

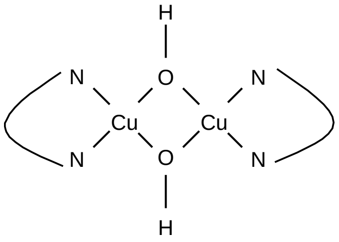

Figure 1 Model of a hydroxide bridged copper dimer

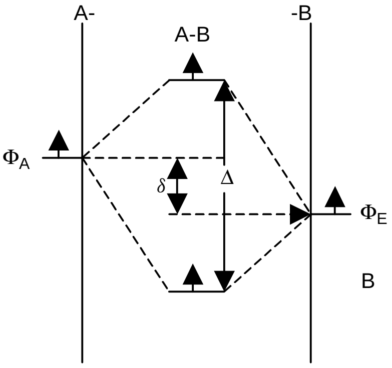

Figure 2 The orbital interaction in a dimer, AB

proportional to the overlap integral so the qualitative picture is not affected by ignoring it. See Reference 11, Chapter 8.)

A similar molecular orbital analysis on the copper dimer system (Figure 1) was performed by Hay *et al.*,**19** leading to the following formula for the singlet-triplet gap,

$$E_S - E_T = 2K_{ab} - \frac{(\varepsilon_S - \varepsilon_A)^2}{J_{aa} - J_{ab}} \tag{26}$$

where K_{ab} is the two-electron exchange integral (equation 24), $\varepsilon_1 - \varepsilon_2$ is the difference between the two orbital energies, and J_{aa} and J_{ab} are the one-center and two-center Coulomb repulsion integrals. These authors focused on the quantity $(\varepsilon_S - \varepsilon_A)$ since the denominator was assumed to vary slowly as a function of distortion for closely related compounds.

The relative order of ε_1 and ε_2, or equivalently ε_S and ε_A, is determined by the metal-bridging ligand overlap. The metal orbitals for Φ_A and Φ_S are required by symmetry to remain *xy* for all M–L–M angles (see Figure 3). On the bridging atoms, there is one symmetry adapted combination of p orbitals $(y_1 + y_2)$ that interacts with Φ_S and another combination $(x1 + x2)$ that interacts with Φ_A. The oxygen 2s orbitals can interact with Φ_S but not with Φ_A.

The relative order of ε_S and ε_A as a function of bridging angle θ will be determined by the metal-bridging ligand overlap. At $\theta = 90°$, the overlaps are equal, the energies of ε_S and ε_A will be equal and one expects ferromagnetic exchange. As θ increases (Figure 4a), the overlap between ⟨xy|x⟩ will increase while the overlap between ⟨xy|y⟩ decreases. This leads to an increase in ε_A and a decrease in ε_S. One then expects to see an increased antiferromagnetic interaction as $(\varepsilon_A - \varepsilon_S)^2$ grows. In Figure 4(b), the energies of the two highest metal orbitals in $Cu_2(OH)_2Cl_4{}^{2-}$ are plotted as a function of bridge angle θ. If the effect of the 2s bridge orbitals are ignored, the energies cross near 107°. Including the ⟨xy|2s⟩ effect lowers ε_S and brings the crossing point to $\theta = 96°$, close to the observed angle for the Hatfield dimers. It is interesting to note the smallest bridge angles structurally accessible closely correspond to the crossover point. The results from Figure 4 predict that the exchange would once again turn antiferromagnetic for angles significantly smaller than 96°, but such compounds have not been discovered.

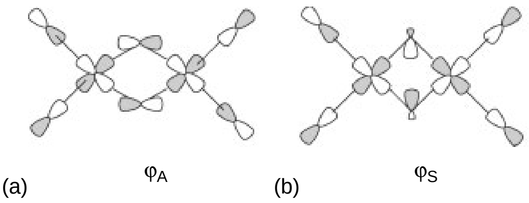

Figure 3 Orbital overlap in copper dimers

The dependence of J_{AF} upon S also provides insight into constructing A–B interactions that are predominately ferromagnetic in character. When the overlap integral is small enough for $J_{\mathrm{F}} > |J_{\mathrm{AF}}|$, the triplet state will be stabilized. The overlap orbital can sometimes be sufficiently tuned by geometrical parameters for this to occur, as illustrated above for Hatfield's dimers. When S vanishes at some special angle, the magnetic orbitals are said to be *accidentally* orthogonal.

A more systematic approach for obtaining ferromagnetic exchange is to make use of magnetic orbitals that are *strictly* orthogonal to one another by symmetry requirements. This will occur when the *a* and *b* orbitals transform as different irreducible presentations of the symmetry group of the system. As was pointed out by Kahn,**11** strict orthogonality is more easily achieved when the two interacting paramagnetic centers are not identical.

An elegant illustration of this principle is found in the binuclear metal complex MM(fsa)$_2$en·MeOH, where

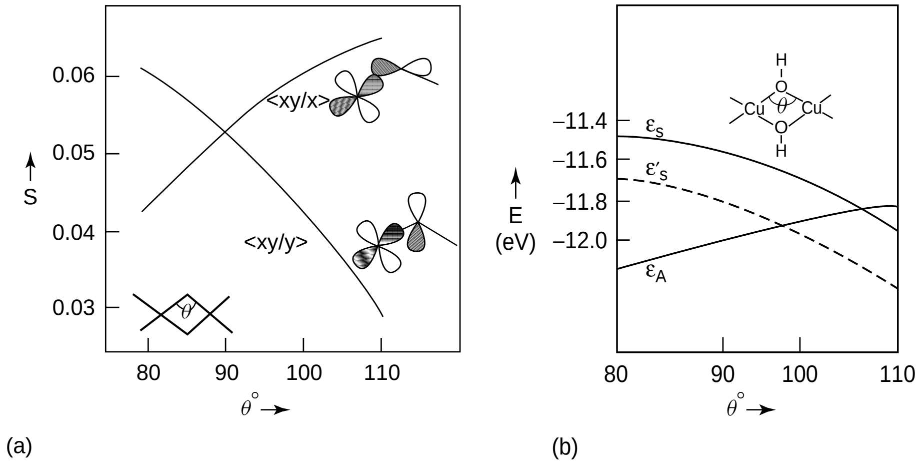

Figure 4 (a) Variation of metal–ligand overlap S in a bibridged dimer geometry as a function of bridging angle. (b) Energies of the highest metal orbitals in $Cu_2(OH)_2Cl_4{}^{2-}$ as a function of bridge angle. The solid line ε_S ignores the 2s bridge orbital effect, the dashed line considers it. The ε_A line does not depend on the oxygen 2s contribution. (Reprinted with permission from Ref. 19 © 1975 American Chemical Society)

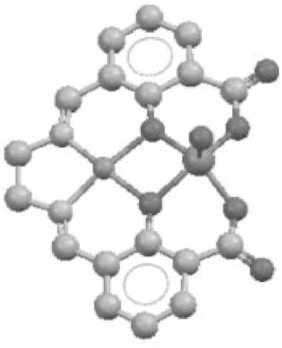

Figure 5 Perspective view of CuVO(fsa)2en·MeOH. The copper site is on the left side of the cage, the vanadyl to the right. The methanol molecule is not shown for clarity[21]

H_4(fsa)2(en)=N,N'-(2-hydroxy-3-carboxybenzilidene) ethylenediamine (see Figure 5).[21] The copper (II) and vanadium(IV) sites, the oxygen atom of the vanadyl group and the methanol oxygen atom weakly bonded to the copper atom (not shown) are very close to forming a mirror plane perpendicular to the plane of the macrocycle. The unpaired copper electron therefore has close to a pure *xy*-type wavefunction transforming as a'' while the unpaired electron around the vanadium is described by a $x^2 - y^2$ magnetic orbital transforming as a'. Strict orthogonality of the two orbitals is obtained and, as expected the triplet state is stabilized by $118\,\text{cm}^{-1}$ below the singlet state. Replacing the vanadyl group with a second copper atom creates a strong overlap of orbitals, with a commensurate antiferromagnetic interaction $2J = -650\,\text{cm}^{-1}$.

The importance of symmetry in determining the sign of the superexchange interaction was first recognized in the late 1950s by Goodenough[22] and Kanamori.[23] Building on Anderson's original theory of superexchange[24] these authors derived qualitative guidelines (known collectively as the 'Goodenough-Kanamori Rules') for predicting the sign of the exchange for different d orbitals bridged by atomic anions though high symmetry bridging angles of 90° or 180°. These rules have more recently been generalized and extended by application of the concepts of natural orbitals to consider molecular bridging units.[11] These results have been particularly useful in the design of bimetallic cyanide compounds with high ordering temperatures (*see* ***Cyanide Complexes of the Transition Metals***).

2.3 The Heisenberg Hamiltonian

The origin of these interactions, called exchange, was first realized by Heisenberg and Dirac in 1926.[1,2] The interpretation of the exchange effect as formally equivalent to the coupling between spins permits the use of a vector-coupling scheme to model the quantitative behavior of coupled spins with the HDVV Hamiltonian[3]

$$H = -2JS_i \cdot S_j = -2J(S_i^x S_j^x + S_i^y S_j^y + S_i^z S_j^z) \tag{27}$$

where the subscripts i and j correspond to the two different spins and J is the exchange coupling constant (the factor of two preceding the exchange strength J is traditional, dating back to Heisenberg's original paper.) The Hamiltonian states that the energy of the interacting spin pair depends only on the *relative* orientation of adjacent spins. No spatial direction is contained in this term so the spins are free to orient themselves along any crystallographic direction, so long as their relative orientation remains the same. An important consequence of this fact is the tendency of antiferromagnetically coupled moments to orient perpendicular to small external fields (see Section 2.8). With the negative sign preceding the dot product, a positive J indicates that a minimum energy is achieved with adjacent spins parallel, that is, in a ferromagnetic alignment.

2.4 Anisotropic Interactions & Spin Dimensionality

The spin angular momentum of an electron is properly described by a three-component vector and an isolated spin is free to orient in any direction in space. Likewise, the magnetic moment of the electron, related to the vector spin through the relation

$$m_S = -g\mu_\beta S \tag{28}$$

is free to point in any direction. However for an ion within a crystalline lattice, the situation is more complex. The total spin of the ion will depend on the number of d-electrons and the crystal field states in which the electrons reside. In addition, for ions with significant amounts of unquenched orbital angular momentum such as Fe^{2+} or Co^{2+}, the moment of the ion can have greatly different values along the different axes of the local coordination sphere. One technique of describing this behavior is to replace the simple scalar g-factor in equation (28) with a g-tensor. A more complete discussion is found in the contribution (*see* ***Magnetism of Transition Metal Ions***).

What is the connection between the HDVV exchange interaction of equation (27) and the complexities of an ion in a crystal field? The isotropic exchange Hamiltonian is always correct since it is a direct consequence of the Pauli Exclusion Principle. However, a modified form of the exchange interaction is frequently used to describe those cases in which the individual moments are no longer isotropic.

$$H = -2J\left[\alpha(S_i^x S_j^x + S_i^y S_j^y) + \beta S_i^z S_j^z\right] \tag{29}$$

The anisotropic exchange Hamiltonian appears as equation (29). It retains the form of a product of spins S_i and S_j but the spin components are given different weights. The x- and

y-components are multiplied by the dimensionless factor α while the z-components are multiplied by β. It is convenient to discuss three limiting classes of spin anisotropy in which one, two, or all three spin components have significant weight. For historical reasons, these classes are known as the one-dimensional Ising case ($\alpha = 0$, $\beta = 1$), the two-dimensional XY case ($\alpha = 1$, $\beta = 0$), and the three-dimensional, or fully isotropic Heisenberg case ($\alpha = \beta = 1$). The dimensionality refers to the number of spin components that have important weight in the Hamiltonian and is known both as the *spin dimensionality* and as the number of spin degrees of freedom. It is determined by the local environment of each ion and is independent of the exchange pathways that can connect any given moment to a one-, two-, or three-dimensional magnetic lattice.

In general, the spin dimensionality classes arise from structural features of materials that govern interactions between paramagnetic ions or from the electronic structure of the single ions.

The physical origins of the α/β ratio are due to the presence of strong internal fields on the ions themselves. Unquenched orbital angular momentum in a ferrous ion can create internal fields greater than 50 tesla along an internal axis. The exchange is always Heisenberg, but the effect of the internal fields can be modeled as $\beta \gg \alpha$, or the Ising interaction. Likewise, cases in which the spins are constrained to lie in a plane can be modeled as $\alpha \gg \beta$, the XY interaction.

2.5 Nonexchange Interactions: Dzialoshinski-Moriya Coupling

If two paramagnetic centers are related to each other by low symmetry, they are subject to an antisymmetric interaction known as Dzialoshinski-Moriya exchange.[25] The strength of the interaction D_{D-M} was shown by Moriya[25b] to be proportional to the exchange constant as follows:

$$H_{anti} = D_{D-M} \cdot S_A \times S_B \tag{30a}$$

$$\text{where} \quad D_{D-M} \propto \frac{\Delta g}{g} J \tag{30b}$$

Δg is the variation of the g-tensor components from 2.0023. This interaction arises from the coupling of the paramagnetic moment to the lattice through spin-orbit coupling as was derived by Moriya by extending Anderson's superexchange model[24] to include the spin-orbit effect.

D_{D-M} equals zero exactly if the two magnetic centers are centrosymmetric or lie on an n-fold axis of C_{nv} symmetry with $n \geq 2$, so many compounds are unaffected by this term. It is most commonly observed when adjacent magnetic sites are related by a screw axis. The effect of this term is to align adjacent spins at right angles to each other, but it only occurs when the exchange interaction is also present and rendering the spins either parallel or antiparallel. The result is for the spins to be canted alternately to either side of their mean axis by an angle Φ whose tangent is proportional to the ratio of the interaction strengths

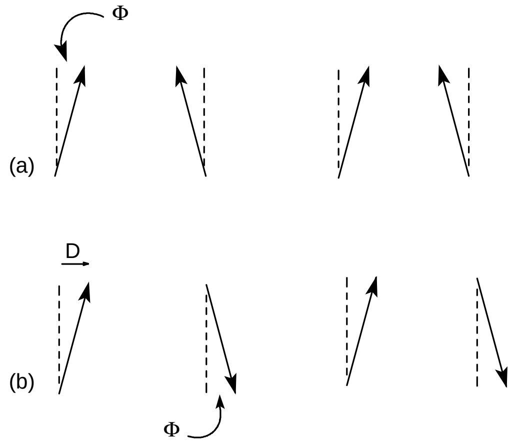

Figure 6 Spin canting in (a) a linear ferromagnet and (b) in a linear antiferromagnet

$$\tan(\Phi) \propto \frac{D_{D-M}}{J} \tag{31}$$

The effect of the canting on ferromagnets is usually minor (Figure 6a) but it can change the behavior of antiferromagnets dramatically. As seen in Figure 6(b), spin canting in an antiferromagnet can lead to the formation of a spontaneous moment along one axis for temperatures below the Néel temperature. This phenomena is know as 'weak ferromagnetism' because the canted moment is much smaller than the full saturated moment.

2.6 Magnetic Correlations and Magnetic Ordering

Magnetic ordering is a cooperative process in which, at some critical temperature, every moment assumes a specific orientation relative to the entire lattice of interacting moments. (The critical temperature for a ferromagnetic transition is historically called the Curie temperature, T_C, while antiferromagnetic transitions occur at the Néel temperature, T_N.) Below T_C, the expectation value of the dot product of a pair of spins, $\langle S_i \cdot S_j \rangle$, will be nonzero for any spin pair, no matter how distant they may be from each other. Above T_C, the expectation value is finite for nearby spins but decreases to zero as the spins become further separated. The *correlation length* is defined as the distance between spins at which the expectation value of the spin pair drops to some stated fraction of its maximum possible value. Using this definition, a magnetic transition to an ordered state can be said to occur when the system's correlation length grows to infinity.

Magnetic correlations are caused by magnetic interactions. The interacting system has a ground state and excited states, with the population of the states determined by the Boltzmann distribution, or a quantum statistical distribution function. The width of the energy spectrum will be proportional to the interaction strength J. When the temperature is reduced, the population of the ground state increases and the correlation length expands. Significant deviations from the behavior of a noninteracting system occur for temperatures $T \approx J$.

Low relative temperatures (T/J) are a necessary, *but not sufficient*, condition for the occurrence of magnetic ordering. As the temperature approaches zero, the correlation length will grow, but if there exist natural limits to the size of the correlation length, it cannot diverge, and magnetic ordering will not occur. The most fundamental limit is the dimensionality of the magnetic lattice itself. As described in the following section, no cluster with a finite number of moments can sustain long-range order, while every three-dimensional lattice can. All one-dimensional systems are prevented from ordering by entropic effects, while the ability of two-dimensional lattices to undergo a magnetic transition depends on the spin dimensionality.

2.7 Lattice Dimensionality

The *lattice dimensionality* of the interacting spin system describes the number of directions in which there are extended interaction pathways. Along with the spin dimensionality, the lattice dimensionality determines if a magnetic system can spontaneously undergo a transition to a magnetically ordered state at a finite temperature (see Section 2.6). Spin and lattice dimensionalities are independent parameters so within each class of lattice dimensionality, the spins can be described by Ising-like, XY-like, or Heisenberg Hamiltonians.

There are four classes of structural dimensionality. The simplest class is that in which the structure is made up of isolated clusters containing a finite number of exchange-coupled paramagnetic ions. Such systems are defined to be zero dimensional, 0D, because of the absence of any direction of extended interactions. If the number of paramagnetic ions in the cluster is small, exact expressions for the thermomagnetic properties of the cluster can be derived for any of the three spin dimensionalities. Small clusters of exchange-coupled paramagnetic ions are frequently used as models for more complicated extended systems. In every cluster, the correlation length is restricted to the size of the cluster; no magnetically ordered state is possible. Clusters with a magnetic ground state are known both as ‘high-spin molecules’ and ‘nanomagnets’ and display many interesting features, including quantum tunneling.[26]

The second structural class is that of infinite chains of exchange-coupled ions (Figure 7). In the simplest example of a one-dimensional (1-D) system, each paramagnetic ion has two nearest neighbors linked by suitable ligand bridges, with the next-nearest neighbors much farther away and not directly bridged to the chain. As always the exchange interactions may have spin dimensionalities of one, two, or three. The study of linear quantum magnets has played an important part in the study of phase transitions with such seminal names as Ising[27] and Bethe[28] being the first scientists to study the 1D $S = 1/2$ Ising and Heisenberg chains, respectively. While it is energetically possible for the correlation of a 1-D system to diverge at low temperatures, entropic effects will induce disorder in the chain and keep the correlation length finite for all nonzero temperatures. No long-range order is possible in purely 1D systems although weak secondary interactions in 2D or 3D may induce order at low temperatures.

The last structural class of *low-dimensional* magnetic systems is an isolated layer or sheet containing exchange-coupled paramagnetic ions (Figure 8). Spin dimensionality plays an important role in determining the nature of long-range cooperative behavior in two-dimensional (2-D) arrays[12,13] with 2D Heisenberg systems unable to sustain an ordered state at any finite temperature owing to the strong effects of their quantum fluctuations. (They are ordered in the absence of all thermal fluctuations at $T = 0$.) 2D Ising magnets spontaneously order as either ferro- or antiferromagnets[29] while 2D XY magnets are predicted to have a special kind of behavior in which the moments align in vortices within

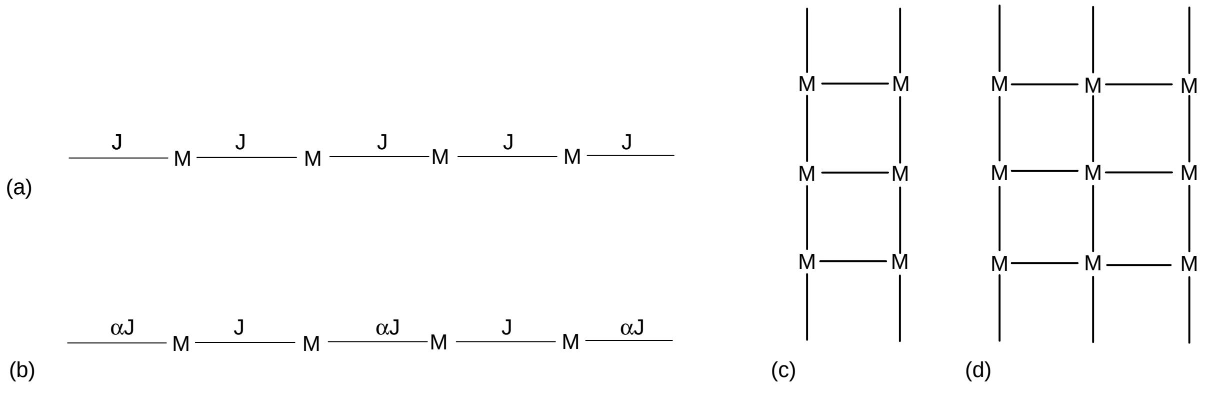

Figure 7 Some low-dimensional magnetic lattices: (a) uniform chain, (b) alternating chain, (c) two-leg ladder, and (d) three-leg ladder

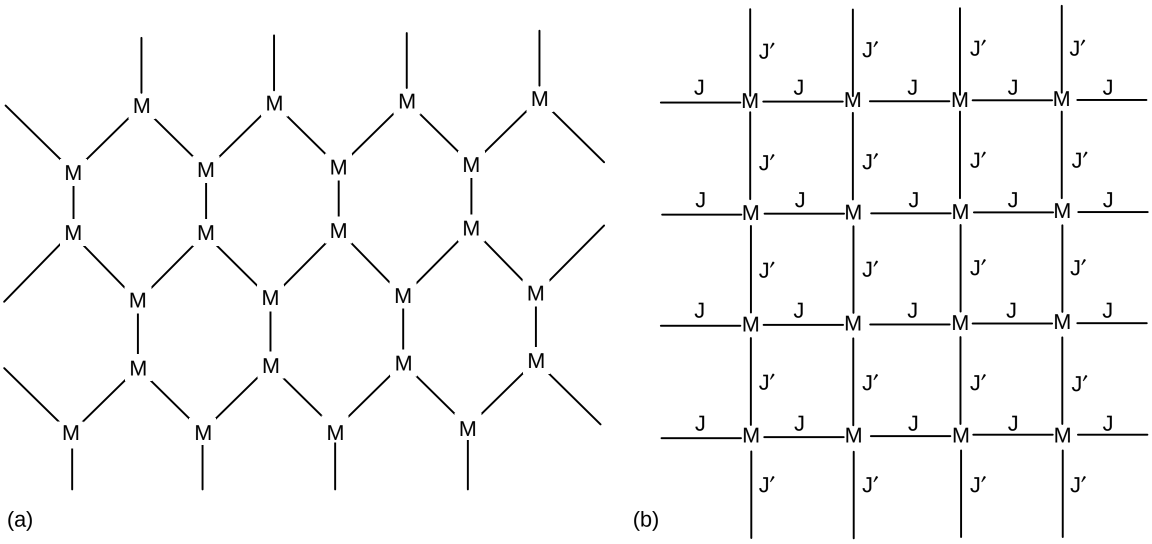

Figure 8 Some two-dimensional magnetic lattices: (a) honeycomb and (b) square (if $J = J'$) or rectangular (if $J > J'$)

the planes.[30] The correlation length is predicted to diverge at the critical temperature but no spontaneous moments appear.

Three-dimensional (3-D) magnetic systems are those in which exchange interactions occur in all directions. These may range from simple cubic systems to very complex arrays that reflect structural details of superexchange pathways and the electronic structures of the paramagnetic ions. A number of fascinating phenomena are exhibited by many of these systems, and a wide range of models for the nature of these interactions has been generated. Theoretical and experimental efforts are synergistic with advances in one area stimulating additional efforts in the other.

2.8 Magnetic Susceptibilities of Exchange-coupled Systems

The essential measurement to characterize a magnetic material is the determination of the temperature dependence of the magnetic susceptibility, χ. Many other experimental techniques will be necessary to understand fully the static and dynamic properties of a magnetic material (isothermal magnetization, specific heat in zero and applied fields, EPR and NMR spectroscopies, and elastic and inelastic neutron scattering) but, following a determination of the structure, no other experiment can yield as much information with as little effort. Analysis of the magnetic susceptibility can reveal the spatial and spin dimensionalities of the magnetic lattice, the sign and magnitude of the exchange strength, the absence or presence of an ordering transition, and even estimates of the internal anisotropies.

By definition, the susceptibility is the ratio of the sample's magnetization per unit volume M_V to the applied field H, in the limit of the field going to zero.

$$\chi_V = \lim_{H \to o} \frac{M_V}{H} \text{ (dimensionless)} \tag{32}$$

The magnetization per unit volume has the same units as the H-field for both cgs and SI units so the volume susceptibility is dimensionless. In practice, it is much more common to work with the molar magnetization $M_{mol} = M_V \times (MW/\rho)$ where MW is the molecular weight and ρ is the density of the material.

$$\chi_{mol} = \lim_{H \to o} \frac{M_{mol}}{H} \left(\frac{\text{vol}}{\text{mol}}\right) \tag{33}$$

The molar susceptibility thus has units of volume per mole for all unit systems. In practice, the molar susceptibility is frequently reported in cgs units as 'emu $\text{Oe}^{-1}\,\text{mol}^{-1}$'. (Scientists studying magnetism continue to utilize an eccentric mix of mostly cgs units in which the unit of magnetic moment, properly '$\text{erg}\,\text{Oe}^{-1}$' is given the name of 'emu'. The volume susceptibility remains dimensionless but is said to have units of '$\text{emu}\,\text{cm}^{-3}\,\text{Oe}^{-1}$' and the molar susceptibility can be expressed as '$\text{emu}\,\text{Oe}^{-1}\,\text{mol}^{-1}$', which is equivalent to '$\text{cm}^3\,\text{mol}^{-1}$'. See Reference 31 for a lucid discussion of SI units.)[31]

2.8.1 Heisenberg 1D Chains: Uniform $S = 1/2$ Antiferromagnets

The uniform Heisenberg magnetic chain has been an object of study for three quarters of a century, dating back to the initial work of Bethe.[28] Unlike the equivalent Ising and XY-chains, the Heisenberg model cannot be solved analytically. The first calculations of the susceptibility and specific heat were reported in a now-celebrated 1964 paper by Bonner and Fisher[32] who used extrapolated results based on computer calculations for finite chains. The revolution in computer technology and numerical methods over the past forty years has led to detailed understanding of the energy spectrum of the 1D quantum Heisenberg antiferromagnet (QHAF) in both zero- and applied fields.

A rigorous examination of the susceptibility and specific heats of the uniform and alternating Heisenberg antiferromagnets was reported by Johnston.[33] As shown in Figure 9, the susceptibility at low relative temperatures shows a rounded maximum, and then decreases to a finite value as the temperature approaches zero. The temperature ($T^{\max}$) at which the maximum susceptibility ($\chi^{\max}$) occurs is proportional to the exchange strength while the value of $\chi^{\max}$ is inversely proportional to the exchange.

The $T^{\max}\chi^{\max}$ product, is a constant now known to nine decimal places. (It is important to note that Figure 9 was prepared using the single J format for the Hamiltonian.)

$$T^{\max} = \frac{0.640\,851\,0(2J)}{k_B} \tag{34}$$

$$\frac{\chi^{\max}(2J)}{Ng^2\mu_\beta^2} = 0.146\,926\,279 \tag{35}$$

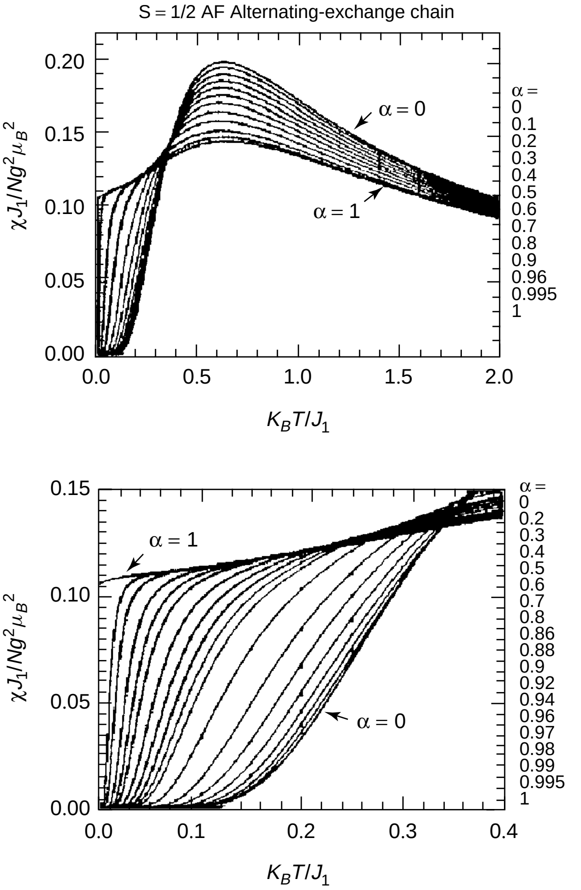

Figure 9 Susceptibility as a function of temperature for Heisenberg alternating chains with different values for α, the alternation parameter. (Reprinted with permission from D.C. Johnston, R.K. Kremer, M. Troyer, X. Wang, A. Klümper, S.L. Bud'ko, A.F. Panchula, and P.C. Canfield, *Phys. Rev. B*, 2000, **61**, 9558. © 2000 by the American Physical Society)

Exchange constants for low-dimensional magnets are most commonly obtained via comparison of experimental data to the predicted behavior of a thermodynamic property for a given model, usually the magnetic susceptibility. Johnston *et al.*[33] showed that the molar susceptibility χ_M of the uniform chain can be expressed as a ratio of polynomials in powers of the reduced temperature t ($t \equiv k_BT/|2J|$). The coefficients N_n and D_n are listed in Table 1.

$$\chi_M = \frac{C}{T}P_r^q(t)\text{where}P_r^q(t) = \frac{1+\sum_{n=1}^{q} N_n/t^n}{1+\sum_{n=1}^{r} D_n/t^n} \tag{36}$$

In the limit of high temperature, $P_r^q(t) \rightarrow 1$, and the molar susceptibility $\chi_{\text{mol}} \rightarrow C/T$, where $C = (N_A g^2\mu_\beta^2/4k_B)$ for the $S = 1/2$ system. When equation (35) is used to determine the exchange strength from comparison to an experimental data set the fitting parameter will be the absolute value $|J|$.

2.8.2 Heisenberg 1D Chains: Alternating Exchange Linear Chains

Inspection of the low-temperature region of Figure 10 shows two distinct types of behavior. If the lattice is uniform, either 1D or 2D, the susceptibility remains finite as the temperature approaches zero. If the lattice consists of a network of dimers, such as an alternating chain or a spin ladder, the ground state is a nonmagnetic singlet separated from the lowest excited state by an energy gap Δ. As the temperature is reduced, the system drops into the ground state and the susceptibility decreases to zero exponentially $\chi \propto 1/\sqrt{T}\exp(-T/\Delta)$

The alternating chain consists of $S = 1/2$ units linked alternately by an exchange strength J and a strength αJ,

Table 1 Coefficients for the expansion of the molar magnetic susceptibility of the $S = 1/2$ Heisenberg antiferromagnetic chain in equation (36).[33] This expression is valid over the temperature range $0.01 < T/|2J| < 5$

Index I	N_i	D_i
1	−0.053837836	0.44616216
2	0.097491365	0.32048245
3	0.014467437	0.13304199
4	0.0013925193	0.037184126
5	0.00011393434	0.0028136088
6		0.00026467228

where $\alpha < 1$ (Figure 7b). In the limit of $\alpha \rightarrow 0$, the chain is reduced to a collection of isolated dimers, while it approaches the uniform chain as $\alpha \rightarrow 1$. The singlet-triplet gap is also a function of the alternation parameter being equal to $2|J|$ for the dimer and zero for the uniform chain. The variation of the susceptibility of the alternating chain as a function of α and temperature is seen in Figure 9. Expressions for the alternating chain susceptibility are considerably more complex than the expression (equation 36) for the uniform chain.[33]

2.8.3 *Heisenberg Antiferromagnetic Spin Ladders*

Spin ladders consist of two uniform chains, exchange strength $2J_{\text{rail}}$, coupled together by a second interaction $2J_{\text{rung}}$ (Figure 7c). When $|J_{\text{rung}}| \gg |J_{\text{rail}}|$, the system can be approximated as nearly independent dimers with $\Delta E_{S-T} = 2|J_{\text{rung}}|$. Consequently the susceptibility will vanish exponentially as $T \rightarrow 0$ (Figure 11). Surprisingly, the gap remains finite even in the opposite limit of $|J_{\text{rail}}| \gg |J_{\text{rung}}|$ and the low-temperature susceptibility of all spin ladders vanishes. Figure 11 shows the variation of susceptibility as a function of temperature and the $|J_{\text{rail}}/J_{\text{rung}}|$ ratio.[34]

Comparison of Figures 9 and 11 shows the susceptibilities of alternating chains and spin ladders are very similar. It is not possible to distinguish between the two models when examining an experimental data set. Additional experiment evidence is required.

2.8.4 *Heisenberg Ferromagnetic S = 1/2 Heisenberg Chains*

Ferromagnetic chains become increasingly easier to magnetize as the temperature is lowered and their correlation length expands. Their susceptibilities increase considerably faster than the Curie-like T^{-1} behavior; Heisenberg $S = 1/2$ ferromagnetic chains have been approximated[32] as diverging as $T^{-1.7}$. This property means the applied external field must be carefully checked to insure that the moment remains linear in field at low temperatures.

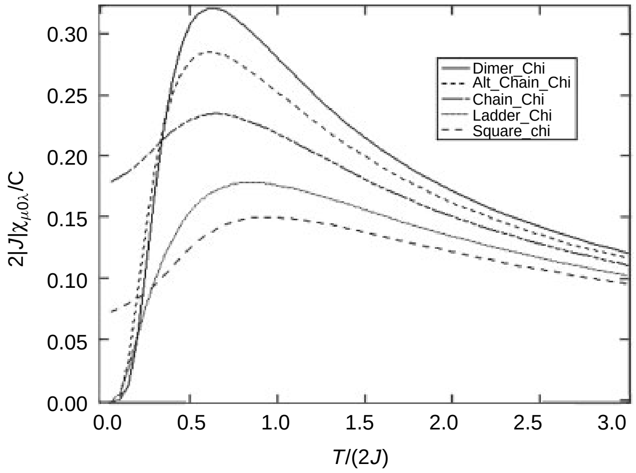

Figure 10 Comparison of the relative molar susceptibilities as a function of relative temperature ($T/2|J|$) for five $S = 1/2$ Heisenberg antiferromagnet lattices: a dimer, an alternating chain with an alternation parameter $\alpha = 0.5$, a uniform chain, a spin ladder with $J_{\text{rung}}/J_{\text{rail}} = 2$, and a square lattice. The value of J is the same for all curves

For comparison to experimental data, the susceptibility of the Heisenberg $S = 1/2$ ferromagnetic chain in zero field can be expressed as a power series expansion in powers of $J/(2T)$ with the coefficients β known for the first one hundred terms.[35]

$$\chi_{\text{mol}} = \frac{C}{T}\sum \frac{\beta_n}{(n+1)!}\left(\frac{J}{2T}\right)^n \qquad (37)$$

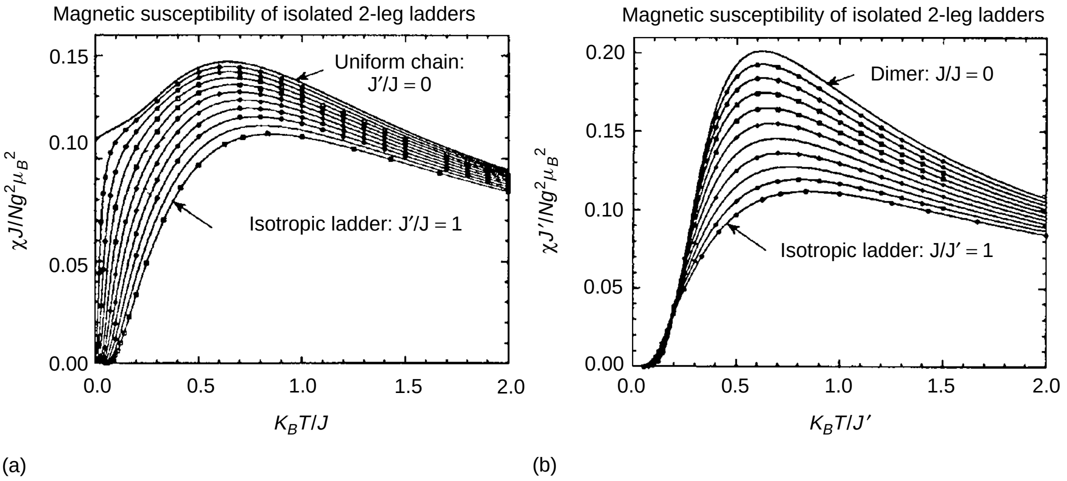

Figure 11 Magnetic susceptibility for two-leg Heisenberg ladders in the (a) weak exchange and (b) strong exchange models. (Ref. 34. Reproduced by permission of Author Matthias Troyer)

where $\beta_0 = 1$, $\beta_1 = 4$, $\beta_2 = 0$, $\beta_3 = -64$, $\beta_4 = 400$, and so on. This J is based on the $2J$ form of the Heisenberg Hamiltonian and is positive.

2.8.5 Heisenberg Chains with S ≥ 1

Understanding of the susceptibility of chains of spins with $S = 1$ or higher underwent dramatic change in 1983. Prior to that year, only the susceptibility of the classical ($S = \infty$) chain was known[36] and, like the $S = 1/2$ susceptibility, it showed a rounded maximum and remained finite at low temperature. Susceptibilities calculated for $S = 1$ and higher values using variations of the Bonner–Fisher technique,[32] or by using high-temperature series expansion techniques also showed the presence of rounded maxima but these techniques were unable to obtain values for lower relative temperature. It was assumed that the antiferromagnetic susceptibilities for all values of S remained finite as temperature declined to zero.

In 1983, Haldane[37] predicted that the ground states for all Heisenberg chains with integer spins were nonmagnetic singlet ground states, with energy gaps Δ to the first excited triplet. These predictions were confirmed by finite-chain calculations[38] that showed the gap was also affected by the presence of single-ion anisotropy D. For the $S = 1$ chain with $D = 0$, $\Delta \approx 0.4(J)$ and decreases as D increases (where J is from the $2J$ format). The presence of the singlet ground state means that for temperatures at or below Δ, the susceptibility will vanish exponentially and will resemble the curves for the alternating chain or spin ladder in Figures 9 and 11.

2.8.6 Bimetallic Spin Chains – 1D Ferrimagnets

Since the 1980s, it has been possible to synthesize site-ordered bimetallic chains in which metal ions of type A and B alternate. A and B are generally coupled antiferromagnetically and will have different moments that will tend to cancel at low temperatures, leaving a net moment within each unit cell. The net moments all have the same orientation, similar to the case of a monometallic ferromagnetic chain, so at low temperature the bimetallic chain has a diverging susceptibility. Materials that contain antiferromagnetically coupled inequivalent moments are known as ferrimagnets.

The susceptibility of a ferrimagnetic chain increases continuously upon cooling, with no obvious features. Their behavior can be identified more clearly by observing the $\chi_M T$ product, which shows a characteristic minimum at low temperatures. The $\chi_M T$ product of noninteracting spins is simply the sum of the Curie constants, C_A and C_B.; this value will be the high-temperature limit for interacting spins. Figure 12 shows that upon cooling the $\chi_M T$ product for each chain first decreases in response to the antiferromagnetic interaction. Upon further cooling, the moments of each unit cell become aligned parallel, leading to a diverging susceptibility. It is noted that the depth of the minimum is largest for the [1/2−1] chain and decreases rapidly with increasing S.

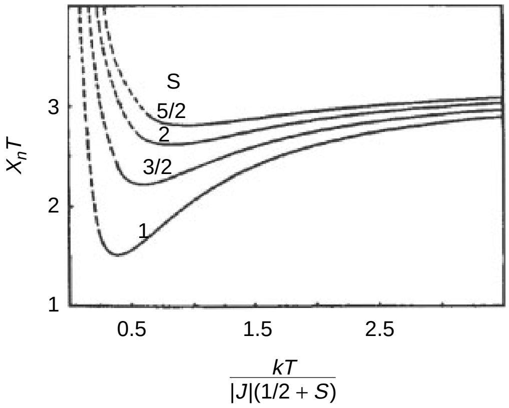

Figure 12 The product of susceptibility time temperature is shown as a function of temperature for four ferrimagnetic spin chains.[39] Each chain alternates a $S = 1/2$ spin and a second, larger spin S. The dashed lines at low temperatures correspond to the $\chi_M T$ values for ferromagnetic spins of S-1/2[39]

2.8.7 Chains with Anisotropic Exchange

When the exchange Hamiltonian is no longer isotropic, that is, when $\alpha \neq \beta$ in the exchange Hamiltonian, the susceptibility is no longer isotropic. The anisotropic Hamiltonian describes a system in which there is a preferred direction (Ising-like, $\alpha < \beta$) or preferred plane (XY-like, $\alpha > \beta$) in space. The magnetic response will be different depending on whether the external field is applied parallel to or perpendicular to the preferred direction(s). These responses correspond to the parallel ($\chi_\parallel$) and perpendicular susceptibilities ($\chi_\perp$).

Anisotropic Antiferromagnetic Exchange. For the isotropic Heisenberg case, the spins are free to rotate in space to remain antiferromagnetic to each other and essentially perpendicular to the field. For a Heisenberg system, there is only a perpendicular susceptibility with its characteristic rounded maximum (Figure 10). The g-factors for the Heisenberg ions can be slightly different in different directions but this difference only affects the magnitudes of the susceptibilities. The temperature dependences of the susceptibility are identical in all directions.

The zero-field susceptibilities for the $S = 1/2$ Ising chain have been derived by Fisher.[40] They have the same form for both antiferromagnetic and ferromagnetic exchange, only the sign of J is different.

$$\chi_\parallel = \frac{N g_\parallel^2 \mu_B^2}{2J} \left(\frac{J}{2kT}\right) \exp\left(\frac{J}{kT}\right) \tag{38}$$

$$\chi_\perp = \frac{N g_\perp^2 \mu_B^2}{4J} \left[\tanh\left(\frac{J}{kT}\right) + \left(\frac{J}{kT}\right) \sec h^2 \left(\frac{J}{kT}\right)\right] \tag{39}$$

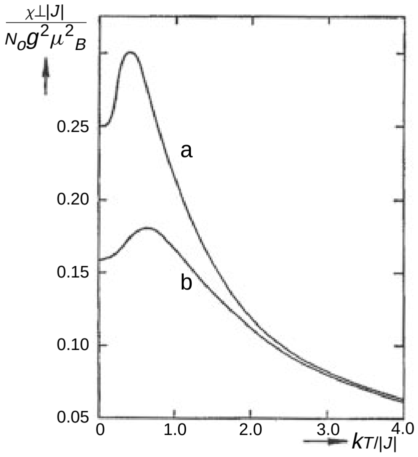

Figure 13 The perpendicular susceptibility as a function of temperature for (a) an Ising antiferromagnet and (b) an XY-antiferromagnet. (Ref. 12. Reproduced by permission of Taylor & Francis)

The perpendicular susceptibilities of the Ising ($\alpha = 0$) antiferromagnetic chain and XY($\beta = 0$) chain likewise have rounded maxima and remain finite as the temperature descends to zero (Figure 13). The parallel susceptibility of the Ising antiferromagnet decreases exponentially to zero as the temperature drops, in response to the energy gap in the Ising spectrum.

The XY magnet ($\beta = 0$) retains isotropic symmetry in the plane, so the spins are free to rotate and align themselves perpendicular to any field lying in the plane, similar to the Heisenberg susceptibility. There is a thus a perpendicular susceptibility[41] (see Figure 13), which has a similar shape to that of the Ising $\chi_\perp$. There is no easy axis in the XY system so there does not exist a true $\chi_\parallel$. A field applied normal to the easy-plane induces a magnetic response at finite temperature, which vanishes at zero temperature, in a manner similar to $\chi_\parallel$ of the Ising magnet.[42] This response is, unfortunately, called the XY parallel susceptibility.

3 EXCHANGE COUPLING IN ONE-DIMENSIONAL LATTICES

The fundamental idea of exchange leads directly to the simple Heisenberg Hamiltonian (equation 1), but numerous variations in magnetic behavior arise as a result of exchange anisotropy, lattice dimensionality, or the presence of more than one exchange constant. The onset of long-range order can obscure some of these variations but low-dimensional magnets that do not spontaneously order (Table 2) permit the development of the characteristic behavior over broad temperature ranges. Since order is most difficult to achieve in one-dimensional systems, the examples below have been selected to illustrate variations of magnetic behavior in one-dimension.

Table 2 Existence (Yes) or absence (No) of spontaneous magnetic order at finite temperature as a function of spin- and lattice dimensionality

	Lattice dimension			
Spin dimension	0D	1D	2D	3D
Ising	No	No	Yes	Yes
XY	No	No	Unusual	Yes
Heisenberg	No	No	At $T = 0$	Yes

Experimental progress in low-dimensional magnetism became possible when what constituted a low-dimensional *magnetic* lattice in a 3D *crystalline* environment was recognized. The key is the existence of moments joined by significant low-dimensional (1D or 2D) superexchange pathways while in the orthogonal direction(s), the interaction strengths are much weaker. Superexchange pathways are commonly provided by bridging anions or coordinating organic groups while the magnetic isolation arises from the presence of large counterions or neutral organic groups. While the crystalline host of the magnetic lattice will always remain three dimensional, the magnetic behavior remains essentially 1D down to low temperatures if the ratio of the 1D exchange J to that of the 3D exchange J_{3D} exceeds $\approx 10^2$.[12]

3.1 Heisenberg 1D Chains: Uniform $S = 1/2$ Antiferromagnets

One of the earliest examples of a 1D antiferromagnet is copper bispyridine dichloride (CPC). Its structure (Figure 14)[43] consists of bichloride-bridged chains of Cu^{II} ions extended along the c-axis, with the two pyridine ligands coordinated to the metal site through the nitrogens. The magnetic interaction is due to the superexchange along the copper chloride spine (intrachain Cu–Cu distance = 3.87 Å). The bridging Cu–Cl–Cu angle (91.1°) is large enough to induce significant antiferromagnetic exchange. The bulk of the pyridine rings forces adjacent chains far apart (interchain Cu–Cu separation = 8.59 Å) and prevents the formation of any interchain superexchange pathway. Susceptibility studies[44] found a rounded maximum in the susceptibility near 18 K; comparison to the Bonner–Fisher calculation for the susceptibility yielded an exchange strength $2J/k_B = -26.8$ K. The experimental susceptibility dropped below the Bonner–Fisher (BF) results below 2 K, an effect attributed to the 3D antiferromagnetic ordering transition found at 1.13 K by specific heat measurements.[44b]

The ideal 1D Heisenberg antiferromagnet becomes increasingly correlated within the chain as the temperature cools but will remain disordered even at $T = 0$ (see Section 2.8). Long-range order arises from the presence of weaker interactions J' between the chains. The ratio of the Néel temperature T_N to the exchange strength ($T_N/|2J|$) is a

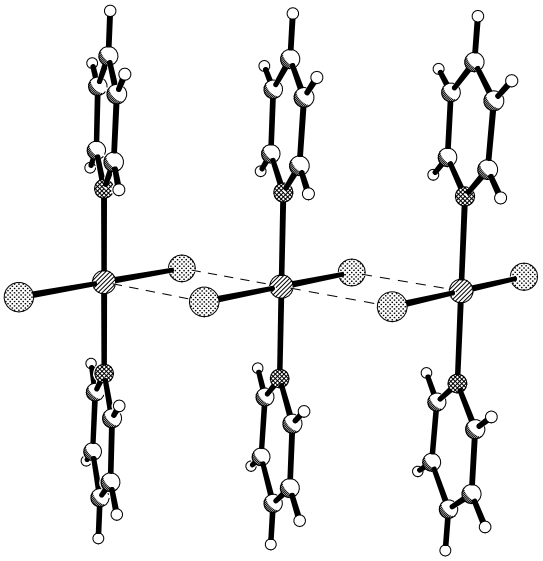

Figure 14 The structure of $Cu(py)_2Cl_2$

sensitive measure of the degree of one-dimensional isolation, decreasingly approximately a factor of 3 for every decade of reduction of the J'/J ratio.[45] The value $T_N/|2J| = 0.042$ for CPC corresponds to a ratio of exchange strengths $J'/J = 7 \times 10^{-3}$ and is sufficiently low for the characteristic behavior of the 1D QHAF to be examined over a wide relative temperature range ($T/|2J|$) without interference from 3D correlations. Neutron scattering studies on CPC were among the earliest and most influential studies of low-dimensional spin dynamics.[46]

Even greater 1D isolation is found in copper pyrazine dinitrate,[47] CuPzN. It consists of chains of Cu^{II} ions bridged by the diazines along the a-axis (see Figure 15). Charge neutrality is achieved by having two nitrate groups chelate to each metal site. Early magnetic studies by Hatfield[48] showed the interaction strength to be $2J/k_B = -10.6(2)$ K and detected no evidence of 3D effects. The specific heat of CuPzN has been measured down to 0.05 K[49] and has been found to agree with the predictions for the 1D QHAF model with $2J/k_B = -10.4(1)$ K down to the lowest measured temperature. No evidence of magnetic ordering was observed so $T_N < 0.05$ K; consequently $T_N/|2J| < 0.005$, one of the lowest ratios found for a 1D QHAF.

Two other 1D QHAF are included in Table 3. They are the copper oxide Sr_2CuO_3, and $KCuF_3$. Copper oxide magnetic systems are renowned for the strength of their magnetic interactions and Sr_2CuO_3 is no exception; based on susceptibility studies[51] its exchange constant has been determined to be $2J/k_B = -2200 \pm 200$ K. While there is a separate section on magnetic oxides found elsewhere in the Encyclopedia (*see* ***Magnetic Oxides***), we mention Sr_2CuO_3 here because it has the lowest critical ratio $k_BT_N/|2J| = 0.0025$ of any linear magnet.

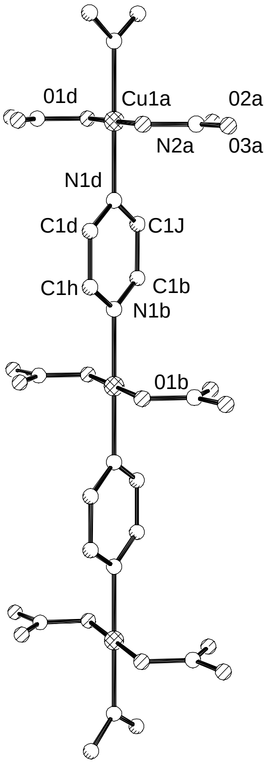

Figure 15 The structure of $Cu(pz)(NO_3)_2$[50]

Table 3 Susceptibility and ordering parameters for a selection of 1D-antiferromagnets

Compound	$\lvert 2J\rvert/k_B$ (K)	T_N (K)	$k_BT_N/\lvert 2J\rvert$	Ref.
$Cu(py)_2Cl_2$	26.8	1.13	0.042	44
$Cu(pz)(NO_3)_2$	10.5	<0.05	$<5 \times 10^{-3}$	49
Sr_2CuO_3	2200	5.4	2.5×10^{-3}	51
$KCuF_3$	375	39	0.104	52
Copper Benzoate	18	0.76	0.042	53,54
$Cu(DMSO)_2Cl_2$	16.5	0.92	0.02	55

Potassium copper fluoride, $KCuF_3$, is a surprising 1D magnet because its structure is closely related to that of the cubic perovskite. The cooperative Jahn–Teller distortion causes the fluorides to move from their midpositions in the (001) plane and leads to a special alignment of the 3d orbitals of the Cu^{2+} ions, giving rise to strong superexchange interactions along the tetragonal c-axis ($2J/kB = -375$ K),[52] and much weaker interactions perpendicular to the chains. The critical ratio, $k_BT_N/|2J| = 0.104$, is higher than that of any other chain in Table 3, but is still a remarkably low value considering the copper–copper distance is very nearly the same in all directions. We find it notable that compounds such as $KCuF_3$ and $SrCuO_3$ can provide such a range of J'/J ratios without the need for organic blocking groups such as those found in CPC.

3.2 Heisenberg 1D Chains: Canted $S = 1/2$ Antiferromagnets

The uniform chain compounds discussed above contained magnetic centers related by unit-cell translations; consequently there is only one exchange constant. When adjacent centers are related by screw axes, there remains only one exchange interaction but the magnetic behavior becomes more complex. Owing to the presence of the screw axis, the local coordination spheres and g-tensors are canted with respect to each other, creating the conditions for the Dzialoshinski-Moriya antisymmetric interaction D_{D-M} (Section 2.5). The DM interaction tends to align adjacent moments perpendicular to each other, in competition with the exchange interaction's effort to align the moments (anti)parallel. The competition between the DM and exchange terms creates a net canted moment (see Figure 6b), whose magnitude depends on the D/J ratio. The canted g-tensors have a similar effect and create an environment in which any uniform field is unable to be parallel to every moment; the parallel susceptibility cannot be measured directly.

$$\begin{aligned} H = -2J \sum_{i} S_i \cdot S_{i+1} - \sum_{j,\alpha,\beta} H^{\alpha}[g^{u}_{\alpha,\beta} + (-1)^{j} g^{s}_{\alpha,\beta}]S^{\beta}_{j} \\ + \sum_{j} (-1)^{j} D \cdot S_{j-1} x S_j \end{aligned} \tag{40}$$

Copper benzoate trihydrate is an example of a uniform chain with a 2_1 screw axes.[53] As seen in Figure 16, the chains are formed by the copper ions aligned along the c-axis. There are two copper sites that alternate along the chain with local symmetry axes that differ by 20°.[53a] The antiferromagnetic interaction along the chain has a strength of $2J/k = -18.2\,\text{K}$ but the characteristic susceptibility maximum is only observed in large fields. Owing to the canting of the moments parallel to the c-axis, in small fields ($H < 50\,\text{Oe}$) χ_c is as much as 10 times bigger than χ_a and one hundred times bigger than χ_b.[53b] Anomalies are observed near 0.8 K for the susceptibility, but specific heat studies at low temperature[54] show no unusual behavior near that temperature.

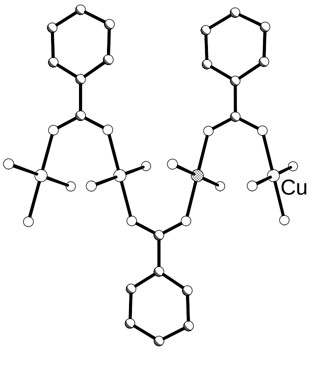

Figure 16 The structure of copper(II) benzoate

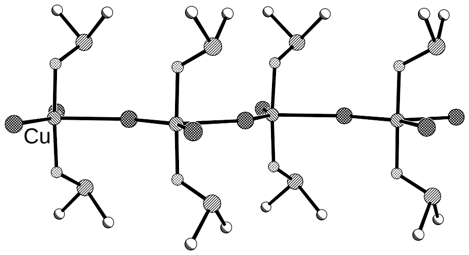

Figure 17 The structure of $CuCl_2(DMSO)_2$

Copper dichloride bisDMSO $Cu(DMSO)_2Cl_2$ (DMSO = dimethylsulfoxide) consists of chains of roughly square planar coordinated copper with the two chloride ions and the two organic molecules in trans positions, and the chloride from an adjacent molecule semicoordinated in an axial site (see Figure 17).[56] Adjacent copper sites are related by a 2_1 axis.

The exchange strength is $2J/k = -16.5\,\text{K}$ for the chloride. While there is no overt canting observed in the data, the presence of the spin-canting terms in the Hamiltonian creates different temperature dependences for each of the three principle susceptibilities.[55]

3.3 Heisenberg 1D Chains: Ferromagnetic $S = 1/2$ Heisenberg Chains

Copper halide chains exhibit ferromagnetic interactions when the coppers are tribridged along the chain axis (see Figure 18). This contrasts with the antiferromagnetic interactions observed when the coppers are distinctly bibridged, as in $Cu(py)_2Cl_2$ (Figure 14). The sensitivity of the ferromagnetic susceptibility to small anisotropic contributions to the exchange Hamiltonian makes ferromagnetic chains particularly good subjects for the study of local coordination upon exchange anisotropy.

Copper(II) chloride tetramethylenesulfoxide[57] consists of the formula units tied together by two chlorine interactions and one oxygen interaction to form chains parallel to the b-axis. The copper coordination sphere has an elongated tetragonal distortion giving the common '4 + 2' coordination geometry. The chains are formed by the action of the 2_1 screw axis parallel to b, leading to a structure with three Cu–ligand–Cu bridges between adjacent Cu ions. The most important is the symmetrical Cu–Cl(1)Cu' bridge with Cu–Cl distances of 2.325 and 2.358 Å and a bridging angle of 86.5° (there are also two asymmetrical bridges with bridging angles of 80.95° and 79.63°). Hatfield had demonstrated that superexchange interactions through symmetrical Cu–Cl–Cu bridges with an angle near 90° gave ferromagnetic interactions[58] and a ferromagnetic interaction was found for $CuCl_2(TMSO)$ with a strength of $2J/k = 78\,\text{K}$. Interactions between the chains lead to a 3D ordered state near 3.9 K. When plotted on a log–log plot, the susceptibility of a Heisenberg ferromagnetic chain is linear, corresponding to a divergence as $T^{-1.7}$. This

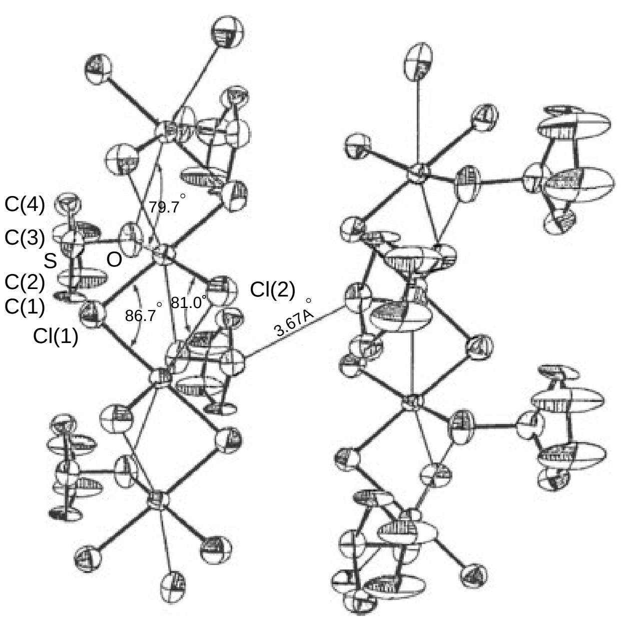

Figure 18 The structure of $CuCl_2(TMSO)$[57]

behavior is seen for $CuCl_2(TMSO)$ and the analogous DMSO in Figure 19,[57] as well as for two other tribridged copper chains, tetramethylammonium copper trichloride (TMCuC) and tris(trimethylammonium)Cu_2Cl_7 (TTMCuC).[59]

Two excellent examples of ferromagnetic chains with measurable exchange anisotropy are the isotropic cyclohexylammonium copper trichloride and tribromide, CHAC and CHAB respectively.[60] The structure of CHAC consist of bibridged linear chains of $CuCl_3^-$ ions parallel to the c-axis, hydrogen bonded together in the b-c plane by the $-NH3^+$ moiety of the organic group, (see Figure 20). The coordination sphere around the copper atom assumes nearly perfect square pyramidal (C_{4V}) geometry. The apical chlorides, related by the 2_1 axis parallel to c are rotated by ±17° out of the b-c plane. Two symmetrical Cu–Cl–Cu bridges are formed, each with a bridging angle of 86.0°, leading to the presence of ferromagnetic interactions.

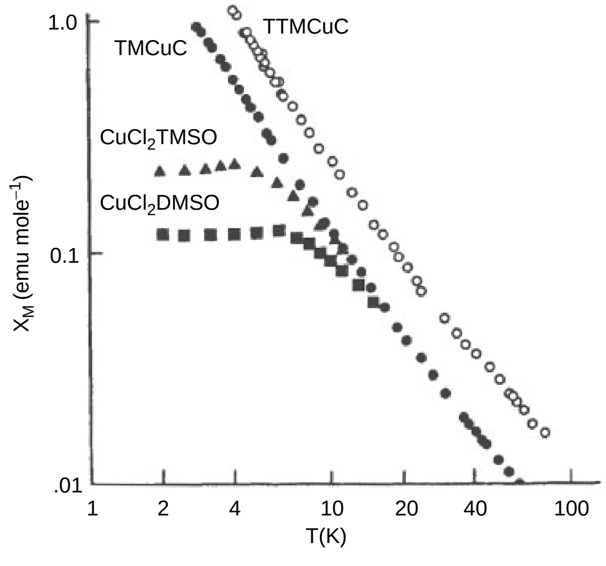

Figure 19 Log–log plot of susceptibility versus temperature for four Heisenberg ferromagnetic chains. Deviations from linearity are due to interchain interactions. (Reprinted with permission from C.P. Landee and R.D. Willett, *Phys. Rev. Lett.*, 1979, **43**, 463. © 1979 by the American Physical Society)

The susceptibility of CHAC above 30 K is well described by the prediction for a ferromagnetic Heisenberg chain with $J/k = 45(5)$ K (Figure 21a), but the single-crystal susceptibilities become increasingly anisotropic below that temperature, indicating the presence of non-Heisenberg behavior. The low-temperature ac-susceptibilities (Figure 21b) shows strong anisotropy in the vicinity of the Néel temperature of 2.18 K. The greatest susceptibility for all $T > T_N$ is found along the b-axis, defining b as the magnetic easy axis. The antiferromagnetic transition is due to the moments of adjacent ferromagnetic chains alternately aligning along the b-axis. Consistent with this assignment is the disappearance of χ_b at the lowest temperature. The susceptibility along c is small at all temperatures and remains finite as $T \rightarrow 0$, marking χ_c as a perpendicular susceptibility. The susceptibility along the a-axis is also small and characteristic of $\chi_\perp$ above 4 K, but it diverges at T_N and a spontaneous moment develops along the a-axis. This weak ferromagnetism is due to the spin canting of each ferromagnetic chain in the same direction along the a-axis. Further examinations of the magnetism and the magnetic specific heat led to a quantitative understanding of the exchange anisotropy in CHAC; it has a slight Ising-like behavior, consistent with a Hamiltonian (equation 29) with $\alpha = 0.98$, $\beta = 1$. In CHAC, the moments point along the local axes defined by the copper and apical chloride.

The isostructural bromide analog CHAB also consists of ferromagnetic chains along c ($J/k = 55(5)$ K), with the easy

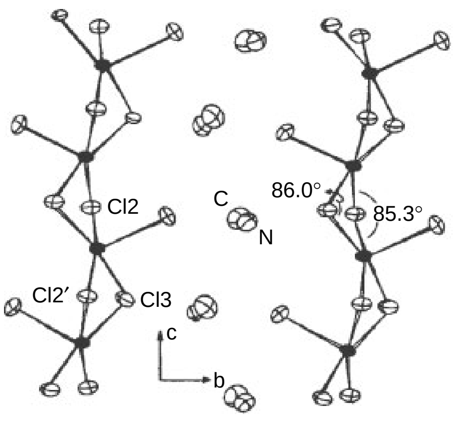

Figure 20 The chain structure of CHAC[60b]

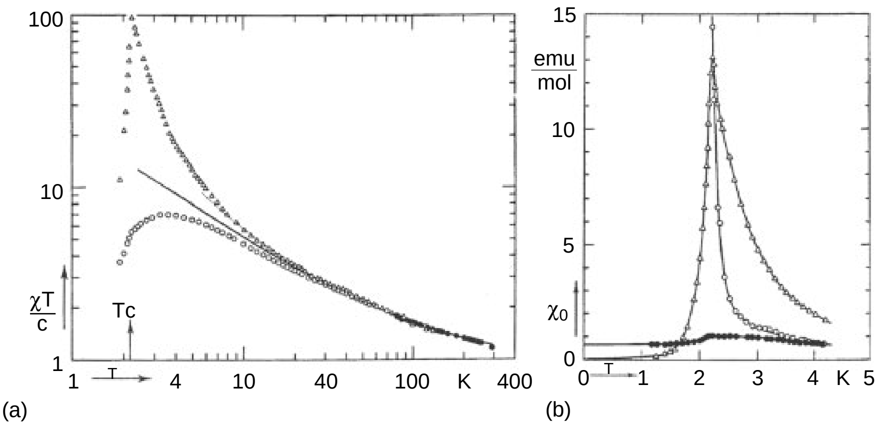

Figure 21 Single-crystal susceptibilities of CHAC. (a) log−log plot of the DC responses along the easy b-axis (Δ) and the hard c-axis ((0) and b) ac responses along the easy b-axis (Δ), the canted a-axis ((0), and the hard c-axis (•)). (Reprinted from Ref. 60a. © 1981, with permission from Elsevier)

axis along b, a canted moment along a, and a Néel temperature of 1.50 K. However, CHAB has an easy-plane anisotropy ($\alpha = 1$, $\beta = 0.95$) with the moments rotating most easily in the bc plane. Such reversals in anisotropy upon substitution of bromide for chloride ligands in copper complexes are common and have been explained[61] as arising from the reversal in sign in the effective spin-orbit coupling of the spins to the lattice upon change of the halide.

3.4 Heisenberg 1D Chains: Alternating Linear Chains

The moments in uniform chains are related by simple crystallographic symmetry such as a unit-cell translation or a screw axis. Consequently the exchange coupling between each pair of nearest neighbors is identical and only one exchange strength is present. For homometallic linear systems containing a basis with more than one magnetic site, there will be two (or more) exchange constants, one within the basis and the second connecting adjacent bases. Such systems are known as alternating chains with the stronger interaction labeled J and the weaker interaction labeled αJ, where $\alpha < 1$ (Section 2.8). When α is positive, the two interactions have the same sign; $\alpha = 0$ or 1 corresponds to the isolated dimer and uniform chain, respectively. Alternation commonly occurs when structural dimers are linked in an end-on fashion to their neighbors, forming a chain of dimers. It is also found when moments are linked by alternating ligands as in . . .M–L–M–L′ – M–L–M–L′. . ..

The temperature dependence of the alternating chain susceptibility as a function of alternation parameter α is shown in Figure 9. The susceptibility for each α displays a rounded maximum at nearly the same relative temperature ($T^{\max} \approx 0.6(2J)/kB$ in our notation), but the maximum susceptibility reached and the low-temperature behavior of the susceptibility are strongly dependent upon α. For all $\alpha < 1$, the ground state is a nonmagnetic singlet separated by an energy gap Δ from the lowest excited state with $\Delta = 0$ or $2|J|$ for $\alpha = 1$ or 0, respectively. Consequently, at low temperatures the susceptibilities for the alternating chains all decrease exponentially to zero with the fastest decrease occurring for small values of α.

Piperazinium hexachlordicuprate (PHCC) consists of trichlorocuprate anions and piperazinium cations.[62] Two contiguous copper atoms are bridged symmetrically by two Cl(1) chlorine atoms into Cu_2Cl_6 dimers, which in turn are linked through semicoordinate Cu–Cl(3) bonds to form chains running along the a-axis (Figure 22).

The symmetric Cu–Cl(1) bridges are 2.32 Å while the asymmetric Cu–Cl(3) bridge contains a long bond of 2.60 Å. The structural alternation is reflected in the magnetic susceptibility that shows a rounded maximum near 15 K and decreases rapidly to zero upon further cooling (see Figure 23).

The magnetic data are well described by an exchange constant $J/k = -12.5$ K and an alternation parameter $\alpha \approx 0.63(4)$. The relatively small exchange for the copper chloride dimeric units has been explained by a molecular overlap analysis of natural magnetic orbitals, similar to that used by Girerd *et al.*[18] The symmetric Cu–Cl(1)–Cu bridging angle $\theta = 96°$ produces an antiferromagnetic contribution

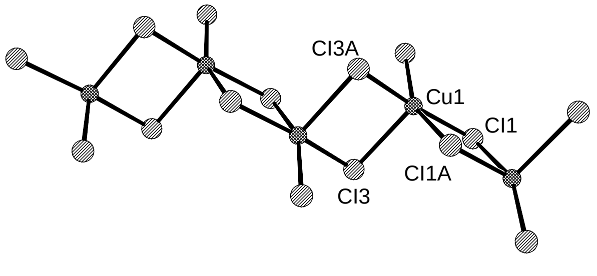

Figure 22 Schematic view of the chain structure of piperazinium hexachlorodicuprate

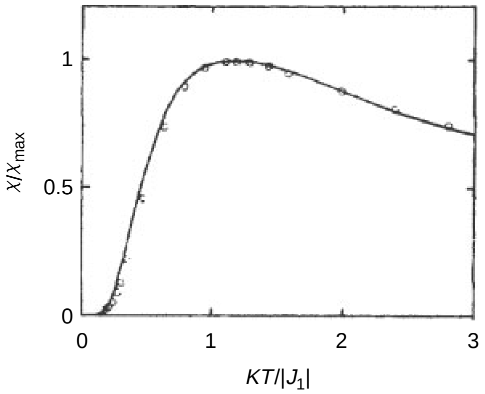

Figure 23 Reduced susceptibility (c/cmax) of piperazinium hexachlordicuprate as a function of the reduced temperature kT/J. The solid curve is the theoretical prediction for $J/k = -12.5\,\text{K}$ and $\alpha = 0.6$ (Reprinted with permission from A. Daoud, A.B. Salah, C. Chappert, J.P. Renard, A. Cheikhrouhou, T. Duc, and M. Verdaguer, *Phys. Rev. B*, 1986, **33**, 6253. © 1986 by the American Physical Society)

approximately equal to that of the ferromagnetic contribution, leading to a near cancellation of exchange. The dimer formed by the Cu–Cl(3)–Cu links is small owing to a poor overlap integral.

The 1980s saw rapid advances in the understanding of coordination compounds with more than one metal or more than one ligand. Techniques were developed by which two different metals M, M' could be inserted *site-specifically* into an extended lattice, forming molecular-based ferrimagnets (see Section 3.7). Concurrently, it was discovered how using *alternating ligands* to link a single type of magnetic moment into an alternating chain. The compound $[Cu_2(bpm)(H_2O)_2(OH)_2(NO_3)_2]2H_2O$ (bpm = 2, 2′-dipyrimidine) consists of discrete, centrosymmetric bis(μ-hydroxo) copper(II) dimers with bpm as terminal ligand, weakly coordinated water molecules, unidentate nitrate anions, and two waters of crystallization (Figure 24).[63]

The Cu(1)–OH–Cu(1a) bridging angle is 95.0°, within the ferromagnetic range for hydroxy-bridged copper dimers (Section 2.8). Each dimeric unit is linked to its neighbor by the unused chelating site of the bpm, forming the alternating ligand exchange.

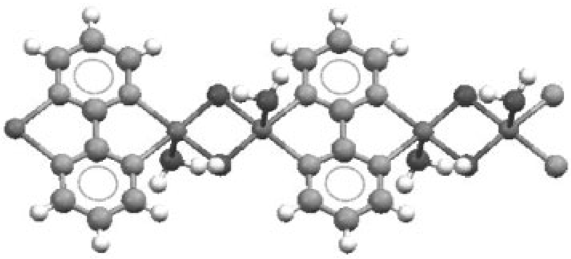

Figure 24 The alternating chain structure of $[Cu_2(bpm)(H_2O)_2(OH)_2(NO_3)_2]\cdot 2H_2O$[63]

Bipyrimidine is known to transfer strong antiferromagnetic interactions while the hydroxo bridge produces ferromagnetic exchange; this compound is thus an alternating exchange alternating chain. Analysis of the magnetic data reveals the ferromagnetic interaction to be $2J/k = +160\ \text{cm}^{-1}$ while the antiferromagnetic interaction $\alpha(2J)/k = -145\ \text{cm}^{-1}$, that is, $\alpha = -0.91$.

Spin-Peierls Chains. The uniform one-dimensional exchange-coupled chain is inherently unstable at low temperatures toward distortion to an alternating exchange chain, because the electronic energy is lowered as the system drops into the nonmagnetic ground state of the distorted chain, separated from excited states by an energy gap Δ. The dimerization will occur if the reduction in magnetic energy is greater than the increase in lattice energy caused by the dimerization. This spontaneous structural transition, known as the spin-Peierls distortion is very rare because the energy requirement is difficult to meet. One of the few examples of a spin-Peierls transition occurs in $CuGeO_3$, with a transition temperature $T_{SP} \approx 14\,\text{K}$.[64] The magnetic susceptibility is dramatically affected at the transition as seen in Figure 25.

The data above T_{SP} cannot be described with a uniform chain model, but can be explained by including the existence of a next-nearest interaction $2J_{nnn}/k = -58\,\text{K}$ to the presence of a nearest neighbor exchange $2J/k = -160\,\text{K}$.[65]

3.5 Spin Ladder Linear Chains

Spin ladders consist of two or more uniform chains, exchange strength $2J_{rail}$, coupled together by a second

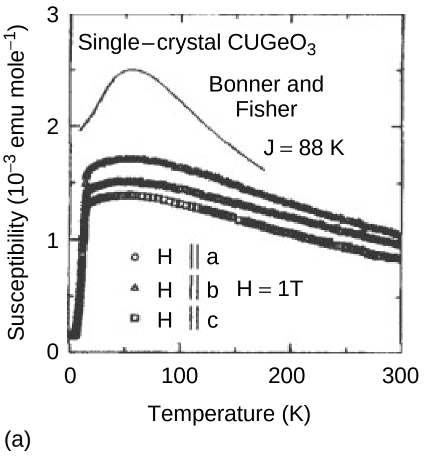

Figure 25 The magnetic susceptibility of single crystals of $CuGeO_3$ measured under $H = 1T$. Note the rapid decrease of the susceptibility towards zero along each axis below 14 K. (Reprinted with permission from M. Hase, I. Terasaki, and K. Uchinokura, *Phys. Rev. Lett.*, 1993, **70**, 3651. © 1993 by the American Physical Society)

interaction $2J_{\text{rung}}$. The ground state for ladders of an even number of rails is a nonmagnetic singlet, separated by an energy gap Δ from the lowest magnetic states. Recent strong interest in two-leg ladders is due to the prediction and discovery of superconductivity in such ladders doped with charge carriers.[66] Only two-leg ladders will be considered further.

A small number of spin ladders is known. An excellent example is $SrCu_2O_3$,[67] but it is characterized by very large exchange ($2J/k \approx -2000$ K) and an energy gap $\Delta = 420$ K but these large magnitudes make field-dependent studies, necessary to distinguish between a ladder or alternating chain, impossible to carry out. Molecular-based ladders are alternatives.

Bis(piperidinium)tetrabromocuprate, BPCB,[68] consists of $CuBr_4$ dianions and organic cations. Hydrogen bonding creates a structure where the $CuBr_4$ groups are packed together in pairs, with adjacent pairs aligned along the a-axis (Figure 26). The copper–copper interactions take place by double-halide superexchange through Cu–Br· · ·Br–Cu pathways.

Such contacts are known to create antiferromagnetic interactions on the order of 10 K, depending on the Br–Br distance and bond angles. The magnetic susceptibility of BPCB[69] has a rounded maximum near 8 K and decreases rapidly towards zero at lower temperatures, characteristic of a singlet ground state. Both the spin ladder and alternating chain models fit this data equally well (Figure 27).

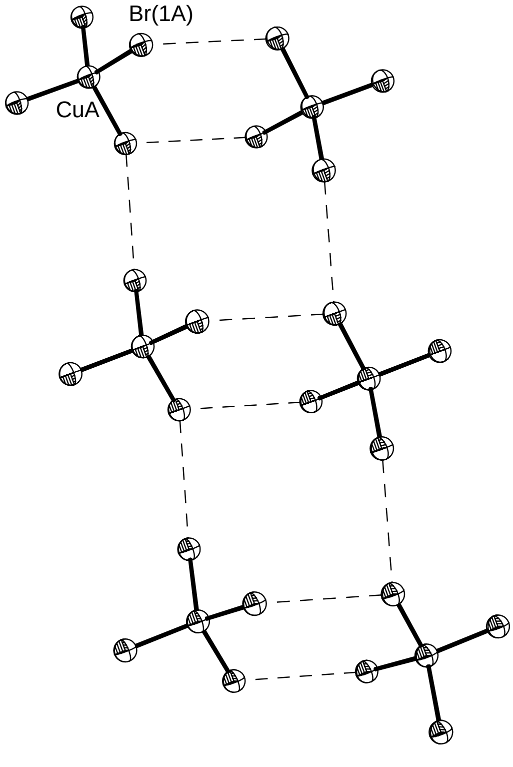

Figure 26 The $CuBr_4{}^{2-}$ packing structure of BPCB[68]

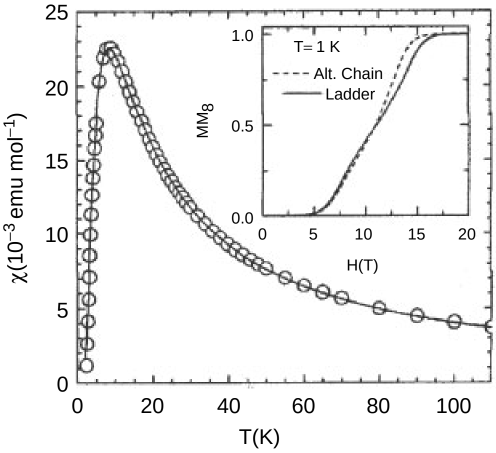

Figure 27 Susceptibility as a function of temperature for BPCB. (Reprinted with permission from B.C. Watson, V.N. Kotov, M.W. Meisel, D.W. Hall, G.E. Granroth, W.T. Monfrooij, S.E. Nagler, D.A. Jensen, R. Backov, M.A. Petruska, G.E. Fanucci, and D.R. Talham, *Phys. Rev. Lett.*, 2001, **86**, 5168. © 2001 by the American Physical Society)

The low-temperature magnetization (insert of previous figure) of BPCB is essentially zero until 5 tesla when the gap is closed by the Zeeman interaction. There is a rapid increase until 17 tesla when the field overcomes both the rung and rail exchanges. The ladder and alternating chain models make different predictions for M(H) leading to the conclusion that BPCB is a spin ladder with $2J_{\text{rung}}/k = -13.3$ K and $J_{\text{rail}}/k = -3.8$ K.

An alternative approach to spin ladders has been taken in the synthesis of Cu(quinoxaline)Br_2.[70] Here the rails are formed by the bridging bidentate quinoxaline with the rungs formed by bridging bromine atoms (Figure 28). The second ring of the quinoxaline projects into the coordination sphere of the copper atom and prevents the formation of an extended $(CuBr_2)_n$ chain orthogonal to the copper/quinoxaline axis. The exchange constants were found to be $2J_{\text{rung}}/k = -35.0$ K through the bromides and $J_{\text{rail}}/k = -30.3$ K through the quinoxalines.

3.6 Chains with $S > 1/2$

$S = 1$: The most well-studied chain compound is $[Ni(en)_2NO_2(ClO_4)]$, en = ethylenediamine, commonly known as NENP.[71] The structure of NENP consists of Ni(II) atoms bridged into chains by nitrite ion (Figure 29). The coordination sphere of the nickel is completed by the two chelating en ligands. The noncoordinating perchlorate groups (not shown) balance the charge and provide isolation between the chains. Adjacent nickel sites are related by a 2_1 screw axis, which creates the condition for spin canting.

When it was first reported, the susceptibility of NENP was a great mystery. While showing a rounded maximum near 50 K, the susceptibility along each of the crystallographic

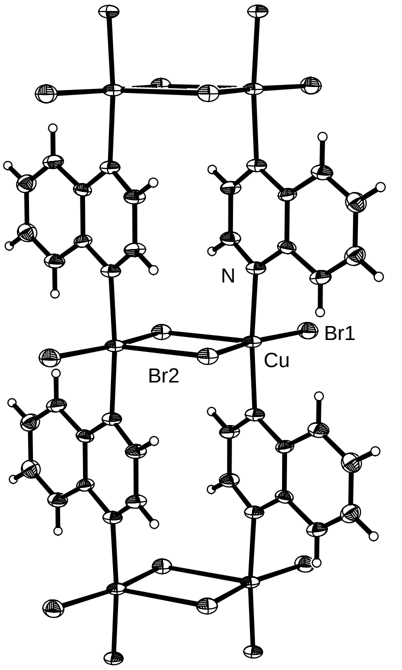

Figure 28 The ladder structure of Cu(quinoxaline)Br_2[70]

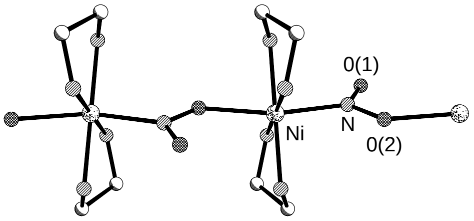

Figure 29 The chain structure of NENP71

axis decreased exponentially (Figure 30),[72] but to a small constant value rather than zero. It was soon realized that the existence of the Haldane gap Δ_H (Section 2.8) could account neither for the decrease at low temperatures nor for the finite values that remained nor for the anisotropy in the rate of decrease. Examination of the low-temperature magnetization for different crystal orientations showed the moment to be zero for fields less than 7 tesla along the b and c axes before increasing sharply at separate larger fields (Figure 31).[73] This behavior is characteristic of a spin singlet state, but with different gap energies for different directions. Inclusion of a single-ion anisotropy D into the Haldane theory led to the following field-dependent energy level diagram of NENP[74] consistent with parameters $2J/k = -45\,\text{K}$, $D/k = 9\,\text{K}$, and which can explain all the susceptibility and magnetization studies as well as the observed NMR T1 studies, plus EPR and inelastic neutron studies (Figure 32). The presence of the spin-canting interaction mixes different eigenstates and accounts for the observed anisotropies.

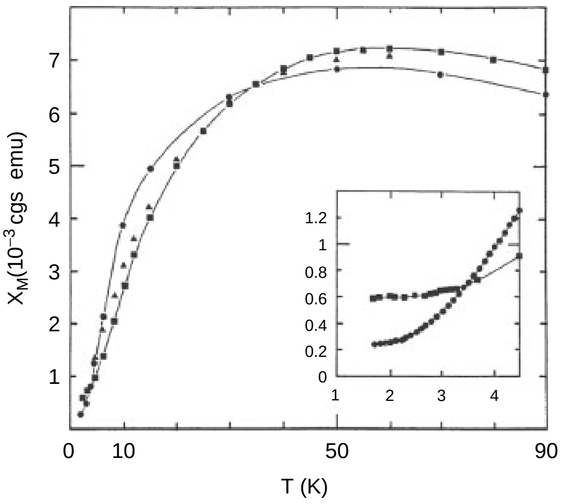

Figure 30 Molar susceptibility of NENP along the three crystal axis: a (squares), b(circles), c (triangles). (Ref. 72 © 1987, with kind permission of Springer Science & Business Media)

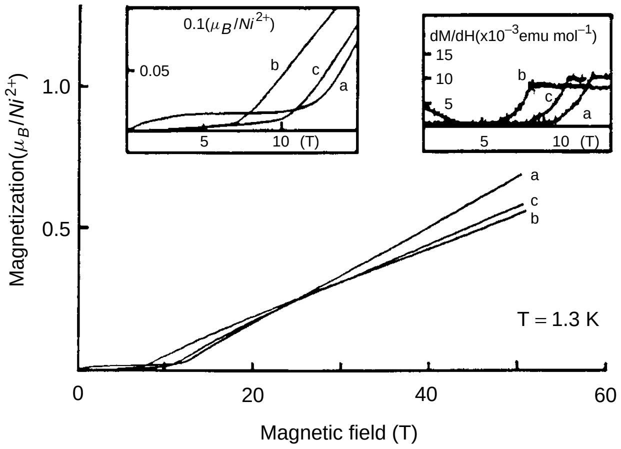

Figure 31 Magnetization of NENP at 1.3 K for different crystal orientations showing the rapid onset of moment for three different critical fields. (Reprinted with permission from K. Katsumata, H. Hori, T. Takeuchi, M. Date, A. Yamagishi, and J.-P. Renard, *Phys. Rev. Lett.*, 1989, **63**, 86. © 1989 by the American Physical Society). The left insert shows the low field behavior

The great interest in NENP led to the development of many other antiferromagnetic nickel chains, as a way of exploring the effects of different D/J ratios and spin-canting effects. Because Haldane gap theory also predicts that the ratio of gap to exchange energy ($\Delta_H/2J$), approximately 0.4 for $S = 1$, should decrease exponentially with the value of the spin, there has been interest in $S = 2$ Heisenberg antiferromagnets. Only one is known, Mn(III)(bipy)$_2$Cl·2H_2O, for which $\Delta_H/2J = 0.07(2)$, consistent with numerical predictions.[75]

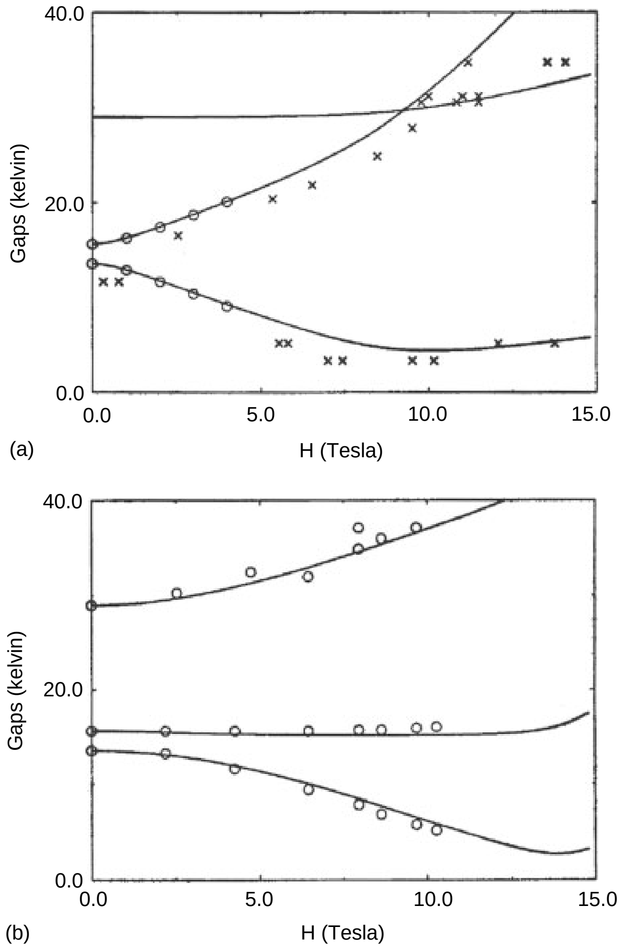

Figure 32 Energy levels for H || to the *b*-axis (upper) and H ⊥ *b*-axis (lower). The circles are energy values determined by neutron scattering; the x's are from values determined by EPR absorption. (Reprinted with permission from P.P. Mitra and B.I. Halperin, *Phys. Rev. Lett.*, 1994, **72**, 912. © 1994 by the American Physical Society)

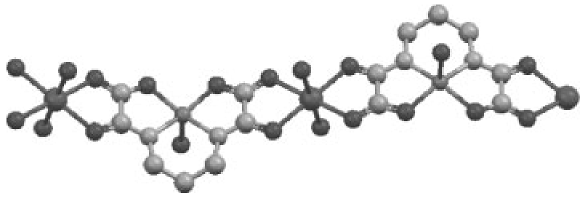

Figure 33 The structure of MnCu(pba)$(H_2O)_3 \cdot 2H_2O$[77]

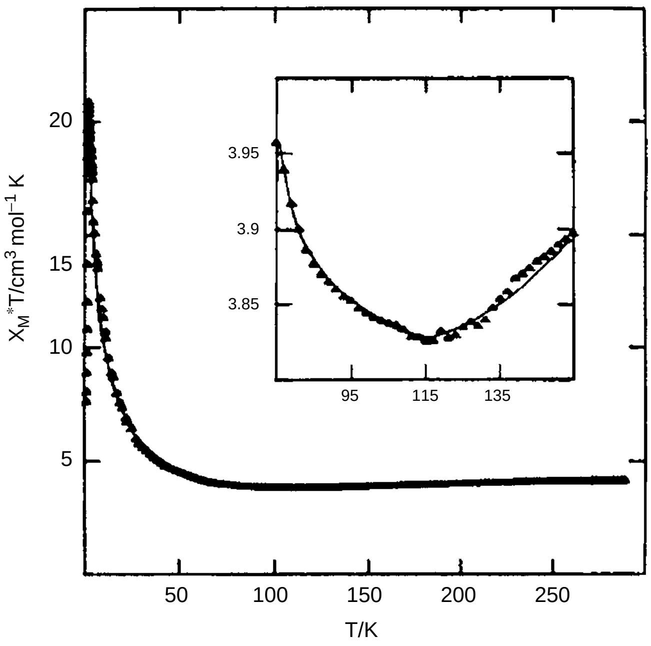

Figure 34 The experimental (Δ) and theoretical (–) $\chi_m T$ product as a function of temperature for MnCu(pba)$(H_2O)_3 \cdot 2H_2O$. (Reprinted with permission from Ref. 77. © 1987 American Chemical Society)

3.7 Bimetallic Spin Chains – 1D Ferrimagnets

Antiferromagnetic chains with alternating inequivalent moments will develop strongly diverging susceptibilities at low temperatures as the net moment of each unit cell aligns parallel to those in adjacent cells. The technique for insuring a site-ordered M, M' bimetallic is to encapsulate one of the metals inside a polydentate ligand, such that the M–L unit remains intact in solution. If the ligand has external binding sites that can (preferably) chelate to the second metal M', the system will self-assemble into the desired chain. This principle was demonstrated in 1981[76] using the unsymmetrical ligand dithiooxalate to bridge Ni(II) and Mn(II) ions in $[Ni(S_2C_2O_2)][Mn(H_2O)_3] \cdot 4.5H_2O$.

An elegant example of this process is the compound MnCu(pba)$(H_2O)_3 \cdot 2H_2O$,[77] where pba = 1, 3-propylenebis(oxamate). This compound contains the mononuclear dianion $[Cu(pba)]^{2-}$ as an unbreakable copper containing unit, the 'brick' out of which the chain is assembled. Crystals are obtained by slow diffusion of aqueous solutions of $Na_2[Cu(pba)] \cdot 2H_2O$ and manganese perchlorate. The Mn^{2+} cation is chelated by the external binding sites of two bricks to serve as the 'mortar' between the bricks, with water molecules filling in the coordination spheres of the two metal atoms (Figure 33).

The magnetic susceptibility of MnCu(pba)$(H_2O)_3 \cdot 2H_2O$ rises continuously upon cooling from room temperature until 2.4 K, where 3D ordering occurs (see Figure 34). Identification of the ferrimagnetic nature of the chain is observed in the characteristic minimum in the χT product near 115 K (insert).

An alternative approach to the formation of ferrimagnetic chains has been to combine transition ions and stable organic radicals in an alternating manner. One such example is the compound Mn(hfac)$_2$(NIT)^{i}Pr, where hfac = hexafluoroacetylacetonate and (NIT)^{i}Pr is the nitronyl nitroxide 2-isopropyl 4,4,5,5-tetramethylimidazoline-1-oxy 3-oxide.[78] An advantage of using the radicals is the very strong antiferromagnetic exchange that occurs between the radical and the transition metal ion. For the Mn(NIT) derivatives, the magnitudes of $2J$ range from 200 to 330 cm^{-1}. Such large exchange causes the ferrimagnetic minimum in χT to occur above 300 K. The excellent 1D isolation of these chains leads to χT values of several hundred before the chains order ferromagnetically between 5 and 10 K.

4 CONCLUDING REMARKS

Magnetic exchange, direct or via superexchange, arises from the overlap of wavefunctions of unpaired electrons and the quantum mechanical requirement that the two-electron wavefunction be antisymmetric. Although simple in concept, exchange is the basis of all useful magnets and magnetic technology. When combined with the diverse properties of transition metal ions and radicals, and the endless imagination of synthetic chemists, it leads to the wide variety of magnetic behavior illustrated above and more.

5 RELATED ARTICLES

Electronic Structure of Solids; Magnetism of Transition Metal Ions; Paramagnetic Organometallic Complexes.

6 REFERENCES

1. W. Heisenberg, *Z. Phys.*, 1926, **38**, 411.
2. P. A. M. Dirac, *Proc. R. Soc.*, 1926, **112A**, 661.
3. J. H. Van Vleck, ‘The Theory of Electric and Magnetic Susceptibilities’, Oxford University Press, London, 1932.
4. D. C. Mattis, ‘The Theory of Magnetism’, Harper & Row, New York, 1968.
5. J. B. Goodenough, ‘Magnetism and the Chemical Bond’, Interscience, New York, 1963.
6. J. S. Smart, ‘Effective Field Theories of Magnetism’, Saunders, Philadelphia, 1966.
7. D. H. Martin, ‘Magnetism in Solids’, The M.I.T. Press, Cambridge, MA, 1967.
8. R. H. White, ‘Quantum Theory of Magnetism’, 2nd edn., Springer-Verlag, Berlin, 1983.
9. The reader is directed to the proceedings of the various International Conferences on Molecule-Based Magnets. a) *Polyhedron*, 2003, **22**, 1725; b) *Polyhedron*, 2001, **20**, 1115; c) *Mol. Cryst. Liq. Cryst.*, 1999, 334; c) *Mol. Cryst. Liq. Cryst.*, 1996, 305; d) *Mol. Cryst. Liq. Cryst.*, 1995, 271; e) *Mol. Cryst. Liq. Cryst.*, 1993, 232.
10. R. L. Carlin, ‘Magnetochemistry’, Springer-Verlag, Berlin, 1986.
11. O. Kahn, ‘Molecular Magnetism’, VCH Publishers, New York, 1993.
12. L. J. De Jongh and A. R. Miedema, *Adv. Phys.*, 1974, **23**, 1.
13. L. J. de Jongh ed., ‘Magnetic Properties of Layered Transition Metal Compounds’, Kluwer Academic Pubublishers, Dordrecht, 1990.
14. A. Bencini and D. Gatteschi, ‘EPR of Exchange Coupled Systems’, Springer-Verlag, Berlin, 1990.
15. K. Itoh and M. Kinoshita eds, ‘Molecular Magnetism’, Gordon and Breach, Amsterdam, 2000.
16. W. H. Crawford, H. W. Richardson, J. R. Wasson, D. J. Hodgson, and W. E. Hatfield, *Inorg. Chem.*, 1976, **15**, 2107.
17. A. Bencini and D. Gatteschi, *Inorg. Chim. Acta*, 1978, **31**, 11.
18. J. J. Girerd, M. F. Charlot, and O. Kahn, *Mol. Phys.*, 1977, **34**, 1063.
19. P. J. Hay, J. C. Thibeault, and R. H. Hoffman, *J. Am. Chem. Soc.*, 1975, **97**, 4884.
20. a) W. E. Marsh, W. E. Hatfield, and D. J. Hodgson, *Inorg. Chem.*, 1982, **21**, 2679; b) W. E. Marsh, K. C. Patel, W. E. Hatfield and D. J. Hodgson, *Inorg. Chem.* 1983, **22**, 511.
21. O. Kahn, J. Galy, Y. Journaux, and I. Morgenstern-Badarau, *J. Am. Chem. Soc.*, 1982, **104**, 2165.
22. a) J. B. Goodenough, *Phys. Rev.*, 1955, **100**, 564; b) J. B. Goodenough, ‘Magnetism and the Chemical Bond’, Interscience, New York, 1963.
23. a) J. Kanamori, *J. Phys. Chem. Solids*, 1959, **10**, 87; b) J. Kanamori, in ‘Magnetism’, eds. G. T. Rado and H. Suhl, Academic Press, New York, 1963, Vol. 1.
24. a) P. W. Anderson, *Phys. Rev.*, 1950, **79**, 350; b) P. W. Anderson, in ‘Magnetism’, eds. G. T. Rado and H. Suhl, Academic Press, New York, 1963, Vol. 1, 25.
25. a) I. E. Dzyaloshinsky, *Sov. Phys. JETP*, 1958, **6**, 621; I. E. Dzyaloshinsky *J. Phys. Chem. Solids*, 1958, **4**, 241; b) T. Moriya, *J. Phys. Chem. Solids*, 1959, **11**, 73; T. Moriya, *Phys. Rev.*, 1960, **117**, 635; T. Moriya *Phys. Rev.*, 1960, **120**, 91.
26. a) J. R. Friedman, M. P. Sarachik, J. Tehada, and R. Ziolo, *Phys. Rev. Lett.*, 1996, **76**, 3830; b) L. Thomas, L. Lionti, R. Ballou, D. Gatteschi, R. Sessoli, and B. Barbara, *Nature (London)* 1996, **383**, 145.
27. E. Ising, *Z. der Physik*, 1925, **31**, 253.
28. H. Bethe, *Z. der Physik*, 1931, **71**, 205.
29. L. Onsager, *Phys. Rev.*, 1944, **65**, 117.
30. J. M. Kosterlitz and D. J. Thouless, *J. Phys. C*, 1973, **6**, 1181.
31. B. N. Taylor, ‘NIST Special Publication 811, 1995 Edition, Guide for the Use of the International System of Units (SI)’, US. Government Printing Office, Washington, DC, 1995.
32. J. C. Bonner and M. E. Fisher, *Phys. Rev. A*, 1964, **135**, 640.

33. D. C. Johnston, R. K. Kremer, M. Troyer, X. Wang, A. Klümper, S. L. Bud’ko, A. F. Panchula, and P. C. Canfield, *Phys. Rev. B*, 2000, **61**, 9558.
34. D. C. Johnston, M. Troyer, S. Miyahara, D. Lidsky, K. Ueda, M. Azuma, Z. Hiroi, M. Takano, M. Isobe, Y. Ueda, M. A. Korotin, V. I. Anisimov, A. V. Mahajan, and L. L. Miller, arXiv:cond-mat/0001147.
35. M. Shiroishi and M. Takahashi, *Phys. Rev. Lett.*, 2002, **89**, 117201.
36. M. E. Fischer, *Am. J. Phys.*, 1964, **32**, 343.
37. a) F. D. M. Haldane, *Phys. Lett.*, 1983, **93A**, 464; b) F. D. M. Haldane, *Phys. Rev. Lett.*, 1983, **50**, 1153; c) F. D. M. Haldane, *Bull. Am. Phys. Soc.*, 1982, **27**, 181.
38. R. Botet, R. Julien, and M. Kolb, *Phys. Rev. B*, 1983, **28**, 3914.
39. M. Drillon, E. Coronado, R. Georges, J. C. Gianduzzo, and J. Curely, *Phys. Rev. B*, 1989, **40**, 10,992.
40. M. E. Fisher, *J. Math. Phys.*, 1963, **4**, 124.
41. P. M. Duxbury, J. Oitmaa, M. N. Barber, A. van der Bilt, K. O. Joung, and R. L. Carlin, *Phys. Rev. B*, 1981, **24**, 5149.
42. S. Katsura, *Phys. Rev.*, 1962, **127**, 1508.
43. J. D. Dunitz, *Acta Crystallogr.*, 1970, **10**, 307.
44. a) K. Takeda, S. Matsukawa, and T. Haseda, *J. Phys. Soc. Jpn.*, 1971, **30**, 1330; b) W. Duffy Jr, J. E. Venneman, D. L. Strandburg, and P. M. Richards, *Phys. Rev. B*, 1974, **9**, 2220.
45. J. P. Renard, in ‘Organic and Inorganic Low-Dimensional Crystalline Materials’, eds. P. Delhaes and M. Drillon, Plenum Press, New York and London, 1987.
46. a) Y. Endoh, G. Shirane, R. J. Birgeneau, P. M. Richards, and S. L. Holt, *Phys. Rev. Lett.*, 1974, **32**, 170; b) I. U. Heilmann, G. Shirane, Y. Endoh, R. J. Birgeneau, S. L. Holt, *Phys. Rev. B*, 1978, **18**, 3530.
47. A. Santoro, A. D. Mighell, and C. W. Reimann, *Acta Crystallogr., B*, 1970, **26**, 979.
48. D. B. Losee, H. W. Richardson, and W. E. Hatfield, *J. Chem. Phys.*, 1973, **59**, 3600.
49. G. Mennenga, L. J. de Jongh, W. J. Huiskamp, and J. Reedijk, *J. Magn. Magn. Mater.*, 1984, **44**, 89.
50. B. R. Jones, P. A. Varughese, I. Olejniczak, J. M. Pigos, J. L. Musfeldt, C. P. Landee, M. M. Turnbull, and G. L. Carr, *Chem. Mater.*, 2001, **13**, 2127.
51. N. Motoyama, H. Eisaki, and S. Uchida, *Phys. Rev. Lett.*, 1996, **76**, 3212.
52. K. Hirakawa and Y. Kurogi, *Prog. Theor. Phys. Suppl.*, 1970, **46**, 147.
53. a) M. Date, H. Yamazki, M. Motokawa, and S. Tazawa, *Suppl. Prog. Theor. Phys.*, 1970, **46**, 194; b) D. C. Dender, D. Davidović, D. H. Reich, C. Broholm, K. Lefmann, and G. Aeppli, *Phys. Rev. B*, 1996, **53**, 2583.
54. K. Takeda, Y. Yoshino, K. Matsumoto, and T. Haseda, *J. Phys. Soc. Jpn.*, 1980, **49**, 162.
55. C. P. Landee, A. C. Lamas, R. E. Greeney, and K. G. Buecher, *Phys. Rev. B*, 1987, **35**, 228.
56. a) R. D. Willett and K. Chang, *Inorg. Chim. Acta*, 1970, **4**, 447; b) W. E. Estes, W. E. Hatfield, J. A. Van Ooijen and J. Reedijk, *J. Chem. Soc., Dalton Trans.*, 1980, 2121.
57. D. D. Swank, C. P. Landee, and R. D. Willett, *Phys. Rev. B*, 1979, **20**, 2154.
58. V. H. Crawford, H. W. Richardson, J. R. Wesson, D. J. Hodgson, and W. E. Hatfield, *Inorg. Chem.*, 1976, **15**, 2107.
59. C. P. Landee and R. D. Willett, *Phys. Rev. Lett.*, 1979, **43**, 463.
60. a) H. A. Groenendijk, H. W. Blöte, A. J. Van Duyneveldt, R. M. Gaura, C. P. Landee, and R. D. Willett, *Physica*, 1981, **106B**, 47; b) K. Kopinga, A. M. C. Tinus, and W. J. M. de Jonge, *Phys. Rev. B* 1982, **25**, 4685.
61. R. D. Willett, *Inorg. Chem.*, 1986, **25**, 1918.
62. A. Daoud, A. B. Salah, C. Chappert, J. P. Renard, A. Cheikhrouhou, T. Duc, and M. Verdaguer, *Phys. Rev. B*, 1986, **33**, 6253.
63. G. De Munno, M. Julve, F. Lloret, J. Faus, M. Verdaguer, and A. Caneschi, *Inorg. Chem.*, 1995, **34**, 157.
64. M. Hase, I. Terasaki, and K. Uchinokura, *Phys. Rev. Lett.*, 1993, **70**, 3651.
65. J. Riera and A. Dobry, *Phys. Rev. B*, 1995, **51**, 16098.
66. a) E. Dagotto and T. M. Rice, *Science*, 1996, **271**, 618; b) E. Dagotto, *Rep. Prog. Phys.* 1999, **62**, 1525.
67. M. Azuma, Z. Hiroi, M. Takano, K. Ishida, and Y. Kitaoka, *Phys. Rev. Lett.*, 1994, **73**, 3463.
68. B. R. Patyal, B. L. Scott, and R. D. Willett, *Phys. Rev. B*, 1990, **41**, 1657.
69. B. C. Watson, V. N. Kotov, M. W. Meisel, D. W. Hall, G. E. Granroth, W. T. Monfrooij, S. E. Nagler, D. A. Jensen, R. Backov, M. A. Petruska, G. E. Fanucci, and D. R. Talham, *Phys. Rev. Lett.*, 2001, **86**, 5168.
70. C. P. Landee, A. Delcheva, C. Galeriu, G. Pena, M. M. Turnbull, and R. D. Willett, *Polyhedron*, 2003, **22**, 2325.
71. A. Meyer, A. Gleizes, J. Girerd, M. Verdaguer, and O. Kahn, *Inorg. Chem.*, 1982, **21**, 1729.
72. J. P. Renard, M. Verdaguer, L. P. Regnault, W. A. C. Erkelens, J. Rossat-Mignod and W. G. Stirling, in ‘Organic and Inorganic Low-dimensional Crystalline Materials’, eds. P. Delhaes and M. Drillon, Plenum 1987.
73. K. Katsumata, H. Hori, T. Takeuchi, M. Date, A. Yamagishi, and J. P. Renard, *Phys. Rev. Lett.*, 1989, **63**, 86.
74. P. P. Mitra and B. I. Halperin, *Phys. Rev. Lett.*, 1994, **72**, 912.
75. G. E. Granroth, M. W. Meisel, M. Chaparala, Th. Jolicoeur, B. H. Ward, and D. R. Talham, *Phys. Rev. Lett.*, 1996, **77**, 1616.
76. A. Gleizes and M. Verdaguer, *J. Am. Chem. Soc.*, 1981, **103**, 7373.
77. Y. Pei, M. Verdaguer, O. Kahn, J. Sletten, and J. P. Renard, *Inorg. Chem.*, 1987, **26**, 138.

78. A. Caneschi, D. Gatteschi, R. Sessoli, and P. Rey, *Acc. Chem. Res.*, 1989, **22**, 392.

Acknowledgment

William E. Hatfield, a pioneer of molecular magnetism, wrote the preceding version of this article in the first edition of the Encyclopedia of Inorganic Chemistry. We have both benefited from his understanding of chemistry and magnetism. We dedicate this article to his memory.

Magnetism of Transition Metal Ions

William E. Hatfield
University of North Carolina, Chapel Hill, NC, USA

1 Introduction 1
2 Analysis of Experimental Data 2
3 Theoretical Analysis of Experimental Data 6
4 Multielectron Transition Metal Complexes and Compounds 9
5 High-spin and Low-spin Complexes and Compounds 9
6 Survey of Typical Results for Transition Metal Compounds 10
7 Related Articles 10
8 References 10

Glossary

Flux density: the number of lines of force per unit area
Lines of force: the free path that would be traced by a unit pole in a magnetic field owing to the forces acting upon it is called the line of force. Consider a unit pole enclosed in a sphere that has a radius of 1.0 cm. For the unit pole, one line of force passes through each square cm of area, and since there are 4π cm^2 of surface area on the sphere, there are 4π lines of force emanating from each unit pole
Magnetic dipole: a magnetic system composed of two poles that are equal in magnitude but opposite in nature, and that are separated by a short distance
Magnetic field: the region surrounding a magnetic body
Magnetic field strength: the force that acts upon a unit pole placed at a fixed point in a magnetic field in a vacuum is a measure of the magnetic field strength. The unit of magnetic field strength is the oersted, although frequently field strengths are given in gauss, an older term
Magnetic flux: the total number of lines of force emanating from the pole face of a magnet is called the total magnetic flux. Magnetic flux is measured in maxwells
Magnetic induction: magnetic induction along a specific direction, say i, is given by $B_i = H_i + 4\pi M_i$
Magnetic permeability: if two poles of strength m_1 and m_2 are placed at a distance r cm apart in a vacuum, the force between them is given by $F = km_1m_2/r^2$. If some material is placed between the poles, then the force will be given by $F = (k/\mu)m_1m_2/r^2$, where μ is the magnetic permeability of the material between the poles. Magnetic permeability is related to magnetic susceptibility by $\mu = 1 + 4\pi\chi$
Magnetic susceptibility: gram magnetic susceptibility is obtained by dividing the volume magnetic susceptibility (see below) by the density of the substance; molar magnetic susceptibility is obtained by multiplying the gram magnetic susceptibility by the molecular weight; when the magnetic induction along a specific direction i is divided by H_i, the result is $B_i/H_i = 1 + 4\pi M_i/H_i$, where the quantity M_i/H_i is the volume susceptibility. Volume magnetic susceptibility is almost always designated as κ_i
Pole strength: the pole strength of a magnet is measured by the number of unit poles to which each pole of the magnet is equivalent
Unit pole: a unit pole is one that will repel with a force of one dyne an equal and similar pole placed 1.0 cm away in a vacuum; the repulsion obeys Coulomb's law; a unit magnetic pole has not been isolated

1 INTRODUCTION

Much chemical information may be obtained from a determination of the response to magnetic fields of complexes or compounds of transition metal ions. This article is devoted to a development of the basis for a discussion of the magnetic susceptibility and magnetization studies of complexes or compounds in which short- or long-range order does not dictate the magnetic behavior. Magnetic susceptibility and magnetization studies are supplemented by electron paramagnetic resonance studies. Substances will be broadly classified as to their response to an inhomogeneous magnetic field. When placed in an inhomogeneous magnetic field, a diamagnetic substance will tend to move towards the weakest region of the inhomogeneous magnetic field, while a paramagnetic substance will tend to move to the strongest region of the magnetic field. These simple observations yield extremely important information about electronic structure, and ultimately bonding, in transition metal complexes and compounds.

Magnetic properties arise from the spin and orbital motions of electrons. If all of the electrons in a substance are paired, then the substance will usually be diamagnetic. However, if unpaired electrons are present, then the substance may be paramagnetic. Cooperative interionic interactions may lead to long-range magnetic ordering resulting in ferromagnetism, antiferromagnetism, or ferrimagnetism among other forms of cooperative magnetic ordering (*see* ***Magnetism of Extended Arrays in Inorganic Solids***).

Useful theory for the description of the properties of transition metal complexes and compounds has been developed in depth in a number of monographs (some classical ones are referenced here; *see* ***Ligand Field Theory & Spectra***).[1–6] Therefore, only a brief outline of theoretical developments will be presented along with some valuable results for the interpretation of magnetic data.

Table 1 Conversion factors for magnetic quantities

Multiply the number for			To obtain the number for	
Gaussian quantity	Unit	By	SI quantity	Unit
Flux density, B	G	10^{-4}	Flux density, B	T ($\equiv$ Wb m^{-2} $\equiv$ V s m^{-2})
Magnetic field strength, H	Oe	$10^3/4\pi$	Magnetic field strength, H	A m^{-1}
Volume magnetic susceptibility, κ	emu cm^{-3} (dimensionless)	4π	Rationalized volume susceptibility, κ	(dimensionless)
Gram magnetic susceptibility, χ_g	emu g^{-1} ($\equiv$ cm^3 g^{-1})	$4\pi \times 10^{-3}$	Rationalized gram susceptibility, κ_g	m^3 kg^{-1}
Molar magnetic susceptibility, χ_M	emu mol^{-1} ($\equiv$ cm^3 mol^{-1})	$4\pi \times 10^{-6}$	Rationalized molar susceptibility, κ_{mol}	m^3 mol^{-1}

There are two systems of units commonly used in publications dealing with magnetic properties. These are the cgs–emu system and the International System of Units (SI). A number of useful conversion factors are collected in Table 1.

1.1 Experimental Techniques

Magnetic susceptibility and magnetization measurements are made by a variety of techniques. These include the Gouy method, the Faraday method, and change in flux methods. Excellent descriptions of the methods as well as their advantages and limitations are available.[7–9]

Absolute values of magnetic susceptibilities are rarely measured in the laboratory. Instead, the apparatus for the measurement of magnetic susceptibilities are usually calibrated with standard substances that have well known values. It is generally advisable to use a standard that has a gram magnetic susceptibility comparable in magnitude to that of the unknown. Thus, for diamagnetic materials, water ($\chi_g = -0.720 \times 10^{-6}$ cgs units at 293 K)[7] is frequently used. The compound HgCo(NCS)$_4$ ($\chi_g = 16.44 \times 10^{-6}$ cgs units at 293 K) is widely used as a standard for paramagnetic substances, even though the gram magnetic susceptibility is rather large. HgCo(NCS)$_4$ can be used over a range of temperatures since the Curie–Weiss parameters are well known.[10,11] The manganese Tutton salt $(NH_4)_2Mn(SO_4)_2 \cdot 6H_2O$ is widely used since the magnetic susceptibility of this compound obeys the Curie law with $C = 4.375$.[12] The compound $(Me_2enH_2)CuC1_4$ ($Me_2enH_2 = [Me_2NHCH_2CH_2NHMe_2]^{2+}$) has been suggested[11] as a calibration standard for work with less paramagnetic materials since the gram magnetic susceptibility is significantly smaller than that of HgCo(NCS)$_4$ or the manganese Tutton salt. The magnetic susceptibility of $(Me_2enH_2)CuC1_4$ obeys the Curie–Weiss law with $C = 0.433$ and $\theta = -0.07$.[11]

2 ANALYSIS OF EXPERIMENTAL DATA

2.1 The Van Vleck Equation

Van Vleck[13] derived an equation for the calculation of magnetic susceptibilities of paramagnetic systems in which the magnetic susceptibility is independent of the magnetic field. The equation is applicable for moderate magnetic fields and temperatures. The system to be described by the theory consists of a series of n states, each of which is m-fold degenerate. The energy of the state $E_{n,m}$ in a magnetic field H is expanded in terms of a power series in H:

$$E_{n,m} = E^{(0)}_{n \cdot m} + HE^{(1)}_{n \cdot m} + H^2E^{(2)}_{n \cdot m} + \mathrm{K} \tag{1}$$

The magnetic moment of the level $E_{n,m}$ in the magnetic field direction ($i = x, y, z$) is given by

$$\begin{aligned} \mu_{n,m} &= \frac{-\mathrm{d}E_{n,m}}{\mathrm{d}H_i} \\ &= \left(\frac{-\mathrm{d}}{\mathrm{d}H_i}\right)(E^{(0)}_{n \cdot m} + HE^{(1)}_{n,m} + H^2E^{(2)}_{n,m} + \mathrm{K}) \\ &= -E^{(1)}_{n,m} - 2HE^{(2)}_{n,m} - \mathrm{K} \end{aligned} \tag{2}$$

The magnetic moment per gram atom for the array of states is obtained by taking a statistical mean over the populated states weighted by a Boltzmann distribution, yielding

$$M_i = \frac{N_A \sum_{n,m} \mu_{n,m} \exp(-E_{n,m}/kT)}{\sum_{n,m} \exp(-E_{n,m}/kT)} \tag{3}$$

where N_A is the Avogadro number. The theory is developed for paramagnetic substances for which there is no magnetization in the absence of an applied field. The magnetic susceptibility, defined as $\chi_i = M_i/H_i$, is given by the Van Vleck equation:

$$\chi_i = \frac{N_\mathrm{A}\sum\limits_{n,m}[E^{(1)^2}_{n,m}/kT - 2E^{(2)}_{n,m}]\exp(-E^{(0)}_{n,m}/kT)}{\sum\limits_{n,m}\exp(-E^{(0)}_{n,m})/kT} \tag{4}$$

The terms $E^{(1)}_{n,m}$ and $E^{(2)}_{n,m}$ in the Van Vleck equation are the first- and second-order Zeeman coefficients obtained from the expansion of the magnetic moment in terms of a power series of the magnetic field.

2.2 The Curie Law

Consider an octahedral molecule with the direction of the applied field H taken parallel to z, so the $L_z + 2S_z$ components of the Zeeman operator $L + 2S$ may be used. Thus

$$E^{(1)}_{n,m} = \langle\psi_{n,m}|L_z + 2S_z|\psi_{n',m'}\rangle\mu_\mathrm{B}H \tag{5}$$

and

$$E^{(2)}_{n,m} = \frac{\sum\limits_{n}|\langle\psi_n|L_z + 2S_z|\psi_0\rangle\mu_\mathrm{B}H|^2}{(E_0 - E_n)} \tag{6}$$

Ignoring the second-order term, the magnetic susceptibility of an orbitally nondegenerate ground state becomes

$$\begin{aligned}\chi_z &= \left(\frac{N\mu_\mathrm{B}}{k_\mathrm{B}T}\right)\frac{|\langle\psi_{n,m}|2S_z|\psi_{n',m'}\rangle|^2}{(2S+1)}\\ &= \left(\frac{N{\mu_\mathrm{B}}^2g^2}{k_\mathrm{B}T(2S+1)}\right)\\ &= \left[\frac{N{\mu_\mathrm{B}}^2g^2}{k_\mathrm{B}T(2S+1)}\right]\left[\left(\frac{1}{3}\right)S(S+1)(2S+1)\right]\\ &= \left(\frac{N{\mu_\mathrm{B}}^2g^2}{3k_\mathrm{B}T}\right)[S(S+1)]\end{aligned} \tag{7}$$

This last equation is the spin-only formula where the Landé g factor has been introduced to take account of any spin–orbit coupling with excited states. The Landé g factor is given by

$$g = \frac{1 + [J(J+1) + S(S+1) - L(L+1)]}{[2J(J+1)]} \tag{8}$$

In the case of spin-only paramagnetism, the Landé g factor is 2, since $L = 0$. The Curie law

$$\chi = \frac{C}{T} \tag{9}$$

where C is the Curie constant, is frequently used. Thus

$$C = \frac{N{\mu_\mathrm{B}}^2g^2S(S+1)}{3k} \tag{10}$$

The Curie law was found experimentally in the 1890s.

2.3 Paramagnetism

In the general case, magnetic properties will depend on the total angular momentum J, the magnetic moment will be μ_J, and the Hamiltonian for a single magnetic ion will be

$$\mathrm{H} = -\mu_J\cdot H_0 \tag{11}$$

where H_0 is the applied magnetic field. Along one direction, say the z direction, the Hamiltonian becomes

$$\mathrm{H} = -\mu_{Jz}H_z \tag{12}$$

The eigenvalues are $-g\mu_\mathrm{B}m_JH_z$, where m_J can take on the values J, $J-1, \ldots, -J$. The partition function is

$$\begin{aligned}Z_J &= \sum_{m_J}\exp\left(\frac{g\mu_\mathrm{B}H_z}{k_\mathrm{B}T}\right)\\ &= \left(\sinh\left[\left\{\frac{(2J+1)}{2J}\right\}x\right]\right)\left(\sinh\left(\frac{x}{2J}\right)\right)\end{aligned} \tag{13}$$

where $x = g\mu_\mathrm{B}JH_z/k_\mathrm{B}T$ is the ratio between magnetic and thermal energies. The magnetic moment becomes

$$M = \frac{N\mu_\mathrm{B}\sum\limits_{m_J}m_J\exp(m_Jx/J)}{Z_J(x)} \tag{14}$$

which can be expressed in terms of the Brillouin function as[14]

$$M = Ng\mu_\mathrm{B}JB_J(x) \tag{15}$$

where

$$\begin{aligned}B_J(x) &= \left[\frac{(2J+1)}{2J}\right]\coth\left[\left\{\frac{(2J+1)}{2J}\right\}x\right]\\ &\quad - \left(\frac{1}{2J}\right)\coth\left(\frac{x}{2J}\right)\end{aligned} \tag{16}$$

There are two limiting cases. In the first case, $x \ll 1$. This would correspond to a typical paramagnetic substance at room temperature. For example, with $J = 1$, $g = 2$, and $H_0 = 10\,000$ Oe at room temperature, x may be calculated to be 5×10^{-3}. In such a case the Brillouin function reduces to

$$B_J(x) = \left[\frac{(J+1)}{3J}\right]x \tag{17}$$

and the magnetic moment is given by

$$M = \frac{Ng^2{\mu_\mathrm{B}}^2J(J+1)H_z}{3k_\mathrm{B}T} \tag{18}$$

Since the magnetic susceptibility is defined by $\chi = M/H$, then

$$\chi = \frac{C}{T} \tag{19}$$

where the Curie constant C is

$$C = \left[\frac{Ng^2\mu_\mathrm{B}{}^2 J(J+1)}{3k}\right] \tag{20}$$

in agreement with the results obtained earlier considering only the spin.

An effective magnetic moment may be defined as

$$\mu_\mathrm{eff} = g[J(J+1)]^{1/2} \tag{21}$$

or, for spin-only paramagnetism, by

$$\mu_\mathrm{eff} = g[S(S+1)]^{1/2} \tag{22}$$

The spin-only formula may also be expressed as

$$\mu_\mathrm{eff} = [n(n+2)]^{1/2} \tag{23}$$

where n is the number of unpaired electrons, and g is taken to be 2.0. Magnetic moments calculated with these simple formulas are compared with experimental magnetic moments in Table 2.

The other limiting case occurs when the magnetic energy is large with respect to the thermal energy, in other words x takes on large values. This corresponds to paramagnetic saturation. The following expression may be written:

$$\frac{M}{Ng\mu_\mathrm{B}J} = B_J(x) = 1 - \left(\frac{1}{J}\right)\exp\left(\frac{-g\mu_\mathrm{B}H_z}{k_\mathrm{B}T}\right) \tag{24}$$

Plots of $B_J(x)$ as a function of x are shown in Figure 1 for several x values. It is clear that magnetization studies can be very useful in determining angular momentum quantum numbers since the shape of the magnetization curves are very sensitive to the value of J.

Table 2 Typical experimental magnetic moments of first-row transition metal-ion complexes compared with theoretical predictions

	Ground state		Free ion				μ_eff expt
Ion	O_h	S	L	J	$\mu_\mathrm{eff} = g[J(J+1)]^{1/2}$	$\mu_\mathrm{eff} = g[S(S+1)]^{1/2}$	(BM)
Ti^{3+}	$^2T_2$	1/2	2	3/2	1.55	1.73	1.8
V^{3+}	$^3T_1$	1	3	2	1.63	2.83	2.8
Cr^{3+}	$^4A_2$	3/2	3	3/2	0.77	3.87	3.8
Mn^{3+}	^5E	2	2	0	0.00	4.90	4.9
Fe^{3+}	$^6A_1$	5/2	0	5/2	5.92	5.92	5.9
Fe^{2+}	$^5T_2$	2	2	4	6.70	4.90	5.4
Co^{2+}	$^4T_1$	3/2	3	9/2	6.63	3.87	4.8
Ni^{2+}	$^3A_1$	1	3	4	5.59	2.83	3.2
Cu^{2+}	^2E	1/2	2	5/2	3.55	1.73	1.9

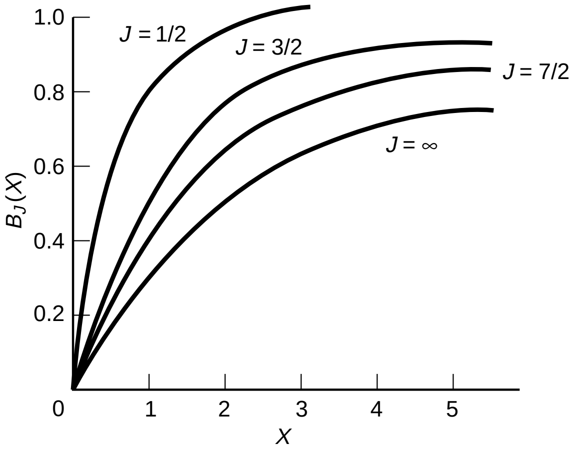

Figure 1 The functional form of the Brillouin function for selected J values

2.4 Data Analysis

Measurements of magnetic properties at one temperature, say room temperature, or over a limited temperature range yield data that may be useful, but generally measurements should be made over wide ranges of temperatures and magnetic field strengths. Such measurements may yield valuable information for detailed descriptions of electronic structure and bonding.**15**

2.5 Diamagnetic Corrections

Experimental magnetic susceptibility data must be corrected for the diamagnetism of the constituent atoms, a quantity that is practically temperature independent. Diamagnetism may be estimated rather precisely by the following procedure developed by Pascal:

$$\chi_\mathrm{M}(\mathrm{dia}) = \sum_i n_i \chi(A)_i + \sum_j n_j \chi(B)_j + \mathrm{K} \tag{25}$$

where n_i is the number of atoms of kind i and diamagnetic susceptibility $\chi(A)_i$, and $\chi(B)_j$ is the susceptibility associated with n_j structural features (such as double or triple carbon–carbon bonds). Extensive self-consistent tables of magnetic susceptibilities of atoms, ions, and structural features have been tabulated.**15** Some commonly used diamagnetic corrections are collected in Table 3.

As an example of the use of Table 3, consider the diamagnetic susceptibility of $[Cu(bipy)_3](ClO_4)_2 \cdot 4H_2O$,

Table 3 Diamagnetic corrections ($\chi_{\text{dia}} \times 10^{-6}$ emu mol^{-1})

Atoms		Anions		Cations	
H	2.93	F^-	9.1	Li^+	1.0
C	6.0	Cl^-	23.4	Na^+	6.8
N (open chain)	5.6	Br^-	34.6	K^+	14.9
N (ring)	4.6	I^-	50.6	Rb^+	22.6
N (monoamide)	1.5	$NO_3{}^-$	18.9	Cs^+	35.0
N (diamide, imide)	2.1	$ClO_3{}^-$	30.3	Tl^+	35.7
O (alcohol, ether)	4.6	$ClO_4{}^-$	32.0	$NH_4{}^+$	13.3
O (ketone, aldehyde)	−1.7	$BrO_3{}^-$	38.8	Hg^{2+}	40
O (carboxyl)	3.4	$IO_4{}^-$	51.9	Mg^{2+}	5
F	6.3	$IO_3{}^-$	51.4	Zn^{2+}	15
Cl	20.1	CN^-	13.0	Ca^{2+}	10.4
Br	30.6	NCS^-	31.0	Fe^{2+}	12.8
I	44.6	$SO_4{}^{2-}$	40.1	Co^{2+}	12.8
S	15.0	$CO_3{}^{2-}$	29.5	Ni^{2+}	12.8
Se	23.0	OH^-	12.0	Cu^{2+}	12.8
Te	37.3				
P	26.3				
As^{III}	20.9				
As^{V}	43.0				
Sb^{III}	74.0				
Li	4.2				
Na	9.2				
K	18.5				
Common ligands		**Constituent corrections**			
Water	13.0	C=C	−5.5		
2,2′-Bipyridine	105.0	C≡C	−0.8		
Phenanthroline	128	C=C–C=C	−10.6		
		C (in aromatic ring)	1.4		
		N=N	−1.9		
		C=N–	−8.2		
		–C≡N	−0.8		
		C–Cl	−3.1		
		C–Br	−4.1		
		C–I	−4.1		

for which

$$\begin{aligned}\chi_M(\text{dia}) &= \chi(\text{Cu}) + 3\chi(\text{bipy}) + 2\chi(\text{ClO}_4{}^-) + 4\chi(\text{H}_2\text{O}) \\ &= 12.8 + 315 + 64 + 52 \\ &= 443.8 \times 10^{-6}\text{cgs units} \qquad (26)\end{aligned}$$

Thus, the quantity 443.8×10^{-6} must be added to the measured magnetic susceptibility in order to arrive at the corrected molar magnetic susceptibility of the compound.

2.6 Graphical Treatment of Experimental Data

The molar magnetic susceptibility, χ_M, which has been corrected for the diamagnetism of the constituent atoms, is plotted versus T^{-1}. If a straight line is obtained, then the data follow the Curie law, $\chi = C/T$. The effective magnetic moment is given by

$$\mu_{\text{eff}} = 2.828(\chi_M \cdot T)^{1/2} \qquad (27)$$

and the Bohr magneton number can be used in the solution of the chemical problem under study.

If a straight line that intercepts the positive χ_M axis at $T^{-1} = 0$ is obtained, then it is possible that temperature-independent paramagnetism (see below) is present, or alternatively, that the diamagnetic correction has been overestimated. If the straight line intercepts the negative χ_M axis at $T^{-1} = 0$, it is likely that the diamagnetic correction has been underestimated.

If the line in the plot of χ_M versus T^{-1} is not straight, then χ_M^{-1} must be plotted versus T. A straight line here indicates that the data obey the Curie–Weiss law

$$\chi = \frac{C}{(T - \theta)} \qquad (28)$$

which, when recast, yields

$$T = \frac{C}{\chi_M + \theta} \qquad (29)$$

The slope of the line is the Curie constant, and the intercept is the Weiss constant.

It is usually instructive to plot $\chi_M \cdot T$ versus T. Curie law behavior holds if a straight line parallel to the T axis is obtained. For orbitally nondegenerate systems, deviations from straight line behavior toward larger $\chi_M \cdot T$ values with decreasing temperature indicate an array of populated electronic states with states of larger spin multiplicity lying lowest. The array of states may arise from ferromagnetic interactions. Deviations of $\chi_M \cdot T$ to smaller values with decreasing temperature indicate the presence of an array of populated electronic states with lower spin multiplicities lying lowest. Such an array of states may arise from antiferromagnetic interactions.

If a straight line is not obtained from the Curie–Weiss plot, then it is clear that more detailed theory is necessary for data analysis, and the Van Vleck equation or other more sophisticated theory must be used.

3 THEORETICAL ANALYSIS OF EXPERIMENTAL DATA

Crystal-field theory and its modifications are very useful in discussions of magnetic properties of transition metal compounds even though the theories are well known to be highly artificial. This arises from the assumption that the bonding between the transition metal ion and the ligands is considered to be totally ionic or can be parameterized. The ligands are assigned a passive role in that they provide a constant electric field that has the symmetry of the ligand nuclei, and this electric field destabilizes the free ion energy levels of the transition metal ion.

3.1 Basic Theoretical Concepts

Crystal-field theory will be briefly described here using a weak-field approach. Those interested in complete treatments beyond the scope of this article are referred to discussions in appropriate monographs.[1–6] Perturbation theory is used assuming free ion eigenfunctions and eigenvalues, and the Hamiltonian is

$$\mathrm{H} = -\left(\frac{h}{8\pi^2 m}\right)\sum_i \nabla_i^2 - \sum_i \left(\frac{Ze^2}{r_i}\right) + \left(\frac{1}{2}\right)\sum_{i \neq k}\left(\frac{e^2}{r_{i,k}}\right) + \sum_i (\zeta_i(r) l_i \cdot s_i) + V_{\mathrm{CF}} \qquad (30)$$

The following cases may be envisaged:

1. $V_{\mathrm{CF}} < l \cdot s$
2. $l \cdot s < V_{\mathrm{CF}} < e^2/r_{ij}$
3. $V_{\mathrm{CF}} > e^2/r_{ij}$

Table 4 Crystal-field splitting of ^{2}D free ion state

$\mathrm{E} = -4\mathrm{Dq}$	$\mathrm{E} = 6Dq$
$\psi_1 = (\lvert 2\rangle - \lvert -2\rangle)/\sqrt{2}$	$\psi_4 = (\lvert 2\rangle + \lvert -2\rangle)/\sqrt{2}$
$\psi_2 = \lvert 1\rangle$	$\psi_5 = \lvert 0\rangle$
$\psi_3 = \lvert -1\rangle$	

Complexes of the rare earth elements provide examples of case (1), many complexes of the first-transition series metals provide examples of case (2), and complexes with covalent bonds provide examples of case (3). Case (2) will be considered here. Excellent monographs cited above are available in which the theory is developed in detail.

The calculation reveals that the octahedral crystal field removes the fivefold orbital degeneracy of the ^{2}D free ion state, yielding a threefold degenerate state at $-4Dq$ and a twofold degenerate state at $+6Dq$. The results of the crystal-field calculation are collected in Table 4. The representations spanned by the crystal-field states are determined by an examination of the transformation properties of $\psi_1, \ldots, \psi_5$ in the point group O, since it is known that d wavefunctions are even under inversion and O_h is $O \times i$. In O_h, these become $\mathrm{T_{2g}}$ and $\mathrm{E_g}$, respectively. In this manner, it has been determined that the octahedral crystal field removes the orbital degeneracy of the ^{2}D free ion state, resulting in the formation of two crystal-field states, those being $^2\mathrm{T_{2g}}$ and $^2\mathrm{E_g}$.

3.2 Spin–Orbit Coupling in Octahedral Crystal-field States

Under certain circumstances, the degeneracies of the crystal-field states are further split by coupling of the orbital angular momenta of the electrons to their spin angular momenta. The splitting of these crystal-field states by spin–orbit coupling can be determined by use of group theory, and in the case of odd numbers of electrons, double groups must be used.

The technique proceeds as follows. The representations spanned by the spin function and by the orbital function in the double group are determined, the direct product of these representations is taken, and the direct product representation is reduced to a sum of irreducible representations. In an octahedral crystal field, the $^2\mathrm{E_g}$ state is not split by spin–orbit coupling but transforms as the irreducible representation Γ_8 in the double group O', while the $^2\mathrm{T_{2g}}$ state is split by spin–orbit coupling giving new states Γ_7 and Γ_8. In many instances, the influence of the $^2\mathrm{E_g}$ state cannot be ignored, since symmetry arguments show that it can mix with the ground state by spin–orbit coupling. For the purposes of this discussion, these interactions will be neglected.

The term that is added to the Hamiltonian to account for spin–orbit coupling is valid for spherical symmetry only, but the error introduced in lower symmetry cases is not great. The spin–orbit coupling constant could be taken from the spectra of gaseous ions, but it is usually treated as a parameter with the fitted parameter in the complex being less than that of the free ion.

If the interactions between different Russell–Saunders states are not large, the spin–orbit coupling operator may be written

$$\mathrm{H}_{LS} = \lambda L\cdot S \tag{31}$$

For a shell less than half filled

$$\lambda_{LS} = \frac{\zeta}{2S} \tag{32}$$

while a shell that is more than half filled has

$$\lambda_{LS} = \frac{-\zeta}{2S} \tag{33}$$

The secular determinantal equation is set up in the usual manner, the wavefunctions corrected for the crystal-field interaction are used in the perturbation treatment, energies are generated, and these are used in conjunction with the secular equations to generate new wavefunctions that have now been corrected for spin–orbit coupling. These corrected wavefunctions are used for the calculation of the Zeeman effect.

3.3 The Zeeman Effect

It is appropriate to use perturbation theory to approximate the Zeeman energies since λ is typically much greater than the quantity $\mu_B H$. The first-order Zeeman energy is the first-order perturbation energy, and the second-order Zeeman energy is the second-order perturbation energy. An energy level diagram that shows the effects of the octahedral crystal field, spin–orbit coupling, and an external magnetic field on the ^{2}D free ion term is shown in Figure 2. An expression for magnetic susceptibility may be generated by substitution of the first- and second-order Zeeman coefficients and the zero-field energies into the Van Vleck equation.

Since

$$\mu_{\mathrm{eff}} = \left(\frac{3k_B T}{N\mu_B{}^2}\right)\chi_M \tag{34}$$

then the temperature variation of the magnetic moment for the $^2T_{2g}$ state arising from the d^1 electronic configuration in an octahedral crystal field is

$$\mu_{\mathrm{eff}} = \left[\frac{\{8 + (3\lambda/k_B T - 8)\exp(-3\lambda/2k_B T)\}}{(\lambda/k_B T) \times \{2 + \exp(-3\lambda/2k_B T)\}}\right]^{1/2} \tag{35}$$

The magnetic moment tends toward zero at low temperatures because, as shown in Figure 2, there is no first-order Zeeman effect in Γ_8. At the level of approximation presented here the moments arising from the orbital and spin motions cancel.

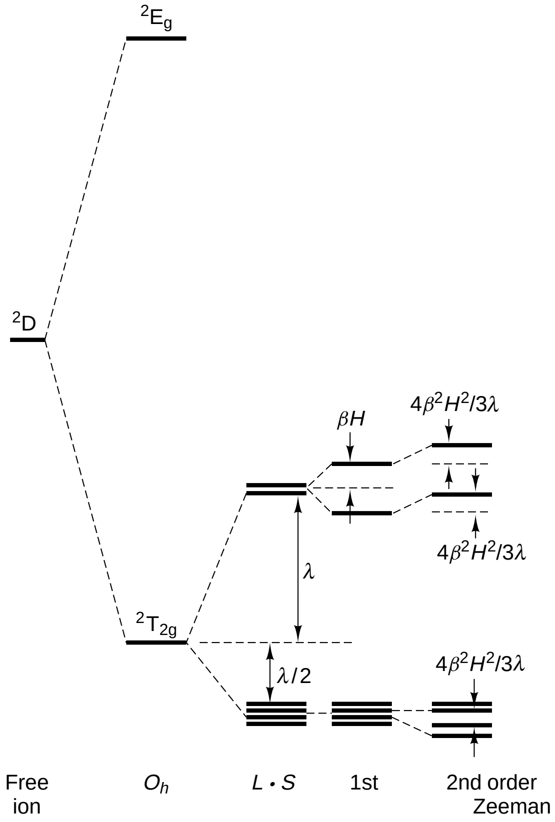

Figure 2 Successive perturbations of an octahedral crystal field, spin–orbit coupling, and the first and second Zeeman interactions on the ^{2}D state

The magnetic susceptibility data for a transition metal complex with a d^1 electronic configuration may obey the Curie–Weiss law above about 200 K, usually with a large θ value. At lower temperatures the magnetic susceptibility deviates from the Curie–Weiss law and becomes constant. This behavior may be understood in terms of the calculation outlined above. At low temperatures, only Γ_8 is populated, and this state exhibits only a second-order Zeeman effect. This example illustrates an important result; large θ values in the Curie–Weiss law are not always associated with long- or short-range cooperative magnetic effects.

3.4 Magnetism of a d^1 Ion in a Tetrahedral Environment

Many of the results obtained for the octahedral crystal-field calculation can be used for the description of the magnetic properties of ions in tetrahedral environments. If an S_4 axis of the tetrahedron is taken as the axis of quantization (being collinear with the C_4 axis of quantization of the octahedron), and the C_3 axes of the tetrahedron are collinear with the C_3 axes of the octahedron, then the crystal-field potential energy operator for the tetrahedral environment is

$$V(T_d) = -\left(\frac{28}{27}\right)\pi^{1/2}\left(\frac{Z_j e^2 r^4}{a^5}\right) \times \left[Y_4{}^0 + \left(\frac{5}{14}\right)^{1/2}(Y_4{}^4 + Y_4{}^{-4})\right] \qquad (36)$$

Comparison of $V(T_d)$ with $V(O_h)$ reveals that $V(T_d) = -(4/9)V(O_h)$. The Y_l^m are spherical harmonics.

The rotation group T is a subgroup of the rotation group O, and the degeneracy of the ^{2}D free ion state is lifted in the point group T yielding $^2T_2$ and ^{2}E, which correlate with $^2T_2$ and ^{2}E of O, respectively. At the same level of approximation described for the d^1 ion in an octahedral environment, the first-order Zeeman effect in the ^{2}E state leads to a doubly degenerate level at $+\mu_B H_z$ and a second doubly degenerate level at $-\mu_B H_z$.

If second-order effects are ignored, substitution into the Van Vleck equation yields for the magnetic susceptibility

$$\chi_M = \frac{N\mu_B{}^2}{k_B T} \qquad (37)$$

This result shows that, to first order, the magnetic susceptibility of a d^1 ion in a tetrahedral environment should exhibit simple Curie law behavior, but this is rarely the case. Second-order effects may arise from interactions with the excited states.

Following the procedures outlined in the calculations presented above, substitution of the Zeeman coefficients and zero-field energies into the Van Vleck equation yields the following expression for the magnetic susceptibility:

$$\chi_M = \frac{N\mu_B{}^2}{k_B T} + \frac{4N\mu_B{}^2}{\Delta_t} \qquad (38)$$

The second term is temperature-independent paramagnetism and can be verified independently if Δ_t is known from spectral studies. This is an excellent example of the complementary data that may be obtained from magnetic susceptibility and electronic spectroscopic studies.

3.5 Example of a Low-symmetry Crystal-field Component

Transition metal complexes rarely have structures that may be classified in high symmetry point groups such as O_h or T_d. The effect of a tetragonal distortion of an octahedron will be discussed here. The most important conclusion from the exercise is that additional parameters must be introduced. In optimum cases, these parameters may be obtained from detailed spectroscopic studies. Consider an elongation or contraction of an octahedron along a C_4 axis such that there are two equivalent metal–ligand bond distances along the z axis with length b, and four equivalent metal–ligand bond distances perpendicular to the z axis with length a. Following the procedures outlined earlier, it may be seen that some combination of $Y_2{}^m$ contributes to the crystal-field potential, as well as $Y_4{}^m$ combinations. Retaining quantization along C_4, it may be shown that only $Y_2{}^0$ contributes to $V(O_h)$.

Since D_4 is a subgroup of the point group O, it may be shown, from symmetry arguments, that the effect of the lower symmetry on the ^2E_g and $^2T_{2g}$ states is removal of some of the degeneracy. The results follow:

$$\begin{aligned} {}^2\mathrm{E_g} &\longrightarrow {}^2\mathrm{A_{1g}} + {}^2\mathrm{B_{1g}} \\ {}^2\mathrm{T_g} &\longrightarrow {}^2\mathrm{B_{2g}} + {}^2\mathrm{E_g} \end{aligned} \qquad (39)$$

The energies of the states must be calculated. For example, for $^2A_{1g}$ the integral $\langle d_0|V(D_{4h})|d_0\rangle$ must be evaluated. $V(D_{4h})$ has additional terms as a result of the lower symmetry, and it is necessary to define new constants in addition to *Dq*. Two popular constants are *Ds* and *Dt*. Other constants appear in the literature, but *Ds* and *Dt* predominate. The energies are

$$\begin{aligned} \mathrm{A_{1g}} &= 6Dq - 2Ds - 6Dt \\ \mathrm{B_{1g}} &= 6Dq + 2Ds - Dt \\ \mathrm{B_{2g}} &= -4Dq + 2Ds - Dt \\ \mathrm{E_g} &= -4Dq - Ds + 4Dt \end{aligned} \qquad (40)$$

Since the low-symmetry component of the crystal-field and spin–orbit coupling are of comparable magnitude, these perturbations to the octahedral results must be applied simultaneously. The spacing and ordering of the array of states will depend on the nature and magnitude of the distortion. Corrections to the energies and corrected wavefunctions may be generated by substitution of the energies into the appropriate secular equations. For the details and solutions, an excellent paper by Figgis**[16]** provides such information and results. It is sufficient to note that the details of the low-lying energy levels, which determine the magnetic properties, are dependent on the spin–orbit coupling constant and the crystal-field component.

Anisotropic magnetic properties are anticipated in the axial system under consideration, where the Zeeman effect in the direction parallel to the C_4 axis may be calculated with

$$(l_z + 2s_z)\mu_B H_z \qquad (41)$$

and in the perpendicular direction by use of

$$(l_x + 2s_x)\mu_B H_x \qquad (42)$$

The steps to be followed may be summarized. Secular determinants must be constructed for each of the doubly degenerate levels in both directions. First-order Zeeman coefficients must be evaluated for each direction. Matrix elements connecting the three secular determinants must be evaluated to yield second-order Zeeman coefficients. The first- and second-order Zeeman coefficients must be substituted into the Van Vleck equation to yield the anisotropic magnetic susceptibilities $\chi_\parallel$ and $\chi_\parallel$. Generally, anisotropic magnetic properties are discussed in terms of $\mu_\parallel$ and $\mu_\parallel$ since the variation of these anisotropic components are much more easily visualized.

4 MULTIELECTRON TRANSITION METAL COMPLEXES AND COMPOUNDS

Important problems arise for complexes and compounds with two or more electrons. It is known that an array of states will arise from interelectronic interactions. Furthermore, the treatment of the magnetic problem depends on the magnitude of the perturbation of the metal-ion electrons by the surrounding ligands. The weak-field approach described above works well for complexes and compounds of transition metal ions with ligands at the weak end of the spectrochemical series. Examples are provided by low-oxidation state complexes of first-transition series metal ions with ligands such as halides, hydroxide, water, and ammonia, among many others. In these complexes and compounds, the spectroscopic terms of the free ion are maintained, but the degeneracies may be lifted by the symmetry provided by the ligands.

At the other end of the scale the perturbation may be very strong, the orbitals of the free ion may be viewed as being highly separated in energy, the electrons may occupy only the lowest lying orbitals, and in some cases the electron may be paired in these low-lying orbitals. As an illustrative example, consider the d^2 electronic configuration in an octahedral environment. Under the influence of a very strong perturbation, the t_{2g} orbitals will lie lowest in energy, the electronic configuration will be $(t_{2g})^2$, and states will arise from interelectronic interactions in these orbitals. Since the e_g level lies at a much higher energy, the next electronic configuration will be $(t_{2g})^1(e_g)^1$, which will give rise to a number of states, and the highest lying configuration will be $(e_g)^2$ with its resultant states. The states that arise from these configurations will correlate exactly with the states that arise from the action of the ligand field on the Russell–Saunders states found in the weak-field approach. It is instructive and useful to construct correlation diagrams linking the states from the weak-field and the strong-field approaches. A lucid description of the procedures to be followed and the application of these diagrams has been given by Cotton.[17]

A third case arises when the perturbation from the ligand field is intermediate between the weak-field case and the strong-field case. There is no sharp dividing line between the three cases given here. The calculational approach to be used depends on the identities of the transition metal ion and the ligands. The results of this third case have been presented by Figgis.[16] Applications have also been discussed by Mabbs and Machin.[18]

4.1 Weak-field Approach for a d^2 Ion in an Octahedral Environment

The Russell–Saunders states that arise from interelectronic interactions in a free ion with an electronic configuration d^2 are ^3F, ^1D, ^3P, ^1G, and ^1S, with the ^3F being the ground state as dictated by Hund's first and second rules. An approximate calculation in which the ^3F state is outlined here.

In an octahedral environment with O_h symmetry, the degeneracy of the ^3F state is lifted and $^3T_{1g}$, $^3T_{2g}$, and $^3A_{2g}$ states arise. A crystal-field calculation shows that the $^3T_{1g}$ state is the ground state with an energy of $-6Dq$, with the $^3T_{2g}$ state lying at $2Dq$, and the $^3A_{2g}$ state at $12Dq$. Since Dq is on the order of $1000\,\mathrm{cm}^{-1}$, then the two higher lying states will be omitted from the calculation of spin–orbit coupling. Precise treatments of data from some experiments may require the mixing in of excited states, especially the $^3T_{1g}$ provided by the ^3P Russell–Saunders state.

A spin–orbit calculation using the crystal-field corrected wavefunctions yields a fivefold degenerate level at $-\zeta/2$, a threefold degenerate level at $\zeta/2$, and a singly degenerate level at ζ. Calculation of the Zeeman coefficients and substitution into the Van Vleck equation is straightforward, and an equation for the temperature variation of the magnetic moment may be generated from the magnetic susceptibility expression. If x is taken to be ζ/k_BT, then the latter equation becomes

$$\mu_{\mathrm{eff}}{}^2 = \frac{3[5x/2 + 15 + (x/2 + 9)\exp(-x) - 24\exp(-3x/2)]}{x(5 + 3\exp(-x) + \exp(-3x/2))} \tag{43}$$

It is instructive to examine the temperature dependence of the magnetic moment. As the temperature approaches 0 K, the magnetic moment approaches $1.2\,\mu_B$, while at very high temperatures the magnetic moment approaches $3.2\,\mu_B$. At room temperature, the magnetic moment given by the above equation is about $2.8\,\mu_B$, a remarkable coincidence with the magnetic moment predicted by the spin-only formula. The calculation proceeds in the same manner for a d^3 ion in an octahedral environment of ligands. The steps of the calculation are described in much detail by Theissing and Caplan.[19] Useful formulas for the analysis of magnetic data for complexes of transition metal ions have been given by König and König.[15]

5 HIGH-SPIN AND LOW-SPIN COMPLEXES AND COMPOUNDS

An interesting situation arises for octahedral complexes in which the metal ion has electronic configurations d^4, d^5, d^6, and d^7. The electronic configurations that may be written for d^4 are $(t_{2g})^3(e_g)^1$ or $(t_{2g})^4$, for d^5 are $(t_{2g})^3(e_g)^2$ or $(t_{2g})^5$, for d^6 are $(t_{2g})^4(e_g)^2$ or $(t_{2g})^6$, and for d^7 are $(t_{2g})^5(e_g)^2$ or $(t_{2g})^6(e_g)^1$. The former in each case is called high spin and the latter is called low spin. To a good approximation, the electronic configuration adopted is determined by the magnitude of the crystal-field splitting Δ as compared to the electron–electron (repulsion) or pairing energy, P. If P is greater than Δ, the high-spin configurations arise, while low-spin configurations arise when Δ is greater than P. As a general rule, ligands at the low end of the spectrochemical series, such as halides, water, and ammonia, give rise to high-spin complexes with first-row transition metal ions, while ligands at the high end of the spectrochemical series, such as nitrite and cyanide, give rise to low-spin complexes for first-row transition series metal ions. There is no hard and fast rule concerning the crossover point and, for example, few ligands give high-spin complexes with cobalt(III).

5.1 Spin Crossover Complexes and Compounds

Very interesting phenomena may occur near the crossover point. There are frequently dramatic changes in magnetism, structure, and electronic, and vibrational spectroscopy of the complexes, and these changes may be continuous or discontinuous.[20] As implied by the nomenclature, in spin crossover compounds the properties of a complex in the continuous class exhibit gradual changes with an external perturbation such as a change in temperature, while those in the discontinuous class show abrupt changes in properties that may be first order in nature. There is frequently hysteresis in properties as the perturbation, say temperature, is cycled from high to low values; the observed changes in properties almost never obey a Boltzmann distribution law expected for two independent states, and frequently the properties reflect incomplete transitions from one state to the other. For example, spin crossover complexes of iron(II), which should be diamagnetic in the low-spin state, often show sizeable magnetic moments. This is an active field of research that has been stimulated recently by the LIESST effect (LIESST is Light Induced Electron Spin State Trapping).[21] In special instances, the excited states in these compounds have very long lifetimes, and, for example, the magnetic properties of these excited states may be determined. The potential for practical applications of these fascinating molecules are great.

6 SURVEY OF TYPICAL RESULTS FOR TRANSITION METAL COMPOUNDS

In view of the thousands of transition metal compounds, it is not possible to discuss here the diverse behavior exhibited by the many different classes of these compounds. The variables are numerous; these include structures, oxidation states, and ligands to name a few. Data for many transition metal compounds have been collected by König and König in a series of volumes.[15] They give the basic theory required for effective use of the tables, often summarize conclusions by the original author or authors, and show structures for complex ligands. This is an extremely valuable collection of data that is the starting point for critical analyses of the properties of the different classes of compounds. Reference to the current literature is necessary, for data on new and fascinating compounds are being generated at a very high rate. The research is stimulated by the invention of new chemistry and by the generation of new models for magnetic behavior. A new monograph has appeared on bioinorganic aspects of the subject,[22] as well as a book on molecular magnets, a topic of great current interest.[23]

7 RELATED ARTICLES

Coordination & Organometallic Chemistry: Principles; Ligand Field Theory & Spectra; Magnetism of Extended Arrays in Inorganic Solids.

8 REFERENCES

1. M. Gerloch, ‘Magnetism and Ligand-Field Analysis’, Cambridge University Press, Cambridge, MA, 1983.
2. J. B. Goodenough, ‘Magnetism and the Chemical Bond’, Interscience, New York, 1963.
3. A. S. Chakravarty, ‘Introduction to the Magnetic Properties of Solids’, Wiley, New York, 1980.
4. B. N. Figgis, ‘Introduction to Ligand Fields’, Interscience, New York, 1966.
5. C. J. Ballhausen, ‘Introduction to Ligand Field Theory’, McGraw-Hill, New York, 1962.
6. J. S. Griffith, ‘The Theory of Transition-Metal Ions’, Cambridge University Press, Cambridge, MA, 1961.
7. L. N. Mulay, ‘Magnetic Susceptibility’, Interscience, New York, 1963.
8. B. N. Figgis and J. Lewis, in ‘Modern Coordination Chemistry, Principles and Methods’, eds. J. Lewis and R. G. Wilkins, Interscience, New York, 1960, Chap. 6, p. 400.
9. W. E. Hatfield, in ‘Solid State Chemistry Techniques’, eds. A. K. Cheetham and P. Day, Clarendon Press, Oxford, 1987, Chap. 4, p. 122.
10. B. N. Figgis and R. S. Nyholm, *J. Chem. Soc.*, 1958, 4190.
11. D. B. Brown, V. H. Crawford, J. W. Hall, and W. E. Hatfield, *J. Phys. Chem.*, 1977, **81**, 1303.
12. B. N. Figgis, M. Gerloch, J. Lewis, F. E. Mabbs, and G. A. Webb, *J. Chem. Soc. A*, 1968, 2086.
13. J. H. Van Vleck, ‘The Theory of Electric and Magnetic Susceptibilities’, Oxford University Press, London, 1932.
14. J. S. Smart, ‘Effective Field Theories of Magnetism’, Saunders, Philadelphia, PA, 1966.
15. E. König and G. König, ‘Magnetic Properties of Coordination and Organometallic Transition-Metal Compounds’, Landolt-Börnstein, New Series, Springer, Berlin, 1981, Vol. II/11 (and earlier volumes).
16. B. N. Figgis, *Trans. Faraday Soc.*, 1961, **57**, 198.
17. F. A. Cotton, ‘Chemical Applications of Group Theory’, 3rd edn., Wiley, New York, 1990, Chap. 9 (earlier editions of this book may also be consulted).
18. F. E. Mabbs and D. J. Machin, ‘Magnetism and Transition-Metal Complexes’, Chapman & Hall, London, 1973.
19. H. H. Theissing and P. J. Caplan, ‘Spectroscopic Calculations for a Multielectron Ion’, Interscience, New York, 1966.
20. E. König, G. Ritter, and S. K. Kulshreshtha, *Chem. Rev.*, 1985, **85**, 219.

21. P. Gütlich and A. Hauser, *Coord. Chem. Rev.*, 1990, **97**, 1.
22. L. Que, ‘Physical Methods in Bioinorganic Chemistry: Spectroscopy and Magnetism’, University Science Books, Sausalito, CA, 2000.
23. P. Day and A. E. Underhill, ‘Metal-Organic and Organic Molecular Magnets’, RSC, Cambridge, 1999.

Manganese: Inorganic & Coordination Chemistry

Marie-Noëlle Collomb & Alain Deronzier
Université Joseph Fourier, Grenoble, France

Based in part on the article Manganese: Inorganic & Coordination Chemistry by Charles A. McAuliffe, Stephen M. Godfrey, & Michael Watkinson which appeared in the Encyclopedia of Inorganic Chemistry, First Edition.

1	Background and General Chemistry	1
2	Manganese (II)	1
3	Manganese (III)	5
4	Manganese (IV)	7
5	Mixed Oxidation State (II–IV)	7
6	Manganese (V) (VI) and (VII)	9
7	References	10

Abbreviations

ntb = tris(2-benzimidazolylmethyl)amine; bpea = N,N bis (2-pyridylmethyl)ethylamine; tpa = tris(2-pyridylmethyl) amine; Hdpm = dipyrazolylmethane; Hdbm = dibenzoyl methane; $dppO_2$ = 1,3-bis(diphenylphosphinoyl)propane; dmu = N,N'-dimethylurea; bipym = $2,2'$-bipyrimidine; bpman = 2,7-bis[bis(2-pyridylmethyl)aminomethyl]-1,8-naphthyridine; bipy = $2,2'$-bipyridine; phen = 1,10-phenantroline; gly = glycine; H_2bamen = 1,2-bis(biacetylmonoximeimino)ethane; 2-OHsalpn = 1,3-bis(salicylideneamino)-2-propanol; py = pyridine; terpy = 2,2′-6′,2″-terpyridine; tacn = 1,4,7-triazacyclononane; pko = $2,2'$-dipyridyl ketonoxime; 3,4-D = 3,4-dichlorophenoxy acetic acid; H_3thme = 1,1,1-tris(hydroxymethyl)ethane; biphen = $2,2'$-biphenoxide; salen = N,N'-bis(salicylidene)ethylenediamine.

1 BACKGROUND AND GENERAL CHEMISTRY

Manganese is a relatively abundant metal, constituting about 0.085% of the earth's crust. Among the transition metals, only iron is more abundant. Manganese minerals are widely distributed; oxides, hydrous oxides, silicates, and carbonates are the most common. Large quantities (more than 10^{12} tons) of 'manganese nodules' that have been discovered on the floor of the oceans may become a source of manganese. These nodules contain about 24% of manganese together with many other metals in lesser abundance. Most manganese today is obtained from ores, pyrolusite (MnO_2) and rhodochrosite ($MnCO_3$) are the most common. The metal is produced by reduction of its oxides with sodium, magnesium, and aluminum, or by electrolysis. Nearly all manganese produced commercially is used in the steel industry as ferromanganese.

Manganese is roughly similar to iron (*see* ***Iron: Inorganic & Coordination Chemistry***) in its physical and chemical properties but is harder and more brittle, though less refractory (mp 1247 °C). At room temperature, manganese metal is not particularly reactive to air, despite it being quite electropositive; however it burns in O_2 to form the manganese oxide Mn_3O_4, in N_2 to yield the nitride Mn_3N_2, and in Cl_2 to form $MnCl_2$, and reacts with Br_2, I_2, or Br_2 to form $MnBr_2$, MnI_2 and both MnF_2 and MnF_3, respectively. It dissolves readily in dilute nonoxidizing acids to form manganese (II) salts ($[Mn(H_2O)_6]^{2+}$) together with H_2 gas.

Manganese resembles Ti, V, and Cr in that the highest oxidation state, Mn^{VII}, corresponds to the loss of all the 3d and 4s electrons. In common with V and Cr, the higher oxidation states form Mn=O and $Mn{=}NBu^t$ multiple bond.**[1,2]** The oxo species are strong oxidants and some are very unstable and explosive. In the oxidation state, the most stable is II, with the +3, +4, +5, and +6 states becoming increasingly less stable. The oxidation states and common stereochemistries are summarized in Table 1 (*see* ***Manganese: Organometallic Chemistry***).

2 MANGANESE (II)

This is the dominant oxidation state and the most stable. In neutral or acidic aqueous solution, very pale pink $[Mn(H_2O)_6]^{2+}$ is present, which is resistant to oxidation, while in basic media, the hydroxide $Mn(OH)_2$ formed is easily oxidized by air (Figure 1).**[2,3]** Manganese (II) is a 'hard' acid and is quite distinctly a class (a) metal. This is manifest, for example, in the preference for O donors rather than N-donor

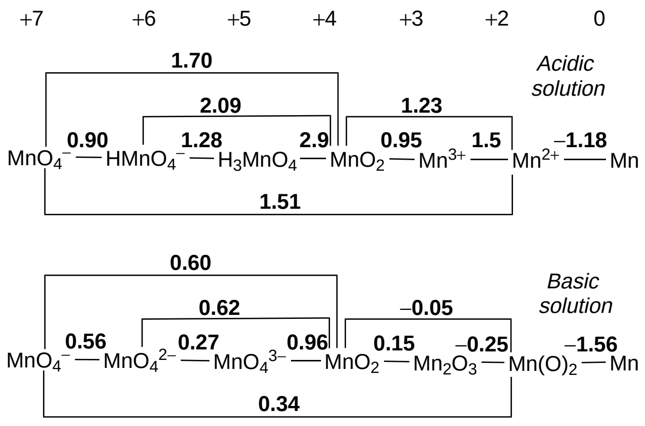

Figure 1 Standard reduction potentials (E^0/V)

Table 1 The oxidation state and geometry of some manganese compounds

Oxidation state	Coord. number	Geometry[a]	Examples
Mn^{II}, d^5	2	Linear	$Mn[C(SiMe_3)_3]_2$
	3	Trig. Planar	$[Mn\{N(SiMe_3)_2\}_3]^-$
	4	Tet	$[MnCl_4]^{2-}$
	4	Square	$[Mn(H_2O)_4]SO_4 \cdot H_2O$
	5	Tbp	$[Mn(trenMe_6)Br]Br$
	5	Dist. Tbp	[Mn(ntb)Cl]Cl
	6	Oct	$[Mn(H_2O)_6]^{2+}$
	6	Dist Oct	$[Mn(bipy)_3]^{2+}$
	7	Pbp	$MnX_2(N_5macrocycle)$
	7	Dist Pbp	$[Mn(dmu)_2(NO_3)_2]$
	8	Dod	$[Mn(NO_3)_2(N_4Schiff\ base)]$
Mn^{III}, d^4	3	Trig. Planar	$Mn[N(SiMe_3)_2]_3$
	4	Square	$[Mn(S_2C_6H_3Me)_2]^-$
	5	Sqpy	$[bipyH_2]MnCl_5$
	5	Tbp	$MnI_3(PMe)_2$
	6	Oct	$Mn(acac)_3$
	6	Dist. Oct	MnF_3, $Mn(terpy)F_3$
	7		$MnH_3(dmpe)_2$
Mn^{IV}, d^3	4	Tet	$Mn(1\text{-}norbornyl)_4$
	6	Oct	MnO_2, $MnCl_6{}^{2-}$
Mn^V, d^2	4	Tet	$MnO_4{}^{3-}$, $[Mn(NBu^t)_2(\mu\text{-}NBu^t)]_2{}^{2-}$
Mn^{VI}, d^1	4	Tet	$MnO_4{}^{2-}$, $[Mn(NBu^t)_2(\mu\text{-}NBu^t)]_2$
Mn^{VII}, d^0	3	Planar	$MnO_3{}^+$
	4	Tet	$MnO_4{}^-$, MnO_3F, $MnCl(NBu^t)_3$

[a] Oct, octahedral; Sqpy, square pyramidal; Tbp, trigonal bipyramidal; Tet, tetrahedral; Pbp, pentagonal bipyramidal; Dod, dodecahedral; Dist, distorted.

ligands. Few compounds are also known with P, As, and S-donor ligands.[4] Manganese(II) compounds are generally quite labile. The spin state of the majority of Mn^{II} complexes is high-spin d^5, because of their stable half-filled d electron shell. Few low-spin compounds have been isolated,[5] for example, $[Mn(CN)_6]^{4-}$. The coordination number and geometries are quite variable because of the lack of ligand-field stabilization energy for the high-spin configuration and appear to depend largely on ligand steric and electronic effects. Manganese (II) is larger (ionic or covalent radii, or metal–ligand distances) than other first-row (+2) transition metals and more 'plastic' (the metal–ligand bond distances are quite variable in response to ligand steric effects). Coordination geometry six appears to be the most common. Lower coordination numbers (three, four, and five) are fairly rare, while higher coordination numbers (seven and eight) are more common than for other first-row (+2) transition elements, a reflection of the larger size of Mn^{II}.[4]

In octahedral fields, the high-spin configuration gives spin-forbidden as well as parity-forbidden transitions, thus accounting for the extremely pale color of such compounds. In tetrahedral environments, the transitions are still spin-forbidden but no longer parity-forbidden; these transitions are therefore ~ 100 times stronger and the compounds have a noticeable pale yellow–green color.[2,4] In low-spin configuration, compounds are strongly colored since a spin-allowed absorption band is expected in the visible region.

Magnetic susceptibilities are easily recorded and the high-spin configuration gives an essentially spin-only, temperature independent magnetic moment of $5.92\mu_B$. The strong paramagnetic behavior unfortunately renders NMR useless, giving broad signals. Single-crystal X-ray diffraction still provides the only unequivocal form of characterization and is now used more and more routinely. The studies in solution remain a major difficulty with these labile systems, and assumptions about the nature of the compounds in solution are often necessary.

Conventional X- and Q-band EPR spectra are generally complex and often difficult to interpret.[6] The recent use of high-field and high-frequency EPR spectroscopy (HF-EPR) has led to simplified spectra with remarkable resolution and provides an accurate determination of the electronic parameters of the studied compounds.[7] Therefore, with this technique, structural information can be afforded both on solid state and in solution.

2.1 Nitrogen Ligands

The solution structure of the Mn^{2+} ion in CH_3CN and five other organic nitriles, as determined by EXAFS spectroscopy, is six-coordinate with Mn–N bond lengths of 2.21(1) Å,[8] while the octahedral $[Mn(CH_3CN)_6][MnI_4]$ crystals are obtained from CH_3CN solutions of MnI_2.[9]

Amine complexes are not particularly stable[2,4] but there are tertiary amine complexes, for example, $[MnI_3(NMe_3)]^-$ and $[Mn_2(\mu\text{-}I)_2I_2(NEt_3)_2]$.[10] The secondary amine can be three-coordinate[11,12] as in $[Mn\{N(SiMe_3)_2\}_3]^-$. Amides can be also three-coordinate with bridges as in $[Mn_2(\mu\text{-}NPr^i_2)_2(NPr^i_2)_2]$[13] and four-coordinate[14] in $[Mn(NPh_2)_4]^{2-}$.

With higher multidentate N-donor ligands, manganese (II) compounds become rather more robust.

Bridging ligands such as cyano[15,16] and azido[17] are used to form one-, two-, and three-dimensional polymeric systems and represent a fast growing research field because of their interesting magnetic properties. In addition to the polymeric binary dicyanamide and azide systems, for example, $[Mn\{N(CN)_2\}_2]$,[18] $[Mn\{N(CN)_2\}_3]^-$,[19] and $[Mn(N_3)_3]^-$,[20] ancillary organic ligands, such as pyrazine, 4,4′-bipy and 2,2′-bipy have been extensively used to create other lattice types.

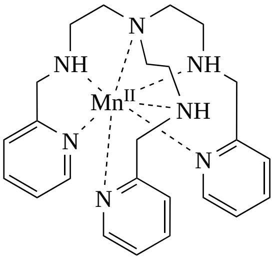

$[MnL^1]^{2+}$

(**1**)

Otherwise, many compounds, generally high-spin, with a variety of open-chain polydentate ligands (bidentate to septadentate) have been isolated with or without additional anion ligands, for example, halides or carboxylates. For example, the tripodal tetradentate ligand ntb with chloride, acetate, or nitride anions, forms the five to seven-coordinate mononuclear complexes, [Mn(ntb)X]Cl (X = Cl, O_2CMe) and $[Mn(ntb)(NO_2)_2]$, having trigonal bipyramidal or distorted octahedral geometries.[21] 8 and 7 N coordinations are found respectively in $[Mn(tpa)_2]^{2+}$,[22] and $[MnL^1]^{2+}$ (**1**);[23] this latter complex has been investigated as superoxide dismutase mimics. The tridentate facially capping bpea ligand affords six-coordinate $[Mn(bpea)_2]^{2+}$, $[Mn_2(\mu\text{-}O_2CMe)_3(bpea)_2]^+$, and $[Mn_2(\mu\text{-}Cl)_2Cl_2(bpea)_2]$ complexes.[24,25] The new structure of a rare low-spin, six-coordinate complex $[Mn(L^2)_2]$ (**2**) has been obtained.[5]

2.2 Phosphorus Ligands

Although complexes of stochiometry $[MnX_2(PR_3)]$ are polymeric with halide bridges, there are also monomers such as the octahedral $[MnX_2(dmpe)_2]$, the distorted tetrahedral $[MnI_2(PEt_3)_2]$, and a dinuclear $[Mn_2I_2(\mu\text{-}I)_2\{P(NMe_2)_3\}_2]$. The complexes $[MnX_2(PR_3)]_n$ have the remarkable ability to reversibly bind O_2, CO, NO, and ethylene in THF at low temperatures and irreversibly bind SO_2 under ambient conditions. The O_2 species are deep blue or purple and probably peroxo ones. Irreversible oxidation of R_3P to R_3PO also occurs slowly to give, for example, $[MnI_2(OPPh_2Me)(PPh_2Me)]$ and $[MnI_2(OPPh_2Me)_2]$, both of which have been structurally characterized.[26]

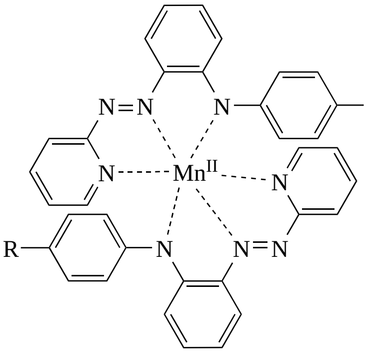

$[Mn(L^2)_2]$

(**2**)

Phosphine complexes with alkyl ligands are discussed in the chapter ***Manganese: Organometallic Chemistry***.

2.3 Oxygen Ligands

Manganese (II) oxide, a dark green powder, has the rock salt structure and is insoluble in water. There is little doubt that the species formed when almost any MnX_2 salt is dissolved in water is $[Mn(H_2O)_6]^{2+}$. Most of the salts crystallize from water as hydrate; those with weakly coordinating anions, such as $Mn(ClO_4)_2\cdot 6H_2O$ and $Mn(SO_4)\cdot 7H_2O$, contain $[Mn(H_2O)_6]^{2+}$.[2] Solutions of MnX_2 in alcohols give $[Mn(ROH)_6]^{2+}$ species or polymeric $MnX_2\cdot nROH$ systems.[4] Few alkoxides are known and are usually made by interaction of MnX_2 with LiOR in the alcohol. Use of bulky OR groups can give monomeric species or bridged dimers such as $[Mn(OC_6Cl_3H_2)(\mu\text{-}OC_6Cl_3H_2)(bipy)]_2$.[2] Several tetrameric alkoxides are known to have the Mn_4O_4 cubane cores (see Section 5). The typical tetranuclear clusters $[Mn(OMe)(MeOH)L]_4$ (L = dpm, dbm) have four μ_3-OMe groups and four Mn^{II} atoms at alternating vertices of the cube with the chelate diketonate L and MeOH bound to the Mn atoms, which are thus octahedrally coordinated.[27] The disc-like molecule $[Mn_{19}O_{12}(moe)_{14}(moeH)_{10}]moeH$ (moe = $OC_2H_5OCH_3$) recently synthesized is the largest alkoxide molecule[28] (others are heterometallic alkoxides containing Mn and Sn or Sb). In solvent ethers such as THF and dioxane, MnX_2 form stable species, which are probably polymeric chain structures such as $[MnCl_2(THF)_{1.6}]_n$.[29]

2.3.1 Oxides of Phosphorus and Arsenic

The air stable tetrahedral $[MnX_2(OEPh_3)_2]$ (E = P, As; X = Cl, Br, I, NCS, NO_3) and the octahedral $[MnX_2(OEPh_3)_4]$ (X = I, NCS) complexes have been known for many years.[4] Some compounds, such as $[MnX_2(OPPh_3)_2]$ (X = Br, I), exhibit triboluminescence properties.[30] Complexes of the type $[Mn(NCS)_2(OPR_3)_n]$ (R = Ph, Et, *n*-Bu, $n = 1-4$) and $[MnX_2(OPR_3)_2]$ (R = Et, *n*-Pr, *n*-Bu, X = Cl, Br, I) have been also synthesized.[31] The new 'Chinese lantern' complexes $[XMn(\mu\text{-dppO}_2)_4MnX]^{2+}$ (X = Cl, Br, I) have been shown to have an increasing affinity for SO_2 across the series $Cl < Br < I$.[32]

2.3.2 Oxyanions

Crystalline borates, carbonates, and silicates of manganese (II) have been characterized for a long time. Manganese (II) nitrites and iodates are only stable at low temperatures. Anhydrous $Mn(NO_3)_2$, $MnSO_4$, and $Mn(ClO_4)_2$ and their hydrates are stable under ambient conditions although manganese(II) nitrates are very hydroscopic.[4] Nitrate[33,34] and sulfate[35–38] groups acting as bidentate or monodentate ligands are also found in various mixed ligand species, and several of these complexes have been explored crystallographically, for example, $[Mn(dmu)_3(NO_3)_2]$,[33] $[Mn(\mu\text{-bipym})(NO_3)_2]_n$, and[34] $[Mn(phen)(H_2O)_3(SO_4)]$[35] and with sulfato bridges $[Mn(H_2O)_4(SO_4)]_2$,[36] $[Mn(phen)(H_2O)_2(SO_4)]_n$[37] and $[Mn_2(bpman)(SO_4)_2]$.[38] Perchlorato coordination exists, for example, $[Mn(bipy)_2(H_2O)(ClO_4)]^+$.[39]

Several new layered manganese(II) phosphates and phosphonates have been synthesized, generally under hydrothermal conditions, and their magnetic properties investigated. Some examples are $NaMnP_2O_7$,[40] $[Mn_3(P_2O_7)_2(H_2O)_2](NH_4)_2$,[41] $[Mn(HPO_4)(H_2O)_3]$, $[Mn_5(\mu\text{-OH})_2(HPO_4)_2(H_2O)_2]$,[42] and $[Mn_3(HPO_3)_4](C_3H_{12}N_2)$.[43] New selenite[44] and selenate[45] species have been crystallographically characterized, for example, $Mn_4(H_2O)_3(SeO_3)_4$, $Mn_3(H_2O)(SeO_3)_3$, and $Mn(H_2O)_4(SeO_4)\cdot H_2O$, and all these show $[MnO_6]$ octahedra as the previous ones.[4]

2.3.3 Monocarboxylates and Multidentate Oxygen Ligands

Mono and dicarboxylates are interesting ligands because of their biological relevance and because their wide variety of coordination modes make them key building blocks for the synthesis of one-, two- and three-dimensional polymeric networks in the presence of other organic nitrogen ligands. Compounds with manganese (II) can be also monomeric, dimeric, or clusters of higher nuclearity and can exist in mixed-valent species (see Section 5). Some examples with monocarboxylate ligands are $[Mn_2(\mu\text{-O}_2CR)_2(bipy)_4]^{2+}$, $[Mn_3(\mu\text{-O}_2CR)_6(bipy)_2]$, and $[Mn(\mu\text{-O}_2CR)_2(bipy)]_n$ with R = 2-ClPh, 3-ClPh, 4-ClPh.[46]

Dicarboxylates such as malonate,[47] adipate,[48] fumarate, and maleate[49] generally produce polymeric compounds with a variety of bridging modes. Mono and binuclear malonate, and adipate complexes with bipy, phen,[50,51] and a high nuclearity cluster with phthalate $[Mn_{10}(OH)_3(phth)_9(bipy)_6][NH_2Et_2]$, with a pinwheel-shaped $[Mn_{10}O_9]$ core, have also been reported.[52]

The oxalate $[Mn(C_2O_4)_3]^{4-}$, like the catecholate $[Mn(cat)_3]^{4-}$ compounds, can be readily oxidized to Mn^{III} state.[2] Otherwise, oxalate can form polymers[53] and the combination of phosphate and oxalate in forming hybrid framework materials has been also explored.[54] Several hydroxycarboxylates exist as monomers or polymers[4] and the first mononuclear manganese citrate complex, $(NH_4)_4[Mn(C_6H_5O_7)_2]$, has been recently isolated and crystallographically characterized.[55]

Multidentate oxygen ligands such as the symmetric tetraketone (H_2L) give an asymmetric complex, $[Mn_3L_3]$, which has been reported as the first asymmetric homometallic helicate formed from a symmetric ligand.[56] A wide variety of compounds have been studied with the β-diketonate monoanions such as acetylacetonate (acac) and hexafluoroacetylacetonate (hfacac) that have been used as ligands in many polymeric systems.[57]

2.4 Sulfur Ligands

Structural data are available for a range of bi-, ter- and quaternary sulfides of manganese (II), which contain four-coordinate $[MnS_4]$ tetrahedral and six-coordinate $[MnS_6]$ octahedral; no other polyhedra have been detected.[4] The thiolates may be tetrahedral complexes of the type $[Mn(SR)_4]^{2-}$,[58] $[Mn_2(SR)_4(\mu\text{-SR})_2]^{2-}$, and $[Mn_4(SPh)_{10}]^{2-}$.[2] Thiolates with bulky aryl groups can stabilize low-coordination numbers as in the three-coordinate $[(ArS)Mn^{II}(\mu\text{-SAr})]_2$, Ar = 2,4,6-$Bu_3{}^tC_6H_2S$. The crystal structure of a five-coordinated compound $[Mn_2(C_3S_5)_4]^{4-}$, $C_3S_5{}^{2-}$ = 4,5-dimercapto-1,3-dithiole-2-dithiole-2-thionate, has also been reported.[59] There are dithiocarbamates, as well as the sulfido anion, $[Mn(S_6)_2]^{2-}$, that are infinite polymers with bridging S atoms. Some Se and Te analogue compounds are also known.[2]

2.5 Halide Ligands

The halide complexes exhibit a wide structural diversity. Anhydrous MnF_2 and $MnCl_2$ have the tetragonally distorted (TiO_2) rutile and the hexagonal layer-type structures (defined first for $CdCl_2$) respectively, while both $MnBr_2$ and MnI_2 have the CdI_2 layer structure.[4]

The formation constants of Mn^{2+} with X^- in aqueous solution are very low, but when ethanol or acetic acid is used as a solvent, salts of complex anions of varying types may be isolated,[2,4] such as $MnX_3{}^-$ (octahedral with perovskite structure), MnX_4^{2-} (tetrahedral or polymeric octahedral with halide bridges),[30] $MnCl_6^{4-}$ (octahedral), $Mn_2Cl_6^{2-}$ (tetrahedral),[60] and $Mn_2Cl_7^{3-}$ (linear chain face-sharing $MnCl_6$ octahedra, also discrete $MnCl_4^{2-}$, tetrahedral). The precise nature of the product obtained depends on the cation used and also on the halide and the solvent. There is a variety of halide complexes containing other ligands present, such as $MnI_2(THF)_3$ trans-$[MnCl_4(H_2O)_2]^{2-}$, and amine and phosphine species.

2.6 Mixed-Donor Atom Ligands

For this area of chemistry, the use of X-ray diffraction is necessary to assign unambiguously which ligand donor atoms are bound. The preference of manganese(II) for O rather than N donors is seen in the amino acid complexes, in which the amino acids generally bind only through the O atoms of the carboxylic acid group. In polymeric species, for example, $[Mn(gly)_2Cl_2]_n$, the carboxylate acts as a bridge between adjacent manganese(II) atoms[61] and in monomeric ones, only one of the O atoms is coordinated.[4] Manganese(II) complexes of several amino acids catalytically disproportionate hydrogen peroxide in the presence of imidazole.[62]

In several multidentate ligands associating one carboxylate and pyridine/imidazole moieties, the coordination involves both the N and O atoms. Dimeric,[63] but also trimeric,[64] or polymeric[65,66] complexes can be formed in which metal centers are linked by one or two oxygen of the carboxylate moiety of the ligand.

Manganese(II) compounds with several types of Schiff-base ligands are known. A linear tetranuclear $[\{Mn_2(L)(O_2CMe)_2(CH_3OH)\}_2]$, where L is a N_2O_2 donor set, has an unprecedented arrangement of five N_2O_3 and six-coordinated O_6 manganese ions.[67] A (pyridylazo)oxime ligand forms the low-spin mononuclear $[Mn(L^3)_2]$ (**3**) complex with the very rare mononuclear oximato-O coordination.[68]

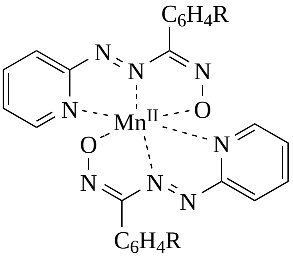

$[Mn(L^3)_2]$

(**3**)

There is sound evidence that mixed O, S donors can bind both donor atoms to manganese(II), while there are few examples of N, S donors.[69,70] A rare example of a complex with N, O, S donors is the octahedral low-spin thioether complexes $[Mn(L^4)]$ (**4**) that can be electrochemically oxidized to $[Mn(L^4)]^+$; one example of each has been structurally characterized.[71]

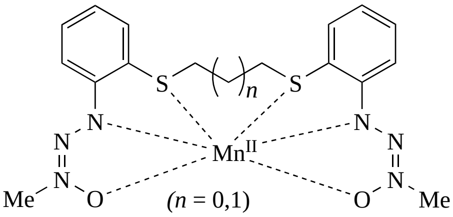

$[MnL^4]$

(**4**)

2.7 Macrocyclic Ligands

There has been a large number of studies involving coordination of Mn(II) by a wide variety of nitrogen and mixed-oxygen nitrogen macrocyclic ligands. Among them, as for the higher oxidation states of manganese, a significant number of investigations were made using pendant arm polyazamacrocycles. For the mixed-donor Schiff-base macrocycles, complexes are formed by a template reaction and the solution complexation properties (determination of the stability constant) of a large range of ligands have been reported. The main applications of those mixed-donor macrocycles and their resulting manganese (II) complexes concern the separation and analysis of Mn^{2+}, the epoxidation of olefin, and modeling of biological redox processes (superoxide dismutase and catalase activities) (*see* ***Manganese Proteins with Mono- & Dinuclear Sites***). All these studies are not detailed here and an extensive review of this topic can be found in Reference 1.

In manganese(II) compounds incorporating crown ether macrocycles, the metal is generally H-bonded to the crown via water molecules, although it has been possible to isolate some compounds such as $[Mn(12\text{-crown-}4)_2]^+$ and $[Mn(15\text{-crown-}5)(CF_3SO_3)_2]$, in which all the ether oxygen atoms of the crown bind directly to manganese(II).[72–74]

3 MANGANESE (III)

The aqua ion of manganese(III) can be obtained by electrolytic or peroxo sulfate oxidation of Mn^{2+} solutions, or by reduction of MnO_4^-.[2] The ion plays a central role in the complex redox reactions of the higher oxidation states of manganese in aqueous solutions, although it is often subject to disproportionation into manganese(IV) (MnO_2) and manganese(II). It is more stable in acidic solution. The chemistry of manganese(III) is dominated by dinuclear, trinuclear, and tetranuclear complexes with oxo, alkoxo, and carboxylates bridges. The propensity of these complexes to be in mixed-valence states such as manganese(II,III) or manganese(III,IV) require the confirmation of their structures by spectroscopic and X-ray structural methods (see Section 5).[1] Mononuclear compounds can be stabilized by Schiff-base ligands, nitrogen-base ligands, and macrocyclic ligands. The most commonly observed coordination numbers of manganese(III) are 5 and 6. Few compounds are known with S and P donors ligands.

The electronic configuration of manganese(III) is $3d^4$, and therefore, the high-spin configuration in an octahedral field is subject to Jahn–Teller distortion like for Cu^{II} and Cr^{II} compounds. Such distortions often serve to identify the Mn^{III} polyhedra in mixed oxidation state compounds (see Section 5). There are few examples of low-spin compounds, for example, $[Mn(CN)_6]^{3-}$, $[MnH_3(dmpe)_2]$, and there are other examples among macrocyclic compounds. The electronic spectra of these d^4 systems have spin-allowed d-d transitions, and accordingly the compounds have more color than those of manganese(II). All high-spin manganese(III) complexes have magnetic moments very close to $4.9\,\mu_B$. The recently developed techniques of HF-EPR have now proven to be effective at elucidating the electronic structure of integer-spin systems such as high-spin manganese(III) ($S = 2$) compounds, which are usually EPR silent at X- and Q-band frequencies. Mononuclear complexes with axial[75,76] (macrocyclic ligands) and rhombic symmetries[77,78] have been studied and this technique has been proposed as a useful tool for the structural investigation of these complexes and also for mixed-valence clusters incorporing manganese (III)[79] (see Section 5).

3.1 Nitrogen Ligands

The chemistry of manganese(III) with nitrogen ligands, other than macrocycles or mixed N, O donors is still quite limited. Amido species include the three-coordinate planar $[Mn\{N(SiMe_3)_2\}_3]$ and the a trigonal pyramidal four-coordinate complex $Mn(N_3N)$, where $N_3N = [(Bu^tMe_2Si)NCH_2CH_2]_3N$.[2] The interaction of alkaline-earth nitrides and manganese nitride at high temperatures leads to compounds such as Ca_3MnN_3 or Ca_6MnN_5 that have sheet structures involving the trigonal planar $[Mn(N)_3]^{6-}$ anion.[80] Octahedral mononuclear complexes with bi- or tridentate N-ligands and halides or pseudohalides have been structurally characterized such as $[Mn(L)(X)_3(H_2O)]$[81–83] (L = bipy, phen; X = Cl, F), $[Mn(phen)_2(Cl)_2]^+$[84] and $[Mn(L)(X)_3]$[77] (L = terpy, bpea; X = F, N_3). Tripodal N-ligands allowed the isolation and structural characterization of very rare mononuclear manganese(III) complexes: the side-on peroxo pyrazolate-pyrazolylborate, $[Mn(\eta^2\text{-}O_2)(3,5\text{-}Pr^i pzH)HB(3,5\text{-}Pr_2{}^i pz)_3]$,[85] the hydroxo, $[Mn(LH_3)(OH)]^-$ (**5**) and the oxo, $[Mn(LH_3)(O)]^{2-}$ (**6**).[86]

Various reactions with open-chain mono to hexadentate N-ligands have produced multinuclear μ-alkoxo, oxo, and/or carboxylato bridged manganese(III) compounds and some examples are given in Section 5.[1]

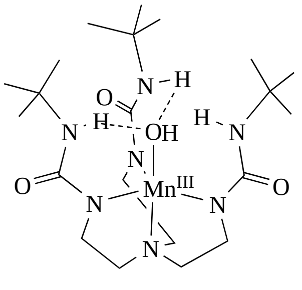

(**5**)

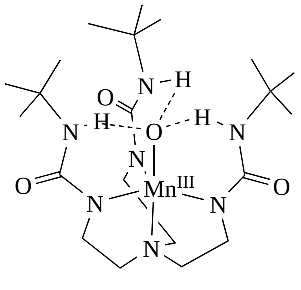

(**6**)

3.2 Oxygen Ligands

Manganese(III) complexes with a variety of oxygen ligands constitute the largest group next to those with mixed-donor ligands. The carboxylate chemistry of manganese(III) is mainly represented by monocarboxylates compounds, such as acetate, benzoate, and their derivatives, while with bidentate carboxylates such as oxalate, malonate, and salicylate, there is a limited number of compounds. This chemistry can be extremely complicated and often has mixed valencies (see Section 5). The chemistry of manganese(III) with monocarboxylates is extensive and results in the formation of clusters with nuclearities of 2, 3, 4, 6, 7, 8, 9, 10, and 18, and polymers with or without coligands such as Schiff bases.[1] Examples of compounds are the elusive manganese(III) formate formed by the reaction of $KMnO_4$ and formic acid that has finally been crystallographically characterized as the polymeric $Mn(\mu\text{-}O_2CH)_3\cdot 5CO_2\cdot 0.25HCO_2H\cdot 0.67H_2O$ with a carboxylate cage encapsulating the other molecules.[87] The 'manganic acetate' still often referred to as $Mn(OCMe)_3\cdot 2H_2O$ has the well-known trinuclear oxocentered core $[Mn_3(\mu_3\text{-}O)(\mu_2\text{-}O_2CMe)_6]^+$.[88] Otherwise, the oxidation of $Mn(OCMe)_2\cdot 4H_2O$ with $KMnO_4$ in acetic acid gives the triply bridged polymer $[\{Mn(\mu\text{-}OH)(\mu\text{-}OCMe)_2\}\cdot MeCO_2H\cdot H_2O]_n$.[89]

Mononuclear complexes are mostly obtained with hydroxycarboxylate (e.g. $(NH_4)_5[Mn(C_6H_5O_7)_2]$[55]) or β-diketones and related ligands.[1] Examples of carboxylate-free complexes of higher nuclearity with diketones are $[Mn_2(OMe)_2(dmb)_4]$ and $[NaMn_6(OMe)_{12}(dmb)_6]^+$, the latter displaying a 12-metallocrown-6 structure.[90] The nonalkoxo $[Mn_6O_4X_4(Me_2\ dbm)_6]$ (X = Cl, Br) has been also structurally characterized.[91] Detailed magnetic studies indicate that these three hexanuclear clusters have ground spin states of 12. Catecholate[92,93] and other diphenolates form manganese(III) complexes.

A rare example of a manganese(III) cluster with phosphinate and phosphonate ligands is $[Mn_6O_2(O_3PPh)_2(O_2PHPh)_2(O_2CPh)_8(py)_2]$ synthesized by the reaction of $[Mn_3O(O_2CPh)_6(py)_2(H_2O)]$ with an equimolar quantities of phenylphosphonic acid.[94]

3.3 Phosphorus, Sulfur, and Halide Ligands

Phosphorus compounds of manganese (III), except for alkyl and hydride species, are still limited to $[MnCl_2(diphos)_2]Cl_2$ and $[MnX_3(PMe_3)_2]$ (X = Cl, Br, I, NCS).**[95]** The tendency of manganese(III) to oxidize sulfur ligands results in the rarity of such compounds. Nevertheless, for simple thiols, a new species has been isolated and characterized such as the dimer with asymmetric Mn–S bridges $[Mn_2(pttd)_2]^{2-}$ ($pttd^{4-}$ = propane-1,2,3-trithiol), which is very similar to the previously reported $[Mn_2(edt)_4]^{2-}$ (edt^{2-} = ethane-1,2-dithiolate) species.**[96]**

The only binary compound of manganese(III) with the halides stable at room temperature is MnF_3. Hydrated salts of the anions $MnF_4{}^-$, $MnF_5{}^{2-}$, and $MnF_6{}^{3-}$ are known.**[97]** The salt $Tl_2MnF_5{\cdot}H_2O$ has chains of $(MnF_5)_n{}^{2n-}$ units, and some other fluoromanganese(III) complexes are $[MnF_3(urea)_3]{\cdot}3H_2O$, $K_3[MnF_2(C_2O_4)_2]{\cdot}3H_2O$ and those with N-donor ligands (see Section 3.1).**[2]** Although several methods of making $MnCl_3$ in solution are known, the best is the interaction of $[Mn_{12}O_{12}(O_2CMe)_{16}(H_2O)_4]$ in acetonitrile or other solvents, with Me_3SiCl. The resulting purple solutions are useful starting materials for synthesis of $(Et_4N)MnCl_5$, or amine complexes such as $[MnCl_3(bipy)]_n$, $[MnCl_3(H_2O)(bipy)]$, and the imido species $MnCl(NBu^t)_3$ (see Section 6). Other important compounds are the Schiff-base species, such as MnCl(salen), porphyrins, and related macrocycles.**[2]**

3.4 Mixed Donors and Macrocycles Ligands

Most of the polydentate ligands that stabilize manganese(III) are Schiff bases and their derivatives. Square planar and pyramidal mononuclear manganese(III) complexes with tetradentate Schiff bases have been extensively investigated for the epoxidation of olefins.**[98]** Other types of mixed N, O-donor ligands form interesting compounds without carboxylates, such as a metallocrown-10 such as the decanuclear complex**[99]** generated from the pentadentate N_2O_3, N-phenylsalicylhydrazidate ligand and a trinuclear oxocentered one,**[100]** $[Mn_3O(bamen)_3]^+$ generated from a hexadentate N_4O_2 ligand.

The preparation and characterization of novel manganese(III) complexes of various porphyrin and porphyrin-likes macrocycles have continued to attract strong attention especially because of their importance in catalytical oxidation processes through the formation of a Mn(V)O intermediate (see Section 6) and as model for metalloenzymes.**[2,101]** In this line, an artificial enzyme formed through a directed assembly of a molecular square that encapsulated a Mn porphyrin has been prepared and investigated as a catalyst.**[102]** In contrast to symmetrical binuclear bis(phenoxo) bridged macrocyclic Mn(III)Mn(III) complexes, unsymmetrical ones are rare. A new series of these kinds of carboxylate-free complexes has been described and their redox properties investigated.**[103]**

4 MANGANESE (IV)

In aqueous solution, the insoluble MnO_2 is formed readily. Much of the manganese (IV) chemistry involves O-donor ligands. The compounds are generally high-spin d^3 ($S = 3/2$) species and many are octahedral showing magnetic moments close to the spin-only value of 3.87 μ_B.

4.1 Nonoxygen Containing Compounds

This class of compounds is relatively limited. Few examples of nonporphyrinic manganese(IV) complexes coordinated solely by nitrogen have been structurally characterized: $\{Mn[HB(3,5\text{-}Me_2Pz)_3]\}^{2+}$, the water stable $[Mn(biguanide)_3]^{4+}$,**[104]** and $Mn(bpy)(N_3)_4$.**[105]**

Compounds with dithiolates have been characterized.**[4]** The only binary halide known is the unstable MnF_4 that decomposes to MnF_3 and F_2. Room temperature syntheses of MnF_4 and hexafluoromanganate(IV) of alkali cations A_2MnF_6 (A = Li–Cs) have been reported.**[106]**

4.2 Oxygen-containing Compounds

These are of great variety and importance. A new tetrachlorocatecholate derivative $[Mn(Cl_4cat)_3]^{2-}$ has been isolated.**[107]** A wide variety of compounds with various multidentate mixed-donor ligands have been synthesized, the majority of which contain N and O donor atoms (see Section 5). Several mononuclear manganese (IV) of the type $Mn(L)_2$ with tridentate O,N,O ligands**[108–110]** and $Mn(L)Cl_2$ with tetradentate Schiff bases have been synthesized.**[1,111]** Complexes with oxo bridges are very characteristic of manganese (IV) chemistry and some examples are given in Section 5. Many porphyrins have Mn=O bonds and have been much studied as oxygen transfer agents, for example, in the epoxidation of C=C bonds.**[101,112]**

5 MIXED OXIDATION STATE (II–IV)

For about twenty years, there have been an increasing number of publications on mixed-valence manganese multinuclear complexes that are relevant to such diverse fields as metalloenzymes and single-molecule magnets (*see* ***Manganese Proteins with Mono- & Dinuclear Sites*** and ***Manganese: The Oxygen-evolving Complex & Models***). Besides the small clusters, comprising two to four metal ions relevant to biological systems such as manganese catalases and the oxygen-evolving complex of Photosystem II, a large interest has been invested in larger clusters, not only for their biological relevance, but also for their interesting magnetic properties. Hundreds of new compounds have been made, those with carboxylate ligands being the most common. However, other ligands employed

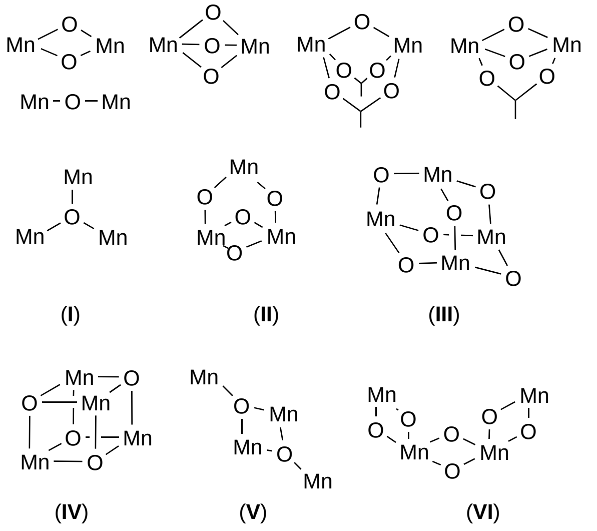

Figure 2 Various types of manganese oxo, alkoxo, or carboxylato core structures

have been pyridine, polypyridyl, pyrazolylborates, triazacyclononanes, and Schiff bases of various sorts. These have been obtained in oxidation states II–IV with both unitary and mixed valencies. The majority of mixed valency complexes form crystallographically valence-trapped species with distinct sites for each oxidation level. The electronic (EPR), magnetic, and electrochemical properties of these compounds have been largely investigated. Some of the core types are shown in Figure 2. The structures vary from quite simple to extremely complicated and the more complex species can have structures built up of different core units. This chemistry is too extensive to detail here and the reader should note the existence of several recent reviews, that cover this literature.[1,79,113–116] Only some recent examples are given here.

5.1 Dinuclear Complexes

The majority of Mn_2(III,IV) and Mn_2(IV,IV) compounds have bis-μ-oxo or bis-μ-oxo mono-μ-carboxylato cores, for example, $[Mn_2^{III,IV}(O)_2(terpy)_2(X)_2]^{n+}$ ($X = H_2O$ or CF_3CO_2),[117,118] $[Mn_2^{IV}(O)_2(terpy)_2(SO_4)_2]$,[119] and $[Mn_2^{IV}(O)_2(O_2CMe)(bpy)_2Cl_2(H_2O)]$,[120] while for Mn_2(III,III) complexes, mono-μ-oxo bis-μ-carboxylato and bis-μ-alkoxo mono-μ-carboxylato cores are the most common, for example, $[Mn_2^{III}O(O_2CMe)_2(HB(pz)_3)_2]$ and $[Mn_2^{III}$(5-Br-salpn)(OMe) $(O_2CMe)(MeOH)_2]^+$.[121] All complexes with a bis-μ-alkoxo mono-μ-carboxylato contain a Schiff-base coligand.[1] The only example of a bis-μ-oxo bis-μ-carboxylato Mn_2(III,IV) complex is $[Mn_2O_2(Ar^{tol}CO_2)_2(bipy)_2]^+$.[122]

Few examples of tris-μ-oxo, di-μ-oxo mono-$\mu_{1,2}$-peroxo, and mono-μ-oxo bridged dinuclear complexes are known. Examples are $[Mn_2^{IV}(O)_3(Me_3tacn)_2]^{2+}$,[123] $[Mn_2^{IV}(O)_2(O_2)(Me_3tacn)_2]^{2+}$, and $[Mn_2^{III}O(L)_2]^{2+}$ with a Schiff-base pentadentate monoanionic ligand (L = *N*,*N*-bis(2-pyridylmethyl)-*N*′-salicyliden-1,2-diaminoethane).[124] The one-electron oxidized complex $[Mn_2^{III,IV}O(L)_2]^{3+}$ has been electrochemically prepared and crystallized and is the only example of a structurally characterized mono-oxo bridged Mn_2(III,IV) complex.

Several Mn_2(II,II) complexes exist with different bridging patterns including solely carboxylates, or those associated with aqua, hydroxo, alkoxo, or phenoxo bridges.[114] Conversely, mixed-valent Mn_2(II,III) derivatives have received much less attention.[125]

Among these numerous dimeric complexes that have been prepared using a variety of ligands, very few exist in more than two stable oxidation states. Examples of complexes with three stable oxidation states are di-μ-oxo bridged dinuclears with tetradentate N-donor ligands such as $[Mn_2O_2(tpa)_2]^{2+,3+,4+}$ where the (III,III), (IIII,IV), and (IV,IV) states can be electrochemically generated. A rare example of complexes isolated and crystallographically characterized at the four oxidation states (II,II), (II,III), (III,III), and (III,IV) is the series $[Mn_2$(2-OHsalpn)$_2]^{2-,-,0,+}$.[126] Otherwise, core interconversions or changes in nuclearity have been observed for a series of compounds at different oxidation states. The complexes $[Mn_2^{III}(\mu\text{-}O)(\mu\text{-}O_2CMe)_2(bpea)_2]^{2+}$ and $[Mn_2^{IV}(\mu\text{-}O)_2(\mu\text{-}O_2CMe)(bpea)_2]^{3+}$ can be selectively and quantitatively electrogenerated from $[Mn_2^{II}(\mu\text{-}O_2CMe)_3(bpea)_2]^+$ in acetonitrile solution and it appears that each substitution of an acetate group by an oxo group is induced by a two-electron oxidation of the corresponding dimanganese complexes.[24] Electrochemical oxidation of $[Mn_2^{III,IV}O_2(bipy)_4]^{3+}$ in water leads to the stable, linear tetranuclear $[Mn_4^{IV}O_6(bipy)_6]^{4+}$.[127]

5.2 Trinuclear and Tetranuclear Complexes

The number of trinuclear manganese(II) complexes with bridging carboxylates is limited and most possess the linear $[Mn_3(\mu\text{-carboxylate})_6]$ core[1] as in $[Mn_3(O_2CMe)_6(bipy)_2]$ and there is only one example of a hydroxocentered complex[128] $[(py)_5(Mn_3(\mu_2\text{-}O_2CMe)_3(\mu_3\text{-}OH)(catechol)]$ (Type I). Several mixed-valence $Mn^{III}Mn^{II}Mn^{III}$ or $Mn^{II}Mn^{III}Mn^{II}$ carboxylato compounds with open structures have been also isolated with Schiff-base ligands.[113] All the trinuclear manganese(III) carboxylate complexes possess the basic manganic acetate oxocentered structure, for example, $[Mn_3O(O_2CBu^t)_6(py)_3]^+$ and $[Mn_3O(O_2CMe)_6(py)_3]^+$, the latter is also crystallized in the $Mn^{III}Mn^{II}Mn^{III}$ oxidation state.[113] All trinuclear Mn_3(IV) complexes have the Mn_3O_4 core, for example, $[Mn_3O_4(phen)_4(H_2O)_2]^{4+}$ (Type II).[113]

Examples of tetranuclear adamantane-shaped complexes (Type III) are $[Mn_4^{IV}O_6(bpea)_4]^{4+}$ and its corresponding one-electron reduced species, while cubane cores (Type IV) are found in $[Mn_2^{III}Mn_2^{IV}O_4(O_2PPh_2)_6]$ and its one-electron reduced species. A large family of tetranuclear clusters is now known with the distorted cubane core $[Mn_3{}^{III}Mn^{IV}O_3X]$ ($X = N_3{}^-$, ${}^-O_2CMe$, ${}^-O_2CPh$, $NO_3{}^-$, OMe...), supported by the chelating dbm$^-$ ligand.[1] The planar or butterfly cores (Type V) are generally found in tetranuclear carboxylato manganese(III) complexes with a $[Mn_4O_2(O_2CMe)_6]^{2+}$ or a $[Mn_4O_2(O_2CMe)_7]^+$ core respectively.[1] The linear tetranuclear complex (Type VI), $[Mn_4{}^{IV}O_6(bipy)_6]^{4+}$ was also reported.[129]

Rare examples of complexes simultaneously containing manganese (II) and manganese (IV) are the trinuclear $Mn^{II}Mn^{IV}Mn^{II}$ $[Mn_3(pko)_4(CH_3O)_2(SCN)_2]$[130] and the tetranuclear $[Mn_3{}^{II}Mn^{IV}(\mu_4\text{-}O)(pko)_4(3,4D)_4]$ complexes.[131]

5.3 Higher Nuclearity Clusters

A novel hexanuclear high-valent species, $[Mn_2{}^{III}Mn_4{}^{IV}O_8(Ar^{tol}CO_2)_2(Me_2bipy)_6)]^{4+}$ where two cuboidal $[Mn_3O_4]$ units are fused together through a pair of 'T-shaped' μ_3-O groups has been isolated.[122] Novel octanuclear[132] and nonanuclear[133] clusters have been also reported, such as $[Mn_2{}^{III}Mn_6{}^{IV}O_{10}(O_2CMe)_6(H_2O)_2(bpy)_4]^{4+}$ ($S = O$) with a 'serpentine' core and $[Mn_9O_7(O_2CMe)_{11}(thme)(py)_3(H_2O)_2]$ ($S = 17/2$) with a $[Mn_4{}^{III}Mn_2{}^{II}O_6]^{4+}$ unit and a smaller $[Mn_3{}^{IV}O]^{10+}$ unit embedded in it. The cluster with one of the largest ground spin states is $[Mn_6{}^{II}Mn_4{}^{III}O_4(biphen)_4X_{12}]$ ($S = 12$) with an adamantine-like inner $[Mn_2{}^{II}Mn_4{}^{III}]$ core connected through the four oxygen atoms to four Mn^{II} atoms (see also Section 3.2).[79] Another class of clusters with a large ground spin state ($S = 10$) that has attracted attention for their unique properties at very low temperatures is the dodecanuclear $[Mn_{12}O_{12}(OCR)_{16}(H_2O)_n]$ cluster ($R = Me$, Et, Ph; $n = 3$, 4). The structure consists of a central $[Mn_4{}^{IV}O_4]^{8+}$ cuboidal unit surrounded by a ring of eight Mn^{III} ions. These molecules possess the useful property of retaining their magnetization in the absence of an applied magnetic field, a classical property of a magnet.[1,79] The monoanions $[Mn_{12}O_{12}(OCR)_{16}(H_2O)_4]^-$ ($R = Et$, Ph) formed by reduction of the neutral molecules have a spin state of 19/2 with the localized ground-state [4Mn(IV)7Mn(III)Mn(II)] for $R = Et$ and with eight delocalized Mn(2.875) centers for $R = Ph$. Higher nuclearity clusters such as $[Mn_6{}^{IV}Mn_{10}{}^{III}O_{16}(OMe)_6(O_2CMe)_{16}(MeOH)_3(H_2O)_3]$, $[Mn_9{}^{IV}Mn_{12}{}^{III}O_{24}(OMe)_8(O_2CCH_2Bu^t)_{16}(H_2O)_{10}]$ ($S = 13/2$) and the largest known $[Mn_3{}^{II}Mn_{26}{}^{III}Mn^{IV}O_{24}(OH)_8(O_2CCH_2Bu^t)_{32}(H_2O)_2(CH_3NO_2)_4]$ ($S = 7$) have also been reported.[1]

6 MANGANESE (V) (VI) AND (VII)

Most of the manganese compounds that have high oxidation states involve oxo compounds; however some other compounds in these oxidation states have been synthesized and characterized, especially those based on nitrodo and imido ligands.

6.1 Oxochemistry

Reduction of the tetraoxomanganates $MnO_4{}^-$, $MnO_4{}^{2-}$, and $MnO_4{}^{3-}$ by pulse radiolytically–generated free organic radicals leads to the unstable $[Mn^VO_3(OH)]^{2-}$ and $[Mn^{VI}O_3(OH)^\bullet]^-$ species. They were characterized by their UV-visible spectra and their corresponding acid dissociation constants have been determined.[134]

The permanganate anion is well-known as a convenient oxidizing agent in inorganic and organic chemistry.[2] Its utilization for synthesis has been investigated following several procedures. The oxidizing properties of $MnO_4{}^-$ have also been applied to the destruction of pollutants in groundwater or as a chemiluminescent analytical agent.[1]

Crystals of $Na_4Mn_{0.5}P_{0.5}O_5$, a mixed-metal Mn(VII)/P(V) oxide, were synthesized via a sodium hydroxide flux.[135]

Manganyl [Mn(V)O] complexes have drawn considerable attention over the past 15 years because they are generally accepted to be the key reactive intermediates in many catalytic oxidation processes, especially those related with biomimicry.[101,112] However, only a few Mn^VO species have been isolated and their structures resolved. Two well-characterized species involving the use of a tetraanionic ligand to stabilize the high-valent manganese center have been reported.[136,137] The very short bond distance suggests a $Mn{\equiv}O$ bond. One of these complexes can be activated for O-atom transfer by the addition of a secondary cation like Na^+. A major advance in this chemistry was made with the isolation and characterization of a porphyrin Mn^VO species.[112,138] Besides studies in the porphyrin series, some oxomanganese (V) corrole complexes have been generated, characterized spectroscopically, and investigated in catalytic oxidations.[139–141] Direct proof of the existence of discrete $[Mn^VO(salen)]^+$ complexes has been obtained by means of electrospray tandem mass spectrometry.[142]

6.2 Nonoxo Chemistry

Nitrido macrocyclic complexes containing a terminal $Mn^V{\equiv}N$ bond have proven to be versatile and effective aminating agents with a different class of olefins;[143] an asymmetric version of this methodology was also reported.[144] The complexes $[L_nMn^VN]$ are usually made by photolysis of azide precursors $[L_nMn^{III}(N_3)]$ (Arshankkow–Poznjak reaction). The ligands L_n are the regular macrocycles: porphyrins, corroles, cyclams, salens. Alternative methods for their synthesis have been developed using an oxidizing agent (e.g. NaOCl), and some of these nitrido manganese complexes have been structurally characterized.[145] An extremely short $Mn{\equiv}N$ bond distance (1.50–1.55 Å) was observed.[146] Since the manganese (V) species have a d^2 electron configuration, they are nonmagnetic with a low-spin ground state. A terminal imido complex of a Mn(V), the postulated intermediate in amination and aziridination reactions with nitrido complexes, has been synthesized and fully characterized.[147]

Ligand substitution by CN^- of nitrido complexes of Mn(V) leads to the simple nitrodo cyanometalate of Mn(V): $[Mn^V(N)(CN)_5]^{3-}$, which has been structurally characterized, together with an assignment of its electronic transitions and orbital energies.[148]

The interaction of $MnCl_3$ with $NHBu^t(SiMe_3)$ gave the thermally and air stable Mn(VII) species $[Mn(NBu^t)_3Cl]$.[149] *Tert*-butyl imido chemistry has been further developed and over 40 imido compounds are now known.[150] The Cl atom of $[Mn(NBu^t)_3Cl]$ can be substituted by, for example, Br, O_2CR, SC_6F_5, and $NHBu^t$; all these compounds are green. Reduction of $[Mn(NBu^t)_3Cl]$ can give the dimers $[Mn^V(NBu^t)_2(\mu\text{-}NBu^t)]_2{}^{2-}$ and $[Mn^{VI}(NBu^t)_2(\mu\text{-}NBu^t)]_2$. Another unusual anion is $[Mn^{VII}(\equiv N)(NBu^t)_3]^{2-}$.

7 REFERENCES

1. D. C. Weatherburn, S. Mandal, S. Mukhopadhyay, S. Bhaduri, and L. F. Lindoy, in ‘Comprehensive Coordination Chemistry II’, eds. J. A. McCleverty and T. J. Meyer, Elsevier Pergamon, Oxford, 2004, Vol. 5, Chap. 1, p. 1.
2. F. A. Cotton, G. Wilkinson, C. A. Murillo, and M. Bochmann, ‘Advanced Inorganic Chemistry’, 6th edn., Wiley, New York, 1999, p. 757.
3. http://www.webelements.com/webelements/compounds/text/Mn.
4. B. Chiswell, E. D. McKenzie, and L. F. Lindoy, in ‘Comprehensive Coordination Chemistry’, ed. G. Wilkinson, Pergamon, Oxford, 1987, Vol. 4, Chap. 41, p. 2.
5. A. Saha, P. Majumdar, and S. Goswami, *J. Chem. Soc., Dalton Trans.*, 2000, 1703, references therein.
6. S. Blanchard, G. Blondin, E. Rivière, N. Nierlich, and J.-J. Girerd, *Inorg. Chem.*, 2003, **42**, 4568.
7. R. M. Wood, D. M. Stucker, L. M. Jones, W. B. Lynch, S. K. Misra, and J. H. Freed, *Inorg. Chem.*, 1999, **38**, 5384.
8. Y. Inada, T. Sugata, K. Ozutsumi, and S. Funahashi, *Inorg. Chem.*, 1998, **37**, 1886.
9. F. Weller, H.-J. Mai, and K. Denicke, *Z. Naturforsch.*, 1996, **51B**, 298.
10. H. P. Lane, S. M. Godfrey, R. G. Pritchard, and C. A. McAuliffe, *J. Chem. Soc., Dalton Trans.*, 1995, 701.
11. M. A. Putzer, B. Neumüeller, K. Dehnicke, and J. Magull, *Chem. Ber.*, 1996, **129**, 715.
12. A. Panda, M. Stender, R. J. Wright, M. M. Olmstead, P. Klavins, and P. P. Power, *Inorg. Chem.*, 2002, **41**, 3909.
13. A. Belforte, F. Calderazzo, U. Englert, J. Straehle, and K. Wurst, *J. Chem. Soc., Dalton Trans.*, 1991, 2419.
14. M. A. Putzer, A. Pilz, U. Müller, B. Neumüller, and K. Dehnicke, *Z. Anorg. Allg. Chem.*, 1998, **624**, 1336.
15. A. Escuer, N. Sanz, R. Vincente, and F. A. Mautner, *Inorg. Chem.*, 2003, **42**, 541.
16. J. L. Manson, Q. Z. Huang, J. W. Lynn, H.-J. Koo, M.-H. Whangbo, R. Bateman, T. Otsuka, N. Wada, D. N. Argyriou, and J. S. Miller, *J. Am. Chem. Soc.*, 2001, **123**, 162.
17. J. Ribas, A. Escuer, M. Montfort, R. Vicente, R. Cortés, L. Lezama, and T. Rojo, *Coord. Chem. Rev.*, 1999, **193**, 1027.
18. J. L. Manson, C. R. Kmety, A. J. Epstein, and J. S. Miller, *Inorg. Chem.*, 1999, **38**, 2552.
19. P. M. van der Werff, S. R. Batten, P. Jensen, B. Moubaraki, and K. S. Murray, *Inorg. Chem.*, 2001, **40**, 1718.
20. F. A. Mautner, S. Hanna, R. Cortés, L. Lezama, M. G. Barandika, and T. Rojo, *Inorg. Chem.*, 1999, **38**, 4647.
21. S. Lah and H. Chun, *Inorg. Chem.*, 1997, **36**, 1782.
22. Y. Gultneh, A. Farooq, K. D. Karlin, S. Liu, and J. Zubieta, *Inorg. Chim. Acta*, 1993, **211**, 171.
23. A. Deroche, I. Morgenstern-Baradau, M. Cesario, J. Guilhem, B. Keita, L. Nadjo, and C. Houée-Levin, *J. Am. Chem. Soc.*, 1996, **118**, 4567.
24. I. Romero, L. Dubois, M.-N. Collomb, A. Deronzier, J.-M. Latour, and J. Pécaut, *Inorg. Chem.*, 2002, **41**, 1795.
25. I. Romero, M.-N. Collomb, A. Deronzier, A. Llobet, E. Perret, J. Pécaut, L. Le Pape, and J. Latour, *Eur. J. Inorg. Chem.*, 2001, **221**, 69.
26. S. M. Godfrey, C. A. McAuliffe, P. T. Ndifon, and R. G. Pritchard, *J. Chem. Soc., Dalton Trans.*, 1993, 3373.
27. L. E. Pence, A. Caneschi, and S. J. Lippard, *Inorg. Chem.*, 1996, **35**, 3069.
28. I. A. M. Pohl, L. G. Westin, and M. Kritikos, *Chem. Eur. J.*, 2001, **7**, 3438.
29. P. Sobota, J. Utko, and L. B. Jerzykiewiez, *Inorg. Chem.*, 1998, **37**, 3428.
30. F. A. Cotton, L. M. Daniels, and P. Huang, *Inorg. Chem.*, 2001, **40**, 3576.
31. S. M. Godfrey, D. G. Kelly, and C. A. McAuliffe, *J. Chem. Soc., Dalton Trans.*, 1992, 1305.
32. W. I. Cross, S. M. Godfrey, C. A. McAuliffe, and R. G. Pritchard, *Chem. Commun.*, 2001, 1764.
33. R. Keuleers, G. S. Papaefstathiuo, C. P. Raptopoulou, V. Tangoulis, H. O. Desseyn, and S. P. Perlepes, *Inorg. Chem. Commun.*, 1999, **2**, 479, references therein.
34. D. M. Dong, H. H. Wei, L. L. Gan, G. H. Lee, and Y. Wang, *Polyhedron*, 1996, **15**, 2335.
35. F. Hueso-Urena, S. B. Jimenez-Pulido, J. N. Low, and M. N. Moreno-Carretero, *J. Coord. Chem.*, 2001, **53**, 317.
36. P. Held and L. Bohaty, *Acta Cryst.*, 2002, **E58**, i121.
37. Y.-Q. Zheng and J.-L. Lin, *Z. Anorg. Allg. Chem.*, 2003, **629**, 185.
38. C. He, V. Gomez, B. Spingler, and S. J. Lippard, *Inorg. Chem.*, 2000, **39**, 4188.

39. Y. Rodriguez-Martin, J. Gonzales-Platas, and C. Ruiz-Perez, *Acta Cryst.*, 1999, **C55**, 186.
40. Q. Huang and S.-J. Hwu, *Inorg. Chem.*, 1998, **37**, 5869.
41. A. M. Chippindale, O. M. Gaslain, A. D. Bond, and A. V. Powell, *J. Mater. Chem.*, 2003, **13**, 1950.
42. C. V. K. Sharma, C. C. Chusuei, R. Clérac, T. Müller, K. R. Dunbar, and A. Clearfield, *Inorg. Chem.*, 2003, **42**, 8300.
43. S. Fernandez, J. L. Pizarro, J. L. Mesa, L. Lezama, M. I. Arriortua, R. Olazcuaga, and T. Rojo, *Inorg. Chem.*, 2001, **40**, 3476, references therein.
44. A. Larranaga, J. L. Mesa, J. L. Pizarro, R. Olazcuaga, M. I. Arriortua, and T. Rojo, *J. Chem. Soc., Dalton Trans.*, 2002, 3447.
45. H. Euler, A. Meents, B. Barbier, and A. Kirfel, *Z. Krist. – New Cryst. Struct.*, 2003, **218**, 9.
46. B. Albela, M. Corbella, J. Ribas, I. Castro, J. Sletten, and H. Stoeckli-Evans, *Inorg. Chem.*, 1998, **37**, 788.
47. Y. Rodriguez-Martin, M. Hernandez-Molina, J. Sanchiz, C. Ruiz-Pérez, F. Lloret, and M. Julve, *Dalton Trans.*, 2003, 2359.
48. P. S. Mukherjee, S. Konar, E. Zangrando, T. Mallah, J. Ribas, and N. R. Chaudhuri, *Inorg. Chem.*, 2003, **42**, 2695.
49. Z. Shi, L. Zhang, S. Gao, G. Yang, J. Hua, L. Gao, and S. Feng, *Inorg. Chem.*, 2000, **39**, 1990.
50. S. Sain, T. K. Maji, G. Mostafa, T.-H. Lu, N. R. Chaudhuri, and R. Nirmalendu, *Inorg. Chim. Acta*, 2003, **351**, 12.
51. Y. Q. Zheng and M.-F. Zheng, *Z. Naturforsch.*, 2003, **B58**, 266.
52. C. Canada-Vilalta, M. Pink, and G. Christou, *Dalton Trans.*, 2003, 1121.
53. Z. A. D. Lethbridge, A. F. Congreve, E. Esslemont, A. M. Z. Slawin, and P. Lightfoot, *J. Solid State Chem.*, 2003, **152**, 212.
54. Z. A. D. Lethbridge, M. J. Smith, S. K. Tiwary, A. Harrison, and P. Lightfoot, *Inorg. Chem.*, 2004, **43**, 11.
55. M. Matzapetakis, N. Karligiano, A. Bino, M. Dakanali, C. P. Raptopoulou, V. Tangoulis, A. Terzis, J. Giapintzakis, and A. Salifoglou, *Inorg. Chem.*, 2000, **39**, 4044.
56. G. Aromi, P. Carrero Berzal, P. Gamez, O. Rouleau, H. Kooijman, A. L. Spek, W. L. Driessen, and J. Reedijk, *Angew. Chem., Int. Ed. Engl.*, 2001, **40**, 3444.
57. L. M. Field, P. M. Lahti, F. Palacio, and A. Paduan-Filho, *J. Am. Chem. Soc.*, 2003, **125**, 10110.
58. H. O. Stephan and G. Henkel, *Polyhedron*, 1996, **15**, 501.
59. H. Tamura, S. Tanaka, G. Matsubayashi, and W. Mori, *Inorg. Chim. Acta*, 1995, **232**, 51.
60. J.-S. Sun, H. Zhao, X. Ouyang, R. Clerac, J. A. Smith, J. M. Clemente-Juan, C. Gomez-Garcia, E. Coronado, and K. R. Dunbar, *Inorg. Chem.*, 1999, **38**, 5841.
61. R. Mrozek, Z. Rzaczynska, M. Sikorska-Jwan, and T. Glowiak, *J. Chem. Crystallogr.*, 1999, **29**, 803.
62. M. Devereux, M. Jackman, M. McCann, and M. Casey, *Polyhedron*, 1998, **17**, 153.
63. L. P. Nielsen, M. Mortensen, S. Kjaergaard Knudsen, K. L. Lund, M.-N. Collomb, C. Baffert, A. Deronzier, J.-M. Latour, N. Thorup, and C. J. McKenzie, *Dalton Trans.*, 2003, 1765.
64. C. Ma, C. Chen, Q. Liu, D. Liab, and L. Li, *Eur. J. Inorg. Chem.*, 2003, **6**, 1227.
65. H. Iikura and T. Nagata, *Inorg. Chem.*, 1998, **37**, 4702.
66. S. Durot, C. Policar, G. Pelosi, F. Bisceglie, T. Mallah, and J.-P. Mahy, *Inorg. Chem.*, 2003, **42**, 8072.
67. S. Theil, R. Yerande, R. Chikate, F. Dahan, A. Bousseksou, S. Padhye, and J.-P. Tuchagues, *Inorg. Chem.*, 1997, **36**, 6279.
68. S. Ganguly, S. Karmakar, C. Kumar, and A. Chakravorty, *Inorg. Chem.*, 1999, **38**, 5984.
69. C. Schmidt, J. Dalkner, D. Schollmeyer, and H. Singer, *Inorg. Chim. Acta*, 1997, **257**, 269.
70. K. Yamoto, I. Miyahara, A. Ichimura, K. Hirotsu, Y. Kojima, H. Sakurai, D. Shiomi, K. Sato, and T. Takui, *Chem. Lett.*, 1999, **4**, 295.
71. P. Chakraborty, S. K. Chandra, and A. Chakravorty, *Inorg. Chem.*, 1993, **32**, 5349.
72. Y. Deng, J. H. Burns, and B. A. Moyer, *Inorg. Chem.*, 1995, **34**, 209.
73. H. O. N. Reid, I. A. Kahwa, A. J. P. White, and D. J. Williams, *Inorg. Chem.*, 1998, **37**, 3868.
74. J. L. Atwood and P. C. Junk, *Polyhedron*, 2000, **19**, 85.
75. S. Mossin, H. Weihe, and A.-L. Barra, *J. Am. Chem. Soc.*, 2002, **124**, 8726.
76. J. Krzystek, J. Telser, B. M. Hoffman, J.-L. Brunel, and S. Licoccia, *J. Am. Chem. Soc.*, 2001, **123**, 7890.
77. C. Mantel, A. K. Hassan, J. Pécaut, A. Deronzier, M.-N. Collomb, and C. Duboc-Toia, *J. Am. Chem. Soc.*, 2003, **125**, 12337.
78. A.-L. Barra, D. Gatteschi, R. Sessoli, G. L. Abbati, A. Cornia, A. C. Fabretti, and M. G. Uytterhoeven, *Angew. Chem., Int. Ed. Engl.*, 1997, **36**, 2329.
79. A. Caneschi, D. Gatteschi, and R. Sessoli, *J. Chem. Soc., Dalton Trans.*, 1997, 3963.
80. D. H. Gregory, M. G. Barker, P. P. Edwards, and D. J. Siddons, *Inorg. Chem.*, 1995, **34**, 5195.
81. C. Philouze, M. Henry, N. Auger, D. Vignier, M. Lance, M. Nierlich, and J.-J. Girerd, *Inorg. Chem.*, 1999, **38**, 4.
82. G. Swarnabala, K. R. Reddy, J. Tirunagar, and M. V. Rajasekharan, *Transition Met. Chem.*, 1994, **19**, 506.
83. P. Nunez, C. Elias, J. Fuentes, X. Solans, A. Tressaud, M. C. Marco de Lucas, and F. Rodriguez, *J. Chem. Soc., Dalton Trans.*, 1997, 4335.
84. K. R. Reddy and M. V. Rajasekharan, *Polyhedron*, 1994, **13**, 765.
85. V. N. Kitojima, H. Komatsuzaki, S. Hikichi, M. Osawa, and Y. Moro-oka, *J. Am. Chem. Soc.*, 1994, **116**, 11596.
86. R. Gupta, C. E. MacBeth, V. G. Young Jr, and A. S. Borovik, *J. Am. Chem. Soc.*, 2003, **125**, 13234, references therein.

87. A. Cornia, A. Caneschi, P. Dapporto, A. C. Fabretti, D. Gatteschi, W. Malavasi, C. Sangregorio, and R. Sessoli, *Angew. Chem., Int. Ed. Engl.*, 1999, **38**, 1780.
88. J. Ribas, B. Albela, H. Stoeckli-Evans, and G. Christou, *Inorg. Chem.*, 1997, **36**, 2352.
89. A. J. Tasiopoulos, N. C. Harden, K. A. Abboud, and G. Christou, *Polyhedron*, 2003, **22**, 133.
90. G. L. Abbati, A. Cornia, A. C. Fabretti, A. Caneschi, and D. Gatteschi, *Inorg. Chem.*, 1998, **37**, 1430.
91. G. Aromi, M. J. Knapp, J.-P. Claude, J. C. Huffman, D. N. Hendrickson, and G. Christou, *J. Am. Chem. Soc.*, 1999, **121**, 5489.
92. S. T. Sheriff, P. Carr, and B. Pigott, *Inorg. Chim. Acta*, 2003, **348**, 115.
93. A. S. Attia and C. G. Pierpont, *Inorg. Chem.*, 1998, **37**, 3051. and.
94. E. K. Brechin, R. A. Coxall, A. Parkin, S. Parsons, P. A. Tasker, and R. E. P. Winpenny, *Angew. Chem., Int. Ed. Engl.*, 2001, **40**, 2700.
95. S. M. Godfrey, C. A. McAuliffe, A. G. Mackie, and R. G. Pritchard, *J. Chem. Soc., Chem. Commun.*, 1992, 483.
96. J. L. Seela, M. J. Knapp, K. S. Kolack, H.-R. Chang, J. C. Huffman, D. N. Hendrickson, and G. Christou, *Inorg. Chem.*, 1998, **37**, 516.
97. P. Nunez, J. C. Ruiz-Morales, A. D. Lozano-Gorrin, P. Gili, V. D. Rodriguez, J. Gonzales-Platas, T. Barriuso, and F. Rodriguez, *Dalton Trans.*, 2004, 273.
98. H. Jacobsen and L. Cavallo, *Chem. Eur. J.*, 2001, **7**, 800.
99. S.-X. Liu, S. Lin, B.-Z. Lin, C.-C. Lin, and J.-Q. Huang, *Angew. Chem., Int. Ed. Engl.*, 2001, **40**, 6.
100. S. G. Sreerama and S. Pal, *Inorg. Chem.*, 2002, **41**, 4843.
101. J. T. Groves, K. Shalyaev, and J. Lee, in 'The Porphyrin Handbook', eds. K. M. Kadish, K. M. Smith, and R. Guilard, Academic Press, San Diego, CA, 2000, Vol. 4, p. 17.
102. M. L. Merlau, M. del Pilar Mejia, S. T. Nguyen, and J. Hupp, *Angew. Chem., Int. Ed. Engl.*, 2001, **40**, 4239.
103. M. Marappan, V. Narayanan, and M. Kandaswamy, *J. Chem. Soc., Dalton Trans.*, 1998, 3405.
104. G. Das, P. K. Bharadwaj, D. Ghosh, B. Chaudhuri, and R. Banerjee, *Chem. Commun.*, 2001, **4**, 323.
105. B. C. Dave and R. S. Czerneswicz, *J. Coord. Chem.*, 1994, **33**, 257.
106. Z. Mazej, *J. Fluorine Chem.*, 2002, **114**, 75.
107. R. Ruiz, A. Caneschi, D. Gatteschi, C. Sangregorio, L. Sorace, and M. Vazquez, *Inorg. Chem. Commun.*, 2000, **3**, 76.
108. M. Mikuriya, D. Jie, Y. Kakuta, and T. Tokii, *Bull. Chem. Soc. Jpn.*, 1993, **66**, 1132.
109. T. Weymüller, T. K. Paine, E. Bothe, E. Bill, and P. Chaudhuri, *Inorg. Chim. Acta*, 2002, **337**, 344.
110. T. M. Rajendiran, J. W. Kampf, and V. L. Pecoraro, *Inorg. Chim. Acta*, 2002, **339**, 497.
111. H. Asada, M. Fijiwara, and T. Matsushita, *Polyhedron*, 2000, **19**, 2039.
112. R. Weiss, A. Gold, A. X. Trautwein, and J. Terner, in 'The Porphyrin Handbook', eds. K. M. Kadish, K. M. Smith, and R. Guilard, Academic Press, San Diego, CA, 2000, Vol. 4, p. 65.
113. D. P. Kessissoglou, *Coord. Chem. Rev.*, 1999, **185**, 837.
114. A. J. Wu, J. E. Penner-Hahn, and V. L. Pecoraro, *Chem. Rev.*, 2004, **104**, 903.
115. M. Yagi and M. Kaneko, *Chem. Rev.*, 2001, **101**, 21.
116. W. Ruettinger and G. C. Dismukes, *Chem. Rev.*, 1997, **97**, 1.
117. J. Limburg, J. S. Vrettos, L. M. Liable-Sands, A. L. Rheingold, R. H. Crabtree, and G. W. Brudvig, *Science*, 1999, **283**, 1524.
118. C. Baffert, M.-N. Collomb, A. Deronzier, J. Limburg, G. W. Brudvig, R. H. Crabtree, and J. Pécaut, *Inorg. Chem.*, 2002, **41**, 1404.
119. J. Limburg, J. S. Vrettos, H. Chen, J. C. de Paula, R. H. Crabtree, and G. W. Brudvig, *J. Am. Chem. Soc.*, 2001, **123**, 423.
120. S. Bhaduri, A. J. Tasiopoulos, M. A. Bolcar, K. A. Abboud, W. E. Streib, and G. Christou, *Inorg. Chem.*, 2003, **42**, 1483.
121. C. Palopoli, B. Chansou, J. P. Tuchagues, and S. Signorella, *Inorg. Chem.*, 2000, **39**, 1458.
122. S. Mukhopadhyay and W. H. Armstrong, *J. Am. Chem. Soc.*, 2003, **125**, 13010.
123. J. H. Koek, S. W. Russell, L. van der Wolf, R. Hage, J. B. Warnaar, A. L. Spek, J. Kerschner, and L. Del Pizzo, *J. Chem. Soc., Dalton Trans.*, 1996, 353.
124. O. Horner, E. Anxolabéhére-Mallart, M.-F. Charlot, L. Tchertanov, J. Guilhem, T. A. Mattioli, A. Boussac, and J.-J. Girerd, *Inorg. Chem.*, 1999, **38**, 1222.
125. L. Dubois, D.-F. Xiang, X. S. Tan, J. Pécaut, P. Jones, S. Baudron, L. Le Pape, J.-M. Latour, C. Baffert, S. Chardon-Noblat, M.-N. Collomb, and A. Deronzier, *Inorg. Chem.*, 2003, **42**, 750, references therein.
126. A. Gelasco, M. L. Kirk, J. W. Kampf, and V. L. Pecoraro, *Inorg. Chem.*, 1997, **36**, 1826.
127. M.-N. Collomb-Dunand-Sauthier, A. Deronzier, X. Pradon, S. Ménage, and C. Philouze, *J. Am. Chem. Soc.*, 1998, **120**, 5373.
128. R. A. Reynolds III, W. O. Yu, W. R. Dunham, and D. Coucouvanis *Inorg. Chem.*, 1996, **35**, 2721.
129. C. Philouze, G. Blondin, J.-J. Girerd, J. Guilhem, C. Pascard, and D. Lexa, *J. Am. Chem. Soc.*, 1994, **116**, 8557.
130. M. Alexiou, C. Dendrinou-Samara, A. Karagianni, S. Biswas, C. M. Zaleski, J. Kampf, D. Yoder, J. E. Penner-Hahn, V. L. Pecoraro, and D. P. Kessissoglou, *Inorg. Chem.*, 2003, **42**, 2185.
131. T. Afrati, C. Dendrinou-Samara, C. P. Raptopoulou, A. Terzis, V. Tangoulis, and D. P. Kessissoglou, *Angew. Chem., Int. Ed. Engl.*, 2002, **41**, 2148.
132. A. J. Tasiopoulos, K. A. Abboud, and G. Christou, *Chem. Commun.*, 2003, 580.

133. E. K. Brechin, M. Soler, J. Davidson, D. N. Hendrickson, S. Parsons, and G. Christou, *Chem. Commun.*, 2002, 2252.

134. J. D. Rush and B. H. J. Bieleski, *Inorg. Chem.*, 1995, **34**, 5832.

135. K. M. S. Etheredge, A. S. Gardberg, and S. J. Hwu, *Inorg. Chem.*, 1996, **35**, 6358.

136. F. M. Mac Donell, N. L. P. Facklet, C. Stern, and T. V. O'Halloran, *J. Am. Chem. Soc.*, 1994, **116**, 7431.

137. C. G. Miller, S. W. Gordon-Wylie, C. P. Horwitz, S. A. Strazisar, P. K. Peraino, G. R. Clark, S. T. Weintraub, and T. J. Collins, *J. Am. Chem. Soc.*, 1998, **120**, 11540.

138. N. Jin and J. T. Groves, *J. Am. Chem. Soc.*, 1999, **121**, 2923.

139. Z. Gross, G. Golubkov, and L. Simkhovich, *Angew. Chem., Int. Ed. Engl.*, 2000, **39**, 4045.

140. B. S. Mandimutsira, B. Ramdhanie, R. C. Todd, H. Wang, A. A. Zareba, R. S. Czernuszewicz, and D. P. Goldberg, *J. Am. Chem. Soc.*, 2002, **124**, 15170.

141. H.-Y. Liu, T.-S. Lai, L.-L. Yeung, and C. K. Chang, *Org. Lett.*, 2003, **5**, 617.

142. D. Feichinger and D. A. Plattner, *Chem. Eur. J.*, 2001, **7**, 591, references there in.

143. J. Du Bois, C. S. Tomooka, J. Hong, and E. Z. M. Carreira, *Acc. Chem. Res.*, 1997, **30**, 364.

144. S. Minakata, T. Ando, M. Nishimurra, I. Ryu, and M. Komatsu, *Angew. Chem., Int. Ed. Engl.*, 1998, **37**, 3392.

145. J. Du Bois, C. S. Tomooka, J. Hong, E. M. Carreira, and M. W. Day, *Angew. Chem., Int. Ed. Engl.*, 1997, **36**, 1645, references therein.

146. K. Meyer, J. Bendix, N. Nietzler-Notte, T. Weyhermüller, and K. Wieghardt, *J. Am. Chem. Soc.*, 1998, **120**, 7260.

147. R. A. Eikey, S. I. Khan, and M. M. Abu-Omar, *Angew. Chem., Int. Ed. Engl.*, 2002, **41**, 3592.

148. J. Bendix, R. J. Deeth, T. Weyhermüller, E. Bill, and K. Wieghardt, *Inorg. Chem.*, 2000, **39**, 930, references therein.

149. A. A. Danopoulos, G. Wilkinson, T. Sweet, and M. B. Hursthouse, *J. Chem. Soc., Chem. Commun.*, 1993, 495.

150. A. A. Danopoulos, J. C. Green, and M. B. Hursthouse, *J. Organomet. Chem.*, 1999, **591**, 36.

Manganese: Organometallic Chemistry

Dwight A. Sweigart & Jeffrey A. Reingold
Brown University, Providence, RI, USA

1	Introduction	1
2	Complexes Without CO Ligands	1
3	Carbonyl Compounds	1
4	Insertion Reactions	3
5	Carbenes and Related Compounds	5
6	Cymantrenes	7
7	Cyclic π-Hydrocarbon Compounds	8
8	Metal-Organometallic Coordination Networks	11
9	Related Articles	13
10	References	13

Glossary

Organomanganese compounds: compounds that contain at least one Mn–C bond, where the carbon donor is CO, alkyl, aryl, π-hydrocarbon, and so on

1 INTRODUCTION

This review summarizes advances in the organometallic chemistry of manganese over the period 1994–2002. As will be shown, there have been very significant advances in this area of organometallic chemistry. Especially noteworthy are novel applications of π-bonded organomanganese complexes in organic synthesis, in the activation of covalent chemical bonds in organic molecules, and in the synthesis of polymeric coordination networks. The low cost of manganese, its many available oxidation states, and the general ease of carrying out transformations involving ligands bonded to the metal suggest that manganese will assume an increasingly important role in synthetic chemistry and will be a vehicle for important technological advances in industrial, biomedical, and materials science.

2 COMPLEXES WITHOUT CO LIGANDS

Treatment of $MnCl_2$ with $MgAr_2$ (Ar = 2,4,6-t-$Bu_3C_6H_2$) affords the thermally stable two-coordinate diaryl $MnAr_2$ (**1**).**[1]** The low-coordination number is a consequence of the sterically demanding t-Bu groups, which also accounts for the lack of any reaction between (**1**) and simple ligands such as THF, pyridine, and MeCN. High yields of benzylic manganese halides, sulfonates, and phosphates can be obtained by the reaction of organic benzylic precursors with highly activated manganese metal prepared via a lithium/naphthalene/THF reduction of Mn(II) halides.**[2]** Such benzylic organometallic reagents play a significant role in organic synthesis. The manganese reagents are quite selective in cross-coupling reactions, one of which is shown in Scheme 1.

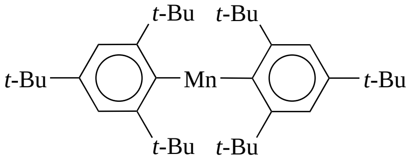

(**1**)

A useful review on organomanganese reagents in organic synthesis has appeared.**[3]** As described therein, one of the most stable alkyl Mn(II) reagents is trialkyl manganate, MnR_3^-, which can be conveniently prepared as the Li^+ or $MgBr^+$ salt and used at 0 °C. These have been utilized for a variety of reactions, such as the stereoselective alkylation of *gem*-dibromocyclopropanes (Scheme 2), the silylation of acetylenes, and the radical cyclization of allylic ethers. Some of these transformations can be made catalytic.**[3]**

3 CARBONYL COMPOUNDS

Simple manganese carbonyl complexes (*see* ***Carbonyl Complexes of the Transition Metals***) containing σ-bonded ligands comprise a vast array of compounds. The ligands, other than CO, include halides, phosphines, amines, alkyls, aryls, and so on. The resultant complex can be neutral, cationic, or anionic and may exhibit a wide range of chemical reactivity centered at the metal or at the ligands. Noteworthy additions to the recent literature in this area include ligands based on antimony**[4]** and tellurium:**[5]** $Mn(CO)_4(SbPh_3)Cl$, $[Mn(CO)_5SbPh_3]^+$, and $Mn(CO)_3$(TeTTe)Cl (**2**). Interestingly, ^{55}Mn NMR of (**2**) indicate the existence of three slowly interconverting stereoisomers based on pyramidal inversion at the Te centers.

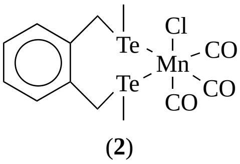

(**2**)

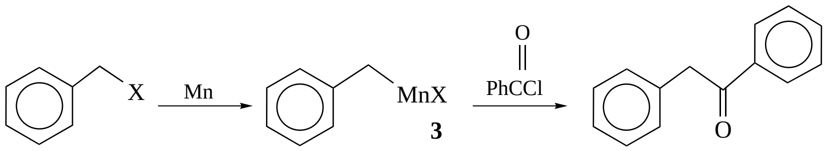

Scheme 1

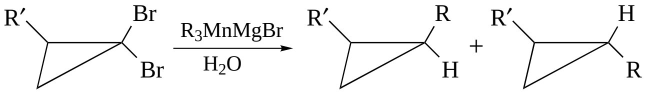

Scheme 2

The aqua complex $[fac\text{-}Mn(CO)_3(dppe)OH_2]^+$ (dppe is bis-diphenylphosphinoethane) contains a fairly labile water that can be conveniently replaced by OMe^--, CN^--, RCN-, and RNC-type ligands.[6] An attempt to prepare the fluoro complex led to the isolation of $[(OC)_3Mn(dppe)OH_2\cdots FMn(CO)_3(dppe)]BF_4$, which is held together by a very strong hydrogen bond ($O\cdots F = 2.46$ Å, *see Hydrogen Bonding*).[7] The nucleophilic carbonyl anion $[Mn(CO)_3(bipy)]^-$ attacks the electrophile $ClCH_2SR$ to afford the alkylthiomethyl complex $fac\text{-}Mn(CO)_3(bipy)CH_2SR$, which is easily methylated at the sulfur.[8] In other work, it was shown that the hexafunctionalized cyclotriphosphazene $N_3P_3(p\text{-}OC_5H_4N)$ reacts with $fac\text{-}Mn(CO)_3(bipy)OClO_3$ to give the interesting hexametallic complex (**3**).[9]

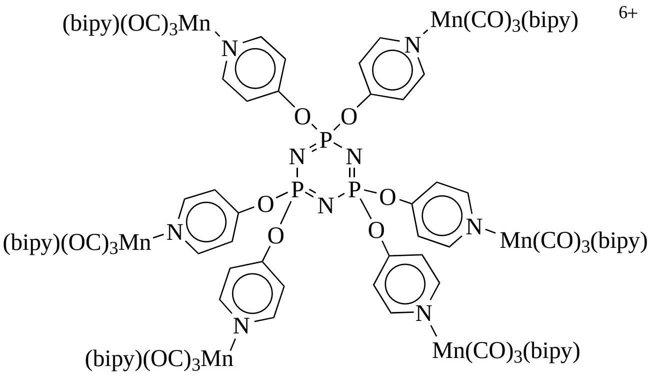

(**3**)

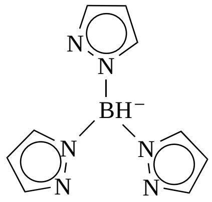

(**4**)

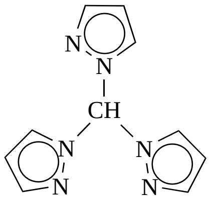

(**5**)

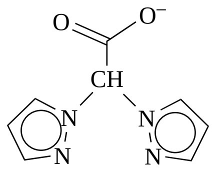

(**6**)

Manganese carbonyl complexes containing σ-bonded ligands that are related to the celebrated tris(pyrazolyl)borate ligand (*see Tris(pyrazolyl)borates*) (**4**) have been reported. These include tris(pyrazolyl)methane[10] (**5**) and bis(pyrazolyl)acetate[11] (**6**), which function as tridentate ligands in complexes $[Mn(CO)_3(\mathbf{5})]^+$ and $[Mn(CO)_3(\mathbf{6})]$. The solvent-coordinated Mn(I) carbonyl (**7**) containing a tied-back phosphite ligand is formed by treating the methyl analogue of (**7**) with trityl cation in CH_2Cl_2.[12] Complex (**7**) is highly electrophilic and readily forms ''σ-bond'' complexes with H_2 and $HSiR_3$, according to Scheme 3. The 'tied-back' nature of the phosphite ligands prevents intramolecular agostic bonding (*see Agostic Bonding*), which would hinder external ligand binding. Other η^2-H_2 complexes of manganese recently reported include $[Mn(CO)(dppe)_2(\eta^2\text{-}H_2)]^+$, $[Mn(CO)_3(PCy_3)_2(\eta^2\text{-}H_2)]^+$, $[Mn(CO)\{P(OEt)_3\}_4(\eta^2\text{-}H_2)]^+$, and $Cp^*Mn(CO)_2(\eta^2\text{-}H_2)$.[13–16]

The boryl complex $Mn(CO)_4(PR_3)(BH_2PMe_3)$ is protonated to the borane analogue,[17] which also contains a σ-bond η^2-ligand (HBH_2PMe_3) similar to that obtained with H_2 and $HSiR_3$ in Scheme 3. In a similar vein, the σ-borane complex

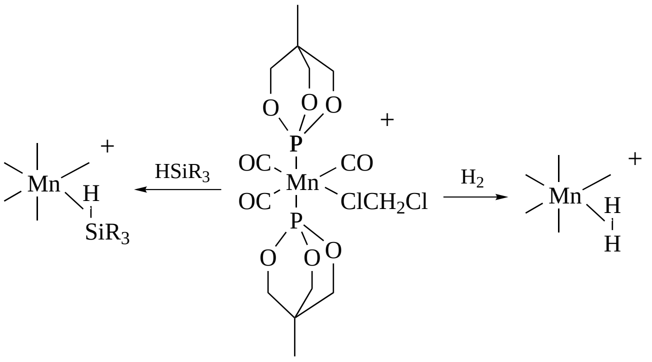

(**7**)

Scheme 3

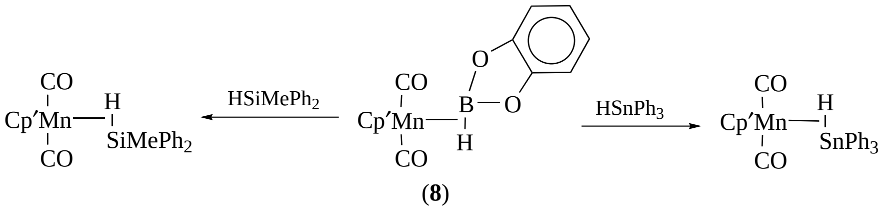

(**8**)

Scheme 4

$CpMn(CO)_2(HBH_2PMe_3)$ has been characterized, with the conclusion that the bonding consists primarily of σ-donation from the B–H bond with little d orbital back donation into the B–H σ^* orbital.[18] An upper limit of 100 kJ has been estimated for the η^2 bond in the σ-borane complex (**8**).[19] The borane ligand in (**8**) is readily replaced by CO, PhC≡CPh, $HSiMePh_2$, and $HSnPh_3$, with the latter two ligands forming H–Si and H–Sn σ-bond complexes, as indicated in Scheme 4.

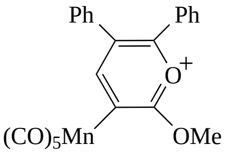

(**9**)

The pyrylium complex (**9**) was found to be surprisingly resistant to protolytic Mn–C bond cleavage and CO insertion reactions.[20] It undergoes electrocatalytic CO substitution upon reduction in the presence of PPh_3. The dimeric complex $[Mn(CO)_4Br]_2$ was found to be a catalyst precursor for the alcoholysis of silanes.[21] Similarly, manganese carbonyl complexes, for example $Mn(CO)_4(PPh_3)C(O)Me$, are very effective catalysts for the hydrosilylation (*see Hydrosilation*) of ketones.[22] Nucleophilic attack of hydride on electrophilic metal carbonyls is a favorite route to formyl complexes. An example is provided by the reaction of borohydride with $[Mn(CO)_4(dppe)]^+$ to generate an observable formyl intermediate, $Mn(CO)_3(dppe)(CHO)$, which slowly decarbonylates to *fac*-$Mn(CO)_3(dppe)H$.[23] Manganese acyls, $(OC)_5MnC(O)CH_2R$, can be converted into the α-ketoacyl derivatives $(OC)_5MnC(O)C(O)CH_2R$ by treatment with $HSiEt_3$, followed by carbonylation and protonlysis.[24]

A rather large number of multimetallic complexes containing manganese carbonyl units have been reported during the last 10 years. The one-pot synthesis of the selenolato-bridged bimetallic (**10**) follows the chemistry shown in Scheme 5.[25] A variety of bimetallic complexes containing one or more bridging μ-PPh_2 phosphido groups have been synthesized,[26–29] including the heteronuclear manganese–tungsten complex (**11**).[26] The latter complex is especially interesting because phosphine and phosphite ligands were found to substitute for a CO ligand at the manganese center only, while ^{13}CO substitutes at both metal centers. New bimetallic complexes containing bridging thiolates have appeared.[30,31] Most significant was the report[32,33] in 2001 of the isolation of the simplest disulfide of manganese carbonyl, $Mn_2(CO)_7S_2$ (**12**), from the reaction of $Mn_2(CO)_9(NCMe)$ and thiirane. Chemical reduction of (**12**) affords[34] the trimetallic carbonyl anion $[Mn_3(CO)_{10}(\mu\text{-}S_2)_2]^-$. Also of interest is the synthesis of the first dinuclear complex with bridging borylene ligands, $Cp_2Mn_2(CO)_4(\mu\text{-}BR)$ (R = NMe_2, CMe_3).[35,36]

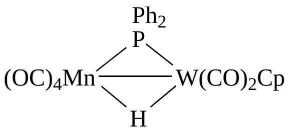

(**11**)

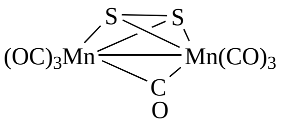

(**12**)

4 INSERTION REACTIONS

The migratory insertion (*see Migratory Insertion*) reactions of manganese carbonyls have been studied for many

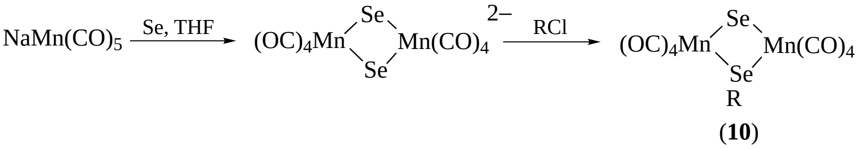

(**10**)

Scheme 5

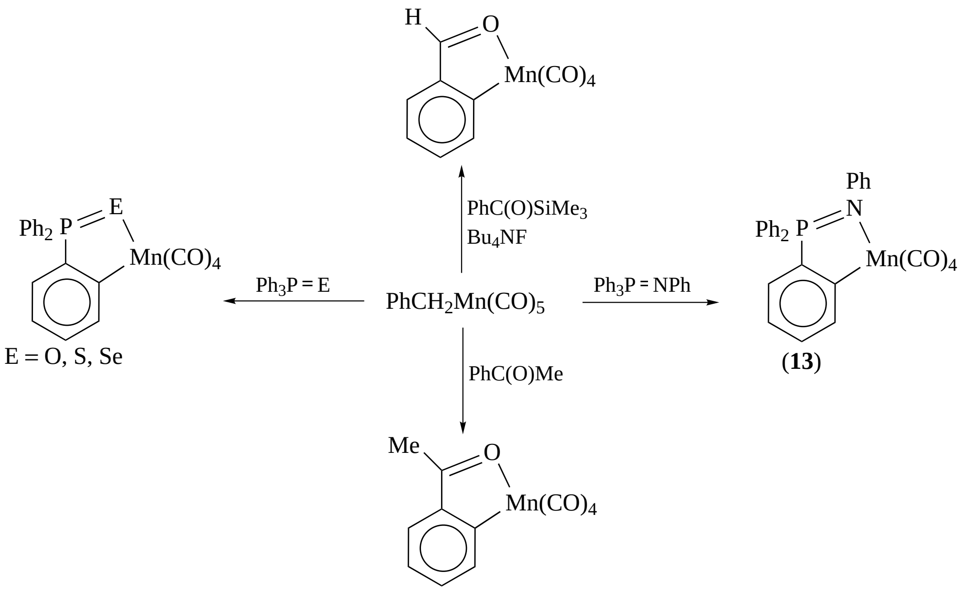
H
O
Mn(CO)4
PhC(O)SiMe3
Bu4NF
Ph2 P
E
Mn(CO)4
Ph3P = E
PhCH2Mn(CO)5
Ph3P = NPh
Ph
N
Ph2 P
Mn(CO)4
E = O, S, Se
PhC(O)Me
(13)
Me
O
Mn(CO)4

Scheme 6

years. A useful starting reagent is $PhCH_2Mn(CO)_5$, which reacts with many suitably substituted aromatic substrates in a 'cyclomanganation' reaction. Scheme 6 provides a number of examples.[37–47] Complex (**13**) is especially interesting because it is thermochromic in solution, changing abruptly from ambient yellow to intense purple as the solution is heated to 100 °C.[39] Cyclomanganated species frequently undergo insertion reactions with a variety of reagents. Scheme 7 illustrates a recently reported typical example of alkyne insertion.[46] Cyclomanganation of aromatic *complexes* of chromium, such as those shown in structures (**14**)– (**16**), hold significant promise.[48–50] In some cases, the use of these bimetallic cyclometallated products allows enhanced diastereoselectivity in subsequent insertive cyclization sequences to generate indanol and other heterocycles.[50]

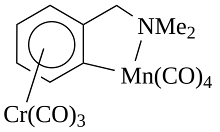
NMe2
Mn(CO)4
Cr(CO)3

(**14**)

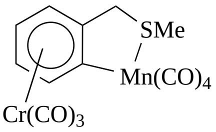
SMe
Mn(CO)4
Cr(CO)3

(**15**)

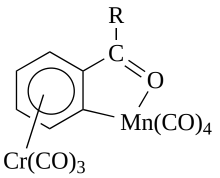
R
C
O
Mn(CO)4
Cr(CO)3

(**16**)

The manganese carbonyl disulfide complex (**12**) inserts various metal fragments into the S–S bond (Scheme 8).[51–55] On the other hand, Me_2S inserts into the Mn–Mn bond and tertiary phosphines substitute CO ligands. *Heterobimetallic* disulfides and diselenides analogous to (**12**) have been reported.[54,55] These fascinating compounds insert ethylene, CO, and $Pt(PPh_3)_2$ according to Scheme 9. Another interesting report concerns the insertion of imines and carbon monoxide into manganese–alkyl bonds. The double insertion of these species into $MeMn(CO)_5$ affords the manganese-chelated amide (**17**).[56]

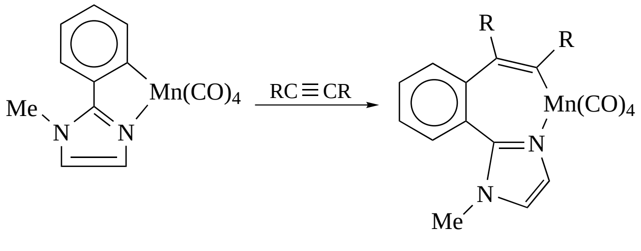
Mn(CO)4
Me
N
N
RC≡CR
R
R
Mn(CO)4
N
N
Me

Scheme 7

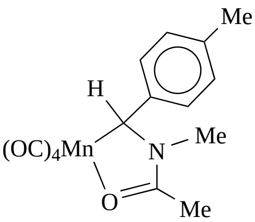
Me
H
(OC)4Mn
N
Me
O
Me

(**17**)

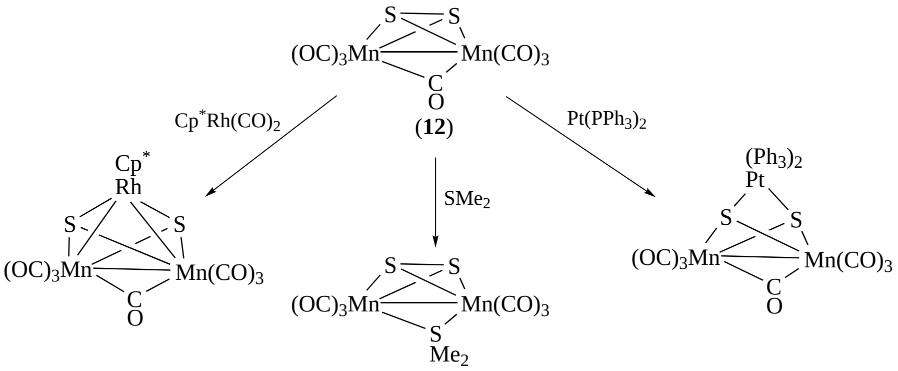

Scheme 8

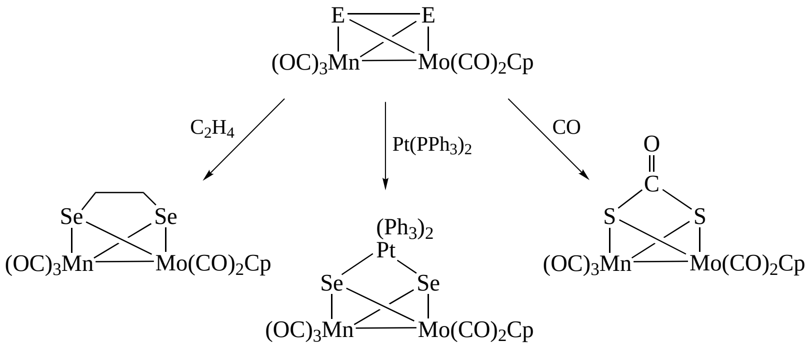

Scheme 9

5 CARBENES AND RELATED COMPOUNDS

Transition metal carbenes constitute a very important class of molecules that have found a multitude of applications. With reference to manganese, a number of new carbene complexes have been reported recently. The η^2-alkyne complex (**18**) was found[57] to undergo oxidation by dimethyldioxirane to afford the α-keto carbene (**19**). The fascinating aspect of this reaction is the likely existence of an oxirene intermediate (**20**). Stable oxirene complexes have never been reported, undoubtedly because of the extreme instability of the antiaromatic oxirene ring. The possibility of trapping an oxirene by epoxidation of a coordinated alkyne is intriguing. Scheme 10 summarizes the chemistry involved.

Chiral-at-the-metal Fischer carbene complexes are formed when the 16-electron fragment $[\mathrm{CpMn(NO)(PPh_3)}]^+$ is treated with hydroxyalkynes.[58] The likely mechanism of this reaction is given in Scheme 11. Abstraction of iodide from precursor (**21**) allows coordination of the alkyne, which rearranges to the vinylidene (**22**). The latter undergoes intramolecular nucleophilic (*see Intramolecular*) attack of the alcohol at the α-carbon to generate the chiral carbene (**23**). The carbene complex $\mathrm{Cp(CO)_2Mn{=}C(OAc)(Ph)}$ reacts with chiral aminoalcohols ($\mathrm{R^*OH}$) to afford $\mathrm{Cp(CO)_2Mn{=}C(OR^*)(Ph)}$ complexes, which are converted diastereoselectively to $\mathrm{Cp(CO)(PR_3)Mn{=}C(OR^*)(Ph)}$ when photolyzed in the presence $\mathrm{PR_3}$ ligands.[59] A number of bis(carbene) complexes of manganese have been synthesized, for example (**24**)

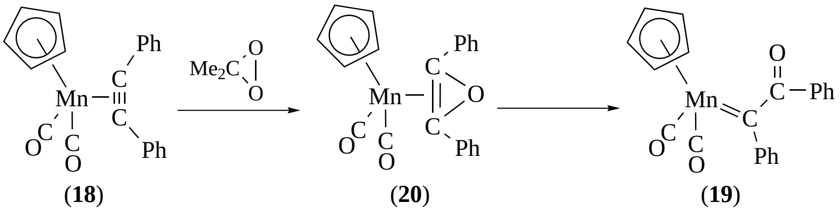

Scheme 10

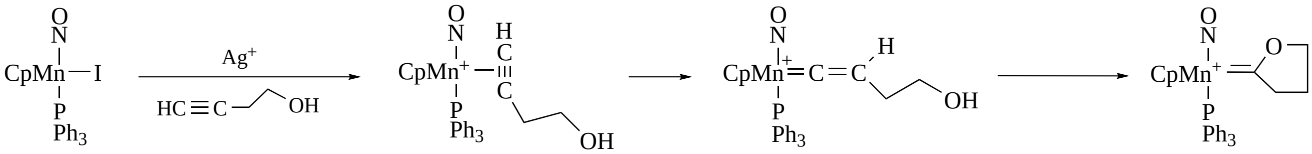

(**21**) (**22**) (**23**)

Scheme 11

and (**25**).[60–62] The coordination of a CpMn(CO)$_2$ fragment to the alkyne in the carbene complex Cp(CO)$_2$Mn=C(R)C$\equiv$CR$'$ yields a highly fluxional (*see Fluxional Molecule*) bimetallic species in which the η^1-carbene and η^2-alkyne moieties rapidly exchange as pictured in Scheme 12.[63]

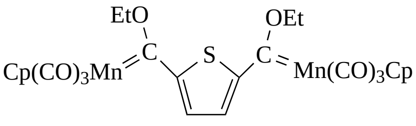

(**24**)

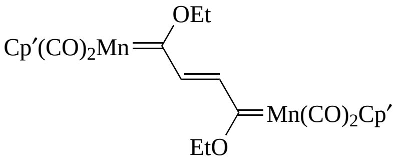

(**25**)

The paramagnetic 17-electron alkynyl complex CpMn(dmpe)(C$\equiv$CPh) reacts with hydride donors to give the vinylidene Cp(dmpe)Mn=C=CHPh or with itself to generate the bimetallic bis-vinylidene [Cp(dmpe)Mn=C=C(Ph)]$_2$.[64] The analogous [Cp(CO)$_2$Mn=C=C(Ph)]$_2$ complex has been made by an oxidative dehydrodimerization process.[65] The alkynyl complex Cp*(CO)$_2$FeC$\equiv$CH combines with Cp$'$Mn(CO)$_2$(THF) to afford the bimetallic vinylidene Cp$'$(CO)$_2$Mn=C=C(H)(Fp*), where Fp* stands for the Cp*Fe(CO)$_2$ fragment.[66] Manganese vinylidene complexes may also be obtained by treating Cp$'$Mn(CO)$_3$ with organolithium reagents to form acyl anions Cp$'$Mn(CO)$_2$C(O)CH$_2$R$^-$ that react with electrophiles such as acetyl chloride to afford the carbenes Cp$'$(CO)$_2$Mn=C(OC(O)Me)(CH$_2$R). The latter complexes eliminate acetic acid and convert to the vinylidenes Cp$'$(CO)$_2$Mn=C=CHR.[67]

Carbyne complexes containing the Mn$\equiv$CR moiety undergo an interesting variety of reactions.[68–70] Scheme 13 provides a sampler of these reactions. The electrophilic nature of the carbyne in the cationic Cp(CO)$_2$Mn$\equiv$CR$^+$ has been exploited in cycloadditions, metatheses, and ketene formation methodologies. Extended chains containing unsaturated carbon networks that are truncated by metal

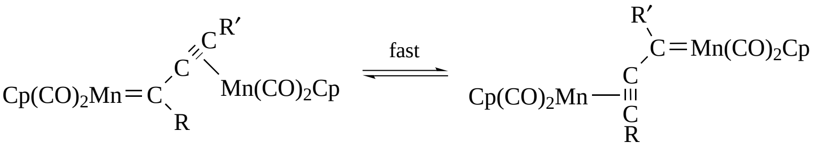

Scheme 12

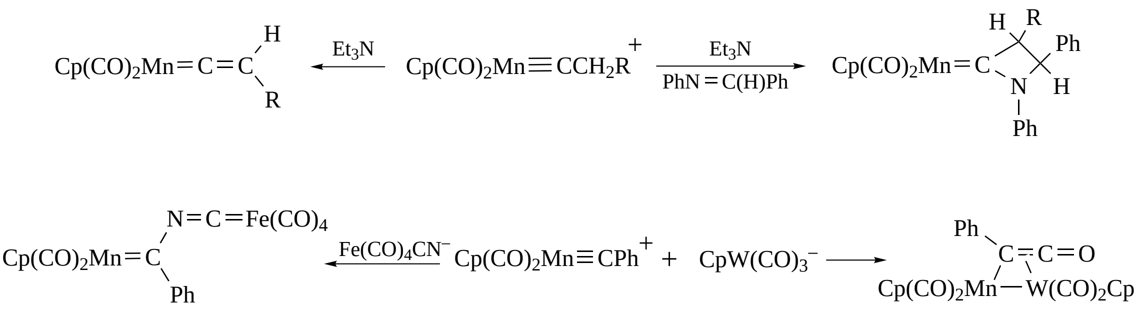

Scheme 13

fragments are being developed as 'molecular wires'.[71–73] Structures (**26**) and (**27**) illustrate two examples of these. In (**26**), the cumulenic chain is capped by different metals. In (**27**), the unsaturation is provided by acetylide linkages.

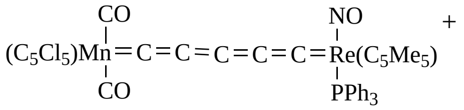

$$(C_5Cl_5)\underset{CO}{\overset{CO}{Mn}}{=}C{=}C{=}C{=}C{=}C{=}\underset{PPh_3}{\overset{NO}{Re}}(C_5Me_5)^{+}$$

(**26**)

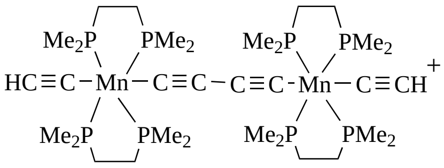

(**27**)

6 CYMANTRENES

$CpMn(CO)_3$, known as cymantrene, is a robust molecule whose chemistry has been extensively developed. The cyclopentadienyl (*see Cyclopentadienyl*) ring in $CpMn(CO)_3$ can be functionalized with alkyl, aryl, and alcoholic substituents.[74,75] Even pentamercuration has been reported, affording (**28**), from which the pentahalo derivatives (**29**) can be obtained.[76] Photolysis of cymantrenes-bearing ring substituents with donor atoms can lead to intramolecular ring closure following CO dissociation to yield products such as (**30**).[77] Photoacoustic calorimetric measurements indicate that the ring closure occurs with a rate constant greater than $10^7\ s^{-1}$ at room temperature. Lithium fluorenide ($LiC_{13}H_9$) reacts with $Mn(CO)_5Br$ to give an η^1 complex, which slowly dissociates CO and rearranges to the η^5 analogue (**31**) shown in Scheme 14.[78] Other noteworthy complexes, recently reported, that are related to cymantrene include the fulvene (**32**), sesquifulvalene (**33**), and the rather bizarre metallacycle (**34**).[79–81]

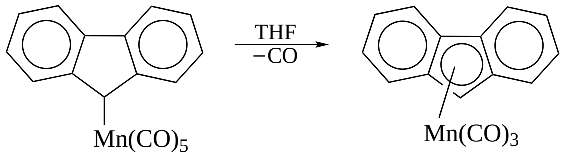

(**31**)

Scheme 14

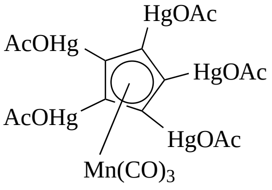

(**28**)

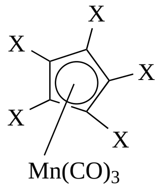

(X = Cl, Br, I)

(**29**)

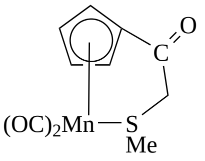

(**30**)

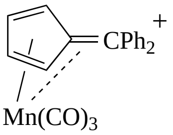

(**32**)

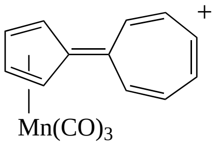

(**33**)

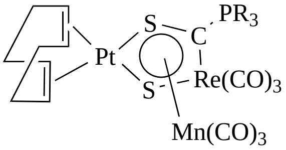

(**34**)

UV photolysis of $CpMn(CO)_3$ in toluene leads to loss of CO and formation of $CpMn(CO)_2(\eta^2$-toluene). Kinetic studies suggest that the binding energy of the toluene is ca. $60\ kJ\ mol^{-1}$.[82] The η^2 binding of H_2 to $CpMn(CO)_2$ has been studied in supercritical CO_2 solvent.[83,84] It has been proposed that pyrylium and pyridinium salts such as (**35**) can be used to label proteins and thereby aid in the detection and characterization of receptor sites.[85] Cymantrene bound to lysine residues of bovine serum albumin (BSA) has been used as a redox label.[86] Electrochemical reduction of the label established an impressive BSA detection limit of 2×10^{-7} M.

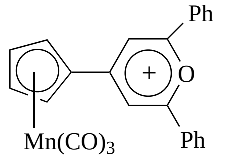

(**35**)

Multimetallic cymantrenes such as (**36**) and (**37**) have recently been reported.[87,88] An especially interesting multimetallic system is (**38**), in which two cymantrene units are linked by a pyrazolate bridge.[89] Electrochemical measurements show that the two metal centers in (**38**) interact

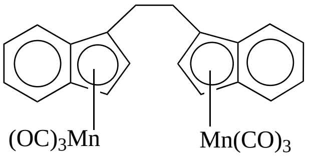

(36)

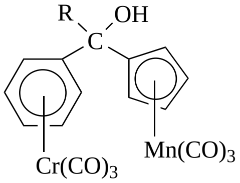

(37)

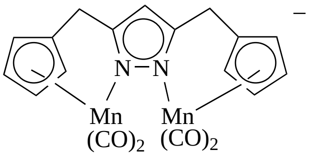

(38)

significantly, which results in a consequent stabilization of the Mn(I)/Mn(II) mixed-valence one-electron oxidation product.

7 CYCLIC π-HYDROCARBON COMPOUNDS

With the possible exception of the cyclopentadienyl ring system, described in the last section, the most important cyclic π-hydrocarbon ligands in manganese chemistry are six-electron donors based on the benzene nucleus. The use of ^{55}Mn NMR in characterizing manganese sandwich complexes has been examined with the series $(\eta^5\text{-}C_5H_4R)Mn(\eta^6\text{-}C_6H_5R')$.**[90]** The ^{55}Mn nucleus has a spin of 5/2 and a sizable quadrupole moment, resulting in line-widths of several kHz in the compounds studied. Nevertheless, the chemical shift δ covers a sufficiently large range that well-resolved spectra may be obtained. The ^{55}Mn chemical shifts were found to be usefully dependent on the nature of the π-hydrocarbon ring substituents R and R′.

The complexes $[(\eta^6\text{-arene})Mn(CO)_3]^+$ constitute a very important class of compounds that have been shown to undergo a rather amazing range of useful chemical reactions.**[91–93]** The synthesis of such complexes is generally straightforward, unless the arene contains an electron-withdrawing substituent.**[94,95]** The most useful reaction of $[(\eta^6\text{-arene})Mn(CO)_3]^+$ is the very facile addition of a wide range of nucleophiles to afford stable cyclohexadienyl complexes, as illustrated in Scheme 15.**[96–108]** The nucleophiles utilized include Grignard reagents, benzylic zinc reagents, stabilized enolates, borohydride, aryl lithium reagents, anionic metal complexes, and so on. The stereoselectivity of these addition reactions is almost always exclusively exo to the metal, as shown in (**40**). The regioselectivity depends on the substituent R′. When R′ in (**39**) is -OMe, for example, the addition is highly selective for the meta position. Ring strain can influence the result in some cases. Thus, $[(\eta^6\text{-tetralin})Mn(CO)_3]^+$ adds nucleophiles α to the bridgehead to give (**41**), while $[(\eta^6\text{-biphenylene})Mn(CO)_3]^+$ prefers to be attacked at the bridgehead (**42**), with concomitant release of ring strain.**[101,102]** Interestingly, it proved possible to functionalize the aromatic steroid estrone and the diterpenoid podocarpic acid by initial complexation of manganese tricarbonyl to the aromatic ring to afford (**43**) and (**44**), respectively.**[103–105]** It was also found that $[(\eta^5\text{-thiophene})Mn(CO)_3]^+$ complexes readily undergo nucleophilic addition (*see Nucleophilic Addition: Rules for Predicting Direction*) at the sulfur atom, which leads to zwitterionic $(\eta^4\text{-}C_4H_4SR)Mn(CO)_3$ products.**[109,110]** Complexes (**39**) that contain a phenolic arene are readily and reversibly deprotonated by weak bases to oxocyclohexadienyl derivatives.**[111,112]**

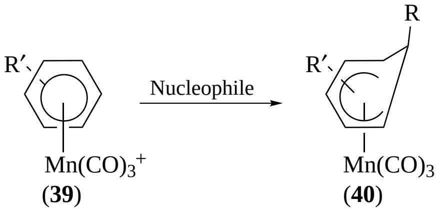

Scheme 15

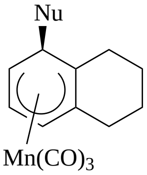

(41)

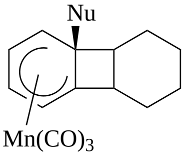

(42)

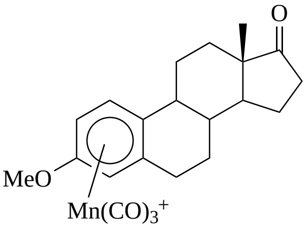

(43)

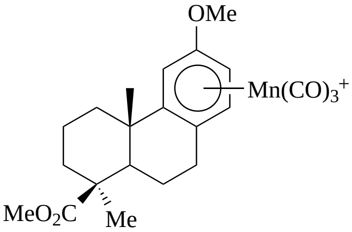

(44)

In a new and significant development, it was found that chlorocyclohexadienyl manganese tricarbonyl complexes undergo palladium-catalyzed coupling reactions with a variety of carbon nucleophiles to afford products from which hydride may be abstracted with trityl cation, thus generating new $[(\eta^6\text{-arene})Mn(CO)_3]^+$ complexes containing substituents that cannot be introduced in any other manner.**[113–117]** This is particularly true of electron-withdrawing substituents. Scheme 16 illustrates the chemistry involved.

One of the most exciting developments in organomanganese chemistry concerns the synthesis of naphthalene and

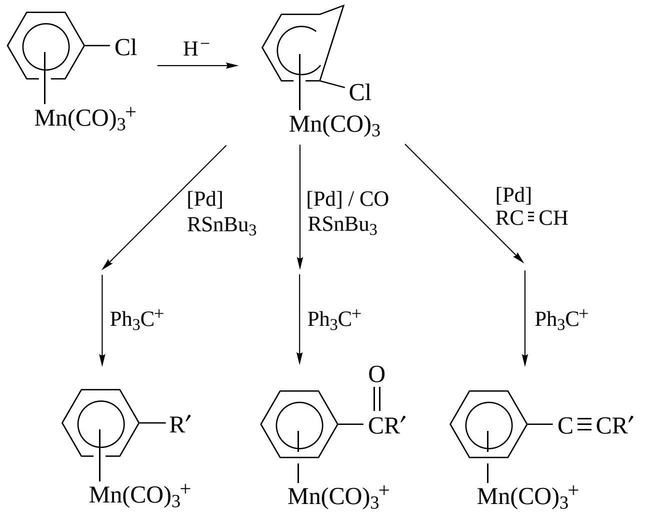

Scheme 16

related complexes (**45**).[118] This compound, although erroneously reported in 1961, had never before been synthesized and characterized in spite of numerous attempts to do so. The reason for the synthetic difficulties becomes apparent when the chemistry of (**45**) is compared to that of the analogue (**46**) having one ring saturated (tetralin). Both complexes react cleanly with acetonitrile with displacement of the arene and formation of $[(MeCN)_3Mn(CO)_3]^+$. However, the half-lives are tremendously different: 2 years for (**46**) and one minute for (**45**)! Thus, it became apparent that the naphthalene-type complexes are generally very sensitive to potential nucleophiles, which accounts for the previous difficulty in synthesis. The use of a nonnucleophilic solvent under moisture-free conditions permits the ready synthesis of (**45**) and its analogues in good yields.[118] The great reactivity of (**45**) does not imply a weak bond. It merely means that a low-energy pathway exists for arene displacement. This pathway involves $\eta^6 \rightarrow \eta^4$ ring slippage that accompanies associative attack by a nucleophile. Such slippage entails a loss in aromatic resonance energy that contributes to the activation energy. However, the loss in resonance energy upon slippage is not nearly as much as that for a monocyclic unsaturated system (benzene, tetralin, etc.). In fact, the differences in ring-displacement rates for complexes containing monocyclic unsaturated arene rings and rates for complexes containing polycyclic unsaturated arene rings almost exactly match the anticipated differential in resonance energy loss upon ring slippage. Relevant to this is the known stability of the slipped $[(\eta^4\text{-naphthalene})Mn(CO)_3]^-$ complex (**47**).[119]

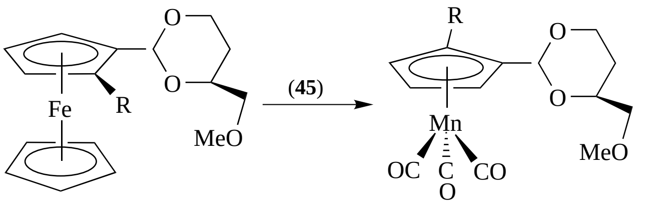

Scheme 17

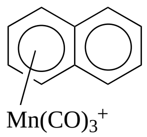

(**45**)

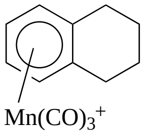

(**46**)

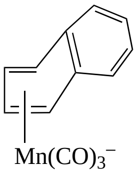

(**47**)

The ease of arene ring displacement from (**45**) makes it an excellent manganese tricarbonyl transfer (MTT) reagent.[118] In particular, many free arenes react readily with (**45**) to generate new $[(arene)Mn(CO)_3]^+$ complexes by a mild and useful synthetic route. In this manner, hydroquinones, centropolyindanes, and even $(\eta^6\text{-biphenyl})Cr(CO)_3$ are readily coordinated to manganese tricarbonyl.[118,120,121] In a dramatic illustration of the utility of (**45**) as an MTT reagent, it was found that merely refluxing equimolar amounts of (**45**) and Cp^*_2M (M = Fe, Ru, Os) produces air-stable capped metallocenes (**48**) as BF_4^- salts.[122] In a similar vein, it has been shown that the reaction of (**45**) with planar chiral ferrocenes (*see Ferrocene*) results in transfer of planar chirality as illustrated in Scheme 17.[123] The resulting chiral cymantrenes are useful as chiral auxiliaries in asymmetric allylic alkylations and other reactions.

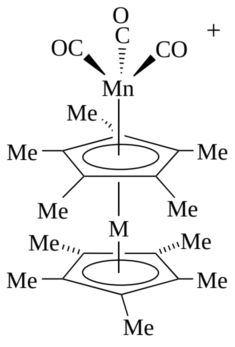

(**48**)

The facile ring slippage that occurs in (**45**) upon nucleophilic attack or upon reduction has been combined in a rather extraordinary reaction that utilizes both types of slippage to produce novel syn-facial and anti-facial bimetallic complexes such as (**49**)– (**52**).[124] In cyclohexadienyl derivative (**53**), ligand addition to the metal occurs reversibly concomitant with $\eta^5 \rightarrow \eta^3$ ring slippage according to Scheme 18.[125–127] Because of the facile ring slippage, (**53**) is an effective catalyst for the hydrosilylation (*see Hydrosilation*) of ketones[126] and also undergoes the rapid 1,4-hydride shift illustrated.[128–130] In an interesting series of reactions,[131–134]

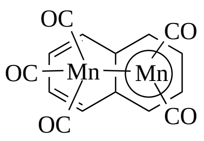
OC
CO
OC
Mn
Mn
OC
CO

(**49**)

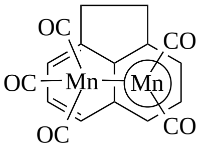
OC
CO
OC
Mn
Mn
OC
CO

(**50**)

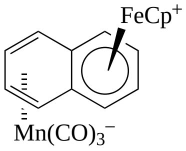

(**51**)

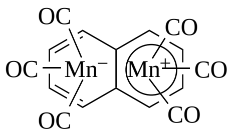
OC
CO
OC
Mn−
Mn+
CO
OC
CO

(**52**)

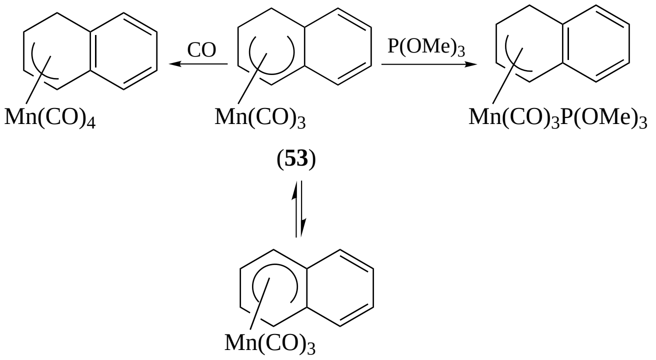
CO
P(OMe)3
Mn(CO)4
Mn(CO)3
Mn(CO)3P(OMe)3
(53)
Mn(CO)3

Scheme 18

it been reported that $[(\eta^6\text{-benzene})\mathrm{Mn(CO)_3}]^+$ (**54**) undergoes two-electron reduction by potassium naphthalenide at low temperatures to afford $[(\eta^4\text{-benzene})\mathrm{Mn(CO)_3}]^-$. The latter complex survives long enough to react with a variety of electrophiles, according to Scheme 19. Cyclohexadienyl complexes $(\eta^5\text{-}\mathrm{C_6H_6R})\mathrm{Mn(CO)_3}$ (**55**) react with $\mathrm{[NO]BF_4}$ to generate $[(\eta^5\text{-cyclohexadienyl})\mathrm{Mn(CO)_2NO}]^+$ cations that add a (second) nucleophile to give neutral difunctionalized cyclohexadiene complexes.[135] Treatment of complexes (**55**) sequentially with a hydride and a proton source leads to hydrodechlorination, hydrodesulfurization (HDS), and so on, when there is a heteroatom substituent present on the cyclohexadienyl ring.[136] Deprotonation of an α-carbon substituent in (**55**) produces a nucleophile that adds to a range of electrophiles, including metallic ones such as (**54**).[137] Single and double cycloaddition of alkynes to (**55**) has been reported.[138]

The ability of the $\mathrm{Mn(CO)_3}^+$ moiety to activate aromatic rings to nucleophilic attack and/or deprotonation of side-chain substituents has been extended to the activation of strong covalent bonds in regions of the molecule adjacent to the coordinated aromatic ring.[139] This is called ‘remote activation’. For example, coordinating $\mathrm{Mn(CO)_3}^+$ to the benzene ring in benzothiophene to give (**56**) activates both C–S bonds to

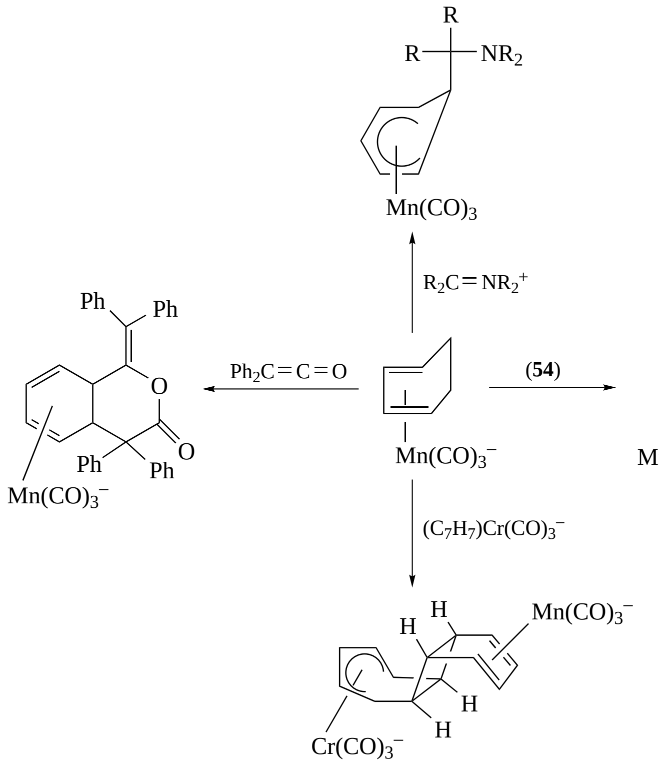
R
R
NR2
Mn(CO)3
R2C=NR2+
Ph
Ph
O
O
Ph
Ph
Mn(CO)3−
Ph2C=C=O
Mn(CO)3−
(54)
H
H
Mn(CO)3−
H
Mn(CO)3−
H
(C7H7)Cr(CO)3−
H
H
Mn(CO)3−
H
H
Cr(CO)3−

Scheme 19

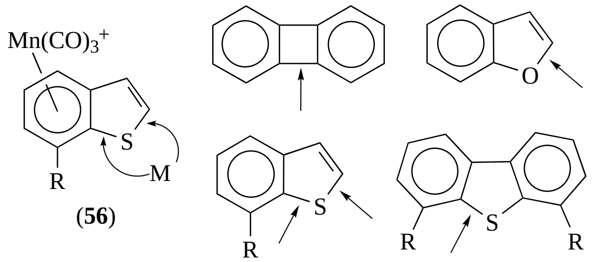

Scheme 20

cleavage upon the addition of a mild metal nucleophile. Which C–S bond is broken depends on the substituent R. Scheme 20 illustrates some of the systems reported, with the arrows indicating which bond is broken after the molecule is activated to bond fission by nucleophilic insertion or by reduction.[139–152] For example, the C–C bond in $[(\eta^6\text{-biphenylene})Mn(CO)_3]^+$ is rapidly broken by the mildly nucleophilic $Pt(PPh_3)_3$. The same is true of the vinylic C–O bond in benzofuran, in which an intermediate could be observed containing the $Pt(PPh_3)_2$ unit π-bonded to the furan C=C prior to fission of the adjacent C–O bond, as shown in Scheme 21.

It is remarkable indeed to observe that precoordination of $Mn(CO)_3^+$ to dibenzothiophenes, even 4,6-dialkylated ones, activates a C–S bond to cleavage by a mild nucleophile within *seconds* at room temperature. C–S bond fission is the first step in sulfur removal, and the methodology described could point the way to catalytic desulfurization of the major and most intractable sulfur-containing contaminant in fossil fuels – alkylated dibenzothiophenes. The removal of sulfur by reaction with hydrogen to yield H_2S is practiced on a massive scale by the petroleum industry. Indeed, HDS is the largest-scale industrial chemical reaction in the world. The removal of sulfur is required for industrial and environmental reasons, and getting the content down to tens of parts-per-million, as soon required by Federal legislation, is a difficult proposition termed ‘deep hydrodesulfurization’. Organometallic model systems such as that described above for manganese may contribute significantly in this regard in the twenty-first century.

8 METAL-ORGANOMETALLIC COORDINATION NETWORKS

An especially interesting example of the use of an MTT reagent is in the high-yield synthesis of π-bonded η^6-hydroquinone and η^6-catechol manganese complexes.[153–155] The transition metal chemistry of π-bonded hydroquinones is little developed because of difficulty in synthesis and/or instability. Furthermore, hydroquinones have a strong propensity to bind through the oxygen atoms rather than through the π system. Nevertheless, η^6-hydroquinone, resorcinol, and catechol π complexes of $Mn(CO)_3^+$ are thermally stable species and undergo interesting reactions. For example, complexes (**57**) and (**60**) are easily deprotonated to afford η^5-semiquinone and η^4-quinone derivatives (Scheme 22). The semiquinone (**58**) exists in linear polymeric arrays in the solid state with a structure

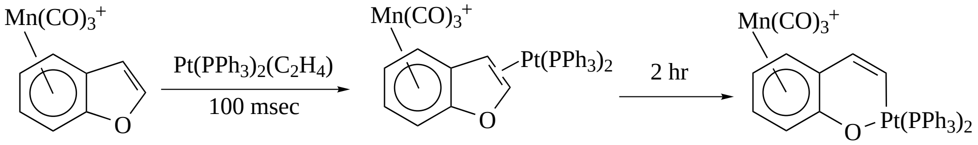

Scheme 21

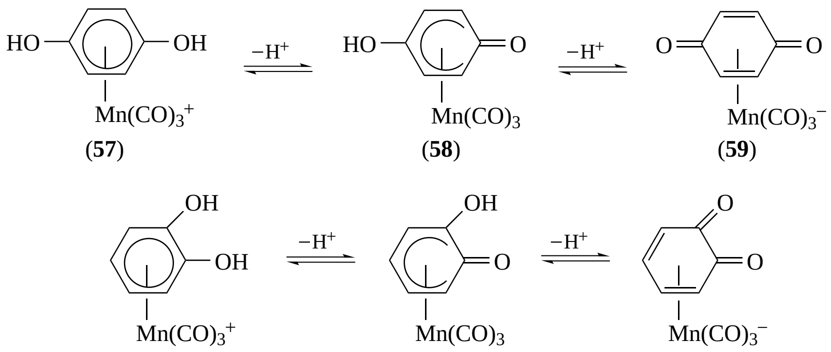

Scheme 22

dictated by strong intermolecular hydrogen bonding. By comparison, the catechol analogue (**61**) exists as discrete hydrogen-bonded dimers.

The anionic η^4-quinone complexes (**59**) and (**62**) have been shown to function as good ligands toward transition metals by σ-binding through the oxygen atoms.[156–160] Accordingly, complexes (**59**) and (**62**) are termed 'organometalloligands'. The catecholate (**62**) functions as a chelating ligand and with divalent metal ions forms complexes $[\mathrm{M}(\mathbf{62})_2(\mathrm{L}_2)]$ (M = Mn, Cd, Co; L_2 = phen, 2,2′-bipy, 2 py). The electron-sink nature of the manganese carbonyl moiety combined with the redox-active nature of quinones make these complexes interesting in the context of 'redox tautomerization', meaning that they show a dynamic electronic environment (oxidation state) at the metal M that self-adjusts to changes in the binding properties of the nonquinonoid ligand L.

In contrast to the discrete complexes formed by organometalloligand (**62**), the benzoquinone complex (**59**) is geometrically prevented from chelating a metal ion and instead functions as a bifunctional ligand to form supramolecular coordination networks. These consist of metal ions, called *nodes*, connected by organometalloligand spacers. The whole assembly is termed a metal-organometallic coordination network (MOMN).[156] For example, in DMSO (**59**) reacts to form the 1-D MOMN (**63**). By using a bifunctional organic spacer as the axial ligand, the 1-D 'string' polymers in (**63**) can be tied together to give the 2-D MOMN (**64**). With suitable experimental conditions, it is possible to construct 3-D MOMNs that contain 2-D quinonoid planes connected by the bipyridine spacers. Significantly, it appears that the architectures that obtain can be rationally designed based upon the coordination number, oxidation state, and geometrical requirements of the metallic nodes that link the organometalloligands.

In other work involving organometallic supramolecular systems containing manganese, the incorporation of the $\mathrm{Mn(CO)_3}^+$ fragment into poly(methylphenylsilane) has been achieved with 10% loading by using the MTT reagent (**45**).[161]

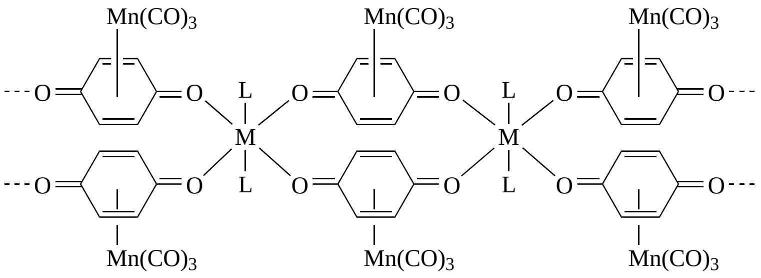

(**63**)

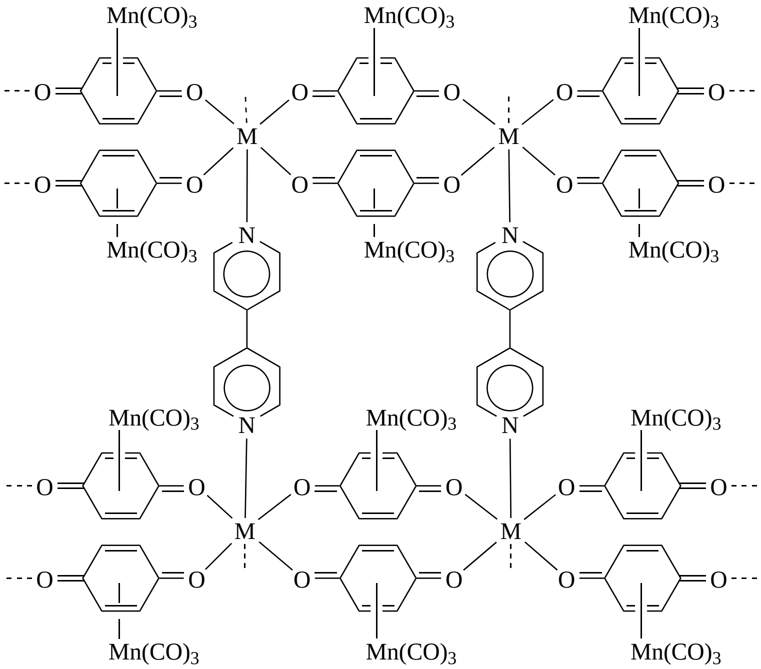

(**64**)

The manganese is η^6-bonded to the silane phenyl groups. Cyclodextrins are known to function as hosts for a variety of guest substrates. Monomeric and dimeric β-cyclodextrins have been shown to bind $CpMn(CO)_3$ as a guest, allowing water solubility and/or photosubstitution to be studied.[162,163]

9 RELATED ARTICLES

Carbonyl Complexes of the Transition Metals; Mechanisms of Reaction of Organometallic Complexes; Osmium: Inorganic & Coordination Chemistry; Semiconductor Interfaces.

10 REFERENCES

1. R. J. Wehmschulte and P. P. Power, *Organometallics*, 1995, **14**, 3264.
2. Y. Suh, J. Lee, S. Kim, and R. D. Rieke, *J. Organomet. Chem.*, 2003, **684**, 20.
3. K. Oshima, *J. Organomet. Chem.*, 1999, **575**, 1.
4. N. J. Holmes, W. Levason, and M. Webster, *J. Organomet. Chem.*, 1998, **568**, 213.
5. W. Levason, B. Patel, G. Reid, and A. J. Ward, *J. Organomet. Chem.*, 2001, **619**, 218.
6. T. M. Becker, J. A. Krause Bauer, C. L. Homrighausen, and M. Orchin, *J. Organomet. Chem.*, 2000, **602**, 97.
7. T. M. Becker, J. A. Krause Bauer, J. E. Del Bene, and M. Orchin, *J. Organomet. Chem.*, 2001, **629**, 165.
8. E. Hevia, J. Pérez, V. Riera, and D. Miguel, *Organometallics*, 2002, **21**, 5312.
9. G. A. Carriedo, P. G. Elipe, F. J. García Alonso, L. Fernández-Catuxo, M. R. Díaz, and S. García Granda, *J. Organomet. Chem.*, 1995, **498**, 207.
10. D. L. Reger, T. Christian Grattan, K. J. Brown, C. A. Little, J. J. S. Lamba, A. L. Rheingold, and R. D. Sommer, *J. Organomet. Chem.*, 2000, **607**, 120.
11. N. Burzlaff, I. Hegelmann, and B. Weibert, *J. Organomet. Chem.*, 2001, **626**, 16.
12. X. Fang, J. Huhmann-Vincent, B. L. Scott, and G. J. Kubas, *J. Organomet. Chem.*, 2000, **609**, 95.
13. W. A. King, B. L. Scott, J. Eckert, and G. J. Kubas, *Inorg. Chem.*, 1999, **38**, 1069.
14. A. Toupadakis, G. J. Kubas, W. A. King, B. L. Scott, and J. Huhmann-Vincent, *Organometallics*, 1998, **17**, 5315.
15. G. Albertin, S. Antoniutti, M. Bettiol, E. Bordignon, and F. Busatto, *Organometallics*, 1997, **16**, 4959.
16. P. A. Hamley, S. G. Kazarian, and M. Poliakoff, *Organometallics*, 1994, **13**, 1767.
17. T. Yasue, Y. Kawano, and M. Shimoi, *Angew. Chem. Int. Ed.*, 2003, **42**, 1727.
18. T. Kakizawa, Y. Kawano, and M. Shimoi, *Organometallics*, 2001, **20**, 3211.
19. S. Schlecht and J. F. Hartwig, *J. Am. Chem. Soc.*, 2000, **122**, 9435.
20. M. J. Shaw and J. Mertz, *Organometallics*, 2002, **21**, 3434.
21. B. T. Gregg and A. R. Cutler, *Organometallics*, 1994, **13**, 1039.
22. M. D. Cavanaugh, B. T. Gregg, and A. R. Cutler, *Organometallics*, 1996, **15**, 2764.
23. S. K. Mandal, J. A. Krause, and M. Orchin, *J. Organomet. Chem.*, 1994, **467**, 113.
24. B. T. Gregg and A. R. Cutler, *Organometallics*, 1998, **17**, 4169.
25. W. Eikens, S. Jäger, P. G. Jones, and C. Thöne, *J. Organomet. Chem.*, 1996, **511**, 67.
26. M. J. Mays, S. M. Owen, P. R. Raithby, P. F. Reinisch, G. P. Shields, and G. A. Solan, *J. Organomet. Chem.*, 1997, **528**, 123.
27. J. T. Lin, A. C. Yeh, Y. C. Chou, T. Y. R. Tsai, and Y. S. Wen, *J. Organomet. Chem.*, 1995, **486**, 147.
28. L. Manojlovic-Muir, K. W. Muir, M. C. Jennings, M. J. Mays, G. A. Solan, and K. W. Woulfe, *J. Organomet. Chem.*, 1995, **491**, 255.
29. V. G. Albano, L. Busetto, M. Monari, and V. Zanotti, *J. Organomet. Chem.*, 1999, **583**, 28.
30. S. T. Liu, D. R. Hou, T. C. Lin, M. C. Cheng, and S. M. Peng, *Organometallics*, 1995, **14**, 1529.
31. G. Canole, J. E. Davies, J. D. King, M. J. Mays, M. McPartlin, H. R. Powell, and P. R. Raithby, *J. Organomet. Chem.*, 1999, **585**, 141.
32. R. D. Adams, O. Kwon, and M. D. Smith, *Inorg. Chem.*, 2001, **40**, 5322.
33. R. D. Adams, O. Kwon, and M. D. Smith, *Inorg. Chem.*, 2002, **41**, 6281.
34. R. D. Adams and S. Miao, *J. Organomet. Chem.*, 2003, **665**, 43.
35. H. Braunschweig and T. Wagner, *Angew. Chem., Int. Ed. Engl.*, 1995, **34**, 85.
36. H. Braunschweig and B. Ganter, *J. Organomet. Chem.*, 1997, **545**, 163.
37. J. M. Cooney, L. H. P. Gommans, L. Main, and B. K. Nicholson, *J. Organomet. Chem.*, 2001, **634**, 157.
38. G. J. Depree, N. D. Childerhouse, and B. K. Nicholson, *J. Organomet. Chem.*, 1997, **533**, 143.
39. M. A. Leeson, B. K. Nicholson, and M. R. Olsen, *J. Organomet. Chem.*, 1999, **579**, 243.
40. R. C. Cambie, L. C. Mui Mui, P. S. Rutledge, and P. D. Woodgate, *J. Organomet. Chem.*, 1994, **464**, 171.
41. W. J. Mace, L. Main, B. K. Nicholson, and M. Hagyard, *J. Organomet. Chem.*, 2002, **664**, 288.

42. J. M. Cooney, L. Main, and B. K. Nicholson, *J. Organomet. Chem.*, 1996, **516**, 191.
43. J. M. Cooney, C. V. Depree, L. Main, and B. K. Nicholson, *J. Organomet. Chem.*, 1996, **515**, 109.
44. M. B. Dinger, L. Main, and B. K. Nicholson, *J. Organomet. Chem.*, 1998, **565**, 125.
45. W. Tully, L. Main, and B. K. Nicholson, *J. Organomet. Chem.*, 1996, **507**, 103.
46. A. Suárez, F. Faraldo, J. M. Vila, H. Adams, A. Fernández, M. Lípez-Torres, and J. J. Fernández, *J. Organomet. Chem.*, 2002, **656**, 270.
47. W. Tully, L. Main, and B. K. Nicholson, *J. Organomet. Chem.*, 2001, **633**, 162.
48. J. P. Djukic, A. Maisse, and M. Pfeffer, *J. Organomet. Chem.*, 1998, **567**, 65.
49. J. P. Djukic, A. Maisse, M. Pfeffer, A. de Cian, and J. Fischer, *Organometallics*, 1997, **16**, 657.
50. G. R. Clark, M. R. Metzler, G. Whitaker, and P. D. Woodgate, *J. Organomet. Chem.*, 1996, **513**, 109.
51. R. D. Adams, O. Kwon, and M. D. Smith, *Inorg. Chem.*, 2002, **41**, 1658.
52. R. D. Adams, O. Kwon, and M. D. Smith, *Inorg. Chem.*, 2002, **41**, 5525.
53. R. D. Adams, O. Kwon, and M. D. Smith, *Organometallics*, 2002, **21**, 1960.
54. R. D. Adams, B. Captain, O. Kwon, and S. Miao, *Inorg. Chem.*, 2003, **42**, 3356.
55. R. D. Adams and O. Kwon, *Inorg. Chem.*, 2003, **42**, 6175.
56. D. Lafrance, J. L. Davis, R. Dhawan, and B. A. Arndtsen, *Organometallics*, 2001, **20**, 1128.
57. S. Sun, J. O. Edwards, and D. A. Sweigart, *Organometallics*, 1995, **14**, 1546.
58. M. F. Semmelhack, A. Lindenschmidt, and D. Ho, *Organometallics*, 2001, **20**, 4114.
59. K. Weßenbach and H. Fischer, *J. Organomet. Chem.*, 2001, **621**, 344.
60. Y. M. Terblans, H. M. Roos, and S. Lotz, *J. Organomet. Chem.*, 1998, **566**, 133.
61. A. Rabier, N. Lugan, R. Mathieu, and G. L. Geoffroy, *Organometallics*, 1994, **13**, 4676.
62. A. Rabier, N. Lugan, and R. Mathieu, *J. Organomet. Chem.*, 2001, **617–618**, 681.
63. Y. Ortin, Y. Coppel, N. Lugan, R. Mathieu, and M. J. McGlinchey, *Chem. Commun.*, 2001, 1690.
64. D. Unseld, V. V. Krivykh, K. Heinze, F. Wild, G. Artus, H. Schmalle, and H. Berke, *Organometallics*, 1999, **18**, 1525.
65. L. N. Novikova, M. G. Peterleitner, K. A. Sevumyan, O. V. Semeikin, D. A. Valyaev, N. A. Ustynyuk, V. N. Khrustalev, L. N. Kuleshova, and M. Y. Antipin, *J. Organomet. Chem.*, 2001, **631**, 47.
66. M. Akita, N. Ishii, A. Takabuchi, M. Tanaka, and Y. Moro-oka, *Organometallics*, 1994, **13**, 258.
67. H. Adams, S. G. Broughton, S. J. Walters, and M. J. Winter, *Chem. Commun.*, 1999, 1231.
68. M. R. Terry, L. A. Mercando, C. Kelley, G. L. Geoffroy, P. Nombel, N. Lugan, R. Mathieu, R. L. Ostrander, B. E. Owens-Waltermire, and A. L. Rheingold, *Organometallics*, 1994, **13**, 843.
69. Y. Tang, J. Sun, and J. Chen, *Organometallics*, 2000, **19**, 72.
70. Y. Tang, J. Sun, and J. Chen, *Organometallics*, 1999, **18**, 4337.
71. K. Venkatesan, F. J. Fernández, O. Blacque, T. Fox, M. Alfonso, H. W. Schmalle, and H. Berke, *Chem. Commun.*, 2003, 2006.
72. W. Weng, T. Bartik, and J. A. Gladysz, *Angew. Chem., Int. Ed. Engl.*, 1994, **33**, 2199.
73. F. J. Fernández, O. Blacque, M. Alfonso, and H. Berke, *Chem. Commun.*, 2001, 1266.
74. M. P. Thornberry, C. Slebodnick, P. A. Deck, and F. R. Fronczek, *Organometallics*, 2000, **19**, 5352.
75. H. Plenio and A. Warnecke, *Organometallics*, 1996, **15**, 5066.
76. S. A. Kur, M. J. Heeg, and C. H. Winter, *Organometallics*, 1994, **13**, 1865.
77. T. Jiao, Z. Pang, T. J. Burkey, R. F. Johnston, T. A. Heimer, V. D. Kleiman, and E. J. Heilweil, *J. Am. Chem. Soc.*, 1999, **121**, 4618.
78. A. Decken, A. J. MacKay, M. J. Brown, and F. Bottomley, *Organometallics*, 2002, **21**, 2006.
79. M. A. O. Volland, S. Kudis, G. Helmchen, I. Hyla-Kryspin, F. Rominger, and R. Gleiter, *Organometallics*, 2001, **20**, 227.
80. M. Tamm, A. Grzegorzewski, T. Steiner, T. Jentzsch, and W. Werncke, *Organometallics*, 1996, **15**, 4984.
81. D. Miguel, D. Morales, V. Riera, and S. García-Granda, *Angew. Chem., Int. Ed.*, 2002, **41**, 3034.
82. A. A. Bengali, *Organometallics*, 2000, **19**, 4000.
83. J. A. Banister, P. D. Lee, and M. Poliakoff, *Organometallics*, 1995, **14**, 3876.
84. P. D. Lee, J. L. King, S. Seebald, and M. Poliakoff, *Organometallics*, 1998, **17**, 524.
85. K. L. Malisza, S. Top, J. Vaissermann, B. Caro, M. C. Sénéchal-Tocquer, D. Sénéchal, J. Y. Saillard, S. Triki, S. Kahlal, J. F. Britten, M. J. McGlinchey, and G. Jaouen, *Organometallics*, 1995, **14**, 5273.
86. M. Hromadová, M. Salmain, R. Sokolová, L. Pospíšil, and G. Jaouen, *J. Organomet. Chem.*, 2003, **668**, 17.
87. R. Khayatpoor and J. R. Shapley, *Organometallics*, 2000, **19**, 2382.
88. T. E. Bitterwolf, S. C. Everly, A. L. Rheingold, and G. Yapp, *J. Organomet. Chem.*, 1997, **531**, 1.
89. J. C. Röder, F. Meyer, I. Hyla-Kryspin, R. F. Winter, and E. Kaifer, *Chem. Eur. J.*, 2003, **9**, 2636.
90. B. Wrackmeyer, T. Hofmann, and M. Herberhold, *J. Organomet. Chem.*, 1995, **486**, 255.

91. S. Sun, C. A. Dullaghan, and D. A. Sweigart, *J. Chem. Soc., Dalton Trans.*, 1996, 4493.

92. R. D. Pike and D. A. Sweigart, *Coord. Chem. Rev.*, 1999, **187**, 183.

93. F. Rose-Munch, V. Gagliardini, C. Renard, and E. Rose, *Coord. Chem. Rev.*, 1998, **178–180**, 249.

94. J. D. Jackson, S. J. Villa, D. S. Bacon, and R. D. Pike, *Organometallics*, 1994, **13**, 3972.

95. S. C. Chaffee, J. C. Sutton, C. S. Babbitt, J. T. Maeyer, K. A. Guy, R. D. Pike, and G. B. Carpenter, *Organometallics*, 1998, **17**, 5586.

96. M. C. P. Yeh, C. C. Hwu, A. T. Lee, and M. S. Tsai, *Organometallics*, 2001, **20**, 4965.

97. F. Rose-Munch, C. Susanne, C. Renard, E. Rose, and J. Vaissermann, *J. Organomet. Chem.*, 1996, **519**, 253.

98. I. Verona, J. P. Gutheil, R. D. Pike, and G. B. Carpenter, *J. Organomet. Chem.*, 1996, **524**, 71.

99. V. Gagliardini, F. Balssa, F. Rose-Munch, E. Rose, C. Susanne, and Y. Dromzee, *J. Organomet. Chem.*, 1996, **519**, 281.

100. D. K. Astley and S. T. Astley, *J. Organomet. Chem.*, 1995, **487**, 253.

101. T. Y. Lee, S. S. Lee, Y. K. Chung, and S. W. Lee, *J. Organomet. Chem.*, 1995, **486**, 141.

102. C. A. Dullaghan, G. B. Carpenter, and D. A. Sweigart, *Chem. Eur. J.*, 1997, **3**, 75.

103. Y. Cao, K. Woo, L. K. Yeung, G. B. Carpenter, and D. A. Sweigart, *Organometallics*, 1997, **16**, 178.

104. K. Woo, P. G. Williard, D. A. Sweigart, N. W. Duffy, B. H. Robinson, and J. Simpson, *J. Organomet. Chem.*, 1995, **487**, 111.

105. K. Woo, Y. Cao, H. Li, K. Yu, G. B. Carpenter, D. A. Sweigart, and B. H. Robinson, *J. Organomet. Chem.*, 2001, **630**, 84.

106. F. Rose-Munch, C. Susanne, F. Balssa, and E. Rose, *J. Organomet. Chem.*, 1994, **476**, C25.

107. J. A. Kim, T. M. Chung, Y. K. Chung, J. H. Jung, and S. W. Lee, *J. Organomet. Chem.*, 1995, **486**, 211.

108. C. Renard, R. Valentic, F. Rose-Munch, and E. Rose, *Organometallics*, 1998, **17**, 1587.

109. J. Chen, V. G. Young Jr, and R. J. Angelici, *Organometallics*, 1996, **15**, 325.

110. S. S. Lee, T. Y. Lee, D. S. Choi, J. S. Lee, and Y. K. Chung, *Organometallics*, 1997, **16**, 1749.

111. S. G. Lee, J. A. Kim, Y. K. Chung, T. S. Yoon, N. Kim, and W. Shin, *Organometallics*, 1995, **14**, 1023.

112. H. Seo, S. G. Lee, D. M. Shin, B. K. Hong, S. Hwang, D. S. Chung, and Y. K. Chung, *Organometallics*, 2002, **21**, 3417.

113. J. F. Carpentier, Y. Castanet, J. Brocard, A. Mortreux, F. Rose-Munch, C. Susanne, and E. Rose, *J. Organomet. Chem.*, 1995, **493**, C22.

114. D. Prim, A. Auffrant, F. Rose-Munch, E. Rose, and J. Vaissermann, *Organometallics*, 2001, **20**, 1901.

115. A. Auffrant, D. Prim, F. Rose-Munch, E. Rose, and J. Vaissermann, *Organometallics*, 2002, **21**, 3500.

116. A. Auffrant, D. Prim, F. Rose-Munch, E. Rose, and J. Vaissermann, *Organometallics*, 2001, **20**, 3214.

117. A. Auffrant, D. Prim, F. Rose-Munch, E. Rose, and S. Schouteeten, *Organometallics*, 2003, **22**, 1898.

118. S. Sun, L. K. Yeung, D. A. Sweigart, T. Y. Lee, S. S. Lee, Y. K. Chung, S. R. Switzer, and R. D. Pike, *Organometallics*, 1995, **14**, 2613.

119. S. Lee, S. R. Lovelace, and N. J. Cooper, *Organometallics*, 1995, **14**, 1974.

120. C. A. Dullaghan, G. B. Carpenter, D. A. Sweigart, D. Kuck, C. Fusco, and R. Curci, *Organometallics*, 2000, **19**, 2233.

121. S. S. Lee, T. Y. Lee, J. E. Lee, I. S. Lee, Y. K. Chung, and M. S. Lah, *Organometallics*, 1996, **15**, 3664.

122. E. J. Watson, K. L. Virkaitis, H. Li, A. J. Nowak, J. S. D'Acchioli, K. Yu, G. B. Carpenter, Y. K. Chung, and D. A. Sweigart, *Chem. Commun.*, 2001, 457.

123. S. U. Son, K. H. Park, S. J. Lee, Y. K. Chung, and D. A. Sweigart, *Chem. Commun.*, 2001, 1290.

124. S. Sun, C. A. Dullaghan, G. B. Carpenter, A. L. Rieger, P. H. Rieger, and D. A. Sweigart, *Angew. Chem., Int. Ed. Engl.*, 1995, **34**, 2540.

125. A. Georg and C. G. Kreiter, *Eur. J. Inorg. Chem.*, 1999, 651.

126. S. U. Son, S. J. Paik, I. S. Lee, Y. A. Lee, Y. K. Chung, W. K. Seok, and H. N. Lee, *Organometallics*, 1999, **18**, 4114.

127. S. U. Son, K. H. Park, and Y. K. Chung, *Organometallics*, 2000, **19**, 5241.

128. J. M. Veauthier, A. Chow, G. Fraenkel, S. J. Geib, and N. J. Cooper, *Organometallics*, 2000, **19**, 3942.

129. J. M. Veauthier, A. Chow, G. Fraenkel, S. J. Geib, and N. J. Cooper, *Organometallics*, 2000, **19**, 661.

130. S. U. Son, S. J. Paik, K. H. Park, Y. A. Lee, I. S. Lee, and Y. K. Chung, *Organometallics*, 2002, **21**, 239.

131. S. Lee, S. J. Geib, and N. J. Cooper, *J. Am. Chem. Soc.*, 1995, **117**, 9572.

132. S. Lee, S. R. Lovelace, D. J. Arford, S. J. Geib, S. G. Weber, and N. J. Cooper, *J. Am. Chem. Soc.*, 1996, **118**, 4190.

133. S. H. K. Park, S. J. Geib, and N. J. Cooper, *J. Am. Chem. Soc.*, 1997, **119**, 8365.

134. L. Shao, S. J. Geib, P. D. Badger, and N. J. Cooper, *J. Am. Chem. Soc.*, 2002, **124**, 14812.

135. S. S. Lee, E. Jeong, and Y. K. Chung, *J. Organomet. Chem.*, 1994, **483**, 115.

136. F. Balssa, V. Gagliardini, F. Rose-Munch, and E. Rose, *Organometallics*, 1996, **15**, 4373.

137. E. Rose, C. Le Corre-Susanne, F. Rose-Munch, C. Renard, V. Gagliardini, F. Teldji, and J. Vaissermann, *Eur. J. Inorg. Chem.*, 1999, 421.

138. H. J. Chung, J. B. Sheridan, M. L. Coté, and R. A. Lalancette, *Organometallics*, 1996, **15**, 4575.

139. M. Oh, K. Yu, H. Li, E. J. Watson, G. B. Carpenter, and D. A. Sweigart, *Adv. Synth. Catal.*, 2003, **345**, 1053.

140. X. Zhang, G. B. Carpenter, and D. A. Sweigart, *Organometallics*, 1999, **18**, 4887.

141. X. Zhang, K. Yu, G. B. Carpenter, and D. A. Sweigart, *Organometallics*, 2000, **19**, 1201.

142. K. Yu, H. Li, E. J. Watson, K. L. Virkaitis, G. B. Carpenter, and D. A. Sweigart, *Organometallics*, 2001, **20**, 3550.

143. H. Li, G. B. Carpenter, and D. A. Sweigart, *Organometallics*, 2000, **19**, 1823.

144. X. Zhang, E. J. Watson, C. A. Dullaghan, S. M. Gorun, and D. A. Sweigart, *Angew. Chem., Int. Ed.*, 1999, **38**, 2206.

145. D. S. Choi, S. H. Hong, S. S. Lee, and Y. K. Chung, *J. Organomet. Chem.*, 1999, **579**, 385.

146. X. Zhang, C. A. Dullaghan, G. B. Carpenter, D. A. Sweigart, and Q. Meng, *Chem. Commun.*, 1998, 93.

147. C. A. Dullaghan, G. B. Carpenter, D. A. Sweigart, D. S. Choi, S. S. Lee, and Y. K. Chung, *Organometallics*, 1997, **16**, 5688.

148. C. A. Dullaghan, X. Zhang, D. Walther, G. B. Carpenter, and D. A. Sweigart, *Organometallics*, 1997, **16**, 5604.

149. X. Zhang, C. A. Dullaghan, E. J. Watson, G. B. Carpenter, and D. A. Sweigart, *Organometallics*, 1998, **17**, 2067.

150. C. A. Dullaghan, S. Sun, G. B. Carpenter, B. Weldon, and D. A. Sweigart, *Angew. Chem., Int. Ed. Engl.*, 1996, **35**, 212.

151. H. Li, K. Yu, E. J. Watson, K. L. Virkaitis, J. S. D’Acchioli, G. B. Carpenter, D. A. Sweigart, P. T. Czech, K. R. Overly, and F. Coughlin, *Organometallics*, 2002, **21**, 1262.

152. M. A. Reynolds, I. A. Guzei, B. C. Logsdon, L. M. Thomas, R. A. Jacobson, and R. J. Angelici, *Organometallics*, 1999, **18**, 4075.

153. S. Sun, G. B. Carpenter, and D. A. Sweigart, *J. Organomet. Chem.*, 1996, **512**, 257.

154. M. Oh, G. B. Carpenter, and D. A. Sweigart, *Organometallics*, 2002, **21**, 1290.

155. M. Oh, G. B. Carpenter, and D. A. Sweigart, *Organometallics*, 2003, **22**, 1437.

156. M. Oh, G. B. Carpenter, and D. A. Sweigart, *Acc. Chem. Res.*, 2004, **37** 1.

157. M. Oh, G. B. Carpenter, and D. A. Sweigart, *Angew. Chem., Int. Ed.*, 2001, **40**, 3191.

158. M. Oh, G. B. Carpenter, and D. A. Sweigart, *Angew. Chem., Int. Ed.*, 2002, **41**, 3650.

159. M. Oh, G. B. Carpenter, and D. A. Sweigart, *Angew. Chem., Int. Ed.*, 2003, **42**, 2025.

160. M. Oh, G. B. Carpenter, and D. A. Sweigart, *Macromol. Symp.*, 2003, **196**, 101.

161. A. J. Wiseman, R. G. Jones, and M. J. Went, *J. Organomet. Chem.*, 1997, **544**, 129.

162. C. Lu, Z. Ni, W. Liu, Y. Zou, J. Xie, C. Ni, H. Zhu, Q. Meng, and Y. Yao, *J. Organomet. Chem.*, 2003, **681**, 269.

163. L. Song, Q. Meng, and X. You, *J. Organomet. Chem.*, 1995, **498**, C1.

Manganese: The Oxygen-evolving Complex & Models

G. Charles Dismukes & Rogier T. van Willigen
Princeton University, Princeton, NJ, USA

Based in part on the article Manganese: Oxygen-Evolving Complex & Models by Lars-Erik Andréasson & Tore Vänngård which appeared in the Encyclopedia of Inorganic Chemistry, First Edition.

1 Introduction: Origin and Significance of Oxygenic Photosynthesis 1
2 The O_2 Clock Reaction Steps: the 'S-State Cycle' 2
3 X-ray Diffraction (XRD) Structure of the PSII Protein Complex 2
4 Atomic Structure of the Inorganic Core from XRD and Spectroscopy 4
5 Insights from Mutagenesis 5
6 Mn Oxidation States and Electronic (Spin) States 6
7 Energetics of S-State Transitions: Free Energy and Activation Energy Barriers 8
8 Substrate Binding, Exchange, and Mechanism of O_2 Evolution 9
9 Why Manganese? Inorganic Mutants 11
10 Functional Manganese Complexes that Split Water 12
11 Related Articles 14
12 References 14

Abbreviations

PSII = Photosystem II; WOC = Water-oxidizing complex; OEC = Oxygen-evolving complex; (B)RC = (Bacterial) Reaction Center; Chl = Chlorophyll; Bchl = Bacteriochlorophyll; XRD = X-ray diffraction; EPR = Electron paramagnetic resonance; EXAFS = Extended X-ray absorption fine structure; ENDOR = Electron-nuclear double resonance; ESEEM = Electron spin echo envelope modulation; ($Tyr_Z = Y_Z$) = D1Tyr161; ATP = Adenosine Triphosphate; KIE = Kinetic isotope effect; UV = UltraViolet; (FT−)IR = (Fourier Transform) InfraRed.

1 INTRODUCTION: ORIGIN AND SIGNIFICANCE OF OXYGENIC PHOTOSYNTHESIS

The production of O_2 by the oxidation of water within photosynthetic organisms is a striking signature of life on Earth. This biological innovation appeared in the precursors to contemporary cyanobacteria circa 2.2−3.8 billion years ago and had profound global geological consequences.[1,2] Very little is known about how water splitting chemistry was invented.[3–5] By using water as an inexhaustible source of electrons and protons, it enabled the proliferation of phototrophic life everywhere on the planet. This event was nature's analog of the 'universal big bang'. It transformed the atmosphere from anaerobic to O_2-rich, perfused phototrophic life throughout the oceans, pigmented the surface of Earth in a carpet of green chlorophyll, and enabled the biogeochemical cycles to develop their present forms. The emergence of atmospheric O_2 permitted the development of respiratory metabolism with its vastly more efficient energy production. This new boost in metabolic energy *supercharged* the engine of life and led to all complex life as we know it.

O_2 is a by-product of splitting water into electrons and protons within a wide variety of photosynthetic organisms, including both prokaryotes (cyano- and oxyphoto-bacteria), and eukaryotes (green algae and higher plants). Water splitting is driven by the membrane pigment-protein complex known as the photosystem II−water oxidizing complex (PSII-WOC) or oxygen-evolving complex (PSII-OEC). The electrons and protons are ultimately used to store energy in the phosphoanhydride bond of ATP and to reduce CO_2 to carbohydrate, the precursors for synthesis of the biopolymers needed by the organism. Some cyanobacteria and green algae also use the protons and electrons to synthesize hydrogen under anaerobic conditions, presumably to eliminate excess reducing capacity.

A single class of PSII-WOC enzymes is found in all O_2-producing (oxygenic) phototrophs that have been studied to date. No variation of the inorganic core $Mn_4Ca_1O_xCl_{1-2}(HCO_3)_y$ has been identified among them. The PsbA gene encoding the D1 reaction center protein subunit that binds this inorganic core is highly conserved in more than 180 sequences. This invariance of both the protein and cofactors is an extraordinary feature that is not found anywhere else in biology. It is as if nature has performed combinatorial synthesis through evolution over 2.2−3.8 billion years, using all possible ecological habitats that are permissive of photosynthetic metabolism and has been able to invent *only one biological blueprint for water splitting.* This lesson is vital to appreciate by all who are engaged in creating biomimetic catalysts or engineered PSII enzymes for practical applications.

Two applications for which catalysts are sought are the direct solar splitting of water for hydrogen production, and the reversible reduction of O_2 to water in fuel cell cathodes. Nature uses abundant metals (Mn, Ca) organized into a novel, self-repairing, cluster to achieve water splitting. By contrast, man-made water splitting catalysts use rare noble metals (Pt) that operate inefficiently and create damaging reactive intermediates. The lessons learned from photosynthetic water splitting are beginning to contribute to more practical solutions.

In this article, we offer a brief and select overview of the literature on the atomic and electronic structure of the water-splitting enzyme,[5–7] the chemical basis of its catalysis, and insights learned from functional model complexes. Citations cover the main review articles that are available rather than primary works.

2 THE O_2 CLOCK REACTION STEPS: THE ‘S-STATE CYCLE’

The PSII-WOC accomplishes a complex task of converting the one-electron photoexcited state of chlorophyll into the concerted four-electron (all-or-nothing) oxidation of two water molecules. The working model used to discuss the intermediate oxidation states of all PSII-WOC enzymes comes from studies of flash O_2 yield measurements by Joliot and coworkers and the interpretation by Kok and coworkers.[8,9] Illumination of dark-adapted chloroplasts or algal cells with saturating flashes of light leads to the production of O_2 in a characteristic pattern peaking on flash #3 and repeating each four flashes. It was therefore concluded that O_2 production takes place at a catalytic center and that each flash advances the oxidation state of the WOC by removal of one electron. O_2 is formed and released only after four oxidation equivalents are accumulated. The ‘S-state cycle’ which describes this sequence is shown in Figure 1. The stoichiometry of the inorganic cofactors which make up the WOC is $Mn_4Ca_1O_xCl_{1-2}(HCO_3)_y$ and has been determined by various spectroscopic, extraction, and reconstitution studies.[10–12] The pattern of proton release during the cycle is also known and changes with the pH of the medium and the number of protein subunits present in the PSII complex.[13] Electrostatic effects on ionizable protein residues are involved (Bohr protons) as well as the intrinsic protons released from substrate water molecules. The latter stoichiometry has been estimated to be 1:0:1:2.[14] One or more essential Cl^- ions bind within the PSII-WOC complex and are postulated to play a role in proton transfer from the Mn cluster to the medium.[15] Additional information about the kinetics of the S-state advances, stoichiometry of proton release, and the rate of substrate (water) exchange with bulk water is given in Table 1.

Table 1 Half-life ($T_{1/2}$) for the S-state transitions $S_i \rightarrow S_{i+1}$,[16] the stoichiometry of proton release[14] and the rate of exchange of the two substrate water molecules with bulk solvent water[17,18]

Reaction		# H^+ pH	H_2O exchange rate in S_i	
$S_i \rightarrow S_{i+1}$	$T_{1/2}$ (μs)	7.4/6.3	Fast (s^{-1})	Slow (s^{-1})
$S_0 \rightarrow S_1$	30	0.5/1.5	>100	13.6
$S_1 \rightarrow S_2$	100	1.0/1.1	>100	0.02
$S_2 \rightarrow S_3$	250	1.5/0.5	>175	2.0
$S_3 \rightarrow S_4$	1300	1.0/0.9	37.5	2.0

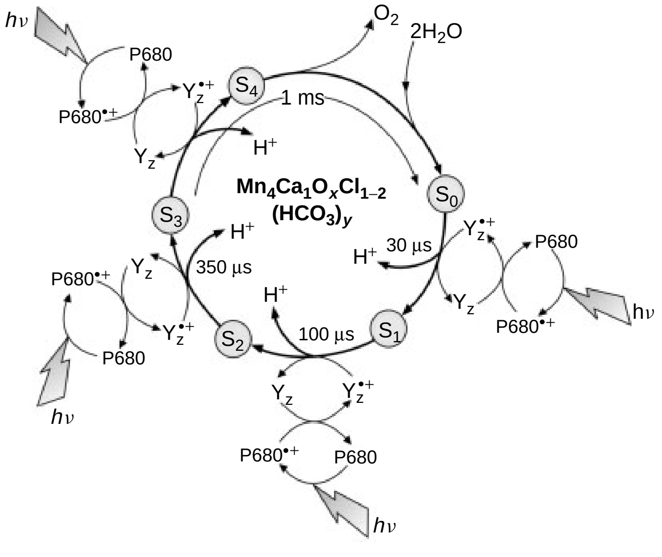

Figure 1 The intermediate oxidation states (S-states) of the PSII-WOC created by single turnover flashes. (Reproduced, with permission, from J. Nield, ‘‘Structural Characterisation of Photosystem II’’ Ph.D. thesis, University of London, 1997)

3 X-RAY DIFFRACTION (XRD) STRUCTURE OF THE PSII PROTEIN COMPLEX

Three XRD models of the PSII-WOC complex from a thermophilic cyanobacterium *Thermosynechococcus* species have been published at resolutions ranging from 3.8 to 3.5 Å.[19–21] The most complete data set was calculated by the method of multiple isomorphus replacement using six heavy atom derivatives and has substantially reduced residuals (R-factor = 30.4% at 3.5 Å resolution vs >53% for the other structures). Hence, we shall discuss this more refined model.[21] The crystallographic asymmetric unit contains a dimer of PSII (640 kDa mass; dimensions: 105 Å depth, 205 Å length, and 110 Å width) with two nearly identical monomers. Within the PSII dimer, monomers are related by noncrystallographic twofold axis perpendicular to the membrane plane. Each monomer consists of 16 integral membrane subunits composed of 35 transmembrane helices and 3 peripheral subunits. The monomer is characterized by pseudo 2-fold symmetry, which rotates the D1, CP47 and *PsbI* subunits into the D2, CP43 and *PsbX* subunits. Each monomer contains 36 chlorophyll *a* (Chl), 7–8 all-trans β-carotene molecules, 1 WOC (Mn_4Ca cluster), 1 heme *b*, one heme *c*, 2 plastoquinones, 2 pheophytins, 1 nonheme Fe, and 2 putative bicarbonate molecules. A stoichiometry of 4Mn and 1 Ca for the WOC was previously established from several lines of evidence, including ^{55}Mn hyperfine structure in EPR,[22] Mn EXAFS and the rate of O_2 evolution activity during light-driven reconstitution of the free inorganic cofactors to apo-WOC-PSII complexes (photoactivation).[12]

3.1 Charge Separation

Light-driven electron-transfer steps among pigments within the reaction center (RC), composed of the D1 and D2 subunits, serve to trap the light energy delivered from the inner antennas (CP43 and CP47) or outer antennas complexes. Figure 2 depicts the cofactors involved in these electron-transfer reactions. Upon illumination, an electron is transferred *ca.* 35 Å across the membrane from the excited primary electron donor P680 – comprising one or more of the four Chls symmetrically positioned with the D1D2 RC subunits near the lumenal surface – to the final electron acceptor plastoquinone Q_B via Chl_{D1}, pheophytin ($Pheo_{D1}$), plastoquinone Q_A, and nonheme Fe(II). After accepting two electrons and undergoing protonation, plastoquinonol $QH_{2(B)}$ is released from PSII into the membrane matrix. The photo-generated cationic radical $P680^{\bullet +}$ is reduced by a tyrosine residue known as Tyr_Z (D1Tyr161) to generate a neutral tyrosine radical $Tyr_Z^{\bullet}$ which acts as an oxidant for the water oxidation process at the WOC.

The radical cation $P680^{\bullet +}$ oxidizing potential, recently estimated to be 1.3–1.4 V, exceeds that required for water splitting and is the highest of all types of reaction centers.[23] The two Chls denoted P_{D1} and P_{D2}, equivalent to the 'special pair' of bacteriochlorophylls (Bchl) in the anoxygenic bacterial reaction center (BRC), are rotated by 20° to the membrane normal and separated slightly further (Mg–Mg distance of 8.2 Å) than in BRC. The tetrapyrrole head groups of P_{D1} and P_{D2} are in van der Waals contact, but do not have appreciable π overlap, which could explain why P680 shows more monomeric character and weaker electronic coupling than its bacterial counterpart. P_{D1} and P_{D2} Chls are close to Chl_{D1} and Chl_{D2}, suggesting that the P680 excited state is delocalized over the four Chls and that Chl_{D1}, which is closest to the active branch $Pheo_{D1}$, participates in the primary charge separation. The electrons are transferred from $Pheo_{D1}$ to Q_A, which is a firmly bound plastoquinone. Even though PSII and BRCs utilize different primary quinone acceptors, the Q_A binding pockets are structurally similar.

3.2 The Water-splitting Center[21]

The Mn_4Ca cluster is asymmetrically located off the pseudo twofold symmetry axis that relates the 4 Chl molecules comprising P680 and approximately 8 Å below the mean interface of the transmembrane domain. The edge of the closest Chl of P680 is located 8.1 Å from the edge of the photooxidizable tyrosyl radical Tyr_Z (closest non-H atoms) and the latter is located 5.1 Å to the Ca atom and 6.5 Å to the closest Mn atom. This asymmetrical location likely contributes to the strong bias for charge separation involving the closest branch of RC Chls. Water molecules are presumed to fill the gap between the Mn and Tyr_Z. The phenoxyl hydrogen of Tyr_Z is hydrogen bonded to D1His190 and is the presumed proton acceptor required for stable photooxidation to form the neutral

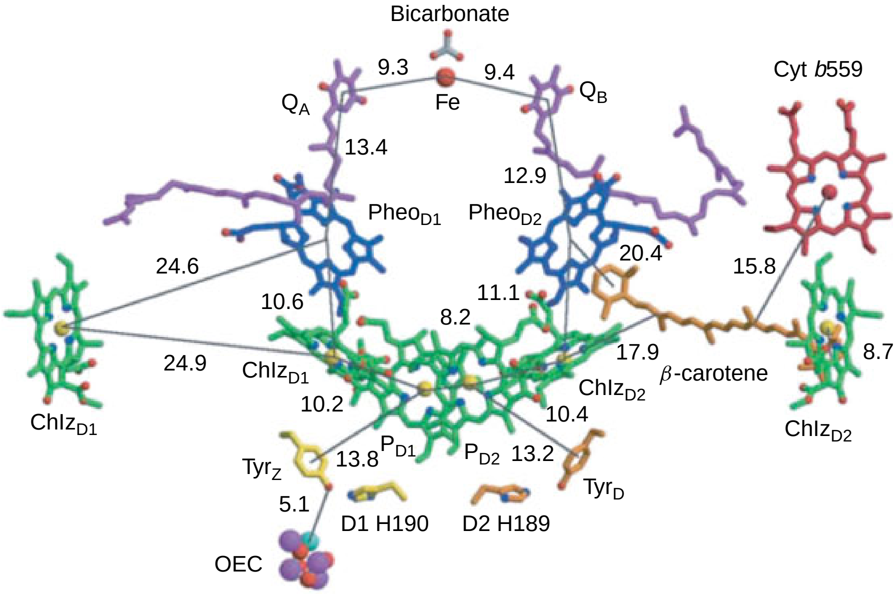

Figure 2 XRD model of the cofactors bound to photosystem II RC core and the water-oxidizing complex. The view is perpendicular to the membrane normal. (Reprinted with permission from K. Ferreira, T. Iverson, K. Maghlaoui, J. Barber and S. Iwata, Science Express, DOI 1093087 (2004). © 2004 AAAS)

tyrosyl radical. Together with the D1Glu189 these residues form hydrogen bonds that have been proposed to be involved in proton ejection into the lumenal space.[24] The distances and geometry provide no support for a mechanism in which Tyr_Z directly abstracts a H atom from substrate water bound to the Mn cluster. However, proton-coupled electron-transfer steps involving other bases in the active site may be involved as proton acceptors.

All of the protein ligands to the Mn_4Ca cluster come from side chains from three different domains of the D1 subunit and one domain of CP43. In D1 these domains are the carboxyl terminus (between H332 and D342), two residues within the interhelical CD luminal loop (D170 and E189), and one residue in the interhelical AB loop (D61). No homology to other protein folding domains is evident.

4 ATOMIC STRUCTURE OF THE INORGANIC CORE FROM XRD AND SPECTROSCOPY

The electron density attributed to the Mn_4Ca cluster is described as 'capped tetrahedral' when contoured at 8σ, with 4 metal atoms in the large end and one in a connected small end (Figure 3). A series of difference Fourier omit maps accommodates a tetrahedral array of 4 metal ions ($3\text{Mn} + \text{Ca}$) in the large end and one Mn in the small end. The small protruding density has been assigned to 1Mn based on comparing the anomalous scattering of X rays that are preferentially absorbed by Mn. A Ca atom is located in one of the corners of the tetrahedron based upon anomalous diffraction data taken at the Ca absorption edge. The presence of Ca is supported also by compelling evidence from three types of EXAFS measurements obtained at the Mn-, Ca- and Sr edges.[25] The EXAFS data clearly show that Ca is located at ~ 3.4 Å to Mn, but had anticipated only 1 or 2Mn scatters at this distance, not 4Mn as proposed in the XRD model. The intermetal distances within the cube are not adequately resolved in the XRD data and have been set equal for simplicity, yielding a symmetrical trigonal prism of CaMn_3. The authors postulate four bridging oxides (not directly observable) linking the tetrahedral array of CaMn_3 atoms, with one of these oxides (μ_4-oxo) bridging to the fourth Mn atom external to the cube (Figures 3 and 4). The resulting CaMn_4O_4 cluster can be classified also in terms of the two types of oxide bridges $(\mu_3\text{-oxo})_3(\mu_4\text{-oxo})$ that make up the core. The resulting CaMn_4O_4 core is novel; no exact structural analogs have been synthesized, although all manganese-oxo cubanes containing the $[\text{Mn}_4\text{O}_4]^{n+}$ are known.[26] Mn EXAFS and ^{55}Mn magnetic hyperfine (EPR) data had previously established the Mn stoichiometry of the WOC and were compatible with 8 possible Mn_4O_x core geometries, one of which has the same topology as the XRD model.[22,25] However, both the EXAFS and EPR data require that a lower symmetry cluster must exist in S_1 and S_2, with Mn EXAFS-derived intermanganese distances of 2.7 Å and 3.3 Å in S_1. This asymmetry could be accommodated if some of the bridging oxygen atoms are water or hydroxide molecules.

The 3Mn atoms within the cubane core each have one terminal carboxylate ligand, two from D1 (D342, E189) and one from CP43 (E354), while one Mn has an additional histidine ligand from D1 (H332). A proposed μ-oxo bridge that lies at the corner of the cube trans to Ca is H-bonded to a histidine of D1 (H337). The Mn atom external to the cube is ligated to two carboxylates from D1 (D170 and E333), two proposed water molecules (one of which is H-bonded to aspartate-61 carboxylate from D1), and an unidentified

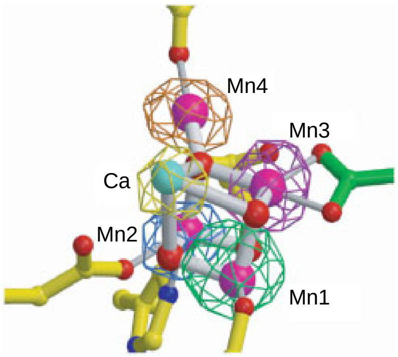

Figure 3 The electron density map of the Mn_4Ca cluster, calculated after omission of each metal of the WOC. The maps are contoured at 8σ for Mn1, Mn2, and Mn3 and 7σ for Mn4 and Ca. (Reprinted with permission from K. Ferreira, T. Iverson, K. Maghlaoui, J. Barber and S. Iwata, Science Express, DOI 1093087 (2004). © 2004 AAAS)

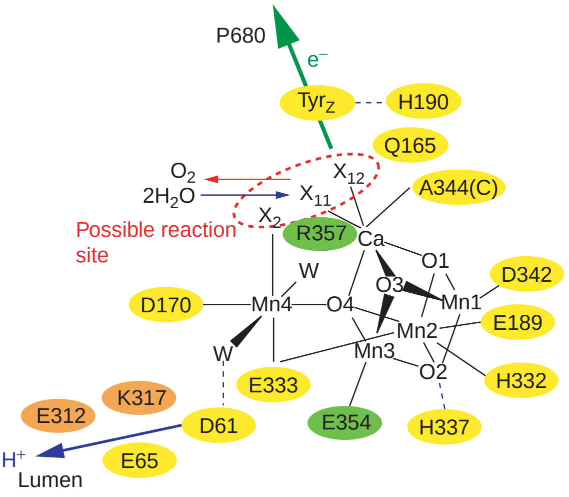

Figure 4 Schematic coordination of the WOC, its protein ligands and other important residues. Residues in D1, D2, and CP43 subunits are shown in yellow, orange, and green, while X_{11}, X_{12}, and X_2 denote nonprotein ligands, possibly substrate water binding positions or bicarbonate site. (Reprinted with permission from K. Ferreira, T. Iverson, K. Maghlaoui, J. Barber and S. Iwata, Science Express, DOI 1093087 (2004). © 2004 AAAS)

heavier scatterer X1 (possibly Cl^-, SO_4^{2-} or CO_3^{2-}). The Ca atom has no protein ligands but is coordinated to two solute molecules X21 and X22 having electron density greater than water (postulated as Cl^-, SO_4^2, or CO_3^{2-}). Arginine residue Arg357 from CP43 is positioned with its side chain fully extended and its cationic guanidinium group interacting with the nonprotein ligand X1 with a $N^{\cdots}X_1$ bond length of 1.9 Å. In the current model the authors have positioned a tridentate carbonate ligand bridging between the exo-cuboidal Mn and Ca at these positions (both X22 and X23 carbonate(O)$^{\cdots}$Ca distances = 2.26 Å). The authors postulate that these sites constitute the likely substrate water sites.

The net charge of the core of the WOC is not known experimentally. The XRD model for the $[Mn_4CaO_4]^n$ core suggests charges of $n = 6+$ or $8+$ for S_1 (assuming $4Mn^{III}$ or $2Mn^{III} + 2Mn^{IV}$ as suggested by EPR and Mn XAS, respectively). Assuming that the coordinated protein carboxylates are ionized, there are a total of 6− charges from the ligands. This leaves a minimal net charge for the WOC of zero or 2+, respectively, and possibly greater assuming that some of the oxo bridges are protonated. Charge neutralization within buried active sites suggests that the nonprotein ligands (X1, X22, X23 and possibly other Mn coordinate sites) are most likely anionic ligands. The possibilities include solute (OH^-), other native cofactors required for water splitting (Cl^-, CO_3^{2-}) or precipitant (SO_4^{2-}).

5 INSIGHTS FROM MUTAGENESIS

The XRD model of the PSII monomer contains assignments for 19 of the 21 known PSII gene products except for the genes PsbW and PsbY. Mutagenesis studies have been carried out on some of these protein subunits, with the majority directed at the D1 protein and more recently CP43.[24,27–29] The consequences of point mutations in selected residues of the D1 and CP43 proteins are summarized in Figure 5 and discussed below.

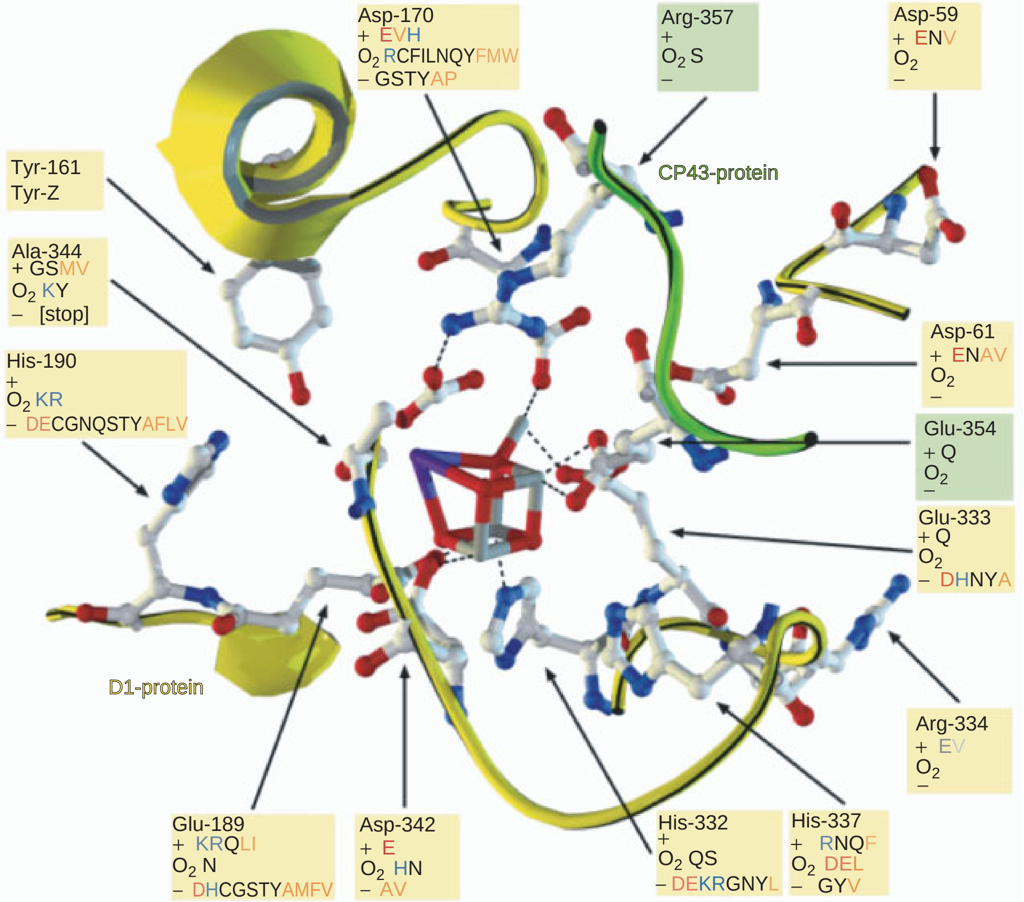
Asp-170
+ EVH
O_2 RCFILNQYFMW
– GSTYAP
Arg-357
+
O_2 S
–
Asp-59
+ ENV
O_2
–
Tyr-161
Tyr-Z
CP43-protein
Ala-344
+ GSMV
O_2 KY
– [stop]
His-190
+
O_2 KR
– DECGNQSTYAFLV
Asp-61
+ ENAV
O_2
–
Glu-354
+ Q
O_2
–
Glu-333
+ Q
O_2
– DHNYA
D1-protein
Arg-334
+ EV
O_2
–
Glu-189
+ KRQLI
O_2 N
– DHCGSTYAMFV
Asp-342
+ E
O_2 HN
– AV
His-332
+
O_2 QS
– DEKRGNYL
His-337
+ RNQF
O_2 DEL
– GYV

Figure 5 Consequences of point mutations in D1 (yellow) and CP43 (green). In the boxes, the first line (+) indicates amino acids mutations that support photoautotrophic growth (light + CO_2) and evolve O_2. The second line (O_2) indicates mutants that do not grow photoautotrophically but retain an initial O_2 evolution rate when grown heterotrophically (≥5% vs. the wild-type strain). The third line (−) indicates lethal mutants that do not grow photoautotrophically, have no O_2 evolution activity, and in some cases no photooxidizable Mn. Amino acid color coding: acidic (red), basic (blue), hydrophobic (brown)

The primary aims of mutagenesis are to identify those amino acid residues that control the assembly and functioning of the $Mn_4Ca_1O_x$ cluster and the reactivity of $D1Tyr_Z161$.

Mutagenesis studies have identified three domains of the D1 protein implicated in assembly of a stable WOC or expression of O_2 evolution activity. In D1 these domains are the carboxyl terminus, the interhelical CD lumenal loop, and residues in the interhelical AB lumenal loop. These loci agree with the amino acid sites identified by XRD.

Within the carboxyl-terminus of D1, multiple residues play a role in stabilizing the WOC by interaction with one or more of the three internal Mn ions of the $Mn_3Ca_1O_x$-cube. Studies have been performed on D1Ala244, D1Asp342, D1His332, D1His337, D1Arg334, and D1Glu333, of which Asp342, His332, and Glu333 ligate the $Mn_4Ca_1O_x$-cluster according to the crystal structure (see Figure 5). There is solid evidence from pulsed EPR studies and FTIR for one histidine ligand to the $Mn_4Ca_1O_x$ cluster which may correspond to D1His332. Most mutants of the ligating amino acid residues do not grow photoautotrophically and possess diminished oxygen evolution rates. Although the Ala344 is not ligating manganese (Reanalysis of the 3.6 A XRD data[30] has shown that two oxos at the corners of the Mn_3CaO_4 cubane-like core (O_1 and O_3, Figure 4) interact by hydrogen bonding to carboxylate residues (D1-Glu189 and D1-Ala 344-C-terminus). These oxos exhibit bonding interactions consistent with identification as water molecules. Mutagenesis studies are consistent with these carboxylate residues serving in proton pathways for substrate water deprotonation. On this basis and other evidence, the O_1 and O_3 corner sites have been proposed as the substrate water oxidation sites[30]), there is a requirement for the presence of an amino acid residue at this position.

The interhelical CD lumenal loop contains the Tyr_Z (D1Tyr161), probably hydrogen bonded to D1His190. It contains the D1Asp170 residue which ligates the high affinity Mn (exocubical Mn). Mutagenesis on this important residue shows that Glu, His, and even Val mutants grow photoautotrophically, while 11 other mutants show at least some oxygen evolution, albeit only when grown heterotrophically on glucose. The latter mutants fail to grow photoautotrophically apparently due to photoinactivation of the WOC. It was concluded from EPR measurements that Asp170 ligates the high affinity Mn site, as the binding and/or photooxidation of Mn(II) was altered in mutants at that site. Remarkably, some positively charged, polar, and hydrophobic mutants of D1Glu189, which is a ligand of the $Mn_4Ca_1O_x$ cluster, show photoautotrophic growth. An hypothesis is that mutants at this residue are involved in a network of hydrogen bonds, possibly in which additional bicarbonate or chloride ions might compensate for loss of the carboxylate charge in some mutants.

According to mutagenesis studies, the amino acid residues in the interhelical AB lumenal loop are involved in coordination of the Ca^{2+}, especially D1Asp59 and D1Asp61. The crystal structure does not yield evidence for direct binding of these residues to Ca. All examined mutants at these positions exhibit an elevated requirement for Ca^{2+} and show photoautotrophic growth. The mutagenesis and XRD results appear inconsistent but may not be. Since the Ca^{2+} binding assays used with the mutants are actually O_2 evolution assays performed in the presence of Mn, these assays reflect the cooperative binding between the high affinity Mn and Ca sites during assembly.[12]

Mutagenesis studies have examined the CP43 protein. First segment deletion studies were conducted, followed by site-directed mutagenesis. The point mutant, Glu354Gln, exhibits reduced photoautotrophic growth rate, although normal PSII content (e.g. no photoinactivation) and an 80% reduction in the O_2 evolution rate due to a specific impairment to the WOC.[31] The Arg357Ser mutant is the only available mutant at this site. It is unable to grow photoautotrophically, but does grow heterotrophically on glucose. It accumulates a normal amount of PSII core proteins, but these exhibit low electron-transfer rates, weak O_2 evolution activity (10%) and strong photoinactivation kinetics (fourfold).[32] These results clearly show an important role that both of these residues play in water-splitting chemistry, as would be expected by the XRD structure (Figure 4).

Mutagenesis studies together with the emerging PSII XRD structures at higher resolution offer future opportunities for detailed mechanistic insight at the molecular level in the coming years.

6 Mn OXIDATION STATES AND ELECTRONIC (SPIN) STATES

The electronic states of the $Mn_4Ca_1O_x$ cluster, for example, the spatial distributions and energies of the electrons in the various S-states are vital to understanding water-splitting chemistry. Tools such as electron paramagnetic resonance (EPR) and X-ray absorption spectroscopies (XAS) have been indispensable to characterize both the redox chemistry of PSII-WOCs and the atomic structure of the inorganic core. Historically, EPR provided the first experiments to identify an electronically coupled Mn cluster at the catalytic site. Shortly thereafter, spectral simulations of the extensive ^{55}Mn hyperfine structure in the S_2 oxidation state indicated electronic coupling of 4Mn ions (Mn^{3+} and Mn^{4+} oxidation states) in a low-spin ground state ($S = 1/2$). EPR signals are now available for four of the five S-states and each in multiple perturbed forms.[22,33–36] An important conclusion is that all of the S-states are formed in low-spin ground electronic states in native (unperturbed) PSII-WOC complexes (Table 2).[22] This conclusion comes from measurements of the electronic Zeeman g−factor and zero-field splittings (for $S > 1/2$). The ^{55}Mn hyperfine structure (magnetic and quadrupole tensors) has given a detailed description of how the unpaired spin density is distributed among the four Mn ions in the S_2 state.

Table 2 Electronic spin states (Zeeman g factors): S ($g_{\text{effective}}$) and changes in the room temperature magnetic susceptibility ($\Delta\chi$) upon advances in oxidation states of the spinach WOC induced by single turnover flashes in PSII complexes. *Syn.* denotes *Synechocystis* 6803[a]

	S_0	S_1	S_2	S_3
S (g_{eff}) ground first excited	1/2 ($g = 2$)	$0 \geq 1$ integer ($g = 4.8$ spinach $g = 12$ *syn*)	1/2 ($g = 2$) 5/2 ($g = 4.1$)[a] 7/2 ($g = 10, 6$)[a]	$0 \geq 1$ integer ($g = 12, 8, 6.7$)
$S_i \rightarrow S_{i+1} \Delta\chi$ (μ_B^2)	∼0	+ (14–17)	∼0	+10 (8 from O_2)

[a] The S = 5/2 and 7/2 spin states become ground states in modified samples.

The resulting spin densities are compatible with a limited set of cluster geometries and Mn oxidation states.

The lowest spin configuration occurs when all 4 paramagnetic Mn ions are coupled by pairwise antiferromagnetic interactions via bridging ligands, corresponding to favorable bonding interactions between the Mn electrons. In addition, low-lying excited electronic states are found to be thermally populated, as revealed by both EPR and magnetic susceptibility measurements in all S-states.

Additionally, the S_2 state (and probably others) can be produced in different ground states having discrete spin values S = 1/2, 5/2 or 7/2, depending upon how it is prepared from the S_1 state. For example, lower temperature illumination favors the S = 5/2 state, while NH_3 inhibition involves binding to a site between Mn ions that forms a different S = 1/2 state characterized by a redistribution of spin densities. Near-IR illumination of Mn^{3+} electronic transition forms an excited state that relaxes to a new ground state either an S = 5/2 or 7/2 state. These conditions change the ordering in energy of these discrete electronic spin states by changing the relative strength or number of intermanganese couplings and by changing the Mn d^n electronic configuration. The former is mediated by the bridging ligands while the latter is determined by the ligand field strength and symmetry. This flexibility of the electronic states does not happen in binuclear clusters or in higher nuclearity clusters that possess only nearest neighbor spins (e.g. linear). Hence, the Mn ions in the Mn_4O_x core are arranged with bridges between more than one other Mn ion. These competing pathways orient the Mn spins such that both low- and intermediate-spin configurations can be produced by modest changes to the intermanganese couplings. This phenomenon is called spin frustration. There are only 8 possible Mn_4O_x geometries which can account for the multiple spin configurations observed for the S_0 through S_3 oxidation states. Three of these cores are depicted in Figure 6. Topologically, they may be called funnel (4), cubane (12), and open cubane (13).

Among these $8Mn_4O_x$ core types, only those that produce the same distribution of unpaired electron spin density need to be considered further as structural models of the WOC. This distribution can be obtained from the ^{55}Mn hyperfine structure observable in EPR and ENDOR measurements of the S_0, S_1, and S_2 states.[22,34] A simple ionic model to predict the Mn spin densities has worked well in simulating the ^{55}Mn hyperfine structure, but not all 8 possible topologies have been fully investigated yet. The S_1 state EPR signal exhibits ^{55}Mn hyperfine structure with 21 lines separated by one observable hyperfine constant and a binomial pattern of intensities consistent with 4 magnetically equivalent ^{55}Mn ions (I = 5/2).[34] This indicates an approximately uniform spin density on all 4Mn ions and thus a single Mn oxidation state is indicated.

The native S_2 state EPR signal (ground spin S = 1/2) illustrates a more asymmetric distribution of spin densities. Assuming the Mn oxidation states are Mn_4(3III,IV) the deduced spin densities that simulate the EPR spectrum are given in Figure 7 (ionic model). This is illustrated using a $Mn_4O_2(OH)_2$ cubane-type model, although other spin-frustrated topologies like the open cubane core (13) in Figure 6 are also suitable. Future EPR simulations should examine the open cubane core (13) and the influence of Ca^{2+} on

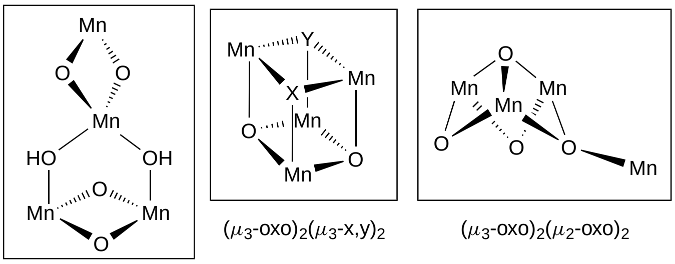

(μ_2-oxo)$_4$(μ_2-hydroxo)$_2$ (μ_3-oxo)$_2$(μ_3-x,y)$_2$ (μ_3-oxo)$_2$(μ_2-oxo)$_2$

Figure 6 Three of the eight possible Mn_4O_x core topologies that could give rise to the observed spin states[22]

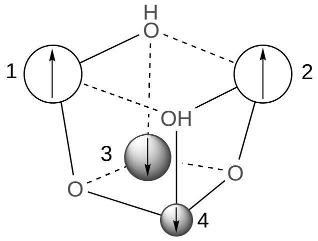

Figure 7 Unpaired spin density distribution on the four Mn ions in the native S_2 state (total spin $S = 1/2$). The size of the spheres reflect the spin densities: 5/3, 5/3, −4/3, −1. The two shades of sphere indicates + and − spin density. A distorted $Mn_4O_2(OH)_2$ cubane core was postulated

spin densities. A higher oxidation state Mn_4(III,3IV) has been proposed for the S_2 state based upon XAS and some EPR experiments, so that the question of Mn oxidation states remains unresolved. A good summary of the debated interpretations can be found in the following articles.[22,34]

Changes in the room temperature magnetic susceptibility upon photooxidation between S-states (Table 2) reveals that the third photooxidation step, for example, $S_3 \rightarrow S_0$, yields a large increase equal to 10 squared Bohr magnetons ($\mu_\beta{}^2$), comprising $8\mu_\beta{}^2$ owing to the O_2 product (proved by use of glucose oxidase trap) and $2\mu_\beta{}^2$ from reduction of the Mn_4 cluster. The O_2 product is therefore formed in the $S = 1$ (ground) triplet spin configuration ($\mu_{\mathrm{eff}}{}^2 = 4S(S + 1)$ for spin-only magnetism), as was anticipated based on thermodynamic predictions. The second and fourth photooxidation steps produce small or no change in $\Delta\chi$, while the first photooxidation step which converts the resting S_1 state to S_2 has a very large increase equal to $14-17\mu_\beta{}^2$. This large increase for S_1(resting) $\rightarrow S_2$ is not cyclic on the second turnover of S_1 and reflects the larger $\Delta\chi$ increase seen when the S_1 state is dark adapted for 15 minutes or longer prior to illumination. Hence, the active S_1 conformation which cycles during continuous O_2 production possesses considerably weaker antiferromagnetic couplings between some of the Mn spins. Studies of Mn_xO_y clusters reveals that ferromagnetic intermanganese pairings are not found between Mn ions in mono- and di-μ_2-oxo bridged Mn^{2+}, Mn^{3+} and Mn^{4+} complexes (dimers), but are observed in μ_3-oxo and μ_4-oxo bridged clusters where three or four Mn ions compete for spin alignment, respectively. These additional couplings produce spin frustration within the trinuclear and tetranuclear Mn-clusters causing a greater density of low-lying electronic spin states and an increase in χ. The very large increase in χ on the S_1(resting) $\rightarrow S_2$ step reflects conversion of a less frustrated, relaxed, $Mn_4Ca_1O_x$ topology to a more frustrated spin topology (exhibiting an increase in the number of Mn-μ-oxo bonds or a more equitable distribution of exchange couplings between the existing Mn-μ-oxo bonds.). Model compounds have shown that a plausible chemical process that could produce such a large increase in χ is the formation a μ_3-hydroxo/oxo bridge between three Mn ions, as occurs upon deprotonation of an aquo/hydroxo ligand.

7 ENERGETICS OF S-STATE TRANSITIONS: FREE ENERGY AND ACTIVATION ENERGY BARRIERS

The kinetics and thermodynamics of individual steps in the catalytic S-state cycle have been measured by time-resolved UV-absorption changes of Mn and lead to the picture shown in Figure 8 and Table 1.[13,37] The half-lives for reduction of the Tyr_Z radical ($Y_z{}^\bullet$) by the Mn cluster after flash excitation in the first three steps ($S_iY_z{}^\bullet \rightarrow S_{i+1}Y_z$; $i = 0,1,2$) are in the range of 30–50 µs, whereas the last step ($S_3Y_z{}^\bullet \rightarrow S_0Y_z + O_2$) is rate-limiting with a half-life for S_3 of 1 ms (Table 1). The H/D kinetic isotope effects using D_2O as substrate have been measured by three different groups and fall in the range for all four steps $k_H/k_D = 1.3-1.4$, $1.3-2.9$, and $1.5-2.3$.[38,39] The UV and near-IR spectral changes during S-state cycling have been attributed to oxidation of high-spin Mn(III) ions.[35]

The thermodynamic driving force (ΔG) for each of the S-state transitions has been estimated from measurements of the temperature-dependent equilibrium constants for the light-induced transient intermediate states: $P680^+/Y_z$ and $Y_z{}^\bullet$/WOC(Mn).[39] These values were then placed on

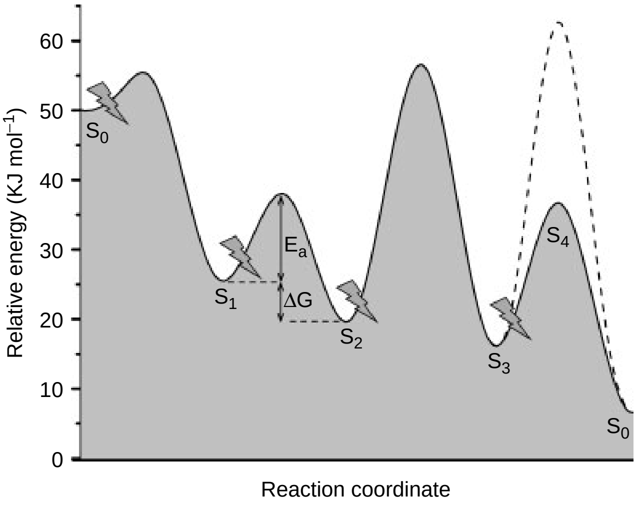

Figure 8 The free-energy changes of the S-state intermediates and their transition states: the reactions $S_iY_z{}^\bullet \rightarrow S_{i+1}Y_z (i = 0-2)$ and $S_3Y_z{}^\bullet \rightarrow S_0Y_z + O_2$ for spinach PSII membrane fragments measured at room temperature. The dashed line indicates a higher energy transition state that exists for $S_3Y_z^\bullet \rightarrow S_0Y_z + O_2$ when measured at $T < 279$ K. E_a = Arrhenius activation energy; ΔG = calculated net free energy change on each turnover. The constant energy offset for the cycle ($\Delta G = 42.9\,\mathrm{kJ\,mol^{-1}}$) reflects the combined effects of oxidation $Y_z \rightarrow Y_z{}^\bullet$ and conversion of dark-adapted (resting) S_0 to active S_0-states

an absolute free energy scale using an estimated value for the P680$^+$/P680 reduction potential. The free energies vary between approximately $-4\,\mathrm{kJ\,mol^{-1}}$ and $-24\,\mathrm{kJ\,mol^{-1}}$ (Figure 8). Also shown are the corresponding experimental activation energies which vary between $+5\,\mathrm{kJ\,mol^{-1}}$ and $+36\,\mathrm{kJ\,mol^{-1}}$.[39] The highest activation barrier is found for the S_2 to S_3 step and was interpreted (together with EXAFS data) as evidence for a structural rearrangement of the Mn cluster which increases the intermanganese distances in two Mn_2 pairs by 0.1–0.15 Å.

8 SUBSTRATE BINDING, EXCHANGE, AND MECHANISM OF O_2 EVOLUTION

^{1}H/^{2}H-ENDOR and ESEEM methods have provided good evidence for water molecules in the active site.[40–42] Two exchangeable protons located at 2.5 Å have been assigned to a water molecule directly bound to a Mn ion in the native S_2 state.[42] A second pair of exchangeable protons lacking scalar hyperfine coupling but with large dipolar coupling is located at 2.7 Å from the nearest spin density center (Mn).[42] The latter water site is unlikely to be on Mn and has been suggested to represent water bound to the Ca^{2+} site. Both sites are located in an aqueous-like environment with additional exchangeable protons attributed to water molecules in the next coordination shell. The assignment of these water ligands as substrate molecules although plausible is speculative.

An alternative approach to characterize the chemical environment of the substrate water molecules is by the rate at which they exchange with bulk water. This experiment has been conducted using rapid-mixing mass spectrometry to measure the isotopic composition of the O_2 product following injection of ^{18}O-water in each S state.[17] Table 1 gives the rate constants for the two exponential kinetic phases that are present in the data. These phases have been attributed to two substrates sites that exchange with bulk water at slow and fast rates. The first conclusion is that there is no evidence for nonexchangeable substrate sites; for example, no irreversible step occurs that is not in equilibrium with bulk water. The authors interpret the rate data as evidence that the slow substrate water is bound to a Mn(III) site in all S-states, while the fast exchange site is unlikely to involve coordination to Mn prior to the S_3 state.

The large (100-fold) decrease in the exchange rate at the slow substrate site in the S_1 state and recovery in S_2 has not been satisfactorily explained, but should prove important in sorting out the correct mechanism. One hypothesis is that the slow exchanging substrate site may help to protect PSII against disassembly of the inorganic core caused by reduction of the S_1 core by diffusible reductants that are present in the cell or chloroplast (H_2O_2, ascorbate, glutathione). Mano *et al*. showed that the reaction of PSII membranes in the S_1 state with H_2O_2 is 100x slower than either the S_2 or S_0 states (catalase activity of PSII) suggesting that the H_2O_2 binding site (catalase dismutation) and the slow substrate site are the same site or are in rapid equilibrium.[12] Both of these sites were found to be distinct from the functional chloride site.

The most recent mass spectrometry data using Sr to replace Ca suggests that the fast exchanging substrate site may involve interaction with Ca.[18] This interpretation agrees with ^{1}H/^{2}H-ENDOR and ESEEM results showing that two water molecules are bound, one to a Mn site and the other to a nonmagnetic site postulated to be Ca.[42]

There has been wide debate about whether the kinetic data for S-state transitions discussed in Section 6 are evidence for concerted H atom transfer or proton-coupled electron transfer (pcet) involving more weakly coupled sites for the proton and electron. The small H/D kinetic isotope effect (KIE) for the S-state transitions (as little as 1.3–1.4) indicates little displacement of the H atom coordinates in the transition state. The 6.5 Å distance between the phenol oxygen of Tyr_Z and the nearest Mn ion observed in the XRD structure of PSII-WOC essentially eliminates a direct concerted H atom transfer mechanism, as the distance is too far for tunneling of H atoms. This has led to two pcet models for the S-state transitions that enable the longer-range, delocalized, electron-transfer pathway to be thermodynamically coupled to the shorter range proton transfer pathway of the reaction.[14,24,28] The first model involves oxidation of the $Mn_4Ca_1O_x$ cluster (molecular orbitals localized thereon) that is coupled to the ionization of substrate protons. The Tyr_Z radical is both the electron and proton acceptor in one view (phenol oxygen proton site). Another view argues that these functions are separated, such that the proton is delivered to other auxiliary proton carriers (water, bicarbonate, amino acids (Reanalysis of the 3.6 A XRD data[30] has shown that two oxos at the corners of the Mn_3CaO_4 cubane-like core (O_1 and O_3, Figure 4) interact by hydrogen bonding to carboxylate residues (D1-Glu189 and D1-Ala 344-C-terminus). These oxos exhibit bonding interactions consistent with identification as water molecules. Mutagenesis studies are consistent with these carboxylate residues serving in proton pathways for substrate water deprotonation. On this basis and other evidence, the O_1 and O_3 corner sites have been proposed as the substrate water oxidation sites[30])) in a distributed hydrogen-bonded network eventually reaching the aqueous lumen. In both cases, the reduction of the Tyr_Z radical is coupled to its protonation, either by a substrate proton or an alternative proton donor, likely D1His190.

No direct evidence for Mn(V) or peroxide-like intermediates have been observed yet in any native S_i state. However, release of hydrogen peroxide occurs in a modified S_2 state formed under a variety of conditions (removal of Cl^-, replacement of Cl^- by F^- and solubilization with lauryl choline chloride)(reviewed in[12]). These results show that the driving force for HO–OH bond formation already exists at the modified S_2 oxidation level.

There is little experimental information about the O–O bond formation step in the native S_4 state. Two general mechanisms for the O–O bond formation step have been postulated (Figure 9), although definitive evidence to distinguish these possibilities or others is still lacking. The first mechanism (Figure 9(a)), involves homolytic intramolecular bond formation from two bridging substrate oxygen atoms in the $Mn_4Ca_1O_4$ core. In this mechanism the O=O bond enthalpy must contribute to overcoming the favorable Mn–O bond enthalpy in the transition state for reaction to occur. There is definitive experimental proof that this reaction coordinate is thermodynamically possible in symmetrical $Mn_4O_4^{6+}$ cubane clusters because they have long (e.g. weak) Mn–O bonds, but not in simpler $Mn_2O_2^{2+/3+/4+}$ cores which have much shorter (e.g. stronger) Mn–O bonds (see final section).**[43]**

A heterolytic pathway, Figure 9(b), has been proposed which involves attack by a nucleophilic OH^-, possibly generated by ionization of water bound to Ca^{2+}, at an electrophilic oxygen atom. The latter oxygen atom has been attributed to either a putative Mn(V)=O 'manganyl oxo' intermediate as envisioned in Figure 9(b),**[44]** or a bridging oxyl radical (μ_2-$O^{\bullet}$).**[45]** The latter proposal is supported by electron structure calculations showing that bridging μ_2-oxos can be sufficiently electron deficient in special Mn_xO_y topologies that nucleophillic attack may be possible by OH^-.**[45]**

Bicarbonate influences the activity of electron donation from Mn^{2+} to apo-WOC-PSII complexes depleted of manganese.**[46]** Photoactivation data show that bicarbonate interacts with the high affinity Mn^{2+} and stabilizes the photooxidized Mn^{3+} product during assembly of the WOC. These data and the hypothesis from XRD allowing the presence of bicarbonate as a core ligand in the holoenzyme (Figure 4) open up interesting new mechanistic possibilities to consider.

An alternative heterolytic pathway shown in Figure 10(a) can be envisioned based on the XRD evidence suggesting a μ_4-oxo (Figure 4). The μ_4-oxo will be electron-deficient and thus forms a potentially reactive site for O–O bond formation with a nucleophilic oxyanion. Here we postulate that the carbonate ion in the active site attached to Ca, Mn, and Arg357 residue serves as the nucleophile by forming peroxycarbonate, transiently as a bound intermediate that decays to the O_2 product. This proposal is supported by the occurrence of carbonates as nucleophiles in organic hydration reactions and the formation of peroxycarbonate as metastable intermediate in carbonate chemistry.**[47]** Unlike pathway Figure 9(b), which must form the Mn(V) oxidation state in order to form an electrophilic manganyl oxo complex, pathway Figure 10(a) produces a highly activated μ_4-O at the Mn(IV) level.

An alternative homolytic pathway shown in Figure 10(b) can also be envisioned in which intramolecular O–O bond formation occurs between the electrophillic μ_4-oxo and a transient nucleophilic μ_2-oxo released from Ca upon rearrangement of the carbonate ligand from monodentate to bidentate coordination. The figure shows the anticipated

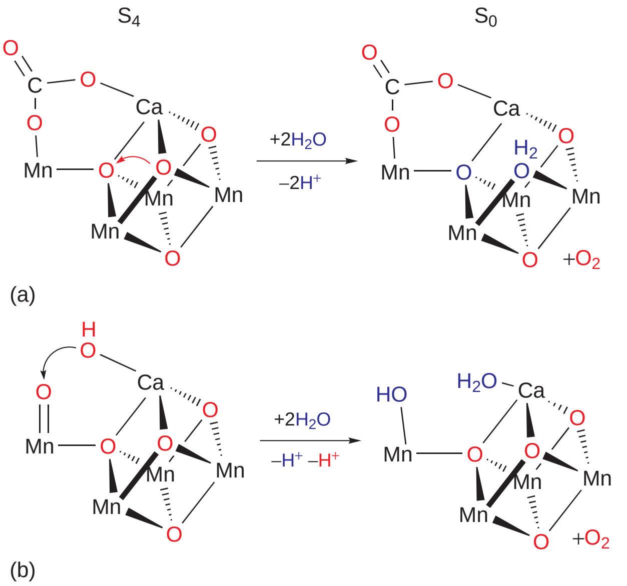

Figure 9 Two general mechanisms postulated for O–O bond formation. (a) involves homolytic intramolecular bond formation from two bridging substrate oxygen atoms, while (b) involves a nucleophilic attack at a an electrophilic oxygen atom

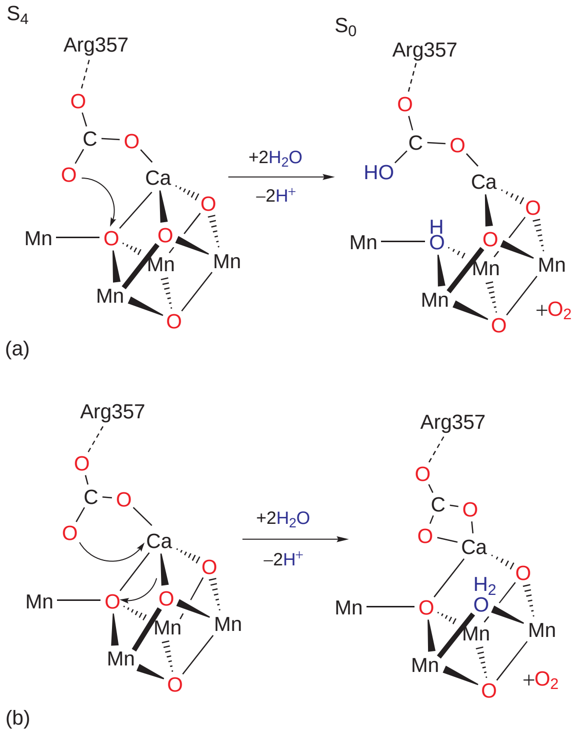

Figure 10 Two alternative hypothesized mechanisms for formation and release of oxygen in the $S_4 \rightarrow S_0$ step, incorporating hints yielded by the emerging crystal structures at higher resolution. (a) shows a heterolytic mechanism in which the electron-deficient μ_4-oxo acts as an electrophile, while (b) shows a mechanism involving the Ca^{2+} ion leading to the formation of a peroxo-intermediate

bond isomerization sequence leading to a transient peroxo-intermediate that decays to the O_2 product. In both of the mechanisms depicted in Figure 10(a) and (b), the Ca^{2+} participates directly in the O–O bond formation step. This key feature is in agreement with the experimental data on O_2 release in inorganic mutants replacing Ca^{2+} with Sr^{2+} (Reference 48).

With the rapid advances in knowledge that are taking place in the chemical basis of PSII catalysis, there will surely be exciting times ahead in sorting out these proposals for the mechanism of water oxidation.

9 WHY MANGANESE? INORGANIC MUTANTS

Several factors may have conspired to make manganese the universal metal for catalyzing water splitting in all oxygenic phototrophs. Transition metals are the clear winners versus main group atoms at storing/delivering large units of energy in the form of redox reactions, for example, atom transfer reactions, in contrast to acid-base chemistry and ion concentration gradients. This preference arises because transition metals store and deliver energy in the form of both charge (the number of electrons) and bond strengths (potential and kinetic energy of electrons and nuclei). Their versatility originates from the greater number and smaller energy spacing of their valence d orbitals which facilitates matching with substrate orbitals for maximal bond strength and accommodates a wider range of geometries. A direct consequence is that the geometrical constraints can be relaxed in cases where the redox changes involve nonbonding d orbitals. For the same reasons, the activation barriers between redox states in multistep catalysis are usually lower.

Phototrophs take up Mn^{2+} but use it in the WOC in the Mn^{3+} and Mn^{4+} oxidation states. Mn^{2+} is highly soluble, has weak or modest affinity for simple ligands, speciates as the simple aquo cation in water over a wide pH range and is readily transported into cells by a variety of redundant transport systems. Mn^{2+} is chemically stable in neutral solutions. It auto-oxidizes in O_2 saturated solutions only above pH 9.5 where most phototrophs do not function, or at ambient pH only if exceptionally strong chelates are accessible to stabilize the resulting Mn^{3+} (e.g. pyrophosphate^{4-}). Hence, there is usually no need for chaperone proteins in the cell to deliver Mn^{2+} or to protect the cellular matrix from auto-oxidation. Mn chaperones have not been identified (yet) for assembly of the WOC during biogenesis. What a great savings in energy and complexity for the primitive phototroph that first used Mn^{2+} over other more abundant redox metals (Fe^{2+}) in the anaerobic world when oxygenic photosynthesis was invented. The redox potential for oxidizing Mn^{2+} (aq) $\rightarrow$ Mn^{3+} (aq) $E^0 = 1.3\,V$ closely matches the redox potential of Chl-a, unlike the majority of other soluble transition ions. Thus, the biogenesis of Chl-a in phototrophs enabled the photooxidation of Mn^{2+} to occur on the surface of Chl-a proteins. The resulting Mn^{3+} binds more tightly by ca. $10^{12}-10^{15}$ and thus would be long-lived at the protein site. Importantly, loss of the redox energy by charge recombination is greatly slowed owing to the energy released upon dissociation of a proton to form $[Mn^{III}(OH^-)]^{2+}$ ($pK_a = 0$). Energetically downhill direct electron-hole recombination without reprotonation is also greatly slowed owing to the unusually large vibronic distortion that Mn^{3+} typically produces with its ligand environment (e.g. 1 eV barrier for pseudorotation of the Jahn–Teller axes in $MnF_6{}^{3-}$). The photooxidation of a second Mn^{2+} is catalyzed by formation of the first $Mn(OH)^{2+}$ photoproduct, as the OH^- can serve as a better ligand than water to template the binding of the next Mn^{2+}. The efficiency of this assembly process increases in the presence of bicarbonate which is a surrogate for hydroxide and can exist in neutral pH solutions at concentrations several orders of magnitude higher than hydroxide.

These properties of aqueous Mn redox chemistry are all utilized during the light-driven biogenesis of the $Mn_4Ca_1O_x$ core from the free inorganic cofactors and apo-WOC-PSII. Measurements of the kinetics of reconstitution of O_2 evolution activity and proton release during this photoactivation process have resolved three kinetic intermediates:**[49]** first $Mn^{II}(OH^-)$ or $Mn^{II}(HCO_3{}^-)$ binds to the high affinity Mn site, involving D1Asp170, followed by a slow (rate-limiting) dark step in which a proton is ejected and the affinity of Ca^{2+} increases substantially. This step is hypothesized to involve a conformational change of the D1 protein (carboxyl terminus or AB loop movement). It is followed by cooperative binding of 3 additional Mn^{2+} and photooxidation steps in rapid succession that are not resolved kinetically. This $1 + 3Mn^{2+}$ sequence and positive cooperativity in Ca^{2+} uptake after the first Mn^{2+} photooxidation step fits well with the XRD structural data. Bicarbonate was shown to specifically increase the affinity of Mn^{2+} at the high affinity site by stabilizing the photooxidized Mn^{3+} state. A second higher affinity bicarbonate site was found that stimulates the rate of photoactivation and was attributed to electrostatic attraction of Mn^{2+} caused by ionization of protein residues or ion-pairing between carbonate and arginine.

A nearly constant yield and rate of photoactivation is found over a 200-fold range in concentrations of Mn^{2+} and Ca^{2+}, provided the ratio is kept nearly constant at about 500 Ca/1Mn. If Ca^{2+} is left out of the solution, binding and photooxidation of many more Mn^{2+} occurs to the apo-WOC-PSII protein and no O_2 evolution activity is observable. Ca^{2+} can be replaced by Sr^{2+} and actually accelerates the assembly process by 4-fold,**[12]** but the O_2 evolution rate is reduced to 40%, apparently due to a slower terminal step $S_3 \rightarrow S_0 + O_2$.**[48]** It can be concluded that Ca^{2+} is specifically involved in the O–O bond formation step.

No functional replacement for manganese during the photoactivation process has been found to be effective (yet).

Several 3d, 4d, and 5d transition ions were tried, all at fixed pH (6) and fixed concentration without success.[12] It appears that manganese may be truly unique for biological water splitting.

10 FUNCTIONAL MANGANESE COMPLEXES THAT SPLIT WATER

There have been a large number of examples of Mn-oxo complexes that have contributed important insights to understanding the structure and function of the $Mn_4Ca_1O_x$ core.[43,50,51] However, only three systems have been shown to produce O_2 and will be highlighted here.

10.1 The Dimanganese(III,III)porhyrin Complex

The dimanganese(III,III)porphyrin complex (**1**) depicted in Figure 11 was shown to catalyze the anodic oxidation of water at low conversion (≤8 turnovers). The mechanism appears to proceed by formation of a [Mn(V)=O]$_2$ intermediate (**2**) which has recently been isolated by chemical oxidation with *m*-chloroperoxybenzoic acid (Figure 11). Subsequent acidification of (**2**) yields O_2 in a stoichiometric reaction that does not occur with the corresponding mono-manganese(V) porphyrin, nor with the corresponding [Mn(IV)]$_2$ dimer species. Two mechanisms were considered based on H/D-water isotopic labeling studies and the observation that the acidified intermediate also converts Cl^- to OCl^- quantitatively. The postulated active intermediate is [H_2O–Mn(V)=O]$_2$. This species may produce O_2 either by intramolecular coupling of the oxo groups, or by [H_2O–Mn(V)=O] reaction with free water. The latter reaction could not be excluded, as the oxo in (**2**) exchanges with water rapidly. This chemistry suggests that the homolytic coupling of two electrophilic oxos is an observable pathway for O–O bond formation with strong π-acceptor porphyrin ligands. Geometrical constraints on the intermanganese distance and orientation imposed by the covalent bridge linking the porphyrin ligands were found important for O_2 formation in earlier work, further implicating a homolytic intramolecular pathway is observed.

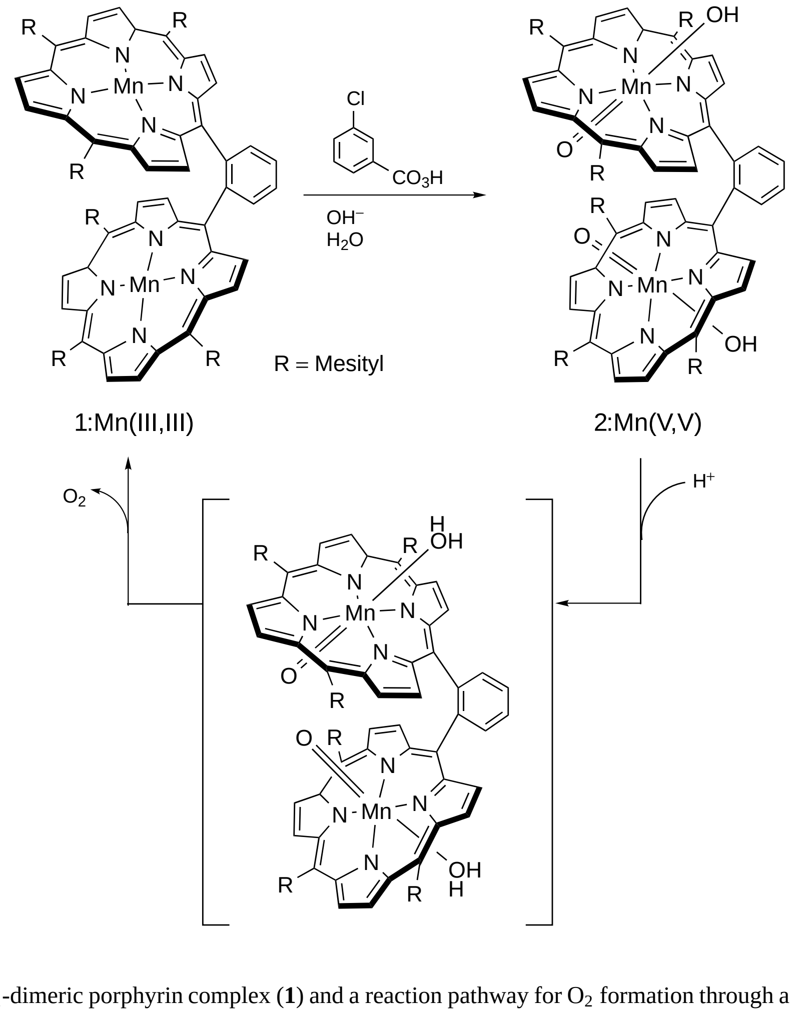

Figure 11 Structure of Mn_2-dimeric porphyrin complex (**1**) and a reaction pathway for O_2 formation through a dimanganyl (V,V) species (**2**)

10.2 Dimanganese(IV,V) Oxo Complexes

Although several examples of complexes containing the $[Mn_2O_2]^{n+}$ core type have been studied, only one has been found to catalyze O_2 evolution in water. The complex $[(terpy)(H_2O)Mn^{III}(\mu\text{-}O)_2Mn^{IV}(OH_2)(terpy)]^{3+}$ contains the tridentate terpyridine ligand that coordinates to three meridional sites on Mn and thus positions the two terminal aquo ligands trans to the μ-oxo bridges. The oxidation of this complex by SO_5^{2-} or OCl^- in water was shown to produce O_2 and permanganate.[52] Steady-state saturation kinetics were observed indicating the formation of an intermediate suggested to be a 1:1 precursor complex that decays to form a postulated manganyl intermediate $(H_2O)Mn^{III}(\mu\text{-}O)_2Mn^V{=}O$ that was not directly observed. The yields of labeled O_2 products were measured using ^{18}O-water by mass spectrometry. The authors show on the basis of the $m/z = 32$, 34, and 36 products that the oxidant SO_5^{2-} is directly responsible for forming O_2 by reacting with the kinetic intermediate which also reforms the starting catalyst $(H_2O)Mn^{III}(\mu\text{-}O)_2Mn^{IV}(OH_2)$. The yield of the m/z 34 and 36 products is argued to favor a second pathway in which (labelled) water or hydroxide is proposed to attack the kinetic intermediate to produce O_2 and a reduced $Mn^{II}Mn^{III}$ intermediate. The latter product is then recycled by reacting with excess oxidant to reform the original catalyst. This mechanism has been offered as indirect evidence for the possible presence of an analogous $Mn^V{=}O$ intermediate in PSII and for a heterolytic pathway for O–O bond formation. Additional evidence to identify the source of the m/z 34 and 36 products would be very helpful. The possibility of rapid exchange of oxygen atoms between water, the putative manganyl oxo and eventually into SO_5^{2-} could also explain the

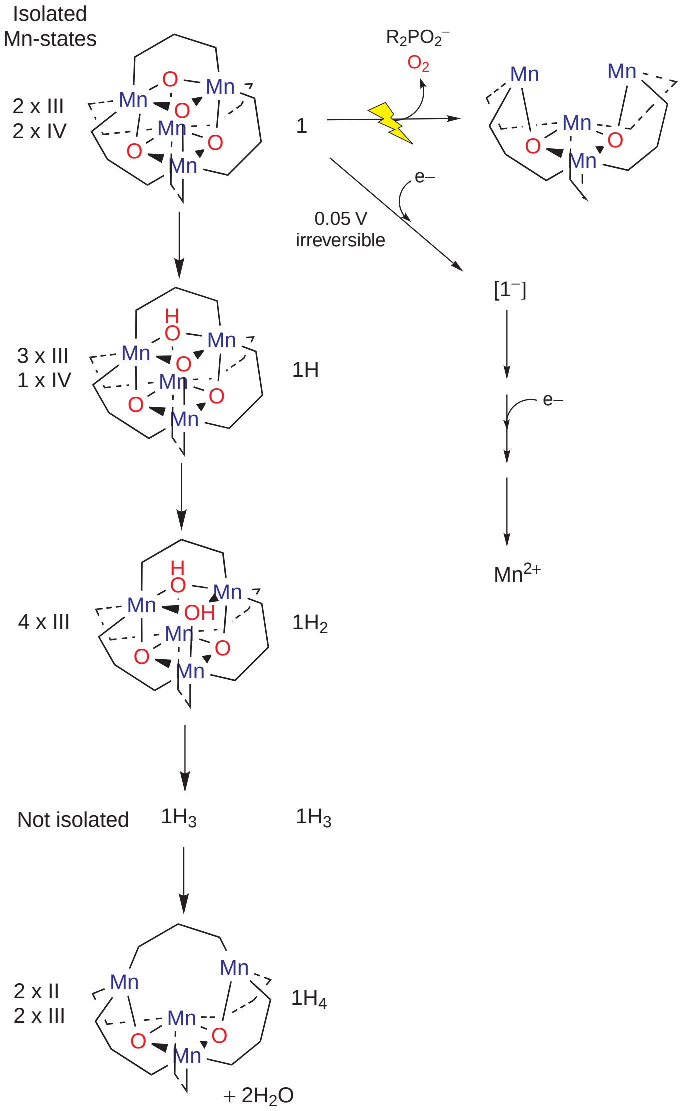

Figure 12 O_2 and water formation from $Mn_4O_4(Ph_2PO_2)_6$ complexes

isotope distribution of the O_2 product without invoking any water oxidation chemistry. The former exchange rate has been shown to be very rapid ($\sim 100\,s^{-1}$) in the case of the porphyrin class of $Mn^V{=}O$. Also, direct evidence to identify the formation of the manganyl intermediate and the use of innocent oxidants that do not deliver active oxygen atoms would also be very helpful in establishing the relevance of this chemistry to PSII-WOC. Recent studies using this same complex did not find evidence for the formation of O_2 in solution, but did find evidence that the complex forms a catalyst capable of low efficiency water splitting if adsorbed onto clays.[53] The active catalyst that produced O_2 was shown to involve two equivalents of the adsorbed dimanganese complex (e.g. 4Mn equiv.).

10.3 Mn_4O_4-Cubane-to-Mn_4O_2-Butterfly

A cubane/butterfly core rearrangement, represented by core type 12 (Figure 6), was proposed in an early hypothesis for the photosynthetic O_2 evolution step. The feasibility of this rearrangement has been demonstrated in a model cluster, as summarized in Figure 12.[26] The molecule $Mn_4O_4(Ph_2PO_2)_6$ can be synthesized from simple monomeric precursors (Mn^{2+} and $MnO_4{}^-$) in the presence of phosphinate anions which have long O–O' chelate distance that bridges between Mn ions. It contains a rare example of the symmetrical $[Mn_4O_4]^{6+}$ cubane core in the formal oxidation state Mn_4(2III, 2IV). The $[Mn_4O_4]^{6+}$ core has longer Mn–O bonds (by 0.15–0.2 Å) than the isoelectronic $[Mn_2O_2]^{3+}$ core complexes. By changing the type of phosphinate ligand, the core geometry changes from tetrahedral with equivalent Mn ions to C_2 with distinct Mn(IV) and Mn(III) sites.[54] Importantly, UV light absorption into a Mn–O charge transfer band efficiently releases an O_2 molecule in the gas phase together with one of the phosphinate chelates, leaving the intact cationic species $[Mn_4O_2(Ph_2PO_2)_5]^+$ (Mn_4O_2-butterfly core). This reaction proceeds with high quantum efficiency (>90%), is the only observable reaction channel (other than decay to the ground state), and is selective to the cubane core type (i.e. not observed for Mn_2O_2, Mn_2O, or Mn_3O_4 core complexes).[43] By comparing the isotopomers synthesized with $[Mn_4({}^{18}O)_4]^{6+}$ and $[Mn_4({}^{16}O)_4]^{6+}$ cores, the mechanism of O_2 formation was shown to proceed via intramolecular coupling of corner oxos. This chemistry illustrates that the cubane topology is intrinsically poised toward O_2 formation, in contrast to the $[Mn_2O_2]^{3+/4+}$ core complexes which do not release O_2 from the μ-oxos.

The mechanism of O–O bond formation has been supported by density functional calculations which show that, following removal of a phosphinate chelate, the resulting core is unstable towards O_2 release via a thermal pathway involving out of plane displacement of the oxygen atoms. This degree of freedom permits the oxygen atoms to approach one another in the transition state (ca 23–30 $kcal\,mol^{-1}$) in route to forming a peroxo-intermediate and O_2 release (F. De Angelis, R. Car, unpublished data). This appreciable activation barrier accounts for why the quantum yield is very low in solution owing to geminate recombination. The longer Mn–O bonds in the $[Mn_4O_4]^{6+}$ cubanes are weaker than those in $[Mn_2O_2]^{3+}$ core complexes, a feature which is believed responsible in part for their reactivity toward forming O_2.

Reduction of the parent cubane in solution using various H atom donors (organoamines and phenols) proceeds via successive intermediates differing by addition of H atoms to the corner oxos. A total of 4 H atoms can be delivered, but the isolated product is not the tetrakis μ-OH species $1H_4$, rather it is the dehydrated 'pinned butterfly' complex $Mn_4O_2(Ph_2PO_2)_6$ and two free water molecules.[55] The rate constants and H/D kinetic isotope effects were also examined. No further reduction below this oxidation state Mn(2II, 2III) is observed, indicating that the butterfly core topology is intrinsically resistant to further reduction.

The chemistry in Figure 12 gives direct experimental proof of the unique properties of the Mn_4O_2-butterfly/Mn_4O_4-cubane topology in the dehydrogenation of water to μ-oxos and coupling to form O_2. The possible relationship between this chemistry and the permissible mechanisms for biological water splitting is illustrated in Figures 9 and 10.

11 RELATED ARTICLES

Manganese: Inorganic & Coordination Chemistry; Manganese Proteins with Mono- & Dinuclear Sites.

12 REFERENCES

1. D. J. Des Marais, *Science*, 2000, **289**, 1703.
2. M. J. Russell and A. J. Hall, *Geochem. News*, 2002, **113**, 6.
3. G. C. Dismukes, V. V. Klimov, S. V. Baranov, Y. N. Kozlov, J. Dasgupta, and A. M. Tyryshkin, *Proc. Natl. Acad. Sci. U.S.A.*, 2001, **98**, 2170.
4. K. Sauer and V. K. Yachandra, *Proc. Natl. Acad. Sci. U.S.A.*, 2002, **99**, 8631.
5. R. E. Blankenship, 'Molecular Mechanisms of Photosynthesis', Blackwell Science, Oxford, 2002.
6. J. Nugent, ed. Photosynthetic Water Oxidation, B.B.A. Bioenergetics, vol. 1503, p. 1.
7. T. Wydrzynski and K. Satoh, eds. 'Photosystem II: The Water/Plastoquinone Oxido-Reductase in Photosynthesis' Springer, The Netherlands, 2005.
8. P. Joliot, *Photosynth. Res.*, 1993, **38**, 214.
9. G. M. Cheniae, *Photosynth. Res.*, 1993, **38**, 225.
10. C. G. Chen and G. M. Cheniae, *Plant Physiol.*, 1995, **108**, 87.
11. J. S. Vrettos, D. A. Stone, and G. W. Brudvig, *Biochemistry*, 2001, **40**, 7937.

12. G. M. Ananyev, L. Zaltsman, C. Vasko, and G. C. Dismukes, *Biochim. Biophys. Acta Bioenergetics*, 2001, **1503**, 52.
13. F. Rappaport and J. Lavergne, *Biochim. Biophys. Acta Bioenergetics*, 2001, **1503**, 246.
14. W. Junge, M. Haumann, R. Ahlbrink, A. Y. Mulkidjanian, and J. Clausen, *Philos. Trans. R. Soc. Lond, Ser. B Biol. Sci.*, 2002, **357**, 1407.
15. K. Olesen and L. E. Andreasson, *Biochemistry*, 2003, **42**, 2025.
16. G. Renger, *Biochim. Biophys. Acta Bioenergetics*, 2001, **1503**, 210.
17. W. Hillier and T. Wydrzynski, *Biochim. Biophys. Acta Bioenergetics*, 2001, **1503**, 197.
18. G. Hendry and W. T. Wydrzynski, *Biochemistry*, 2003, **42**, 6209.
19. A. Zouni, H.-T. Witt, J. Kern, P. Fromme, N. Krauss, W. Saenger, and P. Orth, *Nature*, 2001, **409**, 739.
20. N. Kamiya and J.-R. Shen, *Proc. Natl. Acad. Sci. U.S.A.*, 2003, **100**, 98.
21. K. N. Ferreira, T. M. Iverson, K. Maghlaoui, J. Barber, and S. Iwata, *Science*, 2004, **303**, 1831.
22. T. G. Carrell, A. Tyryshkin, and G. C. Dismukes, *J. Biol. Inorg. Chem.*, 2002, **7**, 2.
23. B. A. Diner and F. Rappaport, *Ann. Rev. Plant Biol.*, 2002, **52**, 551.
24. R. Debus, *Biochim. Biophys. Acta Bioenergetics*, 2001, **1503**, 164.
25. J. H. Robblee, R. M. Cinco, and V. K. Yachandra, *Biochim. Biophys. Acta Bioenergetics*, 2001, **1503**, 7.
26. W. Ruettinger, M. Yagi, K. Wolf, S. Bernasek, and G. C. Dismukes, *J. Am. Chem. Soc.*, 2000, **122**, 10353.
27. R. Debus, ed. The Catalytic Manganese Cluster–Protein Ligation, in 'Photosystem II: The Water/Plastoquinone Oxido-Reductase in Photosynthesis', eds. T. Wydrzynski and K. Satoh, Springer, The Netherlands, 2005, Chap. 11.
28. B. A. Diner, *Biochim. Biophys. Acta Bioenergetics*, 2001, **1503**, 147.
29. B. A. Diner, *Meth. Enzymol.*, 1998, **297**, 337.
30. J. Dasgupta, R. T. van Willigen, and G. C. Dismukes, *Physical Chem. Chem. Phys.*, 2004, **6**, 4793.
31. C. Rosenberg, J. Christian, T. M. Bricker, and C. Putnam-Evans, *Biochemistry*, 1999, **38**, 15994.
32. M. Knoepfle, T. M. Bricker, and C. Putnam-Evans, *Biochemistry*, 1999, **38**, 1582.
33. K. Hasegawa, T.-A. Ono, Y. Inoue and M. Kusunoki, *Bull. Chem. Soc. Jpn.*, 2000, **72**, 1013.
34. J. M. Peloquin and R. D. Britt, *Biochim. Biophys. Acta Bioenergetics*, 2001, **1503**, 96.
35. D. Kuzek and R. J. Pace, *Biochim. Biophys. Acta Bioenergetics*, 2001, **1503**, 123.
36. R. D. Britt, J. M. Peloquin, and K. A. Campbell, *Ann. Rev. Biophys. Biomol. Struct.*, 2000, **29**, 463.
37. M. Karge, K.-D. Irrgang, and G. Renger, *Biochemistry*, 1997, **36**, 8904.
38. K. L. Westphal, C. Tommos, R. I. Cukier, and G. T. Babcock, *Curr. Opin. Plant Biol.*, 2000, **3**, 236.
39. G. Renger, G. Christen, M. Karge, H.-J. Eckert, and K.-D. Irrgang, *J. Biol. Inorg. Chem.*, 1998, **3**, 360.
40. R. Fiege, W. Zweygart, R. Bittl, N. Adir, G. Renger, and W. Lubitz, *Photosynth. Res.*, 1996, **48**, 227.
41. X. S. Tang, M. Sivaraja, and G. C. Dismukes, *J. Am. Chem. Soc.*, 1993, **115**, 2382.
42. C. Aznar and R. Britt, *Philos. Trans. R. Soc. London, Ser. B*, 2002, **357**, 1359.
43. M. Yagi and M. Kaneko, *Chem. Rev.*, 2001, **101**, 21.
44. J. S. Vrettos and G. W. Brudvig, *Philos. Trans. R. Soc. Lond. B Biol. Sci.*, 2002, **357**(1426), 1395.
45. P. E. M. Siegbahn, *Curr. Opin. Chem. Biol.*, 2002, **6**, 227.
46. V. V. Klimov and S. V. Baranov, *Biochim. Biophys. Acta Bioenergetics*, 2001, **1503**, 187.
47. D. E. Richardson, H. Yao, K. M. Frank, and D. A. Bennett, *J. Am. Chem. Soc.*, 2000, **122**, 1729.
48. K. L. Westphal, N. Lydakis-Simantiris, R. I. Cukier, and G. T. Babcock, *Biochemistry*, 2000, **39**, 16220.
49. S. Baranov, A. Tyryshkin, D. Katz, G. Ananyev, V. Klimov, and G. Dismukes, *Biochemistry*, 2004, **43**, 2070.
50. W. Ruettinger and G. C. Dismukes, *Chem. Rev.*, 1997, **97**, 1.
51. R. Manchandra, G. W. Brudvig, and R. H. Crabtree, *Coord. Chem. Rev.*, 1995, **144**, 1.
52. J. Limburg, J. S. Vrettos, H. Chen, J. C. de Paula, R. H. Crabtree, and G. W. Brudvig, *J. Am. Chem. Soc.*, 2001, **123**, 423.
53. M. Yagi and K. Narita, *J. Am. Chem. Soc.*, 2004, **126**, 8084.
54. J.-Z. Wu, E. Selitto, G. Yap, J. Sheats, and G. C. Dismukes, 2004, vol. 43, 5795.
55. M. Maneiro, W. F. Ruettinger, E. Bourles, G. McLendon, and G. C. Dismukes, *Proc. Natl. Acad. Sci. U.S.A.*, 2003, **100**, 3703.

Acknowledgments

We thank M. Yagi and R. Debus for preprints of their work and W. Ruettinger for assistance with figures. RvW acknowledges support by Princeton University, Leiden University, and the Human Frontiers Science Program (RG-P0029-2002). Research in the authors' laboratory has been supported by the National Institutes of Health (GM-39932).

Manganese Proteins with Mono- & Dinuclear Sites

James E. Penner-Hahn
The University of Michigan, Ann Arbor, MI, USA

1 Introduction 1
2 Biological Distribution of Manganese 2
3 Manganese Transport and Regulation 2
4 Manganese-Activated Enzymes 3
5 Metalloproteins with Mononuclear Mn Sites 4
6 Metalloproteins with Dinuclear Mn Sites 6
7 Manganese-substituted Proteins 9
8 Spectroscopy 9
9 Model Compounds 10
10 Related Articles 10
11 References 10

Glossary

Manganese-activated enzyme: an enzyme that does not bind Mn tightly, but for which the enzymatic activity is nevertheless enhanced by addition of Mn. Manganese may or may not be the cation bound in vivo

Manganoenzyme: an enzyme that binds Mn stoichiometrically. Mn is difficult to remove from the protein and is typically required for biological activity

1 INTRODUCTION

In contrast to iron and copper proteins (*see Polypeptide*), which are well-known and well-characterized, relatively little is known about the bioinorganic chemistry of manganese (*see* ***Iron: Heme Proteins & Dioxygen Transport & Storage***; ***Iron: Heme Proteins & Electron Transport***; ***Iron: Heme Proteins, Mono- & Dioxygenases***; ***Iron: Heme Proteins, Peroxidases, Catalases & Catalase-peroxidases***; ***Copper Proteins: Oxidases***; ***Copper Proteins with Type 1 Sites***; ***Copper Proteins with Type 2 Sites***; ***Copper Enzymes in Denitrification***; ***Cytochrome Oxidase*** for examples of some of the well-characterized iron and copper proteins). In part, this is simply a matter of detectability: proteins that have heme-iron or blue copper-active sites (*see Active Site*) are characterized by intense UV–visible absorption bands; Cu proteins often have easily detectable EPR (*see Electron Paramagnetic Resonance*) signals. Manganese, however, is often difficult to detect spectroscopically. In the biological milieu, the accessible Mn oxidation states are $\mathrm{Mn^{II}}$, $\mathrm{Mn^{III}}$, and $\mathrm{Mn^{IV}}$. Of these, $\mathrm{Mn^{II}}$ is by far the most common. Unfortunately, most $\mathrm{Mn^{II}}$ complexes, including $\mathrm{Mn^{II}}$ proteins, have very weak UV–visible transitions. When it is present in a high symmetry environment, $\mathrm{Mn^{II}}$ has an easily detectable EPR signal. In lower symmetry environments, the $\mathrm{Mn^{II}}$ EPR signal can become broad and hard to detect. Nevertheless, EPR studies have been extremely useful in characterizing the role of Mn in proteins.[1,2]

A second difficulty in studying Mn proteins is the lability of protein-bound Mn. Complexes of $\mathrm{Mn^{II}}$ typically have binding constants that are somewhat smaller than those for the corresponding $\mathrm{Fe^{II}}$ complexes and substantially smaller than those for $\mathrm{Cu^{II}}$ and $\mathrm{Zn^{II}}$ complexes (this is the so-called *Irving–Williams Series*). For heme–iron proteins, the porphyrin cofactor (*see* ***Iron Porphyrin Chemistry***) increases the stability of the Fe–protein interaction. No such small molecule cofactors are known for Mn proteins. Small binding constants mean that Mn is readily lost from a protein during purification.

In describing this phenomenon, it is common to distinguish between manganese-activated enzymes and manganoenzymes.[3,4] Manganese-activated enzymes do not contain tightly bound Mn ions, and often contain no Mn whatsoever when they are isolated. The activity of these enzymes is dependent on the amount of free $\mathrm{Mn^{II}}$ in solution, with $\mathrm{Mn^{II}}$ dissociation constants typically in the μM to mM range. In some cases, there is an absolute requirement for Mn. In others, Mn is not essential: either there is activity in the absence of added metal (basal activity) or activation can be observed using divalent cations other than Mn. Unfortunately, it is often difficult to establish that $\mathrm{Mn^{II}}$ is the in vivo activator for a $\mathrm{Mn^{II}}$-activated protein. Since $\mathrm{Mn^{II}}$ and $\mathrm{Mg^{II}}$ have similar chemistry and since intracellular $\mathrm{Mg^{II}}$ concentrations are roughly 10^3 higher than intracellular $\mathrm{Mn^{II}}$ concentrations, the mere observation of activation by $\mathrm{Mn^{II}}$ does not prove that a protein is manganese-activated in vivo.

In contrast to manganese-activated enzymes, manganoenzymes contain tightly bound Mn and it is often quite difficult to remove the Mn from the protein. The activity of manganoenzymes is not enhanced by the addition of free Mn to the assay medium. Both classes of proteins are discussed since the distinction involves only the relative strength of the Mn–protein interaction and not any fundamental properties of the Mn active site.

There have in addition been numerous studies of Mn-substituted proteins. In these, Mn is substituted for a metal found naturally in the protein (most often $\mathrm{Mg^{II}}$, but also $\mathrm{Zn^{II}}$, $\mathrm{Ca^{II}}$, or $\mathrm{Fe^{II}}$). This substitution is generally used to permit spectroscopic characterization of the native metal site, using $\mathrm{Mn^{II}}$ as the reporter. Often (although not always) the Mn-substituted protein is active. Manganese-substituted proteins are discussed briefly where they illustrate important properties of Mn–protein interactions.

2 BIOLOGICAL DISTRIBUTION OF MANGANESE

Manganese is one of the most common elements in the Earth's crust; thus it should not be surprising that manganese is an essential trace element for a variety of organisms (both prokaryotes and eukaryotes (*see Prokaryote* and *Eukaryote*) including humans). Manganese deficiency has been implicated in numerous diseases including skeletal abnormalities and depressed reproductive function.[5] Manganese is distributed throughout mammalian tissues, with the highest concentrations found in the liver, kidney, lung, heart, spleen, and brain. In some cases, it appears that Mn^{II} and Ca^{II} share the same intracellular transport mechanism, which is reasonable given their similar ionic radii (*see Crystallographic Radius*). In other cases, it is Fe^{II} and Mn^{II} that appear to share transport and regulation mechanisms.

Much of the manganese present in tissue can be accounted for by a few proteins: pyruvate carboxylase, superoxide dismutase, and arginase in the liver; glutamine synthetase in the brain. The location and function of the remainder of the Mn remains to be defined, although it may be associated with weak-binding Mn-activated enzymes. The biochemical significance of the 'remainder' Mn is not clear at present, although there is growing evidence (see Section 3) that Mn levels can be critical in determining the pathogenicity of bacteria.

Manganese may play a role in metabolic regulation. For Mn to function in intracellular control, several conditions must be met: (1) The kinetic constants for the interaction of Mn^{II} with the putative control target must approximate the intracellular free Mn^{II} concentration; (2) the binding site for Mn^{II} must discriminate strongly against Mg^{II}; (3) the amount of intracellular exchangeable Mn^{II} must approximate the concentration of target enzyme that is required to account for the observed metabolic flux; and (4) the intracellular free Mn^{II} concentration must change in response to altered physiological or hormonal states. These criteria seem to be met by several protein kinases, synthetases, and phosphatases. There is sufficient Mn in cells to accommodate additional control pathways. However, the putative protein targets remain to be identified.

3 MANGANESE TRANSPORT AND REGULATION

The last decade has seen an explosion of interest in Mn transport and regulation.[6] While this remains poorly characterized in comparison with the much better studied areas of Fe and Cu homeostasis (*see* ***Metallochaperones & Metal Ion Homeostasis***), the basic principles of Mn metabolism are beginning to be worked out. In yeast, there are at least two independent systems for importing Mn into the cell. The high-affinity transporter, operative under conditions of Mn starvation, is an Nramp (Natural resistance-associated macrophage protein) divalent cation transporter. Very recently, the low-affinity transporter has been shown to be a phosphate transporter.[7] In addition to these import systems, there is at least one additional transporter, a P-type ATPase, that is responsible for Mn export, in order to maintain an appropriate intracellular Mn level. Bacterial Mn transport also includes an Nramp protein (known as MntH) and a P-type ATPase, together with an ATP-binding cassette (ABC)-type Mn permease. Although these proteins are beginning to be well-characterized genetically, the details of the Mn sites, and the mechanisms of Mn transport remain to be elucidated. What is clear, however, is that careful control of Mn levels is critical for most cells, at least in part because of the importance of Mn ions and Mn-binding proteins in protecting cells from oxidative stress.[8]

As with transport, the biochemistry of Mn regulation (*see* ***Metalloregulation***) is only beginning to be worked out. In *B. subtilis*, Mn homeostasis appears to be maintained by the regulatory protein MntR. When the Mn^{II} concentration is low, MntR is present as the apo protein. In this form, MntR promotes transcription of an (ABC)-type Mn permease (MntA). At high Mn concentration, Mn binds to MntR, converting the protein to a form that is ineffective at promoting MntA and that in addition inhibits the Nramp transporter MntH.[9] MntR is a member of the diphtheria toxin repressor (DtxR) family of metalloregulatory proteins. Most of the DtxR proteins bind Fe, although they can be activated by Mn under some conditions. Surprisingly, MntR is highly selective for Mn. The basis of this selectivity appears to be the formation of novel dinuclear Mn active site,[10] in which the Mn are bridged by two carboxylates, one in a μ-1,3 geometry and one in a μ-1,1 geometry, with a third bridge provided by a solvent molecule. Although DtxR also binds two metal ions, the irons in DtxR are separated by 9 Å, in comparison with the 3.3 Å Mn–Mn separation in MntR. The presence of a dinuclear site in MntR may be responsible for its Mn selectivity; although it is certainly possible to form dinuclear Fe sites, one of the Mn ions in MntR appears to be 7-coordinate, a relatively uncommon structure for the smaller Fe^{II} ion.

Iron availability is known to limit the pathogenicity of many organisms. It appears that at least some microorganisms have responded to this limitation by evolving metabolic systems that can function with little or no Fe, but that, in many cases, have an absolute requirement for Mn. Examples include *Borrelia burgdorferi* (causative agent of Lyme disease) and *Mycoplasma pneumoniae*. The existence of a unique Mn requirement for some bacteria suggests that it may be possible to develop new drugs that attack selected microorganisms by limiting their Mn transport. For example, a virulence factor in *Enterococcus faecalis* (a cause of infective endocarditis) appears to be an (ABC)-type Mn transporter.

4 MANGANESE-ACTIVATED ENZYMES

Over 150 enzymes have been shown to contain Mn, and in many cases, it seems likely that Mn is the in vivo activator.[11] For example, enzymes that utilize nucleoside triphosphates (e.g. kinases, DNA polymerases) require divalent cations. Often Mn^{II} is just one of several divalent cations that can stimulate activity. In many cases, Mg^{II} is believed to be the physiologically relevant cation. There are, however, many cases in which Mn appears to be preferred, or even essential, for activity. Examples include L-threonine dehydrogenase, which has low basal activity that is significantly enhanced by Mn^{II} and Cd^{II}, but not by any other divalent cations and inorganic pyrophosphatase, which is specifically activated by Mn^{II} and more weakly by Co^{II}. In both cases, Mn^{II} almost certainly is the in vivo activator. Although no structural details are available for the former Mn site, the latter has recently been shown crystallographically to have a dinuclear Mn active site.[12]

Although there have been numerous studies of the interactions of substrates and inhibitors with the Mn^{II} ions in manganese-activated enzymes, structural details of the Mn sites in most Mn-activated enzymes are only beginning to be defined. However, with the growth of structural genomics initiatives, it is clear that the number of known Mn active sites will continue to grow rapidly – there are already over 1000 entries in the protein data bank containing bound Mn. Three Mn-activated enzymes in which the Mn site structure and function are relatively well-characterized are xylose isomerases, glutamine synthetase, and phosphoglycerate mutase.

4.1 Xylose Isomerase

D-Xylose isomerase catalyzes the isomerization of the five-carbon aldose D-xylose to the ketose D-xylulose. The enzyme has an absolute requirement for added divalent cations; however, Mg^{II}, Co^{II}, and Mn^{II} are all effective in stimulating activity. The enzyme has been the object of intensive scrutiny, including numerous crystal structures, because of its industrial importance in the production of fructose from glucose.[13] There are two adjacent metal-binding sites, with the metals sharing a carboxylate ligand. The structure (**1**) features a 1,3-bridging mode for the carboxylate. This gives a long metal–metal distance of ca. 5 Å, with some variation in this distance when substrate is bound. The first cation is believed to bind and orient the sugar, while the metal in the second site is believed to participate directly in the isomerization reaction. This second metal coordinates to O-1 and O-2 of the sugar and, by virtue of its electric field, facilitates hydride transfer between C-1 and C-2. Recently, it has been possible to engineer isomerases having modified metal ion specificity. In particular, modification of a carboxylate that is near, but not at, the cation sites gives a protein that is most active with Mn.

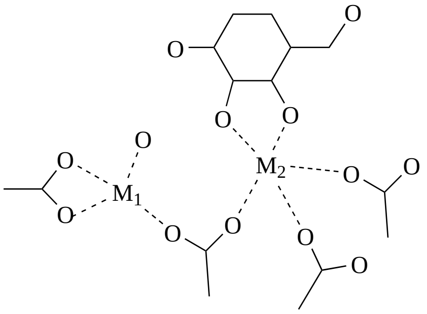

(**1**)

4.2 Glutamine Synthetase

Glutamine synthetase catalyzes the ATP-dependent biosynthesis of glutamine according to equation (1). This enzyme plays a central role in nitrogen metabolism. In mammalian brain tissue, glutamine synthetase converts the neurotransmitter glutamate into glutamine.

$$\text{L-Glutamate} + \text{ATP} + \text{NH}_3 \longrightarrow \text{L-Glutamine} + \text{ADP} + \text{P}_i \qquad (1)$$

At one point, it appeared that the mammalian enzyme contained tightly bound Mn (i.e. was a manganoenzyme). More recently, however, it has been shown that both the mammalian and the bacterial enzyme are manganese-activated (i.e. Mn dissociation constants in the µM range). There are two cation binding sites. As with xylose isomerase, the first site is believed to be responsible for defining the orientation of the substrate binding while the second is directly involved in catalytic activity. Based on a dipolar relaxation mechanism, the EPR spectra of glutamine synthetase indicate a 6–10 Å distance between the two sites, depending on the state of the enzyme. The presence of at least one water in the coordination sphere of one site was inferred from NMR relaxation data. These spectroscopic interpretations were recently confirmed with the determination of the glutamine synthetase crystal structure.[14] Each Mn is coordinated by three or four protein ligands and two water molecules in an approximately octahedral geometry. There is a single bridging water molecule, giving a Mn–Mn distance of 5.8 Å.

4.3 Phosphoglycerate Mutase

Phosphoglycerate mutase (PGM) catalyzes the isomerization of 2- and 3-phosphoglycerate, and is essential for glucose metabolism. There are two major categories of PGM, one dependent on the cofactor 2,3-bisphosphoglycerate, and the other (*i*PGM) that is independent of organic cofactors, but that requires the presence of divalent metal cations. The *i*PGM from *Bacillus stearothermophilus* has an absolute requirement for Mn^{II} and shows dramatic pH sensitivity. Similar, albeit less well-characterized *i*PGMs are found in more dangerous pathogens, including *Bacillus anthracis* (the causative agent of anthrax). Interestingly, the pH sensitivity is significantly enhanced by the presence of low levels of Mn; most likely this reflects the pH dependence of Mn binding, which in turn results from the fact that two protons are released when Mn binds. It is likely that this Mn-dependent pH sensitivity is physiologically important. The decrease in pH during sporulation inactivates *i*PGM and results in the accumulation of a reserve of 3-phosphoglycerate in the developing spore; on spore germination the pH rises, activating *i*PGM and allowing utilization of the 3-phosphoglycerate.[15] Given the large number of Mn-activated enzymes that are involved in the interconversion of phosphoglycerate, pyruvate, and oxaloacetate, it is possible that a mechanism similar to that found in *i*PGM could offer a way for Mn to play a central role in regulating cellular carbon metabolism.

The dramatic pH sensitivity requires that the available Mn concentration match the relatively weak-binding constant of *i*PGM for Mn. If higher Mn levels are present, the pH sensitivity is greatly attenuated. Crystallographic studies have shown that *i*PGM has a dinuclear Mn active site, with an oxygen of the phosphoglycerate forming a bridge between the two Mn, thus orienting the substrate for reaction.[16]

5 METALLOPROTEINS WITH MONONUCLEAR Mn SITES

There are relatively few characterized metalloproteins having mononuclear Mn sites. By far the best characterized mononuclear Mn site is shown in *Superoxide Dismutase*, although there are several other proteins that appear to have tightly bound mononuclear sites, including an extradiol dioxygenase, and several members of the cupin family.

5.1 Superoxide Dismutase

Superoxide dismutase (SOD) catalyzes the disproportionation of superoxide to peroxide and oxygen according to equation (2). Four different types of SOD are known, containing either Cu and Zn (*see* ***Copper Proteins with Type 2 Sites***), Fe, Mn, or Ni (*see* ***Nickel Enzymes & Cofactors***). The Fe and Mn containing SODs have very similar structures and can be further subdivided into metal-specific (i.e. functioning only when the ‘correct’ metal is bound) and cambialistic (functioning with either Fe or Mn bound to the active site).

$$2O_2^- + 2H^+ \longrightarrow H_2O_2 + O_2 \qquad (2)$$

Crystal structures have been determined for both Fe and Mn SODs. These constitute a family of closely related proteins with homologous folding patterns. There is complete conservation of both the metal ligands and the aromatic residues surrounding the metal atom. The metal site has approximate trigonal bipyramidal structure (**2**) with an equatorial plane of two histidine imidazoles and one aspartate carboxylate, and axially coordinated solvent and imidazole.

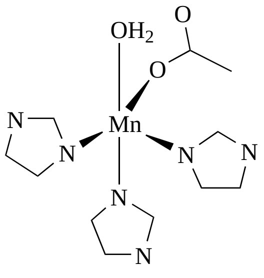

(**2**)

In Mn-activated enzymes, the Mn appears either to play a structural role (e.g. defining the substrate orientation or stabilizing an active conformation of the protein) or to function as a Lewis acid (*see Lewis Acids & Bases*). In contrast, in extensive kinetic studies of Fe, and to a lesser extent Mn, SODs have shown unambiguously that the metal plays a redox role in these proteins, cycling between Mn^{II} and Mn^{III}. There is no significant change in the Mn structure when the metal is reduced; this is typical of redox-active metal sites, since any significant distortion will give rise to a kinetic barrier to reaction (*see* ***Long-range Electron Transfer in Biology***)

Azide is a competitive inhibitor of SOD and is believed to bind analogously to superoxide. The crystal structures of the azide derivative show that azide binding takes place without loss of protein ligands. A plausible kinetic mechanism, combining the kinetic and structural data for Fe and Mn SODs, is shown in Scheme 1. During steady-state turnover, the majority of Mn SOD appears to be present in an inactive

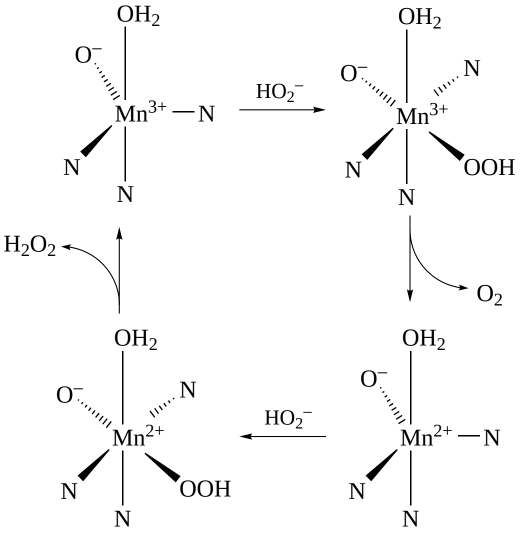

Scheme 1 Possible superoxide dismutase mechanism

dead-end complex that rapidly converts to the active enzyme once superoxide is consumed. Based on the observed *Ligand-to-Metal Charge Transfer* bands, the dead-end complex has been identified as a $Mn^{III}-$peroxo adduct.

One of the most intriguing questions about SOD is the structural basis of the metal specificity. Two limiting mechanisms have been suggested. One is based on redox potential. The midpoint potentials for oxidation and reduction of superoxide are $-160\,mV$ and $+890\,mV$, respectively. In order to have maximum kinetic efficiency, the redox potential for SOD needs to be between these, and consistent with this, the redox potentials for the enzyme are around $+300\,mV$. This is ca. 470 mV below the redox potential of aqueous Fe, but more than 1 V below the redox potential of aqueous Mn. The redox model then suggests that the Mn-specific protein must lower the reduction potential of the metal more than does the Fe-specific protein. Consequently, if Fe is substituted for Mn, the redox potential will be too low to oxidize superoxide. An alternative model is based on structural differences that are seen when Fe is substituted into the Mn site.**[17]** In this case, it appears that the Fe is 6-, rather than 5-coordinate, with the 6th coordination site being occupied by hydroxide, when Fe is substituted into Mn-specific superoxide dismutase. Hydroxide binding, like azide binding, would inhibit the enzyme by blocking access of the superoxide to the metal, and thus would account for the inactivity. Consistent with this, some activity is recovered at lower pH, where the hydroxide concentration is lower.

5.2 3,4-Dihydroxyphenylacetate 2,3-Dioxygenase

Iron-containing extradiol-cleaving dioxygenases are well known (*see* ***Iron Proteins with Mononuclear Active Sites***). These contain a loosely bound Fe^{II} and are readily inhibited by cyanide. In contrast, the dioxygenase from *Bacillus brevis* contains no Fe as-isolated, is not activated by Fe^{II}, and is not inhibited by cyanide. It does contain two tightly bound Mn ions per tetramer. EPR spectra show that the Mn environment changes when inhibitor is bound, thus suggesting a functional role for the Mn, and recent crystallographic studies confirm the presence of Mn rather than Fe.**[18]** For both the Fe and the Mn proteins, the metal is coordinated by two histidines, one glutamic acid, and solvent molecules completing the coordination sphere. The available structures are at fairly low resolution (2.5 Å or worse); thus it is not possible to define the metal ligation in detail; it is possible that Fe and Mn have different coordination numbers. Intriguingly, both the first and the second coordination spheres are essentially identical within the uncertainty of the data. Unlike SOD, it has not been possible to prepare metal substituted samples of the dioxygenases; thus it is not known whether the Fe-enzyme will function with Mn in the active site (and vice versa). The finding that the protein is either Fe-specific or Mn-specific, despite the identical structures and very similar sequences, suggests that metal selectivity may be due to changes in structure that occur during folding.

Since the proposed mechanism involves cycling of the metal between the M^{II} and M^{III} oxidation states, it is somewhat surprising that there is no apparent difference in structure between the Fe and Mn-specific enzymes. As discussed above, one would predict nearly a half-volt difference in reduction potential if Fe and Mn are bound in identical sites. This may mean metal oxidation is not rate limiting, and thus that the reaction can accommodate this shift in potential (in contrast with the case for SOD) or it may mean that there are structural changes (e.g. coordination number) that cannot be detected with the present crystallographic resolution.

5.3 Cupins

The cupin family of proteins form extremely stable beta-barrels. Recently, several cupins have been shown to bind Mn. The best characterized of these is oxalate decarboxylase, which has a $Mn(His)_3(Glu)(H_2O)_2$ binding site. The two water molecules are cis, thus providing a possible bidentate binding site for oxalate, or perhaps more realistically, binding sites for a monodentate oxalate and an O_2.**[19]** Oxalate metabolism is important for maintaining pH and ionic strength in plants, and oxalate production is believed to play an important role in biological defense. In addition to the decarboxylation reaction, in which oxalate is converted to CO_2 and formate, it is also possible to degrade oxalate by oxidation in an O_2-dependent process to give two moles of CO_2 and one mole of H_2O_2, a reaction catalyzed by oxalate oxidase. Recently, germin, a protein implicated in plant response to pathogens, was shown to be an oxalate oxidase, and was found crystallographically to have a structure very similar to that seen in oxalate decarboxylase.**[20]** Oxalate oxidase and oxalate decarboxylase have identical Mn active sites. Both enzymes require O_2 for activity, although only in the oxidase is O_2 consumed. One possible mechanism that could account for the reactivity is shown in Scheme 2. In this mechanism, O_2 binds to the Mn^{II} form of the enzyme, giving a Mn^{III} superoxide intermediate that acts as an electron sink to facilitate decarboxylation of the oxalate, producing a formyl radical-anion intermediate. In the decarboxylase (left-hand side of Scheme 2), the formyl carbon is protonated, while in oxalate oxidase (right-hand side), the intermediate decays with release of H_2O_2. Alternative schemes involving higher oxidation states of Mn have also been proposed,**[21]** but seem less likely given the known ability of histidine ligation to stabilize Mn^{II}. Recently, a new Mn-containing cupin was identified by structural genomics efforts.**[22]** This protein has a novel tetra-histidine Mn site, with two solvent molecules completing the octahedral site, but does not, as yet, have any known biological function. This ligation should significantly favor the Mn^{II} oxidation state, thus it is unlikely that this Mn is redox-active in vivo.

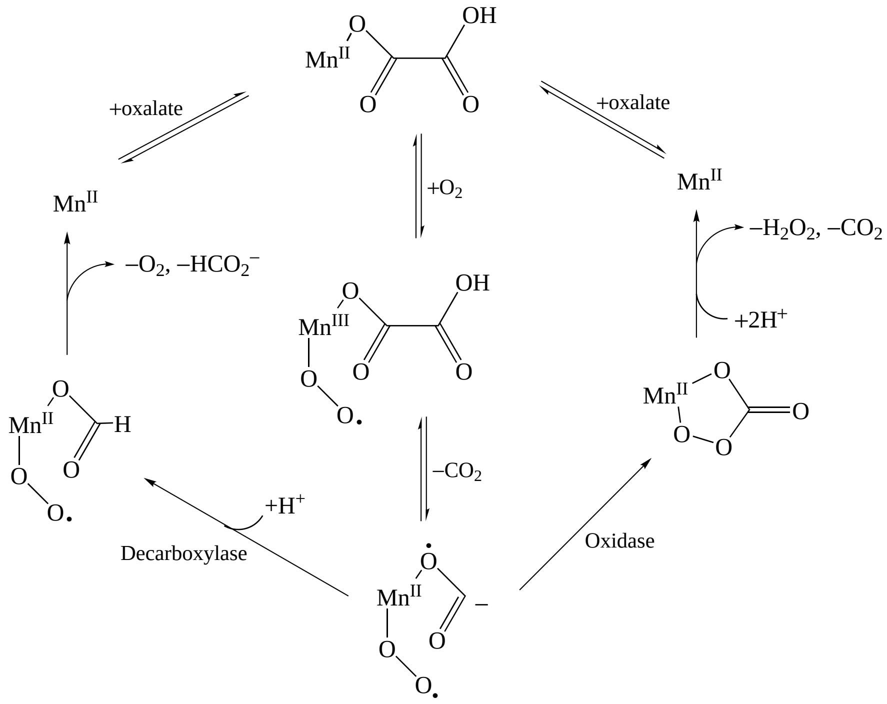

Scheme 2 Possible mechanisms for Mn-mediated oxalate metabolism

6 METALLOPROTEINS WITH DINUCLEAR Mn SITES

Several manganoproteins having dinuclear sites are now known. These include a large number of Mn-activated enzymes, such as phosphoglycerate mutase (discussed above), numerous hydrolytic enzymes, including inorganic pyrophosphatase (above) and arginase, and several proteins where the dinuclear site may play only a structural role, including concanavalin A and MntR (above). One enzyme in which the dimanganese site is unambiguously redox-active is Mn catalase. There are several other proteins that may have redox-active dinuclear sites; however, these have not, in general, been characterized structurally.

6.1 Mn Catalase

The catalases catalyze the disproportionation of hydrogen peroxide (equation 3). Most catalases contain the iron-protoporphyrin IX prosthetic group (*see* ***Iron: Heme Proteins, Peroxidases, Catalases & Catalase-peroxidases***). However, some bacteria are able to synthesize catalases that are not inhibited even by millimolar concentrations of azide and cyanide,[23] suggesting that some catalases are nonheme enzymes; it is now known that these enzymes possess a dinuclear Mn active site.

$$2H_2O_2 \longrightarrow 2H_2O + O_2 \qquad (3)$$

The nonheme catalases are sometimes referred to as pseudocatalases. However, this is inappropriate since there is nothing ‘pseudo’ about their catalase activity. They are better described as Mn catalases. Bacteria that lack Mn catalase (either genetically or through inactivation of the enzyme) show decreased viability, suggesting that Mn catalase does, in fact, play a physiological role in the detoxification of H_2O_2.

6.1.1 Characterization of Mn Catalase

Most of the work on Mn catalases has focused on the enzymes isolated from *Lactobacillus plantarum* and *Thermus thermophilus*. However, numerous putative Mn catalases have been identified from sequence comparisons. Most of these are from stress-tolerant bacteria (heat, salt, pH, etc.) consistent with the suggestion (above) that Mn proteins may be important in stress response. Intriguingly, at least three putative Mn catalases are found in pathogenic organisms: *E. coli* O157:H7, *Salmonella typhimurium*, and *Bacillus anthracis*.

Three Mn catalases have been purified and characterized,[24] including crystals structures for two of the enzymes.[25] Each Mn catalase monomer has four parallel α-helices, similar to the structure found in hemerythrin (*see* ***Iron Proteins with Dinuclear Active Sites***). The crystallography demonstrates that the Mn site is bridged by a single μ-(1,3)-carboxylate ligand and two solvent molecules, and that there is a single histidine coordinated to each Mn. The remainder of the ligation sphere, to give 6-coordinate Mn, is completed by two additional glutamates (one monodentate and one bidentate) together with a third solvent molecule. The Mn–Mn separations are relatively long (3.4–3.6 Å) suggesting that at least one of the bridging solvents must be protonated. One possible scheme invokes oxo, hydroxo bridging in the oxidized Mn^{III}_2 form and hydroxo, aquo bridging in the reduced Mn^{II}_2 form.**[26]** However, despite the availability of several crystal structures, questions remain regarding the structural details owing to the sensitivity of the enzyme to X-ray induced radiation damage, especially in the Mn^{III} oxidation state. Consistent with this, EXAFS (*see Extended X-ray Absorption Fine Structure*) spectra seem to show shorter Mn–Mn separations than are seen crystallographically.

The optical spectrum of as-isolated Mn catalase has a broad weak absorption band at ca. 450–550 nm, similar to the spectra seen for Mn^{III} superoxide dismutase and for a variety of Mn^{III} model complexes, thus suggesting that at least some of the Mn in Mn catalase is present as Mn^{III}. In particular, the absorption maximum at ca. 500 nm is similar in energy and intensity to the transitions seen for oxo-, carboxylato-bridged Mn dimers (see Section 9). The EPR spectrum of the as-isolated enzyme is a complex multicomponent signal. At 50 K, the EPR is dominated by a 16-line signal centered at ca. $g = 2.0$ that is ca. 1300 G wide. This signal is essentially identical to those observed for Mn^{III}/Mn^{IV} mixed-valence compounds (*see **Mixed Valence Compounds***). On treatment with NH_2OH, the Mn^{III}/Mn^{IV} signal disappears and a new, very broad signal, attributed to a Mn^{II}/Mn^{II} form of the enzyme, appears. This signal is quite sensitive to the buffer, the pH, and the anions that are present (i.e. SO_4^{2-}, N_3^-, F^-, CN^-). At temperatures below 50 K, a third EPR signal, attributed to a Mn^{II}/Mn^{III} derivative, is observed. All three signals contribute to the observed spectrum of the as-isolated enzyme but each can be enhanced by selective redox interconversions. Electron Spin Echo Envelope Modulation (ESEEM) (*see Electron Spin Echo Envelope Modulation Spectroscopy*) spectra for the Mn^{III}/Mn^{IV} enzyme show ^{14}N modulations, consistent with the nitrogen ligation seen crystallographically. Interestingly, only one of the two histidines is detectable by ESEEM.

The Mn catalases were originally identified on the basis of their insensitivity to azide and cyanide. However, kinetic studies have subsequently shown that all three Mn catalases are inhibited by azide and other anions, albeit at much higher concentrations than are required for inhibition of heme catalases. In the case of azide, the inhibition is competitive, suggesting that azide and peroxide bind at the same metal site. Azide binding to the reduced (Mn^{II}/Mn^{II}) enzyme appears to cause loss of a coordinated water molecule.

Mn catalase cycles between the Mn^{II}/Mn^{II} and the Mn^{III}/Mn^{III} oxidation states during catalysis and is thus, in some sense, the two-electron analog of Mn superoxide dismutase. One possible mechanistic model, based on the known coordination chemistry of Mn dimers and the crystal structures of Mn catalase, is shown in Scheme 3.**[26]** In this scheme, the bridging solvent molecules play a critical role in proton transfer, with the oxo bridge acting as a Lewis base, facilitating the oxidation of peroxide to dioxygen.

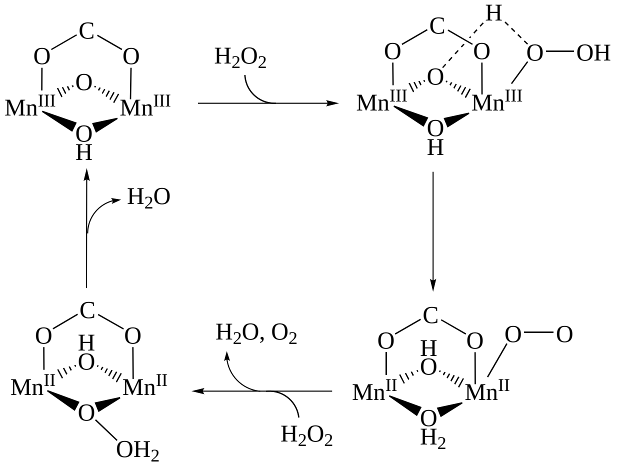

Scheme 3 Possible mechanism for Mn catalase peroxide disproportionation

6.1.2 *Possible Analogies to the Oxygen-Evolving Complex*

The best characterized of the Mn enzymes is the photosynthetic oxygen-evolving complex (OEC, *see **Manganese: The Oxygen-evolving Complex & Models***). On the surface, the OEC would appear to be quite different from any other Mn enzyme, since it contains four tightly bound Mn ions and appears to use only the Mn^{III} and Mn^{IV} oxidation states. However, if Mn catalase is inactivated by the simultaneous addition of μM concentrations of NH_2OH and H_2O_2, a Mn^{III}/Mn^{IV} mixed-valence derivative is formed. This superoxidized catalase has a $Mn^{III}(\mu\text{-}O)_2Mn^{IV}$ structure**[27]** and is spectroscopically (EPR) and structurally (EXAFS) similar to the Mn site in the OEC. With this in mind, it is intriguing to note that the OEC Mn site has been implicated both in the disproportionation of H_2O_2 and in the formation of H_2O_2. It thus seems that the OEC and Mn catalase may not be as different as they first appear.

6.2 Concanavalin A

The lectins are saccharide-binding proteins that cause cell agglutination. The best characterized of the lectins is concanavalin A (Con A). Con A is devoid of carbohydrate binding activity in the absence of added metal. Each monomeric unit of Con A has two binding sites, named S1 (the transition metal site) and S2 (the calcium site). The S1 site binds a variety of divalent transition metals, including Mn, Ni, Co, Cd, Zn, Fe, and Cu, although Mn is probably the metal used in vivo. The S2 site is not formed until S1 is occupied. Both S1 and S2 must be occupied before saccharide will bind.

Crystallographic studies show that the S1 and S2 sites are ca. 4.2 Å apart and are bridged by two carboxylate residues. When Mn^{II} and Ca^{II} are added to the *Apoprotein*, Con A is initially in an inactive conformation. This slowly converts to an active, or 'locked', conformation. In the locked conformation, Mn is tightly bound. The Mn appears to play solely a structural role in Con A. The principal interest in Con A, in the context of understanding dinuclear Mn proteins, is that in the absence of Ca^{II}, two equivalents of Mn^{II} will bind to the apoprotein. This dimanganese protein has an EPR spectrum characteristic of an antiferromagnetically coupled (*see Antiferromagnetism*) Mn dimer. Although the dimanganese protein is active in saccharide binding, it is of particular interest as the first well-characterized spectroscopic model for exchange-coupled di-Mn^{II} sites.

6.3 Arginase

Arginase is the terminal enzyme in the urea cycle. It catalyzes the hydrolysis of L-arginine to L-ornithine and urea (equation 4). Preincubation with Mn^{II} is required for activation. However, in contrast to Mn-activated enzymes, free Mn^{II} is not required in the assay medium. That is, Mn^{II} is apparently lost during purification, but once the Mn site is reformed, the Mn is tightly bound. The EPR spectrum for Mn-saturated arginase is very similar to that for Mn_2Con A, indicating that there are two magnetically coupled Mn ions in the active site.

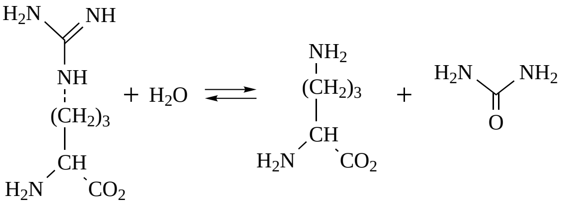

(4)

Crystallography has shown that arginase is structurally quite similar to Mn catalase. The protein provides similar ligands to the Mn: a μ-1,3-carboxylate, together with one histidine and one carboxylate per Mn (aspartates in arginase vs. glutamates in catalase). However, in contrast with the two bridging solvent molecules in catalase, arginase has one bridging solvent and a μ-1,1 bridging carboxylate. This difference in ligation is apparently responsible for the lack of catalase activity, despite the similar ligation. This is consistent with the critical role proposed for the bridging solvent in proton buffering during H_2O_2 disproportionation by Mn catalase.

The concentration of arginase in the liver greatly exceeds that necessary for the observed metabolic flux. For many years, this was taken to indicate that arginase could not be the rate-determining step in urea production, and thus that arginase regulation was unlikely to be important metabolically. Recently, however, it has been shown that, in vivo, arginase operates at well below its maximum capacity owing to subsaturation with Mn^{II}. Arginase has a strong pH dependence that appears to arise from the pH dependence of Mn binding, similar to that described previously for phosphoglycerate mutase, suggesting that arginase is a candidate to be another Mn-regulated enzyme.

6.4 Ribonucleotide Reductase

Ribonucleotide reductase catalyzes the reduction of ribonucleotide diphosphates to the corresponding deoxyribonucleotides and is thus an essential enzyme for all living organisms. The ribonucleotide reductase from *E. coli* has a dinuclear Fe site that has been characterized crystallographically (*see* ***Iron Proteins with Dinuclear Active Sites***). Mn competes with Fe in reconstitution of apo-ribonucleotide reductase and has been shown crystallographically to bind at the same site as Fe. The Mn_2 site in ribonucleotide reductase (**3**) is bridged by two carboxylate groups, giving it a relatively short Mn–Mn distance of 3.6 Å. This is essentially the same as that found in Mn catalase structure, despite the difference in bridging ligation. There is no EPR signal for Mn_2 ribonucleotide reductase at room temperature; however, at low temperature a broad signal consistent with an exchange-coupled Mn dimer is seen. Unlike the native Fe protein, in which the Fe is redox-active, the Mn^{II} in Mn_2 ribonucleotide reductase is not readily oxidized (thus explaining why the Mn-substituted enzyme is catalytically inactive).

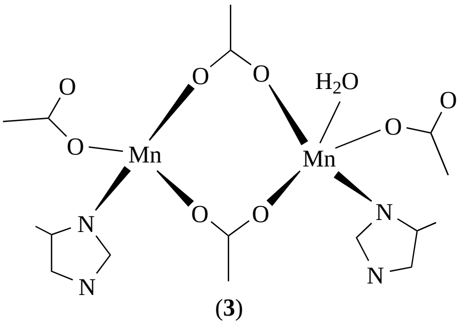

(**3**)

It was suggested, based on UV-visible and EPR spectroscopy, that the ribonucleotide reductase from *Corynebacterium ammoniagenes* contains Mn rather than Fe in its native form. However, more recent crystallographic studies have shown that this protein is structurally identical to the native iron proteins and apparently does not contain a Mn active site.**[28]**

6.5 Other Dinuclear Mn proteins

A wide range of hydrolase enzymes contain dinuclear metal sites, and in many cases these can include dinuclear Mn sites. Phosphotriesterases catalyze the hydrolysis of a wide range of organophosphates and generally bind two divalent cations. The native enzyme typically contains Zn^{II}; however, this can be replaced by $\mathrm{Mn^{II}}$ with no loss of activity. The EPR spectrum of the enzyme is typical of those found for antiferromagnetically coupled $\mathrm{Mn^{II}/Mn^{II}}$ sites with a broad feature near $g = 2$ that shows >26 lines with a hyperfine coupling of ca. 45 G, attributed to an $S = 1$ excited state. These data demonstrate that the two metal ions must be within 3–5 Å, thus indicating that phosphotriesterase is a dinuclear Mn enzyme. Similar behavior is found for glyoxylase II, a member of the metallo-β-lactamase superfamily. In this case, the enzyme is isolated with Zn, Fe, and Mn bound, all of which appear to be active.[29] Other, less well-characterized systems that may contain dinuclear Mn include an enzyme from *Thiobacillus versutus* that oxidizes thiosulfate to sulfate. One of the proteins in this system ('protein B') has an EPR spectrum indicative of an exchange-coupled $\mathrm{Mn^{II}}$ dimer. No structural information is available for this protein.

7 MANGANESE-SUBSTITUTED PROTEINS

Most of the enzymatic reactions that utilize the naturally occurring diamagnetic $\mathrm{Mg^{II}}$ ion still occur when the $\mathrm{Mg^{II}}$ is substituted by the paramagnetic $\mathrm{Mn^{II}}$ ion, often with little or no loss of activity. Since $\mathrm{Mn^{II}}$ is present at much lower concentrations than $\mathrm{Mg^{II}}$ in the cell, $\mathrm{Mn^{II}}$ does not play a role in vivo. The substitution studies are nonetheless useful, since $\mathrm{Mn^{II}}$ can be used as a probe for cation environment.[1] An important class of enzymes that have been studied in this way are those enzymes that utilize nucleoside triphosphates, including elongation factors and kinases.

Transferrin is a reversible iron-binding protein used in vertebrate iron-transport (*see* ***Iron Proteins for Storage & Transport & their Synthetic Analogs***). Manganese will bind to transferrin in vitro to form a $\mathrm{Mn^{III}}$–transferrin complex. Transferrin appears to bind the majority of the serum Mn and may be important in Mn transport.

8 SPECTROSCOPY

Magnetic resonance techniques (EPR, ESEEM, and NMR) have been among the most useful in characterizing Mn proteins. Other techniques, such as *X-Ray Absorption Spectroscopy* are also useful in special cases.

8.1 EPR

As described above, $\mathrm{Mn^{II}}$ is the most common oxidation state for Mn in proteins. In biological complexes, $\mathrm{Mn^{II}}$ is exclusively high-spin ($S = 5/2$) giving it a ^{6}S ground-state. This gives a total of 36 possible states, since m_S and m_I can both range from $-5/2$ to 5/2 (*see Electron Paramagnetic Resonance*). In the most general case, there are five EPR transitions, each split into a sextet by hyperfine coupling to the Mn nucleus. In reality, it is typical to observe only the central $\Delta M_S = \pm 1/2$ transitions since the other allowed transitions have pronounced orientational anistropy (and hence are often too broad to be detected). As a half-integral spin system, $\mathrm{Mn^{II}}$ is always EPR active (although this does not mean that the EPR spectrum is easily detectable). In general, the detectability and interpretability of $\mathrm{Mn^{II}}$ EPR spectra is improved by making measurements at higher fields. The so-called Q-band (35 GHz) is accessible to many investigators, and recent work has demonstrated the value of ultrahigh field EPR (up to ~300 GHz) for making subtle distinctions between different Mn sites. From the EPR spectrum, one can (at least in principle) extract the zero-field-splitting tensor for the Mn ion, and thus learn about the local symmetry of the site. This was shown in a recent ultrahigh field study of superoxide dismutase, where measurements at 285 GHz revealed subtle differences in Mn electronic structure that could be correlated with protein activity.[30]

By judicious use of spin-labeled substrates (often ^{17}O), it has proven possible to extract substantial information about the interactions between the Mn and various substrates.[2] As discussed above, EPR is also a powerful probe for determining the metal–metal distances in proteins having multiple metal sites. A variation on EPR is Electron Nuclear Double Resonance (ENDOR; *see Electron Nuclear Double Resonance Spectroscopy*), in which samples are irradiated by a combination of microwaves and radio waves. ENDOR allows identification of the nuclear spin transitions that are magnetically coupled to the unpaired electron spin, and thus has been extremely useful for identifying ligands to Mn sites (e.g. by identifying protons from solvent and/or nitrogens from histidine ligands).

8.2 ESEEM

ESEEM spectroscopy is a time-domain (i.e. pulsed) analog of EPR (*see Electron Spin Echo Envelope Modulation Spectroscopy*).[31] In principle, ESEEM contains the same information as is found in EPR and ENDOR, although in practice ESEEM is much more sensitive to weakly coupled nuclei that are not easily detected by ENDOR. On the other hand, strongly coupled nuclei can be undetectable by ESEEM, thus the combination of both techniques is often useful.

8.3 NMR

The proton spin–lattice relaxation times for solvent water are strongly perturbed if the water is in rapid exchange with a paramagnet. In particular, $\mathrm{Mn^{II}}$ is a strong relaxer for water protons and thus nuclear magnetic resonance (NMR) spectroscopy provides a sensitive probe for the presence of exchangeable water molecules bound to Mn in Mn proteins.

8.4 UV–Visible Spectroscopy

Since the ligand-field transitions (*see* ***Ligand Field Theory & Spectra***) for Mn^{II} are both spin and orbitally forbidden, Mn^{II} proteins seldom have detectable visible absorption bands. Proteins in which the Mn is oxidized, for example, Mn catalase or Mn transferrin, do have characteristic absorption features, as discussed above. As more Mn proteins are discovered, possibly with redox-active metals, visible spectroscopy may become more important. For paramagnetic species, which includes most Mn proteins, it is also possible to measure *Magnetic Circular Dichroism*. This provides sensitive insight into the electronic structure of the manganese site, and has been used, for example, to investigate the ligation changes that are responsible for the thermochromism in Mn superoxide dismutase.[32]

9 MODEL COMPOUNDS

Until relatively recently, little was known about the coordination chemistry of Mn, particularly in the higher oxidation states. In the last 2 decades, there has been an explosion of interest in synthesizing Mn model compounds (*see* ***Manganese: Inorganic & Coordination Chemistry***). Much of this effort has been devoted to synthesizing models for the oxygen-evolving complex; however, there also now exist a variety of well-characterized Mn dimers, including several Mn^{II} dimers that appear to be good models for the dinuclear sites in Mn catalase, glutamine synthetase, and ribonucleotide reductase. There are, in addition, several well-characterized reactivity models that carry out peroxide disproportionation.

Several conclusions can be drawn from the model studies. First, it is clear that Mn is just as versatile as Fe or Cu and that Mn complexes can, with appropriate design, be synthesized in a variety of oxidation states and coordination environments. A common feature of the model chemistry is the observation of $(\mu\text{-O})(\mu\text{-carboxylate})_2Mn_2$ and $(\mu\text{-O})_2(\mu\text{-carboxylate})Mn_2$ core structures similar to those suggested for Mn catalase. By judicious protonation of the oxo bridge(s), it is possible to vary the Mn reduction potential of these structures over a wide range.

10 RELATED ARTICLES

Manganese: Inorganic & Coordination Chemistry; Manganese: The Oxygen-evolving Complex & Models.

11 REFERENCES

1. G. H. Reed and G. D. Markham, in ‘Biological Magnetic Resonance’, eds. L. J. Berliner and J. Reuben, Plenum, New York, 1984, Vol. 6, p. 73.
2. J. J. Villafranca, S. C. Ransom, C. D. Eads, E. J. Gibbs, and J. L. Singer, in ‘Manganese in Metabolism and Enzyme Function’, eds. V. L. Schramm and F. C. Wedler, Academic Pres7s, Orlando, FL, 1986, p. 357.
3. R. J. P. Williams, *Biol. Rev.*, 1953, **28**, 381.
4. B. G. Malmstrom and A. Rosenberg, *Adv. Enzymol.*, 1959, **21**, 131.
5. C. Kies ed., ‘Nutritional Bioavailability of Manganese’, American Chemical Society, Washington, DC, 1986.
6. D. G. Kehres and M. E. Maguire, *FEMS Microbiol. Rev.*, 2003, **27**, 263.
7. L. T. Jensen, M. Ajua-Alemanji, and V. C. Culotta, *J. Biol. Chem.*, 2003, **278**, 42036.
8. M. J. Horsburgh, S. J. Wharton, M. Karavolos, and S. J. Foster, *Trends Microbiol.*, 2002, **10**, 496.
9. Q. Que and J. D. Helmann, *Mol. Microbiol.*, 2000, **35**, 1454.
10. A. Glasfeld, E. Guedon, J. D. Helmann, and R. G. Brennan, *Nat. Struct. Biol.*, 2003, **10**, 652.
11. J. D. Crowley, D. A. Traynor, and D. C. Weatherburn, in ‘Metal Ions in Biological Systems’, eds. A. Sigel and H. Sigel, Marcel Dekker, New York, 2000, Vol. 37, p. 209.
12. S. Ahn, A. J. Milner, K. Futterer, M. Konopka, M. Ilias, T. W. Young, and S. A. White, *J. Mol. Biol.*, 2001, **313**, 797.
13. R. Bogumil, R. Kappl, and J. Huttermann, ‘Metal Ions in Biological Systems’, Marcel Dekker, New York, 2000, Vol. 37, p. 365.
14. M. M. Yamashita, R. J. Almassy, C. A. Janson, D. Cascio, and D. Eisenberg, *J. Biol. Chem.*, 1989, **264**, 17681.
15. N. J. Kuhn, B. Setlow, P. Setlow, R. Cammack, and R. Williams, *Arch. Biochem. Biophys.*, 1995, **320**, 35.
16. D. J. Rigden, E. Lamani, L. V. Mello, J. E. Littlejohn, and M. J. Jedrzejas, *J. Mol. Biol.*, 2003, **328**, 909.
17. R. A. Edward, M. M. Whittaker, J. W. Whittaker, G. B. Jameson, and E. N. Baker, *J. Am. Chem. Soc.*, 1998, **120**, 9684.
18. M. W. Vetting, L. P. Wackett, L. Que, J. D. Lipscomb, and D. H. Ohlendorf, *J. Bacteriol.*, 2004, **186**, 1945.
19. V. J. Just, C. E. M. Stevenson, L. Bowater, A. Tanner, D. M. Lawson, and S. Bornemann, *J. Biol. Chem.*, 2004, **279**, 19867.
20. E. J. Woo, J. M. Dunwell, P. W. Goodenough, A. C. Marvier, and R. W. Pickersgill, *Nat. Struct. Biol.*, 2000, **7**, 1036.
21. R. Anand, P. C. Dorrestein, C. Kinsland, T. P. Begley, and S. E. Ealick, *Biochemistry*, 2002, **41**, 7659.
22. L. Jaroszewski, R. Schwarzenbacher, F. von Delft, D. McMullan, L. S. Brinen, J. M. Canaves, X. P. Dai, A. M. Deacon, M. DiDonato, M. A. Elsliger, S. Eshagi, R. Floyd, A. Godzik, C. Grittini, S. K. Grzechnik, E. Hampton, I. Levin, C. Karlak, H. E. Klock, E. Koesema, J. S. Kovarik, A. Kreusch, P. Kuhn, S. A. Lesley, T. M. McPhillips, M. D. Miller, A. Morse, K. Moy, O. Y. Jie, R. Page, K. Quijano, R. Reyes, F. Rezezadeh, A. Robb, E. Sims, G. Spraggon, R. C. Stevens, H. van den Bedem, J. Velasquez, J. Vincent, X. H. Wang, B. West, G. Wolf, Q. P. Xu, K. O. Hodgson, J. Wooley, and

I. A. Wilson, *Proteins-Structure Funct. Bioinform.*, 2004, **56**, 611.

23. E. A. Delwiche, *J. Bacteriol.*, 1961, **81**, 416.
24. J. E. Penner-Hahn, in 'Manganese Redox Enzymes', ed. V. L. Pecoraro, VCH Publishers, New York, 1992, p. 29.
25. M. M. Whittaker, V. V. Barynin, S. V. Antonyuk, and J. Whittaker, *Biochemistry*, 1999, **38**, 9126.
26. M. M. Whittaker, V. V. Barynin, T. Igarashi, and J. W. Whittaker, *Eur. J. Biochem.*, 2003, **270**, 1102.
27. G. S. Waldo, S. Yu, and J. E. Penner-Hahn, *J. Am. Chem. Soc.*, 1992, **114**, 5869.
28. Y. Huque, F. Fieschi, E. Torrents, I. Gibert, R. Eliasson, P. Reichard, M. Sahlin, and B. M. Sjoberg, *J. Biol. Chem.*, 2000, **275**, 25365.
29. O. Schilling, N. Wenzel, M. Naylor, A. Vogel, M. Crowder, C. Makaroff, and W. Meyer-Klaucke, *Biochemistry*, 2003, **42**, 11777.
30. S. Un, L. C. Tabares, N. Cortez, B. Y. Hiraoka, and F. Yamakura, *J. Am. Chem. Soc.*, 2004, **126**, 2720.
31. R. D. Britt, 'Paramagnetic Resonance of Metallobiomolecules', American Chemical Society, Washington, DC, 2003, Vol. 858, p. 16.
32. T. A. Jackson, A. Karapetian, A. F. Miller, and T. C. Brunold, *J. Am. Chem. Soc.*, 2004, **126**, 12477.

Mechanisms of Reaction of Organometallic Complexes

Jim D. Atwood[1] & Edward Rosenberg[2]

[1]*State University of New York at Buffalo, Buffalo, NY, USA*
[2]*University of Montana, Missoula, MT, USA*

1 Introduction 1
2 16-Electron Complexes 1
3 18-Electron Complexes 4
4 17-Electron Complexes 15
5 Conclusion 17
6 Related Articles 18
7 References 18

1 INTRODUCTION

This chapter is an update of the chapter appearing in the first edition of the *Encyclopedia*. The literature has been surveyed up through June, 2003 with the intent of including studies that directly relate to the themes put forth in the original chapter.

Reactions of organometallic compounds are of interest because of their role in catalytic reactions and as models for catalytic reactions. An understanding of the chemical transformations that occur may lead to modifications of a catalyst to increase the activity (activity refers to the total amount of product formed) or the selectivity (selectivity refers to the formation of a specific product). Thus, a significant amount of effort has been devoted to understanding the mechanisms of organometallic reactions. In the following sections, the most important aspects of organometallic reactions will be examined.

A very important concept for the interpretation of organometallic reactions is counting electrons (*see Counting Electrons*). A number of years ago, it was suggested that most organometallic reactions occur through complexes that have 16 electrons ($16e^-$) or 18 electrons ($18e^-$).**[1]** This counting refers to the number of metal valence and ligand electrons (*see* ***Bonding Energetics of Organometallic Compounds***). Thus, 16-electron complexes would undergo associative reactions and 18-electron complexes would undergo dissociative reactions. Although exceptions to this scheme exist, it remains a valuable rule and will form the basis for this presentation.

2 16-ELECTRON COMPLEXES

16-electron organometallic complexes exist primarily as square-planar complexes involving Rh^I, Ir^I, Pd^{II}, Pt^{II}, Au^{III}, and Os^0. These d^8 metals coordinated to four $2e^-$ donor ligands give stable $16e^-$ complexes that provide excellent examples of associative reactions and oxidative addition (*see Oxidative Addition*).

2.1 Ligand Substitution

Ligand substitution reactions of square-planar complexes most often occur by associative reaction sequences.**[2,3]** An example of square-planar organometallic complexes that will illustrate this reactivity is *trans*-$Ir(Cl)(CO)(PPh_3)_2$ (frequently referred to as Vaska's Complex), (*see Vaska's Complex*).**[4]** This complex undergoes rapid ligand substitution with ^{13}CO, PR_3, and X^-:**[5]**

$$trans\text{-}Ir(Cl)(CO)(PPh_3)_2 \xrightarrow{PR_3} trans\text{-}Ir(Cl)(CO)(PR_3)_2 \qquad (1)$$

These reactions are sufficiently rapid to preclude kinetic studies. However, the expected associative intermediates, $Ir(Cl)(CO)_2(PPh_3)_2$ and $Ir(Cl)(CO)(PR_3)_3$, can be spectroscopically identified in the presence of CO and PR_3, respectively.

Square-planar substitution reactions can be presented generically as:

$$Ir–X + Y \longrightarrow Ir–Y + X \qquad (2)$$

where Ir represents an iridium(I) center, X is a leaving group, and Y is the incoming ligand. The rate law for such a reaction:

$$\text{rate} = k[Ir][Y] \qquad (3)$$

is dependent on the concentration of the iridium complex and on the concentration of the incoming ligand. As for substitution reactions of other square-planar complexes, square-planar organometallic substitution reactions depend on the nucleophilicity of the entering ligand. Values for substitution of *trans*-$Pt(Cl)(Me)(PEt_3)_2$ are shown in Table 1.**[6]**

$$trans\text{-}Pt(Cl)(Me)(PEt_3)_2 + Y^- \longrightarrow trans\text{-}Pt(Me)(PEt_3)_2Y + Cl^-$$
$$Y = NO_2^-, N_3^-, Br^-, I^-, \text{ or thiourea} \qquad (4)$$

More nucleophilic entering ligands react more readily. Solvent attack may also provide a route for ligand substitution, depending on the nature of Y and the solvent.

When a ligand substitution reaction is carried out in a coordinating solvent, such as methanol, the rate law becomes more complex and involves a first-order term involving only the metal complex, M and the second-order term usually

Table 1 Y group dependence for equation (4) in MeOH at 30 °C

Y	k_2 ($10^2\,M^{-1}\,s^{-1}$)
NO_2^-	1.6
N_3^-	7
Br^-	12
I^-	40
Thiourea	≥ 1500

associated with $16e^-$ complexes. This type of rate law is referred to as a compound rate law:

$$\text{rate} = k_1[M] + k_2[M][Y] \tag{5}$$

Experimental evidence for this type of rate law comes from a study of substitution in the presence of excess Y, when the rate law becomes pseudo−first order:

$$\text{rate} = k_{obs}[M] \qquad k_{obs} = k_1 + k_2[Y] \tag{6}$$

A plot of the observed pseudo-first-order rate constant versus [Y] gives k_2 as the slope of the line and k_1 as the intercept.[7]

Associative reactions of square-planar organometallic complexes are also important in the formation of $18e^-$ complexes. Some of the most valuable studies of unsaturated hydrocarbon binding to transition metal centers have centered on $16e^-$ organometallic complexes:[4,8,9]

$$Ir(CO)(Cl)(PPh_3)_2 + \text{alkene} \rightleftharpoons Ir(\text{alkene})(CO)(Cl)(PPh_3)_2 \tag{7}$$

$$Ir(CO)(Cl)(PPh_3)_2 + \text{alkyne} \rightleftharpoons Ir(\text{alkyne})(CO)(Cl)(PPh_3)_2 \tag{8}$$

$$Ir(CO)(Cl)(PPh_3)_2 + C_{60} \longrightarrow Ir(C_{60})(CO)(Cl)(PPh_3)_2 \tag{9}$$

The stability of the five-coordinate adduct depends on the electron-withdrawing ability of the unsaturated hydrocarbon fragment.[4,9] The adducts are trigonal bipyramidal with the strongly π-accepting groups in equatorial positions.

Reactions of 16-electron *intermediates* with ligands occur very rapidly by an associative reaction. These reactions will be covered in Section 3.1 on dissociation from 18-electron complexes. Evidence for the trigonal bipyramidal complex as an intermediate and for the preference of π-acceptor ligands for the equatorial positions in this geometry comes from the work of Wing and Rettig.[10] A stable trigonal bipyramidal trisolefin complex of Pt(II) with all three olefins in the equatorial positions was isolated by using the chelating and sterically constrained diolefin, 3,7-dimethylene[3.3.1]nonane:[10]

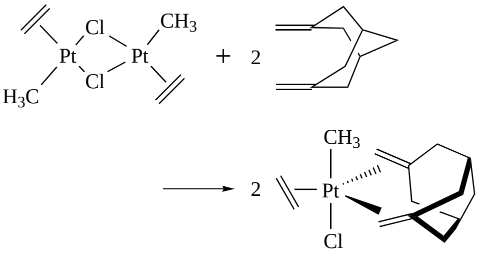

(10)

2.2 Oxidative Addition Reactions

Oxidative addition (*see Oxidative Addition*) is a very important reaction for 16-electron complexes and is involved in many catalytic reactions.[2] Our examples will use stable 16-electron complexes, although in many catalytic reactions a five-coordinate, $18e^-$ complex undergoes ligand dissociation to form the $16e^-$, square-planar complex prior to oxidative addition. Several examples are shown here:

$$Ir(CO)(Cl)(PPh_3)_2 + Cl_2 \longrightarrow Ir(CO)(Cl)_3(PPh_3)_2 \tag{11}$$

$$Rh(Cl)(PPh_3)_3 + H_2 \longrightarrow Rh(Cl)(H)_2(PPh_3)_3 \tag{12}$$

$$Pt(I)(Me)(PPh_3)_2 + MeI \longrightarrow Pt(I)_2(Me)_2(PPh_3)_2 \tag{13}$$

In each of these examples, the metal oxidation state is increased by two, the formed complex contains $18e^-$, and the geometry is octahedral. For oxidative addition of nonpolar molecules, the adding groups occupy cis positions, while for polar molecules the adding groups adopt trans positions.[11] These different stereochemistries are related to mechanistic differences that will be described below.

In a number of cases, oxidative addition reactions are reversible:

$$\textit{trans}\text{-}Rh(CO)(Cl)(PPh_3)_2 + MeI \rightleftharpoons Rh(CO)(Cl)(I)(Me)(PPh_3)_2 \tag{14}$$

$$Rh(Cl)(PPh_3)_3 + H_2 \rightleftharpoons Rh(Cl)(H)_2(PPh_3)_3 \tag{15}$$

The reaction that is the reverse of the oxidative addition reaction is called reductive elimination (*see Reductive Elimination*). In reductive elimination, two ligands are removed from the metal and the metal undergoes a reduction in its oxidation state. Reductive elimination reactions of $18e^-$ complexes will be discussed in Section 3.2.

Enthalpy changes for oxidative addition of different RI groups to *trans*-Ir(CO)(Cl)(PMe$_3$)$_2$ have been reported:[11]

$$\textit{trans}\text{-}Ir(CO)(Cl)(PMe_3)_2 + RI \longrightarrow Ir(CO)(Cl)(I)(R)(PMe_3)_2 \qquad R = I, H, Me, Et, etc. \tag{16}$$

Values are given in Table 2.[11] The enthalpies suggest that the stronger bond of R to Ir gives the larger enthalpy for oxidative addition.

Table 2 Enthalpies[8] for oxidative addition reactions at Ir^I

RI	ΔH (kJ mol^{-1})
I_2	-185 ± 7
HI	-160 ± 3
MeI	-117 ± 7
EtI	-110 ± 3
PrI	-103 ± 4
$PhCH_2I$	-95 ± 7
i-PrI	-88 ± 10
MeC(O)I	-125 ± 4

Table 3 Rates of reaction of MeI with *trans*-$Ir(CO)(Cl)L_2$ for different L groups[a]

L	k (s^{-1} M^{-1})
$P(p\text{-tolyl})_3$	3.3×10^{-2}
PPh_3	3.3×10^{-3}
$P(p\text{-}C_6H_4Cl)_3$	3.7×10^{-5}

[a] Rate $= k[Ir(CO)(Cl)L_2][MeI]$.[12]

Oxidative addition reactions of nonpolar molecules, such as H_2, show quite different characteristics from the oxidative addition reactions of polar molecules, such as MeI. For H_2 addition, the rate is relatively insensitive to the nature of the metal center, although a stable dihydride is formed only for very electron-rich metal centers. For *trans*-$Ir(CO)(X)(PPh_3)_2$, the rate depends on the X group ($X = I > Br > Cl$).[12] The very small deuterium isotope effect ($k_H/k_D = 1.22$) and calculations indicate only slight H–H bond weakening in the transition state.[13,14] Hydrogen addition is best considered as a donation of the H–H σ-bond electron density to the metal (as in molecular hydrogen complexes: *see* ***Hydride Complexes of the Transition Metals***), followed by simultaneous formation of two M–H bonds while the H–H bond weakens. This concerted addition leads to a cis stereochemistry.

Oxidative addition reactions of polar molecules show evidence for a nucleophilic attack mechanism in many cases. Methyl iodide is the most frequently used example. Metal complexes with more electron density react more rapidly with methyl iodide. This effect is shown by changes in the phosphine ligands for $Ir(CO)(Cl)L_2$ (Table 3).[15] For phosphines that only differ in the para substituents on the aryl groups and should be sterically very similar, the more-donating groups lead to appreciably faster reactions with MeI. Since the oxidative addition reaction leads to an increase in coordination number, an increase in steric congestion about the metal center causes a decrease in the rate, as expected. When an alkyl halide with a chiral carbon is used as the adding molecule, an inversion of configuration at carbon is observed,[16] consistent with the nucleophilic attack mechanism. The rate dependence on the alkyl halide is also consistent with nucleophilic attack by the metal on the alkyl halide RX ($R = Me > Et >$ secondary $>$ cyclohexyl; $X = I > Br =$ tosylate $> Cl$).[17]

Alkyl halides that do not readily undergo nucleophilic attack may oxidatively add to a metal by radical mechanisms.[18] Oxidative addition reactions that occur by radical mechanisms show loss of stereochemistry, nonreproducible rates, inhibition by radical inhibitors, and acceleration by O_2 or light. Reactions of $Ir(Cl)(CO)(PMe_3)_2$ with methyl and benzyl halides showed no indication of radical behavior, but other saturated alkyl halides, vinyl, and aryl halides showed characteristics consistent with a radical-chain pathway.[18,19] The following scheme was suggested.

$$\begin{tikzcd}
R\bullet + Ir(Cl)(CO)(PMe_3)_2 \arrow[r] & Ir(Cl)(CO)(PMe_3)_2R \arrow[d, "RX"] \\
 & Ir(Cl)(CO)(PMe_3)_2(R)(X) + R\bullet
\end{tikzcd} \tag{17}$$

In other cases, non-chain radical reactions have been suggested (*see* ***Paramagnetic Organometallic Complexes***).

2.3 Dissociative Processes

Considerable data have now been obtained that show that dissociative processes are possible for square-planar, 16-electron, organometallic complexes.[20] Ligand substitution reactions of *cis*-PtR_2S_2 ($R = Me$, Ph; $S = SMe_2$, $S(O)Me_2$) use the strong labilizing effects of Me and Ph groups to proceed through $14e^-$ intermediates.[20]

The primary evidence cited has been: (1) positive values for the volume of activation, (2) independence of the rate on the nature of the entering group, (3) saturation kinetics, (4) identical rates for dissociation and solvent exchange, and (5) positive values for the entropy of activation.[20]

Dissociative reactions for square-planar organometallic complexes may be more important than for square-planar coordination complexes because a strong donor ligand is important to facilitate dissociation. The characteristics of dissociative processes are quite different from associative reactions. Lack of dependence on the nature of the incoming ligand is shown in the replacement of DMSO from *cis*-$Pt(Ph)_2(DMSO)_2$ with chelating diphosphines.[21] For both dppe and o-phen, the rate constant is 2.0 s^{-1}. Such dissociative processes also have a very small solvent dependence.[21]

Dissociation of ligands from square-planar complexes is also important in ligand redistribution reactions of square-planar complexes:[22,23]

$$\begin{aligned} &Ir(CO)(Cl)L_2 + Ir(CO)(Me)L'_2 \rightleftharpoons Ir(CO)(Cl)LL' + Ir(CO)(Cl)L'_2 \\ &\quad + Ir(CO)(Me)LL' + Ir(CO)(Me)L_2 \quad L,L' = \text{phosphine ligands} \end{aligned} \tag{18}$$

Phosphine ligand dissociation offers the most reasonable explanation for such redistribution reactions.

Most recently, square-planar organometallic complexes of Pd(II) and Pt(II) have been reported whose reactivity incorporates almost all of the reaction pathways discussed in this section (i.e. associative and dissociative ligand exchange, oxidative addition, reductive elimination, and redistribution).[24] Thus, the N,N'-diaryl-α-diimine Pd(II)dimethyl complexes, $({}^{t\mathrm{Bu}_2\mathrm{Ar}}\mathrm{DAB}^{\mathrm{Me}})\mathrm{PdMe}_2$ and $({}^{(\mathrm{CF}_3)_2\mathrm{Ar}}\mathrm{DAB}^{\mathrm{Me}})\mathrm{PdMe}_2$ (${}^{t\mathrm{Bu}_2\mathrm{Ar}}\mathrm{DAB}^{\mathrm{Me}} = \mathrm{ArN{=}C(CH_3)\text{-}C(CH_3){=}NAr}$, Ar = 3,5-di-*tert*-butylphenyl; ${}^{(\mathrm{CF}_3)_2\mathrm{Ar}}\mathrm{DAB}^{\mathrm{Me}}$, Ar = 3,5-bis(trifluoromethyl)phenyl) undergo protonolysis with $\mathrm{HBF_4}$ in trifluoroethanol to form cationic complexes presumably via protonation at the metal followed by reductive elimination:

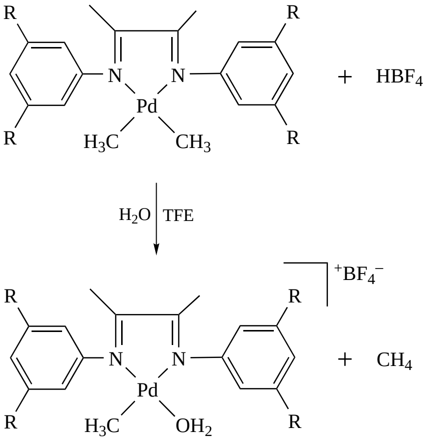

(19)

This complex then undergoes reaction with benzene and a second elimination of methane in a reaction where C–H bond cleavage is rate determining ($K_{\mathrm{H}}/K_{\mathrm{D}} = 4.1$) and which is inhibited by water. The final products are biphenyl and a bis-aquo complex presumably formed by a redistribution reaction of an aquo-phenyl complex followed by reductive elimination of biphenyl and by oxidation by O_2 of the resulting $\mathrm{Pd^o}$ complex (equation 20).

This chemistry not only illustrates the extension of the reactivity of $16\mathrm{e}^-$ complexes but also represents an alternative to more conventional routes for catalytic C–H activation, where the more accessible $\mathrm{Pd^o}$/Pd(II) couple replaces the Pt(II)/Pt(IV) couple.[24]

3 18-ELECTRON COMPLEXES

The majority of organometallic complexes contain 18 electrons (*see* ***Bonding Energetics of Organometallic Compounds***). These complexes undergo ligand substitution, reductive elimination, and electron-transfer reactions (*see* ***Electron Transfer in Coordination Compounds***). Each type of reaction will be covered in the following sections.

Understanding the reactivity of organometallic complexes requires an understanding of ligand bonding. While a full description of the bonding of organometallic ligands is inappropriate in this section, a summary of the σ donation, π acceptance, and size of typical ligands will be very useful to the discussion. There has been much discussion in the literature about the relative amounts of π- and σ-bonding in a given ligand. The separation of these two contributions is a daunting task but two recent studies have used computational and experimental techniques to help define the relative π- and σ-bonding parameters for phosphines and related ligands.[25,26] On the basis of the semi-empirical method known as QALE (Quantitative Analysis of Ligand Effects) the σ-donating abilities of phosphine and related ligands have been estimated:

$$\mathrm{P}(i\text{-}\mathrm{Pr})_3 > \mathrm{P(Me)_3} > \mathrm{P(Ph)_3} > \mathrm{N(R)_3} > \mathrm{PH_3}$$
$$> \mathrm{P(OMe)_3} > \mathrm{P(OPh)_3} > \mathrm{PF_3} > \mathrm{CO}$$

and for π acceptance:

$$\mathrm{PF_3} \gg \mathrm{PCl_3} > \mathrm{P(OPh)_3} > \mathrm{PH_3} > \mathrm{P(OMe)_3} > \mathrm{PPh_3} > \mathrm{P(Me)_3}$$

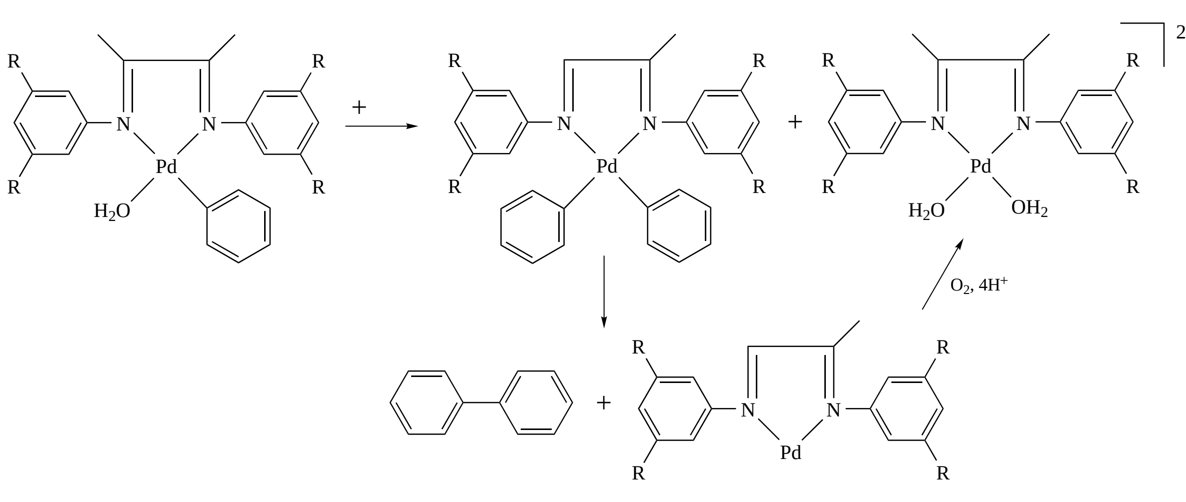

(20)

Table 4 Chromium–PPh_3 bond lengths for different trans ligands

Ligand trans	Cr–PPh_3 bond length (Å)
PBu_3	2.345(3)
$P(OMe)_3$	2.362(2)
$P(OPh)_3$	2.393(1)
CO	2.422(1)

On the basis of QALE alkyl phosphines, PR_3 function only as strong donors.[25] For these ligands, the most accurate statement is that alkyl phosphines have orbitals that may accept electron density. For aryl phosphines such as PPh_3, however, π acceptance may be significant. The most straightforward evidence is from the Cr–PPh_3 bond lengths of *trans*-$Cr(CO)_4LPPh_3$ [L = PBu_3, $P(OMe)_3$, $P(OPh)_3$, CO] (Table 4).[7] The shortening of the Cr–PPh_3 bond as the donor strength of the trans ligand increases is most easily accommodated in terms of π acceptance by PPh_3. However, it should be pointed out that DFT calculations have recently shown that there is no correlation between calculated bond dissociation energies and metal phosphorous bond lengths in this type of complex. Any discussion of the electronic binding of these ligands to an organometallic center is complicated by steric interactions of the rather bulky phosphine and phosphite ligands.[25] The relative size of the ligands is as follows:[25,27]

$$P(^tBu)_3 > P(Cy)_3 > P(^nBu)_3 > P(OPh)_3 > P(OMe)_3 > P(Me)_3 > CO$$

Each of these ligand parameters is important in discussing reactivity of organometallic compounds. As we investigate reactions of organometallic complexes, we shall often refer to σ-bonding ability, π-accepting ability, or size of the ligand.

3.1 Substitution Reactions

3.1.1 Mononuclear Metal Carbonyls

Most studies of organometallic substitution reactions have been accomplished on transition metal-carbonyl complexes (*see* ***Carbonyl Complexes of the Transition Metals***). These complexes are readily prepared and purified, are stable, and have very characteristic IR spectra that allow quantitative analysis. The reactions can be represented by

$$M(CO)_n + L \longrightarrow M(CO)_{n-1} + CO \qquad (21)$$

where M is a transition metal and L is an entering ligand, usually a phosphine or phosphite. Two examples among the first to be investigated kinetically were $Ni(CO)_4$ and $Mn(CO)_5Br$:[28,29]

$$Ni(CO)_4 + L \longrightarrow Ni(CO)_3L + CO \qquad (22)$$

$$Mn(CO)_5Br + L \longrightarrow \textit{cis}\text{-}Mn(CO)_4LBr + CO \qquad (23)$$

Kinetic data indicate that the rate law is independent of the concentration of L and first order in metal-carbonyl complex:

$$\text{rate} = k_1[Ni(CO)_4] \qquad (24)$$

The accepted mechanism involves rate-determining CO dissociation from the 18-electron complex to form a 16-electron intermediate:

$$Ni(CO)_4 \xrightarrow{k_1} Ni(CO)_3 + CO \qquad (25)$$

$$Ni(CO)_3 + L \xrightarrow{\text{fast}} Ni(CO)_3L \qquad (26)$$

such that the substitution can be considered to be a two-step process. The second step (equation 26) is much more rapid, occurring at a rate of $10^6\,M^{-1}\,s^{-1}$, in contrast to the first step (equation 25), which occurs at a rate of $10^{-4}\,s^{-1}$.[12] The activation parameters are in agreement with a dissociative process that has a positive entropy of activation, as shown in Table 5.[28]

Substitution of several metal-carbonyl complexes $Cr(CO)_6$ and $Mn(CO)_5$(amine) show a small dependence on the nature and concentration of the entering ligand. Under pseudo-first-order conditions, the rate laws for these substitutions have two terms, as shown for $Cr(CO)_6$ (as for some substitution reactions with $16e^-$ complexes, see equation 5). The second-order term was always much smaller than the first-order term.[30,31] A mechanism that ascribes the second-order term to dissociative interchange (I_d) has been suggested for the $Mo(CO)_5Am$ system (Am = amine) and involves a solvent-encased substrate and a species occupying a favorable site for exchange.[31] Thus, the body of evidence for the simple metal carbonyls indicates that CO dissociation and is the mechanism of ligand substitution reactions.

Metal Effects on Metal-carbonyl Reactivity. The effect of the metal center on organometallic reactivity is not as clearly defined as for coordination complexes. We will examine: (a) the effect of charge, (b) first-row, second-row, and third-row effects and (c) the effect of d-electron count. As will be discussed in Section 4.1, the enhanced reactivity of odd-electron complexes is a major effect of the metal center.

(a) *Effect of Charge*. The effect of charge on metal–carbon monoxide bonding has been frequently examined, with the extent of π acceptance being greater as the charge on

Table 5 Activation parameters for the reaction of $Ni(CO)_4$ with nucleophiles

L	$\Delta H‡$ (kcal mol^{-1})	$\Delta S‡$ (cal K^{-1} mol^{-1})	k (10^{-4} s^{-1}) at 20 °C
PPh_3	24	13	50
$C^{18}O$	24	14	52

the metal is lowered. The effect of charge on reactivity is not as clear. $V(CO)_6^-$, $Cr(CO)_6$, and $Mn(CO)_6^+$ are relatively inert to CO dissociation. Similarly, $Mn(CO)_5^-$ and $Fe(CO)_5$ are relatively inert, though the fact that $Co(CO)_5^+$ is unknown may indicate that it would have considerable reactivity. The best indication of the expected effect of charge on reactivity is in the greater reactivity of $Ni(CO)_4$ than $Co(CO)_4^-$ (ready substitution versus no reaction in 48 h).**[32]**

The failure (in many cases) to see the expected large increase in rate of CO loss with increase in negative charge must indicate that the destabilization of the ground state is negated by a similar destabilization of the transition state. This suggests that the effect of charge on the bonding of CO in the 16-electron transition state for CO dissociation is similar to that for the 18-electron ground state.

(b) *Row Effects*. In general, the reactivity is greatest for the second-row metal and least for the third-row metal. This order is different from the order of reactivity observed for classical coordination complexes, for which the reactivity decreases down a row for analogous complexes. The change of reactivity across a row has not been examined to any significant extent. The order of reactivity, $Ni(CO)_2L_2 > Cr(CO)_4L_2 > Fe(CO)_3L_2$ (L = CO, phosphine base), does not correlate with effective nuclear charge or steric considerations.**[33]** Further, M–L distance does not correlate with the reactivity toward dissociative loss of L,**[33]** as shown in Table 4.

(c) *Electronic Effects*. The metal-carbonyl compounds offer the best comparative data on rates of reactions:**[33]**

$$\begin{array}{lcccc} \text{Complex} & Co(CO)_4, & Mn(CO)_5 > & V(CO)_6 > & Ni(CO)_4, \\ \text{d electrons} & d^9 & d^7 & d^5 & d^{10} \end{array}$$

$$\begin{array}{ccc} Ti(CO)_3(P\text{–}P)_2 > & Cr(CO)_6 > & Fe(CO)_5 \\ d^4 & d^6 & d^8 \end{array} \tag{27}$$

Table 6 is composed of dissociative reactions for quite different classes of compounds. These data indicate several features, which appear to be general. (i) Organometallic complexes with a d^{10} configuration are relatively labile. (ii) Complexes with a d^6 configuration are relatively inert. (iii) Dissociative reactivity apparently follows the order $d^{10} > d^4 > d^6 > d^8$ for a homologous series.

A comparison of analogous compounds shows no evidence that the observed dependence of the rate on the metal center arises from ground-state properties. Thus, a primary factor in the metal center reactivity is the transition state. This is similar to the conclusions regarding substitutional reactivity of classical coordination complexes, suggesting that similar interpretations may be possible.

Table 6 Rates of reactions at 30 °C for different organometallic complexes compared to the number of d electrons**[33]**

Compound	Rate	d Electrons
$CpMn(CO)_3$	Very slow at 140 °C	6
$CpV(CO)_4$	$4.7 \times 10^{-13}\ s^{-1}$	4
$Cr(CO)_6$	$1 \times 10^{-12}\ s^{-1}$	6
$Fe(CO)_3(PPh_3)_2$	$1 \times 10^{-11}\ s^{-1}$	8
$Cr(CO)_4(PPh_3)_2$	$5 \times 10^{-11}\ s^{-1}$	6
$CpRu(CO)_3Br$	$3 \times 10^{-10}\ s^{-1}$	6
$CpFe(CO)_2I$	$5 \times 10^{-8}\ s^{-1}$	6
$CpMo(CO)_3I$	$6.2 \times 10^{-8}\ s^{-1}$	4
$Ni(P(OEt)_3)_4$	$1.0 \times 10^{-6}\ s^{-1}$	10
$Ti(CO)_3$		
$Ni(CO)_4$	$1 \times 10^{-2}\ s^{-1}$	10

Stereochemistry of CO Dissociation. If a complex has nonequivalent CO groups, the stereochemistry of the dissociative process can be defined. This has prompted many studies of exchange reactions with $Mn(CO)_5Br$.**[34]** Substitution reactions always lead to *cis*-$Mn(CO)_4LBr$,**[29]** but substitution products do not necessarily provide information on the site of CO dissociation. In an exchange reaction, the products must reflect the site of dissociation by the principle of microscopic reversibility. One would predict that the site of CO dissociation would be cis to the bromide in $Mn(CO)_5Br$ since each *cis*-CO (equatorial) is trans to CO and should not be as strongly π bonded as the axial CO, which is trans to Br. However, both the axial and equatorial positions were enriched when reacted with $C^{18}O$ or ^{13}CO:

$$Mn(CO)_5Br + {*}CO \longrightarrow Mn(CO)_n({*}CO)_{5-n}Br + CO \tag{28}$$

This rather surprising result is explained by recognizing that the 16-electron intermediate is five coordinate and could equilibrate the cis and trans carbonyls. A fluxional five-coordinate intermediate (*see Fluxional Molecule*) would allow for enrichment in the axial position without dissociation of the axial CO.**[34]** Thus, the stereochemistry of CO dissociation is consistent with expectations.

The extent of substitution depends on the size of the substituting ligand. A series of substitutions on $Mn(CO)_5Br$ have been studied for the effect of ligand size on the number of ligands that can be substituted and the geometry of substitution.**[35]** These data are shown in Table 7. The smaller ligands are able to substitute to a greater extent than the larger

Table 7 Complexes prepared by ligand substitution on $Mn(CO)_5Br$**[35]**

Complex	L
trans-$Mn(CO)_3L_2Br$	PPh_3, $P(OPh)_3$, $AsPh_3$
mer-$Mn(CO)_2L_3Br$	PMe_2Ph, PMe_3, $P(OMe)_2Ph$
trans-$Mn(CO)_2L_3Br$	$P(OMe)_3$, $P(OEt)_3$
trans-$Mn(CO)L_4Br$	$P(OMe)_3$

ones. Steric effects are certainly significant in complexes of this type.

Dissociation of Other Ligands. There have been relatively few studies of dissociation of ligands other than CO from organometallic complexes. Because many of the ligands are large, one must analyze the data in terms of size as well as σ- and π-bonding ability. Indeed, rates of L dissociation from NiL_4 correlate very nicely with ligand size, suggesting a dominant role for steric effects in dissociation of L from NiL_4:**[36]**

$$NiL_4 + L' \longrightarrow NiL_3L' + L \tag{29}$$

This effect is readily understandable, because tetrasubstituted complexes should have very significant steric interactions. Steric interactions are also shown to be important in dissociations from *cis*-$Mo(CO)_4L_2$ complexes.**[37]**

A systematic investigation of ligand dissociation from chromium carbonyl complexes provided evidence regarding electronic effects. The complexes $Cr(CO)_5L$, *trans*-$Cr(CO)_4L_2$, and *trans*-$Cr(CO)_4LL'$ have been investigated for their reaction with carbon monoxide.**[38]** The order of Cr–L bond stabilities in $Cr(CO)_5L$ is:

$$Cr–PBu_3 \gg Cr–P(OPh)_3 > PPh_3 \approx CO > AsPh_3 > py \tag{30}$$

which indicates that the strength of bonding ability is more significant than whether the bonding is σ or π in nature.**[38]** The order of bond energies for Cr–L bonds, where the ligand is bound to Cr^0 is remarkably similar to the order for *trans*-$MePt(PMe_2Ph)_2L^+$, where the ligand is bound to Pt^{II}.**[39]**

A trans effect (*see Trans Effect*) in octahedral metal-carbonyl substitution reactions was observed in the reactions of $Cr(CO)_4LL'$ with CO:**[38]**

$$trans\text{-}Cr(CO)_4LL' + CO \longrightarrow Cr(CO)_5L + L' \tag{31}$$

The ordering of the trans effect on dissociation of PPh_3 and of $P(OPh)_3$ is identical: $PPh_3 > PBu_3 > P(OPh)_3 > P(OMe)_3 > CO$. Crystal-structure determinations showed no correlation between the Cr–PPh_3 or Cr–$P(OPh)_3$ bond lengths and rates of PPh_3 and $P(OPh)_3$ dissociation from *trans*-$Cr(CO)_4LL'$.**[38]** Thus, the rate acceleration by L from $Cr(CO)_4LL'$ does not arise by a ground-state destabilization, for that would be manifested by a lengthening of the Cr–L′ bonds. Rather, a transition state stabilization by L is indicated. A stabilization of the 16-electron intermediate $Cr(CO)_3$(*o*-phen) by electron-releasing *o*-phenanthroline ligands was noted a number of years ago.**[40]** This simple concept is also applicable to cis labilization of CO dissociation, to the trans effect noted for dissociation from $Cr(CO)_4LL'$, and probably generally to organometallic substitution reactions that proceed through unsaturated intermediates. To completely understand the effect of a ligand on either stereochemistry or reactivity for a given reaction, one must consider both ground and transition state effects. In cis labilization, the increased reactivity arises by stabilization of the 16-electron intermediate attributable to the presence of a donating ligand. The cis stereospecificity results from a stronger M–CO bond trans to the donor ligand (a ground-state effect). A complete interpretation of substitution reactions of metal-carbonyl complexes requires knowledge of site specificity, of steric effects in both the ground and transition states, and of the ground-state bond energies; but the gross effects, especially in a series of complexes, can be accounted for in terms of a stabilization of the electron-deficient transition state by electron-donating groups.

3.1.2 Ligand Substitution Reactions on Alkyl Complexes

Alkyl complexes (*see Alkyl Complexes*) undergo ligand substitution processes:

$$MeMn(CO)_5 + L \longrightarrow MeMn(CO)_4L + CO \tag{32}$$

similar in stoichiometry to other substitution reactions. An important difference is that in many reactions of this type an acyl intermediate is observed:

$$\begin{aligned} MeMn(CO)_5 + L &\longrightarrow MeC(O)Mn(CO)_4L \\ &\longrightarrow MeMn(CO)_4L + CO \end{aligned} \tag{33}$$

Reactions of this type are termed alkyl migration (*see Alkyl Migration*). These reactions are very important in several catalytic reactions, such as hydroformylation, methanol carbonylation, and homogeneous CO reduction (*see **Carbonylation Processes by Homogeneous Catalysis***).

Kinetics and Rate Law. The rate is dependent on the concentration of the metal complex and on the entering ligand.**[2]** The rate law that best accommodates the observations is

$$\text{rate} = \frac{k_1k_2[L][RM]}{k_{-1} + k_2[L]} \tag{34}$$

The mechanism most consistent with this rate law involves a rapid preequilibrium as represented for $RMn(CO)_5$:

$$\begin{gathered} RMn(CO)_5 \underset{k_{-1}}{\overset{k_1}{\rightleftharpoons}} [RC(O)Mn(CO)_4] \\ RC(O)Mn(CO)_4 \xrightarrow[L]{k_2} RC(O)Mn(CO)_4L \end{gathered} \tag{35}$$

followed by the reaction of the 16-electron acyl intermediate with L.

The rate of carbonylation on the alkyl group has been shown to depend on the electron-withdrawing ability of the R group.**[41]** The results of the carbonylation of substituted methylmanganese pentacarbonyl complexes are shown in Table 8. The presence of an electron-withdrawing R group

Table 8 Rates of carbonylation for a series of substituted methylmanganese pentacarbonyl complexes at 30 °C in β,β'-diethoxydiethyl ether[42]

$$RCH_2Mn(CO)_5 + CO \longrightarrow RCH_2C(O)Mn(CO)_5$$

R	$10^5\,k$ ($M^{-1}\,s^{-1}$)
Et	14 000
Me	12 000
Cy	2500
H	1200
MeO	25
Ph	12
HOC(O)	<5

dramatically slows the rate, most likely by affecting the preequilibrium.

Stereochemical Considerations. Much attention has been directed toward the stereochemistry of substitution reactions of alkyl complexes. Substitution of $MeMn(CO)_5$ leads to *cis*-$MeC(O)Mn(CO)_4L$ initially, although the cis complex isomerizes to the trans eventually:

$$\begin{aligned} MeMn(CO)_5 + L &\longrightarrow \textit{cis}\text{-}MeC(O)Mn(CO)_4L \\ &\xrightarrow{\text{slow}} \textit{trans}\text{-}MeC(O)Mn(CO)_4L \end{aligned} \quad (36)$$

The stereochemistry of substitution reactions does not necessarily provide information on the stereochemistry of the intermediates. In this case, however, the formation of a kinetically stable product, *cis*-$MeC(O)Mn(CO)_4L$, indicates that the substitution reaction probably does provide stereochemical information. This is confirmed by carbonylation with ^{13}CO, which leads exclusively to *cis*-$MeC(O)Mn(CO)_4(^{13}CO)$. A more difficult question to answer is whether the methyl group migrates to a CO or whether a CO inserts into the Me–Mn bond. These processes are termed methyl migration and CO insertion (*see CO Insertion*), respectively. The distinction between these two is based on which group is moving during formation of the 16-electron acyl intermediate. The body of evidence shows that alkyl migration is the reaction occurring.[2]

Reaction of optically active alkyl groups shows that the carbonylation proceeds with retention of configuration at the carbon:[43]

$$\begin{aligned} &Me_3CC(H)(D)C(H)(D)FeCp(CO)_2 + PPh_3 \longrightarrow \\ &\qquad Me_3CC(H)(D)C(H)(D)C(O)FeCp(CO)PPh_3 \\ &[\textit{threo}\text{-}3,3\text{-dimethylbutyl-}1,2\text{-}d_2](Cp)\text{dicarbonyliron} + PPh_3 \longrightarrow \\ &\qquad [\textit{threo}\text{-}4,4\text{-dimethylpentanoyl-}2,3\text{-}d_2](Cp)\text{carbonyltriphenyl-} \\ &\qquad \text{phosphineiron} \end{aligned} \quad (37)$$

This suggests that the C–Fe bond remains intact as the C–C bond forms, consistent with the results of an extended Hückel calculation of the reaction coordinate for migration of Me in $MeMn(CO)_5$.[44]

Table 9 Kinetic data for alkyl migration reactions[44]

Lewis acid	k_{obs} (s^{-1})
None	2×10^{-6}
$AlClEt_2$	0.37
$AlCl_2Et$	10
$AlCl_3$	170

Alkyl migration is catalyzed by the presence of Lewis acids, such as $AlCl_3$. The effects of several Lewis acids are shown in Table 9.[44] As shown by the data, a Lewis acid can accelerate the methyl migration by a factor of 10^8.

To summarize the results on substitution of alkyl complexes:

- A preequilibrium exists between the 18-electron alkyl carbonyl complex and a 16-electron acyl, which probably is solvent coordinated.
- The rate of migration depends on the electron-withdrawing ability of the alkyl group, with the more electron-withdrawing groups reacting more slowly.
- More nucleophilic entering ligands accelerate the reaction.
- The reaction proceeds by alkyl migration as the carbanion.
- The migration may be catalyzed by Lewis acids.

Recently, it has been shown that inclusion of (η^5-methylcyclopentadienyl)$Fe(CO)_2Me$ into cyclodextrins allows phosphine substitution to take place both thermally and photochemically without CO insertion/alkyl migration. This compound normally undergoes an irreversible alkyl migration to give the corresponding acyl derivative exclusively. The use of the cyclodextrin inclusion complexes may provide a general method circumventing the alkyl migration.[45]

3.1.3 *Ligand Substitution of Lightly Stabilized Ligands on Mononuclear Carbonyls*

The importance of phosphine ligands to organometallic chemistry has prompted the development of synthetic methodologies that allow more precise control of the degree of substitution via the use of lightly stabilized or labile ligands rather than the direct thermal or photochemical substitution of phosphine for CO. These methods include the use of O-atom transfer reagents such as trimethylamine-N-oxide where one mole of CO is oxidized per mole O-atom transfer reagent and where a labile ligand such as acetonitrile replaces each oxidized CO prior to reaction with the phosphine or the other nucleophile (equation 54).[46] In the absence

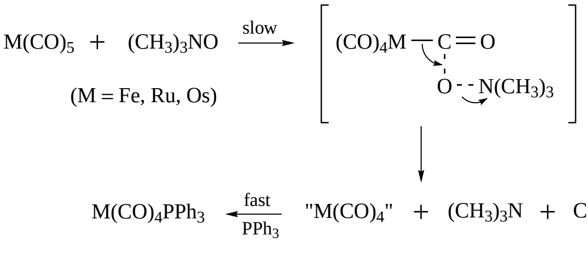

(38)

of the intermediate labile ligand, the reaction is first order in the carbonyl complex, first order in amine oxide, and zero order in phosphine. The mechanism is thought to involve nucleophilic attack on the carbon of the coordinated carbonyl to create the good leaving group, CO_2, followed by rapid reaction of the phosphine or the labile ligand with the $16e^-$ complex (equation 38). The order of reactivity for mononuclear metal carbonyls is W > Mo > Cr and Os > Ru > Fe with the former triad being much less reactive than the latter. This general trend is in agreement with the overall trend that carbonyl complexes with higher infrared stretching frequencies are less reactive towards nucleophiles. The activation parameters for the iron triad all show negative entropies of activation and activation enthalpies in the range of $10-15\,\mathrm{kcal\,mol^{-1}}$. As expected, good hydrogen bonding solvents, such as ethanol, tend to slow the reaction down by bonding to the negatively polarized oxygen on the O-atom transfer reagent.

The labile bidentate ligand, benzylidene acetone (BDA) has been extensively employed in substitution reactions for mononuclear carbonyl complexes. In particular, the reactions of $(BDA)Fe(CO)_3$ with trialkyl phosphines to give *trans*$-(PR_3)_2Fe(CO)_3$ have allowed detailed and quantitative investigations of the enthalpies of the reactions as a function of the steric and electronic nature of the phosphines employed (equation 39).[47,48]

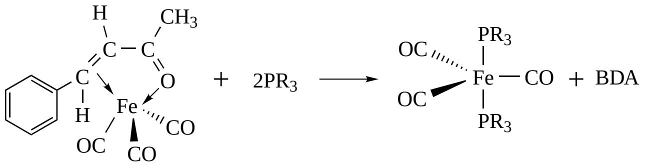

(39)

The enthalpies of this reaction become more negative in the order PPh_3 < PCy2Ph < PCyPh2 < PCy3 < PiPr3 < PPh2Et < PBz3, suggesting that both steric and electronic factors play a role in the formation of these bis phosphines. A QALE treatment of the thermochemical data revealed that the electron-donating parameter, χ is generally dominant but that the reaction has a steric threshold where phosphines with cone angles >135° exhibit a significant steric effect on the thermodynamic stability of the disubstituted complex.[47] In a related study, using isosteric phosphines of the type $(p\text{-}XC_6H_4)_3P$ ($X = H, CH_3O, CH_3, Cl, F, CF_3$), it was shown that, indeed, the electronic factor is the more important factor in determining the enthalpy of this reaction (equation 39).[48]

3.1.4 *Metal-carbonyl Dimers and Clusters*

Substitution reactions on metal-carbonyl dimers (*see* ***Dinuclear Organometallic Cluster Complexes***) and clusters (*see* ***Polynuclear Organometallic Cluster Complexes***) occur by replacement of a CO with an entering ligand:

$$Mn_2(CO)_{10} \xrightarrow{+L,\,-CO} Mn_2(CO)_9L \xrightarrow{+L,\,-CO} Mn_2(CO)_8L_2 \qquad (40)$$

$$Fe_3(CO)_{12} \xrightarrow{+L,\,-CO} Fe_3(CO)_{11}L \qquad (41)$$

There are three features that are different for metal–metal bonded systems than for mononuclear complexes: possible substitution at different metals, fragmentation, and the effect of the metal–metal bond on reactivity.

Metal-carbonyl Dimers. The reactions that have been most often studied are those of the group 7 dimers, $Mn_2(CO)_{10}$, $Tc_2(CO)_{10}$, $Re_2(CO)_{10}$, and $MnRe(CO)_{10}$. Kinetic studies on these dimers show the rate law:

$$\text{rate} = (k_1 + k_2[L])[M_2(CO)_{10}] \qquad (42)$$

where the k_2 term is much smaller than the k_1 term. This rate law is identical to that seen for substitution at $Cr(CO)_6$ and is best ascribed to a dissociative interchange mechanism. Considerable controversy has existed over whether the mechanism involves CO dissociation or homolytic cleavage of the metal–metal bond. The ability to distinguish between the two metal centers in $MnRe(CO)_{10}$ added mechanistic information that ruled out Mn–Re bond homolysis for substitutions on this complex.[49]

The ultimate experiment to differentiate between metal–metal bond homolysis and other routes was performed for $Re_2(CO)_{10}$.[50] Two complexes with different rhenium isotopes were prepared ($^{185}Re_2(CO)_{10}$ and $^{187}Re_2(CO)_{10}$) for use in substitution and exchange reactions. No mixed-isotopic species were observed after several half-lives under the reaction conditions, ruling out the metal–metal bond homolysis mechanism in thermal substitution and CO exchange reactions of $Re_2(CO)_{10}$. The metal isotopes are not available for manganese, but similar reactions of $Mn_2(CO)_{10}$ and $Mn_2(^{13}CO)_{10}$ are fully consistent with CO dissociation and inconsistent with metal–metal bond cleavage. Substitution of $MnRe(CO)_{10}$ leads to predominantly the rhenium isomer $(CO)_5MnRe(CO)_4L$. Comparing the reactivities of $Mn_2(CO)_{10}$ and $Re_2(CO)_{10}$ and analogous mononuclear complexes of manganese and rhenium, one would anticipate that CO dissociation from manganese would occur at a rate about 100 times greater than from rhenium.[49] It has been suggested that CO dissociates from the manganese and that the intermediate/transition state contained a bridging CO such that the unsaturation at one metal center was shared by the other metal. The incoming ligand would then attack at the most favorable site, which for steric reasons would be the rhenium. A mass spectral study of $(CO)_5MnRe(^{13}CO)_5$ has shown preferential loss of CO from manganese.[51]

Substitution reactions of $Co_2(CO)_8$ show more variation than the group 7 dimers. Reaction with ^{13}CO, $AsPh_3$, and H_2 show a rate law that is independent of the concentration of the incoming nucleophile at temperatures from −15 to 30 °C.[52] The activation parameters ($\Delta H\ddagger = 22\,\mathrm{kcal\,mol^{-1}}$ and $\Delta S\ddagger = 10\,\mathrm{cal\,K^{-1}\,mol^{-1}}$) and the lack of dependence on the incoming ligand are consistent with CO dissociation:

$$\begin{tikzcd}\mathrm{Co_2(CO)_8} \arrow[r] & \mathrm{Co_2(CO)_7} + \mathrm{CO} \arrow[d, "\mathrm{AsPh_3,\ rapid}"] \\ & \mathrm{Co_2(CO)_7AsPh_3}\end{tikzcd} \tag{43}$$

Substitution of $Co_2(CO)_8$ by phosphines is quite different:

$$\mathrm{Co_2(CO)_8} + 2\mathrm{PR_3} \longrightarrow [\mathrm{Co(CO)_3(PR_3)_2}]^+[\mathrm{Co(CO)_4}]^- + \mathrm{CO} \tag{44}$$

leading to ionic products at rates that are more rapid than CO dissociation and that depend on the concentration and the nucleophilicity of the entering ligand. In addition, the apparent order with respect to $Co_2(CO)_8$ varies within the range 1.0–1.5, depending on the reaction conditions. A radical-chain mechanism has been suggested to account for these observations in the substitution of phosphine bases on $Co_2(CO)_8$.[52] Thus, two distinct mechanisms exist for $Co_2(CO)_8$: a CO dissociative route for reaction with weak nucleophiles and a radical-chain pathway for reaction with strong nucleophiles.

Transition Metal Clusters. Reactions of Lewis bases with metal clusters may yield either mononuclear or polynuclear products. Substitution reactions on $Fe_3(CO)_{12}$ represent the features that may be seen. Reaction with L at 50 °C leads to substituted metal clusters, but reaction at 80 °C produces substituted mononuclear fragments:[2]

$$\mathrm{Fe_3(CO)_{12}} + n\mathrm{L} \xrightarrow{50\,^\circ\mathrm{C}} \mathrm{Fe_3(CO)_{12-\mathit{n}}L_\mathit{n}} + n\mathrm{CO} \tag{45}$$

$$\mathrm{Fe_3(CO)_{12}} + \mathrm{L} \xrightarrow{80\,^\circ\mathrm{C}} \mathrm{Fe(CO)_4L} + \mathrm{Fe(CO)_3L_2} \tag{46}$$

The ruthenium and osmium analogs have less tendency to fragment, presumably because of the stronger metal–metal bonds.

Substitutions on $Ir_4(CO)_{12}$ and derivatives have been thoroughly studied cluster reactions:[53–59]

$$\mathrm{Ir_4(CO)_{12}} + n\mathrm{L} \longrightarrow \mathrm{Ir_4(CO)_{12-\mathit{n}}L_\mathit{n}} + n\mathrm{CO} \tag{47}$$

The product observed depends on the reaction conditions and on the ligand L. The rate law observed has two terms:

$$\text{rate} = (k_1 + k_2[\mathrm{L}])[\mathrm{Ir_4(CO)_{12}}] \tag{48}$$

This rate law is of the same form as that seen for substitutions on other metal-carbonyl complexes, but the relative values of the two terms are very different from those observed in other systems. The ligand-dependent term predominates for ligands that are reasonably good nucleophiles, such as CNR, PBu_3, PPh_3, and $P(OPh)_3$. The relative values of k_2 show a strong dependence on the nucleophilicity of the entering ligand, indicating nucleophilic attack on the metal complex.

As the tetrairidium cluster is substituted, some changes are noted. Substitution on $Ir_4(CO)_{11}L$ (L = PPh_3, $P(OPh)_3$, and $AsPh_3$) occurs by a primarily ligand-independent mechanism, probably CO dissociation. For more nucleophilic entering ligands (PBu_3, CN-*t*-Bu), the ligand-dependent path still predominates. The CO dissociation rates from $Ir_4(CO)_{11}L$ show the same trends with changes in L as mononuclear complexes and metal-carbonyl dimers.

In metal clusters that are more highly substituted with phosphines, ligand steric effects may be significant. The rates of phosphine dissociation from $Ir_4(CO)_8L_4$ show evidence of a steric effect:[58,59]

$$\mathrm{Ir_4(CO)_8L_4} + \mathrm{CO} \longrightarrow \mathrm{Ir_4(CO)_9L_3} + \mathrm{L} \qquad \mathrm{L} = \mathrm{PMe_3,\ PEt_3,\ PBu_3} \tag{49}$$

The steric interactions in $Ir_4(CO)_8(PMe_3)_4$ are sufficient to cause an elongated Ir–Ir bond.[59]

Mixed metal clusters (clusters containing two different metals) have considerable potential for mechanistic studies. Three separate studies on iron–ruthenium clusters show the possibilities.[60–62] Reactions of $FeRu_2(CO)_{12}$ and $Fe_2Ru(CO)_{12}$ in comparison to $Fe_3(CO)_{12}$ and $Ru_3(CO)_{12}$ show a very interesting activation of the iron center towards CO dissociation by ruthenium centers in the mixed metal-cluster system.[60] Such an activation of the iron center by ruthenium has also been demonstrated for $(\mu\text{-H})FeRu_2(\mu\text{-COMe})(CO)_{10}$.[61] The presence of different metal centers for $H_2FeRu_3(CO)_{12}$ allowed unusually detailed interpretation of the isomerization, substitution, and CO exchange reactions.[62,63]

It is rather surprising that the clusters thus far investigated show the same basic mechanistic features as mononuclear complexes. The primary reaction mode seen is CO dissociation, although large metals are susceptible to nucleophilic attack at the metal.

An interesting case in point where a high nuclearity cluster shows a distinct change in mechanism depending on the steric requirements of the incoming ligand is $Ru_5C(CO)_{15}$.[64] Phosphine ligands with cone angles of <133° show a two-step reaction mechanism, where an intermediate adduct can be detected spectroscopically:

$$\begin{aligned} \mathrm{Ru_5C(CO)_{15}} + \mathrm{L} &\xrightarrow{k_{+\mathrm{L}}} \mathrm{Ru_5C(CO)_{15}L} \\ \mathrm{Ru_5C(CO)_{15}L} &\xrightarrow{k_{-\mathrm{CO}}} \mathrm{Ru_5C(CO)_{14}L} + \mathrm{CO} \end{aligned} \tag{50}$$

Ligands with cone angles >136° show a single-step reaction mechanism:

$$\mathrm{Ru_5C(CO)_{15}} + \mathrm{L} \xrightarrow{k_2} \mathrm{Ru_5C(CO)_{14}L} \tag{51}$$

This distinct switch in the intimate mechanism in response to the steric requirements of the incoming ligand represents a more extreme example of the earlier studies with the tetrairidium clusters and is thought to arise from the ability of this cluster to open to a bridged butterfly structure on adduct formation with the sterically less-demanding ligands.

Coordinately Unsaturated Clusters and Clusters with Hemilabile Ligands. As for mononuclear complexes, the use of lightly stabilized ligand–cluster complexes to afford more control over ligand substitution reactions under milder conditions is widespread.[65,66] For example, a huge literature exists on the use of $M_3(CO)_{10}L_2$ (M = Ru, Os, L = CH_3CN, cyclooctene) for ligand substitution reactions with phosphines as well as alkynes amines and nitrogen heterocycles.[65,66] Recent kinetic studies on the cluster $Rh_6(CO)_{15}L$, where L = the 'lightly bonded ligands' CH_3CN, THF, DMSO, cyclooctene, and ethanol revealed that the reactions of these complexes are primarily dissociative in nature (I_d) and in some cases require stabilization of the intermediate $Rh_6(CO)_{15}$ by solvent or additional CO bridging.[67]

A distinctly different method of activating metal clusters towards precise ligand substitution is illustrated by the complexes $M_3(CO)_{11}X^-$ (M = Ru, Os, X = NCO, Cl, Br, I). Here, intramolecular nucleophilic attack by the metal coordinated halide or psuedohalide on a neighboring metal atom of the metal cluster promotes CO dissociation forming a bridged chloride intermediate, which then undergoes rapid reaction with the incoming ligand:[65,66]

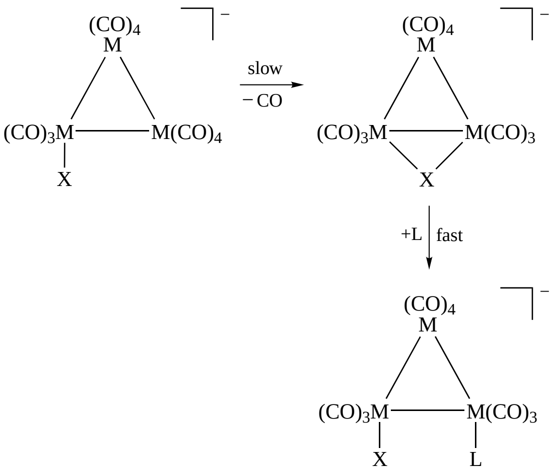

(52)

Kinetic studies have shown that the reaction is first order in cluster and zero order in incoming ligand.[68] The reaction can be carried out catalytically starting with the parent carbonyl cluster and [PPN]X and gives the monosubstituted cluster exclusively.[65,66] The intermediate bridging halide species has been isolated. An alternative catalytic path for obtaining the monosubstituted cluster is the electron-transfer-induced substitution using sodium benzophenone ketyl as the electron-transfer agent.[69]

Coordinately unsaturated clusters are defined as those species that do not obey the effective atomic number rule (EAN) according to the relationship:

$$\text{\# Electrons Required for an EAN Cluster} = 18(\text{\# Metal Atoms}) - 2(\text{\#M–M Bonds}) \quad (53)$$

Thus, for a trinuclear cluster with three metal–metal bonds 48 electrons are required. By far the most well-studied group of coordinately unsaturated clusters are the trinuclear 46 electron species of which $Os_3(CO)_{10}(\mu\text{-H})_2$ is the best-known example.[65] This complex undergoes facile ligand addition reactions with a wide variety of two-electron donors by an associative mechanism and subsequent thermolysis can result in reformation of the 46-electron cluster:

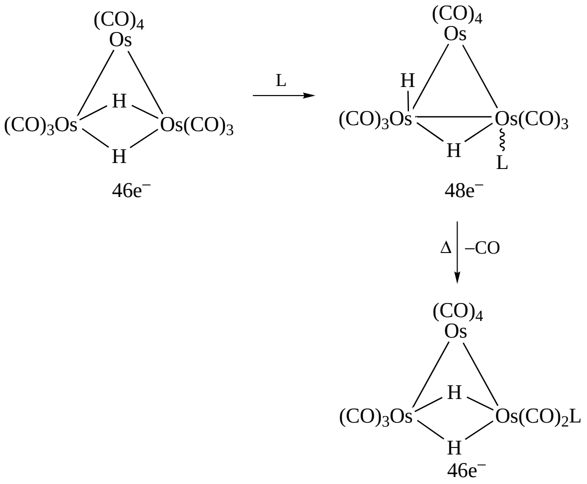

(54)

The mechanism of the ligand addition reactions are associative and a detailed kinetic study of the $Os_3(CO)_{10}(\mu\text{-H})_2 + CO$ system revealed that both the addition of CO and its loss are both single-step concerted processes with the observed rate constant for the system as it approaches equilibrium being:[70]

$$Os_3(CO)_{10}(\mu\text{-H})_2 + CO \underset{k_{-1}}{\overset{k_1}{\rightleftharpoons}} Os_3(CO)_{11}(\mu\text{-H})H;$$
$$k_{obs} = k_{-1} + k_1[CO] \quad (55)$$

Unsaturated trinuclear clusters that undergo similar addition reactions are now known for diphosphine hydride and alkyne clusters of ruthenium[65,66] as well as for triosmium clusters containing nitrogen heterocycles.[71] In the case of the latter systems, the electronic unsaturation is communicated to the heterocycle and completely changes the regiochemistry of the organic ligand, a feature unique to this class of molecules. Coordinately unsaturated clusters that undergo ligand addition reactions are well known for higher nuclearity clusters[72,73] as well as for mixed metal clusters and binuclear clusters.[74]

Electron-precise (*see Electron Precise Compound*) metal clusters that undergo concerted associative ligand addition reactions have become increasingly common in metal-cluster chemistry. A common feature in many of these systems is a hemilabile face-capping ligand whose coordination is partially displaced by the incoming ligand and then recoordinates with loss of CO on subsequent thermolysis to give a substituted product. Two well-studied examples of trinuclear clusters containing ancillary hemilabile ligands are $Ru_3(CO)_9(\mu\text{-H})(\mu_3\text{-}\eta^2\text{-2-amino-pyridyl})$ and $M_3(CO)_9(\mu\text{-H})(\mu_3\text{-}\eta^2\text{-imidoyl})$ (M = Ru, Os):[65,75]

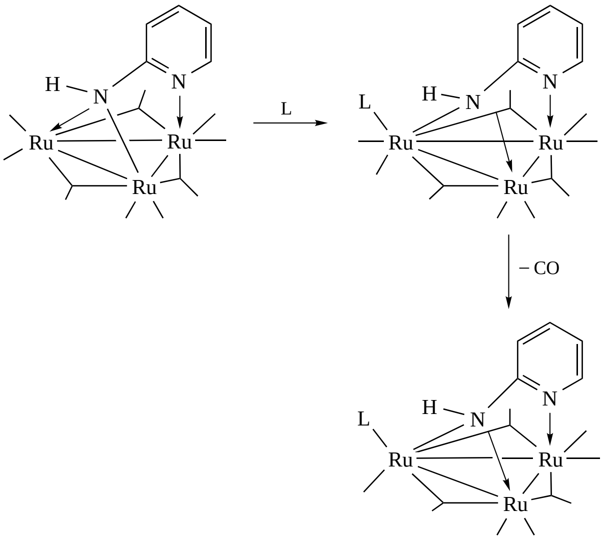

(56)

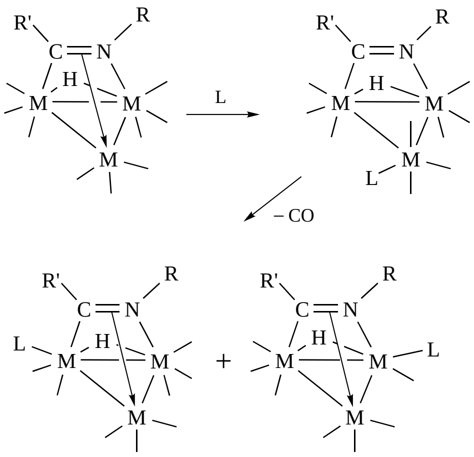

(57)

Kinetic studies on the imidoyl complexes reveal strict second-order rate laws where the observed rate is related to the donor properties of the incoming ligand.[76]

3.1.5 Hydride Complexes

Hydride complexes (*see* ***Hydride Complexes of the Transition Metals***) are important in many reactions catalyzed by organometallic complexes, yet understanding of substitution reactions of hydrides is limited. Metal hydrides are quite sensitive to oxygen, and therefore difficult to study quantitatively. Another difficulty is that the presence of trace impurities leads to rapid reactions by radical-chain mechanisms. Most hydride complexes have been observed to undergo facile ligand substitution reactions, probably by radical reactions like those studied for $HRe(CO)_5$.[2] Under rigorously pure conditions, with the exclusion of light, $HRe(CO)_5$ showed no reaction with PBu_3 in 60 days at 25 °C.[77] When such care was not taken, the reaction yielded $HRe(CO)_4PBu_3$ and $HRe(CO)_3(PBu_3)_2$ at variable rates, and this was explained by a radical-chain process where hydrogen atom abstraction by an initiator produces the $Re(CO)_5\bullet$ radical that acts as a chain carrier. The latter undergoes rapid ligand substitution for CO and then abstracts a hydrogen.

Thus, the substitution reaction is catalyzed by trace impurities ($R^\bullet$), which initiate a self-perpetuating chain mechanism for substitution. Mechanisms of radical reactions will be discussed in Section 4.1.

Metal hydride complexes might undergo substitution by dissociative, associative, or hydride migration processes. Very few studies have been accomplished under conditions that clearly rule out radical mechanisms. The reactions of $HMn(CO)_5$ with L (L = ^{13}CO, $AsPh_3$, PPh_3, and PBu_3) have been carefully investigated and show dependence of the rate on the nature and concentration of the entering ligand.[78] The rates for different ligands are shown in Table 10. The dependence on the nature of the entering ligand is considerably greater than that observed for alkyl migration. At this point, there is no evidence favoring hydride migration over direct nucleophilic attack on the complex in substitution reactions of $HMn(CO)_5$.

The very rapid substitution reactions of hydride complexes $H_2Fe(CO)_4$ and $H_2Ru(CO)_4$ at −70 °C are interpreted in terms of hydride migration.[79]

More recently, the reactions of the of anionic carbonyl hydrides $HFe(CO)_4{}^-$, $HCr(CO)_5{}^-$, and $H(Cr(CO)_5)_2{}^-$ with phosphines and phosphites have been studied over a wide range of conditions.[80,81] Although no kinetic studies have been done, the reactions show significant sensitivity to the stereoelectronic properties of the incoming ligand and also to the nature of the anion. Thus, ligand substitution reactions are much slower when the cation is PPN^+ than with Na^+, and this is thought to be the result of an interaction between the Na^+ and a radial carbonyl (based on infrared studies) that labilizes the axial carbonyl. For the iron complexes in protic solvents, the major product of the reactions is *trans*-$H_2Fe(CO)_4(PR_3)_2$ (*trans*-referring to the phosphine ligands), while in aprotic solvents the major product is $Fe(CO)_3(PR_3)_2$. In the case of the chromium complexes, the major product is *trans*-$Cr(CO)_4(PR_3)_2$ under both photochemical and thermal activation along with the corresponding metal hydride salt. The reactions have been shown to proceed through the anionic monophosphine hydride derivatives in all cases and the most likely mechanism is proposed to involve an associative pathway. Substitution of the first phosphine is thought to

Table 10 Variation in the rate of substitution on $HMn(CO)_5$ with L = ^{13}CO, $AsPh_3$, PPh_3, and PBu_3 at 20 °C[78]

L	Rate ($M^{-1}\,s^{-1}$)
$^{13}CO^a$	1.2×10^{-3}
$AsPh_3{}^b$	3×10^{-4}
PPh_3	1.4×10^{-2}
PBu_3	Fast

[a] At 26 °C. [b] At 28 °C.

weaken the hydride-transition metal interaction and to increase the counter ion hydride interaction, thus favoring hydride loss from the salt.[81]

3.2 Reductive Elimination

Reductive elimination (*see Reductive Elimination*) from an 18-electron complex is the reverse of oxidative addition to a 16-electron complex:

$$\mathrm{CpIr(L)(R)(H)} \longrightarrow [\mathrm{CpIrL}] + \mathrm{R{-}H} \qquad (58)$$
$$\mathrm{L} = \mathrm{CO, PMe_3}$$

These reactions involve a decrease in the oxidation number of the metal (in this case Ir^{III} to Ir^{I}), and a decrease in coordination number for the metal. Reductive elimination reactions are very important in catalysis as the product-removing step. Frequently, the reductive elimination reactions are rapid, making detailed study difficult.

Our examples will first center on the complexes $Ir(CO)(R)(R')L_2X$ (R and R′ = H, alkyl, or alkoxy; L = PPh_3 or $P(p\text{-tolyl})_3$; X = halide or H), which reductively eliminate a number of different products. The reactions are summarized in Table 11. The reactions described in Table 11 show that reductive elimination from Ir^{III} results in formation of different types of bonds. These reductive elimination reactions occur under very similar conditions, indicating that the nature of R and R′ does not significantly affect the rate.[82–86] However, the coupling of two sp^3 carbon centers does not occur. Theoretical studies have suggested that the directionality of the sp^3 hybrid inhibits bond formation.[87,88]

Despite the fact that a coordination site is not formally required for reductive elimination reactions, ligand dissociation from the metal center apparently facilitates reductive elimination.[2] In the iridium examples described in Table 11, halide dissociation is important; in other examples, phosphine ligand dissociation is important.

Table 11 Reductive elimination reactions from $Ir(CO)(R)(R')L_2X$[82–86]

R	R′	X	Product (R–R′)
Me	H	H	CH_4
Me	H	Cl	CH_4
Ph	H	Cl	C_6H_6
OMe	H	H	MeOH
OMe	H	Cl	MeOH
Me	H	$Si(OMe)_3$	CH_4
OMe	$SiPh_3$	H	$Si(OMe)Ph_3$
Me	$SiMe_3$	I	$SiMe_4$
Me	C(O)Me	Cl	MeC(O)Me
OMe	C(O)Me	Cl	MeC(O)OMe
OH	Me	I	MeOH
OH	H	H	H_2O

Until recently, reductive elimination of alkanes from $18e^-$ complexes was not well studied. The reaction of $Rh(PMe_3)_3Cl$ with propylene oxide provides an early example:[89]

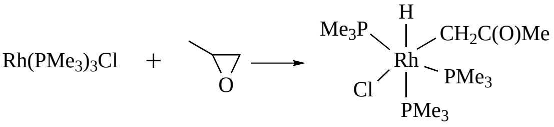

(59)

The stereochemistry was assigned from the ^1H and ^{31}P NMR spectra. Reductive elimination of acetone showed first-order kinetics, with $\Delta H\ddagger = 25.0\,\mathrm{kcal\,mol^{-1}}$ and $\Delta S\ddagger = 5.3\,\mathrm{cal\,K^{-1}\,mol^{-1}}$.[89]

$$cis\text{-}\mathrm{RhH[CH_2C(O)Me](PMe_3)_3Cl} \longrightarrow$$
$$\mathrm{RhCl(PMe_3)_3 + MeC(O)Me} \qquad (60)$$

The presence of PMe_3 inhibits the reaction. Mixtures of *cis*-$RhH(CH_2C(O)CH_3)(PMe_3)_3Cl$ and *cis*-$RhD(CD_2C(O)CD_3)(PMe_3)_3Cl$ led to only $CH_3C(O)CH_3$ and $CD_3C(O)CD_3$, showing that the elimination was intramolecular, which involved reversible dissociation of phosphine followed by an irreversible reductive elimination and reassociation of phosphine.[89]

More recently, the reductive elimination of alkanes from Pt(IV) complexes has become an intense area of investigation as it represents the reverse of the C–H oxidative addition reaction that has been shown to be catalytic in the presence of the Pt(II)/Pt(IV) couple.[90]

The mechanism of ethane and methane reductive elimination from the Pt (IV) complexes P_2PtMe_3R ($P_2 = Ph_2(CH_2)_2Ph_2$, $o\text{-}Ph_2C_6H_4Ph_2$, R = Me, H) has been thoroughly investigated and these studies revealed that ethane elimination occurs from a five-coordinate intermediate formed by partial dissociation of the chelating phosphine, while methane elimination occurs by the direct coupling without ligand loss:[91]

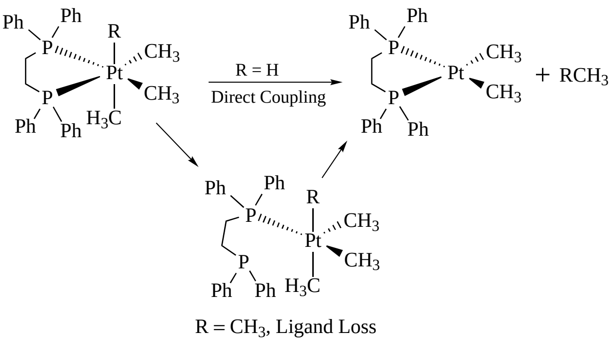

(61)

In a related study, the complex $Tp^{Me_2}Pt^{IV}(CH_3)_2H$ (Tp^{Me_2} = hydridotris(3,5-dimethyl pyrazolyl)borate) undergoes reductive elimination of methane, but here labeling studies revealed that the rate-determining step is loss of methane from an intermediate methane σ complex.[92] Following loss of methane, the $16e^-$ intermediate complex can be trapped with R-D or with CD_3CN to give the corresponding alkyl-deuteride or nitrile complex respectively. The methane reductive elimination is reversible in this Pt(IV) system and an inverse isotope, which is characteristic for a reversible C–H activation, is observed. These results parallel the earlier work of Bergman *et al.* with Ir(III) aryl and alkyl complexes, which also exhibit first-order kinetics in complex and an inverse isotope effect:**[93]**

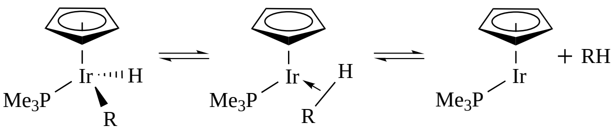

(62)

In a number of cases, dinuclear (*see Dinuclear* and ***Dinuclear Organometallic Cluster Complexes***) reductive elimination, in which two metal centers participate in the reaction, has been observed:**[2]**

$$Cp_2MH_2 + MeMn(CO)_5 \longrightarrow H_2 + CH_4 + Cp(CO)M[\mu\text{-}\eta^5,\eta^1\text{-}C_5H_4)]Mn(CO)_4 \quad M = Mo, W \qquad (63)$$

$$CpMo(CO)_3H + CpMo(CO)_3R \longrightarrow RCHO + Cp_2Mo_2(CO)_4 + Cp_2Mo_2(CO)_6 \qquad (64)$$

The mechanism for the latter reaction was suggested to be:

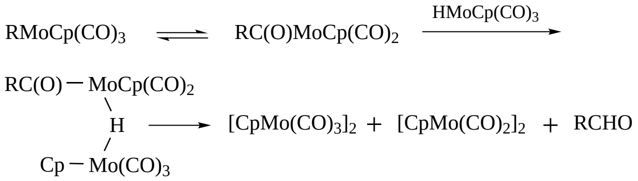

$$RMoCp(CO)_3 \rightleftharpoons RC(O)MoCp(CO)_2 \xrightarrow{HMoCp(CO)_3} \begin{array}{l} RC(O)-MoCp(CO)_2 \\ \quad\quad \backslash \\ \quad\quad H \\ \quad\quad / \\ Cp-Mo(CO)_3 \end{array} \longrightarrow [CpMo(CO)_3]_2 + [CpMo(CO)_2]_2 + RCHO$$

(65)

The reaction sequence is an alkyl migration that opens a coordination site for the bridging hydride, reductive elimination of aldehyde, and the combination of metal-carbonyl fragments to give the products, which have a metal single and triple bond, respectively, $Cp_2Mo_2(CO)_6$ and $Cp_2Mo_2(CO)_4$. The reactions of *cis*-$RMn(CO)_4L$ and *cis*-$HMn(CO)_4L$, where R = benzoyl derivatives and L = CO or $P(p\text{-}MeOC_6H_4)_3$, have been investigated.**[94]** Four distinct pathways have been identified for this dinuclear reductive elimination: (1) CO dissociation from the manganese alkyl followed by a concerted binuclear reductive elimination; (2) the same process but involving solvent displacement of CO by a coordinating solvent; (3) homolysis of the metal alkyl bond followed by H atom abstraction; (4) associative CO insertion followed by reductive elimination to give benzaldehyde instead of toluene. The relatively minor changes involved in the completely different mechanisms for dinuclear reductive eliminations from these manganese systems suggest that reductive elimination reactions may not be easily generalized.

3.3 Electron-transfer Reactions

Electron-transfer reactions of 18-electron organometallic complexes have received growing attention (*see **Paramagnetic Organometallic Complexes***). The field of electron-transfer catalysis where an organometallic complex is activated by oxidation or reduction provides the impetus for such studies (*see* section *Coordinately Unsaturated Clusters and Clusters with Hemilabile Ligands*). Organometallic complexes lie on the border between the fields of inorganic and organic chemistry. The terminology for electron-transfer reactions of organometallic complexes demonstrates the influence of organic (single-electron transfer (SET) and nucleophilic reactions) and inorganic outer and inner sphere (*see Outer-sphere Reaction* and *Inner-sphere Reaction*) electron-transfer nomenclature. For the metal-carbonyl anions whose reactions dominate the electron-transfer reactions of 18-electron organometallic complexes, SET, and outer-sphere terms are equivalent and nucleophilic and inner-sphere reactions are frequently equivalent.

Electron transfer has been frequently observed in catalytic and synthetic reactions of organometallic complexes. Simple reduction:

$$Fe(CO)_5 + 2Na(Hg) \longrightarrow Na_2Fe(CO)_4 + CO \qquad (66)$$

$$Cp_2Fe_2(CO)_4 + Mg \longrightarrow Mg[CpFe(CO)_2]_2 \qquad (67)$$

and oxidation:

$$2Ni(CO)_4 + CS_2 \longrightarrow 2NiS + C + 8CO \qquad (68)$$

$$Fe(CO)_5 + 2CuCl_2 \longrightarrow Cu_2Cl_2 + FeCl_2 + 5CO \qquad (69)$$

reactions are commonly observed and utilized. Disproportionation reactions provide another example of electron transfer.**[95]**

$$Co_2(CO)_8 + 2L \longrightarrow [Co_2(CO)_3L_2][Co(CO)_4] + CO \quad L = \text{phosphine} \qquad (70)$$

$$3V(CO)_6 + 6L \longrightarrow [VL_6][V(CO)_6]_2 + 6CO \quad L = \text{oxygen or nitrogen base} \qquad (71)$$

Reactions between cationic and anionic carbonyls to form metal–metal bonds also involve a formal electron transfer:**[96,97]**

$$[Mn(CO)_6]^+ + [Mn(CO)_5]^- \longrightarrow Mn_2(CO)_{10} + CO \qquad (72)$$

$$[Co(CO)_3(PPh_3)_2][Co(CO)_4] \xrightarrow{\Delta} Co_2(CO)_6(PPh_3)_2 + CO \qquad (73)$$

The primary method of synthesis of heterobimetallic complexes may involve electron transfer between metal halides and metal-carbonyl anions:**[98–101]**

$$CpFe(CO)_2I + NaMn(CO)_5 \longrightarrow Cp(CO)_2FeMn(CO)_5 + NaI \qquad (74)$$

$$Re(CO)_5Cl + NaMn(CO)_5 \longrightarrow MnRe(CO)_{10} + NaCl \qquad (75)$$

$$Mn(CO)_5Cl + NaCo(CO)_4 \longrightarrow MnCo(CO)_9 + NaCl \qquad (76)$$

Table 12 Half-reaction reduction potentials for one-electron and two-electron transitions of metal-carbonyl species[103]

Metal carbonyl, M_2	$M_2 + 2e^- \rightarrow 2M^-$(V)	$M\bullet + e^- \rightarrow M^-$(V)	Nucleophilicity ($\ln k_2$) $M^- + MeI \rightarrow MeM + I^-$
$Co_2(CO)_8$	−0.123	−0.15	−4.7
$Cp_2Cr_2(CO)_6$	−0.639	−0.70	−2.9
$Cp_2Mo_2(CO)_6$	−0.336 (−0.56^a)	−0.79	−0.94
$Cp_2W_2(CO)_6$	−0.330	∼−0.8	−0.67
$Mn_2(CO)_{10}$	−0.400 (−0.69^a)	−0.97	0.41
$Re_2(CO)_{10}$	−0.523	−1.2	4.3
$Cp_2Fe_2(CO)_4$	−1.186 (−1.44^a)	−1.7	Large

[a] Values from Pugh and Meyer,[65] which are probably more accurate and are systematically 0.25 V more negative.

This type of reaction sometimes leads to formation of homobimetallic complexes.

An interesting example of electron transfer from $Mn(CO)_5^-$ to $Cr(\eta^6\text{-}C_6H_6)_2^+$ is shown below:[102]

$$2\,[Cr(\eta^6\text{-}C_6H_6)_2][Mn(CO)_5] \longrightarrow 2Cr(\eta^6\text{-}C_6H_6)_2 + Mn_2(CO)_{10} \quad (77)$$

This reaction occurs at reasonable rates just above ambient temperatures. The one- and two-electron transitions for many neutral carbonyl species have been measured (Table 12).[103]

3.3.1 *Metal-carbonyl Anions*

The electron-transfer reactions of metal-carbonyl anions have been reviewed.[103] Metal-carbonyl anions exhibit one- and two-electron reactions. The two-electron processes involving transfer of groups such as hydrogen, alkyl, and halogen between metal centers are related to the nucleophilicity of the anion involved. The one-electron processes are primarily outer-sphere electron transfers. However, in contrast to organic reactions, the metal-carbonyl anions can also undergo inner-sphere electron transfers. This is usually the case when an anion of low nucleophilicity transfers an electron to a metal-carbonyl cation or halide.

Recently, the thermally and photochemically induced one-electron transfers from the metal-carbonyl anions $A[Mn(CO)_5]$, $A[Co(CO)_4]$, and $A[Re(CO)_5]$ ($A =$ Na and PPN) to fullerene have been studied.[104] In the case of the thermal reactions of the Mn and Re anions, initial electron transfer to form C_{60}^- and the corresponding $17e^-$ $M(CO)_5$ radical is followed by the competitive collapse to the metal dimer and formation of the η^2-C_{60} complexes $A[Mn(CO)_4(\eta^2\text{-}C_{60})]$. Under photochemical conditions, redissociation of the dimer results in exclusive formation of the η^2-complexes, which are thought to be formed by nucleophilic displacement of CO on the substitution labile $M(CO)_5$ fragment by C_{60}^-:

$$Mn(CO)_5^- + CO_{60} \xrightarrow{\Delta \text{ or } h\nu} Mn(CO)_5 + C_{60}^- \longrightarrow [(CO)_4Mn(\eta^2 - C_{60})]^- + CO \quad (78)$$

The kinetics of accumulation and consumption of the iron carbonyl radical anions, $Fe_3(CO)_{12}^{\bullet-}$ and $Fe_3(CO)_{11}^{\bullet-}$ formed by one-electron transfer from $(NH_4)SEt$ have been studied using stopped-flow techniques.[105] The kinetic measurements reveal that initial formation of a thioacetyl adduct is followed by electron transfer to $Fe_3(CO)_{12}$ forming the radical anion, $Fe_3(CO)_{12}^{\bullet-}$, which then undergoes CO loss to give the other spectroscopically characterized radical anion, $Fe_3(CO)_{11}^{\bullet-}$. The formation of these radical anions is followed by a series of reactions involving radical-chain electron transfers and ligand exchange reactions where the main chain carriers are the trimetallic radical anions and where the final major product is the salt $NH_4[Fe_2(CO)_7]$. The significance of this work is that it supports the idea that chain radical processes including preliminary complex formation followed by redox initiation lies at the heart of the interaction of iron carbonyls with Lewis bases, and that ligand substitution takes place via the coordinately unsaturated species created by the radical-chain processes.

4 17-ELECTRON COMPLEXES

17-electron complexes are inherently unstable. However, the huge increase in reactivity for 17-electron complexes offers possibilities for activation of 18-electron complexes through a process called electron-transfer catalysis (*see* ***Paramagnetic Organometallic Complexes***). 17-electron complexes are formed by oxidation of 18-electron complexes, by reduction of 18-electron complexes accompanied by ligand dissociation, and by homolytic cleavage of the metal–metal bond of dimers. The reactions of 17- and 18-electron complexes have recently been reviewed.[106] The two most common reaction pathways for the 17-electron species are ligand substitution and electron transfer. However, some recent work illustrates that 17-electron complexes can undergo other types of reactions as well.

4.1 Ligand Substitution

17-electron complexes undergo ligand substitution through an associative reaction and a 19-electron intermediate.[106,107] This can be illustrated by the reactions of $[V(CO)_6]^\bullet$:

$$[V(CO)_6]^\bullet + L \longrightarrow [V(CO)_6L]^\bullet \xrightarrow{-CO} [V(CO)_5L]^\bullet + CO \quad (79)$$

The activation parameters and dependence on L are shown in Table 13.[108] These data are fully consistent with an associative reaction. The 17-electron complex $V(CO)_6$ has an associative substitution reaction rate that is $>10^{10}$ more facile than for the 18-electron $Cr(CO)_6$ complex. The vanadium complexes are among the most inert of the 17-electron complexes. Table 14 shows the rate constants for substitution of several complexes.[107] As expected from size considerations, substituting a phosphine ligand for a CO decreases the rate for an associative reaction.

The two dominant characteristics for substitution reactions of 17-electron complexes are very rapid reactions and associative mechanisms. Each of these features is in contrast to reactions of 18-electron complexes. The reactivity has been attributed to the formation of a three-electron bond between the entering nucleophile and the 17-electron complex.[109] Electron density analysis supports stabilization of the 19-electron transition state as the primary source for the labilization.[110]

The arene complexes of the early transition metals represent recent extensions 17-electron class of compounds. Thus, the 18-electron half open chromocene carbonyl complexes, (2, 4-dimethylpentadienyl)CpCrCO and the analogous Cp* complex undergo one-electron oxidation with $NOBF_4$ to provide the corresponding cationic 17-electron complexes.[111] These complexes undergo ligand substitution processes:[111]

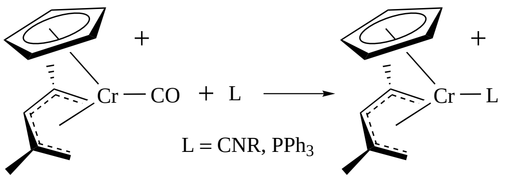

(80)

Table 13 Rate constants and activation parameters for substitution of $V(CO)_6$[108]

L	k ($M^{-1}\,s^{-1}$)	$\Delta H‡$ (kcal mol^{-1})	$\Delta S‡$ (cal $K^{-1}\,mol^{-1}$)
PMe_3	132	7	−23
PBu_3	50	7	−25
$PMePh_2$	4	9	−26
$P(OMe)_3$	0.7	11	−23
PPh_3	0.2	10	−28
$AsPh_3$	0.02	–	–

Table 14 Rate constants for substitution of 17-electron complexes[107,a]

Complex	k ($M^{-1}\,s^{-1}$)
$[V(CO)_6]^•$	100
$[V(CO)_5PBu_3]^•$	5×10^{-4}
$[Re(CO)_5]^•$	2×10^9
$[Mn(CO)_5]^•$	1×10^9
$[Mn(CO)_4PPh_3]^•$	7×10^2

[a] The entering ligand is an alkyl phosphine.

The reactions exhibit second-order kinetics with rate constants on the order of $2.0 \times 10^{-4}\,M^{-1}\,s^{-1}$. This rate of substitution is 6 to 9 orders of magnitude slower than 17-electron binary metal carbonyls but is similar to that observed for phosphine substituted vanadium carbonyls (Table 14). When t-butyl isocyanide is the incoming ligand, the initial slow substitution for CO is followed by rapid displacement of the of the pentadienyl ligand to yield the complex, $CpCr(CN^tBu)_4{}^+$. This is presumably caused by a pentadienyl slippage after the first rate-determining associative ligand addition. Reaction with more electron-donating phosphines results in nucleophilic addition to the C(1) of the pentadienyl ligand by an associative pathway. Interestingly, the CO exchange rate for the cationic 17-electron complex is about the same as for the 18-electron precursor. Taken together, these data indicate that electron count may control reaction pathway (i.e. associative versus dissociative) but steric factors have a dominant influence on rate and on the nature of the product obtained. This steric dependence is exemplified by the different cone angle limits for phosphine substitution on the more sterically encumbered 17-electron systems $Cp^*Cr(CO)_3$ and $(Tp)Mo(CO)_3$ (Tp = hydridotris(pyrazolyl)borate, cone angle limit = 140°) relative to $CpCr(CO)_3$ (cone angle limit = 170°).[112]

An exception to the general rule that 17-electron complexes react by strictly associative mechanisms has been reported.[113] The alkyl for iodide metathesis in the 17-electron complex $CpCr(NO)(PPh_3)I$ is inhibited by excess phosphine. The reaction requires formation of a THF solvate CpCr(NO)(THF)I, which has been characterized. Although the formation of this intermediate takes place by an associative pathway, the requirement that a two-electron ligand dissociate prior to the replacement of iodide by the alkyl group puts this transformation of a 17-electron complex into a different mechanistic class.

The gas-phase reactions of the 17-electron radical anions $Cr(CO)_5{}^-$, $Fe(CO)_4{}^-$, and $Ni(CO)_3{}^-$ with organic electrophiles have been examined.[114] Here, CO substitution takes place by initial charge transfer to the organic electrophile (e. g. maleic anhydride) followed by addition of the resulting anion to the $16e^-$ metal center. The efficiency of the reaction correlates with the electron affinity of the organic ligand. This mechanism is also thought to be operative in the condensed phase reactions of $Fe(CO)_4{}^-$ with similar ligands studied earlier and represents an alternative to the formation of the usual 19-electron intermediate.[115]

4.2 Electron-transfer Reactions

17-electron complexes undergo facile oxidation, reduction, and atom-transfer reactions. The rapidity of these reactions has made the study difficult, but their importance in radical-chain processes warrants discussion. The speed of atom-transfer reactions can be illustrated by the reactions of 17-electron metal-carbonyl complexes with halide complexes.[107] A few reactions with CCl_4 are shown in Table 15.[107]

$$M^{\bullet} + CCl_4 \longrightarrow M\text{–}Cl + [CCl_3]^{\bullet} \qquad (81)$$

Hydrogen-transfer reactions have also been reported. 17-electron complexes may be oxidized or reduced:

$$M^{\bullet} + e^{-} \longrightarrow M^{-} \qquad (82)$$

$$M^{\bullet} \xrightarrow{S} [M - S]^{+} + e^{-} \qquad (83)$$

S = solvent

$M^{\bullet}$ = a 17-electron complex

Burke and Brown examined reactions of $[Re(CO)_4L]^{\bullet}$, L = PMe_3, $P(O\text{-}i\text{-}Pr)_3$, with *N*-methylpyridinium salts.[116] These reactions occur with electron-transfer rate constants in the 10^6–$10^9\,M^{-1}\,s^{-1}$ range. From Marcus-type (*see Marcus Equation*) analysis, an intrinsic barrier of $\sim 3\,kcal\,mol^{-1}$ was obtained for the 17-electron rhenium complexes.[116] The facile oxidation and reduction of 17-electron complexes makes them quite susceptible to disproportionation reactions:

$$3V(CO)_6 \xrightarrow{MeC(O)Me} [V(MeC(O)Me)_6][V(CO)_6]_2 \qquad (84)$$

Such reactions are probably quite important in the disproportionation of dimers. Disproportionation of $V(CO)_6$ was interpreted as an inner-sphere reaction with transfer of an electron through an isocarbonyl (*see Isocarbonyl Complexes*).[117] The observation that $V(CO)_5PBu_3$ disproportionates 10^5 times more slowly than $V(CO)_6$ suggests large ligand effects are possible for such reactions. Atom-transfer and electron-transfer reactions of 17-electron complexes are very important in radical-chain processes. Thus, the radical-initiated substitution of $HRe(CO)_5$ involves the 17-electron electron $Re(CO)_5\bullet$ as the chain propagating intermediate.[95] Chain reactions take advantage of the very rapid atom transfer (in other cases electron transfer) and ligand substitution of 17-electron complexes.

Table 15 Rate constants for equation (81)[107]

$M^{\bullet}$	$k\ (M^{-1}\,s^{-1})$
$Mn(CO)_5$	1×10^6
$Re(CO)_5$	3×10^7
$Re(CO)_4PMe_3$	2×10^9
$CpMo(CO)_3$	2×10^4
$CpW(CO)_3$	1×10^4

The 17-electron bis(mesitylene)vanadium(0) undergoes a one-electron transfer when reacted with difluoro- or trifluoroacetic acid to give the vanadium(I) salt $[V(mes)_2][CF_3CO_2]$ with the liberation of a half mole of hydrogen:[118]

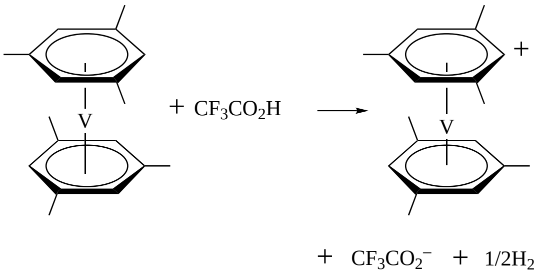

(85)

This species is stable in THF but reacts with excess trifluoroacetic acid to give the protonated vanadium(II) complex $[H(THF)_n][V(CF_3CO_2)_3]$. Similarly, the reaction of $V(mes)_2$ with triphenyl methyl halides in DME gives the vanadium (II) complexes $VX_2(DME)_n$ (X = Cl, $n = 1.1$, X = Br or I, $n = 2$).

5 CONCLUSION

The reaction mechanism expected for an organometallic complex is closely correlated with the electron count at the metal center. This has been recognized for many years as the $16e^{-}$ and $18e^{-}$ rule for organometallic reactions. 18-electron complexes usually undergo transformations (ligand dissociation, alkyl migration, or reductive elimination) that result in a $16e^{-}$ intermediate. 16-electron complexes usually undergo transformations (ligand addition or oxidative addition) that result in 18-electron complexes. However, some very interesting exceptions to this rule now exist. Generation of 14-electron intermediates by ligand dissociation from 16-electron complexes now appears to be a viable alternative for complexes containing very strongly donating ligands. Single-electron transfer reactions of 18-electron complexes can generate $17e^{-}$ and $19e^{-}$ complexes, which are very reactive for a number of reaction types. Such transformations allow the use of electron-transfer catalysis with organometallic complexes.

Furthermore, although electron count can by used to anticipate a mechanistic type for a given complex, the rate of the reaction is strongly influenced by the stereoelectronic factors associated with the complex. Thus, although 17-electron complexes usually react by an associative pathway, the rate of the reaction may be as slow or even slower than the primarily dissociative reactions of their 18-electron counterparts depending on the overall charge, the nature of the incoming ligand, and the nature of the ancillary ligands on the metal(s).

In many respects, the reactivities of organometallic complexes are similar to organic complexes (high reactivity of odd-electron complexes, single-electron transfer, and nucleophilic displacement) and in other respects organometallic complexes are very similar to coordination complexes (ligand substitution and metal effects).

6 RELATED ARTICLES

Bonding Energetics of Organometallic Compounds; Electron Transfer in Coordination Compounds; Paramagnetic Organometallic Complexes; Structure & Property Maps for Inorganic Solids.

7 REFERENCES

1. C. A. Tolman, *Chem. Soc. Rev.*, 1972, **1**, 337.
2. J. D. Atwood, 'Inorganic and Organometallic Reaction Mechanisms', VCH Publishers, Weinheim, 1997.
3. F. Basolo and R. G. Pearson, 'Mechanisms of Inorganic Reactions', Wiley, New York, 1968.
4. L. Vaska, *Acc. Chem. Res.*, 1986, **1**, 335.
5. T. V. Ashworth, J. E. Singleton, D. J. A. de Waal, W. J. Louw, E. Singleton, and E. van der Stok, *J. Chem. Soc., Dalton Trans.*, 1978, 340.
6. U. Belluco, M. Graziani, and P. Rigo, *Inorg. Chem.*, 1966, **5**, 1123.
7. D. F. Shriver and P. W. Atkins, 'Inorganic Chemistry', 3rd edn., Freeman, New York, 1999, p. 471.
8. J. D. Atwood, *Coord. Chem. Rev.*, 1988, **83**, 93.
9. A. L. Balch, V. J. Catalano, J. W. Lee, and M. M. Olmstead, *J. Am. Chem. Soc.*, 1992, **114**, 5455.
10. L. Mink, M. F. Rettig, and R. M. Wing, *J. Am. Chem. Soc.*, 1991, **113**, 2065.
11. G. Yoneda and D. M. Blake, *Inorg. Chem.*, 1981, **20**, 67.
12. P. B. Chock and J. Halpern, *J. Am. Chem. Soc.*, 1966, **88**, 3511.
13. J. Chatt and J. M. Davidson, *J. Chem. Soc.*, 1965, 843.
14. K. Kitaura, S. Ohara, and K. Morokuma, *J. Am. Chem. Soc.*, 1981, **103**, 2891.
15. R. Ugo, A. Pasini, A. Fusi, and S. Cenini, *J. Am. Chem. Soc.*, 1972, **94**, 7364.
16. J. K. Stille and K. S. Y. Lau, *Acc. Chem. Res.*, 1977, **10**, 434.
17. J. P. Collman and M. R. MacLaury, *J. Am. Chem. Soc.*, 1974, **96**, 3019.
18. J. A. Labinger and J. A. Osborn, *Inorg. Chem.*, 1980, **19**, 3230.
19. J. A. Labinger, J. A. Osborn, and N. J. Coville, *Inorg. Chem.*, 1980, **19**, 3236.
20. G. Alibrandi, L. M. Scolaro, and R. Romeo, *Inorg. Chem.*, 1991, **30**, 4007.
21. S. Lanza, D. Minniti, P. Moore, J. Sachinidis, R. Romeo, and M. L. Tobe, *Inorg. Chem.*, 1984, **23**, 4428.
22. R. L. Rominger, J. M. McFarland, J. R. Jeitler, J. S. Thompson, and J. D. Atwood, *J. Coord. Chem.*, 1994, **31**, 7.
23. P. E. Garrou, *Adv. Organomet. Chem.*, 1984, **23**, 95.
24. L. J. Ackerman, J. P. Sadighi, D. M. Kurtz, J. A. Labinger, and J. E. Bercaw, *Organometallics*, 2003, **22**, 3884.
25. D. Woska, A. Prock, and W. P. Giering, *Organometallics*, 2000, **19**, 4629.
26. G. Frenking, K. Wichmann, N. Fröhlich, J. Grobe, W. Golla, D. Le Van, B. Krebs, and M. Läge, *Organometallics*, 2002, **21**, 2921.
27. S. P. Wang, M. G. Richmond, and M. Schwartz, *J. Am. Chem. Soc.*, 1992, **114**, 7595.
28. J. P. Day, F. Basolo, R. G. Pearson, L. F. Kangas, and P. M. Henry, *J. Am. Chem. Soc.*, 1968, **90**, 1925.
29. R. J. Angelici and F. Basolo, *J. Am. Chem. Soc.*, 1962, **84**, 2495.
30. J. R. Graham and R. J. Angelici, *Inorg. Chem.*, 1967, **6**, 2082.
31. W. D. Covey and T. L. Brown, *Inorg. Chem.*, 1973, **12**, 2820.
32. F. Ungvary and A. Wojicki, *J. Am. Chem. Soc.*, 1987, **109**, 6848.
33. J. D. Atwood, *J. Organomet. Chem.*, 1990, **383**, 59.
34. J. D. Atwood and T. L. Brown, *J. Am. Chem. Soc.*, 1975, **97**, 3380.
35. R. H. Reimann and E. Singleton, *J. Chem. Soc., Dalton Trans.*, 1973, 841.
36. C. A. Tolman, *J. Am. Chem. Soc.*, 1970, **92**, 2956.
37. D. J. Darensbourg and A. H. Graves, *Inorg. Chem.*, 1979, **18**, 1257.
38. M. J. Wovkulich, J. L. Atwood, L. Canada, and J. D. Atwood, *Organometallics*, 1985, **4**, 867, references therein.
39. L. E. Manzer and C. A. Tolman, *J. Am. Chem. Soc.*, 1975, **97**, 1955.
40. R. J. Angelici, S. E. Jacobson, and C. M. Ingemanson, *Inorg. Chem.*, 1968, **7**, 2466.
41. J. N. Cawse, R. A. Fiato, and R. L. Pruett, *J. Organomet. Chem.*, 1979, **172**, 405.
42. G. M. Whitesides and D. J. Boschetto, *J. Am. Chem. Soc.*, 1969, **91**, 4313.
43. H. Berke and R. Hoffmann, *J. Am. Chem. Soc.*, 1978, **100**, 7224.
44. T. G. Richmond, F. Basolo, and D. F. Shriver, *Inorg. Chem.*, 1982, **21**, 1272.
45. P. P. Patel and M. E. Walker, *J. Organomet. Chem.*, 1997, **547**, 103.
46. J. K. Shen, Y. C. Gao, Q. Z. Shi, and F. Basolo, *Coord. Chem. Rev.*, 1993, **128**, 69.
47. C. Li, E. D. Stevens, and S. P. Nolan, *Organometallics*, 1995, **14**, 3791.

48. C. Li and S. P. Nolan, *Organometallics*, 1995, **14**, 1327.
49. D. Sonnenberger and J. D. Atwood, *J. Am. Chem. Soc.*, 1980, **102**, 3484.
50. A. M. Stolzenberg and E. L. Muetterties, *J. Am. Chem. Soc.*, 1983, **105**, 822.
51. N. J. Coville and P. Johnston, *J. Organomet. Chem.*, 1989, **363**, 343.
52. M. Absi-Halabi, J. D. Atwood, N. P. Forbes, and T. L. Brown, *J. Am. Chem. Soc.*, 1980, **102**, 6248.
53. K. J. Karel and J. R. Norton, *J. Am. Chem. Soc.*, 1974, **96**, 6812.
54. D. Sonnenberger and J. D. Atwood, *Inorg. Chem.*, 1981, **20**, 3243.
55. D. Sonnenberger and J. D. Atwood, *J. Am. Chem. Soc.*, 1982, **104**, 2113.
56. D. Sonnenberger and J. D. Atwood, *Organometallics*, 1982, **1**, 694.
57. G. F. Stuntz and J. R. Shapley, *J. Organomet. Chem.*, 1981, **213**, 389.
58. D. J. Darensbourg and B. J. Baldwin-Zuschke, *J. Am. Chem. Soc.*, 1981, **104**, 3906.
59. D. J. Darensbourg and B. J. Baldwin-Zuschke, *Inorg. Chem.*, 1981, **20**, 3846.
60. R. Shojaie and J. D. Atwood, *Inorg. Chem.*, 1987, **26**, 2199.
61. D. S. Parfitt, J. D. Jordan, and J. B. Keister, *Organometallics*, 1992, **11**, 4009.
62. J. R. Fox, W. L. Gladfelter, and G. L. Geoffroy, *Inorg. Chem.*, 1980, **19**, 2574.
63. J. R. Fox, W. L. Gladfelter, T. G. Wood, J. A. Smegal, T. K. Foreman, G. L. Geoffroy, I. Tavanaiepour, V. W. Day, and C. S. Day, *Inorg. Chem.*, 1981, **20**, 3214.
64. D. H. Farrar, A. J. Poë, and Y. Zheng, *J. Am. Chem. Soc.*, 1994, **116**, 6552.
65. G. Lavigne, in 'The Chemistry of Metal Clusters', eds. D. Shriver, R. D. Adams, and R. D. Kaesz, Verla Chemie, Berlin, 1990, Chap. 5, p. 201.
66. R. D. Adams and F. A. Cotton, 'Catalysis by Di- and Polynuclear Metal Cluster Complexes', Wiley-VCH, New York, 1998, Chap. 1 and 2.
67. A. J. Poë and S. P. Tunik, *Inorg. Chim. Acta*, 1998, **268**, 189.
68. J. K. Shen and F. Basolo, *Organometallics*, 1993, **12**, 2942.
69. M. I. Bruce, B. K. Nicholson, and M. L. Williams, *Inorg. Synth.*, 1989, **26**, 271.
70. A. J. Poë, C. N. Sampson, R. T. Smith, and Y. Zheng, *J. Am. Chem. Soc.*, 1993, **115**, 3174.
71. J. Abedin, B. Bergman, R. Holmquist, R. Smith, E. Rosenberg, J. Ciurash, K. Hardcastle, J. Roe, V. Vazquez, C. Roe, S. Kabir, B. Roy, S. Alam, and K. A. Azam, *Coord. Chem. Rev.*, 1999, **190–192**, 975.
72. L. J. Farrugia, D. Ellis, and A. M. Senior, in 'Synergy Between Dynamics and Reactivity at Clusters and Surfaces', ed. L. J. Farrugia, Kluwer, Dordrecht, NATO ASI series C, Vol. 465, 1995, p. 141.
73. T. Berenghelli, G. D'Alfonso, and M. Zarini, *J. Chem. Soc., Dalton Trans.*, 1995, **14**, 2407.
74. J. Y. Liu, V. Riera, M. A. Ruiz, M. Lanfranchi, and A. Tiripicchio, *Organometallics*, 2003, **22**, 4500.
75. E. Rosenberg, D. Espitia, S. E. Kabir, T. McPhillips, M. W. Day, K. I. Hardcastle, R. Gobetto, D. Osella, and L. Milone, *Organometallics*, 1991, **10**, 3550.
76. E. Rosenberg, W. Freeman, Z. Carlos, K. I. Hardcastle, Y. J. Yoo, L. Milone, and R. Gobetto, *J. Cluster Sci.*, 1992, **3**, 439.
77. B. H. Byers and T. L. Brown, *J. Am. Chem. Soc.*, 1977, **99**, 2527.
78. B. H. Byers and T. L. Brown, *J. Organomet. Chem.*, 1977, **127**, 181.
79. R. G. Pearson, H. W. Walker, H. Mauermann, and P. C. Ford, *Inorg. Chem.*, 1981, **20**, 2741.
80. J. J. Brunet, R. Chauvin, O. Diallo, F. Kindela, P. Lascale, and D. Neilbecker, *Coord. Chem. Rev.*, 1998, **178–180**, 331.
81. J. J. Brunet, O. Diallo, B. Donnadieu, and E. Roblou, *Organometallics*, 2002, **21**, 3388.
82. J. S. Thompson and J. D. Atwood, *Organometallics*, 1991, **10**, 3525.
83. J. S. Thompson, S. L. Randall, and J. D. Atwood, *Organometallics*, 1991, **10**, 3906.
84. J. S. Thompson, K. A. Bernard, B. J. Rappoli, and J. D. Atwood, *Organometallics*, 1990, **9**, 2727.
85. K. A. Bernard and J. D. Atwood, *Organometallics*, 1989, **8**, 795.
86. B. J. Rappoli, J. M. McFarland, J. S. Thompson, and J. D. Atwood, *J. Coord. Chem.*, 1990, **21**, 147.
87. J. J. Low and W. A. Goddard III, *J. Am. Chem. Soc.*, 1986, **108**, 6115.
88. J. J. Low and W. A. Goddard III, *Organometallics*, 1986, **5**, 609.
89. D. Milstein, *J. Am. Chem. Soc.*, 1982, **104**, 5226.
90. S. S. Stahl, J. A. Labinger, and J. E. Bercaw, *Angew. Chem., Int. Ed. Engl.*, 1998, **37**, 2181, references therein.
91. D. M. Crumpton-Bregel and K. I. Goldberg, *J. Am. Chem. Soc.*, 2003, **125**, 9442.
92. M. P. Jensen, D. D. Wick, S. Reinhartz, P. S. White, J. L. Templeton, and K. I. Goldberg, *J. Am. Chem. Soc.*, 2003, **125**, 8614.
93. J. M. Buchanan, J. M. Stryker, and R. G. Bergman, *J. Am. Chem. Soc.*, 1986, **108**, 1537.
94. M. J. Nappa, R. Santi, S. P. Diefenbach, and J. Halpern, *J. Am. Chem. Soc.*, 1982, **104**, 619.
95. J. E. Ellis, *J. Organomet. Chem.*, 1975, **86**, 1.
96. T. Kruck and M. Hoffer, *Chem. Ber.*, 1964, **97**, 2289.

97. M. Absi-Halabi, J. D. Atwood, N. P. Forbes, and T. L. Brown, *J. Am. Chem. Soc.*, 1980, **102**, 6248.
98. R. B. King, P. M. Treichel, and F. G. A. Stone, *Chem. Ind. (London)*, 1961, 747.
99. N. Flitcroft, D. K. Huggins, and H. D. Kaesz, *Inorg. Chem.*, 1964, **3**, 1123.
100. G. Sbrignaldello, *Inorg. Chim. Acta*, 1981, **48**, 237.
101. P. Chini, G. Longoni, and V. G. Albano, *Adv. Organomet. Chem.*, 1976, **14**, 285.
102. I. Wender and P. Pino, ‘Metal Carbonyls in Organic Synthesis’, Wiley, New York, 1968, Vol. 1.
103. J. D. Atwood, M. S. Morraine-Pandolfino, Y. Zhen, W. S. Striejewske, C. K. Lei, and P. Wang, *J. Coord. Chem.*, 1994, **32**, 65.
104. D. M. Thompson, M. Bengough, and M. C. Baird, *Organometallics*, 2002, **21**, 4762.
105. Y. A. Belousov and E. F. Brin, *Polyhedron*, 2001, **20**, 2765.
106. S. Sun and D. A. Sweigart, *Adv. Organomet. Chem.*, 1996, **40**, 171.
107. T. L. Brown, in ‘Organometallic Radical Processes’, ed. W. C. Trogler, Elsevier, Amsterdam, 1990, p. 67.
108. W. C. Trogler, *Int. J. Chem. Kinet.*, 1987, **19**, 1024.
109. W. C. Trogler, in ‘Organometallic Radical Processes’, ed. W. C. Trogler, Elsevier, Amsterdam, 1990, p. 306.
110. Z. Lin and M. B. Hall, *J. Am. Chem. Soc.*, 1992, **114**, 6574.
111. J. K. Shun, J. W. Freeman, N. C. Halllnan, A. L. Rheingold, A. M. Arlf, R. D. Ernst, and F. Basolo, *Organometallics*, 1992, **11**, 3215.
112. J. H. MacNeil, A. W. Roszak, M. C. Baird, K. F. Preston, and A. Rheingold, *Organometallics*, 1993, **12**, 4402.
113. P. Legzdins and M. J. Shaw, *J. Am. Chem. Soc.*, 1994, **116**, 7700.
114. Y. H. Pan and D. P. Ridge, *J. Am. Chem. Soc.*, 1992, **114**, 2773.
115. P. J. Krusic and J. San Filippo, *J. Am. Chem. Soc.*, 1982, **104**, 2645.
116. M. R. Burke and T. L. Brown, *J. Am. Chem. Soc.*, 1989, **111**, 5185.
117. T. G. Richmond, Q. Z. Shi, W. C. Trogler, and F. Basolo, *J. Am. Chem. Soc.*, 1984, **106**, 76.
118. F. Calderazzo, G. E. De Benedetto, S. Detti, and G. Pampaloni, *J. Chem. Soc., Dalton Trans.*, 1997, 3319.

Mercury: Inorganic & Coordination Chemistry

Deborah C. Bebout
The College of William and Mary, Chemistry Department, Williamsburg, VA, USA

Based in part on the article Mercury: Inorganic & Coordination Chemistry by Gregory J. Grant which appeared in the Encyclopedia of Inorganic Chemistry, First Edition.

1 Introduction 1
2 General Aspects of the Chemistry of Mercury 1
3 Mercury(I): Compounds and Coordination Chemistry 5
4 Mercury(II): Compounds and Coordination Chemistry 8
5 Related Articles 13
6 References 14

Abbreviations

BAL = British antilewisite; DMPS = 2,3-dimercapto-1-propane sulfonic acid, sodium salt; 15S5 = 1,4,7,10,13-pentathiacyclopentadecane; 9S3 = 1,4,7-dithiacyclononane.

1 INTRODUCTION

Mercury has been known for over 4000 years. Its chemistry has many unusual aspects that have resulted in extensive usage by mankind. Mercury is the only common metal that is liquid at room temperature. It is also one of the very few elements that is monoatomic in its vapor phase at low temperatures, an indication of the weak *Intermolecular* forces that are present in mercury. The element exhibits surprisingly different chemistry from its congeners zinc and cadmium, a feature that is probably a consequence of the poor shielding by electrons in the completely filled 4f and 5d sublevels. The metal is used in a number of applications, including thermometers, amalgams, and production of chlor−alkali.

Mercury is the only group 12 member to have a substantial chemistry in the +1 oxidation state, in which Hg_2^{2+}, the most common of all metal polycations, is formed. This ion was the first one known to exhibit metal−metal bonding. Its chloride salt is the material present in the standard calomel reference electrode. In addition to halides and oxy salts, nitrogen and oxygen-donor ligand complexes of mercury(I) are known, but far fewer than of mercury(II).

In the divalent state, mercury forms compounds and complexes with many different CN and geometries. Since Hg^{2+} is a d^{10} metal ion lacking strong coordination geometry preferences, crystallography is critical to definitive structural characterization. Although Hg^{2+} typically makes stronger bonds with S, N, and P donors than any other divalent metal ion, rapid ligand exchange is common for simple complexes. Recent studies with multidentate ligands have revealed slowed exchange and stimulated development of ^{199}Hg NMR methods.

Although mercury has been used medicinally, the element and its compounds are generally very toxic (*see* ***Metal Ion Toxicity***). For reasons of economy, conservation, and public health, mercury use is gradually falling back to instances where no substitute can be found and recovery efforts are becoming more scrupulous.

2 GENERAL ASPECTS OF THE CHEMISTRY OF MERCURY

2.1 Prevalence and Applications

Mercury is the sixty-second most abundant element, with a terrestrial abundance of 5×10^{-5}%. Its abundance is comparable to silver and much less than either zinc or cadmium. Cinnabar (HgS) serves as the only important mercury ore, and droplets of liquid mercury are frequently found in cinnabar veins. The chloride and oxide are also found in nature, and mercury is a by-product from mining of other metals (e.g. copper, zinc, gold, silver). Volcanic activity produces mercury vapor, and the liquid condensate can sometimes be found in association with volcanic flows. Degassing of the earth's crust and oceans places thousands of tons of elemental mercury into the atmosphere each year. Coal-burning power plants, crematoria, and waste incinerators burden the atmosphere with additional elemental mercury. With an estimated residence time of at least one year in the atmosphere, Hg^0 is widely dissipated before deposition as a nonbiodegradable environmental toxin. In the oceans, Hg^{II} is the prevalent form of mercury, but it can be converted to methylmercury (CH_3Hg^+) and dimethylmercury by microorganisms. These lipid soluble compounds are biomagnified in aquatic food chains. All forms of mercury are toxic and the magnitude of the public health risk presented by mercury has spurred development of alternatives to many Hg-containing products.

Mercury and its compounds have a long and rich history. Its atomic symbol is derived from the Greek name *Hydragyrum* meaning watery silver. The English word for the element comes from the name of the Roman messenger god because of mercury's liquid mobility and 'quickness'. As early as the second millennium B.C., mercury may have been recovered and used in Egypt. Recovery of the element from its principal ore, cinnabar (HgS), by smelting in air was known in the Mediterranean region during the fifth century B.C.[1] As early as the second century B.C., alchemists are believed to have used mercury in attempts to convert base metals to gold. In the ancient world, the ink and cosmetic pigment known as vermilion came from the red color of cinnabar. Pharmaceuticals containing mercury have included diuretics, antibacterial agents, antiseptics, and laxatives. Mercury containing treatments for syphilis in the 1500 s led to the discovery of the important toxicological principle, usually credited to Paracelsus, that 'the dose makes the poison'.

Large-scale release of mercury from the earth's crust began about 500 years ago for the mining of gold and silver from Spanish America by a mercury amalgamation process.[2] Historically, the cinnabar mine near the town of Almadén in Spain has dominated global production from the mercuriferous belt between the Western Mediterranean and Central Asia. Mercury was originally smelted by placing cinnabar in a pile of brushwood and burning the wood. Modern smelting techniques (*see Extraction of the Elements*) are still based upon the same chemical reaction (equation 1). The cinnabar ore is concentrated by flotation before smelting. Mercury may also be obtained from cinnabar by roasting the ore in the presence of iron metal or calcium oxide (equations 2 and 3). The initial purification of the crude metal is by filtration, followed by oxidation using dilute nitric acid or air. This removes contaminants of more easily oxidized metals. The final step is usually distillation, taking advantage of the relatively low boiling point of the metal.

$$\mathrm{HgS(s)} + \mathrm{O_2(g)} \xrightarrow{600\,^\circ\mathrm{C}} \mathrm{Hg(g)} + \mathrm{SO_2(g)} \tag{1}$$

$$\mathrm{HgS(s)} + \mathrm{Fe(s)} \longrightarrow \mathrm{Hg(g)} + \mathrm{FeS(s)} \tag{2}$$

$$\mathrm{4HgS(s)} + \mathrm{4CaO(s)} \longrightarrow \mathrm{Hg(g)} + \mathrm{3CaS(s)} + \mathrm{CaSO_4(s)} \tag{3}$$

The industrial age prompted further increases in mercury mining. Cumulative industrial age anthropogenic global production of Hg is estimated at 0.64 million tons through 2000.[3] Diverse applications have been found for metallic mercury in the electrical industry including lamps, switches, relays, and batteries. Control instruments including thermometers, manometers, barometers, and other pressure sensing devices often use mercury in the metal form. Mercurous chloride is a component of the calomel electrode used in pH measurement and mercury cadmium telluride (MCT) (*see* ***Semiconductor Interfaces***) has become the material of choice for a broad range of infrared applications. Inorganic mercury compounds are catalysts for a variety of industrially important processes. Mercury production spiked to approximately 10 000 tons per year during World War II, in part because mercury fulminate was used as a component of detonating devices. Production peaked again in the 1960s and 1970s with discovery of the Castner–Kellner process for production of chlor–alkali (chlorine–NaOH). This process, in which liquid mercury serves as the cathode for electrolysis of brine solutions, remains the largest industrial use of mercury. During this time, mercury batteries were prevalent in which mercury (II) oxide (HgO) served as the cathode and a zinc–mercury amalgam as the anode (only Zn reacts) with a KOH electrolyte. The cell voltage is about +1.3 V, and the overall cell reaction is shown in Scheme 1. The battery has a high conversion of mass of the composite materials to energy, and there are no concentration changes during discharge since the reaction does not involve ions in solution.

Cathode:

$$\mathrm{HgO} + \mathrm{H_2O} + 2\mathrm{e}^- \longrightarrow \mathrm{Hg} + 2\mathrm{OH}^-$$

Anode:

$$\mathrm{Zn} + 2\mathrm{OH}^- \longrightarrow \mathrm{ZnO} + \mathrm{H_2O} + 2\mathrm{e}^-$$

Net:

$$\mathrm{Zn} + \mathrm{HgO} \longrightarrow \mathrm{ZnO} + \mathrm{Hg}$$

$$E^\circ = +1.3\ \mathrm{V}$$

Scheme 1

Mercury production has declined to 2000 tons annually in recent years reflecting conversion of many products and processes to less toxic Hg-free alternatives.[4] For example, the major battery manufacturers have developed mercury-free formulations for nearly every application, decreasing their mercury consumption by 99% since 1985. Pacemaker batteries are notable exceptions that, along with amalgam fillings, contribute mercury to crematoria efflux. Mercury-free membrane and diaphragm processes are available for the production of chlor–alkali, and are economically viable for new units. Mercury compounds are no longer used as antifoulants in paints, seed grain fungicides, nor slimicides in paper pulp factories. In general, mercury-free alternatives for most electromechanical applications of mercury are well established. For products dependent on the unique photoelectronic properties of mercury, designs minimizing mercury use are under development as well as recycling infrastructures.

In spite of the trend toward minimizing mercury use, novel applications are still being discovered. For example, the landmark synthesis of mercury cuprates with superconducting transition onset (T_C) higher than the boiling point of liquid nitrogen was reported in 1993 (*see* ***Superconductivity***).[5] The family of ceramic copper oxide materials based on single mercury-oxide layers in rock salt–like blocks (BaO-HgO_δ-BaO) and variable perovskite type blocks ($\mathrm{CuO_2\text{-}(Ca\text{-}CuO_2)}_{n-1}$) have a general formula $\mathrm{HgBa_2Ca}_{n-1}\mathrm{Cu}_n\mathrm{O}_{2n+2+\delta}$. The material with $n = 3$ has the record-high T_C (onset) > 133 K, which can be raised above 160 K by the application of external pressure. Furthermore, mercury-based films are good candidates for applications demanding high current density since their single blocking layer structure promotes stronger coupling between adjacent

CuO_2 layers. Reviews of the challenging issues relevant to the synthesis, structural chemistry, and properties of critical importance for these superconducting materials have been published.**[6]**

2.2 Chemical Properties

The properties of elemental mercury are summarized in Table 1. Mercury has a *Ground State* configuration of $[Xe]4f^{14}5d^{10}6s^2$ (Ground-state term: $^1S_0$), and its first three ionization energies are 1007, 1809, and 3300 kJ mol^{-1}; it does not commonly form an oxidation state (*see Oxidation Number*) higher than +2 because of its large third ionization potential. In the solid phase, Hg^0 adopts a distorted hexagonal close-packed structure (*see Close Packing*) with significant distortion. The six hexagonal coplanar mercury atoms are at a 16% greater distance than the six proximate, noncoplanar mercury atoms. This distortion from normal hexagonal close packing is the opposite of what is observed for zinc and cadmium. The metal shows limited solubility in both polar and nonpolar solvents, with a solubility in water of 6.1×10^{-6} g per 100 g at 25 °C, and a solubility in n-hexane of 2.7×10^{-7} g per 100 g at 40 °C.

It has been proposed that the contraction of the electron orbitals in mercury due to *Relativistic Effects* are important contributors to the element's unusual physical, chemical, and spectroscopic properties.**[7–9]** Some of these properties include the so-called *Inert Pair Effect*, the difficulty of oxidation of the metal, its unusually low-melting point and electrical conductivity, and the low *Enthalpy* of vaporization, which at 59.1 kJ mol^{-1} is about one-half those of cadmium (100 kJ mol^{-1}) and zinc (114 kJ mol^{-1}). Both NMR shieldings and spin–spin coupling constants with ^{199}Hg are significantly impacted by relativistic effects.**[9]**

Table 1 Properties of elemental mercury

Atomic weight	200.59
Number of natural isotopes	7
Valence configuration and ground-state term	$5d^{10}6s^2$, $^1S_0$
Ionization energies (kJ mol^{-1})	
1st	1007
2nd	1809
3rd	3300
Melting point (°C)	−38.9
Boiling point (°C)	357
Heat of vaporization (kJ mol^{-1})	59.1
Heat of fusion (kJ mol^{-1})	2.30
E°_{red} for Hg^{II}/Hg	+0.854
Radius (pm)	
Hg^{II} (6-coordinate)	116
Hg^{I} (6-coordinate)	133
Hg (12-coordinate)	151
Density (g cm^{-3} at 20 °C)	13.546
Vapor pressure (mm Hg at 20 °C)	2×10^{-3}
Solubility (g per 100 g H_2O at 25 °C)	6×10^{-6}
Pauling electronegativity	2.00
Ohmic resistance (μΩ cm at 20 °C)	95.8
Crystal structure	hcp (distorted)

Mercury has a high density (13.546 g cm^{-3} at 20 °C) and a wide liquid range (mp −38.9 °C; bp 357) over most of which its volume expands uniformly. In addition, the high surface tension of mercury keeps it from sticking to glass surfaces. These properties have contributed to its use in an impressive number of laboratory applications. For a metal, mercury has an unusually high electrical resistivity or specific resistance (95.8 μΩ cm), and this property enables it to be used as an electrical standard. Of all the common metals, only bismuth has a higher resistivity.

Mercury readily dissolves or forms alloys (*see* ***Alloys***) with many metals, including Ag, Au, Na, and Zn, a process known as amalgamation. Mercury amalgams find applications as reducing agents in chemical synthesis (usually Zn or Na amalgam) and in the recovery of Au and Ag from their ores in metallurgy. Perhaps, the most famous historical case is Spain's use of its cinnabar deposits to extract silver from New World mines in the 1500 s. Amalgamation is presently used in the Amazon basin for what has been described as the largest gold rush of the twentieth century.**[10]** Alchemists used amalgams in their search for the transmission of base metals to Au and Ag. Since mercury does not amalgamate iron, iron flasks can be used to store the metal or amalgams. Some amalgams (Hg_2Au, Na_2Hg) exist as stoichiometric compounds with discrete crystalline structures. The solid-state chemical aspects of the six thermodynamically stable binary Na–Hg solids has been reviewed recently with an emphasis on the temperature-dependent polymorphic transitions and their thermodynamics.**[11]**

Mercury is a relatively nonreactive metal and is nobler than its lighter congeners zinc and cadmium; this is reflected in its positive reduction potential. It does not react with HCl under any conditions, but it is oxidized to Hg^{II} by concentrated HNO_3 or hot concentrated H_2SO_4 with production of nitrogen and sulfur oxides, respectively. Cold dilute HNO_3 reacts slowly with Hg^0 to form mercury(I) nitrate, $Hg_2(NO_3)_2$. The metal does not generally react with bases, but does react with aqueous ammonia in the presence of O_2 to form Millon's base, $Hg_2NOH{\cdot}2H_2O$.

2.3 Spectroscopic Properties

Traditionally, spectroscopic studies of mercury compounds have been limited. As a d^{10} metal ion, Hg(II) lacks any *Crystal Field Stabilization Energy*, *Paramagnetism* or d–d absorption spectra (*see d–d Transitions*). Similarly, the $Hg_2{}^{2+}$ ion can be fingerprinted by *Infrared Spectroscopy*, but other spectroscopic methods commonly used to characterize metals are inapplicable. However, since mercury is diamagnetic (*see Diamagnetism*) in the most common oxidation states, its complexes with organic ligands are readily characterized by multinuclear magnetic resonance.**[12]**

Table 2 NMR properties of the magnetic isotopes of mercury

Isotope	Natural abundance (%)	Spin, I	Magnetic moment, μ/μ_N	Magnetogyric ratio, γ	Quadrupole moment, Q (10^7 rad T^{-1} s^{-1})	NMR frequency, Ξ (MHz)	Relative receptivity, D^c
^{199}Hg	16.87	1/2	0.87621937	4.8457916	–	17.910323	5.73
^{201}Hg	13.18	3/2	−0.7232483	−1.788769	0.385	6.611400	1.13

Furthermore, over the last decade, considerable advances in the characterization of mercury compounds by mercury NMR have been made. The properties of the two naturally occurring NMR-active isotopes of mercury, ^{199}Hg and ^{201}Hg, are listed in Table 2.**[13]** Since ^{201}Hg has a large quadrupole coupling constant, efficient relaxation mechanisms leading to severe broadening of NMR transitions and averaging of spin–spin couplings to zero make it generally unsuitable for NMR studies. For example, even though mercury occupies a site of *Tetrahedral* symmetry in $K_4[Hg(CN)_4]$, its solid-state ^{201}Hg NMR signal linewidth was three times larger than the ^{199}Hg signal.**[14]** On the other hand, ^{199}Hg is one of the relatively few metals with a high natural abundance (16.87%) spin $I = 1/2$ isotope that can be exploited for compound characterization. The sensitivity of this nucleus is five times higher than ^{13}C. ^{199}Hg has a relative frequency of 17.9 MHz when ^{1}H has a frequency of 100 MHz. Thus, ^{199}Hg is a very accessible nucleus on most NMR spectrometers. The chemical shift range for ^{199}Hg extends over 5000 ppm, exhibiting extraordinary sensitivity to changes in the coordination environment. The ^{199}Hg chemical shift associated with coordination environments composed of a single ligand type can range more than 1000 ppm.**[15]** In the spectra of other nuclei, satellite peaks reflecting spin–spin coupling to one ^{199}Hg nucleus are 1/5 the size of the main resonance. Coupling to the mercurous ion or any other pair of magnetically inequivalent ^{199}Hg nuclei produces satellites that are each one-quarter the size of the main resonance. Several reviews of the ranges of observed mercury chemical shifts and ^{199}Hg–^{1}H coupling constants have been published.**[15–18]**

The primary reference material for ^{199}Hg NMR spectroscopy is dimethylmercury(II). However, a lethal accident caused by the cutaneous absorption of a few drops of this substance in 1996 cautions against its routine experimental use.**[19]** Calculation of the frequency at 0 ppm for ^{199}Hg from the measured frequency of 0 ppm for protons in the sample is a prudent alternative with modern spectrometers.**[20]** For solid-state NMR, hexakis(dimethylsulphoxide)mercury(II) trifluoromethanesulphonate, $\delta(^{199}\text{Hg}) = -2313$ ppm,**[21]** is a suitable secondary standard. Its high symmetry *Octahedral* coordination environment results in small chemical shift anisotropy and short H–Hg separations lead to high $^1\text{H} \rightarrow {}^{199}\text{Hg}$ polarization transfer efficiency.

Solution-state NMR studies of mercury complexes are most meaningful when taken under slow-exchange conditions. Fast-exchange spectra involving equilibria between several species in solution are common due to the relatively high lability of ligands in mercury complexes. Tridentate coordination appears to be necessary but not sufficient for slow ligand exchange in solution. Furthermore, isolation of a bis-tridentate chelate of (**1**) and $Hg(ClO_2)_4$ that had C_2 symmetry in the solid-state but a single environment for each ligand proton when dissolved in the recrystallization solvent indicates the occurrence of dynamic racemization processes.**[22]** This process was *Intramolecular* since most of the ligand protons remained ^{199}Hg-coupled. The stereochemical nonrigidity of tetrahedral Hg^{II} complexes has also been reviewed.**[23]** In the most spectacular demonstration of slow ligand exchange for Hg^{II} yet reported, as many as five complexes of the sterically demanding multidentate ligand (**2**) were shown to coexist in slow-exchange on the proton chemical shift timescale in acetonitrile-d_3.**[24]**

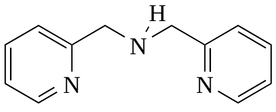

(**1**)

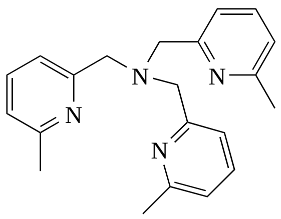

(**2**)

Although the majority of the reported values for heteronuclear coupling with ^{199}Hg are associated with alkylmercurials,**[15]** (**2**) has been used to detect $J(^{199}\text{Hg}^1\text{H})$ between nuclei as many as five bonds apart**[24]** and $J(^{199}\text{Hg}^{13}\text{C})$ over as many as three bonds were detected in the Hg^{2+} complexes of (**3**).**[25]** Indirect nuclear spin–spin coupling constants $^nJ(^{199}\text{Hg-X})$ were reviewed in 1992.**[15]** The additivity of coupling constants is generally accepted, and chelate rings provide multiple coupling paths with the possibility of significant enhancements if contributions are of the same sign. Solution-state proton NMR of isostructural Cd^{II} and Hg^{II} complexes of (**1**) and (**3**) revealed larger and longer-range couplings in Hg^{II} complexes,**[26]** consistent with significant relativistic effects.**[9]** Spin–spin coupling has also been reported for mercurous complexes, with $^1J(^{199}\text{Hg-}^{199}\text{Hg}) > 200\,000$ for asymmetric coordination by *Crown Ethers*, the largest scalar couplings ever recorded.**[27]** The first example of slow-exchange on the $J(^{199}\text{Hg}^1\text{H})$ timescale for a mercurous complex was recently reported for $[Hg_2(\mathbf{2})_2](ClO_4)_2$ in acetonitrile-d_3 solution.**[28]** The methylene

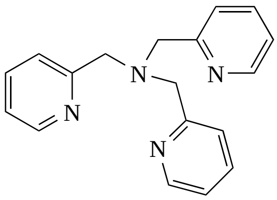

(**3**)

protons of (**2**) were coupled to both metal centers with $^{3,5}J(^{199}\mathrm{Hg}^{1}\mathrm{H}) = 22\,\mathrm{Hz}$ and $^{4,6}J(^{199}\mathrm{Hg}^{1}\mathrm{H}) = 13\,\mathrm{Hz}$.

Over the last decade, developments in high-resolution NMR techniques for solids have been extended to mercury nuclei.[29] Solid-state NMR studies provide more definitive characterization of mercury complexes since their interpretation is not compromised by exchange processes or solvent coordination. While medium effects on spectra are not absent in the solid-state, they are generally more defined and therefore studied more readily. Furthermore, the chemical shift anisotropy, coupling constant anisotropy, and dipolar coupling constants obtained by solid-state NMR provide an additional probes into structure and bonding. Comparison of solid-state NMR spectra of structurally characterized complexes with solution-state NMR spectra promises to reveal significant differences between the solution and solid-state structures.

2.4 Biological Properties

Mercury is the only group 12 member without a known beneficial biological role.[30] Several references discuss the safety precautions and hazards of working with the various forms of mercury.[31,32] The vapor pressure of Hg at 25 °C is high, 1.9×10^{-3} mm; since this is many times the LD_{50}, air saturated with mercury vapor is highly toxic and liquid mercury must only be used in a well-ventilated area and stoppered when not in use. Spills must be collected and removed immediately to prevent prolonged exposure. A common procedure involves the absorption of mercury by a small quantity of elemental sulfur. Even small amounts of mercury can exert potent, detrimental effects. The use of slaves and criminals to mine mercury in ancient times indicates that the toxic properties of mercury were already known. Historically, mercury was used in the production of felt hats, causing hatters of the nineteenth century to exhibit the effects of inorganic mercury poisoning: nervous tremors, loosening of the teeth, mouth soreness, and neurological disorders. The expression ‘mad as a hatter’ is said to have come from the effects of acute mercury poisoning. Alfred Stock, a noted chemist, was a temporary victim of mercury poisoning from the pools of mercury often present around his laboratory vacuum lines. Over 50 fatalities and numerous neurological impairments in a small fishing village on the Minamata Bay of Japan have been attributed to the biotransformation of $\mathrm{Hg}^{\mathrm{II}}$ in industrial effluent to methylmercury ($\mathrm{CH_3Hg^+}$). Bioaccumulation of alkyl mercurials in the aquatic food chain presents a serious risk to the world’s food supply.

Mercury forms strong *Covalent Bonds* in biological systems and competes with physiologically essential metals for binding to organic molecules, resulting in high toxicity. In all its forms, mercury is a cumulative poison because of its slow elimination from the body. While metals cannot be destroyed metabolically, many bacteria are able to convert organomercurials and $\mathrm{Hg}^{\mathrm{II}}$ to less deleterious and volatile Hg^{0}.[33] The most common bacterial resistance mechanism uses specific proteins for mercuric ion transport (MerT and MerP), organomercurial cleavage (MerB or organomercurial lyase) and mercuric ion reduction (MerA or mercuric ion reductase), which are transcriptionally regulated by a $\mathrm{Hg}^{\mathrm{II}}$-activated metalloregulatory switch (MerR). In eukaryotic organisms, sequestration by specific, cysteine-rich enzymes (phytochelatins in plants and metallothioneins in animals), and excretion are the dominant routes for heavy metal removal. The oxidation of elemental mercury to $\mathrm{Hg}^{\mathrm{II}}$ in animals is mediated by catalase. Brain uptake of elemental mercury and subsequent oxidation can lead to mercury accumulation since $\mathrm{Hg}^{\mathrm{II}}$ does not readily cross the blood–brain barrier. Mercury(I) salts disproportionate into Hg^{0} and $\mathrm{Hg}^{\mathrm{II}}$ within organisms. Furthermore, $\mathrm{Hg}^{\mathrm{II}}$ can be reduced to Hg^{0} internally. Treatment for mercury poisoning first involves removal from the exposure source. Metal-mobilizing chelating agents with greater affinity than endogenous ligands may be used to increase water solubility and excretion by the kidney. Standard treatment for mercury poisoning has been dimercaprol (British Antilewisite, BAL, (**4**)). Recently, a challenge test with Dimaval (2,3-dimercapto-1-propane sulfonic acid, sodium salt, DMPS, (**5**)) was found to have high sensitivity for low level mercurialism.[34] DMPS is used for treatment of mercury poisoning by physicians in Europe but is not FDA approved for use in the United States even though it is 300 times less toxic and neither crosses the blood–brain barrier nor redistributes mercury to the brain like BAL.

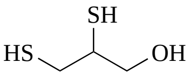

(**4**)

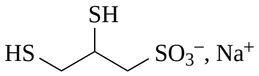

(**5**)

3 MERCURY(I): COMPOUNDS AND COORDINATION CHEMISTRY

3.1 General Aspects

In contrast to zinc and cadmium, mercury has a stable monovalent state, and thus exhibits an appreciable chemistry as Hg^{I}. Both Hg^{I} and $\mathrm{Hg}^{\mathrm{II}}$ are stable in aqueous environments, and Hg^{I} can be prepared by the reduction of $\mathrm{Hg}^{\mathrm{II}}$ in

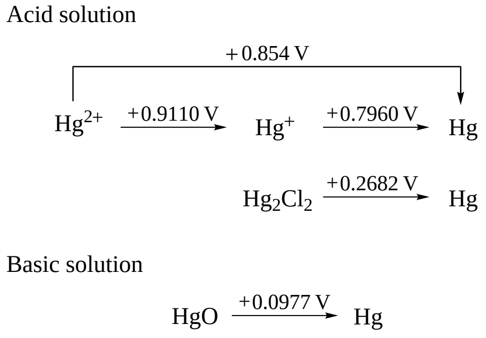

Scheme 2

an aqueous acidic environment. The Latimer diagram (*see Latimer Diagrams*) for mercury is shown in Scheme 2.

A summary of the thermodynamic properties of elemental mercury and its compounds has appeared.[35] Although Hg^I is considered a class b or 'soft' metal ion (*see Class A & Class B Behavior* and ***Hard & Soft Acids and Bases***), its coordination behavior suggests that it functions as a harder acid than the divalent ion. Advanced texts have discussed the chemistry of the element and its compounds.[36,37]

There are no compounds containing the simple Hg^I ion. Instead, a metal-to-metal σ-bond produces the $Hg_2{}^{2+}$ *Cation* through the overlap of the 6s orbitals of two Hg^I ions and occupation of the bonding MO by two electrons. *Disproportionation* of the mercurous ion into Hg^0 and Hg^{II}, as shown in equation (4), has an *Equilibrium Constant* of 1.14×10^{-2} based on standard potentials. Hence, the mercurous ion is stable, but depletion of free Hg^{2+} by complexation or precipitation will result in disproportionation.

$$Hg_2{}^{2+} \rightleftharpoons Hg\,(l) + Hg^{2+} \tag{4}$$

$$E^\circ = -0.115\text{V};\ K = \frac{Hg^{2+}}{Hg_2{}^{2+}} = 1.14 \times 10^{-2}$$

Reviews listing tables of Hg–Hg bond lengths[38–40] (*see Bond Length*) and Hg–Hg stretching frequencies in a series of mercurous compounds have appeared, from which selected values are given in Table 3. The bond distances fall in the range of 245 to 269 pm, while the stretching frequencies range from 113 to 207 cm^{-1}. For the mercury (I) halides, there is an inverse correlation between bond length and stretching frequency, which has been related to the *Electronegativity* of the halogen.

Table 3 Hg–Hg bond lengths and Hg–Hg stretching frequencies in selected mercury(I) compounds

Compound	Hg–Hg (pm)	Hg–Hg (cm^{-1})
Hg_2F_2	251	185.9
Hg_2Cl_2	253	166.5
Hg_2Br_2	249	132.2
Hg_2I_2	269	112.5
$Hg_2(NO_3)_2{\cdot}2H_2O$	254	179.8
$Hg_2(ClO_4)_2{\cdot}2H_2O$	250	181.6
Hg_2SO_4	250	172.2
$Hg_2(BrO_3)_2$	251	183

3.2 Mercury(I) Halides

The four mercury(I) halides have a linear structure X–Hg–Hg–X, the two most common being Hg_2Cl_2 and Hg_2F_2. All the halides are somewhat light sensitive, especially the iodide. The chloride, bromide, and iodide have very low solubility in water, but the fluoride decomposes upon contact with water. Reaction of mercury(I) halides with halogens or oxidizing acids leads to the oxidation of the metal to Hg^{II}. All four halides are oxidized to form mercury(II) oxyhalides. The addition of aqueous ammonia leads to the formation of a black solid, which contains finely divided elemental mercury and a complex mixture of mercury(II) compounds including $HgNH_2Cl$, $Hg_2NCl{\cdot}H_2O$, and $HgCl_2{\cdot}2\,NH_3$. The properties of the four mercury(I) halides are summarized in Table 4.

The chemistry of mercury(I) fluoride, Hg_2F_2, has been reviewed.[41] This yellow solid is prepared by the reaction of Hg_2CO_3 (itself precipitated from aqueous $NaHCO_3$ and $Hg_2(NO_3)_2$) with 40% aqueous HF. It decomposes in water to produce Hg^0 and HgO, and heating of the compound above 570 °C results in a disproportionation to Hg^0 and HgF_2. The higher melting point relative to the other halides indicates a greater *Ionic Character*.

Even though Hg_2Cl_2 is white, its trivial name of calomel is derived from two Greek words meaning 'beautiful' and 'black'. It is possible that the name comes from the black color of elemental mercury formed by the reaction of Hg_2Cl_2 with ammonia. Calomel has been known for many centuries, and it was the first compound known to have a metal–metal bond. It is precipitated from aqueous solutions containing $Hg_2(NO_3)_2$ and chloride ions. All other mercury(I) halides can be prepared similarly, except the fluoride. The Hg–Hg bond length in the compound is 253 pm, with an Hg–Hg stretching frequency of 166.5 cm^{-1}. It was used as a treatment for syphilis before the advent of penicillin, and is the material present in the standard calomel reference electrode.

The bromide and iodide, as well as pseudohalides (*see Pseudohalide*) such as the thiocyanate and azide, all have the general formula Hg_2X_2. Mercury(I) bromide is a white solid that sublimes at 345 °C, while mercury(I) iodide is a yellow solid that sublimes at 140 °C. The crude iodide

Table 4 Halides of mercury(I)

Compound	Color	Mp (°C)	K_{sp}
Hg_2F_2	Yellow	d > 570	Decomposes in water
Hg_2Cl_2	White	383, sublimes	1.1×10^{-18}
Hg_2Br_2	White	345, sublimes	1.3×10^{-22}
Hg_2I_2	Yellow	140, sublimes	4.5×10^{-29}

sometimes appears green because of the presence of fine particles of Hg^0. Mercury(I) iodide reacts with excess iodide ion to disproportionate into Hg^0 and $[HgI_4]^{2-}$. The S-bound mercury (I) thiocyanate, $Hg_2(SCN)_2$, formed by *Metathesis* between mercury(I) nitrate and thiocyanate ion, is very light sensitive (*see Ambidentate Ligand*). The azide can be prepared by a similar metathesis reaction using aqueous azide or HN_3. The colorless crystalline material is very shock sensitive and heat sensitive and explodes violently. The reaction between cyanide ions and mercury(I) results in a disproportionation, forming $Hg(CN)_2$ and Hg^0.

3.3 Mercury(I) Oxy Salts

Numerous salts containing oxoanions (*see Oxoanion*), including the nitrate, perchlorate, chlorate, bromate, iodate, and sulfate, are known. Of these, only the nitrate, chlorate, and perchlorate demonstrate a fair degree of water solubility and these serve as a source of insoluble mercury(I) salts through metathesis reactions in water. The nitrate crystallizes as a dihydrate, $Hg_2(NO_3)_2{\cdot}2H_2O$ (*see Hydrates*), which contains linear O–Hg–Hg–O linkages. The nitrate is stable in acid solution; at higher pH it precipitates as $Hg(OH)(NO_3)$.

Mercury(I) is assumed to be of minor importance as an environmental contaminant due to the instability of Hg^I complexes with common atmospheric ligands (e.g. OH^- and $SO_3{}^{2-}$, etc.). However, reliable trace analytical techniques for Hg^I in the gaseous or aqueous phase are unavailable.

3.4 Mercury(I) Complexes

Complexes of Hg^I are considerably fewer than those of Hg^{II}; the tendency of the ion to disproportionate leads to difficulties in preparation. Decreasing the concentration of Hg^{II} by complexation or precipitation favors disproportionation, as is the case for ligands such as S^{2-}, OH^-, CN^-, NH_3, acac, and thioethers; very few mercury(I) complexes containing these species have been isolated. Similarly, bulky ligands that thwart intermolecular disproportionation processes and form low solubility Hg^I complexes of type $[Hg_2L_2]^{2+}$ can be prepared from Hg^{II}.[28,42] The Latimer diagram for mercury (Scheme 2) reveals that very few oxidizing agents are capable of oxidizing Hg^0 only to Hg^I.

A review of 30 structurally characterized complexes of mercury(I) with organic ligands has been published.[39] Complexes containing nitrogen-donor ligands (*see* ***Ammonia & N-donor Ligands***), principally weakly basic heterocyclic amines (anilines, pyridines, and phenanthroline), commonly have the compositions $[Hg_2L_2]X_2$ or $[Hg_2L_4]X_2$ with mercury coordination numbers of two and three, respectively. Asymmetric coordination is also possible as in $[Hg_2(phen)](NO_3)_2$, where both nitrogens of phenanthroline are bound to one mercury atom. Oxygen-donor complexes are also known with DMSO, polyphosphates, dicarboxylates, and group 15 oxides, including Ph_3PO and Ph_3AsO (*see* ***Water & O-donor Ligands***). These complexes exhibit a linear O-Hg-Hg-O structure. Recently, complexes $[Hg_2(\mathbf{6})_2(Me_2SO)(\mu\text{-}Me_2SO)](O_3SCF_3)_2$ and $[Hg_2(\mathbf{6})(\mathbf{7})(Me_2SO)](O_3SCF_3)_2$ were characterized by X-ray crystallography and ^{199}Hg NMR.[27] Asymmetric coordination permitted detection of $^1J(^{199}Hg^{199}Hg) = 220\,300$ and 284 100 Hz, respectively, the largest scalar couplings ever reported.

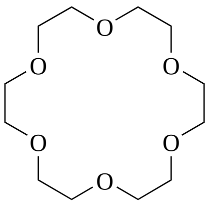

(**6**)

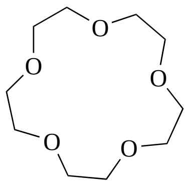

(**7**)

3.5 Mercury Polycations of Lower Oxidation States

A number of salts that contain polycations of mercury in oxidation states less than +1 are known. These lower oxidation state cations are typically generated in molten salt media but are also found in natural minerals. For example, salts containing the polycation $Hg_3{}^{2+}$ (**8**) in the salt $Hg_3(AlCl_4)_2$ can be prepared in molten salt media (Hg, $HgCl_2$, $AlCl_3$). Here, the oxidation state of the mercury is $+2/3$. The same cation, as well as $Hg_4{}^{2+}$ ($Hg = +1/2$) (**9**), can be generated using the correct stoichiometric equivalents of AsF_5 in liquid SO_2. The compound $Hg_4(AsF_6)_2$ is red while $Hg_2(AsF_6)_3$ is orange. A third compound, $Hg_2(AsF_6)_2$, can also be isolated from these reactions. Not surprisingly, it contains the $Hg_2{}^{2+}$ cation and is colorless. Some of these cations can also be prepared in HSO_3F *Superacid* media. Under certain conditions, the reaction of Hg and AsF_5 in liquid SO_2 can also produce a nonstoichiometric compound (*see Nonstoichiometric Compounds*) of the formula $Hg_{2.82}(AsF_6)_{0.94}$, which consists of a ccp array of fluoride ions with infinite chains of mercury atoms. The compound is an anisotropic superconductor. Mercury NMR has proven useful in the study of the previously mentioned mercury polycations in low oxidation states.

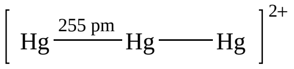

(**8**)

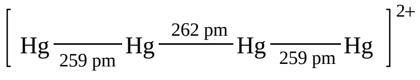

(**9**)

The structures of 13 mixed-valence compounds containing Hg_n groups ($n = 2$ or 3), in which the oxidation state of the mercury atoms is lower than +2, and Hg^{2+} cations have been reviewed.[39] Most of these compounds contain the mercurous ion. However, the first mixed-valence compound characterized by X-ray diffraction was the synthetic analog of the rare mineral terlinguaite $Hg_4O_2Cl_2$. Unusual triangular Hg_3 clusters with Hg–Hg bond lengths of 253 pm and mercury atoms with a formal oxidation state +4/3 were observed. A limited variety of additional compounds containing Hg triangles are known, with Hg–Hg distances of 261–344 pm.[40]

4 MERCURY(II): COMPOUNDS AND COORDINATION CHEMISTRY

4.1 General Aspects

Motivations to investigate the coordination chemistry of Hg(II) include improved understanding of its interactions in physiological systems and development of ligands with potential for selective coordination. Solvent extraction is potentially an effective and energy-saving technique for the recovery of mercury from industrial wastes; however, the complex syntheses of selective extractants and recoverability issues have thus far restricted commercial viability. Recent efforts relying on novel structural modifications of calixarene and crown ether, thiaether and azaether macrocycles have been reviewed.[43] Structural comparisons with other members of the group 12 triad are also common.

Hg^{2+} is about the same size as Ca^{2+}, but it is a much more strongly polarizing ion, which results in greater covalency. Interestingly, Hg^{2+} generally forms stronger bonds with S-, N- and P-ligands than any other divalent metal ion, yet undergoes extraordinarily rapid ligand exchange. The large diameter of Hg^{II}, its ability to form complexes of several different coordination numbers with the same ligand type, and its lack of strong coordination geometry preferences favor associative exchange processes. Although complexes of Hg(II) with monodentate ligands seem to favor linear and tetrahedral geometries, the binding constraints of multidentate ligands have expanded the number of accessible geometries. The coordination chemistry of the group 12 triad has been reviewed annually since 1994.[44–52]

The softness of Hg^{2+} makes it a prototypical class b acceptor. As noted, the ion has a strong tendency to form covalent bonds rather than ionic bonds. Its complexes can be highly colored owing to the presence of *Charge Transfer* bands because of the highly polarizing Hg^{2+} cation. The decreased shielding power of the 14 4f electrons and relativistic effects are the source of the large polarizing ability of Hg^{2+}.

A collection of well-proven syntheses for standard mercury compounds in general use synthetically has been published.[53] Mercury(II) forms both a hydride, HgH_2, and a carbide, HgC_2. These compounds are not stable and decompose rapidly, the carbide explosively.

4.2 Mercury(II) Halide and Pseudohalide Complexes

All four mercury(II) halides are known, and their properties are listed in Table 5. All can be prepared by the direct combination of the appropriate halogen with mercury metal. Except for the fluoride, which has bonds that are predominantly ionic in character, they are characterized by relatively low-melting and boiling points and display surprising solubility in organic solvents such as acetone. Their coordination chemistry has been reviewed.[54] A summary of the structural features of the crystalline mercury(II) halides is given in Table 6.

Mercury(II) fluoride, HgF_2, has the highest melting and boiling point of the mercury(II) halides due to the high degree of ionic character in the Hg–F bonds. It is prepared by the reaction of fluorine gas and Hg^0, and readily hydrolyzes into HgO and HF. It exists in the cubic fluorite structure with Hg–F distances of 240 pm.

Mercury(II) chloride, $HgCl_2$, has a linear structure with significant covalent character. It has a much higher solubility in organic solvents such as methanol (50 g per 100 g at 25 °C)

Table 5 Halides of mercury(II)

Compound	Color	Mp(°C)	Bp(°C)	Solubility (g per 100 g H_2O at 20 °C)
HgF_2	White	d > 645	–	Decomposes
$HgCl_2$	White	280	303	6.6
$HgBr_2$	White as solid, Yellow as liquid	238	318	0.62
HgI_2	Red, yellow	257	351	6×10^{-3}

Table 6 Structural information on crystalline mercury(II) halides

Compound	Crystalline structure, description	Distances of X atoms around Hg
HgF_2	Cubic, fluorite	8 F at 240 pm
$HgCl_2$	Orthorhombic, linear	2 Cl at 225 pm; 2 Cl at 338 pm; 2 Cl at 346 pm
$HgBr_2$	Orthorhombic, distorted O_h	2 Br at 248 pm; 4 Br at 323 pm
HgI_2 (red)	Tetragonal, distorted tetrahedral	4 I at 278 pm
HgI_2 (yellow)	Orthorhombic, distorted O_h	2 I at 262 pm; 4 I at 351 pm

and acetone (55 g per 100 g at 25 °C) than in water. In the solid-state, the Hg–Cl bond length is 225 pm. Historically, $HgCl_2$ has been referred to as 'corrosive sublimate', and small quantities have been used as an antiseptic. However, it is also highly toxic because of its large water solubility.

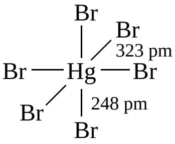

(**10**)

The heavier halides (X = Cl, Br, I) can also be prepared by precipitation from aqueous $Hg(NO_3)_2$ and the halide. The solubility of the mercury(II) halides decreases with increasing molecular weight, and the iodide is highly insoluble. Although the crystalline bromide is colorless, it produces a yellow liquid upon melting. Crystalline $HgBr_2$ (**10**) contains two short Hg–Br distances (248 pm) and four long distances (323 pm). This distortion from octahedral stereochemistry is observed in many mercury(II) compounds. In the vapor phase, the three heavier halides exist as discrete linear molecules with the following bond lengths: Hg–Cl, 228 pm; Hg–Br, 240 pm; Hg–I, 257 pm.

Two mercury(II) iodides exist: the yellow form is the kinetic product and the red is the thermodynamic product from the reaction between Hg^{II} and I^-. Both iodides have very low solubility in water. The red form consists of Hg^{2+} ions in tetrahedral holes in a ccp array of iodide ions with Hg–I distances of 278 pm. The red HgI_2 consists of a layer structure with HgI tetrahedral linked at the apex. Progress in growing single crystals of this form for use at room temperature as X-ray and gamma-ray detectors, as well as photocells with a wide variety of uses, has been reviewed.[55] The yellow HgI_2 is octahedrally coordinated with two short Hg–I distances (262 pm) and four longer ones (351 pm), similar to the observed $HgBr_2$ structure. Reaction of mercury with excess KI forms K_2HgI_4, and reaction of the metal with zinc(II) iodide forms the red HgI_2. Above 126 °C, the red form converts to the less dense yellow form. Evidence for a third metastable form, an orange HgI_2 with Hg–I distances of 268 pm, has been presented.[56]

Addition of excess iodide to the insoluble HgI_2 results in the formation of soluble mercury iodo complex $[HgI_3]^-$, with a trigonal planar structure. The ion is solvated in water and converts to a tetrahedral structure. Further, addition of I^- leads to tetrahedral $[HgI_4]^{2-}$. Reaction of iodide salts with Hg^0 can be used to produce mercury iodo complexes. Other halide and pseudohalides also form $[HgX_3]^-$ and $[HgX_4]^{-2}$. The tetrahalo anions (*see Anion*) are usually tetrahedral, while the trihalo ions readily add solvent molecules to form distorted tetrahedral or *Trigonal Bipyramidal* structures.

The 17 known chloromercury anions of form $Hg_xCl_y{}^{n-}$ ($x = 1–6$; $y = 2–10$; $n = 1–6$) have been reviewed.[57] These anions exhibit diverse configurations that cannot be determined from the analytical stoichiometry, and in many cases multianion combinations are observed. As a result, single-crystal diffraction studies are critical to definitive structural assignment. Many chloro complexes of mercury(II) are based upon distorted $HgCl_6$ units. These units are then linked into chains or layers by sharing edges or corners.

Mercury(II) cyanide, which exists as discrete linear $Hg(CN)_2$ molecules, forms 1:2 and 1:1 adducts (*see Addition Compound*) with soft ligands such as phosphines and thioethers. The cobalt(II) complex $CoHg(SCN)_4$, commonly used as a calibrant in *Magnetic Susceptibility* studies, exhibits a diamond-like structure in which the thiocyanate ligands link the Co and Hg ions into a three-dimensional framework. Furthermore, the Co ion is surrounded by a tetrahedron of four nitrogen atoms while the Hg ion is surrounded by a tetrahedron of four sulfur atoms. Mercury fulminate, $Hg(ONC)_2$, is used as a detonator. The principal component of a child's toy dating from 1865, 'Pharaoh's serpent eggs', is $Hg(SCN)_2$. When the $Hg(SCN)_2$ pellet is ignited, an ash is produced, which curves up into the air as it expands, resembling the movements of a snake. The structure of $Hg(SCN)_2$ (**11**) consists of two short Hg–S bonds (232 pm) and four long Hg–N bonds (281 pm) in a distorted octahedral arrangement around the central metal atom. All the thiocyanate ligands bridge mercury atoms (*see Bridging Ligand*). A highly sensitive spectrophotometric method for the measurement of trace amounts of mercury in solution based upon a colored complex of mercury(II), thiocyanate, and Rhodamine B has recently been reported.[58] Mixed halide and pseudohalide complexes such as [HgCl(SCN)] are known; typically they have linear structures.

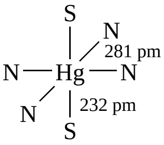

(**11**)

Mercury(II) halides form solvate complexes with a large number of polar organic solvents including methanol, pyridine, acetonitrile, and 1,4-dioxane. These complexes are usually polymeric and octahedral with doubly bridging halides. There are also adducts of the general formula HgX_2L, where X is typically Cl, Br, or I, and L is a soft ligand such as a phosphine, dithiocarbamate, or thioether, a heterocyclic amine, or an As, Se or Te donor. Compounds such as $HgI_2(PPh_3)_2$ display tetrahedral structures with the general formula ML_2X_2 (**12**). Some monomeric and polymeric complexes that do not contain bridging halide groups are also observed, as well as dimeric halogen bridged tetrahedral complexes of the general type $LXHgX_2HgLX$ (**13**). Additionally, some five-coordinate species of the type HgX_2L, where L is a polydentate amine such as dien, are known. Most of these, such as $HgBr_2\cdot$ bipy (**14**), are trigonal bipyramidal, but a few, such as $HgCl_2\cdot$ diphenyl sulfoxide (**15**), are *Square Pyramidal*. Mercury(II) forms some six-coordinate halide complexes with distorted octahedral structures having short axial and long equatorial bonds.

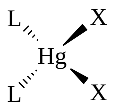

(**12**)

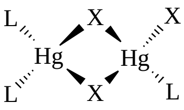

(**13**)

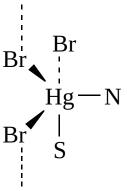

(**14**)

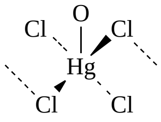

(**15**)

Mercury(II) is known to accelerate *Ligand Substitution* reactions of complexes of formula ML_5X (M = Rh, Cr, Co, Ru; L = H_2O or NH_3; X = bridging halide or pseudohalide), probably by forming an intermediate with a halide bridge between Hg^{II} and M.

4.3 Mercury(II) Oxides, Sulfides, and Other Chalcogenides

Mercury(II) oxide, HgO, is of historical significance since its pyrolysis by Priestley in 1774 led to the discovery of oxygen. Crystalline HgO is orthothombic, and the structure of HgO consists of almost linear O–Hg–O bonds (Hg–O bond length = 205 pm; O–Hg–O bond angle = 180°; Hg–O–Hg bond angle = 107°). These linear Hg–O bonds form a zigzag chain structure (**16**). Like HgI_2, HgO exists in both a red and a yellow form. In this case, however, the red form is prepared by the pyrolysis of $Hg(NO_3)_2$ or by the oxidation of Hg^0 by O_2 at elevated temperatures. The yellow form is precipitated from Hg^{2+} solution by aqueous OH^-. The color difference between the two mercury oxides is due to particle size and not a structural difference. The hydroxide, $Hg(OH)_2$, has never been isolated. The reaction between Hg metal and oxygen is kinetically slow and is usually carried out at 300 to 350 °C. Above 400 °C, however, HgO decomposes into Hg^0 and oxygen. As seen from the reduction potentials (Scheme 2), the reduction of mercury(II) in base, in the form of HgO, occurs less readily than in acidic solutions. Basic solutions therefore stabilize mercury(II) more than acidic solutions do. A less common hexagonal form of HgO that is isostructural with red HgS is known; it is obtained by heating K_2HgI_4 in aqueous NaOH at 50 °C. Mixed metal oxides of mercury(II), such as $Hg_2Nb_2O_7$, also contain linear O–Hg–O linkages, and many have pyrochlore structures.[59]

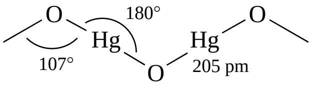

(**16**)

The first systematic structure analysis of mercury oxosalts, salts containing oxygen atoms that are not part of an acid residue, was recently published.[60] Structural description in terms of oxocentered $[OHg_4]$ tetrahedra with nonequivalent Hg–O bonds linked by both vertices and edges efficiently illustrated the unique structures and interrelationships of these compounds.

Mercury(II) suflide, HgS, exists in both zinc blende and rock salt structures. The red cinnabar ore exhibits the rock salt form, which consists of Hg–S helical chains, resulting in a very large optical rotatory power for the crystal. There are three pairs of Hg–S bond distances: 236, 301, and 330 pm. The S–Hg–S bond angles are 172°, and the Hg–S–Hg bond angles are 105°. A less common zinc blende form, the black metacinnabar, is converted to the more stable rock salt structure upon heating. The denser red form is favored at higher pressures. A black precipitate of HgS is produced by the addition of H_2S or sulfide ion to a solution containing Hg^{2+} ions. This compound is highly insoluble ($K_{sp} = 1 \times 10^{-52}$), but the chemistry involved is more complex than a simple ionic precipitation since substantial hydrolysis of both mercury(II) and sulfide ion occurs, and complex polysulfides are formed.[61] Black HgS is an inert material that only very strong concentrated acids such as HBr, HI, and aqua regia will dissolve.

The other chalcogenides (*see Chalcogens*) mercury(II) selenide, HgSe and telluride, HgTe, can be synthesized directly from the elements. Both compounds have a zinc blende structure and function as semiconductors. The selenide is violet–black, and the telluride is black.

4.4 Mercury(II) Oxy Salts

The nitrate, perchlorate, and sulfate salts of mercury(II) are all known. Since mercury(II) is a weak acid, hydrolysis of the ion to form hydroxo-bridged polycations is strongly favored but is inhibited at low pH. In acidic solutions, species such as hydrated mercury(II) and $[Hg(NO_3)]^+$ are formed. The reaction of mercury(II) with excess nitrate leads to the formation of the complex anion $[Hg(NO_3)_4]^{2-}$. This complex is formally eight-coordinate with each nitrate ion coordinating in bidentate fashion through two O donors (*see Bidentate Ligand*). The average Hg–O bond distance in this complex is 240 pm.

Reaction of mercury(II) with carbonate ion produces the insoluble carbonate, $HgCO_3$, in addition to species such as $[Hg(OH)]^+$ and $[Hg(OH)(CO_3)]^-$. The oxalate and phosphate salts are also known, both of low solubility. Mercury forms compounds with a variety of organic carboxylates, and many of these compounds are used as specific reagents or catalysts (*see Catalysis*) in organic reactions. Many of these oxo salts have two short Hg–O bonds and four longer Hg–O bonds, as is typical of mercury(II) coordination in general. When hydroxide is the coordinating ligand, zigzag chains of Hg–(OH)–Hg linkages are formed, similar to what is observed in the structure of HgO.

4.5 Other Complexes of Mercury(II)

The coordination chemistry of mercury has been reviewed.**[44–52,62–64]** Tolerance for different coordination numbers and coordination geometries, even with the same ligand type, is typical of the coordination chemistry of Hg(II) (Table 7). Two coordination is more common for mercury(II) than for any other cation. Tetrahedral mercury(II) complexes are usually more covalent in nature and contain less polar Hg–I or Hg–S bonds as opposed to the more ionic character observed in Hg–O bonds. Monodentate ligands tend to form either linear two-coordinate or tetrahedral four-coordinate complexes. Six coordination is less common than for Zn(II) or Cd(II), but reports of octahedral and higher CN complexes of mercury(II) are increasing in number. Frequently, the otherwise equal bond lengths in six-coordinate complexes are distorted into two short and four long bonds, analogous to linear coordination. Multidentate ligands have permitted isolation of numerous complexes with less common stereochemistry and high coordination numbers. Crystallographic and structural data for mercury coordination compounds have been classified in terms of nuclearity and CN with analysis of isomerism and correlations between ligand donor atoms, bond lengths, and bond angles.**[65]**

4.5.1 Complexes with Sulfur Donor Ligands

Mercury has a strong affinity for sulfur, so it is not surprising that a large number of mercury(II) complexes contain S-donor ligands (*see* ***S-donor Ligands***). In fact, the word ‘mercaptan’ is derived from ‘mercury capturer’ because of the ability of mercury to react readily with thiols. Organic thiols react with HgO to form mercury mercaptides, which are characterized by low-melting points and high solubility in solvents of low polarity such as toluene. The structure and spectroscopy of Hg^{II}−thiolates has been reviewed.**[18]** In physiological systems, proteins with high sulfur content called metallothioneins are responsible for scavenging Hg^{II} and transporting it to the kidney for excretion. The metalloregulatory protein MerR, which regulates metallothionein synthesis at the transcriptional level, is believed to have a trigonal planar sulfur-binding site that exhibits both high affinity and selectivity toward mercury.**[17,18]**

Table 7 Stereochemistries of selected mercury(II) complexes

Coordination number	Stereochemistry	Complex
2	Linear	$[Hg(NH_3)_2]^{2+}$, $HgCl_2$
3	Trigonal planar	$[HgI_3]^-$
	T-shaped	$[Hg(SC_6H_2Bu^t_3)_2(py)]$
4	Tetrahedral	$[Hg(SCN)_4]^{2-}$, $[HgI_2{\cdot}2PPh_3]$
	Square planar	*trans*-$[Hg\{Ph_2PNP(O)Ph_2\text{-}P, O\}_2]$
5	Trigonal bipyramidal	$[Hg(dien)Cl_2]$, $[HgCl_5]^{3-}$
	Square pyramidal	$[Hg(15S5)]^{2+}$, $[HgCl_2{\cdot}$diphenyl sulfoxide$]$
6	Octahedral	$[Hg(en)_3]^{2+}$, $[Hg(9S3)_2]^{2+}$
	Trigonal prism	$[Hg\{Pt(2,6\text{-}Me_2C_6H_3NC)\}_6]$
8	Distorted square antiprism	$[Hg(NO_2)_4]^{2-}$

A number of sulfur containing ligands have been found to complex mercury(II), including thiourea, thiocarboxylic acids, thiocarboxylates, mercaptides, thiones, and thioethers. The remarkable structural diversity of the mercury(II) bis xanthates (S_2COR) and bis dithiocarbamates has been reviewed.**[66]** Dithiolates can function as monodentate, chelating, and bidentate bridging binding ligands of Hg(II), and more than one of these modes can be found in a single structure. Structurally characterized $[Hg(S_2COR)_2]$ complexes have a one-dimensional chain structure (R = Me), a two-dimensional layer structure (R = Et), and a three-dimensional network structure (R = *i*Pr). Variation of remote organic substituents also leads to an intriguing array of five distinct structural motifs for the $[Hg(S_2CNR_2)_2]$ system. The delicate balance between satisfaction of the bonding requirements of the mercury atom and optimization of intermolecular interactions is especially apparent in the existence of two forms of $[Hg(S_2CNEt_2)_2]$, one dimeric and the other essentially monomeric. Interestingly, eight distinct structural motifs have been observed for bis dithiolates of group 12 metals, of which three have only been observed with Hg and three have yet to be observed with Hg.**[67]** Structural assignments for this class of compounds obviously requires definitive crystallographic evidence.

The host−guest chemistry of crown ethers continues to be exploited for the development of new ionophores for the selective recovery of Hg(II). A novel crown ring system containing a redox switchable trithiadiazapentalene/trithiotriuret unit (**17**/**18**) allows control of Hg(II) in solvent extraction experiments between chloroform and water.**[68]** The thiocarbonyl sulfur donor sites outside the macrocyclic cavity of (**18**) are responsible for strong complexation and extractability into chloroform.

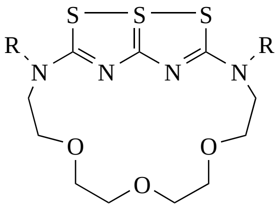

(**17**)

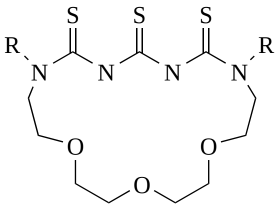

(**18**)

Selective transport of Hg(II) over Cu(II) through chloroform from a solution of these metal ions to an aqueous HCl solution was demonstrated for the troponoid dithiocrown ether (**19**).[69] The benzenoid dithiocrown ether (**20**) was a much less effective transporter in spite of similar cavity size, suggesting protonation of the tropone ring assisted release of the Hg(II) from the complex.

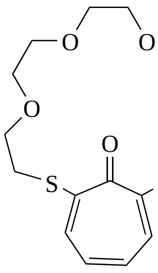

(**19**)

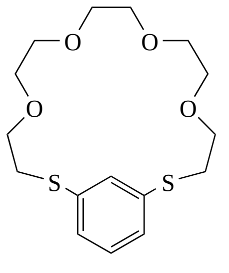

(**20**)

Related complexes containing several cyclic or crown thioethers are known, and the thioether ligands may bind through three, four, or even five sulfur donor sites. For example, unusual octahedral hexakis(thioether) coordination was observed in the single-crystal *X-ray diffraction* structure of [Hg(**21**)$_2$](ClO$_4$)$_2$.[70] Interestingly, no macrocyclic effect is observed for mercury(II) complexes with the two crown tetrathioether ligands (**22**) and (**23**).[71] Indeed, acyclic tetrathioethers such as (**24**) actually have a greater affinity for mercury(II) than do the cyclic thioethers, the converse of what is observed for other transition metal ions. This observation has been attributed to the large size of the mercury(II) ion and the need of a larger and more flexible ligand for better coordination. The stability constants (*see* ***Stability Constants & their Determination***) of many mercury(II) complexes of thioethers have been reported.[72]

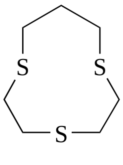

(**21**)

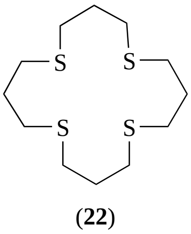

(**22**)

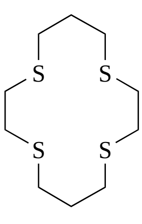

(**23**)

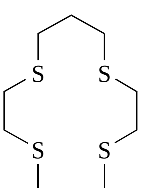

(**24**)

4.5.2 Complexes with Oxygen-donor Ligands

A series of octahedral complex ions with monodentate O-donor ligands, such as [Hg(H$_2$O)$_6$]$^{2+}$ and [Hg(DMSO)$_6$]$^{2+}$, are known, but only in the presence of poorly coordinating *Counter Ions* such as perchlorate or triflate. The Hg–O bond lengths in these complexes average about 234 pm. Related complexes with bidentate O-donor ligands such as oxalate are also known. The ophthalmic preservative known as thimerosal is actually the sodium salt of an anionic mercury complex, which contains a mercury(II) ion center chelated (*see Chelating Ligands*) by a bidentate mixed O,S– donor ligand.

4.5.3 Complexes with Nitrogen-donor Ligands

Alchemists performed reactions between ammonia and mercury compounds, to some of which they gave descriptive names. However, the complex nature of the products prevented their full characterization until more recently. Mercury(II) chloride or bromide reacts with ammonia under differing reaction conditions to form three types of complexes: Hg(NH$_3$)$_2$X$_2$, diammine halides; HgNH$_2$X, amidohalides or aminohalides; and Hg$_2$NHX, iminohaides (equations 5–7). The complex Hg(NH$_3$)$_2$Cl$_2$, known as ‘fusible white precipitate’, consists of a fcc lattice of chloride ions with linear N–Hg–N linkages. The observed Hg–N distance is 203 pm, and the observed Hg–Cl distance is 287 pm. The compound is isolated from the reaction of HgCl$_2$ and a mixture of aqueous ammonia and ammonium ions when a high concentration of ammonium ion and/or nonpolar solvents are present. The amidochloride, HgNH$_2$Cl, ‘infusible white precipitate’, can be isolated under conditions of low ammonia concentration and without NH$_4$$^+$ present. HgNH$_2$Cl has a structure of zigzag chains of Hg–N bonds. In addition, complexation to mercury(II) can activate N–H bonds in these amine halides to form iminohalides (e.g. HgNHCl) (equation 7).

$$\mathrm{HgCl_2(s) + 2NH_3(aq) \rightleftharpoons [Hg(NH_3)_2Cl_2]} \tag{5}$$

$$\mathrm{[Hg(NH_3)_2Cl_2] \rightleftharpoons [Hg(NH_2)Cl] + NH_4Cl} \tag{6}$$

$$\mathrm{2[Hg(NH_2)Cl] + H_2O \rightleftharpoons [Hg_2NCl(H_2O)] + NH_4Cl} \tag{7}$$

$$\mathrm{Hg^{2+} + 2NH_3 \rightleftharpoons [Hg\text{-}NH_2]^+ + NH_4{}^+} \tag{8}$$

The compound [Hg$_2$NCl(H$_2$O)] is the chloride salt of the dihydrate of Millon’s base, [Hg$_2$NOH·2H$_2$O] (see Section 2). Besides air oxidation of Hg^0 in ammonia, Millon’s base can also be prepared by the reaction of yellow HgO with ammonia. The bright yellow product can be converted to [Hg$_2$NCl(H$_2$O)] with HCl. Many salts, called imino derivatives, are known with the general formula [Hg$_2$NX(H$_2$O)]. These compounds have a structure consisting of [Hg$_2$N]$^+$ units with tetrahedra of four Hg$^{\mathrm{II}}$ ions linked to each nitrogen atom, and two nitrogen atoms linearly linked to each Hg$^{\mathrm{II}}$ ion. The structure has open channels and cavities to accommodate anions and water molecules in interstitial sites, and the compounds resemble zeolites (*see* ***Zeolites***) in their ability to function as anion exchangers (*see Ion Exchange*).

Additionally, octahedral tris bidentate complexes of mercury(II) with ligands such as en, bipy, and phen have also been reported. Typically, these must be formed in the presence of excess ligand and must contain poorly coordinating anions such as perchlorate to minimize the formation of amino and imino compounds. Complexes of mercury(II) with aromatic amines, heterocyclic amines, and macrocyclic amines including porphyrins (*see Porphyrin*) are also known. Recent studies with dipodal and tripodal amines bearing pyridyl and imidazoyl appendages (e.g. **1**, **2**, **3**) have provided opportunities to correlate NMR spectra taken under slow-exchange conditions with crystallographically determined structures.**[22,24,25,73]** With (**2**), it was even possible to monitor changing from a tridentate binding mode with pendant lutidyl in [Hg(**2**)Cl_2] to a tetradentate binding mode in $[\text{Hg}(\mathbf{2})\text{Cl}]^+$ through changes in proton chemical shifts and $J(^{199}\text{Hg}^1\text{H})$.**[73]**

Mercury(II) reacts with dithizone to form the mixed N,S-donor complex mercury dithizonate (**25**).**[74]** This complex has interesting photochromic properties (*see Photochromism*). For example, its solutions in a variety of organic solvents are orange in weak illumination, but they turn dark blue in sunlight or intense artificial light. The water-soluble, turn-on florescein-based sensor (**26**) that exhibits environmentally relevant selectivity and sensitivity for Hg was recently reported.**[75]**

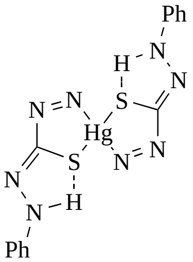

(**25**)

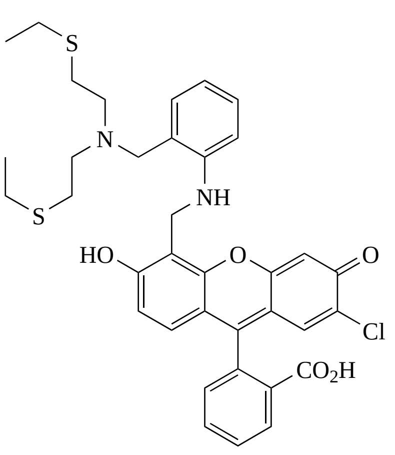

(**26**)

4.5.4 *Complexes with Phosphorus Donor Ligands*

Mercury(II) reacts with phosphines to form 1:1 or 1:2 complexes of the general type $HgLX_2$, where X is an anionic ligand such as halide or nitrate. The values of the $^{31}\text{P}-^{199}\text{Hg}$ coupling constants are useful in elucidating the structures of these compounds. Complexes with bidentate ligands that contain phosphorous and group 16 donor atoms (S, Se) are also known.**[76]** These have been characterized by ^{31}P, ^{77}Se, and ^{199}Se, and ^{199}Hg NMR spectroscopy and by electrochemical studies. Recently, the first true square-planar Hg(II) compound *trans*-$[\text{Hg}\{\text{Ph}_2\text{PNP(O)Ph}_2\text{-}P,\ O\}_2]$ was synthesized and fully characterized.**[77]** Charge delocalization in the ligand appeared to be key to the observed geometry.

4.5.5 *Complexes with Other Donors*

As observed previously for soft donor ligands such as thioethers and phosphines, mercury(II) reacts with selenoethers and telluroethers to form complexes of the general type $HgLX_2$, where X is a halide or pseudohalide. In addition, mercury(II) forms complexes with various Se-donor ligands such as diethylselenocarbamate and selenourea.

Tellurium coordination is seen in a series of acyclic bidentate ligands that coordinate through Te–N donor atoms or Te–O donor atoms.**[78]** An interesting series of adamantane-like cage complex cations that contain mercury(II) have been prepared and have the general formula $[\mu\text{-ER}_2(\text{HgL})_4]^{2+}$ (E = S, Se, or Te; L = phosphine or arsine).**[79,80]** These cations contain a variety of Hg–L bonds and have been characterized using heteronuclear NMR (^{31}P, ^{125}Te, ^{199}Hg).

4.6 Mercury(III) Complexes

There is potentiometric evidence for the formation of a mercury(III) complex by the oxidation of the mercury(II) complex of the cyclam macrocycle 1,4,8,11-tetraazacyclotetradecane.**[81]** There is also some evidence for the biological oxidation of mercury to Hg^{III}.

4.7 Compounds with Metal–Mercury Bonds

Mercury will bond directly to certain metal atoms including Co, Ru, Rh, Fe, Pt, and Mn. Such Hg–metal bonds are usually part of linear M–Hg–M or M–Hg–X linkages, and some clusters containing mercury−metal bonds are also known. These compounds are prepared by the reaction of mercury(II) halides with carbonylmetallates. A rare example of trigonal prismatic (*see Trigonal Prism*) coordination in a mercury complex is exhibited by $[\text{Hg}\{\text{Pt}_3(2,6\text{-Me}_2\text{C}_6\text{H}_3\text{NC})_6\}_2]$, which contains Pt–Hg bonds.**[82]** These types of compound have been reviewed.**[83]**

5 RELATED ARTICLES

Alloys; Ammonia & N-donor Ligands; Hard & Soft Acids and Bases; Mercury: Organometallic Chemistry; Metal Ion Toxicity; S-donor Ligands; Semiconductor Interfaces; Superconductivity; Water & O-donor Ligands; Zeolites.

6 REFERENCES

1. W. V. Farrar and A. R. Williams, The history of mercury, in ‘The Chemistry of Mercury’, ed. C. A. McAuliffe, Macmillan, London, 1977, p. 3.
2. L. D. Hylander and M. Meili, *Sci. Total Environ.* 2003, **304**, 13.
3. F. X. Han, A. Banin, Y. Su, D. L. Monts, M. J. Plodinec, W. L. Kingery, and G. E. Triplett, *Naturwissenschaften*, 2002, **89**, 497.
4. R. M. Randall, *Environ. Prog.*, 1995, **14**, 232.
5. S. N. Putilin, E. V. Antipov, O. Chmaissem, and M. Marezio, *Nature*, 1993, **362**, 226.
6. A. Narlikar, ed., ‘Studies of High Temperature Superconductors: Hg-Based High T_C Superconductors’, Nova Science Publishers, New York, 1997, p. 1.
7. G. Wulfsberg, ‘Principles of Descriptive Inorganic Chemistry’, University Science Books, Mill Valley, CA, 1991, p. 393.
8. L. J. Norby, *J. Chem. Educ.*, 1991, **68**, 110.
9. J. Autschback and T. Ziegler, Relativistic computation of NMR shieldings and spin-spin coupling constants, in ‘Encyclopedia of NMR’, eds. D. M. Grant and R. K. Harris, John Wiley & Sons, Chichester, 2002, p. 306.
10. D. Cleary, ‘Anatomy of the Amazon Gold Rush’, University of Iowa Press, Iowa City, 1990.
11. H. J. Deiseroth, E. Biehl, and M. Rochnia, *J. Alloys Compd.* 1997, **246**, 80.
12. B. E. Mann, NMR in inorganic chemistry, in ‘Encyclopedia of Inorganic Chemistry’, ed. R. B. King, John Wiley & Sons, Chichester, 1994, p. 2615.
13. R. K. Harris, Nuclear spin properties and notation, in ‘Encyclopedia of Nuclear Magnetic Resonance’ eds. D. M. Grant and R. K. Harris, John Wiley & Sons, Chichester, 1996, Vol. 5, p. 3301.
14. G. Wu and R. E. Wasylishen, *Magn. Reson. Chem.* 1993, **31**, 537.
15. B. Wrackmeyer and R. Contreras, ^{199}Hg NMR Parameters, in ‘Annu. Rep. NMR Spectrosc.’, ed. G. A. Webb, Academic Press, New York, 1992, Vol. 24, p. 267.
16. P. Granger, Groups 11 and 12: Copper to mercury, in ‘Transition Metal Nuclear Magnetic Resonance’, ed. P. S. Pregosin, Elsevier, Amsterdam, 1991, p. 264.
17. L. M. Utschig, J. W. Bryson, and T. V. O’Halloran, *Science*, 1995, **268**, 380.
18. J. G. Wright, M. J. Natan, F. M. MacDonnell, D. M. Ralston, and T. V. O’Halloran, Mercury(II)-Thiolate chemistry and the mechanism of the heavy metal biosensor MerR, in ‘Progress in Inorganic Chemistry: Bioinorganic Chemistry’, ed. S. J. Lippard, John Wiley & Sons, New York, 1990, Vol. 38, p. 323.
19. L. Long, *Chem. Eng. News* 1997, **June 16**, 12.
20. D. S. Wishart, C. G. Bigam, J. Yao, F. Abildgaard, H. J. Dyson, E. Oldfield, J. L. Markley, and B. D. Sykes, *J. Biomol. NMR* 1995, **6**, 135.
21. J. M. Hook, P. A. W. Dean, and L. C. M. van Gorkom, *Magn. Reson. Chem.*, 1995, **33**, 77.
22. D. C. Bebout, A. E. DeLanoy, D. E. Ehmann, M. E. Kastner, D. A. Parrish, and R. J. Butcher, *Inorg. Chem.* 1998, **37**, 2952.
23. V. I. Minkin and L. E. Nivorozhkin, ‘Stereodynamics and Degenerated Ligand Exchange in the Solutions of Tetracoordinated Chelate Complexes of Non-Transition Metals in Complex Formation and Stereochemistry of Coordination Compounds’, ed. Y. Beslaev, Nova Science Publishers, Commack, New York, 1996, p. 77.
24. D. C. Bebout, J. F. Bush II, K. K. Crahan, E. V. Bowers, and R. J. Butcher, *Inorg. Chem.*, 2002, **41**, 2529.
25. D. C. Bebout, D. E. Ehmann, J. C. Trinidad, K. K. Crahan, M. E. Kastner, and D. A. Parrish, *Inorg. Chem.* 1997, **36**, 4257.
26. D. C. Bebout, S. W. Stokes, and R. J. Butcher, *Inorg. Chem.* 1999, **38**, 1126.
27. R. Malleier, H. Kopacka, W. Schuh, K. Wurst, and P. Peringer, *Chem. Commun.* 2001, 51.
28. D. C. Bebout, J. F. Bush II, E. M. Shumann, J. A. Viehweg, M. E. Kastner, D. A. Parrish, and S. M. Baldwin, *J. Chem. Crystallogr.* 2003, **33**, 455.
29. G. A. Bowmaker, R. K. Harris, and S.-W. Oh, *Coord. Chem. Rev.* 1997, **167**, 49.
30. H. Strasdeit, *Angew. Chem., Int. Ed. Engl.*, 2001, **40**, 707.
31. W. J. Mahn, ‘Academic Laboratories Chemical Hazards Guidebook’, Van Nostrand Reinhold, New York, 1964, p. 204.
32. H. H. Henning and S. G. Luxon, Hazardous substances, in ‘Hazards in the Chemical Laboratory’, 5th edn., ed. S. G. Luxon, Royal Society of Chemistry, London, 1992, p. 465.
33. M. J. Moore, M. D. Distefano, L. D. Zydowsky, R. T. Cummings, and C. W. Walsh, *Acc. Chem. Res.*, 1990, **23**, 301.
34. H. V. Aposhian, R. M. Mariorino, D. Gonzalex-Ramirez, M. Zuniga-Charles, Z. Xu, K. M. Hurlbut, P. Junco-Munoz, R. C. Dart, and M. M. Aposhian, *Toxicology*, 1995, **97**, 23.
35. L. G. Helper and G. Olfosson, *Chem. Rev.*, 1975, **75**, 585.
36. F. A. Cotton, G. Wilkinson, C. Murillo and M. Bochman, ‘Advanced Inorganic Chemistry’, 6th edn., John Wiley & Sons, New York, 1999, p. 598.
37. N. N. Greenwood and A. Earnshaw, ‘Chemistry of the Elements’, 2nd edn., Butterworth-Heinemann, Oxford, 1997, p. 1201.
38. W. Levason and C. A. McAuliffe, Mercurous mercury Hg_2^{2+}, in ‘The Chemistry of Mercury’, ed. C. A. McAuliffe, Macmillan, London, 1977, p. 51.
39. N. V. Pervukhina, S. A. Magarill, S. V. Borisov, G. V. Romanenko, and N. A. Pal’chik, *Russ. Chem. Rev.* 1999, **68**, 615.
40. N. V. Pervukhina, G. V. Romanenko, S. V. Borisov, S. A. Magarill, and N. A. Palchik, *J. Struct. Chem.* 1999, **40**, 461.
41. D. T. Meshri, ‘Inorganic Fluorine Chemistry: Mercury in Kirk-Othmer Encyclopedia of Chemical Technology’, 3rd edn., eds. R. E. Kirk, D. F. Othmer, John Wiley & Sons, New York, 1985, Vol. 10, p. 763.

42. D. Bravo-Zhivotovskii, M. Yuzefovic, M. Bendikov, K. Klinkhammer, and Y. Apeloig, *Angew. Chem., Int. Ed. Engl.* 1999, **38**, 1100.
43. M. L. P. Reddy and T. Francis, *Solvent Extr. Ion Exch.* 2001, **19**, 839.
44. J. Malito, *Annu. Rep. Prog. Chem., Sect. A*, 2002, **98**, 115.
45. J. Malito, *Annu. Rep. Prog. Chem., Sect. A*, 2001, **97**, 117.
46. J. Malito, *Annu. Rep. Prog. Chem., Sect. A*, 2000, **96**, 147.
47. J. Malito, *Annu. Rep. Prog. Chem., Sect. A*, 1999, **95**, 93.
48. I. B. Gorrell, *Annu. Rep. Prog. Chem., Sect. A*, 1998, **94**, 137.
49. I. B. Gorrell, *Annu. Rep. Prog. Chem., Sect. A*, 1997, **93**, 117.
50. I. B. Gorrell, *Annu. Rep. Prog. Chem., Sect. A*, 1996, **92**, 113.
51. I. B. Gorrell, *Annu. Rep. Prog. Chem., Sect. A*, 1995, **91**, 115.
52. H. Sloan, *Annu. Rep. Prog. Chem., Sect. A*, 1994, **90**, 91.
53. D. K. Breitinger, Mercury and its compounds, in 'Synthetic Methods of Organometallic and Inorganic Chemistry: Copper, Silver, Gold, Zinc, Cadmium and Mercury', eds. D. K. Breitinger and W. A. Herrmann, Georg Thieme Verlag, Stuttgart, New York, 1999, p. 193.
54. P. A. W. Dean, *Prog. Inorg. Chem.*, 1978, **24**, 109.
55. A. Burger, D. Nason, L. van den Berg, and M. Schieber, *Semicond. Semimetals*, 1995, **43**, 85.
56. D. Schwarzenbach, *Z. Kristallogr.*, 1968, **128**, 97.
57. D. A. House, W. T. Robinson and V. McKee, *Coord. Chem. Rev.* 1994, **135/136**, 533.
58. S. Li, S. Li, and F. Ling, *Fenxi Shianshi*, 1991, **10**, 14; *Chem. Abstr.*, 1992, **116**, 206847d.
59. A. F. Wells, 'Structural Inorganic Chemistry', Clarendon Press, Oxford, 1984, p. 604.
60. S. A. Magarill, G. V. Romanenko, N. V. Pervukhina, S. V. Borisov, and N. A. Palchik, *J. Struct. Chem.*, 2000, **41**, 96.
61. K. E. Paquette and G. R. Helz, *Environ. Sci. Technol.*, 1997, **31**, 2148.
62. E. C. Constable, *Coord. Chem. Rev.*, 1982, **45**, 367.
63. M. N. Hughes, *Coord. Chem. Rev.*, 1981, **37**, 323.
64. W. Levason and C. A. McAuliffe, Mercuric mercury Hg^{2+}, in 'The Chemistry of Mercury', ed. C. A. McAuliffe, Macmillan, London, 1977, p. 60.
65. C. E. Holloway and M. Melnik, *Main Group Metal Chem.*, 1994, **17**, 799.
66. E. R. T. Tiekink, *Rigaku J.* 2002, **19**, 14.
67. M. J. Cox and R. T. Tiekink, *Rev. Inorg. Chem.*, 1997, **17**, 1.
68. K. Gloe, H. Graubaum, M. Wüst, T. Rambusch, and W. Seichter, *Coord. Chem. Rev.*, 2001, **222**, 103.
69. A. Mori, K. Kubo, and H. Takeshita, *Coord. Chem. Rev.*, 1996, **148**, 71.
70. M. L. Helm, C. M. Combs, D. G. VanDerveer, and G. J. Grant, *Inorg. Chim. Acta*, 2002, **338**, 182.
71. R. D. Bach and H. B. Vardhan, *J. Org. Chem.*, 1986, **51**, 1609.
72. S. R. Cooper and S. C. Rawle, *Struct. Bonding*, 1990, **72**, 1.
73. D. C. Bebout, J. F. Bush II, K. K. Crahan, M. E. Kastner, and D. A. Parrish, *Inorg. Chem.*, 1998, **37**, 4641.
74. W. L. Jolly, 'The Synthesis and Characterization of Inorganic Compounds', Waveland Press, Prospect Heights, IL, 1991, p. 470.
75. E. M. Nolan and S. J. Lippard, *J. Am. Chem. Soc.* 2003, **125**, 14270.
76. A. M. Bond, R. Colton, and J. Ebner, *Inorg. Chem.*, 1988, **27**, 1697.
77. R. Haid, R. Gutmann, G. Czermak, C. Langes, W. Oberhauser, H. Kopacka, K.-H. Ongania, and P. Brüggeller, *Inorg. Chem. Com.* 2003, **6**, 61.
78. A. K. Singh, S. Thomas, and B. L. Khandelwal, *Polyhedron*, 1991, **10**, 2693.
79. P. A. W. Dean and V. Manivannan, *Can. J. Chem.*, 1990, **68**, 214.
80. P. A. W. Dean, V. Manivannan, and J. J. Vittal, *Inorg. Chem.*, 1989, **28**, 2360.
81. F. A. Cotton, R. N. Grimes, G. Wilkinson, M. Bochman, and C. Murillo, 'Advanced Inorganic Chemistry', 6th edn., John Wiley & Sons, New York, 1999, p. 598.
82. Y. Yamamoto, H. Yamazaki, and T. Sakurai, *J. Am. Chem. Soc.* 1982, **104**, 2329.
83. W. Levason and C. A. McAuliffe, Mercury-metal bonds, in 'The Chemistry of Mercury', ed. C. A. McAuliffe, Macmillan, London, 1977, p. 109.

Mercury: Organometallic Chemistry

Daniela Rais[1] & Ramón Vilar[2,3]
[1]*Institut für Anorganische Chemie, Universität Würzburg, Würzburg, Germany*
[2]*Institució Catalana de la Recerca i Estudis Avançats (ICREA), Barcelona, Spain*
[3]*Institut Català d'Investigació Química (ICIQ), Tarragona, Spain*

Based in part on the article Mercury: Organometallic Chemistry by Richard C. Larock which appeared in the Encyclopedia of Inorganic Chemistry, First Edition.

1 Introduction 1
2 Synthesis of Organomercurials 1
3 Structure 4
4 Reactivity 5
5 References 8

1 INTRODUCTION

In spite of their early discovery by Frankland in 1852, organomercurials have found relatively limited applications with respect to other organometallic compounds. The reason for this can be traced back to their high toxicity, which causes damage to the central nervous system and induces neuropsychiatric disorders in humans.**[1]** Since the publication of the first edition of EIC,**[2]** the chemistry of organomercurials has focused more on development than on innovation. New compounds have been prepared using the general synthetic procedures that had previously been described. The reactivity of organomercurials has been further explored – using established methodologies – leading to interesting applications in organic synthesis. The solvomercuration of alkenes is still the most widely employed organometallic reaction of mercury, although there have been important advances in the use of the mercury-mediated ring opening of cyclopropanes. Structural investigations of organomercurials have received considerable attention over the past 10 years. Several new structures have been crystallographically elucidated providing detailed information on the connectivity of a wide range of mono- and polymercuric complexes. Furthermore, there has been considerable interest in understanding the supramolecular interactions displayed by several organomercurials in the solid state and in solution.

This entry will provide an overview of the most important advances on the organometallic chemistry of mercury between 1993 and 2003. During the past 10 years, several reviews and books on this topic have appeared.**[3–13]** Annual updates can be found in the Specialist Periodical Reports on Organometallic Chemistry published by the Royal Society of Chemistry.**[14–17]**

2 SYNTHESIS OF ORGANOMERCURIALS

2.1 Transmetallation

A general method for the synthesis of organomercurials is the transmetallation of mercury(II) salts with other organometallic species. Organolithium and -magnesium compounds continue to be widely employed for the preparation of complexes with formula RHgX or HgR_2 (see equation 1).

$$\mathrm{HgX_2} \xrightarrow{\mathrm{RM}} \mathrm{RHgX} \xrightarrow{\mathrm{RM}} \mathrm{HgR_2}$$
$$\mathrm{M} = \mathrm{Li, MgX}$$
$$\mathrm{X} = \mathrm{Cl, Br, I} \qquad (1)$$

Selected recent examples of the applicability of this synthetic procedure are shown in equations (2–4).**[18–20]**

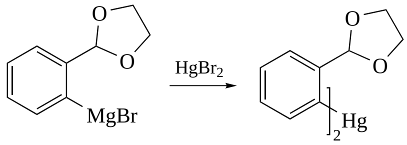

(2)

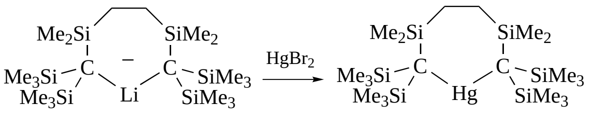

(3)

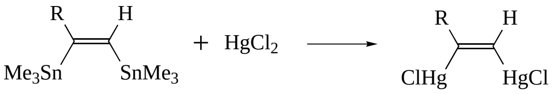

(4)

Organoboranes (such as aryl and vinyl boronic acids) have also demonstrated to be valuable reagents for the synthesis of organomercurials, particularly in the presence of functional groups that are not compatible with the more reactive organolithium or -magnesium reagents.

2.2 Mercuration of C–H Bonds

Mercury salts can react directly with hydrocarbons exchanging hydrogen for mercury. This reaction is an electrophilic substitution (equation 5) and hence can take place with arenes, cyclopentadienyls, terminal alkynes, and also with aliphatic hydrocarbons that contain activated carbon–hydrogen bonds (e.g. carbonyl or nitrile compounds). When the hydrocarbon contains several equivalent hydrogen atoms, polymercuration is often observed.

$$\mathrm{R{-}H} + \mathrm{HgX_2} \longrightarrow \mathrm{RHgX} + \mathrm{HX} \qquad (5)$$

The direct mercuration of arenes is widely used for the synthesis of arylmercurials. The reaction is particularly efficient for activated arenes (such as phenols, anilines, and aryl ethers), while deactivated arenes require the use of stronger electrophiles and higher reaction temperatures. A recent example of the latter is the mercuration of terephthaldehyde reported by Vicente (equation 6).[21]

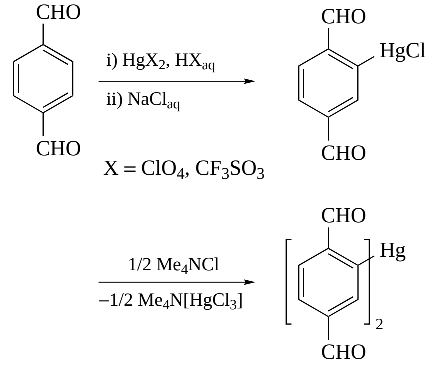

(6)

The mercuration of metallocenes has continued to attract interest due to the potential use of the mercurated species in the synthesis of different metallocene derivatives. New mercurometallocenes, together with some mechanistic studies on their formation,[22] have been reported over the past few years. Besides the monomercurated species, a detailed study has appeared on the permercuration of ferrocene and ruthenocene.[23] For both metallocenes, the decamercurated species shown in equation (7) have been obtained in high yields.

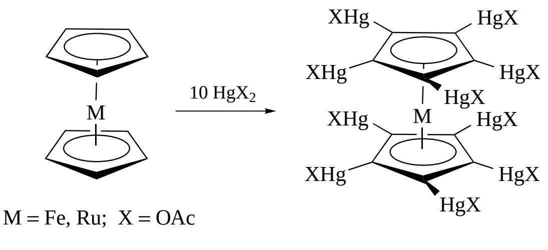

(7)

Direct mercuration of alkynes has also been achieved.[24] The interest in mercury alkynyls stems from their documented applications in the rapid separation and detection of toxic organomercurials (particularly, methylmercury derivatives). Upon reaction with alkynes, samples containing methylmercury salts yield $Hg(C{\equiv}CR)_2$ or $Hg(Me)(C{\equiv}CR)$ species that can then be analyzed using chromatographic techniques.

A series of luminescent mercury(II) bis(alkynyl) complexes containing oligothiophenes have been synthesized by Wong via direct mercuration of the corresponding alkynes (see equation 8).[24] Most importantly, the optical properties of these species have been found to be easily tuned by modifying the nature of the thiophene unit.

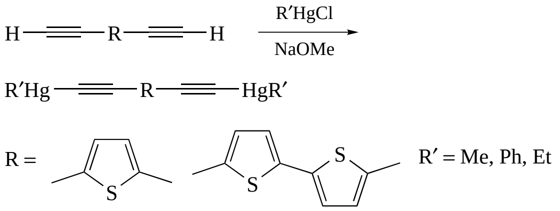

(8)

2.3 Mercuration of Alkenes

The reaction between mercury(II) salts and alkenes is the most important general method for the synthesis of organomercurials.[3] Although there are some examples where mercury reacts directly with olefins to produce vinyl mercurials, the most common reaction is the addition of mercury to the alkene's double bond with the participation of a nucleophile (equation 9).

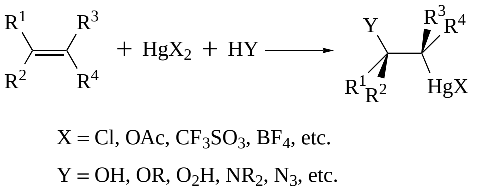
R^1
R^3
R^2
R^4
+ HgX$_2$ + HY
Y
R^3
R^4
R^1
R^2
HgX
X = Cl, OAc, CF$_3$SO$_3$, BF$_4$, etc.
Y = OH, OR, O$_2$H, NR$_2$, N$_3$, etc.

(9)

The proposed mechanism for this reaction involves the electrophilic attack by mercury(II) on the double bond to generate a mercurinium intermediate, followed by attack of the nucleophile (see equation 10).

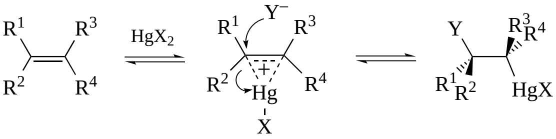

(10)

The solvomercuration of alkenes has an important synthetic value since it allows the asymmetric functionalization of olefins. Although a large number of organomercurials have been isolated from these reactions, more commonly, they are reduced with alkaline $NaBH_4$ to yield the corresponding metal-free organic species (see Section 4.1). In this way, olefins can be converted into a wide range of organic species such as alcohols, ethers, and amines.

2.3.1 *Mercuration in the Presence of Oxygen-containing Nucleophiles*

In the previous edition of EIC, Larock described in detail the hydro-, alkoxo-, peroxo-, and acyloxy-mercuration of olefins. These reactions generally proceed in a Markovnikov fashion yielding products of anti addition, although in some cases (e.g.

with strained olefins such as norbornene), the formation of syn products is observed. For the hydroxy-, alkoxy-, and acyloxy-mercuration reactions, $Hg(OAc)_2$ is the reagent of choice (although other mercury(II) salts such as $Hg(O_2CCF_3)_2$ and $Hg(BF_4)_2$ have been used to modify the rate or selectivity of the reaction). Peroxomercurations usually yield better results with $Hg(NO_3)_2$ or $Hg(O_2CCF_3)_2$.

Since the publication of the previous edition of the EIC, the scope of the mercuration of olefins in the presence of water, alcohols, peroxides, and carboxylic acids has considerably broadened. While studying the deprotection of monoallyloxyalcohols to yield sugar-containing systems, Jarosz optimized the reaction conditions yielding various organomercury compounds (see equation 11).**25** In this reaction, the resulting organomercurial is formed via preferential intramolecular attack of the hydroxy group of the monoprotected diol and not by the water present in the reaction medium. Paquette has reported a very detailed study on the intramolecular oxymercuration of a series of tetraspiro carbinols and trispiro cyclohexanones (equation 12).**26** An interesting conclusion from this work is that the approach of the mercury to the double bond (and consequently the stereochemistry of the final product) is largely governed by the interaction of the metal center with a proximal axially oriented ether oxygen. Similar interactions between the mercury ion and a proximal oxygen atom have been invoked to rationalize the stereochemistry observed in a series of intra- and intermolecular alkoxymercurations reported by Senda (equation 13).**27**

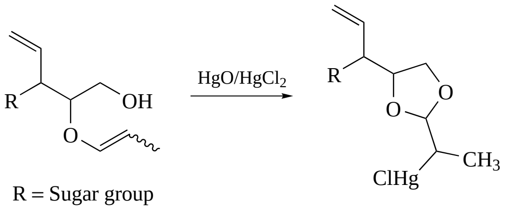

R = Sugar group

(11)

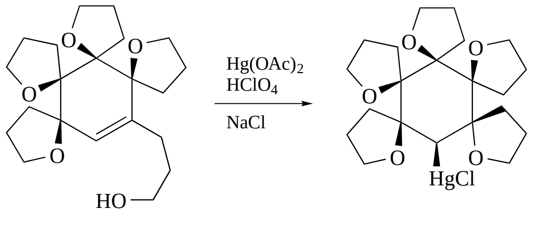

(12)

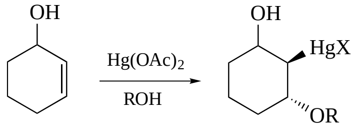

(13)

2.3.2 *Mercuration in the Presence of Nitrogen-containing Nucleophiles*

The mercuration of alkenes in the presence of nitrogen-containing species such as amines, amides, nitriles, azides, or nitro groups has also been studied, although not as systematically as that of the corresponding oxygen-containing species. The reaction can be performed with a variety of mercury salts, $Hg(OAc)_2$ and $HgCl_2$ being the most commonly used. When this reaction occurs in an intramolecular fashion, it provides a route to several heterocycles, such as pyrroles, piperidines, and a variety of polycyclic species. A selection of some recent examples is shown in equations (14–16). An intramolecular stereoselective amidomercuration reaction has been disclosed by Singh as an essential step for the synthesis of polyhydroxylated pirrolidines (equation 14).**28**

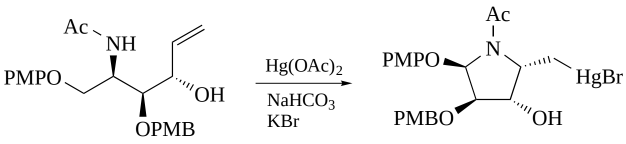

PMP = 4-(*p*-methoxy)phenoxy PMB = *p*-methoxybenzyl

(14)

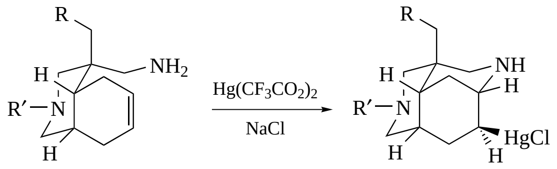

(15)

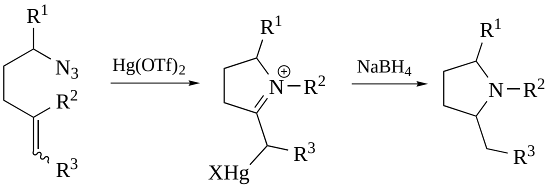

(16)

An example of intramolecular aminomercuration has been reported by Weinreb as part of the synthetic strategy to the tricyclic nucleus of madangamine A – an alkaloid that shows cytotoxicity toward a number of tumor cell lines (equation 15).**29** Pearson has recently reported the first example of an azidomercuration involving aliphatic azides (see equation 16) according to a protocol that exhibits wider applicability and is, therefore, more convenient than the analogous acid-promoted Schmidt reaction.**30**

2.3.3 *Miscellaneous Mercuration Reactions*

Halo-, carbo-, and nitro-mercurations of alkenes (and alkynes) have been previously described. However, these reactions are not as general and have not found as many applications in organic synthesis as the ones described in the previous two sections. Consequently, they will not be discussed any further in this review and the interested readers are directed to previous reviews and some recent references.**31–33**

2.4 Mercuration of Alkynes

Mercury(II) salts react with alkynes in two different ways. As discussed in Section 2.2, terminal alkynes react with mercury under basic conditions to yield species with general formula $Hg(C{\equiv}CR)_2$ or $Hg(X)(C{\equiv}CR)$. Alternatively, under neutral or acidic conditions, alkynes undergo solvomercuration reactions to yield anti addition products (for example, see equation 17).[34]

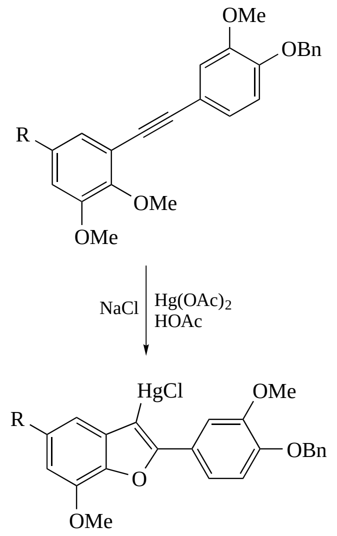

(17)

2.5 Mercuration of Cyclopropanes

The electrophilic ring opening of cyclopropanes is a well-established reaction. Detailed studies have shown that the nature of the electrophile is important in determining the mechanism of the reaction: for electrophiles with the capacity of back-donating (e.g. Pd^{2+} or Pt^{2+}), the reaction involves a stereoregiospecific 'edge attack', whereas a 'corner opening' mechanism is proposed for poor back-donors such as Hg^{2+} (see Scheme 1).[11] In both cases, the stereo- and regioselectivities are consistent with backside attack of the nucleophile on the carbon that can best stabilize a positive charge.

Although the initial interest in this type of reaction was mainly focused on the kinetics, stereochemistry, and mechanism, over the past 10 years, more emphasis has been given to its synthetic applications (see Section 4). As part of these studies, several stable organomercurials have been isolated and characterized (see e.g. equation 18).[35] However, Cossy has focused on reactions that lead to the formation of stereotriads via interaction of cyclopropylcarbinol derivatives with mercuric salts.[36] Some of the intermediate organomercurial species involved in this process have been isolated (see equation 19).

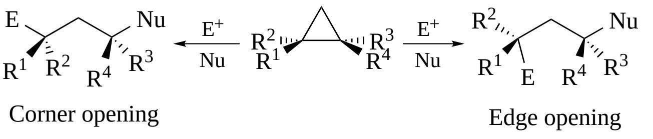

Scheme 1

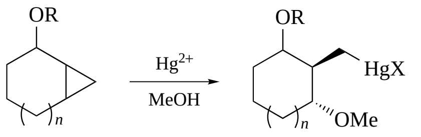

(18)

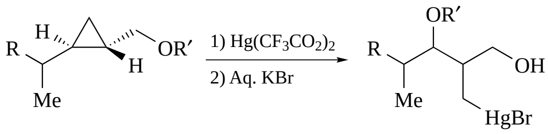

(19)

Barrett has reported a systematic study on the cleavage of multiple cyclopropanes (see e.g. equation 20).[37] Interestingly, it was found that while the mercury-mediated ring opening of monocyclopropanes usually proceeds via a concerted mechanism, in the case of multiple cyclopropanes, it occurs through a stabilized free carbocation. Furthermore, the presence of an adjacent cyclopropane increases the rate of the ring opening of the first cyclopropane.

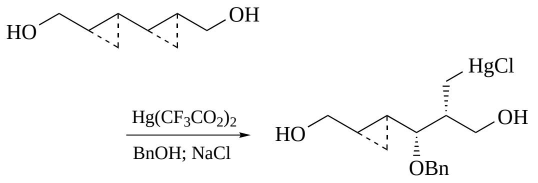

(20)

3 STRUCTURE

3.1 Structural Characterization

To date, the structures of more than four hundred organomercury compounds have been determined by X-ray diffraction methods. Detailed reviews by Wardell, Holloway, and Melkník,[9] and Casas,[6] have already been published covering the relevant literature up to the end of 1997. Consequently, only a representative set of recent examples will be discussed in this section.

A survey of the reported data reveals that, despite the known preference of mercury for linear di-coordination, the metal center generally displays sufficient residual acidity to engage in secondary intra- or intermolecular interactions. As a result, there are relatively few examples of organomercury complexes with coordination number two, while coordination numbers as high as seven can be reached when the groups (mainly oxygen-, nitrogen-, and sulfur-donors) involved in the secondary interactions are sufficiently small. The phenomenon is most pronounced not only for mono-organomercurials but also for the less acidic di-organomercury compounds, particularly when their primary bonds involve perfluorinated ligands. Following Holloway's and Melkník's distinction,[9] monomeric organomercurials can be divided into three subgroups: (a) authentic digonal compounds; and digonal compounds displaying: (b) intramolecular; or (c) intermolecular interactions. The presence of secondary bonding causes a distortion in the L–Hg–L linearity and the L–Hg–L bond angle's mean value decreases from 176.5° to 174.5° to 171° on going from (a) to (b) to (c).

Although a number of intramolecular Hg–π-aryl interactions have been structurally identified, a rare example of unsupported π-aryl complex of Hg has been recently reported. In $[Hg(\eta^2-C_6H_5Me)_2(GaCl_4)_2]$, the two toluene molecules bind to mercury in an asymmetric η^2 fashion, with the Hg–C_{para} bond length of 2.349(9) Å being considerably shorter than the Hg–C_{meta} (2.71(1) Å).[38] Interestingly, coordination to the Hg/GaCl$_4$ system enhances the acidity of the aromatic molecule and catalytic hydrogen/deuterium exchange phenomena are observed in C_6D_6.

The molecular structure of $[Hg(CO)_2][Sb_2F_{11}]_2$, the first example of a thermally stable carbonyl derivative of a posttransition metal, has also recently been reported.[39] The $[Hg(CO)_2]^{2+}$ cation is nearly linear, with the Hg–C–O bond angle of 177.7(7)°. However, the coordination environment around the mercury atom is that of a distorted octahedron due to weak Hg···F interactions producing an extended two-dimensional structure where each anion links a pair of cations and each cation links four anions.

In addition to the 'conventional' secondary interactions described above, the presence of noncovalent mercuriophilic Hg···Hg attractions has been revealed in some organomercury compounds. Loose polymeric assemblies are formed through weak d^{10}-d^{10} Hg···Hg contacts (3.777–3.935 Å) in the solid-state structures of [R′HgC≡CRC≡CHgR′] (R = thiophene-2,5-diyl or [2,2′]bithiophene-5,5′-diyl, R′ = Me)[24] as well as of $[Hg(C{\equiv}CR)_2]$ (R = Ph, SiMe$_3$; Hg···Hg = 3.71–4.25 Å)[40] and [MeHgC≡CRC≡CHgMe] (R = 9,9′-dioctyl-2,7-diethynylfluorene; Hg···Hg = 3.738–4.183 Å).[41]

Clear examples of intermolecular mercuriophilic interactions have been described in $[MeHg(SC_4H_2N_2Me)]$ (Hg···Hg = 3.10 Å),[42] obtained from the reaction of methylmercury(II) hydroxide with 4-methylpyrimidine-2-thione hydrochloride, and in $[L_3Hg_3O][NO_3]$ (L = 1,3-dimethyluracil-5-yl) (Figure 1).[43] The cations $[L_3Hg_3O]^+$ dimerize, in the solid state, through weak Hg···Hg contacts to give hexanuclear compounds. The unit cell of $[L_3Hg_3O][NO_3]$ contains two different $[L_3Hg_3O]^+$ units. Cation **I** has the geometrical arrangement of a very flat pyramid, with intramolecular Hg···Hg distances in the range 3.4705(5)–3.5859(5) Å, while the two intermolecular contacts are of 3.5620(5) Å. In cation **II**, the Hg···Hg distances within the triangle range from 3.4552(6) to 3.5974(5) Å, while the intercationic separation is 3.6728(8) Å.

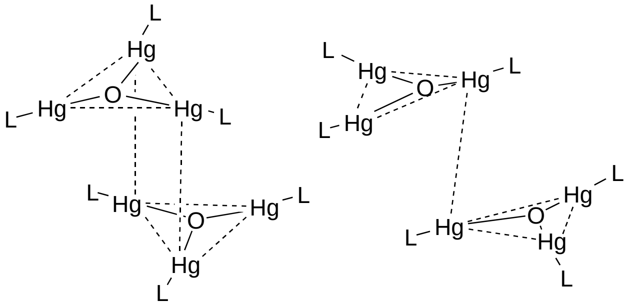
(a) Cation **I** (b) Cation **II**

L = 1,3-dimethyluracil-5-yl

Figure 1 Hexanuclear compounds formed via mercuriophilic interactions in the solid-state structures of $[L_3Hg_3O][NO_3]$[43]

3.2 Organomercurials as Polydentate Lewis Acids

The search for receptors capable of interacting with neutral and anionic substrates has led to the design and development of polydentate Lewis acids. Polyfunctional organomercurials, due to their air and water stability, ease of preparation, and Lewis acidity at mercury, have grown into one of the most prominent classes of Lewis acidic hosts. Much work has focused on derivatives of 1,2-phenylenedimercury (**1**)[13] along with polymercuramacrocycles such as the tetranuclear mercuracarborands (**2**) developed by Hawthorne[7] and the trimeric perfluoro-*ortho*-phenylenemercury (**3**) used by Gabbaï[44] and Shur (Figure 2).[45]

These systems exhibit considerable affinity for halide anions. X-ray analysis ascertained the formation of an anionic 2:1 chloride adduct of (**1**) where the chloride is simultaneously bound by four mercury atoms.[13] In the crystal structures of (**2**) $\cdot Cl^-$ and (**2**) $\cdot I_2^-$, the anions are located within the macrocycle and complexed cooperatively by the four mercury(II) centers.[7] Several anionic complexes of (**3**), including bromide, iodide, and thiocyanide salts, have been isolated. The compounds adopt multidecker structures with the hexacoordinated anions effectively sandwiched between two successive molecules of (**3**). The Lewis acidity of perfluoro-*ortho*-phenylenemercury (**3**) has also been substantiated by its ability to form stable adducts with neutral substrates (HMPA, DMSO, ethyl acetate, and acetonitrile) and arenes. The (**3**) $\cdot C_6H_6$ adduct exists as extended stacks of nearly parallel, staggered molecules of (**3**), which sandwich benzene molecules. Similar structures have been reported for the corresponding adducts with biphenyl, naphthalene, pyrene, and triphenylene.

4 REACTIVITY

A summary of the most important reactions undergone by organomercurials is shown in Schemes 2 and 3. Most of

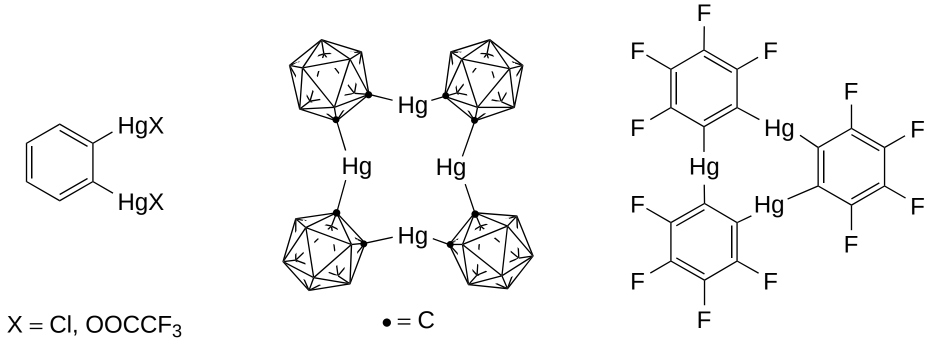

(**1**) (**2**) (**3**)

Figure 2 Examples of mercury-based polydentate Lewis acids[7,44,45]

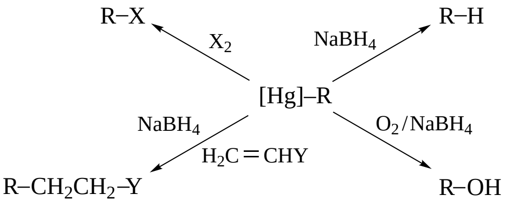

Scheme 2

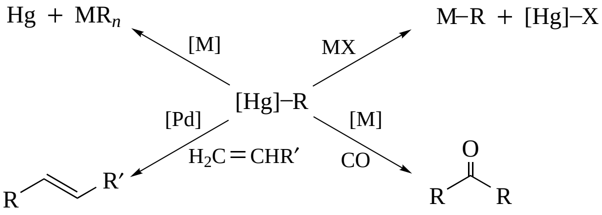

Scheme 3

these reactions were described in detail by Larock in the previous edition of this encyclopedia. Consequently, herein, only a summary of their most relevant features, together with a selection of recent and novel examples, will be presented.

4.1 Substitution of Mercury to Yield Metal-free Products

Many of the organomercurials prepared using the methodologies described in Section 3, are used in situ to effect a transformation on the organic moiety of the complex. The substitution of mercury by hydrogen or halogens continues to be the most important reactions of organomercurials from the synthetic point of view. These two reactions provide general methodologies to yield the corresponding metal-free species. Similarly, the reactions of organomercurials with $NaBH_4$ in the presence of either O_2 or an alkene, have demonstrated to be relatively general procedures to yield alcohols and substituted alkanes, respectively. Selected examples of these different substitution reactions can be found in the references at the end of the review.[36,46–50]

4.2 Transmetallation

Organomercurials are useful reagents for the synthesis of other organometallic complexes. Direct transmetallation is the most common approach and a large number of main group and transition metal organometallic complexes have been prepared in this way from organomercurials.

Organomercurials can also react with other metals by oxidative addition. This has been previously employed for the synthesis of some organopalladium and -platinum compounds. More recently, this approach has been extended to the preparation of a series of novel organo-, organooxo-, and organoamido-lanthanoid complexes. Reaction of the appropriate diorganomercurial [generally $Hg(C_6F_5)_2$ or $Hg(C_6H_5)_2$] with metallic europium or ytterbium in THF leads to isolation of di- or trivalent organolanthanoid complexes (equations 21 and 22).[51,52]

$$\mathrm{Ln} + \mathrm{HgR_2} \longrightarrow \mathrm{LnR_2} + \mathrm{Hg} \qquad (21)$$

$$2\mathrm{Ln} + 3\mathrm{Hg(C_6H_5)_2} \longrightarrow 2\mathrm{Ln(C_6H_5)_3} + \mathrm{Hg} \qquad (22)$$

Protonolysis of the highly reactive Ln–C bond with protic reagents LH ($LH = C_5R_5H$, ArOH, R_2NH) generates cyclopentadienyl, aryloxo, and amido lanthanoids, respectively. The two steps, redox transmetallation and protonolysis, can be carried out separately when the intermediate organolanthanoid complexes are to be isolated, or combined in a convenient ‘one-pot’ synthesis involving Ln metal, HgR_2, and LH. Isolation of the half-sandwich complex $[Yb(C_5Me_5)(C_6F_5)(THF)_3]$ represents a recent extension of this synthetic protocol.[53]

While reactions between lanthanide elements and $Hg(C_6F_5)_2$ proceed smoothly at room temperature, those with $Hg(C_6H_5)_2$ are more difficult to induce and generally require activation of the metal and heating. However, redox transmetallation-ligand exchange reactions with $Hg(C_6H_5)_2$ have proven unique in providing a convenient way of preparing the first lanthanoid(II) pyrazolates.

4.3 Cross-coupling Reactions

The reaction of organomercurials with palladium salts in the presence of alkenes leads to cross-coupling of the two organic species. Over the past few years, several examples of this reaction have been reported. For instance, ferrocenylmercuric derivatives can undergo cross-coupling reactions to form ferrocene-containing conjugated species. Bis(ferrocenyl)mercury in the presence of palladium salts undergoes cross-coupling reactions with aryl, heteroaryl, and acid halides.[54]

A variation of the cross-coupling protocol involving the ring opening of 4-alkenyl-2-azetidinones to yield amides has been recently reported (equation 23). Differently substituted aryl- and vinylmercurials effect the transformation in good yields and stereoselectively.[55]

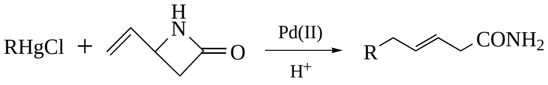

(23)

Cross-coupling of organomercurials has been employed in the generation of soluble, well-characterized poly(3-alkylthiophene) and poly(3-alkylthienyl ketone).[56] Facile mercuration of 3-alkylthiophenes with $HgCl_2$ produces 2,5-bis(chloromercurio)-3-alkylthiophenes. The mercurated intermediates subsequently undergo cross-coupling reactions in the presence of Cu and $PdCl_2$ to yield poly(3-alkylthiophene) and, under CO pressure, poly(3-alkylthienyl ketone) (Scheme 4).

4.4 Carbonylation of Organomercurials

Direct carbonylation of organomercurials is a low yielding process that requires high temperatures and pressures. However, it can be performed efficiently under milder conditions in the presence of transition metal catalysts, particularly, rhodium and palladium.[57,58] Two important applications of this protocol have recently been reported. The Rh^I-catalyzed formylation of organomercurials has been applied to the synthesis of a polyol-derived natural product.[59] The organomercury chloride substrate is synthesized by oxymercuration of the corresponding homoallylic alcohol with Hg(OAc)Cl (Scheme 5).

Subjection of this material to a formylation protocol involving a Rh^I catalyst, a bulky phosphite and DABCO (1,4-diazabicyclo[2.2.2]octane) in the presence of H_2/CO gas mixture, gives a high yield of the desired aldehyde. Iteration of these steps leads to the synthesis of *Tolypothrix* pentaether.

A Pd^{II}-catalyzed carbonylation procedure has been employed for the conversion of organomercurials into 5-membered cis- and trans-annulated lactones in which three consecutive chiral centers are introduced (equation 24).[60,61]

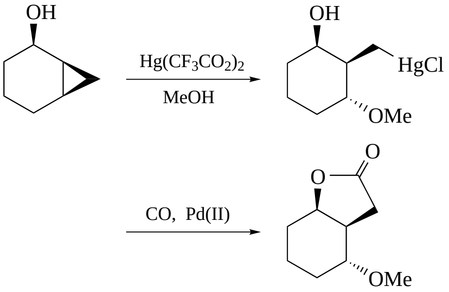

(24)

4.5 Mercury Photosensitized Reactions of Organic Compounds

A procedure for the dehydrodimerization of volatile organic compounds on a preparative scale by Hg photosensitized reactions has been reported by Crabtree and coworkers.[62,63]

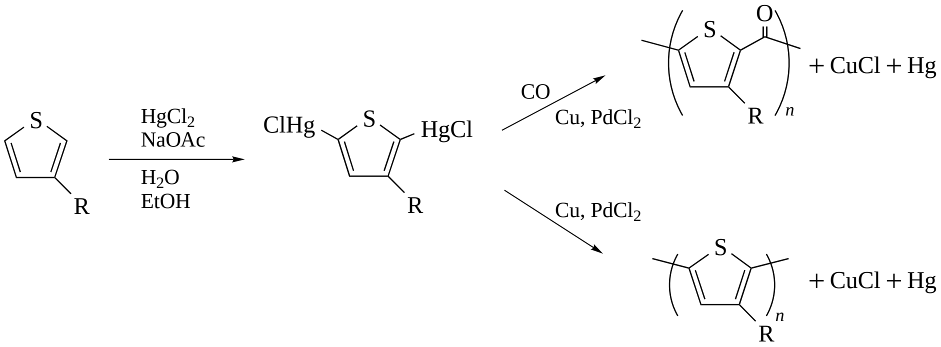

Scheme 4

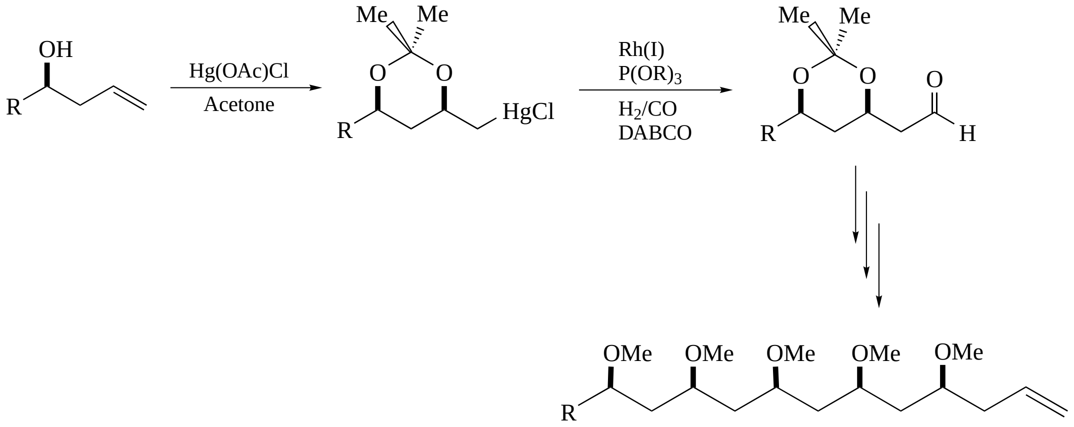

Scheme 5

Detailed theoretical work has shown that alkane C–H activation by the $3P_1$ excited state Hg* proceeds by initial formation of a weak [Hg*(alkane)] exciplex, followed by C–H cleavage via a mechanism described as a mixture of oxidative addition and H atom abstraction. While alkanes react exclusively via C–H bond activation, sensitization of monosubstituted arenes $ArCH_2-X$ (Ar = aryl; X = H, alkyl, OR, NR_2) occurs with substantial C–X bond cleavage (equation 25).

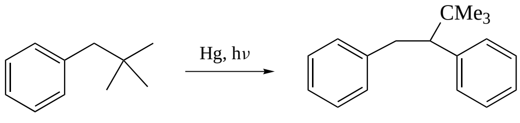

(25)

On the basis of experimental photochemical studies and theoretical calculations, the proposed mechanism involves formation of a [Hg*(arene)] exciplex, energy transfer from Hg* yielding a vibrationally excited triplet arene that spontaneously undergoes C–X bond cleavage.**[64]** Calculations performed on the exciplex between Hg* and benzene point to a structure of the type $^3[Hg(\eta^2\text{-}C_6H_6)]$.

5 REFERENCES

1. M. Morita, J. Yoshinaga, and J. S. Edmonds, *Pure Appl. Chem.*, 1998, **70**, 1585.
2. R. C. Larock, in ‘Encyclopedia of Inorganic Chemistry’, ed. R. B. King, Wiley & Sons, Chichester, 1994.
3. A. G. Davies and J. L. Wardell, in ‘Comprehensive Organometallic Chemistry II’, eds. G. Wilkinson, F. G. A. Stone, and E. W. Abel, Pergamon, Elsevier Science, Oxford, 1995.
4. G. A. Bowmaker, R. K. Harris, and S.-W. Oh, *Coord. Chem. Rev.*, 1997, **167**, 49.
5. D. K. Breitinger, *Synth. Methods Organomet. Inorg. Chem.*, 1999, **5**, 193.
6. J. S. Casas, M. S. Garcia-Tasende, and J. Sordo, *Coord. Chem. Rev.*, 1999, **193–195**, 283.
7. M. F. Hawthorne and Z. Zheng, *Acc. Chem. Res.*, 1997, **30**, 267.
8. P. Hayes, B. D. Suthers, and W. Kitching, *Tetrahedron Lett.*, 2000, **41**, 6175.
9. C. E. Holloway and M. Melnik, *J. Organomet. Chem.*, 1995, **495**, 1.
10. H. Kunkely, O. Horvath, and A. Vogler, *Coord. Chem. Rev.*, 1997, **159**, 85.
11. C. Meyer, N. Blanchard, M. Deffosseux, and J. Cossy, *Acc. Chem. Res.*, 2003, **36**, 766.
12. M. Wills, *Contemp. Org. Synth.*, 1996, **3**, 201.
13. J. D. Wuest, *Acc. Chem. Res.*, 1999, **32**, 81.
14. J. Malito, *Annu. Rep. Prog. Chem. Sect. A: Inorg. Chem.*, 1999, **95**, 93.
15. J. Malito, *Annu. Rep. Prog. Chem. Sect. A: Inorg. Chem.*, 2001, **97**, 117.
16. I. B. Gorrell, *Annu. Rep. Prog. Chem. Sect. A: Inorg. Chem.*, 1997, **93**, 117.
17. I. B. Gorrell, *Annu. Rep. Prog. Chem. Sect. A: Inorg. Chem.*, 1998, **94**, 137.
18. C. Eaborn, Z.-R. Lu, P. B. Hitchcock, and J. D. Smith, *Organometallics*, 1996, **15**, 1651.
19. T. N. Mitchell and B. Kowall, *J. Organomet. Chem.*, 1994, **471**, 39.
20. K. R. Flower, V. J. Howard, S. Naguthney, R. G. Pritchard, J. E. Warren, and A. T. McGown, *Inorg. Chem.*, 2002, **41**, 1907.
21. J. Vicente, J.-A. Abad, B. Rink, F.-S. Hernandez, and M. C. Ramirez de Arellano, *Organometallics*, 1997, **16**, 5269.
22. A. F. Cunningham Jr, *Organometallics*, 1997, **16**, 1114.

23. Y.-H. Han, M. J. Heeg, and C. H. Winter, *Organometallics*, 1994, **13**, 3009.
24. W.-Y. Wong, K.-H. Choi, G.-L. Lu, and Z. Lin, *Organometallics*, 2002, **21**, 4475.
25. S. Jarosz and K. Szewczyk, *Tetrahedron*, 2001, **57**, 7549.
26. L. A. Paquette, D. G. Bolin, M. Stepanian, B. M. Branan, U. V. Mallavadhani, J. Tae, S. W. E. Eisenberg, and R. D. Rogers, *J. Am. Chem. Soc.*, 1998, **120**, 11603.
27. Y. Senda, S. Takayanagi, T. Sudo, and H. Itoh, *J. Chem. Soc., Perkin Trans. 1*, 2001, 270.
28. S. Singh, D. Chikkanna, O. V. Singh, and H. Han, *Synlett*, 2003, 1279.
29. N. Matzanke, R. J. Gregg, S. M. Weinreb, and M. Parvez, *J. Org. Chem.*, 1997, **62**, 1920.
30. W. H. Pearson, D. A. Hutta, and W.-K. Fang, *J. Org. Chem.*, 2000, **65**, 8326.
31. H. Huang and C. J. Forsyth, *J. Org. Chem.*, 1995, **60**, 5746.
32. A. J. Frontier, S. Raghavan, and S. J. Danishefsky, *J. Am. Chem. Soc.*, 2000, **122**, 6151.
33. H. Huang and C. J. Forsyth, *J. Org. Chem.*, 1997, **62**, 8595.
34. C. L. Kao and J. W. Chern, *Tetrahedron Lett.*, 2001, **42**, 1111.
35. P. Kocovsky, J. M. Grech, and W. L. Mitchell, *J. Org. Chem.*, 1995, **60**, 1482.
36. J. Cossy, N. Blanchard, and C. Meyer, *Org. Lett.*, 2001, **3**, 2567.
37. A. G. M. Barrett and W. Tam, *J. Org. Chem.*, 1997, **62**, 4653.
38. A. S. Borovik, S. G. Bott, and A. R. Barron, *Angew. Chem., Int. Ed. Engl.*, 2000, **39**, 4117.
39. M. Bodenbinder, G. Balzer-Joellenbeck, H. Willner, R. J. Batchelor, F. W. B. Einstein, C. Wang, and F. Aubke, *Inorg. Chem.*, 1996, **35**, 82.
40. S. J. Faville, W. Henderson, T. J. Mathieson, and B. K. Nicholson, *J. Organomet. Chem.*, 1999, **580**, 363.
41. W.-Y. Wong, L. Liu, and J.-X. Shi, *Angew. Chem., Int. Ed. Engl.*, 2003, **42**, 4064.
42. J. Bravo, J. S. Casas, Y. P. Mascarenhas, A. Sanchez, C. De, O. P. Santos, and J. Sordo, *J. Chem. Soc., Chem. Commun.*, 1986, 1100.
43. F. Zamora, M. Sabat, M. Janik, C. Siethoff, and B. Lippert, *Chem Commun.*, 1997, 485.
44. M. R. Haneline, R. E. Taylor, and F. P. Gabbai, *Chem. Eur. J.*, 2003, **9**, 5189.
45. I. A. Tikhonova, F. M. Dolgushin, K. I. Tugashov, P. V. Petrovskii, G. G. Furin, and V. B. Shur, *J. Organomet. Chem.*, 2002, **654**, 123.
46. M. Nishizawa, H. Takao, V. K. Yadav, H. Imagawa, and T. Sugihara, *Org. Lett.*, 2003, **5**, 4563.
47. M. Nishizawa, V. K. Yadav, M. Skwarczynski, H. Takao, H. Imagawa, and T. Sugihara, *Org. Lett.*, 2003, **5**, 1609.
48. S. H. Kang, J. H. Lee, and S. B. Lee, *Tetrahedron Lett.*, 1998, **39**, 59.
49. S. H. Kang and S. B. Lee, *Chem. Commun.*, 1998, 761.
50. S. Sakamuri, *Tetrahedron Lett.*, 2001, **42**, 4317.
51. G. B. Deacon, E. E. Delbridge, B. W. Skelton, and A. H. White, *Eur. J. Inorg. Chem.*, 1998, 543.
52. G. B. Deacon, C. M. Forsyth, and S. Nickel, *J. Organomet. Chem.*, 2002, **647**, 50.
53. G. B. Deacon and C. M. Forsyth, *Organometallics*, 2003, **22**, 1349.
54. I. P. Beletskaya, A. V. Tsvetkov, G. V. Latyshev, V. A. Tafeenko, and N. V. Lukashev, *J. Organomet. Chem.*, 2001, **637–639**, 653.
55. R. C. Larock and S. Ding, *J. Org. Chem.*, 1993, **58**, 2081.
56. M. D. McClain, D. A. Whittington, D. J. Mitchell, and M. D. Curtis, *J. Am. Chem. Soc.*, 1995, **117**, 3887.
57. W. C. Baird Jr, R. L. Hartgerink, and J. H. Surridge, *J. Org. Chem.*, 1985, **50**, 4601.
58. K. Fagnou and M. Lautens, *Chem. Rev.*, 2003, **103**, 169.
59. S. T. Sarraf and J. L. Leighton, *Org. Lett.*, 2000, **2**, 3205.
60. P. Kocovsky, *J. Organomet. Chem.*, 2003, **687**, 256.
61. P. Kocovsky, V. Dunn, A. Gogoll, and V. Langer, *J. Org. Chem.*, 1999, **64**, 101.
62. L. A. Fowley, J. C. Lee Jr, R. H. Crabtree, and P. E. M. Siegbahn, *J. Organomet. Chem.*, 1995, **504**, 57.
63. L. A. Fowley, J. C. Lee Jr, R. H. Crabtree, and P. E. M. Siegbahn, *Organometallics*, 1996, **15**, 1157.
64. N. Ichinose, K. Mizuno, Y. Otsuji, and H. Tachikawa, *Tetrahedron Lett.*, 1994, **35**, 587.

Metal Ion Toxicity

R. Bruce Martin
University of Virginia, Charlottesville, VA, USA

1	Introduction	1
2	Interdependencies	2
3	Ionic Radii	2
4	Stability Sequences	3
5	Stability Ruler	3
6	Metal Ion Hydrolysis	4
7	Heavy Metal Ion Complexes	4
8	Aluminum	9
9	Related Articles	10
10	References	10

1 INTRODUCTION

This chapter does not focus primarily on *metal* toxicity, although metals may be toxic and damage lung tissue, especially in particulate form and in industrial settings. For comprehensive coverage of this topic see Reference 1. This chapter deals with *metal ion* toxicity because it is via their ions that metals are presented as toxic substances to most of us.

Figure 1 illustrates the biological response of a tissue to increasing concentrations of essential nutrients and toxic substances.[2] The solid curve for an essential nutrient is deliberately drawn with an immediate positive response above zero concentration as if the nutrient were saturating a site and no nutrient were consumed at the lowest levels by other interactions. The solid curve levels off at an optimal level, the width of which depends on the nutrient. Finally, at excess concentrations, deleterious effects settle in, the biological response becomes unfavorable, and the once nutritious substance becomes toxic.

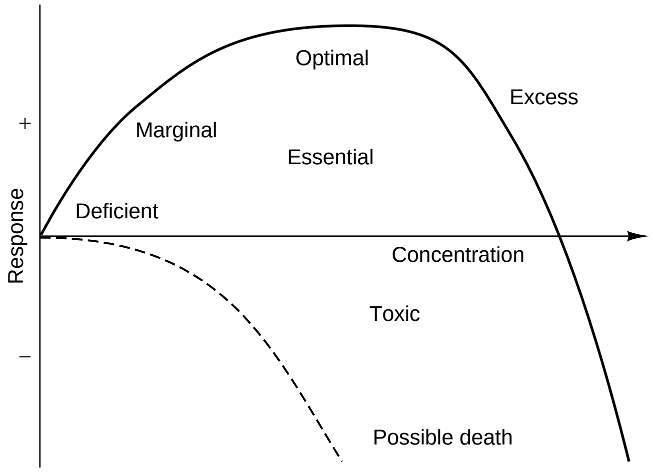

Figure 1 Biological response dependence on tissue concentration of an essential nutrient (solid curve) and of a deleterious substance (dashed curve). The relative position of the two curves on the concentration axis is arbitrary and one of convenience. (Reprinted from Ref. 2 by permission of Marcel Dekker, Inc)

The dashed curve in Figure 1 for a toxic substance shows a lag region under the assumption that an organism can cope with some amount of a substance before toxic effects become evident (threshold). For both essential nutrients and toxic substances, Figure 1 shows general characteristics; each substance has its own specific curve of biological response versus concentration.

Figure 1 emphasizes the point that an essential nutrient may become toxic at sufficiently high concentrations. Almost any substance in excess ultimately becomes harmful, even if the action is indirect, such as limiting absorption of other essential nutrients. The optimal region at the plateau in Figure 1 may be wide as for sodium or narrow as for fluoride and selenium. Animals maintain a concentration within the optimal range by a complex set of physiological reactions termed *homeostasis*. Concentrations of all essential metal ions are under homeostatic control. The detailed mechanism of homeostasis for individual substances remains an area of current research.[3]

Twenty-one elements are essential to humans. An essential nutrient is one for which a deficiency results in an impairment in function that is relieved only by administration of that substance. Vitamins by definition and some minerals are essential. The significance of essentiality may be illustrated by burlesquing an old adage.

> ‘For want of a nail the shoe is lost, for want of a shoe the horse is lost, for want of a horse the rider is lost.’

George Herbert, *Jacula Prudentum* (Outlandish Proverbs), 1640

> ‘For want of a nutrient the enzyme is lost, for want of an enzyme the function is lost, for want of a function the life is lost.’

Bruce Martin, *Summa Veritatis* (Lofty Truth), 1989

Four essential elements, H, O, C, and N, comprise more than 99 atom % and about 96 wt % of the human body. These 4 and 14 other essential elements occur among the first 30 elements (through zinc) of the periodic table. (Uncertainties surround the status of chromium (*see* ***Chromium: Biological Relevance***).[4]) Three heavier trace elements Se, Mo, and I are also essential in humans. For 17 tabulated essential elements, Table 1 shows the predominant elemental form at pH 7, typical adult concentrations in the blood plasma or serum, the approximate amount found in a 70-kg adult, and a recommended adult daily allowance. In addition to

Table 1 Essential elements for humans[a]

Element	pH 7 form	Serum conc.	Human amt.[b]	Daily allowance
Na	Na^+	140 mM	70 g	1–2 g
K	K^+	4 mM	130 g	2–5 g
Mg	Mg^{2+}	0.8 mM	22 g	0.3 g
Ca	Ca^{2+}	2.4 mM	1100 g	0.8 g
Mn	Mn^{2+}	10 nM	12 mg	3 mg
Fe	$Fe(OH)_3\downarrow$	17 μM	4 g	10–20 mg
Co	Co^{2+}	2 nM	1 mg	3 μg vitamin B_{12}
Cu	Cu^{2+}	17 μM	80 mg	3 mg
Zn	Zn^{2+}	14 μM	2.3 g	15 mg
Cr	$Cr(OH)_2{}^+$	3 nM	6 mg	0.1 mg
Mo	$MoO_4{}^{2-}$	6 nM	5 mg	0.2 mg
Cl	Cl^-	104 mM	80 g	2–4 g
P	$HPO_4{}^{2-}$	1.1 mM	600 g	1 g
S	$SO_4{}^{2-}$	24 mM	120 g	0.7 g Met[c]
Se	$HSeO_3{}^-$	1 μM	5 mg	0.1 mg
F	F^-	2 μM	2.5 g	2 mg
I	I^-	0.4 μM	30 mg	0.15 mg

[a]In addition to H, C, N, and O. [b]Approximate amount found in a 70-kg adult. [c]Essential amino acid methionine.

the basic four elements, the essential elements include two alkali metal ions, two alkaline earth metal ions, six first-row transition metal ions (the most common, iron, contributes less than 0.01% of body weight), molybdenum, phosphorus, sulfur, selenium, and three halogens. Thus 11 metal ions are essential. Table 1 shows that most of the remaining 4% of body weight consists of two elements found in bone, Ca and P. Many of the elements do not exist predominantly in their pH-7 forms in the serum as they are combined with other components. For example, Fe^{3+} does not precipitate as the hydroxide but is retained by tightly chelating ligands. There is little free iodide; it occurs as part of the thyroid hormones. For sulfur, Table 1 lists the total serum concentration, most of which appears in proteins; there is only about 1 mM nonprotein sulfur. Sulfur is not important as an inorganic element but only as part of the amino acids cysteine and essential methionine. An additional four elements, B, Si, V, and Ni, not included in Table 1, are essential for other organisms.

2 INTERDEPENDENCIES

Metal ion toxicity does not relate to essentiality. Toxicity and essentiality do share, however, one feature: frequent interdependencies among metal ions, between metal ions and nonmetals, and between both, and organic molecules such as vitamins. For example, excess Zn^{2+} may reduce absorption of essential Cu^{2+}, while a deficiency of Zn^{2+} worsens Cd^{2+} toxicity. Such antagonisms and mutual dependencies produce variable toxicities for like concentrations of an element, and hinder any attempt to formulate simple guidelines for essentiality or toxicity.

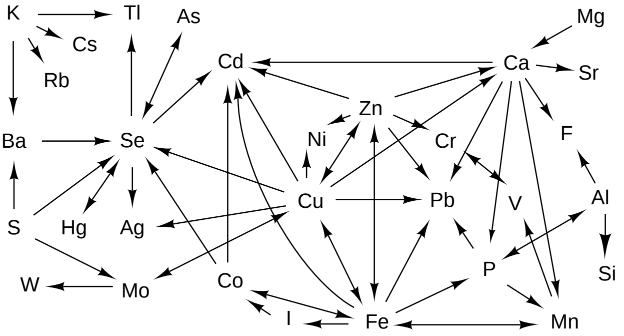

Figure 2 Interdependencies among 30 elements in mammals. An arrow from element A to B indicates that administration of element A may reduce toxicity of element B, low levels of element A may heighten toxicity of element B, or high levels of element B may inhibit salutary effects of element A. (Reprinted from Ref. 2 by permission of Marcel Dekker, Inc)

Interdependencies among 30 elements in mammals are diagrammed in Figure 2.**[5]** The figure does not exhaust all possibilities but serves to show both the commonality and complexity of the interactions among elements. Figure 2 points out that heavily supplementing a diet with one mineral may upset the balances with others.

Figure 2 shows that both Cd^{2+} and Pb^{2+} share interdependencies with several other elements, accounting for some of their toxicities. Cd^{2+} interferes with activities of essential Ca^{2+} and Zn^{2+}, and a low-Ca^{2+} diet enhances Cd^{2+} absorption. Pb^{2+} interacts with systems that use Ca^{2+}, iron, and Zn^{2+}. Ca^{2+}, Cd^{2+}, and Pb^{2+} possess similar ionic radii (Table 2), so that the pair of detrimental metal ions may substitute for Ca^{2+}.

3 IONIC RADII

Like size usually plays a greater role than identical charge in promoting metal ion substitutions in both mineralogy and biology. For example, the plagioclase feldspars display a continuous series of aluminum silicate mixtures in a common lattice from $NaAlSi_3O_8$ to $CaAl_2Si_2O_8$. Neither Mg^{2+} nor Sr^{2+} replace Ca^{2+} in this series. The charge compensation required in minerals is not critical when substitution occurs in a protein or in other biological ligands.

Table 2 presents effective ionic radii for many metal ions.**[6]** For any metal ion, the radius increases with coordination number since the greater number of bonds weakens the strength of any one bond. The radius of the most common coordination number is underlined in Table 2. The alkali and alkaline earth metal ions exhibit variable coordination numbers without strong directionality in bonding. Because they are of similar size, Ca^{2+} and Na^+ of differing charges

Table 2 Effective ionic radii in picometers[a] [6]

	Coordination number					
Ion	4	5	6	7	8	9
Be^{2+}	$\underline{27}$		45			
Al^{3+}	39	48	$\underline{54}$			
Cr^{3+}			$\underline{62}$			
Ga^{3+}	47	55	$\underline{62}$			
Fe^{3+}	49	58	$\underline{64}^{b}$		78	
Ni^{2+}	55	63	$\underline{69}$			
Mg^{2+}	57	66	$\underline{72}$		89	
Cu^{2+}	57	65	73			
Co^{2+}	58	67	$\underline{74}$		90	
Zn^{2+}	$\underline{60}$	68	74		90	
Li^{+}	59		76		92	
Fe^{2+}	63		$\underline{78}^{c}$		92	
Mn^{2+}	66	75	$\underline{83}$	90	96	
Lu^{3+}			86		$\underline{98}$	103
Gd^{3+}			94	100	$\underline{105}$	111
Cd^{2+}	78	87	$\underline{95}$	103	110	
Ca^{2+}			100	106	$\underline{112}$	118
La^{3+}			103	110	116	$\underline{122}$
Na^{+}	99	100	$\underline{102}$	112	118	124
Sr^{2+}			118	121	126	131
Pb^{2+}	98		119	123	129	135
Ba^{2+}			135	138	142	147
K^{+}	137		138	146	$\underline{151}$	155
Tl^{+}			150		159	
Rb^{+}			152	156	161	163
Cs^{+}			167		174	178

[a] The radius of the most common coordination number is underlined. [b] High spin; low spin value is 55. [c] High spin; low spin value is 61.

often interchange in biological systems. Ba^{2+} is poisonous because of its antagonism to K^{+} of similar radius and not to Ca^{2+} of identical charge but smaller radius. Ba^{2+} is a muscle poison for which one antidote is intravenous infusion of K^{+}. Table 2 shows that Co^{2+} and Zn^{2+} exhibit similar radii in all coordination numbers.

4 STABILITY SEQUENCES

From the many studies on stability constants, one finds the order of metal ion stabilities to be dependent on the ligand. Metal ion stabilities increase in the following orders:

$$\text{Glycine: Ca, Mg} \ll \text{Mn} < \text{Fe, Cd, Pb,} < \text{Co, Zn} < \text{Ni}$$
$$\ll CH_3Hg^{+}, \text{Cu} \ll \text{Hg}$$
$$\text{1, 2-Diaminoethane(en)} : \text{Mg} \ll \text{Mn} \ll \text{Fe} < \text{Pb, Cd, Co, Zn}$$
$$\ll \text{Ni} < CH_3Hg^{+} \ll \text{Cu} \lll \text{Hg}$$

The ion Ca^{2+} does not form stable amine complexes. Except for methyl mercury, CH_3Hg^{+}, all the metal ions carry two positive charges. Owing to the strongly chelating bidentate ligands, glycine (gly) and 1,2-diaminoethane (en), CH_3Hg^{+} with only a single, strong binding site is at a competitive disadvantage in the above series. CH_3Hg^{+} binds to a unidentate ligand more strongly than all of the above metal ions except Hg^{2+}.

In the above series, each inequality sign stands for an approximate 10-fold increase in the stability constant. The two series gly and en are similar, their major difference being a stability constant span from Mg^{2+} to Hg^{2+} of 10^{9} for glycine and 10^{14} for en. Generally, the increment between metal ions increases on passing from $O < N < S$ donor atoms. The presence of a sulfur donor promotes Cd^{2+} and Pb^{2+} to higher positions than in the above series. The order of increasing sulfur binding strengths is $Zn^{2+} < Cd^{2+} < Pb^{2+} < CH_3Hg^{+} < Hg^{2+}$. Sulfhydryl group interactions are the main mode of toxicity of the heavy metal ions. These general bonding features are expressed in the concept of the stability ruler.

5 STABILITY RULER

For a single ligand, the Irving–Williams stability sequence of dipositive metal ions is Mg < Mn < Fe < Co < Ni < Cu > Zn, irrespective of ligand. The uniformly progressive part of this sequence from Mg^{2+} to Cu^{2+} defines a *stability ruler* against which more variable metal ions may be compared.[2] The stability ruler appears across the top of Table 3. For several ligand donor sets, Table 3 shows the relative binding strengths of the variable dipositive metal ions Zn^{2+}, Cd^{2+}, Pb^{2+}, and Hg^{2+}. Their placement in Table 3 corresponds to their stability constants compared with those of the metal ions that define the ruler. The entries for glycine and en agree with the series in the previous section. With most of the metal ions in Table 3, histidine will be tridentate.[7,8] The increment between metal ions and hence the length of the stability ruler increases with the substitutions O < N < S. The ruler length for binding to each ligand appears in the next to last column of Table 3 in log K units. The longer the ruler, the more discriminating the ligand in selecting among metal ions. Thus, oxygen donor atoms are the least discriminating among metal ions, nitrogen donors intermediate, and sulfur donors the most discriminating.

From Table 2, we can see that not only do Co^{2+} and Zn^{2+} display nearly identical radii for the same coordination number but they also exhibit similar stabilities for all ligands in Table 3, except for those involving sulfur and hydroxide. The similarities allow the facile and useful substitution of Co^{2+} for Zn^{2+} in many enzymes. When a sulfhydryl group is present, as in 2-mercaptoethylamine, Zn^{2+} binding strengthens, equaling that for Ni^{2+}. Table 3 also shows the relative strengthening of Cd^{2+} and Pb^{2+} binding with the sulfhydryl donor in 2-mercaptoethylamine.

Table 3 Stability ruler[a]

Ligand	Donors	Mg	<	Mn	<	Fe	<	Co	<	Ni	<	Cu	Length[b]	Hg[c]
Hydroxide	OH^-				Cd						Zn	Pb	3.7	1.2
Acetate	O^-									Zn	Cd	Pb	1.3	1.2
Imidazole	=N							Zn	Cd				4.0	1.1
Ammonia	NH_3						Pb		Zn	Cd			4.0	1.1
Oxalate	O^-,O^-				Cd			Zn	Pb				2.1	
Glycine	N,O^-					Cd	Pb	Zn					6.1	0.4
Histidine	N,=N					Cd	Pb	Zn					8.2	0.2
$NH_2(CH)_2\ NH_2$	N,N					Pb	Cd	Zn					10.1	0.4
$NH_2(CH)_2S^-$	N,S^-									Zn	Cd	Pb	12(est.)	0.2

[a] All dipositive cations. [b] Ruler length in difference between log stability constants of Cu^{2+} and Mg^{2+} complexes. [c] Relative magnitude that the Mg^{2+} to Cu^{2+} length must be extended to reach the Hg^{2+} value.

Cd^{2+} binds more strongly than Zn^{2+} to most unidentate ligands. Probably because of an unfavorable ring bite size for the relatively large Cd^{2+} (Table 2), Zn^{2+} chelates more strongly to ligands containing O and N donors in five-membered rings. Table 3 shows that upon introduction of an S donor atom into a chelate, Cd^{2+} becomes the stronger metal ion binder.

For all donor sets in Table 3, Hg^{2+} binds so strongly that it is off the end of the ruler scale. The number under Hg in the last column of Table 3 refers to the relative distance by which the length of the whole log stability constant scale from Mg^{2+} to Cu^{2+} must be extended to reach the value for Hg^{2+}. A telling contrast appears between the length of the extension for most bidentate ligands and that for unidentate ligands. The scale extension for Hg^{2+} amounts to 0.2 to 0.4 log units for bidentate ligands and to 1.1 to 1.2 log units for the three unidentate ligands at the end of Table 3. The difference arises because Hg^{2+} prefers linear, two coordination and binds the second donor atom in small chelate rings much more weakly than it does the first donor atom.

We may generalize the results and conclusions of the stability ruler by noting that alkali metal and alkaline earth metal ions, lanthanides, and Al^{3+} prefer oxygen donors; transition metal ions, oxygen and nitrogen donors; and the heavy metal ions, nitrogen and sulfur donors. For amplification of this topic, (*see* ***Hard & Soft Acids and Bases***).

6 METAL ION HYDROLYSIS

The higher the charge density or charge-to-radius ratio, the more likely a metal ion undergoes hydrolysis in aqueous solutions to give hydroxo complexes. Hydroxo complexes may abruptly form polynuclear complexes and precipitate even in solutions more acidic than the pK_a for the first hydroxo complex formation. The first five small metal ions in Table 2 hydrolyze even in acidic solutions and form precipitates. In six-coordination, the charge-to-radius ratio for the first five metal ions is greater than 0.044, while for all the other metal ions in Table 2, the ratio is less than 0.035. The first five metal ions cannot occur to an appreciable extent in the bloodstream (pH 7.4) as the free aqueous ion and must be complexed in some way. Covalency may also promote complex formation and hydrolysis in acidic solutions, as is the case for Hg^{2+}.

Hydroxo complex formation follows the same stability order as other ligands with the strongest binding at the right of the stability ruler in Table 3, where the hydroxide ion appears as the first entry. The stability ruler in Table 3 shows that both Zn^{2+} and Pb^{2+} exhibit a relatively strong tendency to form hydroxo complexes and precipitates.

7 HEAVY METAL ION COMPLEXES

The most serious side effects of many metal ions result from the inhalation of dusts, usually in an industrial setting. Especially bad are particles 0.1 to 1 μm in diameter, which are effectively absorbed in the lungs. The lungs are 10 times more effective in absorbing most metal ions into body fluids than are the intestines. Thus, the greater danger from radioactive plutonium-239, an emitter of damaging α particles with a half-life of 24 400 years, results not from its ingestion, but from adsorption of its powders onto lung tissue. Volatile metal compounds such as the carbonyls and alkyl compounds of mercury, tin, and lead are readily absorbed via the lungs and may give rise to acute toxicity. Obviously, inhalation of metal ions should be avoided. Since inhalation episodes are local events, we shall not mention them further; they are covered in the compendia.

Fortunately, many metal ions are less harmful than they might be because of their intrinsic chemical behavior, such as formation of insoluble compounds in the gut with subsequent elimination of the metal ion. Other fractions of metal ions travel in the blood to other tissues, where they are immobilized, like lead in bone, or to the liver or kidneys, where they are complexed in a less toxic or disposable form. Even a relatively toxic metal ion (nonradioactive) requires almost a gram amount for lethality, much more than for potent organic toxins.

Sulfhydryl groups of proteins furnish the vehicle for both the toxicity and detoxification of most heavy metal ions. In the stability ruler (Table 3) discussion, we noted the special avidity of heavy metal ions for sulfhydryl groups. Both Cd^{2+} and Pb^{2+} exhibit enhanced binding to sulfhydryl groups compared with that to N or O donor ligands. Still stronger is the binding of both Hg^{2+} and CH_3Hg^+ to sulfhydryl groups.

In response to the presence of detrimental Cd^{2+}, Hg^{2+}, Pb^{2+}, and other heavy metal ions, the human liver and kidneys synthesize more *metallothionein,* an unusual small protein in which approximately one-third of the 61 amino acid residues are cysteine (*see* ***Metallothioneins***). The frequency and juxtaposition of sulfhydryl groups provide strong binding sites for several heavy metal ions. Though not as profusely as metallothionein, many proteins contain sulfhydryl groups that may become metalated by toxic heavy metal ions such as Cd^{2+}, Hg^{2+}, and Pb^{2+}, and it is widely believed that this complex formation explains the toxicity of these metal ions. The exact proteins where the most consequential damage occurs remain uncertain.

Toxic metal ions enter many tissues, and the greatest damage does not always occur where the metal ion is most plentiful. For example, more than 90% of Pb^{2+} may become immobilized in bone, but the toxic effects result from the remaining 10% distributed among other tissues, where it may react with sulfhydryl groups on any number of proteins. The immobilization of Pb^{2+} in bone may act as a detoxifying mechanism even though it is more likely the result of an incidental property of the metal ion rather than a deliberate intent of the organism.

Topics not included here or appearing in more length elsewhere include book-length discussions of concepts and summaries,[9–12] toxic metal ions in the environment[13] and nervous system,[14] and cisplatin as an anticancer agent (*see* ***Platinum-based Anticancer Drugs***).[15] An element by element discussion of toxicity appears in a convenient handbook.[1]

For the purpose of considering their toxicity, metal ions may be divided into three groups. In the first group are the alkali and alkaline earth metal ions and the Al^{3+} group. Of these, most are harmless in the amounts that they usually occur. Be^{2+} is a dangerous substance with latent toxicity and should be handled cautiously or not at all. Fortunately, it is quite rare, and it is not discussed further here. Of this first group, Al^{3+} is common and sometimes occurs in deleterious quantities, and is the only nonheavy metal ion that warrants discussion, in Section 8. The second group consists of the light first-row transition metal ions that are not especially harmful in available quantities and often are essential (Table 1). Finally, the third group consists of heavy second and third row transition metal ions that include toxic Cd^{2+}, Hg^{2+}, Tl^+, and Pb^{2+}, which are discussed below. The emphasis is on toxicity in humans. For many metal ions, *acute* toxicity arising from a sudden exposure to a large dose leads to different effects and symptoms than *chronic* toxicity, which may be due to low-dose exposures over a long time period. The symptomatic descriptions of acute and chronic toxicity rely on two comprehensive compendia.[1,10]

7.1 Cadmium[2]

Relatively rare, Cd^{2+} occurs in minerals and soils in association with zinc to about 0.1%. Like Zn^{2+}, the metal occurs only as a 2+ ion, Cd^{2+}. Cd^{2+} is larger than Zn^{2+} and more nearly the size of Ca^{2+} (Table 2), leading to its use as a Ca^{2+} probe in protein systems. However, in its binding strength to ligands, Cd^{2+} is much more like Zn^{2+} (stability ruler, Table 3), and it is in competition with Zn^{2+} that the greater number of its toxic effects arise (Figure 2). In contrast to Ca^{2+}, both metal ions bind strongly to nitrogen and sulfur donor ligands. Excess Cd^{2+} disturbs mineral metabolism, interferes with Zn^{2+} and other enzymes, and may redistribute Zn^{2+} in the body.

In strong contrast to CH_3Hg^+, Cd^{2+} does not easily cross the placental barrier, and newborns are virtually Cd^{2+} free. For most individuals, Cd^{2+} is slowly accumulated from foods. The body only slowly releases absorbed Cd^{2+}, which has a half-life of 30 years in the kidneys. As a consequence, the Cd^{2+} content of the kidneys increases throughout life from zero at birth to about 20 mg in a middle-aged nonsmoker and more than twice as much in an adult smoker. Much of the Cd^{2+} is bound by metallothionein, a small protein with sulfhydryl binding sites, whose production is stimulated by Cd^{2+}.

Acute Cd^{2+} poisoning, signaled by vomiting, abdominal cramps, and headache, may arise from drinking water or other, especially acidic, liquids that have contacted cadmium-containing solders in water pipes and vending machines with cadmium-glazed pottery. Ingested Cd^{2+} is transported to other organs by the blood, where it is bound by glutathione and hemoglobin in the red cells. The blood of smokers contains about seven times as much Cd^{2+} as that of nonsmokers. Cd^{2+} stimulates metallothionein synthesis in the liver. The metal–protein complex passes through the blood to the kidney. Chronic Cd^{2+} poisoning damages the liver and kidneys, leading to severe kidney malfunction. There is no specific therapy for Cd^{2+} poisoning; chelating agents may harmfully redistribute Cd^{2+} to the kidney. Consuming plentiful quantities of Zn^{2+}, Ca^{2+}, phosphate, vitamin D, and protein may lessen the impact of Cd^{2+} toxicity.

An especially serious form of Cd^{2+} poisoning has been described in Japan as itai-itai (Japanese for ouch-ouch) disease. The name derives from pain in the back and legs due to osteomalacia or bone decalcification (usually in older women) leading to easy fracturing (72 fractures in one victim). There is also severe kidney damage with proteinuria (protein in the urine) persisting even after exposure ceases. This disease leads to early death. In Japan, it was caused by the consumption of Cd^{2+}-laden water, either directly through drinking or through the eating of crops, especially rice, irrigated by the water over a period of many years. Though there was earlier, visible damage to the rice crop, it took 17 years from the first medical studies on humans to the final fixing of legal responsibility on to the zinc-mining company that had discarded the unwanted cadmium by-product into a river used for drinking and irrigation.[16]

7.2 Mercury[2]

Mercury is detrimental to mammals in all of its forms. The global release of mercury by degassing from the earth's crust and oceans exceeds that produced by humans by a factor of at least 5, but industrial discharges are more local and concentrated. The average person carries 13 mg of mercury in the body; this does not serve any useful purpose, although various mercuric salts have been used as therapeutic agents, for example, mercuric benzoate to treat syphilis and gonorrhea. Use of mercury reagents as insecticides and fungicides has led to many small-scale and several disastrous large-scale poisonings involving thousands of people. Mercury poisoning is a worldwide problem.

Mercury occurs in three common forms and in one uncommon form as mercurous ion that disproportionates to two of the common forms, elemental mercury and the mercuric ion:

$$Hg_2{}^{2+} \rightleftharpoons Hg^0 + Hg^{2+} \qquad K = \frac{Hg^{2+}}{Hg_2{}^{2+}} = \frac{1}{170}$$

The value of the equilibrium constant for the reaction indicates that the favored direction of the reaction is actually from right to left. It is driven to the right by the strong complexation of Hg^{2+} with any of a large number of ligands. The third common form of mercury is as organic mercurials such as methyl mercury, CH_3Hg^+.

Mercury is one of the few elements that remains liquid at room temperature. Though its boiling point is 357 °C, it is more volatile and hence more dangerous than generally appreciated. At saturation at 25 °C, a cubic meter of air holds 20 mg of Hg. Spilled mercury is a health hazard in rooms with poor ventilation. Elemental mercury is almost insoluble in water, dissolving to the extent of 0.29 μM at 25 °C, 58 μg liter^{-1}, or 58 ppb.

Both the mercuric ion, Hg^{2+}, and methyl mercury, CH_3Hg^+, prefer linear two-coordination. They form stronger complexes with a single donor atom, especially N and S, than most metal ions. Rare among metal ions, Hg^{2+} in basic solutions substitutes for a hydrogen on amines (in contrast with ammonium ions) as in mercuric amidochloride, $ClHgNH_2$. At high pH values, excess CH_3Hg^+ substitutes for a hydrogen on the $–NH_2$ groups at C4 in cytidine and C6 in adenosine.[17] Hg^{2+} may add third and fourth donor atoms to give a distorted tetrahedron. The last two ligands are bound much more weakly than the first two and exhibit longer Hg^{2+}–donor atom bond lengths. The ability of linear, two-coordinated Hg^{2+} and CH_3Hg^+ to associate weakly with additional donor atoms accounts for the rapid metal ion exchange among donor atoms, as is discussed below.

Because they prefer linear, two-coordination, there is not much chelate effect with Hg^{2+} and CH_3Hg^+. In contrast to most metal ions, the stability constant logarithm for Hg^{2+} and CH_3Hg^+ binding to 1,2-diaminoethane is less than the sum of the values for binding to two ammonia molecules, that to glycine is less than the sum for ammonia and acetate, and that to histidine is less than the sum for ammonia and imidazole. However, owing to the great strength of binding to a single nitrogen donor atom, the stability constants for the weakly chelated Hg^{2+} and CH_3Hg^+ with diaminoethane, glycine, and histidine still exceed those for most metal ions.

In pure water, HgO precipitates at pH > 2 and CH_3HgOH forms at pH > 5. The chloride ion binds with high stability. The first two Cl^- that give linear $HgCl_2$ are bound 10 times more strongly than the last two Cl^- that give tetrahedral $HgCl_4{}^{2-}$.[18] In seawater, with its high 0.56 M Cl^- background, the predominant species are $HgCl_4{}^{2-}$ and CH_3HgCl.

In almost any biological system, an excess of sulfhydryl donors is expected to bind all Hg^{2+} and CH_3Hg^+. The name mercaptan ('mercury capture') derives from the strong Hg^{2+} binding to thiols. In red blood cells, Hg^{2+} links glutathione and hemoglobin sulfhydryl groups in a mixed complex. Only a fraction of body Hg^{2+} remains in the blood. Though the molecular basis of Hg^{2+} toxicity by interaction at sulfhydryl groups is generally understood, the specific proteins undergoing consequential damage remain uncertain. Many proteins contain reactive sulfhydryl groups. Hg^{2+} also forms inert bonds at C5 in pyrimidines. The long retention times of mercury in tissues may result from formation of inert aromatic carbon–mercury bonds involving nucleic bases or amino acid side chains.

In spite of being very strongly bound, ligands show rapid exchange in and out of coordination to Hg^{2+} and CH_3Hg^+. Substitution of inner-sphere water in Hg^{2+} occurs with a half-life of less than 10^{-9} s, as fast as any metal ion. For CH_3Hg^+ binding to the sulfhydryl group of glutathione, the stability constant $\log K = 15.9$. For such strong binding, the half-life for exchange by a dissociation mechanism is about 10 days, yet the average lifetime for the CH_3HgSR complex in the presence of excess glutathione is less than 0.01 s. This comparison shows that the exchange does not occur by a dissociation mechanism. The clue to the exchange mechanism in Hg^{2+} and CH_3Hg^+ compounds is the weak coordination of third and fourth ligands (mentioned near the beginning of this section). Excess ligand participates in a nucleophilic attack at an uncoordinated site on the metal ion, with rearrangement in the coordination geometry and release of a formerly bound ligand. This addition–elimination mechanism accounts for the very rapid exchange in Hg^{2+} and CH_3Hg^+ complexes.

The rapid exchange of Hg^{2+} and CH_3Hg^+ among excess donor ligands such as sulfhydryl groups plays a key role in toxicology. It accounts for the fast partitioning of the mercury among sulfhydryl groups in tissues. In the blood, CH_3Hg^+ partitions in the same proportion as the populations of sulfhydryl groups, about 10% in the plasma and 90% in the erythrocytes, which contain both hemoglobin and glutathione sulfhydryl groups. To be avoided as an antidote for mercury poisoning, British anti-Lewisite or BAL (2,3-dimercaptopropanol) promotes the distribution of mercury throughout the body.

Inhaled mercury vapor is efficiently absorbed and accumulates in the brain, kidneys, and testicles. It also crosses the placental barrier. Acute poisoning causes lung damage. In tissues, elemental mercury is converted to the mercuric ion, which combines with sulfhydryl-containing molecules, including proteins. Chronic poisoning gives rise to permanent nervous system damage, resulting in fatigue, and at higher levels, to a characteristic mercurial tremor in which a fine trembling is interrupted every few minutes by coarse shaking.

Ingestion of even 1 g of a mercuric salt is lethal. Mercuric salts accumulate in the kidneys; in contrast with elemental mercury, they do not readily cross the blood–brain or placental barriers. Acute poisoning by ingestion results in precipitation of proteins from the mucous membranes of the gastrointestinal tract, causing pain, vomiting, and diarrhea. If the patient survives this damage, the kidney becomes the critical organ. There is some red cell hemolysis. Chronic poisoning gives rise to central nervous system damage. The Mad Hatter in *Alice in Wonderland* by Lewis Carroll represents an occupational disease caused by poisoning by $Hg(NO_3)_2$, used in the treatment of furs.

Organic mercurials such as methyl mercury chloride, CH_3HgCl, are highly toxic owing to their high volatility. Microorganisms in polluted waters freely convert various forms of inorganic mercury to methyl mercury, CH_3Hg^+. Most of the mercury in fish occurs as CH_3Hg^+, which is retained for years or until the fish is eaten. High levels of CH_3Hg^+ do not appear as toxic to fish as to humans. In humans, inhaled or ingested CH_3Hg^+ is efficiently absorbed; appears in the red blood cells, liver, and kidneys; and accumulates in the brain, including the fetal brain, where it causes serious, cumulative, irreversible damage to the central nervous system. In the human body, the retention half-life ranges from months to years. The effects are insidious, the appearance of symptoms often delayed for many years.

Two of the most well-known examples of mercury poisoning were both due primarily to CH_3Hg^+. In 1956, ‘Minamata disease’ was discovered near Minamata Bay in southern Japan. In 1959, it was shown that the disease was caused by eating fish contaminated by mercury from CH_3HgCl discharged by a chemical manufacturer into the bay. The mercury load was so great that some fish died, fish-eating birds dropped into the sea, and cats would stagger, ‘whirl violently, then dash away on a zigzag course or collapse’.**[19]** Even as early as 1954, this ‘dancing disease’ had markedly reduced the local cat population. No records of mercury contamination levels in the area were taken before 1959. Owing to the Japanese custom of saving dried umbilical cords of infants, it was possible to demonstrate human mercury contamination as far back as 1947. Not until 1968 was the dumping brought to a halt.

In humans, the onset of Minamata disease due to CH_3Hg^+ begins with numbness in the limbs and face, sensory disturbance, and difficulty with hand movements such as writing. Later there is a lack of coordination, weakness, tremor, uncoordinated walking, mental disturbance, slurred speech, impaired hearing, and constriction of the visual field. Finally, there is general paralysis, limb deformity especially in the fingers, difficulty in swallowing, convulsions, and death. Tragically also, children born of mildly diseased mothers, who may or may not have exhibited symptoms themselves, suffered from cerebral palsy and idiocy. (Normally, cerebral palsy is not associated with significant mental retardation.) Evidently, the mother discharges CH_3Hg^+ through the placental barrier into the highly susceptible fetus.**[19]** Women with more serious disease levels are unable to give birth to live children.

In Iraq, in the winter of 1971 to 1972, ingestion for 2 to 3 months of bread made from seed wheat treated with a CH_3Hg^+ fungicide resulted in over 6000 hospital admissions and 500 deaths. Symptoms were similar to those listed above for Minamata disease. In the United States, registration of CH_3Hg^+ as a seed fungicide was suspended in 1970, but a manufacturer obtained an injunction against the suspension, allowing sales to continue. A suspension by the Environmental Protection Agency was finally made to stick in 1972.**[20]**

7.3 Thallium

This dispersed element occurs with lead in galena, PbS, where Tl^+ and Bi^{3+} (or Sb^{3+}) replace two Pb^{2+}. Tl^+ replaces the similarly sized K^+ and Rb^+ (Table 2) occurring in some feldspars and micas. Thallium usually appears in the 1+ oxidation state, but appears as 3+ in the rare mineral Avicennite, Tl_2O_3, found in Central Asia. If Tl(III) were to appear in the ocean, it would be present as $Tl(OH)_3(aq)$.**[18]** Contrary to the usual principle of hard and soft acids and bases (*see* ***Hard & Soft Acids and Bases***), Tl(III) is softer than Tl(I).**[21]**

Once used as medicinal agents and rodenticides, thallium salts are no longer available in most countries for these purposes owing to their high toxicity. Other uses for thallium salts continue, especially in communication systems where there is an increasing demand for them as an ingredient of fiberglass. The sulfides in coal carry thallium, and coal burning is the major source of thallium release into the environment. A typical coal consists of 1 ppm thallium, but some coals contain more. Except in the vicinity of coal burning plants, thallium release is probably not a hazard to humans. Worldwide, thallotoxicosis from ingestion of thallium-based rodenticides remains one of the most common acute toxic diseases caused by metals.[22]

Both Tl(I) and Tl(III) salts are readily absorbed by the gastrointestinal tract and the skin. Excretion is slow with a half-life of nearly one month. Thallium concentrates in the brain and testes. The lethal dose is less than 1 g of a thallium compound in a single ingestion. Thallotoxicosis involves the nervous system, skin, hair loss, and the cardiovascular system. Tl^+ can substitute for the similarly sized K^+ (Table 2 and Figure 2) and interfere in K^+-dependent processes (Figure 2). Recovery from thallotoxicosis takes months and may be incomplete as nervous system damage may be irreversible.[22] Thallium may be the most toxic nonradioactive metal.

As this summary indicates, thallium compounds are dangerously and cumulatively toxic even at low levels. They should be handled with great care and respect, never being allowed to touch the skin or be ingested.

7.4 Lead[23]

Owing to its easy reduction from its ores upon heating, metallic lead has been known for 6000 years. Wealthy Romans suffered from lead toxicity because their food was cooked, their wine and acidic fruits stored, and their water piped in leaden vessels. What part such lead exposure played in the demise of Roman culture and empire has been debated.[24,25] Under stomach conditions, metallic lead is oxidized to Pb^{2+}, the only important oxidation state under biological conditions. Painters, such as Goya, suffered from inhalation and accidental ingestion of Pb^{2+} from paints. Benjamin Franklin diagnosed himself a ‘lead colic’ because of his long exposure to lead type used in printing.

Today food and water are the main sources of lead in the body, and children are more likely to absorb and retain lead. With the elimination of lead additives in gasoline, their airborne combustion products contribute much less to pollution than in the past. The body burden of lead increases with age, beginning with the fetus as lead crosses the placental barrier. Today, the average adult body contains about 120 mg of lead, 10 times the amount found in Egyptian mummies. More than 95% of the body burden of Pb^{2+} accumulates in bones.

Acute lead toxicity produces appetite loss and vomiting. Chronic toxicity leads to renal malfunction, anemia, gout, and nervous system disorders, including brain damage in children. (Lead inhibits development in fetal and child brains.) The effects are more serious for a patient deficient in calcium, zinc, or iron (see Figure 2). Available Pb^{2+} affects the structure and function of the bone marrow, where it inhibits several enzymes involved in heme synthesis. It also affects mitochondrial functions in diverse ways. It has proven difficult, however, to specify critical interactions in lead toxicity. Pb^{2+} is not particularly carcinogenic but quite toxic. Acute toxicity is dealt with by infusion of Ca^{2+}-EDTA, with the intent of exchanging metal ions on the EDTA, (ethylenedinitrilotetraacetate).

Interactions of Pb^{2+} severely restrict the free Pb^{2+} concentration in body fluids. More than 95% of the Pb^{2+} in blood occurs in the red cells, where glutathione promises to be the strongest small molecule binder. From the limited solubility of insoluble $HOPO_3Pb$, a detailed calculation reveals that the allowed free Pb^{2+} concentration is only about 25 nM for extracellular fluids and 10 nM for intracellular fluids.[23] These very low concentrations indicate that in body fluids any significant quantities of total Pb^{2+} must be complexed in some way.

Pb^{2+} exhibits irregular coordination geometries (often with bridging) and variable coordination numbers, 6 to 10 being common. In a crystal structure of $Pb(H_2PO_4)_2$, bridged Pb^{2+} is surrounded by seven oxygen atoms from seven different $H_2PO_4^-$ groups, five at short distances and two farther away.[26] The variable and adaptive coordination about Pb^{2+} presumably accounts for its ability to interact in biological systems at sites normally harboring smaller metal ions such as Ca^{2+} and Zn^{2+}.[2,5]

Contrary to some expectations, Pb^{2+} is not an extraordinarily strong ligand binder, and (in contrast to the hard and soft precept) favors oxygen as well as sulfur donors over nitrogen (see stability ruler, Table 3). In the calmodulin family of proteins, Pb^{2+} binds more strongly than the native Ca^{2+} to the calcium sites, composed solely of O donors. In oncomodulin and chick vitamin D–induced intestinal calcium-binding protein, Pb^{2+} binding occurs exclusively at the Ca^{2+} sites, despite the presence of a free sulfhydryl group on the proteins.[27] Calmodulin in which Pb^{2+} has replaced Ca^{2+} yields a protein that retains many of its native activities. Such Pb^{2+}-induced activities may be responsible for some of its toxicity. Interactions of Pb^{2+} with a variety of nucleotides have received review.[23] Leadzymes, ribozymes of Pb^{2+}, are RNA molecules that catalyze a number of transformations utilizing Pb^{2+}.[28]

The rate of exchange of ligands into and out of the coordination sphere of Pb^{2+} is among the fastest of any metal ion; there should be a rapidly attained equilibrium distribution of Pb^{2+} among ligand sites not separated by barriers.[2,5]

Aqueous Pb^{2+} undergoes loss of protons from bound water molecules with successive pK_a values of 7.8, 9.4, and 10.7 (at 0.16 ionic strength and 25 °C).[18] Thus, at low total lead concentrations, both intracellular (pH 6.6) and extracellular (pH 7.4) body fluids contain mostly aquated Pb^{2+} with some aquated $Pb(OH)^+$. Assuming that a similar pK_a7.8 value prevails in Pb^{2+} complexes, an hydroxo complex may serve as a general base catalyst, a role that has been proposed several times. (Hydroxo complexes of metal ions may also serve as an effective hydroxide nucleophile.[23]) At the total concentrations of lead prevailing in many experiments, soluble polynuclear complexes form. First to appear at about 0.010 mM total lead is $Pb_3(OH)_4{}^{2+}$, from pH 8 to 10. Greater total lead concentrations yield polynuclear species over the entire pH scale.[18]

8 ALUMINUM[29,30]

Comprising 8% of the earth's crust, aluminum is locked in minerals as oxides and complex aluminosilicates that conceal its status as the most abundant metal and the third most abundant element, after oxygen and silicon. For the first time in the history of the earth, this metal ion is being released by acid rain into water supplies. Until recently, most natural waters contained insignificant amounts of aluminum. With the advent of acid rain, metal ions such as aluminum, mercury, and lead escape from mineral deposits and dissolve in fresh waters. Acid rain serves as the key that springs the lock for metal ion release. The Al^{3+} concentration increases sharply in clear water lakes at $\mathrm{pH} < 6$ where micromolar amounts may occur. Al^{3+} is more damaging to fish than is increased acidity; even 5 μM Al^{3+} kills fish. Humans have set in motion an epic experiment to test the ability of living organisms to cope with higher levels of Al^{3+} activity.

Worldwide, given adequate nutrients, the presence of Al^{3+} is the main limiting factor in plant productivity in acidic soils. Plants such as tea that accumulate Al^{3+} are rare and do so in acidic soils and evidently detoxify the Al^{3+} by storing a chelated version in cell vacuoles of older leaves separate from the more metabolically active parts of the plant.[31] Tea plants have been found with as much as 3% Al^{3+} in older leaves and only 0.01% in younger ones, a 300-fold difference. Typical tea infusions contain about 50 times as much Al^{3+} as do infusions from coffee. Adding milk to tea should immobilize Al^{3+} as an insoluble phosphate, while lemon will strongly complex the Al^{3+} in deleterious soluble citrate complexes described below.

Coupled with the increasing availability of Al^{3+} is the role it plays in several human disorders. Aluminum in antacids and in waters used for dialysis is known to cause dementias, bone deterioration, and even death. Al^{3+} is the likely primary cause of three conditions arising from long-term hemodialysis: vitamin D–resistant osteomalacia, iron-adequate microcytic anemia, and dialysis dementia.[32] Because of the large amounts of dialysis fluid used, even small quantities of Al^{3+} may become deleterious over time. Dialysis centers now test for the Al^{3+} content. A study of 10^4 long-term hemodialysis patients found that a serum Al^{3+} concentration of greater than 1.5 mM increased the mortality risk and that 40% of the patients exceeded this level.[33] In normal individuals, the serum Al^{3+} level is less than 0.4 mM. Similar conditions occur in children suffering from renal failure after prescribed high intakes of Al^{3+} to combine with excess phosphate of hyperphosphatemia. Upon acute ingestion, even normal adults may accumulate Al^{3+} in bones. It is debated whether the presence of Al^{3+} is a coincidence, consequence, or cause of Alzheimer's disease.[34]

Table 4 Aluminum intakes by healthy adults

- Natural sources, about 2–5 mg day^{-1}
  - Tea, typical 0.1% with up to 1% in dry tea, but poorly extracted in steeping, ≈1 mg/cup
  - Drinking water, avg. is 0.02 mg Al liter^{-1}
  - Herbs, many high in Al but little consumed
  - Spinach
- Food additives, about 20 mg day^{-1}
  - Alum baking powder products, corn bread
  - Emulsifier in American cheeses
  - In cream substitutes
  - Aluminum silicates as anticaking agents
  - $Al_2(SO_4)_3$ as anticoagulant for turbid drinking water
- Al containers (new) in stewing of acidic fruits, spaghetti sauce, sauerkraut (<0.1 mg day^{-1})
- Pharmaceuticals, if used, to 4000 mg day^{-1}
  - Antacids, 4000 mg day^{-1} for heavy users
  - Buffered aspirin, 500 mg day^{-1} for arthritics
  - Antiperspirants
  - Vaccines (intramuscular injection bypasses intestinal barrier)

There are four categories of exposure of healthy adults to aluminum. For an individual, wide variations in intakes occur in each category, and some typical values appear in Table 4. Natural sources contribute only about 5 mg day^{-1} and probably even less for nontea drinkers. High aluminum levels occur naturally in only a few foods. Food additives add 5 to 100 mg day^{-1} with the high amounts being due to alum baking powder products and Al^{3+}-containing emulsifiers added to processed cheese. Except in instances of long stewing of acidic or highly salted foods, aluminum cookware, especially if not new, furnishes little aluminum to the diet. As indicated by the last category in Table 4, the greatest potential sources of intake are Al^{3+}-containing antacids and buffered aspirins. Most ingested aluminum is poorly absorbed by the intestine and is eliminated by the body. The last entry in Table 4, vaccines, provides an example of a solution that bypasses the intestinal barrier. Solutions given intravenously to patients may result in significant quantities of aluminum being injected into the blood and may be especially critical in infants.[35]

Appreciation of the basic chemistry of aluminum leads to understanding and prediction of its potential roles in more complex systems.[36] The chemistry of aluminum is relatively simple. It reacts 10^7 times faster than Cr^{3+}, its hydroxide is much more soluble than that of Fe^{3+}, and it exhibits only one oxidation state in biological systems, Al^{3+}. There is no oxidation–reduction chemistry to Al^{3+} in biology. Al^{3+} interactions are primarily ionic, and as can be seen from Table 2, its ionic radius is the second smallest listed (after Be^{2+}) and is smaller but comparable to Fe^{3+} and Mg^{2+}, both of which compete with it in biological systems. Both Al^{3+} and Mg^{2+} favor oxygen donor ligands, especially phosphate groups. Al^{3+} is 10^7 times more effective than Mg^{2+} in promoting polymerization of tubulin to microtubules.[37] Ca^{2+} is much larger with a volume nine times greater than Al^{3+}. Wherever there is a process involving Mg^{2+} (*see* ***Cation-activated Enzymes***), seek there an opportunity for interference by Al^{3+}.[29]

In solutions with $\mathrm{pH} < 5$, aluminum occurs as the octahedral hexahydrate, $Al(H_2O)_6{}^{3+}$, usually abbreviated as Al^{3+}. As a solution becomes less acidic, $Al(H_2O)_6{}^{3+}$ undergoes successive deprotonations to yield $Al(OH)^{2+}$, $Al(OH)_2{}^{+}$, and soluble $Al(OH)_3$, with a decreasing and variable number of water molecules. Neutral solutions give an $Al(OH)_3$ precipitate that redissolves, owing to formation of tetrahedral aluminate, $Al(OH)_4{}^{-}$, the primary soluble Al^{3+} species at $\mathrm{pH} > 6.2$. The four successive deprotonations squeeze into a narrow range $5.5 < \mathrm{pH} < 6.2$; the deprotonations from octahedral hexahydrate to tetrahedral aluminate occur cooperatively.[38,39]

The most likely Al^{3+} binding sites are oxygen atoms, especially if they are negatively charged.[29,40,41] Carboxylate, catecholate, and basic phosphate groups[41–43] are the strongest Al^{3+} binders. In contrast with their reaction with the heavy metal ions discussed above, even when part of a potential chelate ring, sulfhydryl groups do not bind Al^{3+}.[44] Amines do not bind Al^{3+} strongly except as part of multidentate ligand systems such as nitrilotriacetate (NTA) and EDTA. Amino acids are weak binders barely competing with metal ion hydrolysis.[40,45] Neither the nitrogenous bases[36,46] nor the phosphates (nonbasic)[29,40,41] of DNA and RNA bind Al^{3+} strongly. Within a cell, Al^{3+} binds mainly to ATP with a stability constant 4000 times greater than Mg^{2+}, making Al^{3+} at only 0.1 μM competitive with intracellular Mg^{2+} at 1 mM.[29,42]

Fluoride binds Al^{3+} strongly, and at the 1 ppm level where it is added to acidic drinking water, most aluminum appears as $AlF_2{}^{+}$ and as neutral AlF_3.[29,47] In mixed complexes of Al^{3+}, ADP, and F^{-}, the ternary complex appears with the frequency expected statistically on the basis of binary complex stabilities.[48] Contrary to a common misconception, when bound to proteins (such as G-proteins), fluoride complexes of Al^{3+} do not contain a tetrahedral, four-coordinate metal ion but hexacoordinate Al^{3+} with six donor atoms.[29,49]

It is as the citrate complex that Al^{3+} passes the intestinal barrier into the blood. Al^{3+} levels were elevated in both the brain and bones of rats fed a diet containing aluminum citrate or even just citrate. Evidently, citrate alone chelates trace Al^{3+} in the diet. Increased levels of serum Al^{3+} were found in patients with chronic renal failure taking an Al^{3+}-containing phosphate binder with citrate or $Al(OH)_3$ with citrate. A rapidly fatal encephalopathy in human patients with chronic renal failure has been attributed to concomitant ingestion of $Al(OH)_3$ and citrate. Moreover, healthy adults taking $Al(OH)_3$-based antacids along with citric acid, citrate salts, or citrus fruits showed substantial increases in Al^{3+} levels of blood and urine. ‘Only those who cared for children in the late 1970s during the liberal use of aluminum-containing antacids and citrate can appreciate the horror of helplessly watching previously normal children die of severe encephalopathy over months to years.’[50] On the basis of information from equilibrium constants, it was strongly urged in 1986 that people not take Al^{3+} and citrate together.[46]

Citrate exists mainly in the form of the tricarboxylate anion at $\mathrm{pH} > 6$, and at 0.1 mM in the blood plasma, it is the leading small molecule Al^{3+} binder.[29,51] In neutral solutions, the main species is $HOAlLH_{-1}{}^{2-}$ followed by $AlLH_{-1}{}^{-}$ with $\mathrm{p}K_a \approx 6.5$ for the loss of a proton from metal ion–bound water.[29,52] Citrate solubilizes Al^{3+} from both insoluble $Al(OH)_3$ and $AlPO_4$, making it more available to an organism.[40,41,51] Proton nuclear magnetic resonance spectroscopy provides direct evidence that Al^{3+} binds to citrate in human blood plasma.[53] From detailed calculations for several biological fluids, estimates of the free Al^{3+} concentration ranges from $10^{-14.2}$ to $10^{-12.6}$ M.[54]

Transferrin binds to Al^{3+} and is the main protein carrier of Al^{3+} in the plasma.[55,56] Displacement of the 10^9 times stronger binding Fe^{3+} is unnecessary because plasma transferrin is about 50 μM in unoccupied sites. On the basis of values of requisite stability constants, it was suggested that in blood plasma about 89% of Al^{3+} is bound to transferrin and 11% to citrate.[51] This distribution is supported by direct measurements by a variety of methods.[56]

9 RELATED ARTICLES

Aluminum: Inorganic Chemistry; Cadmium: Inorganic & Coordination Chemistry; Chromium: Biological Relevance; Hard & Soft Acids and Bases; Lead: Inorganic Chemistry; Mercury: Inorganic & Coordination Chemistry; Mercury: Organometallic Chemistry; Thallium: Inorganic Chemistry.

10 REFERENCES

1. H. G. Seiler and H. Sigel, ‘Handbook on Toxicity of Inorganic Compounds’, Marcel Dekker, New York, 1988.
2. R. B. Martin, *Metal Ions Biol. Syst.*, 1986, **20**, 21.
3. J. J. R. F. daSilva and R. J. P. Williams, ‘The Biological Chemistry of the Elements’, 2nd edn., Clarendon Press, Oxford, 2001.
4. R. B. Martin, in ‘Handbook on Metalloproteins’, eds. I. Bertini, A. Sigel, and H. Sigel, Marcel Dekker, New York, 2001, p. 181.
5. R. B. Martin, in ‘Handbook on Toxicity of Inorganic Compounds’, eds. H. G. Seiler, H. Sigel, and A. Sigel, Marcel Dekker, New York, 1988, p. 9.
6. R. D. Shannon, *Acta Crystallogr.*, 1976, **A32**, 751.
7. R. J. Sundberg and R. B. Martin, *Chem. Rev.*, 1974, **74**, 471.
8. R. B. Martin, *Metal Ions Biol. Syst.*, 1979, **9**, 1.
9. H. Sigel, ‘Metal Ions in Biological Systems’, Concepts on Metal Ion Toxicity, Vol. 20, Marcel Dekker, New York, 1986.
10. B. Venugopal and T. D. Luckey, ‘Metal Toxicity in Mammals’, Plenum Publishing, New York, 1977 & 1978.

11. E. Ochiai, ‘General Principles of Biochemistry of the Elements’, Plenum Publishing, New York, 1987.
12. B. Sarkar, ‘Heavy Metals in the Environment’, Marcel Dekker, New York, 2002.
13. F. W. Oehme, ‘Toxicity of Heavy Metals in the Environment’, Marcel Dekker, New York, 1978.
14. M. Yasui, M. J. Strong, K. Ota, and M. A. Verity, ‘Mineral and Metal Neurotoxicology’, CRC Press, Boca Raton, 1997.
15. B. Lippert, ‘Cisplatin’, John Wiley & Sons, Weinheim, 1999.
16. J. Kobayashi, in ‘Toxicity of Heavy Metals in the Environment’, ed. F. W. Oehme, Marcel Dekker, New York, 1978, Part 1, p. 199.
17. R. B. Martin and Y. H. Mariam, *Metal Ions Biol. Syst.*, 1979, **8**, 57.
18. C. F. Baes and R. E. Mesmer, ‘The Hydrolysis of Cations’, Wiley-Interscience, New York, 1976.
19. M. Harada, in ‘Toxicity of Heavy Metals in the Environment, Part 1’, ed. F. W. Oehme, Marcel Dekker, New York, 1978, Part 1, p. 261.
20. D. R. Cassidy and A. Furr, in ‘Toxicity of Heavy Metals in the Environment, part 1’, ed. F. W. Oehme, Marcel Dekker, New York, 1978, part 1, p. 303.
21. R. B. Martin, *Inorg. Chim. Acta*, 2002, **339**, 27.
22. L. Manzo and E. Sabbioni, in ‘Handbook on Toxicity of Inorganic Compounds’, eds. H. G. Seiler, and H. Sigel, Marcel Dekker, New York, 1988, p. 677.
23. H. Sigel, C. P. DaCosta, and R. B. Martin, *Coord. Chem. Rev.*, 2001, **219–221**, 435.
24. S. C. Gilfillan, *J. Occup. Med.*, 1965, **7**, 53.
25. J. O. Nriagu, ‘Lead and Lead Poisoning in Antiquity’, Wiley-Interscience, New York, 1983, p. 399.
26. P. Vasic, B. Prelesnik, R. Herak, and M. Curic, *Acta Crystallogr.*, 1981, **B37**, 660.
27. C. S. Fullmer, S. Edelstein, and R. H. Wasserman, *J. Biol. Chem.*, 1985, **260**, 6816.
28. A. M. Pyle, *Metal Ions Biol. Syst.*, 1996, **32**, 479.
29. R. B. Martin, *Acc. Chem. Res.*, 1994, **27**, 204.
30. H. Sigel, ‘Metal Ions in Biological Systems’, Aluminum and its Role in Biology, Vol. 24, Marcel Dekker, New York, 1988.
31. T. P. Flaten, *Coord. Chem. Rev.*, 2002, **228**, 385.
32. M. E. deBroe and J. W. Coburn, ‘Aluminum and Renal Failure’, Kluwer Academic Publishers, Dordrecht, 1990.
33. J. A. Chazan, N. L. Lew, and E. G. Lowrie, *Arch. Intern. Med.*, 1991, **151**, 319.
34. J. Savory, R. B. Martin, O. Ghribi, and M. M. Herman, in ‘Heavy Metals in the Environment’, ed., B. Sarkar, Marcel Dekker, New York, 2002, p. 309.
35. G. L. Klein, *Nutr. Rev.*, 1991, **49**, 74.
36. R. B. Martin, *Metal Ions Biol. Syst.*, 1988, **24**, 1.
37. T. L. Macdonald, W. G. Humphreys, and R. B. Martin, *Science*, 1987, **236**, 183.
38. R. B. Martin, *J. Inorg. Biochem.*, 1991, **44**, 141.
39. R. B. Martin, *Comments Inorg. Chem.*, 1996, **18**, 249.
40. R. B. Martin, in ‘Aluminium in Chemistry, Biology, and Medicine’, eds. M. Nicolini, P. F. Zatta, and B. Corain, Cortina International, Verona; Raven Press, New York, 1991, p. 3.
41. R. B. Martin, ‘Aluminium in Biology and Medicine’, Ciba Foundation Symposium 169, John Wiley & Sons, Chichester, 1992, p. 5.
42. T. Kiss, I. Sovago, and R. B. Martin, *Inorg. Chem.*, 1991, **30**, 2130.
43. K. Atkari, T. Kiss, R. Bertani, and R. B. Martin, *Inorg. Chem.*, 1996, **35**, 7089.
44. I. Toth, L. Zekany, and E. Brucher, *Polyhedron*, 1984, **7**, 871.
45. T. Kiss, I. Sovago, I. Toth, A. Lakatos, R. Bertani, A. Tapparo, G. Bombi, and R. B. Martin, *J. Chem. Soc., Dalton Trans.*, 1997, 1967.
46. R. B. Martin, *Clin. Chem.*, 1986, **32**, 1797.
47. R. B. Martin, ‘Aluminium in Biology and Medicine’, Ciba Foundation Symposium 169, John Wiley & Sons, Chichester, 1992, p. 104.
48. D. J. Nelson and R. B. Martin, *J. Inorg. Biochem.*, 1991, **43**, 37.
49. R. B. Martin, *Coord. Chem. Rev.*, 1996, **149**, 23.
50. A. Sedman, *Pediatr. Nephrol.*, 1992, **6**, 383.
51. L. Ohman and R. B. Martin, *Clin. Chem.*, 1994, **40**, 598.
52. L. Ohman, *Inorg. Chem.*, 1988, **27**, 2565.
53. J. D. Bell, G. Kubal, S. Radulovic, P. J. Sadler, and A. Tucker, *Analyst*, 1993, **118**, 241.
54. R. B. Martin, in ‘Aluminium in Infant’s Health and Nutrition’, eds. P. F. Zatta and A. C. Alfrey, World Scientific Publishing Company, London, 1997, p. 3.
55. R. B. Martin, J. Savory, S. Brown, R. L. Bertholf, and M. Wills, *Clin. Chem.*, 1987, **33**, 405.
56. W. R. Harris and L. Messori, *Coord. Chem. Rev.*, 2002, **228**, 237.

Metal Vapor Synthesis of Transition Metal Compounds

Eckhardt Schmidt, Kenneth J. Klabunde, Aldo Ponce, Alexander Smetana & David Heroux
Kansas State University, Manhattan, KS, USA

1 Introduction 1
2 Early Transition Metals (Sc–Mn Groups) 3
3 Late Transition Elements (Fe–Zn Groups) 8
4 Miscellaneous 10
5 Related Articles 11
6 References 11

1 INTRODUCTION

1.1 Bulk Metals versus Atoms

The chemistry of transition metals with a variety of substrates is now well established. It has been learned that the reactivity and reaction speed of one specific element and an appropriate ligand depends in part on the metal particle size. Freshly prepared metal powders often react differently from aged and passivated metal powders, metal wire, pellets, or ingots. Therefore, the highest reactivity might be expected from single metal atoms. The first steps in the direction of producing metal vapor atoms were taken in the 1920s and 1930s. Those studies began with chemical reactions of high-temperature gas phase Na and K with organohalides. Also, small carbon species ($C_1, C_2, C_3, \ldots$) were prepared in the early 1960s to function as macroscale (>50 mg) synthons. In order to demonstrate the use of single metal atoms in synthetic applications, efforts were made in the early 1970s[1,2] to develop techniques to vaporize metals in macroscale amounts. In a short time, these efforts led to a new important field of research.

This article is organized primarily according to the periodic table and secondarily with regard to the importance of substrates found to react with metal vapor atoms. Tables, lists, and figures will display many of the known compounds prepared via the metal vapor-substrate cocondensation method and give further information about physical properties, chemical behavior, spectroscopic data, and structural details.

1.2 Energetics of Vaporization

Table 1 shows relevant information for the metallic elements.

1.3 Vapor Compositions

There exist more than 100 elements in the periodic table from which high-temperature particles can be formed. In order to generate highly reactive free atoms, a great deal of energy is required. For instance, at least 400 kJ mol^{-1} are necessary in order to break nickel–nickel bonds and allow the escape of nickel atoms. Thus nickel must be under vacuum and heated to about 1400 °C to accomplish this. We must also consider small particles, such as Mn_2, V_3, or Co_2. These clusters might react differently from single metal atoms. As the number of atoms in a metal cluster increases, its chemical behavior resembles active metal powders more and more. The chemistry of small clusters is a rather young field, in that experimental advances in vacuum technology, high-temperature ceramics, and cryochemical techniques have been absolutely necessary. However, cluster chemistry, a major new research field, contributes less to synthetic applications than metal atom chemistry, and therefore will not be emphasized here. Similar considerations preclude much discussion of microscale, low-temperature matrix isolation studies.

1.4 Techniques of Vaporization

The most widely used method of metal vaporization in the laboratory is resistive heating of crucibles consisting of Mo or W coils and an Al_2O_3 coating. Typical transition metals, like Cr, Fe, or Ni, can be vaporized in gram amounts per hour. A freshly prepared single metal atom carries some kinetic energy and has orbitals poised for reaction without steric restrictions. To control the reaction parameters, moderate the vapor pressures for incoming reactants, and minimize gas phase interactions, very low substrate temperatures are desired: in the range −50 to −200 °C. Drawbacks to this method are competition between complex formation and metal aggregation, the frequent low yields, and the large amount of cooling agent required. Figure 1 shows a macroscale stationary cocondensation vessel for macroscale reactions. Only the resistive heating method offers the advantage of low concentrations of metal atom dimers, trimers, oligomers, and metal particles that may react with substrates differently. Other widely used vaporization methods, like electron beams and lasers, are more technologically complex and problematic. Resistively heated Al_2O_3 sources are quite satisfactory for most of the transition metals. Elements with a very high heat of vaporization (W, Re) require more advanced and powerful methods of vaporization, and an electron beam is usually employed.

The electron beam method was developed in the late 1960s and uses a focused electron beam to vaporize the central portion of a metal sample. Despite the necessity of

Table 1 Physical data for the metallic elements

	Sc	Ti	V	Cr	Mn	Fe	Co	Ni	Cu	Zn
Mp (K)	1812	1941	2163	2148	1517	1810	1766	1726	1356	693
Bp (K)	3000	3533	3273	2472	2370	3273	3373	3003	2855	1180
ΔH_{vap} (kJ mol^{-1})	343	473	515	397	280	418	423	431	335	128
d (M–M) (pm)	321.2	289.56	262.24	249.80	273.11	248.23	250.61	249.16	255.60	266.94
	Y	Zr	Nb	Mo	Tc	Ru	Rh	Pd	Ag	Cd
Mp (K)	1782	2123	2741	2883	2443	2583	2233	1825	1234	594
Bp (K)	3473	4650	5200	5833	5303	4392	4000	3020	2483	1040
ΔH_{vap} (kJ mol^{-1})	360	607	720	665	649	649	556	372	285	113
d (M–M) (pm)	355.1	317.9	285.84	272.51	270.3	265.02	269.01	275.11	288.94	297.88
	La	Hf	Ta	W	Re	Os	Ir	Pt	Au	Hg
Mp (K)	1193	2503	3269	3683	3443	3323	2716	2043	1336	234
Bp (K)	3727	5473	5700	6203	5903	4500	4662	4100	3081	630
ΔH_{vap} (kJ mol^{-1})	435	607	782	845	778	782	669	565	368	63
d (M–M) (pm)	373.9	312.73	286	274.09	274.1	267.54	271.4	274.6	288.41	300.5

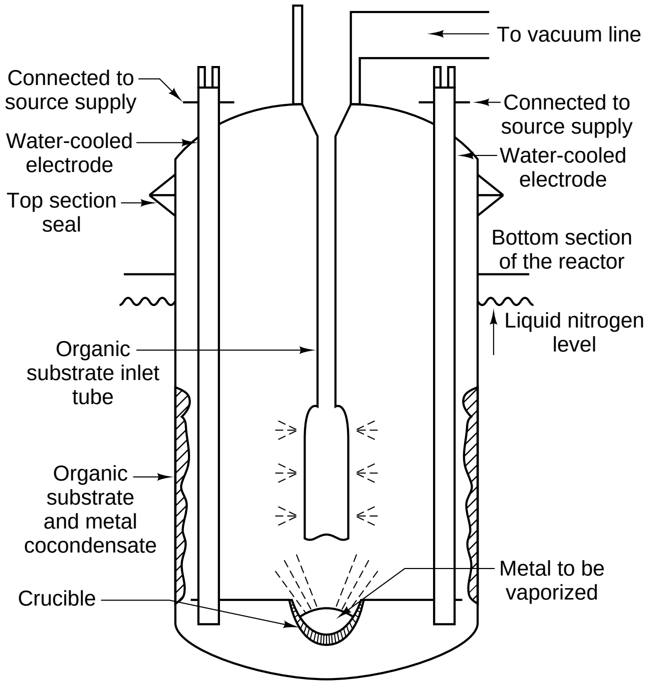
To vacuum line
Connected to source supply
Connected to source supply
Water-cooled electrode
Water-cooled electrode
Top section seal
Bottom section of the reactor
Liquid nitrogen level
Organic substrate inlet tube
Organic substrate and metal cocondensate
Metal to be vaporized
Crucible

Figure 1 Schematic diagram of a cocondensation metal atom (vapor) reactor

an extremely good vacuum (10^{-5} mbar) to avoid arcing and stray electron and X-ray damage of organometallic products, this technique does allow large-scale vaporization (kilograms per hour), and even high-boiling transition metals like W (bp 5660 °C) can be vaporized. Figure 2 illustrates an electron beam apparatus schematically. Only volatile substrates can be conveniently employed in both types of reactors.

A solution metal atom reactor (after Timms), as shown in Figure 3, offers the opportunity to evaporate metal atoms continuously into a substrate dissolved in an inert solvent at low temperature and can be equipped with a crucible or an electron beam heating source. Another, less efficient, evaporation method can be carried out by means of a laser. Figure 4 shows an IR laser beam passing through a window and rapidly heating up a small area on the metal sample. Lasers bring high energy flux densities focused on one point, and stray radiation is less damaging to products than stray electrons and X-rays from electron beam setups. One great disadvantage of the laser method is that molten metals reflect the laser beam like a mirror. Another problem is the need for a window that does not become coated during the metal evaporation and shuts out the light. The latter problem can be partly solved by a slight gas stream near the window keeping

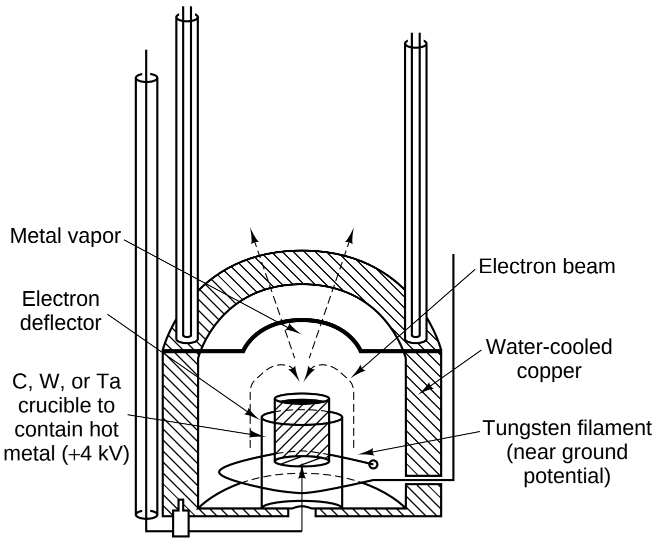
Metal vapor
Electron beam
Electron deflector
Water-cooled copper
C, W, or Ta crucible to contain hot metal (+4 kV)
Tungsten filament (near ground potential)

Figure 2 Schematic diagram for electron beam vaporization of metals

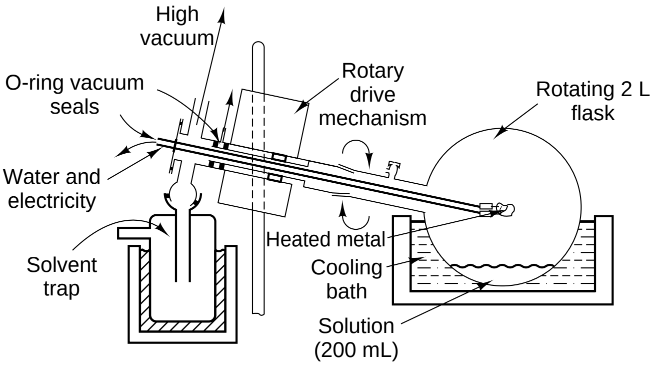

Figure 3 Schematic diagram of a solution metal atom (vapor) reactor

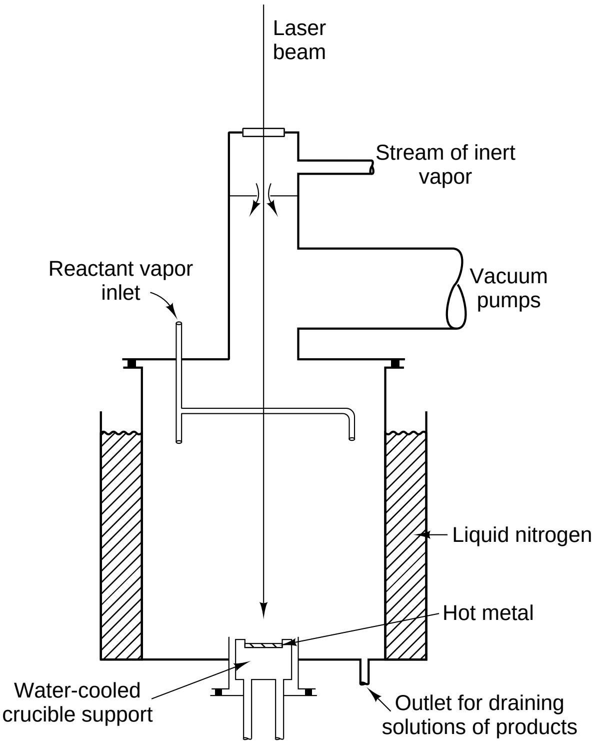

Figure 4 Schematic diagram for laser vaporization and cocondensation of vapor with chemical substrates

it clear of metal deposits. The gas must be continually pumped away, rapidly, and this causes the necessity for faster pumping speed (thus larger pumps).

Other less sophisticated evaporation techniques are, for instance, the wrapping of W coils with Pt wire. Only small amounts of Pt can be vaporized, because alloying with the hot W occurs. The problem is also found with electrodeposited Rh on W coils. Other metal powders like Ru can be glued on W wires with epoxy cement. Slow annealing drives off the carbonaceous residue leaving Ru coated on W. The Ru can then be vaporized with more vigorous resistive heating.

Arc metal vaporization has proven less efficient. Many metals can be vaporized in this way, but metal vapor often condenses on the copper electrode and forms nonvolatile compounds, finally decreasing vaporization rates.

2 EARLY TRANSITION METALS (Sc–Mn GROUPS)

2.1 Chromium–Arene Chemistry

2.1.1 *Bis(benzene)chromium*

The most important ligand for early transition metal atoms is the arene ligand. Bis(benzene)chromium has been known since 1955 (E. O. Fischer) and was prepared first via wet chemical methods. Not all desired substituents on the arene are stable to the extreme conditions employed in the *Fischer–Hafner Synthesis*. The cocondensation technique offers a new synthetic pathway to bis (η^6-arene)metal complexes simply by codepositing Cr atoms together with the appropriate ligand, normally at the temperature of liquid nitrogen ($-196\,°C$). Chromium is quite easy to vaporize, it sublimes before melting, and can be evaporated in gram amounts by resistive heating.

The diamagnetic, air-sensitive, black $(C_6H_6)_2Cr$ is a thermally stable 18-electron complex (mp 284 °C), with D_{6h} symmetry according to electron diffraction and low-temperature X-ray studies. The structure reveals a ring–ring distance of 322 pm, equal to the van der Waals separation of two π-systems, compared to free benzene. The average C–C bond distance of 142 pm is enlarged, compared to the bond parameters in free benzene. The π-bonding alters the reactivity of the arene rings in $(arene)_2Cr$ complexes in several ways. Unlike ferrocene, bis(benzene)chromium undergoes no electrophilic aromatic substitution reactions. Electrophilic attack oxidizes Cr^0 to Cr^I, yielding the paramagnetic cation $[(C_6H_6)_2Cr]^+$, which does not react further. The coordinated benzene is metallated more readily than free benzene by means of n-butyllithium/TMEDA, because of the increased kinetic acidity of benzene upon complexation to chromium. The lithiated product serves as a valuable precursor for substituted $(arene)_2Cr$ compounds (Scheme 1).

2.1.2 *Substituted Arenes and Six-Membered Rings*

Other stable $(arene)_2Cr$ complexes[3] prepared by the metal atom technique are listed in Table 2.

The variously substituted bis(arene)chromium(0) compounds are generally easy to purify by crystallization or sublimation. Bis(arene)chromium complexes with substituents like Cl, F, OMe, or NMe_2 are not preparable by classical means

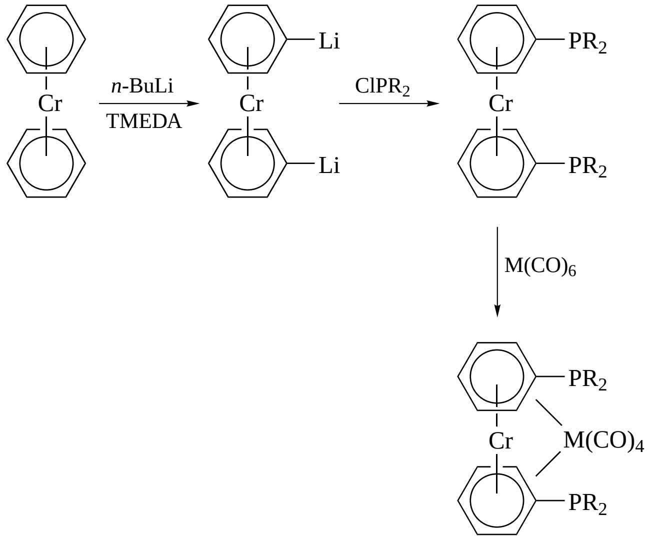

Scheme 1

and show different chemical behavior compared to $(C_6H_6)_2Cr$. While all hydrocarbon-substituted $(arene)_2Cr$ complexes are air sensitive, $(\eta^6\text{-}C_6H_5Cl)_2Cr$ is air stable because of the presence of electron-withdrawing groups. Elschenbroich and his coworkers have prepared a wide series of new Cr sandwich complexes, including arene complexes containing strained-ring substituents, as well as bis(naphthalene)Cr, which serves as an example of a kinetically labile complex (*see Hapticity*). Unlike $(C_6H_6)_2Cr$, $(C_{10}H_8)_2Cr$ undergoes ring exchange under moderate conditions:

$$(C_{10}H_8)_2Cr + 3\text{bipy} \longrightarrow (\text{bipy})_3Cr + 2C_{10}H_8 \qquad (1)$$

For higher polycyclic arenes, like phenanthrene, triphenylene, or coronene, the chromium coordinates preferentially to the ring with the highest index of local aromaticity (usually the terminal ring). The codeposition of a large excess of Cr with biphenyl gives, among other side-products, the interesting bis[μ-(η^6:η^6-biphenyl)]dichromium, whose paramagnetic dication acts as an organometallic triplet species.

The heterobenzene $(\eta^6\text{-}C_5H_5P)_2Cr$ can be directly prepared by the metal–ligand vapor cocondensation technique. This heterocycle is aromatic and prefers η^6-coordination to η^1-coordination. For pyridine, σ-coordination via a lone pair is highly preferred over bonding that utilizes the π-electron system. Therefore the direct synthesis of η^6-pyridine metal complexes requires the N-atom to be blocked by means of substitution in the 2,6-positions:

$$2\ 2,6\text{-}Me_2C_5H_3N(g) + Cr(g) \longrightarrow (2,6\text{-}Me_2C_5H_3N)_2Cr \qquad (2)$$

The labile parent complex bis(η^6-pyridine)chromium can be prepared by occupying the 2,6-positions with protecting

Table 2 Bis(arene)chromium(0) compounds prepared by cocondensation of chromium atoms and ligand vapor

Complex	Yield (%)	Product characteristics
Bis(benzene)chromium	13	Black solid, oxidized by air to cation, volatile (60 °C, 10^{-3} mbar), mp 284 °C
Bis(1,2-dimethylbenzene)chromium	25	Black solid, oxidized by air to cation, volatile (80 °C, 10^{-3} mbar), mp 127–128 °C
Bis(*t*-butylbenzene)chromium	27	Black solid, oxidized by air to cation, volatile (80 °C, 10^{-3} mbar), mp 76–88 °C
Bis(indane)chromium	17	Olive-green solid, oxidized by air to cation, volatile (80 °C, 10^{-3} mbar), mp 107–109 °C
Bis(2,6-dimethylpyridine)chromium	17	Deep-red solid
(η^{12}-[2.2]Paracyclophane)chromium[4]	5	Lemon-yellow solid, volatile (120 °C, 10^{-3} mbar), yield based on unrecoverable ligand
Bis(cyclobuta-η^6-benzene)chromium[5]	12	Reddish-brown solid, volatile (80 °C, 10^{-4} mbar), mp 122 °C
Bis[μ-(η^6:η^6-biphenyl)]dichromium[6]	0.4	Dark brown solid, volatile (180 °C, 10^{-4} mbar)
Bis(naphthalene)chromium	18	Dark brown solid, volatile (80 °C, 10^{-4} mbar), mp 160 °C (dec.), pyrophoric when finely divided
Bis(*p*-methylmethoxybenzene)chromium	12	Brown–black solid, oxidized by air to cation, volatile (130 °C, 10^{-3} mbar), mp 130–133 °C
Bis(*m*-chlorotoluene)chromium	5	Black solid, oxidized by air to cation, volatile (80 °C, 10^{-3} mbar), mp 56–57 °C
Bis(*p*-fluorobenzotrifluoride)chromium[7]	7	Dark green solid, air stable for several days, volatile (56 °C, 10^{-3} mbar), mp 60.5–61 °C
Bis(*p*-difluorobenzene)chromium	12	Dark violet, air stable, volatile (50 °C, 10^{-3} mbar), mp 172–174 °C (dec.)
Bis(phenylether)chromium	3	Olive-green solid, oxidized by air to cation, volatile (130 °C, 10^{-3}, mbar), mp 130–133 °C
Bis(*N*,*N*,-dimethylaniline)chromium	6	Red solid, oxidized by air to chromium oxide, volatile (80 °C, 10^{-3} mbar), mp 87.5–88.5 °C
Bis(trimethylsilylbenzene)chromium	5	Brown solid, oxidized by air to cation, reduced by K to anion, volatile (70 °C, 10^{-3} mbar)
Bis(methyl benzoate)chromium	4	Red solid, moderately air stable, volatile (100 °C, 10^{-3} mbar), mp 111 °C
Bis(arsabenzene)chromium[8]	15	Reddish-black, air-sensitive solid, sublimable, mp 253 °C (dec.)

groups, which can be removed after complex formation:

$$2\ 2,6\text{-}(\mathrm{SiMe_3})_2\mathrm{C_5H_3N(g)} + \mathrm{Cr(g)} \longrightarrow [2,6\text{-}(\mathrm{SiMe_3})_2\mathrm{C_5H_3N}]_2\mathrm{Cr} \xrightarrow[\mathrm{Na_2S_2O_4}]{\mathrm{O_2/5\,min}} (\mathrm{C_5H_5N})_2\mathrm{Cr} \tag{3}$$

The cocondensation of paracyclophane with Cr atoms gives, besides bis(paracyclophane)chromium, (η^{12}-[2.2]paracyclophane)chromium in low yield, which represents a compressed sandwich complex. The average ring–ring distance of 290 pm falls considerably short of the corresponding distance in $(C_6H_6)_2Cr$ (322 pm) (Scheme 2).

2.1.3 *Mixed Arenes*

A series of new mixed bis(arene)Cr complexes have been made by simultaneously codepositing two different arenes. These reactions yield three complexes, $(\mathrm{arene})_2\mathrm{Cr}$, $(\mathrm{arene}')_2\mathrm{Cr}$, and (arene)(arene$'$)Cr, that can be separated by chromatography or sublimation (Table 3). Efforts to prepare bis(arene) complexes from hexafluorobenzene or $C_6(CF_3)_6$ have been unsuccessful because of highly electron-demanding groups like F and CF_3. Neither of those ligands forms thermally stable sandwich complexes with chromium. The mixed (arene)(arene$'$)Cr complex $(C_6H_6)(C_6F_6)Cr$ is surprisingly stable to air and heat. Electrochemical studies show remarkably large variations in $E_{1/2}[(\mathrm{Ar})_2\mathrm{Cr}^0 \rightarrow (\mathrm{Ar})_2\mathrm{Cr}^+]$, ranging from -0.2 V for the electron-rich $(C_6H_5OMe)_2Cr$ to $+1.2$ V for $[(CF_3)_2C_6H_4]_2Cr$. Electron-withdrawing and donating groups greatly affect the σ-framework of the arene ring as well as the π-framework in the M–ring bond. NMR studies by Lagowski on a series of bis(arene)Cr complexes showed that substituent effects are not transmitted through the Cr atom and are confined to the corresponding arene ring.

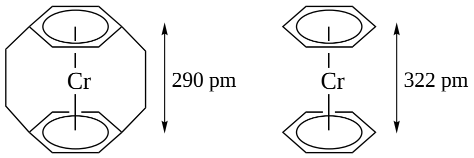

Scheme 2

2.1.4 *Arene/Phosphine/Phosphite Combinations*

Phosphines, particularly PF_3, have been employed for trapping organometallic species generated in low-temperature atom matrices. PR_3 groups are valuable moieties in stabilizing sandwich compounds with potentially labile ligands. Therefore, phosphine ligands act as a stabilizing ancillary ligands in unstable $(Ar)_2Cr$ species. Representative examples for arene–ligand combinations, attached to Cr, are listed in Table 4.

2.2 Other Transition Metals with Arenes

The most important synthetic chemistry of the early transition metal atoms continues to be the preparation of bis(arene)M^0 sandwich complexes, as shown in Table 5:

$$\mathrm{M(g)} + 2\mathrm{Ph(X)} \longrightarrow [\mathrm{Ph(X)}]_2\mathrm{M} \tag{4}$$

The metal vapor–ligand codeposition method has extended the array of such sandwich complexes. A wide range of substituents can be tolerated on the arene ring; unusual arene–M complexes have been prepared. Elschenbroich made the interesting compound bis(η^6-phosphabenzene)vanadium, which is less air sensitive than the ligand itself. It turned out that the phosphorus heteroatom has a much stronger influence on the electron affinity of the free arene than of the bound arene.

Table 3 Mixed bis(arene)chromium compounds prepared by metal vapor–ligand codeposition

Complex	Yield (%)	Product characteristics
$(C_6H_6)(C_6F_6)Cr$	9	Yellow solid, air stable for several weeks, mp 139 °C
$(C_6H_6)(C_6F_5H)Cr$[9]	22	Orange solid, air stable, volatile (35 °C, 0.2 mbar), mp 117 °C
$(C_6H_6)(C_5H_5N)Cr$	2	Red–brown solid, oxidized by air to cation, volatile (50 °C, 10^{-3} mbar)

Table 4 Mixed arene/ligand complexes of Cr prepared via metal vapor–ligand codeposition method

Complex	Yield (%)	Product characteristics
$(C_6H_5Me)Cr[P(OMe_3)_3]_3$[10]		Yellow–orange solid
$(C_6H_6)Cr(PF_3)_3$		Pale yellow solid, air-sensitive, mp 220 °C (dec.)
$(C_6F_6)Cr(PF_3)_3$	1–2	dec. >250 °C
$(C_5H_5N)Cr(PF_3)_3$[11]		
$(C_6H_3Me_3)(PF_3)_3Cr$	10	Cream-colored solid, air-sensitive, mp 130 °C (dec.)

Table 5 Bis(arene)M^0 complexes and properties

Complex	Number of valence electrons	Complex properties
$(C_6H_6)_2Ti$	16	Air sensitive, autocatalytic decomposition in aromatic solvents
$(C_6H_6)_2V$	17	Black solid, very air sensitive, paramagnetic, reducible to $[(C_6H_6)_2V]^-$, mp 227 °C
$(C_6H_5F)_2V$	17	Red solid, air sensitive
$(C_5H_5P)_2V$[12]	17	Reddish-brown solid, mp 210 °C
$(C_6H_6)_2Nb$	17	Purple solid, very air sensitive, paramagnetic, decomposes at ca. 90 °C
$(C_6H_6)_2Mo$	18	Green solid, very air-sensitive, mp 115 °C
$(C_6H_5OMe)_2Mo$	18	Sublimable (50–80 °C, $<10^{-3}$ Torr)
$(C_6H_5CO_2Me)_2Mo$	18	Sublimable (50–80 °C, $<10^{-3}$ Torr)
$(C_6H_5F)_2Mo$	18	Sublimable (50–80 °C, $<10^{-3}$ Torr)
$(C_6H_6)_2$ W	18	Yellow–green solid, less air sensitive than $(C_6H_6)_2Mo$, mp 160 °C
$(C_6H_5F)_2$ W	18	Sublimable (50–80 °C, $<10^{-3}$ Torr)

Table 6 Mono- and bis(arene)/phosphino derivatives of early transition metals prepared by metal vapor synthesis

Metal	Arene	σ-Donor ligand	Product
Zr	Toluene	PMe_3	$(\eta^6\text{-}C_6H_5Me)_2ZrPMe_3$
Hf	Benzene	PMe_3	$(\eta^6\text{-}C_6H_6)_2HfPMe_3$
Mn	Benzene	PMe_3	$(\eta^6\text{-}C_6H_6)Mn(PMe_3)_2H$
Re	Benzene	PMe_3	$[(\eta^6\text{-}C_6H_6)Re(PMe_3)_2]_2$
Mn	Toluene	I_2	$(\eta^6\text{-}C_6H_5Me)_2Mn^+I^-$

The cocondensation of Nb atoms with toluene has yielded bis(η^6-toluene)niobium, which serves as a useful intermediate for the preparation of a wide series of mono- and bis-arene derivatives.[13] While Ti, V, Nb, Cr, Mo, and W form $(Ar)_2M^0$ sandwich complexes, Mn, Tc, and Re appear less promising, because Mn–arene complexes have already been shown to be unstable,[14] Tc is radioactive, and Re remains to be investigated. As already mentioned, Ti forms fairly labile bis(arene)Ti complexes. The unstable 16-electron sandwich complexes from elements of group 4 can be stabilized with phosphine ancillary ligands, yielding bis-arene derivatives as in Table 6.

2.3 Dienes, Trienes, and Tetraenes

Novel organometallics have been prepared via metal atom synthesis since the 1970s. Especially interesting have been diene reactions with early transition metal atoms. Cyclopentadiene on cocondensation with metal atoms reacts with Cr through a bis(cyclopentadienyl)chromiumdihydride intermediate to yield chromocene. For Mo and W, the intermediate species can be isolated. Labeling studies with Cp^*H and Cp^*D indicate that oxidative addition of the C–H bond to M occurs stepwise ($\rightarrow Cp^*MH \rightarrow Cp^*_2MH_2$) (*see Oxidative Addition*).

$$Cr(g) + 2CpH \longrightarrow [Cp_2CrH_2] \longrightarrow Cp_2Cr + H_2 \qquad (5)$$

$$Mo(g) + 2CpH \longrightarrow Cp_2MoH_2 \qquad (6)$$

$$W(g) + 2CpH \longrightarrow Cp_2WH_2 \qquad (7)$$

Ru atom codeposition with dienes at 77 K, followed by warming in the presence of CO, has yielded gram quantities of $Ru(CO)(diene)_2$ complexes (Scheme 3) (*see* ***Hydride Complexes of the Transition Metals***).

The 18-electron complex $(C_6H_6)MnCp$ can be prepared in low yield from the reaction of Mn atoms and a mixture of benzene and cyclopentadiene. 1,3-Butadiene–Mo or –W macroscale depositions yielded unique, stable $(diene)_3Mo/W$ complexes.[15] Those molecules are, according to X-ray crystallography, wrapped cisoid about the Mo and W, so that all 12 carbons are equidistant from the metal.[16] Cyclic dienes like cod are excellent ligands in organometallic chemistry. Pure $(1,5\text{-cod})_nCr$ complexes are unstable, but addition of trapping ligands at low temperature yields stable $(1,5\text{-cod})CrL_4$ complexes. Representative examples are listed in Table 7.

Cyclic triene (nonaromatic) and tetraene reactions form a series of new complexes. While some cyclotrienes yield mostly unstable species, heating or ligand trapping can generally lead to stable, isolable compounds. Hydrogen transfer also plays an important role in the synthesis of $\eta^7-\eta^5$ sandwich complexes. With cot and Cr atoms a Cr≡Cr bonded $Cr_2(C_8H_8)_3$ complex is formed,[17] while in the case of Ti–cot, a novel *Triple Decker Sandwich* is obtained.[18]

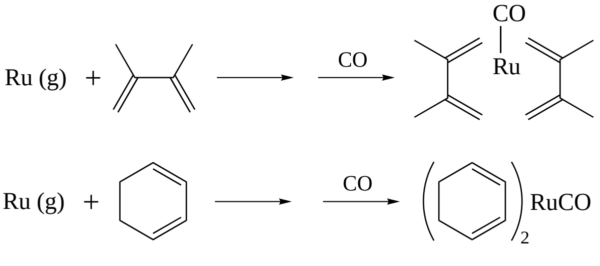

Scheme 3

Table 7 Transition metal complexes of cyclic dienes/trienes/polyenes/σ-donor ligands prepared via the metal vapor–ligand codeposition method

Metal	π-Ligand	σ-Donor ligand	Product
Zr	Cycloheptatriene	–	$(\eta^7\text{-}C_7H_7)Zr(\eta^4\text{-}1,3\text{-}C_7H_{10})$
Hf	Cycloheptatriene	–	$(\eta^7\text{-}C_7H_7)Hf(\eta^4\text{-}1,3\text{-}C_7H_{10})$
Mn	Cycloheptatriene	CO	$(\eta^6\text{-}C_7H_8)_2Mn(CO) + (\eta^5\text{-}C_7H_9)Mn(CO)_3$
Mn	Cycloheptadiene	CO	$(\eta^5\text{-}C_7H_9)Mn(CO)_3 + (\eta^3\text{-}C_7H_{11})Mn(CO)_4$
Mn	Cyclopentadiene	CO	$(\eta^5\text{-}C_5H_5)Mn(CO)_3$
Mn	Cyclohexadiene	CO	$(\eta^4\text{-}C_6H_8)_2Mn(CO)$
Cr	1,5-Cyclooctadiene	PF_3	$(\eta^4\text{-}C_8H_{11})Cr(PF_3)_3H$
Cr	1,3-Cyclohexadiene	PF_3	$(\eta^4\text{-}C_6H_8)_2Cr(PF_3)_2$
Ti	Cycloheptatriene	–	$(\eta^7\text{-}C_7H_7)Ti(\eta^5\text{-}C_7H_9)$
Ti	Cyclooctatetraene	–	$(\eta^8\text{-}C_8H_8)_2Ti_2(\eta^6\text{-}C_8H_8)_3$
Cr	Cyclooctatetraene	–	$Cr_2(C_8H_8)_3$

2.4 Phosphines, Amines, and σ-Donor Combinations

Pure phosphine–metal atom studies with the early transition metals have been lacking. The only complex prepared this way prior to 1978 was $Cr(PF_3)_6$. King and Chang, with the unique aminophosphine systems Me_2NPF_2 and $MeN(PF_2)_2$, have generated a variety of new homoleptic $M{-}(L)_n$ systems (*see Homoleptic Compound*). The codeposition of Cr vapor with these ligands yields the complexes shown:

$$Cr(g) + 6MeN(PF_2)_2 \longrightarrow [MeN(PF_2)_2]_6Cr \tag{8}$$

$$Cr(g) + 6Me_2NPF_2 \longrightarrow (Me_2NPF_2)_6Cr \tag{9}$$

$$Cr(g) + 4Me_2NPF_2 + MeN(PF_2)_2 \longrightarrow Cr(PF_2NMe_2)_4[(PF_2)_2NMe] \tag{10}$$

The chelating ligand $Me_2PCH_2CH_2PMe_2$ (dmpe) is a useful σ-donor ligand and forms complexes with metal vapors of Cr, Mo, W, V, and Nb, to give the corresponding $(dmpe)_3M$ derivatives.[19] Similarly, the codeposition of Cr, Mo, and W vapors with trialkoxyphosphites, $P(OR)_3$, leads to the synthesis of a series of novel zerovalent complexes, such as $Cr[P(OR)_3]_6$. The substituent R = Et yields sterically hindered complexes that are thermally unstable. When R = Me, the zerovalent complex can be isolated.

2.5 Miscellaneous

Codeposition experiments have shown that vapors of the early transition metals Ti, V, and Cr deoxygenate[20] or desulfurate organic compounds. Epoxides yield alkenes with these metal atoms. The early transition metals are generally more efficient for these types of reactions. Aminoxides and DMSO undergo deoxygenation, while nitro compounds and nitroarenes yield coupled azo and azoxy products:

$$(\text{pyridine } N\text{-oxide})_x + Cr(g) \longrightarrow (\text{pyridine})_x + CrO_x \tag{11}$$

Mo is the element of choice for clean and direct sulfur abstractions.[21] A comparison with appropriate C atom reactions, where the ratio cyclopropane/propene was 10:1, indicates an *Insertion* mechanism, in which Mo atoms attack the C–H bond to form an allyl intermediate (*see* ***Mechanisms of Reaction of Organometallic Complexes***).[22]

Mo and W atoms play an important role in oxidative addition to C–H bonds. W activates linear and cyclic saturated hydrocarbons in the presence of PMe_3,[23] while Mo reacts with bidentate phosphine to give a Mo (hydride)phosphine complex:[24]

$$W(g) + C_5H_6 + PMe_3 \longrightarrow C_5H_5WH_5PMe_3 \tag{12}$$

$$Mo(g) + i\text{-}Pr_2PCH_2CH_2P\text{-}i\text{-}Pr_2 \longrightarrow MoH_4(i\text{-}Pr_2PCH_2CH_2P\text{-}i\text{-}Pr_2) \tag{13}$$

Re inserts in pure hydrocarbons and in C–H bonds near an aromatic or triene group. The intermediate metal hydride species react further in order to fill their coordination shell:[25,26]

$$Re(g) + C_6H_{12} + 2C_6H_6 \longrightarrow (\eta^6\text{-}C_6H_6)_2Re_2H_2C_6H_{10} \tag{14}$$

$$Re(g) + C_6H_6 + 2C_6H_5Me \longrightarrow (\eta^6\text{-}C_6H_5Me)_2Re_2H_3C_6H_5 \tag{15}$$

Little is known about the oxidative addition of organohalides to early transition metal atoms. Nevertheless, macroscale amounts of solvated transition metal halides in lower valency states have been obtained. Re yields interesting clusters in reactions with 1,2-dibromoethane and oxalyl chloride:[27]

$$Re(g) + BrCH_2CH_2Br \longrightarrow Re_3Br_9(THF)_3 \tag{16}$$

$$Re(g) + ClOCCOCl \longrightarrow [Re(CO)_4Cl]_2 \tag{17}$$

Pure alkyl transition metal complexes are rare, owing to the *β-Elimination* decay mechanism. An effective strategy to prepare such compounds must therefore aim at blocking possible decomposition pathways. Neopentyl is void of hydrogen in the β-position, and neopentyl bromide with Cr yields the known thermally stable tetrakis(neopentyl)chromium complex:**[28]**

$$2Cr(g) + 4Me_3CCH_2Br \longrightarrow (Me_3CCH_2)_4Cr + CrBr_4 \qquad (18)$$

3 LATE TRANSITION ELEMENTS (Fe–Zn GROUPS)

3.1 Organic and Inorganic Halides

The high-boiling points of the late transition metals, especially the second- and third-row elements, require resistive heating or electron beam vaporization methods.

Organic halides, codeposited with a late transition metal, form the oxidative addition product RMX. Some intermediate products decompose during the macroscale codeposition or, more often, on matrix warm up. The unique ligand bromopentafluorobenzene yields thermally more stable RMX species upon codeposition with Ni, Pd, and Pt. In fact, for Pd the formally coordinatively unsaturated species C_6F_5PdBr, CF_3PdI, C_2F_5PdI, and $CF_3CF_2CF_2PdI$ are isolable as reactive, sensitive, red polymeric solids, which are trimers or tetramers in solution.**[29]** The first step in the reaction mechanism is believed to be formation of a weakly bonded aryl/alkyl halide–Pd complex that gives RPdX. Trapping leads to $RPdXL_2$, while warm up without stabilizing ligands often leads to organic coupling products, PdX_2, and Pd. Suitable trapping ligands are PEt_3, Me_2S, Me_2NH, C_5H_5N, Me_2CO, and others. The corresponding Ni analog, C_6F_5NiBr, is an intriguing system. It is, unlike the Pd complex, not isolable. It decomposes at about −80 °C to form $C_6F_5C_6F_5$, $NiBr_2$, and Ni. It resembles the Pd homolog (dec. 100 °C), but is far less stable. Both intermediates can be trapped at −80 °C or lower with PEt_3. However, in the presence of toluene or other arene systems, C_6F_5NiBr disproportionates and binds an arene molecule, thus forming $(\eta^6\text{-}C_6H_5Me)Ni(C_6F_5)_2$.**[30]** Similar results are obtained in the analogous Co–C_6F_5Br system. These are unique π-systems in that they are the first examples of such complexes for Co^{II} and Ni^{II}. The arene ligand is extremely labile and can be displaced by stronger ligands, such as cot, norbornadiene, butadiene, PEt_3, or even THF. The weakly bonded arene ring is responsible for the catalytic activity of the Ni complex and catalyzes the polymerization of norbornadiene, the trimerization of butadiene, and the *Hydrogenation* of toluene. The formation and the fascinating chemistry of C_6F_5NiBr are shown in Scheme 4.

In related studies, Fe and Ni atoms were found to oxidatively insert Si–H bonds.**[31,32]** In the presence of arenes, η^{6-} complexes are formed that are formally Fe(IV) and Ni(II) complexes:

$$Fe + HSiCl_3 + \text{toluene} \longrightarrow (\eta^6\text{-}C_6H_5CH_3)\text{–}Fe(H)_2(SiCl_3)_2 \qquad (19)$$

$$Ni + HSiF_3 + \text{toluene} \longrightarrow (\eta^6\text{-}C_6H_5CH_3)\text{–}Ni(SiF_3)_2 + H_2 \qquad (20)$$

Several halogenated silanes behaved similarly, including H_2SiCl_2, $HSiF_3$, $HSiCl_3$, and $HSiCl_2CH_3$. In the case of (toluene)$Ni(SiCl_3)_2$, a crystal structure indicated a $p_{\bar{1}}$ space group with two molecules per unit cell. The nickel-silane distances are relatively short, 2.174(4) and 2.182(4) Å, owing to strong Π-backbonding from the Ni to the $SiCl_3$ groups. The toluene possesses a small ‘boat type’ distortion amounting to a rotation of the two end carbons of 5° away from the nickel.

The late transition metals of Groups 11 and 12 can be conveniently vaporized by resistive heating in W–Al_2O_3 crucibles, although many other vaporization techniques have been employed. The d orbitals are filled for these metals, and they have a strong tendency to undergo abstraction and oxidative additions owing to the ease of ionization and loss of electrons from 4s, 5s, or 6s levels. The earliest report of a synthetic application of the macroscale cocondensation was made by Timms in 1968. Copper atoms abstracted halogen very efficiently from BCl_3, forming B_2Cl_4 in high yield:

$$2BCl_3 + 2Cu(g) \longrightarrow 2CuCl + B_2Cl_4 \qquad (21)$$

With PCl_3, Cu atoms yielded smaller amounts of product. Copper also proved useful in dehalogenation reactions with alkyl halides:

$$\begin{aligned}&MeCH_2C^*HClMe + Cu\,(g) \text{ or } Ag\,(g) \longrightarrow\\ &\qquad MeCH_2CH(Me)CH(Me)CH_2Me \qquad (22)\\ &\qquad (S,S)(70\%\ \text{optical purity})\end{aligned}$$

$$\begin{aligned}&MeCH_2C^*HClMe + Na(g) \longrightarrow MeCH_2CH(Me)CH(Me)CH_2Me\\ &\qquad\qquad \text{Same product, but optically inactive} \qquad (23)\end{aligned}$$

Unlike Na, Cu atoms do not generate radical intermediates. Cu or Ag/RX always seem to be associated with $R^\bullet$, which is possibly complexed as RM at low temperatures.

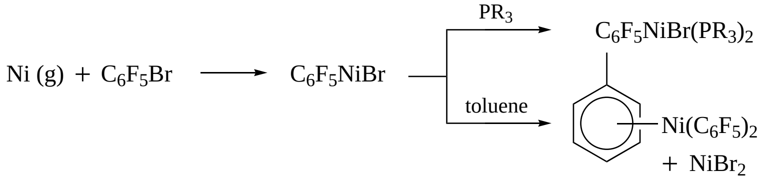

Scheme 4

The first perfluoro $\mathrm{R_fAg}$ and $\mathrm{Ar_fAg}$ compounds have been prepared:

$$\begin{aligned}\mathrm{R_fI} + \mathrm{Ag(g)} &\longrightarrow \mathrm{R_f{-}I\cdots Ag} \longrightarrow \mathrm{R_f}\bullet + \mathrm{IAg}\\ &\longrightarrow \mathrm{R_fI} + \mathrm{R_fAg}\end{aligned} \qquad (24)$$

New, sensitive $\mathrm{R_fAg}$ complexes, such as $\mathrm{CF_3CF_2CF_2Ag}$ and $\mathrm{CF_3Ag}$, are only isolable if complexed to a donor solvent (MeCN). Gold atoms also abstract halide from RX. The resulting complex consists of polymeric $(\mathrm{C_6F_5Au})_n$ units. No abstraction reactions occurred with ground state Zn, Cd, or Hg. However, Zn, codeposited with $\mathrm{R_fI}$ ($\mathrm{R_f} = \mathrm{CF_3}$, $\mathrm{CF_3CF_2}$, $\mathrm{CF_3CF_2CF_2}$, and $\mathrm{(CF_3)_2CF}$) yielded $\mathrm{R_fZnI}$ at low temperatures in a nonsolvated state, which decomposed to ZnIF and [$\mathbf{:}\mathrm{CF_2}$]. The very reactive carbene [$\mathbf{:}\mathrm{CF_2}$] can be trapped by an alkene, to give a cyclopropene:

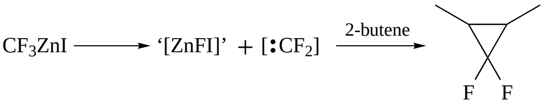

(25)

3.2 Phosphines, Phosphites, and Combinations with Other σ-Donor/π-Ligands

The macroscale codeposition of $\mathrm{PF_3}$ has yielded a series of $\mathrm{M{-}PF_3}$ complexes. Some of these $\mathrm{M{-}PF_3}$ complexes can only be prepared by the metal vapor–ligand cocondensation technique. Very electron-rich M–phosphine and M–phosphite derivatives have been prepared by $\mathrm{M{-}PMe_3}$ and $\mathrm{M{-}P(OMe)_3}$ depositions, as shown in Table 8. A series of new homoleptic compounds have been prepared. Cocondensation of Fe and Ni with some arene systems gives stable $\mathrm{(Ar)_2Fe/Ni}$ species, if maintained at low temperatures. Addition of σ-donor ligands leads to a variety of new ML_n or mixed ArML_n complexes.

Nitric oxide, a three-electron ligand, is too volatile to be cocondensed at −196 °C for macroscale preparations. The $\mathrm{BF_3}$ adduct of NO, which is less volatile, has been used. Deposition of $\mathrm{BF_3{-}NO}$ and appropriate metal/ligand systems yields the corresponding complexes. The codeposition of a wide series of isocyanides gives macroscale amounts of $\mathrm{NiL_4}$ and $\mathrm{FeL_5}$.

3.3 Dienes, Trienes, and Tetraenes

Cyclopentadiene reacts with metal atoms in a combination of oxidative addition and simple orbital mixing processes. The very reactive M–H species form tetrahapto and trihapto complexes under loss of hydrogen. Important representative complexes are listed in Table 9.

The thermally sensitive $\mathrm{(cod)_2Ni}$ has shown unusual reactivity and resembles 'naked nickel' in its chemistry. The chemistry of Ni atoms and $\mathrm{(cod)_2Ni}$ is often very similar. The following examples demonstrate the high reactivity of $\mathrm{(cod)_2Ni}$:

$$\mathrm{(cod)_2Ni} + 3\mathrm{C_2H_4} \longrightarrow \mathrm{(C_2H_4)_3Ni} + 2\mathrm{cod} \qquad (26)$$

$$\mathrm{(cod)_2Ni} + 4\mathrm{PR_3} \longrightarrow \mathrm{(PR_3)_4Ni} + 2\mathrm{cod} \qquad (27)$$

The corresponding paramagnetic complex $\mathrm{(cod)_2Fe}$ decomposes at temperatures above −30 °C. Nevertheless, this weakly bonded Fe complex is an excellent precursor for ligand-exchange reactions. Treatment at low temperatures with a variety of π- and σ-binding ligands leads to partial or complete displacement of the cod units:

$$[\mathrm{(cod)_2Fe}] + 3\mathrm{PF_3} \longrightarrow \mathrm{(cod)Fe(PF_3)_3} \qquad (28)$$

Table 8 M–L_n and ArML_n complexes from the late transition metals prepared by macroscale metal atom methods

Metal	π-Ligand	σ-Donor ligand	Product
Fe	–	$\mathrm{PF_3}$	$\mathrm{Fe(PF_3)_5 + (PF_3)_3Fe(PF_2)_2Fe(PF_3)_3}$
Fe	–	$\mathrm{PMe_3}$	$\mathrm{Fe(PMe_3)_5 + [Me_3Fe(H)CH_2(PMe)_2]}$
Fe	–	$\mathrm{NO, PF_3}$	$\mathrm{(NO)_2Fe(PF_3)_2}$
Fe	$\mathrm{C_6H_6}$	$\mathrm{PF_3}$	$(\eta^6\text{-}\mathrm{C_6H_6})\mathrm{Fe(PF_3)_2}$
Co	–	$\mathrm{PF_3}$	$\mathrm{Co_2(PF_3)_8, HCo(PF_3)_4}$
Co	$\mathrm{C_6H_6}$	NO	$(\eta^6\text{-}\mathrm{C_6H_6})\mathrm{Co(NO)}$
Co	–	$\mathrm{MeN(PF_2)_2, Me_2NPF_2}$	$\mathrm{Co_2(PF_2NMe_2)[(PF_2)_2NMe]_2}$
Co	$\mathrm{C_5H_6}$	$\mathrm{PF_3}$	$\mathrm{C_5H_5Co(PF_3)_2}$
Ni	–	$\mathrm{PF_3}$	$\mathrm{Ni(PF_3)_4}$
Ni	–	$\mathrm{PPh_3}$	$\mathrm{Ni(PPh_3)_4}$
Ni	–	$\mathrm{MeN(PF_2)_2}$	$\mathrm{Ni[(PF_2)_2NMe]}_n$
Ni	–	$\mathrm{C_6F_5Cl, PEt_3}$	$\mathrm{C_6F_5NiCl\ (PEt_3)_2}$
Ni	–	$\mathrm{CF_3COCl, PEt_3}$	$\mathrm{CF_3NiCl(PEt_3)_2}$
Pd	–	$\mathrm{PF_3}$	$\mathrm{Pd(PF_3)_4}$
Pd	–	$\mathrm{CF_3I, PEt_3}$	$\mathrm{CF_3PdI(PEt_3)_2}$
Pd	–	$\mathrm{C_6F_5Cl, PEt_3}$	$\mathrm{C_6F_5PdCl(PEt_3)_2}$
Pd	$\mathrm{CF_3CF{=}CFCF_3}$	$\mathrm{PEt_3}$	$\mathrm{(CF_3CF{=}CFCF_3)\ Pd(PEt_3)_2}$

Table 9 Late transition metal complexes from diene, triene, and tetraene ligands, prepared by the metal atom/ligand cocondensation method

Metal	π-Ligand	σ-Ligand	Complex
Fe	Cyclopentadiene	–	Ferrocene
Co	Cyclopentadiene	–	$(\eta^5\text{-}C_5H_5)Co(\eta^4\text{-}C_5H_6)$
Ni	Cyclopentadiene	–	$(\eta^5\text{-}C_5H_5)Ni(\eta^3\text{-}C_5H_7)$
Ni	1,5-Cyclooctadiene	–	$(\eta^4\text{-}C_8H_8)_2Ni$
Fe	Cycloheptatriene	–	$(\eta^7\text{-}C_7H_7)Fe(\eta^3\text{-}C_7H_{11})$
Co	Cycloheptatriene	PF_3	$(\eta^3\text{-}C_7H_{11})Co(PF_3)_3 + HCo(PF_3)_4$
Ru	Cyclohexadiene	CO	$(\eta^4\text{-}C_6H_8)_2Ru(CO)$

$$[(cod)_2Fe] + 2cot \longrightarrow (cot)_2Fe \qquad (29)$$

$$[(cod)_2Fe] + 2diphos + N_2, CO \longrightarrow (diphos)_2Fe(N_2, CO) \qquad (30)$$

$$[(cod)_2Fe] + 5CO \longrightarrow Fe(CO)_5 \qquad (31)$$

4 MISCELLANEOUS

Very little successful synthetic work with alkynes and metal atoms has been published. Generally, alkynes are efficiently trimerized by group 8 metal atoms, but a few stable metal complexes have been found:

$$M(g) + 6RC{\equiv}CR \longrightarrow (\eta^6\text{-}C_6R_6)_2M \qquad (32)$$

Only a few alkenes form stable homoleptic metal complexes. Norborene allows the formation of relatively stable tris(bicyclo[2.2.1]heptene)palladium. The slight strain energy in the C=C bond results in a stronger π–M interaction.[33] In the past 10 years, examples of synthesis of transition metal compounds have become much less frequent. One reason for this is that other 'wet' methods have been developed to gain access to the desired compounds. Another reason is that the metal vapor method has been adapted for synthesis of metal clusters and nanoscale particles. These are topics of material science rather than organometallic chemistry. However, in some cases, the nanoparticles produced are so monodisperse that they are indeed discrete molecules, although very large ones. For example, gold vapor (atoms) codeposited with acetone (or butanene or 2-pentanone) at 77K leads to colloidal gold with a variety of particle sizes. Treatment with a long chained thiol in refluxing toluene causes a remarkable particle size narrowing so that each gold nanoparticle is 4.6 nm ± 0.1 nm (about 5000 atoms/particle

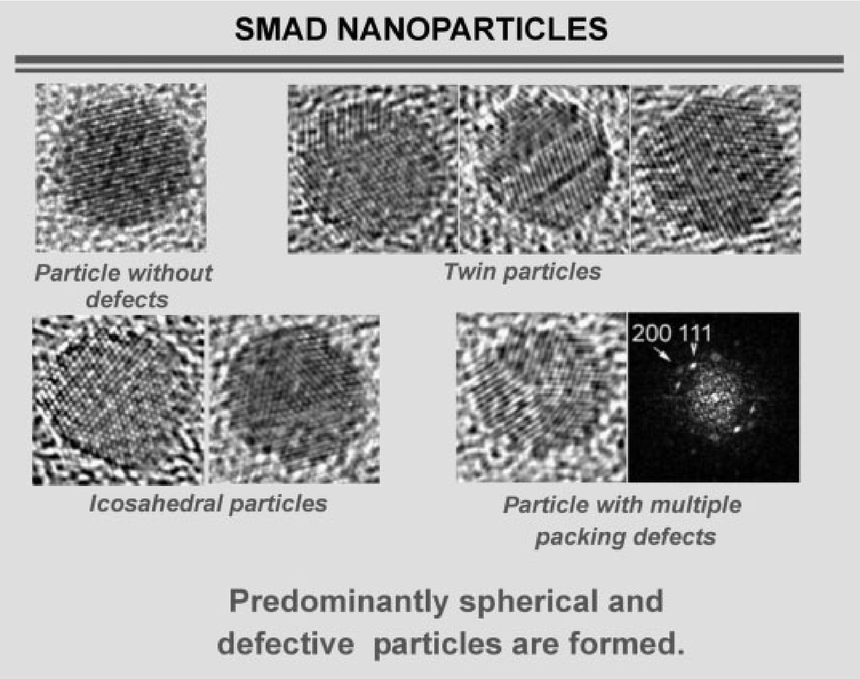
SMAD NANOPARTICLES
Particle without defects
Twin particles
Icosahedral particles
200 111
Particle with multiple packing defects
Predominantly spherical and defective particles are formed.

Figure 5 High-resolution electron microscope images of SMAD gold nanoparticles. Note the rows of gold atoms and the exact monodispersity of the samples. Some of the particles are single crystals, while others are multi-domain

and 300 $C_{12}H_{25}SH$ ligands/particle). This particle narrowing is caused by the transfer of gold atoms/clusters from particle to particle until a thermodynamic equilibrium is achieved between the formation of more gold-sulfur bonds and the size of the particles.[34,35,36]

$$\text{Au vapor} + \text{acetone} \xrightarrow{77\,\text{K}} \text{(Au) (acetone) solvate} \qquad (33)$$

$$\text{Au (acetone)} + C_{12}H_{25}SH \longrightarrow (\text{Au})_x(HSC_{12}H_{25})_y \qquad (34)$$

$$(\text{Au})_x(HSC_{12}H_{25})_y \xrightarrow[\text{reflux (digestive ripening)}]{\text{toluene}} (\text{Au})_{5000}(HSC_{12}H_{25})_{300} \qquad (35)$$

Figure 5 shows high-resolution electron microscope images of several gold nanoparticles formed by this metal vapor synthesis method, often called Solvated Metal Atom Dispersion (SMAD).

5 RELATED ARTICLES

Chromium: Organometallic Chemistry; Metallic Materials Deposition: Metal-organic Precursors.

6 REFERENCES

1. K. J. Klabunde, ‘Chemistry of Free Atoms and Particles’, Academic Press, New York, 1980.
2. Ch. Elschenbroich and A. Salzer, ‘Organometallics’, VCH, Weinheim, 1989.
3. V. Graves and J. J. Lagowski, *Inorg. Chem.*, 1976, **15**, 577.
4. Ch. Elschenbroich, R. Möckel, and U. Zenneck, *Angew. Chem., Int. Ed. Engl.*, 1978, **17**, 531.
5. Ch. Elschenbroich, J. Koch, J. Schneider, B. Spangenberg, and P. Schiess, *J. Organomet. Chem.*, 1986, **317**, 41.
6. Ch. Elschenbroich and J. Heck, *J. Am. Chem. Soc.*, 1979, **101**, 6773.
7. K. J. Klabunde and H. F. Efner, *Inorg. Chem.*, 1975, **14**, 789.
8. Ch. Elschenbroich, J. Kroker, W. Massa, M. Wünsch, and A. J. Ashe, III *Angew. Chem., Int. Ed. Engl.*, 1986, **25**, 571.
9. A. Agarwal, M. J. McGlinchey, and T. S. Tan, *J. Organomet. Chem.*, 1978, **141**, 85.
10. S. D. Ittel, F. A. Van-Catledge, and C. A. Tolman, *Inorg. Chem.*, 1985, **24**, 62.
11. P. L. Timms, in ‘Cryochemistry’, eds. M. Moskovits and G. A. Ozin, Wiley, New York, 1976, p. 61.
12. Ch. Elschenbroich, M. Nowotny, B. Metz, W. Massa, J. Graulich, B. Biehler, and W. Sauer, *Angew. Chem., Int. Ed. Engl.*, 1991, **30**, 547.
13. M. L. H. Green, D. O’Hare, P. Mountford, and J. G. Watkin, *J. Chem. Soc., Dalton Trans.*, 1991, 1705.
14. K. J. Klabunde and H. F. Efner, *J. Fluorine Chem.*, 1974, **4**, 115.
15. P. S. Skell, E. M. Van Dam, and M. P. Silvon, *J. Am. Chem. Soc.*, 1974, **96**, 626.
16. M. Yevitz and P. S. Skell, Symposium on Inter- and Intramolecular Forces, Int. Union Crystallography Intercong. Symp. Intra-Intermol. Forces, 1974, 1974, Ser. 2, Vol. 2, Paper E9.
17. P. L. Timms and T. W. Turney, *J. Chem. Soc., Dalton Trans.*, 1976, 2021.
18. S. P. Kolesnikov, J. E. Dobson, and P. S. Skell, *J. Am. Chem. Soc.*, 1978, **100**, 999.
19. F. G. N. Cloke, P. J. Fyne, M. L. H. Green, M. J. Ledoux, A. Gourdon, and C. K. Prout, *J. Organomet. Chem.*, 1980, **198**, C69.
20. S. Togashi, J. G. Fulcher, B. R. Cho, M. Hasegawa, and J. A. Gladysz, *J. Org. Chem.*, 1980, **45**, 3044.
21. A. H. Reid, P. B. Shevlin, T. R. Webb, and S. S. Yun, *J. Org. Chem.*, 1984, **49**, 4728.
22. J. T. Miller and C. W. DeKock, *J. Org. Chem.*, 1981, **46**, 516; P. S. Skell, K. J. Klabunde, J. H. Plonka, J. S. Roberts, and D. L. Williams-Smith, *J. Am. Chem. Soc.*, 1973, **95**, 1547.
23. M. L. H. Green and G. Parkin, *J. Chem. Soc., Chem. Commun.*, 1984, 1467.
24. F. G. N. Cloke, V. C. Gibson, M. L. H. Green, V. S. B. Mtetwa, and K. Prout, *J. Chem. Soc., Dalton Trans.*, 1988, 2227.
25. J. A. Bandy, F. G. N. Cloke, M. L. H. Green, D. O’Hare, and K. Prout, *J. Chem. Soc., Chem. Commun.*, 1984, 240.
26. M. L. H. Green and D. O’Hare, *J. Chem. Soc., Dalton Trans.*, 1987, 403; M. L. H. Green and D. O’Hare, *J. Chem. Soc., Dalton Trans.*, 1986, 2469.
27. P. R. Brown, F. G. N. Colke, M. L. H. Green, and R. C. Tovey, *J. Chem. Soc., Chem. Commun.*, 1982, 519.
28. T. J. Groshens, 1. Molecular Vapor Synthesis: The Use of Titanium Monoxide and Vanadium Monoxide. 2. Oxidative Insertion Reactions of First Row Early Transition Metal Atoms, Ph. D. Thesis, Kansas State University, 1988.
29. K. J. Klabunde, B. B. Anderson, and K. Neuenschwander, *Inorg. Chem.*, 1980, **19**, 3719.
30. K. J. Klabunde, B. B. Anderson, M. Bader, and L. J. Radonovich, *J. Am. Chem. Soc.*, 1978, **100**, 1313.
31. Z. Yao, K. J. Klabunde, and U. S. Asirvatham, *Inorg. Chem.*, 1995, **34**, 5289.
32. Z. Yao and K. J. Klabunde, *Organometallics*, 1995, **14**, 5013.
33. R. M. Atkins, R. MacKenzie, P. L. Timms, and T. W. Turney, *J. Chem. Soc., Chem. Commun.*, 1975, 764.
34. S. Stoeva, K. J. Klabunde, C. Sorensen, and I. Dragieva, *J. Am. Chem. Soc.*, 2002, **124**, 2305.
35. S. I. Stoeva, B. L. V. Prasad, U. Sitharaman, P. Stoimenov, V. Zaikovski, C. M. Sorensen, and K. J. Klabunde, *J. Phys. Chem. B.* (invited paper for A. Henglein Special Issue), 2003, **107**, 7441.
36. B. L. V. Prasad, S. I. Stoeva, C. M. Sorensen, and K. J. Klabunde, *Langmuir*, 2002, **18**, 7515.

Metallic Materials Deposition: Metal-organic Precursors

Charles H. Winter, Wenjun Zheng & Hani M. El-Kaderi
Wayne State University, Detroit, MI, USA

Based in part on the article Metallic Materials Deposition: Metal-organic Precursors by Herbert D. Kaesz, Alfred Zinn, & Lutz Brandt which appeared in the Encyclopedia of Inorganic Chemistry, First Edition.

---

1 Introduction 1
2 Precursors for Main Group Metals and Lanthanides 3
3 Precursors for Transition Metal Groups 4 and 5 10
4 Precursors for Transition Metal Groups 6 and 7 12
5 Precursors for Transition Metal Groups 8 and 9 13
6 Precursors for Transition Metal Groups 10 and 11 13
7 Related Articles 14
8 Further Reading 15
9 References 15

Glossary

Atomic layer deposition (also termed atomic layer epitaxy): a process in which alternate pulses of two volatile precursors are passed over the substrate to promote layer-by-layer film growth
Chemical beam epitaxy: a process in which one or more beams of volatile metal-organic precursors is directed to the substrate surface to effect film growth
Chemical vapor deposition (CVD; also termed vapor-phase epitaxy): the deposition of a thin film of an element or compound using some form of excitation for the decomposition of a volatile precursor
Laser-assisted chemical vapor deposition: a CVD in which the excitation is delivered from photons delivered from a laser
Metal-organic chemical vapor deposition (MOCVD): the same as CVD, except that the precursor is a volatile organometallic or coordination compound with carbon-containing ligands
Metal-organic vapor-phase epitaxy: the same as MOCVD, but implying specific induced crystalline orientation of the deposited film
Molecular beam epitaxy: a process in which one or more beams of elemental precursors is directed to the substrate surface to effect film growth
Organometallic chemical vapor deposition: the same as MOCVD
Plasma-enhanced chemical vapor deposition (also known as plasma-assisted chemical vapor deposition): a CVD in which the excitation of the material to be deposited is accomplished by thermal means at reduced pressure in the presence of an electric field. This method may also be used for the decomposition of a volatile precursor introduced in a gas stream at low pressure

---

Abbreviations

acac = Acetylacetonato; ALD = Atomic layer deposition; iBu = Isobutyl; nBu = n-butyl; tBu = *Tert*-butyl; CBE = Chemical beam epitaxy; COD = 1,5-cyclooctadiene; dmpy = 3,5-dimethylpyridine; dmen = N,N'-dimethylethylenediamine; DMSO = Dimethylsulfoxide; dmto = 5-N-(N,N-dimethylaminopropyl)-2,2,7-trimethyl-3-octanonato; dpm-CAP-4 = 2,2,25,25-tetramethyl-5,22-di-*tert*-butyl-9,12,15,18-tetraoxa-4,22-diene-6,21-diimino-3,24-hexacosadionato; en = 1,2-ethylenediamine; Et = Ethyl; HBpz$_3$ = Tris(pyrazolyl)borate; hfac = 1,1,1,5,5,5-hexafluoracetylacetonato; LACVD = Laser-assisted chemical vapor deposition; MBE = Molecular beam epitaxy; Me = Methyl; MOCVD = Metal-organic chemical vapor deposition; MOVPE = Metal-organic vapor-phase epitaxy; OMCVD = Organometallic chemical vapor deposition; PACVD = Plasma-assisted chemical vapor deposition; PEB = Pentaethyleneglycol ethyl butyl ether; PECVD = Plasma-enhanced chemical vapor deposition; iPr = Isopropyl; nPr = n-propyl; pz = 3,5-disubstituted pyrazolato; tbaoac = $tert$-butylacetoacetato; tmeda = N,N,N',N'-tetramethylethylenediamine; tmhd = 2,2,6,6-tetramethylheptanedionato; tmp = 2,2,6,6-tetramethylpiperidido; VPE = Vapor-phase epitaxy; VTMOS = Vinyltrimethoxysilane; VTMS = Vinyltrimethylsilane.

---

1 INTRODUCTION

1.1 Scope of This Article

Thin films of metal-containing materials are widely employed in many technological applications ranging from coatings on architectural glass to microelectronics devices.[1–6] While many methods can be used to create thin films, considerable emphasis in recent years has been placed on film growth techniques that use chemical compounds as precursors. These collected techniques are known generally as CVD (chemical vapor deposition), and many different variations of the CVD technique are known.[1–6] However, all CVD methodologies are similar in that they involve the delivery of volatile chemical compounds in the gas phase to the growing film. This article focuses on the chemical compounds that have been used for the growth of metal-containing materials by CVD methods. Specifically, this review describes metal-organic precursors, which contain hydrocarbon groups on the ligands used to satisfy the metal valency and to saturate the coordination sphere. The precursors that are discussed in this article are collected in tables in the subsections. Specific features of the precursors are discussed in the subsections. Wherever possible, volatility data on the precursors are presented, although information on vapor pressures is often limited or not reported. Each entry is accompanied by a leading reference to allow rapid access to the appropriate literature. Recent reviews of metal-organic precursors are cited where appropriate. The major emphasis herein is on precursors that have been reported since 1994, when the last review on metal-organic precursors appeared in this encyclopedia.[7]

$$\mathrm{M\text{-}R} + \mathrm{EH}_n \xrightarrow[-\mathrm{RH}]{\text{CVD Reactor}} \mathrm{M\text{-}EH}_{n-1}$$

M = metal atom or heteratom
E = O, N, S, other heteroatom

Figure 1 Protonolysis reaction in a CVD precursor

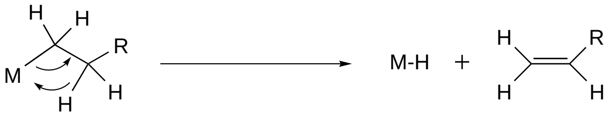

Figure 2 β-Hydrogen elimination

1.2 Advantages of Metal-organic Precursors

Metal-organic precursors have several advantages for film growth, compared to the elemental sources that are used in physical vapor deposition processes. Most importantly, metal-organic precursors tend to be much more volatile than most metals in their elemental form, which allows high film growth rates to be achieved and allows the use of simple precursor delivery systems. Since film growth occurs by a series of chemical reactions, it is possible to design the precursor chemistry to favor the desired inorganic phase, minimize undesirable element incorporation into the final material, control and lower the deposition temperature, and avoid corrosive byproducts that might damage the reactor or the substrate on which the film is grown. Metal-organic precursors can also be obtained in very high chemical purity, which is important for many applications.

1.3 Types of Ligands

Many different types of ligands have been employed to create volatile metal-organic precursors for film growth. In general, the ligands are anionic with carbon, oxygen, or nitrogen donor atoms. In some cases neutral donor ligands are present. The ligand backbone usually consists of a hydrocarbon fragment. Several distinct strategies are used to remove the undesired organic groups during the film growth process. Many CVD processes entail the reaction between a metal-organic precursor with basic ligands and a coreactant that contains acidic element-hydrogen bonds. Mixing of these reactants in the gas phase results in protonation reactions that eliminate the basic ligand in its protonated form and results in the formation of a new metal-element bond (Figure 1).[8] The coreactant with acidic element-hydrogen bonds is generally chosen so that the element corresponds to one of the atoms required for the final thin-film material. Examples of this type of reactant include water and ammonia for the deposition of oxides and nitrides, respectively. A second type of strategy that is used to eliminate excess hydrocarbon groups from the metal-organic precursor is β-hydrogen elimination (Figure 2).[9] Hydrocarbon groups such as ethyl, propyl, isopropyl, *n*-butyl, and isobutyl, when bonded to a metal atom or a heteroatom, can eliminate an alkene through a low-energy decomposition pathway. This β-hydrogen elimination (*see β-Hydride Elimination*) often provides an efficient pathway through which carbon groups are removed from precursors. If a precursor is properly designed, the carbon incorporation in the thin-film material can be minimized. Precursors with hydrocarbon fragments that lack β-hydrogen atoms, such as a methyl or *tert*-amyl groups, are likely to lead to higher carbon incorporation in the thin film.

There are two distinct approaches to metal-organic precursor design. Most commonly, precursors are designed to react with separate gas stream of a reactive element hydride such as ammonia or water, to remove the hydrocarbon ligands and to provide the desired oxide, nitride, or other element needed for the desired thin-film material. The individual precursors are delivered to the reactor chamber as separate gas streams, and are then mixed over the substrate to achieve film growth. Advantages of this approach include being able to maximize the volatility of precursors, greatest flexibility of the deposition variables to achieve the desired outcome, as well as the ability to build desired reactivity paths into the metal-organic precursors. Disadvantages can include poor control over stoichiometry in multicomponent materials and inability to grow desired phases of materials that are not favored thermodynamically. Another approach involves the design of a volatile precursor that contains all of the elements necessary for the desired film material, and which has a low-energy decomposition pathway that affords the desired material. Such compounds are termed single-source precursors.[9] Advantages of single-source precursors can include excellent control over stoichiometry in the thin-film material, reduced incorporation of undesired elements, as well as the ability to deposit kinetic phases that are inaccessible by conventional multi-precursor film growth procedures. Disadvantages of the single-source precursor approach include the low volatility of high molecular weight precursors, attendant low film growth rates, and the expense associated with the synthesis of structurally complex precursors.

1.4 Methods of Deposition

Many different embodiments of the CVD technique are available for the growth of thin films, and the readers is referred to excellent recent monographs for more detail.[1–6] The last review on metal-organic precursors that appeared in this encyclopedia contained a detailed overview of thermal CVD processes, schematics of several reactors, as well as a listing of common variants of thermal CVD processes.[7] In addition to these well-known techniques, several new CVD techniques have gained importance in recent years.

ALD (atomic layer deposition) is a method for the controlled growth of thin films,[10,11] and recent interest in this technique has been driven by the semiconductor industry through its need to decrease feature sizes in integrated circuit manufacturing while increasing aspect ratio and complexity. ALD film growth proceeds by exposing the substrate surface alternatively to the different precursors. It differs from CVD film growth by keeping the precursors strictly separate from each other in the gas phase. There are four distinct steps in an ALD growth cycle: (1) exposure of the substrate surface to a gas stream of the first precursor and formation of a monolayer of this precursor on the substrate, (2) an inert gas purge to remove any excess of the first precursor, (3) introduction of a second precursor to the substrate surface and surface reaction to produce the desired thin-film material, and (4) another inert gas purge to remove the gaseous byproducts. In principle, each growth cycle should produce one monolayer of the desired material. However, the steric bulk of the precursors often reduces the surface density of the adsorbed species, and each growth cycle usually leads to a fraction of a monolayer. Metal-organic precursor design for ALD film growth processes differs from CVD precursor design. In ALD, it is essential that the metal-organic precursor be thermally stable on the surface of the substrate at the deposition temperature to avoid uncontrolled CVD growth. In addition, the metal-organic precursor should be extremely reactive toward the second growth reagent, so that the desired thin-film material forms efficiently and potential film contaminants are removed from the growth ambient. There is an ‘‘ALD window’’, where ALD film growth is surface controlled (Figure 3). Outside of this window, the film growth is limited by insufficient precursor reactivity, formation of greater than one monolayer of precursor through condensation, precursor decomposition, or precursor desorption. Many recently reported metal-organic precursors do not have a distinct ALD window, but still can be useful in film growth by ALD.

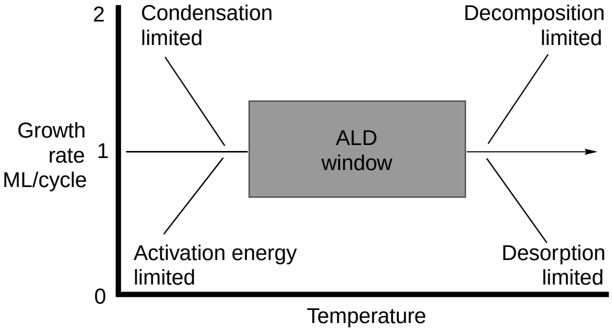

Figure 3 Concept of ALD window, or temperature region for surface-controlled growth

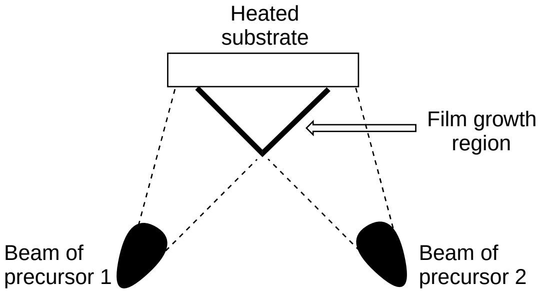

Figure 4 Schematic depiction of CBE film growth

Another emerging film growth technique that employs metal-organic film growth precursors is termed CBE (chemical beam epitaxy).[5] CBE is a variant of the widely used MBE (molecular beam epitaxy) technique, except that metal-organic precursors are used instead of the element sources that are used in MBE. Figure 4 shows a schematic of the basic reactor configuration used in CBE. The film growth process involves decomposition of the precursor beams on the surface of the heated substrate. Since the process occurs at low pressures and the chemical beams are pointed directly at the substrate surface, there is little gas-phase reactivity and the film growth is surface controlled. CBE allows excellent control of film thickness and monolayer abruptness, like the MBE technique. The use of metal-organic precursors with high vapor pressures allows better scale up and reproducibility of precursor delivery, compared to MBE.

2 PRECURSORS FOR MAIN GROUP METALS AND LANTHANIDES

Some main group metal MOCVD (Metal-organic chemical vapor deposition) precursors are listed in Table 1.

2.1 Lithium and Sodium

Film growth precursors for lithium are limited owing to the tendency of lithium compounds to form high nuclearity species

Table 1 MOCVD precursors of main group elements

Compound (mp or bp)	Vapor pressure
Li(tmhd)[12]	bp 295 °C, 760 torr
$[\mathrm{LiO}t\mathrm{Bu}]_6$[13]	0.0016 torr at 70 °C
$\mathrm{Na(OCR(CF_3)_2)}$[14]	subl 75–90 °C at 0.01 torr
$\mathrm{Be(C_2H_5)_2}$[15]	3 torr at 63 °C
$\mathrm{Be(C_5H_5)_2}$[16]	not reported
$\mathrm{Be(C_5H_4CH_3)_2}$[17]	1 torr at 60 °C
$\mathrm{Mg(C_5H_5)_2}$[18,19]	subl 60 °C, 0.01 torr
$\mathrm{Mg(C_5H_4CH_3)_2}$[20,21]	subl 60 °C, 0.01 torr
$\mathrm{Mg(C_5H_4CH_2CH_3)_2}$[22]	0.006 torr at 10 °C
$\mathrm{MgAl_2(CH_3)_8}$[23]	not reported
$[\mathrm{Mg(CH_3)(O}t\mathrm{Bu)}]_4$[24]	subl 140 °C, 1×10^{-6} torr
$\mathrm{Mg(dmto)_2}$[25]	subl 126 °C, 5×10^{-5} torr
$\mathrm{Mg(tmhd)_2(tmeda)}$[26]	subl 120 °C, 5 torr
$\mathrm{Mg(tmhd)_2}$[27]	subl ∼200 °C, 5 torr
$\mathrm{Mg(acac)_2}$[28]	subl 185–240 °C, 10^{-5} torr
$\mathrm{Sr(1,2,4\text{-}C_5}i\mathrm{Pr_3H_2)_2}$[29,30]	subl 100 °C, 10^{-3} torr
$\mathrm{Ba(C_5(CH_3)_5)_2}$[30]	subl 160 °C, 10^{-3} torr
$\mathrm{Sr(tmhd)_2}$[31]	subl 200–225 °C, 10^{-3} torr
$\mathrm{Ba(tmhd)_2}$[32]	prepared in situ at 350 °C from $\mathrm{Ba(OH)_2}$ and tmhdH
$\mathrm{Ba(hfac)_2(PEB)}$[33]	subl 110 °C, 4 torr
$\mathrm{Ba(dpmCAP\text{-}4)_2}$[34]	subl ∼140 °C, 6 torr
$\mathrm{Sr(methd)_2}$ and $\mathrm{Ba(methd)_2}$[35]	liquid injection as solutions in *n*-butyl acetate
$\mathrm{Sr[Ta(OEt)_5(OCH_2CH_2OCH_3)]_2}$[36]	liquid injection as a solution in tetrahydrofuran
$\mathrm{AlMe_3}$[37]	bp 20 °C, 11 torr; 126 °C, 760 torr
$\mathrm{AlEt_3}$[38]	bp 36 °C, 0.1 torr
$\mathrm{AlHMe_2}$[39]	bp 25 °C, 2 torr
$\mathrm{AlH_3(NMe_2Et)}$[40]	bp 24 °C, 1.5 torr
$\mathrm{GaMe_3}$[41]	bp 56 °C, 760 torr
$\mathrm{InMe_3}$[42]	34 torr, 50 °C
$\mathrm{AlMe_3(OEt_2)}$[43]	1 torr, 20 °C
$\mathrm{Al(acac)_3}$[44]	subl 120 °C, low pressure
$\mathrm{Al(OEt)_3}$[45]	subl 137 °C, low pressure
$\mathrm{Mg[(\mu\text{-}O}i\mathrm{Pr)_2AlMe_2]_2}$[46]	subl 60 °C, 10^{-6} torr
$\mathrm{Ga(N_3)_2(CH_2CH_2CH_2NMe_2)}$[47]	2×10^{-3} torr, 25 °C
$\mathrm{In(N_3)(CH_2CH_2CH_2NMe_2)_2}$[48]	subl 70 °C, 0.5×10^{-4} torr
$\mathrm{GaH_2(N_3)}$[49]	bp 40 °C, 0.2 torr
$\mathrm{Ga_2(NMe_2)_6}$[50]	subl 70–80 °C, 10^{-2} torr
$\mathrm{In(C_5Me_5)}$[51]	1.8 torr, 40 °C
$\mathrm{[InMe_2(OC(CF_3)_2CH_2NHMe)]_2}$[52]	subl 120 °C, 0.42 torr
$\mathrm{InMe_2(acac)}$[53]	subl 150 °C, low pressure
$[i\mathrm{Pr_2InOH}\cdot i\mathrm{Pr_2InNH_2}]$[54]	bp 86–88 °C, 10^{-2} torr
$\mathrm{[In(OCMe_2Et)_3]_2}$[55]	subl 95 °C, 10^{-2} torr
$\mathrm{In(OCMe(CF_3)_2)_3(H_2N}t\mathrm{Bu)}$[56]	subl 45–50 °C, 4 torr
$\mathrm{Ga(OCH(CF_3)_2)_3(HNMe_2)}$[57]	subl 100 °C, 0.5 torr
$[\mathrm{Ga(O}t\mathrm{Bu)_3}]_2$[58]	subl 60 °C, 2.5 torr
$\mathrm{In(SOCNEt_2)_3}$[59]	subl 150 °C, 10^{-2} torr
$\mathrm{Ga(SOCNEt_2)_3}$[60]	liquid delivery as tetrahydrofuran solution
$\mathrm{InMe_2(S_2CNEt_2)}$[61]	subl 110 °C, 10^{-2} torr
$\mathrm{In(S_2CNMeBu)_3}$[62]	subl 250 °C, 10^{-2} torr
$\mathrm{Ga(}t\mathrm{Bu)_2(S_2CNMe_2)}$[63]	subl 60 °C, 760 torr
$\mathrm{Ga(SOCMe)_2Me(dmpy)}$[64]	liquid delivery
$\mathrm{[dmpyH]^+\ [In(SOCMe)_4]^-}$[65]	liquid delivery as tetrahydrofuran solution
$\mathrm{[(Me_2EtC)In(\mu_3\text{-}Se)]_4}$[66]	subl 160 °C, 10^{-3} torr
$[(t\mathrm{Bu)Ga(\mu_3\text{-}Se)]_4}$[67]	subl 149 °C, 0.2 torr
$[(t\mathrm{Bu)Ga(\mu_3\text{-}Te)]_4}$[67]	subl 172 °C, 0.2 torr
$\mathrm{SnMe_4}$[68]	108 torr, 25 °C
$\mathrm{SnMe_2Cl_2}$[68]	0.35 torr, 25 °C
$\mathrm{Sn(O}t\mathrm{Bu)_4}$[69]	subl 50–55 °C, 10 torr

(cont’d overleaf)

Table 1 cont'd

Compound (mp or bp)	Vapor pressure
$Sn(OCH(CF_3)_2)_4(HNMe_2)$[70]	subl 70 °C, 0.06 torr
$Sn(NO_3)_4$[71]	subl 0 °C, 0.4 torr
$Sn(SCH_2CH_2S)_2$[72]	liquid delivery as acetone solution
$Sn(SCH_2CF_3)_4$[73]	bp 35 °C, 760 torr
$Sn(NMe_2)_4$[74]	bp 51 °C, 0.15 torr
$Me_3SnCo(CO)_4$[75]	subl 40 °C, 10^{-6} torr
$Pb(tmhd)_2$[76]	subl 128 °C, 0.1 torr
$PbEt_4$[77]	subl 25 °C, 5 torr
SbD_3[78]	bp −18 °C
$SbH_2(CH_2CMe_3)$[79]	5.5 torr, 0 °C
$SbEt_3$[80]	bp 156 °C, 760 torr
$Sb(OEt)_3$[81]	subl 140 °C, 760 torr
$Sb(O_2CNMe_2)_3$[82]	subl 130 °C, 10^{-2} torr
$[AlEt_2(Sb(SiMe_3)_2)]_2$[83]	subl 130 °C, 10^{-3} torr
$BiMe_3$[84]	bp 109 °C, 760 torr
$BiPh_3$[85]	subl 100 °C, 0.2 torr
$Bi(OCMe_2CH_2OMe)_3$[86]	subl 60 °C, 10^{-2} torr
$Bi(tmhd)_3$[87]	subl 150 °C, 0.05 torr
$ZnEt_2$[88]	bp 46 °C
$ZnMe_2$[89]	bp 124 °C
$ZnMe_2(NEt_3)$[90]	11.4 torr, 0 °C
$Zn(acac)_2$[91]	subl 85 °C, 100 torr
$Zn(hfac)_2(H_2O)_2 \cdot diglyme$[92]	subl 70–80 °C, 2–6 torr
$CdMe_2$[93]	bp 106 °C, 760 torr
$Cd(hfac)_2(tmeda)$[94]	subl 70 °C, 10^{-4} torr

with low vapor pressures. Important lithium-containing thin-film materials that have been prepared by CVD methods include $LiNbO_3$, $LiTaO_3$, $LiNb_xTa_{1-x}O_3$, and lithium-doped diamond. Deposition methods to these materials have included CBE, MOCVD, thermal plasma spray CVD, and PECVD (plasma-enhanced chemical vapor deposition). Precursors that have been employed are primarily Li(tmhd)[12] and $[Li(OtBu)]_6$.[13,95] Li(tmhd) decomposes under vacuum, and was suggested as a less useful precursor than $[Li(OtBu)]_6$.[12] Precursors used for thermal plasma spray CVD film growth consisted of commercial 3 wt% solutions of $LiNb(OR)_6$ or $LiTa(OR)_6$ in 3-methylbutyl acetate (R was not identified, but is presumably ethyl).[96]

A series of sodium alkoxide complexes of the formula $Na(OCR(CF_3)_2)$ ($R = H$, CH_3, CF_3) was examined as precursors for the MOCVD growth of sodium fluoride films.[14] Sodium fluoride films were deposited between 255 and 400 °C, and the lowest deposition temperature was obtained where $R = H$.

2.2 Beryllium

Beryllium has few applications in thin-film materials, owing to toxicity issues and the generally high air sensitivity of its compounds. Beryllium is a desirable ablator material in fusion research, and beryllium ion is an excellent p-type dopant in compound semiconductors such as InP and (In,Ga)As. There are limited precursors available for the CVD growth of beryllium-containing materials. $BeEt_2$ has been used to make heavily beryllium-doped (In,Ga)As.[15] $Be(C_5H_5)_2$ was used as a precursor for the growth of beryllium metal thin films.[16] Problems with this precursor included extreme air sensitivity and carbon and oxygen incorporation. $Be(C_5H_4Me)_2$ has been suggested as the best CVD precursor for beryllium.[17] It was used for the growth of beryllium-doped InP films.

2.3 Magnesium

Magnesium has emerged in the past ten years as an important component of certain thin-film materials grown by CVD methods. In particular, magnesium-doped group 13 nitride films grown by MOVPE form the basis of blue and green light emitting diodes and laser diodes.[97] Precursors that have been used to dope GaN and other group 13–15 semiconductors with magnesium ion include $Mg(C_5H_5)_2$,[18,19] $Mg(C_5H_4Me)_2$,[20,21] $Mg(C_5H_4Et)_2$,[22] and $MgAl_2(CH_3)_8$.[23] $Mg(C_5H_5)_2$ is the most widely used metal-organic dopant precursor for the growth of magnesium-doped group 13–15 nitride semiconductors.

MgO has emerged recently as a useful substrate on which to grow perovskite superconductor and ferroelectric materials, because it has a good lattice match with these phases. MgO has also been used as a protective layer in plasma displays. A range of metal-organic precursors has been described, including $Mg(C_5H_5)_2$ in the presence of O_2,[98] $[Mg(CH_3)(OtBu)]_4$,[24] $Mg(dmto)_2$,[25] $Mg(tmhd)_2(tmeda)$,[26]

$[Mg(tmhd)_2]_2$,[27] and $Mg(acac)_2$.[28,99] Use of $Mg(C_5H_5)_2$ and O_2 allowed the growth of epitaxial MgO films by MOCVD. $[Mg(CH_3)(O\mathit{t}Bu)]_4$ has a tetrameric solid-state structure, but is sufficiently volatile to serve as an MOCVD precursor. The precursor $Mg(dmto)_2$ contains a pendant amine donor ligand that is attached to the β-ketiminato ligand core by an alkyl chain. These pendant amine donors lead to octahedral geometry at the magnesium center, which is sterically saturated and prevents formation of an oligomeric, low volatility species. MgO films were grown from this precursor at 450 °C, and there was no need to add additional O_2 to form the oxide. $Mg(tmhd)_2(tmeda)$ is a relatively volatile source compound that was suggested to be superior to $[Mg(tmhd)_2]_2$ owing to its monomeric structure and good thermal stability. By contrast, $[Mg(tmhd)_2]_2$ is dimeric and has a lower vapor pressure than other magnesium precursors owing to its higher molecular weight. $Mg(acac)_2$ is trimeric in the solid state[100] and thus has a very low vapor pressure. It has been used to grow MgO films using MOCVD[28] and PECVD[99] growth techniques.

2.4 Calcium, Strontium, and Barium

The growth of thin films containing calcium, strontium, and barium has been an active area of research in recent years owing to the importance of materials including $SrTiO_3$, $BaTiO_3$, $Ba_xSr_{1-x}TiO_3$, $SrBi_2Ta_2O_9$, $Ba_xPb_{1-x}TiO_3$, $YBa_2Cu_3O_{7-x}$, $Tl_2Ba_2CaCu_2O_{7-x}$, BaB_2O_4, $La_{0.66}Ba_{0.33}MnO_3$, BaS, and other phases. Owing to the high molecular weights, the high coordination numbers, and the low formation constants of complexes containing these elements, it is difficult to identify structures that combine sufficient volatility and thermal stability to serve as film growth precursors. Significant advances have been made in this area, and are overviewed in this section. Several recent reviews have described progress in this area.[101–105]

Metallocenes (*see Metallocene Complexes*) of calcium, strontium, and barium have been the subject of intense basic research scrutiny in recent years, and it is well known that substituted metallocenes are volatile and have vapor pressures that are high enough to be useful in film growth.[101] However, the first reports of film growth using substituted metallocenes have only appeared recently. $Sr(1,2,4\text{-}C_5\mathit{i}Pr_3H_2)_2$ was used as the strontium precursor in the ALD growth of $SrTiO_3$ with titanium tetraisopropoxide and water at temperatures between 250 and 325 °C.[29,30] There was evidence for thermal decomposition of $Sr(1,2,4\text{-}C_5\mathit{i}Pr_3H_2)_2$ during the depositions. $Ba(C_5(CH_3)_5)_2$ was used as a precursor for the ALD growth of $BaTiO_3$ films, along with titanium tetraisopropoxide and water at temperatures at or below 275 °C.[30] Higher deposition temperatures resulted in significant decomposition of $Ba(C_5(CH_3)_5)_2$, and reproducibility of composition and properties were problems even at a growth temperature of 275 °C. It has been reported that thermal decomposition and carbon incorporation are problems associated with the use of strontium and barium metallocene precursors in MOCVD film growth.[106]

Diketonate complexes of calcium, strontium, and barium have been extensively explored as precursors for the growth of oxide materials.[101–105] Two bidentate diketonate ligands are not sufficient to saturate the coordination spheres of the large metal ions, and oligomerization occurs in the absence of neutral donor ligands to provide compounds with very low vapor pressures. Such oligomers have low utility as precursors for film growth, since extensive decomposition can occur at the high temperatures required to achieve volatility. Thermal decomposition is a particularly severe problem with barium precursors. A recent review has summarized the properties and film deposition characteristics of bis(diketonato) precursors of calcium, strontium, and barium.[103] To address the volatility and decomposition problems, a trend in recent years has been to identify neutral donor ligands that can coordination to the bis(diketonato)metal(II) fragment, and thus provide monomeric species with higher vapor pressures. The general features of these adducts will be discussed herein, along with a summary of recent advances in precursor design.

The diketonate ligands that have been employed to create volatile complexes are substituted with alkyl or fluoroalkyl groups to afford steric bulk about the coordination sphere and to minimize intermolecular interactions that reduce volatility. Fluoroalkyl groups, in particular, lead to increased volatility, but can cause problems in film depositions through fluorine incorporation into the film material. The most widely used diketonato ligand is tmhd, which has *tert*-butyl groups attached to the diketonato ligand core. However, the reduced Lewis acidity of the metal center in an alkyl-substituted diketonato ligand means that neutral donor ligands bond less strongly to the metal ion. Thus, such precursors can have reduced thermal stability compared to a precursor containing fluoroalkyl-substituted diketonato ligand. Neutral ligands are generally polyethers or polyamines that can wrap around the metal center to provide complexes with higher formation constants than is possible with monodentate donor ligands.

$Sr(tmhd)_2$ has been used as a precursor for the ALD growth of $SrTiO_3$, along with titanium tetraisopropoxide and ozone at 250–470 °C.[31] The as-deposited films contained some carbon apparently present as $SrCO_3$, but thermal annealing reduced the carbon content and led to good quality $SrTiO_3$. To avoid problems with thermal decomposition, $Ba(tmhd)_2$ was prepared in situ by passage of tmhdH vapor over $Ba(OH)_2$ held at 350 °C.[32] The resultant $Ba(tmhd)_2$ was used to for the ALD growth of BaS at 300–350 °C using hydrogen sulfide as the sulfur source. The precursor $Ba(hfac)_2(PEB)$ contains an unsymmetrical polyether, has a low-melting point of 71 °C, and sublimes at rate useful for CVD film growth at 110–120 °C/4 torr.[33] This precursor was used for the epitaxial growth of $BaTiO_3$ films at substrate temperatures of 700–800 °C by MOCVD using titanium tetraisopropoxide and water as coreactants. The use of water was necessary to avoid the formation of BaF_2 as impurity in the film material. $Ba(dpmCAP\text{-}4)_2$ is a monomeric β-ketiminato complex that contains a polyether ligand tethered to the nitrogen atom by a carbon chain.[34] The polyether fragments provide intramolecular neutral Lewis bases that saturate the coordination sphere of the barium ion. The β-ketiminato ligand backbone is substituted with two *tert*-butyl groups, and thus $Ba(dpmCAP\text{-}4)_2$ represents a fluorine-free volatile film growth precursor. This class of precursors was used to grow epitaxial films of $BaTiO_3$. The complexes $Sr(methd)_2$ and $Ba(methd)_2$ contain a tmhd ligand that has been modified at one methyl group to include a pendant ether donor ligand that caps the coordination sphere of the metal ions, thus affording volatile complexes.[35] These precursors were used for the MOCVD growth of $Ba_xSr_{1-x}TiO_3$ at substrate temperatures of 400–500 °C.

An example of a single-source precursor for the growth of $SrBi_2Ta_2O_9$ films is $Sr[Ta(OEt)_5(OCH_2CH_2OCH_3)]_2$.[36] The fixed Sr/Ta ratio of 1:2 in the precursor is needed for the thin-film material, and presumably a single-source precursor would control this ratio. The growth of $SrBi_2Ta_2O_9$ films was examined using a tetrahydrofuran solution of $Sr[Ta(OEt)_5(OCH_2CH_2OCH_3)]_2$ and $BiPh_3$ with substrate temperatures between 540–580 °C. Use of the single-source precursor afforded excellent control over the Sr/Ta ratio in the thin-film material and provided good quality $SrBi_2Ta_2O_9$ films.

2.5 Aluminum, Gallium, and Indium

There is considerable interest in the CVD growth of thin films containing the group 13 elements aluminum, gallium, and indium. Phases of major interest include oxides, nitrides, sulfides, and the metals. Most film growth procedures for group 13 materials employ group 13 alkyls and hydrides, such as trimethylaluminum,[37] triethylaluminum,[38] dimethylaluminum hydride,[39] alane dimethylethylamine,[40] trimethylgallium,[41] trimethylindium,[42] and related hydrocarbon analogs. These compounds are liquids at ambient temperature or are solids with high vapor pressures and are listed in Table 1. Precursors for the growth of aluminum metal films have been reviewed in a recent monograph.[107] Other precursors that have been employed for CVD film growth are summarized in the following sections.

Many new metal-organic precursors for aluminum-containing materials have been reported recently. The precursors $AlMeCl_2(OEt_2)$, $AlMe_3(OEt_2)$, $AlEtCl_2(OEt_2)$, and $Al(NMe_2)Et_2$ were used to grow (Ti,Al)(O,N) coatings using titanium tetrachloride and hydrogen in a PECVD process.[43] The aluminum precursors have vapor pressures between 0.1–1 torr at 20 °C. $Al(acac)_3$ and $Al(tmhd)_3$ have been used for the growth of Al_2O_3 films by MOCVD.[44,108] $AlMe_2(O\textit{i}Pr)$ has been used for the growth of Cu-Al-O films by MOCVD.[109] $Al(OEt)_3$ and $Al(O\textit{i}Pr)_3$ were used to grow Al_2O_3 films by ALD.[45] Water, dioxygen, and various alcohols were used as added oxygen sources. The single-source precursor $Mg[(\mu\text{-}O\textit{i}Pr)_2AlMe_2]_2$ was used for the MOCVD growth of $MgAl_2O_4$ films.[46]

The growth of gallium and indium nitride, oxide, sulfide, and selenide phases from metal-organic precursors has been intensively studied. An exhaustive listing of precursors is beyond the scope of the present article, but readers are directed toward several recent reviews that summarize progress.[97,110–113]

Growth of epitaxial GaN or InN layers by CVD techniques mostly relies on $GaMe_3$, $InMe_3$, or related alkyl precursors in combination with ammonia.[97,110,111] Several more complex metal-organic precursors have been reported. The azido-based single-source precursor $Ga(N_3)_2(CH_2CH_2CH_2NMe_2)$ was used for the epitaxial growth of GaN layers on sapphire substrates at 850 °C using MOCVD.[47] The related single-source precursor $In(N_3)(CH_2CH_2CH_2NMe_2)_2$ was used for the MOCVD growth of InN films at 300–500 °C.[48] The precursor $GaH_2(N_3)$ has a high vapor pressure, and allows MOCVD growth of GaN films on silicon substrates at temperatures as low as 200 °C.[49] GaN films were grown by MOCVD using $Ga_2(NMe_2)_6$ and ammonia at substrate temperatures of >200 °C.[50] AlN films were grown from the related aluminum dimethylamido precursor. InP films were grown by MOCVD using $In(C_5Me_5)$ and P_4 at temperatures between 150 and 250 °C.[51] It was noted that these alternate precursors avoided the use of pyrophoric $InMe_3$ and toxic PH_3, which are commonly used precursors for the growth of InP films.

Several metal-organic precursors for the CVD growth of Ga_2O_3 and In_2O_3 films have appeared recently. These oxides are of interest for high-temperature gas sensors and as transparent conducting coatings. The precursor $[InMe_2(OC(CF_3)_2CH_2NHMe)]_2$ was used for the MOCVD growth of In_2O_3 films at 400–500 °C.[52] Molecular oxygen was added as a second precursor to induce oxide film growth and to suppress carbon contamination in the film. The precursors $InMe_2(acac)$,[53] $[\textit{i}Pr_2InOH\cdot\textit{i}Pr_2InNH_2]$,[54] and $[In(OCMe_2Et)_3]_2$[55] have been evaluated as MOCVD precursor to In_2O_3 films. MOCVD film growth using $In(OCMe(CF_3)_2)_3(H_2N\textit{t}Bu)$ and molecular oxygen at substrate temperatures of 400–550 °C afforded fluorine-doped In_2O_3 films with 2–3 atom % fluorine.[56] The precursors $Ga(OCH(CF_3)_2)_3(HNMe_2)$[57] and $[Ga(O\textit{t}Bu)_3]_2$[58] were used for the MOCVD growth of Ga_2O_3 films.

There has been considerable development of precursors for the CVD growth of group 13 sulfide and selenide semiconductors.[113] Sulfur precursors that have been reported to date are based upon monothiocarbamato, dithiocarbamato, thiocarboxylato, thiolato, and dialkylselenophosphoryl-amido ligands. In certain cases, selenium analogs of these ligands have been employed to create precursors for the respective selenide phases. In addition, sulfur and selenium tetramers of the formula $[RME]_4$ have been used as precursors to metal sulfide and selenide phases, and have shown phase selectivity that appears to correlate with the cubic cores of the precursors. Monothiocarbamato precursors are exemplified by $In(SOCNEt_2)_3$, which was used for the MOCVD growth of β-In_2S_3 films at substrate temperatures of 350–500 °C.[59] The gallium analog, $Ga(SOCNEt_2)_3$, provided the cubic GaS phase under aerosol-assisted CVD growth conditions.[60] Dithiocarbamato precursors have included $InMe_2(S_2CNEt_2)$, which was used for the MOCVD growth of β-In_2S_3 at 325 °C.[61] The In-S phase that was deposited was found to be sensitive to the substrate temperature as well as the nature of the alkyl group attached to indium. The precursor $In(S_2CNMeBu)_3$ was used in the MOCVD growth of α-In_2S_3 films, and afforded this phase under all growth conditions.[62] $Ga(t\text{Bu})_2(S_2CNMe_2)$ was used for the atmospheric pressure MOCVD growth of GaS films.[63] Dithiocarbamato and diselenocarbamato precursors have been used for the growth of $CuInS_2$ and $CuInSe_2$ films by aerosol-assisted CVD.[114] Thiocarboxylato precursors are exemplied by $Ga(SOCMe)_2Me(dmpy)$[64] and $[dmpyH]^+$ $[In(SOCMe)_4]^-$.[65] Use of $Ga(SOCMe)_2Me(dmpy)$ in aerosol-assisted CVD afforded crystalline Ga_2S_3 films at substrate temperatures of 275–310 °C. The aerosol-assisted CVD of $[dmpyH]^+$ $[In(SOCMe)_4]^-$ gave β-In_2S_3 at temperatures as low as 210 °C. Metal sulfide and selenide films have been grown from a variety of precursors containing cubic M_4E_4 cores. The precursor $[(Me_2EtC)In(\mu_3\text{-Se})]_4$ in low pressure MOCVD film growth afforded stoichiometric InS at temperatures between 260 and 350 °C.[66] Use of $[(t\text{Bu})Ga(\mu_3\text{-Se})]_4$ and $[(t\text{Bu})Ga(\mu_3\text{-Te})]_4$ in MOCVD film growth led to hexagonal GaSe and GaTe films.[67] It was proposed that the cubic cores in these precursors fragment during film growth to afford Ga_3E_3 building blocks that lead to the hexagonal phases. The precursors $Ga_2(S(i\text{Pr}))_6$[115] and $In[SeC(SiMe_3)_3]_3$[116] were used as single-source precursors in the MOCVD growth of Ga_2S_3 and In_2 Se_3 films, respectively. The complex $[InMe_2(SeMe)]_2$ was used as an MOCVD precursor to InSe in the temperature range of 270–370 °C.[117] The dialkylselenophosphorylamide complexes $GaMe_2((SeP\,i\text{Pr}_2)_2N)$ and $InMe_2((SeP\,i\text{Pr}_2)_2N)$ were used as precursors to Ga_2Se_3 and In_2Se_3 films with both aerosol-assisted CVD and low pressure MOCVD.[118] Precursors containing dialkylselenophosphorylamide ligands were used to grow $CuInSe_2$ films by aerosol-assisted CVD.[119]

2.6 Tin and Lead

The main technological application of tin-containing thin-film materials is as transparent conducting oxides for use in computer displays, televisions, and low-emissivity coatings for glass.[120,121] Tin(IV) compounds containing alkyl groups have been widely employed as CVD precursors to SnO_2 and other oxides.[68] $SnMe_4$ was used a dopant source for the atmospheric pressure MOCVD growth of tin-doped CdO films.[122] $SnMe_2Cl_2$ has been evaluated as a source compound for the large area CVD of tin oxide coatings for high volume low-emissivity coatings on commercial glass.[123] Low resistivity tantalum-doped SnO_2 films were grown by MOCVD using $Sn(Ot\text{Bu})_4$ and $Ta(OEt)_5$ as the precursors.[69] Low resistivity fluorine-doped SnO_2 films were grown by low pressure CVD at substrate temperatures of 200–450 °C using $Sn(OCH(CF_3)_2)_4(HNMe_2)$ as the tin and fluorine precursor.[70] $Sn(NO_3)_4$ was used as a source compound for the MOCVD growth of compositional spreads of Ti-Sn-Hf oxides.[71] $Hf(NO_3)_4$ and $Ti(NO_3)_4$ were also used as precursors.

Thin films of tin sulfides are of interest as semiconductors and photovoltaic materials. The precursor $Sn(SCH_2CH_2S)_2$ was used for the aerosol-assisted CVD growth of tin sulfide phases in the presence of hydrogen sulfide.[72] SnS_2, Sn_2S_3, or SnS films were obtained, depending upon the substrate temperature. Tin sulfide films were grown by atmospheric pressure CVD using $Sn(SCH_2CF_3)_4$ and hydrogen sulfide with substrate temperatures of 300–600 °C.[73] The phase of tin sulfide obtained (SnS_2, Sn_2S_3, or SnS) depended upon the growth temperature. SnS films were grown by an atmospheric CVD process using $Sn(n\text{Bu})_3(O_2CCF_3)$ and hydrogen sulfide at 350–600 °C.[124]

Several other precursors to tin phases have been reported. $Sn(NMe_2)_4$ and ammonia were used for the MOCVD growth of Sn_3N_4 films at <200 °C.[74] The single-source precursor $Me_3SnCo(CO)_4$ was used for the growth of CoSn thin films by MOCVD at 250–300 °C.[75] The major phase present in the film was CoSn, suggesting that the precursor controls the final film stoichiometry. Ni-Sn intermetallic particles were made by a CVD process that involved CVD of $SnMe_4$ onto Ni/SiO_2.[125]

Interest in the CVD growth of lead-containing thin films has been driven by the importance of several complex oxides, including $PbTiO_3$, $Pb(Zr,Ti)O_3$, $(Pb,La)(Zr,Ti)O_3$, $Pb(Mg_{0.33}Nb_{0.67})O_3$, and $Pb(Sc_{0.5}Ta_{0.5})O_3$. Lead diketonates have been evaluated for their volatility,[76] and $Pb(tmhd)_2$ is the most widely used of these precursors. $Pb(tmhd)_2$ has been used for the MOCVD growth of $Pb(Sc_{0.5}Ta_{0.5})O_3$ using direct liquid injection of a solution containing Sc and Ta precursors along with $Pb(tmhd)_2$.[126] Many other oxides have been grown with $Pb(tmhd)_2$. $Pb(tmhd)_2$ was used as a source compound for the growth of PbO films by laser-assisted CVD.[127] $PbEt_4$ is another precursor that is widely used for the CVD growth of lead-containing thin-film materials.[77] It is a volatile, air-stable liquid (bp 78 °C, 10 torr), and is commercially available. PbS films have been grown by MOCVD and PECVD from $Pb(S_2CNEt_2)_2$.[128]

2.7 Antimony and Bismuth

A major motivation for the development of antimony metal-organic precursors is the growth of antimony-based semiconductor materials. Advances and problems in this area have been summarized in recent reviews.[129,130] The simplest volatile precursor, SbH_3, is thermally unstable even at −65 °C and rapidly reverts to elemental antimony and hydrogen.[78] However, SbD_3 is more stable thermally, owing to the lowering of the zero point energy (*see Zero*

Point Energy) compared to SbH_3.[78] In fact, SbD_3 shows no signs of decomposition over one week when stored in a glass vessel at 10 torr. Up to 30 wt% of SbD_3 can be stored on solid absorbents, and there was no evidence of decomposition after 2 weeks at 23 °C. SbD_3 was used for the growth of antimony films at temperatures as low as 200 °C.[78] Other antimony hydrides that have been reported as film growth precursors include $SbH_2CH_2CMe_3$,[79] $SbH(CH_2CMe_3)_2$,[79] $SbH_2i\mathrm{Bu}$,[131] and $SbHi\mathrm{Bu}_2$.[131] MOCVD growth with $SbH_2CH_2CMe_3$ and $InMe_3$ afforded InSb films at substrate temperatures as low as 350 °C.[79] Trialkyl-based metal-organic precursors for antimony include $SbEt_3$[80] and $SbMe_2(t\mathrm{Bu})$.[132] $SbEt_3$ is a widely used precursor, and was employed for the MOCVD growth of InAsSb/InPSb strained layer superlattices.[80] Antimony alkoxides $Sb(OR)_3$ ($R = \mathrm{Et}$, $n\mathrm{Bu}$) have been used for the atmospheric pressure CVD growth of antimony oxide films.[81] $Sb(O_2CNMe_2)_3$ was used as a precursor for the low pressure CVD growth of Sb_2O_3 films.[82] The single-source precursor $[AlEt_2(Sb(SiMe_3)_2)]_2$ was employed for the growth of AlSb films by MOCVD.[83]

Development of metal-organic bismuth film growth precursors has been driven by the importance of bismuth-containing ferroelectric and superconducting oxides.[133] $BiMe_3$ is a highly volatile liquid, and has been used recently for the MOCVD growth of $SrBi_2Ta_2O_9$,[84] Bi_2Te_3,[134] and Bi_2Se_3 films.[135] Apparently $BiMe_3$ can explode, so it needs to be handled carefully. $BiPh_3$ is a volatile solid, and is widely used as a metal-organic precursor. Materials that have grown using $BiPh_3$ include $SrBi_2Ta_2O_9$,[85] MoO_3-Bi_2O_3,[136] Bi-doped ZrO_2,[137] and $Bi_4Ti_3O_{12}$.[138] $Bi(OCMe_2CH_2OMe)_3$ has been used for the MOCVD growth of Bi_2O_3[86] and $Bi_4Ti_3O_{12}$.[139] $Bi(tmhd)_3$ was used for the MOCVD growth of $SrBi_2Ta_2O_9$.[87] Bi_2E_3 films ($E = S$ or Se) have been grown from $Bi(S_2CNEt_2)_3$,[140] $Bi(Se_2CNEt_2)_3$,[141] and $Bi[(i\mathrm{Pr}_2PSe)_2N]_3$.[142]

2.8 Zinc and Cadmium

ZnO and CdO are wide bandgap semiconductors, and these materials may serve as transparent conducting oxides for photovoltaics and flat panel displays. ZnO may also have applications in blue and ultraviolet light emitting devices and laser diodes. Thin films of zinc and cadmium chalcogenides also have many potential applications. The technological goals of these materials have been summarized in several recent reviews.[143,144]

Several different classes of precursors have been used for the growth of ZnO films. The most commonly used metal-organic precursor is $ZnEt_2$, in combination with molecular oxygen or water. Many types of deposition processes have been used, and include both thermal and plasma activation of the precursors. For example, ZnO films have been grown from $ZnEt_2$ using MOCVD,[88] PECVD,[145] and ALD[146] methods. $ZnMe_2$ and tBuOH were used as precursors for the MOCVD growth of ZnO films.[89] The amine adducts $ZnMe_2(NR_3)$ are less pyrophoric than $ZnMe_2$, inhibit prereaction with the oxygen source, and facilitate purification. The vapor pressures of some $ZnMe_2(NR_3)$ precursors have been reported.[90] Other zinc alkyl precursors include $ZnEt(NEt_2)$[147] and $ZnMe(OR)$ ($R = i\mathrm{Pr}$, $t\mathrm{Bu}$).[148] Oxygen-based metal-organic precursors to ZnO films include $Zn(acac)_2$,[91] $Zn(hfac)_2(H_2O)_2\cdot$diglyme,[92] $Zn(OAc)_2$,[149] and $Zn_4O(O_2CNEt_2)_6$.[150] Atmospheric pressure CVD of $Zn(dmp)_2$ with dry molecular oxygen afforded ZnO films.[151] Atmospheric pressure CVD using $Zn(N(SiMe_3)_2)_2$ with molecular oxygen afforded Zn_2SiO_4 films owing to the presence of silicon in the metal-organic precursor.[152]

The first CVD growth of CdO films was reported only recently by several groups. Low pressure CVD of $CdMe_2$ with molecular oxygen afforded CdO films at substrate temperatures between 150 and 450 °C.[93] Precursors containing hfac ligands include $Cd(hfac)_2(tmeda)$,[94] $Cd(hfac)_2(H_2O)_2$,[153] and $Cd(hfac)_2(dme)$.[154]

Zinc and cadmium chalcogenide (*see* ***Chalcogenides: Solid-state Chemistry***) films have been grown from several different precursors. $CdMe_2$ has been used along with various chalcogenide precursors to deposit CdS films,[155] CdSe/CdTe films,[156,157] and CdSe/ZnSSe quantum islands.[158] CdSe and ZnSe films have been grown by MOCVD using the single-source precursors $M(Se_2CNMe(n\text{-hexyl}))_2$.[159] CdS films were grown from the related precursor $Cd(S_2CNMe(n\text{-Bu}))_2$.[160] ZnS and CdS films were grown by low pressure MOCVD from $M(S_2Pi\mathrm{Bu}_2)_2$.[161] ZnS, CdS, ZnSe, and CdSe films could be grown by low pressure MOCVD using $M(EPi\mathrm{Pr}_2)_2N_2$ as single-source precursors.[162] CdSe films were also grown from the single-source precursor $Cd(SeR_F)_2$, where $R_F = 2,4,6\text{-}(CF_3)_3C_6H_2$.[163]

2.9 Lanthanides

Some lanthanide MOCVD precursors are listed in Table 2.

Interest in the development of metal-organic precursors for the lanthanide elements is due to the many important applications of lanthanide-containing materials. These include erbium-doped semiconductors for use as optical fiber communications, lanthanide-doped GaN for full color displays, high-temperature superconductors, and lanthanide-doped ferroelectric (*see Ferroelectricity*) phases. Despite the importance of these materials, lanthanide film growth precursors

Table 2 MOCVD precursors of lanthanide metals

Compound (mp or bp)	Vapor pressure
$Er(C_5H_5)_3$[164]	~0.1 torr, 200 °C
$Er(C_5H_4i\mathrm{Pr})_2(C_5H_5)$[164]	0.1 torr, 150 °C
$Er(C_5H_4t\mathrm{Bu})_3$[164]	subl 150 °C, 10^{-4} torr
$Er(tmhd)_3$[165]	subl 150 °C, low pressure
$Eu(tmhd)_3$[166]	subl 135 °C, 0.05 torr
$Er(N(SiMe_3)_2)_3$[167]	subl 160 °C, 75 torr
$Er(t\mathrm{Bu}_2pz)_3(4\text{-}t\mathrm{Bupy})_2$[168]	subl 150 °C, 0.1 torr
$Er(t\mathrm{BuNC}(CH_3)Nt\mathrm{Bu})_3$[169]	subl 140 °C, 760 torr

have not been the subject of intense development. This area was reviewed in 1994,[170] and the following section summarizes the state of metal-organic precursor development. Owing to the common +3 oxidation state of lanthanide metal-organic precursors and the similar sizes of the lanthanide(III) ions, complexes with identical ligands tend to have similar vapor pressures. Thus, in the following sections, film growth precursors are illustrated only for representative lanthanide elements.

Precursors containing cyclopentadienyl (*see Cyclopentadienyl*) and substituted cyclopentadienyl ligands have been the most commonly used for the MOCVD growth of lanthanide-doped semiconductors. Much of the available information is available for erbium, owing to the importance of erbium-doped semiconductors in optical fiber technology. Various cyclopentadienylerbium complexes have been compared with regards to their precursor properties.[164] $Er(C_5H_5)_3$ is polymeric in the solid state through bridging cyclopentadienyl ligands, and as a result, requires heating to 200 °C or higher to achieve vapor transport for film growth.[164] Alkyl substitution on the cyclopentadienyl ligands leads to monomeric complexes that have higher vapor pressures. $Er(C_5H_4{\it i}Pr)_2(C_5H_5)$ and $Er(C_5H_4{\it t}Bu)_3$ were found to be more volatile than $Er(C_5H_5)_3$, and were used as erbium dopant precursors in the MOVPE growth of erbium-doped GaAs epitaxial films.[164] $Er(C_5H_4{\it i}Pr)_2(C_5H_5)$ provided erbium levels that were about one order of magnitude higher than was possible with $Er(C_5H_4{\it t}Bu)_3$, demonstrating that the growth chemistry is subtly affected by the structure of the erbium precursor. $Er(tmhd)_3$ has been used as a precursor for the growth of erbium-doped GaN films, but it was noted that high transport temperatures limited the doping efficiency.[165] $Eu(thmd)_3$ was used as a precursor for the MOCVD growth of europium-doped GaN.[166] $Er(N(SiMe_3)_2)_3$ was used as a dopant precursor for the MOCVD growth of erbium-doped silicon[171] and GaAs.[167] Use of this precursor led to lower carbon and oxygen levels in the GaAs film, but also led to silicon incorporation (an n-type dopant for GaAs).[167] The pyrazolato-based (*see Tris(pyrazolyl)borates*) precursor $Er({\it t}Bu_2pz)_3(4\text{-}{\it t}Bupy)_2$ was used in the growth of erbium-doped GaAs films.[168,172] This precursor gave a better defined erbium emitting center than was obtained with cyclopentadienyl-based precursors. $Er({\it t}BuNC(CH_3)N{\it t}Bu)_3$ and $Er(tmhd)_3$ were employed as precursors for the growth of erbium-doped silicon nanocrystals using a CVD process with disilane as the silicon source.[169] $Er({\it t}BuNC(CH_3)N{\it t}Bu)_3$ gave higher erbium concentrations in the nanoparticles and led to larger nanoparticles, compared to $Er(tmhd)_3$ under identical growth conditions.

3 PRECURSORS FOR TRANSITION METAL GROUPS 4 AND 5

Some MOCVD precursors containing these elements are listed in Table 3.

Table 3 MOCVD precursors of the group 4 and 5 metals

Compound (mp or bp)	Vapor pressure
$Ti(O{\it i}Pr)_4$[173–176]	bp 58 °C, 1 torr
$Ti(O{\it t}Bu)_4$[177]	bp 70 °C, 0.2 torr
$Ti(NO_3)_4$[178]	subl 50 °C, 0.5 torr
$Zr(O{\it t}Bu)_4$[179]	bp 90 °C, 5 torr
$Hf(O{\it t}Bu)_4$[180]	bp 90 °C, 5 torr
$Zr(tmhd)_4$[181]	subl 180 °C, 0.1 torr
$Zr(NO_3)_4$[182]	subl 85 °C, 1.1 torr
$Zr(C_5H_5)_2Me_2$[183]	subl 85 °C, 0.6 torr
$Ti(NMe_2)_4$[184]	bp 50 °C, 0.5 torr
$Ti(NMeEt)_4$[185]	bp 85 °C, 0.05 torr
$Ti(NEt_2)_4$[186]	bp 133 °C, 1.2 torr
$Zr(NEt_2)_4$[187]	bp 112 °C, 0.1 torr
$Hf(NMe_2)_4$[188]	bp 85 °C, 0.1 torr
$TiCl_4(HSC_6H_{11})_2$[189]	2 torr, 23 °C
$TiCl_4(SeEt_2)_2$[190]	2 torr, 23 °C
$TiCl_4(H_2PC_6H_{11})_2$[191]	subl 100 °C, 0.1 torr
$VO(acac)_2$[192]	subl 150–175 °C, 15 torr
$Nb(OEt)_5$[13]	bp 142 °C, 0.1 torr
$Ta(OEt)_5$[193]	bp 145 °C, 0.1 torr
$V(NMe_2)_4$[194]	subl 50 °C, 760 torr
$Nb(NEt_2)_4$[194]	subl 130 °C, 760 torr
$Ta(NMe_2)_5$[194]	subl 100 °C, 0.1 torr

3.1 Titanium, Zirconium, and Hafnium

Titanium is an important component of many oxide materials, including titanium dioxide and various more complex titanates. Several reviews have summarized recent developments in thin-film growth and precursor selection.[195,196] $Ti(O{\it i}Pr)_4$ is the most widely employed metal-organic precursor, and is a liquid at ambient temperature with a boiling point of 58 °C at 1 torr. It has been used for the growth of a range of titanium oxide-containing materials with a variety of CVD deposition techniques. Illustrative examples of film growth with $Ti(O{\it i}Pr)_4$ include MOCVD of TiO_2,[197] LACVD (laser-assisted chemical vapour deposition) of TiO_2,[173] PACVD of $BaTiO_3$,[174] ALD of $SrTiO_3$,[175] and ALD of TiO_2.[176] Related alkoxide precursors that have been used in film growth procedures include $Ti(O{\it t}Bu)_4$,[177] $Ti(OCH_2{\it t}Bu)_4$,[198] $Ti(OEt)_4$,[199] $[Ti(OCH_2CH_2O)(OCH_2CH_2NMe_2)_2]_2$,[200] $Ti(O{\it i}Pr)_2(OCH_2CH_2NMe_2)_2$,[201] $Ti(OCH_2CH_2NMe_2)_4$,[202] and $Ti(HB(pz)_3)(O{\it i}Pr)_3$.[203] A drawback of $Ti(O{\it i}Pr)_4$ and related alkoxo-based precursors is their extreme moisture sensitivity. Thus, one avenue of precursor development has been to explore β-diketonato complexes, which tend to be less reactive toward water. Examples of such precursors include $Ti(tmhd)_2(O{\it i}Pr)_2$,[204] $Ti(tmhd)_2(O{\it t}Bu)_2$,[205] $Ti(tmhd)_2(OMe)_2$,[206] $Ti(acac)_2(O{\it i}Pr)_2$,[207] $Ti(tbaoac)_2(O{\it i}Pr)_2$,[208] and $Ti(tmhd)_3$.[209] β-Ketoiminato complexes of titanium containing pendant alkoxy groups on the nitrogen atoms have been synthesized and were suggested to be good CVD precursors.[210] The nitrato complex $Ti(NO_3)_4$ has a high volatility, and has been demonstrated as a precursor to TiO_2

films.[178] A detailed comparison of TiO_2 MOCVD growth from $Ti(NO_3)_4$ and $Ti(O\textit{i}Pr)_4$ was reported.[211]

Precursors for the growth of zirconium and hafnium oxide materials have been of considerable recent interest, owing to the importance of dielectric and ferroelectric materials that contain these elements. Several reviews have appeared recently that summarize technological progress.[212–214] In the following examples, most of the precursor development has occurred for zirconium. However, zirconium(IV) and hafnium(IV) are very similar chemically, and the properties of many hafnium complexes are usually very close to those of their zirconium analog. Hafnium precursors are mentioned where information is available. The most commonly used precursors for oxide film growth are $Zr(O\textit{t}Bu)_4$[179] and $Hf(O\textit{t}Bu)_4$,[180] since they are liquids at ambient temperature and have convenient volatilities. Other tetraalkoxide precursors that have been reported include $Zr(OCH_2\textit{t}Bu)_4$,[215] $Zr(O\textit{i}Bu)_4$,[216] $Zr(OCH_2CH_2NMe_2)_4$,[217] $Zr(O\textit{t}Bu)_2(OCMe_2CH_2OMe)_2$,[218] $Zr(OCH(CF_3)_2)_4$,[14] and various other $Zr(OR)_4$.[219] Like the titanium alkoxides, the zirconium and hafnium alkoxides are extremely water sensitive, and there has been interest in finding precursors that can be handled more easily. $Zr(tmhd)_4$[181] and $Zr(acac)_4$[220] have been used as film growth precursors. While they possess increased hydrolytic stability, their vapor pressures are very low and they have not seen wide application as a result. A compromise between good vapor pressure and increased hydrolytic stability has been found in mixed diketonato-alkoxo complexes. Precursors of this general class include $Zr_2(tmhd)_2(O\textit{i}Pr)_6$,[221] $Zr(tmhd)_2(OR)_2$ ($R = \textit{i}Pr$, $\textit{t}Bu$),[222] $Zr(acac)_2(OCH(CF_3)_2)_2$,[223] and $Zr(tbaoac)(O\textit{i}Pr)_3$.[224] $Zr(NO_3)_4$[182] and $Hf(NO_3)_4$[225] have been used as precursors to the respective dioxide phases. Dimethylzirconocene ($Zr(C_5H_5)_2Me_2$) has been used for the MOCVD[183] and ALD[226,227] growth of zirconium oxide phases, in combination with molecular oxygen, water, or ozone. $Zr(NMe_2)_4$[228] and $Hf(NEt_2)_4$[229] were used for the growth of oxide films using molecular oxygen as a coreactant. The single-source precursor $Zr(acac)_2(OSiMe_3)_2$ was used for the growth of $Zr_xSi_{1-x}O_2$ films for high dielectric constant gate materials in microelectronics devices.[230]

The growth of group 4 nitride phases have been the subject of intense scrutiny, owing to the importance of TiN as a barrier layer between copper and silicon dioxide in microelectronics devices. Work on metal-organic precursors has been reviewed.[8,231] Amido-based precursors have been examined by many workers. Available precursors include $Ti(NMe_2)_4$,[184] $Ti(NMeEt)_4$,[185] and $Ti(NEt_2)_4$.[186] MOCVD of these precursors in the presence of ammonia or another nitrogen source affords high quality TiN films. The step coverage is greatest with $Ti(NEt_2)_4$,[186] due to its slower reaction with ammonia and resultant higher selectivity. MOCVD film growth using $Ti(NMe_2)_4$, ammonia, and silane affords Ti-Si-N films, which is a promising barrier materials for microelectronics devices.[232] Use of $Ti(NMe_2)_4$ as a single-source precursor yields Ti(C,N) films, which are also of potential use as a barrier material in microelectronics devices.[233] Growth of TiN films from single-source precursors has been reported by several authors,[234–237] but these precursors have not been subject to broad investigation. Available metal-organic film growth precursors for zirconium and hafnium nitride films include $Zr(NMe_2)_4$,[238] $Zr(NMeEt)_4$,[238] $Zr(NEt_2)_4$,[187] $Hf(NMe_2)_4$,[188] and $Hf(NEt_2)_4$.[188] These precursors afford MN or M(C,N) films when used in film growth by various CVD methods.

A few metal-organic precursors to other phases have been reported. $TiCl_4(HSC_6H_{11})_2$[189] and $Cp_2Ti(S\textit{t}Bu)_2$[239] serve as single-source precursors for the growth of TiS_2 films using MOCVD. $TiCl_4(SeEt_2)_2$ functions as a single source for the growth of $TiSe_2$ films by MOCVD.[190] $TiCl_4(H_2PC_6H_{11})_2$ is a single-source precursor for the growth of TiP films by MOCVD.[191,240]

3.2 Vanadium, Niobium, and Tantalum

CVD routes to vanadium oxide phases have employed a limited number of metal-organic precursors. $VO(acac)_2$ is the most widely used, and oxide films have been deposited from it by low pressure MOCVD[241] and PECVD.[192] Other precursor for vanadium oxide film growth include $VO(O\textit{i}Pr)_3$[242] and $VO(OEt)_3$.[243]

Interest in film growth of niobium oxides is driven by the importance of several ferroelectric materials that contain niobium. The most widely used precursor is $Nb(OEt)_5$, which is a volatile liquid. Examples of materials that have been grown by MOCVD with $Nb(OEt)_5$ include $LiNbO_3$,[13] Pb-Ti-Nb-O,[244] and $KNbO_3$.[245] Owing to the extreme reactivity of $Nb(OEt)_5$ with water, attempts have been made to identify precursors that are easier to handle. Examples of such precursors include $Nb(tmhd)(O\textit{i}Pr)_4$,[246] $Nb(N\text{-alkoxo-}\beta\text{-ketoiminato})(OEt)_3$,[247] and $Nb(dbm)(OEt)_4$.[248] $Mg[Nb(OEt)_6]_2\cdot(EtOH)_2$ has been used as a single-source precursor for the growth of $Pb(Mg,Nb)O_3$ films.[249] Owing to their chemical similarity, niobium and tantalum complexes with identical ligands tend to have similar volatilities. As a result, several of the papers noted above have also reported related tantalum precursors.

The major technological impetus for the growth of tantalum oxide materials has been the growth of ferroelectric and high dielectric materials. As with niobium, the most widely used film growth precursor is $Ta(OEt)_5$, which is a volatile liquid. As illustrative examples, Ta_2O_5 films have been grown from $Ta(OEt)_5$ using MOCVD[193,250] and ALD.[251] $Ta(OMe)_5$ has also been used as an MOCVD precursor.[252] Since $Ta(OEt)_5$ is a dimer, several approaches have been pursued to increase the vapor pressure by creating monomeric precursors. $Ta(OEt)_4(OCH_2CH_2NMe_2)$, which contains a chelating aminoethoxy group, has been used in the photo-assisted CVD growth of Ta_2O_5 films.[253] Another approach is to replace one alkoxo ligand with a diketonato ligand, to create a monomeric complex and to increase the hydrolytic stability. Examples of such precursors include Ta(tmhd)$(OMe)_4$,[254] Ta(N-alkoxo-β-ketoiminate)$(OEt)_3$,[247] and Ta(tmhd)$(OEt)_4$.[255] Ta(N*t*Bu)$(NEt_2)_3$ has been used for the MOCVD growth of Ta_2O_5 films.[256] The single-source precursor $Sr[Ta(OEt)_5(OCH_2CH_2NMe_2)]_2$ has been employed in the MOCVD growth of $SrBi_2TaO_9$ films, and helps to control the Sr-Ta stoichiometry.[257] Other tantalum-containing single-source precursors include $Sr[Ta(O\textit{i}Pr)_6]_2{\cdot}2\textit{i}PrOH$,[249] $Sr[Ta(OEt)_6]_2$,[258] and $TaAl(O\textit{i}Pr)_8$.[259]

Interest in the growth of metal nitride films by CVD methods arises from the use of TaN as a diffusion barrier between copper and silicon dioxide in microelectronics devices. TaN is one of the best copper diffusion barrier materials that have been identified. This area has been recently reviewed,[260] and the reader is encouraged to consult this article for a detailed discussion of film growth from metal-organic precursors. The predominant metal-organic precursors for are the dialkylamido complexes $V(NMe_2)_4$, $Nb(NEt_2)_4$, and $Ta(NMe_2)_5$.[194] Atmospheric pressure MOCVD using these precursors with ammonia as the coreactant afforded VN, Nb_3N_4, and Ta_3N_5 films, respectively. Since the original report, $Ta(NMe_2)_5$ has been used extensively for the growth of Ta-N phases by CVD techniques.[261,262] Problems include deposition of the insulating Ta_3N_5 phase (as opposed to the desired metallic TaN), high carbon content in the films, and unacceptably high film resistivities for use as barrier layers. Other precursors that have been evaluated for the growth of Ta-N phases include Ta(N*t*Bu)$(NEt_2)_3$,[263] Ta(NEt)$(NEt_2)_3$,[188] and $Ta(NEt_2)_5$.[264] A niobium imido complex has been used for the growth of superconducting NbN films.[265]

Metal-organic precursors to several other group 5-containing phases have been reported. $V(C_6H_6)_2$ (*see Arene Complexes*) provides V_8C_7 films in an MOCVD process.[266] Ta(CH*t*Bu)$(CH_2\textit{t}Bu)_3$ was used as a single-source precursor to tantalum carbide films.[267] Cp_2VMe_2 was used as a precursor to Ti-V-N-C coatings.[268] A review article lists a range of precursors that have been evaluated as single-source precursors to VC and VN films.[269] $Nb_2Cl_8(PH_2C_6H_{11})_4$ functions as a single-source precursor for the growth of NbP films.[270] $[NbCl_4(S_2\textit{i}Pr_2)_2][NbCl_6]$ served as a single-source precursor to films containing NbS_2 and Nb_2O_5.[271]

4 PRECURSORS FOR TRANSITION METAL GROUPS 6 AND 7

4.1 Chromium, Molybdenum, and Tungsten

Some MOCVD precursors containing these elements are listed in Table 4.

Table 4 MOCVD precursors of the group 6 and 7 metals

Compound	Vapor pressure
$Cr(acac)_3$[272]	3.3 torr, 150 °C
$Cr(CO)_6$[273]	subl 70 °C, 760 torr
$W(CO)_6$[274]	subl 30 °C, 2 torr
$W(OEt)_6$[275]	subl 190 °C, 760 torr
W(N*t*Bu)$_2$(NMe$_2$)$_2$[276]	bp 50 °C, 0.05 torr
W(N*t*Bu)$_2$(NH*t*Bu)$_2$[277]	bp 50 °C, 0.05 torr
W(N*i*Pr)Cl$_4$(NCMe)[278]	liquid delivery in benzonitrile
$Mo(NMe_2)_4$[279]	subl 40 °C, 0.1 torr
$Mn(tmhd)_3$[280]	subl 133 °C, 0.018 torr
$Mn(C_5H_4Me)(CO)_3$[281]	bp 233 °C, 760 torr
$MeReO_3$[282]	subl 65 °C, 10^{-3} torr

There have been relatively few metal-organic precursors reported for chromium materials. $Cr(acac)_3$ and other diketonate derivatives have been employed for the growth of oxide phases by MOCVD techniques.[272,283,284] $Cr(CO)_6$ was used for the MOCVD growth of Cr_2O_3 films by MOCVD.[273] $Cr(NEt_2)_4$ provides Cr(C,N) films when used as a single-source precursor.[285] $Cr(C_6H_6)_2$ (*see Arene Complexes*) serves as a precursor for chromium carbide films, but also provides chromium metal films in the presence of hydrogen or hexachlorobenzene.[286] Thin films of the molecular magnet $[Cr(C_6H_6)_2][TCNE]$ were grown by a CVD process from $Cr(C_6H_6)_2$ and TCNE.[287]

Molybdenum and tungsten oxides have been grown from several different metal-organic precursors. The most widely used precursors are $Mo(CO)_6$ and $W(CO)_6$ (*see* ***Carbonyl Complexes of the Transition Metals***).[274,288] Other precursors that have been employed for the growth of oxide phases include $W(OEt)_6$,[275] $W(OC_6H_5)_6$,[289] $W(CO)_4(P(OEt)_3)_2$,[290] W(methyl vinyl ketone)$_3$,[291] and $W(\eta^3\text{-}C_3H_5)_4$.[292] MoS_2 films have been grown from the single-source precursor Mo(S*t*Bu)$_4$.[293] Tungsten carbide phases have been grown from a range of tungsten carbonyl precursors.[294]

W_2N is one of the most promising copper diffusion barrier materials for future microelectronics devices. Owing to the need for conformal film growth, there has been considerable interest in the growth of W_2N from metal-organic precursors using CVD techniques, particularly ALD. Precursors that have been employed include $W(CO)_6$,[295] W(N*t*Bu)$_2$(NMe$_2$)$_2$,[276] W(N*t*Bu)$_2$(NEt$_2$)$_2$,[296] W(N*t*Bu)$_2$(NH*t*Bu)$_2$,[277] and W(N*i*Pr)Cl$_4$(NCMe).[278] Films with a composition of Mo_2N_3 were grown from $Mo(NMe_2)_4$ and ammonia by atmospheric pressure CVD.[279]

4.2 Manganese and Rhenium

Precursor development for these elements has been limited. Manganese oxide-containing thin films have been the subject of considerable interest, owing to the importance of manganese-containing magnetoresistive perovskite phases. The predominant metal-organic precursor is $Mn(tmhd)_3$, and manganese oxide-containing phases have been grown by ALD,[280] liquid-delivery MOCVD,[297] and low pressure MOCVD[298] using this precursor. MnSe films have been grown by MOCVD using $Mn(C_5H_4Me)(CO)_3$.[281] The single-source

Table 5 MOCVD precursors of the group 8 and 9 metals

Compound	Vapor pressure
$Fe(CO)_5$[300]	bp 103 °C, 760 torr
$Fe(C_5H_5)_2$[301]	subl 120 °C, 75 torr
$Fe(acac)_3$[302]	bp 110 °C, 0.2 torr
$Ru(tmhd)_3$[303]	subl 120 °C, 0.05 torr
$Ru(C_5H_5)_2$[304]	subl 85 °C, 6 torr
$[Os(CO)_3((CF_3)_2pz)]_2$[305]	subl 115 °C, 1.5 torr
$Co(acac)_2$[306]	subl 150 °C, 1 torr
$Co(tmhd)_2$[307]	subl 120 °C, 10^{-2} torr
$Co(tmhd)_2(tmeda)$[308]	subl 125 °C, 0.02 torr
$Co_2(CO)_8$[309]	subl 35 °C, 0.15 torr
$Co(C_5H_5)(CO)_2$[309]	subl 0 °C, 0.11 torr
$Co(CO)_3(NO)$[310]	bp 50 °C, 760 torr
$Rh(acac)(CO)_2$[311]	1.7 torr, 100 °C
$[RhCl(CO)_2]_2$[312]	2.7 torr, 100 °C
$Ir(C_5H_4Me)(COD)$[313]	0.0001 torr, 100 °C

precursor $Ga(Mn(CO)_5)_2(CH_2CH_2CH_2NMe_2)$ was employed to grow Mn-Ga alloy films.[299] $MeReO_3$ has been used for the growth of rhenium-containing films by MOCVD.[282]

5 PRECURSORS FOR TRANSITION METAL GROUPS 8 AND 9

Some MOCVD precursors containing these elements are listed in Table 5.

5.1 Iron

Iron-containing thin films have many applications. Precursors for the MOCVD growth of iron-containing phases have included $Fe(CO)_5$ (*see* ***Carbonyl Complexes of the Transition Metals***),[300] $Fe(C_5H_5)_2$ (*see Ferrocene*),[301] $Fe(acac)_3$,[302] $Fe(tmhd)_3$,[314] $Fe(tbaoac)_3$,[315] and $[Fe(O\mathit{t}Bu)_3]_2$.[316] $Fe_2(CO)_6(\mu\text{-}S_2)$ served as a single-source precursor for the MOCVD growth of FeS films.[317] $Fe(CO)_4(GaCH_2CH_2CH_2NMe_2)_2$ was used as a single-source precursor to Fe-Ga alloy films.[318] $FeSi_2$ films were grown from the single-source precursor $Fe(SiCl_3)_2(CO)_4$.[319]

5.2 Ruthenium and Osmium

Ruthenium dioxide has been of recent interest for use as a conductive material in microelectronics devices. A range of precursors has been used for the growth of ruthenium-containing thin-film materials, including $Ru(tmhd)_3$,[303] $Ru(tmhd)_2(COD)$,[320] $Ru(C_5H_5)_2$,[304] $Ru(C_5H_4Et)_2$,[321] $Ru(C_5H_4Et)(C_7H_{11})$,[322] $Ru(C_7H_{11})_2$,[323] $Ru(COD)(C_3H_5)$,[324] $Ru(hfac)_2(CO)_2$,[325] $Ru(CO)_2(OC(CF_3)_2CH_2NHMe)_2$,[326] $Ru(CF_3CCCF_3)(CO)_4$,[327] and $[Ru(CO)_3((CF_3)_2pz)]_2$.[328] Precursors for the growth of osmium metal thin films have included $Os(hfac)(CO)_3(CO_2CF_3)$[329] and $[Os(CO)_3((CF_3)_2pz)]_2$.[305] The single-source precursor $Ru(C_5H_5)((\eta^5\text{-}C_5H_3CH_2NMe_2)Pt(DMSO)Cl)$ served as a precursor to Ru-Pt alloy films.[330]

5.3 Cobalt

Recent interest in cobalt films has been driven by the importance of cobalt oxides as cathode materials in lithium batteries. Many different precursors have been employed for the MOCVD growth of cobalt-containing thin films. Diketonate-based precursors include $Co(acac)_2$,[306] $Co(tmhd)_2$,[307] $Co(tmhd)_3$,[331] $Co(hfac)_2$,[332] $Co(tmhd)_2(tmeda)$,[308] $Co(hfac)_2(H_2O)_2$,[333] and $Co(hfac)_2(H_2O)_2\cdot$tetraglyme.[334] Carbonyl-based precursors (*see* ***Carbonyl Complexes of the Transition Metals***) include $Co_2(CO)_8$,[309] $Co(C_5H_5)(CO)_2$,[309] various cobalt carbonyl clusters,[335] $Co(CO)_3(NO)$,[310,336] and $Co(CO)_2(NO)L$ ($L = PEt_3$, $TeMe_2$, $TeEt_2$).[337] Other cobalt precursors include $CoH(P(O\mathit{n}Pr)(OMe)_2)_4$,[338] $Co(NO_3)_3$,[339] and $Co(\mathit{t}BuNC(CH_3)N\mathit{t}Bu)_2$.[340]

5.4 Rhodium and Iridium

The MOCVD of platinum group metals, including rhodium and iridium, has been recently reviewed.[341,342] A technological application of the metal films is as electrodes in microelectronics devices. Film growth precursors that have been reported for rhodium include $Rh(C_5H_5)(CO)_2$,[343] $Rh(C_5H_5)(COD)$,[343] $Rh(acac)(CO)_2$,[311] $[RhCl(CO)_2]_2$,[311,312] $Rh(C_3H_5)_3$,[311,343] and $Rh(hfac)(C_2H_4)_2$.[344] MOCVD precursors for iridium include $Ir(C_5H_4Me)(COD)$,[313] $Ir(acac)_3$,[345] $Ir(tmhd)(COD)$,[346] a range of precursors of the formula $Ir(X)(COD)$ ($X =$ *bidentate*, anionic donor),[347] and $[Ir(S\mathit{t}Bu)(CO)_2]_2$.[348] Reference 345 gives a recent comprehensive listing of available iridium precursors.

6 PRECURSORS FOR TRANSITION METAL GROUPS 10 AND 11

Some MOCVD precursors containing these elements are listed in Table 6.

6.1 Nickel

Nickel is an important component in many thin-film materials. Precursors for the growth of nickel metal films have been recently summarized in a review.[360] Recently reported precursors for the CVD growth of nickel-containing materials include $Ni(tmhd)_2$,[349] $Ni(hfac)_2(en)$,[361] a series of nickel dioximato complexes,[362] $Ni(O_2CCF_3)_2(dmen)_2$,[363] $Ni(C_5H_5)_2$,[350] and $Ni(\mathit{t}BuNC(CH_3)N\mathit{t}Bu)_2$.[340] Single-source

Table 6 MOCVD precursors of the group 10 and 11 metals

Compound	Vapor pressure
$Ni(tmhd)_2$[349]	subl 90 °C. 0.1 torr
$Ni(C_5H_5)_2$[350]	subl 102 °C, 760 torr
$Pd(hfac)_2$[351]	subl 60 °C, 10−5 torr
$Pt(hfac)_2$[352]	subl 65 °C, 0.1 torr
$Pt(C_5H_4Me)Me_3$[353]	0.2 torr, 35 °C
Cu(hfac)(VTMS)[354]	1 torr, 60 °C
$Cu(tmhd)_2$[355]	1.75 torr, 107 °C
$Ag(hfac)(PMe_3)$[356]	subl 95 °C, 0.1 torr
Ag(tmhd)[357]	subl 230 °C, 0.01 torr
$Au(hfac)Me_2$[358]	0.5 torr, 23 °C
$Au(acac)Me_2$[359]	subl 25 °C, 0.01 torr

precursors have included $Ni(S_2CNRR')_2$ (for NiS_2 films),[364] $Ni(C_5H_5)(CO)In(CH_2CH_2CH_2NMe_2)_2$ (for Ni/In alloy films),[365] and $Ni(dmg{\cdot}GaEt_2)_2$ (for $NiGa_2$ films).[366]

6.2 Palladium and Platinum

Metal-organic precursors for the CVD growth of palladium and platinum films have been recently reviewed.[341,342,367] An issue for the growth of films of these elements is significant heteroatom incorporation from the precursor ligands. Carbon incorporation is a particular problem. Owing to the importance of palladium and platinum films, this area has seen a large amount of activity in the past ten years. Precursors containing alkyl ligands include $PtMe_2(COD)$,[368] $PdMe_2L_2$ ($L = PMe_3$, PEt_3, 0.5 tmeda),[369] $Pt(CH_2CH_2CH_2CH{=}CH_2)_2$,[370] $Pt(C_5H_4Me)Me_3$,[353,371] and $Pt(C_5H_4Et)Me_3$.[372] Diketonate-based precursors include $Pd(acac)_2$,[373] $Pt(acac)_2$,[374] $Pd(hfac)_2$,[351] $Pt(hfac)_2$,[352] $Pd(hfac)(C_3H_5)$,[375] $Pd(hfac)_2(SEt_2)$,[376] and Pd(β-diketonato)(C_3H_5).[377] Precursors containing various substituted β-ketoiminato ligands have included $Pd(\beta\text{-ketoiminato})_2$[378] and Pd($\beta$-ketoiminato)($C_3H_5$).[379] The allyl ligand-based precursors $Pd(C_5H_4Me)(C_3H_5)$[380] and $Pd(C_5H_5)(C_3H_5)$[381] have also been reported. Finally, the single-source precursor $Ru(C_5H_5)((\eta^5\text{-}C_5H_3CH_2NMe_2)Pt(DMSO)Cl)$ serves as a precursor to Ru-Pt alloy films.[330]

6.3 Copper

Growth of copper metal films by CVD methods is driven by the microelectronics industry, which employs copper as an interconnect metallization material. CVD methods are viewed as very promising by the microelectronics industry, owing to excellent conformal film growth that can be obtained with molecular precursors. Progress in this area has been the subject of several recent reviews.[354,355,382] The most commonly employed precursor is Cu(hfac)(VTMS), owing to its high vapor pressure and low growth temperatures.[354] Cu(hfac)(VTMS), while stable at ambient temperature, disproportionates at moderate temperatures to afford copper metal, $Cu(hfac)_2$, and VTMS. This disproportionation allows lower temperature growth of copper metal films, compared to copper(II) precursors. Related copper(I) precursors that differ in the identity of the neutral ligand include $Cu(hfac)(CH_2 = CHt\text{Bu})$,[383] Cu(hfac)(COD),[384] Cu(hfac)(VTMOS),[385] Cu(hfac)(2-methyl-1-hexen-3-yne),[386] and Cu(hfac)(L) (L = a range of terminal alkenes).[387] In spite of the low-temperature film growth with Cu(hfac)(VTMS), there is some residual fluorine contamination on the film surface, and subsequent layers adhere poorly to the copper film. Accordingly, there is considerable interest in fluorine-free precursors. Such precursors that have been reported include $Cu(acac)_2$,[388] $Cu(tmhd)_2$,[389] $Cu(OC(CF_3)_2CH_2NHCH_2CH_2OMe)_2$,[390] $Cu(OCH(Me)CH_2NMe_2)_2$,[391] $Cu(OC(CF_3)_2CH_2\text{-}NHt\text{Bu})_2$,[392] and $Cu(HBpz_3)(PMe_3)$.[393] In addition, a range of β-diketonate complexes of copper(I) and copper(II) have been evaluated as film growth precursors.[394]

6.4 Silver and Gold

Silver is of potential interest for use as the interconnect metal in microelectronics devices. The most commonly used precursors for the growth of silver containing phases are of the formula Ag(hfac)(L), where L = substituted phosphine,[356,395] SEt_2,[396] bis(trimethylsilyl)acetylene,[397] trans-1,2-bis(trimethylsilyl)ethylene,[398] mono-substituted alkenes,[399] vinyltriethylsilane,[400] tetraglyme,[401] and COD.[402] Ag(tmhd) has been used as a precursor, but has a low vapor pressure.[357] Carboxylate complexes of the formula $Ag(O_2CR_F)(PR_3)$ (R_F = perfluoroalkyl, R = alkyl, aryl) have been employed as precursors for the growth of silver metal films.[403–405] Single-source precursors to Ag-In-S films have included $[Ag(PPh_3)_2][In(SOCMe)_4]$[406] and $[Ag(PPh_3)_2][In(SMe)_4]$.[407] The low volatility of these ionic precursors required aerosol delivery of the precursors.

Gold thin films are of interest as substrates for a variety of applications, and also for metallic contacts. Reports of gold film depositions from metal-organic precursors are limited. Precursors have included $Au(hfac)Me_2$,[358] $Au(acac)Me_2$,[359] $AuMe(PMe_3)$,[408] $AuMe(PEt_3)$,[409] $AuMe(P(OMe)_2Me)$,[410] and $Au(O_2CR_F)(PR_3)$ (R_F = perfluoroalkyl, R = alkyl, aryl).[411]

7 RELATED ARTICLES

Carbonyl Complexes of the Transition Metals; Nitrides: Transition Metal Solid-state Chemistry; Oxygen: Inorganic Chemistry; Short-lived Intermediates.

8 FURTHER READING

P. A. Lane and P. J. Wright, *J. Cryst. Growth*, 1999, **204**, 298.

9 REFERENCES

1. A. Sherman, 'Chemical Vapor Deposition for Microelectronics: Principles, Technology, and Applications', Noyes Publications, New Jersey, NJ, 1992.
2. S. Siviram, 'Chemical Vapor Deposition: Thermal and Plasma Deposition of Electronic Materials', Van Nostrand Reinhold, New York, 1995.
3. M. L. Hitchman and K. F. Jensen, 'Chemical Vapor Deposition: Principles and Applications', Academic Press, London, 1993.
4. G. B. Stringfellow, 'Organometallic Vapor-Phase Epitaxy: Theory and Practice', Academic Press, San Diego, CA, 1999.
5. J. S. Foord, G. J. Davies, and W. T. Tsang, 'Chemical Beam Epitaxy and Related Techniques', Wiley, Chichester, 1997.
6. H. S. Halwa, ed., 'Handbook of Thin Film Materials', Academic Press, New York, 2002, Vol. 1–5.
7. H. D. Kaesz, A. Zinn, and L. Brandt, Metallic Materials Deposition: Metal-Organic Precursors, 'Encyclopedia of Inorganic Chemistry', Wiley, Chichester, 1994, p. 2205.
8. D. M. Hoffman, *Polyhedron*, 1994, **13**, 1169.
9. A. H. Cowley and R. A. Jones, *Angew. Chem., Int. Ed. Engl.*, 1989, **28**, 1208.
10. M. Leskelä and M. Ritala, *Angew. Chem., Int. Ed. Engl.*, 2003, **42**, 5548.
11. L. Niinistö, *Ann. Chim.*, 1997, **87**, 221.
12. Y. S. Shin, M. Yoshida, Y. Akiyama, N. Imaishi, and S. C. Jung, *Jpn. J. Appl. Phys., Part 1*, 2003, **42**, 5227.
13. D. Saulys, V. Joshkin, M. Khoudiakov, T. F. Kuech, A. B. Ellis, S. R. Oktyabrsky, and L. McCaughan, *J. Cryst. Growth*, 2000, **217**, 287.
14. J. A. Samuels, W.-C. Chiang, C.-P. Yu, E. Apen, D. C. Smith, D. V. Baxter, and K. G. Caulton, *Chem. Mater.*, 1994, **6**, 1684.
15. T. Kobayashi, K. Kurishima, and T. Ishibashi, *J. Cryst. Growth*, 1994, **142**, 1.
16. K. V. Salazar, S. G. Pattillo, and M. Trkula, *Fusion Technol.*, 2000, **38**, 69.
17. M. Mitsuhara, M. Ogasawara, and H. Suguira, *J. Cryst. Growth*, 1998, **183**, 38.
18. C.-R. Lee, J.-Y. Leem, S.-K. Noh, S.-E. Park, J.-I. Lee, C.-S. Kim, S.-J. Son, and K.-Y. Leem, *J. Cryst. Growth*, 1998, **193**, 300.
19. G. C. Chi, C. H. Kuo, J. K. Sheu, and C. J. Pan, *Mater. Sci. Eng., B*, 2000, **75**, 210.
20. S. Haffouz, B. Beaumont, M. Leroux, M. Laugt, P. Lorenzini, P. Gibart, and L. G. Hubert-Pfalzgraf, *MRS Internet J. Nitride Semicon. Res.*, 1997, **2**, 27.
21. M. L. Timmons, P. K. Chiang, and S. V. Hattandgady, *J. Cryst. Growth*, 1986, **77**, 37.
22. M. Ohkubo, J. Osabe, T. Shiojima, T. Yamaguchi, and T. Ninomiya, *J. Cryst. Growth*, 1997, **170**, 177.
23. A. Hatano, T. Izumiya, and Y. Ohba, *Appl. Phys. Lett.*, 1991, **58**, 1488.
24. S. Y. Lee, S. H. Lee, E. J. Nah, S. S. Lee, and Y. Kim, *J. Cryst. Growth*, 2002, **236**, 635.
25. J. S. Matthews, O. Just, B. Obi-Johnson, and W. S. Rees Jr, *Chem. Vapor Deposition*, 2000, **6**, 129.
26. J. R. Babcock, D. D. Benson, A. Wang, N. L. Edleman, J. A. Belot, M. V. Metz, and T. J. Marks, *Chem. Vapor Deposition*, 2000, **6**, 180.
27. W. Fan, P. R. Markworth, T. J. Marks, and R. P. H. Chang, *Mater. Chem. Phys.*, 2001, **70**, 191.
28. J. M. Zeng, H. Wang, S. X. Shang, Z. Wang, and M. Wang, *J. Cryst. Growth*, 1996, **169**, 474.
29. M. Vehkamäki, T. Hänninen, M. Ritala, M. Leskelä, T. Sajavaara, E. Rauhala, and J. Keinonen, *Chem. Vapor Deposition*, 2001, **7**, 75.
30. M. Vehkamäki, T. Hatanpää, T. Hänninen, M. Ritala, and M. Leskelä, *Electrochem. Solid-state Lett.*, 1999, **2**, 504.
31. A. Kosola, M. Putkonen, L.-S. Johansson, and L. Niinistö, *Appl. Surf. Sci.*, 2003, **211**, 102.
32. V. Saanila, J. Ihanus, M. Ritala, and M. Leskelä, *Chem. Vapor Deposition*, 1998, **4**, 227.
33. A. R. Teren, J. A. Belot, N. L. Edleman, T. J. Marks, and B. W. Wessels, *Chem. Vapor Deposition*, 2000, **6**, 175.
34. D. B. Studebaker, D. A. Neumayer, B. J. Hinds, C. L. Stern, and T. J. Marks, *Inorg. Chem.*, 2000, **39**, 3148.
35. Y.-S. Min, Y. J. Cho, D. Kim, J.-H. Lee, B. M. Kim, S. K. Lim, I. M. Lee, and W. I. Lee, *Chem. Vapor Deposition*, 2001, **7**, 146.
36. W.-C. Shin, K.-J. Choi, N.-K. Seong, E.-S. Choi, B.-H. Kim, and S.-G. Yoon, *Chem. Vapor Deposition*, 2002, **8**, 221.
37. D. R. Biswas, C. Ghosh, and R. L. Layman, *J. Electrochem. Soc.*, 1983, **130**, 234.
38. N. Kobayashi and T. Fukui, *Electron. Lett.*, 1984, **20**, 887.
39. K. Tsubouchi and K. Masu, *Thin Solid Films*, 1993, **228**, 312.
40. P. R. Chalker, T. B. Joyce, C. Johnston, J. A. A. Crosley, J. Huddlestone, M. D. Whitfield, and R. B. Jackman, *Diamond Relat. Mater.*, 1999, **8**, 309.
41. L. H. Long and J. Sackman, *Trans. Faraday Soc.*, 1958, **54**, 1797.
42. B. R. Butler and J. P. Stagg, *J. Cryst. Growth*, 1989, **94**, 481.
43. C. Täschner, J. Klosowski, A. Leonhardt, and U. Dümichen, *Surf. Coat. Technol.*, 1998, **98**, 925.
44. M. P. Singh and S. A. Shivashankar, *Surf. Coat. Technol.*, 2002, **161**, 135.

45. L. Hiltunen, H. Kattelhus, M. Leskelä, M. Makela, L. Niinistö, E. Nykanen, P. Soininen, and M. Tiitta, *Mater. Chem. Phys.*, 1991, **28**, 379.
46. W. Koh, S.-J. Ku, and Y. Kim, *Chem. Vapor Deposition*, 1998, **4**, 192.
47. A. Devi, W. Rogge, A. Wohlfart, F. Hipler, H. W. Becker, and R. A. Fischer, *Chem. Vapor Deposition*, 2000, **6**, 245.
48. R. A. Fischer, H. Sussek, A. Miehr, H. Pritzkow, and E. Herdtweck, *J. Organomet. Chem.*, 1997, **548**, 73.
49. J. McMurran, D. Dai, K. Balasubramanian, C. Steffek, J. Kouvetakis, and J. L. Hubbard, *Inorg. Chem.*, 1998, **37**, 6638.
50. D. M. Hoffman, S. P. Rangarajan, S. D. Athavale, D. J. Economou, J.-R. Liu, Z. Zheng, and W.-K. Chu, *J. Vac. Sci. Technol., A*, 1996, **14**, 306.
51. H. J. Haughn, W. Yu, S. T. Lee, A. Petrou, B. D. McCombe, K. S. Brewer, J. F. Lees, and O. T. Beachley Jr, *J. Cryst. Growth*, 2002, **244**, 157.
52. T.-Y. Chou, Y. Chi, S.-F. Huang, C.-S. Liu, A. J. Carty, L. Scoles, and K. A. Udachin, *Inorg. Chem.*, 2003, **42**, 6041.
53. J.-H. Park, G. A. Horley, P. O'Brien, A. C. Jones, and M. Motevalli, *J. Mater. Chem.*, 2001, **11**, 2346.
54. P. Lobinger, H. S. Park, H. Hohmeister, and H. W. Roesky, *Chem. Vapor Deposition*, 2001, **7**, 105.
55. S. Suh and D. M. Hoffman, *J. Am. Chem. Soc.*, 2000, **122**, 9396.
56. L. A. Mîinea and D. M. Hoffman, *J. Mater. Chem.*, 2000, **10**, 2392.
57. L. A. Mîinea, S. Suh, S. G. Bott, J.-R. Liu, W.-K. Chu, and D. M. Hoffman, *J. Mater. Chem.*, 1999, **9**, 929.
58. M. Valet and D. M. Hoffman, *Chem. Mater.*, 2001, **13**, 2135.
59. G. A. Horley, M. Chunggaze, P. O'Brien, A. J. P. White, and D. J. Williams, *J. Chem. Soc., Dalton Trans.*, 1998, 4205.
60. G. A. Horley, M. R. Lazell, and P. O'Brien, *Chem. Vapor Deposition*, 1999, **5**, 203.
61. S. W. Haggata, M. A. Malik, M. Motevalli, P. O'Brien, and J. C. Knowles, *Chem. Mater.*, 1995, **7**, 716.
62. P. O'Brien, D. J. Otway, and J. R. Walsh, *Thin Solid Films*, 1998, **315**, 57.
63. A. Keys, S. G. Bott, and A. R. Barron, *Chem. Mater.*, 1999, **11**, 3578.
64. G. Shang, M. J. Hampden-Smith, and E. N. Duesler, *Chem. Commun.*, 1996, 1733.
65. G. Shang, K. Kunze, M. J. Hampden-Smith, and E. N. Duesler, *Chem. Vapor Deposition*, 1996, **2**, 242.
66. S. L. Stoll and A. R. Barron, *Chem. Mater.*, 1998, **10**, 650.
67. E. G. Gillan and A. R. Barron, *Chem. Mater.*, 1997, **9**, 3037.
68. A. M. B. van Mol, J. P. A. M. Driessen, J. L. Linden, M. H. J. M. de Croon, C. I. M. A. Spee, and J. C. Schouten, *Chem. Vapor Deposition*, 2001, **7**, 101.
69. Y.-W. Kim, S. W. Lee, and H. Chen, *Thin Solid Films*, 2002, **405**, 256.
70. S. Suh, D. M. Hoffman, L. M. Atagi, D. C. Smith, J.-R. Liu, and W.-K. Chu, *Chem. Mater.*, 1997, **9**, 730.
71. R. C. Smith, N. Hoilien, J. Chen, S. A. Campbell, J. T. Roberts, and W. L. Gladfelter, *Chem. Mater.*, 2003, **15**, 292.
72. I. P. Parkin, L. S. Price, T. B. Hibbert, and K. C. Molloy, *J. Mater. Chem.*, 2001, **11**, 1486.
73. T. G. Hibbert, M. F. Mahon, K. C. Molloy, L. S. Price, and I. P. Parkin, *J. Mater. Chem.*, 2001, **11**, 469.
74. D. M. Hoffman, S. P. Rangarajan, S. D. Sthavale, D. J. Economou, J.-R. Liu, Z. Zheng, and W.-K. Chu, *J. Vac. Sci. Technol., A*, 1995, **13**, 820.
75. T. H.-W. Sun, H.-F. Wang, and K.-M. Chi, *J. Mater. Chem.*, 2000, **10**, 1231.
76. V. V. Krisyuk, A. E. Turgambaeva, and I. K. Igumenov, *Chem. Vapor Deposition*, 1998, **4**, 43.
77. W. Y. Cheng and L. S. Hong, *Thin Solid Films*, 2002, **415**, 94.
78. M. A. Todd, G. Bandari, and T. H. Baum, *Chem. Mater.*, 1999, **11**, 547.
79. D. G. Hendershot, J. C. Pazik, and A. D. Berry, *Chem. Mater.*, 1992, **4**, 833.
80. R. M. Biefeld, J. D. Phillips, and S. R. Kurtz, *J. Cryst. Growth*, 2000, **211**, 400.
81. C. P. Myers, P. W. Haycock, M. Pichot, G. A. Horley, K. C. Molloy, S. A. Rushworth, and L. M. Smith, *Chem. Vapor Deposition*, 2004, **10**, 35.
82. G. A. Horley, M. F. Mahon, K. C. Molloy, P. W. Haycock, and C. P. Meyers, *Inorg. Chem.*, 2002, **41**, 5052.
83. H. S. Park, S. Schulz, H. Wessel, and H. W. Roesky, *Chem. Vapor Deposition*, 1999, **5**, 179.
84. H. Funakubo, K. Ishikawa, T. Watanabe, M. Mitsuya, and N. Nukaga, *Adv. Mater. Opt. Electron.*, 2000, **10**, 193.
85. J. R. Roeder, B. C. Hendrix, F. Hintermaier, D. A. Desrochers, T. H. Baum, G. Bhandar, M. Chappuis, P. C. Van Buskirk, C. Dehm, E. Fritsch, N. Nagel, H. Wendt, H. Cerva, W. Hönlein, and C. Mazuré, *J. Eur. Ceram. Soc.*, 1999, **19**, 1463.
86. P. A. Williams, A. C. Jones, M. J. Crosbie, P. J. Wright, J. F. Bickley, A. Steiner, H. O. Davies, T. J. Leedham, and G. W. Critchlow, *Chem. Vapor Deposition*, 2001, **7**, 205.
87. H. Bachhofer, H. von Philipsborn, W. Hartner, C. Dehm, B. Jobst, A. Kiendl, H. Schroeder, and R. Waser, *J. Mater. Res.*, 2001, **16**, 2966.
88. C. R. Gorla, N. W. Emanetoglu, S. Liang, W. E. Mayo, Y. Lu, M. Wraback, and H. Shen, *J. Appl. Phys.*, 1999, **85**, 2595.
89. B. Hahn, G. Heindel, E. Pschorr-Schoberer, and W. Gebhardt, *Semicond. Sci. Technol.*, 1998, **13**, 788.
90. P. O'Brien, M. A. Malik, J. R. Walsh, and A. C. Jones, *Adv. Mater. Opt. Electron.*, 1997, **7**, 117.
91. Y. Kashiwaba, K. Sugawara, K. Haga, H. Watanabe, B. P. Zhang, and Y. Segawa, *Thin Solid Films*, 2002, **411**, 87.
92. A. Gulino and I. Fragalà, *Chem. Mater.*, 2002, **14**, 116.

93. X. Li, D. L. Young, H. Moutinho, Y. Yan, C. Narayanswamy, T. A. Gessert, and T. J. Coutts, *Electrochem. Solid-St. Lett.*, 2001, **4**, C43.

94. J. R. Babcock, A. Wang, A. W. Metz, N. L. Edleman, M. V. Metz, M. A. Lane, C. R. Kannewurf, and T. J. Marks, *Chem. Vapor Deposition*, 2001, **7**, 239.

95. H. Sternschulte, M. Schreck, B. Stritzker, A. Germaier, and G. Dollinger, *Diamond Rel. Mater.*, 2000, **9**, 1046.

96. S. A. Kulinich, T. Yamaki, S. Bysakh, H. Yamamoto, K. Mitsuishi, M. Song, K. Terashima, and K. Furuya, *J. Cryst. Growth*, 2003, **247**, 408.

97. S. Nakamura, G. Fasol, and S. J. Pearton, 'The Blue Laser Diode: The Complete Story', Springer-Verlag, Berlin, 2000.

98. W. I. Park, D.-H. Kim, G.-C. Yi, and C. Kim, *Jpn. J. Appl. Phys., Part 1*, 2002, **41**, 6919.

99. E. Fujii, A. Tomozawa, S. Fujii, H. Torii, R. Takayama, and T. Hirao, *Jpn. J. Appl. Phys., Part 1*, 1994, **33**, 6331.

100. E. Weiss, J. Kopf, T. Gardein, S. Corbelin, U. Schumann, M. Kirilov, and G. Petrov, *Chem. Ber.*, 1985, **118**, 3529.

101. T. P. Hanusa, *Organometallics*, 2002, **21**, 2559.

102. J. S. Matthews and W. S. Rees Jr, *Adv. Inorg. Chem.*, 2000, **50**, 173.

103. W. A. Wojtczak, P. F. Pfleig, and M. J. Hampden-Smith, *Adv. Organomet. Chem.*, 1996, **40**, 215.

104. D. Schulz and T. J. Marks, *Adv. Mater.*, 1994, **6**, 719.

105. A. R. Barron and W. S. Rees Jr, *Adv. Mater. Opt. Electron.*, 1993, **2**, 271.

106. A. C. Greenwald, W. S. Rees, and U. W. Lay, *Mater. Res. Soc. Symp. Proc.*, 1993, **301**, 21.

107. T. Kodas and M. Hampden-Smith, 'The Chemistry of Metal CVD', VCH, Weinheim, 1994.

108. A. Devi, S. A. Shivashankar, and A. G. Samuelson, *J. Phys. IV*, 2002, **12**, 139.

109. D. Barreca, G. A. Battiston, U. Casellato, R. Gerbasi, and E. Tondello, *J. Phys. IV*, 2001, **11**, 253.

110. A. C. Jones, C. R. Whitehouse, and J. S. Roberts, *Chem. Vapor Deposition*, 1995, **1**, 65.

111. D. A. Neumayer and J. G. Ekerdt, *Chem. Mater.*, 1996, **8**, 9.

112. P. Zanella, G. Rossetto, N. Brianese, F. Ossola, M. Porchia, and J. O. Williams, *Chem. Mater.*, 1991, **3**, 225.

113. M. Lazell, P. O'Brien, D. J. Otway, and J.-H. Park, *J. Chem. Soc., Dalton Trans.*, 2000, 4479.

114. J.-H. Park, M. Afzaal, M. Kemmler, P. O'Brien, D. J. Otway, J. Raftery, and J. Waters, *J. Mater. Chem.*, 2003, **13**, 1942.

115. S. Suh and D. M. Hoffman, *Chem. Mater.*, 2000, **12**, 2794.

116. J. Cheon, J. Arnold, K.-M. Yu, and E. D. Bourret, *Chem. Mater.*, 1995, **7**, 2273.

117. J. Y. Cho, H.-C. Jeong, K.-S. Kim, D. H. Kang, H.-K. Kim, and I.-W. Shim, *Bull. Korean Chem. Soc.*, 2003, **24**, 645.

118. J.-H. Park, M. Afzaal, M. Helliwell, M. A. Malik, P. O'Brien, and J. Raftery, *Chem. Mater.*, 2003, **15**, 4205.

119. M. Afzaal, D. J. Crouch, P. O'Brien, J. Raftery, P. J. Skabara, A. J. P. White, and D. J. Williams, *J. Mater. Chem.*, 2004, **14**, 233.

120. R. G. Gordon, *MRS Bull.*, 2000, **25**, 52.

121. D. S. Ginley and C. Bright, *MRS Bull.*, 2000, **25**, 15.

122. Z. Zhao, D. L. Morel, and C. S. Kerekides, *Thin Solid Films*, 2002, **413**, 203.

123. V. Hopfe, D. W. Sheel, C. I. M. A. Spee, R. Tell, P. Martin, A. Beil, M. Pemble, R. Weiss, U. Vogt, and W. Graehlert, *Thin Solid Films*, 2003, **442**, 60.

124. L. S. Price, I. P. Parkin, M. N. Field, A. M. E. Hardy, R. J. H. Clark, T. G. Hibbert, and K. C. Molloy, *J. Mater. Chem.*, 2000, **10**, 527.

125. A. Onda, T. Komatsu, and T. Yashima, *Chem. Commun.*, 1998, 1507.

126. A. C. Jones, T. J. Leedham, H. O. Davies, K. A. Fleeting, P. O'Brien, M. J. Crosbie, P. J. Wright, D. J. Williams, and P. A. Lane, *Polyhedron*, 2000, **19**, 351.

127. A. Watanabe, T. Tsuchiya, and Y. Imai, *Thin Solid Films*, 2002, **419**, 76.

128. N. I. Fainer, M. L. Kosinova, Y. M. Rumyantsev, E. G. Salman, and F. A. Kuznetsov, *Thin Solid Films*, 1996, **280**, 16.

129. R. M. Bielfeld, *Mater. Sci. Eng. R*, 2002, **36**, 105.

130. A. Aadvark, N. J. Mason, and P. J. Walker, *Prog. Cryst. Growth Charact.*, 1997, **35**, 207.

131. A. Berry, *Polyhedron*, 1999, **18**, 2609.

132. R. M. Biefeld and K. C. Baucom, *J. Cryst. Growth*, 1994, **135**, 401.

133. A. C. Jones and P. R. Chalker, *J. Phys. D: Appl. Phys.*, 2003, **36**, R80.

134. A. Boulouz, A. Giani, F. Pascal-Delannoy, M. Boulouz, A. Foucaran, and A. Boyer, *J. Cryst. Growth*, 1998, **194**, 336.

135. A. Al Bayaz, A. Giani, M. Al Khalfioui, A. Foucaran, F. Pascal-Delannoy, and A. Boyer, *J. Cryst. Growth*, 2003, **258**, 135.

136. D. Barreca, G. A. Rizzi, and E. Tondello, *Thin Solid Films*, 1998, **333**, 35.

137. A. Gulino, G. Compagnini, E. G. Egdell, and I. Fragalà, *Thin Solid Films*, 1999, **352**, 73.

138. M. Schuisky, K. Kukli, M. Ritala, A. Hårsta, and M. Leskelä, *Chem. Vapor Deposition*, 2000, **6**, 139.

139. Y. J. Cho, Y. S. Min, J. H. Lee, B. S. Seo, J. K. Lee, Y. S. Park, and J. H. Choi, *Integr. Ferroelectr.*, 2003, **59**, 1483.

140. O. C. Monteiro, T. Trindade, J.-H. Park, and P. O'Brien, *Chem. Vapor Deposition*, 2000, **6**, 230.

141. O. C. Monteiro, T. Trindade, F. A. Almeida Paz, J. Klinkowski, J. Waters, and P. O'Brien, *J. Mater. Chem.*, 2003, **13**, 3006.

142. D. J. Crouch, M. Helliwell, P. O'Brien, J.-H. Park, J. Waters, and D. J. Williams, *Dalton Trans.*, 2003, 1500.

143. R. S. Mane and C. D. Lokhande, *Mater. Chem. Phys.*, 2000, **65**, 1.

144. T. J. Coutts, D. L. Young, X. Li, W. P. Mulligan, and X. Wu, *J. Vac. Sci. Technol., A*, 2000, **18**, 2646.

145. B. S. Li, Y. C. Liu, D. Z. Shen, Y. M. Lu, J. Y. Zhang, X. G. Kong, X. W. Fan, and Z. Z. Zhi, *J. Vac. Sci. Technol., A*, 2002, **20**, 265.

146. A. Yamada, B. Sang, and M. Konagai, *Appl. Surf. Sci.*, 1997, **112**, 216.

147. S. Suh, D. M. Hoffman, L. M. Atagi, and D. C. Smith, *J. Mater. Sci. Lett.*, 1999, **18**, 789.

148. J. Auld, D. J. Houlton, A. C. Jones, S. A. Rushworth, M. A. Malik, P. O'Brien, and G. W. Critchlow, *J. Mater. Chem.*, 1994, **4**, 1249.

149. S. Jain, T. T. Kodas, and M. Hampden-Smith, *Chem. Vapor Deposition*, 1998, **4**, 51.

150. A. J. Petrella, H. Deng, N. K. Roberts, and R. N. Lamb, *Chem. Mater.*, 2002, **14**, 4339.

151. S. Suh, L. A. Mîinea, D. M. Hoffman, Z. Zhang, and W.-K. Chu, *J. Mater. Sci. Lett.*, 2001, **20**, 115.

152. S. Suh, D. M. Hoffman, L. M. Atagi, and D. C. Smith, *Chem. Vapor Deposition*, 2001, **7**, 81.

153. A. Gulino, F. Castelli, P. Dapporto, P. Rossi, and I. Fragalà, *Chem. Mater.*, 2002, **14**, 704.

154. A. Gulino, P. Dapporto, P. Rossi, and I. Fragalà, *Chem. Mater.*, 2002, **14**, 1441.

155. H. Uda, H. Yonezawa, Y. Ohtsubo, M. Kosaka, and H. Sonomura, *Sol. Energy Mater. Sol. Cells*, 2003, **75**, 219.

156. D. Noda, T. Aoki, Y. Nakanishi, and Y. Hatanaka, *Vacuum*, 2000, **59**, 701.

157. R. A. Berrigan, N. Maung, S. J. C. Irvine, D. J. Cole-Hamilton, and D. Ellis, *J. Cryst. Growth*, 1998, **195**, 718.

158. U. W. Pohl, R. Engelhardt, V. Turck, and D. Bimberg, *J. Cryst. Growth*, 1998, **195**, 569.

159. M. Chunggaze, J. McAleese, P. O'Brien, and D. J. Otway, *Chem. Commun.*, 1998, 833.

160. P. O'Brien, J. R. Walsh, I. M. Watson, L. Hart, and S. R. P. Silva, *J. Cryst. Growth*, 1996, **167**, 133.

161. C. Byrom, M. A. Malik, P. O'Brien, A. J. P. White, and D. J. Williams, *Polyhedron*, 2000, **19**, 211.

162. M. Afzaal, D. Crouch, M. A. Malik, M. Motevalli, P. O'Brien, J.-H. Park, and J. D. Williams, *Eur. J. Inorg. Chem.*, 2004, 171.

163. H. S. Park, M. Mokhtari, and H. W. Roesky, *Chem. Vapor Deposition*, 1996, **2**, 135.

164. J. M. Redwing, T. F. Kuech, D. C. Gordon, B. A. Vaarstra, and S. S. Lau, *J. Appl. Phys.*, 1994, **76**, 1585.

165. S. J. Pearton, C. R. Abernathy, J. D. MacKenzie, R. N. Schwartz, R. G. Wilson, J. M. Zavada, and R. J. Shul, *Mater. Res. Soc. Symp. Proc.*, 1996, **422**, 47.

166. M. Pan and A. J. Steckl, *Appl. Phys. Lett.*, 2003, **83**, 9.

167. A. C. Greenwald, K. J. Linden, W. S. Rees, Jr, O. Just, N. M. Haegel, and S. Donder *Mater. Res. Soc. Symp. Proc.*, 1996, **422**, 63.

168. D. Pfeiffer, B. J. Ximba, L. M. Liable-Sands, A. L. Rheingold, M. J. Heeg, D. M. Coleman, H. B. Schlegel, T. F. Kuech, and C. H. Winter, *Inorg. Chem.*, 1999, **38**, 4539.

169. J. Ji, R. A. Senter, L. R. Tessler, D. Back, C. H. Winter, and J. L. Coffer, *Nanotechnology*, 2004, **15**, 1.

170. T. S. Lewkebandara and C. H. Winter, *Chemtracts-Inorg. Chem.*, 1994, **6**, 27.

171. P. S. Andry, W. J. Varhue, F. Lapido, K. Ahmed, E. Adams, M. Lavoie, P. B. Klein, R. Hengehold, and J. Hunter, *J. Appl. Phys.*, 1996, **80**, 551.

172. J. G. Cederberg, T. P. Culp, B. Bieg, D. Pfeiffer, C. H. Winter, K. L. Bray, and T. F. Kuech, *J. Appl. Phys.*, 1999, **85**, 1825.

173. A. Watanabe, T. Tsuchiya, and Y. Imai, *Thin Solid Films*, 2002, **406**, 132.

174. T. Chiba, K.-I. Itoh, and O. Matsumoto, *Thin Solid Films*, 1997, **300**, 6.

175. A. Kosola, M. Putkonen, L.-S. Johansson, and L. Niinisto, *Appl. Surf. Sci.*, 2003, **211**, 102.

176. A. Rahtu and M. Ritala, *Chem. Vapor Deposition*, 2002, **8**, 21.

177. M. L. Hitchman and F. Tian, *J. Electroanal. Chem.*, 2002, **538–539**, 165.

178. D. C. Gilmer, D. G. Colombo, C. J. Taylor, J. Roberts, G. Haugstad, S. A. Campbell, H.-S. Kim, G. D. Wilk, M. A. Gribelyuk, and W. L. Gladfelter, *Chem. Vapor Deposition*, 1998, **4**, 9.

179. D. J. Burleson, J. T. Roberts, W. L. Gladfelter, S. A. Campbell, and R. C. Smith, *Chem. Mater.*, 2002, **14**, 1269.

180. Q. Fang, J.-Y. Zhang, Z. M. Wang, J. X. Wu, B. J. O'Sullivan, P. K. Hurley, T. L. Leedham, H. Davies, M. A. Audier, C. Jimenez, J.-P. Sénateur, and I. W. Boyd, *Thin Solid Films*, 2003, **428**, 263.

181. J. A. Belot, R. J. McNeely, A. Wang, C. J. Reedy, T. J. Marks, G. P. A. Yap, and A. L. Rheingold, *J. Mater. Res.*, 1999, **14**, 12.

182. R. C. Smith, N. Hoilien, C. J. Taylor, T. Ma, S. A. Campbell, J. T. Roberts, N. Copel, D. A. Buchanan, M. Gribelyuk, and W. L. Gladfelter, *J. Electrochem. Soc.*, 2000, **147**, 3472.

183. S. Codato, G. Carta, G. Rossetto, G. A. Rizzi, P. Zanella, P. Scardi, and M. Leoni, *Chem. Vapor Deposition*, 1999, **5**, 159.

184. J. N. Musher and R. G. Gordon, *J. Mater. Res.*, 1996, **11**, 989.

185. S. Panda, J. Kim, B. H. Weiler, D. J. Economou, and D. M. Hoffman, *Thin Solid Films*, 1999, **357**, 125.

186. J.-Y. Yun, M.-Y. Park, and S.-W. Rhee, *J. Electrochem. Soc.*, 1999, **146**, 1804.

187. J. Whole, A. Gebauer-Teichmann, and K.-T. Rie, *Surf. Coat. Technol.*, 2001, **142–144**, 661.

188. H. Machida, A. Hoshino, T. Suzuki, A. Ogura, and Y. Ohshita, *J. Cryst. Growth*, 2002, **237–239**, 586.

189. C. H. Winter, T. S. Lewkebandara, J. W. Proscia, and A. L. Rheingold, *Inorg. Chem.*, 1993, **32**, 3807.

190. P. J. McKarns, T. S. Lewkebandara, G. P. A. Yap, L. M. Liable-Sands, A. L. Rheingold, and C. H. Winter, *Inorg. Chem.*, 1998, **37**, 418.

191. T. S. Lewkebandara, J. W. Proscia, and C. H. Winter, *Chem. Mater.*, 1995, **7**, 1053.

192. H. Watanabe, K.-I. Itoh, and O. Matsumoto, *Thin Solid Films*, 2001, **386**, 281.

193. A. Porporati, S. Roitti, and O. Sbaizero, *J. Eur. Ceram. Soc.*, 2003, **23**, 247.

194. R. Fix, R. G. Gordon, and D. M. Hoffman, *Chem. Mater.*, 1993, **5**, 614.

195. R. C. Smith, T. Ma, H. Hoilien, L. Y. Tsung, M. J. Bevan, L. Colombo, J. Roberts, S. A. Campbell, and W. L. Gladfelter, *Adv. Mater. Opt. Electron.*, 2000, **10**, 105.

196. L. G. Hubert-Pfalzgraf, *Inorg. Chem. Commun.*, 2003, **6**, 102.

197. B.-C. Kang, J.-H. Lee, H.-Y. Chae, D.-Y. Jung, S.-B. Lee, and J.-H. Boo, *J. Vac. Sci. Technol., B*, 2003, **21**, 1773.

198. J. J. Gallegos, T. L. Ward, T. J. Boyle, M. A. Rodriguez, and L. P. Francisco, *Chem. Vapor Deposition*, 2000, **6**, 21.

199. W. C. Hendricks, S. B. Desu, and C. H. Peng, *Chem. Mater.*, 1994, **6**, 1955.

200. A. C. Jones, P. A. Williams, J. F. Bickley, A. Steiner, H. O. Davies, T. J. Leedham, A. Awaluddin, M. E. Pemble, and G. W. Critchlow, *J. Mater. Chem.*, 2001, **11**, 1428.

201. A. C. Jones, T. J. Leedham, P. J. Wright, M. J. Crosbie, K. A. Fleeting, D. J. Otway, P. O'Brien, and M. E. Pemble, *J. Mater. Chem.*, 1998, **8**, 1773.

202. J. H. Lee, J. Y. Kim, J. Y. Shim, and S. W. Rhee, *J. Vac. Sci. Technol., A*, 1999, **17**, 3033.

203. E.-C. Plappert, K.-H. Dahmen, R. Hauert, and K.-H. Ernst, *Chem. Vapor Deposition*, 1999, **5**, 79.

204. Y. S. Min, Y. J. Cho, D. Kim, J. H. Lee, B. M. Kim, S. K. Lim, I. M. Kim, and W. I. Lee, *J. Phys. IV*, 2001, **11**, 675.

205. T. Nakamura, S. Momose, and K. Tachibana, *Jpn. J. Appl. Phys., Part 1*, 2001, **40**, 6619.

206. F. Ando, H. Shimizu, I. Kobayashi, and M. Okada, *Jpn. J. Appl. Phys., Part 1*, 1997, **36**, 5820.

207. I. T. Kim, C. H. Lee, and S. J. Park, *Jpn. J. Appl. Phys., Part 1*, 1994, **33**, 5125.

208. R. Bhakta, F. Hipler, A. Devi, S. Regnery, P. Ehrhart, and R. Waser, *Chem. Vapor Deposition*, 2003, **9**, 295.

209. K. Vydianathan, G. Nuesca, G. Peterson, E. T. Eisenbraun, A. E. Kaloyeros, J. J. Sullivan, and B. Han, *J. Mater. Res.*, 2001, **16**, 1838.

210. S. Lim, B. Choi, Y.-S. Min, D. Kim, I. Yoon, S. S. Lee, and I.-M. Lee, *J. Organomet. Chem.*, 2004, **689**, 224.

211. C. J. Taylor, D. C. Gilmer, D. G. Colombo, G. D. Wilk, S. A. Campbell, J. Roberts, and W. L. Gladfelter, *J. Am. Chem. Soc.*, 1999, **121**, 5220.

212. A. C. Jones and P. R. Chalker, *J. Phys. D: Appl. Phys.*, 2003, **36**, R80.

213. A. C. Jones, *J. Mater. Chem.*, 2002, **12**, 2576.

214. X. H. Xu, Y. Hou, M. Wang, H. Wang, and A. Q. Zhou, *Prog. Chem.*, 2002, **14**, 61.

215. J. J. Galegos, III, T. L. Ward, T. J. Boyle, M. A. Rodriguez, and L. P. Francisco *Chem. Vapor Deposition*, 2000, **6**, 21.

216. N. Wakiya, K. Kuroyanagi, Y. Xuan, K. Shinozaki, and N. Mizutani, *Thin Solid Films*, 2000, **372**, 156.

217. D.-H. Kim, W.-Y. Yang, and S.-W. Rhee, *J. Electrochem. Soc.*, 2003, **150**, C516.

218. P. A. Williams, J. L. Roberts, A. C. Jones, P. R. Chalker, N. L. Tobin, J. F. Bickley, H. O. Davies, L. M. Smith, and T. J. Leedham, *Chem. Vapor Deposition*, 2002, **8**, 163.

219. S. P. Krumdieck, O. Sbaizero, A. Bullert, and R. Raj, *Surf. Coat. Technol.*, 2003, **167**, 226.

220. K.-I. Itoh and O. Matsumoto, *Thin Solid Films*, 1999, **345**, 29.

221. A. C. Jones, T. J. Leedham, P. J. Wright, M. J. Crosbie, D. J. Williams, K. A. Fleeting, H. O. Davies, D. J. Otway, and P. O'Brien, *Chem. Vapor Deposition*, 1998, **4**, 197.

222. A. C. Jones, T. J. Leedham, P. J. Wright, M. J. Crosbie, P. A. Lane, D. J. Williams, K. A. Fleeting, H. O. Davies, D. J. Otway, and P. O'Brien, *Chem. Vapor Deposition*, 1998, **4**, 197.

223. M. Morstein, *Inorg. Chem.*, 1999, **38**, 125.

224. U. Patil, M. Winter, H.-W. Becker, and A. Devi, *J. Mater. Chem.*, 2003, **13**, 2177.

225. R. C. Smith, N. Hoilien, J. Roberts, S. A. Campbell, and W. L. Gladfelter, *Chem. Mater.*, 2002, **14**, 474.

226. M. Putkonen and L. Niinistö, *J. Mater. Chem.*, 2001, **11**, 3141.

227. M. Putkonen, T. Tajavaara, J. Niinistö, L.-S. Johansson, and L. Niinistö, *J. Mater. Chem.*, 2002, **12**, 442.

228. Y. Senzaki, G. B. Alers, A. K. Hochberg, D. A. Roberts, J. A. T. Norman, R. M. Fleming, and H. Krautter, *Electrochem. Solid State Lett.*, 2000, **3**, 435.

229. J. Schaeffer, N. V. Edwards, R. Liu, D. Roan, B. Hradsky, R. Gregory, J. Kulik, E. Duda, L. Contreras, J. Christiansen, S. Zollner, P. Tobin, B.-Y. Nguyen, R. Nieh, M. Ramon, R. Rao, R. Hegde, R. Rai, J. Baker, and S. Voight, *J. Electrochem. Soc.*, 2003, **150**, F67.

230. S. Zurcher, M. Morstein, N. D. Spencer, M. Lemberger, and A. Bauer, *Chem. Vapor Deposition*, 2002, **8**, 171.

231. A. E. Kaloyeros and E. Eisenbraun, *Annu. Rev. Mater. Sci.*, 2000, **30**, 363.

232. C. Marcadal, M. Eizenberg, A. Yoon, and L. Chen, *J. Electrochem. Soc.*, 2002, **149**, C52.

233. M. Eizenberg, K. Littau, S. Ghanayem, M. Liao, R. Mosely, and A. K. Sinha, *J. Vac. Sci. Technol., A*, 1995, **13**, 590.

234. J. T. Scheper, P. J. McKarns, T. S. Lewkebandara, and C. H. Winter, *Mater. Sci. Semicond. Proc.*, 1999, **2**, 149.

235. T. S. Lewkebandara, P. H. Sheridan, M. J. Heeg, A. L. Rheingold, and C. H. Winter, *Inorg. Chem.*, 1994, **33**, 5879.

236. C. J. Carmalt, A. C. Newport, I. P. Parkin, A. J. P. White, and D. J. Williams, *J. Chem. Soc., Dalton Trans.*, 2002, 4055.

237. C. J. Carmalt, S. R. Whaley, P. S. Lall, A. H. Cowley, R. A. Jones, B. G. McBurnett, and J. G. Ekerdt, *J. Chem. Soc., Dalton Trans.*, 1998, 553.

238. H. Berndt, H.-R. Stock, P. Mayr, and A.-Q. Zeng, *Surf. Coat. Technol.*, 1995, **74–75**, 369.

239. F. Senocq, N. Viguier, and A. Gleizes, *Eur. J. Solid State Inorg. Chem.*, 1996, **33**, 1185.

240. C. S. Blackman, C. J. Carmalt, I. P. Parkin, L. Apostolico, K. C. Molloy, A. J. P. White, and D. J. Williams, *J. Chem. Soc., Dalton Trans.*, 2002, 2702.

241. M. B. Sahana, M. S. Dharmaprakash, and S. A. Shivashankar, *J. Mater. Chem.*, 2002, **12**, 333.

242. A. Montoux, H. Groult, E. Balnois, P. Doppelt, and L. Gueroudji, *J. Electrochem. Soc.*, 2004, **151**, A368.

243. K. Inumaru, M. Misono, and T. Okuhara, *Appl. Catal., A: General*, 1997, **149**, 133.

244. X.-D. Liu, H. Funakubo, S. Noda, and H. Komiyama, *Chem. Vapor Deposition*, 2001, **7**, 253.

245. M. J. Nystrom, B. W. Wessels, D. B. Studebaker, T. J. Marks, W. P. Lin, and G. K. Wong, *Appl. Phys. Lett.*, 1995, **67**, 365.

246. I.-S. Chen, J. F. Roeder, T. E. Glassman, and T. H. Baum, *Chem. Mater.*, 1999, **11**, 209.

247. S. Lim, J. C. Lee, D. S. Sohn, W. I. Lee, and I.-M. Lee, *Chem. Mater.*, 2002, **14**, 1548.

248. P. A. Williams, A. C. Jones, P. J. Wright, M. J. Crosbie, J. F. Bickley, A. Steiner, H. O. Davies, and T. J. Leedham, *Chem. Vapor Deposition*, 2002, **8**, 110.

249. A. C. Jones, H. O. Davies, T. J. Leedham, P. J. Wright, M. J. Crosbie, A. Steiner, J. F. Bickley, P. O'Brien, A. J. P. White, and D. J. Williams, *J. Mater. Chem.*, 2001, **11**, 544.

250. C. Hcaneliere, S. Four, J. L. Autran, R. A. B. Devine, and N. P. Sandler, *J. Appl. Phys.*, 1998, **83**, 4823.

251. K. Kukli, M. Ritala, and M. Leskelä, *Chem. Mater.*, 2000, **12**, 1914.

252. N. Hara, S. Nagata, N. Akao, and K. Sugimoto, *J. Electrochem. Soc.*, 1999, **146**, 510.

253. P. V. Kelly, M. B. Mooney, J. T. Beechinor, B. J. O'Sullivan, P. K. Hurley, G. M. Crean, J.-Y. Zhang, I. W. Boyd, M. Paillous, C. Jimenez, and J.-P. Sénateur, *Adv. Mater. Opt. Electron.*, 2000, **10**, 115.

254. H. W. Davies, T. J. Leedham, A. C. Jones, P. O'Brien, A. J. P. White, and D. J. Williams, *Polyhedron*, 1999, **18**, 3165.

255. K. D. Pollard and R. J. Puddephatt, *Chem. Mater.*, 1999, **11**, 1069.

256. H.-S. Chiu, C.-N. Wang, and S.-H. Chuang, *Chem. Vapor Deposition*, 2000, **6**, 223.

257. M. J. Crosbie, P. J. Wright, H. O. Davies, A. C. Jones, T. J. Leedham, P. O'Brien, and G. W. Critchlow, *Chem. Vapor Deposition*, 1999, **5**, 9.

258. D. S. Shin, H. S. Choi, Y. T. Kim, and I.-H. Choi, *J. Cryst. Growth*, 2000, **209**, 1009.

259. Y. Takahashi, Y. Nakajima, T. Morishita, and K. Tanabe, *Physica C*, 2002, **378–381**, 1357.

260. C. H. Winter, *Aldrichimica Acta*, 2000, **33**, 3.

261. W. C. Gau, C. W. Wu, T. C. Chang, P. T. Liu, C. J. Chu, C. H. Chen, and L. J. Chen, *Thin Solid Films*, 2002, **420–421**, 548.

262. E. R. Engbrecht, Y.-M. Sun, S. Smith, K. Pfiefer, J. Bennett, J. M. White, and J. G. Ekerdt, *Thin Solid Films*, 2002, **418**, 145.

263. M. H. Tsai, S. C. Sun, C. P. Lee, H. T. Chiu, C. E. Tsai, S. H. Chuang, and S. C. Wu, *Thin Solid Films*, 1995, **270**, 531.

264. S.-H. Kim, S.-J. Im, and K.-B. Kim, *Thin Solid Films*, 2002, **415**, 177.

265. X. Lu, J. R. Babcock, M. A. Lane, J. A. Belot, A. W. Ott, M. V. Metz, C. R. Kannewurf, R. P. H. Chang, and T. J. Marks, *Chem. Vapor Deposition*, 2001, **7**, 25.

266. S. Abisset and F. Maury, *Surf. Coat. Technol.*, 1998, **108–109**, 200.

267. Y.-H. Chang, J.-B. Wu, P.-J. Chang, and H.-T. Chiu, *J. Mater. Chem.*, 2003, **13**, 365.

268. L. Valade, C. Danjoy, B. Chansou, E. Riviere, J.-L. Pellegatta, R. Choukroun, and P. Cassoux, *Appl. Organomet. Chem.*, 1998, **12**, 173.

269. L. Valade, R. Choukroun, P. Cassoux, F. Teyssandier, L. Poirier, M. Cucarroir, R. Feurer, P. Bonnefond, and F. Maury, *Chem. Trans. Met. Carbides Nitrides*, 1996, 290.

270. J. T. Scheper, K. C. Jayaratne, L. M. Liable-Sands, G. P. A. Yap, A. L. Rheingold, and C. H. Winter, *Inorg. Chem.*, 1999, **38**, 4354.

271. P. J. McKarns, M. J. Heeg, and C. H. Winter, *Inorg. Chem.*, 1998, **37**, 4743.

272. B. D. Fahlman and A. R. Barron, *Adv. Mater. Opt. Electron.*, 2000, **10**, 223.

273. T. Ivanova, M. Surtchev, and G. Gesheva, *Phys. Status Solidi A*, 2001, **184**, 507.

274. D. Barreca, S. Bozza, G. Carta, G. Rossetto, E. Tondello, and P. Zanella, *Surf. Sci.*, 2003, **532–535**, 439.

275. T. D. Manning, I. P. Parkin, M. E. Pemble, D. Sheel, and D. Vernardou, *Chem. Mater.*, 2004, **16**, 744.

276. J. S. Becker, S. Suh, S. L. Want, and R. G. Gordon, *Chem. Mater.*, 2003, **15**, 2969.

277. E. L. Crane, H.-T. Chiu, and R. G. Nuzzo, *J. Phys. Chem. B*, 2001, **105**, 3549.

278. O. J. Bchir, S. W. Johnson, A. C. Cuadra, T. J. Anderson, C. G. Ortiz, B. C. Brooks, D. H. Powell, and L. McElwee-White, *J. Cryst. Growth*, 2003, **249**, 262.

279. R. Fix, R. G. Gordon, and D. M. Hoffman, *Thin Solid Films*, 1996, **288**, 116.

280. O. Nilsen, H. Fjellvåg, and A. Kjekhus, *Thin Solid Films*, 2003, **444**, 44.

281. P. Tomasini, A. Haidoux, J. C. Tédenac, and M. Maurin, *J. Cryst. Growth*, 1998, **193**, 572.

282. W. A. Herrmann, W. M. Wachter, F. E. Kühn, and R. W. Fischer, *J. Organomet. Chem.*, 1998, **553**, 443.

283. J. C. Nable, M. K. Gulbinska, M. A. Kmetz, S. L. Suib, and F. S. Galasso, *Chem. Mater.*, 2003, **15**, 4823.

284. S. Mahapatra and S. A. Shivashankar, *Chem. Vapor Deposition*, 2003, **9**, 238.

285. F. Maury and F. Ossola, *Appl. Organomet. Chem.*, 1998, **12**, 189.

286. C. Vahlas, F. Maury, and L. Gueroudji, *Chem. Vapor Deposition*, 1998, **4**, 69.

287. H. Casellas, D. de Caro, L. Valade, and P. Cassoux, *Chem. Vapor Deposition*, 2002, **8**, 145.

288. F. Hamelmann, G. Haindl, J. Schmalhorst, A. Aschentrup, E. Majkova, U. Kleineberg, U. Heinzmann, A. Klipp, P. Jutzi, A. Anopchenko, M. Jergel, and S. Luby, *Thin Solid Films*, 2000, **358**, 90.

289. W. B. Cross, I. P. Parkin, S. A. O'Neill, P. A. Williams, M. F. Mahon, and K. C. Molloy, *Chem. Mater.*, 2003, **15**, 2786.

290. E. Brescacin, M. Basato, and E. Tondello, *Chem. Mater.*, 1999, **11**, 314.

291. T. W. Bitner and J. I. Zink, *Inorg. Chem.*, 2002, **41**, 967.

292. L. Meda, R. C. Bretkopf, T. E. Haas, and R. U. Kirss, *Thin Solid Films*, 2002, **402**, 126.

293. J. Chen, J. E. Gozum, and G. S. Girolami, *Chem. Mater.*, 1997, **9**, 1847.

294. K. K. Lai and H. H. Lamb, *Chem. Mater.*, 1995, **7**, 2284.

295. J. E. Kelsey, C. Goldberg, G. Nuesca, G. Peterson, A. E. Kaloyeros, and B. Arkles, *J. Vac. Sci. Technol., B*, 1999, **17**, 1101.

296. J.-B. Wu, Y.-W. Yang, Y.-F. Lin, and H.-T. Chiu, *J. Vac. Sci. Technol., A*, 2003, **21**, 1620.

297. D. Studebaker, M. Todd, C. Seegel, and T. H. Baum, *Mater. Sci. Eng., B*, 1998, **56**, 168.

298. J. J. Heremans, M. Carris, S. Watts, X. Yu, K. H. Dahmen, and S. von Molnár, *J. Appl. Phys.*, 1997, **81**, 4967.

299. R. A. Fischer, A. Miehr, M. M. Schulte, and E. Herdtweck, *J. Chem. Soc., Chem. Commun.*, 1995, 337.

300. K. Akiyama, S. Ohya, S. Konuma, K. Numata, and H. Funakubo, *J. Cryst. Growth*, 2002, **237–239**, 1951.

301. M. Mukaida, I. Hiyama, T. Tsunoda, and Y. Imai, *Thin Solid Films*, 2001, **381**, 214.

302. B. Meester, L. Reijnen, A. Goossens, and J. Schoonman, *Chem. Vapor Deposition*, 2000, **6**, 121.

303. J. Vertrone, C. M. Foster, G.-R. Bai, A. Wang, J. Patel, and X. Wu, *J. Mater. Res.*, 1998, **13**, 2281.

304. P. Lu, S. He, F. X. Li, and Q. X. Jia, *Thin Solid Films*, 1999, **340**, 140.

305. Y. Chi, H.-L. Yu, W.-L. Ching, C.-S. Liu, Y.-L. Chen, T.-Y. Chou, S.-M. Peng, and G.-H. Lee, *J. Mater. Chem.*, 2002, **12**, 1363.

306. C.-S. Cheng, M. Serizawa, H. Sakata, and T. Hirayama, *Mater. Chem. Phys.*, 1998, **53**, 225.

307. D. Barreca, C. Massignan, S. Daolio, M. Fabrizio, C. Piccirillo, L. Armelao, and E. Tondello, *Chem. Mater.*, 2001, **13**, 588.

308. S. Pasko, A. Abrutis, L. G. Hubert-Pfalzgraf, and V. Kubilius, *J. Cryst. Growth*, 2004, **262**, 653.

309. H. S. Lee, H. S. Rhee, and B. T. Ahn, *J. Electrochem. Soc.*, 2002, **149**, G16.

310. N. R. M. Crawford, J. S. Knutsen, K.-A. Yang, G. Haugstad, S. McKernan, F. B. McCormick, and W. L. Gladfelter, *Chem. Vapor Deposition*, 1998, **4**, 181.

311. J.-C. Hierso, P. Serp, R. Feurer, and P. Kalck, *Appl. Organomet. Chem.*, 1998, **12**, 161.

312. P. Serp, R. Feurer, R. Morancho, P. Kalck, J.-C. Daran, and J. Vaisserman, *J. Organomet. Chem.*, 1995, **498**, 41.

313. F. Maury and F. Senocq, *Surf. Coat. Technol.*, 2003, **163–164**, 208.

314. V. N. Moorthy, S. Dhara, A. C. Rastogi, B. K. Das, and D. V. S. Jain, *J. Mater. Res.*, 1999, **14**, 1865.

315. K. Shalini, G. N. Subbanna, S. Chandrasekaran, and S. A. Shivashankar, *Thin Solid Films*, 2003, **424**, 56.

316. S. Mathur, M. Veith, V. Sivakov, H. Shen, V. Huch, U. Hartmann, and H.-B. Gao, *Chem. Vapor Deposition*, 2002, **8**, 277.

317. S.-G. Shyu, J.-S. Wu, C.-C. Wu, S.-H. Chuang, and K.-M. Chi, *Inorg. Chim. Acta*, 2002, **334**, 276.

318. R. A. Fischer, M. M. Schulte, and T. Priermeier, *J. Organomet. Chem.*, 1995, **493**, 139.

319. C. E. Zybill and W. Huang, *Inorg. Chim. Acta*, 1999, **291**, 380.

320. K. Fröhlich, V. Cambel, D. Machajdik, P. K. Baumann, J. Lindner, M. Schumacher, and H. Juergensen, *Mater. Sci. Semicond. Proc.*, 2003, **5**, 173.

321. J. J. Kim, M. S. Kim, and D. Y. Yoon, *Chem. Vapor Deposition*, 2003, **9**, 105.

322. T. Shibutami, K. Kawano, N. Oshima, S. Yokoyama, and H. Funakobo, *Electrochem. Solid State Lett.*, 2003, **6**, C117.

323. A. Dadgar, O. Stenzel, L. Köhne, A. Näser, M. Strassburg, W. Stolz, D. Bimberg, and H. Schumann, *J. Cryst. Growth*, 1998, **195**, 69.

324. D. Barreca, A. Buchberger, S. Daolio, L. E. Depero, M. Fabrizio, F. Morandini, G. A. Rizzi, L. Sangaletti, and E. Tondello, *Langmuir*, 1999, **15**, 4537.

325. F.-J. Lee, Y. Chi, C.-S. Liu, P.-F. Hsu, T.-Y. Chou, S.-M. Peng, and G.-H. Lee, *Chem. Vapor Deposition*, 2001, **7**, 99.
326. Y.-H. Lai, T.-Y. Chou, Y.-H. Song, C.-S. Liu, Y. Chi, A. J. Carty, S.-M. Peng, and G.-H. Lee, *Chem. Mater.*, 2003, **15**, 2454.
327. Y. Senzaki, W. L. Gladfelter, and F. B. McCormick, *Chem. Mater.*, 1993, **5**, 1715.
328. Y.-H. Song, Y.-L. Chen, Y. Chi, C.-S. Liu, W.-L. Ching, J.-J. Kai, R.-S. Chen, Y.-S. Huang, and A. J. Carty, *Chem. Vapor Deposition*, 2003, **9**, 162.
329. H.-L. Yu, Y. Chi, C.-S. Liu, S.-M. Peng, and G.-H. Lee, *Chem. Vapor Deposition*, 2001, **7**, 245.
330. S.-F. Huang, Y. Chi, C.-S. Liu, A. J. Carty, K. Mast, C. Bock, B. MacDougall, S.-M. Peng, and G.-H. Lee, *Chem. Vapor Deposition*, 2003, **9**, 157.
331. S.-I. Cho and S.-G. Yoon, *J. Electrochem. Soc.*, 2002, **149**, A1584.
332. S. Gu, P. Atanasova, M. J. Hampden-Smith, and T. T. Kodas, *Thin Solid Films*, 1999, **340**, 45.
333. A. Gulino, G. Fiorito, and I. Fragalà, *J. Mater. Chem.*, 2003, **13**, 861.
334. A. Gulino, P. Dapporto, P. Rossi, and I. Fragalà, *Chem. Mater.*, 2003, **15**, 3748.
335. S. W.-K. Choi and R. J. Puddephatt, *Chem. Mater.*, 1997, **9**, 1191.
336. A. R. Londergan, G. Nuesca, C. Goldberg, G. Peterson, A. E. Kaloyeros, B. Arkles, and J. J. Sullivan, *J. Electrochem. Soc.*, 2001, **148**, C21.
337. R. S. Dickson, P. Yin, M. Ke, J. Johnson, and G. B. Deacon, *Polyhedron*, 1996, **15**, 2237.
338. H. Choi and S. Park, *Chem. Mater.*, 2003, **15**, 3121.
339. D. G. Colombo, D. C. Gilmer, V. G. Young, Jr, S. A. Campbell, and W. L. Gladfelter *Chem. Vapor Deposition*, 1998, **4**, 220.
340. B. S. Lim, A. Rahtu, and R. G. Gordon, *Nat. Mater.*, 2003, **2**, 749.
341. C. Vahlas, F. Juarez, R. Geurer, P. Serp, and B. Caussat, *Chem. Vapor Deposition*, 2002, **8**, 127.
342. J.-C. Hierso, R. Feurer, and P. Kalck, *Coord. Chem. Rev.*, 1998, **178–180**, 1811.
343. R. Kumar and R. J. Puddephatt, *Can. J. Chem.*, 1991, **69**, 108.
344. E. L. Crane, Y. You, R. G. Nuzzo, and G. S. Girolami, *J. Am. Chem. Soc.*, 2000, **122**, 3422.
345. Y.-M. Sun, J. P. Endle, K. Smith, S. Whaley, R. Mahaffy, J. G. Ekerdt, J. M. White, and R. L. Hance, *Thin Solid Films*, 1999, **346**, 100.
346. T. Gerfin, W. J. Haelg, F. Atamny, and K.-H. Dahmen, *Thin Solid Films*, 1994, **241**, 352.
347. Y.-L. Chen, C.-S. Liu, Y. Chi, A. J. Carty, S.-M. Peng, and G.-H. Lee, *Chem. Vapor Deposition*, 2002, **8**, 17.
348. P. Serp, R. Feurer, P. Kalck, H. Gomez, J. L. Faria, and J. L. Figueiredo, *Chem. Vapor Deposition*, 2001, **7**, 59.
349. P. A. Lane, M. J. Crosbie, P. J. Wright, P. P. Donohue, P. J. Hirst, C. L. Reeves, C. J. Anthony, A. C. Jones, M. A. Todd, and D. J. Williams, *Chem. Vapor Deposition*, 2003, **9**, 87.
350. L. Brissoneau and C. Vahlas, *Chem. Vapor Deposition*, 1999, **5**, 135.
351. V. Bhaskaran, P. Atanasova, M. J. Hampden-Smith, and T. T. Kodas, *Chem. Mater.*, 1997, **9**, 2822.
352. N. L. Jeon, W. Lin, M. K. Erhardt, G. S. Girolami, and R. G. Nuzzo, *Langmuir*, 1997, **13**, 3833.
353. M. Hiratani, T. Nabatame, Y. Matsui, and S. Kimura, *Thin Solid Films*, 2002, **410**, 200.
354. Y. Senzaki, A. K. Hochberg, and J. A. T. Norman, *Adv. Mater. Opt. Electron.*, 2000, **10**, 93.
355. C. Colominas, K. H. Lau, D. L. Hildenbrand, S. Crouch-Baker, and A. Sanjuro, *J. Chem. Eng. Data*, 2001, **46**, 446.
356. D. A. Edwards, R. M. Harker, M. F. Mahon, and K. C. Molloy, *J. Mater. Chem.*, 1999, **9**, 1771.
357. S. Samoilenkov, M. Stefan, G. Wahl, S. Paramonov, H. Kuzmina, and A. Kaul, *Chem. Vapor Deposition*, 2002, **8**, 74.
358. H. Uchida, N. Saitou, M. Satou, M. Tebakari, and K. Ogi, *Mater. Res. Soc. Symp. Proc.*, 1994, **334**, 293.
359. Y.-J. Chen and C.-T. Yeh, *J. Catalysis*, 2001, **200**, 59.
360. L. Brissonneau and C. Vahlas, *Ann. Chim. Sci. Mater.*, 2000, **25**, 81.
361. M. Urrutigoïty, C. Cecutti, F. Senocq, J.-P. Gorrichon, and A. Gleizes, *Inorg. Chim. Acta*, 1996, **248**, 15.
362. J. D. Martin, P. Hogan, K. A. Abboud, and K.-H. Dahmen, *Chem. Mater.*, 1998, **10**, 2525.
363. F. Senocq, M. Urrutigoïty, Y. Caubel, J.-P. Gorrichon, and A. Gleizes, *Inorg. Chim. Acta*, 1999, **288**, 233.
364. P. O'Brien, J. H. Park, and J. Waters, *Thin Solid Films*, 2003, **431–432**, 502.
365. R. A. Fischer, M. Kleine, O. Lehmann, and M. Stuke, *Chem. Mater.*, 1995, **7**, 1863.
366. B. Fraser, L. Brandt, W. K. Stovall, H. D. Kaesz, S. I. Khan, and F. Maury, *J. Organomet. Chem.*, 1994, **472**, 317.
367. J. R. V. Garcia and T. Goto, *Mater. Trans.*, 2003, **44**, 1717.
368. M. Feng and R. J. Puddephatt, *Chem. Mater.*, 2003, **15**, 2696.
369. Z. Yuan, D. Jiang, S. J. Naftel, T.-K. Sham, and R. J. Puddephatt, *Chem. Mater.*, 1994, **6**, 2151.
370. C. D. Tagge, R. D. Simpson, R. G. Bergman, M. J. Hostetler, G. S. Girolami, and R. G. Nuzzo, *J. Am. Chem. Soc.*, 1996, **118**, 2634.
371. J. Goswami, C.-G. Wang, W. Cao, and S. K. Dey, *Chem. Vapor Deposition*, 2003, **9**, 213.
372. W.-G. Choi, E.-U. Choi, and S.-G. Yoon, *Chem. Vapor Deposition*, 2003, **9**, 321.

373. G. Y. Meng, L. Huang, M. Pan, C. S. Chen, and D. K. Peng, *Mater. Res. Bull.*, 1997, **32**, 385.
374. G. Malandrino, R. Lo Nigro, and I. L. Fragalà, *Chem. Vapor Deposition*, 1999, **5**, 59.
375. J.-C. Hierso, C. Satto, R. Feurer, and P. Kalck, *Chem. Mater.*, 1996, **8**, 2481.
376. C. Xu, M. J. Hampden-Smith, T. T. Kodas, E. N. Duesler, A. L. Rheingold, and G. Yap, *Inorg. Chem.*, 1995, **34**, 4767.
377. Y. Zhang, Z. Yuan, and R. J. Puddephatt, *Chem. Mater.*, 1998, **10**, 2293.
378. Y.-S. Liu, Y.-C. Cheng, Y.-L. Tung, Y. Chi, Y.-L. Chen, C.-S. Liu, S.-M. Peng, and G.-H. Lee, *J. Mater. Chem.*, 2003, **13**, 135.
379. Y.-L. Tung, W.-C. Tseng, C.-Y. Lee, P.-F. Hsu, Y. Chi, S.-M. Peng, and G.-H. Lee, *Organometallics*, 1999, **18**, 864.
380. G. Rossetto, P. Zanella, G. Carta, R. Bertani, D. Favretto, and G. M. Ingo, *Appl. Organomet. Chem.*, 1999, **13**, 509.
381. U. Weckenmann, S. Mittler, S. Kramer, A. K. A. Aliganga, and R. A. Fischer, *Chem. Mater.*, 2004, **16**, 621.
382. V. N. Vertoprakhov and S. A. Krupoder, *Russ. Chem. Rev.*, 2000, **69**, 1057.
383. W. H. Lee, B. S. Seo, I. J. Byun, Y. G. Ko, J. Y. Kim, J. G. Lee, and E. G. Lee, *J. Kor. Phys. Soc.*, 2002, **40**, 107.
384. W. Lee, I. J. Byun, B. Seo, and J. Lee, *Proc. Electrochem. Soc.*, 2001, **2000–27**, 47.
385. C.-H. Jun, Y. T. Kim, J.-T. Baek, H. J. Yoo, and D.-R. Kim, *J. Vac. Sci. Technol., A*, 1996, **14**, 3214.
386. T.-Y. Chen, J. Vaissermann, E. Ruiz, J. P. Sénateur, and P. Doppelt, *Chem. Mater.*, 2001, **13**, 3993.
387. K.-K. Choi and S.-W. Rhee, *Thin Solid Films*, 2002, **409**, 147.
388. G. G. Condorelli, G. Malandrino, and I. L. Fragalà, *Chem. Vapor Deposition*, 1999, **5**, 21.
389. L. Reijnen, B. Meester, A. Goossens, and J. Schoonman, *Chem. Vapor Deposition*, 2003, **9**, 15.
390. P.-F. Hsu, Y. Chi, T.-W. Lin, C.-S. Liu, A. J. Carty, and S.-M. Peng, *Chem. Vapor Deposition*, 2001, **7**, 28.
391. R. Becker, A. Devi, J. Weiss, U. Weckenmann, M. Winter, C. Kiener, H.-W. Becker, and R. A. Fischer, *Chem. Vapor Deposition*, 2003, **9**, 149.
392. Y. Chi, P.-F. Hsu, C.-S. Liu, W.-L. Ching, T.-Y. Chou, A. J. Carty, S.-M. Peng, G.-H. Lee, and S.-H. Chuang, *J. Mater. Chem.*, 2002, **12**, 3541.
393. E. C. Plappert, T. Stumm, H. Van den Bergh, R. Hauert, and K.-H. Dahmen, *Chem. Vapor Deposition*, 1997, **3**, 37.
394. F. Maury, S. Vidal, and A. Gleizes, *Adv. Mater. Opt. Electron.*, 2000, **10**, 123.
395. W. Lin, T. H. Warren, R. G. Nuzzo, and G. S. Girolami, *J. Am. Chem. Soc.*, 1993, **115**, 11644.
396. C. Xu, M. J. Hampden-Smith, and T. T. Kodas, *Chem. Mater.*, 1995, **7**, 1539.
397. K.-M. Chi and Y.-H. Lu, *Chem. Vapor Deposition*, 2001, **7**, 117.
398. A. Itsuki, H. Uchida, M. Satou, and K. Ogi, *Nucl. Instr. Methods Phys. Res. B*, 1997, **121**, 116.
399. N. H. Dryden, J. J. Vittal, and R. J. Puddephatt, *Chem. Mater.*, 1993, **5**, 765.
400. K.-M. Chi, K.-H. Chen, S.-M. Peng, and G.-H. Lee, *Organometallics*, 1996, **15**, 2575.
401. M. E. Fragalà, G. Malandrino, O. Puglisi, and C. Benelli, *Chem. Mater.*, 2000, **12**, 290.
402. E. T. Eisenbraun, A. Klaver, Z. Patel, G. Nuesca, and A. E. Kaloyeros, *J. Vac. Sci. Technol., B*, 2001, **19**, 585.
403. E. Szlyk, P. Piszczeck, A. Grodzicki, M. Chaberski, A. Golinski, J. Szatkowski, and T. Blaszczyk, *Chem. Vapor Deposition*, 2001, **7**, 111.
404. H. Schmidt, Y. Shen, M. Leschke, T. Haase, K. Kohse-Hoinghaus, and H. Lang, *J. Organomet. Chem.*, 2003, **669**, 25.
405. D. A. Edwards, M. F. Mahon, K. C. Molloy, and V. Ogrodnik, *J. Mater. Chem.*, 2003, **13**, 563.
406. T. C. Deivaraj, J.-H. Park, M. Afzaal, P. O'Brien, and J. J. Vittal, *Chem. Mater.*, 2003, **15**, 2383.
407. K. K. Banger, M. H.-C. Jin, J. D. Harris, P. E. Fanwick, and A. F. Hepp, *Inorg. Chem.*, 2003, **42**, 7713.
408. C. Winter, U. Weckenmann, R. A. Fischer, J. Käshammer, V. Scheumann, and S. Mittler, *Chem. Vapor Deposition*, 2000, **6**, 199.
409. D. W. Allen and J. Haigh, *Appl. Organomet. Chem.*, 1995, **9**, 83.
410. F. Jansen and T. Kruck, *Adv. Mater.*, 1995, **7**, 297.
411. E. Szlyk, P. Piszczek, I. Lakomska, A. Grodzicki, J. Szatkowski, and T. Blaszczyk, *Chem. Vapor Deposition*, 2000, **6**, 105.

Acknowledgment

The authors are grateful for grants from the National Science Foundation, the Office of Naval Research, and the Army Research Office that have supported metal-organic precursor development work in their laboratory.

Metalloregulation

Tracey A. Rouault[1] **& Caroline C. Philpott**[2]

[1]*National Institute of Child Health and Human Development, National Institutes of Health, Bethesda, MD, USA*
[2]*National Institute of Diabetes and Digestive and Kidney Diseases, National Institutes of Health, Bethesda, MD, USA*

Based in part on the article Metalloregulation by Robert P. Hausinger which appeared in the Encyclopedia of Inorganic Chemistry, First Edition.

1 Introduction 1
2 Regulation of Iron Metabolism 2
3 Regulation of Zinc Metabolism 13
4 Regulation of Copper, Manganese and Nickel Homeostasis 14
5 Related Articles 14
6 References 14

1 INTRODUCTION

Metalloregulation refers to the concept that living organisms from bacteria to mammals must orchestrate the processes of metal import, utilization, sequestration, and export to optimize availability of metals for use in metabolism, while avoiding the toxicity that may arise from reactivity of free metal ions with the protein, nucleic acid and lipid contents of cells. Metalloregulation is necessary because virtually all cells and organisms require transition metals to facilitate basic cellular processes such as respiration and DNA biosynthesis. Proteins that incorporate metals such as iron, copper, and zinc into their structures gain various chemical reactivity and structural properties that they would not otherwise possess. As an example of how metals contribute to metabolism, iron and copper proteins allow cells to make efficient use of oxygen by activating oxygen and allowing it to readily participate in single electron transfer reactions.[1] Life on earth depends largely on the energy captured from complete oxidation of glucose by oxygen, but direct reactions between oxygen and organic molecules are energetically unfavorable in the absence of transition metals. In respiration, iron and copper proteins capture energy released from oxidation of food by synthesizing high-energy compounds such as NADH that are used to fuel cellular metabolism. Iron also enables hemoglobin in red cells of mammals to bind and transport oxygen to tissues throughout the body.[2]

To ensure that metals are available in non-toxic forms, complex regulatory systems have evolved to promote appropriate acquisition, distribution, and excretion of indispensable metals such as iron, copper, zinc, and manganese in organisms from all the kingdoms of life. In this chapter, we will discuss the mechanisms by which cells and organisms gauge their metal status and how they mobilize an appropriate response. In general, one or several proteins interact directly with the metal that requires regulation, and these metal-binding proteins then effect changes in transcription, mRNA stability, translation, protein stability, or subcellular localization of metal transporters and sequestration proteins. In general, metals are transported across lipid bilayers by unidirectional transporters that discriminate amongst the various metals. The rate of metal transport is determined by the level of expression of the transporter and/or an associated reductase, and expression levels change according to cellular needs.

In different organisms, different combinations of regulatory strategies are employed. As cells and organisms increase in their organizational complexity, more processes are subject to regulation. In prokaryotes, metals that reach the cytosol are readily made available to proteins involved in energy metabolism, replication and other important processes, because all of these processes are carried out within the bacterial cytosolic compartment. In eukaryotes, metals that cross the plasma membrane must traverse another membrane or set of membranes to reach organelles such as mitochondria, chloroplasts, the vacuole, peroxisomes, and endoplasmic reticulum. Not only do these membrane bound compartments require metal importers and exporters, but they must also possess a means of coordinating organellar metal homeostasis. At this point, little is known about the mechanisms by which appropriate organellar metal homeostasis is maintained. As will be discussed later, misregulation of organellar iron homeostasis causes some important human diseases, and elucidation of regulatory mechanisms that govern organellar iron homeostasis represents an important frontier in metalloregulation research.

In multicellular organisms, regulatory challenges are even more complex than those in unicellular eukaryotes, because regulation of metal uptake and excretion must also be exerted at the level of the whole organism. Uptake of dietary metals is regulated in the guts of animals, and uptake of metals from soil is regulated in the roots of plants. Thus, complex organisms need mechanisms that enable them to transmit information about overall organismal metal status to cells that are in direct contact with environmental metal sources. In mammals, tissues such as liver and spleen that are open to circulation of blood can synthesize factors that reflect their iron status, and these factors can then be transported through the circulation to the duodenum, the site of the mammalian gut in which most micronutrients are absorbed. To further add to the complexity of mammalian metalloregulation, some organs are separated from direct contact with circulating blood by layers of epithelial cells that are tightly attached to one another, forming a membrane that factors in the circulating blood cannot freely cross. These epithelial barriers, known as the blood-brain barrier and the blood-testis barrier, protect the brain and testis from exposure to toxins in the bloodstream.

Because these compartments are separated from the rest of the organism by epithelial cell layers with tight junctions between cells, these compartments must manage metal uptake and regulate metal homeostasis to appropriately meet the needs of these tissues.

In this article, we will focus mainly on the mechanisms of iron and zinc regulation, because regulation of these two metals illustrates many basic principles. We will also reference reviews that address regulation of copper and manganese metabolism, but regulation of these metals will not be discussed in depth here, in part because they will be discussed elsewhere.

2 REGULATION OF IRON METABOLISM

2.1 The Importance of Transcriptional Regulation in Unicellular Iron Metabolism

Free-living microorganisms and plants must overcome significant environmental barriers in order to use iron. In an aerobic atmosphere, iron is present in soil and water in the form of ferric oxyhydroxides, which have a very low solubility of 10^{-9} M at neutral pH.[3] This very low solubility means that iron is not typically present at a concentration that permits uptake through permeases that have micromolar or high nanomolar affinity. Three strategies are available to these organisms to increase the solubility of iron: (1) acidification of the environment, (2) reduction of ferric iron to the more soluble ferrous form, and (3) secretion of soluble iron-chelating molecules. All of these strategies are used to varying extents by microorganisms and plants, which often simultaneously employ multiple distinct iron-uptake systems.[4] These systems of iron uptake, as well as other proteins of the iron homeostatic machinery, are precisely regulated to adjust to iron availability and the cellular requirements for iron. In general, high-affinity iron acquisition systems are homeostatically regulated. That is, under conditions of iron scarcity, iron acquisition systems are expressed at high levels, and under conditions of iron abundance, these systems are expressed at very low levels. When iron is freely available, uptake occurs primarily through low-affinity uptake systems that may have broad metal specificity.

2.1.1 Iron Homeostasis in Bacteria

The iron acquisition systems of *E. coli* and many other bacteria are regulated at the level of RNA transcription by Fur (ferric uptake regulator), a transcriptional repressor that exhibits ferrous iron-dependent, DNA-binding activity.[5] Fur is expressed as a 17 kDa homodimer and, under conditions of iron sufficiency, it binds one iron ion per subunit, which increases its affinity for its preferred DNA binding sites by 1000-fold.[6] In some bacteria, Fur also contains one structural zinc ion per dimer. Under iron sufficient conditions, Fe^{2+}-Fur binds to specific promoter regions (known as Fur boxes) and represses the transcription of many genes. The genes directly repressed by Fur binding include those involved in the acquisition of iron, as well as numerous genes involved in other cellular processes. Under conditions of iron scarcity, Fur is present in the iron-free form and does not bind to DNA, thereby allowing the active transcription of the Fur-controlled genes. Fur also indirectly controls the iron-dependent induction of several proteins that store iron or require iron-containing prosthetic groups for activity by regulating transcription of a small regulatory RNA known as RyhB.[7] Under conditions of iron deprivation, *ryhB* is actively transcribed because Fur does not repress transcription from its promoter. This small RNA, RyhB, in conjunction with the RNA binding protein Hfq, mediates the degradation of messages encoding proteins of iron utilization (such as the Fe-S proteins succinate dehydrogenase, fumarase, and aconitase) and storage (such as the ferritins encoded by *ftnA* and *bfr*) by binding to complementary regions of the target RNAs. Because Fe^{2+}-Fur represses the transcription of *ryhB* under iron sufficient conditions, the RyhB target messages are not degraded and can be translated into proteins. The effect of RyhB expression is to prevent the synthesis of non-essential, iron-requiring proteins when iron is scarce.

Gram-positive bacteria utilize several different iron regulatory systems. In some Gram-positive bacteria, the DtxR (diphtheria toxin regulator) controls the expression of iron-regulated genes. Although DtxR exhibits little to no homology to Fur, it also acts as a Fe^{2+}-sensing transcriptional repressor.[8] Thus, different types of bacteria can coordinate the response to iron deprivation through the activity of a single iron-sensing transcription factor.

Under conditions of iron scarcity, bacteria express several high-affinity uptake systems that permit them to utilize iron from a variety of sources. Uptake of siderophore-iron chelates constitutes the primary source of iron for bacteria as well as fungi and some plants. Siderophores are low-molecular weight compounds that chelate ferric iron with very high affinity and specificity (*see* ***Iron Transport: Siderophores***). These compounds are synthesized and secreted in the iron-free form by bacteria, most fungi, and some plants. Secreted siderophores can then bind and solubilize ferric iron in the environment, and iron-siderophore chelates can be captured by specific cellular transport systems. Although microorganisms typically synthesize one or, at most, a few types of siderophores, they often express receptors for a variety of siderophores secreted by other organisms. Siderophores exhibit a variety of chemical structures, but the most common fall into two classes, the hydroxamates, which are synthesized primarily by fungi, and the catecholates, which are synthesized primarily by bacteria (Figure 1) (*see* ***Iron Transport: Siderophores***).

In Gram-negative bacteria, iron uptake is a complex process because siderophore uptake systems must facilitate

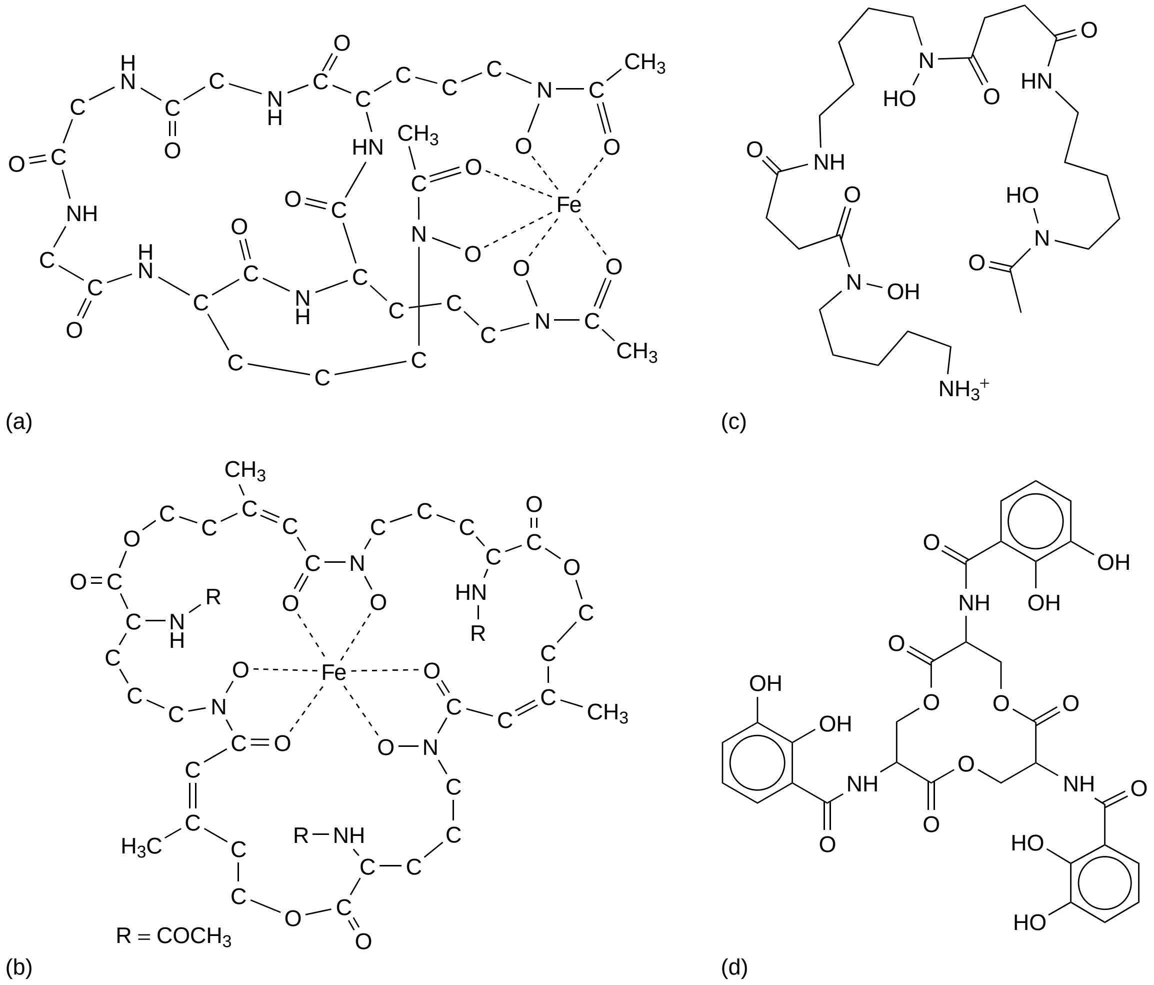

Figure 1 Representative siderophores of the hydroxamate and catecholate classes. The hydroxamates are synthesized from the amino acid ornithine that has been modified through hydroxylation and acetylation. Ferrichrome (a) is a prototypical example of the tri-hydroxamate class. Structurally, ferrichrome is a cyclic hexapeptide that consists of three modified ornithine residues (each of which has a hydroxamate side chain) and three glycines. Ferrichrome coordinates ferric iron through its three bidentate hydroxamate side chains. Triacetylfusarinine C (b) is also a cyclic tri-hydroxamate, but the three modified ornithine residues are joined by ester linkages rather than by peptide linkages. Ferrioxamine B (c) is a linear tri-hydroxamate consisting of three peptide-linked modified ornithine residues. Enterobactin (d) is a prototypical example of a catecholate siderophore. It consists of a tri-ester ring from which extend three side chains of dihydroxybenzoyl serine. Each of these siderophores binds ferric iron in a hexadentate manner, which results in full saturation of d orbitals and a very stable complex. Ferric forms are shown in (a) and (b). Desferri-forms are shown in (c) and (d)

the transport of iron across an outer membrane (OM), the periplasmic space, and an inner cytoplasmic membrane (CM) (Figure 2). Transport processes across the CM can be energized directly through the hydrolysis of cytosolic ATP or through the membrane potential generated by proton-ATPases. The outer membrane contains no energy source, however, and Gram-negative bacteria have evolved a system to overcome this energy barrier to transport. These bacteria have evolved four distinct components that facilitate the process of siderophore transport: 1) outer membrane receptors that bring siderophore-bound iron across the outer membrane to the periplasmic space, 2) an energy transmission system that conveys energy from the CM to the OM, 3) binding proteins that escort ferric siderophores across the periplasmic space to their respective CM transporters, and 4) CM transporters that carry the ferric siderophore into the cytosol of the cell (Figure 2).

Siderophore-bound iron is taken up through specific, high-affinity outer membrane receptors. Although the term ‘receptor’ is used to refer to this group of proteins, their activity goes beyond binding their siderophore ligands, as they also permit the movement of siderophore across the OM to the periplasmic space. *E. coli* K-12 expresses at least six OM receptors that exhibit specificity for a variety of siderophores and iron chelates, including enterobactin, an endogenously produced siderophore, and ferrichrome, a fungal siderophore.[6]

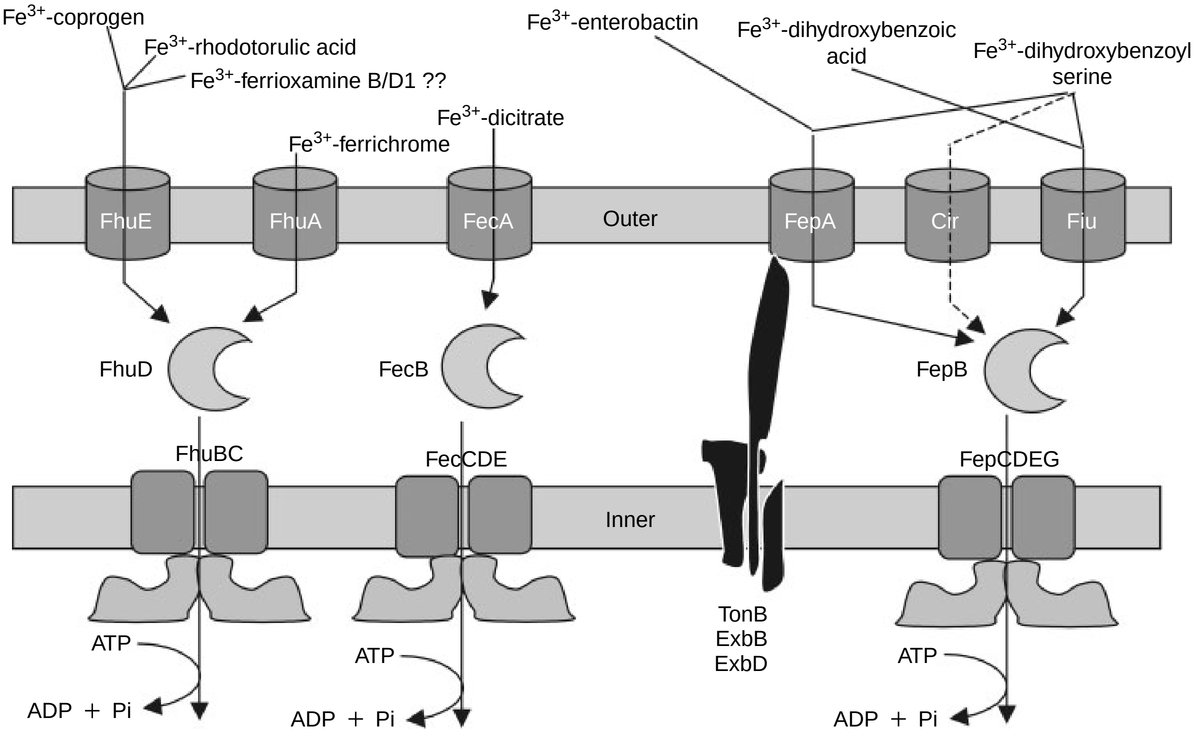

Figure 2 Siderophore-mediated iron-uptake systems in *E. coli*. Siderophore–iron complexes bind to transporter proteins located in the outer membrane (also known as OM), a barrier that is characteristic of Gram-negative bacteria. The region between the outer and inner is known as the periplasmic space. Specific carrier proteins such as FhuD transport iron from the outer membrane to the inner or cytosolic membrane (also known as CM). The TonB/ExbB/ExbD complex spans the inner and outer membranes and interacts with FepA, as shown, as well as all of the outer membrane receptors. The linkage that the TonB/ExbB/ExbD complex provides between the inner or cytosolic membrane to the outer membrane is thought to allow transmission of sufficient energy from the cytosol to drive siderophore-iron uptake across the outer membrane

Microorganisms typically express uptake systems specific for the siderophores that they synthesize as well as siderophores synthesized by other microbes, a strategy that allows them to compete for iron in an environment containing multiple microbial species. The structures of three OM receptors (FecA, FepA, and FhuA) are very similar to one another in that they are all β-barrel proteins containing 22 antiparallel β-strands that form a tube.[9] The N-terminus forms a mobile globular domain that can occupy and occlude the channel formed in the center of the tube. When FhuA binds the ferrichrome near the outer surface of the central channel, major conformational changes occur both at the outer surface and on the periplasmic face of the receptor. The position of the globular ‘cork’ domain then shifts to allow the bound siderophore to translocate across the membrane.

The energy that drives the proposed conformational change of the OM receptor may be transmitted to the OM by a complex of proteins anchored in the CM known as the TonB complex. Energy stored in the proton gradient of the CM may be transmitted to the OM receptors via the TonB/ExbB/ExbD complex.[9] *E. coli* expresses TonB, ExbB, and ExbD in a 1:7:2 ratio and together they form a complex of integral membrane proteins anchored in the CM. TonB extends from the CM across the periplasmic space to contact the periplasmic face of each of the OM siderophore receptors. There, TonB may induce a conformational change in the siderophore-bound form of the receptor that results in the transfer of siderophore to the periplasmic space. ExbB and ExbD form a complex with TonB within the CM and together they may enable TonB to mediate this conformational change.

Siderophores within the periplasmic space interact with periplasmic binding proteins (FhuD, FecB, and FepB in *E. coli*) that recognize a variety of siderophore substrates and bind them with micromolar affinity.[6,9] These periplasmic siderophore binding proteins are required to escort the siderophore-iron chelates to their respective siderophore-specific permease complexes in the CM. Structural studies of FhuD indicate that the periplasmic binding proteins are bilobal structures that bind siderophore in a shallow pocket between the two lobes. Amino acid residues in the binding pocket of FhuD interact with the iron-binding hydroxamate region of the siderophore, rather than its peptide backbone, thereby allowing the binding protein to recognize a variety of hydroxamate-type siderophores.

Uptake of the siderophore across the CM is dependent on specific ABC permease complexes. Each CM permease complex consists of four subunits: two identical or homologous integral membrane permeases and two cytoplasmic ATPases of the ATP-binding cassette (ABC) family that associate with the cytosolic faces of the permeases.[6,9] These complexes transport ferric siderophores, ferric citrate, and heme, although with less specificity than is observed in the OM receptors. Details of the process of siderophore transport across the CM are not known, but these transporters are presumed to operate similarly to the ABC transporters of maltose or vitamin B_{12}. On the basis of the structure of BtuCD, the vitamin B_{12} transporter, the integral membrane permeases are presumed to form a channel that is closed at the cytoplasmic surface.[10] The complex formed by association of the periplasmic binding protein with the ferric siderophore binds to the channel at the outer surface of the integral membrane permease of the CM, forming a cap that prevents leakage of the siderophore back into the periplasm. This binding of the complex also triggers the hydrolysis of ATP by the cytosolic ATP-binding cassettes, resulting in opening of the cytosolic face of the channel and the internalization of the siderophore.

Bacteria without an OM, such as Gram-positives, do not rely on OM receptors or periplasmic binding proteins for siderophore uptake.[6] Instead, extracellular ferric siderophores are bound by CM-anchored binding proteins that are similar to the periplasmic binding proteins, which then interact with ABC-type transport complexes similar to those employed by Gram-negative bacteria. Once internalized, iron is released from ferric siderophores by the activities of specific cytosolic esterases or reductases.

The ferric citrate transport system of *E. coli* is similar to the siderophore transport systems and is also subject to Fur-mediated regulation, but it is also specifically regulated at the transcriptional level by an independent mechanism dependent on the sigma factor FecI.[6] Sigma factors comprise a conserved family of bacterial proteins that specifically interact with promoter regions of genes and with RNA polymerase to stimulate transcription. When ferric citrate binds to its OM receptor (FecA), FecR senses binding, as FecR spans the CM and contains both a periplasmic N-terminal domain that interacts with FecA and a cytosolic C-terminal domain that mediates the activation of FecI. Activated FecI then induces the transcription of *fecABCD*, which encodes the ferric citrate uptake system.

Bacteria also express ferrous iron-uptake systems such as that encoded by *feoABC* of *E. coli* and other enteric pathogens.[6] These are unlike the siderophore-specific systems and are primarily expressed during growth under low oxygen tension, when ferrous iron is much more abundant than the oxidized, ferric form. FeoB contains an N-terminal GTPase domain that is required for ferrous iron uptake. It also contains 8–12 predicted membrane-spanning alpha helices in the C-terminal domain and may employ GTP hydrolysis to energize ferrous iron uptake. Ferrous iron uptake systems can be coupled with extracellular ferric reductases, which enable microbes to convert ferric iron to the reduced form before uptake by ferrous-specific systems. Although many bacteria have biochemically demonstrable ferric reductase activities, the genes encoding these proteins have not been identified.

Pathogenic bacteria are capable of using host iron proteins as nutritional sources of iron. OM receptors for the mammalian ferric iron-binding proteins transferrin and lactoferrin as well as heme and hemoglobin have been identified in a number of bacterial species. In the case of transferrin and lactoferrin, the OM receptors are composed of two subunits, one of which is homologous to the siderophore OM receptors and probably mediates transfer of the iron across the OM, and another that is structurally quite distinct. Initially iron is removed from Fe-transferrin and Fe-lactoferrin by the OM receptor, and the newly released iron is transferred across the periplasmic space via a ferric binding protein to a ferric-iron-specific ABC permease, which transports the iron into cytosol. Heme iron is taken up as an intact molecule after interacting with heme-specific OM receptors in a TonB-dependent manner. No periplasmic binding protein for heme is required and heme, like iron, is transferred into the cytosol by an ABC permease. Cytosolic heme can apparently be incorporated directly into heme proteins, or the iron can be released from heme after degradation by heme oxygenase. Cytosolic iron can then be diverted into ferritins for storage, utilized by heme or iron–sulfur cluster biosynthetic machinery, or directly incorporated into other iron–binding proteins.

2.1.2 *Iron Homeostasis in Fungi*

Unicellular eukaryotes, such as yeast and fungi, differ fundamentally from prokaryotes in that they contain multiple membrane bound organelles. The significance of this difference in terms of iron homeostasis is that fungi must not only coordinate uptake of iron with the metabolic demands of the cell, but they must also coordinate and regulate distribution of iron to different compartments within the cell. Metal metabolism has been studied in greatest detail in the model organism *Saccharomyces cerevisiae*, also known as baker's yeast, although molecular details of metal metabolism in other fungi are beginning to emerge. Under iron replete conditions, yeast import iron through low-affinity metal transporters of low specificity, such as Fet4p.[11] Excess iron and manganese are transferred to the vacuole for storage by the vacuolar transporter Ccc1p.[12] The response of baker's yeast to iron depletion includes up-regulation of high-affinity iron acquisition systems, mobilization of iron stores, sequestration of other metals, reutilization of heme iron, and down-regulation of non-essential, iron-consuming pathways.[13] These responses are primarily controlled at the transcriptional level by the transcriptional activator Aft1p.

Aft1p is a 78 kDa protein that binds to specific sites within the promoters of iron regulated genes and activates

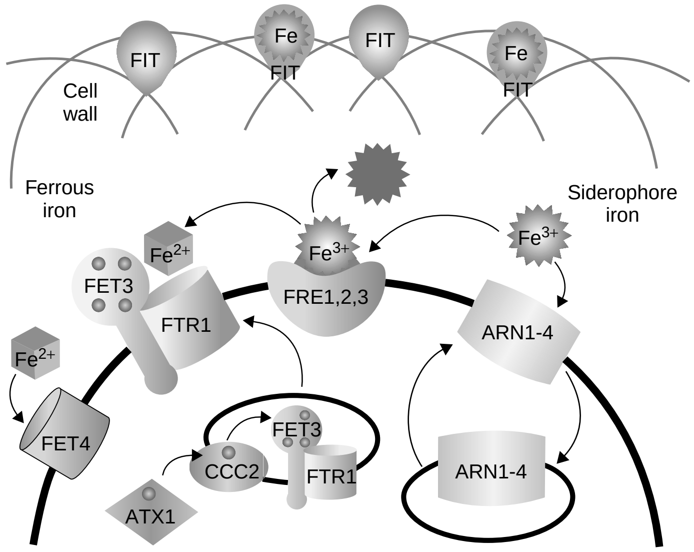

Figure 3 Iron-uptake systems of *S. cerevisiae*. The plasma membrane of yeast is surrounded by a porous cell wall that protects the cell from osmotic lysis and excludes only larger macromolecules. The *FIT* mannoproteins of the cell wall facilitate retention of siderophore-iron in the cell wall, but are not required for siderophore uptake. Many siderophores likely cross the cell wall through nonspecific pores. Siderophore-bound iron can be reduced and released from the siderophore by the *FRE* reductases. Reduced iron can then be taken up through either the high-affinity ferrous iron transporter (the Fet3p and Ftr1p complex) or the low-affinity transporter (Fet4). Ferric iron salts and low-affinity chelates are also reduced by the *FRE* reductases prior to uptake. Fet3p is a ferroxidase that requires copper for function. Fet3p does not become functional until it is loaded with copper intracellularly through the activities of the copper chaperone Atx1p and the copper transporter Ccc2p. Although the Fet3p/ Ftr1p complex mediates uptake of much of the iron released from siderophores, there is also another uptake route. Intact siderophore-iron chelates can be taken up via members of the *ARN* transporter family. The Arn transporter binds siderophore-iron, and the transporter-siderophore complex undergoes endocytosis prior to translocation of the siderophore-iron chelate across the membrane

transcription.[14] The N-terminal half of Aft1p contains a DNA-binding domain and the C-terminal half contains a transcriptional activation domain. Although the levels of Aft1p do not change with iron depletion or iron sufficiency, the subcellular localization and DNA binding activity of Aft1p is regulated by iron.[15] Aft1p is located in the cytosol and is inactive in iron-replete cells. Under conditions of iron deficiency, Aft1p translocates to the nucleus to activate transcription. Aft1p was initially identified as a dominant mutant allele, termed Aft1-1$^{\text{up}}$, which contains a cysteine to phenylalanine mutation in the center of the coding region. Expression of Aft1-1$^{\text{up}}$ results in nuclear localization and transcriptional activation under conditions of iron sufficiency as well as iron deficiency.[15] A recent report indicates that mutant yeast strains with defects in heme biosynthesis are also defective in the transcription of Aft1p target genes, indicating that heme may play a role in Aft1p-dependent transcription.[16] Although Aft1p appears to act as an iron sensor in yeast, it is not known how iron is sensed or whether Aft1p binds iron. A second transcription factor with homology to Aft1p is Aft2p. Aft2p activates the transcription of a subset of the Aft1 target genes as well as a unique set of genes.[14] The role of Aft2p in iron homeostasis is not yet clear.

Aft1p target genes contain a heptanucleotide promoter sequence termed the iron-responsive element, PyPuCACCC. Most of these genes are involved, either directly or indirectly, in the uptake of iron at the plasma membrane (Figure 3). A family of cell wall proteins encoded by *FIT1*, *FIT2*, and *FIT3* is involved in the retention of siderophore-iron complexes in the yeast cell wall and the facilitation of the uptake of iron.[17] Two systems of high-affinity iron uptake are expressed in baker's yeast: one relies on the external reduction of ferric iron before uptake through a ferrous-specific transporter whereas the other relies on the direct uptake of ferric-siderophore complexes (reviewed in[18,19]). The reductive system of uptake begins with the reduction of ferric ions and ferric chelates by members of the *FRE* family of plasma membrane metalloreductases. Four members of this family catalyze the reduction of either ferric ions (Fre1p and Fre2p) or ferric siderophore chelates (Fre1p, Fre2p, Fre3p, and Fre4p). Two additional family members (Fre5p and Fre6p) have not been characterized and a seventh (Fre7p) is regulated by copper through Mac1p and is presumed to function in copper homeostasis. Reduced iron is taken up through a high-affinity transporter complex consisting of the Fet3p multicopper oxidase and the Ftr1p permease.[11] The oxidase activity of Fet3p is required for transport and the activities of the copper chaperone Atx1p and the intracellular copper transporter Ccc2p are required for copper loading of Fet3p.

The nonreductive system of iron uptake in *S. cerevisiae* is specific for ferric-siderophore complexes.[18] Although

S. cerevisiae and *Schizosaccharomyces pombe* do not synthesize or secrete siderophores, both species are capable of taking up siderophore-iron chelates. *S. cerevisiae* relies on a subfamily of four transporters of the major facilitator superfamily for siderophore uptake, and these are termed Arn1p, Arn2p/Taf1p, Arn3p/Sit1p, and Arn4p/Enb1p. These secondary transporters are predicted to contain 14 transmembrane domains and are likely energized by proton symport. Each of the Arn transporters exhibits specificity for different siderophores of the hydroxamate or catecholate class, with some overlapping specificity. Arn1p exhibits specificity for ferrichromes, Arn2p for fusarinines, and Arn3p for both ferrichromes and ferrioxamines. Arn4p exhibits no activity towards these hydroxamate siderophores and exclusively transports enterobactin, a catecholate siderophore.

The siderophore substrates of the Arn transporters influence the intracellular trafficking of the transporters, and this trafficking is important for transporter activity.[20] The ferrichrome transporter Arn1p has been the focus of studies on intracellular trafficking of siderophore transporters. When yeast cells are iron depleted, but there is no ferrichrome available for uptake, Arn1p is not expressed on the plasma membrane, but is instead located intracellularly, cycling between early and late endosomes. Integral membrane proteins of the late endosome can be sorted to the vacuole for degradation, and this is likely the fate of Arn1p when its transport substrate is not available. When ferrichrome is present in the growth medium at low concentrations, Arn1p relocalizes to the plasma membrane, and at higher ferrichrome concentrations, Arn1p begins cycling between the plasma membrane and early endosomes. This plasma membrane cycling is important for Arn1p function, as blocks to endocytosis result in decreased ferrichrome uptake. Arn1p exhibits two surface binding sites for ferrichrome and substrate binding to these sites may control the intracellular trafficking of the transporter.[21]

Aft1p also activates the expression of a group of genes that are not involved in the uptake of iron from the environment (reviewed in[13]). Some of these genes are intracellular metal transporters that are located in the membranes of the vacuole, a site of iron storage in yeast. Fet5p and Fth1 form a vacuolar transporter complex similar to the plasma membrane complex, Fet3p/Ftr1p, which likely functions in the mobilization of iron from the vacuole. Smf3p is a divalent metal ion transporter located in the vacuole with homology to the mammalian iron transporter DMT1. Cot1p is a vacuolar transporter involved in cobalt resistance and zinc transport, and is thought to function in the sequestration of divalent metals in the vacuole. Iron-depleted yeast cells also express a heme-degrading enzyme, Hmx1p, which has similarity to mammalian heme oxygenases. Aft1p also activates the transcription of the biotin permease, Vht1p, thereby linking biotin uptake to iron homeostasis.

Similar to *E. coli*, yeast down-regulate the transcription of non-essential proteins that require iron for activity when the cells become depleted of iron. *BIO2* and *GLT1* encode iron-sulfur cluster proteins that are involved in the synthesis of biotin and glutamate, respectively. These genes plus the remaining genes of the biotin biosynthetic pathway are down-regulated by iron depletion.[13] Yeast can therefore switch from biotin synthesis to biotin uptake when iron becomes limiting. The transcription factors that control this down-regulation in response to iron depletion have not been identified, but this process appears to be independent of Aft1p.

Other species of fungi express reductive and non-reductive systems of iron uptake similar to those of *S. cerevisiae*, including homologues of the *ARN* siderophore transporters, the *FRE* reductases, and the Fet3/Ftr1 oxidase/permease complex.[22] In addition, most species synthesize and secrete one or more types of siderophores, a capacity that *S. cerevisiae* and *S. pombe* lack. *Aspergillus nidulans* seems to lack a reductive system of iron uptake and is completely dependent on siderophores for iron uptake. *S. cerevisiae* also seems to be unique in the use of the transcriptional activator Aft1p. Other fungi, including *S. pombe*, *A. nidulans*, *Neurospora crassa*, and *Ustilago maydis* express an iron-dependent transcriptional repressor of the GATA family of transcription factors. Why these organisms use different transcriptional regulators to express a similar set of genes in response to iron depletion is not known.

2.2 The Challenges of Understanding Plant Iron Homeostasis

Plants also express a precisely controlled system that coordinates the uptake of iron with the nutritional requirements of the plant. A plant can be divided into two organ systems, the root and the shoot. The root includes all structures below ground and is the site of nutrient uptake. The shoot includes all plant structures above ground including stems, leaves, buds, flowers, and fruit. Plants must coordinate the uptake of iron in the root with the nutritional requirements for iron in the shoot to achieve homeostasis. Iron-deficient plants can be readily identified by their chlorosis, a yellowing of the leaf due to a lack of chlorophyll. Higher plants can be separated into two groups according to the primary strategy that they use to obtain iron from the environment (reviewed in[23,24]). Strategy I plants include dicotyledonous and non-graminaceous plants such as pea, tomato, and the model organism *Arabidopsis thaliana*. These plants utilize uptake systems similar to the reductive system of baker's yeast. In this system, ferric iron is solubilized through the pH-lowering activity of a proton-ATPase, the ferric iron is reduced to the ferrous form by a ferric chelate reductase, and the reduced iron is taken up through a high-affinity ferrous transporter. These plants also exhibit morphological changes in response to iron deficiency, with marked increases in root hair density and the appearance of specialized cells in the epidermis. Strategy II plants include the grasses (graminaceous plants) such as maize, rice, and barley. These plants rely on a siderophore-mediated uptake system that is, again, similar to that of baker's yeast. Regulation of these systems occurs through both transcriptional and post-transcriptional mechanisms, although detailed knowledge of these processes is very limited.

mRNA transcripts of the proteins involved in iron transport accumulate rapidly in the roots of strategy I plants in response to iron deficiency. The tomato *FER* gene encodes a candidate transcription factor that may mediate this response.[23,24] *FER* encodes a basic helix-loop-helix transcription factor that is constitutively expressed in the epidermis and pericyte of the root. Absence of the *FER* protein in tomato *fer* mutants results in a complete loss of the iron-deficiency response, including the expression of ferric reductase and ferrous uptake activities and the morphological changes in roots. Whether *FER* interacts directly with promoter elements in the genes induced during the iron-deficiency response or indirectly by altering the transcription of other genes in a signal transduction cascade is not known.

Although the iron-deficiency response in roots may result from localized sensing of iron deficiency, plants must also be able to coordinate root iron uptake with the nutritional needs of the entire plant. Two pea mutants with defects in the root iron-deficiency response make clear that there is a shoot-derived transmissible signal that governs root iron uptake.[23,24] The pea mutants *brz* and *dgl* exhibit constitutively high levels of ferric reductase and ferrous uptake activities in the root, even when iron is abundantly available in the soil and within the plant. Excessive iron uptake results in necrotic bronze-spotted leaves and degenerate leaflets, respectively, due to an over-accumulation of iron in the leaves. These mutations are recessive and non-allelic, and grafting of mutant shoots onto the roots of wild-type plants results in the expression of the mutant phenotype in the roots, thus indicating the existence of a transmissible signal from shoots.[25] The genes that correspond to the *brz* and *dgl* mutations have not been identified. The *Arabidopsi*s mutant *frd3* also exhibits constitutively high levels of ferric reductase and ferrous uptake activities, resulting in accumulation of iron in roots and leaves.[23,24] *FRD3* encodes a polytopic transmembrane protein of the multidrug and toxin efflux (MATE) family and likely facilitates the transport of small molecules across a membrane. *FRD3* is expressed solely in roots and may be involved in the transport of a signaling molecule from the shoot to the root. Alternatively, *FRD3* may act as a receptor for a signaling molecule from the shoot. This molecule might signal iron sufficiency to the root, and, in the absence of *FRD3*, the root fails to receive the iron sufficiency signal and continues to express the iron-deficiency response.

Genes involved in the acquisition of iron in the root have been identified for both strategy I (reductase and ferrous transport) and strategy II (siderophore uptake) plants. In response to iron deficiency, strategy I plants acidify the soil through the activity of a plasma membrane-based, proton-extruding ATPase. A candidate gene encoding this activity is *AHA2*.[23,24] Ferric iron salts and chelates must be reduced prior to uptake and a family of ferric chelate reductases has been identified in *Arabidopsis*. *FRO2* was identified by a PCR-based strategy through its homology to the baker's yeast *FRE* family of plasma membrane metalloreductases. Similar to yeast Fre1p, FRO2 contains putative binding sites for heme and nucleotide cofactors, and expression of FRO2 restores ferric reductase activity in reductase-deficient mutants. *FRO2* is part of a five-member gene family in *Arabidopsis*. Although the other members of this family have not been characterized, they may be involved in reductive iron transport across membranes in other parts of the plant. Iron transport across the plasma membrane of root epidermal cells occurs through the IRT1 ferrous iron transporter. IRT1 is a member of the ZIP family of metal transporters that are found in many eukaryotes, including yeast, plants, worms, and mammals. *Arabidopsis* IRT1 was initially identified through its capacity to restore growth and iron uptake to a yeast *fet3fet4* mutant that completely lacks high-affinity iron uptake. Plants that are homozygous for a deletion mutation in *irt1*exhibit a chlorosis that is typical of iron-deficient plants and a severe growth defect in soil. This growth defect is rescued by the addition of high concentrations of iron to the soil. The roots of *irt1* mutant plants are also defective in the accumulation of zinc, manganese, cadmium and cobalt, indicating that IRT1 has broad transition metal specificity. A homologue of IRT1 from tomato can also restore growth to yeast deficient in copper uptake, although *Arabidopsis* IRT1 cannot. Arabidopsis expresses a second ZIP family member, IRT2, and ZIP family members have been identified in strategy II plants as well. These transporters may have roles in intracellular metal transport or metal transport in other organs of the plant.

Strategy II plants synthesize and secrete iron-chelating phytosiderophores of the mugineic acid (MA) family in response to iron deficiency.[23,24] MA is produced from *S*-adenosyl methionine by the enzymes nicotianamine synthase and nicotianamine aminotransferase, and the levels of these enzymes increase in response to iron deficiency. The molecular details regarding the secretion of MAs are unknown, but the maize mutant *yellow-stripe-3 (ys3)* exhibits an iron-deficient phenotype due to impaired secretion of MAs. Following chelation of iron in the soil, ferric-MAs are taken up by a MA-specific, high-affinity transporter that was identified in the *maize yellow-stripe-1 (ys1)* mutant. Maize *ys1* mutants are iron deficient owing to a defect in the uptake of ferric-MAs, and the *YS1* gene was identified through transposon tagging. YS1 is a member of the oligopeptide transporter family and expression of YS1 in a yeast *fet3fet4* mutant restores growth when cells are exposed to ferric-MAs, but not ferric citrate. Maize YS1 and its homologues are expressed in shoots as well as roots, suggesting that these transporters may have a role in iron transport throughout the plant. The genome of the non-graminaceous plant *Arabidopsis* contains eight genes with homology to YS1, although this plant is not known to secrete or take up MAs. The function of YS1 homologues in these plants is not clear, but the homologues may function in the transport of iron-nicotianamine chelates within and between plant tissues. Nicotianamine, the precursor to MA that is synthesized in all higher plants, is similar to MA in both its structure and capacity to bind iron. The tomato mutant *chloronerva (chln)* is deficient in nicotianamine synthase and completely lacks the capacity to synthesize nicotianamine. The *chln* mutant exhibits constitutively high amounts of iron uptake and accumulates iron-phosphate precipitates in its roots and shoots. Despite high levels of iron uptake, *chln* mutants exhibit an iron-deficient phenotype, including chlorosis in young leaflets and altered root morphology. These data suggest that nicotianamine may be required to keep iron in a form that is metabolically available to cells, or that iron-nicotianamine complexes could act as signaling molecules for the iron-deficiency response. A small iron-binding protein was recently identified in the phloem of castor bean seedlings. ITP (iron transport protein) binds ferric iron in vivo and has the capacity in vitro to bind copper, zinc, and manganese as well. *ITP* was cloned and found to encode a 96-amino acid peptide of the late embryogenesis abundant family and a homologous gene is present in *Arabidopsis*. Thus, ITP may contribute the movement of ferric iron within the vascular system.

Additional genes with homology to mammalian iron transport proteins have been identified in the genome of *Arabidopsis*.[23] These include *NRAMP1*, *3*, and *4*, which exhibit homology to the duodenal iron transporter of mammals, DMT1, and the manganese and iron transporters of baker's yeast, Smf1, 2, and 3. NRAMP1 was shown to rescue the iron-dependent growth defect of a yeast *fet3fet4* mutant as well as to cause increased iron sensitivity when overexpressed in Arabidopsis. The Arabidopsis genome also contains three genes that are homologous to the IREG1/Ferroportin 1/MTP1 iron exporter found in vertebrates. These transporters may have roles in the transport of iron from one cell type to another or in the movement of iron across membranes within the cell.

2.3 Regulation of Mammalian Iron Metabolism

2.3.1 Iron Regulatory Proteins 1 and 2 (IRP1 and 2) are Important Cytosolic Iron Sensors that Regulate Expression of Ferritin, Transferrin Receptor and Other Iron Metabolism Proteins

In the cytosol of mammalian cells, there are two proteins known as iron regulatory proteins 1 and 2 (IRP1 and 2) that are responsible for regulation of several important genes of mammalian iron metabolism. Unlike regulatory factors involved in bacterial and yeast iron homeostasis, IRPs influence the expression of major iron metabolism genes through direct interactions with mRNA transcripts. IRPs are not transcription factors and they do not interact with known transcription factors. These proteins are designed to sense cytosolic iron levels and accordingly regulate expression of major iron metabolism proteins by regulating translation of some new proteins from pre-existing transcripts or by regulating mRNA stability of other transcripts (reviewed in[26–28]).

Before we describe how IRPs function, a description of the proteins encoded by their target transcripts is needed. Two primary targets of IRP regulation are the ferritin genes that encode ferritin H and L subunits (*see* ***Iron Proteins for Storage & Transport & their Synthetic Analogs***). Upon coassembly of ferritin H and L subunits into 24-subunit heteropolymers, iron traverses channels through the ferritin shell into its hollow interior, undergoes oxidation by a ferroxidase activity of the ferritin H subunit, and is deposited as a ferric hydroxyphosphate precipitate within the ferritin heteropolymer. Ferritin molecules can store up to 4,000 atoms of iron. Because the iron is stored as a ferric iron precipitate, the iron is not free to engage in undesirable reactions with lipids, proteins and nucleic acids. Thus, ferritin serves as a safe repository for stored iron (reviewed in[29]). Ferritin iron likely remains unavailable to cellular metabolic processes until ferritin molecules are degraded in lysosomes, an organelle responsible for turnover of many proteins in cells. After degradation of the protein shell by numerous proteases found in lysosomes,[30] the iron precipitate likely gradually solubilizes within the highly acidic interior of the lysosome[31] from whence it may be exported to the cytosol by a metal transporter known as the divalent metal transporter or DMT1.[32] Ferritin competes with other iron metabolism proteins to bind iron, and when excess ferritin is present, the cell can become functionally iron deficient.[33] Thus, cells need to avoid synthesizing ferritin until essential iron proteins such as those involved in the mitochondrial respiratory chain have incorporated sufficient iron for function.

Transferrin receptor is another iron protein that cells express according to their iron needs (*see* ***Iron Proteins for Storage & Transport & their Synthetic Analogs***). There are two transferrin receptors encoded by two different homologous genes. The two transferrin receptors differ in that one is abundantly expressed in virtually all cell types (TfR1) whereas the second (TfR2) is expressed mainly in the liver.[34] TfR1 facilitates the cellular uptake of iron into cells throughout the body by binding serum transferrin, an abundant high-affinity ferric iron-binding protein found in the mammalian bloodstream. Upon binding transferrin, a complex of proteins including the TfR and transferrin internalizes in vesicles that bud from the plasma membrane of the cell. The newly formed vesicle undergoes acidification, whereupon ferric iron is released from transferrin, and newly released free iron is reduced and exported from the vesicle into the mammalian cytosol, most likely by the iron transporter DMT1.[32] When cells are iron-deficient, they synthesize more TfR, resulting in greater uptake of transferrin-bound iron, which in turn leads to an increase in available cytosolic iron.

2.3.2 *IRPs Regulate Expression of Iron Metabolism Proteins Mainly by Enhancing Transcript Stability or Repressing Translation*

Transcripts of both subunits of ferritin and TfR1 contain RNA stem-loop structures known as iron-responsive elements or IREs. Unlike DNA, single-stranded RNA can fold into many complex structures. In the IRE, RNA folds back upon itself to form a structure that consists of a relatively stable base-paired stem and a six-residue loop in which the first five residues have the sequence CAGUG (Figure 4). A solution NMR structure of the IRE revealed that a bulged cytosine that separates the upper and lower stems of the IRE and a guanosine residue in the six-membered loop are unusually mobile, consistent with the possibility that these residues are important recognition sites for RNA binding proteins (Figure 4).[35]

As is shown in (Figure 5), IRE stem-loops are found in the 5’UTR of ferritin transcripts and in the 3’UTR of the TfR1 transcript. In cells that are iron deficient, IRP1 and IRP2 bind to IREs in transcripts. When IRPs bind to IREs that are near the 5’end of the transcript, they interfere with binding of translation initiation factors and association of ribosomes with the transcript, thereby inhibiting new ferritin synthesis.[36] In the 3’UTR of the TfR1 transcript, there are 5 IREs that flank an endonucleolytic cleavage site. When IRPs are bound, access of endonucleases to the potential cleavage site in the transcript is blocked, and the transcript accordingly has a long half-life. When IRPs are not bound, the unprotected site

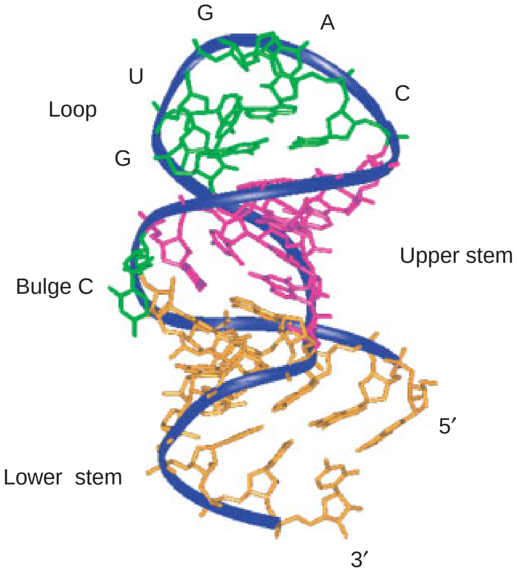
G
A
U
C
Loop
G
Upper stem
Bulge C
5′
Lower stem
3′

Figure 4 Structure of the iron-responsive element. Iron-responsive elements (IREs) are RNA stem-loop structures found in iron metabolism transcripts such as those that encode ferritin and the transferrin receptor. There is base-pairing between residues that creates a lower stem and an upper stem separated by an unpaired cytosine. A six-membered loop is characterized by base-pairing between residues one and five and unusual mobility of the guanosine at position 3[35]

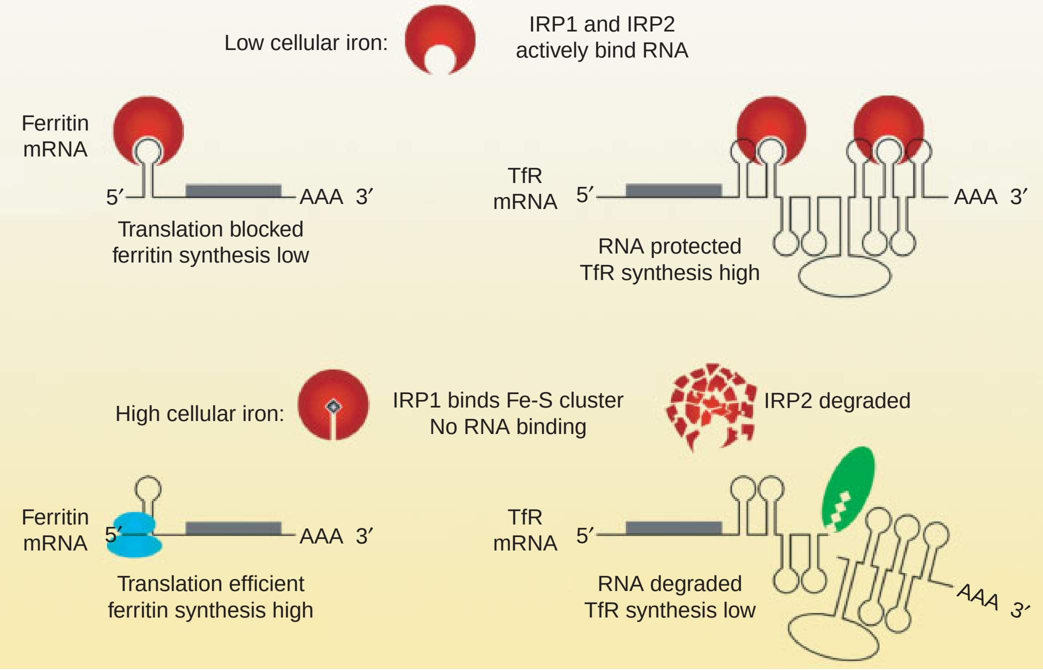
Low cellular iron:
IRP1 and IRP2
actively bind RNA
Ferritin
mRNA
5′
AAA 3′
Translation blocked
ferritin synthesis low
TfR
mRNA
5′
AAA 3′
RNA protected
TfR synthesis high
High cellular iron:
IRP1 binds Fe-S cluster
No RNA binding
IRP2 degraded
Ferritin
mRNA
5′
AAA 3′
Translation efficient
ferritin synthesis high
TfR
mRNA
5′
AAA 3′
RNA degraded
TfR synthesis low

Figure 5 IRP binding to IREs. In cells that are depleted of iron, IRP1 and 2 bind to IREs. When IRPs bind to IREs at the 5′ end of the transcript, they inhibit translation and new protein synthesis from the transcript. When they bind at the 3′ end of the TfR, they protect the transcript from endonucleolytic cleavage. In iron-replete cells, IRPs do not bind to transcripts. Ferritin biosynthesis accordingly increases, whereas TfR biosynthesis drops because the transcript levels decrease

undergoes cleavage and the unprotected ends on both sides of the cleavage site undergo rapid degradation by exonucleases that are common within cells; thus, levels of TfR transcript can decrease significantly without any change in transcription rate. The decrease in transcript levels results in a decrease in the rate of synthesis of new TfR, which in turn leads to a decrease in functional TfR protein and a decrease in uptake of transferrin-bound iron (reviewed in[26–28]).

Several other iron metabolism proteins contain IREs, including ferroportin, an iron exporter,[37] the erythrocyte form of aminolevulinic acid synthase,[38] an enzyme important in heme biosynthesis, an alternatively spliced transcript of the iron transporter DMT1,[32,39] and mammalian mitochondrial aconitase.[40] The importance of these IREs in regulation of these transcripts is the subject of ongoing research.

It is important to note that although much regulation of ferritin and TfR is post-transcriptional, significant transcriptional regulation of ferritin[29] and TfR[41] occurs in some settings.

2.3.3 *Mechanisms of IRP 'Sensing' of Iron Levels*

An important question in metalloregulation is to understand how IRP1 and IRP2 sense iron levels and modify their IRE-binding capability (reviewed in[26,27]). IRP1 and IRP2 are 58% identical to one another at the amino acid level, and inspection of the exon-intron structure suggests that IRP2 arose as a result of duplication of the IRP1 gene. IRP1 is a member of the aconitase gene family.[42] Aconitases are iron-sulfur proteins that interconvert the citric acid cycle intermediates, citrate and isocitrate, and are found in bacteria, yeast, animals and plants.[43] In eukaryotes, the citric acid cycle operates in mitochondria. Mammalian mitochondrial aconitase is the product of a unique gene, and it resides exclusively in mitochondria because the N-terminus of the newly synthesized protein contains information required to target the protein to mitochondria. IRP1 has sequence homology to mitochondrial aconitase, but IRP1 encodes an aconitase that resides in mammalian cytosol rather than mitochondria. Like mitochondrial aconitase, this cytosolic IRP1 contains a cubane [4Fe-4S] cluster (*see* ***Iron–Sulfur Proteins***) at the active site cleft and functions as an aconitase, interconverting citrate and isocitrate in mammalian cytosol. However, when the iron−sulfur cluster is absent, the apo form of IRP1 binds IRE stem-loops with high-affinity. Thus, the presence or absence of the iron−sulfur cluster determines whether IRP1 will function as a cytosolic aconitase or as an IRE-binding protein.[44] In animal tissues, the vast majority of IRP1 is in the form of cytosolic aconitase. IRP1 is highly expressed in brown fat and kidney, two tissues where its role in citrate metabolism could be particularly important. However, animals that lack IRP1 do not have obviously compromised intermediary metabolism, and iron metabolism is minimally compromised in these tissues, suggesting that the functions of IRP1 are not unique and essential.[45]

Although IRP2 is homologous to IRP1, it does not function as an aconitase and does not appear to incorporate an iron−sulfur cluster. Unlike IRP1, IRP2 is degraded and is therefore physically absent in iron-replete cells, whereas IRP1 converts to its aconitase form in iron-replete cells. The rate of IRP2 degradation is enhanced by increases in both iron and oxygen concentrations.[46,47] IRP2 also contains an extra exon that encodes 73 amino acids that are unique to IRP2, and IRP2-like genes that contain this extra exon are found only in mammals.[48] IRP2 degradation is carried out by the ubiquitin-proteasomal degradation system.[49] Proteasomes are cylindrical multimeric proteins that project multiple proteases into the inside of the cylindrical structure. When proteins are marked as abnormal by multiple covalent additions of the peptide ubiquitin, the polyubiquitinated proteins bind to proteasomes. Proteasomes utilize energy captured from ATP hydrolysis to unfold ubiquitinated proteins and thread the denatured peptide through the proteasomal 'cylinder,' where it undergoes proteolysis. IRP2 readily undergoes iron-dependent oxidation and cleavage in vitro,[50] but it is unclear whether direct iron-binding is important an important step in IRP2 degradation in living cells.[47,51] It is also possible that heme binding is important in the ability of IRP2 to correctly sense intracellular iron concentrations.[47,52] Initially, a group of conserved cysteines unique to IRP2 that bind iron and mediate metal-catalyzed oxidation and degradation of the protein in vitro were thought to bind iron and mediate oxidation of IRP2 in vivo. Indeed, mutagenesis of these cysteines inhibits direct iron-dependent oxidation of IRP2 in vitro.[50] However, full-length IRP2 that contained the same cysteine mutations still was iron-dependently degraded when expressed in cells.[47] Thus, function of a well-defined iron-binding site in IRP2 is surprisingly not needed for cellular iron-dependent degradation of IRP2, and the exact molecular mechanisms that enable IRP2 to function as a cytosolic iron sensor remain unclear.

2.3.4 *IRP2 Dominates Regulation of Iron Homeostasis in Mammals*

In mice and many other animals, it is possible through recombinant DNA techniques to assess the role of particular genes by selectively eliminating the ability of mice to manufacture the protein encoded by a specific gene of interest. Mice in which the gene is interrupted are commonly referred to as 'knockout mice' and are said to be 'genetically ablated' or 'null' at a particular locus. Mice that are genetically ablated at the IRP2 locus have been generated and are referred to as IRP2-/- mice.[53] Studies of cells in tissue culture indicate that both IRP1 and IRP2 respond to changes in 'free' iron levels in cells and participate in post-transcriptional gene regulation. To evaluate the role of IRPs in living animals, genetic ablations of IRP1 and IRP2 have been performed. These studies have yielded a somewhat surprising result: they indicate that IRP2 is overwhelmingly responsible for post-transcriptional regulation of iron metabolism in mice, whereas IRP1 contributes much less to mammalian iron homeostasis.[45] IRP2-/- mice over-express ferritin in liver, kidney, spleen and brain, as would be expected if IRP2 is responsible for repressing ferritin translation in these tissues. In the brain, levels of TfR are decreased, consistent with what we expect if there is little IRE-binding protein available to protect the TfR transcript. An unexpected result of the IRP ablation studies was that IRP2-/- mice develop adult-onset neurodegeneration with features of Parkinson's disease.[53,54] This interesting result implies that primary misregulation of iron metabolism in the central nervous system can lead to dysfunction and death in neurons in adult animals.[55] Although these iron metabolism abnormalities affect virtually all tissues, only the central nervous system develops significant pathology, whereas the other tissues such as the liver and kidney continue to function despite abnormalities in iron metabolism. Abnormalities of numerous iron metabolism genes are now implicated in neurodegenerative disease,[56,57] and these results underscore the importance of understanding metal homeostasis in animals.

2.3.5 *Mitochondrial Iron Homeostasis May be Regulated by an Iron-sulfur Protein*

Earlier we mentioned that metalloregulation of organelles is an emerging important topic. Mitochondrial iron homeostasis presents an interesting challenge in metalloregulation. Iron-sulfur clusters are synthesized and inserted as prosthetic groups into mitochondrial proteins, and much iron is needed for assembly and function of these respiratory chain proteins. In addition, insertion of iron by ferrochelatase in the final step of heme biosynthesis also takes place in mitochondria. Yet, we still do not know with certainty how elemental iron enters or exits mitochondria, and we also do not know how heme is exported. In yeast, uptake of elemental iron into mitochondria may be mediated by the Mrs3 and 4 transporters.[58,59] Mammalian counterparts to these genes exist,[60,61] raising the possibility that regulation of mammalian mitochondrial iron import can be studied by analyzing mRNA and protein levels of the mammalian homologue of the Mrs3/4 transporter in various settings. In yeast and mammals, it is now recognized that mutations in genes involved in iron-sulfur cluster assembly genes are associated with marked mitochondrial iron overload.[62–66] Abnormal iron-sulfur cluster biogenesis plays a causal role in several human diseases, including Friedreich's ataxia[67] and some sideroblastic anemias.[68] The observation that abnormalities in iron-sulfur biogenesis lead to mitochondrial iron overload raises the interesting possibility that perhaps an iron-sulfur protein regulates mitochondrial iron homeostasis. When iron-sulfur cluster synthesis is compromised, this proposed regulatory protein registers mitochondrial iron starvation and acts to increase iron uptake and to decrease iron export. Many other possible interpretations are possible, but the fact that IRP1 can become an IRE-binding protein in the absence of an intact iron–sulfur cluster is a reminder that apoproteins can change conformationally and acquire new functions.

2.3.6 *A Peptide Hormone Synthesized in Liver, Hepcidin, Coordinates Mammalian Iron Physiology*

In mammals, multiple tissues must act in concert to ensure that iron is sufficiently available in the bloodstream to support the needs of various tissues and processes. Most circulating transferrin-bound iron gets incorporated into hemoglobin. Red blood cells use hemoglobin to transport iron through the bloodstream, and new red cells are constantly being manufactured in the bone marrow by a process known as erythropoiesis. Red blood cells that are more than 120 days old are phagocytosed by macrophages in spleen and liver.[69] These spleen and liver macrophages comprise the reticuloendothelial system, which plays a major role in retrieving iron from senescent red cells and returning elemental iron to the circulation. Iron exported by macrophages binds to serum transferrin, which transports the iron to tissues that are high iron consumers, such as bone marrow, the site of new red cell synthesis. The rate of red cell turnover by macrophages is so high that macrophage iron-release is the major source of iron used for the manufacture of new red cells. However, about 1 mg of iron is absorbed per day through the duodenum. Duodenal iron transport increases markedly in iron-deficient animals because transcription of proteins involved in iron transport and reduction and oxidation of metal ions increases markedly.[70] Epithelial cells that line the duodenum are highly polarized, and import machinery for free iron and heme is found on the apical membrane of these cells, in direct contact with dietary iron sources. At the opposite end of the cell on the basolateral membrane, iron export machinery operates to release iron to the bloodstream. At the apical membrane, an iron transporter known as DMT1 (Divalent Metal Transporter) was identified recently through a cloning project designed to find a gene responsible for iron-deficiency anemia in mice and also through a project designed to identify iron transporters by expressing mRNAs in Xenopus oocytes.[69] This transporter has multiple membrane-spanning domains and couples transport of Fe^{2+} to transport of a proton. As dietary iron is often found in the Fe^{3+} oxidation state, it is perhaps not surprising that a ferric reductase known as Dcytb is highly regulated by iron status.[71] Dcytb provides Fe^{2+} for transport by DMT1 at the apical surface of epithelial cells.

Recently, a peptide hormone known as hepcidin has been implicated as a major circulating molecule that coordinates iron metabolism responses in the reticuloendothelial system and the duodenum.[72] The presence of a circulating factor helps to explain how sites that are physically distant from one another, such as the duodenum and spleen, can coordinately regulate the amount of iron that they release into the bloodstream. Hepcidin negatively regulates iron absorption through the small intestine, iron transport across the placenta, and iron release from macrophages. Hepcidin is synthesized in hepatocytes, and its synthesis is repressed in anemic animals. Hypoxia directly represses hepcidin synthesis in hepatocytes by unknown mechanisms,[73] but activation could involve an oxygen/iron sensor known as hypoxia inducible factor.[74] Hepatocytic hepcidin transcription can also be activated by signals from adjacent macrophages, which release factors including interleukin-6 that activate the hepcidin promoter. Like many hormones, hepcidin likely binds to specific receptors on the surface of cells that activate or repress transcription of multiple genes in the target cell. The nature of the receptor is still unknown, but another gene likely to be in the same pathway has recently been described.[75] An important future research area will involve determining how interaction of hepcidin with the cells of the duodenum and reticuloendothelial system results in regulation of iron export from these tissues.

3 REGULATION OF ZINC METABOLISM

Zinc is a required cofactor for hundreds of catalytic enzymes (*see* ***Zinc Enzymes***) and a required structural component of numerous proteins such as transcription factors (*see* ***Zinc: DNA-binding Proteins***) in organisms ranging from bacteria to man. Unlike other transition metals, zinc has a stable oxidation state. Zinc can easily shift its coordination number, and through its positive charge, it acts as a Lewis acid, facilitating formation of hydroxide ion from bound water and polarizing various substrate compounds to facilitate chemical rearrangements (*see* ***Zinc Enzymes***). These unique features likely account for the fact that zinc is a cofactor for enzymes from every recognized category, including oxidoreductases, transferases, hydrolases, lyases, isomerases, and ligases.[76,77] In zinc finger domains, zinc provides a structural center which directs folding of proteins into finger-like structures that are well-suited to binding of DNA (*see* ***Zinc: DNA-binding Proteins***). Zinc finger motifs are a common feature of transcription factors as well as numerous other proteins in cells.[78] Zinc is also highly concentrated in synaptic vesicles of some neurons, where its exact role remains unclear.[79] Because zinc is required by numerous proteins, zinc homeostasis is highly regulated in all cells and organisms to optimize availability. Excess zinc is toxic, but unlike some other metals, its toxicity is not directly attributable to redox activity. Rather, it appears likely that excess zinc may compete for the protein binding sites of other metals and thereby interfere with the normal functions of these metalloproteins.[80]

3.1 Regulation of Zinc Homeostasis in Prokaryotes

Much interesting work has been done on zinc regulation in *E. coli*, and this work will serve as the basis for discussion of prokaryotic zinc metalloregulation. In *E. coli*, zinc homeostasis is achieved by independently regulating two separate processes, the import of zinc across the plasma membrane into the bacterial cytosol, and the export of zinc from cytosol. Since there are no membranous organelles within bacteria, sensing of cytosolic zinc levels drives the appropriate regulatory response. There are two known prokaryotic cytosolic sensors: Zur, a protein in which zinc binding leads to dimerization and transcriptional repression of genes involved in zinc uptake, and ZntR, a zinc-binding protein that activates transcription of a zinc efflux gene.

Zinc uptake in *E. coli* is mediated by an import system known as *znuABC* (Zn^{2+} uptake), which encodes a periplasmic binding protein, ZnuA, an ATPase known as ZnuC, and an integral membrane protein, ZnuB.[81,82] Transcription of the *znuACB* gene cluster is regulated by the Zur gene product, which acts as a transcriptional repressor when it binds zinc.

Zinc efflux is mediated by a zinc exporter known as ZntA (Zn^{2+} transport or tolerance), a membrane protein which was identified through studies of bacterial strains that were hypersensitive to zinc and cadmium. Sequence inspection revealed that ZntA was a member of the family of cation transport P-type ATPases,[83] a major family of ion-translocating membrane proteins in which ATPase activity in one portion of the protein is used to phophorylate an aspartate within a highly conserved amino acid sequence, DKTG, in another portion of the protein. The cysteine rich N-terminus of these soft metal transport proteins contains several metal-binding sites.[84] How the chemical energy released by ATP hydrolysis results in metal ion transport is not yet known, in part because there is only partial information about the structures of these proteins.[85] The bacterial zinc exporter also pumps cadmium and lead and is therefore also involved in protection from heavy metal toxicity[84,86] (*see* ***Metal Ion Toxicity***).

The increase in zinc efflux is achieved through transcriptional activation of the *zntA* gene, which in turn leads to increased ZntA protein levels. When cytosolic zinc levels rise beyond a certain point, the transcription factor ZntR[87] activates transcription of the *zntA* gene. ZntR is related to MerR, a mercury binding protein that regulates expression of mercury detoxification genes. Like MerR,[88] ZntR binds constitutively to the promoter of its target gene whether it contains or lacks zinc (apo-ZntR). Apo-ZntR distorts the promoter of *zntA* and inhibits transcription, but when zinc binds, the conformation of the ZntR changes to allow active transcription from the *zntA* promoter.[89]

Until recently, it was difficult to approach the question of how zinc concentrations are sensed within cells. Zinc proteins are abundant, and total zinc concentrations are quite high within cells (0.2 mM), even though most zinc is tightly bound to proteins and is therefore unlikely to be sensed by cytosolic regulatory proteins. The idea that cytosolic regulatory proteins sample a pool of free or loosely bound zinc at micromolar to picomolar concentrations has recently been discarded in favor of a model in which it is postulated that there is virtually no free zinc within the cytosol of bacterial cells.[90] This interesting conclusion was arrived at by performing in vitro transcription assays of Zur and ZntR as a function of free zinc concentrations. Since each of these transcription factors is repressed (Zur) or activated (ZntR) by zinc binding, the amount of zinc required for their activation could be directly assessed. Surprisingly, the sensitivity of these proteins was determined to be in the femtomolar range. The extraordinary affinity of these zinc sensors implies that there is virtually no free zinc in *E. coli*. These results are consistent with the possibility that zinc trafficking proteins exist which escort zinc to recipient proteins, analogous to the situation which has been described for copper trafficking by chaperone proteins (*see* ***Metallochaperones & Metal Ion Homeostasis***).[91] Another impressive and interesting result was that repression of the zinc uptake apparatus by Zur occurred at a free zinc concentration of approximately 2×10^{-16} M, whereas zinc efflux was not activated by ZntR until the concentration of zinc rose to approximately 11×10^{-16} M. If these two values are taken to represent the concentrations that respectively define physiologic zinc deficiency and zinc toxicity, then it is clear that intracellular zinc levels are very tightly controlled. These results also reveal that different affinities for a given metal allow a hierarchy of responses, in which metal uptake is repressed well before the cell goes to the extra effort of actively exporting the metal.[90]

3.2 Eukaryotic Zinc Homeostasis

In yeast, a transcription factor known as Zap1 regulates expression of at least 40 genes in the genome.[80] Intriguingly, Zap1 encodes a zinc finger protein that transcriptionally activates genes that contain a promoter consensus site known as a zinc-responsive element (ZRE). Direct binding of zinc in the zinc fingers determines whether Zap1 is active: in the absence of zinc, Zap1 activates transcription in target genes.[92] Among the targets of Zap1 are transporters in the solute carrier 30 family of proteins (SLC30).[93] All of the members of this large gene family, which has multiple yeast and mammalian examples, mediate zinc efflux from cytosol into intracellular compartments or across the plasma membrane to the external milieu. Another family of proteins known as the SLC39 proteins consists of proteins that transport zinc into cytosol, the opposite direction of the SLC30 family members.

One of these genes encodes a transporter known as Zrt1, which is not only a target of the transcription factor Zap1, but is also regulated post-translationally. When cells are exposed to high levels of zinc, this plasma membrane zinc transporter undergoes ubiquitination, which leads to targeting to the vacuole and degradation. Thus, in yeast, there is a two-tiered regulatory system, in which a transcriptional activator mediates effects on expression of over 40 genes, but the cell can protect itself from toxic zinc uptake almost immediately by degrading zinc importers that are present on the plasma membrane at the onset of zinc stress.[80] The fact that Zap1 activity is determined by zinc-binding is consistent with the recurring theme that regulation of metal homeostasis is usually implemented by a protein that directly binds the metal in question. Plants regulate zinc transport and distribution, but the mechanisms of regulation are not yet well understood.[94] In mammals, there is little known about Zap1 counterparts, but this will represent an interesting area for further research.

4 REGULATION OF COPPER, MANGANESE AND NICKEL HOMEOSTASIS

Recent reviews on copper homeostasis in *E. coli*[95] and yeast are available.[96,97] Copper and iron metabolism are often intertwined. For instance, mammalian iron metabolism depends on the copper protein, ceruloplasmin, a ferroxidase that facilitates iron efflux from cells (*see* ***Copper Proteins: Oxidases***).[98] Several important human diseases, including Menkes disease and Wilson's disease, result from mutations in copper transport (*see* ***Metal-related Diseases of Genetic Origin***).[99]

Less is known about regulation of manganese homeostasis than other metals. However, several recent reviews of regulation of manganese in bacteria are available.[100,101]

The reader is referred to a recent review on bacterial nickel uptake for information on nickel regulation.[102]

5 RELATED ARTICLES

Iron Proteins for Storage & Transport & their Synthetic Analogs; Iron Transport: Siderophores; Metallochaperones & Metal Ion Homeostasis; Zinc: DNA-binding Proteins.

6 REFERENCES

1. A. L. Feig and S. J. Lippard, *Chem. Rev.*, 1994, **94**, 769.
2. D. M. Kurtz Jr, *Essays Biochem.*, 1999, **34**, 85.
3. C. Ratledge and L. G. Dover, *Annu. Rev. Microbiol.*, 2000, **54**, 881.
4. G. L. Challis and D. A. Hopwood, *Proc. Natl. Acad. Sci. U.S.A.*, 2003, **100**(Suppl. 2), 14555.
5. L. Escolar, J. Perez-Martin, and L. de Lorenzo, *J. Bacteriol.*, 1999, **181**, 6223.
6. S. C. Andrews, A. K. Robinson, and F. Rodriguez-Quinones, *FEMS Microbiol. Rev.*, 2003, **27**, 215.
7. E. Masse and S. Gottesman, *Proc. Natl. Acad. Sci. U.S.A.*, 2002, **99**, 4620.

8. K. Hantke, *Curr. Opin. Microbiol.*, 2001, **4**, 172.
9. V. Braun, *Front Biosci.*, 2003, **8**, 1409.
10. K. P. Locher, A. T. Lee, and D. C. Rees, *Science*, 2002, **296**, 1091.
11. H. A. Van, D. M. Ward, and J. Kaplan, *Annu. Rev. Microbiol.*, 2002, **56**, 237.
12. L. Li, O. S. Chen, W. D. McVey, and J. Kaplan, *J. Biol. Chem.*, 2001, **276**, 29515.
13. M. Shakoury-Elizeh, J. Tiedeman, J. Rashford, T. Ferea, J. Demeter, E. Garcia, R. Rolfes, P. O. Brown, D. Botstein, and C. C. Philpott, *Mol. Biol. Cell*, 2004, **15**, 1233.
14. J. C. Rutherford, S. Jaron, and D. R. Winge, *J. Biol. Chem.*, 2003, **278**, 27636.
15. R. Ueta, A. Fukunaka, and Y. Yamaguchi-Iwai, *J. Biol. Chem.*, 2003, **278**, 50120.
16. R. J. Crisp, A. Pollington, C. Galea, S. Jaron, Y. Yamaguchi-Iwai, and J. Kaplan, *J. Biol. Chem.*, 2003, **278**, 45499.
17. O. Protchenko, T. Ferea, J. Rashford, J. Tiedeman, P. O. Brown, D. Botstein, and C. C. Philpott, *J. Biol. Chem.*, 2001, **276**, 49244.
18. C. C. Philpott, O. Protchenko, Y. W. Kim, Y. Boretsky, and M. Shakoury-Elizeh, *Biochem. Soc. Trans.*, 2002, **30**, 698.
19. D. J. Kosman, *Mol. Microbiol.*, 2003, **47**, 1185.
20. Y. Kim, C. W. Yun, and C. C. Philpott, *EMBO J.*, 2002, **21**, 3632.
21. R. E. Moore, Y. Kim, and C. C. Philpott, *Proc. Natl. Acad. Sci. U.S.A.*, 2003, **100**, 5664.
22. H. Haas, *Appl. Microbiol. Biotechnol.*, 2003, **62**, 316.
23. C. Curie and J. F. Briat, *Annu. Rev. Plant Biol.*, 2003, **54**, 183.
24. W. Schmidt, *Trends Plant Sci.*, 2003, **8**, 188.
25. M. A. Grusak and S. Pezeshgi, *Plant Physiol.*, 1996, **110**, 329.
26. M. W. Hentze and L. C. Kuhn, *Proc. Natl. Acad. Sci. U.S.A.*, 1996, **93**, 8175.
27. T. Rouault and R. Klausner, *Curr. Top. Cell Regul.*, 1997, **35**, 1.
28. B. D. Schneider and E. A. Leibold, *Curr. Opin. Clin. Nutr. Metab. Care*, 2000, **3**, 267.
29. F. M. Torti and S. V. Torti, *Blood*, 2002, **99**, 3505.
30. D. C. Radisky and J. Kaplan, *Biochem. J.*, 1998, **336**(Pt 1), 201.
31. Z. Yu, H. L. Persson, J. W. Eaton, and U. T. Brunk, *Free Radic. Biol. Med.*, 2003, **34**, 1243.
32. M. Tabuchi, N. Tanaka, J. Nishida-Kitayama, H. Ohno, and F. Kishi, *Mol. Biol. Cell*, 2002, **13**, 4371.
33. A. Cozzi, B. Corsi, S. Levi, P. Santambrogio, A. Albertini, and P. Arosio, *J. Biol. Chem.*, 2000, **275**, 25122.
34. D. Trinder and E. Baker, *Int. J. Biochem. Cell Biol.*, 2003, **35**, 292.
35. K. J. Addess, J. P. Basilion, R. D. Klausner, T. A. Rouault, and A. J. Pardi, *J. Mol. Biol.*, 1997, **274**, 72.
36. M. Muckenthaler, N. K. Gray, and M. W. Hentze, *Mol. Cell*, 1998, **2**, 383.
37. S. Abboud and D. J. Haile, *J. Biol. Chem.*, 2000, **275**, 19906.
38. N. K. Gray and M. W. Hentze, *EMBO J.*, 1994, **13**, 3882.
39. H. Gunshin, C. R. Allerson, M. Polycarpou-Schwarz, A. Rofts, J. T. Rogers, F. Kishi, M. W. Hentze, T. A. Rouault, N. C. Andrews, and M. A. Hediger, *FEBS Lett.*, 2001, **509**, 309.
40. H. Y. Kim, T. LaVaute, K. Iwai, R. D. Klausner, and T. A. Rouault, *J. Biol. Chem.*, 1996, **271**, 24226.
41. C. N. Lok and P. Ponka, *J. Biol. Chem.*, 2000, **275**, 24185.
42. M. J. Gruer, P. J. Artymiuk, and J. R. Guest, *Trends Biochem. Sci.*, 1997, **22**, 3.
43. H. Beinert, M. C. Kennedy, and D. C. Stout, *Chem. Rev.*, 1996, **96**, 2335.
44. R. D. Klausner and T. A. Rouault, *Mol. Biol. Cell*, 1993, **4**, 1.
45. E. G. Meyron-Holtz, M. C. Ghosh, K. Iwai *et al*., *EMBO J.*, 2004, **23**, 386.
46. E. S. Hanson and E. A. Leibold, *J. Biol. Chem.*, 1998, **273**, 7588.
47. E. Bourdon, D. K. Kang, M. C. Ghosh, S. K. Drake, J. Wey, R. L. Levine, and T. A. Rouault, *Blood Cells Mol. Dis.*, 2003, **31**, 247.
48. K. Iwai, R. D. Klausner, and T. A. Rouault, *EMBO J.*, 1995, **14**, 5350.
49. K. Iwai, *J. Biochem. (Tokyo)*, 2003, **134**, 175.
50. D. K. Kang, J. Jeong, S. K. Drake, N. Wehr, T. A. Rouault, and R. L. Levine, *J. Biol. Chem.*, 2003, **278**, 14857.
51. K. Iwai, S. K. Drake, N. B. Wehr, A. M. Weissman, T. LaVaute, N. Minato, R. D. Klausner, R. L. Levine, and T. A. Rouault, *Proc. Natl. Acad. Sci. U.S.A.*, 1998, **95**, 4924.
52. K. Yamanaka, H. Ishikawa, Y. Megumi, F. Tokunaga, M. Kanie, T. A. Rouault, I. Morishima, N. Minato, K. Ishimori, and K. Iwai, *Nat. Cell Biol.*, 2003, **5**, 336.
53. T. LaVaute, S. Smith, S. Cooperman, K. Iwai, W. Land, E. Meyron-Holtz, S. K. Drake, G. Miller, M. Abu-Asab, M. Tsokos, R. Switzer III, A. Grinberg, P. Love, N. Tresser, and T. A. Rouault, *Nat. Genet.*, 2001, **27**, 209.
54. C. Grabill, A. C. Silva, S. S. Smith, A. P. Koretsky, and T. A. Rouault, *Brain Res.*, 2003, **971**, 95.
55. T. A. Rouault, *Nat. Genet.*, 2001, **28**, 299.
56. C. W. Levenson, *Nutr. Rev.*, 2003, **61**, 311.
57. D. Berg, M. Gerlach, M. B. Youdim, K. L. Double, L. Zecca, P. Riederer, and G. Becker, *J. Neurochem.*, 2001, **79**, 225.
58. F. Foury and T. Roganti, *J. Biol. Chem.*, 2002, **277**, 24475.
59. U. Muhlenhoff, J. A. Stadler, N. Richhardt, A. Seubert, T. Eickhorst, R. J. Schweyen, R. Lill, and G. Wiesenberger, *J. Biol. Chem.*, 2003, **278**, 40612.
60. F. Y. Li, K. Nikali, J. Gregan, I. Leibiger, B. Leibiger, R. Schweyen, C. Larsson, and A. Suomalainen, *FEBS Lett.*, 2001, **494**, 79.

61. F. Y. Li, B. Leibiger, I. Leibiger, and C. Larsson, *Mamm. Genome*, 2002, **13**, 20.
62. B. Schilke, C. Voisine, H. Beinert, and E. Craig, *Proc. Natl. Acad. Sci. U.S.A.*, 1999, **96**, 10206.
63. J. Li, M. Kogan, S. A. Knight, D. Pain, and A. Dancis, *J. Biol. Chem.*, 1999, **274**, 33025.
64. M. Babcock, D. de Silva, R. Oaks, S. Davis-Kaplan, S. Jiralerspong, L. Montermini, M. Pandolfo, and J. Kaplan, *Science*, 1997, **276**, 1709.
65. C. Voisine, Y. C. Cheng, M. Ohlson, B. Schilke, K. Hoff, H. Beinert, J. Marszalek, and E. A. Craig, *Proc. Natl. Acad. Sci. U.S.A.*, 2001, **98**, 1483.
66. H. Puccio, D. Simon, M. Cossee, P. Criqui-Filipe, F. Tiziano, J. Melki, C. Hindelang, R. Matyas, P. Rustin, and M. Koenig, *Nat. Genet.*, 2001, **27**, 181.
67. M. Pandolfo, *Blood Cells Mol. Dis.*, 2002, **29**, 536, discussion 548–52.
68. M. D. Fleming, *Semin. Hematol.*, 2002, **39**, 270.
69. N. C. Andrews, *N. Engl. J. Med.*, 1999, **341**, 1986.
70. N. C. Andrews, *Curr. Opin. Chem. Biol.*, 2002, **6**, 181.
71. A. T. McKie, D. Barrow, G. O. Latunde-Dada, A. Rolfs, G. Sager, E. Mudaly, M. Mudaly, C. Richardson, D. Barlow, A. Bomford, T. J. Peters, K. B. Raja, S. Shirali, M. A. Hediger, F. Farzaneh, and R. J. Simpson, *Science*, 2001, **291**, 1755.
72. T. Ganz, *Blood*, 2003, **102**, 783.
73. G. Nicolas, C. Chauvet, L. Viatte, J. L. Danan, X. Bigard, I. Devaux, C. Beaumont, A. Kahn, and S. Vaulont, *J. Clin. Invest.*, 2002, **110**, 1037.
74. R. K. Bruick, *Genes Dev.*, 2003, **17**, 2614.
75. G. Papanikolaou, M. E. Samuels, E. H. Ludwig, M. L. MacDonald, P. L. Franchini, M. P. Dube, L. Andres, J. MacFarlane, N. Sakellaropoulos, M. Politou, E. Nemeth, J. Thompson, J. K. Risler, C. Zaborowska, R. Babakaiff, C. C. Radomski, T. D. Pape, O. Davidas, J. Christakis, P. Brissot, G. Lockitch, T. Ganz, M. R. Hayden, and Y. P. Goldberg, *Nat. Genet.*, 2004, **36**(1), 77.
76. L. A. Gaither and D. J. Eide, *Biometals*, 2001, **14**, 251.
77. O. Fuchs, M. Babusiak, D. Vyoral, and J. Petrak, *Sb. Lek.*, 2003, **104**, 157.
78. J. M. Matthews and M. Sunde, *IUBMB Life*, 2002, **54**, 351.
79. C. J. Frederickson, S. W. Suh, D. Silva, C. J. Frederickson, and R. B. Thompson, *J. Nutr.*, 2000, **130**, 1471S.
80. D. J. Eide, *J. Nutr.*, 2003, **133**, 1532S.
81. S. I. Patzer and K. Hantke, *Mol. Microbiol.*, 1998, **28**, 1199.
82. S. I. Patzer and K. Hantke, *J. Biol. Chem.*, 2000, **275**, 24321.
83. S. J. Beard, R. Hashim, J. Membrillo-Hernandez, M. N. Hughes, and R. K. Poole, *Mol. Microbiol.*, 1997, **25**, 883.
84. D. K. Blencowe and A. P. Morby, *FEMS Microbiol. Rev.*, 2003, **27**, 291.
85. G. A. Scarborough, *Curr. Opin. Cell Biol.*, 1999, **11**, 517.
86. M. R. Binet and R. K. Poole, *FEBS Lett.*, 2000, **473**, 67.
87. K. R. Brocklehurst, J. L. Hobman, B. Lawley, L. Blank, S. J. Marshall, N. L. Brown, and A. P. Morby, *Mol. Microbiol.*, 1999, **31**, 893.
88. N. L. Brown, J. V. Stoyanov, S. P. Kidd, and J. L. Hobman, *FEMS Microbiol. Rev.*, 2003, **27**, 145.
89. C. E. Outten, F. W. Outten, and T. V. O’Halloran, *J. Biol. Chem.*, 1999, **274**, 37517.
90. C. E. Outten and T. V. O’Halloran, *Science*, 2001, **292**, 2488.
91. D. L. Huffman and T. V. O’Halloran, *Annu. Rev. Biochem.*, 2001, **70**, 677.
92. A. J. Bird, K. McCall, M. Kramer, E. Blankman, D. R. Winge, and D. J. Eide, *EMBO J.*, 2003, **22**, 5137.
93. R. D. Palmiter and L. Huang, *Pflugers Arch.*, 2003, **14**, 769.
94. H. Wintz, T. C. Fox, Y. Y. Wu, V. Feng, W. Chen, H. S. Chang, T. Zhu, and C. D. Vulpe, *J. Biol. Chem.*, 2003, **278**, (48) 47644.
95. C. Rensing and G. Grass, *FEMS Microbiol. Rev.*, 2003, **27**, 197.
96. D. J. Thiele, *J. Nutr.*, 2003, **133**, 1579S.
97. D. R. Winge, *Adv. Protein Chem.*, 2002, **60**, 51.
98. T. Nittis and J. D. Gitlin, *Semin. Hematol.*, 2002, **39**, 282.
99. H. Shim and Z. L. Harris, *J. Nutr.*, 2003, **133**, 1527S.
100. L. E. Chandler, V. V. Bartsevich, and H. B. Pakrasi, *Biochemistry*, 2003, **42**, 5508.
101. N. S. Jakubovics and H. F. Jenkinson, *Microbiology*, 2001, **147**, 1709.
102. S. B. Mulrooney and R. P. Hausinger, *FEMS Microbiol. Rev.*, 2003, **27**, 239.

Metallothioneins

Milan Vašák & Núria Romero-Isart
University of Zürich, Zürich, Switzerland

Based in part on the article Metallothioneins by Milan Vašák & Jeremias H. R. Kägi which appeared in the Encyclopedia of Inorganic Chemistry, First Edition.

1 Introduction 1
2 Occurrence, Definition, and Elementary Structure 1
3 Three-dimensional Structure of M(II)-Bound Metallothioneins 2
4 Three-dimensional Structure of Cu(I)-bound Metallothioneins 6
5 Structural Flexibility 7
6 Reactivity 8
7 Metal-(γ-EC)$_n$G Peptide Complexes (Phytochelatins) 10
9 Related Articles 11
10 References 11

1 INTRODUCTION

Metallothionein (MT) is a generic name for a superfamily of ubiquitous low molecular mass proteins or polypeptides (*see Polypeptide*) possessing a novel type of sulfur-based metal clusters (*see Cluster*; *Polynuclear Complexes*; and ***Polynuclear Organometallic Cluster Complexes***), usually formed by the preferential coordination of d^{10} metal ions (*see d^n Configuration*). The designation 'metallothionein' reflects the extremely high thiolate sulfur and metal content, both of the order of 10% (w/w). More than four decades after their discovery by Margoshes and Vallee in 1957,[1] the biological role of MTs is often considered to be enigmatic. However, in the postgenomic era it is increasingly clear that MT fulfills protein functions, the relative importance of which depends very much on specific evolved requirements of the particular organism. This is not unexpected, as its unique structural characteristics, potent metal binding, and striking chemical reactivity have bearing on numerous biochemical processes. Vital roles for this pleiotropic protein often result from sequestration of environmental toxic metals cadmium and mercury or its involvement in homeostasis of essential trace metals zinc and copper (*see* ***Metal Ion Toxicity*** and ***Metalloregulation***). They also play a critical role in the chemotherapy of certain cancers, both in the development of tolerance to chemotherapeutics and as an adjunct to reduce toxic side effects. In mammalian cells, the binding of copper to MT plays mainly a role in copper sequestration in copper-related disorders such as Menkes and Wilson's disease (*see* ***Metal-related Diseases of Genetic Origin***). In contrast, in lower organisms and fungi, solely copper-containing MT forms are often present, signifying their functional importance. However, it is becoming increasingly clear that MTs, the major intracellular zinc-binding proteins, play an important regulatory role in zinc uptake, distribution, storage, and release. Apart from their role in zinc metabolism, recent studies suggest their involvement in a number of biological processes, among others, protection against reactive oxygen species, adaptation to stress, protection against brain injury, antiapoptotic effects, or regulation of neuronal outgrowth.[2–4]

The purpose of this article is to cover the structure and chemistry of these proteins and related nonproteinaceous polypeptide complexes with divalent and monovalent metal ions, thereby updating our contribution to the first edition of the Encyclopedia of Inorganic Chemistry.[5] The different aspects of MT structures[6,7] and the recent advances in our knowledge regarding their function have been described.[2,3] A number of general reviews and conference proceedings covering all aspects of MT research are also available.[8–11] As the number of references in this contribution is to be kept to a minimum, in many instances only these review articles will be quoted.

2 OCCURRENCE, DEFINITION, AND ELEMENTARY STRUCTURE

2.1 Occurrence and Definition

MTs have been isolated from vertebrates, invertebrates, plants, and eukaryotic microorganisms (*see Eukaryote*) and from some prokaryotes. Most MTs isolated to date are inducible cellular products (*see Gene Expression*). All vertebrates examined contain two or more distinct MT isoforms, designated MT-1 through MT-4. In mammals, MT-1 and MT-2 are expressed in most tissues, whereas MT-3 is primarily confined to the central nervous system (CNS) and MT-4 to the stratified squamous epithelia. The expression of the best studied MT-1 and MT-2 is regulated at the transcriptional level (*see Gene Expression*). They are inducible by a variety of compounds and stress conditions, including glucocorticoids, cytokines, reactive oxygen species, and metal ions. MT-1 and MT-2 induction by zinc is regulated through its binding to the metal-responsive transcription factor (MTF-1). Zinc binding to two out of the six zinc fingers activates MTF-1, which then binds to specific DNA motifs termed metal-responsive elements (MREs). In contrast, the MT-3 and MT-4 isoforms are relatively unresponsive to these inducers. Although MT is a cytoplasmic protein, during development and in regenerative processes it translocates to the nucleus. The significance of the nuclear retention of MT is unknown.[12] The recent introduction of recombinant-DNA technology has proven an effective alternative to their isolation from natural sources, thereby providing a significant stimulus to the further chemical and biological characterization of this family of metalloproteins.

The first MTs isolated were those from mammalian species. They are composed of a single polypeptide chain of 61–68 amino acids, 20 of which are cysteine residues and none of which are aromatic amino acids or histidine, with a molecular mass between 6–8000 Da. All cysteines occur in the reduced form and are usually coordinated to 7 divalent metal ions (Zn^{II}, Cd^{II}) and up to 12 monovalent copper ions through mercaptide bonds, giving rise to spectroscopic features characteristic of metal-thiolate complexes (*see* ***S-donor Ligands***). In view of this distinct common physico-chemical signature, the MTs have been categorized into three different classes.[13] Class I comprises MTs with amino acid sequences related to the mammalian forms. Class II encompasses analogous proteins, which are only distantly related to the mammalian forms. Class III are polydisperse peptides, also known as phytochelatins, produced by plants, algae, and certain fungi to detoxify heavy metal ions. They are atypical, nontranslationally synthesized polypeptides that have a primary structure consisting of repeating sequences of the γ-glutamyl-cysteinyl dipeptide and a carboxyterminal glycine.[14] More recently, on the basis of sequence similarities and phylogenetic relationships a new classification has been proposed (http://www.expasy.ch/cgi-bin/lists?metallo.txt).[13]

2.2 Primary Structure and Metal Content

The characteristic feature of all MTs is the occurrence of Cys-Xaa-Cys tripeptide sequences (*see Sequencing*), where Xaa stands for an amino acid residue other than Cys (Table 1). Interestingly, the amino acid sequence of protist MT (approx. 100 aa) possesses a repeating Cys-Cys-Cys motif.[13] Most MTs are devoid of aromatic and histidine residues. In all mammalian isoforms, MT-1 through MT-4, the Cys are the most highly conserved residues followed by the basic residue Lys. Compared to the amino acid sequences of widely occurring MT-1/MT-2, the primary structure of brain MT-3 shows a novel Cys(7)-Pro-Cys(8)-Pro motif and two inserts that is, an acidic hexapeptide in the C-terminal region and one Thr in the N-terminal region (Table 1).[15] Only this isoform shows a growth inhibitory activity in neuronal assays. Mutational analysis has shown that the unique Thr(5)-Cys-Pro-Cys-Pro(9) motif appears to be necessary and sufficient for the observed bioactivity.[16]

The metal composition of native MTs depends on the natural source and/or on the previous exposure of the organism to metals. The inducible MT-1 and MT-2 isoforms isolated from adult and fetal human livers contain mainly zinc, while those isolated from adult human kidney contain mainly cadmium with some copper or zinc. It may be noted that in higher organisms MTs are the sole proteins in which cadmium accumulates naturally. Both mammalian tissue specific forms MT-3 and MT-4 contain zinc and copper. In contrast to MTs from mammalian sources, in which zinc, cadmium, and copper can be simultaneously bound, yeast (53 aa) and fungal (25 aa) MTs contain exclusively copper. Specific binding of cadmium or copper to different tissue specific MT forms in vivo has been encountered in the snail *Helix pomatia*.[17]

The bound Zn^{II} and/or Cd^{II} ions to MT are readily released from the protein by acidification (pH 2) yielding the metal-free protein designated as thionein or apoMT. The release of tightly bound Cu^{I} from the MT structure requires more harsh conditions such as 0.5 M HCl or treatment with specific copper chelators.[8] From ^{1}H NMR and far-UV CD studies, apoMT was estimated to contain a predominantly disordered structure.[6] From this protein form, a number of various metal derivatives have been prepared through the method of metal reconstitution (see Section 6.1).[8]

3 THREE-DIMENSIONAL STRUCTURE OF M(II)-BOUND METALLOTHIONEINS

3.1 Spatial Structure

In metallothioneins, the metal-free protein or apoMT, appears to possess a predominantly disordered structure. This conclusion has been drawn from ^{1}H NMR studies of apoMT in which the chemical shifts of proton resonances are comparable with those observed in a mixture of the constituent amino acids. In addition, the rapid exchange rate of the amide protons in

Table 1 Comparison of representative amino acid sequences of the mammalian MT isoforms. The conserved Cys residues are in bold

***β*-domain**			
Mouse MT-1	1	MDPN·**C**S**C**STGGS**C**T**C**TSS**C**A**C**KN**C**K**C**TS**C**K	30
rat MT-2	1	MDPN **C**S**C**ATDGS**C**S**C**AGS**C**K**C**KQ**C**K**C**TS**C**K	30
Human MT-3	1	MDPET**C**P**C**PSGGS**C**T**C**ADS**C**K**C**EG**C**K**C**TS**C**K	31
Human MT-4	1	MDPRE**C**V**C**MSGGI**C**M**C**GDN**C**K**C**TT**C**N**C**KT**C**R	31
***α*-domain**			
Mouse MT-1	31	KS**CC**S**CC**PVG**C**SK**C**AQG**C**V**C**KG······AADK**C**T**CC**A	61
rat MT-2a	31	KS**CC**S**CC**PVG**C**AK**C**SQG**C**I**C**KE······ASDK**C**S**CC**A	61
Human MT-3	32	KS**CC**S**CC**PAE**C**EK**C**AKD**C**V**C**KGGEAAEAEAEK**C**S**CC**Q	68
Human MT-4	32	KS**CC**P**CC**PPG**C**AK**C**ARG**C**I**C**KG······GSDK**C**S**CC**P	62

the apoprotein is also consistent with a mainly disordered structure.[18] However, upon binding of metal ions to apoMT a well-defined protein fold develops. The first elucidated three-dimensional (3D) MT structure was that of mammalian MT-2 both by multidimensional/multinuclear NMR (*see Protein Structure by NMR*) and X-ray crystallographic methods (*see* ***Diffraction Methods in Inorganic Chemistry***). The crystal structure of rat Cd_5,Zn_2-MT-2[19] and the solution NMR structures of $^{113}Cd_7$-MT-2 from rabbit,[20] rat,[21] and human[22] sources showed identical metal-thiolate cluster structures and closely similar global polypeptide folds (Figure 1).[23]

Thus, the monomeric proteins possess a dumbbell-like shape with uniformly sized and almost spherical C-terminal α- and N-terminal β-domains, each with a diameter of 15–20 Å and containing at their centers the respective four and three metal clusters: $M^{II}{}_4Cys_{11}$ and $M^{II}{}_3Cys_9$. The metal ions in both clusters are tetrahedrally coordinated by both terminal and μ_2-bridging thiolate ligands and the two-protein domains are connected by a flexible hinge region composed of a conserved Lys–Lys segment (residues 30 and 31) in the middle of the polypeptide chain. The discontinuity in the NMR structure between these two residues (Figure 1(b)) is due to the lack of NOE-based information in the NMR data as to the mutual orientation of the two domains. Comparative 2-D ^1H NMR studies of human Zn_7- and $^{113}Cd_7$-MT-2 revealed closely similar secondary structure elements and $^1H-^2H$ amide exchange properties indicative of a closely similar molecular architecture in the two metal derivatives.[22,24] Also, the NMR solution structure of recombinant mouse $^{113}Cd_7$-MT-1 showed a high similarity to that of Cd_7-MT-2. Within the β-domain, however, evidence for increased flexibility compared to the β-domain of MT-2 was found.[25] Relevant information is also available on the structure of the mammalian isoform MT-3. Spectroscopic data on recombinant human Zn_7- and Cd_7-MT-3 have shown that, similarly to $M^{II}{}_7$-MT-1/-2, $M^{II}{}_7$-MT-3 possesses two-protein domains, each encompassing a metal-thiolate cluster: a 3-metal cluster, $M^{II}{}_3Cys_9$, located in the N-terminal β-domain (residues 1–30) and a 4-metal cluster, $M^{II}{}_4Cys_{11}$, in the C-terminal α-domain (residues 31–68).[26] However, markedly increased structural flexibility and cluster dynamics were observed in this isoform (see Section 5). Consequently, only the solution structure of the α-domain of mouse $^{113}Cd_7$-MT-3 could be determined by NMR,[27] revealing a peptide fold and cluster organization very similar to those found in MT-1 and MT-2. The only exception being a short peptide loop in MT-3 that accommodates the acidic insert (Lys52-Glu60) relative to these isoforms (Figure 2). A β-domain peptide fold of Cd_7-MT-3 similar to that found in Cd_7-MT-1/-2 has been suggested by homology modeling studies.[27]

Complete 3-D solution structures have also been elucidated for a nonmammalian vertebrate and for three invertebrate M^{II}-MT forms: fish Cd_7-MT_nc (*Notothenia coriiceps*, 60 aa), crustacean blue crab Cd_6-MT-1 (*Callinectes sapidus*, 59 aa), lobster Cd_6-MT-1 (*Homarus americanus*, 58 aa), and echinoidal sea urchin Cd_7-MTA (*Strongylocentrotus purpuratus*, 64 aa). By analogy to mammalian MTs, all these structures reveal a monomeric protein composed of two globular domains, each encompassing a metal-thiolate cluster: two 3-metal-thiolate clusters in crustacean MTs, and a 3- and a 4-metal cluster in the same or reverse orientation with respect to mammalian MTs in the fish or urchin protein, respectively.[6,28,29] The recent NMR structure of the bacterial metallothionein SmtA (*Synechococcus* PCC 7942, 56 aa) has provided evidence for the first MT structure in which, besides

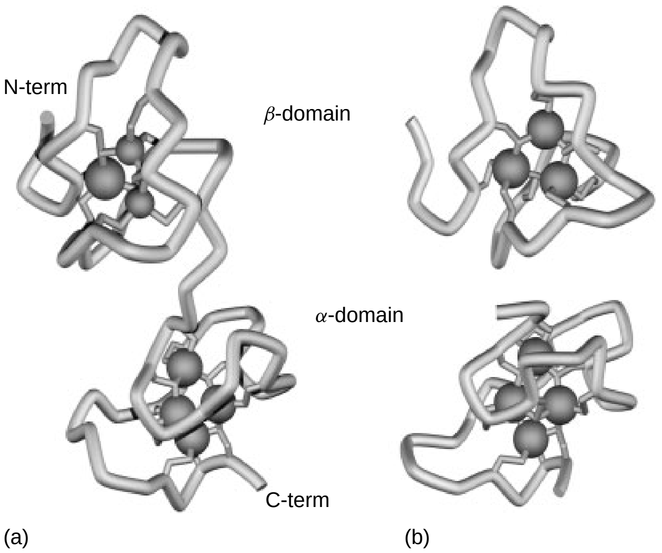

Figure 1 Three-dimensional structure of rat MT-2 as determined (a) by X-ray crystallography, Cd_5,Zn_2-MT-2 and (b) by NMR in aqueous solution, $^{113}Cd_7$-MT-2. Metals are shown as shaded spheres connected to the protein backbone by cysteine thiolate ligands (4mt2, 1mrt, and 2mrt)

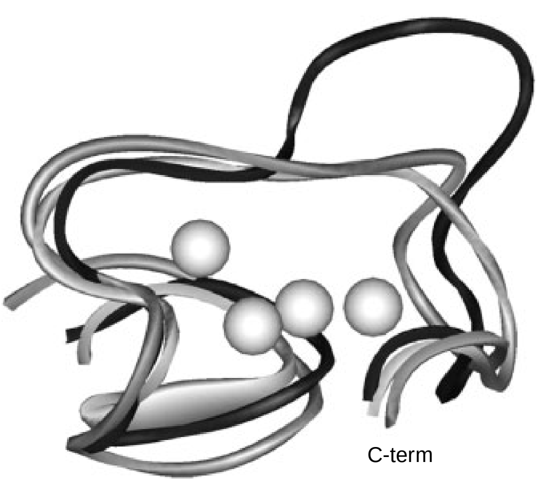

Figure 2 C-terminal α-domain of mouse MT-1 (residues 31–61, light grey), rat MT-2 (residues 31–61, medium grey), and mouse MT-3 (residues 32–68, dark grey). (1dfsa, 1mrt, and 1ji9, respectively)

cysteine thiolates, histidine ligands are also involved in metal binding.[30]

3.2 Geometry of M^{II}-Thiolate Sites and Clusters in Metallothioneins

The general structural properties that characterize all metallothioneins are the formation of metal-thiolate clusters that involve terminal and bridging cysteinyl thiolate ligands of the peptide chain. Consequently, the tertiary structure of the metallated protein is dominated by metal-thiolate clusters, bound in a single domain for the yeast, fungal, or bacterial proteins and in two domains for vertebrate and invertebrate forms. The structure of the M^{II}-clusters in mammalian MT derived from the X-ray diffraction data is shown in Figure 3.[19] The crystallographic structure fully confirmed the geometrical organization of the ligands in the metal binding sites and the topological arrangement of the metal ions in the clusters deduced previously from a number of different spectroscopic and chemical studies, which are discussed below.

The first unambiguous evidence for a pseudo-tetrahedral geometry of metal sites involving the cysteine thiolate ligands was provided by the spin-allowed v_3 $[^4A_2 \rightarrow {}^4T_1(P)]$ ligand field transition (*see Ligand Field Theory*) present in the electronic absorption and magnetic circular dichroism (MCD) spectra of Co^{II}- (*see* ***Cobalt: Inorganic & Coordination Chemistry***) substituted MT (Co_7-MT), displaying well resolved spin-orbit coupling components at 600, 690, and 743 nm (Figure 4), and by the broad v_2 $[^4A_2 \rightarrow {}^4T_1(F)]$ absorption band in the near-IR region at 1275 nm.[31]

The same coordination geometry was also inferred from the analysis of the lowest energy LMCT bands (*see Ligand-to-Metal Charge Transfer*) in the far-UV absorption spectra of Zn_7- and Cd_7-MT, and those of corresponding tetrahedral halide complexes (*see* ***Cadmium: Inorganic & Coordination Chemistry***; *see* ***Zinc: Inorganic & Coordination Chemistry***).[32] Further support came from the presence of the ligand field v_2 $[^5E \rightarrow {}^5T_2]$ transition in the electronic absorption spectrum of Fe_7-MT and from corresponding ^{57}Fe Mössbauer studies (*see* ***Iron: Inorganic & Coordination Chemistry***) in which the zero-field spectrum revealed Mössbauer parameters diagnostic of tetrahedral tetrathiolate metal coordination.[33] The T_d-type of symmetry was also deduced from Zn and Cd K-edge EXAFS (*see Extended X-ray Absorption Fine Structure*) measurements of $M^{II}{}_7$-MT ($M = Zn^{II}$, Cd^{II})[34] (Figure 5) as well as from perturbed angular correlation of gamma-ray (PAC) spectra of ^{111m}Cd-labeled MT.[35]

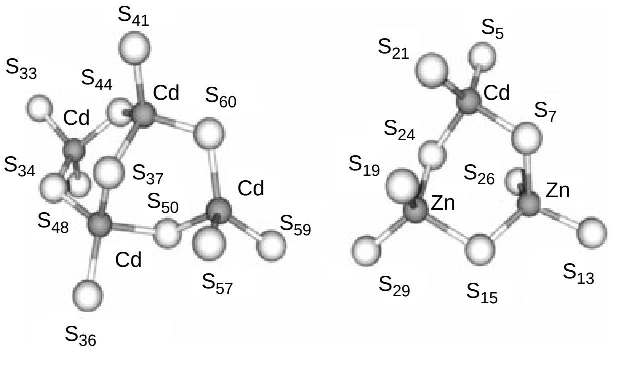

Figure 3 Schematic drawing of the two metal-thiolate clusters in mammalian Zn_2,Cd_5-MT-2: A Cd_4Cys_{11} cluster in the C-terminal α domain and a Zn_2CdCys_9 cluster in the N-terminal β domain. S^{γ} atoms are labeled by Cys residue number (4mt2)

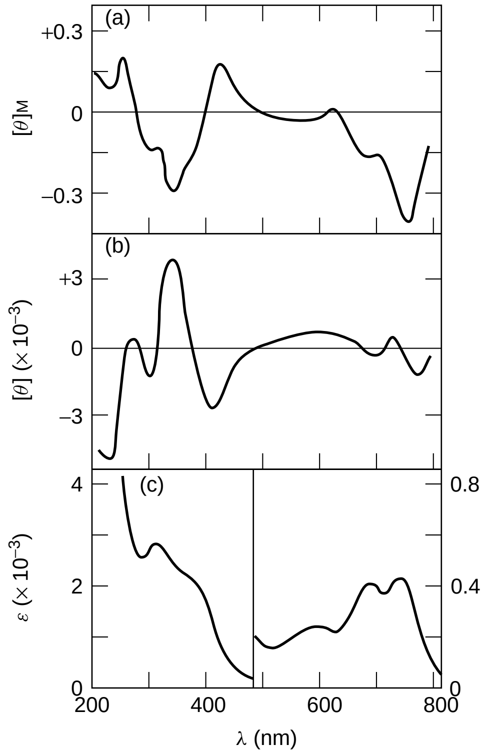

Figure 4 (a) Magnetic circular dichroism, (b) circular dichroism and (c) electronic absorption spectra of Co_7-MT-1 from rabbit liver in 20 mM Tris/HCl, pH 8.6. (Reprinted with permission from Ref. 31. © 1981 American Chemical Society)

Similar spectroscopic approaches provided evidence for a tetrahedral tetrathiolate metal coordination with divalent metal ions in invertebrate MT forms (see Section 3.1).[6,35]

The first and most direct evidence for the existence of the $M^{II}{}_3S_9$- and $M^{II}{}_4S_{11}$-cores in mammalian MTs came from the homonuclear ^{113}Cd NMR decoupling studies on ^{113}Cd reconstituted Cd_7-MT-2.[36] Evidence for a similar cluster organization involving the tetrahedral $M^{II}S_4$ centers was also obtained for Co^{II}- and Fe^{II}-containing MT derivatives. For Co_7-MT such evidence has come indirectly from the temperature dependence of isotropically shifted proton resonances (between −50 and 300 ppm) of the Cys residues of the Co_4-cluster in the C-terminal domain.[37] This was further confirmed by MCD, ESR (*see Electron*

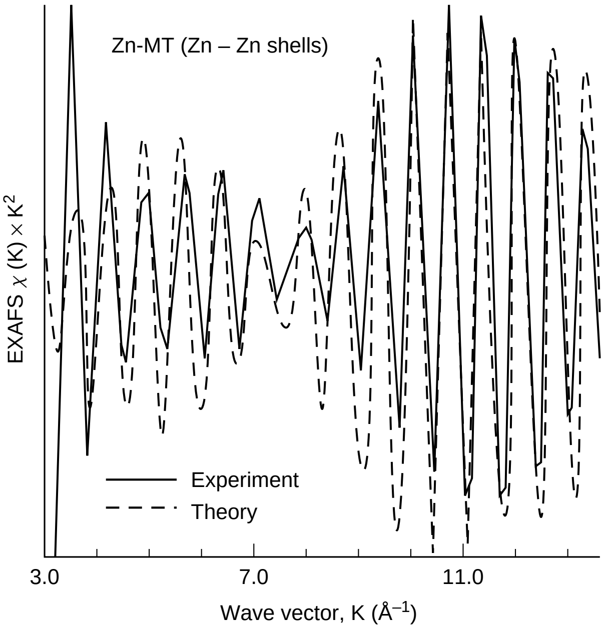

Figure 5 Fourier filtered EXAFS data (R = 4.6–5.8 Å) of Zn_7-MT from rabbit liver and a theoretical simulation with two Zn–Zn separations at 4.8 Å and 5 Å. (Reproduced with permission from Ref. 34. © the Biochemical Society)

Paramagnetic Resonance) and magnetic susceptibility studies of Co_7-MT[35] as well as by ^1H NOESY experiments (*see Paramagnetism*).[38] As for $Fe^{II}{}_7$-MT, the magnetic properties of the Fe^{II} binding sites provided the information concerning the cluster structure (*see Magnetic Susceptibility*). Thus, whereas an adamantane-like 4-metal cluster similar to that found in other $M^{II}{}_7$-MTs (Figure 3) was inferred from strong antiferromagnetic couplings, the weak magnetic exchange couplings between the remaining three adjacent Fe^{II} ions were consistent with a pseudoplanar Fe_3-cluster being present in Fe_7-MT.[39] Analogous magnetic properties have been reported for a number of crystallographically characterized trinuclear $[Fe_3(SR)_3X_6]^{3-}$ clusters ($X = Cl^-$, Br^-; R = Ph, *p*-tolyl, 2,6-$Me_2C_6H_3$) distinguished by the preferential formation of a planar $Fe_3(\mu_2\text{-SR})_3$ ring.[40]

Apart from the 3-metal cluster in Fe_7-MT, which would represent the first example of structural differences in binding divalent metal ions to MT, there is a remarkable overall structure similarity among the 4- and 3-metal clusters in different $M^{II}{}_7$-MT forms. The cluster geometry of the 3-metal clusters can be best described as a distorted boat cyclohexane-like ring, and all 4-metal clusters possess an adamantane-related geometry with the metals and donor atoms arranged in two fused six-membered rings, which almost exclusively adopt distorted boat conformations. A detailed analysis of the metal-thiolate cluster geometries in MTs and inorganic models have recently been reported.[7] This analysis revealed that the predominance of boat-type conformations in MTs contrast with the chair-type usually found in related metal-thiolate complexes. Interestingly, it should be noted that among the extensive family of homoleptic thiolate complexes, those of the formula $[M_3(SR)_9]^{3-}$ and $[M_4(SR)_{11}]^{3-}$ ($M = Zn^{II}$ or Cd^{II}) are unreported.[7] The available inorganic models which approximate best the metal-thiolate clusters in MT are those of adamantane-like cages with monodentate thiolate ligands of the general formula $[M_4(SPh)_{10}]^{2-}$ ($M = Cd^{II}$, Zn^{II}, Co^{II}, Fe^{II}) (Figure 6).[41]

Information on cluster formation in MTs has been forthcoming from various chemical and spectroscopic studies. For instance, by monitoring the intensity of the rhombically distorted Co^{II} EPR signal of Co-MT at pH 8.6 as a function of increasing Co^{II} to apoMT ratios, it was found that cluster formation sets in above four Co^{II} equivalents added, as documented by the occurrence of antiferromagnetic coupling through the bridging μ_2-S-Cys ligands.[35] The transition from mononuclear tetrahedral $M^{II}S_4$ sites to a cluster structure was also manifested by a red shift of the low-energy CysS-M^{II} LMCT bands ($M = Zn^{II}$, Cd^{II}, Co^{II}, Fe^{II}) in the corresponding absorption spectra. Although the electronic basis for the red shift remains to be established, it most likely reflects the reduction of the electronegativity of the thiolate sulfur when μ_2-S-Cys ligands are involved in metal coordination. In the formation of a cluster structure in Cd-MT, this red shift occurred in parallel with a change of the originally monophasic to a biphasic CD profile with a crossover point coinciding with the position of the first LMCT band in the absorption spectrum (at 249 nm). This CD effect has been interpreted in terms of excitonic splitting of the polarized transition dipole moments in the cluster structure (Figure 7).[6,35]

The ^{113}Cd titration studies of apoMT followed by ^{113}Cd NMR measurements both at pH 7.2 and 8.6 showed that at neutral pH the successive addition of $^{113}Cd^{II}$ equivalents leads

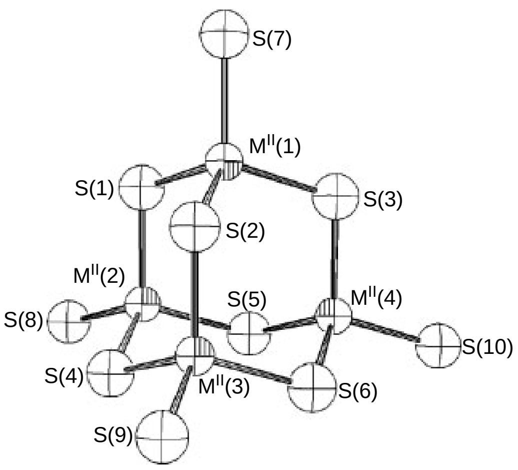

Figure 6 Adamantane-like cage structure of $[M_4(SPh)_{10}]^{2-}$ (phenyl groups omitted) determined with the Cd^{II}, Zn^{II}, and Co^{II} ions. (Reprinted with permission from Ref. 41. © 1982 American Chemical Society)

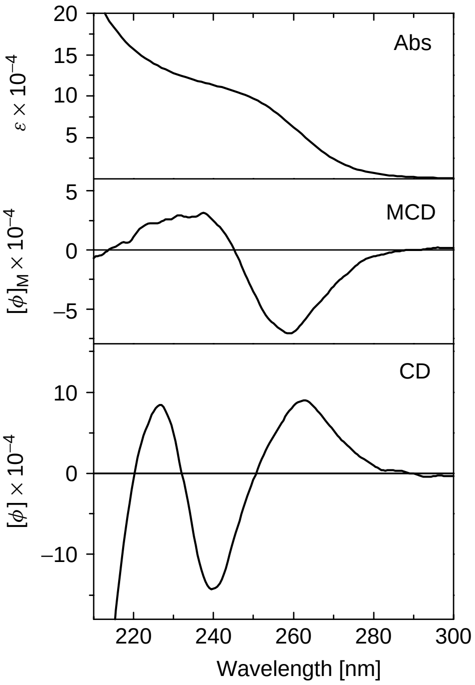

Figure 7 Electronic absorption (Abs), magnetic circular dichroism (MCD), and circular dichroism (CD) spectra of mouse Cd_7-MT-1 in 25 mM Tris/HCl, 50 mM NaCl, pH 8.0.[16] (Reproduced by permission of the American Society for Biochemistry & Molecular Biology)

successively to the cooperative formation of the Cd_4Cys_{11}-cluster followed by the Cd_3Cys_9-cluster. By contrast, under alkaline conditions, $^{113}Cd^{II}$ binds at first to isolated sites and the cluster formation sets in only when at least 4 metal equivalents have been added, again with the 4-metal cluster formation preceding the 3-metal cluster. This observed pH dependence of the cluster formation pathway in MT results from the difference in Gibbs' free energy consumed for the deprotonation of the Cys side chains upon binding of Cd^{II} at the two pH values.[42]

4 THREE-DIMENSIONAL STRUCTURE OF Cu(I)-BOUND METALLOTHIONEINS

The structural features of Cu^I-thiolate clusters in proteins, for example, transcription factors Ace1 and Amt1, MTs, and related proteins have been studied by various spectroscopic techniques including electronic absorption, CD, luminescence, XAS (*see X-ray Absorption Spectroscopy*), and EXAFS.[11] The absorption spectrum of Cu^I-containing MTs shows a broad absorption envelope characterized by a prominent shoulder at 262 nm and a weak shoulder at about 300 nm (Figure 8). The bands in the high-energy region (below 280 nm) originate predominantly from CysS-Cu^I LMCT transitions, whereas those in the low-energy region with very weak molar absorptivities, but rather strong CD bands originate from formally spin-forbidden 3d-4s metal cluster-centered transitions brought about by Cu^I-Cu^I interactions in polynuclear Cu^I complexes.[43] A prominent feature of all Cu-MT complexes is their room temperature luminescence (*see* ***Luminescence***). Upon excitation at 300 nm, yellow or orange emission bands with maxima in the 550 to 650 nm region are observed with a lifetime of about 140 µs at 77 K. The occurrence of an additional high-energy band at 425 nm in the Cu^I luminescence of certain Cu^I-containing MTs at 77 K (lifetime of about 50 µs), has been attributed to the presence of a Cu_4-cluster (Figure 8).[43,44] The measured lifetimes are consistent with the emissions from two distinct triplet excited state manifolds (*see Excited State*). The lower energy emission has been assigned to a triplet LMCT excited state and the higher energy to a triplet cluster-centered excited state, being of mixed d-s/LMCT character.[43]

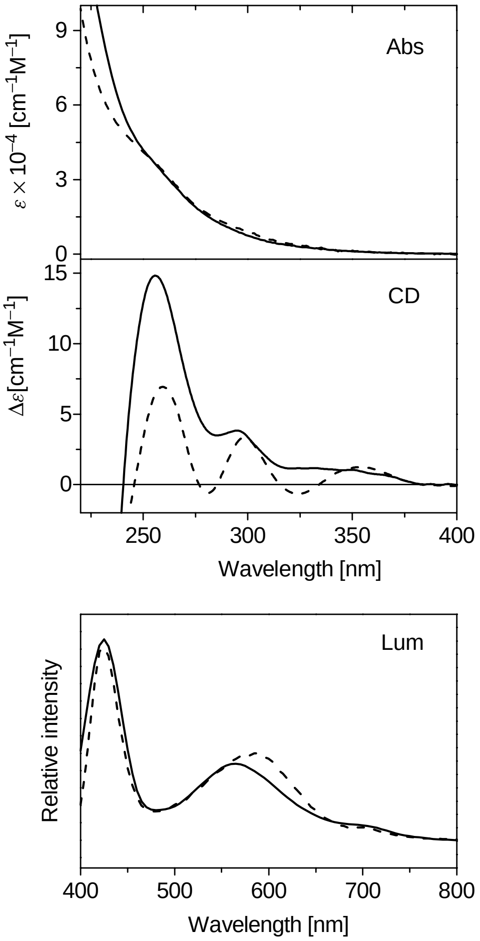

Figure 8 Electronic absorption (Abs), circular dichroism (CD) and luminescence (Lum) spectra, at 77 K and excitation at 300 nm, of human Cu_4,Zn_4-MT-3 (———) and the corresponding Cu_4-cluster in MT-3 (- - - -) at pH 8.0. The spectral features shown originate from the Cu_4-cluster in both species. (Reprinted with permission from Ref. 45. © 2003 American Chemical Society)

At present, our knowledge about the structure of the Cu^I-containing mammalian MT-1 and MT-2 isoforms is limited to the fact that fully Cu-loaded MT form contains 12 Cu^I ions organized in two metal-thiolate clusters, where, in contrast to divalent metal ions, the monovalent copper ions are coordinated by two or three cysteine ligands (*see* ***Copper: Inorganic & Coordination Chemistry***).[11,43] It may be noted that in a number of in vitro studies, even higher Cu^I/MT stoichiometries have been inferred from optical studies.[11,46,47] In MT-3, a mixed Cu^I/Zn MT form, Cu_4,Zn_3-MT-3, was isolated from brains of different mammalian species (see Section 2.2). The EXAFS studies on this species revealed the presence of two homometallic metal-thiolate clusters containing $3Zn^{II}$ and $4Cu^I$ ions with tetrahedral and predominantly trigonal coordination geometry, respectively.[48,49] Evidence for the specific formation of a Cu_4-thiolate cluster in the N-terminal β-domain of MT-3 was obtained by combination of spectroscopic and immunological techniques (Figure 8).[50] A striking feature of this cluster is its remarkable stability against air oxidation. In contrast, the Zn-cluster was found to be air sensitive (see Section 6.3).[45]

The only reported 3-D structure of a Cu^I-containing MT protein is that of yeast (*Saccharomyces cerevisae*) MT of 53 amino acids. The NMR solution structure was determined for the native copper-containing form and for the NMR-active $^{109}Ag^I$ derivative, both showing that 10 out of the 12 available cysteines bind 7 Cu^I or Ag^I ions in a single cluster.[51] However, since it is not certain that Cu/Ag isomorphous replacement can be assumed, a NMR reinvestigation of Cu_7-MT from the same species has been undertaken.[52] In this work, a highly refined structure of the polypeptide chain was determined and the seven Cu^I ions were fitted into the protein cleft formed by a spatial arrangement of the Cys ligands. The subsequent calculations suggested a variety of possible Cu^I-cluster structures fully compatible with the determined geometrical constraints of the protein. Therefore, although no violations of these constraints were found when the previously published sequence specific Cys-Ag^I coordinative bonds were considered, it was concluded that the structure of the Cu_7-cluster derived from the $^{109}Ag_7$-MT derivative is not necessarily correct as the coordination number for Cu^I tends to be larger than that for Ag^I.[52] A recent analysis of the structurally characterized homoleptic thiolate complexes of general formula $M_x{}^I(SR)_y$, $M = Ag^I$ or Cu^I, strongly supports the uncertainty of the Cu^I/Ag^I isomorphous replacement in MTs.[7]

Less detailed structural information is also available for fungal Cu-MT from *Neurospora crassa*, which consists of only 25 amino acids out of which 9 are cysteines. Although the obtained NMR data were not sufficient to permit a structural model to be calculated, they were consistent with the presence of a single protein domain harboring 6 Cu^I ions in a Cu_6Cys_9 cluster.[53]

5 STRUCTURAL FLEXIBILITY

The mobility of the protein backbone structure enfolding the metal core in mammalian MTs is well documented.[54] Both the calculated rmsd values from NMR data and the crystallographic B-factors indicate that a considerable degree of dynamic structural disorder exists (*see Fluxional Molecule*).[19,21] More direct evidence for the nonrigid nature of the MT structure comes from the ^1H NMR $^1H-^2H$ amide exchange studies of Cd_7-MT-1/-2.[25,55] In these studies, the enhanced flexibility of the less constrained β-domain compared to the α-domain in both isoforms has also been demonstrated. Molecular dynamics simulations of the β-domain of rat liver MT-2 in aqueous solution also show that the polypeptide loops between cysteine ligands exhibit an extraordinary flexibility without disrupting the geometry of the 3-metal cluster.[56]

Apart from the conformational flexibility of the polypeptide chain, dynamic processes within the metal-thiolate clusters have also been recognized. Thus, in the Zn K-edge EXAFS studies of Zn_7-MT, substantial movements within the cluster are believed to preclude the observation of Zn–Zn backscattering (second shell) at room temperature.[36] Similarly, in the PAC spectra of ^{111m}Cd-MT, the damping of the major oscillatory component was attributed to inordinately large charge fluctuations in the immediate environment of the ^{111m}Cd nuclei.[35]

The best evidence for metal fluxionality in Cd_7-MT was provided by ^{113}Cd NMR saturation transfer experiments, which established the presence of inter- and/or intramolecular metal exchange within the 3-metal cluster of the β-domain with a half-life of the order of 0.5 s. The confirmation of similar processes taking place within the 4-metal cluster, but with a half-life of about 16 min, was afforded by metal exchange studies using the radioactive ^{109}Cd isotope.[57] In this context, it should be noted that the intersite cadmium exchange measured in the 3-metal cluster of MT-1 was found to be much faster than that in MT-2.[25] This finding was in line with the enhanced backbone flexibility recognized in the NMR studies of the former isoform.[25]

Unprecedented structural flexibility and cluster dynamics was found in the biologically active MT-3 (see Section 3.1). Thus, in the ^{113}Cd NMR spectra of $^{113}Cd_7$-MT-3 (Figure 9(b)), the significant broadening of all ^{113}Cd signals and the very low and temperature-independent intensity of the Cd_3Cys_9-cluster resonances have been interpreted in terms of dynamic events involving *coupled* fast and slow exchange processes, on the ^{113}Cd chemical shift time scale, between conformational and configurational cluster substates in the N-terminal β-domain of the protein.[26] Accordingly, the detected ^{113}Cd signals of the Cd_3Cys_9-cluster in the β-domain reflect only a part of the cluster population, whereas the ^{113}Cd signals of the majority of configurational cluster substates remain undetected, because of an extensive exchange broadening and/or to their low population. The existence of interchanging configurational

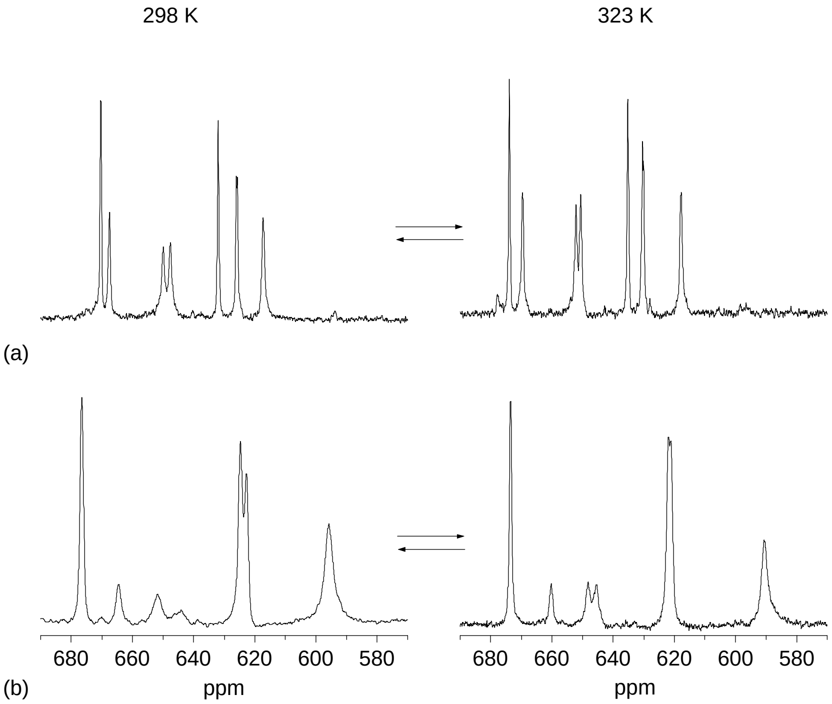

Figure 9 113-MHz ^{113}Cd NMR spectra of (a) mouse ^{113}Cd$_7$-MT-1 and (b) human ^{113}Cd$_7$-MT-3; (a) at 298 and 323 K[16]. (Reproduced by permission of the American Society for Biochemistry & Molecular Biology)

cluster substates, which can be visualized as the temporary breaking and reforming of the metal-thiolate bonds, have already been demonstrated for inorganic adamantane-like metal-thiolate clusters.[41]

Further structural and biological studies on mutated MT-1/-3 forms led to the proposal that the structure/cluster dynamics is required for the biological activity exhibited by MT-3 (see Section 2.2).[16,58] MTs belong to a growing class of proteins with a nonregular protein structure under physiological conditions.[59] In this context, it is worth noting that there is increasing awareness of compact but incompletely folded states of proteins that contain much of the native secondary structure but lack fixed tertiary interactions, playing an important role in many cellular processes.[60]

6 REACTIVITY

6.1 Metal Binding and Exchange

A variety of metal ions has been reported to bind to MT in vivo or in vitro. Homogeneously substituted metal derivatives with stoichiometries, ranging from 7, 10, to 12 and even up to 20 metal ions per protein molecule have been prepared and characterized. These include derivatives containing divalent metal ions such as Zn^{II}, Cd^{II}, Co^{II}, Hg^{II} and trivalent metal ions such as In^{III}, Sb^{III}, Bi^{III}, and TcO^{III}.[7,11] The overwhelming proportion of these metal MT derivatives contain seven metal equivalents, similar to the native Zn$_7$-MT form. Higher metal-to-protein stoichiometries up to 20 are usually observed with monovalent metal ions such as Au^{I}, Ag^{I} and Cu^{I}.[11] As a result of these binding properties different coordination geometries from tetrahedral, square-planar, to linear have been reported. The affinity of the metal ions for the binding sites in MTs follows the order found for inorganic thiolates, that is, Hg^{II} > Ag^{I} ∼ Cu^{I} > Cd^{II} > Zn^{II}.[6] The displacement of one metal by another results in the formation of mixed-metal MT complexes. At neutral pH, closely similar average apparent stability constants have been determined for mammalian M^{II}$_7$-MT by different methods, with values on the order of 10^{11} M^{-1} and 10^{14} M^{-1} for Zn^{II} and Cd^{II}, respectively.[6] The ability of the MT structure to accommodate widely different metal ions led to the suggestion that the protein acts as a ‘metal sponge’ and that no metal selectivity exists.

The metal selectivity of metal-thiolate clusters in MT has been examined by offering seven equivalents of two metal ions in different relative proportions to apoMT that is, Co^{II}/Cd^{II}, Zn^{II}/Cd^{II}, Co^{II}/Zn^{II} and Fe^{II}/Cd^{II}. Subsequently, the respective metal distributions within the clusters were determined using electronic absorption, MCD, ^{113}Cd NMR, ^{57}Fe Mössbauer and EPR spectroscopy, as required.[61,62] The results of the cluster forms in mixed-metal MT derivatives are summarized in Table 2.

Table 2 Cluster types in mixed-metal MT complexes. In parentheses are the spectroscopic methods used in their characterization

MT complexes	Cluster type
Zn_3,$^{113}Cd_4$-MT	distinct heterometallic (^{113}Cd NMR)
Zn_3,Co^{II}_4-MT	distinct heterometallic (MCD, EPR)
Co^{II}_3,$^{113}Cd_4$-MT	distinct homometallic (Absorption, MCD, ^{113}Cd NMR)
Fe^{II}_3,Cd_4-MT	homometallic, Fe_7-, and Cd_7-MT (Mössbauer spectroscopy)

Overall, homometallic clusters were formed with Co^{II}/Cd^{II} or Fe^{II}/Cd^{II}, while heterometallic clusters of distinct composition were formed in MT derivatives incubated with varying proportions of Zn^{II}/Cd^{II} or Co^{II}/Zn^{II}. Thus, an appreciable selectivity in metal partitioning among and within the clusters is indeed observed in this protein. These results are opposite to those obtained in the studies of inorganic adamantane-like cages with monodentate thiolate ligands of the general formula $[M_4(SPh)_{10}]^{2-}$ ($M = Cd^{II}, Zn^{II}, Co^{II}, Fe^{II}$) where, despite the differences in the metal-thiolate affinities and in the homometallic cluster volumes, a simple mixing of two homometallic cages always produced an almost statistical distribution of heterometallic cage complexes.**[41]** Since the same metal ions were employed in the studies of metal selectivity of the protein, properties of the MT structure are responsible for this effect. In these studies, it was concluded that an interplay between both the chemistry of metal ions and the steric requirements of the polypeptide chain would determine the diversity of metal-thiolate cluster structures in MT.

Despite the high thermodynamic stability of metal-thiolate MT complexes, and as a consequence of the dynamic properties of the MT structure (see Section 5), they are kinetically very labile (*see Kinetic Lability*), i.e, the thiolate ligands undergo both metallation and demetallation rapidly. This process is reflected by the facile metal-exchange reactions. MT, with multidentate cysteine thiolates, would resemble chelating inorganic ligands with long bridges, for which a low level of ligand preorganization and hence a high kinetic lability has been shown.**[63]** Qualitatively, the order of the metal replacement in MT follows that of the stability of thiolate model complexes, that is, $Zn^{II} < Cd^{II} < Cu^{I}, Ag^{I}, Hg^{II}, Bi^{III}$. Rapid metal-exchange rate with a half-life of seconds and minutes found in M^{II}_7-MT (see Section 5) also occurs in the binuclear Zn_2Cys_6 cluster of a GAL4 protein involved in the stabilization of the DNA binding domain of this transcription factor as well as in zinc-containing DNA binding proteins, 'zinc-finger proteins' (*see* ***Zinc: DNA-binding Proteins***). By contrast, in zinc enzymes (*see* ***Zinc Enzymes***) for example, alkaline phosphatase, carboxypeptidase, the exchange half-life is on the order of hours and days. Thus, the actual exchange rates of metal ions of protein complexes are not an intrinsic feature of bonding properties of the metal but are determined by the energies and kinetics of protein folding.

Intermolecular metal transfer between MT forms or between MT and other metalloproteins has also been observed.**[6]** Interestingly, in vitro studies have shown that the intermolecular zinc exchange mediated by Zn_7-MT is orders of magnitude faster than the direct exchange between free zinc and a number of other zinc proteins. Moreover, Zn_7-MT has been shown to be able to transfer zinc to apoproteins possessing a much lower affinity for this metal ion, for example, alkaline phosphatase or carboxypeptidase. In this case, however, only one Zn^{II} ion out of the seven in Zn_7-MT was transferred, implying the presence of one weakly bound metal ion.**[64]**

6.2 Ligand Substitution

Studies on ligand-substitution reactivity (*see Ligand Substitution*) have revealed that small multidentate ligands, for example, polyamines, polyaminocarboxylates, bis(thiosemicarbazones), are effective competitors for zinc bound to MT in reactions which are much faster than the dissociation rate constant for zinc in Zn-MTs.**[9]** Biphasic kinetics and differential reactivity of the two metal clusters (α- and β-domain) in mammalian M^{II}_7-MT have been measured with ethylenediaminetetraacetic acid (EDTA) $\beta > \alpha$,**[65]** and, in opposite order $\alpha > \beta$, with nitrilotriacetate (NTA).**[66]** On the other hand, bidentate ligands such as ethylenediamine diacetate and triethylenetetramine were found to be ineffective even at thermodynamically competent concentrations. From these studies, it has been suggested that a tripod configuration of ligands is required in ligand substitution and that only specific regions of the protein domains may provide easy access to the metal clusters.

6.3 Sulfur Reactivity

Although the thiol groups in MT are masked through their interaction with metal ions, they retain a substantial degree of the nucleophilicity (*see Nucleophile*) seen with the metal-free protein. This property is reflected by the extremely high reactivity of the coordinated Cys side chains with alkylating and oxidizing agent such as iodoacetamide or 5,5′-dithiobis-(2-nitrobenzoic acid) (DTNB), respectively.**[6]** Cysteine residues of the zinc-thiolate clusters in Zn_7-MT can also be oxidized by mild cellular oxidants like oxidized glutathione (GSSG),**[64]** releasing bound metal in this process. Experiments in the presence of the GSH/GSSG redox pair gave evidence for an oxidoreductive mechanism modulating the zinc affinity of the cysteine thiolate ligands in vitro.**[67,68]**

Another interesting aspect of MT reactivity is its ability to react with radical species.**[69]** Thus, it has been shown that mammalian M^{II}_7-MT ($M = Zn^{II}$ and/or Cd^{II}) and yeast Cu_7-MT are efficient scavengers of free radicals such as hydroxyl ($OH^{\bullet}$), superoxide ($O_2^{-\bullet}$), or nitric oxide (NO).**[6]** In all cases, the free radical attack occurs at the metal-bound thiolates, leading to protein oxidation and/or modification and subsequent metal release. Interestingly, in many instances these effects could be reversed under reductive conditions and the presence of the appropriate metal ion.

Differential sulfur reactivity of the domains of mammalian MTs has also been reported. Thus, kinetic, mass spectrometric, and NMR studies have shown that the kinetically preferred reaction of mammalian MT with electrophiles may be localized in either the α- or the β-domain depending on the specific attacking reagent. Additionally, modification site selectivity has been observed with some reagents (*see Regiochemistry and Regioselectivity*).**[6]** A redox-labile site in the Zn_4-thiolate cluster containing α-domain of Cu_4,Zn_3-MT-3 and Zn_7-MT-3 has also been observed.**[45]** Thus, while under anaerobic or reducing conditions, a Zn_4-thiolate cluster is formed in the α-domain of MT-3, its oxidation in air resulted in Zn^{II} release giving rise to a Zn_3-cluster.**[45]** These results indicate an increased nucleophilic reactivity of specific thiolate ligands of the protein.

Thiolate coordination is an integral part of a great number of zinc metalloproteins. These sulfur-rich zinc centers fulfill one of two basic roles, either as structural elements, as for example in zinc fingers (*see* ***Zinc: DNA-binding Proteins***), or as a reactive entity for alkyl-group transfer, as for instance in the Ada DNA repair protein. At present, the nondissociative mechanism for alkylation of a specific thiolate ligand is favored. In this context, it is worth noting that studies on inorganic model systems have established that selective reactivity of a bound thiolate in a multithiolate zinc-binding site can be controlled by differences in thiol pK_a.**[70]** Another structural attribute that has been postulated to determine which thiolate ligand in the zinc center is susceptible to modification is its shielding by hydrogen bonding.**[71]** Recent synthetic modeling studies with mononuclear zinc-thiolate complexes have provided quantitative assessment of the role of H-bonding in altering the reactivity of a metal thiolate. Thus, intramolecular hydrogen bonding of an amide N–H to the thiolate sulfur has been shown to reduce the nucleophilicity and consequently the rate of alkylation more than 30-fold at 25 °C.**[72,73]** This would be in line with the presence of deprotonated thiolate ligands in the metal coordination environment as featured by spectroscopic structural analysis of several zinc-binding proteins. However, it is interesting to note that thiol protonation and, thus, electroneutrality of $M^{II}Cys_4$ and $M^{II}Cys_3His$ cores in metalloproteins has also been claimed on the basis of mass spectrometric and alkylation studies.**[6,74]**

7 METAL-(γ-EC)$_n$G PEPTIDE COMPLEXES (PHYTOCHELATINS)

Apart from the widely occurring MTs, some plants and microbial cells have evolved a number of other mechanisms to resist the cytotoxic effect of heavy metal ions. Thus, a family of short gluthatione-related peptides capable of sequestering the metal ions in stable intracellular complexes is synthesized in plants and fungal species exposed to metal salts (see Section 2.1).**[14]** They usually have the general formula (γ-Glu-Cys)$_n$Gly (n is the number of γ-Glu-Cys diisopeptide repeats, typically 2–8) and are designated as γ-EC peptides. In these compounds, the peptide linkages between the glutamate and cysteine residues involves the γ-carboxylate group of glutamate rather than the α-carboxylate group. These γ-EC peptides have been reported under the nondescriptive name phytochelatins. In contrast to metallothioneins, only limited structural data are at present available on metal-γ-EC peptide complexes.

8.1 Cu- and Cd-γ-EC Peptide Complexes

Cu(I)-γ-EC peptide complexes were isolated from the cultured cells of the fission yeast *Schizosaccharomyces pombe* when exposed to copper salts. Based on the similarity of the observed Cu(I) luminescence properties in the 600 nm region with those of Cu-MT (see Section 4), Cu^I-thiolate coordination was suggested.**[75]**

Upon exposure of cultured cells of the yeast *S. pombe* to Cd^{II} ions, two types of Cd-γ-EC complexes were isolated.**[14,76]** The major difference between these two types is the presence of sulfide ions in the structure. The Cd-γ-EC peptide complexes lacking sulfide (M_r between 2500–3500) are characterized by the onset of electronic absorption below 270 nm and a biphasic CD profile (between 270 and 240 nm), features similar to those observed in mammalian Cd_7-MT (Figure 7). Accordingly, for these complexes the presence of bridging μ_2-S-Cys ligands and, hence, a cluster structure was proposed. However, the nonexistence of cluster structure in Cd-γ-EC was claimed by an independent EXAFS study. This discrepancy has recently been reconciled by X-ray absorption spectroscopy of the Cd-γ-EC peptide complexes isolated from maize and their comparison with crystallographically defined inorganic model systems. The studies established the presence of a polynuclear Cd^{II}-cluster in maize phytochelatin with each cadmium being tetrahedrally coordinated by four cysteine ligands.**[77]**

8.2 CdS Crystallites in Yeast

The best studied Cd-γ-EC peptide complexes containing acid labile sulfide as an additional component were isolated from yeasts *S. pombe* and *Candida glabrata* where γ-EC peptides were shown to coat the CdS particles. Ratios of S:Cd in these heterogenous complexes vary from 0.1 to 0.6. This diversity is paralleled by a nondiscrete variation in apparent molecular mass between about 3500–6400 Da, determined by gel exclusion chromatography.**[76,78]** These complexes exhibit a red-shifted absorption profile with a new band in the near-UV region (between 270–320 nm) when compared to the spectrum of complexes lacking CdS centers. The extent of the red shift of the first absorption maximum correlates with increasing particle size. A similar correlation between the location of the red edge of the absorption spectrum and the particle size has been observed with many semiconductor (*see* ***Semiconductors***) crystallites, for example, ZnS and CdS, and is generally referred to as a 'quantum size effect'.[79] In such nanostructures (*see Nanocrystals*), the conducting band continuum of the bulk solid state gives way to more molecular features with discrete excitonic (electron/hole pair) transitions. Owing to the spatial confinement of the exciton in such structures, its energy increases with the reduction of the physical particle size. Photoexcitation of such nanoparticulates also yields luminescence and facilitates electron transfer reactions absent in the bulk solid. Electron transfer reactions of the excited electrons are reflected in the reducing properties of these particles, for example, with electron accepting dyes such as methyl viologen.

The 20 Å diameter monodisperse crystallites isolated from *S. pombe* and *C. glabrata* have been calculated to contain 85 CdS pairs in the lattice coated with approximately 30γ-EC peptides (Figure 10). The particle size was determined using transmission electron microscopy and powder X-ray analysis.[78] The analysis of the X-ray diffraction patterns was inconclusive in discriminating between a four-coordinate zinc blende and six-coordinate rock salt lattice structure. The presence of a short coherence length (8 Å) can be attributed either to internal disorder or to deviation from pure crystallinity. The absorption red edge of the crystallites is located at about 320 nm. The other properties characteristic of semiconductor nanoparticulates such as luminescence with emission near 460 nm, and electron transfer to methyl viologen have also been demonstrated. In vitro reconstitution studies by sulfide ions addition into a Cd-γ-EC peptide mixture led to similar crystallite formation. Thus, the Cd-γ-EC complex provides a matrix for this biomineralization process. Overall, the γ-EC-peptide-metal-sulfide system in yeast offers an interesting possibility to study the initiation and control of metal sulfide biomineralization and may be technically useful in the synthesis of catalytically active nanocrystallites.

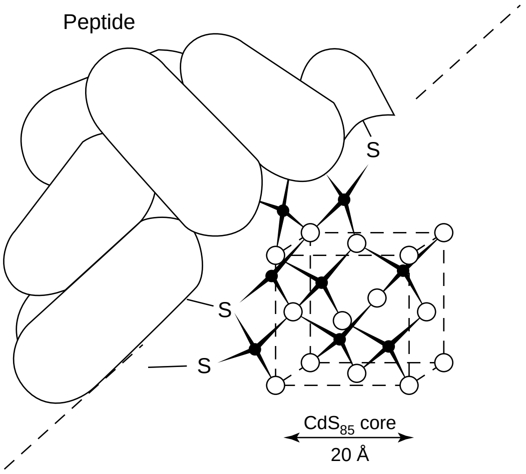

Figure 10 A hypothetical model for the peptide coated CdS crystallite with the cysteinyl thiolates of the peptides providing the surface ligands. The lattice shown is that of a zincblende configuration, but the native particles appear to be more polycrystalline. (Reprinted from Ref. 80. © 1990 with permission from Elsevier)

In summary, MTs represent a ubiquitous but atypical class of diamagnetic metal-thiolate cluster proteins. The unique biological and chemical properties of these proteins have drawn the attention of disciplines as diverse as inorganic chemistry, physics, molecular biology, toxicology, and medicine. The low level of apoprotein preorganization, the abundance and sequence position of cysteine residues, and the chemistry of the bound mono- and divalent d^{10} metal ions provide the highly unusual structural properties of these proteins. The protein fold of a few MTs containing Cu^I-thiolate clusters was determined in solution by NMR. In these NMR structures the precise organization of the corresponding Cu^I-cores is largely unknown. However, during the proofreading of this article the crystal structure of yeast Cu_8-MT was reported.[81] The structure shows the largest known oligonuclear Cu^I-thiolate cluster in biomolecules, consisting of six trigonally and two digonally coordinated Cu^I ions. Although a number of three-dimensional structures of MTs with divalent metal ions are currently available, structural features such as cluster reactivity, dynamics, and metal selectivity of the protein structure remain unexplained. Thus, more studies on the proteins and inorganic models are needed to gain a better understanding of the functional role of MT clusters in biological systems.

9 RELATED ARTICLES

Cadmium: Inorganic & Coordination Chemistry; Cobalt: Inorganic & Coordination Chemistry; Copper: Inorganic & Coordination Chemistry; Diffraction Methods in Inorganic Chemistry; Iron: Inorganic & Coordination Chemistry; Luminescence; Metal Ion Toxicity; Metalloregulation; Polynuclear Organometallic Cluster Complexes; Semiconductors; Zinc: DNA-binding Proteins; Zinc Enzymes; Zinc: Inorganic & Coordination Chemistry.

10 REFERENCES

1. M. Margoshes and B. L. Vallee, *J. Am. Chem. Soc.*, 1957, **79**, 4813.
2. M. Vašák and D. W. Hasler, *Curr. Opin. Chem. Bio.*, 2000, **4**, 177.

3. J. Hidalgo, M. Aschner, P. Zatta, and M. Vašák, *Brain Res. Bull.*, 2001, **55**, 133.
4. J. Hidalgo, M. Penkowa, M. Giralt, J. Carrasco, and A. Molinero, *Methods Enzymol.*, 2002, **348**, 238.
5. M. Vašák and J. H. R. Kägi, Metallothioneins, in ‘Encyclopedia of Inorganic Chemistry’, ed. R. B. King, John Wiley & Sons, New York, 1994, p. 2229.
6. N. Romero-Isart and M. Vašák, *J. Inorg. Biochem.*, 2002, **88**, 388.
7. P. González-Duarte, Metallothioneins, in ‘Comprehensive Coordination Chemistry II’, eds J. A. McCleverty and T. J. Meyer, Elsevier, 2003.
8. J. F. Riordan and B. L. Vallee eds, ‘Methods Enzymol’, Academic Press, San Diego, CA, 1991, p. 201.
9. M. J. Stillman, C. F. Shaw III, and K. T. Suzuki eds, ‘Metallothioneins: Synthesis, Structure, and Properties of Metallothioneins, Phytochelatins and Metal-thiolate Complexes’, VCH, New York, 1992.
10. C. D. Klaasen ed., ‘Metallothionein IV’, Birkhäuser Verlag, Basel 1999.
11. M. J. Stillman, *Coord. Chem. Rev.*, 1995, **144**, 461.
12. M. G. Cherian and M. D. Apostolova, *Cell. Mol. Biol.*, 2000, **46**, 347.
13. P. A. Binz and J. H. R. Kägi, Metallothionein: Molecular Evolution and Classification, in ‘Metallothionein IV’, ed. C. Klaassen, Birkhäuser, Basel, 1999, p. 7.
14. W. E. Rauser, *Plant Physiol.*, 1995, **109**, 1141.
15. Y. Uchida, K. Takio, K. Titani, Y. Ihara, and M. Tomonaga, *Neuron*, 1991, **7**, 337.
16. N. Romero-Isart, L. T. Jensen, O. Zerbe, D. R. Winge, and M. Vašák, *J. Biol. Chem.*, 2002, **277**, 37023.
17. R. Dallinger, B. Berger, P. Hunziker, and J. H. R. Kägi, *Nature*, 1997, **388**, 237.
18. M. Vašák, A. Galdes, J. H. R. Kägi, I. Bremmer, B. W. Young, and H. A. O. Hill, *Biochemistry*, 1980, **19**, 416.
19. A. H. Robbins, D. E. McRee, M. Williamson, S. A. Collett, N. H. Xuong, W. F. Furey, B. C. Wang, and C. D. Stout, *J. Mol. Biol.*, 1991, **221**, 1269.
20. A. Arseniev, P. Schultze, E. Wörgötter, W. Braun, G. Wagner, M. Vašák, J. H. R. Kägi, and K. Wüthrich, *J. Mol. Biol.*, 1988, **201**, 637.
21. P. Schultze, E. Wörgötter, W. Braun, G. Wagner, M. Vašák, J. H. R. Kägi, and K. Wüthrich, *J. Mol. Biol.*, 1988, **203**, 251.
22. B. A. Messerle, A. Schäffer, M. Vašák, J. H. R. Kägi, and K. Wüthrich, *J. Mol. Biol.*, 1990, **214**, 765.
23. W. Braun, M. Vašák, A. H. Robbins, C. D. Stout, G. Wagner, J. H. R. Kägi, and K. Wüthrich, *Proc. Natl. Acad. Sci. U.S.A.*, 1992, **89**, 10124.
24. B. A. Messerle, A. Schäffer, M. Vašák, J. H. R. Kägi, and K. Wüthrich, *J. Mol. Biol.*, 1992, **255**, 433.
25. K. Zangger, G. Öz, J. D. Otvos, and I. M. Armitage, *Protein Sci.*, 1999, **8**, 2630.
26. P. Faller, D. W. Hasler, O. Zerbe, S. Klauser, D. R. Winge, and M. Vašák, *Biochemistry*, 1999, **38**, 10158.
27. G. Öz, K. Zangger, and I. M. Armitage, *Biochemistry*, 2001, **40**, 11433.
28. A. Muñoz, F. H. Forsterling, C. F. Shaw III, and D. H. Petering, *J. Biol. Inorg. Che.(JBIC)*, 2002, **7**, 713.
29. C. Capasso, V. Carginale, O. Crescenzi, D. Di Maro, E. Parisi, R. Spadaccini, and P. A. Temussi, *Structure*, 2003, **11**, 435.
30. C. A. Blindauer, M. D. Harrison, J. A. Parkinson, A. K. Robinson, J. S. Cavet, N. J. Robinson, and P. J. Sadler, *Proc. Natl. Acad. Sci. U.S.A.*, 2001, **98**, 9593.
31. M. Vašák, J. H. R. Kägi, B. Holmquist, and B. L. Vallee, *Biochemistry*, 1981, **20**, 6659.
32. M. Vašák, J. H. R. Kägi, and H. A. Hill, *Biochemistry*, 1981, **20**, 2852.
33. X.-Q. Ding, E. Bill, M. Good, A. X. Trautwein, and M. Vašák, *Eur. J. Biochem.*, 1988, **171**, 711.
34. I. L. Abrahams, I. Bremner, G. P. Diakun, C. D. Garner, S. S. Hasnain, I. Ross, and M. Vašák, *Biochem. J.*, 1986, **236**, 585.
35. M. Vašák and J. H. R. Kägi, Spectroscopic Properties of Metallothioneins, in ‘Metal Ions in Biol. Syst.’, ed. H. Sigel, Marcel Dekker, New York, 1983, p. 213.
36. J. D. Otvos and I. M. Armitage, *Proc. Natl. Acad. Sci. U.S.A.*, 1980, **77**, 7094.
37. I. Bertini, C. Luchinat, L. Messori, and M. Vašák, *J. Am. Chem. Soc.*, 1989, **111**, 7300.
38. I. Bertini, C. Luchinat, L. Messori, and M. Vašák, *Eur. J. Biochem.*, 1993, **211**, 235.
39. X.-Q. Ding, Ch. Buzlaff, E. Bill, D. L. Pountney, G. Henkel, H. Winkler, M. Vašák, and A. X. Trautwein, *Eur. J. Biochem.*, 1994, **220**, 827.
40. M. A. Whitener, J. A. Bashkin, K. S. Hagen, J.-J. Girerd, E. Gamp, N. Edelstein, and R. H. Holm, *J. Am. Chem. Soc.*, 1986, **108**, 5607.
41. K. S. Hagen, D. W. Stephan, and R. H. Holm, *Inorg. Chem.*, 1982, **21**, 3928.
42. M. Good, R. Hollenstein, P. J. Sadler, and M. Vašák, *Biochemistry*, 1988, **27**, 7163.
43. D. L. Pountney, I. Schauwecker, J. Zarn, and M. Vašák, *Biochemistry*, 1994, **33**, 9699.
44. P. C. Ford, E. Cariati, and J. Bourassa, *Chem. Rev.*, 1999, **99**, 3625.
45. B. Roschitzki and M. Vašák, *Biochemistry*, 2003, **42**, 9822.
46. A. R. Green and M. J. Stillman, *Inorg. Chem.*, 1996, **35**, 2799.
47. R. Bofill, M. Capdevila, N. Cols, S. Atrian, and P. González-Duarte, *J. Biol. Inorg. Che. (JBIC)*, 2001, **6**, 405.

48. R. Bogumil, P. Faller, D. L. Pountney, and M. Vašák, *Eur. J. Biochem.*, 1996, **238**, 698.
49. R. Bogumil, P. Faller, P. A. Binz, M. Vašák, J. M. Charnock, and C. D. Garner, *Eur. J. Biochem.*, 1998, **255**, 172.
50. B. Roschitzki and M. Vašák, *J. Biol. Inorg. Che. (JBIC)*, 2002, **7**, 611.
51. C. W. Peterson, S. S. Narula, and I. M. Armitage, *FEBS Lett.*, 1996, **379**, 85.
52. I. Bertini, H.-J. Hartmann, T. Klein, G. Liu, C. Luchinat, and U. Weser, *Eur. J. Biochem.*, 2000, **267**, 1008.
53. J. A. Malikayil, K. Lerch, and I. M. Armitage, *Biochemistry*, 1989, **28**, 2991.
54. J. H. R. Kägi, *Methods Enzymol.*, 1991, **205**, 613.
55. B. A. Messerle, M. Bos, A. Schäffer, M. Vašák, J. H. R. Kägi, and K. Wüthrich, *J. Mol. Biol.*, 1990, **214**, 781.
56. C. D. Berweger, W. Thiel, and W. F. van Gunsteren, *Proteins*, 2000, **41**, 299.
57. J. D. Otvos, X. Liu, H. Li, G. Shen, and M. Basti, Dynamic Aspects of Metallothionein, in ‘Metallothionein III’, eds. K. T. Suzuki, N. Imura, and M. Kimura, Birkhäuser, Basel, 1993, p. 57.
58. D. W. Hasler, L. T. Jensen, O. Zerbe, D. R. Winge, and M. Vašák, *Biochemistry*, 2000, **39**, 14567.
59. E. Smyth, C. D. Syme, E. W. Blanch, L. Hecht, M. Vašák, and L. D. Barron, *Biopolymers*, 2001, **58**, 138.
60. P. E. Wright and H. J. Dyson, *J. Mol. Biol.*, 1999, **293**, 321.
61. M. Good, R. Hollenstein, and M. Vašák, *Eur. J. Biochem.*, 1991, **197**, 655.
62. D. L. Pountney and M. Vašák, *Eur. J. Biochem.*, 1992, **209**, 335.
63. A. E. Martell, R. D. Hancock, and R. J. Motekaitis, *Coord. Chem. Rev.*, 1994, **133**, 39.
64. C. Jacob, W. Maret, and B. L. Vallee, *Proc. Natl. Acad. Sci. U.S.A.*, 1998, **95**, 3489.
65. T. Gan, A. Muñoz, C. F. Shaw III, and D. H. Petering, *J. Biol. Chem.*, 1995, **270**, 5339.
66. H. Li and J. D. Otvos, *J. Inorg. Biochem.*, 1998, **70**, 187.
67. W. Maret and B. L. Vallee, *Proc. Natl. Acad. Sci. U.S.A.*, 1998, **95**, 3478.
68. L. J. Jiang, W. Maret, and B. L. Vallee, *Proc. Natl. Acad. Sci. U.S.A.*, 1998, **95**, 3483.
69. J. P. Fabisiak, G. G. Borisenko, S. X. Liu, V. A. Tyurin, B. R. Pitt, and V. E. Kagan, *Methods Enzymol.*, 2002, **353**, 268.
70. B. S. Hammes and C. J. Carrano, *Inorg. Chem.*, 2001, **40**, 919.
71. C. R. Warthen, B. S. Hammes, C. J. Carrano, and D. C. Crans, *J. Biol. Inorg. Che. (JBIC).*, 2001, **6**, 82.
72. S.-J. Chiou, C. G. Riordan, and A. L. Rheingold, *Proc. Natl. Acad. Sci. U.S.A.*, 2003, **100**, 3695.
73. J. N. Smith, Z. Shirin, and C. J. Carrano, *J. Am. Chem. Soc.*, 2003, **125**, 868.
74. A. T. Maynard and D. G. Covell, *J. Am. Chem. Soc.*, 2001, **123**, 1047.
75. R. N. Reese, R. K. Mehra, E. B. Tarbet, and D. R. Winge, *J. Biol. Chem.*, 1988, **263**, 4186.
76. D. J. Plocke and J. H. R. Kägi, *Eur. J. Biochem.*, 1992, **207**, 201.
77. I. J. Pickering, R. C. Prince, G. N. George, W. E. Rauser, W. A. Wickramasinghe, A. A. Watson, C. T. Dameron, I. G. Dance, D. P. Fairlie, and D. E. Salt, *Biochim. Biophys. Acta*, 1999, **1492**, 351.
78. C. T. Dameron, R. N. Reese, R. K. Mehra, A. R. Kortan, P. J. Carroll, M. L. Steigerwald, L. E. Brus, and D. R. Winge, *Nature*, 1989, **338**, 596.
79. A. Henglein, *Chem. Rev.*, 1989, **89**, 1861.
80. C. T. Dameron and D. R. Winge, *Trends Biotechnol.*, 1990, **8**, 3.
81. V. Calderone, B. Dolderer, H.-J Hartmann, H. Echner, C. Luchinat, C. Del Bianco, S. Mangani and U. Weser, *Proc Natl Acad Sci, U S A.*, 2005, **102**, 51.

Acknowledgment

The financial support of the Swiss National Science Foundation throughout this work is gratefully acknowledged. Núria Romero-Isart thanks Fundación Ramón Areces (Spain) for a postdoctoral fellowship.

Metathesis Polymerization Processes by Homogeneous Catalysis

Kenneth B. Wagener, James M. Boncella & Dennis W. Smith, Jr
University of Florida, Gainesville, FL, USA

---

1 Introduction 1
2 Fundamental Mechanistic Aspects of Metathesis Chemistry 2
3 Ring Opening Metathesis Polymerization (ROMP) Chemistry 4
4 Acyclic Diene Metathesis (ADMET) Polymerization Chemistry 6
5 A Brief Summary Statement 10
6 Related Articles 10
7 References 10

---

1 INTRODUCTION

The term alkene (olefin) metathesis refers to the equilibrium reaction shown in equation (1) in which the alkylidene groups of a pair of alkenes are exchanged with one another in the presence of a transition metal-containing catalyst. The reaction involves the net cleavage of the bonds of the substrate(s) and formation of the new carbon–carbon double bonds of the products. Once equilibrium has been established, the resultant product mixture has a distribution of alkenes (including isomers) that is determined solely by the relative thermodynamic stabilities of the products.

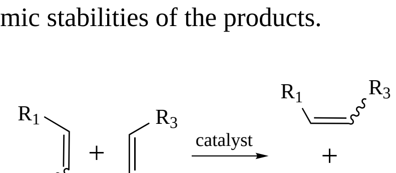

(1)

Both homogeneous and heterogeneous catalysts are effective for this reaction.[1,2] Homogeneous catalysts are usually composed of a transition metal compound combined with a main group metal alkyl cocatalyst, or they consist solely of a well-defined transition metal carbene complex. The most common transition metals used in these catalysts are Mo, W, and Re, although other metals from groups 4–9 have also been used. Literally thousands of different catalyst compositions have been employed in the alkene metathesis reaction, including a variety of heterogeneous catalyst mixtures. An extensive discussion of the properties of all these catalysts is clearly beyond the scope of this review. The discussion presented here will concentrate on the well-defined catalyst systems and their use in polymer synthesis; the extensive literature available on the alkene metathesis reaction provides more detailed information.[1,2]

The metathesis reaction was discovered serendipitously in industrial laboratories in the 1950s during investigations of Zeigler–Natta-type alkene polymerization catalysts,[3] where the surprising observation of ring opening polymerization products (equation 2) rather than the expected addition-type polymers signaled the presence of a new reaction type (*see Ring Opening Metathesis Polymerization Reactions*). This discovery led to the synthesis of numerous polymers via alkene metathesis chemistry using a cyclic alkene monomer as shown in equation (2).

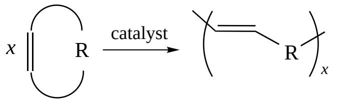

(2)

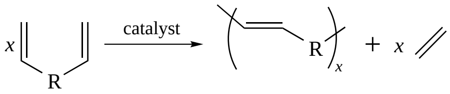

(3)

Ring opening metathesis polymerization, which has been known since the discovery of the alkene metathesis reaction, has been given the acronym ROMP in recent years.[4] In fact, the ROMP reaction was the first observation made in alkene metathesis chemistry, while the discovery of the exchange reaction in equation (1) actually occurred later.[5] Acyclic diene metathesis (ADMET) polymerization (equation 3) has only recently been shown to be a viable method for polymer synthesis, and it has been termed ADMET polymerization.[6] ROMP reactions are driven by the release of ring strain from the monomer, while ADMET polymerization is driven by a shift in the equilibrium caused by the removal of one of the reaction products.

The mechanism of the alkene metathesis reaction is now very well understood and is shown in Scheme 1. The initial mechanistic proposal[7] of a pairwise reaction (the pairwise mechanism) of two alkenes at a transition metal center in a pseudocyclobutane transition metal complex has been discarded in favor of the carbene mechanism (the *Chauvin Mechanism*) of Scheme 1.[8]

Evidence for the carbene mechanism is now so overwhelming (as discussed below) that the pairwise mechanism is only mentioned in this review for historical reasons. All alkene metathesis reactions are catalyzed by a metal carbene complex of some description, and the widely variable compositions used as catalysts are necessary to generate an active metal carbene group.

Alkene metathesis and ROMP reactions have been used industrially to produce a number of chemicals

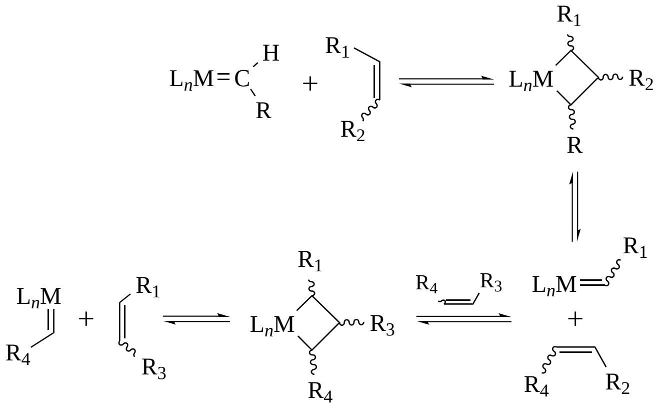

Scheme 1

and polymers.[1,2] Commercial polymers produced using metathesis chemistry include polyoctenamer, polynorbornene, and polydicyclopentadiene,[9] while the metathesis of acyclic alkenes has been used in the synthesis of neohexene and propene, and is a key step in the Shell Higher Olefin Process (SHOP). The polymerization of acyclic dienes has only recently been demonstrated to be feasible, and commercial applications are now under consideration.

2 FUNDAMENTAL MECHANISTIC ASPECTS OF METATHESIS CHEMISTRY

The mechanism described in Scheme 1 (the Chauvin mechanism) is the accepted mechanism of alkene metathesis, and its validity has been demonstrated in two ways. First, classical kinetic studies, including isotopic labeling and crossover experiments performed using poorly defined catalysts, conclusively demonstrated that the carbene mechanism was consistent with the experiments, while the pairwise mechanism was not.[10,11] More recently, the synthesis of isolable carbene complexes that catalyze the reaction has allowed a more direct observation of the reaction.[12,13] Each individual step in the Chauvin mechanism has now been observed spectroscopically for several of the well-defined catalyst systems.

In the mid 1960s, the Goodyear research group led by Calderon recognized that the ring opening polymerization of cyclic alkenes and the alkene exchange chemistry were one and the same reaction.[14] This group coined the term alkene metathesis to describe this chemistry, and soon thereafter an intense amount of study was devoted to understanding the mechanism of this reaction. The 'pairwise mechanism' was proposed in which two substrate alkenes reacted with the transition metal to form a pseudocyclobutane complex (Scheme 2). The exchange of the alkylidene groups was thought to occur by way of the pseudocyclobutane complex to give products. While this was a somewhat appealing explanation of the phenomenon, further mechanistic scrutiny showed that not all the experimental results could be explained with such a simple mechanism.

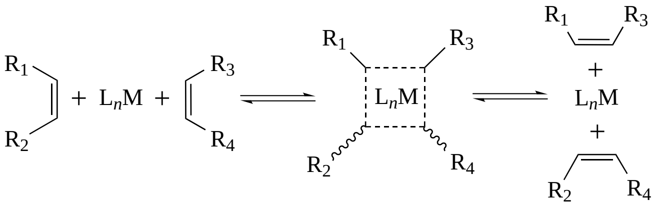

Scheme 2

In 1970, Chauvin[8] proposed a mechanism in which the catalytically active species was a transition metal carbene complex. The carbene mechanism was proposed to account for the products observed when cyclopentene and pent-2-ene were metathesized in the presence of the catalysts WCl_4/Bu_4Sn or $WOCl_4/Et_2AlCl$ (equation 4). The products were observed in a 1:2:1 ratio, even as the initial products. A simple pairwise mechanism, however, would have predicted that compound (**1**) will be the only product initially formed.

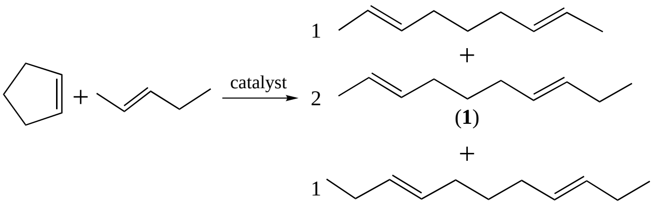

(**1**)

(4)

The suggestion that a metal carbene was the active metal-containing species involved in the reaction inspired an impressive number of elegant experiments, designed to test the validity of this mechanism. The results of double crossover experiments as well as isotopic labeling experiments showed conclusively that a pairwise mechanism could not account for the observed data.[10,11] The reaction shown in equation (5) shows the possible products of the metathesis of two isotopically labeled dienes, and these products include a cyclic alkene derived from the closing of the diene as well as a series of deuterated ethylenes. At very low conversions, the observed ratio of ethylenes was 1:2:1 (d_0:d_2:d_4). A detailed analysis of these results[10] demonstrated that the pairwise mechanism could not possibly account for this result, while the carbene mechanism could.

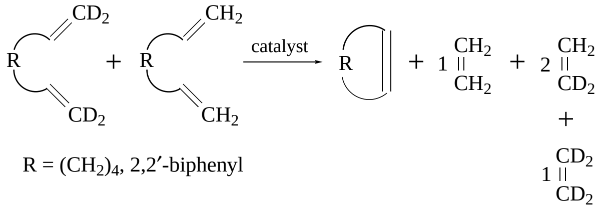

(5)

Although transition metal carbene complexes had been known for six years at the time of Chauvin's proposal, initially there was no evidence that this type of carbene complex would react with an alkene to give metathesis products.[15] Furthermore, the typical alkene metathesis catalysts consisted of metals that were in their highest oxidation states, while the *Fischer-Type Carbene Complexes* complexes (the only ones known at the time) consisted of low-valent metal centers and typically had electron-donating substituents bonded to the carbene carbon. The discovery that the tungsten complex $(CO)_5\,W{=}CPh_2$ could catalyze the polymerization of various cycloalkenes as well as the exchange of the CPh_2 group with ethyl vinyl ether (equation 6) was an example of a single-source metal carbene complex that catalyzed the alkene metathesis reaction.[16] These types of compounds also undergo stoichiometric carbene transfer reactions with alkenes that result in the formation of cyclopropanes, as shown in equation (7). Since 'classical' catalyst systems do not generally give cyclopropanation products, the relevance of the low-valent carbene complexes as models of the typical high-valent transition metal/main group alkyl catalysts was questionable. These complexes did show that isolated metal carbenes could catalyze metathesis reactions and supported the carbene mechanism. The synthesis of better initiators for the metathesis reaction seemed reasonable if the correct type of carbene complex could be synthesized.

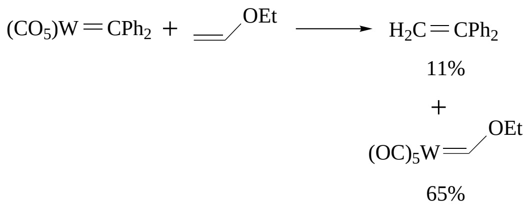

(6)

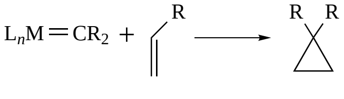

(7)

The synthesis of d^0 *Alkylidene* complexes by Schrock[17] demonstrated that carbene complexes could be isolated that were electronically similar to those postulated to be involved in the alkene metathesis reaction (*see Schrock-type Carbene Complexes*). Eventually, this pioneering work led to the synthesis of a class of compounds that are among the most active catalysts known for metathesis chemistry. The first observation that a d^0 carbene complex was involved in metathesis chemistry was when Tebbe showed that the Ti complex (**2**) would catalyze the degenerate metathesis of deuterated ethylenes (note that this compound can be viewed as a Ti methylene complex that is stabilized by coordination to an aluminum reagent), as shown in equation (8).[18] Reaction of this compound with alkenes in the presence of a Lewis base (equation 9) results in the formation of the metallacyclobutane complexes (**3**).[19] These observations solidified the validity of the carbene mechanism and intensified the search for more efficient, well-defined catalysts.

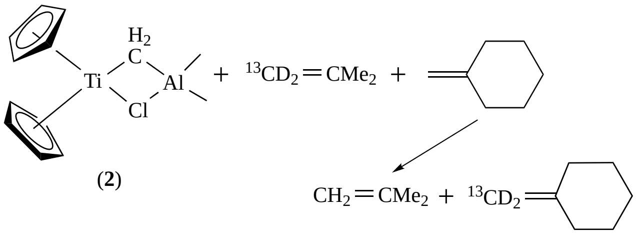

(**2**)

(8)

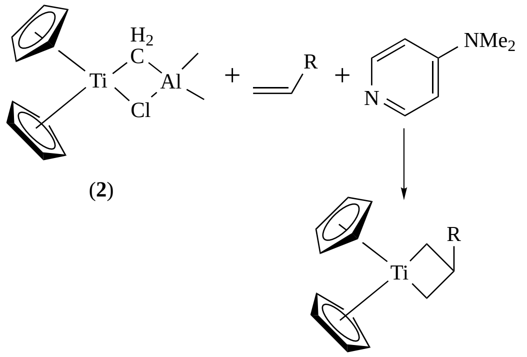

(**2**)

(9)

(**3**)

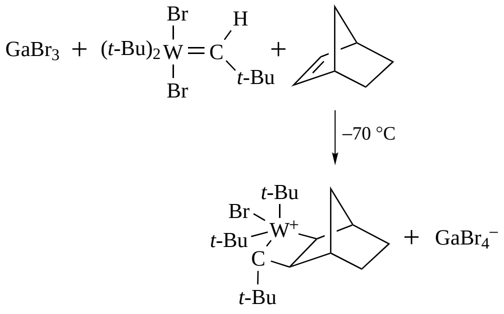

(10)

The initial observation of a metal carbene that reacted with an alkene to give a metallacyclobutane complex was reported by Osborn and coworkers[20] for the reaction shown in equation (10). This reaction was observed by ^{1}H NMR spectroscopy at low temperature (−70 °C). When this reaction mixture was allowed to warm to higher temperature, polynorbornene was produced in high yield. Shortly after this discovery, the titanocene complex (**4**) was shown to be an efficient catalyst for the synthesis of monodisperse polynorbornenes.[21] These discoveries, along with the synthesis of a new family of tungsten (**5a**), molybdenum (**5b**), and rhenium (**6**) catalysts,[22] shown in Figure 1, have opened a new era of ROMP chemistry in which the polymer synthesis is guided by the selection of a catalyst

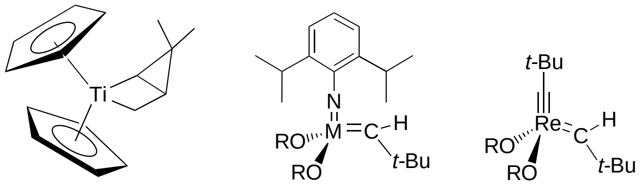

(**4**) (**5a**) M = W, (**5b**) M = Mo (**6**)

Figure 1 A family of well-defined metathesis catalysts

that has a well-defined active site that reacts by way of a well-understood mechanism.

More recent developments in the mechanistic aspects of the alkene metathesis reaction include the observation that the alkene coordinates to the metal carbene complex prior to the formation of the metallacyclobutane complex.[23] Thus a $2 + 2$ addition reaction of the alkene to the carbene is very unlikely, and a vacant coordination site appears to be necessary for catalytic activity. It has also been shown that the metal carbene complex can exist in different rotameric forms (equation 11) and that the two rotamers can have different reactivities toward alkenes.[24] The latter observation may explain why similar ROMP catalysts can produce polymers that have very different stereochemistries.[25] Finally, the synthesis of a well-defined Ru carbene complex (equation 12) that is a good initiator for ROMP reactions suggests that carbenes are probably the active species in catalysts derived from the later transition elements.[26]

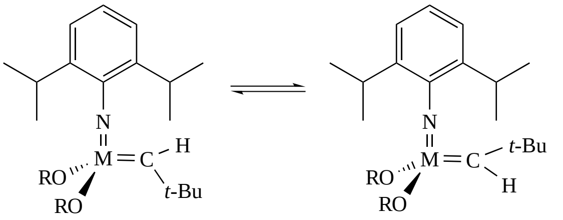

(11)

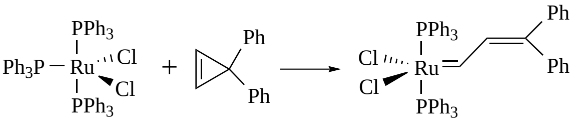

(12)

3 RING OPENING METATHESIS POLYMERIZATION (ROMP) CHEMISTRY

3.1 The Chain Propagation, Addition-type Nature of ROMP Chemistry

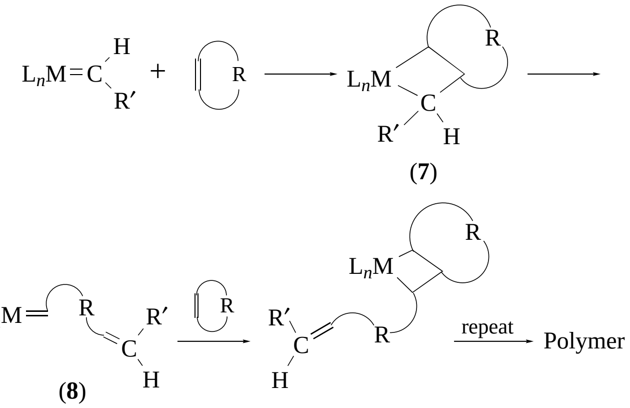

Scheme 3

The ROMP reaction is a special example of the alkene metathesis reaction as shown in equation (2), and the mechanism of the ROMP reaction is shown in Scheme 3. The first step in the reaction involves coordination of the substrate to the metal center, followed by the formation of the metallacyclobutane intermediate (**7**). Opening of the metallacyclobutane ring generates the first new carbene in the system (**8**), and this carbene incorporates the first equivalent of the monomer in what will become the polymer chain. Repetition of the preceding three steps leads to the formation of a polymer that is terminated by the original alkylidene group at one end and by the metal catalyst fragment at the other end. This is chain propagation, addition-type chemistry, where the driving force for the ROMP reaction is the loss of ring strain from the monomer.

In general, the termination reactions of these polymerizations are not well understood but, depending upon the metal and the monomer, reductive coupling of the metal carbene fragments to give alkene and reduced metal complexes is one possibility. Another termination reaction appears to be initiated by *β-Hydride Elimination* from the carbene complex. These mechanisms have been observed in well-defined catalyst systems, and are possible in the ill-defined systems also.[28] The fact that most catalysts are sensitive to oxygen and moisture (or other proton sources) means that termination of the polymer chain by added or adventitious sources of water is a common problem, especially for the ill-defined catalysts.

The details of the ROMP mechanism are useful to help to explain the properties of this reaction. As long as the polymer chain is terminated by the metal carbene, complex (**8**), the growing polymer chain is more reactive toward the monomer than the monomers are with each other. This is one of the necessary requirements for a chain-growth polymerization reaction. The result is that the catalyst will grow a long polymer chain until some reaction occurs to cleave the chain or start a new one (a chain termination, or a chain transfer reaction). In chain propagation chemistry, such as, radical polymerization, the number average molecular weight, M_n, of the polymer is independent of the extent of conversion of the monomer,[27] and this is the behavior of a typical ROMP catalyst, especially the ill-defined catalyst systems, for example, $WCl_6/EtAlCl_2$.[1]

A special case arises when both the rate of chain initiation is greater than the rate of chain propagation and when chain transfer and termination rates are much smaller than the initiation and propagation rates. When such conditions exist during a chain polymerization reaction, the M_n of the polymer is directly proportional to the extent of monomer consumed by each initiator. Thus a plot of M_n verses percent monomer consumed is linear with an intercept of zero.[27] When these conditions are met, a very narrow molecular weight distribution of the polymer results and such polymerization reactions are usually referred to as living polymerizations.

In the context of ROMP chemistry, living polymerization reaction conditions have only been observed when well-defined carbene complexes are used as the catalysts. The first catalyst to behave in this fashion was the titanocene complex (**4**),[21] while more recently, complexes containing Ta, W, and Mo have been shown to be catalysts for the living ROMP of a variety of cyclic alkenes.[22] The Mo complex (**5b**) is an especially promising catalyst since it is compatible with a number of functional groups and thus can be used to synthesize a variety of functionalized polymers.

Another consequence of living polymerization systems is that they can be used to synthesize block copolymers. Under these conditions, once the initial quantity of monomer in a given reaction is consumed, the resultant polymer chains are terminated with metal carbene end groups that are still active for alkene metathesis. As long as these carbenes do not react rapidly with the acyclic alkenes in the polymer chain, addition of a second monomer will result in the synthesis of a block copolymer. This reaction is illustrated in equation (13) for the synthesis of a polymer that consists of block of *x* repeat units of monomer A followed by a block of *y* repeat units of monomer B.

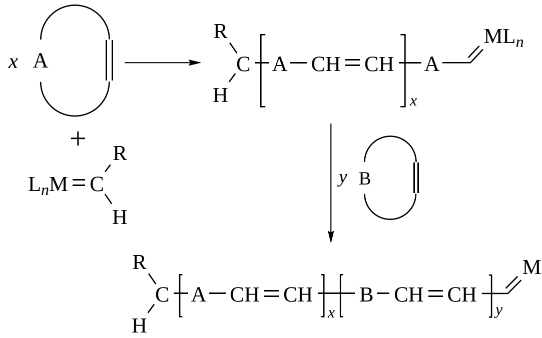

(13)

3.2 Polymers Synthesized by ROMP Chemistry on a Commercial Scale

Concurrent with the development of the mechanistic explanations for the chemistry has been the creation of new polymers based on ROMP chemistry. While a wide variety of strained cyclic monomers have been polymerized with a significant emphasis on monomer structure/reactivity relationships,[1] three ring structures deserve special attention, since they are or have been produced on a commercial scale. These polymers are polyoctenamer (from cyclooctene), polynorbornene (from norbornene), and polydicyclopentadiene (from dicyclopentadiene). The first two structures are linear (thermoplastic) polymers while the last is a network (thermoset) polymer.

The polymerizations yield high molecular weight, linear polymers, under both solution and bulk polymerization conditions. Given their useful physical properties, their commercial synthesis is of particular value. The network polymer, polydicyclopentadiene, is a unique polymer structure (equation 14). This network polymer can be synthesized via bulk polymerization as well and, because of its cross-linked nature, the polymer combines toughness with solvent resistance, chemical inertness, and long-term durability, and its importance in society will continue to grow. The existence of polydicyclopentadiene perhaps is the most important tribute to the success of the ring opening polymerization chemistry done to date.

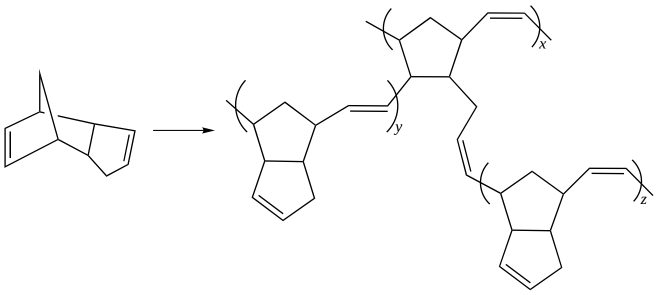

(14)

3.3 Other ROMP Polymers of Particular Interest

Research over the past 30 years has produced a large number of ROMP polymers, and virtually all of these polymerizations have been reviewed elsewhere.[1] The most recent work has revolved about the ‘living’ or ‘pseudoliving’ nature of ROMP polymerization, and a few words regarding this chemistry are worth mentioning here.

The discovery that Ti complex (**4**) was an effective catalyst for living ROMP chemistry resulted in the synthesis of several new types of polymers that were inaccessible with conventional catalysts. Narrow polydispersity polymer and di- and triblock copolymers were synthesized soon after living ROMP was discovered. Because polymer chains that are formed in a living ROMP reaction are terminated with metal carbene groups, functionalization of the chain ends is possible. Reaction of the carbene with an aldehyde occurs in a Wittig-like fashion, making a metal oxo complex that is inert to further metathesis chemistry and terminates the chain with the alkylidene group of the aldehyde.

The living ROMP reactions of norbornene and norbornene derivatives have been used to make a variety of polymers possessing unusual properties. Copolymerization of selected functionalized norbornenes with norbornene has been used to synthesize star polymers[29] and side-chain liquid crystal polymers.[30] This chemistry has also resulted in the preparation of phase separated block copolymers that contain uniform sized metal or semiconductor nanoparticles.[31,32] The synthesis of soluble polyacetylenes[33] and well-defined polyene oligomers[34] has also been achieved using the well-defined tungsten catalysts discussed above.

Clearly, an enormous number of new polymers have and continue to be synthesized using ROMP reactions. The development of the new generation of single-site alkylidene catalysts has introduced a new level of control over ROMP chemistry. Control of polymer microstructure should, in turn, result in a better understanding of the interplay between microstructure and macroscopic properties. The use of living ROMP chemistry is still in its infancy. It will be interesting to observe whether or not useful materials can be developed from this chemistry.

4 ACYCLIC DIENE METATHESIS (ADMET) POLYMERIZATION CHEMISTRY

4.1 The Step Polymerization Mechanism in ADMET Chemistry and Catalyst Selection

The productive metathesis exchange reaction of two acyclic alkenes produces two new alkenes yet, unlike ROMP chemistry, no obvious reference to driving force is noted, except for the increase in entropy associated with an equilibrium process (equation 15).

$$\begin{array}{c}\mathrm{MeCH{=}CH_2}\\+\\\mathrm{MeCH{=}CH_2}\end{array}\ \underset{}{\overset{\text{catalyst}}{\rightleftharpoons}}\ \begin{array}{c}\mathrm{MeCH}\\\|\\\mathrm{MeCH}\end{array}+\begin{array}{c}\mathrm{CH_2}\\\|\\\mathrm{CH_2}\end{array}\qquad(15)$$

If one of the newly formed alkenes is removed selectively from the reaction, however, then the productive metathesis equilibrium is shifted further and faster to product. When applying the scenario to an acyclic reactant containing two metathesizable alkenes (dienes), polymerization should result if high conversions can be achieved. This reaction (equation 16) falls under the category of equilibrium step polymerization chemistry, which, regardless of the chemistry involved, is dictated by strict statistical requirements.[35]

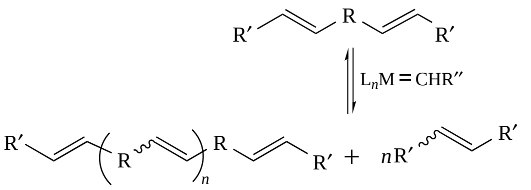

(16)

More specifically, the metathesis polymerization of acyclic alkenes is defined as an equilibrium step propagation, condensation-type polymerization, where the term ‘condensation-type’ arises from the liberation of a by-product that advances the reaction. The other possibility for step polymerization is addition-type, where the resulting polymer linkage is an adduct of the two monomers, and no atoms are lost (e.g. polyurethanes).

Step polymerizations proceed in a stepwise fashion. Monomer is consumed early in the reaction to form dimers, trimers, tetramers, and so on, and the molecular weight is governed by the statistics associated with linking ends of monomer groups. All step polymerizations obey these statistics, oblivious to the nature of the functional groups being connected, and require complete (99.99%) conversions before high molecular weight polymer is formed. In order to achieve these conversions, the stoichiometry of functional groups must be strictly balanced, and side reactions must be completely obviated. The average degree of polymerization (X_n) is dependent upon conversion and stoichiometry, which is governed by the relationship:

$$X_n = \frac{1+r}{(1+r-2r\rho)} \qquad (17)$$

Clearly, the average degree of polymerization, X_n (number of repeat units), depends only on the stoichiometric imbalance ratio, r ($r \le 1$), and the extent of conversion, ρ (expressed as fractional percentage of functional groups consumed). Considering a step polymerization that contains only one type of functional group, as is the case for metathesis polymerization of acyclic dienes, then stoichiometry is perfectly balanced and equation (17) reduces to the Carothers equation.[36]

$$X_n = \frac{1}{(1-\rho)} \qquad (18)$$

A simple plot of the Carothers equation illustrates how functional group conversion governs step polymerization chemistry (Figure 2). Conversions of above 99% are required for high polymer to form.

Although attempts to produce unsaturated polymers by the metathesis of acyclic dienes, using classical-type catalyst systems described earlier, received sparse attention from 1967 to 1987, the strict statistical requirements of step-growth polymer chemistry condemned these early efforts to only limited success.[37–40] Dall’Asta *et al.*[38] were the first to report

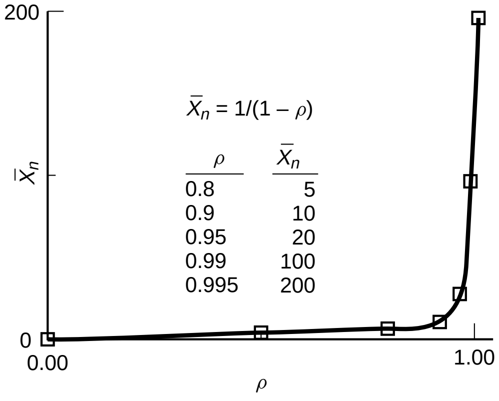

ρ	$\bar{X}_n$
0.8	5
0.9	10
0.95	20
0.99	100
0.995	200

Figure 2 Plot of the Carothers equation in step chemistry

the polycondensation of α,ω-dienes by demonstrating that 1,4-pentadiene and 1,5-hexadiene reacted with traditional Lewis acidic metathesis catalysts to give linear unsaturated oligomers and ethylene. Other early attempts by Doyle[39] and Zuech *et al.*[40] further illustrated the restrictions exhibited by metathesis condensation whereby the use of classical catalyst systems did not result in the formation of high polymer. These Lewis acidic catalysts result in nonselective and highly reactive propagating species where competing reactions destroy the opportunity for the high conversions required for successful step polymerization.

In 1987 it was shown[41] that the early failures of this reaction were due to competing cationic vinyl addition chemistry, and that the elimination of chain propagating carbocations was absolutely essential before successful ADMET polymerization could occur. Attempts to polymerize 1,9-decadiene and 1,5-hexadiene to polyoctenamer and polybutadiene, respectively, using the $WCl_6/EtAlCl_2$ catalyst system, resulted in low conversions of oligomers accompanied by an intractable solid.[41] The solid was rationalized as being a cationically initiated chain polymerization product of the oligomers, where cationic polymerization is done by the Lewis acid. Since most classical catalysts involve a Lewis acid cocatalyst to generate the active alkylidene, the possibility of vinyl addition chemistry had always been present.

To prove the point, model studies were done to demonstrate that crosslinking via cationic initiation was indeed the reaction that competed with metathesis polycondensation.[6,41,42] Substituted styrenes were used to test the hypothesis of cation formation, since styrene is a well-known cationic polymerizable alkene that gives an easily characterized product.[35] When various styrenes were treated with classic Lewis acidic catalyst systems like $WCl_6/EtAlCl_2$, only polystyrene was produced, whereas metathesis products (substituted stilbenes) were not observed (Scheme 4).[41]

These 1987 results concluded that classical metathesis catalyst systems were not sufficient and that Lewis acid cocatalyst-free systems were necessary if successful ADMET condensation polymerization were to become a reality. The key to successful ADMET polymerization was demonstrated[6,42] using the Lewis acid-free tungsten alkylidene metathesis catalyst (**5a**), the structure of which had been reported by Schrock *et al.*[43] just one year earlier. When this catalyst was combined with the styrene model, quantitative metathesis occurred producing only substituted stilbenes.[6,42]

The mechanism of ADMET polymerization (Scheme 5) contains intermediates similar to those found in ROMP chemistry in that both polymerizations contain, inclusively, various metallacyclobutane/carbene species.[44] Although ROMP propagates exclusively via trisubstituted metallacycles, whereas ADMET requires disubstituted metallacycles, the major difference is that ADMET step chemistry is an equilibrium process driven by condensation and ROMP chain chemistry propagates irreversibly owing to the high reactivity of the carbene with strained cycloalkenes. Therefore ROMP is much faster than ADMET simply because competing equilibria, absent during ROMP, decrease the net productive rate in ADMET chemistry.

Studies involving the specific exchange mechanisms,[45,28] as well as theoretical calculations[46–48] of alkene metathesis reactions, generally agree that the mechanism begins with π-coordination of the alkene to the electrophilic metal as shown for a general diene in Scheme 5.

The alkene metal complex (**7**) shown in Scheme 5 undergoes carbene migratory insertion, forming two possible metallacyclobutane complexes (**8a,b**). Cleavage of (**8a**) gives a new carbene (**9**), which is derived from monomer. Productive cleavage of (**8b**), which is not shown in Scheme 5, will generate the methylene complex (**11**). The carbene derived from monomer (**9**) must undergo complexation/metallacycle formation with another equivalent of monomer to generate the α,β-disubstituted metallacycle (**10**). Cleavage of (**10**) gives the methylene complex (**11**), which then reacts with monomer to generate the monosubstituted metallacycle (**12**). Complex (**12**) then extrudes ethylene to regenerate (**9**). These reactions constitute the minimum set of steps that are necessary to form one new C=C double bond and one equivalent of ethylene. The extent of these productive reactions affects the rate of polymerization and depends upon the monomer structure, conversion, and metal catalyst used. Despite the complexity of the catalytic reaction, every reversible condensation cycle gives linear polymer terminated with vinyl end groups.

Summarizing, the mechanism[44] is supported by the following experimental evidence:

1. ethylene is continuously produced during the reaction;

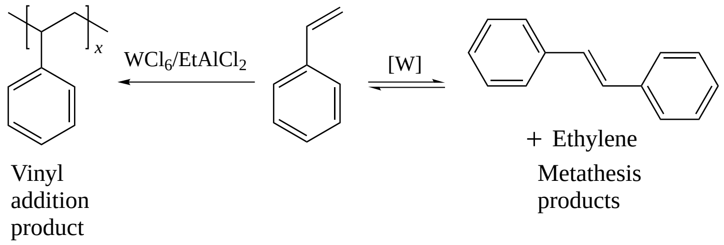

Scheme 4

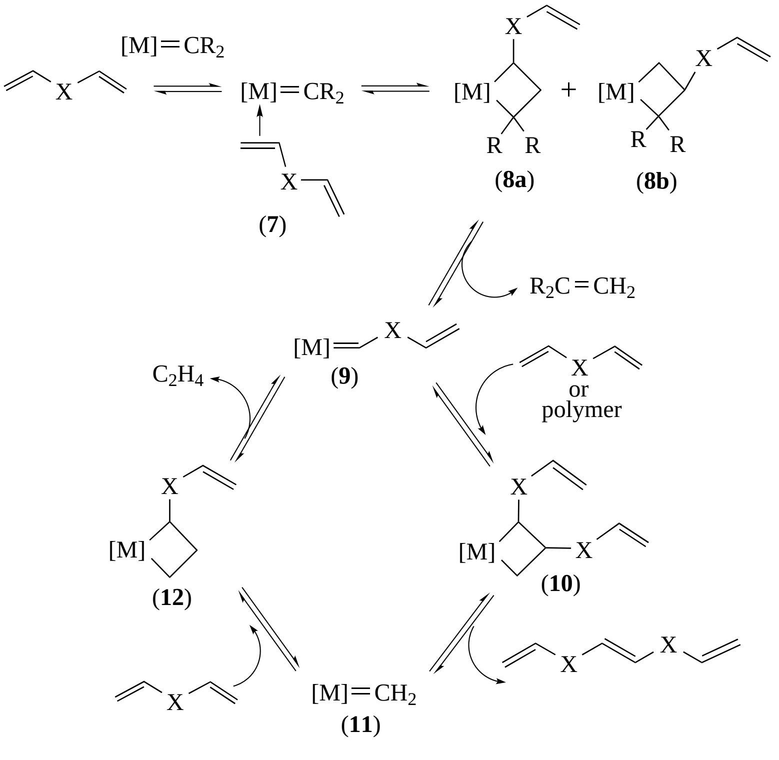

Scheme 5

2. high molecular weight polymer is not observed at low monomer conversions;
3. unpurified polymer reaction mixtures exhibit monomodal molecular weight distributions approaching 2;
4. molecular weight determination by end group analysis (NMR) compare well with colligative property measurements (vapor-pressure osmometry) and relative measurements (gel-permeation chromatography);
5. the average geometric configuration of ADMET polymer increases in trans content as the reaction proceeds, indicative of a dissociative catalysis;
6. an existing ADMET polymer can be polymerized to higher molecular weight or copolymerized with an additional diene by the removal of a monene condensate[49] and;
7. the equilibrium cycle is truly reversible since ADMET polymer can be depolymerized to its original diene monomer by shifting the equilibrium with excess ethylene.[50]

The mechanism sufficiently explains how productive condensation metathesis occurs since terminal alkenes are contained in every step of the productive cycle (Scheme 5). In this kinetically controlled regime (high concentration of terminal alkene present), alkylidene reactions with unsubstituted (terminal) alkenes are favored over interchain redistribution reactions or other degenerate equilibria. However, when terminal alkene concentration decreases near the end of the polycondensation reaction, competing equilibria involving the excess internal alkenes within the polymer are significantly enhanced, and a 'resting state equilibrium' is established. Metathesis reactions that occur in this thermodynamic regime, such as back biting, have been, for the most part, negligible in ADMET chemistry yet do contribute remarkably under some conditions.

4.2 Polymers Synthesized by ADMET Chemistry

Lewis acid-free Schrock alkylidenes provide the means by which successful ADMET polymerization can be achieved, and the scope of this polymerization reaction has been found to be broad. The first high molecular weight polymer was produced by the ADMET condensation of 1,9-decadiene to polyoctenamer (equation 19).[6,42]

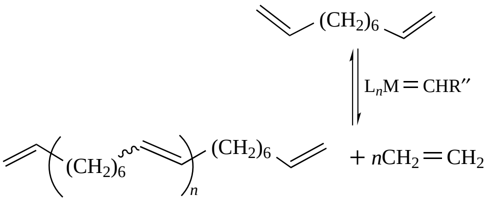

(19)

This polymer is prepared in the bulk by combining rigorously dried and purified monomer in the bulk with the catalyst t-BuCH=M(NC$_6$H$_3$-i-Pr$_2$)[OC(CF$_3$)$_2$Me]$_2$ (equation 1), where M = W or Mo, in the ratio of about 1000/1 monomer to catalyst. Polymerization occurs spontaneously, and high polymer ($M_n = 50\,000$) can be achieved by driving the polymerization via removal of ethylene with a high vacuum.

For ADMET polymerizations in general, the condensation product, ethylene, is observed immediately followed by a rapid increase in viscosity (ca. 30 min). Polymerization reactions are heated to a maximum of 60 °C (generally considered to be catalyst decomposition temperature) and continued for several hours with evacuation of ethylene until stirring is no longer possible owing to formation of the solid state. The ADMET condensation of dienes is an exceptionally clean polymerization reaction and produces a polymer containing only one type of repeat unit and condensate.

1,4-Polybutadiene containing an unprecedented high trans stereochemistry can be synthesized via the ADMET polymerization of 1,5-hexadiene.[44] The extension to other purely hydrocarbon-based homopolymers has shown that (aside from steric factors that influence the formation of the metallacycle in the mechanism) the polymerization method is both trivial and broad in scope.

Random hydrocarbon copolymers can also be produced by this new equilibrium polymerization method.[49] Copolymers containing octenylene and butenylene linkages in a statistical array based on feed ratio result from the cocondensation of the two respective monomers or by the reaction of diene with unsaturated polymer.[49] More controlled polymer structures have also been prepared by the slow addition of a diene solution to an unsaturated polymer containing active catalyst. Substituent effects were shown to dictate the polymerizability of monomers and in some cases selective polymerization of specific alkenes in the monomer resulted in what appears as perfectly alternating copolymers.[51]

As is the case for functional ROMP monomers, the molybdenum-based catalyst used in ADMET chemistry is more tolerant to functionalized dienes than is the tungsten analog. Even so, it is evident that both types of catalysts can be used in the preparation of ADMET polymers possessing various functionalities. For example, ADMET polymers containing the ether functionality can be made (equation 20) if the oxygen atom is placed at least two methylenes apart from the metathesizing alkene ($n = 1$ or greater in the monomer).[52–54] For example, divinyl ether ($n = 0$) and diallyl ether do not polymerize via ADMET techniques, whereas di-n-butenyl ether and higher analogs do, to generate a new class of unsaturated linear polyethers.

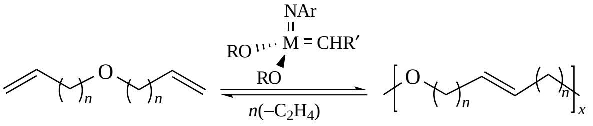

(20)

M = W or Mo

Observations of this nature have also been made for carbonyl-containing monomers (equation 21), and the structure/reactivity relationships for dienes containing esters,[55] carbonates,[56] and ketones[57] have been elucidated. As with previous work, subtle design in monomer structure significantly affects reactivity, and various new unsaturated polymers and copolymers containing these groups were prepared.

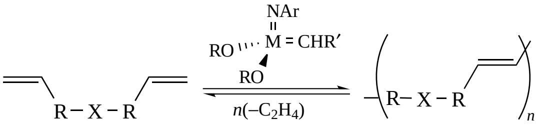

(21)

$X = -CO-, -CO_2-, -OCO_2-; R = -(CH_2)_x-$

The ADMET step condensation polymerization of carbosila- and carbosiloxa-dienes has generated a new class of unsaturated silicon-containing polymers when monomer structure/reactivity relationships, as described earlier for the polar functionalities, are obeyed (equation 22).

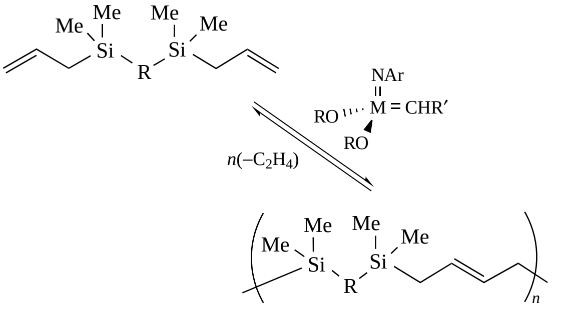

(22)

R = Et, Ph, $-OSiMe_2O-$, $-OSiMe_2PhSiMe_2O-$

Vinylsilane monomers do not homopolymerize owing to steric inhibition within a required catalytic intermediate, yet will specifically copolymerize with an unhindered diene, resulting in isolated units of the vinylsilane within the copolymer. Allylic silanes, however, show no resistance to homometathesis and yield novel high molecular weight, unsaturated polycarbosilanes with low glass transition temperatures and good thermal stability.

4.3 ADMET Depolymerization Chemistry

Scheme 5 suggests that every step of the ADMET polymerization cycle is in equilibrium and that, by shifting the relative concentrations of the condensate and polymer, depolymerization would result. In fact it has been shown that various unsaturated polymers can be depolymerized with excess ethylene,[50] as well as substituted ethylenes. These depolymerizations can be done either with the tungsten or the molybdenum versions of Schrock's catalyst.

Both metathesis degradation (a well documented phenomenon[58]) and metathesis depolymerization offer promise in issues related to chemically recycling discarded unsaturated polymers. However, it should be noted that ADMET depolymerization chemistry is distinguished from metathesis degradation chemistry by virtue of the fact that very specific products result from depolymerization and, in some cases, conversions have been shown to be quantitative. The implications regarding recycling via depolymerization of polymer streams that otherwise would be discarded are clear.

Partial ADMET depolymerizations have been achieved by reaction of ethylene with 1,4-polybutadiene, 1,4-polyisoprene, polyoctenamer, polynorbornene, and poly(styrene-*b*-1,4-butadiene) to yield oligomers of these polymer structures.[50] Polybutadiene also yields 1,5-hexadiene, polyisoprene produces 2-methyl-1,5-hexadiene, and polyoctenamer generates 1,9-decadiene. Depolymerization of the block copolymer demonstrates the potential of directly forming macromers (in this case of polystyrene) from the polymers themselves. These reactions are done in inert solvents such as toluene or chlorobenzene, with a large excess of ethylene being present either at or slightly higher than atmospheric pressure. Generally the reactions are done overnight, and no purification of the products is necessary.

ADMET depolymerizations with substituted alkenes have been done as well, thereby generating perfectly difunctional telechelic molecules. As an example, 1,4-polybutadiene has been depolymerized in an inert atmosphere with a 10-fold molar excess (based on the repeat unit) of either allyltrimethylsilane or allylchlorodimethylsilane (equation 23).[59] In these examples, the chemistry can be driven to complete depolymerization to yield structures with either one, two, three, or four repeat units of 1,4-butadiene. The synthesis of perfectly difunctional oligomers by this chemistry offers significant opportunity, particularly for functional groups such as alcohols, esters, carboxylic acids, and amines.

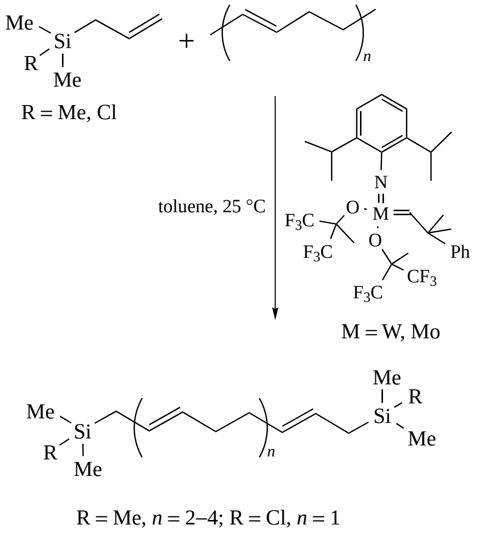

(23)

5 A BRIEF SUMMARY STATEMENT

The past 30 years have produced a wealth of information of both theoretical and practical interest regarding the metathesis reaction. The elegance associated with delineation of the mechanistic details has permitted a high level of sophistication in the synthesis of both conventional polymers as well as previously unknown structures. The key to further advancement in homogeneous metathesis polymerization catalysis will depend upon the creation of stable catalyst structures that can be used at high reaction temperatures. Further, the design of catalysts that are effective under ambient polymerization conditions will be most welcome.

Ultimately the goal of research of this nature is to synthesize polymers possessing a high degree of structural regularity. This goal is not unreasonable, given the rapid advancements in metathesis polymerization, and it is very likely that this method of generating polymers will become as important as the chain and step polymerization schemes that pioneered synthetic polymer chemistry early in this century. We await these developments with a high level of anticipation.

6 RELATED ARTICLES

Molybdenum: Organometallic Chemistry; Oligomerization & Polymerization by Homogeneous Catalysis; Organic Synthesis Using Metal-mediated Metathesis Reactions; Rhenium: Organometallic Chemistry; Titanium: Organometallic Chemistry; Tungsten: Organometallic Chemistry.

7 REFERENCES

1. K. J. Ivin, ‘Olefin Metathesis’, Academic Press, New York, 1983.
2. V. Dragutan, A. T. Balaban, and M. Dimonie, ‘Olefin Metathesis and Ring-Opening Polymerization of Cyclo-Olefins’, Wiley, New York, 1985.
3. H. S. Eleuterio, US Pat. 3 074 918, 1963.
4. T. M. Swager, D. A. Dougherty, and R. H. Grubbs, *J. Am. Chem. Soc.*, 1988, **110**, 2973.
5. G. Natta, G. Dall’Asta, and G. Mazzanti, *Angew. Chem., Int. Ed. Engl.*, 1964, **3**, 723.
6. K. B. Wagener, J. M. Boncella, J. G. Nel, R. P. Duttweiler, and M. A. Hillmyer, *Makromol. Chem.*, 1990, **191**, 365.
7. N. Calderon, E. A. Ofstead, J. P. Ward, W. A. Judy, and K. W. Scott, *J. Am. Chem. Soc.*, 1968, **90**, 4133.
8. J. L. Herisson and Y. Chauvin, *Makromol. Chem.*, 1970, **141**, 161.
9. W. J. Feast, in ‘Comprehensive Polymer Science’, eds. G. Allen, J. C. Bevington, G. C. Eastmond, A. Ledwith, S. Russo, and P. Sigwalt, Pergamon, Oxford, 1989, Vol. 4, p. 135.
10. T. J. Katz, *Adv. Organomet. Chem.*, 1977, **16**, 283.

11. R. H. Grubbs, in 'Comprehensive Organometallic Chemistry', eds. G. Wilkinson, F. G. A. Stone, and E. W. Abel, Pergamon, Oxford, 1982, Vol. 8, p. 449.
12. R. H. Grubbs and W. Tumas, *Science*, 1989, **243**, 907.
13. R. R. Schrock, *Acc. Chem. Res.*, 1990, **23**, 158.
14. K. W. Scott, N. Calderon, E. A. Ofstead, W. A. Judy, and J. P. Ward, *Adv. Chem. Ser.*, 1969, **91**, 399.
15. E. O. Fischer and A. Maasbol, *Angew. Chem., Int. Ed. Engl.*, 1964, **3**, 580.
16. C. P. Casey and T. J. Burkhardt, *J. Am. Chem. Soc.*, 1974, **46**, 7808.
17. R. R. Schrock, *J. Am. Chem. Soc.*, 1974, **96**, 6796.
18. F. N. Tebbe, G. W. Parshall, and D. W. Ovenall, *J. Am. Chem. Soc.*, 1979, **101**, 5074.
19. T. R. Howard, J. B. Lee, and R. H. Grubbs, *J. Am. Chem. Soc.*, 1980, **102**, 6876.
20. J. Kress, J. A. Osburn, R. M. E. Greene, K. J. Ivin, and J. J. Rooney, *J. Am. Chem. Soc.*, 1987, **109**, 899.
21. L. R. Gilliom and R. H. Grubbs, *J. Am. Chem. Soc.*, 1986, **108**, 733.
22. J. Feldman and R. R. Schrock, *Prog. Inorg. Chem.*, 1991, **39**, 1.
23. J. Kress and J. A. Osburn, *Angew. Chem., Int. Ed. Engl.*, 1992, **31**, 1585.
24. J. H. Oskam and R. R. Schrock, *J. Am. Chem. Soc.*, 1992, **114**, 7588.
25. V. C. Gibson and J. Feast, *J. Chem. Soc., Chem. Commun.*, 1992, 1157.
26. S. T. Nguyen, L. K. Johnson, and R. H. Grubbs, *J. Am. Chem. Soc.*, 1992, **114**, 3974.
27. G. Odian, 'Principles of Polymerization', Wiley, New York, 1981.
28. R. R. Schrock, J. S. Murdzek, G. C. Bazan, J. Robbins, M. DiMare, and M. O'Regan, *J. Am. Chem. Soc.*, 1990, **112**, 3875.
29. G. C. Bazan and R. R. Schrock, *Macromolecules*, 1991, **24**, 817.
30. Z. Komiya, C. Pugh, and R. R. Schrock, *Macromolecules*, 1992, **25**, 6586.
31. Y. N. C. Chan, R. R. Schrock, and R. E. Cohen, *J. Am. Chem. Soc.*, 1992, **114**, 7295.
32. C. C. Cummins, R. R. Schrock, and R. E. Cohen, *Chem. Mater.*, 1992, **4**, 27.
33. E. J. Ginsburg, C. B. Gorman, S. R. Marder, and R. H. Grubbs, *J. Am. Chem. Soc.*, 1989, **111**, 7621.
34. K. Knoll and R. R. Schrock, *J. Am. Chem. Soc.*, 1989, **111**, 7989.
35. G. G. Odian, 'Principles of Polymerization', Wiley, New York, 1981.
36. W. H. Carothers, *Trans. Faraday Soc.*, 1936, **32**, 39.
37. K. J. Ivin, 'Olefin Metathesis', Academic Press, New York, 1982.
38. G. Dall'Asta, G. Stigliani, A. Greco, and L. Motta, *Chim. Ind. (Milan)*, 1973, **55**, 142.
39. J. Doyle, *Catalysis*, 1973, **30**, 118.
40. E. A. Zuech, W. B. Hughes, D. H. Kubicek, and E. T. Kittleman, *J. Am. Chem. Soc.*, 1970, **92**, 528.
41. M. Lindmark-Hamberg and K. B. Wagener, *Macromolecules*, 1987, **20**, 2949.
42. J. G. Nel, Acyclic diene metathesis: A new equilibrium step propagation, condensation polymerization, Ph.D. Dissertation, University of Florida, 1989.
43. C. J. Schaverien, J. C. Dewan, and R. R. Schrock, *J. Am. Chem. Soc.*, 1986, **108**, 2771.
44. K. B. Wagener, J. M. Boncella, and J. G. Nel, *Macromolecules*, 1991, **24**, 2649.
45. R. R. Schrock, R. T. DePue, J. Feldman, C. J. Schaverien, J. C. Dewan, and A. H. Liu, *J. Am. Chem. Soc.*, 1988, **110**, 1423.
46. T. R. Cudari and M. S. Gordon, *J. Am. Chem. Soc.*, 1991, **113**, 5231.
47. A. K. Rappé and W. A. Goddard III, *J. Am. Chem. Soc.*, 1982, **104**, 448.
48. T. R. Cundari, *J. Am. Chem. Soc.*, 1992, **114**, 7879.
49. J. G. Nel, J. Konzelman, K. B. Wagener, and J. M. Boncella, *Macromolecules*, 1990, **23**, 5155.
50. K. B. Wagener, R. D. Puts, and D. W. Smith Jr, *Makromol. Chem., Rapid Commun.*, 1991, **12**, 419.
51. J. Konzelman, Acyclic diene metathesis (ADMET) polymerization. A hydrocarbon structure reactivity study, Ph.D. Dissertation, University of Florida, 1993.
52. K. B. Wagener and K. Brzezinska, *Macromolecules*, 1991, **24**, 5273.
53. K. Brzezinska and K. B. Wagener, *Macromolecules*, 1992, **25**, 2049.
54. K. B. Wagener, K. Brzezinska, and C. G. Bauch, *Makromol. Chem., Rapid Commun.*, 1992, **13**, 75.
55. J. T. Patton, J. M. Boncella, and K. B. Wagener, *Macromolecules*, 1992, **25**, 3862.
56. K. B. Wagener and J. T. Patton, *Macromolecules*, 1993, **26**, 249.
57. K. B. Wagener, J. T. Patton, M. D. E. Forbes, T. L. Meyers, and H. D. Maynard, *Polym. Int.*, 1993, **32**, 411.
58. K. Hummel, E. Hubmann, M. Dosinger, and T. Pongratz, *Eur. Polym. J.*, 1991, **27**, 303.
59. J. C. Marmo and K. B. Wagener, *Macromolecules*, 1993, **26**, 2137.

Mixed Donor Ligands

Geoffrey A. Lawrance
University of Newcastle, Callaghan, Australia

Based in part on the article Mixed Donor Ligands by Nikolay N. Gerasimchuk & Kristin Bowman-James which appeared in the Encyclopedia of Inorganic Chemistry, First Edition.

1 Introduction 1
2 Chelating Ligands with Two Types of Donors (A_XB_Y) 2
3 Chelating with Three Types of Donors ($A_XB_YC_Z$) 12
4 Multiple Mixed Donor Ligands 14
5 Common Families of Mixed Donor Ligand 14
6 Polynuclear Systems 18
7 Properties and Reactions 19
8 Related Articles 19
9 References 19

1 INTRODUCTION

Across the enormous range of molecules, including natural molecules, that can act as ligands to metal ions that involve coordination via multiple donors, mixed donor systems predominate and thus represent a vast area of coordination chemistry. The necessary prerequisite is at least didentate capability, the minimum arrangement whereby two different donor atoms are coordinated. A variety of donor atoms, drawn essentially from the p-block of the periodic table, can operate; however, only a small number of atoms are commonly met as donors – predominantly N and O atoms, and to a lesser extent S, P, and heavier elements such as As, Se, and Te. There are also examples of ligands employing C, and heavier elements from group 14. Over 12 000 research papers featuring mixed donor ligands have appeared in the literature in recent decades. For this article, the focus will be on the more commonly met heteroatom donors.

Mixed donor ligands can chelate to metal ions as polydentates, where the heteroatoms bound to the metal center are usually, although not necessarily, linked together via covalent bonding with carbon atoms. The concept of di-, tri-, and tetradentate coordination is illustrated in Figure 1, where A, B, C, and D represent different nonmetals capable of forming coordinate bonds to the central metal atom with significant σ-bond character. The different donor atoms almost invariably lead to different metal-donor distances and consequently distorted geometries about the central metal ion.

A key reason for the predominance of mixed donor systems is that the common donor atoms are met in a number of different donor groups; N in amine or imine, O in alcohol and acid, for example. An example of a classical mixed donor ligand is an amino acid, with both an O and N donor atom; this clearly differs in type from the single N-donor diamine or O-donor dicarboxylate chelates (Figure 2). However, an N-atom donor chelate with one amine group and one pyridine group, or else an O-atom donor chelate with one carboxylate and one alcohol group, are effectively mixed donor ligands, although this is initially less obvious because of the common donor atoms. The two donor groups in each example are distinctly different, even though the two donor atoms are common. It is appropriate to consider such molecules as mixed donor ligands because they present chemical and structural inequivalences in the same way as different groups also containing different donor atoms. The donor groups are related but distinct, like dialects in a language; to identify this particular subclass of mixed donor ligand, where the donor atoms are common but the donor groups differ, we shall classify them as dialectical ligands (Figure 2). They contribute significantly to the family of mixed donor ligands.

For molecules of higher denticity, the presence of mixed donors increases the number of potential ligand topologies as a consequence of the way the component donors may be assembled. This is exemplified for four donor groups in Figure 3, considering a system A_3B with three type A donor groups and a single type B donor group and comparing it with the single donor analogue, A_4. The six topologies illustrated for the A_4 ligand must be expanded to 15 for the A_3B ligand, as a result of considering positional options for the B donor. 'Upgrading' to an A_2B_2 system increases options further. Of course, not all options may be structurally or synthetically practicable, nor even sought, but the enhanced diversity of ligand forms that result as a consequence of introducing mixed donors should be recognized, and is starkly illustrated in Figure 3.

Coordination of a particular mixed donor ligand to a metal ion typically leads to an increase in the number of geometric isomers possible compared with a single donor analogue. This is exemplified with mononuclear tris(didentate) octahedral complexes; a symmetrical ligand like ethane-1,2-diamine exists as a single geometric isomer, whereas a dissymmetric ligand like glycine can form fac and mer isomers. Of course, all the tris(didentate) complexes are also enantiomeric. The potential for a larger number of isomers introduced by coordination of mixed donor ligands (classical or dialectical) rather than single donor ligands should be recognized. For inert metal complexes, separation of isomers is usually practicable; however, with labile metal complexes, isomers may be in dynamic equilibrium and effectively not separable.

Mixed donor ligands present a challenge to the coordination chemist as a result of structural aspects discussed above. Further, the presence of donors of distinctly different character, such as an N-donor and an S-donor, influence the way they select metal ions, and the stability, spectroscopic, and redox properties of their complexes.

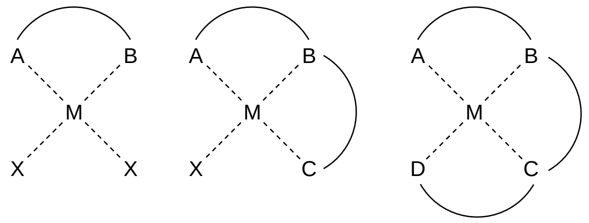

Figure 1 Types of mixed donor ligands

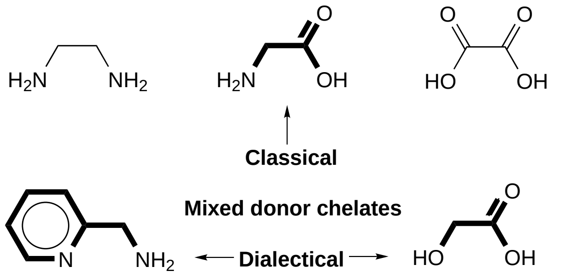

Figure 2 Classes of simple dentate mixed donor ligands

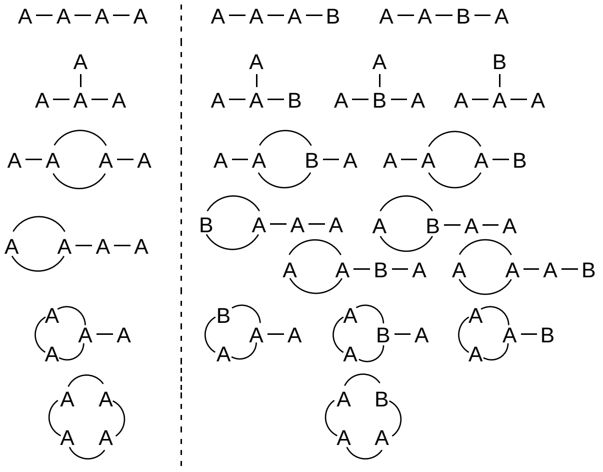

Figure 3 Some topologies for an A_3B mixed donor system compared with an A_4 system

Central to the stability and chemistry of complexes formed by mixed donor ligands are two key concepts of coordination chemistry. The first is the chelate effect, which applies to all polydentate ligands, and reflects the increase in stability of a type of complex as monodentate donor molecules are replaced by polydentates with donors linked by chelate rings. The hard–soft acid–base theory is particularly relevant to mixed donor ligands where donors of distinctly different character may bind to a central metal ion. The 'like prefers like' concept means 'hard' nonpolarizable donor atoms (N and O, for example) bond preferentially to 'hard' nonpolarizable metal ions (high-valent first-row transition metals), whereas 'soft' polarizable ligands (S, P, and As, for example) tend to bond to more polarizable metal ions (low-valent second and third transition metals). For mixed donor ligands with combined hard and soft donors, coordination to a particular metal ion will involve some mismatch, which is reflected in stability and properties of resultant coordination complexes.

The field has been the subject of several reviews of the properties, structures, and stability of numerous ligands and their complexes, including both mixed donor open-chain and macrocyclic polydentates.[1–10] Detailed reports of coordination chemistry that focus on the metal include many examples of mixed donor ligand systems.[11] The nature of this article requires that only limited references are cited herein as examples, but these include some key reviews; readers may access original work through these reviews or else by structure searching from compounds represented in line drawings that appear here.

2 CHELATING LIGANDS WITH TWO TYPES OF DONORS (A_XB_Y)

Ligands with two different types of donors represent the simplest class of mixed donor ligand in principle, but the range and structural diversity is still enormous. Practically, every combination of potential donor groups has been examined; types of donor groups incorporating the four most common donor atoms are exemplified in Table 1. Of course, metal ions play a key role in selection of donors, not only with ambivalent donor groups but also with ligands carrying a surplus of potential donors from which to select.

2.1 Didentate Ligands

Even for simple mixed donor didentate ligands, the scope is virtually limitless. Not only does any combination of two different donor groups lead to a classical or dialectical mixed donor ligand, but also some donor groups are themselves ambivalent donors because they carry two different potential donor atoms in the one group (as exemplified in Table 1), enhancing options for ligand coordination. Chelation to form three-, four-, five-, six-, and higher-membered rings has been observed; this is illustrated with examples in Figure 4, where opening out of the intraligand angle with increasing ring size is also apparent. Didentate mixed N, O, S, and Se donor ligands have been reviewed.[12]

2.1.1 N,O Donor Ligands

α-Amino acids and amino alcohols are the most common examples of N,O donor ligands (Figure 5), and have attracted attention because of potential applications as bioactive

Table 1 Common types of donor groups containing the four most common donor atoms, and examples of ambivalent donors that can bind through one of two potential donor atoms present in a group

Donor Atom	Donor Group	Example
N	Amine	$–NH_2$,–NHR,$–NR_2$
	heterocyclic N-donor	pyridine, imidazole
	Imine	HN=CR–, –N=CR–
	Amido	$–N^-$ –CO–
O	alcohol (or alcoholate)	HO–C (or $^-$O–C)
	Carboxylate	$–COO^-$
	ether (aliphatic, heterocyclic)	C–O–C
	Carbonyl	>C=O
	oxyanions	$–PO_3^-$, $–SO_3^-$, ...
S	Thiol	–SH
	thioether (aliphatic, heterocyclic)	C–S–C
	Thioacid	CSS^-
P	Phosphine	$–PH_3$,$–PRH_2$,$–PR_2H$,$–PR_3$
Ambivalent donors	thioacid (O or S)	HO-C(=S)–
	amide (N or O)	–NH-CO–
	thiophosphate (O or S)	$–PSO_3^-$
	sulfenate (O or S)	–S=O

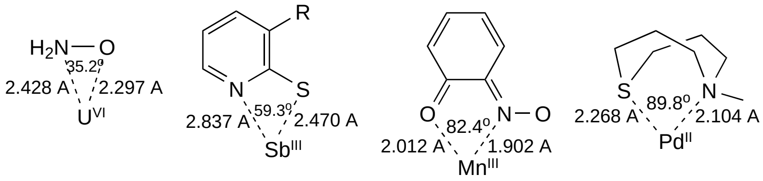

Figure 4 Complexes of mixed donor ligands with from three- to six-membered chelate rings

compounds and catalysts. The simplest member of these two classes are glycine and 2-aminoethanol (**1**; $R = R' = H$; **2**, all $R = H$); substituents introduced in place of the R groups leads to a broad family of compounds. Whereas these two ligands form five-membered chelate rings, the analogues based on the β-amino acid 3-aminopropane (**3**) and 3-aminopropanol (**4**) form six-membered chelate rings; longer chains between donor groups leads to larger chelate rings, but stability diminishes from the five-membered rings upwards; four-membered aminoalcohol rings are rarely met and unstable. Amino acids almost invariably chelate with the carboxylic acid group deprotonated, but some examples of coordinated and protonated acid groups have appeared. In many amino alcohol complexes, both protonated and deprotonated OH groups coexist in the same compound. Monomeric aminoalcohol complexes are well known, and have been well defined by X-ray crystal structures. Polynuclear complexes of the aminoalcohols have been reviewed,[13] and often feature bridging via either deprotonated alkoxides or via hydrogen bonding between an alcohol and alkoxide.

N,O donor molecules where the carboxylic acid group is replaced by another acid group such as sulfonic or phosphonic acid may also chelate efficiently, such as aminophosphonic acids (**5**). Systems with N and O donors bound to an aromatic framework are also well represented, as exemplified by (**6**).

A key characteristic of N-hydroxide, N-oxide, and oxime ligands is the potential for formation of small chelate rings, even the uncommon three-membered chelate rings; while unusual, these have been reported for a number of mixed donor ligands.[14] N-Hydroxides such as hydroxylamine (**7**; $R = R' = H$) and its N-alkylated analogues are capable of forming three-membered chelate rings, although in the presence of alternative larger-ring chelating opportunities three-membered chelate rings may not form, usually being more highly strained. Oximes are molecules with ambidentate groups that can bind to a metal ion via O or N donors, although the majority bind via nitrogen. Amidoximes (**8**), hydroxyoximes (**9**), and nitrosooximes (**10**) are well known as good chelators, and were once widely used as analytical reagents for M^{2+} complexation, the most famous being 'cupron' (**9**; $R = R' = Ph$). Malonamide oximes are N,O didentate ligands, exemplified by the monoanion of the simplest, nitrosomalonodiamide (**11**), which binds Fe^{II} well. The oxime of acetylacetone (**12**) binds to numerous di- and trivalent metal ions. Cyanoximes (**13**), where R is an electron acceptor, can function as ligands but have not been deeply examined. The presence of the nitrile close to the

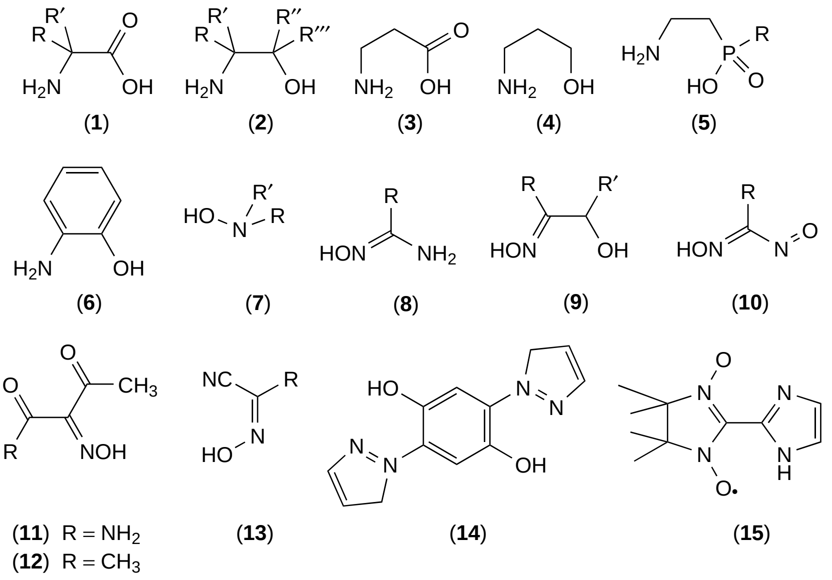

Figure 5 Didentate N,O chelates

oxime functionality leads to greater acidity (pK_a ~ 4.5–5.5) compared to other oxime-containing ligands. Cyanoximes feature in bridging arrangements, but chelation is common for transition metals.

Some N,O ligands reported are formally tetradentate, but contain two didentate compartments, each of which is constrained in such a way that it must bind to different metal ions; they may be termed bis(didentate) ligands. One example is (**14**), which as the dianion binds two $M^{II}(bipy)_2$ fragments (M = Ru, Os), for which ligand-centered oxidations lead to a bridging quinone, while fully oxidized and mixed-valence compounds also form.**[15]** The bridging ligand (**15**) is paramagnetic, and forms one- and two-dimensional polymeric complexes with Mn^{II} involving N,O chelation in opposite directions; some complexes formed display ferromagnetism.**[16]**

2.1.2 N, S and O, S Donor Ligands

Diverse examples of polydentate ligands that feature S-donors in concert with N-, O-, and also P-donors have appeared. Didentate mixed donor sulfur ligands have been reviewed.**[17]**

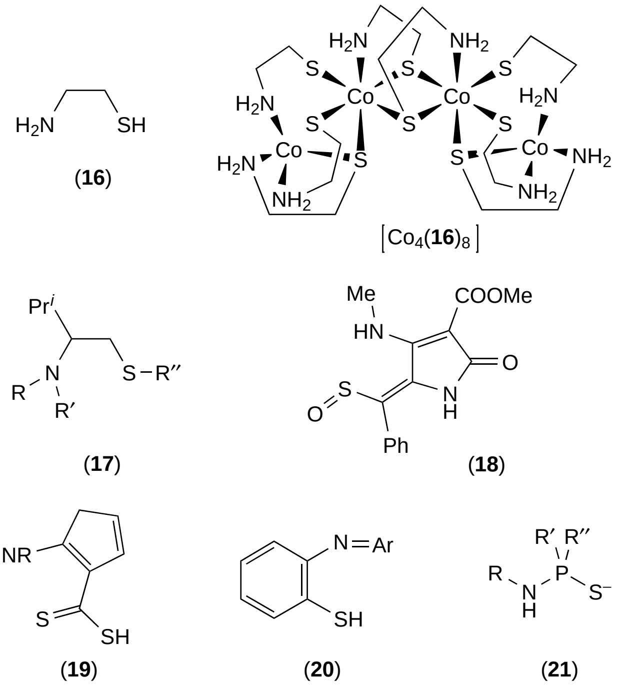

Figure 6 Didentate N,S chelates

N,S donors that bind with chelate ring sizes ranging from six to three are known. Example N,S donors appear in Figure 6. One of the simplest N,S aminothiol chelates is the well known 2-aminoethanethiol (**16**). The deprotonated aminothiolate forms simple ML_2 (M = Cu, Ni, Pd) complexes, but may form polymeric compounds where the S can take on a bridging role. The black tetranuclear compound [Co_4(**16**)$_8$] (Figure 6) features the aminothiolate in simple chelate and bridging roles.**[18]** Chiral aminothiols and aminothioethers (**17**) derived from S-valine have appeared, and are catalysts for asymmetric addition of Et_2Zn to aromatic aldehydes. Oxidation of the thiol donors can occur, leading to ambivalent SO_n-donors, such as (**18**), where coordination of the soft Pt^{II} is still through the soft S atom.**[19]** The aminothioacid (**19**) and its N-alkylated derivatives acts as an N, S chelate, forming six-membered rings with metals like Rh^{III}. The molecules (**20**) are imine-thiol chelates with donor groups attached to a central aromatic ring. Although they form apparently simple

ML_2 complexes with Ni^{II} and Pd^{II}, these complexes show both aromatic stacking interactions and helical distortions.[20] An unusual S,N-chelate, with no carbon atoms in the four-membered chelate ring set, is (**21**); it forms a ‘spirocyclic’ tetrahedral bis Co^{II} complex.

The N,Se donor analogues have been studied selectively. Selenocysteamine has been examined, and its complexation behavior compared with its oxo and thio analogs.[21]

O,S donor chelates include hydroxy-thiols and -thioethers, and thioether-carboxylates (thioacids), such as from (**22**) to (**24**) (Figure 7); these form similar complexes to their amine analogues. Thioacetic acids and their ethers ($RS(CH_2)_nCO_2H$; $n \geq 1$) form at least five-membered chelate rings. Monomeric complexes of 2-mercaptoethanol involve five-membered chelate rings, although these ligands often adopt polymeric structures featuring both O and S bridging. Another simple example of an S,O-chelate is the dianion of 2-mercaptophenol (**25**), which forms strong bis(didentate)metal(II) complexes.

Examples of ligands with a mixed hard–soft O,S donor set that form only four-membered chelate rings are thioacetate (**26**), monothiocarbonate (**27**), and the monothiocarbamates (**28**). Thiohydroxamic acids are long established ligands with wide analytical and biological applications;[3] N-hydroxythiohydroxamic acid (**29**) is an ambivalent ligand, which offer either O,S five-membered rings or N,S four-membered rings. Disulfide donor coordination has been closely examined. Dithiooxamide ligands are other examples of ambivalent ligands, being capable of coordinating either in the S,S or mixed donor modes.[12] Related dithiooxalate (**30**) acts as an O,S didentate chelate when bound to metals as diverse as Ag^{I}, Cu^{II}, and In^{III}.[22] The thiourea monoanion (**31**) has been observed as a chelate in a Tc^{III} phosphine.[23] Pharmacologically active carbazide (**32**; X = O), and related thiosemicarbazides (X = S), and selenosemicarbazides (X = Se) complexes feature N,X (X = O, S, Se) didentate chelation, and the chemistry of this ligand class has been comprehensively reviewed.[24] Selenosemicarbazide (**32**; X = Se, Y = NH_2) has coordination chemistry similar to its thio analog.

2.1.3 Other Didentate Donor Ligands (N,P; O,P; S,P; N,Se; O,Se; S,Se; N,Te; O,Te; N,C)

Simple chelates including soft P, Se, and Te donors with other donors are well known (Figure 8), albeit more often in complexes with heavier and or low-valent metals.

The *N,P donor* didentate ligands are excellent stabilizers of otherwise unstable oxidation states of transition metals. An interest in development of bulky, inert ligands for organometallic chemistry has seen the aminophosphines (**33**) extensively developed.[25] An iminophosphine N,P ligand (**34**) has been reported as a chelate, exemplified by binding to Ni^{II}. The 2-(diphenylphosphino)pyridine ligand (**35**) can chelate simply via a four-membered chelate ring in tetrahedral monomer such as $[Co(\mathbf{35})(NO)_2]^+$, or adopt a bridging mode in dimers (Figure 9).[26] The P,N donor aminophosphine chelate (**36**) exhibits a variety of 4-, 5-, and 6-coordination geometries in divalent metal complexes.

Most *O,P donors* such as (**37**) and (**38**) readily form stable complexes with platinum group metals. Pd complexes of the soft–soft *S,P mixed donor* ligand (**39**) are chiral and resolvable into optical isomers; an As,S analogue is also known. The bicyclo phosphine thiol (**40**) is also chiral, binding Pd^{II} as an S,P chelate.

Mixed donor didentate ligands containing selenium are less well known than their sulfur analogues. A typical example of an *Se,N donor* is (**41**), which coordinates as a didentate chelate; another is (**42**), a selective analytical reagent for platinum group metals. The monoanionic (**43**) forms neutral ML_2 complexes (M^{II} = Zn, Cd, Hg) with an overall N_2Se_2 donor set, with the imine N selected as a much better donor than the alternate ether O.[27] However, *Se,O donor* chelation is displayed by the butane-2,4-dionate analogue (**44**), which forms complexes of Pd^{II}, Hg^{II}, Pb^{II}, Cd^{II}, Co^{III}, and In^{III}. The soft–soft *Se,S donor* simple didentate ligands (**45**) and (**46**; R = H, CH_3) form complexes with Pt^{II} and Pt^{IV}, and the deprotonated ligands stabilize unusual Cu^{III} and Ni^{III}.[28]

Although tellurium chemistry has been reasonably well studied,[29] only relatively few mixed donor ligands have been described. A hard–soft *N,Te donor* didentate is (**47**). An

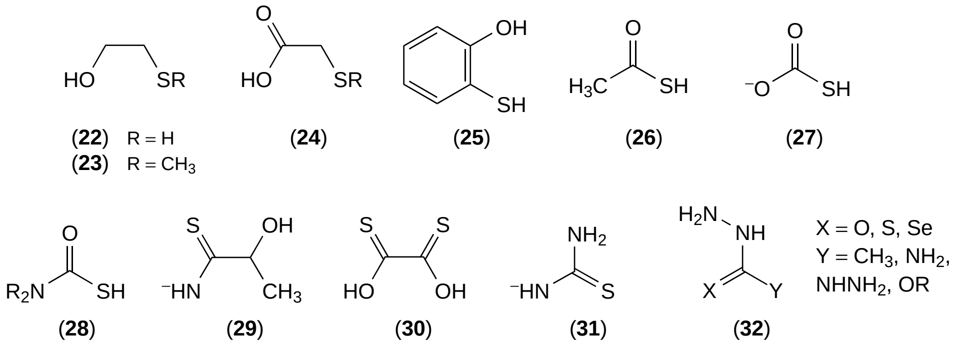

Figure 7 Didentate S,O and S,N chelates

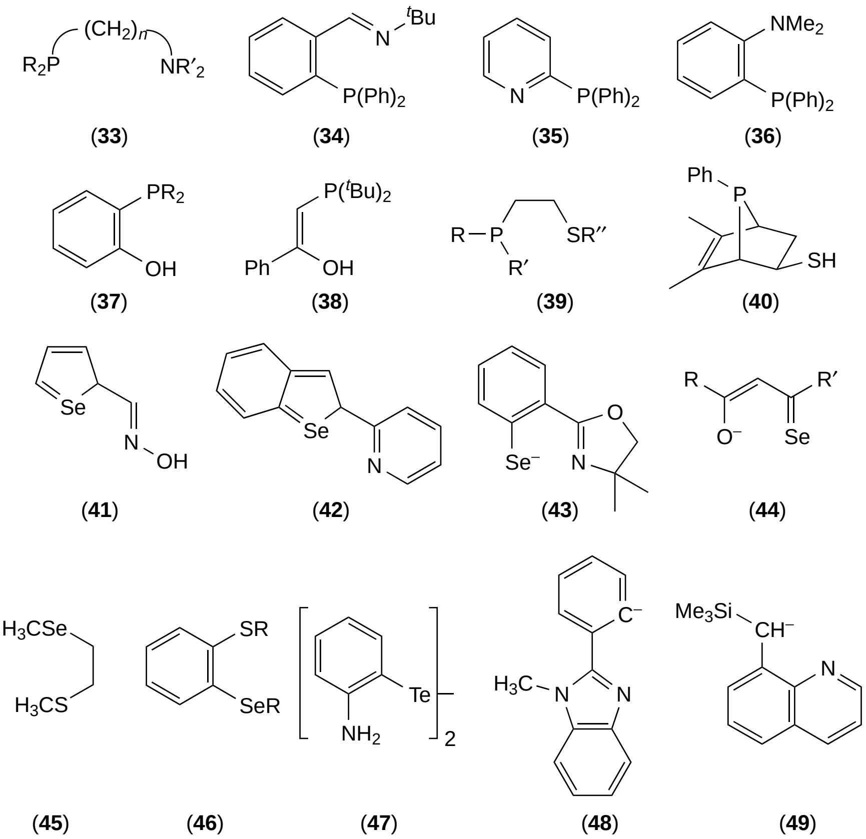

Figure 8 Didentate chelates including a P, Se, Te, or C donor

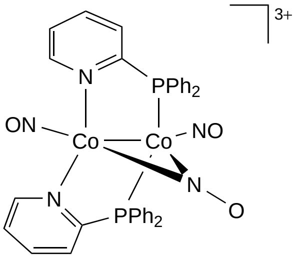

Figure 9 A didentate N,P donor bridging between two metal centers

analogue with an –OMe replacing the amine group is a potential *O,Te donor* didentate ligand.

Chelates with a N and a C donor have been recently reported. An example is (**48**), which binds octahedral Ir^{III} via an imine N as well as a carbanion.[30] Low-spin Co^{II} dialkyls that include the CoL_2 complex of the N,C chelate (**49**) form from organolithium precursor compounds.[31]

2.1.4 Ligands Derived from Nitrogen Heterocycles

Ligands that include nitrogen heterocycles as a component of their molecular structure form an important family of ligands (Figure 10), some of which have already been used as prior examples. Potentially didentate dialectical N_2 donor molecules of aromatic groups are common, exemplified by (**50**). This molecule may chelate or operate in a bridging mode, forming multinuclear complexes in the latter case.

Didentate *N,O and N,S donor* ligands where the N-donor group is aromatic in character (a pyridine, pyrazine, or imidazole, for example) or forms part of a saturated heterocyclic ring (e.g. a pyrimidine) are common. Pyridines feature heavily in ligands of this type. One simple example is 2-pyridinethiolate (**51**). This versatile electron-rich N,S ligand can bind as a monodentate, a chelate, and in bridging modes, and its coordination chemistry has been reviewed.[32,33] The restricted 'bite' of the N,S four-membered ring chelate has obvious structural effects, as observed in the *mer*-$[Co(pt)_3]$ complex, where intraligand S-Co-S angles below 73° and *trans* S–Co–S angles around 166° occur.[34] The ligand, when chelated in $[Co(en)_2(\mathbf{51})]^{2+}$, undergoes a series of stepwise oxidation reactions from thiolato (RS^-) to sulfenato ($R\text{-}SO^-$), sulfinato ($R\text{-}SO_2{}^-$) and sulfonato ($R\text{-}SO_3{}^-$) ligands, with some S,O-isomerization reactions also noted.[35] The 2-hydroxypyridine analogue, which form stable four-membered N,O chelates, is also known. The monoanionic N,O didentate ligand 2-pyridinecarboxylic acid (**52**) forms numerous complexes with five-membered chelate rings,[36] with

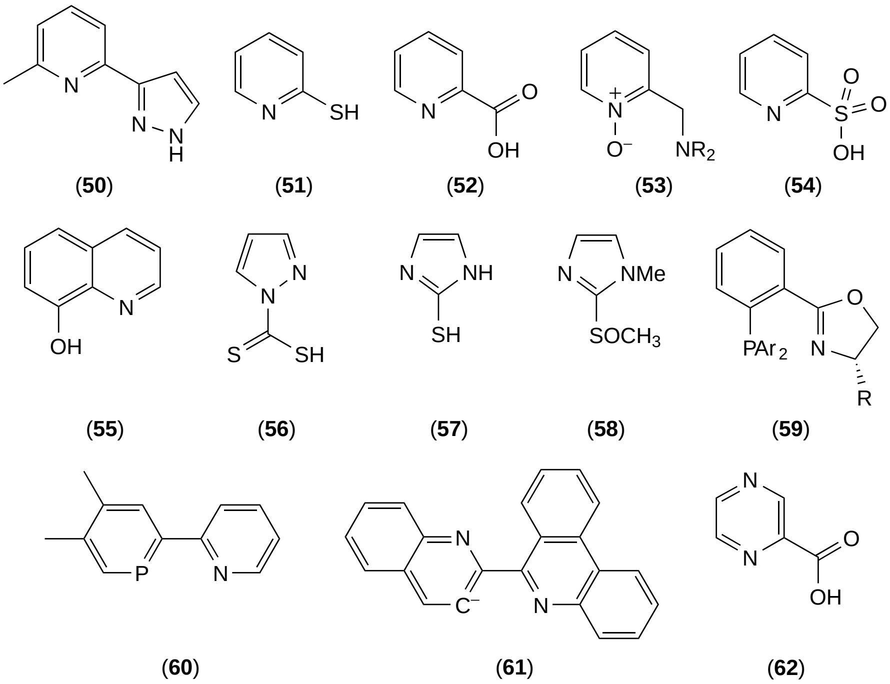
(**50**) (**51**) (**52**) (**53**) (**54**)

(**55**) (**56**) (**57**) (**58**) (**59**)

(**60**) (**61**) (**62**)

Figure 10 Didentate chelates containing N-heterocyclic donors

complexes of the neutral ligand readily isolable. Pyridine N-oxides (**53**) usually form N,O didentates with six-membered chelate rings. The sulfonate analog of picolinic acid (**54**) also acts, albeit in a polymeric Ag^I complex, as an N,O chelating ligand.

Quinolines substituted in the 8-position make excellent ligands and have been used as analytical reagents. The oxine (**55**) is one of the more venerable N,O didentate ligands, observed to form simple mononuclear complexes as well as clusters such as a Mn^{III} tetranuclear complex.[37] The thioxine analogue forms stable, highly colored organic-soluble complexes with five-membered N,S chelates, and a selenium analogue has also been investigated.

Other key heterocyclic rings in mixed donor ligands are pyrazole and imidazole. A review of pyrazole-derived ligands has appeared;[38] an example is 1-thiocarbamylpyrazole (**56**). Ligands with a thiol introduced at the imidazole 2-position form complexes with N,S four-membered chelate rings, as occurs for (**57**). Another example of a N,O chelate is (N-methyl-2-imidazolyl)methylsulfoxide (**58**).

The N,P phosphine-oxazoline chelate (**59**) is chiral, and complexes can act as homogeneous catalysts for asymmetric synthesis; the Ir(I) and Pd(II) complexes promote enantioselective olefin hydrogenation and allylic substitution respectively.[39] An N,P analog of the N,N didentate ligand 2,2′-bipyridine is (**60**), the soft P donor helping to stabilize low-valent metals. Further, 2,2-bipyridine derivatives such as (**61**) can bind metals such as Ir and Ru as N,C^- chelates with one pyridine nitrogen rotated to the opposite side, away from the metal ion.

Numerous pyrazine-containing ligands have been reported, such as (**62**), which displays N,O didentate coordination to transition metals, forming five-membered chelates.[40] Ligands with an N-heterocycle and amide groups can provide N,O chelation, but deprotonation of the amide group leads to a change in the donor set from N,O to dialectical N,N ligation. The monoamides of 2-picolinic acid at high pH demonstrate this characteristic behavior.

2.2 Tridentate Ligands

Ligands with three donor groups may bind to three sites of a metal as a tridentate ligand, although didentate chelation with one donor group pendant and unbound is also observed. Complex stability is usually enhanced by coordination of all three donor groups. Examples appear below in Figures 11, 13, and 14.

There are many examples of N_3– or O_3–donor ligands that are dialectical mixed donors. One example is (**63**), where the central pyridine group and two terminal imidazole groups can be formally considered a mixed donor set. Deprotonation of the imidazole groups causes a significant shift (~0.5 V) in the redox potential of the bis(tridentate)iron(II) complex, whereas substitution on the ring has been used to 'tune' the magnetic properties of the bis Cu^{II} complex.[41] Another example of a dialectical N_3– donor ligands is (**64**), which can form oligomeric complexes through imidazolate bridging.

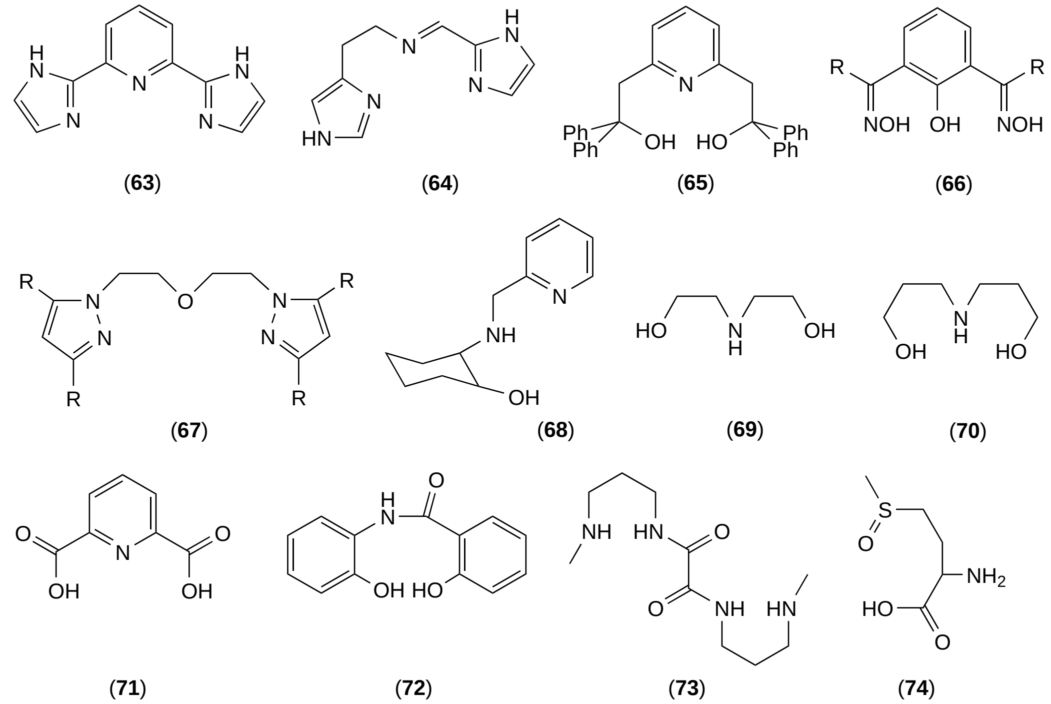

Figure 11 Tridentate (N,N,N), (N,N,O), and (N,O,O) ligands

2.2.1 *N_2O and NO_2 Donors*

N_2O-donors where two arms emanate from a central aromatic component are exemplified by (**65**) and (**66**). The $TiCl_2$ complex of the former is an olefin polymerization catalyst. Rather than form 1:1 complexes, (**66**) acts as a compartment ligand, forming M_2L_2 species (M = Co, Ni, Cu) where the metals, required to be closely confined, exhibit antiferromagnetic exchange.**[42]** 1,2-Pyrazole derivatives (**67**) are also very good N_2O-donor ligands for light transition metals,**[43]** forming two six-membered chelate rings. Analogues with N_2S donor sets are also known. Two types of N-donor are present in the potentially chiral N_2O donor (**68**), which forms distorted octahedral ML_2 complexes with Cu^{II} and Co^{III}, each metal isolated as a different geometric isomer.**[44]**

NO_2-donors often have two identical chains branching from a central amine or aromatic amine group. Examples with alcohol or carboxylic acid arms are most common. The diethanol and dipropanol amines (**69**) and (**70**),**[8,9]** and the well-studied 2,6-pyridinedicarboxylic acid (**71**) exemplify the class. The latter is a good chelating agent for ion chromatographic determination of first-row transition metals. ‘Uneven’ arms can be present, as exemplified in the NO_2 amidodiol (**72**), which stabilizes Co(IV) in the bis complex shown in Figure 12, formed by electrochemical oxidation.**[45]** EPR spectroscopy gave a characteristic 8-line hyperfine coupling pattern due to a single unpaired electron interacting with the ^{59}Co nucleus ($I = 7/2$).

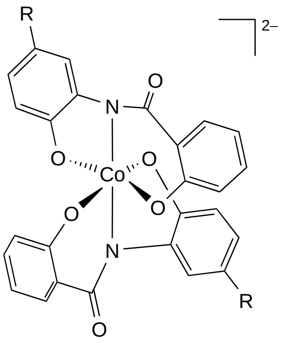

Figure 12 Tridentate bis-mer coordination of a trianionic O,N,O donor amidodiolate ligand to the rare Co^{IV}

More elaborate shapes can initiate more unusual coordination arrangements. The ligand (**73**) exemplifies types that can act as bis tridentates, forming dinuclear complexes with transition metal ions such as Cu^{II}. Amino acid derivatives containing a methyl sulfoxide group (**74**) are rare examples of ambidentate tridentate chelate ligands, offering alternative NO_2 or NOS donor sets, the latter usually found when the NH group is deprotonated.

2.2.2 *N_2S and NS_2 Donors*

Mixed N and S donor ligands (Figure 13) combine hard and soft ligand characteristics, while typically the M−N distance

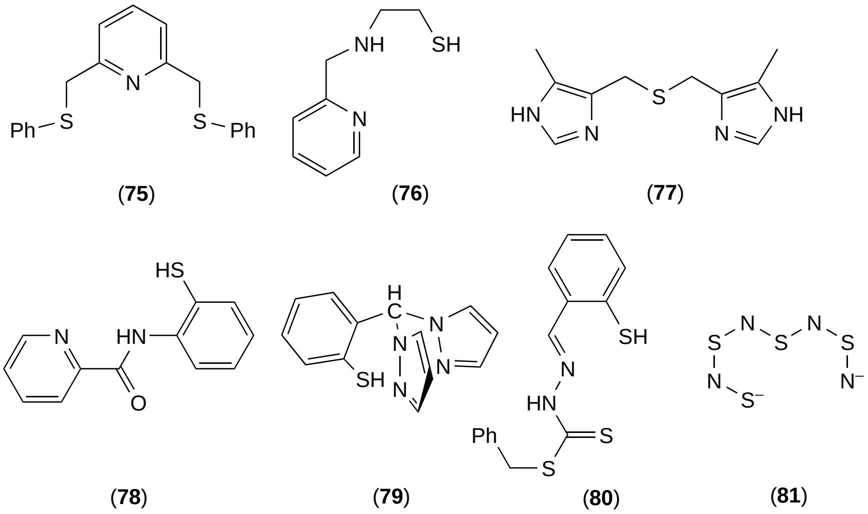

Figure 13 Tridentate chelates with (N,N,S) and (N,S,S) donor sets

is significantly shorter than the M–S distance, particularly with the lighter metal ions.

NS_2 Donor set ligands with two common branches are exemplified by the dithiol analogue of (**65**) and (**75**).[47] The former forms two six-membered chelate rings, whereas the latter forms two five-membered metallocycles. The simple N_2S donor (**76**) and close analogues tend to form oligonuclear complexes with Zn^{II} that feature thiolate bridging. Ligands (**77**) and the analogue with two methylenes in each chain form simple mononuclear complexes with Cu^{II}, featuring five- and six-membered chelate rings, respectively.[48] The unusual pyridine-amide-thiol donor (**78**) forms a very stable $[Fe^{III}L_2]^-$ complex where both amide and thiol are deprotonated.[49] Tripodal N_2S ligands of the type (**79**) have appeared, and form ML_2 complexes, of which the Fe^{III} complex was proposed as a structural model for the *nitrile hydratase* active site.[50] Complexation of (**80**) is as an NS_2 donor, employing two different types of S donors, from a thiol and a thioacid ester. Treatment of the cyclic tetrasulfur tetranitride S_4N_4 with $[PtCl_2(PR_3)_2]_2$ or $Ir(CO)Cl(PPh_3)$ leads to opening of the S_4N_4 ring to form (**81**), a pure inorganic compound that complexes as a tridentate NS_2 ligand.[51]

2.2.3 N_2C, N_2P, P_2O, P_2As, and PAs_2 Donors

Ligands with a carbon anion directly bonded to a metal ion are more common than perhaps supposed. The family of ligands (**82**) (Figure 14) invariably act as a tridentate *N_2C donor* ligand to Pt^{II}, via deprotonation of the carbon marked in the figure. The C-deprotonated N_2C pincer ligand (**83**) forms a totally flat palladacycle with sp^2 hybridization of C and both N donors.[52] A diimine tridentate (**84**) with the carbanion as a terminal rather than central donor of the N_2C ligand has been reported as a Ni^{II} complex;[53] it is an efficient catalyst of ethylene oligomerization.

Phosphorus-containing tridentate ligands are known in a number of donor sets, as exemplified by (**85**) to (**89**), which are excellent chelating agents for particularly platinum group metals. The *PN_2 donor* ligand (**85**) does not display simple coordination, forming a Cu^I complex $[Cu_2(CH_3CN)_2L_2]^{2+}$ where L chelates one metal with both N donors and donates a P donor to the other.[54] The P_2O_4 donor set in (**86**) belies its potential with a tendency to form Pt complexes with only *P_2O donor* coordination, and is a reminder that offering a particular ligand set does not ascertain all are employed. The P_2O donor ligand (**87**) forms a water-soluble Pd^{II} complex that is a catalyst for alkene hydrocarbonylation.[55] The tridentate *P_2As donor* ligand (**88**) binds with four-membered chelates in polynuclear, monovalent complexes. An example of a *PAs_2 donor*, ligand (**89**) binds via six-membered chelate rings to stabilize low-valent metal ions such as Ir^I.[56]

2.3 Tetradentate Ligands

There is a very large literature involving mixed donor tetradentate ligands and their complexes. Some example ligands appear in Figures 15–17.

2.3.1 NO_3 Donors

Linear systems with an NO_3 donor set are exemplified by simple saturated molecules, which show preferences toward lighter, higher charged metal ions, such as linear (**90**). Branched systems include tripodal ligands having different central atoms and O-donors terminating the chains, for example, (**91**) and (**92**). Their coordination chemistry is partly directed by their shape, which tends to support trigonal

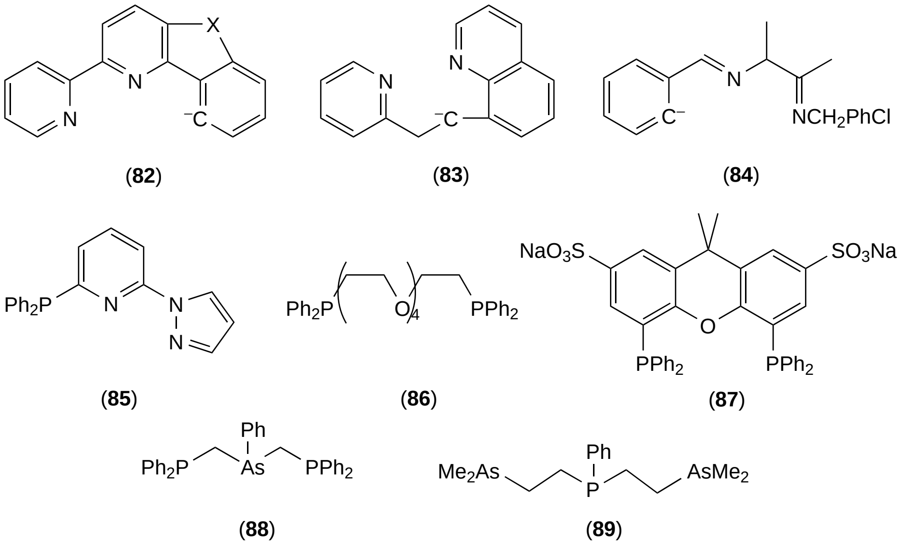

(**82**) (**83**) (**84**) (**85**) (**86**) (**87**) (**88**) (**89**)

X
N
N
⁻C
N
N
⁻C
N
C⁻
NCH₂PhCl
Ph₂P
N
N
N
Ph₂P
O
4
PPh₂
NaO₃S
SO₃Na
O
PPh₂
PPh₂
Ph
Ph₂P
As
PPh₂
Me₂As
Ph
P
AsMe₂

Figure 14 Tridentate ligands that contain one or more C, P, and As donors

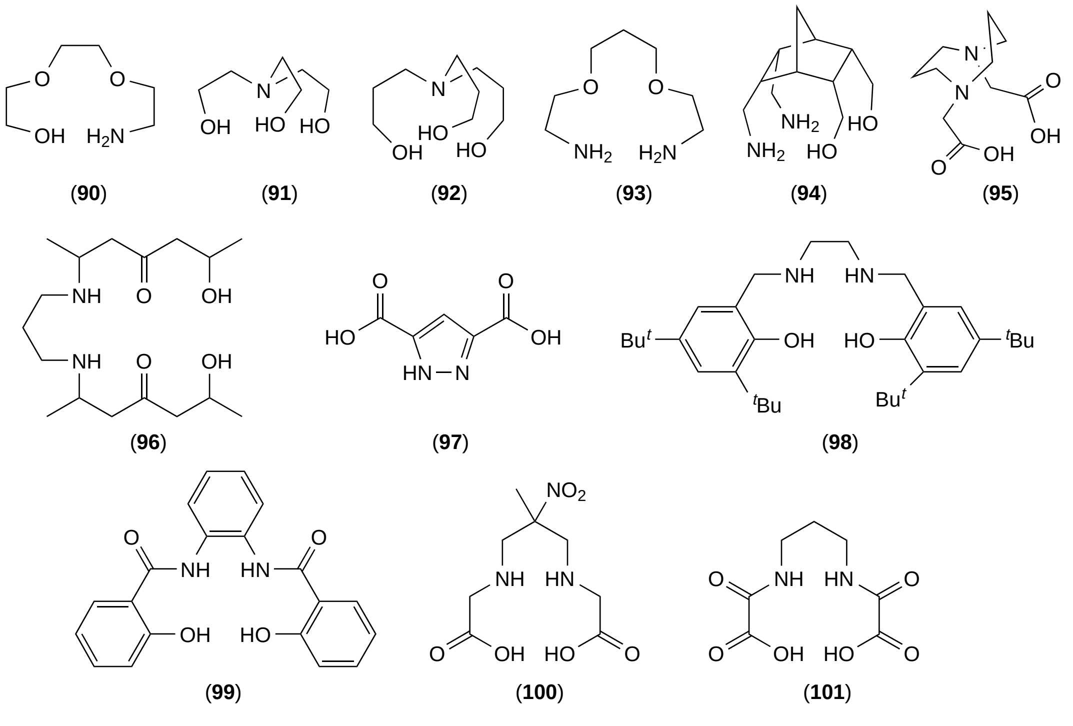

(**90**) (**91**) (**92**) (**93**) (**94**) (**95**) (**96**) (**97**) (**98**) (**99**) (**100**) (**101**)

O
O
OH
H₂N
N
OH
HO
HO
N
HO
OH
HO
O
O
NH₂
H₂N
NH₂
HO
NH₂
HO
N
N
O
OH
O
OH
NH
O
OH
NH
O
OH
O
O
HO
OH
HN
N
NH
HN
Buᵗ
OH
HO
ᵗBu
ᵗBu
Buᵗ
O
O
NH
HN
OH
HO
NO₂
NH
HN
O
OH
HO
O
O
NH
HN
O
O
OH
HO
O

Figure 15 Examples of tetradentate ligands with N,O donor sets

bipyramidal geometries, as found in pentacoordinated Ti^{IV} complexes.[57]

2.3.2 N_2O_2

Ligands with terminal amino groups in different oxo ethers such as (**93**) and analogues with different methylene chain lengths have been studied extensively, and usually exhibit binding of all N_2O_2 donors. They are useful precursors for synthetic macrocycles, and their chemistry has been reviewed.[8,9] The topologically unusual four-strand aminoalcohol (**94**) coordinates to first-row transition metal ions, and may include bis(N_2O_2) coordination. The diacetate (**95**) of a diaza heterocycle, as a tetradentate ligand, features a central ‘butterfly’ six- and two pendant five-membered

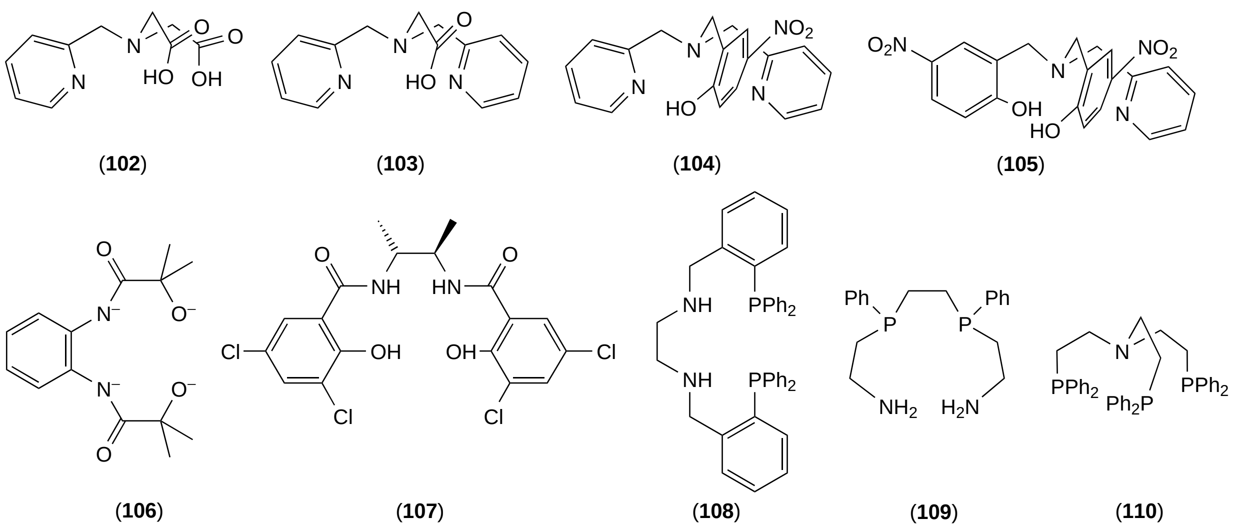

(**102**) (**103**) (**104**) (**105**)

(**106**) (**107**) (**108**) (**109**) (**110**)

Figure 16 Tetradentate mixed donor ligands with N,O and N,P donor sets, including tripodal ligands [(**102**) – (**105**) and (**110**)]

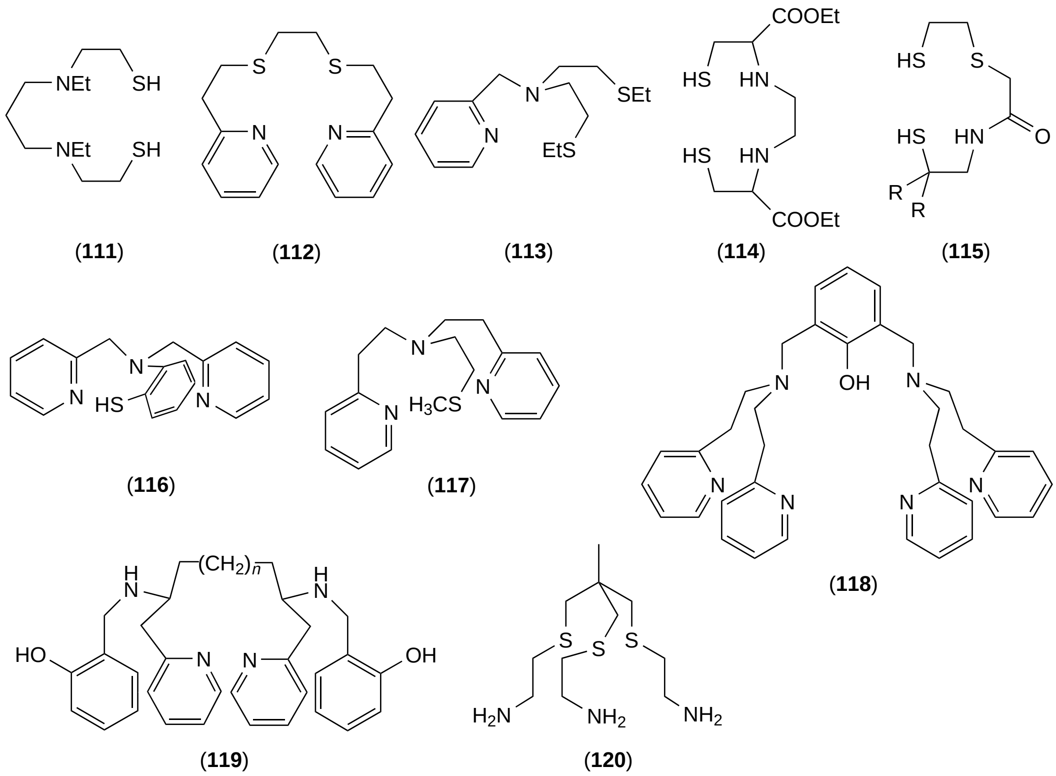

(**111**) (**112**) (**113**) (**114**) (**115**)

(**116**) (**117**) (**118**)

(**119**) (**120**)

Figure 17 Mixed donor tetradentate ligands including at least one S donor, and ligands of higher denticity (5 or 6)

chelate rings. Compound (**96**) exemplifies a large series of ‘compartmental’ ligands, comprehensively reviewed,[58] that may house two different metal ions, one in an N_2O_2 cavity and the other in an O_4 environment. A class of N_2O_2 donor that must bind two metals in a dinuclear bis-chelate arrangement is exemplified by 1,2-pyrazole-3,5-dicarboxylic acid (**97**).

The copper complex of the diaminodiol (**98**) functions as a model for *galactose oxidase*.[59] A related diamidodiol (**99**) has been reported binding to high-valent Os and Ru, as well as in mixed [Cu{L}M(bipy)$_2$] (M = Co, Ni, Zn) compounds, some of the latter being antiferromagnetically coupled.[46] A number of diamine-diacid ligands have appeared, such as (**100**),[60] prepared by a metal-directed template route from α-amino acids. While the amide analogue (**101**) may form simple mononuclear complexes, it may also act as a bis(didentate) bridging ligand, as in $[\mathrm{Mn}_2^{\mathrm{IV}}(\mu\text{-O})_2(\mu\text{-}\mathbf{101})_2]$.[61]

Tripodal N_2O_2 and N_3O iminocarboxylate ligands such as (**102**) and (**103**) have appeared, with the vanadyl complexes acting as *halogenperoxidase* models.[62] Binuclear $\mathrm{Mn^{II}}$ and $\mathrm{Mn^{IV}}$ complexes feature linked MnL units. Related N_3O and N_2O_2 aminoalcohol ligands are known, exemplified by (**104**), which forms a mononuclear trigonal bipyramidal complex with $\mathrm{Cu^{II}}$, with acetate or thiocyanate as the additional donor,[63] and (**105**), which forms a square-pyramidal $\mathrm{Fe^{III}}$ complex that exhibits catalytic activity as a model for *catechol-1,2-dioxidase*.

The sterically crowded ligand (**106**) forms a very rare square-planar $\mathrm{Co^{III}}$ complex, as shown by an X-ray crystal structure,[64] and a spin triplet (paramagnetic) ground state was also identified in the solid state. The $\mathrm{Co^{III}}$ complex of (**107**) catalyzes the epoxidation of norbornene with t-BuOOH or PhI as terminal oxidant,[65] catalysis driven by formation of t-BuOO radicals employing a $\mathrm{Co^{III/II}}$ redox process.

2.3.3 N_2P_2 and NP_3 Donors

The diaminodiphospine ligand (**108**), and analogues with longer methylene chains, is a good example of the N_2P_2 donor set (Figure 16); the $\mathrm{Cu^{II/I}}$ redox potential varies with length of the methylene chain.[66] The diimine precursor of (**108**) forms a rare low-spin and square-pyramidal iodocobalt(III) complex.[67] The linear saturated P_2N_2 tetradentate (**109**) forms *cis*-α- and *cis*-β-$[\mathrm{Co^{III}}(\mathrm{L})(\mathrm{aa})]^{n+}$ (aa = oxalate or acetylacetonate) complexes.[68] The tripodal NP_3 ligand (**110**) shows a propensity to stabilize low-valence oxidation states of Ni and the Co triad,[69] with complexes with metal–metal bonds defined, such as the rather unusual Co-Hg-Hg-Co moiety.

2.3.4 N_2S_2, NS_3 and N_3S Donors

Linear ligands with an N_2S_2 donor set (Figure 17) may have the S donors as terminal thiols or internal thioethers. An example of the former is (**111**), which forms hexanuclear clusters with $\mathrm{Fe^{III}}$.[70] The molecule (**112**) is an example of a simple N_2S_2 donor of the thioether type, and it readily forms mononuclear complexes; the diaquanickel(II) complex has been proposed as a nickel metalloprotein active site model. The copper complex of N_2S_2 ligand (**113**) forms readily, with IR, Raman, and EXAFS supporting it as a model for copper proteins. Ligands from this family, such as (**114**), may have applications in nuclear medicine, since they form robust oxotechnetium complexes.

A simple example of an NS_3 donor is (**115**), which binds to the four coplanar sites in square-pyramidal complexes. A tripodal N_3S donor (**116**) exemplifies this class of donor set, and this is known to form both mononuclear and bridged complexes. Another example of this class is the ligand (**117**), which forms a $\mathrm{Cu^{II}}$(NCMe) complex which is a functional model of the CuB *dopamine β-hydroxylase* center.[71]

2.4 Higher Polydentate Ligands

Molecules with more than four potential donor groups of at least two different types are surprisingly common, with EDTA as the classical example of a hexadentate N_2O_4 donor to a wide range of metal ions. However, increasing the number of donor atoms does not necessarily increase the denticity of the coordinated ligand, and there are many examples of ligands that bind with one or several pendant, uncoordinated groups. Ligand geometry and donor location can be important in directing coordination options. For example, (**118**) can act as bis tetradentate ligands, binding two $\mathrm{Cu^{II}}$ ions via the bridging phenolate and the two sets of three nitrogen atoms,[72] in an arrangement that has been proposed as a model for some dinuclear copper proteins. Alternative behavior is displayed by the structurally related (**119**), which form hexadentate monomer complexes. Usually, the more flexible ligands such as EDTA^{4-} and (**119**) can occupy all coordination sites efficiently.

The tripodal concept featured in (**118**), but without a central donor group, has been used to produce a range of flexible, saturated hexadenate ligands. The tripodal N_3S_3 ligand (**120**) forms robust octahedral complexes with a range of metal ions, and offer distinctive electrochemical properties compared with N_6 analogues, stabilizing lower oxidation states. Ligands with four arms emanating from a head group have also been described recently.[73]

3 CHELATING WITH THREE TYPES OF DONORS ($\mathrm{A_XB_YC_Z}$)

Molecules carrying three different classes of potential donor groups are surprisingly common. They range from simple low-molecular weight compounds to large biomolecules; some examples of the former type appear in Figure 18. Even simple ligands with three different donor groups chelating may form a range of geometrical isomers on coordination; for example, a bis(ABC) octahedral complex will have at least six isomers. Although it is unlikely all possible isomers will form, the prospect will inevitably increase the level of difficulty of their coordination chemistry.

3.1 Tridentate Donors

This group can include dialectical donors such as N_aN_bO (formally N_2O) sets with distinctly different classes of N-donor, such as the N-pyridine, N-amine, alcohol donor (**68**). This can in principal exist as bis(tridentate) octahedral

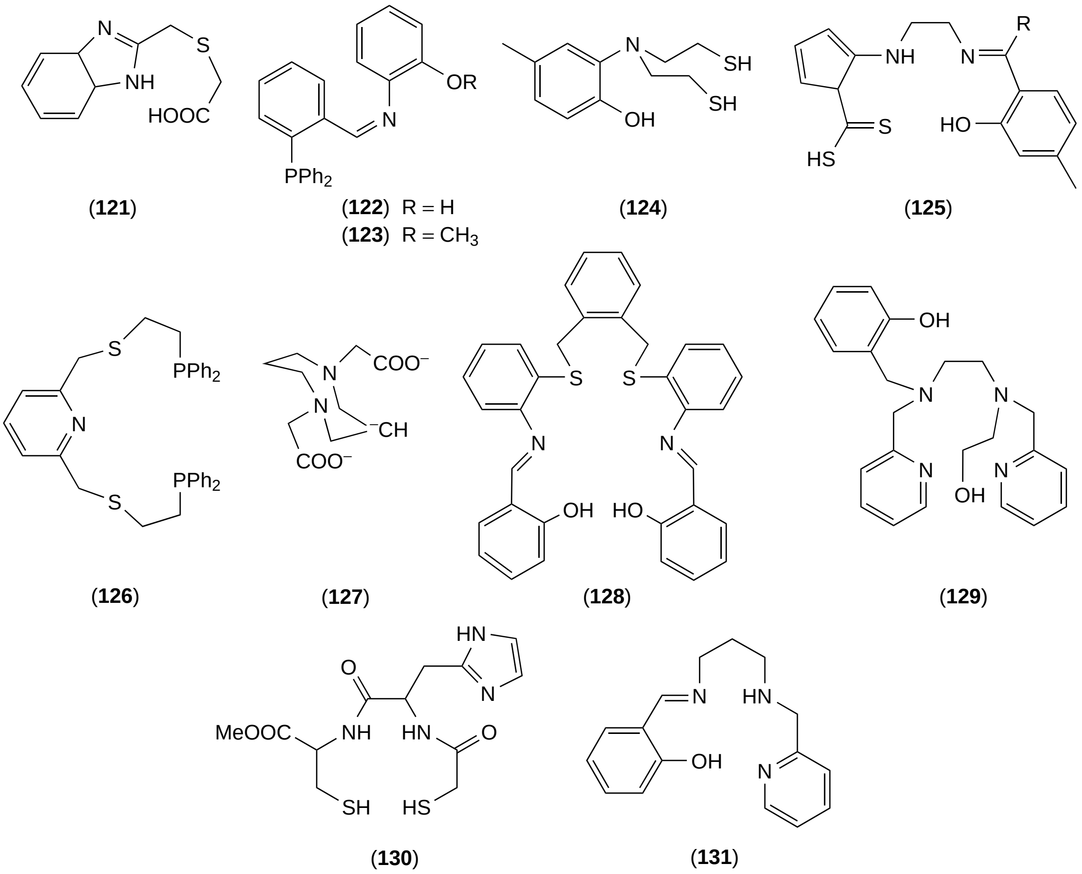

(**121**) (**122**) (**123**) (**124**) (**125**) (**126**) (**127**) (**128**) (**129**) (**130**) (**131**)

Figure 18 Ligands containing three types of potential donor atoms

complexes in any one of six geometrical isomers; the Cu^{II} and Co^{III} complexes were isolated as *trans,trans,trans* and *cis,cis,trans*(N_{py}) *fac* isomers respectively.**44** Dialectical N_3 or O_3 donor sets such as those featuring (N-amine, N-imine, N-amide) and (O-alcohol, O-acid, O-ether) are known. However, we shall subsequently restrict ourselves here to examples that are classical mixed donors with three different donor atoms.

3.1.1 NOS and NOP Donors

The relatively simple tridentate (**121**) presents the same N,O,S donor groups as biological glutamate-methionine-histidine entities. When bound as an octahedral complex, different geometric isomers have been reported, with the octahedral bis(tridentate) complexes of Cu^{II} and Ni^{II} having *trans,cis,cis*- and *cis,cis,cis*-$S_2N_2O_2$ geometries respectively.**74**

The N,O,P phosphine-imine-alcohol donor (**122**) forms simple square-planar complexes with M^{II} ions of the nickel triad. The analogous ether (**123**) acts as a terdentate ligand to Pd^{II}, with CH_3^- in the fourth site of the square-planar complex.**75**

3.2 Tetradentate Donors

A number of tetradentate donor sets featuring three different donors and of varying structural form have been reported over recent decades, and continue to evolve. The mixture of donors of different hard–soft character usually leads to no exceptional preference for a particular metal ion, so the interest in complexes of these ligands must lie in other directions, such as catalysts or biomimics. Examples will be restricted to just a very few.

A simple example of an NS_2O donor ligand is (**124**). Although capable of tetradentate coordination, variable coordination is observed, for example, as a tridentate NS_2 donor to Ni^{II}. Another N_2SO donor is (**125**), which forms tetrahedrally distorted square-planar complexes with Ni^{II}.

3.3 Ligands of Higher Denticity

A simple example of an $A_xB_yC_z$ donor ligand of higher denticity is (**126**), which carries a NS_2P_2 donor set, and binds as a pentadentate in a seven-coordinate bis(triflato)cadmium(II) complex.**76** However, mononuclear Cu^I, Ag^I, and Au^I complexes are four-coordinate with the ligand behaving as a P_2S_2 donor, indicative of the coordination ambivalence of many ligands of potentially high denticity, usually reflecting metal ion preferences. An example of the rare CN_2O_2 donor set (**127**) has been structurally characterized as the aquacobalt(III) complex, with a short Co−C distance of 1.941(4) Å.[77] The $N_2S_2O_2$ donor (**128**) has been characterized binding in the hexadentate coordination mode to first-row transition metal ions. As in other sections, including dialectical ligand systems extends the example set significantly. An example is the $N_{(amine)2}N_{(py)2}O_2$ ligand (**129**); ambivalent denticity may be displayed, such as binding as a pentadentate to vanadyl with a free hydroxyethyl pendant, where only five coordination sites are readily available around the octahedral ion.

4 MULTIPLE MIXED DONOR LIGANDS

Molecules carrying more than three different classes of potential donor groups have not been extensively illustrated, although examples exist, particularly with dialectical mixed donor sets. One dialectical example of a molecule with four different donor groups all in the one molecule is (**130**), which carries imidazole, amide, thiol, and carboxylic acid groups. Its capacity to form a range of geometric isomers upon coordination has been illustrated by actual isolation of isomers of a rhenium complex. Another simple example is (**131**), which offers a pyridine, imine, amine, and alcohol group, allowing it to act as a tetradentate ligand.

At this time, low-molecular weight ligands of high denticity with a large number of different donor groups represent chemical curiosities rather than a target of concerted study, since their complexities in terms of potential isomers, variable coordination modes, and metal ion selection appear to outweigh any short-term potential usefulness.

5 COMMON FAMILIES OF MIXED DONOR LIGAND

Although the above examples have been classified in terms of donor sets, an alternative approach is to report mixed donor ligands in terms of their ‘family’ relationship – as amino alcohols or hydroxyacids, for example; or in terms of the type of complexes they form – as polynuclear systems, for example. Although these have been addressed above in another context, it is appropriate to recognize a few ligand families that are of particular importance (historically, numerically, or in applications) in coordination chemistry. The selection is not designed to be exhaustive, but merely indicative of mixed donor ligand families.

5.1 Schiff Bases

Schiff bases form one of the longest established and most prevalent of the mixed donor systems met in coordination chemistry, with almost all metal ions reported to form complexes with this class of ligand. The usually facile condensation of primary amines with ketones yields imines, featuring a C=N bond. When an aryl group is bonded to the nitrogen or carbon of the imine, it is stabilized somewhat; and this class are then known as Schiff bases (Figure 19). Synthesis by carrying out the condensation reaction in the presence of a metal ion as template is commonly employed, the metal ion both directing the reaction and stabilizing the product. Extensive reviews of the vast chemistry of mixed donor Schiff-base ligands has appeared,[78,79] including acyclic and macrocyclic systems, so only limited examples will be presented. Chirality in Schiff-base ligands has also been described, and will not be elaborated here. Schiff bases are capable of demonstrating tautomerism, probed using IR, UV, and NMR spectroscopy,[78] especially for the numerous derivatives of β-diketones or salicylaldehydes and naphthaldehydes.

Schiff bases commonly employ polyamines as reagents, the donor nature of the ligands depending both on the type of aldehyde or ketone used and the nature of primary amine or diamine. Scheme 1 illustrates some ways of obtaining Schiff bases of different denticities via 1:1 reactions of aldehydes with ketones to yield mixed N, O, S, and Se donor sets. Condensation of aldehydes and ketones with α-amino acids is also known. Where two moles of a carbonyl compounds and one mole of diamine are reacted, more elaborate Schiff bases with higher denticity result, also exemplified in Scheme 1.

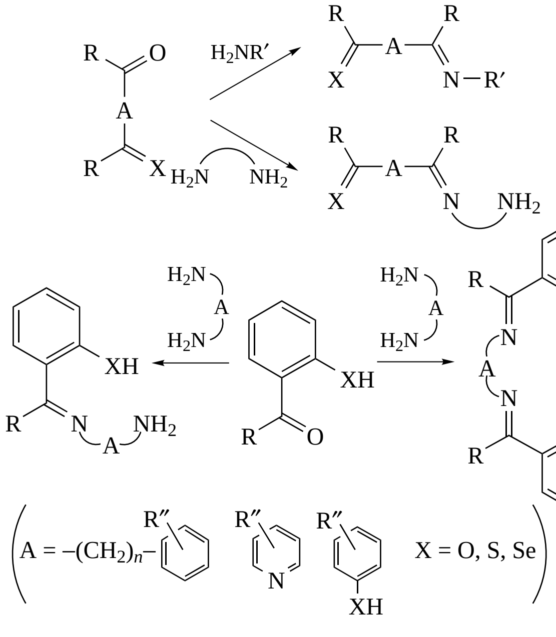

Scheme 1

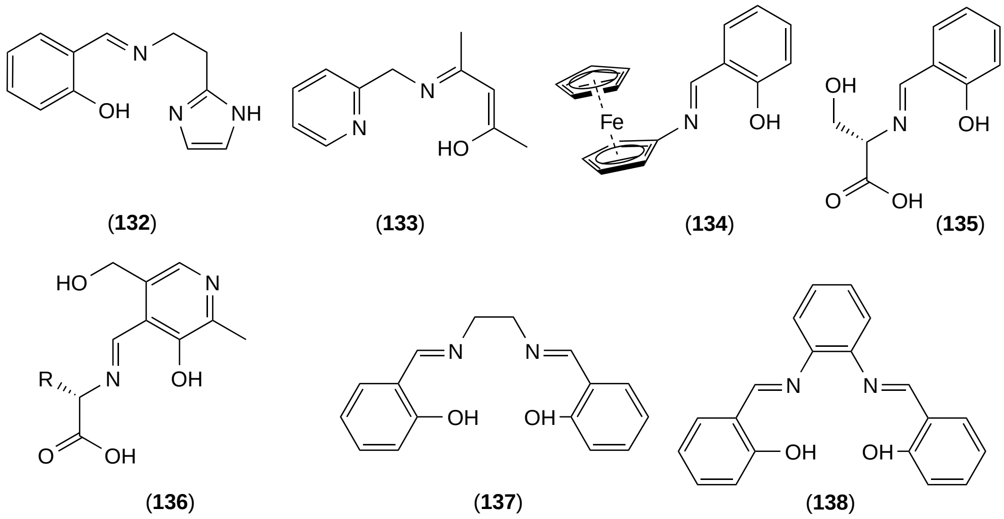

(**132**) (**133**) (**134**) (**135**)

(**136**) (**137**) (**138**)

Figure 19 Di-, tri-, and tetradentate mixed donor Schiff-base ligands

Employing triamines, such as NH_2–$(CH_2)_n$–NH–$(CH_2)_n$–NH_2 ($n = 2-4$), or higher polyamines rather than a diamine leads to pentadentate or higher denticity ligands. Reaction of amines with 2,6-diacetylpyridine or substituted 2,6-phenols leads to high denticity molecules including compartmental ligands.

As Schiff-base denticity increases, coordination can potentially occur in several ways, possibly leading to a number of geometric isomers. Tridentate N_2O donor Schiff bases made from salicylaldehyde (**132**) or a β-diketone (**133**) form stable complexes with transition metals where *fac* or *mer* isomerism may exist. Salicylaldehyde condenses with primary amines (RNH_2) to form didentate monobasic ligands of the form *o*-$(HO)C_6H_4CH{=}NR$. One novel example is the ferrocenylamine adduct (**134**), which forms a bis Co^{II} complex.**[80]** The amino acid serine derivative (**135**), as its $Co^{II}L_2$ complex, is an efficient catalyst for conversion of a number of secondary alcohols to their corresponding ketone in the presence of O_2 and 2-methylpropanal, or ethyl 2-oxocyclopentane-carboxylate, and also oxidizes hydrocarbons such as cyclohexane to cyclohexanol and cyclohexanone. In these reactions, an active Co^{III} superoxo species is implicated.**[81]** The biologically important aromatic aldehyde pyridoxal forms a variety of tridentate Schiff-base ligands (**136**) incorporating amino acids, and their Co complexes bind dioxygen.

One of the classical tetradentate Schiff bases is the open-chain N_2O_2 donor ligand salen (**137**), which has flexibility sufficient to permit it to form different geometric isomers on complexation. The ability of the ubiquitous salen and close analogues to bind O_2 reversibly as its cobalt complex, as in $[(O_2)Co(salen)(py)]$, has been central to most investigations of its coordination chemistry. Complexes of the [Co(salen)] family also mediate the electrocatalytic reduction of O_2 to H_2O_2, whereas those incorporating chiral centers on the ligand backbone are useful in asymmetric synthesis.**[82]** Electrogenerated monovalent Co complexes of salen, salphen (**138**) and their substituted derivatives undergo oxidative additions with alkyl halides.

Pentadentate ligands, as exemplified by the N_3O_2 donor (**139**) also can exist as different geometric isomers, depending on ligand flexibility. Coordination for high denticity ligands (Figure 20) can also involve formation of unusual stereochemistries, such as that observed for the Mn^{II} complex where the pentadentate is practically planar. By way of contrast, a completely nonplanar, twisted coordination appears for the more flexible (**140**) in an oxotechnetium(V) complex.**[83]** Hexadentate Schiff-base complexes are not particularly common, but examples such as the N_4S_2 donor ligand (**141**) bound to Ni^{II}, exist. Schiff bases of high potential denticity may employ some donor atoms as bridging groups to form polynuclear complexes. Many potentially hexadentate Schiff bases actually form bis-tridentate dinuclear or polynuclear complexes.

Condensation of ketones or aldehydes with the methyl ester of dithiocarbazic acid produces ligands with S,N,O or S,N donor sets. An example is (**142**),**[84]** which acts as both a didentate and a tridentate to ReO. Nickel(II)-templated reactions of pentanedione or salicylaldehyde with aminoethanethiol produce N,O,S ligands such as (**143**) and (**144**); these form simple mononuclear complexes or else dinuclear species with thiolate bridging two Ni centers.**[85]** Mixed donor Schiff-base ligands including other heteroatoms such as P (**145**) and Te (**146**) have appeared.

5.2 Macrocycles

Macrocycles are traditionally considered to be ring systems with a chain size of nine atoms or higher. As ligands, they

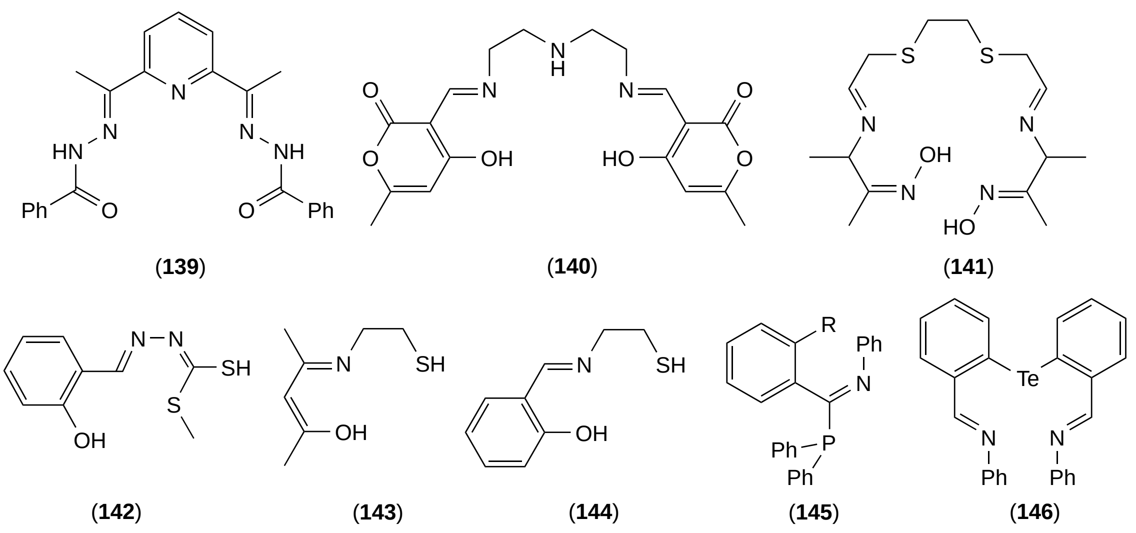
(139) (140) (141) (142) (143) (144) (145) (146)

Figure 20 Mixed donor Schiff-base ligands of higher denticity and or including S, P, or Te donors

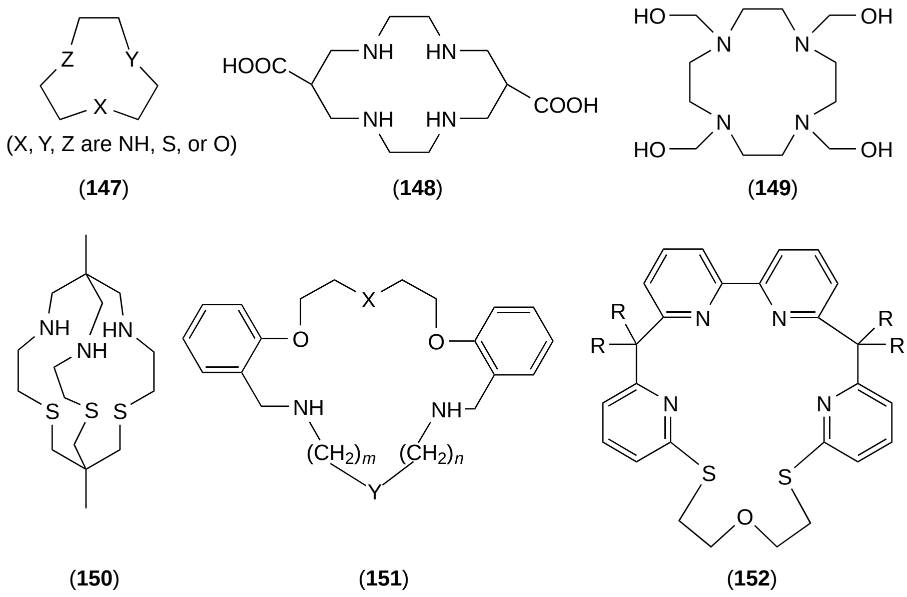
(X, Y, Z are NH, S, or O)

(147) (148) (149) (150) (151) (152)

Figure 21 Macrocyclic mixed donor ligands

contain several heteroatoms within the ring that can act as donors to metals (Figure 21). Additional donors may be introduced as pendants groups attached to either N heteroatoms of the ring or to C atoms of the ring framework. The area has been widely reviewed.[86,87] Many macrocycles that feature a mix of donors in the ring have been described, and include amine, ether, thioether, and phosphine donors, in addition to heavier elements such as Se. A range of N_2X_2 donors (e.g. with X = S) are accessible through metal-templated routes, as illustrated in Scheme 2.

In particular, mixed N,O, N,S, and O,S donor sets are commonly met. The simplest examples are of the 1,4,7-donor cyclononane ring macrocycles (**147**), where examples with N_2O, NO_2, N_2S, and NS_2 donor sets complement N_3, O_3, and S_3 ligands.[88] Mixed donor sets may also be created by the introduction of pendant groups, as exemplified by the N_4O_2 macrocycle (**148**),[89] and the N_4O_4 macrocycle (**149**).[90] Coordination of both ring and pendant donors can enforce unusual properties due to steric and electronic effects within the often rigid complexes.

Macropolycycles, as distinct from the macromonocycles mentioned above, are also well explored. This can be exemplified by the macrobicyclic N_3S_3 donor (**150**), with a ligand shape that is well suited to hexacoordination of

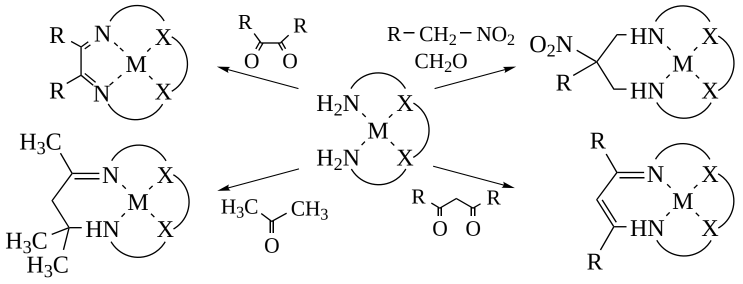

Scheme 2

metals within the cavity, imposing effects of the soft S-donors on physical properties such as redox potentials.

Unsaturated as well as saturated systems can be prepared. Mixed donor dibenzo-substituted macrocycles of type (**151**) (with O_2N_3, O_2N_4, O_3N_2, O_4N_2, and ON_3S donor sets) have been examined to define the effect of variation of ligand structure on metal complex stabilities.**[91]** Ligands with heteroaromatic groups included, such as the potentially N_4S_2O donor ketal coronand (**152**), form complexes, which leads to a change in orientation of the bipyridyl unit from *anti* in the free ligand to *syn* in the complex.

These cyclic systems are an important family of ligands; however, only brief information is presented above, as they can be explored more in the separate entry on macrocyclic ligands.

5.3 Amino Acids and Polyaminoacids

Amino acids and their peptide polymers continue to attract strong interest as ligands because of their biological importance. Detailed treatment of the wide variety of α-amino acids (typically H_2N-CH(R)-COOH), their derivatives and metal complexes is well beyond the scope of this article, so only a few aspects will be noted since comprehensive reviews exist.**[92]** The side chain R may participate in coordination, depending on whether it contains a coordinating heteroatom (Figure 22). For α-amino acids, the pK_a for the first ionization of the carboxylate is 2–3, whereas the ammonium group is deprotonated at about pH ~9 giving the amino form necessary for coordination. Although binding as a monodentate occurs through the amino or carboxyl group, didentate chelation via both N and O donors in a five-membered ring is most common (**153**). Complexes resulting have a rich stereochemistry, and display chirality due at least to the amino acid. In the presence of side chains carrying heteroatoms (such as occurs with histidine, cysteine, methionine, asparagine, glutamine, arginine, lysine, serine, and threonine amino acids), higher denticity is frequently observed.

Amino acids can combine by eliminating water to form di-, tri-, and higher linear or cyclic peptides, featuring –C(O)–NH–C–peptide bonds. The denticity of the ligands usually increases because of the increased possibilities for chelate formation with metal ions. At high pH, the amide nitrogen of the peptide usually is deprotonated during complexation, which leads, as illustrated by tridentate chelation of the GlyAla dipeptide in (**154**), to an increased denticity.

A large class of related polyaminoacid ligands (also called complexones) have been examined for their coordination

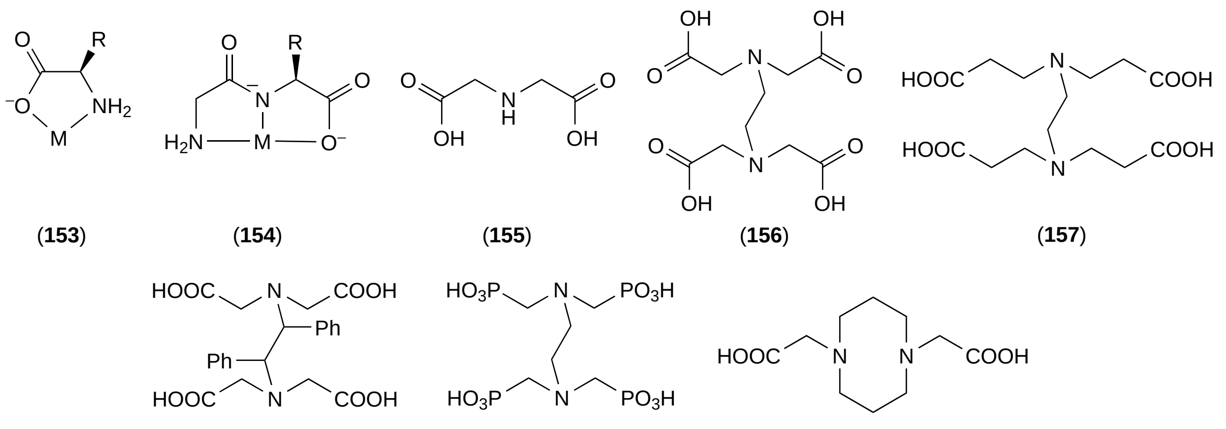

(**153**) (**154**) (**155**) (**156**) (**157**)

(**158**) (**159**) (**160**)

Figure 22 Amino acid and polyaminoacid chelates

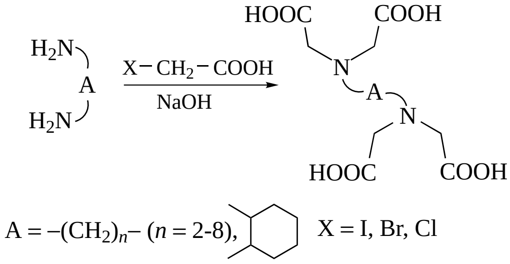

Scheme 3

and analytical chemistry, and are characterized by the presence of the iminodiacetic acid moiety, $–N(CH_2CO_2H)_2$. Complexones, usually prepared in a facile reaction of a diamine and α-halo-substituted acetic acid (Scheme 3), form very stable complexes with almost all metal ions, as detailed elsewhere.[93]

Coordination involves the formation of five- and or six-membered chelates, with polydenticity leading to highly stable and high coordination number complexes, commonly in a 1:1 M:L ratio. The high stability may relate to the flexible, saturated backbone of the ligands and the presence of sets of sterically undemanding carboxylates. Perhaps the simplest examples is iminodiacetic acid itself (**155**), which acts as a tridentate NO_2 donor ligand that forms octahedral bis complexes of *fac* or *mer* geometry. The best-known example is EDTA (**156**), a tetraprotic N_2O_4 donor acid with pK_i values ($pK_1 = 1.99, pK_2 = 2.67, pK_3 = 6.16, pK_4 = 10.26$) typical of this family of ligands, for which a correlation between pK_i and $\log K_{ML}$ has been noted. An array of analogues has resulted from varying the chain length and substituents on the chain between the amine and carboxylate (**157**) or between amine pairs (**158**), or by replacement of carboxylate with other oxoacid groups (**159**). A range of structural variations has been found for complexes of complexones of different potential denticity, leading to NO_2, NO_3, N_2O_3, N_2O_4, and N_3O_4 complexone chelation.

Related synthetic polyaminoacids, which do not feature the iminodiacetate unit but rather are composed of molecules with multiple $–NH-CH_2-COOH$ functionalities, are also common. An example is (**160**), which stabilizes the unusual square-based pyramidal geometry in Co^{III} in conjunction with an axial SO_3^{2-} ion.[94] The macrocycle (**148**) is another example, which binds octahedral metal ions with the pendants in axial sites.[89]

5.4 Biomolecules

Many biomolecules feature metal ions in a mixed donor set, and the area is intensively studied. As an example, the active site of the hydrogenase from *thiocapsa roseopersicina* features nickel in a mixed O,N,S donor environment. Definition of the ligand donor set in biopolymers is not always facile, however, so they tend to be overlooked as examples of mixed donor ligands. There are some small biomolecule examples extant, however. A simple example with dialectical O-donors is the ferrioxamine siderophore *enterobactin,* which features a set of three NO^-, CO chelates binding iron, (Figure 23) the former donors arising from oxidation of an original peptide amine groups.[95] Peptide complexes, of course, usually feature mixed, N,O chelation.

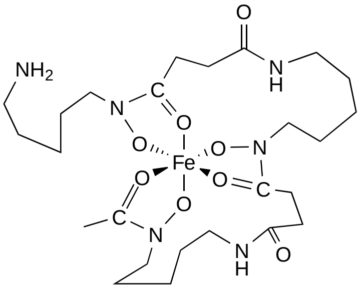

Figure 23 Enterobactin, a catechol siderophore with a dialectical (CO, NO^-) mixed donor ligand

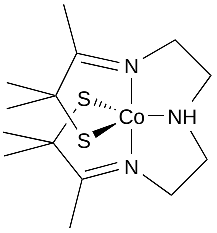

Figure 24 A five-coordinate Co^{III} complex of an N_3S_2 ligand, a proposed model for the active site of *nitrile hydratase*

Many simple complexes have been prepared as models of active sites of biomolecules. For example, a reactive five-coordinate thiolate Co^{III} complex (Figure 24) was prepared to model the active site of *nitrile hydratase,* a Co^{III} or Fe^{III} metalloenzyme that promotes the conversion of nitriles to amides.[96] The synthesized model complex is facile in its uptake and release of azide and thiocyanate, indicating that an appropriate nonleaving group environment enhances ligand displacement sufficiently for catalytic paths in non-redox active Co metalloenzymes. Other examples have appeared earlier in this report.

6 POLYNUCLEAR SYSTEMS

Simple mixed donor ligands are commonly anticipated to form mononuclear complexes. However, many examples of polynuclear complexes that form readily through prior ligand design or via spontaneous self-assembly processes have appeared. A range of shapes, including dendrimers and helical systems, have been identified. One of the

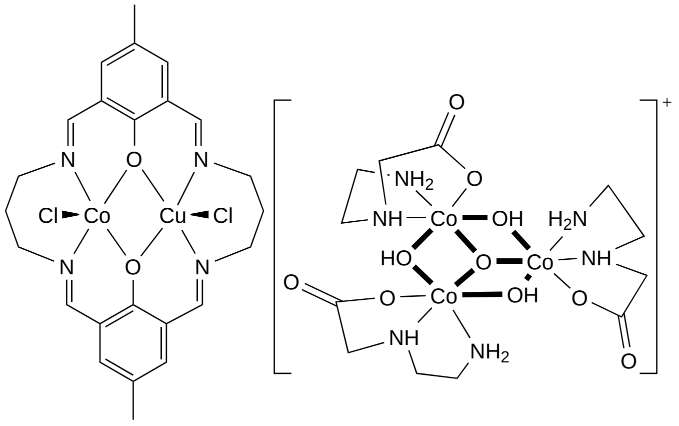

(**161**) (**162**)

Figure 25 Two examples of small polynuclear systems featuring mixed donor ligands

simpler, well-studied designed types are the side-by-side compartment ligands, capable of incorporating two metal ions, one in each compartment (Figure 25). Heterodinuclear complexes such as (**161**) have been made, with two different metal ions in square-pyramidal coordination geometries. Self-assembled clusters such as (**162**),[97] which features amino acid and bridging (μ_2-OH) and (μ_3-O) ligands, are well known with many metal systems. This is a burgeoning area, strongly supported by X-ray structural analysis for characterization.

7 PROPERTIES AND REACTIONS

The presence of mixed donor ligands in metal complexes can complicate or simplify chemical reactions. For example, in an octahedral $[M(NNSN)Cl_2]^{n+}$ complex where the two chloride ions are each opposite different donors means that there is a choice in the site of the first chloride hydrolysis reaction which is absent from the $[M(NNNN)Cl_2]^{n+}$ analogue, while at the same time the electronic effects of the N versus the S donor may direct which site is most reactive clearly in any case. Rearrangement reactions may be more complex, because of the greater number of potential isomers. Redox potentials may be shifted significantly and new oxidation states stabilized; for example, the N_6 versus N_3S_3 macrobicyclic Co(III) complex (**150**) show clearly different redox chemistry, with the latter stabilizing Co(I), an oxidation state not seen in the former complex. Overall, mixed donor ligands are responsible for diversifying the coordination chemistry of metal ions, and changing donor groups can be employed to ‘tune’ the properties and expand applications of complexes. Illustrating the broad field of reactions is beyond this review, so only one aspect peculiar to mixed donor ligands will be exemplified below.

Hemilability refers to polydentate ligands that display facile dissociation–reassociation behavior for part of their donor group set, the rest remaining coordinatively intact. Hemilability of hybrid ligands has been reviewed recently.[98] The property is observed particularly in complexes of mixed donor ligands with a mix of hard and soft donors, as exemplified by a number of studies. Reactions of bis[(benzylthio)methyl]pyridine bound to Rh^I as an S_2N donor ligand with MeI feature reversible release of a thiobenzyl arm and formation of a transient three-coordinate didentate N,S species.[99] The labile nature of specifically the ether donor in the Pd^{II} complex of a P,N,O-donor tridentate ligand is asserted to assist the complex in catalyzing ethylene oligomerization.[100] Solvatochromisim observed in the Ni^{II} complex of the P,O chelate $C_6H_5(CONH)(PPh_2)$ has been assigned to solvent-dependent hemilability of the amide oxygen atom, the P donor remaining intact throughout.[101] Hemilability has also been described for S,O thioether-carboxylate ligands bound to Pd^{II}.[102]

8 RELATED ARTICLES

Ammonia & N-donor Ligands; Macrocyclic Ligands; P-donor Ligands; S-donor Ligands; Water & O-donor Ligands.

9 REFERENCES

1. M. D. Ward, *Annu. Rep. Prog. Chem., Sect. A*, 1999, **95**, 261.
2. A. M. W. C. Thompson, *Annu. Rep. Prog. Chem., Sect. A*, 1996, **92**, 291.

3. J. M. Vila, M. T. Pereira, C. Rodriguez, J. J. Jesus, J. M. Origueira, A. Fernandez, and M. L. Torres, *Recent Res. Dev. Organomet. Chem.*, 2001, **4**, 1.
4. A. J. Barton, A. R. J. Genge, N. J. Hill, W. Levason, S. D. Orchard, B. Patel, G. Reid, and A. J. Ward, *Heteroat. Chem.*, 2002, **13**, 550.
5. Y. Sunatsuki, Y. Motoda, and N. Matsumoto, *Coord. Chem. Rev.*, 2002, **226**, 199.
6. F. T. Edelmann, *Angew. Chem., Int. Ed. Engl.*, 2001, **40**, 1656.
7. B. Gyurcsik and L. Nagy, *Coord. Chem. Rev.*, 2000, **203**, 81.
8. R. D. Hancock and A. E. Martell, *Chem. Rev.*, 1989, **89**, 1875.
9. K. E. Krakowiak, J. S. Bradshaw, and D. J. Zameska-Krakowiak, *Chem. Rev.*, 1989, **89**, 929.
10. W. Levason, S. D. Orchard, and G. Reid, *Coord. Chem. Rev.*, 2002, **225**, 159.
11. J. A. McCleverty and T. J. Meyer eds, (editors-in-chief) ‘Comprehensive Coordination Chemistry II: From Biology to Nanotechnology’, Elsevier Science Ltd, Oxford, 2004.
12. R. S. Vagg, in ‘Comprehensive Coordination Chemistry’, eds. G. Wilkinson, R. D. Gillard, and J. A. McCleverty, Pergamon, Oxford, 1987, Vol. 2, Chap. 20.4, p. 793.
13. J. A. Bertrand and P. G. Eller, *Prog. Inorg. Chem.*, 1976, **21**, 29.
14. A. Chakravorty, *Coord. Chem. Rev.*, 1974, **13**, 1.
15. T. E. Keyes, R. J. Forster, P. M. Jayaweera, C. G. Coates, J. J. McGarvey, and J. G. Vos, *Inorg. Chem.*, 1998, **37**, 5925.
16. K. Fegy, D. Luneau, E. Belorizky, M. Novak, J.-L. Tholence, C. Paulsen, T. Ohms, and P. Rey, *Inorg. Chem.*, 1998, **37**, 4524.
17. K. G. Orrell, *Coord. Chem. Rev.*, 1989, **96**, 1.
18. T. Konno, J. Hidaka, and K.-I. Okamoto, *Bull. Chem. Soc. Jpn.*,1995, **68**, 1353.
19. H.-D. Stackel, E. Immerz-Winkler, H. Poschenrieder, A. Windt, W. Weigand, N. Drescher, and R. Wuensch, *Helv. Chim. Acta*, 2003, **86**, 2471.
20. I. Nagasawa, T. Kawamoto, H. Kuma, and Y. Kushi, *Bull. Chem. Soc. Jpn.*, 1998, **71**, 1337.
21. Y. Sugiura, T. Kikuchi, and H. Tanaka, *Adv. Chem. Ser.*, 1980, **191**, 393.
22. W. Dietzsch, P. Strauch, and E. Hoyer, *Coord. Chem. Rev.*, 1992, **121**, 43.
23. P. L. Watson, J. A. Albanese, J. C. Calabrese, D. W. Ovenall, and R. G. Smith, *Inorg. Chem.*, 1991, **30**, 4638.
24. M. J. M. Campbell, *Coord. Chem. Rev.*, 1975, **15**, 279.
25. A. Bader and E. Lindner, *Coord. Chem. Rev.*, 1991, **108**, 27.
26. J. L. Roustan, N. Ansari, and F. R. Ahmed, *Inorg. Chim. Acta*, 1987, **129**, L11–L12.
27. G. Mugesh, H. B. Singh, R. P. Patel, and R. J. Butcher, *Inorg. Chem.*, 1998, **37**, 2663.
28. C. G. Pierpont, B. J. Gorden, and R. Eisenberg, *J. Chem. Soc., Chem. Commun.*, 1969, 401.
29. I. D. Sadekov, B. B. Rivkin, and V. I. Minkin, *Usp. Khim.*, 1987, **56**, 586.
30. F. Menges, M. Neuburger, and A. Pfaltz, *Org. Lett.*, 2002, **4**, 4713.
31. W.-P. Leung, H. K. Lee, L.-H. Weng, A.-Y. Zhou, and T. C. W. Mak, *J. Chem. Soc., Dalton Trans.*, 1997, 779.
32. E. S. Raper, *Coord. Chem. Rev.*, 1997, **165**, 475.
33. E. S. Raper, *Coord. Chem. Rev.*, 1996, **153**, 199.
34. E. C. Constable, C. A. Palmer, and D. A. Tocher, *Inorg. Chim. Acta*, 1990, **176**, 57.
35. M. Murata, M. Kojima, A. Hioki, M. Miyagawa, M. Hirotsu, K. Nakajima, M. Kita, S. Kashino, and Y. Yoshikawa, *Coord. Chem. Rev.*, 1998, **174**, 109.
36. K. A. Jorgensen, *Chem. Rev.*, 1989, **89**, 438.
37. E. Bouwman, M. A. Bolcar, E. Libby, J. Huffman, K. Folting, and G. Christou, *Inorg. Chem.*, 1992, **31**, 5185.
38. S. Trofimenko, *Chem. Rev.*, 1972, **72**, 497.
39. A. Lightfoot, P. Schnider, and A. Pfaltz, *Angew. Chem., Int. Ed. Engl.*, 1998, **37**, 2897.
40. G. A. Foulds, *Coord. Chem. Rev.*, 1990, **98**, 1.
41. N. K. Solanki, E. J. L. McInnes, F. E. Mabbs, S. Radojevic, M. McPartlin, N. Feeder, J. E. Davies, and M. A. Halcrow, *Angew. Chem., Int. Ed. Engl.*, 1998, **37**, 2221.
42. D. Black, A. J. Blake, K. P. Dancey, A. Harrison, M. McPartlin, S. Parsons, P. A. Tasker, G. Whittaker, and M. Schroder, *J. Chem. Soc., Dalton Trans.*, 1998, 3953.
43. C. Kutal, *Coord. Chem. Rev.*, 1990, **99**, 213.
44. M. J. Robertson, G. A. Lawrance, M. Maeder, and P. Turner, *Aust. J. Chem.*, 2004, **57**, 483.
45. M. Koikawa, M. Gotoh, H. Okawa, S. Kida, and T. Kohzuma, *J. Chem. Soc., Dalton Trans.*, 1989, 1613.
46. Y. Sunatsuki, T. Matsuo, M. Nakamura, F. Kai, N. Matsumoto, and J.-P. Tuchagues, *Bull. Chem. Soc. Jpn.*, 1998, **71**, 2611.
47. R. H. Holm, *Chem. Rev.*, 1987, **87**, 1401.
48. F. Mani, *Coord. Chem. Rev.*, 1992, **120**, 325.
49. J. C. Noveron, M. M. Olmstead, and P. K. Mascharak, *Inorg. Chem.*, 1998, **37**, 1138.
50. T. C. Higgs, D. Ji, R. S. Czernuscewicz, B. F. Matzanke, V. Schunemann, A. X. Trautwein, M. Helliwell, W. Ramirez, and C. J. Carrano, *Inorg. Chem.*, 1998, **37**, 2383.
51. M. G. Barker, *Coord. Chem. Rev.*, 1990, **103**, 162.
52. C. S. Consorti, G. Ebeling, F. Rodembusch, V. Stefani, P. R. Livotto, F. Rominger, F. H. Quina, C. Yihwa, and J. Dupont, *Inorg. Chem.*, 2004, **43**, 530.
53. R. M. Ceder, G. Muller, M. Ordinas, M. Font-Bardia, and X. Solans, *Dalton Trans.*, 2003, 3052.

54. S.-M. Kuang, Z.-Z. Zhang, Q.-G. Wang, and T. C. W. Mak, *J. Chem. Soc., Dalton Trans.*, 1998, 1115.
55. M. S. Goedheijt, J. N. H. Reek, P. C. J. Kamer, and P. W. N. M. van Leeuwen, *J. Chem. Soc., Chem. Commun.*, 1998, 2431.
56. N. M. Doherty and N. W. Hoffman, *Chem. Rev.*, 1991, **91**, 553.
57. W. M. P. B. Menge and J. G. Verkade, *Inorg. Chem.*, 1991, **30**, 4628.
58. J. G. H. Du Preez, T. I. A. Gerber, and O. Knoesen, *J. Coord. Chem.*, 1987, **16**, 285.
59. E. Saint-Aman, S. Ménage, J.-L. Pierre, E. Defrancq, and G. Gellon, *New J. Chem.*, 1998, **22**, 393.
60. P. Comba, T. W. Hambley, G. A. Lawrance, L. L. Martin, P. Renold, and K. Varnagy, *J. Chem. Soc., Dalton Trans.*, 1991, 277.
61. R. Ruiz, A. Aukauloo, Y. Journaux, I. Fernández, J. R. Pedro, A. L. Roselló, B. Cervera, I. Castro, and M. C. Muñoz, *Chem. Commun.*, 1998, 989.
62. B. J. Hamstra, G. J. Colpas, and Vl. Pecoraro, *Inorg. Chem.*, 1998, **37**, 949.
63. M. Vaidyanathan, R. Viswanathan, M. Palaniandavar, T. Balasubramanian, P. Prabhaharan, and T. P. Muthiah, *Inorg. Chem.*, 1998, **37**, 6418.
64. T. J. Collins, T. G. Richmond, B. D. Santarsiero, and B. G. R. T. Treco, *J. Am. Chem. Soc.*, 1986, **108**, 2088.
65. J. D. Koola and J. K. Kochi, *J. Org. Chem.*, 1987, **52**, 4545.
66. F. Tisato, G. Pilloni, F. Refosco, G. Bandoli, C. Corvaja, and B. Corain, *Inorg. Chim. Acta*, 1998, **275**, 401.
67. H. P. Lane, M. Watkinson, N. Bricklebank, C. A. McAuliffe, and R. G. Pritchard, *Inorg. Chim. Acta*, 1995, **232**, 145.
68. K. Kashiwabara, M. Jung, and J. Fujita, *Bull. Chem. Soc. Jpn.*, 1991, **64**, 2372.
69. C. Mealli, C. Ghilardi, and A. Orlandini, *Coord. Chem. Rev.*, 1992, **120**, 361.
70. F. Osterloh, W. Saak, S. Pohl, M. Kroeckel, C. Meier, and A. X. Trautwein, *Inorg. Chem.*, 1998, **37**, 3581.
71. F. Champloy, N. Benali-Chérif, P. Bruno, I. Blain, M. Pierrot, M. Réglier, and A. Michalowicz, *Inorg. Chem.*, 1998, **37**, 3910.
72. S. Schindler, D. J. Szalda, and C. Creutz, *Inorg. Chem.*, 1992, **31**, 2255.
73. C. Zimmermann, W. Bauer, F. W. Heinemann, and A. Grohmann, *Z. Naturforsch. B*, 2002, **57**, 1256.
74. C. J. Matthews, S. L. Heath, M. R. J. Elsegood, W. Clegg, T. A. Leese, and J. C. Lockhart, *J. Chem. Soc., Dalton Trans.*, 1998, 1973.
75. P.-Y. Shi, Y.-H. Liu, S.-M. Peng, and S.-T. Liu, *J. Chin. Chem. Soc. (Taipei, Taiwan)*, 2003, **50**, 89.
76. S.-M. Kuang, Z.-Z. Zhang, and T. C. W. Mak, *J. Chem. Soc., Dalton Trans.*, 1998, 317.
77. D. E. Richardson and P. Sharpe, *Inorg. Chem.*, 1993, **32**, 1809.
78. M. Calligaris and L. Randaccio, in ‘Comprehensive Coordination Chemistry’, eds. G. Wilkinson, R. D. Gillard, and J. A. McCleverty, Pergamon, Oxford, 1987, Vol. 2, Chap. 20.1, p. 715.
79. R. Hernandez-Molina and A. Mederos, in ‘Comprehensive Coordination Chemistry II’, eds. J. A. McCleverty and T. J. Meyer, Elsevier Science, Oxford, 2003, Vol. 1, p. 411.
80. M. Bracci, C. Ercolani, B. Floris, M. Bassetti, A. Chiesi-Villa, and C. Guastini, *J. Chem. Soc., Dalton Trans.*, 1990, 1357.
81. T. Punniyamurthy, B. Bhatia, M. M. Reddy, G. C. Maikap, and J. Iqbal, *Tetrahedron*, 1997, **53**, 7649.
82. L. Canali and D. C. Sherrington, *Chem. Soc. Rev.*, 1999, **28**, 85.
83. S. Liu, S. J. Rettig, and C. Orvig, *Inorg. Chem.*, 1991, **30**, 4915.
84. F. Mevellec, A. Roucoux, N. Noiret, and H. Patin, *Inorg. Chim. Acta*, 2002, **332**, 30.
85. V. E. Kassjager, J. van der Broeke, R. K. Henderson, W. J. J. Smeets, A. L. Spek, W. L. Driessen, E. Bouwman, and J. Reedijk, *Inorg. Chim. Acta*, 2001, **316**, 99.
86. L. F. Lindoy, ‘The Chemistry of Macrocyclic Ligand Complexes’, Cambridge University Press, Cambridge, MA, 1989.
87. D. Parker, ‘Macrocycle Synthesis: A Practical Approach’, Oxford University Press, Oxford, 1996.
88. P. Chaudhuri and K. Weighardt, *Prog. Inorg. Chem.*, 1987, **35**, 329.
89. P. V. Bernhardt and G. A. Lawrance, *Coord. Chem. Rev.*, 1990, **93**, 297.
90. K. P. Wainright, *Coord. Chem. Rev.*, 1997, **166**, 35.
91. C. A. Davis, A. J. Leong, L. F. Lindoy, J. Kim, and S.-H. Lee, *Aust. J. Chem.*, 1998, **51**, 189.
92. S. H. Laurie, in ‘Comprehensive Coordination Chemistry’, eds. G. Wilkinson, R. D. Gillard, and J. A. McCleverty, Pergamon, Oxford, 1987, Vol. 2, Chap. 20.2, p. 739.
93. G. Anderegg, in ‘Comprehensive Coordination Chemistry’, eds. G. Wilkinson, R. D. Gillard, and J. A. McCleverty, Pergamon, Oxford, 1987, Vol. 2, Chap. 20.3, p. 777.
94. W. E. Broderick, K. Kanamori, R. D. Willett, and J. I. Legg, *Inorg. Chem.*, 1991, **30**, 3875.
95. H. Boukhalfa and A. L. Crumbliss, *Biometals*, 2002, **15**, 325.
96. J. Shearer, I. Y. Kung, S. Lovell, W. Kaminsky, and J. A. Kovacs, *J. Am. Chem. Soc.*, 2001, **123**, 463.
97. T. Ama, J. Miyazaki, K. Hamada, K. Okamoto, T. Yonemura, H. Kawaguchi, and T. Yasui, *Chem. Lett.*, 1995, 267.
98. P. Braunstein and F. Naud, *Angew. Chem., Int. Ed. Engl.*, 2001, **40**, 680.
99. G. Sanchez, J. Garcia, D. Meseguer, J. L. Serrano, L. Garcia, J. Perez, and G. Lopez, *Dalton Trans.*, 2003, 4709.
100. P.-Y. Shi, Y.-H. Liu, S.-M. Peng, and S.-T. Liu, *Organometallics*, 2002, **21**, 3203.

101. P. Bhattacharyya, T. Q. Ly, A. M. Z. Slawin, and J. D. Woollins, *Polyhedron*, 2001, **20**, 1803.

102. W. H. Meyer, R. Brull, H. G. Raubenheimer, C. Thompson, and G. J. Kruger, *J. Organomet. Chem.*, 1998, **553**, 83.

Mixed Valence Compounds

John P. Fackler, Jr
Texas A&M University, College Station, TX, USA

1 Introduction 1
2 Historical Observations 3
3 Theoretical Developments 4
4 Molecular Orbital Treatment 5
5 Minerals with Mixed Valence Ions 6
6 Biological Systems with Mixed Valence 8
7 Conductors and Related Mixed Valence Materials 10
8 Miscellaneous Mixed Valence Species 11
9 Related Articles 12
10 References 12

Glossary

Delocalized valency: valency not confined to single atomic center
Fourfold symmetry: rotation by 90° produces an identical arrangement
Ligand fields: the perturbation of the electronic structure of an ion or atom by the surrounding ligands
Superconductivity: electrical conductance without energy loss
Valency: the electronic structure of a compound or metal ion

Abbreviations

Ln = A general abbreviation for lanthanide elements;
PKS model = The model developed by Piepho, Krausz, and Schatz for treating the electronic structure of mixed valence compounds.

1 INTRODUCTION

A survey of the literature[1] from 1980 to 1993 shows that over 2500 articles have been published during this period that contain ‘mixed valence’ or ‘mixed valent’ in the title. From 1994–2003, ‘Mixed Valence’ was in 3988 titles and there were an additional 1095 that contain ‘Mixed Valent’. Four of these are reviews.[2] Thus, the 1967 statement of Robin and Day[3] that stated mixed valence chemistry represented a ‘neglected class of inorganic compounds’ is no longer valid. Mixed valency, the name used to describe compounds containing ions of the same element in two different oxidation states, has come of age.[4–6]

Mixed valence compounds have been used since antiquity as components in pigments such as the oxides of Fe, compounds that can produce red to black colorations in pigments. Today, biologists, as well as chemists, physicists, and geologists, study mixed valence materials. Biological systems have given us an opportunity to explore the ways in which mixed valency is used to store and transfer energy, convert light to chemical reactivity in photosynthesis, and in general utilize mixed valency in redox reactions. Physicists and chemists have been particularly involved with the high-temperature superconducting ceramics. They hold great promise for reducing energy consumption in the future for transport and use of electricity. To date, ***Superconductivity*** has been observed at temperatures above 100 K in mixed valent copper-containing oxides.

Mixed valency is not limited to consideration of individual ions in different oxidation states. Delocalized systems also exist that exhibit properties of mixed valency, as in many organometallic mixed valence compounds. For example, phthalocyanine, Pc (**1**), sandwich compounds of the lanthanides, $Ln(Pc)_2$, are best described as containing the two Pc anionic ligands in mixed valent charge states of -2 and -1 with the metal ion Ln^{3+}.

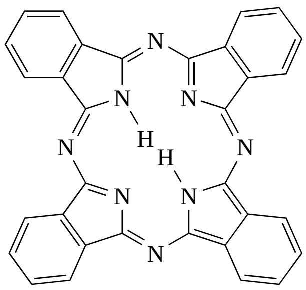

(**1**) H_2Pc

Mixed valency[5,7] benefitted from a classification scheme developed by Robin and Day,[3] which was based upon the symmetry and strength of the ligand fields about the metal ions. This scheme, which remains widely utilized today, divides mixed valence compounds into four classes. By definition, class I systems are those in which the ions of different valence are in sites A and B of very different symmetry and ligand field strength. Class I compounds have trapped valencies for the ions. Conversion from one state to the other requires substantial reorganization of the structure about both ion species. The coefficient, α, which describes the degree of mixing of the states, is zero. The energy difference between states associated with sites A and B is large. There is no symmetry operation that will take site A into site B (Table 1).

An interesting example of a class I mixed valence species is found in the intensely blue, diamagnetic (*see Diamagnetism*) anion $[(Cu^I)_4Cu^{III}(S_3CR_2)]^-$, which has been reported by

Table 1 Characteristics of the four classes of mixed valence compounds[3]

Class I	Class II	Class III-A	Class III-B
Metal ions in ligand fields of very different symmetry and/or strength, that is, tetrahedral vs. octahedral	Metal ions in ligand fields of nearly identical symmetry, differing from one another by distortions of only a few tenths Å	Metal ions indistinguishable but grouped into polynuclear clusters	All metal ions indistinguishable
$\alpha = 0$; valences very firmly trapped	$\alpha > 0$; valences distinguishable, but with slight delocalization	α maximal locally	α maximal; complete delocalization over the cation sublattice
Insulator; resistivity of $10^{10}\ \Omega$ cm or greater	Semiconductor; resistivity in the range $10-10^7\ \Omega$ cm	Probably insulating	Metallic conductivity; resistivity in the range $10^{-2}-10^{-6}\ \Omega$ cm
No mixed valence transitions in the visible region	One or more mixed valence transitions in the visible region	One or more mixed valence transitions in the visible region	Absorption edge in the IR, opaque with metallic reflectivity in the visible region
Clearly shows spectra of constituent ions, IR, UV, Mössbauer	Shows spectra of constituent ions at very nearly their normal frequencies	Spectra of constituent ions not discernible	Spectra of constituent ions not discernible
Magnetically dilute, paramagnetic or diamagnetic to very low temperatures	Magnetically dilute, with both ferromagnetic and antiferromagnetic interactions at low temperatures	Magnetically dilute	Either ferromagnetic with a high Curie temperature or diamagnetic, depending upon the presence or absence of local moments

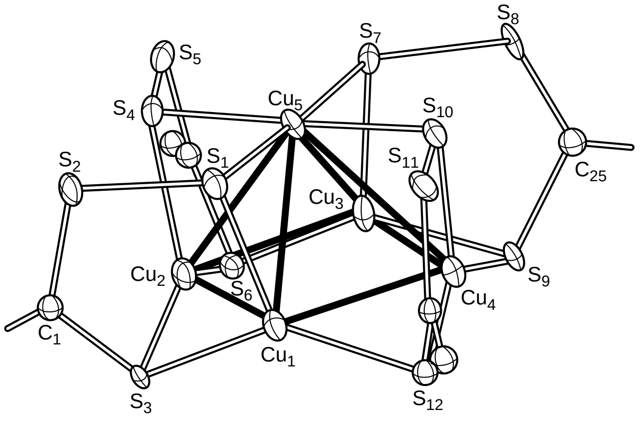

Figure 1 Molecular structure[8] of the $[Cu_8(t\text{-}Bu_2DEDS)_4]^-$ cluster ($DEDS = [S_2C(S)C(CO_2Et)_2]^{2-}$)

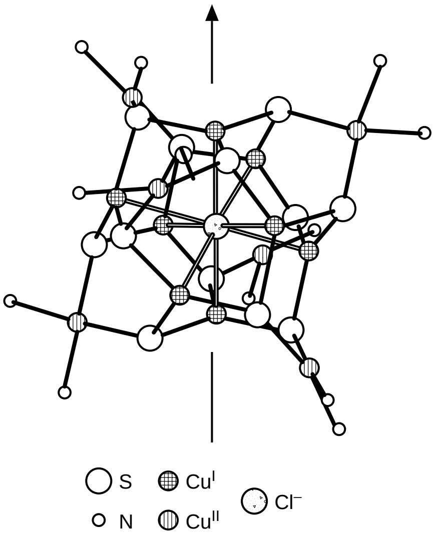

Figure 2 The Cu–Cl–N–S framework of the copper−penicillaminate cluster, showing the threefold axis through two Cu^I atoms and the central Cl. (Ref. 8. Reproduced by permission of Royal Society of Chemistry)

Coucouvanis (Figure 1).[8a] The Cu^{III} ion is in a site with fourfold symmetry, a square-planar environment that is often found for metal ions with the d^8 valence shell electronic structure of Cu^{III}. Each Cu^I ion is found in a site wherein the metal ion is bonded to three sulfur atoms. The Cu^I sites are all equivalent and related to each other by the fourfold symmetry of the complex. Hence the two types of copper ions are in very different coordination environments. This is typical class I behavior since the copper ion sites are not interconvertible by symmetry. The intense blue coloration of the complex, the spectrum of which has not been completely assigned, presumably arises because of the mixed valency of the system. It is especially interesting that D-penicillamine, a drug used in the treatment of Wilson's disease, a genetic disorder that prevents the body from removing excess copper, also produces[8b] an intensely purple mixed valence cluster anion $[Cu^I_8Cu^{II}_6L_{12}Cl]^{5-}$ ($L = –S–CMe_2CH(NH_2)CO_2–$) in which eight Cu^I atoms surround the central Cl$^-$, with six nearly square-planar Cu^{II} ions outside the chloride's centered cubic cluster surface (Figure 2).

Class III mixed valence species are strongly delocalized systems (*see Delocalized Bonding*) in which the symmetry and ligand environment of the two states A and B are identical. Hence the energy difference between the two sites giving rise to electron transfer is zero and the coefficient α that describes the mixing of the states is maximal. It is possible to further divide class III into III-A and III-B, depending upon whether or not discrete polynuclear groupings of indistinguishable metal ions can be distinguished in the crystal (Table 1).

Class II compounds represent an intermediate classification in which delocalization ($\alpha > 0$) does take place but the two types of site remain distinguishable. An optical electron, the electron associated with the transition between the states represented by A and B, does not have an equal probability of being in each site. Unlike the localized class I example presented above, a class II system might have two metal ions in nearly identical octahedral environments with somewhat different metal–ligand distances in each site. Upon electron interchange, the metal–ligand distances must change as the sites interchange. Such transitions are therefore strongly dependant upon vibronic potentials (*see Vibronic Coupling*) connecting the two states.**[9,10]**

It is not easy to draw a clear demarcation between class II and class III behavior.**[11]** Indeed the Creutz–Taube ion (**2**) (*see Creutz–Taube Complex*) caused considerable concern for both experimentalists and theoreticians when it was discovered in 1969, until it was recognized**[12]** that it 'lay at the point where electronic coupling strengths and vibrational properties were of similar magnitude, so precluding any simple perturbation treatment'. The problem was partially solved both by decreasing and by increasing the complexity of the bridging group between the ions. For further elaboration of the complexity of electron transfer communication associated with bridging ligand structure, the recent study by Cotton**[13]** should be consulted. The review by Kaim**[2a]** also should be consulted regarding a wide variety of factors such as the medium, the charge, the nuclearity, and so on, which influence the observed coupling in mixed valence compounds. In general, class II compounds have a bonding atom or group that couples the mixed valence ions or mixed valence molecular units.

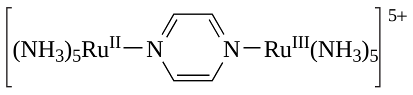

(**2**)

2 HISTORICAL OBSERVATIONS[2]

Prussian blue, $K[Fe^{III}Fe^{II}(CN)_6]$, was the first mixed valent inorganic complex to be synthesized. This deep blue colored material, first recorded in 1704, has been used in pigments and inks since early in the eighteenth century. Other double salts of Fe^{II} and Fe^{III} were described in the middle 1800s. By the late 1800s, other compounds such as the Pt^{II}, Pt^{IV} oxalates of Alfred Werner and the tungsten bronzes were recognized**[11]** to contain both oxidizing and reducing components. By the beginning of the twentieth century, it was recognized that most of these intensely colored inorganic species contain metal ions in two different oxidation states.

Hofmann**[12]** first formulated the concept of mixed oxidation states for Prussian blue and other iron-containing mixed valence species. The electronic origin of the color, of course, remained obscure until the development of quantum mechanics. Another concept, described as 'valence oscillation', was used by Hofmann and Höschele**[12]** following the realization that organic dyes were often found to be unsaturated species with 'valence resonance'; an example is 'cerium–uranium blue' (**3**).

$$Ce^{IV}{}_2O_6U^{IV} \rightleftharpoons Ce^{III}{}_2O_6U^{VI}$$

(**3**)

Shortly after this work, Wells**[14]** came to the same conclusion about valence oscillation and further suggested that enhanced electrical conductivity also resulted. Earlier studies had shown that inorganic powders that were lightly colored (white, pink, gray, and yellow) do not conduct electricity but that intensely colored ions such as the tungsten bronzes often do. As a consequence, most strongly colored inorganic salts were described during the early part of this century in terms of mixed valency. This erroneous conclusion was not satisfactorily rectified until the crystal field and ligand field concepts using wave mechanics became widely known. In fact, 'resonance' ideas continued to be used for an explanation of the colors of inorganic species, especially among chemists, for at least 20 years beyond the time of Bethe's seminal work on crystal field effects.**[15]**

Historically, Stieglitz**[16]** is credited with recognition that interactive oxidation–reduction can produce the intense colors observed in many mixed valence inorganic compounds. There was no compelling reason to continue to introduce valence oscillations to describe these inorganic substances. By 1967, when Robin and Day surveyed**[3]** the chemistry of mixed valence systems, and Allen and Hush independently**[7]** described these systems using quantum mechanics, the concepts of ligand field theory were firmly established. Robin and Day therefore developed a model based on ligand field theory that produced the classification scheme (Table 1) still used today. They introduced the idea of a molecular orbital that contained an optical electron spanning both types of site, A and B, in a mixed valence system. The electron can be completely delocalized into both sites only if the orbitals on both A and B have the same site symmetry, a class III structure. Class II compounds are intermediate between completely localized class I compounds and the class III species.

An important qualitative description of the spectral behavior of class II compounds was presented by Robin and Day.[3] This 'simple model' has found applicability to the discussion of the spectra of numerous mixed valence compounds in which some delocalization occurs. In this model, it is assumed that the ground-state wave function ψ_0 contains the function, α, which describes mixing of the wave function for site A with the wave function ψ_0' of site B. Assuming that these wave functions are linear combinations of atomic functions, ϕ_i, Robin and Day showed that the wave function describing the optical electron spanning sites A and B is given by equation (1). In this equation,

$$\psi_0 = \frac{\kappa}{N}\left[\sqrt{(1-\alpha^2)}\phi^*_{\mathrm{A}} + \alpha\sum_j c_{ij}\phi^*_{\mathrm{B}_j}\right] \tag{1}$$

ϕ_i^* represents the orbitals outside the closed-shell core for sites A and B. Since sites A and B are distinguishable, a fragment of A, ϕ_A^*, and of B, $\sum_j c_j\phi^*_{\mathrm{B}_j}$ must have the same symmetry to be mixed by the coefficient α. N is a normalization constant and κ is a product of all the closed-shell core functions. The mixing coefficient α tends to 0 for large differences in energy between the two sites.

For class I systems, $\alpha = 0$ and the mixed valence absorption bands observed generally fall at frequencies larger than 27 000 cm^{-1}, except when the system contains a colored ion as a constituent. Intervalence interactions (*see Intervalence Transfer Transition*) can provide a source for intensification of such ligand field transitions, however, in class I systems. The mixed valence electronic transition is given by equation (2), where β has the same meaning for the excited state as α does for the ground state. Hence $\alpha = \beta = 0$ for true class I behavior.

$$\frac{\kappa}{N}\left[\sqrt{(1-\alpha^2)}\phi^*_{\mathrm{A}} + \alpha\sum_j c_{ij}\phi^*_{\mathrm{B}_j}\right] \longrightarrow \frac{\kappa}{N'}\left[\beta\phi^*_{\mathrm{A}} - \sqrt{(1-\beta^2)}\sum_j c_{ij}\phi^*_{\mathrm{B}_j}\right] \tag{2}$$

For class II mixed valence systems, the absorption band that is generally observed in the visible region, 14 000–27 000 cm^{-1}, is absent in the spectra of the constituent ions taken individually. The energy of this transition is a function of the changes in the energies of the two sites, along with a term arising from the transfer of the optical electron in the electrostatic field of all the changes in the system.

Robin and Day[3] presented a particularly helpful molecular orbital description of the hypothetical $\mathrm{Cu^IY_2X_2Cu^{II}X_3}$ mixed valence system (Figure 3). This model indicates that the difference in energy between the mixed valence transitions 1 and 2 is equal in energy to the lowest energy ligand field transition in Cu$^{\mathrm{II}}$. Unlike, the localized square-planar Cu$^{\mathrm{II}}$ complexes where three transitions occur, four are expected, 1–4, for the mixed valence system. The intensities of these mixed valence transitions are usually much larger (100–1000 times) than the ligand field transitions.

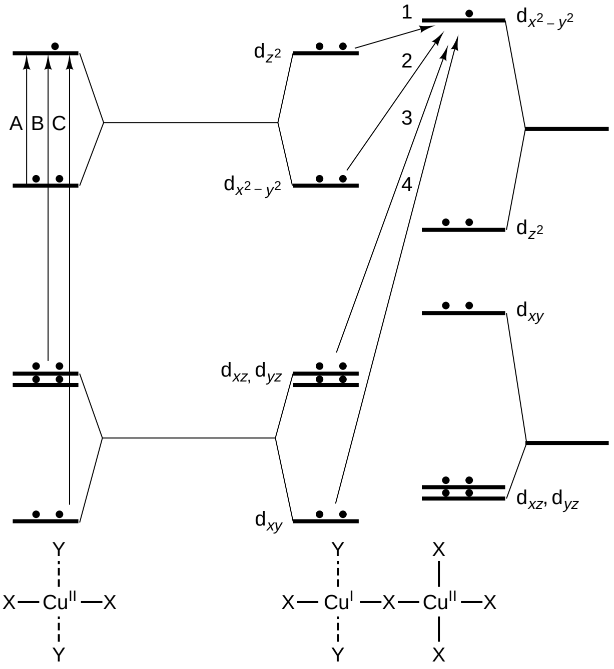

Figure 3 The molecular orbital scheme for the hypothetical class II mixed valence system $\mathrm{Cu^IY_2X_2Cu^{II}X_3}$, showing how the energy difference between the two mixed valence transitions 2 and 1 is equal to the crystal field transition A in $\mathrm{Cu^{II}X_2Y_2}$, and so on. (Ref. 3. Reproduced by permission of Elsevier)

It is recognized that the wave function mixing required for class II mixed valence behavior is governed by the vibrational, magnetic, and electronic features of the system.[17]

3 THEORETICAL DEVELOPMENTS

Following the work of Robin and Day,[3] and Allen and Hush,[7] the first rigorous solution to the vibronic Schrödinger equation for a mixed valence system was formulated by Piepho, Krausz, and Schatz.[18] This model, based on the valence bond approach, is known as the PKS model. It is a model that has been modified[19] to include orbital vibronic constants. A fully equivalent molecular orbital model developed by Piepho[20] is easier to conceptualize, however. The Piepho model also was the first to take advantage of the concept of orbital vibronic constants[8,9] developed by Bersuker for Jahn–Teller systems (Figure 4). The Jahn–Teller theory is the basis for the PKS model.

The PKS model has been shown to be identical[19] with the MO model for one- and two-electron cases provided that the potential function connecting states is expanded to include first- and second-order terms (a Taylor series expansion).

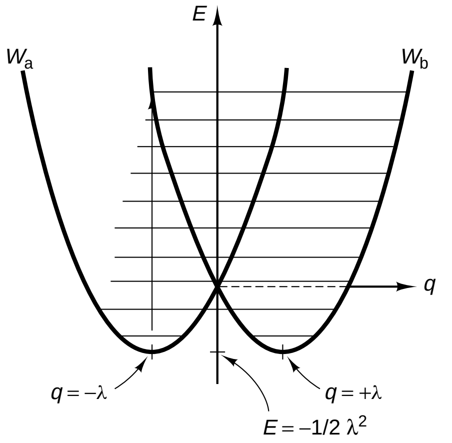

Figure 4 The potential energy surfaces in cross-section of a Jahn–Teller system utilized in the PKS model $\lambda = (8\pi^2 h\nu^3)^{-1/2} l$ (l = vibronic coupling parameter, $\nu = (1/2\pi)k^{1/2}$, k = harmonic vibrational constant). (Ref. 19. Reproduced by permission of Kluwer Academic Publishers)

Several representative examples have been presented by Schatz[19] of the results of the modified PKS model. One of these is reproduced in Figure 5 for a two-electron system.

Although the extended valence bond PKS model probably can always be shown to be equivalent to a molecular orbital model for mixed valency systems involving complex bridging ligands such as found in the Creutz–Taube ion, these systems are best treated using a MO approach. A qualitative description is now given of the MO ideas developed by Piepho.[17]

4 MOLECULAR ORBITAL TREATMENT

The vibronic coupling model of Piepho uses standard MO theory involving MOs of the valence delocalized system. Electron coupling between the metal ion centers requires a coupling with the bridging ligand. The Creutz–Taube ion is described here with this model. A schematic diagram by Piepho[17a] for this prototypical mixed valence complex is shown in Figure 6. In this model, at least two vibronic modes are active that couple the states $\phi_1{}^{\pm} = |\mathrm{b}_{3\mathrm{u}}^2\mathrm{b}_{2\mathrm{g}}{}^{\pm}\rangle$ and $\phi_2{}^{\pm} = |\mathrm{b}_{3\mathrm{u}}{}^{\pm}\mathrm{b}_{2\mathrm{g}}^2\rangle$. The pseudo Jahn–Teller coupling[9] of the states for a given energy splitting, Δ, leads to delocalization. However, the larger the value of Δ for a given coupling, determined by the orbital vibronic constants, the less valence trapped the system becomes. In the Creutz–Taube ion, the unoccupied $\mathrm{b}_{2\mathrm{u}}$ orbital on the bridging pyrazine ligand mixes strongly with a $\mathrm{b}_{3\mathrm{u}}$ metal symmetry orbital thereby producing a large splitting, Δ, of the symmetry orbitals. Hence it is not surprising that the species is valence delocalized.

In the delocalized class III limit, the band shape for electron transfer between mixed valence states is nearly entirely a result of the vibronic coupling associated with the totally symmetric, multicenter, A-bridge-B stretching mode. This mode was omitted[18] from the first PKS model and can be given by – $\langle \mathrm{b}_{2\mathrm{g}}|(\partial V(i)/\partial Q_2)_{Q0}|\mathrm{b}_{3\mathrm{u}}\rangle$, where $(\partial V(i)/\partial Q_2)_{Q0}$ is the matrix element described as the orbital vibronic constant connecting the two states. In the model[20] of Piepho, this strong coupling leads to a symmetric, relatively intense band centered approximately at Δ. Piepho[20] has suggested a number of band contours for different parameter sets. One of these (Figure 7) illustrates how the band shape contours for electronic transitions in mixed valence compounds are related to valence trapping. The parameters λ_n relate to the wavelengths associated with the orbital vibronic constants used and Δ is the energy separation between the mixed valence states. In the Creutz–Taube ion (**2**), the vibronic coupling parameter of importance, λ_1,[9] appears to be 0.70 for a

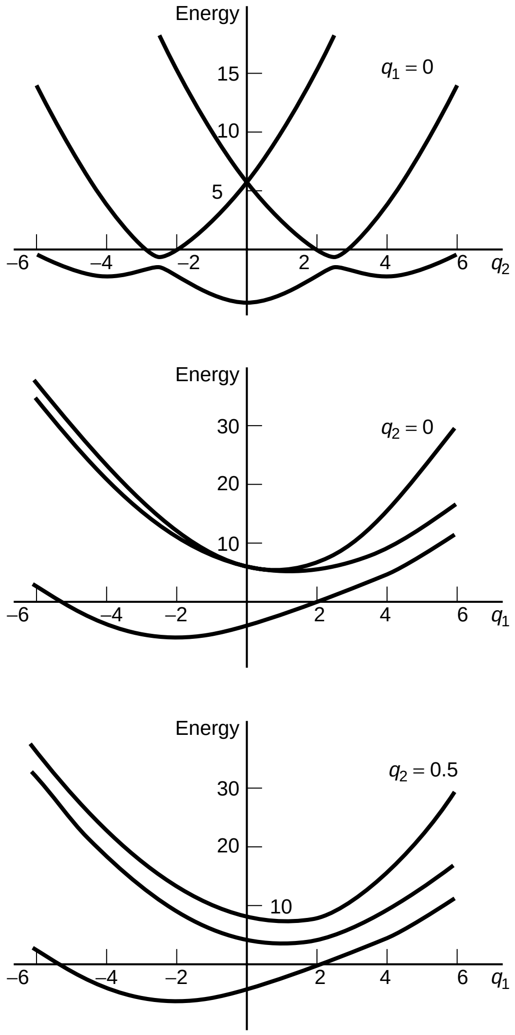

Figure 5 Potential surfaces for a two-electron system in which the covalent state is lowest ($W = -1$). See Schatz[19] for a discussion of the parameters. (Ref. 19. Reproduced by permission of Kluwer Academic Publishers)

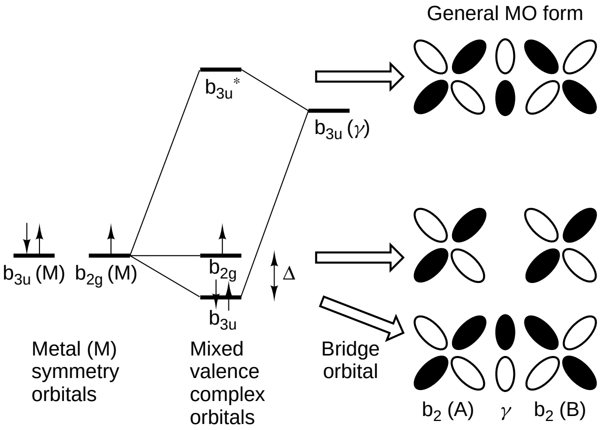

Figure 6 Schematic MO diagram for a prototype mixed valence complex in which an unoccupied b_{3u} bridge orbital interacts with a b_{3u} metal symmetry orbital.[17] (Reprinted with permission from Ref. 20. © 1988 American Chemical Society)

frequency in the 600–800 cm^{-1} range, matching the 701 cm^{-1} band observed experimentally.[14b] Figure 8 is a schematic MO diagram for the Creutz–Taube ion with sketches of the orbitals on the pyrazine bridging ligand and on the metal atoms that are important to the delocalization of the mixed valence.

5 MINERALS WITH MIXED VALENCE IONS

The colors and other physical properties of numerous oxide and silicate minerals are complex facets of mixed valence chemistry. Structural diversity and the frequency of defects complicates the understanding of the electronic properties of such minerals. However, considerable progress has been made, much of which has been described by Burns.[21]

Since biologically important mixed valence systems may have developed in living organisms from mineral systems, it is not surprising that the litany of mixed valence systems in both biology and in minerals largely encompass the same ion states: Fe^{II}, Fe^{III} (magnetite, for example); Ti^{III}, Ti^{IV} (sapphire and other minerals); Mn^{II}, Mn^{III}, Mn^{IV}; Mo^{V}, Mo^{VI}; Co^{II}, Co^{III}; Cu^{I}, Cu^{II}.

Striking examples of ligand field spectral intensity enhancement caused by mixed valency have been observed in mineral

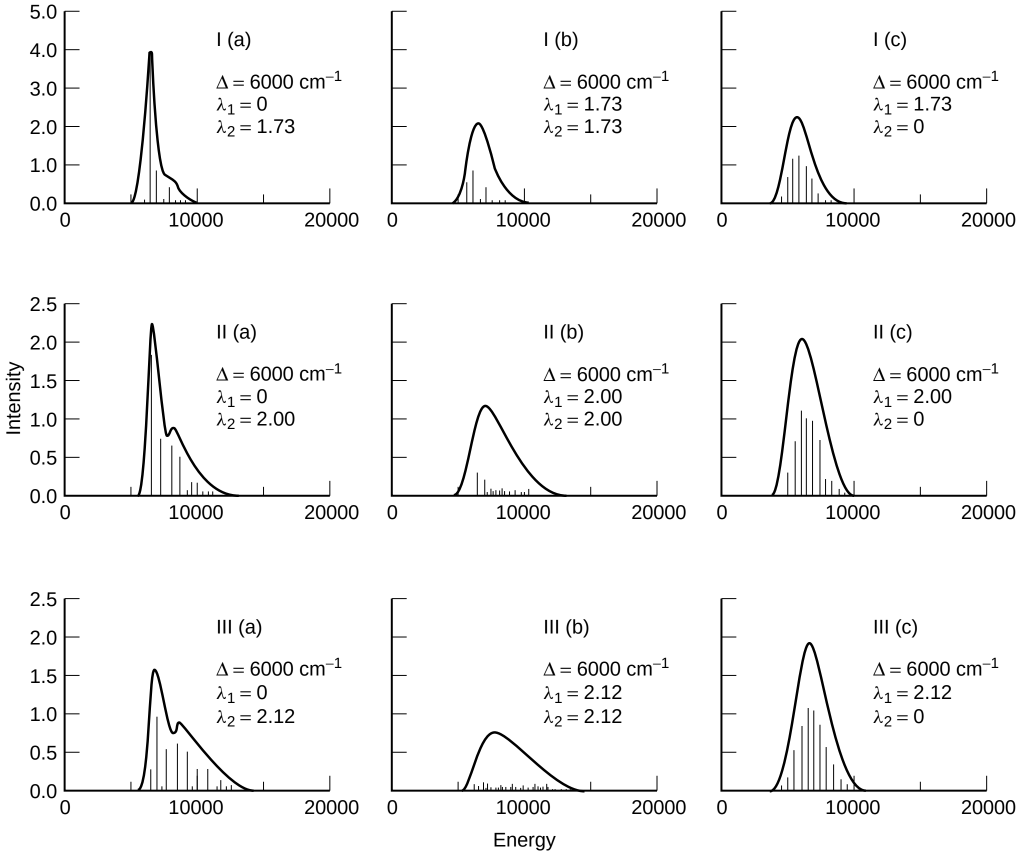

Figure 7 Calculated absorption contours at 298 K for different values of Δ and λn. (Reprinted with permission from Ref. 20. © 1988 American Chemical Society)

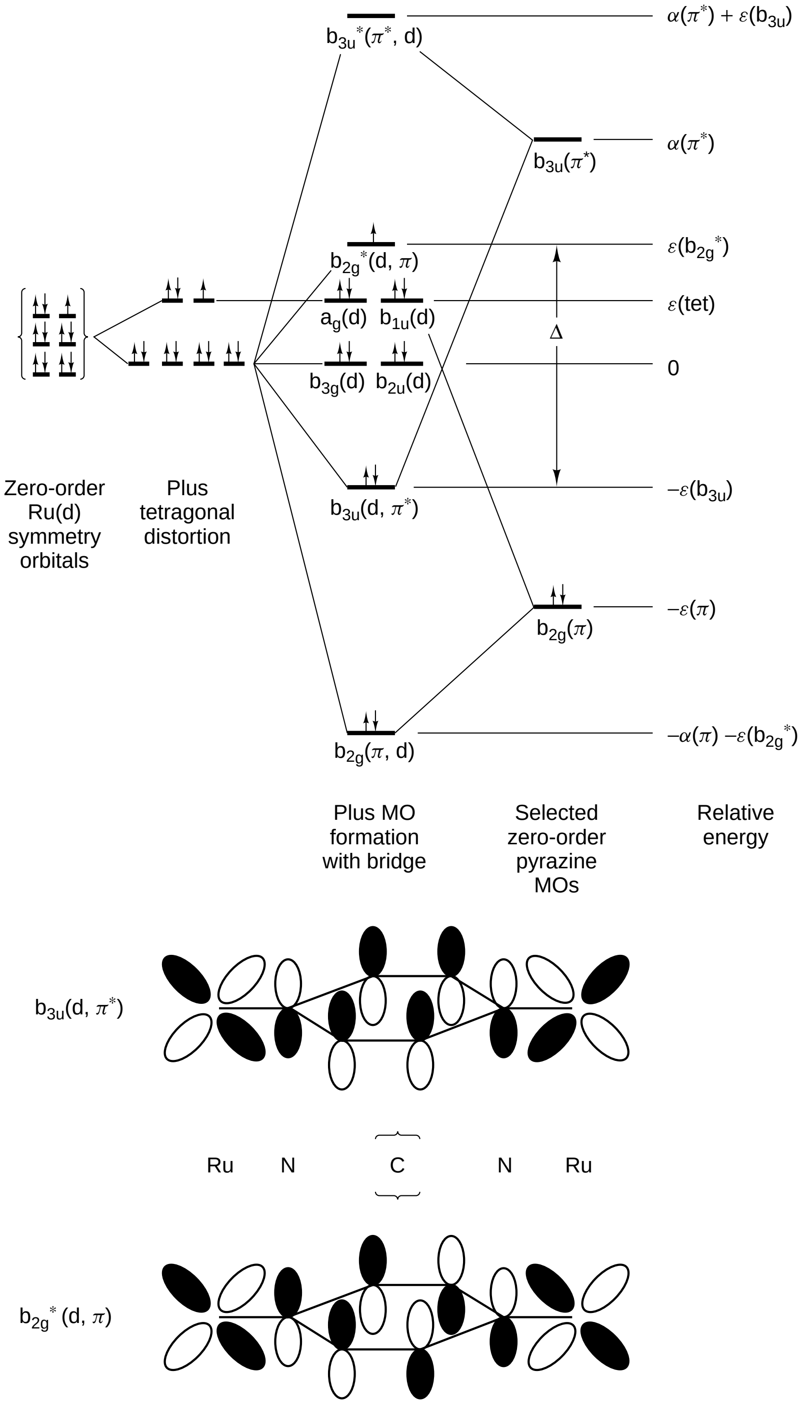
b3u*(π*, d)
α(π*) + ε(b3u)
b3u(π*)
α(π*)
b2g*(d, π)
ε(b2g*)
ag(d) b1u(d)
ε(tet)
Δ
b3g(d) b2u(d)
0
b3u(d, π*)
−ε(b3u)
b2g(π)
−ε(π)
b2g(π, d)
−α(π) −ε(b2g*)
Zero-order Ru(d) symmetry orbitals
Plus tetragonal distortion
Plus MO formation with bridge
Selected zero-order pyrazine MOs
Relative energy
b3u(d, π*)
Ru N C N Ru
b2g* (d, π)

Figure 8 Schematic MO diagram for the Creutz–Taube ion and sketches of the molecular orbitals on the bridging pyrazine and the metal atoms that are important to the mixed valence delocalization.[20] (Reprinted with permission from Ref. 17b. © 1990 American Chemical Society)

studies. Recent observations made in vivianite, a mineral phosphate of composition $Fe^{II}_3(PO_4)_2{\cdot}8H_2O$, upon increasing the degree of oxidation, are shown in Figure 9. This $Fe^{II} \rightarrow Fe^{III}$ intervalence charge-transfer band is the standard against which electron interaction parameters are compared in other mineral systems.

Intervalence charge-transfer energies of various mixed valence minerals can be found in the review by Burns.[21] A few of these minerals are listed in Table 2.

Thermally activated electron delocalization also is observed in some minerals. The silicate mineral ilvanite with its Fe^{II}–Fe^{III} mixed valency has been extensively studied.

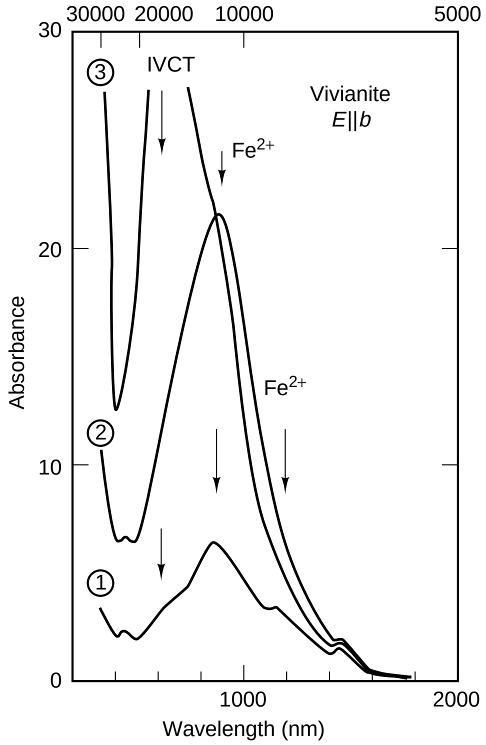

Figure 9 A $Fe^{II}-Fe^{III}$ intervalence charge-transfer band in the mineral vivianite, $Fe_3{}^{II}(PO_4)_3{\cdot}8H_2O$ upon oxidation. (Ref. 22. Reproduced by permission of Kluwer Academic Publishers)

Mössbauer, magnetic, and electronic studies implicate interactions between Fe^{II} and Fe^{III} in neighboring sites. A phase change between 335 and 343 K is accompanied by thermally activated electron delocalization between 300 and 400 K. Below 120 K, ilvanite is ordered antiferromagnetically. Mössbauer studies[21] (*see Mineralogy*) have helped elucidate this mixed valence behavior.

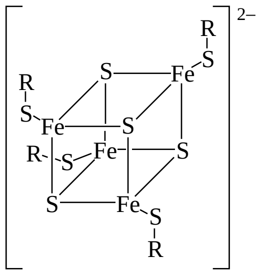

(**4**)

6 BIOLOGICAL SYSTEMS WITH MIXED VALENCE

Mixed valency is well established in biology.[23] Clusters have been identified involving several different combinations of metal ions in various oxidation states. The tetranuclear iron–sulfur system[24] and closely related Fe_2 and Fe_3 complexes[25] are associated with redox processes in proteins in which the enzyme is either mobile or fixed to a membrane. The cluster unit in the oxidized form of the ferrodoxin proteins (*see* ***Iron–Sulfur Proteins***) is made up of mixed valence $[Fe_4S_4(SR)_4]$ units that have been modeled by Holm and coworkers[24] as $[Fe^{II}{}_2Fe^{III}{}_2S_4(SR)_4]^{2-}$ (**4**) clusters. A related 'cubane' Fe_4S_4 unit also is present in the high potential iron proteins (HPIP). However, even with the structural knowledge obtained from model studies, the origin of the potential differences associated with these clusters in the proteins is not fully understood: HPIP, −150/+400 MV; ferrodoxins, −300/−600 MV. The protein apparently controls the cluster structure sufficiently well that the redox potential is different from one protein to another.

Table 2 Some examples from Burns[21] of intervalence charge-transfer energies in minerals

Mineral	M–M distances (pm)[a]	IVCT energy (cm^{-1})	Molar absorptivity ($M^{-1}cm^{-1}$)	Half-width (cm^{-1})
		$Fe^{2+} \rightarrow Fe^{3+}$ IVCT		
Aegerine-augite	320	13 700	160	–
Babingtonite	330	14 710	60	5500
Euclase	294	14 930	–	4600
Glaucophane	309	16 130	–	6600
Glaucophane	331	18 520	–	7000
Ilvaite	283	12 300	150	–
Ilvaite	283	14 500	–	–
Taramellite	339	14 290	–	–
Vivianite	285	15 870	–	–
		$Fe^{2+} \rightarrow Ti^{4+}$ IVCT		
Taramellite	339	21 740	450–1300	9000
Tourmaline	304	24 100	–	4000
Traskite	–	22 730	75	7000
Ti-augite	313	20 600	–	–
		$Ti^{3+} \rightarrow Ti^{4+}$ IVCT		
Ti-augite	315	15 000	–	–
		$Mn^{2+} \rightarrow Ti^{4+}$ IVCT		
Tourmaline	304	30 770	450	7000
		$Mn^{3+} \rightarrow Fe^{3+}$ IVCT		
Babingtonite	330	18 020	–	–

As Blondin and Girerd point out,[25] a 100 MV separation corresponds to an energy of 800 cm^{-1}. This energy difference is assumed to be associated with the vibronic trapping of the mixed valency. This energy separation is of the same order of magnitude as the Fe–S stretching vibrations required to interconvert structural states. Even in the $[Fe_2S_2]^+$ mixed valence systems with bridging S atoms, the valences are localized on a Mössbauer timescale. Hence the trapping parameter Δ cannot be exactly zero. While this conclusion is quite reasonable in the protein environment, it is somewhat surprising that the model compounds show valence trapped class II behavior. The origin of this effect appears to be vibronic.[25]

The electronic structure of the cluster component of metalloenzymes (*see Metalloprotein*) that contain mixed valence clusters can be described using three parameters: a delocalization parameter, an electron exchange parameter, and a trapping energy parameter. As pointed out by Zener[26a] and Anderson[26b] in the 1950s and discussed by Blondin and Girerd,[25] electron transfer between magnetic ions is spin dependent. Magnetic and electronic properties are coupled in these systems. A double exchange occurs with the magnetic coupling energy, it being approximately the same order of magnitude as the vibronic coupling energy. These magnetic systems therefore become very complicated to unravel. Further, it has been shown that if double-exchange is the leading term, then the spins can be aligned parallel even with intrinsic antiferromagnetic coupling. A $[\mathrm{LFe^{II}(OH)_3Fe^{III}L}]$ complex (L = a polydentate ligand) studied by Wieghardt,[27] in which the valences are delocalized, demonstrates the existence of parallel spins in an intrinsically antiferromagnetically coupled system. In related recent work, Wieghardt[23b] has demonstrated that in several *o*-phenylenediamine complexes of Ni, Pd, and Pt, which might otherwise be considered mixed valent, the oxidations and reductions are invariably ligand centered.

Other important mixed valence biological systems under intense study include the dinuclear Mn catalases (*see* ***Manganese Proteins with Mono- & Dinuclear Sites***) and the tetranuclear Mn site for photosynthetic water oxidation (*see* ***Manganese: The Oxygen-evolving Complex & Models***).[28] Progress here has been complicated by the lack of good models although considerable progress is being made particularly using the characterization of materials by ESR spectroscopy. In the dinuclear Mn catalase system, four oxidation states of the *thermous* enzyme are produced: $\mathrm{Mn^{II}Mn^{II}}$; $\mathrm{Mn^{II}Mn^{III}}$; $\mathrm{Mn^{III}Mn^{III}}$; $\mathrm{Mn^{III}Mn^{IV}}$. The mixed valence states are essentially inactive for H_2O_2 disproportionation. Dismukes[28] has proposed a manganese catalase mechanism involving these various oxidation state species (Figure 10). The tetranuclear Mn photosystem II (*see Photosystem I*) is even more complex and less well established although oxide bridges presumably couple mixed valence states.[29]

Other biological mixed valence systems are known but an understanding of their electronic structures is even less well

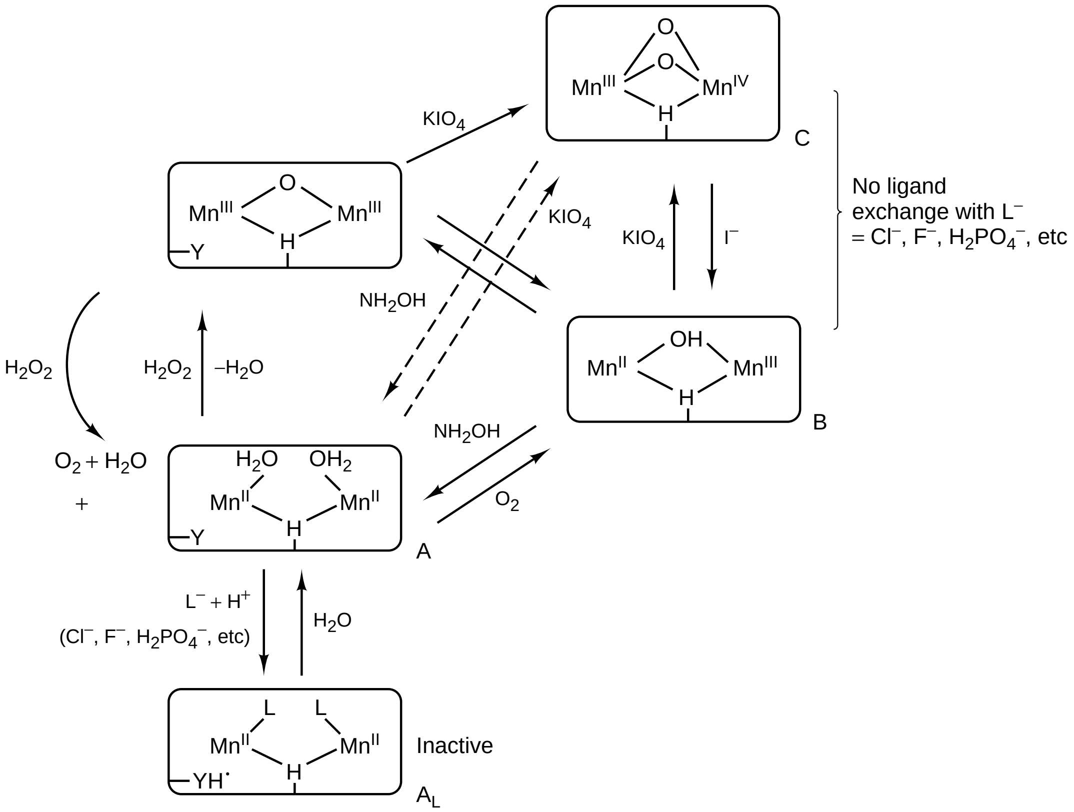

Mn^{III} O O Mn^{IV} H
C
KIO$_4$
Mn^{III} O Mn^{III} H Y
KIO$_4$
KIO$_4$
I$^-$
No ligand exchange with L$^-$ = Cl$^-$, F$^-$, H$_2$PO$_4$$^-$, etc
NH$_2$OH
Mn^{II} OH Mn^{III} H
B
H$_2$O$_2$
H$_2$O$_2$
–H$_2$O
O$_2$ + H$_2$O
+
NH$_2$OH
O$_2$
H$_2$O OH$_2$ Mn^{II} Mn^{II} H Y
A
L$^-$ + H$^+$
(Cl$^-$, F$^-$, H$_2$PO$_4$$^-$, etc)
H$_2$O
L L Mn^{II} Mn^{II} H YH$^\cdot$
Inactive
A$_L$

Figure 10 Proposed mechanism of action for the enzyme catalase involving mixed valence states of manganese. (Ref. 28. Reproduced by permission of Kluwer Academic Publishers)

developed than in the iron and manganese systems described above. An example involving copper has been studied by Karlin.[30]

7 CONDUCTORS AND RELATED MIXED VALENCE MATERIALS

In class I mixed valence species, electron transitions between sites are energetically difficult to accomplish. In the solid state, these materials are generally insulators. However, with class II and class III compounds, electron transfer becomes much easier so that conducting and superconducting materials are obtained (*see* ***Sulfur: Organic Polysulfanes***).

A wide range of optically interesting bronze materials such as $LiFe^{II}Fe^{III}F_6$ have been described.[31] Although architecturally and magnetically of interest, typical resistivity is high at room temperature, $10^9\,\Omega\,cm$. The factors that influence the rates of intramolecular electron transfer in solids have been discussed by Hendrickson.[32] Intramolecular electron transfer in this area is being intensely examined for possible application in molecular electronics.

Mixed valence linear chain materials have proved to be fascinating solid-state species with unusual and interesting properties. Studies range from organic metals such as TTF–TCNQ (**5**) to linear chain metal complexes. In the latter area, the three volume series by Miller[33] is an informative source of material through 1983. Since that date, superconductivity has been observed in TCNQ-type organic materials with the highest T_c found as of 1993 to be about 11–12 K.

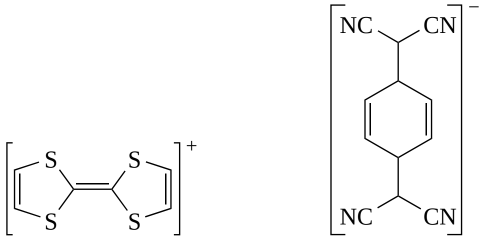

TTF
Tetrathiofulvalene

TCNQ
7,7,8,8-Tetracyano-*p*-quinodimethane

(**5**)

Inorganic–organic composites are receiving close study.[34] In these compounds, as in the mixed valence copper sulfides,[35] the nonmetallic moiety is the mixed valent species. Superconductivity also is known with the sulfides in the *Chevrel Phases*.[36a] In 1991, the pure fullerene phase of carbon, C_{60} (Figure 11), was observed to become superconducting upon doping with alkali metals.[36] This organic–inorganic area is an exciting new field for investigation since conductivity can be dominated by electron delocalization in the organic moieties while magnetic properties are generally associated with the metal centers.

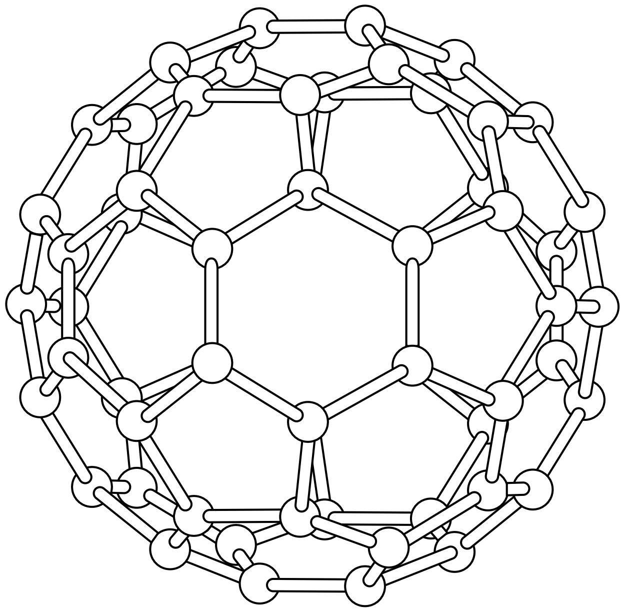

Figure 11 A sketch of the C_{60} fullerene

The discovery of mixed valent oxide superconductors[37] opened up the possibility that room temperature superconducting materials may one day be obtained. Although T_c values around 10 K have been known for many years, the $YBa_2Cu_3O_7$ and $Tl_2Ba_2CaCu_2O_8$ phases have yielded superconducting critical temperatures of 75–91 K and 102 K, respectively (above the boiling point of liquid nitrogen). Evidence even has been presented for filamentary superconductivity in

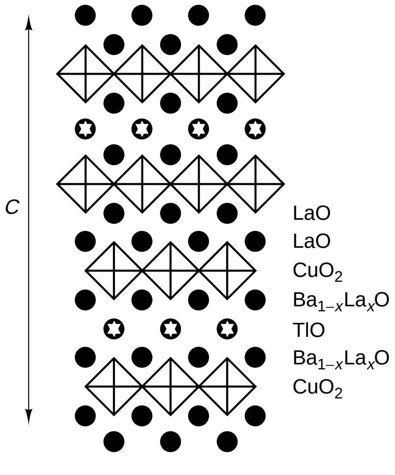

Figure 12 Schematic representation, projected along [010], of the structure of $TlBa_{2-x}La_{2+x}Cu_2O_{9\pm\delta}$ showing the intergrowth of La_2CuO_4 and $TlBa_2CuO_5$ type structures

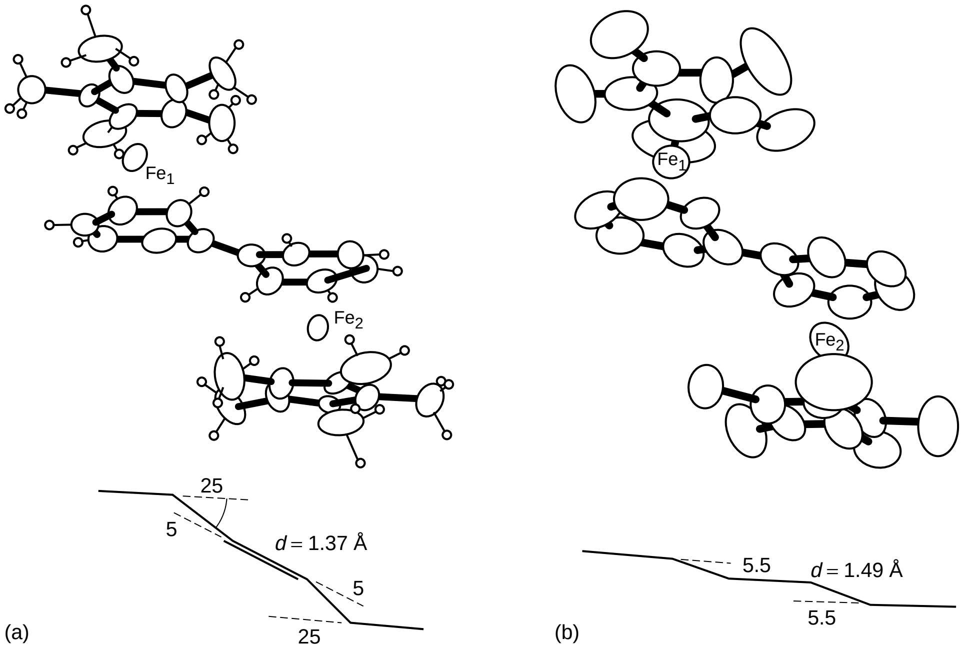

Figure 13 X-ray crystal structures of $[(FeC_5Me_5)_2(\text{diphenyl})]^{n+}$ $(PF_6{}^-)_2$; $(PF_6{}^-)_2$; $n = 0$ (a), 1 (b)

Table 3 Relationship between resonance Raman, conductivity, and electronic spectroscopic results on complexes of the sort $[Pt^{II}(en)_2][Pt^{IV}(en)_2X_2][ClO_4]_4$

	Resonance Raman data			Conductivity data^b	Electronic data IVCT
X	ω_1 (cm^{-1})	ν_1 (max)^a	ν_1 (max) (cm^{-1})	E_a (cm^{-1})	(max) (cm^{-1})
Cl	311.3	14^6	≈4120	10 970	22 750
Br	173.2	10^6	1697	6780	15 170
I	122.6	9^{42}	1053	3390	12 340

[a] Highest harmonic of ν_1 detected in a resonance Raman spectrum of the complex specified. [b] Two-probe, single-crystal data.**41**

specially treated $YBa_2Cu_3O_7$ films at 220 K, and reproducible resistive transitions between 160 and 200 K have been reported for films of $Y_5Ba_6Cu_{11}O_2$ subjected to He and O_2 anneals. Structural patterns from X-ray diffraction implicate copper oxide phases similar to those presented for $TlBa_{2-x}La_{2+x}Cu_2O_{9\pm\delta}$ in Figure 12. Superconductivity in another oxide, $Na_xCoO_2{\cdot}1.3H_2O$, has been related to chemical doping as observed in the high-T_c copper oxides, although the microscopic origin of high T_c in superconductivity is still under active study.**38**

8 MISCELLANEOUS MIXED VALENCE SPECIES

The Creutz–Taube ion (**2**) can be described as the prototypical mixed valent system in which a delocalized formulation best describes the electron transfer between charge centers. Bruns and Kaim**39** described another pyrazine complex that displays delocalized behavior, [*mer*-$(OC)_3$(P-*i*-$Pr_3)_2$ W(μ-pyrazine)W(P-*i*-$Pr_3)_2(CO)_3]^+$. Connecting two organometallic centers with different metal valencies together by delocalized organic spacers becomes a general way to accomplish fast one- and two-electron transfer. This approach has been taken by Astruc,**22** who has described the electrochemistry of mixed valent Fe^IFe^{II} complexes of the π 'sandwich' cyclopentadiene (*Ferrocene*) type, bridged by fulvalene and by diphenyl. The $[Fe_2(Fv)(Cp)_2]^{2+}$ (Fv = fulvalene) system is one where the Fe^IFe^{II} system undergoes a two-electron reduction as measured by cyclic voltammetry. However, Astruc and his colleagues have characterized the $[Fe_2(\text{diphenyl})(C_5R_5)_2]^{2+}$ (R = Me) complex, which, unlike the related $[Fe_2(\text{diphenyl})(C_5H_5)_2]^{2+}$, undergoes a reversible one-electron reduction. Structural comparisons have been made (Figure 13) between the one- and two-electron reduction species in a system giving two close one-electron transfers. The electronic energy difference between the two one-electron reductions is compensated by the energy gained in the structural rearrangement, which intervenes in the two-electron reduction product. Astruc suggests that these types of species are useful 'two-electron transfer mediators'.

The tools used to explore mixed valency over the past few years have been able to give new understanding to these complex inorganic and organometallic systems. Various spectroscopies have been used. Of particular use for studying inorganic compounds is resonance Raman spectroscopy, which gains its very existence from the coupling of electronic and vibrational spectroscopies. In particular, Clark[40] used this tool with considerable success to explore the behavior of linear chain mixed valent species. Multiple harmonic vibrational levels (overtones) of these materials are observed to increase in number with decreasing conductivity. Excitation to the intervalence state requires less nuclear motion in the more highly conducting mixed valent species. Thus, fewer overtone bands are observed in those more highly conducting species where the conductivity obeys the relationship $\sigma = \sigma_0 \exp(-E_a/kT)$ (Table 3).

9 RELATED ARTICLES

Iron−Sulfur Proteins; Manganese Proteins with Mono- & Dinuclear Sites; Manganese: The Oxygen-evolving Complex & Models; Superconductivity.

10 REFERENCES

1. I am indebted to Shannon Geigenmueller and Ahmed Mohamed for these searches.
2. a) W. Kaim, A. Klein, and M. Glockle, *Acc. Chem. Res.*, 2000, **33**, 755; b) D. G. Nocera, *Acc. Chem. Res.*, 1995, **28**, 209; c) R. Nage, *Coord. Chem. Res.*, 1991, **111**, 161; d) W. Kaim, W. Brans, J. Poppe, and V. Kasack, *J. Mol. Struct.*, 1993, **292**, 221.
3. M. B. Robin and P. Day, *Adv. Inorg. Chem. Radiochem.*, 1967, **10**, 247.
4. K. Prassides ed., 'Mixed Valence Systems: Applications in Chemistry, Physics and Biology', NATO ASI Series, Kluwer Academic, Amsterdam, 1990, Vol. 343.
5. D. B. Brown ed., 'Mixed Valency Compounds', Riedel, Dordrecht, 1980.
6. C. G. Young, *Coord. Chem. Rev.*, 1989, **96**, 89.
7. G. C. Allen and N. S. Hush, *Prog. Inorg. Chem.*, 1967, **8**, 357.
8. (a) D. Coucouvanis, *Prog. Inorg. Chem.*, 1979, **26**, 301; (b) P. J. M. W. L. Birker and H. C. Freeman, *J. Chem. Soc., Chem. Commun.*, 1976, 312.
9. I. B. Bersuker, 'The Jahn-Teller Effect and Vibronic Interactions in Modern Chemistry', Plenum, New York, 1984.
10. I. B. Bersuker and V. Z. Polinger, 'Vibronic Interactions in Molecules and Crystals', Springer-Verlag, Berlin, 1989.
11. M. B. Robin and P. Day, *Acc. Chem. Res.*, 2000, **33**, 755; b) D. G. Nocera, *Acc. Chem. Res.*, 1995, **28**, 209; c) R. Nage, *Coord. Chem. Res.*, 1991, **111**, 161; d) W. Kaim, W. Brans, J. Poppe, and V. Kasack, *J. Mol. Struct.*, 1993, **292**, 2.
12. V. A. Hofmann and K. Höschele, *Ber. Deut. Chem. Ges.*, 1915, **48**, 20.
13. F. A. Cotton, C.-Y. Liu, C. A. Murillo, D. Villagren, and X. Wang, *J. Am. Chem. Soc.*, 2003, **125**, 13564.
14. H. L. Wells, *Am. J. Sci.*, 1922, **3**, 417.
15. H. Bethe, *Ann. Phys.*, 1922, **3**, 417; J. P. Fackler Jr, 'Symmetry in Chemical Theory', Dowden Hutchinson and Ross, 1973.
16. J. Stieglitz, *Proc. Natl. Acad. Sci. U.S.A.*, 1923, **9**, 308.
17. (a) S. B. Piepho, *J. Am. Chem. Soc.*, 1981, **103**, 369; (b) S. B. Piepho, *J. Am. Chem. Soc.*, 1990, **112**, 4197.
18. S. B. Piepho, E. R. Krausz, and P. N. Schatz, *J. Am. Chem. Soc.*, 1978, **100**, 2996.
19. P. N. Schatz, in 'Mixed Valence Systems: Applications in Chemistry, Physics and Biology', NATO ASI Series, ed. K. Prassides, Kluwer Academic, Amsterdam, 1990, p. 7.
20. S. B. Piepho, *J. Am. Chem. Soc.*, 1988, **110**, 6319.
21. R. G. Burns, in 'Mixed Valence Systems: Applications in Chemistry, Physics and Biology', NATO ASI Series, ed. K. Prassides, Kluwer Academic, Amsterdam, 1990, p. 175.
22. D. Astruc, M.-H. Desbois, M. Lacoste, N. Ardoin, L. Toupet, and F. Varret, *Adv. Inorg. Chem. Radiochem.*, 1967, **10**, 107.
23. (a) K. Wieghardt, in 'Mixed Valence Systems: Applications in Chemistry, Physics and Biology', NATO ASI Series, ed. K. Prassides, Kluwer Academic, Amsterdam, 1990, p. 447; (b) D. Herbian, E. Bothe, F. Neese, T. Weyhermüller, and K. Weighardt, *J. Am. Chem. Soc.*, 2003, **125**, 9116.
24. S. Ciurli, M. Carric, J. A. Weihel, M. J. Carney, T. D. P. Stack, G. G. Papaefthymion, and R. H. Holm, *J. Am. Chem. Soc.*, 1990, **112**, 2654.
25. G. Blondin and J. J. Girerd, in 'Mixed Valence Systems: Applications in Chemistry, Physics and Biology', NATO ASI Series, ed. K. Prassides, Kluwer Academic, Amsterdam, 1990, p. 119.
26. (a) C. Zener, *Phys. Rev.*, 1951, **82**, 403; b) (P. W. Anderson and H. Hasegawa, *Phys. Rev.*, 1955, **100**, 675.
27. L. Bominaar, X.-Q. Ding, E. Bill, H. Winkler, A. X. Trautwein, S. Drüeke, and K. Wieghardt, in 'Mixed Valence Systems: Applications in Chemistry, Physics and Biology', NATO ASI Series, ed. K. Prassides, Kluwer Academic, Amsterdam, 1990, p. 377.

28. G. C. Dismukes, in ‘Mixed Valence Systems: Applications in Chemistry, Physics and Biology’, NATO ASI Series, ed. K. Prassides, Kluwer Academic, Amsterdam, 1990, p. 137.
29. G. Christou, *Acc. Chem. Res.*, 1989, **22**, 328.
30. M. Mahroof-Tahir and K. D. Karlin, *J. Am. Chem. Soc.*, 1992, **114**, 7599.
31. G. Fe’rey, in *Adv. Inorg. Chem. Radiochem.*, 1967, **10**, 155.
32. D. N. Hendrickson, *Adv. Inorg. Chem. Radiochem.*, 1967, **10**, 67.
33. J. S. Miller, ‘Extended Linear Chain Compounds’, Plenum, New York, 1982–83, Vols. 1–3.
34. M. Kurmoo, D. Kanazawa, and P. Day, *Adv. Inorg. Chem. Radiochem.*, 1967, **10**, 419.
35. H. K. Ro and W. E. Hatfield, *Adv. Inorg. Chem. Radiochem.*, 1967, **10**, 407.
36. (a) R. B. King, ‘Applications of Graph Theory and Topology in Inorganic Cluster and Coordination Chemistry’, CRC Press, Boca Raton, FL, 1993, p. 149, p. 168; (b) C. Greaves, *Annu. Rep. Prog. Chem., Sect. A*, 1991, **88**, 419.
37. A. W. Sleight, *Thermochim. Acta*, 1991, **174**, 1.
38. R. E. Schaak, T. Klimczuk, M. L. Foo, and R. J. Cava, *Nature*, 2003, **424**, 527.
39. W. Bruns and W. Kaim, *Adv. Inorg. Chem. Radiochem.*, 1967, **10**, 365; W. Kaim, A. Klein, and M. Glockle, *Acc. Chem. Res.*, 2000, **33**, 755.
40. R. J. H. Clark, *Adv. Inorg. Chem. Radiochem.*, 1967, **10**, 273.
41. Y. Hamaue, R. Aoki, M. Yamashita, and S. Kida, *Inorg. Chim. Acta*, 1981, **54**, L13.

Molecular Orbital Theory

Paul T. Czech
Providence College, Providence, RI, USA

1 Introduction 1
2 Valence Bond Theory 2
3 Hybridization 4
4 Molecular Orbital Theory: The H_2^+ Molecular Ion 4
5 Pictorial Representations of Orbitals 7
6 Molecular Orbitals and Symmetry 8
7 Improvements to the Wavefunction 9
8 Homonuclear Diatomic Molecules 10
9 Heteronuclear Diatomics 12
10 The Self-consistent Field Approach 14
11 The Hückel and Extended Hückel Methods 15
12 Group Theory and Molecular Orbital Theory 18
13 Related Articles 23
14 References 23

1 INTRODUCTION

Molecular orbital theory is a quantum mechanically based model used for the description of the behavior of electrons in molecules. The essence of the approach is that electronic wavefunctions are built from the commonly used s, p, d, and f hydrogen-atom based atomic orbitals and can range through an entire molecule. These molecular orbitals (MOs) can be constructed using detailed mathematical formalisms and high-speed supercomputers, or with pen and paper using rough approximations. Experimental inorganic chemists are familiar with some of the most notable historical successes of the MO approach, especially in treatments of molecular spectra, the shapes of molecules, and their magnetic character. The types of important subjects that are being treated today using MO calculations include determinations of charge distributions in molecules, details of molecular collisions, descriptions of molecular geometry in the ground and excited states, optical properties, and potential energy surface diagrams for reactions, among many other applications. Several undergraduate chemistry textbooks review MO theory from an inorganic chemists' point of view;[1–4] many other texts treat the method from a more mathematical point of view.[5–12] A large percentage of the supercomputer cpu time in the United States is expended solving electronic structure calculations, a large majority of which uses the many variations of MO theory.

The aforementioned areas of study can be treated with a rigor that would have seemed impossible even a few years ago. This is due principally to the amazing development of efficient, graphically based software and high-speed computer hardware. As a result, rather than electronic structure calculations being in the exclusive realm of the theoretician, it is a matter of routine that experimental chemists make use of the many commercial theoretical chemistry packages for their own purposes. Though there is little chance that the chemical discipline will evolve from an experimental science into a purely theoretical endeavor, quantum chemical calculations play a growing role in chemical inquiry and chemical education.

Our current understanding of chemical bonding in molecules was developed in the late 1920s and early 1930s immediately after the quantum mechanical revolution of thought that revealed a new way of describing energy and matter. It had been known prior to the establishment of the new mechanics that covalent bonds could be described as shared electron pairs while the other electrons in a molecule were characterized as 'lone pairs' or core electrons not involved with bonding.[13,14] The arrangement of the valence electrons in the vast majority of main group compounds could be accounted for using the model that was based on the inherent stability in a 'filled octet' of electrons. Lewis dot structures that use these concepts are highly successful in rationalizing connectivity in molecules and are still used extensively in organic chemistry today (see **1**).

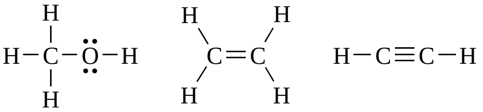

(**1**)

A three-dimensional extension of the same approach was developed in the 1950s as X-ray crystal structures of molecules became more easily available. The valence-shell electron pair repulsion theory (VSEPR) rules modeled the structural influence of bonding pairs and lone pairs of electrons.[15] A set of simple guidelines is used to provide the basis for a great number of structures. For example, the bond angles in the isoelectronic series CH_4 (109.4°), NH_3 (107.3°), and H_2O (104.5°) can be rationalized by attributing a larger repulsive force to lone electron pairs as compared to bond electron pairs (see (**2**)). Another particular success was the accurate model of the structure of the noble gas halides XeF_2 and XeF_4 even before their synthesis.

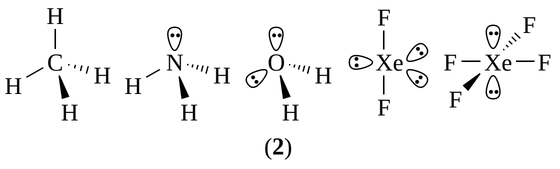

(**2**)

However, to go a step further and identify the physical forces that keep molecules together, as well as to develop a quantitative understanding of molecular structure, a quantum mechanical treatment was required. In 1926, Schrödinger's equation was proposed to relate the energy of a quantum mechanical system to the motions of its constituent particles and all the forces acting upon them. In a chemical system, we are ultimately interested in the mathematical representation of the kinetic and potential energies of an electron under the influence of attractive nuclear forces and the repulsive forces of the other electrons. This representation is called the wavefunction and can be expressed in a variety of ways, some of which will be described in this article. The most general form of the Schrödinger equation is:

$$\widehat{H}\Psi = E\Psi \tag{1}$$

where $\widehat{H}$ represents the Hamiltonian operator, being the sum of the kinetic and potential energy operators. Ψ represents the wavefunction of the system (also known as the eigenfunction) and E the total energy of the system (an eigenvalue). If each side of the equation is multiplied by Ψ and integrated over all space, the equation may be arranged to solve for the total energy:

$$E = \frac{\int \Psi^* \widehat{H} \Psi \mathrm{d}\tau}{\int \Psi^* \Psi \mathrm{d}\tau} \tag{2}$$

Knowledge of the physical forces that influence the total energy of a system thus reveals the theoretical underpinnings of nearly all of experimental chemistry. In fact, much of the early activity in chemical bonding theory was the result of attempts to understand the results of molecular spectroscopy experiments. The developers of what came to be called molecular orbital theory, Robert Mulliken (US) and Friedrich Hund (Germany), established a professional and personal relationship based on their common interest in the spectra of diatomic molecules especially in the influence of isotope effects. When compared to other theories of the time, a major advantage of their theoretical approach was the ability to directly apply the results to the elucidation of molecular spectra.**[16]**

Although equation (2) appears concise in the form above, it cannot be solved exactly for a molecular system. Electron–electron repulsions present a practical problem in the same way that they do in many-electron atoms; the repulsive interaction between two electrons is a function of the position coordinates of each electron and cannot be separated into two functions dependent on each set of coordinates individually. However, even if a complicated wavefunction that was expressed in the coordinates of all the electrons in a molecule could be developed, it would have to be reported as an extensive grid of points in 3-D space, each associated with a different potential energy with unique solutions for each and every molecule. This would clearly be an unwieldy and ineffective way of reporting electronic structure. For this reason, quantum chemists quickly learned that in order for the MO theory to be accepted by chemists at large, a judicious choice of these 'molecular wavefunctions' would need to have transferability between molecules and be easily represented, ideally in a straightforward pictorial fashion.

There are two guiding principles that direct the generation of the solutions to the Schrödinger equation. First, in order to avoid the inconvenient wavefunctions mentioned above, the method takes advantage of a technique analogous to the so-called 'orbital approximation' in atomic structure. In this approximation, a many-coordinate function is expressed as a linear combination of products of one-electron wavefunctions.

$$\begin{aligned}\Psi(\text{electron 1, electron 2, electron 3 K}) &= \psi(\text{electron 1})\\ &\times \psi(\text{electron 2})\psi(\text{electron})K\end{aligned} \tag{3}$$

Secondly, the quality of a wavefunction in any quantum mechanical system is influenced by the variation principle, which states that a normalized, acceptable trial wavefunction will always yield an eigenvalue larger than the true energy provided that the exact Hamiltonian is used. One wavefunction is considered 'better' than another if it yields a lower energy. An alternative way expressing this idea is to say that a means of setting an 'upper bound' is easily achieved. Specifically, a trial wavefunction is designed in terms of parameters that can be varied so that the optimal wavefunction emerges when the lowest eigenvalue is attained.

These guidelines enable the chemist to use a set of common 'building block' functions for all molecules and to make small adjustments as they are warranted in accord with the variation principle. Many methods of calculating the electronic structure of molecules have been proposed since the advent of quantum mechanics but nearly all that are used today are derivatives of two approaches that were proposed in the flurry of activity after Schrödinger introduced his equation.

2 VALENCE BOND THEORY

The application of Walter Heitler and Fritz London's valence bond theory was the first description of the binding forces in the H_2 molecule, the simplest neutral molecule.**[17]** Linus Pauling and John Slater later extended the principles to larger molecules.**[18,19]** The key element in their proposal was the synthesis of a 'bonding' wavefunction resulting from a combination of atomic orbitals that link the two atoms in a bond. It was hugely important that this localized approach concurred with the Lewis dot model. For the simplest neutral molecule, H_2, the Hamiltonian operator may be written

$$\widehat{H} = -\frac{h^2}{2M}(\nabla_{\mathrm{A}}^2 + \nabla_{\mathrm{B}}^2) - \frac{h^2}{2m}(\nabla_1^2 + \nabla_2^2) - \frac{e^2}{4\pi\varepsilon_0}$$

$$\times\left(\frac{Z}{r_{1A}}+\frac{Z}{r_{1B}}+\frac{Z}{r_{2A}}+\frac{Z}{r_{2B}}-\frac{Z}{r_{12}}-\frac{Z^2}{R}\right) \qquad (4)$$

where M is the mass of hydrogen nucleus, m is the electronic mass, Z is the atomic number of the nucleus ($Z = 1$ for hydrogen), ∇_A^2 and ∇_B^2 are the kinetic energy operators for the nuclei A and B, ∇_1^2 and ∇_2^2 are the kinetic energy operators for the electrons 1 and 2, and the various distances are illustrated in (**3**).

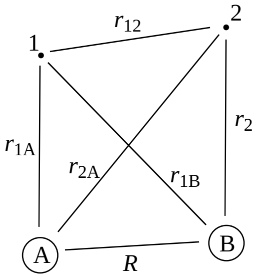

(**3**)

In order to simplify the expression, the motion of the nuclei is neglected by implementing the Born–Oppenheimer approximation, which is justified because of the large difference in mass between the nuclei and the electrons. In fact, atomic nuclei are in constant motion, but their velocity is a fraction of the velocity of the electrons. Thus, the electrons are assumed to quickly adjust to any motion by the nuclei, essentially freezing the nuclei in space relative to the electrons, so R may be considered a constant.

The resulting Hamiltonian for H_2 can be simplified using atomic units:

$$\widehat{H} = -\frac{1}{2}(\nabla_1^2+\nabla_2^2)-\frac{1}{r_{1A}}+\frac{1}{r_{1B}}+\frac{1}{r_{2A}}+\frac{1}{r_{2B}}-\frac{1}{r_{12}}-\frac{1}{R} \qquad (5)$$

In the light of the orbital approximation, a total wavefunction for the 'system' of two separated hydrogen atoms can be written as

$$\Psi = 1s_A(1)1s_B(2) \qquad (6)$$

Each electron occupies a 1s orbital on its 'home' hydrogen, electron 1 on H_A and electron 2 on H_B. This distinction, however, is lost when the nuclear centers are brought within bonding distance of each other. At this close proximity, quantum mechanics requires that electrons be indistinguishable from one another. The simplest function in the valence bond description that accounts for this behavior is a linear combination of two possibilities (**4**).

$$\Psi = c_1\psi_1 + c_2\psi_2$$
where $\psi_1 = 1s_A(1)\,1s_B(2)$ and $\psi_2 = 1s_A(2)1s_B(1)$

(**4**)

An electron described by this new molecular wavefunction could 'belong' to either atom at a given moment while the second electron is associated with the other nuclear center. A calculation of probability density of the electron reveals that there is a buildup of electron density in the internuclear region for the bonding interaction that exceeds the density normally found at the same distance from the nucleus in the separated atoms.

Electrons described by bonding wavefunctions, that is, those that occupy bonding orbitals are more energetically stable than those electrons described by atomic orbitals in the separated atoms. Owing to the fact that an electron in this region has an attractive interaction with the two positively charged nuclei, it might appear reasonable to attribute the stability of a chemical bond to a 'classical' electrostatic attraction. However, as will be shown below, the term that describes stability of the molecule relative to the two separated nuclei is a purely quantum mechanical quantity.

This simplest valence bond description of the chemical bond can be improved (yielding a lower energy via the variation principle) using two straightforward techniques. The first considers the possibility that at a given moment both electrons can be found on a single atom. That is, the wavefunction can include ionic components written as in (**5**):

$$H_A^-H_B^+ \quad \text{or} \quad H_A^+H_B^-$$

(**5**)

This distribution of electron density can be accounted for by rewriting an unnormalized function in the form

$$\begin{aligned}\Psi &= 1s_A(1)1s_B(2) + 1s_A(2)1s_B(1)\\ &\quad + \lambda[1s_A(1)1s_A(2) + 1s_B(1)1s_B(2)] \qquad (7)\end{aligned}$$

where λ is a weighting factor. Calculations using the variational principle have established that the optimum value for λ for the wavefunction in this form is less than one, meaning that the covalent description that places one electron on each nucleus is more important. The other improvement for a valence wavefunction is based upon the observation that, for many polyatomic molecules, a large number of Lewis dot structures may obey the filled octet prescription. This is addressed by identifying the overall wavefunction as a weighted superposition of all the electron-paired structures that obey the Lewis filled octet criterion. The structure of a molecule becomes a resonance combination of the contributing structures. A common example is ozone, O_3 (**6**).

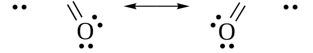

(**6**)

These adjustments rapidly increase the number of terms in the linear combination as the molecules under consideration became larger (as does the amount of time required to calculate a solution), but they all contribute toward lowering the total energy in the direction of the 'true' value.

3 HYBRIDIZATION

The hybrid orbital scheme that is introduced to all student chemists was developed originally in the context of the valence bond description. Early dipole moment measurements had determined the nonlinearity of H_2O and NH_3, and the totally symmetric distribution of the C–H bonds in CH_4. It was not clear, however, how the atomic orbitals on the central atom could be responsible for the required bond angles. The tetrahedral (109.5°) geometry necessary for the nonpolar methane molecule is quite different from the 90° spacing of the lobes of the carbon 2p atomic orbitals. Pauling proposed that the bonding interactions were formed from the overlap of hybrids constructed in a hypothetical prebonding 'valence state'. The wavefunctions of the carbon 2s and 2p orbitals were combined into a linear combination of four mutually orthogonal sp^3 hybrids. Each orbital contains a mixture of 25% of each component atomic orbital (2s, $2p_x$, $2p_y$, $2p_z$), giving a total distribution of s character to p character in the ratio of 1:3. This combination of atomic functions ensures that each orbital is directed toward the corners of a tetrahedron, 109.5° apart (see (**7**)). The atomic functions can be mixed in other ratios in order to produce different angular distributions for other bonding hybrids.

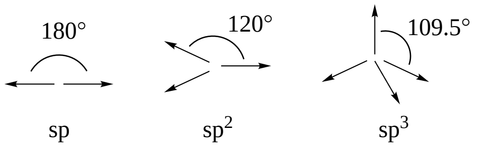

(**7**)

Atomic orbitals that do not participate in the hybridization are then used for bonding with other atomic orbitals on adjacent centers as long as there is nonzero overlap of the atomic orbitals. For example, a hybridization description for the bonding in ethylene accounts for a so-called sigma (σ) framework of bonding utilizing sp^2 hybrids and a second interaction called a pi (π) interaction between pure p atomic orbitals on the carbon atoms (**8**).

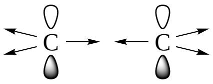

(**8**)

The hybridization scheme also allows for the population of the hybrids by lone pairs. In H_2O and NH_3, nonbonding sp^3 lone pairs account for the approximately tetrahedral geometry about the central atom. A more rigorous approach rehybridizes the central atom where the correct hybridization is determined by finding the lowest energy as the character of the hybrids is varied. The N–H bond hybrids in NH_3 are more accurately described as $sp^{3.4}$, a ratio that contains more than 75% atomic p character in the hybrid, while the lone pair hybrids contain a greater percentage of s character than the tetrahedral hybrids. This process also more accurately reproduces the observed bond angles.

The valence bond hybridization description for atoms with coordination number greater than four is accomplished by the inclusion of atomic d orbitals in the linear combination of the hybrids. Six equivalent d^2sp^3 orbitals are constructed for molecules with six-coordinate 'expanded octets', for example, SF_6. This combination uses 33% atomic d character to direct the lobes of the six hybrids 90° apart in an octahedral arrangement. The use of d orbitals as a major component necessary to account for the bonding in these molecules is not required and has been discredited.**[20]** A detailed description of the MO treatment of hypervalent molecules will be examined later in this article. The simple valence bond picture has been extended in an approach with much wider applicability than second row main group compounds. The generalized valence bond (GVB) method (*see Valence Bond Theory*) uses Pauling's concepts as a starting point for a method that has been used to consider transition metal bond lengths, orbitals, and energies.**[21]**

4 MOLECULAR ORBITAL THEORY: THE $H_2{}^+$ MOLECULAR ION

Mulliken and Hund, along with important contributions from Herzberg and Lennard-Jones, developed an alternative method that does not give the localized electron pair special priority.**[22–26]** This approach was originally referred to as 'Hund–Mulliken' theory although the two friends never wrote a joint paper. The most significant characteristic of the method is that the electronic wavefunctions or 'molecular orbitals' (MOs) are not restricted to two nuclear centers. Thus it is viewed as a delocalized description of electronic structure because MOs are often constructed from many of the atomic centers in a molecule. It is instructive to begin with a simple system, however, in order to develop the vocabulary that is used and build the basis orbitals for larger molecules of chemical interest in the same manner that the exact one-electron hydrogen-like atomic orbitals form the basis for the orbitals in many-electron atoms. Mulliken introduced the method by looking at the simplest 'molecular' system, the hydrogen molecule ion $H_2{}^+$. The Hamiltonian for this system in a simplified form using atomic units is:

$$\widehat{H} = -\frac{1}{2}\nabla^2 - \frac{1}{r_A} - \frac{1}{r_B} + \frac{1}{R} \tag{8}$$

where ∇^2 is the kinetic energy operator, r_A is the distance from the single electron to atom A, r_B is the distance from the single electron to atom B, and R is the nuclear–nuclear separation. Again, the Born–Oppenheimer approximation has been utilized allowing the separation of the nuclear motion from the electronic motion. In order to calculate the total energy for the molecular system, this nuclear kinetic energy term would need to be added to the electronic energy. The first three components of this operator lead to stabilization while the $1/R$ term is a repulsive term.

Mulliken proposed a different trial function than that used in the valence bond approach. In general, this function is a normalized sum of hydrogen-atom orbitals and is written in the form

$$\Psi_{MO} = c_1\phi_1 + c_2\phi_2 + K \quad \text{so that } \Psi_{MO} = \sum_i c_1\phi_1 \tag{9}$$

The procedure is called the linear combination of atomic orbitals (LCAO) approximation and can be used for molecules of any size. $H_2{}^+$ is a special case in that a wavefunction can be found that will solve the Schrödinger equation exactly, yet the MO approach will be used so that molecular orbitals can be derived. The simplest trial function for the $H_2{}^+$ system is written:

$$\Psi_{MO} = c_1 1s_A + c_2 1s_B \tag{10}$$

The $1s_A$ and $1s_B$ atomic orbitals are the building blocks (basis set) for the molecular orbitals. The wavefunction of the electron in the molecule is simply the normalized sum of the 1s atomic orbitals. In this case the function is said to be constructed from a ‘minimal’ basis set because only the atomic orbitals that contain electrons in the separated atoms are allowed to be part of the overall function. If higher energy, unfilled atomic orbitals (2s, 2p, etc.) are allowed to contribute to the LCAO description of the molecular orbital, the term ‘expanded’ basis set is used.

Both rigorous and approximate levels of theory express molecular orbitals as LCAOs, thus a short description of the AOs is commonly used. The hydrogen-like AOs that are used in the MO and VB approaches are expressed in the form

$$\Phi_{AO} = R_{n,l}(r) \cdot Y_{l,m}(\theta, \phi) \tag{11}$$

As can be seen, these orbitals are the product of a radial part R dependent on r, the distance from the electron to the nucleus, and Y, called a spherical harmonic, a function detailing the angular dependence of the atomic wavefunction. For all many-electron atoms, the radial term must be approximated because of the aforementioned problem of electron–electron repulsions.

Many theoretical methods use Slater-type orbitals (STOs) to approximate this term. STOs contain an exponential term of the form

$$\Phi(r, \theta, \phi) \propto e^{-\zeta r} \tag{12}$$

where ζ is an orbital exponent that is determined in a variational approach. The results of many calculations indicate that wavefunctions built from this form are very accurate approximations of true atomic wavefunctions. They are used quite extensively in semiempirical methods but their form is quite unwieldy for use in the complex multicenter integrals that need to be solved in rigorous theoretical methods.

Boys proposed the use of Gaussian-type orbitals (GTOs) of the form

$$\Phi(x, y, z) \propto e^{-\alpha r^2} \tag{13}$$

where α is the variational parameter.[27] The great advantage of GTOs is that they are able to be solved much more quickly than STOs in computer calculations. Unlike STOs, a single GTO does not reproduce a ‘true’ atomic orbital wavefunction with great accuracy. Investigators that use Gaussians in their basis set must use a number of GTOs that are combined to simulate the behavior of a single STO. A simple form of this basis set might be labeled ‘STO-nG’, with $n = 3, 4, \ldots$ where n is the number of Gaussian functions overlayed to mimic a single STO. These basis sets however are not very accurate for nonlinear molecules. ‘Split valence’ basis sets use sums of Gaussians to describe better less symmetric molecular environments. Multiple sets of AOs are used describe the core and valence atomic orbitals. For example, a ‘6–31G’ basis set uses a set of six Gaussians to represent the core orbitals and sets of three and one Gaussians to describe the valence functions. Another improvement involves including ‘polarization’ functions in a set of Gaussians. These functions utilize a larger angular momentum value than the electron that is being described. Thus a 2p polarization function might be added to a 1s basis set in order to depict the deformation of the orbital by the other nuclei away from what would be expected for a spherically symmetric free atom. An asterisk (*) is commonly used to refer to basis sets that use these functions so that a ‘6–31G*’ designation indicates a split valence plus polarization basis set.

Above, the equation for the total energy for a molecular system was expressed (these functions are real so the complex conjugate symbol may be dropped):

$$E = \frac{\int \Psi \widehat{H} \Psi \, d\tau}{\int \Psi^2 \, d\tau} \tag{14}$$

The numerator in this energy term can be expanded using the minimal $H_2{}^+$ basis set (**9**).

$$
\begin{aligned}
\Psi &= c_1 1\mathrm{s}_\mathrm{A} + c_2 1\mathrm{s}_\mathrm{B} \\
\int \Psi \hat{H} \Psi \mathrm{d}\tau &= \int (c_1 1\mathrm{s}_\mathrm{A} + c_2 1\mathrm{s}_\mathrm{B}) \hat{H} (c_1 1\mathrm{s}_\mathrm{A} + c_2 1\mathrm{s}_\mathrm{B}) \mathrm{d}\tau \\
&= c_1^2 \int 1\mathrm{s}_\mathrm{A} \hat{H} 1\mathrm{s}_\mathrm{A} \mathrm{d}\tau + c_1 c_2 \int 1\mathrm{s}_\mathrm{A} \hat{H} 1\mathrm{s}_\mathrm{B} \mathrm{d}\tau \\
&\quad + c_1 c_2 \int 1\mathrm{s}_\mathrm{B} \hat{H} 1\mathrm{s}_\mathrm{A} \mathrm{d}\tau + \mathrm{c}_2^2 \int 1\mathrm{s}_\mathrm{B} \hat{H} 1\mathrm{s}_\mathrm{B} \mathrm{d}\tau \\
&= c_1^2 H_\mathrm{AA} + c_1 c_2 H_\mathrm{AB} + c_1 c_2 H_\mathrm{BA} + c_2^2 H_\mathrm{BB} \\
\text{where } H_\mathrm{AA} &= \int 1\mathrm{s}_\mathrm{A} \hat{H} 1\mathrm{s}_\mathrm{A} \mathrm{d}\tau = H_\mathrm{BB} \\
&\text{(if A and B are equivalent nuclei),} \\
H_\mathrm{AB} &= \int 1\mathrm{s}_\mathrm{A} \hat{H} 1\mathrm{s}_\mathrm{B} \mathrm{d}\tau \text{ and } H_\mathrm{BA} = \int 1\mathrm{s}_\mathrm{B} \hat{H} 1\mathrm{s}_\mathrm{A} \mathrm{d}\tau
\end{aligned}
$$

(**9**)

It is a characteristic of the Hamiltonian that $H_\mathrm{AB} = H_\mathrm{BA}$; therefore

$$\int \Psi \widehat{H} \Psi \mathrm{d}\tau \quad \text{becomes} \quad c_1^2 H_\mathrm{AA} + 2c_1 c_2 H_\mathrm{AB} + c_2 H_\mathrm{BB} \tag{15}$$

The denominator can be written in the same manner (**10**).

$$
\begin{aligned}
\int \Psi_2 \mathrm{d}\tau &= c_1^2 S_\mathrm{AA} + 2c_1 c_2 S_\mathrm{AB} + c_2^2 S_\mathrm{BB} \\
\text{where } S_\mathrm{AA} &= \int 1\mathrm{s}_\mathrm{A} 1\mathrm{s}_\mathrm{A} \mathrm{d}\tau,\ S_\mathrm{BB} = \int 1\mathrm{s}_\mathrm{B} 1\mathrm{s}_\mathrm{B} \mathrm{d}\tau, \\
\text{and } S_\mathrm{AB} &= \int 1\mathrm{s}_\mathrm{A} 1\mathrm{s}_\mathrm{B} \mathrm{d}\tau
\end{aligned}
$$

(**10**)

Now the energy E can be rewritten as a function of the variational parameters c_1 and c_2:

$$E(c_1, c_2) = \frac{c_1^2 H_\mathrm{AA} + 2c_1 c_2 H_\mathrm{AB} + c_2^2 H_\mathrm{BB}}{c_1^2 S_\mathrm{AA} + 2c_1 c_2 S_\mathrm{AB} + c_2^2 S_\mathrm{BB}} \tag{16}$$

Note that the energy is a function of the coefficients of each function in the basis set.

The goal at this stage is to determine the coefficients. Mathematics provides a straightforward way for minimizing the energy by varying the coefficients, keeping in mind the tenet of the variation principle that an improvement to a wavefunction leads to a lower energy (more accurate) wavefunction. Differentiation with respect to c_1 gives

$$
\begin{aligned}
E(c_1^2 S_\mathrm{AA} + 2c_1 c_2 S_\mathrm{AB} + c_2^2 S_\mathrm{BB}) &= c_1^2 H_\mathrm{AA} + 2c_1 c_2 H_\mathrm{AB} + c_2^2 H_\mathrm{BB} \\
E(2c_1 S_\mathrm{AA} + 2c_2 S_\mathrm{AB}) + \frac{\mathrm{d}E}{\mathrm{d}c_1}&(c_1^2 S_\mathrm{AA} + 2c_1 c_2 S_\mathrm{AB} + c_2^2 S_\mathrm{BB}) \\
&= 2c_1 H_\mathrm{AA} + 2c_2 H_\mathrm{AB}
\end{aligned} \tag{17}
$$

Because E is being minimized, then

$$\frac{\mathrm{d}E}{\mathrm{d}c_1} = 0, \text{ therefore } c_1(H_\mathrm{AA} - ES_\mathrm{AA}) + c_2(H_\mathrm{AB} - ES_\mathrm{AB}) = 0 \tag{18}$$

Similarly, differentiating with respect to c_2 gives

$$c_1(H_\mathrm{AB} - ES_\mathrm{AB}) + c_2(H_\mathrm{BB} - ES_\mathrm{BB}) = 0 \tag{19}$$

In this case, the coefficients c_1 and c_2 for each solution are found by solving simultaneous so-called secular equations in which the factors multiplying the unknowns (c_1 and c_2) include the energy of the system E. Because our trial function has two basis functions there will be two roots for the system (hence two values of E). The set of simultaneous equations must be solved to find the roots and has a nontrivial solution only if the $N \times N$ determinant of the factors is zero (see (**11**)). Both roots of the determinant are then used to solve for the coefficients:

$$
\begin{vmatrix}
H_\mathrm{AA} - E & H_\mathrm{AB} - S_\mathrm{AB} \\
H_\mathrm{AB} - ES_\mathrm{AB} & H_\mathrm{BB} - E
\end{vmatrix} = 0
$$

(**11**)

$$E_+ = \frac{H_\mathrm{AA} + H_\mathrm{AB}}{1 + S_\mathrm{AB}} \qquad E_- = \frac{H_\mathrm{AA} - H_\mathrm{BB}}{1 - S_\mathrm{AB}}$$

(**12**)

The lower value for E is the lowest energy attainable with the trial basis set. The corresponding coefficients give the character of the most bonding orbital. It should be noted that a secular determinant must be solved whenever a linear combination of wavefunctions is optimized.

A few of the characteristics of the integrals that need to be solved in the secular determinant should be outlined. H_AA and H_BB are called coulomb integrals and are described as the energy of an electron occupying the basis orbital A or B. The resonance integral, H_AB, is the quantum mechanical interaction term of basis orbital A with basis orbital B. S_AB is the overlap integral, the quantitative measure of the volume in space where the two basis functions interact. Basis functions that have zero overlap are said to be mutually orthogonal while two functions that are exactly coincident have an overlap value equal to 1 ($S_\mathrm{AA} = S_\mathrm{BB} = 1$, hence the simplification in the secular determinant above). In the secular determinant for the $\mathrm{H_2}^+$ system or any homonuclear diatomic system, $H_\mathrm{AA} = H_\mathrm{BB}$.

The two roots for the determinant give (**12**):

By substituting these into the first secular equation, it is found that for E_+, $c_1 = c_2$, and for E_-, $c_1 = -c_2$. Thus the two solutions for the Schrödinger equation can be written:

$$\Psi_+ = c_1 1\mathrm{s}_\mathrm{A} + c_1 1\mathrm{s}_\mathrm{B} \quad \text{and} \quad \Psi_- = c_1 1\mathrm{s}_\mathrm{A} - c_1 1\mathrm{s}_\mathrm{B} \tag{20}$$

Quantum mechanics requires that the wavefunction be normalized over all space such that $\int \Psi^2 \mathrm{d}\tau = 1$ (which is

$$\begin{aligned}\int \Psi^2 \mathrm{d}\tau = 1 &= c_1^2 \int 1s_A^2\, \mathrm{d}\tau \pm 2c_1^2 \int 1s_A 1s_B \mathrm{d}\tau + c_1^2 \int 1s_B^2 \mathrm{d}\tau \\ &= c_1^2 S_{AA} \pm 2c_1^2 S_{AB} + c_1^2 S_{BB} \\ &= c_1^2 (2 + 2S_{AB}) \\ \text{thus } c_1 &= \pm \frac{1}{\sqrt{2+2S}} \qquad \text{where } S = S_{AB}\end{aligned}$$

(**13**)

equivalent to stating that the probability of finding the electron in all space is equal to 1). For this system we have (**13**):

The bonding molecular orbital and the antibonding orbital are designated as:

$$\Psi_+ = \Psi_{\text{bond}} = \frac{1}{\sqrt{2+2S}}(1s_A + 1s_B) \tag{21}$$

$$\Psi_- = \Psi_{\text{anti}} = \frac{1}{\sqrt{2-2S}}(1s_A - 1s_B) \tag{22}$$

5 PICTORIAL REPRESENTATIONS OF ORBITALS

The combination of two atomic orbital basis functions has generated two molecular orbitals. There are a number of ways that MOs can be portrayed in a pictorial fashion to provide a connection between their functional form and their relative energies. It is easy to see why Ψ_+ is a bonding function: when the value of the function or, more importantly, the value of the function squared (the probability) is projected along the internuclear axis, a buildup of electron density is seen in the internuclear region (Figure 1). When the Ψ_- function is squared, the electron density in the internuclear region is diminished with a nodal plane of zero density bisecting the internuclear axis. An electron described by the Ψ_+ function is more stable than its energy relative to the separated nuclei, whereas an electron described by the Ψ_- function is less stable. This is illustrated in a plot of the energy of the two molecular orbitals versus interatomic distance (Figure 2). An electron occupying Ψ_+ favors a bound structure rather than the separated H· · ·H.

The most commonly used pictorial representation for a wavefunction is called the boundary surface and it is used to give a three-dimensional perspective of most of the electron density in an orbital. Usually these shapes are drawn so that their volume contains about 95% of the electron density in a molecular orbital. It is instructive to draw them in a process that first sketches the atomic orbitals as separated functions and then brings them together, allowing mixing to occur via the secular determinant (see (**14**)).

The areas of overlap suggest constructively and destructively interfering classical waves. The buildup of density in the internuclear region of the Ψ_+ orbital shows the connection of the atoms. Yet another frequently used pictorial view of a molecular orbital is as a set of contour diagrams. These are simply planar slices of the aforementioned boundary surfaces chosen to again illustrate the bonding/antibonding characteristics of a particular orbital. A plane is usually chosen so that it contains the internuclear axis (although this is not done exclusively). In larger molecules, a plane can be chosen to contain more than one nuclear center and thereby view more than one bonding/antibonding interaction within the same orbital. The sketch in Figure 3 approximates the contour plots for Ψ_+ and Ψ_-.

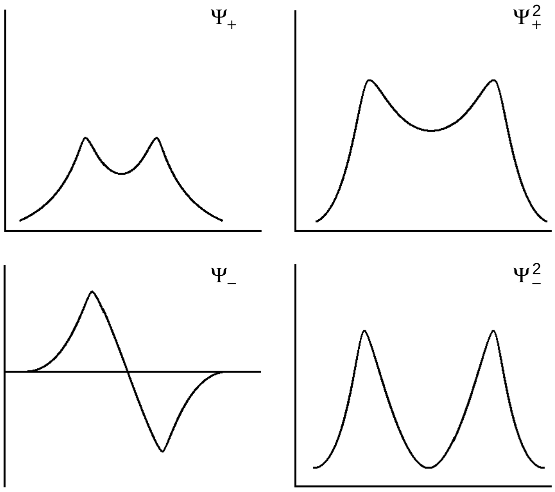

Figure 1 Value of Ψ_+, Ψ_+^2, Ψ_-, and Ψ_-^2 sketched along the internuclear axis

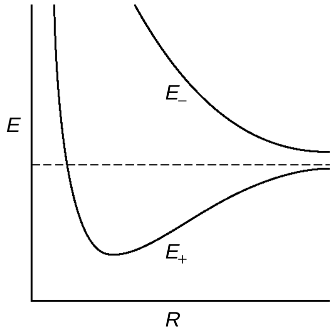

Figure 2 Plot of E_+ (bonding orbital) and E_- (antibonding orbital) as a function of internuclear distance in $H_2{}^+$

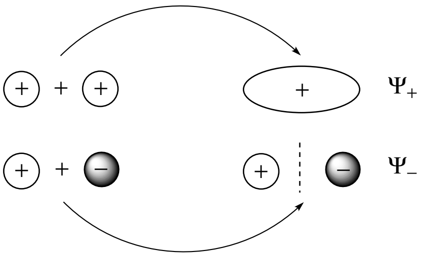

(**14**)

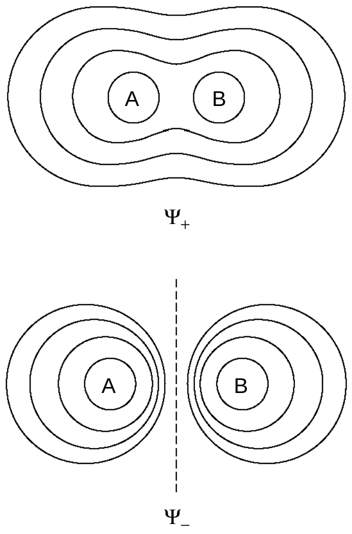

Figure 3 Contour diagrams sketched for Ψ_+ and Ψ_- for the $H_2{}^+$ molecular ion

These contour diagrams illustrate the probability of finding the electron per unit volume; this quantity should be distinguished from the region in space where the electron density is greatest. In order to determine that quantity, a spatial factor needs to be included in a function analogous to the radial distribution function that is used to illustrate the highest regions of electron density in atoms. A 'circular distribution function' has been proposed and identifies a cylindrical region encircling the bond axis as the region of greatest electron density.[28]

6 MOLECULAR ORBITALS AND SYMMETRY

MO theory has developed a strong connection with mathematical group theory and the elements of symmetry. Because of the delocalized nature of the wavefunction, reference to the overall symmetry of the molecule is extremely helpful in differentiating one MO from another and provides a convenient convention for labelling. This system will eventually lead to the much more useful task of establishing a criterion for allowing MOs from separate atoms or molecules to come together in new bonding and antibonding interactions. As can be seen in the boundary surface diagrams, each of the two MOs that we have constructed is invariant to rotations about the internuclear axis. MOs with this characteristic are labelled as σ (sigma) orbitals. If the MO is antibonding with respect to the two basis functions, the label is modified using an asterisk; the antibonding overlap of two H 1s atomic functions is designated σ^* (sigma star) (see (**15**)).

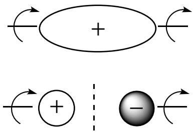

(**15**)

The two energy levels associated with Ψ_σ and Ψ_{σ^*} can be used to sketch yet another pictorial representation of information derived from the secular determinant. A qualitative MO energy level diagram is sketched for the $H_2{}^+$ system in Figure 4.

H_{AA} and H_{AB} are each negative numbers while S_{AB} is positive and less than one; as a result, E_σ (formerly E_+) is lower in energy than H_{AA} and H_{BB} while E_{σ^*} (E_-) is higher in energy than the basis functions. A careful look at the denominator for each term shows that in this model the overlap term forces the antibonding orbital farther away from the basis functions energetically than the bonding orbital. Now that the atoms are within bonding distance, electrons can fill these orbitals in accord with the Pauli principle. This diagram can be used as a qualitative energy level diagram for homonuclear diatomic systems up to four electrons. Because Ψ_+ is the molecular orbital associated with the bonding interaction of the atomic orbitals, the ground state of the H_2 molecule may be described by placing two electrons in the MO with one spin up and one spin down, resulting in a molecular electron configuration, written $1\sigma^2$. The 'complete' molecular wavefunction would need to include information about spin; it is usually written as a Slater determinant in order to ensure that the Pauli principle is satisfied (α for spin up, β for spin down) (see (**16**)).

$$\Psi_{MO} = \frac{1}{\sqrt{2}}\begin{vmatrix} \psi_\sigma\alpha(1) & \psi_\sigma\beta(1) \\ \psi_\sigma\alpha(2) & \psi_\sigma\beta(2) \end{vmatrix}$$

$$\Psi_{MO} = \psi_\sigma(1)\psi_\sigma(2)\left[\frac{1}{\sqrt{2}}[\alpha(1)\beta(2) - \alpha(2)\beta(1)]\right]$$

(**16**)

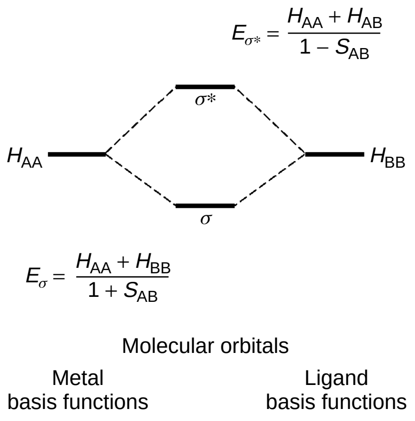
$E_{\sigma*} = \frac{H_{AA} + H_{AB}}{1 - S_{AB}}$
$\sigma*$
H_{AA}
H_{BB}
σ
$E_\sigma = \frac{H_{AA} + H_{BB}}{1 + S_{AB}}$
Molecular orbitals
Metal basis functions
Ligand basis functions

Figure 4 Molecular orbital energy level diagram for $H_2{}^+$

The spatial and spin parts can be viewed separately for our purposes, however, because the Hamiltonain that is being used yields energy values that are independent of spin. The unnormalized spatial part of the function is used frequently to avoid clutter:

$$\Psi_{\mathrm{MO}} = \frac{1}{2(1+S)}[1\mathrm{s}_{\mathrm{A}}(1) + 1\mathrm{s}_{\mathrm{B}}(2)][1\mathrm{s}_{\mathrm{A}}(2) + 1\mathrm{s}_{\mathrm{B}}(1)] \tag{23}$$

The next two electrons are placed into the σ^* antibonding orbital using a molecular (*Aufbau Principle*). Note that the diagram suggests that this will be an unfavorable configuration because of the net instability of the whole molecule. The instability of diatomic helium He_2 can be rationalized with this diagram because two electrons are required to occupy the highly destabilizing Ψ_- energy level. Recent experimental and theoretical work has confirmed, however, that long-range Van der Waals attractions are responsible for a He_2 dimer with a internuclear separation of 55 Å, much longer than a standard chemical bond owing to the overlap of atomic orbitals.**[29]**

7 IMPROVEMENTS TO THE WAVEFUNCTION

The model that is outlined above is generated from a one-electron Hamiltonian and is only an approximation to the true wavefunction for a multielectron system. As suggested earlier, other components may be added as a linear combination to the wavefunction that has just been derived. There are many techniques used to alter the original trial wavefunction. One of these is frequently used to improve wavefunctions for many types of quantum mechanical systems. Typically a small amount of an excited-state wavefunction is included with the minimal basis trial function. This process is called configuration interaction (CI) because the new trial function is a combination of two molecular electron configurations. For example, in the H_2^+ system a new trial function can take the form

$$\Psi = c_1\psi_1 + c_2\psi_2 \quad \text{where} \quad \psi_1 = \psi_\sigma(1)\psi_\sigma(2) \quad \text{and} \quad \psi_2 = \psi_{\sigma^*}(1)\psi_{\sigma^*}(2) \tag{24}$$

where ψ_2 represents the functional form of the antibonding orbital populated by two electrons. (It can be shown that a singly excited state of the type $1\sigma^1 1\sigma^{*^1}$ yields a value $H_{\mathrm{AB}} = 0$). If the solution of a secular determinant and its component integrals yield a nonzero coefficient for the so-called doubly excited state, the overall energy will be lowered to a more accurate value. Therefore, the linear combination given in

$$\Psi_{\mathrm{CI}} = c_1\psi_1 + c_2\psi_2 = c_\sigma\psi_\sigma(1)\psi_\sigma(2) + c_{\sigma*}\psi_{\sigma^*}(1)\psi_{\sigma^*}(2) \tag{25}$$

is the CI ground state. It would be incorrect to interpret this result as proposing that all H_2 molecules spend an amount of time in this doubly excited state; rather, the small addition of this particular orbital's functional form to the original trial function produces a more accurate reproduction of the true wavefunction's behavior than the first function alone.

It is instructive to examine the differences between the original function and the new one. The minimal basis, unnormalized wavefunction for H_2 can be written as (**17**).

$$\begin{aligned}\Psi_{\mathrm{MO}} &= c^2[1\mathrm{s}_{\mathrm{A}}(1) + 1\mathrm{s}_{\mathrm{B}}(1)][1\mathrm{s}_{\mathrm{A}}(2) + 1\mathrm{s}_{\mathrm{B}}(2)]\\ &= \underset{\text{covalent term}}{\underline{c^2[1\mathrm{s}_{\mathrm{A}}(1)1\mathrm{s}_{\mathrm{B}}(2) + 1\mathrm{s}_{\mathrm{B}}(1)1\mathrm{s}_{\mathrm{A}}(2)}}\\ &\qquad \underset{\text{ionic term}}{\underline{+ 1\mathrm{s}_{\mathrm{A}}(1)1\mathrm{s}_{\mathrm{A}}(2) + 1\mathrm{s}_{\mathrm{B}}(1)1\mathrm{s}_{\mathrm{B}}(2)]}}\end{aligned}$$

(**17**)

The first two terms are exactly the wavefunction for the valence bond description while the last two terms are the type of ionic components that were described earlier. In the MO wavefunction, these ionic terms are given much more weight (50%) than in the valence bond wavefunction. This is exactly the improvement that the configuration interaction procedure makes. If the CI wavefunction described above is expanded as in (**18**)

$$\begin{aligned}\Psi_{\mathrm{CI}} &= c_\sigma[1\mathrm{s}_{\mathrm{A}}(1)1\mathrm{s}_{\mathrm{A}}(2) + 1\mathrm{s}_{\mathrm{A}}(1)1\mathrm{s}_{\mathrm{B}}(2) + 1\mathrm{s}_{\mathrm{B}}(1)1\mathrm{s}_{\mathrm{A}}(2)\\ &\quad + 1\mathrm{s}_{\mathrm{B}}(1)1\mathrm{s}_{\mathrm{B}}(2)] + c_{\sigma*}[1\mathrm{s}_{\mathrm{A}}(1)1\mathrm{s}_{\mathrm{A}}(2) - 1\mathrm{s}_{\mathrm{A}}(1)1\mathrm{s}_{\mathrm{B}}(2)\\ &\quad - 1\mathrm{s}_{\mathrm{B}}(1)1\mathrm{s}_{\mathrm{A}}(2) + 1\mathrm{s}_{\mathrm{B}}(1)1\mathrm{s}_{\mathrm{B}}(2)]\\ \Psi_{\mathrm{CI}} &= (c_\sigma - c_{\sigma*})[1\mathrm{s}_{\mathrm{A}}(1)1\mathrm{s}_{\mathrm{B}}(2) + 1\mathrm{s}_{\mathrm{B}}(1)1\mathrm{s}_{\mathrm{A}}(2)]\\ &\quad + (c_\sigma + c_{\sigma*})[1\mathrm{s}_{\mathrm{A}}(1)1\mathrm{s}_{\mathrm{A}}(2) + 1\mathrm{s}_{\mathrm{B}}(1)1\mathrm{s}_{\mathrm{B}}(2)]\\ \Psi_{\mathrm{CI}} &= c_1\Psi_{\mathrm{valence}} + c_2\Psi_{\mathrm{ionic}}\end{aligned}$$

(**18**)

the VB description and the MO description are seen to approach each other. The wavefunctions are formally the same for this simple system. In practice, when considering larger systems, huge numbers of ionic terms in the valence approach and many excited state terms in the MO description would need to be included in order for this convergence to reappear. As time has gone on, however, the MO description with configuration interaction added has come to be the more popular method of choice. The minimal basis set of atomic 1s orbitals has provided a justification for the stability of a chemical bond; however, the use of a CI wavefunction is necessary to approach exact total energy values.

Another technique that is used is to simply increase the number of basis orbitals in the Slater determinant. This is easily done by including a larger number of the hydrogen-like atomic orbitals in the trial function. If the entire $n = 2$ set of atomic orbitals (2s, $2p_x$, $2p_y$, $2p_z$) is included in a linear combination with the 1s orbital for each atomic center, when the atoms are brought together in a bonding interaction the trial function becomes

$$\Psi = c_1 1s_A + c_2 2s_A + c_3 2p_{x_A} + c_4 2p_{y_A} + c_5 2p_{z_A} + c_6 1s_B + c_7 2s_B + c_8 2p_{x_B} + c_9 2p_{y_B} + c_{10} 2p_{z_B} \qquad (26)$$

As a result, the secular determinant for this function becomes a 10 by 10 matrix, the solution of which is not trivial; however, the value of the lowest energy term, E, gives a more accurate value which is in accord with the variational principle. The use of still larger basis sets will push the value even lower.

Yet another means of generating more accurate wavefunctions in terms of reproducing the experimental value for bond dissociation energies is to explicitly include the interelectronic distance r_{12}. A calculation that included this term as well as polarization functions and CI reproduced the H_2 experimental bond dissociation energy to seven significant figures.**[30]** However, beyond the problem of being too computationally intensive for molecules of larger size, this technique does not have the advantage of transferability to other molecules. Thus, in the next section our focus will be on standard MO principles using a minimal basis set.

8 HOMONUCLEAR DIATOMIC MOLECULES

The solution of the many types of coulomb, exchange, and overlap integrals in the 100-term matrix described above will be detailed below, but at this point two valuable principles will allow the neglect many of the terms and yet develop a good qualitative idea of what the resultant molecular orbitals look like as well as their relative energy ordering. The first of these principles is that atomic orbitals must have significant overlap with each other if they are going to contribute to the same molecular orbital. In the expanded basis, in addition to the s–s σ overlap that has already been illustrated, there are two other types of σ interactions: two p orbitals may overlap end-on to produce a bonding/antibonding interaction, or s and p orbitals centered on adjacent atoms may have a nonzero overlap (Figure 5).

Other types of bonding are also present. If the z-axis is the internuclear axis, the p_x and p_y atomic orbitals can have a side-to-side nonzero overlap with the p_x and p_y orbitals on the adjacent atom (Figure 6). These bonding/antibonding interactions are labelled π and π^*, respectively. In general, these side-to-side π-type overlaps are smaller than σ-type overlaps. Note that the nodal plane of the atomic functions that contains the internuclear axis is maintained in the molecular wavefunction. There is an additional nodal plane, however, bisecting the internuclear axis in the π^* molecular orbital. This is the nodal plane that identifies the antibonding character of this type of orbital. Orbitals that combine to give bonding/antibonding MOs are often said to 'have the right symmetry' to interact. An example of a pair of orbitals that do not have the right symmetry to interact (or rather, do not contribute to the same MO) is the side-on overlap of a p orbital with an s orbital (Figure 7). This interaction has a net zero overlap because any constructive bonding interaction of the s orbital with the upper lobe of the p orbital will be exactly compensated for by a negative interaction with the lower lobe of the p orbital.

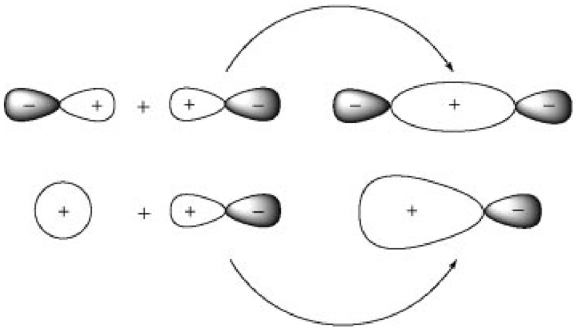

Figure 5 Boundary surface diagrams for p–p and s–p σ molecular orbitals

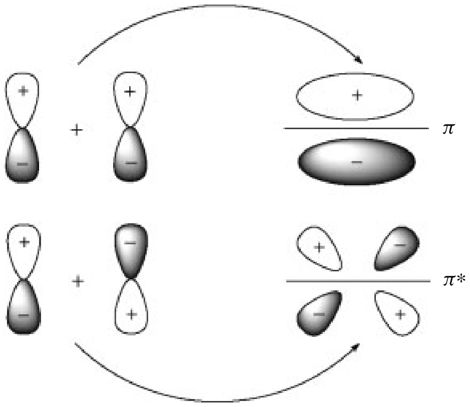

Figure 6 Boundary surface diagrams for π/π^* molecular orbitals

The second criterion for a significant interaction in the secular determinant is that the contributing orbitals must be near in energy to each other. For example, though a $2s_A$–$1s_B$ overlap may be nonzero, the much lower energy of the $1s_B$

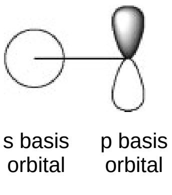

Figure 7 Boundary surfaces for nonbonding s–p interaction

orbital will cause a very small H_{AB} value and the resultant bonding orbital will be overwhelmingly 1s in character while the antibonding orbital will have almost exclusively $2s_A$ character (Figure 8). The conclusion that can be made from these criteria is that when the 10×10 matrix is solved, each MO that is constructed will contain significant character of only a few functions in the AO basis.

Even though the one-electron $H_2{}^+$ Hamiltonian has been used to derive all 10 molecular orbitals (only one of which is even half-filled in $H_2{}^+$), a MO diagram built from the expanded basis will enable us to draw quite accurate boundary surfaces and relative energy separations for all the second row homonuclear diatomics. (This has been verified by the more rigorous approaches that are detailed later.) The figures sketched in Figure 9 show the MO diagrams that result from the 10×10 secular determinant.

Tie lines are drawn between the MOs and the AOs that have the largest coefficients in each linear combination. As expected from the criteria detailed above, each set of 1s and 2s orbitals is split into σ and σ^* molecular orbitals, although the 1s functions are so stable that they are called core orbitals and make no contribution to the bonding in the molecule. However, there are two possibilities for the ordering of the p orbitals. In general, p_π overlap is poorer than the p_σ overlap between adjacent atoms; using this criterion, the p_σ bonding orbital should appear below the p_π bonding orbitals; likewise the p_{σ^*} orbital will appear above the $p_{\pi*}$ as seen in Figure 9(a). This model for ordering assumes that the 2s atomic basis orbitals are too far removed in energy to mix significantly with the 2p functions. It turns out that this model is accurate for highly electronegative atoms such as oxygen and fluorine, where the 2s orbitals are particularly stable because of their higher penetration into the highly stable regions close to the nucleus. When the 2s and 2p atomic functions are closer in energy, for those atoms of average or low electronegativity, the interaction term H_{AB} and overlap terms S_{AB} allow mixing of 2s and 2p basis functions to the same molecular orbital as shown in Figure 9(b). This effect is called s–p mixing and leads to a small stabilization of the $2s_{\sigma^*}$ MO and a destabilization of the $2p_\sigma$ molecular orbital. Because of this mixing, the orbitals are no longer pure s or p, thus labelings such as $2s_\sigma$ or $2p_\pi$ are no longer allowed. Each MO is identified as simply σ- or π-type with each of these sets numbered with integers from the lowest energy to the highest energy.

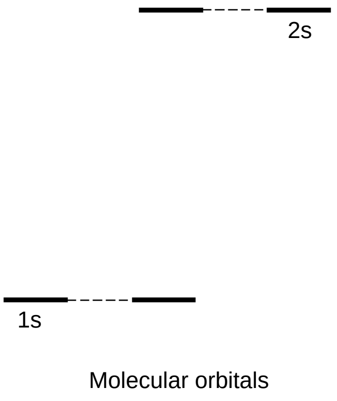

Figure 8 Molecular orbital energy level diagram for 2s–1s. There is virtually no interaction

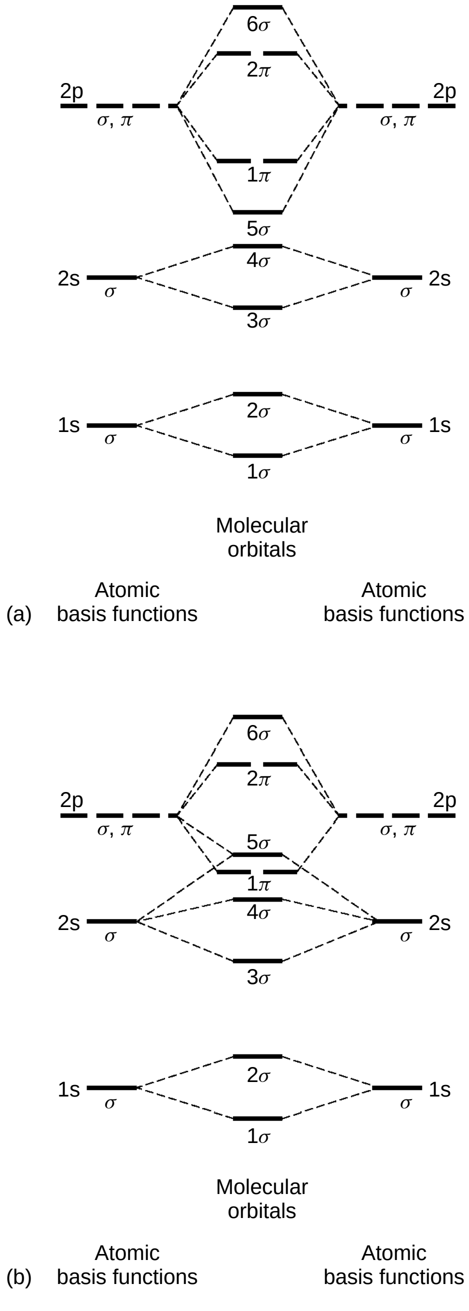

Figure 9 Molecular orbital energy level diagram for homonuclear diatomics: (a) without s–p mixing, (b) with s–p mixing

Now that the orbitals are arranged with respect to energy, a molecular electron configuration may be predicted. Electrons fill lower energy orbitals first, two electrons at a time. If the level is doubly degenerate, the electrons are placed in separate orbitals first. The bond order (B.O.) of a molecule is an accounting of the number of electrons that contribute to bonding minus the number of electrons that destabilize the molecule by filling antibonding levels. In a mathematical form:

$$\text{B.O.} = \frac{(\text{\# of bonding electrons} - \text{\# of antibonding electrons})}{2}$$

Extensive mixing between many basis orbitals can make this assignment difficult and of limited predictive value, but for diatomic molecules bond order correlates well with experimentally determined bond lengths and strengths. In Table 1, higher bond order values are associated with large dissociation energies and short bond lengths.

Working across the first row of the periodic table, the Li_2 molecule has a total of six electrons and a $1\sigma^2 2\sigma^2 3\sigma^2$ configuration, giving four electrons in bonding MOs and two electrons in antibonding MOs for a bond order of one. Be_2 has two additional electrons that must occupy the $4\sigma^2$ orbital, giving a bond order of zero and the prediction that the species is unstable. Spectroscopic investigations indicate that B_2 has two unpaired electrons (a triplet state) whereas C_2 has no unpaired electrons (a singlet). This fits nicely with the strong mixing model for low electronegativity atoms that places the 3σ level above the 1π. In molecular nitrogen, N_2, a bond order of three is calculated. This accounts for the largest homonuclear diatomic dissociation energy and the shortest bond length of the second-row diatomics.

There is still significant 2s–2p mixing in N_2, as is evidenced by the results from photoelectron spectroscopy (PES). In a procedure that revisits the classic photoelectric effect, UV radiation irradiates the sample of interest, and a detector measures the kinetic energy of the electron that is ejected from the molecule. The kinetic energy of the electron is the difference between the energy of the original photon and the energy required to ionize that particular electron. The peaks in Figure 10 correspond to the energy ordering of the orbitals in the MO diagram. Use of higher energy radiation identifies the ionization energy of nitrogen 1s orbitals as approx 400 eV. This verifies the earlier prediction of the high stability of the 1s atomic orbitals and the assumption that they are too localized to take part in bonding for the second-row diatomics. PES thus demonstrates that MO theory provides an accurate description of electronic structure.

Table 1 Bond orders of second-row homonuclear diatomic molecules with bond lengths and energies

Molecule	Bond order	Bond length (pm)	Bond energy (kJ mol^{-1})
H_2	1	74.2	458
He_2	0	–	–
Li_2	1	267.2	105
Be_2	0	–	–
B_2	1	159	289
C_2	2	134	630
N_2	3	109.8	941
O_2	2	120.7	494
F_2	1	141.8	153
Ne_2	0	–	–

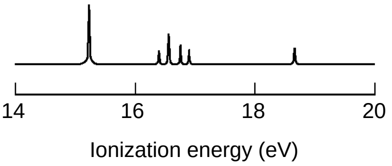

Figure 10 Sketch of photoelectron spectra (PES) of N_2

For oxygen, O_2, each of the 2π levels is occupied by a single electron with their spins matched in accord with Hund's rules. The bond order is now reduced to two, with an accompanying increase in bond length and decrease in bond strength. The two unpaired, parallel spin electrons account for the paramagnetic behavior of molecular oxygen, as evidenced by its attraction to a magnetic field. The prediction of the paramagnetic behavior of oxygen was one of MO theory's chief accomplishments and a motivation for its acceptance as a distinct improvement over the valence bond method.

The 2π antibonding level is filled in F_2, yielding a bond order of one. Finally, the complete occupation of the molecular orbitals with 20 electrons in the Ne_2 dimer is overall destabilizing; this element, like the rest of the noble gases, prefers to exist in the form of isolated atoms.

9 HETERONUCLEAR DIATOMICS

Similar qualitative MO diagrams for heteronuclear diatomic molecules identify some new bonding combinations and rationalize physical characteristics and chemical reactivity of these species. The key difference in the character of the MOs that result from the secular determinant is that much more mixing of multiple AOs occurs. This is a result of the differing electronegativities of the atoms. Comparable AOs, for example, the 1s on atom A and the 1s on atom B, may not have any interaction at all due to the high electronegativity of atom B. The MO diagram for HF is shown in Figure 11.

The fluorine 1s orbital is several eV more stable than the F 2s. It has essentially no interaction at all with the H 1s orbital. Of the 10 electrons in the system, the first two are in this low-energy core orbital. The next two electrons are placed in the 2σ orbital that includes some of the H basis function and therefore has a slight degree of bonding character. This bond is considered to be highly polarized toward fluorine because of its high F 2s character. The 3σ orbital has more

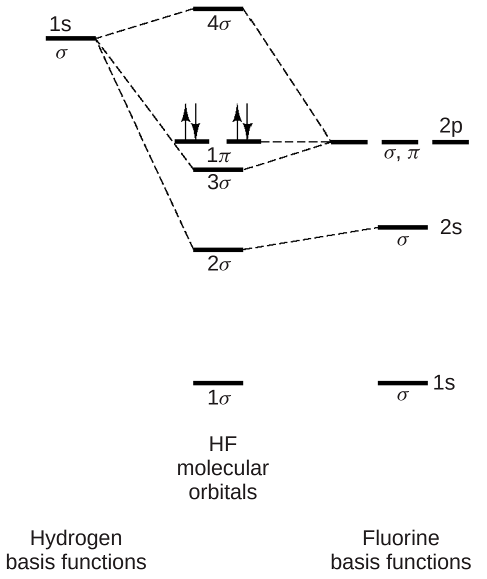

Figure 11 Molecular orbital energy level diagram for HF

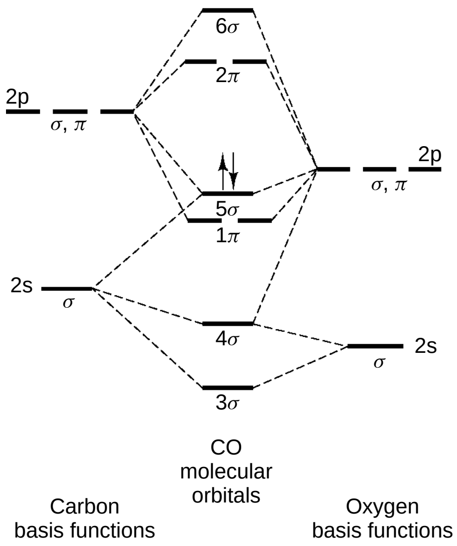

Figure 12 Molecular orbital energy level diagram for CO

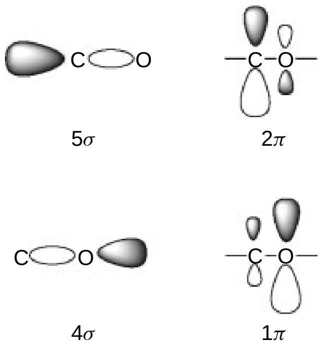

Figure 13 Sketch of boundary surfaces for CO valence orbitals

F 2p character than F 2s character and is also bonding with respect to the H orbital. This set of orbitals (2σ, 3σ) illustrates a central feature of the MO approach. Whereas a simple Lewis structure or valence picture would draw a localized electron pair interaction between two orbitals, the MO picture attributes some bonding character to two separate molecular orbitals. This simple MO diagram illustrates the difficulty of determining a meaningful definition for bond order in a polyatomic molecule. No single MO completely represents the bonding between two atoms.

The F 2p$_x$ and F 2p$_y$ atomic orbitals (a doubly degenerate set) are each filled with two electrons and come across as unperturbed 'molecular orbitals' in a π symmetry set. This type of orbital is said to be nonbonding as its entire character (electron density) remains on the fluorine center.

The heavy weighting of the MO coefficients toward the F atom is observed experimentally in dipole moment measurements. For HF, the value is 1.91 D toward the fluorine atom. Finally, the unoccupied 4σ orbital is predominantly H 1s in character and is populated in excited states of the molecule where the measured dipole is much less.

The MO sketched in Figure 12 is that for the ubiquitous inorganic ligand, carbon monoxide, CO. The chief difference between this diagram and that for the homonuclear diatomic molecules encountered above is that the oxygen atomic basis orbitals are significantly lower in energy than their carbon counterparts. There are 14 electrons in the molecule, making CO isoelectronic with N_2. The σ and π labeling system is still applicable and identifies the atomic functions that are allowed to combine using symmetry criteria (Figure 13). The molecular electronic configuration is $1\sigma^2 2\sigma^2 3\sigma^2 4\sigma^2 1\pi^4 5\sigma^2$ (the 1σ and 2σ levels are essentially core O 1s and C 1s orbitals, respectively, and are not shown in the diagram). The 3σ orbital shows fairly good bonding overlap, has mostly C 2s and O 2s character and is polarized heavily toward oxygen. The 4σ orbital has large amounts of 2p$_z$ mixed in with the 2s for each atom and can best be described as weakly bonding but primarily a lone pair on the oxygen atom. The doubly degenerate 1π levels are π-type bonding levels again polarized toward the more electronegative oxygen atom. The highest occupied molecular orbital (HOMO) is essentially nonbonding and is mostly comprised of the C 2s and C 2p$_z$ basis functions. It can be viewed as essentially a lone pair on the carbon atom. Coincidentally, this accounting of three bonding orbitals, one lone pair centered on carbon, and one lone pair on oxygen, coincides with the Lewis dot structure.

It is the 5σ 'lone pair' that enables the molecule to act as a Lewis base and donate electron density to an acceptor orbital of the appropriate energy and symmetry on another atom or molecular fragment. Later in this article the donation of electron density from the 5σ orbital to transition metal d orbitals will be discussed. The distribution of the polarization of the filled MOs (some toward carbon, some toward oxygen) is responsible for the small measured dipole of CO (0.1 D toward the oxygen atom).

10 THE SELF-CONSISTENT FIELD APPROACH

Until this point, the consideration of electron–electron repulsion terms has been neglected in the molecular Hamiltonian. Of course, an accurate molecular Hamiltonian must account for these forces, even though an explicit term of this type renders exact solution of the Schrödinger equation impossible. The way around this obstacle is the same Hartree–Fock technique that is used for the solution of the Schrödinger equation in many-electron atoms. A Hamiltonian is constructed in which an 'effective' potential of the other electrons substitutes for a true electron–electron repulsion term. The new operator is called the Fock operator, $\widehat{F}$. The orbital approximation is still used so that $\widehat{F}$ can be separated into i (the total number of electrons) 'one-electron' operators, $\widehat{F_i}$ (**19**).

$$\hat{F}(1, 2, 3, K, i)\,\Psi\,(1, 2, 3, K, i) = E\,\Psi\,(1, 2, 3, K, i)$$

$$\hat{F} = \sum_i \hat{F}_i$$

$$\hat{F}_i = -\frac{1}{2}\nabla_i^2 - \sum_{\mathrm{A}} \frac{Z_{\mathrm{A}}}{r_{i\mathrm{A}}} + \sum_j^{n/2} (2J_{ij} - K_{ij})$$

$$\text{where } J_{ij} = \int \psi_i(1)\psi_i(2)\frac{1}{r_{i2}}\psi_j(1)\psi_j(2)\mathrm{d}\tau$$

$$\text{and } K_{ij} = \int \psi_i(1)\psi_j(2)\frac{1}{r_{i2}}\psi_j(1)\psi_i(2)\mathrm{d}\tau$$

(**19**)

The Fock operator determines three sets of information for each electron i: (1) the kinetic energy term of the electron ($-1/2\nabla^2$), (2) an attraction term with each nucleus, A, ($-\Sigma Z_{\mathrm{A}}/r_{i\mathrm{A}}$), and (3) the interaction of the electron with all the other electrons in the molecule. This average force is treated by the $(2J_{ij} - K_{ij})$ term and can be described as the potential felt by a single electron in the 'field' of the other $i - 1$ electrons in the molecule. A few words about the components of this last term in the Fock operator are in order. J is called the coulomb operator and is identified as the classical repulsion between electrons. The exchange integral K is due to the quantum mechanical effect of spin correlation, an intrinsic property of the electron that keeps apart electrons of the same spin. This operator has a stabilizing effect on the energy of the system.

The matrix elements in the secular determinant now rapidly increase in complexity because a single H_{AB} value (now F_{ij}) can be composed of hundreds or thousands of coulomb and exchange integrals for even a modest organic molecule using a minimal basis set. In addition, a new difficulty arises in the actual solution of the integrals because the new 'average potential' operators are dependent on the wavefunctions (hence, the electron density) of the other $n - 1$ electrons. The procedure to solve the quandary is the Hartree–Fock–Roothaan (HFR) self-consistent field (SCF) method. An initial guess is given for the wavefunctions, usually a linear combination of all the basis Slater or Gaussian orbitals, which is used to build the Fock operator which then operates on all of the original wavefunctions to give new molecular orbitals. These MOs are utilized in a 'new' Fock operator which is used to calculate better molecular orbitals. In practice, the variational parameters are the coefficients of the STOs or GTOs and their orbital exponents. They are varied in order to find an energy minimum as prescribed by the variational principle. When this iterative process reaches a point at which the new MOs differ little from their input MOs within some selected tolerance, the calculation is said to be converged.

The so-called 'Hartree–Fock limit' is the energy that is approached in the limit of an infinite number of basis functions using the Fock operator form above. A true 'full' Hartree–Fock calculation would not expand the wavefunctions into a LCAO basis set and therefore would need to be solved numerically in order to achieve the exact Hartree–Fock limit. This limit is not the true upper limit to the energy of the exact Hamiltonian that the variational principle aims for because of the approximation that uses the average potential field. This gap in energy is referred to as the 'correlation energy' and can be treated in a number of ways. The typical way is to expand the basis set even further using excited states (the CI technique applied to molecular orbitals). The size of the molecules that can be treated by calculational approaches that use these large expanded basis sets (usually with Gaussian functions) is ever increasing with the advent of easily accessible computational capacity and speed.

As a group, these calculations are called (*Ab Initio Calculations*) (roughly translated: from the beginning) because all interaction integrals are explicitly calculated and no experimental data are used to adjust F_{ij} or S_{ij} values. These rigorous approaches can achieve remarkable accuracy in the calculation of bond lengths and angles for organic and inorganic molecules. Explicit treatment of the correlation energy problem is required in order to assure quantitative precision in orbital or total energy calculations. These techniques will be summarized later in this section; however, some important steps in the development of current electronic structure methods were the advancements put forth by many inorganic chemists in the later part of the 20th century. Several excellent sources detail the procedures used in ab initio calculations, the history of their development as well as the accuracy of computation versus experiment.[31–38]

For many years however, the chief problem in the application of ab initio methods to many problems of interest for the inorganic chemist was that many chemical systems were simply intractable using these rigorous means owing to the sheer number of integrals that need to be solved. Many 'semiempirical' theories have been developed in order to shorten the process and yet derive valuable and accurate information. Occasionally, adjustments are made in the form of the operators to simplify the calculations. Other approaches set criteria for neglecting some terms in the now massive secular determinants, while still others do both. For example, when a coulomb integral of the type written earlier is expanded in the LCAO approximation, integrals of this type result:

$$\iint \phi_A(1)\phi_B(1)\frac{1}{r_{12}}\phi_C(2)\phi_D(2)\mathrm{d}\tau_1\mathrm{d}\tau_2 \tag{27}$$

The most difficult of these to calculate are the multiple center integrals that contain atomic orbitals of as many as four atomic centers (in the case when A, B, C, and D are atomic orbitals on different nuclei). Since these centers may be quite distant from each other in the molecule, most of the terms of this type are quite small. The zero differential overlap (ZDO), complete neglect of differential overlap(CNDO), moderate neglect of differential overlap (MNDO), intermediate neglect of differential overlap (INDO), and partial retention of diatomic differential overlap (PRDDO) approaches differ in the types of integrals that are ignored.[39–41] An INDO approach labelled INDO/1 or ZINDO has found wide utility with particular success in answering structural and spectroscopic questions in transition metal systems. Of note, a relationship between second order nonlinear optical characteristics and electronic structure in organometallic chromaphores has been examined.[42–44] Certain types of 'differential overlap' within the coulomb and exchange integrals are set to zero where the differential overlap of electron (1) is defined as $\phi_A(1)\phi_B(1)\ \mathrm{d}\tau_1$. This procedure is not the same as setting the overlap integrals, S_{AB}, within a secular determinant equal to zero, an approximation which will be covered below.

An alternative SCF approach frequently used to study orbital interactions in inorganic and organometallic systems is the method of Fenske, Hall, and coworkers.[45,46] A simplified Fock operator is used to eliminate the need for calculating the more difficult multicenter integrals. Coulomb and exchange terms are estimated using the point-charge and Mulliken approximations.[47] The explicit use of CI is eliminated by using Slater's average of configurations.[48] Studies using approximate methods should be approached with some caution; in assessing the justification by any calculational approach of the use of the total energy in a structure or reactivity argument, it should be noted that any procedure that changes the Hartree–Fock Hamiltonian, whether by eliminating terms or approximating them, eliminates the applicability of the variational principle in choosing one structure or mechanism versus another.

Yet another way of treating electron correlation is found in the density functional theory (DFT) of Hohenberg, Kohn, and Sham.[49–53] Though it is not strictly a version of molecular orbital theory, this approach has been hugely influential in inorganic chemistry especially in its highly precise geometry optimizations and in its accurate description of the thermochemistry of reactions principally in the calculation of absolute activation energies. Simply, DFT focuses on the electron density in the molecule, ρ(r), rather than a many electron wavefunction. It is based on the idea that the total energy of the molecule is conveyed as a 'functional' of ρ(r), that is, a function of the electron density that of course is dependent on the coordinates of the electrons as are molecular orbitals. Other marked similarities among the wavefunction-based methods and DFT is that some of the same orbitals are used as building blocks and that SCF methodologies are used that require the solution of closely related Fock matrices. A chief difference is found in the DFT version of the exchange term K_{ij} in the Fock operator. The 'exchange correlation energy' term in DFT does not have an exact expression but is approximated in a variety of ways. Most versions of DFT use a 'gradient correction' term that is a sum of local and exchange terms weighted to fit the properties of well-known molecules. Unfortunately, there is no systematic way to improve the functionals to achieve an arbitrary level of accuracy like those seen in ab initio methods that are bond by the variational principle. Still, a crucial advantage for DFT methods is that they provide highly accurate results at a cost significantly less than computationally intensive perturbation theory methods.

11 THE HÜCKEL AND EXTENDED HÜCKEL METHODS

By far, the theoretical approaches that experimental inorganic chemists are most familiar with and in fact use to solve questions quickly and qualitatively are the simple Hückel method and Hoffmann's extended Hückel theory.[54–56] These approaches are used in concert with the application of symmetry principles in the building of symmetry adapted linear combinations (SALCs) or group orbitals. The ab initio and other SCF procedures outlined above produce MOs that are treated by group theory as well, but that type of rigor is not usually necessary to achieve good qualitative pictures of the character and relative orderings of the molecular orbitals.

Hückel's treatment of delocalized electrons in conjugated organic systems was introduced just as MO theory was being developed. Many approximations are made and the first of these is to separate the σ framework of bonding away from the π framework orbitals. Electrons occupying the σ bonds are in localized two-electron bonds that the hybrid description would label as sp^2–$sp^2\sigma$ bonds. The π electrons are not perturbed by the σ framework because their energies are too far apart and of the wrong symmetry to interact. Thus only the out of plane $2p_z$ orbitals are used as basis functions for the wavefunctions of these electrons. The allyl system is a good first example (Figure 14 and equation 28):

$$\Psi_\pi = c_1\phi_1 + c_2\phi_2 + c_3\phi_3 \tag{28}$$

where ϕ_1, ϕ_2, and ϕ_3 are carbon $2p_z$ orbitals. This system yields the secular determinant given in (**20**):

$$\begin{vmatrix} H_{11} - ES_{11} & H_{21} - ES_{21} & H_{31} - ES_{31} \\ H_{12} - ES_{12} & H_{22} - ES_{22} & H_{32} - ES_{32} \\ H_{13} - ES_{13} & H_{23} - ES_{23} & H_{33} - ES_{33} \end{vmatrix} = 0$$

(**20**)

The appeal of the Hückel approach is that no integrals need to be solved. If we make the assumptions that (a) the diagonal terms $H_{11} = H_{22} = H_{33} = \alpha$ are equal, (b) the off-diagonal H_{ij} values for adjacent atoms (all carbon) are set to a single value, β, while nonadjacent H_{ij} values are set to zero, and (c) the overlap is simplified such that $S_{ii} = 1$ and $S_{ij} = 0$, the secular equation becomes much less complex. The 3×3 determinant is written as in (**21**):

$$\begin{vmatrix} \alpha - E & \beta & 0 \\ \beta & \alpha - E & \beta \\ 0 & \beta & \alpha - E \end{vmatrix} = 0$$

(**21**)

To solve the determinant the matrix must be expanded so that three roots give three energies for the system, that is, N AOs give N MOs (**22**):

$$\alpha - E \begin{vmatrix} \alpha - E & \beta \\ \beta & \alpha - E \end{vmatrix} - \beta \begin{vmatrix} \beta & \beta \\ 0 & \alpha - E \end{vmatrix} = 0$$

$$(\alpha - E)^3 - (\alpha - E)\,\beta^2 - (\alpha - E)\beta^2 = 0$$

let $x = \alpha - E$

$$x^3 - 2\beta^2 x = 0$$

$$x(x^2 - 2\beta^2) = 0$$

$$\text{gives} \quad x = 0, \pm\sqrt{2}\beta$$

(**22**)

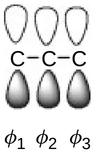
C–C–C
ϕ_1 ϕ_2 ϕ_3

Figure 14 Basis set orbitals for the allyl system in Hückel calculations

Substituting the energies into the secular equations and then solving the equations to get the wavefunctions (and accounting for normalization) gives (**23**):

$$\alpha - E = 0, \pm\sqrt{2}\beta$$

$$\text{thus} \quad E = \alpha, \alpha \pm \sqrt{2}\beta$$

(**23**)

Qualitative drawings of the orbitals are sketched with the relative coefficients represented by the size of the basis orbital in the overall molecular orbital (Figure 15). The α value is set to a relative zero of energy while the β values are derived from experimental data. For our purposes, this value is around 75 kJ mol^{-1}.

Even this very approximate procedure uncovers the inherent stability of a delocalized system that is not obvious in this single example. The solution of the 2×2 determinant for a system of two p_z orbitals, such as the p system in ethylene, yields two MOs with energy values of $\alpha + \beta$ (bonding) and $\alpha - \beta$ (antibonding). This means that the energy for two electrons in the allyl system $(2\alpha + 2\sqrt{2}\beta)$ is more stable than two electrons in the ethylene π system. Thus, the

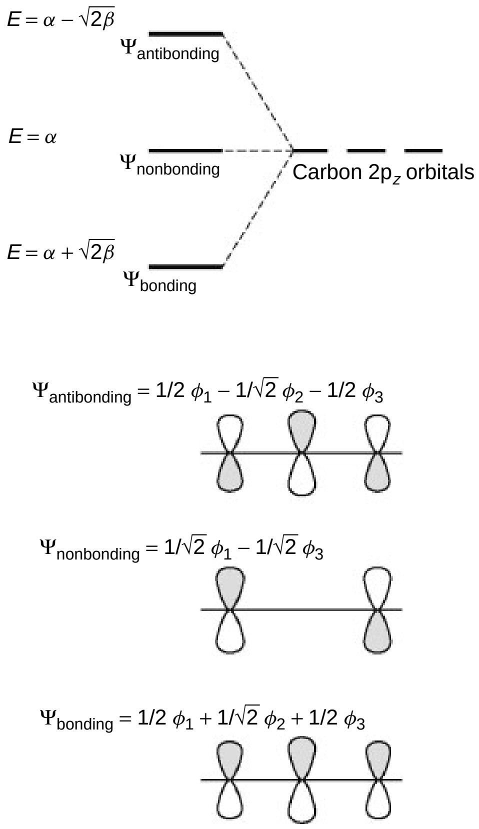
$E = \alpha - \sqrt{2}\beta$
$\Psi_{\text{antibonding}}$
$E = \alpha$
$\Psi_{\text{nonbonding}}$
Carbon $2p_z$ orbitals
$E = \alpha + \sqrt{2}\beta$
Ψ_{bonding}
$\Psi_{\text{antibonding}} = 1/2\ \phi_1 - 1/\sqrt{2}\ \phi_2 - 1/2\ \phi_3$
$\Psi_{\text{nonbonding}} = 1/\sqrt{2}\ \phi_1 - 1/\sqrt{2}\ \phi_3$
$\Psi_{\text{bonding}} = 1/2\ \phi_1 + 1/\sqrt{2}\ \phi_2 + 1/2\ \phi_3$

Figure 15 Hückel π-system energy level diagram, energies, and wavefunctions for the allyl system

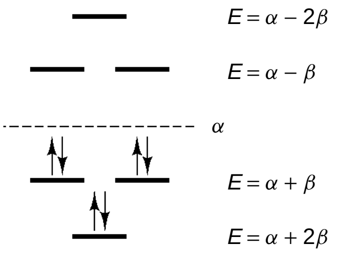

Total π-orbital energy = $6\alpha + 8\beta$

Figure 16 Hückel π-system energy level diagram and energies for C_6H_6

delocalization energy for two electrons in the allyl system is 0.828β.

In benzene, solution of the 6×6 secular determinant using the same procedure gives the energies shown in Figure 16. Each carbon atom supplies one electron to the energy level diagram, giving a π electron energy for benzene of $6\alpha + 8\beta$. If delocalization is ignored and the system is treated as three isolated double bonds, the Hückel approximations give a p electron energy of $6\alpha + 6\beta$. The delocalization energy is 2β. Unfortunately, α and β values differ from system to system which restricts the method's predictive value.

An interesting general result is derived using the Hückel model for a ring system of N p orbitals. For a ring of N atoms, the orbital energies using the Hückel approximations fit the algebraic formula

$$E_j = \alpha + 2\beta \cos\left(\frac{2j\pi}{N}\right) \tag{29}$$

where j runs from 0, $\pm 1, \pm 2 \ldots$ to $\pm N/2$ (N even) or $\pm$ $(N - 1)/2$ (N odd). The relative spacings of the orbitals can be reproduced by inscribing an N-fold regular polygon in a circle of radius 2β with a point at the bottom of the circle (Figure 17). The lowest lying MO is thus always singly degenerate and accommodates two electrons. The remaining orbitals occur in doubly degenerate pairs and may be filled with four electrons.

Using this approach, if this approximation is extended to the infinite limit of n basis orbitals, the resultant energy level diagram would be a tightly packed 'band' of doubly degenerate MOs that are delocalized around the whole ring (except for the lowest bonding orbital and half the highest antibonding orbitals). Bands of orbitals are tightly packed groups of delocalized 'molecular' orbitals and may be empty, filled, or partially filled depending on the number of electrons contributed by the basis set orbitals. The number of nodes increases going from lower energy to higher energy. This process of making bands is the first stage in the MO treatment of solids.[57–59]

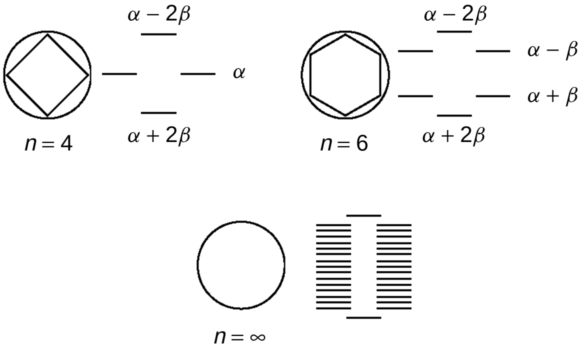

Figure 17 Hückel π-system energy level diagram progression, $n = 4, n = 6, n = \infty$

Though clearly useful for many applications in organic chemistry, the simple Hückel theory has little utility in inorganic chemistry. Hoffmann's extended Hückel theory is able to treat s, p, and d basis sets while evaluating all overlaps. Slater-type basis functions are used in a LCAO expansion of the molecular orbitals but as in the Hückel approach the integrals in the Hamiltonian are not explicitly evaluated. The H_{AA} terms, the basis orbital energies, are estimated using spectral data and are called valence state ionization potentials (VSIPs). The off-diagonal terms are determined using a modified version of the Wolfsberg–Helmholtz formula:

$$1.75\left(\frac{H_{AA} + H_{AB}}{2}\right)S_{AB} \tag{30}$$

where S_{AB} is the calculated orbital overlap.

Whenever overlaps are explicitly calculated, atomic charges can be assigned in a straightforward manner. For a particular orbital interaction, $\Psi_1 = c_1\phi_1 + c_2\phi_2$, the total electron density in that molecular orbital is as shown in (**24**).

$$\begin{aligned}\int \Psi_1^2 \mathrm{d}\tau &= c_1^2 \int \phi_1^2 \mathrm{d}\tau + 2c_1c_2 \int \phi_1\phi_2 \mathrm{d}\tau + c_2^2 \int \phi_2^2 \mathrm{d}\tau \\ &= c_1^2 + 2c_1c_2 + c_2^2\end{aligned}$$

$$\text{if } \phi_1 \text{ and } \phi_2 \text{ are normalized and } S_{12} = \int \phi_1\phi_2 \mathrm{d}\tau$$

(**24**)

The popular Mulliken population analysis assigns the electron density of the MO that 'belongs' to A as the coefficient of that atomic orbital on center A squared plus half the 'overlap population':

$$\text{density on center A} = c_A^2 + c_{12}S_{12} \tag{31}$$

The even splitting of the overlap is arbitrary and works reasonably for covalent bonds. However, it is a poor approximation in more polar interactions and many theorists have proposed alternative ways of calculating distributions of density (although none nearly as simply). Extended Hückel theory has been quite useful for predicting the ground-state conformations of transition metal systems.[60,61]

12 GROUP THEORY AND MOLECULAR ORBITAL THEORY

Until this point only a limited connection to the relationship between 'symmetry' and molecular orbitals has been established. Symmetry concepts provide a good tool for building energy level diagrams and drawing the shapes of orbitals.[62–64] In order to extend the process of drawing qualitative MO diagrams and using them to predict some physical observables for molecules larger than diatomics, a more thorough consideration of symmetry must be undertaken. We have used the terms sigma and pi to label orbitals that are symmetric (σ) or antisymmetric (π) with respect to a 180° rotation about the internuclear axis. As might be expected, more complex molecules may contain other symmetry elements. For example, rotations other than 180°, reflections through planes, inversions through a center of symmetry, or mixtures of these enable quite precise labeling of MOs with respect to their behavior when operated on by a symmetry element. The framework for the classification of MOs by symmetry is called group theory. Detailed proofs for all the techniques illustrated here can be found in other sources.[65]

There are five general types of symmetry elements that are used to classify objects. The first is the identity element, E, in which nothing at all is done. All objects are unchanged under operation by the identity element; however, this element contains important information and is necessary for decomposing large basis sets into smaller units of interacting orbitals. Rotations about an axis are labelled C_n where the degree of rotation is $360°/n$. A C_2 axis is a 180° rotation (exactly that used for the σ, π designations in diatomics). A 120° rotation is done about a C_3 axis, while a 90° rotation is coupled with a C_4 axis. Reflections (σ) are associated with planes that act as mirrors exchanging one side of the plane with the other. Atoms that are contained in the planes are unchanged. Inversions (i) exchange the positions of two points through a point, the inversion center. Improper rotation axes (S_n) combine an n-fold rotation followed by a reflection through a plane perpendicular to the rotation axis.

All objects can be categorized by the list of symmetry elements that they contain. The complete list of symmetry elements for a given molecule identifies its point group classification. The use of the term 'point' refers to the fact that all the planes, axes, and inversion points intersect through a single point that may or may not be the location of an atom in a molecule. This classification is distinguished from that used for crystallographic space groups of repeating unit cells in two or three dimensions. There are approximately 47 chemically important point groups. Some have very little symmetry; the C_s point group contains the identity element and a mirror plane. Others have much more, that is, the tetrahedral group T_d has a total of 24 separate elements: the identity element, eight different C_3 axes, three C_2 axes, six S_4 axes, and six σ planes. The identification of a molecule as belonging to one particular point group or another does have chemical utility. For example, a molecule is nonpolar if its list of symmetry elements contains a mirror plane or rotation axis perpendicular to the principal axis. Also, a molecule is chiral if no improper rotation axis is present.

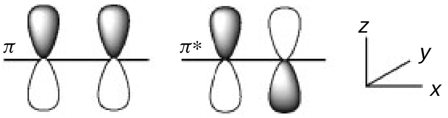

Figure 18 π/π^* orbitals in a homonuclear diatomic molecule. Both orbitals are unchanged upon operation by the σ (xz) reflection plane; π is antisymmetric upon operation by an inversion center, π^* is symmetric upon operation by an inversion center

Most chemists are interested, however, in the connection between the symmetry operations and the classification and construction of molecular orbitals. A first step to this end is that within a point group designation there can be different responses to the individual symmetry elements. A π bonding orbital in N_2 (point group $D_{\infty h}$) changes sign upon operation of i while the π^* antibonding orbital remains unchanged (Figure 18). Each of these orbitals, however, is unchanged upon reflection in a plane that bisects the orbitals lengthwise (xz plane).

The entire list of information that details all the responses to all the symmetry elements in a point group for a basis set of atomic or molecular orbitals is called a reducible representation. Reducible representations, however, are not useful in determining the criteria for deciding which orbitals will participate in bonding/antibonding interactions. These representations must be factored (reduced) into smaller groups. It can be shown with a little effort that a total wavefunction for a molecule, and in turn the set of all the molecular orbitals for a molecule in a certain point group, can be expressed as a simple sum of irreducible representations. There are a only a limited number of irreducible representations for each point group.

12.1 H_2O

A detailed description of each irreducible representation is found in a character table. The table for the C_{2v} point group (that for H_2O) is shown in Figure 19. It shows that there are only four symmetry elements in this point group ($E, C_2, \sigma_v(xz)$, and $\sigma_v(yz)$), each a member of a different

C_{2v}	E	C_2	$\sigma_v\,(xz)$	$\sigma'_v\,(yz)$	
A_1	1	1	1	1	z
A_2	1	1	−1	−1	
B_1	1	−1	1	1	x
B_2	1	−1	−1	−1	y

Figure 19 Character table for C_{2v} point group

class. (By convention, the planar water molecule is found in the *xz* plane.) Occasionally, a point group will contain multiple numbers of the same symmetry element. In ammonia, there are three mirror planes that are grouped in the same class because their effect on a basis set (representation) is the same regardless of which particular symmetry element is used. In the C_{2v} point group, there are four irreducible representations, with the names A_1, A_2, B_1, and B_2. The letters A and B are used for singly degenerate representations (one-dimension) while E and T (not used in the C_{2v} point group) are used for doubly and triply degenerate representations, respectively. The full names (including subscripts) have precise definitions; however, for most purposes they simply serve the same function as the σ and π labels did for the diatomic MOs.

The numbers in the table, the characters, detail the effect of the symmetry operation at the top of the column on each representation labelled at the front of the row. The mirror plane that contains the H_2O molecule, σ (*xz*), leaves an orbital of b_1 symmetry unchanged while a C_2 operation on the same basis changes the sign of the wavefunction (orbital representations are always written in the lower case). An orbital is said to span an irreducible representation when its response upon operation by each symmetry element reproduces the same characters in the row for that irreducible representation. For atoms that fall on the central 'point' of the point group, the character table lists the atomic orbital subscripts (e.g. x, y, z as p_x, p_y, p_z) at the end of the row of the irreducible representation that the orbital spans. A central s orbital always spans the totally symmetric representation (all characters = 1). For the central oxygen atom in H_2O, the 2s orbital spans a_1 and the $2p_x$, $2p_y$, and $2p_z$ span the b_1, b_2, and a_1 representations, respectively (see (**25**)). If two or more atoms are symmetry equivalent such as the H atoms in H_2O, the orbitals must be combined to form symmetry adapted linear combinations (SALCs) before mixing with functions from other atoms. A handy mathematical tool, the projection operator, derives the functions that form the SALCs for the hydrogen atoms.

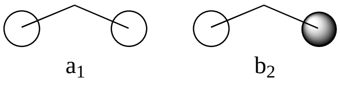

(**25**)

After all the basis orbitals have been labelled by their symmetry behavior, a qualitative molecular orbital diagram may be drawn (Figure 20).

Three orbitals of a_1 symmetry interact in H_2O (a fourth, the O 1s is so low in energy that it is not able to interact and is unperturbed in the diagram). The $2a_1$, largely O 2s in character, has a slight stabilization owing to the combination with the higher energy a_1 orbitals but is essentially nonbonding. The $3a_1$ MO contains a mixture of the O 2s and $2p_z$ as well as the H a_1 SALC. It shows moderate bonding character with a significant amount of electron density pointing away from the bonding region. The $4a_1$ is an antibonding mixture of the entire a_1 basis set. The O $2p_x$ and the H b_2 SALC form a strongly interacting bonding/antibonding set. The O $2p_x$ is the highest occupied molecular orbital (HOMO) in H_2O; it spans the b_1 basis and has no other orbitals to interact with so retains its full atomic character as a nonbonding lone pair.

The Lewis structure idea of equivalent lone electron pairs in water is at odds with the MO diagram. The $2a_1$ and $1b_1$ MOs can be identified as lone pairs but are not equivalent with respect to energy or atomic character and are quite unlike the 'rabbit ear' lone pairs drawn using the VSEPR approach. Though these conclusions are made from qualitative MO diagrams based on symmetry principles and work quite well, it must be noted that quantitative values for the energies and atomic coefficients for the MOs must be generated from a secular determinant using one of the approximation methods detailed above.

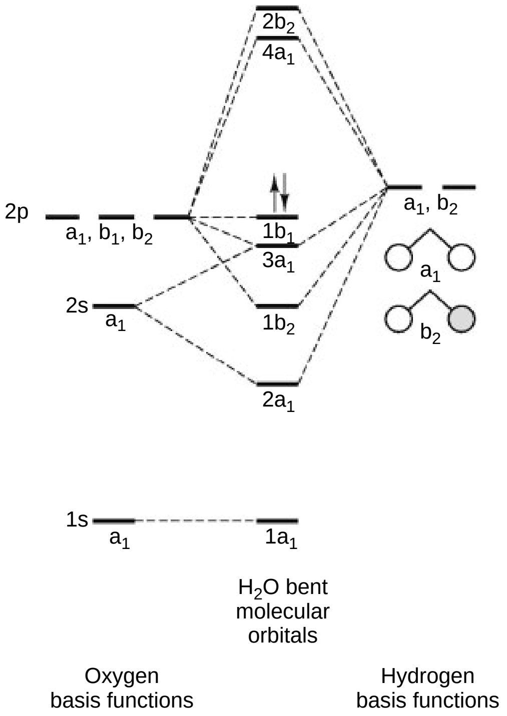

Figure 20 Molecular orbital energy level diagram of bent H_2O

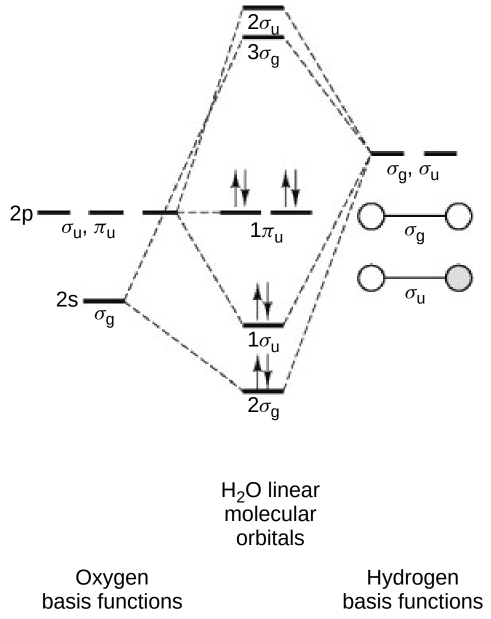

Figure 21 Molecular orbital energy level diagram of linear H_2O

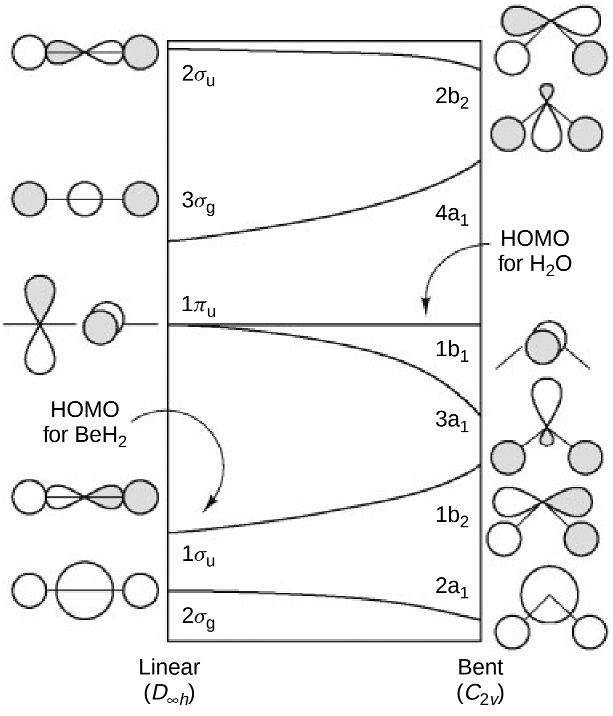

Figure 22 Walsh diagram for AH_2 system

In order to illustrate a powerful predictive application of this qualitative MO approach, it is instructive to generate the energy diagram for the water molecule in a linear geometry. The point group symmetry for the linear arrangement ($D_{\infty h}$) results in changes for the labelling of the same basis orbitals that were used in the bent geometry (Figure 21).

The identical H 1s SALCs are labelled σ_u and σ_g. The O 2s now spans σ_g while the O 2p set spans σ_u ($2p_x$) and a degenerate π_u set ($2p_y$ and $2p_z$). The σ_u and σ_g sets form bonding/antibonding MOs as shown, but there are now two nonbonding p orbitals that cannot interact with orbitals of appropriate symmetry. Using the aufbau method for H_2O (10 electrons total), this linear arrangement is less stable than a bent geometry because the O $2p_z$ orbital is not allowed to take part in any stabilizing interactions with the hydrogen orbitals whereas it makes a contribution to the $3a_1$ bonding orbital in the bent structure. Even though the bonding character of this orbital is not particularly strong, the stabilization does control the geometry in H_2O.

Some of the information contained in each MO diagram can be reexpressed in a comparative pictorial form called a Walsh correlation diagram (Figure 22).[21] The MOs and their relative energy spacings for the linear form are reproduced on the left side of the diagram, while the MOs for the C_{2v} bent geometry are reproduced on the right. Lines are drawn between the MOs that 'correlate' in the two point group designations. The $2\sigma_g{-}2a_1$, $1\sigma_u{-}1b_2$, and $2\sigma_u{-}2b_2$ connections are straightforward, but the $1\pi_u$ orbitals of the linear molecule lose their degeneracy upon a bending distortion. The O $2p_y$ orbital is unaffected (as it is out of the plane of the molecule) and becomes the unperturbed $1b_1$ MO in the bent geometry, but the O $2p_z$ is of a_1 symmetry and can mix with orbitals of like symmetry (the former $2\sigma_g$ in the linear arrangement) to acquire some bonding character, thus stabilizing the orbital. This same correlation diagram can be used to predict the geometries of AH_2 molecules with other electron counts as well. BeH_2 places only four electrons in the valence orbitals, filling the bottom two orbitals in the diagram. The relative stability of the $1\sigma_u$ MO in the linear arrangement, when compared to the $1b_2$ MO in the bent geometry, rationalizes the linear structure observed for BeH_2.

12.2 AH_3

The Walsh diagram for AH_3 systems is shown in Figure 23. BH_3 has six valence electrons and has a planar geometry. This preference is driven by the population of the degenerate 1e' set of MOs, which have better overlap in the planar geometry as illustrated. NH_3, on the other hand, has eight valence electrons to place in valence MOs and prefers the pyramidal C_{3v} geometry because of the very high stability of the $3a_1$ orbital in that arrangement. As for any qualitative interaction diagram, a calculation must be carried out to determine quantitatively preferences in geometries and actual bond angles.

12.3 CH_4

A symmetry analysis of the basis orbitals for methane (T_d point group) identifies the representations for the central

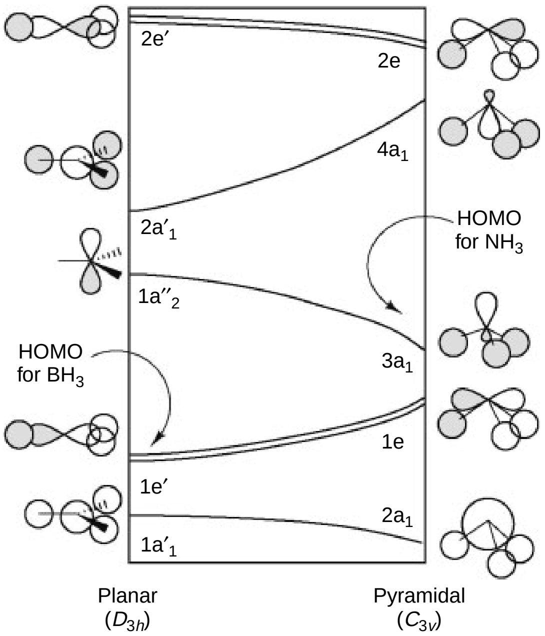
2e′
2e
4a1
2a′1
HOMO for NH3
1a″2
3a1
HOMO for BH3
1e
1e′
2a1
1a′1
Planar (D3h)
Pyramidal (C3v)

Figure 23 Walsh diagram for AH_3 system

carbon basis orbitals as C 2s (a_1) and C 2p (t_2). The four symmetry equivalent H 1s orbitals are reexpressed as a_1 and t_2 SALCs. The a_1 H combination interacts strongly with the C 2s orbital and a triply degenerate t_2 set forms bonding/antibonding combinations with the C 2p orbitals (Figure 24).

The MO diagram shows that the eight valence electrons in methane all occupy orbitals with bonding character, two in the a_1 orbital and a total of six in the t_2 set. Because the carbon basis orbitals and the SALCs for the hydrogen basis set are so close in energy, these bonding interactions are particularly strong. An interesting outcome of the MO description is that although the four bonds have equivalent lengths and strengths there are two types of bonding electrons, each with different ionization energies. Photoelectron spectroscopy verifies that the t_2 set has an ionization potential of 15 eV while the a_1 electrons require 23 eV to be ejected. The spectrum also displays a roughly 3:1 intensity of the peaks, consistent with the predicted populations.

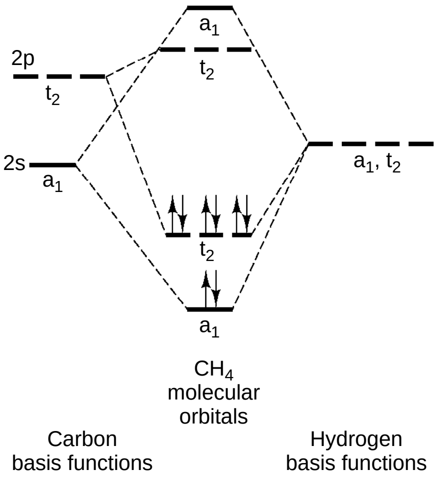
a1
2p
t2
t2
2s
a1
a1, t2
t2
a1
CH4
molecular
orbitals
Carbon
basis functions
Hydrogen
basis functions

Figure 24 Molecular orbital energy level diagram for CH_4

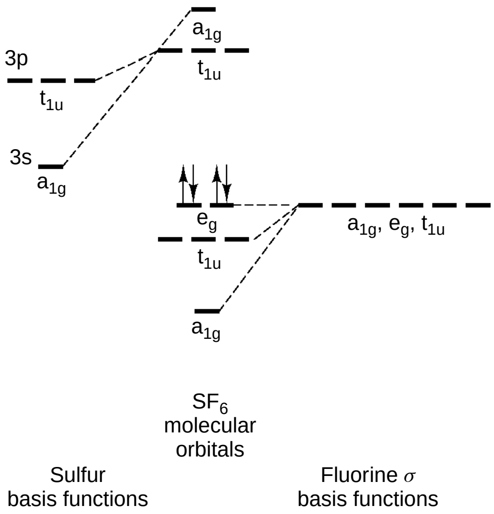
a1g
3p
t1u
t1u
3s
a1g
eg
a1g, eg, t1u
t1u
a1g
SF6
molecular
orbitals
Sulfur
basis functions
Fluorine σ
basis functions

Figure 25 Molecular orbital energy level diagram for ‘hypervalent’ SF_6

12.4 SF_6

As a last example of bonding in a main group system, let us revisit the SF_6 ‘hypervalent’ molecule. A symmetry analysis of the atomic orbitals in this system indicates that a minimal basis set of the 3s and 3p orbitals on sulfur and one σ-type donor SALC from each fluorine atom is sufficient to account for the stability of this molecule (Figure 25). The other SALCs on fluorine do not contribute to the bonding and are omitted from the figure.

The 10 atomic orbitals in the basis set yield a set of 10 molecular orbitals. There are 12 valence electrons available (six from S, one each from the F SALCs) that are assigned to the available orbitals giving a molecular electron configuration of $a_{1u}^2 t_{1u}^6 e_g^4$. The delocalized character of the MO allows for the construction of six ‘bonds’ from only eight ‘bonding’ electrons. Sulfur atomic d orbitals are not necessary to account for the stability of the molecule; however, rigorous calculations with an expanded basis set do indicate that a slight population ($\approx$0.25 electrons total) of the d orbitals does lower the calculated energy.

12.5 Transition Metal Systems

The group theory analysis of molecular orbitals holds an important historical role in the understanding of absorption spectra of transition metal complexes. In principle, rigorous calculations should be able to provide accurate energies for the filled and unfilled molecular orbitals; however, the basis sets that are required to perform an ab initio SCF determination of orbital energies were simply beyond the capabilities of the computer technology in the 1950s and 1960s. This difficulty was the primary motivation behind the development of the many approximate methods (many by inorganic chemists), reviewed earlier in this article.

A symmetry analysis is usually performed to identify the orbitals that interact, then secular determinants are solved to generate energies and coefficients. Octahedral coordination complexes of the type ML_6, ($M =$ transition metal, $L =$ ligand) are representative of the systems that are treated in this way. The metal is typically a d^6–d^8 transition metal (Cr, Fe, etc.) while the ligands fall into three categories: (1) σ-donor ligands, such as NH_3 or H_2O, that have a lone pair that donates electron density to the metal center using σ-type overlap; (2) π-donor ligands that have filled orbitals with local π symmetry with respect to the M–L axis as well as low-energy σ orbitals; the halide ions (F^-, Cl^-, Br^-, I^-) are typical of this category of ligand; (3) π acceptors like CO that have low-lying π^* orbitals that can accept electron density from d orbitals of appropriate symmetry. Figure 26 illustrates the energy level diagram for π donors and Figure 27 illustrates the levels for π acceptors with a first row transition metal (a MO diagram for a σ donor can be easily generated by eliminating the π basis functions from one of the other diagrams). The most important transition in the visible absorption spectra for these complexes is labelled with Δ_0 in each of the diagrams.

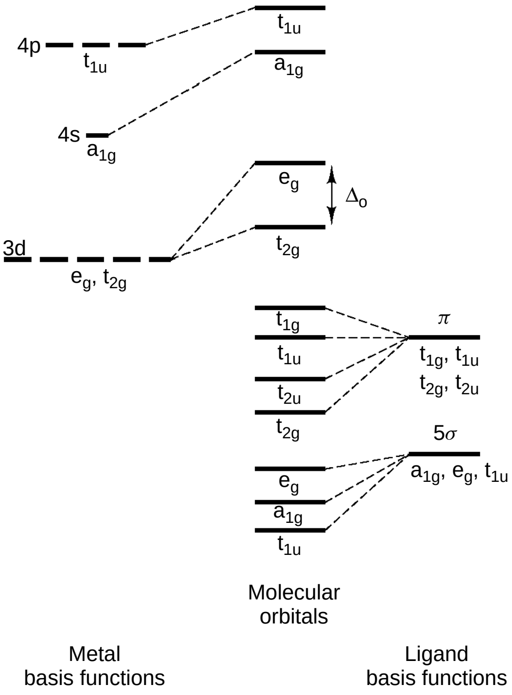

Figure 26 Molecular orbital energy level diagram for first-row transition metal with π-donor type ligand

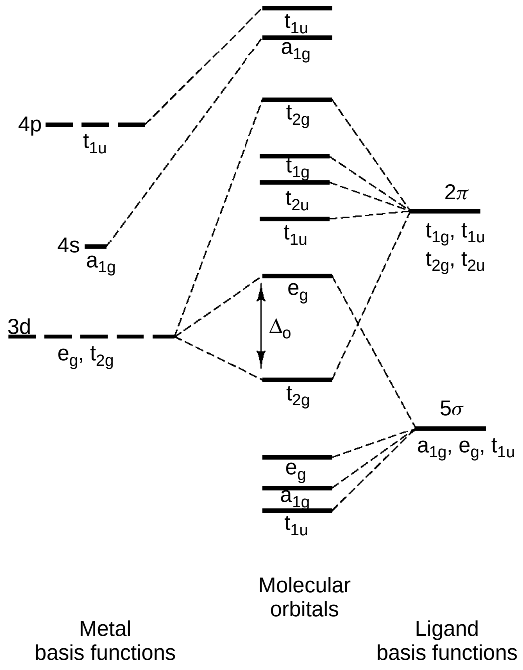

Figure 27 Molecular orbital energy level diagram for first-row transition metal with π-acceptor type ligand

π-Donor ligands (the halides) have completely filled valence orbitals that interact with all of the atomic orbitals on the metal. The ligand SALCs are generally lower in energy than the important d levels; as a result, the majority of the character of the bonding interactions (t_{2g}, e_g) lies on the ligands. The antibonding interactions are principally of metal d character and are of course destabilized relative to the d basis orbitals. An important distinction among the ligands can be made when comparing the σ-only ligands (NH_3, H_2O) to the π-donor ligands. The triply degenerate t_{2g} set of metal d orbitals will be unperturbed by σ-donors. Thus the Δ_o gap is generally smaller for π donors than for σ donors. If the gap is small enough, electrons may preferentially singly occupy the e_g levels rather than expend the energy necessary to pair in the same t_{2g} orbital, giving up to as many as five unpaired electrons in a single molecule. Ligands of this type are called high spin.

In π-acceptor ligands, low-energy basis orbitals again destabilize the metal e_g set, but now the t_{2g} set is stabilized by the accessible π^* ligand basis orbitals. This opens up the Δ_o gap, resulting in relatively larger transition energies. Ligands with this character are called low-spin because the electrons will pair in the t_{2g} levels before entering the e_g set. This variation in Δ_o is assembled in the (*Spectrochemical Series*), which is generalized: π donor $<$ σ donor $<$ π acceptor.

As mention earlier in this article, recent progress in computational chemistry has had a tremendous impact on our understanding of the theoretical underpinnings of larger chemical systems of interest. Several important recent reviews have detailed the application of ab initio MO and DFT methods to the reactions of main group and transition metals.[28] The field of theoretical chemistry has now reached a fully mature stage in theory and application. Chemists are now able to use electronic structure calculations as a reliable, practical tool for the study of the structure and function of important molecular units and provide important evidence for the rational design of new chemical systems.[66–68]

13 RELATED ARTICLES

Bonding Energetics of Organometallic Compounds; Coordination & Organometallic Chemistry: Principles; Electronic Structure of Main-group Compounds; Electronic Structure of Organometallic Compounds; Electronic Structure of Solids; Electronic Structure of Clusters; Ligand Field Theory & Spectra.

14 REFERENCES

1. D. F. Shriver, P. W. Atkins, and C. H. Langford, 'Inorganic Chemistry', Oxford University Press, Oxford, 2001.
2. R. S. Drago, 'Physical Methods for Chemists', Saunders, Philadelphia, PA, 1992.
3. J. E. Huheey, E. A. Keiter, and R. L. Keiter, 'Inorganic Chemistry: Principles of Structure and Reactivity', Addison-Wesley, New York, 1997.
4. W. L. Jolly, 'Modern Inorganic Chemistry', McGraw-Hill, New York, 1984.
5. P. W. Atkins and R. S. Friedman, 'Molecular Quantum Mechanics', Oxford University Press, New York, 1999.
6. R. L. DeKock and H. B. Gray, 'Chemical Structure and Bonding', University Science Books, Mill Valley, CA, 1989.
7. D. A. McQuarrie, 'Quantum Chemistry', University Science Books, Mill Valley, CA, 1983.
8. F. L. Pilar, 'Elementary Quantum Chemistry', Dover Publications, Mineola, NY, 2001.
9. I. N. Levine, 'Quantum Chemistry', Prentice Hall, Upper Saddle River, NJ, 2000.
10. J. P. Lowe, 'Quantum Chemistry', Academic Press, New York, 1993.
11. M. A. Ratner and G. C. Schatz, 'Introduction to Quantum Mechanics in Chemistry', Prentice Hall, Upper Saddle River, NJ, 2001.
12. J. Simons and J. Nichols, 'Quantum Mechanics in Chemistry', Oxford University Press, New York, 1997.
13. G. N. Lewis, *J. Am. Chem. Soc.*, 1916, **38**, 762.
14. J. Langmuir, *J. Am. Chem. Soc.*, 1919, **41**, 868.
15. R. J. Gillespie and R. S. Nyholm, *Quart. Rev. Chem. Soc.*, 1957, **11**, 339.
16. R. S. Mulliken, 'Life of a Scientist', Springer-Verlag, Berlin Heidelberg, 1989.
17. W. Heitler and F. London, *Z. Phys.*, 1927, **44**, 455.
18. L. Pauling, *J. Am. Chem. Soc.*, 1931, **53**, 1367.
19. L. Pauling, 'The Nature of the Chemical Bond', 3rd edn., Cornell, Ithaca, NY, 1960.
20. A. E. Reed and F. Weinhold, *J. Am. Chem. Soc.*, 1986, **108**, 3586.
21. G. Ohanessian and W. A. Goddard III, *Acc. Chem. Res.*, 1990, **23**, 386.
22. R. S. Mulliken, *Rev. Mod. Phys.*, 1930, **2**, 60.
23. R. S. Mulliken, *Rev. Mod. Phys.*, 1930, **2**, 506.
24. R. S. Mulliken, *Rev. Mod. Phys.*, 1930, **3**, 89.
25. R. S. Mulliken, *Rev. Mod. Phys.*, 1930, **4**, 1.
26. F. Hund, *Z. Phys.*, 1928, **51**, 759.
27. S. F. Boys, *Proc. Roy. Soc.*, 1950, **A200**, 542.
28. C. J. Willis, *J. Chem. Educ.*, 1991, **68**, 743.
29. W. R. Gentry, C. F. Giese, F. Luo, G. Kim, and G. McBane, *J. Chem. Phys.*, 1993, **98**, 3564.
30. W. Kolos and L. Wolniewicz, *J. Chem. Phys.*, 1968, **49**, 404.
31. W. J. Hehre, 'A Guide to Molecular Mechanics and Quantum Chemical Calculations', Wavefunction, 2003.
32. W. J. Hehre, L. Radom, P. V. R. Schleyer, and J. A. Pople, 'Ab Initio Molecular Orbital Theory', Wiley, New York, 1986.
33. J. N. Murrell, S. F. A. Kettle, and J. M. Tedder, 'The Chemical Bond', Wiley, Chichester, 1985.
34. W. G. Richards and D. L. Cooper, 'Ab Initio Molecular Orbital Theory Calculations for Chemists', Clarendon Press, Oxford, 1983.
35. H. F. Schaefer III, 'Quantum Chemistry: The Development of Ab Initio Methods in Molecular Electronic Structure Theory', Clarendon Press, Oxford, 1984.
36. H. F. Schaefer III, 'The Electronic Structure of Atoms and Molecules: A Survey of Rigorous Quantum Mechanical Results', Addison Wesley, Reading, 1972.
37. A. Szabo and N. S. Ostland, 'Modern Quantum Chemistry: Introduction to Advanced Electronic Structure Theory', Dover Publications, Mineola, NY, 1996.
38. T. Helgaker, P. Jorgensen, and J. Olsen, 'Molecular Electronic Structure Theory', Wiley, New York, 2000.
39. T. A. Halgren, D. A. Kleier, J. H. Hall, L. D. Brown, and W. N. Lipscomb, *J. Am. Chem. Soc.*, 1978, **100**, 6595.
40. M. J. S. Dewar and G. P. Ford, *J. Am. Chem. Soc.*, 1979, **101**, 5558.
41. J. A. Pople and D. L. Beveridge, 'Approximate Molecular Orbital Theory', McGraw-Hill, New York, 1970.

42. M. C. Zerner, G. H. Loew, R. F. Kirchner, and U. T. Mueller-Westerhoff, *J. Am. Chem. Soc.*, 1980, **102**, 589.
43. W. P. Anderson, T. R. Cundari, R. S. Drago, and M. C. Zerner, *Inorg. Chem.*, 1990, **29**, 1.
44. D. R. Kanis, M. A. Ratner, and T. J. Marks, *J. Am. Chem. Soc.*, 1992, **114**, 10338.
45. M. B. Hall and R. F. Fenske, *Inorg. Chem.*, 1972, **11**, 768.
46. R. F. Fenske, *Prog. Inorg. Chem.*, 1976, **21**, 179.
47. R. S. Mulliken, *J. Chem. Phys.*, 1955, **23**, 1841.
48. J. C. Slater, 'Quantum Theory of Atomic Structure', McGraw-Hill, New York, 1960, Vol. I, p. 322.
49. P. Hohenberg and W. Kohn, *Phys. Rev.*, 1934, **46**, 618.
50. W. Kohn and L. J. Sham, *Phys. Rev.*, 1965, **A140**, 1133.
51. R. G. Parr and W. Yang, 'Density Functional Theory of Atoms and Molecules', Oxford University Press, New York, 1989.
52. J. K. Labanowski and J. W. Andzelm eds, 'Density Functional Methods in Chemistry', Springer-Verlag, New York, 1991.
53. J. M. Seminario and P. Politzer eds, 'Modern Density Functional Theory: A Tool for Chemistry', Elsevier, Amsterdam, NY, 1995.
54. E. Hückel, *Z. Phys.*, 1931, **70**, 204.
55. E. Hückel, *Z. Phys.*, 1932, **76**, 628.
56. R. Hoffmann, *J. Chem. Phys.*, 1963, **39**, 1397.
57. P. A. Cox, 'The Electronic Structure and Chemistry of Solids', Oxford University Press, New York, 1987.
58. J. K. Burdett, 'Chemical Bonding in Solids', Oxford University Press, New York, 1995.
59. J. A. Duffy, 'Bonding Energy Levels and Bands in Inorganic Solids', Longman, London, 1990.
60. T. A. Albright, J. K. Burdett, and M. H. Whangbo, 'Orbital Interactions in Chemistry', Wiley, New York, 1985.
61. J. K. Burdett, 'Molecular Shapes', Wiley, New York, 1980.
62. F. A. Cotton, 'Chemical Applications of Group Theory', Wiley, New York, 1990.
63. R. L. Carter, 'Molecular Symmetry and Group Theory', John Wiley & Sons, Inc., New York, 1998.
64. D. M. Bishop, 'Group Theory and Chemistry', Dover Publications, Mineola, NY, 1993.
65. A. D. Walsh, *J. Chem. Soc.*, 1953, 2260.
66. S. Niu and M. B. Hall, *Chem. Rev.*, 2000, **100**, 353.
67. K. Koga and K. Morokuma, *Chem. Rev.*, 1991, **91**, 823.
68. T. Ziegler, *Chem. Rev.*, 1991, **91**, 651.

Molybdenum: Inorganic & Coordination Chemistry

Jon A. McCleverty
University of Bristol, Bristol, UK

1 Introduction 1
2 Halide and Cyanide Complexes 1
3 Complexes with O-donor Atoms 2
4 Complexes with Sulfur, Selenium, and Tellurium Donor Atoms 5
5 Complexes with N-donor Atoms 10
6 Complexes with P- and As-donor Atoms 18
7 Metal–Metal Bonds and Clusters 18
8 Related Articles 27
9 References 27

Abbreviations

abt = 1-iminobenzene-2-thiolate (2−); acac = Pentane-2,5-dionate (2−); bdt = Benzene-1,2-dithiolate (2−); cat = Catecholate (2−), benzene-1,2-diolate (2−); cyclam = 1,4,8,11-tetraazacyclotetradecane; depe = Bis(diethylphosphino)ethane; dmit = 4,5-dithiolato-1,3-dithiolene-2-thionate (2−); dppe = Bis(diphenylphosphino)ethane; dppee = 1,2-bis(diphenylphosphino)ethene; diphos = Chelating bis(dialkyl)– or (diaryl)-phosphine; dme = 1,2-dimethoxyethane; en = 1,2-diaminoethane; mnt = Maleonitriledithiolate (2−); *cis*-1,2-dicyanoethene-1,2-dithiolate (2−); OTf = Trifluoromethanesulfonate (1−) (triflate (1−)); pc = Phthalocyaninate (2−); porph = Porphyrinate (2−); pz = Pyrazine; py = Pyridine; qdt = Quinoxaline-1,2-dithiolate (2−); tdt = Toluene-3,4-dithiolate (2−); tmeda = 1,2-bis(dimethylamino)ethane; ttp = 5,10,15,20-tetra-*p*-tolylporphyrinato(2−); XAS = X-ray absorption spectroscopy.

1 INTRODUCTION

Molybdenum compounds play a significant role in industrial catalysis, in particular, in alkene metathesis, ammoxidation, epoxidation, hydrodesulfurization, hydroformylation, and in chemical and photooxidation processes.[1,2] Molybdenum is also an essential trace element encountered in a wide variety of enzymes. These enzymes are responsible for the growth and health of organisms, and the cyclic of nitrogen, sulfur, and carbon in the bio−geo-spheres.[3–5]

During the last decade of the twentieth century, the inorganic and coordination chemistry of molybdenum has expanded substantially. Among the major developments in this period have been (1) the introduction of a versatile range of polydentate ligands, including the tripodal tris(amido), triamidoamine, and tris(pyrazolyl)borato species which have enabled the stabilization of novel species and chemistry; (2) continuing development of the chemistry and catalytic applications of a range of complexes containing oxo and imido ligands (*see*, e.g. ***Oxidation Catalysis by Transition Metal Complexes***; ***Hydrodesulfurization & Hydrodenitrogenation***), (3) increased activity and substantial sophistication in the chemical modeling of molybdo-enzymes structure, function, and spectroscopy (*see*, e.g. ***Molybdenum: MPT-containing Enzymes***), (4) a substantial growth of interest in the electro-optical and nonlinear optical behavior of molybdenum compounds, and (5) the development and rationalization of major areas of cluster chemistry, including the assembly of mesoscopic polyoxoanions and rational construction of chalcogenide-containing clusters.

Molybdenum coordination has recently been comprehensively reviewed in *Comprehensive Coordination Chemistry*, particularly in the areas of mononuclear complexes,[6] polyoxometallate synthesis, structure, and reactivity[7,8] (*see also* ***Polyoxometalates***), and in chalcogen-containing cluster complexes.[9]

2 HALIDE AND CYANIDE COMPLEXES

Most synthetic routes to Mo^{III} complexes utilized *mer*-$[MoX_3(solvent)_3]$ species, the general preparations of these species having been reviewed.[6] A complex containing a cyano-Mo^{III} complex, $[Mn^{II}L]_6[Mo^{III}(CN)_7][Mo^{IV}(CN)_8]_2\cdot 19.5\ H_2O$ (L = N_5-donor ligand) has been described.

Reduction of $K[MoF_6]$ with KI in anhydrous HF afforded the molybdenum(IV) salt $K_2[MoF_6]$, while reduction of $[MoOCl_3]$ or $MoCl_5$ with TlCl at 350 °C afforded $Tl_2[MoCl_6]^{2-}$. The salts $[ECl_3]_2[MoCl_6]$ were also prepared in reactions of $MoCl_4$ with ECl_4 (E = Se, Te). All the hexahalide Mo^{IV} anions had octahedral geometries. Complete loss of ether from $[MoCl_4(OEt_2)_2]$ afforded amorphous $MoCl_4$ and this adduct was an important and versatile precursor for most halo-molybdenum(IV) chemistry.

Liquid $[MoF_6]$ is a powerful oxidising agent and its reduction with KBr in anhydrous HF or I_2 in acetonitrile afforded molybdenum(V) salts of $[MoF_6]^-$. Molybdenum pentachloride in the gas phase was shown to be monomeric and has C_{4v} symmetry, but is unstable with respect to $[MoCl_6]^-$.

Salts of molybdenum(VI) fluoride, $[MoF_7]^-$ were prepared by reaction of $[MoF_6]$ with F^- under appropriate conditions. These anions have capped octahedral structures in agreement with theoretical predictions. Radiotracer experiments using

^{18}F established that there is rapid and complete intermolecular fluoride exchange between $[MoF_7]^-$ and $[MoF_6]$.

3 COMPLEXES WITH O-DONOR ATOMS

3.1 Molybdates and Oxomolybdenum Complexes

Dioxo-Mo^{IV} complexes are very rare and almost invariably adopt trans-octahedral structures. Examples include matrix-isolated *trans*-$[MoO_2(CO)_4]$, *trans*-$[MoO_2(CN)_4]^{4-}$, and *trans*-$[MoO_2(dppe)_2]$.

Careful crystallographic and spectroscopic studies have shown that the 'green' bond-stretch isomer of *cis,mer*-$[MoOCl_2(PMe_2Ph)_3]$ is in fact a binary mixture of blue *cis,mer*-$[MoOCl_2(PMe_2Ph)_3]$ and yellow *mer*-$[MoCl_3(PMe_2Ph)_3]$, and this area has been thoroughly reviewed.[10–12] The separation of conformational isomers of *cis,mer*-$[MoOBr_2(PMe_2Ph)_3]$ has been achieved.

The complicated and difficult reactions of ethanol with $MoCl_5$ have been unravelled, the products being found to depend on stoichiometry and temperature. Unstable monomers containing the molybdenyl Mo^{3+} core were detected, for example, $H[MoOCl_4]\cdot 2EtOH$ and $[MoOCl_3(HOEt)]$, which have square-pyramidal structures with an apical oxo group. In the absence of other ligands, these species eliminated HCl, ultimately forming $[(Mo_2O_2Cl_4)\mu\text{-}(OEt)_2\mu\text{-}(HOEt)]$. Addition of ethene, CO, or $OPPh_3$ (L) to $[MoOCl_3(HOEt)]$ afforded $[MoOCl_3L(HOEt)]$ which also eliminated HCl, giving dinuclear species.

Dinuclear fragments, linear polymers, and clusters were found in solid-state materials such as $KMoOCl_4$, $E_2[MoOCl_4]_2$, $[ECl_3][MoOCl_4]$ (E = Se or Te), and $[Te_{15}X_4][MoOX_4]_2$ (X = Cl, Br).

Complexes of the type $[MoOX_4L]^-$ were generated by ligand association or displacement reactions affording numerous salts, where X = halide and L = H_2O, THF, DMF, or NCMe. Ligand exchange at molybdenum centers also afforded a general route to the species $[MoOCl_3L_2]$, which usually adopted a mer structure.

The tetrahedral molybdate(VI) ion, $[MoO_4]^{2-}$ is stable and inert under basic conditions but was readily protonated on acidification.[13] The first protonation afforded $[HMoO_4]^-$, and the second resulted in an increase in coordination number, giving $[MoO_3(OH_2)_3]$, $[MoO_2(OH)_2(OH_2)_2]$, or $[Mo(OH)_6]$. Subsequent protonation produced $[MoO_2(OH)(OH_2)_3]^+$ and $[MoO_2(OH_2)_4]^{2+}$, these last species being observed only at very low Mo concentrations ($<10^{-4}$ M). At higher concentrations, condensation leads to polyoxomolybdate formation (see Section 7.2). The existence of six-coordinate dioxo-Mo^{VI} species has been supported by EXAFS studies and by the isolation of $[MoO_2X_2(OH_2)_2]$ (X = Cl, Br).

The intensely yellow/red tetrahedral thiomolybdates, $[MoO_xS_{4-x}]^{2-}$ ($x = 0–3$) were formed by the reaction of $[MoO_4]^{2-}$ with H_2S or sulfiding reagents in basic solutions. These salts are interesting because of their roles in Cu–Mo antagonism in ruminants, and their potential as treatments for Wilson's disease. Several alkylammonium salts of $[MoS_4]^{2-}$ have been reported, which has facilitated the study of the nonaqueous chemistry of this dianion.

Reaction of the hydroxylamido complexes $[MoO_2(ONR_2)_2]$ (R = Et, Bz) with $B(C_6F_5)_3$ gave the pseudo-octahedral species $[MoO\{OB(C_6F_5)_3\}(ONR_2)_2]$.

The colorless $[MoO_3(R_3tacn)]$ was obtained from MoO_3 and R_3tacn (**1**) in hot water or by oxidative decarbonylation of *fac*-$[Mo(CO)_3(R_3tacn)]$ using HNO_3 or H_2O_2/THF. The crystal structure determinations of several of these species as solvates confirmed their octahedral geometries.[1] In aqueous protic media, $[MoO_3(R_3tacn)]$ (R = H, Me) underwent quasi-reversible reduction ($2e^-$, $4H^+$) to $[Mo(O)(OH_2)_2(R_3tacn)]^{2+}$, which underwent further reduction affording di- and trinuclear species. A variety of related trioxo species have been reported, for example, $[MoO_3(Bu^t_3tch)]$ and $[MoO_3L]^-$, L = Tp^-, Tp^*, Tm^*, (**2**); tpa (**3**). A number of these complexes crystallized as aqua solvates and exhibited extensive networks of H-bonding.

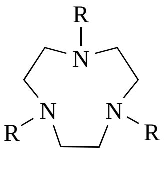

(**1**)

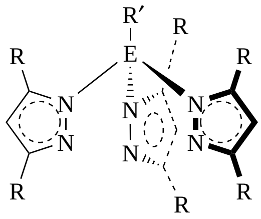

(**2**)

Tp^-, E = H, R′ = R = H

Tp^{*-}, E = H, R′ = H, R = Me

Tpm^{*-}, E = H, R = Me

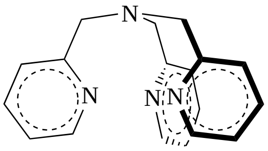

(**3**)

Many dioxo complexes of Mo^{VI} are used in oxidation catalysis as enzymes, and in metal oxide surface modes as sensors and drugs. These have been prepared by ligand addition, exchange, and/or metathesis using *cis*-$[MoO_2]^{2+}$ precursors such as $[MoO_2X_2]$, $MoO_2X_2L_2$ (X = halide; L = H_2O, DMSO, $OPPh_3$, etc.), or $[MoO_2(acac)_2]$. The oxo groups were invariably cis and usually had four- or six-coordination. The four-coordinate species $[MoO_2X_2]$ are tetrahedral and X is almost always a π-donor ligand, for example, $[MoO_2S_2]^{2-}$. Five-coordination in dioxomolybdenum(VI) chemistry is rare but examples included trigonal bipyramidal $[MoO_2(OSiPh_3)_2(PPh_3)]$ and square-pyramidal $[MoO_2(bdt)X]$ (bdt = benzene-1,2-dithiolate; X = $OSiPh_3$, $SC_6H_2Pr^i$-2,4,6).

The majority of dioxo-Mo^{IV} complexes have distorted octahedral geometries, with the weakest π-donor ligands (L) being trans to the oxo ligands, whereas stronger π-donor ligands (X) are mutually trans and cis to the oxo groups, for example, *cis,trans,cis*-(**4**). Exceptions included $[MoO_2Cl_2(tmeda)]$ and $[MoO_2Cl_2(Me_4cyclam)]$ where steric demands of the N-ligands enforced the electronically unfavorable cis,cis,cis geometry (**5**).

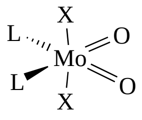

(**4**)

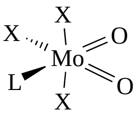

(**5**)

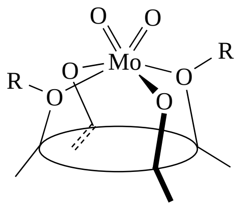

(**6**)

3.2 Alkoxide, Aryloxide, and Catecholate Complexes

3.2.1 Alkoxide Complexes

Distorted octahedral species $[Mo(OCH_2CH_2O)_3]$ and $[Mo(OC_2Me_4O)_3]$ were formed in the reactions of nitrido-Mo^{VI} complexes with 1,2-ethanediol and 2,3-dimethyl-2,3-butanedione in basic media. Reaction of $[MoO(OEt)_4]$ with $MeOCH_2CH_2OH$ afforded liquid $[MoO(OCH_2CH_2OMe)_4]$ which solidified on standing to afford the distorted octahedral complex of the same formula.

Reaction of Ag_2MoO_4 with Ph_3SiCl afforded tetrahedral $[MoO_2(OSiPh_3)_2]$ which reacted with PPh_3 to give the trigonal bipyramidal $[MoO_2(OSiPh_3)_2(PPh_3)]$. Six-coordinate species of the type $[MoO_2(OSiPh_3)_2(N–N)]$ (N–N = phen, Me_4phen, 4,4′-Me_2bipy, 5,5′-bipy) were also reported. Both $[MoO_2(OSiPh_3)_2]$ and $[MoO_2(OC_6H_3Bu^t{}_2\text{-}2,6)_2]\cdot 2HOC_6H_3Bu^t{}_2$-2,6, obtained by reaction of $[MoO_2Cl_2]$ with $LiOC_6H_3Bu^t{}_2$-2,6 were stabilized by significant π-donation from the OR^- ligands. Octahedral $[Mo(OTeF_5)_6]$ has been synthesized and its structure determined crystallographically.

3.2.2 Aryloxide Complexes

Paramagnetic *trans*-$[Mo^{IV}(OPh)_4(PMe_3)_2]$ was obtained from reaction of $[Mo(PMe_3)_6]$ with an excess of phenol in benzene. Red–purple-$[Mo^{IV}Cl_2\{O_2(OR)_2^{Bu}cal\}]$ was formed in the reactions of $[MoOCl_4]$ with 1,3-dialkyl-*p-t*-butylcalix[4]arenes in hexane. A generalized structure for calixarenes is shown in Figure 1.

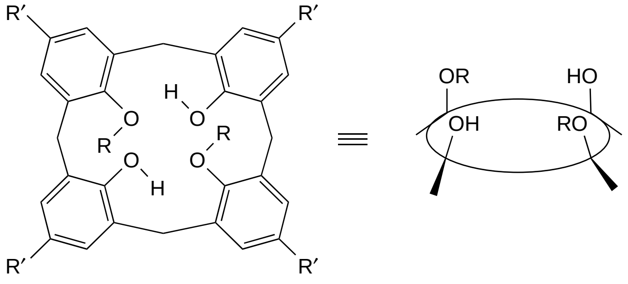

Figure 1 Calixarene ligands

Only one dioxomolybdenum(VI) monocalixarene complex, (**6**) (R = Me) has been reported. The dioxomolybdenum(VI) bis-calixarene complexes $[Mo(O_4^{Bu}cal)\{O_2(OH)_2^{Bu}cal\}]$ and $[Mo_2(O_4^{Bu}cal)_2]^{2-}$ were formed in the reactions of $[MoCl_4L_2]$ (L = OEt_2, SEt_2) with $(HO)_4^{Bu}cal$ and NEt_3 in toluene. The octahedral geometry of $[Mo(O_4^{Bu}cal)\{O_2(OH)_2^{Bu}cal\}]$ was defined by alkoxide O-donor atoms from tetradentate $O_4^{Bu}cal$ and bidentate $[1,2\text{-}O_2(OH)_2^{Bu}cal]^{2-}$. This complex reacted with HCl to give *cis*-$[MoCl_2(O_4^{Bu}cal)]$. Oxo-calixarene complexes are of interest as models of heterogeneous metal oxide catalyst surfaces, centers that may be capable of supporting organometallic transformation, and as building blocks for supramolecular species.

3.2.3 Catecholate Complexes

Reaction of $[MoOCl_3(dme)]$ with 9,10-phenanthrenequinone (O–O) afforded the quinone-stabilized Mo^V species $[MoOCl_3(O–O)]$. Related semiquinone, $[Mo^VCl_4(O–O^-)]$ and Mo^{VI} complexes containing arenediolato ligands have also been prepared.

A range of siderophore-like complexes containing dioxomolybdenum(VI), including $[MoO_2(btrencam)]^{2-}$, $[MoO_2(bta)_2]^{2-}$, and $[MoO_2(bdax)]^{2-}$ have been prepared, (btrencam, (**7**); bta, (**8**); bdax, (**9**)). The *cis*-$MoO_2{}^{2+}$ group in $[MoO_2(btrencam)]^{2-}$ was accommodated outside the macrobicyclic cavity by two catecholate units H-bonded to adjacent amido NH groups, while the third catecholate group was protonated and directed away from the octahedral Mo^{VI} center.

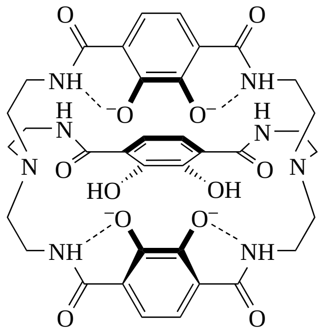

(**7**)

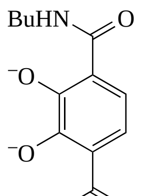

(**8**)

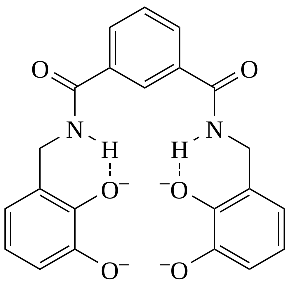

(**9**)

Molybdate binds to the aminochelin siderophore of *Azotobacter vinelandii*, and quenches the fluorescence of attached Ru(bipy)-chromophores, this affording a sensitive probe for the oxoanion.

Hydroxamic acids and their amino acid derivatives formed a series of dioxomolybdenum(VI) complexes of the type *cis*-$[MoO_2(hdx)_2]$ and $[MoO_2(hdxamc)_2]$ (hdxH, (**10**); hdxamcH, (**11**)), which are attractive as models for siderophores and for the development of metal-chelating drugs.

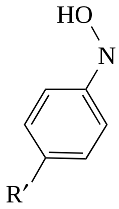

(**10**)

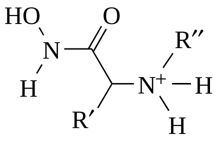

(**11**)

3.2.4 Peroxide Complexes

Reaction of $[MoCl_4(NCMe)_2]$ with a variety of Schiff base ligands, LH_2 in the presence of a base in THF afforded *trans*-$[Mo^{IV}Cl_2L]$, where L is as shown in Figure 2.[1] These Mo^{IV} complexes have octahedral structures although the equatorially disposed N_2O_2 ligand exhibited slight tetrahedral distortion.

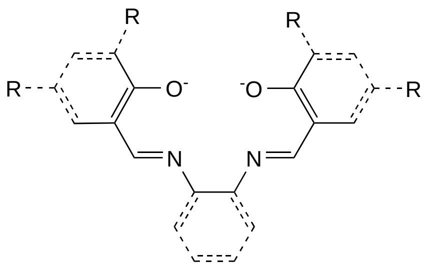

Acen: rings absent
Salen: phenolato rings present, dimino rings absent
Salphen: all rings present, R = H
Bu^t_4salphen: as salphen, R = Bu^t

Figure 2 Tetradentate Schiff base ligands

Peroxide complexes of molybdenum(VI) are intermediates in industrially important epoxidation reactions. The so-called ‘Mimoun-type’ complexes $[Mo^{VI}O(O_2)_2L_{ax}L_{eq}]^{0/n-}$ (**12**) generally exhibit pentagonal-bipyramidal structures, with an axial oxo group trans to L_{ax} and L_{eq}, and two peroxo groups in the equatorial plane. These complexes are effective reagents for the selective oxidation of alcohols to aldehydes, amines to nitroso compounds, sulfides to sulfoxides and then to sulfones, phenols to *o*-quinones, and in the sulfoxidation of thianthrene-5-oxide.[14]

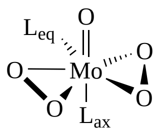

(**12**)

Chiral ligands such as (*R*)/(*S*)-(**13**), (*R*)/(*S*)-(**14**), and (*R*,*R*,*S*)/(*R*,*S*,*R*)-(**15**) form ‘Mimoun-type’ complexes $[MoO(O_2)_2L]$ and $[MoO(O_2)_2L(OH_2)]$, the structure of $[Mo(O_2)_2(\mathbf{C})][(OH_2)]$ revealing that the phosphoryl donor occupied the equatorial position (L_{eq}). Enantioselectivity in the stoichiometric epoxidation of prochiral olefins was marginal (<10%) except in the case of the complex containing (**14**), where e.e.s of up to 39% were noted. An efficient biphasic catalytic epoxidation system based on $[MoO(O_2)_2(OPR_3)]$ (R = *n*-dodecyl) has been developed.

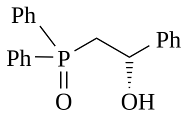

(*R*)-(**13**)

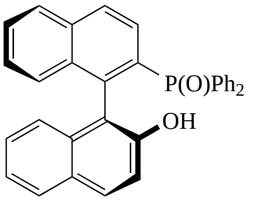

(*S*)-(**14**)

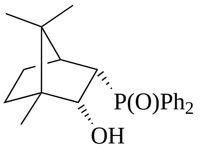

(*R*,*R*,*S*)-(**15**)

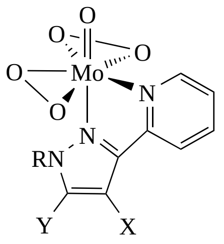

(**16**)

Complexes containing 2-(pyrazol-3-yl)pyridines (R = alkyl; X/Y = H, C, Br, Me, NO_2, CF_3, Ph), (**16**), were effective

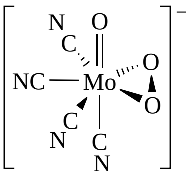

(**17**)

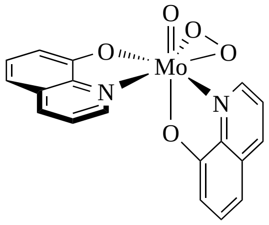

(**18a**)

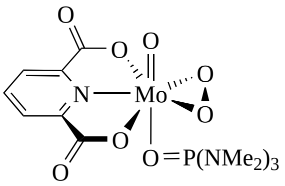

(**18b**)

epoxidation catalysts. Such complexes were also photoactive, producing both singlet and triplet O_2 on irradiation.

Oxo-monoperoxo Mo^{VI} complexes are relatively uncommon. $[MoO(CN)_5]^{3-}$ reacted with O_2 giving $[MoO(O_2)(CN)_4]^{2-}$ (**17**), which was also formed by autoxidation of $[MoO(CN)_4(pz)]^{2-}$. An ill-defined species $[MoO(O_2)_2\cdot 2quinH]$ was formed by reaction of MoO_3 with 8-hydroxyquinoline in 30% H_2O_2, but this converted to pentagonal-bipyramidal $[MoO_2(quin)_2]$, (**18a**), on recrystallization. This species was a catalyst precursor for the autoxidation of methylbenzenes. An X-ray structural determination of $[MoO(O_2)(pdc)\{OP(NMe_2)_3\}]$, (**18b**) (pdc = pyridine-2,5-di(carboxylate)), revealed that it had pseudo-octahedral geometry with a symmetrical sideways-bound (κ^2) peroxido group cis and orthogonal to the Mo=O group. Related oxaziridine complexes [MoO(ONAr)(hmpa)] were effective catalysts for the oxidation of aryl amines to nitroso compounds by H_2O_2.

4 COMPLEXES WITH SULFUR, SELENIUM, AND TELLURIUM DONOR ATOMS

4.1 Thiolato Complexes

Diamagnetic molybdenum(IV) thiolato complexes of the type $[MoO(SR)_4]^{2-}$ were prepared by BH_4^- reduction of corresponding Mo^V precursors, by thiol exchange with $[MoO(SC_6H_4Cl\text{–}4)_4]^{2-}$, or by reaction of $[MoOCl(PPh_2Me)_3]$ with HSC_6F_5 in the presence of NEt_3. X-ray crystallographic examination of a selection of these oxo-Mo^{IV} complexes established that the coordination sphere had expanded slightly with respect to their oxo-Mo^V analogues.

Two types of hydrido Mo^{IV} thiolato complexes have been described (i) 6-coordinated 14-electron species $[MoH(SR)_3(PMe_2Ph)_2]$ (R = mes, $C_6H_2^{i\mathrm{Pr}}{}_3$-2,4,6) and (ii) 5-coordinated, 12-electron complexes containing bulkier phosphines, $[MoH(SR)_3(PR'Ph_2)_2]$ (R = Mes, R′ = Me; R = $C_6H_2^{i\mathrm{Pr}}{}_3$, R′ = Et). The first group was prepared by reaction of $[Mo(NNH_2)Br_2(PMe_2Ph)_3]$ with RSH/NEt_3, and the structure of $[MoH(SC_6H_2^{i}Pr_3)_2(PMe_2Ph)_2]$ was trigonal bipyramidal, with apical phosphine and equatorial thiolate ligands, the H atom not being located. The second group was obtained from the reaction of $[MoH_4(PR'Ph_2)_4]$ or $[Mo(N_2)_2(PR'Ph_2)_4]$ with RSH, and was also trigonal bipyramidal, with an apical H atom trans to $PR'Ph_2$. These complexes afforded a variety of complexes by phosphine displacement, thiol elimination, hydride exchange with deuterium, hydrazine disproportionation, and/or ligand addition.

A distorted octahedral complex $[Mo^{IV}(dmsp)_2(S^tBu)_2]$ (dmsp = $Ph_2PCH_2CH_2S^-$) was obtained by reaction of $[Mo(S^tBu)_4]$ with dmsp. It formed heterobimetallic clusters with iron and copper species. Tridentate $PhP(C_6H_4SH)_2$ reacted with $[MoCl_4(PPh_3)_2]$ in methanol/NEt_3 to give diamagnetic $[Mo^{IV}\{PhP(C_6H_4S)_2\}]$ and when this reaction was carried out in acetonitrile, $[Mo\{PhP(C_6H_4S)_2\}(NCMe)]$ was produced. Reaction of $[MoCl_2(CO)_2(PPh_3)_2]$ with the same ligand in methanol/base afforded $[Mo(CO)\{PhP(C_6H_4S)_2\}_2]$.

The oxomolybdenum(V) thiolato species $[MoO(SR)_4]^-$ was obtained by several different routes: (1) reactions of thiols with precursors containing Mo^V, including $[MoOCl_3(thf)_2]$, (2) thiol exchange with $[MoO(SPh)_4]^-$, (3) reaction of $[MoO_2(acac)_2]$ or $[MoOCl_4]$ with thiolates, (4) reaction of $[MoCl_3(thf)_3]$ with thiols and 4-methylpyridine-*N*-oxide, or (5) reaction of $[MoCl_4(NCMe)_2]$ with thiolates in wet acetonitrile. These complexes carried a range of aryl substituents. Complexes have been prepared containing chelating dithiolato ligands, $[MoO(S\text{–}S)_2]^-$, where S–S = $S(CH_2)_nS$ with $n = 2$ or 3, α-2-toluenedithiolate (**19**), tri- and tetrapeptides, and 2,2′-dimercaptodiphenyl (**20**). These complexes are characterized by intense low-energy (500–650 nm) charge transfer bands mainly comprising multiple $S \rightarrow Mo(d_{xy})$ transitions, the transition energies being strongly dependent on the orientation of the orbitals containing the S lone-pair electrons with respect to the magnetic orbital.

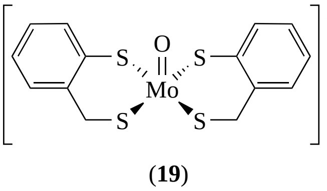

(**19**)

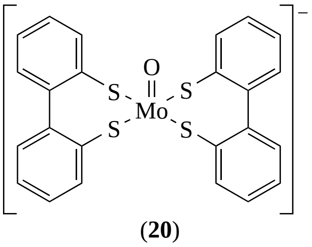

(**20**)

The syntheses of paramagnetic *cis*,*cis*-$[Mo^VOCl(L\text{–}N_2S_2)]$ ($H_2L\text{–}N_2S_2\equiv$ (**21**)) and its thermal isomerization to the cis,trans isomer have been described, and a series of derivatives of *cis,cis*- and *cis,trans*-[$MoOX(L–N_2S_2)$] (X = Br, NCS, $OSiMe_3$, OPh, SPh), and [$MoO(L–N_2S_2)$]$^+$ have also been reported. Reactions of [$MoOCl_5$]$^{2-}$ with $dttdH_2$ ($dttd^{2-} \equiv$ (**22**), R = H) afforded the paramagnetic [MoOCl(dttd)], while reactions of [$MoO(SR)_4$]$^-$ with N-salicylidene(2-mercaptoaniline) (L–$NSOH_2$, (**23**)) gave [$MoO(L–NSO)(SR)_2$] (R = Ph, C_6H_4Me-4).

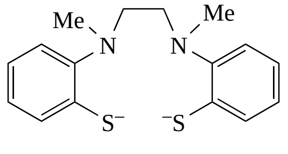
(**21**)

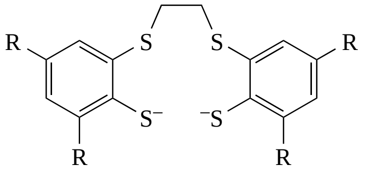
(**22**)

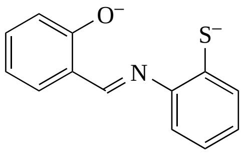
(**23**)

Nitrosyl complexes containing $dttd^{2-}$ (**22**) are described in Section 5.8.

4.2 Thioether Complexes

Tripodal S_3-donor ligands afforded a wide variety of complexes, including the tetra(methylthiomethyl)borate species [$Mo(CO)_2\{\kappa^3\text{-}S,S',S''\text{-}(MeSCH_2)_3BCH_2SMe\}$]$^-$, [$Mo(CO)_3\{\kappa^3\text{-}S,S',S''\text{-}(RSCH_2)_3ER'\}$] (R = alkyl, mainly Me, or aryl; ER = CMe, SiMe, and SnBu). Long Mo–S bonds (>2.6 Å) and ready ligand displacement indicated that these ligands were relatively weakly bound to the molybdenum tricarbonyl center. Thione ligands, based on the tris(pyrazolyl)borate motif, (**24**), were also used to form tricarbonyl anionic derivatives. A variety of linear and macrocyclic thioethers have also been coordinated by tricarbonyl molybdenum fragments, including [$Mo(CO)_2(MeSCH_2CH_2SCH_2CH_2SMe)$], [$Mo(CO)_3$(ttcn)], and [$Mo(CO)_3$(ttob)] (ttcn, (**25**); ttob, (**26**)).

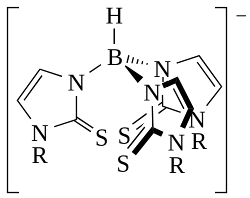
(**24**)

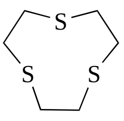
(**25**)

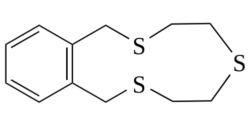
(**26**)

The Mo^{II} complex *trans*-[$MoBr_2\{Me_8[16]aneS_4\}$] (**27**) was prepared by reaction of the macrocyclic tetrathioether with [$\{MoCO_4Br_2\}_2$] and this could be oxidized by Ag^+ to *trans*-[$MoBr_2\{Me_8[16]aneS_4\}$]$^+$ in which the ligand adopted a syn–anti conformation. Reduction of *trans*-[$MoBr_2\{Me_8[16]aneS_4\}$] by sodium amalgam under nitrogen in thf afforded the Mo^0 complexes, *trans*-[$Mo(N_2)_2\{Me_8[16]aneS_4\}$], the macrocyclic thioether adopting a syn conformation.

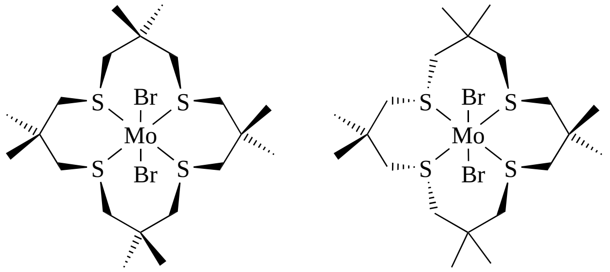
syn conformation *syn-anti* conformation

(**27**)

Reactions of [$MoCl_3(thf)_3$] with cyclic trithioethers c-S_3 afforded the Mo^{III} complexes, [$MoCl_3(c\text{-}S_3)$] and [$MoCl_3$(ttob)], and with neat tetrahydrothiophene (tht), *mer*-[$MoCl_3(tht)_3$] was formed. This latter complex was an active catalyst for the selective polymerization and cyclotrimerization of alkynes.

Reaction of *trans*-[$Mo(N_2)_2\{Me_8[16]aneS_4\}$] with S_8 afforded *trans*-[$Mo^{IV}(S)_2\{Me_8[16]aneS_4\}$] which, on treatment with RX, was converted to *trans*-[$Mo(S)(SR)\{Me_8[16]aneS_4\}$]X. Protonation of [$Mo(S)_2\{Me_8[16]aneS_4\}$] by HBF_4 gave [$Mo_2(S)_3\{Me_8[16]aneS_4\}_2$]$^{2+}$ (containing a near-linear $\{S{=}Mo–S–Mo{=}S\}^{2+}$ group) and *trans*-[$Mo(S)F\{Me_8[16]aneS_4\}$]$^+$. All of these complexes contained the macrocyclic tetrathioether in the syn conformation.

The distorted octahedral oxomolybdenum(V) complexes [MoO(S–S–X–S–S)] were prepared by reaction of [$MoCl_4(NCMe)_2$] with the free pentadentate ligand (HS–S–X–S–SH, (**28**)) or its Ni^{2+} complex in wet thf, or by oxidation in air of [$Mo(CO)_2$(S–S–X–S–S)]. Related dioxomolybdenum(VI) species [MoO_2(S–S–X–S–S)] were also reported.

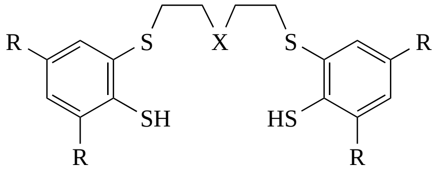
(**28**) (X = S, R = H; X = O, R = H; X = S, R = Bu^t; X = NH, R = H)

4.3 Dithiocarbamato and Related Dithioacid Complexes

Reaction of [$MoI_2(CO)_3(NCMe)L$] (L = EPh_3, E = P, As, Sb) with NaS_2CNR_2 (R = Me, Et, Bz) afforded

$[Mo^{II}I(CO)_3(S_2CNR_2)]$, and similar ethyl xanthate and pyridine- and pyrimidine-2-thiolates have been reported. Treatment of $[MoX_2(CO)_3(NCMe)L]$ with S-donor ligands, including $RS(CH_2)_2SR(R = Ph, C_6H_4X\text{-}4$ where $X = Me$ or F)[7], ttcn (**25**), and related tridentate ligands, afforded di- and tricarbonyl derivatives, $[MoX_2(CO)_3\{RS(CH_2)_2SR\}]$, and $[MoI_2(CO)_2(MeSCH_2CH_2SCH_2CH_2SMe)]$.

Reaction of $[MoX_2(CO)_3(NCMe)_2]$ with two equivalents of dithioacid ligands affords complexes of the type $[Mo(CO)_n(S_2CX)_2]$, for example, $[Mo(CO)_3\{S_2P(OEt)_2\}_2]$, which reacted with tertiary phosphines forming $[Mo(CO)_2(PPh_3)\{S_2P(OEt)_2\}_2]$ and $[Mo(CO)(diphos)\{S_2P(OEt)_2\}_2]$. Similar species containing S_2CPCy_3 were also prepared.

Reactions of $[Mo_2(\mu\text{-}S_2)_2(S_2CNR'_2)_4]^{2+}$, $[Mo(O)(S_2)(S_2CNR'_2)_2]$ ($R' = Me$ or Et) or $[Mo(S_2)(S_2CNEt_2)_2]$ with alkynes ($RC{\equiv}CR$) afforded a variety of mixed ligand ethenedithiolato dithiocarbamato complexes containing Mo^{IV}, including (**29**) and (**30**). The iminothiolene complexes (**31**) and (**32**) were obtained by reaction of alkynes with $[Mo(NPh)(S_2)(S_2CNEt_2)_2]$

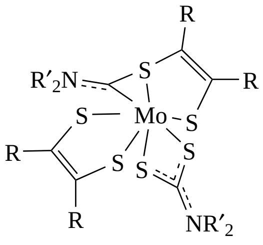

(**29**)

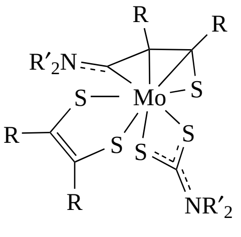

(**30**)

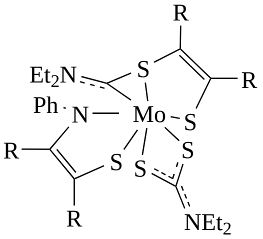

(**31**)

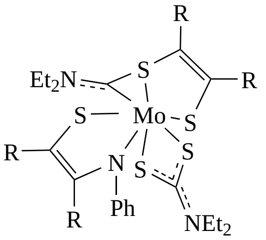

(**32**)

Reaction of $[MoCl(S_2CNR_2)_3]$ (R = Me, Et) with silver triflate afforded diamagnetic $[Mo_2(dtc)_6][OTf]_2$ which could act as the source of tris(dithiocarbamato)Mo^{IV} cations in the synthesis of $[MoL(dtc)_3]^{n+}$ ($n = 0$, L = Cl, I, N_3; $n = 1$, L = O, NCMe, PR_3). The molybdenum atom in paramagnetic seven-coordinate $[Mo(PMe_2Ph)(S_2CNEt_2)_3][OTf]$ has pentagonal-bipyramidal coordination with an apical phosphine ligand.

Reaction of $[NEt_4]_2[MoS_4]$ with tetraethylthiuramdisulfide afforded the paramagnetic molybdenum(V) complex $[Mo(S_2)(S_2CNEt_2)_3]$ ($S = 1/2$). This reacted with 3-chloroperoxybenzoic acid to give $[Mo(S_2O\text{–}S,S')(S_2CNEt_2)_3]$ which also had one unpaired electron. Both molecules have a pentagonal-bipyramidal structure, the former with an apical S_2^{2-} group. Ferrocenium oxidation of $[Mo(S_2)(S_2CNEt_2)_3]$ afforded either $[Mo(S_2CNEt_2)_4]^+$ or $[MoO(S_2CNEt_2)_3]^+$, depending on whether the solvent was dry or wet.

Reaction of $[Mo(S_2CNR_2)_4]$ with TCNQ and TCNE produced radical cation–anion salts $[Mo(S_2CNR_2)_4]Z$ (Z = TCNQ or TCNE). The TCNQ salt reacted with additional TCNQ giving $[Mo(S_2CNR_2)_4][TCNQ]_2$ which contained neutral and anionic forms of TCNQ. The crystal structures of $[Mo(S_2CNR_2)_4][TCNQ]$ (R = Me or Et) showed that the cation in each has an eight-coordinate dodecahedral structure, but that the anion packings are distinctly different. These complexes have interesting optical, magnetic, and electrical properties.

Reaction of $[MoO_2(S_2CNR_2)_2]$ with silanes afforded siloxo, halide, pseudohalide, and tris(dithiocarbamato species, $[Mo^{VI}OX_2(S_2CNEt_2)_2]$ (X = I, NCS), $[MoO(OSiMe_3)(S_2CNEt_2)_2]^+$, and pentagonal-bipyramidal $[MoO(OSiMe_3)(CN)(S_2CNEt_2)_2]$.[3]

The 2-aminocyclopent-1-ene-1-dithiocarboxylato complex $[MoO_2(acpd)_2]$ (acpd, (**33**)) afforded access to a wide range of Mo^{VI}, Mo^V, Mo^{IV}, and Mo^{III} complexes, including $[Mo^VO(acpd)_3]$, $[Mo^VOX_2(acpd)_2]$ (X = halide), $[Mo^{VI}O(acpd)_3]^+$, $[Mo^{VI}O(cat)(acpd)_2]$, and $[Mo(N_2R)(acpd)_3]$. Reaction of $[Mo^VOX(acpd)_2]$ with Hacpd, RSH, RNHOH, and Ph_3PNR gave $[Mo^{IV}(acpd)_4]$, $[Mo^VO(SR)(acpd)_2]$ (R = Ph, $C_6H_4NH_2\text{-}2$, $CH_2CH_2NH_2$), $[Mo^{VI}(ONR)X_2(acpd)_2]$, and $[Mo^{VI}(NR)X_2(acpd)_2]$. The complexes $[Mo^{IV}(SC_6H_4NH_2\text{-}2)(acpd)_3]$ and $[Mo^{III}(PPh_3)(acpd)_3]$ were obtained from $[Mo^{VI}O(acpd)_3]^+$, while $[Mo(acpd)_2(S_2CNR_2)_2]$ and $[Mo(acpd)(S_2CNR_2)_3]$ were prepared from $[MoOCl_2(S_2CNR_2)_2]$ and $[MoO(S_2CNR_2)_3]^+$, respectively.

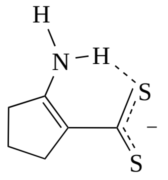

(**33**)

The complexes $[MoO(S_2)(S_2CNR_2)_2]$ are effective catalysts for the episulfurization of (*E*)-cycloalkenes by elemental sulfur. Oxidation of the same complex by 3-chloroperoxybenzoic acid, or reaction of $[Mo_2O_3(S_2CNEt_2)_4]$ or $[MoO(S_2CNEt_2)_2]$ with 'S_2O' sources, afforded the pentagonal-bipyramidal $[MoO(S_2O\text{-}S,S')(S_2CNEt_2)_2]$ which contains axial Mo=O and equatorial $\kappa^2\text{-}S_2O^{2-}$.

Reaction of $[MoS_4]^{2-}$ with tetraalkythiuramdisulfides afforded $[Mo(S_2)(S_2CNR_2)_3]$, while reaction with disulfides, RSSR, gave dinuclear $[Mo_2S_2(\mu\text{-}S)_2(S_2)_2]^{2-}$.

4.4 Dithiolene Complexes

4.4.1 Dicarbonyl Bis(Dithiolene) Complexes and their Reactions

All three members of the electron transfer chain $[Mo(CO)_2(S_2C_2Me_2)]^{n-}$ ($n = 0, 1, 2$) were isolated and characterized. The complexes have trigonal prismatic geometries, and structural, spectral, and electrochemical properties that are consistent with the redox orbital having predominantly sulfur-ligand based character (>80%); behavior consistent also with DFT calculations. Closely related benzene- and 2,4-di-*t*-butyl-benzene-dithiolene complexes, $[Mo(LL')(bdt)_2]$ ($L = O$, $L = PPh_3$, $L = L' = PMeR_2$ (R = Me or Ph)) were obtained by thioether S-dealkylation of appropriate $dttd^{2-}$ (**22**) complexes of molybdenum carbonyls and oxo species. $[Mo(CO)(PPh_3)\{S_2C_6H_2(Bu^t)_2\}_2]$ and $[Mo(PMe_3)_2(bdt)_2]$ have trigonal prismatic structures in the solid state, similar to $[Mo(CO)_2(S_2C_2Me_2)_2]$, although, in solution, it is possible that $[Mo(CO)(PR_3)\{S_2C_6H_2(Bu^t)_2\}_2]$ could have an octahedral structure (*trans* CO/PR$_3$). Reaction of $[MoCl_4(NCMe)_2]$ with $Na_2S_2C_2H_2$ or Na$_2$bdt in the presence of PMePh$_2$ or isocyanides afforded trigonal prismatic $[MoL_2(S_2C_2H_2)_2]$ and $[MoL_2(bdt)_2]$ ($L = PMePh_2$ or CNR (R = Me or Bu^t)), also with structures analogous to $[Mo(CO)_2(S_2C_2Me_2)_2]$.

Reaction of $[Mo(CO)_2(S_2C_2R_2)_2]$ with OR'^- afforded $[Mo(OR')(S_2C_2R_2)_2]^-$ (R = Me, R' = Pr^i, Ph, Ar, 2-Ad, C$_6$F$_5$; R = Ph, R' = Ph, Ar), and with Et$_4$NOH $[MEt_4N]_2[Mo(O)(S_2C_2R_2)_2]$ (R = Me, Ph) was formed. Related complexes $[Mo(OSiBu^tPh_2)(SCH_2CH_2S)_2]^-$ and $[Mo(OSiBu^tPh_2)(bdt)_2]^-$ were formed in the reaction of $[Mo(O)(dithiolate)_2]^{2-}$ with ClSiBu^{t}Ph$_2$. All of these complexes have square-pyramidal structures with axial alkoxide groups. Kinetic and isotope-labeling studies of the oxygen-atom transfer reactions of $[NEt_4][Mo(OR')(S_2C_2Ph_2)_2]$ with Se-, N-, and S-oxides were consistent with the initial formation of $[Mo(O)(OR')(S_2C_2Ph_2)_2]^-$ which decayed by internal redox processes to the final product, $[Mo(O)(S_2C_2Ph_2)_2]^-$. These complexes and the reactions are regarded as excellent models for dmso reductases and, in this context, the large reduction potentials required to reduce $[Mo(OR')(S_2C_2R_2)_2]^-$ may account for the absence of Mo^{III} enzyme states.

Reaction of $[Mo(CO)_2(S_2C_2R_2)_2]$ with SR'^- and SeR'^- were more complicated, producing two types of complexes depending on ligand and reaction conditions: trigonal prismatic $[Mo(ER')(CO)(S_2C_2R_2)_2]^-$ (R = Me, E = S or Se, R' = Ph'R = Me or Ph, E = Se, R' = $C_6H_2Pr^i_3$-2,4,6) and square-pyramidal $[Mo(ER')(S_2C_2R_2)_2]^-$ (R = Me, E = S, R' = 2-Ad, $C_6H_2Pr^i_3$-2,4,6; E = Se, R' = 2-Ad; R = Ph, E = S, R' = $C_6H_2Pr^i_3$-2,4,6; R = Me, E = Se, R' = 2-Ad).

4.4.2 Dianionic Tris(Dithiolene) Complexes

The complexes (**34**–**39**) were prepared by a variety of methods, including reaction of the dithiolato ligand salt (S–S)$^{2-}$ or a precursor mixture involving $[MoS_4]^{2-}$ or MoCl$_5$, or by reaction of Mo^{VI} or Mo^{V} derivatives. All of these complexes are members of at least a three-membered electron transfer chain (equation 1):

$$[Mo(S\text{–}S)_3]^0 \rightleftharpoons [Mo(S\text{–}S)_3]^{-1} \rightleftharpoons [Mo(S\text{–}S)_3]^{-2} \qquad (1)$$

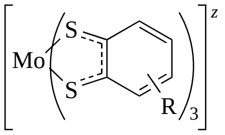

(**34**)

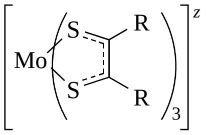

(**35**)

Many of the dianionic species ($z = 2$) have trigonal prismatic geometries which may partly be defined by the twist angle ϕ, shown in Figure 3, for example, (**35**), R = CO$_2$Me, $\phi = 10.6^\circ$, R = CF$_3$, $\phi = 0^\circ$ as Fc$^+$ salt, 16° as NEt$_4$$^+$ salt, R = Me, $\phi = 2.6^\circ$; (**36**) E = S, $\phi = 11^\circ$; (**39**), $\phi = 4.5^\circ$ as $[PPh_4]^+$ salt. Reaction of $[MoO_2(acac)_2]$ with H$_2$qdt in concentrated sulfuric acid gave $[Mo(qdt)_2]^{2-}$. Protonation of the N atoms in this complex caused a marked change in its electrochemical behavior.

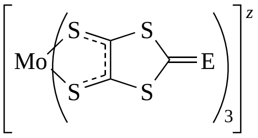

(**36**) E = O, S

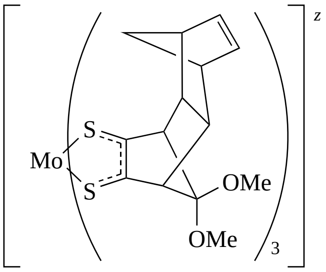

(**37**)

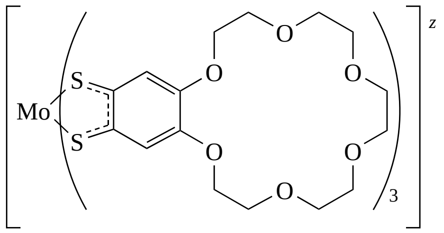

(**38**)

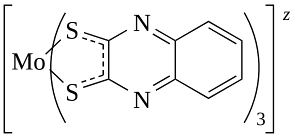

(**39**)

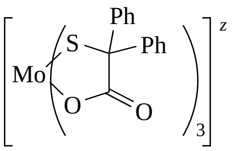

(**40**)

The complex (**40**) is diamagnetic, has a trigonal prismatic geometry and could be oxidized to a monoanion which was

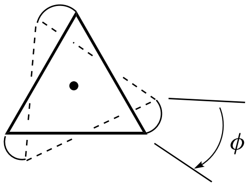

Figure 3 Idealized trigonal prism distortions as defined by angle

described as containing Mo^{V}. This species, however, did not exhibit dithiolenic behavior.

4.4.3 *Monoanionic Tris(Dithiolene) Complexes*

Monoanionic tris(dithiolene) complexes exhibited distorted trigonal prismatic geometries, for example, $[Mo(S_2C_2Me_2)_3]^-$ ($\phi = 1.6°$, as NEt_4^+ salt) and $[Mo(bdt)_3]^-$ ($\phi = 33.5°$ as NBu_4^+ salt), and are paramagnetic (one unpaired electron) exhibiting characteristic EPR spectra ($g \approx 2.002$). These results indicated that the complexes were not appropriately described as containing Mo^{V}. Iodine or ferrocenium cation oxidation of dianionic tris(dithiolene) complexes afforded salts of $[Mo\{S_2C_2(CF_3)_2\}_3]^-$ (**35**) $z = -1$, ϕ ca. 0° as Fc^+ salt; $[Mo(qdt)_3]^-$ (**39**) $z = -1$; $\phi = 14.6°$ as PPh_4^+ salt, and $[Mo(dmit)_3]^-$ (**36**) Z = E). Multifunctional EPR spectra studies of the iminothiolene complex $[Mo(abt)_3]^-$ and computational studies of other related species provided information on the delocalized nature of the ground state of these unusual complexes.

4.4.4 *Neutral Tris(Dithiolene) Complexes*

Tris(dithiolene) complexes carrying no formal charge were produced by reacting dithiolato ligands or their precursors with MoO_4^{2-}, $[MoO_2(acac)_2]$, $MoCl_5$, or $[MoCl_4(thf)_2]$, or via oxidation of Mo^{V} or Mo^{IV} counterparts. Among the complexes generated were $[Mo(bdt)_3]$, $[Mo(S_2C_2H_2)_3]$, $[Mo\{S_2C_2(SR')_2\}_3]$, $[Mo(S_2C_2S_2CE)_3]$ [E = O, S, (**37**) and (**38**) (dmit)]. These complexes had trigonal prismatic geometries, again characterized by a twist angle, ϕ (Figure 3), approaching 0° as observed in $[Mo\{S_2C_2(CF_3)_2\}_3]$ and $[Mo(S_2C_2Me_2)_3]$ ($\phi = 5.4°$). Nuclear magnetic resonance (NMR) and other spectroscopic studies confirmed substantial electron delocalization in the ground states of these complexes, it being suggested that the metal has a formal +4 oxidation state. The complexes, of course, existed within at least a three-membered electron transfer series as shown above. Detailed structural, spectroscopic, and DFT studies of isolated members of the three-membered electron transfer chain $[Mo(S_2C_2Me_2)_3]^z$ ($z = 0, -1, -2$) established that the redox orbital in all members of the series was predominantly ligand based (ca. 80%).

4.4.5 *Oxo Bis(Dithiolene) Complexes*

Square-pyramidal $[MoO(S–S)_2]^{2-}$ (S–S is a wide range of 1,2-dithiolato ligands), formally containing Mo^{IV}, could be prepared by a variety of routes: by reaction of the dithiolate ligand with Mo^{IV} starting materials such as $[MoO_2(CN)_4]^{2-}$, $[MoO(SC_6H_4Cl\text{-}4)_4]^{2-}$, or $[MoOCl(CNMe)_4]^+$, by reaction of the dithiolate ligand with Mo^{VI} or Mo^{V} precursors in the presence of reducing agents, by induced internal redox reactions involving $[MoO_2S_2]^{2-}$ with the dithiete $[S_2C_2(CCF_3)_2]$, by reaction of $[MoO(S_4)_2]^{2-}$ with alkynes, reduction of oxomolybdenum(V) or dioxomolybdenum(VI) dithiolene complexes, by reaction of $[Mo(CO)_2(S_2C_2R_2)_2]$ with $[Et_4N]OH$, or by treatment of nitrido-dithiolene species with dioxygen. These complexes were reversibly oxidized to Mo^{V} counterparts and some belong to a three-membered electron transfer chain (equation 2):

$$[MoO(S–S)_2]^0 \rightleftharpoons [MoO(S–S)_2]^{-1} \rightleftharpoons [MoO(S–S)_2]^{-2} \qquad (2)$$

Many of these complexes also participated in oxygen-atom transfer reactions, giving dioxomolybdenum(VI) species and reduced substrates, and associated kinetic studies have been reviewed.**[15]**

Iodine oxidation of $[MoO(S_2C_2R_2)_2]^{2-}$ afforded $[MoO(S_2C_2R_2)_2]^-$ (R = H, Me, Ph; H/CN), the central member of the electron transfer chain $[MoO(S_2C_2R_2)_2]^z$ shown in equation (2). Similarly, ferrocenium ion oxidation of $[MoO\{SC(H)C(R)S\}_2]^{2-}$ [R = Ph, pyridinyl, quinoxalin-2-yl, 2(dimethylaminomethyleneamino)-3-methyl-4-oxopteridin-6-yl] and $[MoO(qdt)_2]^{2-}$ afforded monoanions. $[MoO(qdt)_2]^-$ was thermochromic due to thermally driven intramolecular charge transfer processes. However, chemical or electrochemical oxidation of $[MoO(mnt)_2]^{2-}$ to the corresponding monoanion resulted in its disproportionation to $[Mo(mnt)_3]^{2-}$ (formally containing Mo^{IV}) and MoO_3. When generation of $[MoO(mnt)_2]^-$ was carried out in the presence of Cl^-, $[MoOCl(mnt)_2]^{2-}$ was formed. Oxidation of $[MoO(dmit)_2]^{2-}$ likewise afforded $[MoO(dmit)_2]^-$, fully or partially oxidized salts of this monoanion exhibiting interesting electrical properties.

Reaction of $[MoO(S–S)_2]^-$ (S–S = $S_2C_2Me_2$, bdt) with SR'^- gave $[MoO(SR')_2(S–S)_2]^-$ (R = 2-Ad, $C_6H_2Pr^i_3$-2,4,6), which exhibited rhombic EPR spectra and underwent reversible electrochemical reduction.

Modeling of the pterin-dithiolate center in Mo enzymes has provided the spur for much work of oxodithiolene complexes in which the metal is formally in oxidation state VI. This included the synthesis of $[MoO_2(mnt)_2]^{2-}$, $[MoO_2\{S_2C_2(CO_2Me)_2\}_2]^{2-}$, $[MoO_2(bdt)_2]^{2-}$, $[MoO_2(S_2C_6H_3R)_2]^{2-}$ [R = H (≡bdt), R = 4-Me (≡tdt), R = 3-$SiPh_3$]. These complexes have distorted octahedral structures with cis-dioxo groups, and resonance Raman spectral studies showed that the sulfur ligands exerted a trans influence on the oxo ligands, and not *vice versa*, as might have been expected. Mo K- and $L_{2,3}$-edge X-ray absorption spectroscopy (XAS) data for these and related complexes have been reported. Some of these complexes reacted with silyl chlorides giving mono(oxo) silyloxo species, for example, $[MoO(OSiBu^tPh_2)(bdt)_2]^-$, and $[Mo(OPh)(S_2C_2Me_2)_2]^-$ reacted with Me_3NO giving $[MoO(OPh)(S_2C_2Me_2)_2]^-$. These species also have octahedral structures in which the oxo and alkoxo groups are mutually cis. Reaction of $[MoO_2(OSiPh_3)_2]$ with Li_2bdt afforded $[MoO_2(OSiPh_3)(bdt)]^-$ which reacted further with $(SC_6H_2Pr^i_3\text{-}2,4,6)^-$ giving $[MoO_2(bdt)(SC_6H_2Pr^i_3\text{-}2,4,6)]^-$, a structural model for sulfite oxidase. These anions have square-pyramidal (pseudotetrahedral) structures.

4.5 Complexes with N/S-Donor Atom Sets

Cis-dioxomolybdenum(VI) complexes of sterically bulky (thiolato)pyridine (**41**) and bi(thiolato)pyridine (**42**) ligands were designed to prevent comproportionation and maintain mononuclearity during oxygen-atom transfer reactions. The complex with (**41**) had a distorted octahedral structure and achieved its designed objective, whereas that with (**42**) did not, having trigonal bipyramidal structure with axial thiolate donors.

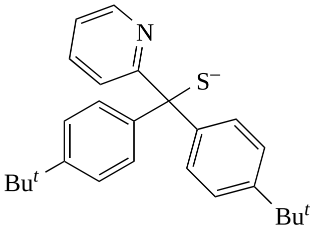

(**41**)

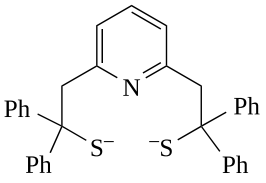

(**42**)

The Schiff bases (**23**), (**43**), and (**44**) formed Mo^{VI} complexes of the type *cis,mer*-$[MoO_2(ligand)]$ (which was associated in the solid state) and *cis,mer*-$[MoO_2(ligand)L]$ (L = neutral donor). The structures, electrochemical and chemical properties of these complexes, and their oxygen-atom transfer capabilities were extensive studies. These species were generally more active catalysts than their N–O–O-donor atom Schiff base counterparts, but oxygen-atom abstraction reactions with tertiary phosphines led to dinuclear Mo^V species rather than monomeric Mo^{IV} complexes.

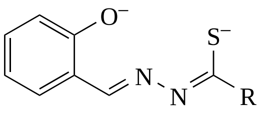

(**43**)

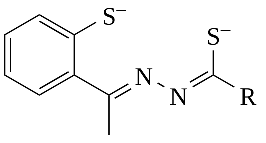

(**44**)

4.6 Complexes of Chalcogenide, Persulfide, and Polychalcogenide Ions

Thio Mo^V centers are implicated in the turnover of industrial catalysts and enzymes, but mononuclear thiomolybdenyl complexes are rare. Examples include $[MoSTp^*X_2]$, where X = OPh, OC_6H_4X-2 (X = SEt, Pr); X_2 = catecholate, tdt, bdt. These species have octahedral structures with short Mo=S bonds ($d_{Mo\text{–}S} = 2.13$ Å).

Reaction of $[Mo(NRAr)_3]$ with S_8, ethylene sulfide, Se, and Te/PEt_3 afforded $[MoE(NRAr)_3]$ (E = Ss, Se, Te). These species were paramagnetic ($\mu = 1.6\text{–}1.9$ BM) and have distorted tetrahedral structures ($d_{Mo\text{–}E} = 2.17$ (S), 2.31 (Se), 2.54 (Te) Å), respectively. A pentagonal-bipyramidal persulfide complex, $[MoO(S_2)_2(bipy)]$ has also been described ($d_{S\text{–}S} = 2.04\text{–}2.06$ Å).

Reaction of $[Mo(CO)_3Tp^z]^-$ (Tp^z = Tp, Tp*) with S_8 afforded $[MoSTp^z(S_4)]$ which has a distorted octahedral geometry. Treatment of $[Mo(=O)_2Tp^*X]$ with B_2S_3 and H_2S mixtures afforded $[MoTp^*X(S_4)]$ (X = halide, NCS). These complexes have very short Mo–S distances ($d_{Mo\text{–}S} = 2.19$ Å), and the alternation of the S–S distances within and the planarity of the MoS_4 ring system implied strong Mo–S $d_\pi\text{–}p_\pi$ bonding.

Nonoxo, mixed-cage ligand complexes, $[Mo(AsSe_5)_2]^{2-}$, $[Mo(CO)_2(As_3Se_5)_2]^{2-}$ have been described, the first containing long intramolecular Se···Se interactions indicative of partial internal redox behavior.

5 COMPLEXES WITH N-DONOR ATOMS

Although complexes containing C-donor atoms (except occasionally carbonyls and isonitriles) are not the subject of this section, a major aspect of the chemistry of molybdenum with particular N-donor atom ligands involves carbide, {Mo≡C:}, alkylidyne, {Mo≡CR}, alkylidene {Mo=CRR′} and alkyl, {Mo–R}, species. These species, and in particular, the alkylidyne and alkylidenes, are extremely important as catalysts for olefin metathesis, ‘living’ ring-opening metathesis polymerization, ring-closing metathesis reactions, and other processes of industrial significance. Many aspects of the chemistry of these have been extensively reviewed[16–18] and comprehensive reports published, so they are not described in detail here.[6,19]

5.1 Carbido Complexes

The carbido anion $[MoC(NRAr)_3]^-$ (R = $C(CD_3)_2CH_3$; Ar = $C_6H_3Me_2$-2,5) was obtained from three-coordinate $[Mo(NRAr)_3]$ (**45**) via $[Mo(CO)(NRAr)_3]$ and the latter's decarbonylation and reduction using sodium amalgam, followed by deprotonation of $[Mo(CH)(NRAr)_3]$ using KBz. The carbide anion is a strong reductant and nucleophile, forming alkylidyne derivatives readily.

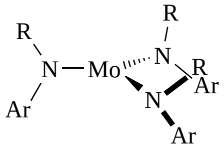

(**45**)

5.2 Nitrido Complexes

The structures and spectroscopic properties of, and aspects of bonding in molybdenum nitrido complexes have been reviewed.**[6,18,20,21]** Generally, the {Mo≡N} group only occurs in relatively simple mononuclear compounds or complexes, but $[MoN_4]^{6-}$ occurred in melt products, stabilized by Ba^{2+} or Sr^{2+}. Nitrido complexes may have tetrahedral, square-pyramidal, or octahedral geometries, and the nitrido ligand normally occupies apical or axial positions, exerting a strong trans influence. The nitrido ligands themselves may interact with neighboring metal centers, counterions, or lattice molecules.

Nitrido–Mo^V complexes are restricted to porphyrin and phthalocyanine derivatives and are discussed in Section 5.7.

Reaction of the Mo^0 bis(dinitrogen) complex containing tetradentate 3,3,7,7,11,11,15,15-octamethyl-1,5,9,13-tetrathiacyclhexadecane, $Me_8[16]aneS_4$ with Me_3SiN_3 afforded the molybdenum(VI) complex *trans*-$[MoN(N_3)\{Me_8[16]aneS_4\}]$. Protonation or reaction of this with acetone or benzaldehyde afforded *trans*-$[Mo(NH^+\cdots{}^-OTf)(OTf)\{Me_8[16]aneS_4\}]$ and *trans*-$[Mo\{NCRR'(OH^+\cdots{}^-OTf)(OTf)\}\{Me_8[16]aneS_4\}]$ ($R = R' = Me$; $R = H$, $R' = Ph$), respectively, these complexes having $\angle Mo{=}N{-}C > 174°$. Treatment of *trans*-$[Mo(N_2)_2(depe)_2]$ with Me_3SiN_3 also gave *trans*-$[MoN(N_3)(depe)_2]$ and the mixed-valence species $[\{Mo^{IV}N(N_3)(depe)_2\}_2\{\mu\text{-}Mo^{V}N(N_3)_2\}]$.

Reaction of $[Mo(NRAr)_3]$ with many simple nitrogen-containing molecules, for example, N_2O, arylazides, and following reduction, N_2, resulted in formation of the molybdenum(VI) nitride $[MoN(NRAr)_3]$. These species are diamagnetic and have tetrahedral geometries, as shown by $[MoN(NBu^tPh)_3]$. Cleavage of N_2 by $[Mo(NRAr)_3]$ was catalyzed by N/Hg, and unusual intermediates, such as $[Mo(N_2)(NRAr)_3]^-$ (stabilized by coordination of $[Na(thf)_x]^+$) and $[\{Mo(NPr^iAr)_3\}_2(\mu\text{-}N)]$, have been characterized. Treatment of $[MoCl\{N(CH_2CH_2NR)_3\}]$ (**46**), ($R = SiMe_3$, Ar) with Me_3SiN_3 also afforded nitrido complexes, $[MoN\{N(CH_2CH_2NR)_3\}]$.

Treatment of $[\{MoNCl_3\}_4]$ with $LiOBu^t$ afforded $[MoN(OBu^t)_3]$ which readily underwent ligand exchange reactions giving $[MoN(OR)_3]$ ($R = Et$, Pr^i, CH_2Bu^t). These species are monomeric in solution but form linear polymers in the solid state. Anionic species such as $[MoN(OPh)_4]^-$ were obtained by treatment of $[MoNCl_4]^-$ with NaOPh. Relatively few thiolato nitrides are known, $[MoN(SR)_3]$ being prepared by reaction of $[MoN(OBu^t)_3]$ with RSH ($R = Pr^i$, Bu^t).

5.3 Imido Complexes

Although there are some parallels between imido and oxo-Mo^{IV} chemistries, the differences are more pronounced. Thus, there are many tetrahedral bis(imido) complexes of Mo^{IV} and apparently only one oxo counterpart. Reduction of $[Mo(NAr)_2Cl_2(dme)]$ by Mg in the presence of PMe_3 afforded $[Mo(NAr)_2(PMe_3)_2]$, which has a distorted tetrahedral geometry with linear Mo=N–C bonds. This complex, and its *t*-butyl analog $[Mo(NBu^t)_2(PMe_3)_2]$, underwent phosphine exchange reactions, and reaction with the diphosphene $Ar'P{=}PAr'$ ($Ar' = C_6H_2(CF_3)_3$-2,4,6) afforded the unusual species $[Mo(NR)_2(PMe_3)(\eta^2\text{-}Ar'P{=}PAr')]$, which has a pseudotetrahedral structure.

Trans-$[Mo^{IV}N(N_3)(depe)_2]$ and $[\{Mo^{IV}N(N_3)(depe)_2\}_2\{\mu\text{-}Mo^{V}N(N_3)_2\}]$ acted as precursors for *trans*-$[Mo(NH)X(depe)_2]^+$ ($X = Cl$, N_3) and *trans*-$[Mo(NMe)(N_3)(depe)_2]^+$, and an electrochemical study established that related dppe complexes would be reduced in an overall four-electron process releasing RNH_2 and regenerating *trans*-$[Mo(N_2)_2(dppe)_2]$. Protonation of the nitrile α-carbon atom in $[Mo(N_2)(NCR)(dppe)_2]$ afforded alkyl- and benzylimido complexes, $[Mo(NCH_2R)X(dppe)_2]^+$.

Sodium amalgam reduction of *cis,mer*-$[Mo(NR)Cl_2L]$ ($L = 2PR'_3$ or dme) in the presence of PR'_3 gave $[Mo(NR)Cl_2(PR')_3]$, which has an octahedral geometry and an essentially linear Mo=N–C bond angle. Oxidation addition of RNCO ($R = Bu^t$, C_6H_4Me-*p*) to $[MoCl_2(PMePh_2)_4]$ afforded $[Mo(NR)Cl_2(CO)(PMePh_2)_2]$, although reaction of *p*-MeC_6H_4NCO with $[MoCl_2(PMe_3)_4]$ afforded an equilibrium mixture of $[Mo(NC_6H_4Me\text{-}p)Cl_2(CO)(PMe_3)_2]$ and $[Mo(NC_6H_4Me\text{-}p)Cl_2(PMe_3)_3]$. Reaction of *mer*-$[Mo(NPh)\{(Me_3SiN)_2C_6H_4\}(PMe_3)_3]$ with H_2 at −10 °C gave $[Mo(NPh)(\kappa^2\text{-}H_2)\{(Me_3SiN)_2C_6H_4\}(PMe_3)_3]$, (**47**) ($d_{H-H} = 1.17$ Å), which transformed into *mer*-$[Mo(NPh)\{(Me_3SiN)(NH)C_6H_4\}(PMe_3)_3]$, with loss of $SiHMe_3$, at 30 °C.

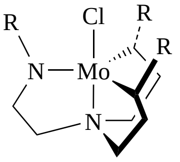

(**46**)

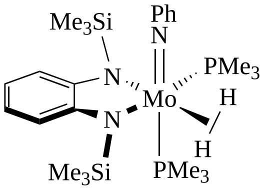

(**47**)

The most common imido-$\mathrm{Mo^{V}}$ species are of the type *mer*-$[\mathrm{Mo(NR)Cl_3L_2}]$ (L = neutral ligand, $\angle\mathrm{Mo{=}N{-}C} > 175°$). A general synthetic route involved the comproportionation of $[\mathrm{Mo^{VI}(NR)_2Cl_2(dme)_2}]$ with $[\mathrm{Mo^{IV}Cl_4(thf)_2}]$, which gave *mer*-$[\mathrm{Mo(NR)Cl_3(dme)}]$.

Phosphiniminato $\mathrm{Mo^{V}}$ complexes are relatively rare, but include *trans*-$[\mathrm{Mo(NPPh_3)Cl_4py}]\cdot\mathrm{CH_2Cl_2}$ ($\angle\mathrm{Mo{=}N{-}C}$ 177°) and $[\mathrm{Mo(NPPh_3)Cl_5}]^-$.

Research on imido complexes has been stimulated by the role of imido molybdenum(VI) species in ammonia and amine oxidation, and because of the isolobal relationship between $[\mathrm{Mo(NR)_2X_2}]$ and the catalytically active Ti and Zr catalysts $[\mathrm{M}(\eta^5\text{-}\mathrm{C_5H_5})_2\mathrm{X_2}]$.**18** The $\mathrm{NR^{2-}}$ ligand may be regarded as a four-electron π-donor, being isoelectronic with the widely encountered oxo ligand. There are many parallels between the chemistry of molybdenum oxo and imido species, but imido species having four-coordination and the metal in a low oxidation state have no counterpart in oxomolybdenum chemistry. Imido ligands are classified as bent ($\angle\mathrm{Mo{=}N{-}R} < 150°$) with an $\mathrm{sp^2}$-hybridized N atom, or essentially linear, with an sp-hybridized N atom. The only two substantiated cases of bent, nonchelating imido ligand complexes are $[\mathrm{Mo(NPh)_2(S_2CNEt_2)_2}]$ and $[\mathrm{Mo(NAr)_2(pdpe)}]$ [$\mathrm{pdpeH_2}$ = pyridine-2,6-bis(2,2-diphenylethanol)], although there are some borderline cases. Mono(imido) complexes may be five-, six-, or seven-coordinate, with trigonal bipyramidal, octahedral, or pentagonal-bipyramidal geometries. Bis(imido) complexes may adopt, four-, five-, or seven-coordination, and tetrahedral, trigonal bipyramidal, square-pyramidal, or octahedral geometries are common. The two imido ligands adopt a cis arrangement, like all other π-donor ligand complexes of $\mathrm{Mo^{VI}}$, in order to facilitate effective π-donation into empty metal orbitals. In addition, π-donor ligands prefer to be *cis* to the imido groups, the weakest π-donors binding to sites trans to the $\mathrm{NR^{2-}}$ ligand.**18,22**

Deprotonation of $[\mathrm{Mo^{VI}(NBu^t)_2(NHBu^t)_2}]$ by LiMe in ether afforded $\mathrm{Li_4[Mo_2(NBu^t)_8]}$ and reaction with $\mathrm{AlX_3}$ (X = Me, Cl) afforded monomeric $[\mathrm{Mo}(\mu\text{-}\mathrm{NBu^t})_4(\mathrm{AlX_2})_2]$. Reaction of $[\mathrm{Mo(NAr)_2Cl_2(thf)_2}]$ with two equivalents of LiNHAr afforded the kinetically unstable $[\mathrm{Mo(NAr)_3Cl}]^-$, which provided access to $[\mathrm{Mo(NAr)_3(PMe_3)}]$ and $[\mathrm{Mo(NAr)_3Br}]^-$.

Bis(imido) complexes, *cis*-$[\mathrm{Mo(NR)_2Cl_2L_2}]$ (R = alkyl, aryl) were obtained from molybdate, amines, or anilines, $\mathrm{Me_3SiCl}$ and $\mathrm{NEt_3}$ in solvents such as dme ($\mathrm{L_2}$), pyridine, or thf (L). These were useful for the formation of other complexes by metathesis or ligand exchange, giving species such as $[\mathrm{Mo(NR)_2(OBu^t)_2}]$, $[\mathrm{Mo(NAr)_2Cl(NEt_2)}]$, and $[\mathrm{Mo(NAr)_2(NHAr)_2}]$. Thiolato species $[\mathrm{Mo(NR)_2(SAr)_2}]$ (R = Mes, Ar) have also been described. Monoanionic bidentate ligands such as deprotonated 8-hydroxyquinoline, $[\mathrm{OC_6H_4CH_2NMe_2\text{-}2}]^-$ and a range of bidentate pyrrolide or arene species carrying $\mathrm{NMe_2}$ groups (L–L) formed $[\mathrm{Mo(NR)_2Cl(L{-}L)}]$ and $[\mathrm{Mo(NR)_2(L{-}L)_2}]$.

Chelating imides have been generated by reaction of *o*-$\mathrm{(Me_3SiNH)_2C_6H_4}$ with $[\mathrm{Mo(NPh)_2Cl_2(dme)}]$. Complexes such as $[\mathrm{Mo(NPh)_2\{(Me_3Si)(H)NC_6H_4\}Cl_2}]$ exist in an equilibrium such as that shown in Figure 4, and reaction with Lewis bases caused displacement of the aniline.

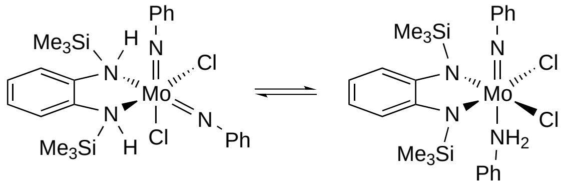

Figure 4 Imide/amine equilibria in $[\mathrm{Mo(NPh)_2\{(Me_3Si)(H)NC_6H_4\}Cl_2}]$

Because ansa metallocenes had been found to be effective polymerization catalysts, exploration of chelating bis(arylimido) complexes has been undertaken, typical examples being (**48**–**51**). In general, these have distorted octahedral structures with $d_{\mathrm{Mo{-}N}}$ in the range 1.73–1.75 Å and $\angle\mathrm{Mo{=}N{-}R}$ in the range 155–162°. Complex (**51**), which is chiral, catalyzed the kinetic resolution of styrene oxide with an e.e of 30%.

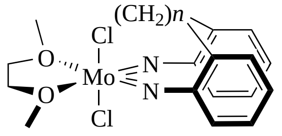

(**48**)

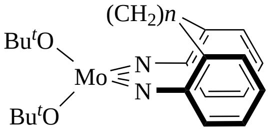

(**49**)

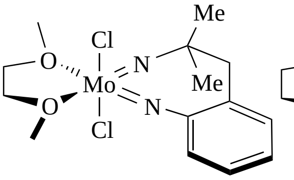

(**50**)

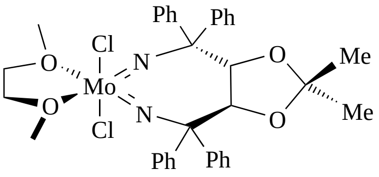

(**51**)

Reaction of $[\mathrm{MoCl_4(thf)_2}]$ with *p*-tolylazide afforded $[\mathrm{Mo(Ntol)Cl_4(thf)}]$ in which the thf is trans to the imido group, as expected.

The calix[4]arenes, $\mathrm{(HO)_4R'cal}$ (Figure 1, R = H; R′ = H or $\mathrm{Bu^t}$), reacted with $\mathrm{Mo^{VI}}$ imido species $[\mathrm{Mo(NAr)_2(OBu^t)_2}]$, $[\mathrm{Mo(NBu^t)_2(NHBu^t)_2}]$, $[\mathrm{Mo(NMes)_2Cl_2(dme)}]$ giving calixarene complexes $[\mathrm{Mo(NR')(O_4R'cal)L}]$ (R′ = H, R″ = Ar, L = NCMe; R′ = $\mathrm{Bu^t}$, R″ = Ar, $\mathrm{Bu^t}$, Mes, L = NCMe, $\mathrm{CNBu^t}$, $\mathrm{OH_2}$), (**52**).

Reaction of substituted anilines with $[\mathrm{MoOCl_2(S_2CNEt_2)_2}]$ afforded $[\mathrm{Mo(NAr)Cl_2(S_2CNEt_2)_2}]$, the X-ray structural determination of the complexes with Ar = $\mathrm{C_6H_4NH_2\text{-}2}$ confirming the expected pentagonal-bipyramidal geometry and an axial imido group ($\angle\mathrm{Mo{=}N{-}C}$ 178°.). Similarly, seven-coordinate $[\mathrm{Mo(NR)(S_2)(S_2CNEt_2)_2}]$ (R = alkyl, aryl) was obtained by reaction of $[\mathrm{MoO_2(S_2CNR'_2)_2}]$ with RNCO

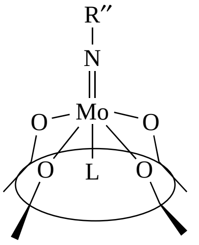

(**52**)

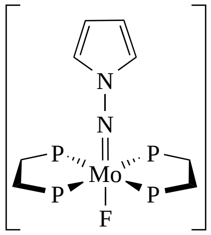

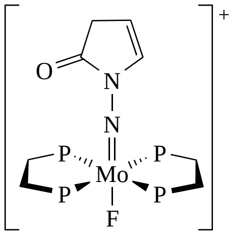

(**53**) (**54**)

or $[Mo(NR)_2(S_2CNEt_2)_2]$ with H_2S or Lawesson's reagent. The Mo=N–C bond angles in these species varied from 165 to 179°.

Reaction of $[Mo(NSCl)Cl_4]$, $[Mo(N_3S_2)Cl_3]$, or $[\{MoNCl_3\}_4]$ with fluorine afforded $[Mo(=NCl)F_4]$ which converted to the octahedral $[Mo(NCl)F_4(solvent)]$ (solvent = NCMe or thf) in solution. The Mo=N–Cl bond angle in this and the related anion $[Mo(NCl)F_5]^-$ (as the Na{15-C-5}$^+$ salt), was in the range 176−177°.

Mixed imido-oxo complexes are relatively rare, but could be obtained by incomplete reaction of some amines and anilines with molybdate, Me_3SiCl, and NEt_3 in dme or pyridine, by reaction of $[MoO_2Cl_2(NCMe)_2]$ with one equivalent of RNCO followed by derivatization, or oxo/imido ligand metathesis of $[Mo(NMes)_2Cl_2(dme)]$ and $[MoO_2Cl_2(dme)]$. These complexes generally adopted distorted octahedral structures with cis imido and oxo ligands, with ∠Mo=N–C >154° (mostly >168°).

5.4 Hydrazido and Organohydrazido Complexes

There are parallels between the chemistry of imido and hydrazido complexes, mainly because of the common Mo=N– link. Nitrosyl hydrazido complexes are described in Section 5.8.

Hydrazido and organohydrazido ligands are important intermediates in the reduction or utilization of N_2 in biological and chemical systems, and their molybdenum complexes are potential catalysts for alkene polymerization and metathesis reactions.

Continued work on the protonation of dinitrogen complexes has afforded a range of complexes, including *syn,trans*-$[Mo(NNH_2)X(bdpe)(PPh_3)]^+$ [bdpe = $(Ph_2PCH_2CH_2)_2PPh$], and closely related derivatives. There has also been further development of electrochemical methods for the cleavage of hydrazido ligands to form ammonia. Reaction of *trans*-$[Mo(NNH_2)F(dppe)_2]^+$ with tetrahydro- and dihydrofurans afforded (**53**) and (**54**), work which led to the development of a system for the conversion of dinitrogen to pyrrole and *N*-aminopyrrole.

Alkylation of $[Na(thf)_n{}^+][Mo(N_2{}^-)(NRAr)_3]$ afforded $[Mo(NNR')(NRAr)_3]$. A range of *cis*-bis(diazenido) complexes containing bidentate S–S, N–S, S–O, N–O, and O–O ligands, or tetradentate N_2S_2 and N_4 macrocyclic ligands have been characterized. These are of the form $[Mo(NNAr)_2(L–L)_2]$, where L–L is a bidentate ligand or $[Mo(NNAr)_2](Q)$ (Q a tetradentate ligand), and they generally have distorted octahedral structures. Pentagonal-bipyramidal mono(diazenido) species $[Mo(NNAr)L_2]$ are also well-characterized.

Hydrazido(2−) complexes of Mo^V are uncommon, but include $[Mo(NNRR')X_3]$, $[Mo(NNRR')X_3L]$, and $[Mo(NNRR')X_3(L–L)]$ (R, R′ = Me, Ph, X = halide, L = PR_3, and L–L = dppe and other chelating diphosphines). Treatment of $[Mo(N_2)_2(dppe)(MePPh_2)_2]$ with HX/ZnX_2 afforded $[Mo(NNH_2)X_3(dppe)]$ (X = Cl, Br), the species with X = Br containing a linear hydrazido(2−) ligand, (∠Mo=N–N 173°). This complex reacted with further acid to release N_2, NH_3, and H_2NNH_2.

Molybdenum(VI) hydrazido(2−) complexes are frequently generated by the condensation of alkyl or aryl hydrazines with dioxomolybdenum precursors. Such reactions usually afforded mixed hydrazido or bis(hydrazido) species. $[Mo(NBu^t)_2Cl_2(dme)]$ reacted with $H_2NNPh_2{\cdot}HCl$ in refluxing dme to give *cis,trans*-$[Mo(NNPh_2)_2Cl_2(dme)]$ which, on treatment with Mg in the presence of PMe_3, afforded $[Mo(NNPh_2)_2Cl_2(PMe_3)_2]$. This latter species had an unexpected cis,cis,trans structure with linear hydrazido(2−) groups. Attempts to prepare it in a 'one-pot' procedure gave $[Mo(NNPh_2)(NHNPh_2)Cl_4]^-$, which contained both hydrazido(2−) and hydrazido(1−) ligands. The similar mixed ligand species *cis,trans*-$[Mo(NNRPh)(NHNRPh)X_2(acac)]$ was formed by reaction of $[MoO_2(acac)_2]$ with $H_2NNRPh{\cdot}HX$ (R = Me, Ph; X = halide).

Monohydrazido complexes, formulated either as $[Mo(NNRR')Cl_4]$ or $[Mo(NNRR')Cl_3]$, were formed by reaction of $MoCl_5$ with H_2NNRR' (R = R′ = Ph; R = Me, R′ = Ph), but their precise structure remains uncertain.

Like their imido analogues, mixed hydrazido(2−) oxomolybdenum complexes have been prepared, including *cis,trans*-$[Mo(NNRPh)](O)X_2(bipy)$ (X = halide) and $[Mo(NNRPh)(O)(acac)_2]$.

5.5 Amido Complexes

The important compound $[Mo^{III}(NRAr)_3]$ (**45**) is conveniently made by reaction of $[MoCl_3(thf)_3]$ with $Li[NRAr](OEt_2)$ under argon. This species has a trigonal planar structure with $d_{Mo–N} = 1.96$ Å, the steric bulk of the R/Ar groups being extremely important in preventing dinucleation and formation of Mo≡Mo bonds. These three-coordinate complexes are paramagnetic, $\mu = 3.4–3.9$ BM, consistent with an $S = 3/2$ ground state $\{a(\text{n})^1e(\text{n})^2$ configuration$\}$. However, the complex formally represented as [Mo(NPr^{i}Ar)$_3$] contains a cyclometalated group and a hydride ligand, (**55**), but remains paramagnetic, $\mu = 2.1$ BM. This remarkable complex induced the cleavage of N_2 giving [{Mo(NPr^{i}Ar)$_3$}$_2$(μ-N)] which could be reduced by sodium amalgam to a monoanion. This monoanionic species reacted further with N_2 to give [Mo(N$_2$)(NPr^{i}Ar)$_3$]$^-$ and [MoN(NPr^{i}Ar)$_3$].[Mo(NPr^{i}Ar)$_3$] also effected the reductive coupling of nitriles.

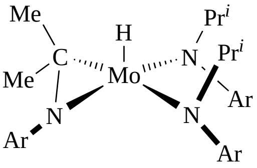

(**55**)

Reduction of (**46**) with magnesium in the presence of N_2 afforded [(thf)$_2$Mg{–N=N–Mo^{III}[N(CH$_2$CH$_2$NR)$_3$]}$_2$] which, on treatment with Pd^{II} species, was converted to [Mo^{III}(N$_2$){N(CH$_2$CH$_2$NR)$_3$}]. Reaction of this last compound with CO gave the corresponding carbonyl [Mo^{III}(CO){N(CH$_2$CH$_2$NR)$_3$}] which was converted by SiClMe$_3$ into [Mo^{VI}{≡C(OSiMe$_3$)}{N(CH$_2$CH$_2$NR)$_3$}]. Dinitrogen was displaced by isonitriles from [Mo^{III}(N$_2$){N(CH$_2$CH$_2$NR)$_3$}] giving [Mo^{III}(CNR){N(CH$_2$CH$_2$NR)$_3$}] which, on heating, afforded [Mo^{IV}(CN){N(CH$_2$CH$_2$NR)$_3$}] and which could be oxidized to [Mo^{IV}(CNR){N(CH$_2$CH$_2$NR)$_3$}]$^+$.

Treatment of [Mo(NMe$_2$)$_4$] with LiNMe$_2$ in thf afforded [Li(thf)$_2$][Mo^{IV}(NMe$_2$)$_6$] in which octahedral {Mo(NMe$_2$)$_6$} units are associated with two opposite face-capping Li(thf)$_2$ groups. Reaction of [Mo(NMe$_2$)$_4$] with PHPh$_2$ or LiPBu$^t_2$ gave [Mo(NMe$_2$)$_2$(PR$_2$)$_2$] which had a tetrahedral structure.

Direct protonation of *trans*-[MoN(N$_3$)(dppe)$_2$] or *trans*-[Mo(NH)(OMe)(dppe)]$^+$ by triflic acid afforded *trans*-[Mo(NH$_2$)(OH)(dppe)$_2$]$^+$ which was octahedral, with $d_{\text{Mo–N}} = 2.05$ Å.

Paramagnetic [Mo(NBu^{t}Ar)$_3$X] (X = Cl, Br) was formed in reaction of [Mo(NBu^{t}Ar)$_3$] with X$_2$ or CH$_2$Cl$_2$. This tetrahedral species was an active catalyst for many alkyne metathesis reactions. The related triamidoamine complex (**46**) was obtained by reaction of [MoCl$_4$(thf)$_2$] or [MoCl$_3$(thf)$_3$] with Li[N(CH$_2$CH$_2$NR)$_3$]. This complex is paramagnetic ($\mu = 2.92$ BM) and has a trigonal bipyramidal structure. Reaction of (**46**) with LiNMe$_2$, ferrocenium triflate, and Me$_3$SiN$_3$ afforded [Mo^{IV}(NMe$_2$){N(CH$_2$CH$_2$NR)$_3$}], [Mo^{IV}(OTf){N(CH$_2$CH$_2$NR)$_3$}], and [Mo^{VI}N{N(CH$_2$CH$_2$NR)$_3$}], respectively. Treatment of (**46**) with Me$_3$SiN$_3$ and with LiPHPh gave [Mo^{VI}E{N(CH$_2$CH$_2$NR)$_3$}] (E = N or P), and reaction of [Mo^{VI}N{N(CH$_2$CH$_2$NR)$_3$}] with ROTf afforded the imido species [Mo^{VI}(NR){N(CH$_2$CH$_2$NR)$_3$}][OTf] which could be reduced by lithium cyclooctatetraenide to give the Mo^V complex [Mo^V(NR){N(CH$_2$CH$_2$NR)$_3$}].

Oxidation of [Mo(NRAr)$_3$] with pyridine N-oxide afforded the paramagnetic tetrahedral oxomolybdenum(V) compound [MoO(NRAr)$_3$]. Alkyl elimination from this afforded [MoO(NAr)(NRAr)$_2$] while oxidation gave [MoO(NRAr)$_3$]$^+$.

Reaction of [Mo(NMe$_2$)$_4$] with dry oxygen afforded blue [Mo(NMe$_2$)$_6$] whose X-ray crystal structure confirmed its octahedral structure (overall T_h symmetry, $d_{\text{Mo–N}} = 2.03$ Å). Reaction of [{MoNCl$_3$}$_4$] with Me$_3$SiN=PR$_3$ (R = Me, Ph) produced [Mo(N=PR$_3$)$_4$]$^{2+}$, while reaction of [MoN(N=PPh$_3$)$_3$] with BF$_3$OEt$_2$ afforded [Mo(N=PPh$_3$)$_4$][BF$_4$]$_2$. Phosphiniminato complexes have been reviewed.**[23]**

5.6 Tris(pyrazolyl)borato and Related Triaza Ligand Complexes

5.6.1 Tris(pyrazolyl)borato Complexes

The chemistry of complexes containing a variety of tris(pyrazolyl)borato ligands (**56**) expanded substantially during the past decade, primarily in connection with oxomolybdenum(V), {MoO}$^{3+}$, and nitrosyl complexes containing the groups {Mo(NO)}$^{3+}$ and {Mo(NO)}$^{2+}$. These two sets of complexes were characterized by their ability to undergo reversible or quasi-reversible electron transfer processes which, in some cases, involved ligand redox behavior in addition to oxidation or reduction of the metal. Tris(pyrazolyl)borato ligands afforded a remarkable series of complexes where the interrelationship between electronic and magnetic behavior could be linked to the topology of the bridging ligands. The chemistry and physical behavior of this group of complexes has been extensively reviewed.**[24–27]**

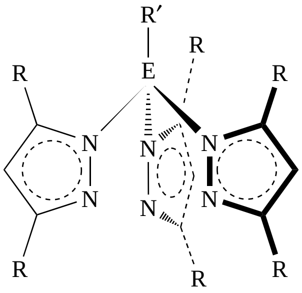

(**56**)

Tp$^-$, E = H, R′ = R = H

Tp*$^-$, E = H, R′ = H, R = Me

Tpm*$^-$, E = H, R = Me

Oxidation of [Mo(CO)$_3$Tp*]$^-$ by ferrocenium salts afforded the paramagnetic mononuclear Mo^I species [Mo(CO)$_3$Tp*] ($\mu = 2.13$ BM) which was octahedral (pseudo C_{3v} symmetry).

Related phosphine-substituted complexes $[Mo(CO)_2(PR_3)Tp]$ have also been described.

The largest range of complexes containing molybdenum in the formal oxidation state I are the nitrosyls $[Mo(NO)Tp^*XL]$ (L = pyridines, pyrrolidine, and related species). These complexes are octahedral, with linear Mo–N–O bond arrangements, and are paramagnetic (1 unpaired electron). These complexes underwent one-electron oxidation and one-electron reduction, achieved chemically and electrochemically, spectroelectrochemical examination revealing that the former process was largely metal-based, whereas the latter had substantial ligand involvement.**[24,27]**

Paramagnetic di-, tri- and tetranuclear species containing the $\{Mo(NO)Tp^*X\}$ core linked by a range of oligopyridines have also been described, these complexes also exhibiting extensive redox behavior. For example, complexes containing the dipyridyl ligand 4,4′-$NC_5H_4CH{=}CHC_5H_4N$ (dpe) existed within a five-membered electron transfer chain, (equation 3). Spectroelectrochemical studies of the reduced species showed that electron addition afforded metal-stabilized radical anion and dianionic ligands. Oxidation to the mono- and dicationic species was mainly a metal-based process and usually appeared in cyclic voltammograms as two coincident oxidation waves. An exception occurred with the pyrazine complex $[\{Mo(NO)Tp^*Cl\}_2pz]$, where all five species could be identified electrochemically and were characterized by EPR and IR spectrometry. Species containing $\{Mo(NO)\}^{2+}$ have one unpaired electron (17 valence electrons), and in the oligonuclear species, there was substantial evidence for long range (up to 30 Å) but weak coupling between the unpaired spins. The magnetic behavior of dinuclear complexes was examined extensively, leading to reliable predictions of antiferromagnetic and ferromagnetic coupling between the unpaired spins on each $\{Mo(NO)\}^{2+}$ center.**[24,26,27]**

$$\begin{aligned}[\{Mo(NO)Tp^*Cl\}_2(dpe)]^{2+} &\rightleftharpoons [\{Mo(NO)Tp^*Cl\}_2(dpe)]^{+}\\ &\rightleftharpoons [\{Mo(NO)Tp^*Cl\}_2(dpe)]^{0}\\ &\rightleftharpoons [\{Mo(NO)Tp^*Cl\}_2(dpe)]^{1-}\\ &\rightleftharpoons [\{Mo(NO)Tp^*Cl\}_2(dpe)]^{2-} \qquad (3)\end{aligned}$$

Halogen oxidation of $[Mo(CO)_3Tp]^-$ afforded the Mo^{II} complex $[Mo(CO)_3TpX]$ (X = Br, I), and oxidation of the Tp^* analogue by $PhCl_2$ or I_2 afforded the unstable $[Mo(CO)_3Tp^*X]$ which converted to paramagnetic $[Mo(CO)_2Tp^*X]$ ($\mu = 2.8{-}3.0$ BM) on standing. The hydride ligand in the unstable $[Mo(CO)_3Tp^*H]$ was located between a pair of CO ligands, giving an overall 3:4 coordination environment.

A very large series of nitrosyl complexes, $[Mo(NO)Tp^*XY]$ has been described where X and Y are halide, alkoxide, aryloxide, alkyl or arylamide, alkyl or aryl thiolate groups. These diamagnetic $\{Mo(NO)\}^{3+}$ species are regarded as containing 16 valence electrons, with a formal metal oxidation state of II, assuming NO^+ binding, and the metal center could be regarded as electron-deficient. As a consequence, there is substantial p_π–d_π bonding between the donor atoms of X and Y and the metal. The complexes adopt octahedral structures, and may be reversibly reduced to paramagnetic (17 valence electron) monoanionic species, the potentials for this electron transfer process being dependent on the donor atoms and their substituents, occurring over a range of at least 2000 mV, probably currently the largest range for a single family of compounds.**[24]** A substantial number of di- and trinuclear species containing the redox-active $\{Mo(NO)\}^{3+}$ core, in which the bridging ligands are di or tri-hydroxy benzene and naphthalene derivatives, or their amino analogues, were also prepared. These complexes could be reduced electrochemically in at least two reversible or quasi-reversible one-electron steps, and several mixed-valence (mono-reduced) species exhibiting Class 1, 2, and 3 behavior were identified using a combination of spectroelectrochemical, EPR, and IR spectral techniques. Ferrocene moieties have been attached to the $\{Mo(NO)Tp^*X\}$ core giving, for example, $[FeC_6H_4CH{=}CHC_6H_4NHMo(NO)Tp^*X]$. These complexes were also redox active, the ferrocenyl group undergoing one-electron oxidation and the $\{Mo(NO)\}^{2+}$ group a one-electron reduction. These complexes were dipolar and solvatochromic, some of them exhibiting nonlinear optical behavior (frequency doubling) which could be switched on and off chemically and electrochemically.**[6]**

Treatment of $[MoO_2Tp^*X]$ with one equivalent of PR_3 in a donor solvent such as pyridine, NCMe, or DMF afforded mono-oxo Mo^{IV} complexes $[MoOTp^*X(solvent)]$, via a transient phosphine oxide adduct. One such adduct, $[MoOTp^{Pr}(OPh)(OPEt_3)]$ was structurally characterized, and a number of more stable oxo-Mo^{IV} species, such as $[MoOTp^*X(py)]$ (X = OPh or SPh), have also been prepared. All have distorted octahedral geometries, with short Mo=O bonds. Dinuclear Mo^{IV} species $[\{MoOTp^*Cl\}_2(\mu\text{-N–N})]$ (N–N = dipyridines) are apparently diamagnetic, but could be oxidized electrochemically in two steps corresponding to $Mo^{IV}Mo^V$ and Mo^VMo^V species. Reduction appeared to mainly involve the bridging dipyridine ligands.

As mentioned above, $[Mo^{VI}O_2Tp^xX]$ (x various pyrazolyl ring substituents) was readily reduced to relatively stable Mo^V species, $[MoO_2Tp^xX]^-$. These species exhibited broad anisotropic EPR signals at g 1.92, but readily protonated affording the conjugate acids $[MoOTp^x(OH)X]$ whose EPR signals are less anisotropic (g ca. 1.94). Treatment of $[MoO_2Tp^xX]$ with SH^- caused reduction to $[MoO_2Tp^xX]^-$ and then replacement of one oxo group by a sulfido group, giving $[MoOSTp^xX]^-$. The EPR spectra of these species were characterized by a larger g-value and reduced anisotropy compared to their dioxo-analogues.

An extensive range of complexes of the type $[MoOTp^*XY]$ (X, Y = halide and/or alkoxide, aryloxide, alkyl or arene thiolate, bidentate 1,2-arenediolates, arenedithiolates, ethane diolates, and dithiolates) has been prepared. These octahedral species underwent quasi-reversible one-electron reductions affording Mo^{IV} species, and, depending on the attached ligands, could also be oxidized to a monocation formally containing Mo^{VI}. These species have been studied by a range of spectroscopic and structural techniques partly because of their biological relevance. A large range of di- and trinuclear complexes containing the {MoOTp*Cl} fragment connected by bis- and tris-phenolato bridging ligands has also been prepared and characterized. These complexes exhibited a rich electrochemistry, like their $\{Mo(NO)\}^{2+/1+}$ analogues described above.**[24]** From spectroelectrochemical studies, it was established that oxidation of the dinuclear species could involve metal- or ligand-based processes, this system demonstrating 'non-innocent' behavior analogous to dithiolene and related complexes.**[25]** These complexes also displayed significant electronic and magnetic interactions between the metal centers which are controlled by the structure and properties of the bridging ligand. Detailed magnetic studies led to an understanding of the relationship between bridging ligand topology and magnetic coupling between the paramagnetic $\{MoO\}^{3+}$ ($S = 1/2$) centers, thereby facilitating the prediction of antiferromagnetic or ferromagnetic behavior.**[26,27]** The oxidized forms of some of the polynuclear complexes showed intense near-IR absorptions, behavior which lead to the construction of an embryonic electrochromic device.**[28]**

Thio-Mo^V species are implicated in the turnover of industrial catalysts and enzymes, but mononuclear thiomolybdenyl complexes are very rare. $[MoSTp^*Cl_2]$, one of the first complexes of this type, was obtained by reaction of $[MoOTp^*Cl_2]$ with B_2S_3, and related species $[MoSTp^*X_2]$ (X = aryloxide, alkane thiolate, X_2 = catecholate, benzene dithiolate) have been described.

The Mo^{IV} complex $[MoOTp^z(S_2PR_2)]$ reacted with B_2S_3 affording the thio analog, $[Mo^{IV}STp^z(S_2PR_2)]$. Both the oxo and thio complexes could be oxidized in a reversible one-electron step, affording monocationic Mo^V species. Oxidation of $[MoSTp^z(S_2PR_2)]$ afforded the Mo^{VI} complex $[MoOSTp^z(S_2PR_2)]$, which was also electrochemically active, reducing in a one-electron process to the corresponding Mo^V monoanion.

The Mo^{VI} and related Mo^V species $[MoNTp^*Cl_2]$ and $[MoNTp^*Cl_2]^-$ were formed when $[MoNCl_5]^{2-}$ was treated with Tp^{*-}. However, only $[MoNTp^*(N_3)_2]$ was formed when $[MoN(N_3)_4]^-$ reacted with Tp^{*-}.

Oxidative decarbonylation of $[Mo(CO)_3Tp^x]^-$ (Tp^x = Tp or Tp*, (**56**)) by dimethyldioxirane, $[Mo(CO)_3Tpm^*]^-$ or $[Mo(CO)_3(tpa)]$ by HNO_3 afforded $[MoO_3L]^z$, $z = -1$, where L = Tp, Tp*, or Tpm; $z = 0$, L = tpa (**57**).

A very large number of dioxo-Mo^{VI} species have been prepared in the development of biomimicry of Mo^{VI}–Mo^{IV} interconversion. Reaction of $[MoO_2X_2]$ (X = halide), $[MoO_2X_2L_2]$ (L = $OPPh_3$, dmso), or $[MoO_2(NCS)_4]^{2-}$ with Tp^x – afforded *fac*-$[MoO_2Tp^xX]$, from which closely related alkoxides or thiolates (X = OR, OAr, SR, SAr) were obtained by metathetical exchange. These complexes have distorted octahedral geometry and, unlike most dioxo-Mo^{VI} complexes, underwent reversible or pseudoreversible one-electron reductions, affording stable, epr-active Mo^V species. The redox potentials were influenced strongly by the nature of X, and correlated with Hammett functions. These Mo^{VI} complexes are extremely important models in the development of synthetic enzyme models encompassing many biologically relevant oxidation states, oxo centers, and reactions, and provided vital information on electronic structures. The oxygen-atom and coupled electron–proton transfer chemistries of this and related systems have been reviewed.**[29]**

$[MoOSTp^xX]$ was formed by O-atom abstraction from $[MoO_2Tp^xX]$ using PR_3. $[MoOTp^x(OPR_3)X]$ was formed initially, and treatment of this with sulfur-donors ultimately afforded the oxo-thio complex. Sulfur donation from propylene sulfide to $[Mo^{IV}OTp^x(S_2PR_2)]$ afforded $[MoOSTp^x(\kappa^1\text{-}S_2PPr_2)]$ whose structure was confirmed crystallographically, the oxo-thio center being stabilized by an S···S interaction. Reduction or oxidation of these complexes afforded corresponding Mo^V complexes, $[MoOSTp^x(\kappa^1\text{-}S_2PPR_2)]^-$ and $[MoOTp^x(S_3PR_2)]^-$ with concomitant S–S bond formation. The related $[MoOSTp^{Pr}(OPh)]$ was formed in a reaction of $[MoOTp^{Pr}(OPh)(OPEt_3)]$ with propylene sulfide, preedge XAS studies indicating that this species was monomeric in solution. On isolation as a solid, it afforded the redox-active dinuclear species $[\{MoOTp^{Pr}(OPh)\}_2(\mu\text{-}S_2)]$.

Reaction of primary amines with $[Mo^VOTp^*Cl_2]$ in the presence of air and NEt_3 afforded the mixed oxo-imido species $[Mo(NAr)OTp^*Cl]$. The hydrazido(2–) complexes $[Mo(NNR_2)Tp^xCl]$ (Tp^x≡Tp, Tp*) have also been structurally characterized.

5.6.2 *Cyclic Triaza Ligand and Related Complexes*

Halogenation of $[Mo(CO)_3(R_3tacn)]$ (**58**) (R = H, Me) afforded $[Mo(CO)_3(R_3tacn)X]^+$ (X = Br, I) analogous to $[Mo(CO)_3TpX]$ and which may have 3:4 'piano stool' geometry.

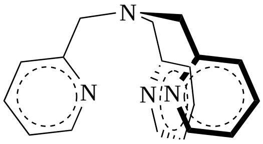

(**57**)

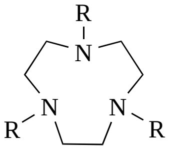

(**58**)

The cationic species $[Mo(CO)_2(NO)(R_3tacn)]^+$, obtained by reaction of $[Mo(CO)_3(R_3tacn)]$ with HNO_3 or with $NOBF_4$, could be converted into $[Mo(NO)(R_3tacn)X_2]^+$ and $[Mo(NO)(R_3tacn)X(OR')]^+$, but these complexes did not exhibit the rich electrochemistry of their tris(pyrazolyl)borato analogues $[Mo(NO)Tp^*X_2]$ and $[Mo(NO)Tp^*X(OR)]$.

Oxidation of $[Mo(CO)_3(R_3tacn)]$ ($R = Me, Pr^i$) by $SOCl_2$, Br_2, or HI afforded paramagnetic $[Mo^{III}(R_3tacn)X_3]$, ($\mu = 3.9-4.7$ BM), many of which species exhibited phosphorescence. Less sterically hindered triazacyclononanes gave dinuclear compounds. The related complexes $[MoTpm^*X_3]$ were obtained similarly, and underwent reversible oxidation to Mo^{IV} species.

Nitric acid oxidation of $[Mo(R_3tacn)X_3]$ afforded $[Mo^VO(Me_3tacn)X_2]^+$ which could be converted to $[MoO(Me_3tacn)(OMe)_2]$. These complexes, like their Tp* analogues, could be reduced to Mo^{IV} species, and dinuclear Mo^V and mixed-valence species were also isolated.

The structures of $[Mo^{VI}O_3(tacn)]\cdot 3H_2O$ (tacn = (**58**), R = H) and related species where $R = Pr^i$, have been confirmed crystallographically as octahedral with C_{3v} symmetry, and $[MoO_3(R_3tacn)]$ could function as a tridentate O-donor ligands to Co^{II} and Fe^{II}. Salts of $[MoO_2(Me_3tacn)X]^+$ ($Me_3tacn \equiv$ (**58**), R = Me) have also been characterized.

5.7 Porphyrin, Phthalocyanine, and Related Macrocyclic Complexes

Reduction of $[Mo^{IV}Cl_2(porph)]$ by Zn/Hg under CO afforded diamagnetic *cis*-$[Mo^{II}(CO)_2(porph)]$ which has trigonal prismatic geometry (porph = ttp) with the CO ligands staggered with respect to the Mo–N vectors. An additional ligand L (1-methylimidazoles, py, OMe^-, etc.) could bind trans to the CO ligands giving $[Mo(CO)_2(porph)L]^{n-}$, and the CO groups could be displaced by pyridine giving octahedral $[MoL_2(porph)]$. The metal–metal bonded $[\{Mo(pc)\}_2]$, obtained by reacting $[Mo(O)(pc)]$ with molten PPh_3, reacted with molten $[NBu_4]CN$ giving paramagnetic *trans*-$[Mo(CN)_2(pc)]^{2-}$ ($\mu = 3.15$ BM).

Reaction of bromine-activated $[Mo(O)(pc)]$ or $[MoN(pc)]$ with molten PPh_3 yielded the molybdenum(III) complex *trans*-$[MoBr_2(pc)]^-$, which was paramagnetic ($\mu = 3.84$ BM) and had an octahedral geometry. This complex underwent pc-centered and metal-centered electrochemical oxidation.

Reaction of $[Mo^{IV}Cl_2(porph)]$ with Li_2S and Na_2Se afforded $[Mo^{IV}E(porph)]$ (E = S or Se), both of which reacted with PPh_3 giving $[Mo^{II}(porph)(PPh_3)_2]$.

Reaction of $[\{Mo(porph)\}_2]$ with Me_3SiN_3 affords the nitrido species $[Mo^VN(porph)]$ which had a square-pyramidal structure ($d_{Mo-N} = 1.63$ Å). The nitrido group was reactive, treatment of $[MoN(porph)]$ with H^+, S_8, and RI affording $[Mo(NH)(porph)]^+$, $[Mo(NS)(porph)]$, and $[Mo(NR)(porph)]I$, respectively. Related phthalocyanine complexes, $[MoN(pc)]$ were also described.

A wide range of five- and six-coordinate species $[Mo^VO(porph)]^+$ and *trans*-$[Mo^VO(porph)X]^{0,+1}$, where $X = OH^-$, alkoxide, halide, H_2O, dmso, and so on, were prepared. These complexes have characteristic EPR spectral properties and their electro-, photo-, and catalytic chemistry have been reviewed.**[30]** Similar phthalocyanine complexes, $[Mo(O)(pc)X]$ (X = Cl, Br, OH) may be prepared by treatment of $[MoO(pc)]$ with $FeCl_3$ or Br_2 or by oxidation of $[MoO(pc)]$ in the presence of OH^-. Black–purple $[Mo(O)(pc)]I_3$ was obtained by reaction of 1,2-dicyanobenzene, MoO_3, and iodine at 210°, had a square-pyramidal structure, and was paramagnetic ($\mu = 1.72$ BM).

Three types of Mo^{VI} porphyrin complexes are well-established: *cis*-$[MoO_2(porph)]$, *cis*-$[MoO(O_2)(porph)]$, and *trans*-$[Mo(O_2)_2(porph)]$ (porph(2−) = 5, 10, 15, 20-R_4-porphyrinato(2−); R = mes, Ph, tol, etc.).**[30]** These complexes could be oxidized and/or reduced in processes which involved both the metal and the porphyrinato ligands, leading to radical cation and radical anion complexes. $[Mo^{VI}O(O_2)(porph)]$, obtained by reaction of $[Mo^{IV}(O)(porph)]$ with O_2, was stable in the dark but lost O_2 on irradiation, with full or partial regeneration of $[MoO(porph)]$.

5.8 Nitrosyl Complexes

Tris(pyrazolyl)borato and related cyclic triaza ligand complexes of the general class $[Mo(NO)Tp'XY]$, in which the metal adopts a formal oxidation state of 0, I, or II, have been described above in Section 5.6.

Dinitrosyl complexes of the type $[Mo^0(NO)_2X_2]$ were obtained by reduction of $[MoO_4]^{2-}$ by hydroxylamine in the presence of added anionic ligands X, where X = dithiocarbamate, dithiocarboxylate, alkoxide, $2\text{-}NH_2C_6H_4E^-$ (E = O or S), hydroxamic acids. Reaction of $[Mo(NO)_2(dttd)]$ ($dttd^{2-}$ = (**22**)) with hydrazine or $NaBH_4$ gave the κ^2-hydroxylamide, $[Mo(NO)(ONH_2)(dttd)]$.

$[Mo(NO)Cl(dttd)]$ reacted with R_3O^+ giving the alkyl complex $[Mo(NO)(R)Cl(dttd)]^+$ (R = Me or Et). Treatment of $[Mo(NO)Cl(dttd)]$ with LiSR afforded the thiolato complexes $[Mo(NO)(SR)(dttd)]$ which could be reduced by $LiBu^n$ affording paramagnetic $[Mo^I(NO)(SR)(dttd)]^-$. Reaction of $[Mo(NO)(SPh)(dttd)]$ with S_8 afforded a species containing a κ^2-S–SPh, a sulfur atom being readily extracted by PPh_3 to regenerate the starting phenylthiolato species. Treatment of $[Mo(NO)(SAr)(dttd)]$ with PR_3 caused elimination of ArSSAr and reduction of the metal center, affording $[Mo^I(NO)(PR_3)(dttd)]$, and oxidation of this with halogen caused regeneration of Mo^{II} species, $[Mo(NO)X(dttd)]$. Treatment of $[Mo(NO)(PR_3)(dttd)]$ with R'_3O^+ effected alkylation of the sulfur macrocycle, giving $[Mo^I(NO)(PR_3)(R'dttd)]^+$. Similar behavior occurred when $[Mo(NO)(SPh)(dttd)]$ was treated with HBF_4. Reaction of $[Mo(NO)Cl(dttd)]$ with NH_2NR_2 gave the κ^2-hydrazido(1−) species $[Mo(NO)(NHNR_2)(dttd)]$, which has pseudo-octahedral structure with $d_{Mo-NH} = 2.10$ Å, $d_{Mo-NR_2} =$

2.17 Å (R = Me), and ∠N–Mo–N = 38°, with a linear Mo–N–O bond. Reaction of this species with HCl caused regeneration of the nitrosyl chloro precursor without cleavage of the hydrazido N–N bond. Other hydrazido complexes are described in Section 5.4.

6 COMPLEXES WITH P- AND As-DONOR ATOMS

6.1 Phosphido and Arsenido Complexes

The first terminal phosphido complexes containing $\mathrm{Mo^{VI}}$, $[\mathrm{MoP(NRAr)_3}]$, were prepared by reacting $[\mathrm{Mo(NRAr)_3}]$ with $\mathrm{P_4}$ in diethyl ether (R = $\mathrm{Bu}^{t,\mathrm{Pr}^i}$, 2-Ad; Ar). These complexes have pseudotetrahedral structures with $d_{\text{Mo–P}} = 2.11–2.20$ Å. They reacted with $\mathrm{Ar'N_3}$ (Ar′ = mesityl) and with dimethyldioxirane and $\mathrm{S_8}$ or episulfides to give $[\mathrm{Mo(P{=}NAr')(NRAr)_3}]$ and $[\mathrm{Mo({-}P{=}E)(NRAr)_3}]$ (E = O or S), respectively. Related five-coordinate complexes $[\mathrm{MoE\{N(CH_2CH_2NR)_3\}}]$ were obtained by reaction of $[\mathrm{MoCl\{N(CH_2CH_2NR)_3\}}]$ (**46**) with LiEHPh (E = P or As). Trigonal bipyramidal $[\mathrm{MoAs\{N(CH_2CH_2NR)_3\}}]$ has an axial terminal arsenido group, $d_{\text{Mo–As}} = 2.25$ Å.

6.2 Tertiary Phosphine and Related Complexes

A convenient synthesis of the $\mathrm{Mo^0}$ species $[\mathrm{Mo(PMe_3)_6}]$ was developed, involving reaction of $\mathrm{MoCl_5}$ dissolved in $\mathrm{PMe_3}$ with Na/K. In solution, this species was in equilibrium with $[\mathrm{MoH(CH_2PMe_2)(PMe_3)_4}]$. The chelating diphosphine complexes $[\mathrm{Mo(dmpe)_3}]$ and $[\mathrm{Mo(tmbp)_3}]$ (tmbp = 4,4′-5,5′-tetramethyl-2,2′-diphosphine) have trigonal prismatic structures and significant $\mathrm{Mo} \rightarrow \mathrm{P}$ electron transfer was inferred from structural and computational studies. The thermally stable phosphinine complex, $[\mathrm{Mo(PC_5H_5)_6}]$ was prepared by reduction of $\mathrm{MoCl_5}$ with Mg in the presence of the ligand in THF. It has an almost ideal octahedral geometry, with $d_{\text{Mo–P}} = 2.38$ Å.

Molybdenum(II) complexes containing CO, $\mathrm{PR_3}$, and halides is very extensive, and research continued to consolidate this area, which has been comprehensively reviewed.[31,32] A significant number of complexes in this group are seven-coordinate, adopting distorted capped octahedral structures.

The molybdenum(III) complexes $[\mathrm{MoCl_4(PRR'_2)_2}]^-$ (R = Et, R′ = Ph; R = Ph, R′ = Et; R = R′ = Et) were obtained by ligand exchange at $[\mathrm{MoCl_4(thf)_2}]^-$ or by phosphine reduction and ligand exchange at $[\mathrm{MoCl_4(thf)_2}]$. Treatment of $[\mathrm{MoX_3(thf)_3}]$ with dppe afforded the paramagnetic *mer*-$[\mathrm{MoX_3(dppe)(thf)}]$ ($\mu = 3.13–3.81$ BM), the thf being readily displaced by acetonitrile of $\mathrm{PMe_3}$. $[\mathrm{MoI_3(dppe)(PMe_3)}]$ has a very rare fac structure, most other species, for example, $[\mathrm{MoI_3(PMe_3)_3}]$ adopting a mer geometry.

Protonation of $[\mathrm{MoH_4(PR_3)_4}]$ ($\mathrm{PR_3} = \mathrm{PEt_3}$, $\mathrm{PBu_3}$, PMe $\mathrm{Ph_2}$) by anhydrous HX gave paramagnetic $\mathrm{Mo^{IV}}$ species $[\mathrm{MoHX_4(PR_3)_2}]^-$, $[\mathrm{PHBu_3}][\mathrm{MoXCl_3(PBu_3)_2}]$ having pentagonal-bipyramidal structure with apical Cl and the hydride ligand located between the equatorial $\mathrm{PBu_3}$ ligands.

Reaction of $[\mathrm{MoH_4(dppe)_2}]$ with $\mathrm{EH_2Ph_2}$ (E = Si or Ge) afforded either the $\mathrm{Mo^{IV}}$ complexes (**59**) or ((**60**)) (X = H), depending on reaction conditions. Complex (**60**) (E = Si, X = H) reacted with $\mathrm{O_2}$ or $\mathrm{SiH_3Ph}$ giving (**61**) (E = Si) and (**60**) (E = Si; X = $\mathrm{SiH_2Ph}$). Complexes (**60**) and (**61**) (E = Si) catalyzed the formation of dmf from $\mathrm{NHMe_2}$ and $\mathrm{CO_2/H_2}$ in benzene at 110 °C.

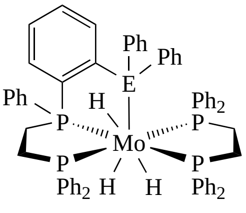

(**59**)

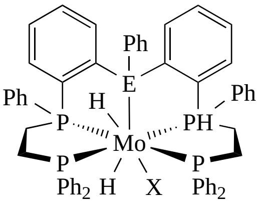

(**60**)

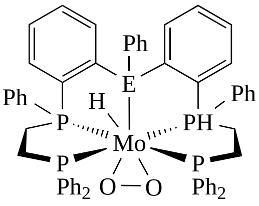

(**61**)

Trans-bis(oxo) and bis(chalcogenido) $\mathrm{Mo^{IV}}$ complexes $[\mathrm{MoE_2(L_4)}]$, where E = O, S, Se, L = $\mathrm{PMe_3}$, or L–L = dppe or dppee, have distorted octahedral structures. Those where E = O (L = dppe, dppee) have tetragonally compressed structures with axial oxo groups, $d_{\text{Mo–O}} = 1.80–1.82$ Å, ∠O–Mo–O = 180°. Reaction of $[\mathrm{MoO_2(dppe)_2}]$ with non-coordinating acids afforded $[\mathrm{MoO(OH)^*(dppe)_2}]^+$ whereas, with coordinating acids or acid/$\mathrm{X^-}$ mixtures, *trans*-$[\mathrm{MoOX(dppe)_2}]^+$ was formed. *Trans*-$[\mathrm{MoE_2(PMe_3)_4}]$ (E = S, Se, Te) was prepared by reaction of $[\mathrm{Mo(PMe_3)_6}]$ with $\mathrm{H_2S}$, $\mathrm{H_2Se}$, Se, or Te/$\mathrm{PMe_3}$.

7 METAL–METAL BONDS AND CLUSTERS

7.1 Dinuclear Complexes

Several reviews of dimolybdenum compounds having multiple bonds have delineated this area comprehensively.[33–36] In very general terms, the formal bond order for dimolybdenum compounds ranges from four to less than unity. The range of bond lengths is wide, from ca. 2.06 Å, representative formally of a quadruple bond, to ca. 3.27 Å, formally representing a single bond, although significant variations occur depending on the nature of the terminal and bridging ligands. Quadruply bonded species are normally encountered in $\mathrm{Mo^{II}Mo^{II}}$ complexes, triply bonded species in $\mathrm{Mo^{III}Mo^{III}}$ compounds, and doubly bonded species in $\mathrm{Mo^{IV}Mo^{IV}}$ complexes. Dinuclear complexes containing the $\mathrm{Mo^{V}Mo^{V}}$ core usually have Mo–Mo single bonds. A great many multiply bonded dimolybdenum complexes carry the η^5-$\mathrm{C_5H_5}$ or related ligands, which are not discussed here.

7.1.1 *Complexes Containing $\mathrm{Mo^{I}Mo^{I}}$*

This is a relatively small group of complexes. Reaction of $[2,6\text{-}(\mathrm{Ph_2P})_2\mathrm{C_6H_3NMe}]^-$, the anion of 2,6-bis(diphenylphosphino)-N-methylaniline, with $[\mathrm{Mo(CO)_6}]$ gave the bridged species $[(\mathrm{OC})_4\mathrm{Mo}\{\mu\text{-}\mathrm{PPh_2(C_6H_3NMe)PPh_2}\}\mathrm{Mo(CO)_4}]^-$. Oxidation of this by bromine afforded $[(\mathrm{OC})_3\mathrm{Mo}(\mu\text{-Br})\{\mu\text{-}\mathrm{PPh_2(C_6H_3NMe)PPh_2}\}\mathrm{Mo(CO)_3}]$, which contains a Mo–Mo bond ($d_{\text{Mo–Mo}} = 2.99$ Å).

7.1.2 *Complexes Containing $\mathrm{Mo^{II}Mo^{II}}$*

A very wide range of compounds containing the $\mathrm{Mo_2}^{4+}$ core have been synthesized, including halides, mono- and bidentate tertiary phosphines, alkoxides, carboxylates, calixarenes, formamidinates, and related ligands. Most of these may be described as containing quadruply bonded dimolybdenum cores, having an eclipsed geometry, as represented by (a) in Figure 5. The normal range of metal–metal bond distances in this category of compounds is 2.06–2.17 Å. The dinuclear acetonitrile complex, $[\mathrm{Mo_2(NCMe)_8}]^{4+}$ was a particularly useful precursor, and also could bind one or two additional acetonitrile ligands in the axial positions.

Potentially bidentate ligands, such as the formamidinates $[\mathrm{RNCR'NR}]^-$, the monoanion derived from 2,6-bis(phenylamino)pyridine and 7-methyl-1,8-naphthyridin-2-one, and others, formed complexes with a 'paddle wheel' structural motif, Figure 5(d), and some of these complexes could be oxidized by ferrocenium cations to give mixed-valent species. Generally, such oxidation led to a slight lengthening of the metal–metal bond.

7.1.3 *Complexes Containing $\mathrm{Mo^{III}Mo^{III}}$*

Dinuclear thiolato bridged complexes play a key role in the synthesis of cluster compounds and in biological and catalytic applications.[37] A common structural motif in this group of dinuclear complexes is the edge-sharing bioctahedral geometry, represented by (b) in Figure 5, which can be derived directly from molecular constituents or by oxidative addition across a dinuclear $\mathrm{Mo^{II}}$ quadruple bond. This group of complexes has an ethane-like geometry. Typical species included $[\mathrm{Mo_2}(\mu\text{-Cl})_2(\mu\text{-OAc})_2\mathrm{Cl_2(PEt_3)_2}]$ ($d_{\text{Mo–Mo}} = 2.61$ Å), $[\mathrm{Mo_2}(\mu\text{-O})(\mu\text{-OMe})(\mathrm{en})_4]^{3+}$ ($d_{\text{Mo–Mo}} = 2.44$ Å), and $[\mathrm{Mo_2(OCMe_2Ph)_6}]$ ($d_{\text{Mo–Mo}} = 2.24$ Å).

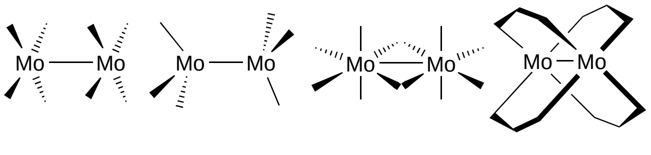

Figure 5 Structural types containing Mo–Mo quadruple bonds

Oxidation of $[\mathrm{Mo_2^{II}(hpp)_4}]$ by $\mathrm{Ag^+}$ afforded $[\mathrm{Mo_2(hpp)_4}]^{2+}$ (hppH = (**62**)) ($d_{\text{Mo–Mo}} = 2.14$ Å as $\mathrm{BF_4}^-$ salt), which formally contains the $\mathrm{Mo^{III}Mo^{III}}$ core. Reaction of $[\mathrm{Mo_2(NCMe)_8}]^{4+}$ with bis(diphenylphosphine)amine, dppa, in acetonitrile containing water generated $[\mathrm{Mo_2}(\mu\text{-}\eta^2\text{-NCMe})(\mu\text{-O})(\mu\text{-dppa})_2(\mathrm{NCMe})_4]^{2+}$ ($d_{\text{Mo–Mo}} = 2.42$ Å, but in the absence of water, $[\mathrm{Mo_2}(\mu\text{-}\eta^2\text{-NCMe})\{\mu\text{-NC(Me)PPh_2N PPh_2}\}(\mu\text{-dppa})(\mathrm{NCMe})_5]^{3+}$ ($d_{\text{Mo–Mo}} = 2.49$ Å) was formed. Reaction of $[\mathrm{Mo_2(OCH_2Bu^{\mathit{t}})_6}]$ with $\mathrm{PMe_3}$ led to the formation of a mixed-valent compound containing $\mathrm{Mo^{II}}$ and $\mathrm{Mo^{IV}}$, $[\mathrm{Mo_2}(\mu\text{-}\mathrm{OCH_2Bu^{\mathit{t}}})(\mathrm{OCH_2Bu^{\mathit{t}}})_3(\mu\text{-O})(\mathrm{PMe_3})_4]$. This species, which contains a formal Mo=Mo bond ($d_{\text{Mo–Mo}} = 2.49$ Å), has one six-coordinate metal center, formally $\mathrm{Mo^{II}}$, and one trigonal bipyramidal center, formally $\mathrm{Mo^{IV}}$. The compound reacted with CO to give $[\mathrm{Mo_2(CO)}(\mu\text{-}\mathrm{OCH_2Bu^{\mathit{t}}})(\mathrm{OCH_2Bu^{\mathit{t}}})_3(\mu\text{-O})(\mathrm{PMe_3})]$, in which the CO group is bonded to the $\mathrm{Mo^{II}}$ site.

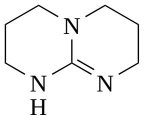

(**62**)

7.1.4 *Complexes Containing $\mathrm{Mo^{IV}Mo^{IV}}$*

The imido-formamidinato complex $[\mathrm{Mo_2(Ph_2NCHNPh_2)_2}(\mu\text{-NPh})\mathrm{Cl_5}]^-$ ($d_{\text{Mo–Mo}} = 2.53$ Å) could be prepared by cleavage of the formamidinate ligand in the reaction between $[\mathrm{MoCl_3(thf)_3}]$ or $[\mathrm{MoCl_4(NCMe)_2}]$ and diphenylformamidine and $\mathrm{Cl^-}$ in refluxing dichlorobenzene. Treatment of $\mathrm{Mo_2S_2Cl_6}$ with tetrahydrothiophene (tht, $\mathrm{SC_4H_8}$) afforded $[\mathrm{Mo_2}(\mu\text{-}\mathrm{S_2})(\mu\text{-tht})\mathrm{Cl_6(tht)_2}]$ ($d_{\text{Mo–Mo}} = 2.77$ Å), but reaction with $\mathrm{Me_2S}$ gave a paramagnetic mixed-valence $\mathrm{Mo^{V}Mo^{IV}}$ complex $[\mathrm{Mo_2}(\mu\text{-S})(\mu\text{-}\mathrm{S_2})\mathrm{Cl_5(SMe_2)}]$ ($d_{\text{Mo–Mo}} = 2.74$ Å).

7.1.5 *Complexes Containing $\mathrm{Mo^{V}Mo^{V}}$*

Reaction of $[\mathrm{MoOI_4(H_2O)}]^-$ with $\mathrm{Ph_3PO}$ in acetonitrile afforded a mixture of $[\mathrm{MoOI_3(OPPh_3)_2}]$ and the dinuclear $[\mathrm{Mo_2(O)_4I_2(OPPh_3)_3}]$ ($d_{\text{Mo–Mo}} = 2.56$ Å). In the latter, each metal center is coordinated by two bridging and one terminal oxo ligand, with the iodo ligand and three phosphine oxides unsymmetrically coordinated, resulting in different coordination environments for each metal atom, *viz.*

$[\mathrm{MoO_3I_2}]$ and $\{\mathrm{MoO_3(OPPh_3)_3}\}$. Reaction of $[\mathrm{Mo_2(NMe_2)_6}]$ with $\mathrm{C_6F_5OH}$ afforded the anion $[\mathrm{Mo_2O_2}(\mu\text{-O})_2(\mathrm{OC_6F_5})_4]^{2-}$ ($d_{\mathrm{Mo–Mo}} = 2.56$ Å).

When $[\mathrm{Mo_2(OAc)_4}]$ reacted with $\mathrm{Na_2mnt}$ (mnt = *cis*-1,2-dithiolato-1,2-dicyanoethene) in dry methanol, the species $[\mathrm{Mo_2}(\mu\text{-S})_2(\mathrm{O})(\mathrm{S})(\mathrm{mnt})_2]^{2-}$ ($d_{\mathrm{Mo–Mo}} = 2.86$ Å) was formed. Reduction of $[(\mathrm{MoO_3})_2(\mu\text{-edta})]^{4-}$ by dithionite at pH = 6 afforded $[\mathrm{Mo_2}(\mu\text{-S})(\mu\text{-O})\mathrm{O_2}(\mu\text{-}N,N'\text{-}\mathrm{C_{10}H_{12}N_2O_8})]^{2-}$ ($d_{\mathrm{Mo–Mo}} = 2.67$ Å), which contains the $\{\mathrm{Mo_2}(\mu\text{-S})(\mu\text{-O})\mathrm{O_2}\}$ core, and by refluxing $[\{\mathrm{Mo_2S_7Br_4}\}_n]$ in $\mathrm{PBu_3}^n$, $[\mathrm{Mo_2}(\mu\text{-S})_2\mathrm{O_2Br_4}]^{2-}$ ($d_{\mathrm{Mo–Mo}} = 2.86$ Å) could be formed.

Addition of benzene dithiol to $[\mathrm{Mo_2(S_2)_6}]^{2-}$ under slightly different conditions afforded $[\mathrm{Mo_2S_2(bdt)_2}]^{2-}$ ($d_{\mathrm{Mo–Mo}} = 2.87$ Å) and $[\mathrm{Mo_2S_4(S_2)_2}]^{2-}$ ($d_{\mathrm{Mo–Mo}} = 2.82$ Å).

7.2 Polyoxoanions

Polyoxometallate ions containing molybdenum form an enormous range of compounds which have been reviewed extensively[7,8] (*see also* ***Polyoxometalates***). They may be subdivided into (i) isopolyanions containing only Mo and (ii) heteropolyanions where other metal and/or nonmetal atoms may be present in the core structure.

7.2.1 Isopolyanions

The $\mathrm{Mo^{VI}}$ isopolyanions $[\mathrm{Mo_7O_{24}}]^{5-}$, $[\mathrm{Mo_8O_{26}}]^{4-}$, and their protonated analogs,[38] exist in aqueous NaCl/NaClO$_4$ media, and salts of $[\mathrm{Mo_{36}O_{110}(H_2O)_{16}}]^{8-}$ have been isolated from such solutions. Salts of the octamolybdate ion occur in at least six different structural forms, containing $\{\mathrm{MoO_4}\}$, $\{\mathrm{MoO_5}\}$, and $\{\mathrm{MoO_6}\}$ coordination units in various combinations. The structure of $[\mathrm{Mo_{36}O_{110}(H_2O)_{16}}]^{8-}$ consisted of four pentagonal-bipyramidal Mo centers, and was loosely described as a centrosymmetric dimer of $\{\mathrm{Mo_{17}}\}$ units linked by two *cis*-MoO$_2$ groups. The nitrosyl species $[\mathrm{Mo_{36}(NO)_4O_{108}(H_2O)_{16}}]^{12-}$ is isostructural with $[\mathrm{Mo_{36}O_{110}(H_2O)_{16}}]^{8-}$, with four $\{\mathrm{MoO_6}\}$ units being substituted by $\{[\mathrm{Mo(NO)}^{3+}]\mathrm{O_6}\}$.

Mixed-valence species, often referred to as heteropoly blues or browns, were generated by reduction of stable polyoxomolybdates. These anions contain a significant number of $\mathrm{Mo^V}$ centers, typically 12 in $[(\mathrm{H_2})\mathrm{Mo_{12}O_{28}(OH)_{12}}(\mathrm{Mo^{VI}O_3})_4]^{6-}$, 26 in $[\mathrm{H_{14}Mo_{37}O_{112}}]^{14-}$, and 38 in $[\mathrm{H_{13}Mo_{43}O_{112}}\{(\mathrm{OCH_2})_3\mathrm{CMe}\}_7]^{10-}$, but may have six diamagnetic $\{\mathrm{Mo^V_2O_4}\}^{2+}$ units assembled into an ε-Keggin conformation.

7.2.2 Heteropolyanions

The Keggin-structure anions α-$[\mathrm{XMo_{12}O_{40}}]^{n-}$ are frequently investigated because of their potential and real catalytic applications.[8] A number of capped Keggin structures have been identified in which the α-Keggin core carries one or two VO units, as in $[\mathrm{PMo_5V_7O_{40}(VO)}]^{7-}$, $[\mathrm{PMo^V_6Mo^{VI}_6O_{40}}(\mathrm{V^{IV}O})_2]^{5-}$, and the extended chain structure $[\{(\mathrm{V^VO_4})\mathrm{Mo^{VI}_8V^{IV}_4O_{36}}(\mathrm{V^{IV}O})_2\}_n]^{7n-}$. Species capped by $\mathrm{As^{III}}$ and *cis*-$\mathrm{MoO_2}^{2+}$ groups, for example, $[\mathrm{H_4As^VMo^V_8Mo^{VI}_4OP_{40}As^{III}_2}]^{-}$ and $[\mathrm{SiMo^V_4Mo^{VI}_8O_{40}}(\mathrm{Mo^{VI}O_2})_2]^{4-}$ have also been characterized.

The diphosphate anions $[\mathrm{O_3PXPO_3}]^{4-}$ (X = O or CH$_2$) have been incorporated into polymolybdate structures. The species $[(\mathrm{O_3PXCPO_3})\mathrm{Mo_6O_{18}(H_2O)}]^{4-}$ has an unsymmetrical structure in which one PO$_3$ group is centered in a ring consisting of six-corner- and edge-shared $\{\mathrm{MoO_6}\}$ octahedra. This complex may be an intermediate in the molybdate-catalyzed hydrolysis of $[\mathrm{P_2O_7}]^{4-}$. In aqueous organic solvents, the diphosphate anion reacted with molybdate giving $\{(\mathrm{P_2})\mathrm{PMo_{18}}\}$, $\{(\mathrm{P_2})\mathrm{Mo_{15}}\}$, and $\{(\mathrm{P_2})\mathrm{Mo_{12}}\}$-complex oxyanions. The first of these was shown to be $[\mathrm{P_2Mo_{18}O_{61}}]^{4-}$, a structure based on the fusion of two $\{\mathrm{PMo_9O_{34}}\}$ units, whereas the $(\mathrm{P_2})\mathrm{Mo_{15}}$-species was shown to be a dimer of the lacunary ion, namely, $[(\mathrm{P_2O_7})_2\mathrm{Mo_{30}O_{90}}]^{8-}$, at least in the solid state.

7.2.3 Mesoscopic Polyoxomolybdate Anions

Increasing numbers of extremely large polyoxomolybdate anions, with ring-shaped and hollow structures have been described. These contain mixed-valence polymolybdate anions that are constructed using common building blocks containing Mo$_2$, Mo$_6$, and Mo$_8$ units, some of which have no independent stable existence. This area of cluster molybdenum chemistry has been extensively reviewed.[39–42]

These extremely large structures are reproducibly generated by self-assembly processes involving careful reduction of aqueous molybdate solutions. The most common building block in these species is a cluster generated by an $\{\mathrm{MoO_4(NO)}\}$ or $\{\mathrm{MoO_5}\}$ pentagonal bipyramid surrounded by five edge-shared MoO$_6$ octahedra. Depending on the solution acidity, the degree of reduction, and the presence of appropriate linker groups, pentagonal $\{\mathrm{Mo}\}_6$ clusters could be induced to form spherical (icosahedral) ‘Keplerates’ $[\{\mathrm{Mo^V_2O_4(OAc)}\}_{30}\{(\mathrm{Mo})\mathrm{Mo_5O_{21}}\}(\mathrm{H_2O})_{612}]^{42-}$ containing the $\{\mathrm{Mo_{72}}(\mathrm{Mo^V_2})_{30}\}$ core, and $[\mathrm{Mo_{72}Fe_{30}O_{252}(OAc)_{12}}\{\mathrm{Mo_2O_7(H_2O)}\}\{\mathrm{H_2MoO_8(H_2O)}\}(\mathrm{H_2O})_{91}]$ containing the $\{\mathrm{Mo_{72}}(\mathrm{Fe^{III}})_{30}\}$ core, or cyclic $[(\mathrm{Mo_{154}O_{420}(NO)_{14}})(\mathrm{OH})_{28}(\mathrm{H_2O})_{70}]^{28-}$.

Surfactant-encapsulated $[\{\mathrm{Mo^V_2O_4(OAc)}\}_{30}\{(\mathrm{Mo})\mathrm{Mo_5O_{21}}\}(\mathrm{H_2O})_{612}]^{42-}$ and $\{\mathrm{Mo_{57}V_6}\}$oxyanions have been obtained using dimethyldioctylammonium ions and have been fully characterized, and a Keggin molybdophosphate anion has been incorporated within $[\mathrm{Mo_{72}Fe_{30}O_{252}(OAc)_{12}}\{\mathrm{Mo_2O_7(H_2O)}\}\{\mathrm{H_2MoO_8(H_2O)}\}(\mathrm{H_2O})_{91}]$. Furthermore, a two-dimensional layer structure has been generated using two $\{\mathrm{Mo_{72}}(\mathrm{Fe^{III}_{30}})\}$ units linked via an Fe–O–Fe bond. The species $[\mathrm{Mo_{72}Fe_{30}O_{252}(OAc)_{12}}\{\mathrm{Mo_2O_7(H_2O)}\}\{\mathrm{H_2MoO_8(H_2O)}\}(\mathrm{H_2O})_{91}]$ contains 30 $\mathrm{Fe^{III}}$ $S = 5/2$ centers, and the magnetic properties of this highly complex polyoxoanion have been satisfactorily explained using classical and quantum Heisenberg models.

Even larger species have been generated by ageing solutions containing $[(MoO_3)_{176}(H_2O)_{80}H_{32}]$ species, which then acquired two $\{Mo_{36}\}$ 'hubcaps' assembling a giant $\{Mo_{248}\}$ cluster. Crystallization of an acidified solution containing sodium molybdate and sodium dithionite afforded an even more massive $\{Mo_{368}\}$ 'hedgehog' cluster anion, $[H_nMo_{368}O_{1032}(H_2O)_{240}(SO_4)_{48}]^{48-}$.**[43]**

7.3 Cluster Compounds Containing Chalcogenide Atoms

There are three main cluster types encountered in this group of important compounds: the incomplete cuboid $\{Mo_3(\mu_3\text{-}E)(\mu\text{-}E)_3\}^{4+}$, the sulfur-rich incomplete cuboid $\{Mo_3(\mu_3\text{-}E)(\mu,\mu'\text{-}E)_3\}^{4+}$, and the cuboid$\{Mo_4E_4\}^{5+}$.**[9]** These species are described as 'cuboidal' since this illustrates the best approximation in what are usually somewhat distorted structures. Several other cluster types, including $\{Mo_3E_7\}^{4+}$, $\{Mo_4S_6\}^{2+}$, and a range of heterometallic species $\{Mo_3M'E_4\}^{4+}$, $\{Mo_6M'_2E_8\}^{8+}$, and $\{Mo_6M'E_8\}^{4+}$ are also known.

7.3.1 Trinuclear Clusters, $[Mo_3E_4]^{4+}$

Improved methods of generating the green cluster $[Mo_3S_4(H_2O)_9]^{4+}$ (**63**) have been developed. New routes have been discovered involving reduction of $[NH_4]_2[Mo_2(S_2)_2Cl_8]$ by Pb or In in concentrated HCl, reaction of $[NH_4]_2[MoS_4]$ with $NaBH_4$, or abstraction of sulfur from S_2 bridges in $[Mo_3(S)(S_2)_3Cl_6]^{2-}$ by PPh_3, followed by cation-exchange chromatography – the yields from this last process being almost quantitative. The cluster $[Mo_3S_4(H_2O)_9]^{4+}$ could be a source of the mixed oxo-sulfido species $[Mo_3O_nS_{3-n}(H_2O)_9]^{4+}$ ($n = 1\text{–}3$), since it reacted with an excess of $NaBH_4$ to give mainly $[Mo_3OS_3(H_2O)_9]^{4+}$ together with a smaller amount of the other species. In all of these clusters, the capping position is occupied by a sulfur atom.

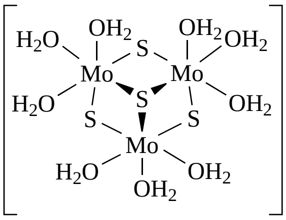

(**63**)

Brown $[Mo_3Se_4(H_2O)_9]^{4+}$ was obtained by aquation of $[Mo_3Se_7Br_6]^{2-}$ and subsequent Se abstraction from the resulting $[Mo_3Se_7(H_2O)_6]^{4+}$ by PPh_3. It could also be produced by reduction of $[Mo_2O_2Se_2(cys)_2]^{2-}$ (cys = cysteinate) by $NaBH_4$ in HCl solutions, the products from cation-exchange chromatography of this reaction mixture also affording $[Mo_3O_2Se_2(H_2O)_9]^{4+}$, $[Mo_3OSe_3(H_2O)_9]^{4+}$, and $[Mo_4Se_4(H_2O)_{12}]^{5+}$. The cluster $[Mo_3O_2Se_2(H_2O)_9]^{4+}$ was also obtained by reduction of $[Mo_2O_2Se_2(cys)_2]^{2-}$ with $[MoCl_6]^{3-}$ in HCl solution, while $[Mo_3O_3Se(H_2O)_9]^{4+}$ was formed by electrochemical reduction of $[Mo_2O_2(cys)_2]^{2-}$ in the presence of grey Se powder, or by reduction of $[Mo_3O_2Se_2(H_2O)_9]^{4+}$ with a very large excess of $NaBH_4$.

The mixed metal clusters $[Mo_2WS_4(H_2O)_9]^{4+}$ and $[MoW_2S_4(H_2O)_9]^{4+}$ were obtained by reaction of an equimolar mixture of $[WS_4]^{2-}$ and $[Mo_2O_2S_2(cys)_2]^{2-}$ with $NaBH_4$, followed by chromatographic separation of the resulting mixtures. However, an alternative method of synthesis made use of selective oxidative degradation of mixed metal tetranuclear clusters $[Mo_xW_{4-x}S_4(H_2O)_{12}]^{5+}$, where invariably only one W atom was lost, this procedure avoiding tedious chromatographic separations.

Water-exchange ligand substitution studies with $[Mo_3S_4(H_2O)_9]^{4+}$ using ^{17}O nmr studies showed that there are two types of kinetically distinct water ligands. Those trans to the capping S (c-H_2O) exchanged about 10^5 times more slowly than those trans to the bridging S and cis to the capping S atoms (d-H_2O). Replacement of μ_3-O by μ_3-S and then by μ_3-Se in $[Mo_3O_4(H_2O)_9]^{4+}$ resulted in a retardation in substitution of the d-H_2O by factors of 6 and 11, respectively. However, replacement of μ-O by μ-Se and μ-Se resulted in labilization with a factor of 10 (S) and 20 (Se) for each μ-O replaced.

The labile formato complex $[Mo_3S_4(O_2CH)_8(H_2O)]^{4-}$ was obtained by elution of $[Mo_3S_4(H_2O)_9]^{4+}$ on a cation-exchange column with formate in aqueous formic acid. The acetylacetonato complexes $[Mo_3E_4(acac)_3(py_3)]^+$ (E = S, Se) were obtained by reacting $[Mo_3E_4(H_2O)_9]^{4+}$ with Hacac and pyridine; the py ligands being trans to the μ_3-S atom. In acidic solution, $[Mo_3S_4(H_2O)_9]^{4+}$ reacted with the monovacant lacunary anions $[SiW_{11}O_{39}]^{8-}$ and $[P_2W_{17}O_{61}]^{10}$ giving $[\{(SiW_{11}O_{39})Mo_3S_4(H_2O)_3(\mu\text{-}OH)\}_2]^{10-}$ and $[\{(P_2W_{17}P_{61})Mo_3S_4(H_{21}O)_3(\mu\text{-}OH)\}_2]^{14-}$. The central core of these clusters consisted of two $\{Mo_3S_4(H_2O)_3\}^{4+}$ units connected by two OH^- groups that were cis to the μ_3-S units. A series of clusters containing the nitrilotriacetate ion (nta^{3-}) were also prepared, including $[Mo_3S_4(Hnta)_3]^{2-}$, $[Mo_3S_4(Hnta)_2(nta)]^{3+}$, $[Mo_2WS_4(Hnta)_3]^{2+}$, and $[MoW_2S_4(Hnta)_3]^{2+}$. The coordination mode of the $Hnta^{2-}$ ligand was tridentate, with one CO_2H group remaining unbound to the cluster core. The complexes were redox active, undergoing three consecutive one-electron reductions representing formal oxidation state changes from M_3^{IV} to M_3^{III}. Coordination of the $\{Mo_3S_4\}^{4+}$ core by 1,3,5-triamino-1,3,5-trideoxy-*cis*-inositol (taci) and its methylated (tris-dimethylamino) analogue (tdci) was achieved by reaction of taci and tdci with $[Mo_3S_7Br_6]^{2-}$ and PPh_3 in ethanol. This afforded $[Mo_3S_4(taci)_3]^{4+}$ and $[Mo_3S_4(tdci)_3]^{4+}$.

In solution, isomers were observed, corresponding to the binding of taci and tcdi in N,N,N, N,N,O, and N,O,O coordination modes, but no evidence for O,O,O-bonding was detected. Reaction of polymeric [$\{Mo_3S_7Cl_4\}_n$] with PPh_3 in refluxing pyridine afforded [$Mo_3S_4py_5Cl_5$], which reacted with I_2 giving [$Mo_3S_4py_6Cl_3$]I.

A range of diethyldithiophosphato ([$S_2P(OEt)_2$]$^-$, dtp) complexes have been characterized, including [Mo_3S_4(dtp)$_3$ ($O_2C_6H_4X$-*o*)py] (X = OH, NO_2) (**64**), [Mo_3S_4(dtp)$_3$(O_3S C_6H_4Me)py], and [Mo_3Se_4(dtp)$_3$(OAc)py]. In most of these complexes, the $\{Mo_3(\mu_3\text{-}S)(\mu\text{-}S)_3\}^{4+}$ core is preserved, each Mo atom carrying a bidentate dtp, the carboxylate or sulfonate group bridging two of the Mo atoms and the remaining Mo atom being coordinated by the py ligand. When more than one dtp ligand was substituted by a carboxylato ligand, the latter functioned as bridging groups, as in [$Mo_3(\mu_3\text{-}O)(\mu\text{-}S)_3(dtp)_2$($\mu$-$O_2CR$)$_2$(py)] (R = Me, Ph). Reaction of [$Mo_3ES_3(H_2O)_9$]$^{4+}$ (E = O or S) with Hdtp, followed by recrystallization from acetonitrile, afforded [Mo_3ES_3(dtp)$_4$(NCMe)]. Treatment of $MoCl_3{\cdot}3H_2O$, P_4S_{10}, and H_2S in ethanol under conditions less acidic than those used to prepare [Mo_3S_4(dtp)$_3$(μ-dtp)(H_2O)] afforded [Mo_3OS_3(dtp)$_3$(μ-dtp)(H_2O)] in which the cluster core was identified as $\{Mo(\mu_3\text{-}O)(\mu\text{-}S)\}^{4+}$, isomeric with the more commonly encountered $\{Mo_3(\mu_3\text{-}S)(\mu\text{-}O)(\mu\text{-}S)_2\}^{4+}$.

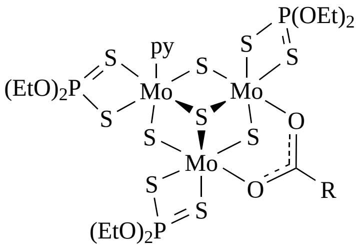

(**64**)

Reaction of [$Mo_3Se_7(S_2CNEt_2)_3$]$^+$ with PPh_3 afforded [$Mo_3Se_4(S_2CNEt_2)_4(PPh_3)$], and treatment of [$Mo_3Te_7\{S_2P(OPr)_2\}_3$]$^+$ with PBu_3 in the presence of benzoates gave [$Mo_3Te_4\{S_2P(OPr)_2\}_3(\mu\text{-}O_2C_6H_4X)(PBu_3)$] (X = X or *o*-$NH_2$) whose structure was similar to that of (**64**) shown above.

Reaction of [$Mo_3S_7X_6$]$^{2-}$ (X = Cl, Br) with PPh_3 or dppe in methanol afforded [$Mo_3S_4X_4(PPh_3)_3$] and [$Mo_3Se_4X_4$(dppe)$_3$]X in good yields, an improvement on reactions involving polymeric [$\{Mo_3Se_7X_4\}_n$].

Treatment of [$\{Mo_3S_7Cl_4\}_n$] with PEt_3 followed by reduction with Mg at −20 °C and addition of dppe, afforded the paramagnetic [$Mo_3S_4Cl_3$(dppe)$_2$(PEt_3)] which contains the $\{Mo_3S_4\}^{3+}$ core. The Mo–Mo bonds in the reduced species (2.81 Å) are longer than those in analogous phosphine complexes of $\{Mo_3S_4\}^{4+}$.

Addition of KCN in hot aqueous solution to [$\{Mo_3Se_7Br_4\}_n$] gave [$Mo_3Se_4(CN)_9$]$^{5-}$ which is redox active, undergoing a one-electron reduction process affording a species with a formal $Mo^{III}Mo_2^{IV}$ core.

7.3.2 Trinuclear Complexes, [Mo_3E_7]$^{4+}$

The chalcogen-rich [$Mo_3S_7X_6$]$^{2-}$ (X = Cl, Br, I) (**65**) could be prepared either by melting the polymer [$\{Mo_3S_7X_4\}_n$] with PPh_4X at 300 °C or grinding with NEt_4X in a ball mill. However, these anions could also be obtained by treatment of [$Mo_3S_7(S_2)_3$]$^{2-}$ with hot concentrated HX or by treatment with Cl_2 or Br_2 in acetonitrile. Reaction of [$Mo_3S_7(S_2)_3$]$^{2-}$ with Me_3CBr in DMF provided a high-yield route to [$Mo_3S_7Br_6$]$^{2-}$, which was an important precursor to the formation of other species containing the $\{Mo_3(\mu_3\text{-}S)(\mu,\mu'\text{-}S_2)_3\}^{4+}$ core. In some structures of [$Mo_3S_7X_6$]$^{2-}$, there was weak secondary coordination of an additional halide ion to the three axial atoms of the S_2 groups (**66**).

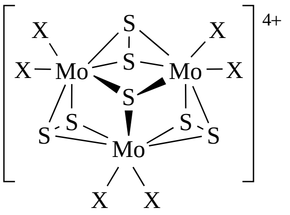

(**65**)

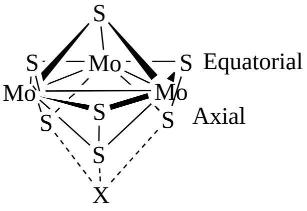

(**66**)

A range of complexes containing the $\{Mo_3S_7\}^{4+}$ core have been described, including [$Mo_3S_7(NCS)_6$]$^{2-}$, [$Mo_3S_7(S_2CNEt_2)_3$]$^+$, [Mo_3S_7(dtp)$_3$]$^+$, and [$Mo_3S_7(S_2PR_2)_3$]$^+$. Most of these clusters, in which the chelating ligands form a four-membered ring with each metal, were obtained from [$Mo_3S_7Br_6$]$^{2-}$, although the last was produced by reaction of [$Mo(CO)_6$] with $R_2P(S)SSP(S)R_2$ in refluxing toluene. Cluster complexes containing chelating ligands which formed a six-membered ring with each metal included [$Mo_3S_7\{Ph_2P(E)NPPh_2(E)\}_3$]$^+$ (E = O or S), [Mo_3S_7(tdt)$_3$]$^{2-}$ (tdt = toluene-3,4-dithiolate), and [Mo_3S_7(cat)$_3$]$^{2-}$ (cat = benzene-1,2-diolate, catecholate).

The main characteristic of the Mo_3S core was found in the distinction between the equatorial and axial chalcogen atoms in the μ_2-S ligands (see (**66**) without additional X). Generally, the equatorial Mo–S bond distance was longer than the Mo–S axial distance. Consequently, the equatorial S atoms were more labile towards abstraction and substitution, as was demonstrated by the preparation of S^{32}/S^{34}-labelled isotopomers of [$Mo_3S_7(S_2)_3$]$^{2-}$. Vibrational spectra of a range of salts of [Mo_3S_{13}]$^{2-}$ established that they are correctly represented as [$Mo_3(\mu_3\text{-}S)(\mu\text{-}S)_3(\mu,\mu'\text{-}S_2)_3$]$^{2-}$.

The selenium clusters [$Mo_3Se_7X_6$]$^{2-}$ were obtained by reaction of [$\{Mo_3Se_7X_4\}_n$] with X^- in the same way as their sulfur analogues. Complexes containing chelating ligands analogous to their sulfur counterparts were also characterized, for example, $[Mo_3Se_7(S_2CNR_2)_3]^+$ and $[Mo_3Se_7(dtp)_3]^+$, while $[Mo_3Se_7(phen)_3]^{4+}$ was obtained by melting $[\{Mo_3Se_7X_4\}_n]$ with 1,10-phenanthroline.

Reaction of alkali metal polyselenides with MoO_3 under hydrothermal conditions afforded, inter alia, $[Mo_3Se_7(Se_2)_3]^{2-}$, whose structure is similar to its sulfur analog, $[Mo_3OSe_6(Se_2)_3]^{2-}$ and $[Mo_6Se_{27}]^{6-}$. The last species consists of an Se^{2-} ion sandwiched between two $[Mo_3Se_7(Se_2)_3]^{2-}$ units, a structure similar to that found in $[\{Mo_3Se_7(S_2CNEt_2)_3\}_2Se]$ ($Se^{2-}\cdots Se_{ax} = 2.81-3.04$ Å). Calculations showed that there is significant electron transfer from the Se^{2-} ion to the antibonding orbitals of the μ-Se_2 groups. $K_8[Mo_9Se_{40}]$, obtained by reaction of MoO_3, K_2Se_2, and water at 135 °C contains $[Mo_3Se_{13}]^{2-}$, an aggregate of three $\{Mo_3Se_7\}$ clusters linked by two Se^{2-}. One of the latter is the capping μ_3 atom of an Mo_3Se_7 cluster ($Se\cdots Se = 3.13$ Å). Another Se^{2-} is sandwiched between two Mo_3Se_7 clusters as in $[Mo_6Se_{27}]^{6-}$ described above. The cluster can be described therefore as three $[Mo_3Se_{13}]^{2-}$ and one Se^{2-}, linked by short $Se\cdots Se$ contacts. A related anion, $[Mo_3Se_{18}]^{2-}$, obtained under the same conditions as $[Mo_9Se_{40}]^{8-}$ but using a different reagent ratio, contained the $\{Mo_3Se_7\}^{4+}$ core, coordinated by a $Se_3{}^{2-}$ and bridging $Se_4{}^{2-}$, thereby generating infinite chains, $[\{Mo_3Se_7(Se_3)(Se_4)_{4/2}\}_n]^{2n-}$. Reaction of Mo metal with K_2Se_4 in water at 140 °C afforded $K_{12}[Mo_{12}Se_{56}]$. In this species, the $\{Mo_3Se_7\}^{4+}$ cluster units are bound into tetrameric aggregates (clusters of clusters) via Se_3 bridges. The Mo atoms, which do not participate in the intercluster bridging, are coordinated by terminal $Se_2{}^{2-}$, each of them bound to the three axial Se atoms in the cluster. The cluster anion $[Mo_3Se_{42}]^{6-}$ contained $[\{Mo_3(\mu_3\text{-}Se)(\mu\text{-}\kappa^2\kappa'^2\text{-}Se_2)_3(\kappa^2\text{-}Se_2)(\mu\text{-}\kappa^2\text{-}Se_5)(\kappa^1\text{-}Se_5)\}_2(\mu\text{-}\kappa^2\text{-}Se_4)]$.

The tellurium cluster anion $[Mo_3Te_7(CN)_6]^{2-}$ was prepared by heating Mo, Te, and I_2 in appropriate atomic ratios at 380 °C, followed by abstraction of the amorphous powder so formed with aqueous cyanide. In contrast to its sulfur and selenium analogues, this cyano cluster was inert to exchange of the Te atoms. The cluster core $\{Mo_3Te_7\}^{4+}$ has a strong affinity for I^-, via $Te_{ax}\cdots I$ contacts. In the reaction of $Mo_3Te_{10}I_{10}$ with $K_2S_2P(OR)_2$, $[Mo_3Te_7\{S_2P(OR)_2\}_3]^+$ ($R = Et, Pr^i$) was formed.

Clusters containing the $\{Mo_3O(S_2)_3\}^{4+}$ core are only known with dtp^-, *viz.* $[Mo_3O(S_2)_3(dtp)_3]^+$. Substitution of the axial S atom by O led to contraction of the Mo–Mo distances, from 2.72 to 2.63 Å. The $\{Mo_3O(Te_2)_3\}^{4+}$ core was found in $[Mo_3O(Te_2)_3(en)_3][In_2Te_6]$, which was formed by solvothermal reaction of Li_2Te, K_2Te, $MoCl_5$, $InCl_3$, and Te in ethylenediamine at 180 °C. Replacement of the apical Te by O resulted in contraction of the Mo–Mo distances.

Clusters containing the cores $\{Mo_3S(S_{eq}\text{–}Se_{ax})_3\}^{4+}$ and $\{Mo_3Se(S_{eq}\text{–}Se_{ax})_3\}^{4+}$ have been identified. Thus, chalcogen-exchange reactions between $[Mo_3S_7Cl_6]^{2-}$ and $P(Se)Ph_3$ or KNCSe resulted in selective substitution of the equatorial S atoms, giving, for example, $[Mo_3S(SSe)_3Cl_6]^{2-}$. With KNCSe, $[Mo_3S_7(SSe)_3(NCSe)_6]^{2-}$ was formed. These reactions were irreversible and the $\{Mo_3S(SSe)_3\}^{4+}$ core did not revert to $\{Mo_3S(S_2)_3\}^{4+}$ even when treated with an excess of $P(S)Ph_3$ or KNCS. Reaction of $[Mo_3S_7(S_2CNR_2)_3][S_2CNR_2]$ with KNCSe afforded $[Mo_3S(SSe)_3(S_2CNR_2)_3][SeCN]$ which contained essentially linear polymer chains $\{S\text{–}Se\cdots Se\cdots S\text{–}Se\cdots Se\cdots\}_n$ due to short (2.9–3.3 Å) cation–anion interactions. Aquation of $[Mo_3S(SSe)_3Br_6]^{2-}$ afforded $[Mo_3S(SSe)_3(H_2O)_6]^{4+}$ which reacted with PPh_3 to give $[Mo_3S_4(H_2O)_9]^{4+}$. Reaction of $[Mo_3Se_4(H_2O)_9]^{4+}$ with P_4S_{10} in ethanolic HCl afforded $[Mo_3Se(S_{eq}\text{–}Se_{ax})_3(dtp)_3]Cl$.

Reaction of $[NH_4]_2[Mo_3S_{13}]$ with an excess of PMe_3 in thf produced $[Mo_3(\mu_3\text{-}S)_2(\mu\text{-}S)_3(PMe_3)_6]$. This symmetrical species contains a trigonal bipyramidal core, in which an equilateral triangle of Mo atoms is capped by two S atoms and bridged by three other S atoms. All six PMe_3 groups were equivalent and showed only one sharp ^{31}P NMR signal in solution. This species was electroactive, underwent quasi-reversible one-electron reduction and oxidation. Reaction of $MoCl_3\cdot 3H_2O$ with H_2S in ethanolic HCl afforded $[Mo_3(\mu_3\text{-}S)_2(\mu\text{-}S)_3Cl_6]^{3-}$ which reacted with $(dtp)^-$ giving $[Mo_3S_2(dtp)_3]$.

7.3.3 *Tetranuclear Cubic $\{Mo_4E_4\}^{5+}$ Clusters*

The structure of $[Mo_4S_4(H_2O)_{12}]^{5+}$ consisted of two interpenetrating Mo_4 and S_4 tetrahedra of different sizes, leading to a distorted pseudocubic geometry. The Mo–Mo distances are 2.80 Å, the cluster is paramagnetic, exhibiting Curie-like behavior with $\mu = 1.78$ BM between 300 and 20 K. The corresponding selenium cluster $[Mo_4Se_4(H_2O)_{12}]^{5+}$ was made in low yield by reaction of $[Mo_2O_2Se_2(cys)_2]^{2-}$ with $NaBH_4$ and is less stable than its sulfur analog in air, degrading to $[Mo_3Se_4(H_2O)_9]^{4+}$. Both pentacationic clusters are redox active, being reversibly reduced to $[Mo_4E_4(H_2O)_{12}]^{4+}$ and reversibly oxidized to $[Mo_4E_4(H_2O)_{12}]^{6+}$. The air-sensitive $[Mo_4S_4(H_2O)_{12}]^{4+}$ was prepared by reduction of $[Mo_4S_4(H_2O)_{12}]^{5+}$ electrochemically or using $NaBH_4$ or $[M(H_2O)_6]^{2+}$ (M = V or Cr). Oxidation of $[Mo_4S_4(H_2O)_{12}]^{5+}$ to $[Mo_4S_4(H_2O)_{12}]^{6+}$ was achieved by controlled stoichiometric addition of *cis*-$[VO_2(H_2O)_4]^+$, but it was not very stable, decaying spontaneously with formation of $[Mo_3S_4(H_2O)_9]^{4+}$. Controlled electrolytic oxidation of $[Mo_4S_4(H_2O)_{12}]^{5+}$ afforded only $[Mo_3S_4(H_2O)_9]^{4+}$ and $[Mo_2O_2S_2(H_2O)_6]^{2+}$. The oxo-cluster $[Mo_4OS_3(H_2O)_{12}]^{5+}$ was prepared by reduction of $[Mo_3OS_3(H_2O)_9]^{4+}$ by iron wire, its constitution being confirmed crystallographically.

Reaction of $[MM'_2E_4(H_2O)_9]^{4+}$ (M, M′ = Mo, W) with $K_4Mo_2Cl_8$ afforded the heterometallic cubes $[MoW_3S_4(H_2O)_{12}]^{5+}$, $[Mo_3WS_4(H_2O)_{12}]^{5+}$, $[Mo_2W_2S_4(H_2O)_{12}]^{5+}$, and $[MoW_3Se(H_2O)_{12}]^{5+}$. Air-oxidation or oxidation by $[Fe(H_2O)_6]^{3+}$ initially afforded $[Mo_nW_{4-n}E_4(H_2O)_{12}]^{6+}$ ($n =$ 1, 2 or 3), but these subsequently exclusively lost one W atom giving trinuclear clusters of the type $[Mo_nW_{3-n}S_4(H_2O)_9]^{4+}$.

Electrochemical studies of the mixed metal cuboidal clusters revealed that, like $[Mo_4S_4(H_2O)_{12}]^{5+}$, they could be reversibly reduced and oxidized in one-electron steps. The corner-shared double cube $[Mo_7S_8(H_2O)_{18}]^{8+}$ is described in the Section 7.3.5.

Reaction of the reduced cluster $[Mo_4S_4(H_2O)_{12}]^{4+}$ with concentrated aqueous ammonia afforded $[Mo_4S_4(NH_3)_{12}]^{4+}$ which reverted to $[Mo_4S_4(H_2O)_{12}]^{5+}$ in air in acidic solutions.

Reduction of $[Mo_2O_2S_2(edta)_2]^{2-}$ with aqueous $NaBH_4$, followed by acidification and air-oxidation, afforded $[Mo_4S_4(edta)_2]^{3-}$. From the crystal structure determinations of the Na^+ and Ca^{2+} salts, it was established that the hexadentate edta was tridentate with respect to two Mo centers and the Mo–Mo distances were in the range 2.76–2.88 Å. $[Mo_4Se_4(edta)_2]^{3-}$ (Mo–Mo, 2.81–2.92 Å) was obtained similarly from $[Mo_2O_2Se_2(cys)_2]^{2-}$. Reduction of $[Mo_4S_4(edta)_2]^{3-}$ by $NaBH_4$ afforded $[Mo_4S_4(edta)_2]^{4-}$ (60-electron cluster) in which the Mo–Mo distances fell in the range 2.77–2.79 Å. Oxidation afforded $[Mo_4S_4(edta)_2]^{2-}$ ($\{Mo_4S_4\}^{6+}$ core) in which the Mo–Mo distances were in the range 2.74–2.87 Å. It was observed that the mean values of the Mo–Mo bond lengths and the volumes of the Mo_4 tetrahedra decreased on progressing from the reduced $\{Mo_4S_4\}^{4+}$ through $\{Mo_4S_4\}^{5+}$ to the oxidized $\{Mo_4S_4\}^{6+}$ cluster core. The tetra- and dianionic species were diamagnetic while the 3−ion was paramagnetic (one unpaired electron). The related selenium clusters $[Mo_4Se_4(edta)_2]^{3-}$ exhibited similar redox behavior.

The diethyldithiophosphato (dtp) clusters $[Mo_4S_4(\mu\text{-}dtp)_2(dtp)_4]$, $[Mo_4OS_3(\mu\text{-}dtp)_2(dtp)_4]$, and $[Mo_4OS_3(\mu\text{-}dtp)_3(dtp)_3]$ were obtained by reaction of $MoCl_3{\cdot}3H_2O$ with P_4S_{10} in ethanol, with or without HCl, or by reaction of $[Mo(CO)_6]$ with the disulfide $(dtp)_2$. The bridging dtp ligand in $[Mo_4S_4(\mu\text{-}dtp)_2(dtp)_4]$ could be displaced by acetate or benzoate giving $[Mo_4S_4(\mu\text{-}OCOR)_2(dtp)_4]$. All these clusters contain the cluster core $\{Mo_4S_4\}^{6+}$. However, reaction of $[Mo_3S_4(\mu\text{-}dtp)(dtp)_4(H_2O)]$ with $[Mo(CO)_6]$ in acetic acid/acetic anhydride, or of $[Mo_3S_7(dtp)_3]Cl$, PPh_3, $[Mo(CO)_6]$ and dtp^-, afforded the $\{Mo_4S_4\}^{5+}$ cluster species $[Mo_4S_4(\mu\text{-}OAc)(dtp)_4]^-$. The dithiocarbamato species $[Mo_4S_4(\mu\text{-}S_2CNR_2)_2(S_2CNR_2)_4]$ were obtained from reactions of $[Mo(CO)_6]$ with appropriate thiuram disulfides $R_2NC(S)SSC(S)NR_2$ (R = alkyl). The crystal structure determination of the cluster with R = Et revealed that the Mo–Mo bonds bridged by the two S_2CNEt_2 ligands contracted to 2.74 Å, whereas the other four intermetallic distances were in the range 2.85–2.87 Å. The ^1H NMR spectrum of this cluster in solution revealed two nonequivalent S_2CNEt_2 ligands indicating that the species was stereochemically rigid in solution. The cluster was also paramagnetic ($\mu = 2.96$ BM). Related xanthato complexes $[Mo_4S_4(\mu\text{-}S_2COR)_2(S_2COR)_4]$ have also been described. This group of tetranuclear clusters containing chelating sulfur ligands bound to a $\{Mo_4S_4\}^{6+}$ core were electroactive, undergoing two quasi-reversible one-electron reduction processes, corresponding to the formation of $\{Mo_4S_4\}^{5+}$ and $\{Mo_4S_4\}^{4+}$, and two quasi-reversible one-electron oxidations, corresponding to the formation of $\{Mo_4S_4\}^{7+}$ and $\{Mo_4S_4\}^{8+}$. The potentials for these processes varied by as much as 670 mV depending on the ligand bridging the cube, with the relative ease of reduction being in the order $(S_2COR)^- > [S_2P(OR)_2]^- > (S_2CNR_2)^-$.

High-temperature treatment of polymeric $[\{Mo_3E_7Br_4\}_n]$ with KCN gave the cyano complexes $[Mo_4E_4(CN)_{12}]^{6-}$ (E = S, Se) and $[Mo_4Te_4(CN)_{12}]^{7-}$. The last was oxidized by bromine water to give a hexa-anionic cluster ($\{Mo_4Te_4\}^{6+}$ core). The clusters $[Mo_4E_4(CN)_{12}]^{6-}$ were redox active, undergoing two reversible or quasi-reversible electron transfers corresponding to the generation of seven- and eight-species containing $\{Mo_4E_4\}^{5+}$ and $\{Mo_4E_4\}^{4+}$ cores.

7.3.4 Raft-like Clusters $[Mo_4(\mu_3\text{-}S)_2)\ (\mu\text{-}S)_4]^{2+}$

Reaction of $[Mo_3S_7(S_2)_3]^{2-}$ with PMe_3 in *n*-butylamine gave a raft-like Mo_4 cluster $[Mo_4(\mu_3\text{-}S)_2(\mu\text{-}S)_4(SH)_2(PMe_3)_6]$. The idealized cluster core, $\{Mo_4S_6\}^{2+}$ core (**67**) has five Mo–Mo bonds, including one between the ‘hinge’ metal atoms (2.83–2.85 Å). Treatment of this cluster with $SnCl_2$ in THF caused displacement of the SH groups and formation of $[Mo_4(\mu_3\text{-}S)_2(\mu\text{-}S)_4Cl_2(PMe_3)_6]$.

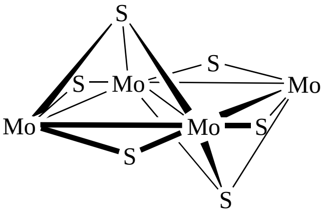

(**67**)

7.3.5 Heterometallic Derivatives of $[Mo_3E_4(H_2O)_9]^{4+}$

The incomplete cubes $[Mo_3E_4(H_2O)_9]^{4+}$ (E = S, Se) reacted with metal ions to generate cuboidal species. These are generally of three types, shown in (**68**–**70**).**[9]** The cluster (**68**) utilizes a heterometal atom with variable coordination preferences (usually octahedral or tetrahedral), constituting a cuboidal species. However, when M′ prefers tetrahedral geometry, the edge-linked double cube (**69**) can be formed. The incomplete cube can also function as a pair of tridentate ‘ligands’, generating a corner-shared cube, (**70**).

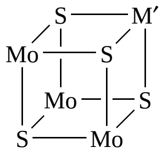

(**68**)

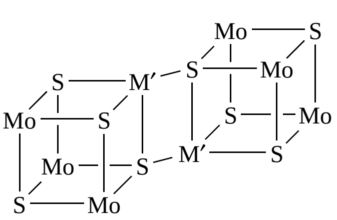

(**69**)

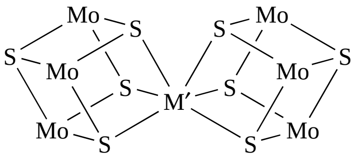

(**70**)

The conversion of (**68**) to (**69**) occurred when the anions accompanying the reaction were normally noncoordinating, such as ClO_4^- or p-$MeC_6H_4SO_3^-$, and regeneration of (**68**) would occur when ligands such as CO, PR_3, Cl^-, or NCS^- were added and attached to M′. An excess of $[Mo_3S_4(H_2O)_9]^{4+}$ and a reducing agent such as BH_4^- or H_3PO_2 was necessary to convert (**68**) into (**70**), a reaction which could be reversed using oxidants such as $[Fe(H_2O)_6]^{3+}$. In general, short Mo–M bonds (ca. 2.7 Å) are observed in (**68**) and (**69**), but relatively long nonbonding separations (>3.5 Å) are detected in (**68**) and (**70**), when M′ is a metal from groups 12–15. All of the corner-shared double cubes (**70**) carry an 8+ charge, and a formal charge distribution, $\{Mo_3S_4\}^{4+}\{M'\}^0\{Mo_3S_4\}^{4+}$ has been deemed useful. However, $[Mo_7S_8(H_2O)_{18}]^{8+}$, described in Section ‘Corner-sharing Cubic Clusters $\{Mo_6M'E_8\}^{8+}$’, is an exception in that an alternative distribution of charge seems to apply. In the single cubes (**68**), where M′ = Co, Ni, Pd, or Cu, there are relatively short Mo–M′ distances, the formalism $\{Mo_3S_4\}^{4+}\{M'\}^0$ seeming reasonable particularly in view of the synthesis of these clusters from metallic M′. Single cubes of type (**68**), where M′ is Hg, Ga, Ge, and Sb, have been formulated as $\{Mo_4S_4\}^{4+}Hg^0$, $\{Mo_4S_4\}^{4+}Ga^I$, $\{Mo_4S_4\}^{4+}Ge^{II}$, and $\{Mo_4S_4\}^{4+}Sb^{III}$, respectively.

These air-sensitive heterometallic species were isolated using cation-exchange chromatography, especially when the aqua clusters were required. The species were handled in acidic solutions in order to avoid acid dissociation involving the H_2O ligands, and many of the complexes were isolated as p-$MeC_6H_4SO_3^-$ salts.

Single Cube $\{Mo_3M'E_4\}^{4+}$ and Double Cube $\{Mo_6M'_2E_8\}^{8+}$ Species. Reaction of $[Mo_3S_4(H_2O)_9]^{4+}$ with $[Cr(H_2O)_6]^{2+}$ afforded $[Mo_3CrS_4(H_2O)_{12}]^{4+}$ [**68**, M′ = $Cr(H_2O)_3$], which was air-sensitive, degrading into $[Mo_3S_4(H_2O)_9]^{4+}$ and $[Cr(H_2O)_6]^{3+}$. This cluster has been described as $[Mo_3^{III}Cr^{III}S_4(H_2O)_{12}]^{4+}$. Reaction of $[Mo_3S_4(H_2O)_9]^{4+}$ with $[Re(CO)_5Br]$ afforded $[Mo_3\{Re(CO)_3\}S_4(H_2O)_9]^{5+}$.

Treatment of $[Mo_3S_4(H_2O)_9]^{4+}$ with iron wire in acid afforded $[Mo_3FeS_4(H_2O)_{10}]^{4+}$ [**68**, M′ = $Fe(H_2O)$] in which the Fe atom was tetrahedrally coordinated. This species did not react with CO or water-soluble tertiary phosphines, but addition of Cl^- gave $[Mo_3(FeCl)S_4(H_2O)_{10}]^{3+}$. Solid samples of $[Mo_3FeS_4(H_2O)_{10}]^{4+}$ were paramagnetic ($\mu = 2.83$ BM at 22 °C) and magnetic susceptibility data over a temperature range of 2–270 K could be fitted to a model having a $Fe^{II}Mo^{IV}Mo_2^{III}$ core. However Mössbauer spectra at 4.2 K were thought to be more consistent with the presence of Fe^{III} ($S = 3/2$), effectively spin-coupled at the lowest temperatures. With concentrated NH_3, $[Mo_3\{Fe(H_2O)\}S_4(NH_3)_9]^{4+}$ was formed, a crystal structure of the p-$MeC_6H_4SO_3^-$ salt showing Mo–Mo, 2.68–2.69 Å and Mo–Fe, 2.77–2.83 Å.

Metallic cobalt reacted with $[Mo_3S_4(H_2O)_9]^{4+}$ to give air-sensitive solutions from which the edged-linked double cube $[\{Mo_3CoS_4(H_2O)_9\}_2]^{8+}$ [**69**, M′ = Co] was isolated, (Co–Co, 2.50 Å). Reaction of this species with CO afforded air-stable $[Mo_3\{Co(CO)\}S_4(H_2O)_9]^{4+}$. Reaction of $[Mo_3S_4(H_2O)_9]^{4+}$ with $RhCl_3$ in aqueous HCl gave $[Mo_3(RhCl_3)S_4(H_2O)_9]^{4+}$ [**68**, M′ = $RhCl_3$] which, on standing in dilute HCl for a few days, was converted into $[Mo_3RhS_4(H_2O)_{12}]^{4+}$ [**68**, M′ = $Rh(H_2O)_3$].

Reaction of metallic nickel with $[Mo_3S_4(H_2O)_9]^{4+}$ or $[Mo_4S_7Cl_6]^{2-}$, or reduction of Ni^{2+} by BH_4^- in the presence of $[Mo_3S_4(H_2O)_9]^{4+}$, afforded $[Mo_3NiS_4(H_2O)_{10}]^{4+}$. The mixed metal clusters $[Mo_2WNiS_4(H_2O)_{10}]^{4+}$ and $[MoW_2NiS_4(H_2O)_{10}]^{4+}$ have also been prepared, and in all of these species the nickel atom had a tetrahedral geometry. Both $[Mo_3NiS_4(H_2O)_{10}]^{4+}$ and $[Mo_2WNiS_4(H_2O)_{10}]^{4+}$ formed single cubes [**68**, M′ = $Ni(H_2O)$] as their crystalline p-$MeC_6H_4SO_3^-$ salts, the di-tungsten cluster adopting a double cubic arrangement, $[\{MoW_2NiS_4(H_2O)_9\}_2]^{8+}$ [**69**, M′ = Ni] with Ni–Ni, 2.55 Å. Solutions of $[Mo_3NiS_4(H_2O)_{10}]^{4+}$ were stable in air for short periods, but on heating degraded to Ni^{2+} and $[Mo_3S_4(H_2O)_9]^{4+}$. In HCl, $[Mo_3(NiCl)S_4(H_2O)_9]^{3+}$ was formed, and treatment of this with nitrilotriacetate, nta^{3-}, caused substitution at the Mo centers rather than Ni, giving $[Mo_3(NiCl)S_4(Hnta)(nta)_2]^{5-}$. Reaction of $[Mo_3(NiCl)S_4(H_2O)_9]^{3+}$ with dppe in methanol afforded $[Mo_3(NiCl)S_4Cl_3(dppe)_3]$, and the Cl coordinated by the Ni center could not be replaced by CO, PMe_3, or PMe_2Ph. However, the nickel atom in $[Mo_3NiE_4(H_2O)_{10}]^{4+}$ (E = S, Se) readily coordinated CO, ethene, and tertiary phosphines, affording $[Mo_3(NiL)S_4(H_2O)_9]^{4+}$, the CO being eliminated by passing N_2 through aqueous solutions, leading to regeneration of $[Mo_3NiE_4(H_2O)_{10}]^{4+}$.

$[Mo_3NiS_4(H_2O)_{10}]^{4+}$, as its p-$MeC_6H_4SO_3^-$ salt, exhibited antiferromagnetism ($\mu = 0.11$ BM at 2.0 K and 1.26 BM at 260.7 K) and was described formally as containing $Ni^{II}Mo^{IV}Mo^{III}{}_2$. However, this contrasted with the substitution behavior at the nickel center, which appeared to function more like Ni^0, showing that it is difficult to precisely assign formal oxidation states in these clusters.

Reaction of $[Mo_3S_4Cl_4(PEt_3)_4(MeOH)]$ with $[Ni(cod)_2]$ (cod = cycloocta-1,5-diene) afforded the pentanuclear $[Mo_3(NiPEt_3)_2S_4Cl_4(PEt_3)_3]$, whose X-ray structure revealed that the cluster had a square-pyramidal core with an Mo_2Ni_2 base and the third Mo at the apex. The metal–metal distances were relatively short (Mo–Mo, 2.65–2.67 Å; Mo–Ni, 2.5–2.67 Å; Ni–Ni, 2.71 Å), and the XPS spectrum was interpreted in terms of a $Mo_3Ni_2^0$ formalism.

$[Mo_3E_4(H_2O)_9]^{4+}$ (E = S, Se) reacted with Pd in dilute HCl solutions giving $[Mo_3(PdCl)E_4(H_2O)_9]^{3+}$ [**68**, M′ = PdCl] which, when Cl^- was abstracted in the presence of p-$MeC_6H_4SO_3H$, afforded the double cube $[\{Mo_3PdS_4(H_2O)_9\}_2]^{8+}$ [**69**, $M' = Pd$]. In these complexes, the Pd geometry was essentially tetrahedral, implying a formal oxidation state of 0 rather than II. This double cube reacted with halide ions, NCS^-, CO, and tertiary phosphines, with cleavage to give mono-cubic species $[Mo_3(PdL)S_4(H_2O)_9]^{n+}$. Treatment of $[Mo_3(PdCl)S_4(H_2O)_9]^{3+}$ with $HP(O)(OH)_2$ gave $[Mo_3\{Pd[P(OH)_3]\}S_4(H_2O)_9]^{4+}$, a unique example of coordinated $P(OH)_3$, and its $As(OH)_3$ analogue was also prepared. Treatment of $[Mo_3(PdCl)S_4(H_2O)_9]^{3+}$ with tacn (**58**) ($R = H$) afforded $[Mo_3(PdCl)S_4(tacn)_3]^{3+}$. The Pd site in this complex could bind π-acids such as CO, isonitrile, alkene, and alkynes.

Reaction of $[Mo_3S_4(H_2O)_9]^{4+}$ with $[PtCl_4]^{2-}$ in the presence of $HP(O)(OH)_2$ as reductant, afforded the edge-linked double cube $[\{Mo_3PtS_4(H_2O)_9\}_2]^{8+}$ [**69**, $M' = Pt$], which was air-stable and much more inert to substitution than its Ni and Pd analogs. Treatment of $[Mo_3S_4(H_2O)_9]^{4+}$, as the Cl^- salt, with $[Pt(dba)_2]$ (dba = 1,5-diphenyl-1,4-pentadiene-3-one) afforded a brown precipitate which, on treatment with dppe, provided $[Mo_3(PtCl)S_4Cl_3(dppe)_3]$. This species contained Mo atoms coordinated by Cl, chelating dppe and S, and the $\{PtS_3Cl\}$ group had tetrahedral geometry (Mo–Mo, 2.81–2.82 Å; Pt–Mo, 2.74–2.76 Å). $[Mo_3\{Pt(\kappa^1\text{-}dppe)\}S_4Cl_3(dppe)]^+$ could also be obtained from this reaction, and both species were electroactive, the former undergoing reversible oxidation, and the second irreversible oxidation. The Cl ligand in $[Mo_3(PtCl)S_4Cl_3(dppe)_3]$ could not be displaced by CO or tertiary phosphines.

Metallic copper reacted with $[Mo_3S_4(H_2O)_9]^{4+}$ giving air-sensitive paramagnetic $[Mo_3CuS_4(H_2O)_{10}]^{4+}$, [**68**, $M' = Cu(H_2O)$] which, on recrystallization from aqueous p-$MeC_6H_4SO_3H$, afforded the edge-linked double cube $[Mo_3CuS_4(H_2O)_9]^{8+}$ [**69**, $M' = Cu$]. This species was EPR-silent and exhibited $\mu = 0.48$ BM. The single cube $[Mo_3CuS_4(H_2O)_{10}]^{4+}$ was also formed on addition of CuCl to $[Mo_3S_4(H_2O)_9]^{4+}$ or by reduction of Cu^{2+} by BH_4^- in the presence of the incomplete trinuclear cluster. The single cube (**68**), $M = Cu$ was unstable in solution, breaking up into Cu^{2+} and reforming $[Mo_3S_4(H_2O)_9]^{4+}$, but was stabilized in aqueous dilute HCl, when $[Mo_3(CuCl)S_4(H_2O)_9]^{3+}$ was formed. Reaction of $[Mo_3(FeCl)S_4(H_2O)_9]^{3+}$ with a large excess of aqueous Cu^{2+} afforded a mixture of $[Mo_3(CuCl)S_4(H_2O)_9]^{3+}$, $[Mo_3(CuCl)S_4(H_2O)_9]^{4+}$ (containing a $\{Mo_3CuS_4\}^{5+}$ core) and $[Mo_3S_4(H_2O)_9]^{4+}$. Addition of nitrilotriacetate to $[Mo_3(CuCl)S_4(H_2O)_9]^{4+}$ gave $[Mo_3(CuCl)S_4(Hnta)_3]^{2-}$, whose structure was determined as K^+ and NH_4 salts; Mo–Mo, 2.75 Å; Mo–Cu, 2.85 Å, the core being formulated as $Mo_3{}^{IV}Cu^{I}$ which is formally isoelectronic with Mo_3Ni^0. The trinuclear clusters $[Mo_3E_4X_3(dmpe)_3]^+$ reacted with Cu^I halides or with $[Cu(NCMe)_4]^+$ giving $[Mo_3(CuX)E_4X_3(dmpe)_3]^+$ (as PF_6^- salts: $X = Cl$, $E = S$; Mo–Mo, 2.78 Å, Mo–Cu, 2.82 Å; $X = Cl$, $E = Se$; Mo–Mo, 2.84 Å, Mo–Cu, 2.84 Å). Dithiophosphate complexes of the $\{Mo_3CuS_4\}^{5+}$ cluster core were also prepared, that is, $[Mo_3(CuI)(\mu\text{-}OCOR)(dtp)_3L]$ ($R = Me$ or CF_3, $L = DMF$, DMSO, MeCN) and $[Mo_3(CuI)(\mu_3\text{-}OS_3)(\mu\text{-}OAc)(dtp)_3L]$ ($L = py$, dmf). The dithiocarbamate $[Mo_3(CuI)(S_4)(\mu\text{-}S_2CNEt_2)(S_2CNEt_2)_3(py)]$, was also isolated. Diamagnetic dithiophosphinates, $[Mo_3(CuI)S_4(\mu\text{-}S_2PR_2)(S_2PR_2)_3(py)]$ ($R = Et$, Pr^n) were obtained by reacting $[Mo_3S_4(\mu\text{-}S_2PR_2)(S_2PR_2)_3]$ with CuI and pyridine ($R = Pr^n$: Mo–Mo, 2.76–2.78 Å, Mo–Cu, 2.84–2.87 Å).

Corner-sharing Cubic Clusters $\{Mo_6M'E_8\}^{8+}$. The single cube $[Mo_3CdS_4(H_2O)_{12}]^{4+}$ [**68**, $M' = Cd(H_2O)_3$] was obtained by addition of Cd to $[Mo_3S_4(H_2O)_9]^{4+}$, and corner-sharing double cubes $[Mo_6CdS_8(Hnta)_6]^{4-}$ and $[Mo_6CdS_8(dtp)_8(NCMe)_2]$ [**70**, $M' = Cd$] were formed by addition of Cd metal powder to $[Mo_3S_4(Hnta)_3]^{2-}$ and $[Mo_3S_4(dtp)_4(NCMe)_2]$, respectively. When mercury was added to $[Mo_3S_4(H_2O)_9]^{4+}$, only the corner-sharing double cube $[Mo_6HgS_4(H_2O)_{18}]^{8+}$ was formed, the crystal structure of selected clusters indicating Mo–Mo bonding but no Mo–Hg bonding. The structural data were consistent with Hg^0 coordinated by two $\{Mo_3S_4\}^{4+}$ 'ligands', that is, [**70**, $M' = Hg$]. The related Se cluster $[Mo_6HgS_4(H_2O)_{18}]^{8+}$ was also prepared. Addition of the group 13 elements Ga, In, or Tl, either directly as metal powders or generated in situ by BH_4^- reduction of appropriate aqueous salts to $[Mo_3S_4(H_2O)_9]^{4+}$ afforded the single cubes $[Mo_3M'S_4(H_2O)_{12}]^{5+}$ and double, corner-sharing cubes $[Mo_6M'S_8(H_2O)_{18}]^{8+}$, $M' = Ga$, In, or Tl. The oxygen-containing cube $[Mo_6InO_2S_6(H_2O)_{18}]^{8+}$ was also isolated. The group 14 metal clusters $[Mo_3M'E_4(H_2O)_{12}]^{8+}$ and $[Mo_6M'E_8(H_2O)_{18}]^{8+}$ ($E = S$, Se, $M' = Ge$, Sn, Pb) were also prepared by addition of the appropriate metal to $[Mo_3S_4(H_2O)_9]^{4+}$. The germanium clusters could also be generated from GeO or GeO_2. Again, there was no evidence for Mo–M′ bonding in these clusters. The corner-sharing cube $[Mo_6SnE_8(H_2O)_{18}]^{8+}$ [**70**, $M' = Sn^{II}$] could be oxidized to give $[Mo_3SnE_4(H_2O)_{12}]^{6+}$ (**68**), [$M' = Sn^{II}(H_2O)_3$] and then $[Mo_3E_4(H_2O)_9]^{4+}$ and Sn^{IV}, whereas the single cube $[Mo_3SnS_4(H_2O)_{12}]^{6+}$ could be made by direct addition of Sn^{II} to $[Mo_3S_4(H_2O)_9]^{4+}$. Treatment of $[Mo_3SnE_4(H_2O)_{12}]^{6+}$ ($E = S$ or Se) with aqueous Cl^- afforded $[Mo_3(SnCl_3)E_4(H_2O)_9]^{3+}$, but addition of NCS^- to this resulted in substitution of the H_2O molecules at Mo only, the product being $[Mo_3(SnCl_3)E_4(NCS)_9]^{6-}$. Reaction of $[Mo_3S_4(S_2PEt_2)_4]$ with Sn powder and $[Et_2P(S)SSP(S)Et_2]$ in toluene afforded air-stable $[Mo_3SnS_4(\mu\text{-}S_2PEt_2)_3(S_2PEt_2)_3]$, which was also produced by direct addition of $[Sn(S_2PEt_2)_2]$ to $[Mo_3S_4(S_2PEt_2)_4]$. The related species containing the $\{Mo_3(\mu_3\text{-}O)(\mu\text{-}S_3)\}^{4+}$ core, *viz.* $[Mo_3(SnCl_3)OS_3(dtp)_3(py)_3]$ was prepared by reaction of $[Mo_3OS_3(dtp)_4(H_2O)]$ with $[SnCl_3]^-$ and pyridine. No single cube derivatives of $[Mo_3PbE_4(H_2O)_{12}]^{6+}$ have been prepared, and the corner-sharing double cubes $[Mo_6PbS_8(H_2O)_{18}]^{8+}$ [**70**, $M' = Pb$] are air-sensitive. However, reaction of $[PbI_3]^-$ with $[Mo_3S_4(H_2O)_9]^{4+}$ and dtp^- in the presence of pyridine afforded $[Mo_3(PbI_3)S_4(dtp)_3(py)_3]$. Similar chemistry of the group 15 element-containing (As, Sb, Bi) clusters has been reported, both single and corner-sharing double cubes having been characterized. The redox chemistry of $[Mo_6AsS_8(H_2O)_{18}]^{8+}$ was consistent with the formalism $\{Mo_3S_4\}^{4+}As^0\{Mo_3S_4\}^{4+}$. The same was suggested for $[Mo_6SbS_8(H_2O)_{18}]^{8+}$ although the ^{121}Sb Mössbauer spectrum of this compound was regarded as more consistent with Sb^{III}; a situation also thought to be relevant to $[Mo_3SbS_4(H_2O)_{12}]^{4+}$. Addition of SbX_3 to $[Mo_3S_4(dtp)_4(H_2O)]$ in various organic solvents gave $[Mo_3(SbX_3)(dtp)_4L]$ (L = EtOH, py). No single cube derivative of Bi has been reported although $[Mo_3(BiI_3)S_4(\mu\text{-OAc})(dtp)_3(py)]$ has been described.

$[Mo_7S_8(H_2O)_{18}]^{8+}$ is also a double cube (**70**), M′ = Mo in which a single Mo atom is bonded to two $[Mo_3S_4(H_2O)_9]^{4+}$ units, the octacation having a $\{Mo_3S_4(Mo)S_4Mo_3\}$ core. Distances from the unique Mo atom to the other Mo atoms, 3.03–3.06 Å, are longer than the other Mo–Mo bond lengths within each subcluster (2.77 Å). Related clusters $[Mo_7Se_8(H_2O)_{18}]^{8+}$, $[MoW_6S_8(H_2O)_{18}]^{8+}$, and $[MoW_6Se_8(H_2O)_{18}]^{8+}$ have also been prepared. As was mentioned above, the formulation of this species as containing Mo^0 seems inappropriate but no alternative description has been established.

7.3.6 *Octahedral Clusters, Mo_6E_8*

Reduction of $[Mo_3E_4Cl_4(PEt_3)_n]$ (E = S, Se; $n = 3$, 4) afforded the molecular clusters $[Mo_6E_8(PEt_3)_6]$ in which E bridges the triangular faces of the octahedral Mo_6 core, the metal–metal distances being 2.66–2.67 Å (S) and 2.70–2.71 Å (E = Se). Related pyridine, pyrrolidine, and piperidine complexes have been described. $[Mo_6E_8(PEt_3)_6]$ is electroactive, undergoing a single one-electron oxidation and two one-electron reduction steps. Sodium amalgam reduction of the clusters afforded $[Mo_6E_8(PEt_3)]^-$, the octahedral structure becoming slightly distorted, and the Mo–Mo distances slightly longer than in the neutral precursor. Reaction of $[Mo_6S_8(PEt_3)_6]$ with NO^+ afforded paramagnetic $[Mo_6S_8(NO)(PEt_3)_5]$, which has a distorted octahedral metal core, the Mo–Mo bonds involving the Mo atom bound to NO (Mo–N–O 175°) being much longer than the others (2.63 Å). A second product obtained from this reaction, $[Mo_{12}S_{16}(PEt_3)_{10}]$ consists of two octahedral $\{Mo_6S_8\}$ cores connected to each other by two Mo–μ_4–S bonds, which is similar to the bridging mode found in solid-state Chevrel phases. This dodecanuclear cluster, and its selenium analog $[Mo_{12}Se_{16}(PEt_3)_{10}]$, could also be made by abstraction of PEt_3 by S_8 (giving $SPEt_3$) from $[Mo_6E_8(PEt_3)_6]$.

Reaction of the Chevrel phase $[Mo_6Se_8]$ with KCN at 650 °C gave the water-soluble paramagnetic $[Mo_6Se_8(CN)_6]^{7-}$ which could be oxidized in air to the hexa-anionic species. This reaction also afforded insoluble paramagnetic $[Mo_6Se_8(CN)_5]^{6-}$, whose structure shows that the Mo atoms in the basal plane of each $\{Mo_6Se_8\}$ cluster are bound to four terminal CN^- ligands, with the clusters being linked by CN groups into linear chains, represented as $\{Mo_6Se_8(\mu\text{-CN})\}^{6-}$. This species exhibits normal Curie–Weiss behavior over the temperature range 1.8–400 K, with $\mu = 1.99$ BM.

Other octahedral clusters were encountered in $[Mo_6\{Se_2Cl_6\}Cl_3]^{3-}$ and $[Mo_6(TeCl_7)Cl_6]^{3-}$.

7.3.7 *$Mo_6E_8{}^{6+}$ Clusters with Raft-like Structures*

Reaction of $[Mo_3E_4Cl_4L_5]$ (E = S, Se; L = PEt_3 and/or THF) with Mg in THF and −20 °C gave $[Mo_6E_8Cl_6(PEt_3)_6]$, (**71**). This species contains seven Mo–Mo single bonds and the structure was described as formed by two reduced $\{Mo_3E_4\}^{3+}$ triangular clusters held together via a Mo–Mo bond (E = S, 3.00 Å; E = Se, 3.06 Å). A similar structure was encountered in $[Mo_6S_{10}(SH)_2(PEt_3)_6]$, prepared by reaction of $[NH_4]_2[Mo_3S_{13}]$ with PEt_3 in THF. In this cluster a Mo–Mo bond again links the two $\{Mo_3S_4\}$ triangles (2.95 Å).

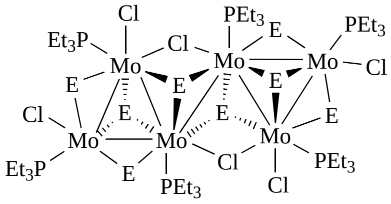

(**71**)

8 RELATED ARTICLES

Hydrodesulfurization & Hydrodenitrogenation; Molybdenum: MPT-containing Enzymes; Molybdenum: Organometallic Chemistry; Oxidation Catalysis by Transition Metal Complexes; Polyoxometalates.

9 REFERENCES

1. E. I. Stiefel, Molybdenum, in ‘Kirk Othmer Encyclopedia of Chemical Technology’, 4th ed., Wiley, New York, 1995, Vol. 16, p. 940.
2. E. R. Braithwaite and J. Haber eds, ‘Molybdenum: An Outline of its Chemistry and Uses’, Elsevier, Amsterdam, 1994.
3. R. Hille, *Chem. Rev.*, 1996, **96**, 2757.
4. R. S. Pilato and E. I. Stiefel, Molybdenum and Tungsten Enzymes, in ‘Bioinorganic Catalysis’, 2nd Ed., eds J. Reedijk and E. Bouwman, Marcel Dekker, New York, 1999, p. 81.
5. A. Sigel and H. Sigel eds, ‘Molybdenum and Tungsten: Their Roles in Biological Processes’, Marcel Dekker, New York, 2002, Vol. 39.

6. C. G. Young, Molybdenum, in ‘Comprehensive Coordination Chemistry II’, eds. J. A. McCleverty and T. J. Meyer, Elsevier, Amsterdam, 2004, Vol. 4, p. 415.
7. M. T. Pope, Polyoxo Anions: Synthesis and Structure, in ‘Comprehensive Coordination Chemistry II’, eds. J. A. McCleverty and T. J. Meyer, Elsevier, Amsterdam, 2004, Vol. 4, p. 635.
8. C. L. Hill, Polyoxometallates: Reactivity, in ‘Comprehensive Coordination Chemistry II’, eds. J. A. McCleverty and T. J. Meyer, Elsevier, Amsterdam, 2004, Vol. 4, p. 679.
9. M. N. Sokolov, V. P. Fedin, and A. G. Sykes, Chalcogenide-Containing Metal Clusters, in ‘Comprehensive Coordination Chemistry II’, eds. J. A. McCleverty and T. J. Meyer, Elsevier, Amsterdam, 2004, Vol. 4, p. 761.
10. G. Parkin, *Acc. Chem. Res.*, 1992, **25**, 455.
11. G. Parkin, *Chem. Rev.*, 1993, **93**, 887.
12. M.-M. Rohmer and M. Bénard, *Chem. Soc. Rev.*, 2001, **30**, 340.
13. J. J. Cruywagen, *Adv. Inorg. Chem.*, 200, **49**, 127.
14. J. P. Caradonna, Oxidation Catalysis by Transition Metal Complexes, in ‘Encyclopedia of Inorganic Chemistry’, ed. R. B. King, John Wiley & Sons, Chichester, 1994, Vol. 6, p. 2866.
15. C. G. Young, in ‘Biomimetic Oxidations Catalysed by Transition Metal Complexes’, ed. B. Meunier, ICP, London, 2000, p. 415.
16. R. R. Schrock, *J. Chem Soc., Dalton Trans.*, 2001, 2541.
17. R. R. Schrock, *Chem. Rev.*, 2002, **102**, 145.
18. W. A. Nugent and J. M. Mayer, ‘Metal-Ligand Multiple Bonds’, Wiley, New York, 1988.
19. E. W. Abel, F. G. A. Stone, and G. Wilkinson, ‘Comprehensive Organometallic Chemistry’, Pergamon, Oxford, 1995.
20. E. I. Stiefel, Molybdenum (VI), in Comprehensive Coordination Chemistry, eds. G. Wilkinson, R. D. Gillard and J. A. McCleverty, Pergamon Press, London, 1986, Vol.6, 630.
21. K. Dehnicke and J. Strähle, *Chem. Soc. Rev.*, 2001, **30**, 125.
22. D. E. Wigley, *Prog. Inorg. Chem.*, 1994, **42**, 239.
23. K. Dehnicke, M. Krieger, and W. Massa, *Coord. Chem. Rev.*, 1999, **182**, 19.
24. J. A. McCleverty, M. D. Ward, and C. J. Jones, *Comments Inorg. Chem.*, 2001, **22**, 293.
25. M. D. Ward and J. A. McCleverty, *J. Chem Soc., Dalton Trans.*, 2002, 275.
26. J. A. McCleverty and M. D. Ward, *Acc. Chem. Res.*, 1998, **31**, 842.
27. J. A. McCleverty and M. D. Ward, in ‘Comprehensive Coordination Chemistry II’, eds. J. A. McCleverty and T. J. Meyer, Elsevier, Amsterdam, 2004, Vol. 2.63.
28. A. M. McDonagh, S. R. Bayly, D. J. Riley, M. D. Ward, J. A. McCleverty, M. A. Cowan, C. N. Morgan, R. Varrazza, R. V. Penty, and I. H. White, *Chem. Mater.*, 2000, **12**, 2523.
29. C. G. Young, in ‘Biomimetic Oxidations Catalysed by Transition Metal Complexes’, ed. B. Meunier, ICP, London, 2000, p. 415.
30. H. Brand and J. Arnod, *Coord. Chem. Rev.*, 1995, **140**, 137.
31. P. K. Baker, *Adv. Organomet. Chem.*, 1996, **40**, 45.
32. P. K. Baker, *Chem. Soc. Rev.*, 1998, **27**, 125.
33. F. A. Cotton and R. A. Walton, ‘Multiple Bonds Between Metal Atoms’, 2nd Ed., Oxford University Press, Oxford, 1993.
34. J. Manna, K. D. John, and M. D. Hopkins, *Adv. Organomet. Chem.*, 1995, **38**, 79.
35. M. H. Chisholm, *Pure Appl. Chem.*, 1991, **63**, 665.
36. J. L. Eglin, in ‘Comprehensive Coordination Chemistry II’, eds. J. A. McCleverty and T. J. Meyer, Elsevier, 2004, Vol. 4.9, p. 603.
37. F. Y. Petillon, P. Schollhammer, J. Talarmin, and K. W. Muir, *Coord. Chem. Rev.*, 1998, **178–180**, 203.
38. F. Taube, I. Andersson, and L. Pettersson, in ‘Polyoxometallate Chemistry: From Topology via Self-assembly to Applications’, eds. M. T. Pope and A. Müller, Kluwer, Dordrecht, 2001, p. 7.
39. A. Müller, F. Peters, M. T. Pope, and D. Gatteschi, *Chem. Rev.*, 1998, **98**, 239.
40. A. Müller, P. Kögerler, and C. Kuhlmann, *Chem. Commun.*, 1999, 1247.
41. A. Müller, P. Kögerler, and H. Bögge, *Struct. Bonding*, 2000, **96**, 203.
42. A. Müller and C. Serain, *Acc. Chem. Res.*, 2000, **33**, 2.
43. A. Müller, E. Beckmann, H. Bögge, M. Schmidtmann, and A. Dress, *Angew. Chem., Int. Ed. Engl.*, 2002, **41**, 1162.

Molybdenum: MPT-containing Enzymes

Charles G. Young
University of Melbourne, Australia

1	Introduction	1
2	Distribution, Classification, and General Chemistry of Mo-MPT Enzymes	2
3	Molybdenum Cofactors (Moco's) and MPT Ligands	3
4	The Dimethyl Sulfoxide (DMSO) Reductase Family	5
5	The Sulfite Oxidase Family	6
6	The Xanthine Oxidase Family	8
7	Synthetic Analogue Chemistry	10
8	A Combined OAT/CEPT Model	13
9	Models for the DMSO Reductase Family	13
10	Models for the Sulfite Oxidase Family	15
11	Models for the Xanthine Oxidase Family	16
12	Conclusion	17
13	Related Articles	18
14	References	18

1 INTRODUCTION

The group 6 elements molybdenum (Z 42) and tungsten (Z 74) are the only second and third row transition metals (*see Transition Metals*) essential to all forms of life on Earth (*see also* ***Tungsten Proteins*** and ***Nutritional Aspects of Metals & Trace Elements***). Molybdenum is found at the active sites (*see Active Site*) of nitrogenase (*see* ***Nitrogenase: Metal Cluster Models*** and ***Nitrogenase Catalysis & Assembly***) and all of the more than 50 known Mo-MPT enzymes (*see Enzyme*).[1–7] The Mo-MPT enzymes feature active sites composed of a single (mononuclear) Mo atom coordinated by one or two MPT-based ligands (*see Ligand*) (MPT = 'molybdopterin' or *M*etal-binding *P*terin ene-1,2-di*T*hiolate); tungsten is also associated with MPT-based ligands in all its known biological manifestations (*see* ***Tungsten Proteins***). The Mo-MPT enzymes are important in the metabolism (*see Metabolism*) of small molecules and anions containing nitrogen, sulfur, carbon, selenium, arsenic, and chlorine, and in the global biogeochemical cycles of these elements. The attributes of selected enzymes are summarized in Table 1; details can be found in Sections 4–6.

There have been tremendous developments in this area since the publication of EIC-I.[1] Advances include: (1) the classification of the enzymes into three families based on sequence and structural comparisons, (2) confirmation of the presence of mononuclear Mo active sites, (3) establishment of the binding mode, redox state, and structural attributes of MPT-based ligands, (4) determination of the composition and structures of the active sites and the emergence of clear targets for model studies, (5) delineation of electron-transfer pathways and reaction mechanisms, and (6) the identification of the genes and proteins involved in MPT biosynthesis and Mo transport, homeostasis (*see Homeostasis*), and regulation.[2–7] Advances in Mo bioinorganic chemistry, particularly the development of OAT/CEPT models and dithiolene (*see Dithiolenes*) synthetic analogues, have accompanied developments on the biological front.[7] Progress in both spheres, viz. enzymatic and synthetic, has depended largely on the continual refinement and application of structural and spectroscopic methods, particularly X-ray crystallography (*see X-ray Crystallography*),[8–11] X-ray absorption spectroscopy (*see X-ray Absorption Spectroscopy*) (especially Extended X-ray Absorption Fine Structure (EXAFS) analysis, *see Extended X-ray Absorption Fine Structure*),[12,13] paramagnetic resonance techniques (Electron Paramagnetic Resonance (EPR), *see Electron Paramagnetic Resonance*; Electron Nuclear Double Resonance (ENDOR), *see Electron Nuclear Double Resonance Spectroscopy*; and Electron Spin Echo Envelope Modulation (ESEEM), *see Electron Spin Echo Envelope Modulation Spectroscopy*),[13–16] resonance Raman spectroscopy (*see Resonance Raman Spectroscopy*),[7,13] Magnetic Circular Dichroism spectroscopy (MCD) (*see Magnetic Circular Dichroism*),[7,13] and advanced electrochemical methods.[17,18]

This account focuses on the Mo bioinorganic chemistry (*see Bioinorganic Chemistry*) of the Mo-MPT enzymes and selected synthetic analogues. It is divided into two main parts. Part 1 (Sections 2–6) provides an overview of the enzyme systems, their distribution, roles, and essential chemistry, as well as a discussion of consensus structures and likely mechanisms. The genes and proteins involved in Mo trafficking and Mo-cofactor biosynthesis are also briefly described. Part 2 (Sections 7–11) summarizes important developments in the production of synthetic analogues, with a focus on new dithiolene, scorpionate (including trispyrazolylborate (*see Tris(pyrazolyl)borates*)) and other complexes sharing the structural, spectroscopic, or chemical attributes of the enzymes.

Current knowledge permits a more definitive description of the enzymes than was possible in EIC-I;[1] however, the fundamental chemistry described therein provides valuable context and valid background for the present account. Since 1994, many reviews of the Mo-MPT enzymes and/or their Mo chemistry have appeared; the major reviews of Hille,[2,3] Pilato and Stiefel,[4] and more recently, Tunney, McMaster, and Garner,[5] deserve special mention (focused reviews are cited in the text). Molybdenum-MPT enzymes and metallodithiolenes were the subjects of recent thematic issues of *Metal Ions in*

Table 1 Properties of selected Mo-MPT enzymes

Enzyme	Source	Subunits, mass (kDa)[a]	Composition[b]	Conversion catalyzed	PDB code[c]
DMSO Reductase Family					
DMSO reductase	*R. sphaeroides*	α, 85	$MoO(OSer)(MGD)_2$	$Me_2SO \rightarrow Me_2S$	1EU1
DMSO reductase	*E. coli* (dmsABC)	$\alpha\beta\gamma$, 140	$MoO(OSer)(MGD)_2$ $[Fe_4S_4]$	$Me_2SO \rightarrow Me_2S$	
Trimethylamine *N*-oxide reductase	*S. massilia*	α, 94	$MoO(OSer)(MGD)_2$	$Me_3NO \rightarrow Me_3N$	1TMO
Nitrate reductase (dissimilatory)	*E. coli* (NarGHI)	$\alpha\beta\gamma_2$, 200	$MoO(SCys)(MGD)_2$ $3[Fe_4S_4]$, $[Fe_3S_4]$, 2 heme	$NO_3^- \rightarrow NO_2^-$	1Q16
Formate dehydrogenase	*E. coli* (FdhF)	α, 79	$MoO(SeCys)(MGD)_2$ $[Fe_4S_4]$	$HCO_2^- \rightarrow HCO_3^-$	1AA6
Polysulfide reductase	*W. succinogenes*	$\alpha\beta\gamma$, 90	$MoX(SCys)(MGD)_2$	$S_n^{2-} \rightarrow S_{n-1}^{2-} + SH^-$	
Arsenite oxidase	*A. faecalis*	$\alpha\beta$, 85	$MoO(OH)(MGD)_2$ $[Fe_3S_4]$ or $[Fe_2S_2]$	$AsO_3^{3-} \rightarrow AsO_4^{3-}$	1G8K
Sulfite Oxidase Family					
Sulfite oxidase	Chicken liver	α_2, 106	$MoO_2(SCys)(MPT)$ b_5-heme	$SO_3^{2-} \rightarrow SO_4^{2-}$	1SOX
Sulfite oxidase	*A. thaliana*	α_2, 88	$MoO_2(SCys)(MPT)$	$SO_3^{2-} \rightarrow SO_4^{2-}$	1OGP
Sulfite dehydrogenase	*Starkeya novella*	$\alpha\beta$, 50	$MoO_2(SCys)(MPT)$ heme *c*	$SO_3^{2-} \rightarrow SO_4^{2-}$	
Nitrate reductase (assimilatory)	Plants	α_2, 228	$MoO_2(SCys)(MPT)$ cyt b, 2FAD	$NO_3^- \rightarrow NO_2^-$	
Xanthine Oxidase Family					
Xanthine oxidoreductase	Cow's milk	α_2, 290	MoOS(OH)(MPT) $2[Fe_2S_2]$, FAD	xanthine → uric acid (see Equation 9)	1FIQ 1FO$_4$
Xanthine dehydrogenase	*R. capsulatus*	$(\alpha\beta)_2$, 275	MoOS(OH)(MPT) $2[Fe_2S_2]$, FAD	xanthine → uric acid (see Equation 9)	
Aldehyde oxidoreductase	*D. gigas*	α_2, 200	MoOS(OH)(MCD) $2[Fe_2S_2]$	RCHO → RCOOH	1HLR
CO dehydrogenase	*O. carboxidovorans*	$(\alpha\beta\gamma)_2$, 277	(MCD)MoO(OH)(SCu) $2[Fe_2S_2]$, FAD	$CO \rightarrow CO_2$	1N5W

[a] Total mass. [b] Per subunit. [c] Structural data can be obtained from the Brookhaven Protein Data Bank (PDB) at http://www.rcsb.org/pdb. Other Mo-MPT enzyme PDB codes include: *Hydrogenophaga pseudoflava* CO dehydrogenase, 1FFV; *Desulfovibrio desulfuricans* aldehyde oxidoreductase, 1DGJ; *Rhodobacter capsulatus* DMSO reductase, 4DMR; *R. sphaeroides* nitrate reductase (dissimilatory), 1OGY; *D. sulfuricans* nitrate reductase (dissimilatory), 2NAP.

Biological Systems[6] and *Progress in Inorganic Chemistry*,[7] respectively.

2 DISTRIBUTION, CLASSIFICATION, AND GENERAL CHEMISTRY OF Mo-MPT ENZYMES

2.1 General Distribution

The enzymes are widely distributed in microorganisms, plants, and animals.[1–6] Three Mo-MPT enzymes have been found in mammals: (1) xanthine dehydrogenase (*see Dehydrogenase*) has many, varied roles in purine catabolism, drug metabolism, and oxidative stress response, (2) aldehyde oxidase is important in drug metabolism and the synthesis of retinoic acid from retinal, and (3) sulfite oxidase plays a crucial role in the detoxification of sulfite produced in the degradation of cysteine and methionine. Genetic Mo-MPT deficiency in humans results in serious neurological disorders and infant death, while enzyme dysfunction manifests in a variety of afflictions.[19] Four MPT enzymes have been found in plants:[20] (1) nitrate reductase (*see Reductase*) catalyzes the conversion of nitrate to nitrite, a key step in the assimilation of nitrogen, (2) aldehyde oxidase catalyzes steps in the formation of phytohormones such as abscisic acid and indole-3-acetic acid, (3) xanthine dehydrogenase is involved in ureide synthesis, purine catabolism, senescence, and oxidative stress response, and (4) sulfite oxidase is responsible for the detoxification of sulfite, produced during sulfur assimilation or from air pollution. Molybdenum deficiency in plants affects many species, causing poor vigor and chlorosis (yellowing) of the leaves, whereas Mo-MPT deficiency causes loss of function and death. The majority of Mo-MPT enzymes (including all those in the DMSO reductase family) are found in microbes. They are responsible for metabolic functions and the adaptation of the organism to available nutrient levels and environmental conditions.[1–6]

2.2 Classification and General Chemistry

The Mo-MPT enzymes are classified into two broad functional types: oxotransferases and hydroxylases (Figure 1). Oxotransferases catalyze oxygen atom transfer (*see Atom Transfer* and *Oxo Transfer*) (OAT) to (for oxidases) or from (for reductases) the central atom of simple oxoanions (*see Oxoanion*), and *S*- and *N*-oxides, employing water as the source or destination of active oxygen (*O). The mediating role of molybdenum in oxygen transfer is obvious from equations (1) and (2), which combine to give the overall catalytic reaction in equation (3). The hydroxylases generally catalyze the insertion of an oxygen atom into C–H bonds of heterocyclic aromatic compounds and aldehydes, the oxygen atom again being derived from water (equation 4). The nature of the active oxygen atom varies by enzyme family (vide infra) as discussed in Sections 4–6. The enzyme reactions couple a two-electron net OAT process (equation 1) with sequential one-electron coupled electron-proton transfer (*see Proton Coupled Electron Transfer*) (CEPT) processes, centered on Mo/water and regenerating the active site (equation 2). Enzyme prosthetic groups (*see Prosthetic Group*) and physiological redox partners are responsible for electron transfer to or from the Mo center as required by equation (2).

$$\mathrm{X + Mo^{VI}[^{*}O] = X^{*}O + Mo^{IV}} \tag{1}$$

$$\mathrm{Mo^{IV} + H_2{}^{*}O = Mo^{VI}[^{*}O] + 2H^{+} + 2e^{-}} \tag{2}$$

$$\mathrm{X + H_2{}^{*}O = X^{*}O + 2H^{+} + 2e^{-}} \tag{3}$$

$$\mathrm{X\text{–}H + H_2{}^{*}O = X^{*}OH + 2H^{+} + 2e^{-}} \tag{4}$$

The enzymes are subdivided into three families based on structural and sequence comparisons (Figure 1, Table 1).[2] Oxotransferases isolated from prokaryotes (*see Prokaryote*) belong to the DMSO reductase family. These enzymes include DMSO reductase, biotin *S*-oxide reductase, trimethylamine *N*-oxide reductase, dissimilatory nitrate reductase, formate dehydrogenase, selenate reductase, and arsenite oxidase; they feature distorted trigonal prismatic $[\mathrm{Mo^{VI}O(AA)L_2}]^-$ (AA = serinate, cysteinate, selenocysteinate, and so on; L = MPT-based ligand (see Section 3)) oxidized active sites (**1**). Some members of the DMSO reductase family, such as formate dehydrogenase and polysulfide reductase, catalyze reactions other than net OAT (see Section 4). Only two oxotransferases, sulfite oxidase and assimilatory nitrate reductase, have been identified in eukaryotes (*see Eukaryote*); they are members of the sulfite oxidase family and contain square-pyramidal *cis*-$[\mathrm{Mo^{VI}O_2L(cysteinate)}]^-$ oxidized active sites (**2**) (see Section 5). The hydroxylases are all members of the xanthine oxidase family. These unique enzymes contain square-pyramidal $[\mathrm{Mo^{VI}OS(OH)L}]^-$ oxidized active sites (**3**) featuring a catalytically essential terminal sulfido ligand (or bridged Mo–S–Cu) moiety. Again, several members of this family catalyze unusual reactions, including the conversion of CO to CO_2 by CO dehydrogenase, hydroxyl group transfer by pyrogallol transhydroxylase, and dehydroxylation by 4-hydroxybenzolyl-CoA reductase (see Section 6). The properties of selected enzymes are presented in Table 1.

3 MOLYBDENUM COFACTORS (Moco's) AND MPT LIGANDS

3.1 Moco's and the Structure and Function of MPT Ligands

The presence of a pterin-dithiolene (MPT-based) ligand at Mo is the unifying feature of the various molybdenum cofactors (Moco's) and enzymes.[1–7] The chemical nature of the pterin-dithiolene ligand was defined by degradative and spectroscopic studies performed by Rajagopalan, Johnson, and coworkers. They proposed the bicyclic structure (**4**) and

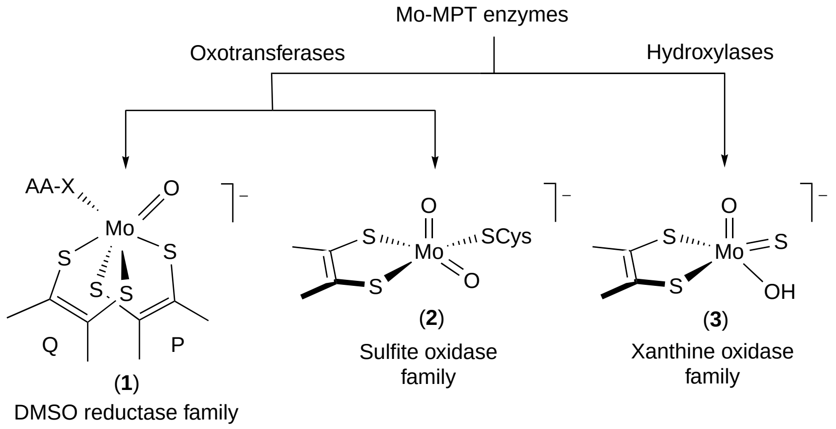

Figure 1 Classification of Mo-MPT enzymes. Structures (**1**)–(**3**) represent oxidized active-site structures (only the dithiolene moiety of each MPT-based ligand is shown)

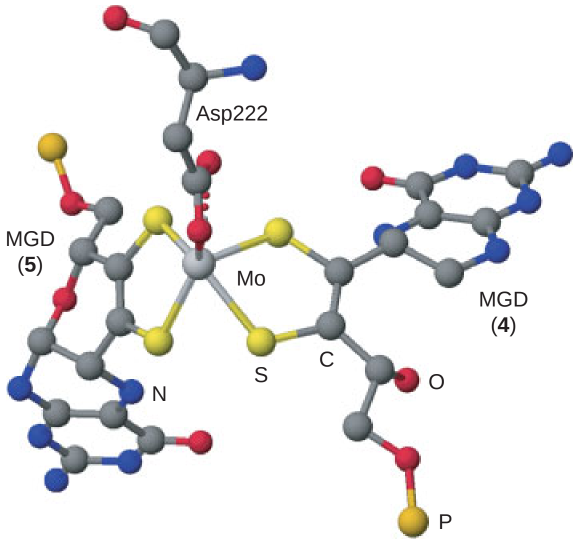

Figure 2 Active site of *E. coli* nitrate reductase, showing pterin forms (**4**) and (**5**). Only the pterin-dithiolene portions of the MGD ligands are shown

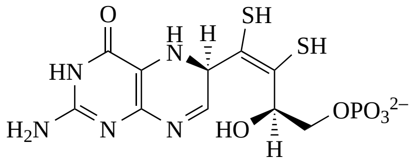

(**4**)

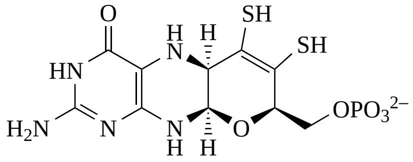

(**5**)

suggested that the dithiolene unit functions as a bidentate ligand (*see Bidentate Ligand*) to Mo. This form was recently identified in *Escherichia coli* nitrate reductase (see Figure 2)[21] and was invoked to explain the electrochemical behavior of *R. capsulatus* xanthine dehydrogenase.[18] Subsequent X-ray crystal structures (*see Crystal Structures*)[8–10] confirmed the general validity of these proposals but revealed an unexpected tricyclic ‘pyranopterin’ form of the ligand (**5**; see also Figures 2, 3, 5, and 7). ‘Molybdopterin (MPT)’ was the name originally coined for the pterin-dithiolene ligand, but the fact that it contains no Mo and binds equally well to W has prompted calls for improved nomenclature. *M*etal-binding *P*terin di*T*hiolate[4] or *M*etal-binding pyrano*P*terin ene-1,2-di*T*hiolate[5] have been proposed as alternative names allowing retention of the widely used MPT abbreviation (the former has the advantage of encompassing both ligand forms (**4**) and (**5**)). In prokaryotic enzymes, the phosphate group of MPT is usually linked to the phosphate group of a 5′-nucleotide of cytidine, guanosine, adenosine, or inosine; these are commonly referred to as ‘dinucleotides,’ and are abbreviated, for example, as MGD (*M*PT-*G*uanosine *D*inucleotide). Although conformationally flexible, MPT-based ligands adopt remarkably similar structures at enzyme active sites. In ubiquitous (**5**), the pyrazine and pyran rings of MPT are nonplanar, the three chiral (*see Chiral*) carbon atoms adopting the (*R*)-configuration. The pyran ring adopts a half-chair conformation and the mean planes defining the pterin and pyran moieties are related by an angle of ca. 40°. The polar groups of MPT (and any nucleotide appendage) are involved in an array of hydrogen bonds that anchor the ligand to the polypeptide chain. Crystallographic data are consistent with dihydropterin (**4**), or equivalent fully reduced tetrahydropterin (**5**) ligand redox levels.[8–10]

As well as its clearly established Moco-anchoring role, it is likely that the ‘noninnocent’ MPT ligand facilitates electron and proton transfer to and from the Mo center (possibly via structural changes modulating the covalency of the Mo–S bonds), the fine-tuning of redox potentials (*see Redox Potential*), and the buffering of oxidation state changes during turnover.[1–7]

3.2 Biosynthesis of MPT and Moco

3.2.1 Molybdate Uptake and Storage

Molybdate is transported into bacteria (*see Bacteria*) and plants by low affinity pathways (on the back of Fe, phosphate, and sulfate uptake) and by specific proteins showing a high selectivity and affinity for $[MoO_4]^{2-}$ over closely related oxoanions. Molybdate transport proteins, designated ModABC, are part of an ATP-binding cassette transporter in the periplasm. Inside the cell, so-called molbindins (Mop-type proteins) store molybdenum and regulate its uptake and utilization. The genes and proteins involved in molybdate transport, homeostasis, and regulation have been reviewed by Pau and Lawson[22] (*see also* ***Metalloregulation***). Animals and humans require Mo as a trace element (*see Trace Element*) in their diets (*see* ***Nutritional Aspects of Metals & Trace Elements***).

3.2.2 Biosynthesis of MPT and Moco

The evolutionarily conserved Moco biosynthetic pathway consists of three steps (Scheme 1): (1) the conversion of a guanosine derivative (probably guanosine triphosphate) into sulfur-free Precursor Z via insertion of C-8 between the ribose C-2′ and C-3′ atoms, (2) sulfurization and transformation of Precursor Z into MPT, catalyzed by MPT-synthase, and (3) metal incorporation through chelation of the dithiolene moiety. Additional steps are involved in the attachment of a nucleotide to generate the dinucleotide forms found

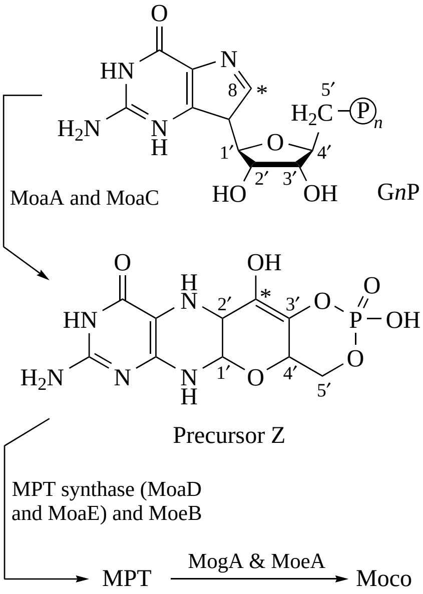

Scheme 1

in bacteria. The biosynthetic pathway in *E. coli* has been extensively studied and many of the proteins involved have been structurally characterized. The multifunctional gephyrin protein is involved in Moco biosynthesis in mammalian and plant cells. The incorporation of the other (nonprotein) ligands at the Mo sites is not well understood; however, some of the enzymes responsible for the terminal sulfido ligand in hydroxylases have been identified. Moco deficiency in humans is a rare autosomal recessive condition marked by severe neurological abnormalities, ocular lens dislocation, and infant death.[19] The burial of Moco deep inside the holoenzymes implicates its incorporation prior to or during protein folding or aggregation, but the details of its incorporation remain unknown. Excellent reviews of Moco biosynthesis are available[9,23] (*see also* ***Metalloregulation***).

4 THE DIMETHYL SULFOXIDE (DMSO) REDUCTASE FAMILY

Enzymes in this family include DMSO reductase, biotin *S*-oxide reductase, dissimilatory nitrate reductase, trimethylamine *N*-oxide reductase, and formate dehydrogenase; they are found exclusively in bacteria and fungi and act as terminal respiratory reductases during anaerobic growth in the presence of their respective substrates.[1–4,24,25] DMSO reductases catalyze the reaction shown in equation (5); the water-soluble enzymes from the purple phototrophic bacteria *R. capsulatus* and *R. sphaeroides* are among the simplest Mo-MPT enzymes, being relatively small (ca. 85 kDa), single subunit (*see Subunit*) enzymes with the Mo center as the only prosthetic group. In contrast, the DMSO reductase from *E. coli* is a heterotrimeric membrane-bound enzyme that couples via the quinol pool to nitrate reductase, thus producing a transmembrane proton gradient for ATP synthesis. The production of dimethyl sulfide by bacteria in the world's oceans has a profound effect on marine life (influencing, e.g., the feeding behavior of sea birds) and global albedo (reflectance) and climate (through its role in cloud formation).[26]

$$\mathrm{Me_2SO(DMSO)} + 2\mathrm{H}^+ + 2\mathrm{e}^- \longrightarrow \mathrm{Me_2S(DMS)} + \mathrm{H_2O} \qquad (5)$$

The enzymes from *Rhodobacter* sp. have been isolated and crystallized under a variety of conditions. A number of crystal structures have revealed the presence of two MGD ligands, designated P and Q, a serinate-147 ligand, and a variable number of water-based ligands; pterin Q displays a range of complexation and redox modes as a result of sample degradation and active-site heterogeneity/disorder.[8–10] EXAFS[27] and resonance Raman[28,29] results provide strong evidence for the presence of distorted trigonal prismatic (*see Trigonal Prism*) monooxo-Mo(VI) (**1**) and square-pyramidal desoxo-Mo(IV) (see species (**c**) in Scheme 2) sites in the oxidized and reduced enzymes, respectively. The active site of the trimethylamine *N*-oxide from *Shewanella massilia* exhibits a closely related structure.[9,10] Substrate specificities in these and related enzymes are determined by the nature of the protein surface, substrate access channel, and the active-site pocket; side-chain (Tyr114 in DMSO reductases, Trp90 in *R. sphaeroides* biotin sulfoxide reductase) interactions with the oxo group, or their absence (in TMSO reductase), are particularly important in fine-tuning redox potentials.

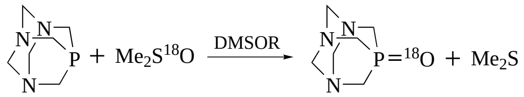

(6)

There is strong evidence for a direct OAT mechanism for DMSO reductases. Schultz *et al.*[30] have demonstrated that *R. sphaeroides* dimethyl sulfoxide reductase catalyzes the reaction in equation (6), an archetypal OAT reaction in synthetic chemistry (Sections 7–9). An intermediate along the OAT reaction coordinate has also been structurally characterized in the form of DMSO-bound *R. capsulatus* DMSO reductase (see species (**d**) in Scheme 2), the DMSO being generated in the reaction of DMS with the terminal oxo ligand.[9,10] Structural data from other techniques (EXAFS, Raman, EPR) have also contributed to the consensus mechanism in Scheme 2. Here, the oxidized oxo-Mo(VI) site (**a** = (**1**)) undergoes CEPT reactions, via Mo(V) (**b**) forms, converting the oxo group to labile water with formation of the desoxo-Mo(IV) active site (**c**). DMSO interacts with (**c**) giving (**d**) – this facilitates direct OAT to produce reduced

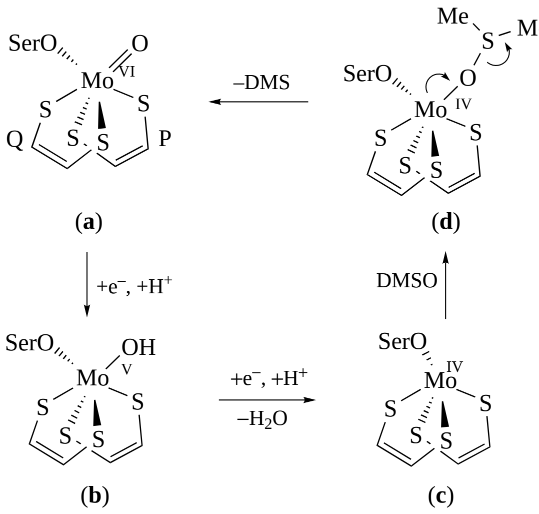

Scheme 2

substrate (DMS) and regenerate the oxo-Mo(VI) site (**a**) (cf. Scheme 3).

Two types of dissimilatory nitrate reductases, localized in either the cytoplasmic membrane or the periplasm, are widespread among bacteria.[1–5,25,31] The cytoplasmic membrane-bound nitrate reductase (Nar) catalyzes the first steps of denitrification ($NO_3^- \rightarrow NO_2^- \rightarrow NO \rightarrow N_2O \rightarrow N_2$) and nitrate ammonification ($NO_3^- \rightarrow NO_2^- \rightarrow NH_3$). These reactions are the terminal electron-transfer reactions during anaerobic respiration, the enzymes being part of a redox loop generating a proton-motive force capable of driving ATP synthesis.[25,31] Periplasmic nitrate reductase (Nap) participates in cellular redox processes, aerobic denitrification, and nitrate scavenging.[25,31]

The heterotrimeric NarGHI from *E. coli* is composed of an $Mo(MGD)_2$ unit (NarG), an [Fe-S] cluster-containing electron-transfer unit (NarH), and a heme-containing membrane anchor (NarI). The Mo active site is remarkable in containing MGD in forms (**4**) and (**5**) and an unsymmetrically bound, bidentate Asp222 ligand (Figure 2).[21] The coupling of formate oxidation (by FdnGHI) and nitrate reduction (by NarGHI) by membrane-soluble menaquinol and/or ubiquinol drives proton translocation across the membrane.[21,25] The Asp222 ligand may function as an ambidentate ligand (*see Ambidentate Ligand*) during catalysis.

The periplasmic nitrate reductases are generally heterodimers, the larger unit (NapA, 90 kDa) binding catalytic $Mo(MGD)_2$ and $[Fe_4S_4]$ centers and the small unit (NapB, 15 kDa) a pair of *c*-type heme groups. A membrane-anchored *c*-type cytochrome (NapC) uses the menaquinol pool to reduce the soluble NapAB complex. The X-ray structures of monomeric Nap from *D. desulfuricans* ATCC 27774 and heterodimeric NapAB from *R. sphaeroides* have been determined.[9,10] The trigonal prismatic oxidized Mo active sites are similar and contain two bidentate MGD ligands, an amino acid thiolate donor (Cys140 and Cys152, respectively), and a water-based ligand. EXAFS studies are consistent with the presence of monooxo (**1**) and desoxo Mo (cf., species (**c**) in Scheme 2) centers in the oxidized Mo(VI) and reduced Mo(IV) forms of the enzyme, respectively. In these enzymes, nitrate is proposed to bind through oxygen to an $Mo^{IV}(Cys)(MGD)_2$ center and undergo direct OAT via O–N bond cleavage, producing nitrite and an $Mo^{VI}O(Cys)(MGD)_2$ center. Regeneration of the active site occurs through proton and electron-transfer processes leading to dissociation of water from the coordination sphere (cf. Scheme 2).

The structure of another member of this family, the selenocysteine-containing formate dehydrogenase H from *E. coli*, has also been determined; it contains an $[Mo^{VI}O(SeCys)(MGD)_2]^-$ oxidized active site (*see* ***Selenium Proteins Containing Selenocysteine***).[8–10] Formate dehydrogenases catalyze the interconversion of formate and carbon dioxide and play an important role in global fixation of carbon dioxide.[32]

Enzymes catalyzing the oxidation of arsenite (AsO_3^{3-}) to arsenate (AsO_4^{3-}) have been identified or isolated from archaea, bacteria, and algae. The active site of arsenite oxidase from *Alcaligenes faecalis*[9,10] contains inequivalent P and Q pterins and two nonpeptide ligands, proposed to be oxo and hydroxo ligands on the basis of EXAFS studies.[33] *Chrysiogenes arsenatis* respires anaerobically using arsenate as the terminal electron acceptor and acetate as electron donor. Reduction of arsenate to arsenite is effected by a periplasmic heterodimeric enzyme, arsenate reductase. Enzymes metabolizing analogous selenium-containing species are also known.[2,3]

Reductive cleavage of sulfur–sulfur bonds in inorganic sulfur species is exploited in terminal electron transfer in some bacteria. The tetrathionate and thiosulfate reductases of the enteric bacterium *Salmonella enterica* LT2 and the polysulfide reductase of the rumen bacterium *Wolinella succinogenes* effect such reactions.[24]

5 THE SULFITE OXIDASE FAMILY

This family includes the sulfite oxidases and dehydrogenases of prokaryotes (*Thiobacilli* sp.), plants, birds, and animals, and the assimilatory nitrate reductases from bacteria, algae, fungi, and plants.[1–5,24] The sulfite oxidases of higher eukaryotes are 100–110 kDa homodimers (Table 1); they are located in the mitochrondrial intermembrane space and catalyze the oxidation of toxic sulfite to innocuous sulfate (equation 7). Human sulfite oxidase deficiency leads to major neurological abnormalities, mental retardation, dislocation of the ocular lenses, and early death.[19]

$$SO_3^{2-} + H_2O + 2\ \text{cyt}\ c^{III} \longrightarrow SO_4^{2-} + 2H^+ + 2\ \text{cyt}\ c^{II} \qquad (7)$$

The crystal structure of chicken liver sulfite oxidase revealed a five-coordinate, square-pyramidal (*see Square Pyramidal*) Mo center coordinated by a bidentate MPT ligand, a cysteine thiolate (from Cys185, conserved in all active enzymes from this family), and two O-donor ligands (Figure 3).**[9,10]** EXAFS**[34]** and resonance Raman**[35]** studies indicate the presence of two oxo ligands in the oxidized enzyme ($\nu(MoO_2)$ 903, 881 cm^{-1}); only one of these is exchanged into $H_2{}^{18}O$ buffer during redox cycling, the other being retained in Mo(V) and Mo(IV) forms. Paramagnetic resonance studies have defined the pH dependent nature of the active site and various anion (*see Anion*) bound forms of the enzyme.**[24]** The types of centers formed under various conditions are shown in Figure 4.

Comprehensive laser flash photolysis studies on chicken and human SO have probed the rates of *intermolecular* electron transfer (IET, *see Intermolecular*) between the Mo and heme centers. Data are consistent with a CEPT mechanism interconverting $Fe^{II}/[MoO_2]^{2+}$ and $Fe^{III}/[MoO(OH)]^{+}$ centers. To account for the wide range of IET rates (20–1400 s^{-1}), it has been proposed that protein conformational changes effectively gate IET by changing the Fe$\cdots$Mo distance.**[24,36]**

The existence of sulfite oxidase in plants such as *Arabidopsis thaliana* (wall or thule cress), tobacco, pea, spinach, barley, carrot, and poplar trees has now been confirmed,**[37]** and the enzyme from *A. thaliana* has been structurally characterized.**[38]** The homodimeric, peroxisomal enzyme lacks the heme domain observed in animal sulfite oxidases, making it the simplest Mo-MPT enzyme yet isolated from eukarya. The animal and plant sulfite oxidases have an overall 47% sequence identity. The detoxification of sulfite, produced in the assimilation of sulfate into sulfur-containing amino acids and membrane components (sulfatides) and from environmental sources (acid rain), is also the principal role of the plant enzymes.

$$NO_3^- + NAD(P)H + H^+ \longrightarrow NO_2^- + H_2O + NAD(P)^+ \qquad (8)$$

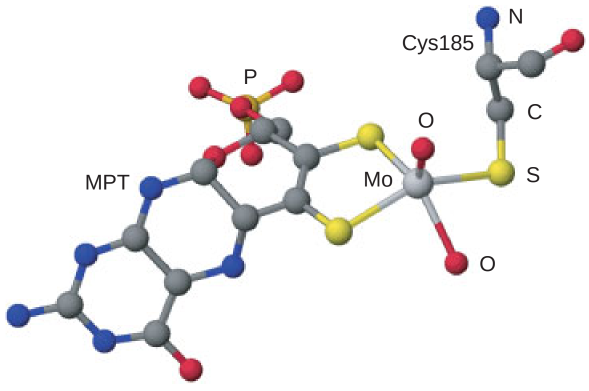

Figure 3 Active site of chicken liver sulfite oxidase. The apical group is a terminal oxo ligand, the second oxygen is an oxo ligand in the oxidized enzyme

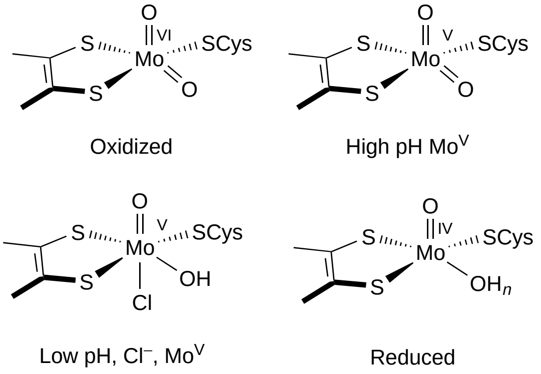

Oxidized

High pH Mo^V

Low pH, Cl^-, Mo^V

Reduced

Figure 4 Important active-site states of sulfite oxidase

Assimilatory nitrate reductases catalyze the first step of nitrate assimilation by bacteria, fungi, algae, and plants (equation 8; Reductant: NADH in plants and most algae, NADPH in fungi); they are estimated to transform ca. 10^7 tons of inorganic nitrogen per year, as a prelude to nitrogen incorporation into proteins and nucleic acids.**[1–5,25,31]** Eukaryotic assimilatory nitrate reductases are cytosolic homodimers (ca. 220 kDa) containing one *b*-type cytochrome, one FAD, and one Mo-MPT center per subunit (Table 1). Two types of assimilatory nitrate reductases, ferredoxin/flavodoxin- and NADH-dependent (Nas) enzymes, are found in bacteria; these cytosolic enzymes contain Mo-MGD and Fe/S groups but not the heme groups found in eukaryotic enzymes. EPR and EXAFS studies of chicken liver sulfite oxidase and *Chlorella vulgaris* nitrate reductase indicate that both enzymes possess similar active sites.**[25,31]**

With respect to the molybdenum center, it appears that a spectator oxo ligand (*see Spectator Ligand (Ion)*) controls the electronic structure allowing the second oxo ligand to participate in OAT reactions with the substrate (*see Substrate*), X = $SO_3{}^{2-}$ for sulfite oxidase (Scheme 3, **a** → **b**); the substrate enters the enzyme via a substrate (solvent) access channel directed toward the exchangeable oxo group. Egress of the oxidized substrate, XO = $SO_4{}^{2-}$, permits the

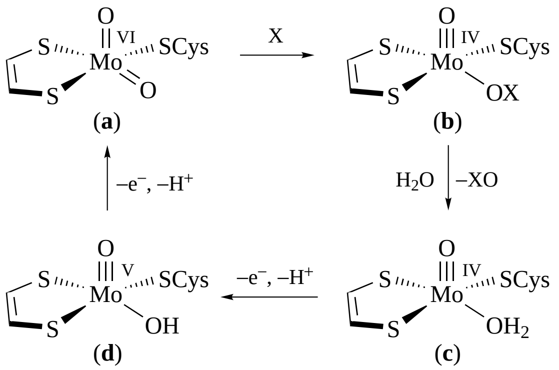

Scheme 3

generation of an *aqua*-Mo(IV) (*see Aqua*) species (**b** → **c**) that undergoes CEPT reactions leading to the regeneration of the active site (**c** → **d** → **a**).[1–4,24] Nitrate reductases would cycle in the opposite direction (cf. Scheme 2 for dimethyl sulfoxide reductase).[1–4,25] The OAT chemistry is represented as a concerted two-electron event, the CEPT chemistry as two consecutive (e^-, H^+) transfers. Other possible mechanisms involve oxoanion binding to Mo prior to OAT or attack of sulfite by activated water (or hydroxide) within the active-site pocket.[2–4,24]

6 THE XANTHINE OXIDASE FAMILY

These enzymes (hydroxylases) are distributed across all phyla and include xanthine oxidoreductase (*see Oxidoreductase*) (oxidase and dehydrogenase),[1–5,39–41] aldehyde oxidoreductase,[1–5,41,42] and a host of lesser known enzymes like 4-hydroxybenzolyl-CoA reductase,[2–4] pyrogallol transhydroxylase,[2–4] picolinate dehydrogenase,[39] CO dehydrogenase,[32] and various quinoline[43] and nicotinate oxidoreductases.[44] They generally catalyze net OAT reactions through the insertion of an oxygen atom into a C–H bond in aromatic heterocycles (e.g., purines, pyrimidines, pterins) and aldehydes, yielding hydroxylated products and carboxylic acids, respectively. Some enzymes catalyze the translocation of hydroxy groups on aromatic substrates and many are selenium-dependent.[45]

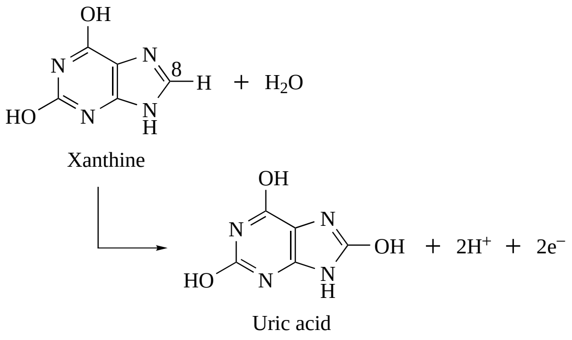

(9)

The xanthine oxidoreductases are large, complex molybdoflavoproteins with roles in the catabolism of purines, for example, oxidizing hypoxanthine to xanthine and xanthine to uric acid (equation 9).[39–41] Xanthine oxidase can also catalyze the reduction of nitrate to nitrite (or in the presence superoxide, peroxynitrite) and the reduction of nitrite to nitric oxide. Peroxynitrite, a powerful and destructive oxidant, has been implicated in diseases such as arthritis, atherosclerosis, multiple sclerosis, and Alzheimer's and Parkinson's diseases. The microbicidal role of milk and intestinal xanthine oxidase may also involve the generation of peroxynitrite in the gut. The high levels of the enzyme in the mammary glands of pregnant or lactating animals suggests a possible role for xanthine oxidoreductases in mammogenesis and lactogenesis.[41] A genetic deficiency of xanthine dehydrogenase leads to the rare but benign condition of xanthinuria (type 1) in humans, whereas enzyme overactivity is associated with hyperuricemia and gout. Allopurinol, a drug for these conditions, acts to suppress xanthine dehydrogenase activity. An excellent review of the potential pathophysiological roles of xanthine oxidase has been prepared by Harrison.[46]

Aldehyde oxidases oxidize azaheterocycles and aldehydes and are involved in the biosynthetic pathways producing retinoic acid and various phytohormones including abscisic acid and indole-3-acetic acid. Aldehyde oxidase and xanthine dehydrogenase both play vital roles in the metabolism of drugs and pollutants, for example, in the metabolism of famciclovir to the antiviral agent penciclovir. Aldehyde oxidoreductase is also important in the metabolism of alcohol (following its transformation to acetaldehyde) and the antimigraine agent almotriptan.[42,46]

The cytosolic, mammalian hydroxylases are homodimeric, with three distinct binding domains for $[Fe_2S_2]$ (20 kDa, N-terminus), FAD (40 kDa), and Mo-MPT (85 kDa, C-terminus) centers.[39–42] Mammalian xanthine oxidoreductases exist in two interconvertible forms, a dehydrogenase (dominant in vivo) employing NAD^+ as electron acceptor and an oxidase employing dioxygen as electron acceptor; the dehydrogenase/oxidase transformation is induced by proteolytic cleavage or cysteine modification.[47] The generation of superoxide and hydrogen peroxide by xanthine oxidase is believed to be responsible for tissue damage due to postischaemic reperfusion injury. The avian and bacterial (*R. capsulatus*) enzymes are stable dehydrogenases. The xanthine dehydrogenase from *R. capsulatus* is unusual for a bacterial Mo-MPT enzyme in that it contains MPT (as in eukaryotic enzymes) rather than a nucleotide derivative.

The presence of a catalytically essential active-site sulfur atom was demonstrated by cyanide deactivation/sulfide reactivation studies performed around 1970. In the 1980s, EXAFS revealed the presence of terminal oxo (Mo=O = 1.73 Å) and terminal sulfido (Mo=S = ca. 2.15–2.18 Å) ligands, as well as two additional sulfur donor atoms. Enzymes from a number of sources have now been structurally characterized (Table 1). These include bovine milk xanthine dehydrogenase and its BOF-4272-inhibited form, the active and alloxanthine-inhibited xanthine dehydrogenase from *R. capsulatus*, the aldehyde oxidoreductases from *D. gigas* and *D. desulfuricans*, and the CO dehydrogenases from *Oligotropha carboxidovorans* and *H. pseudoflava*.[8–10] Crystallographic and spectroscopic data together indicate the presence of five-coordinate, square-pyramidal (or pseudotetrahedral (*see Tetrahedral*)) $[Mo^{VI}OS(OH_n)(MPT)]^{0/-}$ ($n = 1, 2$) oxidized active sites. Resonance Raman studies have allowed the assignment of bands at 899 and $474\,cm^{-1}$ to ν(Mo=O) and ν(Mo=S), respectively; the oxo O atom is nonlabile.[48] Crystallographic evidence supports the presence of an apical terminal

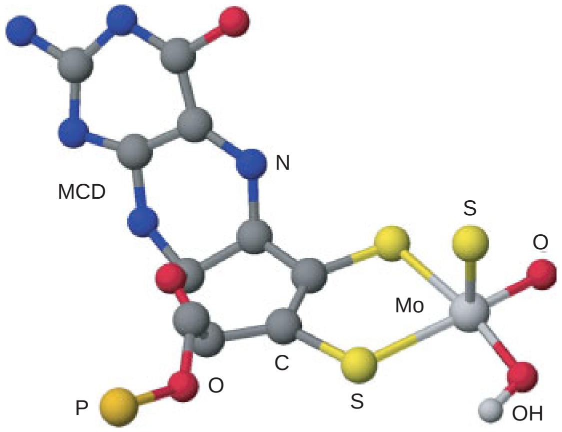

Figure 5 The active site of *D. gigas* aldehyde oxidoreductase. An apical sulfido group is indicated by crystallographic studies but its position remains ambiguous. Although labeled as a hydroxy group, the second oxygen donor may be an aqua ligand. Only the pterin-dithiolene portion of the MCD ligand is shown

sulfido ligand in the square-pyramidal description (Figure 5), but the oxo ligand may in fact be the apical ligand (Figure 6, cf. position of ligand S in CO dehydrogenase (Figure 7)). (Evidence of an equatorial sulfido group has been presented by Okamoto *et al*. Proc. Natl. Acad. Sci. U.S.A., 2004, 101, 7931). The Very Rapid EPR signal of xanthine oxidase ($t_{1/2} \sim 10$ ms) appears during turnover under substrate *limiting* conditions and is assigned to an $[\mathrm{Mo^{V}OS(urate)(MPT)}]^{2-}$ species on the basis of ^{17}O and ^{33}S superhyperfine and ^{13}C-8 ENDOR coupling data (see Section 11.2).[1,40] The unpaired electron is highly delocalized, with ca. 35% sulfido ligand character. In the presence of *excess* substrate, the Rapid signal also appears; ^{1}H and ^{33}S superhyperfine coupling data suggest the presence of an $[\mathrm{Mo^{V}O(SH)}]^{2+}$ center. The presence of bound urate in the Mo(IV) state has been inferred from EXAFS and resonance Raman studies; an $[\mathrm{Mo^{IV}O(SH)(urate)(MPT)}]^{2-}$ center is postulated.[1,40] The detection of intermediates during a *single* catalytic turnover of xanthine oxidase shows that the oxygen atom transferred to substrate originates from the enzyme center and not directly from solvent water.[49] Proposed structures for the important states of active xanthine oxidase are shown in Figure 6. The mechanism shown in Scheme 4 is supported by many lines of evidence but is not the only one possible.[2,4,40] Outstanding mechanistic questions include the nature of the active oxygen, the role of the terminal oxo and thio ligands, and the choreography of proton and electron transfer.

The carbon monoxide dehydrogenase from aerobic, carboxidotropic bacteria catalyzes the oxidation of CO to CO_2, and thereby contributes to the maintenance of subtoxic concentrations of CO in the lower atmosphere. The enzymes are included in the xanthine oxidase family because of sequence similarities and their conversion to inactive ‘desulfo’ (and/or ‘decupro’) forms upon cyanolysis. However, and quite remarkably, the CO dehydrogenase from the bacterium *O. carboxidovorans* (formally *Pseudomonas carboxidovorans*) contains an $\{\mathrm{(MCD)Mo^{VI}({=}O)(OH)(\mu\text{-}S)Cu^{I}(S\text{-}Cys388)}\}$ active site featuring an unprecedented Mo–S–Cu unit (Figure 7).[10,50] The

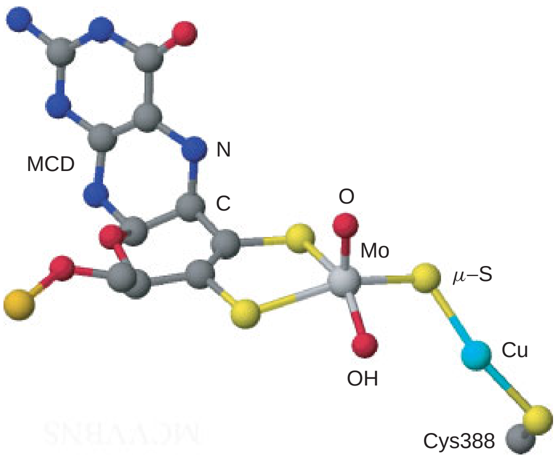

Figure 7 The active site of *O. carboxidovorans* CO dehydrogenase. Although labeled as a hydroxy group, the second oxygen donor may be an aqua ligand. Only the pterin-dithiolene portion of the MCD ligand is shown

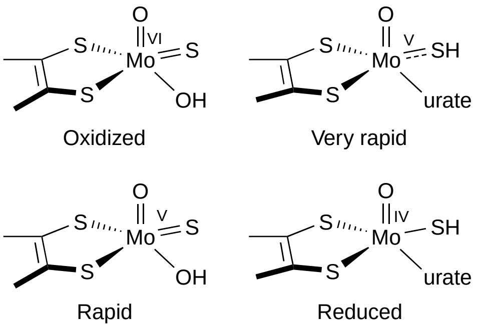

Oxidized Very rapid

Rapid Reduced

Figure 6 Important active-site states of xanthine oxidoreductase

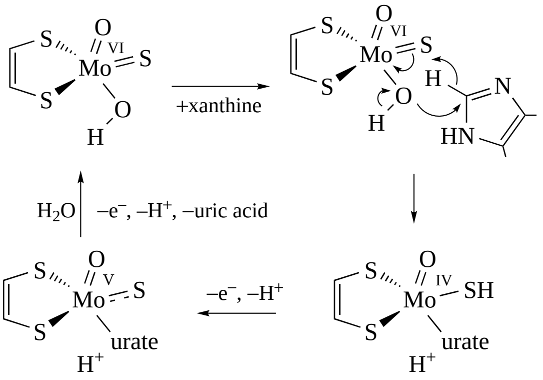

Scheme 4

five-coordinate, square-pyramidal Mo center closely resembles that of active xanthine oxidase, with an oxo ligand in the *apical* site and a longer (as expected) Mo–(μ-S) distance; the geometry at the Cu(I) center is close to linear. The presence of the binuclear heterometallic unit has been confirmed by complementary EXAFS studies.**51** A mechanism involving a thiocarbonate intermediate formed by cooperative binding of the polar CO molecule by the two metal centers has been proposed.

7 SYNTHETIC ANALOGUE CHEMISTRY

7.1 The Contribution of Synthetic Analogues

The synthetic analogue or model approach provides insights into bioinorganic systems through the synthesis and study of closely related 'model' compounds. It garners structural, electronic, spectroscopic, and chemical information crucial to a complete understanding of enzyme behavior.**4,52** This section begins with some general observations relating to biologically relevant ligands and OAT and CEPT reactions. Selected chemistry relating to specific enzyme families is then presented. An exhaustive review of mononuclear Mo chemistry can be found in *Comprehensive Coordination Chemistry II***53** (*see also* ***Molybdenum: Inorganic & Coordination Chemistry***).

7.2 Ligands Important in Biomolybdenum Chemistry

7.2.1 Ligands Derived from Water: Oxo, Hydroxo, Aqua

High-valent molybdenum chemistry is dominated by oxo complexes.**53** The terminal oxo group is characterized by multiple bonding (one σ and up to two π components) to the metal, a short Mo=O distance (1.64–1.72 Å), and group-specific IR absorptions. The strong trans influence (*see Trans Influence*) of the oxo ligand is responsible for lengthening (by 0.15–0.3 Å) or disfavoring *trans* Mo–L interactions. Complexes containing *fac*-MoO_3, *cis*-$[MoO_2]^{2+}$, and $[MoO]^{4+}$ units are common in oxo-Mo(VI) chemistry. Dioxo complexes are very common and tetrahedral, trigonal bipyramidal, and (in the main) distorted octahedral (*see Octahedral*) geometries are observed. Seven-coordinate, pentagonal bipyramidal (*see Pentagonal Bipyramid*) peroxo complexes currently constitute the largest class of monooxo-Mo(VI) complexes. A wide variety of O-, N-, S-, and mixed-donor ligands serve as coligands in these oxo complexes. Mononuclear Mo(V) and Mo(IV) complexes generally contain a single oxo group and exhibit square-pyramidal or distorted octahedral structures. The highly reactive *cis*-dioxo-Mo(V) complexes, $[(L\text{-}N_2S_2)MoO_2]^-$ and $[Tp^*MoO_2X]^-$ (see (**6**) and (**7**) for ligand structures), are rare exceptions (but EPR signals from such centers have never been observed in enzymes). In the absence of steric protection, Mo(V) complexes exhibit a marked tendency for di- or polynucleation reactions. The chemical reactions of oxo-Mo(VI–IV) complexes have been extensively reviewed.**53,54**

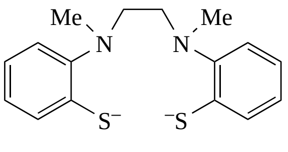

(**6**) L-N_2S_2

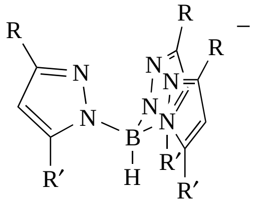

(**7**) Tp*: R = R′ = Me
Tp^{Pr}: R = ^{i}Pr, R′ = H

Mo-MPT enzymes mediate formal exchange of an oxygen atom between the substrate and water (equation 3), and at some stage water is bound to the Mo center. CEPT reactions are responsible for the interconversion of aqua, hydroxo, and oxo ligands upon the oxidation state change; hydroxo ligation is inferred from enzyme EPR spectra, but direct evidence for aqua ligation is lacking. Aqua(oxo) complexes, exemplified by *cis*-$Mo^{VI}O_2(OH_2)_2Cl_2$, $[Mo^VOX_4(OH_2)]^-$, and $[Mo^{IV}O(OH_2)(dppe)_2]^+$, generally possess trans aqua(oxo) arrangements. However, certain coligands can induce a cis geometry, as observed in six-coordinate (L-N_2S_2)MoO(OH) and Tp*MoO(OH)X (X = monodentate anion).**53**

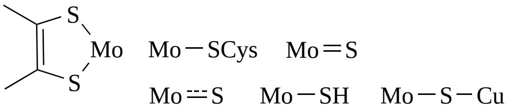

(**8**)

7.2.2 Sulfur Ligands

The Mo–S linkages shown in (**8**) are found at the active sites of Mo–MPT enzymes. Dithiolene, thiolate, and hydrosulfido complexes are known for all common Mo oxidation states, although the latter are extremely rare; terminal thio ligation is restricted to Mo(VI-IV) complexes.**53** Metallodithiolenes have been extensively studied and reviewed.**7,53** Biologically relevant dithiolene complexes feature two types of ligands: arene-1,2-dithiolates (where the 'ene' function is part of an aromatic ring) and authentic dithiolenes (see Sections 9 and 10). Two structural motifs are encountered in ternary oxo bis(dithiolene)-Mo complexes. Firstly, distorted octahedral geometries are observed for *cis*-dioxo-Mo(VI) complexes; here, the longest Mo–S distances (ca. 2.6 Å vs 2.4 Å) are trans to the terminal oxo ligands (d(Mo=O) = 1.70–1.73 Å). Secondly, square-pyramidal complexes with apical oxo ligands are characteristic of both Mo(V) and Mo(IV) complexes.[53] The study of these and related complexes is relevant to the modeling of the DMSO reductase family of enzymes (see Sections 7.3 and 9.1). Mono(dithiolene) complexes relevant to the other two enzyme families are still quite rare and generally do not participate in clean OAT reactions.[53] Very recent progress in this area is described in Section 10.

The synthesis of Moco's (Mo-MPT complexes) presents significant challenges, however, progress is being made.[4,52,55] A general strategy for the synthesis of asymmetrically substituted dithiolenes, involving the generation of dimethylamino- or thione-protected 1,3-dithiolates and their subsequent deprotection by alkaline hydrolysis (Scheme 5), has been developed by Garner, Joule, and coworkers. In the presence of $[MoO_2(CN)_4]^{4-}$, square-pyramidal oxo-Mo(IV) complexes of the type $[MoO(dithiolene)_2]^{2-}$ are formed (R = phenyl, pyridyl, quinoxalinyl, or pterinyl derivatives). These are stepping stones to Mo(V) complexes and may serve as precursors to the Mo(VI) species.[55] The reactions of alkynes with polysulfido complexes (*EIC-1*)[1] or α-bromo ketones with $Cp_2Mo(SH)_2$,[56] have also been exploited in the synthesis of unsymmetrical dithiolenes, including some pterin derivatives. Some of these undergo oxidative decomposition producing molecules closely related to urothione, the excretory by-product of MPT degradation.

Investigations by Enemark, Kirk, and coworkers have provided insights into the electronic structure and function of dithiolene- and thiolato-Mo complexes and Mo-MPT enzymes.[7] For example, Tp*MoOL (L = arene dithiolate, e.g., benzene-1,2-dithiolate (bdt)) and related nitrosyl complexes feature a highly covalent, three-center, pseudo-σ bonding interaction between the redox-active Mo ϕ_{xy} and S (dithiolene) in-plane $\phi^{a'}$ orbitals; this interaction is optimized when the strong-field ligand is cis and perpendicular to the MoS_2 plane. A π interaction between the Mo ϕ_{xy} and S $\phi^{a'}$ out-of-plane orbitals is also possible depending on the electronic requirements of the metal; here, the degree of orbital interaction is determined by the fold angle of the Mo-dithiolene unit along the S$\cdots$S vector. The redox potentials and rates of electron transfer to or from enzyme Mo-MPT centers may be controlled by variations in interactions of this type.[7,57] Related studies have defined the covalency and electronic structures of thiolate complexes, including known $[MoO(SR)_4]^{-}$[58,59] and $(L\text{-}N_2S_2)MoO(SR)$[60] complexes.

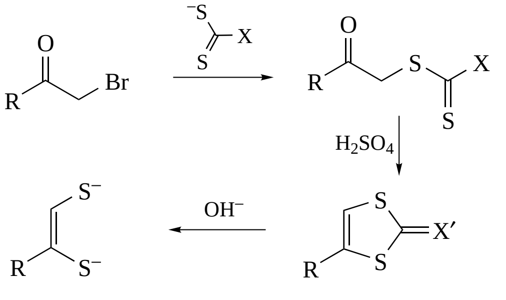

$X = OPr \rightarrow X' = O$; $X = NMe_2 \rightarrow X' = NMe_2{}^+HSO_4{}^-$

Scheme 5

Only a handful of pseudotetrahedral or octahedral oxosulfido-Mo(VI) and -Mo(V) complexes are known, and their chemistry is described in Section 11. Mononuclear sulfido-Mo(V) complexes are unstable due to their susceptibility to redox, polynucleation, and hydrolysis reactions. Trispyrazolylborate derivatives such as structurally characterized $Tp^*Mo^{V}SX_2$ (X = Cl, OPh derivative; X_2 = bdt, catecholate) are most commonly encountered. The Tp* complexes exhibit short Mo=S bonds (ca. 2.13 Å), intense S(1s) $\rightarrow \pi^*$ (Mo=S) XAS transitions characteristic of terminal thio ligands, and EPR g_{iso} (*see g-Factor*) values substantially lower than their oxo analogues.[53]

Speculation about the precise roles of active-site sulfur is tempered by an appreciation of the redox versatility and interplay of sulfur and molybdenum. This is evident from synthetic systems, where the catenation of sulfur (with attendant redox and/or ligand elaboration) and induced internal electron-transfer reactions are frequently observed. The redox interplay of Mo and S, reflected in 'undesirable synthetic outcomes,' may prove crucial to a full description of enzyme behavior.[61,62] (*see also* ***Sulfur: Inorganic Chemistry***)

7.3 Atom Transfer Chemistry

Molybdenum has a marked predilection for OAT reactions[53] and biomimetic systems have been reviewed.[54] OAT is a concerted two-electron process that results in the oxidation of the oxygen atom acceptor and the reduction of the donor. The most common reactions for Mo are shown in equations (10) and (11). Catalysis results from the coupling of these reactions, leading to net oxidation of X by X′O (equation 12, cf. equation 6). Transformations involving oxo-Mo(VI) and desoxo-Mo(IV) complexes are recent and important developments (see Section 9).

$$Mo^{VI}O_2L_n + X \longrightarrow Mo^{IV}OL_n + XO \tag{10}$$

$$Mo^{IV}OL_n + X'O \longrightarrow Mo^{VI}O_2L_n + X' \tag{11}$$

$$X + X'O \longrightarrow XO + X' \tag{12}$$

Comproportionation and concomitant formation of μ-oxo (*see μ-Oxo Bridge*)-Mo(V) species (equation 13) is a prevalent complication in Mo OAT chemistry; the formation of dinuclear (*see Dinuclear*) complexes can be reversible or irreversible, allowing access to both Mo(IV) and Mo(V) complexes or only Mo(V) species, respectively.[54]

$$Mo^{VI}O_2L_n + Mo^{IV}OL_n = Mo^{V}_2O_2(\mu\text{-}O)L_{2n} \tag{13}$$

For neutral complexes, comproportionation is usually encountered when L is not sufficiently bulky to prevent close approach of the Mo atoms. Complexes containing dithio acid, cysteine ester (CysOEt), tridentate Schiff base (hpd), and 2,6-bis(2,2-diphenyl-2-thioethyl)pyridine(2−) ($L\text{-}NS_2$) ligands readily participate in comproportionation/dinucleation reactions.[54] Dinucleation must be prevented in the development of valid enzyme models and steric, electrostatic, and/or immobilizing strategies have been successful in this regard. Comproportionation to monomeric Mo(V) species is also observed but this can be controlled and exploited to produce models for the EPR-active Mo(V) states of enzymes.[54]

The ligands Tp* (and derivatives) (**7**), 2,2-diphenyl-2-mercaptoethanoate(2-) (L-SO), bis(4-*t*-butylphenyl)-2-pyridylmethanethiolate(1-) (L-NS), and various dithiolenes support clean OAT reactions between monomeric species (equations 10 and 11); the reactions have been extensively studied by kinetic methods (*see Kinetic Methods*).[54] The rate constants for these reactions span a ca. 10^6 range depending on the nature of the substrate and ligand (Table 2). In substrate oxidation reactions (equation 10), phosphines feature prominently as oxygen atom acceptors (X). Generally, these reactions are first order in both the phosphine and Mo complex; they are proposed to proceed by an associative mechanism involving nucleophilic attack of the phosphine lone pair on the π^* Mo=O orbital. Theoretical studies have shown these reactions are facilitated, both electronically and energetically, by the presence of a 'spectator oxo group,' and phosphine oxide intermediates have now been isolated and structurally characterized.[63] The mechanism of sulfite oxidation by dioxo-Mo(VI) complexes is less certain (see Section 10.2).

A much broader range of substrates is amenable to reduction by oxo-Mo(IV) complexes (equation 11). These include many biological substrates such as *S*- and *N*-oxides and nitrate, and species related to selenate and arsenate. These reactions are also first order in both the substrate and metal complex; they are proposed to proceed by associative mechanisms involving coordination of substrate to Mo and concomitant OAT.[54] A thermodynamic scale for OAT reactions has been described by Holm and Donahue.[64]

More recently, simple complexes such as $MoO_2X_2(DMSO)_2$ (X = Cl, Br), $(PPh_4)_2[MoO_2(NCS)_4]$, $MoO_2(NCS)_2(Bu^t_2bpy)$, and $MoO_2(acac)_2$ have been shown to catalyze OAT without apparent comproportionation.[54] These observations have challenged the accepted 'design criteria' for efficient OAT catalysis.

7.4 Coupled Electron-proton Transfer (CEPT) Reactions

Regeneration of enzyme active sites is proposed to take place via two one-electron CEPT reactions, accounting for the detection of EPR-active Mo(V) enzyme states. CEPT reactions are facilitated by the quite general interconversion of water-based (oxo, hydroxo, aqua) ligands induced by changes to the oxidation state of the metal. Related transformations interconverting thio and hydrosulfido coligands at oxo-Mo centers are envisaged in hydroxylases. The electron density at the metal center is communicated to the donor oxygen atom via the π-bonding framework; reduction of the center increases the basicity and level of protonation (*see Protonation*) of oxygen while oxidation decreases the basicity and level of protonation of oxygen. While detailed mechanistic information is often lacking, CEPT processes remain the most logical explanation for many synthetic outcomes and the generally irreversible reduction of high-valent oxo-Mo species.[53] The stoichiometries of the synthetic reactions represented by equations (14), (15), and (16) (E = electrophile (*see Electrophile*) (H^+, $SiMe_3$), vide infra) are well established and hint at CEPT or, more broadly, coupled electron-electrophile transfer (CEET) processes.[1] The literature should be consulted for a full overview of OAT and CEPT reactions.[4,53,54]

$$[Mo^{VI}O_2(L\text{-}SO)_2]^{2-} + RSH + H^+ \longrightarrow [Mo^{V}O(L\text{-}SO)_2]^{-} + H_2O + \frac{1}{2}RSSR \tag{14}$$

$$Mo^{VI}O_2\{L\text{-}(NH)_2S_2\} + e^- \longrightarrow [Mo^{V}O\{L\text{-}N_2S_2\}]^- + H_2O \tag{15}$$

$$Tp^*Mo^{VI}O_2(SPh) + e^- \longrightarrow [Tp^*Mo^{V}O_2(SPh)]^- \longrightarrow (+E^+) \longrightarrow Tp^*Mo^{V}O(OE)(SPh) \tag{16}$$

Table 2 Selected kinetics data for OAT from Mo(VI) complexes to PPh_3[a]

Complex	k, $M^{-1}\,s^{-1}$	Complex	k, $M^{-1}\,s^{-1}$
$MoO_2(NCS)_2(Bu^t_2bpy)^b$	22	$MoO_2(L\text{-}NS)_2$	$5.6(1) \times 10^{-3}$
$(PPh_4)_2[MoO_2(NCS)_4]^b$	1.7	$(NEt_4)_2[MoO_2(bdt)_2]^{d,f}$	3.9×10^{-3}
$MoO_2(S_2CNEt_2)_2{}^{c,*}$	0.071(3)	$MoO_2(CysOEt)_2{}^{g,*}$	2.9×10^{-4}
$MoO_2Cl_2(DMSO)_2$	0.043(1)	Tp^*MoO_2X	
$(NBu_4)_2[MoO_2(mnt)_2]^d$	0.056(1)	$X = S_2P(OEt)_2{}^{-h}$	$3.4(1) \times 10^{-3}$
$MoO_2(Me\text{-}hpd)(dmf)^*$	0.0149(2)	$X = SPh^-$	$5.9(2) \times 10^{-4}$
$MoO_2(Bz\text{-}hpd)(dmf)^*$	$8.9(2) \times 10^{-3}$	$X = S_2PPr^i_2{}^{-f,h}$	$2.5(3) \times 10^{-4}$
$MoO_2(L{-}NS_2)^{e,*}$	$7(1) \times 10^{-3}$	$X = OPh^-$	$2(1) \times 10^{-6}$

[a] Reactions at 25 °C in *N*,*N*-dimethylformamide (dmf) unless indicated.[54] Monomer products are not the final products of asterisked reactants. [b] In dichloromethane. [c] In 1,2-dichloroethane. [d] In acetonitrile. [e] At 23 °C. [f] At 30 °C. [g] At 35 °C. [h] In toluene.

8 A COMBINED OAT/CEPT MODEL

The Mo-Tp* and Mo-Tp$^{\mathrm{Pr}}$ chemistry summarized in Scheme 6 represents a unique, holistic model of an important paradigm in Mo-MPT enzymes, the coupling of OAT and CEPT reactions during substrate turnover.[54,65]

The complexes *cis*-Tp*Mo$^{\mathrm{VI}}$O$_2$X (X = halide, monoanionic O-, N- or S-donor) react with PPh$_3$ to produce OPPh$_3$ and a variety of Mo-containing products, depending on the conditions (particularly the solvent) of the reaction (see Table 2 for rate constants); oxo-Mo(IV) complexes, Tp*MoOX(solv), are generated when coordinating solvents like dmf, MeCN, and pyridine are employed (cf. equation 1). Both types of complexes exhibit six-coordinate octahedral structures, as exemplified by the structure of Tp*MoO$_2$(SPh) in Figure 8. Complexes containing ambidentate dithiophosphate and -phosphinate complexes undergo similar reactions, the dithio ligands being monodentate and bidentate in the dioxo-Mo(VI) and oxo-Mo(IV) species, respectively.[54] An associative mechanism, in which the nucleophilic phosphine attacks a terminal oxo ligand, is supported by kinetics and computational studies.[54,66] The phosphine oxide intermediates in such reactions have now been isolated and structurally characterized.[63] The oxo-Mo(IV) complexes react with a variety of S- and N-oxides and nitrate to reform the dioxo-Mo(VI) species and catalyze the oxidation of phosphines by S- and N-oxides (equation 12, cf. equation 6).

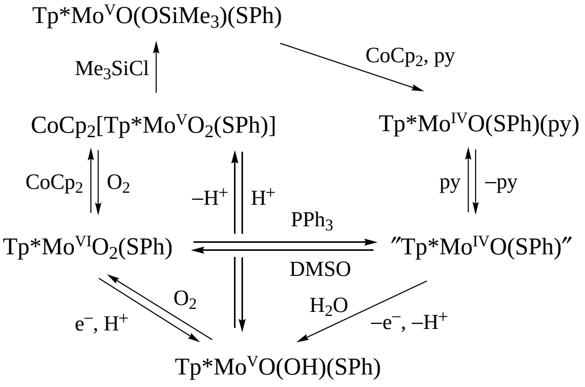

Scheme 6

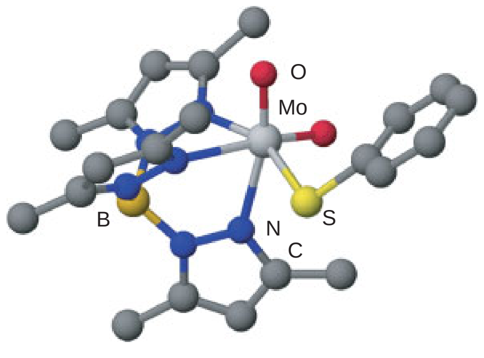

Figure 8 Structure of Tp*MoO$_2$(SPh)

One-electron redox processes (effected electrochemically or chemically) permit Mo(V) states to be accessed and facilitate the coupling of the two-electron OAT reactions to (regenerative) one-electron CEPT reactions. The dioxo-Mo(VI) complexes undergo electrochemically reversible one-electron reductions producing dioxo-Mo(V) species, for example, [Tp*MoO$_2$X]$^-$, characterized by broad and anisotropic EPR spectra; these are readily protonated to give Tp*MoO(OH)X, which feature less-anisotropic doublet EPR signals (due to ^{1}H superhyperfine coupling) similar to those exhibited by enzymes. Chemical reduction permits the isolation of salts such as CoCp$_2$[Tp*MoO$_2$(SPh)], Tp*MoO(OH)(SPh) and derivatives of the type Tp*MoO(OSiMe$_3$)X. The dioxo-Mo(V) complexes support a variety of one-electron processes but do not participate in two-electron OAT reactions.

The generation of oxo(hydroxo)-Mo(V) species, for example, Tp*MoO(OH)X, in the reactions of Tp*MoO$_2$X with half an equivalent of PPh$_3$ in wet solvents is interpreted in terms of combined OAT/CEPT reactions. Thus, water is an effective ligand for the binding site of putative Tp*MoOX, formed upon OAT from Mo to phosphine, and unreacted Tp*MoO$_2$X is an effective oxidant for Tp*MoOX(OH$_2$). Hence, comproportionation (equation 17) mimics oxidation of reduced enzymes by external oxidants.[54]

$$\mathrm{Tp^*Mo^{IV}OX(OH_2) + Tp^*Mo^{VI}O_2X \longrightarrow 2Tp^*Mo^{V}O(OH)X} \qquad (17)$$

Combined with the ready autoxidation (*see Autoxidation*) of the oxo(hydroxo) complex, it is possible to effect the catalytic aerial oxidation of substrates with this system. ^{18}O and ^{17}O-labeling studies have confirmed that the oxygen atom transferred to PPh$_3$ comes from Tp*MoO$_2$X, and that like the enzyme systems water, not dioxygen, is the source of active oxygen. Overall, the oxidation of PPh$_3$ by Tp*MoO$_2$X in wet aerobic solvents is represented by equation (18) (cf. equation 3).[65] An OAT/CEPT system interconverting monooxo and desoxo complexes, viz, [Tp*Mo$^{\mathrm{VI}}$OX$_2$]$^+$ to [Tp*Mo$^{\mathrm{IV}}$(OPPh$_3$)X$_2$]$^+$ (thence to [Tp*Mo(OH$_2$)X$_2$]$^+$), is under development by Basu and coworkers.[67]

$$\mathrm{PPh_3 + H_2{}^*O + 2O_2 \longrightarrow {}^*OPPh_3 + 2HO_2} \qquad (18)$$

9 MODELS FOR THE DMSO REDUCTASE FAMILY

9.1 Functional Models

The OAT reactions of bis(dithiolene) complexes are of interest from a biological perspective (nb. DMSO reductase enzymes); here, comproportionation and dinucleation appear to be prevented by electrostatic factors.[54] Dioxobis(dithiolene) complexes react with oxygen atom acceptors (X) according to equation (10), and kinetics data are available for the reactions of $[MoO_2(bdt)_2]^{2-}$ with PPh_3[68] (Table 2) and $(NBu_4)_2[MoO_2(mnt)_2]$ (mnt = 1,2-dicyanoethenedithiolate) with HSO_3^- (Section 10.2), phosphites,[69] and phosphines[70] (Table 3). For phosphine reactions, OAT rates increase as the basicity of the substrate increases (inversely to the parameter χ; see Table 3). The rate ratio k_{Mo}/k_W of ca. 10^2-10^3 (Table 3) indicates that Mo complexes are more effective oxidants than their W analogues; the same is true of Mo-MPT enzymes and their W analogues (*see* ***Tungsten Proteins***).[55,71] Oxidation of benzoin by $[MoO_2L_2]^{2-}$ (L = bdt derivatives) proceeds according to equation (19); a deuterium isotope effect (*see Isotope Effect*), $k_H/k_D \sim 4.0$, is consistent with α-hydrogen atom abstraction by an oxo ligand in the rate-determining step.[68] Mo-MPT enzymes catalyze the conversion of $RCH(OH)CO_2^-$, a substrate similar to benzoin, to $RCOCO_2^-$.

$$[MoO_2L_2]^{2-} + PhCH(OH)COPh \longrightarrow [MoOL_2]^{2-} + PhCOCOPh + H_2O \qquad (19)$$

The reactions of $[MoOL_2]^{2-}$ with Me_3NO to give $[MoO_2L_2]^{2-}$ and Me_3N (cf. equation 11) are pseudo-first-order with k_{obs} values in the range $2.6(5) \times 10^{-3}$ to $5.7(4) \times 10^{-3}\ s^{-1}$ for L = bdt derivatives.[54] The reactions are proposed to occur via binding of Me_3NO to the trans vacant site (*see Vacant Site*) of $[MoOL_2]^{2-}$, followed by a *trans* → *cis* rearrangement and cleavage of the N–O bond. A dramatic rate enhancement (ca. 10^4-10^5) is observed for complexes stabilized by ligand NH···S(dithiolene) hydrogen bond interactions.[73]

9.2 Structural and Functional Models

The synthesis and study of monooxo-Mo(VI) and desoxo-Mo(IV) bis(dithiolene) complexes are recent developments in this area; associated chemistry is summarized in Scheme 7. The oxo-Mo(VI) complexes, $NEt_4[MoO(OR)L_2]$, are prepared by silylation of $(NEt_4)_2[MoO_2L_2]$ with $ClSi^tBuPh_2$ ($R = Si^tBuPh_2$) or by OAT to the Mo(IV) complexes $NEt_4[Mo(OR)L_2]$ ($R = {}^iPr$, 2-Ad, Ph etc.; L = bdt, $S_2C_2R'^{2-}_2$ (R′ = H, Me, Ph)).[74] Structurally characterized $NEt_4[MoO(OSi^tBuPh_2)(bdt)_2]$ (Figure 9) exhibits a severely distorted octahedral structure, with *cis* O-donors and *d*(Mo=O) 1.715(2) Å, *d*(Mo–O) 1.932(2) Å, and ∠(Mo–O–C) = 160.0(2)°; the Mo–S bond 'trans' to oxo is longer than the others present. Complexes containing authentic dithiolene ligands are unstable to hydrolysis but their W analogues have been isolated and structurally characterized.

The desoxo-Mo(IV) complexes, $NEt_4[Mo(OR)L_2]$, can be prepared by several methods. These include the silylation of $(NEt_4)_2[MoOL_2]$[74] or the reaction of the synthetically versatile complexes, $Mo(CO)_2L_2$, with aryloxide (RO^-), then NEt_4^+ salts.[75] Many of these compounds have been structurally

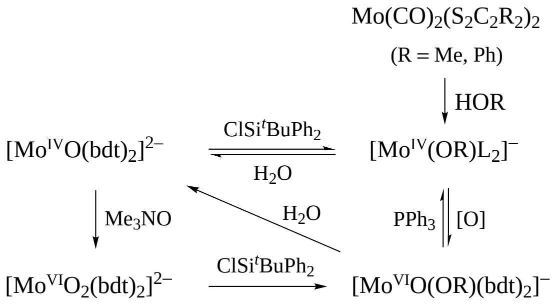

Scheme 7

Table 3 Kinetics data for OAT from $(NBu_4)_2[MO_2(mnt)_2]$ to X[a]

X	M	$k\ (M^{-1}\ s^{-1})^b$	$\Delta H^{\ddagger c}$	$\Delta S^{\ddagger d}$	k_{Mo}/k_W or χ
HSO_3^-	Mo	87[e]	–	–	
	W	No reaction	–	–	
$PPh(OMe)_2$	Mo	0.45(2)	8.2(4)	−33(1)	1000[f]
	W	$4.5(2) \times 10^{-4}$	11(1)	−38(2)	
$PMe(OEt)_2$	Mo	1.1	–	–	320[f]
	W	0.0034	–	–	
$P(OMe)_3$	Mo	0.025(1)	10(1)	−32(1)	2500[f]
	W	9.7×10^{-6}	14(1)	−33(2)	
PEt_3	Mo	0.109(5)	62(6)	−56(20)	6.30[g]
$PPhEt_2$	Mo	0.0784(5)	–	–	9.30[g]
PPh_2Et	Mo	0.061(3)	–	–	11.30[g]
PPh_3	Mo	0.056(1)	45(4)	−119(10)	13.25[g]

[a] Bisulfite,[72] phosphite,[69] and phosphine[70] reactions in $MeCN/H_2O$ (1:1), DMF and MeCN respectively. [b] Measured at 298 K. [c] $\Delta H^\ddagger$ in kcal mol^{-1}. [d] $\Delta S^\ddagger$ in eu. [e] k'_2/K_M from Michaelis–Menten kinetics performed in $MeCN/H_2O$ (1:1) at 293 K. [f] Ratio of k values, k_{Mo}/k_W. [g] Value of relative σ donor capability, χ (cm^{-1}).

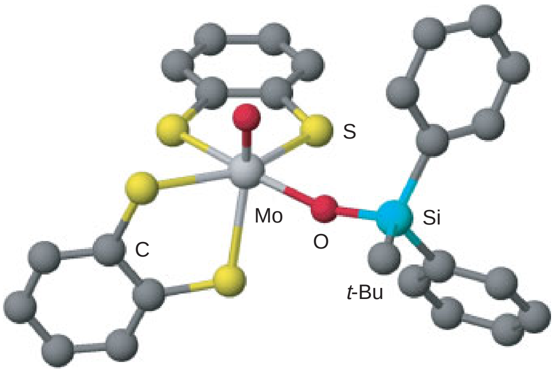

Figure 9 Partial structure of the anion of $NEt_4[MoO(OSi^tBuPh_2)(bdt)_2]$ (^{t}Bu methyl groups excluded)

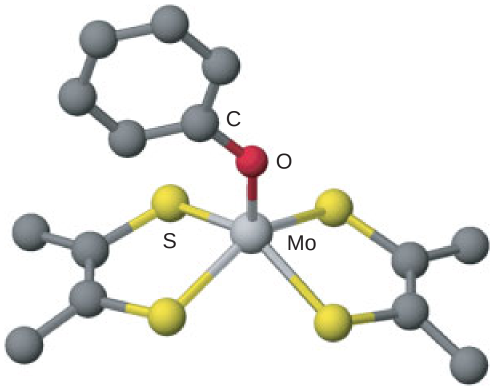

Figure 10 Structure of the anion of $NEt_4[Mo(OPh)(S_2C_2Me_2)_2]$

characterized and they all contain square-pyramidal anions with apical RO^- (d(Mo–O) ca. 1.84 Å, ∠(Mo–O–C) >166°), and basal S-donor ligands (see Figure 10);[74–76] they are prone to hydrolysis according to Scheme 7.[76] Various *S*-, *N*- and *Se*-oxides react with $NEt_4[Mo(OR)(S_2C_2Ph_2)_2]$ to produce $NEt_4[MoO(OR)(S_2C_2Ph_2)_2]$, which subsequently converts to $NEt_4[MoO(S_2C_2Ph_2)_2]$. Kinetics and isotope labeling studies are consistent with initial OAT through associative mechanisms (Table 4).[76] The desoxo-W(IV) analogues are oxidized at significantly increased rates compared to the Mo complexes (Table 4).[77] Similar comparative rates are observed for Mo-MPT enzymes and their W analogues.[55,71] Theoretical studies have shown that the OAT reactions of $[Mo(OR)L_2]^-$ complexes are favored over those of $[MoOL_2]^{2-}$ species by a lower-energy transition state and more stable products.[78,79] The Mo(VI) and Mo(IV) complexes above are excellent structural and functional models for the oxidized and reduced states of DMSO reductase. They also reproduce absorptions at similar wavelengths to those observed for the enzyme from *R. sphaeroides*. The desoxo-Mo(IV) complexes are reduced only at very negative potentials, a fact likely to account for the absence of Mo(III) enzyme states.

Table 4 Kinetics data for OAT from XO to $NEt_4[Mo(OPh)(S_2C_2Me_2)_2]$[76]

XO	k ($M^{-1}\,s^{-1}$)^a	$\Delta H^{\ddagger b}$	$\Delta S^{\ddagger c}$
Me_3NO	$2.0(1) \times 10^2$	8.1(6)	−21(2)
$O(CH_2)_4N(Me)O$	$1.8(1) \times 10^2$	–	–
$(PhCH_2)_3NO$	16(6)	9.5(1)	−21(1)
$C_4H_8SO^d$	$1.5(2) \times 10^{-4}$	10.1(4)	−39(1)
$DMSO^d$	1.3×10^{-6}	14.8(5)	−36(1)

^{a}Measured at 298 K. $^b\Delta H^\ddagger$ in $kcal.mol^{-1}$. $^c\Delta S^\ddagger$ in eu. ^{d}For analogous reactions of $[W(OPh)(S_2C_2Me_2)_2]^-$ (units as above): C_4H_8SO, k $9.0(3) \times 10^{-4}$, $\Delta H^\ddagger 11.6(4)$, $\Delta S^\ddagger$ −33(1); DMSO, k $3.9(4) \times 10^{-5}$, $\Delta H^\ddagger 14.4(2)$, $\Delta S^\ddagger$ −30(1).[77]

Thiolates and selenolates react with $Mo(CO)_2(S_2C_2Me_2)_2$, allowing the isolation of compounds of the type $NEt_4[Mo(ER)(S_2C_2Me_2)_2]$ (E = S, R = $C_6H_2{}^iPr_3$-2,4,6, 2-Ad; E = Se, R = 2-Ad).[75,76] Like the desoxo complexes above, these exhibit square-pyramidal structures, with apical RE^- groups and basal S-donor ligands. Interestingly, the Mo–E–C angles are considerably more bent (at ca. 102°) than the corresponding angles in RO^- complexes. These compounds are valuable structural and spectroscopic models for the active sites of dissimilatory nitrate reductases (E = S) and formate dehydrogenases (E = Se). Analogous W complexes are known.

10 MODELS FOR THE SULFITE OXIDASE FAMILY

10.1 Structural and Spectroscopic Models

Holm and coworkers have very recently described advanced structural models for the Mo(VI) and Mo(V) states of sulfite oxidase. Thus, the reaction sequence shown in Scheme 8 yields dioxo mono(dithiolene) complexes bearing either silyloxo or thiolate ligands. The thiolate complex, $[MoO_2(SC_6H_2{}^iPr_3\text{-}2,4,6)(bdt)]^-$, exhibits a square-pyramidal (pseudotetrahedral) structure closely related to that of oxidized sulfite oxidase (Figure 11).

The reaction represented by equation (20) is key to the generation of mono(dithiolene)-Mo(V) complexes that

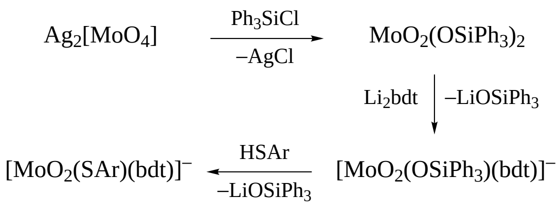

Scheme 8

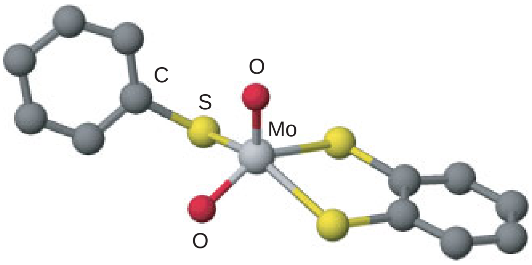

Figure 11 Partial structure of the anion of $NEt_4[MoO_2(SC_6H_2{}^iPr_3\text{-}2,4,6)(bdt)]\cdot MeCN$ (${}^iPr$ groups not shown)

model the intermediate states of sulfite oxidase. Thereafter, chloride ligand exchange yields thiolate complexes such as $[MoO(SAd)_2(S_2C_2Me_2)]^-$, $[MoO(SR)_2(bdt)]^-$, and $[MoOCl(SC_6H_2{}^iPr_3\text{-}2,4,6)(bdt)]^-$. These exhibit square-pyramidal geometries with apical oxo groups and rhombic EPR spectra similar to the low-pH and high-pH forms of sulfite oxidase (Figure 4).[80]

$$NEt_4[MoOL_2] + 2PhSeCl \longrightarrow NEt_4[MoOCl_2L] + C_6H_4(SSePh)_2$$
$$(L = \text{bdt, and likewise } S_2C_2Me_2) \qquad (20)$$

The energy and profile of the X-ray absorption edges of the above mono(dithiolene) complexes are sensitive to the oxidation state and ligands present. In particular, the Mo K-edge XAS and EXAFS spectra of $NEt_4[MoO_2(SC_6H_2{}^iPr_3\text{-}2,4,6)(bdt)]$ are remarkably similar to the corresponding spectra of oxidized sulfite oxidase. Further developments in this area, including biomimetic chemistry, are eagerly anticipated.

The most recent oxo-Mo(V) models for sulfite oxidase include $(L\text{-}N_2S)MoO(SPh)_2$ and $(L\text{-}N_2S)MoO(bdt)$, prepared by thiolate ligand exchange at $[MoO(SPh)_4]^-$, then $(L\text{-}N_2S)MoO(SPh)_2$, respectively ($L\text{-}NS_2$ = anion of (2-dimethylethanethiol)bis(3,5-dimethylpyrazolyl)methane). Both complexes exhibit distorted octahedral structures and *facial* $L\text{-}N_2S$ ligands and have been characterized by electronic and EPR spectroscopy.[81]

10.2 Functional Models

Functional models for sulfite oxidase are extremely uncommon. A well-studied example is the reaction of $(NBu_4)_2[MoO_2(mnt)_2]$ with $NaHSO_3$ in acetonitrile/water mixtures, which proceeds smoothly according to equation (21). However, the mechanism of this 'simple' reaction remains controversial.[54]

$$[Mo^{VI}O_2(mnt)_2]^{2-} + HSO_3{}^- \longrightarrow [Mo^{IV}O(mnt)_2]^{2-} + HSO_4{}^- \qquad (21)$$

The reaction exhibits substrate saturation kinetics, consistent with a pre-equilibrium between $[MoO_2(mnt)_2]^{2-}$ and $HSO_3{}^-$, rather than the substrate first-order dependence typical of direct OAT reactions (Section 7.3). Originally, Sarkar and coworkers proposed that $HSO_3{}^-$ binds to Mo via its anionic oxygen, prior to nucleophilic attack by sulfur at an oxo group of putative $[Mo^{VI}O_2(HSO_3)(mnt)_2]^{3-}$, giving bound $HSO_4{}^-$, that then dissociates.[72] This mechanism was later challenged by Lorber *et al.*,[70] who suggested the direct nucleophilic attack by the sulfur lone pair on a terminal oxo ligand, giving $[Mo^{IV}O(HSO_4)(mnt)_2]^{3-}$, followed by product dissociation. The recent observation that neutral dimethylsulfite fails to react with $[MoO_2(mnt)_2]^{2-}$ supports the mechanism involving oxoanion coordination to Mo prior to OAT.[82] Similar uncertainties surround the mechanism of the enzyme itself (Section 5). The oxidation of $[MoO(mnt)_2]^{2-}$ using $[Fe(CN)_6]^{3-}$ /H_2O results in partial reclamation (ca 10%) of $[MoO_2(mnt)_2]^{2-}$, possibly via CEPT reactions mimicking the regeneration of the active site of sulfite oxidase.[54] The reduction of nitrate by several oxo-Mo(IV) complexes has been described.[54]

11 MODELS FOR THE XANTHINE OXIDASE FAMILY

11.1 Models of the Oxidized Active Enzyme

The Mo hydroxylases are difficult to model because of the general redox incompatibility of the reducing sulfide and oxidizing Mo(VI) moieties found in the enzymes. The outcomes and directions of modeling endeavors up to 1997 have been reviewed by Young.[61]

Pseudotetrahedral complexes, such as $[MoO_{4-n}S_n]^{2-}$ ($n = 1$–3), $MoOS(ONR_2)_2$ and $Cp^*MoOS(CH_2SiMe_3)$, are well known; their stability may be ascribed to the low effective coordination number and consequently large HOMO-LUMO gap (*see HOMO–LUMO Gap*). Compounds of this type are prepared by sulfidation (oxo → sulfido) reactions but decomposition, upon reduction or attempted biomimetic transformations (e.g. cyanolysis), limits their biomimetic chemistry.[61] The first six-coordinate oxosulfido-Mo(VI) complex, $Tp^*MoOS(S_2P^iPr_2)$, was prepared by sulfur atom transfer to the Mo(IV) precursor, $Tp^*MoO(S_2P^iPr_2)$. Metrical parameters were consistent with an oxosulfido-Mo(VI) formulation, the 'terminal' sulfido ligand being stabilized by a weak interaction with the uncoordinated sulfur of the monodentate dithiophosphinate ligand; regardless, the complex is cleanly reduced to an oxosulfido-Mo(V) species and undergoes cyanolysis/sulfidation reactions that mimic those of the hydroxylases.[83] The complexes, $MoOS(OSiPh_3)_2L$ (L = bpy or phen derivative), prepared by reaction of $K_2[MoO_3S]$, $ClSiPh_3$, and L in basic (NEt_3) acetonitrile, contain an unperturbed oxosulfido unit. The structures of the complexes were defined by X-ray diffraction and EXAFS spectroscopy d(Mo=O ca. 1.71 Å, d(Mo=S) ca. 2.18 Å).[84] Exploitation of the sterically demanding $\mathrm{Tp^{Pr}}$ ligand has now permitted the synthesis of a series of oxosulfido-Mo(VI) complexes of the type $\mathrm{Tp^{Pr}MoOS(OR)}$ (OR = phenolate derivative). The parent complex, $\mathrm{Tp^{Pr}MoOS(OPh)}$, is monomeric in solution but crystallizes as a dimer, the two units being linked by a S–S bond formed with concomitant reduction of Mo(VI) to Mo(V).[85] Complexes that are monomeric in both the solution and solid states have now been isolated and structurally characterized (Figure 12); these are amenable to a reversible reduction producing Mo(V) species (vide infra). Oxosulfido-Mo(VI) complexes undergo sulfur rather than oxygen atom transfer to phosphines and cyanide.[83–85] This observation argues against enzyme mechanisms postulating direct involvement of the terminal oxo group in OAT.

11.2 Models of Mo(V) States

Oxosulfido-Mo(V) complexes are relevant models of the Very Rapid Mo(V) enzyme center but these too are extremely rare. The in situ generation and EPR characterization of complexes such as $[\mathrm{(L\text{-}N_2S_2)Mo^VOS}]^-$ and $[\mathrm{Tp^*Mo^VOSX}]^-$ was summarized in *EIC-1*.[1] Identification of $[\mathrm{(L\text{-}N_2S_2)Mo^VOS}]^-$ rests upon multifrequency EPR studies employing complexes isotopically labelled with ^{98}Mo ($I = 0$), ^{33}S ($I = 3/2$), and/or ^{1}H ($I = 1/2$). In particular, the distinctive pattern of anisotropic ^{33}S coupling (dominated by a single direction) observed in the Very Rapid signal of xanthine oxidase is reproduced so convincingly by $[\mathrm{(L\text{-}N_2S_2)^{98}MoO^{33}S}]^-$ that there can be little doubt that an $[\mathrm{Mo^VOS}]^+$ center (Figure 6) is responsible for the enzyme signal. In addition, the Mo-sulfido interaction is highly delocalized with a spin density of 0.3–0.4 of an electron on the sulfido ligand. The EPR parameters of natural abundance $[\mathrm{Tp^*Mo^VOSX}]^-$ are very similar to those of $[\mathrm{(L\text{-}N_2S_2)Mo^VOS}]^-$.[53]

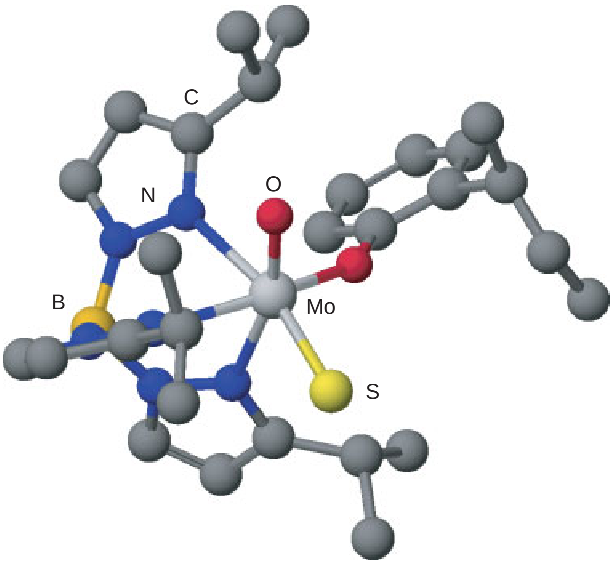

Figure 12 Structure of $\mathrm{Tp^{Pr}MoOS(OC_6H_4{}^sBu\text{-}2)}$

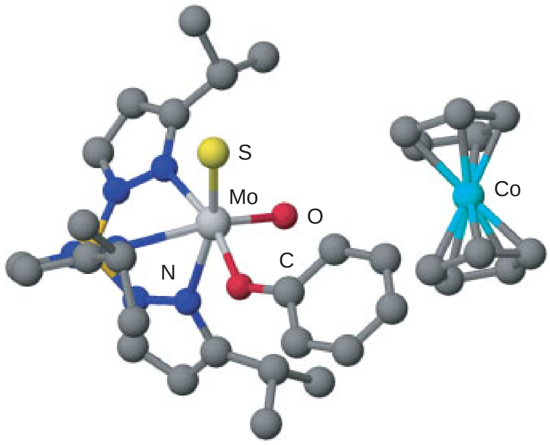

Figure 13 Structure of $\mathrm{CoCp_2[Tp^{Pr}MoOS(OPh)]}$

Protonation of the synthetic species to *cis*-$[\mathrm{MoO^V(SH)}]^{2+}$ collapses both the magnitude and the anisotropy of the ^{33}S coupling in addition to inducing the appearance of ^{1}H coupling.[1,53] These features are characteristic of the centers responsible for the Rapid EPR signals (Figure 6). The delocalized nature of the Mo–S bond in *cis*-$[\mathrm{Mo^VOS}]^+$ has been rationalized in terms of a highly covalent Mo(d_{xy})–S(p_y) interaction perpendicular to the strong-field oxo ligand (z). Claims that $\mathrm{(L\text{-}N_2S_2)Mo^VO(SH)}$ and salts of $[\mathrm{(L\text{-}N_2S_2)Mo^VOS}]^-$ have been isolated are doubtful. In contrast, salts such as $\mathrm{CoCp_2[Tp^{Pr}MoOS(OR)]}$ (OR = phenolate derivative) are tractable and a preliminary (O/S disordered) X-ray crystal structure of $\mathrm{CoCp_2[Tp^{Pr}MoOS(OPh)]}$ has been achieved (see Figure 13). EXAFS results are indicative of Mo=O and Mo=S distances of 1.72 Å and 2.23 Å respectively, while a strong S K pre-edge XAS feature is associated with the π-bonded sulfido group.

12 CONCLUSION

The Mo-MPT enzymes play vital roles in metabolism and global biogeochemical cycles, their myriad functions being facilitated by the chemical versatility of Mo on one hand and the substrate specificity induced by the structure of the active site and the protein on the other. In recent years, our knowledge of these enzymes has increased dramatically, thanks to insights from advanced structural, spectroscopic, and molecular biological techniques. The intrinsic OAT and CEPT capabilities of Mo appear to be central to the function of many enzymes but complete mechanistic descriptions await the results of ongoing investigations. Model studies have made vital contributions to our appreciation of the enzyme active sites and accurate active-site models are now emerging.

Exploration of the structure and function of Mo-MPT enzymes, from (inter alia) molecular, cellular, environmental, and evolutionary perspectives, promises to fully inform our knowledge of these important and interesting biomolecules.

13 RELATED ARTICLES

Molybdenum: Inorganic & Coordination Chemistry; Nitrogenase Catalysis & Assembly; Nitrogenase: Metal Cluster Models; Selenium Proteins Containing Selenocysteine; Tungsten Proteins.

14 REFERENCES

1. C. G. Young and A. G. Wedd, Molybdenum: Molybdopterin-Containing Enzymes, in ‘Encyclopedia of Inorganic Chemistry’, ed. R. King, Wiley, New York, 1994, p. 2330.
2. R. Hille, *Chem. Rev.*, 1996, **96**, 2757.
3. R. Hille, Molybdenum Enzymes Containing the Pyranopterin Cofactor: An Overview, in ‘Metal Ions in Biological Systems’, eds. A. Sigel and H. Sigel, Marcel Dekker, New York, 2002, Vol. 39, p. 187.
4. R. S. Pilato and E. I. Stiefel, Molybdenum and Tungsten Enzymes, in ‘Bioinorganic Catalysis’, eds. J. Reedijk and E. Bouwman, Marcel Dekker, New York, 1999, p. 81.
5. J. M. Tunney, J. McMaster, and C. D. Garner, Molybdenum and Tungsten Enzymes, in ‘Comprehensive Coordination Chemistry II’, eds. J. A. McCleverty and T. J. Meyer, Elsevier Pergamon, Amsterdam, 2004, Vol. 8, Chap. 8.18, p. 459.
6. A. Sigel and H. Sigel eds, ‘Metal Ions in Biological Systems (Molybdenum and Tungsten: Their Roles in Biological Processes)’, Marcel Dekker, New York, 2002, Vol. 39.
7. E. I. Stiefel and K. D., Karlin eds, ‘Progress in Inorganic Chemistry (Dithiolene Chemistry: Synthesis, Properties, and Applications)’, Wiley-Interscience, New York, 2004, Vol. 52.
8. C. Kisker, H. Schindelin, D. Baas, J. Rétey, R. U. Meckenstock, and P. M. H. Kroneck, *FEMS Microbiol. Rev.*, 1999, **22**, 503.
9. H. Schindelin, C. Kisker, and K. V. Rajagopalan, *Adv. Protein Chem.*, 2001, **58**, 47.
10. H. Dobbek and R. Huber, The Molybdenum and Tungsten Cofactors: A Crystallographic Overview, in ‘Metal Ions in Biological Systems’, eds. A. Sigel and H. Sigel, Marcel Dekker, New York, 2002, Vol. 39, p. 227.
11. P. Basu, J. F. Stolz, and M. T. Smith, *Curr. Sci.*, 2003, **84**, 1412.
12. G. N. George, *J. Biol. Inorg. Chem.*, 1997, **2**, 790.
13. L. J. Que Jr ed., ‘Physical Methods in Bioinorganic Chemistry: Spectroscopy and Magnetism’, University Science Books, Sausalito, 2000.
14. Y. Deligiannakis, M. Louloudi, and N. Hadjiladis, *Coord. Chem. Rev.*, 2000, **204**, 1.
15. T. Prisner, M. Rohrer, and F. MacMillan, *Annu. Rev. Phys. Chem.*, 2001, **52**, 279.
16. M. Ubbink, J. A. R. Worrall, G. W. Canters, E. J. J. Groenen, and M. Huber, *Annu. Rev. Biophys. Biomol. Struct.*, 2002, **31**, 393.
17. F. A. Armstrong and G. S. Wilson, *Electrochim. Acta*, 2000, **45**, 2623.
18. K. F. Aguey-Zinsou, P. V. Bernhardt, and S. Leimkühler, *J. Am. Chem. Soc.*, 2003, **125**, 15352.
19. J. L. Johnson and S. K. Wadman, in ‘The Metabolic and Molecular Bases of Inherited Disease’, ed. C. R. Scriver, McGraw Hill, New York, 1995, p. 2271.
20. R. Mendel and R. Hänsch, *J. Exp. Botany*, 2002, **53**, 1689.
21. M. G. Bertero, R. A. Rothery, M. Palak, C. Hou, D. Lim, F. Blasco, J. H. Weiner, and N. C. J. Strynadka, *Nat. Struct. Biol.*, 2003, **10**, 681.
22. R. N. Pau and D. M. Lawson, Transport, Homeostasis, Regulation, and Binding of Molybdate and Tungstate to Proteins, in ‘Metal Ions in Biological Systems’, eds. A. Sigel and H. Sigel, Marcel Dekker, New York, 2002, Vol. 39, p. 31.
23. R. R. Mendel and G. Schwarz, Biosynthesis and Molecular Biology of the Molybdenum Cofactor (Moco), in ‘Metal Ions in Biological Systems’, eds. A. Sigel and H. Sigel, Marcel Dekker, New York, 2002, Vol. 39, p. 317.
24. J. H. Enemark and M. M. Cosper, Molybdenum Enzymes and Sulfur Metabolism, in ‘Metal Ions in Biological Systems’, eds. A. Sigel and H. Sigel, Marcel Dekker, New York, 2002, Vol. 39, p. 621.
25. P. M. H. Kroneck and D. J. Abt, Molybdenum in Nitrate Reductase and Nitrite Oxidoreductase, in ‘Metal Ions in Biological Systems’, eds. A. Sigel and H. Sigel, Marcel Dekker, New York, 2002, Vol. 39, p. 369.
26. E. I. Stiefel, The Biogeochemistry of Molybdenum and Tungsten, in ‘Metal Ions in Biological Systems’, eds. A. Sigel and H. Sigel, Marcel Dekker, New York, 2002, Vol. 39, p. 1.
27. G. N. George, J. Hilton, C. Temple, R. C. Prince, and K. V. Rajagopalan, *J. Am. Chem. Soc.*, 1999, **121**, 1256.
28. S. D. Garton, J. Hilton, H. Oku, B. R. Crouse, K. V. Rajagopalan, and M. K. Johnson, *J. Am. Chem. Soc.*, 1997, **119**, 12906.
29. A. F. Bell, X. He, J. P. Ridge, G. R. Hanson, A. G. McEwan, and P. J. Tonge, *Biochemistry*, 2001, **40**, 440.
30. B. E. Schultz, R. Hille, and R. H. Holm, *J. Am. Chem. Soc.*, 1995, **117**, 827.
31. C. Moreno-Vivián, P. Cabello, M. Martínez-Luque, R. Blasco, and F. Castillo, *J. Bacteriol.*, 1999, **181**, 6573.
32. J. A. Vorholt and R. K. Thauer, Molybdenum and Tungsten Enzymes in C1 Metabolism, in ‘Metal Ions in Biological Systems’, eds. A. Sigel and H. Sigel, Marcel Dekker, New York, 2002, Vol. 39, p. 571.

33. T. Conrads, C. Hemann, G. N. George, I. J. Pickering, R. C. Prince, and R. Hille, *J. Am. Chem. Soc.*, 2002, **124**, 11276.

34. G. N. George, I. J. Pickering, and C. Kisker, *Inorg. Chem.*, 1999, **38**, 2539.

35. S. D. Garton, R. M. Garrett, K. V. Rajagopalan, and M. K. Johnson, *J. Am. Chem. Soc.*, 1997, **119**, 2590.

36. C. Feng, H. L. Wilson, J. K. Hurley, J. T. Hazzard, G. Tolin, K. V. Rajagopalan, and J. H. Enemark, *Biochemistry*, 2003, **42**, 12235.

37. T. Eilers, G. Schwarz, H. Brinkmann, C. Witt, T. Richter, J. Nieder, B. Koch, R. Hille, R. Hänsch, and R. R. Mendel, *J. Biol. Chem.*, 2001, **276**, 46989.

38. N. Schrader, K. Fischer, K. Theis, R. R. Mendel, G. Schwarz, and C. Kisker, *Structure*, 2003, **11**, 1251.

39. E. F. Pai and T. Nishino, The Molybdenum-Containing Xanthine Oxidoreductases and Picolinate Dehydrogenases, in ‘Metal Ions in Biological Systems’, eds. A. Sigel and H. Sigel, Marcel Dekker, New York, 2002, Vol. 39, p. 431.

40. D. J. Lowe, Enzymes of the Xanthine Oxidase Family: The Role of Molybdenum, in ‘Metal Ions in Biological Systems’, eds. A. Sigel and H. Sigel, Marcel Dekker, New York, 2002, Vol. 39, p. 455.

41. E. Garattini, R. Mendel, M. J. Ramão, R. Wright, and M. Terao, *Biochem. J.*, 2003, **372**, 15.

42. M. J. Romão, C. A. Cunha, C. D. Brondino, and J. J. G. Moura, Molybdenum Enzymes in Reactions Involving Aldehydes and Acids, in ‘Metal Ions in Biological Systems’, eds. A. Sigel and H. Sigel, Marcel Dekker, New York, 2002, Vol. 39, p. 539.

43. R. Kappl, J. Hüttermann, and S. Fetzner, The Molybdenum-Containing Hydroxylases of Quinoline, Isoquinoline, and Quinaldine, in ‘Metal Ions in Biological Systems’, eds. A. Sigel and H. Sigel, Marcel Dekker, New York, 2002, Vol. 39, p. 481.

44. J. R. Andreesen and S. Fetzner, The Molybdenum-Containing Hydroxylases of Nicotinate, Isonicotinate, and Nicotine, in ‘Metal Ions in Biological Systems’, eds. A. Sigel and H. Sigel, Marcel Dekker, New York, 2002, Vol. 39, p. 405.

45. V. N. Gladyshev, Comparison of Selenium-Containing Molybdoenzymes, in ‘Metal Ions in Biological Systems’, eds. A. Sigel and H. Sigel, Marcel Dekker, New York, 2002, Vol. 39, p. 655.

46. R. Harrison, *Free Radical Biol. Med.*, 2002, **33**, 774.

47. Y. Kuwabara, T. Nishino, K. Okamoto, T. Matsumura, B. T. Eger, E. F. Pai, and T. Nishino, *Proc. Natl. Acad. Sci. U.S.A.*, 2003, **100**, 8170.

48. N. C. Maiti, T. Tomita, T. Kitagawa, K. Okamoto, and T. Nishino, *J. Biol. Inorg. Chem.*, 2003, **8**, 327.

49. R. Hille and H. Sprecher, *J. Biol. Chem.*, 1987, **262**, 10914.

50. H. Dobbek, L. Gremer, R. Kiefersauer, R. Huber, and O. Meyer, *Proc. Natl. Acad. Sci. U.S.A.*, 2002, **99**, 15971.

51. M. Gnida, R. Ferner, L. Gremer, O. Meyer, and W. Meyer-Klaucke, *Biochemistry*, 2003, **42**, 222.

52. B. Fischer and S. J. N. Burgmayer, Models for the Pyranopterin-Containing Molybdenum and Tungsten Cofactors, in ‘Metal Ions in Biological Systems’, eds. A. Sigel and H. Sigel, Marcel Dekker, New York, 2002, Vol. 39, p. 265.

53. C. G. Young, Molybdenum, in ‘Comprehensive Coordination Chemistry II’, eds. J. A. McCleverty and T. J. Meyer, Elsevier Pergamon, Amsterdam, 2004, Vol. 4, Chap. 4.7, p. 415.

54. C. G. Young, Biomimetic Chemistry of Molybdenum, in ‘Biomimetic Oxidations Catalyzed by Transition Metal Complexes’, ed. B. Meunier, Imperial College Press, London, 2000, p. 415.

55. J. McMaster, J. M. Tunney, and C. D. Garner, *Prog. Inorg. Chem.*, 2004, **52**, 539.

56. J. K. Hsu, C. J. Bonangelino, S. P. Kaiwar, C. M. Boggs, J. C. Fettinger, and R. S. Pilato, *Inorg. Chem.*, 1996, **35**, 4743.

57. H. K. Joshi, J. J. A. Cooney, F. E. Inscore, N. E. Gruhn, D. L. Lichtenberger, and J. H. Enemark, *Proc. Natl. Acad. Sci. U.S.A.*, 2003, **100**, 3719.

58. R. L. McNaughton, A. A. Tipton, N. D. Rubie, R. R. Conry, and M. L. Kirk, *Inorg. Chem.*, 2000, **39**, 5697.

59. J. McMaster, M. D. Carducci, Y.-S. Yang, E. I. Solomon, and J. H. Enemark, *Inorg. Chem.*, 2001, **40**, 687.

60. M. L. Mader, M. D. Carducci, and J. H. Enemark, *Inorg. Chem.*, 2000, **39**, 525.

61. C. G. Young, *J. Biol. Inorg. Chem.*, 1997, **2**, 810.

62. E. I. Stiefel, *J. Chem. Soc., Dalton Trans.*, 1997, 3915.

63. (a) P. D. Smith, A. J. Millar, C. G. Young, A. Ghosh, and P. Basu, *J. Am. Chem. Soc.*, 2000, **122**, 9298; (b) A. J. Millar, C. J. Doonan, P. D. Smith, V. N. Nemykin, P. Basu, and C. G. Young, *Chem. Eur. J.*, 2005, in press.

64. R. H. Holm and J. P. Donahue, *Polyhedron*, 1993, **12**, 571.

65. Z. Xiao, M. A. Bruck, J. H. Enemark, C. G. Young, and A. G. Wedd, *Inorg. Chem.*, 1996, **35**, 7508.

66. M. A. Pietsch and M. B. Hall, *Inorg. Chem.*, 1996, **35**, 1273.

67. V. N. Nemykin, S. R. Davie, S. Mondal, N. Rubie, M. L. Kirk, A. Somogyi, and P. Basu, *J. Am. Chem. Soc.*, 2002, **124**, 756.

68. N. Ueyama, H. Oku, M. Kondo, T.-A. Okamura, N. Yoshinaga, and A. Nakamura, *Inorg. Chem.*, 1996, **35**, 643.

69. G. C. Tucci, J. P. Donahue, and R. H. Holm, *Inorg. Chem.*, 1998, **37**, 1602.

70. C. Lorber, M. R. Plutino, L. I. Elding, and E. Nordlander, *J. Chem. Soc., Dalton Trans.*, 1997, 3997.

71. C. D. Garner and L. J. Stewart, Tungsten-Substituted Molybdenum Enzymes, in ‘Metal Ions in Biological Systems’, eds. A. Sigel and H. Sigel, Marcel Dekker, New York, 2002, Vol. 39, p. 699.

72. S. K. Das, P. K. Chaudhury, D. Biswas, and S. Sarkar, *J. Am. Chem. Soc.*, 1994, **116**, 9061.

73. H. Oku, N. Ueyama, and A. Nakamura, *Inorg. Chem.*, 1997, **36**, 1504.

74. J. P. Donahue, C. R. Goldsmith, U. Nadiminti, and R. H. Holm, *J. Am. Chem. Soc.*, 1998, **120**, 12869.

75. B. S. Lim, J. P. Donahue, and R. H. Holm, *Inorg. Chem.*, 2000, **39**, 263.

76. B. S. Lim and R. H. Holm, *J. Am. Chem. Soc.*, 2001, **123**, 1920.

77. K.-M. Sung and R. H. Holm, *J. Am. Chem. Soc.*, 2001, **123**, 1931.

78. C. E. Webster and M. B. Hall, *J. Am. Chem. Soc.*, 2001, **123**, 5820.

79. A. Thapper, R. J. Deeth, and E. Nordlander, *Inorg. Chem.*, 2002, **41**, 6695.

80. B. S. Lim, M. W. Willer, M. Miao, and R. H. Holm, *J. Am. Chem. Soc.*, 2001, **123**, 8343.

81. K. Peariso, B. S. Chohan, C. J. Carrano, and M. L. Kirk, *Inorg. Chem.*, 2003, **42**, 6194.

82. K. Nagarajan, P. K. Chaudhury, B. R. Srinivasan, and S. Sarkar, *Chem. Commun.*, 2001, 1786.

83. A. A. Eagle, L. J. Laughlin, C. G. Young, and E. R. T. Tiekink, *J. Am. Chem. Soc.*, 1992, **114**, 9195.

84. A. Thapper, J. P. Donahue, K. B. Musgrave, M. W. Willer, E. Nordlander, B. Hedman, K. O. Hodgson, and R. H. Holm, *Inorg. Chem.*, 1999, **38**, 4104.

85. P. D. Smith, D. A. Slizys, G. N. George, and C. G. Young, *J. Am. Chem. Soc.*, 2000, **122**, 2946.

Molybdenum: Organometallic Chemistry

Kevin R. Flower
UMIST, Manchester, UK

Based in part on the article Molybdenum: Organometallic Chemistry by M. David Curtis which appeared in the Encyclopedia of Inorganic Chemistry, First Edition.

1 Introduction 1
2 σ-Ligand-Containing Complexes 1
3 π-Ligand-Containing Complexes 7
4 Polymetallic Complexes 15
5 Related Articles 16
6 References 16

1 INTRODUCTION

Molybdenum is a transition metal that is found in group 6 of the periodic table and has a ground-state electronic configuration of $4d^5 5s^1$. It has a crustal abundance of ∼1.2 ppm. The most important molybdenum ore is molybdenite, MoS_2, with the largest known deposit in Colorado, USA. Other less important ores include wulfenite, $PbMoO_4$, and powellite, $Ca(Mo,W)O_4$. It was first isolated by P. J. Hjelm in the late eighteenth century by heating the oxide MoO_2 with charcoal. The name molybdenum is derived from the Greek word for lead (μόλυβδος, molybdos). This naming arose because of the ancient confusion of soft black minerals that were used for writing. It has an atomic number 42, atomic weight 95.94, mp 2617 °C, and bp 4612 °C. Molybdenum has found extensive use in the steel industry where it is used in high temperature cutting steel, its compounds find use as lubricants, for example, MoS_2, as pigments and catalysts.

Since this article is concerned with molybdenum organometallic chemistry and owing to the immense number of publications each year in this area of science, the author has had to be selective in the areas that are covered. For compounds to be given initial consideration for inclusion, they have to contain a direct molybdenum-to-carbon bond. This article is organized on the basis of the type of carbon-based ligand and the number of atoms directly bound to the molybdenum center. Where there are two or more carbon-based ligands in the compound, the compound is placed in the section perceived to be most relevant. The reader will find that some areas were covered in the Encyclopedia of Inorganic Chemistry, First Edition,[1] and others are new to this edition. The two articles are therefore complimentary. The same referencing policy is used in this article as in the previous edition. Citations are made to review articles wherever possible and where none are available to lead references.

2 σ-LIGAND-CONTAINING COMPLEXES

2.1 Alkyl Complexes

2.1.1 *Homoleptic Complexes*

In 1973, Wilkinson reported the preparation of the homoleptic methyl compounds (*see Homoleptic Compound*) $[W(CH_3)_6]$ and $[Re(CH_3)_6]$. Later, theoretical calculations suggested that these compounds should be based upon trigonal prismatic geometry rather than octahedral as is common in six-coordinate coordination chemistry, and the structure of $[W(CH_3)_6]$ was subsequently shown to be strongly distorted C_{3v} trigonal prismatic.[2] The structure is of particular interest because it contains three long W–C bonds at a narrow angle to each other and three shorter W–C bonds at a larger angle. Recently, the compounds $[Mo(CH_3)_5]$, $[Mo(CH_3)_6]$, and $[Mo(CH_3)_7]$ have been prepared and structurally characterized.[3,4] Blue $[Mo(CH_3)_5]$ is prepared through reaction of $MoCl_5$ with $ZnMe_2$. The compound is paramagnetic and has a square pyramidal geometry with Mo–C_{apical} 2.068(1) Å and Mo–C_{basal} 2.111(1) Å. Orange–brown $[Mo(CH_3)_6]$ is prepared on treatment of MoF_6 with $Zn(CH_3)_2$ and is thermally stable up to 10 °C and very sensitive toward oxygen. Its solid-state structure is similar to its tungsten analog. The structure is strongly distorted trigonal prismatic with three short Mo–C bonds 2.111(3) Å with C–Mo–C 94.9° and three long Mo–C bonds 2.190(3) Å with C–Mo–C 75.7°. Red $[Li\{O(CH_2CH_3)_2\}][Mo(CH_3)_7]$ was prepared on treatment of $[Mo(CH_3)_6]$ with MeLi and is isostructural with its tungsten analog $[Li\{O(CH_2CH_3)_2\}][W(CH_3)_7]$. The structure is best described as a capped octahedron. In none of the reported structures was there any evidence for an agostic interaction (*see Agostic Bonding*), and the relative stability of all these compounds stems from the fact that the methyl group does not contain any β-hydrogen atoms.

2.1.2 *Nonhomoleptic Complexes*

Alkyl-, aryl-, and acetylide-containing compounds that have additional ligands such as phosphines and cyclopentadienyl, amongst others, are far more common than their homoleptic congeners. Examples of this type of compound will be found in other sections of the article.

2.2 Carbonyl Derivatives

2.2.1 Mononuclear Complexes

The starting point for most molybdenum-based carbonyl chemistry is the white crystalline air stable hexacarbonyl [$Mo(CO)_6$], which is commercially available. Low valent compounds that are derived from this starting material tend to give products that obey the Effective Atomic Number Rule (EAN Rule). Since Mo^0 has a d^6 configuration, six two-electron ligands are required to obey the EAN rule.

Bonding Considerations. [$Mo(CO)_6$] is stabilized by back bonding of electrons from the d_π orbitals (d_{xy}, d_{xz}, d_{yz}) into the π^*-molecular orbitals of the carbon monoxide ligands (*see* ***Molecular Orbital Theory***). This back donation of electrons serves to lower the negative charge at the molybdenum center and so strengthens the σ-donation (*see* ***S-donor Ligands***) from the ligand to the molybdenum atom. The compound [$Mo(CO)_6$] has strict O_h symmetry (*see Group Theory*) and all six d-electrons are involved in back donation to the π^*-molecular orbitals of the carbonyl ligands. This results in three identical pairs of *trans*-carbonyl ligands that each competes with each other for the available electron density (see Figure 1a). When the first carbonyl is substituted by another two-electron donor ligand that is a poorer π-acceptor (this will generally be the case), then the carbonyl ligand trans to this ligand will obtain a greater share of the electron density with the overall result that the Mo–CO bond trans to the ligand L is strengthened relative to the cis carbonyl ligands (see Figure 1b). The outcome of this strengthening of the bond is that on substitution of a second carbonyl ligand *cis*-[$Mo(CO)_4L_2$] and a third *fac*-[$Mo(CO)_3L_3$] respectively are obtained. Facile substitution ceases at this point because all of the remaining carbonyl ligands are trans (generally) to poorer π-acceptor ligands. Further substitution can be facilitated under more forcing conditions or through the use of chelating ligands (*see Chelating Ligands*) and/or good π-acceptors (*see* ***Carbonyl Complexes of the Transition Metals***).

In [$Mo(CO)_6$], the Mo–CO bond length is 2.06 Å and the average Mo–CO bond energy (*see* ***Bonding Energetics of Organometallic Compounds***) is 150 kJ mol^{-1}.

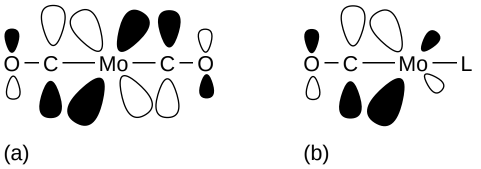

Figure 1 (a) Portion of a molecular orbital that distributes electron density between two *trans*-carbonyl groups. (b) electron density concentrated in M–CO bond trans to poor π-acceptor

Spectral Characteristics. IR spectra (*Infrared Spectroscopy*) are particularly useful for making gross structural assignments in mononuclear carbonyl derivatives. [$Mo(CO)_6$] is octahedral and has a single carbonyl stretching frequency at 2004 cm^{-1}. The δ–M–C–O bending mode appears at 593 cm^{-1} and the M–C stretch (t_{1u}) occurs at 368 cm^{-1}. Substitution of one carbonyl ligand lowers the effective symmetry to C_{4v} (*see Group Theory*), and three ν(CO) bands become IR active ($2a + e$) in the 2050 to 1850 cm^{-1} range. *cis*-[$Mo(CO)_4L_2$] has effective C_{2v} symmetry, and four ν(CO) modes ($2a_1 + b_1 + b_2$) are active. *trans*-[$Mo(CO)_4LL'$] has either D_{4h} ($L = L'$) or C_{4v} ($L \neq L'$) symmetry, with one (e_u) or two (a_1(weak) $+ e$) ν(CO) bands respectively. *Tri*-substituted *fac*-[$Mo(CO)_3L_3$] has C_{3v} symmetry with two ($a_1 + e$) ν(CO) bands. The average ν(CO) frequency decreases with increasing substitution.**5**

In ^{13}C NMR spectra, the carbonyl carbon resonance appears typically in the 200–230 ppm region. If the compound contains phosphine ligands, then the carbonyl signals couple with the spin active phosphorus atom and can be used to complement geometry assignment made using IR spectroscopy. ^{1}H NMR is also useful for characterizing these compounds due to the signals of the organic moieties in the ligands. Typically, the signals are slightly shifted from those observed for the noncomplexed ligand.**6**

2.2.2 Reductive Substitution

Molybdenum carbonyls react with strong reducing agents to give carbonyl metallates in which the molybdenum is formally reduced.**7** Thus, [$Mo(CO)_6$] or [$Mo(CO)_5L$] reacts with strong reducing agents in liquid ammonia or THF to form [$Mo(CO)_5$]$^{2-}$ and [$Mo_2(CO)_{10}$]$^{2-}$ respectively. The dimeric dianion is best obtained with sodium in the presence of a catalytic amount of bipyridine or from $NaBH_4$ at 60 °C in ammonia. [$Mo(CO)_5$]$^{2-}$ is best prepared from the dimer on treatment with CO (equation 1). The [$Mo(CO)_6$] obtained as a side product is readily removed by sublimation.

$$[(OC)_5Mo{-}Mo(CO)_5]^{2-} \longrightarrow [Mo(CO)_5]^{2-} + [Mo(CO)_6] \quad (1)$$

Reduction of [$Mo(CO)_4$(TMEDA)] with sodium in liquid ammonia affords excellent yields of $Na_4[Mo(CO)_4]^{4-}$, which can be isolated as a pyrophoric yellow–orange powder. In this compound, molybdenum shows its lowest formal oxidation state as evidenced by the very low value of ν(CO) 1471 cm^{-1}.

These carbonyl anions are strong nucleophiles (*see Nucleophile*) and can be used to form a diverse range of new compounds. Protonation gives the μ-hydride (*see Bridging Ligand*) [(μ-H){$Mo(CO)_5$}]. Reactions with other metal carbonyls lead to CO substitution and the formation of metal – metal-bonded heteronuclear anions, for example, [$Mo(CO)_5$–$Fe(CO)_4$]$^{2-}$ and [$Mo(CO)_5$-$Co(CO)_4$]$^{2-}$. Reaction with main group halides is shown in Scheme 1. The dianion reacts similarly.

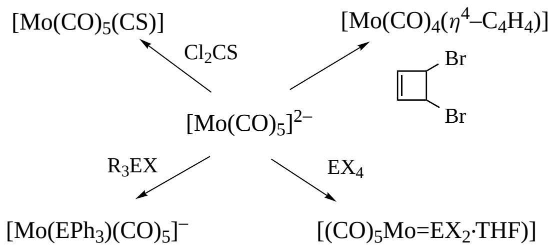

Scheme 1 Selected reactions of $[Mo(CO)_5]^-$

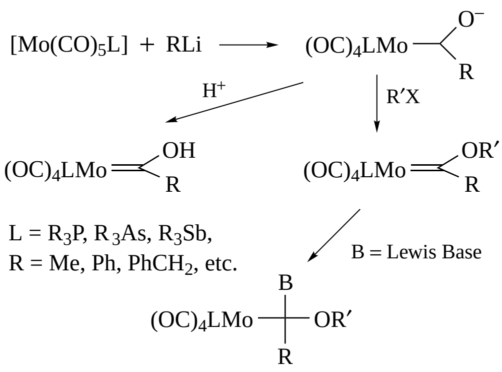

Scheme 2 Preparation of fischer carbene complexes

2.3 Carbene and Carbyne Complexes

The carbon atom of the carbonyl ligand in $[Mo(CO)_6]$ or its derivatives may be attacked by strong nucleophiles (*see Nucleophile*) like organo–lithium reagents. The resulting anion from this nucleophilic attack can be quenched with an electrophilic reagent (*see Electrophile*), for example, trialkyloxonium methylfluorosulfonates (Scheme 2). The resultant neural species are known as carbene complexes (*see* ***Carbene Complexes***) or Fischer-type carbene complexes.[8] The related Cr and W analogs and to a lesser extent the Mo analogs have found utility as reagents in organic syntheses (*see* ***Organic Synthesis using Transition Metal Carbonyl Complexes***) and as catalysts for alkene metathesis (*see* ***Metathesis Polymerization Processes by Homogeneous Catalysis***). Alternative routes to Mo–carbene complexes include the treatment of $[Mo(CO)_6]$ with electron-rich alkenes and reaction of the carbonylate anion $[Mo(CO)_5]^{2-}$ with various substrates such as 3,3-dichlorocyclopropenes or iminium salts.[9]

These Fischer-type carbene complexes can be readily converted to Fischer-type carbyne complexes, and this material has been reviewed.[10] Methods to remove the α-alkoxy group include treatment with BBr_3, oxide abstraction from acyl ligands, and electrophilic attack on the β-carbon of metal acetylides (equations 2–4).

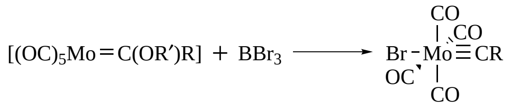
$$[(OC)_5Mo{=}C(OR')R] + BBr_3 \longrightarrow Br{-}Mo(CO)_4{\equiv}CR$$
(2)

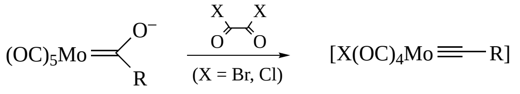

(3)

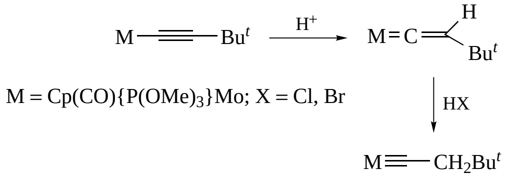

(4)

2.3.1 *Heavier Group 14 Analogs of Carbene and Carbyne Complexes*

Multiple bonds are readily formed with the 2p elements carbon, nitrogen, and oxygen; however, the heavier main group elements only reluctantly participate in multiple bonding[11] (*see* ***Main Group: Multiple Bonding***) since the mid-1960s, considerable effort has been expended to generate heavier group 14 analogs and investigate their coordination chemistry. Some dated reviews are available.[12,13] On complexation of the divalent group 14 element moiety (Figure 2a), it retains its Lewis acid characteristics and often coordinates a Lewis base (Figure 2b), and there are even examples of the coordination of two Lewis bases (Figure 2c) (*see Lewis Acids & Bases*). The reversal of this process to generate the base-free species has always failed and results in compound decomposition. More recently, attempts to prepare heavier group 14 analogs of carbyne complexes have resulted in the preparation of silylyne- and germylyne-containing molybdenum complexes and a stannylyne-containing complex of tungsten.

Silicon. The first base-stabilized silylene complex $[Cp^*Ru\{=Si(Ph)_2NCMe\}(PMe_3)_2]$ was reported in 1987, and the first base-free silylene-containing complexes $[Cp^*Ru{=}Si(SR)_2(PMe_3)_2]$ (R = Me or Ph) were not synthesized until 1990, much later than for the heavier congeners Ge, Sn, and Pb. Recently, the silylene-containing

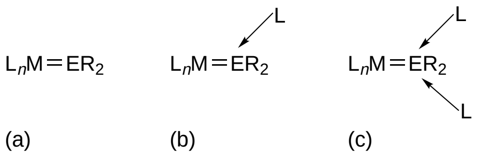

Figure 2 Representation of different classes of double-bonded group 14 fragments

compound [$Cp^*Mo{=}SiCl(C_6H_2$-2,4,6-$Me_3)H(dmpe)$] (**1**) has been prepared**[14]** and structurally characterized. In this compound, the sum of the angles about the silicon atom is 359.8(3)°, which is indicative of a base-free silylene complex that is sp^2 hybridized (*see Hybridization*) at the silicon center. The Mo–Si bond length is short (2.288(2) Å), which confirms its multiple bond character. Compound (**1**) was then treated with $Li[B(C_6F_5)_4]$ to facilitate chloride abstraction and generation of the cationic silylyne-containing complex [$Cp^*Mo{\equiv}Si(C_6H_2$-2,4,6-$Me_3)H(dmpe)][B(C_6F_5)_4]$ (**2**), which has also been structurally characterized. In the solid-state structure of (**2**), the Mo–Si bond length shortened to 2.219(2) Å and the Mo–Si–C angle is 170.9(2)° and is comparable to analogous carbyne-containing compounds.**[10]**

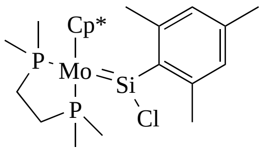
(**1**)

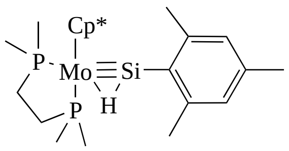
(**2**)

Another interesting feature in the solid-state structure of (**2**) is the presence of a bridging hydride (*see Bridging Ligand*): Mo–H 1.85(5) Å, Si–H 1.39(5) Å, although in heavy metal structures it is often difficult to make too much comment on the location of a hydrogen atom this close to a metal center (*see* ***Diffraction Methods in Inorganic Chemistry***). Density Functional Theory (DTF) (*see Density Functional Theory*) calculations were carried out and suggest the presence of a nonclassical bridging hydride (*see Bridging Ligand*) and support the position of the hydrogen atom observed in the solid-state structure.

Germanium. The compounds [$Mo(CO)_5(GeX_2{\cdot}THF)$] (X = Cl, Br) were prepared on treatment of the decacarbonyldimolybdate dianion with GeX_4 in THF.**[12]** They were, however, originally erroneously reported as base-free species. Many more examples of this type of germylene-containing complex have been prepared where the central metal is Cr or W. Recently, the *tris*-carbene-containing molybdenum (0) complex [$Mo(Ge\{N(CH_2{}^tBu)C_2H_2N(CH_2{}^tBu)\})_3(CO)_3$] was synthesized and structurally characterized. The average Mo–Ge bond length is 2.537(2) Å, which is shorter than the sum of the covalent radii.**[15]** Lengthening of the Ge–N bond lengths and shortening of other bond lengths in the cyclic germylene ligand suggest that it is a good π-acceptor (*see* ***Bond Lengths in Inorganic Solids & Liquids***).

Compounds that contain a germylyne ligand, that is, a metal–germanium triple bond have also been synthesized. Treatment of $Na[CpMo(CO)_3]$ with 2,6–$Mes_2C_6H_3GeCl$ at low temperature in THF afforded the germylyne-containing complex [$Cp(CO)_2Mo{\equiv}GeC_6H_3$-2,6-$Mes_2$](**3**), which has been structurally characterized.**[16]** The Mo–Ge–C angle of 172.2(2)° is similar to what is observed in carbyne-containing complexes and the related silylyne complex (**2**). The Mo–Ge bond length in (**3**) (2.271(1) Å) is significantly shorter (0.35 Å) than the predicted single bond length of 2.62 Å (covalent radii Mo 1.4 Å and Ge 1.22 Å). Unlike in the structure of (**2**), there are no close intramolecular approaches. Another synthetic strategy has also been described**[17]** for the preparation of the germylyne-containing compounds [$(dppe)XMo{\equiv}Ge(\eta^1$-$Cp^*)$] (X = Cl, Br, I) (equation 5). The compound [$(dppe)BrMo{\equiv}Ge(\eta^1$-$Cp^*)$] has also been structurally characterized and found to have a linear Mo–Ge–C geometry 171.6(2)° and a short Mo–Ge bond length 2.310(1) Å, which are comparable to those observed for (**3**).

$$[Mo(N_2)_2(dppe)_2] + Cp^*GeX \longrightarrow [(dppe)XMo{\equiv}GeCp^*] \qquad (5)$$

Analogous Cr and W compounds have been prepared by the same methodology; however, in certain cases the tricarbonyl intermediates [$Cp(CO)_2M(GeC_6H_3$-2,6-$Trip_2)$] (M = Cr **4**, W **5**; Trip = –$C_6H_2$2,4,6-${}^iPr_3$) that contain a M–Ge single bond were isolated. Both compounds have been structurally characterized and shown to have a stereochemically active lone pair at germanium and a bent M–Ge–C = 117.9(3)° (Cr) 114.7(6)° (W) geometry. Gentle heating of these compounds caused elimination of one carbonyl ligand and the formation of the triply bonded species [$Cp(CO)M{\equiv}GeC_6H_3$-2,6-$Trip_2$] (M = Cr **6**, W **7**). Compounds (**6**) and (**7**) have both been structurally characterized and shown to have linear M–Ge–C geometry (175.9(6)° Cr; 170.9(3)° W) and significantly shorter M–Ge bond lengths (2.166(4) Å Cr; 2.277(1) Å W respectively).

Tin and Lead. A small number of molybdenum complexes containing stannylene and plumbylene ligands are known.**[12,13]** The tin and lead compounds [$Cp(CO)_3Mo$-EC_6H_3-2,6-Mes_2] (E = Sn, Pb) have been prepared but do not appear to lose CO and generate the stannylyne**[18]** or plumbylyne analogs of (**3**).**[19]** Very recently, however, the preparation of the tungsten complex [$W{\equiv}Sn(C_6H_3$-2,6-$Mes)Cl(dppe)_2$], that does contain a stannylyne ligand, has been described.**[20]**

2.4 Halocarbonyl Complexes

2.4.1 Six- and Seven-Coordinate Complexes[21,22]

Halocarbonyl complexes of molybdenum have been known since Wilkinson and Piper reported the preparation of [$MoX(CO)_3Cp$] (X = Cl, Br, I) in 1956 with the first dihalocarbonyl donor ligand complex [$MoI_2(CO)_3(diars)$] reported by Nyholm and Nigram in 1957. Pioneering work by Colten in the 1960s led to the development of the halide-bridged dimers [$\{Mo(\mu$–$X)X(CO)_4\}_2$] via an oxidative elimination reaction between the halogen and [$Mo(CO)_6$]. In general, seven-coordinate halocarbonyl complexes have been shown to have one of the following structures: (i) capped octahedral, (ii) capped trigonal prismatic, (iii) pentagonal bipyramidal, (iv) or the so-called 4:3 geometry. Indeed, ^{13}C NMR spectroscopy has been used to correlate the solid-state structures with solution state structures. In the case of capped octahedral structures, there is a shift to low field for the carbonyl in the capping position. Because these compounds are generally fluxional in solution (*see* ***Stability Constants & their Determination***), to observe the capping carbonyl resonance the spectrum needs to be run at low temperature.

An early method for the preparation of a range of six- and seven-coordinate halocarbonyl complexes was the addition of soft donor ligands (*see* ***Hard & Soft Acids and Bases***) to the halide-bridged dimer $[\{Mo(\mu–X)X(CO)_4\}_2]$ to give $[MoX_2(CO)_3L_2]$; however, addition of weaker field ligands led to disproportionation and isolation of the non-carbonyl-containing compounds $[MoX_3L_3]$ (L = py, THF, NCMe). An equally effective alternative to this method of preparation was oxidative elimination of the halogen to zero-valent molybdenum precursors such as $[Mo(CO)_4(bpy)]$ to give $[MoX_2(CO)_3(bpy)]$ (X = Cl, Br). The synthesis of the seven-coordinate halocarbonyl complexes $[MI_2(CO)_3(NCMe)_2]$ (M = Mo, W) through the oxidative elimination of I_2 to $[M(CO)_3(NCMe)_3]$ (M = Mo or W) dissolved in acetonitrile has been described.**[23]** This is a particularly noteworthy observation because, when the compounds $[M(CO)_3(NCMe)_3]$ (M = Mo or W) were originally prepared in 1962 and isolated, I_2 was added to them in refluxing methanol and, under these reaction conditions, only an insoluble non-carbonyl-containing compound was obtained. Recently, the addition of half-a-mole equivalent of I_2 to $[MoI_2(CO)_3(NCMe)_2]$ in refluxing acetonitrile yielded the crystallographically characterized non-carbonyl-containing product $[MoI_3(NCMe)_3]$ and confirms that careful control of reaction conditions is required to prevent significantly different products being obtained. $[MoI_2(CO)_3(NCMe)_2]$ has been crystallographically characterized and shown to have the capped octahedral geometry.**[24]**

Since its preparation, the compound $[MoI_2(CO)_3(NCMe)_2]$ has been shown to display a diverse range of reactivity. The acetonitrile ligands are particularly labile and are readily substituted by a range of neutral donor ligands. Addition of 1 equivalent of ligand L displaces 1 acetonitrile molecule and yields initially the seven-coordinate complexes of type $[MoI_2(CO)_3(NCMe)L]$ (L = phosphines, arsines, stibines) (**4**), which depending on the steric and electronic properties of the ligand may lose the second NCMe ligand to afford the iodide-bridged dimers $[\{Mo(\mu\text{-}I)(CO)_3L\}_2]$. A wide range of mixed ligand systems $[MoI_2(CO)_3(L)(L')]$ (L′ = phosphines, arsines, stibines, ureas, thioureas, pyridines etc.) have been prepared through treatment of (**4**) with a second equivalent of a different monodentate ligand L′. $[MoI_2(CO)_3(NCMe)_2]$ also reacts with a wide range of neutral bidentate ligands to yield *bis*-nitrile substituted products $[MoI_2(CO)_3(L–L)]$ (phosphines, bpy etc.). The halide ligands can also be substituted through use of anionic ligands such as thiolates, dithiocarbamates, acac, and so on. The reactivity of this compound is summarized in Scheme 3.

The compounds $[M(CO)_3(NCMe)_3]$ have also been shown to undergo oxidative elimination with a range of other halogen-based oxidants including Br_2, ICl, and IBr, to afford analogous seven-coordinate complexes. The reactivity of these compounds has been less extensively investigated than $[MoI_2(CO)_3(NCMe)_2]$.

2.4.2 Group 14–Containing Halocarbonyl Complexes

These compounds are of particular interest as they have been shown to be active Ring Opening Metathesis Polymerization (ROMP) catalysts (*see* ***Metathesis Polymerization Processes by Homogeneous Catalysis***). They are not, however, as effective as imido-based alkylidene systems (see next section).

Routes for the preparation of these types of compound are similar to the dihalo analogs in the previous section. Thus, the heterobimetallic complexes $[MoX(MX_3)(CO)_3(bpy)]$

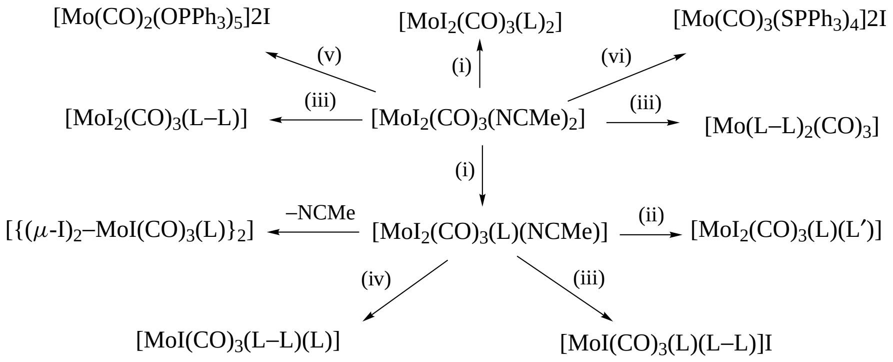

Scheme 3 (i) L = PR_3, AsR_3, SbR_3, BiR_3, $OPPh_3$, $SPPh_3$; (ii) L′ = PR_3, AsR_3, SbR_3, BiR_3, $OPPh_3$, $SPPh_3$, $SC(NR_2)_2$; (iii) L-L = bpy, 1,10-phen, $Ph_2P(CH_2)_nPPh_2$ ($n = 1–6$); (iv) NaS_2CNR_2, KS_2COEt, acac; (v) $OPPh_3$ (vi) $SPPh_3$

(M = Ge, Sn; X = Cl, Br) are prepared through oxidative elimination of MX_4 to the zero-valent precursor $[Mo(CO)_4(bpy)]$. Oxidative elimination of MCl_4 (M = Sn, Ge) to $[Mo(CO)_3(NCMe)_3]$ gives the more versatile, as they contain labile readily substitutable acetonitrile ligands, seven-coordinate complexes $[MoX(MX_3)(CO)_3(NCMe)_2]$;[21] these compounds have been shown to undergo a wide range of molybdenum-centered substitution chemistry analogous to that reported for $[MoI_2(CO)_3(NCMe)_2]$. Oxidative elimination has also been shown to be facile with $[Mo(CO)_4(NCEt)_2]$,[25] and the solid-state structure of $[MoX(MX_3)(CO)_3(NCEt)_2]$ has been determined.[26] The structure was shown to contain a chloride ligand bridging the Mo–Sn bond (*see Bridging Ligand*). The reaction between $[Mo(CO)_6]$ and $SnCl_4$ under photochemical conditions has also been described and shown to yield the crystallographically characterized complex $[(CO)_4Mo(\mu\text{-}Cl_3)Mo(SnCl_3)(CO)_3]$.

2.5 Alkylidene Complexes

Alkylidene complexes are typically carbene-containing complexes of transition metals in high oxidation states as opposed to low oxidation state Fischer-type carbenes (*see* ***Carbene Complexes***). They tend to be nucleophilic (*see Nucleophile*) in nature as opposed to the electrophilic (*see Electrophile*) Fischer-type carbenes. By far, the most important alkylidene complexes of molybdenum are the imido-containing complexes $[Mo(CHR')(NAr)(OR)_2]$ originally reported by Schrock, and some good reviews of this chemistry are available.[27–29] The synthetic relevance of these compounds means also that some are now commercially available. These compounds have been used successfully for ROMP and Ring Closing Metathesis Polymerization (RCMP) (*see* ***Metathesis Polymerization Processes by Homogeneous Catalysis***). One of the problems, however, associated with these alkylidene complexes is their lack of tolerance to many functional groups. This problem can often be overcome by using ruthenium-based alkylidene systems (*see* ***Ruthenium: Organometallic Chemistry*** and ***Carbene Complexes***). A significant advance made recently is the preparation of chiral alkylidene complexes (Figure 3) that act as catalysts for asymmetric ring closing metathesis (*see* ***Metathesis Polymerization Processes by Homogeneous Catalysis***).[30,31] Another is that $[Mo\{CH(CMe_2Ph)\}(NC_6H_3\text{-}2,3\text{-}{}^iPr_2)\{OC(Me)(CF_3)_2\}_2]$ is capable of effecting both ROMP and RCMP in liquid and supercritical CO_2.[32] This approach has particular attractions: the ease with which CO_2 can be removed from the polymer and there is no waste organic solvent that needs to be disposed of.

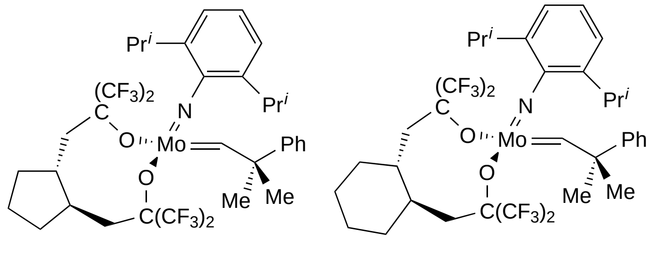

Figure 3 Chiral molybdenum alkylidene complexes used in asymmetric ring closing metathesis polymerization

2.6 Alkylidyne Complexes[33]

$[Mo(CBu^t)(CH_2Bu^t)_3]$ was first prepared in a low yield from the reaction between ${}^tBuCH_2Li$ and $MoCl_5$. An improved synthesis is available in which MoO_2Cl_2 is added to the Grignard reagent ${}^tBuCH_2MgBr$ at −78° in diethylether. It is most likely that the alkylidyne ligand is formed through successive α-elimination processes (*see α-Elimination*). Another route to alkylidyne complexes is through alkyne metathesis reactions (*see* ***Metathesis Polymerization Processes by Homogeneous Catalysis***) with the triply bonded dimer $[Mo_2(OBu^t)_6]$ and alkynes to give $[Mo\equiv CR(OBu^t)_3]$, however, terminal alkynes are not successfully converted to alkylidyne complexes by this method. This type of complex has been shown to be important as ROMP and RCMP catalysts (*see* ***Metathesis Polymerization Processes by Homogeneous Catalysis***); however, their use has been severely limited as a result of the difficulty in their synthesis. This situation may soon change because of the discovery of a new and effective route to their preparation (equation 6).The ene-dialkylidyne complex 1,2,-di(–$C\equiv MoL_n$)cyclohex-1-ene has recently been synthesized and crystallographically characterized and the average $Mo\equiv C$ bond length was found to be 1.753(5) Å (Figure 4).[34]

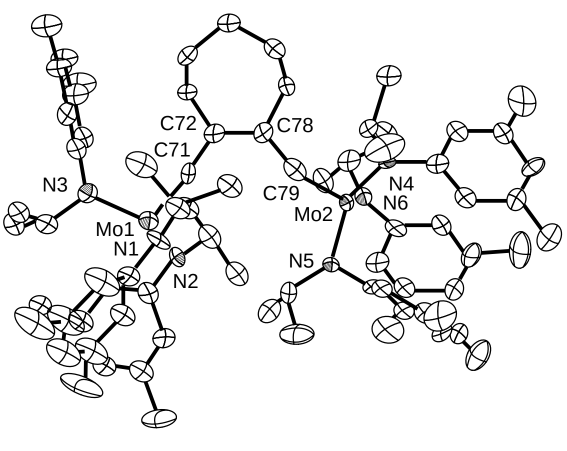

Figure 4 Molecular structure of 1,2,-di(–$C\equiv MoL_n$)cyclohex-ene. (Reprinted with permission from Ref. 34. © 2003 American Chemical Society)

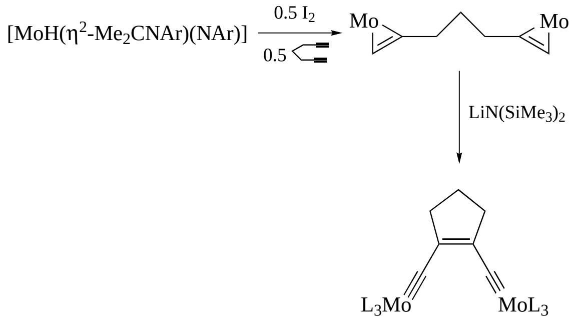

(6)

3 π-LIGAND-CONTAINING COMPLEXES

3.1 Alkene and Allyl Complexes

Alkene complexes of the type $[Mo(CO)_{(6-n)}(\eta^2\text{-}H_2C{=}CH_2)_n]$ ($n = 1, 2$) have been known since 1963 and are prepared by the photolysis of $[Mo(CO)_6]$ (*see* ***Photochemistry of Transition Metal Complexes***) in the presence of an alkene. The geometry of the *bis*-alkene complexes synthesized is trans, with the alkenes orientated orthogonal to each other. Matrix isolation studies (*see Matrix Isolation*) suggest that on photodissociation of CO from $[Mo(CO)_5(\eta^2\text{-alkene})]$ it is a cis carbonyl ligand that dissociates. This means that there is subsequent rearrangement to the observed trans product. The original assignment of the trans geometry was based upon the observation of a single ν(CO) band in the IR spectrum, which is consistent with gross D_{4h} symmetry (*see* ***Surfaces***); the cis geometry has C_{2v} symmetry and would be expected to give rise to four bands. When butadiene, which is a conjugated diene and has the potential to act as a chelating ligand, is the alkene ligand only one of the double bonds is initially involved in bonding to the metal center and the *bis-trans*-$[Mo(CO)_4(\eta^2\text{-}CH_2{=}CHCH{=}CH_2)_2]$ complex can be prepared. This compound can be transformed into the *bis-cis*-$[Mo(CO)_2(\eta^2\text{-}CH_2{=}CHCH{=}CH_2)_2]$ complex on warming.[35]

The analogous *bis*-ethene-containing complex *trans*-$[Mo(PMe_3)_4(\eta^2\text{-ethene})_2]$ is prepared on bubbling ethene through a solution of $[Mo(PMe_3)_4(N_2)_2]$, and it has been crystallographically characterized (Figure 5).[36] It can be clearly seen that the ethene ligands are trans and orthogonal to each other. This means each ligand accepts electron density from a different metal dπ orbital and so maximizes π-backbonding into its π^*-antibonding molecular orbital. Each ethene ligand also orientates so it eclipses a P–Mo–P vector. The average Mo–C bond length is 2.270(6) Å.

The reactivity of $[Mo(PMe_3)_4(\eta^2\text{-ethene})_2]$ has been much studied and, for example, the *tris*-alkene-containing compound $[Mo(PMe_3)(\eta^n\text{-}H_2C{=}CH\text{-}COOMe)_3]$ is prepared on treatment with $H_2C{=}CH\text{-}COOMe$ and it has been crystallographically characterized (Figure 6). The structure shows two of the methylacrylate ligands coordinate through their C=C and C=O bonds and the third through the C=C bond only. It is noteworthy that in this structure, as in the parent compound, the mutually trans alkene ligands are again orientated orthogonal to each other.[37]

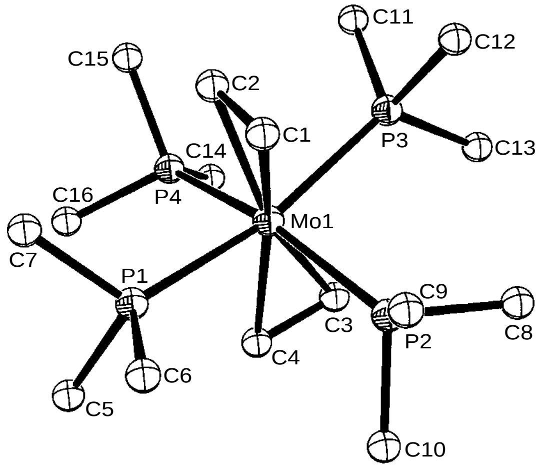

Figure 5 Molecular structure of $[Mo(PMe_3)_4(\eta^2\text{-}H_2C{=}CH_2)_2]$. (Reprinted with permission from Ref. 36. © 2003 American Chemical Society)

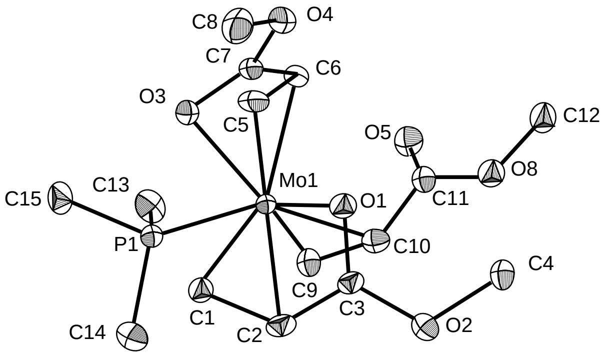

Figure 6 Molecular structure of $[Mo(PMe_3)(H_2C{=}CHCO_2Me)_3]$. (Reprinted from Ref. 37, with permission from Elsevier)

Since its discovery in the 1980s, C_{60} (Buckminsterfullerene) (*see* ***Carbon: Fullerenes***) has captured the imagination. It has been shown to coordinate to many transition metals including molybdenum centers as a two-electron donor alkene ligand. For example, the reaction between *mer*-$[Mo(CO)_3(NCMe)_3]$ with dppb (*bis*-diphenylphosphinobutane) followed by C_{60} gives *mer*-$[Mo(CO)_3(\eta^2\text{-}C_{60})(dppb)]$.[38] C_{60} has been shown to coordinate up to three $[Mo(CO)_2(phen)(dbm)]$ moieties and each of the compounds is electrochemically active at C_{60} (*see* ***Electrochemistry: Applications in Inorganic Chemistry***) and at more negative potentials than for uncoordinated C_{60}. *mer*-$[Mo(CO)_3(\eta^2\text{-}C_{60})(dppb)]$ shows three one-electron reduction potentials associated with the C_{60} ligand. A fourth one-electron reduction is also observed, which is metal centered and causes dissociation of the C_{60} ligand. Similar behavior is seen when the fullerene C_{70} is coordinated to a metal center.[39]

The reaction between chelating-unconjugated dienes like norbornadiene (NBD) or cycloocta-1,5-diene (COD) yields the compounds *cis*-[$Mo(CO)_4(\eta^2, \eta^2$-alkene)]. These products are considerably more stable than their mono-ene analogs due to the chelate effect (*see Chelate Effect*). They are often used as precursors for the preparation of [$Mo(CO)_4L_2$] complexes as better yields and purer products are obtained than from the direct reaction between [$Mo(CO)_6$] and L at elevated temperatures. For example, the fluorophosphine complex [$Mo(CO)_4\{PF_2(CPh_3)\}_2$] can be prepared on stirring [$Mo(CO)_4$(NBD)] with $PF_2(CPh_3)$ at room temperature for 1 h. The solid-state structure of this compound reveals very short Mo–P bonds (2.429 Å) (expected ≈ 2.58 Å) and is due to the presence of the electronegative (*see Electronegativity*) fluorine atoms.[40] Dienes are also known to coordinate to molybdenum in higher oxidation states. The seven-coordinate complex [$Mo(SnCl_3)Cl(CO)_3(\eta^4$-NBD)] was prepared on reaction between [$(CO)_4Mo(\mu\text{-}Cl)_3MoSnCl_3(CO)_3$] with a stoichiometric amount of NBD (equation 7). Its solid-state structure shows some interesting structural features, the most significant being the asymmetry in the bond lengths to the NBD ligand. The alkene trans to the Cl ligand has Mo–C bond lengths of 2.330(3) Å and 2.335(3) Å respectively, which are approximately 0.1 Å shorter than those trans to CO, 2.431(3) Å and 2.423(3) Å. This is consistent with the relative π-acidities of the ligands $CO > R_2C{=}CR_2 > Cl^-$ and equally accounts for the differences in the bound C=C bond lengths, 1.388(4) Å and 1.362(4) Å trans to Cl and CO respectively. [$Mo(SnCl_3)Cl(CO)_3(\eta^4$-NBD)] has also been shown to initiate ROMP of NBD when treated with an excess of NBD (*see* ***Metathesis Polymerization Processes by Homogeneous Catalysis***). The propagation step in the polymerization was found to be slower than the initiation step, which requires decomplexation of one alkene moiety of the NBD ligand followed by rearrangement to an alkylidene ligand with subsequent ring opening followed by a 1,2-hydrogen shift.[41,42]

$$\begin{aligned}&[(CO)_4Mo(\mu\text{-}Cl)_3Mo(SnCl_3)(CO)_3] + 2NBD\\ &\longrightarrow [Mo(\mu\text{-}Cl)(SnCl_3)(CO)_2(\eta^4\text{-NBD})]\\ &\quad + [MoCl_2(CO)_3(\eta^4\text{-NBD})] + CO \qquad (7)\end{aligned}$$

The compounds [$CpMo^{(II)}(\eta^4\text{-}C_4H_6)_2]^+$, [$CpMo^{(III)}(\eta^3\text{-}C_3H_5)_2$], [$CpMo^{(II)}(\eta^3\text{-}C_3H_5)(\eta^4\text{-}C_4H_6)$], [$CpMo^{(III)}(\eta^3\text{-}C_3H_5)(\eta^4\text{-}C_4H_6)]^+$ have all been prepared.[43,44] For [$CpMo^{(III)}(\eta^3\text{-}C_3H_5)(\eta^4\text{-}C_4H_6)]^{n+}$ ($n = 0$, 1), four different isomeric forms are possible (Figure 7a–d). The allyl ligand adopts a *prone* or *exo* (Figure 7a and 7d) *supine* or *endo* (Figure 7b and 7c) geometry, whereas the butadiene ligand takes either *s-cis supine* (Figure 7a and 7d) or *s-trans* (Figure 7c and 7d). The *s-cis prone* butadiene ligand geometry has not been observed for this system. Depending upon the oxidation state $Mo^{(II)}$ versus $Mo^{(III)}$ diamagnetic, 18-valence electron or 17-valence electron paramagnetic species are obtained. This change in electronic configuration and metal oxidation state has a profound effect on their reactivity, for example see Scheme 4.[43] The related diene complexes [$CpMoCl_2(\eta^4$-diene)] (diene = butadiene, isoprene) react with Grignard reagents in a metathetical reaction to yield dialkyl complexes of the type [$CpMoR_2(\eta^4$-diene)] (R = Me, CH_2Ph, CH_2SiMe_3), note the absence of β-hydrogen atoms, rather than nucleophilic (*see Nucleophile*) attack at the diene ligand. The new Mo–C bonds are stable to weak acids but are cleaved by HCl, HBF_4, and CF_3CO_2H.[45]

An example of nucleophilic attack (*see Nucleophile*) on a π-bound diene is illustrated in Scheme 5. The incoming nucleophile adds on the face exo (*see Exo & Endo Substituents*) to the metal, meaning the metal has an antidirecting effect (*see* ***Organic Synthesis using Transition Metal Complexes Containing π-Bonded Ligands***). The functionalized organic molecule can then be obtained through oxidative cleavage; note the iodide enters on the same face as the nucleophile.[46]

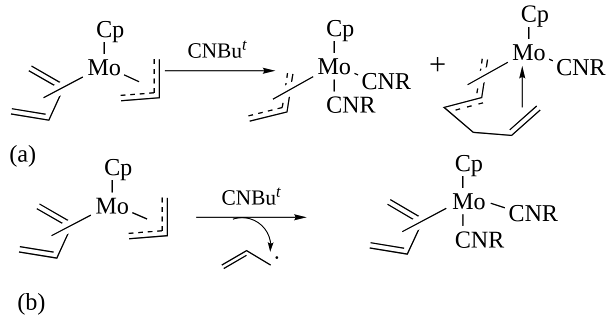

Scheme 4 Different reactivity caused by change in oxidation state (a) Mo^{II}, (b) Mo^{III}

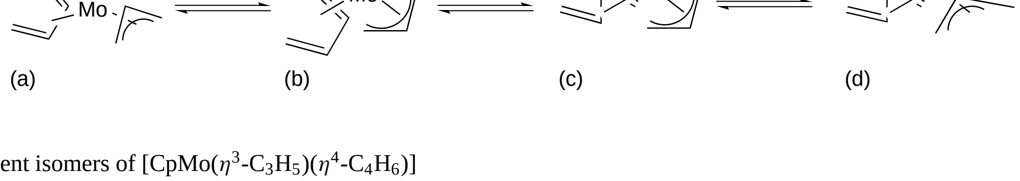

Figure 7 Different isomers of [$CpMo(\eta^3\text{-}C_3H_5)(\eta^4\text{-}C_4H_6)$]

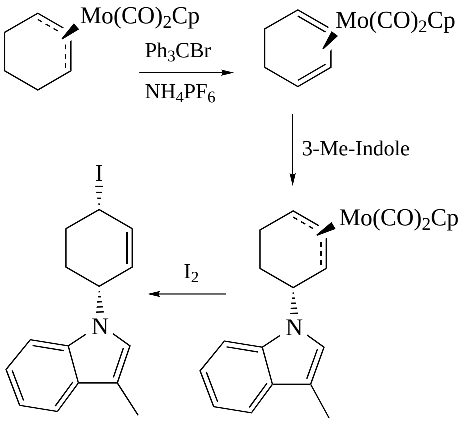

Scheme 5 An example of a nucleophilic attack on a π-bound diene

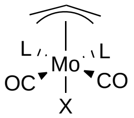

Figure 8 General structure of $[MoX(CO)L_2(\eta^3\text{-}C_3H_5)]$

π-Allyl complexes of the type $[MoX(CO)_2(L)_2(\eta^3\text{-allyl})]$ behave similarly to diene complexes. They show both metal- and ligand-centered reactivity. One method used to prepare this class of compound is by an oxidative elimination reaction between $[Mo(CO)_3(L)_3]$ (L = DMF, NCMe, Py) and a suitable allyl halide or allyl acetate to give $[MoX(CO)_2(L)_2(\eta^3\text{-allyl})]$ (X = Cl, Br, acetate).[47] The ligands L maybe exchanged for a range of monodentate (L′) and bidentate ligands (L-L); nucleophiles (*see Nucleophile*) may also attack the allyl moiety leading to functionalized allylic products.[48] These pseudooctahedral complexes are also known to be fluxional in solution with three different processes having been identified using VT NMR spectroscopy (*see* ***Stability Constants & their Determination***), a pivoted double-switch mechanism, intramolecular trigonal twist, and slow dissociative ligand exchange.[49] They also all generally have the same solid-state geometry (Figure 8). Another interesting use that has recently been found for compounds of the type $[CpMo(CO)_2(\eta^3\text{-allyl})]$ is as robust markers in peptide systems.[50]

Complexes of cycloheptatriene (C_7H_8) and the tropylium cation $(C_7H_7)^+$ are also known and their chemistry mirrors that of the smaller polyene-containing systems, namely, metal-centered ligand exchange reactions and ligand-centered nucleophilic attack. A detailed review of this chemistry is available.[51]

3.2 Alkyne-containing Complexes

Alkyne complexes of molybdenum are common and there are several approaches to their preparation. They are of particular interest as the alkyne has the potential to act as a variable electron donor to the metal center: 4-e, 3-e or 2-e. The alkyne is able to act as a variable electron donor as it has two orthogonal π-systems, which may participate in bonding to the metal center. This makes them noticeably different from mono-alkene ligands, which can behave only as 2-e donors.

Much work has centered on coordination of alkynes to the $[(\eta^5\text{-}C_5H_5)Mo]$ moiety. *Bis*-alkyne-containing complexes of the type $[CpMo(CO)(\eta^2\text{-alkyne})_2]$ are readily synthesized, for example, on reaction of $[\{CpMo(CO)_3\}_2]$ with 2 Mole equivalents of alkyne in the presence of Ag^+. The alkyne ligands in these complexes are formally 3-e donors, if the complex is to obey the EAN (*see Effective Atomic Number Rule*). The compounds show a wide range of metal-centered ligand substitution reactions with, for example, phosphines and phosphites. It has also been shown that it is possible to react the coordinated alkyne with a range of nucleophiles (*see Nucleophile*). The related mono-alkyne-containing complexes $[CpMoL(\eta^2\text{-}RC_2R)_2]$ (L = phosphine or phosphite) are readily converted to either allyl- or metallacyclopropene-containing complexes on treatment with nucleophiles. The *bis*-alkyne-containing complexes undergo a diverse array of ligand coupling reactions and some reviews with regard to these reactions are available.[19,52,53] $[Mo(CO)(\eta^2\text{-PhC}\equiv\text{CPh})Cp][BF_4]$ reacts with 3 equivalents of $CNBu^t$ to give $[Mo(CNBu^t)_3(\eta^2\text{-PhC}\equiv\text{CPh})Cp][BF_4]$, where the alkyne has switched from a 4-e to a 2-e donor. Addition of a fourth equivalent of $CNBu^t$ causes a coupling reaction to occur ultimately affording a vinylcarbene. Reduction with Na/Hg has been shown to give different products that are condition dependent (Scheme 6).[54] Heptamethylindenyl analogs have also recently been prepared and shown to display similar reactivity to the parent cyclopentadienyl complexes.[55]

Making use of the isolobal analogy (*see Isolobal Analogy*), it has been shown that the imido group (NR) is isolobal with the cyclopentadienyl moiety. Bearing this relationship in

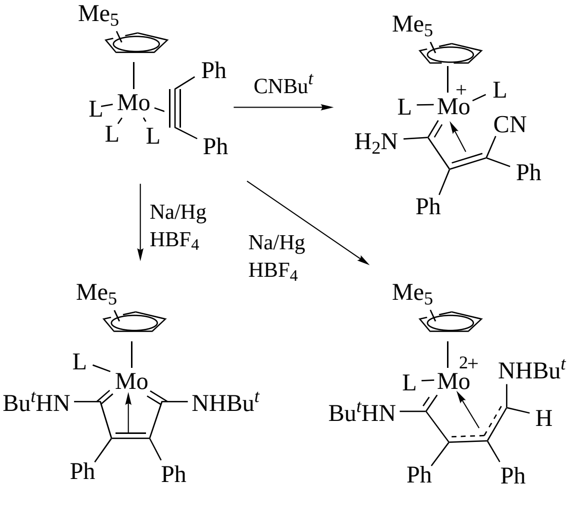

Scheme 6 Isonitrile/alkyne coupling reactions; L = $CNBu^t$

mind, the *bis*-imido alkyne complexes [Mo(NR)$_2$(PMe$_3$)(η^2-R′C≡CR″)] (R = Ph or adamantyl, R′ = R″ = Ph; R = ^{t}Bu, R′ = Ph, R″ = H) were prepared by displacement of ethene from the analogous alkene complexes [Mo(NR)$_2$(PMe$_3$)(η^2-H$_2$C=CH$_2$)] in hot heptane. The solid-state structure of [Mo(N^{t}Bu)$_2$(PMe$_3$)(η^2-PhC≡CPh)] was reported and shows the molecule is pseudo-tetrahedral. The alkyne contact carbon atoms and phosphorus atoms are all coplanar and this plane is perpendicular to the plane defined by N-Mo-N. Analogous structural characteristics are observed in the related solid-state structure of [Mo(N^{t}Bu)$_2$(PMe$_3$)(η^2-HC=CMe)] and in zirconocene systems (*see* ***Zirconium & Hafnium: Organometallic Chemistry***). These data add strong support for the isolobal relationship between zirconocenes and four-coordinate *bis*-imido complexes of molybdenum.**56**

The preparation of the *bis*-alkyne complexes [WI$_2$(CO)(NCMe)(η^2-RC≡CR)$_2$] was reported in 1988 and their reactivity has been reviewed.**21** The analogous molybdenum complexes [MoXX′$_2$(CO)(NCMe)(η^2-RC≡CR′)$_2$] (X = X′ = I, Br; X = I, X′ = Cl; R = R′ = Me, Ph; R = Me, R′ = Ph), which are less stable than the related tungsten analogs, were isolated and structurally characterized in 1998.**57** The structure of [MoI$_2$(CO)(NCMe)(η^2-MeC≡CMe)$_2$] shows the molecule to be pseudooctahedral, if the alkyne ligands are assumed to occupy one coordination site. The C≡C vectors run parallel to the M–CO axis, which is a common structural feature in compounds of this type. The methyl groups bend away from the linear conformation expected in alkynes due to back bonding from suitable metal dπ orbitals into the π^*-antibonding molecular orbitals of the alkyne ligands. The reactivity of these compounds with regard to ligand substitution reactions has been described and reviewed.**21** For example, on reaction with the monodentate phosphite ligands, initial substitution of an alkyne occurs affording [MoI$_2$(CO){P(OR)$_3$}(NCMe)(η^2-RC$_2$R)] that on subsequent treatment with a second equivalent gives rise to a mixture of *cis*- and *trans*-phosphite isomers [MoI$_2$(CO){P(OR)$_3$}$_2$(η^2-RC$_2$R)]; in neither isomer is the alkyne found trans to the carbonyl ligand.**58** The alkyne ligand in *cis*-[MoI$_2$(CO){P(OMe)$_3$}$_2$(η^2-MeC$_2$Me)] was shown to be fluxional and undergoing propeller-like rotation, which could be frozen out at low temperature (*see* ***Stability Constants & their Determination***). The barrier to rotation $\Delta G^\ddagger$ was calculated to be 55 kJ mol^{-1}.

In the compounds [CpMoL$_2$(η^2-MeC$_2$Me)]$^{z+}$ (L = phosphorus donor, z = 0, 1), the but-2-yne ligand was shown to undergo propeller-like rotation (Figure 9a): at high temperature a single methyl resonance was observed in the ^{1}H NMR spectrum and at low temperatures gave two signals for the methyl groups due to the asymmetric environment. The solid-state structures of this class of compound, that have been determined crystallographically, all have the C≡C vector of the alkyne parallel to an Mo–P vector. This means, if the alkyne propeller-like rotation is frozen out, two signals should be evident in the ^{31}P NMR spectrum due to the presence of inequivalent phosphorus environments. For these compounds, this was found not to be the case and a second associated oscillation was shown to be taking place (Figure 9b) (*see* ***Stability Constants & their Determination***).**59**

3.3 Phosphaalkyne Complexes of Molybdenum

Phosphaalkynes (RC≡P) are phosphorus analogs of nitriles and have been shown to display a diverse range of organic- and inorganic-based chemistry including the preparation of phosphaalkyne-containing-transition metal complexes. This work has been reviewed.**60** Photoelectron spectroscopy has shown that the Highest Occupied Molecular Orbital (HOMO) is the phosphorus-carbon triple bond. It is this that influences the coordination chemistry of these molecules and why π-coordination is found to dominate σ-coordination. As a result, these complexes tend to parallel the well-known π-bound alkyne systems rather than their lighter congeners, the nitriles, which generally prefer the σ-ligation mode, for example, in [Mo(CO)$_3$(NCMe)$_3$]. However, π-bound nitriles are known and the first crystallographically characterized example was [Cp$_2$Mo(η^2-NCMe)] reported by Wilkinson in 1986. The related compound [(η^5-C$_5$H$_4$Bu^t)$_2$Mo(η^2-NCMe)] has recently been synthesized and crystallographically characterized. The lone pair at nitrogen has been shown to react with alkyl halides to give the cationic iminoacyl products [(η^5-C$_5$H$_4$Bu^t)$_2$Mo(η^2-RN=CMe)][I] (R = Me, Et).**61**

End-on σ-coordination of phosphaalkynes has been affected by careful control of the steric environment (*see Steric Effect*) at the metal center or the steric bulk of the phosphaalkyne, thus treatment of [Mo(N$_2$)$_2${Et$_2$P(CH$_2$)$_2$PEt$_2$}$_2$] with 2 equivalents of ^{t}BuCP afforded the dinitrogen displaced product [Mo(P≡CBu^t)$_2${Et$_2$P(CH$_2$)$_2$PEt$_2$}$_2$]. More recently, the very bulky supermesityl-phosphaalkyne P≡CMes* (Mes* = –C$_6$H$_2$Bu$^t_3$) has been reacted with [Mo(CO)$_3$(PCy$_3$)$_2$] to give the η^1-phosphaalkyne bound compound [Mo(CO)$_3$(PCy$_3$)$_2$(η^1-P≡CMes*)].**62** The crystal structure of the analogous tungsten complex shows that

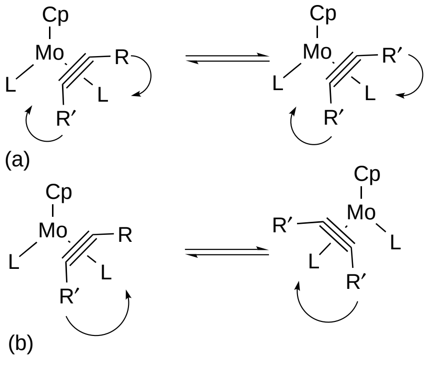

Figure 9 Two fluxional processes present in [CpMoL$_2$(η^2-RC$_2$R)]

the P–C triple bond length (1.54 Å) is little affected on coordination.

The first example of a π-bond phosphaalkyne complex was $[\mathrm{Pt(PPh_3)_2}(\eta^2\text{-}\mathrm{PCBu}^t)]$. The lone pair located at the phosphorus atom allows further elaboration. Thus, treatment with $[\mathrm{Mo(CO)_5(THF)}]$ afforded the bimetallic complex $[\mathrm{Pt(PPh_3)_2}\{\eta^2\text{-}\mathrm{Bu}^t\mathrm{CP} \rightarrow \mathrm{Mo(CO)_5}\}]$. In other parallels to alkyne chemistry treatment of $[\{\mathrm{CpMo(CO)_2}\}_2]$ with ${}^t\mathrm{BuCP}$ affords the four-electron donor phosphaalkyne complex $[\{\mathrm{CpMo(CO)_2}\}(\mu\text{-}\eta^2{:}\eta^2\text{-}\mathrm{PCBu}^t)\{\mathrm{CpMo(CO)_2}\}]$. This compound was shown to undergo further reaction at the phosphorus lone pair, including the formation of adducts with $[\mathrm{Fe_2(CO)_9}]$, $[\mathrm{W(CO)_5(THF)}]$ and $[\mathrm{Os_3(CO)_{11}(NCMe)}]$.

In addition to affording analogous products of the alkyne-containing complexes, some significant differences are also noted. Treatment of $[(\eta^5\text{-}\mathrm{C_9H_7})\mathrm{Mo(CO)_2(NCMe)_2}][\mathrm{BF_4}]$ with 2 equivalents of $\mathrm{MeC_2Me}$ affords the *bis*-alkyne complex $[(\eta^5\text{-}\mathrm{C_9H_7})\mathrm{Mo(CO)}(\eta^2\text{-}\mathrm{MeC_2Me})_2][\mathrm{BF_4}]$ in which the alkynes behave on average as 3e-donors. Whereas treatment of $[(\eta^5\text{-}\mathrm{C_9H_7})\mathrm{Mo(CO)_2(NCMe)_2}][\mathrm{BF_4}]$ with 2 Molar equivalents of ${}^t\mathrm{BuCP}$ afforded a η^3-ligated 1,3-diphosphacyclobutadiene-containing complex, which in the solid-state has a nonplanar diphosphacyclobutadiene ring. The loss of planarity is caused by one of the phosphorus atoms in the diphosphacyclobutadiene ring interacting with the $[\mathrm{BF_4}]^-$ counteranion: P–F 1.536(5) Å (Figure 10a). This interaction leads to the positive charge residing at phosphorus and an elongation of the B–F bond to 1.477(11) Å with the average of the other three B–F bonds being 1.333 Å. It was proposed from the spectroscopic data that in solution the molecule adopts an η^4-ligation of the diphosphacyclobutadiene moiety due to the presence of a singlet resonance in its ${}^{31}\mathrm{P}\text{-}\{{}^1\mathrm{H}\}$ NMR spectrum δ-121.1 ppm.**63**

It is well known that alkynes may behave as variable electron donors to metal centers and efforts have been made to prepare (nonbridging) 4e-donor phosphaalkyne-containing complexes. Treatment of the *trans*-stilbene complex (**5**) with a stoichiometric amount of ${}^t\mathrm{BuCP}$ afforded the low-melting green solid (**6**). Further, treatment of this 4e-donor phosphaalkyne complex with another molar equivalent of ${}^t\mathrm{BuCP}$ afforded the 1,3-diphosphacyclobutadiene-containing complex (**7**) in good overall yield and showed the possibility of the stepwise formation of 1,3-diphosphacyclobutadiene complexes (Scheme 7).**64**

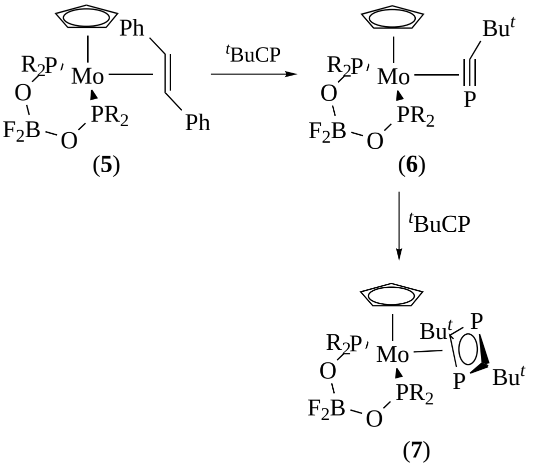

Scheme 7 Stepwise formation of a diphosphabutadiene ring

Using a similar approach, the *bis*-trimethylphosphite-containing complex $[\mathrm{CpMo}\{\mathrm{P(OMe)_3}\}_2(\eta^2\text{-}\mathrm{P{\equiv}CBu}^t)]$, analog of (**6**), was obtained in good yield. Unfortunately, a solid-state structure could not be obtained, for what is rare example of a 4e-donor phosphaalkyne complex of $\mathrm{Mo^{II}}$, so a theoretical calculation on the model compound $[(\eta^5\text{-}\mathrm{C_5H_5})\mathrm{Mo}\{\mathrm{P(OH)_3}\}_2(\eta^2\text{-}\mathrm{P{\equiv}CMe})]^+$ was carried out and the data obtained were comparable to that obtained for the crystallographically determined solid-state structure of the analogous alkyne-containing complex $[\mathrm{CpMo}\{\mathrm{P(OMe)_3}\}_2(\eta^2\text{-}\mathrm{HC_2Bu}^t)]^+$, where the alkyne is orientated parallel to a Mo–P vector. The short nature of the calculated Mo–C bond distance (2.06 Å) to the ligated phosphaalkyne is consistent with the phosphaalkyne being considered a 4e-donor and indeed is comparable to the structural characterization of a 4e-donor phosphaalkyne in the related tantalum complex $[(\eta^5\text{-}\mathrm{C_5Me_5})\mathrm{TaCl_2}(\eta^2\text{-}\mathrm{P{\equiv}CBu}^t)]$ (*see* ***Niobium & Tantalum: Inorganic & Coordination Chemistry***). Further, treatment of $[\mathrm{CpMo}\{\mathrm{P(OMe)_3}\}_2(\eta^2\text{-}\mathrm{PCBu}^t)][\mathrm{B(C_6F_5)_4}]$ with a stoichiometric amount of PCBu^t afforded the 1,3-diphosphacyclobutadiene-containing complex $[\mathrm{CpMo}\{\mathrm{P(OMe)_3}\}(\eta^4\text{-}\mathrm{P_2C_2Bu}^t_2)][\mathrm{B(C_6F_5)_4}]$. The mechanism of the reaction was suggested to be associative because of the potential of the 4e-donor phosphaalkyne to switch to

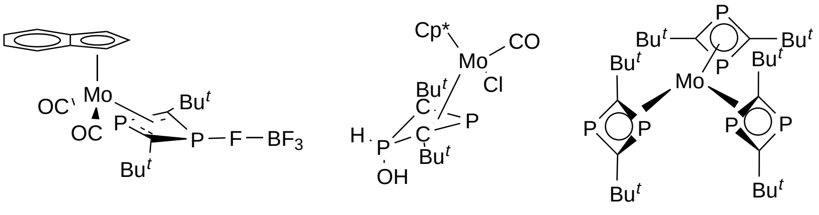

(a) (b) (c)

Figure 10 1,3-Diphosphacyclobutadiene complexes of molybdenum become a 2e-donor, which is common behavior for 4e-donor alkyne ligands in equivalent alkyne-containing complexes, thus forming a site of attack for the incoming phosphaalkyne. These data add additional support to the stepwise formation of 1,3-diphosphacyclobutadiene rings at molybdenum.[65]

Other routes to 1,3-diphosphacyclobutadiene-containing complexes of molybdenum have been described. Treatment of $[(\eta^5\text{-C}_5R_5)\text{MoCl(CO)}_3]$ (where R = H, Me) with PCBu^t afforded the 1,3-diphosphacyclobutadiene-containing complexes $[(\eta^5\text{-C}_5R_5)\text{MoCl(CO)}(\eta^4\text{-1,3-P}_2\text{C}_2\text{Bu}^t_2)]$ (where R = H, Me) (**8**), (**9**) in reasonable yield. Again this mode of reactivity differs from that of alkynes, where on treatment of $[(\eta^5\text{-C}_5R_5)\text{MoCl(CO)}_3]$ (where R = H, Me) with RC_2R affords the 4e-donor alkyne-containing complexes $[(\eta^5\text{-C}_5R_5)\text{MoCl(CO)}(\eta^2\text{-RC}_2\text{R})]$. The asymmetry at the metal center gives rise to two Bu^t signals in the ^{1}H NMR spectrum at room temperature, which on warming begin to coalesce at 60 °C at 400 MHz (*see* ***Stability Constants & their Determination***). Compound (**8**) reacts slowly with water at one of the coordinated phosphorus atoms in an oxidative addition reaction to give compound (**10**) (Figure 10b), which has been crystallographically characterized showing the hydroxyl moiety to be exo (*see Exo & Endo Substituents*).[66]

Metal centers are known to trimerize alkynes to give functionalized arenes and attempts, using molybdenum-based systems, have been made to try and prepare triphosphabenzenes. An early and unsubstantiated report for the preparation of a 1,3,5-triphosphabenzene–containing complex was reported in the 1980s.[67] An alternative approach used was Metal Vapor Synthesis (*see* ***Metal Vapor Synthesis of Transition Metal Compounds***) in which molybdenum atoms were cocondensed with PCBu^t at 77 K. The resulting product was $[\text{Mo}(\eta^4\text{-1,3-P}_2\text{C}_2\text{Bu}^t_2)_3]$ that contains three 1,3-diphosphacyclobutadiene rings rather than the hoped for $[\text{Mo}(\eta^6\text{-P}_3\text{CBu}^t_3)_2]$, which would contain two 1,3,5-triphosphabenzene ligands. The compound has been crystallographically characterized and shows that one of the four-membered rings is rotated through 90° relative to the other two, presumably to reduce steric pressure within the coordination sphere, Figure 10(c).[68]

3.3 Cyclopentadienyl-containing complexes

3.3.1 Monocyclopentadienyl Complexes

Molybdenum complexes that contain the cyclopentadienyl ligand $(\text{C}_5\text{H}_5)^-$ are very common and the cyclopentadienyl ligand (Cp) is often present as a spectator ligand occupying three coordination sites. Precursor compounds that are often used in Cp-containing molybdenum chemistry are the dimeric complex $[\{\text{CpMo(CO)}_3\}_2]$, which contains an unsupported metal–metal bond (3.24 Å), $[\text{CpMoX(CO)}_3]$ (X = halogen), the anion $[\text{CpMo(CO)}_3]^-$, and $[\text{Cp}_2\text{MoX}_2]$ (X = halogen, hydride etc.).

Preparation and Reactivity of $[\{\text{CpMo(CO)}_3\}_2]$. $[\{\text{CpMo(CO)}_3\}_2]$ can be prepared from the reaction between $[\text{Mo(CO)}_6]$ and dicyclopentadiene at 110 to 120 °C; however, this is only really effective for small scale preparations. Better yields are obtained from the reaction between $[\text{Mo(CO)}_3(\text{NCMe})_3]$ with C_5H_6 monomer or through oxidation of $[\text{CpMo(CO)}_3]^-$ with iron (III) sulfate.[69] These latter routes are particularly effective for substituted cyclopentadienyls and indenyl.

The reactivity of $[\{\text{CpMo(CO)}_3\}_2]$ centers around CO substitution by two-electron donors such as phosphines, phosphites, or isonitriles. Typically, one or two carbonyl groups are substituted to give the following compounds $[\text{CpMo(CO)}_3\text{-Mo(CO)}_2\text{LCp}]$ and $[\text{CpMo(CO)}_2\text{L-Mo(CO)}_2\text{LCp}]$. These reactions can be affected either photochemically or thermally (*see* ***Photochemistry of Transition Metal Complexes***). A competing reaction that is often present and difficult to predict is heterolytic cleavage (*see Heterolytic Cleavage*) of the Mo–Mo bond (equation 8).

$$[\text{Cp(CO)}_3\text{Mo} - \text{Mo(CO)}_3\text{Cp}] \xrightarrow{2\text{L}} [\text{CpMo(CO)}_3]^- + [\text{CpMo(CO)L}_2]^+ \quad (8)$$

One carbonyl ligand can also be lost from each molybdenum center in $[\{\text{CpMo(CO)}_3\}_2]$ in the absence of nucleophiles (*see Nucleophile*), affording the compound $[\text{Cp(CO)}_2\text{Mo}{\equiv}\text{Mo(CO)}_2\text{Cp}]$, which contains a Mo–Mo triple bond. Analogous systems where the Cp ligand is replaced by indenyl and a variety of substituted cyclopentadienes are known and react similarly.[70] This unsaturated compound is very reactive and adds nucleophiles (*see Nucleophile*) under very mild conditions. For example, alkynes add across the triple bond to give $[\text{Cp(CO)}_2\text{Mo}(\mu\text{-}\eta^2:\eta^2\text{-RC}_2\text{R})\text{Mo(CO)}_2\text{Cp}]$ and in turn are reactive species. Recently, heterobimetallic complexes of the type $[\text{Cp(CO)}_2\text{Mo}(\mu\text{-}\eta^2:\eta^2\text{-RC}_2\text{R})\text{Co(CO)}_3]$ (*see* ***Dinuclear Organometallic Cluster Complexes***) have been prepared and shown to undergo the Pauson–Khand reaction (*see* ***Organic Synthesis using Transition Metal Complexes Containing π-Bonded Ligands***) to make cyclopent-2-enones.[71] The chirality (*see Chiral*) of the tetrahedral metal-alkyne core in these compounds has been shown to give good stereocontrol in asymmetric variants.[72] Reaction with sulfur-containing compounds gives rise to compounds of type (**11**), (**12**), and (**13**). This work has been developed because of its relevance to sulfur rich metal centers in enzymes and important industrial desulfurization processes (*see* ***Hydrodesulfurization & Hydrodenitrogenation***) and has been reviewed.[73]

The reducing agents Na/Hg, $[\text{HBEt}_3]^-$, or Na/K alloy will reduce $[\{\text{CpMo(CO)}_3\}_2]$ to give the anionic complex $[\text{CpMo(CO}_3)]^-$, which can also be prepared through reaction between $[\text{Mo(CO)}_6]$ and LiCp in THF. Corresponding alkylated cyclopentadiene analogs can also be synthesized in an analogous manner. This anion reacts with a wide range of electrophiles (*see Electrophile*) such as alkyl halides, alkenyl

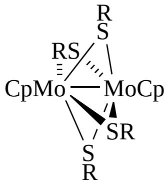

(**11**)

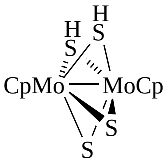

(**12**)

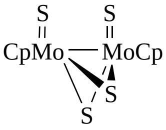

(**13**)

halides, acyl halides, and other main group element halides to give products of the type [CpMo(CO)$_3$E]. Protonation of [CpMo(CO$_3$)]$^-$ gives the hydride [CpMoH(CO)$_3$], which has a pK$_a$ of 13.9 in acetonitrile.[74]

3.3.2 Preparation and Reactivity of [CpMoX(CO)$_3$]

The halide compounds [CpMoX(CO)$_3$] (X = Cl, Br, I) are prepared through treatment of [{CpMo(CO)$_3$}$_2$] with the halogen or through reaction of [CpMoH(CO)$_3$] with a halogenating agent such as MeI, CH$_2$Br$_2$, or CCl$_4$. These compounds are good starting materials for the preparation of [CpMoX(L)$_n$(CO)$_{3-n}$] through simple CO substitution reactions using two-electron donors such as phosphines. Reaction with additional halogen leads to the higher oxidation state compounds [CpMoX$_3$(CO)$_2$]. The halide ligand can be replaced by alkyl or allyl groups to give compounds of the type [CpMoR(CO)$_3$]. Photolysis of the σ-allyl complex facilitates the σ-to-π rearrangement of the allyl ligand, due to dissociation of a carbonyl ligand, affording [CpMo(CO)$_2$(η^3-C$_3$H$_5$)]. Substitution of the halide may also be affected by carbonylate anions to give Mo-transition metal bonds. The halide atom may also be abstracted by strong Lewis acids (*see Lewis Acids & Bases*), like AgBF$_4$, in the presence of CO to give the cation [CpMo(CO)$_4$]$^+$ or if the reaction is carried out in the absence of a donor ligand, the [BF$_4$]$^-$ anion may act as a weekly coordinating ligand to give a masked source of the strong Lewis acid [CpMo(CO)$_3$]$^+$ (*see Lewis Acids & Bases*).

3.3.3 Monocyclopentadienylhalide Complexes

A slightly dated, but exhaustive, review is available on complexes of the type [CpMoX$_n$]. Cyclopentadienyl halide complexes of molybdenum in the +6 and +2 oxidation states are not known.[75]

CpMoX$_n$ and Derivatives. [CpMoX$_4$] (X = Cl, Br) are best synthesized by oxidation of [CpMoMe(CO)$_3$] with PCl$_5$ or PBr$_5$. The tetrachloride may also be prepared on treatment of [CpMoO(Cl)$_2$] with HCl. These Mo$^{\text{V}}$ compounds may be reduced to lower valent species. Thus, treatment of [CpMoCl$_4$] with zinc affords the insoluble molybdenum(III) compound [(CpMoCl$_2$)$_n$]. Enhanced solubility is obtained through the use of alkylated cyclopentadienyl ring systems. The Mo$^{\text{IV}}$ complexes are best prepared by one of two methods: conproportionation of [CpMoCl$_4$] and [CpMoCl$_2$] or by oxidation of [CpMoCl$_2$] with PhICl$_2$ and the reactivity of these compounds has been reviewed.[44]

Cyclopentadienyl Nitrosyl Halides[76]. [CpMoCl(NO)$_2$] is obtained on treatment of [CpMo(CO)$_2$(NO)] with NOCl or from the reaction between [CpMoCl$_2$] and NO. Oxidation of [CpMo(CO)$_2$(NO)] with halogens affords the compounds [{CpMoX$_2$(NO)}$_2$], which contain bridging halides (*see Bridging Ligand*). Subsequent reaction with Grignard reagents gives the corresponding mono and dialkyl complexes with hydrolysis of the latter affording the μ-oxo dimer [{CpMoR(NO)}$_2$(μ-O)] (*see μ-Oxo Bridge*).

3.4 Dicyclopentadienyl Complexes[77,78]

The molybdenum analog of chromocene (*see Metallocene Complexes*) [Cp$_2$Mo] (molybdenocene) is not stable and has only been isolated using matrix isolation techniques (*see Matrix Isolation*). The IR, magnetic circular dichroism spectra of the matrix isolated [Cp$_2$Mo] were interpreted in terms of a paramagnetic metallocene, with parallel rings.

The bent metallocenes [Cp$_2$MoX$_2$] normally have a Cp–Mo–Cp (Cp = ring centroid) angle near 130°, but the X–Mo–X angle depends upon the number of d-electrons. For d^0 complexes, the angle is approximately 97°, for d^1 it is lowered to 86 to 88° and further still to approximately 82° for d^2 systems. These structural features are consistent with the lone pair of d^2 electrons being in an orbital that lies in the MoX$_2$ plane with major lobes lying outside the MoX$_2$ triangle.

3.4.1 Preparation and Reactivity

The dihydride [CpMoH$_2$] was first prepared in 1959 on treatment of MoCl$_5$ and NaCp in the presence of [BH$_4$]$^-$, and its chemistry has been extensively developed since then.[77] It behaves as a Lewis base (*see Lewis Acids & Bases*) and is readily protonated to give the cation [Cp$_2$MoH$_3$]$^+$. This cation has been shown to reduce unsaturated organic fragments such as imines, aldehydes, and ketones.[79] Reaction of [CpMoH$_2$] with methyl triflate (CH$_3$OS(O)$_2$CF$_3$) gives [Cp$_2$MoH{OS(O)$_2$CF$_3$}] and CH$_4$. This compound is water-soluble and undergoes hydride deuteride exchange in D$_2$O and is capable of readily reducing ketones in water under the mild conditions of 40 °C and pH 7 (*see* ***Organic Synthesis using Transition Metal Complexes Containing π-Bonded Ligands***).[79] [Cp$_2$MoH$_2$] also shows its ability to behave as a base by forming adducts with Lewis acids (*see Lewis Acids & Bases*), for example, reaction with AgBF$_4$ in the presence of pseudohalide ligands gives the adducts [(Cp$_2$MoH$_2$)$_2$AgX] (X = SCN$^-$, OCN$^-$, CN$^-$, and SCF$_3$$^-$). The compound [(Cp$_2MoH_2$)$_2$AgSCN] has been crystallographically characterized and has an average Mo–Ag bond length of 2.963 Å.[80] Like the parent compound,

$[\text{Cp}_2\text{MoH}_2]$ substituted cyclopentadienyl ligands can be introduced and the incorporation of alkyl groups onto the Cp ring enhances the complex's solubility in organic solvents. Recently, the compound $[(^t\text{BuCp})_2\text{MoH}_2]$ (**14**) has been prepared and its chemistry extensively investigated.[61] (**14**) can be converted to $[(^t\text{BuCp})_2\text{MoX}_2]$ (X = Cl **15**, Br **16**) on treatment with CCl_4 and CH_2Br_2 respectively. Reaction with MeI gives $[(^t\text{BuCp})_2\text{MoHI}]$.

As is generally the case, generation of the dihalides opens up a vast array of chemistry. Thus, treatment of (**15**) with RLi or RMgX gives the dialkyl complexes $[(^t\text{BuCp})_2\text{MoR}_2]$ (R = Me, CH_2Ph, CH_2SiMe_3); reaction with LiOH gives the oxo-containing complex $[(^t\text{BuCp})_2\text{Mo{=}O}]$; reduction with Na/Hg in the presence of L (L = CO, PMe_3, C_2H_4, C_2H_2, NCMe) gives the formally Mo^{II} adducts $[(^t\text{BuCp})_2\text{MoL}]$. Reaction of $[(^t\text{BuCp})_2\text{Mo(CO)}]$ with elemental S, Se, or Te gives the compounds $[(^t\text{BuCp})_2\text{Mo}(\eta^2\text{-E}_2)]$, where E = S or Se; the compounds have been crystallographically characterized (Figure 11) and both the S–S (2.04 Å) and Se–Se (2.322 Å) bond lengths are close to those in S_8 (2.060 Å) and Se_8 (2.34 Å) suggesting strong back bonding and a Mo^{IV} metallacyclopropane type structure. These reactions mirror those of the parent complex $[\text{Cp}_2\text{MoCl}_2]$.

$[\text{Cp}_2\text{MoCl}_2]$ has been shown to hydrolyze phosphoesters under aqueous conditions through the intermediate compound (**16**), which forms from the reaction between $[\text{Cp}_2\text{Mo(OH}_2)_2]$, generated from the hydrolysis of $[\text{CpMoCl}_2]$, and the phosphoester.[81] This work has been further developed and the organophosphate pesticides Paraoxon (**17**) and Parathion (**18**) have also been shown to be hydrolyzed by $[\text{CpMoCl}_2]$ with an enhanced rate.[82]

The compounds $[(\eta^5\text{-C}_9\text{H}_7)(\text{Cp})\text{MoX}_2]$ (C_9H_7 = indenyl) have been prepared and show comparable reaction chemistry to the parent $[\text{Cp}_2\text{MoX}_2]$ compounds; however, on reduction a noticeable difference occurs. The ring-slipped products $[(\eta^3\text{-C}_9\text{H}_7)(\text{Cp})\text{MoL}_2]$ are obtained rather than the expected $[(\eta^5\text{-C}_9\text{H}_7)(\text{Cp})\text{MoL}]$. This work has been reviewed[83] and studied theoretically.[84]

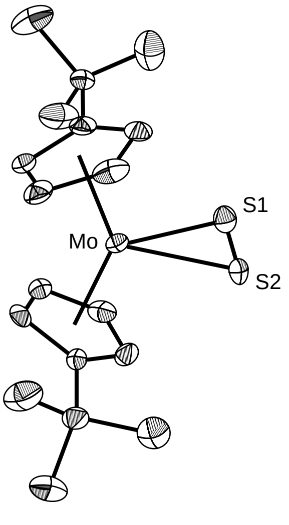

Figure 11 Molecular structure of $[\text{Mo}(\eta^2\text{-S}_2)(\eta^5\text{-}^t\text{BuCp})_2]$. (Reproduced by permission of The Royal Society of Chemistry)

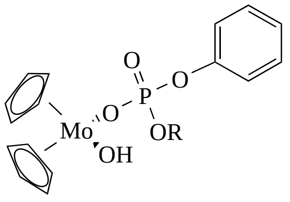

(**16**)

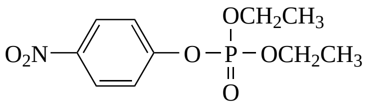

(**17**)

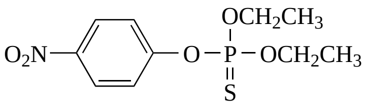

(**18**)

3.5 Arene-containing Complexes

There are two different general classes of π-bound arene-containing complexes of molybdenum: the monoarene complexes $[(\eta^6\text{-arene})\text{Mo(CO)}_3]$ or the *bis*-arene complexes $[(\eta^6\text{-arene})_2\text{Mo}]$. The solid-state structures of both classes of compound show that the bond lengths around the arene ligand are equivalent. This clearly means that the arene does not bond as a triene through localized electron pairs.

The monoarene complexes can be synthesized directly from $[\text{Mo(CO)}_6]$, but the reaction of an arene with $[\text{Mo(CO)}_3\text{L}_3]$ (L = NCMe or py in the presence of BF_3) tend to give better yields and at lower reaction temperatures. The Mo–arene bond strength appears to be greater than for the analogous Cr–arene ($280\ \text{kJ mol}^{-1}$ vs $191\ \text{kJ mol}^{-1}$ (*see* ***Bonding Energetics of Organometallic Compounds***)),[85] however; the molybdenum complexes are thermally less stable and kinetically more labile. The analogous chromium–arene complexes have found much utility in organic synthesis[86] (*see* ***Asymmetric Synthesis by Homogeneous Catalysis*** and ***Organic Synthesis using Transition Metal Complexes Containing π-Bonded Ligands***), in particular utilizing the planar chirality imposed by π-complexation of the $[\text{Cr(CO)}_3]$ fragment on one face of the arene ring.[87] The compound $[\text{Mo(CO)}_3(\eta^6\text{-C}_6\text{H}_3\text{-1,3,5-Bu}^t_3)]$ and its heteroarene analog $[\text{Mo(CO)}_3\ (\eta^6\text{-1,3,5-P}_3\text{C}_3\text{Bu}^t_3)]$ were both prepared from $[\text{Mo(CO)}_3(\text{NCMe})_3]$ and studied by Photoelectron Spectroscopy (*see* ***Photoelectron Spectroscopy of Transition Metal Systems***) and Density Functional Theory (*see Density Functional Theory*). It was found that the 1,3,5-triphosphabenzene ligand is more strongly bound to the molybdenum center because the phosphorus atoms cause a lowering of the energy of the π-acceptor orbitals, and hence allow more π-backbonding and so strengthening the molybdenum arene bond.**88**

The *bis*-arene complexes $[(\eta^6\text{-arene})_2Mo]$ can be prepared in two principally different ways. The Fischer–Hafner synthesis: The reaction between $MoCl_5$ and an arene in the presence of Al and $AlCl_3$. The problems associated with this method are long reaction times, poor yields, and the limitation on the arenes that may be used. Arenes that have lone pairs such as halobenzenes, anilines, or phenols cannot be used as they form Lewis adducts with $AlCl_3$ (*see Lewis Acids & Bases*). Equally, the use of polyalkylated arenes is not possible due to isomerization catalyzed by $AlCl_3$. The parent compound $[Mo(\eta^6\text{-}C_6H_6)_2]$ is green, very air sensitive, and a diamagnetic 18 valence electron species with a melting point of 115 °C.

An alternative synthetic procedure is to use Metal Vapor Synthesis (MVS) (*see* ***Metal Vapor Synthesis of Transition Metal Compounds***). This method of preparation is hindered by the high boiling point of molybdenum and the expense of the MVS apparatus. It does, however, allow a greater range of functionalized *bis*-arene complexes to be synthesized.**89**

bis-Heteroarene complexes, like $[Mo(\eta^6\text{-}C_5H_3N\text{-}2,6\text{-}Me_2)_2]$, can also be prepared using this methodology and their reactivity mirrors that of the *bis*-arene molybdenum complexes.**90** The reactivity of $[Mo(\eta^6\text{-}C_5H_3N\text{-}2,6\text{-}Me_2)_2]$ is summarized in Scheme 8. The solid-state structure of $[\{Mo(\mu\text{-}Cl)(\eta^3\text{-}C_3H_5)(\eta^6\text{-}C_5H_3N\text{-}2,6\text{-}Me_2)\}_2]$ has been determined and shows that the 2,6-lutidine ring is not planar. The nitrogen atom and the *para*-carbon bend in toward the metal center and the two-methyl groups bend away, and differs from the arene systems where the ring remains planar on complexation.

4 POLYMETALLIC COMPLEXES

4.1 Multiply Bonded Dimers

Molybdenum(II) and molybdenum(III) form an extensive array of multiply bonded dimers, which contain Mo–Mo quadruple and triple bonds respectively.**91** Much of the organometallic chemistry of this class of compound has come principally from the work of one research group.**92** Homoleptic compounds such as $[Mo_2Me_8]^{4-}$, $[Mo(\eta^n\text{-allyl})_4]$, which contains bridging and terminal allyl ligands (*see Bridging Ligand*), are readily synthesized from $[Mo_2(OAc)_4]$

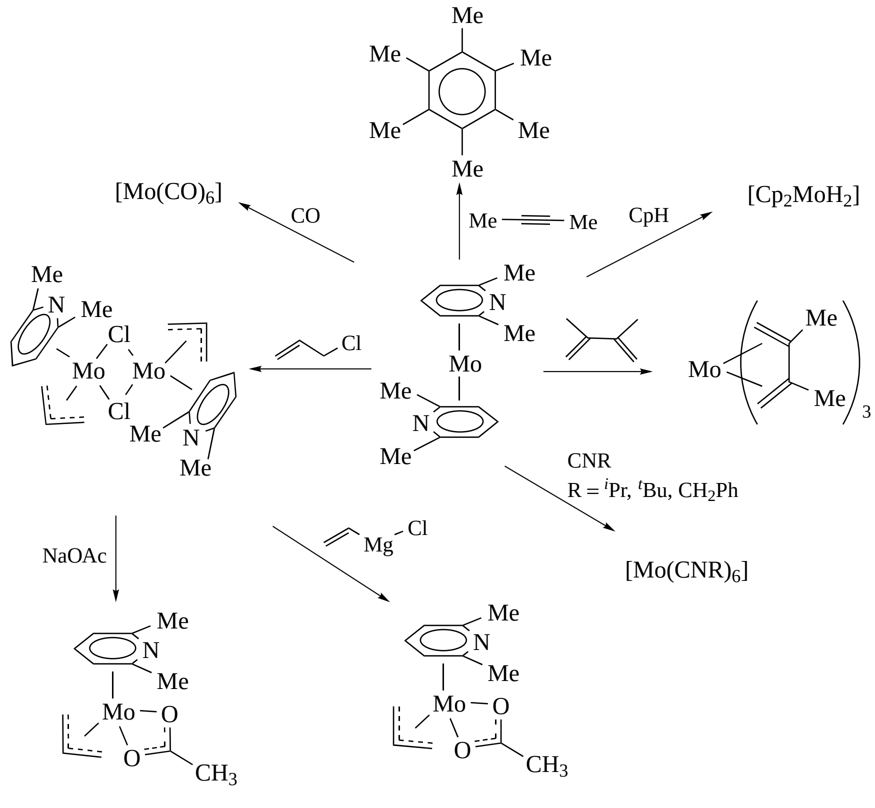

Scheme 8 Summary of the reactions of $[(\eta^6\text{-}2,6\text{-}Me_2NC_5H_3)_2Mo]$

on reaction with either MeLi or allyl Grignard respectively. Treatment of $[Mo_2(OAc)_4]$ with sources of Cp^- does not generate the expected η^5-Cp coordination rather many compounds that contain bridging (η^5:η^1-)cyclopentadienyl ligands and other coupled Cp bound systems (*see **Dinuclear Organometallic Cluster Complexes***).

4.2 Cluster Compounds

As used here cluster refers to molecules that contain at least 3 metal atoms and electron configurations suitable for the formation of metal–metal bonds. Molybdenum readily forms strong homoleptic metal–metal bonds (*see Homoleptic Compound*) and so it is not surprising that molybdenum is readily incorporated into cluster structures (*see **Polynuclear Organometallic Cluster Complexes***).

Early work in this area was often serendipitous but as the field has developed, underpinned concepts such as cluster *Electron Counting* rules and Hoffman's *Isolobal Analogy*, rational cluster syntheses have begun to appear.[93]

4.3 Homometallic Complexes

$[M_3(CO)_{12}]$ (M = Fe, Ru or Os) are derived formally from $[M(CO)_5]$ by replacing 1 of the CO ligands with the formation of 2 metal–metal bonds. However, there are no known analogous molybdenum-centered clusters derived from $[Mo(CO)_6]$ in similar fashion. This is likely to be the result of steric congestion (*see Steric Effect*); however, replacement of the CO ligand with smaller groups allows cluster formation as in $[\{MoH(CO)_3\}_4]^{4-}$.

4.4 Clusters with Bridging Ligands

Replacement of CO groups with functionalities that are capable of forming bonds between 2 or 3 metal atoms is an effective strategy in cluster synthesis. Good bridging groups include: P, As, S, Se, Te, PR, RS (*see **Cluster Compounds: Inorganometallic Compounds Containing Transition Metal & Main Group Elements***). There is particular interest in building clusters that contain sulfur due to their potential importance in processes such as hydrodesulfurization processes (*see **Hydrodesulfurization & Hydrodenitrogenation***) important in fossil fuel refining. Additional interest is as models of active sites of metalloenzymes such as nitrogenase (*see **Metalloprotein Design & Engineering***).[94–96]

Stone's group have been particularly active in the synthesis of molybdenum- and tungsten-centered heteronuclear complexes making effective use of the Isolobal Analogy (*see Isolobal Analogy*).[97]

5 RELATED ARTICLES

Asymmetric Synthesis by Homogeneous Catalysis; Bond Lengths in Inorganic Solids & Liquids; Bonding Energetics of Organometallic Compounds; Carbene Complexes; Carbon: Fullerenes; Carbonyl Complexes of the Transition Metals; Chromium: Organometallic Chemistry; Cluster Compounds: Inorganometallic Compounds Containing Transition Metal & Main Group Elements; Diffraction Methods in Inorganic Chemistry; Dinuclear Organometallic Cluster Complexes; Electrochemistry: Applications in Inorganic Chemistry; Electronic Structure of Organometallic Compounds; Hard & Soft Acids and Bases; Hydrodesulfurization & Hydrodenitrogenation; Main Group: Multiple Bonding; Metal Vapor Synthesis of Transition Metal Compounds; Metalloprotein Design & Engineering; Metathesis Polymerization Processes by Homogeneous Catalysis; Niobium & Tantalum: Inorganic & Coordination Chemistry; Organic Synthesis Using Metal-mediated Metathesis Reactions; Organic Synthesis using Transition Metal Carbonyl Complexes; Organic Synthesis using Transition Metal Complexes Containing π-Bonded Ligands; P-donor Ligands; Photochemistry of Transition Metal Complexes; Photoelectron Spectroscopy of Transition Metal Systems; Polynuclear Organometallic Cluster Complexes; Ruthenium: Organometallic Chemistry; S-donor Ligands; Stability Constants & their Determination; Surfaces; Tungsten: Organometallic Chemistry; Zirconium & Hafnium: Organometallic Chemistry.

6 REFERENCES

1. M. D. Curtis, Molybdenum organometallic chemistry, in 'Encyclopaedia of Inorganic Chemistry', John Wiley & Sons, New York, 1994, p. 2346.
2. V. Pfennig and K. Seppelt, *Science*, 1996, **271**, 626.
3. B. Roessler and K. Seppelt, *Angew. Chem., Int. Ed. Engl.*, 2000, **39**, 1259.
4. B. Roessler, S. Kleinhenz, and K. Seppelt, *Chem. Commun.*, 2000, 1039.
5. D. F. Shriver, P. W. Atkins, and C. H. Langford, 'Inorganic Chemistry', 2nd edn., Oxford University Press, Oxford, 1994, p. 670.
6. G. O. Spessard and G. L. Meissler, 'Organometallic Chemistry', Prentice Hall, New Jersey, 2000, p. 108.
7. J. E. Ellis, *Organometallics*, 2003, **22**, 3322.
8. E. O. Fischer, *Adv. Organomet. Chem.*, 1976, **14**, 1.
9. H. Rudler, M. Andouin, E. Chalain, B. Denise, R. Goumont, A. Massoud, A. Parlier, A. Pacman, and M. Rudler, *Chem. Soc. Rev.*, 1991, **20**, 503.
10. A. Mayr and H. Hoffmiester, *Adv. Organomet. Chem.*, 1991, **32**, 227.

11. P. P. Power, *Chem. Rev.*, 1999, **99**, 3463.
12. W. Petz, *Chem. Rev.*, 1986, **86**, 1019.
13. M. F. Lappert and R. S. Rowe, *Coord. Chem. Rev.*, 1990, **100**, 267.
14. B. V. Mork and T. D. Tilley, *Angew. Chem., Int. Ed. Engl.*, 2003, **42**, 357.
15. O. Kuhl, P. Lönnecke, and J. Heinicke, *Inorg. Chem.*, 2003, **42**, 2836.
16. L. Pu, B. Twamley, S. T. Haubrich, M. M. Olmstead, B. V. Mork, R. S. Simons, and P. P. Power, *J. Am. Chem. Soc.*, 2000, **122**, 650.
17. A. C. Filippou, P. Portius, and A. I. Philippopoulos, *Organometallics*, 2002, **21**, 653.
18. B. E. Eichler, A. D. Phillips, T. S. Haubrich, V. Benjamin, and P. P. Power, *Organometallics*, 2002, **21**, 5622.
19. L. Pu, P. P. Power, I. Boltes, and R. Herbst-Irmer, *Organometallics*, 2000, **19**, 352.
20. A. C. Filippou, P. Portius, A. I. Philippopoulos, and H. Rohde, *Angew. Chem., Int. Ed. Engl.*, 2003, **42**, 445.
21. P. K. Baker, *Adv. Organomet. Chem.*, 1996, **40**, 45.
22. P. K. Baker, *Chem. Soc. Rev.*, 1998, **27**, 125.
23. P. K. Baker, M. M. Meehan, H. Kwen, A. Abbote, and A. E. Maatta, *Inorg. Synth.*, 2002, **33**, 239.
24. P. K. Baker, M. M. Meehan, and M. G. B. Drew, *Transition Met. Chem.*, 1999, **24**, 333.
25. T. Szymańska-Buzar, *Math. Phys. Sci. Ser. C*, 2002, 349.
26. T. Szymańska-Buzar, T. Głowiak, and I. Czelusniak, *Inorg. Chem. Commun.*, 2000, **3**, 102.
27. W. A. Herrmann, T. Weskamp, and V. P. W. Böhm, *Adv. Organomet. Chem.*, 2002, **48**, 1.
28. R. R. Schrock, *Tetrahedron*, 1999, **55**, 8141.
29. R. H. Grubbs, S. J. Miller, and G. Fu, *Acc. Chem. Res.*, 1995, **28**, 446.
30. J. B. Alexander, D. S. La, D. R. Cefalo, A. H. Hoveyda, and R. R. Schrock, *J. Am. Chem. Soc.*, 1998, **120**, 4041.
31. O. Fujimura and R. H. Grubbs, *J. Org. Chem.*, 1998, **63**, 824.
32. A. Fürstner, L. Ackermann, K. Beck, H. Hori, D. Koch, L. Langemann, M. Liebl, C. Six, and W. Leitner, *J. Am. Chem. Soc.*, 2001, **123**, 9000.
33. R. R. Schrock, *Chem. Rev.*, 2002, **102**, 145.
34. J. M. Blackwell, J. S. Figueroa, F. H. Stephens, and C. C. Cummins, *Organometallics*, 2003, **22**, 3351.
35. I. W. Stolz, G. R. Dobson, and R. K. Sheline, *Inorg. Chem.*, 1963, **2**, 1264.
36. E. Carmona, J. M. Marin, M. L. Poveda, J. L. Atwood, and R. D. Rogers, *J. Am. Chem. Soc.*, 1983, **105**, 3014.
37. A. Pastor, A. Galindo, E. Gutiérrez-Puebla, and A. Monge, *J. Organomet. Chem.*, 1998, **566**, 211.
38. L.-C. Song, J.-T. Liu, Q.-M. Hu, and L.-H. Weng, *Organometallics*, 2000, **19**, 1633.
39. P. Zanello, F. Laschi, A. Cinquantini, M. Fontani, K. Tang, X. Jin, and L. Li, *Eur. J. Inorg. Chem.*, 2000, 1345.
40. V. Plack, P. Sakhaii, M. Freytag, P. G. Jones, and R. Schmutzler, *J. Fluorine Chem.*, 2000, **101**, 125.
41. T. Szymańska-Buzar, T. Głowiak, and I. Czeluśniak, *J. Organomet. Chem.*, 2001, **640**, 72.
42. T. Szymańska-Buzar, T. Głowiak, and I. Czeluśniak, *Polyhedron*, 2002, **21**, 2505.
43. R. Poli and L.-S. Wang, *Coord. Chem. Rev.*, 1998, **178–180**, 169.
44. R. Poli, *Acc. Chem. Res.*, 1997, **30**, 494.
45. E. Le Grognec, R. Poli, and P. Richard, *Organometallics*, 2000, **19**, 3842.
46. E. Bjurling, M. H. Johansson, and C.-M. Andersson, *Organometallics*, 1999, **18**, 5606.
47. A. J. Pearson and E. Schoffers, *Organometallics*, 1997, **16**, 5365.
48. L. S. Hegedus, 'Transition Metals in the Synthesis of Complex Organic Molecules', University Science Books, Mill Valey, CA, 1994.
49. P. Espinet, R. Hernando, G. Iturbe, F. Villafańe, A. G. Orpen, and I. Pascual, *Eur. J. Inorg. Chem.*, 2000, 1031.
50. N. Metzler-Nolte, *Organomet. Chem.*, 2002, 34.
51. M. L. H. Green and D. K. P. Ng, *Chem. Rev.*, 1995, **95**, 439.
52. M. Green, *J. Organomet. Chem.*, 1986, **300**, 93.
53. J. L. Templeton, *Adv. Organomet. Chem.*, 1989, **29**, 1.
54. M. Green, T. D. McGrath, R. L. Thomas, and A. P. Walker, *J. Organomet. Chem.*, 1997, **532**, 61.
55. C. J. Adams, K. M. Anderson, I. M. Bartlett, N. G. Connelly, A. G. Orpen, and T. J. Paget, *Organometallics*, 2002, **21**, 3454.
56. P. W. Dyer, V. C. Gibson, J. A. K. Howard, B. Whittle, and C. Wilson, *Polyhedron*, 1995, **14**, 103.
57. N. G. Aimeloglou, P. K. Baker, M. M. Meehan, and M. G. B. Drew, *Polyhedron*, 1998, **19**, 3455.
58. P. K. Baker, M. G. B. Drew, D. S. Evans, A. W. Johans, and M. M. Meehan, *J. Chem. Soc., Dalton Trans.*, 1999, 2541.
59. C. J. Adams, N. G. Connelly, and P. H. Reiger, *Chem. Commun.*, 2001, 2458.
60. J. F. Nixon, *Coord. Chem. Rev.*, 1995, **145**, 201.
61. J. H. Shin, W. Savage, V. J. Murphy, J. B. Bonanno, D. D. Churchill, and G. Parkin, *J. Chem. Soc., Dalton Trans.*, 2001, 1732.
62. T. Gröer, G. Baum, and M. Sheer, *Organometallics*, 1998, **17**, 5916.
63. P. B. Hitchcock, M. J. Maah, J. F. Nixon, and M. Green, *J. Organomet. Chem.*, 1994, **466**, 153.
64. G. Brauers, M. Green, C. Jones, and J. F. Nixon, *J. Chem. Soc., Chem. Commun.*, 1995, 1125.

65. A. D. Burrows, N. Carr, M. Green, J. M. Lynam, M. F. Mahon, M. Murray, B. Kiran, M. T. Nguyen, and C. Jones, *Organometallics*, 2002, **21**, 3076.
66. A. S. Weller, C. D. Andrews, A. D. Burrows, M. Green, J. Lynam, M. F. Mahon, and C. Jones, *Chem. Commun.*, 1999, 2147.
67. A. R. Baron and A. H. Cowley, *Angew. Chem., Int. Ed. Engl.*, 1987, **26**, 907.
68. F. G. N. Cloke, K. R. Flower, P. B. Hitchcock, and J. F. Nixon, *J. Chem. Soc., Chem. Commun.*, 1994, 489.
69. M. D. Curtis and M. S. Hay, *Inorg. Synth.*, 1990, **28**, 150.
70. M. J. Winter, *Adv. Organomet. Chem.*, 1989, **29**, 101.
71. D. T. Rutherford and S. D. R. Christie, *Tetrahedron Lett.*, 1998, **39**, 9805.
72. R. Rios, M. A. Pericá, A. Moyano, M. A. Maestro, and J. Mahría, *Org. Lett.*, 2002, 1205.
73. F. Y. Pétillon, P. Schollhammer, J. Talarmin, and K. W. Muir, *Coord. Chem. Rev.*, 1998, **178–180**, 203.
74. R. F. Jordan and R. J. Norton, *J. Am. Chem. Soc.*, 1982, **104**, 1255.
75. R. Poli, *Chem. Rev.*, 1991, **91**, 509.
76. T. W. Hayton, P. Legzdins, and W. B. Sharp, *Chem. Rev.*, 2002, **102**, 935.
77. M. J. Morris, 'Comprehensive Organometallic Chemistry II', eds. J. A. Labinger and M. J. Winter, Pergamon, New York, 1995, Vol. 5, Chap. 5.
78. H. H. Brintzinger, L. L. Lohr, and K. L. T. Wong, *J. Am. Chem. Soc.*, 1975, **97**, 5146.
79. Y. Kuo, T. J. R. Weakly, K. Awana, and C. Hsia, *Organometallics*, 2001, **20**, 4969.
80. H. Brunner, A. Hollman, B. Nuber, and M. Zabel, *J. Organomet. Chem.*, 2001, **633**, 1.
81. L. Y. Kuo and L. A. Barnes, *Inorg. Chem.*, 1999, **38**, 814.
82. L. Y. Kuo and N. M. Perera, *Inorg. Chem.*, 2000, **39**, 2103.
83. C. C. Romão, *Appl. Organomet. Chem.*, 2000, **14**, 539.
84. M. J. Calhorda, C. A. Gamelas, C. C. Romão, and L. F. Veiros, *Eur. J. Inorg. Chem.*, 2000, 331.
85. S. L. Mukerjee, R. F. Lang, T. Ju, G. Kiss, and C. D. Hoff, *Inorg. Chem.*, 1992, **31**, 4885.
86. A. C. Comely and S. E. Gibson, *J. Chem. Soc., Perkin Trans. 1*, 1999, 223.
87. S. E. Gibson and H. Ibrahim, *Chem. Commun.*, 2002, 2465.
88. S. B. Clendenning, J. C. Green, and J. F. Nixon, *J. Chem. Soc., Dalton Trans.*, 2000, 1507.
89. F. G. N. Cloke, K. A. E. Courtney, A. A. Sameh, and A. C. Swain, *Polyhedron*, 1989, **8**, 1641.
90. C. P. Mehert, A. N. Chernega, and M. L. H. Green, *J. Organomet. Chem.*, 1996, **513**, 247.
91. F. A. Cotton and R. Walton, 'Multiple Bonds between Metal Atoms', John Wiley & Sons, New York, 1982.
92. M. H. Chisholm, *J. Organomet. Chem.*, 1990, **400**, 235.
93. R. Hoffmann, *Angew. Chem., Int. Ed. Engl.*, 1982, **21**, 711.
94. S. Kuwata and M. Hidai, *Coord Chem. Rev.*, 2001, **87**, 211.
95. B. C. Wiegand and C. M. Friend, *Chem. Rev.*, 1992, **92**, 491.
96. S. M. Waterman, N. T. Lucus, and M. G. Humphrey, *Adv. Organomet. Chem.*, 2000, **46**, 47.
97. F. G. A. Stone, *Adv. Organomet. Chem.*, 1990, **31**, 53.

Mössbauer Spectroscopy

Volker Schünemann

University of Kaiserslautern, Kaiserslautern, Germany

Hauke Paulsen

University of Lübeck, Lübeck, Germany

Method Summary 1
1 Introduction 2
2 Technical Background 2
3 Applications 8
4 Acknowledgments 25
5 End Note 25
6 Abbreviations and Acronyms 25
7 Further Reading 25
8 References 25

METHOD SUMMARY

Acronyms, Synonyms

- Recoilless nuclear resonance absorption of γ-radiation (used by Mößbauer in his Nobel lecture 1961)

Measured physical quantities

- Mössbauer spectroscopy is a nuclear probe and works best with ^{57}Fe. Other Mössbauer-active isotopes are, among many others, ^{61}Ni and ^{67}Zn.
- In case of ^{57}Fe, the resonant absorption of 14.4 keV γ-rays emitted by a radioactive ^{57}Co source is measured. The spectra are determined by the hyperfine interactions (isomer shift, quadrupole splitting, and magnetic hyperfine field) of the Mössbauer nucleus caused by the surrounding electron shell.

Information available

- spin state as well as oxidation state of the Mössbauer atom
- fine structure parameters like zero-field splitting D and rhombicity E/D
- hyperfine coupling tensor $\overleftrightarrow{A}$, respectively magnetic hyperfine field B_{hf}
- phase transitions in solids
- coordination number and geometry
- dynamic properties: mean-square displacement of the Mössbauer atom, Debye temperature of solids.

Information not available, limitations

- Coordination number and geometry cannot be determined directly; comparison with model complexes is necessary.
- If several iron species are present in the sample, deconvolution of signals can be tedious.
- Exchange coupling constants J of polynuclear species can only be estimated, because in addition to D and E/D, at least the hyperfine coupling constants of the single sites have to be determined.

Examples of questions that can be answered

- Is there high-spin Fe(II) in the sample? What is the ratio of Fe(II) to Fe(III)?
- What are the values of D and E/D of a high-spin Fe(II)?
- Is there a $[2Fe-2S]^+$ or a $[4Fe-4S]^{2+}$ center in this protein?

Major advantages

- Method ''sees'' all Mössbauer atoms in the sample and works very well with ^{57}Fe. There is no Mössbauer-silent ^{57}Fe.

Major disadvantages

- For solution studies, enrichment with ^{57}Fe is necessary and relatively high ^{57}Fe concentrations (≥ 1 mM) are needed.

Sample constraints

- Sample must be in the solid state: powders, foils, and frozen solutions can be studied. Surface layers can be measured by special techniques (CEMS).
- Sample volume of frozen solutions: typically 0.2–1 mL.
- Thickness of iron foils (not enriched in ^{57}Fe): 5–25 µm.

1 INTRODUCTION

This article introduces the reader to basic fundamentals and in quite a general way to applications of Mössbauer spectroscopy within inorganic and bioinorganic chemistry. The idea is to allow scientists dealing with metal sites, especially iron chemistry, to decide whether Mössbauer spectroscopy will help in solving their problems. A huge amount of Mössbauer work on almost all iron-containing materials ranging from iron-containing alloys, oxides, ionic as well as coordination compounds[1–6] and metal sites in proteins does exist.[7–11] Mössbauer spectroscopy has also been applied to study nano-sized particles both in solution and heterogeneous catalysts.[12] Special experimental techniques like conversion electron Mössbauer spectroscopy (CEMS) allow us to study surfaces and thin films even down to the monolayer regime.[13,14] The same sensitivity has been reached very recently in experiments on iron monolayers with Mössbauer spectroscopy with synchrotron radiation, also called nuclear forward scattering (NFS) (*see* ***Nuclear Resonance Vibrational Spectroscopy (NRVS)***).[15]

Because of the broad coverage of this article, we will limit ourselves to the study of structural and electronic properties of iron centers by ^{57}Fe Mössbauer spectroscopy. If the reader is interested in the determination of dynamic properties both by conventional and synchrotron-based Mössbauer spectroscopy, we refer them to the articles by Parak,[16] and Paulsen *et al.*,[17] as well as to the contribution of Scheidt and Sage in this volume (*see* ***Nuclear Resonance Vibrational Spectroscopy (NRVS)***).

2 TECHNICAL BACKGROUND

2.1 Recoil-free Absorption of γ-Rays

The term Mössbauer effect describes the recoil-free resonant absorption of γ quanta by nuclei of the same kind as the emitters. If a free nucleus undergoes a transition from an excited state by emission of a γ quantum, it suffers a recoil. The energy of this quantum in the laboratory frame is given as $E_\gamma^0 = E^0 - E_R$, where E^0 is the nuclear transition energy and E_R is the recoil energy of the nucleus after the emission of the γ quantum. It can be expressed as

$$E_R = \frac{E_\gamma^{0^2}}{2Mc^2} \approx \frac{E^{0^2}}{2Mc^2} \tag{1}$$

with M being the nuclear mass and c the speed of light. The recoil energy of the nucleus E_R is approximately 10^6 larger than the energy width Γ of the excited nuclear state. Thus the lifetime broadening of the nuclear transition cannot exceed the recoil energy and therefore resonance absorption of γ quanta emitted by free nuclei is not possible.

Rudolf Mössbauer found during work on his PhD thesis in 1953 that, if ^{191}Ir nuclei are embedded in a crystal lattice, there is a certain probability for recoil-free emission and absorption of γ quanta.[18] Later he received the Nobel prize because in the meantime it had been found that recoil-free emission and absorption of γ quanta also worked for ^{57}Fe and this boosted the application of the technique in physics, material science, and chemistry. A very instructive description of these investigations can be found in his Nobel lecture.[19]

Qualitatively the effect can be explained by a simple picture: the recoil energy of a single nucleus is taken up by the whole lattice and the expression for the recoil energy (equation 1) does not contain the mass M of the nucleus anymore, but contains the mass of the whole lattice M_{lattice}:

$$E_R^{\text{Moss}} = \frac{E^{0^2}}{2M_{\text{lattice}}c^2} \cong 0 \tag{2}$$

Because M_{lattice} is much larger than the nuclear mass M, the recoil energy is negligible and resonance absorption takes place. In terms of quantum mechanics, there is a probability f for a zero-phonon process, where no lattice vibrations are excited. Rudolf Mössbauer showed that the probability f for a zero-phonon process is given by the subsequently named Lamb–Mössbauer factor:

$$f = \exp\{-k^2\langle x^2\rangle\} \tag{3}$$

The quantity $\langle x^2\rangle$ denotes the mean-square displacement of the Mössbauer nucleus in the direction of the incoming γ-ray and $k = 2\pi/\lambda$ is the wave number of the γ-ray. The decrease of the mean-square displacement $\langle x^2\rangle$ with decreasing temperature leads to an increase of the Lamb–Mössbauer factor f and thus the Mössbauer effect.

2.2 Experimental Setup and Spectral Line Shape

2.2.1 Transmission Geometry

A setup in transmission geometry is the standard implementation of ^{57}Fe Mössbauer spectroscopy. In a transmission experiment, the γ-rays emitted by the radioactive source are registered by a detector after they have passed the absorber. This method works with powders, foils, and frozen solutions. In order to investigate the energy spectrum of the absorber nuclei, the energy of the emitted γ-ray is modulated by moving the source relative to the absorber with a velocity V according to $E_\gamma = \left(1 + \frac{V}{c}\right) E^0_{\text{source}}$. The source is mounted on the Mössbauer drive, which is basically a loudspeaker driven either by a sinusoidal or triangular shaped current (Figure 1).

The magnitude of the observed Mössbauer effect is determined by the effective thickness of the absorber, which is a dimensionless quantity given by

$$t_{\text{eff}} = f\sigma_0 N_{\text{A}}\beta\rho\frac{\Delta x}{A} \tag{4}$$

with f being the Lamb–Mössbauer factor and σ_0 denoting the resonance cross section for absorption of γ quanta. N_{A} is the Avogadro constant, β is the relative isotopic abundance of the Mössbauer-active element in the absorber, ρ is the mass density of the sample, Δx is the geometric thickness of the absorber, and A is the molar mass of the Mössbauer isotope.

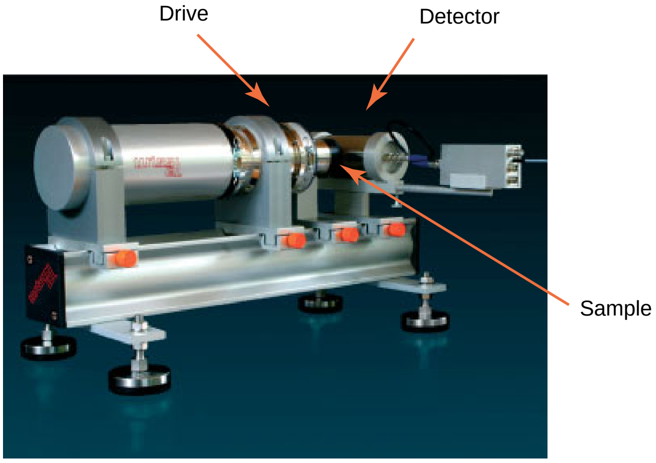

Figure 1 Mössbauer spectrometer with velocity calibrator Mössbauer drive and detector. The sample is placed between drive and detector. For measurements at cryogenic temperatures, the sample is mounted in a cryostat equipped with Mylar or beryllium windows. (Reproduced with permission Wissel Gmbh)

The transmission through an absorber of thickness t_{eff} as a function of the relative velocity V between source and absorber is given by the evaluation of the transmission integral discussed, for example, in Ref. 2. In case of ^{57}Fe Mössbauer spectroscopy for almost all samples which are not enriched in the Mössbauer isotope ^{57}Fe (the natural abundance of ^{57}Fe is 2%), the evaluation of the transmission integral leads to Lorentzian line shape with a minimum linewidth of $0.19\,\text{mm}\,\text{s}^{-1}$, which is twice the natural linewidth of the ^{57}Fe Mössbauer transition. The absorption cross section as a function of source velocity is then given as (with $\sigma_0 = 2.56 \cdot 10^{-18}\,\text{cm}^{-2}$ for ^{57}Fe)

$$\sigma(V) = \frac{\Gamma^2/4}{(V - V_{\text{res}})^2 + (\Gamma/2)^2}\sigma_0 \tag{5}$$

2.2.2 Backscattering Geometry

This technique measures the radiation emitted by the sample after the excited Mössbauer nuclei have returned to their ground state. Backscattered radiation consists of X rays originating from the electron shell, γ-rays from the nucleus, or conversion electrons. Since self absorption prevents γ or X rays from escaping from the inner part of the sample, only a layer at the surface contributes to the backscattered spectrum. The thickness of this layer depends on the energy range and the kind of detected radiation. If one detects γ and/or X rays in backscattering geometry, the escape depth is approximately 10^{-6} m for ^{57}Fe Mössbauer spectroscopy. It is also possible to detect conversion electrons, and in this case the surface layer is even smaller and one can reach monolayer sensitivity. This technique is called *conversion electron Mössbauer spectroscopy* (CEMS). By detecting the electrons in an energy dispersive fashion, Mössbauer spectra from surface layers of varying thickness can be obtained.

Although chemical and biological samples are routinely measured in transmission geometry, the detection of backscattered Mössbauer radiation may also be considered when thin films of bioinorganic complexes or samples that cannot be moved to a laboratory should be studied. The group of G. Klingelhöver has designed such a transportable miniaturized Mössbauer spectrometer (MIMOS), which contains all necessary mechanical and electronic parts (including a Mössbauer drive and radiation detector) in a box that can be held in one hand (Figure 2). This spectrometer has even been used to perform Mössbauer measurements on the planet Mars.**[20,21]** Other applications of this spectrometer, which is commercially available, are, for example, the destruction-free examination of artwork and field studies of soil.

2.2.3 Sample Requirements and Pitfalls during Sample Preparation

Metallic foils can be conveniently measured in absorption geometry. An α-Fe foil of $25\,\mu\mathrm{m}$ thickness and an area of $\sim 1\,\mathrm{cm}^2$ is often used as a calibration standard. With such a foil and using a ^{57}Co source with an activity of $\sim$50 mC, it is possible to acquire a decent spectrum at room temperature in less than 1 h.

Powder samples of inorganic iron compounds can be conveniently measured with sample holders that have a sample thickness of $\sim$0.5 mm and an area of $\sim 1\,\mathrm{cm}^2$. This makes a total sample volume of $\sim 50\,\mu\mathrm{L}$. Some Mössbauer groups prefer to measure pressed pellets, but this decision depends often on history and individual laboratory habits. If sample holders like those displayed in Figure 3 are used, one has to take special care that there are no holes in the sample. This would mean that the γ-rays go through the sample holder but do not penetrate sample material and can lead to a drastic decrease in the intensity of the Mössbauer lines. A simple test is to check whether light is shining through the sample holder. This is especially important when only a tiny amount of sample is present. In such a case, it also helps to put a thin sheet of paper in between the sample holder and the sample. If the sample holder is prepared correctly, it is possible that there is only a very weak Mössbauer spectrum at room temperature. In this case, the Mössbauer–Lamb factor f is small and therefore it is advisory to measure at cryogenic temperatures $\leq$120 K. The experience in our laboratory is that measuring a powder sample of an iron compound with an atomic mass of around 500–1000 amu at 77 K in a sample holder made of Delrin©, like those displayed in Figure 3, normally takes not more than 24 h.

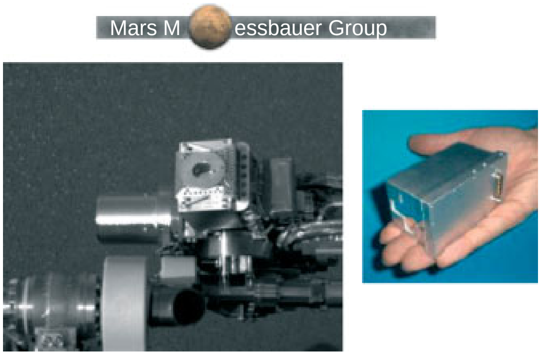

Figure 2 The Mars Exploration Rover Spirit's Mössbauer spectrometer. The hydroxyl containing mineral goethite (FeOOH) has been identified with this spectrometer in the ''Columbia Hills'' of Mars. This finding produced strong evidence for past water activity in the area that Spirit has been exploring.**[22]** (Reproduced from web page with permission G Klingelhofer)

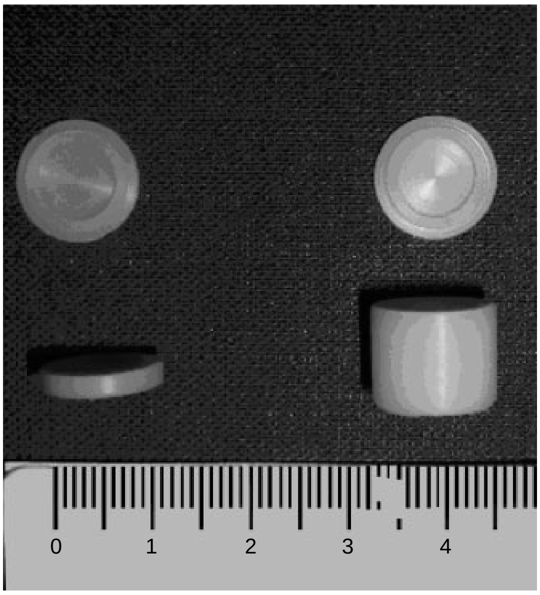

Figure 3 Sample holders made of Delrin© for Mössbauer spectroscopy of powders (left) and frozen solutions (right). The measurement rule has units of centimeters

For liquid solutions containing iron compounds or proteins, the Mössbauer–Lamb factor goes to zero, and therefore ^{57}Fe Mössbauer spectroscopy on solutions is only possible in the frozen state. Since the natural abundance of ^{57}Fe is only 2%, it is advisable to perform Mössbauer studies on solutions with ^{57}Fe-enriched samples. For protein studies, ^{57}Fe enrichment is essential. Typical sample volumes can range from 0.25–1.0 mL. In some cases, frozen solution studies can be performed down to an ^{57}Fe concentration of $\sim$0.1 mM, but taking a Mössbauer spectrum of such a sample can take weeks depending on the shape of the spectrum and the outcome is uncertain. Therefore, it is strongly recommended that the concentration of ^{57}Fe be at least 1 mM. Samples with ^{57}Fe concentrations of, for example, 10 mM can very conveniently be measured in a couple of hours—such samples the Mössbauer spectroscopists like the most. In any case, for

^{57}Fe-enriched iron proteins a general rule exists: the higher the protein concentration the better.

2.3 Hyperfine Structure of ^{57}Fe Mössbauer Spectra

Mössbauer spectroscopy senses the hyperfine interactions, which are present at the nucleus of the Mössbauer isotope. The electrical monopole interaction causes the isomer shift and the electric quadrupole interaction leads to the quadrupole splitting, which in the case of ^{57}Fe causes a two-line Mössbauer pattern. The magnetic dipole interaction leads to a magnetically split six-line pattern (Figure 4). In the following text, these interactions and their deduction from Mössbauer spectra will be discussed.

2.3.1 *The Isomer Shift δ*

The electric monopole interaction is proportional to the s-electron density at the iron nucleus $|\varphi(0)|^2$ and can be expressed by

$$E = \frac{2}{3}\pi \cdot Z^2 e^2 |\varphi(0)|^2 \cdot \langle r^2 \rangle \tag{6}$$

with $\langle r^2 \rangle$ being the mean-square nuclear radius and Ze being the nuclear charge. In general, source and absorber nuclei are embedded in different matrices, which leads to different s-electron densities at the source and the absorber nuclei. As a consequence, the energy of the Mössbauer nuclei in the source and in the absorber have slightly different energy

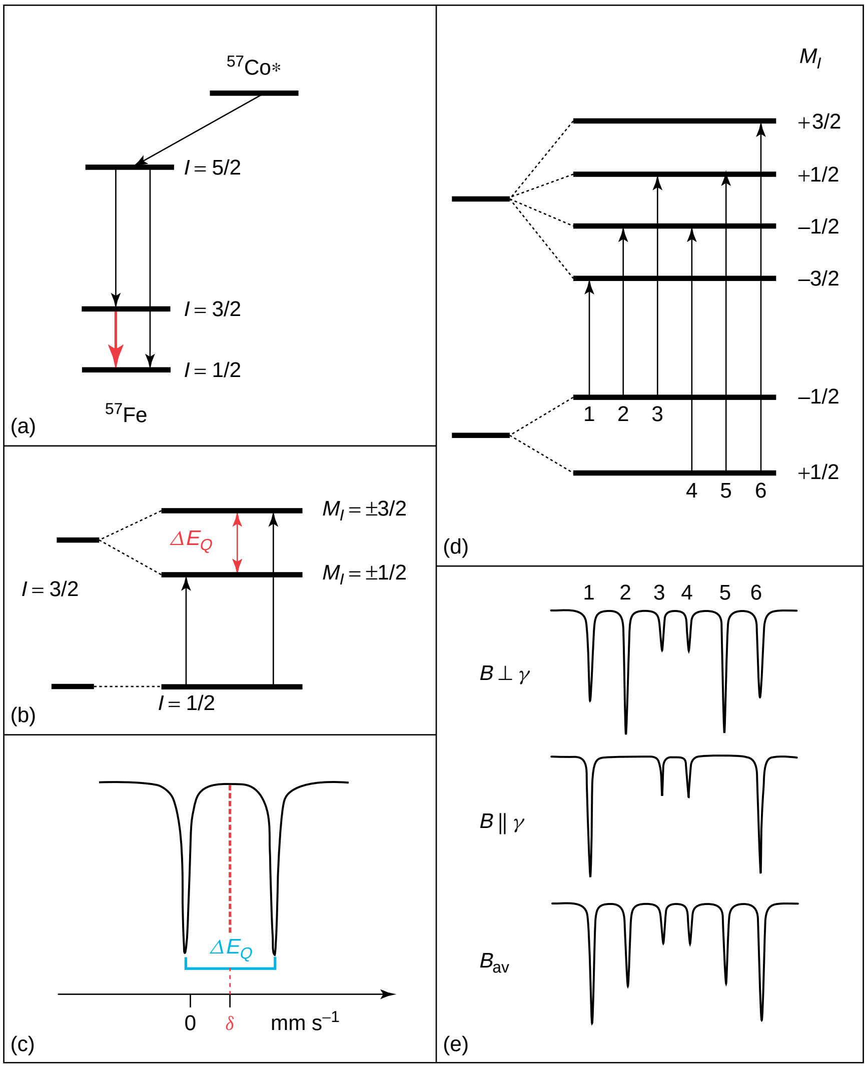

Figure 4 (a) Decay scheme of ^{57}Co. The 14.4-keV transition used for ^{57}Fe Mössbauer spectroscopy is shown in red. (b) Mössbauer transitions without magnetic field. (c) Mössbauer spectrum with quadrupole doublet. (d) Energy levels of the ^{57}Fe states and Mössbauer transitions in the presence of a magnetic field. (e) Magnetic Mössbauer spectra for different orientations of the magnetic field relative to the propagation direction of γ-ray. The quadrupole interaction has been neglected in (d) and (e). (Reprinted with permission from Krebs, Price, Baldwin, Saleh, Green and Bollinger.[23] © 2005 American Chemical Society)

shifts of δE_{source} and $\delta E_{\text{absorber}}$. Therefore, the isomer shift δ is expressed as

$$\delta = \delta E_{\text{source}} - \delta E_{\text{absorber}} \tag{7}$$

For a homogenous charge distribution, the isomer shift is given as

$$\delta = \frac{4}{5}\pi Ze^2R^2\frac{\delta R}{R}[|\varphi(0)_{\text{absorber}}|^2 - |\varphi(0)_{\text{source}}|^2] \tag{8}$$

with $R = \frac{1}{2}(R_e + R_g)$ and $\delta R = R_e - R_g$, where R_g and R_e are the nuclear radii of the ground and excited state, respectively.

For iron, $\delta R = R_e - R_g$ is negative and therefore a more positive isomer shift implies a lower value of $|\varphi(0)_{\text{absorber}}|^2$. This may be caused either from a decrease in the total s-electron population or from shielding of s electrons by the 3d electrons. The isomer shift is sensitive to the oxidation state of the iron and typical values against metallic iron at 300 K are given in Figure 5.

The experimentally observed isomer shift can be expressed as a sum of the temperature-independent term δ_0 and the temperature-dependent second-order Doppler shift δ_{SOD}

$$\delta = \delta_0 + \delta_{\text{SOD}} \quad \text{with} \quad \delta_{\text{SOD}} = -\frac{E_\gamma \langle v^2 \rangle}{2c^2} \tag{9}$$

with $\langle v^2 \rangle$ denoting the mean-square velocity of the iron atom and c denoting the speed of light.

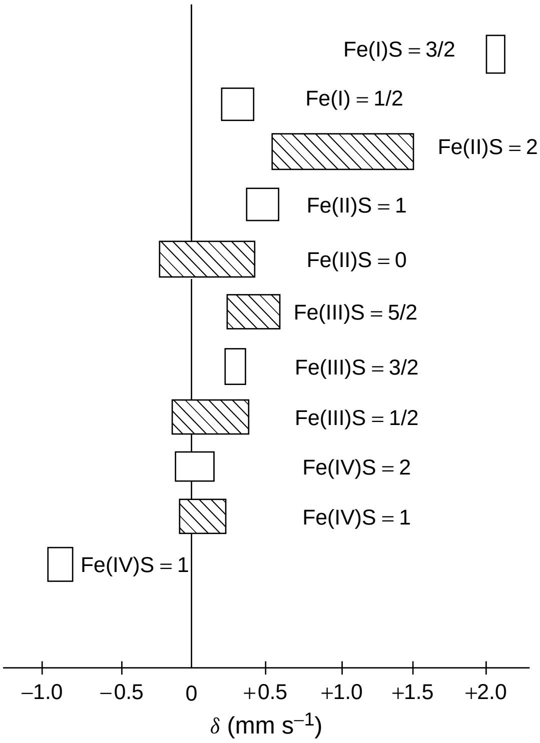

Figure 5 Ranges of isomer shifts observed in various oxidation and spin states of iron (given relative to α-iron at 300 K). Shadowing indicates the most frequently observed configurations. (From Greenwood and Gibb.[3] With kind permission from Springer Science & Business Media)

2.3.2 *The Electric Quadrupole Splitting ΔE_Q*

The electric quadrupole interaction is described by the Hamiltonian

$$\hat{H}(E2) = \frac{eQV_{zz}}{4I(2I-1)}\left[3\hat{I}_z^2 - I(I+1) + \eta(\hat{I}_x^2 - \hat{I}_y^2)\right] \tag{10}$$

with Q being the nuclear quadrupole moment and I being the nuclear spin of the nuclear state. $\hat{I}_x^2$, $\hat{I}_y^2$, and $\hat{I}_z^2$ being the corresponding spin operators. The coordinate frame of the electric field gradient (EFG) tensor $\overleftrightarrow{V}$ is conventionally chosen in such a way that $|V_{xx}| \leq |V_{yy}| \leq |V_{zz}|$. The asymmetry parameter η is generally defined as

$$\eta = \frac{V_{xx} - V_{yy}}{V_{zz}} \tag{11}$$

Since the electric quadrupole moment of the nuclear ground state of iron ^{57}Fe with $I_g = 1/2$ is zero, the quadrupole interaction does not affect the ground state, but splits the first excited nuclear state with $I_e = 3/2$ into two sublevels. As a result, it produces, in the case of ^{57}Fe, a two-line Mössbauer absorption pattern (Figure 4) with a corresponding quadrupole splitting ΔE_Q given by

$$\Delta E_Q = \frac{1}{2}eQV_{zz}\sqrt{1 + \frac{\eta^2}{3}} \tag{12}$$

The largest component of the EFG tensor V_{zz} and the asymmetry parameter η can only be determined separately when a magnetic interaction is present in addition. They reflect the population of the iron 3d orbitals as well as the ligand charges surrounding the iron. For a more detailed description, see Ref. 2 as well as a review on iron porphyrins by Debrunner.[24]

2.3.3 *The Magnetic Splitting B_{hf}*

The third term of the nuclear Hamiltonian contains two contributions. The nuclear Zeeman term couples the magnetic moment of the nucleus to the external magnetic field $\vec{B}_0$. Furthermore, there is a term that describes the interaction of the nuclear spin with the internal magnetic hyperfine field. For paramagnetic samples this is often done in terms of the hyperfine coupling tensor $\overleftrightarrow{A}$, which multiplied by the spin expectation value $\langle\vec{S}\rangle$ of the corresponding electronic state of, for example, the iron ion, that produces the internal magnetic hyperfine field

$$\vec{B}_{\mathrm{hf}} = -\langle\vec{S}\rangle \cdot \overleftrightarrow{A}/(g_{\mathrm{N}}\mu_{\mathrm{N}}) \tag{13}$$

Therefore the hyperfine coupling $\overleftrightarrow{A}$ tensor is often given in units of Tesla ($\overleftrightarrow{A}/g_{\mathrm{N}}\mu_{\mathrm{N}}$; $1\,\mathrm{T} \mathrel{\hat{=}} 1.36\,\mathrm{MHz}$ for ^{57}Fe). The magnetic Hamiltonian is given as

$$\hat{H}(M1) = \langle\vec{S}\rangle \cdot \overleftrightarrow{A} \cdot \vec{I} - g_{\mathrm{N}}\mu_{\mathrm{N}}\vec{B}_0 \cdot \vec{I} = -g_{\mathrm{N}}\mu_{\mathrm{N}}(\vec{B}_{\mathrm{hf}} + \vec{B}_0) \cdot \vec{I} \tag{14}$$

where g_{N} is the nuclear g factor and μ_{N} is the nuclear magneton. If the internal hyperfine field is zero as is the case of diamagnetic ions, the energy eigenvalues of a nuclear spin I in a magnetic field B_0 are given as

$$E_{\mathrm{M}}(m) = -m g_{\mathrm{N}}\mu_{\mathrm{N}} B_0 \tag{15}$$

This leads to the energy differences between nuclear ground and excited state

$$\Delta E_{\mathrm{M}}(m_{\mathrm{e}}; m_{\mathrm{g}}) = B_0(m_{\mathrm{e}} g_{\mathrm{N}}^{e}\mu_{\mathrm{N}} - m_{\mathrm{g}} g_{\mathrm{N}}^{g}\mu_{\mathrm{N}}) \tag{16}$$

For ^{57}Fe with a ground state nuclear spin of $I_{\mathrm{g}} = 1/2$ and $I_{\mathrm{e}} = 3/2$ for the excited state and taking into account the dipole selection rules $\Delta M = 0, \pm 1$, one gets six transitions of different energy, which means a six-line pattern as shown in Figure 4.

For most cases, the internal field is much higher than the external magnetic fields. Metallic iron for example exhibits a magnetic hyperfine field ($-33\,\mathrm{T}$ at $300\,\mathrm{K}$) that is oriented opposite to the magnetization of the sample. The internal hyperfine field contains particularly valuable information about the electronic configuration of the iron atom and is determined by four contributions:

$$\vec{B}_{\mathrm{hf}} = \vec{B}_{\mathrm{fc}} + \vec{B}_{\mathrm{ls}} + \vec{B}_{\mathrm{dd}} + \vec{B}_{\mathrm{latt}} \tag{17}$$

$\vec{B}_{\mathrm{fc}}$ is due to the Fermi-contact interaction, which is caused by the core polarization of the s-electron density at the nucleus. The sign of $\vec{B}_{\mathrm{fc}}$ is negative, which can qualitatively be rationalized in the following way: in the case of iron, the unpaired 3d electrons attract the spin parallel s electrons via exchange interaction. This leaves an excess of antiparallel s-electron spin density at the nucleus, which leads to the negative sign of $\vec{B}_{\mathrm{fc}}$. $\vec{B}_{\mathrm{fc}}$ dominates, for instance, in high-spin ferric Fe(III), whereas low-spin ferric iron shows a considerable contribution of $\vec{B}_{\mathrm{ls}}$ due to spin-orbit interaction. The dipole field $\vec{B}_{\mathrm{dd}}$ originating from the electron shell as well as lattice contributions $\vec{B}_{\mathrm{latt}}$ are normally of the order of 1 T and therefore negligible in most cases.

2.3.4 *The Spin Hamiltonian Formalism: Determination of Zero-Field Splitting D and Rhombicity E/D of Paramagnetic Iron Centers by Mössbauer Spectroscopy*

Mössbauer spectroscopy can also be used to obtain information about fine structure parameters like zero-field splitting D and rhombicity parameter E/D. The zero-field splitting is a second-order effect, which can be classically visualized as resulting from the circular currents generated in the atomic shell by the electron spin. In Section 3.10.5, we describe how D and E/D can be calculated.

The spin Hamiltonian formalism, which is also needed to interpret, for example, electron paramagnetic resonance or magnetic circular dichroism spectra (*see* ***Magnetic Circular Dichroism (MCD) Spectroscopy***), was first applied to the interpretation of magnetic Mössbauer spectra by Wickmann, Klein and Shirley**[25]** and was implemented into a computer program by Münck *et al.* in the early 1970s.**[26]** For most studies of mononuclear iron centers with electron spin quantum number S, the following electronic Hamiltonian is used:

$$\hat{H}_{\mathrm{fs}} = D\left[\hat{S}_z^2 - \frac{1}{3}S(S+1) + \frac{E}{D}(\hat{S}_x^2 - \hat{S}_y^2)\right] + \mu_{\mathrm{B}}\vec{S}\overleftrightarrow{g}\vec{B} \tag{18}$$

Here $\hat{S}_x^2$, $\hat{S}_y^2$, $\hat{S}_z^2$, and $\vec{S}$ are the corresponding quantum mechanical spin operators, $\vec{B}$ is the external magnetic field, and $\overleftrightarrow{g}$ denotes the electronic g tensor. After diagonalization of equation (18) in the spin space, the spin expectation values $\langle\vec{S}_i\rangle$ can be calculated for every fine structure sublevel i. The fine structure levels are separated by energy gaps, which are a function of D, E/D, and the external field $\vec{B}$. The energy gaps between the fine structure sublevels are of the order of some wave numbers. According to equation (13), the spin expectation values $\langle\vec{S}_i\rangle$ lead to a characteristic magnetic hyperfine field B_{hf} at the iron nucleus, which manifests itself in a magnetic splitting of the spectrum. In order to simulate spectra of frozen solutions or powder samples by the spin Hamiltonian formalism, spectra for all orientations of the molecule with respect to the external field have to be calculated and summed up (powder average). Details of this procedure will not be discussed here, but can be found in Refs. 7, 8, 11, and 24. Nowadays several program packages are available. We are using the package VINDA, which runs under Windows environments and is available free of charge via the web site of Palle Gunnlaugson.**[27]** While working at the laboratory of Prof. Alfred X. Trautwein, Dr. Gunnlaugson had included the code that had been used at that time in the Trautwein group in VINDA. Some Mössbauer groups use the package WMOSS, which is distributed by Web Research Co.,**[28]** and others use their own codes. Unfortunately, the broadly used software package NORMOS does not have the option to evaluate paramagnetic Mössbauer spectra by full diagonalization of the spin Hamiltonian matrix to date, but this might be included in the future.

3 APPLICATIONS

3.1 Metallic Iron, Iron Nanoparticles, and Thin Films

3.1.1 Metallic Iron

The Mössbauer spectrum of metallic α-iron at room temperature is used as a velocity calibration standard in almost every Mössbauer laboratory. Therefore most isomer shift values published to date are given relative to metallic iron at room temperature.[a] The ferromagnetism of α-Fe is caused by unpaired spin density in its electronic band structure. The unpaired electronic spin density is able to couple to the nucleus via magnetic hyperfine interactions. This leads to a magnetic six-line pattern which reflects a very high magnetic hyperfine field of $B_{\text{hf}} = -33\,\text{T}$ at the iron nucleus. In the case of metallic iron and iron-containing alloys as well as minerals, the interaction between electron spin $\vec{S}$ and nuclear spin $\vec{I}$ proceeds predominantly via isotropic Fermi-contact interaction. Therefore, the magnetic hyperfine field at the iron nucleus B_{hf} is proportional to the magnetization of the sample and temperature-dependent measurements of B_{hf} can be regarded as complementary to magnetization measurements. The determination of the temperature dependence of the magnetic hyperfine field of α-Fe and its saturation magnetization (Figure 6) was one of the very first applications of ^{57}Fe-Mössbauer spectroscopy. Figure 6 shows that the magnetic hyperfine field does indeed scale very nicely with data from magnetic measurements. It should be noted that such measurements can be performed on any magnetic material to investigate magnetic phase transitions no matter whether the iron atom is present in an alloy, in an oxide or as an impurity in normally non-iron-containing materials. This is always true if the Fermi-contact interaction is the dominant contribution to the magnetic hyperfine field, which holds for metallic iron and ferric high-spin iron having $S = 5/2$.

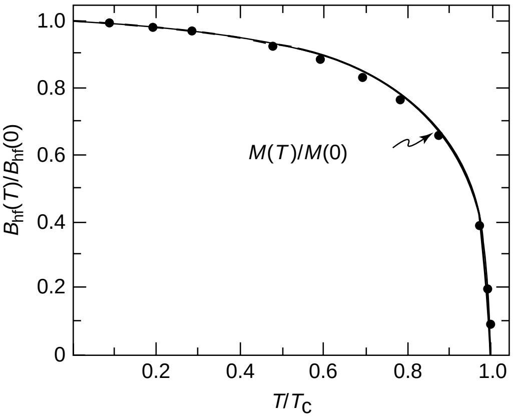

Figure 6 Temperature dependence of the magnetic hyperfine field $B_{\text{hf}}(T)$ of α-Fe as a function of T/T_{c} with T_{c} being the Curie Temperature. Note that $B_{\text{hf}}(T)$ is scaled with the value extrapolated to 0 K which is denoted as $B_{\text{hf}}(0)$. The dots represent Mössbauer data and the solid line represents saturation magnetization data. (Redrawn after Greenwood and Gibb.**[3]** With kind permission from Springer Science & Business Media)

3.1.2 Iron Nanoparticles

If the dimension of a metallic α-Fe-particle (or any ferro-, antiferro-, or ferrimagnetic material) reaches the dimensions of magnetic domains, the particle turns into a single-domain particle. Owing to thermal excitation, the magnetization of the single-domain particle can relax between the axes of easy magnetization. Such a magnetic behavior of small single-domain particles is called *superparamagnetic*. If the relaxation rate of a superparamagnetic particle is fast with respect to the lifetime of the excited state of the ^{57}Fe nucleus ($\sim 10^{-7}$ s), the nucleus sees on average no magnetic field and only a quadrupole doublet occurs.**[12]** This is often the case if small nanoparticles of metallic iron or iron oxides are measured at room temperature. In order to unambiguously identify the magnetic phase of these systems, measurements at cryogenic temperatures are helpful. By lowering the temperature, the relaxation rate of the superparamagnetic particles is slowed down and a magnetically split pattern occurs (Figure 7).**[29]**

In the simplest case of uniaxial relaxation, a relaxation process where the magnetization flips around an angle of 180°, the relaxation rate of a single-domain particle with the saturation magnetic moment $\vec{\mu}$ in a magnetic field $\vec{B}$ at a given temperature T is expressed as

$$\nu = \nu_{\text{o}} \cdot \exp\left(-\frac{KV + \vec{\mu} \cdot \vec{B}}{k_{\text{B}}T}\right) \tag{19}$$

The energy barrier $E_a = KV$ is called the *anisotropy energy* and describes the strength of the pinning of the single-domain particle magnetization. The anisotropy energy KV can be determined by analyzing temperature-dependent Mössbauer measurements in zero magnetic field with suitable relaxation models (Figure 8).**[30]** A simpler approach is the determination of the superparamagnetic blocking temperature T_{B}. For this temperature one assumes $k_{\text{B}}T_{\text{B}} \cong KV$. By definition the blocking temperature of an ensemble of superparamagnetic particles is the temperature where half of the spectral area of the Mössbauer spectrum shows magnetic splitting and the other half of the spectrum shows a doublet or a single line depending on the size of the quadrupole splitting. An approach to determine T_{B} is to fit the temperature-dependent spectra with at least two components: a simple quadrupole doublet with Lorentzian line shape and a spectrum

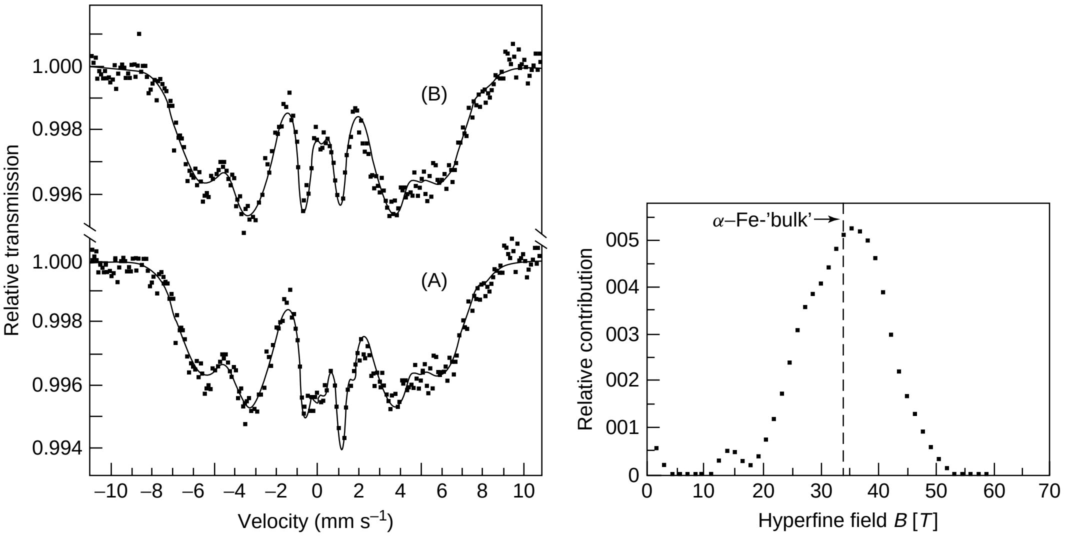

Figure 7 Mössbauer spectrum of nanometer-sized metallic iron particles in zeolite NaX obtained at $T = 4.2\,\mathrm{K}$ before (A) and after (B) subtraction of two Fe(II) contributions with $\delta_1 = 0.75\,\mathrm{mm\,s^{-1}}$ and $\Delta E_{Q1} = 0.8\,\mathrm{mm\,s^{-1}}$ (5% relative contribution) and $\delta_2 = 0.85\,\mathrm{mm\,s^{-1}}$ and $\Delta E_{Q2} = 1.85\,\mathrm{mm\,s^{-1}}$ (6% relative contribution). The analysis of the magnetic hyperfine field distribution identifies metallic α-Fe-nanoparticles. (From Schünemann, Winkler, Butzlaff and Trautwein.[29] With kind permission from Springer Science & Business Media)

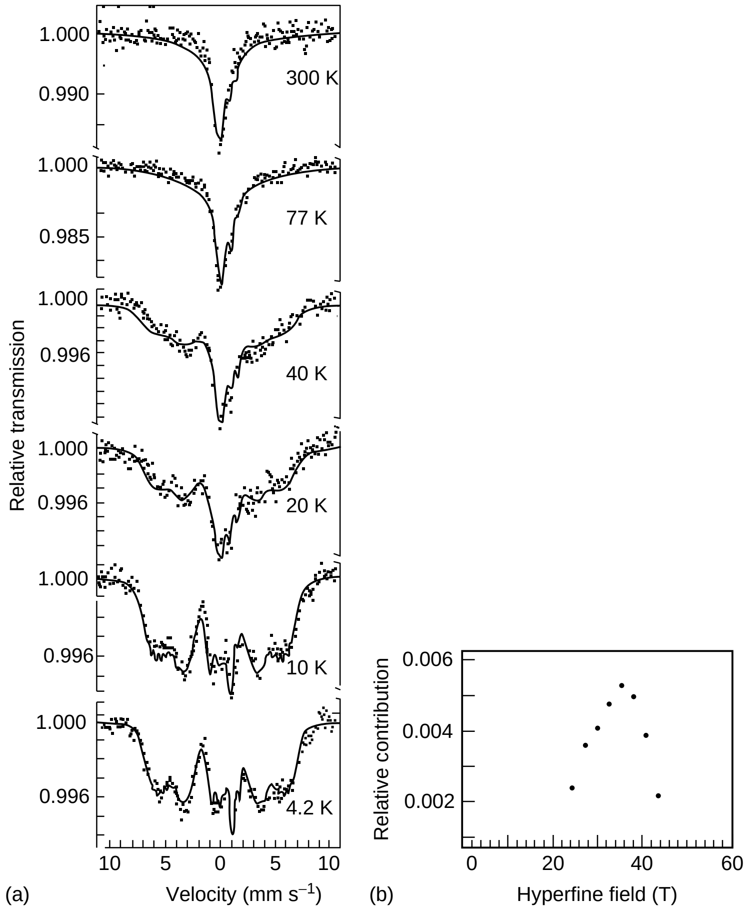

Figure 8 Temperature-dependent Mössbauer spectra of metallic iron nanoparticles in zeolite NaX (a). The superparamagnetic blocking temperature T_c is around 40 K. The solid lines have been calculated by a relaxation formalism[30] assuming a hyperfine field distribution as shown in (b) with a bimodal size distribution of metallic iron particles. (Reprinted from Schünemann, Winkler, Butzlaff and Trautwein.[29] With kind permission from Springer Science & Business Media)

generated by a hyperfine field distribution that represents the magnetically blocked particles. Fitting of Mössbauer spectra with hyperfine field distributions has been pioneered by Le Caer *et al.*[31] Nowadays the software packages NORMOS and VINDA allow us to calculate hyperfine field distributions.[27]

As an example, temperature-dependent Mössbauer spectra of nanometer-sized metallic iron particles prepared by thermal decomposition of $Fe(CO)_5$ on a zeolitic support are shown in Figure 8(a). The analysis of the 4.2 K spectrum by a distribution of hyperfine fields (Figure 7) according to the method of Le Caer *et al.*[31] shows that 90% of the iron is in a magnetically ordered state, with the maximum of the distribution corresponding to metallic iron, whereas 10% remained paramagnetic Fe(II). The spectra could be simulated by an algorithm for uniaxial relaxation[30] assuming two particle fractions with different anisotropy energies and different isomer shifts (0.1 and $0.25\,\mathrm{mm\,s^{-1}}$ at 4.2 K for the larger and smaller particle fraction, respectively) but with the same hyperfine field distribution (Figure 8b). This analysis has been motivated by ferromagnetic resonance results.[32] The anisotropy energies $E_{ai} = K_i V_i (i = 1, 2)$ were determined from the temperature-dependent relaxation rates $\nu(T)$ by assuming the Neel equation (equation 19). Values of $(2.7 \pm 0.4) \cdot 10^{-22}$ J and $(9.8 \pm 1.5) \cdot 10^{-22}$ J were obtained. Using the values of $K_1 = (1.45 \pm 0.2) \cdot 10^5\,\mathrm{J\,m^{-3}}$ and $K_2 = (1.21 \pm 0.18) \cdot 10^5\,\mathrm{J\,m^{-3}}$ obtained from ferromagnetic resonance measurements one obtains, under the assumption that the particles are spherical and have the saturation magnetization of the bulk α-Fe, the diameters of $d_1 = (1.53 \pm 0.15)$ nm and $d_2 = (2.50 \pm 0.25)$ nm. Obviously, one fraction of particles is in the large zeolite cavities, which have a diameter of 1.3 nm. The other fraction of particles is located in defect sites of the zeolite lattice and/or on the surface of the microcrystalline zeolite support.

Another very elegant method to determine the magnetic moment μ of superparamagnetic particles involves Mössbauer spectroscopic measurements above the blocking temperature T_c in varying external magnetic fields, a method that had been first introduced by Steen Morup.[12] In this case, the magnetic energy of the particles μB is much larger than the anisotropy energy, so $\mu B \gg KV$ holds. The observed magnetic hyperfine field $\vec{B}_{\mathrm{obs}}$ at the iron nucleus is expressed as

$$\vec{B}_{\mathrm{obs}} = \vec{B}_0 L\left(\frac{\mu B}{k_{\mathrm{B}} T}\right) + \vec{B} \tag{20}$$

Here $\vec{B}_0$ is the saturation hyperfine field, L is the Langevin function, and k_{B} is the Boltzmann constant. If the condition $\mu B / k_{\mathrm{B}} T \gg 1$ is fulfilled (e.g., for particles having particle magnetizations of 1000–10 000 μ_{B} and external fields B on the order of 1 T as well as temperatures around 80 K), equation (20) simplifies to

$$|\vec{B}_{\mathrm{obs}} - \vec{B}| = B_0 \left(1 - \frac{k_{\mathrm{B}} T}{\mu B}\right) \tag{21}$$

Figure 9 shows a plot of $|\vec{B}_{\mathrm{obs}} - \vec{B}|$ against $1/B$ for metallic α-Fe particles in zeolite NaX.[32] From the slope of the curve, a mean magnetic moment of $\mu = 916 \pm 180\,\mu_{\mathrm{B}}$ has been obtained. With the saturation magnetization of α-Fe and assuming spherical particle sizes with body-centered cubic structure, one obtains a mean diameter of $d = 2.1 \pm 0.1$ nm.

3.1.3 *Thin Films*

Some bioinorganic chemists may also be interested in the characterization of bioinorganic or inorganic complexes on surfaces or in thin films. Such studies are rare to date, but we refer to reviews by Shinjo and Przybylski, which deal with the characterization of iron monolayers and multilayers by CEMS.[13,14] During the last two decades Mössbauer spectroscopy with synchrotron radiation has also been developed, which gives information about the magnetization of thin iron films with a sensitivity down to the monolayer range.[15]

3.2 Covalent Iron Compounds

Iron organometallic compounds are diamagnetic and highly covalent. The parent compounds of this class of molecular compounds are $Fe(CO)_5$ and the cyclopentadienyl complex ferrocene $(\pi\text{-}C_5H_5)_2Fe$. Since no internal hyperfine field is present owing to the diamagnetism of the compounds, indications of the type of sterochemistry and bonding can be inferred only from their isomer shifts and quadrupole splittings. Their isomer shifts range from $-0.18\,\mathrm{mm\,s^{-1}}$ to $+0.54\,\mathrm{mm\,s^{-1}}$ and the quadrupole splittings from 0 up to $2.8\,\mathrm{mm\,s^{-1}}$.[3]

Since iron carbonyls are not only involved in chemical synthesis (of e.g., iron nanoparticles) but also can occur in heterogenous iron catalysts during reaction conditions (e.g., Fischer–Tropsch reactions), we will briefly discuss the Mössbauer parameters of this class of compounds.

Iron pentacarbonyl has $\delta = -0.35\,\mathrm{mm\,s^{-1}}$, which reflects the strong covalency of the Fe–CO bonds. The high value of the quadrupole splitting ($\Delta E_Q = 2.57\,\mathrm{mm\,s^{-1}}$) is explained by the noncubic iron site geometry. The $Fe(CO)_4^{2-}$ anion has a perfect tetrahedral coordination of CO and therefore no detectable quadrupole splitting is observed in $Na_2[Fe(CO)_4)]$. The isomer shift of this compound is $\delta = -0.45\,\mathrm{mm\,s^{-1}}$, which reflects the empirical rule that decreasing the coordination number of the iron center by one leads to a decrease of the isomer shift by $\Delta\delta \approx 0.1\,\mathrm{mm\,s^{-1}}$. $Fe_2(CO)_9$ has axial symmetry with three bridging CO groups and an Fe–Fe bond. The two iron sites are equivalent and

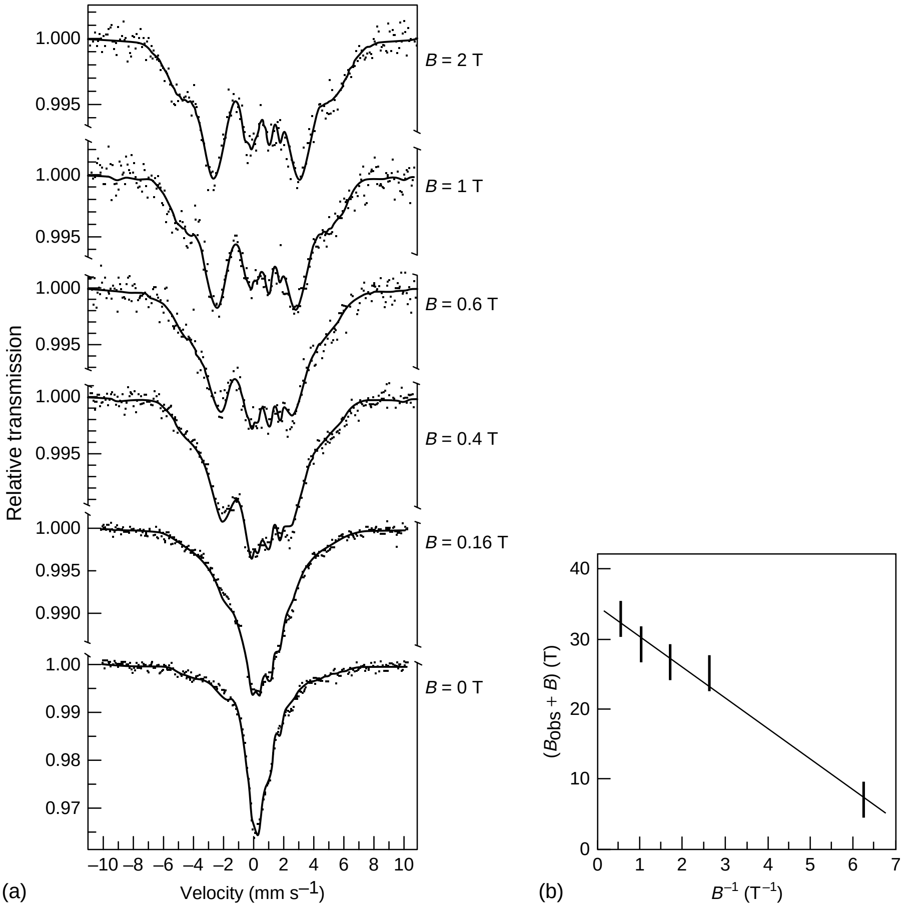

Figure 9 Mössbauer spectra of metallic iron nanoparticles in zeolite NaX taken at T = 77 K and different external fields (a). The analysis of the field dependence of the magnetic hyperfine field according to equation (21) yields a mean particle size of $d = 2.1 \pm 0.1$ nm (b). (Reprinted from Schünemann[32])

Table 1 Isomer shifts δ and quadrupole splittings ΔE_Q of some selected iron carbonyls. These compounds are diamagnetic and therefore do not have an internal magnetic hyperfine field. (From Greenwood and Gibb.[3] With kind permission from Springer Science & Business Media)

Compound	δ [mm s^{-1}]	ΔE_Q [mm s^{-1}]
$Fe(CO)_5$	−0.35	2.57
$Fe_2(CO)_9$	−0.42	0.42
$Fe_3(CO)_{12}$	−0.15	1.13(64%)
	−0.21	0.13(33%)
$Na_2[Fe(CO)_4]$	−0.45	0

the axial symmetry leads to a low quadrupole splitting of $\Delta E_Q = 0.42\,\mathrm{mm\,s^{-1}}$ (Table1).

The Mössbauer spectrum of $Fe_3(CO)_{12}$ shows two distinct iron sites, with a relative ratio of 2:1. In fact, this result led to the refinement of a crystal structure that had reported three equivalent iron sites. Although this happened in the early days of Mössbauer spectroscopy, that is, the 1960s, it is an example of how Mössbauer spectroscopy can help refine crystal structure data. Later the correct structure of $Fe_3(CO)_{12}$ had also been determined by X-ray diffraction and can be pictured as a Fe_2 $(CO)_9$ where a CO-bridge is replaced by a $Fe(CO)_4$ group.[3]

3.3 Iron(I) Compounds

Iron(I) compounds are quite rare. Münck *et al.* have recently reported a Mössbauer study of the mononuclear low-coordinate iron(I) compound LFe(HCCPh).[33] They show by a combined Mössbauer and electron paramagnetic resonance (EPR) study that the complex has a high-spin $3d^7$ configuration ($S = 3/2$) with near orbital degeneracy. The complex shows a sharp magnetic six-line pattern at 4.2 K and an external field of 50 mT. It exhibits an extraordinarily high hyperfine field of $B_{\mathrm{hf}} = +68.8$ T. The positive sign of B_{hf} has been determined from the observation that the magnetic splitting increases with increasing external fields. This behavior is completely different from the situation of most iron compounds and shows that, in the case of LFe(HCCPh), B_{hf} is clearly dominated by orbital contributions.

3.4 Iron(II) Compounds

3.4.1 *Low-Spin Iron(II)*

Low-spin iron(II) ions are d^6 with no unpaired electrons and are diamagnetic. The t_{2g} subshell is fully occupied, which leads to a symmetric charge distribution around the iron nucleus. Therefore, the electronic contribution to the electric field gradient should diminish and as a consequence low-spin iron(II) complexes are expected to have a very small or even undetectable quadrupole splitting. However, this is not always the case. Note that some low-spin ferrous heme proteins as well as heme model complexes have $\Delta E_Q > 1\,\mathrm{mm\,s^{-1}}$. For example, for the heme model complex [TMPFe(II)(1,2-$\mathrm{Me_2Im}$)$_2$], $\Delta E_Q = 1.73\,\mathrm{mm\,s^{-1}}$ has been reported.[34]

Because the shielding of the nucleus by the fully occupied t_{2g} subshell of low-spin iron(II) is less effective than in the case of high-spin iron(II) compounds (*see* Section 3.4.2), the charge density at the nucleus caused by the s electrons is increased compared to high-spin iron(II). This leads to isomer shifts ranging from $-0.258\,\mathrm{mm\,s^{-1}}$ at 298 K for sodium nitroprusside $\mathrm{Na_2[Fe(CN)_5NO]\cdot 2H_2O}$ up to $0.31\,\mathrm{mm\,s^{-1}}$ for $\mathrm{[Fe(phen)_3](ClO_4)_2}$ or even $0.46\,\mathrm{mm\,s^{-1}}$ for several ferrous low-spin heme models and cytochromes.[34]

The very low isomer shift of $\mathrm{Na_2[Fe(CN)_5NO]\cdot 2H_2O}$, a compound that has been often used as calibration standard, can be understood on the basis of the strong covalent effects present in the Fe–NO bond. The ground state of the iron in the nitroprusside molecules is $(d_{xz}, d_{yz})^4(d_{xy})^2$. The electrons in the orbitals with (d_{xz}, d_{yz}) character are delocalized by back donation to the 2p orbitals of the NO ligand. In addition, as in the cyanides shown in Table 2, there is also some slight delocalization from the d_{xy} orbital to the equatorial cyanides. Since there is also considerable 4s population, the electron density at the nucleus is much higher than usual, which manifests itself in the unusually low isomer shift.[3]

For the identification of low-spin iron(II), a low value of the quadrupole splitting is generally not enough. As an example, the Mössbauer spectrum of the reduced low-spin ferrous form of cytochrome c_{552} is shown in Figure 10. The reduced heme iron has $\delta = 0.46\,\mathrm{mm\,s^{-1}}$ and $\Delta E_Q = +1.30\,\mathrm{mm\,s^{-1}}$.[35] These values are characteristic for the low-spin ferrous forms of several electron transfer heme proteins like cytochromes c and b.[34]

Measurements at 4.2 K and large external fields are the experimental choices to unambiguously identify diamagnetic iron species. A diamagnetic iron species exhibits a splitting of the Mössbauer spectrum in a high-field experiment, which is due only to the external field since the internal magnetic hyperfine field at the iron nucleus is zero. The Mössbauer spectrum of ^{57}Fe-enriched cytochrome c_{552} obtained at 7 T is displayed in Figure 10(b). Note that the spectrum originates from a frozen protein solution. Therefore, the distribution of the molecules with respect to the direction of the external field is random (or powderlike) and hence the distribution of the electric field gradient tensor of the iron centers is also random. This fact has to be regarded if one wants to simulate high-field Mössbauer spectra of diamagnetic complexes. Such a situation can conveniently be handled in spin Hamiltonian simulations by setting all elements of the hyperfine coupling tensor $\overleftrightarrow{A}$ to zero for an arbitrary spin S.

3.4.2 *High-Spin Iron(II) Compounds*

High-spin iron(II) compounds with the iron in the $S = 2$ state have rather high isomer shifts up to $1.3\,\mathrm{mm\,s^{-1}}$ at room temperature (Table 3), depending on the coordination

Table 2 Mössbauer parameters of some six-coordinate low-spin Fe(II) ions. Note that the isomer shift decreases if the Fe–ligand bonds become more covalent in character. Mössbauer parameters for the cyanide complexes, as well as those for the phenanthroline complex, were taken from Greenwood and Gibb,[3] which the reader may consult for further references

Compound	Iron coordination	δ [$\mathrm{mm\,s^{-1}}$]	ΔE_Q [$\mathrm{mm\,s^{-1}}$]	T [K]
Cytochrome c_{552}[35]	Heme iron with histidine/methione coordination	0.46	+1.40	4.2
Cytochrome b_{552} from spinach[36]	Histidine/histidine	0.49	1.08	4.2
Cytochrome f from spinach[36]	Heme iron with histidine/N-terminal tyrosine	0.43	1.10	4.2
$\mathrm{[Fe(phen)_3](ClO_4)_2}$	6 N	0.341	0.28	77
$\mathrm{K_4[Fe(CN)_6]\cdot 3H_2O}$	6 CN	−0.047	0	298
		−0.016	0	77
$\mathrm{Al_4[Fe(CN)_6]_3}$	6CN	−0.157	0	300
		−0.080	0	80
$\mathrm{Na_2[Fe(CN)_5NO]\cdot 2H_2O}$	5 CN/1 NO	−0.258	+1.705	298

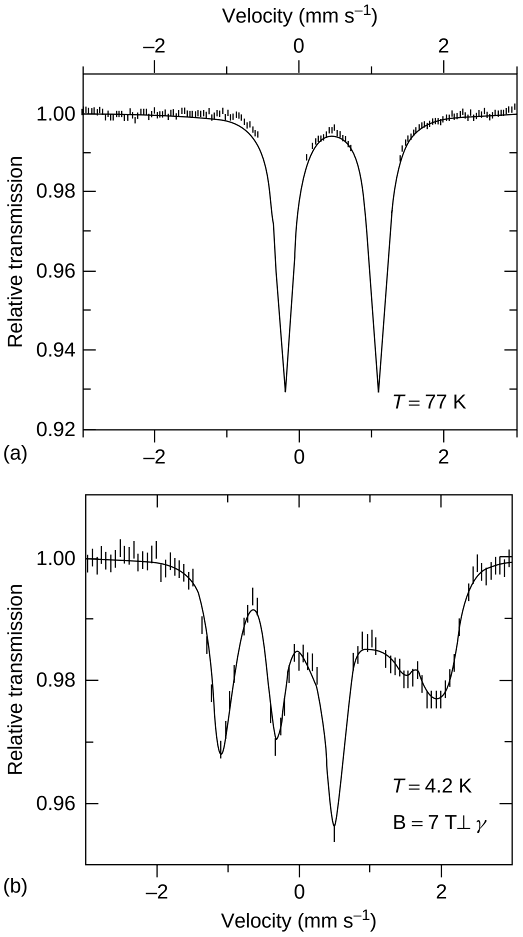

Figure 10 Mössbauer spectra of ferrous cytochrome c_{552} (a) Mössbauer spectrum of reduced cytochrome c_{552} obtained at $T = 77\,\mathrm{K}$. The solid line represents a Lorentzian fit with $\delta = 0.46\,\mathrm{mm\,s^{-1}}$, $\Delta E_Q = 1.30\,\mathrm{mm\,s^{-1}}$, and $\Gamma = 0.27\,\mathrm{mm\,s^{-1}}$. (b) Field-dependent Mössbauer spectrum of reduced cytochrome c_{552} obtained at $T = 4.2\,\mathrm{K}$ in a field of 7 T perpendicular to the γ beam. The shape of the spectrum is characteristic of a diamagnetic powder or frozen solution sample with a positive sign of ΔE_Q. For a negative ΔE_Q, a reversed pattern would be observed. The solid line corresponds to a simulation with $S = 0$, $\delta = 0.46\,\mathrm{mm\,s^{-1}}$, $\Delta E_Q = 1.30\,\mathrm{mm\,s^{-1}}$, $\eta = 0.3$, and $\Gamma = 0.24\,\mathrm{mm\,s^{-1}}$. (From Zoppellaro, Teschner, Harbitz, Schünemann, Karlsen, Arciero, Ciurli, Trautwein, Hooper and Andersson.[35] Reprinted by permission of Wiley-VCH)[35]

number and the type of ligand. The high isomer shift is caused by the shielding of the outer s-electron charge density (mostly of 2s type) by the inner 3d electron charge density. In addition, the spin-down electron in the doubly occupied 3d orbital contributes significantly to the EFG. This leads to the fact that most high-spin iron(II) compounds have quadrupole splittings of around $2-3\,\mathrm{mm\,s^{-1}}$.

The identification of high-spin iron(II) is one of the most straightforward problems to solve with Mössbauer spectroscopy. As an example, we will discuss the native form of human tyrosine hydroxylase (hTH), which catalyzes the rate-limiting reaction in the biosynthesis of dopamine, noradrenaline, and adrenaline. The enzyme contains a nonheme iron center that is required for enzymatic function. All isoforms of hTH exhibit a quadrupole doublet with isomer shift $\delta(1.6-77\,\mathrm{K}) = 1.26-1.24\,\mathrm{mm\,s^{-1}}$ and temperature-independent quadrupole splitting $\Delta E_Q = 2.68\,\mathrm{mm\,s^{-1}}$.[37] These values are characteristic of high-spin Fe(II) in six-coordination with oxygen or nitrogen ligands. Shorter bond lengths in four-coordination with respect to six-coordination, as well as the presence of covalent ligands like sulfur as opposed to oxygen or nitrogen, would increase the s density at the Fe nucleus. This in turn would reduce the isomer shift. For four-coordination with ionic ligands, one would expect isomer shifts $\leq 1\,\mathrm{mm\,s^{-1}}$ below 77 K while alternatively six-coordination yields isomer shifts $> 1.2\,\mathrm{mm\,s^{-1}}$. The empirical rule that reduction of the coordination number by one leads to a decrease of the isomer shift by an amount of $\sim 0.1\,\mathrm{mm\,s^{-1}}$ as discussed in Section 3.2 for covalent iron(0) compounds also holds here. In the same way, a substitution of one oxygen or nitrogen by one sulfur ligand would reduce the isomer shift by about $0.1\,\mathrm{mm\,s^{-1}}$.

An X-ray crystallography study, on the related enzyme from rat reported a five-coordinate iron center. Since nuclear magnetic resonance (NMR) studies indicated the presence of a water molecule loosely bound to the iron, a Mössbauer study of dehydrated hTH was undertaken. Indeed, it has been found that 63% of the spectral area can be attributed to five-coordinate high-spin Fe(II) ($\delta = 1.07\,\mathrm{mm\,s^{-1}}$). After rehydration of hTH the spectroscopic changes were completely reversed.[38] The X-ray absorption spectra (*see* ***X-Ray Absorption Spectroscopy***) of hTH corroborate the findings derived from the Mössbauer spectra. Thus, it was concluded that the active-site iron can exist in different coordination states, which can be interconverted depending on the hydration state of the protein, indicating the presence or absence of a water molecule as a coordinating ligand to the iron.

As a second example, Mössbauer spectra of a rubredoxin-type protein mutant from *Pyrococcus abyssi* are shown in Figure 11. This protein contains a tetrahedral sulfur-coordinated high-spin ferrous site. Owing to the covalent character of the Fe–S bond, an isomer shift of $\sim 0.70\,\mathrm{mm\,s^{-1}}$ is observed at 4.2 K. This value is characteristic for almost all tetrahedral sulfur-coordinated high-spin ferrous sites.

Although the high-spin ferrous site with $S = 2$ is paramagnetic, no magnetic splitting is observed at 4.2 K. The reason is that the ground state spin expectation value of ions having integer spin in small magnetic fields goes to zero. The application of a moderate field of 1 T induces significant spin expectation values and therefore a magnetically split pattern is observed (Figure 11).[39]

The spin Hamiltonian analysis of the field-dependent Mössbauer spectra has been performed by a simultaneous fitting procedure of all spectra displayed in

Table 3 Mössbauer parameters of some high-spin Fe(II) compounds (taken from Greenwood and Gibb[3]) in comparison to the ferrous high-spin site of human tyrosine hydroxylase. Note the decrease in isomer shift with decreasing coordination number

Compound	Iron coordination	δ [mm s^{-1}]	ΔE_Q [mm s^{-1}]	T [K]
Human tyrosine hydroxylase[37]	6N and/or O	1.26	2.68	4.2
Dehydrated human tyrosine hydroxylase[38]	5N and/or O	1.07	2.89	77
FeF_2	6F	1.48	2.92	78
$FeCl_2$	6Cl	1.10	+0.90	78
$FeCl_22H_2O$	4Cl/2O from H_2O	1.08	+2.70	78
$FeCl_24H_2O$	2Cl/4O from H_2O	1.361	+3.117	5
$(Me_4N)_2FeCl_4$	$4Cl^-$	0.76	−0.72	293
		0.86	−2.61	77
		0.90	−3.27	4.2
$(Me_4N)_2Fe(NCS)_4$	4N	0.82	2.83	4.2

Figure 11. The best fit has been found for $\delta = 0.7 \pm 0.01\,\mathrm{mm\,s^{-1}}$, $\Delta E_Q = -3.25 \pm 0.01\,\mathrm{mm\,s^{-1}}$, $\overleftrightarrow{g} = (2.11, 2.19, 2.00)$, $\overleftrightarrow{A}/g_N\mu_N = (-45, 10, 19)\,\mathrm{T}$, $\eta = 0.74 \pm 0.1$, $D = 7.2 \pm 0.5\,\mathrm{cm^{-1}}$, and $E/D = 0.16 \pm 0.02$. The zero-field splitting parameter $D = 7.2 \pm 0.5\,\mathrm{cm^{-1}}$ is comparable to that found for rubredoxin from *Clostridium pasteurianum* ($D = 7.6\,\mathrm{cm^{-1}}$).[40] Surprisingly, the rhombicity parameter $E/D = 0.16 \pm 0.02$ differs somewhat from that of rubredoxin from *C. pasteurianum* ($E/D = 0.28$). The hyperfine coupling tensor has been determined to be $\overleftrightarrow{A} = (-14.5, -9.2, -27.5)\,\mathrm{T}$. The anisotropy of the hyperfine coupling tensor is caused by spin-orbit contributions to the internal magnetic hyperfine field.

It should be noted here that a correct determination of fine and hyperfine structure parameters should be done in such a way that spectra taken under different experimental conditions (variable external fields and/or variable temperatures) are reproduced with the same parameter set. This reproduction of the experimental data is often a bit less accurate than when one fits only a single experimental spectrum. However, owing to the many parameters involved in the simulation it makes absolutely no sense to deduce a complete spin Hamiltonian parameter set of a paramagnetic iron center from just one Mössbauer spectrum.

3.5 Iron(III) Compounds

3.5.1 *Low-Spin Iron(III) Compounds*

Low-spin iron(III) ions have an electron hole in the t_{2g} orbitals. Therefore, these centers have $S = 1/2$ and spin-orbit interaction contributes considerably to the magnetic hyperfine field. Low-spin iron(III) compounds in solution always show a rather complicated magnetic Mössbauer pattern at temperatures around 4.2 K and low external fields, which means that the relaxation rate of these centers is lower than the nuclear precession rate of $\sim 10^{-7}$ s. Sometimes a magnetic splitting is observed even at 77 K. Therefore, in order to pin down δ and ΔE_Q, it is advisory to measure between 100 and 200 K, where the electronic relaxation rate becomes fast with respect to the Mössbauer time window and the limit of fast relaxation applies. Spin–spin interaction in microcrystals can also enhance the electronic relaxation rate and therefore some low-spin iron(III) compounds show quadrupole doublets even at 4.2 K.[41]

Since the iron 4s orbitals are involved in covalent bonding with the ligands, the s-electron density at the iron nucleus is increased compared to high-spin iron(II) compounds. This is even more true if π-accepting ligands like CN^- are present. Therefore the difference in isomer shift between low-spin iron(II) and low-spin iron(III) is much less pronounced than between high-spin iron(II) and high-spin iron(III).

As an example of how to determine the electronic ground state of a low-spin iron(III) compound, we present work on the ferric low-spin heme complex $[TPPFe(NH_2PzH)_2]Cl$, which has been shown to have a $(d_{xy})^2(d_{xz}, d_{yz})^3$ electronic ground state.[42] The field-dependent Mössbauer spectra of $[TPP^{57}Fe(NH_2PzH)_2]Cl$ displayed in Figure 12 are well reproduced by simulations, which yield $\delta = 0.25\,\mathrm{mm\,s^{-1}}$, $\Delta E_Q = (+)2.50\,\mathrm{mm\,s^{-1}}$, an asymmetry parameter $\eta = -3$, and an anisotropic A tensor of $\overleftrightarrow{A}/g_N\mu_N = (-47.6, 6.7, 18.3)\,\mathrm{T}$. The g values necessary for the $S = 1/2$ spin Hamiltonian ($g_{zz} = 2.39$, $g_{yy} = 2.28$, and $g_{xx} = 1.87$) have been taken from a combined EPR and electron spin echo envelope modulation spectroscopy ESEEM analysis.

The calculation of the corresponding A tensor according to the model of Oosterhuis and Lang[43] in the reference frame chosen by Taylor[44] yields $\overleftrightarrow{A}/g_N\mu_N = (-47.6, 11.7, 18.3)\,\mathrm{T}$, which is in very good agreement with the experimental values. The fact that the electronic ground state predominantly exhibits d_{yz} character also allows determination of the anisotropy parameter η, if one neglects the ligand contribution to the EFG.[24] A value of $\eta \cong -3$ has been obtained, which is in excellent agreement with the experiment. The EFG is nearly axially symmetric around the x axis of the molecular frame. The coordinate system of the EFG tensor (x', y', z') is commonly chosen in such a way

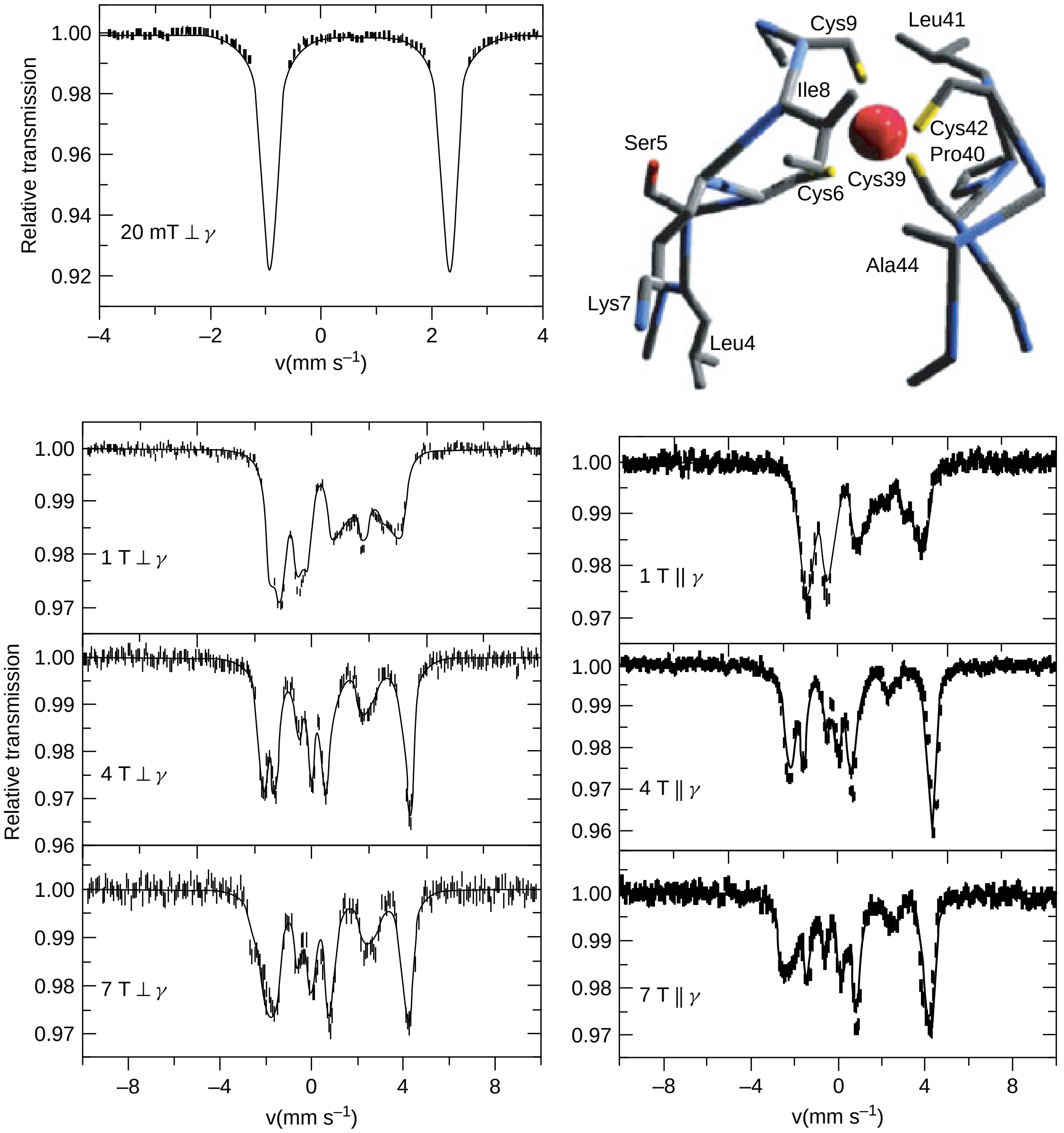

Figure 11 Mössbauer spectrum of the rubredoxin-type protein mutant RM-2–4 from the archaeon *P. abyssi* taken at 4.2 K and fields indicated. The structure of the iron site is shown at top right. The solid lines have been obtained by simultaneous fitting of the Mössbauer spectra with the software package VINDA for an $S = 2$ ground state. The parameters obtained are described in the text. (From Wegner *et al*.[39] With kind permission from Springer Science & Business Media)

that $|V_{z'z'}| \geq |V_{y'y'}| \geq |V_{x'x'}|$, which means that the coordinate system of the EFG tensor is turned around the y axis of the molecular frame by the Euler angle $\beta = 90°$. In this coordinate system, $\eta' \approx 0$ and $\Delta E'_Q = (-)2.50\,\mathrm{mm\,s^{-1}}$. A hole in the t_{2g} orbitals contributes to the quadrupole splitting by an amount of $\sim 3\,\mathrm{mm\,s^{-1}}$.[24] The experimental value of $\Delta E_Q = 2.50\,\mathrm{mm\,s^{-1}}$ for [TPP^{57}Fe(NH$_2$PzH)$_2$]Cl confirms this empirical observation.

Thus, Mössbauer spectroscopy corroborates the results of the ESEEM studies, which give $\overleftrightarrow{g} = (2.39, 2.28, 1.87)$ and clearly show an electronic ground state with major d_{yz} character. The hyperfine coupling constants of the bis-3-aminopyrazole complex are, in fact, very similar to those of the low-spin form of cytochrome P450$_{\mathrm{cam}}$, for which Debrunner *et al*. reported $\overleftrightarrow{A}/g_{\mathrm{N}}\mu_{\mathrm{N}} = (-45, 10.2, 19.1)\,\mathrm{T}$.[45] In spite of the similarity in A values, the g values of the P450$_{\mathrm{cam}}$ species are 2.45, 2.26, and 1.91, somewhat different from those of the 3-aminopyrazole complex discussed here. The largest component of the electric field gradient tensor with respect to the molecular frame is the x component and is negative. The z component of the hyperfine coupling tensor is positive and only about half the magnitude of the

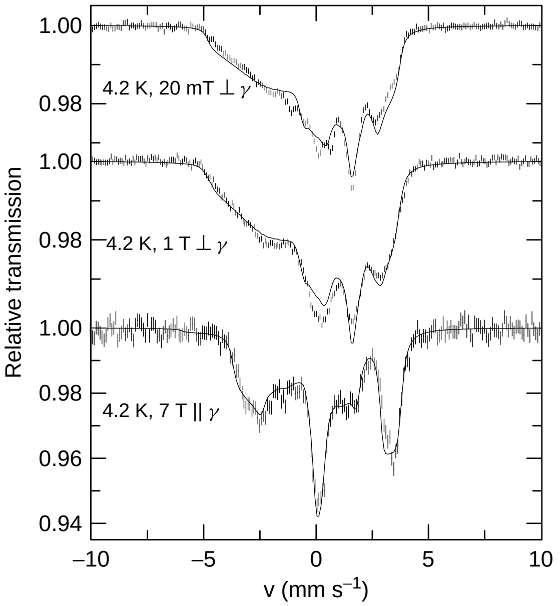

Figure 12 Field-dependent Mössbauer spectra of the ferric low-spin heme complex $[TPPFe(NH_2PzH)_2]Cl$. The solid lines are spin Hamiltonian simulations for $S = 1/2$ with parameters discussed in the text and given in Ref. 42 (From Schünemann *et al.*[42] With kind permission from Springer Science & Business Media)

x component. This is also consistent with a singly occupied d_{yz} orbital, although most other $(d_{xy})^2(d_{xz}, d_{yz})^3$ electronic ground state systems except for cytochrome $P450_{cam}$ have A_{zz} as the largest component.

3.5.2 *High-Spin Iron(III) Compounds*

The iron centers of high-spin iron(III) compounds have a half-filled 3d electron shell with each 3d orbital singly occupied. This electron configuration leads to a symmetric charge distribution around the iron nucleus. Therefore, highly symmetric high-spin iron(III) compounds in general exhibit low values of the quadrupole splitting. This holds specially for highly symmetric octahedral halogen iron compounds like FeF_3 and $FeCl_3$ which have almost zero quadrupole splittings. The isomer shifts of octahedrally coordinated high-spin iron(III) complexes are in general around $0.5\,\mathrm{mm\,s^{-1}}$ at cryogenic temperatures except if sulfur ligands are present, which tends to decrease the isomer shift.

Octahedral iron(III) complexes with nitrogen and/or oxygen as ligand have isomer shifts ranging from 0.4 to $0.6\,\mathrm{mm\,s^{-1}}$. Tetrahedral coordination enhances the electron density at the nucleus and therefore leads to slightly reduced isomer shifts but this effect is not as pronounced as in high-spin iron(II) complexes. Therefore, it is not straightforward to distinguish between different coordination numbers of ferric high-spin iron. An exception is tetrahedral ferric high-spin centers in iron–sulfur proteins. They exhibit an isomer shift of $0.24\,\mathrm{mm\,s^{-1}}$ at 4.2 K, and it has been shown that a 2N2S coordination leads to a slight increase in isomer shift by about $0.08\,\mathrm{mm\,s^{-1}}$. For example, the Mössbauer spectrum of the oxidized Rieske cluster from *Thermus thermophilus*[46] consists of two doublets, which reflects the difference in ligand geometry of the two tetrahedral high-spin iron(III) sites. One doublet has $\delta_1 = 0.24\,\mathrm{mm\,s^{-1}}$ and $\Delta E_{Q1} = 0.52\,\mathrm{mm\,s^{-1}}$ and the other has $\delta_2 = 0.32\,\mathrm{mm\,s^{-1}}$ and $\Delta E_{Q2} = 0.91\,\mathrm{mm\,s^{-1}}$ at 4.2 K. The former values are practically identical with those found for oxidized rubredoxin, which has a tetrahedral sulfur-coordinated ferric high-spin iron site. The latter values are still comparable with $S = 5/2$ ferric irons and represent a tetrahedral iron(III) site with 2N2S coordination. This was proposed on the basis of the Mössbauer data and was confirmed by X-ray crystallography almost a decade after the initial Mössbauer study by Münck *et al.*[46]

In the following text, we discuss the extraction of D from field-dependent Mössbauer spectra recorded at $T = 4.2\,\mathrm{K}$ by means of the spin Hamiltonian formalism for a single iron center in the Fe(III) $S = 5/2$ state. The variation of parameters was carried out by simultaneous simulation of the spectra shown in Figure 13 and of spectra recorded at 4.2 K in a field of 20 mT (data not shown). It should be noted that the rhombicity parameter E/D has been determined from a complementary EPR measurement, which is advisory if spin Hamiltonian simulations of $S = 5/2$ systems are performed to decrease the number of parameters. The EPR spectrum of oxidized RM-2−4 exhibits a broad distribution of effective g values around 4.3 consistent with $E/D = 0.28$. Therefore, this value was taken as initial input parameter for the simulations of the Mössbauer spectra. The best fit has been found for $\delta = 0.24 \pm 0.01\,\mathrm{mm\,s^{-1}}$, $\Delta E_Q = -0.36 \pm 0.01\,\mathrm{mm\,s^{-1}}$, $\overleftrightarrow{g} = (2.0, 2.0, 2.0)$ (fixed), $\overleftrightarrow{A}/g_N\mu_N = (-17.7,\ -15.7,\ -16.4)\,\mathrm{T}$, $\eta = 0.80 \pm 0.2$, $D = 2.13 \pm 0.6\,\mathrm{cm^{-1}}$, and $E/D = 0.23 \pm 0.03$. The hyperfine coupling tensor $\overleftrightarrow{A}$ is almost isotropic, which means that the isotropic Fermi-contact interaction is dominant and spin-orbit interaction contributes only marginally to the anisotropy of $\overleftrightarrow{A}$. The mean value of the hyperfine coupling tensor $A/\mu_N g_N = -16.6\,\mathrm{T}$ (corresponding to $B_{hf} = -41.5\,\mathrm{T}$) is characteristic for iron in tetrahedral sulfur coordination. This value is considerably smaller than $A/\mu_N g_N = -22\,\mathrm{T}$ (corresponding to $B_{hf} = -55\,\mathrm{T}$) typically found for ferric high-spin ions with oxygen and/or nitrogen coordination.

3.6 Iron(IV) Compounds

Four-valent iron centers are well known as catalytic intermediates in enzymatic heme catalysis. The catalytic cycles of, for example, catalase, peroxidase, and cytochrome P450, all have in common an intermediate that is comprised of a ferryl Fe(IV) and a further oxidation equivalent located either on the heme ring or on the protein moiety. This reaction intermediate is called compound I (cpd I) and has a system spin of $S = 1/2$ (e.g., in chloroperoxidase) or $S = 3/2$ (e.g.,

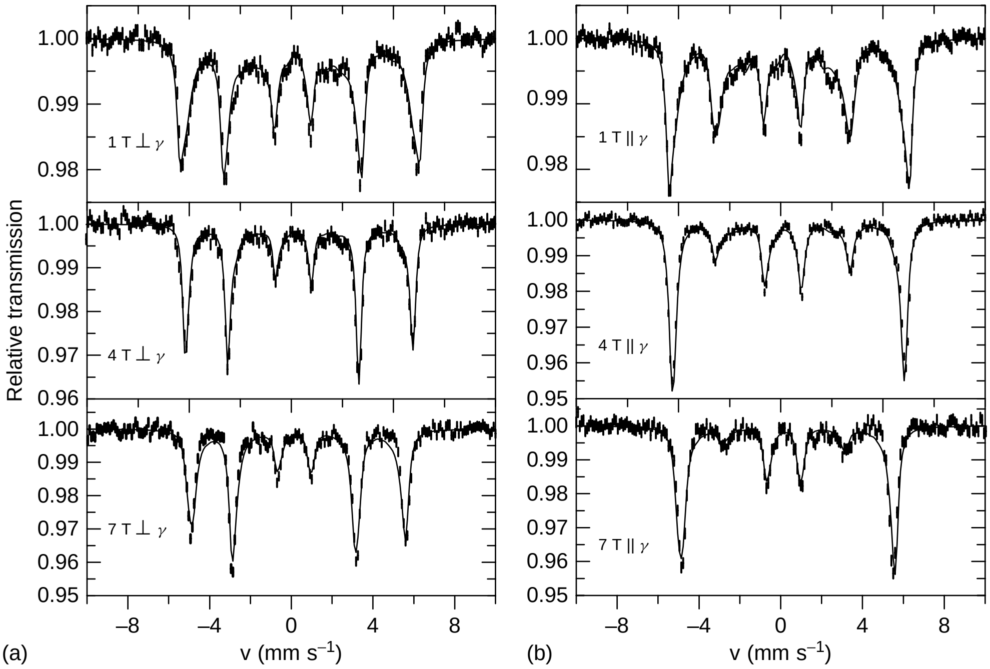

Figure 13 Mössbauer spectra of the oxidized rubredoxin-type protein mutant RM-2−4 from the archaeon *Pyrococcus abyssi* taken at 4.2 K in applied field perpendicular (a) and parallel (b) to γ-ray. The solid lines have been obtained by simultaneous fitting of the Mössbauer spectra with the software package VINDA assuming an $S = 5/2$ ground state.[27] The parameters are described in text. (From Wegner *et al.*[39] With kind permission from Springer Science & Business Media)

in catalase and many heme model compounds). Mössbauer spectroscopy continues to contribute to the understanding of the formal oxidation state of these intermediates. The reduction of cpd I by one electron equivalent leads to a ferryl Fe(IV) heme complex with almost the same isomer shift as cpd I. Heme iron(IV) compounds are characterized by their low isomer shifts around $0\,\mathrm{mm\,s^{-1}}$. Ferryl heme iron has a d^4 configuration with the lowest lying d_{xy} orbital being doubly occupied and the d_{yz} and d_{xz} orbitals being singly occupied. This leads to a total spin of $S = 1$. As an overview, the isomer shifts and quadrupole splittings of some Fe(IV) hemes are displayed in Table 4.

The situation in the case of nonheme Fe(IV) intermediates is somewhat different. It has been recently shown by Krebs and coworkers that a catalytically competent Fe(IV) intermediate in the α-ketoglutarate-dependent dioxygenase TauD has a high-spin $S = 2$ configuration.[48] TauD is a member of a large family of enzymes that catalyze reactions in the biosynthesis of antibiotics, collagen, degradation of xenobiotics, and biosynthesis of antioxidants. Mössbauer spectroscopy of rapid-freeze-quenched (RFQ) samples identified an intermediate named J upon the reaction of a TauD−Fe(II): α-ketoglutarate−taurine complex in the time regime from 20 to 200 ms. The time dependence of the concentration of J correlates with a UV-absorption band at 320 nm. The intermediate J showed a quadrupole doublet with $\delta = 0.31\,\mathrm{mm\,s^{-1}}$ and $\Delta E_Q = 0.88\,\mathrm{mm\,s^{-1}}$ even at $T = 4.2\,\mathrm{K}$ in a weak field of 40 mT (Figure 14).[49]

Table 4 Mössbauer parameters of high-valent intermediates of peroxidases, met-myoglobin treated with H_2O_2 and two tetramesitylporphyrin(TMP) model systems[47]

	δ ($\mathrm{mm\,s^{-1}}$)	ΔE_Q ($\mathrm{mm\,s^{-1}}$)
P450$_{\mathrm{cam}}$	0.13	1.94
JRP[(a)] Cpd I	0.10	1.33
HRP[(b)] Cpd I	0.08	1.25
CPO[(c)] Cpd I	0.14	1.02
CCP[(d)] Cpd ES	0.05	1.55
JRP Cpd II	0.03	1.59
HRP Cpd II	0.03	1.61
Mb[(e)] (H_2O_2)	0.09	1.43
$[\mathrm{Fe^{IV}{=}O(TMP)}]^+$	0.08	1.62
$\mathrm{Fe^{IV}{=}O(TMP)}$	0.04	2.3

(a) Japanese radish peroxidase.
(b) Horseradish peroxidase.
(c) Chloroperoxidase.
(d) Cytochrome c peroxidase compound ES
(e) Myoglobin complexed with H_2O_2.

The application of external fields up to 8 T induced a magnetic splitting, which has been analyzed assuming an $S = 2$ ground state. This example is a very nice piece of work illustrating how the spin and oxidation state can be deduced from Mössbauer spectroscopy. Therefore, we will explain these assignments in more detail by raising some questions:

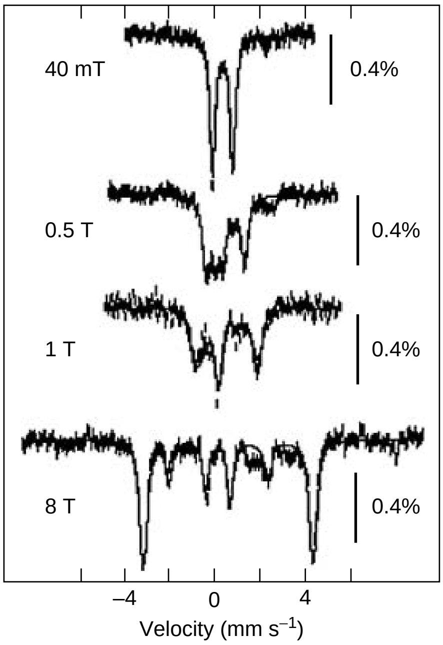

Figure 14 Mössbauer spectra of intermediate J of α-ketoglutarate-dependent dioxygenase TauD obtained at 4.2 K and fields indicated. The solid line represents a simulation using an $S = 2$ spin Hamiltonian and the parameters $\delta = 0.31\,\mathrm{mm\,s^{-1}}$, $\Delta E_Q = -0.88\,\mathrm{mm\,s^{-1}}$, $\eta = 0.0$, $\overleftrightarrow{A}/g_\mathrm{N}\mu_\mathrm{N} = (-18, -18, -18)\,\mathrm{T}$, $g = (2.3, 2.3, 2)$, $E/D = 0.03$, and $D = 10.5\,\mathrm{cm^{-1}}$. (Reprinted with permission from Krebs, Price, Baldwin, Saleh, Green and Bollinger.[48] © 2005 American Chemical Society)

Question 1: Both δ and ΔE_Q are within the range of Fe(III) species with an $S = 5/2$ ground state. Could J have this kind of ground state?

Answer: No! The Mössbauer spectrum of J does not show magnetic splitting at $T = 4.2\,\mathrm{K}$ and weak external field, which would be expected for an isolated ferric high-spin iron.

Question 2: Why does J have an integer spin?

Answer: Spin expectation values (and therefore the magnetic hyperfine field) of half-integer spin systems can be saturated in low fields (*see* Section 3.5.2). This is not the case here. In order to drive the magnetic splitting to its saturation, fields of up to 8 T have been applied. In addition, J is EPR silent, which points to an integer-spin species.

Question 3: Can J be an exchange-coupled Fe(III) dimer? These are EPR silent and also show only a doublet at 4.2 K and weak field.

Answer: Although this may be ruled out from the biochemistry perspective, it is worth considering this question from the Mössbauer spectroscopic point of view: Strongly exchange-coupled ferric iron dimers like those in methane monooxygenase, ribonucleotide reductase, and $\mathrm{Fe_2S_2}$ iron–sulfur proteins all have a diamagnetic ground state. The magnetic splitting of J clearly exceeds that of the applied external fields. Therefore J cannot be diamagnetic.

Question 4: Ultrasmall superparamagnetic particles can relax faster than the time window of Mössbauer spectroscopy even at 4.2 K and such ferric nanoparticles also show similar δ and ΔE_Q values.

Answer: The relaxation rate of superparamagnetic particles would be slowed down by the application of large external fields. What one normally observes is a magnetically split spectrum with broad lines and almost negligible quadrupole splitting (see e.g., Figure 7). The reason is that the main axis of the electric field gradient tensor of the surface atoms of such clusters is oriented in all directions with respect to the direction of the magnetic hyperfine field. This is often observed in reconstitution experiments of iron–sulfur proteins. If the reader is interested, Figure 4 of the work on anaerobic ribonucleotide reductase by Ollagnier *et al.*,[50] which serves as an example of small superparamagnetic iron–sulfur agglomerates, may be referred to.

Question: How can a spin state of S = 1 be ruled out from the spectra?

Answer: The authors did indeed evaluate the Mössbauer data by spin Hamiltonian simulations assuming an $S = 2$ as well as an $S = 1$ ground state. In this way they could deduce two sets of hyperfine and fine structure parameters: simulations assuming an $S = 1$ ground state yield an axial hyperfine tensor $\overleftrightarrow{A}_{x,y}/g_\mathrm{N}\mu_\mathrm{N} = -33.3\,\mathrm{T}$. Such a high hyperfine coupling tensor has never been observed for ferryl iron species having $S = 1$. The isotropic hyperfine coupling tensor $\overleftrightarrow{A}/g_\mathrm{N}\mu_\mathrm{N} = -18\,\mathrm{T}$ which has been obtained assuming an $S = 2$ ground state is in the range of hyperfine coupling tensors observed for ferryl iron species.

The groups of Que and Münck have reported the synthesis of the nonheme Fe(IV)=O model compound $[\mathrm{(Fe(IV){=}O)(TMC)(NCCH_3)}](\mathrm{OTf})_2$, which contains a nonheme macrocyclic ligand.[51] In zero applied field, the complex exhibits a Mössbauer spectrum consisting of a doublet with $\delta = 0.17\,\mathrm{mm\,s^{-1}}$ and $\Delta E_Q = 1.24\,\mathrm{mm\,s^{-1}}$. The spin Hamiltonian analysis of the Mössbauer spectra in high fields between 4.2 and 100 K shows that $[\mathrm{(Fe(IV){=}O)(TMC)(NCCH_3)}](\mathrm{OTf})_2$ has integer electronic spin. Spectral simulations using an $S = 1$ spin Hamiltonian yield $\delta = 0.17(1)\,\mathrm{mm\,s^{-1}}$, $\Delta E_Q = +1.24\,\mathrm{mm\,s^{-1}}$, $\eta = 0.5$, $\overleftrightarrow{A}/g_\mathrm{N}\mu_\mathrm{N} = (-25, -20, -3)\,\mathrm{T}$, $g = (2.3, 2.3, 2)$, $E/D = 0$, and $D = 29\,\mathrm{cm^{-1}}$. In their analysis, the z component of the g tensor was set to 2.0 and the x and y components were calculated according to $g_{x,y} = 2.0 + 4D/\zeta$, with ζ being the single-electron spin-orbit coupling constant. This parameter set compares well with those of Fe(IV)=O complexes having $S = 1$, which show $A_{x,y} \sim 17 - 25\,\mathrm{T}$ and a relatively large zero-field splitting $D \sim 20–37\,\mathrm{cm^{-1}}$.

It is instructive to compare the Mössbauer properties of $[\mathrm{(Fe(IV){=}O)(TMC)(NCCH_3)}](\mathrm{OTf})_2$ with those of the

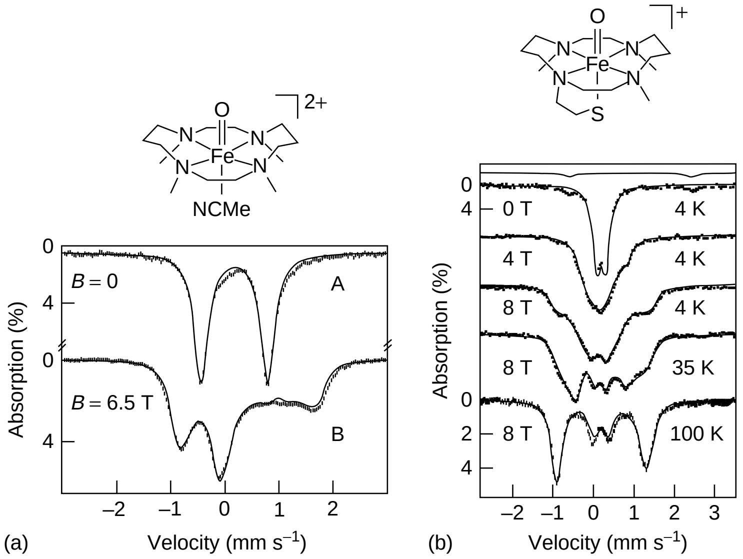

Figure 15 (a) The 4.2 K Mössbauer spectra of [(Fe(IV)=O)(TMC)(NCCH$_3$)](OTf)$_2$ in acetonitrile recorded in (A) zero field and (B) a parallel field of 6.5 T. The solid line represents a spin Hamilton simulation with the parameters described in the text. (b) Mössbauer spectra of [Fe(IV)=(O)(TMCS)] recorded at temperatures and applied fields that are indicated. The solid lines represent spin Hamiltonian simulations with parameters described in the text. The spectra were simulated in the slow (at 4.2 K) and fast (at 30 K) spin fluctuation limit. The applied field was directed parallel to the observed γ radiation. The doublet drawn above the topmost experimental spectrum (0 T, 4 K) represents a 7% Fe(II) contribution from the starting complex. (From J. U. Rohde *et al.* (2003) *Science* **299**:1037–1039. Reprinted with permission from AAAS)

complex [Fe(IV)=(O)(TMCS)].[52] TMCS, the monoanion of 1-mercaptoethyl-4,8,11-trimethyl-1,4,8,11-tetraaza cyclotetradecane, is a pentadentate ligand that provides a square pyramidal N4(SR) ligand environment about the iron center, which is similar to that of cytochrome P450, containing an axial RS$^-$ ligand. At zero field, [Fe(IV)=(O)(TMCS)] exhibits a doublet with $\delta = 0.19\,\mathrm{mm\,s^{-1}}$ and $\Delta E_Q = 0.22\,\mathrm{mm\,s^{-1}}$. A spin Hamiltonian analysis of the high-field Mössbauer spectra (Figure 15) assuming $S = 1$ yields a negative sign for the quadrupole splitting and an asymmetry parameter $\eta = 0$. The hyperfine coupling tensor has been determined as $\overleftrightarrow{A}/g_N\mu_N = (-23,\ -22,\ -5)$ T and the fine structure parameters as $E/D = 0$ and $D = 35\,\mathrm{cm^{-1}}$. Surprisingly, the isomer shift of [Fe(IV)=(O)(TMCS)] is comparable with that of [(Fe(IV)=O)(TMC)(NCCH$_3$)](OTf)$_2$ within the experimental error of $\pm 0.01\,\mathrm{mm\,s^{-1}}$. However the quadrupole splitting is significantly smaller and even reverses its sign in the thiolate complex ($\Delta E_Q = -0.22\,\mathrm{mm\,s^{-1}}$ for [Fe(IV)=(O)(TMCS)] versus $\Delta E_Q = +1.25\,\mathrm{mm\,s^{-1}}$ in [(Fe(IV)=O)(TMC)(NCCH$_3$)](OTf)$_2$).

3.7 Iron(V) Compounds

Iron(V) complexes are very rare, but recently two examples involving the characterization of these compounds with Mössbauer spectroscopy have been reported in the literature. Meyer *et al.* reported on the spectroscopic characterization of a nitridoiron(V) species prepared by photolysis of [Fe(III)(cyclam)(N$_3$)$_2$]$^+$ complexes.[53] Mössbauer spectroscopy of this species yields $\delta = -0.04\,\mathrm{mm\,s^{-1}}$ and $\Delta E_Q = -1.90\,\mathrm{mm\,s^{-1}}$ at 80 K and it has a spin state $S = 3/2$ (determined by EPR). The spin Hamiltonian parameters obtained by Mössbauer spectroscopy are consistent with this picture. The analysis yields $D = -0.37\,\mathrm{cm^{-1}}$, $E/D = 0.095$, $g = 2.0$ (isotropic), $\overleftrightarrow{A}/g_N\mu_N - 13.3,\ -10.6,\ 2.5)$ T and $\eta = 0.6$.

Very recently, chemical and spectroscopic evidence for an Fe(V)-oxo-complex has been reported by de Oliveira *et al.*[54] Field- and temperature-dependent Mössbauer as well as X-ray absorption (*see* ***X-Ray Absorption Spectroscopy***) and EPR spectroscopies in combination with density functional theory DFT calculations show that [Fe(TAML)(O)]$^-$ with TAML being a macrocyclic tetraamide ligand is a d^3 system with spin $S = 1/2$ and $\delta = -0.42\,\mathrm{mm\,s^{-1}}$, $\Delta E_Q = +14.25\,\mathrm{mm\,s^{-1}}$, $\eta = 0.65$, $A/\mu_N g_N = (-49.3, -1.5, -16.3)$ T and $g = (1, 99, 1.97, 1.74)$. The hyperfine parameters have also been determined by DFT using Gaussian with the functional B3LYP and the basis set G-311G with admirable accuracy ($\delta = -0.39\,\mathrm{mm\,s^{-1}}$, $\Delta E_Q = +4.51\,\mathrm{mm\,s^{-1}}$, $\eta = 0.72$, $\overleftrightarrow{A}_{\mu_N} g_N = (-43.6, -0.5, -15.0)$ T).

3.8 Iron(VI) Compounds

Until very recently, only a single Fe(VI) species, the ferrate ion [Fe(VI)O$_4$]$^{2-}$, was known. This species is a strong oxidant and used not only in organic synthesis but also in waste water treatment, batteries, and disinfectants. The Fe(VI) compound K_2FeO_4 has a single-line resonance at $-0.78\,\mathrm{mm\,s^{-1}}$ at 78 K.

Very recently, a photochemical synthesis of an Fe(VI) compound has been reported by the Wieghardt group.[55] The octahedrally coordinated iron in $[(Me_3cy\text{-}ac)FeN](PF_6)_2$ has a Fe≡N triple bond of 1.57 Å as shown by X-ray absorption spectroscopy. Mössbauer spectroscopy in a field of 7 T shows that the iron is diamagnetic and that the sign of ΔE_Q is positive (Figure 16).

DFT calculations reproduce the positive sign of ΔE_Q and indicate that $[(Me_3cy\text{-}ac)FeN](PF_6)_2$ has a doubly occupied nonbonding d_{xy} orbital and a strong covalent iron–nitrogen bond. Surprisingly the isomer shift of this complex ($\delta = -0.29\,\mathrm{mm\,s^{-1}}$) is much higher than that of $[Fe(VI)O_4]^{2-}$, which has δ values between -0.79 and $-0.85\,\mathrm{mm\,s^{-1}}$, depending on the type of salt.

In such a situation, the only clear cut strategy that leads to a definite answer concerning the valence state of the iron is not only to apply spectroscopic methods complementary to Mössbauer spectroscopy but also to investigate complexes with similar ligands but different electronic configurations. In order to clarify the electronic configuration of $[(Me_3cy\text{-}ac)FeN](PF_6)_2$, X-ray absorption spectroscopy (XAS) has been chosen as a method complementary to Mössbauer spectroscopy and the spectroscopic signatures of a series of iron complexes with valence states ranging from Fe(II) to Fe(VI) have been studied. Figure 17 displays a plot of the isomer shifts versus iron oxidation states for a series of low-spin iron complexes with cyclam-related ligands having oxidation states from II to VI. Not only the isomer shift scales beautifully with the oxidation number, but also the XAS pre-edge-energy, which is also an indicator for iron oxidation states, exhibits a linear correlation with the iron oxidation states of the complexes.

Together with the reproduction of δ and ΔE_Q values by DFT calculations, this piece of work is a beautiful example of how Mössbauer spectroscopy can be used to determine spin and oxidation states of high-valent iron. The authors do claim that in fact Fe(VI) intermediates that are undetected until now might exist in chemical and/or enzymatic reactions.

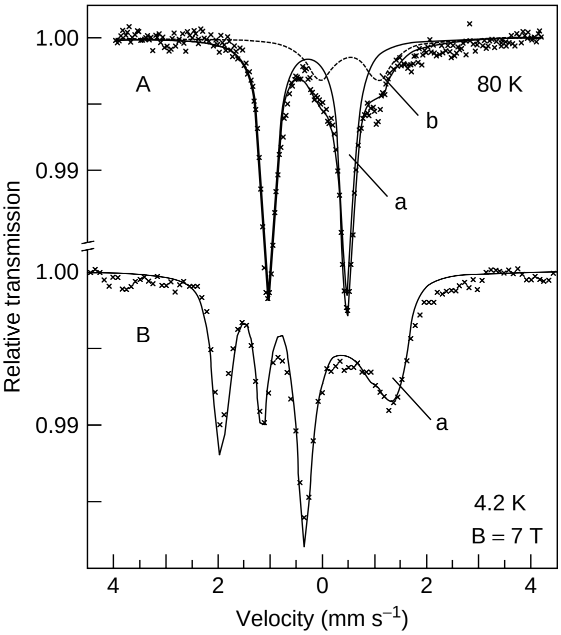

Figure 16 Mössbauer spectra of a acetonitrile solution of $[(Me_3cy\text{-}ac)Fe(VI)N](PF_6)_2$ measured at 80 K (A) and at 4.2 K in a magnetic field of 7 T (B). The magnetic splitting in B corresponds to the external field. The simulation has been performed by assuming a diamagnetic species. Subspectrum (a) corresponds to a stable $[(Me_3cy\text{-}ac)Fe(IV)N_3](PF_6)_2$ and was the only subspectrum that was fitted in (B). (From J. F. Berry *et al.* (2006) *Science* **312**:1937–1941. Reprinted with permission from AAAS)

3.9 Molecules with Iron Centers of Higher Nuclearity

There are many iron proteins and corresponding model complexes that have more than one iron site. Dinuclear iron centers are present in 2Fe–2S electron transfer proteins or in enzymes like methane monoxygenase and ribonucleotide reductases. Even high-valent reaction intermediates have been detected by the RFQ Mössbauer studies of Huynh *et al.*[56] A broad variety of 3Fe–4S and 4Fe–4S proteins exist and enzymes like hydrogenases and nitrogenases have even more complex iron centers. Mössbauer spectroscopy detects all ^{57}Fe in the sample, which is a big advantage if compared, for example, with EPR, and therefore all the systems mentioned above have been and are still investigated using this technique.[7,8,11]

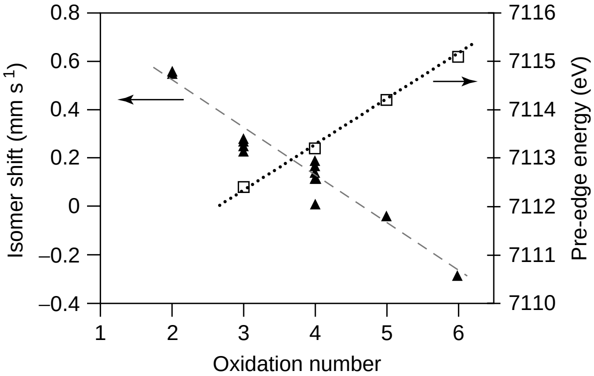

Figure 17 Plot of the isomer shifts versus Fe oxidation state of a series of low-spin Fe(III) Fe(IV), Fe(V), and Fe(VI) complexes with cyclam-related ligands. A plot of the Fe X-ray absorption spectroscopy (XAS) pre-edge peak energies of some complexes versus Fe oxidation state is also shown (open squares). The lines with dashes and dots represent least squares fits. (From J. F. Berry *et al.* (2006) *Science* **312**:1937–1941. Reprinted with permission from AAAS)

Mössbauer spectra of exchange-coupled iron centers having a paramagnetic ground state are almost exclusively evaluated in the strong-exchange limit. This implies that all exchange interactions are assumed to be strong and that no excited states are populated under the conditions at which the Mössbauer spectra are recorded. Only in this case is it justified to assume that the center can be described by a system spin S. Therefore, it is possible to evaluate the Mössbauer spectra in terms of the conventional spin Hamiltonian (equation 18). This procedure yields the system spin S as well as the parameters D, E/D, g, and A. The parameters of the single iron sites can be obtained by the spin-projection technique, which is also used in evaluating EPR spectra of strongly exchange-coupled systems. Instructive examples of this procedure can be found in Ref. 57.

Here we limit ourselves to an example of a 4Fe−4S center from the radical S-adenosyl-L-methionine (SAM) enzyme oxygen-independent coproporphyrinogen III oxidase HemN.**[58]** This enzyme catalyzes the oxidative decarboxylation of coproporphyrinogen III to protoporphyrinogen IX during bacterial heme biosynthesis. The crystal structure of *Escherichia coli* HemN revealed the presence of an unusually coordinated iron−sulfur cluster and two molecules of SAM.

The Mössbauer spectra of HemN without further additions are shown in Figure 18(a) and the parameters obtained are summarized in Table 5. The corresponding three iron atoms are ligated by cysteines ($\delta_1 = 0.43(1)\,\mathrm{mm\,s^{-1}}$, $\Delta E_{Q1} = 1.17(1)\,\mathrm{mm\,s^{-1}}$) whereas the fourth is not ($\delta_2 = 0.57(3)\,\mathrm{mm\,s^{-1}}$, $\Delta E_{Q2} = 1.23(2)\,\mathrm{mm\,s^{-1}}$). A value of $\delta \sim 0.45\,\mathrm{mm\,s^{-1}}$ is typical for valence-delocalized $\mathrm{Fe^{2.5+}}$−$\mathrm{Fe^{2.5+}}$ pairs with one electron being delocalized over the two iron sites. The value $\delta_2 = 0.57(3)\,\mathrm{mm\,s^{-1}}$ is clearly outside this range. Therefore, the ligand of the fourth iron site is unknown in the absence of SAM. Possible candidates could be either an amino acid residue of the polypeptide other than cysteine or alternatively any molecule contained within the buffer solution. These results are consistent with the finding that only the three cysteine residues C62, C66, C69 within the CXXXCXXC motif of *E. coli* HemN are involved in iron−sulfur cluster coordination.

Figure 18(b) shows the Mössbauer spectra of HemN plus SAM. As in the case of HemN, two different iron sites of a $[\mathrm{4Fe{-}4S}]^{2+}$ cluster were identified for the HemN spectra in the presence of SAM. However, for the latter spectra, a change in the isomer shift of the non-cysteine-ligated iron atom (from $\delta_2 = 0.57(3)\,\mathrm{mm\,s^{-1}}$ to $\delta_2 = 0.68(3)\,\mathrm{mm\,s^{-1}}$) was observed, which indicates that SAM only binds at one iron of the cluster, namely this unique, non-cysteine-ligated iron atom. This is consistent with the observed coordination of SAM to the iron−sulfur cluster in the crystal structure of *E. coli* HemN, in which it was observed that SAM binds at the iron by means of the carboxy and the amino group of the methionine part of SAM. Thus SAM coordination to the fourth iron site of the cluster is analogous in solution and in the crystalline state of HemN. The isomer shift value for the SAM ligated iron site can be directly correlated with specified distances between the iron and the ligand atoms in the case of HemN. Thus, the observed isomer shift of $\delta_2 = 0.68(3)\,\mathrm{mm\,s^{-1}}$ is

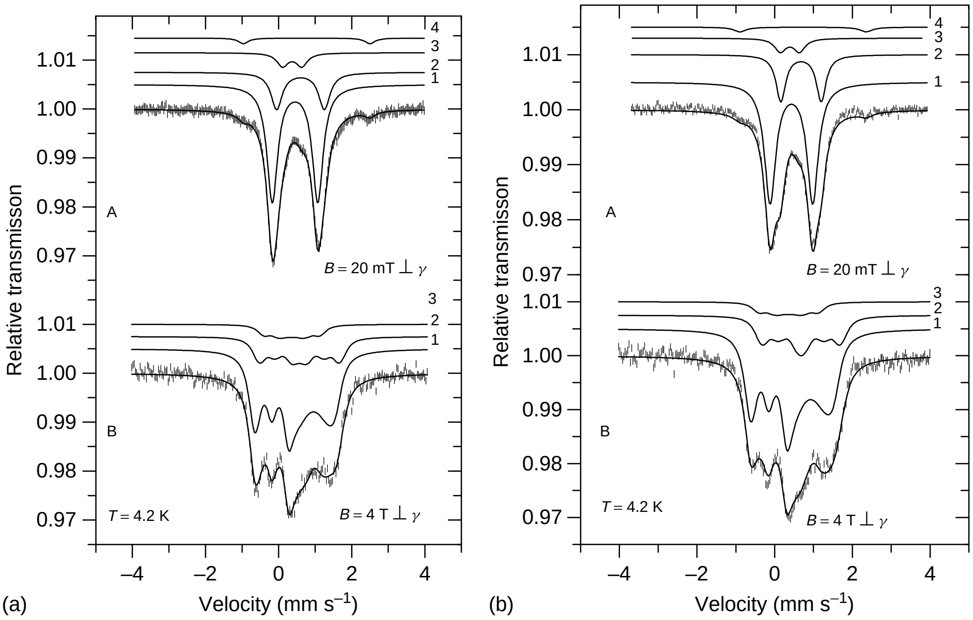

Figure 18 Mössbauer spectra of HemN in the absence (a) and in the presence of SAM (b). Spectra were obtained at $T = 4.2\,\mathrm{K}$ in an external magnetic field of (A) 20 mT and (B) 4 T perpendicular to the γ beam. The parameters are given in Table 5. (From Layer, Grage, Teschner, Schünemann, Breckau, Masoumi, Jahn, Heathcote, Trautwein and Jahn.**[58]** Reproduced by permission of American Society for Biochemistry & Molecular Biology)

Table 5 Mössbauer parameters obtained from the fit and simulation of HemN spectra in the absence or presence of SAM (Figure 18). (From Layer, Grage, Teschner, Schünemann, Breckau, Masoumi, Jahn, Heathcote, Trautwein and Jahn.[58] Reproduced by permission of American Society for Biochemistry & Molecular Biology)

HemN in the Absence of SAM				
	$[4Fe-4S]^{2+}$ Cysteine ligated (solid line 1)	$[4Fe-4S]^{2+}$ Non-cysteine-ligated (solid line 2)	Fe^{3+} (S = 0) (solid line 3)	$Fe^{2+}-4S^{(a)}$ (S = 2) (solid line 4)
δ [mm s^{-1}]	0.43(1)	0.57(3)	0.36(2)	0.73(1)
ΔE_Q [mms^{-1}]	1.17(1)	1.23(2)	0.49(4)	3.25(1)
η	0.0(1)	1.0(1)	1.0(1)	—
Γ [mm s^{-1}]	0.34(1)	0.35(1)	0.35(1)	0.31
Area [%]	67(2)	22(2)	8(2)	3(2)
HemN in the Presence of SAM				
δ [mm s^{-1}]	0.43(1)	0.68(3)	0.36(2)	0.73
ΔE_Q [mm s^{-1}]	1.10(1)	1.04(2)	0.49(4)	3.25
η	0.0(1)	1.0(1)	1.0(1)	—
Γ [mm s^{-1}]	0.35(2)	0.30(3)	0.31(2)	0.40(2)
Area [%]	67(2)	22(2)	8(2)	3(1)

[a] The $Fe^{2+}-4S$ component was not resolved in the 4T measurement.

associated with the iron site, which is ligated by the O- (2.3 Å) and the N-ligand (2.6 Å) of the methionine part of SAM as observed in the crystal structure of HemN. Therefore, the Mössbauer results provide essential information in correlation with the structural data, namely the possibility to combine the structural features (distances between the atoms) with the electronic properties (Mössbauer parameters) of the [4Fe–4S] cluster of HemN.

3.10 Prediction of Mössbauer Parameters by Density Functional Calculations

Since the early days of application of Mössbauer spectroscopy in solid state physics and inorganic chemistry, electronic structure calculations have been performed to rationalize and predict the Mössbauer parameters obtained. In the beginning, calculations were applied to single ions, but later semiempirical methods could be applied to small molecules, too. Early density functional theory (DFT) methods, like the self-consistent charge (SCC)-Xα method could be successfully applied to larger molecules. For more than a decade, DFT methods with all-electron basis sets have also been applied to large bioinorganic molecules. These methods allow the determination of Mössbauer parameters with impressive accuracy and have become a valuable tool for the interpretation of Mössbauer spectra.

3.10.1 Density Functional Calculations

Density functional theory is based on the Hohenberg–Kohn theorems,[59] which state (i) that there is a one-to-one mapping between the electronic charge density ρ_0 and the wavefunction Ψ_0 of the ground state and (ii) that there is a functional $E[\rho]$ that maps the density on the molecular energy and that is minimized by the ground state density ρ_0. In this way, the solution of the Schrödinger equation for an N-particle wavefunction is reduced to the problem of minimizing the energy functional $E[\rho]$ by a one-particle charge density. The price for this reduction of complexity is that only approximations for the functional $E[\rho]$ are available, the exact form being unknown. Actually, Before the formulation of the Hohenberg–Kohn theorems, Slater had already proposed the SCC-Xα method,[60,61] which is now regarded as the first DFT method. For most of the problems that are addressed by electronic structure calculations, DFT methods became the method of choice. Although ab initio methods can, in principle, give results with any desired accuracy, they are at the current stage for most purposes computationally too demanding to compete with DFT methods in the field of transition metal compounds.

3.10.2. Electric Field Gradient and Quadrupole Splitting

The quadrupole splitting ΔE_Q is the first Mössbauer parameter that could be predicted with reasonable accuracy by electronic structure calculations. The quadrupole splitting can be related to the EFG at the Mössbauer nucleus according to equation (12). Since the nuclear quadrupole moment Q is very difficult to determine by experiment alone, the combination of Mössbauer spectroscopy and density functional calculations is currently the most accurate approach to estimate Q. A linear regression of measured quadrupole splittings and calculated electric field gradients has been performed by Blaha *et al.*[62] for a large series of compounds

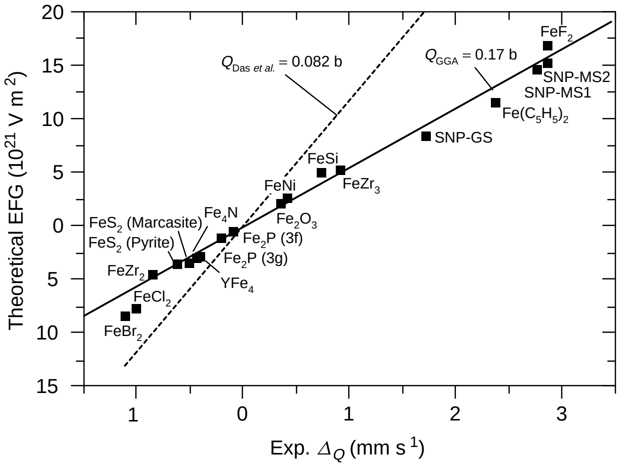

Figure 19 Calculated electric field gradients versus observed quadrupole splittings ΔE_Q. The solid line represents a linear regression with a ^{57}Fe nuclear quadrupole moment of 0.17 barns. (From Blaha, Schwarz, Faber and Luitz.[62] With kind permission from Springer Science & Business Media)

covering a wide range of different quadrupole splittings (Figure 19). According to these calculations, a value of the nuclear quadrupole moment of the ^{57}Fe nucleus of 0.15–0.17 barn is commonly accepted, with an uncertainty of about 10%.

Successful calculations of the quadrupole splitting have been performed with a variety of density functional methods. Among the currently most popular functionals—like the gradient corrected functionals BP86 or BPW91 or the hybrid functional B3LYP—there are no apparent differences in the quality of the predicted field gradients. Zhang and Oldfield[63] demonstrated that wrong iron–ligand bond lengths are a major source of error for calculated field gradients. Methods employing the local density approximation, which are notorious for underestimating metal–ligand bond lengths, are in principle expected to give less accurate field gradients than corrected gradient functionals. However, this effect may be canceled by other sources of error working in the opposite direction.

Several studies[63–65] have shown that the calculated field gradients are sensitive to the quality of the size of the basis set. The type of basis set, for example, Gaussian-type orbitals (GTOs) or Slater-type orbitals (STOs), does not seem to influence the field gradient, provided the basis set is large enough.[63] For this reason, the computationally more efficient GTOs are usually preferred to STOs, which give a better representation of the cusp of the charge density at the nucleus. Since relativistic calculations give no significant improvement of the calculated electric field gradients,[66] most of the reported EFG calculations have been performed with nonrelativistic methods.

3.10.3 Isomer Shift

According to equation (8), the absolute value of the isomer shift, δ_{abs}, depends linearly on the electronic charge densities $\rho_S(0) = e|\varphi(0)_{source}|^2$ and $\rho_{\text{A}}(0) = e|\varphi(0)_{absorber}|^2$ at the Mössbauer nuclei in the source and in the absorber, respectively.[67] Usually, nonrelativistic electronic structure calculations are performed, giving an electronic charge density $\rho_{\text{nr}}(0)$ that is smaller than the true value (nonrelativistic $\sim 1.2 \cdot 10^4$ au as compared to relativistic $\sim 1.5 \cdot 10^4$ au in case of ^{57}Fe). Fortunately, the relativistic charge density $\rho(0)$ can in good approximation be retrieved from the nonrelativistic charge density $\rho_{\text{nr}}(0)$ by multiplication with a so-called relativity factor $S(Z)$:

$$\rho(0) = S(Z)\rho_{\text{nr}}(0) \tag{22}$$

This factor is about 1.32 in the case of iron and about 2.48 in the case of tin. One may conclude that—like for the quadrupole splitting—for the prediction of the isomer shift also nonrelativistic calculations are fully sufficient. Since it is quite difficult to determine the absolute isomer shift as defined in equation (8), it is common practice to give the isomer shift as the difference, $\delta = \delta_{\text{abs, sample}} - \delta_{\text{abs, standard}}$, compared to a given standard (e.g., α-iron foil or sodium nitroprusside in case of iron). In principle, one could try to predict the isomer shift directly, using equation (8) and the relativity factor $S(Z)$. However, it turns out that the accuracy of the calculated charge densities as well as the accuracy of the experimentally observed radii of the Mössbauer nuclei in the ground and excited state is not sufficient for this approach. Therefore, it is common to use linear regression on a large data set containing measured isomer shifts and calculated charge densities. For this purpose, the isomer shift can be written as

$$\delta = \alpha[\rho_{\text{A,nr}}(0) - b] \tag{23}$$

where α and b are parameters that have to be determined by linear regression. A large number of studies have been performed to estimate α and b by semiempirical molecular orbital, ab initio and DFT calculations, first for free atoms[68–73] (see also Ref. 74 for a review), and also later for molecules.[64,65,75–79] A detailed description of the technical details of the calculation of charge densities and an extensive review of previously published work on this subject have been given by Neese.[80]

With increasing computational resources, the correlation between calculated charge densities and measured isomer shifts has improved significantly. A benchmark for the calibration of the parameters α and b in equation (24) has been given by Neese,[80] who compiled data for 15 iron-containing compounds that cover a range of the isomer shift from $-0.87\,\text{mm}\,\text{s}^{-1}$ to $+1.39\,\text{mm}\,\text{s}^{-1}$. The linear regression of the measured isomer shifts with respect to nonrelativistic charge densities calculated with B3LYP gives a remarkable correlation and a standard deviation between measured

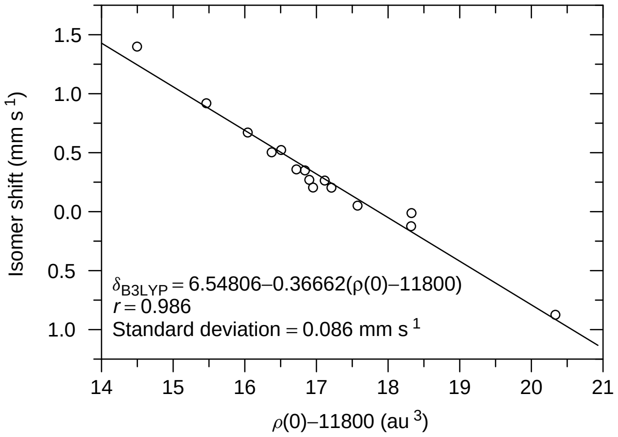

Figure 20 Calibration of the B3LYP method for the prediction of ^{57}Fe isomer shifts. The calculated electron density at the iron nucleus is plotted versus the experimentally determined isomer shift for a series of 15 iron-containing compounds. (Reprinted from Neese.[80] © 2002, with permission from Elsevier)

and predicted isomer shifts of about $0.1\,\mathrm{mm\,s^{-1}}$ (Figure 20). Similar results were obtained with the BP86 method.[80]

It is important to note that, although different DFT and ab initio methods can be used for the prediction of the isomer shift with comparable accuracy, these methods nevertheless give quite different values for the charge densities at the Mössbauer nucleus. The linear regression parameters α and b obtained with a particular method are therefore not useful for charge densities that have been calculated with any other method.

There is a long-standing tradition to correlate the measured isomer shifts with calculated orbital populations of the Mössbauer isotope, especially with the populations of the valence orbitals. The first reason for this tradition is the restricted computational resources that did not allow full electron basis sets. A second reason is the intention to rationalize the relation between physical and chemical concepts like spin and oxidation state of the Mössbauer atom. While the first argument is becoming obsolete even for large bioinorganic molecules, the second argument is as appealing as ever, since the prediction of isomer shifts by DFT methods has to some extent the character of a ‘‘black box’’, despite its remarkable accuracy. However, the correlation of orbital populations and isomer shifts is hindered by several problems. The first problem is that orbital populations may significantly depend on the basis set employed. A second problem is that the relation between the orbital populations and the charge density at the nucleus is fairly complex since core and valence orbitals change their shape owing to shielding and covalency effects. An authoritative analysis of these complex relations has been given by Neese.[80] Vrajmasu *et al.* have combined DFT calculations with a semiempirical model that is able to predict the influence of redox states on the isomer shift in iron proteins.[81]

Instructive examples for the possible benefit of isomer shift calculations using DFT are some recently investigated high-valent iron complexes like those that are described in Sections 3.7 and 3.8. For instance, the Fe(VI) complex $[(\mathrm{Me_3cy\text{-}ac})\mathrm{FeN}](\mathrm{PF_6})_2$, reported by Berry *et al.*[55] (*see* also Section 3.8), exhibits a surprisingly high isomer shift. For this reason, a series of similar complexes with different electronic configuration was investigated by spectroscopic and by theoretical methods in order to confirm the oxidation state VI of this complex. DFT calculations were able to accurately reproduce the spectroscopic results for the investigated series of complexes and they confirmed that the electronic configurations that have been assigned to the complexes as a result of the spectroscopic data were consistent with the calculated electronic structures.

3.10.4. Lamb–Mössbauer Factor

The Lamb–Mössbauer factor f_{LM}, which is difficult to determine experimentally as well as computationally, does not belong to the most common Mössbauer parameters in the field of inorganic chemistry. It can be of importance, however, when Mössbauer spectra are used to determine for a given sample the fractions of different species containing the same Mössbauer isotope. This is the case, for instance, for iron spin-crossover complexes where Mössbauer spectroscopy can be used to measure the temperature- or pressure-dependent fraction of different spin isomers.[82] The first approach to estimate the change of the Lamb–Mössbauer factor upon spin crossover has been restricted to molecular vibrations, neglecting the important contribution that arises from intermolecular vibrations.[83,84]

3.10.5 Spin Hamiltonian Parameters

In case of paramagnetic compounds in high magnetic fields, it is common to use the spin Hamiltonian formalism to interpret the Mössbauer spectra (compare Section 2.3.4). This formalism employs adjustable parameters like the g tensor, the hyperfine coupling tensor $\overleftrightarrow{A}$, the zero-field D splitting, and the rhombicity E/D, in order to simulate the measured spectra. The interpretation of these parameters in terms of geometric and electronic structure can be supported by DFT calculations. In general, g tensors can be calculated quite accurately by DFT methods. Unfortunately, in the case of transition metal complexes sometimes only qualitative agreement can be achieved. Currently, the best results seem to be obtained by a combination of nonrelativistic DFT methods and second-order perturbation theory.[85] The calculation of the hyperfine coupling tensor $\overleftrightarrow{A}$ (consisting of the Fermi-contact contribution, a spin dipolar contribution, and an orbital contribution) of iron is currently less advanced than the g tensor. The first results have been published by Neese.[85] In the meantime, algorithms for the calculation of the hyperfine coupling tensor are implemented in many quantum chemistry program packages. A recent application to an oxoiron(IV) complex is described in Ref. 52. In order to calculate the zero-field splitting D and the rhombicity E/D, the ground state wavefunction has to be mixed with wavefunctions of different multiplicities. This has first been achieved at the semiempirical level.[86] Only recently, very accurate calculations of the zero-field splitting using DFT have been presented.[87–89] While the zero-field splitting parameter D is currently systematically underestimated by DFT calculations,[87,88] more accurate results have been obtained by ab initio methods.[90]

4 ACKNOWLEDGMENTS

We would like to dedicate this contribution to our academic teacher Ali Trautwein, who introduced us to the fascinating field of Mössbauer spectroscopy.

5 END NOTE

[a] In the older literature isomer shifts are often reported relative to $Na_2[Fe(CN)_5NO]$ (Table 2) sodium nitroprusside. The values are related by $\delta_{\mathrm{NP}} = \delta_{\alpha-Fe} + 0.26\,\mathrm{mm\,s^{-1}}$.

6 ABBREVIATIONS AND ACRONYMS

CEMS = conversion electron Mössbauer spectroscopy; DFT = density functional theory; EFG = electric field gradient; EPR = electron paramagnetic resonance; ESEEM = electron spin echo envelope modulation spectroscopy; GTO = Gaussian-type orbitals; hTH = human tyrosine hydroxylase; MIMOS = miniaturized mössbauer spectrometer; NFS = nuclear forward scattering; NMR = nuclear magnetic resonance; RFQ = rapid freeze quench; SAM = *S*-adenosyl-L-methionine; SCC = self-consistent charge; STOs = slater-type orbitals; TMP = tetramesitylporphyrin; XAS = X-ray absorption spectroscopy.

7 FURTHER READING

P. G. Debrunner, in ‘Iron Porphyrins Part III, Physical Bioinorganic Chemistry Series’, eds. A. B. P. Lever and H. B. Gray, VCH Publishers, New York, 1989, p. 139. Although focused on iron porphyrins a very instructive introduction into hyperfine interactions and Mössbauer parameters.

N. N. Greenwood and T. C. Gibb, ‘Mössbauer Spectroscopy’, Chapman & Hall, London, 1971, Although from 1971, this is a classic with an overwhelming amount of Mössbauer data and a solid introduction to the technique.

P. Gütlich, R. Link and A. X. Trautwein, ‘Mössbauer spectroscopy and Transition Metal Chemistry’, Springer-Verlag, Berlin, Heidelberg, New York, 1978, Very useful for starters in the field. From the many books on Mössbauer spectroscopy the only one where a new edition is foreseen.

B.-H. Huynh, ‘Advances in Inorganic Biochemistry’, eds. G.-L. Eichhorn and L.-G. Marzilli, Elsevier, New York, Amsterdam, Oxford, 1984, Vol. 6, p. 164. Very nice for those who are also interested in EPR of iron complexes.

F. Neese, *Inorg. Chim. Acta*, 2002, **337C**, 181. Authoritative analysis of the correlation between measured isomer shifts and calculated charge densities and orbital populations.

A. X. Trautwein, E. Bill, E. L. Bominaar and H. Winkler, *Struct. Bonding*, 1991, **78**, 1. A thorough overview on spin-Hamiltonian parameters and Mössbauer spectroscopy with a lot of examples of spin-coupled systems.

8 REFERENCES

1. V. I. Goldanskii and R. H. Herber eds., ‘Chemical Applications of Mössbauer Spectroscopy’, Academic Press, London, 1968.
2. P. Gütlich, R. Link and A. X. Trautwein, ‘Mössbauer Spectroscopy and Transition Metal Chemistry’, Springer-Verlag, Berlin, Heidelberg, New York, 1978.
3. N. N. Greenwood and T. C. Gibb, ‘Mössbauer Spectroscopy’, Chapman & Hall, London, 1971.
4. T. E. Cranshaw, B. W. Dale, G. O. Longworth and C. E. Johnson, ‘Mössbauer Spectroscopy and its Applications’, Cambridge University Press, Cambridge, 1985.
5. G. J. Long ed., ‘Mössbauer Spectroscopy Applied to Inorganic Chemistry’, Plenum Press, New York, 1984–1989, 1–3 Vols.
6. D. P. E. Dickson and F. J. Berry, ‘Mössbauer Spectroscopy’, Cambridge University Press, Cambridge, 1986.
7. B.-H. Huynh, ‘Advances in Inorganic Biochemistry’, eds. G.-L. Eichhorn and L.-G. Marzilli, Elsevier, New York, Amsterdam, Oxford, 1984, Vol. 6, p. 164.
8. A. X. Trautwein, E. Bill, E. L. Bominaar and H. Winkler, *Struct. Bonding*, 1991, **78**, 1.
9. P. G. Debrunner, in ‘Biological Magnetic Resonance’, ‘Vol 13: EMR of Paramagnetic Molecules’, eds. L.-J. Berliner and J. Reuben, Plenum Press, New York, 1993, p. 59.
10. E. Münck and A. Stubna, ‘Comprehensive Coordination Chemistry II’, ed. B. Lever, Elsevier, Vol. 2, p. 279.
11. V. Schünemann and H. Winkler, *Rep. Prog. Phys.*, 2000, **63**, 263.

12. S. Mørup, J.-A. Dumesic and H. Topsøe, in ‘Applications of Mössbauer spectroscopy’, ed. R. L. Cohen, Academic Press, New York, 1980, Vol. II, p. 1.
13. T. Shinjo, *Surf. Sci. Rep.*, 1991, **12**, 51.
14. M. Przybylski, *Hyperfine Interact.*, 1998, **113**, 135.
15. R. Röhlsberger, ‘Nuclear Condensed Matter Physics with Synchrotron Radiation’, Springer-Verlag, Berlin, Heidelberg, New York, 2004.
16. F. G. Parak, *Rep. Prog. Phys.*, 2003, **66**, 103.
17. H. Paulsen, V. Schünemann, A. X. Trautwein and H. Winkler, *Coord. Chem. Rev.*, 2005, **249**, 255.
18. R. L. Mössbauer, *Naturwissenschaften*, 1958, **45**, 538.
19. http://nobelprize.org/physics/laureates/1961/mossbauer-lecture.pdf.
20. R. V. Morris, G. Klingelhöfer, B. Bernhardt, C. Schröder, D. S. Rodionov, P. A. de Souza, Jr, A. Yen, R. Gellert, E. N. Evlanov, J. Foh, E. Kankeleit, P. Gütlich, D. W. Ming, F. Renz, T. Wdowiak, S. W. Squyres and R. E. Arvidson, *Science*, 2004, **305**, 833.
21. G. Klingelhöfer, R. V. Morris, B. Bernhardt, C. Schröder, D. S. Rodionov, P. A. de Souza, Jr, A. Yen, R. Gellert, E. N. Evlanov, B. Zubkov, J. Foh, U. Bonnes, E. Kankeleit, P. Gütlich, D. W. Ming, F. Renz, T. Wdowiak, S. W. Squyres and R. E. Arvidson, *Science*, 2004, **306**, 1740.
22. http://iacgu32.chemie.uni-mainz.de/main.php.
23. C. Krebs, J. C. Price, J. Baldwin, L. Saleh, M. T. Green and J. M. Bollinger, Jr, *Inorg. Chem.*, 2005, **44**, 742.
24. P. G. Debrunner, in ‘Iron Porphyrins Part III, Physical Bioinorganic Chemistry Series’, eds. A. B. P. Lever and H. B. Gray, VCH Publishers, New York, 1989, p. 139.
25. H. H. Wickman, M. P. Klein and D. A. Shirley, *Phys. Rev.*, 1966, **152**, 345.
26. E. Münck, J. L. Grover, T. A. Tumolillo and P. G. Debrunner, *Comput. Phys. Commun.*, 1973, **5**, 225.
27 http://whome.phys.au.dk/∼hpg/vinda.htm.
28 http://www.webres.com/software/software.html.
29. V. Schünemann, H. Winkler, C. Butzlaff and A. X. Trautwein, *Hyperfine Interact.*, 1994, **93**, 1427.
30. H. H. Wickman, in ‘Mössbauer Effect Methodology’, ed. I. J. Gruverman, Plenum Press, New York, 1996, Vol. 2, p. 39.
31. C. Le Caer and J. M. Dubois, *J. Phys. E: Sci. Instrum.*, 1979, **12**, 1083.
32. V. Schünemann, ‘Magnetisches und katalytisches Verhalten von Eisenteilchen im Zeolith NaX (Magnetic and catalytic properties of iron particles in zeolite NaX)’, PhD-thesis, Medical University of Lübeck, Lübeck, 1993.
33. S. Stoian, Y. Yu, J. M. Smith, P. A. Holland, E. L. Bominaar and E. Münck, *Inorg. Chem.*, 2005, **44**, 4915.
34. J. R. Polam, J. L. Wright, K. A. Christensen, F. A. Walker, H. Flint, H. Winkler, M. Grodzicki and A. X. Trautwein, *J. Am. Chem. Soc.*, 1996, **118**, 5272.
35. G. Zoppellaro, T. Teschner, E. Harbitz, V. Schünemann, S. Karlsen, D. M. Arciero, S. Ciurli, A. X. Trautwein, A. B. Hooper and K. Andersson, *Chem. Phys. Chem.*, 2006, **7**, 1258.
36. V. Schünemann, A. X. Trautwein, J. Illerhaus and W. Haehnel, *Biochemistry-US*, 1999, **38**, 8981.
37. W. Meyer-Klaucke, H. Winkler, V. Schünemann, A. X. Trautwein, H. F. Nolting and J. Haavik, *Eur. J. Biochem.*, 1996, **241**, 432.
38. V. Schünemann, C. Meier, W. Meyer-Klaucke, H. Winkler, A. X. Trautwein, P. M. Knappskog, K. Toska and J. Haavik, *J. Biol. Inorg. Chem.*, 1999, **4**, 223.
39. P. Wegner, M. Bever, V. Schünemann, A. X. Trautwein, C. Schmidt, H. Bönisch, M. Gnida and W. Meyer-Klaucke, *Hyperfine Interact.*, 2004, **156–157**, 293.
40. C. E. Schulz and P. G. Debrunner, *J. Phys.*, 1976, **C6–37**, 153.
41. G. Simmoneaux, V. Schünemann, C. Morice, L. Carel, L. Toupet, H. Winkler, A. X. Trautwein and F. A. Walker, *J. Am. Chem. Soc.*, 2000, **122**, 4366.
42. V. Schünemann, A. M. Raitsimring, R. Benda, A. X. Trautwein, T. K. Shokireva and F. A. Walker, *J. Biol. Inorg. Chem.*, 1999, **4**, 708.
43. W. T. Oosterhuis and G. Lang, *J. Chem. Phys.*, 1969, **50**, 4381.
44. C. P. S. Taylor, *Biochim. Biophys. Acta*, 1977, **491**, 137.
45. M. Sharrock, P. G. Debrunner, C. Schulz, J. D. Lipscomb, V. Marshall and I. C. Gunsalus, *Biochim. Biophys. Acta*, 1976, **420**, 8.
46. J. A. Fee, K. L. Findling, T. Yoshida, R. Hille, G. E. Tarr, D. O. Hearshen, W. R. Dunham, E. P. Day, T. A. Kent and E. Münck, *J. Biol. Chem.*, 1984, **259**, 124.
47. V. Schünemann, C. Jung, A. X. Trautwein, D. Mandon and R. Weiss, *FEBS Lett.*, 2000, **179**, 149.
48. C. Krebs, J. C. Price, J. Baldwin, L. Saleh, M. T. Green and J. M. Bollinger, Jr, *Inorg. Chem.*, 2005, **44**, 742.
49. J. C. Price, E. W. Barr, B. Tirupati, J. M. Bollinger, Jr and C. Krebs, *Biochemistry-US*, 2003, **42**, 7497.
50. S. Ollagnier, C. Meier, E. Mulliez, J. Gaillard, V. Schünemann, A. X. Trautwein, T. Mattiolo, M. Lutz and M. Fontecave, *J. Am. Chem. Soc.*, 1999, **121**, 6344.
51. J. U. Rohde, J. H. In, M. H. Lim, W. W. Brennessel, M. R. Bukowski, A. Stubna, E. Münck, W. Nam and L. Que, Jr, *Science*, 2003, **299**, 1037.
52. M. R. Bukowski, D. Kevin, K. D. Koehntop, A. Stubna, E. L. Bominaar, J. A. Halfen, E. Münck, W. Nam and L. Que, Jr, *Science*, 2005, **310**, 1000.
53. K. Meyer, E. Bill, B. Mienert, T. Weyhermüller and K. Wieghardt, *J. Am. Chem. Soc.*, 2000, **121**, 4859.
54. F. Tiago de Oliveira, A. Chanda, D. Banerjee, S. Mondal, E. L. Bominaar, E. Münck and T. C. Collins, *Science*, 2007, **315**, 835.
55. J. F. Berry, E. Bill, E. Bothe, S. DeBeer George, B. Mienert, F. Neese and K. Wieghardt, *Science*, 2006, **312**, 1937.

56. N. Ravi, J. M. Bollinger, B. H. Huynh, D. E. Edmondson and J. Stubbe, *J. Am. Chem. Soc.*, 1994, **116**, 8007.

57. A. Bencini and D. Gatteschi, 'EPR of Exchange Coupled Systems', Springer-Verlag, Berlin, Heidelberg, New York, 1990.

58. G. Layer, K. Grage, T. Teschner, V. Schünemann, D. Breckau, A. Masoumi, M. Jahn, P. Heathcote, A. X. Trautwein and D. Jahn, *J. Biol. Chem.*, 2005, **32**, 29038.

59. P. Hohenberg and W. Kohn, *Phys. Rev.*, 1964, **136B**, 864.

60. J. C. Slater, *Phys. Rev.*, 1951, **81**, 385.

61. K. Schwartz, *Phys. Rev. B*, 1972, **5**, 2466.

62. P. Blaha, K. Schwarz, W. Faber and J. Luitz, *Hyperfine Interact.*, 2000, **126**, 389.

63. Y. Zhang and E. Oldfield, *J. Phys. Chem. B*, 2003, **107**, 7180.

64. T. Lovell, J. Li., T. Liu, D. A. Case and L. Noodleman, *J. Am. Chem. Soc.*, 2001, **123**, 12392.

65. Y. Zhang, J. Mao and E. Oldfield, *J. Am. Chem. Soc.*, 2002, **124**, 7829.

66. P. Schwerdtfeger, T. Söhnel, M. Pernpointner, J. K. Laerdahl and F. E. Wagner, *J. Chem. Phys.*, 2001, **115**, 5913.

67. P. Gütlich, R. Link and A. X. Trautwein, 'Mössbauer Spectroscopy and Transition Metal Chemistry', Springer-Verlag, Berlin, Heidelberg, New York, 1978.

68. R. E. Watson, *Phys. Rev.*, 1960, **118**, 1036.

69. L. R. Walker, G. K. Wertheim and V. Jaccarin, *Phys. Rev. Lett.*, 1961, **6**, 98.

70. S. L. Ruby and G. K. Shenoy, *Phys. Rev.*, 1969, **186**, 326.

71. J. B. Mann, *J. Chem. Phys.*, 1969, **51**, 841.

72. J. P. Desclaux, *At. Data Nucl. Data Tables*, 1973, **12**, 311.

73. J. P. Desclaux, *Comput. Phys. Commun.*, 1975, **9**, 31.

74. A. J. Freeman and D. Ellis, in 'Mössbauer Isomer Shifts', eds. G. K. Shenoy and F. E. Wagner, North Holland, Amsterdam, 1978, p. 111.

75. A. X. Trautwein, E. Bill, R. Bläs, S. Lauer and H. Winkler, *J. Chem. Phys.*, 1985, **82**, 3584.

76. A. X. Trautwein and H. Winkler, *Z. Naturforsch*, 1987, **42a**, 211.

77. Q. M. Zhang, Y. L. Zhang and D. S. Wang, *Commun. Theor. Phys.*, 1987, **8**, 139.

78. N. Jansen, H. Spiering, P. Gütlich, D. Stahl, R. Kniep, V. Eyert, J. Kübler and P. C. Schmidt, *Angew. Chem.*, 1992, **104**, 1632.

79. Y. Yamada and T. Tominaga, *Radiochim. Acta*, 1998, **80**, 163.

80. F. Neese, *Inorg. Chim. Acta*, 2002, **337C**, 181.

81. V. Vrajmasu, E. Münck and E. L. Bominaar, *Inorg. Chem.*, 2003, **42**, 5974.

82. P. Gütlich and H. A. Goodwin eds., 'Spin Crossover in Transition Metal Compounds I-III', Springer-Verlag, Berlin, Heidelberg, New York, 2004.

83. H. Paulsen, H. Winkler, A. X. Trautwein, H. Grünsteudel, V. Rusanov and H. Toftlund, *Phys. Rev. B*, 1999, **59**, 975.

84. H. Paulsen, H. Grünsteudel, W. Meyer-Klaucke, M. Gerdan, H. Winkler, H. Toftlund and A. X. Trautwein, *Eur. Phys. J. B*, 2001, **23**, 463.

85. F. Neese, *Curr. Opin. Chem. Biol.*, 2003, **7**, 125.

86. F. Neese and E. I. Solomon, *Inorg. Chem.*, 1998, **37**, 6568.

87. R. Reviakine, A. V. Arbuznikov, J. C. Tremblay, C. Remenyi, O. L. Malkina, V. G. Malkin and M. Kaupp, *J. Chem. Phys.*, 2006, **125**, 054110.

88. S. Sinnecker and F. Neese, *J. Phys. Chem. A*, 2005, **110**, 12267.

89. J. C. Schöneboom, F. Neese and W. Thiel, *J. Am. Chem. Soc.*, 2005, **127**, 5840.

90. D. Ganyushin and F. Neese, *J. Chem. Phys.*, 2006, **125**, 024103.

Nickel Enzymes & Cofactors

Stephen W. Ragsdale
University of Nebraska, Lincoln, NE, USA

1 Introduction 1
2 Urease (EC 3.5.1.5) 3
3 NiFe Hydrogenases (EC 1.12.1.2, 1.2.2.1, or 1.18.99.1) 5
4 Carbon Monoxide Oxidoreductases (CODH, EC 1.2.99.2) 7
5 Acetyl-CoA Synthase (ACS) (EC 2.3.1) 7
6 Methyl-Coenzyme M Reductase (MCR) (EC 2.8.4.1) 10
7 Superoxide Dismutase (SOD) (EC 1.15.1.1) 11
8 Glyoxalase-I (EC 4.4.1.5) 12
9 Aci-Reductone Dioxygenase 12
10 Related Articles 13
11 References 13

Abbreviations

CoA = Coenzyme A; CoM = Coenzyme M, 2-thioethanesulfonate; ENDOR = Electron nuclear double resonance; EPR = Electron paramagnetic resonance; H_4MPT = Tetrahydromethanopterin; HS-HTP = N-7-mercaptoheptanoyl-O-phosphothreonine; MCR = Methyl-CoM reductase; MRF = Methyl-reducing factor; XAS = X-ray absorption spectroscopy; GSH = Glutathione.

1 INTRODUCTION

The nickel enzymes covered in this article can be divided into two groups: redox enzymes and hydrolases. The five Ni redox enzymes are hydrogenase, CO dehydrogenase (CODH), acetyl-CoA synthase (ACS), methyl-Coenzyme M reductase (MCR), and superoxide dismutase (SOD). Glyoxalase-I and urease are Ni hydrolases. Ni proteins that are not enzymes are not covered, because they have been recently reviewed.[1,2] These include regulatory proteins (NikR) and chaperonins and metal uptake proteins (CooJ, CooE, UreE, and ABC transporters). A recent crystal structure of NikR, shown in Figure 1(i), is a notable recent achievement in this area.[3]

1.1 Biology of Nickel

Derived from the German word meaning Devil's copper, Ni is an essential element that, at elevated levels, is toxic, causing skin allergies, lung fibrosis, and cancer of the respiratory tract (*see* ***Metal Ion Toxicity***).[10,11] While the total Ni concentration in most natural environments is in the low nM range (e.g. ∼20 nM in freshwater or seawater and 0.5 nM in the human bloodstream),[12] industrial workers like welders are exposed to atmospheric Ni levels that have been determined to be a cancer risk ($>1\,\mathrm{mg\,m^{-3}}$). Ni becomes toxic at relatively high levels (oral LD50 in rats for nickel acetate = $350\,\mathrm{mg\,kg^{-1}}$). Based on studies of Ni depletion in rats as early as 1920, it was suggested that Ni is an essential element for higher animals;[11] however, the source of the Ni requirement has not yet been uncovered. Following the initial discovery of a microbial Ni requirement for hydrogenase activity in 1965,[13] a Ni requirement for many microbes as an essential prosthetic group in key enzymes has been described. The diverse structures of Ni active sites are shown in Figure 1 and summarized in Table 1. Some general properties of the Ni enzymes are described in Table 2. Reviews on the bioinorganic chemistry of Ni are available.[2,14]

1.2 Chemistry of Nickel

Nickel (relative atomic mass = 58.69) is a first-row transition metal in group VIIIb of the periodic table. Although there are five natural isotopes, ^{58}Ni (68.3%) and ^{60}Ni (26.1%) are the most abundant. Proteins are often labeled with ^{61}Ni (nuclear spin, I, is 3/2) to identify the nickel site by EPR spectroscopy, since paramagnetic species with significant spin on ^{61}Ni exhibit a four-line splitting. ^{63}Ni, which is a beta emitter with a relatively long half-life of 100 years, can be used to identify Ni-containing proteins and to measure Ni uptake in cells.

Nickel can exist in oxidation states from 0 to +4 and all but the +4 state have been observed in biology. Although the 2+ state ($3d^8$) is most common, the Ni redox enzymes described here appear to access either the 2+/1+ and/or the 3+/2+ redox couples. It has been proposed that the 0 state is important during catalysis by acetyl-CoA synthase. The hydrolases appear to only use Ni^{2+}, which is a Lewis acid. Since Ni^{1+} and Ni^{3+} are paramagnetic, electron paramagnetic resonance (EPR) and related advanced methods like electron nuclear double resonance (ENDOR) and electron spin echo envelope modulation (ESEEM) are valuable spectroscopic methods used to study Ni redox enzymes. Some Ni enzymes have rather strong UV-visible and magnetic circular dichroism (MCD) bands that are redox- and coordination-dependent. X-ray absorption spectroscopic (XAS) methods are often used to assess the oxidation state and geometry of the Ni active site in proteins.

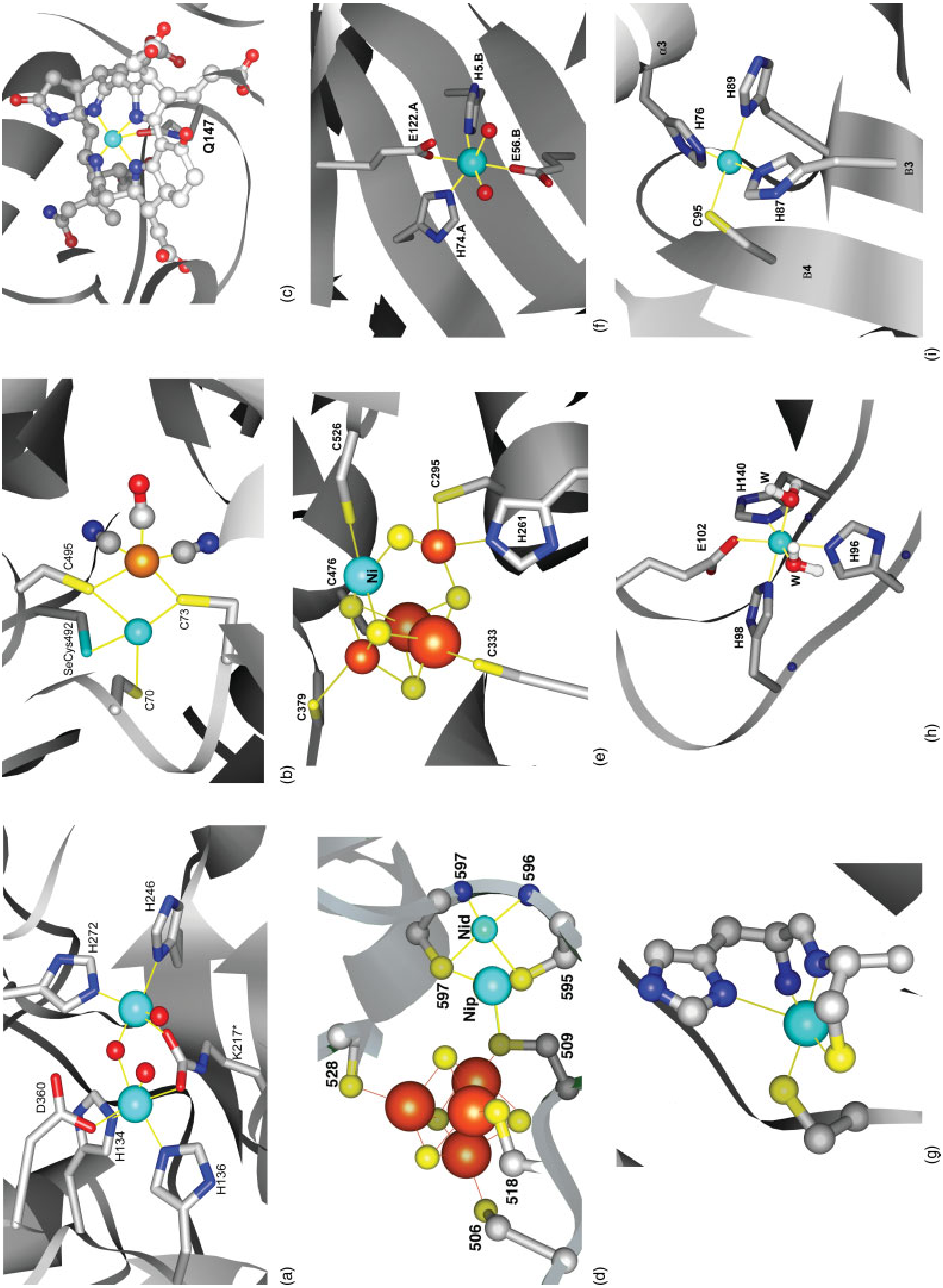
(a)
D360
H134
H136
K217*
H246
H272
(b)
SeCys492
C70
C73
C495
(c)
Q147
(d)
506
518
528
509
597
Nip
Nld
595
597
596
(e)
C379
C476
Ni
C526
C333
C295
H261
(f)
H74.A
E122.A
E56.B
H5.B
(g)
(h)
H98
W
E102
H140
W
H96
(i)
B4
C95
H87
H76
H89
B3
α3

Table 1 Reactions covered in this review

Urease	$\text{Urea} + H_2O \rightarrow 2NH_3 + H_2CO_3$	(1)
Hydrogenase	$2H^+ + 2e^- \leftrightarrow H_2$	(2)
CO Dehydrogenase	$CO + H_2O \leftrightarrow 2H^+ + CO_2 + 2e^-$	(3)
Acetyl-CoA Synthase	$CH_3\text{–CFeSP} + \text{CoASH} + CO \rightarrow CH_3\text{–CO–SCoA} + \text{CFeSP}$	(4)
Methyl-CoM Reductase	$\text{Methyl-SCoM} + \text{CoBSH} \rightarrow CH_4 + \text{CoBS-SCoM}$	(5)
Superoxide Dismutase	$2O_2{}^- + 2H^+ \rightarrow H_2O_2 + O_2$	(6)
Gloxylase I	$\text{Methylglyoxal} + \text{glutathione} \leftrightarrow \text{GS-derivative}$	(7)
Aci-reductone dioxygenase	$\text{Aci-reductone} + O_2 \rightarrow \text{methylthiopropionate}$	(8)

Table 2 Nickel Enzymes

Enzyme	Source	Composition	Ni center	Other groups
Urease	Plants	6×91 kDa	High-spin Ni^{II} dimer	
	K. pneumoniae	$60.3 + 11.7 + 11$ kDa	High-spin Ni^{II} dimer	
Hydrogenase	*D. gigas*	$61 + 28$ kDa	NiFe Center	2[4Fe–4S] + [3Fe–4S]
	Wolinella succinogenes	$64 + 32 + 19$ kDa		2[4Fe–4S] + cytochromeb
CO dehydrogenase	*M. thermoacetica*	71 kDa	$NiFe_4S_4$ cluster	2[4Fe–4S] + 1 *bridged* [4Fe–4S]
	Rhodospirillum rubrum	61.8 kDa	$NiFe_4S_4$ cluster	2[4Fe–4S] + 1 *bridged* [4Fe–4S]
	C. hydrogenoformans	64.5 kDa (CODHII)	$NiFe_4S_5$ cluster	2[4Fe–4S] + 1 *bridged* [4Fe–4S]
Acetyl-CoA Synthase	*M. thermoacetica*	78 kDa	$NiNiFe_4S_4$ cluster	
	C. hydrogenoformans	73.3 kDa (CODHIII)	$NiNiFe_4S_4$ cluster	
Methyl-CoM reductase	Methanogenic bacteria	65 (Ni protein), 46, and 35 kDa	Ni tetrapyrrole (hydrocorphin)	
Superoxide Dismutase	Streptomyces		4–5 coordinate Ni site	
Gloxylase I	*E. coli*	14.9 kDa	6-coordinate Ni site	
Aci-reductone dioxygenase	*K. pneumonia*	20.2 kDa	6-coordinate Ni site	

Ni^{2+} generally adopts octahedral or tetragonally distorted octahedral geometry, but square-planar (diamagnetic) and tetrahedral (high-spin) geometries are well known. It forms tight complexes with histidine ($\log K_f = 15.9$), a property exploited in affinity tagging of engineered proteins for easy purification, and, among the first-row transition metals, is second only to Cu(II) in its ability to complex with acidic amino acids ($\log K_f = 6–7$).**[15]** Square-pyramidal and trigonal bipyramidal Ni^{2+} complexes have also been reported. Ni^{1+} generally contains distorted octahedral or square-planar geometry, while Ni^{3+} is usually low spin, with distorted octahedral or trigonal bipyramidal geometry. Redox changes in Ni during redox activation and catalysis are often accompanied by changes in the geometry and spin state.

2 UREASE (EC 3.5.1.5)

Urease, which catalyzes the reaction described by equation (1) (Table 1), was the first Ni enzyme to be identified.**[16]** A relatively recent review on urease is available.**[17]** Ironically, although urease was the first enzyme to be crystallized, it was not recognized at that time to be a metalloenzyme. A di-Ni hydrolase, urease catalyzes the

Figure 1 Nickel centers in Enzymes. (a) dinuclear center of urease (1EJX). The two nickel ions are bridged by a hydroxide bridge and the two oxygens from K217*, which is a carbamylated lysine residue. Each Ni ion binds an additional water ligand. (b) The dinuclear NiFe center of the reduced active state of the NiFe–Se hydrogenase from *desulfomicrobium baculatum* (1CC1).**[4]** The Se–Cys residue corresponds to C543 in *D. fructosovorans* and appears to be the general base in the heterolytic H_2 cleavage reaction. The Fe site contains 2 CN and 1 CO ligands. Besides the NiFe dinuclear center, this enzyme contains 3 [4Fe–4S] clusters. (c) The Ni tetrahydrocorphinoid active site of MCR (1HBN).**[5]** The oxygen from the side chain of glutamine-147 axially coordinates to the Ni. (d) The [2Ni–4Fe–4S] site of the *M. thermoacetica* ACS (1MJG).**[6]** A tetragonally distorted Ni ion, called the proximal Ni (Ni_p) bridges the [4Fe–4S] cluster and the square-planar Ni, called the distal Ni (Ni_d). Although Cu was present in the original structure, Ni has been shown to be the active metal at the Ni_p site (see text). (e) The [Ni–4Fe–5S] site of the *C. hydrogenoformans* CODH (1JJY).**[7]** In the *R. rubrum* CODH, the sulfur from the homolog of C526 replaces the sulfide bridge in the Ni–Fe subsite (1JQK).**[8]** (f) The Ni active-site of E. coli glyoxylase-I (1F9Z) (g) The square-planar Ni active site of superoxide dismutase (1G0D). (h) The octahedral Ni site of aci-reductone dioxygenase (1M4O).**[9]** (i) The Ni-bound regulatory domain of NikR (1Q5Y).**[3]** The Ni ions are shown in cyan, sulfur in yellow, and iron in red

hydrolysis of urea to yield two moles of ammonia and carbonic acid. The ammonia can then serve as a nitrogen source. Urease also is a virulence factor that participates in GI tract infection by *Helicobacter pylori*. Urease is found in bacteria, plants, fungi, and invertebrates. Jack bean urease has a 545 kDa hexameric quaternary structure, with six identical 91 kDa subunits, while the *Klebsiella aerogenes* urease consists of three copies each of three smaller subunits (UreABC) (i.e. it is a homotrimer of the heterotrimeric unit), in which the larger UreC subunit (60.3 kDa) contains the dinuclear active site.

The structures of the ureases from *Klebsiella aerogenes*,**[18,19]** *Bacillus pasteurii*,**[20]** *H. pylori*,**[21]** and jack bean are known. The active site contains a dinuclear Ni–Ni center bridged by a carbamylated lysine residue and a hydroxy group (Figure 1(a)). Based on MCD and magnetic susceptibility measurements, the two Ni ions appear to be high spin Ni(II) ($S = 1$) and become strongly antiferromagnetically coupled when the inhibitor β-mercaptoethanol is bound ($J = -40\,\text{cm}^{-1}$).**[22]** Synthesis of this metallocenter is a multistep process that has been recently reviewed**[1,2]** in which several accessory proteins (UreDFG) form a complex with apourease (UreABC in bacteria like *K. aerogenes*) and promote assembly of the Ni ions into the urease apoenzyme by UreE, carbamylation of lysine with carbon dioxide, and GTP hydrolysis by UreG. In bacteria, the accessory proteins are encoded adjacent to the urease structural genes, and, in some organisms, the gene cluster contains a Ni permease. The following complexes have been characterized: UreABCD, UreABCDF, and UreABCDFG. UreE, whose structure is known,**[23,24]** appears to be the metallochaperone that donates Ni to apourease. UreE contains a metal-binding domain and a Hsp40 chaperone domain. In *H. pylori*, there is evidence that the hydrogenase accessory proteins HypA and HypB are involved in urease assembly.

What features of the active site are responsible for the 10^{14}-fold rate enhancement over the uncatalyzed reaction? Urease can hydrolyze 3500 molecules of urea per second.**[25]** The bridging electrophilic carbamate group on the modified lysine residue stabilizes the dinickel center, which appears to be mechanistically significant since the enzyme is only active when both Ni are present in the active site. The Ni_2 ion has a nearly perfect octahedral coordination while Ni_1 shows a slightly distorted square-pyramidal coordination. The two Ni are bridged by the carbamate of lysine and by a hydroxide bridge. A proposed bimetallic mechanism (Figure 2) is based on computational studies,**[26,27]** model studies,**[28]** on the 2.0 Å X-ray structure of the diamidophosphoric acid-inhibited form of the enzyme (regarded as a transition state analogue),**[20]** and the 1.85 Å structure of the phosphate-inhibited form.**[29]** It appears that urea binds in a bidentate manner based on the X-ray crystallographic structure of the DAP-inhibited urease and on computational studies as shown in Figure 2. The urea carbonyl group is expected to bind to the most electrophilic Ni_1 while one amino group of urea would coordinate to Ni_2. The hydroxide bridge between Ni_1 and Ni_2 is apparently parallel to the bound urea, which would facilitate nucleophilic attack of the bridging hydroxide on urea carbonyl carbon atom to give a tetrahedral intermediate. Replacement of the hydroxide bridge by fluoride inhibits urease, suggesting that the bridging hydroxide is responsible for hydrolysis of urea. Either the bridging hydroxide or His320 would then protonate the leaving ammonia molecule. However, it remains possible that a metal bound water molecule (W2) would act as the nucleophile. Figure 2 shows attack by the bridging OH to generate an OH^- nucleophile that attacks bound urea, liberating NH_2, which is protonated by an active-site histidine residue (or perhaps the proton release to form ammonia, and carbamate, which spontaneously and nonenzymatically hydrolyzes to another mol of ammonia and carbonic acid. Alternatively, it has been suggested that one of the bound water molecules facilitates the hydrolysis of the first product, carbamate.

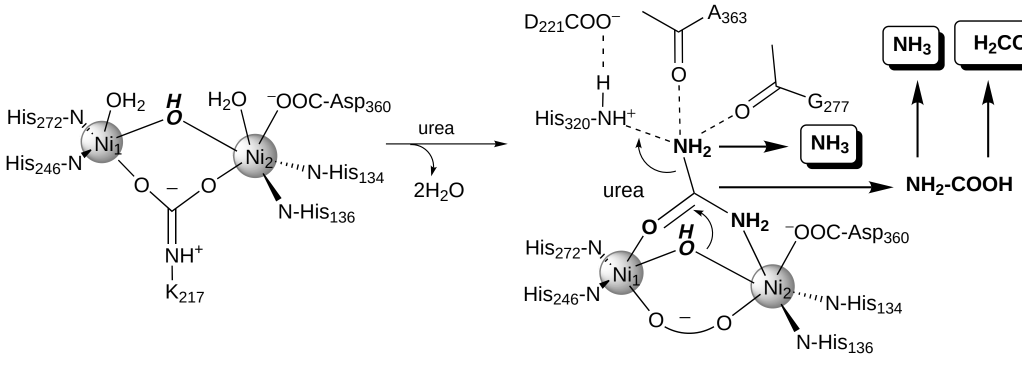

Figure 2 Mechanism of urease. This proposed mechanism features binding of urea through its carbonyl group to one of the Ni ions, making the carbon subject to nucleophilic attack by the bridging hydroxide leading to liberation of NH_2, which is protonated by $H^{32}0$ to form ammonia, and carbamate, which hydrolyzes to another mole of ammonia and carbonic acid. The same mechanism with proton transfer from water (instead of histidine) to ammonia is another possibility. Another possibility would be urea binding in a monodentate manner with a terminal hydroxide on Ni2 as the nucleophile

3 NiFe HYDROGENASES (EC 1.12.1.2, 1.2.2.1, OR 1.18.99.1)

Marjory Stephenson and Leonard Stickland proposed the name in 1931 for the enzyme that catalyzes equation (1), the oxidation of H_2 gas (Reaction 2, Table 1).[30] Hydrogenases are essential and versatile components of microbial metabolism that can catalyze the consumption as well as the production of H_2 gas.[31] Hydrogenases have been recently reviewed.[32,33] Uptake hydrogenases generate energy by coupling H_2 oxidation to the reduction of terminal electron acceptors like oxygen, nitrate, sulfate, CO_2, and fumarate. Hydrogenotrophic organisms catalyzing H_2 oxidation are important in the global carbon cycle because elevated H_2 levels inhibit the anaerobic biodegradation of biomass. On the other hand, evolving hydrogenases siphon off excess reducing equivalents by transferring electrons to protons. Hydrogenases also are key to the processes of interspecies H_2 transport and H_2 cycling, which have been studied in sulfate reducers that generate a proton gradient during growth on organic substrates in the presence of SO_4.[34] Efficient utilization of H_2 is accomplished by growth of microbes growing syntrophically, for example, by fatty- and aromatic acid-degrading fermentative bacteria growing in syntrophic association with a hydrogen-using microbes.[35] This association is important because fatty/aromatic acid degradation is thermodynamically unfavorable only at very low H_2 concentrations (equation (1)).

$$2H^+ + 2e^- \longleftrightarrow H_2 \quad \Delta E^{\circ\prime} = -414\,\text{mV} \tag{1}$$

Hydrogenases are classified into four categories: the NiFeSe, NiFe, Fe-only, and one represented by N^5,N^{10}-methylenetetrahydromethanopterin dehydrogenase that was previously thought to lack metals[36] but now has been shown to contain a metallic cofactor.[37] The immediate electron donors/acceptors are metalloproteins like ferredoxin or cytochromes or an organic cofactor, like NAD. When the natural electron acceptors are limiting, some metalloenzymes in their reduced states, like pyruvate:ferredoxin oxidoreductase and carbon monoxide dehydrogenase, can reduce protons to H_2.[38] Nitrogenase also generates H_2 with each cycle of N_2 reduction. This review will focus on the Ni enzymes.

All [NiFe]-hydrogenases contain at least two subunits ('large' and 'small') of approximately 60 and 30 kDa, containing a nickel center and at least one [4Fe−4S] cluster. The active site of H_2 oxidation/reduction by the Ni hydrogenases, located in the large subunit, is shown in Figure 1(b). This binuclear NiFe center is coupled to a 'wire' within the small subunit which is usually composed of three Fe–S clusters. The enzyme from *Desulfomicrobium baculatum*, shown in Figure 1(b), contains 3[4Fe−4S] clusters, although 2[4Fe−4S] and one [3Fe−4S] clusters are frequently observed. The hydrogenase shown here is a member of the subclass of the nickel-hydrogenases that contain a selenocysteine ligand.

Besides the reactions described above, hydrogenases also catalyze hydrogen isotope exchange, for example, between $^1H_2$ gas and deuterium oxide (equation (2)) and interconversion of *ortho-* and *para*-hydrogen.[39] These reactions are expected to proceed through a metal-hydride intermediate, as first proposed in 1959 based on studies of the H-D exchange reaction using D_2 and H_2O.[40] It is now generally accepted that hydrogenase catalyzes heterolytic cleavage of H_2 (equation (3)) followed by electron transfer to an external acceptor (equation (4)).[41] Electron transfer from the bound hydride to an external electron carrier protein is believed to be the function of the FeS clusters, which form an intramolecular 'wire'.

$$D_2O + H_2 \longleftrightarrow HDO + HD \tag{2}$$

$$\text{E–Ni} + H_2 \longleftrightarrow \text{E–Ni–H}^- + H^+ \tag{3}$$

$$\text{E–Ni–H}^- + \text{Acceptor}_{\text{ox}} \longleftrightarrow \text{E–Ni} + H^+ + \text{Acceptor}_{\text{red}} \tag{4}$$

The structure of the catalytic center of the NiFe hydrogenase is shown in Figure 1(b). X-ray crystallographic studies showed that the Fe site of the binuclear NiFe center contains three nonexchangeable diatomic ligands[42] that were identified as one CO and two cyanide ligands by FTIR spectroscopy,[43] and assigned in the structure by their interaction with the protein (hydrogen bonds in the case of CN, a hydrophobic pocket in the case of CO).[42,43]

EPR spectroscopic studies have uncovered various redox states of the Ni hydrogenases (Scheme 1). The oxidized state of the [Ni]-hydrogenases exhibit EPR signals (called Ni-A and Ni-B) that disappear on reduction and have been attributed to the Ni^{3+} oxidation state, with a $(d_{z}^{2})^1$ ground state (*see Splitting, Crystal Field & Molecular Orbital*).[44] The states of the enzyme that elicit these signals are called Form A and Form B. Neither Form A (an already oxidatively inactivated form) nor Form B is catalytically active, and neither is sensitive to inactivation by O_2, indicating that both are oxidized forms.

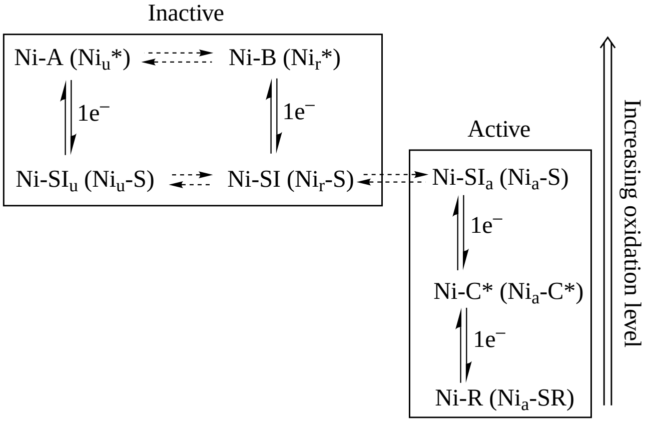

Scheme 1 The states of hydrogenase described here. Only the Ni–C* and Ni–R states appear to be in equilibrium with H_2. This scheme is revised from Ref. 49

Form A has been called the unready state (Ni_u) because it requires prolonged treatment with a reductant (like H_2) to undergo conversion to an EPR-silent state called SI_r (where the 'r' designates 'ready'), which is in redox equilibrium with Form B. Apparently this is a self-activation that occurs by electron transfer from the small amount of active enzyme present in the solution. An oxidizing agent is required to oxidize SI_r to Form B, indicating that Form B contains a Ni^{3+} state and SI_r contains a Ni^{2+} state. Form A and B are not in equilibrium; Form A must be reduced and reoxidized to convert it to Form B. SI_r is in equilibrium with SI_a, which is an active form that can be reduced to Form C, another EPR-detectable state, called Ni-C.

In the Ni-A state, the binuclear center appears to contain a hydroxide ligand that points toward a gas channel.[45] H_2 treatment generates an EPR-detectable species (Ni-C) that appears to contain a bound state of hydrogen, based on ENDOR and ESEEM spectroscopy.[46] ENDOR studies demonstrate that an OH^- ligand bridges the Ni and Fe sites in the Ni-A and Ni-B states and is lost upon reduction to the Ni-C state.[47] This is consistent with XAS[48] and electrochemical[49] studies indicating that a hydroxo ligand present in Form A, Form B and SI_u, is removed during activation at the SI_r level. Photolysis of the Ni-C state at low temperatures alters its EPR signal to form the Ni-L state at a rate that is six-fold slower when $^2H_2$ is used.[50] Ni-C forms and decays to an EPR-silent state at rates consistent with its involvement in catalysis.[51] The properties just described indicate that Ni-C is an intermediate state in the catalytic cycle. Although whether or not Ni-C contains a hydride species remains controversial, single-crystal EPR studies were interpreted to indicate that Ni-C can be described as a Ni(III) species with a bridging hydride between the Ni and the Fe atoms and that the photolysis product, Ni-L, is a Ni(I) species with a proton removed from the bridging position[52] or from one of the Cys ligands. If Ni-C does contain a hydride, perhaps it can be described in one of the following formulations: $Ni^I \cdot 2H^+$, or $Ni^{III} \cdot H_2$, or $Ni^{III} \cdot H^-$, although a Ni(I) state appears to be ruled out by XAS experiments.[48]

One of the shocking discoveries in the hydrogenase field was that the active site contains diatomic ligands, which were identified by IR spectroscopy.[53] The IR bands from the diatomic ligands are sensitive indicators of the state of the enzyme. In the Ni-A state of the *D. fructosovorans* [NiFe] hydrogenase, the CO stretching mode appears at $1947\,cm^{-1}$, while the CN bands appear at 2096 and $2084\,cm^{-1}$.[54] These bands appear at 1938, 2060, and $2074\,cm^{-1}$ in the Ni-R state and at 1951, 2074, and $2086\,cm^{-1}$ in the Ni-C state. These strong-field ligands are thought to maintain the Fe atom in the binuclear site in its low-spin ferrous state as indicated by Mössbauer spectroscopy.[55] This type of coordination appears to favor the binding of molecular hydrogen or hydride to the active site.

Besides identifying the tightly bound intrinsic CO and CN ligands to the Fe site of the NiFe center, IR studies provide evidence that another CO can interact weakly with Ni in the reduced Ni-C state, which blocks both electron and proton transfer at the active site.[54]

The biosynthesis of all the [NiFe] hydrogenases, including the H_2-sensing regulatory protein,[56] requires the function of seven Hyp proteins (HypA, HypB, HypC, HypD, HypE, HypF, and HypX) to assemble the [NiFe] active site. Their functions and the assembly process has been reviewed.[1,57] Before Ni is incorporated, the $Fe(CO)(CN)_2$ site appears to be assembled by HypD, E, and F, the diatomic ligands apparently derived from carbamoyl phosphate.[58] The other Hyp proteins, two of which are similar to UreE and UreG and a protease (HyaC, D, and I) are involved in Ni incorporation and maturation of hydrogenase to its active state.

H_2 accesses the active site through a tunnel in the protein,[59] where it forms a complex with the NiFe catalytic center buried 30 Å beneath the surface and then catalyzes heterolytic cleavage to form a Ni-hydride and a proton. Isotope effect studies indicate that electron transfer is rate limiting in H_2 oxidation and proton transfer is rate limiting in proton reduction.[60] When the NiFe hydrogenase is absorbed to a pyrolytic graphite edge-plane (PGE) electrode and studied by voltammetric methods, the rate of H_2 oxidation is diffusion-controlled (k_{cat}/K_m of 10^8–$10^9\,M^{-1}\,s^{-1}$), with a turnover number reaching $9000\,s^{-1}$ at $30\,°C$; thus the NiFe center has a similar catalytic activity to platinum.[61]

After binding and heterolytically cleaving H_2, the Ni-C state apparently is formed, which contains the bound hydride. One of the terminal cysteine ligands of the active-site nickel atom (the Se–Cys residue in Figure 1(b)) is considered to be the general base in the heterolytic cleavage reaction by binding the released proton. This conclusion is based on X-ray diffraction data, X-ray absorption spectroscopic studies, EPR, model complex studies, and theoretical calculations. A conserved glutamic residue (E25 in *D. fructosovorans* or E18 or *D. gigas*) that forms a hydrogen bond with this cysteine/selenocysteine residue[62] appears to be the first step in a proton transfer chain that couples the base catalyst to eventual proton release to the solvent.

A fifth type of hydrogenase is in the NiFe class, but is oxygen insensitive and has very low catalytic activity, functioning not as an enzyme, but as a hydrogen sensor.[63] Like the catalytic hydrogenases, this class of proteins contains two subunits encoded by *hupUV* in *Rhodobacter capsulatus* or *hoxBC* in *R. eutropha*). Remarkably, this protein has spectroscopic properties similar to the standard NiFe hydrogenase with 2 CN and 1 CO bound to the low-spin Fe site, indicating high structural homology between the two enzyme classes.[64] Why isn't this enzyme active? It apparently is blocked in the Ni-C state. Further reduction to the Ni-R is apparently required for catalytic turnover (above).[64] The regulatory mechanism involves interaction between the NiFe protein with histidine kinase and response regulator proteins, which modulate transcription of the hydrogenase-related genes.[65]

4 CARBON MONOXIDE OXIDOREDUCTASES (CODH, EC 1.2.99.2)

CODH is at the heart of the ability of microbes to use CO as a sole carbon and electron source. CODH rapidly and efficiently oxidizes CO at rates between 4000 and 40 000 s^{-1}, depending on the source, and reduces CO_2 ($\sim 11\ s^{-1}$) with virtually no overpotential and under mild conditions. CO biochemistry and bioinorganic chemistry has been most thoroughly studied in enzymes from the anaerobic microbes, *Moorella thermoacetica. Rhodospirillum rubrum, Carboxydothermus hydrogenoformans*, and the aerobic carboxydobacterium, *Oligotropha carboxidovorans*. Only the anaerobic CODHs will be discussed here since the aerobic CODHs lack Ni and have a Mo-pterin active site (*see* ***Molybdenum: MPT-containing Enzymes***). CODH and ACS have been the subjects of several reviews.[66–68]

There are two types of Ni-CODHs: one class is a homodimer and catalyzes only CO oxidation, while the other also contains acetyl-CoA synthase activity on a separate subunit. The *R. rubrum* CODH is encoded by *cooS*, which is part of the *coo* regulon consisting of at least two operons whose expression is induced at least 1000-fold when the microbe senses the presence of CO. CO is sensed and the *coo* gene cluster is regulated by the heme protein, CooA, which is a member of a large family of transcriptional activators that includes the cAMP regulatory protein (CRP) and fumarate nitrate regulatory protein (FNR).[69] The first operon in the *coo* gene cluster includes a NiFe hydrogenase and proteins just described that are involved in generating the mature enzyme, while the second operon consists of CODH (*cooS*), a membrane-associated electron transfer FeS protein (*cooF*), and genes involved in generating the NiFeS active site of CODH. Metal center assembly proteins include CooC, a Ni insertase similar to UreG, and CooJ, which is similar to UreE.[70] The proteins involved in Ni incorporation into CODH and their functions have been reviewed.[71]

The CODHs from *R. rubrum, C. hydrogenoformans*, and *M. thermoacetica* have been most extensively studied and structures are known for each of these proteins. All ligands at the active site, as well as some residues proposed to facilitate acid-base chemistry at the active site, are conserved among these proteins, even those that associated with ACS. The X-ray crystal structure of CODH reveals a mushroom-shaped homodimeric enzyme containing 5 metal clusters (Clusters B, C, and D).[6–8,72] Electrons generated during CO oxidation at the C-Cluster are transferred to a ‘wire’ consisting of the B-, a typical [4Fe–4S] cluster, and the D-Cluster, a [4Fe–4S] cluster with two cysteine ligands contributed by each subunit. As shown in Figure 1(e), the C-Cluster is a $NiFe_4S_{4-5}$ cluster that can be viewed as a [3Fe–4S] cluster bridged to a binuclear NiFe center. Controversy remains about whether the Ni and Fe are bridged by a sulfide or by a cysteine sulfide (C526 in *C. hydrogenoformans*). Adopting a distorted five-coordinate geometry with 4S and another unidentified ligand, the Ni site is part of the cube. In the *C. hydrogenoformans* structure, all 4Fe atoms are bridged to Ni through inorganic sulfide ligands, with Ni–Fe distances distributed over 1 Å (2.8, 2.9, 3.3, and 3.7 Å),[7] while in the 2.8 Å resolution structure of CO-treated Rr-CODH,[8] all four Ni–Fe distances are clustered within a much tighter range between 2.6 and 2.8 Å and the external Fe is bridged to the Ni by a cysteine S ligand. Ni EXAFS studies of ‘as-isolated’ and CO-treated *C. hydrogenoformans* CODH indicate that CO treatment and/or reduction induces a major structural rearrangement of the C-Cluster to adopt a conformation similar to that observed in the *R. rubrum* structure.[73]

Like the NiFe center of hydrogenase, the C-Cluster exists in several redox states, including C_{ox}, C_{red1}, C_{int}, and C_{red2}. C_{red1} and C_{red2} can be observed by EPR spectroscopy. The [3Fe4S] component is proposed to remain in the 1- redox state ($2Fe^{2+}/1Fe^{3+}/4S^{-2}$) throughout most of the catalytic mechanism, except in the C_{red2} and C_{int} states where it undergoes 1 electron reduction to the 2- state ($3Fe^{2+}$), with most of the redox changes occurring at the NiFe center (Figure 3).

The *C. hydrogenoformans* CODH can catalyze CO oxidation with a turnover number of 39 000 s^{-1} and a k_{cat}/K_m of over $10^9\ M^{-1}\ s^{-1}$.[78] The first step in the CODH reaction is binding of substrates, CO and H_2O or CO_2 and protons to Cluster C. Dobbek *et al*. described a hydrophobic CO channel in the COOH-terminal domain of ACS and a hydrophilic positively charged water channel that connects the surface and the C-Cluster in the *C. hydrogenoformans* CODH II.[7]

Then, after CO and water bind, it is proposed that the water molecule binds to a metal center, presumably Fe and perhaps in a bridging position. The active metal-hydroxide is then proposed to attack the M-CO complex to form M-COOH. Elimination of CO_2 and a proton would leave the C-Cluster two-electrons more reduced, presumably in the Cred2 state. Conversion of Cred1 to Cred2 occurs very rapidly, as studied by rapid quench EPR.[75] Several basic residues near the C-Cluster, including Lys563, His93, and His261 and several other histidine residues, described as a histidine tunnel, were proposed to participate in these acid-base reactions. The His tunnel leading from the active site to the surface is proposed to deliver protons that are liberated during the reaction to the solvent. Cred2 then transfers its electrons to the B and D clusters, which in turn reduce the external electron carriers. The scheme shown in Figure 3 indicates the existence of a diamagnetic form of the C-Cluster (Cint)[77] as an intermediate in the reduction of the B and D clusters.

5 ACETYL-CoA SYNTHASE (ACS) (EC 2.3.1)

ACS catalyzes the synthesis of acetyl-CoA from CO, CoA, and a methyl group donated by a methylated corrinoid iron–sulfur protein (Reaction 4, Table 1). In the CODH-only enzymes like CODHI and II from *C. hydrogenoformans* and *R. rubrum*, there is evidence for a channel between the surface and the C-cluster (above). On the other hand, in CODH/ACS,

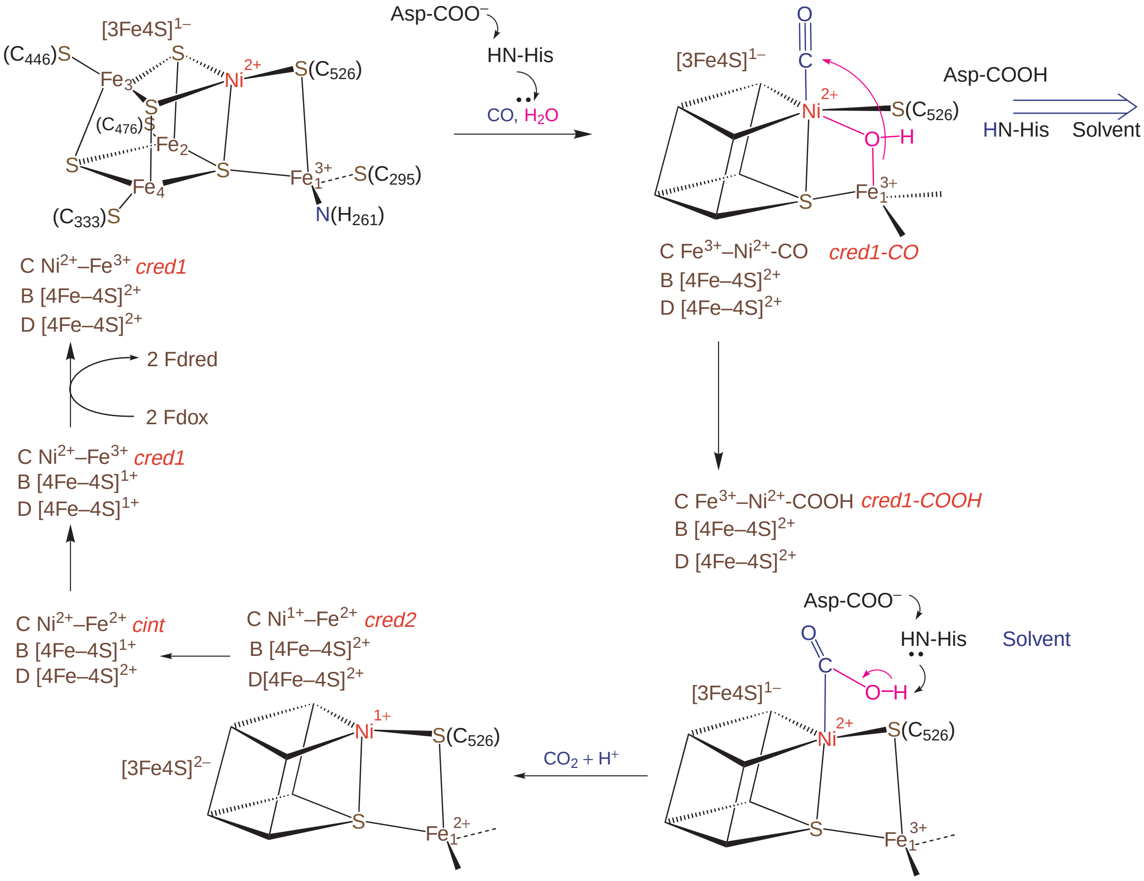
[3Fe4S]1–
(C446)S
Fe3
S
Ni 2+
S(C526)
(C476)S
S
Fe2
S
Fe4
S
Fe1 3+
S(C295)
(C333)S
N(H261)
Asp-COO–
HN-His
CO, H2O
C Ni2+–Fe3+ cred1
B [4Fe–4S]2+
D [4Fe–4S]2+
2 Fdred
2 Fdox
C Ni2+–Fe3+ cred1
B [4Fe–4S]1+
D [4Fe–4S]1+
[3Fe4S]1–
O
C
Ni 2+
S(C526)
O–H
Fe1 3+
S
Asp-COOH
HN-His Solvent
C Fe3+–Ni2+-CO cred1-CO
B [4Fe–4S]2+
D [4Fe–4S]2+
C Fe3+–Ni2+-COOH cred1-COOH
B [4Fe–4S]2+
D [4Fe–4S]2+
Asp-COO–
HN-His
Solvent
O
C
O–H
[3Fe4S]1–
Ni 2+
S(C526)
S
Fe1 3+
CO2 + H+
C Ni2+–Fe2+ cint
B [4Fe–4S]1+
D [4Fe–4S]2+
C Ni1+–Fe2+ cred2
B [4Fe–4S]2+
D[4Fe–4S]2+
[3Fe4S]2–
Ni 1+
S(C526)
S
Fe1 2+

Figure 3 Proposed CODH mechanism. This mechanism proposes that the active state is Cred1, consistent with recent electrochemical studies,[74] which contains a bridging hydroxide at the binuclear NiFe center that serves as the nucleophile to attack a Ni-bound carbonyl forming a Ni-carboxylate. This OH, which is formed by acid-base catalysis by indicated acid-base residues, is in the position of the bridging sulfide in the *C. hydrogenoformans* structure.[7] The enzyme is proposed to remain in the Cred1 redox state until formation of CO_2 when it becomes two-electrons reduced to the Cred2 state. Conversion of Cred1 to Cred2 occurs faster than electron transfer from Cred2 to the FeS clusters,[75,76] which in turn reduce external electron acceptors. The electron transfer reactions are proposed to occur through a diamagnetic Cint state.[77]

such a channel would be detrimental, since the purpose of these proteins is to generate CO from CO_2 and utilize the CO in acetyl-CoA synthesis. Accordingly, there is both biochemical[79,80] and structural[6,72] evidence for a CO channel or tunnel between the C-Cluster in the CODH subunit and the A-Cluster in the ACS subunit. Such a channel would couple CO production to its utilization, explain why only very low levels of CO escape during growth of acetogenic bacteria, and protect host organisms that harbor the microbes from being exposed to potentially toxic CO levels.

The X-ray crystal structures of ACS both free[81] and bound to CODH[6,72] are available. The active site, called the A-Cluster, is present in a domain that is most distant from the interface with the CODH subunit separating the A- and C-Clusters by over 75 Å. The A-Cluster (Figure 1(d)) consists of a [4Fe−4S] cluster bridged to a Ni site (Ni_p) that is bridged by a cysteine thiolate to another Ni ion in a square-planar thiolato- and carboxamido-type N_2S_2 coordination environment. The distal site resembles the mononuclear Fe site of nitrile hydratase in which two Cys side chains and two backbone N atoms coordinate the Fe with a Cys-X-Cys motif.[82] Thus, one can describe the A-Cluster as a binuclear NiNi center bridged to a [4Fe−4S] cluster, similar to the Fe-only hydrogenases in which a Cys residue bridges a [4Fe−4S] cluster and a binuclear Fe site. The distal Ni atom is coordinated by the side chains of two Cys residues and by two backbone N atoms. When CO binds to CODH/ACS, an EPR signal, called the NiFeC signal is elicited, which appears to reflect the active state of the enzyme.

There has been controversy about the metal occupying the proximal metal center. In one structure, Cu was in high occupancy,[6] while, in another structure, Ni was in one molecule and Zn in the other.[72] There was evidence that the CuNi enzyme is active;[6,83] however, several papers insisted that only the NiNi form is active.[72,81,84–86] Recent spectroscopic, enzymatic, and computational studies provide further evidence that the NiNi enzyme is active and that the CuNi and ZnNi forms are not.[87]

A longstanding problem in studies of ACS are the heterogeneous composition of the protein, with only 20–30% activity, reflected in the intensity of the NiFeC EPR signal, described above. After recognition that the vulnerability of the proximal metal site in the A-Cluster to substitution with different metals underlies this heterogeneity, a protocol was developed in which a Cu^{+1}-specific chelator is used to remove the Cu and Ni is added to reconstitute the di-Ni center, resulting in nearly homogeneous preparations of ACS with a NiFeC signal intensity of ~0.8 spins per mol.[87] Recent DFT calculations[88] indicate that the NiFeC signal derives from a $[4Fe{-}4S]^{2+}$ (net $S = 0$) cluster bridged to a Ni(I)($S = 1/2$) at M_p that is bridged to square-planar Ni(II) ($S = 0$) at M_d, with the spin predominantly on the Ni(I).

Figure 4 summarizes two proposed catalytic cycles for ACS. In a mechanistically related reaction sequence, called

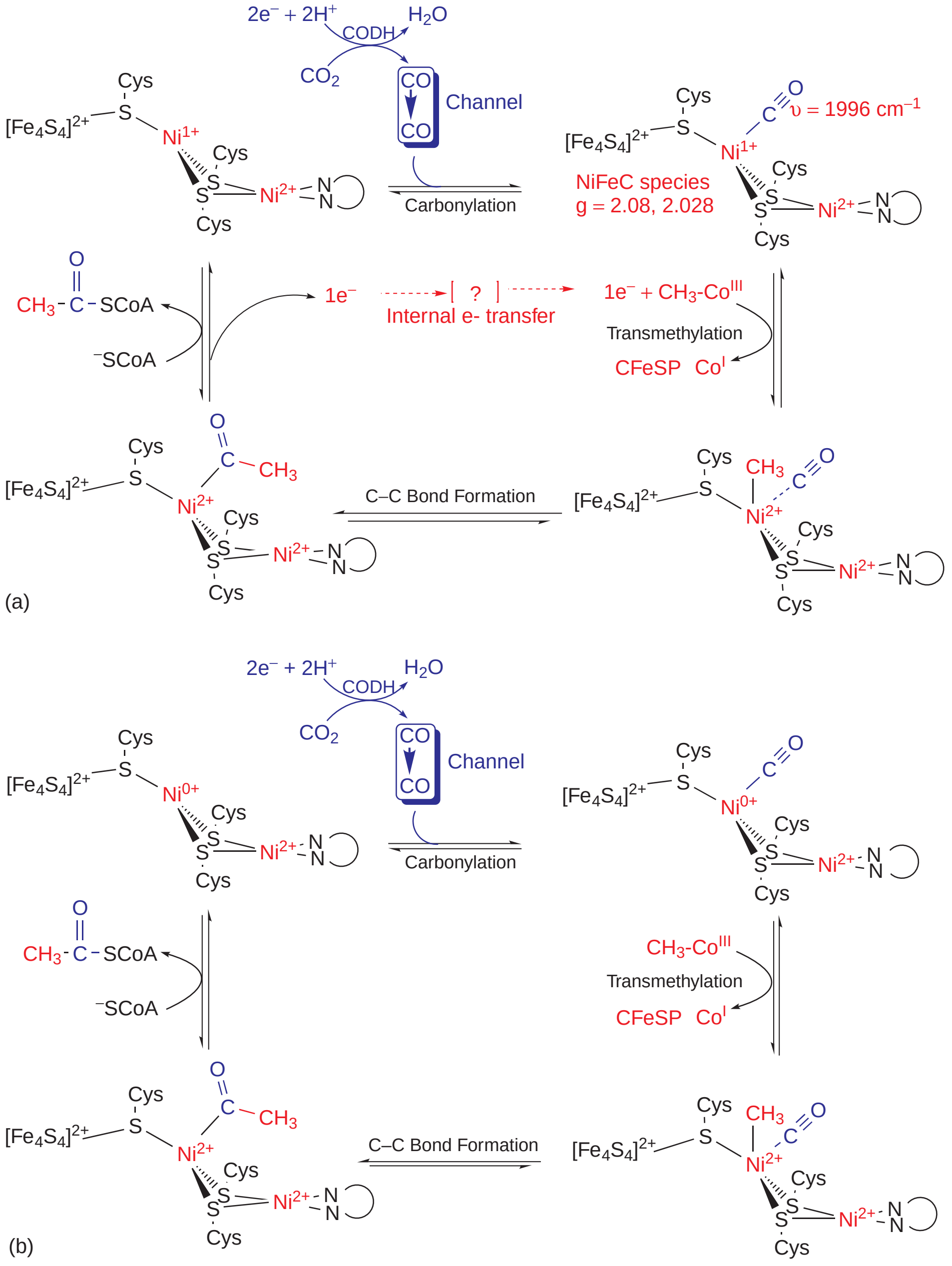
2e⁻ + 2H⁺
CODH
H2O
CO2
CO
CO
Channel
Carbonylation
Cys
[Fe4S4]2+
S
Ni1+
Cys
S
S
Ni2+
N
N
Cys
υ = 1996 cm−1
NiFeC species
g = 2.08, 2.028
CH3-C-SCoA
⁻SCoA
1e⁻
[?]
Internal e- transfer
1e⁻ + CH3-CoIII
Transmethylation
CFeSP CoI
C–C Bond Formation
CH3
Ni2+
(a)
Ni0+
CH3-CoIII
(b)

Figure 4 Proposed ACS mechanisms. The major difference between the two mechanisms is the oxidation state of the proximal Ni. In both cases, CO emerges from the channel and binds to the proximal metal of the A-Cluster to form a Ni–CO intermediate. Then, the Ni center performs nucleophilic attack on the methyl group of methylated CFeSP to form a $(CH_3)(CO)$ intermediate state of the A-Cluster. Then, carbon–carbon bond formation occurs by condensation of the methyl and carbonyl groups to form an acetyl-metal species. Finally, CoA binds to cleave the acetyl group as acetyl-CoA. See text for more details

the Monsanto or Reppe process, a rhodium complex catalyzes acetate formation from methanol and CO in the presence of HI through methyl-Rh, Rh-CO, and acetyl-Rh organometallic intermediates. ACS catalyzes the final steps of a biological process called the Wood–Ljungdahl pathway in which a methyl group, CO, and CoA are condensed to form acetyl-CoA at the A-Cluster of ACS. Although it also has been proposed that the methylation precedes carbonylation,[89] the first step in both reaction sequences proposed here is the binding of CO, emerging from the protein channel, to the A-Cluster to form a Ni–CO intermediate. In the top mechanism, the carbonylated enzyme is a Ni^{1+}-CO intermediate, the NiFeC species, which has been characterized by IR[90,91] and EPR[92] spectroscopy and has been shown to be catalytically competent in the pathway.[93] In the bottom mechanism, a diamagnetic Ni^0 active enzyme has also been proposed.[72] The next step is nucleophilic attack of the A-Cluster on the methyl group of methylated CFeSP to form a methylated state of the A-Cluster.[93] This reaction generates a diamagnetic product, which is easily accommodated into the bottom mechanism; however, this would require a one-electron reduction to accompany methylation if a diamagnetic CH_3–Ni^{+2} species is the product. This is proposed to occur through an internal electron transfer reaction, which could involve the FeS cluster. Then, carbon–carbon bond formation occurs by condensation of the methyl and carbonyl groups to form an acetyl-metal species. Finally, CoA would bind and cleave the acetyl group as acetyl-CoA. This would liberate two electrons, which would regenerate the Ni^0 state in the bottom mechanism. In the top mechanism, the electron transferred during the methylation would be returned and the other electron would be used to regenerate the Ni^{1+} active site. The overall reaction sequence is strongly inhibited by CO[94] and it appears that it is the methylation step that is inhibited.[93]

Based on the crystal structures, it is clear that the ACS subunit assumes two conformations: one in which the A-Cluster is inaccessible and the channel accessible to solvent and another in which the A-Cluster is accessible and the CO channel is inaccessible to solvent. Recent biochemical evidence indicates that major conformational changes occur during the catalytic cycle of acetyl-CoA synthesis.[95]

6 METHYL-COENZYME M REDUCTASE (MCR) (EC 2.8.4.1)

MCR catalyzes the final step in the biological synthesis of methane. Methanogenesis occurs in a unique group of microbes, called methanogens, which are members of the so-called third kingdom of life, the archaea. These organisms use very simple substrates as a source of carbon and energy, including H_2/CO_2, methanol, CO, methylamines, acetic acid, and methyl mercaptans. All biologically produced methane is the result of MCR activity and has reached a global emission rate of 560 million metric tons per year and a 2002 level of 1.75 ppm.

MCR catalyzes the conversion of methyl-coenzyme M (methyl-SCoM) and N-7-mercaptoheptanoylthreonine phosphate (CoBSH) to methane and the mixed disulfide CoBS-SCoM (Reaction 5, Table 1). Methanogenesis and MCR have both been reviewed fairly recently.[96,97] At the active site of MCR is Coenzyme F_{430} (Figure 1(c)), which is a nickel tetrapyrrole (specifically, a tetrahydrocorphin), exhibiting a maximum absorption at ∼430 nm in its Ni^{2+} state, making it bright yellow. F_{430}, like porphyrin, chlorophyll, and vitamin B_{12}, is derived from 5-aminolevulinic acid. The structure of free F_{430} was elucidated by X-ray crystallographic and NMR methods. It is the most reduced tetrapyrrole in nature, containing four conjugated double bonds linking Rings B, C, and D and one isolated double bond in Ring A. Based on X-ray crystallographic studies of the protein, F_{430} forms the base of a narrow well that accommodates the two substrates and shields the reaction from solvent.[5] The Ni site is ligated by the four tetrapyrrole N atoms, a side chain oxygen of a glutamine residue, and a sixth ligand that differs with the state of the enzyme. The structures of the inactive nickel (II) enzyme in complex with CoM and CoB ($MCR_{ox1-silent}$) and in complex with the heterodisulfide CoM-S-S-CoB product (MCR_{silent}) have been resolved at 1.16 Å and 1.8 Å resolution, respectively.[98]

Several states of MCR exhibit EPR signals. This includes MCR_{red1}, which is accepted to contain Ni^{1+} and is the active state of the enzyme. This assignment is well accepted based on the similarity of its UV-visible and EPR spectra with isolated Ni^IF_{430} and on DFT computations.[99,100] Several spectroscopic characteristics led to the hypothesis that red1 may also have undergone tetrapyrrole ring reduction; however, electrochemical,[101] and MCD and computational studies[100] demonstrate that this is incorrect – red1 retains the five double bonds present in the Ni^{2+} states. Another important form is MCR_{ox1}, which retains the basic symmetry of the red1 EPR signal and similar nitrogen hyperfine splitting constants. Recent computational studies indicate that the ox1 state should be described as a Ni^{2+} state coupled to a thiyl radical (formally equivalent to a Ni^{3+} state).[100]

EPR spectroscopic studies with ^{33}S-labeled coenzyme M demonstrate that, when CoBSH and CoMSH are both present, the thiol group of CoMSH interacts with the Ni(I) of F_{430}.[102] Apparently, CoBSH is required for MCR to exhibit this interaction.

Steady-state kinetic and crystallographic studies support an ordered ternary complex mechanism in which first methyl-SCoM and then CoBSH must bind before methane is formed. Presteady-state kinetic studies indicate that CoBSH is required for even a single turnover of methane formation, suggesting that CoBSH is integrally involved in the steps leading up to cleavage of the C–S bond of methyl-SCoM.[103] This may indicate that CoBSH forms an adduct with methyl-SCoM (a methylsulfuranyl species) before the methyl group is cleaved or that CoBSH is an obligate proton donor for the reaction. In many proposed mechanisms, a methyl-Ni intermediate is

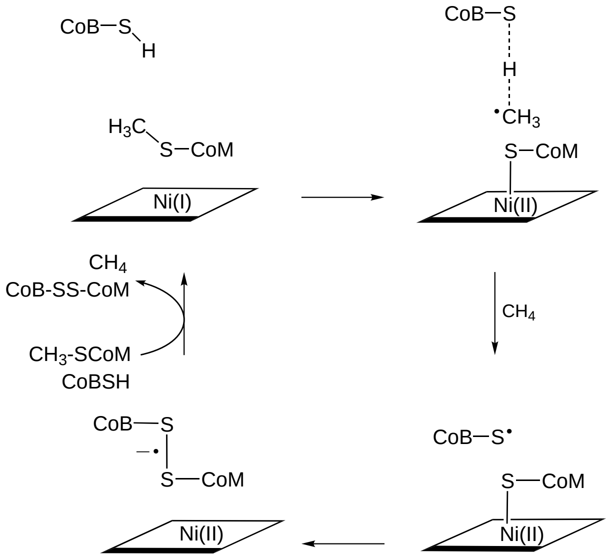

Figure 5 Proposed MCR mechanism. See text for details

included based on studies demonstrating that the Ni(I) form of the pentamethyl ester of F_{430} reacts with activated methyl donors (e.g. methyl sulfonium ions and methyl iodide) to yield methane through protonation of a methylnickel intermediate (*see* ***Nickel: Organometallic Chemistry***).

Density functional calculations indicate that a methyl-Ni species could not be part of the catalytic cycle of methane formation; instead methane formation occurs through a radical mechanism (Figure 5) in which a methyl radical abstracts a hydrogen atom from CoBSH to form methane.[104] *Step 1* involves homolytic cleavage of the C-S bond of methyl-CoM to generate a methyl radical and a thiyl radical on CoM. The thiyl radical is then proposed to accept an electron from Ni(I) to generate Ni(II) and the CoM-S^- thiolate. Negative charge on the thiolate is proposed to be stabilized by H bonding interactions from two active site tyrosine residues. In *Step 2*, the methyl radical is proposed to abstract a H-atom from CoBSH to form methane and a thiyl radical on CoB. This step should lead to inversion of stereochemistry at carbon. If so, the H-atom transfer to the methyl radical must occur before the methyl group has a chance to rotate in the active site. *Step 3* involves formation of a S–S bond between CoBS and $CoMS^-$, to generate a disulfide anion radical, while *Step 4* involves reduction of Ni(II) to regenerate active Ni(I) F430, release of products, and binding of substrates.

7 SUPEROXIDE DISMUTASE (SOD) (EC 1.15.1.1)

SOD protects cells against the detrimental effects of superoxide, a reactive oxygen species, by catalyzing the conversion of superoxide to hydrogen peroxide and oxygen (Reaction 6, Table 1).[105] The dismutation reaction catalyzed by SODs proceeds via a mechanism wherein the metal is first reduced and then reoxidized by superoxide (Figure 6). Since the potentials involved in the oxidation and reduction of superoxide at pH = 7 are −0.33 and 0.87 V, respectively,[106] the metal center must have a redox potential between these extremes. Four types of SODs are known and are typically classed by their active-site metal composition: MnSOD, FeSOD, CuZnSOD, and NiSOD. The NiSOD, which has been identified in some Streptomyces[107] and cyanobacteria, has approximately the same catalytic rate constant as the CuZn enzyme, about $10^9\ M^{-1}\ s^{-1}$.[108]

$$M^{(n+1)} + O_2^{\bullet -} \longrightarrow M^{(n+)} + O_2$$
$$M^{(n+)} + O_2^{\bullet -} + 2H^+ \longrightarrow M^{(n+1)} + H_2O_2$$
$$2O_2^{\bullet -} + 2H^+ \longrightarrow O_2 + H_2O_2$$

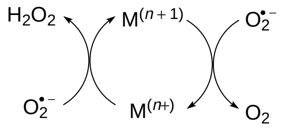

$$2O_2^{\bullet -} + 2H^+ \longrightarrow O_2 + H_2O_2$$

Figure 6 SODs catalyze the formation of hydrogen peroxide and oxygen from superoxide in a two-step reaction in which the metal is first reduced and then reoxidized by superoxide

Like the NiFe hydrogenase, NiSOD is translated as a pro-protein that requires processing to become an active enzyme. While the large subunit of hydrogenase requires processing of the C-terminal, 14 residues must be cleaved from the N-terminal of Ni SOD to generate an N-terminal histidine residue. Because active NiSOD could not be obtained without correct N-terminal processing, Maroney developed a strategy for heterologous expression of the SOD as a C-terminal fusion with a leader sequence containing a cleavable his tag sequence.[109]

Based on the XAS and EPR spectral changes associated with the reduction of NiSOD, it appears that it is the $Ni^{3+/2+}$ couple that is involved in superoxide disproportionation.[110] Spectroscopic studies indicated that the SOD active site could be either a mononuclear or a binuclear Ni site;[110,111] however, the X-ray crystallographic studies indicate a mononuclear Ni center (Figure 1(g)) that is coordinated by the N-terminal amino group of His1 and the amide nitrogen of Cys2, and the side-chain thiolate sulfurs of Cys2 and Cys6.[112,113] EPR and XAS studies indicate that the reduced 2+ state consists of a square-planar Ni ion that becomes square pyramidal in the 3+ state, as the side-chain ring nitrogen of His1 becomes a fifth ligand.[111] The existence of an axial nitrogen ligand in the five-coordinate Ni(III) state appears to be responsible for the nitrogen hyperfine splittings observed by EPR,[110] however, it is puzzling that the H1Q mutant still exhibited nitrogen hyperfine splittings. The sulfur ligands have been proposed to play a major role in poising the $Ni^{3+/2+}$ redox couple in the appropriate range for catalyzing both the reduction and

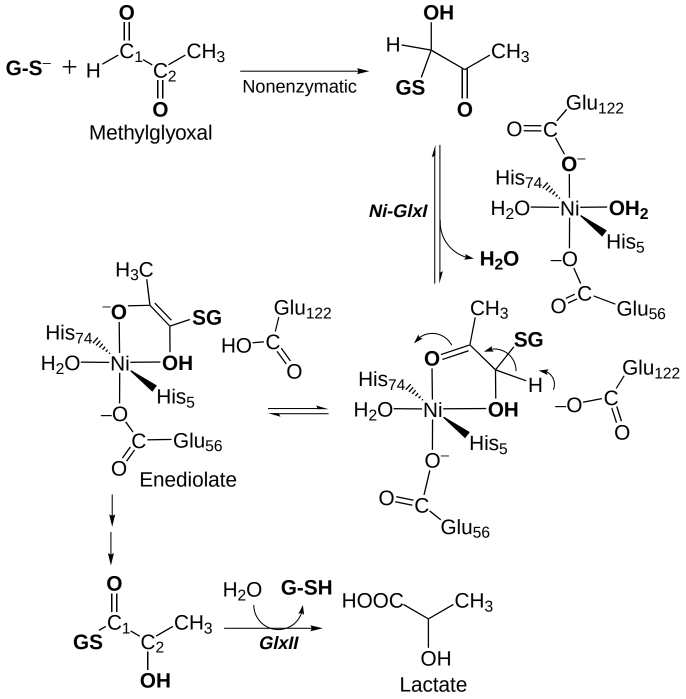

Figure 7 Mechanism of gloxylase I in methylglyoxal degradation. See text for details

the oxidation of superoxide,[110] and may also play a role as a source of protons in catalysis.[111]

8 GLYOXALASE-I (EC 4.4.1.5)

Methylglyoxal, which is a toxic species produced by several cellular reactions including the misfiring of triosephosphate isomerase during glycolysis, is hydrolyzed by the two-component glyoxalase system (GlxI and GlxII). As shown in Figure 7, after glutathione (GSH) reacts nonenzymatically with methylglyoxal to form a hemithioacetal, GlxI, the Ni component, catalyzes an isomerization reaction forming S-D-lactoylglutathione, which is hydrolyzed to lactate and GSH by GlxII. Glyoxal is harmful because it forms covalent adducts with DNA and proteins.

Although the yeast and human glyoxalases are Zn-dependent enzymes, the *E. coli* enzyme is specific for Ni.[114] The Ni site exhibits octahedral Ni coordination (Figure 1(f)), which is similar to the Zn coordination environment in the human enzyme.[115] *Yersinia pestis*, among other pathogens, are predicted to contain a Ni-dependent glyoxalase-I species.[116]

A suggested mechanism (Figure 7) for the *E. coli* GlxI[115] based on the X-ray structure (Figure 1(f)) includes binding of substrate to displace one of the water molecules and Glu122, which would allow Glu122 to act as a general base to abstract a proton from the substrate, which would lead to formation of the enediolate intermediate still coordinated to the Ni ion. For the Zn enzyme, it was pointed out that displacement of the Glu122 from coordination with the metal would increase the pK_a of the carboxyl group, while coordination of the substrate should decrease the pK_a of C1-H and that these combined effects would promote catalysis.[117] Reprotonation at C2 would form the product, which will then dissociate from the metal and leave the active site to serve as substrate for Glx2.

9 ACI-REDUCTONE DIOXYGENASE

During polyamine and ethylene biosynthesis, *S*-adenosylmethionine (AdoMet) is converted to methylthioadenosine.

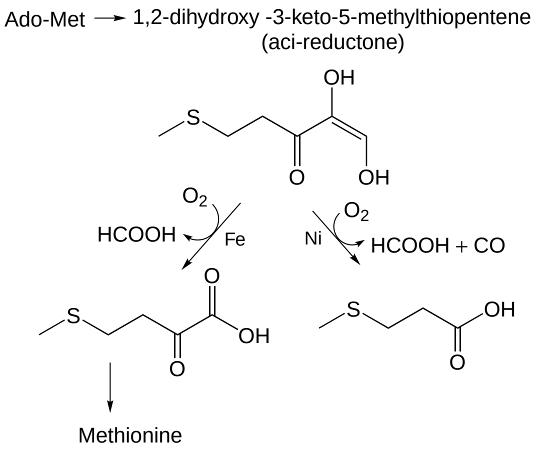

Figure 8 Role of aci-reductone dioxygenase in methionine salvage

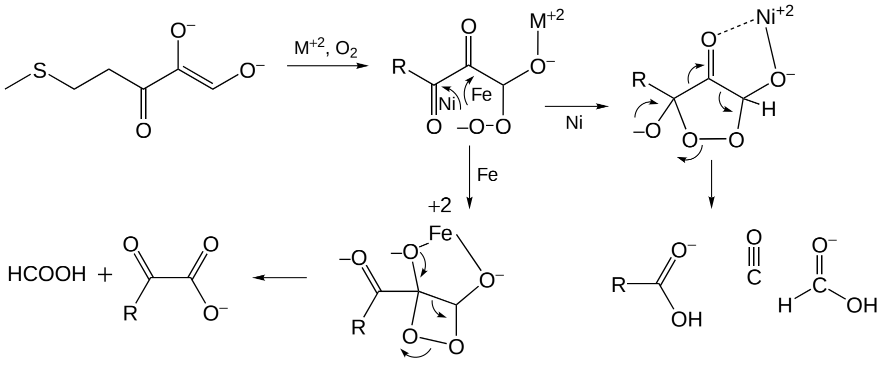

Figure 9 Proposed mechanism of aci-reductone dioxygenase. See text for details[9]

Regeneration of AdoMet is accomplished by the methionine salvage pathway, which converts methylthioadenosine to methionine. Besides regenerating methionine, this pathway functions to control the concentration of methylthioadenosine, which is a powerful inhibitor of polyamine biosynthesis and transmethylation reactions.[118] A key intermediate in the methionine salvage pathway is 1,2-dihydroxy-3-keto-5-methylthiopentene (aci-reductone), which is oxidized to the α-ketoacid precursor of methionine by aci-reductone dioxygenase (Figure 8). This dioxygenase catalyzes competing reactions, depending on its metal composition. The Fe-enzyme forms the methionine precursor, while the Ni enzyme generates methylthiopropionate, which is cytotoxic.

Aci-reductone dioxygenase folds into a beta-sandwich or jellyroll structure. The Ni active site (Figure 1(h)) is located at the loops connecting several of the beta sheets in a pseudo-octahedral environment consisting of oxygen and nitrogen ligands donated by the nitrogen atoms of three histidine residues, the oxygens from one glutamate residue, and the oxygens of two water molecules.

Figure 9 describes a proposed mechanism for the dioxygenase reaction based on enzymatic and structural studies.[9,118] It is proposed that the substrate binds as a dianion, which ligates the metal ion. Oxygen would then react to form an organic peroxide anion, which would then form a cyclic peroxide intermediate. The different reaction specificity is proposed to result from attack of the peroxide oxygen on alternative carbons. For example, the Ni-ARD would direct attack of the peroxide anion at the C3 carbonyl to form a five-membered peroxide intermediate, while the Fe-ARD would attack at carbon 2 to form a four-membered cyclic peroxide.

10 RELATED ARTICLES

Cobalt: B_{12} Enzymes & Coenzymes; Iron–Sulfur Proteins; Metallocenter Biosynthesis & Assembly; Nickel: Models of Protein Active Sites.

11 REFERENCES

1. J. Kuchar and R. P. Hausinger, *Chem. Rev.*, 2004, **104**, 509.
2. S. B. Mulrooney and R. P. Hausinger, *FEMS Microbiol. Rev.*, 2003, **27**, 239.
3. E. R. Schreiter, M. D. Sintchak, Y. Guo, P. T. Chivers, R. T. Sauer, and C. L. Drennan, *Nat. Struct. Biol.*, 2003, **10**, 794.
4. E. Garcin, X. Vernede, E. Hatchikian, A. Volbeda, M. Frey, and J. Fontecilla-Camps, *Structure*, 1999, **7**, 557.
5. U. Ermler, W. Grabarse, S. Shima, M. Goubeaud, and R. K. Thauer, *Science*, 1997, **278**, 1457.
6. T. I. Doukov, T. Iverson, J. Seravalli, S. W. Ragsdale, and C. L. Drennan, *Science*, 2002, **298**, 567.
7. H. Dobbek, V. Svetlitchnyi, L. Gremer, R. Huber, and O. Meyer, *Science*, 2001, **293**, 1281.
8. C. L. Drennan, J. Heo, M. D. Sintchak, E. Schreiter, and P. W. Ludden, *Proc. Natl. Acad. Sci. U.S.A.*, 2001, **98**, 11973.
9. T. C. Pochapsky, S. S. Pochapsky, T. Ju, H. Mo, F. Al-Mjeni, and M. J. Maroney, *Nat. Struct. Biol.*, 2002, **9**, 966.
10. M. Costa, *Biol. Chem.*, 2002, **383**, 961.
11. E. Denkhaus and K. Salnikow, *Crit. Rev. Oncol. Hematol.*, 2002, **42**, 35.
12. J. O. Nriagu, The Global Cycle of Nickel, in ‘Nickel in the Environment’, ed. J. O. Nriagu, John Wiley & Sons, New York, 1980, p. 1.
13. R. Bartha and E. J. Ordal, *J. Bacteriol.*, 1965, **89**, 1015.
14. J.-C. Fontecilla-Camps, *Struct. Bonding*, 1998, **91**, 160.
15. M. N. Hughes and R. K. Poole, *J. Gen. Microbiol.*, 1991, **137**, 725.
16. N. E. Dixon, C. Gazzola, R. L. Blakeley, and B. Zerner, *J. Am. Chem. Soc.*, 1975, **97**, 4131.
17. R. P. Hausinger and P. A. Karplus, Urease, in ‘Handbook of Metalloproteins’, eds. K. Wieghardt, R. Huber, T. L. Poulos, and A. Messerschmidt, John Wiley & Sons, West Sussex, 2001, p. 867.

18. E. Jabri, M. B. Carr, R. P. Hausinger, and P. A. Karplus, *Science*, 1995, **268**, 998.
19. M. A. Pearson, L. O. Michel, R. P. Hausinger, and P. A. Karplus, *Biochemistry*, 1997, **36**, 8164.
20. S. Benini, W. R. Rypniewski, K. S. Wilson, S. Miletti, S. Ciurli, and S. Mangani, *Structure*, 1999, **7**, 205.
21. N. C. Ha, S. T. Oh, J. Y. Sung, K. A. Cha, M. H. Lee, and B. H. Oh, *Nat. Struct. Biol.*, 2001, **8**, 505.
22. E. P. Day, J. Peterson, M. Sendova, M. J. Todd, and R. P. Hausinger, *Inorg. Chem.*, 1993, **32**, 634.
23. H. K. Song, S. B. Mulrooney, R. Huber, and R. P. Hausinger, *J. Biol. Chem.*, 2001, **276**, 49359.
24. H. Remaut, N. Safarov, S. Ciurli, and J. Van Beeumen, *J. Biol. Chem.*, 2001, **276**, 49365.
25. M. J. Todd and R. P. Hausinger, *J. Biol. Chem.*, 1987, **262**, 5963.
26. F. Musiani, E. Arnofi, R. Casadio, and S. Ciurli, *J. Biol. Inorg. Chem.*, 2001, **6**, 300.
27. D. Suarez, N. Diaz, and K. M. Merz Jr, *J. Am. Chem. Soc.*, 2003, **125**, 15324.
28. A. M. Barrios and S. J. Lippard, *J. Am. Chem. Soc.*, 2000, **122**, 9172.
29. S. Benini, W. R. Rypniewski, K. S. Wilson, S. Ciurli, and S. Mangani, *J. Biol. Inorg. Chem.*, 2001, **6**, 778.
30. M. Stephenson and L. H. Stickland, *Biochem. J.*, 1931, **25**, 205.
31. M. W. W. Adams, L. E. Mortenson, and J.-S. Chen, *Biochim. Biophys. Acta*, 1981, **594**, 105.
32. D. J. Evans and C. J. Pickett, *Chem. Soc. Rev.*, 2003, **32**, 268.
33. J.-C. Fontecilla-Camps and S. W. Ragsdale, Nickel-Iron-Sulfur Active Sites: Hydrogenase and CO Dehydrogenase, in ‘Advances in Inorganic Chemistry’, eds. A. G. Sykes and R. Cammack, Academic Press, San Diego, CA, 1999, Vol. 47, p. 283.
34. J. M. Odom and H. D. Peck Jr, *Annu. Rev. Microbiol.*, 1984, **38**, 551.
35. B. E. Jackson, V. K. Bhupathiraju, R. S. Tanner, C. R. Woese, and M. J. McInerney, *Arch. Microbiol.*, 1999, **171**, 107.
36. G. C. Hartmann, A. R. Klein, M. Linder, and R. K. Thauer, *Arch. Microbiol.*, 1996, **165**, 187.
37. E. J. Lyon, S. Shima, G. Buurman, S. Chowdhuri, A. Batschauer, K. Steinbach, and R. K. Thauer, *Eur. J. Biochem.*, 2004, **271**, 195.
38. S. Menon and S. W. Ragsdale, *Biochemistry*, 1996, **35**, 15814.
39. C. Navarro, L.-F. Wu, and M.-A. Mandrand-Berthelot, *Mol. Microbiol.*, 1993, **9**, 1181.
40. T. Yagi, *Biochim. Biophys. Acta*, 1959, **30**, 194.
41. A. I. Krasna and D. Rittenberg, *J. Am. Chem. Soc.*, 1954, **76**, 3015.
42. A. Volbeda, E. Garcia, C. Piras, A. L. deLacey, V. M. Fernandez, E. C. Hatchikian, M. Frey, and J. C. FontecillaCamps, *J. Am. Chem. Soc.*, 1996, **118**, 12989.
43. R. P. Happe, W. Roseboom, A. J. Pierik, S. P. Albracht, and K. A. Bagley, *Nature*, 1997, **385**, 126.
44. J. R. Lancaster Jr, *FEBS Lett.*, 1980, **115**, 285.
45. B. Bleijlevens, B. W. Faber, and S. P. Albracht, *J. Biol. Inorg. Chem.*, 2001, **6**, 763.
46. C. Fan, M. Teixeira, J. Moura, I. Moura, H. B. Hanh, J. L. Gall, J. Harry, D. Peck, and B. M. Hoffman, *J. Am. Chem. Soc.*, 1991, **113**, 20.
47. M. Carepo, D. L. Tierney, C. D. Brondino, T. C. Yang, A. Pamplona, J. Telser, I. Moura, J. J. Moura, and B. M. Hoffman, *J. Am. Chem. Soc.*, 2002, **124**, 281.
48. G. Davidson, S. B. Choudhury, Z. J. Gu, K. Bose, W. Roseboom, S. P. J. Albracht, and M. J. Maroney, *Biochemistry*, 2000, **39**, 7468.
49. A. K. Jones, S. E. Lamle, H. R. Pershad, K. A. Vincent, S. P. Albracht, and F. A. Armstrong, *J. Am. Chem. Soc.*, 2003, **125**, 8505.
50. J. W. Van der Zwaan, S. P. J. Albracht, R. D. Fontijn, and Y. B. M. Roelofs, *Biochim. Biophys. Acta*, 1986, **872**, 208.
51. R. P. Happe, W. Roseboom, and S. P. Albracht, *Eur. J. Biochem.*, 1999, **259**, 602.
52. S. Foerster, M. Stein, M. Brecht, H. Ogata, Y. Higuchi, and W. Lubitz, *J. Am. Chem. Soc.*, 2003, **125**, 83.
53. K. A. Bagley, C. J. V. Garderen, M. Chen, E. C. Duin, S. P. J. Albracht, and W. H. Woodruff, *Biochemistry*, 1994, **33**, 9229.
54. A. L. De Lacey, C. Stadler, V. M. Fernandez, C. Hatchikian, H. J. Fan, S. Li, and M. B. Hall, *J. Biol. Inorg. Chem.*, 2002, **7**, 318.
55. K. K. Surerus, M. Chen, J. W. van der Zwaan, F. M. Rusnak, M. Kolk, E. C. Duin, S. P. Albracht, and E. Munck, *Biochemistry*, 1994, **33**, 4980.
56. T. Buhrke, B. Bleijlevens, S. P. Albracht, and B. Friedrich, *J. Bacteriol.*, 2001, **183**, 7087.
57. T. Eitinger and B. Friedrich, Microbial Nickel Transport and Incorporation into Hydrogenases, in ‘Transition Metals in Microbial Metabolism’, eds. G. Winkelmann and C. J. Carrano, Harwood Academic Publishers, Amsterdam, 1997, p. 235.
58. S. Reissmann, E. Hochleitner, H. Wang, A. Paschos, F. Lottspeich, R. S. Glass, and A. Bock, *Science*, 2003, **299**, 1067.
59. Y. Montet, P. Amara, A. Volbeda, X. Vernede, E. C. Hatchikian, M. J. Field, M. Frey, and J. C. Fontecilla-Camps, *Nat. Struct. Biol.*, 1997, **4**, 523.
60. P. Bertrand, F. Dole, M. Asso, and B. Guigliarelli, *J. Biol. Inorg. Chem.*, 2000, **5**, 682.
61. H. R. Pershad, J. L. Duff, H. A. Heering, E. C. Duin, S. P. Albracht, and F. A. Armstrong, *Biochemistry*, 1999, **38**, 8992.
62. P. M. Matias, C. M. Soares, L. M. Saraiva, R. Coelho, J. Morais, J. Le Gall, and M. A. Carrondo, *J. Biol. Inorg. Chem.*, 2001, **6**, 63.

63. O. Lenz and B. Friedrich, *Proc. Natl. Acad. Sci. U.S.A.*, 1998, **95**, 12474.

64. A. J. Pierik, M. Schmelz, O. Lenz, B. Friedrich, and S. P. J. Albracht, *FEBS Lett.*, 1998, **438**, 231.

65. M. Bernhard, T. Buhrke, B. Bleijlevens, A. L. De Lacey, V. M. Fernandez, S. P. Albracht, and B. Friedrich, *J. Biol. Chem.*, 2001, **276**, 15592.

66. P. A. Lindahl, *Biochemistry*, 2002, **41**, 2097.

67. S. W. Ragsdale, Nickel Containing CO Dehydrogenases and Hydrogenases, in 'Enzyme-Catalyzed Electron and Radical Transfer', eds. A. Holzenburg and N. Scrutton, Plenum Press, New York, 2000, Vol. 35, p. 487.

68. S. W. Ragsdale, Anaerobic One-Carbon Catalysis, in 'Encyclopedia of Catalysis', eds. I. T. Horvath, E. Iglesia, M. T. Klein, J. A. Lercher, A. J. Russell, and E. I. Stiefel, John Wiley & Sons, New York, 2003, Vol. 1, p. 665.

69. S. Aono, *Acc. Chem. Res.*, 2003, **36**, 825.

70. R. K. Watt and P. W. Ludden, *J. Biol. Chem.*, 1998, **273**, 10019.

71. R. K. Watt and P. W. Ludden, *Cell. Mol. Life Sci.*, 1999, **56**, 604.

72. C. Darnault, A. Volbeda, E. J. Kim, P. Legrand, X. Vernede, P. A. Lindahl, and J. C. Fontecilla-Camps, *Nat. Struct. Biol.*, 2003, **10**, 271.

73. W. Gu, J. Seravalli, S. W. Ragsdale, and S. P. Cramer, *Biochemistry*, 2004, **43**, 9029.

74. J. Feng and P. A. Lindahl, *Biochemistry*, 2004, **43**, 1552.

75. M. Kumar, W.-P. Lu, L. Liu, and S. W. Ragsdale, *J. Am. Chem. Soc.*, 1993, **115**, 11646.

76. J. Seravalli, M. Kumar, W.-P. Lu, and S. W. Ragsdale, *Biochemistry*, 1997, **36**, 11241.

77. D. M. Fraser and P. A. Lindahl, *Biochemistry*, 1999, **38**, 15706.

78. V. Svetlitchnyi, C. Peschel, G. Acker, and O. Meyer, *J. Bacteriol.*, 2001, **183**, 5134.

79. E. L. Maynard and P. A. Lindahl, *J. Am. Chem. Soc.*, 1999, **121**, 9221.

80. J. Seravalli and S. W. Ragsdale, *Biochemistry*, 2000, **39**, 1274.

81. V. Svetlitchnyi, H. Dobbek, W. Meyer-Klaucke, T. Meins, B. Thiele, P. Romer, R. Huber, and O. Meyer, *Proc. Natl. Acad. Sci. U.S.A.*, 2004, **101**, 446.

82. S. Nagashima, M. Nakasako, N. Dohmae, M. Tsujimura, K. Takio, M. Odaka, M. Yohda, N. Kamiya, and I. Endo, *Nat. Struct. Biol.*, 1998, **5**, 347.

83. J. Seravalli, W. Gu, A. Tam, E. Strauss, T. P. Begley, S. P. Cramer, and S. W. Ragsdale, *Proc. Natl. Acad. Sci. U.S.A.*, 2003, **100**, 3689.

84. R. P. Hausinger, *Nat. Struct. Biol.*, 2003, **10**, 234.

85. S. Gencic and D. A. Grahame, *J. Biol. Chem.*, 2003, **278**, 6101.

86. M. R. Bramlett, X. Tan, and P. A. Lindahl, *J. Am. Chem. Soc.*, 2003, **125**, 9316.

87. J. Seravalli, Y. Xiao, W. Gu, S. P. Cramer, W. E. Antholine, V. Krymov, G. J. Gerfen, and S. W. Ragsdale, *Biochemistry*, 2004, **43**, 3944.

88. R. P. Schenker and T. C. Brunold, *J. Am. Chem. Soc.*, 2003, **125**, 13962.

89. X. S. Tan, C. Sewell, and P. A. Lindahl, *J. Am. Chem. Soc.*, 2002, **124**, 6277.

90. M. Kumar and S. W. Ragsdale, *J. Am. Chem. Soc.*, 1992, **114**, 8713.

91. J. Chen, S. Huang, J. Seravalli, H. Gutzman Jr, D. J. Swartz, S. W. Ragsdale, and K. A. Bagley, *Biochemistry*, 2003, **42**, 14822.

92. S. W. Ragsdale, H. G. Wood, and W. E. Antholine, *Proc. Natl. Acad. Sci. U.S.A.*, 1985, **82**, 6811.

93. J. Seravalli, M. Kumar, and S. W. Ragsdale, *Biochemistry*, 2002, **41**, 1807.

94. E. L. Maynard, C. Sewell, and P. A. Lindahl, *J. Am. Chem. Soc.*, 2001, **123**, 4697.

95. X. Tan, M. R. Bramlett, and P. A. Lindahl, *J. Am. Chem. Soc.*, 2004, **126**, 5954.

96. R. K. Thauer, *Microbiology*, 1998, **144**, 2377.

97. S. W. Ragsdale, Biochemistry of Methyl-CoM Reductase and Coenzyme F_{430}, in 'The Porphyrin Handbook', eds. K. M. Kadish, K. M. Smith, and R. Guilard, Academic Press, New York, 2003, Vol. 11, p. 205.

98. W. G. Grabarse, F. Mahlert, E. C. Duin, M. Goubeaud, S. Shima, R. K. Thauer, V. Lamzin, and U. Ermler, *J. Mol. Biol.*, 2001, **309**, 315.

99. J. L. Craft, Y.-C. Horng, S. W. Ragsdale, and T. C. Brunold, *J. Am. Chem. Soc.*, 2004, **126**, 4068.

100. J. L. Craft, Y. C. Horng, S. W. Ragsdale, and T. C. Brunold, *J. Biol. Inorg. Chem.*, 2004, **9**, 77.

101. R. Piskorski and B. Jaun, *J. Am. Chem. Soc.*, 2003, **125**, 13120.

102. C. Finazzo, J. Harmer, C. Bauer, B. Jaun, E. C. Duin, F. Mahlert, M. Goenrich, R. K. Thauer, S. Van Doorslaer, and A. Schweiger, *J. Am. Chem. Soc.*, 2003, **125**, 4988.

103. Y.-C. Horng, D. F. Becker, and S. W. Ragsdale, *Biochemistry*, 2001, **40**, 12875.

104. V. Pelmenschikov, M. R. A. Blomberg, P. E. M. Siegbahn, and R. H. Crabtree, *J. Am. Chem. Soc.*, 2002, **124**, 4039.

105. I. Fridovich, *Annu. Rev. Biochem.*, 1995, **64**, 97.

106. J. S. Valentine, Dioxygen Reactions, in 'Bioinorganic Chemistry', eds. I. Bertini, H. B. Gray, S. J. Lippard, and J. S. Valentine, University Science Books, Mill Valley, CA, 1994, p. 37.

107. H.-D. Youn, H. Youn, J.-W. Lee, Y.-I. Yim, J. K. Lee, Y. C. Hah, and S.-O. Kang, *Arch. Biochem. Biophys.*, 1996, **334**, 341.

108. H.-D. Youn, E.-J. Kim, J.-H. Roe, Y. C. Hah, and S.-O. Kang, *Biochem. J.*, 1996, **318**, 889.

109. P. A. Bryngelson, S. E. Arobo, J. L. Pinkham, D. E. Cabelli, and M. J. Maroney, *J. Am. Chem. Soc.*, 2004, **126**, 460.

110. S. B. Choudhury, J. W. Lee, G. Davidson, Y. I. Yim, K. Bose, M. L. Sharma, S. O. Kang, D. E. Cabelli, and M. J. Maroney, *Biochemistry*, 1999, **38**, 3744.

111. R. K. Szilagyi, P. A. Bryngelson, M. J. Maroney, B. Hedman, K. O. Hodgson, and E. I. Solomon, *J. Am. Chem. Soc.*, 2004, **126**, 3018.

112. J. Wuerges, J. Lee, Y. Yim, S. Kang, H. Yim, and K. Djinovic-Carugo, *Proc. Natl. Acad. Sci. USA*, 2004, **101**, 8569.

113. D. P. Barondeau, C. J. Kassmann, C. K. Bruns, J. A. Tainer, and E. D. Getzoff, *Biochemistry*, 2004, **43**, 8038.

114. S. L. Clugston, J. F. Barnard, R. Kinach, D. Miedema, R. Ruman, E. Daub, and J. F. Honek, *Biochemistry*, 1998, **37**, 8754.

115. M. M. He, S. L. Clugston, J. F. Honek, and B. W. Matthews, *Biochemistry*, 2000, **39**, 8719.

116. S. L. Clugston and J. F. Honek, *J. Mol. Evol.*, 2000, **50**, 491.

117. A. D. Cameron, M. Ridderstrom, B. Olin, M. J. Kavarana, D. J. Creighton, and B. Mannervik, *Biochemistry*, 1999, **38**, 13480.

118. Y. Dai, T. C. Pochapsky, and R. H. Abeles, *Biochemistry*, 2001, **40**, 6379.

Acknowledgments

I thank Andy Karplus, Bob Hausinger, Juan Fontecilla–Camps, and Mike Maroney for their helpful comments during preparation of this manuscript.

Nickel: Inorganic & Coordination Chemistry

Simon R. Collinson & Martin Schröder
University of Nottingham, Nottingham, UK

1	Introduction	1
2	General Features	1
3	Nickel(0)	5
4	Nickel(I)	6
5	Nickel(II)	10
6	Nickel(III)	25
7	Nickel(IV)	26
8	Biological Chemistry	26
9	Related Articles	28
10	References	28

Abbreviations

[9]aneN_3 = 1,4,7-triazacyclononane; [9]aneS_3 = 1,4,7-trithiacyclononane; cat = Catechol (1,2-dihydroxybenzene); dad = Diazadiene; EPR = Electron paramagnetic spectroscopy; imid = Imidazole; NMR = Nuclear magnetic resonance; pc = Phthalocyanine.

1 INTRODUCTION

Ni has the atomic number 28, atomic weight 58.69, and electron configuration $[Ar]3d^8 4s^2$, and has five naturally occurring isotopes, ^{58}Ni 68.27%, ^{60}Ni 26.10%, ^{61}Ni 1.13%, ^{62}Ni 3.59%, and ^{64}Ni 0.91%. Ni is the 22nd most common element in the Earth's crust, with an estimated abundance of 99 ppm. The element was isolated in 1751 by A. F. Cronsted and named after the ore '*Kupfernickel*'. Ni is widely distributed in silicate, sulfide, oxide, and arsenide ores; commercially important ores include garnierite, $(Ni,Mg)_6Si_4O_{10}(OH)_8$, limonite, $(Fe,Ni)O(OH){\cdot}xH_2O$, and pentlandite, $(Ni,Fe)_9S_8$. The element is ferromagnetic and has a face-centered cubic structure.

2 GENERAL FEATURES

The literature on the coordination chemistry of Ni is immense, and this article can only summarize general features and properties. Comprehensive reviews of the literature up to 1984 and up to 2002 have appeared,**[1,2]** while general summaries of Ni chemistry are given in inorganic textbooks**[3]** (*see also* ***Nickel: Organometallic Chemistry*** for descriptions of the organometallic and cluster chemistry of Ni).

The coordination chemistry of Ni features a very wide variety of mono- and polydentate ligands, with metal oxidation states ranging from 0 to +IV, although organometallic Ni^{-I} and Ni^{-II} species have been reported. The most common oxidation state by far is Ni^{II}, although Ni^0 complexes are also well known. Ni^I and Ni^{III} species are less common, while Ni^{IV} complexes are established only for certain ligand types. Table 1 summarizes typical data on the oxidation states and stereochemistries of Ni complexes. The basic electronic and spectral features of Ni complexes have been reviewed.**[4]**

2.1 Nickel(0)

Ni^0 complexes have a d^{10} electron configuration and are typically stabilized by π-acceptor ligands such as PR_3, CO, alkenes, N_2, and CN^-. Thus, bonding in Ni^0 species is usually highly covalent, with strong π-backdonation from the electron-rich metal center to the π-acceptor ligand orbitals. Many Ni^0 complexes are organometallic species (*see* ***Nickel: Organometallic Chemistry***) and often have four-coordinate, tetrahedral geometries with an overall closed-shell 18-electron configuration, for example, $[Ni(CO)_4]$ (**1**) and $[Ni(PF_3)_4]$ (**2**). With more bulky tertiary phosphine ligands, three-co-ordinate Ni^0 complexes can be prepared, for example, $[Ni(PPh_3)_3]$ and $[Ni(PCy_3)_3]$. Square-planar adducts with O_2, CO_2, CS_2, and SO_2 have also been reported; this stereochemistry maximizes orbital overlap between the metal center and the adduct molecule(s) and may also reflect a degree of oxidative addition at Ni^0 to afford a formal Ni^{II} species. Ni^0 complexes are diamagnetic and generally highly reactive via oxidative-addition reactions to give octahedral Ni^{II} products (*see Catalysis*).

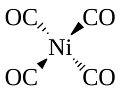

(**1**)

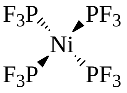

(**2**)

2.2 Nickel(I)

Ni^I complexes are relatively rare and are often stabilized by specialized ligands such as N-donor macrocycles and P-donor tripodal systems. Ni^I has a d^9 electron configuration and its complexes are therefore paramagnetic with one unpaired electron. They show a variety of stereochemistries depending upon the ligands present, although four or five

Table 1 Nickel complexes

Metal oxidation state	Complex
0	$[Ni(PR_3)_3]$, $[Ni(PR_3)_4]$, $[Ni(CO)_4]$, $[Ni(CN)_4]^{4-}$, $[Ni(N_3P)](N_3P = \text{tripod})$
+1	$[Ni(PR_3)_3Br]$, $[Ni(L)]^+$ (L = tetraaza macrocycle), $[Ni(PR_3)_2\{N(SiMe_3)_2\}]$, $[Ni_2(CN)_6]^{4-}$
+2	$[Ni(NPh_2)_3]^-$, $[Ni_2(NR_2)_4]$, $[Ni(CN)_4]^{2-}$, $[NiCl_4]^{2-}$, $[NiX_2(PR_3)_2]$, $[Ni(CN)_5]^{3-}$, $[Ni(H_2O)_6]^{2+}$, $[Ni(bipy)_3]^{2+}$
+3	$[NiCl_2([14]aneN_4)]^+$, $[NiX_3(PR_3)_2]$, $[Ni([9]aneX_3)_2]^{3+}$ (X = N, S)
+4	$[NiF_6]^{2-}$

coordination is most common. Their general reactivity is based upon disproportionation to Ni^0 and Ni^{II}, electron-transfer reactions, and dimerization to give diamagnetic metal–metal bonded products.

2.3 Nickel(II)

By far the most common oxidation state for Ni is the +II state with a d^8 electron configuration. Four, five, and particularly six coordination are all common geometries for Ni^{II} and depend upon the ligands present. Scheme 1 shows the d-orbital splitting pattern for tetrahedral, square-planar, tetragonal, and octahedral Ni^{II}.

2.3.1 *Four Coordination*

Four coordination for Ni^{II} is relatively common, with tetrahedral and square-planar geometries representing the two extreme possibilities. Good π-donor ligands such as halides tend to stabilize tetrahedral geometries, for example, $[NiCl_4]^{2-}$ (**3**), while π-acceptor ligands such as PR_3 and CN^- afford square-planar geometries, for example, $[Ni(CN)_4]^{2-}$ (**4**).

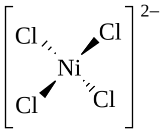
(**3**)

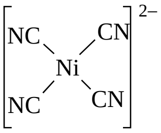
(**4**)

Tetrahedral complexes are usually highly colored (blue or green) with three expected d–d transitions, $^3T_1(F) \rightarrow {}^3T_2(F)$ (ν_1), $^3T_1(F) \rightarrow {}^3A_2(F)$ (ν_2), and $^3T_1(F) \rightarrow {}^3T_1(P)$ (ν_3), although the observed spectra tend to be complicated by spin–orbit coupling effects. Scheme 2 shows a simplified Orgel diagram (*see Tanabe–Sugano Diagram*) for tetrahedral and octahedral Ni^{II} complexes. The ligand field splitting parameter (*see Ligand Field Theory*) $10Dq$ for the complexes $[NiX_4]^{2-}$ varies from 4090, to 3790, to 3820 cm^{-1} for X = Cl, Br, I, respectively. Tetrahedral Ni^{II} would be expected to have two unpaired electrons, and such complexes do indeed show experimentally temperature-dependent magnetic behavior with μ_{eff} in the range 3.2 to 4.2 BM, consistent with a T ground-state for a $e_g^4t_{2g}^4$

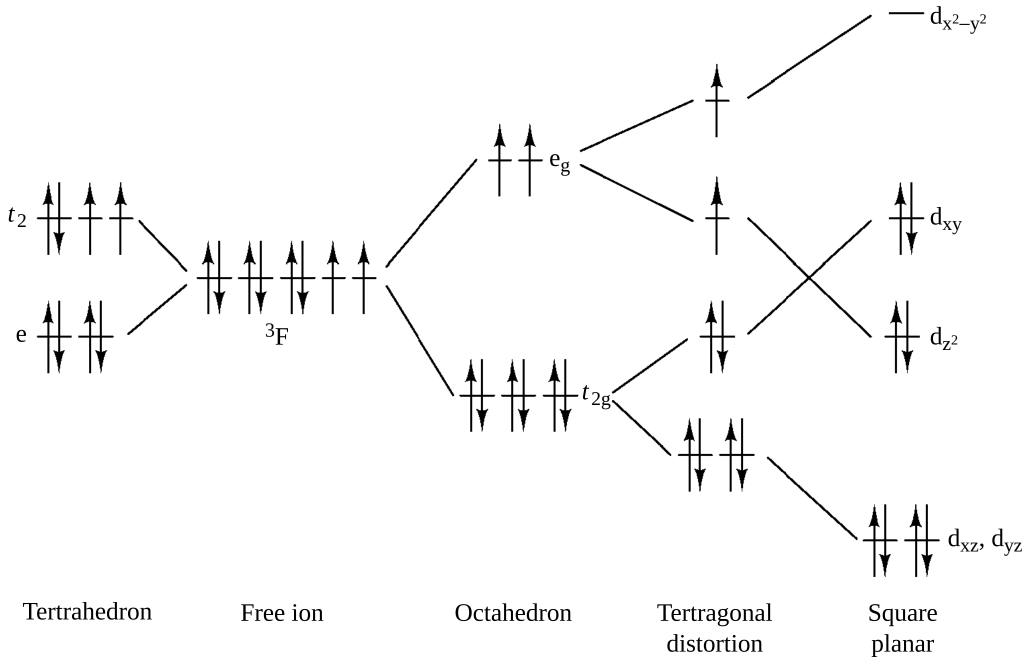

Scheme 1

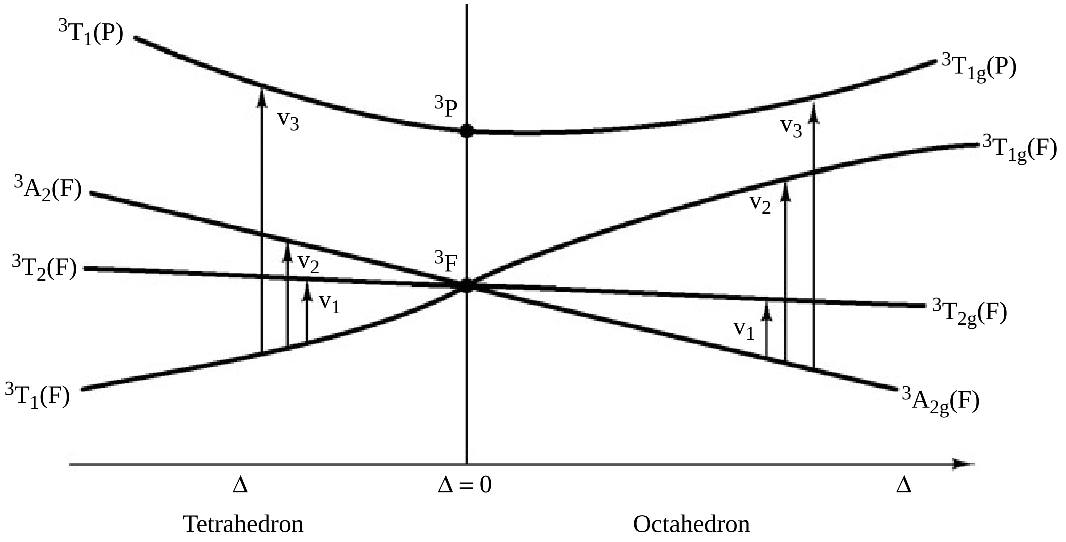

Scheme 2

configuration. The observed values of μ_{eff} for these complexes are related to the degree of distortion from pure tetrahedral coordination.

Square-planar Ni^{II} complexes are typically yellow, red, or brown in color, and are invariably diamagnetic with a spin-paired configuration, although there is one report of paramagnetic planar Ni^{II} species.**5** Planar coordination for Ni^{II} is common and is linked to the stabilization of this geometry for d^8 metal ions (*see* ***Palladium: Inorganic & Coordination Chemistry*** and ***Platinum: Inorganic & Coordination Chemistry***). Typical examples of square-planar Ni^{II} complexes include $[Ni(CN)_4]^{2-}$ (**4**), $[Ni(dmgH)_2]$ (**5**), $[Ni(Me\text{-}salen)_2]$ (**6**) and $[Ni(t\text{-}Bu_2acac)_2]$ (**7**).

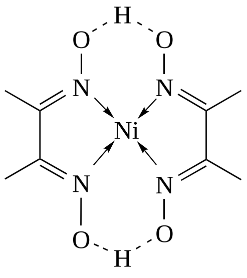

(**5**)

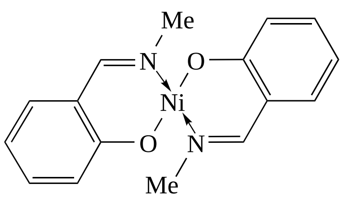

(**6**)

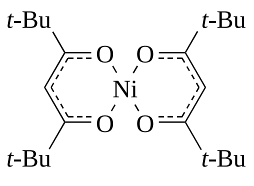

(**7**)

An interesting feature in four-coordinate Ni^{II} chemistry is the interconversion of paramagnetic, tetrahedral, and diamagnetic square-planar geometries.**6** Thus, complexes of the type $[NiX_2(PR_3)_2]$ can be tuned towards one stereochemistry rather than another by variation of X (halide) and PR_3 ligands. For example, $[NiCl_2(PPh_3)_2]$ is tetrahedral, while $[NiBr_2(PEt_3)_2]$ is square-planar. Temperature-dependent equilibria between tetrahedral (blue or green) and square-planar (yellow or red) geometries are also seen for related complexes incorporating PCy_3 and PPh_2Bu ligands. Moreover, in the solid-state structure of $[NiBr_2(PPh_2Bz)_2]$ both tetrahedral and square-planar forms are observed. These changes from tetrahedral to square-planar geometries are influenced by the steric bulk of the ligands, with tetrahedral coordination favored in general by highly bulky ligands.

Another common feature of square-planar Ni^{II} complexes is their ability to coordinate extra ligands in solution to set up equilibria between four-, five-, and six-coordinate complexes (equation 1). Thus, diamagnetic square-planar complexes can be transformed in coordinating solvents, or in the presence of extra ligands, to paramagnetic, octahedral Ni^{II} species. These transformations can be monitored by electronic spectroscopy. Aggregation of planar units can also occur in both solid state and solution, to form paramagnetic polymers. Thus, $[Ni(Me\text{-}salen)_2]$ forms dimeric and polymeric oligomers via bridging of the O-donor across planar units (**8**).**7** Another example is the structure of $[Ni(acac)_2]$ (**9**), which is actually trimeric with bridging acac ligands between octahedral, paramagnetic Ni^{II} centers.**8** Thus, in addition to tetrahedral ⟷ square-planar ⟷ five-coordinate ⟷ octahedral equilibria, monomer ⟷ oligomer/polymer equilibria may also exist for Ni^{II} complexes.

$$[Ni(L)_4] \rightleftharpoons [Ni(L)_4X] \rightleftharpoons [Ni(L)_4X_2] \qquad (1)$$

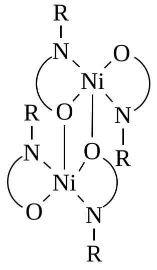

(**8**)

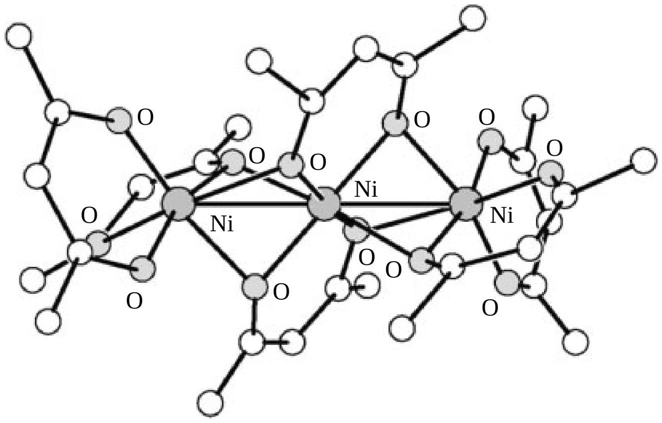

(**9**)

2.3.2 Five Coordination

Five-coordinate complexes usually incorporate polychelate or tripodal N-, P-, and As-donor ligands,**9** but are also observed in simpler systems such as $[Ni(CN)_5]^{3-}$ and $[Ni(PPhMe_2)_3(CN)_2]$. Interestingly, $[Ni(CN)_5]^{3-}$ has been crystallized and characterized as a square-based pyramidal and a trigonal bipyramidal species; this is consistent with facile Berry rotation (*see Berry Pseudorotation*) interconverting square-based pyramidal and trigonal bipyramidal geometries in five-coordinate transition metal complexes.**10** Five-coordinate complexes can be paramagnetic (high spin, $\mu_{eff} = 3.2$–$3.5\,BM$), for example, $[NiBr(tren)]^+$ (**10**), or diamagnetic (low spin), for example, $[NiBr(NP_3)]^+$ (**11**).

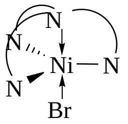

(**10**)

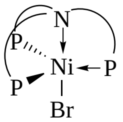

(**11**)

2.3.3 Six Coordination

Octahedral coordination is the most common geometry for Ni^{II} and is observed in a host of complexes with an extremely wide range of mono- and polydentate ligands, for example, $[Ni(L)_6]^{2+}$ (L = H_2O, py, NH_3 (**12**)), $[Ni(LL)_3]^{2+}$ (LL = en (**13**), bipy, phen), and $[Ni(terpy)_2]^{2+}$. Three d–d transitions, $^3A_{2g}(F) \rightarrow {}^3T_{2g}(F)$ (ν_1, $10Dq$), $^3A_{2g}(F) \rightarrow {}^3T_{1g}(F)$ (ν_2), and $^3A_{2g}(F) \rightarrow {}^3T_{1g}(P)$ (ν_3) (see Scheme 2), are expected for Ni^{II} in an octahedral field and these are usually observed. The value of $10Dq$ varies as a function of ligand donor set, with values of 7730 for $[Ni(DMSO)_6]^{2+}$, 8500 for $[Ni(H_2O)_6]^{2+}$, 10 750 for $[Ni(NH_3)_6]^{2+}$, 11 200 for $[Ni(en)_3]^{2+}$, and 12 500 cm^{-1} for $[Ni([9]aneN_3)_2]^{2+}$. The magnetic susceptibility of octahedral Ni^{II} is typically in the region $\mu_{eff} = 2.9$–$3.3\,BM$. Octahedral Ni^{II} ($S = 1$) has a large zero-field splitting and so these complexes do not generally show EPR spectra, although paramagnetically shifted Nuclear magnetic resonance (NMR) spectra are observed in many cases.

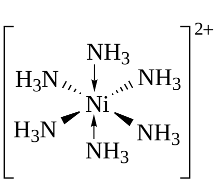

(**12**)

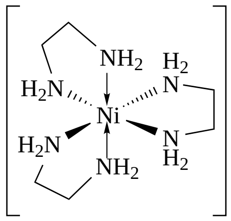

(**13**)

2.3.4 Other Coordination

Three coordination is very rare and has been observed in sterically hindered phosphine and amide complexes of type $[Ni(PPh_3)_3]$, $[Ni(NPh_2)_3]^-$, and $[(R_2N)Ni(\mu^2\text{-}NR_2)_2Ni(NR_2)]$.**11** Seven coordination, although rare, is observed in pentagonal bipyramidal complexes incorporating pentadentate chelate and macrocyclic complexes, for example, $[Ni(\mathbf{14})(L)_2]$**12** and $[Ni(\mathbf{15})(L)_2]^{2+}$.**13**

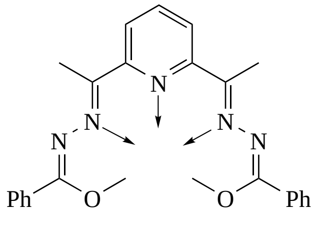

(**14**)

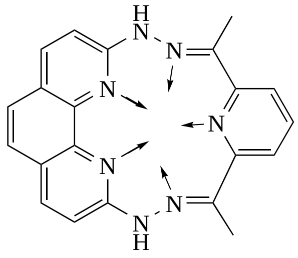

(**15**)

2.4 Nickel(III)

Ni^{III} complexes have a d^7 electron configuration [cf. Co^{II}] and are usually five-coordinate or Jahn–Teller distorted octahedral species (*see Jahn–Teller Effect*) with characteristic EPR spectra. Ni^{III} is stabilized by halides, as in $[NiF_6]^{3-}$ (**16**), and by strong σ-donor N- or P-ligands, as in $[Ni([9]aneN_3)_2]^{3+}$ (**17**) and $[NiBr_3(PR_3)_2]$ (**18**), and is usually prepared by chemical or electrochemical oxidation of the Ni^{II} precursors. Ni^{III} is still a relatively rare oxidation state, although increasingly more examples are being reported, particularly with polyaza macrocyclic ligands.**[14]** More recently, Ni^{III} centres have been implicated in the activity of [NiFe]hydrogenase enzymes (see Section 8).

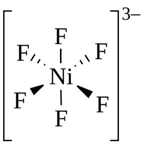

(**16**)

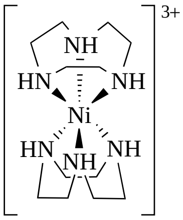

(**17**)

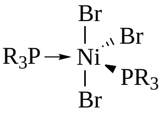

(**18**)

2.5 Nickel(IV)

Ni^{IV} complexes have a d^6 electron configuration and are invariably octahedral and diamagnetic. They are stabilized by strong σ- and π-donors such as halide, O- and N-donor oxime, amino acid, and amido ligands. Ni^{IV} species are very highly oxidizing and often transient species. Several complexes assigned originally as Ni^{IV} species have been reformulated as ligand-oxidized products.

3 NICKEL(0)

Ni^0 complexes are frequently highly reactive, air- and temperature-sensitive species, which undergo facile oxidative-addition reactions with a range of external substrates.

3.1 C-donor Complexes

The majority of Ni^0 complexes are organometallic species incorporating CO and related π-acceptor ligands, the best known being the tetracarbonyl species $[Ni(CO)_4]$ (**1**). Related isocyanide and cyanide complexes such as $[Ni(CN\text{-}t\text{-}Bu)_4]$ and $[Ni(CN)_4]^{4-}$ have also been prepared. Both of these complexes are highly reactive and undergo substitution reactions with alkenes, alkynes, tertiary phosphines, CO, NO, and O_2.**[15]** $[Ni(CN\text{-}t\text{-}Bu)_2(O_2)]$ (**19**) is a highly reactive complex and shows a square-planar stereochemistry at Ni with the O_2 ligand bound side-on (*see Side-on Coordination*).**[16]** The first stable complex of CO_2, $[Ni(\eta^2\text{-}CO_2)(PCy_3)_2]$, has been structurally characterized. Such electron-rich Ni^0 complexes undergo a host of oxidative coupling reactions with unsaturated organic molecules.**[17]** For an account of organometallic complexes and clusters of Ni, *see* ***Nickel: Organometallic Chemistry***.

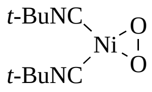

(**19**)

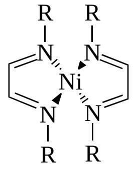

(**20**)

3.2 N-, P-, As-, and Sb-donor Complexes

In general, N-donors are not sufficiently strong π-acceptors to stabilize low-valent states such as Ni^0. However, the diimine ligand dad can form stable tetrahedral Ni^0 complexes $[Ni(dad)_2]$ (**20**).**[18]**

A wide range of Ni^0 phosphine and arsine complexes, $[Ni(L)_3]$, $[Ni(L)_4]$ ($L = PR_3$, AsR_3, SbR_3), and $[Ni(LL)_2]$ (LL = chelate ligand), can be prepared by reduction of Ni^{II} precursors in the presence of excess phosphine and arsine ligands. Alternatively, ligand replacement on $[Ni(cod)_2]$ or directly on to nickel sponge affords the same products (equations 2–4).**[19]**

$$\begin{tikzcd} NiX_2 \arrow[r, "2\,L"] & {[Ni(L)_2X_2]} \arrow[r, "2\,L", "{[H]}"'] & {[Ni(L)_4]} \arrow[r, leftrightharpoons] & {[Ni(L)_3] + L} \arrow[d, shift left] \\ NiX_2 \arrow[r, "LL"] & {[Ni(LL)X_2]} \arrow[r, "LL", "{[H]}"'] & {[Ni(LL)_2]} & {[Ni(L)_2] + L} \arrow[u, shift left] \end{tikzcd} \qquad (2)$$

$$[Ni(cod)_2] + 4L \longrightarrow [Ni(L)_4] + 2\,cod \qquad (3)$$

$$[Ni] + 4L \longrightarrow [Ni(L)_4] \qquad (4)$$

With bulky PR_3 ligands, dissociation of ligand occurs to give the highly reactive $[Ni(PR_3)_3]$ and even $[Ni(PR_3)_2]$.**[20]** A range of mixed PR_3 and CO complexes $[Ni(CO)_{4-x}(PR_3)_x]$ ($x = 1-4$) and alkene complexes $[Ni(PR_3)_2(alkene)]$ have been reported. The complex [Ni(triphos)(CO)] (**21**) and related tripodal complexes can be readily isolated by reduction of Ni^{II} precursors in the presence of CO and triphos;**[21]** the analogous nitrosyl complex $[Ni(triphos)(NO)]^+$ (**22**) (NO is coordinated as NO^+ in this complex) can be prepared by a similar route.**[22]** A wide range of related tetrahedral nitrosyl complexes of Ni^0 incorporating bent NO, NO^-, and/or linear NO^+ ligands have been synthesized (*see Nitrosyl Complexes*).**[23]**

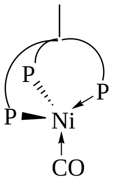

(**21**)

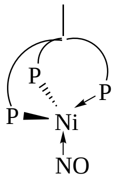

(**22**)

Reaction of [Ni(PR$_3$)$_4$] or [Ni(PR$_3$)$_2$(C$_2$H$_4$)] with O$_2$ affords the highly reactive species [Ni(PR$_3$)$_2$O$_2$] (**23**) which is related to the isocyanide complex (**19**). Ni^0–phosphine adducts of CO$_2$ (**24**),[24] CS$_2$ (**25**),[25] and SO$_2$ (**26**)[26] can also be prepared,[17] while the formation of mononuclear N$_2$ adducts has been proposed (equation 5).[27] The binuclear complex [Ni(PCy$_3$)$_2$]$_2$N$_2$ (**27**) has been structurally characterized and shows a μ^2-bridging N$_2$ ligand, N–N = 1.12 Å, with the sterically bulky cyclohexyl groups stabilizing the general structure.[28]

$$[\mathrm{Ni(PR_3)_3}] \overset{\mathrm{N_2}}{\rightleftharpoons} [\mathrm{Ni(PR_3)_3N_2}] \rightleftharpoons [\mathrm{Ni(PR_3)_3}]_2\mathrm{N_2} \qquad (5)$$

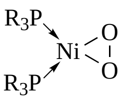

(**23**)

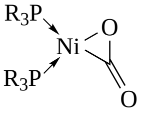

(**24**)

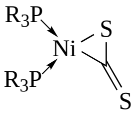

(**25**)

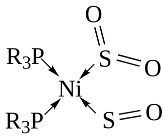

(**26**)

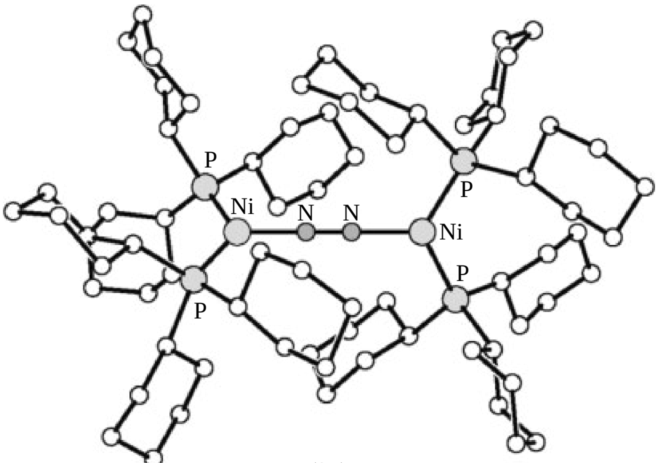

(**27**)

The tripodal Ni^0 complex [Ni(NP$_3$)] (**28**) can be prepared by reaction of Ni^{II} salts with NP$_3$ in the presence of reducing agents such as BH$_4{}^-$.[29] A series of related tripodal Ni^0 have been reported. The complex (**28**) and related tripodal species are highly reactive and add H$^+$ to form complexes of the type [Ni^{II}H(NP$_3$)]$^+$ (**29**), add CO to form [Ni(NP$_3$)CO] (**30**), and add P$_4$ to form [Ni(NP$_3$)(η^1-P$_4$)] (**31**).[30] Related P$_3$- and As$_3$-bridged dimers [Ni$_2$(triphos)$_2$(P$_3$)]$^{2+}$ (**32**), [Ni$_2$(triphos)$_2$(As$_3$)]$^{2+}$, and related mixed-metal complexes can be prepared by reaction of Ni^{II} salts with triphos in the presence of white phosphorus P$_4$ or yellow arsenic As$_4$.[31] The same reaction with P$_4$S$_3$ and As$_4$S$_3$ in place of P$_4$ and As$_4$, respectively, affords the mononuclear species [Ni(triphos)(P$_3$)]$^+$ (**33**) and [Ni(triphos)(As$_3$)]$^+$.[32] A fascinating complex [Ni(P-t-Bu)$_6$] (**34**) containing a planar P$_6$ ring has been reported from the reaction of NiCl$_2$ with (P-t-Bu)$_3$. By considering intramolecular P–P interactions, [Ni(P-t-Bu)$_6$] can be regarded as an 18-electron species.[33]

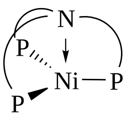

(**28**)

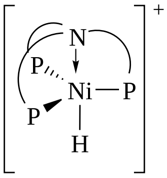

(**29**)

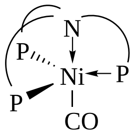

(**30**)

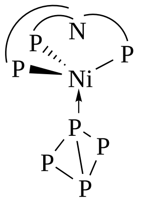

(**31**)

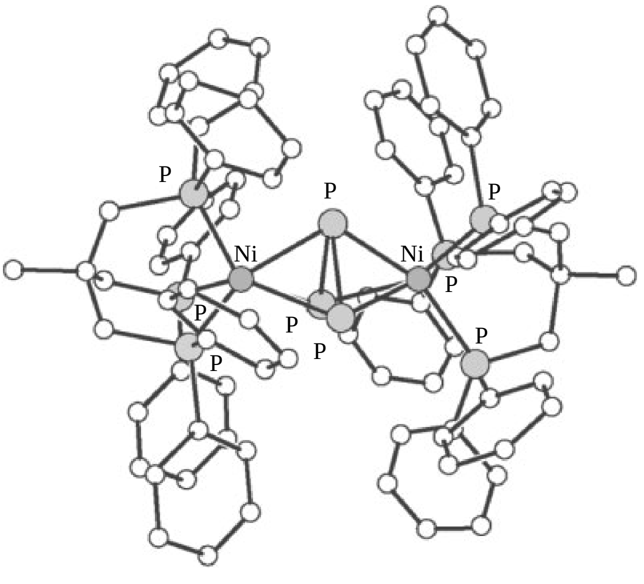

(**32**)

4 NICKEL(I)

In comparison with the relatively large number of Ni^0 complexes that have been reported, relatively few Ni^I compounds

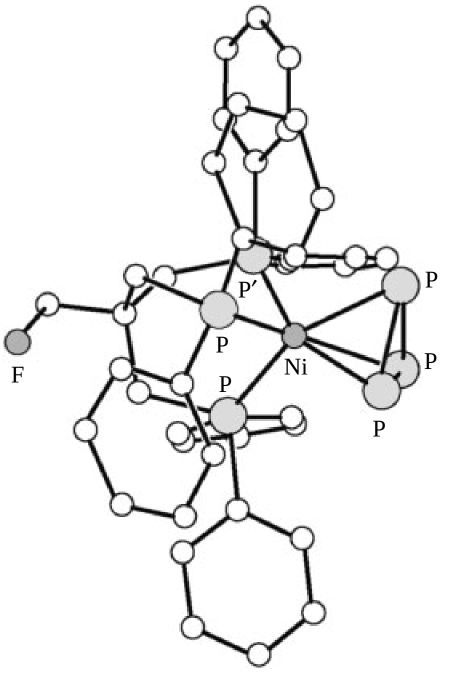

(**33**)

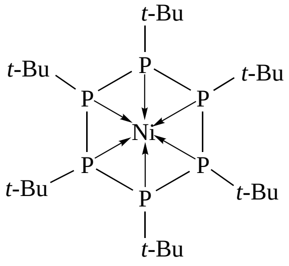

(**34**)

have been well characterized. $\mathrm{Ni^I}$ species are generally prepared via chemical or electrochemical reduction of $\mathrm{Ni^{II}}$ precursors, and are almost invariably highly reducing and air sensitive. They are often postulated as radical intermediates in electron-transfer reactions of $\mathrm{Ni^0}$ and $\mathrm{Ni^{II}}$ and have been implicated in the Ni-L form of [NiFe]hydrogenase. Mononuclear $\mathrm{Ni^I}$ species formally have a d^9 electron configuration and have magnetic susceptibilities corresponding to one unpaired electron, $\mu_{\mathrm{eff}} = 1.7$ to 2.3 BM. Mononuclear $\mathrm{Ni^I}$ complexes are EPR active and often show $g_{\parallel} > g_{\perp} > 2.0023$ for a $(d_{x^2-y^2})^1$ ground-state configuration. The stereochemistries of $\mathrm{Ni^I}$ species vary from sterically hindered three-co-ordinate species, to four- and five-coordinate complexes. The chemistry of $\mathrm{Ni^I}$ complexes has been reviewed.**14**

4.1 C-donor Complexes

Reduction of $\mathrm{K_2[Ni(CN)_4]}$ with $\mathrm{K/NH_3}$ or Na/Hg affords $\mathrm{K_2[Ni(CN)_3]}$, which has been shown to be a $\mathrm{Ni^I}$–$\mathrm{Ni^I}$ bonded dimer $\mathrm{[Ni_2(CN)_6]^{4-}}$ (**35**). The complex is diamagnetic with a Ni–Ni distance of 2.32 Å and the $\mathrm{Ni(CN)_3}$ units twisted by 82° to one another.**34**

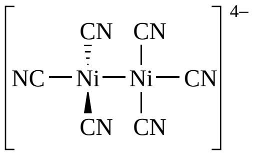

$$\left[\begin{array}{c}\mathrm{CN\quad CN}\\ \mathrm{NC{-}Ni{-}Ni{-}CN}\\ \mathrm{CN\quad CN}\end{array}\right]^{4-}$$

(**35**)

4.2 N-donor Complexes

Electrochemical reduction of $\mathrm{[Ni(bipy)_3]^{2+}}$ affords $\mathrm{[Ni(bipy)_3]^{+}}$ and $\mathrm{[Ni(bipy)_3]}$, which are formulated as $\mathrm{Ni^I}$ and $\mathrm{Ni^I}$-$\mathrm{bipy^-}$ radical anion complexes, respectively.**35** These species are highly reactive and illustrate the problems of assigning redox products as genuine metal-based or ligand-based radicals.

A very wide range of tetraaza macrocyclic complexes of $\mathrm{Ni^{II}}$ have been prepared and studied. An important feature of many $\mathrm{Ni^{II}}$ macrocycles is their high stability and inertness. Macrocyclic ligands can therefore be regarded as protecting groups for the metal center, and this has led to the study of metal redox properties and the electrochemical generation of $\mathrm{Ni^I}$ products.**36** Some of the ligands that have been studied for $\mathrm{Ni^I}$ complexation are listed in Scheme 3.

The redox properties of the complexes (the reversibility and potential of the $\mathrm{Ni^{II/I}}$ couple) are related to the ring size, the donor atoms, the unsaturation, and the degree of functionalization of the macrocyclic ring. EPR spectroscopy has been particularly useful in differentiating between metal- and ligand-based radical species. Interestingly, the degree of alkylation at the N-donor ligands enhances the stabilization of $\mathrm{Ni^I}$ species by shifting the $\mathrm{Ni^{II/I}}$ couple to more anodic potentials; this effect has been ascribed to solvation and stereochemical effects.**37** Interestingly, $\mathrm{Ni^I}$ species can also be generated from pentagonal bipyramidal $\mathrm{Ni^{II}}$ precursors.**13** Reduction of the $\mathrm{[Ni(\mathbf{36})]^{2+}}$ by one electron affords a ligand-based radical species; addition of CO to these reduced solutions gives a metal-based $\mathrm{Ni^I}$ product $\mathrm{[Ni(\mathbf{36})CO]^{+}}$, which has been assigned by EPR spectroscopy. This is an example of intramolecular electron transfer within a macrocyclic complex (equation 6).**38**

$$\mathrm{[Ni^{II}(36^{\bullet-})]^{+}} \underset{-\mathrm{CO}}{\overset{+\mathrm{CO}}{\rightleftharpoons}} \mathrm{[Ni^{I}(36)(CO)]^{+}} \qquad (6)$$

The single-crystal X-ray structures of macrocyclic $\mathrm{Ni^I}$ species showing square-planar coordination at the metal center have been reported. The complexes (**37**)**39** and (**38**)**40** both show $\mathrm{Ni^I}$ bound to four aza N-donors of a saturated macrocycle to give square-planar coordination at the metal center. The electrochemistry of a wide range of $\mathrm{Ni^{II}}$–porphyrin complexes

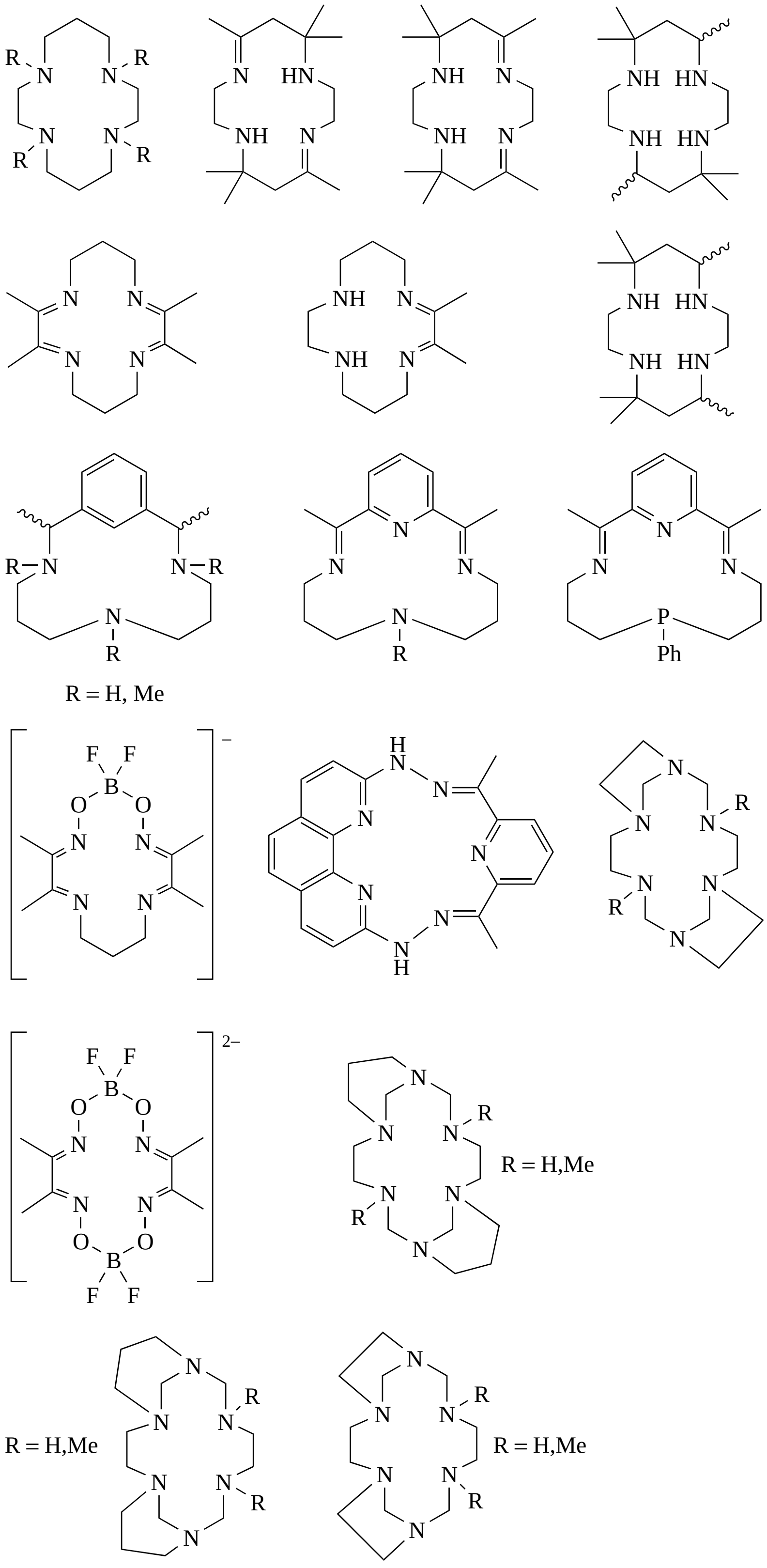
R = H, Me
−
2−
R = H,Me
R = H,Me
R = H,Me

Scheme 3

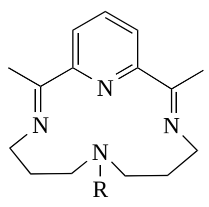

(**36**)

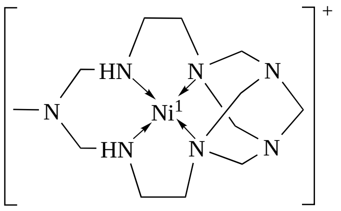

(**37**)

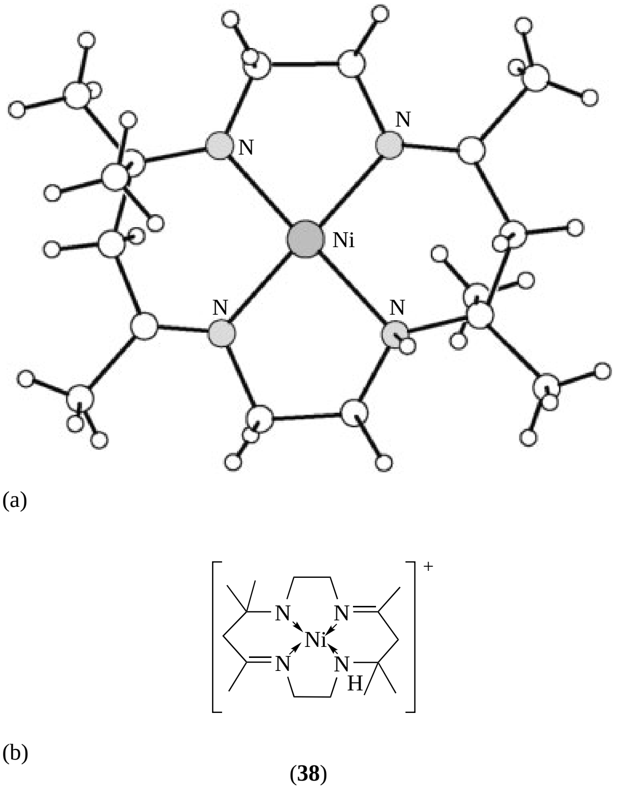

(**38**)

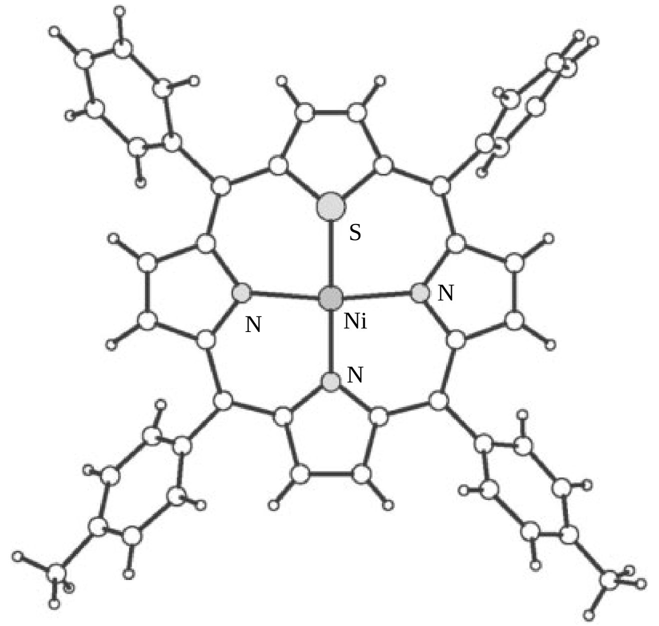

(**39**)

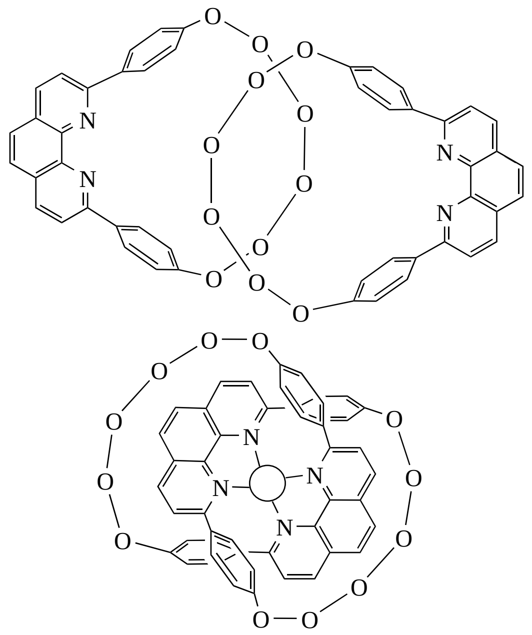

(**40**)

has been investigated, particularly with regard to the formation of Ni$^{\mathrm{I}}$ and ligand-based ligand-radical anions.[41] The structure of a Ni$^{\mathrm{I}}$ complex of a modified porphyrin has been reported; in (**39**), one of the N-donors of the porphyrin has been replaced by an S-donor, with the resultant SN$_3$-donor ligand binding to Ni$^{\mathrm{I}}$ in a square plane. Interestingly, the S-donor acts as a long-range bridging ligand to another [Ni(L)] unit to give an overall binuclear structure.[42]

A highly unusual air-stable Ni$^{\mathrm{I}}$ species has been produced using an interlocking catenane ligand (**40**). The Ni$^{\mathrm{II}}$ precursor has an enforced tetrahedral geometry and shows a particularly anodic Ni$^{\mathrm{II/I}}$ couple. The resultant Ni$^{\mathrm{I}}$ species, which is assumed to be tetrahedral, is stable in air for extended periods.[43] The electrochemical generation and stabilization of Ni$^{\mathrm{I}}$ centres by 2,6-diiminopyridyl ligands (**41**) in [Ni(**41**)$_2$]$^{2+/+}$ has been reported.[44]

The mechanisms and kinetics of CO$_2$ reduction by Ni$^{\mathrm{I}}$ macrocycles have been investigated.[45]

An electrochemical study of Ni$^{\mathrm{II}}$ meso-tetraphenylhomoporhyrins, -secochlorins, and -chlorophin has shown that the rigid homoporphyrin complexes are reduced at the ligand sites. In contrast, the more flexible chlorin and secochlorin complexes form Ni^I complexes upon reduction as the increased flexibility can better accommodate the larger Ni^I ion.**46**

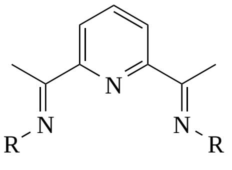

(**41**)

4.3 P- and As-donor Complexes

A series of air-sensitive trigonal bipyramidal and trigonal pyramidal Ni^I complexes, $[Ni(PR_3)_4]^+$, $[NiX(PR_3)_3]$, $[NiX(AsR_3)_3]$ (X = halide), and $[Ni(tripod)]^+$ and [NiX(tripod)] (tripod = face-capping tripodal P, As ligand), have been reported.**47** The methods of synthesis of these species are varied, but essentially are based on the reduction of Ni^{II} or oxidation of Ni^0 precursors. A range of four- and five-coordinate Ni^I complexes have been structurally characterized and some of these are illustrated in (**42**)–(**46**).

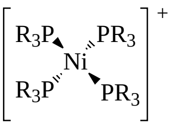

(**42**)

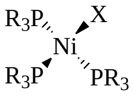

(**43**)

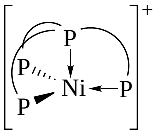

(**44**)

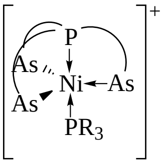

(**45**)

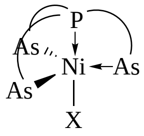

(**46**)

The magnetic moments of these complexes are consistent with the presence of one unpaired electron. Unusual three-coordinate Ni^I species (**47**) and (**48**) have been isolated using sterically hindered amido ligands.**48**

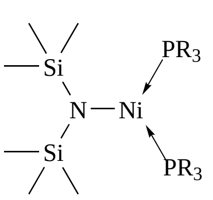

(**47**)

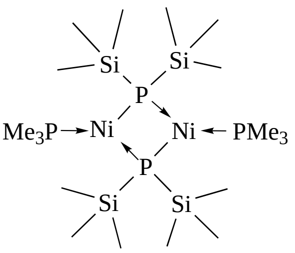

(**48**)

4.4 S-donor Complexes

The reductive electrochemistry of several Ni^{II} complexes of unsaturated dithiolate ligands has been examined.**49** On the basis of the electrochemical redox potentials, EPR spectral evidence, and SCF calculations, these reduction products are best formulated as Ni^I complexes for dithiocarbamate and 1,2-dithiolene ligands, and as Ni^{II} stabilized ligand-radical anions for dithiodiketonate species. It is often difficult to assign electron-density distributions within a molecule, particularly with delocalized ligands such as dithiolenes.

5 NICKEL(II)

The literature on the coordination chemistry of Ni^{II} is vast, and this brief review can only cover aspects of this chemistry. Essentially, all types of ligands that have been used for metal coordination chemistry have been investigated with Ni^{II}.

5.1 Cyanide Complexes

$[Ni(CN)_2]$ is a polymeric material with the CN^- ligand bridging between Ni^{II} ions (**49**). $[Ni(CN)_4]^{2-}$ (**50**) is a particularly stable, yellow Ni^{II} species with a formation constant of some 10^{30}. The complex is diamagnetic and square-planar at Ni^{II} with Ni–C = 1.86 Å.**50** The solid-state structure also shows stacking of these planar layers to give a Ni^{II}–Ni^{II} interaction with a 3.30 Å separation. This type of stacking interaction is relatively common for square-planar Ni^{II} complexes. Addition of another CN^- ligand to $[Ni(CN)_4]^{2-}$ affords $[Ni(CN)_5]^{3-}$, which shows square pyramidal (**51**) or trigonal bipyramidal (**52**) structures depending upon the counterion (equation 7, $K_{eq} = 0.28$ at 298 K).**51**

$$[Ni(CN)_4]^{2-} \rightleftharpoons [Ni(CN)_5]^{3-} \qquad (7)$$

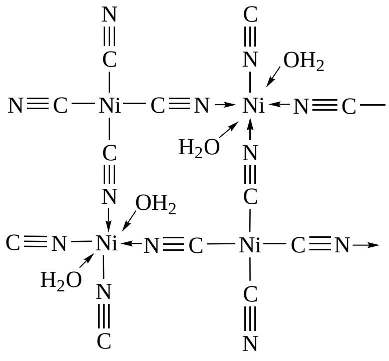

(**49**)

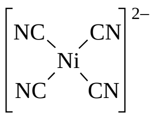

(**50**)

Recent work has indicated that Ni^{II} complexes can interact with buckminsterfullerene, C_{60}, and related fullerenes**50** (*see* ***Carbon: Fullerenes*** and Section 5.2).

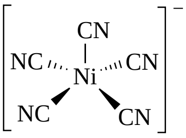

(**51**)

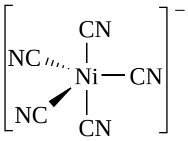

(**52**)

5.2 N-donor Complexes

Ni^{II} amine chemistry was investigated by Werner as part of his classic experiments on metal coordination chemistry.[52] This work led to an understanding of ligand field and the chelate effects, and pioneered the modern era of coordination, organometallic, and bioinorganic chemistry.[53] The chelate effect is illustrated by comparison of the stepwise stability constants for $[Ni(NH_3)_6]^{2+}$ (**53**) ($\log K_1 - \log K_6 = 2.36$, 1.90, 1.55, 1.23, 0.85, 0.42, respectively) and $[Ni(en)_3]^{2+}$ (**54**) ($\log K_1 - \log K_3 = 7.66, 6.40, 4.55$, respectively), which shows greater stability for the latter bidentate five-membered chelate system. Further, replacement of en by pn leads to the formation of $[Ni(pn)_3]^{2+}$ (**55**), which is less stable owing to the larger six-membered chelate ring. A wide variety of substituted amine complexes of the type $[Ni(en)_2X_2]^{x+}$ have been reported.

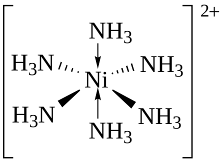

(**53**)

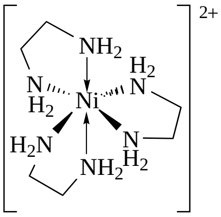

(**54**)

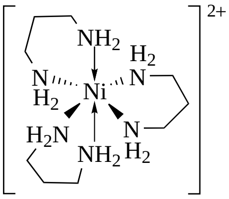

(**55**)

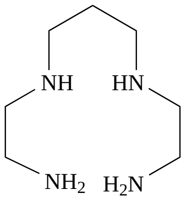

(**56**)

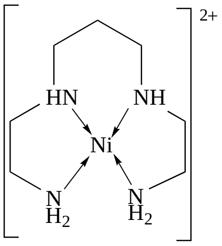

(**57**)

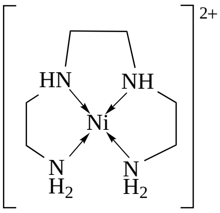

(**58**)

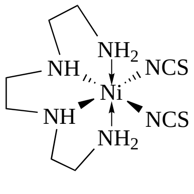

(**59**)

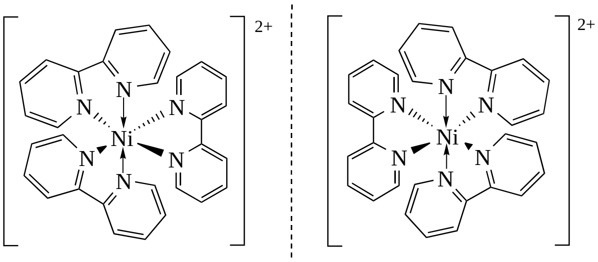

(**60**)

Polychelate triamine and tetraamine ligands can form even more stable complexes with Ni^{II}. For example, 2,3,2-tet (**56**) forms a particularly stable, yellow, square-planar Ni^{II} complex, $[Ni(2,3,2\text{-tet})]^{2+}$ (**57**), which is some 10^2 times more stable than the corresponding $[Ni(2,2,2\text{-tet})]^{2+}$ (**58**). This illustrates the variation of stability constant with ligand size. Interestingly, $[Ni(2,2,2\text{-tet})]^{2+}$ can be regarded as somewhat strained owing to the presence of three, five-membered ring chelates within an equatorial plane. This strain can be released by formation of the *cis* octahedral species $[Ni(2,2,2\text{-tet})(NCS)_2]$ (**59**), which is formed readily on addition of ^{-}NCS to a solution of $[Ni(2,2,2\text{-tet})]^{2+}$.[54]

Many examples of Ni^{II} complexes containing pyridyl, substituted pyridyl, imidazoles, pyrazoles, and related heterocyclic N-donor ligands have been reported, for example, $[Ni(L)_4X_2]$ (X = halide, L = monodentate N-donor), $[Ni(LL)_3]$, $[Ni(LL)_2X_2]$ (LL = chelate N-donor, for example, bipy, phen).[55] These compounds can be very readily prepared by reaction of NiX_2 and related Ni^{II} starting materials with L and LL. The complexes $[Ni(LL)_3]^{2+}$ (LL = bipy (**60**), phen) are normally isolated as racemic mixtures of (+) and (−) enantiomers, which can be resolved by crystallization with chiral counter anions.[56] Sterically hindered heterocyclic chelates or chelates with a small bite angle tend to form binuclear and polynuclear structures. For example, reaction of Ni^{II} salts with 1,8-naphthyridine (**61**) affords an unusual species in which the tight chelate bite of the ligand leads to the formation of a Ni^{I}–Ni^{II}-bonded dimer $[Ni_2(\mathbf{61})_4Br_2]^+$ (**62**). The Ni–Ni distance in (**62**) is 2.41 Å with Ni–N(av) = 2.11 Å.[57] Magnetic and EPR data on this complex suggest that it is a spin-delocalized system with an average oxidation state of +1.5 on each Ni. Second-sphere coordination of $[Ni(H_2O)_5py]^{2+}$ in a calixarene host has been reported.[58]

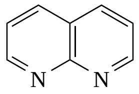

(**61**)

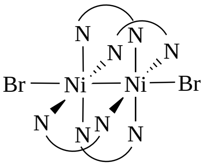

(**62**)

The tetradentate amine ligand (**63**) (L) displays an unusual binding to Ni^{II} ions to form the complex $[Ni_2L_3]^{4+}$. This species does not show the expected helical structure but incorporates two ligands each bound to a Ni^{II} ion in a tetradentate manner with the third ligand L in a bis-bidentate bridging mode.[59] Such a structure has been previously observed for the binding of siderophore alcilagin to Fe^{III}.

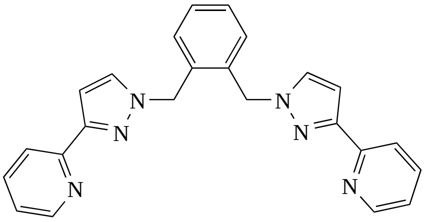

(**63**)

The structural trends and magnetic behavior of polynuclear Ni(II) and Mn(II) azido bridged complexes have been assessed.[60]

A very wide range of Schiff-base polychelate ligand complexes of Ni^{II} have been reported. These complexes can be prepared by reaction of Ni^{II} with the preformed ligand. More frequently, however, the complex is prepared in one step by Schiff-base condensation of the free aldehyde or ketone with the corresponding amine in the presence of Ni^{II}. The Ni^{II} ion thereby acts as a template, bringing together and stabilizing the intermediates and final product of the reaction.[61] Scheme 4 illustrates some of the ligands that have been prepared and complexed to Ni^{II}.

The report by Curtis[62] of the condensation of $[Ni(en)_3]^{2+}$ with acetone to give the open-chain condensation product and subsequently the macrocyclic complex (equation 8) was the first example of the synthesis of N-donor macrocycles by a metal template, and predates work on the oxycrown ligands such as 18-crown-6 ($[18]aneO_6$).

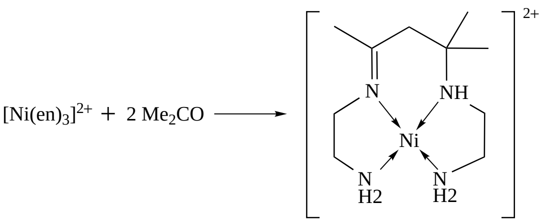

(8)

An enormous, wide-ranging literature on Ni^{II} macrocyclic chemistry is now available (see Section 5.7). The H-bonded dimethylglyoxime complex $[Ni(dmgH)_2]$ (**64**) is one of the more important, since this species is used for the gravimetric determination of Ni. Like many square-planar Ni^{II} complexes it stacks in the solid state with a Ni–Ni separation of 3.24 Å.[63] Related Ni^{II} complexes of functionalized dmg ligands frequently show this type of stacking interactions.

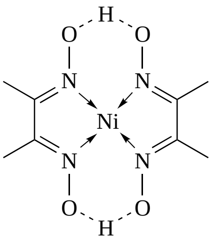

(**64**)

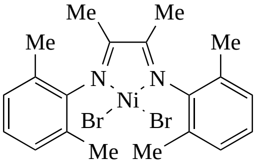

(**65**)

There has been an explosion in interest in diimine Ni^{II} complexes such as (**65**) since the report of Brookhart and coworkers detailing[64] their activity in the polymerization of alkenes with toleration of functional groups such as ethers, esters, and carboxylic acids. The incorporation of steric bulk within the ligand framework,that is, alkyl groups on the aromatic rings, is crucial for efficient polymerization rather than oligomerization.[64]

Ni^{II} octaethylporphyrin has been cocrystallized with C_{70}, in which the eight ethyl groups are arranged so that they encircle the C_{70}. This allows the close face–face contact of two flat Ni^{II} porphyrins.[65] This contrasts with the structure of Ni^{II} octakis(dimethylamino)porphyrazinato with C_{60} in which the porphyrazinato ligand is warped to a significant degree with each C_{60} lying in a cleft formed by two steeply inclined Ni^{II} porphyrazinates; there is additional π-stacking between the C_{60} molecules to produce a zig-zag chain. By contrast the analogous copper octakis(dimethylamino)porphyrazinato complex remains flat when cocrystallized with C_{60}.[66]

The tetraazamacrocyclic complex (**66**) adopts a saddle shape about Ni^{II} and allows the formation of a 1:1 supramolecular complex with C_{60} and a 2:1 complex with other

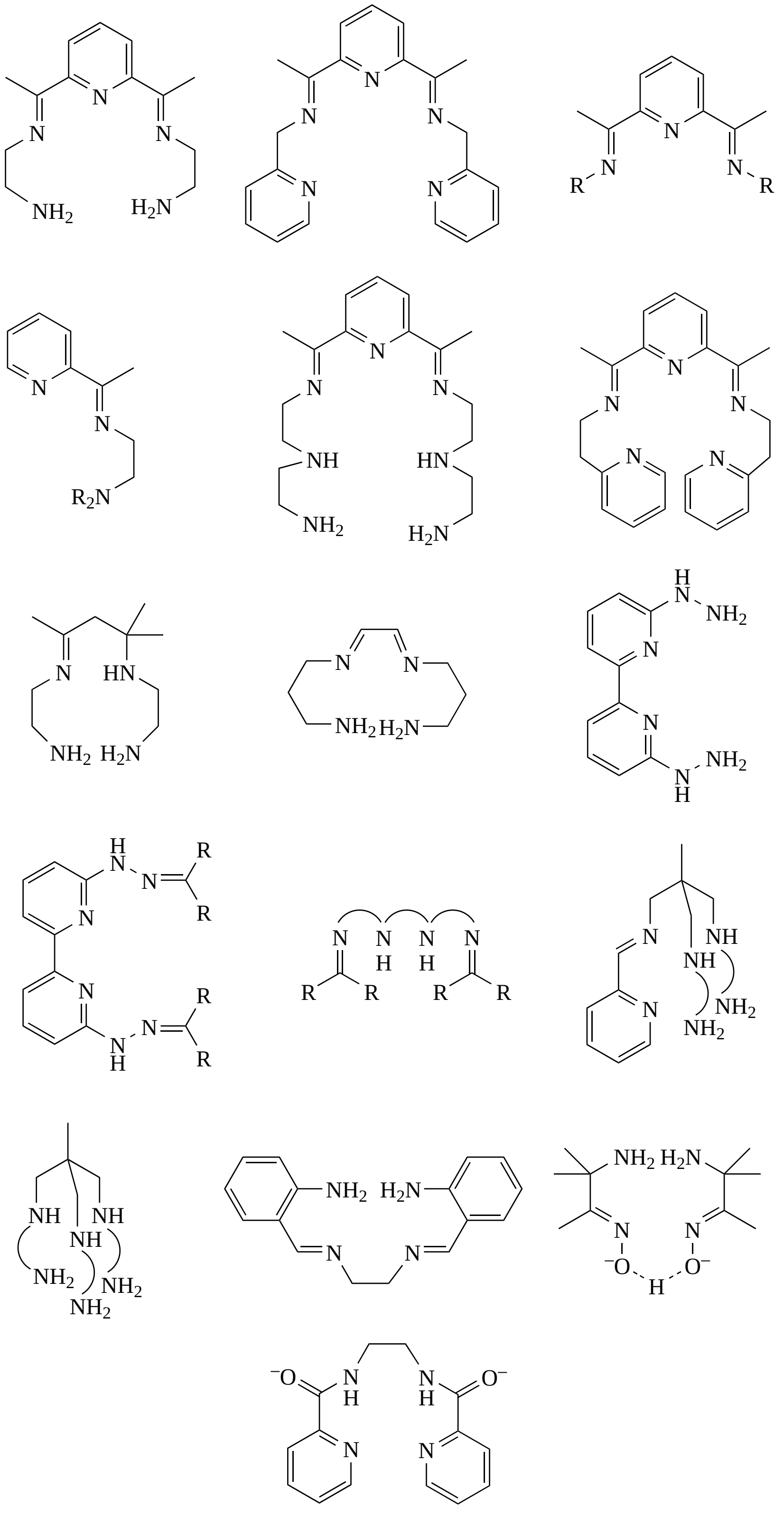

Scheme 4

globular molecules for example, 1,2-dicarbadodecaborane and the phosphorus chalcogenide P_4S_3.[67]

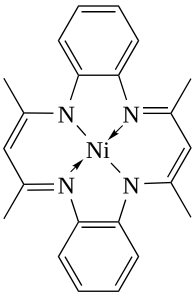

(**66**)

A range of complexes incorporating organic nitriles, nitrosyls, cyanates, thiocyanates, pyrazolyl borates, and azides have been reported.[1,2]

5.3 P-, As-, and Sb-donor Complexes

A very large number of phosphine, phosphite, stibine, and arsine complexes of type four-coordinate $[NiX_2(ER_3)_2]$ and five-coordinate $[NiX_2(ER_3)_3]$ ($X =$ halide) have been reported, although this area is dominated by complexes of tertiary phosphines. The complexes $[NiX_2(ER_3)_2]$ can be either tetrahedral (**67**) or square-planar (**68**), depending upon the electronic and steric effect of the coordinated phosphine, arsine, and stibine ligands (see Section 2).[68]

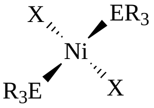

(**67**)

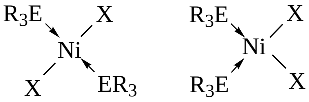

(**68**)

1,5,9,-Triethyl-1,5-9-triphospacyclododecane reacts with $NiBr_2$ to form an unusually distorted four-coordinate complex (**69**) as a result of constraints imposed by the macrocyclic ligand.[69] Indeed, the coordination geometry at Ni can best be described as a trigonal bipyramidal with a vacant vertex. Surprisingly, this apparent vacancy only leads to low activity in the polymerization of ethane.[69]

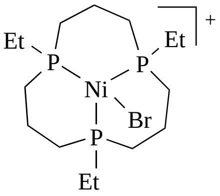

(**69**)

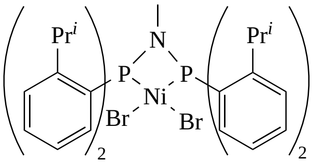

(**70**)

The square-planar complex (**70**) incorporating a C_2 symmetric diphosphine catalyzes the polymerization of ethene,[70] which is somewhat surprising as diphosphine complexes tend to be much less active than related diimine complexes (see Section 5.2).

The Ni^{II} complex incorporating mixed-donor P/O-ligands find industrial application in the Shell Higher Olefin Process (SHOP) to yield α-alkenes, while the complex (**71**) has been shown to be active in the polymerization of olefins and will also tolerate functionalized monomers such as methyl methacrylate.[71] Grubbs and coworkers have adapted the standard SHOP catalyst to yield a highly active family of catalysts (e.g. **72**) for the polymerization of low-branched polyethylene.[72] This is in contrast to the diimine catalysts (Section 5.2) which lead to a more highly branched polyethylene.

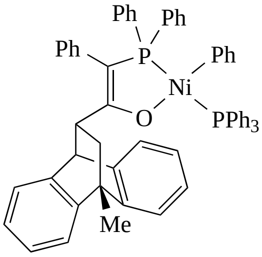

(**71**)

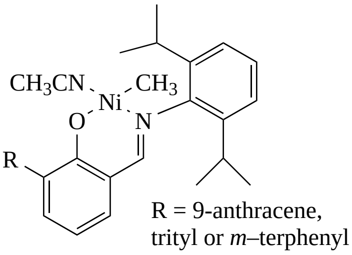

(**72**)

An extensive range of polychelate P-donor and mixed P/N-, P/S-, P/O-, and P/C-donor ligand complexes have been

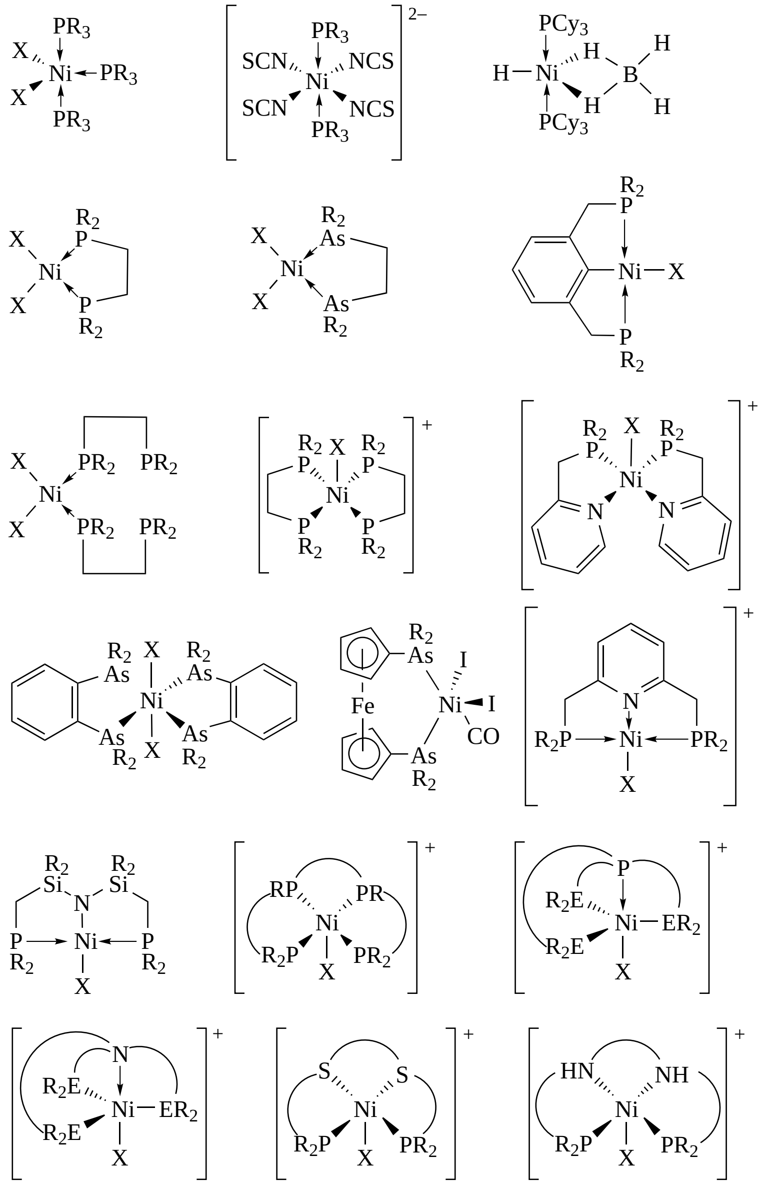

Scheme 5

prepared.[1,2] Their complexation to Ni^{II} is based, in general, on four-coordinate Ni^{II} species in equilibrium, in the presence of other ligands, with five- and six-coordinate products. Some of the complexes that have been prepared are illustrated in Scheme 5.

5.4 O-donor Complexes

$[Ni(H_2O)_6]^{2+}$ (**73**) is the main cation formed when Ni^{II} is dissolved in aqueous solution in the absence of other coordinating ligands; a second hydration sphere of some 15 water molecules has been proposed.[73] In addition, most simple salts written as $NiX_2{\cdot}xH_2O$ actually contain the hexaaqua ion $[Ni(H_2O)_6]^{2+}$. Under alkaline conditions, Ni^{II}–hydroxy species are formed, including $[Ni(OH)_6]^{4-}$, $[Ni(OH)_4]^{2-}$, and $[Ni_4(OH)_4]^{4+}$ (**74**), which presumably has a cubane structure.[74]

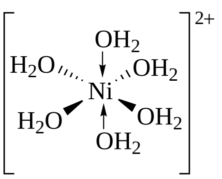

(**73**)

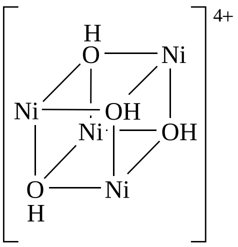

(**74**)

Complexes such as $[Ni(ROH)_6]^{2+}$ and $[NiX_2(ROH)_4]$ can be generated under anhydrous conditions, although they tend to be water sensitive and can be readily hydrolyzed.[75] O-Donor ligands such as alcohols, ethers, and ketones are in general very poor donors to Ni^{II} and so their complexes are labile and often unstable. The structure of $[NiBr(EtOH)_4]^+$ (**75**) shows it to be a halo-bridged dimer.

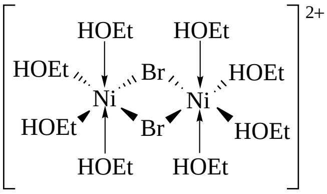

(**75**)

Alkoxide complexes of stoichiometry $[Ni(OR)_2]$ can be prepared by reaction of simple Ni^{II} salts NiX_2 with RO^-.[73] In general, the structures of these complexes are not known for certain, although the X-ray structure of $[Ni_4(OMe)_4(acac)_4(MeOH)_4]$ (**76**) confirms[76] it to be based on a $Ni_4(OMe)_4$ cube. Similar cubane structures have been proposed for a variety of other Ni^{II} alkoxide complexes.

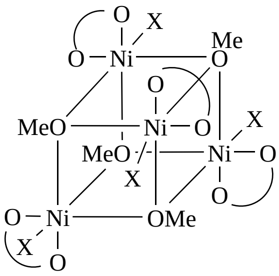

(**76**)

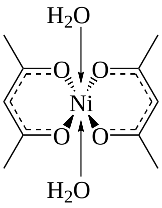

(**77**)

Reaction of Ni^{II} with acac affords *trans*-$[Ni(acac)_2(H_2O)_2]$ (**77**), which can be dehydrated to $[Ni(acac)_2]$ (**78**). $[Ni(acac)_2]$ is actually trimeric with bridging acac ligands.[77] The complexes $[Ni(acac)_2(L)_2]$ (L = py and related amine ligands) have been prepared, and some structurally characterized. Related tropolone, quinone, and catechol complexes have been reported.[1,2] Coupled electronic states in the complexes *trans*-$[MCl_2(H_2O)_4]^{n+}$ complexes (M = Ni^{2+}, Co^{2+}, V^{3+} and Cr^{3+}) have been probed by absorption and luminescence spectroscopy. The strongest interaction occurs for the Ni^{II} complex, where the lowest energy singlet state is very close in energy to a spin allowed crystal field band, giving rise to intense vibronic patterns.[78]

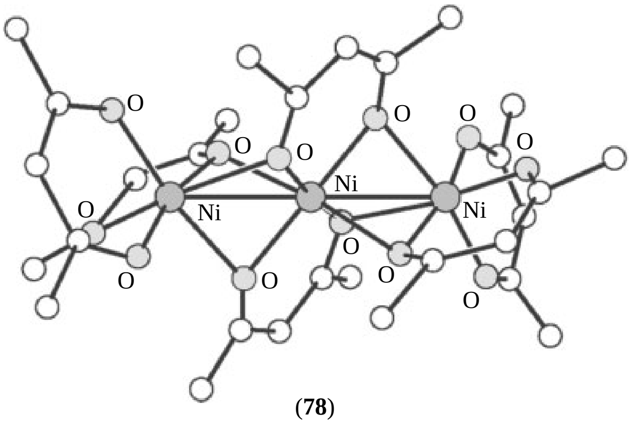

(**78**)

Treatment of Ni^{II} salts with acetic acid affords *trans*-$[Ni(O_2CMe)_2(H_2O)_4]$ (**79**) incorporating monodentate acetate ligands. By altering the reaction conditions and the carboxylic acid, complexes of type *trans* and *cis* $[Ni(O_2CR)_2(L)_2]$ (**80**) (L = N-, O-donor ligands) in which the carboxylate moiety is acting as a bidentate ligand can be prepared.[79] Binuclear species of the type $[Ni_2(O_2CR)_4(L)_2]$ (**81**) can also be synthesized,[80] and a cubane complex $[Ni_4(OMe)_4(O_2CMe)_2(L)_4]^{2+}$ (L = dinitrile ligand) (**82**) has been reported.[81]

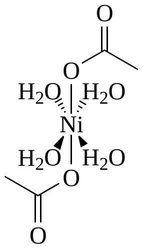

(**79**)

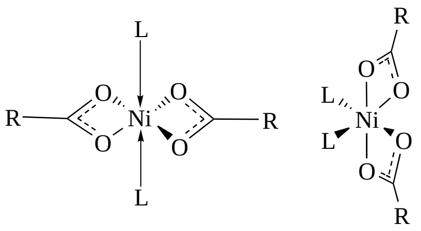

(**80**)

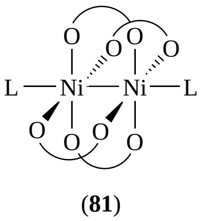

(**81**)

$[Ni(NO_3)_2]$ is a common starting material for Ni^{II} coordination chemistry, since the nitrato ion is not a very strong donor. However, many nitrato[82] and nitrito[83] complexes are known in which these ligands are bound directly to

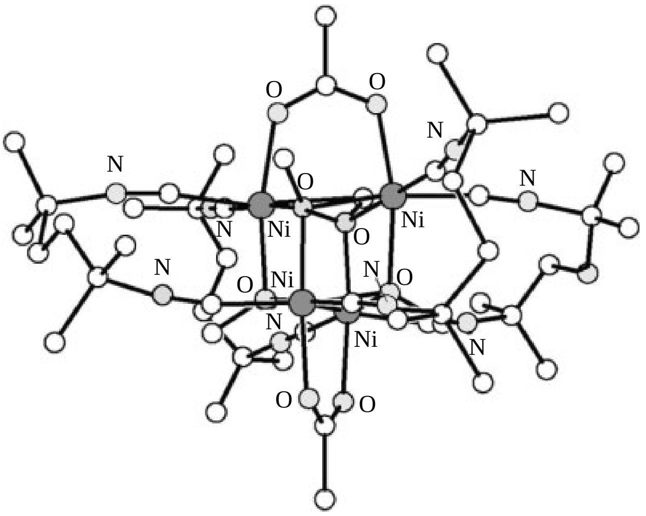

(**82**)

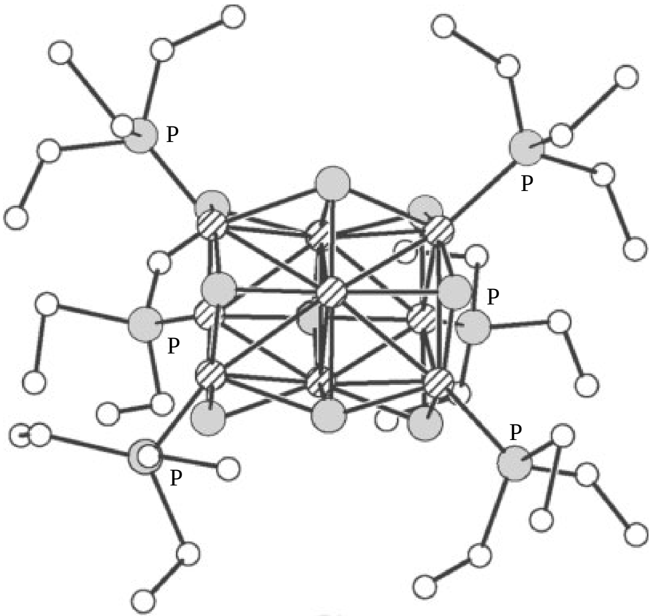

(**83**)

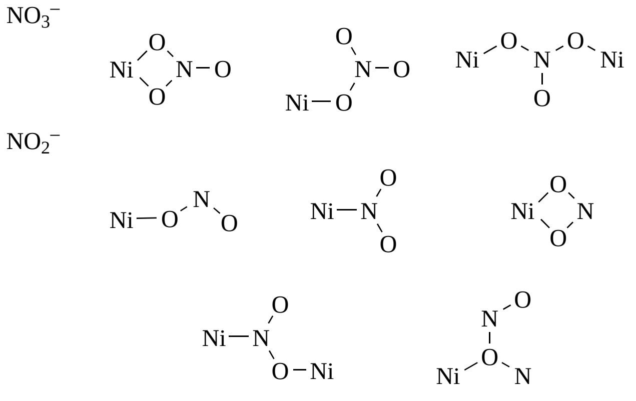

Scheme 6

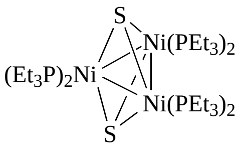

(**84**)

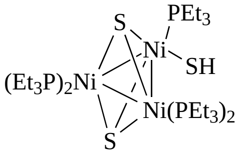

(**85**)

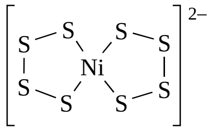

(**86**)

Ni^{II} either as monodentate, bidentate, or bridging ligands. Differentiation between these modes of coordination can be difficult in the absence of good X-ray structural data, although IR spectroscopy has been used effectively. The different bonding modes of NO_3^- and NO_2^- ligands are summarized in Scheme 6.

5.5 S-, Se-, and Te-donor Complexes

The chemistry of Ni^{II} with S-ligands is not as well-developed as for N- and O-donor ligands. This is partly due to the formation of insoluble Ni^{II} sulfide polymers. The ability of S^{2-} to act as a bridging and capping ligand has led to the formation of polynuclear cluster species such as $[Ni_9(\mu^4\text{-}S)_3(\mu^3\text{-}S)_6(PEt_3)_6]^{2+}$ (**83**),**[84]** $[Ni_3(\mu^3\text{-}S)_2(PEt_3)_6]^{2+}$ (**84**), and $[Ni_3(\mu^3\text{-}S)_2(SH)(PEt_3)_5]^{2+}$ (**85**).**[85]** Reaction of $[Ni(OAc)_2]$ with ammonium polysulfide affords $[Ni(S_4)_2]^{2-}$ (**86**) in good yield as a square-planar, diamagnetic product.**[86]**

A range of dithiocarboxylate, dithiocarbamate, xanthate, dithioformate, thioformate, and sacsac complexes have been reported for Ni^{II}.**[1,2]** These ligands are illustrated in Scheme 7. Many of the complexes are square-planar of type $[Ni(L)_2]$ with the mono negatively charged ligand chelating to the Ni^{II} center, although there are examples where the complexes stack in the solid state. Dithiolene complexes of Ni^{II} are of particular interest since they are generally redox active at the metal and/or ligand centers.

Work on Ni-thiolate complexes has focused on the synthesis of mononuclear, S-bridged polynuclear, cluster, and cubane model complexes of relevance to active site in biological systems (see Section 8).**[87,88]** Scheme 8 illustrates some of the thiolate complexes that have been prepared.

The synthesis of homoleptic Ni-thiolate complexes $[Ni(L)_4]$ ($L =$ hindered thiolate) has been reported by Armstrong and coworkers.**[89]** Preparations of Ni^{II} thiolates

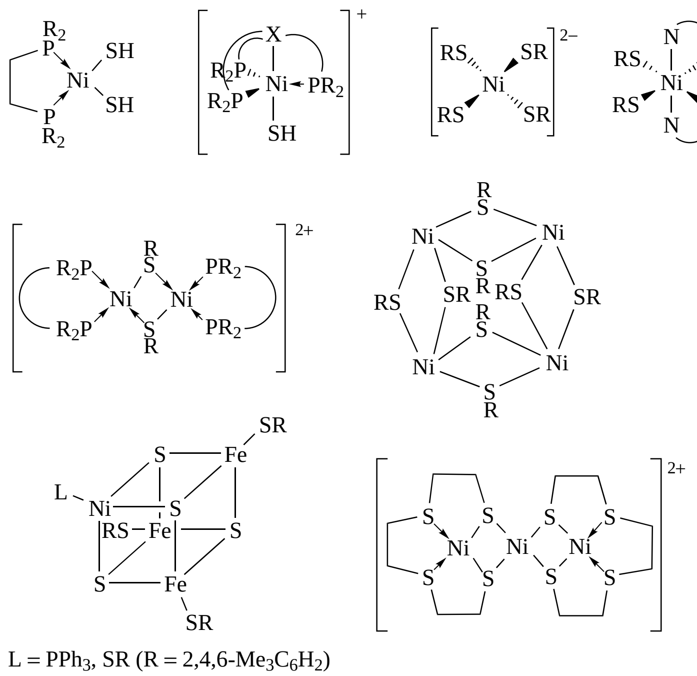

L = PPh_3, SR (R = 2,4,6-$Me_3C_6H_2$)

Scheme 8

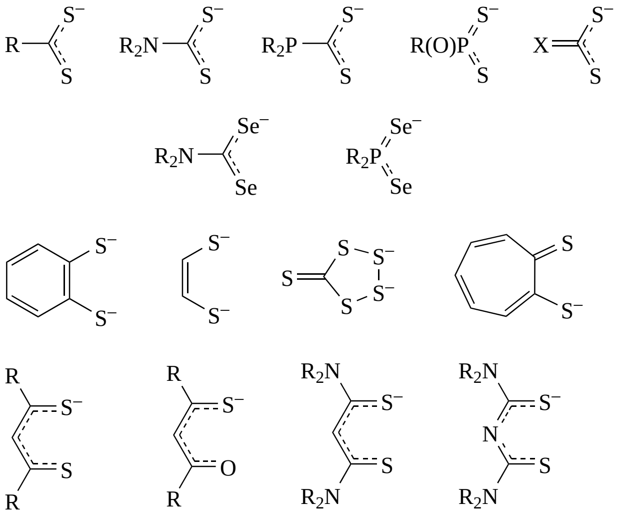

Scheme 7

are very solvent dependent particularly when synthesizing coordinatively unsaturated metal complexes, and can be highly O_2 sensitive with the required synthetic procedure varying according to the thiolate used.

Recently, interest in Ni^{II} thiolate chemistry has increased owing to the recognition that certain enzymes incorporate mixed N/S coordination at Ni^{II}. Several mixed N/S-donor complexes have been prepared and characterized, including $[Ni(terpy)(SPh)_2]_2$ (**87**), $[Ni(terpy)(SC_6F_5)_2(NCMe)]$ (**88**), and $[Ni(terpy)(SR)_2]$ [$R = 2,4,6\text{-}i\text{-}Pr_3C_6H_2$ (**89**), 2,6-$Me_2C_6H_3$ (**90**)], and their chemical and redox properties related to the in vivo systems.**90** More recent examples of low molecular weight model complexes are described in Section 8.

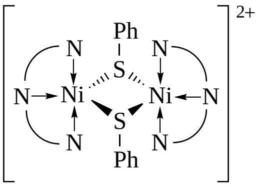

(**87**)

Oxidation of a series of Ni-bound thiolates (such as **91**) demonstrate the formation of sulfones and further oxidation to give sulfoxides.**91** The oxidation of thiolates was found not to occur for the analogous Fe or Zn

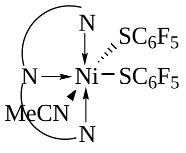
N
SC6F5
N
Ni
SC6F5
MeCN
N

(**88**)

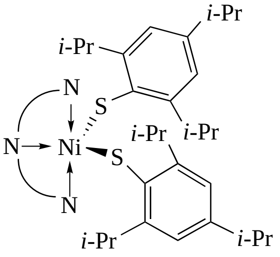
i-Pr
i-Pr
N
S
N
Ni
S
i-Pr
i-Pr
N
i-Pr
i-Pr

(**89**)

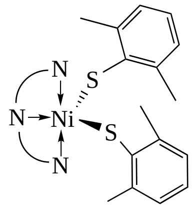

(**90**)

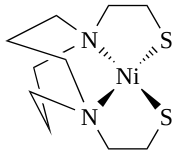

(**91**)

complexes. By cyclic voltammetry, the Ni complexes display a reversible Ni^{II}–Ni^{I} reductions and irreversible ligand-based oxidation presumably to give unstable thiyl radical intermediates. The bis(sulfone) complexes, however, show reversible Ni^{II}–Ni^{III} oxidative processes as do the analogous complexes where the S-centres have been alkylated.[91] The possibility for a two centred Ni-SR site to function in an oxidative-addition mode was suggested as an intriguing solution developed by Nature to achieve the desired reactivity.

Holm and coworkers have investigated the structural and redox properties of mixed N/S-donor and related oxime Ni^{II} complexes, for example, (**92**) and (**93**), and have generated and studied the corresponding Ni^{III} species.[92]

Significantly, Ni^{II} dithiolenes have been shown to be effective for the electrochemical separation of alkenes from complex streams. No poisoning was observed with common impurities including hydrogen, carbon monoxide, acetylene, or hydrogen sulfide. Reactivity of these complexes occurs via alkene binding to S-centres rather than at the Ni (Scheme 9) reflecting the radical nature of these ligands.[93]

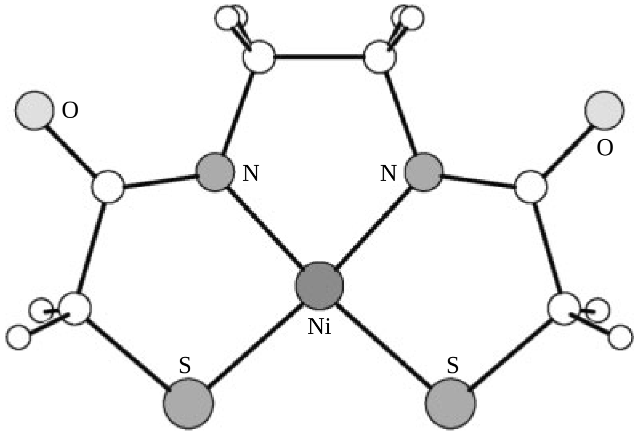

(**92**)

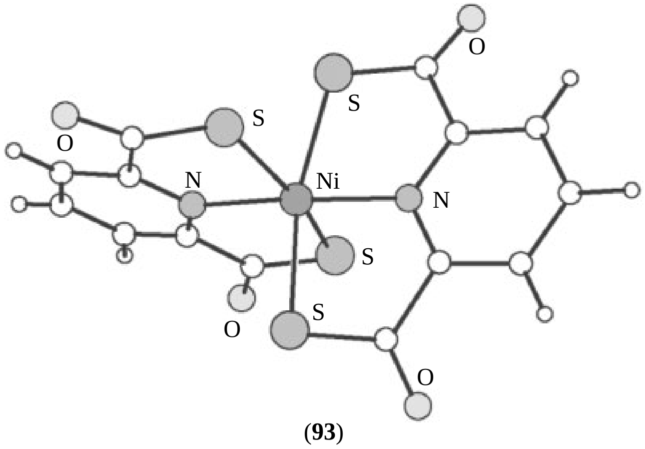
O
S
S
O
N
Ni
N
S
S
O
O

(**93**)

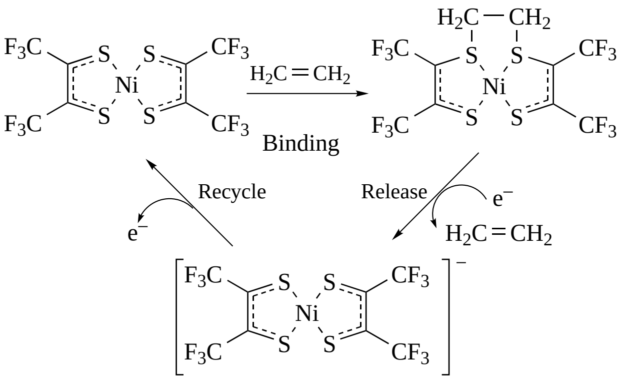
F3C
S
S
CF3
Ni
F3C
S
S
CF3
H2C=CH2
Binding
H2C—CH2
F3C
S
S
CF3
Ni
F3C
S
S
CF3
Recycle
e−
Release
e−
H2C=CH2
F3C
S
S
CF3
Ni
F3C
S
S
CF3
−

Scheme 9

5.6 Halide Complexes

Anhydrous NiX_2 (X = F, Cl, Br, I) can be prepared by reaction of elemental Ni with the free halide.[94] These species are polymeric and show octahedral coordination at Ni^{II}. The trihalo complexes $[NiX_3]^-$ also show octahedral coordination at Ni^{II} via bridging μ^2-Cl_3 units. The tetrahedral tetrahalo complexes $[NiX_4]^{2-}$ are readily prepared by reaction of NiX_2 with excess X^-. Substituted species $[NiX_3(L)]^-$ (L = py, substituted py, PPh_3) have been isolated as tetrahedral complexes.

5.7 Open-chain Mixed Donor and Macrocyclic Complexes

The redox noninnocence of the 2-mercapto-3,5-di-tert-butylaniline ligand has recently been investigated with Ni^{II} ions.[95] The spectroelectrochemistry of the complex displays a range of electron transfers where the monocation, the neutral species, and the mono- and dianions have been characterized. In a related manner, Wieghardt and coworkers have reported the first example of a stable N, O-coordinated *o*-iminobenzoquinone via air oxidation of the initial Ni^{II} complex with 2-anilino-4,6-di-tert-butylphenol (**94**).[96] The analogous *o*-iminobenzosemiquinonate π-radical complex was also isolated for this system and earlier for the bis-(*o*-iminobenzosemiquinonate)nickel(II) complex.[97]

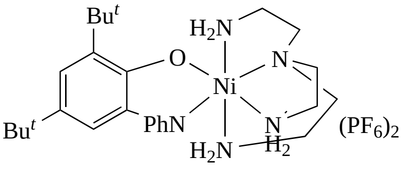

(**94**)

In recent years, the development of new concepts for the rational design of larger, more complex molecules has led to considerable progress in supramolecular chemistry to afford structures of a variety of symmetries, sizes, and stoichiometries. Ni^{II} complexes have provided versatile molecular tectons in a plethora of such structures.

The aggregation of Ni^{II} complexes using amine-thiolate ligands such as (**95**) has been observed to yield homo-hexanuclear complexes. Fascinating pinwheel motifs have been observed where two Ni centres bridge four Ni amino-thiolate complexes.[98] Here, both the bite angle of the S^-–Ni–S^- unit and the choice of bridging metal ion influence whether a simple trinuclear aggregate is favoured or a higher motif.[98]

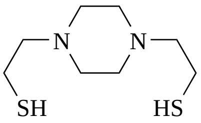

(**95**)

The imino-carboxylate ligand (**96**) coordinates to Ni^{II} in an equatorial manner to yield the monomer tecton $[Ni(L)(MeOH)_2]$. Subsequently, in the presence of templating lanthanide or group II metal ion these Ni^{II} complexes aggregate into an octahedral cage $\{M[Ni(L)]_6\}^{x+}$ (M = Sr^{II} or Ba^{II}, $x = 2$, M = La^{III}, Ce^{III}, Pr^{III} or Nd^{III}, $x = 3$).[99] However, in the presence of group I metal ions, aggregates of the alkaline metal-oxide cations template various cage compounds. For example, Na^+ forms the trigonal bipyramidal $[Na_5O]^{3+}$ core within a tricapped trigonal prismatic $[Ni(L)]_9$ aggregate to yield $\{(Na_5O) \subset [Ni(L)]_9(MeOH)_3\}(BF_4)_2{\cdot}OH{\cdot}CH_3OH$, whilst Li^+ forms a tetrahedral $[Li_4O]^{2+}$ core within a hexanuclear open cage $[Ni(L)]_6$ in $\{(Li_4O) \subset [Ni(L)]_6(MeOH)_3\}(ClO_4)_2{\cdot}1.85\ CH_3OH$.[99]

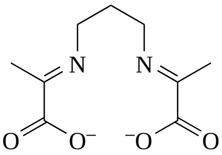

(**96**)

Complexes of $Ni(OAc)_2$ with 6-chloro-2-pyridonate (**97**) have been organized into an elegant Ni_{12} wheel, which has been investigated as a 'single-molecule magnet'.[100,101] With 3-methyl-3-pyrazol-5-one (**98**) the larger Ni_{24} wheel has been assembled.[102]

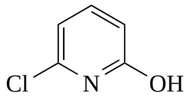

(**97**)

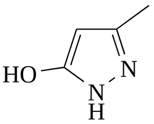

(**98**)

Bis(thiosemicarbazide)nickel(II) forms charge augmented double hydrogen-bonded chains with 1,4-terephthalate and trans-fumarate anions, which are further linked into sheets by hydrogen bonds between the N–H···O units. The methylation of the primary amine disrupts these interactions markedly so that hydrogen-bonded sheets result, involving now molecules of water.[103]

Crystals of $Ni(NO_3)_2$ with 4,4′-bipyridine produce a ladder type framework polymer, which can be desolvated to yield a stable porous solid.[104] The adsorption of methanol has then been studied and shown to cause a guest-driven solid-to-solid transformation. Fascinatingly, this material is able to accept toluene into its pores, in spite of the pore window being lower than the cross-sectional area of toluene.[105] Molecular frameworks which grow as homochiral single crystals have been realized through the use of 1,3,5-benzenetricarboxylic acid, nickel(II) nitrate and 1,2-propanediol. The chiral 1,2-propanediol represents the first demonstration that chiral molecules can specifically template helix handedness in a chiral porous framework solid.[106]

Van Koten and coworkers have described the first example of a dendrimer employed as a catalyst support (Scheme 10).[107] This system is based upon diaminoarylnickel(II) complexes attached to the dendrimer surface and catalyze the Kharasch-type additions of polyhalogenoalkanes to alkenes. There is a clear advantage with regard to catalyst recovery, although in comparison to the analogous mononuclear catalyst the activity of the supported material was reduced.[107]

Supramolecular interactions have been exploited in the extraction of Ni^{II} salts using ditopic ligands (e.g. **99)** with specific binding sites for both the cation, in the salen $N_2O_2{}^{2-}$, and the anion being hydrogen-bonded to the external protonated amines.[108] The formation of metallomacrocycles and the supramolecular chemistry of salen type complexes for cation binding studies with alkaline-earth metal ions has been investigated.[109]

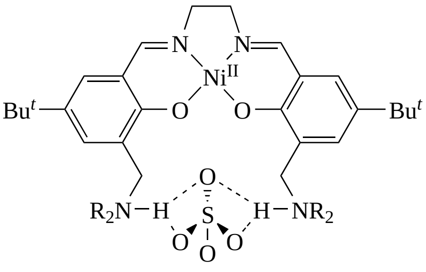

(**99**)

A very extensive and wide-ranging literature has built up around the coordination chemistry of Ni^{II} about N-donor Schiff-base ligands (see Section 5.2), open-chain mixed-donor ligands, and macrocyclic ligands. This burgeoning area is based on the ease of complexation of Ni^{II} by these types of ligands. Interest in these types of complexes derives from their potential and practical uses in metal extraction processes, metal ion transport and recognition, for the stabilization of unusual oxidation state and stereochemistries at the metal center, as models for biological systems, in host–guest chemistry, and for small molecule binding and catalysis. Several reviews and texts specifically dealing with polydentate and macrocyclic complexes, porphyrins, and phthalocyanins have been published.[110–112] Scheme 11 illustrates some of the open-chain mixed-donor ligands and metal complexes that have been investigated.

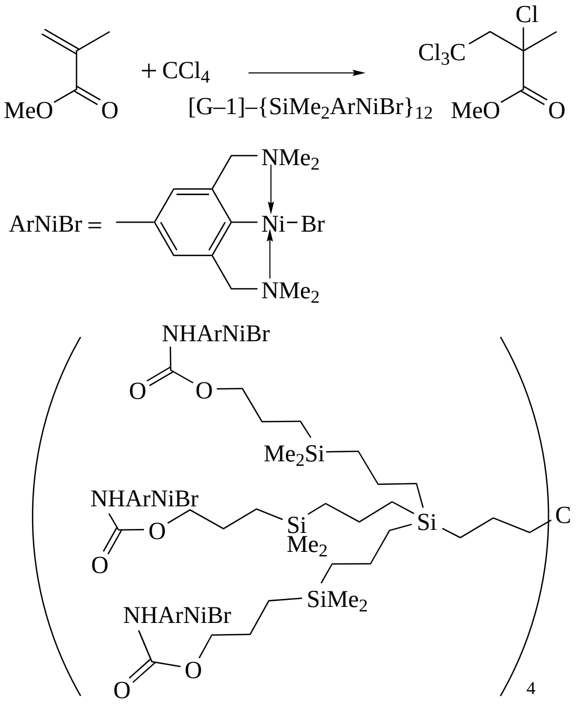

Scheme 10

Much of the macrocyclic chemistry of Ni^{II} is based on Schiff-base template condensation reactions. The pioneering work of Curtis[62] showed that the condensation of en and acetone could be templated by Ni^{II} to afford the corresponding tetraaza macrocycle (equation 9). Related template condensation reactions are illustrated in Scheme 12.

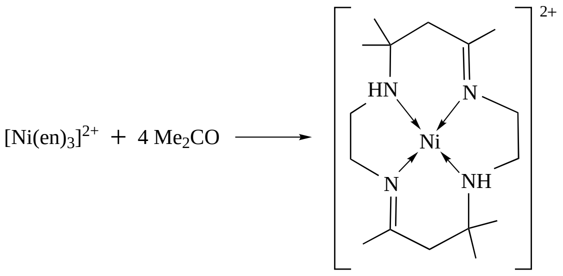

(9)

Subsequently, syntheses of tri-, tetra-, penta-, and hexaaza macrocycles, using methods developed by Richman and Atkins, have been published.[113] More recently, methods have been developed for the synthesis of polythioether macrocyclic ligands, some of which complex Ni^{II} very strongly.[114,115] This is particularly significant since monodentate thioether ligands are notoriously poor ligands for Ni^{II}.[116] Scheme 13 illustrates some of the macrocyclic ligands that have been coordinated to Ni^{II} and some of the complexes derived from them (see also Scheme 3). Of particular interest has been the determination of conformations of the coordinated rings, the stereochemistry and configuration at the metal center, and the assignment of configuration at the coordinated N-donors,that is, whether the side groups are ‘up’ or ‘down’ relative to one another. The coordination geometry and electronic environment at Ni^{II} can be specifically controlled by the protecting macrocyclic

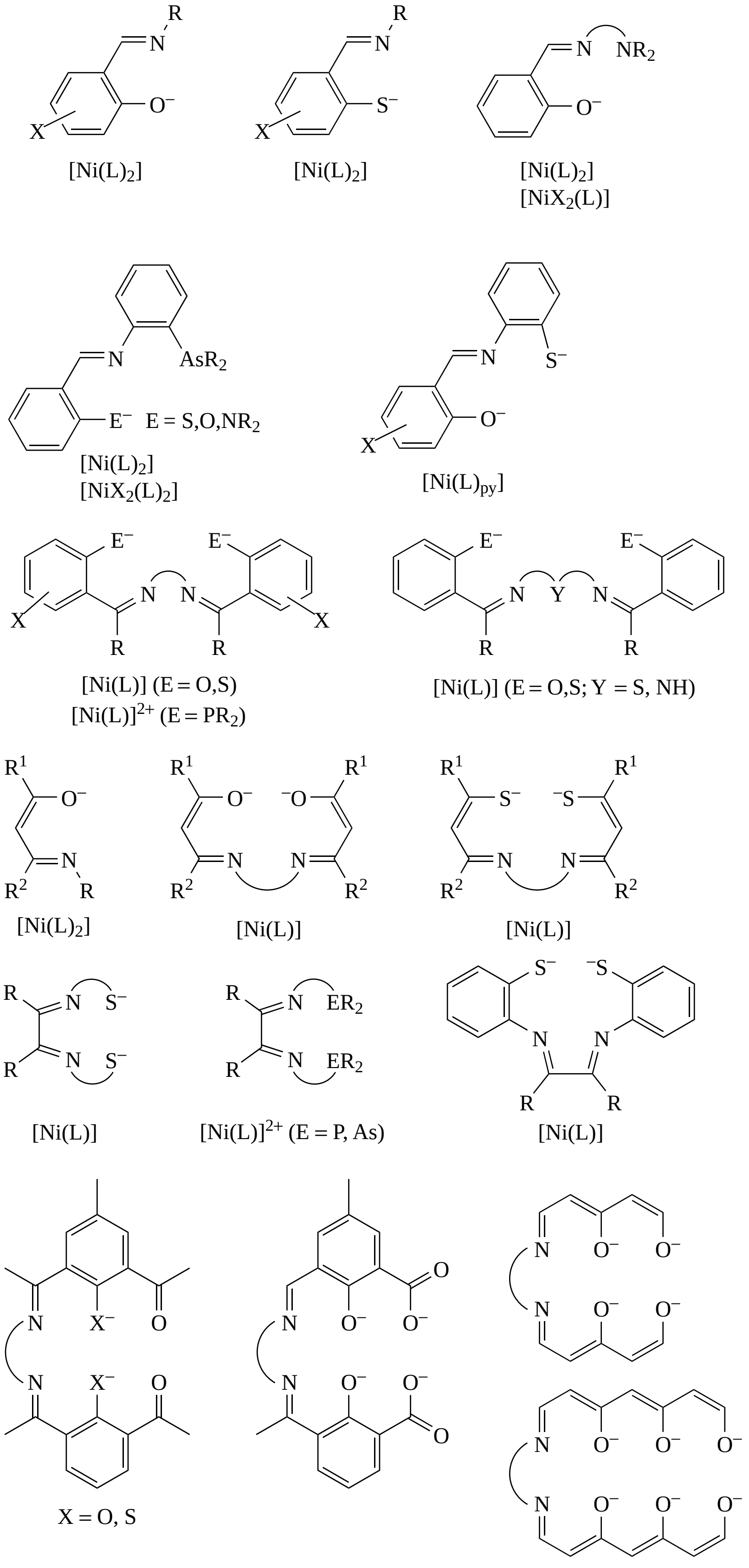
R
N
O⁻
X
[Ni(L)₂]
R
N
S⁻
X
[Ni(L)₂]
N
NR₂
O⁻
[Ni(L)₂]
[NiX₂(L)]
N
AsR₂
E⁻
E = S,O,NR₂
[Ni(L)₂]
[NiX₂(L)₂]
N
S⁻
O⁻
X
[Ni(L)py]
E⁻
E⁻
X
N
N
X
R
R
[Ni(L)] (E = O,S)
[Ni(L)]²⁺ (E = PR₂)
E⁻
E⁻
N
Y
N
R
R
[Ni(L)] (E = O,S; Y = S, NH)
R¹
O⁻
R²
N
R
[Ni(L)₂]
R¹
O⁻
⁻O
R¹
N
N
R²
R²
[Ni(L)]
R¹
S⁻
⁻S
R¹
N
N
R²
R²
[Ni(L)]
R
N
S⁻
R
N
S⁻
[Ni(L)]
R
N
ER₂
R
N
ER₂
[Ni(L)]²⁺ (E = P, As)
S⁻
⁻S
N
N
R
R
[Ni(L)]
N
X⁻
O
N
X⁻
O
X = O, S
N
O⁻
O
O⁻
N
O⁻
O⁻
O
N
O⁻
O⁻
N
O⁻
O⁻
N
O⁻
O⁻
O⁻
N
O⁻
O⁻
O⁻

Scheme 11

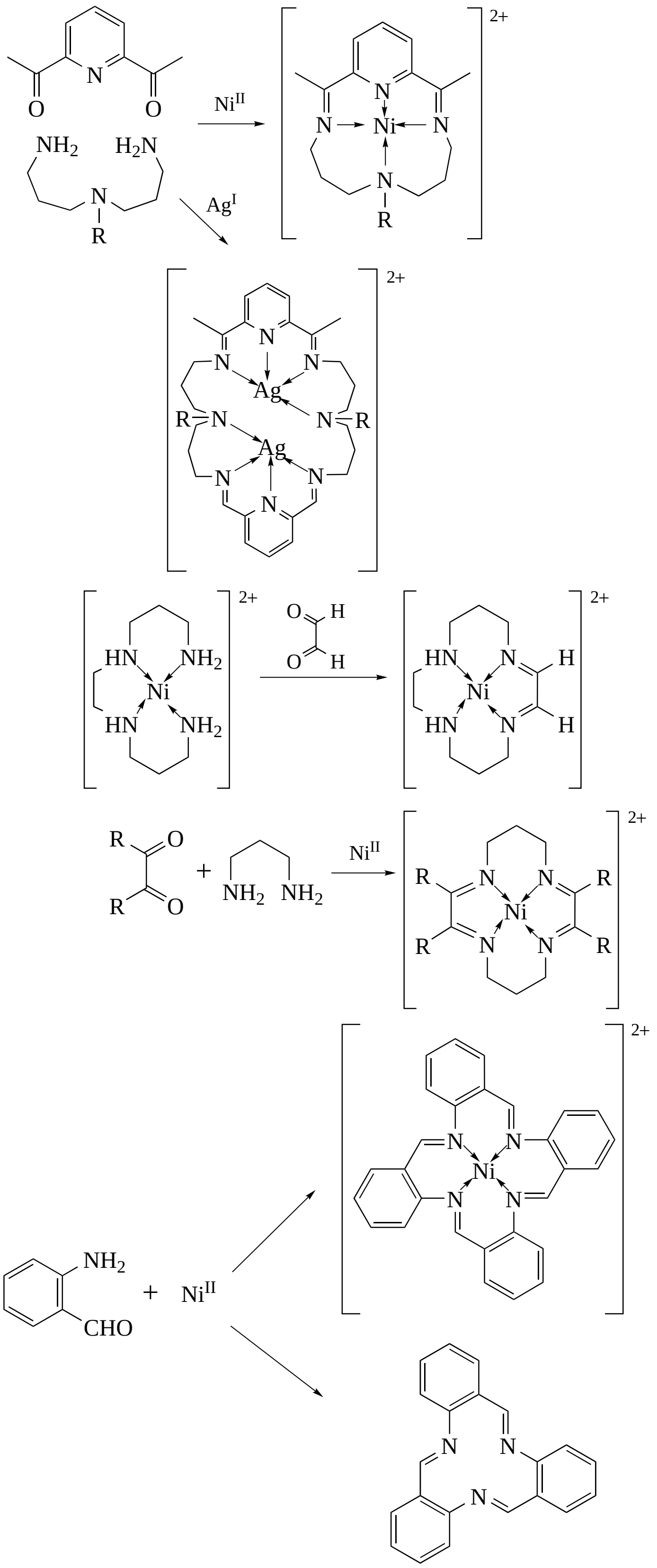
Ni^II
Ag^I
2+
Ni^II
Ni^II

Scheme 12

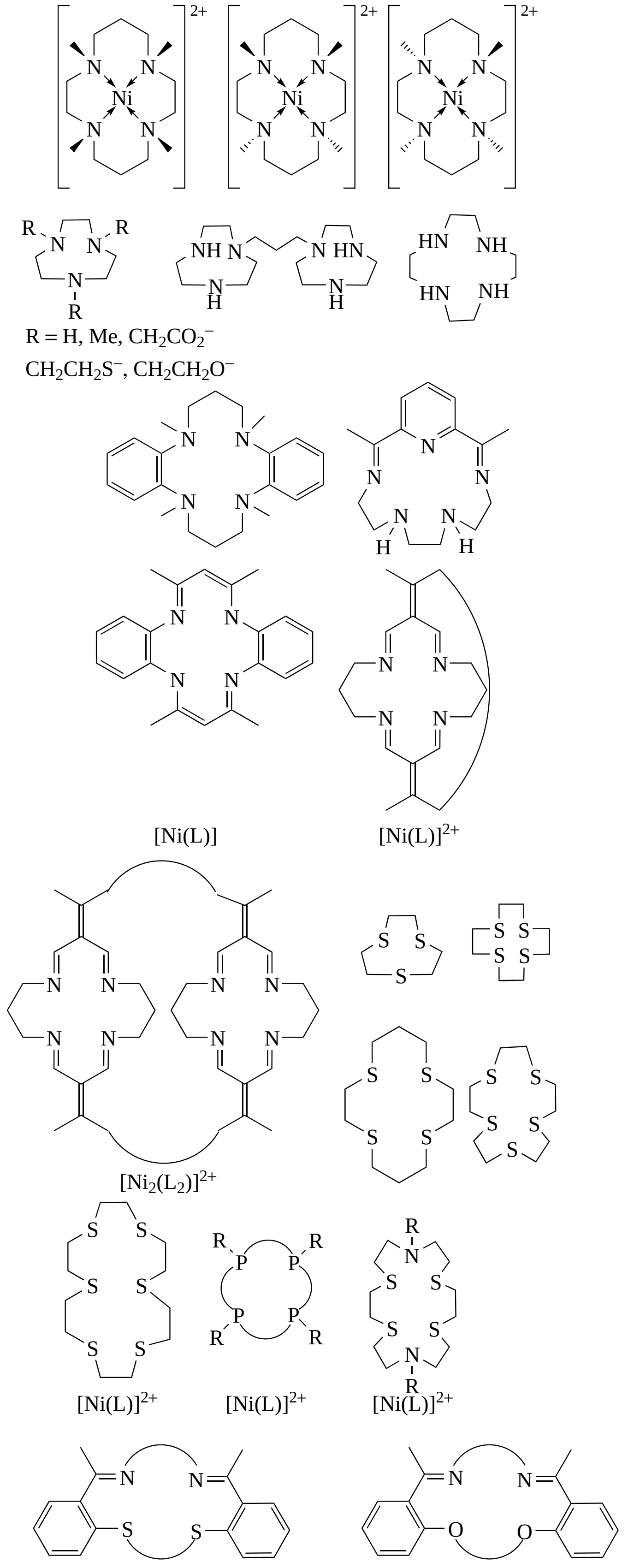
2+
2+
2+
Ni
R = H, Me, CH₂CO₂⁻
CH₂CH₂S⁻, CH₂CH₂O⁻
[Ni(L)]
[Ni(L)]2+
[Ni2(L2)]2+
[Ni(L)]2+
[Ni(L)]2+
[Ni(L)]2+

Scheme 13

ligand, and this has led to the stabilization of a range of Ni^{I} and Ni^{III} centers (see Sections 4 and 6, respectively).[111,112]

For example, an electrochemical investigation on [Ni[18]aneN$_2$S$_4$]$^{2+}$ confirms a reversible Ni(II)–Ni(III) couple and an irreversible reduction. In contrast, [Ni(Me$_2$[18]aneN$_2$S$_4$)]$^{2+}$ shows an irreversible Ni(II)–Ni(III) couple but a reversible Ni(II)–Ni(I) process. This contrasting redox behavior can be rationalized by the different binding characteristics of the ligands (**100**).[117]

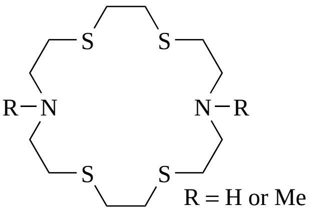

(**100**)

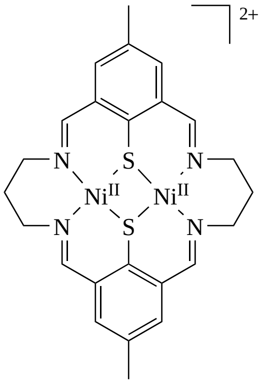

(**101**)

The binuclear nickel-thiolate macrocyclic complex (**101**) displays noteworthy redox behavior, in which one-electron oxidation yields a Ni^{III}. Ni^{II} product with significant delocalization of the unpaired electron density onto the bridging thiolate ligands and not onto the second nickel ion.[118] The charge delocalization consequently lies between the two redox extremes of nickel(III)-thiolate and nickel(II)-thiyl radical, thus mimicking the Ni-C state in [NiFe]hydrogenase (see Section 8).

Ni^{II} macrocyclic complexes have also been investigated as covalent attachments to photosensitizers such as [Ru(bipy)$_3$]$^{2+}$,[119] and as interchelating agents for the cleavage of DNA.[120]

6 NICKEL(III)

The coordination chemistry of Ni^{III} has been reviewed,[14] and electron-transfer reactions of Ni^{III} and Ni^{IV} complexes assessed.[121] Ni^{III} species are stabilized by σ-donor ligands and are excellent oxidizing agents. The complexes usually show tetragonally distorted octahedral geometries consistent with a d^7 electron configuration; the EPR spectra of Ni^{III} species show $g_\perp > g_\parallel \sim 2.0023$ assigned to a $d^1_{z^2}$ ground-state configuration for an axially elongated octahedron. Coordination of solvent molecules such as MeCN to apical sites leads to hyperfine coupling to N in the $g_\parallel$ component of the EPR spectrum.[122] Many Ni^{III} species have relatively short half-lives for decomposition and may be regarded as transient species.

The oxidation of a range of Ni^{II} complexes of open-chain mixed-donor ligands (Scheme 14) has generated Ni^{III} complexes that have been characterized by EPR spectroscopy.[123] Many of these complexes incorporate deprotonated amide and amino acid functionalities. The stabilization of Ni^{III} by diimino ligands has also been reported.[44,92]

A wide range of Ni^{III} complexes of aza macrocyclic[124] and porphyrin[125] ligands has been reported. The structures of [Ni([9]aneN$_3$)$_2$]$^{3+}$ (**102**), the thioether analogue [Ni([9]aneS$_3$)$_2$]$^{3+}$ (**103**), [Ni([14]aneN$_4$)Cl$_2$]$^+$ (**104**), [Ni(R$_3$[9]aneN$_3$)] (R = CH$_2$CO$_2$$^-$) (**105**), and the Ni^{III} analogue of (**92**) confirm the stereochemical preference of Ni^{III} for distorted octahedral coordination.[92,126] The oxidation of organic substrates and biological materials by Ni^{III} macrocyclic species (generated by oxidation of Ni^{II} precursors) has been reported.[127] The generation of Ni^{III} species by pulse radiolysis has been a particularly useful technique for the study of kinetics and mechanism,[128] while the oxidative addition of R–X to Ni^{I} to form Ni^{III} species has been described (equation 10).[129]

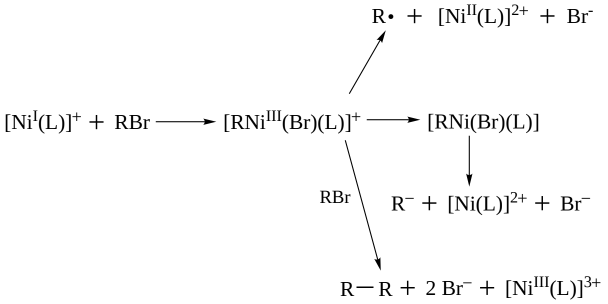
R• + [Ni^{II}(L)]$^{2+}$ + Br$^-$
[Ni^{I}(L)]$^+$ + RBr
[RNi^{III}(Br)(L)]$^+$
[RNi(Br)(L)]
RBr
R$^-$ + [Ni(L)]$^{2+}$ + Br$^-$
R−R + 2 Br$^-$ + [Ni^{III}(L)]$^{3+}$

(10)

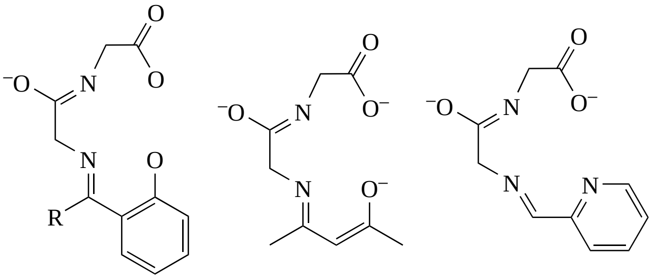

Scheme 14

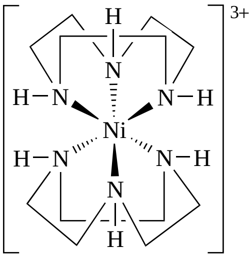

(**102**)

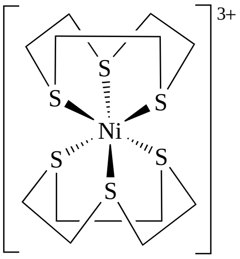

(**103**)

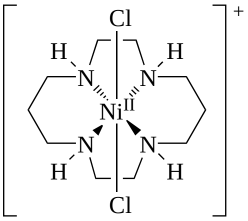

(**104**)

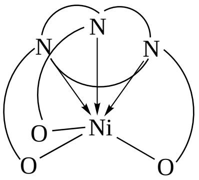

(**105**)

The ability of tetraazamacrocycles (**106**) to stabilize nickel ions in the $+3$ oxidation state has been employed to demonstrate redox switching of fluorescence. The wavelength of the emitted light is controlled through the choice of pendant group X.[130]

A limited series of phosphine and thiolene complexes of $\mathrm{Ni^{III}}$ have been generated. These include the species $[\mathrm{NiX_3(PR_3)_2}]$ and $[\mathrm{M(L)_2}]^-$ (L = dithiolene), although in the latter complexes the formation of $\mathrm{Ni^{III}}$-stabilized ligand-radical cations has been observed. The synthesis of $[\mathrm{NiF_6}]^{3-}$ has been reported.

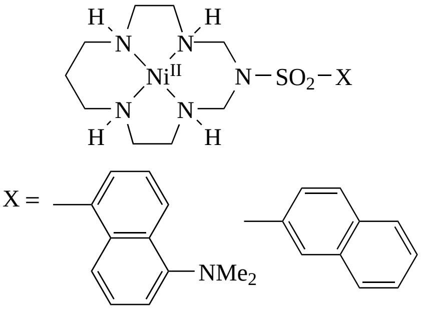

(**106**)

7 NICKEL(IV)

$\mathrm{Ni^{IV}}$ complexes are relatively rare and very few have been characterized fully. The structure of $[\mathrm{NiF_6}]^{2-}$ shows octhedral coordination with Ni–F = 1.72, 1.76 Å.[131] With $\mathrm{Ni^{III}}$ and $\mathrm{Ni^{IV}}$ centers deprotonation of coordinated amine occurs very readily, reflecting the requirement of these metal ions for electronegative ligands. $\mathrm{Ni^{IV}}$ has been stabilized by polydentate oxime, amide, and amino acid ligands (see Scheme 14). Examples of $\mathrm{Ni^{IV}}$ stabilized by dithiocarbamate and dithiolene ligands are now believed to be ligand-oxidized complexes. The stabilization of $\mathrm{Ni^{IV}}$ in molybdates and niobates is also known. A highly unusual $\mathrm{Ni^{IV}}$ cubane complex $[\mathrm{Ni_4Se_4(Se_3)_5(Se_4)}]^{4-}$ (**107**) has been isolated and characterized.[132]

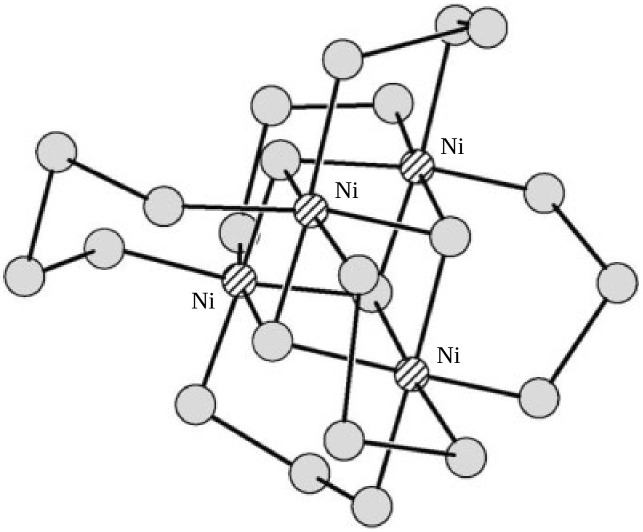

(**107**)

8 BIOLOGICAL CHEMISTRY

A major impetus for the study of Ni redox chemistry has been provided by the discovery of paramagnetic Ni centers in several biological systems.[133,134] Several enzymes are now known to contain Ni and in a number of these the Ni is thought to take part in redox reactions.[135,136]

Urease catalyzes the hydrolysis of urea to NH_3 and CO_2 and incorporates Ni^{II} in an octahedral environment.[137] The function of the Ni center(s) in these enzymes is thought to be analogous to that of Zn^{II} in carbonic anhydrase, to activate the urea substrate electrostatically to nucleophilic attack.[138] The binuclear Ni^{II} complex (**108**) displays urease activity, firstly via conversion of urea to ammonia and cyanate, followed by a second step involving the hydrolysis of the cyanate.[139,140] In addition, a related asymmetric complex reacts with urea and allows the structural characterization of the isocyanate product.

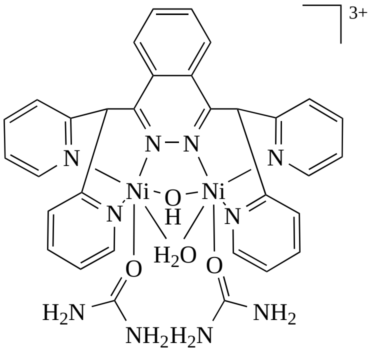

(**108**)

Methyl-coenzyme M reductase requires a Ni-containing prosthetic group for activity, Factor F_{430}. This is a Ni complex of a tetrahydroporphyrin which forms an octahedral Ni complex in the intact protein. The active ('reduced') form of this enzyme is EPR active ($g_{\perp} = 2.23$, $g_{\parallel} = 2.17$),[141] which is consistent with the formation of a d^9 Ni^I center. A recent X-ray structure of methyl-coenzyme M reductase shows the octahedral Ni^{II} ion bound in a tetrapyrrole hydrocorphin ring and the oxygen from a glutamine residue at the 5th site. The sixth site is occupied by either a thiol group of coenzyme M in the methyl-coenzyme M reductase$_{\text{ox1-silent}}$ structure or a sulfonate oxygen of coenzyme M in the methyl-coenzyme M reductase$_{\text{silent}}$ structure.[142,143]

Carbon monoxide dehydrogenase is a bacterial enzyme that catalyzes the interconversion of CO and CO_2, the active site has been shown to contain an asymmetric [Ni-4Fe-5S] cluster.[144,145] There have been two recent independent reports of X-ray structures for the bifunctional enzyme carbon monoxide dehydrogenase/acetyl-coenzyme A synthase. In both structures Ni^{II} is present bound within a N_2S_2 polychelate, which via the thiolate donors bridges to either a Cu, Zn, or Ni ion, which in turn is bound to a 4Fe4S cluster.[146,147] Helix-loop-helix peptides have been designed as scaffolds for the stabilization of Ni^{II}-Fe_4S_4 bridged assemblies to model the active site of the A-cluster of carbon monoxide dehydrogenase. Herein, the Fe_4S_4 is incorporated in the flexible loop of the peptide and is bridged by a cysteine residue to the bound Ni^{II}; this Ni^{II} appears to be in equilibrium with a peptide free Ni^{II} species.[15,148] Low molecular weight models for the active site of acetyl-coenzyme A synthase have been prepared (**109**,[149] **110**,[150] **111**,[151]), and these are also able to form higher aggregates containing more metal ions in the centre of the complexes.

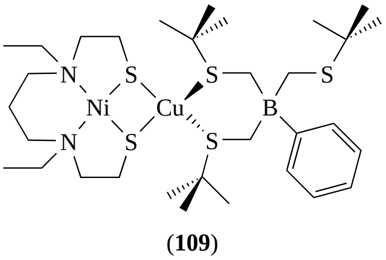

(**109**)

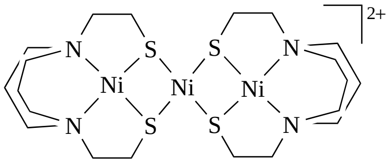

(**110**)

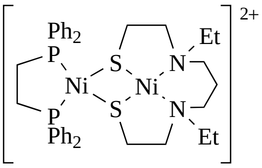

(**111**)

Hydrogenase enzyme catalytically interconvert H_2 and $2H^+$. The X-ray structure of [NiFe] hydrogenase has been solved for Desulfovibrio gigas to a resolution of 2.85 and 2.54 Å.[152,153] The active site comprises a heterobimetallic [NiFe] center, with the Ni ligated by four cysteines, two of which are terminal and two which bridge to iron (**112**). The Fe is ligated further by three nonprotein diatomics, namely, two cyanide and one carbonyl, a third bridging group completes the octahedral coordination sphere and is assigned as an oxo-oxygen more closely associated with the Ni than the Fe. Activation of the enzyme is believed to involve loss of the oxo-ligand and contraction of the nickel–iron separation to some 2.5–2.6 Å.[154]

The precise mechanistic detail of the enzymic reaction is not fully understood, although a $Ni^{III}-(H_2)$ complex appears to be involved;[155,156] Crabtree and coworkers have published evidence for the first example of a Ni^{II} complex that interacts directly with H_2,[157] while Lubitz and coworkers have proposed using multi-frequency EPR analysis a reaction scheme for H_2 and H^+ interconversion at the biosite (see Scheme 15).[158]

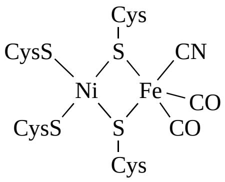
Cys
CysS
S
CN
Ni
Fe
CO
CysS
S
CO
Cys

(**112**)

The active site of [NiFe] hydrogenase

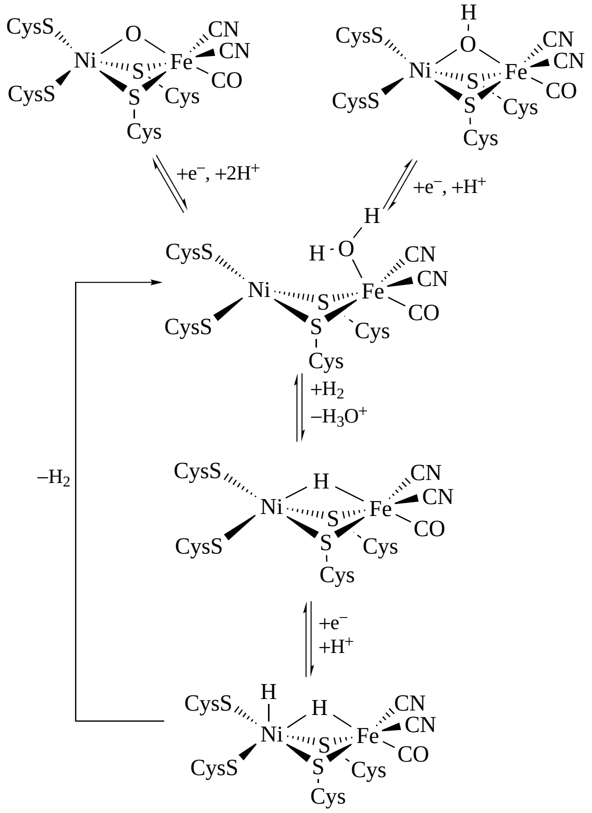
CysS
O
CN
CN
Ni
S
Fe
CO
CysS
S
Cys
Cys
H
+e⁻, +2H⁺
+e⁻, +H⁺
H
H-O
+H₂
−H₃O⁺
−H₂
+e⁻
+H⁺

Scheme 15

The synthesis and study of low molecular weight model complexes that mimic the electronic structure and coordination chemistry of the hydrogenase active site is a timely area of research and has been reviewed.[159] Typical examples of mixed Ni-Fe complexes that have been prepared include complexes (**113**),[160] (**114**),[159] (**115**),[159] and (**116**).[161]

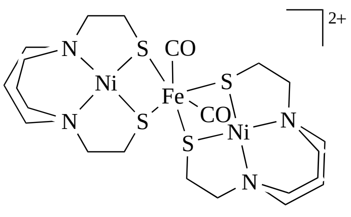
2+
N
S
CO
Ni
Fe
S
CO
N
S
Ni
N
S
N

(**113**)

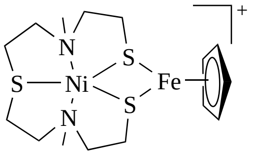

(**114**)

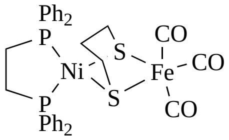
Ph₂
P
S
CO
Ni
Fe
CO
P
S
CO
Ph₂

(**115**)

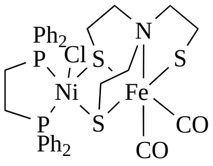
Ph₂
P
Cl
S
N
S
Ni
Fe
P
S
CO
Ph₂
CO

(**116**)

9 RELATED ARTICLES

Macrocyclic Ligands; Nickel Enzymes & Cofactors; Nickel: Models of Protein Active Sites; Nickel: Organometallic Chemistry.

10 REFERENCES

1. L. Sacconi, F. Mani, and A. Bencini, in ‘Comprehensive Coordination Chemistry’, eds. G. Wilkinson, R. D. Gillard, and J. A. McCleverty, Pergamon, Oxford, 1987, Vol. 5.
2. F. Meyer and H. Kozlowski, in ‘Comprehensive Coordination Chemistry’, 2nd edn., eds. J. A. McCleverty and T. J. Meyer, Pergamon, Oxford, 2003, Vol. 5.
3. F. A. Cotton, G. Wilkinson, C. A. Murillo, and M. Bochmann, ‘Advanced Inorganic Chemistry’, 6th edn., Wiley Interscience, 1999.
4. E. Uhlig, *Coord. Chem. Rev.*, 1973, **10**, 227; M. Campiolini, *Struct. Bonding (Berlin)*, 1969, **6**, 52.
5. T. Frömmel, W. Peters, H. Wunderlich, and W. Kuchen, *Angew. Chem., Int. Ed. Engl.*, 1992, **31**, 612.
6. R. H. Holm and M. J. O. Connor, *Prog. Inorg. Chem.*, 1971, **14**, 241.
7. R. H. Holm, *J. Am. Chem. Soc.*, 1961, **83**, 4683.
8. W. C. Fernelius and B. E. Bryant, *Inorg. Synth.*, 1978, **5**, 105.

9. R. Morassi, I. Bertini, and L. Sacconi, *Coord. Chem. Rev.*, 1973, **11**, 343.
10. J. S. Wood, *Prog. Inorg. Chem.*, 1972, **16**, 227; R. R. Holmes, *Prog. Inorg. Chem.*, 1984, **32**, 119.
11. H. Hope, M. M. Olmstead, B. D. Murray, and P. P. Power, *J. Am. Chem. Soc.*, 1985, **107**, 712.
12. M. G. B. Drew, J. Nelson, and S. M. Nelson, *J. Chem. Soc., Dalton Trans.*, 1981, 1685.
13. C. W. G. Ansell, J. Lewis, P. R. Raithby, J. N. Ramsden, and M. Schröder, *J. Chem. Soc., Chem. Commun.*, 1982, 546.
14. K. Nag and A. Chakravorty, *Coord. Chem. Rev.*, 1980, **33**, 87; R. I. Haines and A. McAuley, *Coord. Chem. Rev.*, 1981, **39**, 77; A. G. Lappin and A. McAuley, *Adv. Inorg. Chem.*, 1988, **32**, 241.
15. L. Malatesta, *Prog. Inorg. Chem.*, 1959, **1**, 283.
16. M. Matsumoto and K. Nakatsu, *Acta Crystallogr., Sect. B*, 1975, **31**, 2711.
17. X. Yin and J. R. Moss, *Coord. Chem. Rev.*, 1999, **181**, 27.
18. M. Svoboda, H. Tom Dieck, C. Krueger, and Y.-H. Tsay, *Z. Naturforsch., Teil B*, 1981, **36**, 814.
19. C. A. Tolman, W. C. Seidel, and D. H. Gerlach, *J. Am. Chem. Soc.*, 1972, **94**, 2669.
20. T. T. Tsou, J. C. Huffman, and J. K. Kochi, *Inorg. Chem.*, 1979, **18**, 2311.
21. J. Chatt and F. A. Hart, *J. Chem. Soc.*, 1965, 812.
22. K. S. Chong, S. J. Rettig, A. Storr, and J. Trotter, *Can. J. Chem.*, 1979, **57**, 3099.
23. J. A. McCleverty, *Chem. Rev.*, 1979, **79**, 53.
24. M. Aresta, C. Nobile, V. G. Albano, E. Forni, and M. Manassero, *J. Chem. Soc., Chem. Commun.*, 1975, 636.
25. C. Bianchini, C. A. Ghilardi, A. Meli, S. Midollini, and A. Orlandini, *J. Chem. Soc., Chem. Commun.*, 1983, 753.
26. L. Vaska, *Acc. Chem. Res.*, 1976, **9**, 175; R. W. Erskine and B. O. Field, *Struct. Bonding (Berlin)*, 1976, **28**, 3.
27. P. Dapporto, S. Midollini, A. Orlandini, and L. Sacconi, *Inorg. Chem.*, 1976, **15**, 2768.
28. P. W. Jolly, K. Jonas, C. Krüger, and Y. H. Tsay, *J. Organomet. Chem.*, 1971, **33**, 109.
29. L. Sacconi, C. A. Ghilardi, C. Mealli, and F. Zanobini, *Inorg. Chem.*, 1975, **14**, 1380.
30. M. Di Vaira, M. Peruzzini, and P. Stoppioni, *Inorg. Chem.*, 1983, **22**, 2196.
31. M. Di Vaira, S. Midollini, and L. Sacconi, *J. Am. Chem. Soc.*, 1979, **101**, 1757.
32. M. Di Vaira, L. Sacconi, and P. Stoppioni, *J. Organomet. Chem.*, 1983, **250**, 183.
33. R. Ahrlichs, D. Fenske, H. Oesen, and U. Schneider, *Angew. Chem., Int. Ed. Engl.*, 1992, **31**, 323.
34. O. Jarchow, H. Schuttz, and R. Nast, *Angew. Chem., Int. Ed. Engl.*, 1970, **9**, 71.
35. N. Tanaka, T. Ogata, and S. Niizuma, *Inorg. Nucl. Chem. Lett.*, 1972, **8**, 965.
36. F. V. Lovecchio, E. S. Gore, and D. H. Busch, *J. Am. Chem. Soc.*, 1974, **96**, 3109; A. M. Tait, M. Z. Hoffmann, and E. Hayon, *Inorg. Chem.*, 1976, **15**, 934.
37. G. Golub, H. Cohen, and D. Meyerstein, *J. Chem. Soc., Chem., Commun.*, 1992, 397.
38. J. Lewis and M. Schröder, *J. Chem. Soc., Dalton Trans.*, 1982, 1085.
39. M. P. Suh, H. K. Kim, M. J. Kim, and K. Y. Oh, *Inorg. Chem.*, 1992, **31**, 3620.
40. L. R. Furenlid, M. W. Renner, D. J. Szalda, and E. Fujita, *J. Am. Chem. Soc.*, 1991, **113**, 883.
41. G. K. Lahiri, L. J. Schlussel, and A. M. Stolzenberg, *Inorg. Chem.*, 1992, **31**, 4991; K. M. Kadish, *Prog. Inorg. Chem.*, 1987, **34**, 435.
42. L. Latos-Grazynski, M. M. Olmstead, and A. L. Balch, *Inorg. Chem.*, 1989, **28**, 4066.
43. C. O. Dietrich-Buchecker, J.-M. Kern, and J.-P. Sauvage, *J. Chem. Soc., Chem. Commun.*, 1985, 760.
44. A. J. Blake, A. J. Lavery, T. I. Hyde, and M. Schröder, *J. Chem. Soc., Dalton Trans.*, 1989, 965.
45. M. H. Schmidt, G. M. Miskelly, and N. S. Lewis, *J. Am. Chem. Soc.*, 1990, **112**, 3420.
46. C. J. Campbell, J. F. Rusling, and C. Brückner, *J. Am. Chem. Soc.*, 2000, **122**, 6679.
47. L. Sacconi, P. Dapporto, and P. Stoppioni, *Inorg. Chem.*, 1976, **15**, 325; 1977, **16**, 224; A. Gleizes, M. Dartiguenave, Y. Dartiguenave, J. Galy, and H. F. Klein, *J. Am. Chem. Soc.*, 1977, **99**, 5187; F. Cecconi, S. Midollini, and A. Orlandini, *J. Chem. Soc., Dalton Trans.*, 1983, 2263.
48. D. C. Bradley, M. B. Hursthouse, R. J. Smallwood, and A. J. Welch, *J. Chem. Soc., Chem. Commun.*, 1972, 872.
49. G. A. Bowmaker, P. D. W. Boyd, and G. K. Campbell, *Inorg. Chem.*, 1982, **21**, 2403; G. A. Bowmaker, P. D. W. Boyd, M. Zvagulis, K. J. Cavell, and A. F. Masters, *Inorg. Chem.*, 1985, **24**, 401.
50. A. L. Bach and M. M. Olmstead, *Chem. Rev.*, 1998, **98**, 2123; B. Chase and P. J. Fagan, *J. Am. Chem. Soc.*, 1992, **114**, 2252; Y. Huang and B. S. Freiser, *J. Am. Chem. Soc.*, 1991, **113**, 8186.
51. K. N. Raymond, P. W. R. Corfield, and J. A. Ibers, *Inorg. Chem.*, 1968, **7**, 1362.
52. A. Werner, *Z. Anorg. Allg. Chem.*, 1899, **21**, 229.
53. D. H. Busch, *Chem. Rev.*, 1993, **93**, 847.
54. A. Cristini, G. Ponticelli, and A. Diaz, *J. Chem. Soc., Dalton Trans.*, 1972, 1361.
55. L. F. Lindoy and S. E. Livingstone, *Coord. Chem. Rev.*, 1967, **2**, 173; W. R. McWhinnie and J. D. Miller, *Adv. Inorg. Chem. Radiochem.*, 1969, **12**, 135; E. D. McKenzie, *Coord. Chem. Rev.*, 1971, **6**, 187.

56. G. B. Kauffman and L. T. Takahashi, *Inorg. Synth.*, 1966, **8**, 227.
57. L. Sacconi, C. Mealli, and D. Gatteschi, *Inorg. Chem.*, 1974, **13**, 1985.
58. J. L. Atwood, G. W. Orr, F. Hamada, R. L. Vincent, S. G. Bott, and K. D. Robinson, *J. Am. Chem. Soc.*, 1991, **113**, 2760.
59. S. Fleming, K. L. V. Mann, C.-A. Carraz, E. Psillakis, J. C. Jeffery, J. A. McCleverty, and M. D. Ward, *Angew. Chem., Int. Ed. Engl.*, 1998, **37**, 1279.
60. J. Ribas, A. Escuer, M. Montfort, R. Vicente, R. Cortes, L. Lezama, and T. Rojo, *Coord. Chem. Rev.*, 1999, **195**, 1027.
61. R. C. Stoufer and D. H. Busch, *J. Am. Chem. Soc.*, 1956, **78**, 6016.
62. N. F. Curtis, *J. Chem. Soc.*, 1960, 4409; M. M. Blight and N. F. Curtis, *J. Am Chem. Soc.*, 1962, **1204**, 3016; D. A. House and N. F. Curtis, *J. Am. Chem. Soc.*, 1964, **86**, 1331.
63. D. E. Williams, G. Wohlauer, and R. E. Rundle, *J. Am. Chem. Soc.*, 1959, **81**, 755.
64. L. K. Johnson, C. M. Killian, and M. Brookhart, *J. Am. Chem. Soc.*, 1995, **117**, 6414; S. D. Ittel, L. K. Johnson, and M. Brookhart, *Chem. Rev.*, 2000, **100**, 1169.
65. M. M. Olmstead, D. A. Costa, K. Maitra, B. C. Noll, S. L. Phillips, P. M. Van Calcar, and A. L. Balch, *J. Am. Chem. Soc.*, 1999, **121**, 7090.
66. D. H. Hochmuth, S. L. J. Michel, A. J. P. White, D. J. Williams, A. G. M. Barrett, and B. M. Hoffman, *Eur. J. Inorg. Chem.*, 2000, 593.
67. P. C. Andrews, J. L. Atwood, L. J. Barbour, P. J. Nichols, and C. L. Raston, *Chem. – Eur. J.*, 1998, **4**, 1384.
68. H. A. Mayer and W. C. Kaska, *Chem. Rev.*, 1994, **94**, 1239.
69. R. J. Baker and P. G. Edwards, *J. Chem. Soc., Dalton Trans.*, 2002, 2960.
70. N. A. Cooley, S. M. Green, D. F. Wass, K. Heslop, G. A. Orpen, and P. G. Pringle, *Organometallics*, 2001, **20**, 4769.
71. V. C. Gibson, A. Tomov, A. J. P. White and D. J. Williams, *Chem. Commun.*, 2001, 719; V. C. Gibson and A. Tomov, *Chem. Commun.*, 2001, 1964.
72. T. R. Younkin, E. F. Connor, J. I. Henderson, S. K. Fridrich, R. H. Grubbs, and D. A. Bansleben, *Science*, 2000, **287**, 460.
73. R. C. Mehrotra, *Adv. Inorg. Chem. Radiochem.*, 1983, **26**, 269; J. P. Hunt and H. L. Friedman, *Prog. Inorg. Chem.*, 1983, **30**, 359.
74. B. W. Clare and D. L. Kepert, *Aust. J. Chem.*, 1975, **28**, 1489.
75. L. G. L. Oward and J. R. Pipal, *Inorg. Synth.*, 1972, **13**, 154.
76. J. A. Bertrand, A. P. Ginsberg, R. I. Kaplan, C. E. Kirkwood, R. L. Martin, and R. C. Sherwood, *Inorg. Chem.*, 1971, **10**, 240.
77. R. E. Cramer, S. W. Cramer, K. F. Cramer, M. A. Chudyk, and K. Seff, *Inorg. Chem.*, 1977, **16**, 219.
78. G. Bussiere, R. Beauclac, B. Cardinal-David, and C. Reber, *Coord. Chem. Rev.*, 2001, **219**, 509.
79. C. Oldham, *Prog. Inorg. Chem.*, 1968, **10**, 223.
80. A. Bencini, C. Benelli, D. Gatteschi, and Z. Zanchini, *J. Am. Chem. Soc.*, 1980, **102**, 5820.
81. W. L. Gladfelter, M. W. Lynch, W. P. Schaefer, D. N. Hendrickson, and H. B. Gray, *Inorg. Chem.*, 1981, **20**, 2390.
82. C. C. Addison, N. Logan, S. C. Wallwork, and C. D. Garner, *Q. Rev., Chem. Soc.*, 1971, **25**, 289.
83. M. A. Hitchman and G. L. Rowbottom, *Coord. Chem. Rev.*, 1982, **42**, 55.
84. F. Cecconi, C. A. Ghilardi, and S. Midollini, *Inorg. Chem.*, 1983, **22**, 3802.
85. H. Vahrenkamp and L. F. Dahl, *Angew. Chem., Int. Ed. Engl.*, 1969, **8**, 144.
86. A. Muller, E. Krickmeyer, H. Bogge, W. Clegg, and G. M. Sheldrick, *Angew. Chem., Int. Ed. Engl.*, 1983, **22**, 1006.
87. J. R. Dilworth and J. Hu, *Adv. Inorg. Chem.*, 1994, **40**, 411.
88. T. Krüger, B. Krebs, and G. Henkel, *Angew Chem., Int. Ed. Engl.*, 1992, **31**, 55; J. Zhou, M. J. Scott, Z. Hu, G. Peng, E. Münck, and R. H. Holm, *J. Am. Chem. Soc.*, 1992, **114**, 10843.
89. S. G. Rosenfield, W. H. Armstrong, and P. K. Mascharak, *Inorg. Chem.*, 1986, **25**, 3014.
90. N. Baidya, M. M. Olmstead, J. P. Whitehead, C. Bagyinka, M. M. Maroney, and P. K. Mascharak, *Inorg. Chem.*, 1992, **31**, 3612.
91. C. A. Grapperhaus and M. Y. Darensbourg, *Acc. Chem. Res.*, 1998, **31**, 451.
92. H.-J. Krüger, G. Peng, and R. H. Holm, *Inorg. Chem.*, 1991, **30**, 734; H.-J. Krüger and R. H. Holm, *J. Am. Chem. Soc.*, 1990, **112**, 2955; *Inorg. Chem.*, 1987, **26**, 3645.
93. K. Wang and E. I. Stiefel, *Science*, 2001, **291**, 106.
94. J. R. Miller, *Adv. Inorg. Chem. Radiochem.*, 1962, **4**, 133.
95. D. Herebain, E. Bothe, E. Bill, T. Weyhermüller, and K. Wieghardt, *J. Am. Chem. Soc.*, 2001, **123**, 10012.
96. K. S. Min, T. Weyhermüller, and K. Wieghardt, *Dalton Trans.*, 2003, 1126.
97. P. Chaudhuri, C. N. Verani, E. Bill, E. Bothe, T. Weyhermüller, and K. Wieghardt, *J. Am. Chem. Soc.*, 2001, **123**, 2213.
98. A. J. Amoroso, S. S. M. Chung, D. J. E. Spencer, J. P. Danks, M. W. Glenny, A. J. Blake, P. A. Cooke, C. Wilson, and M. Schröder, *Chem. Commun.*, 2003, 2020.
99. X. Lin, D. M. J. Doble, A. J. Blake, A. Harrison, C. Wilson, and M. Schröder, *J. Am. Chem. Soc.*, 2003, **125**, 9476.

100. A. J. Blake, C. M. Grant, S. Parsons, J. M. Rawson, and R. E. P. Winpenny, *Chem. Commun.*, 1994, 2363.

101. H. Andres, R. Basler, A. J. Blake, C. Cadiou, G. Chaboussant, C. M. Grant, H.-U. Güdel, M. Murrie, S. Parsons, C. Paulsen, F. Semadini, V. Villar, W. Wernsdorfer, and R. E. P. Winpenny, *Chem. – Eur. J.*, 2002, **8**, 4867.

102. L. Dearden, S. Parsons, and R. E. P. Winpenny, *Angew. Chem., Int. Ed. Engl.*, 2001, **40**, 152.

103. M. T. Allen, A. D. Burrows, and M. F. Mahon, *J. Chem. Soc., Dalton Trans.*, 1999, 215.

104. A. J. Fletcher, E. J. Cussen, T. J. Prior, M. J. Rosseinsky, C. J. Kepert, and K. M. Thomas, *J. Am. Chem. Soc.*, 2001, **123**, 10001.

105. E. J. Cussen, J. B. Claridge, M. J. Rosseinsky, and C. J. Kepert, *J. Am. Chem. Soc.*, 2002, **124**, 9574.

106. C. J. Kepert, T. J. Prior, and M. J. Rosseinsky, *J. Am. Chem. Soc.*, 2000, **122**, 5158.

107. J. W. J. Knapen, A. W. van der Made, J. C. de Wilde, P. W. N. M. van Leeuwen, P. Wijkens, D. M. Grove, and G. van Koten, *Nature*, 1994, **372**, 659.

108. N. Akkus, J. C. Campbell, J. Davidson, D. K. Henderson, H. A. Miller, A. Parkin, S. Parsons, P. G. Plieger, R. M. Swart, P. A. Tasker, and L. C. West, *Dalton Trans.*, 2003, 1932.

109. F. C. J. M. van Veggel, W. Verboom, and D. N. Reinhoudt, *Chem. Rev.*, 1994, **94**, 279.

110. L. F. Lindoy, 'The Chemistry of Macrocyclic Ligand Complexes', Cambridge University Press, 1989; P. V. Bernhardt and G. A. Lawrence, *Coord. Chem. Rev.*, 1990, **104**, 297; R. M. Izatt, K. Pawlak, J. S. Bradshaw, and R. L. Bruening, *Chem. Rev.*, 1991, **91**, 1721.

111. A. Ingham, M. Rodopoulos, K. Coulter, T. Rodopoulos, S. Subramanian, and A. McAuley, *Coord. Chem. Rev.*, 2002, **233**, 255.

112. J. D. Chartres, L. F. Lindoy, and G. V. Meehan, *Coord. Chem. Rev.*, 2001, **216**, 249.

113. J. E. Richman and T. J. Atkins, *J. Am. Chem. Soc.*, 1974, **96**, 2268.

114. A. J. Blake and M. Schröder, *Adv. Inorg. Chem.*, 1990, **35**, 1.

115. S. R. Cooper and S. C. Rawle, *Struct. Bonding (Berlin)*, 1990, **72**, 1.

116. S. G. Murray and F. R. Hartley, *Chem. Rev.*, 1981, **81**, 365.

117. A. J. Blake, G. Reid, and M. Schröder, *J. Chem. Soc., Dalton Trans.*, 1994, 3291.

118. N. D. Branscombe, A. J. Atkins, A. Marin-Becerra, E. J. L. McInnes, F. E. Mabbs, J. McMaster, and M. Schröder, *Chem. Commun.*, 2003, 1098.

119. S. C. Rawle, P. Moore, and N. W. Alcock, *J. Chem. Soc., Chem. Commun.*, 1992, 684; E. Fujita, S. J. Milder, and B. S. Brunschwig, *Inorg. Chem.*, 1992, **31**, 2079.

120. J. G. Muller, X. Chen, A. C. Dadiz, S. E. Rokita, and C. J. Burrows, *J. Am. Chem. Soc.*, 1992, **114**, 6407.

121. S. Bhattacharya, B. Saha, A. Dutta, and P. Banerjee, *Coord. Chem. Rev.*, 1998, **170**, 47.

122. F. V. Lovecchio, E. S. Gore, and D. H. Busch, *J. Am. Chem. Soc.*, 1974, **96**, 3109.

123. T. Sakurai, J.-I. Hongo, A. Nakahara, and Y. Nakao, *Inorg. Chim. Acta*, 1980, **46**, 205.

124. M. C. Rakowski, M. Rychek, and D. H. Busch, *Inorg. Chem.*, 1975, **14**, 1194; L. Fabrizzi, A. Perotti, and A. Poggi, *Inorg. Chem.*, 1983, **22**, 1411; A. McAuley, P. R. Norman, and O. Olubyide, *J. Chem. Soc., Dalton Trans.*, 1984, 1501.

125. D. Dolphin, T. Niem, R. H. Felton, and I. Fujita, *J. Am. Chem. Soc.*, 1975, **97**, 5288; P. Cocolios and K. M. Kadish, *Isr. J. Chem.*, 1985, **25**, 138; P. A. Connick and K. A. Macor, *Inorg. Chem.*, 1991, **30**, 4654.

126. A. J. Blake, R. O. Gould, M. A. Halcrow, A. J. Holder, T. I. Hyde, and M. Schröder, *J. Chem. Soc., Dalton Trans.*, 1992, 3427.

127. H. Yoon, T. R. Wagler, K. J. O'Connor, and C. J. Burrows, *J. Am. Chem. Soc.*, 1990, **112**, 4568.

128. H. Cohen, L. J. Kirschenbaum, E. Zeigerson, G. Ginsberg, M. Jaacobi, E. Fuchs, and D. Meyerstein, *Inorg. Chem.*, 1979, **18**, 2763; D. G. Kelley, J. H. Espenson, and A. Bakac, *J. Chem. Soc., Chem. Commun.*, 1991, 546.

129. G. Smith and J. K. Kochi, *J. Organomet. Chem.*, 1980, **198**, 199.

130. V. Amendola, L. Fabbrizzi, M. Licchelli, C. Mangano, P. Pallavicini, L. Parodi, and A. Poggi, *Coord. Chem. Rev.*, 1999, **192**, 649.

131. P. Charpin, M. Lance, T. B. Huy, and R. Bougon, *J. Fluorine Chem.*, 1981, **17**, 479.

132. J. M. McConnachie, M. A. Ansari, and J. A. Ibers, *J. Am. Chem. Soc.*, 1991, **113**, 7078.

133. R. Cammack, *Adv. Inorg. Chem.*, 1988, **32**, 297.

134. L. R. Furenlid, M. W. Renner, and J. Fajer, *J. Am. Chem. Soc.*, 1990, **112**, 8987.

135. R. K. Thauer, *Science*, 2001, **293**, 1264.

136. J. C. Fontecilla-Camps and S. W. Ragsdale, *Adv. Inorg. Chem.*, 1999, **47**, 283.

137. N. E. Dixon, R. L. Blakeley, and B. Zerner, *Can. J. Biochem.*, 1980, **58**, 469.

138. L. Alagna, S. S. Hasnain, B. Piggott, and D. J. Williams, *Biochem. J.*, 1984, **220**, 591.

139. A. M. Barrios and S. J. Lippard, *J. Am. Chem. Soc.*, 2000, **122**, 9172.

140. S. Uozumi, H. Furutachi, M. Ohba, H. Okawa, D. E. Fenton, K. Shindo, S. Murata, and D. J. Kitko, *Inorg. Chem.*, 1998, **37**, 6281.

141. S. P. J. Albracht, D. Ankel-Fuchs, J. W. Van der Zwaan, R. D. Fontijn, and R. K. Thauer, *Biochim. Biophys. Acta*, 1986, **870**, 50.

142. U. Elmer, W. Grabarse, S. Shima, M. Goubeaud, and R. K. Thauer, *Science*, 1997, **278**, 1457.

143. W. G. Grabarse, F. Mahlert, E. C. Duin, M. Goubeaud, S. Shima, R. K. Thauer, V. Lamzin, and U. Ermler, *J. Mol. Biol.*, 2001, **309**, 315.

144. H. Dobbek, V. Svetlitchnyi, L. Gremer, R. Huber, and O. Meyer, *Science*, 2001, **293**, 1281.

145. S. W. Ragsdale, H. G. Wood, and W. E. Antholine, *Proc. Natl. Acad. Sci. U.S.A.*, 1985, **82**, 6811.

146. T. I. Doukov, T. M. Iverson, J. Seravalli, S. W. Ragsdale, and C. L. Drennan, *Science*, 2002, **298**, 567.

147. C. Darnault, A. Volbeda, E. J. Kim, P. Legrand, X. Vernede, P. A. Lindahl, and J. C. Fontecilla-Camps, *Nat. Struct. Biol.*, 2003, **10**, 271.

148. C. E. Laplaza and R. H. Holm, *J. Am. Chem. Soc.*, 2001, **123**, 10255; K. B. Musgrove, C. E. Laplaza, R. H. Holm, B. Hedman, and K. O. Hodgson, *J. Am. Chem. Soc.*, 2002, **124**, 3083.

149. R. Krishnan, J. K. Voo, C. G. Riordan, L. Zahkarov, and A. L. Rheingold, *J. Am. Chem. Soc.*, 2003, **125**, 4422.

150. M. L. Golden, M. V. Rampersad, J. H. Reibenspies, and M. Y. Darensbourg, *Chem. Commun.*, 2003, 1824.

151. Q. Wang, A. J. Blake, E. S. Davis, E. J. L. McInnes, C. Wilson, and M. Schröder, *Chem. Commun.*, 2003, 3012.

152. A. Volbeda, M.-H. Charon, C. Piras, E. C. Hatchikian, M. Frey, and J. C. Fontecilla-Camps, *Nature*, 1995, **373**, 580.

153. A. Volbeda, E. Garain, C. Piras, A. L. Delacey, V. M. Fernandez, E. C. Hatchikian, M. Frey, and J. C. Fontecilla-Camps, *J. Am. Chem. Soc.*, 1996, **118**, 12989.

154. G. Davidson, S. B. Choudhury, Z. Gu, K. Bose, W. Roseboom, S. P. J. Albracht, and M. J. Maroney, *Biochemistry*, 2000, **39**, 7468.

155. H. Wang, C. Y. Ralston, D. S. Patil, R. M. Jones, W. Gu, M. Verhagen, M. Adams, P. Ge, C. Riordan, C. A. Marganain, P. Mascharak, J. Kovacs, C. G. Miller, T. J. Collins, S. Brooker, P. D. Croucher, K. Wang, E. I. Stiefel, and S. P. Cramer, *J. Am. Chem. Soc.*, 2000, **122**, 10544.

156. R. Cammack, D. S. Patil, E. C. Hatchikian, and V. M. Fernandez, *Biochim. Biophys. Acta*, 1987, **912**, 98.

157. M. Zimmer, G. Schulte, X.-L. Luo, and R. H. Crabtree, *Angew. Chem., Int. Ed. Engl.*, 1991, **30**, 193.

158. M. Stein, E. van Lenthe, E. J. Baerends, and W. Lubitz, *J. Am. Chem. Soc.*, 2001, **123**, 5839.

159. A. C. Marr, D. J. E. Spencer, and M. Schröder, *Coord. Chem. Rev.*, 2001, **219**, 1055.

160. C. H. Lai, J. H. Reibenspies, and M. Y. Darensbourg, *Angew. Chem., Int. Ed. Engl.*, 1996, **35**, 2390.

161. M. C. Smith, J. E. Barclay, S. P. Cramer, S. C. Davis, W. W. Gu, D. L. Hughes, and S. Longhurst, *J. Chem. Soc., Dalton Trans.*, 2002, 2641.

Nickel: Models of Protein Active Sites

Wen-Feng Liaw
National Tsing Hua University, Hsinchu, Taiwan

Based in part on the article Nickel: Models of Protein Active Sites by Michael J. Maroney which appeared in the Encyclopedia of Inorganic Chemistry, First Edition.

1 Introduction 1
2 Hydrogenase 1
3 Urease 5
4 Carbon Monoxide Dehydrogenase/acetyl Coenzyme A Synthase (CODH/ACS) 7
5 Methyl Coenzyme M Reductase 11
6 Related Articles 15
7 References 15

Abbreviations

H_{2ase} = hydrogenase; Hbsms = 4-mercapto-3,3-methyl-1-phenyl-2-thiabutane; S_{cys} = cysteine thiolate; psnet = bis(5-(diphenylphosphino)-3-thiapentanyl)amine; bdptz = 1,4-bis (2,2′-dipyridylmethyl)phthalazine; OTs = *p*-toluenesulfonate; tmen = N,N,N',N'-tetramethylethylenediamine; AA = acetohydroxamate anion; $[PhTt^{tBu}]$ = phenyltris((*tert*-butylthio)-methyl)borate; bipy = bipyridine.

1 INTRODUCTION

Recently, major progress has been made in solving the active-site structures of the nickel-containing metalloenzymes by single-crystal X-ray diffraction (the unsolved problem of bioinorganic chemistry as it exists in the 1980s–1990s) and in deducing the ways that nature activates/catalyzes reversible hydrogen oxidation (hydrogenases), hydrolysis of urea to ammonia and carbamate (ureases), reversible CO oxidation (carbon monoxide dehydrogenases), acetyl coenzyme assembly (acetyl coenzyme A synthase), and the formation of methane by the methanogens (methyl coenzyme M reductase). The high-resolution X-ray crystal structures of the active sites of the nickel-containing hydrogenases, carbon monoxide dehydrogenases (CODH/ACS), ureases, methyl coenzyme M reductase (MCR), as well as the role(s) of nickel in these enzymes have now been explored in detail. In such pursuit, extensive spectroscopic experiments and kinetic measurements on these enzymes have also been performed, as a background for the subsequent modeling studies. Since the mechanism(s) of catalytic reactions by the microorganisms remain elusive at the present time, modeling approaches have been adopted to correlate the spectral and reactivity parameters of model compounds with those of Ni-containing enzymes and to derive conclusions regarding mechanistic and functional characteristics of the biological nickel site.

2 HYDROGENASE

2.1 Background

Hydrogen metabolism (reversibly catalyzed oxidation of H_2 molecules) in the biological energy cycle is mostly mediated by two types of metal-containing enzymes, [NiFe] hydrogenases, and [Fe] hydrogenases.[1–5] [NiFe] hydrogenase containing a [Ni–Fe] center that is believed to be the catalytic site for hydrogen activation functions more effectively in the direction of H_2 oxidation. The recent X-ray crystallographic studies of the active-site structure of [NiFe] hydrogenases isolated from *Desulfovibrio gigas*, *Desulfovibrio vulgaris*, *Desulfovibrio fructosovorans*, and *Desulfovibrio desulfuricans* ATCC27774 in combination with infrared spectroscopy have revealed an active site comprised of a heterobimetallic $(S_{cys})_2Ni(\mu\text{-}S_{cys})_2(\mu\text{-}X)Fe(CO)(CN)_2$ (X = O, OH) cluster (Figure 1). The bridging ligand X was proposed to be an oxide or hydroxide in the oxidized state, and was found to be absent in the reduced state. Three nonprotein diatomic groups (two cyanide and one carbonyl ligands) ligate the iron center.[4–21]

The nickel site has been proposed to be redox active and changes between Ni(III) and Ni(II), while the iron site remains as Fe(II) in all spectrally defined redox states of the enzyme.[11–21,25–41] The EXAFS/EPR studies indicate that the formal oxidation state of the Ni center is paramagnetic Ni(III) in Ni–A, Ni–B and Ni–C states.[28–41] Actually, the active form Ni–C (the paramagnetic Ni–C intermediate) of [NiFe] H_{2ase} was proposed to exist as the $[(S_{cys}\text{-}H)Ni^{III}\text{-}H^{-}\text{-}Fe]$ intermediates after an active state Ni–SIa (silent-active $[(S_{cys}\text{-}H)Ni^{II}(S_{cys})_3]$) is passed. Ni–C is believed to be an intermediate in the catalytic cycle. Upon illumination,

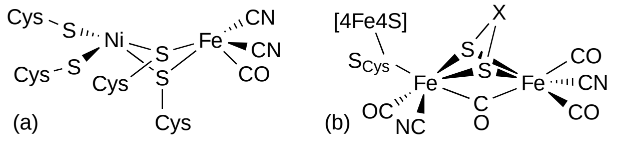

Figure 1 (a) A schematic drawing of the active site of [NiFe] hydrogenases as deduced from the crystallographic studies.[6–10] (b) A schematic drawing of the H-cluster of the CO-inhibited form of the *Clostridium pasteurianum* [Fe] hydrogenases as deduced from the recent X-ray crystallographic studies[22–24]

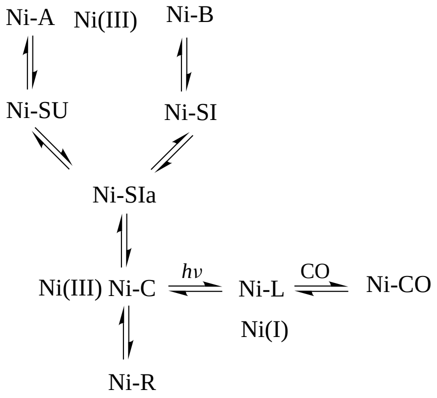

Scheme 1 The possible redox states of the active center of [NiFe] hydrogenases.[11–21,25–43]

the Ni–C state is transformed into a fourth paramagnetic Ni–L state. These conversions are considered to correspond to photodissociation of proton species from the [Ni–Fe] center.[28–41] Interestingly, the recent X-ray crystal structures of CO-inhibited forms and single-crystal EPR studies of the reduced active site of [NiFe] H_{2ase} isolated from *D. vulgaris Miyazaki F* implicate that the Ni–C intermediate is a formal Ni(III) oxidation state with a hydride (H^-) bridging between the Ni and the Fe atoms and the sulfur atom of Cys 546 hydrogenated for the catalytic reaction of the enzyme.[40,41] In addition, the active form Ni–C has also been shown to contain a solvent exchangeable proton, assigned as an in-plane hydride, as a S–H proton directly interacting with nickel, or as H_2 from ENDOR studies.[42,43] Interpretations of these results tend to favor the assignment of a Cys–SH proton directly interacting with nickel. The redox states of the active center of [NiFe] hydrogenases are shown in Scheme 1.

The recent report of high-quality X-ray crystal structures of [Fe]-only hydrogenases isolated from *D. desulfuricans* (DdH_{2ase})/*Clostridium pasteurianum* (CpH_{2ase}) revealed that the active sites are composed of a conventional [4Fe-4S] subcluster linked by a bridging cysteine to a dinuclear iron subcluster.[22–24,44,45] The crystal structures, in combination with FTIR data, suggest that the dinuclear iron subcluster is ligated by terminal CO and CN^- diatomic molecules with the two iron atoms linked by a di(thiomethyl)-amine ligand (DdHase)/two thiolate ligands (CpHase) and a carbonyl group. Upon reduction, FTIR spectra and crystal structure show that the previously bridging CO shifts toward the distal iron that most likely serves as the primary hydrogen binding site.[22–24,44,45] Mössbauer studies of the H-cluster in [Fe] hydrogenases isolated from *C. pasteurianum* (CpII) showed that the dinuclear Fe subcluster contains a low-spin $Fe^{II}-Fe^{II}$ site in the reduced state (H_{red}), while it is in the mixed-valence $Fe^{III}-Fe^{II}$ form in the oxidized state (H_{ox} and H_{ox}–CO).[46] It is generally believed that the dinuclear Fe subcluster of DdH_{2ase} and CpH_{2ase} may be assigned as $[Fe^{II}Fe^{II}]$, $[Fe^{I}Fe^{II}]$, and $[Fe^{I}Fe^{I}]$ in the fully oxidized (inactive), the oxidized (active), and reduced states, respectively.[45,47–51]

2.2 Structural Models

Designing and synthesizing structural model complexes, in addition to serving as spectroscopic references, may provide an essential understanding about the active-site construction and function of [Fe] and [NiFe] hydrogenases, and the role/function of CO, CN^- ligands, and may elucidate the electronic structure of active centers of the binuclear subcluster.[52–54] Examples of structurally characterized, thiolate-bridged heterobimetallic NiFe complexes with iron coordinated by CO/NO ligands are few. $[Ni\{Fe(NS_3)(CO)–S,S'\}_2]$ ($NS_3{=}[N(CH_2CH_2S)_3]^{3-}$) (**1**) is made up of two trigonal bipyramidal $Fe(NS_3)(CO)$ units bridging to a central Ni(II) atom.[55] A review of the heterobimetallic NiFe compounds finds Ni–Fe distances ranging from 2.80 to 3.323 Å (Ni–Fe distance: **2**, 3.323(1) Å; **3**, 3.308(2) Å; **4**, 3.10 Å; **5**, 2.80 Å; **6**, 2.80 Å), far beyond the enzyme Ni–Fe distance. $[(C_6H_4S_2)Ni(\mu\text{-}`S_3')Fe(CO)(PMe_3)_2]$ ('S_3'=bis(2-mercaptophenyl)sulfide (2−)) (**2**) nearly duplicates the donor atom set of [NiFe] hydrogenases centers with the ν(CO) frequency 1948 cm^{-1} (KBr) corresponding to the most reduced Ni–R state of hydrogenases.[56] The Ni of $[Fe(CO)_2\{N(CH_2CH_2S)_3\text{-}S,S'\}NiCl(dppe)]$ (**3**) is five-coordinate in a square pyramidal pattern and is displaced 0.307(2) Å from the base plane towards the chloride ligand in the apical site.[57] The unique NiFe heterotrimetallic (**4**) is formed by two $\{NiN_2S_2\}$ fragments serving as a bidentate metallothiolate ligand bound to $\{Fe(CO)_2\}$ motif.[58] Formation of $[Ni^{II}(N_2S_2)Fe(NO)_2]$ (**5**) and $[(NO)Ni^0(S_3)Fe(NO)_2]$ (**6**) may be rationalized according to the ability of the chalcogenolate (or metal-modified calcogenolate) ligand to stabilize the oxidized, $\{Fe(NO)_2\}^9$, or reduced, $\{Fe(NO)_2\}^{10}$ forms.[59,60] The Ni^{II}-bound dichalcogenolate stabilizes the electron-rich or reduced form and the $[Ni^0NO^+]$ unit effectively generates a monoanionic dithiolate ligand donor set that stabilizes the oxidized form.

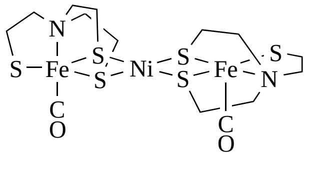

(**1**)

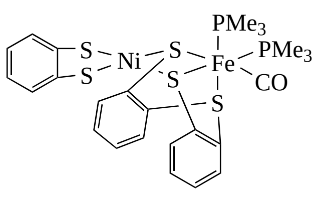

(**2**)

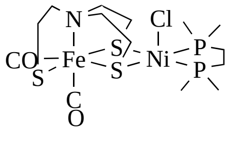

(**3**)

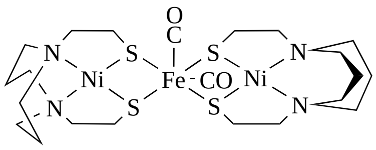

(**4**)

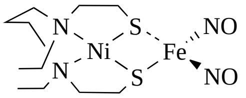

(**5**)

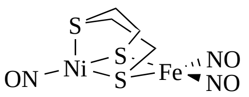

(**6**)

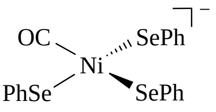

(**7**)

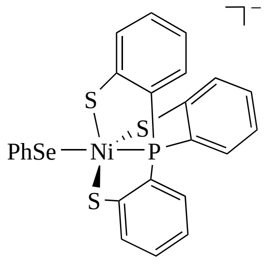

(**8**)

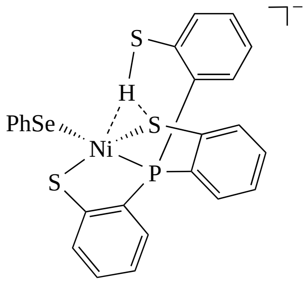

(**9**)

Mononuclear nickel-thiolate complexes may serve as precursors for synthetic goals of preparing Ni–Fe heterometallics in biological-type ligation settings. Structural models as $[\mathrm{Ni(CO)(SPh)}_n\mathrm{(SePh)}_{3-n}]^-$ ($n = 0, 1, 2$) (**7**), a distorted square-planar $\mathrm{Ni^{II}}$–CO complex, may be appreciated as possibilities for intermediates in biological reaction pathways or as structures important to CO-inhibitory processes in the [NiFe] enzyme.[61,62] Interestingly, the mononuclear $\mathrm{Ni^{III}}$ $[\mathrm{Ni(SePh)(P(}o\text{–}\mathrm{C_6H_4S)_3)}]^-$ complex (**8**) with S-donor ligands has been structurally characterized recently.[63] Complex (**8**) is five-coordinate with three equatorial S-donors, one axial selenolate Se-donor and one axial P-donor. The distorted square-planar $[\mathrm{Ni(SePh)(P\text{–}(}o\text{-}\mathrm{C_6H_4S)_2(}o\text{-}\mathrm{C_6H_4SH))}]^-$ (**9**) with the thiol proton interacting with both the nickel and sulfur sites was verified in the solid state by the observation of one $\nu_{\mathrm{S–H}}$ stretching band ($2274\,\mathrm{cm^{-1}}$) in its IR spectrum and subsequently confirmed by an X-ray diffraction study.[63] The H/D exchange reaction between complex (**9**) and D_2O occurred in CH_3CN as indicated by IR and ^{2}H NMR. The facile conversion of complex (**9**) into complex (**8**) accompanied by by-product H_2O was observed upon exposure of complex (**9**) to O_2. In $[\mathrm{Ni(bsms)_2}]$ (**10**), a promising complex for new structural models of [NiFe] hydrogenases, the two ligands are coordinated with the thiolates in trans positions to each other.[64] $[\mathrm{Ni_2(L)}]^{3+}$, the one-electron oxidation product of $[\mathrm{Ni_2(L)}]^{2+}$ (**11**), can be described with a proportion (ca. 30%) of the unpaired electron density delocalized onto the bridging thiolate ligands, that is, the charge delocalization lies between the $[\mathrm{Ni^{III}}\text{-(–SR)}]$ and $[\mathrm{Ni^{II}}\text{-}(\cdots\mathrm{SR})]$ redox extremes.[65]

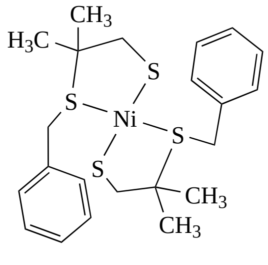

(**10**)

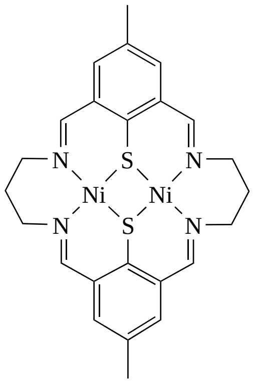

(**11**)

2.3 Models of Hydrogenase Catalysis

Hydrogenases catalyze the heterolytic cleavage of the hydrogen molecule. During catalysis, the Ni ion in [NiFe] hydrogenase has been proposed to serve as the catalytic site, heterolytically splitting the H_2 molecule into hydride and proton with the thiolate of $\mathrm{Cys_{530}}$ serving as a base. In model compounds, an electrochemical study provided evidence for such a Ni(III)-H species generated by one-electron reduction of a nickel(II) macrocyclic complex accompanied by protonation.[66] Recently, two elegant examples have been provided, $[\mathrm{Ni(diphosphine)_2}]^{2+}$ containing ligand-appended nitrogen bases (**12**) and $[\mathrm{Ni(NHP}n\mathrm{Pr_3)(`S_3')}]$ (‘$\mathrm{S_3}$’$^{2-}$=bis(2-sulfanylphenyl)sulfide(2−)) (**13**).

In one interesting model compound, complex $[\mathrm{Ni(PNP)_2}]^{2+}$ (PNP = $\mathrm{Et_2PCH_2NMeCH_2PEt_2}$) (**12**) is an electrocatalyst for the oxidation of hydrogen to protons, and stoichiometric reaction with hydrogen forms $[\mathrm{HNi(PNP)(PNHP)}][(\mathrm{BF_4})_2]$ in which the hydride ligand is associated with nickel and the proton is bound by nitrogen.[67,68] Complex $[\mathrm{HNi(PNP)(PNHP)}]^{2+}$ undergoes reversible deprotonation to yield $[\mathrm{HNi(PNP)_2}]^+$. Meanwhile, the hydride ligand and the NH proton of $[\mathrm{HNi(PNP)(PNHP)}]^{2+}$ undergo rapid intramolecular exchange with each other and intermolecular exchange with protons in solution. The proposed electrocatalytic reaction sequences are summarized in Scheme 2.[67,68] The one-electron oxidation of $[\mathrm{HNi^{II}(PNP)_2}]^+$

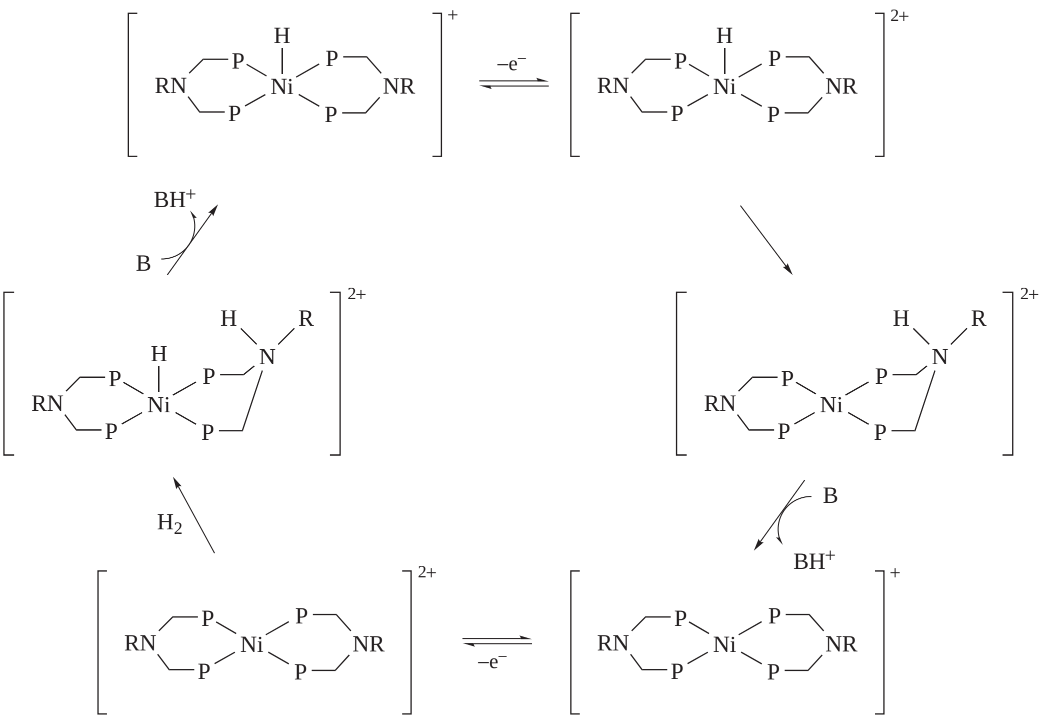

(**12**)

Scheme 2 A proposed mechanism for the oxidation of hydrogen. (Reprinted from *Inorg. Chem.*, 2003, **42**, 216–227. © 2003 American Chemical Society)

to $[HNi^{III}(PNP)_2]^{2+}$ is followed by rapid transfer of the proton bound to Ni in $[HNi^{III}(PNP)_2]^{2+}$ to the N atom of the chelating PNP ligand. A proton transfer occurs from the diphosphine ligand to give $[Ni^{I}(PNP)_2]^{+}$ and $HNEt_3^{+}$ in the presence of triethylamine. Oxidation of $[Ni^{I}(PNP)_2]^{+}$ to $[Ni^{II}(PNP)_2]^{2+}$ completes the two-electron oxidation process.

Model compound $[Ni(NHPnPr_3)(‘S_3’)]$ (**13**) was presumed to catalyze the heterolytic cleavage of H_2 (reaction of H_2 and D_2O yielding HD and HDO). Reactions of $[Ni(NHPnPr_3)(‘S_3’)]$ with D_2 and D_2O yielding $[Ni(NDPnPr_3)(‘S_3’)]$/HD, and $[Ni(NDPnPr_3)(‘S_3’)]$/HDO, individually, demonstrate that complex (**13**) is able to exchange NH protons with molecular D_2 and with H^+ or D^+.**69** The proposed mechanism of the catalyzed D_2/H^+ exchange is shown in Scheme 3.**69**

Recent kinetics studies on protonation of $[Ni(SEt)((Ph_2PCH_2CH_2)_2PPh)]^+$ (**14**) proposed that the proton interacts with both the nickel and sulfur sites,**70** consistent with the proposal of intramolecular proton transfer between cysteinate sulfur and Ni atom in the Ni-based hydrogenases. Additionally, the mononuclear complex $[Ni(psnet)]^+$ (**15**) of known structure and a mildly negative redox potential can stoichiometrically evolve H_2 from protic sources. On the basis of kinetics analysis, the reaction paths considered most probable involve steps of protic oxidative addition to Ni(I) to generate Ni^{III}-H^-, and electron transfer to Ni(III) followed

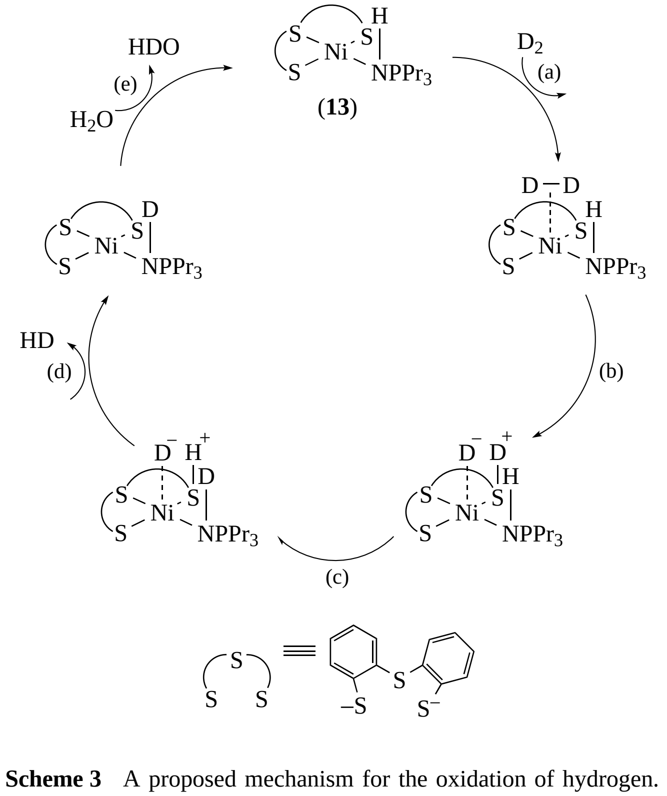

Scheme 3 A proposed mechanism for the oxidation of hydrogen. (Reprinted from *Angew. Chem. Int. Ed. Engl.*, 2000, **39**, 561–563. © 2000 John Wiley & Sons, Ltd)

by protonation of bound hydride or the bimolecular reaction $2Ni^{III}\text{-}H^- \rightarrow 2Ni^{II} + H_2$ to yield H_2.[71]

2.4 Models for the Iron Site of [NiFe] Hydrogenase

Examples of cyanide (CN^-) coordination to iron(II) and the spectroscopic signals of dicyanide iron(II) thiolate carbonyl complexes ($[(CN)_2(CO)Fe^{II}(SR)_2]^{n-}$) are of much interest, particularly in catalytically active-site construction of the $(CysS)_2Ni(\mu\text{-}Scys)_2Fe(CN)_2(CO)$ active site of [NiFe] hydrogenases. In the iron-site architecture of the [NiFe] hydrogenase active site, a vacant coordination site around iron, trans to the carbonyl ligand, may serve as a potential H_2-binding site and presumably plays an important role in biological hydrogen activation. By application of oxidative addition and stepwise ligand exchange route, *trans, cis*-$[(CN)_2(CO)_2Fe(S, S\text{–}C\text{–}R)]^-$ (R = OEt **16**, R = $N(Et)_2$ **17**) were isolated and characterized by X-ray crystallography and infrared spectroscopy.[72] Photolysis of THF solutions of complexes (**16**/**17**) led to the formation of coordinatively unsaturated iron(II) dicyanocarbonyl thiolate complexes $[(CN)_2(CO)Fe(S, S\text{–}C\text{–}R)]^-$ (R = OEt **18**, R = $N(Et)_2$ **19**, respectively), with two cyanides occupying cis positions and a vacant site preferably trans to the CO ligand. Complexes (**18**/**19**) and Ni–A/Ni–C states of [NiFe] hydrogenases from *D. gigas* exhibit a similar one-band pattern in the ν_{CO} region and two-band pattern in the ν_{CN} region, individually, but in different positions, which may be accounted for by the distinct electronic effects between $[S, S\text{–}C\text{–}R]^-$ and cysteine ligands.[72] Also, two particularly elegant model compounds $[Fe(CO)_2(CN)_2(SPh)_2]^{2-}$ (**20**) and $[Fe(CO)(CN)_2(S,S\text{–}C_6H_4)]^{2-}$ (**21**) have been characterized by IR and X-ray diffraction, recently.[73] Scrutiny of the coordination chemistry of iron(II)-thiolate species $[Fe^{II}(CO)_x(CN)_y(SR)_z]^{n-}$ reveals that certain combinations of thiolate and cyanide ligands ($3 \le y + z \le 4$) ligated to the Fe(II) center provide significant stabilization to the iron(II)-thiolate cyanocarbonyl species $[Fe^{II}(CO)_x(CN)_y(SR)_z]^{n-}$.[74,75]

3 UREASE

3.1 Background

The metalloenzyme urease catalyzes the hydrolysis of urea to ammonia and carbamate (equation 1).[76]

$$H_2NCONH_2 + H_2O \longrightarrow NH_3 + H_2NCOOH \qquad (1)$$

The X-ray crystallographic studies of the enzyme isolated from *Klebsiella aerogenes* reveals an active site composed of a dinickel center with 3.5-Å Ni···Ni separation. A schematic view of the active site of urease isolated from *K. aerogenes* is shown in Figure 2.[77,78] The two nickel ions are bridged by a carboxylate group of a carbamylated lysine residue (*see* ***Metal-mediated Protein Modification***) and one water molecule or hydroxide ion.[77–81] The geometry around one nickel ion (Ni(1)) is best described as a distorted square pyramidal with further coordination of two histidine residues from the protein and one terminally coordinated water molecule; the position is only partially occupied by a water molecule and considered to be a likely candidate for binding urea in the catalysis. One terminally coordinated water molecule, one additionally ligated aspartate residue, and two histidine residues complete the coordination spheres of the second nickel ion (Ni(2)), resulting in a pseudooctahedral geometry for Ni(2). The nickel centers are in the stable diamagnetic Ni(II) state; thus the role of Ni in urease may be essentially catalytic without necessarily redox chemistry.

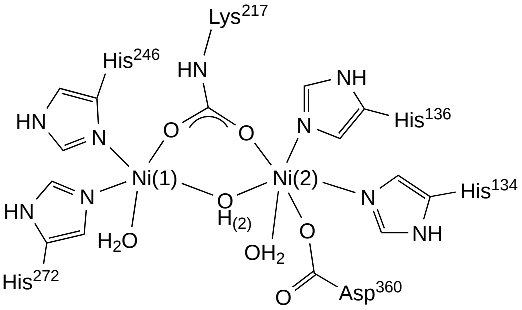

Figure 2 A schematic drawing of the active site of urease isolated from *K. aerogenes*[77–79]

Urease catalyzes hydrolysis of urea to ammonia and carbamate at a rate at least 10^{14} times faster than the spontaneous hydrolysis rate of urea in aqueous solution between pH 2 to 12.[82,83] The stability of urea is attributed to its resonance energy, which has been estimated at 30–40 kcal mol^{-1}.[84] The zwitterionic resonance forms of urea donate electrons to the carbonyl carbon, causing it to be less reactive toward nucleophiles.

It is considered that urease employs such an unsymmetric dinuclear core to promote the concerted binding of the substrate at one nickel center and a hydroxide nucleophile at the other nickel center.[80] There are many studies of urease[77–85] and model dinickel complexes to elucidate the relationship between the structure and function of the dinickel active site.[86–91] The generally accepted mechanism has suggested that both nickel ions are involved in the hydrolysis of urea. Several key features of the molecular geometry at the active site are essential for the function of the enzyme: (i) an open coordination site at each nickel center, (ii) the generation of a Ni-bound hydroxyl group resulting from removal of a proton from coordinated water by the assistance of a basic histidine residue located in proximity to the dinickel core, and (iii) polarization of the urea substrate through oxygen binding

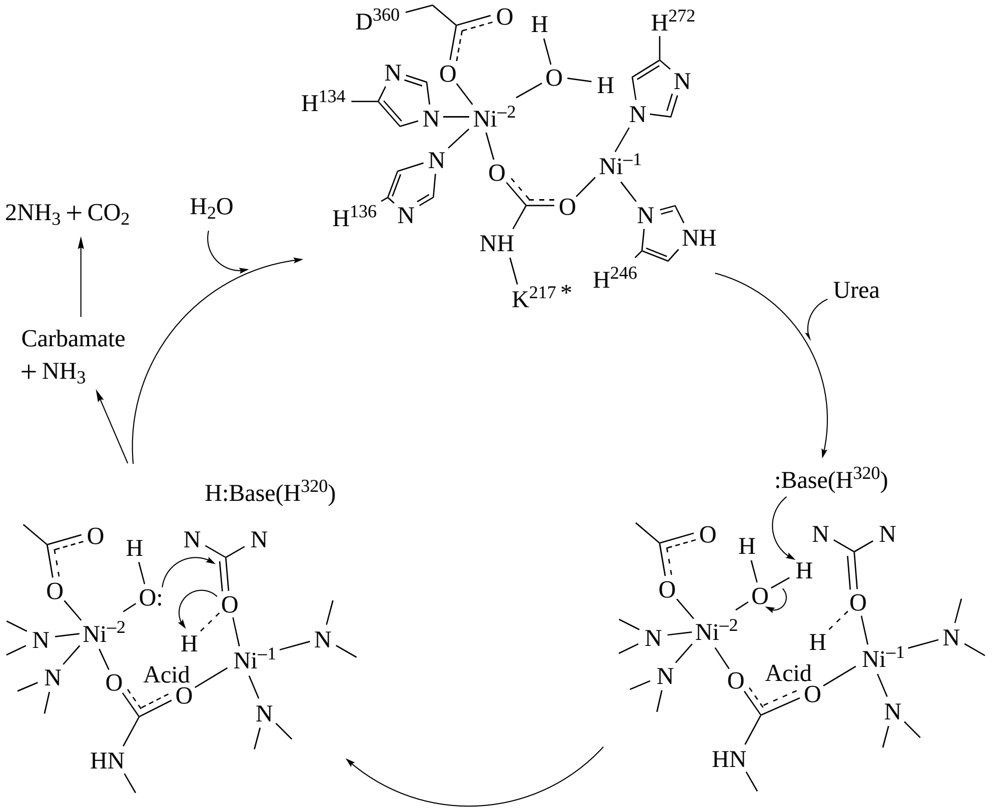

Scheme 4 A mechanism for the hydrolysis of urea by urease

to one Ni center followed by nucleophilic attack by a Ni-bound hydroxyl group.[77–92] The choice of Ni for this catalytic hydrolysis reaction may be attributed to the high affinity of the urea-Ni binding and the stability of the urease Ni-containing active site. The proposed catalytic cycle of ureases is shown in Scheme 4.[80]

3.2 Structural and Functional Models

Numerous dinickel complexes have been reported as models for urease. As depicted in Scheme 5, a dinickel complex $[Ni_2(\mu\text{-OH})(\mu\text{-}H_2O)(bdptz)(H_2O)_2][OTs]_3$ is capable of hydrolyzing a bound amide substrate by intramolecular nucleophilic attack of a coordinated hydroxide ion, either from a bridging position or from a transient terminally bound form.[86] This amide hydrolysis mimics the hydrolysis of urea by urease in that a hydroxide nucleophile is generated by the dinickel center, and the coordination of the substrate to the dinickel center as well as a nickel-bound hydroxide ion serving as the nucleophile are crucial to hydrolysis. Protonation of the amine group by an acidic residue in the active-site results in loss of ammonia.

A number of dinickel urease models with urea bound to the dinickel center implicate preferential binding of urea via the carbonyl oxygen atom;[87–91] this coordination mode is believed to be a species formed for the urea substrate binding to Ni(1) by replacing the terminally bound water molecule in the catalytic cycle of urease.[77,79] In addition to these model complexes, catalytic ethanolysis of urea by a (μ-alkoxo)(μ-carboxylato)dinickel(II) complex, presumably taking place via nucleophilic attack of ethanol solvent on coordinated urea, was also reported.[88,90]

An alternative mechanism for the urease-catalyzed hydrolysis of urea is hydrolysis of urea to ammonia and carbon dioxide through formation of a cyanate intermediate.[92–95] This reaction proceeds via a pathway, which is distinct from the proposed enzymatic hydrolysis of urea shown in Schemes 4 and 5. Upon heating, a dinickel complex $[Ni_2(\mu\text{-OH})(\mu\text{-urea})(bdptz)(urea)(CH_3CN)][ClO_4]_3$ containing a bridging urea molecule promotes the hydrolysis of urea in a two-step reaction; a molecule of ammonia is eliminated from urea with concomitant formation of a cyanate intermediate and, subsequently, the cyanate-containing intermediate is hydrolyzed by an external water molecule upon further heating. In this catalytic reaction, it is proposed that the coordinated hydroxide ion is not sufficiently nucleophilic to hydrolyze the coordinated urea molecule. On the contrary, the coordinated hydroxide ion serves as a base aiding in the deprotonation of urea to favor elimination. These results establish the precedence for hydrolysis of urea via a cyanate

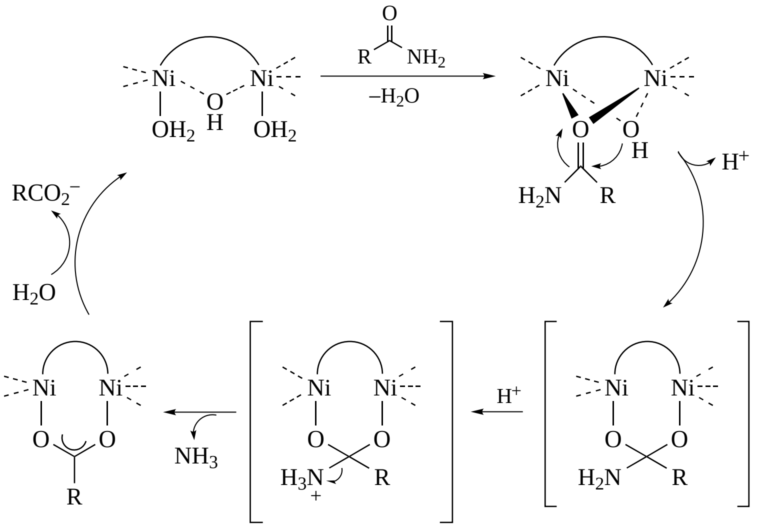

Scheme 5 A mechanism for the hydrolysis of urea. (Reprinted from *J. Am. Chem. Soc*, 1999, **121**, 11751–11757. © 1999 American Chemical Society)

intermediate for the urease-catalyzed hydrolysis of urea, as shown in Scheme 6.[92]

In addition, urease is inhibited by a variety of agents including fluoride[96] and disulfides,[97] as observed recently in the acetohydroxamate-inhibited C319A variants of *K. aerogenes* urease.[78] It is proposed that this mode of inhibition involves coordination of the inhibitor to only one nickel center, while another involves the inhibitor bridging the dinickel center. Urease is slowly inhibited by fluoride in both the presence and absence of substrate, and fluoride binding rates are directly proportional to inhibitor concentration. Fluoride inhibition is pH-dependent due to a protonation event linked to fluoride dissociation. That fluoride binding is pH-independent suggests that fluoride anion, not HF, is the actual inhibitor.[96] Reaction of the model complex $[Ni_2(OAc)_3(urea)(tmen)_2][OTf]$ ($OAc = CH_3COO^-$) with acetohydroxamic acid (AHA) gives the monobridged hydroxamate complex $[Ni_2(OAc)_2(AHA)(urea)(tmen)_2][OTf]$, a close model of the proposed mode of urease inhibition by hydroxamic acids.[78,89,98] In particular, only one bridging hydroxamate for the inhibited urease was suggested.[98]

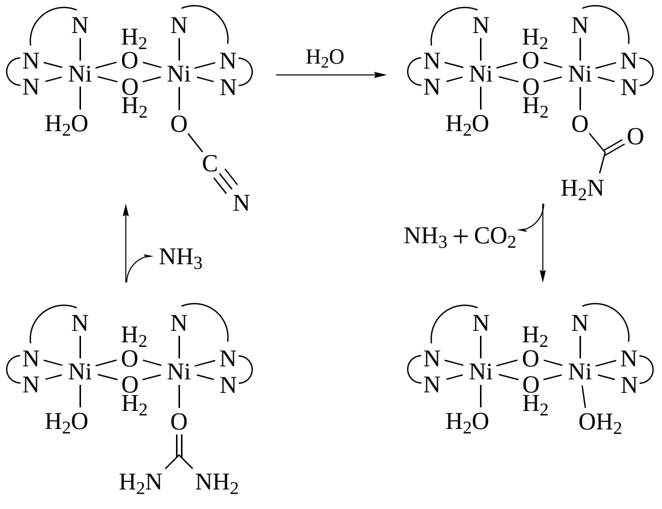

Scheme 6 A mechanism for the hydrolysis of urea. (Reprinted from *J. Am. Chem. Soc.*, 2000, **122**, 9172–9177. © 2000 American Chemical Society)

4 CARBON MONOXIDE DEHYDROGENASE/ ACETYL COENZYME A SYNTHASE (CODH/ACS)

4.1 Background

Carbon monoxide dehydrogenase/acetyl coenzyme A synthase (CODH/ACS) describes two different classes of enzymes; carbon monoxide dehydrogenase (CODH) isolated from *Rhodospirillum rubrum* or *Carboxydothermus hydrogenoformans* reversibly oxidizes CO to CO_2 according to equation (2), and the bifunctional CODH/ACS enzyme from *Moorella thermoacetica* catalyzes the reversible reduction of CO_2 to CO (CODH) and acetyl coenzyme assembly/disassembly (ACS) (equation 3).[99–101]

$$CO + H_2O \rightleftharpoons CO_2 + 2H^+ + 2e^- \qquad (2)$$

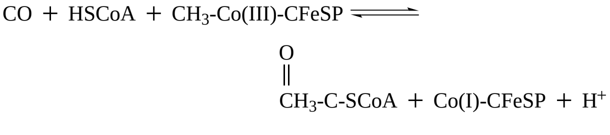

$$CO + HSCoA + CH_3\text{-Co(III)-CFeSP} \rightleftharpoons CH_3\text{-}\overset{\overset{\large O}{\|}}{C}\text{-SCoA} + \text{Co(I)-CFeSP} + H^+ \qquad (3)$$

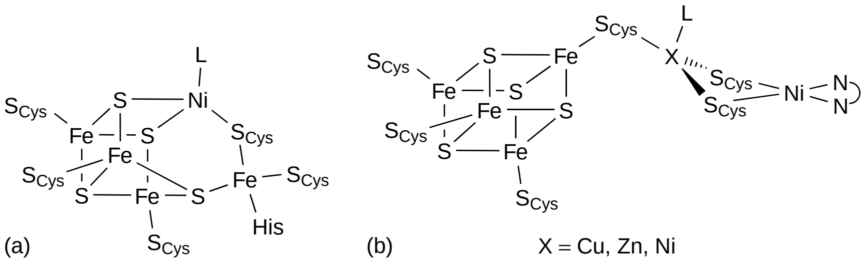

Figure 3 (a) A schematic drawing of the active-center C-cluster of CODH isolated from *R. rubrum* or *C. hydrogenoformans*.[102–104] (b) A schematic drawing of the active site of the ACS enzyme isolated from *C. thermoaceticum*[104–106]

Recent X-ray crystallographic studies indicated that the dimeric CODH isolated from *R. rubrum* or *C. hydrogenoformans* contains two [Fe-NiFe$_3$S$_4$] C-clusters, two conventional cysteine-ligated [Fe$_4$S$_4$] B-clusters, and a D-cluster that bridges the two subunits.[102–104] The B-cluster is involved in electron transfer and the *R. rubrum* enzyme catalyzes the biological oxidation of CO at the C-cluster. The active-center C-cluster is composed of the mononuclear Fe site and the four-metal cubane cluster [NiFe$_3$S$_4$] bridged by cysteine and one of the sulfides of the cube, as shown in Figure 3(a). Recently, the crystallographic characterization of the ACS enzyme isolated from *C. thermoaceticum* revealed an unprecedented hexametallic active site, a cuboidal [Fe$_4$S$_4$] unit linked via cysteine to a binuclear [CuNi] subcluster. The proximal copper atom is coordinated by three cysteine sulfur atoms and the unidentified fourth ligand. The distal Ni is in a square-planar environment with two amide nitrogens (deprotonated protein backbone) and two cysteine thiolates coordination (Figure 3(b)).[104–106]

The amount of Cu in CODH/ACS directly correlates with ACS activity. However, Cu is not the only metal that can occupy the Cu site. The negative correlation between Zn content and ACS activity suggests that Zn can replace Cu and inhibit the enzyme.[106] In contrast, the active-site structure from *M. thermoacetica* ACS enzyme (an $\alpha_2\beta_2$ tetramer) shows that the two α-subunits display different conformations (open and closed conformations). One α- subunit contains one Zn, located in the proximal site, and one Ni at its active-site metal cluster (α-closed form), while the A-cluster of the other α subunit contains two Ni ions at the corresponding positions (α-open form).[107,108] These investigations also demonstrate that Cu-containing ACS is inactive and only the A-cluster containing two Ni ions are responsible for the observed catalytic activity.[107,108] Such a Ni(μ-Cys)$_3$ low-coordinate site may be susceptible to demetalation by 1,10-phenanthroline, accounting for the observation that 1,10-phenanthroline removes some of the Ni in the protein resulting in loss of ACS activity and the correlated spectroscopic signals.[107,108]

The CODH from *R. rubrum* catalyzes both the oxidation of CO as well as the reduction of CO$_2$, and does not synthesize acetyl CoA. A mechanism for CO/CO$_2$ oxidation catalyzed by the C-center of CODH has been proposed in which the C-center can be stabilized in three states. The detailed electronic structures of the various [Fe-NiFe$_3$S$_4$] oxidation states remain ambiguous. As shown in Scheme 7, CO binding to the Fe site and subsequent nucleophilic attack of OH$^-$ on the CO or CO insertion into the Ni–OH bond leads to the release of CO$_2$. In this catalytic cycle, it is proposed that CO is bound to a unique Fe site of the C-cluster and at least two sites of the C-cluster are essential for the catalytic interconversion of CO and CO$_2$. Meanwhile, the Ni ion is proposed to be redox active.[109–111] On the basis of recent studies, a model for the mechanism of CO$_2$ reduction was proposed. In this model, fully oxidized CODH ($[(\mathrm{CO_L})\mathrm{Fe}^{2+}\text{-}\mathrm{Ni}^{2+}]^{4+}$) and CODH at the C$_{\mathrm{red1}}$ state ($[(\mathrm{CO_L})\mathrm{Fe}^{3+}\text{-}\mathrm{Ni}^{2+}\text{-}\mathrm{H}^-]^{4+}$) are unable to reduce CO$_2$ to CO. CO$_2$ reduction only occurs effectively when the putative [Fe-NiFe$_3$S$_4$] subcluster is fully reduced $[(\mathrm{CO_L})\mathrm{Fe}^{2+}\text{-}\mathrm{Ni}^{2+}\text{-}\mathrm{H}^-]^{3+}$ (C$_{\mathrm{unc}}$ state).[111–114] The B-cluster mediates electron flow from the C-center to the external electron acceptors in *R. rubrum* CODH and to the A-cluster via the 13.8-Å-long hydrophobic channel in *M. thermoacetica* CODH.[115] Cyanate, thiocyanate, and azide have been shown to bind to the C-center and inhibit CO oxidation.[116]

In addition to the CO oxidation occurring at the C-center, the *M. thermoacetica* enzyme is also capable of catalyzing the synthesis of acetyl coenzyme A at the A-center located in the α subunit.[117] The bifunctional enzyme CODH/ACS plays a central role in the Wood–Ljungdahl pathway of autotrophic CO$_2$ fixation.[99] In the acetate-production pathway, one CO$_2$ molecule is reduced to a methyl group in a set of enzymatic reactions. CO generated from CO$_2$ reduction at the C-cluster travels through a 70-Å channel and binds to Cu to generate a paramagnetic species NiFeC observed by FTIR and EPR spectroscopy.[105,118–120] The proposed mechanism of acetyl CoA synthesis is shown in Scheme 8. Methylation of Ni by the methyl group of protein-bound methylcob(III)amide yields cob(I)amide and a diamagnetic state, a transient methyl-Ni(III) species.[121,122] Electron transfer from [Fe$_4$S$_4$]$^+$ to the transient methyl-Ni(III) species generates methyl-Ni(II). The reaction of CO and the methyl group could proceed through an alkyl migration yielding an acetyl-metal-bound intermediate, and then HSCoA is deprotonated and acetylated.[123]

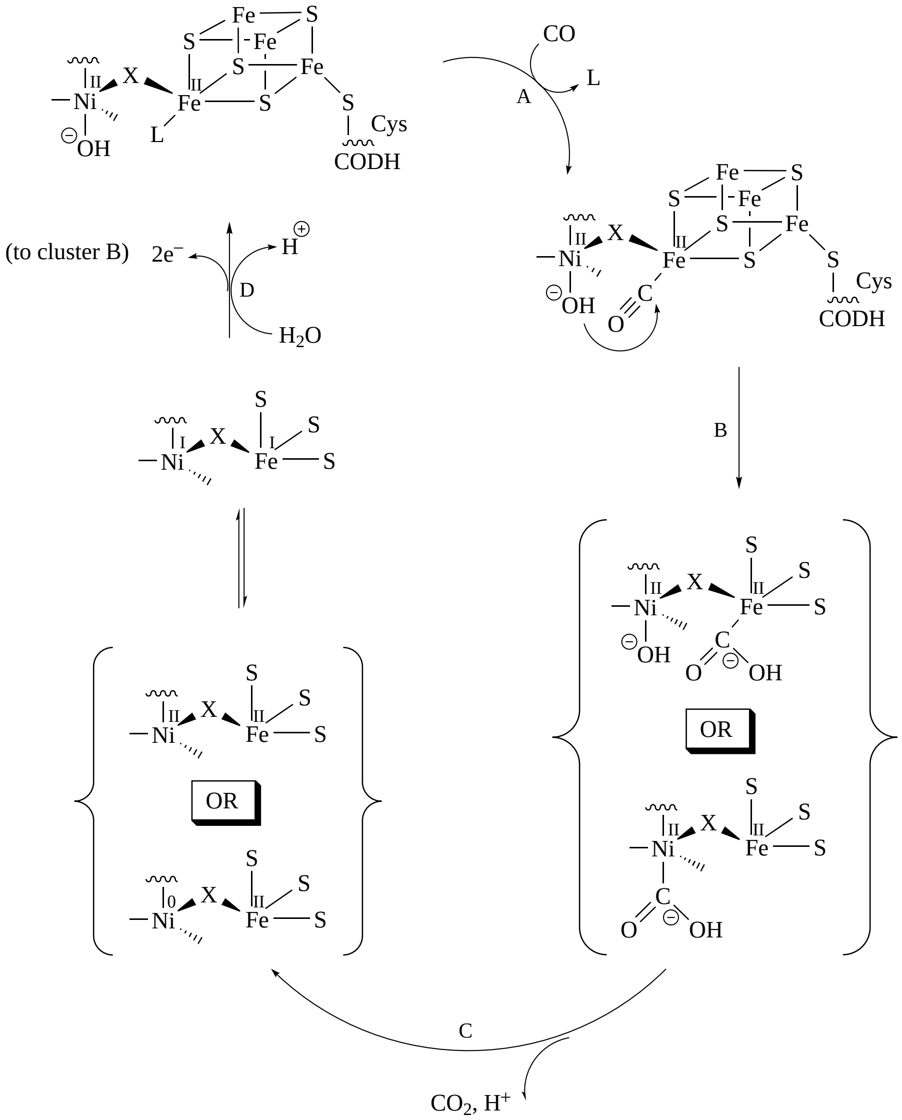

Scheme 7 A proposed mechanism for CO/CO_2 oxidation catalyzed by the C-center of CODH. (Reprinted from *J. Am. Chem. Soc*, 1996, **118**, 10 429–10 435. © 2003 American Chemical Society)

4.2 Structural Models

There are several bimetallic systems bearing a stoichiometric and structural resemblance to the bimetallic site of ACS. Structures of the binuclear complexes (**22**) and (**23**) show that the adjacent thiolate donors of the $[N_2S_2]$Ni motif can serve as a chelate in coordinating to a single Cu metal. Reactivity studies confirm that the binuclear complexes (**22**) and (**23**) bind CO, and subsequently, generate the respective mononuclear species, $[N_2S_2]$Ni and $[PhTt^{tBu}]$Cu(CO) resulting from the rupture of the thiolate bridges,[124,125] as observed in the paramagnetic NiFeC species. The NiFeC species, produced from reductive carbonylation of the A-cluster, indicates Cu-CO and acetyl-Cu intermediates characterized by EPR, IR, and Mössbauer studies.[105,126–128] The dimeric ‘staircase’ structure $[Cu_2\{NiS_2N_2\}_2]^{2+}$ (**24**), structurally analogous to the ACS active site, was obtained by reaction of $[Cu(NCMe)_4]^+$ and the nickel hexamethylated diamino dithiolate ($[NiS_2N_2]$).[129] Treatment of complex (**24**) with PR_3 (R = *i*Pr, NMe_2) yielded the bimetallic derivative $[\{(R_3P)(MeCN)Cu\}\{NiS_2N_2\}]^+$ (**25**).

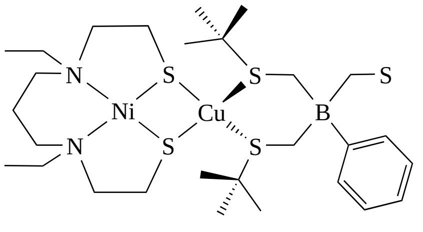

(**22**)

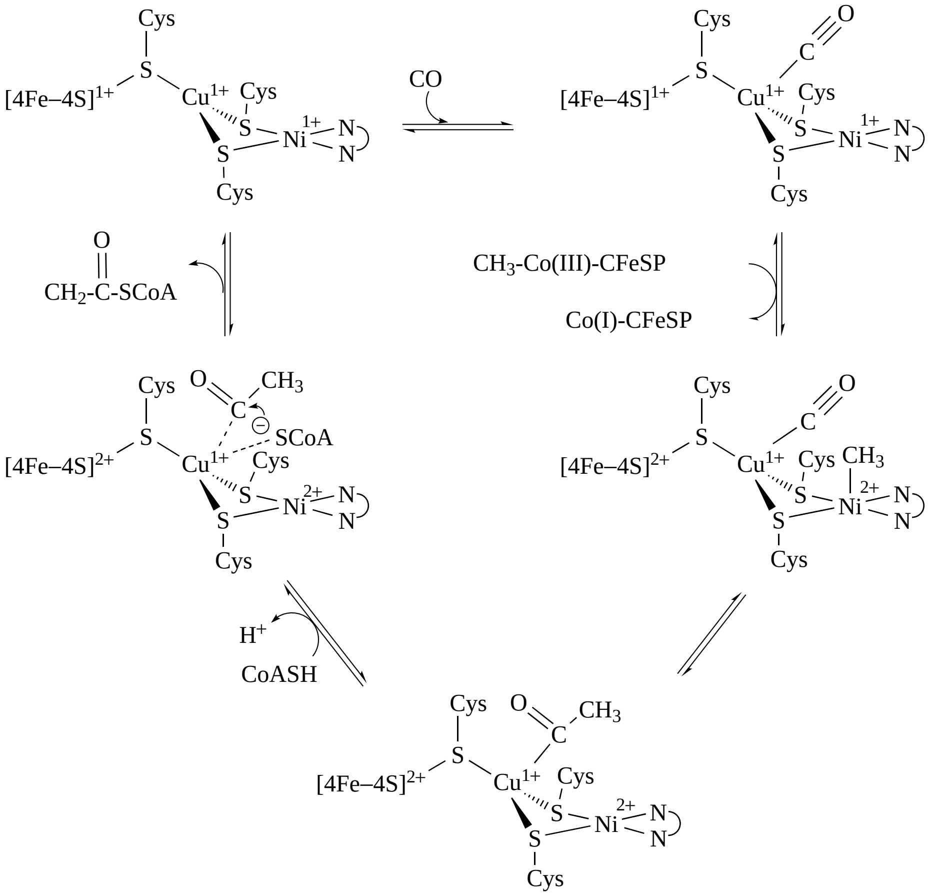

Scheme 8 A proposed mechanism of acetyl CoA synthesis. (Reprinted from *Proc. Natl. Sci. U.S.A.*, 2003, **100**, 3689–3694. © 2003 National Academy of Science, U.S.A)

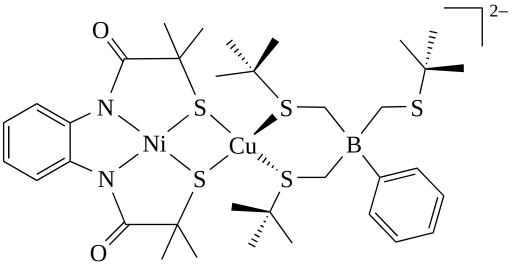

(**23**)

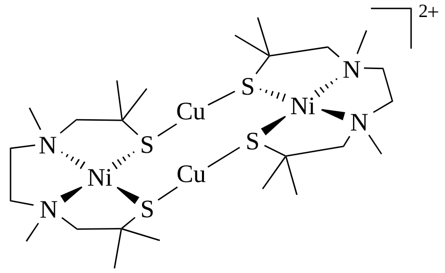

(**24**)

Relevant to the conflicting reports of copper versus nickel requirements for enzyme activity,[106,130] biochemical studies demonstrated the existence of a labile nickel associated with the α subunit of ACS/CODH.[131] Very recently, model studies on a metal-ion capture of a peptide-backbone, nonlabile $[NiN_2S_2]$ (**26**) unit have established the capability of such a nickel dithiolate to bind exogeneous metals. A qualitative ranking of the binding ability of complex (**26**) with Zn^{2+}, Cu^+, and Ni^{2+} was established by a metal-ion displacement experiment ($Zn^{2+} < Ni^{2+} < Cu^+$), as shown in Scheme 9.[132] A concept that the chemically most reasonable dinickel ACS

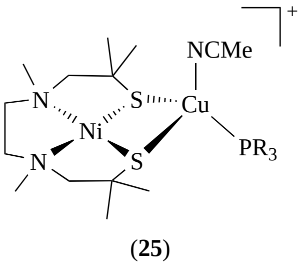

(**25**)

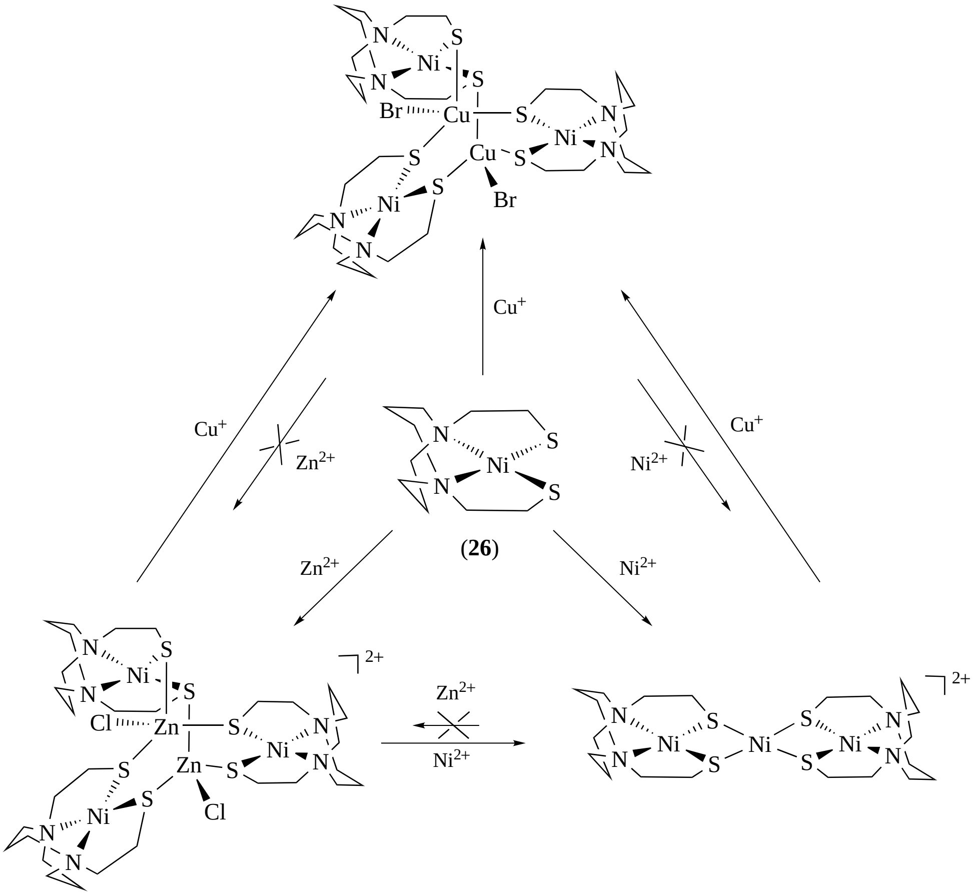

Scheme 9 The binding ability of complex (**26**) with Zn^{2+}, Cu^+ and Ni^{2+}

active site could be compromised by copper replacement has been derived from the lability study of both Zn and Ni bound by the model complex (**26**). This accounts for the possibility of exclusion of inappropriately associated metals to ultimately achieve functioning active sites in the nickel enzyme.[133]

On the other hand, the A-cluster in the ACS subunit of the protein is also proposed to bind CO via the Ni atom prior to CO migratory insertion into a H_3C–Ni bond.[99,134] The four-coordinate [(bipy)Ni(CH_3)(SR)] and [(bipy)Ni($SCH_2CH_2CH_2$)] complexes provide a possible model for CO insertion into the H_3C–Ni bond yielding the stable acetylthiolatonickel,[135] and thialactones under CO atmosphere,[136] respectively.

5 METHYL COENZYME M REDUCTASE

5.1 Background

Methyl coenzyme M reductase (MCR) is the enzyme responsible for the microbial formation of methane by the methanogens, a class of strictly anaerobic archaebacteria.[137–140] A key component of the active site of MCR is cofactor F_{430} (Figure 4), a nickel tetrahydrocorphinoid cofactor.

X-ray crystallographic studies reveal that MCR is composed of three different subunits in an $\alpha_2\beta_2\gamma_2$ arrangement containing tightly bound 2 mol of the nickel porphinoid

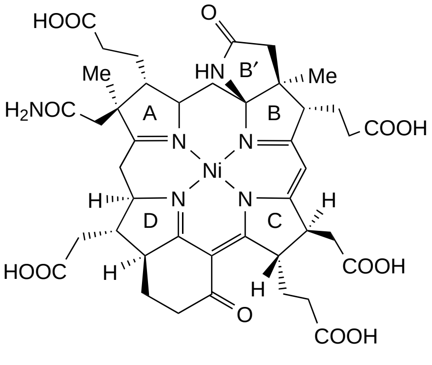

Figure 4 A schematic drawing of the active site of MCR[139,141–143]

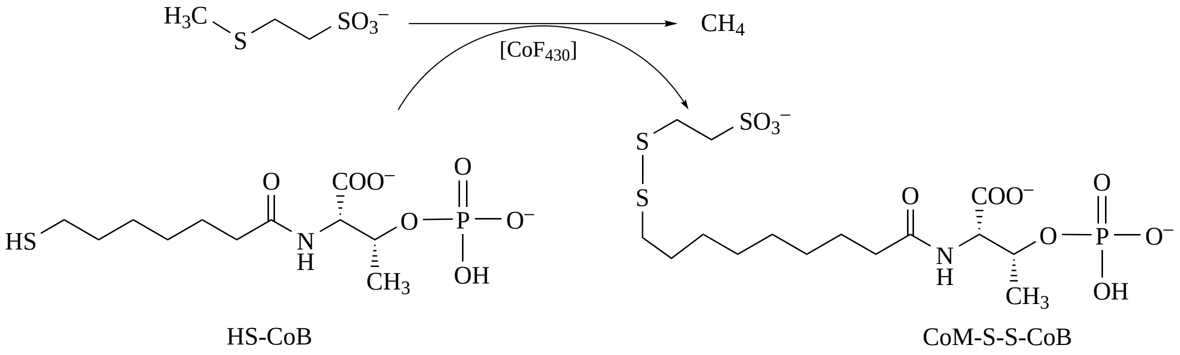

Scheme 10 The production of methane and CoM-S-S-CoB catalyzed by methyl coenzyme M reductase

F_{430}, and cofactor F_{430} forms the base of a narrow well accommodating the two substrates.[141–143] The phosphate group of HS-CoB binds at the upper lip of the well with its thiol group located 6 Å from the central Ni atom of F_{430}.[141–143] Synthesis of methane and the heterodisulfide CoM-S-S-CoB is achieved by two-electron reduction of MeS-CoM (2-(methylthio)ethanesulfonate) by HS-CoB (7-thioheptanoylthreonine phosphate) (Scheme 10). HS-CoB serves as the electron donor, and the heterodisulfide CoM-S-S-CoB is the product of the oxidative half-reaction.[137–140]

A variety of nickel oxidation states (Ni(I), low-spin Ni(II), high-spin Ni(II) and Ni(III)) have been characterized for F_{430}.[141–146] High-resolution X-ray crystallographic structures of EPR-silent high-spin Ni(II) forms of the inactive enzyme show that the Ni sites are six-coordinate with four tetrapyrrole nitrogen ligands in the plane, the carbonyl oxygen of a side-chain glutamine in the lower axial position, and the thiolate of $^{-}$S-CoM as the upper ligand in the $MCR_{red1\text{-}silent}$ and $MCR_{ox1\text{-}silent}$ states. A sulfonate oxygen from the CoM-S-S-CoB disulfide is the upper axial ligand in MCR_{silent} state.[141–143] For the enzyme to be active, the prosthetic group has to be in the Ni(I) oxidation state, and EPR, ENDOR, resonance Raman, and X-ray absorption studies demonstrate that both the MCR_{ox1} and MCR_{red1} are Ni(I) states.[145–147] Meanwhile, XAS results indicate that the Ni(I) sites in both MCR_{ox1} and MCR_{red1} are six-coordinate. On the basis of X-ray crystallographic structures of two Ni(II) inactive forms of the enzyme, a proposed catalytic mechanism is shown in Scheme 11.[141] A nucleophilic attack of coenzyme F_{430} Ni(I) form on the methyl group of CoM leads to a Me-Ni(III) complex (Scheme 11a). Here the nucleophilic reaction of Ni(I) resulting in the activation of the carbon–sulfur bond is presumed to be facilitated by protonation of MeS-CoM. Electron transfer from the protonated CoM to the strongly oxidative Ni(III) results in the formation of a CoM thiyl radical and Me-Ni(II) intermediate. Protonolysis of the methyl group of the Me-Ni(II) intermediate, the concomitant coupling of the CoM thiyl radical and the thiolate group of CoB, accompanied by electron transfer from the generated disulfide anion radical to the Ni(II), generates methane, CoM-S-S-CoB and the second Ni(I) intermediate (Scheme 11b–c). It is proposed that a coordination of the sulfonate oxygen to nickel is prevented when nickel is present as nucleophilic Ni(I). The repulsion between Ni(I) and the sulfonate oxygen molecules might act as a driving force to push the heterodisulfide out of the channel (Scheme 11d).[141]

Density functional theory (DFT) computations suggest that either Ni(I) or Ni(III) formulations for MCR_{ox1} states are conceivable.[148,149] EPR/ENDOR studies and analyses of the XANES/EXAFS/RR data indicate that both the MCR_{ox1} and MCR_{red1} states are best described as a hexacoordinate Ni(I) species, and that the main difference between MCR_{ox1} and MCR_{red1} is a change of one axial ligand from a S donor to an O/N donor.[149,150] Studies also imply that conversion from MCR_{ox1} to MCR_{red1} involves conformational rearrangements resulting from a two-electron reversible reduction of the hydrocorphin ring of F_{430}, and these changes trigger the activation to a MCR_{red1} state that can react productively with the methyl group of Me-SCoM.[148–150] In addition, recent studies implicate that the six-coordinate Ni(I) centers in the MCR_{ox1} and MCR_{red1} states exhibit markedly different reactivities and the enhanced reactivity of MCR_{red1} is due to the replacement of a relatively exchange-inert thiol ligand in MCR_{ox1} with a weakly coordinating upper axial ligand in MCR_{red1} that can be easily replaced by incoming ligands.[148–150] Furthermore, HS-CoB is required as a second substrate and induces a change forcing the real substrate, Me-S-CoM, and Ni(I) of the prosthetic group to interact in the active enzyme MCR_{red1}.[151–154]

5.2 Structural and Functional Models

Ni^{I}-F_{430} reacting directly with MeS-CoM before/after the substrate activation, the role of the thiol cofactor HS-HTP, and the reason(s) for the enzyme specifically directing the C–S bond cleavage to the Me–S bond of Me-CoM are the principal questions to be resolved to understand how the enzyme methyl coenzyme M reductase functions.

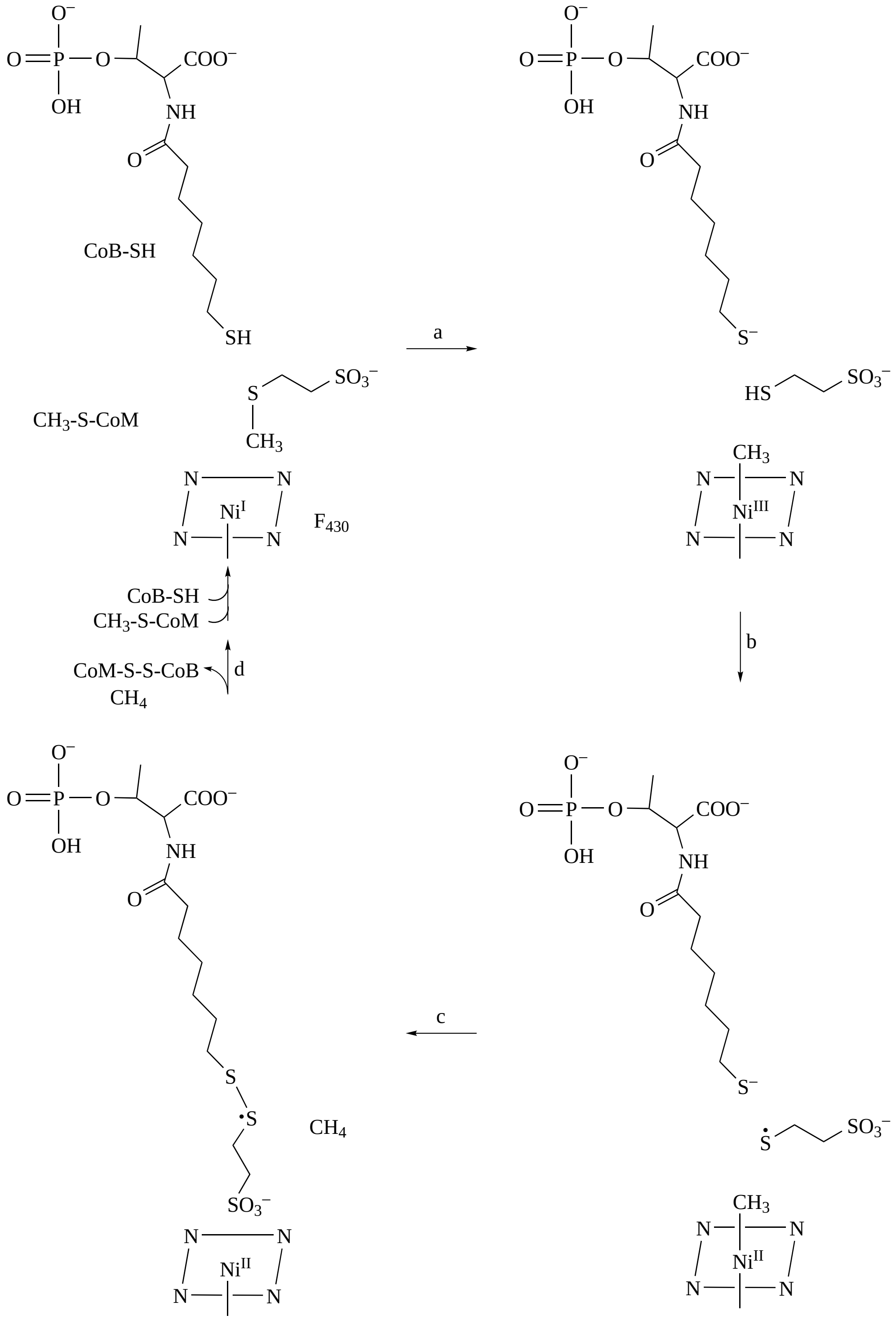

Scheme 11 A proposed catalytic mechanism for the formation of methane and CoM-S-S-CoB by methyl coenzyme M reductase

Numerous mononuclear Ni complexes have been synthesized to investigate the possible mechanism for the formation of disulfide and methane catalyzed by the enzyme.[155–159] Two models that are perhaps relevant to the mechanistic situation of MCR are complexes (**27**) and (**28**) that feature square-planar Ni site coordinated through both the thiolate and the methyl thioether sulfur atoms,[155] and four N-donors,[156] respectively.

As interpreted in Scheme 12,[155] a sterically shielded, bifunctional model substrate containing a methyl thioether and sulfhydryl functional group could form a five-membered

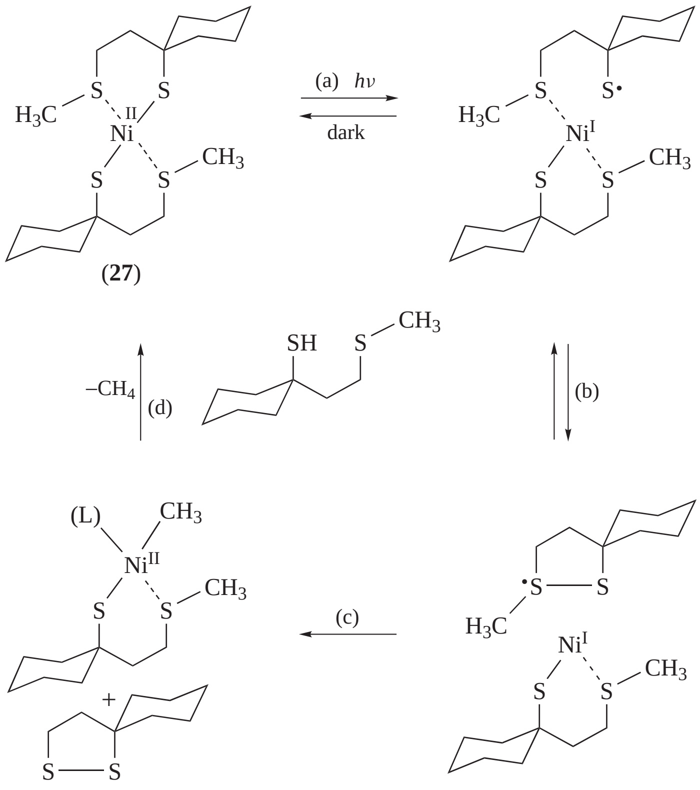

Scheme 12 A proposed mechanism for methane formation involving C–S bond cleavage. (Reprinted with permission from *Chem. – Eur. J.*, 2000, **6**, 3508–3516. © 2000 John Wiley & Sons, Ltd)

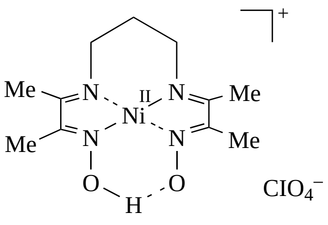

(**28**)

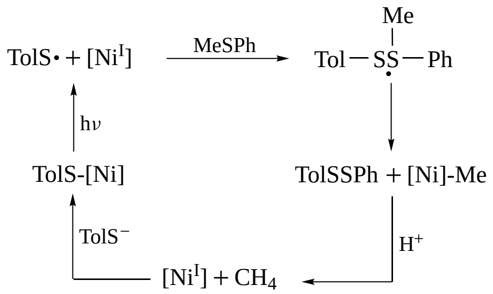

Scheme 13 A mechanism for methane formation involving a Ni–Me intermediate

cyclic sulfuranyl radical when this complex was irradiated with light of $\lambda > 300$ nm. The role of irradiation is interpreted as the formation of a Ni^{I}-thiyl radical pair upon excitation of a charge-transfer band of the Ni^{II}-dithiolate compound (Scheme 12a). Cyclization of the photochemically generated thiyl radical yields a sulfuranyl radical accompanied by transfer of a methyl group to Ni(I) to produce a methyl-Ni(II) intermediate (Scheme 12b–c). Here the addition of a thiyl radical to the sulfur atom of the thioether giving a sulfuranyl radical intermediate is the central step. The methyl-Ni(II) intermediate dissociates to methane and complex (**27**) through protonation. In particular, the cleavage of the carbon–sulfur bond of the aliphatic sulfide described in Scheme 12 occurred only in the presence of nickel and after excitation of the Ni^{II}-thiolate charge-transfer band.

A similar, but bimolecular, photoinduced reaction was observed on the basis of the nickel complex (**28**), *p*-toluene thiolate, and thioanisole reactants to generate methane and disulfide.[156] The thiyl radical and Ni(I) complex was prepared by the photolysis of the Ni(II) complex (**28**) and *p*-toluenethiolate anion in acetonitrile solution. Upon irradiation ($\lambda = 350$ nm) of the mixture of complex (**28**), *p*-toluenethiolate ion, and thioanisole in acetonitrile under argon, gas chromatography-mass spectral analysis showed the formation of methane, ditolyl disulfide $(TolS)_2$, and a mixed disulfide TolSSPh. The proposed catalytic mechanism is depicted in

Scheme 13.[156] The catalytic reaction was proposed to go through a sulfuranyl radical by addition of a thiyl radical to the sulfur atom of the thioether MeSPh. Interestingly, these studies are consistent with the proposed mechanism of the enzyme; the thiyl radical of cofactor HS-CoB resulting from one-electron reduction of F_{430} by $^{-}$S-CoB couples with Me-CoM to afford the sulfuranyl radical, CoB-S-S·(Me)-CoM. The sulfuranyl radical transfers a methyl radical to Ni^{I}-F_{430} to generate Me-Ni^{II}-F_{430} and the heterodisulfide CoM-S-S-HTP.[160,161]

6 RELATED ARTICLES

Nickel Enzymes & Cofactors.

7 REFERENCES

1. J. R. Lancaster Jr, 'The Bioinorganic Chemistry of Nickel', VCH Publishers, New York, 1988.
2. S. P. J. Albracht, *Biochim. Biophys. Acta*, 1994, **1188**, 167.
3. J. J. G. Moura, M. Teixeira, I. Moura, and J. LeGall, in 'The Bioinorganic Chemistry of Nickel', ed. J. R. Lancaster Jr, VCH Publishers, New York, 1988, Chap. 9.
4. Y. Nicolet, B. J. Lemon, J. C. Fontecilla-Camps, and J. W. Peters, *Trends Biochem. Sci.*, 2000, **25**, 138.
5. J. W. Peters, *Curr. Opin. Struct. Biol.*, 1999, **9**, 670.
6. A. Volbeda, M. H. Charon, C. Piras, E. C. Hatchikian, M. Frey, and J. C. Fontecilla-Camps, *Nature*, 1995, **373**, 580.
7. E. Garcin, X. Vernede, E. C. Hatchikian, A. Volbeda, M. Frey, and J. C. Fontecilla-Camps, *Structure*, 1999, **7**, 557.
8. R. P. Happe, W. Roseboom, A. J. Pierik, and S. P. J. Albracht, *Nature*, 1997, **385**, 126.
9. Y. Higuchi, T. Yagi, and N. Yasuoka, *Structure*, 1997, **5**, 1671.
10. Y. Higuchi, H. Ogata, K. Miki, N. Yasuoka, and T. Yagi, *Structure*, 1999, **7**, 549.
11. M. Rousset, Y. Montet, B. Guigliarelli, A. Forget, M. Asso, P. Bertrand, J. C. Fontecilla-Camps, and E. C. Hatchikian, *Proc. Natl. Acad. Sci. U.S.A.*, 1998, **95**, 11625.
12. M. Carepo, D. L. Tierney, C. D. Brondino, T. C. Yang, A. Pamplona, J. Telser, I. Moura, J. J. G. Moura, and B. M. Hoffman, *J. Am. Chem. Soc.*, 2002, **124**, 281.
13. M. W. W. Adams and E. I. Stiefel, *Curr. Opin. Chem. Biol.*, 2000, **4**, 214.
14. M. Frey, *Struct. Bonding*, 1998, **90**, 98.
15. J. C. Fontecilla-Camps, *Struct. Bonding*, 1998, **91**, 1.
16. M. J. Maroney, *Curr. Opin. Chem. Biol.*, 1999, **3**, 188.
17. M. J. Maroney, G. Davidson, C. B. Allan, and J. Figlar, *Struct. Bonding*, 1998, **92**, 1.
18. A. J. Pierik, W. Roseboom, R. P. Happe, K. A. Bagley, and S. P. J. Albracht, *J. Biol. Chem.*, 1999, **274**, 3331.
19. E. Garcin, X. Vernede, E. C. Hatchikian, A. Volbeda, M. Frey, and J. C. Fontecilla-Camps, *Struct. Fold. Des.*, 1999, **7**, 557.
20. Y. Higuchi, H. Ogata, K. Miki, N. Yasuoka, and T. Yagi, *Struct. Fold. Des.*, 1999, **7**, 549.
21. H. Wang, C. Y. Ralston, D. S. Patil, R. M. Jones, W. Gu, M. Verhagen, M. Adams, P. Ge, C. Riordan, C. A. Maganian, P. K. Mascharak, J. Kovacs, C. G. Miller, T. J. Collins, S. Brooker, P. D. Croucher, K. Wang, E. I. Stiefel, and S. P. Cramer, *J. Am. Chem. Soc.*, 2000, **122**, 10544.
22. J. W. Peters, W. N. Lanzilotta, B. J. Lemon, and L. C. Seefeldt, *Science*, 1998, **282**, 1853.
23. Y. Nicolet, C. Piras, P. Legrand, C. E. Hatchikian, and J. C. Fontecilla-Camps, *Structure*, 1999, **7**, 13.
24. B. J. Lemon and J. W. Peters, *J. Am. Chem. Soc.*, 2000, **122**, 3793.
25. S. Niu, L. M. Thomson, and M. B. Hall, *J. Am. Chem. Soc.*, 1999, **121**, 4000.
26. F. Dole, A. Fournel, V. Magro, E. C. Hatchikian, P. Bertrand, and B. Guigliarelli, *Biochemistry*, 1997, **36**, 7847.
27. L. De Gioia, P. Fantucci, B. Guigliarelli, and P. Bertrand, *Inorg. Chem.*, 1999, **38**, 2658.
28. P. M. Matias, C. M. Soares, L. M. Saraiva, R. Coelho, J. Morais, J. Le Gall, and M. A. Carrondo, *J. Biol. Inorg. Chem.*, 2001, **6**, 63.
29. G. Davidson, S. B. Choudhury, Z. Gu, K. Bose, W. Roseboom, S. P. J. Albracht, and M. J. Maroney, *Biochemistry*, 2000, **39**, 7468.
30. P. Amara, A. Volbeda, J. C. Fontecilla-Camps, and M. J. Field, *J. Am. Chem. Soc.*, 1999, **121**, 4468.
31. A. L. De Lacey, E. C. Hatchikian, A. Volbeda, M. Frey, J. C. Fontecilla-Camps, and V. M. Fernandez, *J. Am. Chem. Soc.*, 1997, **119**, 7181.
32. A. Volbeda, E. Garcin, C. Piras, A. de Lacey, V. M. Fernandez, E. C. Hatchikian, M. Frey, and J. C. Fontecilla-Camps, *J. Am. Chem. Soc.*, 1996, **118**, 12989.
33. L. De Gioia, P. Fantucci, B. Guigliarelli, and P. Bertrand, *Inorg. Chem.*, 1999, **38**, 2658.
34. F. Dole, A. Fournel, V. Magro, E. C. Hatchikian, P. Bertrand, and B. Guigliarelli, *Biochemistry*, 1997, **36**, 7847.
35. S. Niu, L. M. Thomson, and M. B. Hall, *J. Am. Chem. Soc.*, 1999, **121**, 4000.
36. S. Li and M. B. Hall, *Inorg. Chem.*, 2001, **40**, 18.
37. M. Stein, E. van Lenthe, E. J. Baerends, and W. Lubitz, *J. Am. Chem. Soc.*, 2001, **123**, 5839.
38. M. Stein and W. Lubitz, *Curr. Opin. Chem. Biol.*, 2002, **6**, 243.
39. M. J. Maroney and P. A. Bryngelson, *J. Biol. Inorg. Chem.*, 2001, **4**, 453.

40. H. Ogata, Y. Mizoguchi, N. Mizuno, K. Miki, S.-I. Adachi, N. Yasuoka, T. Yagi, O. Yamauchi, S. Hirota, and Y. Higuchi, *J. Am. Chem. Soc.*, 2002, **124**, 11628.
41. S. Foerster, M. Stein, M. Brecht, H. Ogata, Y. Higuchi, and W. Lubitz, *J. Am. Chem. Soc.*, 2003, **125**, 83.
42. C. Fan, M. Teixeira, J. Moura, I. Moura, B. H. Huynh, J. Le Gall, H. D., Peck Jr, and B. M. Hoffman, *J. Am. Chem. Soc.*, 1991, **113**, 20.
43. J. P. Whitehead, R. J. Gurbiel, C. Bagyinka, B. M. Hoffman, and M. J. Maroney, *J. Am. Chem. Soc.*, 1993, **115**, 5629.
44. B. J. Lemon and J. W. Peters, *Biochemistry*, 1999, **38**, 12969.
45. Y. Nicolet, A. L. de Lacey, X. Vernéde, V. M. Fernandez, E. C. Hatchikian, and J. C. Fontecilla-Camps, *J. Am. Chem. Soc.*, 2001, **123**, 1596.
46. C. V. Popescu and E. Münck, *J. Am. Chem. Soc.*, 1999, **121**, 7877.
47. A. L. De Lacey, C. Stadler, C. Cavazza, E. C. Hatchikian, and V. M. Fernandez, *J. Am. Chem. Soc.*, 2000, **122**, 11232.
48. A. J. Pierik, M. Hulstein, W. R. Hagen, and S. P. Albracht, *Eur. J. Biochem.*, 1998, **258**, 572.
49. D. S. Patil, J. J. G. Moura, S. H. He, M. Teixeira, B. C. Prickril, D. V. Der Vartanian, H. D. Peck Jr, J. Legall, and B. H. Huyanh, *J. Biol. Chem.*, 1988, **263**, 18732.
50. Z. X. Cao and M. B. Hall, *J. Am. Chem. Soc.*, 2001, **123**, 3734.
51. Z.-P. Liu and P. Hu, *J. Am. Chem. Soc.*, 2002, **124**, 5175.
52. M. Y. Darensbourg, E. J. Lyon, and J. Smee, *J. Coord. Chem. Rev.*, 2000, **206**, 533.
53. A. C. Marr, D. J. E. Spencer, and M. Schröder, *Coord. Chem. Rev.*, 2001, **219**, 1055.
54. J. C. Fontecilla-Camps, *J. Biol. Inorg. Chem.*, 1996, **1**, 91.
55. M. C. Smith, S. Longhurst, J. E. Barclay, S. P. Cramer, S. C. Davies, D. L. Hughes, W.-W. Gu, and D. J. Evans, *J. Chem. Soc., Dalton Trans.*, 2001, 1387.
56. D. Sellmann, F. Geipel, F. Lauderbach, and F. W. Heinemann, *Angew. Chem., Int. Ed. Engl.*, 2002, **41**, 632.
57. S. C. Davies, D. J. Evans, D. L. Hughes, S. Longhurst, and J. R. Sanders, *Chem. Commun.*, 1999, 1935.
58. C.-H. Lai, J. H. Reibenspies, and M. Y. Darensbourg, *Angew. Chem., Int. Ed. Engl.*, 1996, **35,**, 2390.
59. F. Osterloh, W. Saak, D. Hasse, and S. Pohl, *J. Chem. Soc., Chem. Commun.*, 1997, 979.
60. W.-F. Liaw, C.-Y. Chiang, G.-H. Lee, S.-M. Peng, C.-H. Lai, and M. Y. Darensbourg, *Inorg. Chem.*, 2000, **39**, 480.
61. W.-F. Liaw, Y.-C. Horng, D.-S. Ou, C.-Y. Ching, G.-H. Lee, and S.-M. Peng, *J. Am. Chem. Soc.*, 1997, **119**, 9299.
62. W.-F. Liaw, C.-H. Chen, C.-M. Lee, G.-H. Lee, and S.-M. Peng, *J. Chem. Soc., Dalton Trans.*, 2001, 138.
63. C.-M. Lee, C.-H. Chen, S.-C. Ke, G.-H. Lee, and W.-F. Liaw, *J. Am. Chem. Soc.*, 2004, **126**, 8406.
64. J. A. W. Verhagen, D. D. Ellis, M. Lutz, A. L. Spek, and E. Bouwman, *J. Chem. Soc., Dalton Trans.*, 2002, 1275.
65. N. D. J. Branscombe, A. J. Atkins, A. Marin-Becerra, E. J. L. McInnes, F. E. Mabbs, J. McMaster, and M. Schröder, *Chem. Commun.*, 2003, 1098.
66. L. L. Efros, H. H. Thorp, G. W. Brudvig, and R. H. Crabtree, *Inorg. Chem.*, 1992, **31**, 1722.
67. C. J. Curtis, A. Miedaner, R. Ciancanelli, W. W. Ellis, B. C. Noll, M. R. DuBois, and D. L. DuBois, *Inorg. Chem.*, 2003, **42**, 216.
68. C. J. Curtis, A. Miedaner, W. W. Ellis, and D. L. DuBois, *J. Am. Chem. Soc.*, 2002, **124**, 1918.
69. D. Sellmann, F. Geipel, and M. Moll, *Angew. Chem., Int. Ed. Engl.*, 2000, **39**, 561.
70. W. Clegg and R. A. Henderson, *Inorg. Chem.*, 2002, **41**, 1128.
71. T. L. James, L. Cai, M. C. Muetterties, and R. H. Holm, *Inorg. Chem.*, 1996, **35**, 4148.
72. W.-F. Liaw, J.-H. Lee, H.-B. Gau, C.-H. Chen, S. -J. Jung, C.-H. Hung, W.-Y. Chen, C.-H. Hu, and G. -H. Lee, *J. Am. Chem. Soc.*, 2002, **124**, 1680.
73. T. B. Rauchfuss, S. M. Contakes, S. C. N. Hsu, M. A. Reynolds, and S. R. Wilson, *J. Am. Chem. Soc.*, 2001, **123**, 6933.
74. W.-F. Liaw, N.-H. Lee, C.-H. Chen, C.-M. Lee, G. -H. Lee, and S.-M. Peng, *J. Am. Chem Soc.*, 2000, **122**, 488.
75. C.-H. Chen, Y.-S. Chang, C.-Y. Yang, T.-N. Chen, C.-M. Lee, and W.-F. Liaw, *Dalton Trans.*, 2004, 137.
76. P. A. Karplus, M. A. Pearson, and R. P. Hausinger, *Acc. Chem. Res.*, 1997, **30**, 330.
77. E. Jabri, M. B. Carr, R. P. Hausinger, and P. A. Karplus, *Science*, 1995, **268**, 998.
78. M. A. Pearson, L. O. Michel, R. P. Hausinger, and P. A. Karplus, *Biochemistry*, 1997, **36**, 8164.
79. S. Benini, W. R. Rypniewski, K. S. Wilson, S. Miletti, S. Ciurli, and S. Mangani, *Structure*, 1999, **7**, 205.
80. S. J. Lippard, *Science*, 1995, **268**, 996.
81. S. Benini, W. R. Rypniewski, K. S. Wilson, S. Miletti, S. Ciurli, and S. Mangani, *J. Biol. Inorg. Chem.*, 2000, **5**, 110.
82. R. L. Blakeley, A. Treston, R. K. Andrews, and B. Zerner, *J. Am. Chem. Soc.*, 1982, **104**, 612.
83. B. Zerner, *Bioorg. Chem.*, 1991, **19**, 116.
84. G. W. Wheland, ‘Resonance in Organic Chemistry’, John Wiley & Sons, New York, 1955.
85. H. L. T. Mobley, M. D. Island, and R. P. Hausinger, *Microbiol. Rev.*, 1995, **59**, 451.
86. A. M. Barrios and S. J. Lippard, *J. Am. Chem. Soc.*, 1999, **121**, 11751.
87. T. Koga, H. Furutachi, T. Nakamura, N. Fukita, M. Ohba, K. Yakahashi, and H. Okawa, *Inorg. Chem.*, 1998, **37**, 989.
88. K. Yamaguchi, S. Koshino, F. Akagi, M. Suzuki, A. Uehara, and S. Suzuki, *J. Am. Chem. Soc.*, 1997, **119**, 5752.

89. M. Arnold, D. A. Brown, O. Deeg, W. Errington, W. Hasse, K. Herlihy, T. J. Kemp, H. Nimir, and R. Werner, *Inorg. Chem.*, 1998, **37**, 2920.

90. M. Konrad, F. Meyer, A. Jacobi, P. Kircher, P. Rutsch, and L. Zsolnai, *Inorg. Chem.*, 1999, **38**, 4559.

91. H. E. Wages, K. L. Taft, and S. J. Lippard, *Inorg. Chem.*, 1993, **32**, 4985.

92. A. M. Barrios and S. J. Lippard, *J. Am. Chem. Soc.*, 2000, **122**, 9172.

93. S. Uozumi, H. Furutachi, M. Ohba, H. Okawa, D. E. Fenton, K. Shindo, S. Murata, and D. J. Kitko, *Inorg. Chem.*, 1998, **37**, 6281.

94. L. Roecker, J. Akande, L. N. Elam, I. Gauga, B. W. Helton, M. C. Prewitt, A. M. Sargeson, J. H. Swango, A. C. Willis, T. Xin, and J. Xu, *Inorg. Chem.*, 1999, **38**, 1269.

95. F. Meyer, E. Kaifer, P. Kircher, K. Heinze, and H. Pritzkow, *Chem. – Eur. J.*, 1999, **5**, 1617.

96. M. J. Todd and R. P. Hausinger, *Biochemistry*, 2000, **39**, 5389.

97. M. J. Todd and R. P. Hausinger, *J. Biol. Chem.*, 1991, **266**, 24327.

98. A. J. Stemmler, J. W. Kampf, M. L. Kirk, and V. L. Pecoraro, *J. Am. Chem. Soc.*, 1995, **117**, 6368.

99. S. W. Ragsdale and M. Kumar, *Chem. Rev.*, 1996, **96**, 2515.

100. J. G. Ferry, *Annu. Rev. Microbiol.*, 1995, **49**, 305.

101. P. A. Lindahl, *Biochemistry*, 2002, **41**, 2097.

102. C. L. Drennan, J. Heo, M. D. Sintchak, E. Schreiter, and P. W. Ludden, *Proc. Natl. Acad. Sci. U.S.A.*, 2001, **98**, 11973.

103. J. Heo, C. M. Halbleib, and P. W. Ludden, *Proc. Natl. Acad. Sci. U.S.A.*, 2001, **98**, 7690.

104. H. Dobbek, V. Svetlitchnyi, L. Gremer, R. Huber, and O. Meyer, *Science*, 2001, **293**, 1281.

105. T. I. Doukov, T. M. Iverson, J. Seravalli, S. W. Ragsdale, and C. L. Drennan, *Science*, 2002, **298**, 567.

106. J. Seravalli, W. Gu, A. Tam, E. Strauss, T. P. Begley, S. P. Cramer, and S. W. Ragsdale, *Proc. Natl. Acad. Sci. U.S.A.*, 2003, **100**, 3689.

107. C. Darnault, A. Volbeda, E. J. Kim, P. Legrand, X. Vernede, P. A. Lindahl, and J. C. Fontecilla-Camps, *Nat. Struct. Biol.*, 2003, **10**, 271.

108. M. R. Bramlett, X. Tan, and P. A. Lindahl, *J. Am. Chem. Soc.*, 2003, **125**, 9316.

109. D. Qiu, M. Kumar, S. W. Ragsdale, and T. Spiro, *J. Am. Chem. Soc.*, 1996, **118**, 10429.

110. J. Heo, C. R. Staples, J. Telser, and P. W. Ludden, *J. Am. Chem. Soc.*, 1999, **121**, 11045.

111. J. Heo, C. R. Staples, C. M. Halbleib, and P. W. Ludden, *Biochemistry*, 2000, **39**, 7956.

112. J. Heo, C. R. Staples, and P. W. Ludden, *Biochemistry*, 2001, **40**, 7604.

113. W. K. Russell and P. A. Lindahl, *Biochemistry*, 1998, **37**, 10016.

114. M. E. Anderson and P. A. Lindahl, *Biochemistry*, 1996, **35**, 8371.

115. N. J. Spangler, P. A. Lindahl, V. A. Bandarian, and P. W. Ludden, *J. Biol. Chem.*, 1996, **271**, 7973.

116. M. Kumar, W. P. Lu, A. Smith, S. W. Ragsdale, and J. McCraken, *J. Am. Chem. Soc.*, 1995, **117**, 2939.

117. J. W. Peters, *Science*, 2002, **298**, 552.

118. M. Kumar and S. W. Ragsdale, *J. Am. Chem. Soc.*, 1992, **114**, 8713.

119. S. W. Ragsdale, L. G. Ljungdahl, and D. V. DerVartanian, *Biochem. Biophys. Res. Commun.*, 1982, **108**, 658.

120. S. W. Ragsdale, L. G. Ljungdahl, and D. V. DerVartanian, *Biochem. Biophys. Res. Commun.*, 1983, **115**, 658.

121. D. P. Barondeau and P. A. Lindahl, *J. Am. Chem. Soc.*, 1997, **119**, 3959.

122. S. Menon and S. W. Ragsdale, *J. Biol. Chem.*, 1999, **274**, 11513.

123. S. W. Ragsdahl and H. G. Wood, *J. Biol. Chem.*, 1985, **260**, 3970.

124. R. Krishnan, J. K. Voo, C. G. Riordan, L. Zahkarov, and A. L. Rheingold, *J. Am. Chem. Soc.*, 2003, **125**, 4422.

125. J. L. Craft, B. S. Mandimutsira, K. Fujita, C. G. Riordan, and T. C. Brunold, *Inorg. Chem.*, 2003, **42**, 859.

126. S. W. Ragsdale, H. G. Wood, and W. E. Antholine, *Proc. Natl. Acad. Sci. U.S.A.*, 1985, **82**, 6811.

127. J. Q. Xia, Z. G. Hu, C. V. Popescu, P. A. Lindahl, and E. Münck, *J. Am. Chem. Soc.*, 1997, **119**, 8301.

128. W. K. Russell, C. M. V. Stalhandske, J. Q. Xia, R. A. Scott, and P. A. Lindahl, *J. Am. Chem. Soc.*, 1998, **120**, 7502.

129. R. C. Linck, C. W. Spahn, T. B. Rauchfuss, and S. R. Wilson, *J. Am. Chem. Soc.*, 2003, **125**, 8700.

130. S. Gencic and D. A. Grahame, *J. Biol. Chem.*, 2003, **278**, 6101.

131. W. Shin, M. E. Anderson, and P. A. Lindahl, *J. Am. Chem. Soc.*, 1993, **115**, 5522.

132. M. L. Golden, M. V. Rampersad, J. H. Reibenspies, and M. Y. Darensbourg, *Chem. Commun.*, 2003, 1824.

133. R. P. Hausinger, *J. Biol. Inorg. Chem.*, 1997, **2**, 279.

134. J. Seravalli, M. Kumar, and S. W. Ragsdale, *Biochemistry*, 2002, **41**, 1807.

135. G. C. Tucci and R. H. Holm, *J. Am. Chem. Soc.*, 1995, **117**, 6489.

136. P. T. Matsunaga and G. L. Hillhouse, *Angew. Chem., Int. Ed. Engl.*, 1994, **33**, 1748.

137. R. K. Thauer, *Microbiology*, 1998, **144**, 2377.

138. A. A. DiMarco, T. A. Bobik, and R. S. Wolfe, *Annu. Rev. Biochem.*, 1990, **59**, 355.

139. J. Telser, *Struct. Bonding*, 1998, **91**, 31.

140. S. W. Ragsdale, in ‘The Porphyrin Handbook’, eds. K. M. Kadish, K. M. Smith, and R. Guilard, Academic Press, New York, 2002, Vol. 2.
141. U. Ermler, W. Grabarse, S. Shima, M. Goubeaud, and R. K. Thauer, *Science*, 1997, **278**, 1457.
142. W. G. Grabarse, F. Mahlert, E. C. Duin, M. Goubeaud, S. Shima, R. K. Thauer, V. Lamzin, and U. Ermler, *J. Mol. Biol.*, 2001, **309**, 315.
143. W. G. Grabarse, F. Mahlert, S. Shima, R. K. Thauer, and U. Ermler, *J. Mol. Biol.*, 2000, **303**, 329.
144. M. Goubeaud, G. Schreiner, and R. K. Thauer, *Eur. J. Biochem.*, 1997, **243**, 110.
145. J. Telser, R. Davydov, Y.-C. Horng, S. W. Ragsdale, and B. M. Hoffman, *J. Am. Chem. Soc.*, 2001, **123**, 5853.
146. J. Telser, Y.-C. Horng, D. Becker, B. Hoffman, and S. W. Ragsdale, *J. Am. Chem. Soc.*, 2000, **122**, 182.
147. Q. Tang, P. E. Carrington, Y.-C. Horng, M. J. Maroney, S. W. Ragsdale, and D. F. Bocian, *J. Am. Chem. Soc.*, 2002, **124**, 13242.
148. T. Wondimagegn and A. Ghosh, *J. Am. Chem. Soc.*, 2001, **123**, 1543.
149. T. Wondimagegn and A. Ghosh, *J. Am. Chem. Soc.*, 2000, **122**, 6375.
150. K. Singh, Y.-C. Horng, and S. W. Ragsdale, *J. Am. Chem. Soc.*, 2003, **125**, 2436.
151. C. Finazzo, J. Harmer, C. Bauer, B. Jaun, E. C. Duin, F. Mahlert, M. Goenrich, R. K. Thauer, S. V. Doorslaer, and A. Schweiger, *J. Am. Chem. Soc.*, 2003, **125**, 4988.
152. Y.-C. Horng, D. F. Becker, and S. W. Ragsdale, *Biochemistry*, 2001, **40**, 12875.
153. E. C. Duin, N. J. Cosper, F. Mahlert, R. K. Thauer, and R. A. Scott, *J. Biol. Inorg. Chem.*, 2002, **8**, 141.
154. F. Mahlert, W. Grabarse, J. Kahnt, R. K. Thauer, and E. C. Duin, *J. Biol. Inorg. Chem.*, 2002, **7**, 101.
155. L. Signor, C. Knuppe, R. Hug, B. Schweizer, A. Pfaltz, and B. Jaun, *Chem. – Eur. J.*, 2000, **6**, 3508.
156. M. Tada and Y. Masuzawa, *Chem. Commun.*, 1997, 2161.
157. A. M. Stolzenberg and Z. Zhang, *Inorg. Chem.*, 1997, **36**, 593.
158. Z. Zhang, J. L. Petersen, and A. M. Stolzenberg, *Inorg. Chem.*, 1996, **35**, 4649.
159. P. J. Chmielewski, L. Latos-Grazynski, and T. Glowiak, *J. Am. Chem. Soc.*, 1996, **118**, 5690.
160. B. Jaun, *Helv. Chim. Acta*, 1990, **73**, 2209.
161. A. Berkessel, *Bioorg. Chem.*, 1991, **19**, 101.

Acknowledgments

The author would like to thank Prof. Robert A. Scott for helpful suggestions and Mr. Chien-Ming Lee, Mr. Chien-Hong Chen for their assistance during the preparation of this manuscript.

Nickel: Organometallic Chemistry

Davit Zargarian
Université de Montréal, Montréal, QC, Canada

Based in part on the article Nickel: Organometallic Chemistry by Clifford P. Kubiak which appeared in the Encyclopedia of Inorganic Chemistry, First Edition.

1	Introduction	1
2	Allyl, Cyclopentadienyl, Indenyl, and Tris(Pyrazolyl)Borate Complexes	2
3	Hydrido, Alkyl, Alkenyl, and Silyl Complexes	5
4	Ni(0) Complexes	8
5	Catalytic Polymerization and Copolymerization of Olefins	12
6	Other Catalytic Reactions	16
7	Related Articles	17
8	References	18

Abbreviations

acac = Acetylacetonate, $[CH_3C(O)CH{=}C(O)CH_3]^-$; Ar = aryl fragment; *t*-Bu = tertiary butyl radical, $C(CH_3)_3$; Bipy = bipyridine; COD = 1, 5-cyclooctadiene; Cp = cyclopentadienyl radical; Cp* = pentamethylcyclopentadienyl radical; Cy = cyclohexyl radical; Dmpe = bis(dimethylphosphino) ethane, $(Me_2PCH_2)_2$; Dmpm = bis(dimethylphosphino)methane, $(Me_2P)_2CH_2$; Et = ethyl radical, CH_3CH_2; HOMO = highest occupied molecular orbital; Ind = indenyl radical; LUMO = lowest unoccupied molecular orbital; Me = methyl radical, CH_3; *i*-Pr = *iso*-propyl radical, $CH(CH_3)_2$; Ph = phenyl radical, C_6H_5; Tp = tris(pyrazolyl)borate anion; Triphos = $\{PPh_2(CH_2)_2\}PPh$.

1 INTRODUCTION

The organometallic chemistry of nickel has experienced rapid growth over the past decade. A number of exciting new areas have emerged, such as the reactivities of Ni(0)-carbene complexes (*see* ***Carbene Complexes***) and the polymerization of olefins catalyzed by nickel complexes (*see* ***Oligomerization & Polymerization by Homogeneous Catalysis***) of nitrogen-based ligands. In addition, the traditionally rich area of Ni-catalyzed organic transformations has undergone major developments that have expanded the scope of their applications. Altogether, the synthesis and characterization of new complexes, the discovery of new reactions, and the development of new catalytic processes has meant that a bright future awaits this area of inorganic chemistry.

The material presented in this chapter is organized in various sections according to the main ligands coordinated to the Ni atom or the type of reaction being discussed. Thus, there will be a section on the complexes of allyl, Cp, Ind, and Tp ligands (*see Tris(pyrazolyl)borates*). The increasing number of reports that have appeared on these complexes over the past decade show that they have a rich array of interesting structural and reactivity features. The main structural and bonding properties of these complexes are presented and their major reactivities are outlined.

Section 3 is devoted to the complexes of hydride, alkyl, alkenyl, and silyl ligands. Hydrido (*see* ***Hydride Complexes of the Transition Metals***) and alkyl complexes of most transition metals, and in particular those of nickel, are often involved in many catalytic processes of commercial importance; therefore, an in-depth understanding of the fundamental reactivities of these complexes is crucial to expanding their practical applications. Silyl complexes are involved in the transformations of organosilicon compounds, and for this reason their basic reactivities and structural properties are of interest.

The chemistry of zerovalent nickel complexes will be discussed in Section 4. One of the most exciting developments in this area is the recent introduction of N-heterocyclic carbene ligands. Ni complexes of these ligands have been shown to be important catalysts and reagents for a number of important organic transformations. This section will describe briefly the practical methods for preparing Ni-carbene complexes and will outline some of the catalytic reactions promoted by these complexes. This section will also describe the preparation and reactivities of other types of Ni(0) complexes.

Section 5 is dedicated to discussing the polymerization and copolymerization of olefins. This aspect of the chemistry of Ni complexes has experienced a phenomenal growth and development over the past decade, beginning with the discovery of a family of diimine complexes that catalyze the polymerization of aliphatic olefins. A series of new and highly efficient catalysts were introduced in rapid progression, a great deal of new chemistry has been discovered, and a number of industrial processes have been developed on the basis of these nickel complexes. In contrast, nickel-based catalysts are not very efficient in the alternating copolymerization of CO/ethylene, but studies of this reaction have revealed very interesting patterns of reactivity which appears to be fairly unique to nickel.

The last section of this chapter is dedicated to an overview of a number of coupling reactions catalyzed by nickel complexes. Thus, we will discuss the emergence of new strategies for the efficient cross-coupling of alkyl halides with organozinc and Grignard reagents, as well as the coupling of dienes with CO_2.

2 ALLYL, CYCLOPENTADIENYL, INDENYL, AND TRIS(PYRAZOLYL)BORATE COMPLEXES

2.1 Allyl Complexes

Allyl complexes (*see Allyl Complexes*) have occupied an important position in the development of the organometallic chemistry of nickel. Thus, allylnickel complexes have had numerous applications in organic synthesis (e.g. nucleophilic attack on coordinated allyl ligands) and have been identified as key intermediates in the oligomerization and cyclization of olefins and dienes; moreover, the η^3/η^1 rearrangements of allylnickel species has helped explain the facile isomerization of olefins in the presence of nickel complexes. The vast majority of allylnickel complexes are 4-coordinate, 16-electron complexes of the type (allyl)Ni(L)X, $[(allyl)NiLL']^+$, or $(allyl)_2Ni$ (L and X are neutral and anionic two-electron donor ligands, respectively). A recent report has shown, however, that formally 5-coordinate and 18-electron species are thermally stable but highly reactive catalysts (turnover frequency of up to 2000/min) for the oligomerization of styrene (equation 1).[1] The unusual coordination of three $SbPh_3$ ligands and their great lability are due, presumably, to the longer, less robust Ni–Sb bonds.

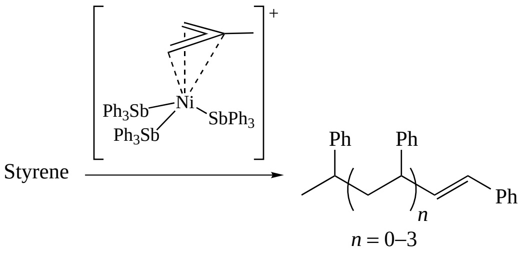

(1)

In comparison to the allyl complexes, the analogous cyclopentadienyl (Cp) complexes, with the exception of nickelocene, Cp_2Ni (*see Nickelocene*), have played a less prominent role. However, there has been a resurgence of interest over the past decade in the reactivities of CpNi complexes and this interest has extended into the chemistry of the analogous indenyl (Ind) and tris(pyrazolyl)borate (Tp) (*see Tris(pyrazolyl)borates*) complexes. Some of the major developments in this area are outlined in the following sections.

2.2 Cp Complexes

The reaction of nickelocene with primary phosphines has allowed the preparation of the phosphido-bridged dimers (**1**); deprotonation and methylation of the phosphido moiety results in the formation of the methylated derivatives (**2**) (Scheme 1).[2]

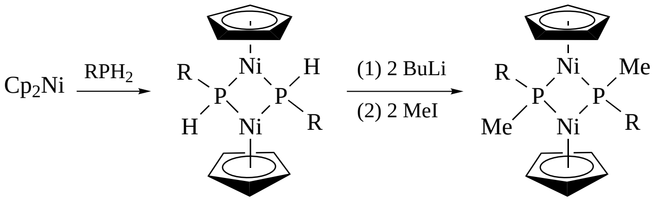

(**1**) (**2**)

Scheme 1

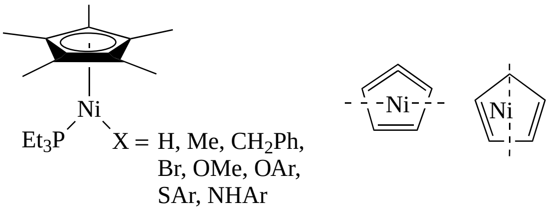

Scheme 2

A large series of pentamethylcyclopentadienyl (Cp^*) derivatives have been prepared by reacting PEt_3 with $Cp^*Ni(acac)$, which was shown to be a paramagnetic, 18-electron, spin-equilibrium molecule,[3] followed by addition of a variety of reagents (e.g. MeLi, LiBr, PR_3, NaOMe, etc.).[4,5] Systematic structural studies of these complexes have led to interesting generalizations about the haptotropic distortions observed in the Cp^* ring; these distortions range from a symmetrical allyl-ene to diene-yl type distortions (Scheme 2). In addition, the impact on the Ni–Cp interactions of the ligand trans influence exerted by the other auxiliary ligands has been discussed and the following approximate trans influence order has been suggested: alkyl, hydride > phosphine, methoxide > arylamide, aryloxide, arylthiolate, bromide. A study of the Ni-amido derivatives with Bronsted acids HX has led to the observation that the Ni–X bonds have a significant electrostatic component.

A number of interesting complexes bearing hemilabile (dimethylamino)ethyl-Cp has been reported. The tethered, hemilabile amino moiety either coordinates to the Ni center or to an unsaturated group 13/14 ligand (Scheme 3); in the absence of such unsaturated ligands or when the Ni center is coordinatively saturated, the amino moiety remains dangling.[6–8]

2.3 Indenyl Complexes

An extensive series of indenyl complexes has been prepared and their structural and reactivity features studied in-depth.[9] The detailed characterization, in solution and solid state, of complexes IndNi(L)X ($L = PR_3$ and N-heterocyclic carbenes; X = halides, imidates, alkyl, alkynyl, thienyl, triflate, etc.) and $[IndNi(PR_3)L]^+$ ($L = PR'_3$, PR_3, MeCN, CN(t-Bu)) has allowed an analysis of the factors affecting the Ni–Ind interaction.[10–12] As was seen for the Cp^* complexes discussed

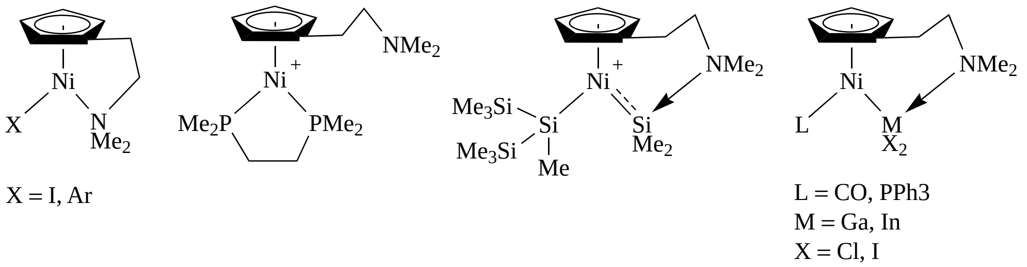
Ni
X
N
Me2
X = I, Ar
NMe2
Ni +
Me2P
PMe2
Me3Si
Me3Si
Si
Me
Ni +
Si
Me2
NMe2
Ni
L
M
X2
NMe2
L = CO, PPh3
M = Ga, In
X = Cl, I

Scheme 3

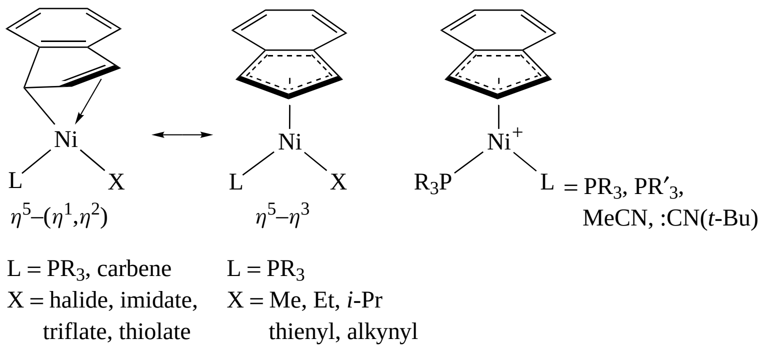
Ni
L
X
η5–(η1,η2)
L = PR3, carbene
X = halide, imidate,
triflate, thiolate
Ni
L
X
η5–η3
L = PR3
X = Me, Et, i-Pr
thienyl, alkynyl
Ni+
R3P
L = PR3, PR′3,
MeCN, :CN(t-Bu)

Scheme 4

above, the trans influence differences of the ligands L and X is responsible for the Ind–Ni bonding mode: ligands of widely different trans influence values (e.g. PPh_3 and Cl) lead to a nonsymmetric hapticity approaching η^1, η^2-Ind, whereas ligands of similar trans influence values (e.g. PPh_3 and Me) give a symmetrical interaction ($\eta^5 - \eta^3$, Scheme 4).[13] Interestingly, the more strongly donor and covalent ligands such as Me and PPh_3 result in stronger Ni–Ind interaction (less slip-folded, shorter Ni–C bonds), whereas weaker and more ionic ligands such as halides result in weaker Ni–Ind interactions (large slip-fold distortions, longer Ni–C bonds).[14] In general, these Ind complexes appear to be less stable and more reactive than the corresponding Cp* analogues.

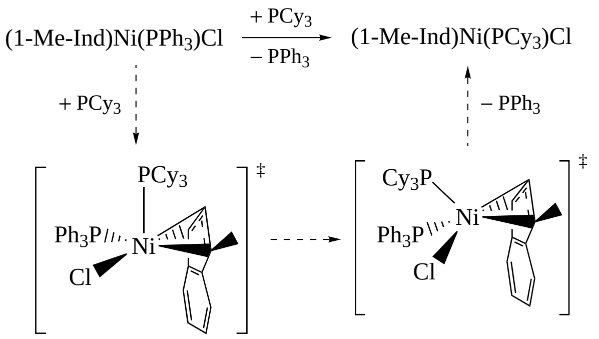
(1-Me-Ind)Ni(PPh3)Cl
+ PCy3
− PPh3
(1-Me-Ind)Ni(PCy3)Cl
+ PCy3
− PPh3
PCy3
Ph3P
Ni
Cl
‡
Cy3P
Ph3P
Ni
Cl
‡

Scheme 5

The neutral Ni–Cl or Ni–R complexes undergo associative ligand substitution reactions (Scheme 5, *see Associative Substitution*; ***Mechanisms of Reaction of Organometallic Complexes***),[15] and react with methylaluminoxane (MAO) to generate intermediates that polymerize ethylene to high MW poly(ethylene),[16] and alkynes to *cis, transoid*-poly(alkynes) (Scheme 6).[17–20]

On the other hand, the cationic bis(phosphine) complexes $[IndNi(PR_3)_2]^+$ and the highly electrophilic, in situ generated cations $[Ind(PR_3)]^+$ catalyze the dimerization of ethylene[21] and oligo- and polymerization of other olefins (Scheme 7).[22,23]

The reaction of $PhSiH_3$ with the Ni–Me precursors has been shown to result in the formation of oligosilanes $(PhSiH)_n$.[24] The initial step of this reaction is believed to go through a concerted σ-bond metathesis ($K_H/K_D \sim 10$), but multiple intermediates are formed in the later stages of the catalysis, some of which result from the reductive elimination (*see Reductive Elimination*) of the indenyl ligand (Scheme 8).[25]

The indenyl complexes are also efficient precatalysts for the hydrosilylation (*see Hydrosilation*) of olefins, alkynes, and ketones.[26] This reaction is believed to involve a hydrido intermediate, which can be generated initially via different routes (Scheme 9).

A few interesting dinuclear complexes bearing $CpCMe_2Ind$ or $IndCMe_2Ind$ ligands have also been prepared (Scheme 10),[27] as have complexes bearing aminoindenyl

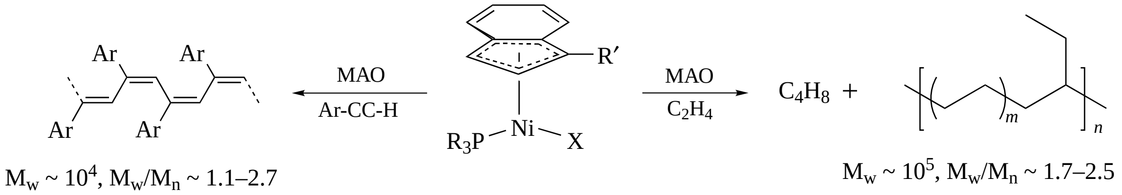
Ar
Ar
Ar
Ar
MAO
Ar-CC-H
R′
R3P
Ni
X
MAO
C2H4
C4H8 +
m
n
Mw ~ 10^4, Mw/Mn ~ 1.1–2.7
Mw ~ 10^5, Mw/Mn ~ 1.7–2.5

Pre-catalyst			Polymerisation Activity
R	R′	X	Kg of PE (mol of Ni.h)$^{-1}$
Ph	Me	Cl	40
Me	Me	Cl	325
Cy	Me	Cl	310
Ph	*i*-Pr	Cl	550
Ph	Me	Me	275
Ph	Me	CC-Ph	550

Scheme 6

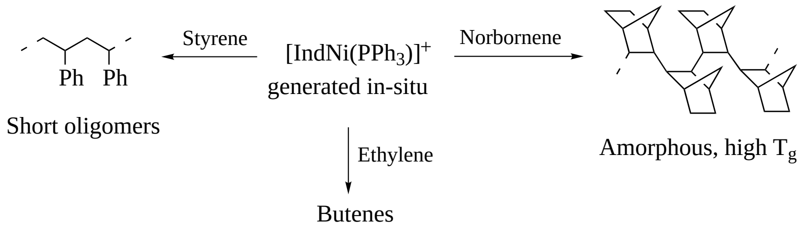
Styrene
[IndNi(PPh3)]+
generated in-situ
Norbornene
Ph Ph
Short oligomers
Amorphous, high Tg
Ethylene
Butenes

Scheme 7

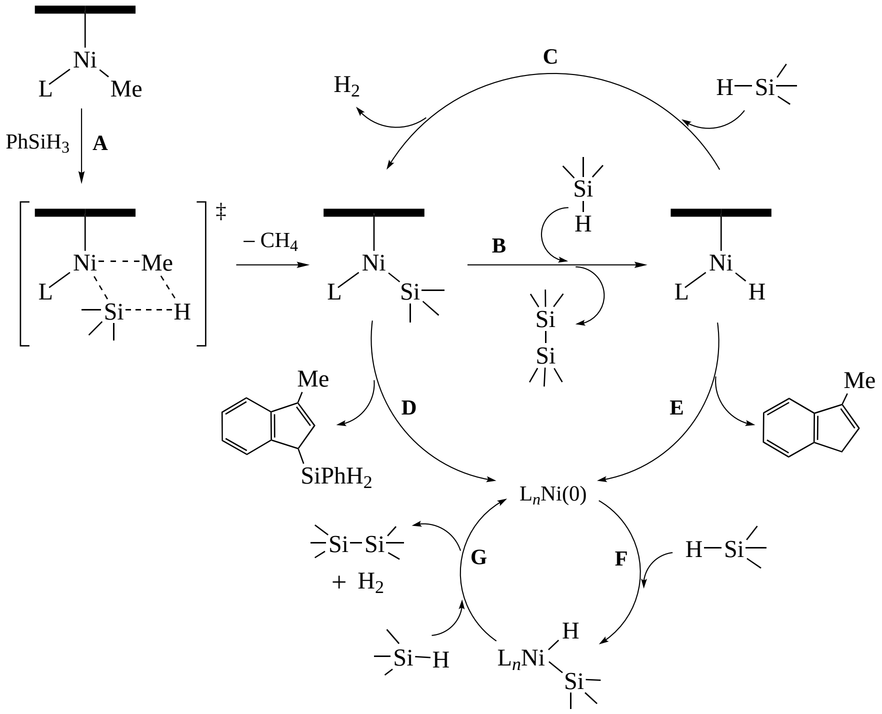
Ni
L
Me
PhSiH3
A
‡
Ni
Me
L
Si
H
– CH4
Ni
L
Si
C
H2
H–Si
B
Si
H
Si
Si
Ni
L
H
Me
D
E
Me
SiPhH2
LnNi(0)
Si–Si
+ H2
G
F
H–Si
Si–H
LnNi
H
Si

Scheme 8

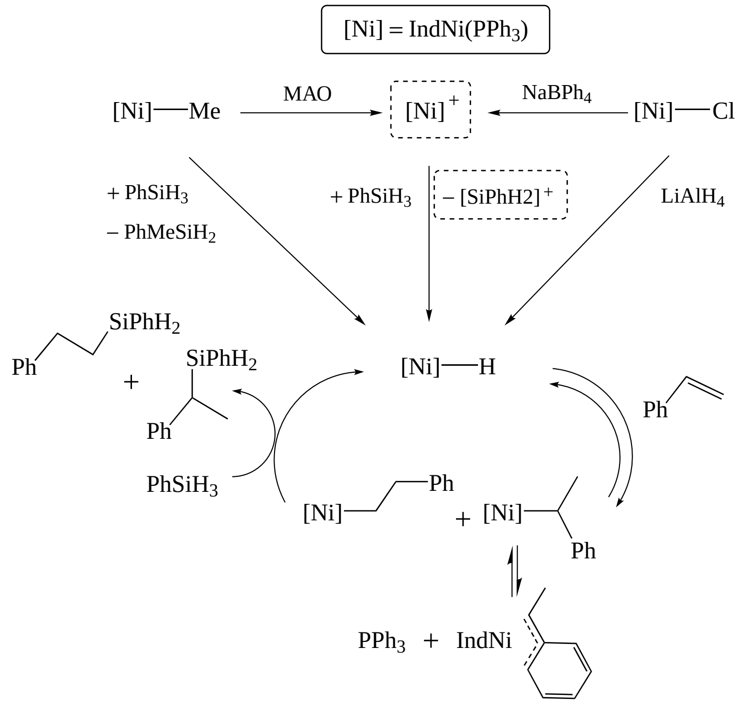
[Ni] = IndNi(PPh3)
[Ni]—Me
MAO
[Ni]+
NaBPh4
[Ni]—Cl
+ PhSiH3
− PhMeSiH2
+ PhSiH3
− [SiPhH2]+
LiAlH4
SiPhH2
Ph
+
SiPhH2
Ph
PhSiH3
[Ni]—H
Ph
[Ni]
Ph
+ [Ni]
Ph
PPh3 + IndNi

Scheme 9

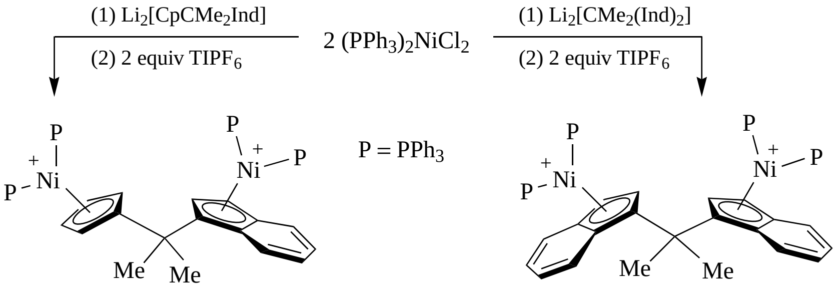
(1) Li2[CpCMe2Ind]
(2) 2 equiv TIPF6
2 (PPh3)2NiCl2
(1) Li2[CMe2(Ind)2]
(2) 2 equiv TIPF6
P
P
Ni
+
P
Ni
P
+
Me
Me
P = PPh3
P
P
Ni
+
P
Ni
P
+
Me
Me

Scheme 10

ligands (Scheme 11); the hemilabile nature of the amine moiety in the latter complexes facilitates a number of interesting catalytic reactions.[28–32]

2.4 Tp Complexes

A recent report has shown that tris(pyrazolyl)borate (Tp) (*see Tris(pyrazolyl)borates*) complexes of Ni tend to form 5-coordinate, formally 18-electron complexes. The hapticity of the tris(pyrazolyl)borate ligand in these complexes appears to be more sensitive to the steric environment around the Ni center as opposed to the electronic factors (i.e. formal electron count of the complex).[33] Thus, the η^3-allyl derivative of tris{(3,5-*i*-Pr$_2$-pyrazolyl)borate}NiR (**3**) displays a κ^3-coordination, whereas the η^3-prenyl derivative (**4**) adopts a κ^2-coordination (Scheme 12); interestingly, carbonylation of the 4-coordinate complex (κ^3-Tp)Ni-Et (**5**) gave the 5-coordinate complex (κ^3-Tp)Ni(CO){C(=O)Et} (**6**) underlining the readiness with which extra pairs of electrons are accommodated in the presence of Tp ligands.

3 HYDRIDO, ALKYL, ALKENYL, AND SILYL COMPLEXES

3.1 Hydride Complexes

Nickel hydride (*see Hydrides*) species are thought to be involved in a number of catalytic reactions, and so an intimate knowledge of the thermodynamics of Ni–H

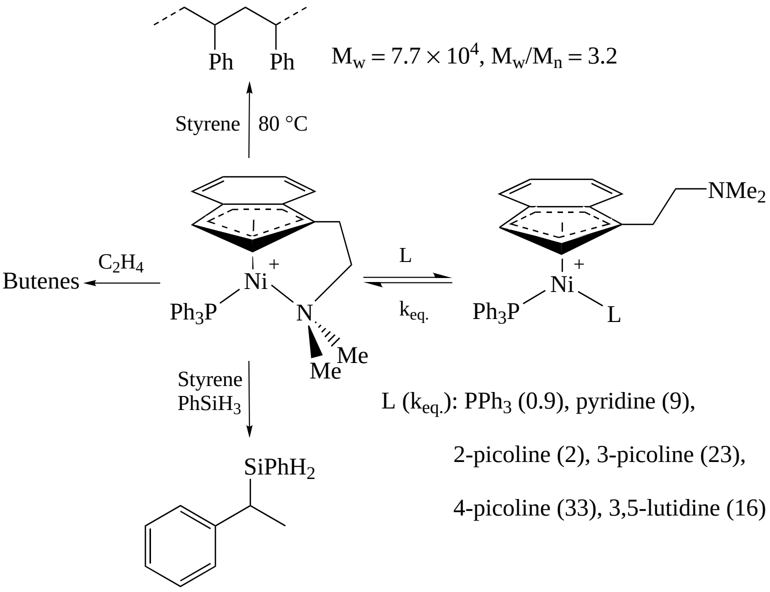
Ph
Ph
Mw = 7.7 × 10^4, Mw/Mn = 3.2
Styrene
80 °C
NMe2
C2H4
Butenes
Ni
+
Ph3P
N
Me
Me
L
keq.
Ni
+
Ph3P
L
Styrene
PhSiH3
SiPhH2
L (keq.): PPh3 (0.9), pyridine (9),
2-picoline (2), 3-picoline (23),
4-picoline (33), 3,5-lutidine (16)

Scheme 11

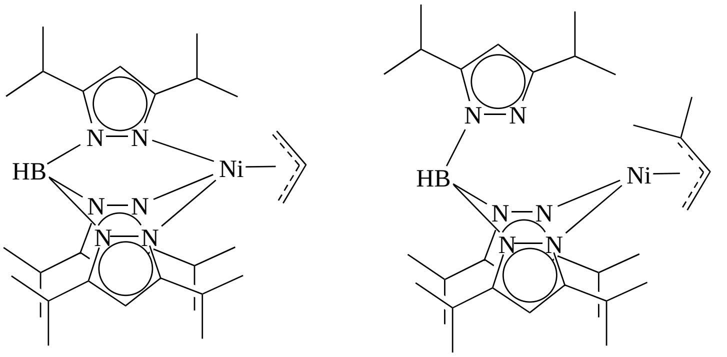
N—N
HB
Ni
N—N
N—N
N—N
HB
Ni
N—N
N—N

(**3**)

(**4**)

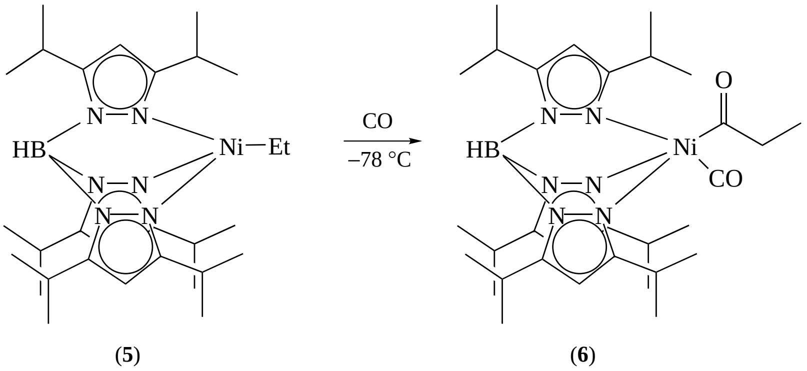
N—N
HB
Ni—Et
N—N
N—N
CO
−78 °C
O
N—N
HB
Ni
CO
N—N
N—N

(**5**)

(**6**)

Scheme 12

bonds (e.g. homolytic dissociation energy, acidity, etc.) can be valuable in understanding the mechanisms of their reactivities. A convenient method for determining metal hydride bond energies (*see* ***Bonding Energetics of Organometallic Compounds***) is based on a thermodynamic cycle that uses the pK_a values of the hydride complex and the one-electron reduction potentials of its conjugate base to estimate the free energies of all three M-H bond cleavage reactions ($\Delta G^\circ_{\mathrm{H}^-}$, $\Delta G^\circ_{\mathrm{H}^\circ}$, $\Delta G^\circ_{\mathrm{H}^+}$).[34] Thus, electrochemical and pK_a studies can help establish the energetics of the Ni–H bond in complexes such as $[\mathrm{HNi(diphosphine)_2}]^+$, whose p$K_a$ values can be measured fairly accurately and whose conjugate bases, $\mathrm{Ni(diphosphine)_2}$, undergo two reversible, one-electron oxidations (Ni(II)/Ni(I), Ni(I)/Ni(0)). A number of these studies have shown that more electron-donating diphosphine ligands and those with smaller bite angles (*see Bite Angle*) increase the hydride donor ability of the Ni–H bond; the acidities are also affected by the basicity of the ligand but not the bite angles.[35]

Moreover, it has been shown that a free-energy relationship exists between the $E_{1/2}$(II/I) values and the hydride donor abilities ($\Delta G^\circ_{\mathrm{H}^-}$) of $\mathrm{Ni(diphosphine)_2}$; this can be justified by considering that the $E_{1/2}$(II/I) values reflect the energy of the LUMO (*see LUMO*) in $[\mathrm{Ni(diphosphine)_2}]^{2+}$. Since the LUMO in these complexes is the antibonding $d_{x^2-y^2}$ orbital, which is the orbital involved in hydride transfer reactions, it stands to reason that the energy of this ligand (and the $E_{1/2}$(II/I) value) should correlate with the hydride donor/acceptor properties of $[\mathrm{Ni(diphosphine)_2}]^{2+}$. The more electron-donating substituents on the ligands increase the energy of the LUMO and make the reduction potentials more negative; therefore, $[\mathrm{HNi(diphosphine)_2}]^+$ becomes a better hydride donor. On the other hand, larger bite angles lead to greater tetrahedral distortion of the structures and lower the energy of the $d_{x^2-y^2}$ orbital; the resulting reduction in the antibonding nature of the P_σ-$d_{x^2-y^2}$ interaction increases the hydride acceptor properties of the complex. A free-energy relationship also exists between the $E_{1/2}$(I/0) values of $\mathrm{Ni(diphosphine)_2}$ and acidities ($\Delta G^\circ_{\mathrm{H}^+}$) of the corresponding $[\mathrm{HNi(diphosphine)_2}]^+$; this can be justified by considering that, to a first approximation, the $E_{1/2}$(I/0) values represent the energy of the HOMO (*see HOMO*), which would be expected to influence the basicity of $\mathrm{Ni(diphosphine)_2}$.

An interesting, and somewhat counter-intuitive, finding of the above studies is that the values of ν(Ni–H) obtained from IR spectra correlate best with $E_{1/2}$(II/I) and $\Delta G^\circ_{\mathrm{H}^-}$ values; in other words, the stretching frequencies correspond more closely to the hydride transfer reaction (equation 2) than to the homolytic cleavage (*see Homolytic Cleavage*). Altogether, these findings demonstrate that $E_{1/2}$(II/I) and $E_{1/2}$(I/0) values measured for a given complex can give fairly accurate estimates of the pK_a values and the energetics of the corresponding Ni–H complex. This information is useful when selecting appropriate acids for generating Ni–H species by protonation and for predicting the stability of the Ni–H bond toward decomposition by deprotonation or formation of H_2.

$$[\mathrm{HNi(diphosphine)_2}]^+ \longrightarrow [\mathrm{Ni(diphosphine)_2}]^{2+} + \mathrm{H}^- \qquad (2)$$

3.2 Alkyl Complexes

The complex $[\mathrm{Li(THF)}]_4[\mathrm{Ni_2(CH_3)_8}]$ (**7**) is a rare example of simple, anionic Ni-alkylate complexes. It has been prepared by reacting excess MeLi with a Ni(II) complex bearing oxalic amidinate (oxam) ligands (equation 3).[36] The stability of this homoleptic (*see Homoleptic Compound*) methyl complex towards reductive elimination is thought to be due to ineffective stabilization of the resulting Ni(0) complexes by the oxam ligands, which are poor π-acceptors. The ^{1}H and ^{13}C NMR spectra of this compound show singlets for the $\mathrm{C}H_3$ (ca. −0.6 ppm) and $C\mathrm{H_3}$ nuclei (ca. −6 ppm), respectively. The geometry around each Ni center is square planar and the relatively long Ni–Ni distance of ca. 3.17 Å indicates little or no bonding interaction. The methyl ligands occupy the vertices of a cube and the dimeric structure is maintained by Li–H–C α agostic interactions (Li–H = 2.05–2.08 Å; Li–H–C = 95–96°). The Ni–C (ca. 1.99–2.01 Å) and Li–C (2.34–2.37 Å) distances are fairly symmetrical. These complexes are thought to offer a glimpse into the presumed intermediates of cross-coupling reactions between R-X and R′M (X = halide; M = Li, MgX).

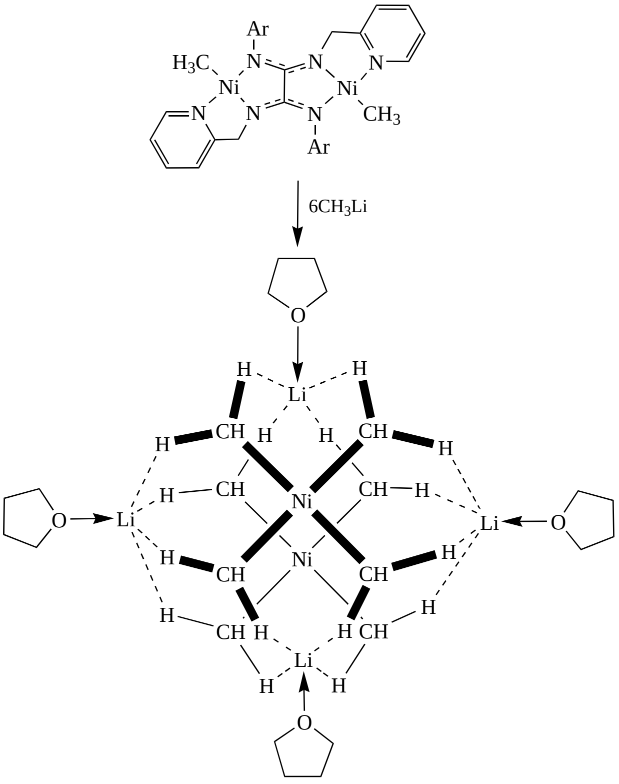

(3)

(**7**)

3.3 Protonation of Ni–R Moieties

Protonation of organometallic complexes, L_nM-R, is a reaction of fundamental importance both in the industrial applications of organometallic complexes and also in

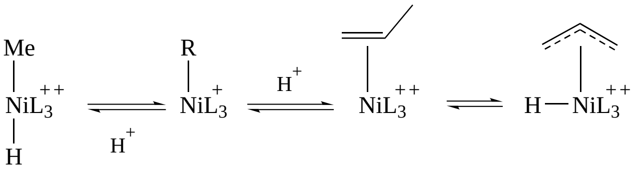

Scheme 13

bioinorganic chemistry. In principle, protonation can occur at either the metal center or the (formally anionic) R ligand; moreover, since the added proton can move rapidly between the two sites, determining the initial site of protonation is often a complicated task.[37–39] A number of recent studies have examined the kinetics of protonating a series of $[L_3Ni–R]^+$ complexes (L_3 = triphos; R = Me, η^3-allyl) with the following findings (Scheme 13).[40,41] The Ni center in the η^3-allyl derivative was found to be ca. 10^6 times more basic than that of the analogous Me complex; this is presumably due to the electronically saturated configuration of the Ni-η^3-allyl species (18 electron). Interestingly, however, the much less basic Ni center in the Ni–Me complex is protonated first to give the (formally) Ni(IV) dication $[(triphos)Ni(H)Me]^{2+}$, whereas the precise site of attack for the Ni-η^3-allyl complex could not be determined because of the relatively small difference (ca. 30 times) between the basicities of the metal/ligand sites.

3.4 Alkenyl Complexes

The reactions of alkynes or alkenes with Ni–R bonds are important in organic synthesis, particularly when they involve metallacyclic precursors because these reactions lead to synthetically valuable poly- or heterocyclic derivatives. A crucial question in this context is the regioselectivity of the insertion reaction. To address this issue, a systematic study has been carried out on the insertion of various unsymmetrical alkynes into the Ni–C(sp^2) bond of the nickellacycle (**8**) (Scheme 14); structural analysis of the fairly stable 7-membered ring Ni-alkenyl products (**9**) indicates that the insertions are primarily governed by electronic factors.[42]

3.5 Silyl Complexes

Transition metal-catalyzed transformations of organosilicon compounds continue to make important contributions to organic synthesis and hold great promise for developing efficient routes to Si-based functional materials. The need to understand the mechanisms of these transformations and develop new methodologies has inspired researchers to probe the fundamental reactivities of silanes with a variety of transition metal complexes. The reactivities of Ni complexes with hydrosilanes have been studied quite vigorously and a number of interesting transformations have been reported recently, some of which are described below.

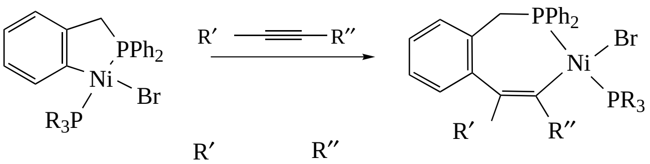

(**8**) (**9**)

R′	R″
H	Ph
Et	Ph
COOEt	Ph
COOMe	Me
CF_3	COOEt
H	$COOBu^t$
H	*t*-Bu
H	$SiMe_3$

Scheme 14

The reaction of $Ni(dmpe)_2$ (dmpe = bis(dimethylphosphino)ethane) with 1,2-disilylbenzene (**10**) has formed a number of interesting bis(silyl) species (**11–13**) that seem to be intermediates leading to the rare tetrasilyl Ni(IV) complex (**14**) and the (apparently) Ni(III)-Ni(III) dimer bearing μ-silylene moieties (**15**), as shown in Scheme 15.[43,44]

Solid-state structure determinations carried out on (**13–15**) have provided useful data for Ni–SiR_3 bond lengths. For instance, the longer Ni–Si bonds for the mutually *trans* silyl moieties in (**14**) compared to those of the silyl ligands *trans* from the phosphine ligands (2.29 Å vs. 2.25 Å) confirms the very strong *trans* influence of silyl ligands. On the other hand, the Ni–Si distances in (**15**) are fairly long (2.21–2.30 Å) even though they are not *trans* from one another; in addition, the Ni–Ni distance (ca. 2.70 Å) is longer than a usual Ni–Ni single bond, while the adjacent Si–Si distances are short enough for a weak bonding interaction (ca. 2.69 Å). The latter observations might imply that complex (**15**) can be viewed alternatively as a Ni(I)–Ni(I) species bearing two μ-silyl moieties formed by the dimerization of (**10**) (dehydrogenative formation of two Si–Si bonds), as shown in Scheme 16.

The validity of this alternative view is supported by the finding that reacting Ni(0) species with (**16**), the dimethyl analogue of (**10**), allowed the isolation of a new product (**17**) containing an 8-membered cyclic disilyl ligand that has formed by the dimerization of (**16**) (Scheme 17). The Si–Si bonds in this species (ca. 2.36 Å) were shorter than the analogous distances in (**15**).

4 Ni(0) COMPLEXES

Organometallic complexes of Ni(0) display a rich array of reactivity both in stoichiometric reactions (e.g. oxidative additions (*see Oxidative Addition*), cycloadditions, etc.)

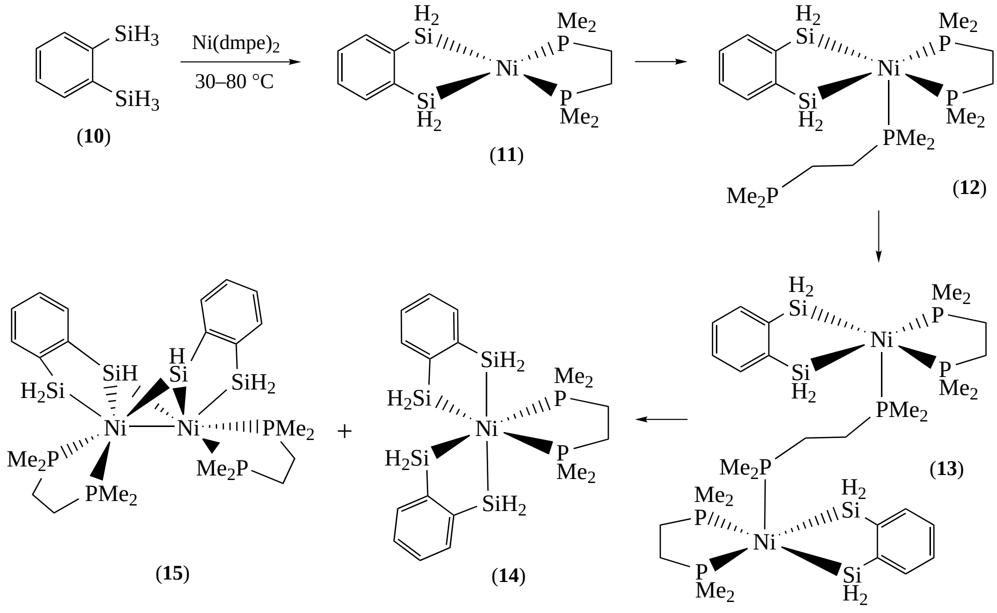

Scheme 15

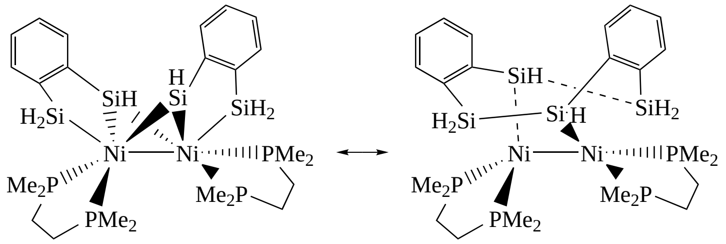

Scheme 16

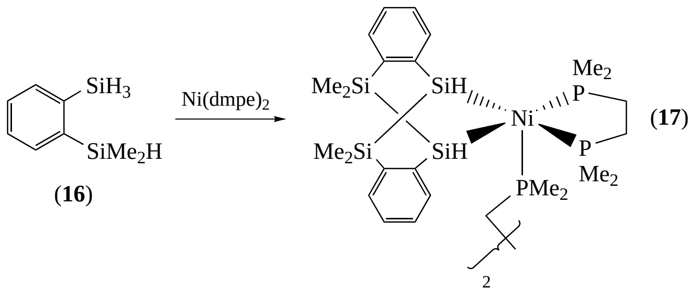

Scheme 17

and in catalysis (e.g. cross-coupling reactions). Curiously, however, a relatively small number of Ni(0) complexes have found practical utility as versatile precatalysts or stoichiometric reagents in organic transformations (e.g. $Ni(PR_3)_n$, $Ni(PR_3)_n(CH_2{=}CH_2)_m$, $Ni(COD)_2$, $Ni(bipy)_2$, etc.), while the reactivities of most complexes of zerovalent nickel remains unexplored. A significant development in this context has been the introduction of Ni(0) complexes bearing N-heterocyclic carbenes (*see* ***Carbene Complexes***),[45] which have spearheaded a renewal of interest in the catalytic chemistry of Ni(0) in many different directions. Some of these developments are described below, followed by an overview of the reactivities of a number of other Ni(0) species introduced recently.

4.1 N-heterocyclic Carbene Complexes

N-heterocyclic carbenes have been used extensively over the past decade as versatile alternatives to the ubiquitous tertiary phosphines. These ligands are strongly electron donor, weakly π-acceptor, and in most cases quite bulky.[46–48] The stoichiometric reactions of Ni-carbene complexes are quite similar to those of analogous phosphine complexes; for example, oxidative addition of aryl- or alkyl-halides gives square planar bis(carbene)Ni(R)X species.[49] On the other hand, a number of side-reactions have been observed for the carbene complexes, such as the addition of electrophiles like alkyl halides to the carbene ligand instead of the metal center; it is believed that the imidazolium salts produced in this reaction form as a result of the elimination of the hydrocarbyl (*see Hydrocarbyl*) and carbene ligands. This is an important reactivity since many catalytic reactions are believed to go through such square planar Ni(II) intermediates bearing hydrocarbyl moieties; hence, side-reactions such as this might undermine the potential of carbenes in catalysis. Nevertheless, an increasing number of important reactions have already been catalyzed efficiently by Ni-carbene precursors. For instance, it has been shown that the cross-coupling of aryl bromides with phenylboronic acids (the Ni-analogue of the well-known Suzuki coupling) is catalyzed by (carbene)$_2$Ni(Ar)Br with a catalytic turnover of ca. 2000.[50]

A series of Ni(0)-carbenes have been studied in order to determine the level of electron-donation of heterocarbenes as well as the Ni-carbene bond dissociation energies. Thus, the ν(CO) values for (carbene)Ni(CO)$_3$ were used to show that the heterocarbene ligands bearing N-mesityl substituents are at least as donating as P(t-Bu)$_3$; on the other hand, the carbenes bearing N-adamantyl and N-t-Bu substituents appear to form relatively labile C–Ni bonds (BDE = ca. 40 kcal mol^{-1}) in (carbene)Ni(CO)$_2$.[51] These findings should prove important in interpreting the catalytic reactivities of Ni-carbene complexes.

Ni(0)-carbene complexes (*see* ***Carbene Complexes***) can be prepared in situ by mixing a Ni(0) precursor with the desired carbene ligand (Scheme 18). This protocol can be further simplified by the in situ generation of both the Ni(0) species and the carbene ligand from readily available starting materials, as shown below; the distinct ^{13}C NMR signal for the carbene carbon (ca. 220 ppm) can be used to monitor the formation of the target complex.[52]

Ni(carbene)$_n$ species generated in situ have been used to effect the catalytic coupling of dienes and variously substituted benzaldehydes in the presence of HSiEt$_3$ to give the Z-homoallylic silyl ethers (**18**) in 5–20 catalytic turnovers (equation 4);[53] it is interesting to note that using PPh$_3$ analogues of the Ni(0) complexes ($n = 2$) gives the E-isomer.[54]

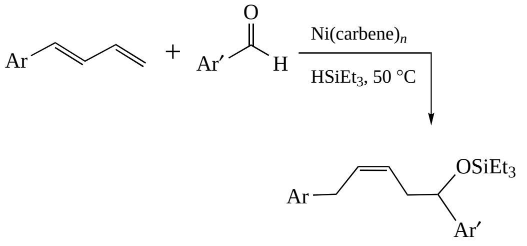

(4)

(**18**)

Ni(0) carbenes are also effective for the Kumada–Corriu coupling reaction between arylmagnesium reagents and aryl chlorides[55] or fluorides[56] in ca. 35 catalytic turnovers (equation 5). The yields are generally high even at room temperature (ca. 30 turnovers over 18 h); only when the aryl chloride is congested (substituents ortho to Cl) does the yield suffer. It is noteworthy, however, that very similar yields were obtained when the N-heterocarbene ligands were replaced by t-Bu$_3$P.

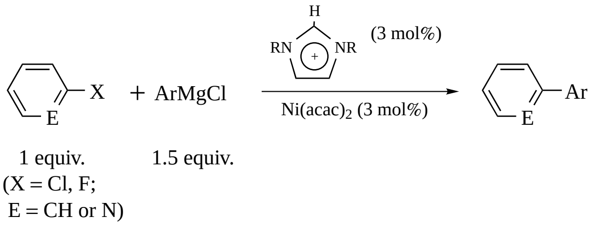

(5)

4.2 Phosphorous-containing Complexes

Phosphines provide suitable coordination environments for the preparation of stable yet reactive Ni(0) species. A recently introduced member of this family of complexes contains a cyclic oligophosphine ligand and was prepared by reacting the cyclic pentaphosphanide anion (**19**), [P$_5$(t-Bu)$_4$]$^-$, with a source of Ni(II) (Scheme 19); given the isolobal analogy between P and C–H, the resulting complex (**20**) can be viewed

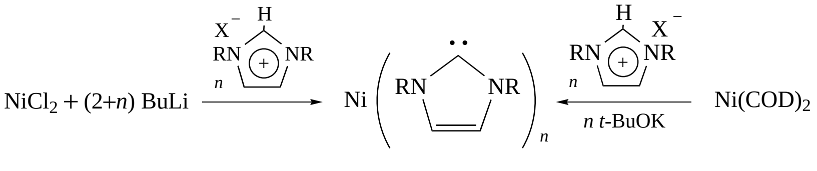

Scheme 18

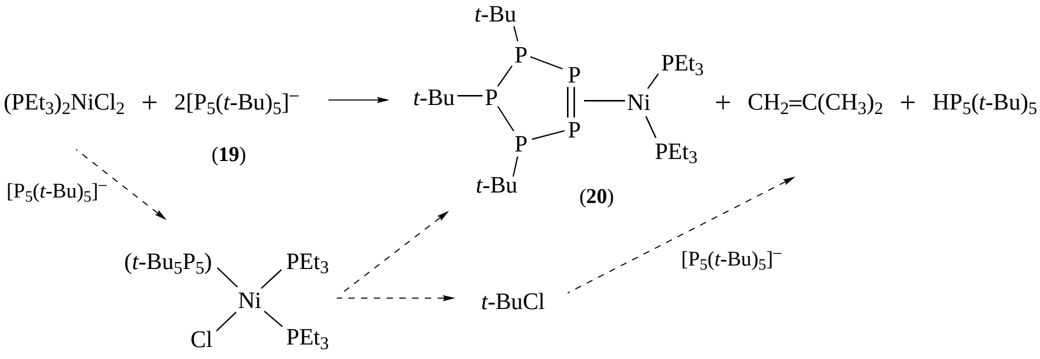

(PEt3)2NiCl2 + 2[P5(t-Bu)5]⁻
(19)
t-Bu
P
P
Ni
PEt3
PEt3
(20)
+ CH2=C(CH3)2 + HP5(t-Bu)5
[P5(t-Bu)5]⁻
(t-Bu5P5)
Cl
t-BuCl
[P5(t-Bu)5]⁻

Scheme 19

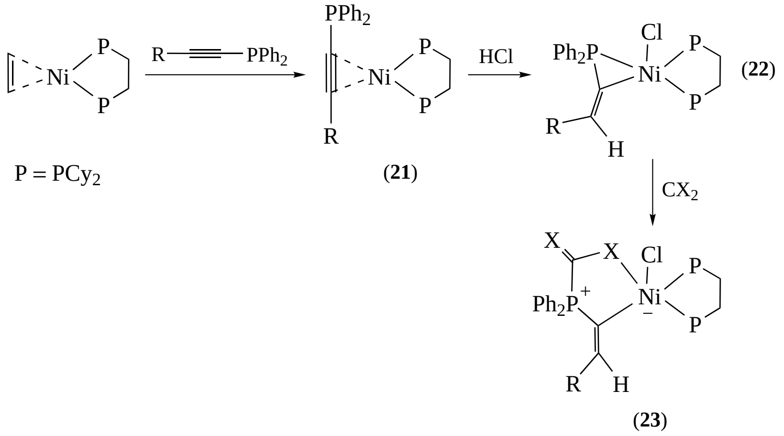

P = PCy2
R—≡—PPh2
PPh2
R
(21)
HCl
Ph2P
Cl
Ni
(22)
H
CX2
X
Ph2P+
(23)

Scheme 20

as an analogue of $(PR_3)_2Ni$(cycloalkene). The solid-state structure of (**20**) has been studied by X-ray crystallography, which showed that the geometry of the Ni center is distorted trigonal planar (Et_3P–Ni–PEt_3 ca. 108°; P–Ni–P ca. 56°). The average (*t*-Bu)P–P(*t*-Bu) distance of 2.20 Å is in the expected range for P–P single bonds, whereas the shorter P–P distance of 2.12 Å implies that the P atoms bonded to Ni are multiply bonded; therefore, (**20**) can be justifiably considered a formally 16-electron Ni(0) species.

A recent report has described a series of Ni(0)-alkynylphopshine complexes (**21**) featuring the unusual coordination of the alkyne moiety in preference over the phosphine moiety (Scheme 20).[57] The reaction of these Ni(0)-alkyne complexes with HCl and the isolation of the resulting Ni(II) η^2-vinyl complexes (**22**) has provided a rare opportunity to study alkyne insertion reactions. The Ni–P bond in (**22**) undergoes another insertion (*see Insertion*) by CO_2 or CS_2 to give 5-coordinate, zwitterionic (*see Zwitterion*) complexes (**23**).

Alkynylphosphines have also been shown to undergo an interesting double insertion with Ni(0)-benzyne complexes. Thus, two equivalents of Ph_2P-CC-R insert into the Ni-benzyne bond in (**24**) to form a series of novel naphthalene-based bis(phosphine) ligands coordinated to the Ni center (**25**, equation (6)).[58]

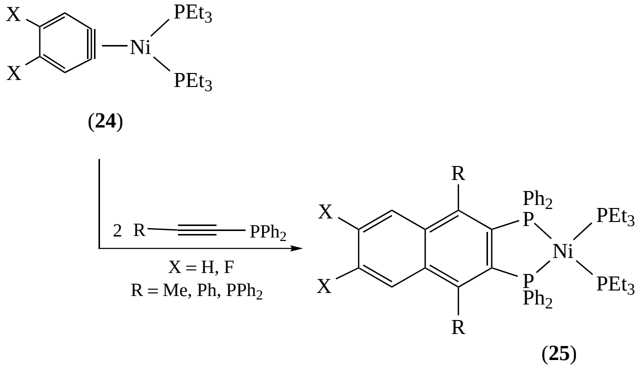

X
PEt3
Ni
PEt3
(24)
2 R—≡—PPh2
X = H, F
R = Me, Ph, PPh2
R
Ph2
P
(25)

(6)

4.3 Cyclopropene-containing Complexes

A number of Ni(0) complexes containing a cyclopropene ligand have been prepared and shown to catalyze the oxidative coupling of cyclopropene derivatives to compounds with a cyclobutane core (Scheme 21). A recent study of the kinetics of these reactions has led to the isolation

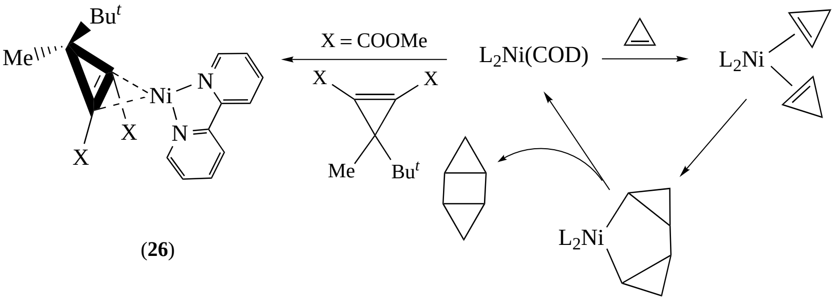

Scheme 21

of a putative intermediate (**26**).[59] Thus, the reaction of (bipy)Ni(COD) with 3-methyl-3-(*t*-Butyl)-1-cyclopropene-1,2-dimethyl dicarboxylate forms the Ni(0)-cyclopropene compound (**26**), which crystallizes in a trigonal planar structure. It is interesting to note that the carboxylate substituents are bent out of the coordination plane, while the *t*-Bu group is *endo* with respect to the Ni center; this orientation is presumably favored over the alternative *cis* disposition of the *t*-Bu and carboxylate substituents, which would engender greater steric (*see Steric Effect*) repulsions.

5 CATALYTIC POLYMERIZATION AND COPOLYMERIZATION OF OLEFINS

The study of olefin polymerization reactions catalyzed by complexes (*see* ***Oligomerization & Polymerization by Homogeneous Catalysis***) of late transition metals experienced a significant progress during the 1990s and the rapid pace of progress continues unabated during the present decade. The driving force for the intense activity in this area is the belief that, in comparison to catalytic systems based on early metal complexes (e.g. group 4 metallocenes), systems based on the less electrophilic late transition metal complexes will allow the development of polymerization protocols that are tolerant of olefinic monomers possessing polar functional groups. The incorporation of such units in ethylene-based copolymers is expected to furnish new macromolecules possessing novel structural properties and promising applications. On the other hand, the main obstacle for the development of efficient catalytic systems based on late metals was the well-documented propensity of late transition metal complexes in general, and Ni-based catalysts, in particular, to favor oligomerization over polymerization.[60] This behavior stems from the readiness with which alkyl complexes of nickel (and of most late transition metals) undergo β-H elimination (*see β-Hydride Elimination*) reactions; these reactions in effect rearrange the alkyl moiety into a (new) olefin, which is then expelled from the metal's coordination sphere, as shown in Scheme 22. The L$_n$M-H species generated in this sequence can then undergo an insertion reaction with another molecule of olefin to restart the oligomerization process; this olefin is usually the monomer, which is present in the reaction mixture in higher concentrations and is less bulky.

In light of the above, it is generally assumed that the key to extending the olefin homologation (*see Homologation Reactions*) process beyond dimerization or oligomerization is to retard the above-described β-H elimination (*see β-Hydride Elimination*) (or de-insertion) and chain-transfer reactions. This objective was achieved most spectacularly when it was demonstrated, in 1995, that a family of Ni(II) complexes bearing α-diimine ligands (**27**) had unexpectedly

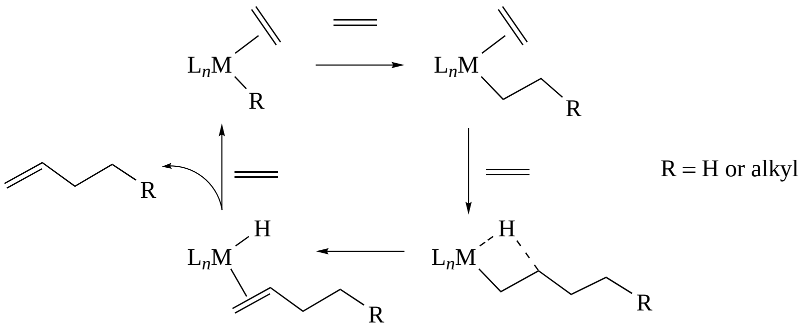

Scheme 22

high activities for the polymerization of ethylene.[61] (NB: These complexes and their Pd(II) analogues have been trademarked Versipol catalyst systems by DuPont.) This reactivity was later extended to other terminal, aliphatic olefins (propylene, 1-hexene, 1-octene, etc.).[62]

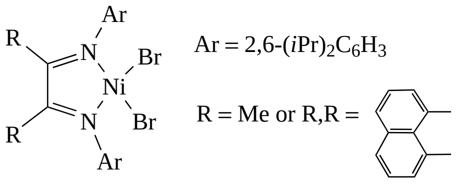

(**27**)

It is noteworthy that this family of complexes had been known for decades,[63] but what made the newly introduced derivatives excellent catalysts for polymerizing ethylene was the incorporation of very bulky aryl substituents (e.g. 2, 6-(i-Pr)$_2$C$_6$H$_3$) on the diimine nitrogens. Solid-state structural and computational studies have indicated that the aryl substituents orient themselves approximately perpendicular to the coordination plane, thus placing the ortho substituents above and below this plane. It seems, therefore, that the role of these substituents is to provide steric crowding around the axial plane above the Ni center, which in effect blocks the interaction of the growing alkyl chain with the d_{z^2} orbital, thereby hindering the β-H elimination step. Other crucial features of these systems include their cationic nature and the use of noncoordinating counter anions during the ionization step; together, these factors increase the electrophilicity of the central metal and provide an open coordination site for the uptake and insertion of the monomer.

In a typical polymerization experiment, the (diimine)NiX$_2$ precursor is generated in situ and reacted with 100–1000 equivalents of methylaluminoxane (MAO, $\{MeAlO\}_n$) in toluene (μmol conc. in Ni) under a small pressure of ethylene (typically 1 atm) at about 35 °C (Scheme 23). Typical activities are hundreds of kg of poly(ethylene) (PE)/mol Ni.h, although they can be one or two orders of magnitude higher under optimized conditions. The molecular weights of the resulting PE can range from 3 to 1000 × 10^3 Daltons, and the polymer

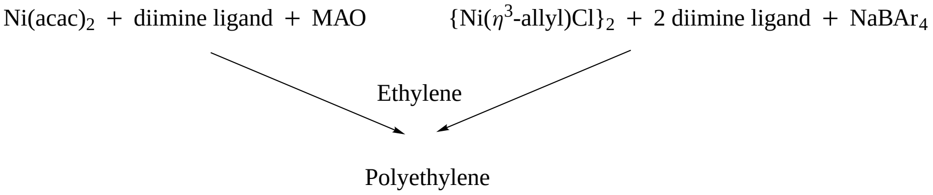
Ni(acac)2 + diimine ligand + MAO
{Ni(η3-allyl)Cl}2 + 2 diimine ligand + NaBAr4
Ethylene
Polyethylene

Scheme 23

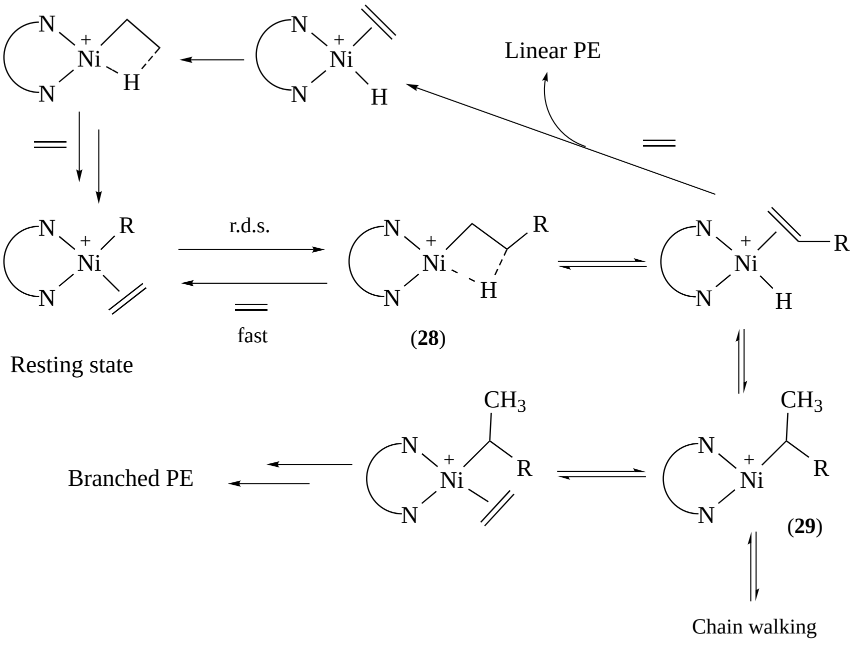

Scheme 24

microstructure can vary from highly linear and crystalline to fairly branched and amorphous. In general, PE samples obtained with Ni catalysts are less branched in comparison to the corresponding Pd systems.

The mechanism of the polymerization reactions catalyzed by the Ni(diimine) system has been studied in detail both experimentally[64] and by computational methods.[65–69] Since a number of cationic species of the type [(diimine)Ni(n-alkyl)(olefin)]$^+$ can be observed throughout the reaction, it is believed that these intermediates are formed in relatively rapid steps (e.g. rapid monomer uptake) and consumed in relatively slow steps (e.g. the migratory insertion of the monomer into the Ni-alkyl bond). Therefore, such species represent the catalyst resting state and their reactions are considered to be rate-limiting (Scheme 24). This type of reactivity also implies that the chain growth is zero-order with respect to the concentration of ethylene, although this is not the case with higher α-olefins. The barrier to the insertion reaction has been estimated (by low-temperature NMR techniques (*see* ***Structure & Property Maps for Inorganic Solids***)) to be ca. 13–14 kcal mol^{-1}, which is ca. 4–5 kcal mol^{-1} lower than the barrier for the insertion step for the analogous Pd complexes. Some of the computational studies[70] have produced rate data that are in close agreement with these values.

As mentioned earlier, the very bulky N-substituents tend to hinder the chain-transfer or β-H elimination (*see β-Hydride Elimination*) steps; moreover, the larger steric bulk is thought to destabilize the resting state with respect to the insertion transition state. In other words, the bulky substituents favor the chain growth process by both accelerating the propagation step (insertion of the monomer) and by retarding the termination steps (the chain-transfer or β-H elimination steps). The formation of branched PE can be rationalized as follows: the 14-electron intermediate [(diimine)Ni(n-alkyl)]$^+$ generated by the insertion process (**28**) can either trap a monomer and undergo another insertion reaction leading to linear chain growth, or it can be stabilized by agostic C–H–Ni interactions (*see Agostic Bonding*) that can produce [(diimine)Ni(branched-alkyl)]$^+$ intermediates (**29**) via successive β-H elimination/reinsertion steps. The intermediate with the branched-alkyl moieties can then trap monomer and undergo insertion to give branched PE. This process is dubbed 'chain-walking'.

Another remarkable character of this class of Ni complexes is their tendency to promote living polymerization of α-olefins at low temperatures and with low concentrations of the monomer. Thus, the low-temperature polymerization of propylene leads to a material whose number average molecular weight (M_n) increases almost linearly as a function of time and propylene consumption, reaching values of $M_n = 160\,000$ Daltons and polydispersities of ca. 1.13.[71] This character allows these Ni catalysts to produce A-B-A type block copolymers composed of semicrystalline and amorphous segments, which is used to prepare thermoplastic elastomeric polymers. The Ni catalysts can also polymerize internal cyclic olefins such as cyclopentene, giving high molecular weight materials ($M_w \sim 250\,000$ Daltons) that are melt-processable to strong, clear films.

The relative insensitivity of this class of Ni catalysts to polar functional groups, and especially their low oxophilicity, is another important characteristic. This property has been exploited for the development of novel polymeric materials that might find new applications. For example, 1-hexene has been copolymerized with 6-(2-ureido-4-[1H]-pyrimidinone)hex-1-ene (**30**) to generate a new poly(olefin) elastomer (equation 7).[72] The dimerization (through H-bonding) of the pyrimidinone moieties forms noncovalent crosslinks that bestow unique properties to the otherwise amorphous poly(1-hexene) matrix.

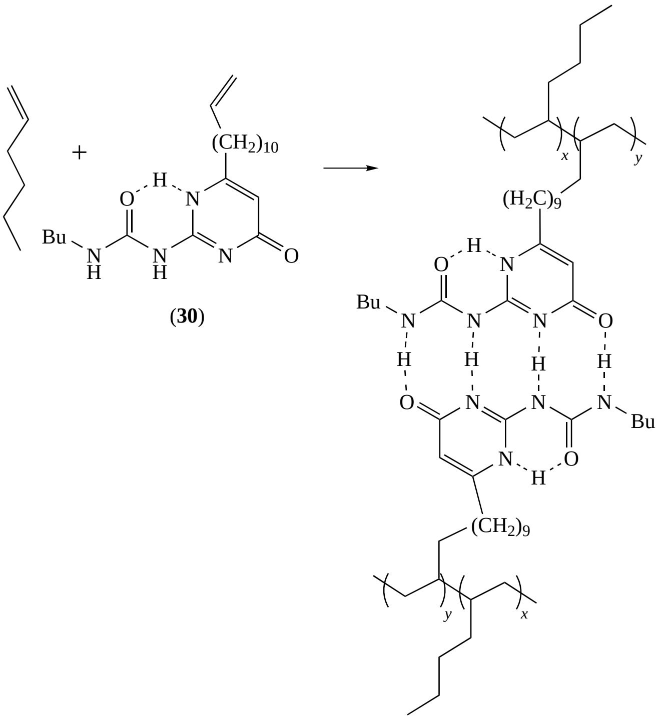

(7)

5.1 Ni-based Neutral Catalysts for Olefin Polymerizations

Following the successful development of the above-discussed cationic systems, there has been a surge of interest to develop neutral, single-component systems not requiring cocatalysts such as MAO. As before, it was anticipated that the reduced electrophilicity of noncationic systems and their tolerance for polar functionalities on the olefinic monomers will further facilitate the use of olefinic monomers bearing polar groups. The Ni complexes (**31**) based on the salicylaldiminato ligand were found to be promising catalysts for this purpose,[73] particularly when a bulky substituent was placed *ortho* to the OAr position, because this feature allowed the catalysis to proceed without the customarily required initiators/cocatalysts.[74] Evidence from experimental studies indicates that the main role of the bulky Ar-substituent is to induce the dissociation of the PPh_3 ligand, thereby opening up a coordination site around the Ni center; computational studies are in accord with this proposal.[75]

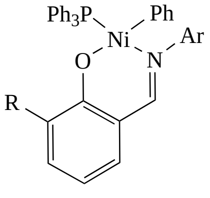

(**31**)

Ar = 2,6-(iPr)$_2$C$_6$H$_3$

R = H, Ph, *t*-Bu, 9-phenathrenyl, 9-anthracenyl

In addition to ethylene, the precatalysts (**31**) homo- and copolymerize styrene and norbornene and copolymerize ethylene with α-olefins (e.g. 1-hexene, 1-octene, etc.) or functionalized norbornenes (e.g. 5-norbornen-2-ol). Remarkably, the polymerization of ethylene can proceed in the presence of various polar molecules such as ethers, ketones, esters, amines, alcohols, and even water! This tolerance of extremely polar media has been exploited to carry out Ni-catalyzed polymerization of ethylene in aqueous emulsions.[76–78] This type of polymerization protocol leads to so-called polymer latexes, which consist of stable aqueous dispersions of surfactant-stabilized microparticles of the polymer having diameters in the range of tens or hundreds of nm. In addition to the obvious advantage of using aqueous media for polymer synthesis, the polymer latexes produced by emulsion polymerizations have also many varied applications (e.g. in coatings). In a particularly attractive approach to applying emulsion polymerization protocols to metal-catalyzed reactions, hydrocarbon solutions of the Ni-based system (**32**) were dispersed in water/surfactant mixtures and exposed to ethylene pressure; this led to PE latexes consisting of long chains (M_w ca. 10^5 Daltons) and having average particle sizes of 50–350 nm in diameter.[79]

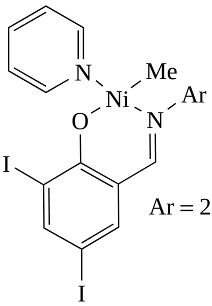

Ar = 2,6-(iPr)$_2$C$_6$H$_3$

(**32**)

Recent reports have described other neutral, single-component Ni catalysts based on the N–O ligands 2-anilinotropone (**33**)[80] and 2-anilinoperinaphtenone (**34**).[81] There are a number of structural similarities between these and the above-described salicylaldiminato-based systems in that they all incorporate N–O ligands in addition to PPh_3 and Ph ligands (Ph *trans* to O, PPh_3 *trans* to N). On the other hand, there are also important differences such as (a) the greater localization of the negative charge on the N-atom in the new systems as opposed to on the O atom in the salicylaldiminato system, and (b) the formation a 5- as opposed to 6-membered chelate metallacycles (*see Metallacycle*). The latter feature results in different bite angles: O-Ni-N angles of ca. 83° vs. ca. 94° and O-Ni-P angles of ca. 95° vs. ca. 87° for the 2-anilinotropone (**33**) and salicylaldiminato (**34**) systems, respectively. The activities of the new complexes are up to ca. 60 000 kg PE/h.mol of Ni, which is comparable to, or higher than, those of the best salicylaldiminato systems, but their lifetimes are shorter. The tropolone system (**33**) has the interesting property of tolerating many functional groups (ether, THF, water, NEt_3, etc.) in addition to being fairly insensitive to the presence of added PPh_3 ligand; thus, even the presence of 5 equivalents of PPh_3 has essentially no effect on the activities.

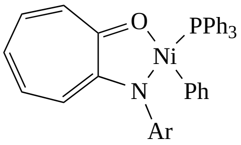

Ar = 2,6-(iPr)$_2$C$_6$H$_3$

(**33**)

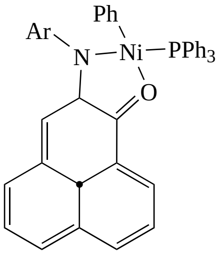

(**34**)

Although most of the Ni-based catalyst systems displaying high activities in the polymerization of ethylene bear N-based ligands, there have been a few reports on the catalytic reactivities of P-based Ni complexes. Recall that the nickel indenyl complexes IndNi(PR_3)X discussed earlier polymerize ethylene to high MW PE with activities ranging from 50 to 700 kg PE/mol of Ni.h ($P_{ethylene} = 5–10$ atm).[16] Higher activities up to 2000 kg PE/mol of Ni.h ($P_{ethylene} = 8$ atm) have been obtained from $LNiBr_2$ (**35**) with L representing the chelating bis(phosphine) $MeN\{P(2\text{-}i\text{-}Pr\text{-}C_6H_4)_2\}_2$.[82] Both of these systems require cocatalysts/activators such as MAO, and in both cases it has been shown that the presence of $AlMe_3$ in the reaction mixture lowers polymerization activities. Like the other Ni-based systems described above, these catalysts are fairly insensitive to polar functional moieties present in the polymerization medium.

As discussed earlier, the electronically and coordinatively unsaturated cations $[IndNi(PR_3)]^+$, which are generated from the corresponding Ni-X precursors in the presence of excess MAO or other halide abstractors such as $AgBF_4$, promote exclusively the dimerization of ethylene. The 1-butene

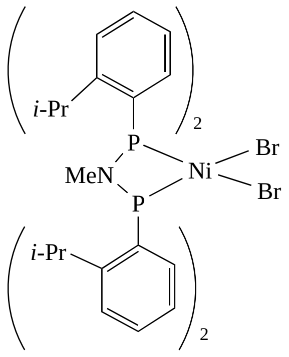

(**35**)

produced during the polymerization reaction is incorporated into the PE chains, leading to ca. 5% ethyl branches along the essentially linear PE produced by this system. The PE obtained from the bis(phosphine) system is also essentially linear but contains a small number of different branches (mostly Me branches but longer homologues are also detected), indicative of the chain-walking mechanism.

5.2 Alternating Copolymerization of CO and Ethylene

The alternating copolymerization of CO and ethylene has been studied in much detail over the past two decades.[83] Although a number of Ni-based systems are known to catalyze this reaction,[84,85] comparative studies have shown that Pd-based systems are by far the most active catalysts for this reaction. The lower activity of the Ni-based systems is somewhat surprising because the requisite CO and ethylene insertion steps are expected to be energetically more facile for the Ni-based systems. A recent study has shown that the energy barrier for CO insertion into the Ni–Me bond is less than 10 kcal mol^{-1} (Scheme 25),[86] significantly lower than the barrier of ca. 15 kcal mol^{-1} in the analogous Pd complexes; this finding supports the results of computational studies that predict barriers on the order of 4–7 kcal mol^{-1} for simplified Ni systems.[87] The reaction of the Ni-acyl complex (**37**), which is formed from the initial CO insertion into the Ni–Me bond in (**36**), with ethylene gives a new Ni-acyl species (**38**) instead of the expected Ni-alkyl intermediate; this is presumably caused by the very facile insertion of CO into the Ni-alkyl bond arising from the ethylene insertion. Since the CO insertion is reversible, argon-purging of the reaction solution for an extended period produces a new Ni-alkyl species bearing a pendant, chelating acyl moiety (**39**). It appears, therefore, that the facile uptake and insertion of CO stabilizes the catalyst resting state in the Ni-based systems, making these systems less efficient catalysts relative to the Pd-based systems. Moreover, the Ni-catalyzed copolymerization reaction seems to involve stable, 5-coordinate intermediates, in contrast to the almost exclusive involvement of 4-coordinate species in the Pd-based systems.

6 OTHER CATALYTIC REACTIONS

6.1 Ni-catalyzed Cross-coupling Reactions

The Ni-catalyzed cross-coupling of organic halides with various other organometallic reagents (e.g. RLi, RMgX, XZnR, etc.) plays an important role in organic synthesis. A number of recent reports have introduced important developments in this area, which promise to improve the potential of Ni-catalyzed routes for making new C–C bonds. For example, it was shown in 1998 that diorganozinc (*see* ***Zinc: Organometallic Chemistry***) reagents can be coupled with alkyl halides (Negishi reaction) if a suitable π-donor

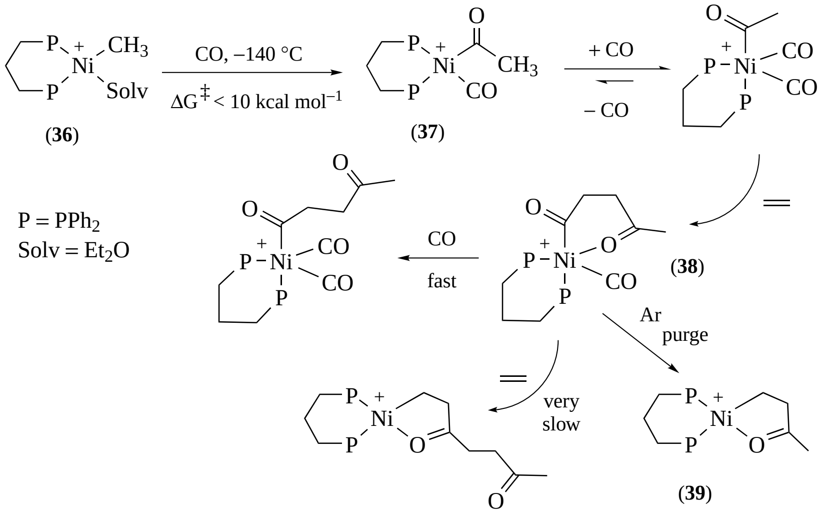

Scheme 25

ligand was used to induce the reductive elimination of the product from the postulated diorganonickel intermediates (equation 8).**88** This protocol has been revised more recently to extend the coupling reaction to RZnI, which are less reactive than ZnR_2 but also more tolerant of functional groups; thus, ethers, esters, ketones, amides, and nitriles can be tolerated.**89** The presence of Bu_4NI is essential for this protocol; the role of this additive is not clear, but it might coordinate to RZnI to form a more nucleophilic organozinc anion.

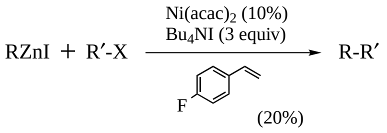

(8)

R = alkyl; X = Br, I
R′ = alkyl groups bearing functional groups

The cross-coupling of more hindered secondary and tertiary alkyl halides has also been studied. Thus, secondary alkyl halides can be cross-coupled with organozinc reagents in the presence of the so-called 'pybox' ligands (equation 9).

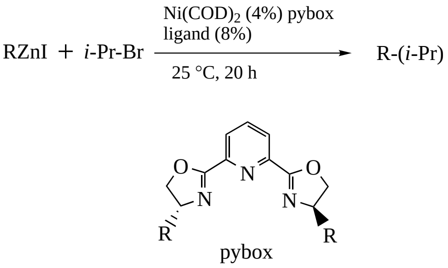

(9)

An interesting development concerning the mechanistic aspects of the Negishi cross-coupling reaction was the recent report that $ZnBr_2$ can abstract a bromide atom from $L_2Ni(R)Br$, generating $[L_2NiR]^+$ cations (Scheme 26). Since both ZnX_2 and organyl halides of nickel are proposed intermediates in the Negishi reaction, this finding is likely to have important consequences for the future developments in this area.

In another development, it was shown that simple Ni(II) or Ni(0) precursors (e.g. $NiCl_2$, $Ni(acac)_2$, $Ni(COD)_2$, etc.) can catalyze the coupling of primary alkyl halides with Grignard reagents (Kumada–Corriu reaction).**90** This otherwise challenging coupling of two sp^3-C centers is facilitated by the presence of various 1,3-butadienes; this feature allows even the normally unreactive alkyl chlorides to be coupled in very good yields and low catalyst loadings (equation 10). The precise mechanism of this reaction is not known, but free radical-based routes have been excluded; a tentative proposal has invoked the involvement of Ni(IV) intermediates.

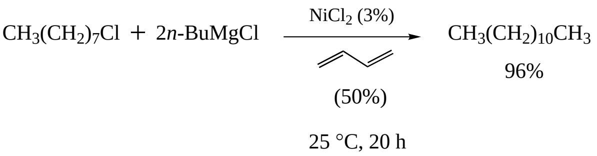

(10)

6.2 Ni-catalyzed Coupling of Carbonyl Compounds with Alkynes or 1,3-dienes

A number of new Ni-catalyzed protocols have been developed recently for the coupling of carbonyl compounds and unsaturated substrates such as alkynes or 1,3-dienes.**91–94** For instance, a three-component intramolecular coupling (alkyne/aldehyde/hydrosilane) has led to the formation of bicyclic N-heterocycles. A number of similar inter- and intramolecular coupling reactions have been developed into useful synthetic routes (Scheme 27).

6.3 Ni-catalyzed CO_2 Additions

A novel Ni-promoted route has been developed for using CO_2 as a natural source of acid/ester moieties in building organic molecules. This reaction, which provides an attractive method for preparing a number of mono- and di-carboxylic acid derivatives, proceeds by the oxidative cycloaddition of CO_2 to conjugated dienes as exemplified in the transformations shown in Scheme 28.**95** The reaction of $Ni(COD)_2$ (in stoichiometric amounts) with the diene and CO_2 (1 atm) is believed to produce the oxo-π-allyl nickel intermediates (**40**) that can be hydrolyzed or transmetallated (*see Transmetalation*) with zinc reagents; the presence of two equivalents of 1,8-diazabicylco-[5.4.0]undec-7-ene (DBU) is essential for the success of the transformation. It is not known why $ZnMe_2$ leads to dicarboxylation whereas $ZnAr_2$ gives arylative carboxylation.

7 RELATED ARTICLES

Carbene Complexes; Carbonylation Processes by Homogeneous Catalysis; Coordination Numbers & Geometries; Coordination & Organometallic Chemistry: Principles.

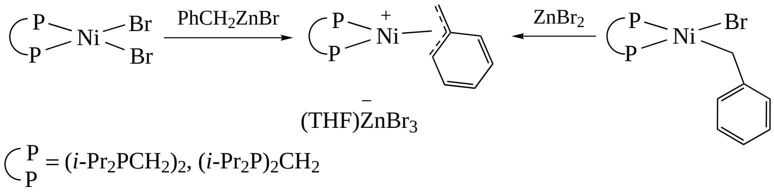

Scheme 26

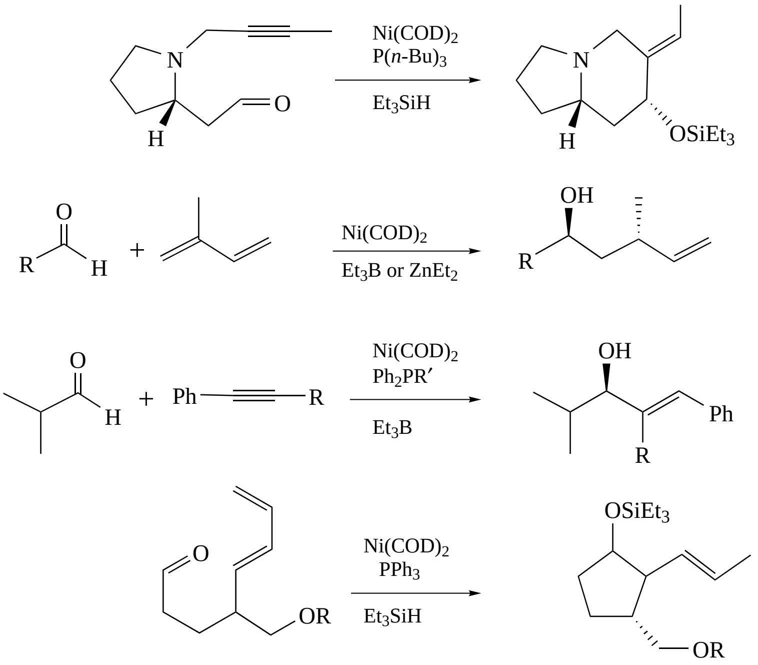
N
O
H
Ni(COD)$_2$
P(n-Bu)$_3$
Et$_3$SiH
N
H
OSiEt$_3$
O
R
H
+
Ni(COD)$_2$
Et$_3$B or ZnEt$_2$
OH
R
O
H
+
Ph
R
Ni(COD)$_2$
Ph$_2$PR′
Et$_3$B
OH
Ph
R
O
OR
Ni(COD)$_2$
PPh$_3$
Et$_3$SiH
OSiEt$_3$
OR

Scheme 27

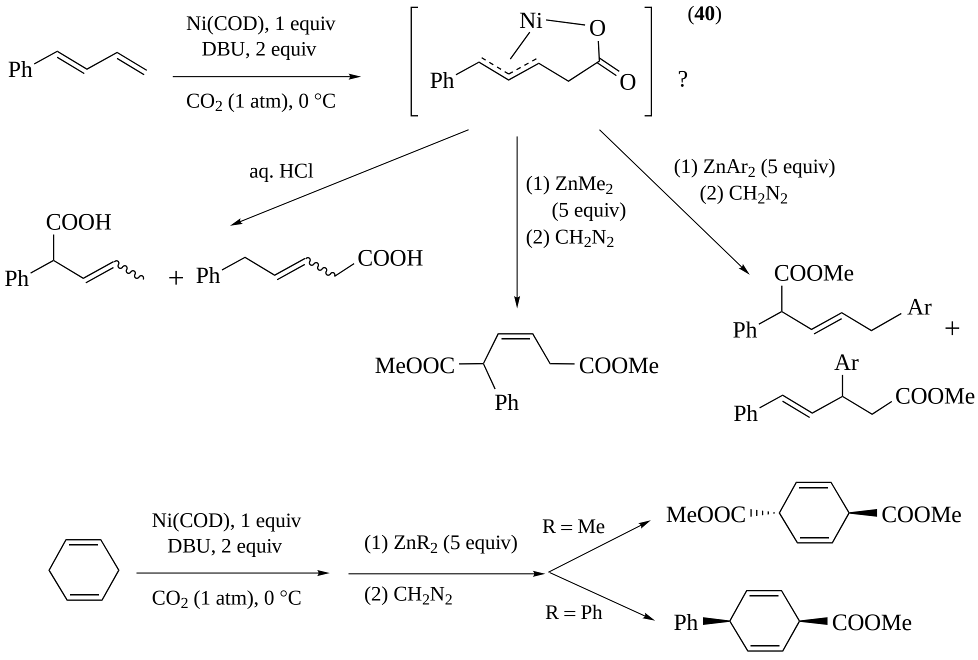
Ph
Ni(COD), 1 equiv
DBU, 2 equiv
CO$_2$ (1 atm), 0 °C
Ni
O
Ph
O
(40)
?
aq. HCl
COOH
Ph
+
Ph
COOH
(1) ZnMe$_2$
(5 equiv)
(2) CH$_2$N$_2$
MeOOC
COOMe
Ph
(1) ZnAr$_2$ (5 equiv)
(2) CH$_2$N$_2$
COOMe
Ph
Ar
+
Ar
Ph
COOMe
Ni(COD), 1 equiv
DBU, 2 equiv
CO$_2$ (1 atm), 0 °C
(1) ZnR$_2$ (5 equiv)
(2) CH$_2$N$_2$
R = Me
R = Ph
MeOOC
COOMe
Ph
COOMe

Scheme 28

8 REFERENCES

1. M. Jiménez-Tenorio, M. C. Puerta, I. Salcedo, P. Valerga, S. I. Costa, P. T. Gomes, and K. Mereiter, *Chem. Commun.*, 2003, 1168.
2. S. V. Maslennikov, D. S. Glueck, G. P. A. Yap, and A. L. Rheingold, *Organometallics*, 1996, **15**, 2483.
3. M. E. Smith and R. A. Andersen, *J. Am. Chem. Soc.*, 1996, **118**, 11119.
4. P. L. Holland, R. A. Andersen, R. G. Bergman, J. Huang, and R. G. Bergman, *J. Am. Chem. Soc.*, 1997, **119**, 12800.
5. P. L. Holland, M. E. Smith, R. A. Andersen, and R. G. Bergman, *J. Am. Chem. Soc.*, 1997, **119**, 12815.

6. R. A. Fischer, S. Nlate, H. Hoffmann, E. Herdtweck, and J. Blümel, *Organometallics*, 1996, **15**, 5746.
7. S. Nlate, E. Herdtweck, and R. A. Fischer, *Angew. Chem., Int. Ed. Engl.*, 1996, **35**, 1861.
8. O. Segnitz, M. Winter, K. Merz, and R. Fischer, *Eur. J. Inorg. Chem.*, 2000, 2077.
9. D. Zargarian, *Coord. Chem. Rev.*, 2002, **233–234**, 157.
10. T. A. Huber, F. B. Gariépy, and D. Zargarian, *Organometallics*, 1995, **14**, 4997.
11. M. Bayrakdarian, M. J. Davis, C. Reber, and D. Zargarian, *Can. J. Chem.*, 1996, **74**, 2115.
12. M. Jiménez-Tenorio, M. C. Puerta, I. Salcedo, and P. Valerga, *J. Chem. Soc., Dalton Trans.*, 2001, 653.
13. T. A. Huber, M. Bayrakdarian, S. Dion, I. Dubuc, F. B. Gariépy, and D. Zargarian, *Organometallics*, 1997, **16**, 5811.
14. I. Dubuc, M.-A. Dubois, F. B. Gariépy, and D. Zargarian, *Organometallics*, 1999, **18**, 30.
15. F.-G. Fontaine, M.-A. Dubois, and D. Zargarian, *Organometallics*, 2001, **20**, 5156.
16. M.-A. Dubois, R. Wang, D. Zargarian, J. Tian, R. Vollmerhaus, Z. Li, and S. Collins, *Organometallics*, 2001, **20**, 663.
17. R. Wang, F. Bélanger-Gariépy, and D. Zargarian, *Organometallics*, 1999, **18**, 5548.
18. R. Wang, L. F. Groux, and D. Zargarian, *J. Organomet. Chem.*, 2002, **660**, 98.
19. R. Wang, L. F. Groux, and D. Zargarian, *Organometallics*, 2002, **21**, 5531.
20. E. Rivera, R. Wang, X. X. Zhu, D. Zargarian, and R. Giasson, *J. Mol. Catal. A*, 2003, **204–205**, 325.
21. R. Vollmerhaus, F. Bélanger-Gariépy, and D. Zargarian, *Organometallics*, 1997, **16**, 4762.
22. H. Sun, W. Li, X. Han, Q. Shen, and Y. Zhang, *J. Organomet. Chem.*, 2003, **668**, 132.
23. M. Jiménez-Tenorio, M. C. Puerta, I. Salcedo, P. Valerga, S. I. Costa, L. C. Silva, and P. T. Gomes, *Organometallics*, 2004, **23**, 3139.
24. F.-G. Fontaine, T. Kadkhodazadeh, and D. Zargarian, *J. Chem. Soc., Chem. Commun.*, 1998, 1253.
25. F.-G. Fontaine and D. Zargarian, *Organometallics*, 2001, **20**, 401.
26. F.-G. Fontaine, R.-V. Nguyen, and D. Zargarian, *Can. J. Chem.*, 2003, **81**, 1299.
27. J. R. Ascenso, A. R. Dias, M. T. Duarte, P. T. Gomes, J. N. Marote, and A. F. G. Ribiero, *J. Organomet. Chem.*, 2001, **632**, 164.
28. L. F. Groux, F. Bélanger-Gariépy, D. Zargarian, and R. Vollmerhaus, *Organometallics*, 2000, **19**, 1507.
29. L. F. Groux and D. Zargarian, *Organometallics*, 2001, **20**, 3811.
30. (a) L. F. Groux, D. Zargarian, *Acta Crystallogr.* 2001, **E57**, m547; (b) L. F. Groux, D. Zargarian, *Organometallics* 2003, **22**, 4759.
31. L. F. Groux and D. Zargarian, *Organometallics*, 2003, **22**, 3124.
32. L. F. Groux, D. Zargarian, L. C. Simon, and J. B. P. Soares, *J. Mol. Catal. A*, 2003, **193**, 51.
33. N. Shirasawa, T. T. Nguyet, S. Hikichi, Y. Moro-oka, and M. Akita, *Organometallics*, 2001, **20**, 3582.
34. D. E. Berning, B. C. Noll, and D. L. Dubois, *J. Am. Chem. Soc.*, 1999, **121**, 11432.
35. D. E. Berning, A. Miedaner, C. J. Curtis, B. C. Noll, M. C. R. Dubois, and D. L. Dubois, *Organometallics*, 2001, **20**, 1832.
36. D. Walther, M. Stollenz, and H. Görls, *Organometallics*, 2001, **20**, 4221.
37. K. W. Kramarz and J. R. Norton, *Prog. Inorg. Chem.*, 1994, **42**, 1.
38. R. A. Henderson, *Angew. Chem., Int. Ed. Engl.*, 1996, **35**, 946.
39. B. Åkermark, J. Martin, J.-E. Nyström, S. Strömberg, M. Svensson, K. Zetterberg, and M. Zuber, *Organometallics*, 1998, **17**, 5367.
40. R. A. Henderson and K. E. Oglieve, *J. Chem. Soc., Chem. Commun.*, 1999, 2271.
41. W. Clegg, G. Cropper, R. A. Henderson, C. Strong, and B. Parkinson, *Organometallics*, 2001, **20**, 2579.
42. A. J. Edwards, S. A. Macgregor, A. D. Rae, E. Wenger, and A. C. Willis, *Organometallics*, 2001, **20**, 2864.
43. S. Shimada, M. L. N. Rao, and M. Tanaka, *Organometallics*, 1999, **18**, 291.
44. S. Shimada, M. L. N. Rao, T. Hayashi, and M. Tanaka, *Angew. Chem., Int. Ed. Engl.*, 2001, **40**, 213.
45. A. J. Arduengo III, S. F. Gamper, J. C. Calabrese, and F. Davidson, *J. Am. Chem. Soc.*, 1994, **116**, 4391.
46. W. A. Herrmann, G. Gerstberger, and M. Spiegler, *Organometallics*, 1997, **16**, 2209.
47. W. A. Herrmann, M. Elison, J. Fischer, C. Köcher, and G. R. J. Artus, *Angew. Chem., Int. Ed. Engl.*, 1995, **34**, 2371.
48. N. Fröhlich, U. Pidun, M. Stahl, and G. Frenking, *Organometallics*, 1997, **16**, 442.
49. D. Sellmann, C. Allmann, F. Heinman, F. Knoch, and J. Sutter, *J. Organomet. Chem.*, 1997, **541**, 291.
50. D. S. McGuinness, K. J. Cavell, B. W. Skelton, and A. H. White, *Organometallics*, 1999, **18**, 1596.
51. R. Dorta, E. D. Stevens, C. D. Hoff, and S. P. Nolan, *J. Am. Chem. Soc.*, 2003, **125**, 10490.
52. P. F. Arnold, F. G. N. Cloke, T. Geldbach, and P. B. Hitchcock, *Organometallics*, 1999, **18**, 3238.
53. Y. Sato, R. Sawako, and M. Mori, *Organometallics*, 2001, **20**, 5510.
54. M. Takimoto, Y. Hiraga, Y. Sato, and M. Mori, *Tetrahedron Lett.*, 1998, **39**, 4543.
55. V. P. W. Böhm, T. Weskamp, C. W. K. Gstöttmayr, and W. A. Herrmann, *Angew. Chem., Int. Ed. Engl.*, 2000, **39**, 1602.

56. V. P. W. Böhm, C. W. K. Gstöttmayr, T. Weskamp, and W. A. Herrmann, *Angew. Chem., Int. Ed. Engl.*, 2001, **40**, 3387.
57. M. A. Bennett, J. Castro, A. J. Edwards, M. R. Kopp, E. Wenger, and A. C. Willis, *Organometallics*, 2001, **20**, 980.
58. M. A. Bennett, C. J. Cobley, A. D. Rae, E. Wenger, and A. C. Willis, *Organometallics*, 2000, **19**, 1522.
59. H. Weiss, F. Hempel, W. Donaubauer, M. A. Grundl, J. W. Bats, A. S. K. Hashmi, and S. Schindler, *Organometallics*, 2001, **20**, 1713.
60. The reader is invited to consult the chemistry of the so-called SHOP (Shell Higher Olefin Process) catalysts that are used for the large-scale oligomerization of ethylene to long-chain terminal olefins (C_{6-20}): D. Vogt, in 'Applied Homogeneous Catalysis with Organometallic Complexes', eds. B. Cornils and W. A. Hermann, VCH, Weinheim, 1996, Vol. 1, p. 245.
61. L. K. Johnson, C. M. Killian, and M. Brookhart, *J. Am. Chem. Soc.*, 1995, **117**, 6414.
62. D. P. Gates, S. A. Svejda, E. Oñate, C. M. Killian, L. K. Johnson, P. S. White, and M. Brookhart, *Macromolecules*, 2000, **33**, 2320.
63. G. Van Koten and K. Vrieze, *Adv. Organomet. Chem.*, 1982, **21**, 151.
64. S. A. Svejda, L. K. Johnson, and M. Brookhart, *J. Am. Chem. Soc.*, 1999, **121**, 10634.
65. L. Deng, P. Margl, and T. Ziegler, *J. Am. Chem. Soc.*, 1997, **119**, 1094.
66. D. G. Musaev, R. D. J. Froese, and K. Morukoma, *Organometallics*, 1998, **17**, 1850.
67. T. K. Woo, P. E. Blöchl, and T. Ziegler, *J. Phys. Chem. A.*, 2000, **104**, 121.
68. T. K. Woo, P. M. Margl, E. Blöchl, and T. Ziegler, *J. Phys. Chem. B.*, 1997, **101**, 7877.
69. T. K. Woo and T. Ziegler, *J. Organomet. Chem.*, 1999, **591**, 204.
70. L. Deng, T. K. Woo, L. Cavallo, P. M. Margl, and T. Ziegler, *J. Am. Chem. Soc.*, 1997, **119**, 6177.
71. C. Pellechia and A. Zambelli, *Macromol. Rapid Commun.*, 1996, **17**, 333.
72. L. R. Rieth, R. F. Eaton, and G. W. Coates, *Angew. Chem., Int. Ed. Engl.*, 2001, **40**, 2153.
73. C. Wang, S. Friedrich, T. R. Younkin, R. T. Li, R. H. Grubbs, D. A. Bansleben, and M. W. Day, *Organometallics*, 1998, **17**, 3149.
74. T. R. Younkin, E. F. Connor, J. I. Henderson, S. Friedrich, R. H. Grubbs, and D. A. Bansleben, *Science*, 2000, **287**, 460.
75. M. S. W. Chan, L. Deng, and T. Ziegler, *Organometallics*, 2000, **19**, 2741.
76. A. Held, F. M. Bauers, and S. Mecking, *Chem. Commun.*, 2000, 301.
77. F. M. Bauers and S. Mecking, *Macromolecules*, 2001, **34**, 1166.
78. A. Tomov, J.-P. Broyer, and R. Spitz, *Macromol. Symp.*, 2000, **150**, 53.
79. F. M. Bauers and S. Mecking, *Angew. Chem., Int. Ed. Engl.*, 2001, **40**, 3020.
80. F. A. Hicks and M. Brookhart, *Organometallics*, 2001, **20**, 3217.
81. J. C. Jenkins and M. Brookhart, *Organometallics*, 2003, **22**, 250.
82. N. A. Cooley, S. M. Green, D. F. Wass, K. Heslop, A. G. Orpen, and P. Pringle, *Organometallics*, 2001, **20**, 4769.
83. E. Drent and P. H. M. Budzelaar, *Chem. Rev.*, 1996, **96**, 663.
84. S. Y. Desjardins, K. J. Cavell, J. L. Hoare, B. W. Skelton, A. N. Sobolev, A. H. White, and W. Keim, *J. Organomet. Chem.*, 1997, **544**, 163.
85. B. Domhöver, W. Kläui, A. Kremer-Aach, R. Bell, and D. Mootz, *Angew. Chem., Int. Ed. Engl.*, 1998, **37**, 3050.
86. C. S. Shultz, J. M. DeSimone, and M. Brookhart, *Organometallics*, 2001, **20**, 16.
87. F. Bernardi, A. Bottoni, M. Nicastro, I. Rossi, J. Novoa, and X. Prat, *Organometallics*, 2000, **19**, 2170.
88. R. Giovannini, T. Stüdemann, G. Dussin, and P. Knochel, *Angew. Chem., Int. Ed. Engl.*, 1998, **37**, 2387.
89. A. E. Jensen and P. Knochel, *J. Org. Chem.*, 2002, **67**, 79.
90. J. Terao, H. Watanabe, A. Ikumi, H. Kuniyasu, and N. Kambe, *J. Am. Chem. Soc.*, 2002, **124**, 4222.
91. J. Montgomery, *Acc. Chem. Res.*, 2000, **33**, 467.
92. J. Montgomery and M. Song, *Org. Lett.*, 2002, **4**, 4009.
93. M. Sato, M. Takimoto, and M. Mori, *J. Am. Chem. Soc.*, 2000, **122**, 1624.
94. M. Kimura, S. Matsuo, K. Shibata, and Y. Tamaru, *Angew. Chem., Int. Ed. Engl.*, 1999, **38**, 3386.
95. M. Takimoto and M. Mori, *J. Am. Chem. Soc.*, 2001, **123**, 2895.

Niobium & Tantalum: Inorganic & Coordination Chemistry

Liliane G. Hubert-Pfalzgraf
Université Claude Bernard Lyon 1, Villeurbanne, France

1 Introduction: Survey and General Trends 1
2 Oxidation State V 3
3 Oxidation State +IV 13
4 Oxidation State +III 16
5 Clusters with Nonintegral Oxidation States 19
6 Molecular Compounds in Oxidation States II and Lower 21
7 Related Articles 23
8 Further Reading 23
9 References 23

Abbreviations

β-dikH = β-diketone; silox = OSitBu$_3$; thdH = 2,2,6,6-tetramethylheptane-3,5-dione; THT = tetrahydrothiophene, Tp* = hydridotris(3,5-dimethylpyrazolyl)borate, Tp = hydridotris(pyrazolyl)borate, R$_2$-dad = N,N'-substituted 1,4-diaza-1,3-diene, R$_2$pz = alkyl-substituted pyrazolato, salophen = N,N'-o-phenylenebis(salicyldeneaminato) dianion.

1 INTRODUCTION: SURVEY AND GENERAL TRENDS

Niobium (formerly called columbium) and tantalum are *Transition Metals* having a considerable affinity for oxygen donor groups; they are thus called oxophilic (*see Oxophilic Character*). They occur as mixed-metal oxides such as columbites (Fe/Mn)(Nb/Ta)$_2$O$_6$ and pyrochlore NaCaNb$_2$O$_6$F. Their discovery in minerals extends back to the beginning of the nineteenth century, when they were believed to be identical and called tantalum. Rose showed that at least two different elements were involved in the minerals, and named the second one niobium. Their separation was resolved around 1866, especially by Marignac. These metals often display similar chemical behavior as a result of nearly identical atomic radii (1.47 Å) due to the lanthanide contraction (*see* ***Periodic Table: Trends in the Properties of the Elements***) and of similar ionization energies (*see Ionization Potential*); (Nb 6.67 eV, Ta 7.3 eV). Their separation is, nevertheless, possible and was long based on the greater tendency of tantalum to form insoluble anionic MF_7^{2-} complexes. Their modern separation uses liquid–liquid extraction into isobutyl methyl ketone from hydrofluoric acid.**[1]**

The chemistry of niobium and tantalum ranges from oxidation states +V to −III. No species of oxidation state −II is known so far (Table 1) and the chemistry is dominated by the higher oxidation states, especially V. By contrast with the 3d transition metals, the $[M(H_2O)_6]^{n+}$ ions are unknown and the aqueous chemistry of the higher valence states is dominated by the formation of homo- and heteroisopolyanions (*see* ***Polyoxometalates***). They have an extensive lower oxidation state aqueous chemistry based on hexanuclear clusters. Most recent developments have been in their nonaqueous chemistry in intermediate oxidation states since these species are able to promote C–E (E = O, S, N) cleavage and N$_2$ activation reactions. Niobium is more prone to reduction than tantalum. In their higher oxidation states, niobium and tantalum tend to resemble titanium and zirconium (*see* ***Titanium: Organometallic Chemistry*** and ***Zirconium & Hafnium: Inorganic & Coordination Chemistry***) rather than vanadium, but in their lower states they are closer to molybdenum and tungsten (*see* ***Molybdenum: Inorganic & Coordination Chemistry*** and ***Tungsten: Inorganic & Coordination Chemistry***). This is illustrated by their tendency to give multiple bonds with nonmetals such as oxygen, sulfur, nitrogen, or carbon (for the last *see* ***Niobium & Tantalum: Organometallic Chemistry***) and to form hexanuclear clusters. Niobium and tantalum are among the largest early transition metals; they can easily accommodate a large number of ligands and display large coordination numbers (*see* ***Coordination Chemistry: History***).**[1]** Hexacoordination and heptacoordination are the most common, but higher coordination numbers such as eight or even nine and ten have been observed; as a result, their derivatives often have a dynamic coordination sphere and are fluxional (*see Fluxional Molecule* and *Stereolability*).**[1,2]**

Niobium finds use in the production of stainless steels for high temperatures, and in superconducting magnets. The high corrosion resistance of tantalum results in its use for chemical plants. The binary and ternary oxides of these elements arouse increasing interest as electronic ceramics. Their full potential as reagents in organic synthesis lies in the development of their lower oxidation state chemistry as compared to other oxophilic early transition metals. Niobium pentoxide has been used in heterogeneous *Catalysis* either as catalyst or as support (*see* ***Oxygen: Inorganic Chemistry***).

Both metals are active in NMR (spin 9/2 for ^{93}Nb, 7/2 for ^{181}Ta) and have high sensitivities, but their major drawbacks are their large quadrupole moments that often result in broad signals (several kHz) in low symmetry environments, and thus application of NMR remains limited, especially for tantalum. ^{181}Ta is a nucleus with interesting characteristics

Table 1 Oxidation states and common stereochemistries of Nb and Ta compounds

Oxidation state	Coordination number	Idealized geometry	Examples
M^{V}	4	Tetrahedron	NbE_4^{3-} (E = O, S), $NbO[N(SiMe_3)_2]_3$, $Ta(NR)(NMe_2)_3$
	5	Trigonal bipyramid	$Ta(NEt_2)_5$, $MS(S\text{-}t\text{-}Bu)_4^-$, $(py)_2MeTa({=}NSi\text{-}t\text{-}Bu_3)_2$, $MCl_{5(vap)}$, $Ta(NMe_2)_3[O_2S(NtBu)_2]$ $MCl_2(NPR_3)_3$
	5	Square-based pyramid	$Nb(NMe_2)_5$, $NbS(SPh)_4^-$, $NbOCl_4^-$, $NbSCl_3(Ph_3PS)$
	6	Octahedron	M_2X_{10}, $[MOX_3]_\infty$, $NbAlCl_8$, $[LiNb(OEt)_6]_\infty$, $[Nb(OMe)_5]_2$
	6	Trigonal prism	$[M(S_2C_6H_4)_3]^-$, $M(CH_3)_6^-$ $[Nb(SC_6H_4Me\text{-}p)_6]^-$, $[Nb(SC_2H_4S)_3]^-$
	7	Capped octahedron	$NbOCl_3(PMe_3)_3$
	7	Pentagonal bipyramid	$[NbO(C_2O_4)_3]^{3-}$, $Ta(NMe_2)_3(\eta^2\text{-}tBupz)_2$ $ME(R_2NCS_2)_3$ (E = O, S), $NbOF_6^{3-}$, $M(O_2)F_5^{2-}$, $MS(\eta^2\text{-}SCNEt_2)(\eta^2\text{-}S_2CNEt_2)_2$ $Ta(NMe_2)_3[SO_2(NCMe_3)_2]$
	8	Capped trigonal prism	MF_7^{2-}
	8	Bicapped trigonal prism	TaF_8^{3-}, $Ta(PS_4)S_2$
	8	Dodecahedron	$[MCl_4(diars)_2]^+$, $[M(\eta^2\text{-}O_2)_4]^{3-}$, $[Ta(S_2CNEt_2)_4]^+$, $[M(\eta^2\text{-}O_2)_3(phen)]^-$, $[M(\eta^2\text{-}O_2)_2(C_2O_4)_2]^{3-}$
	9		$[NbCl_3(Cp)_2]_2O$
M^{IV}	4	Tetrahedron	$M(NR_2)_4$, $M(NR_2)_2Cl_2$
	5	Trigonal bipyramid	$[MH_2(OSi\text{-}t\text{-}Bu_3)_2]_2$
	6	Octahedron	NbX_4L_2, MCl_6^{2-} $Nb_2Cl_4(OMe)_4(MeOH)_2$
	7	Pentagonal bipyramid	NbF_7^{3-}, $Ta(PhNCHNPh)_3(NPh)$
	7	Capped octahedron	$NbBr_4(PPhMe_2)_3$
	8	Dodecahedron	$Nb[S_2P(OR)_2]_4$, $Nb(CN)_8^{4-}$ $Nb(dtc)_4$, $TaH_2Cl_2(dmpe)_2$
	8	Square antiprism	$Nb(thd)_4$, $TaCl_4(dmpe)_2$
	8		$Nb_2(\mu\text{-}Cl)_4Cl_4(PhPMe_2)_4$, $Nb_2(\mu,\eta^2\text{-}S_2)_2(dtcR_2)_4$ $Nb(SCN)_4(bipy)_2$
	9		$Nb(acac)_4(dioxane)$
M^{III}	3		$Ta(silox)_3$
	4	Tetrahedron (flattened)	$Nb(silox)_3(PMe_3)$
	6	Octahedron	$MCl_3(py)_3$, $Nb_2X_9^{3-}$, $[M_3X_{10}L_3]^-$, $M_2(\mu\text{-}Cl)_2Cl_4L_4$, $Nb_2Cl_5(O\text{-}i\text{-}Pr)(i\text{-}PrOH)_4$
	7	Pentagonal bipyramid	$Ta(PMe_3)_3(\eta^2\text{-}CH_2PMe_2)(\eta^2\text{-}CHPMe_2)$, $TaH(PPh_2)_2(dmpe)_2$
	8	Dodecahedron	$Nb(CN)_8^{5-}$ (solid)
	8	Square antiprism	$Nb(CN)_8^{5-}$ (solution) $[Ta(\eta^2\text{-}C_4H_5\ NS)_4]^-$
M^{II}	6	Octahedron	$MCl_2(PMe_3)_4$, $t\text{-}NbCl_2(py)_4$
M^{I}	5	Trigonal bipyramid	$TaL_2R(C_2H_4)_2$,
	7	Capped octahedron	$TaH(CO)_2(dmpe)_2$ $Ta(CO)_4(acac)(THF)$
	7	Capped trigonal prism	$TaX(CO_2)(dmpe)_2$, $MCl(CO)_3(PMe_3)_3$
	7	'Four-legged piano stool'	$Nb(CO)_4(\eta^5\text{-}Cp)$
M^{0}	6	Octahedron	$M(dmpe)_3$, $M(CO)_2(NO)(PPP)$ $Ta(CO)_4(dppe)$,
	6	Sandwich	$M(\eta^6\text{-}arene)_2$
M^{-I}	6	Octahedron	$M(CO)_6^-$, $M(CO)_2(NO)(PPP)$ $HM(PF_3)_6$
M^{-III}	5		$M(CO)_5^{3-}$
	6		$M(CO)_3(\eta^5\text{-}Cp)^{2-}$

for *Mössbauer Spectroscopy* and this technique has been applied for the study of sulfide intercalation compounds.[2]

2 OXIDATION STATE V

2.1 Halogens as Ligands: Pentahalides and their Anionic and Neutral Adducts

Niobium and tantalum pentahalides MX_5 are known for all halogens including iodine.[1] They are predominantly covalent (*see Covalent Bonds*), and all are sensitive to moist air, water, or hydrolytic solvents. Pentahalides, especially chlorides, provide the most convenient entry to the molecular chemistry of these elements. They are commercially available and can be prepared by reactions between metals, oxides, or halides and the appropriate halogenation reagent at high temperatures. NbI_5 is the less stable pentahalide (dissociation at 200 °C) and must be prepared and sublimed in the presence of excess iodine. In the solid state, the metals are hexacoordinate; this is achieved by association of MX_5 units as tetramers for MF_5, as discrete dimers for MCl_5 and MBr_5, and as layers of dimers for TaI_5 and β-$NbBr_5$. The dimers can be viewed as two octahedra sharing an edge (Figure 1). In the vapor phase, dissociation into monomers occurs for the dimers, while the pentafluorides exist as a mixture of monomers, dimers, and trimers.

MF_5 and MCl_5 are strongly electrophilic (*see Electrophile* and *Electrophilic Reaction*) and catalyze Friedel–Crafts reactions. The HF/TaF_5 system is a superacid catalyst and has been used in the selective acid-catalyzed isomerization and hydrogenolysis of cycloalkanes. Oligomerization and polymerization of alkynes with Nb^V and Ta^V halides as catalysts have been reported (*see* ***Oligomerization & Polymerization by Homogeneous Catalysis***).[1]

Pentahalides form adducts with nearly all types of neutral or anionic donors.[1–5] The high Lewis acidity of MF_5 is illustrated by facile fluoride transfer and formation of anionic adducts. Species such as MF^{n-}_{5+n} ($n = 1$–4) and $M_2F_{11}^-$ have been detected in HF solutions of the metals using a selective fluoride ion electrode or by ^{19}F NMR. These complexes can be extracted by organic solvents. Niobium and tantalum pentafluorides form double salts (*see Double Salt*) with most ionic fluorides (*see Ionic Bonds*) by mixing of the constituents in the molten state, or by addition of a fluoride to the oxides in aqueous HF. The fused salt baths used in the electrolytic production of the metals contain mainly the MF_7^{2-} and MF_8^{3-} anions, whose structure has been solved by X-ray diffraction (*see* ***Diffraction Methods in Inorganic Chemistry***). MF_7^{2-} display luminescence properties (*see* ***Luminescence***). Mixed-metal fluoroanions and mono- or dioxofluoro complexes are known.[1–5] Facile corrosion of borosilicate glass by $Cp_2{}^*TaF_3$ giving a ionic tetrafluoroborate complex has been observed.[6]

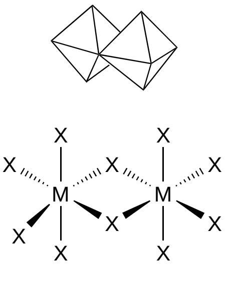

Figure 1 Association of octahedra: molecular structure of the dimeric pentahalides $M_2(\mu$-$X)_2X_8$ (X = Cl, Br, I)

The higher halides MCl_5 and MBr_5 show much less affinity for Cl^- and Br^- than does MF_5 for F^-. Halogen transfer reactions are nevertheless observed, mostly when these MX_5 halides are allowed to react with AX ($A^+ =$ alkali metals, NH_4, NR_4, PPh_4, $AsPh_4$), thus giving $A^+MX_6^-$. The octahedral symmetry of the MX_6^- anions is favorable for obtaining sharp ^{93}Nb or ^{181}Ta NMR lines and explains their use as NMR references for these nuclei. Mixed-halide anions have been recognized by ^{93}Nb NMR on mixtures of $NbCl_5$ and $NbBr_5$ in acetonitrile.

The pentahalides form coordination compounds MX_5L_n ($n = 1$ or 2, generally) with a large variety of Lewis bases L. The monoadducts MX_5L are octahedral, monomeric, and generally nonelectrolytes. Stability constants have been determined by proton NMR (*see* ***Stability Constants & their Determination***). Bis adducts MX_5L_2 have also been isolated for many oxygen, sulfur, nitrogen, and phosphorus donors. The MF_5L_2 adducts are mostly ionic in solution, while molecular seven-coordinate species appear to be equally likely in the solid. IR data have shown greater acceptor capacity for NbF_5 than for TaF_5 toward the phosphoryl ligands.[3] Analogous chloride and bromide complexes are essentially molecular.

The pentahalides form mono or bis adducts with O-donors such as aliphatic or crown ethers, phosphine or arsine oxides, ketones, dialkyl esters, and amides. These reactions have mostly been investigated with MCl_5. Abstraction of oxygen from the ligands giving oxotrihalide adducts, $MOCl_3L_2$, can be promoted by heating (for ethers), by an appropriate solvent, or by an excess of ligand as for ketones or phosphine oxides (equation 1). The formation of oxychlorides appears more favorable in the case of niobium.

$$\begin{gathered} M_2X_{10} + 6O{=}ER_n \longrightarrow 2MOX_3(O{=}ER_n)_2 \\ X = Cl, Br;\ E = P, As(n = 3), S(n = 2) \end{gathered} \qquad (1)$$

Pentahalides form essentially 1:1 adducts with sulfur, selenium, and tellurium donors, including phosphine sulfides and selenides. IR, Raman (*see Raman Spectroscopy*), and NMR studies of the complexes formed with mixed-donor O,S ligands showed bonding to occur via sulfur exclusively.[1] The ionic $[NbCl_4(\eta^2$-$S_2R_2)][NbCl_6]$ complexes are volatile and act as a single-source precursor to mixed-Nb_2O_5/NbS_2 films using *Metal–Organic Chemical Vapor Deposition* (MOCVD; *see* ***Tin: Inorganic Chemistry***) techniques.[7]

Niobium and tantalum halides also form adducts with numerous N-donors. Their reactions with pyridine and related ligands (bipyridine, phenanthroline, 7-azaindole[3]) depend critically on the reaction conditions. Indeed, aromatic amines have a tendency to reduce the metal to oxidation state IV especially for niobium but the reduction can be prevented, even at rt, by an appropriate choice of the solvent (equations 2a–c). Imide adducts $M(NR)Cl_3L_2$ are obtained with primary or secondary amines.[8]

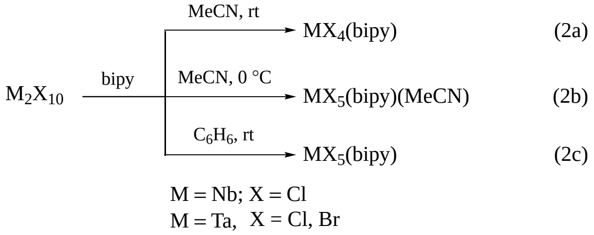

Complexes with P- or As-donors are obtained in nonpolar media. The tendency toward increasing coordination numbers follows the decrease in the ligand's *Cone Angle* (*see* ***P-donor Ligands***). $NbCl_5$ forms adducts with β-P_4S_4 and P_4Se_3, coordination occurs via the phosphorus atom.[3] Complexes such as $TaBr_5$(diars) have been reformulated as ionic $[TaBr_4(diars)_2][TaBr_6]$ species.

2.2 Oxygen Donors

Anionic oxygen donors include ligands derived from dioxygen, that is, oxo (O^{2-}) and peroxo ($O_2{}^{2-}$) groups (*see* ***Dioxygen & Related Ligands***), alkoxides, and potential chelating ligands such as β-diketonates, carboxylates, or oxyanions of inorganic acids.

2.2.1 Compounds Containing the Oxo Ligand: Oxyhalides and Derivatives

Oxyhalides such as MOX_3 (X = F, Cl, Br, I) or MO_2X may be prepared by halogenation of the oxides or controlled reaction of the pentahalides with dioxygen. $NbOCl_3$, the most studied, is a *Polymer* in the solid state as characterized by a strong, broad IR band at $770\,cm^{-1}$ attributed to Nb–O–Nb stretching. A band at $997\,cm^{-1}$ in the Raman spectrum of gaseous $NbOCl_3$ is attributed to a terminal Nb=O, consistent with a monomeric *Square Pyramidal* geometry.[1] As a result of the oxophilic character of Nb and Ta, incorporation of oxygen into the coordination sphere is frequent. Its origin can result from adventitious water or oxygen or from oxo abstraction reactions involving the solvent or a ligand. Most of the compounds that can be formally considered as resulting from substitution of MOX_3 thus derive from more complex reactions involving precursors without metal oxo bonds.

A variety of anionic oxohalo complexes has been reported. Oxofluoro complexes are formed more readily for Nb than for Ta, this difference is the basis of the classical method of separation of the two metals. K_2TaF_7 precipitates before $K_2NbOF_5{\cdot}H_2O$ during the concentration of the oxides in aqueous HF. Oxo anions of the higher halides include mainly $[MOX_5]^{2-}$ (X = Cl, Br), $[MOCl_4]^-$, $[MO_2Cl_2]^-$. The oxo ligand can adopt a variety of coordination modes. Dinuclear anions such as $[Ta_2Cl_{10}O]^{2-}$ and $[M_2Cl_9O]^-$ with nearly linear M–O–M bridges have been obtained, mostly by adventitious hydrolysis.[1–5] The latter is characterized by an asymmetrical M···O–M bond (1.76 and 2.08 Å) and can be seen as a complex between $NbOCl_4{}^-$ and $NbCl_5$.[7] A tetranuclear niobium–alkyne anion was shown to encapsulate a μ_4-O oxo ligand with an uncommon planar *Stereochemistry*.[2]

Numerous 1:1, 1:2, and 1:3 neutral adducts are known for $NbOCl_3$. While complexes with N-donors such as amines, nitriles, or with phosphines derive mostly from direct reaction between oxyhalides and the ligands, many MOX_3L_2 complexes have been obtained by oxygen abstraction from O-donors by pentahalides. This reactivity can be exploited for an easy entry into oxychloride chemistry via the *Labile* $NbOCl_3(MeCN)_2$ complex (**1**) (equation 3).[1,2]

$$Nb_2Cl_{10} + 2(Me_3Si)_2O \xrightarrow{\text{MeCN, rt}} \underset{\textbf{(1)}}{2NbOCl_3(MeCN)_2} + 4Me_3SiCl \qquad (3)$$

Tetranuclear monoadducts with asymmetrical M···O–M bridges related to those of $[M_2OCl_9]^-$ have been characterized; but most structural data concern monomeric $NbOCl_3$ bis adducts. In such derivatives, the metal is octahedrally surrounded with the neutral ligands cis to each other, one being trans to the oxo bond, which is short (typical Nb=O *Bond Length* ~1.70 Å). The coordination polyhedron is distorted as a result of the niobium–oxygen multiple bond (*see Valence Shell Electron Pair Repulsion Model*).[1]

The stabilizing effects of the bulky and strong electron donor pentamethylcyclopentadienyl ligand Cp* permitted investigation of the stepwise hydrolysis, in the solid state as well as in solution, of Cp^*MCl_4. The oxide ligand can be progressively introduced via hydrates or hydroxo derivatives, giving structurally characterized dinuclear or trinuclear aggregates.[9] These bulky ligands were also able to stabilize the simultaneous presence of oxo and hydride ligands on tantalum. Nonhalide oxo derivatives can be stabilized as monomers with bulky O- or N-donor ligands such as tri-*t*-butylsiloxide (silox), bistrimethylsilylamide, tropolone,[1,2] or as tetramers with trispyrazolylborate ligands.[10]

In aqueous solutions, numerous orthometallates ($MO_4{}^{3-}$), metametallates (MO^{3-}), and polyoxometallates, especially $[Nb_6O_{19}]^{8-}$, are known (*see* ***Polyoxometalates***). Peroxo derivatives are other species obtained from aqueous solutions. Orthoperoxometallates precipitate from alkaline solutions of

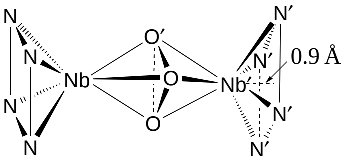

Figure 2 Coordination polyhedron of the $M_2(\mu\text{-}O)_3(\text{porp})_2$ dimers

niobates or tantalates on addition of H_2O_2.[1] In the $Nb(\eta^2\text{-}O_2)_4{}^{3-}$ ion, all peroxide groups are linked side-on to the metal (*see Side-on Coordination*). Perhydrolysis of alkoxides in the presence of organic bases provides a clean route to peroxo anions. The peroxometallates release O_2 progressively in mild conditions, and explosively at 80 °C. They are converted into orthoperoxo acids by H_2SO_4. The yellow color that is developed for niobium has been used in colorimetric titration. Displacement of the peroxo ligands with chelating O- or N-donors (*see Chelating Ligands*) gives di- and triperoxo complexes. For the bisperoxo compounds, the coordination polyhedron corresponds to a distorted dodecahedron (*see Dodecahedral*), the two peroxo groups displaying an unusual cis geometry. Peroxo complexes with N-oxide derivatives of polycarboxylic acids, $[Nb(\eta^2\text{-}O_2)_2(LO_2)]^{3-}$ (L = edta) or pdta (propylenediaminetetracetate) have been reported.[11] Anionic and neutral peroxohalo derivatives, mainly peroxofluoro ones, are known; their structure has been investigated by X-ray diffraction as well as by ^{19}F NMR. A cyclopentadienyl monoperoxide catalyzes the conversion of cyclohexene into its epoxide in the presence of H_2O_2.[1]

Most *Porphyrin* complexes are niobium oxo derivatives such as NbOZ(porp) (Z = F, OAc, acac). Tantalum porphyrin derivatives are scarcer. The hydrolysis of $M(\text{porp})Cl_3$ afforded oxo dimers, $M_2(\text{porp})(\mu\text{-}O)_3$ (**2**) of an unusual structure since two M(porp) units are linked together through three oxo bridges (Figure 2). Structure determinations by X ray have shown that the metal lies always above the plane of the porphyrin ring and that the axial ligands have a cis geometry with respect to the ring. The redox chemistry of the Nb oxo dimer (**2**) was investigated by chemical and electrochemical means (*see* ***Electrochemistry: Applications in Inorganic Chemistry***). The photochemically reduced Nb porphyrin derived from (**2**) is able to reduce O_2 and to achieve the catalytic and exclusive epoxidation of alkenes, without additional reactant;[9,12] it is the first example of such an activation (*see* ***Oxygen: Inorganic Chemistry***). Attempts to get $Ta(OEP)Cl_3$ from $TaCl_5$ lead to $[Ta(OEP)_2][TaCl_6]$, a sandwich compound (OEP = octaetylporphyrin). Half-sandwich alkyl Ta compounds including a cationic species were also prepared.[13]

2.2.2 Alkoxides

Homoleptic alkoxides (*see Homoleptic Compound*) $M(OR)_5$ (**3**; R = Me, Et, Pr, etc.) derive from MCl_5 by reaction with alcohols (the reaction is driven to completion by a base that acts as proton acceptor) or with alkali alkoxides (equation 4) or from anodic dissolution of the metal in alcohol.[1] Transesterification reactions extend the range of available alkoxides, giving, for instance, trialkylsiloxides $M(OSiR_3)_5$ and heteroleptic alkoxides $M(OR)_{5-x}(OR')_x$ (*see Heteroleptic Compound*).

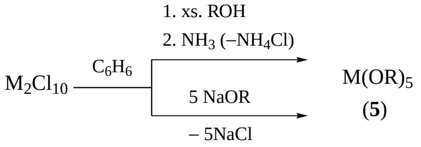

$$M_2Cl_{10} \xrightarrow{C_6H_6} \left\{ \begin{array}{l} \xrightarrow[\text{}]{\text{1. xs. ROH} \atop \text{2. NH}_3\ (-\text{NH}_4\text{Cl})} \\ \xrightarrow[-\ 5\text{NaCl}]{5\ \text{NaOR}} \end{array} \right. \underset{(\mathbf{5})}{M(OR)_5} \qquad (4)$$

Alkoxides are usually highly soluble, volatile, monomeric (R = 2,6-dialkylaryl) or dimeric (R = Me, Et, Ph), depending on the size of the R group. The terminal M–OR bond lengths (about 1.90 Å) are shorter than the sum of the covalent radii (2.27 Å). This suggests electron donation from oxygen p_π orbitals to the metal empty d_π orbitals $[O(p_\pi) \rightarrow M(d_\pi)]$ and thus π-bonding (*see π-Bond*). π-Bonding is confirmed by rather large M–O–C angles. Despite a high thermodynamic stability, the M–OR bond is labile; for the dimers, bridges may open and close reversibly, leading to fluxional behavior in solution. The electroattractive OR groups make metal alkoxides very prone to nucleophilic attack (*see Fluxional Molecule*) and they react with a variety of organic hydroxy derivatives such as β-diketones (*see Diketones*), thio-β-diketones, β-hydroxyesters, diols and polyols, silanols, alkoxyamines, Schiff bases (*see Schiff Base*), and simple and functional, including polymerizable, carboxylic acids.[14,15]

Metal alkoxides are extremely sensitive to hydrolysis, and one of their applications is their use as precursors for advanced materials via hydrolysis–polycondensation reactions and the formation of polynuclear oxoalkoxides as intermediates in the ***sol–gel*** process (*see* ***Sol–Gel Synthesis of Solids***). Most of their modification by hydroxy derivatives has been related to the need to reduce their reactivity for those applications.[16] Their volatility, comparable to the β-diketonates, makes them suitable for the elaboration of coatings by MOCVD.[16,17] By contrast with the pentahalides, alkoxides (**3**) do not easily form complexes with Lewis bases, although complexes can be detected in solution in the presence of the parent alcohol or hard donors (amines, phosphine oxides) (*see* ***Hard & Soft Acids and Bases***). However, they react easily with other metallic derivatives (alkoxides, carboxylates, β-diketonates, etc.) giving heterometallic (mixed-metal) oxo or non-oxoalkoxides[14–17] Such derivatives are attractive precursors for ternary or quaternary oxides by sol–gel reactions as they allow homogeneity to be achieved at a molecular level and their structure may preform the macromolecular framework of the ceramic. $[LiNb(OEt)_6]_\infty$ (**4**) and (**5**) are examples of compounds having structures related to the materials lithium niobate and $M'Nb_2O_6$ (M′ = Mg, Cd, Pb), respectively. Scheme 1 collects some of their reactivity patterns.

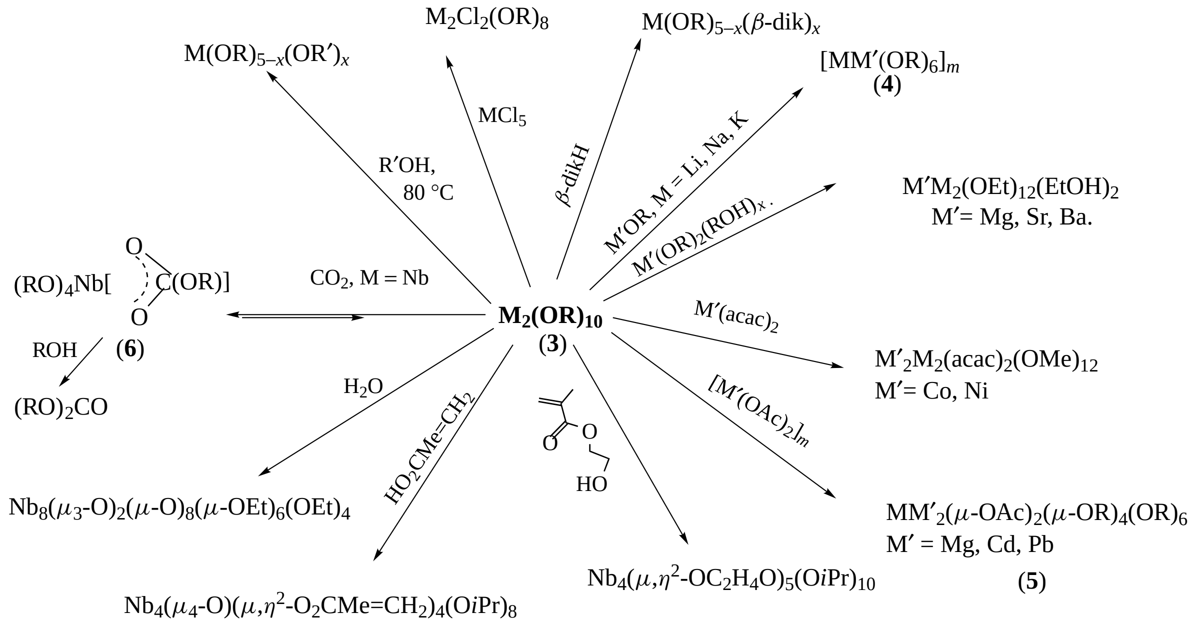

Scheme 1 Some examples of the reactivity of $M(OR)_5$ (all reactions at rt unless otherwise stated)

$[Nb(OR)_5]_2$ (R = Me, Et, allyl) react reversibly with carbon dioxide to form an O,O-hemicarbonate (**6**) then the organic carbonate.[18] $Ta(OEt)_5$ was reported as a catalyst for lactide polymerization whereas $(EtO)_2TaL$ (L = tris(2-oxy-3,5-dimethylbenzyl)amine) failed to act as a single site initiator.[19] The homoleptic Nb and Ta alkoxides have also been used for access to mesoporous (*see **Porous Inorganic Materials***) oxides using surfactants,[20] or to nanostructured oxides using organogelators as structure-directing agents.[21] Mesoporous Nb_2O_5 could be converted into a metallic niobium oxide molecular sieve which, reacting at rt with N_2 to form a nitride, provides the first example of such a process mediated by a molecular sieve.

Halide alkoxides $M(OR)_{5-x}X_x$ ($x = 1-4$, X = Cl or Br mainly) result essentially from reaction of MX_5 with ROH or with trimethylsilyl reactants. They display reactivity patterns comparable to (**3**) but they are more prone to form complexes. $M(OR)_4Cl$ species are the least common. The most relevant results in organometallic chemistry of Nb and Ta have been associated with ancillary, bulky alkoxide ligands (*see **Niobium & Tantalum: Organometallic Chemistry***).[22] Of particular interest are the halide alkoxides based on groups such as 2,6-alkylaryloxides[14] or tri-t-butylsiloxide.[14,23] They are able to sterically saturate metal centers in monomers while leaving them electron deficient (*see Electron Deficient Compound*), and unusual structural and reactivity patterns have been observed in different oxidation states. Substitution reactions of the halides afforded alkylaryloxides, which catalyze the hydrogenation of arylphosphines. Stable aryloxide hydrides such as $TaH_2(2,6\text{-}t\text{Bu}_2C_6H_3O)_2Cl(PMe_2Ph)_2$ for instance have been isolated.[14,24] They react with olefins and alkynes, the product depending on the ancillary ligand. A Ta^V hydride showing hydrodeoxygenation (HDO) of the tridentate aryloxide has been reported.[25] The isolation of Ta^V species containing resolved 3,3′-disubstituted-1,1′-bi-2,2′-naphtoxides has been achieved with chloride or dimethylamide as ancillary ligands.[26] Nb aryloxides associated with AlR_3 or *Grignard Reagents* are catalyst precursors for the polymerization of monoalkyl-substituted alkynes. The bulkiness around the metal (controlled by the number of OAr- ligands) prevents side reactions and enhances the molecular weight (MW) of the polymer.[14] The reduction of $(silox)_3TaCl_2$ under H_2 offered a mononuclear dihydride (**7**) in high yield (equation 5).[24] The presence of terminal hydride ligands for (**7**) is supported by a vibration at 1725 cm^{-1} in the IR and a signal at low field in the NMR (*see **Hydride Complexes of the Transition Metals***).

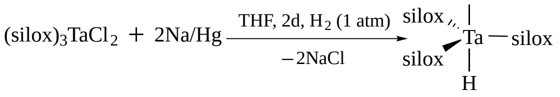

$$(silox)_3TaCl_2 + 2Na/Hg \xrightarrow[-2NaCl]{\text{THF, 2d, } H_2 \text{ (1 atm)}} (silox)_3TaH_2 \qquad (5)$$

(**7**)

Calix[4]arenes have been used as a preorganized set of O-donor atoms. Monomeric or dimeric species were obtained depending on the calixarene substituents.[27] They were used to develop the organometallic chemistry of Nb and Ta in various oxidation states, the electron reservoir of the Nb=Nb bond is able to activate small molecules including N_2 (*see **Niobium & Tantalum: Organometallic Chemistry***).

2.2.3 Diketonates, Carboxylates, and Related Derivatives

Homoleptic pentavalent β-diketonates are unknown, the volatility of heteroleptic derivatives such as $M(thd)_4X$ ($X = Cl$, OR) allows their use as a source of the metal oxides in MOCVD.[16,17] Ionic species such as $[Ta(thd)_4][TaCl_6]$ have also been obtained.

The reaction between pentahalides or alkoxides and carboxylic acids gives oxochloro- or oxoalkoxocarboxylates. *Chiral* tantalum cyclopentadienyl carboxylates mediate acylation reactions of amides, giving dipeptides in good yield with high stereochemical purity.[28]

Derivatives of heterocyclic carboxylic or α-hydroxyacids have been obtained in aqueous media. For instance, niobic and tantalic acids dissolve in aqueous solutions of oxalic acid giving mono-, bis-, or trisoxalato compounds, depending on pH and concentrations.[1,2] The species isolated for Nb are oxooxalato derivatives with the oxo ligand in the axial position of a pentagonal bipyramid (*see Pentagonal Bipyramid*).[1] The solubility of Ta_2O_5 in oxalic acid solutions is much lower than that of Nb_2O_5 due to polymeric species. The intense coloration of the complexes formed with ligands such as 4-(2-pyridylazo) resorcinol or ascorbic acid are interesting for the spectrophotometric determination of Nb or Ta[1,2] (*see* ***Analytical Chemistry of the Transition Elements***). Compounds with inorganic oxyanions (*see Oxoanion*) (nitrates, sulfates, phosphates, etc.) have been reported. The interest in the sulfates arises from processes using sulfuric acid in the treatment of minerals.[1] Various sulfato species (mainly oxo ones) were isolated from the $M_2O_5{-}SO_3{-}H_2O$ system.[1] The coordination polyhedron of $K_7M(SO_4)_6$, obtained from solutions of M_2O_5 in molten $K_2S_2O_7$, consist of six monodentate sulfato ligands.[2] Crystalline phosphate hydrates display a layer structure able of hosting various molecules.[1] An NbX_6^- anion based on the 'teflate' $OTeF_5$ ligand has been reported; the steric hindrance provides kinetic stabilization in the presence of electrophilic cations that might expand its use as a counterion (*see Counter Ions*).

2.3 Complexes with Sulfur, Selenium, and Tellurium Donors

Numerous neutral complexes of the pentahalides with S-donors have been described. Anionic S-donor ligands are mainly represented by sulfides (S^{2-}), disulfides ($S_2{}^{2-}$), thiolates (RS^-), dialkyldithiocarbamates ($R_2dtc = S_2CNR_2{}^-$; *see Dithiocarbamate*), and dialkyl thiophosphates ($S_2P(OR)_2{}^-$) (*see* ***S-donor Ligands***).

2.3.1 Thio-, Seleno- and Tellurohalides Derivatives

Thio- and selenohalides MEX_3 ($E = S$, Se) are accessible by the reaction of antimony chalcogenides with pentahalides at rt in CS_2. $NbSCl_3$ can also be conveniently obtained by reacting the pentachloride with hexamethyldisilathiane in CH_2Cl_2;[1,2] the reaction is comparable to that depicted in equation (3). A few neutral mono or bis adducts of the thiohalides have been described. X ray has established the presence of a terminal Nb=S bond (2.09 Å). Vibrations of the M=S moiety in the IR have been reported around 550 cm^{-1} for Nb, while a wider range (435–505 cm^{-1}) has been observed for the tantalum derivatives. Multidendate amino ligands $[(NH)_3N = (Me_3SiNHC_3H_6)_3N]$ allowed to stabilize $TaE(N_3N)$ derivatives ($E = S$, Se, Te) prepared by reacting the Ta chloroamide and $(THF)_2LiESi(SiMe_3)_2$.[3] The one-dimensional solid $[Ta(Te_2)_2]_4[PtI_6]I_2$ synthesized from the elements at high temperature consists of $[Ta(\mu, \eta^2\text{-}Te_2)_2]$ chains separated by PtI_6 groups and iodine atoms.[3,4]

2.3.2 Thiolate, Dithiocarbamate Derivatives, and Chalcogenometallates

Anionic six-coordinate homoleptic thiolates were isolated with monodentate arenethiolate or with bidentate ethylene-1,2-dithiolate ligands and with various cations.[29] The coordination sphere often tends toward a trigonal prismatic geometry (*see Trigonal Prism*), as observed for $[Nb(SC_2H_4S)_3]^-$ or for $[Nb(SC_6H_4Me\text{-}p)_6]^-$. Neutral homoleptic thiolates $M(SR)_5$ are limited ($R = C_6F_5$ or $SC_6H_3Me_2$-2,6). The Nb arylthiolate was converted into NbS_2 by thio sol-gel whereas it acted as a precursor to NbS films by chemical vapor deposition (CVD).[30] Oxo- and halothiolates have also been reported. X-ray data have shown that the extent of the S to M π-bonding in these electron-deficient thiolates is reduced compared to the O to M π-bonding in aryloxides. Reactions with thiolates (equation 6) or dialkyldithiocarbamates are often versatile and compounds having M=S or $M(S_2)$ bonds might be obtained by activation and cleavage of the C–S bond.[1,29] These reactions are dependent on the experimental conditions;[1] they might be assisted by water and be relevant to hydrodesulfurization (*see* ***Hydrodesulfurization & Hydrodenitrogenation***). Niobium sulfido and bis-sulfido dithiocarbamates were obtained by reacting $NbO(dtcEt_2)_3$ with boron sulfide.[4,29]

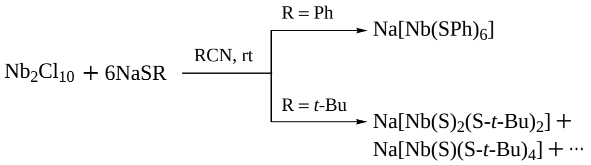

$$Nb_2Cl_{10} + 6NaSR \xrightarrow{RCN,\ rt} \begin{cases} \xrightarrow{R = Ph} Na[Nb(SPh)_6] \\ \xrightarrow{R = t\text{-}Bu} Na[Nb(S)_2(S\text{-}t\text{-}Bu)_2] + Na[Nb(S)(S\text{-}t\text{-}Bu)_4] + \cdots \end{cases}$$

(6)

Homoleptic Ta dithiocarbamates result from *Insertion* of CS_2 into the tantalum–nitrogen bond of $Ta(NR_2)_5$; in the case of niobium, similar reactions proceed with reduction to Nb^{IV}.[1] Halodithiocarbamates can be either molecular or ionic and the existence of *Coordination Isomers* $NbCl_3(Et_2dtc)_2$ and $[Nb(Et_2dtc)_4][NbCl_6]$ has been established.[2,31] ^{93}Nb NMR spectroscopy has been used to identify the various dithiocarbamates in solution. The dithiocarbamate ligand is bidentate and its small bite (*see Bite Angle*) favors high coordination numbers of seven or eight.

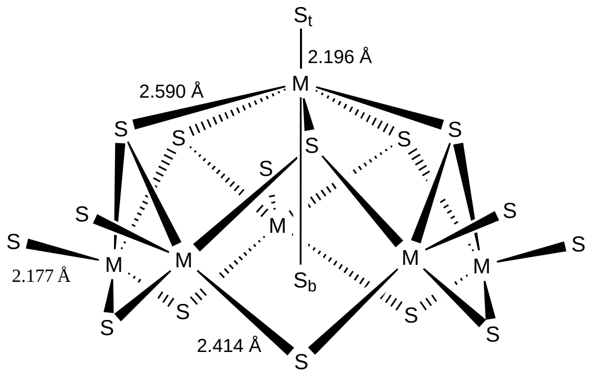

Figure 3 Structure of the $M_6S_{17}{}^{4-}$ thiometallates. The bond length order is M–S terminal $<$ M-μS $<$M-μ_3-S $<$ M–S_b (S_b being inside the cage)

The lability of the pentalkoxides has been exploited for the synthesis of *Thiometallates* at rt. This is an interesting alternative to the high-temperature reaction between the elements, often difficult to control. Hexamethyldisilathiane is used as a source of sulfur, and soluble $[MS_4]^{3-}$ (**8**) and $[M_6S_{17}]^{4-}$ (Figure 3) salts were obtained depending on the counterion (equation 7). Li^+ allows the stabilization of small, highly charged, nucleophilic $[MS_4]^{3-}$ species, the simplest chalcogenoniobates and -tantalates structurally characterized.[1,29]

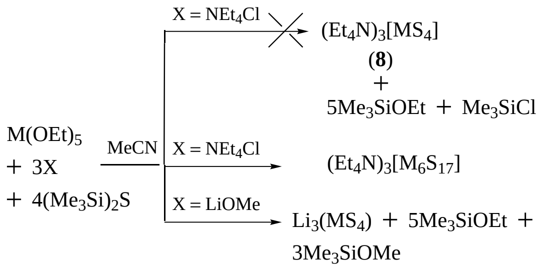

(7)

Thiometallates (**8**) and $Ta_6S_{17}{}^{4-}$ serve as synthons, for instance, for the preparation of mixed-metal clusters involving iron[2] or copper and silver, respectively.[1,32] The discrete polynuclear $Ta_2S_{11}{}^{4-}$ and $Nb_4Se_{22}{}^{6-}$ anions, prepared by traditional solid-state routes, have a structure related to that of polynuclear Mo oxysulfide anions. Nb–Cu chalcogenido clusters stabilized by phosphines could be prepared directly from $NbCl_5$ (equation 8). The anion (**9**), for instance, is based on two Cu_3NbS_3Cl heterocubane units linked by three μ_3-chlorine.[33]

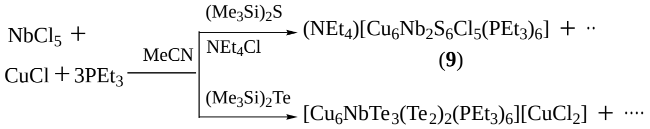
NbCl5 +
CuCl + 3PEt3
MeCN
(Me3Si)2S
NEt4Cl
(NEt4)[Cu6Nb2S6Cl5(PEt3)6] + ··
(9)
(Me3Si)2Te
[Cu6NbTe3(Te2)2(PEt3)6][CuCl2] + ····

(8)

Soluble mixed-chalcogenido Nb/Se/E complexes (E = S, O) have been reported.[34] The differences in structures and *coordination geometries* between sulfides and selenides as ligands for Nb have been attributed to their redox properties as well as to size. The presence of terminal Se–H ligands in the metal coordination sphere might be due to the need to avoid accumulation of excessive negative charge around the $Nb(Se)_3L^{2-}$ units (L = SH, SeH, OMe).

A variety of sulfide and selenide clusters have been obtained from $CpMCl_4$ and silylated or Li chalcogenides.[32] The $Cp^*TaS_3{}^{2-}$ unit offers an example of a moiety with three terminal sulfides that might serve as a building block for more complex structures.[9] The presence of the bridging pentasulfide μ, η^2-$S_5{}^{2-}$ ligand, derived from octasulfur, has been established by X-ray diffraction in dinuclear anionic or neutral niobium derivatives such as $[Nb_2(OMe)_2(\eta^2\text{-}S_2)_2(\mu, \eta^2\text{-}S_2)(\mu\text{-}O)(\mu\text{-}\eta^2\text{-}S)_5]^-$.[2,9,35]

2.4 Nitrogen Donors

Anionic N-donor ligands comprise essentially amido ($NR_2{}^-$), imides or nitrenes (NR^{2-}); amidinates or guanidinates [$(RN)_2CX{}^-$, X = R′ or NR′ respectively]; azides ($N_3{}^-$); or nitrides (N^{3-}).

2.4.1 Amido and Imido Derivatives

Homoleptic Nb^V and Ta^V dialkylamides, $M(NR_2)_5$, have been obtained from the pentahalides and lithium amides. By contrast with alkoxides, they are generally monomers (even for NMe_2) as a result of the steric demand of the dialkylamido ligand. They are volatile but less stable thermally than the pentaalkoxides. The steric congestion around the metal is reduced during thermolysis by loss of ligands. This is achieved for niobium by reduction to $Nb(NR_2)_4$ (favored by the length of the alkyl chain); in the case of tantalum, oxidation state V is retained and the pentaamides are converted into a mixed imido amide $Ta(NR)(NR_2)_3$ (**10**) (equation 9). Formation of the imide ligand occurs through β-H abstraction and intramolecular metallation although *Cyclometallation* reactions are uncommon with metals having a d^0 electronic configuration (*see Electron Configuration*). The azametallacycle (**11**) was isolated and used as a MOCVD metal source for obtaining films of cubic TaN as well as of amorphous Ta_2O_5 at low temperature.[35]

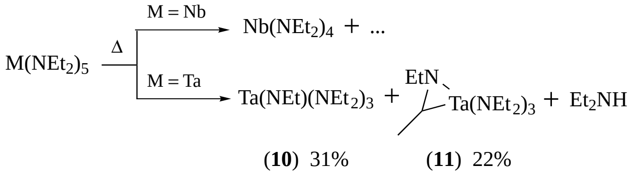

(9)

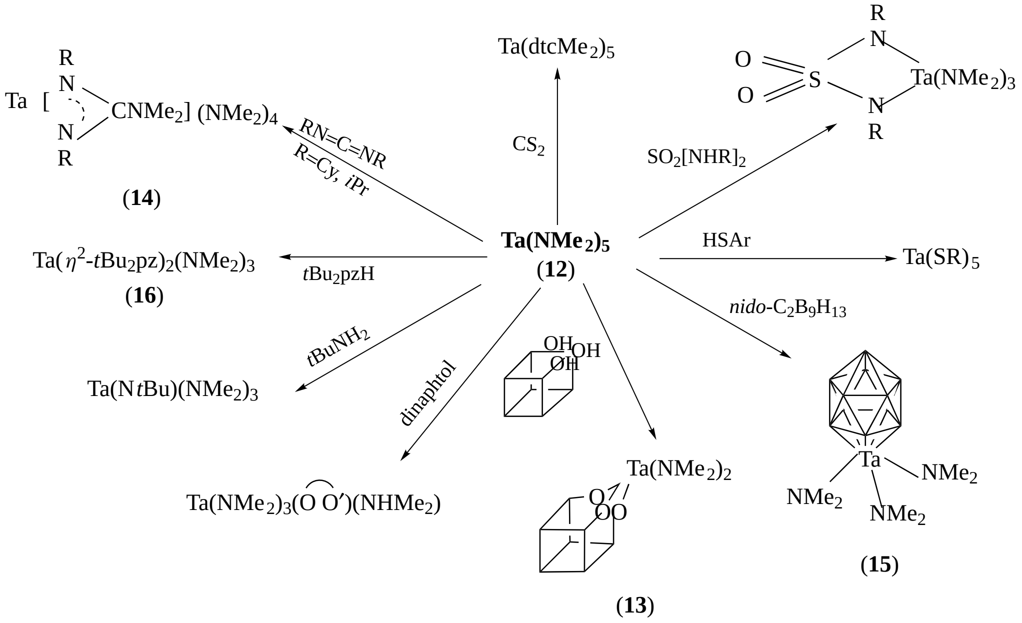
Ta(NMe2)5
(12)
Ta(dtcMe2)5
CS2
SO2[NHR]2
Ta(NMe2)3
HSAr
Ta(SR)5
nido-C2B9H13
NMe2
(15)
Ta(NMe2)2
(13)
dinaphtol
Ta(NMe2)3(O O′)(NHMe2)
tBuNH2
Ta(NtBu)(NMe2)3
tBu2pzH
Ta(η2-tBu2pz)2(NMe2)3
(16)
RN=C=NR
R=Cy, iPr
CNMe2] (NMe2)4
(14)

Scheme 2 Some reactions of $Ta(NMe_2)_5$ (all reactions at rt unless otherwise stated)

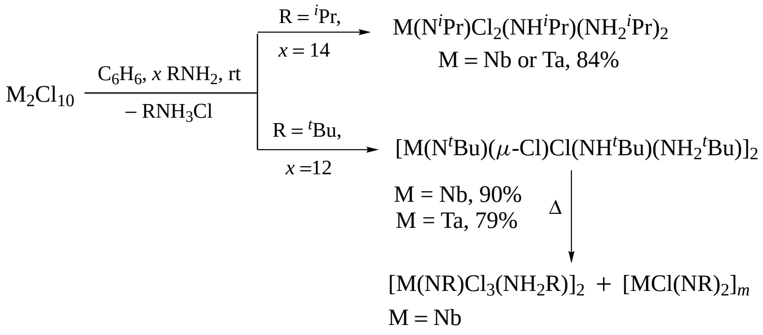
M2Cl10
C6H6, x RNH2, rt
– RNH3Cl
R = iPr,
x = 14
M(NiPr)Cl2(NHiPr)(NH2iPr)2
M = Nb or Ta, 84%
R = tBu,
x =12
[M(NtBu)(μ-Cl)Cl(NHtBu)(NH2tBu)]2
M = Nb, 90%
M = Ta, 79%
Δ
[M(NR)Cl3(NH2R)]2 + [MCl(NR)2]m
M = Nb

Scheme 3 Synthesis and reactivity of chloroimide complexes

Halodialkylamido derivatives are accessible by several methods, especially reactions between pentahalides and amines or trimethylsilyl reactants. They are obtained as dimers or as monomeric adducts in the presence of an excess of amines. A common feature of these derivatives is the hexacoordination of the metal. The MNC_2 units are planar with short M–N distances ($\approx$1.86 Å), and thus suggest strong π-bonding by interaction of the nitrogen p_π orbitals and empty d_π orbitals of the metal.

The $M–NR_2$ bond is labile and Nb and Ta dialkylamides $M(NR_2)_5$ (**12**) are valuable starting materials (Scheme 2). They can easily undergo substitution or *Insertion* reactions. Insertion of CO_2, CS_2, and COS in $M(NR_2)_5$ has been observed, giving dialkylcarbamates, dithiocarbamates, or monothiocarbamate derivatives, respectively. In the case of niobium, the insertion of CS_2 is accompanied by reduction. Insertion of CO_2 is catalyzed by amines resulting from adventitious hydrolysis. Monodentate as well as bidentate carbamato ligands have been observed by X ray and can be distinguished in solution by IR, but not by NMR owing to fluxionality.[9,36] Nb and Ta derivatives based on bidentate or polydentate amido ligands have been reported. (**12**) allowed access to the first tantalasilsesquioxanes (**13**) (*see* ***Silicon: Organosilicon Chemistry***).[37] (**12**) are source to guanidinate(−1) (**14**) or to guanidinate(−2) complexes by reaction with carbodiimides, or by protonation of the amido groups with trialkylguanidines respectively.[38] The acidic *carborane nido*-$C_2B_9H_{13}$ (*see* ***Boron: Metallacarbaboranes***) reacts with (**12**) to generate three-legged piano stool $M(C_2B_9H_{11})(NMe_2)_3$ complexes (**15**), where the dicarbollide acts as a *spectator ligand*.[39]

Imido ligands are implicated in catalytic processes; they may act as NR transfer reactants or as intermediates on chemical routes to nitrides by CVD. Among the variety of routes available, reactions between MCl_5 and primary amines (Scheme 3), trimethylsilyl or lithium reactants and aminolysis of $M(NR_2)_5$ with primary amines are the most selective ones. The formation of the M≡NR bond proceeds via H abstraction. It is favored by proton acceptors, either excess of the amines, of ligands such as phosphines, or of an inorganic base (silicates, $ZnCl_2$, ...)[40] and many efforts have been devoted to high-yield syntheses of $M(NR)Cl_3L_x$ complexes ($R = Ar$, *t*Bu, $SiMe_3$) with labile, inert ligands. The donor capability of the various R groups have been compared, *t*Bu is more efficient toward d^0 metals than $SiMe_3$, itself better than the Cp ligand.[41] Decomposition patterns of chloroimide complexes have been examinated in relation to CVD of metal nitrides.[8] The decomposition of $MNCl_2$ into NbN and Ta_3N_5 respectively, is consistent with the CVD results.

The reaction between $Ta(NMe_2)_5$ and silanes yielded an unusual dihydride imine complex (**17**) through β-H abstraction between amide ligands (equation 10).[42] The first Cp-free silyl (**18**) and disilyl Ta derivatives have been reported. They are potential precursors to Ta–N–Si ternary materials. Unusual oxidation products such as (**19**) could be stabilized (equation 11).[43]

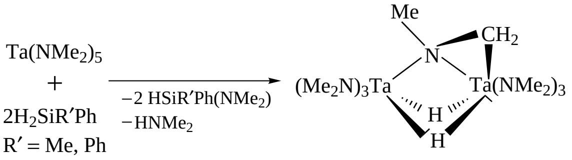

(**17**)

(10)

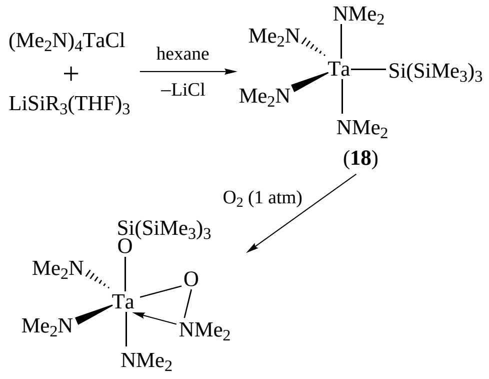

(**18**)

(**19**)

(11)

Imido amides or imido alkoxides are known, especially with bulky NAr groups.[1,22] Their utility has been demonstrated in the preparation of M^{III} imido alkyne compounds. The electrophilic, transient $(t\text{-Bu}_3SiNH)Ta(=NSi\text{-}t\text{-Bu}_3)_2$ was active in hydrocarbons C–H activation reactions.[22] Metal–imide bonds are short (1.75 Å) with M–N–C angles close to linearity. These data are consistent with an M–N *Bond Order* somewhat greater than two, and reflect the π donation of the nitrogen lone pair with a formal bonding M≡NR, the imido ligand being described as a 4e donor. In the imido alkoxides, the OR ligand is oriented cis to the imide, thus allowing to maximize the number of interactions between these ligands, and the d^0 metal is thus able to reach 18e (*see Effective Atomic Number Rule*).

The oxo and organoimide ligands are *Isoelectronic*, but imides have higher thermal stability and solubility than their oxo analogs. They are characterized by a vibration around 1350 cm^{-1} in the IR. ^{15}N NMR data have been reported for M^V and M^{III} imides, the latter appear at higher fields. The action of alcohols generally removes the imido ligand, giving alkoxides, while that of carboxylic compounds results in the formation of oxo derivatives.[1]

2.4.2 Dinitrogen Activation

Niobium and tantalum belong to the metals that are able to bind dinitrogen.[44] The development of this area was first due to Schrock and coworkers, who in 1982 could obtain stable tantalum μ-N_2 compounds in high yields by reducing *Alkylidene* complexes under dinitrogen at normal pressure.[1,22] This route can be circumvented in a ‘single pot’ synthesis by reacting the pentahalides with silylated hydrazines (equation 12).

$$\begin{array}{l} \mathrm{M_2Cl_{10}} \\ \quad + \\ \mathrm{(Me_3Si)XNNX(SiMe_3)} \end{array} \xrightarrow{\mathrm{CH_2Cl_2,\ THF}} [\mathrm{MCl_3(THF)_2}](\mu\text{-}\mathrm{N_2})$$

M = Nb, X = $SiMe_3$, (**20**) (60%)

M = Ta, X = H (**21**) (30%) (12)

Complexes (**20**) and (**21**) are *synthons*, either by *Ligand* exchange or by chlorine substitution. The latter reactions offered, for instance, thiolate or diethyldithiocarbamate (**22**) derivatives (Figure 4); the first dinitrogen complexes in which the coligands are exclusively S-donors, significant in light of the predominant sulfur ligation of the enzyme nitrogenase (*see* ***Nitrogenase: Metal Cluster Models***).

The usual structural feature of Nb or Ta nitrogen complexes is the presence of a bridging μ-η^2:η^2 dinitrogen ligand (*see Bridging Ligand*) involved in a nearly linear M–N–N–M arrangement. The N–N bond lengths (1.39–1.25 Å) are longer than in free dinitrogen (N≡N, 1.0976 Å), suggesting a bond order between one and two. The M–N bonds (1.85 – 1.75 Å) are also much shorter than the usual M–N single bond (typically 1.95–2.05 Å) and close to the

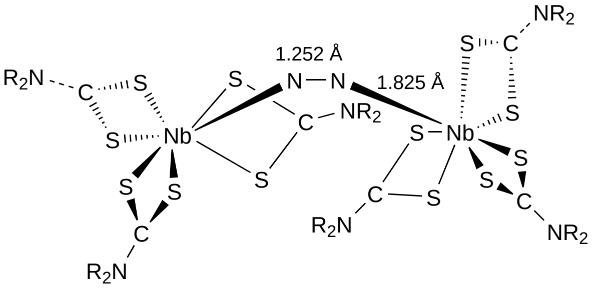

Figure 4 Molecular structure of the dinitrogen complex $Nb_2(\mu\text{-}N_2)_2(dtcR_2)_6$ (**22**)

distances found in imido derivatives. As a result, these dinitrogen complexes, which are specific for early transition metals, have been formulated as M=N–N=M systems or hydrazido(4−) derivatives. ^{15}N labeling has established that the Ta=N–N=Ta group is characterized in the IR by an absorption around 845 cm^{-1}, consistent with partial reduction of N_2. This description of the Mμ-N_2 bridge is supported by the reactivity of these adducts, which behave as imido complexes. Protonation of bridging dinitrogen by various hydracids gives hydrazine only (equation 13) and has been studied kinetically in the dithiocarbamates (**22**).**[44]** In the presence of excess acid, protonation proceeds irreversibly via hydrazido(2−) complexes that have been detected in the case of niobium (Scheme 4).**[1,2,9]** Ta complexes containing the methylhydrazido(1−) ligand have been studied with the aim of understanding the role of related derivatives as intermediates in the conversion of hydrazido(2−) complexes to hydrazine. A 4e reduction of N_2, as well as further reduction into a nitride, has also been achieved with a Nb^{III}-calix[4]arene containing a very reactive Nb≡Nb unit.**[45]** Cleavage of N_2 was also promoted by the low-valent species derived from the reduction of [Nb(^{R}-L)Cl$_2$]$_2$ (^{R}-L^{3-} = linked aryloxide). The reactions are dependent on the nature of the R substituent.**[46]**

$$\underset{(\mathbf{22})}{[\mathrm{Ta(Et_2dtc)_3}]_2(\mu\text{-}\mathrm{N_2})} + 4\mathrm{HX} \xrightarrow{\mathrm{S,\ rt}} \underset{100\%}{2\mathrm{Ta(Et_2dtc)_3X_2}} + \mathrm{N_2H_4}$$

$$\mathrm{X = Cl, Br, I;\ S = CH_2Cl_2,\ THF\ or\ MeCN} \qquad (13)$$

A facile process for the preparation of Nb and Ta dinitrogen complexes supported by aminophosphine ligands was reported recently.**[47]** The reaction of the Ta^{IV} diamagnetic hydride ([NPN]$_2$Ta$_2$(μ-H)$_4$) (**23**) ([NPN] = PhP(CH$_2$SiMe$_2$NPh)$_2$) with N_2 provided a Ta^{V} species (**24**) with an unprecedented side-on end-on dinuclear bonding mode. The N–N distance (1.319 Å) is consistent with the bridging dinitrogen as $(N_2)^{4-}$. The hydride ligands force the metal centers so close together (Ta···Ta 2.830 Å) that the usual end-on dinuclear bonding mode becomes impossible (Scheme 5). This strongly activated N_2 is amenable to functionalization such as Si–N (**25**) or B–N (**26**) bond formation for instance.

2.4.3 Miscellaneous

The azides and nitrides (*see* ***Nitrogen: Inorganic Chemistry***) further illustrate the ability of niobium and tantalum to form M–N multiple bonds. The stability of the azides, although poor, is higher for Ta and for ionic derivatives than for Nb and neutral ones.**[1]** Their M–N distances are longer than expected for a single bond. Reactions analogous to the Staudinger reaction (*see* ***Phosphorus: Organophosphorus Chemistry***), giving compounds containing the phosphineiminato M=N=P group, are the salient feature of their reactivity. These heteroimido derivatives could also be obtained from penta- or oxyhalides and trimethylsilyl or lithium reagents.**[48]**

Nitrides can be obtained by decomposition of the azides, but thermolysis of the pentahalides with ammonium salts appears more general. Recent synthetic pathways involve the cleavage of N_2**[45]** or decarboxylation of a Nb isocyanate.**[49]** The solid-state characterization of the [M$_2$NX$_{10}$]$^{3-}$ anions shows a linear symmetrical M=N=M bridge. Neutral halide nitrides are polymeric.**[1,2]** Heterometallic nitrides based on a corner-shared double cube NbTi$_6$N$_8$ core (**27**) have been described (equation 14).**[50]**

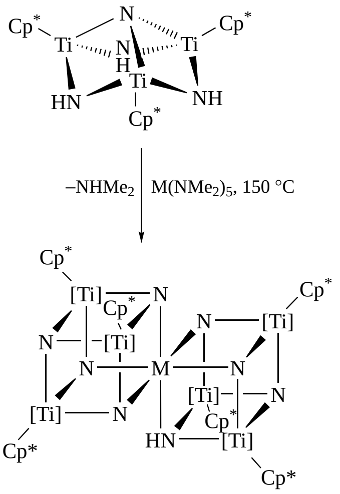

(14)

(**27**)

M(μ_3-N)(μ_3-NH{Ti$_3$(η^5-Cp*)(μ_3-N)}$_2$

A number of pentavalent trispyrazolylborate derivatives (*see Tris(pyrazolyl)borates*) have been reported, especially for niobium.**[51]** Most of them are monomeric Tp*MCl$_2$X (X = O, NR) derivatives. η^1 and η^2-pyrazolato (**16**) or 1,2,4-triazolato derivatives have been prepared as potential sources of nitrides for CVD.**[52]** The reactions between dilithium 1,4-diaza-1,3-diene and pentachlorides have been investigated.**[53]**

Ammonolysis of NbBr$_5$ followed by heat treatment was used for access to ceramics, that is, nitrides or carbonitrides. Applied to Ta alkyl derivatives, ammonolysis provides a low temperature route to TaN; the cubic form is obtained instead of the more stable hexagonal one.**[54]** Similar reactions for Cp*TaMe$_4$ give a cyclic trimer (**28**) (equation 15), whose delocalized six-membered ring (Ta–N av. 1.88 Å) is related to that of phosphazenes (*see* ***Phosphorus–Nitrogen Compounds***). The thermal ring opening of the chloride analog of (**28**) offered the first soluble polymer based on a Ta–N backbone.**[2,3]**

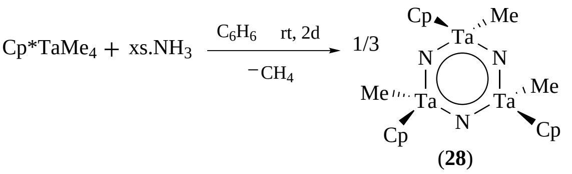

(15)

(**28**)

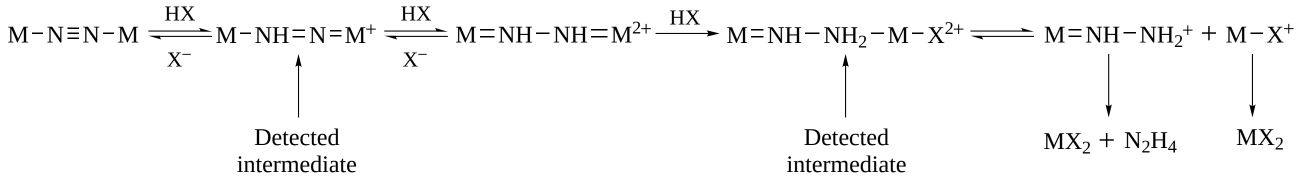
M−N≡N−M
HX
X⁻
M−NH=N=M⁺
HX
X⁻
M=NH−NH=M²⁺
HX
M=NH−NH₂−M−X²⁺
M=NH−NH₂⁺ + M−X⁺
Detected intermediate
Detected intermediate
MX₂ + N₂H₄
MX₂

Scheme 4 Mechanism of the production of bridging dinitrogen in niobium and tantalum dithiocarbamate complexes (R_2dtc, etc. Omitted for clarity)

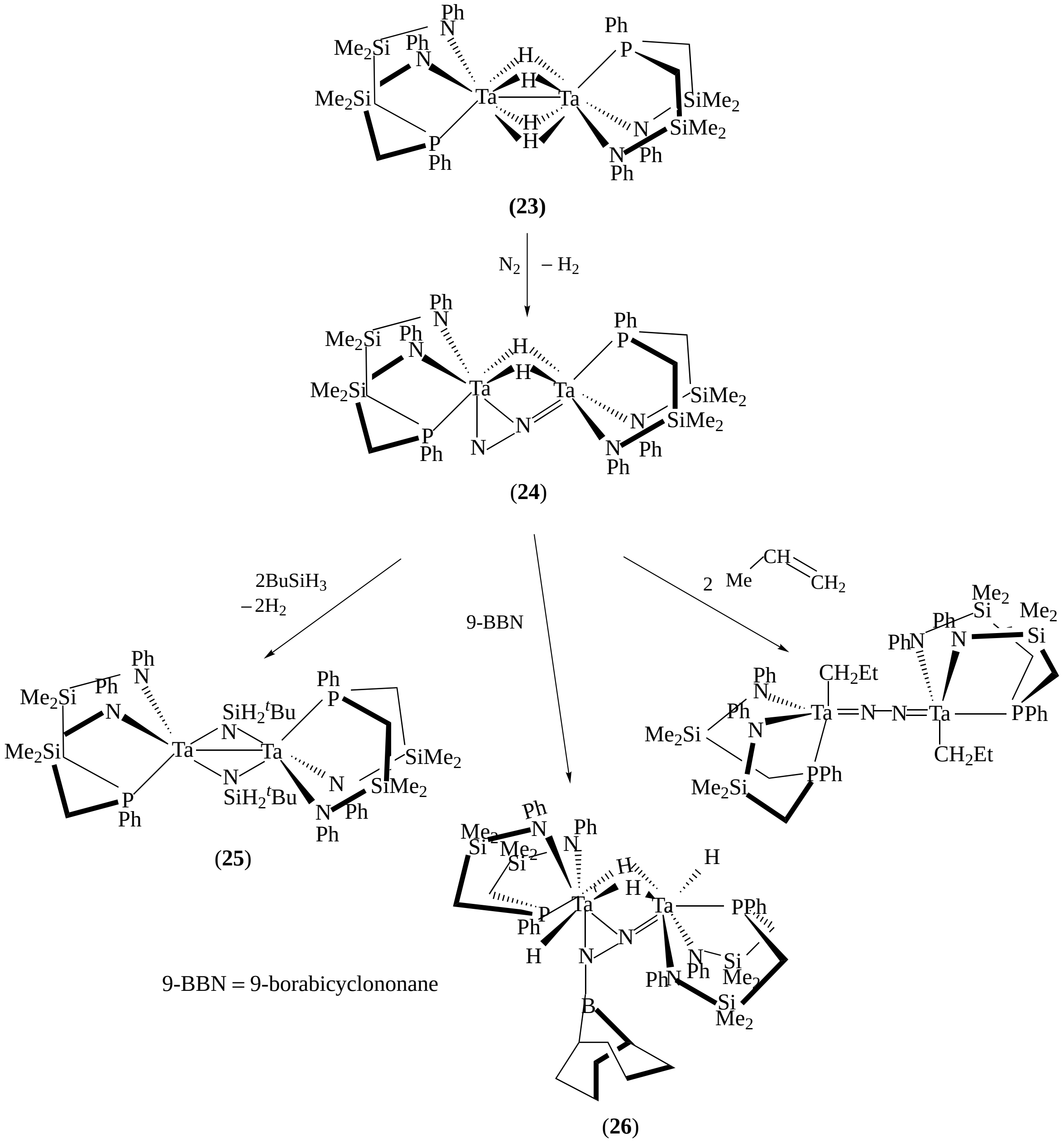
(23)
N₂
− H₂
(24)
2BuSiH₃
− 2H₂
9-BBN
2 Me CH=CH₂
(25)
(26)
9-BBN = 9-borabicyclononane
Ta
Ph
N
Me₂Si
P
SiMe₂
SiH₂ᵗBu
CH₂Et
PPh
H
B

Scheme 5 Activation and functionalization of dinitrogen by Ta derivatives[47]

Neutral and anionic *Pseudohalide* complexes have been reported. While most of the thiocyanates were considered to be N-coordinated, ^{93}Nb NMR spectra of $Nb(NCS)_6^-$ were reinterpreted in terms of a mixture of N- and S-coordinated isomers.[1,2]

2.5 Phosphorus and Arsenic Donors

Nb^V and Ta^V derivatives are hard acids and their complexes with P- or As-donors are limited. Tertiary phosphines, especially PMe_3, have been widely used to stabilize low-valent derivatives. C–H activation reactions, promoted by the formation of thermodynamically stable Ta–H, Ta–C, and Ta=C bonds have resulted in metallacycles based on unusual anionic phosphorus donors.[22] Nucleophilic Ta^V phosphinidene complexes could be stabilized by a tripodal tetradentate $[NN_3]$ amido ligand.[9,55] The terminal PR ligand reacts smoothly with aldehydes, providing a general synthesis of phosphaalkenes $RP{=}C(H)R'$ and act thus as a phospha-Wittig reactant (*see* ***Phosphorus: Organophosphorus Chemistry***).

3 OXIDATION STATE +IV

The niobium and tantalum tetrahalides MX_4 are all known, except TaF_4, whose nonexistence is consistent with the fact that $[TaF_5]_4$ should be the least reducible halide of these elements.[1] They are dark solids, obtained by reduction of the pentahalides by H_2 or more often by metals (Al or M) at high temperatures. With the exception of NbF_4, all tetrahalides disproportionate thermally (*see Disproportionation*); this can be overcome by a high pressure of the pentahalides during the preparation. Except NbF_4, they are all essentially diamagnetic (*see Diamagnetism*) as a result of a one-dimensional (1D) polymeric structure based on dinuclear M_2X_8 units with two types of metal bridging (short and long), being responsible for their semiconducting properties (*see* ***Semiconductors***).

3.1 Halogens as Ligands: Tetrahalides and their Adducts

Numerous adducts, mostly of type MX_4L_2 (X = Cl, Br, I), are known with nitrogen, phosphorus, arsenic, oxygen, and sulfur donors. They are synthesized by reaction of solid tetrahalides with the ligand or by reduction of pentahalides with the ligand, mainly bidentate or heterocyclic N-donors or phosphines. $NbCl_4(THF)_2$ (**29**) is of particular value since the lability of the THF molecules makes it a useful *synthon* in Nb^{IV} chemistry.

The MX_4L_2 adducts with monodentate ligands are generally monomeric, and thus paramagnetic (*see Paramagnetism*). In the absence of X ray, electron spin resonance (ESR) (*see Electron Paramagnetic Resonance*) can be used to gain structural information. The ESR spectra of the Nb derivatives, for instance, are characterized by 10 lines as a result of the coupling of the unpaired electron with the metal of spin $I = 9/2$. The hyperfine coupling parameters of the d^1 distorted octahedral MX_4L_2 complexes generally decrease with increasing ligand basicity. Reduction of $NbCl_5$ with primary phosphines (equation 16) gave dinuclear diamagnetic Nb^{IV} adducts (**30**) whose structure is similar to that of the $Nb_2(\mu\text{-}Cl)_4Cl_4(PR_3)_4$ derivatives obtained from $NbCl_4$.[1] (**30**) were used as precursors to NbP films by CVD.[56] Octacoordination is also found for monomeric MX_4 bisadducts involving bidentate ligands such as $MCl_4(dmpe)_2$, which have been widely used for access to lower oxidation states.

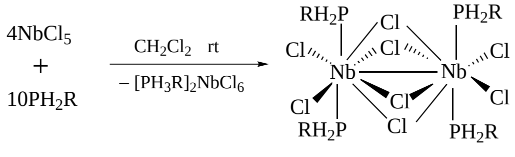

(**30**)

(16)

3.2 Solvolysis Products of the Tetrahalides

Compounds that can be considered as *Solvolysis* products from the tetrahalides can result from direct substitution reactions of MX_4 or their complexes but also from the reduction of M^V derivatives or from oxidative addition of M^{III} complexes especially in the case of Ta.[1]

Nb^{IV} alkoxides were first reported to form during the electrochemical synthesis of $Nb(OEt)_5$, starting from the metal or during the electrolytic reduction of $NbCl_5$ in alcohols. Alcoholysis of $Nb(NR_2)_4$ generally leads to $Nb(OR')_5$, but oxidation state IV could be retained with bulky R′ groups such as adamantyl. Structurally characterized diamagnetic dimeric Nb chloroalkoxides and tetrameric oxochloroalkoxides have been obtained from trivalent halide adducts and alcohols.[1,2,9] $[Nb_2(OMe)_9]^-$ results from further substitution. All compounds have a Nb–Nb single bond (2.78–2.89 Å). The first Nb^{IV} enolate has been reported.[57] The reductive coupling of Nb^V salophen derivatives led to dimers linked through C–C and Nb–Nb bonds. Each of those bonds can be used as a reversible source of a pair of electrons for reduction, for instance, of diphenyldiazomethane.[58] These reactions offer a close analogy with those observed for the reduced Nb calix[4]arene species.[45]

The reduction of $MCl_3(silox)_2$ in the presence of H_2 (1 atmosphere) gives siloxohydrides (**31**), shown by MW measurements to be dinuclear (Scheme 6).[23,24] Multinuclear NMR (^{1}H, ^{13}C, ^{29}Si) and IR account for an unusual geometry: M–M bonding without bridging ligands. The Ta species is able to promote CO deoxygenation, and C–H and C–C bond formation, and thus tracks the

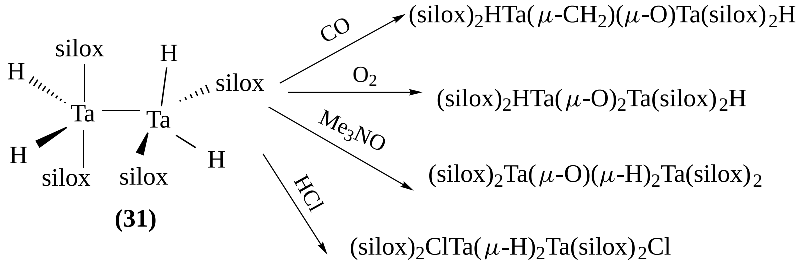
silox
H
H
Ta
Ta
silox
H
H
silox
silox
(31)
CO
(silox)₂HTa(μ-CH₂)(μ-O)Ta(silox)₂H
O₂
(silox)₂HTa(μ-O)₂Ta(silox)₂H
Me₃NO
(silox)₂Ta(μ-O)(μ-H)₂Ta(silox)₂
HCl
(silox)₂ClTa(μ-H)₂Ta(silox)₂Cl

Scheme 6 Some reactions of the dinuclear Ta^{IV} hydridosiloxide (**31**)

critical sequence of the *Fischer–Tropsch Process* (*see* ***Carbonylation Processes by Homogeneous Catalysis***). The reduction of Nb 2,6- or 2,4,6-aryloxides under H_2 gave η^4-cyclohexadiene complexes by intermolecular hydrogenation. Hydrogenation occurs exclusively at the ortho-Ph group.[14]

Monomeric, paramagnetic chlorohydrides such as $MH_2Cl_2(PR_3)_4$ derive from facile oxidative addition of H_2 to $MCl_2(PR_3)_4$ complexes. Of these 17e dodecahedral complexes, (**32**) is the most interesting (equation 17). Its thermolysis in solution offers a quadruply bridged hydride (**33**) and it can also be reduced to a monomeric Ta^{III} 16e species (**34**).[1,22] Ta^{IV} hydrides display a hydridic character (*see* ***Hydride Complexes of the Transition Metals***), as shown by the reduction of CO by cyclopentadienyl derivatives.[1] (*see* ***Niobium & Tantalum: Organometallic Chemistry***)

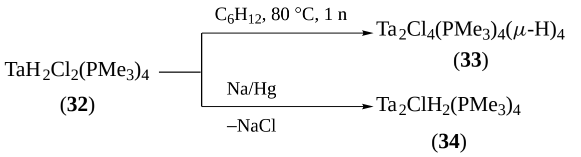

(17)

Homoleptic and chloro β-diketonates have been reported for both metals. They derive from the reaction of β-diketones (or their alkali derivatives) with either M^{IV} or M^{III} halide complexes. They are generally monomeric and thus paramagnetic; their structures have been proposed on the basis of UV or ESR data and less often X-ray data.

Monomeric, paramagnetic Nb^{IV} dialkylamides $Nb(NR_2)_4$ have been obtained as highly air-sensitive liquids by spontaneous reduction of the pentaamides. The thermal decomposition of $Nb(NEt_2)_4$ in the presence of ammonia gave Nb_3N_4 films.[35] Whereas Nb^{IV} amides (**35**) can also be obtained from $NbCl_4(THF)_2$,[59] those of Ta^{IV} derive mostly from the reduction of $Ta(NR_2)_2Cl_3$ by Na/Hg.[60] Organometallic $Nb(NR_2)_2R'_2$ species as well as compounds based on terdentate diphosphino- and diamidoamido ligands are known for Nb.[5,59] Reaction of (**29**) with three equivalents of Cy_2NLi afforded the first Nb^{IV} aziridine (**36**) by metallation of one of the cyclohexyls. Attempts to reduce (**36**) with $LiBEt_3H$ under N_2 lead to a Nb^{V}–N_2 end-on complex.[61] Scheme 7 summarizes some examples of the reactivity of $NbCl_4(THF)_2$. An amide based on staggered $TaCl(NCy_2)_2$ moieties first considered as a Ta^{III} species has been reformulated as a Ta^{IV}one, $Ta_2(\mu\text{-}H)_2Cl_2(NCy_2)_4$, because of hydride ligands.[62] The high reactivity of the dinuclear Ta amide supported by the bulky $9H$-carbazole is illustrated by its hydrogenolysis giving a hexahydride,[9,22] whose structure is representative of the $Ta_2{}^{IV}(\mu\text{-}H)_4$ core observed with the chlorides (**33**). Eight-coordinate arylformamidinates $M[ArNC(H)NAr]_4$ have been reported for both metals.[63] Binuclear Nb^{IV} bis-pyrazolylborate derivatives are known.[54] A paramagnetic Nb_2–N_2 complex was obtained by reduction of a Nb^{III} chloride precursor supported by a bis-(amidophosphine) $[N_2P_2]$ macrocycle.[64]

The unstable $Nb(PCy_2)_4$ derived from a Nb^{III} precursor remains the only homoleptic dialkylphosphide of those elements.[1] Ta^{IV} phosphinidene bridged dimers stabilized by CpR or Cp* ligands are known.[55]

The few data available on thiocyanates indicate N-coordination in the solid.[1] The octacyanometallate $Nb(CN)_8{}^{4-}$ has been used for supramolecular magnetic architectures by self assembly with ML^{2+} complexes ($M = Ni^{II}$, Mn^{II}, $L =$ N-donor macrocycle).[65]

3.3 Sulfur, Selenium, and Tellurium Donors: Chalcogenohalides and their Adducts

The interest in the chalcogenides has been stimulated by a possible use of disulfides as cathodes in lithium batteries. Niobium and tantalum homoleptic ME_4 chalcogenides are only stable as tetratellurides; large halide anions are, however, able to stabilize a variety of chalcogenohalides, especially for Nb, the corresponding Ta chemistry being less developed.[2,65] The synthetic and structural chemistry of chalcogenide-rich derivatives is complex. Many of them are low-dimensional solids and display interesting physical properties (*see* ***Chalcogenides: Solid-state Chemistry***). As for most Nb^{IV} halides, a common feature is the occurrence of chains in which the metal is present as pairs (alternate short and long Nb–Nb distances, about 3.1 and 3.7–3.9 Å, respectively) that causes diamagnetism as well as semiconducting properties. These chains are connected by a wide variety of fragments. IR and Raman studies established the presence of E–E or M–E

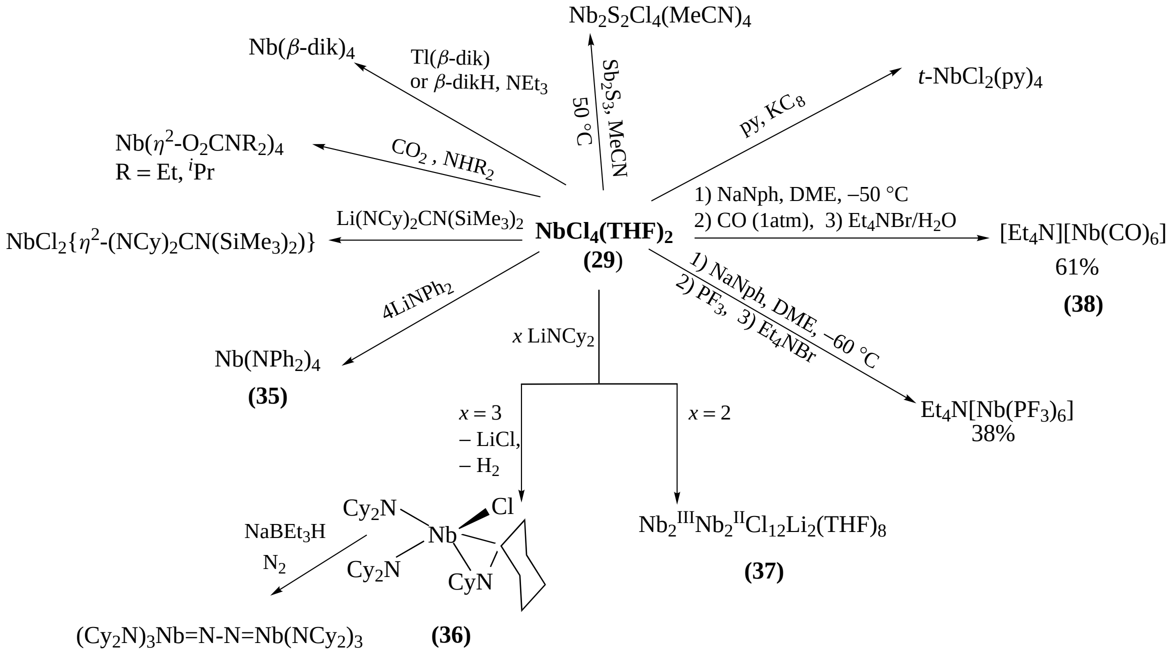
Nb2S2Cl4(MeCN)4
Sb2S3, MeCN
50 °C
Nb(β-dik)4
Tl(β-dik)
or β-dikH, NEt3
t-NbCl2(py)4
py, KC8
Nb(η2-O2CNR2)4
R = Et, iPr
CO2, NHR2
1) NaNph, DME, –50 °C
2) CO (1atm), 3) Et4NBr/H2O
[Et4N][Nb(CO)6]
61%
(38)
NbCl2{η2-(NCy)2CN(SiMe3)2)}
Li(NCy)2CN(SiMe3)2
NbCl4(THF)2
(29)
1) NaNph, DME, –60 °C
2) PF3, 3) Et4NBr
Et4N[Nb(PF3)6]
38%
4LiNPh2
Nb(NPh2)4
(35)
x LiNCy2
x = 3
– LiCl,
– H2
x = 2
Cy2N
Cl
Nb
Cy2N
CyN
NaBEt3H
N2
Nb2IIINb2IICl12Li2(THF)8
(37)
(Cy2N)3Nb=N-N=Nb(NCy2)3
(36)

Scheme 7 Some reactions of $NbCl_4(THF)_2$

bonds that were confirmed by X-ray studies. Compounds such as NbS_3, for instance, have to be considered formally (they are covalent) as $Nb^{IV}(S–S)_2{}^{2-}S^{2-}$.

Chalcogenohalides have been synthesized by solid-state high-temperature reactions. A series of isomorphous $Nb(E_2)X_2$ (E = S or Se, X = Cl, Br, I) halides have been obtained.[1,2] The molecules may be described as cage-shaped $Nb_2(E_2)_2$ units with μ-η^2:η^2 dichalcogeno ligands between adjacent Nb atoms and an extended $[Nb_2(\mu\text{-}E_2)_2Cl_{8/2}]_\infty$ structure by sharing all chlorine. The vibrations of the S_2 groups of NbS_2Cl_2 occur at 588 cm^{-1} in the IR; they are higher than those of the Nb=S group. Chalcogenohalides containing selenium are often mixed-valence (*see* ***Mixed Valence Compounds***) $Nb^{IV}Nb^{V}$ derivatives, as established by X-ray and photoelectron spectroscopy (*see* ***Photoelectron Spectroscopy of Transition Metal Systems***).[1] Compounds such as $Nb_3Se_5Cl_7$ or $Nb_6Se_{20}Br_6$, actually $Nb_2{}^{IV}Nb^{V}(Se_2)_2SeCl_7$ and $Nb_4{}^{IV}Nb_2{}^{V}(Se_2)_{10}Br_6$, respectively, illustrate this behavior. $NbSe_2Br_2$ was obtained in conditions that lead to $[Ta(Se_2)_2]_2[TaBr_6]$ for Ta.[5] The structure of the latter is based on 1D positively charged chains of $Ta(Se_2)_2$ (and thus oxidation state of 4.5 for Ta, which leaves 0.5 e for the Ta–Ta bond) separated by $TaBr_6{}^-$ anions.

NbS_2Cl_2 has been used as starting material. It gave access to thiocyanates and to $[Nb_2(\mu, \eta^2\text{-}S_2)_2(H_2O)_8]^{4+}$, the first structurally characterized, in 1997 only, aqua-Nb^{IV} complex. The water molecules are labile and the $Nb_2(\mu, \eta^2\text{-}E_2)_2{}^{4+}$ core (E = S, Se) afforded a new series of Nb^{IV} diamagnetic β-diketonates dithiocarbamates, dithiophosphates, and xanthates.[66] Depopulation of π^* orbitals leaves the $S_2{}^{2-}$ ligands susceptible to nucleophilic attack giving a product assumed to be $[Nb_2(\mu\text{-}S)_2(H_2O)_8]^{4+}$.

The first Nb or Ta tellurium halide, $Nb_2Te_8I_{12}$ was described in 1993. Its structure is characterized by two $[Te_2(\mu\text{-}I)_2I_4]^{2-}$ ligands coordinated to a $Nb_2(\mu\text{-}Te_2)_2{}^{4+}$ center. The discrete $Nb_2Se_4(Te_2I_6)_2$ molecule has a similar structure.[67] New types of structures have been reported for instance for $Nb_4(\mu, \eta^{2-}Te_2)_4Te_4I$: tetranuclear butterfly clusters are assembled via iodide bridges into 1D infinite chains.[3,4]

Chalcogenide halide adducts obtained directly from M^{IV} compounds remain scarce. $Nb_2(\mu\text{-}S)_2X_4(MeCN)_4$ (**39**), result from reaction between NbX_4 (X = Cl, Br) and Sb_2S_3 in MeCN. Attempts to synthesize $NbSeBr_2$ adducts led to reduction of the metal and formation of a mixed valence cluster (**40**) (equation 18). Formally, two Se^{2-} ions form an $(Se_2)^{2-}$ ion with release of 2e, which reduce two Nb^{IV} to Nb^{III} atoms, giving a $Nb^{IV}_2Nb^{III}_2$ aggregate. (**40**) is best described as a central $(MeCN)_2Br_2Nb^{IV}(\mu, \eta^2\text{-}Se_2)(\mu\text{-}Se)Nb^{IV}Br_2(MeCN)_2$ fragment linked by long bromide bridges to two $NbBr_3$ units (Figure 5). The tetravalent metals Nb(1) are connected by Nb–Nb bonding but no interaction is observed between the Nb^{III} centers, Nb(2) and Nb(3).

$$\begin{array}{ccc} 4NbBr_4(MeCN)_2 & \xrightarrow[-SbBr_3]{MeCN,\ 50\,^{\circ}C,\ 7\ d} & 2Nb_4Br_{10}(Se_2)(Se)(MeCN)_4 \\ + & & (\mathbf{40}) \\ Sb_2Se_3 & & \end{array} \qquad (18)$$

The reaction of $NbSBr_3$ in neat THT proceeds with disproportionation; two S^{2-} ligands are oxidized to $(S_2)^{2-}$

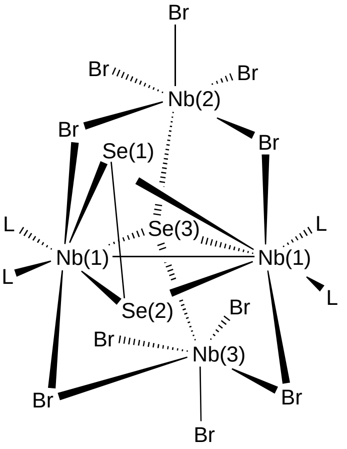

Figure 5 Molecular structure of the mixed-valence cluster (**40**)

giving (**41**) (equation 19). Its most salient structural feature is the Nb(μ-S)(μ-S_2) ring. While similar reactivity patterns were observed for $NbSX_3$ and other S-donors such as Me_2S, no evidence for reduction was found in the case of Ta.[1]

$$\mathrm{NbSBr_3(THT)_2} \xrightarrow{\mathrm{THT}} \underset{(\mathbf{41})}{\mathrm{Nb_2(\mu\text{-}S)(\mu\text{-}S_2)Br_4(THT)_4}} + \mathrm{NbBr_5(THT)_2} \tag{19}$$

The $TaCp_2$ or Nb(tBuC_5H_4)$_2$ moieties allowed to stabilize a number of telluride and selenide units such as Te_n^{2-} ($n = 1,4$), η^2-$TeCH_2$, η^2- Se_2H, and so on, which were used as ligands toward metal carbonyls.[2,68] ^{77}Se and ^{125}Te NMR data were reported.

4 OXIDATION STATE +III

The development of the chemistry of niobium and tantalum in their lower oxidation states, three or less, has long been precluded by the lack of convenient starting materials. Indeed, stoichiometric trihalides MX_3 (X = Cl, Br) are only incidental compositions. They are obtained by reduction of the pentahalides or disproportionation of the tetrahalides, and are polymeric and rather inert.

4.1 Halogen as Ligands

4.1.1 Anionic and Neutral Complexes: Synthesis and Characterization

A new area in niobium and tantalum chemistry was opened with the discovery that the reduction of MX_5, MX_4, or their complexes to yield molecular trihalides can be achieved easily by reductants such as sodium amalgam in the presence of ligands when carried out in strictly anaerobic conditions. The first trivalent complexes, $Nb_2X_6(THT)_3$ (X = Cl, Br, I), based on tetrahydrothiophene, were obtained in high yield (equation 20) in 1973.

$$\mathrm{2NbX_4(THT)_2 + 2Na/Hg} \xrightarrow[\mathrm{rt}]{\mathrm{C_6H_6}} \mathrm{Nb_2X_6(THT)_3 + 2NaX + THT}$$
$$\mathrm{X = Cl, Br, I} \tag{20}$$

Similar reductive routes allowed to obtain a large variety of soluble Nb and Ta complexes, mostly chlorides, involving monodentate sulfur, nitrogen, or phosphorus donors. The complexes formed can be highly dependent on the experimental conditions, especially the nature of the starting material, of the solvent, or of the reductant. Borohydrides that act as dual reagents can give access to metallic species incorporating various boron ligands.[63,69] The Ta^V Lewis acid–base adduct (**42**) (equation 21) with a Li···H–Ta interaction[24] and the *nido*-metalloborane $Ta_2(\mu, \eta^4$-$B_2H_6)[ArNC(H)NAr]_4$ formed by reacting $TaCl_5$ with $LiBH_4$ and N,N'-diarylformamidinato lithium are examples of complex reactivity patterns. THF ring opening also can generate unanticipated products such as the Ta^{III} [(η^5-Cp)$_2$Ta(μ-H)$_2$AlH]$_2$(μ-O-n-Bu)$_2$ adduct, where the butoxides bridge the Al centers.[24]

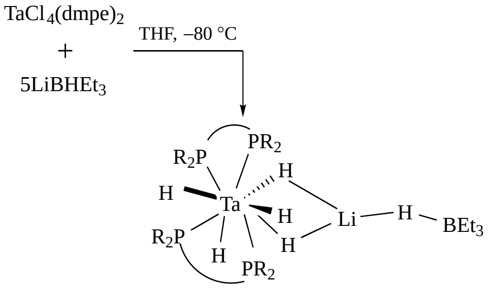

(21)

(**42**)

Although stable, monomeric, paramagnetic MX_3L_3 adducts could be isolated and characterized (ESR, X ray), the formation of diamagnetic compounds involving M–M bonding is more frequent affording di- or tetranuclear neutral adducts[70] or anionic trinuclear clusters. Indeed, while the TaX_n–PR_3 (R = Et, Me) system offers mono- or dinuclear derivatives, the niobium system appears more prone to formation of discrete di or trinuclear anions, the counterion being derived either from the reductant (as $[Mg_2(\mu\text{-}Cl)_3(THF)_6]^+$) or from the ligand (as the phosphonium cation HPR_3^+). The metal is generally heptacoordinate, counting the M–M bond. Dinuclear adducts are the most common with monodentate as well as with bidentate LL donors, their formulation being $M_2X_6L_n$ ($n = 3$ or 4) and $M_2X_6(LL)_2$, respectively. Their structure is based on confacial or edge-sharing bioctahedra (Figure 6), as also found for the anionic complex $M_2X_9^{3-}$. The short

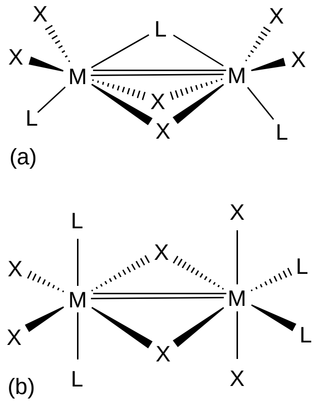

Figure 6 Frameworks of the dinuclear M^{III} halide adducts: (a) $M_2X_4(\mu\text{-}X)_2(\mu\text{-}L)L_2$ (L = Me_2S, THT); (X = Cl, Br, I); (b) structure of $Ta_2Cl_4(\mu\text{-}Cl)_2(PR_3)_4$

M–M distances (2.7 Å) were considered to reflect the strong metal–metal bonding of a formal double bond. Longer M–M distances (≈2.97 Å) are found in the trinuclear monocapped clusters $[M_3(\mu_3\text{-}Cl)(\mu\text{-}Cl)_3Cl_6L_3]^-$, which have a structural unit related to that of the Nb_3X_8 (X = Cl, Br, I) halides.[1] The solubility (in nonpolar media) and diamagnetism of the dinuclear $M_2X_6L_n$ adducts allowed their characterization in solution by NMR (^{1}H, ^{31}P). By contrast, the complexes formed with bidentate ligands are often of poor solubility. The trivalent adducts display a wide range of colors, but information on their electronic absorption spectra remains scarce.

4.1.2 Reactivity of the Halide Complexes

The $M_2Cl_6L_n$ complexes with monodentate S or P ligands were first used as starting materials. The lability of the M–S bond allowed to expand the range of M^{III} adducts, especially with bidentate donors, by ligand exchange reactions. The formation of mixed ligand adducts in which the bridging S-donor is retained suggests that the terminal ligands are more labile than the bridging ones.[1,70] Exploration of the reactivity of adducts based on O- or N-donors such as $NbCl_3$(dme) or $Nb_2Cl_6(tmeda)_2$ is more recent.

Oxidative addition represents the main trend in the reactivity of the d^2 complexes, either as monomers or dimers, and these compounds are thus good precursors of M^V and dinuclear M^{IV} derivatives. Oxidative reactions can occur in the course of ligand exchange reactions, such as with hydrazines[2] or nitriles, as well as during chlorine substitution. They are assisted by the tendency to form strong M=E multiple bonds (E = O, S, or N) and can lead to novel ligands either by C–E cleavage or by C–C coupling, the latter being favored by unsaturated ligands (isonitriles, nitriles, alkynes, etc.). This results in a rich inorganic and organometallic chemistry with applications in organic synthesis.[22]

The reaction between $Ta_2Cl_6(THT)_3$ and acetonitrile illustrates these features. It proceeds quantitatively with formation of a new bridging ligand 1,2-dimethyl-1,2-diimidoethylene, which formally derives from the coupling of two MeCN molecules (equation 22). The M–N bond distances imply an imide character.[1] The reaction between (**43**) and Na diethyldithiocarbamate provides another example of unusual reactivity with formation of a sulfide S^{2-} and a thiocarbamyl $SCNEt_2^-$ ligand as a result of the oxidative addition of one C–S bond to the M^{III} metal (equation 23).[1] By contrast, similar reactions applied to $NbCl_3(dme)(RC{\equiv}CR')$ afforded $Nb(dtcR''_2)_3(RC{\equiv}CR')$.[31] C–S cleavage is also observed for the synthesis of thiolates from $Nb_2Cl_6(SMe_2)_3$ (equation 24). The square $Nb_4(\mu_4\text{-}S)_2$ core of (**44**) is also found in Nb^{III} thiolate phosphine complexes obtained from $NbCl_5$.[29] Similar reactions applied to $TaCl_5$ lead to $Ta_2S_2Cl_4(PR_3)_4$. Numerous investigations with the formamidinate $[ArNC(H)NAr]^-$ ligand have illustrated its versatility resulting in C–N cleavage with formation of arylimido NAr^{2-} or formimidoyl $HCNAr^{3-}$ ligands, and coupling reactions.[71] All these reactivity patterns show the difficulty of an unequivocal formulation of the compounds in the absence of an X-ray structure.

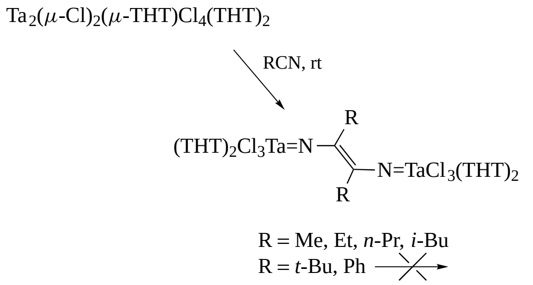

(22)

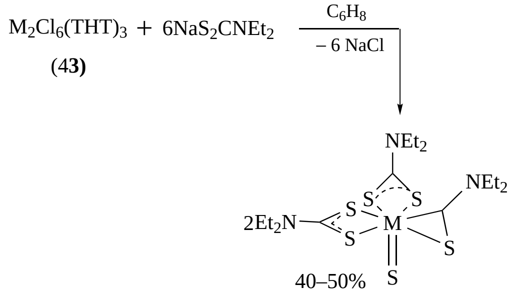

(23)

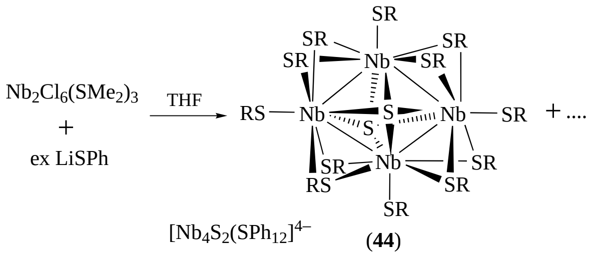

(24)

The easy access, on a large scale, to $NbCl_3$(dme), by reduction of $NbCl_5$ by tributyltin hydride, has prompted its use as a reactant in organic chemistry; it offers a convenient route to 2-amino alcohols via the coupling of imines with aldehydes or ketones.[22] Other low-valent derivatives promote the stereoselective functionalization of C≡C bonds.

M^{III} halide complexes based on mononuclear, dinuclear, tetranuclear, and hexanuclear frameworks polymerize and cyclize alkynes via different activation modes. The reactivity of the THT adducts (**43**) with alkynes RC≡CR′ depends on R and R′.[1] A common feature is the formation of strong M–C bonds and thus of a metallacycle exhibiting properties of a metallacyclopropene. A manifestation of the reactivity of the coordinated alkyne as a dianionic ligand is its reductive coupling with ketones or aldehydes. Such reactions may be applicable for C–C bond formation in the synthesis of new carbonyl compounds. The $Ta(OAr)_3$ fragment provides a template for alkyne cyclotrimerization via metallacyclopentadiene and arene derivatives (*see Arene Complexes*); such reactions can provide some insight into the mechanism of the C−C coupling of alkynes (*see* ***Niobium & Tantalum: Organometallic Chemistry***).

The dinuclear M=M chloride adducts with monodentate phosphines react cleanly with H_2, Cl_2, or HCl, giving dinuclear diamagnetic M^{IV}derivatives. The oxidative addition of H_2 to $Ta_2(\mu\text{-}Cl)_2Cl_4(PMe_3)_4$, for instance, occurs under mild conditions, giving an air-stable dinuclear Ta^{IV} hydride $Ta_2(\mu\text{-}Cl)_2(\mu\text{-}H)_2Cl_4(PMe_3)_4$. This reactivity is associated with the presence of a M=M bond and is not a general property of Nb^{III} or Ta^{III} derivatives. The monomeric hydride (**34**), resulting from reduction of (**32**) (equation 17) and characterized by neutron diffraction (*see* ***Diffraction Methods in Inorganic Chemistry***), is a useful synthon in Ta^{III} and Ta^{I} chemistry.[1]

Substitution reactions generally proceed with retention of the M–M bond (*see* ***Polynuclear Organometallic Cluster Complexes***). Trivalent compounds derived from such reactions are represented mainly by chloroalkoxides, chlorocarboxylates, carbamates, and formamidinates. A chiral, ionic Ta^{III} compound $[K(THF)_6][Ta(pyt)_4]$ (pyt = Pyridine-2-thiol) has been isolated starting from $TaCl_5$.[63] The reaction between $M_2Cl_6L_3$ (L = THT or Me_2S) and alkali carboxylates provides either dinuclear derivatives resulting from substitution or, in the case of niobium, bi-oxo-capped trinuclear clusters such as $[Nb_3(\mu_3\text{-}O)_2(O_2CR)_6(THF)_3]^+$. The reaction between $Nb_2Cl_6(THT)_3$ and inorganic aqueous acids (with exclusion of O_2) has extended this class of compounds, well known in the chemistry of molybdenum and tungsten. In all compounds with a $Nb_3(\mu_3\text{-}O)_2$ framework known presently, the number of core electrons available for Nb–Nb bonding is four, giving a bond order of 2/3 (Nb–Nb 2.84 Å av) (*see* ***Metal-mediated Protein Modification***). Among these complexes, the red−brown sulfato compound, which can be obtained by reduction of Nb^V in aqueous sulfuric acid, has a history that goes back to early attempts to separate and characterize niobium and tantalum; it was reported as early as 1912 but its formulation, $[Nb_3(\mu_3\text{-}O)_2(\mu,\eta^2\text{-}SO_4)_6(H_2O)_3]^{5-}$ (**45**), was only established by X-ray studies.[9] Electrochemical data on (**45**) and on the oxomethanesulfonate analog are available.[72] The air-sensitive trinuclear cluster (**46**) derived from $NbCl_3$(dme) and aqueous HCl gives, by reacting with KTp, a μ_3-hydroxotrioxoborate-capped mixed-valence $Nb^VNb_2^{IV}$ cluster (**47**) (equation 25). The borate cap is lost by oxidation, thus affording the $[Nb(=O)(\mu\text{-}O)Tp]_4$ species.[10]

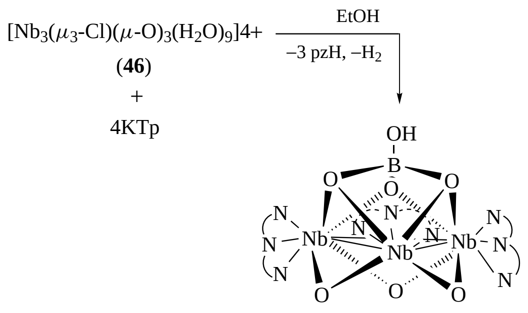

(25)

$(Tp)_3Nb_3\{\mu_3\text{-}BO_3(OH)\}(\mu\text{-}O)_3$ (**47**)

$NbCl_3$(dme) (**48**) is an useful starting material (Scheme 8). The reaction between KTp (or Tp*) and $NbCl_3(dme)(PhC{\equiv}CR)$ (**49**) afforded an entry into Nb^{III} trispyrazolylborate chemistry.[51] As for other M^{III} alkyne species, metallocyclopropene tautomeric forms with a d°, Nb^V configuration should be taken into account. An α-agostic interaction is preferred over the more common β-one due to the bulky Tp* ligand in their alkyl derivatives. Alkyne coupling products have been obtained. Some of those derivatives polymerize ethylene at rt in the presence of $B(C_6F_5)_3$. $NbCl_3$(dme) and $NbCl_3(dme)(PhC{\equiv}CR)$ were also used to form complexes of α-keto stabilized phosphorus ylides.[73] Ta-alkyne analogs $TaCl_3(RC{\equiv}CR')(LL)$ LL = dme, bipy, tmeda, $(py)_2$ have only become available recently.[74]

4.2 Reactivity of d^2 Derivatives Supported by Ligands other than Halogens

The monomeric M^{III} centers supported by bulky O-donors such as siloxide or aryloxide are extremely effective in reduction, cleaving numerous C–E bonds (E = O, S, halides, etc.), and exhibit unusual coordination behavior. A manifestation of the electrophilic behavior of $Ta(silox)_3$ (**51**) is its cleavage of CO (equation 26), giving an oxo derivative and a dinuclear carbide (**53**). The reducing power of (**52**) is also illustrated in the unusual coordination found for both pyridine and benzene. In coordination to these aromatics in a η^2 fashion (η^2-N,C for pyridine as shown in Figure 7), the metal can achieve its highest formal oxidation state. X-ray as well as NMR data indicate an interruption of the heterocycle π-system.[22,23] The nucleophilic attack on a similar η^2-N,C coordinated pyridine supported by a Ta aryloxide fragment led to a regioselective C–N bond cleavage, providing models for hydrodenitrogenation (HDN).[22] Oxygen vs sulfur ligation for the ancillary ligands has been discussed.[75] $Nb(silox)_3(PMe_3)$ (**54**), a masked Nb^{III} species, promoted ring

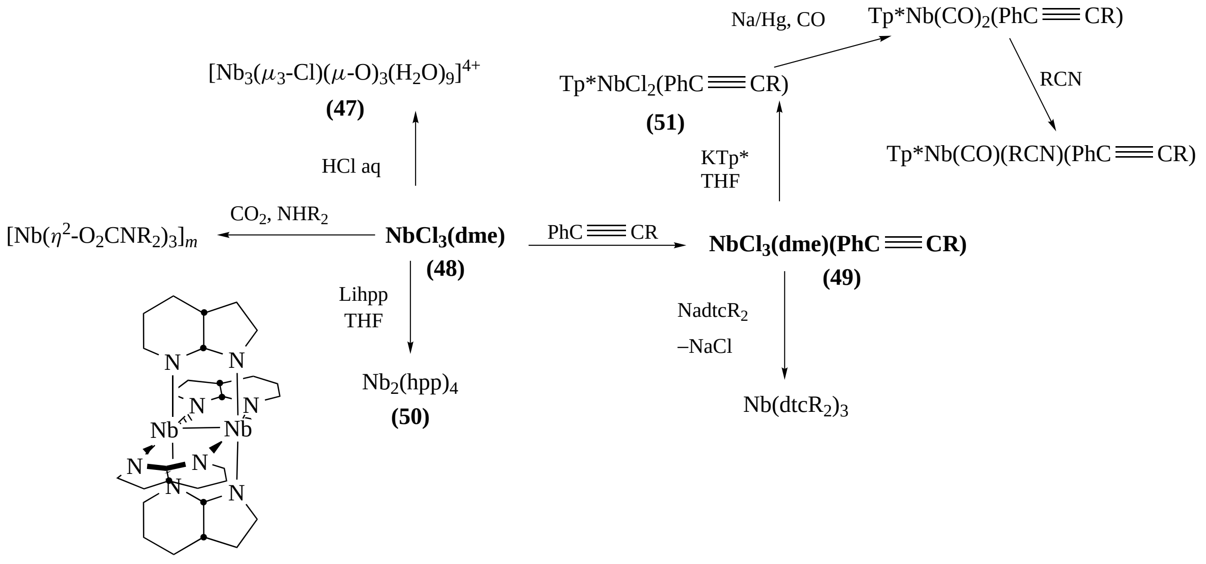

[Nb3(μ3-Cl)(μ-O)3(H2O)9]4+
(47)
HCl aq
CO2, NHR2
[Nb(η2-O2CNR2)3]m
NbCl3(dme)
(48)
Lihpp
THF
Nb2(hpp)4
(50)
PhC≡CR
NbCl3(dme)(PhC≡CR)
(49)
NadtcR2
−NaCl
Nb(dtcR2)3
KTp*
THF
Tp*NbCl2(PhC≡CR)
(51)
Na/Hg, CO
Tp*Nb(CO)2(PhC≡CR)
RCN
Tp*Nb(CO)(RCN)(PhC≡CR)
N
Nb

Scheme 8 Reactivity of Nb^{III} dme halide adducts

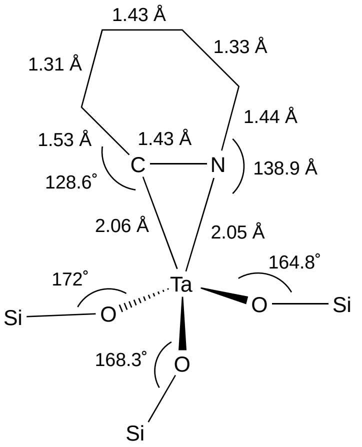

1.43 Å
1.31 Å
1.33 Å
1.44 Å
1.53 Å
1.43 Å
C
N
138.9 Å
128.6°
2.06 Å
2.05 Å
164.8°
172°
Ta
Si
O
O
Si
168.3°
O
Si

Figure 7 The unusual η^2-N,C coordination mode for pyridine in $Ta(silox)_3$(pyridine)

opening of 3,5-lutidine with participation (cyclometallation) of a silox ligand, a rare example for this typically ancillary ligand.[76] Although desoxygenation of small molecules such as CO or NO (**52**) is very fast, (**54**) was more effective for desoxygenation of OPR_3 (R = Me, Ph) giving $MO(silox)_3$.[23]

$$\underset{\mathbf{(52)}}{Ta(silox)_3} + CO \xrightarrow[1\ atm]{C_6H_6,\ rt} (silox)_3Ta{=}O + \underset{\mathbf{(53)}}{(silox)_3Ta{=}C\text{-}C{=}Ta(silox)_3} \qquad (26)$$

As already mentioned, stepwise cleavage of the N≡N bond was assisted by the very reactive Nb=Nb unit (2.659 Å) of a Nb^{III}-calix[4]arene.[45] A 4e reduction gives a Nb^{IV} complex with a bridging hydrazido N_2^{4-} anion [Nb≡N 1.747 Å, N–N 1.390 Å], further 2e reduction using Na lead to a nitride.

5 CLUSTERS WITH NONINTEGRAL OXIDATION STATES

The chemistry of reduced Nb and Ta halides is rich in clusters with various structures. The metal atoms assemble with metal–metal distances close to those in the metal into triangular and tetranuclear clusters but the dominant structural motif is that of the octahedral M_6X_{12} and Nb_6I_8 types.[1,2] Binary, ternary, and quaternary compounds all crystallize in that type. The M_6 clusters are characteristic of the chemistry of the lower oxidation states of Nb and Ta, although not restricted to them. These electron-deficient clusters are based on metal ions with average oxidation numbers between III and I.

The trinuclear clusters derive formally from the M_3X_8 halides, which remain unknown for tantalum.[1] Coordination compounds whose structure is related to that of these halides are represented by tetranuclear clusters such as the $Nb_4Cl_{10}(PMe_3)_6$ complex, the $CsNb_4Cl_{11}$ subhalide,[1] or the mixed–valence $Nb_2^{II}Nb_2^{III}Cl_{12}Li_2(THF)_8$ (**37**) cluster.[77] Their structure consists of Nb_3 units fused into a centrosymmetric rhombus with the capping μ_3-ligands on opposite sides and a planar Nb_4 arrangement (Figure 8).[1] Trimetallic halide cations stabilized by hexamethylbenzene have been obtained by Friedel–Crafts reductive synthesis.[1] Similar frameworks have been observed for oxo Cp*Nb derivatives obtained by reductive aggregation, although their metal oxidation state is higher (Nb_3^{13+} core).

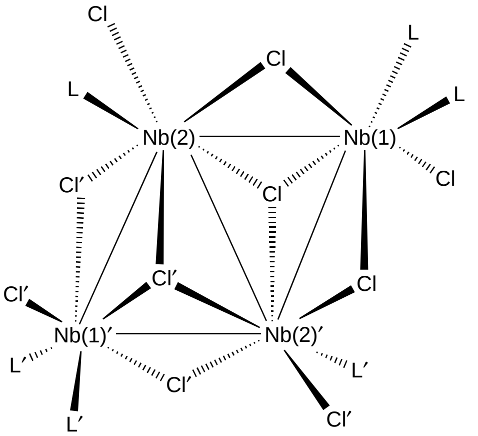

Figure 8 Assembly of trinuclear monocapped units into tetranuclear frameworks: the structure of $Nb_4Cl_{10}(PMe_3)_4$

The lowest halides obtained under strongly reducing conditions, often in aqueous media, or by thermal disproportionation of the higher halides, correspond mostly to the compositions M_6X_{15} (M = Nb, X = F; M = Ta, X = Cl, Br, I), M_6X_{14} (M = Nb, X = Cl, Br; M = Ta, X = Br, I), and Nb_6I_{11}. These high-electron density metal complexes are either insulators or semiconductors[78] and have attracted attention recently for their potential as X-ray contrasting agents.[79] They are actually built up of two types of octahedral clusters; $[M_6X_{12}]^{q+}$ ($q = 2-4$) units can be described as M_6 clusters whose edges are capped by 12 'inner' (bridging) ligands X^i and, in addition, six 'outer' or 'centrifugal' ligands X^a occupy the pseudo quaternary axes of the M_6 core (Figure 9a), thus leading to the general formula $[M_6X^i_{12}]X^a_6$. The $[M_6X_8]^{q+}$ (q = 2, 3) cluster is built up of an M_6 core whose faces are capped by eight inner (μ_3-) ligands and six outer ligands (Figure 9b). Since these compounds can be obtained in aqueous media, their discovery is old, but their correct formulation had to await modern structural X-ray methods. $[Ta_6Cl_{14}]\cdot 8H_2O$, the first subhalide hydrate, was prepared as early as 1907, but it was formulated as $TaCl_2\cdot 2H_2O$.

The fast and quantitative *Disproportionation* of Nb or Ta with their pentahalides in the presence of an alkali halide has long been used. This synthesis is assisted by the stabilization of the cluster through complexation with the $[M_6X_{18}]^{4-}$ anion. The relative stabilities of the other possible clusters depend on the alkali metal.[1] Replacement of the group V metals as reductant by gallium or Ga_2Cl_4 (actually Ga^+ $GaCl_4^-$) has afforded a convenient, cheap, lower temperature route to the $[M_6X_{12}]^{2+}$X = Cl, Br core.[79]

$[Nb_6X_{12}]^{q+}$ and $[Ta_6X_{12}]^{q+}$ clusters are redox-promiscuous possessing five ($q = 1-5$) and four ($q = 1-4$) accessible oxidation states respectively. Disproportionation reactions therefore complicate ligand-substitution chemistry. The hydrates, being more soluble than the anhydrous lower halides, are useful starting materials. The high lability of the 'centrifugal' ligands allows access to mixed halides, hydrates, and oxygen; nitrogen or phosphorus donors complexes of the form $[(M_6X^i_{12})X^a_{6-x}L_x]^{(q-x)+}$ with X^i = Cl, Br, X^a = halide, CN, OSO_2CF_3, OH, BF_4, OMe, and L = H_2O, DMSO, DMF, $OPPh_3$, $OAsPh_3$, NH_3, MeCN, pyridine, PR_3. The stability of $[M_6X_{12}]^{q+}$ compounds toward hydrolysis decreases in the order Ta > Nb, Cl > Br, and with increasing oxidation states. Moisture- and oxygen-sensitive alkoxides of M_6 units have been obtained by substitution reactions; their hydrolysis offers a clean route to cluster hydroxides.[78]

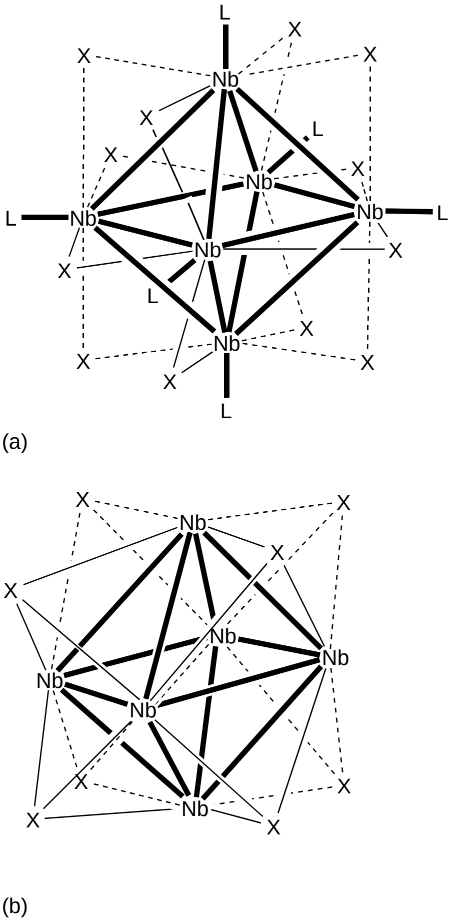

(a)

(b)

Figure 9 Octahedral clusters: (a) the $[M_6X_{12}]^{q+}$ core with additional centrifugal ligands L; (b) the $[M_6X_8]^{q+}$core

The preparation of pure $[M_6X_{12}]^{2+}$ complexes from aqueous solutions is not easy, as oxidation to $[M_6X_{12}]^{3+}$ occurs with air. Oxidation is slow in neutral solution, but fast in acidic or basic media. The presence of $[M_6X_{12}]^{3+}$ may be detected by a band in the UV–vis spectra near 8000 cm^{-1}. Addition of reductants ($SnCl_2$ or Cd) to oxidized solutions allows a return of the green color of the $[M_6X_{12}]^{2+}$ clusters. In the solid state, $Ta_6Cl_{14}\cdot 8H_2O$ undergoes reversible oxidation by *Topotactic* electron–proton transfer. While oxidation under mild conditions (iodine) leads to the paramagnetic yellow $[M_6X_{12}]^{3+}$ clusters, two or more moles of strong oxidants (H_2O_2, Ce^{IV}) led to the red–brown diamagnetic $[M_6X_{12}]^{4+}$

($X = Cl$, Br) derivatives. Oxidation is faster for the chloride than for the bromide clusters. No redox chemistry has yet been reported for the fluoride or iodide clusters. Spontaneous reduction is observed for all $[M_6X_{12}]^{4+}$ clusters, except $[Ta_6Br_{12}]^{4+}$, upon redissolution. Examples of reduction by ligands appear limited to that of $Nb_6Cl_{15}{\cdot}7H_2O$ by phosphines to give $(Nb_6Cl_{12})Cl_2(PR_3)_4$. Its cyclic voltammetry in nonaqueous media revealed three monoelectronic reductions (*see* ***Electrochemistry: Applications in Inorganic Chemistry***). The stabilizing effect of PR_3 leads to a redox chemistry that is more extensive than that in aqueous media. Indeed the monoanions $[(M_6Cl_{12})Cl_2(PR_3)_4]^-$ (**55**), formally derived from the previously unknown $[M_6X_{12}]^+$ core, are detected; attempts to synthesize them have failed so far. The average oxidation state of the metal in (**55**) remains higher than for $[Nb_6I_8]^{2+}$. The $[M_6X_{12}]^{q+}$ clusters displaying several oxidation states with small differences in redox potentials are attractive candidates for multielectron transfer reactions. In addition, the delocalization of the redox orbitals over the clusters might reduce their sensitivity to decomposition. Irradiation (*see* ***Photochemistry of Transition Metal Complexes***) of $[Ta_6Br_{12}]^{2+}$ in oxygen-free HCl solution led to $[Ta_6Br_{12}]^{3+}$ and H_2. An application of these clusters is their intercalation and subsequent oxidation to metal oxide aggregates in pillared clays such as montmorillonite[1] (*see* ***Intercalation Chemistry***).

$[M_6X_{12}]^{q+}$ clusters have been studied by X-ray diffraction, far-IR, UV–vis, XPS, and NQR.[1] The influence of the oxidation state on their structures can be evaluated from comparison of the X-ray data. The regular octahedral symmetry usually considered for the isolated clusters is an oversimplified view and five structural types can be distinguished. A contraction of the M–M bonds is observed upon increase of the number of valence electrons on the metal available for M–M bonding (valence electron count or VEC).[78] The Nb–Nb intracluster distances increase from 2.91, to 2.97, and 3.02 Å when the VEC decreases. The M–M stretching vibration in the IR has been located around $140\,cm^{-1}$ or in the $60-110\,cm^{-1}$ range. *DFT* calculations provide a better description of the relationships between the structural arrangement and the number of valence electron count (VEC) than extended hückel molecular orbital (EHMO) calculations. The observation that both the $[M_6X_{12}]^{2+}$ (16e) and $[M_6X_{12}]^{4+}$ (14e) clusters are diamagnetic and the values of the magnetic moments (*see* ***Magnetism of Transition Metal Ions***) found for the $[M_6X_{12}]^{3+}$ clusters show that the 15th and 16th electrons occupy a nondegenerate molecular orbital. A compilation of visible spectra on the solid state or in solution is available.[1]

A growing chemistry of niobium oxide clusters continues to emerge.[78] The reduced niobates and the NbO suboxide are also built up from condensation of M_6 units through shared vertices, namely, Nb_6O_{12}. Although the inner halides within the $[M_6X_{12}]^{q+}$ core are relatively inert to substitution, Nb_6 and Ta_6 oxohalides, such as $[Nb_6Cl_{12-m}O_m]^{n+}$ ($m = 1-4$) and even Nb_6 oxohydroxohalides, could be obtained by excision reactions.[80] Oxyhalide $A_xLnM_6X_{18-x}O_x$ compounds containing paramagnetic as well as nonparamagnetic lanthanide cations could also be prepared.

The $Rb_3[Nb_6SBr_{17}]$ salt is the first example of an isolated trigonal-primatic Nb_6 cluster. The Nb_6 units (distortion of structure of Figure 9(a)) enclosing an interstitial sulfide are linked through two terminal bromine.[78]

Nb_6I_{11} (**56**) and Nb_6I_9S are the lowest subhalides reported so far for niobium and tantalum. The structure of Nb_6I_{11} is atypical, since it is based on a $[Nb_6I_8]^{3+}$ unit and can be written as $[Nb_6I_8]I_{6/2}$. The $[Nb_6I_8]^{3+}$ moiety is paramagnetic and above 300 °C (**56**) absorbs H_2, giving diamagnetic $Nb_6I_{11}H$, where the hydrogen occupies the center of the Nb_6 cluster, as shown by neutron diffraction. A discrete complex possessing the $[Nb_6I_8]^0$ core, $Nb_6I_8(NH_2Me)_6$, was obtained by reacting (**56**) with the amine in ethanol.[1,78] Unlike Nb_6I_{11} and related compounds, it does not form an extended lattice. It represents the lowest oxidation state yet observed in a Nb_6 cluster.

6 MOLECULAR COMPOUNDS IN OXIDATION STATES II AND LOWER

The number of niobium and tantalum coordination compounds in oxidation states lower than II is limited, and they often are organometallic derivatives involving carbonyl, cyclopentadienyl, or alkenic ligands.

The first member of the series where the metal has a d^3 configuration, $TaCl_2(dmpe)_2$, was reported in 1977. Mononuclear paramagnetic halide adducts such as $MX_2(PMe_3)_4$ and $MCl_2(dmpe)_2$ have been isolated by reduction of monomeric M^Vor M^{IV} phosphine complexes. $TaCl_2(PMe_3)_4$ opens up access to Ta^{IV} and Ta^{III} chlorohydrides.[1] The niobium aryloxide (**57**), whose structure is related to that of $TaCl_2(dmpe)_2$, gives, by oxidation by the parent phenol, an ionic mixed-valence species (**58**) (equation 27). Monomeric t-$NbCl_2(py)_4$ is easily accessible by reduction of (**29**) (Scheme 7).[63] Reduction of $TaCl_5$ in similar condition gave a Ta^{III} species.

$$\underset{\textbf{(57)}}{2Nb(OAr)_2(dmpe)_2} + 2ArOH \xrightarrow[-H_2,\,-dmpe]{} \underset{\textbf{(58)}}{[Nb(OAr)_2(dmpe)_2][Nb(OAr)_6]} \qquad (27)$$

$$Ar = 3,5\text{-}Me_2C_6H_3$$

Species with M≡M triple bonds are recent. Although dinuclear M^{II} species such as $Cp_2Nb_2L_4(\mu\text{-}Cl)_2$ ($L = CO$, $RC{\equiv}CR'$) were known, their Nb–Nb distance is that of a single bond. The synthesis of $TaCl_2(PMe_3)_4$ requires excess of PMe_3 in order to preclude the formation of the M=M bonded dimers $Ta_2Cl_6(PMe_3)_4$ that cannot be reduced by

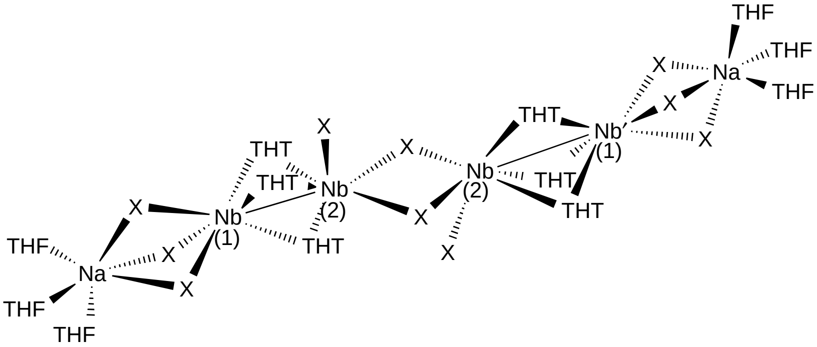

Figure 10 Structure of (**61**) with alternate M–M distances (2.6 Å) for the outer two pairs and more than 3.9 Å for the inner pair ($\mathrm{Nb^2,Nb'^2}$)

Na/Hg. By contrast, reduction of the $\mathrm{M^{III}}$ dimers based on THT (**43**) could be achieved by Na/Hg (equation 28). The metal–metal bond is retained with formation of ionic, diamagnetic, dimers $[\mathrm{M_2X_6(\mu\text{-}THT)_3}]^{2-}$ (**59**), $[\mathrm{Nb_2(\mu\text{-}Cl)_2(\mu\text{-}THT)Cl_3(py)_3}]^-$ (**60**) or tetramers $[\mathrm{Nb_4X_{10}(\mu\text{-}THT)_6}]^{4-}$ (**61**; X = Cl, Br).[69] Their common structural unit is a confacial bioctahedral dimer analogous to that depicted in Figure 6(a). MO calculations have confirmed the presence of a M≡M triple bond for the short M–M distance of (**59**) (≈2.61 Å). (**59**) were the first dimers with Nb or Ta M≡M bonds. Unlike most $\mathrm{M^{II}}$ complexes, which are very reactive, they are unreactive to most donor ligands, and can even be recrystallized unchanged from degassed water. However, the unstability of their sodium salts in THF lead to an insoluble derivative, identified by X ray as a centrosymmetric tetramer (**61**) (Figure 10). It results from the junction of two dinuclear units (**59**) with extrusion of NaX. The X-ray data of (**61**) as well as MO calculations support a M≡M···M≡M bonding sequence.

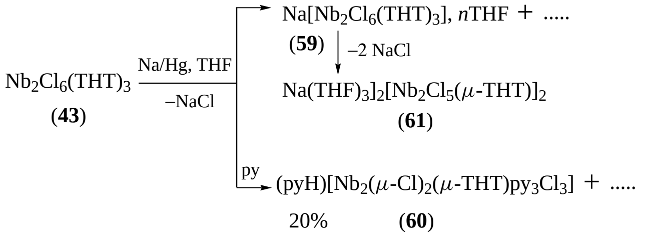

$$\mathrm{Nb_2Cl_6(THT)_3}\ (\mathbf{43}) \xrightarrow[-\mathrm{NaCl}]{\mathrm{Na/Hg,\ THF}} \begin{cases} \mathrm{Na[Nb_2Cl_6(THT)_3]},\ n\mathrm{THF} + \ldots\ (\mathbf{59}) \xrightarrow{-2\,\mathrm{NaCl}} \mathrm{Na(THF)_3]_2[Nb_2Cl_5(\mu\text{-}THT)]_2}\ (\mathbf{61}) \\ \xrightarrow{\mathrm{py}} \mathrm{(pyH)[Nb_2(\mu\text{-}Cl)_2(\mu\text{-}THT)py_3Cl_3]} + \ldots\quad 20\%\ (\mathbf{60}) \end{cases}$$

(28)

Triply bonded dimers where Nb has a $\sigma^2\pi^4$ configuration could also be stabilized with anionic ligands having N–C–N moieties such as 7-azaindolyl or hpp (1,3,4,6,7,8-hexahydropyrimido[1,2-a]pyrimidinate). The tetragonal lantern $\mathrm{Nb_2(hpp)_4}$ compound (**50**) with a Nb–Nb distance of 2.035(9) Å represents the shortest triple bond reported so far for niobium.[81] This distance is much shorter than that found in the metal (2.85 Å). Attempts to reduce (**50**) with $\mathrm{NaBEt_3H}$ afforded an adduct with a B–H···Na interaction. The diamagnetic $\mathrm{Nb_2Cl_5Li(tmeda)_3}$ (**62**) cluster obtained by reacting $\mathrm{Nb_2Cl_6(tmeda)_2}$ with Li diisopropylamide provides another example of a Nb≡Nb triple bond. Its formation was attributed to disproportionation of a $\mathrm{Nb^{III}}$ intermediate since $\mathrm{Nb^{IV}}$ species were isolated with other Li amides. The reaction of (**62**) with alkali 7-azaindolyl affords dia- or paramagnetic $\mathrm{Nb^{II}}$ dimers depending on the alkali metal.[82] Coordination of LiCl for the azaindolyl $\mathrm{Nb^{II}}$ species or of Na with the 'pseudo-allylic' units of hpp for (**50**) occurs at the expenses of the Nb≡Nb bond.

Other examples of $\mathrm{M^{II}}$ species are dialkylcarbamates $\mathrm{M(\eta^6\text{-}C_6Me_6)(O_2CNiPr_2)_2}$[36] and the $\mathrm{Nb(TCNE)}_x$ molecular magnets[83] grown as films by CVD (XPS accounts for $\mathrm{Nb^{2+}}$ species).

Compounds in oxidation state +1 generally derive from reduction (often reductive *Carbonylation*) of $\mathrm{M^{II}}$ complexes such as the seven-coordinate $\mathrm{M(CO)_3X(PMe_3)_3}$ (X = Cl, Br) complexes or of $\mathrm{M^{III}}$ ones such as $\mathrm{Tp^*M(CO)_2(PhC{\equiv}CR)}$ (Scheme 8). Complexes such as $\mathrm{NbX(CO)_2(dppe)_2}$ (X=Cl, Br), $\mathrm{NbI(CO)_2(CNR)_2(dppe)}$ and $\mathrm{TaH(CO)_4(dppe)}$ have been reported.[22] The one-electron oxidation of bis-mesitylene Nb in the presence of ligands (L = CO, alkyne) giving the bent $[\mathrm{Nb(Mes)_2L}]^+$ cation is another approach. Heating of the alkyne derivative results in total mesitylene displacement and formation of a neutral species with two η^6-aryl bonds of the $\mathrm{BPh_4}$ original counterion (*see* ***Niobium & Tantalum: Organometallic Chemistry***). Well-characterized noncarbonyl compounds are $\mathrm{Ta[H_2Al(OC_2H_4OMe)_2(dmpe)_2]}$, obtained through the reduction of $\mathrm{TaCl_2(dmpe)_2}$ by vitride[1] or the $\mathrm{M(\mathit{i}Pr_2\text{-}dad)_3}^+$ cation.[84] Reduction of $\mathrm{TaCl_5}$ with $\mathrm{LiBH_4}$ in the presence of bis(dimethylphosphino)methane gave (**63**), the first structurally characterized metalloborane complex with a $\mu\text{-}\mathrm{BH_3}$ ligand (equation 29). Donation of d electrons from the $\mathrm{Ta^I}$ center to the electron-deficient $\mu\text{-}\mathrm{BH_3}$ provides the best explanation for the X-ray data. A Ta=Ta bond is consistent with the Ta–Ta distance (≈2.78 Å) and the diamagnetism.[67] Protonation of $[\mathrm{M(PF_3)_6}]^-$ by $\mathrm{H_2SO_4}$

afforded the $M(PF_3)_6H$ hydrides, the Nb one being quite unstable.[85]

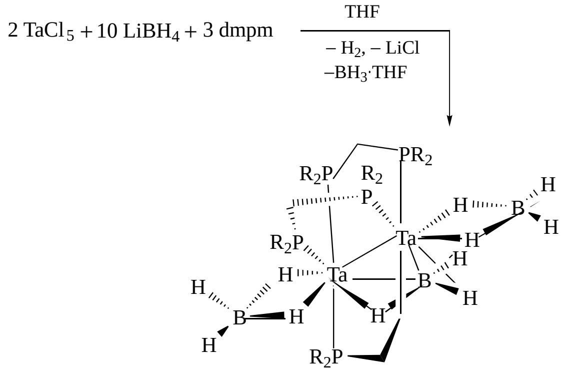

(29)

$Ta_2(\mu\text{-}BH_3)(\mu\text{-dmpm})_3(\eta^2\text{-}BH_4)_2$ (**63**)

Two-electron transfer processes applied to the hexacarbonyl $[M(CO)_6]^-$ (**38**) anions using reactants such as hydracids, nickel acetylacetonate, or metal halides offered $[M_2Cl_3(CO)_8]^-$, the first halocarbonyl complexes without ancillary ligands (*see Ancillary Ligand*), or the β-diketonate $Ta(acac)(CO)_4(THF)$.[1,22] The cothermolysis of $Cp''Ta(CO)_4$ ($Cp'' = 1,3\text{-}t\text{Bu}_2C_5H_3$) with As_4 or $(RAs)_n$ afforded polynuclear Ta derivatives with As_n moieties ($n = 3$, 6 or 8) as ligands. The phosphido-phosphinidene coordination mode of a P_2 ligand has been realized in the trinuclear complex $(Cp''Ta)_3(P_4)(P_2)$ obtained by thermolysis of $Cp''Ta(CO)_4$ and P_4.[86]

Metal vapor synthesis techniques (*see* ***Metal Vapor Synthesis of Transition Metal Compounds***) are the most convenient access to M^0 derivatives, solution routes being limited to the synthesis $Nb(Mes)_2$.[5] Highly air-sensitive, paramagnetic but crystalline $M(dmpe)_3$ with a distorted octahedral geometry were isolated in good yields. The formally zerovalent 17e $M(i\text{Pr}_2\text{-dab})_3$ species were shown by *DFT calculations* to be actually $[Ta]^+ [(i\text{Pr}_2\text{dad})_3]^-$ rather than Ta^0 species.[84] The 17e species, $Ta(CO)_4(dppe)$, has been the first Ta^0 carbonyl isolated. The first nitrosyl complexes of Nb and Ta were reported in 1998.[87] They were obtained in high yields according to equation (30). Diazald (N-methyl-N-nitroso-p-toluenesulfonamide) was the source of the nitrosyl. The M–N bond distances suggest multiple M–N bonding due to M → NO back bonding.

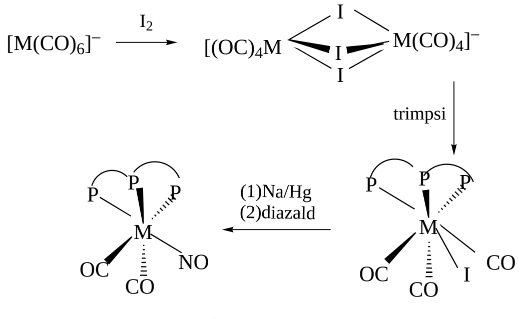

(30)

trimpsi = $t\text{BuSi}(CH_2PMe_3)_3$

$[Nb(CO)_6]^-$ (**38**) has become accessible in high yield by reduction of $NbCl_4(THF)_2$ at atmospheric pressure (Scheme 7).[85] $[Nb(PF_3)_6]^-$ is accessible either by photolysis (*see* ***Photosynthesis***) of $[Nb(CO)_6]^-$ under PF_3 or by a reductive route similar to that of (**38**). The ^{93}Nb NMR chemical shifts suggest weaker Nb–PF_3 bonds than Nb–CO ones.[1]

No derivative in which niobium or tantalum displays an oxidation state of −II has been reported so far, while carbonyl complexes derived from $[M(CO)_5]^{3-}$ represent the only coordination compounds for these metals in oxidation state −III.

7 RELATED ARTICLES

Metal-mediated Protein Modification; Niobium & Tantalum: Organometallic Chemistry; Polynuclear Organometallic Cluster Complexes.

8 FURTHER READING

J. Rouxel, *Acc. Chem. Res.*, 1992, **25**, 328.

9 REFERENCES

1. L. G. Hubert-Pfalzgraf, M. Postel, and J. G. Riess, in ‘Comprehensive Coordination Chemistry’, eds. G. Wilkinson, R. D. Gillard, and J. A. McCleverty, Pergamon, London 1987, Vol. 3, Chap. 34, p. 585.
2. R. W. Berg, *Coord. Chem. Rev.*, 1992, **113**, 1.
3. T. P. Kee, *Coord. Chem. Rev.*, 1995, **146**, 17.
4. T. P. Kee, *Coord. Chem. Rev.*, 1997, **162**, 255.
5. J. Malito, *Annu. Rep. Prog. Inorg. Chem. A: Inorg. Chem.*, 2000, **96**, 175.
6. J. H. Shin and G. Parkin, *Organometallics*, 1998, **17**, 5689.
7. P. J. McKarns, M. J. Heeg, and C. H. Winter, *Inorg. Chem.*, 1998, **37**, 4743.
8. K. C. Jayaratne, G. P. A. Yap, B. S. Hagerty, A. L. Rheingold, and C. H. Winter, *Inorg. Chem.*, 1996, **35**, 4910.
9. L. G. Hubert-Pfalzgraf, ‘Encyclopedia of Inorganic Chemistry’, Wiley, New York 1994, Vol 5, p. 2444.
10. S. Minhas, A. Devlin, D. T. Richens, A. C. Benyei, and P. Lightfoot, *Dalton Trans.*, 1998, 953.
11. D. Bayot, B. Tinant, B. Mathieu, J. P. Declercq, and M. Devillers, *Eur. J. Inorg. Chem.*, 2003, 737.
12. Y. Matsuda and Y. Murakami, *Coord. Chem. Rev.*, 1988, **92**, 157.
13. D. Y. Dawson, H. Brand, and J. Arnold, *J. Am. Chem. Soc.*, 1994, **116**, 9797.

14. D. C. Bradley, R. C. Mehrotra, I. P. Rothwell, and A. Singh, 'Alkoxo and Aryloxo Derivatives of Metals', Academic Press, London, 2001.
15. N. Y. Turova, E. P. Turevskaya, V. G. Kessler, and M. I. Yanovskaya, 'The Chemistry of Metal Alkoxides', Kluwer Academic Publishers, Boston, MA, 2002.
16. L. G. Hubert-Pfalzgraf, *Inorg. Chem. Commun.*, 2003, **6**, 102.
17. A. C. Jones, *J. Mater. Chem.*, 2002, **12**, 2576.
18. M. Aresta, A. Dibenetto, and C. Pastore, *Inorg. Chem.*, 2003, **42**, 3256.
19. Y. Kim, P. N. Kapoor, and J. G. Verkade, *Inorg. Chem.*, 2002, **41**, 4834.
20. X. Hun and D. Antonelli, *Angew. Chem., Int. Ed. Engl.*, 2002, **41**, 214.
21. S. Kobayashi, N. Hamasaki, M. Suzuki, M. Kimura, H. Shirai, and H. Hanabusa, *J. Am. Chem. Soc.*, 2002, **124**, 6550.
22. D. E. Wigley and S. D. Gray, in 'Comprehensive Organometallic Chemistry', 2nd edn., eds. E. W. Abel, F. G. A. Stone, and G. Wilkinson, Oxford, 1995.
23. A. S. Veige, Le. Grande. M. Slaughter, E. B. Lobovsky, P. T. Wolczanski, N. Matsunaga, S. A. Decker, and T. R. Cundari, *Inorg. Chem.*, 2003, **42**, 6204.
24. A. J. Hoslin and D. W. Stephan, *Coord. Chem. Rev.*, 2002, **233–234**, 107.
25. H. Kawaguchi and T. Matsuo, *J. Am. Chem. Soc.*, 2003, **125**, 14254.
26. C. S. Weinert, P. E. Fanwick, and I. P. Rothwell, *Organometallics*, 2002, **21**, 484.
27. B. Castellano, E. Solari, C. Floriani, N. Re, A. Chiesi-Villa, and C. Rizzoli, *Chem. Eur. J.*, 1999, **5**, 722.
28. K. Joshi, J. Bao, A. S. Goldman, and J. Kohn, *J. Am. Chem. Soc.*, 1992, **114**, 6649.
29. D. W. Stephan and T. T. Nadasdi, *Coord. Chem. Rev.*, 1996, **147**, 147.
30. C. J. Carmalt, C. W. Dinnage, I. V. Parkin, A. J. P. White, and D. J. Williams, *Inorg. Chem.*, 2002, **41**, 3668.
31. J. Fernandez-Baeza, F. A. Jalon, A. Otero, M. E. Rodrigo-Blanco, and M. Etienne, *J Chem Soc, Dalton Trans.*, 1998, 769.
32. R. Patov and D. Fenske, *Z. Anorg. Allg. Chem.*, 2002, **628**, 2790.
33. A. Lorenz and D. Fenske, *Angew. Chem., Int. Ed. Engl.*, 2001, **40**, 4402.
34. B. S. Mandimutsira, S. J. Chen, R. A. Reynolds, and D. Coucouvanis, *Polyhedron*, 1997, **16**, 3911.
35. H. T. Chiu, C. N. Wang, and S. H. Chuang, *Chem. Vap. Dep.*, 2000, **6**, 223.
36. D. Belli Dell'Amico, F. Calderazzo, L. Labella, F. Marcheti, and G. Pampaloni, *Chem. Rev.*, 2003, **103**, 3857.
37. Z. Fei, S. Busse, and F. T. Edelmann, *JCS Dalton Trans.*, 2002, 2587.
38. P. J. Bailey and S. Pace, *Coord. Chem. Rev.*, 2001, **214**, 91.
39. A. S. Batsanov, A. V. Churakov, J. A. K. Howard, A. K. Hughes, A. L. Johnson, A. J. Kingsley, I. S. Neretin, and K. Wade, *Dalton*, 1999, 3867.
40. A. V. Korolev, A. L. Rheingold, and D. S. Williams, *Inorg. Chem.*, 1997, **36**, 2647.
41. A. Schorm and J. Sundermeyer, *Eur. J. Inorg. Chem.*, 2001, 2947.
42. H. Cai, T. Chen, X. Wang, A. J. Schultz, T. F. Koetzle, and Z. Xue, *Chem. Commun.*, 2002, 230.
43. Z. Wu, H. Cai, X. Yu, J. R. Blanton, J. B. Diminnie, H. J. Pan, Z. Xue, and J. C. Brian, *Organometallics*, 2000, **21**, 3973.
44. S. Gambarotta, *J. Organomet. Chem.*, 1995, **500**, 117; M. D. Fryzuk, *Inorg. Chem. Highlights*, 2002, **216**, 73.
45. A. Caselli, E. Solari, R. Scopelliti, C. Floriani, N. Re, C. Rizzoli, and A. Chiesi-Villa, *J. Am. Chem. Soc.*, 2000, **122**, 3652.
46. H. Kawaguchi and T. Matsuo, *Angew. Chem., Int. Ed. Engl.*, 2002, **41**, 2792.
47. M. D. Fryzuk, B. A. McKay, and B. O. Patrick, *J. Am. Chem. Soc.*, 2003, **125**, 3234.
48. K. Weber, K. Korn, M. Schulz, K. Korth, and J. Sundermeyer, *Z. Anorg. Allg. Chem.*, 1999, **625**, 1315.
49. M. G. Fickes, A. L. Odon, and C. C. Cummins, *Chem. Commun.*, 1997, 1993.
50. A. Abarca, M. V. Galakhov, J. Gracia, A. Martin, M. Mena, J. M. Poblet, J. P. Sarasa, and C. Yelamos, *Chem. Eur. J.*, 2003, **9**, 2337.
51. M. Etienne, *Coord. Chem. Rev.*, 1996, **156**, 205.
52. C. Yelamos, K. R. Gust, A. G. Baboul, M. J. Heeg, H. B. Schlegel, and C. H. Winter, *Inorg. Chem.*, 2001, **40**, 6451.
53. T. Spaniel, H. Gorls, and J. Scholz, *Angew. Chem., Int. Ed. Engl.*, 1998, **37**, 1862.
54. M. M. Banaszak Holl, P. T. Wolczanski, D. Properpio, A. Bielecki, and D. B. Zax, *Chem. Mater.*, 1996, **8**, 2468.
55. S. Blaurock and E. Hey-Hawkins, *Eur. J. Inorg. Chem.*, 2002, 2975.
56. J. T. Scheper, K. C. Jayaratne, L. M. Liable-Sands, G. P. A. Yap, A. L. Rheingold, and C. H. Winter, *Inorg. Chem.*, 1999, **38**, 4354.
57. K. B. P. Ruppa, S. Gambarotta, and G. P. A. Yap, *Inorg. Chim. Acta*, 1998, **280**, 143.
58. C. Floriani, E. Solari, F. Franceschi, R. Scopelliti, P. Belanzoni, and M. Rosi, *Chem. Eur. J.*, 2001, **7**, 3052.
59. S. Suh and D. M. Hoffman, *Inorg. Chem.*, 1996, **35**, 5015.
60. S. G. Bott, D. M. Hoffman, and S. P. Rangarajan, *Dalton*, 1996, 1979.
61. P. Berno and S. Gambarotta, *Organometallics*, 1995, **14**, 2159.
62. F. A. Cotton, L. M. Daniels, and C. A. Murillo, *J. Am. Chem. Soc.*, 1996, **118**, 12449.
63. F. A. Cotton, J. H. Matonic, C. A. Murillo, and X. Wang, *Bull. Soc. Franc. Chim.*, 1996, **133**, 711.

64. M. D. Fryzuk, C. M. Kozak, and B. O. Patrick, *Inorg. Chim. Acta*, 2003, **345**, 53.
65. R. Pradham, C. Desplanches, P. Guionneau, and J. P. Sutter, *Inorg. Chem.*, 2003, **42**, 6607.
66. M. Sokolov, O. Gerasko, A. Virovets, V. Fedorov, and K. Hegetschweiler, *Inorg. Chim. Acta*, 1998, **271**, 222.
67. V. P. Fedin, V. E. Fedorov, H. Imoto, and T. Saito, *Polyhedron*, 1997, **16**, 995.
68. H. Brunner, H. Cattey, D. Evrard, M. Kubicki, Y. Mugnier, E. Vigier, J. Wachter, R. Wanninger, and M. Zabel, *Eur. J. Inorg. Chem.*, 2002, 1315.
69. F. A. Cotton, C. A. Murillo, and X. Wang, *J. Am. Chem. Soc.*, 1998, **120**, 9594.
70. F. A. Cotton and M. Shang, *Inorg. Chim. Acta*, 1994, **227**, 191.
71. F. A. Cotton, L. M. Daniels, L. M. Daniels, C. A. Murillo, and X. Wang, *Inorg. Chem.*, 1997, **36**, 896.
72. M. May, M. Gantt, C. Hoadley, T. Batten, W. Sayers, and V. Katovic, *Inorg. Chem.*, 2003, **42**, 7137.
73. A. Spannenberg, W. Baumann, and U. Rosenthal, *Appl. Organomet. Chem.*, 2000, **14**, 611.
74. T. Oshiki, K. Tanaka, J. Yamada, T. Ishiyama, Y. Kataoka, K. Mashima, K. Tani, and K. Takai, *Organometallics*, 2003, **22**, 464.
75. J. B. Bonanno, A. S. Veige, P. T. Wolczanski, and E. B. Lobovsky, *Inorg. Chim. Acta*, 2003, **345**, 173.
76. P. A. Fox, M. A. Bruck, S. D. Gray, N. E. Gruhn, C. Grittini, and D. E. Wigley, *Organometallics*, 1998, **17**, 2720.
77. M. Tayebani, G. Aharonian, K. Feghali, S. Gambarotta, and G. P. A. Yap, *Inorg. Chem.*, 2001, **40**, 2442.
78. T. G. Gray, *Coord. Chem. Rev.*, 2003, **243**, 213.
79. D. N. T. Hay, D. Swenson, and L. Messerlé, *Inorg. Chem.*, 2002, **41**, 4700.
80. N. G. Naumov, S. Cordier, F. Gulo, T. Roisnel, V. E. Federov, and C. Perrin, *Inorg. Chim. Acta*, 2003, **350**, 503.
81. F. A. Cotton, J. H. Matonic, and C. A. Murillo, *J. Am. Chem. Soc.*, 1998, **120**, 6047.
82. M. Tayebani, K. Feghali, S. Gambarotta, and G. P. A. Yap, *Inorg. Chem.*, 2001, **40**, 1399.
83. E. Lamouroux, E. Alric, H. Casellas, L. Valade, D. de Caro, M. Etienne, and D. Gatteschi, *Electrochem. Soc., Proc. Chem. Vapor Depos. XVI and EuroCVD 14*, 2003, **2**, 1040.
84. P. J. Daff, M. Etienne, B. Donnadieu, S. Z. Knottenbelt, and J. E. McGrady, *J. Am. Chem. Soc.*, 2002, **124**, 3818.
85. M. V. Barybin, J. E. Ellis, M. K. Pomije, M. L. Tinkham, and G. F. Warnock, *Inorg. Chem.*, 1998, **37**, 6518.
86. K. Mast, J. Meiers, O. J. Scherer, and G. Wolmerhauser, *Z. Anorg. Allg. Chem.*, 1999, **625**, 70.
87. J. P. Daff, P. Legzdins, and S. J. Rettig, *J. Am. Chem. Soc.*, 1998, **120**, 2688.

Niobium & Tantalum: Organometallic Chemistry

Ruitao Wang & Ziling Xue
The University of Tennessee, Knoxville, TN, USA

Based in part on the article Niobium & Tantalum: Organometallic Chemistry by David E. Wigley which appeared in the Encyclopedia of Inorganic Chemistry, First Edition.

1	Introduction	1
2	Carbonyls, Isocyanides, Phosphaalkynes, and Azides	1
3	η^1-Complexes	3
4	Alkylidenes and Alkylidynes	7
5	η^2-Complexes	9
6	Metallacyclic Complexes	12
7	π-Complexes of Carbocyclic, Ene, Enyl and Related Ligands	16
8	Heterometal Clusters	19
9	Niobium and Tantalum Complexes in Catalysis and Metal-Mediated Organic Synthesis	19
10	Related Articles	22
11	References	23

Abbreviations

cb = carbazole; [CNN] = $[C_6H_4(CH_2N(Me)CH_2CH_2NMe_2)\text{-}2]^-$; COT = cyclooctatetraene; Cp = η^5-C_5H_5; Cp* = η^5-C_5Me_5; Cp′ = η^5-$C_5H_4SiMe_3$; Cy = cyclohexyl; DME = 1,2-dimethoxyethane; dmpe = $Me_2PCH_2CH_2PMe_2$; dppe = 1,2-bis(diphenylphosphino)ethane; $Et_2C_2B_4H_4^{2-}$ = nido-carborane ligand; Mes = mesitylene; $[N_3N]^{3-}$ = $[N(CH_2CH_2NSiMe_3)_3]^{3-}$; $[N_3N^*]^{3-}$ = $[N(CH_2CH_2NSiEt_3)_3]^{3-}$; [NCN] = $[2,6\text{-}(CH_2NMe_2)_2\text{-}C_6H_3]^-$; Np = CH_2Bu^t; $^R[P_2N_2]$ = $RP(CH_2SiMe_2NSiMe_2CH_2)_2PR$ (R = Ph, Cy); silox = $Bu^t{}_3SiO$; THT = tetrahydrothiophene; TMEDA = N,N,N',N'-tetramethyethylenediamine; Tol = tolyl, Tp = hydrotris(pyrazolyl)borate; Tp* = hydrotris(3,5-dimethylpyrazolyl)borate; Xyl = 2,6-dimethylphenyl.

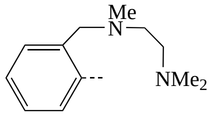

CNN

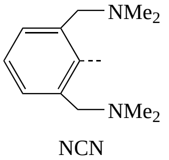

NCN

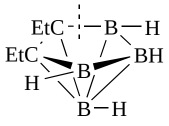

$Et_2C_2B_4H_4$

1 INTRODUCTION

Organometallic chemistry of niobium and tantalum has developed rapidly over the past ten years, as judged by the number of papers published in the field. This review covers the literature between 1993 to early 2003. *SciFinder* (*Chemical Abstracts*) searches were conducted on ‘‘niobium (Nb) or tantalum (Ta)’’ between 1993 and early 2003. The hits were then sorted so that those in Section 29 (Organometallic and Organometalloidal Compounds) were selected. In addition, hits in Sections 78 (Inorganic Chemicals and Reactions) and 67 (Catalysis, Reaction Kinetics, and Inorganic Reaction Mechanisms) were also reviewed. This paper is primarily based on the literature from these searches. Because of the limit of space, the current paper highlights leading literature during this period. General references for niobium and tantalum organometallic chemistry include the chapter by Wigley and Gray in *Comprehensive Organometallic Chemistry II*, which reviews the literature through 1993.**[1]** M refers to Nb and Ta throughout this chapter.

2 CARBONYLS, ISOCYANIDES, PHOSPHAALKYNES, AND AZIDES

2.1 Carbonyls and Substituted Carbonyls

2.1.1 *Carbonyl Complexes without Cyclopentadienyl Ligands*

Unlike stable $V(CO)_6$, neutral $M(CO)_6$ (M = Ta, Nb) have not been characterized (except in matrix-isolation experiments,**[2]** *see Matrix Isolation*). Neutral mixed-ligand complexes were unknown until 1996. The first Ta(0) carbonyl complex $Ta(CO)_4(dppe)$ was synthesized by the reaction of hydride $TaH(CO)_4(dppe)$ with the $(p\text{-}Bu^tC_6H_4)_3C\bullet$ radical.**[3]** This complex exists as a CO-bridged dimer in solid and, in solution, as an equilibrium mixture of the monomer and dimer.**[4]**

Density functional theory calculations of 17-electron (*see Seventeen Electron Configuration*), metal-centered radical $Ta(CO)_6$ and its dimer $[Ta(CO)_6]_2$ show that the dimer is energetically bound with respect to the monomer. The bidentate phosphine ligand in $Ta(CO)_4(H_2PCH_2CH_2PH_2)$ leads to several energetically competitive chelated dimers. In these dimers, linear semibridging carbonyls (*see Semibridging Carbonyl Ligand*) support a weak, delocalized Ta−Ta interaction.**[5]**

A recent review gives a chronological survey of the syntheses and characterizations of homoleptic mononuclear metal-carbonyl (*see* ***Carbonyl Complexes of the Transition Metals***) anions.**[6]** $[M(CO)_6]^-$ is a key precursor to niobium and tantalum carbonyls. More reliable synthesis of $[Ta(CO)_6]^{-}$**[7]**

and a higher yield route to $[Nb(CO)_6]^-$[8] are now available. Reduction of $[Nb(CO)_6]^-$ by sodium in liquid ammonia affords $[Nb(CO)_5]^{3-}$, the only known Nb^{3-} species.[8] Treatment of $[Et_4N][M(CO)_6]$ with I_2 produces $[M_2(\mu\text{-}I)_3(CO)_8]^-$. Addition of trimpsi [trimpsi = $Bu^tSi(CH_2PMe_2)_3$] to $[M_2(\mu\text{-}I)_3(CO)_8]^-$ affords (trimpsi)$M(CO)_3I$ (**1**). Treatment of (**1**) with Na/Hg followed by diazald results in the formation of (trimpsi)$M(CO)_2(NO)$, the first nitrosyl complexes of niobium and tantalum.[9]

Vibronic structure and coupling (*see Vibronic Coupling*) in the electronic spectra of $[Ph_4P][Ta(CO)_6]$ have been studied. The emission spectrum originates from a ligand field transition. There is an apparent energy gap between the red and the blue regions of the spectrum, and this is interpreted in terms of Herzberg–Teller coupling of the ligand field state, with an allowed Ta-to-CO charge-transfer (*see Charge Transfer*) excited state.[10]

2.1.2 Cyclopentadienyl Carbonyl Complexes

The cyclopentadienyl carbonyl derivatives $(C_5R_5)M(CO)_4$ are easily prepared by reductive carbonylation (*see Reductive Carbonylation*) of $(C_5R_5)MCl_4$ under CO. $[M_2(\mu\text{-}Cl)_3(CO)_8]^-$ readily reacts with NaC_5H_4R to give $(C_5H_4R)M(CO)_4$.[11] Reduction of the borollide complex Cp*$[C_4H_4B\text{-}NPr^i{}_2]TaCl_2$ with Mg under CO gives Cp*$[C_4H_4B\text{-}NPr^i{}_2]Ta(CO)_2$.[12] Carbonylation of CpTa(η^4-butadiene)(η^2-C_2H_4)(PMe_3) afforded monocarbonyl CpTa(η^4-butadiene)(CO)(PMe_3) and dicarbonyl CpTa(η^4-butadiene)$(CO)_2$.[13]

Gas-phase photoelectron spectroscopy has been used to study the bonding in $CpM(CO)_4$, $Cp'M(CO)_4$, and (η^5-C_5H_4COMe)$Nb(CO)_4$. The character of two overlapping ionizations in the lowest ionization energy region is dominated by the carbonyls rather than by the metals. The second group of ionizations corresponds to orbitals with predominantly cyclopentadienyl π character that donate to empty metal d orbitals. A much larger shift of these ionizations is observed upon cyclopentadienyl substitution.[14]

μ-Phosphido complex $Cp''CpTa(\mu\text{-}CO)(\mu\text{-}PMe_2)W(CO)_4$ ($Cp'' = 1\text{-}Bu^t\text{-}3,4\text{-}Me_2\text{-}C_5H_2$) reacts with an optically active phosphine (PRR′R″) to give a pair of optically active diastereoisomers $Cp''CpTa(CO)(\mu\text{-}PMe_2)W(CO)_4$(PRR′R″). X-ray structure determinations of these diastereoisomers lead to the assignment of absolute configurations of the Ta chiral centers.[15]

2.2 CO Reductive Coupling

The reductive coupling (*see Reductive Coupling*) of CO ligands in $M(CO)_2(dmpe)_2Cl$ (M = V, Nb, or Ta) to form $M(R_3SiOC{\equiv}COSiR_3)(dmpe)_2X$ occurs via sequential formation of $Na[M(CO)_2(dmpe)_2]$ and $M({\equiv}COSiR_3)(CO)(dmpe)_2$ complexes. Reactions of siloxycarbynes (*see Carbyne Complexes*) $M({\equiv}COSiR_3)(CO)(dmpe)_2$ ($R_3 = Pr^i{}_3$, **2a**; Bu^tPh_2, **2b**; Ph_3, **2c**) with, for example, Me_3SiCl afford CO reductive coupling products $Ta(R_3SiOC{\equiv}COSiMe_3)(dmpe)_2Cl$. Kinetic studies of carbyne/CO coupling in the reaction of $Ta({\equiv}COSiPr^i{}_3)(CO)(dmpe)_2$ with Me_3SiCl to form $Ta(Me_3SiOC{\equiv}COSiPr^i{}_3)(dmpe)_2Cl$ show that the reaction is first order in both the Ta complex and Me_3SiCl in the presence of excess $Bu^n{}_4NBPh_4$, suggesting that initial electrophilic attack of the silyl reagent occurs at the O atom of the carbonyl ligand.[16,17] Reactions of carbon-based electrophiles (e.g. AcCl) with the siloxycarbynes such as (**2b**) and $M(COSiBu^tPh_2)(CO)(depe)_2$ give mixed siloxy/alkoxyacetylene complexes $M(Ph_2Bu^tSiOC{\equiv}COAc)(P_2)_2Cl$ (P_2 = dmpe, depe).[18] Similarly, AcCl reacts with $Na[Ta(CO)_2(P_2)_2]$ to yield $Ta(AcOC{\equiv}COAc)(P_2)_2Cl$ through direct alkylation at the terminal CO ligands.[18] Treatment of methylene $Cp_2Ta({=}CH_2)Me$ with carbonyls $Co_2(CO)_8$ and $Fe_2(CO)_9$ results in CO coupling reactions to yield trinuclear complexes (**3**).[19,20]

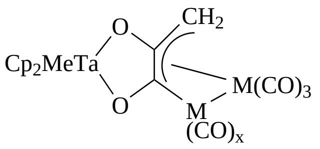

(**3**) M = Co, x = 3
M = Fe, x = 4

Reaction of Cp*$TaMe_2$(=NXyl) with CO gives an ene diolate [Cp*Ta(=NXyl)Me]$_2${μ-η^2-OC(Me)=C(Me)O} via intermolecular coupling between acyls of an intermediate Cp*TaMe{=NXyl}{η^2-C(Me)=O} (**4**).[21,22] In comparison, the reaction of the chloro analog Cp*TaMeCl(=NXyl) with CO yields an unexpected oxo η^2-iminoacyl complex Cp*TaCl(O)[η^2-C(Me)=NXyl] through an intermediate Cp*TaCl(=NXyl)[η^2-C(Me)=O].[21]

Similar coupling reactions were observed when $[Ta(OEP)Me_2](BPh_4)$ (OEP = octaethylporphyrin) and a bis (amidinate) complex $[PhC(NSiMe_3)_2]_2TaMe_3$ were added CO to give {Ta(OEP)[OC(Me)=CMe(O)]}(BPh_4),[23] and $[PhC(NSiMe_3)_2]_2Ta[OC(Me)=C(Me)O]Me$,[24] respectively.

2.3 Complexes of Isocyanides, Phosphaalkynes, Azides, and the Reductive Coupling of the Ligands

The interests in homoleptic (*see Homoleptic Compound*) isocyanide (‘isonitrile,’ *see Isocyanide Ligands*) complexes of transition metals have largely been associated with their similarities to metal carbonyls. The greater versatility of isocyanide ligands in comparison to CO makes isocyanide complexes potentially valuable reagents in synthetic chemistry and catalysis. The dication $[V(CNBu^t)_6]^{2+}$ reported in 1980 remained the sole example of a homoleptic group 5 metal isocyanide until 1999, when the first binary

Nb and Ta isocyanides were isolated.[25] Two-electron oxidation of anions $[M(CO)_6]^-$ by $AgBF_4$ in the presence of CNXyl and a mixture of CNXyl and I_2 yields $[M(CNXyl)_7](BF_4)$ and $MI(CNXyl)_6$, respectively.[25] Direct reactions of $[M(CO)_6]^-$ with CNR and X_2 also yield halo isocyanide complexes such as $[I_2M^{III}(CNBu^t)_6]I$ and $ITa(CO)_3(CNBu^t)_3$. In the presence of a small amount of water, the reaction of $[Nb(CO)_6]^-$ gives aminoalkyne complexes $[X_2Nb(CNBu^t)_4(Bu^tHNC{\equiv}CNHBu^t)]X$ (X = I, Br), suggesting successive protonation and intramolecular reductive isocyanide coupling (*see Reductive Coupling*) mediated by a Nb^I center.[26] Direct nitrosylation of $[M(CO)_6]^-$ with $(NO)^+$ in the presence of CNXyl yields *cis*-$[M(NO)_2(CNXyl)_4]^+$, the first dinitrosyls of niobium and tantalum.[27]

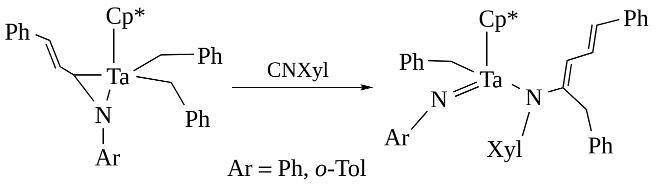

(**5**) (**6**)

In the reactions of dibenzyl 1-aza-1,3-butadiene complexes (**5**) with CNXyl, alkyl-insertion followed by coupling with the 1-aza-1,3-butadiene ligand affords amido-imido complexes (**6**).[28] The reaction of $Cp^*TaMe_2(SCH_2CH_2)_2O$ with CNXyl yields $Cp^*Ta(\eta^2\text{-}XylNCMe_2)(SCH_2CH_2)_2O$, which undergoes a second isocyanide insertion to yield (**7**).[29] A similar reaction of $Cp^*TaMe_3(SC_6H_7N_2)$ with CNXyl gives (**8**).[30]

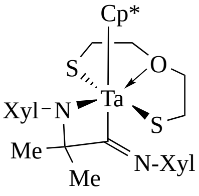

(**7**)

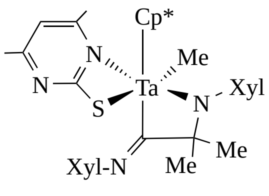

(**8**)

The Ta hydride compound $Ta(OAr)_2Cl_2(H)(PMe_2Ph)_2$ (Ar = 2,6-$Pr^i{}_2$-C_6H_3, **9**) reacts with RNC (R = Xyl, 2,6-$Pr^i{}_2$-C_6H_3) to yield the ylide (*see Ylide*) derivatives (**10a**). The reaction of (**9**) with Bu^tNC gives the keteneimine complex (**10b**).[31]

$Cp_2Ta({=}CH_2)Me$ reacts with 1 and 2 equiv of $HB(C_6F_5)_2$ to give $Cp_2Ta[CH_2B(C_6F_5)_2](\mu\text{-}H)Me$ (**11**) and $Cp_2Ta[CH_2B(C_6F_5)_2](\mu\text{-}H)(H)$, respectively. Reductive elimination (*see Reductive Elimination*) of CH_4 from (**11**) in the presence of Bu^tNC (or CO) and R′NC (R′ = Cy, $PhCH_2$) leads to the formation of $Cp_2Ta^{III}[\eta^2\text{-}CH_2B(C_6F_5)_2](L)$ (L = Bu^tNC, CO),[32] and unusual η^3-1-azaallyl Ta^{III} complexes (**12**).[33]

Substitution of CO ligands in $Cp^*TaCl_2(CO)_2(THF)$ with phosphaalkynes $RC{\equiv}P$ (R = Bu^t, adamantyl) gives η^2(4e)-bonded $Cp^*TaCl_2(P{\equiv}CR)$. Treating $Cp^*TaCl_2(P{\equiv}CBu^t)$ with additional $P{\equiv}CBu^t$ gives the 1,2-diphosphacyclobutadiene complex (**13**).[34]

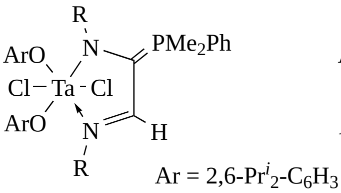

Ar = 2,6-$Pr^i{}_2$-C_6H_3

(**10a**) R = Xyl, Ar

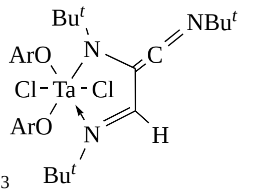

(**10b**)

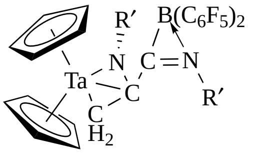

(**12**) (R′ = Cy, CH_2Ph)

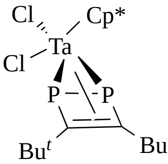

(**13**)

Aryl azides ArN_3 (Ar = Ph, *p*-$CF_3C_6H_4$, *p*-$Me_2NC_6H_4$) replace PMe_3 in $Cp_2TaMe(PMe_3)$, affording rare examples of terminal phenylazido complexes $Cp_2TaMe(N_3Ar)$, which under heating or UV irradiation give imides $Cp_2TaMe({=}NAr)$ and N_2. Thermolysis of $Cp_2TaMe(NN^{15}NPh)$ yields $Cp_2TaMe(^{15}NPh)$. Crossover (*see Crossover Experiment*) and kinetic studies reveal that this is a unimolecular decomposition.[35]

3 η^1-COMPLEXES

3.1 Alkyls, Aryls, Silyl, and Related σ-Complexes

3.1.1 *Synthesis and Complexes*

Metathesis reactions (*see Metathesis*) of Nb and Ta halide complexes with main group alkyls or milder alkylating reagents such as organozinc, -tin and -aluminum compounds (*see* ***Zinc: Organometallic Chemistry***; ***Tin: Organometallic Chemistry***, and ***Aluminum: Organometallic Chemistry***), continue to be the most common approach to the formation of Nb– and Ta–C bonds. NaCp was used, for example, to give the η^1-C_5H_5 ligands in $Cp_2Nb(\eta^1\text{-}C_5H_5)_2$[36] and $Cp_2M({=}NSiMe_3)(\eta^1\text{-}C_5H_5)$.[37]

Migratory insertions (*see Migratory Insertion*) of alkenes or alkynenes into M–H bonds are also a common method to form the Nb and Ta alkyls. Such reactions with activated alkynes lead to the formation of $Cp'_2Nb(CNR)(\eta^1\text{-}CR'{=}CHR')$ and $Cp'_2Nb(CO)(\eta^1\text{-}CR'{=}CHR')$ (R = Xyl, Cy, Bu^t; $R' = CO_2Me$, CO_2Bu^t) from $Cp'_2Nb(H)(CNR)$ and $Cp'_2Nb(H)(CO)$, respectively.[38]

A less common method to give η^1-alkyl or aryl complexes is the C–H bond activation reactions. Elimination of $HNMe_2$ from $Ta(O\text{-}2\text{-}Ind\text{-}4,6\text{-}Bu^t_2\text{-}C_6H_3)(NMe_2)_4$ yields (**14**).[39] Activation of a C–H bond in a $Ta \leftarrow NMe_2$ group led to the formation of the $\overline{Ta \leftarrow NMe\text{-}CH_2}$ moiety, as discussed in Section 9.1.[40,41]

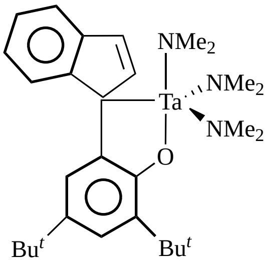

(**14**)

Reactions of $TaMe_5$ with triamines $(Me_3SiNHCH_2CH_2)_2NH$ and $(Me_3SiNH\text{-}o\text{-}C_6H_4)_2NH$ yield $[(Me_3SiNCH_2CH_2)_2N]TaMe_2$ and $[(Me_3SiN\text{-}o\text{-}C_6H_4)_2N]TaMe_2$, respectively. $(C_6F_5NHCH_2CH_2)_2NH$ reacts with $TaMe_5$, yielding first $[(C_6F_5NCH_2CH_2)_2NH]TaMe_3$, which then decomposes to $[(C_6F_5NCH_2CH_2)_2N]TaMe_2$.[42]

A review by Eisen summarizes chemistry of transition metal silyl chemistry between 1992 and mid-1996.[43] Earlier general references in this field include the reviews by Tilley and Schubert for the literature before 1992.[44] Nb silyl complexes $Cp'_2NbH_2(SiR_3)$ ($SiR_3 = SiMe_2Ph$, $SiMePh_2$, $SiPhH_2$, $SiPh_2H$, $SiPh_3$) have been prepared from the reactions of Cp'_2NbH_3 with silanes $HSiR_3$.[45] In these silyl complexes, the silyl ligands occupy the central equatorial position. Reactions of Cp_2NbH_3 or Cp_2NbBH_4 with $HSiR_3$ [R_3=, for example, Me_2Cl, $(OEt)_3$] yield $Cp_2Nb(SiR_3)H_2$.[46] Disilyl hydrides $Cp_2NbH(SiMe_2X)_2$ are obtained by reactions of $Cp_2NbH(CH_2{=}CHPh)$ with $HSiMe_2X$ (X = Cl, Ph),[47] or reactions of $NbCp_2(SiMe_2Cl)_2H$ with $XSiMe_3$ (X = Br, I).[48] Similar reactions of Ph_3EH (E = Ge, Sn) with Cp'_2NbH_3 lead to the formation of $Cp'_2NbH_2(EPh_3)$ (E = Ge, Sn).[49]

$(RCH_2)_3TaCl_2$ ($R = Bu^t$, Me_3Si) react with $LiSi(SiMe_3)_3$, affording Cp-free silyl alkylidene (*see Alkylidene*) complexes $(RCH_2)_2Ta({=}CHR)Si(SiMe_3)_3$ ($R = Bu^t$, Me_3Si).[50,51] Mechanistic studies (*see* ***Mechanisms of Reaction of Organometallic Complexes***) of the formation of $(Me_3SiCH_2)_2Ta({=}CHSiMe_3)Si(SiMe_3)_3$ suggest that the intermediate $(Me_3SiCH_2)_3Ta[Si(SiMe_3)_3]Cl$ undergoes α-H abstraction (*see α-Elimination*) with the elimination of $HSi(SiMe_3)_3$ to give '$(Me_3SiCH_2)_2Ta({=}CHSiMe_3)Cl$.'[51,52] Subsequent chloride replacement by the second equiv of $Si(SiMe_3)_3^-$ gives the silyl alkylidene complex.

3.1.2 Reactions

Alkyl ligands in niobium and tantalum complexes are susceptible to attack by electrophiles (*see Electrophilic Reaction*). Hydrogenation (*see Hydrogenation*) of niobium or tantalum M–R bonds to provide the metal hydrides is an important reaction of synthetic utility. Insertion reactions of unsaturated reagents into Nb– or Ta–C bonds are common. The unsaturated reagents include alkenes, alkynes, CO, NO, RN=C=NR, CNR, and others.

Photolysis of $Ta(O\text{-}2,6\text{-}Ph_2\text{-}3,5\text{-}R_2\text{-}C_6H)_2(CH_2SiMe_3)_3$ and ${}^{Ph}[P_2N_2]TaMe_3$ yields alkylidenes $Ta(O\text{-}2,6\text{-}Ph_2\text{-}3,5\text{-}R_2\text{-}C_6H)_2({=}CHSiMe_3)(CH_2SiMe_3)$[53] and ${}^{Ph}[P_2N_2]Ta({=}CH_2)(Me)$,[54] respectively. In the presence of ethylene, ${}^{Ph}[P_2N_2]Ta({=}CH_2)(Me)$ is slowly converted to ${}^{Ph}[P_2N_2]Ta(C_2H_4)Et$ and ${}^{Ph}[P_2N_2]Ta(C_2H_4)Me$.[54]

Transition structures of CH_4 elimination in MMe_5 have been investigated in detail with *ab initio* (*see Ab Initio Calculations*) quantum mechanics calculations. The most favorable transition structure for the elimination is close to a trigonal-bipyramidal geometry. A dimeric mechanism through intermolecular hydrogen abstraction is found to be much lower in activation free energy than the unimolecular mechanism. The dimeric transition structure is mainly stabilized by an $M\text{–}CH_2\text{–}M$ bridge.[55]

Reactions of the silyl complex $Cp_2Ta^{III}(PMe_3)(SiBu^t_2H)$ with $L \rightarrow BH_3$ ($L = NEt_3$, N-methylmorpholine) give $Cp_2Ta(\mu\text{-}H)_2B(SiBu^t_2H)H$ containing a B–Si bond.[56]

3.2 Hydride Complexes

Transition metal hydride (*see Hydrides*) derivatives are thought to be responsible for a plethora of organic transformations and catalytic cycles. The chemistry of Nb and Ta hydrides has developed rapidly in the past ten years. This part will focus on the synthetic and reactivity studies of these hydride complexes. A recent review surveyed the synthesis and reactivity of early metal hydride complexes.[57]

3.2.1 Cyclopentadienyl-free Hydride Complexes

Phosphines and alkoxides constitute common ancillary ligands in Cp-free hydride complexes. A Ta^{IV} penta-hydride $[TaH_5(dmpe)_2](LiHBEt_3)$ has been reported.[58] Hydrogenation of arenes is catalyzed by Nb and Ta hydrides with ancillary aryloxide ligation.[59] Reactions of alkynes and olefins with hydrides such as $Ta(O\text{-}2,6\text{-}Ph_2\text{-}C_6H_3)_2(H)_2Cl(PMe_3)_2$ were studied to explore the mechanistic pathways.[60] Reaction of $[(silox)_2TaH_2]_2$ with ethylene gives $[(silox)_2HTaEt]_2$ and $[(silox)_2EtTa](\mu\text{-}CHCH_2)(\mu\text{-}H)_2[Ta(silox)_2]$.[61]

Hydrogenation of $[NPN]TaMe_3$ $\{[NPN] = PhP(CH_2SiMe_2NPh)_2\}$ yields an interesting series of hydride-bridged dimers such as $\{[NPN]Ta\}_2(\mu\text{-}H)_4$.[62] This Ta^{IV} complex, upon exposure to N_2, loses H_2 to give a dinitrogen complex

$\{[NPN]Ta(\mu\text{-}H)\}_2(\mu\text{-}\eta^1{:}\eta^2\text{-}N_2)$ (**15**).**63** Reactions of silanes with the amido complex $Ta(NMe_2)_5$ have been reported to give the dihydride η^2-imine complex (**16**).**64**

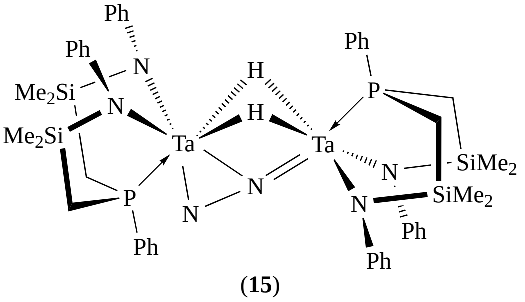

(**15**)

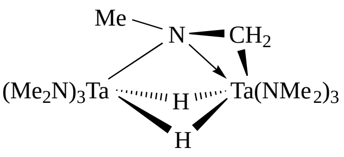

(**16**)

The niobaziridine-hydride $Nb(H)[\eta^2\text{-}Bu^t(H)C{=}NAr]\text{-}[N(Np)Ar]_2$ ($Ar = 3,5\text{-}Me_2\text{-}C_6H_3$), acting as a reactive synthon for its tautomer, the three-coordinate, trisamide $Nb[N(Np)Ar]_3$, reveals divergent reactivity for 2-electron reduction chemistry. It reacts with P_4, forming bridging diphosphide complex $(\mu_2{:}\eta^2,\eta^2\text{-}P_2)\{Nb[N(Np)Ar]_3\}_2$. In demonstrations of dual pathways of reactivity, nitriles and aldehydes insert into the Nb–H bond, leaving the niobaziridine ring intact.**65**

3.2.2 *Cyclopentadienyl Hydrides*

Important references of cyclopentadienyl hydrides include a review by Otero and coworkers, which covered the literature till mid-1998.**66**

$(\eta^5\text{-}C_5R_5)_2MH_3$ are useful stating hydrides of these two elements. Preparation of Nb silyl complexes from Nb hydrides is discussed in Section 3.1.1. In the studies of hydridosilyl complexes $Cp(ArN{=})Ta(PMe_3)(H)(SiCl_nR_{3-n})$ [$Ar = 2,6\text{-}Pr^i{}_2\text{-}C_6H_3$, $SiCl_nR_{3-n} = SiHMePh$, (**17a**); $SiClMe_2$, (**17b**); $SiCl_2Me$, (**17c**); $SiCl_3$, (**17d**)], an unprecedented increase of the $J_{\text{Si–H}}$ coupling constants between the hydride and silyl ligands from 14 Hz for (**17a**) to 50 Hz in (**17d**) was observed. This work shows that the increase in the magnitude of $J_{\text{Si–H}}$ does not necessarily correspond to stronger bonding interaction between these two ligands.**67** The nature of possible $H\cdots SiR_3$ interligand interactions in the complexes $Cp_2MXH(SiR_3)$ ($X = SiR_3$, Cl, H, Me) has been studied by *ab initio* calculations at the MP2 level. These theoretical studies indicate that the presence of a Si–Cl bond trans to hydride is crucial to developing shortened $H\cdots Si$ contacts and gives a concomitant lengthening of the Si–Cl bond.**68**

cis-$[Cp'_2Nb(HD)(PMe_2Ph)](CF_3CO_2)$ exhibits hindered rotation of the coordinated H-D. At 203 K, the *endo* H and *exo* H rotamers are observed, and they interconvert by rotation of the HD ligand reaching the coalescence at 233 K. This is the first observation of a freezing of H-D rotation on a transition metal complex.**69**

Insertion of $ClPPh_2$ into M–H bonds in Cp_2MH_3 and Cp'_2NbH gives phosphines $[Cp_2MH_2(PHPh_2)]Cl$ (M = Nb,**70** Ta**71**) and $[Cp'_2NbH_2(PHPh_2)]Cl$,**72** which undergo deprotonation to yield $Cp_2Nb^{III}H(PHPh_2)$, $Cp_2Ta^VH_2(PPh_2)$, and $Cp'_2NbH(PHPh_2)$, respectively. Similar reactions give $Cp_2NbH_2AsR_2$,**73** $Cp_2NbH_2SbPh_2$,**74** $Cp_2NbH_2PbMe_3$,**75** $Cp_2NbH_2BiPh_2$,**76** and $Cp_2NbH_2GeR_3$.**77** Protonation of $Cp'_2NbH(L)$ ($L = PHPh_2$, CNXyl) with CF_3COOH gives dihydrogen complexes $[Cp'_2Nb(\eta^2\text{-}H_2)(L)](CF_3CO_2)$.**72,78** Upon heating, $[Cp'_2Nb(\eta^2\text{-}H_2)(PHPh_2)](CF_3CO_2)$ is converted to its transoiddihydride isomer. Reactions of $(C_5H_4R)_2MH_3$ ($R = H$, $SiMe_3$) with PH_2R' afford $(C_5H_4R)_2\text{-}MH[(PR')_2]$ ($R' = Ph$, Cy) with a MP_2 ring, while the reaction of Cp_2TaH_3 with white phosphorus gives $Cp_2TaH[(PH)_2]$.**79**

Reactions of silanes with cyclopentadienyl Ta imides are a new method to yield hydrides. Addition of the Si–H bond in $PhSiH_3$ across the Ta=N double bond in $Cp^*\overline{Ta[{=}N(C_6H_3Me)_2N}SiMe_3]X$ (X = Cl, Me) yields hydrides (**18**).**80** The reaction of $Cp^*Ta({=}N\text{-}Ar)[Si(SiMe_3)_3]H$ ($Ar = 2,6\text{-}Pr^i{}_2\text{-}C_6H_3$) with $PhSiH_3$ gives a mixture of hydrides $[Cp^*(ArN{=})TaH(\mu\text{-}H)]_2$, (**19**), and (**20**).**81**

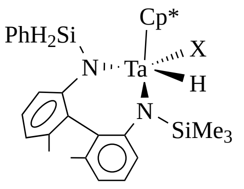

X = Cl, Me (**18**)

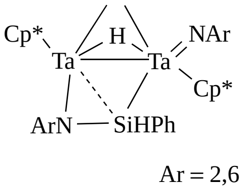

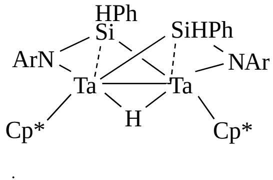

$Ar = 2,6\text{-}Pr^i{}_2\text{-}C_6H_3$

(**19**) (**20**)

$(Bu^tC_5H_4)_2NbBH_4$ or $(Bu^tC_5H_4)_2TaH_3$ reacts with Se to afford $(Bu^tC_5H_4)_2Nb(\eta^2\text{-}SeSeH)$ and $(Bu^tC_5H_4)_2Ta(\eta^2\text{-}Se_2)H$.**82** Similar reactions of $(Bu^tC_5H_4)_2NbH_3$ and $Cp^*{}_2TaH_3$

with Te give $(Bu^tC_5H_4)_2Nb(\eta^2\text{-}Te_2)H$[83] and $Cp^*{}_2Ta(\eta^2\text{-}Te_2)H$.[84] The telluroformaldehyde complex $Cp^*{}_2Ta(\eta^2\text{-}TeCH_2)H$ has been prepared by the PMe_3-catalyzed addition of Te to the $Ta{=}CH_2$ bond in $Cp^*{}_2Ta({=}CH_2)H$.[84]

Insertion of alkynes $RC{\equiv}CR'$ bearing electron-withdrawing substituents into Nb–H bonds in $Cp'_2NbH(L)$ ($L = CO$, isocyanide) and Cp'_2NbH_3 were found to give alkenyl complexes $Cp'_2Nb(CR{=}CHR')L$ and hydride olefin derivatives $Cp'_2Nb(CHR{=}CHR')(H)$.[38] The formation of the latter is believed to occur via initial stereospecific *trans*-insertion, followed by intramolecular rearrangement. Reactions of olefins $RCH{=}CH_2$ with Cp'_2NbH_3 yield $Cp'_2Nb(H)(\eta^2\text{-}RCH{=}CH_2)$.[85] Such olefin hydrides are also prepared from the alkylation of $(Cp'_2NbCl)_2$ with Grignard reagents RMgX ($R = Et$, CH_2CH_2Ph), followed by β-hydrogen elimination (*see β-Elimination*).[86]

Recent studies of the rates of H-exchange following intramolecular ethylene insertion into the M–H bond in *ansa*-metallocene (*see Metallocene Complexes*) complexes, $[Me_2Si(\eta^5\text{-}C_5H_4)(\eta^5\text{-}3\text{-}R\text{-}C_5H_3)]Nb(CH_2CH_2)H$ ($R = Pr^i$, Bu^t), *rac*- and *meso*-$[Me_2Si(\eta^5\text{-}3\text{-}Bu^t\text{-}C_5H_3)_2]Nb(CH_2CH_2)H$, and $[(1,2\text{-}SiMe_2)_2(\eta^5\text{-}3,5\text{-}Pr^i{}_2\text{-}C_5H)(\eta^5\text{-}4\text{-}Bu^t\text{-}C_5H_2)]Ta(CH_2CH_2)H$, show that the singly bridged *ansa*-niobocenes exchange up to three orders of magnitude faster than unbridged complexes. The doubly bridged *ansa*-tantalocene complex exchanges at a rate comparable to that previously reported for $Cp^*{}_2Ta(CH_2CH_2)H$ and much slower than the singly bridged complex $[Me_2Si(\eta^5\text{-}C_5Me_4)_2]Ta(CH_2CH_2)H$. DFT calculations on model complexes indicate the presence of an agostic (*see Agostic Bonding*) ethyl intermediate in the computed exchange pathway.[87]

Reactions of Cp_2NbH_3 with catecholborane or 9-borabicyclononane HBR_2 yield disubstituted hydridoborates $Cp_2Nb(H_2BR_2)$ via loss of H_2.[88] Ta boryl complexes *endo*- and *exo*-$Cp_2Ta(H)_2(BO_2C_6H_4)$ are prepared from the reaction of chlorocatecholborane with $(Cp_2TaH_2Li)_x$.[89] *ansa*-Niobiocene tetrahydroborate complexes $[(C_5H_4)X(C_5H_4)]Nb(\eta^2\text{-}BH_4)$ ($X =$ *ansa*-bridging unit) are prepared as well,[90] and the barrier to bridge-terminal hydrogen exchange is considerably reduced when the bridging unit imposes significant structural changes in the metallocene (*see Metallocene Complexes*). Theoretical studies of catecholborane adducts of hydride complexes $Cp_2M(H)$ that are obtained from $Cp_2M(H)(\eta^2\text{-}CH_2{=}CH_2)$ show that there are structural isomers of the O- and N-substituted borane adducts including boryl, hydridoborate, and σ-complex structures. These structures are related to how the electron-deficient (*see Electron Deficient Compound*) B atom is electronically saturated.[91]

Dianionic borollide complexes $Cp^*(C_4H_4B\text{-}R)TaMe_2$ have been prepared and found to undergo hydrogenolysis in the presence of PMe_3 to give $Cp^*(C_4H_4B\text{-}R)Ta(H)_2(PMe_3)$ (**21a**).[92,93] $[C_4H_4BNPr^i{}_2](C_5H_5BPh)Ta(H)_2PEt_3$ (**21b**) is similarly prepared.[12]

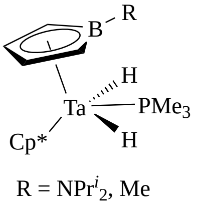

(**21a**)

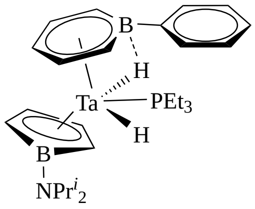

(**21b**)

Treatment of the imide hydride $Cp^*{}_2Ta({=}NBu^t)H$ with $[Ph_3C][B(C_6F_5)_4]$ yields the cationic imide $[Cp^*{}_2Ta({=}NBu^t)(THF)][B(C_6F_5)_4]$ (**22**). (**22**) reacts cleanly with H_2 to yield $[Cp^*{}_2Ta(NHBu^t)H][B(C_6F_5)_4]$, and undergoes C–H bond activation reactions with propyne or phenylacetylene to afford $[Cp^*{}_2Ta(NHBu^t)(C{\equiv}CR)][B(C_6F_5)_4]$ ($R = Me$, Ph). The heterolytic cleavage reactions of (**22**) may be the result of the presence of both electrophilic and nucleophilic sites of reactivity in the same molecule. Intramolecular activation of a C–H bond of a Cp* ligand yields $[Cp^*\overline{Ta(\eta^5\text{-}C_5Me_4CH_2N}Bu^t)H][B(C_6F_5)_4]$ with the methylene group attached to the N rather than the Ta atom. Dealkylation of the imido group is observed in an unusual reaction of (**22**) with CO_2 giving isobutylene and the isocyanate complex $[Cp^*{}_2Ta(OH)(NCO)][B(C_6F_5)_4]$.[94]

Reactions of $(C_5H_4Bu^t)_2Ta({=}S)H$ with PhNCS and HCl exhibit a surprisingly low hydride reactivity. The $Ta{=}S$ bond is involved either in a $[2 + 2]$ cycloaddition giving $(C_5H_4Bu^t)_2\overline{Ta(H)[S\text{-}C({=}S)\text{-}N}Ph]$ or in a protonation yielding $(C_5H_4Bu^t)_2Ta(H)Cl_2$.[95]

Reduction of the allene complex $Cp^*{}_2Ta_2(\mu\text{-}X)X_3(\mu\text{-}\eta^1,\eta^3\text{-}C_3H_4)$ ($X = Cl$, Br) with Na/Hg gives $Cp^*{}_2Ta_2(\mu\text{-}H)_2X_2(\mu\text{-}HCCCH)$ (**23**). The reactions proceed via a double 1,3-C-H activation, with C_3H_2 and two μ-hydride ligands instead of an allenyl hydride.[96]

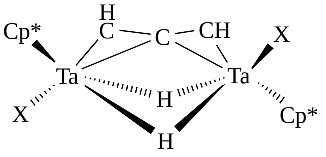

(**23**)

Selective conversion of an ethylene to an ethylidene ligand in reactions of a $Cp_2Ta(C_2H_4)H$ with iodofluorocarbons has been reported. Reactions of $Cp_2Ta(C_2H_4)H$ with perfluorobutyl iodide or perfluorobenzyl iodide, and perfluoro-*iso*-Pr iodide or pentafluorophenyl iodide are found to yield the ethylene complex $Cp_2Ta(C_2H_4)I$ and the ethylidene complex $Cp_2Ta(CHMe)I$, respectively. No interconversion of these two isomers is observed under these reaction conditions, indicating that each is formed under conditions of kinetic control.[97]

Thermodynamic studies of hydride transfer from $Cp_2M(H)L$, $Cp^*{}_2M(H)L$, $Cp'_2M(H)L$ [$L = CO$, PEt_3, $(H)_2$, $PhC{\equiv}CPh$, $CH_2{=}O$, ${=}O$], and $Cp'_2Nb(Cl)(L')$ ($L' =$

O=C=CEtPh, O=C=CEt$_2$) to Ar$_3$C$^+$ indicate that the free energies of hydride transfer are heavily influenced by coligands, but less so by 4d versus 5d effects in isostructural Nb or Ta complexes.[98]

3.2.3 *Heterobimetallic Complexes*

Hydride complexes discussed here include both μ-hydride heterobimetallic complexes, and bimetallic complexes with Nb–H or Ta–H ligands.

Reduction of Cp$_2$Nb(SiMe$_2$Cl)H$_2$ with LiAlH$_4$ gives [Cp$_2$Nb(μ-H)$_2$AlH(μ-H)]$_2$.[48] Reactions of Cp$_2$TaH$_3$ with M(CO)$_6$ also give μ-hydride heterobimetallic complexes Cp$_2$TaH$_2$(μ-H)M(CO)$_5$ (M = Cr, Mo, W).[99] [(Cp$'_2$NbH$_3$)$_2$M](PF$_6$) (M = Cu, Ag, Au) are prepared via the reactions of Cp$'_2$NbH$_3$ with [Cu(MeCN)$_4$]PF$_6$, AgBF$_4$, or ‘Au(THT)PF$_6$’.[100] Tantalum analogues [(C$_5$H$_4$Bu^t)$_2$TaH$_3$-MPPh$_3$](PF$_6$) (M = Cu, Au) have also been prepared from the reactions of (C$_5$H$_4$Bu^t)$_2$TaH$_3$ with (MPPh$_3$)(PF$_6$).[101] NMR studies are consistent with two bridging hydride ligands between the disparate metals centers. Cp$'_2$NbH(CO) reacts with [Cu(MeCN)$_4$]BF$_4$, CuPPh$_3$Cl/TlPF$_6$, AgBF$_4$, AgPPh$_3$Cl/TlPF$_6$, and Au(THT)Cl/TlPF$_6$, giving [{Cp$'_2$Nb(CO)}$_2$(μ-H)$_2$M]$^+$ (M = Cu, Ag, Au), whereas the reaction with [Au(PPh$_3$)]$^+$ leads to [{Cp$'_2$Nb(CO)}(μ-H)Au]PF$_6$.[102]

Electrophilic addition of the Lewis acid B(C$_6$F$_5$)$_3$ to Cp$_2$TaH$_3$ yields Cp$_2$TaH$_2$[η^1-HB(C$_6$F$_5$)$_3$].[103] Protonation of Cp$_2$TaH(CO) by HBF$_4$·Et$_2$O gives a dihydrogen complex Cp$_2$TaH$_2$(CO)$^+$BF$_4$$^-$. This complex exists as two isomers. The minor isomer is a *trans*-dihydride, and the major isomer is [Cp$_2$Ta(η^2-H$_2$)(CO)]BF$_4$, the first thermally stable group 5 dihydrogen complex. Protonation of the silyl hydride Cp$_2$TaH$_2$(SiMe$_2$Ph) gives a dinuclear complex [(Cp$_2$TaH$_2$)$_2$(μ-H)]{B[3,5-(CF$_3$)$_2$-C$_6$H$_3$]$_4$}.[104] Organocyclichydroborate complexes of niobiocenes Cp$_2$Nb$^{\text{III}}$(μ-H)$_2$BR$_2$, where R$_2$ is, for example, *cyclic*-(CH$_2$)$_n$- ($n = 4$, 5), are prepared from the reductions of Cp$_2$Nb$^{\text{IV}}$Cl$_2$ with the hydroborate salts.[105] Reactions of Cp$_2$Nb$^{\text{III}}$(μ-H)$_2$B(C$_5$H$_{10}$) with B(C$_6$F$_5$)$_3$ are solvent-dependant, yielding cationic [Cp$_2$Nb(μ-H)(η^5, η^1-C$_5$H$_4$)Nb(η^5, η^1-C$_5$H$_4$)$_2$Nb{(μ-H)(η^5-C$_5$H$_4$B(C$_6$F$_5$)$_2$)}]$^+$ in toluene and neutral CpNb(C$_6$F$_5$){(μ-H)[η^5-C$_5$H$_4$B(C$_6$F$_5$)$_2$]} in diethyl ether.[106]

4 ALKYLIDENES AND ALKYLIDYNES

4.1 Synthesis and Complexes

A recent paper by Schrock reviewed chemistry of complexes with high-oxidation-state metal-carbon multiple bonds.[107]

The most common approach to alkylidene (*see Alkylidene*) and alkylidyne (*see Alkylidyne*) complexes involves α-hydrogen abstraction from bis(alkyl) and alkyl-alkylidene complexes to give alkylidenes and alkylidynes, respectively. Short-lived TaNp$_5$ is directly observed as an intermediate in the formation of the first alkylidene Np$_3$Ta=CHBu^t from the alkylation of TaNp$_4$Cl.[108] Ta(CH$_2$SiMe$_3$)$_5$, which is less bulky and thus more stable than TaNp$_5$, is isolated. It converts to alkylidene (Me$_3$SiCH$_2$)$_3$Ta=CHSiMe$_3$ and then to bridging alkylidyne (Me$_3$SiCH$_2$)$_4$Ta$_2$(μ-CSiMe$_3$)$_2$. The first and second conversions follow first-order [$\Delta H_1 = 21.6(1.4)\ \text{kcal mol}^{-1}$ and $\Delta S_1 = -5(5)$ e.u.] and second-order kinetics [$\Delta H_2 = 6.2(0.3)\ \text{kcal mol}^{-1}$ and $\Delta S_2 = -61.6(0.8)$ e.u.], respectively.[108] Dialkylation of [N$_3$N]TaCl$_2$ and [N$_3$N*]TaCl$_2$ with RCH$_2$Li or RCH$_2$MgCl (R = for example, Et, Pr^n,and Bu^i) yields [N$_3$N]Ta=CHR and [N$_3$N*]Ta=CHR, respectively. Alkylation of [N$_3$N]TaCl$_2$ and [N$_3$N*]TaCl$_2$ with EtMgCl gives ethylene complexes [N$_3$N]Ta(C$_2$H$_4$) and [N$_3$N*]Ta(C$_2$H$_4$).[109–111] Reactions of Cp*Ta(N=PR$_3$)Cl$_3$ (R = Bu^t, Pr^i) with PhCH$_2$MgCl similarly afford Cp*Ta(N=PR$_3$)(=CHPh)(CH$_2$Ph).[112]

Reactions of phenols (ArOH) with (RCH$_2$)$_4$Ta$_2$(μ-CR)$_2$ (R = SiMe$_3$) lead to the substitution of an alkyl ligand to give (ArO)(RCH$_2$)$_3$Ta$_2$(μ-CR)$_2$. Such a reaction follows second-order kinetics with a strong kinetic isotope effect ($k_{\text{H}}/k_{\text{D}}$), and the rates strongly depend on the nature of the phenol substituents.[113]

The alkylidenes or alkylidynes can also be prepared by the intermolecular deprotonation reactions. Reaction of [PhC(NSiMe$_3$)$_2$]TaCl(CH$_2$Ph)$_3$ with LiN(SiMe$_3$)$_2$ affords [PhC(NSiMe$_3$)$_2$]Ta(=CHPh)(CH$_2$Ph)$_2$.[24] An unusual alkylidene complex CpTa(NEt$_2$)$_2$(=C$_5$H$_4$) was prepared from the reaction of CpTa(NEt$_2$)$_2$Cl$_2$ with MeLi.[114]

Phosphorus ylides (*see Ylide*) are useful reagents to introduce alkylidene groups to Nb or Ta complexes. Ph$_3$P=CH$_2$ reacts with Cp$_2$M(=NBu^t)Cl$_2$ (M = Ta, Nb) yielding Cp$_2$M(=NBu^t)(CHPPh$_3$)Cl. Treatment of the Nb complex with an excess of Ph$_3$P=CH$_2$ leads to Cp$_2$Nb(=NBu^t)(CHPPh$_3$)$_2$.[115]

Alkene metathesis (*see Alkene Metathesis*) reactions have also been used to give isolable alkylidenes. Reactions of Ta(=CHBu^t)[NCN](OBu^t)X (X = Cl, **24a**; OBu^t; **24b**) with Me$_3$SiCH=CH$_2$ afford Ta(=CHSiMe$_3$)[NCN](OBu^t)X stabilized by *ortho*-chelating arylamine ligands.[116]

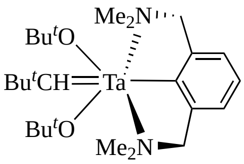

(24b)

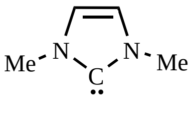

(25)

Several other approaches have led to the formation of alkylidene and carbene complexes. Substitution of pyridine ligands in $MCl_4(py)_2$ by nucleophilic cyclocarbene 1,3-dimethylimidaxolin-2-ylidene (**25**) gives MCl_4L_2.**117**

Rearrangement of the ethylene ligand in $[N_3N]Ta(H_2C{=}CH_2)$ affords $[N_3N]Ta{=}CHMe$, and this reaction is catalyzed by $PhPH_2$.**109,110** Reaction of Cp^*TaCl_4 with phosphavinyl Grignard reagent (*Z*)-$MgCl\{C(Bu^t){=}PCy\}$ gives a novel bis(phosphinoalkylidene) complex $\{Cp^*TaCl_2[{=}C(Bu^t)\text{-}P(Cy)\text{-}]\}_2$ (**26**).**118**

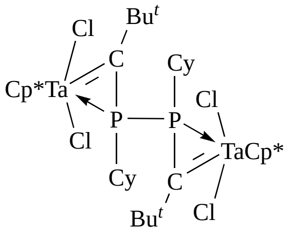

(**26**)

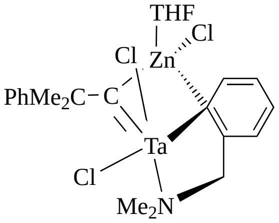

(**27**)

Bimetallic complexes containing bridging alkylidene and alkylidyne ligands have been prepared using alkylating reagents. Ta–Zn neophylidyne $\{[TaCl_2(\mu\text{-}CCMe_2Ph)(\mu\text{-}Cl)(THF)_2][Zn(\mu\text{-}Cl)]\}_2$ is a good starting material for the synthesis of alkylidynes such as the Ta–Zn neophylidynes (**27**) and (**28a**), where the alkylidyne functionality and the aryl ipso-carbon bridge between the Zn and Ta centers. The reaction of $TaCl_2[NCN]({=}CHBu^t)$ with NpZnCl affords (**28b**), an analog of (**28a**).**41** (**28a-b**) react with TMEDA leading to C–H activation of the methyl group in $\text{–}NMe_2$, a subject discussed in Section 9.1.**119**

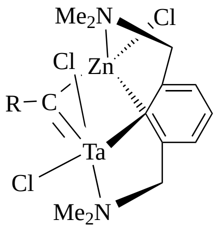

(R = CMe_2Ph, **28a**; Bu^t, **28b**)

4.2 Reactions

The reactions of alkylidenes (*see Alkylidene*) and alkylidynes (*see Alkylidyne*) of niobium and tantalum are typically characterized by nucleophilic alkylidene and alkylidyne ligands. $Cp^*Ta(CH_2SiMe_3)_2({=}CHSiMe_3)$ reacts with PhOH to give alkyl phenoxo $Cp^*Ta(CH_2SiMe_3)_3(OPh)$, and is hydrolyzed in the presence of a trace amount of H_2O to give the oxo dialkyl derivative $[Cp^*Ta(CH_2SiMe_3)_2O]_n$.**120**

Nb and Ta alkylidenes readily undergo metathesis reactions (*see Alkene Metathesis*) with carbonyl functionalities or imines to form alkene and M=O or M=NR bonds. Reactions of $(Me_3SiCH_2)(ArN{=})Ta(\mu\text{-}CHSiMe_3)(\mu\text{-}\eta^1{:}\eta^3\text{-}Pr^i{}_2\text{-tacn})Li$ ($Pr^i{}_2\text{-tacn}^-$ = anionic triazacyclononane, **29**) with $Ph_2C{=}O$ give $[(Me_3SiCH_2)(RN{=})Ta(\mu\text{-}O)(\mu\text{-}\eta^1{:}\eta^3\text{-}Pr^i{}_2\text{-tacn})Li]_2$.**121**

In some cases, hydrogenation of the alkylidenes and alkylidynes reduces the metal-carbon multiple bonds to single bonds. The alkylidene ligand in (**29**) is converted to an alkyl group when exposed to H_2, leading to the formation of an interesting tantalum–lithium bridging hydride complex.**122**

The reactions of alkylidene with alkenes typically afford metallacyclic complexes (*see Metallacycle*), a subject discussed in Section 6.1. $Ta({=}CHR)[CNN](OBu^t)_2$ (R = Bu^t, **30a**; CMe_2Ph, **30b**) reacts with ethene to afford the tantalacyclobutane complex $Ta[(CH_2)_3\text{-}1,3][CNN](OBu^t)_2$ (**31a**) at room temperature. Under heating, (**30b**) reacted with ethene to give $Ta[CNN](OBu^t)_2(H_2C{=}CH_2)$.**123**

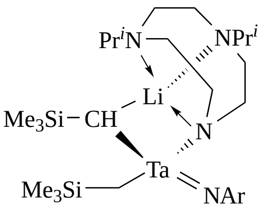

(**29**) Ar = 2,6-$Pr^i{}_2$-C_6H_3

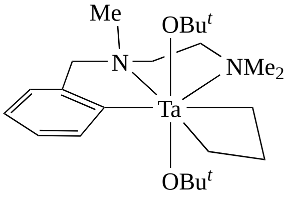

(**31a**)

Reactions of $[TolC(NSiMe_3)_2]_2Ta({=}CH_2)Me$ with pyridine N-oxides proceed via regioselective methylene transfer to afford 2-methylpyridines and $[TolC(NSiMe_3)_2]_2Ta({=}O)CH_3$, while the reaction with the nitrone $PhCH{=}N(\rightarrow O)Bu^t$ leads to $[TolC(NSiMe_3)_2]_2Ta({=}O)(NMeBu^t)$ and $PhCH{=}CH_2$.**124**

The mechanism of H_2 addition to $Cp^*{}_2Ta({=}CH_2)H$ has been studied using parahydrogen-induced polarization (PHIP), ^{13}C labeling, and comparison to the related complex $Cp^*{}_2Ta({=}CH_2)Me$. The reaction of *para*-enriched H_2 with labeled $Cp^*{}_2Ta({=}^{13}CH_2)H$ leads to polarized resonances for both $Cp^*{}_2TaH_3$ and $Cp^*{}_2Ta(CH_3)H_2$, where the polarized resonances correspond to the two hydride ligands. The results thus support a pathway of H_2 addition to a Ta(III) intermediate $Cp^*{}_2TaCH_3$, rather than addition directly across the Ta=C bond.**125**

Surface chemistry of the alkyl/alkylidene complexes has been studied by ^{13}C CPMAS NMR spectroscopy. $Cp_2Ta({=}^{13}CH_2)(^{13}CH_3)$ is converted predominantly to a stable cation-like $Cp_2Ta(^{13}CH_3)_2{}^+$ species on partially dehydroxylated SiO_2 (PDS) presumably via electrophilic addition of a proton from the PDS surface. The formation of cation-like $Cp_2Ta(^{13}CH_3)_2{}^+$ and $CpTa(^{13}CH_3)_3{}^+$ is observed when $Cp_2Ta(^{13}CH_3)_3$ and $CpTa(^{13}CH_3)_4$ are chemisorbed on PDS and dehydroxylated SiO_2 (DS), and on dehydroxylated γ-alumina, respectively. In comparison, $(Bu^{t\,13}CH_2)_3Ta{=}^{13}CHBu^t$ forms predominantly a $Ta(^{13}CHBu^t)(^{13}CH_2Bu^t)_2O$-Si, μ-oxo-alkylidene species on PDS.[126]

The conversion of NH_3 and pentamer $[Np_2TaN]_5$, which had been prepared from $Np_3Ta{=}CHBu^t$ and NH_3, to cubic $TaN_{0.8}$ is found to proceed via precipitate $1/n[TaC_{1.41}H_{3.90}N_{1.90}]_n$ at 80 °C and amorphous TaN at 400 °C. The latter was then converted to cubic $TaN_{0.8}$ at 820 °C.[127]

5 η^2-COMPLEXES

5.1 Alkene Complexes

Alkene complexes of niobium and tantalum are of great interest in large part because they are implicated in polymerization, metathesis, and dimerization reactions of alkenes (*see* ***Oligomerization & Polymerization by Homogeneous Catalysis*** and ***Metathesis Polymerization Processes by Homogeneous Catalysis***). Nb and Ta alkene complexes are usually prepared from: (i) direct alkene coordination to metal centers. Substitution of the 4-picoline ligand in $(silox)_3Nb(\eta\text{-}C,N\text{-}$4-picoline) by COT, followed by dehydrogenation, gives the cyclooctatrieneyne complex $\{(silox)_3Nb\}_2(\eta\text{-}1,2;\eta\text{-}5,6\text{-}C_8H_6)$. Treatment of this complex with H_2 leads to a rearrangement to the alkylidene-yne $\{(silox)_3Nb\}_2(\eta^1;\eta^2\text{-}4,5\text{-}C_8H_6)$.[128] (ii) β-Hydrogen abstraction (*see α-Elimination*) in dialkyl complexes. One such example is the reaction of $[N_3N]TaCl_2$ with 2 equiv of EtMgCl to give $[N_3N]Ta(H_2C{=}CH_2)$.[109,110] The presence of a catalytic amount of $PhPH_2$ leads to the conversion of $[N_3N]Ta(H_2C{=}CH_2)$ to the ethylidene complex $[N_3N]Ta{=}CHMe$.[110] Alkylation of $Cp^*Ta(NPR_3)Cl_3$ ($R = Bu^t$, Pr^i) with 2 equiv of EtMgCl results in formation of $Cp^*Ta(NPR_3)(\eta^2\text{-}C_2H_4)Cl$. Substitution of the remaining chloride by EtMgCl affords $Cp^*Ta({=}NPBu^t{}_3)(\eta^2\text{-}C_2H_4)(Et)$.[112] (iii) β-Hydride elimination in unsaturated d^3 complexes. The olefin-hydride complexes *endo*-$Cp'_2Nb(H)(\eta^2\text{-}RHC{=}CH_2)$ ($R = H$, Ph) are prepared by alkylation of $(Cp'_2NbCl)_2$ with RCH_2CH_2MgX followed by a stereoselective β-H elimination from $Cp'_2Nb(CH_2CH_2R)$. In comparison, reactions of Cp'_2NbH_3 with styrene or other olefins give a mixture of *endo*- and *exo*-isomers.[85,86] Similarly, $Cp'_2NbR'[\eta^2\text{-}(C,Z)\text{-}ZCCRPh]$ ($Z = NPh$, $R = Ph$, Me, Et, H; $Z = O$, $R = Ph$; $R' = H$, Me, Et), prepared from $Cp'_2NbCl[\eta^2\text{-}(C,Z)\text{-}ZCCRPh]$ and $R'MgI$ or R'_2Mg, readily undergo the loss of the ketene ligand and subsequent β-hydride elimination to form $Cp'_2NbH(\eta^2\text{-}CH_2{=}CH_2)$.[129] (iv) Reductive addition of alkynes to the hydride complexes. $Cp'_2Nb(H)[\eta^2\text{-}RO_2C(H){=}C(H)CO_2R]$ ($R = Me$, Bu^t) and $Cp'_2Nb(H)(\eta^2\text{-}MeO_2CH{=}CH_2)$ are prepared from Cp'_2NbH_3 and active alkynes $RO_2CC{\equiv}CCO_2R$ or $MeO_2CC{\equiv}CH$.[38]

Substitution of two chloride ligands in $[\eta^5\text{-}C_4H_4BN(CHMe_2)_2]TaCl_3$ by methylcyclopentadienyl $MeC_5H_4^-$ affords η^2 borollide $(MeC_5H_4)_2[\eta^2\text{-}C_4H_4BN(CHMe_2)_2]TaCl$.[12]

5.2 Alkyne and Benzyne Complexes

Nb and Ta alkyne complexes are of interest in part because they have found use in organic synthesis and cyclooligermerization (*see Cyclodimerization & -trimerization Reactions*) of alkynes.

5.2.1 Alkyne Complexes without Cyclopentadiene Ligands

Reactions of low-valent Nb and Ta complexes with alkynes are one of the simplest methods to prepare the alkyne complexes. Substitution of a CO and PR_3 ligand in $INb(CO)_3(PR_3)_3$ by diynes gives $INb(CO)_2(PR_3)_2$(diyne) ($PR_3 = PEt_3$; diyne = 2,4-hexadiyne, 1,5-hexadiyne; $PR_3 = PMe_2Ph$, diyne = 2,6-octadiyne). When $Ph_2PCCPPh_2$ is used, its reaction with $INb(CO)_3(PMe_2Ph)_3$ affords $INb(CO)_2(PMe_2Ph)_2(Ph_2PC{\equiv}CPPh_2)$.[130] $[Nb(\eta^2\text{-}F_3CC{\equiv}CCF_3)(py)Br_4]^-$ is obtained from the reaction of $[Nb(CO)_6]^-$, $F_3CC{\equiv}CCF_3$, and [Hpy]Br.[131] Treatment of alkynes with low-valent Ta species derived from the reduction of $TaCl_5$ with Zn yields $TaCl_3(R^1C{\equiv}CR^2)$(dme) ($R^1 = Et$, $n\text{-}C_5H_{11}$, Ph; $R^2 = Et$, $n\text{-}C_5H_{11}$, Me, Ph).[132] Tp^*NbCl_2(alkyne) (alkyne = $PhC{\equiv}CMe$, $PhC{\equiv}CEt$, $PhC{\equiv}CPr^n$, $MeC{\equiv}CMe$, $PhC{\equiv}CPh$) have been prepared from the high-yield, one-pot reaction of $NbCl_3$(DME) first with an alkyne and then with KTp^*.[133,134] Alkyne adducts $Tp^*Nb(CO)(PhC{\equiv}CMe)(L)$ ($L = RCN$, PMe_2Ph) have also been prepared by ligand exchanging reactions. $PhC{\equiv}N$ is thermally displaced from $Tp^*Nb(CO)(PhC{\equiv}CMe)(PhC{\equiv}N)$ by $PhC{\equiv}CMe$ to give $Tp^*Nb(CO)(PhC{\equiv}CMe)_2$.[135]

β-Hydrogen abstraction from η^1-alkene ligands is another method to yield alkyne complexes. $[N_3N]Ta(C_2H_2)$ is obtained, for example, from the reaction of $[N_3N]TaCl_2$ with 2 equiv of $CH_2{=}CHMgBr$.[110]

Unique reversible migratory insertion/β-alkyl elimination (*see Migratory Insertion*) in Nb alkyl alkyne complexes has been reported. $Tp^*Nb(Cl)(CH_2R)(PhC{\equiv}CMe)$ ($R = Me$, **32a**; Et, **32b**; $SiMe_3$, **32c**) undergo a thermally induced, first-order rearrangement, yielding methyl complexes $Tp^*Nb(Cl)(Me)(PhC{\equiv}CCH_2R)$ (**32d-f**), respectively. $Tp^*Nb(Cl)(Pr^n)(PhC{\equiv}CEt)$ is in a 1:1 equilibrium with $Tp^*Nb(Cl)(Et)(PhC{\equiv}CPr^n)$. $Tp^*Nb(Cl)(Et)(PhC{\equiv}CEt)$ reacts with $PhC{\equiv}CMe$ yielding $Tp^*Nb(Cl)(\eta^1\text{-}CPh{=}CEt_2)(PhC{\equiv}CMe)$, demonstrating that alkyl migration is a key step of the rearrangement. Kinetic and trapping studies indicate that the migratory insertion of the alkyl group onto the alkyne is the rate-determining step of the reactions.[136]

The *iso*-propyl complex $Tp^*Nb(Cl)(Pr^i)(PhC{\equiv}CMe)$ (**33a**) exhibits an unusual equilibrium between its β- (**33a**-β)

and minor α-agostic (*see Agostic Bonding*) rotamer (**33a**-α) in solution ($\Delta G^{\neq}{}_{193\,\mathrm{K}} = 11.4 \pm 0.6\,\mathrm{kcal\,mol^{-1}}$; $\Delta G^{\circ}{}_{193\,\mathrm{K}} = -0.53\,\mathrm{kcal\,mol^{-1}}$) as the result of the restricted rotation about the Nb–C bond. This is a case that steric factors overcome the intrinsic electronic preference for the β-agostic structure. In solid state, the β-agostic isomer (**33a**-β) is observed. This secondary alkyl complex thermally rearranges via a first-order reaction ($\Delta G^{\neq}{}_{323\,\mathrm{K}} \approx 25.8\,\mathrm{kcal\,mol^{-1}}$) to the linear, α-agostic n-propyl isomer Tp*Nb(Cl)(Pr^n)(PhC≡CMe) (**33b**), which undergoes another first-order isomerization ($\Delta G^{\neq} = 27.0\,\mathrm{kcal\,mol^{-1}}$) to methyl complex (**33e**).[137] In the cyclopropyl complex Tp*Nb(Cl)(*cyclo*-C_3H_5)(MeC≡CMe), an unprecedented α-C–C agostic interaction is observed to be preferred over both α- and β-C–H agostic alternatives.[138]

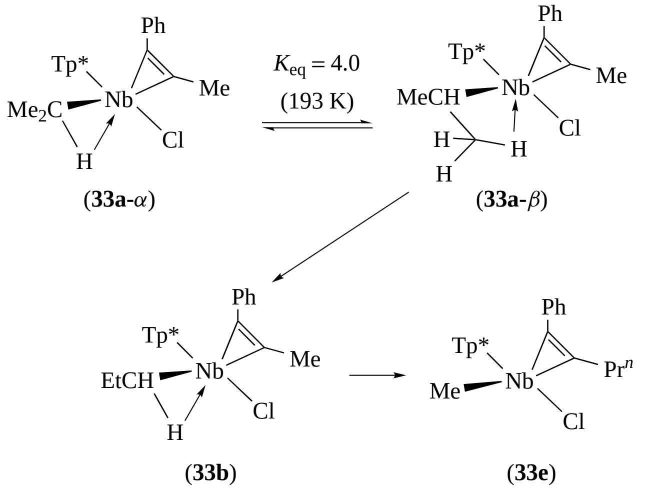

5.2.2 *Cyclopentadienyl Alkyne Complexes*

Reduction of niobocene dichlorides in the presence of RC≡CR is one common path to niobocene alkyne complexes such as Cp_2Nb^{V}(RC≡CR)Cl,[139–141] and Cp'_2Nb^{IV}(η^2-RC≡CR).[142] Direct reactions of $Cp'_2Nb^{III}Cl$ with the diynes or alkyne-alkenes give, for example, $Cp'_2NbCl[\eta^2(C,C)$-PhC≡$CCH_2CH{=}CH_2$]. Hydrogenation of the enyne-containing products occurs at the C=C bond using Pd/C as catalyst to give the alkyne complexes such as $Cp'_2NbCl[\eta^2(C,C)$-PhC≡$CCH_2CH_2CH_3$].[143]

The deprotonation with BuLi at the propargylic site of the coordinated alkyne in Tp′Nb(Cl)(X)(PhC≡CMe) (X = Cl, OMe) followed by the reaction with MeI or $PhCH_2Br$ affords the alkylated alkyne complexes Tp′Nb(Cl)(X)(PhC≡CCH_2R) (R = Me, CH_2Ph). Adding $PhCH_2Br$ and MeI to the deprotonated Tp′Nb(Cl)(OMe)(PhC≡CCH_2Me) and Tp′Nb(Cl)(OMe)(PhC≡CCH_2CH_2Ph), respectively, gives 4:1 and 1:6 diastereomeric mixtures of Tp′Nb(Cl)(OMe)[PhC≡CCHMe(CH_2Ph)].[144]

5.2.3 *Benzyne Complexes*

Benzyne complexes contain η^2-benzyne, a moiety not stable in its free state, and are relatives of the alkyne complexes. Several methods have been used to prepare these complexes. Refluxing $[N_3N]TaCl_2$ with PhLi affords $[N_3N]Ta(C_6H_4)$.[110] Thermolysis of the methyl phenyl complex Cp*TaMe(Ph)(η^4-butadiene) gives the benzyne complex Cp*Ta(η^4-butadiene)(η^2-C_6H_4), the first example of the parent benzyne complex bearing a metallocene-like MCp(diene) fragment.[145] The η^2-benzyne complex CpTa(η^2-C_6H_4)(PMe_3)($Et_2C_2B_4H_4$) (**34**), an analogue of tantalocenes, is prepared from $CpTaPh_2(Et_2C_2B_4H_4)$ and excess PMe_3. In a striking demonstration of the electronic influence of the carborane ligand, the properties of (**34**) contrast dramatically with those of normal metal (η^2-benzyne) complexes. (**34**) is air-stable, does not undergo coupling with unsaturated substrates such as acetone, and is not protonated by MeOH.[146]

The mechanism of H_2 addition to benzyne complex $Cp^*{}_2Ta(\eta^2\text{-}C_6H_4)H$ has been investigated by parahydrogen-induced polarization (PHIP). This hydrogenation (*see Hydrogenation*) gives $Cp^*{}_2Ta(Ph)H_2$, which then adds another equiv of H_2 to give Cp^*TaH_3. Addition of *para*-H_2 leads to strong polarization in the hydride resonances of $Cp^*{}_2Ta(Ph)H_2$, providing evidence for a 16-electron intermediate in the reaction. In the formation of Cp^*TaH_3 with *para*-H_2, polarization of the hydride resonances is observed. D-labeling studies also indicate H_2 addition to the 16-electron monohydride ‘$Cp^*{}_2TaH$’ intermediate. This work provides definitive evidence of pairwise, concerted H_2 oxidative addition to two Ta^{III} complexes in the hydrogenation reactions.[147]

5.3 η^2-Acyls, η^2-Iminoacryls, and Related Complexes

The η^2-acyls, η^2-iminoacryls and related complexes originate from the migratory insertion (*see Migratory Insertion*) of C≡O or isocyanides C≡NR into a metal–alkyl bond. These complexes are of interest mainly because of their relevance to catalytic CO reduction and the C–C bond formation in Fischer–Tropsch (*see Fischer–Tropsch Process*) reactions.

A large number of η^2-iminoacyl complexes have been reported. A series of η^2-iminoacyl derivatives CpMX(NXyl)[η^2-C(R)=NXyl] (X = Cl, R) are prepared by reactions of chloro alkyl or dialkyl imides CpMX(R)(NXyl) with 1 equiv of CNXyl. Reaction of Cp*TaRMe(NXyl) with CNXyl involves the migration of alkyl or Me group, giving a mixture of Cp*TaMe(NXyl)[η^2-C(R)=NXyl] and Cp*TaR(NXyl)[η^2-C(Me)=NXyl].[22] The following complexes are prepared similarly: Cp*Ta(CH_2SiMe_3)($CHSiMe_3$)-[η^2-C(CH_2SiMe_3)=NXyl],[120] Cp*Ta(η^2-MeCNR)(η^2-PhCCPh)Me (R = Bu^t, Me),[148] Cp*TaR(η^2-CR=NXyl)-(NXyl) (R = Et, Pr^n),[149] and $Cp'_2Ta[\eta^2\text{-}Bu^tN{=}CCH_2B(C_6F_5)_3]$.[150]

The carborane (*see Carborane*) complex $(Et_2C_2B_4H_4)CpTaMe_2$ is found to undergo insertion reactions with isocyanides under UV-visible irradiation to afford both isomers of $(Et_2C_2B_4H_4)CpTaMe[\eta^2\text{-}C,N\text{-}C(=NR)Me]$ (R = Bu^t, Xyl). The isomers interconvert under heat. The diphenyl complex $(Et_2C_2B_4H_4)CpTaPh_2$ generally reacts at elevated temperatures to give only one isomer of $(Et_2C_2B_4H_4)CpTaPh[\eta^2\text{-}C,N\text{-}C(=NXyl)Ph]$.[151]

Reactions of $Cp^*TaMe_2X_2$ [$X_2 = Cl_2$, $(SCH_2CH_2)_2O$] with 1 equiv of isocyanides occur with double migration of Me, giving imine complexes $Cp^*TaX_2(\eta^2\text{-}Me_2CNR)$ [R = Xyl, 2,4,6-Me_3-C_6H_2, $X_2 = Cl_2$;[152,153] R = Xyl, $X_2 = (SCH_2CH_2)_2O$].[29] Mono- and dimethylated imines $Cp^*TaCl_nMe_{2-n}(\eta^2\text{-}XylN{=}CMe_2)$ were similarly prepared. They react with second equiv of isocyanide to give imido alkenylamido species $Cp^*TaX(=NXyl)(NR'CMe{=}CMe_2)$ (X = Cl, Me; R′ = Xyl, 2,4,6-$Me_3C_6H_2$, **35**). Reactions of (**35**) with third equiv of R″NC (R″ = Xyl, 2,4,6-$Me_3C_6H_2$, Bu^t) afford η^2-imino acyl compounds $Cp^*TaX(=NXyl)(\eta^2\text{-}NR''{=}CCMe_2CMe{=}NR')$.[154] It is interesting to note that insertion of CNXyl into the Ta–Me bond in $Cp^*Ta(=NBu^t)Me(NR_2)$ (R = Ph, $SiMe_3$) gives $Cp^*Ta(=NBu^t)(NR_2)[\eta^1\text{-}C(Me){=}NXyl]$, and CNXyl inserts into the Ta–N bond in $Cp^*Ta(=NBu^t)Me(NMeR)$ (R = H, Me) to give $Cp^*Ta(=NBu^t)Me[\eta^2\text{-}C(NRMe){=}NXyl]$.[155] When the reaction of $Cp^*TaMe_2Cl_2$ with CNXyl is carried out in the presence of a trace amount of H_2O, a cyclic η^2-amido-carbene species $Cp^*TaCl_3[\eta^2\text{-}N(Xyl)CMe_2CNHR]$ was produced.[154] η^2-Iminoacyl complexes $Cp^*Ta(NBu^t)(NHBu^t)\{\eta^2\text{-}C(Me){=}NR\}$ react with one equiv of CNXyl to give the double insertion imine-η^2-iminoacyl complexes $Cp^*Ta(NBu^t)(NHBu^t)\{\eta^2\text{-}C[C(Me){=}NR]{=}NR\}$, which when heated undergo an intramolecular H migration to yield η^2-diamidoalkenes $Cp^*Ta(NBu^t)\{\eta\text{-}NBu^t\text{-}C(NHR){=}C(Me)\text{-}\eta\text{-}NR\}$.[156]

In the reactions of $(Me_2S)_2Cl_4Ta_2(\mu\text{-}Me_2S)(\mu\text{-}Cl)_2$ with formamidinate anions, $[ArNC(H)NAr]^-$, C–N bond cleavage is observed. The reaction of $[PhNC(H)NPh]^-$ ($DPhF^-$) with $(Me_2S)_2Cl_4Ta_2(\mu\text{-}Me_2S)(\mu\text{-}Cl)_2$ and Zn yields the CNPh-containing compound $(\eta^2\text{-}DPhF)_2Ta(\mu\text{-}NPh)(\mu\text{-}\eta^2\text{-}CNPh)Ta(\eta^2\text{-}DPhF)_2$. When $[TolNC(H)NTol]^-$ ($DTolF^-$) and Na/Hg are used, the isolated product is $(\eta^2\text{-}DTolF)Ta(\mu\text{-}NTol)(\mu\text{-}\eta^2\text{-}CNTol)(\mu\text{-}DTolF)_2Ta(\eta^2\text{-}DTolF)$. In the absence of a reducing agent, the reaction with LiDTolF produces $Cl_2(\eta^2\text{-}DTolF)Ta(\mu\text{-}NTol)(\mu\text{-}\eta^2,\eta^2\text{-}HCNTol)Ta(\eta^2\text{-}DTolF)_2$ in which a tolylformimidoyl fragment ($HCNTol^{3-}$) binds to the Ta atoms through both C and N atoms in an η^2,η^2 mode.[157]

5.4 CO_2, Isocyanate, and Related Complexes

Olefin-hydride complexes such as $Cp'_2Nb(H)(\eta^2\text{-}H_2C{=}CH_2)$ react with CO_2 to afford, for example, $Cp'_2Nb(Et)(\eta^2\text{-}CO_2)$ (**36**). When $B(C_6F_5)_3$ is added to (**36**), the adduct $Cp'_2Nb(Et)[\eta^2\text{-}CO_2\text{-}B(C_6F_5)_3]$ is yielded in the first step, which subsequently evolves to give the oxo-alkyl complexes $Cp'_2Nb(Et)[O\text{-}B(C_6F_5)_3]$ with the loss of CO.[86] Upon heating, the coordinated CO_2 ligand in $(MeC_5H_4)_2Nb(\eta^2\text{-}CO_2)(CH_2R)$ (R = $SiMe_3$, Bu^t, Ph, H) splits, giving $(MeC_5H_4)_2Nb(=O)(CH_2R)$ and CO.[158] As in the formation of (**36**), reactions of CS_2 with $Cp'_2Nb(H)(\eta^2\text{-}RHC{=}CH_2)$ (R = H, Ph) afford $Cp'_2Nb(\eta^2\text{-}CS_2)(CH_2CH_2R)$. Interaction of $Cp'_2NbX(\eta^2\text{-}CS_2)$ (X = Cl, carboxylate) with alkynes $R'C{\equiv}CR'$ bearing electron-withdrawing groups gives 1,3-dithiol-2-ylidene complexes $Cp'_2NbX[=\overline{CS(R')C{=}C(R')S}]$.[159]

Nb and Ta complexes with other η^2-ligands such as η^2-COS, η^2-OCN and η^2-COTe have also been reported. $(Cp'_2NbCl)_2$ reacts with phenyl isocyanate PhN=C=O to give the adduct $Cp'_2NbCl(\eta^2\text{-}N,C\text{-}OCNPh)$. Similar dinuclear adducts are obtained from the reactions of $(Cp'_2NbCl)_2$ with 1,3- and 1,4-phenylenedi-isocyanate.[160]

5.5 Ketene and Ketenimine Complexes

Complexation of the ketene C=O bonds in, for example, $Cp'_2Nb(Cl)[\eta^2\text{-}O{=}C{=}CMe_2]$ (**37**) is usually observed. Ketene complexes are prepared from coordination of ketenes to Cp'_2NbCl[161] or deprotonation of η^2-acyl in $Cp'_2NbCl(\eta^2\text{-}O{=}C\text{–}CHEtPh)$.[162] Treatment of (**37**) with $(Ph_3C)(BF_4)$ leads to γ-hydride abstraction to give η^2-enacyl salts $[Cp'_2Nb(Cl)(\eta^2\text{-}OCCMe{=}CH_2)](BF_4)$.[163] The ketene complex $Cp'_2Nb(H)(\eta^2\text{-}C,O\text{-}O{=}C{=}CPh_2)$ reacts with MeCN or Bu^tNC to yield isocyanate and $Cp'_2Nb(H)(=C{=}CPh_2)$.[164] A synthetic strategy involving sequential hydride abstraction and proton abstraction has been developed to convert the η^2-C, O ketene ligand in $Cp'_2Nb(Cl)(\eta^2\text{-}OC{=}CREt)$ (R = Ph, Et) into a vinylketene ligand $\eta^2\text{-}OC{=}C(R)CH{=}CH_2$. These are the first vinylketene complexes exhibiting the η^2-C,O bonding mode.[165]

Ketenimine complexes such as $Cp'_2NbCl(\eta^2\text{-}C,N\text{-}Ph_2C{=}C{=}NPh)$ (**38**) reacts with $HBF_4{\cdot}OEt_2$ to give η^2-iminoacyl $[Cp'_2NbCl(\eta^2\text{-}C,N\text{-}Ph_2CHC{=}NPh)]^+$ BF_4^-.[166] Reduction of (**38**) with Na/Hg yields $Cp'_2Nb^{IV}(\eta^2\text{-}C,N\text{-}Ph_2C{=}C{=}NPh)$, which is oxidized by Cp_2Fe^+ in the presence of nitriles or isonitriles L to give $[Cp'_2Nb(\eta^2\text{-}C,N\text{-}Ph_2C{=}C{=}NPh)(L)]^+$, cationic derivatives of (**38**).[167]

5.6 Ketone, Aldehyde, Imine, and Related Complexes

Ketone and aldehyde complexes have been prepared from deprotonation of the relatively strong C–H acid $Cp'_2Nb(Cl)(OMe)^+$ to give $Cp'_2Nb(Cl)(\eta^2\text{-}OCH_2)$,[162] reaction of $Nb(NPr^iAr)_3Cl$ (Ar = 3,5-Me_2-C_6H_3) with $O{=}CPh_2$ to yield $Nb(\eta^2\text{-}OCPh_2)(NPr^iAr)_3$,[168] and double migration of alkyl groups in $Ta\{p\text{-}Bu^t\text{-}calix[4]\text{-}(OMe)(O)_3\}R_2$ (R = Me, Bz, p-MeC_6H_4, η^3-allyl **39**) in their reactions with CO to form $(calix[4]OMe)Ta(\eta^2\text{-}OCR_2)$. Reactions of (**39**) with

Bu^tNC yields related imine complexes (calix[4]OMe)Ta(η^2-$Bu^tN{=}CR_2$).[169,170] Although butadiene is π^2,η^4-bonded to the metal in Ta{p-Bu^t-calix[4]-(OMe)$(O)_3$}(η^4-C_4H_6), it behaves as if it were η^4,σ^2-π bonded in the migratory insertion reaction with Bu^tNC to afford an η^2-imine derivative.[169]

The η^2-formaldehyde complex $Cp'_2Nb(Cl)(\eta^2\text{-}CH_2O)$ undergoes facile Na/Hg reduction to produce the radical $Cp'_2Nb^{IV}(\eta^2\text{-}CH_2O)$, which then reacts with H_2 to give $Cp'_2Nb^{V}({=}O)Me$. In the presence of added alcohol, this reduction yields diamagnetic hydride $Cp'_2Nb(H)(\eta^2\text{-}CH_2O)$.[171]

Telluroformaldehyde complex $Cp^*_2Ta(\eta^2\text{-}TeCH_2)H$ (**40**) is prepared by the PMe_3-catalyzed addition of Te to the $Ta{=}CH_2$ in $Cp^*_2Ta({=}CH_2)H$. (**40**) is converted to its more stable isomer $Cp^*_2Ta({=}Te)CH_3$ under heating.[84]

5.7 η^2-Arene, η^2-Pyridine, and Related Complexes

In contrast to some η^2-C,C-heterocycles containing other metals, Nb and Ta prefer to bind N-heterocycles in the η^2-C,N mode. The very first complex of this type, $(silox)_3Ta(\eta^2\text{-}N,C\text{-py})$, was reported by Wolczanski and coworkers in 1988.[172] Its Nb analogs $(silox)_3Nb(\eta^2\text{-}N,C\text{-L})$ (L = py, 4-picoline, 3,5-lutidine) are prepared by reduction of $(silox)_3NbCl_2$ with Na/Hg in pyridine or 4-picoline.[173–175] Heating the pyridine and lutidine adducts leads to the cleavage of the C=N bond. Similar reduction of $(silox)_2TaCl_2(NR_2)$ (NR_2 = pyrrolidide, piperidide) with Na/Hg in pyridine gives $(silox)_2Ta(NR_2)(\eta^2\text{-}N,C\text{-py})$, which react with $MeNH_2$ to yield imides $(silox)_2Ta(NR_2)({=}NMe)$.[175] Reduction of $(ArO)_3TaCl_2(\eta^1\text{-}N\text{-L})$ (L = quinoline, 6-methylquinoline; Ar = 2,6-Pr^i_2-C_6H_3) leads to an $\eta^1(N) \rightarrow \eta^2(N,C)$ bonding rearrangement to give $(ArO)_3Ta(\eta^2\text{-}N,C\text{-L})$.[176] Reaction of $NbCl_4(THF)_2$ with $LiNCy_2$ leads to the formation of imine $Nb(\eta^2\text{-}N,C\text{-}CyN{=}C_6H_{10})(NCy_2)_2Cl$ containing one metallated cyclohexyl ring.[177]

6 METALLACYCLIC COMPLEXES

Metallacyclic (*see Metallacycle*) complexes of niobium and tantalum play an important role in understanding several catalytic and stoichiometric transformations of organic compounds. Some group 5 metallacycles are formed from the inter- or intramolecular hydride abstraction reactions. Most of the Nb and Ta metallacycles are prepared, however, from reductive coupling (*see Reductive Coupling*) of unsaturated organic substrates. To be included in this section, the metallacyclic ligand must have at least one M–C bond.

6.1 Metallacyclobutanes and Other Four-member Rings

Metallacyclobutanes are important intermediates in alkene metathesis (*see Alkene Metathesis*). Many Ta and Nb alkylidene complexes do not readily afford metathesis products upon reactions with alkenes. These reactions often lead to the formation of metallacyclobutanes. The alkylidene $Ta({=}CHSiMe_3)[NCN]Cl(OBu^t)$ is prepared from the metathesis of $Ta({=}CHBu^t)(NCN)Cl(OBu^t)$ (**24a**, Section 4.1) with $CH_2{=}CHSiMe_3$, and yet it does not undergo further metathesis with ethene. This reaction instead leads to the formation of the tantalacyclobutane complex (**41**).[116] Similarly, the dialkoxides $Ta({=}CHBu^t)[CNN](OBu^t)_2$ (**30b**) reacts with ethene to afford the tantalacyclobutane (**31a**) (Section 4.2).[123] (**30b**) and (**31a**) initiate ring-opening metathesis polymerization (*see Ring Opening Metathesis Polymerization Reactions*) of strained cyclic olefins such as dicyclopentadiene and norbornene. Metathesis of (**31a**) with propene and styrene gives substituted tantalacyclobutane complexes (**31b-c**). Insertion of Bu^tNC into the Ta–C bonds in (**31a–c**) affords $Ta[C({=}NBu^t)CH_2CHRCH_2\text{-}1,4][CNN](OBu^t)_2$ (R = H, Me, Ph, **42a–c**).[178]

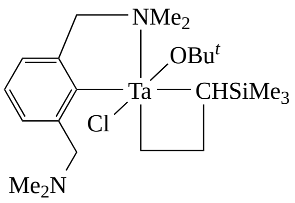

(**41**)

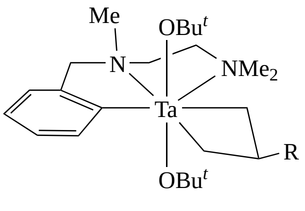

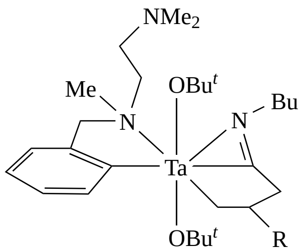

R = H, Me, Ph

(**31a-c**) (**42a-c**)

Ta alkylidenes $(RCH_2)_3Ta(L){=}CHR$ and $RCH_2Ta(L)_2\text{-}({=}CHR)_2$ (R = $SiMe_3$, L = PMe_3) react with phenylsilanes $H_2SiR'Ph$ (R′ = Me, Ph) and $(PhSiH_2)_2CH_2$ to give bis(silyl)-substituted alkylidene complexes $(RCH_2)_3Ta{=}CR(SiHR'Ph)$ and novel metallasilacyclobutadiene (**43a**) and metalladisilacyclohexadiene complexes (**44**). Reactions of the mixed-ligand trimethylsilylmethyl neopentylidene complex $RCH_2Ta(L)_2({=}CHBu^t)_2$ with $H_2SiMePh$ also yield a metallasilacyclobutadiene complex (**43b**).[179,180]

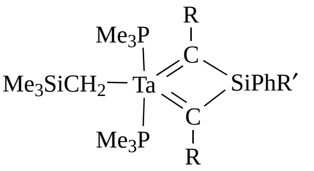

R = SiMe$_3$; R′ = Me, Ph, (**43a**)
R = Bu^t; R′ = Me, (**43b**)

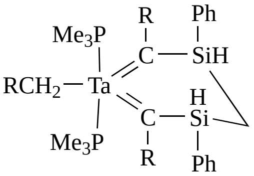

R = SiMe$_3$, (**44**)

6.2 Metallacyclopentanes, Metallacyclopentadienes, and Other Five-member Rings

Metallacyclopentanes are of considerable importance as intermediates in catalytic alkene dimerization (*see* ***Oligomerization & Polymerization by Homogeneous Catalysis***).

The tantalacyclopentane $\mathrm{Cp^*(DippN{=})Ta[CH_2CH_2CH_2CH_2]}$ (**45**) and tantalacyclopentadiene $\mathrm{Cp^*(DippN{=})Ta[CPh{=}CPh\text{-}CPh{=}CPh]}$ are obtained when $\mathrm{Cp^*(DippN{=})Ta[Si(SiMe_3)_3]H}$ (Dipp = 2,6-$\mathrm{Pr^i_2\text{-}C_6H_3}$) is treated with ethylene and diphenylacetylene, respectively.[181] $\mathrm{Cp^*Ta({=}NDipp)Cl_2}$ reacts with excess EtMgCl in the presence of $\mathrm{CH_2{=}CH_2}$, giving (**45**) as well. (**45**) undergoes exchange with $\mathrm{C_2D_4}$ to give (**45**-d$_8$), and double CO insertion to yield a cyclic diacyl complex in which CO has inserted into both of the metallacyclic Ta–C bonds.[182]

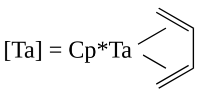

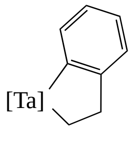

(**46a**)

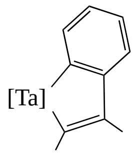

(**46b**)

Insertion of ethylene and 2-butyne into the Ta benzyne bond of $\mathrm{Cp^*Ta(\eta^4\text{-butadiene})(\eta^2\text{-}C_6H_4)}$ affords the metallacycles (**46a**) and (**46b**), respectively. Similar insertion of acetonitrile and carbon dioxide gives metallacycles (**46c**) and (**46d**).[145]

Alkylation of $\mathrm{Cp^*Cp'TaCl_2}$ with $\mathrm{LiCH_2CMe_2Ph}$ gives the benzocyclic complex $\mathrm{Cp^*Cp'Ta(H)(\eta^2\text{-}CH_2\text{-}CMe_2\text{-}}o\mathrm{\text{-}C_6H_4)}$ (**47**). In comparison, the alkylation with $\mathrm{Mg(CH_2Ph)_2(THF)_2}$ or $\mathrm{LiCH_2R}$ (R = SiMe$_3$, Bu^t) gives bis(μ-alkylidene) complexes $\mathrm{(Cp^*Cp'Ta)_2(\mu\text{-}CHR)_2}$ (R = Ph, SiMe$_3$, Bu^t).[183]

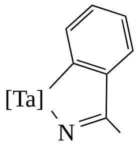

(**46c**)

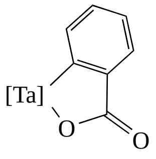

(**46d**)

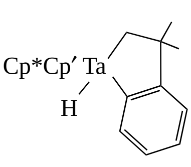

(**47**)

Thermolysis of $\mathrm{(Et_2C_2B_4H_4)CpTaPh_2}$ (**48**) in the presence of alkynes and 1,4-diphenylbutadiyne leads to the formation of the five-membered metallacycles (**49a–b**). (**49a**) reacts with excess $\mathrm{(Et_2C_2B_4H_4)CpTaPh_2}$, giving a bis-insertion product (**50**).[184] Reaction of (**48**) with excess styrene $\mathrm{PhCH{=}CH_2}$ results in a novel triple-insertion process in which styrene units are added to both ortho positions of an aryl ligand and to the central B atom of the $\mathrm{C_2B_3}$ ring in (**51**).[184]

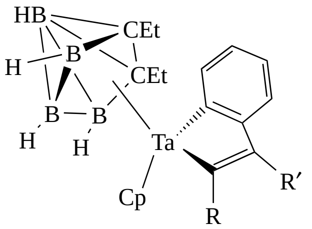

e.g., R = R′ = Et, Ph (**49a**)
R = Ph, R′ = PhC≡C- (**49b**)

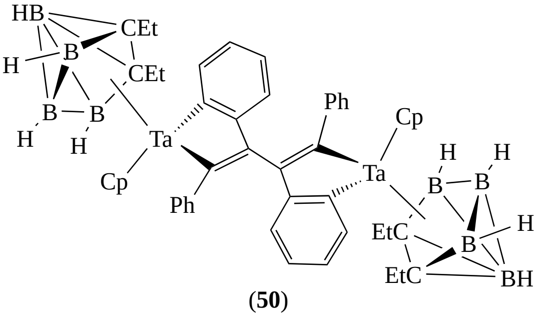

(**50**)

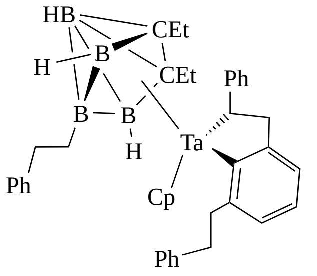

(**51**)

$\mathrm{Tp^*NbCl_2(PhC{\equiv}CR)}$ (R = Me, **52a**; Ph, **52b**) reacts with allyl Grignard giving the five-membered niobacycles $\mathrm{Tp^*(Cl)Nb({=}CPh–CR{=}CH–CHMe)}$.[185] When (**52a**) is treated with EtMgCl, the formal dehydrogenation of an ethyl group gives the alkyne-coupled product $\mathrm{Tp^*NbEt({=}CPh–CMe{=}CHCH_2)}$.[133]

Protonation of the 3e-alkyne-η^2(3e)-nitrile complex $\mathrm{Tp^*Nb(CO)(PhC{\equiv}CMe)(EtC{\equiv}N)}$ with $\mathrm{HBF_4}$ induces nitrile/alkyne coupling to give $\mathrm{Tp^*NbF({=}CPh\text{-}CMe{=}CPhNH)}$

via $[\mathrm{Tp^*Nb(CO)(\eta^2\text{-}CPh{=}NH)(PhC{\equiv}CMe)](BF_4)}$. Protonation of $\mathrm{Tp^*Nb(CO)(PhC{\equiv}CMe)_2}$ with $\mathrm{HBF_4}$ leads to the niobacycle $\mathrm{Tp^*NbF[{=}CPh\text{–}CMe{=}C(\text{–}CMe{=}CHPh)O]}$ in which CO is included in the alkyne coupling reaction.[135] Similar five-membered oxaniobiacycles $\mathrm{Tp'Nb(OMe)({=}CPh\text{–}CR{=}CMe\text{–}O)}$ (R = Me, Et) and $\mathrm{Tp'Nb(OMe)({=}CPh\text{–}CEt{=}CPh\text{–}O)}$ are prepared from the regioselective coupling of the coordinated alkyne with an acetyl or benzoyl group in the reactions of $\mathrm{Tp'NbMe(OMe)(PhC{\equiv}CR)}$ and $\mathrm{Tp'NbPh(OMe)(PhC{\equiv}CEt)}$ with CO.[186]

Reaction of $\mathrm{Cp^*Ta(CH_2SiMe_3)_2({=}CHSiMe_3)}$ with $\mathrm{2,6\text{-}Me_2\text{-}C_6H_3OH}$ leads to H abstraction from the methyl group in $\mathrm{Ta\text{-}(O\text{-}2,6\text{-}Me_2C_6H_3)}$, giving the cyclic alkyl-alkoxo derivative $\mathrm{Cp^*Ta(CH_2SiMe_3)_2\{\eta^2\text{-}O(2\text{-}CH_2\text{-}6\text{-}MeC_6H_3)\}}$ with the elimination of $\mathrm{SiMe_4}$.[120]

$\mathrm{Cp'_2Ta[CH_2B(C_6F_5)_2](\mu\text{-}H)(Me)}$, generated via treatment of $\mathrm{Cp'_2Ta({=}CH_2)Me}$ with $\mathrm{HB(C_6F_5)_2}$, undergoes irreversible methane loss in the presence of an excess of $\mathrm{MeC{\equiv}CMe}$ and $\mathrm{PhC{\equiv}CH}$, giving the tantala-3-boratacyclopentene compounds (**53a–b**). The kinetic product (**53b**) thermally rearranges to the thermodynamic product (**53c**).[187]

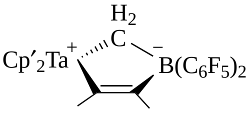

(**53a**)

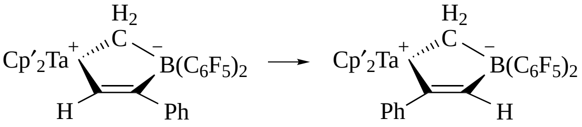

(**53b**) (**53c**)

$\mathrm{(silox)_3TaH_2}$ thermally cyclometallates to $\mathrm{(silox)_2(H)\text{-}TaOSiBu^t{}_2CMe_2CH_2}$, but is reconstituted with $\mathrm{H_2}$. Reduction of $\mathrm{(silox)_3(H)TaI}$ with Na/Hg in THF produces a ring-opened THF complex $\mathrm{(silox)_3Ta(H)[\mu\text{-}CH_2(CH_2)_3O\text{-}]\text{-}Ta(H)(silox)_3}$.[188]

6.3 Other Metallacycles

Reaction of $\mathrm{Cp^*TaCl_3[\eta^2\text{-}C_6H_4(2\text{-}CH_2NMe_2)]}$ with 1 and 3 equiv of $\mathrm{Li[2\text{-}(Me_2NCH_2)C_6H_4]}$ causes successive β-H abstraction at one of the methylamino groups, giving the cyclometallated (**54**) and alkylidene (**55a**). Similarly, the reactions of (**54**) with 2 equiv of $\mathrm{LiNMe_2}$ and 1 equiv of $\mathrm{LiN(SiMe_3)_2}$ yield the tantalacycloalkylidenes (**55b**) and (**55c**), respectively.[189]

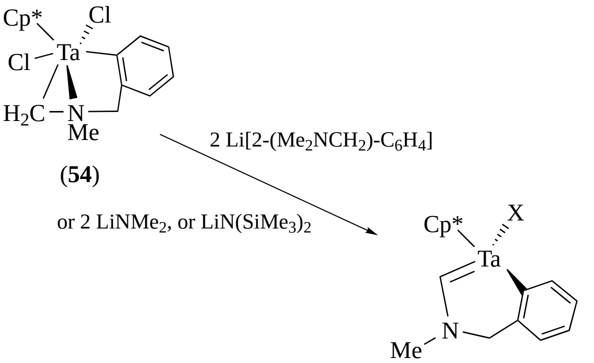

(**54**)

$\mathrm{X = \eta^2\text{-}C_6H_4(2\text{-}CH_2NMe_2)}$ (**55a**)
$\mathrm{= NMe_2}$ (**55b**)
$\mathrm{= Cl}$ (**55c**)

On standing at room temperature, the $\mathrm{d^0}$ carbonyl complex $\mathrm{Cp^*(ArN{=})Ta(CO)[Si(SiMe_3)_3]H}$ transforms into the tantalacycle (**56**).[190]

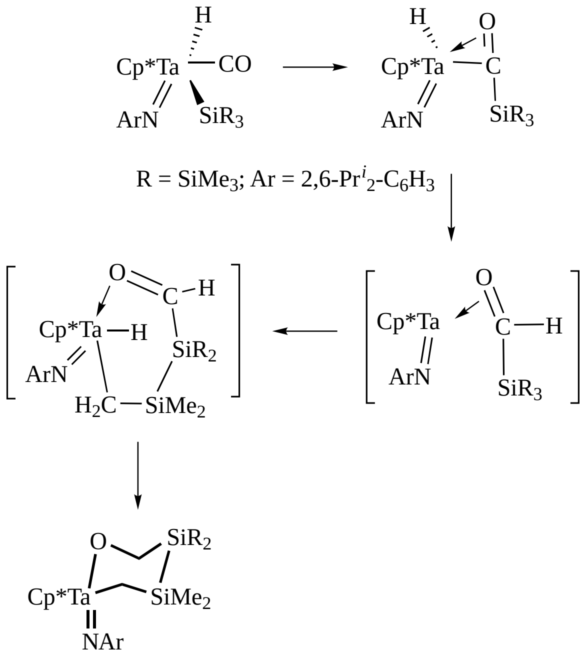

(**56**)

Photolysis of $\mathrm{Ta(OAr)_2(CH_2SiMe_3)_3}$ ($\mathrm{Ar = 2,6\text{-}Ph_2\text{-}3,5\text{-}R_2\text{-}C_6H}$; R = H, Ph, Me, $\mathrm{Pr^i}$) generates alkylidenes $\mathrm{Ta(OAr)_2({=}CHSiMe_3)(CH_2SiMe_3)}$, which undergo intramolecular cyclometallation (*see Cyclometalation*) of the aryloxide ligand, through the addition of an aromatic C–H bond to the Ta alkylidene, to form (**57**).[53]

The cation complex $\mathrm{[(\mathit{s\text{-}trans}\text{-}\eta^4\text{-}butadiene)TaCp^*Cp]^+}$ (**58**) was found to react with ketones such as acetone and adamantanone, as well as 1-cyanoadamantane to yield seven-membered 2-tantalatetrahydrooxepine (**59a-b**) and 2-tantala-3,6-dihydro-2H-azepine (**59c**) cation complexes, respectively. Activation of (**58**) with methylalumoxane gives an active ethene polymerization (*see* ***Oligomerization & Polymerization by Homogeneous Catalysis***) catalyst.[191]

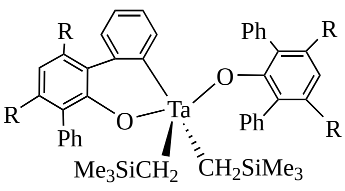
R
R
Ph
Ta
O
O
Ph
R
Ph
R
Me_3SiCH_2
CH_2SiMe_3

(**57**)

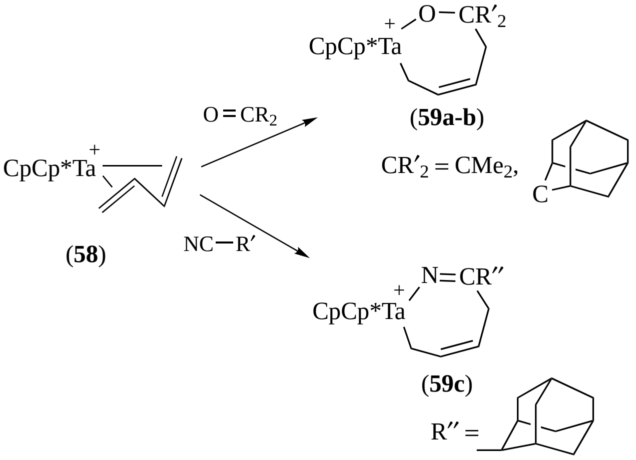
CpCp*Ta
+
O=CR2
NC−R′
+ O−CR′2
CpCp*Ta
CR′2 = CMe2,
C
+ N=CR″
CpCp*Ta
R″ =

(**58**)

(**59a-b**)

(**59c**)

In the course of the model studies of hydrodenitrogenation (HDN) reactions (See Section 9.5), thermolysis of (η^2-N,C-2,4,6-Bu^t_3-NC_5H_2)$Ta(OAr)_2X$ (**60**) leads to migration of alkyl (Me, Et, Pr^n, Bu^n) and aryl ligands from metal to ligand, giving the ring-opened compounds (**61**).[192] The reaction of (**60-Cl**) (X = Cl) with hydride $LiBEt_3H$ similarly affords the C–N bond scission product (**61-H**) (X = H).[193] (**61-Me**) undergoes thermal decomposition in THF to give the metallapyridine (**62**) through elimination of $Bu^tCH{=}CH_2$. (**62**) reacts with electrophiles such as isocyanates and carbodiimides to afford insertion products (**63**) and (**64**).[194]

$Ta(OAr)_2Cl_2(H)(PMe_2Ph)_2$ (Ar = 2,6-Pr^i_2-C_6H_3) reacts with RNC (R = Ar, Xyl, Bu^t) to produce phosphine adduct η^2-iminoformyl complexes (**65**). Further reactions of XylNC with (**65-Xyl**) (R = Xyl) and of Bu^tNC with (**65-Bu^t**) (R = Bu^t) yield the ylide derivative (**66a**) and (**66b**), respectively. $Ta(OAr')_2Cl_2(H)(PMePh_2)$ (Ar′ = 2,6-Bu^t_2-C_6H_3) reacts with RNC (R = Xyl, Bu^t) to produce monocyclometalated complex (**67**) in which three H atoms have been transferred to the isocyanide substrate to give the amido ligand.[31]

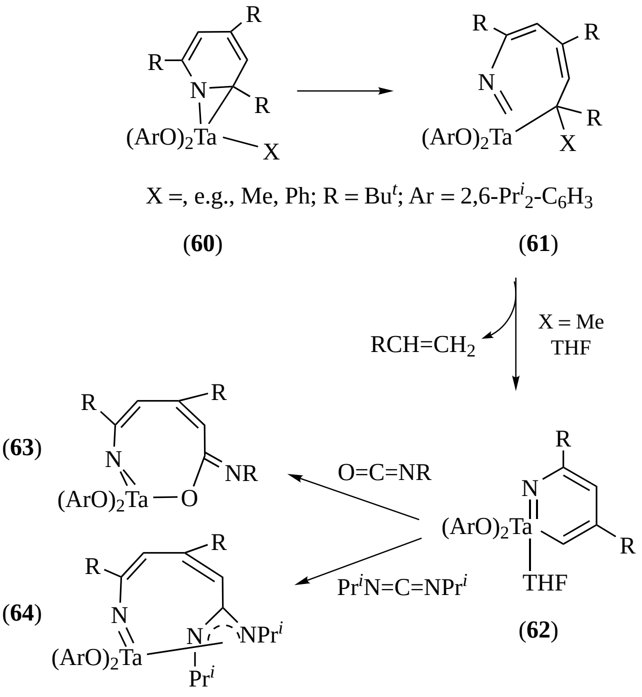
R
R
N
R
$(ArO)_2Ta$
X
R
R
N
R
$(ArO)_2Ta$
X
$RCH{=}CH_2$
X = Me
THF
R
R
N
NR
$(ArO)_2Ta$—O
O=C=NR
R
N
$(ArO)_2Ta$
R
THF
$Pr^iN{=}C{=}NPr^i$
R
R
N
N
NPr^i
$(ArO)_2Ta$
Pr^i

X =, e.g., Me, Ph; R = Bu^t; Ar = 2,6-Pr^i_2-C_6H_3

(**60**) (**61**)

(**63**)

(**64**)

(**62**)

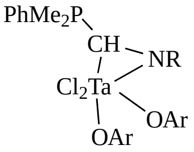
$PhMe_2P$
CH
NR
Cl_2Ta
OAr
OAr

(**65**)

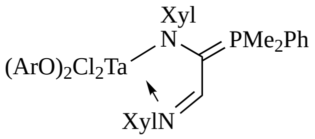
Xyl
N
PMe_2Ph
$(ArO)_2Cl_2Ta$
XylN

(**66a**)

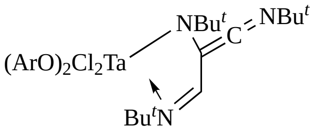
NBu^t
C
NBu^t
$(ArO)_2Cl_2Ta$
Bu^tN

(**66b**)

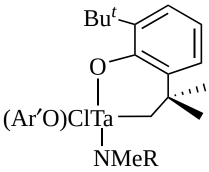
Bu^t
O
$(Ar'O)ClTa$
NMeR

(**67**)

Reduction of $Nb(OAr)_3Cl_2$ (Ar = 2,6-Pr^i_2-C_6H_3) by Na/Hg in the presence of donor ligands leads to dehydrogenation of the *ortho*-isopropyl group of an aryloxide group yielding η^2-α-methylvinyl complex (**68**). The metallacyclopropane ring in (**68-THF**) (L_n = THF) undergoes ring expansion (coupling of the olefin) with unsaturated substrates such as $Ph_2C{=}O$ and $PhC{\equiv}CR$ (R = H, Ph) to give 2-oxaniobacyclopentane (**69a**) and niobacyclopentene derivatives (**69b**).[195]

Bridging alkylidynes $(cb)_2M(\mu$-$CSiMe_3)_2M(cb)_2$ (**70**) react rapidly with isocyanide XylNC to give bridging amidoalkyne complexes (**71**) through coupling of the isocyanide with one of the alkylidyne bridges in (**70**).[196] Similar coupling of alkynes with (**70**) yields nonplanar six-membered dimetallacycles (**72**).[197]

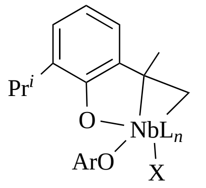

L_n = Py$_2$, (Bu^{t}NC)$_2$, THF; X = OAr
L_n = PMe$_2$Ph; X = Cl

(**68**)

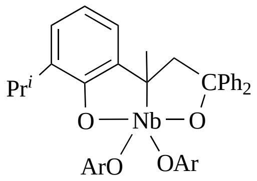

(**69a**)

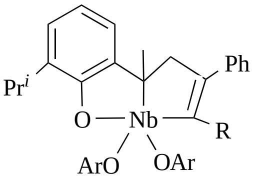

R = H, Ph

(**69b**)

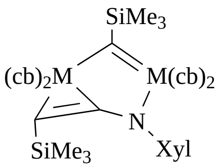

(**71**)

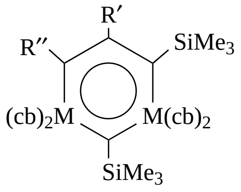

R′= R″ = Et
R′ = H, R″ = SiMe$_3$

(**72**)

7 π-COMPLEXES OF CARBOCYCLIC, ENE, ENYL AND RELATED LIGANDS

7.1 η^3-Complexes

The stable bis(allyl)tantalum complex Cp*Ta(η^3-1-phenylallyl)$_2$ obtained from the reaction of Cp*TaCl$_4$ with PhCH=CHCH$_2$MgCl. Cp*Ta(η^3-allyl)$_2$ was only characterized by ^{1}H NMR and MS. In the formation of Cp*Ta(η^3-1-phenylallyl)$_2$, tantalum is reduced from Ta(V) to Ta(III), and dienes such as (PhCH=CHCH$_2$)$_2$ from the coupling of the allyl ligands are observed.**198** The presence of an imido ligand in Cp*Ta$^{\mathrm{V}}$(=NR)Cl$_2$ prevents the reduction of the metal in its reaction with (allyl)MgBr, yielding the fluxional bis(allyl) complex Cp*Ta$^{\mathrm{V}}$(=NR)(η^1-C$_3$H$_5$)(η^3-C$_3$H$_5$) (R = Bu^t, 2,6-Pr$^i{}_2$-C$_6$H$_3$).**199**

Nb(III) allyl and 1-azaallyl complexes Cp′$_2$Nb(η^3-CH$_2$CRCH$_2$) (R = H, Me, **73a**), Cp′$_2$Nb(η^3-CHR′CHCHR″) (R′ = R″ = SiMe$_2$Bu^t; R′ = H, R″ = SiPh$_3$, **73b**) and Cp′$_2$Nb[N(SiMe$_3$)C(Bu^t)-CH$_2$] (**73c**) have been prepared from reactions of (Cp′$_2$NbCl)$_2$ with the corresponding allyl Grignard (for **73a**), allyl potassium (for **73b**), and Li(1-azaallyl) reagents.**140,200** (**73a**) reacts with O$_2$ giving η^1-allyl oxo complexes Cp′$_2$Nb(=O)(η^1-CH$_2$CRCH$_2$).

Thermolysis of (η^5-C$_5$H$_4$CMe$_2$R)Nb(NMe$_2$)$_2$(=NAr) (R = CH$_2$CH=CH$_2$, Ph, CH$_2$Ph; Ar = 2,6-Pr$^i{}_2$-C$_6$H$_3$) leads to interesting intramolecular C–H activation with elimination of HNMe$_2$ to give *ansa*-type half-sandwich (*see Half-sandwich Complexes*) niobiocenes (**74a–c**).**201**

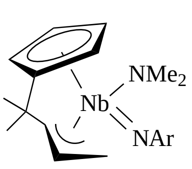

(**74a**)

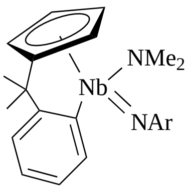

(**74b**)

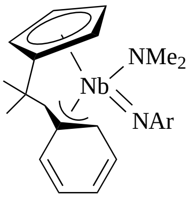

(**74c**) Ar = 2,6-Pr$^i{}_2$-C$_6$H$_3$

In addition to (**73c**), other heteronucles η^3 complexes have also been reported. Protonation of M(NMe$_2$)$_5$ with trialkylguanidines (RNH)$_2$C=NR produces dianionic guanidinate complexes M(NMe$_2$)$_3$[η^3-*N*,*C*,*N*-(RN)$_2$C=NR] (R = Pr^i, **75**, Cy).**202** Reaction of (**75**) with Me$_3$SiCl yields monoanionic guanidinate complex Ta(NMe$_2$)$_3$Cl[(Pr^{i}N)$_2$-CN(SiMe$_3$)Pr^i].**203** Carbodiimide insertion into M−amide bonds occurs in the reactions of M(NMe$_2$)$_5$ with RN=C=NR (R = Cy, Pr^i), yielding monoanionic guanidinate [η^3-*N*,*C*,*N*-(RN)$_2$C(NMe$_2$)]M(NMe$_2$)$_4$.**204** Benzamidinate complexes [PhC(NSiMe$_3$)$_2$]$_2$TaMe$_3$**24** and Nb(=ER)-[ArC(NSiMe$_3$)$_2$]$_2$Cl (ER = O, NBu^t; Ar = Ph, 4-Me-C$_6$H$_4$)**205** have been prepared from the reactions of Li[ArC(NSiMe$_3$)$_2$] with TaMe$_3$Cl$_2$ and Nb(=ER)Cl$_3$(py)$_2$, respectively. The reaction of Nb(=NBu^t)Cl$_3$(py)$_2$ with Li[PhC(NSiMe$_3$)$_2$] yields Nb(=NBu^t)[PhC(NSiMe$_3$)$_2$]-Cl$_2$(py).

Cyclooctatetraene (COT) binds to the early d-block metals in a variety of coordination modes. η^8-, η^4- η^3- and η^2-COT ligands have been reported. These include a series of η^3-COT Ta complexes such as (η^5-$^{\mathrm{R}}$Cp)Ta(η^4-diene)(η^3-COT) (diene = butadiene, isoprene, 2,3-dimethylbutadiene; $^{\mathrm{R}}$Cp = Cp*, C$_5$H$_4$Me, Cp). They are prepared from the reactions of (η^5-$^{\mathrm{R}}$Cp)TaCl$_2$(η^4-diene) with (COT)Li$_2$. The addition of B(C$_6$F$_5$)$_3$ to Cp*Ta(η^4-C$_4$H$_6$)(η^3-COT) affords Cp*Ta(η^4-C$_4$H$_6$)[C$_8$H$_8$B(C$_6$F$_5$)$_3$] containing a substituted bicyclo[5.1.0]octadienyl ligand.**206**

7.2 η^4-Complexes

Chemistry of Nb and Ta complexes with η^4-ligands has grown considerably. Among the η^4 complexes, those with η^4-butadiene (η^4-C$_4$H$_6$) are the best characterized, and they are the subject of a review by Nakamura and Mashima.**207** This paper focuses on complexes with other η^4-ligands such as η^4-arene, η^4-cyclodiene, and η^4-diazabutadiene.

η^4-Butadiene complex CpTaCl$_2$(η^4-C$_4$H$_6$), prepared from the reaction of CpTaCl$_4$ with (C$_4$H$_6$)Mg, is treated with NaCp to yield the η^2-butadiene complex Cp$_2$Ta(η^1-Cp)(η^2-C$_4$H$_6$) (**76**). Treatment of (**76**) and CpCp*TaCl(η^2-C$_4$H$_6$) with (Cp$_2$ZrMe)$^+$[MeB(C$_6$F$_5$)$_3$]$^-$ results in formation of Cp$_2$Ta(η^4-C$_4$H$_6$)$^+$ (**77a**) and CpCp*Ta(η^4-C$_4$H$_6$)$^+$ (**77b**). In reactions of (**77a**) with ketones and nitriles, and (**77b**) with ketones, insertion of ketones and nitriles into the butadiene ligands is observed, giving cationic seven-membered metallacyclic σ-allyl complexes.[191,208] Similar reactions of (**77a**) with alkynes give metallacyclic (π-allyl)metallocene cations.[208]

When the dialkylated complexes Cp′NbR′$_2$(RCCR) (R = SiMe$_3$, R′ = Me, CH$_2$SiMe$_3$, Np) are treated with 1 equiv of isocyanide XylNC under heat, hydrogen migration occurs, giving diene complexes Cp′Nb(=NXyl)[η^4-CHRCRCR′CHR″] (R′ = Me, R″ = H; R′ = CH$_2$R, R″ = R) and the niobacyclohept-2-ene Cp′Nb(=NXyl)[η^2-CH$_2$CMe$_2$-CH$_2$CH(Np)CR=CR].[209]

In the Na/Hg reduction of aryloxides Nb(OAr)$_3$Cl$_2$ (Ar = 2,6-Ph$_2$-C$_6$H$_2$R, R = H, Ph) under H$_2$, 1,2-hydrogenation of an *ortho*-phenyl substituent occurs, leading to a cyclohexadiene group in Nb(OC$_6$H$_2$RPh-η^4-C$_6$H$_7$)(OAr)$_2$.[210] In the presence of 1,3-cyclohexadiene (C$_6$H$_8$), the Na/Hg reduction of M(OAr′)$_n$Cl$_{5-n}$ ($n = 2$, 3, Ar′ = 2,6-Pr$^i_2$-C$_6$H$_3$) leads to formation of cyclohexadiene adducts M(OAr′)$_n$Cl$_{3-n}$(η^4-C$_6$H$_8$), respectively. The cyclohexadiene ligand binds strongly in the complexes, and does not readily undergo displacement with added reagents such as PMe$_2$Ph. One of the adducts, Ta(OAr′)$_3$(η^4-C$_6$H$_8$), catalyzes the disproportionation of 1,3-cyclohexadiene into cyclohexene and benzene as well as the hydrogenation of 1,3-cyclohexadiene and cyclohexene into cyclohexane. Addition of 1,3-cyclohexadiene to Ta(OAr″)$_2$(H)$_3$(PMe$_2$Ph)$_2$ (Ar″ = 2,6-Cy$_2$-C$_6$H$_3$, 2,6-Cy$_2$-3,5-Ph$_2$-C$_6$H) leads to Ta(OAr″)$_2$(η^1-C$_6$H$_{10}$-η^4-C$_6$H$_7$) (**78**) containing a partially hydrogenated non-Diels–Alder dimer of 1,3-cyclohexadiene.[211]

The first tris(arene)niobium complex, [Nb(1-4-η^4-anthracene)$_3$]$^-$, prepared by the Na or K anthracene reduction of NbCl$_4$(THF)$_2$, undergoes facile anthracene displacement in the presence of CO to afford [K(18-crown-6)(THF)$_2$][Nb(CO)$_6$].[212] Reduction of TaCl$_5$ by sodium naphthalene provides [Na(THF)][Ta(η^4-naphthalene)$_3$], the first homoleptic naphthalene complex of a third row transition metal. This complex reacts with CO and anthracene to give [Ta(CO)$_6$]$^-$ and [Ta(1-4-η^4-anthracene)$_3$]$^-$, respectively. The latter product reacts with cyclooctatetraene (COT) to give [Ta(COT)$_3$]$^-$.[213]

Half-sandwich (*see Half-sandwich Complexes*) complexes Cp*Nb{η^4-*o*-(CH$_2$)$_2$C$_6$H$_4$}Cl$_2$ and Cp*Ta(η^4-C$_{14}$H$_{10}$)Cl$_2$ with an extended conjugated η^4-diene ligand such as *o*-xylylene and anthracene have been prepared from the reactions of Cp*MCl$_4$ with *o*-C$_6$H$_4$(CH$_2$MgCl)$_2$ and Mg(anthracene)(THF)$_3$, respectively.[214]

The germole reagent C$_4$Me$_4$Ge(Me)SiMe$_3$ reacts with TaCl$_5$ to give [(η^4-C$_4$Me$_4$GeMeCl)TaCl$_3$(Et$_2$O)$_x$]$_2$ (x = 0.5–1.0), which reacts with CpTl to give air-stable Cp(η^4-C$_4$Me$_4$GeMeCl)TaCl$_2$ (**79**).[215]

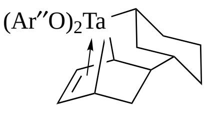

(**78**)

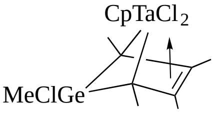

(**79**)

Cp*Ta(R$_2$-dad)Cl$_2$ (R$_2$-dad = RN-CH=CH-NR^{2-}; R = Pr^i, Bu^t, **80**) are prepared from the reactions of Cp*TaCl$_4$ with Li$_2$(R$_2$-dad). The N,N'-disubstituted diazabutadiene (R$_2$-dad) ligands in these complexes are bound to the metal center with a $\sigma^2(N,N')$, $\pi(C,C')$-coordination mode.[216] The Nb ene-diamido ene-diolato complexes Cp′NbCl$_2$(Me,Ph-dad) and Cp′NbCl$_2$[O(R)C=C(R)O] are prepared from the reactions of Cp′NbCl$_2$(Me$_3$SiCCSiMe$_3$) with Me,Ph-dad (PhN=CMe–CMe=NPh) and diketones R–CO–CO–R (R = Me, Ph).[217] Similarly, Cp*TaCl$_4$ reacts with *o*-C$_6$H$_4$(NLiSiPr$^i_3$)$_2$ giving (**81**), where the diamide ligand is coordinated in an η^4-fashion via donation of electron density from the phenylene ring to the metal.[218]

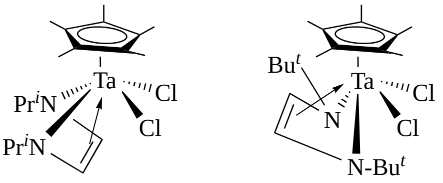

(**80**)

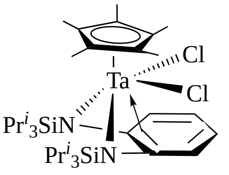

(**81**)

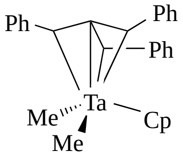

(**82**)

A neutral group 5 bent metallocene analog (**82**) containing the unusual η^4-TBM dianion (TBM = tribenzylidenemethane) has been prepared from the reaction of (TBM)TaMe$_2$Cl and LiCp.[219] Both TBM^{2-} and Cp$^-$ ligands are formally six-electron donors but differ in their respective charges. Compounds such as (**82**) are of interest as neutral group 4 counterparts of cationic metallocene alkyls that important homogeneous Ziegler–Natta polymerization catalysts (*see Ziegler–Natta Catalysts*).

7.3 η^5-Complexes

Many Nb and Ta complexes containing cyclopentadienyl ligands have been described in other sections. 3-D metallasiloxanes, prepared from reactions of Cp^*TaMe_4 with organosilanetriols $RSi(OH)_3$, as models for catalytically useful transition metals supported on silica was recently reviewed.[220] In this section, the η^5-ligands obtained from the reduction of arene rings will be described.

$M(\eta^5\text{-9-Ph-}C_{13}H_8)(CO)_4$ (9-Ph-$C_{13}H_8$ = phenylfluorenyl) have been prepared from $[M_2(\mu\text{-Cl})_3(CO)_8]^-$ and Li(9-phenylfluorenyl).[221]

Hydrogenolysis of $^R[P_2N_2]NbCH_2SiMe_3$ (R = Cy, Ph) in benzene and toluene causes hydride addition to the aromatic solvent, resulting in the formation of $^R[P_2N_2]Nb(\eta^5$-cyclohexadienyl) and $^R[P_2N_2]Nb(\eta^5$-methylcyclohexadienyl), respectively.[222] One-electron reduction of the P–Ph group in $^{Ph}[P_2N_2]NbCl$ yields (**83**) containing a cyclohexadienyl moiety formed via a C–C bond formation between the ipso carbons of the two Ph groups.[223] (ArN=)(ArNH)TaMe(OTf) (Ar = 2,6-dimesitylphenyl, **84a**) reacts with H_2 to convert one mesityl group into a η^5-cyclohexadienyl ligand, forming (ArN=)[2-(η^5-2,4,6-Me_3-C_6H_3)-6-mesitylC_6H_3NH]Ta(OTf) (**84b**).[224,225] D-labeling studies indicate that reaction proceeds through a hydride intermediate (ArN=)(ArNH)TaH(OTf) (**84c**), and a reversible intramolecular hydride transfer between Ta and the aromatic ring.

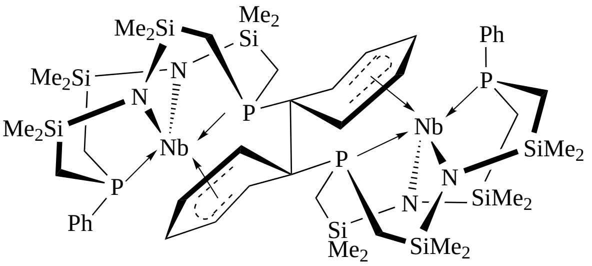

(**83**)

Reactions of 17-e $Nb^{II}(2,4\text{-}C_7H_{11})_2(L)$ species ($C_7H_{11}^-$ = dimethylpentadienyl; L = PEt_3, PMe_2Ph) with CO lead to spontaneous reduction of these complexes and formation of 18-e $Nb^I(2,4\text{-}C_7H_{11})(L)(CO)_3$. These products are also susceptible to reduction by alkali metals, presumably leading to the dianion $Nb(2,4\text{-}C_7H_{11})(CO)_3^{2-}$, which is oxidized under CO to give $Nb^I(2,4\text{-}C_7H_{11})(CO)_4$.[226]

7.4 η^6-Complexes

η^6-Arene complexes are usually prepared by the following methods: (i) metal vapor synthesis (*see* ***Metal Vapor Synthesis of Transition Metal Compounds***).[227] (ii) Al/AlX_3 reduction of a metal halide in the presence of the arene; and (iii) alkyne cyclotrimerization (*see Cyclodimerization & -trimerization Reactions*). Synthetic procedures to obtain η^6-arene derivatives have been reviewed by Pampaloni and Calderazzo.[228] Over the past ten years, studies in this area have been focused on the reactivities of η^6-arene complexes.

Reaction of $(TMEDA)_2Nb^{II}{}_2Cl_5Li(TMEDA)$ with the amide Ph_2NK leads to the formation of several compounds including the Nb^{III} anion (**85a**) and neutral, diamagnetic Nb^0 (**85b**). (**85a**) is the product of oxidative addition (*see Oxidative Addition*) of two Nb centers to the *ortho* C–H bond of a Ph group. (**85a**) then undergoes reductive elimination (*see Reductive Elimination*) to restore the C–H bond to form (**85b**).[229]

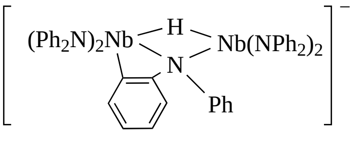

(**85a**)

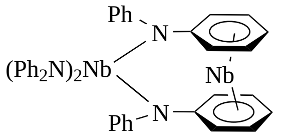

(**85b**)

$[Nb(Mes)_2]^+$, produced from the 1-e oxidation of bis(mesitylene) complex Mes_2Nb, adds alkynes to give $[Nb(Mes)_2(RC{\equiv}CR)]^+$ (R = Me, Ph). Thermal treatment of $[Nb(Mes)_2(RC{\equiv}CR)](BAr_4)$ gives $(RC{\equiv}CR)Nb(\eta^6\text{-}C_6H_4X)_2B(C_6H_4X)_2$ (R = Me, X = H, *p*-F, **86a**; R = Ph, X = H, **86b**) containing Nb bonded to two of the four aromatic rings of the tetraphenylborato ligand in a bent fashion. Alkyne displacement in (**86a**) by CO gives $Nb(CO)(\eta^6\text{-}C_6H_4X)_2B(C_6H_4X)_2$ (X = H, *p*-F).[230] Mes_2Nb is oxidized by $XMn(CO)_5$ (X = Cl, I) and $XRe(CO)_5$ (X = Br, I) to give Mes_2NbX and $Mes(CO)_2Nb(\mu\text{-}X)_2Re(CO)_3$, respectively.[231]

η^6-Hexamethylbenzene alkyl and aryl Ta(III) complexes supported by aryloxide and arenethiolate ligands have been reported. These include $(\eta^6\text{-}C_6Me_6)Ta(OAr)_2Me$, $(\eta^6\text{-}C_6Me_6)Ta(OAr)RR'$ (R = R′ = Me, Et, CH_2SiMe_3, Ph; R = H, R′ = CH_2SiMe_3), $(\eta^6\text{-}C_6Me_6)Ta(OAr)(R)X$ (X = Cl, R = CH_2SiMe_3, Ph; X = Br, R = Me, Et) (Ar = 2, 6- $Pr^i{}_2$-C_6H_3).[232]

7.5 η^8-Complexes

$Ta(\eta^8\text{-}COT')Me_3$ (**87**) was prepared from the reaction of $TaCl_2Me_3$ with $Li_2(COT')$ [COT′ = 1,4-bis(trimethylsilyl)cyclooctatetraene]. It reacts with $(NHPr^i{}_2Et)Cl$ to yield η^8-pentalene (**88**).[233]

Complexes (**89**) containing a noncyclic η^8-tetraene ligand are prepared from reactions of $(RC_5H_4)NbCl_4$ with dimethylpentadienyl (dienyl) anion. The reactions initially give $(RC_5H_4)Nb(\eta^5\text{-dienyl})(\eta^3\text{-dienyl})$, which subsequently undergo intramolecular coupling between the two dienyl ligands, yielding (**89**).[234]

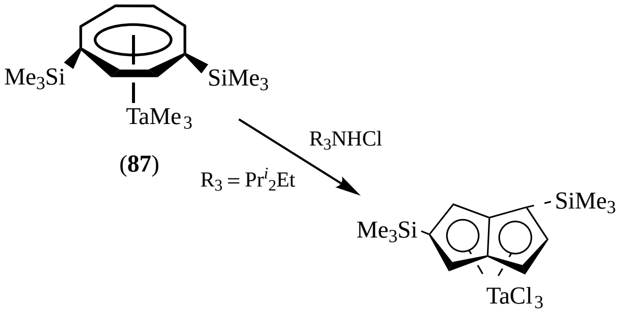

(**87**)

(**88**)

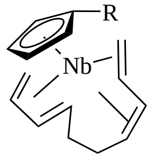

(**89**) R = H, Me

8 HETEROMETAL CLUSTERS

Heterobimetallic hydride and alkylidyne complexes are discussed in Sections 3.2.3 and 4.1, respectively. C–H activation of the alkylidyne (*see Alkylidyne*) complexes are discussed in Section 9.1 below.

The Ta–Li alkylidene (**29**) (Section 4.2) containing an anionic triazacyclononane ligand ($Pr^i{}_2$-tacn$^-$) reacts with $FeCl_2$(TEMDA) or $[RhCl(COD)]_2$ to form bimetallic (**90**) and (**91**), respectively.[121] In both products, the two metals in close proximity and linked by single-atom bridges.

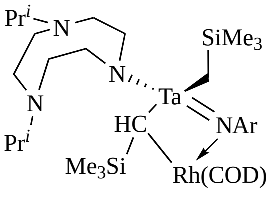

(**90**)

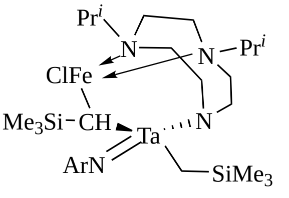

(**91**)

9 NIOBIUM AND TANTALUM COMPLEXES IN CATALYSIS AND METAL-MEDIATED ORGANIC SYNTHESIS

9.1 C–H Bond Activation

This section reviews C–H activation reactions that have not been discussed in earlier sections.

Silyl complexes, $Cp_2Ta^{III}(L)SiR_3$ (L = PMe_3, CO), activate C–H bonds of unhindered arenes such as benzene, toluene, and *m*-xylene. $Cp_2Ta(PMe_3)(SiBu^t{}_2H)$ reacts in neat arenes (ArH) to produce aryl complexes $Cp_2Ta(PMe_3)Ar$. Complexes with smaller silyl ligands give equilibrium mixtures of silyl and aryl complexes in which the silyl is favored. Thermodynamic studies reveal that the Ta–Si bonds in $Cp_2Ta(PMe_3)SiR_3$ (R_3 = $Bu^t{}_2H$; Me_3) are 5.4–7.9 kcal mol^{-1} weaker than the Ta–Ph bond in $Cp_2Ta(PMe_3)Ph$, and suggest that the strength of the Ta–Si bonds are probably comparable to or greater than that of a Ta–alkyl bond.[235]

Bridging alkylidyne (*see Alkylidyne*) complexes (**28a–b**) (Section 4.1) react with TMEDA, leading to C–H activation of the methyl group in $-NMe_2$ and the elimination of $ZnCl_2$, giving the alkylidene (**92a–b**).[41,119]

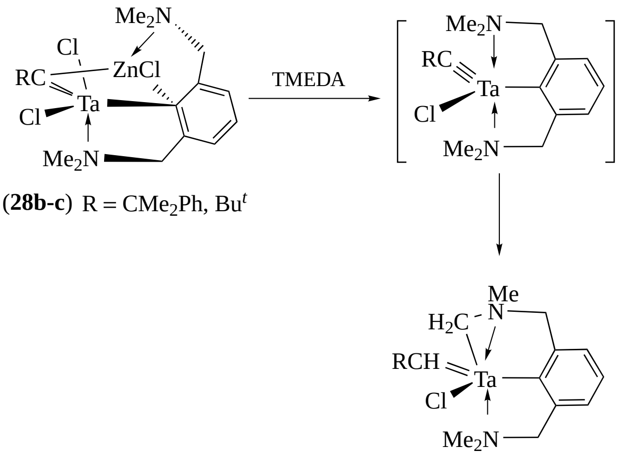

(**28b-c**) R = CMe$_2$Ph, Bu^t

(**92a-b**)

Silica-supported Ta hydride ($(\equiv SiO)_2Ta-H$ (**93a**) presents unusual properties in the activation of alkanes. It catalyzes the metathesis reaction of alkanes to give higher and lower molecular weight alkanes, and the hydrogenolysis of alkanes such as ethane to methane.[236] This hydride also activates the C–H bonds of cycloalkanes to form the corresponding surface metal-cycloalkyl complexes, and catalyses the H/D exchange reaction between CH_4 and CD_4, producing the statistical distribution of methane isotopomers.[237]

C–H activation using the aryloxide supported Ta complexes has been discussed in Section 6.3.[53,238,239] Additional examples include the thermal conversion of the hydride Ta(O-2,6-Ph_2-$C_6H_3)_2(H)_2Cl(PMe_3)_2$ into the monocyclometalated complex (**94**).[60] Reaction of Cp^*TaCl_4 with (cb)K (>3 equiv) leads to the species $(C_5Me_4CH_2)Ta(cb)_2Cl$, in which one of the ring methyl C–H bonds of the Cp* ligand has been cleaved.[240]

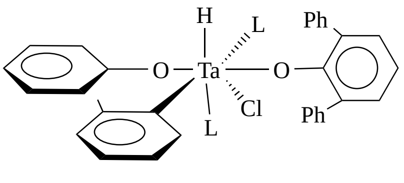

(**94**) L = PMe$_3$

Ta amide (**14**) and *ansa*-type half-sandwich (*see Half-sandwich Complexes*) niobiocenes (**74a–c**) from intramolecular C–H activation with elimination of $HNMe_2$ are discussed in Sections 7.1 and 3.1.1. The $-NMe_2$ group in (**95**) undergoes β-H abstraction by a benzyl ligand to give (**96**).[40] Alkylidyne-mediated C–H activation in the $-NMe_2$ group is observed in the formation of alkylidenes (**92a–b**) (Section 8).[41]

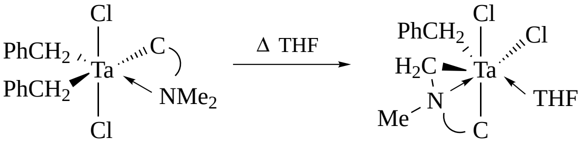

(**95**) (**96**)

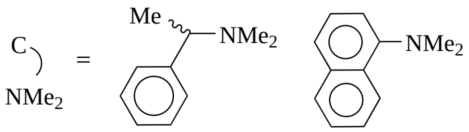

9.2 Alkene Polymerization

The use of Nb and Ta cyclopentadienyl complexes as catalysts for olefin polymerization has been actively studied (*see* ***Oligomerization & Polymerization by Homogeneous Catalysis***). These complexes include $(\eta^5\text{-}C_5R_5)(\eta^4\text{-diene})TaMe_2$ (R = H, Me),[241] $(\eta^5\text{-}C_5R_5)(TBM)TaMe_2$ and (fluorenyl)(TBM)$TaMe_2$ (TBM = tribenzylidenemethane),[242] borollide $Cp^*[\eta^5\text{-}C_4H_4BN\text{-}(CHMe_2)_2]TaCl_2$,[243] and $Cp^*Ta({=}NAr)(\eta^1\text{-}C_3H_5)(\eta^3\text{-}C_3H_5)$ (Ar = 2,6-Pr^i_2-C_6H_3).[199] They are typically activated with methylaluminoxane (MAO),[241–243] $(Ph_3C)^+[B(C_6F_5)_4]^-$, or $B(C_6F_5)_3$.[199]

The catalytic activities of Nb and Ta complexes $Cp^*M(\eta^4\text{-diene})Cl_2$ (M = Nb, Ta; diene = 1,3-butadiene, isoprene, 2,3-dimethyl-1,3-butadiene) activated by MAO have been compared. They both give polyethylene with very narrow polydispersities at low temperature (M_w/M_n as low as 1.05). The Nb complexes are superior to the Ta complexes in terms of the catalyst activity and the polydispersity.[244,245] Cp^*Ta(*o*-xylylene)Cl_2/MAO is twice as catalytically active and the molecular weight distribution of the polyethylene is much narrower than that using $Cp^*M(\eta^4\text{-1,3-butadiene})Cl_2$/MAO as catalysts.[246]

Substituted hydridotris(pyrazolyl)borato (Tp′) complexes $Tp'NbMe_2(PhC{\equiv}CMe)$, when treated with $B(C_6F_5)_3$, polymerize ethylene. It is interesting to note that bulky $(Tp^{Me2,4-Cl})NbMe_2(PhC{\equiv}CMe)$ yields a catalyst that is far more active than $TpNbMe_2(PhC{\equiv}CMe)$.[247]

Insertion of $H_2C{=}CHX$ (X = OR; R = Me, Et, Pr^n, Pr^i, $CH{=}CH_2$, Ph) into $(Bu^t{}_3SiO)_3TaH_2$ affords $(Bu^t{}_3SiO)_3(H)\text{-}TaCH_2CH_2X$, which β-X-eliminates to give ethylene and $(Bu^t{}_3SiO)_3HTaX$. These reactions and their relevance to incorporation of functionalized monomers in Ziegler–Natta (*see Ziegler–Natta Catalysts*) copolymerizations have been studied. β-X-elimination rates are found to be inversely proportional to the size of R.[248]

9.3 Alkene Dimerization

Reduction of $TaCl_5$ with Zn in the presence of alkyne $RC{\equiv}CR$ and solvents (L) is believed to yield Ta chloro alkyne complexes, which react with lithium alkoxides tethered to alkenyl groups to give chemo- and stereoselective addition of terminal alkenyl groups.[249] Alkoxy-directed insertion of C=C bonds into Ta-alkyne complexes plays a critical role through the following mechanism.

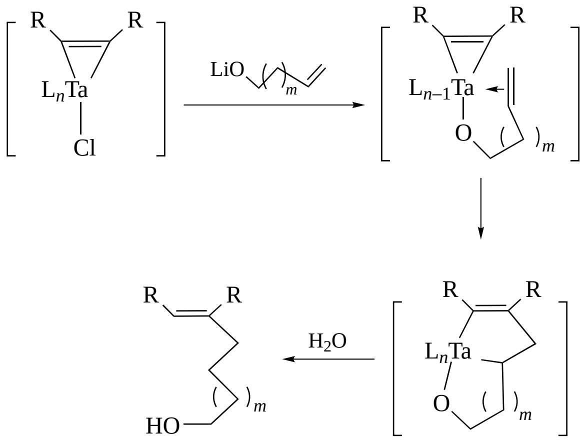

Reactions of $TaCl_5$ with alkylating agents such as MeLi are believe to give in situ $TaCl_3Me_2$, which catalyzes selective trimerization of ethene to 1-hexene.[250] Theoretical studies of the detailed mechanism of the olefin trimerization provide insights why this catalyst selectively trimerizes rather than dimerizes or polymerizes ethene.

The theoretical studies confirm intermediacy of tantalacycloheptane in the trimerization process. The conversion of tantalacycloheptane to the Ta-(1-hexene) complex follows. The dimerization is disfavored by the nonexistence of such concerted reductive elimination process for the tantalacyclopentane. The bimolecular process of tetramerization and possible higher oligomerization cannot compete with the facile reductive elimination (*see Reductive Elimination*).[251]

The silica-supported Ta hydride $({\equiv}SiO)_2Ta{-}H$ (**93a**) reacts with PMe_3 to give $({\equiv}SiO)_2Ta(H)(PMe_3)$ (**93b**). In comparison to (**93a**), the phosphine hydrid (**93b**) is inactive toward metathesis of acyclic alkanes, but affords the oligomerization of ethylene into 1-butene and higher oligomers.[252]

9.4 Metathesis of Alkanes and Alkenes and Metathesis Polymerization

C–C and C–H bond activation of alkanes by silica-supported group 4 and 5 hydrides is the subject of a recent review by Lefebvre and Basset.[253] Alkane metathesis catalyzed by $(\equiv SiO)_2Ta–H$ (**93a**) is discussed briefly in Section 9.1. Over (**93a**), ethane is transformed into an equimolar mixture of propane and methane.[236] ^{13}C-monolabeled ethane is converted, in addition to higher alkanes, to its unlabeled and dilabeled isotopomers.[254] The relative reactivity of Ta^{III} (**93a**) and Ta^{V} $(\equiv SiO)_xTa(=CHCMe_3)(CH_2CMe_3)_{3-x}$ ($x = 1$, 2, **97**) toward alkanes has been studied. The reaction of C–C bonds with a surface Ta complex containing both neopentyl and neopentylidene groups gives cross-metathesis products with the Bu^t markers. The studies using (**97**) as catalysts provide the first evidence for alkane cross-metathesis.[255]

As discussed in Sections 4.2 and 6.1, alkylidenes (**30a–b**) and tantalacyclobutane (**31a**) initiate ring-opening metathesis polymerization with strained cyclic olefins.[123] *cis*-Dialkyl Ta complexes $Cp^*TaR_2(\eta^4\text{-butadine})$ [$R_2 = (CH_2Ph)_2$, $(CH_2SiMe_3)_2$, Me(Np)] are catalyst precursors for ring-opening metathesis polymerization (ROMP) of norbornene to poly(norbornene) with a high *cis*-vinylene double-bond (97–99%) content. The *o*-xylylene analog $Cp^*Ta(CH_2Ph)_2[\eta^4\text{-}o\text{-}(CH_2)_2C_6H_4]$ is also an initiator to give poly(norbornene) with a high *trans*-vinylene double-bond (92–95%) content. These results indicate the control of stereoselectivity in the ROMP of norbornene by butadiene and *o*-xylylene ligands, as a result of the congestion between Cp* and these auxiliary ligands.[256]

$NbCl_3(DME)$ and *mer*-$(DME)Cl_3Nb{=}NPh$ serve as effective catalysts or precatalysts in imine metathesis of aldimines $RCH{=}NR'$ and $R''CH{=}NR^x$ to give $RCH{=}NR^x$ and $R''CH{=}NR'$.[257]

9.5 Hydrodenitrogenation and Hydrodeoxygenation

Catalytic hydrodenitrogenation (HDN) and hydrodeoxygenation (HDO) are the processes of removing nitrogen and oxygen, respectively, from petroleum feedstocks to provide more processable and environmentally compatible liquid fuels. A review of heterogeneous HDN process and homogeneous models summarized the research till ca. 1997.[258]

β-H abstraction of amide ligands to give $\eta^2\text{-}N,C$-heterocyclic complexes is discussed in Section 5.7. Thermolysis of $Ta(NC_9H_{10})(O\text{-}2,6\text{-}Pr^i{}_2\text{-}C_6H_3)R_2Cl$ ($NC_9H_{10}{}^- =$ tetrahydroquinolinyl; R = Me, Et), which are reactivity models for fundamental HDN reactions of pyridines, however, shows no evidence for the formation of $\eta^2\text{-}N,C$-heterocycles arising from metallation of a tetrahydroquinolinyl ligand.[259]

Treatment of $(silox)_3Ta$ with arylamines $H_2NC_6H_4X$ leads to the oxidative addition of N–H bonds to give $(silox)_3$-$Ta(H)[NH(C_6H_4X)]$ and/or C–N activation to yield $(silox)_3$-$Ta(NH_2)(C_6H_4X)$ (X = 4-NMe_2, 4-OMe, 4-Me, 4-F, 3-F, 3-CF_3, 3,5-CF_3, 4-CF_3, 4-Ph). $(silox)_3Ta$ activates the C–O bonds in 1,2-dihydrofuran and 3,3-dimethyloxetane, forming the cyclic complexes (**98a–b**).[260] These reactions mimic key steps in HDN and HDO processes.

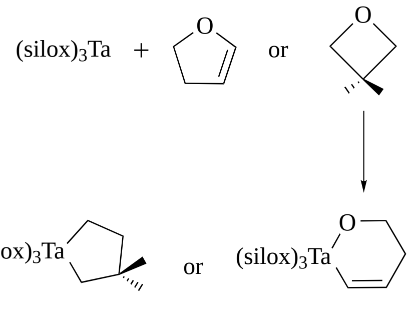

(**98b**) (**98a**)

Structural models for the substrate-catalyst adduct in HDN catalysis have been prepared and compared with respect to O versus S-ancillary ligands. $\eta^2\text{-}N,C$-1,3,5-tributylpyridine complexes $(\eta^2\text{-}N,C\text{-}NC_5Bu^t{}_3H_2)Ta(OAr)_2X$ ($X = OBu^t$, SBu^t, Br) show a severe interruption of aromaticity within the pyridine heterocycle, different rotational preferences of the NC_5 plane with respect to the $Ta(OAr)_2X$ moiety, and structural differences in the aryloxide ligand. The comparison here support the ancillary ligand π-donor ability decreasing as $OBu^t > OAr > SBu^t > Cl \sim Br > Et$.[261]

9.6 Epoxidation of Olefins

Silica-supported chiral tantalum alkoxides and $Ta(=CHCMe_3)(CH_2CMe_3)_3$ are, in the presence of (+)-tartrate, active catalysts for the asymmetric epoxidation of 2-propenol and *trans*-hex-2-en-1-ol by Bu^tOOH.[262,263] The enantioselective (*see Enantioselectivity*) catalytic epoxidation of unfunctionalized alkyl and aryl olefins by H_2O_2 was conducted using niobocene peroxide complex (R, R)-(+)-$Cp''_2Nb(O_2)Cl$ containing the C_2-symmetrical binaphthylcyclopentadienyl ligand (Cp″).[264] Enantiomeric excesses and activities range between 2–20% and 10–55 turnovers are observed in these epoxidation reactions.

9.7 Hydrogenation of Alkenes and Arenes

As discussed in Section 7.3, $(ArN{=})(ArNH)TaMe(OTf)$ (Ar = 2,6-dimesitylphenyl, **84a**) reacts cleanly with H_2 to convert one mesityl group to a η^5-cyclohexadienyl complex (**84b**) (Section 7.3). (**84b**) is in equilibrium with the hydride $(Ar^*N{=})(Ar^*NH)TaH(OTf)$ (**84c**). (**84b-c**) catalyze olefin hydrogenation, diene cyclization, and silane deuteration.[225] As discussed in Section 7.3 as well, hydrogenolysis of $^{R}[P_2N_2]NbCH_2SiMe_3$ (R = Cy, Ph) in, for example, benzene gives $^{R}[P_2N_2]Nb(\eta^5\text{-cyclohexadienyl})$. At a higher H_2 pressure, this hydrogenolysis causes the catalytic hydrogenation of benzene to cyclohexane and toluene to methylcyclohexane.[222]

Treatment of a mixture of $Nb(O\text{-}Ar)_2(CH_2SiMe_3)_2$, $Nb(O\text{-}Ar)_2(CH_2SiMe_3)(=CHSiMe_3)$ (Ar = 2,3,5,6-Ph_4-C_6H), and PMe_3 under 1200 psi of H_2 leads to hydrogenolysis of Nb alkyl/alkylidene bonds but also the intramolecular hydrogenation of the *ortho*-phenyl rings of the aryloxide ligands to give $Nb(O\text{-}2,6\text{-}Cy_2\text{-}3,5\text{-}Ph_2\text{-}C_6H)_2(H)_2(PMe_3)_2$.**265** Similar reactions are discussed in Section 7.2. These hydride derivatives containing bulky ancillary aryloxide ligands are catalysts for high regio- (*see Regioselectivity*) and stereoselective (*see Stereoselectivity*), all-*cis* hydrogenation of benzenes and polynuclear aromatic hydrocarbons. The Nb complexes also rapidly hydrogenate arylphosphine ligands such as PPh_3 to PPh_2Cy, $PPhCy_2$ and PCy_3 as a new procedure for the synthesis of cyclohexylphosphines.**59** As discussed in Section 7.2, $Ta(OAr')_3(\eta^4\text{-}C_6H_8)$ catalyzes the hydrogenation of 1,3-cyclohexadiene and cyclohexene into cyclohexane.**211**

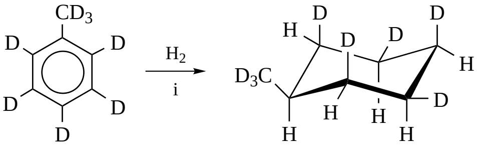

i, $Nb(O\text{-}2,3,5,6\text{-}Ph_4\text{-}C_6H)_2Cl_3$ / $3Bu^nLi$

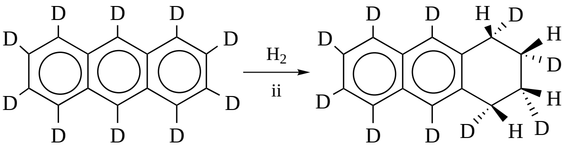

ii, $Ta(O\text{-}2,6\text{-}Pr^i{}_2\text{-}C_6H_3)_2(H)_3(PMePh_2)$

The bridging alkylidyne compounds $(Me_3SiCH_2)_4M_2(\mu\text{-}CSiMe_3)_2$ supported on silica catalyze the exhaustive hydrogenation of a variety of aromatic substrates. Hydrogenation of benzene at 1200–1400 psi of H_2, for example, gave 100% cyclohexane.**266**

9.8 Metal-mediated Hydroboration of Olefins

Olefin complexes $Cp^*{}_2M(CH_2{=}CHR)(H)$ (R = H, Me) react with catecholborane (HBCat) and $HBO_2C_6H_3\text{-}4\text{-}Bu^t$ (HBCat′) to give $Cp^*{}_2M(H_2BCat)$ and $Cp^*{}_2M(H_2BCat')$ and the anti-Markovnikov hydroboration (*see Hydroboration*) products $CatBCH_2CH_2R$ and $Cat'BCH_2CH_2R$, respectively. D-labeling studies suggest a mechanism through which HBCat reacts with the alkyl intermediates $Cp^*{}_2MCH_2CH_2R$, via σ-bond metathesis (*see σ-Bond Metathesis*) or oxidative-addition (*see Oxidative Addition*) and reductive elimination (*see Reductive Elimination*) sequences, to generate the alkylboranes and the hydride $Cp^*{}_2MH$.**267**

9.9 Cross-coupling of Unsaturated Organic Substrates

$NbCl_3(DME)$ is found to be a useful reagent for the intermolecular pinacol coupling of aliphatic aldehydes RCHO to give diols RCH(OH)–RCH(OH). The high anti-diastereoselectivity (*dl meso* $\geq 9/1$) is consistent with the mechanism involving an insertion of the oxo-group into the Nb–C bond of the intermediate niobiooxirane $[Nb](\eta^2\text{-}C,O\text{-}CHR{=}O)$.**268**

Reaction of $Cp^*{}_2Nb^{III}({=}O)H$ with excess isocyanate PhN=C=O gave a mixture of heterocycles $(PhNCO)_2$ and $(PhNCO)_3$.**269** Cp^*Ta^{III}(1-phenylallyl)$_2$ is also a catalyst for the dimerization of isocyanates RN=C=O (R = Et, Bu^t, Cy) to $(RNCO)_2$.**198**

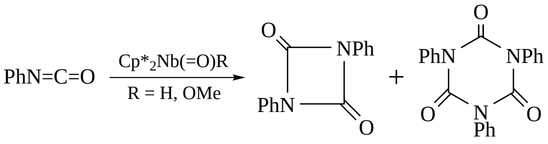

Treatment of tantalum-alkyne complexes, prepared in situ from $TaCl_5$, Zn and RC≡CR ($R = n\text{-}C_5H_{11}$), with the lithio-imine Li–N=CR′Me ($R' = n\text{-}C_8H_{17}$), followed by aqueous NaOH, gives primary (E)-allylic amines E-RCH=CR–CR′Me(NH_2).**270** Treatment of these complexes with the terminal alkyne R″C≡CH ($R'' = n\text{-}C_6H_{13}$), followed by aqueous NaOH, yields tetrasubstituted benzene derivatives (**99a-d**).**271**

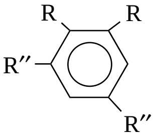

(**99a**)

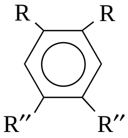

(**99b**)

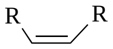

(**99c**)

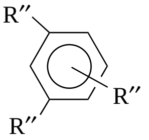

(**99d**)

Ta reagents ‘Ta–Nu’, prepared by the transmetallation of organotin compounds ($Bu^nSn\text{-}Nu$) with $TaCl_5$, promote the conjugate allylation of enones RC(=O)CH=CR′R″. The reactions, followed by treating with MeOH, give $RC({=}O)CH_2CR'R''(Nu)$ (e.g., R = Me, R′ = Ph, R″ = H, Nu = allyl).**272**

$TaCl_5\text{-}SiO_2$ has been used as an efficient Lewis acid (*see Lewis Acids & Bases*) catalyst for the three-component coupling (*see Coupling*) of aldehydes or ketones, aromatic amines, and $HOP(OEt)_2$ to produce α-amino phosphonates. Thus, coupling reaction of PhCH=O, $PhNH_2$, and $HOP(OEt)_2$ is catalyzed by $TaCl_5\text{-}SiO_2$, forming PhNHCH(Ph)–P(=O)$(OEt)_2$ in 90% yield.**273**

10 RELATED ARTICLES

Aluminum: Organometallic Chemistry; Carbene Complexes; Carbon–Carbon & Carbon–Heteroatom Activation;

Carbonyl Complexes of the Transition Metals; Mechanisms of Reaction of Organometallic Complexes; Metal Vapor Synthesis of Transition Metal Compounds; Metathesis Polymerization Processes by Homogeneous Catalysis; Oligomerization & Polymerization by Homogeneous Catalysis; Organic Synthesis using Transition Metal Carbonyl Complexes; Tin: Organometallic Chemistry; Vanadium: Organometallic Chemistry; Zinc: Organometallic Chemistry.

11 REFERENCES

1. D. E. Wigley and S. D. Gray, in ‘Comprehensive Organometallic Chemistry’, eds. E. W. Abel, G. Wilkinson, F. G. A. Stone, V. Editor, J. A. Labinger, and M. J. Winter, Pergamon Press, Oxford, 1995, *Vol. 5* p. 57.
2. M. Zhou and L. Andrews, *J. Phys. Chem. A*, 1999, **103**, 7785.
3. M. D. Koeslag and M. C. Baird, *Organometallics*, 1994, **13**, 11.
4. M. A. Koeslag, M. C. Baird, S. Lovelace, and W. E. Geiger, *Organometallics*, 1996, **15**, 3289.
5. T. F. Miller, III, D. L. Strout, and M. B. Hall, *Organometallics*, 1998, **17**, 4164.
6. J. E. Ellis, *Organometallics*, 2003, **22**, 3322.
7. J. E. Ellis, G. F. Warnock, M. V. Barybin, and M. K. Pomije, *Chem. – Eur. J.*, 1995, **1**, 521.
8. M. V. Barybin, J. E. Ellis, M. K. Pomije, M. L. Tinkham, and G. F. Warnock, *Inorg. Chem.*, 1998, **37**, 6518.
9. P. J. Daff, P. Legzdins, and S. J. Rettig, *J. Am. Chem. Soc.*, 1998, **120**, 2688.
10. T. W. Bitner and J. I. Zink, *J. Am. Chem. Soc.*, 2000, **122**, 10631.
11. T. E. Bitterwolf, S. Gallagher, A. L. Rheingold, and G. P. A. Yap, *J. Organomet. Chem.*, 1997, **545–546**, 27.
12. C. K. Sperry, W. D. Cotter, R. A. Lee, R. J. Lachicotte, and G. C. Bazan, *J. Am. Chem. Soc.*, 1998, **120**, 7791.
13. K. Mashima, Y. Tanaka, and A. Nakamura, *J. Organomet. Chem.*, 1995, **502**, 19.
14. D. L. Lichtenberger, H.-J. Fan, N. E. Gruhn, T. E. Bitterwolf, and S. Gallagher, *Organometallics*, 2000, **19**, 2012.
15. P. Sauvageot, O. Blacque, M. M. Kubicki, S. Juge, and C. Moise, *Organometallics*, 1996, **15**, 2399.
16. J. D. Protasiewicz, A. Masschelein, and S. J. Lippard, *J. Am. Chem. Soc.*, 1993, **115**, 808.
17. J. D. Protasiewicz, B. S. Bronk, A. Masschelein, and S. J. Lippard, *Organometallics*, 1994, **13**, 1300.
18. B. S. Bronk, J. D. Protasiewicz, L. E. Pence, and S. J. Lippard, *Organometallics*, 1995, **14**, 2177.
19. G. Proulx and R. G. Bergman, *Science*, 1993, **259**, 661.
20. G. Proulx and R. G. Bergman, *J. Am. Chem. Soc.*, 1996, **118**, 1981.
21. M. Gomez, P. Gomez-Sal, G. Jimenez, A. Martin, P. Royo, and J. Sanchez-Nieves, *Organometallics*, 1996, **15**, 3579.
22. A. Castro, M. V. Galakhov, M. Gomez, P. Gomez-Sal, A. Martin, and F. Sanchez, *J. Organomet. Chem.*, 2000, **595**, 36.
23. D. Y. Dawson, H. Brand, and J. Arnold, *J. Am. Chem. Soc.*, 1994, **116**, 9797.
24. D. Y. Dawson and J. Arnold, *Organometallics*, 1997, **16**, 1111.
25. M. V. Barybin, V. G. Young Jr, and J. E. Ellis, *J. Am. Chem. Soc.*, 1999, **121**, 9237.
26. D. Rehder, C. Bottcher, C. Collazo, R. Hedelt, and H. Schmidt, *J. Organomet. Chem.*, 1999, **585**, 294.
27. M. V. Barybin, V. G. Young Jr, and J. E. Ellis, *Organometallics*, 1999, **18**, 2744.
28. Y. Matsuo, K. Mashima, and K. Tani, *Organometallics*, 2002, **21**, 138.
29. R. Fandos, C. Hernandez, I. Lopez-Solera, A. Otero, A. Rodriguez, M. J. Ruiz, and P. Terreros, *Organometallics*, 2000, **19**, 5318.
30. R. Fandos, C. Hernandez, A. Otero, A. Rodriguez, M. J. Ruiz, and P. Terreros, *Eur. J. Inorg. Chem.*, 2003, 493.
31. J. R. Clark, P. E. Fanwick, and I. P. Rothwell, *Organometallics*, 1996, **15**, 3232.
32. K. S. Cook, W. E. Piers, T. K. Woo, and R. McDonald, *Organometallics*, 2001, **20**, 3927.
33. K. S. Cook, W. E. Piers, P. G. Hayes, and M. Parvez, *Organometallics*, 2002, **21**, 2422.
34. A. D. Burrows, A. Dransfeld, M. Green, J. C. Jeffery, C. Jones, J. M. Lynam, and M. T. Nguyen, *Angew. Chem., Int. Ed. Engl.*, 2001, **40**, 3221.
35. G. Proulx and R. G. Bergman, *Organometallics*, 1996, **15**, 684.
36. F. Calderazzo, C. Giardi, U. Englert, and G. Pampaloni, *J. Organomet. Chem.*, 2001, **630**, 275.
37. A. Schorm and J. Sundermeyer, *Eur. J. Inorg. Chem.*, 2001, 2947.
38. A. Antinolo, F. Carrillo-Hermosilla, M. Fajardo, S. Garcia-Yuste, M. Lanfranchi, A. Otero, M. A. Pellinghelli, S. Prashar, and E. Villasenor, *Organometallics*, 1996, **15**, 5507.
39. M. G. Thorn, P. E. Fanwick, I. P. Rothwell, and R. W. Chesnut, *Chem. Commun.*, 1999, 2543.
40. H. C. L. Abbenhuis, R. Van Belzen, D. M. Grove, A. J. A. Klomp, G. P. M. Van Mier, A. L. Spek, and G. Van Koten, *Organometallics*, 1993, **12**, 210.
41. H. C. L. Abbenhuis, N. Feiken, H. F. Haarman, D. M. Grove, E. Horn, A. L. Spek, M. Pfeffer, and G. van Koten, *Organometallics*, 1993, **12**, 2227.
42. R. R. Schrock, J. Lee, L.-C. Liang, and W. M. Davis, *Inorg. Chim. Acta*, 1998, **270**, 353.

43. M. S. Eisen, in 'The Chemistry of Organic Silicon Compounds', eds. Z. Rappoport and Y. Apeloig, Wiley, New York, 1998, Vol. 2, p. 2037.

44. (a) T. D. Tilley, in 'The Chemistry of Organic Silicon Compounds', eds. S. Patai, Z. Rappoport, Wiley, New York, 1989, Part 2, p. 1415; (b) T. D. Tilley, in 'The Silicon-Heteroatom Bond', eds. S. Patai, Z. Rappoport, Wiley, New York, 1991, p. 245 and p. 309; (c) U. Schubert, *Transition Met. Chem.* 1991, **16**, 136.

45. A. Antinolo, F. Carrillo, M. Fajardo, A. Otero, M. Lanfranchi, and M. A. Pellinghelli, *Organometallics*, 1995, **14**, 1518.

46. G. I. Nikonov, L. G. Kuzmina, S. F. Vyboishchikov, D. A. Lemenovskii, and J. A. K. Howard, *Chem. – Eur. J.*, 1999, **5**, 2947.

47. G. I. Nikonov, L. G. Kuzmina, D. A. Lemenovskii, and V. V. Kotov, *J. Am. Chem. Soc.*, 1995, **117**, 10133.

48. G. I. Nikonov, L. G. Kuzmina, and J. A. K. Howard, *J. Chem. Soc., Dalton Trans.*, 2002, 3037.

49. A. Antinolo, F. Carrillo-Hermosilla, A. Castel, M. Fajardo, J. Fernandez-Baeza, M. Lanfranchi, A. Otero, M. A. Pellinghelli, G. Rima, J. Satge, and E. Villasenor, *Organometallics*, 1998, **17**, 1523.

50. Z. Xue, L. Li, L. K. Hoyt, J. B. Diminnie, and J. L. Pollitte, *J. Am. Chem. Soc.*, 1994, **116**, 2169.

51. L. Li, J. B. Diminnie, X. Liu, J. L. Pollitte, and Z. Xue, *Organometallics*, 1996, **15**, 3520.

52. L. Li, Z. Xue, G. P. A. Yap, and A. L. Rheingold, *Organometallics*, 1995, **14**, 4992.

53. J. S. Vilardo, M. A. Lockwood, L. G. Hanson, J. R. Clark, B. C. Parkin, P. E. Fanwick, and I. P. Rothwell, *J. Chem. Soc., Dalton Trans.*, 1997, 3353.

54. M. D. Fryzuk, S. A. Johnson, and S. J. Rettig, *J. Am. Chem. Soc.*, 2001, **123**, 1602.

55. Y.-D. Wu, K. W. K. Chan, and Z. Xue, *J. Am. Chem. Soc.*, 1995, **117**, 9259.

56. Q. Jiang, P. J. Carroll, and D. H. Berry, *Organometallics*, 1993, **12**, 177.

57. A. J. Hoskin and D. W. Stephan, *Coord. Chem. Rev.*, 2002, **233–234**, 107.

58. D. M. Dawson, A. Meetsma, J. B. Roedelof, and J. H. Teuben, *Inorg. Chim. Acta*, 1997, **259**, 237.

59. I. P. Rothwell, *Chem. Commun.*, 1997, 1331.

60. D. R. Mulford, J. R. Clark, S. W. Schweiger, P. E. Fanwick, and I. P. Rothwell, *Organometallics*, 1999, **18**, 4448.

61. R. L. M. Chamberlin, D. C. Rosenfeld, P. T. Wolczanski, and E. B. Lobkovsky, *Organometallics*, 2002, **21**, 2724.

62. M. D. Fryzuk, S. A. Johnson, and S. J. Rettig, *Organometallics*, 2000, **19**, 3931.

63. M. D. Fryzuk, S. A. Johnson, B. O. Patrick, A. Albinati, S. A. Mason, and T. F. Koetzle, *J. Am. Chem. Soc.*, 2001, **123**, 3960.

64. H. Cai, T. Chen, X. Wang, A. J. Schultz, T. F. Koetzle, and Z. Xue, *Chem. Commun.*, 2002, 230.

65. J. S. Figueroa and C. C. Cummins, *J. Am. Chem. Soc.*, 2003, **125**, 4020.

66. A. Antinolo, F. Carrillo-Hermosilla, M. Fajardo, J. Fernandez-Baeza, S. Garcia-Yuste, and A. Otero, *Coord. Chem. Rev.*, 1999, **193–195**, 43.

67. S. R. Dubberley, S. K. Ignatov, N. H. Rees, A. G. Razuvaev, P. Mountford, and G. I. Nikonov, *J. Am. Chem. Soc.*, 2003, **125**, 642.

68. M.-F. Fan and Z. Lin, *Organometallics*, 1998, **17**, 1092.

69. F. A. Jalon, A. Otero, B. R. Manzano, E. Villasenor, and B. Chaudret, *J. Am. Chem. Soc.*, 1995, **117**, 10123.

70. G. I. Nikonov, D. A. Lemenovskii, and J. Lorberth, *Organometallics*, 1994, **13**, 3127.

71. G. I. Nikonov, L. G. Kuzmina, P. Mountford, and D. A. Lemenovskii, *Organometallics*, 1995, **14**, 3588.

72. A. Antinolo, F. Carrillo-Hermosilla, J. Fernandez-Baeza, S. Garcia-Yuste, A. Otero, J. Sanchez-Prada, and E. Villasenor, *Eur. J. Inorg. Chem.*, 2000, 1437.

73. G. I. Nikonov, J. Lorberth, K. Harms, and D. A. Lemenovskii, *Inorg. Chem.*, 1995, **34**, 2461.

74. G. I. Nikonov, L. G. Kuzmina, and J. A. K. Howard, *Organometallics*, 1997, **16**, 3723.

75. G. I. Nikonov, E. V. Avtomonov, and W. Massa, *Chem. Ber. Recl.*, 1997, **130**, 1629.

76. G. I. Nikonov, D. A. Lemenovskii, and J. Lorberth, *Polyhedron*, 1996, **15**, 1565.

77. G. I. Nikonov, A. V. Churakov, and M. Y. Antipin, *Organometallics*, 2003, **22**, 2178.

78. A. Antinolo, F. Carrillo-Hermosilla, M. Fajardo, S. Garcia-Yuste, A. Otero, S. Camanyes, F. Maseras, M. Moreno, A. Lledos, and J. M. Lluch, *J. Am. Chem. Soc.*, 1997, **119**, 6107.

79. N. Etkin, M. T. Benson, S. Courtenay, M. J. McGlinchey, A. D. Bain, and D. W. Stephan, *Organometallics*, 1997, **16**, 3504.

80. T. I. Gountchev and T. D. Tilley, *J. Am. Chem. Soc.*, 1997, **119**, 12831.

81. U. Burckhardt, G. L. Casty, T. D. Tilley, T. K. Woo, and U. Rothlisberger, *Organometallics*, 2000, **19**, 3830.

82. H. Brunner, M. M. Kubicki, J.-C. Leblanc, W. Meier, C. Moise, A. Sadorge, B. Stubenhofer, J. Wachter, and R. Wanninger, *Eur. J. Inorg. Chem.*, 1999, 843.

83. H. Brunner, H. Cattey, D. Evrard, M. M. Kubicki, Y. Mugnier, E. Vigier, J. Wachter, R. Wanninger, and M. Zabel, *Eur. J. Inorg. Chem.*, 2002, 1315.

84. J. H. Shin and G. Parkin, *Organometallics*, 1994, **13**, 2147.

85. A. Antinolo, F. Carrillo, S. Garcia-Yuste, and A. Otero, *Organometallics*, 1994, **13**, 2761.

86. A. Antinolo, F. Carrillo-Hermosilla, I. del Hierro, A. Otero, M. Fajardo, and Y. Mugnier, *Organometallics*, 1997, **16**, 4161.

87. L. J. Ackerman, M. L. H. Green, J. C. Green, and J. E. Bercaw, *Organometallics*, 2003, **22**, 188.
88. J. F. Hartwig and S. R. De Gala, *J. Am. Chem. Soc.*, 1994, **116**, 3661.
89. D. R. Lantero, D. H. Motry, D. L. Ward, and M. R. Smith III, *J. Am. Chem. Soc.*, 1994, **116**, 10811.
90. S. L. J. Conway, L. H. Doerrer, and M. L. H. Green, *Organometallics*, 2000, **19**, 630.
91. D. Liu, K.-C. Lam, and Z. Lin, *J. Organomet. Chem.*, 2003, **680**, 148.
92. C. M. Kowal and G. C. Bazan, *J. Am. Chem. Soc.*, 1996, **118**, 10317.
93. C. K. Sperry, G. C. Bazan, and W. D. Cotter, *J. Am. Chem. Soc.*, 1999, **121**, 1513.
94. R. E. Blake, Jr, D. M. Antonelli, L. M. Henling, W. P. Schaefer, K. I. Hardcastle, and J. E. Bercaw, *Organometallics*, 1998, **17**, 718.
95. H. Brunner, M. M. Kubicki, J. C. Leblanc, C. Moise, F. Volpato, and J. Wachter, *J. Chem. Soc., Chem. Commun.*, 1993, 851.
96. J.-H. Huang, J. J. Luci, T.-Y. Lee, D. C. Swenson, J. H. Jensen, and L. Messerle, *J. Am. Chem. Soc.*, 2003, **125**, 1688.
97. R. P. Hughes, S. M. Maddock, A. L. Rheingold, and I. A. Guzei, *Polyhedron*, 1998, **17**, 1037.
98. N. Sarker and J. W. Bruno, *Organometallics*, 2001, **20**, 55.
99. V. I. Bakhmutov, E. V. Vorontsov, G. Boni, and C. Moise, *Inorg. Chem.*, 1997, **36**, 4055.
100. A. Antinolo, F. Carrillo-Hermosilla, B. Chaudret, M. Fajardo, J. Fernandez-Baeza, M. Lanfranchi, H.-H. Limbach, M. Maurer, A. Otero, and M. A. Pellinghelli, *Inorg. Chem.*, 1996, **35**, 7873.
101. V. I. Bakhmutov, E. V. Vorontsov, E. V. Bakhmutova, G. Boni, and C. Moise, *Inorg. Chem.*, 1999, **38**, 1121.
102. A. Antinolo, F. Carrillo, B. Chaudret, M. Fajardo, S. Garcia-Yuste, F. J. Lahoz, M. Lanfranchi, J. A. Lopez, A. Otero, and M. A. Pellinghelli, *Organometallics*, 1995, **14**, 1297.
103. L. H. Doerrer, A. J. Graham, D. Haussinger, and M. L. H. Green, *J. Chem. Soc., Dalton Trans.*, 2000, 813.
104. S. Sabo-Etienne, V. Rodriguez, B. Donnadieu, B. Chaudret, H. Abou el Makarim, J.-C. Barthelat, S. Ulrich, H.-H. Limbach, and C. Moise, *New J. Chem.*, 2001, **25**, 55.
105. F. C. Liu, C. E. Plecnik, S. Liu, J. Liu, E. A. Meyers, and S. G. Shore, *J. Organomet. Chem.*, 2001, **627**, 109.
106. S. Liu, F.-C. Liu, G. Renkes, and S. G. Shore, *Organometallics*, 2001, **20**, 5717.
107. R. R. Schrock, *Chem. Rev.*, 2002, **102**, 145.
108. L. Li, M. Hung, and Z. Xue, *J. Am. Chem. Soc.*, 1995, **117**, 12746.
109. J. S. Freundlich, R. R. Schrock, C. C. Cummins, and W. M. Davis, *J. Am. Chem. Soc.*, 1994, **116**, 6476.
110. J. S. Freundlich, R. R. Schrock, and W. M. Davis, *J. Am. Chem. Soc.*, 1996, **118**, 3643.
111. J. S. Freundlich, R. R. Schrock, and W. M. Davis, *Organometallics*, 1996, **15**, 2777.
112. S. Courtenay and D. W. Stephan, *Organometallics*, 2001, **20**, 1442.
113. P. N. Riley, M. G. Thorn, J. S. Vilardo, M. A. Lockwood, P. E. Fanwick, and I. P. Rothwell, *Organometallics*, 1999, **18**, 3016.
114. P. M. Briggs, V. G. Young Jr, and D. E. Wigley, *Chem. Commun.*, 1997, 791.
115. S. Schmidt, J. Sundermeyer, and F. Moeller, *J. Organomet. Chem.*, 1994, **475**, 157.
116. H. C. L. Abbenhuis, M. H. P. Rietveld, H. F. Haarman, M. P. Hogerheide, A. L. Spek, and G. van Koten, *Organometallics*, 1994, **13**, 3259.
117. W. A. Herrmann, K. Oefele, M. Elison, F. E. Kuehn, and P. W. Roesky, *J. Organomet. Chem.*, 1994, **480**, C7.
118. C. Jones, A. F. Richards, S. Fritzsche, and E. Hey-Hawkins, *Organometallics*, 2002, **21**, 438.
119. M. H. P. Rietveld, P. Lohner, M. G. Nijkamp, D. M. Grove, N. Veldman, A. L. Spek, M. Pfeffer, and G. Van Koten, *Chem. – Eur. J.*, 1997, **3**, 817.
120. I. de Castro, M. V. Galakhov, M. Gomez, P. Gomez-Sal, A. Martin, and P. Royo, *J. Organomet. Chem.*, 1996, **514**, 51.
121. J. A. R. Schmidt and J. Arnold, *J. Am. Chem. Soc.*, 2001, **123**, 8424.
122. J. A. R. Schmidt and J. Arnold, *Organometallics*, 2002, **21**, 3426.
123. M. H. P. Rietveld, W. Teunissen, H. Hagen, L. van de Water, D. M. Grove, P. A. van der Schaaf, A. Muehlebach, H. Kooijman, W. J. J. Smeets, N. Veldman, A. L. Spek, and G. van Koten, *Organometallics*, 1997, **16**, 1674.
124. S. M. Mullins, R. G. Bergman, and J. Arnold, *Organometallics*, 1999, **18**, 4465.
125. D. Bregel, C. S. Oldham, and M. R. Eisenberg, *J. Am. Chem. Soc.*, 2002, **124**, 13827.
126. H. Ahn and T. J. Marks, *J. Am. Chem. Soc.*, 2002, **124**, 7103.
127. M. M. Banaszak Holl, P. T. Wolczanski, D. Proserpio, A. Bielecki, and D. B. Zax, *Chem. Mater.*, 1996, **8**, 2468.
128. A. S. Veige, P. T. Wolczanski, and E. B. Lobkovsky, *Angew. Chem., Int. Ed.*, 2001, **40**, 3629.
129. A. Antinolo, A. Otero, M. Fajardo, R. Gil-Sanz, M. Jose Herranz, C. Lopez-Mardomingo, A. Martin, and P. Gomez-Sal, *J. Organomet. Chem.*, 1997, **533**, 87.
130. D. Rodewald, C. Schulzke, and D. Rehder, *J. Organomet. Chem.*, 1995, **498**, 29.
131. C. Felten, F. Olbrich, and D. Rehder, *Organometallics*, 1993, **12**, 982.
132. T. Oshiki, K. Tanaka, J. Yamada, T. Ishiyama, Y. Kataoka, K. Mashima, K. Tani, and K. Takai, *Organometallics*, 2003, **22**, 464.

133. M. Etienne, F. Biasotto, R. Mathieu, and J. L. Templeton, *Organometallics*, 1996, **15**, 1106.

134. M. Etienne, B. Donnadieu, R. Mathieu, J. F. Baeza, F. Jalon, A. Otero, and M. E. Rodrigo-Blanco, *Organometallics*, 1996, **15**, 4597.

135. M. Etienne, C. Carfagna, P. Lorente, R. Mathieu, and D. de Montauzon, *Organometallics*, 1999, **18**, 3075.

136. M. Etienne, R. Mathieu, and B. Donnadieu, *J. Am. Chem. Soc.*, 1997, **119**, 3218.

137. J. J. Jaffart, M. Etienne, F. Maseras, J. E. McGrady, and O. Eisenstein, *J. Am. Chem. Soc.*, 2001, **123**, 6000.

138. J. Jaffart, M. Etienne, M. Reinhold, J. E. McGrady, and F. Maseras, *Chem. Commun.*, 2003, 876.

139. A. Antinolo, T. Exposito, I. del Hierro, D. Lucas, Y. Mugnier, I. Orive, A. Otero, and S. Prashar, *J. Organomet. Chem.*, 2002, **655**, 63.

140. A. Antinolo, C. Huertas, Id. Hierro, M. F. Lappert, A. Otero, S. Prashar, A. M. Rodriguez, and E. Villasenor, *Organometallics*, 1998, **17**, 5874.

141. A. Antinolo, M. Martinez-Ripoll, Y. Mugnier, A. Otero, S. Prashar, and A. M. Rodriguez, *Organometallics*, 1996, **15**, 3241.

142. A. Antinolo, M. Fajardo, M. Galakhov, R. Gil-Sanz, C. Lopez-Mardomingo, A. Otero, D. Lucas, H. Chollet, and Y. Mugnier, *J. Organomet. Chem.*, 1994, **481**, 27.

143. C. Garcia-Yebra, F. Carrero, C. Lopez-Mardomingo, M. Fajardo, A. Rodriguez, A. Antinolo, A. Otero, D. Lucas, and Y. Mugnier, *Organometallics*, 1999, **18**, 1287.

144. M. Etienne, P. Zeline, J. L. Templeton, and P. S. White, *New J. Chem.*, 1993, **17**, 515.

145. K. Mashima, Y. Tanaka, and A. Nakamura, *Organometallics*, 1995, **14**, 5642.

146. K. L. Houseknecht, K. E. Stockman, M. Sabat, M. G. Finn, and R. N. Grimes, *J. Am. Chem. Soc.*, 1995, **117**, 1163.

147. S. P. Millar, D. L. Zubris, J. E. Bercaw, and R. Eisenberg, *J. Am. Chem. Soc.*, 1998, **120**, 5329.

148. W. Hirpo and M. D. Curtis, *Organometallics*, 1994, **13**, 2706.

149. P. Royo, J. Sanchez-Nieves, M. A. Pellinghelli, and A. Tiripicchio, *J. Organomet. Chem.*, 1998, **563**, 15.

150. K. S. Cook, W. E. Piers, S. J. Rettig, and R. McDonald, *Organometallics*, 2000, **19**, 2243.

151. E. Boring, M. Sabat, M. G. Finn, and R. N. Grimes, *Organometallics*, 1997, **16**, 3993.

152. M. V. Galakhov, M. Gomez, G. Jimenez, M. A. Pellinghelli, P. Royo, and A. Tiripicchio, *Organometallics*, 1994, **13**, 1564.

153. M. V. Galakhov, M. Gomez, G. Jimenez, P. Royo, M. A. Pellinghelli, and A. Tiripicchio, *Organometallics*, 1995, **14**, 1901.

154. M. V. Galakhov, M. Gomez, G. Jimenez, P. Royo, M. A. Pellinghelli, and A. Tiripicchio, *Organometallics*, 1995, **14**, 2843.

155. F. Amor, J. Sanchez-Nieves, P. Royo, H. Jacobsen, O. Blacque, H. Berke, M. Lanfranchi, M. A. Pellinghelli, and A. Tiripicchio, *Eur. J. Inorg. Chem.*, 2002, 2810.

156. J. Sanchez-Nieves, P. Royo, M. A. Pellinghelli, and A. Tiripicchio, *Organometallics*, 2000, **19**, 3161.

157. F. A. Cotton, L. M. Daniels, C. A. Murillo, and X. Wang, *Inorg. Chem.*, 1997, **36**, 896.

158. P.-F. Fu, M. A. Khan, and K. M. Nicholas, *J. Organomet. Chem.*, 1996, **506**, 49.

159. A. Antinolo, Id. Hierro, M. Fajardo, S. Garcia-Yuste, A. Otero, O. Blacque, M. M. Kubicki, and J. Amaudrut, *Organometallics*, 1996, **15**, 1966.

160. A. Antinolo, F. Carrillo-Hermosilla, A. Otero, M. Fajardo, A. Garces, P. Gomez-Sal, C. Lopez-Mardomingo, A. Martin, and C. Miranda, *J. Chem. Soc., Dalton Trans.*, 1998, 59.

161. M. C. Fermin, A. S. Hneihen, J. J. Maas, and J. W. Bruno, *Organometallics*, 1993, **12**, 1845.

162. M. E. Kerr, X.-M. Zhang, and J. W. Bruno, *Organometallics*, 1997, **16**, 3249.

163. M. E. Kerr, N. Sarker, A. S. Hneihen, G. K. Schulte, and J. W. Bruno, *Organometallics*, 2000, **19**, 901.

164. M. C. Fermin and J. W. Bruno, *J. Am. Chem. Soc.*, 1993, **115**, 7511.

165. M. E. Kerr and J. W. Bruno, *J. Am. Chem. Soc.*, 1997, **119**, 3183.

166. A. Antinolo, M. Fajardo, R. Gil-Sanz, C. Lopez-Mardomingo, P. Martin-Villa, A. Otero, M. M. Kubicki, Y. Mugnier, S. El Krami, and Y. Mourad, *Organometallics*, 1993, **12**, 381.

167. A. Antinolo, M. Fajardo, R. Gil-Sanz, C. Lopez-Mardomingo, A. Otero, A. Atmani, M. M. Kubicki, S. El Krami, Y. Mugnier, and Y. Mourad, *Organometallics*, 1994, **13**, 1200.

168. D. J. Mindiola and C. C. Cummins, *Organometallics*, 2001, **20**, 3626.

169. B. Castellano, E. Solari, C. Floriani, N. Re, A. Chiesi-Villa, and C. Rizzoli, *Chem. – Eur. J.*, 1999, **5**, 722.

170. B. Castellano, A. Zanotti-Gerosa, E. Solari, C. Floriani, A. Chiesi-Villa, and C. Rizzoli, *Organometallics*, 1996, **15**, 4894.

171. B. Thiyagarajan, L. Michalczyk, J. C. Bollinger, J. C. Huffman, and J. W. Bruno, *Organometallics*, 1996, **15**, 1989.

172. D. R. Neithamer, L. Parkanyi, J. F. Mitchell, and P. T. Wolczanski, *J. Am. Chem. Soc.*, 1988, **110**, 4421.

173. T. S. Kleckley, J. L. Bennett, P. T. Wolczanski, and E. B. Lobkovsky, *J. Am. Chem. Soc.*, 1997, **119**, 247.

174. A. S. Veige, T. S. Kleckley, R. M. Chamberlin, D. R. Neithamer, C. E. Lee, P. T. Wolczanski, E. B. Lobkovsky, and W. V. Glassey, *J. Organomet. Chem.*, 1999, **591**, 194.

175. J. B. Bonanno, A. S. Veige, P. T. Wolczanski, and E. B. Lobkovsky, *Inorg. Chim. Acta*, 2003, **345**, 173.

176. K. D. Allen, M. A. Bruck, S. D. Gray, R. P. Kingsborough, D. P. Smith, K. J. Weller, and D. E. Wigley, *Polyhedron*, 1995, **14**, 3315.

177. P. Berno and S. Gambarotta, *Organometallics*, 1995, **14**, 2159.
178. M. H. P. Rietveld, H. Hagen, L. van de Water, D. M. Grove, H. Kooijman, N. Veldman, A. L. Spek, and G. van Koten, *Organometallics*, 1997, **16**, 168.
179. J. B. Diminnie and Z. Xue, *J. Am. Chem. Soc.*, 1997, **119**, 12657.
180. J. B. Diminnie, J. R. Blanton, H. Cai, K. T. Quisenberry, and Z. Xue, *Organometallics*, 2001, **20**, 1504.
181. U. Burckhardt, G. L. Casty, J. Gavenonis, and T. D. Tilley, *Organometallics*, 2002, **21**, 3108.
182. V. C. Gibson and A. D. Poole, *J. Chem. Soc., Chem. Commun.*, 1995, 2261.
183. A. Castro, M. V. Galakhov, M. Gomez, P. Gomez-Sal, and A. Martin, *Eur. J. Inorg. Chem.*, 2002, 1336.
184. E. Boring, M. Sabat, M. G. Finn, and R. N. Grimes, *Organometallics*, 1998, **17**, 3865.
185. F. Biasotto, M. Etienne, and F. Dahan, *Organometallics*, 1995, **14**, 1870.
186. M. Etienne, P. S. White, and J. L. Templeton, *Organometallics*, 1993, **12**, 4010.
187. K. S. Cook, W. E. Piers, and R. McDonald, *J. Am. Chem. Soc.*, 2002, **124**, 5411.
188. R. L. Miller, R. Toreki, R. E. LaPointe, P. T. Wolczanski, G. D. Van Duyne, and D. C. Roe, *J. Am. Chem. Soc.*, 1993, **115**, 5570.
189. I. de Castro, M. V. Galakhov, M. Gomez, P. Gomez-Sal, and P. Royo, *Organometallics*, 1996, **15**, 1362.
190. U. Burckhardt and T. D. Tilley, *J. Am. Chem. Soc.*, 1999, **121**, 6328.
191. H. C. Strauch, G. Erker, R. Frohlich, and M. Nissinen, *Eur. J. Inorg. Chem.*, 1999, 1453.
192. K. J. Weller, S. D. Gray, P. M. Briggs, and D. E. Wigley, *Organometallics*, 1995, **14**, 5588.
193. S. D. Gray, K. J. Weller, M. A. Bruck, P. M. Briggs, and D. E. Wigley, *J. Am. Chem. Soc.*, 1995, **117**, 10678.
194. K. J. Weller, I. Filippov, P. M. Briggs, and D. E. Wigley, *Organometallics*, 1998, **17**, 322.
195. J. S. Yu, L. Felter, M. C. Potyen, J. R. Clark, V. M. Visciglio, P. E. Fanwick, and I. P. Rothwell, *Organometallics*, 1996, **15**, 4443.
196. P. N. Riley, R. D. Profilet, P. E. Fanwick, and I. P. Rothwell, *Organometallics*, 1996, **15**, 5502.
197. P. N. Riley, R. D. Profilet, M. M. Salberg, P. E. Fanwick, and I. P. Rothwell, *Polyhedron*, 1998, **17**, 773.
198. K. Mashima, Y. Yamanaka, Y. Gohro, and A. Nakamura, *J. Organomet. Chem.*, 1993, **459**, 131.
199. D. M. Antonelli, A. Leins, and J. M. Stryker, *Organometallics*, 1997, **16**, 2500.
200. I. del Hierro, R. Fernandez-Galan, S. Prashar, A. Antinolo, M. Fajardo, A. M. Rodriguez, and A. Otero, *Eur. J. Inorg. Chem.*, 2003, 2438.
201. L. Djakovitch and W. A. Herrmann, *J. Organomet. Chem.*, 1997, **545–546**, 399.
202. M. K. T. Tin, G. P. A. Yap, and D. S. Richeson, *Inorg. Chem.*, 1998, **37**, 6728.
203. N. Thirupathi, G. P. A. Yap, and D. S. Richeson, *Organometallics*, 2000, **19**, 2573.
204. M. K. T. Tin, G. P. A. Yap, and D. S. Richeson, *Inorg. Chem.*, 1999, **38**, 998.
205. P. J. Stewart, A. J. Blake, and P. Mountford, *Inorg. Chem.*, 1997, **36**, 1982.
206. H. C. Strauch, K. Bergander, G. Kehr, R. Frohlich, and G. Erker, *Eur. J. Inorg. Chem.*, 1999, 1461.
207. A. Nakamura and K. Mashima, *J. Organomet. Chem.*, 1995, **500**, 261.
208. H. C. Strauch, G. Erker, and R. Frohlich, *Organometallics*, 1998, **17**, 5746.
209. A. Galindo, M. Gomez, P. Gomez-Sal, A. Martin, D. Del Rio, and F. Sanchez, *Organometallics*, 2002, **21**, 293.
210. M. A. Lockwood, M. C. Potyen, B. D. Steffey, P. E. Fanwick, and I. P. Rothwell, *Polyhedron*, 1995, **14**, 3293.
211. V. M. Visciglio, J. R. Clark, M. T. Nguyen, D. R. Mulford, P. E. Fanwick, and I. P. Rothwell, *J. Am. Chem. Soc.*, 1997, **119**, 3490.
212. W. W. Brennessel, J. E. Ellis, S. N. Roush, B. R. Strandberg, O. E. Woisetschlaeger, and V. G. Young, *Chem. Commun.*, 2002, 2356.
213. W. W. Brennessel, J. E. Ellis, M. K. Pomije, V. J. Sussman, E. Urnezius, and V. G. Young, Jr, *J. Am. Chem. Soc.*, 2002, **124**, 10258.
214. K. Mashima, Y. Nakayama, M. Kaidzu, N. Ikushima, and A. Nakamura, *J. Organomet. Chem.*, 1998, **557**, 3.
215. J. M. Dysard and T. D. Tilley, *Organometallics*, 2000, **19**, 4720.
216. H. Kawaguchi, Y. Yamamoto, K. Asaoka, and K. Tatsumi, *Organometallics*, 1998, **17**, 4380.
217. A. Galindo, M. Gomez, D. Del Rio, and F. Sanchez, *Eur. J. Inorg. Chem.*, 2002, 1326.
218. K. Aoyagi, P. K. Gantzel, and T. D. Tilley, *Polyhedron*, 1996, **15**, 4299.
219. G. Rodriguez and G. C. Bazan, *J. Am. Chem. Soc.*, 1995, **117**, 10155.
220. R. Murugavel, M. Bhattacharjee, and H. W. Roesky, *Appl. Organomet. Chem.*, 1999, **13**, 227.
221. F. Calderazzo, F. Marchetti, M. Moreno, G. Pampaloni, and F. Tumminia, *J. Organomet. Chem.*, 2001, **631**, 110.
222. M. D. Fryzuk, C. M. Kozak, M. R. Bowdridge, and B. O. Patrick, *Organometallics*, 2002, **21**, 5047.
223. M. D. Fryzuk, C. M. Kozak, P. Mehrkhodavandi, L. Morello, B. O. Patrick, and S. J. Rettig, *J. Am. Chem. Soc.*, 2002, **124**, 516.
224. J. Gavenonis and T. D. Tilley, *J. Am. Chem. Soc.*, 2002, **124**, 8536.

225. J. Gavenonis and T. D. Tilley, *Organometallics*, 2002, **21**, 5549.
226. T. E. Waldman, B. Waltermire, A. L. Rheingold, and R. D. Ernst, *Organometallics*, 1993, **12**, 4161.
227. D. L. Clark, J. C. Gordon, J. T. McFarlan, R. L. Vincent-Hollis, J. G. Watkin, and B. D. Zwick, *Inorg. Chim. Acta*, 1996, **244**, 269.
228. F. Calderazzo and G. Pampaloni, *J. Organomet. Chem.*, 1995, **500**, 47.
229. M. Tayebani, K. Feghali, S. Gambarotta, and G. Yap, *Organometallics*, 1998, **17**, 4282.
230. F. Calderazzo, G. Pampaloni, L. Rocchi, and U. Englert, *Organometallics*, 1994, **13**, 2592.
231. F. Calderazzo, G. E. De Benedetto, G. Pampaloni, L. Rocchi, and U. Englert, *J. Organomet. Chem.*, 1993, **462**, C10.
232. D. S. J. Arney, P. A. Fox, M. A. Bruck, and D. E. Wigley, *Organometallics*, 1997, **16**, 3421.
233. Q. A. Abbasali, F. G. N. Cloke, P. B. Hitchcock, and S. C. P. Joseph, *Chem. Commun.*, 1997, 1541.
234. A. M. Arif, R. D. Ernst, E. Melendez, A. L. Rheingold, and T. E. Waldman, *Organometallics*, 1995, **14**, 1761.
235. Q. Jiang, D. C. Pestana, P. J. Carroll, and D. H. Berry, *Organometallics*, 1994, **13**, 3679.
236. V. Vidal, A. Theolier, J. Thivolle-Cazat, and J.-M. Basset, *Science*, 1997, **276**, 99.
237. L. Lefort, C. Coperet, M. Taoufik, J. Thivolle-Cazat, and J.-M. Basset, *Chem. Commun.*, 2000, 663.
238. J. R. Clark, A. L. Pulvirenti, P. E. Fanwick, M. Sigalas, O. Eisenstein, and I. P. Rothwell, *Inorg. Chem.*, 1997, **36**, 3623.
239. M. A. Lockwood, J. R. Clark, B. C. Parkin, and I. P. Rothwell, *Chem. Commun.*, 1996, 1973.
240. P. N. Riley, J. R. Parker, P. E. Fanwick, and I. P. Rothwell, *Organometallics*, 1999, **18**, 3579.
241. K. Mashima, S. Fujikawa, and A. Nakamura, *J. Am. Chem. Soc.*, 1993, **115**, 10990.
242. G. Rodriguez, J. P. Graham, W. D. Cotter, C. K. Sperry, G. C. Bazan, and B. E. Bursten, *J. Am. Chem. Soc.*, 1998, **120**, 12512.
243. G. C. Bazan, S. J. Donnelly, and G. Rodriguez, *J. Am. Chem. Soc.*, 1995, **117**, 2671.
244. K. Mashima, S. Fujikawa, Y. Tanaka, H. Urata, T. Oshiki, E. Tanaka, and A. Nakamura, *Organometallics*, 1995, **14**, 2633.
245. K. Mashima, S. Fujikawa, H. Urata, E. Tanaka, and A. Nakamura, *J. Chem. Soc., Chem. Commun.*, 1994, 1623.
246. K. Mashima, Y. Nakayama, N. Ikushima, M. Kaidzu, and A. Nakamura, *J. Organomet. Chem.*, 1998, **566**, 111.
247. J. Jaffart, C. Nayral, R. Choukroun, R. Mathieu, and M. Etienne, *Eur. J. Inorg. Chem.*, 1998, 425.
248. S. A. Strazisar and P. T. Wolczanski, *J. Am. Chem. Soc.*, 2001, **123**, 4728.
249. K. Takai, M. Yamada, H. Odaka, and K. Utimoto, *J. Org. Chem.*, 1994, **59**, 5852.
250. C. Andes, S. B. Harkins, S. Murtuza, K. Oyler, and A. Sen, *J. Am. Chem. Soc.*, 2001, **123**, 7423.
251. Z.-X. Yu and K. N. Houk, *Angew. Chem., Int. Ed.*, 2003, **42**, 808.
252. M. Taoufik, A. de Mallmann, E. Prouzet, G. Saggio, J. Thivolle-Cazat, and J.-M. Basset, *Organometallics*, 2001, **20**, 5518.
253. F. Lefebvre and J. M. Basset, *J. Mol. Catal. A: Chem.*, 1999, **146**, 3.
254. O. Maury, L. Lefort, V. Vidal, J. Thivolle-Cazat, and J.-M. Basset, *Angew. Chem., Int. Ed.*, 1999, **38**, 1952.
255. C. Coperet, O. Maury, J. Thivolle-Cazat, and J.-M. Basset, *Angew. Chem. Int. Ed.*, 2001, **40**, 2331.
256. K. Mashima, M. Kaidzu, Y. Tanaka, Y. Nakayama, A. Nakamura, J. G. Hamilton, and J. J. Rooney, *Organometallics*, 1998, **17**, 4183.
257. J. W. Bruno and X. J. Li, *Organometallics*, 2000, **19**, 4672.
258. K. J. Weller, P. A. Fox, S. D. Gray, and D. E. Wigley, *Polyhedron*, 1997, **16**, 3139.
259. P. A. Fox, S. D. Gray, M. A. Bruck, and D. E. Wigley, *Inorg. Chem.*, 1996, **35**, 6027.
260. J. B. Bonanno, T. P. Henry, D. R. Neithamer, P. T. Wolczanski, and E. B. Lobkovsky, *J. Am. Chem. Soc.*, 1996, **118**, 5132.
261. P. A. Fox, M. A. Bruck, S. D. Gray, N. E. Gruhn, C. Grittini, and D. E. Wigley, *Organometallics*, 1998, **17**, 2720.
262. D. Meunier, A. de Mallmann, and J.-M. Basset, *Top. Catal.*, 2003, **23**, 183.
263. D. Meunier, A. Piechaczyk, A. De Mallmann, and J.-M. Basset, *Angew. Chem., Int. Ed.*, 1999, **38**, 3540.
264. S. L. Colletti and R. L. Halterman, *J. Organomet. Chem.*, 1993, **455**, 99.
265. S. W. Schweiger, M. M. Salberg, A. L. Pulvirenti, E. E. Freeman, P. E. Fanwick, and I. P. Rothwell, *J. Chem. Soc., Dalton Trans.*, 2001, 2020.
266. R. D. Profilet, A. P. Rothwell, and I. P. Rothwell, *J. Chem. Soc., Chem. Commun.*, 1993, 42.
267. D. R. Lantero, D. L. Ward, and M. R. Smith, III, *J. Am. Chem. Soc.*, 1997, **119**, 9699.
268. J. Szymoniak, J. Besancon, and C. Moise, *Tetrahedron*, 1994, **50**, 2841.
269. O. Blacque, H. Brunner, M. M. Kubicki, J.-C. Leblanc, W. Meier, C. Moise, Y. Mugnier, A. Sadorge, J. Wachter, and M. Zabel, *J. Organomet. Chem.*, 2001, **634**, 47.
270. K. Takai, H. Odaka, Y. Kataoka, and K. Utimoto, *Tetrahedron Lett.*, 1994, **35**, 1893.

271. K. Takai, M. Yamada, and K. Utimoto, *Chem. Lett.*, 1995, 851.

272. I. Shibata, T. Kano, N. Kanazawa, S. Fukuoka, and A. Baba, *Angew. Chem., Int. Ed.*, 2002, **41**, 1389.

273. S. Chandrasekhar, S. J. Prakash, V. Jagadeshwar, and C. Narsihmulu, *Tetrahedron Lett.*, 2001, **42**, 5561.

Nitrogen Monoxide (Nitric Oxide): Bioinorganic Chemistry

Jack R. Lancaster Jr & Gregory I. Giles
The University of Alabama at Birmingham, Birmingham, AL, USA

1	Introduction	2
2	Nitric Oxide Chemistry	4
3	Nitric Oxide and Biology Prior to 1980	5
4	Cell-Mediated Immunity, Cytotoxic Activated Macrophages, and Cytokines	5
5	Metabolic Basis of Activated Macrophage Cytotoxicity Toward Tumor Cells: Studies Prior to 1987	6
6	Macrophage Production of Nitrogen Oxides	7
7	Nitric Oxide as a Messenger Molecule	8
8	Posttranslational Covalent Protein Modification by •NO-derived Species	9
9	EPR of Biological Iron-nitrosyl Complexes	10
10	Nitric Oxide Synthesis	11
11	Nitric Oxide Diffusion	12
12	Nitric Oxide in Pathophysiology	13
13	Novel Biological Roles of •NO	15
14	Related Articles	15
15	References	15

Glossary

Activation: a characteristic phenotypic change in immune cells (including macrophages) upon specific stimulation by cytokines and/or bacterial products that renders them able to recognize and kill foreign or abnormal cells, through mechanisms that can involve production of •NO
Agonist: a general biological term for certain substances that activate a given biological response
Autocrine: a mechanism whereby one cell affects itself
Calmodulin: a soluble protein present in all types of cells that binds calcium. The calcium complex binds to and affects the activity of a variety of enzymes
Cellular immunity: recognition and neutralization of foreign cells, pathogenic organisms, and abnormal host cells through a mechanism that is typically triggered by antibody but, once activated, does not involve antibody; also termed nonspecific immunity
Complement: a series of proteins that bind to foreign antigens or cells, and that can induce lysis or activate other immunological processes
Cytokines: a family of small soluble proteins that are 'immune hormones', that is, they are produced under specific conditions of immune activity and act to transmit messages from one immune cell to another. They are extraordinarily important to the control of the complex repertoire of the entire immune defense mechanism
Cytostatic: does not kill cells, but inhibits their proliferation (division and growth)
Cytotoxic: kills cells
Cytotoxic activated macrophages (CAMs): macrophages that have been treated either in vivo or in vitro by exposure to a combination of bacterial products (such as endotoxin) plus cytokines (particularly interferon-γ), rendering them able to kill or damage abnormal cells (cancerous or infected with pathogenic microbe or virus) or pathogen. An important component of the CAMs armamature for this cytotoxic mechanism is production of •NO
Cytotoxic effector: substances produced by certain immune cells (such as •NO) that result in killing of their targets, typically abnormal cells or invading pathogen
Denitrification: the microbial transformation of nitrite and nitrate to N_2
Digitonin: a mild detergent that permeabilizes the plasma membrane of most mammalian cells without affecting organelles such as the mitochondria
Endothelial cells: cells that line the inside (lumen) of the blood vessels, that produce •NO for the regulation of blood pressure
Endothelial-derived relaxing factor (EDRF): a small, diffusible molecule that is released by the vascular endothelial cell and diffuses to the overlying smooth muscle cell, where it induces relaxation and resulting vasodilation. EDRF is either •NO alone or a bound form of •NO
Endotoxin: a molecular component of certain bacteria that is recognized by certain cells of the immune system (most especially macrophages) and triggers the activation of many immune functions, including synthesis of •NO; also called lipopolysaccharide
EPR: electron paramagnetic resonance spectroscopy
Guanylyl cyclase: a heme-containing enzyme that is stimulated by •NO and results in the formation of cyclic guanosine monophosphate, which signals a variety of processes in the cell including relaxation of smooth muscle cells in the vasculature
Hepatic: pertaining to the liver
Homodimers: a protein composed of two identical protein subunits tightly bound to each other
Humoral immunity: immune defense mechanisms that involve the participation of antibodies against foreign antigens; also termed specific immunity
Hypotension: low blood pressure
Immune surveillance: the hypothesis that cancerous cells are continually developing, but that the body's immune system normally is capable of identifying and removing these dangerous cells
Immunohistochemical method: a method using specific antibodies to detect the presence and microscopic location of

individual proteins or groups (e.g. nitrotyrosine) microscopically in tissues or cells

Interferons: a class of cytokines that were originally discovered because they interfered with viral replication inside mammalian cells, but are now known to perform many other functions, including transmission of information from one immune cell to another; interferon-γ is the most potent cytokine known to induce ·NO formation by activated macrophages

Interleukins: a subset of the cytokines, denoted by the designation IL-1, IL-2, and so on, and each has specific functions in regulating the immune reaction

Lymphotoxin: a cytokine, similar to tumor necrosis factor

Lipopolysaccharide: a molecular component of certain bacteria, that is recognized by certain cells of the immune system (most especially macrophages) and triggers the activation of many immune functions, including synthesis of ·NO; also called endotoxin

Lymphocytes: immune cells that orchestrate the immune response

Macrophages: a phagocytic cell of the immune system that performs many functions critical to defense against foreign or pathogenic organisms

Murine: from a mouse

Necrosis: a type of cell death or nonspecific tissue decay

Neoplastic: cancerous

Neurotransmitter: a molecular messenger that is released by one cell of the nervous system and induces a specific signal in another cell

Neutrophils: a phagocytic immune cell, whose central function is to kill invading organisms

Nitrovasodilators: certain compounds such as nitroglycerine, nitroprusside, and isosorbide dinitrate, that act to cause decrease in blood pressure by releasing ·NO

Nonspecific immunity: recognition and neutralization of foreign cells, pathogenic organisms, and abnormal host cells through a mechanism that is typically triggered by antibody but, once activated, does not involve antibody; also termed cellular immunity

Paracrine: a mechanism whereby one cell affects another

Peritoneal cavity: the body cavity that houses the organs of the gut

Phagolysosome: a membrane-surrounded compartment in phagocytic cells where certain products are assembled for further processing and secretion; the pH of this compartment is low (4 or less)

Posttranslational Protein Modification: a mechanism of biological control of protein activity by covalent modification after protein synthesis

Reactive Oxygen Species: intermediates of O_2 between O_2 and H_2O that are involved in oxidative cellular injury ($\cdot O_2^-$, H_2O_2, ·OH)

Sepsis: a serious infection that results in the presence of bacteria and bacterial products in the circulation

Septic shock: a serious and life-threatening clinical condition where massive bacterial products and bacteria in the circulation results in an excessive immune response

Specific immunity: immune defense mechanisms that involve the participation of antibodies against foreign antigens; also termed humoral immunity

Transformed: a term applied to mammalian cell cultures that have become ‘immortalized’, that is, they grow and divide and thus resemble cancerous cells

Tumor necrosis factor (TNF): a multifunctional cytokine that is capable of specifically stimulating certain cells to perform a wide variety of immune functions, and also induces a ‘suicide’ response in many abnormal cells (cancerous, infected with pathogenic microbe or virus)

Vascular smooth muscle cells: the cells that surround the blood vessels and control blood pressure by relaxing or contracting in response to specific signals, including ·NO

Vascular tone: the degree of contraction of the vascular smooth muscle cells that regulates blood pressure

Vasodilation or vasodilatation: expansion of the blood vessels as a result of relaxation of the smooth muscle cells that overlie the vessels, resulting in decreased blood pressure

Abbreviations

BH_4 = Tetrahydrobiopterin; CAM = Cytotoxic activated macrophage; cNOS = Constitutive nitric oxide synthase; CPR = Cytochrome P450 reductase; EDRF = Endothelial-derived relaxation factor; EPR = Electron paramagnetic resonance spectroscopy; IL-1 = Interleukin-1; iNOS = Inducible nitric oxide synthase; LPS = Lipopolysaccharide, or endotoxin; NMMA = N^G-monomethyl-L-arginine; NOS = Nitric oxide synthase; ROS = Reactive oxygen species; SOD = Superoxide dismutase; TNF = Tumor necrosis factor.

1 INTRODUCTION

As documented by the selection of nitric oxide (·NO, nitrogen monoxide) by *Science* as ‘Molecule of the Year’ for 1992, followed by the 1998 Nobel Prizes for Physiology or Medicine, research into the remarkable and multiple roles of ·NO in biology has exploded since 1987 (with nearly 70 000 publications, most appearing within the last five years). It is probably true that ·NO is involved in one way or another in virtually every common pathophysiological state by virtue of its importance in the normal maintenance of many important physiological phenomena (such as blood pressure, neurotransmission, and gastrointestinal function) as well as in the host response to disease (immune and inflammatory stimulation, cancer, and cardiovascular disease) (Figure 1).

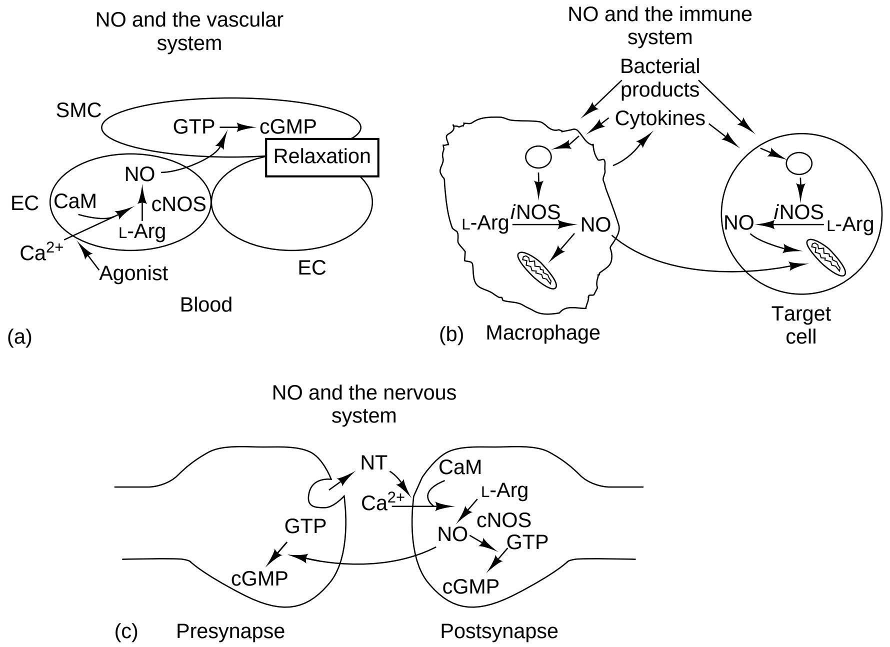

Figure 1 Schematic representation of the three major roles of ·NO in mammalian biology. (a) As the messenger responsible for vascular dilation (EDRF), ·NO is produced in the endothelial cell (EC) that line the lumen of the blood vessels upon stimulation with certain specific agonists (and also, although not shown in the diagram, physical changes in the flow of blood). These agonists act by stimulating an influx of Ca^{2+} into the EC, which binds to calmodulin and this calcium-calmodulin complex binds to the constitutive nitric oxide synthase (cNOS), which catalyzes the formation of ·NO and citrulline from L-arginine. The ·NO diffuses into the surrounding vascular smooth muscle cell (SMC), and stimulates the enzyme guanylyl cyclase to produce cyclic GMP cyclic guanosine monophosphate (cGMP) from guanosine triphosphate (GTP); this stimulation occurs because ·NO binds to a heme group, specifically required for maximal enzymatic activity. The increase in cGMP acts upon the contractile apparatus of the SMC (by a largely unknown mechanism) to induce relaxation. (b) In the immune system, particularly the macrophage, activation by exposure to bacterial products and/or cytokines induces the de novo transcription and translation of the gene for the inducible isoform of nitric oxide synthase (iNOS), which produces ·NO and citrulline from L-arginine in a largely calcium-independent manner. The ·NO interferes with the normal energetic metabolism of both the macrophage and the target cell, by inhibiting iron-containing enzyme function. (c) In the neural system, the production of ·NO resembles that for the vascular system in that ·NO is synthesized by a constitutive NOS (although it is different from the enzyme in EC cells) in response to increased internal Ca^{2+}; however, the signals that trigger this response are certain neurotransmitters, that are released by the presynaptic terminal and diffuse to another adjacent cell at the postsynaptic terminal. ·NO produced in the postsynaptic cell affects that cell and possibly also the presynaptic cell in a ‘feedback’ manner, in both cases through the heme-mediated stimulation of guanylyl cyclase

This article is written as a general review that is intended to bridge many interdisciplinary gaps ranging from chemistry, biochemistry, and spectroscopy to physiology, neuroscience, immunology, and biomedicine. Because of the extraordinary range of scientific literature on ·NO, it is possible to obtain great insight into this unique molecule’s multiple actions by combining concepts on this multifaceted molecule from these disciplines. The trade-off for such an approach, however, is that a sufficient amount of background material must be provided for the nonspecialist in each area. Although we will provide the reader with appropriate citations for entry into the original literature and reviews in the many fields that have been affected by this fast-moving area, our focus will be upon what is presently known about the molecular mechanisms of action of ·NO in mammalian physiology and pathophysiology, much of which has come from studies in immunology. We will not attempt to cover the entire range of biological roles of ·NO, which is covered in many books and reviews,[1–38] including methods for measurement and preparation and handling of ·NO[39–43] and the chemistry and biochemistry of its reactions with biological targets.[44–47] There are also three books of proceedings of international conferences that have appeared on the biology of ·NO,[48–50] and volumes 268, 269, 301, and 359 of *Methods in Enzymology* are devoted to various aspects of ·NO chemistry and biochemistry. There are also books dealing with metal-nitrosyls[51] and their electron paramagnetic resonance (EPR) spectroscopy[52] as well as various biomedical aspects of ·NO.[53–55] In addition, a recent book on ·NO, its chemistry, and its biochemistry has appeared[56] and is a superb resource, especially for chemists interested in the biological roles of ·NO and the basics of its mechanistic actions. Finally, Carl Djerassi has written an entertaining fictional (but chemically informative and historical) novel entitled ‘NO’.

As we shall see, a thorough appreciation for the chemistry and biochemistry of ·NO is essential for any fundamental understanding of its critical roles in a multitude of biologically and medically important areas and can provide important new insights and tools for its study.

2 NITRIC OXIDE CHEMISTRY

Owing to its unpaired electronic configuration, the reactions of •NO with the highest rate constants involve either its association with a transition metal ion or recombination reactions with other radical and paramagnetic species. Iron is the most prevalent transition metal ion, being required for a variety of essential functions. In addition, several iron-containing proteins such as hemoglobin, myoglobin, the cytochromes P450, and cytochrome oxidase are specifically designed to bind O_2 and since •NO is similar in structure, it can bind to these proteins as an oxygen surrogate (*see* ***Iron: Heme Proteins & Dioxygen Transport & Storage***, ***Iron: Heme Proteins, Mono- & Dioxygenases***, ***Cytochrome Oxidase***). Under physiological conditions, most heme in hemoglobin is oxygenated. In this case, •NO reacts extremely rapidly, essentially ‘extracting’ the equivalent of superoxide from the ferroheme and generating nitrate and the oxidized heme:[57–59]

$$\bullet NO + O_2 - Fe^{2+} \longrightarrow NO_3^- + Fe^{3+} \qquad (1)$$

Quantitatively, this reaction probably represents the major in vivo route for •NO conversion into stable metabolites.[60] •NO also reacts with oxygen complexes of other metalloproteins, including lipoxygenase[61] and myeloperoxidase (*see* ***Iron: Heme Proteins, Peroxidases, Catalases & Catalase-peroxidases***).[62,63] When •NO encounters hemoglobin in the reduced deoxy state (in the absence of O_2), it binds to the heme iron atom in a fashion very similar to that of O_2. Under physiological conditions, this reaction is probably not functionally relevant given the respective concentrations of O_2 and •NO. However, the inhibitory effects of •NO on cytochrome oxidase, involving binding to both heme and copper, may have important regulatory effects on mitochondrial electron transfer[34] and also diffusion of •NO and O_2 away from the blood vessel.[64]

In addition to hemoproteins, the other major metabolically active pool of intracellular iron is the nonheme iron-sulfur proteins (*see* ***Iron–Sulfur Proteins***), which function primarily as electron carriers, most especially in the mitochondrial electron transfer chain. In vitro treatment with •NO has been shown to result in conversion of the iron in these clusters into dinitrosyliron thiol complexes ($(RS\text{-})_2Fe(NO)_2$).[65] As described in more detail below, these complexes exhibit a characteristic EPR signal, which has been observed in both •NO-producing activated macrophages and their tumor cell targets, suggesting that such complexes may also be formed in vivo.

In addition to transition metals, •NO also reacts with biological radicals. •NO reacts with dioxygen in aqueous solution via a fairly complex reaction to eventually produce nitrous acid (called autoxidation) with an overall stoichiometry:

$$4\bullet NO + O_2 + 2H_2O \longrightarrow 4H^+ + 4NO_2^- \qquad (2)$$

The kinetic expression for •NO autoxidation is rate $= 4k[\bullet NO]^2[O_2]$ with $k = 2\text{–}2.9 \times 10^6\,M^{-2}\,s^{-1}$.[66–68] Thus, for physiological concentrations of •NO (1–50 nM) the consumption of •NO via autoxidation is slow (half-life 2–100 h) and will not account for the loss of significant amounts. However, this reaction may have enormous biological consequences as it results in the formation of species with potent biological activities. In addition, this reaction is accelerated by a factor of nearly 300-fold (on a per volume basis) when it occurs in hydrophobic compartments such as membranes.[69]

In contrast, the reaction of •NO with superoxide is extremely rapid ($k = 1.9 \times 10^{10}\,M^{-1}\,s^{-1}$):[70]

$$\bullet NO + \bullet O_2^- \longrightarrow ONOO^- \qquad (3)$$

After much confusion over the past 10 years, it is now clear that in aqueous buffer in the absence of another reactant, peroxynitrous acid (ONOOH, $pK_a = 6.8$) undergoes two subsequent reactions, isomerization to produce nitrate (yield 71%) and homolysis to produce hydroxyl radical (•OH) and nitrogen dioxide (•NO_2) (yield 29%).[71] Both of these species are highly oxidizing and much speculation has been directed toward their involvement in biologically damaging actions of •NO production (see below). However, under biological conditions, peroxynitrite will undergo at least two other reactions long before isomerization and homolysis, two-electron oxidation of cellular thiol (forming the sulfenic acid and nitrite),[72] and reaction with CO_2 to form the nitrosoperoxocarbonate anion ($ONOOCO_2^-$). This extremely short-lived species undergoes either heterolytic scission, producing nitrate and CO_2 (67% yield) or homolytic scission producing •NO_2 and the carbonate anion radical (•CO_3^-) (33% yield).[73] Thus, in the biological milieu, reaction of •NO with superoxide generates two potent oxidants, linking •NO and cellular oxidizing species with mild activity to form potent new stressors. The production of both •NO and •O_2^- are deliberately upregulated in locations of inflammatory stimulation, indicating that this reaction plays a key role in oxidative stress (and also, perhaps, signaling).

NO also undergoes radical recombination reactions. Reaction with •CO_3^- yields CO_2 and HNO_2.[74] The reaction with •NO_2, produced from the reaction of •NO with both O_2 and •O_2^-, yields the potent nitrosating agent nitrous anhydride (N_2O_3).[75] N_2O_3 reacts with water, which, in addition to the nitrosation reaction, generates nitrite. The two most important targets for nitrosation are amines and thiols.[76] In the case of amines, the subsequent chemistry is different for each type of amine. For primary amines, the nitrosamine is the initial product that rapidly forms a diazo compound. The diazo is an excellent leaving group, which results in the formation of an alcohol and so the net result is the conversion of a primary amine into an alcohol. For secondary amines, the nitrosamine is stable but is metabolized in cells to yield a variety of highly reactive and mutagenic species.[77] Correspondingly thiols also are excellent nitrosation acceptors, yielding nitrosothiols. As described below, this covalent modification has been proposed to be an important mechanism of posttranslational protein modification. In addition, ·NO (and also $\cdot NO_2$) reacts with radical species produced by one-electron oxidation. One important species is the initial product of lipid peroxidation (e.g. peroxyl species), which results in the formation of several different nitrolipid species.[23] This action represents a potent antioxidative activity of ·NO and $\cdot NO_2$ since it results in radical chain termination, and there is also recent evidence that these species may possess specific regulatory and anti-inflammatory signaling activity as well.[23,78] Finally, $\cdot NO_2$ will recombine with tyrosyl radical thus resulting in the formation of stable nitrotyrosine. Nitrotyrosine can also be formed from an ill-defined reaction of peroxynitrite with metals[79] and also metals (including peroxidases) in the presence of nitrite and H_2O_2.[80,81]

The biological transformations of ·NO described above are all oxidative. Although chemical studies have shown that reduction of ·NO to form nitroxyl (HNO) can occur via some biochemical mechanisms (e.g. superoxide dismutase (SOD),[82] ·NO synthase,[83] mitochondrial metabolism,[84] and reaction of nitrosothiols with thiols[85]), little evidence has been presented to suggest that functionally relevant quantities of nitroxyl are produced in vivo.[86,87]

3 NITRIC OXIDE AND BIOLOGY PRIOR TO 1980

Nitric oxide is one of the most extensively investigated molecules in inorganic and bioinorganic chemistry, having been originally discovered in 1620 by the Belgian chemist Jan Baptist van Helmont when an ‘air’ was generated upon pouring nitric acid over metal filings.[88] Priestley is generally credited with the original discovery of ·NO,[89] and this is correct in the sense that he recognized it as distinct from other gases. It is noteworthy that Dalton utilized the reactions of ·NO with air to perform the first accurate determination of the content of oxygen in the atmosphere,[90] which of course requires a proper appreciation of the concepts of reaction stoichiometry. Because of its close resemblance to dioxygen (one atomic number different) and its paramagnetism (15 total electrons), ·NO has been used extensively as an O_2 surrogate to probe the metal environment of a variety of metalloproteins. In particular, ·NO has been shown to bind to Fe^{2+} in heme-containing oxygen transporting proteins (*see* ***Iron: Heme Proteins & Dioxygen Transport & Storage***) in a fashion nearly identical to O_2, with the important consequence of rendering the complex paramagnetic and so visible by EPR spectroscopy.[91] Because the unpaired electron assumes appreciable iron d orbital character, analysis of the EPR characteristics of hemoprotein nitrosyl complexes yields a great deal of information on both the ligand binding environment around the heme and on the conformational states of the protein (*see* ***Iron Porphyrin Chemistry***). Indeed, much of the classic work delineating the ligand-induced T to R allosteric transitions in hemoglobin were based on EPR studies of nitrosylhemoglobin,[92,93] first described in detail by Hideo Kon in a classic paper in 1968.[94]

Prior to the 1980s, studies on the biological roles of ·NO were confined almost exclusively to five areas: its actions as an atmospheric pollutant,[95] as a potent stimulator of the mammalian enzyme soluble guanylyl cyclase[96] (which presaged its roles as an intercellular messenger as described below), its properties as a food preservative,[97] and its roles in the microbial nitrogen cycle[98] and in the actions of certain nitrogen-containing carcinogenic compounds.[95] However, as described in more detail below, there was EPR evidence for endogenous nitrosyl production of unknown origin in mammals in the late 1960s and early 1970s. In an early study published in 1916, Mitchell, Shonle, and Grindley[99] provided evidence that more nitrate is excreted in the urine of Man than is ingested, suggesting the presence of an endogenous mechanism for production of inorganic nitrogen oxides. This one paper presaged the remarkable discoveries of ·NO in mammalian biology that occurred more than 60 years later.

Data published in the 1970s[100,101] indicated that ·NO may be a protein-bound (although probably not freely released) intermediate in the assimilatory reduction of nitrite to ammonia in plants. Nitrite and nitrate, the one- and three-electron oxidation products of ·NO, respectively, are the precursors for microbial denitrification, which is the reduction of these nitrogen oxides to N_2. Early reports described a red haze over molasses vats where denitrification occurs, suggesting ·NO production and subsequent oxidation to $\cdot NO_2$ and N_2O_4.[102] ·NO production was also observed in soil samples during denitrification,[103] and in extracts of certain denitrifying bacteria[104–106] and purified heme-containing nitrite reductases.[107–109] As described in several studies,[110,111] it is only recently that ·NO has been shown to be a true intermediate in this process, as opposed to a transient, protein-bound and only slowly releasable intermediate, as mentioned above for plants.

4 CELL-MEDIATED IMMUNITY, CYTOTOXIC ACTIVATED MACROPHAGES, AND CYTOKINES

As we will describe in more detail below, ·NO has been shown to play an important role in (among other areas) mammalian immunology, and it is these studies that have provided most of the information about the molecular mechanisms of ·NO effects upon cells (the central focus of this article). In this section, we provide a brief overview for the nonspecialist of the principal components of cellular immunity specifically related to ·NO; readers familiar with this area should skip to the next section.

There are two 'arms' to the immune defense mechanism. Humoral (or specific) immunity, the most familiar, is the production of specific antibody to foreign antigen, which triggers a panel of different immune responses including lysis of invading cells by the complement cascade and opsonization (specific adsorption of antibody or complement components to the foreign material), which enables recognition by specific phagocytosing cells that engulf and inactivate the antigen. No detailed studies have linked ·NO to the mechanisms of antibody production.

Cellular (or nonspecific) immunity, on the other hand, does not involve the active participation of antibody, although antigenic stimulation activates it.[112] The historical development of the concept of nonspecific immunity lies in studies carried out in the 1950s and 1960s, which demonstrated that once an immune reaction occurs against a specific antigen, oftentimes certain cells of the immune system (most especially the macrophage) become 'activated' and are capable of recognizing and killing not only the pathogen that initiated the response but also unrelated organisms.[113,114] Remarkably, isolated macrophages that have been activated in vivo by infection with microbes and intracellular pathogens (such as *Corynebacterium parvum*, Bacillus Calmette-Guérin, or *Toxoplasma*) are capable of inactivating in vitro not only the pathogen that initiated the activation, but also unrelated pathogenic microbes, viruses, and even tumor cells. Indeed, Hibbs, in particular, has championed the notion that this killing of tumor cells by macrophages serves as an 'immune surveillance' mechanism whereby cancerous transformation is continually opposed in vivo.[115] Subsequent research demonstrated that purified components of bacterial cell walls (including lipopolysaccharide (LPS) from gram-negative organisms, also called endotoxin) will replace intact microbes in inducing this cross-resistance.[112]

At the turn of the century, Dr. William B. Coley, a young surgeon in New York City, made the remarkable discovery that injection of live or inactivated pathogenic bacteria into patients with otherwise incurable cancers would oftentimes induce dramatic necrosis (a specific type of cell death) and regression of the tumors.[116,117] Owing to a number of factors including lack of standardization of the potency of the bacterial injections, toxic side effects, variability and sometimes total lack of effect, and the simultaneous advent of radiotherapy, these intriguing results were not followed up until much later.

In 1975, Lloyd Old and colleagues discovered that transfer of serum from the blood of donor mice that had been previously injected with endotoxin into recipient mice harboring tumors would induce necrosis of the tumors.[118] They dubbed the transferrable substance responsible 'tumor necrosis factor', or TNF. Remarkably, TNF was also shown to induce killing in vitro of two different neoplastic cell lines in tissue culture, but had no effect on normal mouse embryo fibroblast cultures. TNF is now known to be a member of an extraordinarily important family of small, soluble proteins called cytokines.[119] These proteins (most of which have been cloned and pure recombinant proteins are now available) function as 'immune hormones', and act as messengers to relay information between different cells involved in the immune response. In this capacity, cytokines orchestrate the incredibly complex immune response to infection and inflammation. In addition, several cytokines (including TNF, interferons α and γ, interleukin-1β, and lymphotoxin) are capable of inducing a 'suicide' response in vitro in cultured cells that are abnormal (infected with virus or pathogenic microbe, or transformed to a cancerous phenotype). Because this effect obviously does not involve antibody, cytokines are usually considered key components of nonspecific immunity; however, this distinction is not strict because antibody production is also regulated by cytokine production and by cell-specific responses to specific cytokines.[112] Cytokines act by binding to specific receptors on the surface of the responding cell, and act via receptor-mediated signal transduction. Different cells have different receptors for different cytokines, and there can be considerable interaction between different cytokine actions on even the same cell. The result of this complexity is redundancy, synergism, or antagonism of different cytokine effects on a given cell type, conferring exquisite control over the signals transmitted depending on the cytokine(s) present and the cell type as target. Nitric oxide plays an important role in many cytokine actions on isolated cells, as well as on the nonspecific mechanism of macrophage injury and killing of pathogens and tumor cells.

5 METABOLIC BASIS OF ACTIVATED MACROPHAGE CYTOTOXICITY TOWARD TUMOR CELLS: STUDIES PRIOR TO 1987

What are the specific intracellular derangements that occur in target cells (specifically, tumor cells) in response to activated macrophages? In 1980, Krahenbuhl[120] studied the in vitro (in culture) effects of murine cytotoxic activated macrophages (CAMs, produced by injection of killed *C. parvum*) on EMT-6 cells, a murine cell line originally derived from explantation of a mammary tumor. These and subsequent studies on the mechanism of CAM-induced injury were greatly facilitated by the fact that this and certain other tumor cell lines are 'injured' by CAMs (do not proliferate) but not 'killed' (do not lyse). He observed a dramatic and early (within 2 h) inhibition of DNA synthesis in the CAM-injured EMT-6 cells. Shortly thereafter, Granger, Taintor, Cook, and Hibbs[121] examined murine L1210 tumor cells after incubation with macrophages isolated from the peritoneal cavity of mice after they had been pretreated with endotoxin to induce the activated state. Like EMT-6 cells, CAMs are cytostatic against L1210 cells but not cytotoxic.

The striking results revealed that survival of the L1210 cells after CAM coincubation exhibited an absolute requirement for exogenous glucose in the medium, whereas uninjured L1210 cells had no such requirement. The ability of other sugars to substitute (mannose and fructose) correlated quantitatively with their capacity to support glycolytic metabolism, and inhibition of glycolysis with 2-deoxyglucose prevented the ability of glucose and mannose to prevent eventual lysis of the cells. Also, unlike control cells (not pretreated with CAMs), injured cells exhibited no Pasteur effect, meaning lactate production was the same in the presence or absence of oxygen. Finally, oxygen consumption by the injured L1210 cells was 85% inhibited compared to the control cells. These results suggested that CAMs induce an inhibition in mitochondrial oxygen consumption leading to energetic deprivation that can be partially alleviated by glycolytic metabolism.

There are several possibilities for the decreased oxygen consumption in CAM-injured L1210 cells, including defects in required substrate uptake from the medium, imbalances in intracellular ion homeostasis, and critical cofactor depletion. In 1982, Granger and Lehninger**[122]** performed a careful analysis, using now classic techniques, for determining whether the lesion is a direct inhibition of mitochondrial electron transfer. Using digitonin to selectively permeabilize the L1210 plasma membrane (thus allowing direct measurement of mitochondrial respiration with exogenously added substrates) and selective inhibitors and electron donors of segments of the electron transfer chain, it was found that oxygen reduction from NADH and from succinate as electron donors was inhibited in mitochondria in CAM-injured L1210 cells. However, electron transfer to O_2 from α-glycerophosphate, which donates electrons on the oxygen side of coenzyme Q, or from the addition of ascorbate plus tetramethylphenylenediamine, which donates electrons at the level of cytochrome *c*, was relatively unaffected. This suggests that there is a site-specific malfunction in the mitochondrial electron transfer chain, localized to complexes I (NADH-coenzyme Q reductase) and II (succinate-coenzyme Q reductase). It is important to point out here that these regions of the chain are especially rich in nonheme iron-sulfur centers. Importantly, simple cessation of cell division does not induce mitochondrial inhibition, and the time course of this inhibition resembled that for inhibition of DNA synthesis. In addition, mitochondrial respiration in the presence of oligomycin (an inhibitor of the proton-translocating adenosine triphosphate (ATP) synthase) was low and similar in both untreated and CAM-injured cells, indicating that there is no defect in the energy-coupling ability of the mitochondria but rather a direct inhibition of electron transfer.

In 1984, Hibbs, Taintor, and Vavrin**[123]** reported that CAMs cause L1210 cells to lose up to 64% of their intracellular iron, and the time course of this release is similar to that of CAM-induced mitochondrial inhibition. In 1986, Drapier and Hibbs**[124]** showed that aconitase (an iron-sulfur-containing enzyme (*see* ***Iron–Sulfur Proteins***)) is also a target for CAM injury, and that the injured cells recover aconitase activity upon addition of Fe^{2+} to the medium. It was speculated that the inhibition of DNA synthesis may be due to inhibition of ribonucleotide reductase, which catalyzes the rate-limiting step in this pathway and which contains nonheme iron essential for activity. Wharton, Granger, and Durack**[125]** subsequently found that NADH dehydrogenase and succinate dehydrogenase are depleted of iron, as judged by ^{55}Fe radioactivity in isoelectric focusing gel slices corresponding to these complexes. These results indicated that iron-sulfur-containing enzymes are important targets for the CAM-induced injury.

6 MACROPHAGE PRODUCTION OF NITROGEN OXIDES

In the early 1980s, Tannenbaum's laboratory definitively showed that humans and rats excrete more urinary nitrate than is ingested,**[126,127]** as originally suggested for humans in the early study by Mitchell *et al.***[99]** A clue to the formation of the nitrate came from work by Tannenbaum's group**[128]** as well as Hegesh and Shiloah**[129]** who found that urinary nitrate levels are much higher than normal in infants or adults with diarrhea, suggesting an origin related to infection. Indeed, Tannenbaum and colleagues subsequently demonstrated that nitrate levels in rat urine are elevated also by injection of endotoxin.**[128,130]**

Stuehr and Marletta and colleagues provided key insight into this phenomenon in the mid-1980s by demonstrating that isolated mouse macrophages, when activated in vivo by injection with *Mycobacterium bovis* or Bacillus Calmette-Guérin or treated in vitro with endotoxin and/or cytokines (including interferon-γ), are stimulated to produce nitrite and nitrate.**[131–134]** In addition, it was shown that these activated macrophages cause N-nitrosation of morpholine, which is not induced by the addition of nitrite to macrophages that had not been activated.**[135]** This result suggests that the active agent responsible for N-nitrosation is an active precursor of nitrite + nitrate, and Marletta *et al.***[136]** showed that in macrophages •NO is indeed the precursor to nitrite and nitrate, which are produced by the reaction of •NO with O_2.

In 1987, Hibbs, Taintor, and Vavrin published a seminal paper in the field of mammalian nitric oxide production.**[137]** By using a medium that was depleted in specific components, it was found that the formation of nitrite + nitrate in CAMs requires L-arginine, produces L-citrulline, and is inhibited by the L-arginine analog N^G-monomethyl-L-arginine (NMMA) (Figure 2). Importantly, addition of NMMA prevents not only formation of nitrogen oxides and citrulline but also inhibition of aconitase and DNA synthesis in tumor cells cocultured with the CAMs. Subsequent studies by Hibbs' laboratory demonstrated that the macrophages themselves are also subject to the same L-arginine-dependent damaging effects that occur in the tumor target cells**[138]** as well as cytokine-treated isolated tumor cells (in the absence of CAMs) under certain conditions.**[139,140]** Thus, macrophage activation

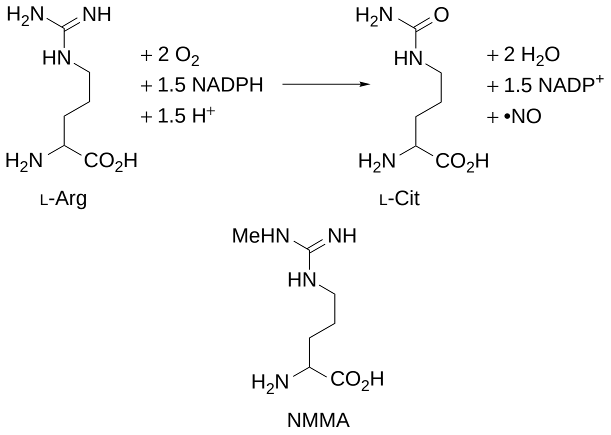

Figure 2 Stoichiometry of the enzymatic mechanism of formation of •NO, and the structure of a competitive inhibitor, N^G-monomethyl-L-arginine (NMMA). •NO is synthesized by all NOS's by a similar mechanism, involving the NADPH-dependent mixed-function oxidation of a guanidino nitrogen of the amino acid L-arginine (L-arg) to produce L-citrulline (L-cit) and •NO. The nonintegral stoichiometries are explained in the text. NMMA inhibits NOS as a competitive inhibitor

or treatment of isolated cells with cytokines under certain conditions involves the deimination of L-arginine to form L-citrulline and an active precursor to nitrite + nitrate that inhibits intracellular iron-containing enzyme function in either tumor target cells or pathogenic organisms (although there are L-arginine-independent effects of CAMs and cytokines[112]). As we shall see, this intermediate is nitric oxide.

7 NITRIC OXIDE AS A MESSENGER MOLECULE

Unexpectedly, parallel research in two separate fields, vascular physiology and neurophysiology, converged with these immunological studies in 1987 and 1988, united by the demonstration that the L-arginine-dependent pathway also produces •NO as a messenger molecule for intercellular signal transmission. Although there are distinct differences in the enzymological regulation of •NO formation when it functions as a cytotoxic effector (immune) versus a messenger (vasodilation and neural signal transmission), the fundamental biochemistry of the formation of •NO and its interactions with its targets are similar, namely, synthesis from the mixed-function oxidation of a guanidino nitrogen of L-arginine and cellular effects exerted by interaction with iron-containing proteins.

The vasculature is composed of two principal cell layers, an endothelial cell lining the lumen and a surrounding layer of smooth muscle cells (SMC) (Figure 1). Vascular relaxation/contraction (vascular tone) is effected by relaxation/contraction of the smooth muscle layer. In 1867, Brunton reported the use of amyl nitrite for the treatment of angina.[141] Since that time, nitrovasodilators have been one of the most commonly prescribed pharmacologic agents, including the compounds nitroglycerin and nitroprusside. These compounds are potent inducers of systemic decrease in blood pressure (hypotension) and their mechanism of action has been a major area of research in cardiovascular physiology. In the 1970s, Murad's laboratory provided convincing evidence that the ability of this heterogenous class of compounds to induce vasodilatation is determined by their ability to release nitric oxide, either by cellular metabolism or by spontaneous liberation, and stimulate the intracellular synthesis of the messenger molecule cyclic cGMP.[142,143] Craven and DeRubertis showed that •NO and •NO-liberating compounds stimulate guanylyl cyclase through binding to heme.[144] In 1980, Furchgott and Zawadzki discovered that the endothelial cell layer releases a diffusible substance (termed Endothelial-Derived Relaxing Factor or EDRF) that travels to the overlying smooth muscle cell layer and induces relaxation.[145] Combining these observations with the stimulatory actions of nitrovasodilators, in 1986 Furchgott and Ignarro simultaneously proposed that EDRF is nitric oxide, although no biochemical mechanism was then known to account for the production of •NO in mammals.[146,147]

One year later, Ignarro[148,149] and Palmer, Ferrige, and Moncada[150] demonstrated that EDRF, produced by endothelial cells (EC), has properties indistinguishable from •NO, using the analytical techniques employed. It was shown soon thereafter that, like Hibbs demonstrated for the activated macrophage, L-arginine is the precursor, L-citrulline is formed, and NMMA inhibits both •NO formation and the production of EDRF.[151–153] It is important to point out that there are also other important molecules produced by the endothelium that regulate vascular tone, including the potent prostaglandin prostacyclin and the small peptide endothelin as well as a so far unidentified mediator of dilation *via* smooth muscle cell membrane hyperpolarization.[154] Nevertheless, substantial modulation of blood pressure in vivo can be accomplished by administration of agents that activate (nitrovasodilators) or attenuate (NMMA) this mechanism of vasorelaxation.[10,11] The importance of •NO in the vascular system was highlighted in 1998 when the Nobel Prize for Physiology or Medicine was awarded to Furchgott, Ignarro, and Murad 'for their discoveries concerning nitric oxide as a signaling molecule in the cardiovascular system'.

The stimulation of soluble guanylate cyclase (sGC) by •NO is arguably the most physiologically important reaction of •NO. Early work had demonstrated that isolated sGC contains heme, which is a requirement for stimulation by •NO, and that various heme species stimulate the activity of the enzyme.[144] Further work has led to the hypothesis that •NO stimulates the enzyme by binding to the distal position and inducing formation of a pentacoordinate complex, thus resulting in breakage of the proximal histidine bond to the iron (*see* ***Iron Porphyrin Chemistry***).[155] Although this model still holds generally, there is evidence that •NO may also exert a modulatory effect on activity, presumably at a second site, although this point is in contention.[156,157]

In 1988, Garthwaite demonstrated that cultured cerebellar neurons stimulated with the neurotransmitter glutamate release ·NO, providing an explanation for the previously established glutamate-induced elevation in neuronal cGMP levels[158] (Figure 1). Soon thereafter, it was shown that brain extracts[159] and slices[160,161] synthesize ·NO from L-arginine. As described in more detail below, these results sparked a series of studies on the physiological and pathological roles of ·NO in neurotransmission, an area that is one of the most intensely investigated in the biological roles of this molecule.

Remarkably, a critical target of ·NO is the cytosolic form of aconitase, which in fact possesses either of two biological activities; in one form, which is dominant under conditions of cellular iron depletion, the protein functions as iron regulatory protein-1 (IRP-1) and is a key control in regulation of iron homeostasis (*see* ***Metalloregulation***) by acting as a transcription factor increasing expression of transferrin receptor and ferritin.[162] This form possesses no aconitase activity; however, under conditions of iron repletion the protein acquires aconitase activity and loses IRP-1 activity. The mechanism of this conversion involves the presence (aconitase active, IRP-1 inactive) or absence (aconitase inactive, IRP-1 active) of an intact iron-sulfur center (*see* ***Iron–Sulfur Proteins***). Cellular ·NO formation, by disrupting the intactness of the iron-sulfur cluster, thus induces a cellular response (in terms of iron homeostasis) similar to iron depletion. Indeed, there is evidence that at least part of the effect of ·NO on the IRP system is due to its depletion of cellular iron pools.[163–165] ·NO also activates the iron-sulfur-containing bacterial transcription factor SoxR, which is involved in regulating defensive responses to oxidative stress (*see* ***Iron–Sulfur Proteins***).[166] The precise mechanism of action of ·NO in protein-bound iron-sulfur centers is not clear, with the three possibilities being disruption of the cluster via direct attack of ·NO, as described above,[163,167] similar direct disruption via reactive nitrogen oxide products resulting from ·NO (e.g. peroxynitrite[167]), and loss of activity from nitrogen oxide-induced thiol modification.[168] It is, however, difficult to demonstrate experimentally direct effects of ·NO (as compared to actions of higher nitrogen oxides) since such a demonstration would require anoxic, unphysiological conditions, which among other effects would dramatically increase the concentration of ·NO.[64] In any event, it does appear that disruption of iron-sulfur center function can be a deleterious cellular injury since cells possess mechanisms for their repair (*see* ***Iron–Sulfur Proteins***).[123,169,170]

8 POSTTRANSLATIONAL COVALENT PROTEIN MODIFICATION BY ·NO-DERIVED SPECIES

Nitrosation of thiols to form nitrosothiols as a result of endogenous ·NO synthesis can occur for both small molecules such as glutathione and large molecules, especially the cysteine residues of proteins. In an analogous manner to nitration, not all cellular thiol groups are equally susceptible to nitrosation[171–173] and there is evidence that nitrosation of protein thiols may serve as a mechanism for regulation of protein function.[174] However, a critical unresolved issue is the mechanism of this nitrosation, which is largely unknown.[175] The direct reaction of ·NO with thiols, which results in disulfide formation, is too slow to be of biological relevance with physiological ·NO concentrations.[176] Espey *et al.* have demonstrated that under conditions of slight excess of ·NO production over superoxide production, rapid nitrosative chemistry can occur.[177] Thus, peroxynitrite acts to oxidize a target, which then reacts with ·NO, presenting a plausible pathway for nitrosothiol formation. Once formed, the nitrosothiol group can be exchanged between thiols via transnitrosation. Therefore following an initial reaction such as nitrosoglutathione (GSNO) formation, different nitrosothiols can readily be formed downstream of the original nitrosation event. The stability of nitrosothiols is also heavily dependent on the nature of the substituent group, generating a large variation in half-lives and corresponding biological effects. Additionally nitrosothiols, in the presence of even trace amounts of transition metals (especially Cu^{1+}), will break down to liberate ·NO.[178] Overall, there is at present little to no unequivocal evidence for a functional role for thiol nitrosation as a widespread and physiologically significant mechanism of regulation of protein function.[179]

A mechanism of protein thiol nitrosation of special interest is hemoglobin (*see* ***Iron: Heme Proteins & Dioxygen Transport & Storage***), wherein nitrosation of cysβ-93 has been proposed to serve a function as ‘preserver’ of ·NO biological activity in the face of the very rapid irreversible consumption of ·NO via oxidation.[180] In addition, since changes in the accessibility of this thiol to covalent modification upon changes in the oxygenation state of hemoglobin has been known for many years,[181] a respiratory cycle has been proposed where uptake of O_2 and ·NO are proposed to exhibit positive cooperativity and so hemoglobin will deliver both O_2 and ·NO from the lung to O_2-deficient tissues.[174,182] However, important mechanistic details regarding formation, movement to the target (smooth muscle cell guanylate cyclase), and vasodilation from the nitrogen oxide species responsible are lacking. This controversy is still very much ongoing, with several recent reviews pro[183,184] and con.[36,185,186] Very recently, a novel interaction between nitrite and deoxyhemoglobin has been reported that could accomplish delivery of ·NO to tissue that is low in O_2.[187]

Metallothionein (MT) is a small protein ($\sim$6 kDa) that binds zinc tightly via cysteine residues (*see* ***Metallothioneins***).[188] The ability of these thiolate clusters to bind zinc is dependent on the redox states of the sulfur ligands, with oxidation resulting in expulsion of the zinc ion. Control of zinc homeostasis (*see* ***Metallochaperones & Metal Ion Homeostasis***) is an important regulatory function, as zinc is an essential component of many protein structures including DNA transcription factors and metabolic enzymes. Nitrosation of the MT cysteine ligands as a result of ·NO formation releases the chelated metal and so allows ·NO to regulate zinc concentration.[189] This provides an elegant example of transduction of the nitrosative stimulus from a short-lived redox active species to the more stable, redox inert, zinc ion. In addition to the regulation of iron homeostasis via aconitase this provides another mechanism whereby the effects of ·NO production can continue to exert an effect on the cell long after the actual stimulus has finished.

9 EPR OF BIOLOGICAL IRON-NITROSYL COMPLEXES

Nitric oxide has been a favorite tool of biochemical spectroscopists, dating back to at least 1937 when Keilin and Hartree demonstrated nitrosylation of the heme group of cytochrome *c* (*see* ***Iron: Heme Proteins & Electron Transport***) under anaerobic conditions.[190] Numerous studies have employed ·NO as an oxygen surrogate for O_2-carrying hemoproteins, most especially utilizing the fact that ·NO binds to the heme ferrous iron in hemoglobin and myoglobin in a configuration essentially identical to O_2 with the added 'bonus' that the complex is paramagnetic and EPR visible (*see* ***Iron: Heme Proteins & Dioxygen Transport & Storage***). As described in more detail below, these findings provided a spectroscopic tool to examine whole blood by EPR from animals stimulated to produce ·NO endogenously by immune stimulation or in humans administered ·NO-donating nitrovasodilators.

The first detailed EPR studies of biological nonheme iron-nitrosyl complexes were carried out primarily by the laboratories of Commoner, Kayushin, and Vanin. Utilizing the results of a study by McDonald *et al.* on small inorganic complexes,[191] the characteristic axial $g = 2.04$ signal resulting from the exposure of biological samples to ·NO or ·NO-generating systems,[192–197] as well as feeding of animals nitrite or nitrate plus or minus iron[196–204] (and in some cases untreated yeast cells[205] or animals[202,206]), was attributed to the formation of complexes of the general formula $[(RS)_2Fe(NO)_2]$ with the iron in approximately tetrahedral geometry.[207,208] Similar complexes are formed in cells stimulated by cytokines to produce ·NO endogenously by ·NO synthase, as described below. Early studies by Dervartanian *et al.*[209] and Salerno *et al.*[65] demonstrated the appearance of these signals in ·NO-treated isolated mitochondrial Complexes II and III. Since then, similar signals have been reported for other purified iron-sulfur-containing enzymes (*see* ***Iron–Sulfur Proteins***),[210–212] and numerous studies have shown that this complexation results in destruction of enzymatic activity. Indeed, destruction of the native chromophoric iron-sulfur cluster of *Clostridial* ferredoxin has been used as a spectrophotometric assay to detect cellular ·NO formation in vitro.[213]

What is the physiological relevance of this damaging reaction in the biological actions of ·NO? In the late 1960s Commoner showed the formation of these EPR-detectable complexes in the liver of rats fed carcinogenic compounds in the diet; the signal appeared and then disappeared many weeks prior to the appearance of hepatic tumors and so generated a great deal of interest because of its potential use as an early indication of neoplastic transformation. This conclusion is bolstered by the observation of similar signals (as well as heme-nitrosyl signals) in other tumors of noncarcinogenic compound origin including stably transformed transplantable tumor cells.[214,215] However, Commoner and others subsequently demonstrated that the carcinogen-induced appearance of the $g = 2.04$ signal is dependent on high dietary nitrate consumption, which is apparently not consistent with an origin of ·NO from the L-arginine-dependent ·NO synthase reaction.[216] In addition, it was shown that similar iron-nitrosyl signals are observed in nonspecifically necrotic tissues.[215,217] These results, combined with the lack of indication at that time for a mechanism of mammalian nitrogen oxide synthesis, unfortunately discouraged further research on this interesting phenomenon.

Sodium nitrite is commonly utilized in food preservation.[218] In spite of its known potential for metabolism to carcinogenic nitrosamines, nitrite supplementation is still in widespread use in nutrition because the addition of nitrite (plus a reducing agent such as ascorbate) has two desirable effects: it imparts a red color to meats (primarily a result of the production of nitrosylheme from myoglobin[219]) and, perhaps more importantly, the organism responsible for botulism (*Clostridium botulinum*) is exquisitely sensitive to this treatment.[220] There is indeed a massive literature on the role of ·NO and its reactions in foods in the nutrition fields and is worthy of scrutiny by researchers in the biological effects of endogenously produced ·NO in mammalian systems.

Capitalizing on the facts that nonheme iron-sulfur proteins are critically important to the anaerobic metabolism of *Clostridia* in general[221] and the earlier EPR studies showing destruction of these centers by nitrite addition in vitro, in 1983 we performed an EPR examination of whole cells of *C. botulinum* under conditions approximating those during food preservation.[222] We indeed observed the formation of an intense $g = 2.04$ signal in these cells when treated with nitrite. The facts that the formation of these signals is increased when ascorbate is also added and that the EPR signal from the native intracellular iron-sulfur clusters are concomitantly decreased suggested that the antibotulinal mechanism involves the ·NO-mediated destruction of nonheme iron-containing enzymes. Although the mechanism of formation of these nonheme iron-nitrosyl complexes may not be as straightforward as direct reaction with iron-sulfur proteins,[211,223] these results indicate that disruption in cellular iron functions by ·NO complexation is damaging to the cell, a mechanism that is also important when ·NO is produced by mammalian cells as described below.

In 1990, we[224] and simultaneously Drapier and Henry and colleagues[225] showed that similar $g = 2.04$ signals are observed in CAMs, and subsequently Drapier and Henry showed similar signals in the injured tumor cell targets of CAMs[212] providing a similar rationale for the destruction of mitochondrial activity that is responsible for the cytostatic and cytotoxic activity of immune-produced endogenous •NO synthesis (Figure 1). Although it appears likely that these signals do not in all cases represent direct observation of nitrosylated iron-sulfur proteins (as opposed to other cytosolic forms of nonheme iron), similar signals are indeed observed in several different cell types exposed to inflammatory stimuli.[52,53]

10 NITRIC OXIDE SYNTHESIS

Because of the extraordinary range of clinically significant actions of •NO in pathophysiology (see below), numerous research groups have been mobilized to investigate the fundamental enzymatic mechanism(s) and regulation of •NO synthesis.[30,226] Insight into these mechanisms holds great promise for the design of new effective therapies ranging from carcinogenesis to cardiovascular disease and immunity.

There are three major isoforms of nitric oxide synthase (NOS). The first to be described is termed inducible, because inflammatory agents such as endotoxin and/or cytokines trigger the de novo transcription and translation of inducible nitric oxide synthase (iNOS) molecules. It is likely that, at least in rodents, every nucleated cell is capable of being triggered to produce iNOS; the different sensitivities to signals probably lie only in the differing mechanisms of signal transduction between cell types.

The two other major types of NOS are constitutive, that is, present continually, and both produce much smaller quantities of •NO. Here, •NO acts as a diffusible intracellular and intercellular messenger to stimulate soluble guanylyl cyclase in both the source cell and its neighbors thus effecting both autocrine (one cell affecting itself) and paracrine (one cell affecting another) signal transmission. The two primary physiological functions of •NO as a messenger are in control of vascular tone and in neurotransmission.

The first NOS to be isolated and the gene sequenced was the rat cerebellar enzyme, by Bredt and Snyder in 1991.[227,228] Since then, the sequences for all three isoforms have been determined: human brain, human and bovine endothelial, mouse macrophage, and recently the cytokine-inducible NOS from human hepatocytes. There is substantial sequence identity between the same isoforms in different species: rat and human brain (93%[229]) and bovine and human endothelial (94%[230]). The identity between different isoforms (even in the same species) is substantially less, between 50 and 60%.[228,230–236] An exception is the homology between the human hepatocyte and the mouse macrophage enzymes, which is only 80%,[236] a puzzling result because both enzymes are induced by cytokines and LPS and thus are of the ‘inducible’ type.

A key observation made by Bredt and Snyder during the purification of the constitutive NOS from rat cerebellum was that this enzyme is greatly stimulated by calcium plus the calcium binding regulatory protein calmodulin (*see* ***Calcium-binding Proteins***).[227] It is now known that the mechanism of stimulation of all constitutive signal-transducing NOS’s involves the induction by specific extracellular agonists of increased levels of cytosolic calcium that binds to calmodulin and activates the enzyme. Nathan’s laboratory[237] showed that even the highly purified inducible isoform contains tightly bound calmodulin, even though this enzyme is not generally thought to be regulated by intracellular calcium levels. Indeed, the sequences for all three isotypes contain consensus regions for calmodulin binding. Structural and functional analysis has revealed the presence of an autoinhibitory control element in the constitutive enzymes that is released upon calmodulin binding, which is a major factor in the mechanism of calcium regulation of activity.[238]

As illustrated in Figure 2, the basic reaction of •NO formation is identical for all three isoforms, involving a three-electron mixed-function oxidation of a guanidino nitrogen of L-arginine to produce citrulline and •NO.[239] The reaction consumes three electrons from 1.5 NADPH equivalents and two moles of O_2. Two of these oxygen atoms are reduced to water, and one is incorporated into citrulline and one into •NO.[240,241] Thus, since only three electrons are donated by NADPH, as pointed out by Stuehr and Griffith[239] L-arginine must provide the fourth electron for the reduction of the two O atoms to $2H_2O$. The fact that NADPH is an obligatory two-electron donor means that during catalytic turnover the enzyme must cycle between two oxidation states differing by one electron. Indeed, EPR studies of the resting enzyme has revealed the presence of a flavin radical,[242] suggesting that flavins function as electron reservoirs and are capable of stabilizing odd-electron states as in other flavin-containing oxidoreductases.[243]

Beginning with the first NOS sequence published by Bredt and Snyder,[227] all sequences so far reveal consensus regions for the binding of NADPH, FMN, and FAD, and analysis of purified enzymes confirms the presence of one FMN and one FAD per monomer.[239] The stimulation of the enzyme by added FAD suggests weak binding of this cofactor. Thus, NOS is the only mammalian enzyme known besides cytochrome P450 reductase (CPR) that contains both FAD and FMN, as evidenced by the substantial sequence homology between the two enzymes in addition to the consensus regions for flavin binding.[228,239] Indeed, like CPR, NOS reduces several artificial electron acceptor dyes (‘diaphorase’ activity) as well as molecular oxygen and also cytochrome P450. The deduced molecular weights from the cloned sequences of the endothelial and inducible enzymes from all species examined so far are comparable, approximately 133 kDa; the brain enzymes from rat and human are larger, 160 kDa, primarily resulting from a substantial N-terminal segment. This segment contains a PDZ domain that targets nNOS for binding to a variety of other proteins within the cell and may well be an important factor in certain diseases such as Duchenne muscular dystrophy.[244,245] All NOS isoforms are composed of specific domains, and catalytic reactivity involves two of these, a reductase domain (containing the NADPH, FMN, and FAD binding sites where electron flow enters the protein and electrons are 'stored' during turnover) and an oxidase domain (containing the substrate, heme, and tetrahydrobiopterin (BH_4) binding sites). All NOS isoforms are functionally active as homodimers and, remarkably, arranged 'head-to-tail' such that electrons from the reductase domain of one subunit flow to the oxidase domain of the other subunit.[246]

Early studies by Stuehr and Nathan and colleagues[247,248] demonstrated a specific stimulation of NOS activity in crude subcellular fractions by BH_4, which is true for all purified NOS enzymes to date. BH_4 is important both as a stabilizer of protein conformation and also as an electron transfer component.[226,249] The activity of the enzyme intracellularly can be affected by modulations in cellular BH_4 levels, and this may have important consequences under physiological and pathophysiological conditions.[250–252]

All NOS proteins contain a cytochrome P450-type heme.[242,253–255] Because of the well-established functions of cytochromes P450 in mixed-function hydroxylations (*see* ***Iron: Heme Proteins, Mono- & Dioxygenases***),[256] most attention is now directed toward the potential role of this prosthetic group in carrying out an O-atom transfer reaction in the enzyme (thermodynamically driven by the reduction of O to H_2O), supported by the inhibition of enzymatic activity by carbon monoxide[242,253,254] and nitrogenous bases,[257] which are heme-binding ligands.

The first step in •NO synthesis is hydroxylation of a guanidino nitrogen of L-arginine to produce N^G-hydroxy-L-arginine:[239] during turnover a relatively small but significant quantity of this intermediate is released from the enzyme and it is a competent substrate for •NO production. Like L-arginine, •NO formation from N^G-hydroxy-L-arginine requires the presence of BH_4 and consumes NADPH, but the stoichiometry for NADPH is 0.5 mol per •NO instead of 1.5. Thus, the overall reaction for L-arginine is a two-electron hydroxylation to produce N^G-hydroxy-L-arginine followed by another that reduces O to H_2O from one electron from NADPH (probably through the intermediacy of a semiquinone flavin(s)) and one electron from the N^G-hydroxy-L-arginine and forms •NO and citrulline. The kinetic characterization of each of the individual reaction steps is well under way, and a particularly important concept is that the newly synthesized •NO binds to ferriheme and is an important regulator of activity.[226]

There is increasing attention to the biological importance of mechanisms of •NO formation not involving •NO synthase. Although it has been known for decades that nitrosothiols can produce •NO, and could be important in certain circumstances as a source for vasodilation,[258] it is only recently that •NO formation from these species has been characterized. Probably the most important mechanism for •NO formation from nitrosothiols in the biological milieu involves metal catalysis.[259,260] Another mechanism, first identified by Furchgott,[261] is via photoactivation; it has recently been demonstrated that this phenomenon is in all probability due to photolysis of nitrosothiol.[262] A major problem with the possibility that nitrosothiol represents a physiologically significant 'reservoir' for •NO (other than under inflammatory conditions where massive amounts of •NO are formed) is that no specific protein-mediated mechanism for •NO formation from nitrosothiol has been identified that could fulfill the requirement for regulation. Another potential mechanism for non-NOS •NO production is through acidification of nitrite, which has attracted attention in regards to acidic compartments biologically (in the stomach and in acidic phagolysosomes),[263] although this has been questioned on kinetic grounds.[264]

11 NITRIC OXIDE DIFFUSION

The chemistry of •NO at any specific biological location will be defined not only by the rates of •NO formation but also by the diffusion of •NO from distal locations. Since •NO is freely permeable through biological membranes and exhibits one of the highest diffusion constants known, its actions are not confined to a specific cellular compartment or even a single cell producing it.[265,266] This property places •NO in a unique category of cellular messengers in that it is able to transmit its signal virtually instantaneously after it is produced by •NO synthase. In addition, because of its reactivity, •NO will disappear relatively rapidly and so there is no need for a mechanism of deactivation.

The rapid diffusibility of •NO has critically important implications for its chemistry in the biological setting. The speed with which •NO moves by random diffusion can be illustrated by consideration of its root mean square distance of displacement, which describes the distance a single •NO molecule will move in any time interval based on its diffusion constant D (which is similar for aqueous solution and also tissue (brain)[267]):

$$\langle \Delta \bar{x} \rangle^2 = 2Dt \qquad (4)$$

An illustration of the extraordinarily rapid diffusibility of •NO is given by applying this relationship to ask how long, on average, it takes before •NO will escape a cell that produces it. For a cell of 5 μm diameter, equation (4) reveals that, on average, this time will be no more than:

$$t = \frac{(2.5\ \mu\mathrm{m})^2}{2 \times 3300\ \mu\mathrm{m}^2\mathrm{s}^{-1}} \approx 0.001\ \mathrm{s} \qquad (5)$$

In terms of chemical reactivity, we can now ask how rapid an intracellular reaction must be in order to prevent this ‘escape’. To a first approximation, the half-life of such a reaction should be in the range of this ‘escape’ time, and so we calculate the rate for a reaction with this half-life:

$$rate = \frac{\ln 2}{0.001\ \mathrm{s}} = 6.93 \times 10^2\ \mathrm{s}^{-1} \qquad (6)$$

Assuming a second-order reaction between ·NO and a reactant R (rate $= k[\cdot\mathrm{NO}][\mathrm{R}]$) and a very high intracellular R concentration (1 mM), the value for the rate constant k is given by:

$$k = \frac{6.93 \times 10^2\ \mathrm{s}^{-1}}{10^{-3}\ \mathrm{M}} = 6.93 \times 10^5\ \mathrm{M}^{-1}\ \mathrm{s}^{-1} \qquad (7)$$

This is the rate constant for a quite rapid reaction. In addition, in order to provide continual inhibition of ·NO escape the reactant R must be continually maintained at this high concentration. Experimental support for the general concept that ·NO will rapidly escape a cell producing it is provided by the observation that coincubation of ·NO-producing isolated rat hepatocytes with intact erythrocytes eliminates the reaction of ·NO with targets within the ·NO-producing hepatocyte; it can be shown from first principles that the only explanation for this effect is if, on average, any individual ·NO molecule that acts within an ·NO-producing cell had at some time previously existed in the volume outside the cell.[268,269] Similar conclusions have recently been reported for formation of intracellular nitrosothiol.[270] In vivo, different cell types produce different reactive oxygen and nitrogen species. Spatially, this means that the appearance (flux) of these reactive species at any point location will be determined by the distance from this point to the cells producing these species. Thus, the precise chemistry that occurs at different locations can be very different, especially when dealing with highly interactive networks of interreacting species.

12 NITRIC OXIDE IN PATHOPHYSIOLOGY

Without doubt, the action of ·NO that has provided the single most attention in human disease is its role in penile erection,[271] thus providing the mechanistic basis for the most widely prescribed oral agent in medicine, Viagra (Sildenafil).[272] Production of ·NO by the corpus cavernosum results in relaxation of the vessels and engorgement of the organ with blood and consequent erection. The dilating action of ·NO lies at the beginnings of the realization of its biological actions and its clinical applications, since the use of nitrovasodilators to attenuate a variety of cardiovascular problems is nearly 140 years old.[141]

Abnormal production of ·NO, either too much or too little, has been linked to a remarkable number of clinically important conditions. In two important early papers, it was shown by Kilbourn and Lodato that excessive ·NO contributes to the serious and life-threatening hypotension (loss of blood pressure) that occurs during systemic bacterial infection (sepsis).[273,274] Prior to these studies it had been demonstrated that severe hypotension accompanying sepsis is a result of the stimulation of lymphocytes and macrophages by bacterial products (most notably endotoxin), which results in massive production of circulating cytokines.[275] Indeed, injection of two cytokines (TNF and IL-1), in particular, in animals and humans produces many symptoms that are identical to septic shock, including hypotension, and administration of neutralizing antibodies or antagonists to these cytokines is capable of marked attenuation in the hypotensive response to injection of bacterial products. Kilbourn and Lodato showed that a similar protective response occurs against TNF or endotoxin injection in dogs when NMMA is administered to inhibit ·NO formation and this restoration in blood pressure is reversed (blood pressure again decreases) when L-arginine is subsequently injected.[273,274] The effect of NMMA is attributable to its prevention of ·NO formation by NOS and its reversal by excess substrate (L-arginine) is a classic example of competitive enzyme inhibition (Figure 2).

Some 600 000 patients annually are stricken with septic shock, with an estimated in-hospital mortality rate of 18%.[276] In humans, the importance of ·NO in maintaining normal vascular tone (blood pressure) was originally demonstrated by Vallance *et al.*,[277] and several early reports demonstrated restoration of near normal blood pressure in humans with sepsis, including one report where it appears to have saved a life.[278] In addition, it has been shown that septic patients have high circulating $\mathrm{NO_3}^-$ levels[279] (indicating excess ·NO formation). In the only large-scale clinical trial of the effects of NOS inhibitors on septic shock, NMMA was tested on a total of 797 patients[280] and, in spite of initial trials indicating beneficial effects,[281] patients administered NMMA exhibited increased mortality. Unfortunately, this has been a severe setback for further studies of the use of NOS inhibitors for this dread affliction, and investigators have been disappointed that this study using such a nonselective NOS inhibitor was pursued; as has been pointed out,[282] it is still quite possible that a new generation of iNOS-selective inhibitors could provide beneficial results.

A central paradigm in the field is that ·NO is ‘Janus-faced’[1] in its roles in pathophysiology, exhibiting protective actions under some conditions and damaging effects in others. The possible mechanistic explanations for this paradoxical result can be viewed from two perspectives, cellular/tissue and molecular. In terms of cellular/tissue actions, one of the most important biological actions of ·NO is its potent inhibition of vascular coagulation and aggregation, which was reported more than 20 years ago.[283] This is a very important biological effect that will be protective in the many disorders involving aggregation and adhesion of blood cells, which interrupts the free flow of blood and results in sites of vascular plugging and local inflammation.[284] Additional salutatory effects of •NO in the vascular system are the inhibition of smooth muscle cell proliferation (thus attenuating disorders such as restenosis) and also promotion of angiogenesis (the growth of new blood vessels).[284] This latter action is an excellent illustration of the ‘Janus-faced’ roles of •NO, where new blood vessel formation is beneficial for wound healing but •NO has been implicated in the formation of new vessels to supply blood to tumors.[285]

The most commonly cited mechanistic explanation for the paradoxical roles of •NO in cell and organ injury involves the interaction of •NO with reactive oxygen species (ROS). The complexity of these reactions, many of which are mentioned above, leaves ample room to interpret results in terms of ‘good’ versus ‘bad’ by emphasizing one or another collection of reactions. Central to ROS biological actions is the metal-catalyzed Haber-Weiss reaction:[286,287]

$$\begin{array}{l}
\cdot O_2^- + Fe^{3+} \longrightarrow O_2 + Fe^{2+} \\
H_2O_2 + Fe^{2+} \longrightarrow \cdot OH + OH^- + Fe^{3+} \\
\hline
\cdot O_2^- + H_2O_2 \longrightarrow O_2 + \cdot OH + OH^-
\end{array} \tag{8}$$

According to this mechanism, it is actually the highly toxic and reactive hydroxyl radical (•OH) that causes most damage, produced by the interaction of •O_2^-, H_2O_2, and iron. The reaction that actually produces •OH (the Fenton reaction) is the reduction of H_2O_2 by Fe^{2+}. The function of •O_2^- is twofold, both as a reductant for Fe^{3+} and also because it is a source for H_2O_2, either enzymatically (SOD) or by spontaneous dismutation. Although there is disagreement about how literally this scheme should be taken, it is a good paradigm within which to discuss •NO/ROS interactions.

It is well-established that a major response to septic stimuli in general is the activation (primarily by cytokines and bacterial products, conditions that as described above also can induce •NO synthesis) of phagocytic cells (neutrophils, macrophages) to produce ROS, through the respiratory burst mechanism;[288,289] this is a major immune mechanism for combating infectious agents but also can be damaging to the host.

In terms of potential chemical interactions, the effects of •NO on ROS-induced injury are multiple, and some effects can be classified as ‘prooxidant’ and others may be classified as ‘antioxidant’; still others can be classified as both. In terms of the metal-catalyzed Haber-Weiss reaction, there are two primary effects of •NO. The binding of •NO to metal ions will prevent the Fenton reaction and thus results in an antioxidant action.[290–292] Another important antioxidant action of •NO (and its oxidized product •NO_2) is its reaction with lipid radicals, thus resulting in radical chain termination.[23]

One of the first pieces of evidence supporting the identification of EDRF as •NO was the demonstration that •O_2^- reacts rapidly with EDRF.[293] Early work suggested that •NO could be protective against oxidative injury by reacting with, and thus scavenging, ROS.[294] However, in a landmark paper in 1990, Beckman *et al.*[295] brought attention to the fact that the product of the •NO/•O_2^- reaction, peroxynitrite, possesses highly oxidizing properties, thus, •NO effectively converts a rather mild oxidant (•O_2^-) into a strong oxidant ($ONOO^-$). This concept has become a central paradigm for interpretation of all prooxidant effects of •NO, although its validity has been questioned.[296] In particular, since the rate of reaction of superoxide with •NO is similar in magnitude to the rate of reaction with SOD, appreciable $ONOO^-$ formation will occur only at locations where the •NO concentration is greater than SOD concentration. The concentration of SOD inside most cells is quite appreciable (in the micromolar range) and so relatively high •NO concentration would be required. This may be less of a problem extracellularly, where SOD levels are lower and also where appreciable superoxide is formed from phagocytic cells.[297] Nevertheless, in at least one case (motor neuron death in a model of amyotrophic lateral sclerosis, Lou Gehrig’s disease) there is good evidence that intracellular peroxynitrite formation from •NO and •O_2^- is responsible for toxic effects.[298]

The major ‘curse’ of working with short-lived species such as radicals and oxidants is the dirth of methods to unambiguously demonstrate their existence and actions in situ (i.e. biologically). This has been especially true for peroxynitrite. In 1994 Beckman *et al.* introduced the use of antibodies directed to protein nitrotyrosines as an immunohistochemical method.[299] This was a very exciting development because at the time it was believed that this was a specific marker for peroxynitrite, based on the demonstration of nitrotyrosine formation from $ONOO^-$.[300] This has been followed by a deluge of papers using this method to demonstrate nitrotyrosine formation in a vast array of inflammatory disease states, thus inferring the presence of peroxynitrite in vivo. Unfortunately, it is now known that nitrotyrosine can be formed from a variety of mechanisms, involving principally metals (including peroxidases) in the presence of nitrite and H_2O_2.[80,81] The mechanistic link between these various conditions is the formation of •NO_2, which combines with tyrosyl radical (formed from a number of possible oxidants) to form nitrotyrosine.[301]

In summary, in terms of chemistry the interactions of •NO with ROS are many and complex.[38] The general paradigm that has emerged is that at low levels •NO exerts beneficial effects, through several mechanisms including cellular signaling (e.g. inhibition of vascular aggregation and adhesion, vasodilation) and radical chain termination. At higher levels, and especially in the context of increased ROS (specifically, •O_2^-) formation, •NO can greatly contribute to cellular injury. The chemical bases and understanding for this paradigm (if indeed accurate) in terms of reaction patterns of the network of reactive oxygen and nitrogen chemistry are largely unexplored.

13 NOVEL BIOLOGICAL ROLES OF ·NO

Researchers in many previously unrelated fields of biology have recently become united by the discovery that ·NO plays important roles in their systems. The typical experimental tools used in these numerous studies are the modulation of the observed biological effects by the addition of agents that attenuate (NMMA, hemoglobin, $\cdot O_2^-$) or potentiate (·NO donors, L-arginine) ·NO production, as well as the correlation of ·NO formation (NO_2^-, NO_3^- appearance) with the biological phenomenon of interest. In addition, it is possible to identify specific cells that are exceptionally rich in NOS and thus correlate the specific sites of ·NO production with microanatomical function. In this last section, we briefly describe a few of these novel findings.

The endogenous production of ·NO appears to be a phylogenetically widespread phenomenon. The initial reports of endogenous ·NO in nonmammalian systems involved birds[302] and invertebrates.[303] It has also been shown that certain blood-sucking insects produce ·NO in their salivary glands, and that it is delivered to the blood stream of its victims as a complex to a ferric iron-containing protein named nitrophorin (*see* ***Iron Porphyrin Chemistry***).[304,305] Since ·NO binds relatively poorly to Fe^{3+} (compared to Fe^{2+}),[207] the ·NO dissociates and induces vascular dilation at the site of the bite. ·NO is also involved in the mechanism of control of firefly flashing[306] as well as in other insects (including *Drosophila*) where it appears to perform a variety of signaling and immune roles,[307] as well as in plants where in fact the first enzymatic formation of ·NO was reported.[100,101] ·NO also plays a biological role in unicellular organisms, including protozoa; one clinically important aspect is that many pathogenic organisms produce ·NO for unknown reasons.[308] ·NO has been known for many years to be a component of the biological nitrogen cycle, being produced by bacteria during denitrification (*see* ***Copper Enzymes in Denitrification***).[309] However, its role as a messenger in these bacteria is only now being appreciated.[310] Remarkably, *C. botulinum* has recently been shown to possess an ·NO sensor that detects ·NO down to the femtomolar range.[311] As described above, this organism, which produces the most toxic substance known to humans (the botulinum toxin), is extremely sensitive to nitrite and this sensitivity has been proposed to involve ·NO.[222]

Undoubtedly other novel roles for ·NO in biology will be discovered; its chemical properties are indeed unique and Nature will always find ways to exploit any chemical opportunity.

14 RELATED ARTICLES

Copper Enzymes in Denitrification; Iron: Heme Proteins & Dioxygen Transport & Storage; Iron: Heme Proteins & Electron Transport; Iron: Heme Proteins, Mono- & Dioxygenases; Iron: Heme Proteins, Peroxidases, Catalases & Catalase-peroxidases.; Iron Porphyrin Chemistry; Iron–Sulfur Proteins.

15 REFERENCES

1. J. R. Lancaster Jr, *Am. Sci.*, 1992, **80**, 248.
2. S. H. Snyder and D. S. Bredt, *Sci. Am.*, 1992, **266**, 68.
3. M. A. Marletta, *Chem. Res. Toxicol.*, 1988, **1**, 249.
4. M. A. Marletta, *Trends Biochem. Sci.*, 1989, **14**, 488.
5. S. Moncada, R. M. Palmer, and E. A. Higgs, *Biochem. Soc. Trans.*, 1989, **17**, 642.
6. L. J. Ignarro, *FASEB J.*, 1989, **3**, 31.
7. S. Moncada, R. M. Palmer, and E. A. Higgs, *Biochem. Pharmacol.*, 1989, **38**, 1709.
8. L. J. Ignarro, *Annu. Rev. Pharmacol. Toxicol.*, 1990, **30**, 535.
9. R. A. Johns, *Anesthesiology*, 1991, **75**, 927.
10. L. J. Ignarro, *Biochem. Pharmacol.*, 1991, **41**, 485.
11. S. Moncada, R. M. Palmer, and E. A. Higgs, *Pharmacol. Rev.*, 1991, **43**, 109.
12. S. J. Green, C. A. Nacy, and M. S. Meltzer, *J. Leukocyte Biol.*, 1991, **50**, 93.
13. C. F. Nathan and J. B. Hibbs Jr, *Curr. Opin. Immunol.*, 1991, **3**, 65.
14. S. L. James, *Exp. Parasitol.*, 1991, **73**, 223.
15. S. Moncada and E. A. Higgs, *Eur. J. Clin. Invest.*, 1991, **21**, 361.
16. T. M. Dawson, V. L. Dawson, and S. H. Snyder, *Ann. Neurol.*, 1992, **32**, 297.
17. L. J. Ignarro, *Biochem. Soc. Trans.*, 1992, **20**, 465.
18. D. S. Bredt and S. H. Snyder, *Neuron*, 1992, **8**, 3.
19. H. Kolb and V. Kolb-Bachofen, *Immunol. Today*, 1992, **13**, 157.
20. J. A. Corbett and M. L. McDaniel, *Diabetes*, 1992, **41**, 897.
21. C. J. Lowenstein and S. H. Snyder, *Cell*, 1992, **70**, 705.
22. C. Nathan, *FASEB J.*, 1992, **6**, 3051.
23. V. B. O’Donnell and B. A. Freeman, *Circ. Res.*, 2001, **88**, 12.
24. K. D. Kroncke, K. Fehsel, and V. Kolb-Bachofen, *Clin. Exp. Immunol.*, 1998, **113**, 147.
25. C. Bogdan, *Nat. Immunol.*, 2001, **2**, 907.
26. J. Torreilles, *Front. Biosci.*, 2001, **6**, D1161.
27. L. J. Ignarro, *J. Physiol. Pharmacol.*, 2002, **53**, 503.
28. G. B. Richter-Addo, P. Legzdins, and J. Burstyn, *Chem. Rev.*, 2002, **102**, 857.
29. P. C. Ford and I. M. Lorkovic, *Chem. Rev.*, 2002, **102**, 993.
30. L. J. Roman, P. Martasek, and B. S. Masters, *Chem. Rev.*, 2002, **102**, 1179.

31. I. M. Wasser, S. de Vries, P. Moenne-Loccoz, I. Schroder, and K. D. Karlin, *Chem. Rev.*, 2002, **102**, 1201.
32. B. Demple, *IUBMB Life*, 2004, **56**, 59.
33. K. Bian and F. Murad, *Front. Biosci.*, 2003, **8**, d264.
34. M. Brunori, A. Giuffre, E. Forte, D. Mastronicola, M. C. Barone, and P. Sarti, *Biochim. Biophys. Acta*, 2004, **1655**, 365.
35. L. J. Hofseth, S. P. Hussain, G. N. Wogan, and C. C. Harris, *Free Radical Biol. Med.*, 2003, **34**, 955.
36. M. T. Gladwin, J. R. Lancaster Jr, B. A. Freeman, and A. N. Schechter, *Nat. Med.*, 2003, **9**, 496.
37. L. A. Ridnour, D. D. Thomas, D. Mancardi, M. G. Espey, K. M. Miranda, N. Paolocci, M. Feelisch, J. Fukuto, and D. A. Wink, *Biol. Chem.*, 2004, **385**, 1.
38. J. R. Lancaster Jr, in 'Signal Transduction by Reactive Oxygen and Nitrogen Species: Pathways and Chemical Principles', eds. H. J. Forman, J. M. Fukuto, and M. Torres, Kluwer Academic Publishers, Dordecht, 2003, p. 53.
39. M. Feelisch, *J. Cardiovasc. Pharmacol.*, 1991, **17**,(Suppl. 3), S25.
40. S. Archer, *FASEB J.*, 1993, **7**, 349.
41. J. Everse and M. B. Grisham, eds. 'Measurement of Nitric Oxide', Academic Press, San Diego, CA, 1995.
42. M. Feelisch and J. Stamler, eds. 'Methods in Nitric Oxide Research', John Wiley & Sons, Chichester, 1996.
43. M. A. Titheradge, ed. 'Nitric Oxide Protocols', Humana Press, Totowa, NJ, 1998.
44. Y. Henry, C. Ducrocq, J. C. Drapier, D. Servent, C. Pellat, and A. Guissani, *Eur. Biophys. J.*, 1991, **20**, 1.
45. J. S. Stamler, D. J. Singel, and J. Loscalzo, *Science*, 1992, **258**, 1898.
46. Nitric Oxide, 'Principles and Actions', Academic Press, San Diego, CA, 1996.
47. Nitric Oxide, 'Biology and Pathobiology', Academic Press, San Diego, CA, 2000.
48. S. Moncada and E. A. Higgs eds, 'Nitric Oxide from L-Arginine: A Bioregulatory System', Elsevier Science Publishers B.V., Amsterdam, 1990.
49. S. Moncada, M. A. Marletta, J. B. Hibbs, Jr and E. A. Higgs, eds. 'The Biology of Nitric Oxide. I. Physiological and Clinical Aspects', Portland Press, London, 1992.
50. S. Moncada, M. A. Marletta, J. B. Hibbs, Jr and E. A. Higgs, eds. 'The Biology of Nitric Oxide. II. Enzymology, Biochemistry and Immunology', Portland Press, London, 1992.
51. G. B. Richter-Addo and P. Legzdins, 'Metal Nitrosyls', Oxford University Press, New York, 1992.
52. Y. Henry, A. Guissani and B. Ducastel, eds. 'Nitric Oxide Research from Chemistry to Biology: EPR Spectroscopy of Nitrosylated Compounds', Chapman & Hall/Landes Bioscience, Austin, MN, 1997.
53. S. Lukiewicz and J. L. Zweier, eds. 'Nitric Oxide in Transplant Rejection and Anti-Tumor Defense', Kluwer Academic Publishers, Boston, MA, 1998.
54. F. C. Fang, ed. 'Nitric Oxide and Infection', Kluwer Academic/Plenum Publishers, New York, 1999.
55. P. J. Kadowitz and D. B. McNamara, eds. 'Nitric Oxide and the Regulation of the Peripheral Circulation', Birkhauser, Boston, MA, 2000.
56. A. R. Butler and R. Nicholson, 'Life, Death, and Nitric Oxide', Royal Society of Chemistry, Cambridge, MA, 2003.
57. M. P. Doyle and J. W. Hoekstra, *J. Inorg. Biochem.*, 1981, **14**, 351.
58. R. F. Eich, T. Li, D. D. Lemon, D. H. Doherty, S. R. Curry, J. F. Aitken, A. J. Mathews, K. A. Johnson, R. D. Smith, G. N. J. Phillips, and J. S. Olson, *Biochemistry*, 1996, **35**, 6976.
59. S. Herold, *FEBS Lett.*, 1999, **443**, 81.
60. A. Wennmalm, G. Benthin, A. Edlund, N. Kieler-Jensen, S. Lundin, A. S. Petersson, and F. Waagstein, *Ann. N.Y. Acad. Sci.*, 1994, **714**, 158.
61. M. J. Coffey, R. Natarajan, P. H. Chumley, B. Coles, P. R. Thimmalapura, M. Nowell, H. Kuhn, M. J. Lewis, B. A. Freeman, and V. B. O'Donnell, *Proc. Natl. Acad. Sci. U.S.A.*, 2001, **98**, 8006.
62. H. M. Abu-Soud and S. L. Hazen, *J. Biol. Chem.*, 2000, **275**, 37524.
63. J. P. Eiserich, S. Baldus, M. L. Brennan, W. Ma, C. Zhang, A. Tousson, L. Castro, A. J. Lusis, W. M. Nauseef, C. R. White, and B. A. Freeman, *Science*, 2002, **296**, 2391.
64. D. D. Thomas, X. Liu, S. P. Kantrow, and J. R. Lancaster Jr, *Proc. Natl. Acad. Sci. U.S.A.*, 2001, **98**, 355.
65. J. C. Salerno, T. Ohnishi, J. Lim, and T. E. King, *Biochem. Biophys. Res. Commun.*, 1976, **73**, 833.
66. D. A. Wink, R. W. Nims, J. F. Darbyshire, D. Christodoulou, I. Hanbauer, G. W. Cox, F. Laval, J. Laval, J. A. Cook, and M. C. Krishna, *Chem. Res. Toxicol.*, 1994, **7**, 519.
67. S. Goldstein and G. Czapski, *J. Am. Chem. Soc.*, 1995, **117**, 12078.
68. P. C. Ford, D. A. Wink, and D. M. Stanbury, *FEBS Lett.*, 1993, **326**, 1.
69. X. Liu, M. S. Miller, M. S. Joshi, D. D. Thomas, and J. R. Lancaster Jr, *Proc. Natl. Acad. Sci. U.S.A.*, 1998, **95**, 2175.
70. R. Kissner, T. Nauser, P. Bugnon, P. G. Lye, and W. H. Koppenol, *Chem. Res. Toxicol.*, 1997, **10**, 1285.
71. J. W. Coddington, J. K. Hurst, and S. V. Lymar, *J. Am. Chem. Soc.*, 1999, **121**, 2443.
72. M. G. Bonini and O. Augusto, *J. Biol. Chem.*, 2001, **276**, 9749.
73. S. V. Lymar and J. K. Hurst, *J. Am. Chem. Soc.*, 1995, **117**, 8867.
74. G. Czapski, J. Holcman, and B. H. Bielski, *J. Am. Chem. Soc.*, 1994, **116**, 11465.

75. S. Goldstein and G. Czapski, *Chem. Res. Toxicol.*, 2000, **13**, 736.
76. D. L. H. Williams, 'Nitrosation', Cambridge University Press, Cambridge, MA, 1988.
77. I. T. Vermeer and J. M. van Maanen, *Rev. Environ. Health*, 2001, **16**, 105.
78. B. Coles, A. Bloodsworth, S. R. Clark, M. J. Lewis, A. R. Cross, B. A. Freeman, and V. B. O'Donnell, *Circ. Res.*, 2002, **91**, 375.
79. J. S. Beckman, H. Ischiropoulos, L. Zhu, M. van der Woerd, C. Smith, J. Chen, J. Harrison, J. C. Martin, and M. Tsai, *Arch. Biochem. Biophys.*, 1992, **298**, 438.
80. D. D. Thomas, M. G. Espey, M. P. Vitek, K. M. Miranda, and D. A. Wink, *Proc. Natl. Acad. Sci. U.S.A.*, 2002, **99**, 12691.
81. F. J. Schopfer, P. R. Baker, and B. A. Freeman, *Trends Biochem. Sci.*, 2003, **28**, 646.
82. M. E. Murphy and H. Sies, *Proc. Natl. Acad. Sci. U.S.A.*, 1991, **88**, 10860.
83. A. J. Hobbs, J. M. Fukuto, and L. J. Ignarro, *Proc. Natl. Acad. Sci. U.S.A.*, 1994, **91**, 10992.
84. E. Cadenas, J. J. Poderoso, F. Antunes, and A. Boveris, *Free Radical Res.*, 2000, **33**, 747.
85. D. R. Arnelle and J. S. Stamler, *Arch. Biochem. Biophys.*, 1995, **318**, 279.
86. M. Espey, K. Miranda, D. Thomas, and D. Wink, *Free Radical Biol. Med.*, 2002, **33**, 827.
87. M. D. Bartberger, W. Liu, E. Ford, K. M. Miranda, C. Switzer, J. M. Fukuto, P. J. Farmer, D. A. Wink, and K. N. Houk, *Proc. Natl. Acad. Sci. U.S.A.*, 2002, **99**, 10958.
88. J. P. van Helmont, 'Oriatricke, or Physick Refined, the Common Errors therein Refuted, and the Whole Art Reformed and Rectified: Being a New Rise and Progress of Phylosophy and Medicine, for the Destruction of Diseases and Prolongation of Life', Elsevier, Amsterdam, 1648.
89. J. Priestley, *Philos. Trans.*, 1772, **62**, 147.
90. J. Dalton, *Mem. Lit. Philos. Soc. Manch.*, 1805, **1**, 244.
91. W. E. Blumberg, *Methods Enzymol.*, 1981, **76**, 312.
92. R. Hille, J. S. Olson, and G. Palmer, *J. Biol. Chem.*, 1979, **254**, 12110.
93. S. R. Louro, P. C. Ribeiro, and G. Bemski, *Biochim. Biophys. Acta*, 1981, **670**, 56.
94. H. Kon, *J. Biol. Chem.*, 1968, **243**, 4350.
95. 'The Health Effects of Nitrate, Nitrite, and N-Nitroso Compounds', National Academy Press, Washington, DC, 1981.
96. F. Murad, C. K. Mittal, W. P. Arnold, S. Katsuki, and H. Kimura, *Adv. Cyclic Nucl. Res.*, 1978, **9**, 145.
97. R. G. Cassens, M. L. Greaser, T. Ito, and M. Lee, *Food Technol.*, 1979, **33**, 46.
98. J. I. Sprent, 'The Ecology of the Nitrogen Cycle', Cambridge University Press, Cambridge, MA, 1987.
99. H. H. Mitchell, H. A. Shonle, and H. S. Grindley, *J. Biol. Chem.*, 1916, **24**, 461.
100. R. Cammack, D. P. Hucklesby, and E. J. Hewitt, *Biochem. J.*, 1978, **171**, 519.
101. J. R. Lancaster Jr, J. M. Vega, H. Kamin, N. R. Orme-Johnson, W. H. Orme-Johnson, R. J. Krueger, and L. M. Siegel, *J. Biol. Chem.*, 1979, **254**, 1268.
102. H. Jensen, *Handbuch der Technologischen Mykologie*, 1904, **3**, 182.
103. J. Wijler and C. C. Delwiche, *Plant Soil*, 1954, **5**, 155.
104. V. A. Najjar and M. B. Allen, *J. Biol. Chem.*, 1954, **295**, 209.
105. C. W. Chung and V. A. Najjar, *J. Biol. Chem.*, 1956, **218**, 617.
106. T. Matsubara and H. Iwasaki, *J. Biochem.*, 1971, **69**, 859.
107. M. Miyata and T. Mori, *J. Biochem.*, 1968, **64**, 849.
108. H. Iwasaki and T. Matsubara, *J. Biochem.*, 1971, **69**, 847.
109. H. Iwasaki and T. Matsubara, *J. Biochem.*, 1972, **71**, 645.
110. O. C. Zafiriou, Q. S. Hanley, and G. Snyder, *J. Biol. Chem.*, 1989, **264**, 5694.
111. J. Goretski, O. C. Zafiriou, and T. C. Hollocher, *J. Biol. Chem.*, 1990, **265**, 11535.
112. A. K. Abbas, 'Cellular and Molecular Immunology', W. B. Saunders, Philadelphia, PA, 1991.
113. S. S. Elberg, *J. Bacteriol.*, 1960, **24**, 67.
114. G. B. Mackaness, *J. Exp. Med.*, 1964, **120**, 105.
115. J. B. Hibbs Jr, H. A. Chapman Jr, and J. B. Weinberg, *J. Retic. Soc.*, 1978, **24**, 549.
116. H. C. Nauts and J. R. McLaren, *Adv. Exp. Med. Biol.*, 1990, **267**, 483.
117. C. O. Starnes, *Nature*, 1992, **357**, 11.
118. E. A. Carswell, L. J. Old, R. L. Kassel, S. Green, N. Fiore, and B. Williamson, *Proc. Natl. Acad. Sci. U.S.A.*, 1975, **72**, 3666.
119. A. Cerami, *Clin. Immunol. Immunopathol.*, 1992, **62**, S3.
120. J. L. Krahenbuhl, *Cancer Res.*, 1980, **40**, 4622.
121. D. L. Granger, R. R. Taintor, J. L. Cook, and J. B. Hibbs Jr, *J. Clin. Invest.*, 1980, **65**, 357.
122. D. L. Granger and A. L. Lehninger, *J. Cell Biol.*, 1982, **95**, 527.
123. J. B. Hibbs Jr, R. R. Taintor, and Z. Vavrin, *Biochem. Biophys. Res. Commun.*, 1984, **123**, 716.
124. J. C. Drapier and J. B. Hibbs Jr, *J. Clin. Invest.*, 1986, **78**, 790.
125. M. Wharton, D. L. Granger, and D. T. Durack, *J. Immunol.*, 1988, **141**, 1311.
126. L. C. Green, S. R. Tannenbaum, and P. Goldman, *Science*, 1981, **212**, 56.
127. L. C. Green, K. Ruiz de Luzuriaga, D. A. Wagner, W. Rand, N. Istfan, V. R. Young, and S. R. Tannenbaum, *Proc. Natl. Acad. Sci. U.S.A.*, 1981, **78**, 7764.
128. D. Wagner and S. R. Tannenbaum, in 'Nitrosamines and Human Cancer', ed. P. N. Magee, Cold Spring Harbor Press, New York, 1982, p. 437.

129. E. Hegesh and J. Shiloah, *Clin. Chim. Acta*, 1982, **125**, 107.
130. D. A. Wagner, V. R. Young, and S. R. Tannenbaum, *Proc. Natl. Acad. Sci. U.S.A.*, 1983, **80**, 4518.
131. D. J. Stuehr and M. A. Marletta, *Proc. Natl. Acad. Sci. U.S.A.*, 1985, **82**, 7738.
132. D. J. Stuehr and M. A. Marletta, *J. Immunol.*, 1987, **139**, 518.
133. D. J. Stuehr and M. A. Marletta, *Cancer Res.*, 1987, **47**, 5590.
134. A. H. Ding, C. F. Nathan, and D. J. Stuehr, *J. Immunol.*, 1988, **141**, 2407.
135. M. Miwa, D. J. Stuehr, M. A. Marletta, J. S. Wishnok, and S. R. Tannenbaum, *Carcinogenesis*, 1987, **8**, 955.
136. M. A. Marletta, P. S. Yoon, R. Iyengar, C. D. Leaf, and J. S. Wishnok, *Biochemistry*, 1988, **27**, 8706.
137. J. B. Hibbs Jr, R. R. Taintor, and Z. Vavrin, *Science*, 1987, **235**, 473.
138. J. C. Drapier and J. B. Hibbs Jr, *J. Immunol.*, 1988, **140**, 2829.
139. I. J. Amber, J. B. Hibbs Jr, R. R. Taintor, and Z. Vavrin, *J. Leukocyte Biol.*, 1988, **43**, 187.
140. I. J. Amber, J. B. Hibbs Jr, R. R. Taintor, and Z. Vavrin, *J. Leukocyte Biol.*, 1988, **44**, 58.
141. T. L. Brunton, *Lancet*, 1867, **ii**, 97.
142. F. Murad, C. K. Mittal, W. P. Arnold, S. Katsuki, and H. Kimura, *Adv. Cycl. Nucl. Res.*, 1978, **9**, 145.
143. R. M. Rapoport and F. Murad, *J. Cycl. Nucl. Prot. Phosph.*, 1983, **9**, 281.
144. P. A. Craven and F. R. DeRubertis, *Biochim. Biophys. Acta*, 1983, **745**, 310.
145. R. F. Furchgott and J. V. Zawadzki, *Nature*, 1980, **288**, 373.
146. R. F. Furchgott, in ‘Vasodilatation: Vascular Smooth Muscle, Peptides, Autonomic Nerves, and Endothelium’, ed. P. M. Vanhoutte, Raven Press, New York, 1988, p. 401.
147. L. J. Ignarro, R. E. Byrns, and K. S. Wood, in ‘Vasodilatation: Vascular Smooth Muscle, Peptides, Autonomic Nerves, and Endothelium’, ed. P. M. Vanhoutte, Raven Press, New York, 1988, p. 427.
148. L. J. Ignarro, R. E. Byrns, G. M. Buga, and K. S. Wood, *Circ. Res.*, 1987, **61**, 866.
149. L. J. Ignarro, G. M. Buga, K. S. Wood, R. E. Byrns, and G. Chaudhuri, *Proc. Natl. Acad. Sci. U.S.A.*, 1987, **84**, 9265.
150. R. M. Palmer, A. G. Ferrige, and S. Moncada, *Nature*, 1987, **327**, 524.
151. R. M. J. Palmer, D. D. Rees, D. S. Ashton, and S. Moncada, *Biochem. Biophys. Res. Commun.*, 1988, **153**, 1251.
152. I. Sakuma, D. J. Stuehr, S. S. Gross, C. Nathan, and R. Levi, *Proc. Natl. Acad. Sci. U.S.A.*, 1988, **85**, 8664.
153. H. H. Schmidt, H. Nau, W. Wittfoht, J. Gerlach, K. E. Prescher, M. M. Klein, F. Niroomand, and E. Bohme, *Eur. J. Pharmacol.*, 1988, **154**, 213.
154. H. Ding and C. R. Triggle, *J. Pharmacol. Toxicol. Methods*, 2000, **44**, 441.
155. L. J. Ignarro, *Semin. Hematol.*, 1989, **26**, 63.
156. D. P. Ballou, Y. Zhao, P. E. Brandish, and M. A. Marletta, *Proc. Natl. Acad. Sci. U.S.A.*, 2002, **99**, 12097.
157. T. C. Bellamy, J. Wood, and J. Garthwaite, *Proc. Natl. Acad. Sci. U.S.A.*, 2002, **99**, 507.
158. J. Garthwaite, S. L. Charles, and R. Chess-Williams, *Nature*, 1988, **336**, 385.
159. R. G. Knowles, M. Palacios, R. M. Palmer, and S. Moncada, *Proc. Natl. Acad. Sci. U.S.A.*, 1989, **86**, 5159.
160. J. Garthwaite, G. Garthwaite, R. M. Palmer, and S. Moncada, *Eur. J. Pharmacol.*, 1989, **172**, 413.
161. D. S. Bredt and S. H. Snyder, *Proc. Natl. Acad. Sci. U.S.A.*, 1989, **86**, 9030.
162. R. S. Eisenstein, *Annu. Rev. Nutr.*, 2000, **20**, 627.
163. S. L. Wardrop, R. N. Watts, and D. R. Richardson, *Biochemistry*, 2000, **39**, 2748.
164. R. Oria, L. Sanchez, T. Houston, M. W. Hentze, F. Y. Liew, and J. H. Brock, *Blood*, 1995, **85**, 2962.
165. K. Pantopoulos, G. Weiss, and M. W. Hentze, *Mol. Cell. Biol.*, 1996, **16**, 3781.
166. P. J. Pomposiello and B. Demple, *Trends Biotechnol.*, 2001, **19**, 109.
167. G. Cairo, R. Ronchi, S. Recalcati, A. Campanella, and G. Minotti, *Biochemistry*, 2002, **41**, 7435.
168. L. Oliveira, C. Bouton, and J. C. Drapier, *J. Biol. Chem.*, 1999, **274**, 516.
169. E. Clementi, G. C. Brown, M. Feelisch, and S. Moncada, *Proc. Natl. Acad. Sci. U.S.A.*, 1998, **95**, 7631.
170. W. Yang, P. A. Rogers, and H. Ding, *J. Biol. Chem.*, 2002, **277**, 12868.
171. S. R. Jaffrey, H. Erdjument-Bromage, C. D. Ferris, P. Tempst, and S. H. Snyder, *Nat. Cell Biol.*, 2001, **3**, 193.
172. D. T. Hess, A. Matsumoto, R. Nudelman, and J. S. Stamler, *Nat. Cell Biol.*, 2001, **3**, E46.
173. A. J. Gow, Q. Chen, D. T. Hess, B. J. Day, H. Ischiropoulos, and J. S. Stamler, *J. Biol. Chem.*, 2002, **277**, 9637.
174. J. S. Stamler, S. Lamas, and F. C. Fang, *Cell*, 2001, **106**, 675.
175. M. G. Espey, K. M. Miranda, D. D. Thomas, and D. A. Wink, *J. Biol. Chem.*, 2001, **276**, 30085.
176. W. A. Pryor, D. F. Church, C. K. Govindan, and G. Crank, *J. Org. Chem.*, 1982, **47**, 156.
177. M. G. Espey, D. D. Thomas, K. M. Miranda, and D. A. Wink, *Proc. Natl. Acad. Sci. U.S.A.*, 2002, **99**, 11127.
178. D. L. H. Williams, *Acc. Chem. Res.*, 1999, **32**, 869.
179. J. R. Lancaster Jr and B. Gaston, *Am. J. Physiol. Lung Cell Mol. Physiol.*, 2004, **287**, L465.
180. A. J. Gow, B. P. Luchsinger, J. R. Pawloski, D. J. Singel, and J. S. Stamler, *Proc. Natl. Acad. Sci. U.S.A.*, 1999, **96**, 9027.
181. A. F. Riggs, *J. Biol. Chem.*, 1961, **236**, 1948.
182. S. S. Gross, *Nature*, 2001, **409**, 577.
183. J. S. Stamler, *Circ. Res.*, 2004, **94**, 414.

184. E. J. Frehm, J. Bonaventura, and A. J. Gow, *Free Radical Biol. Med.*, 2004, **37**, 442.

185. A. Hobbs, M. Gladwin, R. Patel, D. Williams, and A. Butler, *Trends Pharmacol. Sci.*, 2002, **23**, 406.

186. Y. Zhang and N. Hogg, *Free Radical Biol. Med.*, 2004, **36**, 947.

187. K. Cosby, K. S. Partovi, J. H. Crawford, R. P. Patel, C. D. Reiter, S. Martyr, B. K. Yang, M. A. Waclawiw, G. Zalos, X. Xu, K. T. Huang, H. Shields, D. B. Kim-Shapiro, A. N. Schechter, R. O. Cannon III, and M. T. Gladwin, *Nat. Med.*, 2003, **9**, 1498.

188. N. Romero-Isart and M. Vasak, *J. Inorg. Biochem.*, 2002, **88**, 388.

189. A. Gow and H. Ischiropoulos, *Am. J. Physiol. Lung Cell Mol. Physiol.*, 2002, **282**, L183.

190. D. Keilin and E. F. Hartree, *Nature*, 1937, **139**, 548.

191. C. C. Mcdonald, W. D. Phillips, and H. F. Mower, *J. Am. Chem. Soc.*, 1965, **87**, 3319.

192. Y. I. Azhipa, L. P. Kayushin, and E. I. Nikishkin, *Biophysica (USSR)*, 1965, **10**, 167.

193. A. F. Vanin, *Biochemistry (USSR)*, 1967, **32**, 228.

194. J. C. Woolum, E. Tiezzi, and B. Commoner, *Biochim. Biophys. Acta*, 1968, **160**, 311.

195. J. C. Woolum and B. Commoner, *Biochim. Biophys. Acta*, 1970, **201**, 131.

196. R. W. Chiang, J. C. Woolum, and B. Commoner, *Biochim. Biophys. Acta*, 1972, **257**, 452.

197. A. F. Vanin, A. N. Osipov, L. N. Kubrina, D. S. Burbaev, and R. M. Nalbandyan, *Stud. Biophys.*, 1975, **49**, 13.

198. A. F. Vanin and V. Y. Varich, *Biophysica (USSR)*, 1980, **24**, 686.

199. V. Y. Varich, *Biophysica (USSR)*, 1980, **24**, 1146.

200. A. F. Vanin and V. Y. Varich, *Stud. Biophys.*, 1981, **86**, 177.

201. V. Y. Varich and A. F. Vanin, *Biophysica (USSR)*, 1983, **28**, 1125.

202. M. A. Foster and J. M. Hutchison, *Phys. Med. Biol.*, 1974, **19**, 289.

203. V. Y. Varich, A. F. Vanin, and L. M. Ovsyannikova, *Biophysica (USSR)*, 1987, **32**, 1158.

204. A. F. Vanin, L. N. Kubrina, I. S. Kurbanov, P. I. Mordvintsev, N. V. Khrapova, M. E. Galagan, and E. I. Matkhanov, *Biokhimiia*, 1989, **54**, 1974.

205. A. F. Vanin and R. M. Nalbandyan, *Biophysica (USSR)*, 1965, **10**, 184.

206. J. M. Hutchison, M. A. Foster, and J. R. Mallard, *Phys. Med. Biol.*, 1971, **16**, 655.

207. J. H. Enemark and R. D. Feltham, *Coord. Chem. Rev.*, 1974, **13**, 339.

208. A. R. Butler, C. Glidewell, and M.-H. Li, *Adv. Inorg. Chem.*, 1988, **32**, 335.

209. D. V. Dervartanian, S. P. J. Albracht, J. A. Berden, B. F. Van Gelder, and E. C. Slater, *Biochim. Biophys. Acta*, 1973, **292**, 496.

210. M. R. Hyman, L. C. Seefeldt, T. V. Morgan, D. J. Arp, and L. E. Mortenson, *Biochemistry*, 1992, **31**, 2947.

211. M. J. Payne, C. Glidewell, and R. Cammack, *J. Gen. Microbiol.*, 1990, **136**, 2077.

212. J. C. Drapier, C. Pellat, and Y. Henry, *J. Biol. Chem.*, 1991, **266**, 10162.

213. D. J. Stuehr, S. S. Gross, I. Sakuma, R. Levi, and C. F. Nathan, *J. Exp. Med.*, 1989, **169**, 1011.

214. M. J. Brennan, T. Cole, and J. A. Singley, *Proc. Soc. Exp. Biol. Med.*, 1966, **123**, 715.

215. T. Maruyama, N. Kataoka, S. Nagase, H. Nakada, H. Sato, and H. Sasaki, *Cancer Res.*, 1971, **31**, 179.

216. B. Commoner, J. C. Woolum, B. H. Senturia Jr, and J. L. Ternberg, *Cancer Res.*, 1970, **30**, 2091.

217. A. F. Vanin, L. V. Vakhina, and A. G. Chetverikov, *Biophysics USSR (Engl. Trans.)*, 1970, **15**, 1082.

218. E. F. Binkerd and O. E. Kolari, *Food Cosmet. Toxicol.*, 1975, **13**, 655.

219. G. G. Giddings, *J. Food Sci.*, 1977, **42**, 288.

220. R. C. Benedict, *J. Food Prot.*, 1980, **43**, 877.

221. H. Beinert, *FASEB J.*, 1990, **4**, 2483.

222. D. Reddy, J. R. Lancaster Jr, and D. P. Cornforth, *Science*, 1983, **221**, 769.

223. M. J. Payne, L. F. Woods, P. Gibbs, and R. Cammack, *J. Gen. Microbiol.*, 1990, **136**, 2067.

224. J. R. Lancaster Jr and J. B. Hibbs Jr, *Proc. Natl. Acad. Sci. U.S.A.*, 1990, **87**, 1223.

225. C. Pellat, Y. Henry, and J. C. Drapier, *Biochem. Biophys. Res. Commun.*, 1990, **166**, 119.

226. D. J. Stuehr, J. Santolini, Z. Q. Wang, C. C. Wei, and S. Adak, *J. Biol. Chem.*, 2004, **279**, 36167.

227. D. S. Bredt and S. H. Snyder, *Proc. Natl. Acad. Sci. U.S.A.*, 1990, **87**, 682.

228. D. S. Bredt, P. M. Hwang, C. E. Glatt, C. Lowenstein, R. R. Reed, and S. H. Snyder, *Nature*, 1991, **351**, 714.

229. H. Schworer, A. Clemens, S. Katsoulis, H. Kohler, W. Creutzfeldt, and W. E. Schmidt, *Scand. J. Gastroenterol.*, 1993, **28**, 625.

230. P. A. Marsden, K. T. Schappert, H. S. Chen, M. Flowers, C. L. Sundell, J. N. Wilcox, S. Lamas, and T. Michel, *FEBS Lett.*, 1992, **307**, 287.

231. S. P. Janssens, A. Simouchi, T. Quertermous, D. B. Bloch, and K. D. Bloch, *J. Biol. Chem.*, 1992, **267**, 22694.

232. M. Nakane, H. H. Schmidt, J. S. Pollock, U. Forstermann, and F. Murad, *FEBS Lett.*, 1993, **316**, 175.

233. W. C. Sessa, J. K. Harrison, C. M. Barber, D. Zeng, M. E. Durieux, D. D. D'Angelo, K. R. Lynch, and M. J. Peach, *J. Biol. Chem.*, 1992, **267**, 15274.

234. S. Lamas, P. A. Marsden, G. K. Li, P. Tempst, and T. Michel, *Proc. Natl. Acad. Sci. U.S.A.*, 1992, **89**, 6348.

235. Q. W. Xie, H. J. Cho, J. Calaycay, R. A. Mumford, K. M. Swiderek, T. D. Lee, A. Ding, T. Troso, and C. Nathan, *Science*, 1992, **256**, 225.

236. D. A. Geller, C. J. Lowenstein, R. A. Shapiro, A. K. Nussler, M. Di Silvio, S. C. Wang, D. K. Nakayama, R. L. Simmons, S. H. Snyder, and T. R. Billiar, *Proc. Natl. Acad. Sci. U.S.A.*, 1993, **90**, 3491.

237. H. J. Cho, Q. W. Xie, J. Calaycay, R. A. Mumford, K. M. Swiderek, T. D. Lee, and C. Nathan, *J. Exp. Med.*, 1992, **176**, 599.

238. J. C. Salerno, D. E. Harris, K. Irizarry, B. Patel, A. J. Morales, S. M. Smith, P. Martasek, L. J. Roman, B. S. Masters, C. L. Jones, B. A. Weissman, P. Lane, Q. Liu, and S. S. Gross, *J. Biol. Chem.*, 1997, **272**, 29769.

239. D. J. Stuehr and O. W. Griffith, *Adv. Enz.*, 1992, **65**, 287.

240. N. S. Kwon, C. F. Nathan, C. Gilker, O. W. Griffith, D. E. Matthews, and D. J. Stuehr, *J. Biol. Chem.*, 1990, **265**, 13442.

241. A. M. Leone, R. M. Palmer, R. G. Knowles, P. L. Francis, D. S. Ashton, and S. Moncada, *J. Biol. Chem.*, 1991, **266**, 23790.

242. D. J. Stuehr and M. Ikeda-Saito, *J. Biol. Chem.*, 1992, **267**, 20547.

243. S. Ghisla and V. Massey, *Eur. J. Biochem.*, 1989, **181**, 1.

244. K. S. Christopherson and D. S. Bredt, *J. Clin. Invest.*, 1997, **100**, 2424.

245. B. C. Kone, T. Kuncewicz, W. Zhang, and Z. Y. Yu, *Am. J. Physiol. Renal Physiol.*, 2003, **285**, F178.

246. U. Siddhanta, A. Presta, B. Fan, D. Wolan, D. L. Rousseau, and D. J. Stuehr, *J. Biol. Chem.*, 1998, **273**, 18950.

247. D. J. Stuehr, N. S. Kwon, S. S. Gross, B. A. Thiel, R. Levi, and C. F. Nathan, *Biochem. Biophys. Res. Commun.*, 1989, **161**, 420.

248. N. S. Kwon, C. F. Nathan, and D. J. Stuehr, *J. Biol. Chem.*, 1989, **264**, 20496.

249. M. Sorlie, A. C. Gorren, S. Marchal, T. Shimizu, R. Lange, K. K. Andersson, and B. Mayer, *J. Biol. Chem.*, 2003, **278**, 48602.

250. G. Werner-Felmayer, E. R. Werner, G. Weis, and H. Wachter, *J. Natl. Cancer Inst.*, 1992, **84**, 1671.

251. R. G. Kilbourn and O. W. Griffith, *J. Natl. Cancer Inst.*, 1992, **84**, 1672.

252. E. R. Werner, G. Werner-Felmayer, and H. Wachter, *Proc. Soc. Exp. Biol. Med.*, 1993, **203**, 1.

253. K. A. White and M. A. Marletta, *Biochemistry*, 1992, **31**, 6627.

254. K. McMillan, D. S. Bredt, D. J. Hirsch, S. H. Snyder, J. E. Clark, and B. S. Masters, *Proc. Natl. Acad. Sci. U.S.A.*, 1992, **89**, 11141.

255. P. Klatt, K. Schmidt, and B. Mayer, *Biochem. J.*, 1992, **288**, 15.

256. M. J. Coon, X. X. Ding, S. J. Pernecky, and A. D. Vaz, *FASEB J.*, 1992, **6**, 669.

257. D. J. Wolff, G. A. Datto, R. A. Samatovicz, and R. A. Tempsick, *J. Biol. Chem.*, 1993, **268**, 9425.

258. L. J. Ignarro, J. C. Edwards, D. Y. Gruetter, B. K. Barry, and C. A. Gruetter, *FEBS Lett.*, 1980, **110**, 275.

259. J. McAninly, D. L. H. Williams, S. C. Askew, A. R. Butler, and C. Russell, *J. Chem. Soc., Chem. Commun.*, 1993, 1758.

260. K. Inoue, T. Akaike, Y. Miyamoto, T. Okamoto, T. Sawa, M. Otagiri, S. Suzuki, T. Yoshimura, and H. Maeda, *J. Biol. Chem.*, 1999, **274**, 27069.

261. R. F. Furchgott, S. J. Ehrreich, and E. Greenblatt, *J. Gen. Physiol.*, 1961, **44**, 499.

262. J. Rodriguez, R. E. Maloney, T. Rassaf, N. S. Bryan, and M. Feelisch, *Proc. Natl. Acad. Sci. U.S.A.*, 2003, **100**, 336.

263. A. Samouilov, P. Kuppusamy, and J. L. Zweier, *Arch. Biochem. Biophys.*, 1998, **357**, 1.

264. A. R. Butler and J. H. Ridd, *Nitric Oxide*, 2004, **10**, 20.

265. J. R. Lancaster Jr, *Nitric Oxide*, 1997, **1**, 18.

266. J. R. Lancaster Jr, in 'Nitric Oxide: Biology and Pathobiology', ed. L. J. Ignarro, Academic Press, San Diego, CA, 2000, p. 209.

267. A. Meulemans, *Neurosci. Lett.*, 1994, **171**, 89.

268. J. Stadler, H. A. Bergonia, M. Di Silvio, M. A. Sweetland, T. R. Billiar, R. L. Simmons, and J. R. Lancaster Jr, *Arch. Biochem. Biophys.*, 1993, **302**, 4.

269. J. R. Lancaster Jr, *Meth. Enzymol.*, 1996, **268**, 31.

270. Y. Zhang and N. Hogg, *Am. J. Physiol. Lung Cell Mol. Physiol.*, 2004, **287**, L467.

271. L. J. Ignarro, P. A. Bush, G. M. Buga, K. S. Wood, J. M. Fukuto, and J. Rajfer, *Biochem. Biophys. Res. Commun.*, 1990, **170**, 843.

272. D. G. Hatzichristou, *Int. J. Impot. Res.*, 2002, **14**,(Suppl 1), S43.

273. R. G. Kilbourn, S. S. Gross, A. Jubran, J. Adams, O. W. Griffith, R. Levi, and R. F. Lodato, *Proc. Natl. Acad. Sci. U.S.A.*, 1990, **87**, 3629.

274. R. G. Kilbourn, A. Jubran, S. S. Gross, O. W. Griffith, R. Levi, J. Adams, and R. F. Lodato, *Biochem. Biophys. Res. Commun.*, 1990, **172**, 1132.

275. R. M. J. Palmer, *Arch. Surg.*, 1993, **128**, 396.

276. R. Bucala, *J. Leukoc. Biol.*, 2004, **75**, 398.

277. P. Vallance, J. Collier, and S. Moncada, *Cardiovasc. Res.*, 1989, **23**, 1053.

278. A. Petros, D. Bennett, and P. Vallance, *Lancet*, 1991, **338**, 1557.

279. J. B. Ochoa, A. O. Udekwu, T. R. Billiar, R. D. Curran, F. B. Cerra, R. L. Simmons, and A. B. Peitzman, *Ann. Surg.*, 1991, **214**, 621.

280. A. Lopez, J. A. Lorente, J. Steingrub, J. Bakker, A. McLuckie, S. Willatts, M. Brockway, A. Anzueto, L. Holzapfel, D. Breen, M. S. Silverman, J. Takala, J. Donaldson, C. Arneson, G. Grove, S. Grossman, and R. Grover, *Crit. Care Med.*, 2004, **32**, 21.

281. J. Bakker, R. Grover, A. McLuckie, L. Holzapfel, J. Andersson, R. Lodato, D. Watson, S. Grossman, J. Donaldson, and J. Takala, *Crit. Care Med.*, 2004, **32**, 1.

282. R. P. Dellinger and J. E. Parrillo, *Crit. Care Med.*, 2004, **32**, 282.

283. B. T. Mellion, L. J. Ignarro, E. H. Ohlstein, E. G. Pontecorvo, A. L. Hyman, and P. J. Kadowitz, *Blood*, 1981, **57**, 946.

284. G. Walford and J. Loscalzo, *J. Thromb. Haemost.*, 2003, **1**, 2112.

285. D. A. Wink and J. B. Mitchell, *Free Radical Biol. Med.*, 2003, **34**, 951.

286. B. Halliwell and J. M. Gutteridge, *FEBS Lett.*, 1992, **307**, 108.

287. W. H. Koppenol, *Redox Rep.*, 2001, **6**, 229.

288. B. M. Babior, *Adv. Enz.*, 1992, **65**, 49.

289. R. A. Clark, *J. Infect. Dis.*, 1999, **179**,(Suppl 2), S309.

290. J. Kanner, S. Harel, and R. Granit, *Lipids*, 1992, **27**, 46.

291. D. A. Wink, K. M. Miranda, M. G. Espey, R. M. Pluta, S. J. Hewett, C. Colton, M. Vitek, M. Feelisch, and M. B. Grisham, *Antioxid. Redox Signal.*, 2001, **3**, 203.

292. V. E. Kagan, A. V. Kozlov, Y. Y. Tyurina, A. A. Shvedova, and J. C. Yalowich, *Antioxid. Redox Signal.*, 2001, **3**, 189.

293. R. J. Gryglewski, R. M. Palmer, and S. Moncada, *Nature*, 1986, **320**, 454.

294. G. Johnson, P. Tsao, and A. M. Lefer, *Am. Heart J.*, 1990, **119**, 530.

295. J. S. Beckman, T. W. Beckman, J. Chen, P. A. Marshall, and B. A. Freeman, *Proc. Natl. Acad. Sci. U.S.A.*, 1990, **87**, 1620.

296. J. M. Fukuto and L. J. Ignarro, *Acc. Chem. Res.*, 1997, **30**, 149.

297. G. Czapski and S. Goldstein, *Free Radical Biol. Med.*, 1995, **19**, 785.

298. A. G. Estevez, J. B. Sampson, Y. X. Zhuang, N. Spear, G. J. Richardson, J. P. Crow, M. M. Tarpey, L. Barbeito, and J. S. Beckman, *Free Radical Biol. Med.*, 2000, **28**, 437.

299. J. S. Beckman, Y. Z. Ye, P. G. Anderson, J. Chen, M. A. Accavitti, M. M. Tarpey, and C. R. White, *Biol. Chem. Hoppe-Seyler*, 1994, **375**, 81.

300. H. Ischiropoulos, L. Zhu, J. Chen, M. Tsai, J. C. Martin, C. D. Smith, and J. S. Beckman, *Arch. Biochem. Biophys.*, 1992, **298**, 431.

301. S. Goldstein, G. Czapski, J. Lind, and G. Merenyi, *J. Biol. Chem.*, 2000, **275**, 3031.

302. Y. J. Sung, J. H. Hotchkiss, R. E. Austic, and R. R. Dietert, *J. Leukocyte Biol.*, 1991, **50**, 49.

303. M. W. Radomski, J. F. Martin, and S. Moncada, *Proc. R. Soc. London, Ser. B*, 1991, **334**, 129.

304. J. M. C. Ribeiro, J. M. H. Hazzard, R. H. Nussenzveig, D. E. Champagne, and F. A. Walker, *Science*, 1993, **260**, 539.

305. F. A. Walker, J. M. Ribeiro, and W. R. Montfort, *Met. Ions Biol. Syst.*, 1999, **36**, 621.

306. B. A. Trimmer, J. R. Aprille, D. M. Dudzinski, C. J. Lagace, S. M. Lewis, T. Michel, S. Qazi, and R. M. Zayas, *Science*, 2001, **292**, 2486.

307. S. Davies, *Insect Biochem. Mol. Biol.*, 2000, **30**, 1123.

308. M. Masetti, T. Locci, A. Cecchettini, P. Lucchesi, M. Magi, G. Malvaldi, and F. Bruschi, *Int. J. Parasitol.*, 2004, **34**, 715.

309. J. Goretski and T. C. Hollocher, *J. Biol. Chem.*, 1990, **265**, 889.

310. W. G. Zumft, *J. Mol. Microbiol. Biotechnol.*, 2002, **4**, 277.

311. P. Nioche, V. Berka, J. Vipond, N. Minton, A. L. Tsai, and C. S. Raman, *Science*, 2004, **306**, 1550.

Nitrides: Transition Metal Solid-state Chemistry

Walter Lengauer & Alexander Eder
Vienna University of Technology, Vienna, Austria

Based in part on the article Nitrides: Transition Metal Solid State Chemistry by Peter Ettmayer & Walter Lengauer which appeared in the Encyclopedia of Inorganic Chemistry, First Edition.

---

1 Introduction 1
2 Structure and Bonding 1
3 Preparation 3
4 Characterization 4
5 Thermodynamics 5
6 Properties of fcc Transition Metal Nitrides 10
7 Uses 15
8 References 15

---

1 INTRODUCTION

Together with the transition metal carbides and borides, the transition metal nitrides belong to a family of materials that features an unusual combination of outstanding properties, among which are exceptional hardness, high melting point, metallic luster with sometimes vivid colors, and simple metallic structures combined with excellent electrical and thermal conductivities. This combination of these properties has attracted considerable attention and has resulted in numerous technical applications.[1–4] Lengauer[5] has recently compiled several features of transition metal nitrides and carbonitrides. Many of the nitride phases closely resemble metallic alloys, with broad ranges of homogeneity, particularly if the structure of the metallic host lattice is one of the types encountered in typical metals. They often form solid solutions with structurally related compounds such as other transition metal nitrides or carbides and are easily wetted by liquid metals of the iron group.

The chemical stability of transition nitrides is considerable; they are not readily attacked by dilute acids except by oxidizing acids and hydrofluoric acid or alkaline solutions. The thermal stability is determined by their free energies of formation; the stability decreases with increasing group number. While TiN, ZrN, and HfN can be melted without decomposition at ambient pressure, the nitrides of the other groups decompose by liberating nitrogen before melting points are reached.

Table 1 gives a brief survey of the most important properties of the well-characterized binary transition metal nitrides. It should, however, be emphasized that practically all properties are significantly influenced by the nitrogen to metal ratio (Section 6) and by impurities.

2 STRUCTURE AND BONDING

2.1 Structures: General Features

Transition metal nitrides together with the structurally closely related transition metal carbides belong to the family of ‘interstitial compounds’ or alloys. The common features of this class of materials are the very simple metallic structures with the smaller nitrogen atoms in the interstitial voids of the frequently dense-packed host lattice. The simple conceptual Hägg model in which the basically metallic character of the host metal is thought to be only modified by insertion of nonmetal atoms into the voids had to be substantially restructured in the light of modern bonding theories in order to account for the strong binding energies observed between transition metal atoms and nonmetal atoms. Nevertheless, the rather approximate interstitial alloy concept has proved helpful for gaining insight into the basic principles governing the structures of interstitial alloys and compounds.

Because of structural similarities, transition metal nitrides usually form solid solutions with transition metal carbides. However, there are important differences, possibly owing to the different bonding character of nitrogen as compared to that of carbon. Transition metal carbides and nitrides generally have face-centered cubic (fcc) or hexagonal close-packed (hcp) metal lattices with nonmetal atoms more or less randomly distributed on the interstitial sites; deviations from this simple concept are much more frequently encountered with nitrides. If the immediate neighborhood of the nonmetal X ($X = C$, N) is considered, one can define the structural elements of interstitial alloys.[6] In the group 4 and 5 transition metals, the common structural element of the nitrides and carbides is the T_6X octahedron. With increasing radius ratio r_X/r_T, the trigonal prismatic group T_6X is favored over the octahedral group. Therefore, the transition metal carbides of groups 6–9 feature trigonal prismatic T_6X elements in different crystallographic arrangements. In transition metal nitrides, a third structural element is occasionally observed, particularly in group 5 compounds, consisting of T_5X square pyramids. These prevail even in the complex nitrides, such as the Z-phases NbCrN, TaCrN, NbMoN, and TaMoN with the filled Θ-CuTi-type structure. With this square pyramid, which has lower symmetry than an octahedron, such nitrides have more complicated structures (Section 5.2) than the corresponding carbides.

Because of the formation of structural elements other than T_6N octahedra, the fcc structure of δ-nitrides is destabilized increasingly with increasing group number and, within a group, with increasing periodic number. For example, the nitrides of group 4, δ-TiN_{1-x}, δ-ZrN_{1-x} and

δ-HfN_{1-x} crystallize in the sodium chloride structure. No low-temperature modifications of these stoichiometric nitrides are known. In group 5, all three metals form stoichiometric fcc nitrides, too, but δ-$VN_{1.00}$ transforms below 205 K into a tetragonal modification,[7] δ-$NbN_{1.00}$ below around 1320 °C into hexagonal η-NbN,[8] and δ-$TaN_{1.00}$ below around 1920 °C congruently into hexagonal ε-TaN.[9] In group 6, these fcc nitrides are increasingly less stable: fcc CrN is nearly a line compound at low temperature with a reduced thermochemical stability and transforms below approximately 280 K into a tetragonal antiferromagnetic compound,[10] and fcc γ-MoN_{1-x} apparently does not even occur with a nitrogen content approaching the ideal composition $MoN_{1.00}$ (except perhaps at very high pressures) but rather in the vicinity of $MoN_{0.50}$. Face-centered cubic $MoN_{0.50}$ also transforms into a tetragonal modification with an ordered arrangement of nitrogen atoms in the interstitial sites. This tendency proceeds further in the Mn–N and Fe–N systems, where ferromagnetic fcc phases with the stoichiometry T_4N are observed with an ordered arrangement of N atoms.[11] Ordered manganese nitride phases with respect to the arrangements of nitrogen and a concurrent tetragonal distortion of the metal host lattice are found. An fcc MnN_{1-x} was recently prepared by high-rate reactive sputtering.[12]

An extensive compilation of nitride phases is contained in Pearson's handbook[13] and in the ASM binary phase diagram compilation.[11]

The different stacking of close-packed metal layers can be described by the Jagodzinski–Wyckoff notation, where close-packed stacking ABC,ABC, ... is designated as 'c' and hexagonal close-packed stacking AB,AB, ... is designated as 'h'. Figure 1 shows these structures and lists several metal nitride and carbide phases that can be described with this formalism.

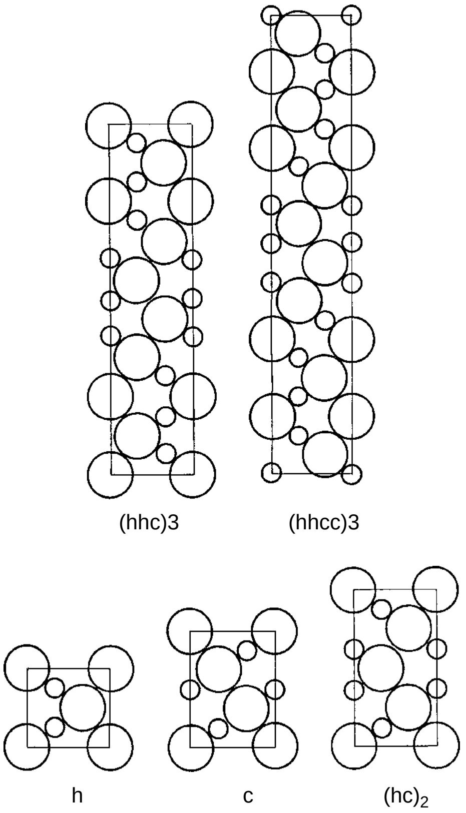

Figure 1 Close-packed structure types observed for various transition metal nitrides. Large circles designate metal atoms, small circles designate nitrogen atoms. In h sequences, only 50% of the interstices can be occupied. The following transition metal nitrides crystallize in these structures: h: β-V_2N, β-Nb_2N, β-Ta_2N, ε-Cr_2N, ζ-Mn_2N, ε-Fe_2N; c: δ-TiN_{1-x}, δ-ZrN_{1-x}, δ-HfN_{1-x}, δ-VN_{1-x}, δ-NbN_{1-x}, δ-TaN_{1-x}, γ-MoN_{1-x}; $(hc)_2$: ScNbN, ScTaN, Mn_3TaN_{4-x}; $(hc)_2$ with metal and nonmetal sites exchanged: η-NbN, η-TaN; $(hhc)_3$: η-Ti_3N_{2-x}, η-Hf_3N_{2-x}; $(hhcc)_3$: ζ-Ti_4N_{3-x}, ζ-Hf_4N_{3-x}

2.2 Bonding

The bonding in transition metal carbides and nitrides can be described as a mixture of metallic, covalent, and ionic components.

The metallic character is immediately noticed in the high electrical conductivities of these compounds. The bonding mechanism has been described extensively by a variety of approaches for calculating the density of states (DOS) and hence the electron density in fcc transition metal nitrides, carbides and oxides.[14] In the DOS of these compounds, there is a minimum at a valence electron concentration (VEC) of eight that corresponds to the stoichiometric composition of group 4 carbides TiC, ZrC and HfC. Figure 2 compares the decomposed and the total DOS of TiN and TiC[15] with respect to the s, p, and d bands. At low energies of <0Ryd the s band is characterized by a large contribution of the nonmetal 2s state. Above 0Ryd the p band follows and there is a significant contribution of d states to this band, too. At higher energies, the d band composed of d states follows with the Fermi energy E_F located well within this band. The DOS at E_F is higher for TiN than for TiC, consistent with the observed superconducting properties (TiN, $T_C = 5.4$ K; TiC, $T_C < 1.2$ K) and room-temperature electrical conductivities (Section 6.3).

An illustrative picture of covalent bonding in these compounds can be drawn in the molecular orbital (MO) scheme[16] where atomic orbitals of atoms are combined to form bonding and antibonding states. Figure 3 shows a schematic drawing of these bonds between metal d and nonmetal p orbitals in the (100) plane of the fcc structure, which can be decomposed into two different bonding symmetries, t_{2g} and e_g. It can be shown that the calculated electron densities in this plane reflect the change of e_g bonding symmetry in TiC to t_{2g} bonding symmetry in TiN. Thus the exchange in bonding strength from a strong Ti–C interaction in TiC toward a more pronounced Ti–Ti interaction in TiN is to be expected.

The ionic contribution to the binding mechanism of transition metal nitrides and carbides can be estimated from

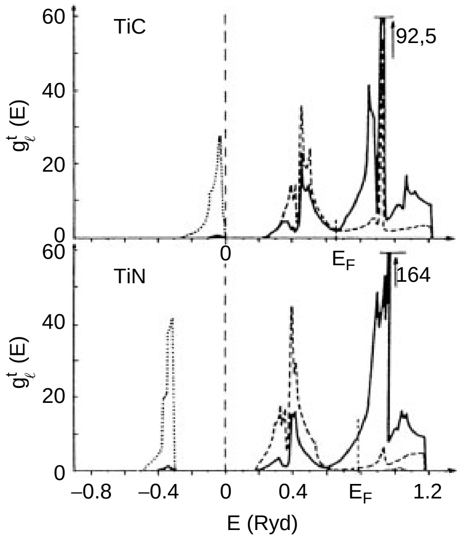

Figure 2 Density of states (DOS) for TiC and TiN. (Ref. 15. Reproduced by kind permission of Kluwer Academic Publishers)

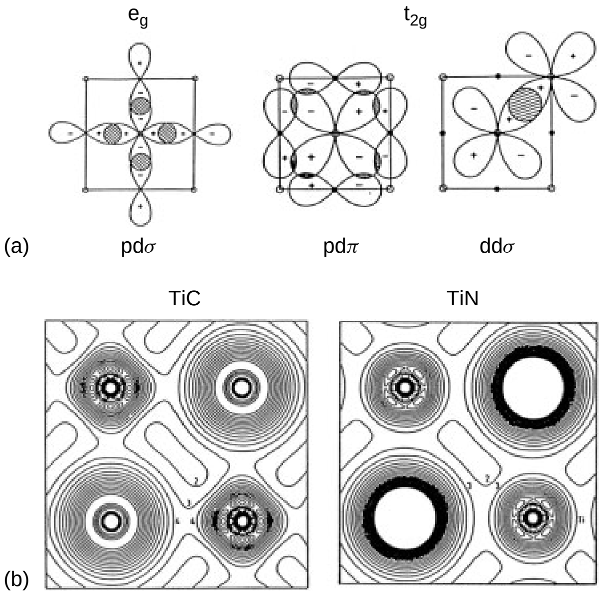

Figure 3 Bonding schemes: (a) of different symmetries in the (100) plane and calculated electron densities and (b) of TiN and TiC showing the change around Ti from e_g symmetry TiC to t_{2g} bonding symmetry in TiN. (Ref. 16. Reproduced by permission of Wiley, Inc)

the charge transfer from the metal atom to the nonmetal atom. It is about half an electron per atom, which contributes to the electrostatic interaction of metal and nonmetal.

The bonding of 4d transition metal nitrides and carbides can be treated in a very similar way; the nonmetal contribution to the electron density is about the same, whereby the contribution from 4d electrons causes a more spatial extension of electron density than in 3d compounds. In 5d transition metal nitrides and carbides, relativistic effects due to the heavy cores have to be taken into account.

3 PREPARATION

Transition metal nitrides can be prepared by allowing the metal or the metal hydride in powdered or compact form to react with molecular or atomic nitrogen or flowing ammonia:

$$\mathrm{Ti} + \frac{1}{2}\mathrm{N_2} \longrightarrow \mathrm{TiN} \tag{1}$$

$$\mathrm{ZrH_2} + \frac{1}{2}\mathrm{N_2} \longrightarrow \mathrm{ZrN} + \mathrm{H_2} \tag{2}$$

$$\mathrm{Mo} + \mathrm{NH_3} \longrightarrow \mathrm{MoN} + \frac{3}{2}\mathrm{H_2} \tag{3}$$

The pressure of molecular nitrogen at a given temperature that is necessary to obtain a specific nitride phase is defined by the nitrogen potential (partial free energy of nitrogen) of the nitride. In flowing ammonia, very high nitrogen potentials can be maintained as long as the thermal decomposition of ammonia into $N_2 + 3H_2$ can be minimized.

The formation of nitrides from oxides is performed in the presence of carbon as a reducing agent, according to the overall reaction

$$\mathrm{TiO_2} + 2\mathrm{C} + \tfrac{1}{2}\mathrm{N_2} \longrightarrow \mathrm{TiN} + 2\mathrm{CO} \tag{4}$$

This reaction usually proceeds over several intermediate products and the resulting nitride may contain oxygen and carbon.

For the preparation of nitrides from metal powders, the exothermic heat of formation can be utilized in the self-sustaining high-temperature synthesis (SHS) process. If the reaction is exothermic enough, that is, if the heat generated is sufficient to reach the reaction temperature, then the starting material is converted to the nitride and the heat is dissipated. For the preparation of large crystals, zone-annealing techniques have been developed.**[17]** Similar to the zone-melting process, a heated zone is passed along a rod in a nitrogen atmosphere. The starting materials are either solid-state sintered nitride powders or metal powders pressed into rods. The applied temperatures must be very high (ca. 3000 °C) in order to overcome the low diffusivity of nitrogen in nitrides, but they must not exceed the melting temperatures of the compounds in order to avoid incongruent melting and decomposition. Crystals on the order of 1 cm^3 have been produced by this technique. While they still may show some concentration gradients, they are suitable for solid-state investigations such as neutron diffractometry.

A great variety of methods have been applied to the preparation of nitride layers. These can be divided into three main groups (Section 7.1 gives more details).

- Chemical vapor deposition (CVD) – a volatile transition metal compound such as a chloride is reacted in the gas phase with ammonia, nitrogen/hydrogen or ammonia/hydrogen/nitrogen mixtures. The high-melting nitride that forms as a reaction product in the gas phase nucleates on any solids present, for example, hard metals, and forms compact strongly adhering layers at temperatures around 1000 °C.
- Physical vapor deposition (PVD) – the transition metal is evaporated by electron beam or plasma heating or sputtered by glow discharge and reacted with low-pressure nitrogen (typically in the range of 10^{-4} mbar). Numerous modifications of PVD methods have been developed. The nitride layers that are deposited on the substrate often have high lattice defect concentrations and hence exhibit significant deviations from generally known bulk values (lattice parameters, hardness, composition, etc.).
- Surface nitridation is widely used for surface hardening and can be achieved by subjecting the material surface to the action of ammonia, molecular or atomic nitrogen, or nitrogen ions. Case-hardening techniques also make use of cyanide salt baths to form nitrides or carbonitrides on material surfaces. Reactive plasma techniques and high-pressure techniques have been developed to keep the workpiece temperature low and to avoid thermally induced changes in the workpiece. Laser irradiation together with an N_2 jet directed on the heated spot is employed for locally limited heating of the sample. This nitridation method is applicable to titanium alloys (e.g. Ti6Al4V) used to create wear- and corrosion-resistant layers on steam turbine blades for protection against droplets having supersonic velocity.

4 CHARACTERIZATION

4.1 Chemical Analysis

Several procedures have been applied for the analysis of nitrogen and impurities such as oxygen and carbides in nitrides.

- Combustion analysis[18] according to the Dumas method – the sample is heated at temperatures of up to 1200 °C in oxygen and/or with oxidizing agents such as V_2O_5, CuO, or Cu_2O. The evolved N_2 is either measured volumetrically in an azotometer or via a gas chromatograph[19] equipped with a thermoconductivity detector. With the latter equipment, C and H can also be determined simultaneously via the combustion products CO_2 and H_2O. The accuracy of the method is better than 1 rel %N for finely powdered samples if combustion can be completed within a rather short time span.
- Carrier gas hot extraction – the sample is heated to more than 2000 °C in the presence of carbon and an auxiliary bath of metal such as platinum and in a stream of a carrier gas such as He. Nitrogen is liberated as N_2 and is usually measured in a thermoconductivity cell. Oxygen combines with C to give CO and can thus be analyzed. Because of the high temperatures involved, the method is suitable for powder samples with larger grain size or even for small solid pieces. The accuracy of the method is on the order of 1–2 rel %N.
- Kjehldahl analysis – this involves the dissolution of nitrides in acids whereby the nitrogen is converted into ammonium ions. The dissolution process may be time consuming since some nitrides, such as δ-TiN_{1-x}, are chemically very stable against acids and must be dissolved using severe conditions such as by the action of hydrofluoric acid in Polytetraflourethylene (PTFE) containers at 100–200 °C. It is doubtful whether all of the nitrogen can be converted into NH_4^+ so systematic errors may arise.

4.2 Physical Analysis

Among the microphysical methods used for the analysis of nitrogen in nitrides, e.g. electron probe microanalysis (EPMA), Auger electron spectroscopy (AES), ultraviolet X-ray spectroscopy (UPS) and X-ray spectroscopy (XPS), secondary ion- or neutral mass spectrometry (SIMS, SNMS) and Rutherford backscattering (RBS), EPMA is considered to have the highest reproducibility and accuracy, provided that the lateral resolution of only a few microns is sufficient. The main problem in EPMA is the rather low energy of $N_{K\alpha}$ radiation. Even with windowless detector systems, a high background-to-peak ratio together with low net intensities are the result.[20] High-accuracy EPMA requires external or internal standardization[21] together with a wavelength-dispersive spectrometer equipped with high-quality crystals (e.g. W-Si multilayer or lead stearate crystals). For standardization, diffusion couples have been used in which diffusion layers are broadened.[22–24] Such samples can even be prepared in single-phase form upon increase of diffusion time so that the gross chemical composition is the same as the phase composition, a necessary prerequisite for application of different analyzing techniques and for true standardization.[25] By such a method, single-phase standards of TaN,[26] CrN,[27] and ζ-Hf_4N_{3-x}[28,29] have been prepared. These phases have a very narrow homogeneity range at least at a certain temperature.

Neutron activation analysis (NAA) making use of the nuclear reaction $^{14}N(n,2n)^{13}N$ can be applied for bulk determination of nitrogen.

5 THERMODYNAMICS

5.1 Nitrogen Partial Pressure

The nitrogen partial pressure of the transition metal nitrides is a function of temperature and increases substantially with increasing group number. This is reflected in the Richardson diagram shown in Figure 4. The lower (the more negative) the free energy of formation the lower is the equilibrium nitrogen pressure of the nitride. Group 4 nitrides can easily be obtained by nitridation of the metals with molecular nitrogen under low pressures even at high temperatures, whereas for the group

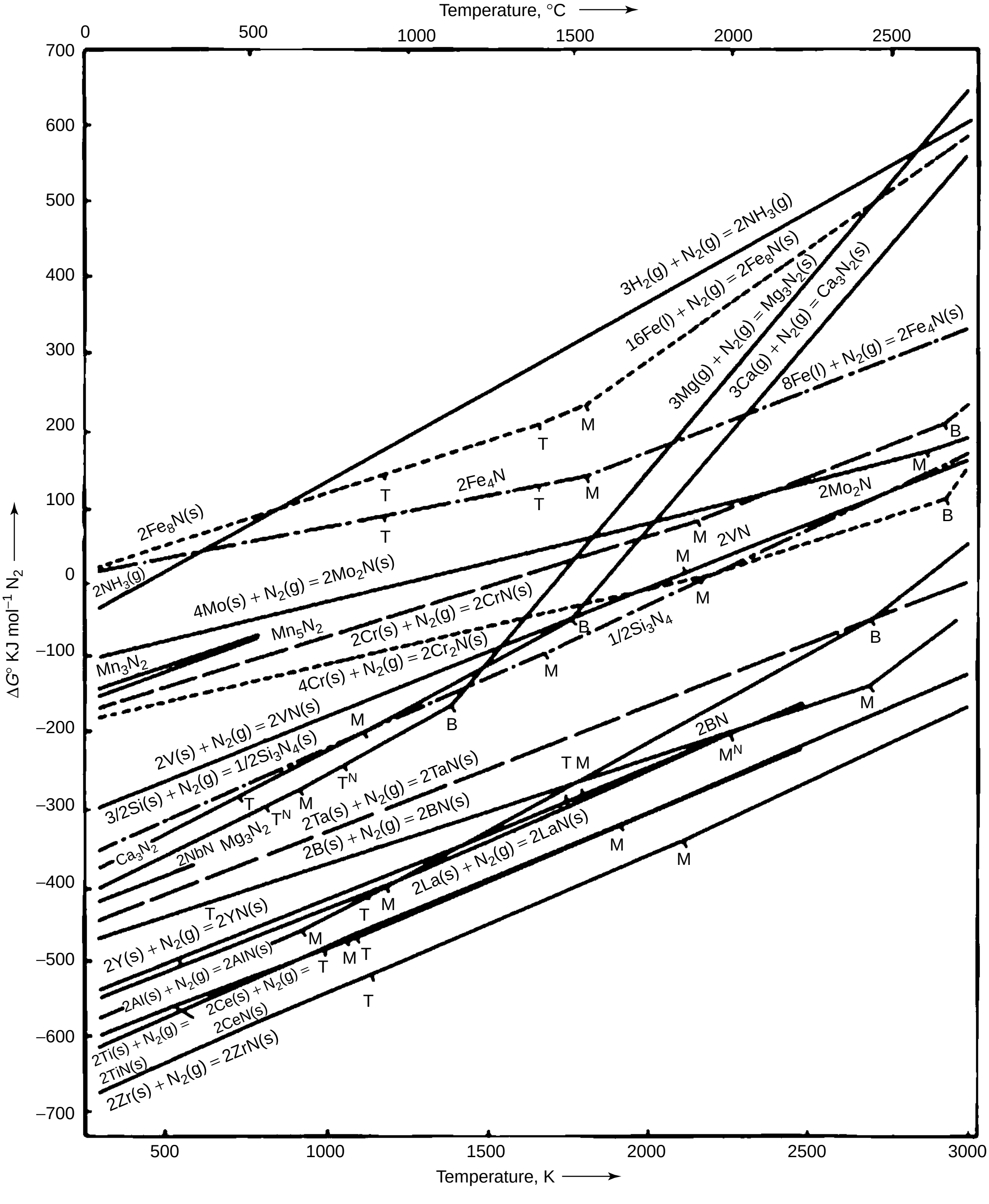

Figure 4 Richardson diagram of various transition metal mononitrides (together with other nitrides) giving the free energy of formation as a function of temperature. (Ref. 4. Reproduced by permission of Wiley VCH)

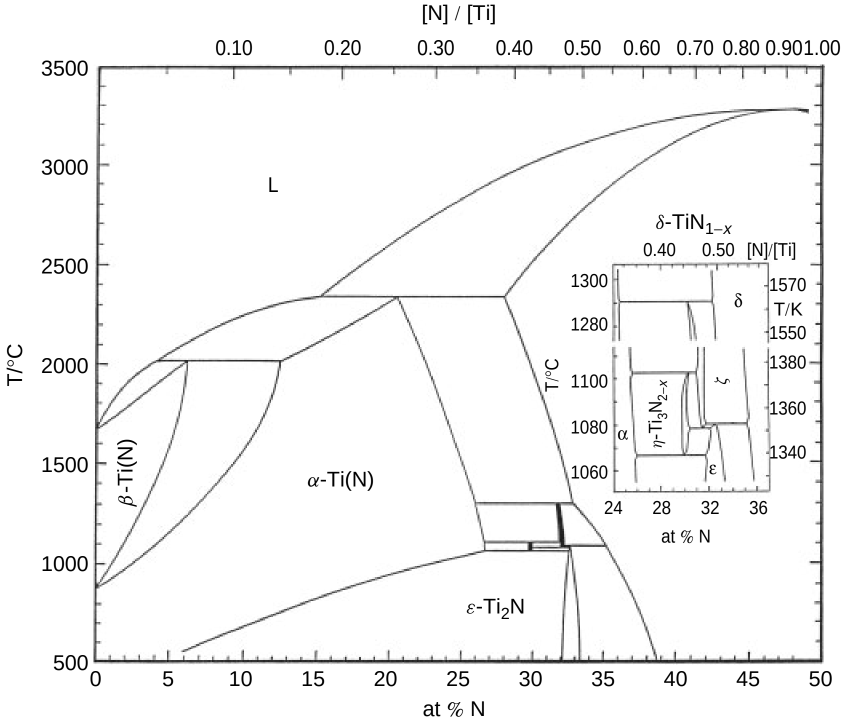

Figure 5 Phase diagram of the Ti–N system. (Reprinted from Ref. 31. © 1991, with permission from Elsevier)

5 nitrides the nitrogen pressure must already exceed normal pressure at temperatures above 1400 °C, and even higher pressures or more energetic nitriding conditions must prevail for the preparation of group 6 nitrides.

The nitrogen pressure determines the composition of the nitride if equilibrium is attained. Thermochemical models have been established that correctly predict pressure-temperature-composition (p-T-x) relationships for nitride phases.[30]

Nitride phases with a nonmetal to metal ratio greater than one have been obtained with high-pressure nitrogen or at high nitrogen potentials, such as those prevailing in flowing ammonia or ionic nitrogen atmospheres. Either an extension of the mononitride phase field to compositions N/T >1 has been observed such as in the Nb–N, Hf–N, and Ta–N systems, or distinct nitride phases are observed such as in the Zr–N, Nb–N, and Ta–N systems.

Ion implantation techniques can lead to nitrides having extremely high nitrogen to metal ratio such as $TiN_{1.5}$ but these phases are probably metastable.

5.2 Phase Equilibria and Structural Features

Several of the transition metal-nitrogen systems are not yet fully established. This is especially the case for some of the metals in groups 6–9, probably because of the lower technical relevance of the nitrides and the high nitrogen pressures needed for equilibrium investigations.

5.2.1 *The Ti–N System*

The Ti–N system[31] features a high solubility of nitrogen in α-Ti, the three subnitride phases η-Ti_3N_{2-x}, ζ-Ti_4N_{3-x} and ε-Ti_2N, and the fcc phase δ-TiN_{1-x} with the sodium chloride structure. η-Ti_3N_{2-x} and ζ-Ti_4N_{3-x} have been found to be isostructural with the hafnium subnitride phases and are characterized by metal atom layers comprising cubic- and hexagonal stacking sequences (Figure 1). Figure 5 shows the phase diagram of the Ti–N system.

In δ-$TiN_{0.50}$, the random distribution of nitrogen atoms undergoes an ordering process[32] below about 880 °C with a concurrent tetragonal distortion of the metal lattice.[33] The so-formed δ'-$TiN_{0.5}$ phase is only formed from δ-TiN_{1-x} by lattice distortion and is not an equilibrium phase (e.g. it is not formed in isothermal diffusion couples in the form of a phase band).

5.2.2 *The Zr–N System*

If the solid solution of nitrogen in Zr, α-Zr(N), which exists up to a composition 'Zr_2N', is not considered as a nitride phase, the Zr–N system is characterized by the presence of only one nitride phase, δ-ZrN_{1-x} up to a composition of approximately [N]/[Zr] = 1. It should be mentioned that none of the subnitride phases that exist in the neighboring systems Ti–N and Hf–N occur here. In Massalski's compilation[11]

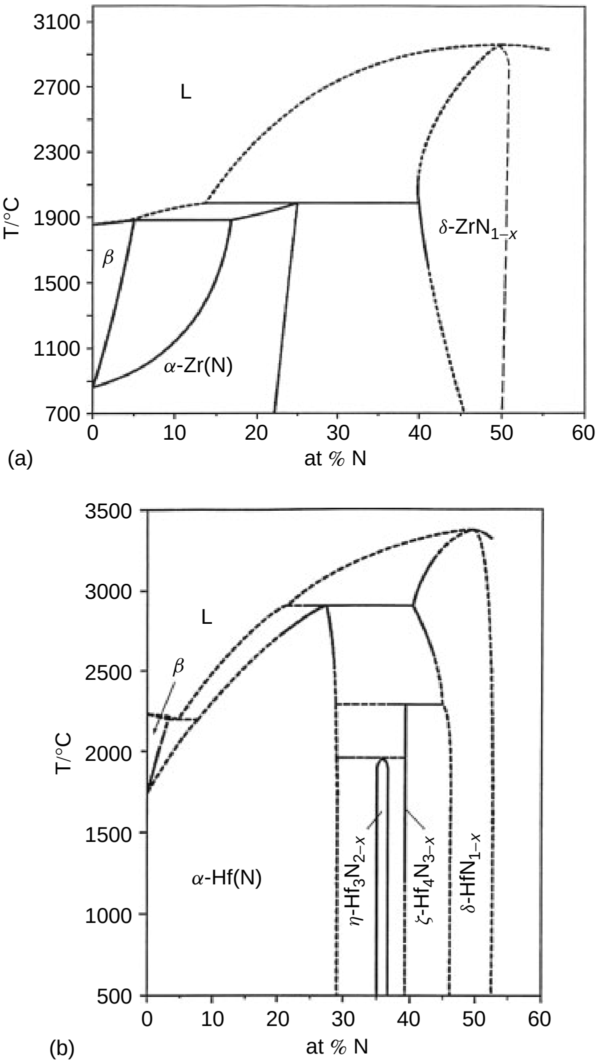

Figure 6 Phase diagrams of group 4 transition metal-nitrogen systems. (a) Zr–N. (Ref. 11. Reproduced by permission of Materials Information Society/ASM International), (b) Hf–N. (Reprinted from Ref. 28. © 1991, with permission from Elsevier)

(Figure 6), the Zr_3N_4 phase[34] that can be obtained by reacting $ZrCl_4$ with NH_3 has not been included.

5.2.3 *The Hf–N System*

Besides the fcc δ-HfN_{1-x}, the Hf–N system contains two subnitride phases,[35] η-Hf_3N_{2-x} and ζ-Hf_4N_{3-x}. Only a few phase equilibria studies have been performed for this system. Figure 6 shows the compiled phase diagram together with results from diffusion couples.[28,29] The homogeneity ranges of the subnitride phase could be established. The decomposition temperatures of these phases need to be reinvestigated.

5.2.4 *The V–N System*

In the vanadium–nitrogen system, the phases β-V_2N and δ-VN_{1-x} have cph and fcc structures, respectively. Carlsson *et al.*[36] have reviewed the V–N system and reinvestigated the vanadium-rich portion. Compiled data and results of a phase diagram study based on diffusion couples[37] have been used to construct the phase diagram shown in Figure 7.

Stoichiometric VN undergoes a phase transition into a tetragonal phase below 205 K.[7] At a composition of around $VN_{0.80}$, a transition into a tetragonal phase occurs at 500 °C. Two different versions of the phase diagram at temperatures below 500 °C have been reported,[39,40] one with a eutectic and one with a peritectic phase reaction between tetragonal $VN_{0.83}$ and δ-VN_{1-x}.

5.2.5 *The Nb–N System*

Brauer *et al.*[41,42] made careful studies on p-T-x relationships in the Nb–N system. In recent years, the phase reactions in this system have been investigated by high-temperature X-ray diffraction as well as by use of diffusion couples.[38,43,44] The phase reactions could be assumed as established (Figure 7). Interestingly, γ-Nb_4N_{3-x} is formed by a martensitic transformation from δ-NbN_{1-x}, hence an interface between δ-NbN_{1-x} and γ-Nb_4N_{3-x} does not form in diffusion couples.[38]

Near the composition NbN, at least three phases have been observed. For η-NbN, two different structures have been proposed with respect to the nitrogen positions. It contains trigonal prismatic and octahedral T_6N structure elements and features a metal layer sequence AABB. η-NbN undergoes a phase transition at about 1320 °C (depending on the nitrogen pressure) into fcc δ-NbN_{1-x} with a sodium chloride structure. Another phase, δ'-$NbN_{0.97}$ is most probably oxygen stabilized or occurs as metastable phase with phase transitions and is not included in the phase diagram. By reacting Nb powder with nitrogen under high pressure, the composition of the δ-NbN_{1-x} phase can be extended beyond N/Nb = 1. At even higher nitrogen pressure, the phase Nb_5N_6 can be prepared. Nb_5N_6 is isotypic with Ta_5N_6 and features T_5N square pyramides structural elements. These structural elements have not been observed in the analogous carbide systems and are probably linked to the higher electron concentration in nitrides.

5.2.6 *The Ta–N System*

The lower stability of the tantalum nitride phases as compared to the nitrides of the group 4 metals is reflected in the substantially higher equilibrium pressures (Figure 7).[45] In order to prepare the high-temperature fcc phase δ-TaN_{1-x}, the nitrogen pressure must exceed 10 bar but can be stabilized at lower pressures and temperatures by minute amounts of carbon. It is the hardest known transition metal nitride phase. The Ta_2N phase belongs to the ε-Fe_2N type at low temperatures and undergoes an order-disorder transition to

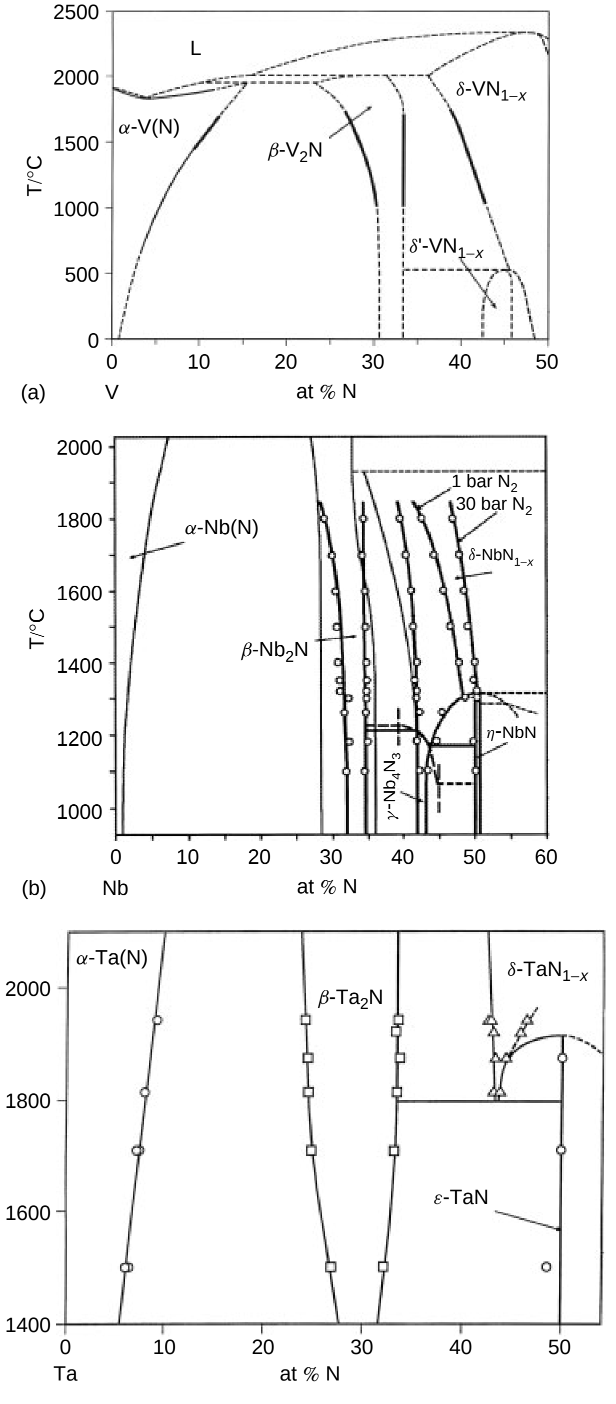

Figure 7 Phase diagram of group 5 transition metal-nitrogen systems. (a) V–N. (Ref. 37. Reproduced by permission of Materials Information Society/ASM International); (b) Nb–N. (Reprinted from Ref. 38. © 2000, with permission from Elsevier); and (c) Ta–N. (Reprinted from Ref. 38. © 2000, with permission from Elsevier)

an L′3 type between 1600 and 2000 °C. The often cited melting point of TaN of 2950 °C is probably incorrect and has to be attributed to Ta$_2$N. TaN is expected to melt at about 2800–3000 °C and nitrogen equilibrium pressures of 1–3 kbar. The θ-TaN phase with a WC-type structure is often observed in the reaction products of Ta powder with nitrogen or ammonia at temperatures below 1100 °C and is believed by Brauer *et al.*[46] to be a high-pressure phase that is metastable under normal conditions. ε-TaN has a structure not encountered in carbides, featuring an arrangement of Ta$_5$N squared pyramids. There are three stoichiometric phases in the Ta–N system with decreasing metallic character. The one with the highest nitrogen content, red Ta$_3$N$_5$ is nonmetallic and has been synthesized by the reaction of TaCl$_5$ with NH$_3$. In this rhombohedral phase, the nitrogen atoms are situated in the centers of tetrahedra while the tantalum atoms are still sixfold coordinated by nitrogen atoms in the form of slightly distorted octahedra.

5.2.7 The Cr–N System

The Cr–N system is characterized by the nitride phases Cr$_2$N$_{1-x}$ and CrN. The former has an appreciable homogeneity range. The arrangement of the metal atoms is cph and the nitrogen atoms are distributed in an ordered arrangement in the interstitial voids corresponding to the ε-Fe$_2$N-type structure. CrN crystallizes in the sodium chloride type structure and its homogeneity range at low temperature is rather narrow whereas it is substantially broadened above about 1230 °C.

Cr$_2$N$_{1-x}$ is readily dissolved by dilute acids, whereas CrN appears to withstand acid attack for prolonged periods. CrN is paramagnetic at room temperatures and undergoes a paramagnetic-antiferromagnetic first-order transition at temperatures between 276 and 286 K, depending on the composition.[10] The phase equilibria in the Cr-N system are strongly dependent on the nitrogen pressure. A phase diagram based on literature compilation and a study by diffusion couples is shown in Figure 8.[27]

5.2.8 The Mo–N and W–N Systems

In the Mo–N system (phase diagram[47] in Figure 8), three nitride phases have been reported. An fcc phase, originally named γ-Mo$_2$N because of its composition around 33 at %N, should instead be written as δ-MoN$_{1-x}$ to be consistent with the notation for other fcc nitrides. Diffusion couple studies gave a homogeneity range at 1000 °C of 28.5–38.2 mol %N.[48] Since fcc–Mo$_2$N$_{1-x}$ has been reported to exist at nitrogen contents above 33 at % and since it forms solid solutions with fcc δ-CrN, it can be assumed to be basically of the fcc δ-nitride type. This compound undergoes an ordering transition of the nitrogen atoms and a concurrent tetragonal distortion of the metal lattice into β-Mo$_2$N between 400 and 850 °C, depending on the composition. A hexagonal phase, Mo$_2$N, which would be expected by analogy with the other transition metal nitride systems, appears to be thermodynamically less stable than the cubic phase because in the ternary system Mo–C–N the

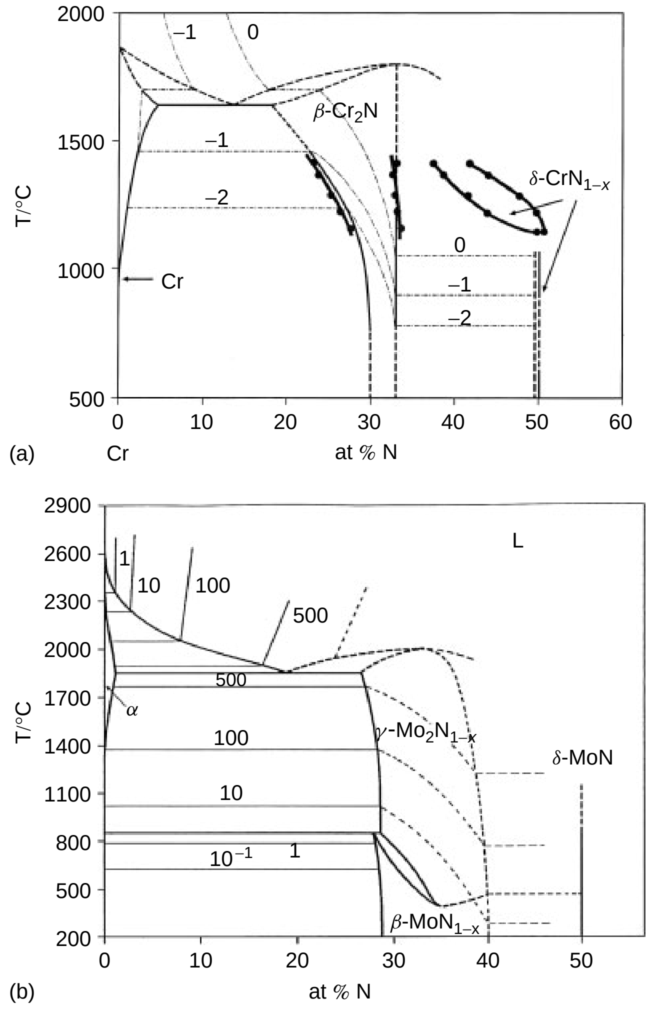

Figure 8 Phase diagrams of group 6 transition metal-nitrogen systems. (a) Cr–N system. (Ref. 11. Reproduced by permission of Materials Information Society/ASM International December, with results from diffusion couples[27]), (b) Mo–N; isobar pressures are given in bar. (Ref. 47. Reproduced by kind permission of Springer Science & Business Media)

compositional range of the hexagonal solid solution $Mo_2(C,N)$ extends from Mo_2C to approximately $Mo_2(C_{0.35},N_{0.65})$.[49]

Another phase, δ-MoN, with a structure similar to that of WC, has been prepared by various methods including nitridation of Mo powder with flowing ammonia and reaction of $MoCl_5$ with NH_3. It has been structurally characterized to have several types of ordered arrangements of nitrogen in the centers of trigonal prismatic structure elements.[50]

While at least 15 different nitride phases with compositions ranging between W_2N and WN_2 have been reported, none of them appear to be very well characterized. As for the Mo–N system, an fcc nitride WN_{1-x} appears to exist since nitridation experiments[51] under pressure in the Mo–W–N system have shown that the fcc MoN_{1-x} phase is able to form extended solid solutions with the isotypic phase WN_{1-x}. The pressure required to bring molecular nitrogen to reaction with tungsten powder at such temperatures, where kinetics are favourable, appears to be beyond the pressures available in standard laboratories. It is quite probable that another phase, WN with a WC-type structure, exists; it has at least been shown that nitrogen stabilizes the quaternary solid solution (Mo,W)(C,N) with a WC-type structure. Except for the solubility of nitrogen in bcc WN, no reliable data for this system are available.

5.2.9 The Mn–N, Fe–N, Ni–N and Co–N Systems

The Mn–N system[11] bears some resemblance to the Cr and Fe nitride systems. The correspondence to the Cr–N system manifests itself by the existence of the Mn_2N_{1-x} phase with a cph arrangement on Mn atoms as well as two nearly cubic phases with compositions η-Mn_4N_3 and δ-Mn_6N_5.

Similarity to the Fe–N system is reflected by the extensive solid solubility of nitrogen, particularly in the fcc manganese (austenite) phase and the occurrence of a ferromagnetic Mn_4N phase. The nitrides with higher nitrogen contents, η-Mn_4N_3 and δ-Mn_6N_5, can only be prepared by the reaction of ammonia with manganese powder at rather low temperature, suggesting that the equilibrium pressures of nitrogen are very high even at moderate temperatures. η-Mn_4N_3 resembles in its structure the ordered phases Mn_4N_3 and β-Mn_2N, where ordering of the nitrogen atoms at the interstitial sites is accompanied by a tetragonal distortion of the cubic lattice. The θ-Mn_6N_5 phase comes very close to the stoichiometric composition MnN but still has a clearly visible tetragonality of the basically fcc lattice. CrN apparently stabilizes an fcc solid solution extending from CrN up to $(Cr_{0.2}Mn_{0.8})N_{1-x}$ at 1000 °C and 800 bar N_2.[52]

The solubility of nitrogen in austenite (γ-Fe) is much higher than that in α-Fe, and in this respect nitrogen behaves similarly to carbon. Upon cooling of nitrogen−containing austenite, a structure develops that is similar to pearlite and is consequently called *nitrogen pearlite*. Unlike carbon, nitrogen forms an ordered Fe_4N phase that is ferromagnetic below 480−508 °C. At about 680° Fe_4N transforms into ε-Fe_2N_{1-x} and in that respect the close similarity to the Mn–N system becomes apparent. Besides ε-Fe_2N with an ordered arrangement of nitrogen atoms on the interstitial sites between the hexagonal arranged metal atoms, the ζ-Fe_2N phase with a slightly higher nitrogen content and an orthorhombic distortion of the cph metal lattice has been reported. Figure 9 presents the Fe–N system with pressure isobars.[53]

Various iron nitrides and carbonitrides are formed during case hardening of steels and alloyed steels.[54] These iron nitrides are hard, highly wear resistant and usually do not lead to dimensional changes in the case-hardened items.

While there are no phase diagrams available for the Co–N and Ni–N systems, it can be supposed that they are similar to the Fe–N system but with even higher equilibrium pressures. Several phases have been prepared by the reaction of flowing ammonia with Co and Ni powder.

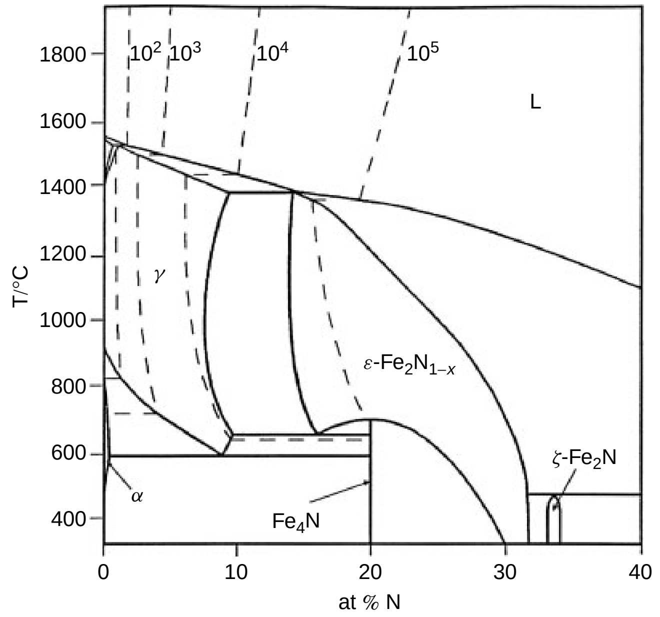

Figure 9 Phase diagram of the Fe–N system: isotherm pressures are in bar; the region around the ζ-Fe_2N phase has been modified. (Ref. 53. Reproduced by permission of Royal Institute of Technology, Stockholm)

5.2.10 Ternary and Higher-order Nitride Systems

Binary transition metal nitrides can form ternary solid solutions with each other if they are isostructural and if their lattice parameters differ by no more than about 10–15%. δ-VN_{1-x} and δ-ZrN_{1-x} do not form extensive solid solutions with each other and the intersolubility of δ-VN_{1-x} and δ-HfN_{1-x} is not complete.

Ternary phases with structures different from those of the phases of the binary boundary systems are more the exception than the rule. Such phases have been reported in the systems Nb–Mo–N, Ta–Mo–N, Nb–Ta–N, Zr–V–N, Nb–Cr–N, and Ta–Cr–N. Information about ternary transition metal-nitrogen systems is often available for specific temperatures only.[55] This is even more the case for quaternary nitride systems, which play a role in the production of carbonitride cermets where quaternary compounds of the types (Ti,Mo)(C,N) and (Ti,W)(C,N) are of interest (*see* ***Carbides: Transition Metal Solid-state Chemistry***), as well as in layer technology where titanium nitride-based coatings of the type Ti(C,B,N) are prepared by magnetron sputtering. Layers consisting of ternary compounds of the type (Ti,Al)N and (Ti,V)N also have favorable properties[56] with respect to abrasion resistance.

A further group of ternary nitrides are of the type $R_2Fe_{17}N_x$ where R is a rare earth element such as Sm, Ce or Nd, and x indicates the variable nitrogen content. These phases have been prepared, by nitridation at relatively low temperatures and up to 15 MPa N_2, under which conditions the nitrogen content can reach $x = 3$. They are closely related to borides and carbides with the similar formula and have attracted considerable interest for hard-magnetic applications.[57] It has been reported that these phases can reach compositions where $x = 6$, using a combination of hydrogen and nitrogen treatments.

Additional generally interesting phases from the crystal chemistry viewpoint are the H-phases,[58] for example, Ti_2AlN, nitrogen perovskites, filled β-manganese-type phases, and Nowotny[6] phases.

6 PROPERTIES OF fcc TRANSITION METAL NITRIDES

For carbonitrides, (*see* ***Carbides: Transition Metal Solid-state Chemistry***).

6.1 Melting Points

Melting points of various nitrides[59] have been measured under nitrogen pressures up to 300 bar. The nitrogen pressure has to be chosen in such a way as to be equal to the nitrogen equilibrium pressure of the nitride at its melting point. The melting point temperatures of the various nitrides can reach more than 3000 °C and can be read from the phase diagrams given in Section 5.2.

6.2 Color

Many mononitrides exhibit vivid colors of a bright metallic appearance that depends on the N/T ratio. Table 1 lists the colors of the mononitrides and gives some idea on their color-composition interdependency. These colors can be observed in bulk samples, and also have an important role when thin films[60] are produced for ornamental purposes.

6.3 Thermal and Electrical Properties

Interestingly, the transition metal carbides and nitrides do not show the expected decrease in heat conductivities with temperature but instead an increase.[61] Figure 10 illustrates this property for the group 4 nitrides and shows a comparison with group 4 carbides and carbonitrides. The substitution of nitrogen by carbon in group 4 transition metal nitrides significantly reduces the heat conductivities.

The electrical conductivities of transition metal carbides and nitrides are greatly influenced by the nonmetal/metal ratio; as this ratio approaches unity the electrical conductivity reaches a maximum. This is shown for δ-TiN_{1-x} in Figure 11.[63] A similar behavior can be observed for other carbides and nitrides. The electrical conductivities of these compounds decrease linearly with increasing temperature.[62]

The phenomenon of superconductivity is common for all fcc transition metal nitrides of groups 4 and 5 and is also observed in fcc MoN_{1-x} and hexagonal MoN. δ-NbN_{1-x}

Table 1 Bulk properties of important transition metal nitrides

Nitride	Homogeneity range[a] $1-x$ at 1700 K	Structure (Bravais lattice)	Lattice parameter (room temp.) (nm)	Density ($g\,cm^{-3}$)	Color	Microhardness (room temp.) (GPa)	Melting point[b] (K)	Heat conduct.[b] (room temp.) ($W\,m^{-1}\,K^{-1}$)	Thermal exp. coefficient at 1000 K ($10^6\,K^{-1}$) comp. $(1-x)$	Electr. resistance (room temp.)[b] ($\mu\Omega$ cm)	Supercond. transition temp. T_c (K) comp. $(1-x)$
TiN_{1-x}	0.50	fcc	0.4215	–	Metallic gray	23	–	–	–	–	<1
	1.00		0.4242	5.39[c]	Golden yellow	17	3050	29	9.5	27	5.8
ZrN_{1-x}	0.72	fcc	0.4585	–	Yellow	–	–	–	–	–	–
	1.00		0.4570	7.32[c]	Yellow	13	3000	25	7.8	24	10.47
HfN_{1-x}	0.85	fcc	0.4523	–	Light yellow	13.9 (0.94)	–	–	–	–	8.7 (0.85)
	1.06		0.4516	13.83[c]	Dark green yellow	16	3330	31	8.5	27	6.92
VN_{1-x}	0.70	fcc	0.4060	6.05	Brown yellow	13.0	–	–	11.0	–	2.7 (0.76)
	1.00		0.4138	6.04	Brown	5.7	2350	11	10.8	65	8.9
NbN_{1-x}	0.70	fcc	0.4380	8.24 (0.92)	Pale yellow	13.0	–	–	9.5 (0.92)	–	13.8 (0.84)
	1.00		0.4392	8.16	Pale yellow	11.0	[d]	3.8	10.2 (0.95)	60	17.2
TaN_{1-x}	0.72 (2200 K)	fcc	0.4345	–	–	–	–	–	–	–	–
	1.00		0.4238	15.9[c]	Gray yellow	32	[d]	–	8.0	–	8.9 (0.94)
TaN	1.00	hex	a0.5190 c0.2911	–	–	–	[d]	9.5	–	128	–
CrN	1.00 (1500 K)	fcc	0.4148	6.14	Gray	11	1300[d]	11.7	2.3	640	[f]
CrN_{1-x}	0.31[e]	hcp	a0.4750[g] c0.4430[g]	6.51	Gray	12[g]	–	–	–	–	[f]
	0.50		a0.4796 c0.4470	–	–	14[b]	1800	–	–	81	–
MoN_{1-x}	0.40	fcc	0.4139	–	–	–	–	–	–	–	–
	0.62 (1200 K)		0.4162	9.84[c]	Gray	17[b]	–	–	9.3	–	5.08
MoN	–	hex	a0.5745 c0.6122	9.1[c]	Gray	–	–	–	–	–	15.1

[a] Nitrogen-rich phase boundary depends on nitrogen pressure. [b] Exact composition unknown, probably close to 2:1 (CrN_{1-x}, MoN_{1-x}) or 1:1 (all others) stoichiometry. [c] X-ray density. [d] Decomposes. [e] Calculated. [f] Not superconducting. [g] Exact composition unknown.

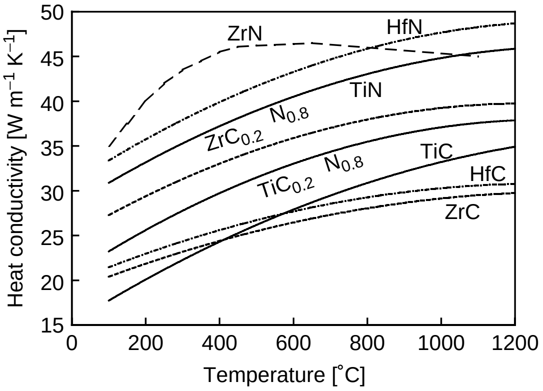

Figure 10 Heat conductivities of nearly stoichiometric and substoichiometric δ-TiN_{1-x}, δ-ZrN_{1-x} and δ-HfN_{1-x} compared with δ-TiN_{1-x}, δ-ZrC_{1-x}, δ-HfC_{1-x} and δ-$Ti(C_{0.2}N_{0.8})$ and δ-$Zr(C_{0.2}N_{0.8})$ as a function of temperature. δ-$Hf(C_{0.2}N_{0.8})$ coincides closely with the curve for TiN[62]

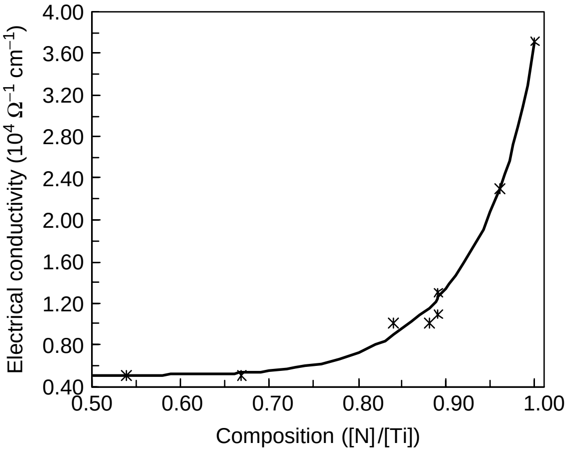

Figure 11 Electrical conductivity at room temperature of δ-TiN_{1-x} as a function of stoichiometry. (Reprinted from Ref. 63. © 1992, with permission from Elsevier)

shows the highest superconducting transition temperature of 17 K, which was the highest known of any material for several decades. It is noteworthy that hexagonal δ-MoN also has one of the highest superconducting transition temperatures (15 K) of these materials,[50] and fcc γ-$MoN_{1.00}$, although never prepared with a stoichiometric composition, was predicted theoretically to have a T_c of up to 30 K. All transition metal nitrides are type II (hard) superconductors. For several fcc nitrides, such as δ-TiN_{1-x}, δ-ZrN_{1-x} and δ-VN_{1-x}, T_c increases linearly with increasing nitrogen content up to $[N]/[T] = 1$;[64] δ-NbN_{1-x} shows a much weaker increase. The T_c data reported for δ-HfN_{1-x} are contradictory as to whether an increase or a decrease occurs. This is probably due to the fact that δ-HfN_{1-x} can apparently exist with a hyperstoichiometric composition. T_c is expected to be reduced significantly by unoccupied metal sites in the hyperstoichiometric δ-VN_{1+x}. Figure 12 shows the normalized T_c of several fcc nitrides (where the highest T_c of each compound is equal to 1) and Table 1 shows the highest T_c for each compound for the given composition.

6.4 Thermal Expansion

The thermal expansion of various transition metal nitrides has been measured at both low temperatures[65] (8 K) and high temperatures[66] (up to 1500 K). δ-VN_{1-x} exhibits a very low or even negative thermal expansion at temperatures below 70 K. The high-temperature thermal expansion data are summarized in Figure 13.[66] Interestingly, considering its low-temperature

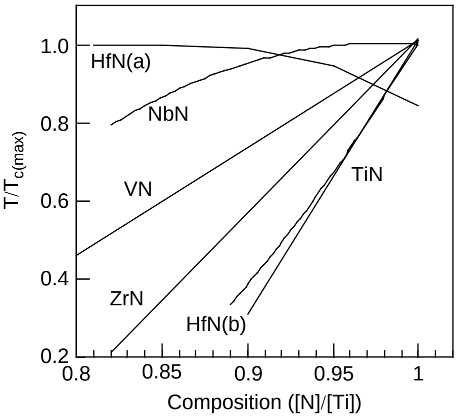

Figure 12 Superconducting transition on temperatures (normalized relative to maximum T_c) as a function of stoichiometry for various transition metal nitrides. For δ-HfN_{1-x}, different functions have been reported (a,b). (Ref. 64. Reproduced by permission of Wiley)

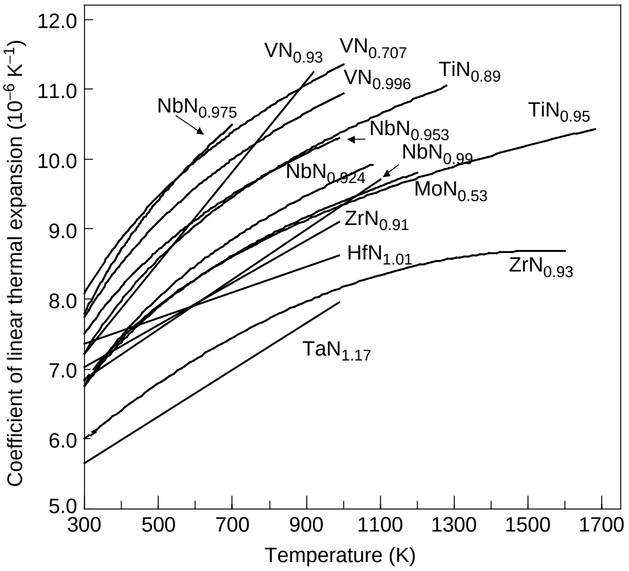

Figure 13 High-temperature thermal expansion of various transition metal nitrides. (Ref. 54. Reproduced by permission of Materials Information Society/ASM International)

thermal expansion behavior, δ-VN$_{1-x}$ has the highest high-temperature expansion coefficient among these compounds, up to $11 \cdot 10^{-6}$K^{-1} at 1100 K.

6.5 Diffusivities

In transition metal nitrides, nitrogen diffusion proceeds via a vacancy mechanism in the nonmetal sublattice. The vacancy concentration is a function of composition within the homogeneity range of the fcc phases and hence the nitrogen diffusivity is most probably composition-dependent as well. However, this has not been generally investigated in transition metal nitrides.[67] In this respect, the Cr–N system has been investigated in detail.[27] Figure 14 shows the concentration-dependent diffusivity in CrN. Generally, diffusivity studies were conducted by investigating nitride layer growth[62] as a function of time, which gives the average nitrogen diffusivity in the various phases. A parabolic relationship, $d = k \cdot t^{0.5}$, holds for this layer growth, where d is the layer thickness, k is a constant, and t the diffusion time. The parabolic behavior indicates that the nitride layer growth is indeed diffusion controlled. By use of wedge-type samples, the thickness of diffusion layers is increased if the sample thickness increases. Such a deviation from the parabolic law (if different thicknesses are compared) can be used to establish the nitrogen diffusivities in all the phases at a given temperature.[22,24] An example of such a wedge-type sample is shown in Figure 15 for the Hf–N system.[28]

Nitrogen diffusion in nitrides such as δ-TiN$_{1-x}$,[68] δ-ZrN$_{1-x}$ and δ-HfN$_{1-x}$ has an activation energy of 2–3 eV. Although the metal diffusivity in transition metal nitrides has not yet been investigated in detail, the activation energy of that process is probably much higher and can be estimated to be ca. 7–8 eV. Table 2 shows diffusivity data of transition metal nitrides.

The diffusivity versus composition has been investigated for δ-TiN$_{1-x}$, δ-HfN$_{1-x}$,[28] and δ-NbN$_{1-x}$.[69] A modified Boltzmann–Matano analysis, carried out on nitrogen diffusion profiles measured by EPMA, yielded a composition-dependent diffusion coefficient for N diffusion expressed as

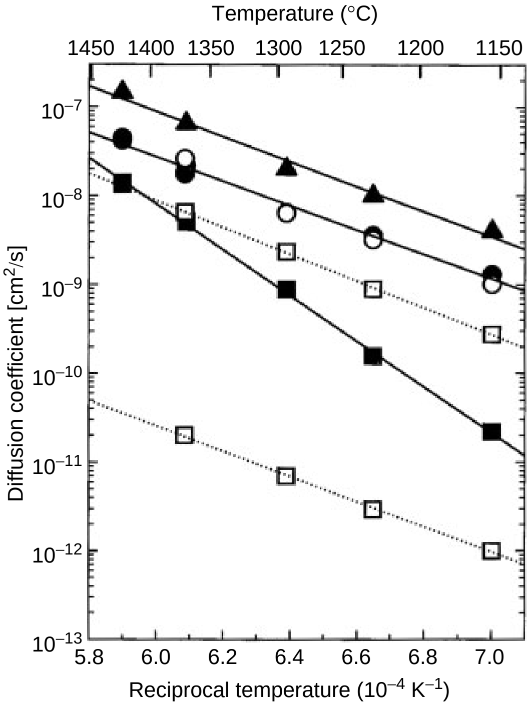

Figure 14 Temperature dependence of diffusion coefficients for the Cr–N system obtained from layer growth and concentration profiles,[27] ■/□: δ-CrN$_{1-x}$, ○/●: β-Cr$_2$N, ▲: α-Cr(N)

$$D = f\nu^2 d \exp\left(\frac{-E}{k_B T}\right) \exp(A(c^+ - c))\ \mathrm{cm^2\,s^{-1}} \tag{5}$$

where f = 1/12, for fcc compounds, ν is the jump frequency of the N atom, d is the mean distance between lattice planes, E is the activation energy, k_B is the Boltzmann constant, A is a parameter for the steepness of concentration dependency, c is the concentration and c^+ is the maximum concentration.

6.6 Elastic Properties

Transition metal nitrides exhibit high Young's moduli, appreciably higher than the elastic moduli of the transition

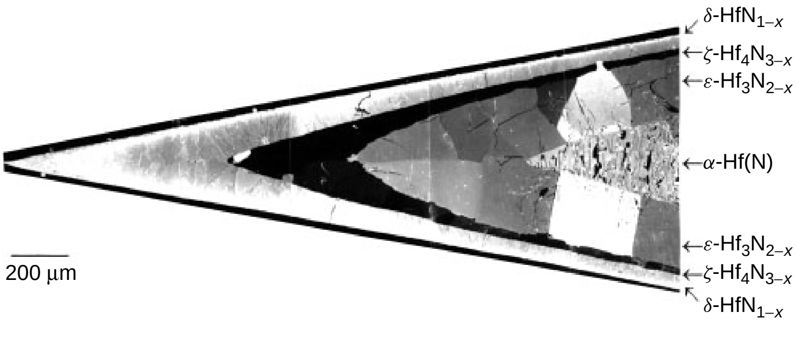

Figure 15 Wedge-type sample of the Hf–N system with various diffusion layers[28]

Table 2 Diffusion data for nitrogen in fcc transition metal nitrides

Compound	D_0 (cm^2 s^{-1})	E (eV)	A (cm^3 mol^{-1})
δ-NbN$_{1-x}$	0.68–1.10	3.2	20
β-Ta$_2$N	1.40	3.3	0
δ-CrN$_{1-x}$	0.018	2.92	183.7
δ-HfN$_{1-x}$	0.02	2.7	–
ζ-Hf$_4$N$_{3-x}$	0.14	2.74	–
η-Hf$_3$N$_{2-x}$	0.54	2.73	–
δ-VN$_{1-x}$	12.7	2.93	–
β-V$_2$N	13.6	2.92	–
δ-TaN$_{1-x}$	3.4	3.6	–
β-Nb$_2$N	120	4.0	–
β-Cr$_2$N	3.51	2.68	–

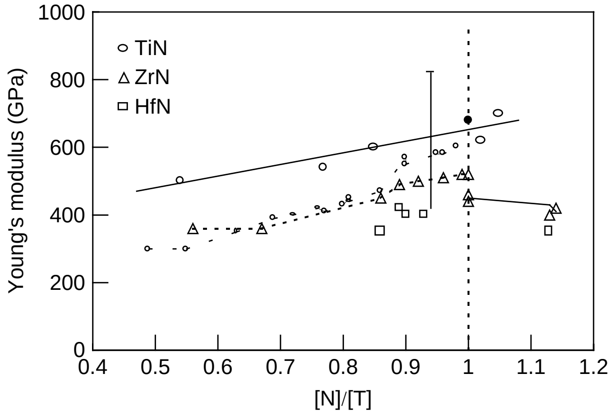

Figure 16 Young's modulus of bulk and layered group 4 transition metal nitrides. (Reprinted from Ref. 73. © 1987, with permission from Elsevier)

metals. As can be seen from Figure 16,[73] the Young's moduli of δ-TiN$_{1-x}$ and δ-ZrN$_{1-x}$ increase with increasing nitrogen to metal ratio, whereas for δ-HfN$_{1-x}$ the modulus remains approximately constant. Several of these data were obtained from thin layers. It is well known that in layers large deviations from bulk properties (lattice parameter, composition) may occur, due probably to the high concentration of defects particularly in PVD layers, while in bulk samples, pores can drastically influence the results.[72]

The elastic properties were critically reviewed by Kral *et al.*[71]

6.7 Hardness

Some transition metal nitrides are among the hardest materials known. Figure 17 shows hardness versus composition for δ-TiN$_{1-x}$ and for the group 5 transition metal nitrides. The hardness decreases with increasing nitrogen content for the group 5 nitrides.[66,70,74] This behavior can probably be explained by electronically induced lattice softening as a result of the generation of antibonding states. It is known from band structure calculations that in fcc transition metal compounds with more than eight valence electrons, antibonding states are successively occupied. An increasing valence electron concentration arising from increasing nitrogen content would then lead to a decrease in hardness when the number of valence electrons exceeds eight. Indeed, in δ-TiN$_{1-x}$ a maximum in microhardness is found at the composition δ-TiN$_{0.67}$, corresponding to 7.3 valence electrons. For δ-HfN$_{1-x}$, a smooth

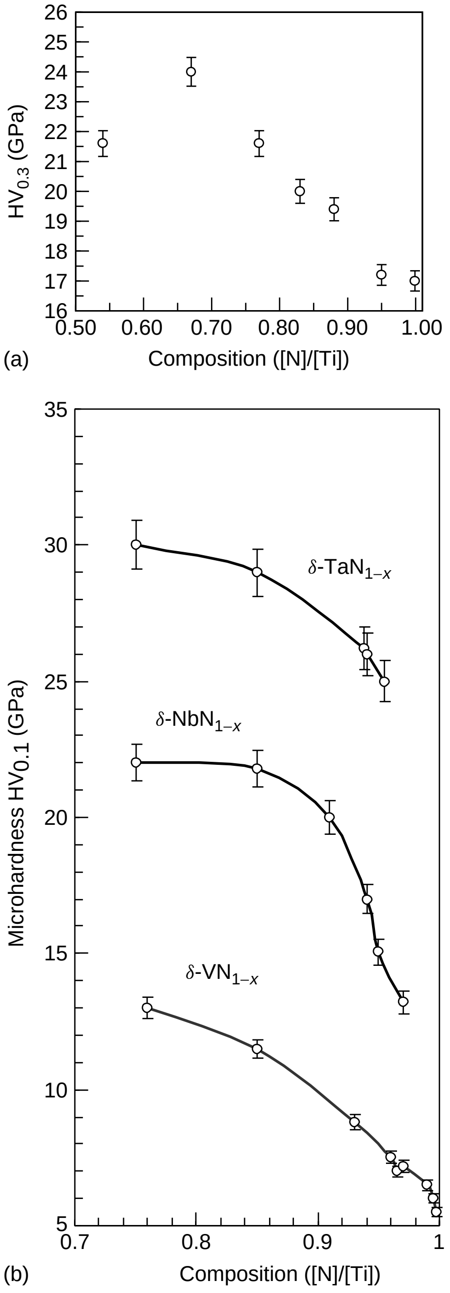

Figure 17 (a) Microhardness of δ-TiN. (Reprinted from Ref. 73. © 1992, with permission from Elsevier) and (b) group 5 transition metal nitrides as a function of composition. (Ref. 5. Reproduced by permission of Wiley VCH)

increase in microhardness with increasing nitrogen content is observed. This, however, is probably a result of the difference in electronic states owing to 5f electrons.

7 USES

Nitrides and carbonitrides in form of powders play some role in hardmetals (cemented carbides). The reader is referred to the article on Carbides of this Encyclopedia (*see* ***Carbides: Transition Metal Solid-state Chemistry***). There, also nitrided hardmetals to form functionally graded hardmetals (FGHM) are discussed.

7.1 Wear-resistant and Ornamental Layers

CVD and PVD transition metal nitride layers composed mainly of δ-TiN$_{1-x}$ and Ti(C,N) are produced in order to increase the service life of hardmetal tools for cutting and milling operations. Nitride-coated tool tips result in a better surface finish of the workpiece owing to both a decrease in diffusion welding between tool tip and workpiece and an increase in thermal oxidation resistance. The layer thickness is generally 1–10 µm. Typically, multilayer tools feature layers of TiN, TiC, TiCN, and Al_2O_3.[75] Figure 18 shows a multilayer coating including δ-TiN$_{1-x}$ on a WC-Co hardmetal. Bright golden yellow δ-TiN$_{1-x}$ is also used for ornamental layers, for example, on watch cases where the combination of color with increased scratch resistance is exploited.

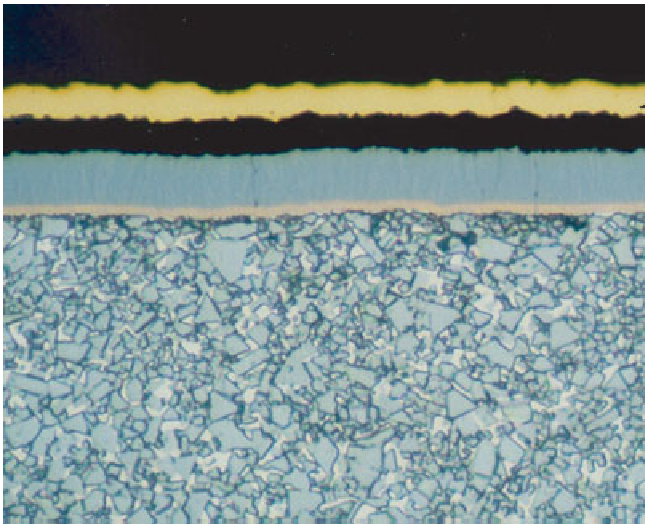

Figure 18 CVD multilayer coating on WC–Co hardmetal with TiN$_{1-x}$ as top and bottom layer

7.2 Cemented Carbonitrides

δ-TiN is used as one of the hard components in sintered hardmetal or cermet compositions containing TiC, Mo_2C, WC, TaC and other compounds. Such cermets can be produced by liquid phase sintering of blends of TiN and TiC with Mo_2C and WC and with Ni and/or Co as a binder phase. The modern titanium carbonitride cermets[76] are characterized microstructurally by a structured hard phase featuring a core-rim structure embedded in a tough Co/Ni binder alloy. In steel-cutting applications, such cermets appear to outperform even nitride-coated hardmetal tools.

7.3 Diffusion Barriers

Because of their chemical inertness, their high electrical conductivities and the ease with which they can be deposited as layers, transition metal nitrides are excellent candidates for use in multilayer metallizations of integrated circuits.[77,78] In these devices, interdiffusion between the different metals, compound layers or thin metal wires during thermal load with soldering and packaging operations must be avoided, otherwise degradation of the multilayer arrangement will occur. In order to protect these layers against interdiffusion, very thin nitride layers (<100 nm) can be deposited by PVD methods. These layers are stable up to 600 °C (depending on the time and the substrate) and prevent the layers from undergoing structural changes.

8 REFERENCES

1. P. Schwarzkopf and R. Kieffer, ‘Refractory Hard Metals’, Macmillan, 1953.
2. H. J. Goldschmidt, ‘Interstitial Alloys’, Butterworths, London, 1967.
3. L. E. Toth, ‘Transition Metal Carbides and Nitrides’, Academic Press, New York-London, 1971.
4. P. Ettmayer and W. Lengauer, Nitrides, in ‘Ullmann’s Encyclopedia of Industrial Chemistry’, Verlag Chemie, 1991, Vol. A17, p. 341.
5. W. Lengauer, in ‘Handbook of Ceramic Hard Materials’, ed. R. Riedel, Wiley-VCH, Weinheim, 2000, Vol. I, p. 202.
6. H. Nowotny and F. Benesovsky, in ‘Phase Stability in Metals and Alloys’, eds. P. S. Rudman, J. Stringer, and R. I. Jaffee, McGraw-Hill, New York, 1967, p. 319.
7. F. Kubel, W. Lengauer, K. Yvon, A. Junod, and K. Knorr, *Phys. Rev. B*, 1988, **38**, 12908.
8. G. Brauer and H. Kirner, *Z. Anorg. Allg. Chem.*, 1964, **328**, 34.
9. J. Gatterer, G. Dufek, P. Ettmayer, and R. Kieffer, *Monatsh. Chem.*, 1975, **106**, 1137.
10. J. D. Browne, P. R. Lidell, R. Street, and T. Mills, *Phys. Status Solidi*, 1970, **A1**, 715.

11. T. B. Massalski ed., ‘Binary Alloy Phase Diagrams’, 2nd edn, ASM International, Metals Park, OH, 1990.
12. K. Suzuki, T. Suzuki, Y. Fujinaga, T. Kaneko, H. Yoshida, Y. Obi, and S. Tomiyoshi, *J. Alloys Compd.*, 2002, **360**, 34.
13. P. Villars and L. D. Calvert eds, ‘Pearson’s Handbook of Crystallographic Data for Intermetallic Phases’, 2nd edn., ASM, Metals Park, OH.
14. K. Schwarz, *CRC Crit. Rev. Solid State Mater. Sci.*, 1987, **13**(3), 211.
15. A. Neckel, in ‘The Physics and Chemistry of Carbides, Nitrides and Borides’, ed. R. Freer, Kluwer Academic Publishers, Dordrecht, 1990, p. 485.
16. P. Blaha and K. Schwarz, *Int. J. Quantum Chem.*, 1983, **23**, 1535.
17. A. N. Christensen and S. Fregerslev, *Acta Chem. Scand. A*, 1978, **A31**, 861.
18. W. Lengauer, *Talanta*, 1991, **38**(6), 659.
19. R. Täubler, S. Binder, M. Groschner, W. Lengauer, and P. Ettmayer, *Mikrochim. Acta I*, 1992, **107**, 337.
20. G. F. Bastin and H. J. M. Heijligers, ‘Quantitative Electron Probe Microanalysis of Nitrogen’, University of Technology, Eindhoven, 1988.
21. W. Lengauer, J. Bauer, A. Guillou, J.-P. Bars, M. Bohn, E. Etchessahar, J. Debuigne, and P. Ettmayer, *Mikrochim. Acta I*, 1992, **107**, 303.
22. W. Lengauer, *J. Alloys Compd.*, 1995, **229**, 80.
23. D. Rafaja, W. Lengauer, and P. Ettmayer, *Acta Mater.*, 1996, **44**(12), 4835.
24. D. Rafaja and W. Lengauer, *Mater. Struct. Chem., Biol. Phys. Technol.*, 1997, **4**(2), 43.
25. W. Lengauer, J. Bauer, M. Bohn, H. Wiesenberger, and P. Ettmayer, *Mikrochim. Acta*, 1997, **126**, 279.
26. M. Dopita, B. Wollein, D. Rafaja, W. Gruner, and W. Lengauer, *Defect Diff. Forum*, 2001, **194–199**, 1613; ‘Proc. DIMAT 2000’, Scitec Publications, Uetikon-Zürich, Paris, 2000, Part 2, 17.
27. W. Mayr, W. Lengauer, D. Rafaja, J. Bauer, and M. Bohn, *J. Phase Equilib.*, 1999, **20**, 35.
28. W. Lengauer, D. Rafaja, R. Täubler, C. Kral, and P. Ettmayer, *Acta Metall. Mater.*, 1993, **41**(12), 3505.
29. W. Lengauer, D. Rafaja, G. Zehetner, and P. Ettmayer, *Acta Mater.*, 1996, **44**(8), 3331.
30. M. Hoch, in ‘Phase Stability in Metals and Alloys’, eds. P. S. Rudman, J. Stringer, and R. I. Jaffee, McGraw-Hill, New York, 1967, p. 419.
31. W. Lengauer, *Acta Metall. Mater.*, 1991, **39**, 2985.
32. G. Lobier and J. P. Marcon, *Compt. Rend. Acad. Sci. Ser. C (Paris)*, 1969, **268**, 1132.
33. W. Lengauer, *J. Alloys Compd.*, 1992, **179**, 289.
34. P. Kroll, *Phys. Rev. Lett.*, 2003, **90**(12), 125501-1.
35. E. Rudy, *Metall. Trans.*, 1970, **1**, 1249.
36. O. N. Carlsson, J. F. Smith, and R. H. Nafziger, *Metall. Trans. A*, 1986, **A17**, 1647.
37. C. Teichmann, W. Lengauer, P. Ettmayer, J. Bauer, and M. Bohn, *Metall. Mater. Trans. A*, 1997, **28A**, 837.
38. W. Lengauer, M. Bohn, B. Wollein, and K. Lisak, *Acta Mater.*, 2000, **48**(6), 2633.
39. T. Onozuka, *J. Appl. Crystallogr.*, 1978, **11**, 132.
40. T. Onozuka, *Trans. Jap. Inst. Met.*, 1982, **23**, 315.
41. G. Brauer and W. Kern, *Z. Anorg. Allg. Chem.*, 1983, **507**, 127.
42. G. Brauer and W. Kern, *Z. Anorg. Allg. Chem.*, 1984, **512**, 7.
43. R. Berger, W. Lengauer, and P. Ettmayer, *J. Alloys Compd.*, 1997, **259**, L9.
44. M. Joguet, W. Lengauer, M. Bohn, and J. Bauer, *J. Alloys Compd.*, 1998, **269**, 233.
45. H. Wiesenberger, W. Lengauer, and P. Ettmayer, *Acta Mater.*, 1998, **46**(2), 651.
46. G. Brauer, E. Mohr, A. Neuhaus, and A. Skokan, *Monatsh. Chem.*, 1972, **103**, 794.
47. P. Ettmayer and A. Vendl, in ‘Science of Hard Materials’, eds. R. K. Viswanadham, D. J. Rowcliffe, and J. Gurland, Plenum Publication Corp., 1983, p. 47.
48. V. Ucakar, F. Cheviré, F. Tessier, N. Krendelsberger, R. Marchand, and W. Lengauer, *Defect Diff. Forum*, 2001, **194–199**, 1607; ‘Proc. DIMAT 2000’, Paris, Scitec Publications, Uetikon-Zürich, 2000, Part 2, 17.
49. P. Ettmayer, *Monatsh. Chem.*, 1970, **101**, 1720.
50. A. Bezinge, K. Yvon, J. Muller, W. Lengauer, and P. Ettmayer, *Solid State Commun.*, 1987, **63**, 141.
51. G. Banik, P. Ettmayer, A. Vendl, and R. Kieffer, *High Temp. -High. Press.*, 1979, **11**, 349.
52. P. Ettmayer, A. Vendl, E. Horvath, and R. Kieffer, *Monatsh. Chem.*, 1978, **109**, 1277.
53. K. Frisk, A thermochemical evaluation of the Cr–N, Fe–N, Mo–N and Cr–Mo–N systems, Report TRITA-MAC-0393, Materials Research Center, Royal Institute of Technology, Stockholm, 1989.
54. S. Lampman, ‘ASM Handbook’, Heat Treating, ASM International, 1991, Vol. 4.
55. H. Holleck, Inst. Mater. Festkoerperforsch., Kernforschungszent. Karlsruhe G.m.b.H., Karlsruhe, Fed. Rep. Ger. Avail. INIS. Report (1981), (KFK-3087-B) 353 pp., From: INIS Atomindex 1982, 13(8), Abstr. No. 664151. Report written in German. CAN 97:79764 AN 1982:479764 CAPLUS.
56. O. Knotek, W. D. Münz, and T. Leyendecker, *J. Vac. Sci. Technol.*, 1987, **A5**, 2173.
57. K. H. J. Buschow, *Rep. Prog. Phys.*, 1991, **54**, 1123.
58. R. Ward, in ‘MTP International Rewiev of Science’, Inorganic Chemistry Series One, ed. D. W. A. Sharp, Butterworths, London, 1972, Vol. 5.
59. P. Ettmayer, R. Kieffer, and F. Hattinger, *Metall(Berlin)*, 1974, **28**, 1151.

60. A. J. Perry, M. Georgson, and W. D. Sproul, *Thin Solid Films*, 1988, **157**, 255.
61. W. Lengauer, S. Binder, K. Aigner, P. Ettmayer, A. Guillou, J. Debuigne, and M. Bohn, *J. Alloys Compd.*, 1995, **217**, 137.
62. V. S. Eremeyev, Y. M. Iwanov, and A. S. Panov, *Izv. Akad. Nauk. SSSR, Metall.*, 1969, **4**, 262.
63. W. Lengauer, *J. Alloys Compd.*, 1992, **186**, 293.
64. W. Lengauer, *Surf. Interface Anal.*, 1990, **15**, 377.
65. W. Lengauer, P. Ettmayer, and K. Yvon, *J. Less-Common Met.*, 1991, **168**, L7.
66. W. Lengauer and P. Ettmayer, *Monatsh. Chem.*, 1986, **117**, 275.
67. H. Matzke, in 'The Physics and Chemistry of Carbides, Nitrides and Borides', ed. R. Freer, Kluwer Academic Publishers, Dordrecht, 1990, p. 357.
68. F. W. Wood and O. G. Paasche, *Thin Solid Films*, 1970, **40**, 131.
69. D. Rafaja, W. Lengauer, H. Wiesenberger and M. Joguet, *Metallurgical and Materials Transactions A: Physical Metallurgy and Materials Science*, 1998, **29A**(2), 439.
70. C. Politis and G. Rejman, Kernforschungszentrum Karlsruhe GmbH, Karlsruhe (D), KfK Report Ext6/78-1, 1978.
71. C. Kral, W. Lengauer, D. Rafaja, and P. Ettmayer, *J. Alloys Compd.*, 1998, **265**(1–2), 215.
72. Q. Yang, W. Lengauer, T. Koch, M. Scheerer, and I. Smid, *J. Alloys Compd.*, 2000, **309**, L5.
73. E. Török, A. J. Perry, L. Chollet, and W. D. Sproul, *Thin Solid Films*, 1987, **153**, 37.
74. W. Lengauer and P. Ettmayer, *J. Less-Common Met.*, 1985, **109**, 351.
75. H. Westphal and V. Sottke, Patent PCT Int. Appl., WO 00017416 A1, 2002.
76. P. Ettmayer, Hardmetals and Cermets, *Annu. Rev. Mater. Sci.*, 1989, **19**, 145.
77. S. P. Murarka, *Defect Diffus. Forum*, 1988, **59**, 99.
78. H. von Seefeld, N. W. Cheung, M. Mäenpää, and M.-A. Nicolet, *IEEE Trans. Electron. Devices*, 1980, **ED-27**, 873.

Nitrogen: Inorganic Chemistry

Anton Hammerl & Thomas M. Klapötke
Universität München Butenandtstr, Munich, Germany

Based in part on the article Nitrogen: Inorganic Chemistry by Harry H. Sisler which appeared in the Encyclopedia of Inorganic Chemistry, First Edition.

1	Introduction	1
2	Dinitrogen	1
3	Atomic Nitrogen	5
4	Polynitrogen	5
5	Binary Compounds of Nitrogen and Hydrogen	11
6	Nitrogen Oxides	28
7	Oxoacids of Nitrogen	38
8	Nitrogen Halides	52
9	Oxohalides of Nitrogen	62
10	Related Articles	66
11	References	66

1 INTRODUCTION

Nitrogen, as an element of the first period, has a tendency to form $p_\pi - p_\pi$ double bonds like its neighbors carbon and oxygen. Nitrogen chemistry is therefore different from the chemistry of the heavier homologues (*see* ***Periodic Table: Trends in the Properties of the Elements***). Nitrogen forms element chains (catenation) more easily than its right neighbor oxygen, but less easy than the other neighbors carbon and phosphorus. With the appropriate substituents, nitrogen chains containing up to eight nitrogen atoms are known (see Table 1). Average nitrogen−nitrogen bond distances are 148 pm for single bonds, 120 pm for double bonds, and 110 pm for triple bonds (*see* ***Bond Lengths in Inorganic Solids & Liquids***).

As shown in Scheme 1, nitrogen compounds are known with nitrogen in the oxidation states between −3 and +5:

In compounds with moderately electropositive bonding partners, nitrogen has the coordination number one (N_2, HCN), two (angular in HN=NH, linear in Cl–N=O), three (pyramidal in NH_3; planar in $N(SiMe_3)_3$),[1] and four (tetrahedral in NH_4^+, NF_4^+). With more electropositive bonding partners, the higher coordination numbers five (quadratic-pyramidal in $[Fe_5(CO)_{14}H(\mu_5\text{-}N)]$), six (octahedral in MN, M = Sc, Ti, V, Cr, Th, U; trigonal prismatic in $[Co_6(CO)_{15}(\mu_6\text{-}N)]^-$) and eight (cubic in BeLiN, $AlLi_3N_2$; hexagonal-bipyramidal in Li_3N) are known (*see* ***Coordination Numbers & Geometries***). Nitrogen compounds of all nonradioactive elements except helium, neon, and argon have been isolated, although compounds such as XN^+ with helium, neon, and argon have been detected using mass spectrometry.

Two isotopes of nitrogen are found in nature, ^{14}N (99.634%, magnetic dipole moment $\mu_N = +0.403761$, electrical quadrupole moment 1.60×10^{-30} m^{-2}) and ^{15}N (0.366%, magnetic dipole moment $\mu_N = -0.28319$, no electrical quadrupole moment).[2] The average mass is 14.00674 atomic mass units. The relation between the isotopes may be different by up to 1.5% for nitrogen from other sources than air, for example, in natural gas or in gas pockets in the Earth's crust. ^{15}N is used for labeling in NMR spectroscopy and mass spectrometry. All other nitrogen isotopes have half-lives that are much too short to be of use in labeling experiments (see Table 2).

Fractional distillation of ^{15}NO is an effective method for concentrating ^{15}N. Chemical exchange processes for nitrogen isotope separation include the following:

$$^{15}NH_3(g) + {}^{14}NH_4{}^+(aq) \longrightarrow {}^{14}NH_3(g) + {}^{15}NH_4{}^+(aq) \tag{1}$$

$$^{15}NO(g) + {}^{14}NO_3{}^-(aq) \longrightarrow {}^{14}NO(g) + {}^{15}NO_3{}^-(aq) \tag{2}$$

The NO–NO_2 equilibrium can be used in thermal diffusion separation.

$$^{14}NO_2(g) + {}^{15}NO(g) \longrightarrow {}^{15}NO_2(g) + {}^{14}NO(g) \tag{3}$$

2 DINITROGEN

In 1772, the German Carl Scheele, the Englishman Henry Cavendish, the Scotsman Daniel Rutherford, and Joseph Priestley, who was also English, all independently discovered dinitrogen or studied its equivalent, 'burnt' air or air where the oxygen was removed. A. L. Lavoisier named it azôte (from the Greek word meaning 'lifeless'). After niter (potassium nitrate) and nitric acid were recognized as compounds of the element, the name nitrogenium (Latin, 'niter former') was introduced by the French J. A. C. Chaptal.[3,4]

Nitrogen occurs almost exclusively in nature as dinitrogen N_2. It is the main part of dry air (78.09% by volume, 75.52% by weight), which accounts for more than 99% of the approximately 10^{15} tons of nitrogen on earth. At higher altitudes, dinitrogen is partly dissociated to nitrogen by ultraviolet radiation. Other nitrogen species with very short lifetimes are also formed under stratospheric conditions. The high solubility of nitrogen salts makes minerals containing nitrogen, mainly nitrates, rare. The major minerals are saltpeter KNO_3, occurring in large deposits in India and Chile saltpeter $NaNO_3$, which can be found in the desert sections of northern Chile. Calcium nitrate, ammonium chloride, and several other compounds can occasionally be found in small amounts. Another 10^{13} tons of dinitrogen are

−3	−2	−1	±0	+1	+2	+3	+4	+5
NH_3	N_2H_4	N_2H_2	N_2	N_2O	NO	N_2O_3	NO_2	N_2O_5

Scheme 1 Examples of nitrogen compounds in various oxidation states

Table 1 Examples of nitrogen chains

n(N)	Bonding pattern	Examples
3	N–N=N	$\mathrm{HN(CH_3)–N{=}NH}$
3	N=N=N	HN=N=N
4	N–N=N–N	$\mathrm{H_2N–N{=}N–NH_2}$
4	N–N–N–N	$\mathrm{(CF_3)_2N–(CF_3)N–(CF_3)N–N(CF_3)_2}$
5	N=N–N–N=N	$\mathrm{PhN{=}N–N(CH_3)–N{=}NPh}$
5	N≡N–N–N≡N	$\mathrm{N{\equiv}N–N–N{\equiv}N^+\ SbF_6^-}$
6	N=N–N–N–N=N	PhN=N–N(Ph)–N(Ph)–N=NPh
8	N=N–N–N=N–N–N=N	PhN=N–N(Ph)–N=N–N(Ph)–N=NPh

dissolved in the oceans. Like many other gaseous compounds, dinitrogen is also included in water clathrate complexes, for example $(H_2O)_{136}(N_2)_{9.4}$, which was found in Greenland. Extraterrestrially, nitrogen has been detected in the atmosphere of Mars (2.7 vol%), Venus (3.5 vol%), Pluto, and possibly in traces on Mercury. Nitrogen also occurs in proteins and other organic compounds in the biosphere (10^{10} t). It is an essential element for humans; the human body contains about 3% nitrogen, which is found in proteins, DNA, and many coenzymes. There are several processes, referred to as nitrogen fixation, making dinitrogen available to biological species. In lightning, enough energy is set free to activate dinitrogen molecules for the reaction with dioxygen, forming nitrogen oxides. Industrial nitrification is discussed in Section 5.1.1. Some bacteria can form ammonia from dinitrogen (*see* ***Nitrogenase: Metal Cluster Models*** and ***Nitrogenase Catalysis & Assembly***). In the nitrification process, ammonia is converted to nitrate via nitrite by bacteria under aerobic conditions. In anaerobic conditions, bacteria convert nitrate via nitrite to the gaseous compounds NO, N_2O, and N_2.

2.1 Production of Dinitrogen

The technical production of dinitrogen and other nitrogen compounds is discussed in great detail in the literature.**[5]** A compilation of physical data for many compounds is published.**[6]** For all technical processes, dinitrogen is obtained from air, where cryogenic (low temperature), adsorption, and membrane separation processes are used. The chemical removal of dioxygen from air is an older method that is of secondary importance. The cryogenic production is based on the fractionized distillation of liquid air. Nitrogen production by pressure-swing adsorption (PSA) employs carbon or zeolitic molecular sieves. Separation of air components with zeolites is based on differences in adsorption capacity; carbon molecular sieves employ differences in diffusion rates. In

Table 2 Properties of nitrogen isotopes

	Mass [amu]	Spin	Mode of decay	$t_{1/2}$	Decay energy [MeV]
^{10}N	10.0426180 ± 0.0004290	–		39.70 s	–
^{11}N	11.0267962 ± 0.0001932	+1/2	p^+	5×10^{-22} s	2.290
^{12}N	12.0186132 ± 0.0000011	+1	e^- capture	11 ms	17.338
			e^-capture + 3α (3%)		
^{13}N	13.0057386 ± 0.0000003	−1/2	e^- capture	9.965 min	2.220
^{14}N	14.0030740 ± 0.0000000	+1	stable	–	–
^{15}N	15.0001089 ± 0.0000000	+1/2	stable	–	–
^{16}N	16.0061014 ± 0.0000028	−2	β^-	7.13 s	10.419
^{17}N	17.0084497 ± 0.0000161	−1/2	β^-	4.173 s	8.680
			$\beta^- +$ n		4.536
^{18}N	18.0140818 ± 0.0000215	−1	β^-	624 ms	13.899
			$\beta^- + \alpha$		7.672
^{19}N	19.0170269 ± 0.0000176	–	β^-	290 ms	12.527
			$\beta^- +$ n (64%)		8.571
^{20}N	20.0233673 ± 0.0000565	–	β^-	142 ms	17.970
			$\beta^- +$ n (66.1%)		10.360
^{21}N	21.0270876 ± 0.0000959	−1/2	β^-	89 ms	17.170
			$\beta^- +$ n (80%)		13.360
^{22}N	22.0344403 ± 0.0002103	–	β^-	18 ms	22.800
			$\beta^- +$ n (35%)		15.950
^{23}N	23.0405100 ± 0.0007600	–	–	15 ms	–
^{24}N	24.0505000 ± 0.0005400	–	N	<52 ns	1.200

carbon molecular sieves, the unadsorbed N_2-rich gas product is withdrawn at the discharge end of the adsorber during the adsorption phase. In the zeolite process, previously adsorbed nitrogen is recovered by lowering the pressure during the regeneration phase. The membrane separation process uses membranes that have different permeabilities for different gases. The total nitrogen production in Europe, the United States, and Japan amounted to $59.6 \times 10^9\,m^3$ in 1996. The production of gaseous nitrogen is growing more rapidly than that of liquid nitrogen. The largest applications need dinitrogen gas and have, therefore, always been most economically served by gas. Today, noncryogenic production technologies such as membranes and PSA are making gas production economical at customer sites.

Nitrogen from the cryogenic distillation of air has an inherent high purity since virtually all bulk gases with higher boiling points (methane, water, carbon dioxide) are removed to less than ppb levels by volume. The very low boiling gases helium, hydrogen, and neon are not removed by standard single-column cryogenic processes, nor is carbon monoxide, which is difficult to separate by cryogenic fractionation because of its boiling point of 81.6 K. CO and H_2 can be removed from the compressed air before distillation by oxidation in an upstream catalytic reactor with a noble metal catalyst. The oxidation products are water and carbon dioxide, which can be removed by the conventional air-purification system. Downstream purifier systems operate by oxidation over metal oxides and chemisorption by transition metals. Thus, nickel at ambient temperature eliminates oxygen as the oxide and hydrogen as the hydride.

In a chemical process, oxygen can be removed from air ($4N_2 + O_2$) by oxidation with carbon, propane gas, or ammonia and successive removal of carbon dioxide and water. Because air also contains noble gases, chemical processes do not yield pure dinitrogen but a mixture of dinitrogen and noble gases.

$$4N_2 + O_2 + C \longrightarrow 4N_2 + CO_2 \tag{4}$$

Partial burning of carbon produces carbon monoxide (see Section 5.1.1):

$$4N_2 + O_2 + 2C \longrightarrow 4N_2 + 2CO \tag{5}$$

In the laboratory, copper can be used to bind oxygen at red heat:

$$4N_2 + O_2 + 2Cu \longrightarrow 4N_2 + 2CuO \tag{6}$$

Pure dinitrogen can be obtained from nitrogen compounds, for example, the oxidation of ammonia with CaCl(OCl) or bromine. More often, nitrous acid is used to include the nitrogen of the acid:

$$NH_3 + HNO_2 \longrightarrow N_2 + 2H_2O \tag{7}$$

The thermal decomposition of azides, especially of sodium azide, is used to produce spectroscopically pure dinitrogen:

$$2NaN_3 \longrightarrow 2Na + 3N_2 \tag{8}$$

The largest-volume of dinitrogen is used for the synthesis of ammonia. As an alloying element in steel, nitrogen serves to improve hardness and corrosion resistance. The inert dinitrogen is used as a blanketing gas to prevent oxidation or fire. It is also used for the processing, cooling, storage, and transportation of food. Liquid nitrogen provides the cryogenic temperature necessary for freezing, and nitrogen vapor as an inert medium inhibits oxygen-dependent ripening and decay processes. Embrittlement of grinding feed, shrink fitting of metal parts, cryosurgery, or the conservation of biological samples are only a few examples of the many uses of liquid nitrogen.

2.2 Physical Properties of Dinitrogen

Dinitrogen is a colorless, odorless, noncombustible gas with a density of $1.2505\,g\,dm^{-3}$ at standard conditions ($C_p = 29.12\,J\,mol^{-1}\,K^{-1}$). The boiling point is 77.36 K (enthalpy of vaporization: $5.577\,kJ\,mol^{-1}$) and the melting point is 63.15 K (enthalpy of fusion: $0.7196\,kJ\,mol^{-1}$) (see Table 3). Two solid phases of dinitrogen exist (see Table 4), the standard β-phase (hexagonal close-packed N_2 molecules) and the α-phase (cubic close-packed N_2 molecules). The standard enthalpy of transition is $228.9\,kJ\,mol^{-1}$. At pressures above 350 Mpa, tetragonal γ-N_2 is formed. Gaseous dinitrogen has a specific heat capacity of $1.040\,J\,g^{-1}\,K^{-1}$, a dynamic viscosity of 15.9×10^{-6} Pa and a thermal conductivity of $25.9\,mW\,m^{-1}\,K^{-1}$ (298).

The bond distance in N_2 is 109.75 pm and the bond dissociation energy of the N–N triple bond is $945.33\,kJ\,mol^{-1}$.

N_2 is soluble in metal melts, for example, 4% dinitrogen can be solved in iron melts. Dinitrogen is only half as soluble as dioxygen in water (see Table 5). This is important for

Table 3 Properties of N_2[7]

	Triple point	Critical point	Boiling point
T [K]	63.15	126.2	77.35
p [MPa]	12.463×10^{-3}	3.39908	0.1013
ρ [$g\,dm^{-3}$]	0.6803 (g) 867.7 (l) 947 (s)	314.03	4.61 (g) 808.6 (l)

Table 4 Properties of solid dinitrogen

Modification	Existence range [K]	ρ [$g\,dm^{-3}$]	p_{vapor} [kPa]
α	0–35.6	1027	1.47×10^{-11}
β	35.6–63.15	948	6.3

Table 5 Solubility of nitrogen in different solvents

Solvent	T[K]	$p(N_2)$ [MPa]	Solubility [mol N_2 kg^{-1}]
Water	273	0.1	1.04×10^{-3}
	298	0.1	6.2×10^{-4}
	298	10	5.6×10^{-2}
	298	100	0.32
Ethanol	293	0.1	6.8×10^{-3}
Blood	311	0.1	6.2×10^{-4}
γ-Iron	1273	0.1	8×10^{-3}

the breathing of marine life. Dinitrogen has no apparent effect on plants, animals, or humans. Suffocation in dinitrogen atmosphere is due to the lack of dioxygen. The higher solubility of dinitrogen in blood at high pressures is responsible for decompression sickness and nitrogen narcosis, known as the ‘bends’, in divers.

2.3 Chemical Properties of Dinitrogen

Dinitrogen is relatively inert under standard conditions due to the high stability of the nitrogen–nitrogen triple bond. This makes most reactions of dinitrogen endothermic. Exothermic reactions of dinitrogen have high activation barriers. Unlike dioxygen (IE 13.618 eV), dinitrogen cannot be oxidized chemically to the cation N_2^+ because of the high ionization energy of dinitrogen (15.576 eV).**4**

The reactivity of the N_2 molecule increases rapidly as the temperature is increased. At higher temperatures, compounds with many metals and nonmetals are formed. Binary nitrogen compounds, which sometimes cannot be obtained by the direct reaction, have been found for most elements. Binary noble-gas nitrogen compounds have been detected mass spectrometrically (e.g. XN^+, XN_2^+). Among the prominent reactions of dinitrogen are the reaction of dinitrogen with hydrogen to form ammonia (in detail see Section 5.1.1), the reaction of dinitrogen with dioxygen at elevated temperatures to form NO (in details see Section 7.8.1), and the reaction of dinitrogen with calcium carbide at 1300 K ($\Delta H = -296\,\text{kJ mol}^{-1}$) to form calcium cyanamide, which is used for nitrogen fixation.

$$CaC_2 + N_2 \longrightarrow CaCN_2 + C \tag{9}$$

While the latter reactions are no longer used for nitrogen fixation, the reaction of dinitrogen with dihydrogen to form ammonia is among the most important industrial processes. The alkaline-earth metals react readily with dinitrogen at elevated temperatures to form nitrides; lithium reacts even at room temperature with dinitrogen.

The nitrides (*see* ***Nitrides: Transition Metal Solid-state Chemistry***) can be divided roughly into ionic nitrides (e.g. alkali and alkaline-earth nitrides), covalent nitrides (e.g. BN (*see* ***Boron: Inorganic Chemistry***), S_4N_4 (*see* ***Sulfur–Nitrogen Compounds***), CN_2 (*see* ***Carbon: Inorganic Chemistry***), S_2N_2 (*see* ***Sulfur–Nitrogen Compounds***), As_4N_4, P_3N_5, Ge_3N_4, Se_4N_4 (*see* ***Selenium: Inorganic Chemistry***), Te_4N_4 (*see* ***Tellurium: Inorganic Chemistry***)), and semimetallic phases (VN, CrN, W_2N). In semimetallic phases, the nitrogen atoms are interstitial or included in more complex structures. The nitride ion, N^{3-}, is only stable with very Lewis basic cations. Even in the alkaline-earth metal nitrides M_2N_3 (M = Be–Ba), the metal–nitrogen bond has a covalent contribution.

Nitrogen can form complexes with compounds of most transition metals. These play an important role in the biological nitrogen fixation process (*see* ***Nitrogenase: Metal Cluster Models*** and ***Nitrogenase Catalysis & Assembly***), where bacteria use dinitrogen complexes to form other nitrogen compounds. Metal complexes of dinitrogen can be synthesized directly from the reaction of dinitrogen with metal salts in a reducing environment (10) or by the oxidation of metal coordinated ammonia (11) or hydrazine (12).

$$[MoCl_4(PR_3)_2] \xrightarrow[-NaCl]{Na,\ N_2} Mo(N_2)(PR_3)_4 \tag{10}$$

$$[C_5H_5Mn(CO)_2(N_2H_4)] + H_2O_2 \longrightarrow [C_5H_5Mn(CO)_2(N_2)] + 4H_2O \tag{11}$$

$$[Os(NH_3)_5(N_2)]^{2+} + HNO_2 \longrightarrow [Os(NH_3)_4(N_2)_2]^{2+} + 2H_2O \tag{12}$$

The dinitrogen ligand is often easily displaced by other ligands. Some dinitrogen complexes can be reduced to ammonia or hydrazine complexes and are model compounds for the biological nitrogen fixation process. Homoleptic metal dinitrogen complexes $M(N_2)_x$ are not stable at standard conditions but can be obtained by the rapid chilling of metal/dinitrogen gas mixtures below 10 K (e.g. $Ti(N_2)_6$, $V(N_2)_6$, $Cr(N_2)_6$, $Rh(N_2)_4$, $Ni(N_2)_4$, $Pd(N_2)_3$, $Pt(N_2)_3$). These compounds are metastable at low temperatures and loose dinitrogen upon warming. $Ti(N_2)_6$ decomposes at 40 K.

As shown in Scheme 2, most dinitrogen complexes show a σ end-on coordination of the dinitrogen molecule (**1**) (e.g. octahedral $[Os(NH_3)_4(N_2)_2]^{2+}$). The end-on coordination (**2**) is also found for bridging dinitrogen ligands (e.g. $[\{Ru(NH_3)_5\}_2N_2]^{2+}$). Side-on coordination via the $N_2\pi$-orbitals has been found in very few complexes. Planar side-on coordinated dinitrogen (**3**) is found in $\{(C_5Me_5)_2Sm\}_2(N_2)$. In some zirconium complexes, for example, $[(i\text{Pr}_2PCH_2SiMe_2)_2N]ZrCl_2(\mu\text{-}\eta^2\text{:}\eta^2\text{-}N_2)$, a bent coordination (**4**) is found. (*see* ***Nitrogenase: Metal Cluster Models*** and ***Nitrogenase Catalysis & Assembly***).

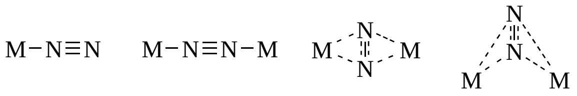

(1) **(2)** **(3)** **(4)**

Scheme 2 Coordination of dinitrogen in transition metal complexes

3 ATOMIC NITROGEN

An electric discharge in a N_2 atmosphere in the pressure range 1.0–0.1 hPa splits dinitrogen molecules to atomic nitrogen. This is accompanied by a peach–yellow glow that persists for up to 6 h after stopping the discharge.**[8]**

Atomic nitrogen ($\Delta H_f = 472.7\,\mathrm{kJ\,mol^{-1}}$) is very reactive. It reacts with many metals to form nitrides at room temperature.

$$3\mathrm{Mg} + 2\mathrm{N} \longrightarrow \mathrm{Mg_3N_2} \qquad (13)$$

Atomic nitrogen also reacts with nonmetals like phosphorus and sulfur (*see* ***Phosphorus–Nitrogen Compounds*** and ***Sulfur–Nitrogen Compounds***).

Recombination of the nitrogen atoms to N_2 is a slow process since it requires a three-body collision of the nitrogen atoms with the walls of the container or a termolecular, homogeneous second-order association of the nitrogen atoms. This can result in excited dinitrogen molecules that are responsible for the yellow glow.

$$\mathrm{N(^4S)} + \mathrm{N(^4S)} \xrightarrow{\mathrm{(M)}} \mathrm{N_2^*} \longrightarrow \mathrm{N_2} + h\nu(\text{yellow}) \qquad (14)$$

The excited dinitrogen molecules N_2^* can break bonds in other molecules:

$$\mathrm{N_2^*} + \mathrm{CO_2} \longrightarrow \mathrm{N_2} + \mathrm{CO} + \mathrm{O(^3P)} \qquad (15)$$

Nitric oxide NO molecules can be used to determine the concentration of the nitrogen atoms.

$$\mathrm{N(^4S)} + \mathrm{NO} \longrightarrow \mathrm{N_2} + \mathrm{O(^3P)} \qquad (16)$$

This rapid reaction stops the yellow glow. If excess NO is present, the oxygen atoms react with NO to form NO_2 under emission of a green–yellow light:

$$\mathrm{NO} + \mathrm{O(^3P)} \longrightarrow \mathrm{NO_2^*} \longrightarrow \mathrm{NO_2} + h\nu(\text{green–yellow}) \qquad (17)$$

whereas a blue light is emitted if not enough nitrogen oxide is present:

$$\mathrm{N(^4S)} + \mathrm{O(^3P)} \longrightarrow \mathrm{NO^*} \longrightarrow \mathrm{NO} + h\nu(\text{blue}) \qquad (18)$$

4 POLYNITROGEN

In contrast to the other elements, the homonuclear single-bond energies of nitrogen (159 kJ mol^{-1}) (and oxygen) are significantly less than one-third of their triple (945.33 kJ mol^{-1}) or one-half of their double-bond (466 kJ mol^{-1}) energies (*see* ***Main Group: Multiple Bonding***). Compounds with high nitrogen content are synthesized for use as high-energy materials.**[9]** The nitrogen–nitrogen double bond energy is also less than two-thirds of the triple bond energy. As a consequence, ordinary nitrogen consists of diatomic molecules, which are very stable and remarkably unreactive and reluctant, in particular, to bind to other N atoms to give N_n species with $n > 2$. Homonuclear polynitrogen species are thermodynamically highly unstable, since invariably their dissociation into N_2 is highly exothermic, and there are only very few compounds known.**[10]** Owing to the highly endothermic heats of formation, their syntheses and handling present great challenges. No nitrogen compounds are known that can be isolated in bulk, while most other elements can exist in the form of many stable allotropes. Owing to the great experimental difficulties, most polynitrogen species have only been studied theoretically. Molecular nitrogen forms a non-molecular superconductor that exists at equilibrium over a very large range of pressures, from below 100 GPa to at least 240 GPa.

4.1 Trinitrogen

The azide radical $N_3\bullet$ (linear, ground state $^2\Pi_g$, d(N–N) 118.1 pm) is produced in the reaction of HN_3 with fluorine atoms ($\Delta H_r = -180\,\mathrm{kJ\,mol^{-1}}$):

$$\mathrm{F\bullet} + \mathrm{HN_3} \longrightarrow \mathrm{N_3\bullet} + \mathrm{HF} \qquad (19)$$

The enthalpy of formation of the azide radical is 467 ± 8 kJ mol^{-1}. The spin-allowed dissociation to $\mathrm{N(^2D)}$ and $\mathrm{N_2(X\ ^1\Sigma_g^+)}$ is endoergic by 225 kJ mol^{-1}, the dissociation enthalpy to $\mathrm{N(^4S)} + \mathrm{N_2(X^1\Sigma_g^+)}$ is – 0.5 ± 1 kJ mol^{-1}.**[11]** The azide radical is only stable because this spin-forbidden decomposition pathway has an appreciable energy barrier. In aqueous solution, it primarily exists as a monomer, in contrast to other halide or pseudohalide radicals that exist as the less reactive dimers (e. g. $\mathrm{Br_2^{-\bullet}}$, $\mathrm{(SCN)_2^{-\bullet}}$). Reaction of the azide radical with halogen atoms or other small molecules like O_2, NO, CO, and CO_2 produces molecules in electronically excited states because of propensity rules, which can be used for chemically pumped lasers.**[12]** The azide ion is also formed during high-pressure photolysis of sodium azide.

4.1.1 N_3^+

The trinitrogen cation is produced in nitrogen plasmas through the reaction of energized N_2^+ ions with N_2 molecules. Formation in the atmosphere probably involves ternary reactions of N^+ and N_2.[13] In the atmosphere, it reacts with H_2O to form H_2NO^+ and with O_2 to form NO^+. N_3^+ ($X\,^1\Sigma g^+$) has a linear, centrosymmetric structure like the azide radical and the azide anion ($D_{\infty h}$, d(N–N) $= 119.3$ Å). It is quite strongly bound with a dissociation energy of about 3.5 eV:

$$N_3^+(X\,^3\Sigma_g) \longrightarrow N^+(^3P) + N_2(X\,^1\Sigma_g^+) \tag{20}$$

Attempts to remove the fluorine atom of N_3F with the strong fluorine acceptors AsF_5, SbF_5, or BF_3 only yielded the adducts $N_3F{\cdot}AsF_5$ and $FN_3{\cdot}BF_3$ and explosions in the case of SbF_5. The N_3^+ cation was not observed in this reaction.[14] Electrostatically bound $(N_3)^+$-$(N_2)_n$ clusters have been observed mass spectrometrically.[15]

The azide ion is discussed in Section 5.8.

4.2 Tetranitrogen

The metastable singlet T_4 species tetraazatetrahedrane (**5**) shown in Scheme 3 is the best theoretically investigated N_4 species. The dissociation to N_2 has an activation energy of 54 kJ mol^{-1} to release as much as 800 kJ mol^{-1} of energy. Density functional calculations show the open-chain C_{2h} triplet (**6**), which releases 505 kJ mol^{-1} upon decomposition, to be the global minimum structure whereas a MP4 study shows it to be a transition state and identifies the C_s triplet (**7**) as the global minimum. The metastable D_{2h} singlet (**8**), which releases 766 kJ mol^{-1} upon decomposition, was also found at the B3LYP level.

A van-der-Waals dimer $(N_2)_2$ with a dissociation energy of only about 1 kJ mol^{-1} has been detected experimentally. Another N_4 species, which was prepared by neutralizing N_4^+, was detected mass spectrometrically,[16] and is believed to be the C_s triplet because of its fragmentation pattern. The geometry of the starting material N_4^+ also points to a linear structure.

4.2.1 N_4^+

The N_4^+ cation is formed in electric discharges through nitrogen.[17] N_2^+ is formed by interaction of cosmic rays with N_2 in the stratosphere and can, in denser regions of the ionosphere, form N_4^+, which might play a role as an intermediate that reacts very rapidly with other species in the atmosphere. N_4^+ ($X\,^2\Sigma_u^+$) has a linear, centrosymmetric structure. The dissociation energy to N_2 ($X\,^1\Sigma_g^+$) and N_2^+ ($X\,^2\Sigma_u^+$) is only slightly higher than 96 kJ mol^{-1}. The terminal N–N bond is with 110.9 pm slightly longer than in N_2 and slightly shorter than in N_2^+ (111.6 pm). The inner N–N bond is with 200.4 pm rather long. Mass spectrometrically observed $(N_2)_n^+$ clusters contain a N_4^+ core.

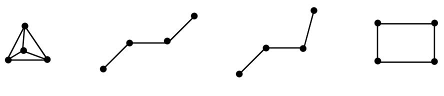

(5) T_4 **(6)** C_{2h} **(7)** C_s **(8)** D_{2h}

Scheme 3 Connectivity of theoretically predicted N_4 isomers

4.3 Pentanitrogen

While the symmetric, weak complex between a $N_3{\bullet}$ radical and N_2 (**9**) in Figure 1 was shown to be minimum on the potential surface, higher-level computations indicate that this complex is not stable.[18]

4.3.1 N_5^+

The pentanitrogen cation has an essentially planar V-shape structure (C_{2v}). The exceptional stability of N_5^+ is largely due to resonance stabilization shown in Scheme 4, resulting in relatively high bond orders for all the bonds.[19] The additional, higher charged Lewis structures in the second row have to be included to account for the charge distribution of N_5^+.[20] The geometrical parameters of the pentanitrogen cation in $N_5^+Sb_2F_{11}^-$ are shown in Table 6.

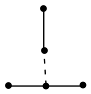

(9)

Figure 1 Connectivity of N_5 minimum structure

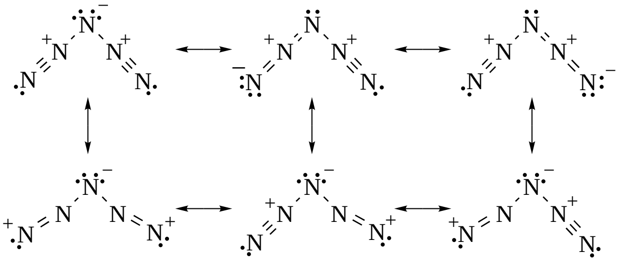

Scheme 4 Mesomeric structures of N_5^+

Table 6 Geometrical parameters of the pentanitrogen cation in $N_5^+Sb_2F_{11}^-$

d(N1-N2) [pm]	110(2)	d(N4-N5) [pm]	111(2)
d(N2-N3) [pm]	130(2)	<(N1-N2-N3) [°]	168(2)
d(N3-N4) [pm]	130(2)	<(N2-N3-N4) [°]	111(1)

The reaction of $N_2F^+MF_6^-$ salts (M = As, Sb) with HN_3 yields the N_5^+ cation (C_{2v}).[21]

$$N_2F^+MF_6^- + HN_3 \xrightarrow[195\,K]{HF} N_5^+MF_6^- + HF \tag{21}$$

Using the insolubility of $KSbF_6$ in SO_2 and of $CsSbF_6$ in HF, salts of N_5^+ have been prepared in metathetical reactions:

$$N_5^+SbF_6^- + K[B(CF_3)_4] \xrightarrow[214K]{SO_2} N_5^+[B(CF_3)_4]^- + KSbF_6 \tag{22}$$

$$2N_5^+SbF_6^- + Cs_2SnF_6 \xrightarrow[195\,K]{HF} (N_5^+)_2SnF_6^{2-} + 2CsSbF_6 \tag{23}$$

$(N_5^+)_2SnF_6^{2-}$ is only marginally stable at room temperature and decomposes at slightly higher temperatures yielding $N_5^+ SnF_5^-$ and FN_5, which has a lifetime of nanoseconds and decomposes instantly to dinitrogen and fluorine azide, whose further decomposition yields several NF compounds (see Section 8.6).

$$(N_5^+)_2SnF_6^{2-} \longrightarrow N_5^+SnF_5^- + N_2 + FN_3 \tag{24}$$

While $N_5^+AsF_6^-$ and $(N_5^+)_2SnF_6^{2-}$ are only marginally stable at room temperature and decompose at slightly elevated temperatures, the decomposition of N_5^+ $[B(CF_3)_4]$ starts at 323 K and the decomposition of N_5^+ SbF_6^- and $N_5^+Sb_2F_{11}^-$ at 343 K, thus indicating the limits of the thermal stability of the N_5^+ ion.

$N_5^+SbF_6^-$ oxidizes NO, NO_2, and Br_2, but does not oxidize Cl_2, O_2, or Xe, indicating an ionization potential between 10.52 and 11.48 eV.

So far, N_5^+ has not been combined with a polynitrogen anion to form a new modification of nitrogen. Theoretical consideration and experimental investigations agree that $N_5^+N_3^-$ is not stable. However, calculations indicate that the salt $N_5^+N_5^-$ may be stable.[22]

4.3.2 N_5^-

Both pentazole N_5H and the pentazole anion N_5^- consist of a five-membered ring of nitrogen atoms. Huisgen and Ugi synthesized the first pentazole derivatives RN_5 with substituted phenyl rings.[23] Tetrazolylpentazole and imidazolylpentazole, the pentazole derivatives of five-membered aromatic rings, are also known.[24] The geometry of the pentazole ring system was determined from the crystal structures of *p*-dimethylaminophenylpentazole, which decomposes at 340 K, and phenylpentazole (see Table 7). The pentazole ring system is planar with almost equal N–N distances.

Table 7 Geometrical parameters of the pentazole ring system in phenylpentazole

d(N1-N2) [pm]	132(1)	N1-N2-N3 [°]	105.3(1)
d(N2-N3) [pm]	130.8(2)	N2-N3-N4 [°]	108.9(1)
d(N3-N4) [pm]	133.7(6)	N3-N4-N5 [°]	109.0(1)
d(N4-N5) [pm]	130.7(8)	N4-N5-N1 [°]	105.3(1)
d(N1-N5) [pm]	132.2(2)	N2-N1-N5 [°]	111.5(1)

Kinetic studies on *p*-substituted phenylpentazoles have demonstrated that electron-donating substituents on the phenyl ring such as NMe_2 and electron-withdrawing substituents such as NO_2, respectively increase and decrease the stability of pentazole with respect to decomposition. Thus, maximum negative charge in the pentazole ring leads to the most stable compounds. Therefore, the pentazole anion N_5^- is the most stable pentazole species with an estimated activation energy of decomposition of 116 kJ mol^{-1}, and a reaction enthalpy of 60 kJ mol^{-1} for the decomposition forming the azide ion and N_2.[25] Pentazole N_5H has an estimated activation energy of 68 kJ mol^{-1} for the decomposition to dinitrogen and hydrazoic acid. NMR spectroscopic studies yielded accurate kinetic data for the decomposition of arylpentazoles (see Scheme 5), and proved that the pentazole ring is relatively stable in solution. On reaction of an azide ion with an aryl diazonium compound, three open-chain ArN_5 compounds are formed.[26] One isomer (Z, E) decomposes instantly to phenylazide and dinitrogen, another (E, E) can rearrange to a third isomer (E, Z), which can also be formed directly and undergoes cyclization to form a pentazole. Decomposition follows a different mechanism: phenylpentazole is involved in a 1,3-dipolar cycloreversion with elimination of dinitrogen to form phenylazide.

With negative ion electrospray ionization of *p*-hydroxyphenylpentazole and laser desorption ionization of *p*-dimethylaminophenylpentazole, it was possible to cleave the C–N bond between the aromatic substituent and the pentazole in $R-N_5$ and to observe the pentazole anion mass spectrometrically.[27]

4.4 Hexanitrogen

Quantum chemical calculations of the N_6 potential-energy hypersurface have shown that the qualitative shape strongly depends on the choice of the theoretical method and basis set. All the geometries represented in Scheme 6 have been shown to be minima on the potential surface, but most of them do not possess minima at all the levels of theories applied. Hexaazabenzene (**13**), for example, has a minimum for a D_{6h} structure at the HF level of theory. However, this geometry is a second-order saddle point with the density functional theory (DFT) and also at the MP2 level of theory. D_2 hexaazabenzene has a minimum structure at DFT, but at the CCSD(T)/aug-cc-pVDZ level, the D_2 geometry resembles a van der Waals complex of two N_3 units, whereas it is a minimum structure at the CCSD(T)/cc-pVTZ level of theory. Similar behavior has been observed for most of the other isomers.

Only the first two compounds, an open-chain diazide (**10**)[28] and hexaazadewarbenzene (**11**) have minima at all levels of

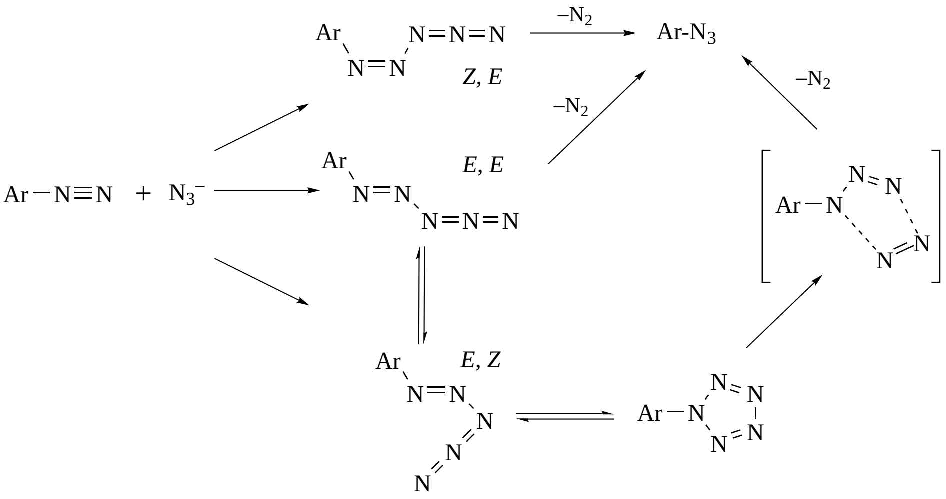

Scheme 5 Formation and decomposition of the pentazole ring system

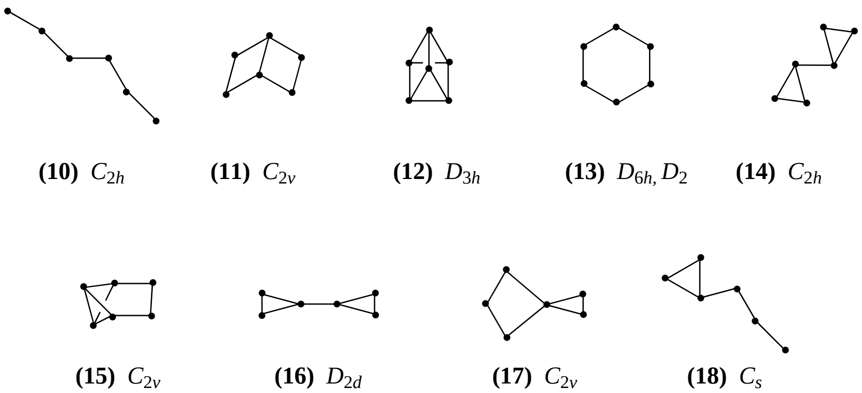
(10) C_{2h} **(11)** C_{2v} **(12)** D_{3h} **(13)** D_{6h}, D_2 **(14)** C_{2h}

(15) C_{2v} **(16)** D_{2d} **(17)** C_{2v} **(18)** C_s

Scheme 6 Connectivity for calculated geometries of N_6

theory applied. The diazide (**10**) has a planar *trans-* C_{2h} structure and is the global minimum structure for N_6, the C_{2v} hexaazadewarbenzene (**11**) is 230 kJ mol^{-1} higher in energy. The diazide (**10**) decomposes with a concerted elimination of two N_2 molecules. The decomposition barrier is estimated to be about 70–80 kJ mol^{-1}.[18]

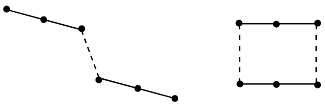
(**19**) (**20**)

Scheme 7 Connectivity of calculated N_6^- isomers

4.4.1 N_6^-

The reaction of the azide radical $N_3\bullet$ with excess azide ions in solution forms the hexanitrogen radical anion ($\Delta H = 18$ kJ mol^{-1}).[29]

$$N_3\bullet + N_3^- \rightleftharpoons N_6^{-}\bullet \tag{25}$$

The hexanitrogen radical anion is more stable in acetonitrile solution compared to water. In the absence of added quenchers, it decays with approximately second-order kinetics with a half-life of 10 µs. During the high-pressure photolysis (1.1 GPa) of sodium azide, N_6^- ions have also been detected.

Using quantum chemical calculations, the two minima in Scheme 7 have been found for N_6^-. Both are formal dimers of N_3 with large distances between the azide units.

At the highest level of theory applied, the *trans* form (**19**) was calculated to be more stable than the rectangular form (**20**) by about 2 kJ mol^{-1}.[18]

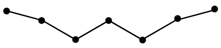

(**21**) C_{2v}

Figure 2 Connectivity of N_7 minimum structure

4.5 Heptanitrogen

A C_{2v} open-chain structure (**21**) in Figure 2 was found to be the global minimum structure for N_7, but complications of the calculations suggest that neutral N_7 does not have a significant dissociation barrier similar to N_5.**[30]**

For N_7^+, an open-chain structure (**22**) shown in Figure 3 and similar to (**21**), which was found for N_7, was calculated. The decomposition of the open-chain N_7^+ to the N_5^+ cation and dinitrogen has a calculated activation barrier of 13 kJ mol^{-1}.**[31]**

For N_7^-, the open-chain C_2 structure (**23**) in Scheme 8 is the global minimum. It is favored by 36 kJ mol^1 over the complex C_s structure (**25**) and 45 kJ mol^{-1} over the C_s ring structure (**24**). The activation energy for the decomposition was calculated to be 5 kJ mol^{-1} for the open-chain structure (**23**), which decomposes to the azide anion and two molecules of dinitrogen and to 18 kJ mol^{-1} for the ring structure (**24**).**[31]**

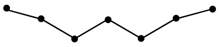

(**22**) C_{2v}

Figure 3 Connectivity of N_7^+ minimum structure

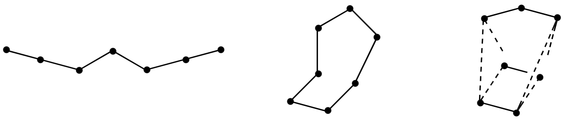

(**23**) C_2 (**24**) C_s (**25**) C_s

Scheme 8 Connectivity of calculated N_7^- isomers

4.6 Octanitrogen

Several isomers of N_8 have been studied theoretically (see Scheme 9).**[32]** Azidopentazole (**26**) is the global minimum structure (964 kJ mol^{-1} above 4 N_2). Octaazapentalene (**27**) is 72 kJ mol^{-1} higher in energy, *cis*-(**29**) and *trans*-(**28**) diazidodiimide ($N_3{-}N{=}N{-}N_3$) are 58 kJ mol^{-1} and 63 kJ mol^{-1} higher in energy and octaazacubane (**30**) is 939 kJ mol^{-1} higher in energy.

Azidopentazole (**26**) is believed to decompose forming four dinitrogen molecules (activation energy 59 kJ mol^{-1}). The violently explosive tetrazolylazide, which is derived from azolylpentazole by the exchange of one nitrogen with a carbon atom and the addition of a hydrogen atom, shows the high-energy content of these systems.**[33]** Octaazapentalene (**27**) decomposes by rearrangement to azidopentazole (**26**) (activation energy 37 kJ mol^{-1}) and the diazodiimides (**28**) and (**29**) decompose via elimination of a dinitrogen molecule (activation energies: *cis* 80 kJ mol^{-1}, *trans* 91 kJ mol^{-1}). The least motion unimolecular decomposition of octaazacubane (**30**) to four dinitrogen molecules is spin forbidden, as is the case also for its hydrocarbon analogue cubane C_8H_8. However, a non-least-motion pathway was found that reduces the activation barrier to less than 80 kJ mol^{-1}.

4.7 Nonanitrogen

For the decomposition of the C_{2v} open-chain nonanitrogen N_9 (**31**), in Figure 4 to open-chain N_7 (**28**) and N_2, a dissociation barrier of 69 kJ mol^{-1} was calculated.**[34]** Bearing in mind that no true minimum structures for N_5 and N_7 have been found, the calculated dissociation barrier for N_9 seems to be too high.

4.8 Decanitrogen

The C_{3v} triazidoamine (**33**) in Scheme 10 represents a minimum structure at lower levels of theory; at the MP2 level, however, it does not represent a minimum. Dipentazole (D_{2d}) (**32**) decomposes to azidopentazole (**26**) and dinitrogen

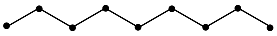

(**31**)

Figure 4 Connectivity of N_9 minimum structure

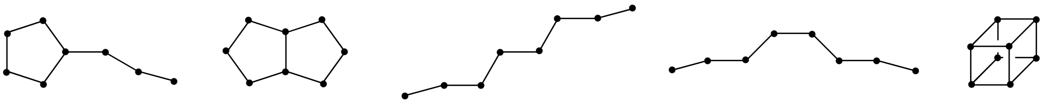

(**26**) C_s (**27**) D_{2h} (**28**) C_{2v} (**29**) C_{2h} (**30**) O_h

Scheme 9 Connectivity of calculated N_8 isomers

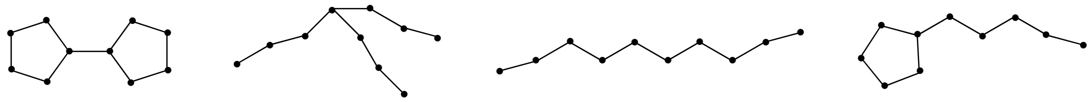

(**32**) D_{2d} (**33**) C_{3v} (**34**) C_{2h} (**35**) C_s

Scheme 10 Connectivity of calculated N_{10} isomers

with an activation barrier of 21.2 kJ mol^{-1}.[25] It is very improbable that dipentazole (**32**) can be isolated, because the activation energy for the decomposition of the experimentally known tetrazolylpentazole, where one nitrogen atom is exchanged by carbon, was calculated by the same method to be 48 kJ mol^{-1}, and tetrazolylpentazole decomposes at temperatures above 220 K.[24] Calculations have shown that the activation energy for the decomposition of azolylpentazoles decreases with an increasing number of nitrogen atoms in the five-membered ring. Imidazolylpentazole, which has two nitrogen atoms, decomposes above 248 K. Therefore, dipentazole could only be observed at temperatures that are below 200 K, maybe much below 200 K. The activation energy for the decomposition of open-chain C_{2h} N_{10} (**34**) to open-chain N_8 (**28**) and dinitrogen was calculated to be 64 kJ mol^{-1}. The C_s pentazole isomer (**35**) has an activation energy of 49 kJ mol^{-1} for the decomposition to open-chain N_8 (**28**) and dinitrogen. Calculations also indicate that salts of the type $N_5^+N_5^-$ with the experimentally known N_5^+ and N_5^- ions are stable against charge transfer reactions between the ions. A $N_5^+N_5^-$ salt is the most likely candidate for the synthesis of solid nitrogen.[22]

4.9 Undecanitrogen

The C_s isomer (**36**) containing two pentazole ring systems in Scheme 11 was calculated to be 180 kJ mol^{-1} lower in energy than the C_2 isomer (**37**) and 312 kJ mol^{-1} lower than the open-chain C_{2v} isomer (**38**). For the decomposition of the C_{2v} open-chain undecanitrogen (**38**) a dissociation barrier of 59 kJ mol^{-1} to open-chain N_9 (**31**) and N_2 was calculated.[34] As remarked for the dissociation barrier of nonanitrogen, this activation barrier for the decomposition of (**38**) also seems to be too high.

The open-chain N_{11}^+ cation (**40**) in Scheme 12 is 30 kJ mol^{-1} higher in energy than the pentazole derivative (**39**), which is the lowest energy N_{11}^+ structure reported.

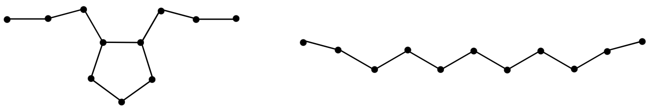

(**39**) C_{2v} (**40**) C_{2v}

Scheme 12 Connectivity of calculated N_{11}^+ isomers

For N_{11}^-, an open-chain global minimum structure with the connectivity of (**40**) was reported.[35]

4.10 Dodecanitrogen

Several minima have been found on the N_{12} energy hypersurface (see Scheme 13).[36] The azobispentazole C_{2h} structure (**41**) is the global minimum structure. It has an activation energy of 17 kJ mol^{-1} for the decomposition to the N_{10} pentazole isomer (**35**) and dinitrogen.[37] The C_s pentazole derivative (**42**) decomposes to open-chain N_{10} (**34**) and N_2 with an activation energy of 39 kJ mol^{-1} and the open-chain C_{2h} N_{12} (**43**) decomposes to the open-chain N_{10} (**34**) and dinitrogen with an activation energy of 61 kJ mol^{-1}. Further reported N_{12} isomers have activation energies of less than 5 kJ mol^{-1}. The azobistetrazolate dianion, where one nitrogen atom of each pentazole ring of (**41**) is formally exchanged with C^-, is a remarkably stable species that is used in high-energy materials.[38]

Higher polynitrogen species have also been calculated, but only at lower levels of theory because of computational cost. As was discussed above for the hexanitrogen isomers, the results of the calculation on polynitrogen energy hypersurfaces are heavily dependant on the method employed and the basis set used. Lower level calculations of the structures and properties of polynitrogen species have not given accurate results in the past. Therefore, polynitrogen species larger than dodecanitrogen are not discussed here.

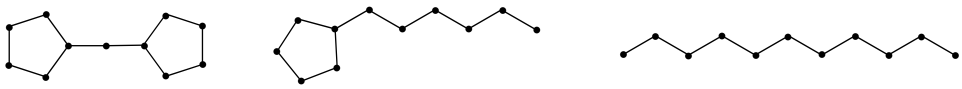

(**36**) C_s (**37**) C_2 (**38**) C_{2v}

Scheme 11 Connectivity of calculated N_{11} isomers

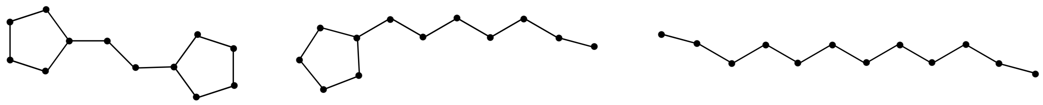

(**41**) C_{2h} (**42**) C_s (**43**) C_{2h}

Scheme 13 Connectivity of calculated N_{12} isomers

Table 8 Binary compounds of nitrogen and hydrogen

Saturated	Cyclic	Unsaturated	Polyunsaturated	Salts
NH_3		NH		$NH_4^+N_3^-$
N_2H_4		$H_2N{=}NH_2$		$N_2H_5^+N_3^-$
$H_2N–NH–NH_2$	$(NH)_3$	$H_2N–N{=}NH$	HN=N=N	$N_2H_5^+N_3^-{\cdot}N_2H_4$
$H_2N–NH–NH–NH_2$		$H_2N–N{=}N–NH_2$		

Table 9 Physical properties of ammonia

m.p. [K]	195.42	$S°(g)$ [J mol^{-1} K^{-1}]	192.77(5)
b.p. [K]	239.72	Dielectric constant	25
ΔH_f [kJ mol^{-1}]	−45.94	μ [D]	1.47
ΔG_f [kJ mol^{-1}]	−16.391	Ionization energy [kJ mol^{-1}]	979.7
ΔH_{fusion} [kJ kg^{-1}]	332.3	Proton affinity [kJ mol^{-1}]	841
$\Delta H_{vaporization}$ [kJ kg^{-1}]	1373		

5 BINARY COMPOUNDS OF NITROGEN AND HYDROGEN

Nitrogen forms several binary compounds with hydrogen (see Table 8). A review of binary nitrogen–hydrogen compounds can be found in the literature.[39,40] Substitution of hydrogen atoms by organic substituents leads to organic derivatives that are often more stable than the binary nitrogen–hydrogen compounds. Ammonia, hydrazine, diazene (diimine), hydrazoic acid, and tetrazene have been isolated so far. Ammonia and hydrazine also form salts with hydrazoic acid, that is, ammonium azide and hydrazinium azide. Hydrazinium azide forms an adduct with another hydrazine molecule, resulting in hydrazinium azide hydrazinate. Other binary nitrogen compounds, which have not been isolated but have been detected experimentally include nitrene, triazane, *cyclo*-triazane, tetrazane, and triazene. Hydrogenpentazole is discussed in Section 4.3.2.

5.1 Ammonia

Ammonia is a colorless, diamagnetic gas with a characteristic, penetrating odor that is irritating to the eyes and mucous membranes at concentrations higher than 100 ppm. At higher concentrations, ammonia paralyzes the breathing organs which may be fatal.[4,40] Some physical properties of ammonia are given in Table 9.

The ammonia molecule has a pyramidal structure (see (26)) with C_{3v} symmetry (d(N–H) 101.1 pm, $<$(H–N–H) 106.18°). Solid ammonia crystallizes in a distorted cubic close packed structure, where every nitrogen atom is surrounded by six other nitrogen atoms with N–N distances of 338 pm, thus every nitrogen atom is involved in six hydrogen bonds. Upon melting, about 27% of the hydrogen bonds are broken. Another 7% are broken while heating to the boiling point (see Table 10). The high vaporization enthalpy is the result of breaking the remaining hydrogen bonds, and it allows the use of ammonia as a refrigerant. Ammonia shows anomalies in its melting and boiling point as well as in the enthalpies of fusion and vaporization compared to the heavier homologues PH_3, AsH_3, SbH_3, and BiH_3. As for H_2O and HF, which show similar anomalies in their periodic group, these anomalies are explained by hydrogen bonding.

The ammonia molecule can undergo inversion of configuration with a planar transition state (activation energy

Table 10 Characteristics of ammonia

	Triple point	Critical point	Boiling point
T [K]	195.44	405.4	239.72
p [MPa]	6.077	11.35	0.1013
ρ [g cm^{-3}]	0.2362	0.235	0.682(l) 0.000888 (g)

24.5 kJ mol^{-1}).

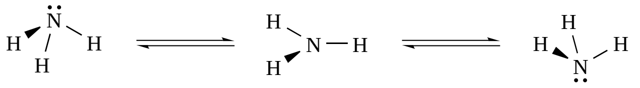

(26)

The observed microwave frequency of $2.387 \times 10^{10}\,s^{-1}$ for the inversion of ammonia is higher than the frequency calculated from the inversion barrier. The reason is quantum chemical tunneling through the inversion barrier. Because tunneling is proportional to the weight of the atoms, the inversion of ND_3 with the heavier deuterium atoms has a frequency of $1.591 \times 10^{9}\,s^{-1}$, roughly 1/15 of the frequency of ammonia. Derivatives of ammonia are also subject to this inversion with higher or lower activation energies depending on the substituent. Highly electronegative substituents increase the inversion barrier (250 kJ mol^{-1} in NF_3), π-bonding of the nitrogen lone pair to the substituent decreases the activation barrier (5.6 kJ mol^{-1} in H_2NCN).

Ammonia is stable at ambient conditions, but decomposes to the elements in the presence of catalysts at higher temperatures ($\Delta H = 92.28\,kJ\,mol^{-1}$). This decomposition also takes place under UV irradiation or in electric discharges.

$$2NH_3 \rightleftharpoons N_2 + 3H_2 \qquad (27)$$

In the presence of catalysts, ammonia reacts with oxygen to form nitrogen oxide at relatively low temperatures of 500–700 K ($\Delta H = -906.1\,kJ\,mol^{-1}$).

$$4NH_3 + 5O_2 \longrightarrow 4NO + 6H_2O \qquad (28)$$

This reaction is used for the synthesis of nitric acid in the Ostwald process (see Section 7.8.1). Without catalysts, and at higher temperatures, ammonia burns in an oxygen atmosphere with a pale yellow flame forming the thermodynamically favorable products dinitrogen and water ($\Delta H = -1267\,kJ\,mol^{-1}$). At high pressures, mixtures of ammonia and oxygen are explosive.

$$4NH_3 + 3O_2 \longrightarrow 2N_2 + 6H_2O \qquad (29)$$

Strong oxidants like H_2O_2, $KMnO_4$, HOCl, HNO_2, or Cl_2 oxidize ammonia to dinitrogen ($E^\circ = 0.27\,V$ at pH 1, see Scheme 26).

$$2NH_4^+ \rightleftharpoons N_2 + 8H^+ + 6e^- \qquad (30)$$

If chlorine is passed through a concentrated solution of ammonia or through ammonia gas, ammonia starts to burn and dinitrogen and HCl are formed.

$$2NH_3 + 3Cl_2 \longrightarrow N_2 + 6HCl \qquad (31)$$

The reaction of dilute chlorine with dilute ammonia yields chloramine, which can, under the right conditions, react with excess ammonia to form hydrazine (see Section 5.2.1). Fluorine reacts more vigorously than chlorine with ammonia. Bromine shows about the same reactivity and iodine reacts less vigorously. Ammonia reacts with phosphorus to form PH_3 and N_2 (*see* ***Phosphorus–Nitrogen Compounds***), with sulfur to form H_2S and S_4N_4 (*see* ***Sulfur–Nitrogen Compounds***) and with red-hot carbon to form NH_4CN and H_2 (*see* ***Carbon: Inorganic Chemistry***).

Ammonia and all other amines, NR_3, are bases. A solution of ammonia in water is mildly alkaline ($pK_b = 4.75$). Ammonia dissolves readily in water (1.176 m^3 at 273 K, 0.702 m^3 at 298 K in 1 L of water) under evolution of heat ($\Delta H = -37.1\,kJ\,mol^{-1}$). Hydrogen bonds are formed between water and ammonia. Two hydrogen-bonded ammonium hydrates have been isolated, $NH_3{\cdot}H_2O$ (m.p. 194.15 K) and $2NH_3{\cdot}H_2O$ (m.p. 194.32 K). In the solid state, both compounds have a three-dimensional extended hydrogen bond network.

$$NH_3 + H_2O \rightleftharpoons NH_4^+ + OH^- \qquad (32)$$

The equilibrium (32) lies to the left side, a 0.1 mol L^{-1} solution of ammonia in water is less than 1% dissociated into ions. The undissociated ammonia forms hydrogen-bonded hydrates $NH_3{\cdot}xH_2O$. For comparison, a potassium hydroxide solution is dissociated quantitatively. Ammonium hydroxide NH_4^+ OH^- is only found dissociated in solution, the undissociated form does not exist. Addition of stronger acids than water, for example, hydrochloric acid, sulfuric acid, or nitric acid, shifts the equilibrium (32) to the right side, that is, the side of the salts. The reaction of ammonia with hydrochloric acid vapors forms a white nebula in humid air, and white smoke in dry air.

$$NH_3 + HCl \longrightarrow NH_4Cl \qquad (33)$$

Heating of the ammonium salts shifts the formation equilibrium to the ammonia side, the ammonium salts sublime under dissociation. Ammonium salts with oxidizing anions (NO_2^-, NO_3^-, $Cr_2O_7^{2-}$) decompose under oxidation of the ammonium nitrogen to N_2 or N_2O.

Ammonia also has a low acidity (34) and a very slight oxidizing character (35).

$$NH_3 \longrightarrow NH_2^- + H^+ \qquad (34)$$

$$NH_3 + e^- \longrightarrow NH_2^- + 0.5H_2 \qquad (35)$$

Step-by-step replacement of the hydrogen atoms in ammonia with metal atoms according to (34) or (35) leads to the amides MNH_2, the imides M_2NH, and the nitrides M_3N. The alkali and alkaline-earth amides can be obtained from the reaction of the hot metals with ammonia.

$$2Na + 2NH_3 \longrightarrow 2NaNH_2 + H_2 \qquad (36)$$

Imides are formed during heating of the amides, further heating results in the nitrides.

$$M(NH_2)_2 \longrightarrow MNH + NH_3 \qquad (37)$$

$$3MNH \longrightarrow M_3N_2 + NH_3 \qquad (38)$$

The alkali and alkaline-earth amides, imides, and nitrides are immediately decomposed by water to ammonia and the metal hydroxides.

Ammonia and its organic, H_2NR, HNR_2, and NR_3, derivatives have a lone pair and can act as Lewis bases. The trialkylated derivatives of ammonia form the well-known trialkylammonium oxides R_3NO with the Lewis acid oxygen. Ammonia oxide H_3NO is less stable than the alkylated compounds, it rearranges to the more stable hydroxylamine NH_2OH. Two H_3NO^+ species have been identified mass spectrometrically.[41] Neutralization of the ion beam and subsequent reionization of the H_3NO^+ cations have shown that the neutral ammonia oxide H_3NO also has an inherent stability.

Lewis acids like boron trifluoride form Lewis acid–Lewis base complexes such as $H_3N{\cdot}BF_3$ with ammonia. Ammonia also forms metal complexes, the aminocomplexes (*see* ***Ammonia & N-donor Ligands***).[42] Deprotonation leads to amido, imido, and nitridocomplexes (see Scheme 14).

The nitrogen lone pair can be included in the metal–nitrogen bonds, decreasing the bond length and increasing the bond angle at the nitrogen atom.

5.1.1 *Production of Ammonia*

Ammonia is the second largest synthetic chemical product by mass and the largest by molar units.[5] Almost all the world consumption is manufactured from the elements nitrogen and hydrogen in a catalytic process originally developed by Fritz Haber and Carl Bosch using a promoted iron catalyst discovered by Alwin Mittasch. This process has remained largely unchanged since its discovery. A hydrogen–nitrogen mixture reacts over the iron catalyst at an elevated temperature in the range of 673–773 K and pressures above 10 MPa ($\Delta H = -46.22\,\mathrm{kJ\,mol^{-1}}$). The unreacted portion of the synthesis gas is recycled and the ammonia product separated under high pressure.

$$0.5N_2 + 1.5H_2 \longrightarrow NH_3 \qquad (39)$$

Even though this reaction is exothermic, the dinitrogen molecule, which has a very high dissociation energy of 945.33 kJ mol^{-1}, has to be activated. A purely thermal activation would require temperatures well above 800–1200 K under the most favorable conditions to achieve measurable reaction rates. However, at such high temperatures and industrially reasonable pressures, the theoretically possible ammonia yield is extremely small because of the unfavorable position of the thermodynamic equilibrium. At pressures above 200 MPa, the synthesis of ammonia proceeds even in the absence of specific catalysts, here the vessel walls appear to catalyze the formation of ammonia. Electrical energy or ionizing radiation, so-called plasma processes, can also be employed to provide the activation energy. The principal difficulty is that a great part of the supplied energy is transformed either into heat, which is undesirable, or unusable incidental radiation.

In the catalytic combination of nitrogen and hydrogen, the molecules lose their translational degrees of freedom by fixation on the catalyst surface. This drastically reduces the required energy of activation. The reaction may then proceed in the temperature range 520–670 K. Electron donor–acceptor complexes allow the synthesis of ammonia at room temperature with a measurable reaction rate. Since the beginning of commercial ammonia synthesis, iron catalysts that are composed in an unreduced form of iron oxides (mainly magnetite) and a few percent of Al, Ca, and K, are generally used. Other elements such as Mg and Si may also be present in small amounts. The catalysts are usually activated in situ by reduction with synthesis gas. The added elements perform different functions. Structural stabilizers like Al_2O_3 produce high inner surfaces during reduction and stabilize it under thermal stress by restraining iron crystallite growth.

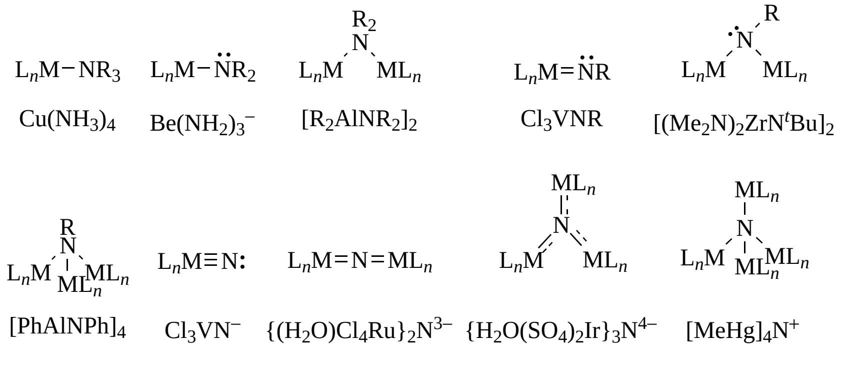

Scheme 14 Connectivity of amido, imido, and nitridocomplexes (R = H or organyl substituent)

Electronic promoters, for example, the alkali oxides, enhance the specific activity of iron–alumina catalysts. However, they reduce the inner surface or lower the thermal stability and the resistance to oxygen-containing catalyst poisons. Promoter oxides that are reduced to the metal during the activation process, and form an alloy with the iron, are a special group in which cobalt is an example that is in industrial use. Oxygen-containing compounds such as H_2O, CO, CO_2, and O_2 only temporarily poison the iron catalysts in low concentrations. Sulfur, phosphorus, arsenic, and chlorine compounds poison the catalyst permanently.

Ruthenium on a graphite or basic oxide support is also used as a catalyst in industrial synthesis. A Co–Mo–N system has also been investigated as a potential catalytic material, however, it has to be improved to compete with the already available catalysts.[43]

The mechanism of the ammonia synthesis by the Haber–Bosch process includes the following steps:

1. transport of the reactants by diffusion and convection out of the bulk gas stream, through a laminar boundary layer, to the outer surface of the catalyst particles, and further through the pore system to the inner surface;
2. adsorption on the inner surface;
3. reaction of the adsorbed species, if necessary with participation by hydrogen from the gas phase, to form activated intermediate compounds;
4. desorption of the formed ammonia into the gas phase;
5. transport of the ammonia through the pore system and the laminar boundary layer into the bulk gas stream.

The nitrogen adsorption and dissociation is the rate-determining step for the intrinsic reaction for iron catalysts. The mechanism of the catalytic reaction includes adsorption of dinitrogen in the molecular state followed by chemisorption in the atomic state. Hydrogen has a direct transition from the gaseous H_2 molecule into the chemisorbed atoms. The chemisorbed nitrogen atoms are then stepwise hydrogenated via N, NH, NH_2 species to NH_3. After the ammonia synthesis, ammonia is recovered from the synthesis loop by cooling the synthesis gas to condense the ammonia under synthesis pressure. The liquid ammonia product is separated from the gas, which is again fed into the synthesis loop.

Industrial ammonia production contains the following steps:

1. Synthesis gas production
   (a) Feedstock pretreatment and gas generation
   (b) Carbon monoxide conversion
   (c) Gas purification
2. Compression
3. Synthesis and purge gas management

Over the years, the most fundamental changes were made in the synthesis gas production and gas compression. These steps still have the highest potential for improvement. Some progress has been made in the synthesis section, especially in converter design and optimization of heat recovery.

The goal of synthesis gas production is a pure mixture of nitrogen and hydrogen in the stoichiometric ratio of 1:3. The raw materials are water, air, and a carbon-containing reducing medium that may contain hydrogen (natural gas, CH_4, naphtha, petroleum) and nitrogen. Normally natural gas and sometimes naphtha is used as a reducing medium. Depending on special economic circumstances, other media are used, for example, coal, which is used for most of the ammonia production in China. The capital cost and the specific energy requirement (i.e. feed and fuel) largely depend on the raw material employed. Both are lowest for natural gas. The term feedstock is often applied to the total consumption of fossil fuel, although strictly speaking a distinction should be made between gasification feed and fuel for energy generation. The chemical reaction of hydrocarbons with water, oxygen, air, or any combination of these is generally referred to as gasification. It produces a gas mixture of CO and H_2 in various proportions along with carbon dioxide and, where air is used, some nitrogen. Any carbon-containing feedstock reacts according to (40) ($\Delta H > 0$) or (41) ($\Delta H < 0$) or both simultaneously.

$$[CH_x] + H_2O \rightleftharpoons CO + H_2 + \frac{x}{2}H_2 \qquad (40)$$

$$[CH_x] + 0.5O_2 \rightleftharpoons CO + \frac{x}{2}H_2 \qquad (41)$$

Light hydrocarbons from natural gas (methane) to naphtha (max. C_{11}) are reacted with steam over a catalyst according to (40), a process usually called steam reforming. In (40), the proportion of hydrogen supplied by the feedstock increases with its hydrogen content with a theoretical maximum of 66% for methane. The higher bond energy of a hydrogen–oxygen bond compared to a carbon–hydrogen bond decreases the positive reaction enthalpy of (40) with increasing hydrogen content. Natural gas consists predominantly of methane and is therefore the most hydrogen-rich and energetically the best raw material for the steam-reforming route. In the partial-oxidation route, less hydrogen is produced in the primary gasification step and the raw synthesis gas has a rather high CO content. The catalytic steam-reforming technology can only be applied to light hydrocarbon feedstock (up to naphtha) but not for heavy hydrocarbons such as fuel oil or vacuum residue. These materials contain a substantial amount of sulfur and also minor quantities of heavy metals, which would poison the sensitive reforming catalyst, thus heavy feedstocks are processed by partial oxidation.

In the steam-reforming process, any sulfur compounds present in the hydrocarbon feedstock have to be removed because the nickel-containing catalysts are sensitive to poisons. This is either achieved by hydrodesulfurization (*see* ***Hydrodesulfurization & Hydrodenitrogenation***), generally with a combination of cobalt–molybdenum and zinc oxide catalysts, or by adsorption on activated carbon when the feed is natural gas with a rather low sulfur content.

The primary reformer consists of a multitude of reformer tubes loaded with the nickel catalyst (15–25% NiO on aluminum oxide, calcium aluminate, or magnesium aluminum spinel support) in a furnace box, in which the heat needed for the reaction is transferred to the tubes by radiation. The heat is generated in burners, generally gas-fired in the furnace box.

While only light hydrocarbons can be used for the steam-reforming process, all carbon-containing feedstocks can be processed in a noncatalytic reaction with oxygen according to (41), which is referred to as partial oxidation or coal gasification for coal feedstocks. A minor amount of water is added for process reasons and gives rise to a simultaneous reaction according to (40).

For the exothermic reaction no external heat supply is necessary.

As the synthesis of ammonia needs only nitrogen and hydrogen, all carbon oxides must be removed from the raw synthesis gas of the gasification process. Depending on feedstock and process technology, this gas contains 10–50% carbon monoxide and also varying amounts of carbon dioxide. In the water gas shift reaction, traditionally known as carbon monoxide shift conversion, the carbon monoxide serves as a reducing agent for water, to yield hydrogen and carbon dioxide ($\Delta H = -41\,\mathrm{kJ\,mol^{-1}}$). In this way, not only is the carbon monoxide converted to readily removable carbon dioxide but also additional hydrogen is produced:

$$\mathrm{CO + H_2O \rightleftharpoons CO_2 + H_2} \tag{42}$$

This reaction is without volume change and is therefore independent of pressure. As an exothermic process, it is favored by lower temperatures, which shift the equilibrium to the right side. Even with a low excess of steam in the gas, the equilibrium concentrations of CO are low, for example, 0.2 vol% at 220 °C and 0.12 vol% at 200 °C for a steam/gas ratio of 0.4. The heat formed in the reaction has to be removed to keep the temperature low, and effective catalysts have to be applied to achieve a sufficient reaction rate. The process is therefore performed in steps. Heat is removed between the individual catalyst beds in which the reaction runs adiabatically. Quasi-isothermal reactors with cooling tubes through the catalyst layers are used. The process configuration and catalysts of steam reforming and partial oxidation are somewhat different. The raw synthesis gases from the partial oxidation of heavy hydrocarbons and coal differ mainly in two aspects from that produced from light hydrocarbons by steam reforming. First, depending on the feedstock composition, the gas may contain a rather high amount of sulfur compounds (mainly H_2S with smaller quantities of COS); second, the CO content is much higher, in some cases in excess of 50%. The high initial carbon monoxide concentration means that the reaction has to be performed in steps with intermediate cooling. In steam-reforming plants, the gas from the secondary reformer enters the high-temperature shift reactor loaded with an iron–chromium catalyst at 600–630 K. After a temperature increase of around 50–70 K, depending on the initial CO concentration, the process gas has a residual CO content of around 3%. It is then cooled to 470–480 K for the low-temperature shift, which is carried out on a copper–zinc–alumina catalyst in a downstream reaction vessel and achieves a carbon monoxide concentration of 0.1–0.3 vol%.

After shift conversion, carbon dioxide, residual carbon monoxide, and sulfur compounds (only present in the synthesis gas from partial oxidation) have to be removed as they are not only a useless ballast but, more importantly, can poison the ammonia synthesis catalyst.

CO_2 is removed by scrubbing the synthesis gas under pressure with a solvent capable of dissolving carbon dioxide in sufficient quantity and at a sufficient rate, usually in countercurrent in a column equipped with trays or packings. The CO_2 saturated solvent is flashed, often in steps, to around atmospheric pressure, and the spent scrubbing liquid is subsequently heated and regenerated in a stripping column before being recycled to the pressurized absorption column. Today, physical or chemical solvents are used. In physical solvents, carbon dioxide dissolves without forming a chemical compound, allowing a recovery by flashing. In chemical solvents, carbon dioxide becomes fixed as a chemical compound. Heat is needed for its decomposition. In the first ammonia plants, water was used for scrubbing. Today ethyl or diethyl amine as well as potassium carbonate solutions are used. As the acidic gases CO_2 and H_2S are both soluble in the solvents applied, special process configurations are required to recover a separate pure CO_2 fraction and an H_2S-rich fraction suitable for sulfur disposal from partial-oxidation gases.

After this bulk removal of the carbon oxides, the typical synthesis gas still contains 0.2–0.5 vol% CO and 0.005–0.2 vol% CO_2. All oxygen-containing compounds have to be reduced to a very low ppm level, as they are poisonous toward the ammonia synthesis catalysts. Methanation is the simplest method to reduce the concentrations of the carbon oxides well below 10 ppm, and is widely used in steam-reforming plants.

$$\mathrm{CO + 3H_2 \rightleftharpoons CH_4 + H_2O} \tag{43}$$

$$\mathrm{CO_2 + 4H_2 \rightleftharpoons CH_4 + 2H_2O} \tag{44}$$

The advantages of simplicity and low cost more than outweigh the disadvantages of hydrogen consumption and production of additional inert gases in the makeup gas to the synthesis loop. Water is absorbed on molecular sieves. Other final purification methods are pressure-swing adsorption, or washing with liquid nitrogen.

Of the world energy consumption, 1.6% is used for the production of ammonia. In 2000, 108 megatons of ammonia were produced. About 85% is used for fertilizer production as urea, which accounts for 40% of the fertilizer production, and ammonium nitrate, phosphate, and sulfate. Ammonia is also used as a solvent, for the nitriding of steel, and as a refrigerant, due to its low boiling point and high heat of evaporation.

5.1.2 Ammonia as a Solvent

Ammonia possesses similar physical properties to that of water, which is similarly highly associated.**44** It is a good solvent for many compounds. Owing to the lower dielectric constant (NH_3: 16.9, H_2O: 78.3 at 298 K) of ammonia in comparison with water, less polar compounds are more soluble in ammonia and polar compounds, for example, salts, are more soluble in water. Organic compounds tend to have a higher solubility in ammonia than in water. Ammonium salts, nitrates, nitrites, cyanides, and thiocyanates dissolve readily in ammonia. The solubility increases from fluorides to chlorides, bromides, and iodides. Salts with higher charged ions dissolve only poorly in ammonia. This results in the reversal of some precipitation reactions in ammonia compared to water.

$$Ba(NO_3)_2 + 2AgBr \xrightarrow{NH_3} BaBr_2 + 2AgNO_3 \qquad (45)$$

As a hard base, water prefers to coordinate to the harder acid Ba^{2+}, the softer base ammonia prefers to coordinate the softer acid Ag^+ to form $Ba(OH_2)_n{}^{2+}$ and $Ag(NH_3)_2{}^+$, respectively. Sulfates, sulfites, carbonates, phosphates, arsenates, oxides, and sulfides are virtually insoluble in ammonia. Hydroxides and amides are also very poorly soluble.

In ammonia, the $NH_4{}^+$ ion is the strongest available acid and the $NH_2{}^-$ ion the strongest available base. Compounds of the type HX that produce $NH_4{}^+$ ions are acids in this system, MR compounds such as $LiCH_3$ or $NaSiH_3$ are bases as they produce $NH_2{}^-$ ions.

$$NH_3 + HX \longrightarrow NH_4{}^+ + X^- \qquad (46)$$

$$NH_3 + MR \longrightarrow NH_2{}^- + M^+ + RH \qquad (47)$$

Ammonia is an attractive solvent if strong bases are required, since $NH_2{}^-$ is more basic than OH^-, but is less useful for reactions requiring strong acids. Acids like acetic acid that are weak acids in water are strong acids in ammonia and dissociate fully to form ammonium ions. Strong bases like $C{\equiv}C^{2-}$, Ph_3Ge^-, or R_2P^-, that are immediately hydrolyzed in water, can be handled in ammonia. Complexation is an important factor for the solution of metal salts in ammonia. $Zn(NH_2)_2$, which is insoluble in ammonia, is like the hydroxocomplex $Zn(OH)_2$, which is insoluble in water, amphoteric. It dissolves in acidic solution to form $Zn(NH_3)_4{}^{2+}$ or in basic solution to form $Zn(NH_2)_4{}^{2-}$.

Elements that are above H_2/H^+ are oxidized under evolution of dihydrogen, elements below NH_3/N_2 are reduced under evolution of dinitrogen (see Table 11). This leaves a range of only +0.04 V in which oxidizing agents more powerful than N_2, and reducing agents more powerful than H_2 are thermodynamically stable. However, kinetic effects leading to overvoltages of H_2 and N_2 extend the range from +1.0 V to −1.0 V in basic solution and from −2.05 V to +0.6 V in acidic solution. Therefore, even strong reductants like $[M^0(CN)]^{4-}$ (M = Ni, Pd, Pt) and strong oxidizers like $O_2{}^-$ or $O_3{}^-$ can be handled in liquid ammonia.

Alkali and alkaline-earth metals dissolve in ammonia, in contrast to water, without the evolution of dihydrogen, forming intensely colored solutions that are strong reducing agents. The solutions, which have lower densities than ammonia, are metastable in the absence of water and dioxygen. Over time, or in the presence of catalysts such as $FeCl_2$, these solutions decompose to the metal amides and dihydrogen. Beryllium and magnesium do not dissolve because metal ionization and lattice energies are too high, but solutions of these metals in ammonia can be prepared by the electrochemical reduction of solutions of their salts in ammonia. The color of the solutions depends on concentration; dilute solution are intense blue and salt-like, concentrated solutions bronze–gold and truly metallic. At intermediate concentrations, there is a concentration-dependent metal–nonmetal transition, which is associated with a remarkable liquid–liquid phase transition and unusual critical properties. In one mol of ammonia, the following amounts of metals are dissolved at 223 K: Li 0.27 mol, Na 0.19 mol, K 0.20 mol, Rb 0.3 mol, Cs 0.43 mol.

Saturated solutions of lithium in ammonia have the lowest density ($\rho = 0.48\,\mathrm{g\,cm^{-1}}$) of any known liquid at room temperature and provide the lowest-temperature liquid metals with a deep pseudoeutectic extending to 88 K.**45** Dissolution of lithium atoms in ammonia produces a rich variety of solvated electronic and ionic species. At very low concentrations (c < 0.01 mole percent metal, MPM),

Table 11 Standard potentials in liquid ammonia compared to standard potentials in liquid water in parentheses

	$E°$ [V]		$E°$ [V]		$E°$ [V]
Li/Li^+	−2.28 (−3.01)	H/H^+	±0 (±0)	$N_2/NO_3{}^-$	+1.17 (+1.25)
K/K^+	−1.98 (−2.92)	NH_3/N_2	+0.04 (+0.28)	I^-/I_2	+1.26 (+0.54)
Cs/Cs^+	−1.95 (−2.92)	Pb/Pb^{2+}	+0.35 (−0.13)	H_2O/O_2	+1.28 (+1.23)
Na/Na^+	−1.85 (−2.71)	Cu/Cu^+	+0.41 (+0.52)	$ClO^-/ClO_3{}^-$	+1.47 (+1.45)
Ca/Ca^{2+}	−1.64 (−2.84)	Cu/Cu^{2+}	+0.43 (+0.34)	Br^-/Br_2	+1.73 (+1.07)
Zn/Zn^{2+}	−0.49 (−0.76)	Hg/Hg^{2+}	+0.75 (+0.85)	Cl^-/Cl_2	+1.91 (+1.36)
Cd/Cd^{2+}	−0.2 (−2.84)	Ag/Ag^+	+0.83 (+0.80)	F^-/F_2	+3.50 (+3.05)

the solutions are essentially electrolytic, and contain solvated ions and isolated electrons. The latter are localized within polaronic solvent cavities with an approximate radius of 3 Å, causing the decrease in density of the metal solutions compared to ammonia and the paramagnetism of the solutions. At intermediate concentrations (0.01 MPM to 2 MPM), the electronic and magnetic properties are dominated by spinpaired species, for example, peanut-shaped bipolarons. These species account for about 90% of the excess electrons at 1 MPM. A metal–nonmetal transition takes place at around 4 MPM, with the onset of liquid–liquid phase separation below 210 K. At higher concentrations, the excess electronic states become more extended and itinerant, forming solutions that are good metals. Saturated solutions of lithium in ammonia have a concentration of 22 MPM, and an electrical conductivity that exceeds that of liquid mercury. The lithium cations are strongly solvated by four ammonia molecules, forming $Li(NH_3)_4^+$. This suggests that the excess electrons are almost fully dissociated from lithium and trapped in polaronic cavities formed by free-solvent molecules. The nonmetal-to-metal transition is explained as the lack of enough free-solvent molecules to fully solvate all excess electrons and the resulting overlap of the solvation shells of different electrons. The alkaline-earth metal solutions in ammonia contain hexacoordinated cations $M(NH_3)_6^{2+}$.

5.1.3 Ammonium Salts

The ammonium ion NH_4^+ has a tetrahedral structure and is slightly acidic ($pK_a = 9.25$). If no strong hydrogen bonds are present, like in NH_4F, the properties of ammonium salts, for example, the solubility and the structure, are similar to the corresponding potassium and rubidium salts. The reasons are similar ionic radii of the ammonium (143 pm), potassium (137 pm), and rubidium ions (148 pm). The oxonium salts $H_3O^+X^-$, which have lower melting points, are also similar to the ammonium salts. The similar properties of element-hydrogen compounds have been rationalized by the hydride displacement law shown in Table 12.

Accordingly, the isoelectronic FH_2, OH_3, NH_4, as well as Na form cations, for example, in $Na^+ClO_4^-$, $FH_2^+ClO_4^-$, $OH_3^+ClO_4^-$, and $NH_4^+ClO_4^-$. NeH has only been observed in the gas phase. The saturated molecules HF, H_2O, NH_3, and CH_4 correspond to the noble gas neon and OH, NH_2, and CH_3 are found either single bonded or anionic like the fluorine atom. Examples are the ionic compounds Na^+F^-, Na^+OH^-, $Na^+NH_2^-$, $Na^+CH_3^-$ or the covalent compounds CH_3F, CH_3OH, CH_3NH_2, and CH_3CH_3. The ammonium radical $NH_4•$, which is isosteric to the alkali metals, has so far not been isolated.

Table 12 Hydride displacement law

C	**N**	**O**	**F**	**Ne**	**Na**
	CH	NH	OH	FH	NeH
		CH_2	NH_2	OH_2	FH_2
			CH_3	NH_3	OH_3
				CH_4	NH_4

Ammonium ions can coordinate up to four ammonia molecules via hydrogen bonds, for example, $NH_4I{\cdot}4NH_3$ (m.p. 268). The ionic, hydrogen-bonded structure $NH_4{\cdots}X$ shifts to an adduct structure $NH_3{\cdots}HX$ with weaker acids HX. For an explanation of hydrogen bonds, *see* ***Hydrogen Bonding & Dihydrogen Bonding***. Some properties of important ammonium salts are given in Table 13.

Ammonium Chloride. Ammonium chloride, which occurs naturally in volcanic material, forms two solid phases. The α-modification (cubic, CsCl type), which is stable at room temperature, changes reversibly to the β-modification (cubic, NaCl type) at 457.6 K. The slightly hygroscopic ammonium chloride sublimes easily, the dissociation to ammonia and HCl is complete at 520 K. It is very soluble in water.**[5]**

Ammonium chloride is produced in a modified Solvay process, which is used for the production of sodium carbonate.

$$2NH_3 + CO_2 + H_2O + 2NaCl \longrightarrow 2NH_4Cl + Na_2CO_3 \qquad (48)$$

If HCl is available cheaply, ammonium chloride can also be produced from ammonia and HCl. Ammonium chloride as gas, solid, or in solution is corrosive because it is acidic, it complexes metal ions and it contains the corrosive chloride ion.

The 150 kilotons of ammonium chloride that are produced per year are mostly used as fertilizer and, in order of importance, for solid electrolytes in dry cell batteries, a component of quarrying explosives, hardeners for formaldehyde-based adhesives, one component of etching solutions in the manufacture of printed circuit boards, and a component, along with zinc chloride, of fluxes in tin and zinc plating.

Table 13 Properties of important ammonium salts

	NH_4Cl	$(NH_4)_2SO_4$	NH_4NO_3	NH_4HCO_3
m.p. [K]	dissoc. 520	decomp. > 575	442.8	decomp. 309–333
ΔH_f [kJ mol^{-1}]	−314.6	−1180.9	−365.1	−849
ρ [g cm^{-3}]	1.530	1.77	1.725	1.58
C_p [J g^{-1} K^{-1}]	1.63	1.423	1.70	1.53

Ammonium Sulfate. The colorless, crystalline ammonium sulfate cannot be melted at atmospheric pressure without decomposition at 508 K, releasing ammonia and forming NH_4HSO_4. After cleavage of water, ammonium bisulfate $(NH_4)_2S_2O_7$ is left. However, the ammonia vapor pressure of pure, anhydrous ammonium sulfate is effectively zero up to 350 K. Above 573 K, decomposition yields N_2, SO_2, SO_3, and H_2O in addition to ammonia.[5]

Ammonium sulfate is synthesized from ammonia, which stems from either coke oven gas or the Haber–Bosch process, and sulfuric acid.

$$2NH_3 + H_2SO_4 \longrightarrow (NH_4)_2SO_4 \tag{49}$$

Ammonium sulfate is a coproduct in the production of synthetic-fiber intermediates, such as caprolactam, acrylonitrile, and methyl methacrylate, and in the production of formic acid and acrylamide. The recovery of ammonium sulfate form these syntheses has gained importance in the last thirty years. Almost all of the 2.8 megatons of ammonium sulfate produced annually is used as fertilizer. In industrial countries, ammonium sulfate is almost always a coproduct or by-product in other processes and can only be sold as fertilizer, mostly in developing countries. In these countries, its low nitrogen content makes the transportation cost per unit of nitrogen higher than for other nitrogen fertilizers.

Ammonium Nitrate. Ammonium nitrate is a colorless, deliquescent crystalline salt. At standard pressure, five modifications of ammonium nitrate exist (Table 14). The phase change at 305.5 K is of particular importance for the handling of ammonium nitrate fertilizer. On passing through the phase change repeatedly, granules of ammonium nitrate lose strength and finally disintegrate because of the differing densities.[5]

Ammonium nitrate dissolves readily in water; in addition, the salt is hygroscopic. Therefore, care must be taken to avoid moisture during transportation and storage. When the salt dissolves in water, heat is absorbed ($\Delta H = 26\,\text{kJ mol}^{-1}$). Therefore, ammonium nitrate can be used in freezing mixtures, for example, in mixtures with sodium chloride and ice.

In the synthesis of ammonium nitrate from the neutralization of 45–65% HNO_3 with gaseous NH_3, the considerable heat of the reaction is used for the partial or complete evaporation of the water.

$$NH_3 + HNO_3 \longrightarrow NH_4NO_3 \tag{50}$$

Table 14 Modifications of ammonium nitrate

Modification	Existence range [K]	Crystal system
α	<256.2	tetragonal
β	305.5–256.2	orthorhombic
γ	357.5–305.5	orthorhombic
δ	398.4–357.4	tetragonal
ε	442.8–398.4	cubic

Depending on the reaction conditions, 95–97% solutions of ammonium nitrate can be obtained. Quick and thorough mixing of the compounds is necessary to avoid local overheating, losses of nitrogen, and decomposition of the ammonium nitrate. Ammonium nitrate has to be prevented from caking during storage by a final surface treatment (coating). The earlier practice of powdering with inorganic substances to separate the grains mechanically has mostly been replaced by treatment of the grain with effective organic surfactants, such as cationic long-chain fatty amines or anionic alkylarylsulfonates.

Ammonium nitrate undergoes several decomposition processes. At 442.8 K, ammonium nitrate starts to melt and at 443.2 K endothermic dissociation takes place ($\Delta H = +175\,\text{kJ mol}^{-1}$):

$$NH_4NO_3 \xrightarrow{442.8\,\text{K}} HNO_3 + NH_3 \tag{51}$$

On careful heating to 473 K, N_2O is eliminated ($\Delta H = -37\,\text{kJ mol}^{-1}$).

$$NH_4NO_3 \xrightarrow{473\,\text{K}} N_2O + 2H_2O \tag{52}$$

Above 503 K, dinitrogen and NO_2 are eliminated ($\Delta H = -102\,\text{kJ mol}^{-1}$).

$$4NH_4NO_3 \xrightarrow{503\,\text{K}} 3N_2 + 2NO_2 + 8H_2O \tag{53}$$

Further heating results in the formation of dinitrogen and dioxygen accompanied by detonation ($\Delta H = -118.5\,\text{kJ mol}^{-1}$).

$$NH_4NO_3 \xrightarrow{>>503\,\text{K}} N_2 + 0.5O_2 + 2H_2O \tag{54}$$

Hydrogen ions, chlorides, and heavy metals catalyze the decomposition of ammonium nitrate.

Pure ammonium nitrate, highly concentrated hot solutions of ammonium nitrate, various mixtures of ammonium nitrate, and ammonium nitrate fertilizer can be detonated by shock waves unless stabilized. Several times, huge amounts of ammonium nitrate have exploded, causing severe damage. One of the latest accidents happened in Toulouse in 2001, where 200 to 300 tons of ammonium nitrate exploded in a warehouse. The blast blew out windows in the city center 3 km away and created a crater with a diameter of 50 meters and more than 10 meters deep.

For safety reasons, solidified ammonium nitrate should not be broken up by blasting. Products containing ammonium nitrate must be stored separately from oxidizable and inflammable materials and, if ammonium nitrate must be heated (during production, evaporation, etc.), the quantity must be kept small and catalysts avoided. In several countries, inert materials such as limestone powder, dolomite, or precipitated calcium carbonate, are added to ammonium nitrate for fertilizer use (calcium ammonium nitrate). Such fertilizers, containing no more than 80% ammonium nitrate, no more than 0.4% combustible constituents, and no less than 18% magnesium or calcium carbonate, are considered nondetonatable.

The 15 megatons of ammonium nitrate produced annually are used mainly as fertilizer, either pure, diluted, or in multinutrient mixtures. It is used in liquid fertilizers with urea.

Safety explosives for mining are produced from ammonium nitrate. Owing to its low explosion temperature in mixtures with NaCl, the temperature is not high enough to set off the much-feared firedamp. For greater explosive power, for example, for mining (rock explosives), porous-prilled ammonium nitrate containing approximately 6% diesel oil is used.

Ammonium Carbonates. In the ternary system, $NH_4^+/H_2O/CO_2$ four compounds are found: ammonium hydrogencarbonate NH_4HCO_3 ($\rho = 2.4\,\mathrm{g\,cm^{-3}}$), ammonium carbonate $(NH_4)_2CO_3{\cdot}H_2O$ (m.p. 316.2 K), ammonium sesquicarbonate $(NH_4)_2CO_3{\cdot}2NH_4HCO_3{\cdot}H_2O$, and ammonium carbamate $NH_4CO_2NH_2$ (m.p. 402 K).[5] Ammonium hydrogencarbonate, also called ammonium bicarbonate is the only compound soluble in water without decomposition. $(NH_4)_2CO_3{\cdot}H_2O$ is only formed under precisely defined conditions, which are difficult to achieve in production. Therefore, usually equimolar mixtures of ammonium carbamate and ammonium hydrogencarbonate are used and sold as ammonium carbonate. In the presence of air, ammonium carbonate $(NH_4)_2CO_3$ forms ammonium bicarbonate NH_4HCO_3, which decomposes at temperatures higher than 333 K to ammonia and CO_2. Owing to this decomposition, ammonium bicarbonate is mainly used as an expanding agent for baked goods. It is also used in buffer solutions for the neutralization of acids when additional anions are undesirable. Further uses include an ammonization agent for the humic acid in turf, a nitrogen source for yeast cultures, and blowing agents for foam rubber and poly(vinyl chloride). Ammonium carbamate is used as an insecticide for cereals, a neutralization agent in the chemical industry, and as feedstock for ammonium carbonate production. Ammonium carbonate is used in the manufacture of catalysts, as a blowing agent in foam rubber and foam plastic, and as an additive in photographic developers. In a number of countries, it is also used as an expanding agent in certain baked goods.

5.2 Hydrazine

Hydrazine is a colorless, viscous liquid that fumes in air. A comprehensive review of the chemistry, properties, and production of hydrazine can has been produced.[46] The toxic substance has an odor reminiscent of ammonia and forms a hydrate $N_2H_4{\cdot}H_2O$. A $2s2p^3$ hybridization of the nitrogen atoms in hydrazine leads to a tetrahedral arrangement similar to that of saturated carbon atoms, where a lone pair of electrons replaces one ligand of the carbon atom. The repulsion of these lone pairs destabilizes the N–N single bond. Rotation of one-half of the hydrazine molecule around the N–N bond leads to three different conformations, which are shown in Scheme 15.

The unsymmetrical *gauche* conformation (**46**) is the most stable structure. The staggered (anti) chair structure (**45**) is about $3\,\mathrm{kJ\,mol^{-1}}$ higher in energy, and the eclipsed (syn) boat structure (**44**) represents a transition state that was found to be $25-41\,\mathrm{kJ\,mol^{-1}}$ higher in energy by spectroscopic and dipole measurements. The high rotation barrier compared to ethane ($10.7-13.8\,\mathrm{kJ\,mol^{-1}}$) was explained by the repulsion of the nitrogen lone pairs. Hydrogen peroxide (*see* ***Oxygen: Inorganic Chemistry***) is another example of this lone pair interaction. At room temperature, hydrazine does not rotate freely in the gas phase, the NH_2 groups only twist and oscillate against each other.

The bonding parameters of hydrazine as obtained by various experimental investigations are in the expected range for an sp^3 hybridized nitrogen atom (see Table 15).

In liquid hydrazine, hydrogen bonding occurs between the hydrazine molecules similar to the hydrogen bonding in liquid water. In solid hydrazine, the hydrogen bonds have NH-N distances between 319 and 367 pm. In hydrazine hydrate, each hydrazine molecule is linked via six hydrogen bonds to surrounding water molecules so that the hydrazine molecules are separated from each other by water molecules.[47] Some physical properties of hydrazine and hydrazine hydrate are shown in Table 16.

5.2.1 *Production of Hydrazine*

For a long time, the Raschig process, which was discovered in 1907, was used for the production of hydrazine.[5] Here, ammonia is oxidized with sodium hypochlorite in alkaline solution (pH = 8–11). In the initial rapid reaction, (55) sodium hypochlorite reacts with ammonia, forming chloramine. Chloramine then reacts with ammonia in a slower second reaction.[5,46]

$$NaOCl + NH_3 \longrightarrow H_2NCl + NaOH \qquad (55)$$

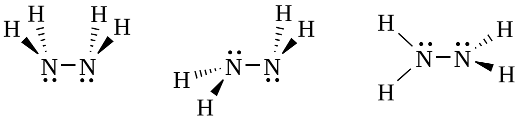
(**44**) eclipsed (**45**) staggered (**46**) gauche

Scheme 15 Rotamers of hydrazine

Table 15 Bonding parameters of hydrazine

	IR	X-ray	GED
d(N–H) [pm]	1.014 to 1.025	–	1.022(6)
d(N–N) [pm]	1.449 to 1.453	1.46	1.449(4)
<(N–N–H) [°]	108 to 112	–	112.0

Table 16 Physical properties of hydrazine and hydrazine hydrate

	N_2H_4	$N_2H_4{\cdot}H_2O$
m.p. [K]	275.16	221.5
b.p. [K]	387.37	389.55
ρ [g cm^{-3}]	1.0037	1.032
Viscosity [cP]	0.913	1.50
Surface tension [mN cm^{-1}]	0.6645	0.743
C_p [J g^{-1} K^{-1}]	3.0778	3.360
ΔH_f [kJ mol^{-1}]	50.63	−242.7
ΔG_f [kJ mol^{-1}]	149.2	−109.2
ΔH_{fusion} [kJ mol^{-1}]	12.657	–
$\Delta H_{\text{vaporization}}$ [kJ mol^{-1}]	39.079	47.7
$S°$ (l) [J mol^{-1}K^{-1}]	121.15	–
$S°$ (g) [J mol^{-1}K^{-1}]	238.4	265.3
Dielectric constant	51.7	61.2
μ [D]	1.84	–
Index of refraction n_D	1.4683	1.4644

$$NH_2Cl + NH_3 + NaOH \longrightarrow N_2H_4 + NaCl + H_2O \qquad (56)$$

Chloramine reacts preferentially with the produced hydrazine, thus limiting the stationary hydrazine concentration in solution.

$$2NH_2Cl + N_2H_4 \longrightarrow 2NH_4Cl + N_2 \qquad (57)$$

To avoid this decomposition, an excess of ammonia has to be present. Transition metal ions, which are generally present as contaminants in the starting materials and the process water, catalyze this reaction and have to be removed by complexation with glue, gelatin, or albumin. One of the main disadvantages of the Raschig process is the high dilution of the obtained hydrazine (3% solution in water). To obtain hydrazine hydrate, an energy-intensive multistage distillation is necessary. The Bergbau–Bayer–Whiffen or ketazine process solves some of these disadvantages. Here a ketone, typically acetone, reacts with hydrazine forming a ketazine $Me_2C{=}N{-}N{=}CMe_2$ or acetone hydrazone $Me_2C{=}NNH_2$. In contrast to hydrazine, ketazines are not oxidized by chloramine, thus improving the yield. The liberation of hydrazine from the ketazine is dependant on further use. For hydrazinium(I) sulfate, the azine is hydrolyzed with dilute sulfuric acid; for hydrazine hydrate, a high-pressure steam hydrolysis is used.

In anhydrous systems, the low hydrazine concentration is avoided.[48] Chlorine and ammonia can react in the gas phase to form chloramine, which then reacts with ammonia to form hydrazine. As in the Raschig process, the reaction (57) of chloramine with hydrazine limits the yields. Substituted hydrazines can be prepared using this process with the appropriate substituted amines.

In the PCUK process (introduced by Produits Chimiques Ugine Kuhlmann), ammonia is oxidized with hydrogen peroxide in the presence of a ketone. A ketazine is formed as in the ketazine process, which is then processed similarly. Ketones with many different substituents, even aldehydes, have been examined for this reaction. Normally acetone, methylethylketone, or diethylketone are employed.

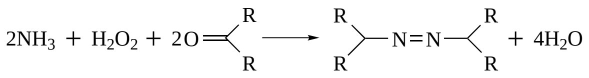

(58)

The PCUK process is used for most of the newly built hydrazine plants. Its main advantages are higher yield (close to 90% compared to 60–70% with Raschig technology) and lower energy consumption. Furthermore, no sodium chloride has to be disposed off.

The production of hydrazine from urea by treatment with sodium hypochlorite is no longer used. Here urea was oxidized with sodium hypochlorite followed by hydrolysis and decarboxylation to yield hydrazine.

$$(H_2N)_2CO + NaOCl \xrightarrow[-NaCl\ -CO_2]{H_2O} N_2H_4 \qquad (59)$$

Many other processes have been investigated. Attempts to synthesize hydrazine from nitrogen and hydrogen gave only traces of hydrazine. In the biological nitrogen fixation process (*see* ***Nitrogenase Catalysis & Assembly***), hydrazine is an intermediate. The oxidation of ammonia has been investigated by photolysis, γ-radiolyses, glow discharge, arc plasma electrolysis, chemonuclear processes, and chemical oxidation. Also, other starting materials such as semicarbazide, nitramide, nitrosamines, nitroso compounds, and nitrogen oxides were used. These processes are not used on an industrial scale. About 74 kilotons of hydrazine hydrate were produced in 2000.

Hydrazine is mostly sold as an aqueous solution; anhydrous hydrazine is only used as a rocket fuel or as a mono- or bipropellant for satellites and spacecrafts. About 80–90% of the hydrazine produced is converted into organic derivatives. Other applications are based on its use as a reducing agent, as an energy-rich compound, or on its hydrogen storage capacity.

5.2.2 *Anhydrous Hydrazine*

All technical processes for the synthesis of hydrazine yield either hydrazine in aqueous solution or hydrazine hydrate. Most applications can use hydrazine hydrate, but for some applications, for example, rocket propulsion, anhydrous hydrazine is necessary. The water can be removed by a chemical reaction followed by distillation or by azeotropic distillation with an auxiliary fluid. As water binding chemicals, calcium carbide, sodium hydroxide, calcium oxide, calcium hydride, barium oxide, barium hydroxide, and barium pernitride Ba_3N_4 have been used. The use of sodium or calcium metal and sodium amide is best avoided because of the formation of explosive hydrazides. Starting from hydrazine hydrate (64% hydrazine), sodium hydroxide is generally used to obtain 90% hydrazine. The rest of the water can be removed by repeated treatment with barium oxide and recondensation. The separation of the drying agent and hydrazine by distillation has resulted in many explosions in the past and is, if possible, best avoided. In technical processes, hydrocarbons with similar boiling points as hydrazine, for example, *n*-heptane, are used as blanketing fluids to dilute the hydrazine vapor and prevent explosions. Upon recondensation, they are immiscible with hydrazine and are easily siphoned off. Another approach for drying hydrazine uses an entrainer, a fluid that forms an azeotrope with water, boiling at a temperature different from hydrazine or hydrazine hydrate. Aniline is ideally suited for this purpose.[46]

For liquid–liquid extraction, fluids that have a high affinity for hydrazine and are immiscible with water were found. Fluoroalcohols, typically $H(CF_2)_6CH_2OH$, are ideally suited for this purpose. Anhydrous hydrazine can also be prepared by reacting hydrazinium salts with strong bases.

$$N_2H_5HSO_4 + 2NH_3 \longrightarrow N_2H_4 + (NH_4)_2SO_4 \qquad (60)$$

The equilibrium of the reaction of hydrazinium hydrogensulfate with liquid ammonia (60) is shifted to the product side by the precipitation of $(NH_4)_2SO_4{\cdot}3NH_3$. Organic amines that are weaker bases than hydrazine but have higher boiling points than hydrazine can also be used for the production of anhydrous hydrazine. In a mixture with these bases, hydrazine always has a small equilibrium concentration and can be distilled off under reduced pressure. It is also possible to thermally decompose some hydrazinium salts, yielding anhydrous hydrazine. Here hydrazinium tetraborate $(N_2H_5)_2(B_4O_7)_3$, the hydrazinium salt of carbazic acid $N_2H_5{}^+H_2NNHCO_2{}^-$, and the hydrazinium salt of cyanuric acid have been used. Further purification by fractional crystallization, sublimation, or distillation at low pressure is possible.

5.2.3 *Chemical Properties of Hydrazine*

Hydrazine is an endothermic compound that decomposes at higher temperatures, sometimes explosively, to form dinitrogen and ammonia.[46]

$$3N_2H_4 \longrightarrow 4NH_3 + N_2 \qquad (61)$$

Hydrazine and aqueous solutions of hydrazine are strong reducing agents. Depending on the oxidizing agent, catalysts, pH, and temperature, hydrazine can react in different ways. In aqueous solution, hydrazine can be oxidized in a one, two, or four electron oxidation to form dinitrogen, a mixture of dinitrogen and ammonia or ammonium azide.[49] Hydrazoic acid (63) is only formed in a highly acidic solution with strong oxidants like H_2O_2, $ClO_3{}^-$, or $S_2O_8{}^2$. The oxidation potentials are given in Table 17.

$$N_2H_5{}^+ \longrightarrow 0.5N_2 + NH_4{}^+ + H^+ + e^- \qquad (62)$$

$$N_2H_5{}^+ \longrightarrow 0.5HN_3 + 0.5NH_4{}^+ + 2.5H^+ + 2e^- \qquad (63)$$

$$N_2H_5{}^+ \longrightarrow N_2 + 5H^+ + 4e^- \qquad (64)$$

Reactions (63) and (65) often occur simultaneously. For example, iodate or iodine in acidic conditions and cyanoferrate(III) in alkaline solutions prefer reaction (62), while iron(III) or manganate prefer reaction (64). The oxidation to dinitrogen either takes place directly or stepwise in a one-electron oxidation with hydrazyl radicals $N_2H_3{\bullet}$ ($\Delta H_f = 231\,kJ\,mol^{-1}$) as intermediates.

$$N_2H_4 \longrightarrow N_2H_3{\bullet} + H^+ + e^- \qquad (65)$$

The hydrazyl radicals either dimerize to form tetrazane, which then decomposes to form dinitrogen and ammonia (62), or are oxidized further to diazene, which disproportionates to dinitrogen and hydrazine, thus yielding (64).

$$N_2H_3{\bullet} \longrightarrow N_2H_2 + H^+ + e^- \qquad (66)$$

Under atmospheric conditions, an autoxidation of hydrazine takes place:[50]

$$N_2H_4 + O_2 \longrightarrow N_2 + 2H_2O \qquad (67)$$

While autoxidation is undesirable during storage, it limits the environmental damage after spillage and is the driving force in hydrazine-air fuel cells, which have a standard potential of 1.56 V, which is split into 1.16 V for the oxidation of hydrazine (68) and 0.4 V for the reduction of dioxygen (69).

$$N_2H_4 + 4OH^- \longrightarrow N_2 + 4H_2O + 4e^- \qquad (68)$$

$$O_2 + 2H_2O + 4e^- \longrightarrow 4OH^- \qquad (69)$$

Hydrazinium salts do not show autoxidation. When ignited in air, hydrazine burns rapidly and completely with a high-energy release ($\Delta H = -625.1\,kJ\,mol^{-1}$).

When hydrazine is combined with strong oxidizers (N_2O_4, HNO_3, and $HClO_4$), spontaneous ignition takes place. These hypergolic mixtures are used for rocket propulsion. The end stage of the European Ariane 5, for example, uses a bipropellant mixture of methylhydrazine and N_2O_4.[51]

Reaction with CO_2 gives hydrazinocarboxyclic acid (carbazidic acid) H_2NNCO_2H and ammonia. The reaction of hydrazine with carbon monoxide at high pressure and temperature in the presence of iron pentacarbonyl leads

Table 17 Oxidation potentials of hydrazine

	pH = 0	pH = 14
(62)	$E° = -1.74\,V$	$E° = -2.42\,V$
(63)	$E° = +0.11\,V$	$E° = -0.92\,V$
(64)	$E° = -0.23\,V$	$E° = -1.16\,V$

to semicarbazide $H_2NCONHNH_2$. Thiocarbonohydrazide $S{=}C(NHNH_2)_2$ is prepared by reacting carbon disulfide with excess hydrazine in aqueous solution. Hydrazine also reacts with many nitrogen compounds, where it is almost always oxidized.[52] Nitrite, nitrite esters, and occasionally also nitrates can oxidize hydrazine to azides, which are often unwanted because of their explosive hazards. The reaction of hydrazine and its derivatives with many organic compounds are used for analytical purposes.[53]

Pure hydrazine undergoes an autionization according to the following equation

$$N_2H_4 \rightleftharpoons N_2H_5^+ + N_2H_3^- \qquad (70)$$

with an equilibrium constant $K = 2 \times 10^{-25}$.

This is nine orders of magnitude less than the corresponding constant of water and eight orders of magnitude larger than the self-ionization constant of ammonia. Each nitrogen atom of hydrazine can accept one proton, thus two series of salts can be formed ($pK_1 = 6.07$, $pK_2 = 15.1$). With a pK_1 of 6.07, hydrazine is a weaker base than ammonia. The second nitrogen atom is only protonated by strong bases like H_2SO_4 or $HClO_4$. The diprotonated salts are not stable in aqueous solution; they hydrolyze with water acting as a base according to equation (71).

$$N_2H_6^{2+} + H_2O \longrightarrow N_2H_5^+ + H_3O^+ \qquad (71)$$

A solution of hydrazinium(2+) chloride in water is thus equivalent to a solution of hydrazinium(1+) chloride with an equimolar excess of HCl. Hydrazinium salts are similar to ammonium salts, they are colorless and crystallize well. The difference is their lower stability due to the lower basicity of hydrazine and their reducing nature. Salts with strong oxidizing acids like nitric or perchloric acid may be explosive and require careful handling. The salts are characterized by strong hydrogen bonding between the hydrazinium ions and the anions. Some hydrazinium salts crystallize as hydrates.

Hydrazine only acts as a base with very strong bases, for example, sodium amide or sodium hydride.

$$N_2H_4 + NaNH_2 \longrightarrow Na^+N_2H_3^- + NH_3 \qquad (72)$$

Hydrazine can occupy the space commonly occupied by water in crystallization. These compounds are sometimes called hydrazinates in analogy to hydrates. This addition is reversible. Hydrazinium salts and their hydrazine adducts can be used as gas generators, for example, $(N_2H_5)_2(N_2H_4)_2C_2N_{10}$ as they release huge amounts of gas upon decomposition.[54]

The two lone electron pairs of the nitrogen atoms make hydrazine a good ligand for complex formation.[55] One or both nitrogen atoms of hydrazine can be bound to a metal center (*see* ***Ammonia & N-donor Ligands***). Complexes of deprotonated hydrazine are also known, thus giving hydrazine a great structural variety as shown in Scheme 16.

Hydrazine forms Lewis acid–Lewis base adducts with electron-deficient compounds, for example, $BF_3{\cdot}N_2H_4$.

5.3 Triazane and Tetrazane

Triazane and *cyclo*-triazane form in the capillaries of fully Ag^+-exchanged zeolite after exposure to NH_3 gas at ambient temperature. The N_3H_5 molecules (d(N–N) 160(10) pm, <(N–N–N) 107(8)°) form triple bridges via the terminal

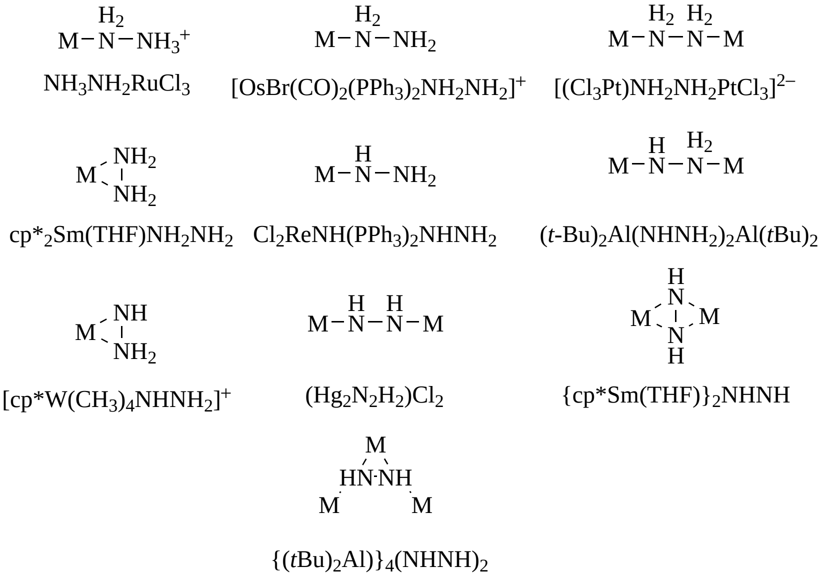
$NH_3NH_2RuCl_3$
$[OsBr(CO)_2(PPh_3)_2NH_2NH_2]^+$
$[(Cl_3Pt)NH_2NH_2PtCl_3]^{2-}$
$cp^*{}_2Sm(THF)NH_2NH_2$
$Cl_2ReNH(PPh_3)_2NHNH_2$
$(t\text{-}Bu)_2Al(NHNH_2)_2Al(tBu)_2$
$[cp^*W(CH_3)_4NHNH_2]^+$
$(Hg_2N_2H_2)Cl_2$
$\{cp^*Sm(THF)\}_2NHNH$
$\{(tBu)_2Al)\}_4(NHNH)_2$

Scheme 16 Coordination of hydrazine ligands in complexes nitrogen atoms in the complex $Ag(N_3H_5)_3{}^{2+}$.[56] *Cyclo*-triazane acts as a η^3 ligand in $Ag(N_3H_5)^+$ (d(N–N) 149(8) pm). The triazane molecules are further stabilized by hydrogen bonds to the oxygen atoms of the surrounding zeolite framework. Weak $N_3H_5{}^+$ and $N_3H_4{}^+$ peaks were observed in the mass spectrum of the zeolite crystal. Organic derivatives of *cyclo*-triazane (triaziridine) are known, for example, *trans*-diisopropyltriaziridine.[39]

Triazane and tetrazane ($\Delta H_f = 293(10)\,\text{kJ mol}^{-1}$) were observed mass spectrometrically in a continuous-flow microwave plasma discharge excited in hydrazine gas in helium.[57] Tetrazane is formed from the dimerization of N_2H_3 radicals and decomposes to dinitrogen and ammonia.

$$2N_2H_3\bullet \longrightarrow N_4H_6 \tag{73}$$

$$N_4H_6 \longrightarrow N_2 + 2NH_3 \tag{74}$$

Otherwise the free bases have not yet been observed. In the case of triazane, only the decomposition products were observed.

$$H_2NNHNH_2 \longrightarrow HN{=}NH + NH_3 \tag{75}$$

Substitution of the hydrogen atom of the central nitrogen atom leads to more stable organyltriazanes H_2NNRNH_2.[58]

5.3.1 Triazanium Salts

The Raschig hydrazine synthesis can be extended one further step. Reaction of chloramine with hydrazine in ether yields triazanium chloride, which decomposes instantaneously.[39] This is responsible for hydrazine decomposition during the Raschig synthesis (see Section 5.2.1):

$$H_2NNH_2 + NH_2Cl \longrightarrow H_2NNHNH_2{\cdot}HCl \tag{76}$$

Hydroxylamine-*O*-sulfonic acid reacts with hydrazine to form a precipitate of triazanium hydrogensulfate $(H_2NNH_2\ NH_2)^+$ $HSO_4{}^-$. Reaction of this solution with an appropriate barium salt in 0.1 M aqueous solution yielded solutions of the nitrate, perchlorate, chlorate, acetate, cyanide, bromide, and hydroxide salts.[59] The stability of the salts decreases in the order hydrogen sulfate > nitrate > perchlorate > chlorate > acetate > azide > cyanide > bromide > hydroxide. The stability of the solutions decreases with decreasing H^+ concentration, thus stronger acids form more stable salts.

5.4 Nitrene

Nitrene ($\Delta H_f = 357(1)\,\text{kJ mol}^{-1}$, $S^\circ = 181.253\,\text{J mol}^{-1}\,\text{K}^{-1}$), also called imidogen radical, nitrogen monohydride, and azene has a triplet ground state ($X^3\Sigma^-$).[39] The reactivity of the first excited singlet state ($a^1\Delta$) is different from ground-state nitrene because of the difference in its electronic structure. In thermal systems below 1000 K, the ground state is the dominant state. At very high temperatures or in nonthermal systems (photolytic, radiolytic), higher electronic states can be populated. The controlled formation of NH in the electronic ground state is difficult. Thermal decomposition of NH_3, NH_2Cl, N_2H_4, and HNCO yields NH in different electronic states. Photolysis of NH_3 and HN_3 produces NH in the first excited state ($a^1\Delta$). Ground-state nitrene is formed in the multiphoton dissociation of NH_3 at 193 nm. A two-step process also produces ground-state nitrene: first UV photolysis of HN_3 or HNCO that yields NH ($a^1\Delta$) followed by quenching in a Xe or N_2 matrix to yield NH ($X^3\Sigma^-$).

Ground-state nitrene decomposes to dinitrogen and dihydrogen ($\Delta H = -331\,\text{kJ mol}^{-1}$)

$$NH(X^3\Sigma^-) \longrightarrow 0.5N_2 + 0.5H_2 \tag{77}$$

Nitrene can be stored for some time below 40 K. At room temperature, nitrene dimerizes very quickly to diimine according to (77).

$$2NH \longrightarrow N_2H_2 \tag{78}$$

Nitrene reacts with dioxygen to form nitrous acid and has been observed in a variety of environments including astrophysical studies. It is a key for understanding the fate of nitrogen in combustion systems regardless of the source of nitrogen: dinitrogen, air, or fuel.

5.5 Diazene

At low-pressure diazene ($\Delta H_f = 219.2(8)\,\text{kJ mol}^{-1}$), also called diimine, is a moderately stable, yellow compound with a lifetime of several minutes at room temperature. It is metastable as a solid below 93 K and very light sensitive.[39]

Evidence for both *cis*-(**47**) and *trans*-(**48**) diazene shown in Scheme 17 has been found in IR studies. *Trans*-diazene (**48**) (d(N–N) 124.7(1) pm, d(N–H) 102.9(1) pm, <(H–N–N) 106.3(2)°) is the dominant structure in the gas phase and has been unambiguously identified. There is evidence that the *cis* isomer (**47**) is the reactive species in many reactions, for example, in the hydrogenation of organic compounds. A third isomer, the blue–violet, photolabile 1,1-diazene or isodiazene (**49**) has been detected in matrix-isolation studies at 12 K. It was prepared from aminoisocyanate. Irradiation

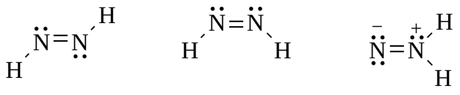

(**47**) C_{2h} (**48**) C_{2v} (**49**) C_{2v}

Scheme 17 Isomers of diazene

of isodiazene (**49**) at 80 K leads to quantitative formation of dihydrogen and dinitrogen.

The major decomposition path of solid *trans*-diazene (**48**) is the disproportionation to dinitrogen and hydrazine:

$$2N_2H_2 \longrightarrow N_2 + N_2H_4 \qquad (79)$$

The dissociation to dinitrogen and dihydrogen, the dimerization to ammonium azide, and the cleavage to ammonia and dinitrogen are only of minor importance.

$$N_2H_2 \longrightarrow N_2 + H_2 \qquad (80)$$

$$2N_2H_2 \longrightarrow NH_4N_3 \qquad (81)$$

$$3N_2H_2 \longrightarrow 2NH_3 + 2N_2 \qquad (82)$$

Below 400 K, dissolved or gaseous diazene decomposes according to (79). Above 400 K, (80) is the major decomposition path. Gaseous diazene can be stored for some time at room temperature at very low pressures because the decomposition reaction is a bimolecular reaction. The photolytic decomposition of *trans*-N_2H_2 occurs according to (80) with a radical mechanism via NNH•.

Diazene can be prepared by a microwave discharge of hydrazine at low pressures. It is accompanied by an excess of NH_3 and can be frozen out with ammonia at lower temperatures. Diazene is more stable in ammonia than in the gas phase at room temperature.

The thermal decomposition of tosylhydrazides $H_2NNXM (X = p\text{-}CH_3\text{-}C_6H_4SO_2, \quad M = \text{alkali metal})$ at temperatures between 373 and 393 K, and trapping at 77 K produces diazene, which is almost free of ammonia.[60]

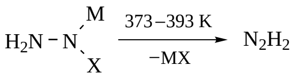

$$H_2N{-}N\begin{smallmatrix}M\\ \\ X\end{smallmatrix} \xrightarrow[-MX]{373-393\,K} N_2H_2 \qquad (83)$$

In solution, diimine can be conveniently generated by the protolysis of azodicarbonate:

$$-OOC{-}N{=}N{-}COO^- \xrightarrow[-2CO_2]{H^+} N_2H_2 \qquad (84)$$

Diazene is a reducing agent. In the absence of reactive substances, solid or dissolved diazene decomposes in a self-reduction (79). At 77 K, it reacts with dioxygen to form H_2O_2 and with CCl_4 to form $HCCl_3$, H_2CCl_2, and HCl. At 173 K, it reduces sulfuric acid to SO_2 and P_2O_5 to P_4. It does not react with SiO_2, therefore, glass equipment can be used for the handling of N_2H_2. In organic chemistry, solutions of diazene are used for the hydrogenation of unsaturated compounds, N=N, C≡N, C=N, S=O, and C=O bonds.

Trans-diazene can be stabilized in complexes (see Scheme 18), where it is normally found as a bridging ligand (**51**). Only one complex is known where it has a monodentate configuration, as in (**50**) (*see* ***Ammonia & N-donor Ligands***). Diazene complexes are intermediates in biological nitrogen fixation (*see* ***Nitrogenase: Metal Cluster Models*** and ***Nitrogenase Catalysis & Assembly***).[61]

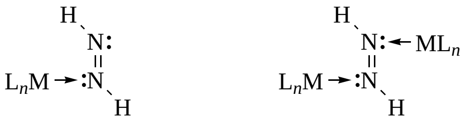

(**50**) $[Co(CO)_5]_2HNNH$

(**51**) $[(PPh_3)_2(CO)_2NO\,W(HNNH)]^+$

Scheme 18 Coordination of diazene in complexes

5.6 Triazene

Triazene $HN{=}N{-}NH_2$ is formed in the pulse radiolysis of aqueous solutions of hydrazine.[62] In the radiolysis, hydrazyl radicals N_2H_3• are formed that dimerize to tetrazane, which decomposes under elimination of ammonia to form triazene.[39]

$$N_4H_6 \longrightarrow HN{=}N{-}NH_2 + NH_3 \qquad (85)$$

Triazene has only a limited lifetime, milliseconds in an acidic medium and up to 100 seconds in a basic environment. It decomposes to form ammonia and dinitrogen.

$$HN{=}N{-}NH_2 \longrightarrow N_2 + NH_3 \qquad (86)$$

The amphiprotic triazene forms both $N_3H_4{}^+$ ($pK_1 = 4.95$) and $N_3H_3{}^-$ ($pK_2 = 11.35$).

$$N_3H_3 + H^+ \rightleftharpoons N_2H_4{}^+ \qquad (87)$$

$$N_2H_3 \rightleftharpoons N_2H_2{}^- + H^+ \qquad (88)$$

5.7 Tetrazene

Trans-2-tetrazene (**52**), which is shown in Scheme 19, forms colorless needles that decompose, sometimes explosively, at 273 K to form dinitrogen and a liquid phase

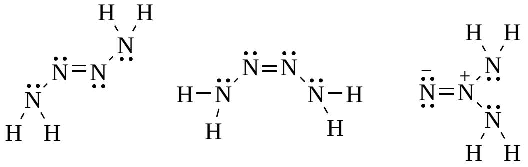

(**52**) C_{2h} (**53**) C_{2v} (**54**)

Scheme 19 N_4H_4 isomers

containing hydrazine and ammonium azide. At temperatures below 243 K, tetrazene can be stored indefinitely.[39] It is soluble in methanol, less soluble in dichloromethane, THF, or trimethylamine. The density of 1.40 g cm^{-3} is higher than the density of hydrazine (1.00 g cm^{-3}) and is similar to the density of ammonium azide, another N_4H_4 isomer. In the solid state, *trans*-2-tetrazene (**52**) is found in a gauche conformation. The nitrogen atoms belong to one plane, the lone pairs of all nitrogen atoms are orthogonal to each other (d(N=N) 121(2) pm, d(N–N) 142.9(5) pm, <(H–N–H) 109.8°, <(H1–N–N) 101(4)°, <(H2–N–N) 118(3)°, <(N–N=N) 109(2)°).[63] Hydrogen bonds with NH···N distances of 303–342 pm form a three-dimensional network of tetrazene molecules.

Gaseous 2-tetrazene decomposes only slowly at low pressures to form hydrazinium azide. In solution, 2-tetrazene decomposes above 253 K. It can disproportionate to form dinitrogen and hydrazine or to ammonium azide.

$$N_4H_4 \longrightarrow N_2 + N_2H_4 \qquad (89)$$

$$N_4H_4 \longrightarrow NH_4N_3 \qquad (90)$$

Tetrazene can be obtained from the reaction of tetrazenium salts $N_4H_7^+X^-$ with bases. The tetrazenium salts are formed in small amounts in the decomposition of diazene, which is catalyzed by acids. For the bulk preparation of *trans*-2-tetrazene, the trimethylsilylderivative of tetrazene is reacted with trifluoroacetic acid at 195 K.[64]

$$\begin{aligned}&(Me_3Si)_2N–N{=}N–N(SiMe_3)_2 + 4F_3CCOOH\\ &\longrightarrow H_2N–N{=}N–NH_2 + 4F_3CCOOSiMe_3 \qquad (91)\end{aligned}$$

Tetrazene can be purified by sublimation at 253 K. Tetrazenes with organic substituents can be obtained by oxidation of organically substituted hydrazines.

Tetrazene is a weaker base than hydrazine and forms salts $N_4H_5^+X^-$ with strong acids. The salts decompose at temperatures above 253 K to the respective ammonium salt and hydrazoic acid.

$$N_4H_5^+X^- \longrightarrow NH_4X + HN_3 \qquad (92)$$

Tetrazene is a strong reducing agent that readily forms dinitrogen.

$$N_4H_4 \longrightarrow N_2 + 4H^+ + 4e^- \qquad (93)$$

Table 18 Properties of hydrazoic acid

b.p. [K]	308.85	$S°$ [J mol^{-1} K^{-1}]	214.35
m.p. [K]	193	ΔH_{vap} [kJ mol^{-1}]	30.5
ρ (l) [g cm^{-3}]	1.127	ΔH_{fusion} [kJ mol^{-1}]	6.0
ΔH_f [kJ mol^{-1}]	263(3)	dipole moment [D]	1.70
ΔG_f [kJ mol^{-1}]	327.3		

cis-2-tetrazene (**53**), the product of protolysis of a cyclic silyl derivative of tetrazene, decomposes instantly at 195 K to form ammonium azide. 1-Tetrazene HN=N–NH–NH_2 is known in form of some unstable organic derivatives that can be synthesized from the reaction of diazonium salts with organic hydrazine derivatives $RNHNH_2$. Isotetrazene $(H_2N)_2N{=}N$ (**54**) is only known in the form of the complex $[(Cl_5WN)_2NN]^-AsPh_4^+$ (*see* ***Ammonia & N-donor Ligands***) (d(N–N) 148(2), 159(2), 123(2) nm, <(N–N–N) 125(2) and 126(1)°).

5.8 Hydrazoic Acid and Azide Salts

Hydrazoic acid is a volatile, endothermic liquid of unbearably acrid odor. Some of its properties are given in Table 18. Hydrazoic acid and its salts are very toxic. Inhalation of small quantities causes the blood pressure to drop and damages the mucous membranes. Exposure to HN_3 vapors can be recognized by reddening of the eyes. Pure, liquid hydrazoic acid is very sensitive and explodes with slight mechanical stress.[39] It is completely miscible with water and soluble in alcohols and ethers. Tests have shown that aqueous solutions with less than 20% hydrazoic acid do not detonate. Diethylether, which has almost the same boiling point (307.7 K) as HN_3 can be used as a blanketing fluid.

The N_3 unit of HN_3 (C_s) is angular (d(H–N_α)101 pm, d(N_α–N_β)124 pm, d(N_β–N_γ)113 pm, <(H–N–N) 109°, <(N–N–N) 171°). The unsymmetrical structure of covalent azides can be explained by mesomeric resonance, the triple bond structure is the more important Lewis structure.

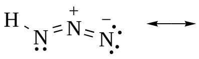
(94)

The bond distances of hydrazoic acid suggest a bond order greater than one for the N_α–N_β bond. This fact is explained better by the extended valence bond theory.[65] In (95), two different mesomeric structures are used to explain the bonding properties of HN_3.[66] The middle structure describes a three-electron bond between N_α–N_β, whereas the right (Dewar) structure describes a long bond.

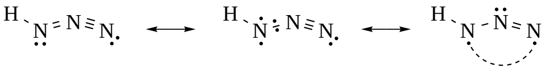
(95)

The azide anion, which has a symmetric, linear arrangement of the nitrogen atoms ($D_{\infty h}$, d(N–N) 118 pm, <(N–N–N) 180°), is a pseudohalide (*see Pseudohalide*).

HN_3 was first obtained as a product of the oxidation of hydrazine by nitrous acid in aqueous solution:

$$N_2H_4 + HNO_2 \longrightarrow HN_3 + 2H_2O \qquad (96)$$

Today, hydrazoic acid is obtained by the reaction of sodium azide, which is the precursor for all azide compounds, with a stronger acid. Several procedures have been developed for this reaction. Hydrazoic acid has been generated by the reaction of ion-exchange resins, mineral acids, or stearic acid. A convenient way to synthesize anhydrous HN_3 solutions is the reaction of HBF_4 with sodium azide in diethylether followed by recondensation of the HN_3 solution.**[67]**

$$HBF_4 + NaN_3 \xrightarrow[200\,K]{Et_2O} HN_3 + NaBF_4 \qquad (97)$$

5.8.1 *Production of Azides*

For the synthesis of sodium azide, precursors with two nitrogen atoms, hydrazine N_2H_4 and N_2O, are used.**[5]** In the technical process, sodium azide is obtained from dry N_2O, which is passed through a sodium amide melt.

$$NaNH_2 + N_2O \xrightarrow{460\,K} NaN_3 + H_2O \qquad (98)$$

Water reacts with a second molecule of sodium amide to form sodium hydroxide and ammonia.

$$NaNH_2 + H_2O \longrightarrow NaOH + NH_3 \qquad (99)$$

Since N_2O is formed from sodium amide and sodium nitrate, sodium azide can also be obtained from the reaction of sodium amide and sodium nitrate in liquid ammonia under pressure at 370 K.

$$3NaNH_2 + NaNO_3 \longrightarrow NaN_3 + 3NaOH + NH_3 \qquad (100)$$

5.8.2 *Chemical Properties of Hydrazoic Acid and Azide Salts*

Hydrazoic acid is a weak acid, comparable in strength to acetic acid ($pK_a = 4.64$).

$$HN_3(aq) \rightleftharpoons H^+(aq) + N_3^-(aq) \qquad (101)$$

HN_3 only acts as a base with very strong acids, for example:

$$HN_3 + HF/SbF_5 \longrightarrow H_2N_3^+SbF_6^- \qquad (102)$$

The C_s $N_3H_2^+$ ion ($d(N_\alpha–N_\beta)$ 1.295(5) pm, $d(N_\beta–N_\gamma)$ 1.101(6) pm, $<$(H–N–N) 107(6)°, $<$(N–N–N) 175.3(5)°) has a pyramidal NH_2 group. The N–N bond distances show that the mesomeric formula with an N–N triple bond is the dominant mesomeric structure.

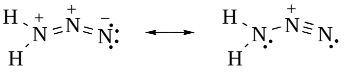
(103)

The weak acid HN_3 can also react with another azide ion to form the hydrogendiazide anion $N_3HN_3^-$.**[68]** The second azide ion is bound to hydrazoic acid via hydrogen bonding with a short NH···N distance of 272(1) pm.

The sometimes explosive decomposition of HN_3 releases huge amounts of heat ($\Delta H = -528\,kJ\,mol^{-1}$):

$$HN_3(l) \longrightarrow 0.5H_2 + 1.5N_2 \qquad (104)$$

At high temperatures and low pressures, HN_3 decomposes to form nitrene.

$$HN_3 \longrightarrow HN + N_2 \qquad (105)$$

Hydrazoic acid is a strong oxidant ($E° = 1.96\,V$):

$$HN_3 + 3H^+ + 2e^- \longrightarrow N_2 + NH_4^+ \qquad (106)$$

It dissolves some metals (M = Zn, Fe, Mn, and Cu) without evolution of dihydrogen:

$$M + 3HN_3 + H^+ \longrightarrow M(N_3)_2 + N_2 + NH_4^+ \qquad (107)$$

In the presence of oxidants, hydrazoic acid is a strong reducing agent ($E° = -3.09\,V$).

$$2HN_3 \longrightarrow 2H^+ + 3N_2 + 2e^- \qquad (108)$$

Iodine and Ce(IV) salts reduce HN_3 to dinitrogen. Nitrous acid oxidizes hydrazoic acid to dinitrogen and dinitrogen oxide:

$$HN_3 + HNO_2 \longrightarrow N_2O + N_2 + H_2O \qquad (109)$$

Hydrazoic acid can be reduced electrochemically to hydrazine and ammonia.

$$HN_3 + 6H^+ + 6e^- \longrightarrow N_2H_4 + NH_3 \qquad (110)$$

The salts of hydrazoic acid, the azides, have similar properties as the respective chlorides, for example, AgN_3, $Hg_2(N_3)_2$, $Pb(N_3)_2$, CuN_3, TlN_3 have only low solubility in water. The alkali- and alkaline earth azides have ionic structures. With the exception of CsN_3 (m.p. 483 K), they do not melt without decomposition. Upon heating, they decompose under evolution of dinitrogen.

$$3Ba(N_3)_2 \xrightarrow[-7N_2]{473\,K} Ba_3N_4 \xrightarrow[-N_2]{523\,K} Ba_3N_2 \qquad (111)$$

$$2NaN_3 \xrightarrow{573\,K} 2Na + 3N_2 \qquad (112)$$

The thermal decomposition of sodium azide is used for the preparation of spectroscopically pure dinitrogen.

Heavy metal azides have more covalent structures and detonate upon heating or mechanical stress. Lead diazide $Pb(N_3)_2$ is used as an initiator for explosives. Like chlorine, azide can act as a ligand in complexes. The complex azido anions are often more stable than binary azide complexes (*see* ***Ammonia & N-donor Ligands***).**69** Dinuclear azide complexes are found with two coordination modes of the azide ion, (**56**) and (**57**) depicted in Scheme 20.

Anhydrous azide salts or moisture sensitive azides can easily be prepared by the reaction of HN_3 with the respective metal hydrides, of sodium azide with the respective metal chlorides, or of trimethylsilyl azide with the respective metal fluorides:

$$n\mathrm{HN_3} + \mathrm{MH}_n \longrightarrow \mathrm{M(N_3)}_n + \frac{n}{2}\mathrm{H_2} \qquad (113)$$

$$n\mathrm{NaN_3} + \mathrm{MCl}_n \longrightarrow \mathrm{M(N_3)}_n + n\mathrm{NaCl} \qquad (114)$$

$$n\mathrm{(CH_3)_3SiN_3} + \mathrm{MF}_n \longrightarrow \mathrm{M(N_3)}_n + n\mathrm{(CH_3)_3SiF} \qquad (115)$$

5.8.2 Covalent Azides

In covalent azides, the pseudohalogen azide RN_3 has an angular structure as in HN_3.**70** Triazidoborazine $[H_3N_3B_3(N_3)_3]$ and other boron azides, for example, salts of the tetraazidoborate ion $B(N_3)_4{}^-$**67** have been considered as boron nitride precursors (*see* ***Boron–Nitrogen Compounds***). The $M(N_3)_3$ azido complexes of the other group 13 elements (Al, Ga, In, Tl) and their $M(N_3)_4{}^-$ tetraazido anions are all known. They and their derivatives are also used as precursors for the nitrides.

In group 14, the triazidocarbenium ion $C(N_3)_3{}^+$ and cyanuric azide $C_3N_3(N_3)_3$ are molecules with a high-energy content. The triazidocarbenium dinitramide and perchlorate have high positive heats of formation. Nitrophenylazides like 1,3,5-trinitro-2,4,6-triazidobenzene were recently reinvestigated as high-energy materials that produce only gaseous products (CO and N_2).**71** While $Si(N_3)_4$ has been reported,**72** no other tetraazides of group 14 are known. The hexaazides $M(N_3)_6{}^{2-}$ of Si–Pb are remarkably stable when accompanied by large cations, for example, $AsPh_4{}^+$.**73** Organic derivatives of germanium, tin, and lead diazides and triazides are known, but only lead diazide, which is used as a primary explosive, has been isolated. Silicon and tin azides have been reported as versatile reagents in main group element and organic chemistry.**74**

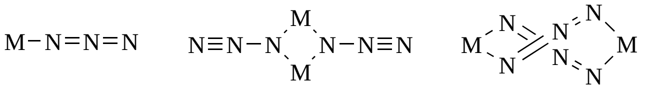

(**55**) $As(N_3)_6{}^-$

(**56**) $[Cu_2(N_3)_6]^{2-}$

(**57**) $[(PPh_3)_2Cu]_2(\mu N_3)_2$

Scheme 20 Coordination of the azide ion in complexes

Table 19 Physical properties of ammonium azide

	NH_4N_3
m.p. [K]	433
ΔH_f [kJ mol^{-1}]	+114.1(9)
ΔG_f [kJ mol^{-1}]	274.2
$S°$ [J mol^{-1} K^{-1}]	112.5
ρ [g cm^{-3}]	1.350
c_p [J g^{-1} K^{-1}]	2.1 (4)
n_D	1.573
ΔH_{sub} [kJ mol^{-1}]	73.6

The phosphorus azides $P(N_3)_3$, $P(N_3)_4{}^+$, $P(N_3)_5$, and $P(N_3)_6{}^-$ have long been known (*see* ***Phosphorus–Nitrogen Compounds***). More recently, the binary arsenic, antimony, and bismuth $M(N_3)_3$, the cations $As(N_3)_4{}^+$ and $Sb(N_3)_4{}^+$, and the arsenic and antimony $M(N_3)_4{}^-$ and $M(N_3)_6{}^-$ anions have been synthesized.**75** While the cations and binary azides are very sensitive(the bismuth compound has not been isolated), the anions, in combination with sufficiently large cations such as $As(Ph)_4{}^+$, are less sensitive. Attempts to prepare the As(V) and Sb(V) pentaazides resulted in explosions.

In group 16, the intermediate existence of $O(N_3)_2$ as an intermediate in the reaction of OF_2 with CsN_3 has been proposed.**76** Many sulfur azides are known, for details see (*see* ***Sulfur: Inorganic Chemistry***). Binary selenium and tellurium azides are not known, but several organic derivatives of the azides have been synthesized.**77,78** For a description of the halogen azides, see Section 8.6.

5.9 Ammonium Azide

Ammonium azide is a colorless, crystalline substance. Some of its properties are given in Table 19. No phase transitions are found between 90 and 348 K. Sublimation of ammonium azide begins at 406 K, recondensation of the vapors at 418 K. Ammonium azide vapors decompose, similar to other ammonium salts, to ammonia and HN_3 at 418 K ($\Delta H = +67.7\,\mathrm{kJ\,mol^{-1}}$). In the solid state, all ammonium ions are tetrahedrally connected to azide ions via hydrogen bonds with an NH···N distance of 297.5(4) and 296.7(3) pm.**39**

Ammonium azide is synthesized either by reacting solutions of HN_3 with ammonia:

$$\mathrm{NH_3} + \mathrm{HN_3} \longrightarrow \mathrm{NH_4{}^+N_3{}^-} \qquad (116)$$

or by dry heating of sodium azide with ammonium nitrate, whereby the produced ammonium azide sublimes to colder parts of the reaction vessel. Great care has to be taken in this reaction because of the thermal sensitivity of ammonium nitrate.

$$\mathrm{NH_4NO_3} + \mathrm{NaN_3} \longrightarrow \mathrm{NH_4{}^+N_3{}^-} + \mathrm{NaNO_3} \qquad (117)$$

The reaction of sodium azide with ammonium sulfate or ammonium chloride in dimethylformamide at 358–393 K under reduced pressure also leads to ammonium azide:

$$NH_4Cl + NaN_3 \xrightarrow{DMF} NH_4{}^+N_3{}^- + NaCl \quad (118)$$

The detonation of ammonium azide produces a huge amount of gas ($\Delta H = -158\,\mathrm{kJ\,mol^{-1}}$).

$$NH_4N_3 \longrightarrow NH_3(g) + 0.5H_2(g) + 1.5N_2(g) \quad (119)$$

An activation energy of $110\,\mathrm{kJ\,mol^{-1}}$ was found for the explosion of ammonium azide. Irradiation at wavelengths <300 nm results in decomposition to ammonia and dinitrogen:

$$3NH_4N_3 \xrightarrow{h\nu} 4NH_3 + 4N_2 \quad (120)$$

5.10 Hydrazinium Azide

Hydrazinium azide ($\Delta H_f = +246.6\,\mathrm{kJ\,mol^{-1}}$, $\Delta H_{\mathrm{fusion}} = +15.8\,\mathrm{kJ\,mol^{-1}}$, $\rho = 1.40\,\mathrm{g\,cm^{-3}}$) is the salt of the weak acid HN_3 with the weak base hydrazine. It is a colorless, hygroscopic solid (m.p. 348 K, b.p. 443 K) that easily sublimes.**38** A phase change between 268 and 273 K has been detected. The hydrazinium ions in the crystal structure have a staggered configuration, and every hydrogen atom of the hydrazinium ions is involved in hydrogen bonding with azide ions. The NH···N distances of the hydrogen bonds between hydrazinium ions and azide ions are between 282.4 and 291.8 pm. There is also a weak hydrogen bond between the hydrazinium ions with an NH···N distance of 338 pm. Table 20 shows a comparison of the bonding parameters between ammonium azide, hydrazinium azide, and its hydrazine adduct.

Hydrazinium azide is prepared by the reaction of hydrazine with hydrazoic acid. To avoid the handling of the hazardous HN_3, which is generally synthesized by the reaction of sodium azide with an acid, several procedures have been developed for this reaction. Hydrazoic acid has been generated by the reaction of ion-exchange resins, mineral acids, or stearic acid. It was then either passed through a solution of hydrazine in an inert gas stream or a solution of hydrazoic acid was added to a solution of hydrazine. Especially pure hydrazinium azide can be obtained by the reaction of anhydrous solutions of HN_3 in diethyl ether with a suspension of anhydrous hydrazine in diethyl ether (97). Hydrazinium azide was also observed in the decomposition of 5-aminotetrazole and *trans*-2-tetrazene.

Table 20 Bonding parameters of $N_2H_5N_3$ and $N_2H_5N_3{\cdot}N_2H_4$

	NH_4N_3	$N_2H_5N_3$	$N_2H_5N_3{\cdot}N_2H_4$
d(N–N) [pm]	–	144.5	145.3(2)
d(N1=N2) [pm]	118.6(4)	117.4	118.0(2)
d(N2=N3) [pm]	118.6(4)	116.4	117.4(2)
<(N1=N2=N3) [°]	180.0	179.21	179.5(2)

The first step in the decomposition of liquid hydrazinium azide is the dissociation to hydrazine and HN_3.

$$N_2H_5N_3 \longrightarrow N_2H_4 + HN_3 \quad (121)$$

HN_3 reacts with hydrazinium azide to form NH_3 and N_2.

$$N_2H_5N_3 + HN_3 \longrightarrow 2NH_3 + 3N_2 \quad (122)$$

The overall equation for the decomposition of hydrazinium azide between 400 and 570 K was found to be:

$$N_2H_5N_3 \longrightarrow 0.25N_2H_4 + 1.33NH_3 + 1.58N_2 \quad (123)$$

Detonation of hydrazinium azide in an argon atmosphere under 3 MPa pressure produces ammonia, dinitrogen, and dihydrogen.

$$N_2H_5N_3 \xrightarrow{3MPa} 2.18N_2 + 1.52H_2 + 0.65NH_3 \quad (124)$$

Both hydrazinium azide and its hydrazinate have been tested in explosive mixtures and as gas generators, but so far they are not in use.

5.11 Hydrazinium Azide Hydrazinate

The hydrazine adduct of hydrazinium azide, hydrazinium azide hydrazinate ($\Delta H_f = +294(3)\,\mathrm{kJ\,mol^{-1}}$, $\rho = 1.320\,\mathrm{g\,cm^{-3}}$) is a colorless solid (m.p. 338 K).**79** Every hydrogen atom of the hydrazine molecules is involved in hydrogen bonding. The NH···N distances are between 294.5(2) and 313.5(2) pm. The hydrazinium ion and the hydrazine molecule are connected by a long hydrogen bond with an NH···N distance of 313.5(2) pm, forming a formal $(N_2H_4)_2H^+$ cation.

Hydrazinium azide hydrazinate can be synthesized by heating a mixture of hydrazinium azide and an equimolar amount of hydrazine to 333 K for several days.

$$N_2H_5N_3 + N_2H_4 \xrightarrow{333\,K} N_2H_5N_3{\cdot}N_2H_4 \quad (125)$$

The detonation of hydrazinium azide hydrazinate under pressure produces ammonia, dinitrogen, and dihydrogen.

$$N_2H_5N_3{\cdot}N_2H_4 \xrightarrow{3MPa} 2.63N_2 + 1.91H_2 + 1.73NH_3 \quad (126)$$

6 NITROGEN OXIDES

The nitrogen oxides, shown in Table 21, except N_2O_4 (l) and N_2O_5 (s), are endothermic compounds and all nitrogen

Table 21 Binary nitrogen oxides

Ox. state	NO_x	N_2O_{2x}	N_3NO_x
+1	N_2O		
+2	NO	N_2O_2	N_3NO
+3		N_2O_3	
+4	NO_2	N_2O_4	N_3NO_2
+5		N_2O_5	
+5	NO_3		

compounds are endergonic compounds ($\Delta G_f > 0$) and should therefore decompose to the elements at room temperature.[5] Owing to kinetic barriers, decomposition begins only at higher temperatures. The monomeric nitrogen oxides NO, NO_2, and NO_3 are radicals.[65] Some properties of the nitrogen oxides are summarized in Table 22.

The nitrogen oxides NO_x are important in globally relevant tropospheric and stratospheric processes. Their life and fate is related to the ozone molecule due to manifold interactions both between the neutral and charged species. The anthropogenic emission of nitrogen oxides is now in the same order of magnitude as the natural emission of nitrogen oxides. Bacteria produce dinitrogen oxide from NH_4^+ during nitrification, and from NO_3^- in the denitrification process. N_2O ($t_{1/2}$ about 100 years) is inert under tropospheric conditions, but reacts in the stratosphere under the influence of oxygen radicals and ultraviolet radiation.

$$N_2O \xrightarrow[\lambda < 240\,\text{nm}]{h\nu} NO\cdot + O\cdot \tag{127}$$

$$N_2O + O\cdot \longrightarrow 2NO\cdot \tag{128}$$

Nitric oxide radicals ($t_{1/2}$ about 2–3 years) destroy ozone in a catalytic process. In the stratosphere, they also stem from emissions from planes and rockets, and reactions of N_2O with solar protons

$$NO\cdot + O_3 \longrightarrow NO_2\cdot + O_2 \tag{129}$$

$$NO_2\cdot + O\cdot \longrightarrow NO\cdot + O_2 \tag{130}$$

The overall reaction of this process is:

$$O_3 + O\cdot \longrightarrow 2O_2 \tag{131}$$

Ozone is formed by the photolytic decomposition of NO_2 yielding oxygen radicals and by the reaction sequence $NO_2 \rightarrow HNO_3 \rightarrow NO_3 \rightarrow O_3$. In particular, the reaction of NO_2 with hydroxyl radicals to form HNO_3 increases ozone concentration because two radicals, $NO_2\cdot$ and $\cdot OH$, which catalyze ozone decomposition, are removed. Other radicals are also important for ozone destruction in the stratosphere, especially chlorine oxides (*see* ***Chlorine, Bromine, Iodine, & Astatine: Inorganic Chemistry***). The mechanism of ozone destruction is complicated as there many compounds involved. Chlorine nitrate and dinitrogen pentoxide can act as reservoir species for $ClO\cdot$, $NO_2\cdot$, and $NO_3\cdot$ radicals.

Nitric oxide in the troposphere ($t_{1/2}$ about 1 day) stems from bacteria, lightning and for the main part from emissions of combustion engines.

The oxidation of nitric oxide in small concentrations in the troposphere by dioxygen is very slow. As shown in Scheme 21, nitric oxide is oxidized to nitrogen dioxide ($t_{1/2}$ several days) either by $HOO\cdot$ radicals or by ozone. Reaction of nitrogen dioxide with hydroxide radicals forms nitric acid ($t_{1/2}$ several days). Rain washes nitric acid out, thus acidic rain is formed.

$$CO + HO\cdot \longrightarrow CO_2 + H\cdot \tag{132}$$

$$H\cdot + O_2 \xrightarrow{(M)} HO_2\cdot \tag{133}$$

$$HO_2\cdot + NO\cdot \longrightarrow NO_2\cdot + HO\cdot \tag{134}$$

Table 22 Properties of nitrogen oxides

	N_2O	NO	N_2O_3	NO_2/N_2O_4	N_2O_5
$T_{crit.}$ [K]	309.45	180	–	431.4	–
$p_{crit.}$ [MPa]	7.245	6.485	–	10.132	–
$\rho_{crit.}$ [kg m^{-3}]	452	520	–	570	–
C_p [kJ kg^{-1} K^{-1}]	0.879	0.996	0.862	1.326	0.782
m.p. [K]	182.3	115.5	172.6	262	306 (subl.)
b.p. [K]	184.7	121.38	233 to 276	294.3	–
ΔH_f [kJ mol^{-1}]	+82.10	+90.25	+86.6	+34.2/+11.1	−43.1
ΔG_f [kJ mol^{-1}]	104.2	86.6	139.4	52.30/97.83	113.8
ΔS [kJ mol^{-1} K^{-1}]	219.7	210.7	139.4	−/304.2	178.2
ΔH_{fusion} [kJ kg^{-1}]	287.4	270.4	40.5[a]	318.5	–
$\Delta H_{vaporization}$ [kJ kg^{-1}]	376.07	459.031	517.416	414.257	–
ρ_{gas} (273 K)[kg m^{-3}]	1.9775	1.3402	1.447	3.4	2.05
ρ_{liquid} (293 K)[kg m^{-3}]	793	–	1446.8	–	solid
Dynamic viscosity gas [mPa s]	14.874	19.184	–	12.838	–
Thermal conductivity gas (293 K) [W m^{-1} K^{-1}]	0.01718	0.02573	–	0.1124	–

[a] Dissociation to NO and NO_2.

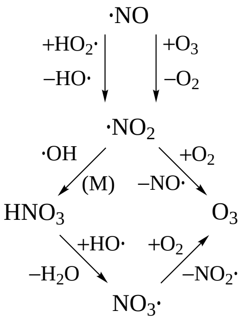

Scheme 21 Reactions of tropospheric nitrogen oxides

$$NO_2\bullet + O_2 \xrightarrow{h\nu} NO\bullet + O_3 \qquad (135)$$

$$HO_2\bullet + O_3 \longrightarrow HO\bullet + 2O_2 \qquad (136)$$

Carbon monoxide is oxidized in the troposphere ((133) and (134)). With a high concentration of nitric oxide in the troposphere, reactions (135) and (136) take place. This sequence is a formation of ozone catalyzed by nitric oxide. If the nitric oxide concentration is too low, the perhydryl radicals decompose ozone to form hydroxyl radicals (136). Ozone and peroxyacylnitrates PAN are the major toxins of smog. Peroxyacylnitrates are formed from aldehydes in a reaction catalyzed by nitric oxide.

6.1 Nitrosyl Azide

Nitrosyl azide is formed in the reaction of an excess of activated sodium azide with nitrosyl chloride at 218 K.[80]

$$NOCl + NaN_3 \xrightarrow{218\,K} NaCl + ONN_3 \qquad (137)$$

Nitrosyl azide can be sublimed under partial decomposition at low temperatures to form a pale yellow solid. Upon warming, it decomposes to form dinitrogen oxide and dinitrogen.

$$ONN_3 \longrightarrow N_2O + N_2 \qquad (138)$$

Calculations indicate the formation of a cyclic N_4O isomer as an intermediate during this decomposition.[81] A N_3O^+ cation has been detected mass spectroscopically in the detonation products of nitromethane.[82]

6.2 Nitryl Azide

The reaction of nitronium hexafluoroantimonate with sodium azide at 223 K in carbon dioxide yields nitryl azide.[83]

$$NO_2{}^+SbF_6{}^- + NaN_3 \xrightarrow[223\,K]{CO_2} NaSbF_6 + O_2NN_3 \qquad (139)$$

On warming up to room temperature, nitryl azide decomposes to dinitrogen oxide.

$$O_2NN_3 \longrightarrow 2N_2O \qquad (140)$$

6.3 Dinitrogen Monoxide

Dinitrogen monoxide ($\Delta H_f^\circ = +82.10\,kJ\,mol^{-1}$), also called nitrous oxide, is a colorless, diamagnetic gas with a weak, pleasant odor, and a sweet taste. The melting point of N_2O is 182.3 K; its boiling point is 184.7 K. It is insoluble in water.[4]

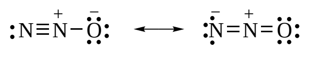
(141)

N_2O has a linear geometry with an N–O distance of 118.6 pm and an N–N distance of 112.6 pm. The N–N bond can be regarded to be between a double and triple bond, the N–O bond is between a single and a double bond. The extended valence bond structures in (142) describe the observed N–N and N–O bond lengths in N_2O better. The right structure gives is the best representation of the actual bonding situation.[84]

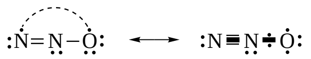
(142)

A cyclic N_2O isomer has not been detected yet,[81] but theoretical calculations indicate its formation in the decomposition of nitrosyl azide and in the reaction of OF_2 with cesium azide. Dinitrogen monoxide is only metastable at lower temperatures, at temperatures above 870 K it decomposes to the elements ($\Delta H = +82.10\,kJ\,mol^{-1}$):

$$N_2O \longrightarrow N_2 + 0.5O_2 \qquad (143)$$

Dinitrogen monoxide is relatively unreactive at room temperature; it does not react with alkaline metals, ozone, chlorine, bromine, or iodine. Easily flammable materials (phosphorus (*see* ***Phosphorus–Nitrogen Compounds***), sulfur (*see* ***Sulfur–Nitrogen Compounds***), coal (*see* ***Carbon: Inorganic Chemistry***)) burn in a dinitrogen oxide atmosphere as in an oxygen atmosphere, though it is more difficult to start the combustion in dinitrogen monoxide. A mixture of N_2O and dihydrogen (*see* ***Hydrogen: Inorganic Chemistry***) explodes with slightly less force than a dioxygen/dihydrogen mixture because of the formation of dinitrogen ($\Delta H = +1012.1\,kJ\,mol^{-1}$).

$$3N_2O + 2NH_3 \longrightarrow 4N_2 + 3H_2O \qquad (144)$$

Under UV irradiation, N_2O reacts with difluorine to form nitrosodifluoramine (see Section 9.4). Dinitrogen monoxide is synthesized by the thermal decomposition of ammonium nitrate or mixtures of sodium nitrate and ammonium sulfate at about 500 K:

$$NH_3 + HNO_3 \longrightarrow N_2O + 2H_2O \qquad (145)$$

At first, this process used solid ammonium nitrate and great care had to be taken to avoid an explosive decomposition of ammonium nitrate (54), which starts at higher temperatures. Now aqueous solutions of ammonium nitrate are used. By-products in this reaction are N_2 and NO.

Laboratory syntheses of nitrous oxide include the decomposition of hyponitrous acid (236) or nitramide (314), the reaction of nitrous acid with hydroxylamine (146) or hydrazoic acid, (147) and the reaction of amidosulfonic acid with concentrated nitric acid (148):

$$HNO_2 + NH_2OH \longrightarrow N_2O + 2H_2O \qquad (146)$$

$$HNO_2 + HN_3 \longrightarrow N_2O + H_2O + N_2 \qquad (147)$$

$$H_2NSO_3H + HNO_3 \longrightarrow N_2O + H_2SO_4 + H_2O \qquad (148)$$

Dinitrogen monoxide can act as a Lewis base in complexes (monodentate in $[Ru(NH_3)_5(N_2O)]^{2+}$). It can also act as a Lewis acid with strong Lewis bases, for example, in the reaction with amides to form azides.

$$NH_2^- + N_2O \longrightarrow N_3^- + H_2O \qquad (149)$$

Dinitrogen monoxide is used in medicine as an anesthetic because, when inhaled, it can bring about a spasmodic inclination to laugh and a condition resembling drunkenness, which explains its historic name, laughing gas. It is also used as a propellant in the munitions industry and a foaming agent for whipped cream in the food industry.

6.4 Nitrogen Monoxide and Dinitrogen Dioxide

Nitrogen monoxide ($\Delta H_f = +90.25\,kJ\,mol^{-1}$), also called nitric oxide, is a colorless, paramagnetic, and toxic gas. Impurities of N_2O_3 can cause a blue color of the liquid (b.p. 121.38 K, m.p. 115.5 K). It is only slightly soluble in water. Nitrogen monoxide is the simplest known, thermally stable molecule (d(N–O) 114 pm) with an odd number of electrons (*see* ***Electronic Structure of Main-group Compounds***) and is a chemical messenger in biological systems. NO helps to regulate a diverse array of physiological processes, such as neurotransmission and blood pressure, and prevents blood clots (*see* ***Nitrogen Monoxide (Nitric Oxide): Bioinorganic Chemistry***).

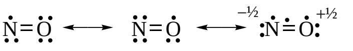

(150)

The structure with the three electron bond between nitrogen and oxygen is the best description of the bonding situation in nitric oxide.

Nitrogen monoxide partly dimerizes upon condensation. At room temperature the dimerization equilibrium is on the side of NO ($\Delta H = -10.5\,kJ\,mol^{-1}$).

$$2NO \rightleftharpoons N_2O_2 \qquad (151)$$

In the liquid and especially in the solid state (diamagnetic), the equilibrium is on the side of the diamagnetic dimer.

As the MO scheme (Scheme 22) shows, the unpaired electron in nitric oxide is in an antibonding MO, thus the bond order is 2.5 and the ionization energy is rather low compared to dinitrogen, dioxygen or carbon monoxide (IE(NO) = 9.25 eV, IE(N_2) = 15.6 eV, IE(CO) = 14.0 V, IE(O_2) = 12.1 eV). The two antibonding $\pi*$ orbitals of NO form a bond in the dimer (see Figure 5). The antibonding $\pi*$ orbital is closer to nitrogen, thus explaining the shorter nitrogen–nitrogen bonds.**[65]**

While both the *cis* (**58**) and the *trans* (**59**) isomer in Scheme 23 have been observed, the *cis* isomer (**58**) (d(N–O) 112(2) pm, d(N–N) 218(3) pm, d(O–O) 2.62(3) pm)**[85]** is more stable. A red asymmetric dimer (**60**) has been detected when NO is condensed in the presence of Lewis acids like BX_3 (X = Hal), SiF_4, $SnCl_4$, $TiCl_4$, SO_2, or HCl.

NO can form a molecule with an even number of electrons either by oxidation to the NO^+ cation (d(N–N) 106 pm), which is isoelectronic with CO and N_2 and has a nitrogen–oxygen triple bond or by reduction to form the nitroxyl anion NO^-, which is isoelectronic to dioxygen O_2.

The highly endothermic nitric oxide can be synthesized from the elements dinitrogen and dioxygen in an electric arc ($\Delta H = 180.6\,kJ\,mol^{-1}$). This also takes place in the natural nitrogen fixation by lightning.

$$N_2 + O_2 \rightleftharpoons 2NO\bullet \qquad (152)$$

Nitric oxide is only formed at very high temperatures (equilibrium concentration about 10^{-7} vol% NO (500 K), 0.04% (1000 K), 0.1% (1500 K), 0.5% (1800 K), and 1% at 2100 K). Around 2300 K, the NO concentration reaches a maximum; at higher temperatures the NO decomposition is faster than the NO formation. The nitric oxide formation has a radical mechanism, starting with the homolytic dissociation of dioxygen to form oxygen radicals.

$$O_2 \overset{(M)}{\rightleftharpoons} 2O\bullet \qquad (153)$$

The chain reaction consists of oxygen radicals reacting with dinitrogen molecules to form NO and nitrogen radicals, which

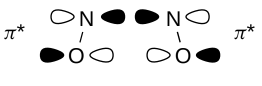

Figure 5 Bonding in the NO dimer

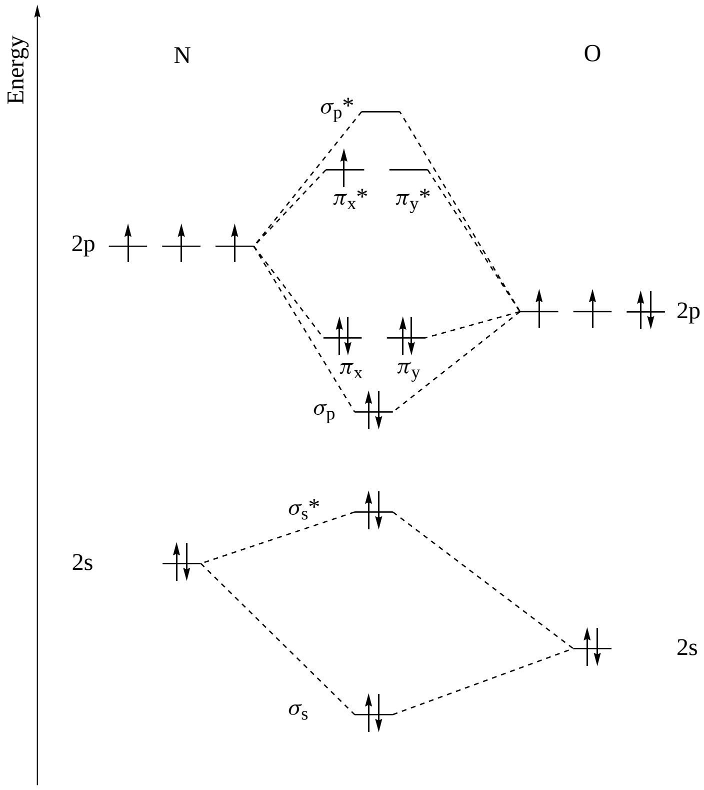

Scheme 22 MO scheme of nitric oxide

react with dioxygen to form NO and oxygen radicals.

$$\text{O}\bullet + \text{N}_2 \overset{\text{(M)}}{\rightleftharpoons} \text{NO}\bullet + \text{N}\bullet \qquad (154)$$

$$\text{N}\bullet + \text{O}_2 \overset{\text{(M)}}{\rightleftharpoons} \text{NO}\bullet + \text{O}\bullet \qquad (155)$$

The process stops on the combination of nitrogen and oxygen radicals.

$$\text{O}\bullet + \text{N}\bullet \overset{\text{(M)}}{\rightleftharpoons} 2\text{NO}\bullet \qquad (156)$$

In former technical processes for the synthesis of nitric oxide, the reaction gases had to be rapidly cooled below 725 K. Slow cooling would give the equilibrium concentration of nitric oxide at the appropriate temperature. At temperatures lower than 725 K, nitric oxide is metastable and does not decompose to dinitrogen and dioxygen. Careful control of the reaction conditions can yield nitric oxide concentrations of about 3%. Nitric oxide is a side product in all combustion processes that employ air and has to be disposed off to avoid pollution of air and the detrimental effects of nitric oxide in the atmosphere (see Section 6). Owing to the preventive energy consumption, the process was only ever practiced in countries with cheap waterpower like Norway and Switzerland and has been completely replaced by the catalytic combustion of NH_3 in the Ostwald process (see Section 7.8.1).[5]

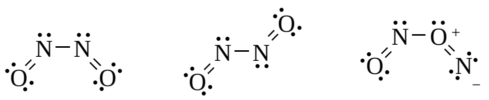
(**58**) *cis* C_{2v} (**59**) *trans* C_{2h} (**60**)

Scheme 23 N_2O_2 isomers

$$4\text{NH}_3 + 5\text{O}_2 \longrightarrow 4\text{NO} + 6\text{H}_2\text{O} \qquad (157)$$

Nitric oxide can be obtained conveniently in the laboratory by the reduction of nitric acid with copper, mercury, or iron(II) salts.

$$\text{NO}_3^- + 4\text{H}^+ + 3e^- \rightleftharpoons \text{NO} + \text{H}_2\text{O} \qquad (158)$$

A very pure nitric oxide is available from the reduction of acidic nitrite solutions with iodide or iron(II) salts.

$$\text{HNO}_2 + \text{H}^+ + e^- \longrightarrow \text{NO} + 2\text{H}_2\text{O} \qquad (159)$$

Nitric oxide decomposes at temperatures higher than 725 K in the reverse of its formation (152) to dinitrogen and dioxygen.

Compressed, liquid, and nitric oxide included in zeolites decompose slowly in an exothermic process:

$$4NO \longrightarrow N_2O_3 + N_2O \tag{160}$$

At higher pressures and temperatures above 323 K it decomposes to:

$$3NO \longrightarrow NO_2 + N_2O \tag{161}$$

In the presence of air or dioxygen, nitric oxide is oxidized to the brown nitrogen dioxide ($\Delta H = 114.2\,\text{kJ mol}^{-1}$).

$$NO + 0.5O_2 \longrightarrow NO_2 \tag{162}$$

The equilibrium of this exothermic reaction is shifted to the left side at higher temperatures. At temperatures higher than 925 K, almost all nitrogen dioxide has decomposed to nitric oxide and dioxygen. The mechanism of the oxidation of NO with dioxygen is assumed to have an ONOONO intermediate that isomerizes to the nitrite isomer of N_2O_4. It has not been proven whether a ONOO intermediate is formed in the first step.**[86]**

Nitric oxide forms nitrosyl halides in the reaction with chlorine and bromine (see Section 9.1); in the reaction with fluorine, both nitrosyl fluoride and trifluoramine oxide are formed (see Section 9.3).

$$NO + 0.5X_2 \longrightarrow XNO \quad X = Cl, Br \tag{163}$$

Strong oxidizing agents such as $KMnO_4$, HOCl, or K_2CrO_4 oxidize nitric oxide to nitrate (158) in acidic solution ($E° = 0.96\,V$). Strong reducing agents reduce nitric oxide to dinitrogen or ammonia. Coal, phosphorus, and magnesium burn vigorously in nitric oxide atmosphere.

Nitric oxide, in contrast to nitrogen dioxide, does not react with water. It reacts with concentrated solutions of strong bases or with alkali metal oxides at 373 K to form nitrite and hyponitrite, which decomposes under these conditions forming N_2O and Na_2O.

$$4NO + 2Na_2O \longrightarrow 2NaNO_2 + N_2O + Na_2O \tag{164}$$

In coordination compounds, NO is more electronegative than CO and a weaker σ-donor than CO, but a stronger π-acceptor. In mononuclear complexes, NO is found either in a linear geometry (**61**) (which can still have small deviations) or in an angular geometry (**61**). In the linear geometry, the NO ligand coordinates as NO^+ and is considered a three-electron donor. In the angular geometry, the NO ligand coordinates as NO^- and is considered a one-electron donor. Scheme 24 summarizes different modes of no coordination.

In multinuclear complexes, NO can act as a bridging ligand, bridging two (**63**) or three metal atoms (**64**). NO has one electron more than CO, therefore the atomic number of the metal centers of NO complexes are lower than in similar CO complexes (*see* ***Carbonyl Complexes of the Transition Metals***), for example, $Ni(CO)_4$, $Co(CO)_3NO$, $Fe(CO)_2(NO)_2$, $Mn(CO)(NO)_3$, and $Cr(NO)_4$. For more information on nitrosyl complexes, see Reference 87.

6.5 Dinitrogen Trioxide

Pure dinitrogen trioxide ($\Delta H_f = +86.6(1)\,\text{kJ mol}^{-1}$) is a pale blue solid ($\rho = 1.781\,\text{g cm}^{-3}$) that melts at 172.6 K to form an intensively blue liquid. N_2O_3 partially decomposes in the range of 233 K to 270 K. At 233 K, the vapor phase contains NO and N_2O_3, while the liquid phase contains N_2O_3 and the equilibrium mixture of NO_2 and N_2O_4. The liquid assumes a green hue due to the mixed colors of blue N_2O_3 and brown NO_2. At higher temperatures, NO_2 is also found in the vapor phase and at ambient temperatures N_2O_3 vapors only contain about 10% undissociated N_2O_3. Solutions of N_2O_3 in organic solvents also have a blue color.

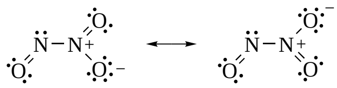

(165)

Dinitrogen trioxide has a planar C_s structure.**[88]** The nitrogen–nitrogen bond in N_2O_3 of 186 pm in the gas phase and 189 pm in the solid state is significantly longer than the bond distances found for N–N single bonds, for example, in hydrazine. It corresponds to a Pauling bond order of 0.2. N_2O_3 can be described as nitrosyl nitrite $NO^+NO_2^-$. The N1–O1 distance is with 112 pm between the N–O distance of NO of 115 pm and NO^+ with 106.5 pm. The N–O bond length of 121 pm and the O–N–O bond angle of 129° of the NO_2 group are in good agreement with N_2O_4 (d(N–O) =

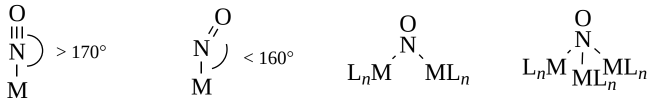

(**61**) (**62**) (**63**) (**64**)

$[Fe(CN)_5(NO)]^{2-}$ $[Co(NH_3)_5NO]^{2-}$ $\{cpCo\}_2NO$ $\{cp(NO)Mn\}_3NO$

Scheme 24 Coordination of NO in nitrosyl complexes

118 pm, <(O–N–O) = 134°) and NO_2^- (d(N–O) = 124 pm, <(O–N–O) = 115°). A comparison between solid-state and gas-phase bonding parameters is shown in Table 23.

A second isomer (**65**) of N_2O_3 shown in Figure 6 with the connectivity ONONO was detected in matrix-isolation experiments.

It is assumed to be an intermediate in the nitration of organic compounds in solution. After irradiation at 380 nm, it reverts to the $ONNO_2$ structure.

Nitric oxide and nitrogen dioxide form N_2O_3 upon cooling ($\Delta H = +40.6(1)\ \mathrm{kJ\,mol^{-1}}$).

$$NO\bullet + NO_2\bullet \rightleftharpoons N_2O_3 \tag{166}$$

Therefore, dinitrogen trioxide can be synthesized by adding an equimolar amount of NO to liquid NO_2 or by adding a stoichiometric amount of dioxygen to NO_2.[5]

$$2NO + 0.5O_2 \longrightarrow N_2O_3 \tag{167}$$

The equilibrium (166) is easily shifted to either side, therefore an equimolar mixture of NO and NO_2 has the same reactivity as N_2O_3, the anhydride of nitrous acid:

$$N_2O_3 + H_2O \rightleftharpoons 2HNO_2 \tag{168}$$

In basic solutions, NO and NO_2 are absorbed to form nitrites. N_2O_3, which is responsible for the nitrite formation, is formed according to the equilibrium (166).

$$NO + NO_2 + 2NaOH \longrightarrow 2NaNO_2 + H_2O \tag{169}$$

In strong acids, the nitrosyl cation NO^+ is formed from N_2O_3.

$$HONO + HClO_4 \longrightarrow NO^+ClO_4^- + H_2O \tag{170}$$

Table 23 Bonding parameters of N_2O_3

	X-ray	Microwave
d(N1–N2) [pm]	189.06(6)	186.4
d(N1–O1) [pm]	111.96(6)	114.2
d(N2–O2) [pm]	120.87(6)	121.7
d(N2–O3) [pm]	120.57(5)	120.2
<(O1–N1–N2) [°]	105.12(4)	105.05
<(O2–N2–O3) [°]	128.61(5)	129.8
<(O2–N2–N1) [°]	119.55(4)	117.47
<(O3–N2–N1) [°]	111.84(3)	112.72

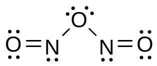

(**65**)

Figure 6 ONONO Isomer of N_2O_3

N_2O_3 is used as a powerful nitrosating agent in organic chemistry. It is also used for preparing high-purity alkali nitrites.

6.6 Nitrogen Dioxide and Dinitrogen Tetroxide

Nitrogen dioxide ($\Delta H_f = +34.2(5)\ \mathrm{kJ\,mol^{-1}}$) is a brown, paramagnetic, corrosive, and highly toxic gas with a characteristic pungent odor. Below the melting point of 262 K, it forms a brown liquid that loses its intensity upon cooling, until at 258 K a colorless solid is formed. The color change is due to the equilibrium of the NO_2 radical (brown) with its dimer N_2O_4 (colorless).

$$N_2O_4 \rightleftharpoons 2\bullet NO_2 \tag{171}$$

The dissociation enthalpy in the gas phase is 57.3(1) kJ mol^{-1}. Below the freezing point, only N_2O_4 exists. The pale yellow liquid at the freezing point contains 0.01% NO_2. At the boiling point, the liquid changes to an intense red–brown color with 0.1% NO_2, the vapor phase contains 20% NO_2. At 373 K, the vapor phase contains 90% NO_2 and at 413 K N_2O_4 is completely dissociated. At temperatures higher than 423 K, NO_2 starts to decompose ($\Delta H = +114.2\ \mathrm{kJ\,mol^{-1}}$), and decomposition is complete at 873 K.

$$2NO_2 \longrightarrow 2NO + O_2 \tag{172}$$

Paramagnetic nitrogen dioxide is, like nitric oxide, a molecule with an odd number of electrons (*see* ***Electronic Structure of Main-group Compounds***) and has an angular structure (C_{2v}, d(N–O) = 119.5(3) pm (GED), 119.455(3) (MW); <(O–N–O) = 133.7(2)° (GED), 133.852(2) (MW)).[89] The repulsive interaction of lone pairs of electrons can be observed in the bond angles of NO_2^+, NO_2, and NO_2^-. NO_2^+, which has no lone electrons and has a linear structure; NO_2, which has one lone electron has a O–N–O angle of 133.7° and NO_2^-, which has a lone pair, has a O–N–O angle of 115.4°.

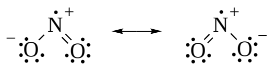

(173)

A better bonding description is given by the extended valecence bond structures:

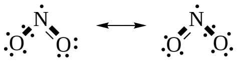

(174)

Diamagnetic dinitrogen tetroxide ($\Delta H_f(g) = +11.1(1)$ kJ mol^{-1}) has a planar (D_{2h}) geometry (**66**). The activation energy for internal rotation is estimated to be 40 kJ mol^{-1}, the twisted isomer has been detected under nonequilibrium conditions. Table 24 shows a comparison of the bonding parameters of N_2O_4 in the solid state and in the gas phase.

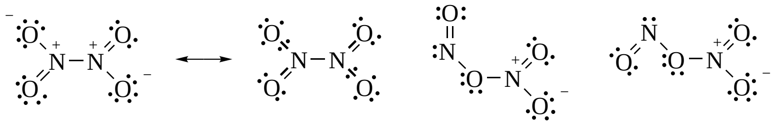

(**66**) D_{2h} (**67**) *syn* (**68**) *anti*

Scheme 25 Isomers of dinitrogen tetroxide

Table 24 Bonding parameters of N_2O_4

	X-ray	GED	IR	$NO^+NO_3^-\cdot IF_5$
d(N–N) [pm]	175.96(7)	177.6(4)	176(1)	–
d(N–O) [pm]	119.02(3)	119.1(4)	119.6(5)	106.2(4) 126.1(3) 125.3(4) 126.8(4)
<(O–N–N) [°]	112.6	–	–	–
<(O–N–O) [°]	134.3(1)	134.6(5)	133.7(5)	120.0(3) 119.6(3) 120.4(3)

N_2O_4 forms two phases in the solid state, a cubic and a monoclinic phase.[90] The monoclinic phase is only formed during crystallization from liquid N_2O_4 with small impurities and can transform to the standard cubic phase, whereas the cubic phase does not transform to the monoclinic phase The *syn* (**67**) and *anti* (**68**) nitrite isomers of N_2O_4 shown in Scheme 25 were identified in low-temperature matrices of N_2 and O_2.[91] The less stable of these forms converts to the ionic form of N_2O_4 and $NO^+NO_3^-$ upon warming. Self ionization of N_2O_4 has been implicated in the solution chemistry of N_2O_4, and occurs as a reversible phase transition at 2.5 GPa for solid N_2O_4, although the molecular form O_2NNO_2 is metastable to very high pressures when compressed as a single crystal.[92] Self oxidation of NO at 80 K also results in a red solid that is described as $NO^+NO_3^-$ on the basics of its IR spectrum. If N_2O is compressed to 10–30 GPa at temperatures of 1000–2000K, $NO^+NO_3^-$ is formed in the following reaction:

$$4N_2O \longrightarrow NO^+NO_3^- + 3N_2 \qquad (175)$$

Once formed, $NO^+NO_3^-$ is stable below 180 K. At room temperature, it is stable with a pressure greater than 1.0 GPa. At higher temperatures/lower pressures, NO^+ NO_3^- transforms to molecular N_2O_4 (**66**).[93] Weak electron donor solvents can form complexes of the type D-N_2O_4 and strong electron donor solvents stabilize the ionic form of N_2O_4: $NO^+NO_3^-$. N_2O_4 dissolves in IF_5 with a yellow color, forming an adduct of the type $NO^+NO_3^-\cdot IF_5$.[94] An ONOONO isomer of N_2O_4 is assumed to be an intermediate in the oxidation of NO with dioxygen, and isomerizes to the nitrite isomers of N_2O_4, (**67**) and (**68**).

In nitrogen dioxide, one electron is in a $\pi*$ antibonding orbital like in nitric oxide. A bonding interaction between two dinitrogen oxide molecules with partly filled $\pi*$ antibonding orbitals leads to a six center three-electron interaction (see Figure 7), explaining the planar structure and the long N–N bond of 176 pm in dinitrogen tetroxide.

NO_2/N_2O_4 is produced industrially by the Ostwald process (see Section 7.8.1),[5] by the catalytic oxidation of ammonia to NO, and oxidation of NO with dioxygen.[5] Other commercial processes for producing NO_2/N_2O_4 are the oxidation of nitrosyl chloride yielding chlorine as by-product and the treatment of sodium nitrite with nitric acid followed by oxidation of the liberated nitrogen monoxide to nitrogen dioxide. High-purity NO_2/N_2O_4 is obtained in the production of sodium nitrate from sodium chloride and nitric acid. In the laboratory, NO_2 is accessible by the reduction of concentrated nitric acid with copper:

$$2NO_3^- + 4H^+ + Cu \longrightarrow 2NO_2 + Cu^{2+} + 2H_2O \qquad (176)$$

Even more convenient is dry heating of heavy metal nitrates, especially lead(II)nitrate to 620–850 K:

$$Pb(NO_3)_2 \xrightarrow{>620\,K} PbO + 2NO_2 + 0.5O_2 \qquad (177)$$

Dinitrogen oxide is a strong oxidizing agent ($E° = 1.03$ V) (see Scheme 26 and Scheme 27) with a similar oxidation potential to Br_2.

$$NO_2 + 2H^+ + 2e^- \rightleftharpoons NO + H_2O \qquad (178)$$

Potassium, sulfur (*see* ***Sulfur–Nitrogen Compounds***), phosphorus (*see* ***Phosphorus–Nitrogen Compounds***), coal (*see* ***Carbon: Inorganic Chemistry***), and dihydrogen (*see* ***Hydrogen: Inorganic Chemistry***) burn in an NO_2 atmosphere more intensively than in an NO or N_2O atmosphere. NO_2 forms explosive mixtures with hydrogen; mixtures with ammonia

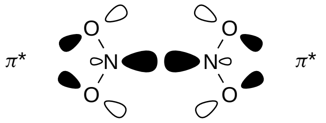

Figure 7 Bonding in dinitrogen tetroxide

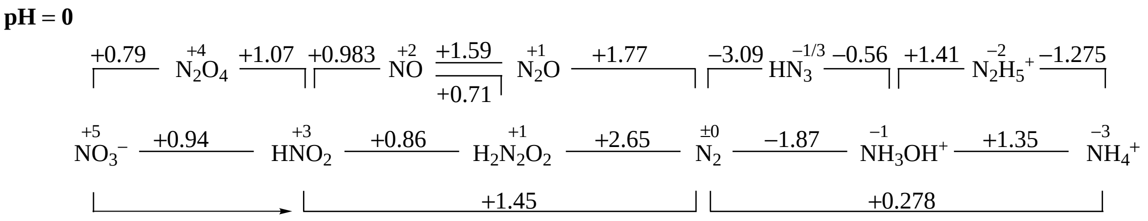

Scheme 26 Standard potentials for nitrogen compounds at pH = 0

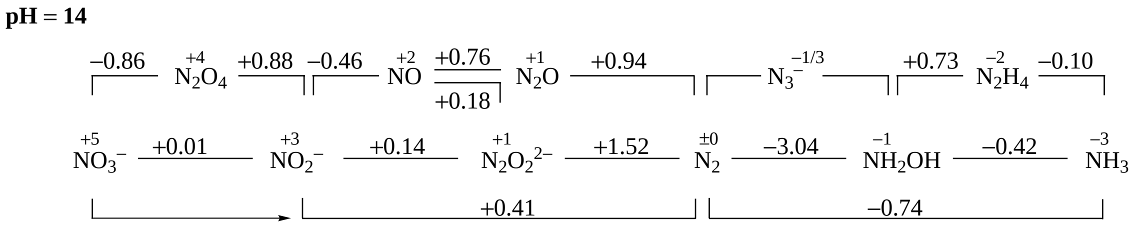

Scheme 27 Standard potentials for nitrogen compounds at pH = 14

explode even at low temperature. It can also react explosively with organic compounds in a radical chain reaction with the first step:

$$\bullet NO_2 + RH \longrightarrow ONOH + R\bullet \qquad (179)$$

NO_2 can also act as a reducing agent with powerful oxidizing agents like O_3 or H_2O_2.

$$NO_2 + H_2O \longrightarrow NO_3^- + 2H^+ + e^- \qquad (180)$$

The reaction of NO_2 with fluorine or chlorine yields nitryl halides (see Section 9.2).

N_2O_4 is between the anhydride of nitrous acid, N_2O_3, and the anhydride of nitric acid, N_2O_5, and is the anhydride of both nitrous and nitric acid:

$$N_2O_4 + 2H_2O \longrightarrow HNO_2 + HNO_3 \qquad (181)$$

In the reaction with bases, nitrates and nitrites are formed.

Liquid N_2O_4 can be used as a nonaqueous solvent.[95] The low electric conductivity $1.3 \times 10^{-13}\ \Omega^{-1}\ \mathrm{cm}^{-1}$ indicates that autodissociation to nitrosonium and nitrate ions does not take place in liquid N_2O_4.

$$N_2O_4 \rightleftharpoons NO^+ + NO_3^- \qquad (182)$$

Weak electron donor solvents can form complexes of the type D-N_2O_4 and strong electron–donor solvents stabilize the ionic form of N_2O_4:$NO^+NO_3^-$. N_2O_4 dissolves in IF_5 with a yellow color, forming an adduct of the type $NO^+NO_3^-\cdot IF_5$. It consists of double chains of alternating NO^+ and NO_3^- ions separated by layers of IF_5 molecules. Distillation of the IF_5 adduct returns covalent N_2O_4.

The nitrosonium cations in liquid N_2O_4 react as oxidizing agents, for example, for the oxidation of metals.

$$NO^+ + e^- \longrightarrow NO \qquad (183)$$

Nitrosonium ions also react as Lewis bases with Lewis acids like halides or oxides.

$$NO^+ + X^- \longrightarrow XNO \qquad (184)$$

$$ZnCl_2 + 2N_2O_4 \longrightarrow 2NOCl + Zn(NO_3)_2 \qquad (185)$$

$$CaO + 2N_2O_4 \longrightarrow Ca(NO_3)_2 + N_2O_3 \qquad (186)$$

The nitrate ions remaining from the dissociation of N_2O_4 react as Lewis bases with metal cations.

$$M^{n+} + nNO_3^- \longrightarrow M(NO_3)_n \qquad (187)$$

Many metal salts dissolve in N_2O_4. Sn, Cu, and Zn dissolve in N_2O_4 to form the metal dinitrates.

$$M + 2N_2O_4 \longrightarrow M(NO_3)_2 + 2NO \qquad (188)$$

These reactions are a convenient preparation of anhydrous nitrates, especially if the metal bromides or iodides are dissolved in N_2O_4.

$$TiI_4 + 4N_2O_4 \longrightarrow Ti(NO_3)_4 + 4NO + 2I_2 \qquad (189)$$

Often nitrato complexes with nitrosonium cations $(NO^+)_m$ $M(NO_3)_n{}^{(n-m)-}$ are formed.

$$Zn(NO_3)_2 + 2N_2O_4 \longrightarrow (NO)^+{}_2[Zn(NO_3)_4]^{2-} \qquad (190)$$

Another example is the intriguing $[(NO^+)_3NO^-]^+$ $[Fe(NO_3)_4]_2{}^-$. Here the cation consists of a nitrate anion surrounded by three NO^+ cations.

N_2O_4 is a donor for nitronium and nitrite ions:

$$N_2O_4 \rightleftharpoons NO_2{}^+ + NO_2{}^- \tag{191}$$

An example is the reaction with BF_3, where $NO_2{}^+$ $[NO_2{}^-{\cdot}BF_3]^-$ is formed.

$$BF_3 + N_2O_4 \longrightarrow NO_2{}^+[NO_2{\cdot}BF_3]^- \tag{192}$$

The strong oxidizing agent dinitrogen tetroxide is used for many applications. It is employed as a catalyst in oxidation reactions and as an inhibitor in the distillation of acrylates. It is also used in the manufacture of explosives and as bleach. In rocket propellants, it is used in a hypergolic mixture with hydrazine derivatives.[51] The command module of the Apollo mission used a 1:1 mixture of hydrazine and *N*,*N*′-dimethylhydrazine with N_2O_4 as the oxidant.

6.7 Dinitrogen Pentoxide

Dinitrogen pentoxide ($\Delta H_f = -43.1\,kJ\,mol^{-1}$) is a colorless, light, and heat sensitive solid that is deliquescent in air and sublimes at 305.5 K. It melts under pressure at 314 K and decomposes at room temperature. The decomposition is sometimes explosive, especially at higher temperatures.

$$N_2O_5 \longrightarrow 2NO_2 + 0.5O_2 \tag{193}$$

In the gas phase and in unpolar solvents like CCl_4, N_2O_5 consists of two NO_2 groups linked by a bridging oxygen atom with a nonlinear N–O–N group.[96] The equilibrium structure has a torsion angle of 30° (C_2); the rotation along the N–O single bonds has an activation barrier of about $4-8\,kJ\,mol^{-1}$.

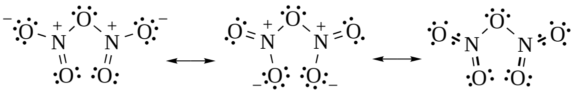
(194)

In the solid state, ($\rho(78\,K) = 2.175\,g\,cm^{-3}$; $\rho(288\,K) = 2.05\,g\,cm^{-3}$) and when dissolved in strong acids like nitric acid, N_2O_5 has an ionic nitronium nitrate $NO_2{}^+NO_3{}^-$ structure. When gaseous N_2O_5 is rapidly cooled below 80 K, the molecular structure is conserved. Upon reheating to 200 K, the ionic structure is formed. Table 25 shows a comparison of the bonding parameters of N_2O_5 in the solid state and in the gas phase.

In the gas phase, N_2O_5 dissociates ($\Delta H = 95.6(1.5)\,kJ\,mol^{-1}$) to nitrogen dioxide and nitrogen trioxide, which can decompose further according to (202) and (203). This makes N_2O_5 an important nighttime reservoir in atmospheric chemistry for the reactive $NO_2{\bullet}$ and $NO_3{\bullet}$ species.[97]

Table 25 Bonding parameters of N_2O_5

	X-ray	GED
d(N–O) [pm]	123.4	1.505(4) 1.495(4)
d(N=O) [pm]	115.4	1.188(1) 1.188(2)
<(N–O–N) [°]	–	112(2) 112(2)
<(N–O=N) [°]	–	134.2(4) 133.2(6)

$$N_2O_5 \rightleftharpoons NO_3{\bullet} + NO_2{\bullet} \tag{195}$$

Dinitrogen pentoxide is the anhydride of nitric acid, and was industrially prepared by the careful dehydration of nitric acid with phosphorus pentoxide.

$$6HNO_3 + P_2O_5 \xrightarrow{263\,K} 3N_2O_5 + 2H_3PO_4 \tag{196}$$

A newer synthesis produces 10–20% solutions of N_2O_5 in nitric acid by electrolysis of nitric acid in the presence of N_2O_4.

$$2HNO_3 + 2e^- \xrightarrow{N_2O_4} N_2O_5 + H_2O \tag{197}$$

Pure and almost acid free N_2O_5 is obtained from the oxidation of dinitrogen tetroxide with ozone.

$$N_2O_4 + O_3 \longrightarrow N_2O_5 + O_2 \tag{198}$$

N_2O_5 is a strong oxidant and reacts violently with many types of reductants, including metals, nonmetals, and numerous organic compounds.

$$N_2O_5 + I_2 \longrightarrow I_2O_5 + N_2 \tag{199}$$

The dissociation to $NO_2{}^+NO_3{}^-$ in strong acids is a convenient pathway to nitronium salts like $(NO_2{}^+)_2S_2O_7{}^{2-}$ from the reaction with SO_3 or $NO_2{}^+FSO_3{}^-$.

Dinitrogen pentoxide forms an adduct $N_2O_5{\cdot}BF_3$ ($NO_2{}^+$ $(BF_3{\cdot}ONO_2{}^-)$) with boron trifluoride, which is a good nitrating reagent. The reaction of N_2O_5 with halogens X_2 (X = F, Cl) forms nitryl halides XNO_2.

N_2O_5 is slowly replacing nitrating acid ($HNO_3 + 2H_2SO_4$) in some applications, because nitration with pure nitrogen pentoxide is acid free and can take place in an anhydrous solvent. For nitration, a dilute solution of N_2O_5 in chlorinated organic solvents like CH_2Cl_2 is used.

6.8 Nitrogen Trioxide

NO_2 and excess dioxygen form nitrogen trioxide ($\Delta H_f = 74(1)\,kJ\,mol^{-1}$) in a glow discharge.

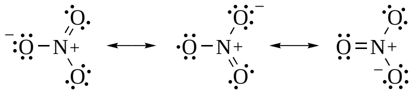

(200)

The nitrogen trioxide radical has a D_{3h} structure (d(N–O) = 120.4 pm). The spin density of nitrogen is zero for symmetrical reasons and the unpaired electron is located at the oxygen atoms.

The reaction of NO_2 and N_2O_5 with ozone as well as the decomposition of N_2O_5 yields NO_3. $NO_3\cdot$ decomposes according to two dissociation channels:

$$NO_3\cdot \longrightarrow NO_2\cdot + O\cdot \qquad (201)$$

$$NO_3\cdot \longrightarrow NO\cdot + O_2 \qquad (202)$$

The mechanism for the formation of nitric oxide (202) is still unclear.

The formation of an intermediate ONOO (**69**) species in Figure 8 has been claimed in a spectroscopic study but was later questioned due to multireference calculations.[98] NO_3 reacts with NO_2 to form dinitrogen pentoxide.[97]

$$NO_3\cdot + NO_2\cdot \rightleftharpoons N_2O_5 \qquad (203)$$

N_2O_5 acts as a reservoir species in atmospheric chemistry making NO_3, formed by the dissociation of N_2O_5, the major nighttime oxidant in the stratosphere.

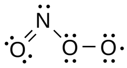

(**69**)

Figure 8 ONOO isomer of NO_3

A mass spectrometric investigation of $NO_2/O_3/O_2$ mixtures with chemical ionization has identified the NO_5^+ cation from the reaction of NO_2^+ with ozone.[99] The decomposition products NO_4^+ and NO_3^+ indicate an O_nNO_2 connectivity of NO_5^+ and its decomposition products.

Mixtures of $NO/O_3/O_2$ also produce NO_4^+ ions under the conditions described above, but their decomposition products indicate an O_3NO connectivity. Three isomeric NO_3^+ cations have been detected in the mixtures described above under different conditions: one has O_2NO connectivity and two share $O{-}NO_2$ connectivity, but with different structures. One NO_3^+ cation has a trigonal structure like the radical $NO_3\cdot$, the other corresponds to a weakly bound species that undergoes a near threshold decomposition and is assumed to have ONOO connectivity. Neutralisation-reionization mass spectrometry of this NO_3^+ isomer shows weak evidence for a neutral ONOO isomer (**69**) with a lifetime exceeding 1 μs.

7 OXOACIDS OF NITROGEN

The strength of the nitrogen oxoacids given in Table 26 increases with higher oxidation numbers of nitrogen. While hydroxylamine is only a very weak acid, nitrous acid is an acid of medium strength and nitric acid is a very strong acid. The anions of orthonitric acid HNO_4 and oxohyponitric acid $H_2N_2O_3$ are known, but the free acids have not yet been observed. HNO and HNOO are not stable at standard conditions and are metastable at lower temperatures. Salts with the formula M_3NO_3, formally salts of orthonitrous acid H_3NO_3, are obtained from the reaction of equimolar amounts of alkali metal nitrites with alkali metal oxides M_2O.[100]

$$MNO_2 + M_2O \longrightarrow M_3NO_3 \qquad (204)$$

Yellow Na_3NO_3, red K_3NO_3, and red-brown Rb_3NO_3 do not contain the orthonitrite anion NO_3^{3-}, but are mixed crystals of the salts MNO_2 and M_2O with an anti-perovskite $(NO_2)OM_3$

Table 26 Oxoacids of nitrogen in different oxidation states

Oxidation state	Formula	Name	Salt
−1	H_2NOH	hydroxylamine	hydroxylamide
0	HNOO	imine peroxide	–
+1	HNO	nitrosyl hydride (nitroxyl)	nitroxyl anion
	HONNOH	hyponitrous acid	hyponitrite
+2	$H_2N_2O_3$	oxohyponitric acid, only salts	hyponitrate, trixodinitrate
+3	HNO_2	nitrous acid	nitrite
	HONOO	peroxonitrous acid	peroxonitrite
+5	HNO_3	nitric acid	nitrate
	H_3NO_4	orthonitric acid, only salts	orthonitrate
	HNO_4	peroxonitric acid	peroxonitrate
–	H_2NNO	nitrosamine	–
–	H_2NNO_2	nitramide	–
–	$HN(NO_2)_2$	dinitramic acid	dinitramide

structure.[101] The trialkoxyamines $(RO)_3N$, organic derivatives of orthonitric acid, are also unstable species.

Reduction of a solution of sodium nitrite in ammonia with sodium produces a deep yellow solid with the formula Na_2NO_2, sodium nitroxylate.

$$2NaNO_2 + 2Na \longrightarrow 2Na_2NO_2 \qquad (205)$$

The compound has only a small paramagnetic susceptibility. The unexpected low paramagnetic susceptibility suggests that the compound dimerizes to $Na_4N_2O_4$, and is dissociated to about 20% to Na_2NO_2 at room temperature. The structure of this salt is unknown.[102]

The oxidation potentials of nitrogen compounds in different oxidation states are shown in Scheme 26 and Scheme 27. The oxidants are stronger in acidic solution and the reductants are stronger in basic solution. The strongest oxidants are hyponitrous acid $H_2N_2O_2$ and HNO_3, the strongest reductants NH_2OH and $N_2O_2{}^{2-}$. It follows that dinitrogen N_2 cannot disproportionate to compounds with any oxidation state. Nitrogen fixation is not possible this way. On the other hand, depending on the pH of the medium, hydroxylamine can disproportionate to form ammonia and dinitrogen, and hyponitrous acid can disproportionate to form nitrous acid and dinitrogen. Nitrous acid can disproportionate to form nitric acid and dinitrogen.

7.1 Hydroxylamine

Hydroxylamine crystallizes as colorless needles ($\Delta H_f^\circ = -114\,\text{kJ mol}^{-1}$), which melt at 305 K. The boiling point of liquid hydroxylamine is 329.5 K at 22 HPa and the density is $1.204\,\text{g cm}^{-1}$ at 306 K. The N–O bond distance is 146 pm in the gas phase and 147 pm in the solid state. Other gas-phase bonding parameters include: d(O–H) = 96 pm, d(N–H) = 101 pm, $<$(H–O–N) = 103°, $<$(H–N–O) = 105°, $<$(H–N–H) = 107°. In the solid state (Figure 9), hydrogen bonds connect hydroxylamine molecules with a *trans* conformation (**70**). The NH···O distance is 274 pm.

Hydroxylamine can disproportionate to form ammonia and dinitrogen or dinitrogen oxide:

$$3NH_2OH \longrightarrow NH_3 + N_2 + 3H_2O \qquad (206)$$

$$4NH_2OH \longrightarrow 2NH_3 + N_2O + 3H_2O \qquad (207)$$

Pure hydroxylamine or its aqueous solutions can be stored for several weeks in the absence of oxygen at low temperatures. The decomposition rate increases with increasing pH. In the presence of oxygen, for example, in air, pure hydroxylamine or its aqueous solution decompose rapidly, especially at slightly elevated temperatures. At temperatures above 373 K, hydroxylamine decomposes explosively. Autoxidation takes place in basic solutions in the presence of transition metals and dioxygen. Hydroxylamine is oxidized to nitrite via nitrosyl and peroxonitrite ions.

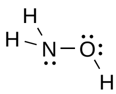

(**70**)

Figure 9 Structure of hydroxylamine molecules in the solid state

$$NH_2O^- + O_2 \longrightarrow H_2O_2 + NO^- \qquad (208)$$

$$NO^- + O_2 \longrightarrow ONOO^- \qquad (209)$$

$$ONOO^- + NH_2O^- \xrightarrow{[Cu^{2+}]} NO_2{}^- + NO^- + H_2O \qquad (210)$$

7.1.1 Production of Hydroxylamine

Hydroxylamine is prepared by reducing nitrogen oxides in higher oxidation states, for example, nitric oxide, nitrous acid, or nitric acid.[5]

For reduction of nitric oxide, a mixture of nitric oxide and dihydrogen is passed through a suspension of a platinum (BASF process) or palladium in sulfuric acid. Ammonium sulfate and dinitrogen oxide are by-products.

$$2NO + 3H_2 + H_2SO_4 \longrightarrow (NH_3OH)_2SO_4 \qquad (211)$$

Nitrous acid can be reduced to hydroxylamine with sulfurous acid:

$$HNO_2 + 2H_2SO_3 + H_2O \longrightarrow NH_2OH + 2H_2SO_4 \qquad (212)$$

In the Raschig process, ammonium nitrite is converted to ammonium hydroxylamine disulfonate with sulfur dioxide in sulfuric acid at 273 K:

$$2SO_2 + NH_4NO_2 + NH_3 + H_2O \longrightarrow (NH_4)_2[HO\text{–}N(OSO_2)_2] \qquad (213)$$

The sulfonate is then hydrolyzed at 373 K to form hydroxylammonium sulfate and ammonium sulfate.

A phosphoric acid/ammonium nitrate buffer solution with a suspended noble metal catalyst can be reduced with hydrogen to hydroxylammonium dihydrogenphosphate:

$$\begin{aligned} NH_4NO_3 + 2H_3PO_4 + 3H_2 \longrightarrow {} & [NH_3OH]^+[H_2PO_4]^- \\ & + NH_4H_2PO_4 + 2H_2O \qquad (214) \end{aligned}$$

The hydroxylammonium solution is then directly used for oxime formation and the consumed nitrate ions are replaced by addition of nitric acid.

Nitric acid can also be reduced between lead electrodes in the presence of hydrochloric or sulfuric acid:

$$HNO_3 + 6H^+ + 6e^- \longrightarrow NH_2OH + 2H_2O \qquad (215)$$

The acidic cleavage of nitroalkanes has only found limited use due to its cost and the limited availability of the raw materials.

$$\mathrm{2RCH_2NO_2 \xrightarrow[H_2SO_4]{H_2O} (NH_3OH)_2SO_4 + 2RCOOH} \tag{216}$$

7.1.2 *Anhydrous Hydroxylamine*

All hydroxylamine syntheses yield hydroxylammonium salts. Free hydroxylamine can be prepared by adding a strong base to the hydroxylammonium salts. Sodium methanolate $NaOCH_3$ can be used for this purpose:

$$\mathrm{NH_3OH^+X^- + NaOCH_3 \longrightarrow NH_2OH + NaX + CH_3OH} \tag{217}$$

After the reaction, the solid sodium salt is filtered off and methanol is distilled off under reduced pressure. Hydroxylamine can also be prepared by the ammonolysis of hydroxylammonium salts in liquid ammonia. The ammonium salt precipitates and is filtered off. Hydroxylamine is obtained after evaporating the excess ammonia.

7.1.3 *Chemical Properties of Hydroxylamine*

As a hydroxyderivative of ammonia, hydroxylamine is a weak base ($pK_b = 8.2$) and forms hydroxylammonium salts with acids:

$$\mathrm{NH_2OH + HX \longrightarrow NH_3OH^+X^-} \tag{218}$$

In contrast to free NH_2OH, the hydroxylammonium salts are relatively stable. Dry hydroxylammonium salts disproportionate upon heating to form the ammonium salts and dinitrogen.**[4]**

The hydroxylammonium salts ($pK_a = 5.8$) are more acidic in aqueous solution than the ammonium salts ($pK_a = 9.25$) because NH_2OH is less basic than NH_3. NH_2OH is a weak acid ($pK_a = 13.7$), only slightly more acidic than water. The hydroxylamides NH_2O^-, of which the sodium, calcium, and zinc salts are known, are very unstable and explosive.

Like ammonia, hydroxylamine can form complexes in basic solution (*see* ***Ammonia & N-donor Ligands***), coordinating via the nitrogen atom as in (**71**) in Scheme 28. Complexes of the deprotonated hydroxylamides show N,O coordination as in (**72**). Both coordination modes are found in $[UO_2(ONH_2)(HONH_2)]$.

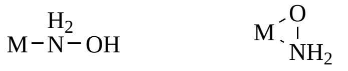

(**71**) (**72**)

$[Ni(NH_2OH)_6]^{2+}$ $Mo(N_3)_4(NO)(NH_2O)$

Scheme 28 Coordination of hydroxylamine and the hydroxylamide ion in complexes

Hydroxylamine ($E° = 1.87\,V$) is a strong reducing agent (see Scheme 26 and Scheme 27).

$$\mathrm{2NH_3OH^+ \longrightarrow N_2 + 2H_2O + 4H^+ + 2}e^- \tag{219}$$

N_2 and N_2O are the products of the oxidation of hydroxylamine. With an excess of oxidizing agent, NO, NO_2^-, NO_2, as well as NO_3^- are formed. Hydroxylamine reacts as an oxidant with reducing agents ($E° = 1.35\,V$).

$$\mathrm{NH_3OH^+ + 2H^+ + 2}e^- \longrightarrow \mathrm{NH_4^+ + H_2O} \tag{220}$$

One-electron oxidants like Ce^{4+}, Mn^{3+}, Fe^{3+}, Co^{3+}, Cu^{2+}, Ag^+, or Ag^{2+} generate the intermediate radical •NHOH that can react with Ce^{4+}, Mn^{3+}, or Cu^{2+} to form HNO:

$$\mathrm{NHOH\bullet \longrightarrow HNO + H^+} + e^- \tag{221}$$

which in turn forms N_2O

$$\mathrm{2HNO \longrightarrow N_2O + H_2O} \tag{222}$$

or decomposes directly to form dinitrogen (with Co^{3+}, $Fe(CN)_6{}^{4-}$).

$$\mathrm{2NHOH\bullet \longrightarrow HONHNHOH \longrightarrow N_2 + 2H_2O} \tag{223}$$

Two-electron oxidants such as $CrO_4{}^{2-}$, $MnO_4{}^-$, or ClO^- produce N_2O via HNO.

Sn(II), V(II), or Cr(II) salts can reduce hydroxylamine to ammonia, here the amino radical NH_2• is an intermediate.

$$\mathrm{NH_2OH} + e^- \longrightarrow \mathrm{NH_2\bullet + OH^-} \tag{224}$$

$$\mathrm{NH_2\bullet + H^+} + e^- \longrightarrow \mathrm{NH_3} \tag{225}$$

Reaction of hydroxylamine with ketones or aldehydes yields oximes, aldoximes RHC=NOH, or ketoximes R_2C=NOH. Almost all the hydroxylamine production (95%) is used for the production of either cyclohexanone oxime or caprolactam, both of which are intermediates for polyamide synthetics. The remainder of the hydroxylamine production is used as an anticreaming agent in paints and coatings, as an auxiliary in refining fats for soap production, as a regulator or inhibitor for various polymerizations, as a stabilizer for developers, and as an additive for color emulsions. Oximes are also used as pharmaceuticals or in crop protection.

7.2 Nitrosyl Hydride (Nitroxyl)

The reaction of atomic hydrogen with NO at 77 K yields a pale yellow substance with the composition HNO that condenses on the walls of the reaction vessel ($\Delta H_f = +107\,\mathrm{kJ\,mol^{-1}}$). At 178 K, it decomposes to form hyponitrous acid $H_2N_2O_2$ (80%) and dinitrogen oxide (20%). HNO is also a reactive intermediate of the oxidation of hydroxylamine NH_2OH and the reduction of nitrous acid HNO_2. It dimerizes to hyponitrous acid $H_2N_2O_2$. HNO is also formed during the decomposition of Angeli's salt $Na_2N_2O_3$:

$$N_2O_3{}^{2-} + H^+ \longrightarrow HNO + NO_2{}^- \qquad (226)$$

The weak acid HNO ($pK_a = 11.4$) has a singlet ground state ($X\ ^1A'$).[103] The nitroxyl anion NO^- has a triplet ground state ($X\ ^3\Sigma^-$), therefore the dissociation of HNO to NO^- and H^+ is spin forbidden and inherently slow. In physiological systems, HNO is the dominant form, but NO^-, once formed, has sufficient lifetime to react with other species. HNO is like NO a transient intermediate in physiological systems.

$$HNO \rightleftharpoons H^+ + NO^- \qquad (227)$$

The nitroxyl anion dimerizes to form hyponitrite:

$$2NO^- \longrightarrow N_2O_2{}^{2-} \qquad (228)$$

The isomer HON was detected in matrix isolation and is in a photoequilibrium with HNO.[104]

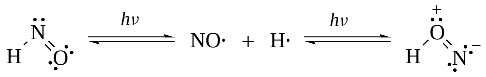

(229)

Reaction of the nitroxyl anion NO^- with dioxygen O_2 forms peroxonitrite, which isomerizes in acidic solution to nitrate.

$$NO^- + O_2 \longrightarrow OONO^- \qquad (230)$$

The presence of HNO as an intermediate in this reaction can be verified with the violet complex $[Ni(CN)_3NO]^{2-}$:

$$Ni(CN)_4{}^{2-} + NO^- \longrightarrow [Ni(CN)_3NO]_2{}^- + CN^- \qquad (231)$$

In HNO complexes, the HNO molecule (d(N=O) 120 pm, <(H–N–O) 99°) is bonded via nitrogen and has a bent conformation.

7.3 Imine Peroxide

The reaction of ground-state nitrene NH($X\ ^3\Sigma^-$) with molecular oxygen in argon or xenon matrices at temperatures of 20 K yields imine peroxide:[105]

$$NH(X^3\Sigma^-) + O_2(X^3\Sigma_g{}^-) \longrightarrow HNOO(X^1A) \qquad (232)$$

It is also formed in the photodissociation of matrix-isolated methyl nitrate that yields either HNO_2 (hydrogen nitryl) or imine peroxide HNOO.[106]

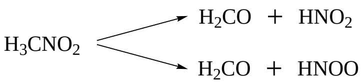

$$H_3CNO_2 \longrightarrow H_2CO + HNO_2; \quad H_3CNO_2 \longrightarrow H_2CO + HNOO \qquad (233)$$

Theoretical calculations suggest that HNOO has a singlet electronic ground state with considerable diradical character, similar to ozone. HNOO is, therefore, a member of the group of 1,3-dipole molecules whose electronic structure has been described as a resonance of the zwitterionic versus the radical structure.

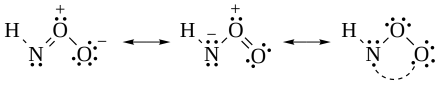

(234)

A *cis* and a *trans* form are possible for HNOO. However, only one form, probably the *trans* form, was detected in the matrix-isolation experiments. Imine peroxide isomerizes to nitrous acid upon irradiation with UV or IR light.

7.4 Hyponitrous Acid

The hydroxygroups of hyponitrous acid are found in a *trans* (**73**) and a *cis* (**74**) conformation (Scheme 29). The nitridonitrate isomer (**75**) is only known in form of its tautomer, nitramide.

While *trans*-hyponitrous acid has been known for a long time, only salts of *cis*-hyponitrous acid are stable. The isolated $N_2O_2{}^{2-}$ dianion, which was insulated from stabilizing cations in solid argon, has been observed with matrix-isolation techniques and is one of the smallest known dianions that is stable toward electron loss.[107]

7.4.1 *trans-Hyponitrous Acid*

trans-Hyponitrous acid forms colorless rods, which are very sensitive when dry and decompose violently.[108] A comparison of the bonding parameters of several $N_2O_2{}^{2-}$ compounds is given in Table 27.

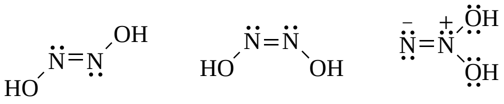

(**73**) *trans* C_{2h} (**74**) *cis* C_{2v} (**75**) C_{2v}

Scheme 29 Isomers of hyponitrous acid

Table 27 Structural data of $N_2O_2{}^{2-}$ compounds

	trans-$H_2N_2O_2{}^a$	*trans*-$HN_2O_2{}^{-a}$	*trans*-$N_2O_2{}^{2b}$	*cis*-$N_2O_2{}^{2-c}$
d(N=N) [pm]	122.6(4)	123.2(3)	1.233(2)	120(3)
d(N–O) [pm]	136.3(3)	NOH 140.2(3) NO 137.1(3)	1.389(1)	140(1)
<(N–N–O) [°]	109.0(3)	NNOH 110.1(2) NNO 108.2(2)	107.6(1)	120.8(4)

[a] $[HEt_2NCH_2CH_2NEt_2H][HN_2O_2]_2 \cdot H_2N_2O_2$; [b] [2,2′-bipyridinium]$[N_2O_2]$; [c] *cis*-$Na_2N_2O_2$.

trans-$H_2N_2O_2$ is obtained by reducing nitrous acid with sodium amalgam at 273 K:

$$2NaNO_2 + 4Na/Hg \longrightarrow trans\ Na_2N_2O_2 + 2Na_2O + 4Hg \qquad (235)$$

After the reaction is finished, the insoluble silver hyponitrite $Ag_2N_2O_2$ is precipitated with $AgNO_3$. $H_2N_2O_2$ is accessible by treating the silver salt with a solution of HCl gas in diethyl ether, or by oxidation of hydroxylamine with copper, silver, or mercury oxide.

Aqueous solutions of *trans*-hyponitrous acid are acidic ($pK_1 = 7.21$, $pK_2 = 11.54$) and decompose slowly, faster at higher temperatures, via HO–N=N–O^- to form water and dinitrogen oxide ($t_{1/2}$ (298 K) = 16 days at pH = 1−3, at higher pH values *trans*-$H_2N_2O_2$ is unstable).

$$H_2N_2O_2 \longrightarrow N_2O + H_2O \qquad (236)$$

This reaction is not reversible, and dissolving of N_2O in water does not give hyponitrous acid. As a dibasic acid, *trans*-hyponitrous acid forms two types of salts: acidic hyponitrites $M^+\ HN_2O_2{}^-$ that decompose readily and are more stable, and neutral hyponitrites $M_2{}^+N_2O_2{}^{2-}$. Both types of salts react basic, are reductants, and are remarkably stable against reduction.

Reaction of iodine with *trans*-hyponitrous acid yields nitrous acid and nitric acid:

$$trans\ H_2N_2O_2 + 3I_2 + 3H_2O \longrightarrow HNO_3 + HNO_2 + 6HI \qquad (237)$$

Nitrous acid reduces *trans*-hyponitrous acid to dinitrogen:

$$trans\ H_2N_2O_2 + HNO_2 \longrightarrow N_2 + HNO_3 + H_2O \qquad (238)$$

Liquid N_2O_4 oxidizes *trans*-hyponitrous acid stepwise: $N_2O_2{}^{2-} \rightarrow N_2O_3{}^{2-} \rightarrow N_2O_4{}^{2-} \rightarrow N_2O_5{}^{2-} \rightarrow N_2O_6{}^{2-}$.

7.4.2 *cis-Hyponitrites*

Disodium *cis*-hyponitrite can be obtained by passing NO through a solution of sodium in liquid ammonia:

$$2NO + 2Na \xrightarrow{NH_3(l)} cis\text{-}Na_2N_2O_2 \qquad (239)$$

Reaction of disodium oxide and dinitrogen oxide at 633 K also yields disodium *cis*-hyponitrite.[109]

$$N_2O + Na_2O \xrightarrow{633\,K} cis\text{-}Na_2N_2O_2 \qquad (240)$$

Disodium *cis*-hyponitrite is very sensitive to moisture and CO_2.

$$cis\text{-}Na_2N_2O_2 + H_2O \longrightarrow N_2O + 2NaOH \qquad (241)$$

$$cis\text{-}Na_2N_2O_2 + CO_2 \longrightarrow N_2O + Na_2CO_3 \qquad (242)$$

Thermal decomposition of *cis*-$Na_2N_2O_2$ leads to sodium orthonitrite.

$$3cis\text{-}Na_2N_2O_2 \longrightarrow 2NaNO_2 + 2N_2 + 2Na_2O \qquad (243)$$

$$NaNO_2 + Na_2O \longrightarrow Na_3NO_3 \qquad (244)$$

cis-Hyponitrite is found in transition metal complexes as a chelating ligand in the yellow $(PH_3)_2Pt(N_2O_2)$ with a PtO_2N_2 five-membered ring and as a bridging ligand that is coordinated via one nitrogen atom and one oxygen atom in red $[(H_3N)_5Co(N_2O_2)Co(NH_3)_5]^{4+}$. The reaction of diazenium diolates with metal chlorides can be used for the synthesis of chelating *cis*-hyponitrite complexes.[110]

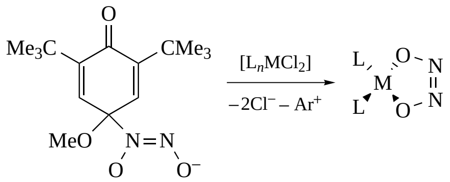

(245)

7.5 Oxohyponitrous Acid

Oxohyponitrous acid is not known. The trioxodinitrate anion (**76**) in Figure 10 is planar (d(N1–O1) 131.0(4) pm, d(N2–O2/3) 132.2(4) pm, d(N–N) 126.4(5) pm, <(O2–N2–O3) 119.1(5)°, <(O1–N–N) 118.4(3)°).

It is relatively stable in very basic solutions and forms insoluble precipitates with alkaline earth, lead, and cadmium dications. Dioxygen oxidizes the trioxodinitrate anion.

The monoanion $HN_2O_3{}^-$ is found in mildly basic to mildly acidic solution and is very sensitive toward oxidation by

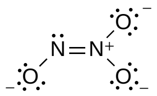

(**76**)

Figure 10 Structure of the trioxodinitrate dianion

dioxygen. It is unstable and decomposes via HNO to form N_2O and nitrite:[111]

$$HN_2O_3^- \rightleftharpoons HNO + NO_2^- \tag{246}$$

$$2HNO \longrightarrow N_2O + H_2O \tag{247}$$

The proton of $HN_2O_3^-$ is bound to a nitrogen atom according to $O_2N\text{–}NH\text{–}O^-$. Addition of nitrite to an aqueous solution of $HN_2O_3^-$ shifts the dissociation equilibrium (246) to the left side and stabilizes the protonated anion.

Oxohyponitrous acid, an acid of medium strength ($pK_1 = 2.4$, $pK_2 = 9.4$), is unstable like the $HN_2O_3^-$ anion. The same is true for very acidic solutions of $N_2O_3^{2-}$. The decomposition of the free acid is catalyzed by nitrite ions, traces of which are initially formed during decomposition of $HN_2O_3^-$.

$$H_2N_2O_3 \xrightarrow{[NO_2^-]} 2NO + H_2O \tag{248}$$

This reaction is not reversible, therefore, NO is not the anhydride of oxohyponitrous acid.

The disodium salt of oxohyponitrous acid, Angeli's salt, is formed by the nitration of hydroxylamine $HONH_2$ with alkylnitrates RNO_3 in methanol with sodium methanolate at 273 K.

$$O_2N\text{–}OR + H_2N\text{–}OH \xrightarrow[-HOR]{} (O_2N\text{–}NH\text{–}OH) \xrightarrow[-2CH_3OH]{+2CH_3ONa} (Na^+)_2N_2O_3^{2-} \tag{249}$$

7.6 Nitrous Acid

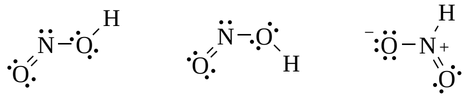

(**77**) *trans, C_s* (**78**) *cis, C_s* (**79**) C_{2v}

Scheme 30 Isomers of nitrous acid

Planar nitrous acid forms two isomers (Scheme 30). The *trans* form (**77**) ($\Delta H_f = -80.18\ \text{kJ mol}^{-1}$, d(N=O) 117.7 pm, d(N–O) 143.3 pm, d(O–H) 95.4 pm), <(O–N–O) 110.7°, d(N–O–H) 102.1° is more stable than the *cis* isomer (**78**) ($\Delta H_f = -78.04\ \text{kJ mol}^{-1}$) in the gas phase and is the only one observed in the gas phase.[4] Another tautomeric form, the C_{2v} structure (**79**), was detected as an intermediate in the photodissociation of nitric acid in noble gas matrices. Organic derivatives of both forms play important roles in industrial chemistry. Organic derivatives $R\text{–}NO_2$ of the C_{2v} structure (**79**) are called nitro compounds; derivatives ONOR of the C_s structures (**77**) and (**78**) are called nitrite esters. Nitro complexes (**80**) that contain the $\text{–}NO_2$ ligand (e.g. $K_3[Co(NO_2)_6]$) are more stable than nitrito complexes (**81**) with the –ONO ligand. Because nitrito complexes are usually less dense, nitro and nitrito complexes can be transformed into each other. The red nitro complex $[Ni(en)_2(NO_2)_2]$ is converted to the violet nitrito complex $[Ni(en)_2(ONO)_2]$ on raising the temperature from room temperature to 400 K. Application of 2 MPa pressure at 400 K reverses the change. An in plane rotation of the nitro group is responsible for theses changes. The nitrite ion also shows chelating (**82**) ($[Cu(ONO)(2,2'\text{-bipy})_2]NO_3$), unsymmetrical bridging (**83**) ($[Ni(en)_2NO_2]^+$), and η^1 bridging (**84**) coordination ($\{Cu(2,2'\text{-dipyridylamine})NO_2\}_2(\mu^1NO_2)_2$) (see Scheme 31).

The nitrite ion is isoelectronic to ozone and NOF, and has an angular structure (d(N–O) = 123.6 pm, <(O–N–O) 115.4°).

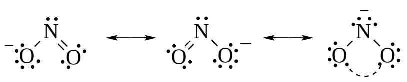

(250)

Nitrous acid is only stable in dilute, cold aqueous solution and in the form of its salts, the nitrites. Upon heating or increasing the concentration, the following equilibria are in effect:

$$2HNO_2 \rightleftharpoons N_2O_3 + H_2O \tag{251}$$

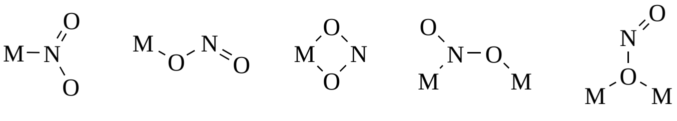

(**80**) nitro (**81**) nitrito (**82**) chelating (**83**) unsymmetrical bridging (**84**) η^1 bridging

Scheme 31 Coordination modes of nitrite ligands

$$N_2O_3 \rightleftharpoons \bullet NO + \bullet NO_2 \qquad (252)$$

$$2\bullet NO_2 \rightleftharpoons N_2O_4 \qquad (253)$$

$$N_2O_4 + H_2O \rightleftharpoons HNO_3 + HNO_2 \qquad (254)$$

The equilibrium constant K of (251) at room temperature is around 0.2, therefore a 0.1 mol L^{-1} solution of nitrous acid contains 0.002 mol L^{-1} N_2O_3. In total, nitrous acid disproportionates to nitric acid and NO.

$$3HNO_2 \rightleftharpoons HNO_3 + 2NO + H_2O \qquad (255)$$

Aqueous solutions of nitrous acid are synthesized by the reaction of nitrite salts with strong acids. The reactions of silver nitrite with HCl and barium nitrite with sulfuric acid both produce insoluble precipitates that can easily be separated from the nitrous acid solution.

$$Ba(NO_2)_2 + H_2SO_4 \longrightarrow 2HNO_2 + BaSO_4 \qquad (256)$$

$$AgNO_2 + HCl \longrightarrow HNO_2 + AgCl \qquad (257)$$

Anhydrous nitrous acid can be prepared in the gas phase; liquid HNO_2 has not been isolated.

$$N_2O_3 + H_2O \rightleftharpoons 2HNO_2 \qquad (258)$$

The disproportion reaction (255) shows that nitrous acid can react both as an oxidizing or reducing agent. In combination with strong oxidizing agents like MnO_4^-, BrO_3^-, O_2, H_2O_2, or PbO_2, nitrous acid acts as a reducing agent ($E° = 0.949$ V).

$$HNO_2 + H_2O \rightleftharpoons NO_3^- + 3H^+ + 2e^- \qquad (259)$$

Nitrous acid acts as an oxidizing agent toward iodides, iron(II) salts, and oxalates. ($E° = 0.996$ V).

$$HNO_2 + H^+ + e^- \longrightarrow NO + H_2O \qquad (260)$$

Other compounds reduce nitrous acid to $H_2N_2O_2$ (sodium amalgam, H_2NOH), N_2O (Sn(II) salts), N_2 (NH_3), HN_3 (N_2H_4), H_2NOH (H_2SO_3), or NH_3 (H_2S).

Nitrous acid is a moderately weak acid ($pK_a = -3.35$ at 291 K). Aqueous solutions of nitrite salts contain nitrous acid and are therefore not very stable. Nitrous acid is an extremely weak base:

$$HNO_2 \underset{-H^+}{\overset{+H^+}{\rightleftharpoons}} H_2NO_2^+ \underset{+H_2O}{\overset{-H_2O}{\rightleftharpoons}} NO^+ \qquad (261)$$

Only very strong, concentrated acids produce the nitrosyl cation in small concentrations (e.g. 9 mol L^{-1} sulfuric acid). NO^+ reacts with nitrous acid to form N_2O_3.

$$NO^+ + HNO_2 \longrightarrow N_2O_3 + H^+ \qquad (262)$$

Therefore, pouring sulfuric acid over nitrites results in the formation of both NO and NO_2. Nitrates do not form brown gases on reaction with sulfuric acid, a reaction that is used for the analytic distinction between nitrates and nitrites.

With the exception of silver nitrite, which is only slightly soluble, nitrite salts readily dissolve in water. The alkali metal nitrites and ammonium nitrite are hygroscopic. While sodium nitrite melts without decomposition, most other nitrites decompose before reaching the melting point ($Ba(NO_2)_2 > 593$ K, $AgNO_2 > 413$ K, $Hg(NO_2)_2 > 348$ K). Ammonium nitrite decomposes above 333 K, sometimes explosively, to dinitrogen and water:

$$NH_4NO_2 \longrightarrow N_2 + 2H_2O \qquad (263)$$

Ammonium nitrite is only stable as a dry solid; it can be used to prepare very pure nitrite salts on reaction with hydroxides.

The reaction of alkali metal nitrites with alkali metal oxides M_2O yields salts M_3NO_3 that do not contain the orthonitrite anion NO_3^{3-} but are mixed crystals of the salts MNO_2 and M_2O with anti- perovskite structure $(NO_2)ONa_3$.[100,101] Some properties of important nitrite salts are given in Table 28.

$$MNO_2 + M_2O \longrightarrow M_3NO_3 \qquad (264)$$

Sodium nitrite, the most important nitrite salt, is produced by the reaction of nitrogen oxides with sodium carbonate or sodium hydroxide solution.[5] Formation of nitrates can be inhibited by using an excess of NO and working with a pH higher than 8.

Sodium nitrite is still the most reliable agent for preventing botulism, a dangerous bacterial contaminant of meats and in curing salts is used in the food industry. High nitrite concentrations can, however, lead to the formation of carcinogenic nitrosamines. Nitrous acid and its salts are used in nitrosation reactions. The nitrosation of aromatic amines leads to diazonium compounds (for dyes). Primary aliphatic amines form the corresponding alcohol and dinitrogen upon nitrosation with nitrous acid. Secondary aliphatic amines form *N*-nitrosamines and R_2NNO and tertiary aliphatic alcohols form trialkylammonium nitrites R_3NH^+ NO_2^-, which react further to an alcohol and the dialkylnitrosamines R_2NNO upon warming.

7.7 Peroxohyponitrous Acid

The peroxonitrite ion has a partial double bond between nitrogen and the first peroxide oxygen. As shown in

Table 28 Properties of important nitrite salts

	NH_4NO_2	$NaNO_2$	KNO_2
m.p. [K]	–	557	714 (decomp.)
ΔH_f [kJ mol^{-1}]	−260(5)	−358(2)	−375(5)
ρ [g cm^{-3}]	1.69	2.168	1.915

Scheme 32, the molecule exists in a *cis* (**85**) and a *trans* form (**86**).[112]

The *cis* form (**85**) is predicted to be more stable than the *trans* form (**86**) by 12–17 kJ mol^{-1} by quantum chemical calculations. Tetramethylammonium peroxonitrite crystallizes in the *cis* form (**85**) (d(O=N) 116 pm, d(N–O) 135 pm, d(N–O) 141 pm)[113] and is nearly flat with a torsion angle of 22°. In a solid argon matrix, both conformers show a reversible photoisomerism.

$$\textit{cis}\ \mathrm{ONOO^-} \underset{\text{vis, near IR}}{\overset{\text{near UV, vis}}{\rightleftharpoons}} \textit{trans}\ \mathrm{ONOO^-} \qquad (265)$$

Peroxonitrous acid is an acid of medium strength (p$K_a = 6.8$), which rapidly decomposes in neutral conditions ($t_{1/2} = 1$s at pH = 7.4). Peroxonitrite can isomerize to nitrate or decompose to nitrite and dioxygen. Isomerization to nitrate is a major pathway in acidic media. The mechanism for the decomposition is still in doubt, but it is believed that HOONO homolyzes to give the NO_2/OH radical pair.[114] Peroxonitrites are stable in basic solution. Peroxonitrous acid is formed as a yellow intermediate in the reaction of nitrite solutions with hydrogen peroxide that leads to nitrates.

$$\mathrm{HNO_2 + H_2O_2 \longrightarrow ONOOH + H_2O} \qquad (266)$$

It is a powerful oxidizing agent, stronger than nitric acid or hydrogen peroxide. The two-electron reduction potential of peroxonitrous acid is 1.68 V.

Tetramethylammonium *cis*-peroxonitrite, which decomposes at 383 K, is prepared by reacting tetramethylammonium superoxide with nitric oxide in liquid ammonia at 195 K.[115]

$$\mathrm{NMe_4{}^+O_2{}^- + NO \xrightarrow{NH_3(l)} NMe_4{}^+ONOO^-} \qquad (267)$$

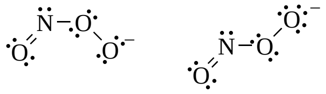

(**85**) *cis* (**86**) *trans*

Scheme 32 Isomers of peroxonitrite

Peroxonitrous acid reacts with azide to form dinitrogen oxide, nitrous acid, and N_2.

$$\mathrm{ONOOH + N_3{}^- \longrightarrow N_2O + 0.5N_2 + HNO_2} \qquad (268)$$

It is believed that in biological systems NO reacts with superoxide $O_2{}^-$ to form the cytotoxic $ONOO^-$. In biological media, low concentration levels of $HCO_3{}^-$ prevent the toxic effects of $ONOO^-$, due to the formation of an unstable adduct with the composition $ONO_2CO_2{}^-$, which homolyzes to give the $NO_2/CO_3{}^-$ radical pair.[116]

7.8 Nitric Acid

Pure, anhydrous nitric acid is a colorless liquid that fumes when exposed to air. Some of its physical properties are summarized in Table 29.[4,5]

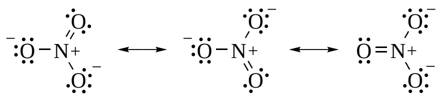

(269)

The nitrate ion has a symmetrical, trigonal planar structure (D_{3h}, d(N–O) 121.8 pm, <(O–N–O) 120°). In nitric acid (**86**) (C_s) (Figure 11), the N–O bond of the N–OH group with 140.5 pm is longer than the N–O bond lengths with 120.6 pm.

Nitric acid can be mixed with water in all proportions. It forms two hydrates, a monohydrate $HNO_3{\cdot}H_2O$ (m.p. 236 K), and a trihydrate $HNO_3{\cdot}3H_2O$ (m.p. 255 K). A third hydrate, the dihydrate $HNO_3{\cdot}2H_2O$ (m.p. 233 K) can be obtained by careful thermal treatment. In all three crystal structures, hydrogen bonds connect the oxygen atoms of planar $NO_3{}^-$ ions with pyramidal H_3O^+ ions. In the monohydrate layers of hydrogen, bonded H_3O^+ and $NO_3{}^-$ ions are formed, the other two hydrates have three-dimensional hydrogen-bonded networks. At a concentration of 69.2 wt%, nitric acid forms a maximum-boiling azeotrope with water with a boiling point

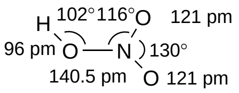

(**86**)

Figure 11 Structure of the nitric acid

Table 29 Physical properties of nitric acid

m.p. [K]	231.56	$\Delta H_{\mathrm{vap.}}$ [kJ mol^{-1}]	39.465 kJ mol^{-1}
b.p. [K]	355.8	$S°$ (l) [J mol^{-1} K^{-1}]	155.6 J mol^{-1}K^{-1}
ρ [g cm^{-3}]	1.504	Dielectric constant	50(10)
Thermal conductivity [W m^{-1} K^{-1}]	0.343	μ[D]	1.84 D
C_p [J g^{-1} K^{-1}]	1.7481	Index of refraction n_D	1.3970
ΔH_f [kJ mol^{-1}]	−174.1[1]		

of 395 K.[117] The azeotropic mixture is known as concentrated nitric acid ($\rho = 1.410\,\mathrm{g\,cm^{-3}}$). Some physical properties of aqueous nitric acid in different concentrations are given in Table 30.

Nitric acid decomposes thermally in the reverse reaction of its formation:

$$2HNO_3 \rightleftharpoons 2NO_2 + H_2O + 0.5O_2 \qquad (270)$$

In ambient light, this decomposition already takes place at room temperature so that pure nitric acid has to be stored at temperatures below 273 K. At 303 K, the equilibrium contains 98% HNO_3, at 323 K 89% HNO_3. The photodissociation of the nitrate anion in aqueous solution may proceed according to one of the following three paths:[118]

$$NO_3^- \xrightarrow{h\nu} {\bullet}NO_2 + {\bullet}O^- \qquad (271)$$

$$NO_3^- \xrightarrow{h\nu} ONOO^- \qquad (272)$$

$$NO_3^- \xrightarrow{h\nu} NO_2^- + O \qquad (273)$$

Decomposition occurs to the same extent for pathways (272) and (273), whereas path (273) is of very minor importance. No peroxonitrite is formed in a cage-recombination reaction of the products of (271). The oxygen anion of (271) reacts further with water to form hydroxyl radicals that can oxidize nitrite anions back to NO_2.

$$O^-{\bullet} + H_2O \longrightarrow OH{\bullet} + OH^- \qquad (274)$$

$$OH{\bullet} + NO_2^- \longrightarrow NO_2{\bullet} + OH^- \qquad (275)$$

Reaction of the peroxonitrite $ONOO^-$ anion with OH• radicals from (274) forms the peroxonitrite radical ONOO•, that decomposes to dioxygen and NO, the major source for the formation of nitrite ions NO_2^- in the system.

Dissolved nitrogen dioxide gives nitric acid a yellow color (fuming nitric acid). Higher concentrations of nitrogen dioxide give the nitric acid a red color (red fuming nitric acid). If the oxygen produced is allowed to dissipate, even aqueous nitric acid solutions can decompose in this manner.

Table 30 Physical properties of aqueous nitric acid as a function of composition

Concentration [wt%]	ρ[g cm^{-3}]	m.p. [K]	b.p. [K]
0	0.99823	273	373
10	1.0543	266	374.2
20	1.1150	256	376.4
30	1.1800	237	380
40	1.2463	243	385
50	1.3100	253	389.4
60	1.3667	251	393.4
70	1.4134	232	394.4
80	1.4521	234	389.6
90	1.4826	213	375
100	1.5129	232	359

The chemistry of nitric acid is characterized by its acidity and oxidation strength. In dilute solutions of nitric acid, the acidity is more important for its chemical behavior, in concentrated nitric acid the oxidizing character dominates its chemical behavior.

Nitric acid is a strong acid ($\mathrm{p}K_a = -1.44$).

$$HNO_3 \rightleftharpoons NO_3^- + H^+ \qquad (276)$$

Dilute solutions of nitric acid are almost completely dissociated. In concentrated nitric acid, which dissociates according to (277), the nitracidium ion $H_2NO_3^+$ is formed:

$$2HNO_3 \rightleftharpoons H_2NO_3^+ + NO_3^- \qquad (277)$$

In the gas phase, two isomeric structures of the neutral radical H_2NO_3 are found,[119] $(HO)_2NO$ and the more stable $H_2O{\cdot}NO_2$. $H_2NO_3^+$, which decomposes under elimination of water in analogy to the isoelectronic H_2CO_3:

$$H_2NO_3^+ \rightleftharpoons NO_2^+ + H_2O \qquad (278)$$

$H_2NO_3^+$ is formed by adding a strong acid to nitric acid (279).

$$HClO_4 + HNO_3 \rightleftharpoons H_2NO_3^+ + ClO_4^- \qquad (279)$$

The decomposition of the nitracidium ion (278) shifts the dissociation equilibrium (276) to the right side.

$$2HNO_3 \rightleftharpoons NO_2^+ + NO_3^- + H_2O \qquad (280)$$

The formation of nitronium ions NO_2^+ and of water, that further reacts to

$$H_2O + HNO_3 \rightleftharpoons H_3O^+ + NO_3^- \qquad (281)$$

with a net equation of

$$3HNO_3 \rightleftharpoons NO_2^+ + 2NO_3^- + H_3O^+ \qquad (282)$$

explains the high electric conductivity ($3.7210^{-2}\Omega\ \mathrm{cm}^{-1}$) of anhydrous nitric acid. These equilibria are also responsible for a rapid exchange of nitrogen atoms in nitric acid.

$$NO_3^- + 4H^+ + 3e^- \longrightarrow NO + 2H_2O \qquad (283)$$

Nitrate has an oxidation potential of +0.96 V. Copper (+0.342 V) and silver (+0.799 V) are dissolved by nitric acid under formation of NO (which is instantly oxidized to NO_2 in air), gold (+1.498 V) and platinum (+1.118 V) are not attacked. The oxidation of metals yields different products depending on the concentration of nitric acid. In dilute solutions of nitric acid, NO is formed, whereas in concentrated solutions, NO is oxidized by nitric acid to NO_2. Moderately concentrated nitric acid oxidizes metals under formation of a mixture of NO and NO_2. A 50% solution of HNO_3 (aqua fortis) is used to separate silver from gold. The oxidation power of nitric acid increases with increasing concentration. Dilute solutions of nitric acid do not attack copper and more noble metals.

Some metals (Al, Cr, and Fe) are not oxidized by concentrated nitric acid even though they would be expected to be oxidized based on their oxidation potentials. These metals form thin oxide layers that protect the metal core (passivation). As a result, alloyed steel equipment can be used in nitric acid technology.

In concentrated nitric acid, the $NO_2{}^+$ ion has the highest oxidation potential. Increasing its concentration increases the oxidizing power of nitric acid. This is commonly achieved by adding a strong acid, normally sulfuric acid:

$$HNO_3 + 2H_2SO_4 \rightleftharpoons H_3O^+ + NO_2{}^+ + 2HSO_4{}^- \qquad (284)$$

The mixture of nitric acid and two parts of sulfuric acid is known as nitrating acid and is mainly used in organic chemistry for nitration reactions. In the mixture of one part nitric acid and three parts hydrochloric acid, NOCl and active chlorine (chlorine radicals) are formed:

$$HNO_3 + 3HCl \longrightarrow NOCl + 2Cl\bullet + 2H_2O \qquad (285)$$

This mixture dissolves almost all metals, even gold (aqua regia) but not niobium, tantalum, and tungsten.

In pure nitric acid, dissolved N_2O_4 dissociates completely to NO^+ and $NO_3{}^-$, and N_2O_5 dissociates to $NO_2{}^+$ and $NO_3{}^-$.

7.8.1 Production of Nitric Acid

Historically, nitric acid was synthesized by adding sulfuric acid to Chile saltpeter:[5]

$$NaNO_3 + H_2SO_4 \longrightarrow HNO_3 + NaHSO_4 \qquad (286)$$

The process of Birkeland and Eyde involved the direct combination of dinitrogen, dioxygen, and water ($\Delta H = -30.3$ kJ):

$$N_2 + 2.5O_2 + H_2O \longrightarrow 2HNO_3 \qquad (287)$$

This reaction requires an electric arc to provide the high activation energy and is therefore quite expensive. The availability of cheap ammonia synthesized by the Haber–Bosch process signaled the demise of this process.

Today, nitric acid is produced by the Ostwald process, which involves three chemical steps:

First, ammonia is catalytically oxidized to nitric oxide with atmospheric oxygen ($\Delta H = -904\,\text{kJ mol}^{-1}$):

$$4NH_3 + 5O_2 \longrightarrow 4NO + 6H_2O \qquad (288)$$

This is one of the most efficient catalytic processes known. With a suitable catalyst, 93–98% of ammonia is oxidized to NO. Side reactions include the formation of dinitrogen oxide ($\Delta H = -1105\,\text{kJ mol}^{-1}$) (289) and the formation of dinitrogen (290) ($\Delta H = -1268\,\text{kJ mol}^{-1}$).

$$4NH_3 + 4O_2 \longrightarrow 2N_2O + 6H_2O \qquad (289)$$

$$4NH_3 + 3O_2 \longrightarrow 2N_2 + 6H_2O \qquad (290)$$

Decomposition of the formed NO (291) ($\Delta H = -90\,\text{kJ mol}^{-1}$) and its reaction with ammonia (292) ($\Delta H = -1808\,\text{kJ mol}^{-1}$) also occur:

$$2NO \longrightarrow N_2 + O_2 \qquad (291)$$

$$4NH_3 + 6NO \longrightarrow 5N_2 + 6H_2O \qquad (292)$$

A short reaction time (in the order of 10^{-3} s) is necessary to avoid the decomposition of the metastable NO according to (291). Closely stacked, fine mesh gauzes of platinum, usually alloyed with 5–10% of rhodium to improve its mechanical strength, are used as catalysts. The loss of precious metal catalysts has a significant effect on the operating costs, therefore great efforts are made to recover the catalyst loss by filters and recovery gauzes. In the technical process, a 1:10 mixture of ammonia and oxygen is pressed at high velocity at temperatures between 973 K and 1223 K and pressures between 0.1 and 1.2 MPa through the catalyst gauzes.

The nitrogen oxide gas is then cooled down and, if necessary, compressed. Here the nitrogen oxide is partly oxidized by the dioxygen in air to NO_2 (293) ($\Delta H = -113.6\,\text{kJ mol}^{-1}$), which dimerizes to N_2O_4 (294) ($\Delta H = -58.08\,\text{kJ mol}^{-1}$):

$$2NO + O_2 \longrightarrow 2NO_2 \qquad (293)$$

$$2\,\bullet NO_2 \rightleftharpoons N_2O_4 \qquad (294)$$

Dinitrogen trioxide is also formed ($\Delta H = -40\,\text{kJ mol}^{-1}$):

$$NO + NO_2 \longrightarrow N_2O_3 \qquad (295)$$

The absorption of this complex mixture of gases and the formation of nitric acid follows a complicated mechanism. The main route involves two steps in the liquid phase. First, dinitrogen tetroxide reacts with water to form nitric acid and nitrous acid ($\Delta H = -87\,\text{kJ mol}^{-1}$):

$$N_2O_4 + H_2O \longrightarrow HNO_3 + HNO_2 \qquad (296)$$

Nitrous acid then disproportionates to nitric acid and NO ($\Delta H = -15.3\,\mathrm{kJ\,mol^{-1}}$), which again enters the oxidation process.

$$3HNO_2 \longrightarrow HNO_3 + H_2O + 2NO \tag{297}$$

Absorption is normally performed in plate columns. Nitrogen monoxide is constantly reformed in this step and prevents the complete absorption of the inlet gases. Oxidation of nitrogen monoxide mainly occurs in the gas phase between the plates, but also in the bubble layer on the plates. The absorption efficiency increases at lower temperatures (higher N_2O_4 concentration) and higher pressures. Temperatures of 293 to 303 K and pressures of 5–10 MPa are used. The emission of nitrous gases is an environmental problem, which led to the design of advanced absorption towers and the development of different scrubbing processes for the stack gas. Nitric acid produced in technical processes has concentrations of 50–70%, depending on the absorption process. This is enough for most uses, including the production of fertilizers. Some processes require 100% nitric acid, which cannot be obtained by distillation because of the formation of an azeotropic mixture with water containing 68.4% HNO_3. Greater concentrations are obtained in a direct process by reacting liquid dinitrogen under pressure with pure oxygen and a certain quantity of dilute nitric acid. In an indirect process, either sulfuric acid or magnesium nitrate is added to commercial nitric acid. Distillation of these mixtures yields 99% nitric acid.

The principal use of nitric acid is the production of fertilizers, which uses between 75 and 85% of the total nitric acid production. Further uses include the production of organic nitro compounds that are used as explosives and rocket fuels. In 1987, 26.5 megatons of nitric acid were produced worldwide.

7.8.2 Nitrates

The reaction of nitric acid with metal oxides, hydroxides, or carbonates yields metal nitrates.**[5]** Hydrogendinitrates $H(NO_3)_2^-$ and dihydrogentrinitrates $H_2(NO_3)_3^-$ that contain nitrogen ions bound by hydrogen bonds are also known. $H(NO_3)_2^-$ has a symmetrical hydrogen bond between the nitrate ions with an O–O distance of 245 pm, the hydrogen bonds in $H_2(NO_3)_3^-$ are asymmetrical with O–O distances of 260 pm. Nitrates of the alkali and alkaline-earth metals as well as ammonium nitrate contain discrete NO_3^- ions; transition metal nitrates show a coordinative bond to the nitrate group. All nitrates dissolve readily in water. Heating results in decomposition under elimination of dioxygen. Alkali and alkaline-earth nitrates form nitrites, heavy metal nitrites form oxides and NO_2.

$$KNO_3 \xrightarrow{\Delta} KNO_2 + 0.5O_2 \tag{298}$$

$$Cu(NO_3)_2 \xrightarrow{\Delta} CuO + 2NO_2 + 0.5O_2 \tag{299}$$

For the complex decomposition processes of ammonium nitrate, see section 'Ammonium Nitrate'.

Alkali metal nitrates have comparatively low-melting points and the solid nitrates are excellent oxidizers at higher temperatures. Potassium nitrate is used as an oxidizer in black powder (75 wt% KNO_3, 15% charcoal, 10% sulfur). Fertilizer mixtures commonly contain ammonium nitrate or potassium nitrate, sometimes sodium or calcium nitrate as nitrogen compounds. Ammonium nitrate is also used as an explosive or as an oxidizer in an explosive mixture. Some properties of important nitrate fertilizers are summarized in Table 31.

In nitrate complexes, the nitrate ligand is found in the different coordination modes shown in Scheme 33:

7.9 Orthonitrates

Free orthonitric acid H_3NO_4, which would be analogous to H_3PO_4, has not been observed yet. The salts of orthonitric acid, the orthonitrates, contain tetrahedral T_d NO_4^{3-} (d(N–O) 139 pm) with somewhat smaller N–O distances than expected for N–O single bonds.**[120]**

Sodium orthonitrate is prepared by the reaction of sodium nitrate and sodium oxide at 573 K for one week:**[100]**

$$NaNO_3 + Na_2O \longrightarrow Na_3NO_4 \tag{300}$$

Water decomposes the orthonitrate ion to nitrate:

$$Na_3NO_4 + 2H_2O \longrightarrow 2NaOH + NaH_2NO_4 \tag{301}$$

$$NaH_2NO_4 \longrightarrow NaNO_3 + H_2O \tag{302}$$

The orthonitrates, for example, sodium orthonitrate, readily react with atmospheric water vapor and carbon dioxide:

$$Na_3NO_4 + H_2O + CO_2 \longrightarrow NaNO_3 + NaOH + NaHCO_3 \tag{303}$$

7.10 Peroxonitric Acid

In the reaction of pure hydrogen peroxide with dinitrogen pentoxide at 195 K, peroxonitric acid is formed:

$$N_2O_5 + H_2O_2 \longrightarrow O_2NOOH + HNO_3 \tag{304}$$

Peroxonitric acid is very unstable**[121]** and decomposes explosively at temperatures above 243 K. It has a pK_a of

Table 31 Properties of important nitrate fertilizers

	NH_4NO_3	$NaNO_3$	KNO_3	$Ca(NO_3)_2$
m.p. [K]	443	579.9	607	834
ΔH_f [$\mathrm{kJ\,mol^{-1}}$]	−365.1	−466.8	−492.8	−937.4
ΔH_{fusion} [$\mathrm{kJ\,mol^{-1}}$]	13.55	15.7	11.9	21.3
ρ [$\mathrm{g\,cm^{-3}}$]	1.725	2.261	2.109	2.504

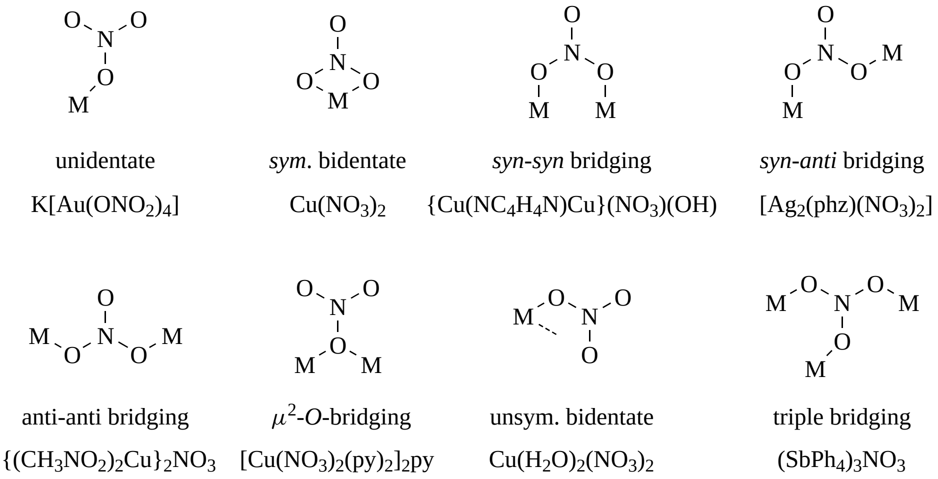
unidentate
$K[Au(ONO_2)_4]$

sym. bidentate
$Cu(NO_3)_2$

syn-syn bridging
$\{Cu(NC_4H_4N)Cu\}(NO_3)(OH)$

syn-anti bridging
$[Ag_2(phz)(NO_3)_2]$

anti-anti bridging
$\{(CH_3NO_2)_2Cu\}_2NO_3$

μ^2-*O*-bridging
$[Cu(NO_3)_2(py)_2]_2py$

unsym. bidentate
$Cu(H_2O)_2(NO_3)_2$

triple bridging
$(SbPh_4)_3NO_3$

Scheme 33 Coordination modes of nitrate ligands

5.9, which is similar to the pK_a of peroxonitrous acid of 6.8. In dilute solutions, peroxonitric acid can be stored for a short time at 293 K. In contrast to peroxonitrous acid, which is stable in basic solution and decomposes in acidic solution, peroxonitric acid is relatively stable at moderate to low pH. Under these conditions, a slow N–O bond cleavage reaction gives the OOH/NO_2 radical pair. If peroxonitric acid is diluted too much, it hydrolyzes to form hydrogen peroxide and nitric acid. At a pH higher than 5, peroxonitrates decompose rapidly as follows:

$$O_2NOO^- \longrightarrow NO_2^- + O_2 \qquad (305)$$

The decomposition either follows homolysis, initially to NO_2/O_2^-, or heterolysis, initially to $^1O_2/NO_2^-$. In contrast to peroxonitrous acid, peroxonitric acid is insensitive to the presence of CO_2. Peroxonitric acid is a strong oxidizer with a two-electron reduction potential of 1.83 V.

7.11 Nitrosamine

NH_2NO is a transient intermediate in the reaction,

$$NH_2 + NO \longrightarrow H_2NNO \qquad (306)$$

which is part of the deNOx process. In the deNOx process, nitrogen oxides are reduced to dinitrogen with either ammonia or urea. The process works both catalytically (SCR, selective catalytic reduction) or noncatalytically (SNCR, selective non-catalytic reduction). In the noncatalytic process, temperatures have to be between 1025 and 1300 K, at lower temperatures the reduction does not work. The noncatalytic process follows a radical mechanism. In the catalytic process, lower temperatures between 473 and 573 K are sufficient. Titanium oxide catalysts are used with promoter oxides like V_2O_5. The process is used in large industrial plants and for diesel engines. Depending on the composition of the exhaust, different reactions occur:

$$6NO + 4NH_3 \longrightarrow 5N_2 + 6H_2O \qquad (307)$$

$$6NO_2 + 8NH_3 \longrightarrow 7N_2 + 12H_2O \qquad (308)$$

$$4NO + 4NH_3 + O_2 \longrightarrow 4N_2 + 6H_2O \qquad (309)$$

$$2NO + 4NH_3 + 2O_2 \longrightarrow 3N_2 + 6H_2O \qquad (310)$$

Under the reaction conditions in the NO_x removal process, H_2NNO is very short-lived because it is formed in a vibrationally excited state. The highly carcinogenic organic derivatives of nitrosamine R_2NNO are more stable and can be isolated in bulk.

7.12 Nitramide

Nitramide[122] (**87**) is a structural isomer of hyponitrous acid HON=NOH ($H_2N_2O_2$) (Figure 12).

It is a colorless solid, which melts in the range of 354–359 K. In a dry environment, it is stable up to 393 K, in the presence of moisture the decomposition may begins at 343 K.

The N–N bond in nitramide is shorter than a typical N–N single bond (145 pm in hydrazine) (see Table 32). The N–O bonds are also shorter than typical N–O single bonds. Both bonds have a greater bond order than one. In the solid state, hydrogen bonds connect the NH hydrogen atoms to

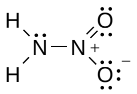
(**87**)

Figure 12 Lewis structure of nitramide

Table 32 Bonding parameters of nitramide in the gas phase and the solid state

	X-ray	GED	Microwave
d(N–N) [pm]	131.9(2)	138.1	142.7(2)
d(N–O) [pm]	123.3(1)	123.2	120.6
d(N–H) [pm]	0.86(2)	–	1.01(1)
<(H–N–H) [°]	–	120.9	115(2)
<(O–N–O) [°]	123.2(1)	132.7	130.1(3)
<(O–N–N) [°]	118.4(6)	–	–
<(H–N–N) [°]	117(1)	109.7	109

the oxygen atoms of the nitro group of another molecule, building a structure of hydrogen-bonded nitramide molecules. This hydrogen bonding results in a planar structure and a shorter N–N bond length in the solid phase. In the gas phase, the amino and nitro groups are twisted.

Aqueous solutions of nitramide are slightly acidic ($pK_a = 6.6$). The nitramide anion is not stable in salts, and the sodium, potassium, and ammonium salts decompose in solution. Nitramide, like hyponitrous acid, decomposes slowly forming N_2O and water. The decomposition is base-catalyzed and proceeds faster with stronger bases OR^-,

$$O_2NNH_2 + OR^- \overset{\text{slow}}{\rightleftharpoons} O_2NNH^- + HOR \qquad (311)$$

$$O_2NNH^- \xrightarrow{\text{fast}} N_2O + OH^- \qquad (312)$$

$$OH^- + OHR \xrightarrow{\text{very fast}} H_2O + OR^- \qquad (313)$$

thus giving the overall reaction:

$$O_2NNH_2 \longrightarrow N_2O + H_2O \qquad (314)$$

The nitramide anion O_2NNH^- can rearrange to imidonitric acid $HNN(OH)O^-$, which in turn decomposes to N_2O. In mildly acidic solution, the decomposition is nonetheless base-catalyzed with water acting as a base.

Nitramide can be prepared by the decomposition of potassium nitrocarbamate in an acidic medium:

$$K_2[O_2N\text{–}NCO_2] + 2H_2SO_4 \longrightarrow O_2NNH_2 + CO_2 + 2KHSO_4 \qquad (315)$$

Other preparations include the hydrolysis of nitrocarbamic acid (316), the reaction of $NaSO_3\,NH_2$ with concentrated nitric acid, (317) and the reaction of N_2O_5 with two equivalents of ammonia (318) (see Scheme 34).

$$O_2N\text{–}NHCOOH \longrightarrow O_2NNH_2 + CO_2 \qquad (316)$$

$$NaSO_3NH_2 + HNO_3 \longrightarrow O_2NNH_2 + NaHSO_4 \qquad (317)$$

$$N_2O_5 + 2NH_3 \longrightarrow O_2NNH_2 + NH_4NO_3 \qquad (318)$$

7.13 Dinitramic Acid

Dinitramic acid[123] (**88**) and the dinitramide anion were discovered in 1971 (Figure 13). However, it was then only known in the former Soviet Union and was independently discovered in the United States in 1989.

In the gas phase, the dinitramide ion $N(NO_2)_2^-$ has C_s symmetry. In the solid state, the symmetry is often distorted by interactions with the counterion, for example, hydrogen bonding with the ammonium ion in ammonium dinitramide (see Table 33). The N–NO_2 rotation barrier is very low. In fact, though the bond lengths of the nitramide ion remain fairly constant, no two-dinitramide crystal structures show the same geometry of the dinitramide anion.[124] The crystal structure of lithium dinitramide shows the symmetric anion.

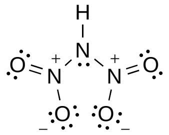

(**88**)

Figure 13 Lewis structure of dinitramic acid

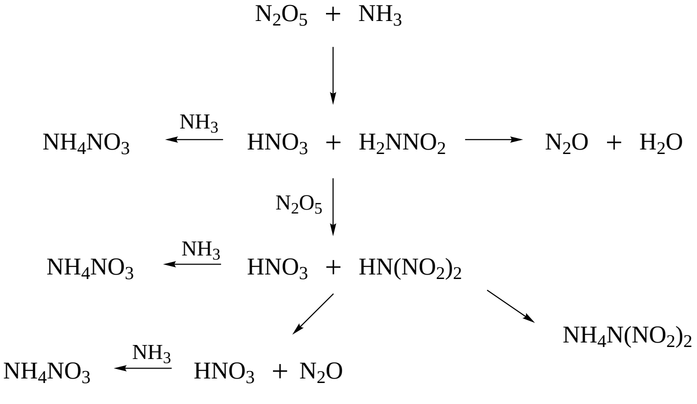

Scheme 34 Reactions of N_2O_5 with ammonia

Table 33 Bonding parameters of the dinitramide anion in ammonium and lithium dinitramide

	$NH_4N(NO_2)_2$	$LiN(NO_2)_2$		$NH_4N(NO_2)_2$	$LiN(NO_2)_2$
d(N1–N2) [pm]	1.376(1)	1.366(1)	<(N2–N1–N3) [°]	113.20(8)	114.5(2)
d(N1–N3) [pm]	1.359(1)	1.366(1)	<(N1–N2–O1) [°]	123.38(1)	126.6(2)
d(N2–O1) [pm]	1.227(1)	1.227(1)	<(N1–N3–O3) [°]	125.14(9)	126.6(2)
d(N2–O2) [pm]	1.236(1)	1.254(1)	<(N1–N2–O2) [°]	113.03(8)	111.7(2)
d(N3–O3) [pm]	1.223(1)	1.227(1)	<(N2–N3–O4) [°]	114.40(8)	111.7(2)
d(N3–O4) [pm]	1.252(1)	1.254(1)	<(O1–N2–O2) [°]	123.35(9)	121.5(2)
			<(O3–N3–O4) [°]	122.18(9)	121.5(2)

The N–N bonds of dinitramide are shorter than N–N single bonds (145 pm in N_2H_4).

Dinitramic acid (**88**) is a strong acid ($pK_a = -5.62$). Aqueous solutions of dinitramic acid with a concentration of 7–10% can be safely and easily prepared by passing a solution of $KN(NO_2)_2$ through a protonated ion-exchange resin. A nonaqueous solution is obtained by passing HCl through a suspension of $KN(NO_2)_2$ in ether at 273–278 K. Removal of ether yields a viscous yellow liquid that still contains some ether and is very shock and heat sensitive. After removal of the solvent at 273 K, dinitramic acid decomposes, often explosively, to a mixture of nitrogen oxides. Slow decomposition in air results in nitric acid as the major product. Solutions of dinitramic acid, either in water or in organic solvents, can be stored without noticeable decomposition if their concentration is less than 20%. The dinitramide anion is stable in the pH range 0–15. In concentrated acids, the dinitramide anion decomposes slowly at room temperature.

Solutions of dinitramic acid can be used to synthesize dinitramide salts with metal hydroxides, carbonates or oxides, and the salts of amine bases:

$$HN(NO_2)_2 + MOH \longrightarrow M^+N(NO_2)_2^- + H_2O \qquad (319)$$

$$HN(NO_2)_2 + RNH_2 \longrightarrow RNH_3^+N(NO_2)_2^- \qquad (320)$$

The metal dinitramides are crystalline substances that are generally stable at 298 K and have low-melting points. They are usually nicely soluble in water, alcohols, acetonitrile, and other polar solvents. Heavy metal dinitramides like silver dinitramide are sensitive to friction. Silver dinitramide is used in metathesis reactions with halides to produce dinitramide salts.

$$nAgN(NO_2)_2 + MX_n \longrightarrow M^{n+}(N(NO_2)_2^-)_n + nAgX \qquad (321)$$

7.13.1 Ammonium Dinitramide

Ammonium dinitramide ($\rho = 1.82\,\mathrm{g\,cm^{-3}}$, $\Delta H_f = 148(10)\,\mathrm{kJ\,mol^{-1}}$) is a colorless solid with a melting point of 365 K. The four hydrogen atoms of the ammonium ion form hydrogen bonds to oxygen atoms of surrounding dinitramide ions (d(N–O) 215.3 to 223.0 pm). These tetrahedrally arranged hydrogen bonds set up a three-dimensional network of hydrogen bonds. Slow decomposition of ammonium dinitramide begins above the melting point. The salt decomposes, often explosively, at 408 K. Like many other ammonium salts, the first step in the volatization (ΔH_{sub} between 125 and $185\,\mathrm{kJ\,mol^{-1}}$, $\Delta H_{fusion} = 130\,\mathrm{kJ\,kg^{-1}}$) of ammonium dinitramide is proton transfer from the ammonium NH_4^+ cation to the dinitramide anion $N(NO_2)^-$, to form a hydrogen-bonded acid base pair ($NH_3{\cdot}HN(NO_2)_2$).

Depending on the temperature, ammonium dinitramide can then decompose in two different ways. At temperatures between 328 K and 373 K, N_2O is eliminated from the molecule:**125**

$$NH_3{\cdot}HN(NO_2)_2 \longrightarrow NH_3{\cdot}HNNO_2 + NO_2 \qquad (322)$$

Above 383 K, the favored decomposition pathway produces NO_2 in a homolytic bond fission reaction:

$$NH_3{\cdot}HN(NO_2)_2 \longrightarrow NH_4NO_3 + N_2O \qquad (323)$$

$HNNO_2$ further decomposes to N_2O and OH or NH and NO_2. The decomposition to N_2O is slow, whereas the decomposition forming NO_2 is rapid.

Ammonium dinitramide can be obtained in low yields of 13–30% by the nitration of ammonia with N_2O_5, and extraction of the solid products with ethyl acetate. The main product of this reaction is ammonium nitrate. Nitramide or ammonium dinitramide can be obtained by careful control of the reaction conditions (see Scheme 34).

Organic dinitramines of the type $RCH_2CH_2N(NO_2)_2$ with an electron accepting group (R = CN, CHO, COR, COOR, or NO_2) eliminate ammonium dinitramide and acrylic compounds $H_2C{=}CHR$ during decomposition in aqueous solutions of ammonia.

The nitration of deactivated amines H_2NR (R = NO_2, $OOCC_2H_5$, $H_4NO(O)C$, $H_4NOS(O)_2$, H_2NCO) with strong nitrating agents (N_2O_5, NO_2BF_4, $O_2NS_2O_7H$, $HNO_3/SO_3/H_2SO_4$) and neutralization of the reaction mixture with ammonia or aqueous solutions of ammonia also yields ammonium dinitramide.

All nitration reactions are highly exothermic and require temperatures below 273 K to achieve good yields and to avoid decomposition of ammonium dinitramide to gaseous products and ammonium nitrate.

Current research aims to establish ammonium dinitramide as a replacement for ammonium perchlorate as an oxidizer

Table 34 Properties of nitrogen halides

	F	Cl	Br	I
NH_2X	colorless gas m.p. 173 K	colorless gas m.p. 203 K decomp. $>$ 163 K	red–violet substance decomposes easily	black substance decomp. $>$ 183 K
NHX_2	colorless gas m.p. 156.6 K b.p. 249.4 K $\Delta H_f = -67\,kJ\,mol^{-1}$	yellow gas	orange substance	black substance decomp. $>$ 213 K
NX_3	colorless gas m.p. 63.4 K b.p. 144.2 K $\Delta H_f = -132\,kJ\,mol^{-1}$	yellow liquid m.p. 233 K b.p. 344 K $\Delta H_f = +232\,kJ\,mol^{-1}$	red crystals explosion $>$ 173 K	red substance decomp. $>$195 K $\Delta H_f = +290\,kJ\,mol^{-1}$
N_2X_4	colorless gas m.p. 108.5 K b.p. 200 K $\Delta H_f = -7.1\,kJ\,mol^{-1}$			
N_2X_2	*trans*/*cis* colorless gas m.p. 101/78 K b.p. 161.6/167.3 K $\Delta H_f = +81/+69\,kJ\,mol^{-1}$			
N_3X	yellow–green gas m.p. 119 K b.p. 191 K $\Delta H_f = +343\,kJ\,mol^{-1}$	yellow gas m.p. ca. 173 K b.p. ca. 258 K $\Delta H_f = +389\,kJ\,mol^{-1}$	red–brown liquid m.p. 228 K – $\Delta H_f = +426\,kJ\,mol^{-1}$	yellow solid – – $\Delta H_f = +435\,kJ\,mol^{-1}$

in rocket propellants and other explosive formulations to avoid the environmental problem of chlorine emission. Unfortunately, ammonium dinitramide is thermally and mechanically more sensitive than ammonium perchlorate.

Hydroxylammonium dinitramide is not stable at ambient conditions. However, a salt with the formula $(H_3NOH)_2[N(NO_2)_2]\cdot 2H_2NOH$ is known. All hydroxylamine species in this salt are involved in hydrogen bonding, and one of the coordinated hydroxylamine molecules shows zwitterionic behavior. The salt resembles the formula $(H_3NOH)_2[N(NO_2)_2]\cdot H_2NOH\cdot H_3N^+O^-$. Hydrazinium dinitramide $(N_2H_5)_2[N(NO_2)_2]$ also has a three-dimensional hydrogen bond network, but is less stable than ammonium dinitramide.

8 NITROGEN HALIDES

The properties of nitrogen halides are summarized in Table 34.

8.1 Nitrogen Fluoride compounds

All NCl, NBr, and NI compounds are thermodynamically unstable ($\Delta H_f > 0$). Some, but not all binary NF compounds are exothermic species, with NF_3 as the most stable species. During the 1960s, NF compounds were investigated as rocket propellants. Today, NF compounds are used in chemical lasers and as high-energy density materials, but no compound has achieved widespread use.[126,127] The bonding situation in nitrogen fluorides is explained in the literature.[128] The N–F bond lengths are given in Table 35, the other bonding parameters in Table 36.

8.1.1 *Fluoramine*

Fluoramine is synthesized by vaporizing the adduct $NH_2F\cdot 2HF$ ($NH_3F^+\ HF_2^-$) in a dynamic vacuum. The reaction gas is passed through activated, powdered KF to absorb HF and is collected at 76 K.[126]

$$\text{RO–CO–NH}_2 \xrightarrow[-HF]{F_2/N_2} \text{RO–CO–NHF}$$

$$\xrightarrow[-RCO_2^-]{HF/H_2O} FNH_3^+HF_2^- \xrightarrow[-2KHF_2]{+2KF,\ \Delta} NH_2F \qquad (324)$$

Table 35 N–F bond lengths in binary N–F compounds

	Symmetry	d(N–F) [pm]
NF_3	C_{3v}	137
NF_4^+	T_d	130
N_2F_4	C_2	137
$N_2F_3^+$	C_s	130–133 (calc.)
cis-N_2F_2	C_{2v}	141
trans-N_2F_2	C_{2h}	140
N_2F^+	$C_{\infty v}$	122
NF^{2+}	$C_{\infty v}$	110 (calc.)
FN_3	C_s	144

Table 36 Bonding parameters of fluorinated and chlorinated derivatives of ammonia.[129]

	d(N–H) [pm]	d(N–X) [pm]	<(H–N–H) [°]	<(X–N–X) [°]	<(H–N–X) [°]
NH_3	101.1	–	106.18	–	–
NH_2F	102.25(3)	142.39(3)	106.27(8)	–	101.08(7)
NHF_2	102.6(2)	gas: 140.0(2) solid: 139.4	–	gas: 102.9(2) solid: 102.4(1)	99.8(2)
$ClNF_2$	N–Cl: 173.0	N–F 138.2	F–N–Cl: 105(1)	F–N–F: 103(1)	
NF_3	–	136.5(2)	–	102.37(3)	–
NH_2Cl	101.9	174.8	106.4	103.5	102
$NHCl_2$	–	176	–	106	102
NCl_3	–	gas: 176 solid: 171 to 177	–	gas: 107 solid: 105.1 to 109.6	–

Above 173 K fluoramine decomposes:

$$3NH_2F \longrightarrow NH_4F + 2HF + N_2 \tag{325}$$

As a weak base, fluoramine reacts with strong acids HX (X e.g. HF_2^-, SO_3F^-,ClO_4^-, and HSO_4^-) forming fluorammonium salts $NH_3F^+X^-$. The stability of the NH_3F^+ salts is influenced by the acidity of the anion and increases in the order $SO_3Cl^- < ClO_4^- < H_3CSO_3^- < SO_3F^- < F_3CSO_3^-$.

8.1.2 *Difluoramine*

Difluoramine has a melting point of 156.6 K and a boiling point of 249.4 K. The boiling point is considerably higher than the boiling point of NF_3 (144.2 K) due to hydrogen bonding in the liquid.[130] It is an unstable compound that requires very careful handling since it often explodes spontaneously, especially on freezing or melting.[126]

Difluoramine can be obtained by the hydrolysis of *N*,*N*-difluorourea with concentrated sulfuric acid.

$$H_2NCO\text{–}NH_2 \xrightarrow[-2HF]{F_2/N_2} H_2NCO\text{–}NF_2$$

$$\xrightarrow{\text{conc. } H_2SO_4} NHF_2 + NH_4^+ + CO_2 \tag{326}$$

Other preparations include the hydrolysis of *N*,*N*-difluorosulfamide ($F_2NSO_2NH_2$) or trityldifluoramine ($(C_6H_5)_3CNF_2$).

Anhydrous difluoramine decomposes thermally (in the presence of KF as HF absorber) to dinitrogen difluoride.

$$2NHF_2 \xrightarrow{(KF)} N_2F_2 + 2HF \tag{327}$$

Difluoramine is a versatile reagent in organic synthesis and is used, among others, to synthesize organic difluoramino and geminal bis(difluoramino) derivatives of organic compounds. Reaction of NHF_2 with ClF at low temperatures leads to chlorodifluoramine.

$$HNF_2 + ClF \longrightarrow ClNF_2 + HF \tag{328}$$

Reaction of difluoramine with ClO^- also yields chlorodifluoramine NF_2Cl, and reaction with bromine yields bromodifluoramine NF_2Br.

Difluoramine is a weak base that can form adducts with Lewis acids (BF_3, BCl_3, PF_5, SO_2) that are formed at 195 K and decompose well below ambient temperature. NHF_2 reacts with AsF_5 in anhydrous HF below 195 K to $NH_2F_2^+$ AsF_6^-. Otherwise difluoramine reacts as an acid:

$$NHF_2 \rightleftharpoons NH_2^- + H^+ \tag{329}$$

In the absence of other reaction partners the diflouroamide anion reacts to form *cis*/*trans*-N_2F_2.

$$2NF_2^- \longrightarrow N_2F_2 + 2F^- \tag{330}$$

Fe^{3+} oxidizes NF_2^- to tetrafluorohydrazine.

$$NF_2^- + Fe^{3+} \longrightarrow NF_2\bullet + Fe^{2+} \tag{331}$$

$$2\,NF_2\bullet \rightleftharpoons N_2F_4 \tag{332}$$

8.1.3 *Nitrogen Trifluoride*

Nitrogen trifluoride is a colorless, odorless gas with a boiling point of 144.2 K and a melting point of 66.4 K. It has a trigonal pyramidal structure with a F–N–F angle of 102.1°. The dipole moment of NF_3 (0.2340 D) is lower than the dipole moment of ammonia (1.47 D), which can be explained by the reversed polarity of nitrogen. NF_3 has a positively polarized nitrogen atom and the dipole moment of the lone pair is in opposite direction to the dipole moment along the same axis associated with the three N–F bonds. In ammonia, the polarities are reversed and the dipole moments, of the NH bonds and the lone pair operate in the same direction. Compared to other fluoramines, the N–F bond in NF_3 is relatively short (see Table 35). This can be explained by an electrostatic model. The partial charges in NF_3 ($N^{\delta+}$ $F^{\delta-}$) indicate a strong attractive interaction, a weak attraction in HNF_2, and a repulsive electrostatic interaction ($N^{\delta-}$ $F^{\delta-}$) in H_2NF.[126,127]

NF_3 is synthesized by the melt electrolysis of NH_4F/HF mixtures, or by the fluorination of ammonia catalyzed by copper.

$$4NH_3 + 3F_2 \xrightarrow{[Cu]} NF_3 + 3NH_4F \tag{333}$$

At low temperatures, NF_3 reacts only sluggishly, giving no reaction with H_2, CO, CH_4, H_2S and many other compounds. Although these reactions are in fact thermodynamically favored, they are prevented at ambient temperatures by the kinetic stability of NF_3. When the activation energy is provided by heating or an electric spark, NF_3 reacts readily and sometimes explosively.

At higher temperatures, NF_3 reacts with metals (e.g. Li, Na, K, Cu, Ag, Mg, Ca, Ba, Zn, Cd, Hg, Sn, Pb) and nonmetals (e.g. H_2, B, Si, As, Sb) to form fluorides. In the reaction with the metals Bi, Sb, Cu, or As in a flow reactor, the metals are converted to the respective fluorides and NF_3 is reduced to tetrafluorohydrazine.

$$2NF_3 + Cu \longrightarrow N_2F_4 + CuF_2 \tag{334}$$

After ignition with a spark, the reaction with dihydrogen proceeds with a sharp bang and a red–violet glow (*see* ***Hydrogen: Inorganic Chemistry***). Ignition of a mixture of NF_3 and water vapor gives a slow reaction that is accompanied by a blue glow, and leads to hydrogen fluoride and nitrous acid. At room temperature, NF_3 does not react with water.

$$2NF_3 + 3H_2 \longrightarrow N_2 + 6HF \tag{335}$$

$$NF_3 + 2H_2O \longrightarrow HNO_2 + 3HF \tag{336}$$

NF_3 shows low inclination toward coordination and is a poor ligand.

The reaction of NF_3 with AsF_5, SbF_5 or BF_3, and fluorine leads to salts of the tetrahedral $NF_4{}^+$ ion (d(N–F) 130 pm).

$$NF_3 + F_2 + BF_3 \xrightarrow{80\,K,\,UV} NF_4{}^+BF_4{}^- \tag{337}$$

$NF_4{}^+$ is one of the strongest fluorinating agents known.

Metathesis reactions that form $CsSbF_6$, which is almost insoluble in HF, can be used to obtain different $NF_4{}^+$ salts.

$$NF_4{}^+SbF_6{}^- + CsHF_2 \xrightarrow[195\,K]{HF} NF_4{}^+HF_2{}^- + CsSbF_6 \tag{338}$$

$NF_4{}^+$ $HF_2{}^-$ cannot be obtained in a pure form, as it always contains some HF. It decomposes at room temperature to form NF_3, F_2, and HF. The HF solution of this salt is stable at room temperature. Theoretical calculations indicate that a hypothetical NF_5 has a decomposition barrier of 69 kJ mol^{-1} but so far no experimental evidence has been found for this species.**131** For more information on hypervalent compounds, *see* ***Hypervalent Compounds***.

In the thermal decomposition of $NF_4{}^+H^{18}F_2{}^-$, the fluorine atom of $HF_2{}^-$ only attacks fluorine atoms and not the central nitrogen atom.

$$NF_4{}^+H^{18}F_2{}^- \xrightarrow{\Delta} NF_3 + H^{18}F + {}^{18}F\text{–}F \tag{339}$$

8.1.4 Tetrafluorohydrazine

Tetrafluorohydrazine is a colorless gas with a melting point of 108.7 K and a boiling point of 200 K. The structure of tetrafluorohydrazine (microwave: d(N–N) 140(2) pm, d(N–F) 135 pm, <(F–N–F) 107(2)°, electron diffraction: d(N–N) 148(2) pm, d(N–F) 139(1) pm, <(F–N–F) 103.0(1)°) resembles hydrazine. In the temperature range of 123–193 K, the staggered (C_{2h}) and gauche (C_2) isomers of tetrafluorohydrazine are in equilibrium both in the condensed phase and the vapor phase. The staggered conformation is favored by about 2 kJ mol^{-1} and a barrier of 12.5 kJ mol^{-1} hinders the free rotation of the NF_2 groups. N_2F_4 is synthesized by fluorine abstraction from NF_3 with metals, or by the oxidation of difluoramine with an alkaline solution of hypochlorite.**126**

$$2NF_3 + M \longrightarrow N_2F_4 + MF_2 \tag{340}$$

$$(NH_2)_2CO \xrightarrow{F_2/N_2} NH_2CONF_2 \xrightarrow{H_2SO_4} HNF_2 \xrightarrow[pH12]{NaOCl} 0.5N_2F_4 \tag{341}$$

Tetrafluorohydrazine is a strong fluorinating agent.

$$N_2F_4 + 10Li \longrightarrow 4LiF + 2Li_3N \tag{342}$$

$$S_8 \xrightarrow[N_2F_4]{383-413\,K} \left\{\begin{array}{l} SF_4 \\ SF_5NF_2 \end{array}\right. \tag{343}$$

Tetrafluorohydrazine has a long and weak nitrogen–nitrogen bond and dissociates easily into deep blue $\cdot NF_2$ radicals (d(N–F) 136.3 pm, <(F–N–F) 102.5°).

$$2NF_2\bullet \rightleftharpoons N_2F_4 \tag{344}$$

The easy dissociation (K = 0.03 at 43K, $\Delta H° = 83.2$ kJ mol^{-1}) into radicals explains the higher reactivity of N_2F_4 compared to NF_3. Reaction of N_2F_4 with chlorine yields chlorodifluoramine. In the reaction with NO, the purple, easily dissociating nitrosodifluoramine NF_2NO is formed and reaction with S_2F_{10} yields the colorless NF_2SF_5.

$$N_2F_4 + Cl_2 \longrightarrow 2NF_2Cl \tag{345}$$

$$N_2F_4 + 2NO \longrightarrow F_2NNO \tag{346}$$

$$N_2F_4 + S_2F_{10} \longrightarrow 2NF_2SF_5 \tag{347}$$

The highly unstable F_2NNO_2 is formed in the reaction with NO_2 at 583 K and rapid quenching at 77 K.

$$N_2F_4 + NO_2 \longrightarrow F_2NNO_2 \tag{348}$$

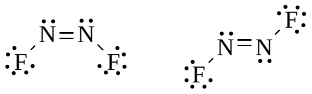

(89) **(90)**

Scheme 35 N_2F_2 isomers

Tetrafluorohydrazine is used for the synthesis of organic compounds containing the -NF_2 or =NF group, for example, it adds to olefines.

$$R_2C{=}CR_2 + N_2F_4 \longrightarrow R_2C(NF_2)\text{–}C(NF_2)R_2 \qquad (349)$$

The reaction of tetrafluorohydrazine with strong fluorine acceptors (AsF_5, SbF_5) forms salts of the planar C_s cation $N_2F_3^+$.**132**

$$N_2F_4 + 2SbF_5 \xrightarrow{HF} N_2F_3{}^+Sb_2F_{11}{}^- \qquad (350)$$

8.1.5 Difluorodiazene

Two planar isomers of N_2F_2 are known (Scheme 35), the *cis* (**89**) (C_{2v}, m.p. <78 K, b.p. 167.3 K, μ 0.18D) and *trans* isomers (**90**) (C_{2h}, m.p. 101 K, b.p. 161.8 K, μ 0 D).**126** Their bonding parameters are given in Table 37.

The shortening of the N–N bond in the *cis* isomer (**89**), which is accompanied by a lengthening of the N–F bond, can be explained by negative hyperconjugation. This corresponds to the partial delocalization of the nitrogen lone pair into the antibonding $\sigma*$ orbital of the neighboring N–F group. This donor–acceptor interaction is only present in the *cis* isomer. The *cis* isomer (**89**) is thermodynamically favored by 13 kJ mol^{-1}. At 298 K, the equilibrium has about 90% *cis* and 10% *trans*, and at about 342 K the *trans* isomer (**90**) rearranges to the *cis* form (**89**). At 570 K, N_2F_2 dissociates to the elements. The equilibrium is only slowly attained at lower temperatures without catalysts. Therefore, the pure isomers of N_2F_2 can be obtained.

The two isomers react very differently. The *cis* form is more stable as well as more reactive. The *trans* form can be stored in glass vessels, whereas the *cis* form reacts slowly with glass to form SiF_4 and N_2O.

Dinitrogen difluoride is best synthesized by passing difluoramine over KF.

$$HNF_2 + KF \xrightarrow{193\,K} HNF_2{\cdot}KF \xrightarrow{293\,K} 0.5N_2F_2 + KHF_2 \qquad (351)$$

Table 37 Bonding parameters of N_2F_2 compounds

	cis	*trans*
d(N–F) [pm]	140.9	139.8
D(N–N) [pm]	120.9	122.4
<(F–N–N) [°]	114	106

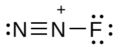

(**91**)

Figure 14 Lewis structure of the N_2F^+ cation

The thermal decomposition of fluorine azide also yields N_2F_2.

$$2FN_3 \longrightarrow 2N_2 + N_2F_2 \qquad (352)$$

These preparations, as well as the reaction of nitrogen trifluoride with mercury vapor in an electric discharge, and the fluorination of sodium azide yield mixtures of both isomers. The pure *trans* isomer is produced in 45% yield by the reaction of tetrafluorohydrazine with aluminum trichloride, or by the reaction of a mixture of the N_2F_2 isomers with aluminum trichloride.

$$2N_2F_4 + 2AlCl_3 \longrightarrow \textit{trans}\text{-}N_2F_2 + 3Cl_2 + 2AlF_3 + N_2 \qquad (353)$$

$$3\ \textit{cis}\text{-}N_2F_2 + 2AlCl_3 \longrightarrow 3Cl_2 + 2AlF_3 + N_2 \qquad (354)$$

$$3\ \textit{trans}\text{-}N_2F_2 + 2AlCl_3 \longrightarrow \text{no reaction} \qquad (355)$$

Only the *cis* isomer reacts with AsF_5 to form the linear fluorodiazenium ion N_2F^+ (**90**) in Figure 14 that has the shortest known N–F bond (d(N–F) 122 pm, d(N–N) 109.9 pm). N_2F^+ is isoelectronic to $NO_2{}^+$.**133**

$$\textit{cis}\text{-}N_2F_4 + AsF_5 \longrightarrow N_2F^+AsF_6{}^- \qquad (356)$$

In the reaction of N_2F^+ (**91**) with NaF and HF, only *cis*-N_2F_2 is formed.

Heating a mixture of FN_3 and ClN_3 to 393K results in a yellow, highly explosive substance that has not been isolated so far. It is assumed to be ClNNF.**134**

$$FN_3 \longrightarrow N_2 + NF \qquad (357)$$

$$ClN_3 \longrightarrow N_2 + NCl \qquad (358)$$

$$NF + NCl \longrightarrow FNNCl \qquad (359)$$

8.2 Nitrogen Chlorides

8.2.1 Chloramine

Chloramine has a melting point of 203 K. Decomposition begins at 163 K, and above 233 K the decomposition is explosive. Gaseous NH_2Cl at low pressures and dissolved NH_2Cl at low concentrations are thermally slightly more stable. NH_2Cl is readily soluble in water and ether, but less soluble in $CHCl_3$ and CCl_4. In aqueous solution, it decomposes according to (360):

$$3NH_2Cl \longrightarrow N_2 + NH_4Cl + 2HCl \qquad (360)$$

This decomposition occurs in a neutral, or mildly alkaline (up to $pH = 11$) medium. The reaction is slow, only a few percent of a 0.1 M solution of NH_2Cl in water decompose according to (360) in several weeks. At pH values above 11, the equilibrium for the synthesis (365) is shifted to the hypochlorite side and the following reaction slowly occurs:

$$3NH_2Cl + 3OH^- \longrightarrow NH_3 + N_2 + 3Cl^- + 3H_2O \qquad (361)$$

In an acidic medium at pH values of around 4, chloramine disproportionates to form dichloramine (362), which in turn disproportionates at pH values below 3 (363), so that at low pH values, NCl_3 dominates and between pH 3–5 $NHCl_2$ dominates.

$$2NH_2Cl + H^+ \rightleftharpoons NHCl_2 + NH_4{}^+ \qquad (362)$$

$$3NHCl_2 + H^+ \rightleftharpoons 2NCl_3 + NH_4{}^+ \qquad (363)$$

These equilibria are disturbed by the irreversible decomposition of $NHCl_2$ and NCl_3:

$$NHCl_2 + NCl_3 + 2H_2O \longrightarrow N_2 + 3HCl + 2HOCl \qquad (364)$$

In dilute aqueous solution, chloramine is prepared by the reaction of ammonia with sodium hypochlorite:

$$NH_3 + OCl^- \rightleftharpoons NH_2Cl + HO^- \qquad (365)$$

As a result of the decomposition reactions shown above, the reaction has to be carried out in a slightly alkaline medium ($pH = 8.5$ to 11). This is also the first step of the Raschig hydrazine synthesis. The acting chlorinating agent in this reaction is hypochloric acid HOCl, which has to be generated by protonation of hypochlorite, and then reacts in a nucleophilic substitution of the hydroxo against the amino group. The reaction occurs quickest at around $pH = 8$, at higher pH values the concentration of hypochloric acid is lower, at lower pH values ammonia NH_3 is protonated to form ammonium ions $NH_4{}^+$, which do not react further. The NH_2Cl solutions can be concentrated by vacuum distillation, and passing the vapor through potassium carbonate which absorbs the water. NH_2Cl can be extracted with ether. Gaseous chloramine can be obtained from the reaction of gaseous ammonia with chlorine gas that is diluted with nitrogen gas in molar ratios of 20:1 to 6:1.[135]

$$2NH_3(g) + Cl_2(g) \rightleftharpoons NH_2Cl(g) + NH_4Cl(s) \qquad (366)$$

By passing the effluent from the gas-phase reaction into a solvent at 253 K and then removing the ammonia by warming up the solution or passing it through a column with anhydrous copper(II) sulfate, solutions of chloramine in various solvents can be obtained. Almost pure (97%) NH_2Cl is obtained by the fractional low-temperature condensation of the effluent. Pure NH_2Cl is synthesized by passing pure fluoramine through a layer of $CaCl_2$:

$$2NH_2F + CaCl_2 \longrightarrow NH_2Cl + 2CaF_2 \qquad (367)$$

Chloramine is both a very weak base and a very weak acid ($pK_a = 14$, $pK_b = 15$). In water NH_2Cl acts neutral. It is an oxidizing agent (acidic solution: $E^\circ = -1.48$ V, in basic solution $E^\circ = -0.81$ V)

$$NH_2Cl + 2H^+ + 2e^- \longrightarrow NH_4{}^+ + Cl^- \qquad (368)$$

Reactions of chloramine include radical, nucleophilic, and electrophilic substitution of chlorine, electrophilic substitution of hydrogen, and oxidative additions, for example:

$$Ph_2C{=}C{=}O + NH_2Cl \longrightarrow Ph_2CCl\text{–}CONH_2 \qquad (369)$$

Chloramine can, like HOCl, donate positively charged chlorine Cl^+ in reactions with nucleophiles Nu^-.

$$Nu^- + NH_3Cl^+ \longrightarrow Nu\text{–}Cl + NH_3 \qquad (370)$$

These reactions follow the S_N2 mechanism at the chlorine atom of NH_2Cl or NH_3Cl^+. An example is the chlorination of the hydroxide ion OH^- in highly alkaline solution (reverse of (365)).

$$NH_2Cl + HO^- \rightleftharpoons NH_3 + OCl^- \qquad (371)$$

Another chlorination is the reaction of chloramine to form dichloramine, which starts the decomposition in an acidic medium.

$$2NH_2Cl \rightleftharpoons NHCl_2 + NH_3 \qquad (372)$$

This equilibrium lies to the left side under normal conditions, but can be shifted to the right side by removing ammonia, for example, by protonation. Hydrazine is chlorinated in acidic solution:

$$NH_2Cl + N_2H_4 \rightleftharpoons NH_3 + N_2H_3Cl \qquad (373)$$

Chlorohydrazine, like all chloro-, bromo- or iodohydrazines, is not stable and immediately decomposes to diimine,

$$N_2H_3Cl \longrightarrow N_2H_2 + HCl \qquad (374)$$

which in turn disproportionates to dinitrogen and hydrazine.

$$2N_2H_2 \longrightarrow N_2 + N_2H_4 \qquad (375)$$

The overall equation of the reaction of chloramine with hydrazine is as follows (Raschig process, see Section 5.2.1):

$$2NH_2Cl + N_2H_4 \longrightarrow N_2 + 2NH_4Cl \qquad (376)$$

Nucleophiles can also react according to an S_N2 mechanism at the nitrogen atom. This is an amination reaction, where the NH_2^+ group is transferred to the nucleophile.

$$Nu^- + NH_2Cl \longrightarrow Nu\text{–}NH_2 + Cl^- \qquad (377)$$

The reaction is also called electrophilic amination and amino donors like NH_2Cl or NH_2OSO_3H are called electrophilic amination agents.

The amination of ammonia with chloramine to form hydrazine is an example of this mechanism (Raschig process):

$$NH_2Cl + NH_3 \longrightarrow N_2H_5^+Cl^- \qquad (378)$$

This reaction can also be carried out with substituted amines RNH_2, R_2NH, and R_3N to form the corresponding substituted hydrazines $RNH\text{–}NH_2$, $R_2NH\text{–}NH_2$, or $R_3N^+\text{–}NH_2$ salts.

Chloramine electrophilically aminates itself in neutral and alkaline media to start its decomposition.

$$2NH_2Cl \longrightarrow N_2H_3Cl + HCl \qquad (379)$$

Chlorohydrazine decomposes as described above (374), the net reaction of this decomposition is given by equation (360).

Hydrazine can also be aminated by chloramine, but only in alkaline solution:

$$NH_2Cl + H_2N\text{–}NH_2 \longrightarrow [H_2N\text{–}NH_2^+\text{–}NH_2]Cl^- \qquad (380)$$

In acidic solution, the chlorination to form chlorohydrazine (373) is much faster. Triazanium chloride is only stable at temperatures below 223 K, otherwise it decomposes under cleavage of NH_4Cl to diimine.

$$H_2N\text{–}NH_2\text{–}NH_2^+Cl^- \longrightarrow N_2H_2 + NH_4Cl \qquad (381)$$

In turn, diimine disproportionates according to (375), thus giving an overall equation that is identical to the reaction in the acidic medium (376):

The reaction of chloramine with *N*,*N*-disubstituted hydrazines R_2NNH_2 yields stable triazanium salts:

$$NH_2Cl + R_2N\text{–}NH_2 \longrightarrow [H_2N\text{–}NR_2^+\text{–}NH_2]Cl^- \qquad (382)$$

In the reaction of $(CH_3)_2NNH_2$ with chloramine, $(CH_3)_2NN{=}CH_2$ and $(CH_3)_2NN{=}NN(CH_3)_2$ were found as side products, indicating the intermediate formation of dimethyldiazine.

$$NH_2Cl + (CH_3)_2N\text{–}NH_2 \longrightarrow (CH_3)_2NN + NH_4Cl \qquad (383)$$

Amination of the hydroxide ion to form hydroxylamine is only fast enough in very basic solutions (here chloramine has already partly decomposed to hypochlorite and ammonia according to (372)):

$$NH_2Cl + OH^- \longrightarrow NH_2OH + Cl^- \qquad (384)$$

Hydroxylamine cannot be isolated because it is rapidly aminated by chloramine to form the unstable hydroxylhydrazine H_2NNHOH, which eliminates water and forms diimine, whose decomposition has been described above (375). The net equation of the amination of hydroxide ions is therefore (361).

Analogous to the amination of NH_3, NH_2Cl, N_2H_4, sulfanes R_2S are aminated to $[R_2S\text{–}NH_2]^+Cl^-$, phosphanes R_3P are aminated to $[R_3P\text{–}NH_2]^+Cl^-$, arsanes R_3As are aminated to $[R_3As\text{–}NH_2]^+Cl^-$, and the cyanide ion CN^- is aminated to form cyanamide $NC\text{–}NH_2$.

Nucleophiles Nu^- attack the N–Cl bond ((371) and (378)), formally an electrophilic or nucleophilic substitution of chlorine. In the reaction of electrophiles E^+ with chloramine NH_2Cl, a nitrogen bound proton is substituted. This results in the transfer of the $NHCl^-$ to E^+.

$$E^+ + NH_2Cl \longrightarrow E\text{–}NHCl + H^+ \qquad (385)$$

Examples for this reaction are the chloramidation of chlorine in hypochloric acid

$$NH_2Cl + HOCl \rightleftharpoons NHCl_2 + H_2O \qquad (386)$$

or of chloramine (372).

In radicalic reactions, NH_2Cl can react as a chlorinating agent:

$$H_2C{=}C(CH_3)_2 \xrightarrow[NH_2Cl]{UV} H_2C{=}C(CH_3)CH_2Cl + CH_2Cl\text{–}CCl(CH_3)_2 \qquad (387)$$

Saturated hydrocarbons react similarly:

$$HC(CH_3)_3 \xrightarrow[NH_2Cl]{UV} (CH_3)_3CCl + (CH_3)_2CHCH_2Cl \qquad (388)$$

These reactions are believed to have a free radical mechanism where the neutral amino radical abstracts a hydrogen atom from the hydrocarbon.

$$NH_2Cl \longrightarrow H_2N\bullet + Cl\bullet \qquad (389)$$

$$RH + H_2N\bullet \longrightarrow R\bullet + NH_3 \qquad (390)$$

$$R\bullet + H_2NCl \longrightarrow RCl + H_2N\bullet \qquad (391)$$

$$R\bullet + Cl\bullet \longrightarrow R\text{–}Cl \qquad (392)$$

The oxidative power of chloramine has been used for the oxidative coupling of X–H bonds (X = nonmetal).

$$2Ph_2PH + NH_2Cl \longrightarrow Ph_2P\text{–}PPh_2 + NH_4Cl \qquad (393)$$

$$5PhPH_2 + 5NH_2Cl \longrightarrow [PhP]_5 + 5NH_4Cl \qquad (394)$$

Chloramine is used as a disinfectant for water because it is less aggressive than Cl_2 and more stable against light than ClO^-.

8.2.2 *Dichloramine*

Dichloramine is highly unstable and has not been isolated as a pure substance yet. Its yellow aqueous solutions are almost undissociated ($pK_a = 7$) and unprotonated.[135]

$$HNCl_2 \rightleftharpoons NCl_2^- + H^+ \tag{395}$$

$$HNCl_2 + H^+ \longrightarrow H_2NCl_2^+ \tag{396}$$

It is less polar than chloramine and has a higher solubility in unpolar solvents. Solutions containing NH_4^+ are relatively stable at pH = 3.5–4 with about 10% decomposition per day, whereas solutions without NH_4^+ ions decompose totally within hours. The ammonium ions inhibit the decomposition by reacting with hypochloric acid HOCl, which is formed in small amounts by the hydrolysis of $NHCl_2$ and accelerates the decomposition of dichloramine.

$$NH_4^+ + HOCl \longrightarrow NH_2Cl + H_3O^+ \tag{397}$$

The decomposition of dichloramine without NH_4^+ ions is dependant on the pH of the solution. In very acidic solution (pH < 4), dichloramine disproportionates to trichloramine:

$$3HNCl_2 + H^+ \rightleftharpoons 2NCl_3 + NH_4^+ \tag{398}$$

In mildly acidic solution (pH = 4), dinitrogen and trichloramine are formed.

$$3HNCL_2 \longrightarrow NCl_3 + N_2 + 3HCl \tag{399}$$

At pH 12, hypochlorite is formed:

$$2HNCl_2 + 4OH^- \longrightarrow N_2 + 3Cl^- + ClO^- + 3H_2O \tag{400}$$

In the pH range of 4 to 12, both reactions (400) and (401) take place, for example, at pH = 7 the ratio of (400) and (401) is 1:10.

Dichloramine is an intermediate in the chlorination of NH_3 in acidic solution that leads to NCl_3 (see Section 8.2.3), but the best synthesis is the chlorination of ammonium ions with hypochloric acid (ratio NH_4^+:HOCl = 1:2) in dilute aqueous solution at pH values around 4. NH_2Cl is an intermediate in this reaction since the chlorination of NH_2Cl is slower than the chlorination of NH_3.

$$NH_4^+ + 2HOCl \rightleftharpoons NHCl_2 + H_3O^+ + H_2O \tag{401}$$

Dichloramine can be extracted with organic solvents. Comproportionation of NH_2Cl and NCl_3 in organic solvents at 195 K also gives dichloramine:

$$NCl_3 + NH_2Cl \rightleftharpoons 2NHCl_2 \tag{402}$$

As explained above, dichloramine is formed during the disproportionation of chloramine at pH 3.5–4, thus it can be obtained by adding perchloric acid to a solution of chloramine:

$$2NH_2Cl + H^+ \rightleftharpoons NHCl_2 + NH_4^+ \tag{403}$$

Pure, ammonia-free solutions of dichloramine can be obtained by passing chloramine through an acidic ion-exchange column (which exchanges NH_4^+ ions from the disproportionation reaction (403) against H^+).

In analogy to chloramines, dichloramine can react as a chlorinating agent and can transfer positive chlorine to ammonia or water.

$$HNCl_2 + NH_3 \longrightarrow 2NH_2Cl \tag{404}$$

$$HNCl_2 + H_2O \rightleftharpoons NH_2Cl + HOCl \tag{405}$$

The equilibrium of hydrolysis is on the side of $HNCl_2$. Hypochloric acid, which is formed during the hydrolysis of $HNCl_2$, chlorinates $HNCl_2$ to NCl_3.

$$HNCl_2 + HOCl \rightleftharpoons NCl_3 + H_2O \tag{406}$$

This reaction is much faster than the hydrolysis and lowers the HOCl concentration so that the hydrolysis equilibrium is shifted to the HOCl side. Excess $HNCl_2$ then reacts with the formed trichloramine to form decomposition products.

$$HNCl_2 + NCl_3 + 2H_2O \longrightarrow N_2 + 3HCl + 2HOCl \tag{407}$$

The formed hypochloric acid further accelerates the decomposition. The reaction rate of (407) increases rapidly with increasing pH so that the decomposition of NCl_3 according to (407) is faster than the formation of NCl_3, thus producing only a small static concentration and a small yield of NCl_3. In acidic solution, the decomposition of NCl_3 is slower, NCl_3 is formed in good yield.

8.2.3 *Nitrogen Trichloride*

Nitrogen trichloride is a dark yellow liquid ($\rho = 1.65\,\mathrm{g\,cm^{-3}}$) that is only poorly soluble in water but dissolves well in nonpolar solvents like CCl_4 or CS_2. For the same reasons as for NF_3, NCl_3 has a low polarity ($\mu = 0.6(2)\,\mathrm{D}$). NCl_3 is a highly endothermic compound ($\Delta H_f = 229\,\mathrm{kJ\,mol^{-1}}$) that explodes when heated to 363 K, after slight mechanical stress or by contact with oxidizable organic matter. The low solubility in water can cause the formation of droplets of NCl_3 in the aqueous solution that readily explode. The explosive decomposition produces dinitrogen and Cl_2 via a radical decomposition mechanism.

$$2NCl_3 \longrightarrow N_2 + 3Cl_2 \tag{408}$$

Nitrogen trichloride is more stable than chloramine and dichloramine. Decomposition occurs only slowly at room temperature. The decomposition is accelerated by light, arsenic trifluoride, or silver halides.

Nitrogen trichloride is formed in the reaction of chlorine with solutions of ammonium chloride in water at pH 3–4.**[135]**

$$NH_3 + 3Cl_2 \rightleftharpoons NCl_3 + 3HCl \qquad (409)$$

Nitrogen trichloride is also produced by electrolysis of NH_4Cl solutions. The reaction is carried out in a buffer system because of the formed HCl. NCl_3 can be extracted with organic solvents like carbon tetrachloride. Ammonium ions can be chlorinated with hypochloric acid at pH 3–4:

$$NH_4^+ + 3HOCl \rightleftharpoons NCl_3 + H_3O^+ + 2H_2O \qquad (410)$$

In this reaction, NH_2Cl and $NHCl_2$ are intermediates, the chlorination speed decreases from NH_4^+ over NH_2Cl to $NHCl_2$. Quantitative yields are not achieved because the NCl_3 formed can be attacked by $NHCl_2$ according to (407).

NCl_3 has a low basicity and decomposes on reaction with very strong acids HX, forming NH_4X and Cl_2. HCl reacts with NCl_3 to form ammonium chloride and chlorine:

$$NCl_3 + 4HCl \longrightarrow NH_4Cl + 3Cl_2 \qquad (411)$$

Salts of $HNCl_3^+$ have not been isolated, but $HNCl_3^+$ has been observed mass spectrometrically. Addition of the Lewis acid Cl^+ to NCl_3 in SO_2 yields colorless NCl_4^+ ions (T_d symmetry):

$$2NCl_3 + Cl_2 + 3AsF_5 \longrightarrow 2NCl_4^+AsF_6^- + AsF_3 \qquad (412)$$

Oxygen can also react with NCl_3, but $ONCl_3$ is only known in the form of the light yellow, planar cation $NOCl_2^+$ (d(N–Cl) 161 and 172 pm, d(N–O) 130 pm, <(ONCl) 118.5/117.9°, <(ClNCl) 118.5°):**[136]**

$$NCl_3 + SOCl_2 + SbCl_5 \longrightarrow NOCl_2^+SbCl_6^- + SCl_2 \qquad (413)$$

A quaternary $ONCl(F)^+$ cation was formed in the reaction of NOCl with NF_2^+.

$$ONCl + N_2F^+AsF_6^- \xrightarrow{195\,K} ONCl(F)^+AsF_6^- + N_2 \qquad (414)$$

$ONClF^+$ decomposes in SO_2 solution at 195 K in the course of several days to form NO^+ and ClF. The stability of the NOX_2^+ salts decreases in the order $NOF_2^+ > NOCl_2^+ \sim NOCl(F)^+$.

The reactions of NCl_3 with water and ammonia proceed as follows:

$$2NCl_3 + 3H_2O \longrightarrow N_2 + 3HOCl + 3HCl \qquad (415)$$

$$2NCl_3 + 3NH_3 \longrightarrow N_2 + 3NH_2Cl + 3HCl \qquad (416)$$

In these reactions, NCl_3 acts as a chlorinating agent by transferring positively charged chlorine Cl^+. During the slow hydrolysis of NCl_3, $NHCl_2$ and hypochloric acid are initially formed:

$$NCl_3 + H_2O \rightleftharpoons HNCl_2 + HOCl \qquad (417)$$

The equilibrium is on the left side, but the $NHCl_2$ formed decomposes by the reaction with NCl_3 according to (407) to yield the overall equation (415).

The first step in the reaction of $HNCl_2$ and NCl_3 is the formation of tetrachlorohydrazine from the reaction of NCl_3 with the nucleophile NCl_2^-, which is formed from $HNCl_2$. Here NCl_3 is an electrophilic amination agent that transfers NCl_2^+.

$$NCl_3 + NCl_2^- \longrightarrow Cl_2NNCl_2 + Cl^- \qquad (418)$$

The tetrachlorohydrazine formed is not stable, and instantly decomposes via the unstable dichlorodiazene N_2Cl_2 to dinitrogen.

$$Cl_2NNCl_2 + OH^- \longrightarrow ClNNCl + Cl^- + HOCl \qquad (419)$$

$$ClNNCl + OH^- \longrightarrow N_2 + Cl^- + HOCl \qquad (420)$$

The reaction of NCl_3 with bromide anions in aqueous solution proceeds via an $NBrCl_2$ intermediate to form dinitrogen and Br_2.**[137]**

8.3 Nitrogen Bromides

Aqueous solutions of bromamine NH_2Br are formed during the bromination of NH_3 with hypobromite:**[4]**

$$NH_3 + BrO^- \rightleftharpoons NH_2Br + OH^- \qquad (421)$$

Ethereal solutions can be obtained by passing ammonia through an ethereal solution of Br_2.

$$2NH_3 + Br_2 \longrightarrow NH_2Br + NH_4Br \qquad (422)$$

After the removal of insoluble NH_4Br, the ethereal solution is poured into pentane at 153 K, and black–violet NH_2Br precipitates.

NH_2Br is a weak base ($pK_b = 7.7$). In absence of ammonia, NH_2Br reacts in an equilibrium in aqueous and ethereal solutions to form dibromamine $NHBr_2$.

$$2NH_2Br \rightleftharpoons NHBr_2 + NH_3 \qquad (423)$$

The equilibrium can be shifted to the right side by removing ammonia with $CaCl_2$ or acid. Solutions of $NHBr_2$ in ether are short-lived.

NH_2Br decomposes in the presence of ammonia more or less rapidly like chloramine ($t_{1/2} = 580$ min at 203 K, $t_{1/2} = 124$ min at 273 K, $t_{1/2} = 6.9$ min at 297 K).

$$3NH_2Br + 2NH_3 \longrightarrow N_2 + 3NH_4Br \qquad (424)$$

In this reaction hydrazine is an intermediate, but contrary to chloramine, hydrazine reacts rapidly with NH_2Br, so that hydrazine can not be isolated as in the NH_2Cl/NH_3 system.

The equilibria between the various bromination products of ammonia are strongly influenced by the pH value. At pH values above 9, the equilibria are displaced almost totally toward $BrNH_2$. With high NH_3:Br_2 ratios and pH values between 6.3 and 5.8, the very unstable $NHBr_2$ is the main species. At low NH_3:Br_2 ratios and pH values lower than 6, NBr_3 is the dominant product. NBr_3 can be extracted with various solvents such as chloroform, carbon tetrachloride, or ether. Pure NBr_3 is available by treating $(Me_3Si)_2NBr$ with BrCl in pentane at 286 K. NBr_3 is a deep red, insoluble substance in pentane that explodes easily even at 173 K.**[138]**

$$(Me_3Si)_2NBr + 2BrCl \longrightarrow NBr_3 + 2Me_3SiCl \qquad (425)$$

8.4 Nitrogen Iodides

Addition of I_2 to liquid ammonia at temperatures below 240 K results in the precipitation of green $NI_3{\cdot}3NH_3$. The reaction proceeds via ammonia-iodine charge transfer complexes ($I_2{\cdot}NH_3$ and $I_2{\cdot}2NH_3$ are known), to iodamine, diiodamine, and to triiodamine. At temperatures below 200 K, red $NI_3{\cdot}5NH_3$ is obtained.**[4]**

$$2I_2 + 2NH_3 \xrightleftharpoons{\pm 2NH_3} 2H_3N{\cdot}I_2 \xrightleftharpoons[\pm 2NH_4I]{\pm 2NH_3} 2NH_2I \xrightleftharpoons{\pm NH_3} NHI_2$$
$$\xrightleftharpoons{\pm NH_2I} NI_3{\cdot}NH_3 \xrightleftharpoons{\pm 2NH_3} NI_3{\cdot}3NH_3 \qquad (426)$$

At temperatures above 40 K, $NI_3{\cdot}3NH_3$ loses ammonia to form the red–brown to black $NI_3{\cdot}NH_3$. The ammonia adduct $NI_3{\cdot}NH_3$ precipitates when ammonia is passed through an aqueous solution of potassium triiodide. In an atmosphere with a high partial pressure of ammonia, it can be stored in the dark for a long time. The dry compound is extremely sensitive and explodes after the slightest mechanical stress, slight heating, or irradiation.

$$8NI_3{\cdot}NH_3 \longrightarrow 5N_2 + 6NH_4I + 9I_2 \qquad (427)$$

The equilibria (426) are reversible, and on the side of the ammonia-iodine charge transfer complex. Solvation of $NI_3{\cdot}NH_3$ in diethylether in the presence of ammonium iodide yields the ether-soluble charge transfer complex $NH_3{\cdot}I_2$.

$$NI_3{\cdot}NH_3 + 3NH_4I \rightleftharpoons 3NH_3{\cdot}I_2 + 2NH_3 \qquad (428)$$

Removal of ammonia from $NI_3{\cdot}NH_3$ in vacuo results in the decomposition to dinitrogen and iodine.

$$2NI_3{\cdot}NH_3 \longrightarrow 2NH_3 + N_2 + 3I_2 \qquad (429)$$

In $NI_3{\cdot}NH_3$, slightly distorted NI_4 tetrahedra are linked by shared corners into indefinite I–N–I–N–I chains ($d(N–I_{bridge})$ 230 pm, $d(N–I_{term})$ 214 pm). Ammonia forms a charge transfer complex with the terminal iodine atoms ($d(N–I{\cdots}NH_3)$253 pm).

When a saturated solution of $NI_3{\cdot}3NH_3$ in liquid ammonia in the presence of NH_4I is cooled to below 198 K, a red adduct $NH_2I{\cdot}NH_3$ (see (426)) precipitates. Storing this adduct at 183 K in vacuo results in the removal of ammonia to form the black iodamine NH_2I. Warming up NH_2I to 213 K in vacuo removes another ammonia molecule and yields the very unstable diiodamine NHI_2.

Pure nitrogen triiodide ($\Delta H_f = +290$ kJ mol^{-1})**[139]** can be obtained by the reaction of iodine fluoride with boron nitride at 263 K in CF_3Cl.

$$BN + 3IF \longrightarrow NI_3 + BF_3 \qquad (430)$$

The deep red substance can be purified by sublimation at 253 K under partial decomposition. It decomposes fast and often explosively. This makes NI_3 thermally more stable than NBr_3 but less stable than NCl_3.

8.5 Mixed Nitrogen Halides

8.5.1 Dichlorofluoramine

Dichlorofluoramine has a boiling point of 270 K and is explosive in the liquid as well as in the solid state. $FNCl_2$ can be prepared by passing a ClF/N_2 mixture over sodium azide:

$$2ClF + NaN_3 \xrightarrow{-N_2} Cl_2NF + NaF \qquad (431)$$

The low-temperature chlorination of $FC(O)NF_2$ is also a convenient method for the synthesis of Cl_2NF.**[140]** Alternatively, $FNCl_2$ can be obtained from ClF and ClN_3 in perfluorinated ether. Irradiation of $FNCl_2$ with a high-pressure Hg lamp leads to the formation of *cis*-N_2F_2.

8.5.2 Chlorodifluoramine

Chlorodifluoramine ($\Delta H_f >= -104$ kJ mol^{-1}) boils at 207.1 K, and has a melting point below 78 K. In Pyrex glass, it is thermally stable up to 393 K, where it decomposes to NF_3, N_2, and Cl_2. Irradiation at wavelengths < 300 nm results in the reversible photochemical decomposition to N_2F_4 and Cl_2.**[141]**

$$2ClNF_2 \rightleftharpoons 2{\bullet}NF_2 + 2Cl{\bullet} \rightleftharpoons N_2F_4 + Cl_2 \qquad (432)$$

As a Lewis base, chlorodifluoramine is intermediate in strength between HNF_2 and NF_3. It reacts vigorously with NO even at low temperatures:

$$ClNF_2 + NO \longrightarrow NOCl + 0.5N_2F_4 \qquad (433)$$

Chlorodifluoramine is accessible by chlorinating HNF_2 with gaseous Cl_2 in CCl_4 solutions or with aqueous NaOCl at 273 K and pH 6–6.5. At pH 12, the major product is N_2F_4, whereas between pH 6–12 both $ClNF_2$ and N_2F_4 result. Difluoramine also reacts with HOCl, *t*BuOCl, $SOCl_2$, $COCl_2$, HCl, ClF_3, and ClF to form $ClNF_2$.

Tetrafluorohydrazine is converted to $ClNF_2$ by chlorine under UV irradiation. Reaction of fluorine with chlorine azide also yields chlorodifluoramine.

8.5.3 Bromodifluoramine

Bromodifluoramine ($\Delta H_\mathrm{f} > = -39\ \mathrm{kJ\ mol^{-1}}$) is a colorless liquid with a boiling point of 237 K and decomposes rapidly on warming.[142] Bromodifluoramine is prepared by the reaction of aqueous bromine with HNF_2 in the presence of HgO.

$$HNF_2 + Br_2 \xrightarrow{HgO} BrNF_2 + HBr \qquad (434)$$

It was also prepared from $NF_2\bullet$ and bromine radicals, which were generated by microwave discharge in an atmosphere of N_2F_4 and Br_2:

$$\bullet NF_2 + Br\bullet \longrightarrow BrNF_2 \qquad (435)$$

8.5.4 Dibromoiodamine

The reaction of tribromamine with iodine in dichloromethane yields red–brown NBr_2I, which is stable up to 253 K.[138]

$$2NBr_3 + I_2 \longrightarrow 2NBr_2I + Br_2 \qquad (436)$$

8.6 Halogen Azides

In the gas phase, the halogen azides have a *trans Cs*-configuration like HN_3 with an N–N–N bond angle around 171°.[127,143] The N–N bond lengths are significantly different. The N_α–N_β bond length is around 124 pm and N_β–N_γ is around 113 pm. The N_α–N_β bond can be considered as a long double bond, and the N_β–N_γ bond is a weak triple bond. The azides show a strong delocalization of the π-electron density over the complete molecule. A donor–accepter interaction leads to electron donation from a filled bonding σ(X–N_α) orbital to an empty antibonding $\pi*$(N_β–N_γ) orbital (see Figure 15).[144] The consequences of this negative hyperconjugation are the long and weak X–N_α bond, the short and strong N_α–N_β bond, the weak N_β–N_γ triple bond and the angle at the central N2 nitrogen atom.[145]

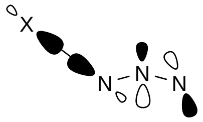

Figure 15 Negative hyperconjugation ion halogen azides XN_3

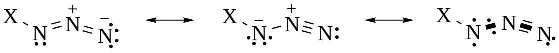

(437)

The crystal structure of iodine azide is polymeric with longer N–I distances than in the gas phase, because the IN_3 units are connected by linear coordinated iodine atoms.[146] Structural data of the halogen azides are summarized in Table 38.

The halogen azides are prepared by the reaction of metal azides with halogens or the hypohalogenic acids.

$$NaN_3 + HOCl \xrightleftharpoons{H_2O} ClN_3 + NaOH \qquad (438)$$

$$NaN_3 + Cl_2 \longrightarrow ClN_3 + NaCl \qquad (439)$$

$$AgN_3 + I_2 \longrightarrow IN_3 + AgI \qquad (440)$$

All halogen azides are sensitive and explode easily. The sensitivity decreases in the order $FN_3 > ClN_3 > BrN_3 > IN_3$. Fluorine azide decomposes to form dinitrogen difluoride and dinitrogen.

$$FN_3 \longrightarrow N_2F_2 + N_2 \qquad (441)$$

The thermal decomposition of the other halogen azides is not initiated by the breaking of the X–N_3 bond, but, at least in

Table 38 Structural data of halogen azides compared to HN_3

	HN_3 (g)	FN_3 (g)	ClN_3 (g)	BrN_3 (g)	IN_3 (g)	IN_3 (s)
d(X–N1) [pm]	101	144	175	190	212	228
d(N1–N2) [pm]	124	125	125	123	126	123
d(N2–N3) [pm]	113	113	113	113	115	107
<(X–N1–N2) [°]	109	104	109	110	107	116
<(N1–N2–N3) [°]	171	171	172	171	170	172

the gas phase, by dissociation into XN(X $^3\Sigma^-$) and N_2(X $^1\Sigma_g^+$).[147]

$$XN_3(XA') \longrightarrow XN(X^3\Sigma^-) + N_2(X^1\Sigma_g{}^+) \qquad (442)$$

Even though this decomposition is spin forbidden, pyrolysis experiments have clearly shown the fragmentation into XN(X $^3\Sigma^-$) fragments and N_2. The end products of the decomposition of chlorine, bromine, and iodine azide are dinitrogen and the dihalides. Iodine also forms other azide species, the orange $I(N_3)_2{}^-$, the deep violet $I_2N_3{}^-$,[148] the deep carmine–red $I_2N_3{}^+$,[149] and the yellow $I(N_3)_2{}^+$.[150]

$$NMe_4{}^+N_3{}^- + IN_3 \longrightarrow NMe_4{}^+[I(N_3)_2]^- \qquad (443)$$

$$NMe_4{}^+I^- + IN_3 \longrightarrow NMe_4{}^+[I_2N_3]^- \qquad (444)$$

$$AgN_3 + I_3SbF_6{}^- \xrightarrow[SO_2]{223\,K} AgI + [I_2N_3]^+SbF_6{}^- \qquad (445)$$

$$ICl_2AsF_6{}^- + 2AgN_3 \longrightarrow 2AgCl + [I(N_3)_2]^+AsF_6{}^- \qquad (446)$$

Chlorine, bromine, and iodine azide can act as donors of positive halides. The reaction of chlorine azide with water yields hydrazoic acid and hypochloric acid:

$$ClN_3 + H_2O \rightleftharpoons HN_3 + HOCl \qquad (447)$$

The halogen azides XN_3 (X = Cl, Br, I) react with element chlorides (e.g. BX_3, AlI_3, $SnCl_4$, $SbCl_5$, $TiCl_4$, $NbCl_5$, $TaCl_5$, $CrCl_3$, WCl_6, $ReCl_5$, UCl_6) under halogen elimination to form the element halogenide azides.[151]

$$X_{n-1}EX + XN_3 \longrightarrow X_{n-1}EN_3 + X_2 \qquad (448)$$

With other element halides ($SnCl_2$, PCl_3, and $SbBr_3$) oxidative addition occurs:

$$X_nE + XN_3 \longrightarrow X_{n+1}EN_3 \qquad (449)$$

9 OXOHALIDES OF NITROGEN

9.1 Nitrosyl Halides

The nitrosyl halides all assume an angular structure. In the gas phase, the nitrogen–halogen bond distances are quite long (see Table 39) compared to NF_3 (136.5(2) pm) and NCl_3 (175.9(2) pm) and the nitrogen–oxygen bond distances are so short that they are in the range of triple bonds.

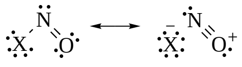

(450)

Table 39 Physical properties and bonding parameters of nitrosyl halides

	FNO	ClNO	BrNO
Color of gas	Colorless	Orange-yellow	Red
m.p. [K]	140	214	217
b.p. [K]	213	268	297
ΔH_f [kJ mol^{-1}]	−66.6	+51.8	+82.2
ΔG_f [kJ mol^{-1}]	−51.0	+66.1	+82.4
$S°$ [J mol^{-1} K^{-1}]	248.0	+261.6	+273.5
d(X–N) [pm]	solid 165.1(3) gas 151.67(5)	solid 218.7(4) gas 197.45(3)	gas 214(2)
d(N–O) [pm]	solid 108.3(3) gas 113.15(4)	solid 105.2(6) gas 113.13(3)	gas 115(4)
X–N–O angle [°]	solid 109.7(2) gas 109.91(1)	solid 111.1(4) gas 113.32(1)	gas 114
μ [D]	1.81	0.42	–

The bond polarity has a strong influence on the N–X bond length, for less basic groups X^- a complete shift to NO^+X^- is observed (e.g. NO^+ $PF_6{}^-$, NO^+ $ClO_4{}^-$). In the solid state, both NOF and NOCl show longer N–X bonds and shorter N–O bonds. The effect is more pronounced for chlorine and is explained in terms of a stronger ionic character in the solid state.[152] IR data indicate a similar behavior of NOBr.[153] For a detailed analysis of the bonding situation, see Ref. 154.

Nitrosyl halides can be obtained by the direct reaction of the respective halides with nitrogen monoxide at slightly elevated temperatures (310–320 K).

$$2NO + X_2 \longrightarrow 2NOX \qquad (451)$$

In the case of fluorine, NOF_3 is also produced during this reaction. The stability of the nitrosyl halides decreases in the order F > Cl > Br. NOCl is 0.5% decomposed at 298 K, NOBr is 7% decomposed, and nitrosyl iodide is unstable and decomposes rapidly to nitrogen monoxide and iodine, and has so far only been observed in matrix isolation at 9K.

$$2NOI \longrightarrow 2NO + I_2 \qquad (452)$$

NOCl decomposes at 373 K to form NO and chlorine. NOCl is present in aqua regia and is responsible for its red–yellow color. In the presence of traces of water, NOCl is very aggressive and can only be stored in Tantalum or glass vessels. Dry NOCl does not attack nickel, lead, platinum, and some polymers.

NOCl is the mixed anhydride of nitrous acid and hydrochloric acid and is easily hydrolyzed by water.

$$NOCl + H_2O \rightleftharpoons HNO_2 + HCl \qquad (453)$$

Therefore, water has to be excluded during the synthesis, for example, by passing HCl gas into liquid N_2O_3 in the presence of P_2O_5 as a dehydrating agent.

$$N_2O_3 + 2HCl \longrightarrow 2NOCl + H_2O \qquad (454)$$

In another synthesis, sodium chloride reacts with nitrosyl hydrogensulfate to form NOCl:

$$NO^+HSO_4^- + NaCl \longrightarrow NOCl + NaHSO_4 \qquad (455)$$

A laboratory synthesis uses sodium nitrite and hydrochloric acid:

$$NaNO_2 + 2HCl \longrightarrow NOCl + NaCl + H_2O \qquad (456)$$

Other preparations include the treatment of KNO_2–$AlCl_3$ melts with ammonium chloride, reaction of nitric acid with HCl in aqua regia, or the reactions of metal chlorides with nitric acid.

NOF, NOCl, and NOBr form NO^+ salts in reactions with halogen acceptors:

$$NOF + BF_3 \longrightarrow NO^+BF_4^- \qquad (457)$$

$$NOCl + SbCl_5 \longrightarrow NO^+SbCl_6^- \qquad (458)$$

NOBr has been obtained from nitrogen dioxide and potassium bromide:

$$2NO_2 + KBr \longrightarrow NOBr + KNO_3 \qquad (459)$$

In the system, NO/Br_2 $NOBr_3$ is the main compound found below 293 K, above 313 K NOBr is the main compound.[155]

The photosensitive isonitrosylhalides NOX (X = Cl, Br) can be obtained using matrix-isolation technique by irradiation of the nitrosyl halides.[156]

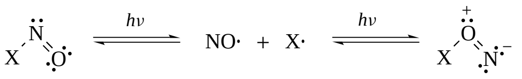

(460)

9.2 Nitryl Halides

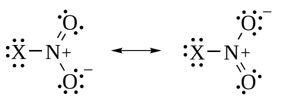

(461)

The nitryl halides (C_{2v} symmetry) are planar in analogy to the isoelectronic CO_3^{2-}. The gas phase and solid-state structures for $ClNO_2$ both show covalently bound molecules (see Table 40).[154] In contrast to the nitrosyl halides, the halogen–nitrogen bond distances in the gas phase and in the solid state are similar.[152] The nitryl halides NO_2F and NO_2Cl are the mixed anhydrides of nitric acid and hydrofluoric or hydrochloric acid, respectively.

$$XNO_2 + H_2O \rightleftharpoons HNO_3 + HX \qquad (462)$$

Table 40 Properties and bonding parameters of nitryl halides

	FNO_2	$ClNO_2$
Color of gas	Colorless	Colorless
m.p. [K]	107	128
b.p. [K]	201	258
ΔH_f [kJ mol^{-1}]	−80	+12.6
ΔG_f [kJ mol^{-1}]	−37.2	+54.4
$S°$ [J mol^{-1} K^{-1}]	+258.0	+272.0
d(X–N) [pm]	135	gas: 184.0(2) solid: 181.7(1), 183.3(1)
d(N–O) [pm]	123	gas: 120.2(1) solid: 119.7(1), 119.3(2) 119.2(1), 119.0(1)
<(X–N–O) [°]	118	gas: 115 solid:114.57(8), 115.04(9) 114.24(8), 114.71(8)
<(O–N–O) [°]	125	gas: 130.6(2) solid: 130.4(1), 131.1(1)
μ [D]	0.47	0.42

Similar to the nitrosyl halides, the nitryl halides are easily hydrolyzed. During the synthesis, water has to be excluded, either by removing it:

$$HNO_3 + HCl + H_2SO_4 \longrightarrow ClNO_2 + H_3O^+SO_4H^- \qquad (463)$$

$$HNO_3 + HSO_3Cl \longrightarrow ClNO_2 + H_2SO_4 \qquad (464)$$

or by using a synthetic route that does not produce water:

$$N_2O_5 + NaF \longrightarrow FNO_2 + NaNO_3 \qquad (465)$$

The oxidation of nitrosyl chloride with ozone, N_2O_5, Cl_2O, and ClO_2 also yields nitryl chloride.

$$NOCl + N_2O_5 \longrightarrow ClNO_2 + 2NO_2 \qquad (466)$$

Nitrosyl fluoride was also made from NO_2 and CoF_3 and by the reaction of nitryl chloride with hydrogen fluoride:

$$NO_2 + CoF_3 \longrightarrow FNO_2 + CoF_2 \qquad (467)$$

$$ClNO_2 + HF \longrightarrow FNO_2 + HCl \qquad (468)$$

The stability of the nitryl halides follows the stability of the nitrosyl halides, F > Cl > Br > I. Nitryl bromide $BrNO_2$ exists in equilibrium with NO_2/N_2O_4 at room temperature and can be studied spectroscopically.[157] INO_2 has a lifetime of only a few seconds at room temperature.

$$2NO_2Br \rightleftharpoons 2NO_2 + Br_2 \qquad (469)$$

Reaction of the nitryl halides with strong Lewis acids yields nitryl salts with the linear NO_2^+ cation (**92**) (d(N=O) 115.4 pm) (see Figure 16).

$$NO_2F + BF_3 \longrightarrow NO_2^+BF_4^- \qquad (470)$$

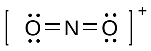

(**92**)

Figure 16 Lewis structure of the NO_2^+ cation

At low temperatures, the structural isomers, the halogen nitrites (nitrosyl hypohalides) XONO can be observed in the photolysis reaction of X_2/NO_2 mixtures.

$$2NO_2 + X_2 \xrightarrow{h\nu} 2ONOX \qquad (471)$$

Nitryl chloride reacts with zinc, mercury, and bismuth to form mixtures of the metal chlorides and nitrates, but does not react with copper, magnesium, iron, aluminum, or tin at 243 K. In the reaction with ammonia, nitryl chloride acts as a source of positive chlorine:

$$ClNO_2 + 2NH_3 \longrightarrow ClNH_2 + NH_4NO_2 \qquad (472)$$

9.3 Trifluoramine Oxide

Trifluoramine oxide (**93**) (Figure 17) is a colorless and highly toxic gas ($\Delta H_f = -71\,\mathrm{kJ\,mol^{-1}}$) with a melting point of 113 K and a boiling point of 185.6 K. It has a tetrahedral structure (C_{3v} symmetry) and is isoelectronic to NF_4^+.[154] The NF bond length (143 pm) is significantly longer than in NF_4^+ (130 pm), the NO bond length (116 pm) is shorter than the NO bond length in HNO (121 pm), thus indicating a bond order of around 2.

The bonding situation can be explained by negative hyperconjugation. Electron density is transferred from the oxygen p lone pairs to one of the antibonding $\sigma*$ (N–F) orbitals, thus strengthening the NO bond and weakening the NF bonds. The reaction of NF_3 and O_2 in electric discharge results in formation of NOF_3.

$$2NF_3 + O_2 \xrightarrow{77\,K} 2ONF_3 \qquad (473)$$

ONF_3 is also accessible from the reaction of nitrosyl fluoride with iridium hexafluoride:

$$3NOF + 2IrF_6 \longrightarrow ONF_3 + 2(NO)IrF_6 \qquad (474)$$

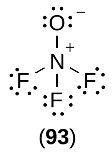

(**93**)

Figure 17 Lewis structure of F_3NO

Other methods for the preparation of ONF_3 include the fluorination of NO and the reaction of NF_3 with N_2O.[158]

$$2NO + 3F_2 \longrightarrow 2ONF_3 \qquad (475)$$

$$NF_3 + N_2O + 2SbF_5 \xrightarrow{423\,K} 2ONF_2^+Sb_2F_{11}^- + N_2 \qquad (476)$$

$$ONF_2^+Sb_2F_{11}^- \xrightarrow{>450\,K} ONF_3 + 2SbF_5 \qquad (477)$$

Irradiation with ultraviolet light forms the $NOF_2\bullet$ radical. NOF_3 decomposes at temperatures above 600 K to yield NOF, NO, NO_2, and NO_2F. It is a strong oxidizing agent toward organic and inorganic compounds.

As for NF_3, reactions with NOF_3 require an activation energy and do not occur spontaneously at room temperature, even though they are thermodynamically favored. In many instances, reactions result in fluorination rather than oxygenation, in keeping with the greater strength of the N–O bond.

$$NF_3O + SF_4 \xrightarrow{h\nu} NOF + SF_6 \qquad (478)$$

On reaction with strong fluorine acceptors (BF_3, AsF_5, SbF_5), NOF_3 can loose fluoride and form the planar ONF_2^+ cation (d(N–F) 128.4 pm, d(N–O) 111.4 pm, <(F–N–F) 107.9°, <(F–N–O) 126.0°).[159]

$$ONF_3 + AsF_5 \longrightarrow ONF_2^+AsF_6^- \qquad (479)$$

The NOF_2^+ cation reacts with HN_3 to form the N_3NOF^+ cation:

$$NOF_2^+SbF_6^- + HN_3 \longrightarrow N_3NOF^+SbF_6^- + HF \qquad (480)$$

9.4 Nitrosodifluoramine

The reaction of the normally relatively unreactive N_2O with difluorine gas at 77 K under UV irradiation yields a dark blue liquid, nitrosodifluoramine F_2NNO (**94**) (Figure 18).[160]

$$F_2 + N_2O \xrightarrow{77\,K,\ UV} F_2NNO \qquad (481)$$

Nitrosodifluoramine (**94**) can also be obtained by reacting tetrafluorohydrazine with a tenfold excess of NO at 583 K followed by quenching at 77 K.

$$N_2F_4 + 2NO \xrightarrow{77\,K,\ UV} 2F_2NNO \qquad (482)$$

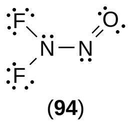

(**94**)

Figure 18 Lewis structure of F_2NNO

Table 41 Properties and bonding parameters of halogen nitrates

	$FONO_2$	$ClONO_2$	$BrONO_2$	$IONO_2$
Color	colorless gas	colorless gas	yellow liquid	yellow
m.p. [K]	98	166	231	–
b.p. [K]	227.1	291	decomp > 273 K	decomp. > 268 K
d(N=O) [pm]	129(5)	gas: 119.4(1) solid: $120.23(7)_{trans}$ $118.74(8)_{cis}$	gas: 120.5(3) solid: $121.3(8)_{trans}$ $119.2(8)_{cis}$	–
d(N–O) [pm]	139(5)	gas: 149.6(3) solid: 146.98(7)	gas: 145.6(5) solid: 141.4(7)	–
d(X–O) [pm]	1.42(5)	gas: 166.5(2) solid: 168.38(6)	gas: 182.9(4) solid: 186.0(5)	–
$O–N=O_{trans}$ angle [°]	–	gas: 108.8(2) solid: 109.33(5)	gas: 119.5(6) solid: 120.0(5)	–
$O–N=O_{cis}$ angle [°]	–	gas: 118.6(3) solid:118.36(5)	gas: 106.6(5) solid: 110.1(5)	–
O=N=O angle [°]	125(5)	gas: 132.6(5) solid: 132.31(6)	gas: 133.9(8) solid: 130.0(6)	–
X–O–N angle [°]	105(5)	gas: 113.0(3) solid:112.47(4)	gas: 113.9(5) solid: 113.8(4)	–

Nitrosodifluoramine (**94**) decomposes at 133 K to form tetrafluorohydrazine and NO, the reverse of the formation reaction (481).

$$F_2NNO \xrightarrow{133\,K} F_2 + N_2O \qquad (483)$$

9.5 Halogen Nitrates

The halogen nitrates have planar C_s structures (see Table 41). The dissociation to XO and NO_2 gets easier from fluorine to iodine.

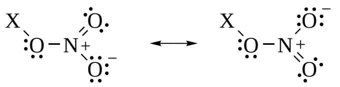

(484)

In the gas phase, the N–O bonds of chlorine and bromine nitrate are shorter and the O–X bonds longer than in the crystal structure.[154,161] In the solid state of the halogen nitrates, as for the nitrosyl halides, the contribution of the ionic $X^+ \; NO_3^-$ structure is higher.[152] This makes the N–O bond shorter and the O–X bond longer. The crystal structures can be considered as adducts of the halogen oxide XO• and the NO_2• radicals.

Fluorine nitrate is best prepared by the fluorination of nitric acid:

$$F_2 + HNO_3 \longrightarrow FONO_2 + HF \qquad (485)$$

The chlorine compound can by synthesized from nitric acid and ClF:

$$ClF + HNO_3 \longrightarrow ClONO_2 + HF \qquad (486)$$

or by reacting N_2O_5 with Cl_2O at 253 K:

$$Cl_2O + N_2O_5 \longrightarrow 2ClONO_2 \qquad (487)$$

The chlorine, bromine, and iodine nitrates (X = Cl, Br, I) can also be prepared by the reaction of silver nitrate with the halides.

$$X_2 + AgNO_3 \longrightarrow XONO_2 + AgX \qquad (488)$$

Bromine nitrate reacts with N_2O_5 to form an adduct.

$$BrONO_2 + N_2O_5 \longrightarrow NO_2^+[Br(ONO_2)_2^-] \qquad (489)$$

Bromine nitrate disproportionates to bromine, oxygen, and N_2O_5 at 273 K:[162]

$$2BrONO_2 \longrightarrow Br_2 + 0.5O_2 + N_2O_5 \qquad (490)$$

The unstable chloryl nitrate was detected in the reaction of ClO_2 with NO_3:[163]

$$ClO_2 + NO_3 \xrightarrow{(M)} O_2ClONO_2 \qquad (491)$$

and bromyl nitrate from the ozonization of bromine nitrate at 196 K:

$$BrONO_2 + 2O_3 \longrightarrow O_2BrONO_2 + 2O_2 \qquad (492)$$

Bromyl nitrate thermally decomposes to dibromine, dioxygen, and nitrogen dioxide.

$$2O_2BrONO_2 \longrightarrow Br_2 + 2NO_2 + 3O_2 \qquad (493)$$

The high levels of chlorine radicals ClO_x observed in the polar stratosphere couple with nitrogen oxides NO_x, resulting in the removal of reactive chlorine species by conversion into temporary reservoir species. The association reaction between ClO and NO_2 forming chlorine nitrate has been considered the most significant:

$$ClO\bullet + NO_2\bullet \xrightarrow{(M)} ClONO_2 \tag{494}$$

Chlorine nitrate and HCl are considered to be the most important chlorine reservoir species in the stratosphere.[164] Iodine nitrate has also been considered as a reservoir species for iodine radicals that could destroy tropospheric ozone, but photodissociation of $IONO_2$ to form iodine radicals is only effective at temperatures below 290 K, at higher temperatures thermal decomposition takes place which does not yield iodine radicals.[165]

Several iodine nitrates in the oxidation state +III are known: $I(ONO_2)_3$ and $CF_3I(ONO_2)_2$.[166] The other halogens do not form binary nitrates in the oxidation state +III. Iodine (III) nitrates are available by substitution of iodine(III)compounds

$$ICl_3 + 3ClONO_2 \longrightarrow I(ONO_2)_3 + 3Cl_2 \tag{495}$$

or by the oxidation of iodine(I) compounds:

$$CF_3I + 2ClONO_2 \longrightarrow CF_3I(ONO_2)_2 + Cl_2 \tag{496}$$

$I(ONO_2)_3$ has also been prepared by the oxidation of iodine with $ClONO_2$ at 238 K:

$$I_2 + 6ClONO_2 \longrightarrow 2I(ONO_2)_3 + 3Cl_2 \tag{497}$$

Vibrational spectra indicate a polymeric structure with bridging nitrate ligands for $I(ONO_2)_3$. The fluffy light yellow solid decomposes at 273 K to form N_2O_5 and $IONO_2$, which is only marginally stable and decomposes under formation of N_2O_5.

$$I(ONO_2)_3 \longrightarrow OINO_3 + N_2O_5 \tag{498}$$

The $XeNO_3^+$ cation, which is isoelectronic to the halogen nitrates has been detected in a mass spectrometer and seems to have the same connectivity as the halogen nitrates, but can isomerize to an $OXeNO_2$ structure. $XeNO_2^+$ was also detected, here xenon acts as a ligand of the nitronium ion. In the solid state, $NO_2^+Xe_2F_{13}^-$ consists of $X_2F_{13}^-$ and nitronium ions. In solution, the reaction of xenon difluoride with a HNO_3/NO_2 mixture produces the neutral species $Xe(ONO_2)_2$.[167]

10 RELATED ARTICLES

Ammonia & N-donor Ligands; Bond Lengths in Inorganic Solids & Liquids; Boron–Nitrogen Compounds; Carbon: Inorganic Chemistry; Coordination Numbers & Geometries; Electrochemistry: Applications in Inorganic Chemistry; Electronic Structure of Main-group Compounds; Hydrogen: Inorganic Chemistry; Hypervalent Compounds; Mixed Donor Ligands; Nickel: Inorganic & Coordination Chemistry; Nitrides: Transition Metal Solid-state Chemistry; Nitrogen Monoxide (Nitric Oxide): Bioinorganic Chemistry; Nitrogenase: Metal Cluster Models; Periodic Table: Trends in the Properties of the Elements; Phosphorus–Nitrogen Compounds; Selenium: Inorganic Chemistry; Sulfur–Nitrogen Compounds; Tellurium: Inorganic Chemistry.

11 REFERENCES

1. H. Schmidbaur, *Organometallics*, 1994, **13**, 1762.
2. G. Audi and A. H. Wapstra, *Nucl. Phys.*, 1995, **595A**, 409.
3. K. Jones, Nitrogen, in ‘Comprehensive Inorganic Chemistry’, ed. R. Lide, Pergamon, Oxford, 1973, Vol. 2, p. 147.
4. N. Wiberg, ‘Inorganic Chemistry’, 101st edn., Walther de Gruyter, Berlin, 1995.
5. W. Gerhertz, ed., ‘Ullmann’s Encyclopedia of Industrial Chemistry’, 7th edn., Wiley-VCH, Weinheim, 2003, chapters: Ammonia; Ammonium Compounds; Hydrazoic Acid and Azides; Hydrazine; Hydroxylamine; Nitrates and Nitrites; Nitric Acid, Nitrous Acid and Nitrogen Oxides; Nitrogen.
6. D. R. Lide, ed., ‘CRC Handbook of Chemistry and Physics’, 83rd edn., CRC-Press, London, 2002–2003.
7. R. T. Jacobsen, R. B. Stewart, and M. Jahangiri, *J. Phys. Chem. Ref. Data*, 1986, **15**, 735.
8. G. R. Brown and C. A. Winkler, *Angew. Chem.*, 1970, **82**, 187; *Angew. Chem., Int. Ed. Engl.*, **9**, 181.
9. A. Hammerl, G. Holl, K. Hübler, T. M. Klapötke, and P. Mayer, *Eur. J. Inorg. Chem.*, 2001, 755.
10. T. M. Klapötke, *Angew. Chem.*, 1999, **111**, 2694; *Angew. Chem., Int. Ed. Engl.*, 1999, **38**, 2536.
11. R. E. Continetti, D. R. Cyr, D. L. Osborn, D. J. Leahy, and D. M. Neumark, *J. Chem. Phys.*, 1993, **99**, 2616.
12. K. B. Hewett and D. W. Setser, *J. Phys. Chem. A*, 1998, **102**, 6274.
13. A. Friedmann, A. M. Soliva, S. A. Nizkorodov, E. J. Bieske, and J. P. Maier, *J. Phys. Chem.*, 1994, **98**, 8896.
14. G. Schatte and H. Willner, *Z. Naturforsch.*, 1991, **46b**, 483.
15. A. A. Friedmann, S. Nizkorodov, E. J. Bieske, and J. P. Maier, *Chem. Phys. Lett.*, 1994, **224**, 16.
16. F. Cacace, *Chem. Eur. J.*, 2002, **8**, 3838.
17. T. Ruchti, T. Speck, J. P. Connelly, E. J. Bieske, H. Linnartz, and J. P. Maier, *J. Chem. Phys.*, 1996, **105**, 2591.
18. M. T. Nguyen and T.-K. Ha, *Chem. Phys. Lett.*, 2001, **335**, 311.
19. A. Vij, W. W. Wilson, V. Vij, F. S. Tham, J. A. Sheehy, and K. O. Christe, *J. Am. Chem. Soc.*, 2001, **123**, 6308.

20. R. D. Harcourt and T. M. Klapötke, *Z. Naturforsch. B.*, 2002, **57b**, 983.
21. W. W. Wilson, A. Vij, V. Vij, E. Bernhardt, and K. O. Christe, *Chem. Eur. J.*, 2003, **9**, 2840.
22. S. Evangelisti and T. Leininger, *J. Mol. Struct. (THEOCHEM)*, 2003, **621**, 43.
23. R. Huisgen and I. Ugi, *Chem. Ber.*, 1957, **90**, 2914.
24. A. Hammerl and T. M. Klapötke, *Inorg. Chem.*, 2002, **41**, 906.
25. A. Hammerl, T. M. Klapötke, and P. Schwerdtfeger, *Chem. Eur. J.*, 2003, **9**, 5511.
26. R. N. Butler, A. Fox, S. Collier, and L. A. Burke, *J. Chem. Soc. Perkin Trans. 2*, 1998, 2243.
27. A. Vij, J. G. Pavlovich, W. W. Wilson, V. Vij, and K. O. Christe, *Angew. Chem.*, 2002, **114**, 3177; *Angew. Chem., Int. Ed. Engl.*, 2002, **41**, 3051.
28. T. M. Klapötke, *J. Mol. Struct. (THEOCHEM)*, 2000, **499**, 99.
29. M. S. Workentin, B. D. Wagner, F. Negri, M. Z. Zgierski, J. Lusztyk, W. Siebrand, and D. D. M. Wayner, *J. Phys. Chem.*, 1995, **99**, 94.
30. J. F. Zhao and Q. S. Li, *Chem. Phys. Lett.*, 2003, **368**, 12.
31. Q. S. Li and J. F. Zhao, *J. Phys. Chem. A*, 2002, **106**, 5928.
32. G. Chung, M. W. Schmidt, and M. S. Gordon, *J. Phys. Chem. A*, 2000, **104**, 5647.
33. A. Hammerl, G. Holl, T. M. Klapötke, H. Nöth, and M. Warchhold, *Propell. Explos. Pyrot.*, 2003, **28**, 165.
34. M. D. Thompsson, T. M. Bledson, and D. L. Strout, *J. Phys. Chem. A*, 2002, **106**, 6880.
35. Y. D. Liu, P. G. Yiu, J. Guan, and Q. S. Li, *J. Mol. Struct. (THEOCHEM)*, 2002, **588**, 37.
36. Q. S. Li and J. F. Zhao, *J. Phys. Chem. A*, 2002, **106**, 5367.
37. T. M. Klapötke and R. D. Harcourt, *J. Mol. Struct. (THEOCHEM)*, 2001, **541**, 237.
38. A. Hammerl, T. M. Klapötke, P. Mayer, H. Nöth, H. Piotrowski, and M. Warchhold, *Eur. J. Inorg. Chem.*, 2002, 834.
39. L. Gmelin, A. Kotowski, E. H. E. Pietsch, and M. Becke-Goehring, eds, ‘Gmelin Handbook of Inorganic and Organometallic Chemistry, Nitrogen’, Suppl. Vol. B1 and B2, Compounds with nitrogen and hydrogen, Springer, Berlin, 1993.
40. E. Dietsch, ed., ‘Gmelins Handbuch der anorganischen Chemie, Stickstoff’, 8th edn., Verlag Chemie, Berlin, 1936.
41. M. Brönstrup, D. Schröder, I. Kretzschmar, C. A. Schalley, and H. Schwarz, *Eur. J. Inorg. Chem.*, 1998, 1529.
42. M. F. Lappert, P. P. Power, A. R. Sanger, and R. C. Srivastasta, ‘Metal and Metalloid amides’, Ellis Horwood, Chichester, 1980.
43. R. Schlögl, *Angew. Chem.*, 2003, **115**, 2050; *Angew. Chem., Int. Ed. Engl.*, 2003, **42**, 2004.
44. J. Jander, Chemistry in Anhydrous Liquid Ammonia, in ‘Chemistry in Nonaqueous Ionizing Solvents’, eds. G. Jander, H. Spandau, and C. C. Addison, Wiley & Sons, New York, 1966, Vol. I.
45. S. Hayama, N. T. Skipper, J. C. Wasse, and H. Thompson, *J. Chem. Phys.*, 2002, **116**, 2991.
46. E. W. Schmidt, ‘Hydrazine and its Derivatives: Preparation, Properties, Applications’, 2nd edn., John Wiley & Sons, New York, 2001, Vol. 1 and 2.
47. D. Giordano, *J. Chem. Eng. Data*, 2001, **46**, 486.
48. H. H. Sisler, F. T. Neth, and F. R. Hurley, *J. Am. Chem. Soc.*, 1954, **76**, 3906.
49. D. M. Stanbury, *Prog. Inorg. Chem.*, 1998, **47**, 511.
50. V. Andries and D. Couturier, *Mat. Perform.*, 2000, **39**, 58.
51. O. de Bonn, A. Hammerl, T. M. Klapötke, P. Mayer, H. Piotrowski, and H. Zewen, *Z. Anorg. Allg. Chem.*, 2001, **627**, 2011.
52. G. Stedman, *Adv. Inorg. Chem. Radiochem.*, 1979, **22**, 113.
53. M. Vogel, A. Buldt, and U. Karst, *Fresen. J. Anal. Chem.*, 2000, **366**, 781.
54. A. Hammerl, G. Holl, M. Kaiser, T. M. Klapötke, H. Nöth, U. Ticmanis, and M. Warchhold, *Inorg. Chem.*, 2001, **40**, 3570.
55. J. R. Dilworth, *Coord. Chem. Rev.*, 1976, **21**, 29.
56. Y. Kim, J. W. Gije, and K. Seff, *J. Am. Chem. Soc.*, 1977, **99**, 7057.
57. T. Fujii, C. P. Selvin, M. Sablier, and K. Iwase, *J. Phys. Chem. A*, 2002, **106**, 3102.
58. K.-H. Linke and H. J. Göhausen, *Chem. Ber.*, 1971, **104**, 301.
59. K.-H. Linke and R. Turley, *Z. Anorg. Allg. Chem.*, 1970, **377**, 139.
60. N. Wiberg, G. Fischer, and H. Bachhuber, *Angew. Chem.* 1977, **89**, 828; *Angew. Chem., Int. Ed. Engl.*, 1977, **16**, 780.
61. M. R. Smith, T.-Y. Cheng, and G. L. Hillhouse, *J. Am. Chem. Soc.*, 1993, **115**, 8638.
62. J. Sutherland, *J. Phys. Chem.*, 1979, **83**, 789.
63. M. Veith and H. Schlemmer, *Z. Anorg. Allg. Chem.*, 1982, **494**, 7.
64. N. Wiberg, H. Bayer, and H. Bachhuber, *Angew. Chem.* 1975, **87**, 202; *Angew. Chem., Int. Ed. Engl.*, 1975, **14**, 177.
65. T. M. Klapötke, A. Schulz, and R. D. Harcourt, ‘Quantum Chemical Methods In Main-Group Chemistry’, John Wiley & Sons, Chichester, 1998.
66. R. D. Harcourt, *J. Mol. Struct.*, 1993, **300**, 245.
67. W. Fraenk, T. Habereder, A. Hammerl, T. M. Klapötke, B. Krumm, P. Mayer, H. Nöth, and M. Warchhold, *Inorg. Chem.*, 2001, **40**, 1334.
68. B. Neumüller, F. Schmock, and K. Dehnicke, *Z. Anorg. Allg. Chem.*, 1999, **625**, 1243.
69. A. Kornath, *Angew. Chem.*, 2001, **113**, 3231; *Angew. Chem., Int. Ed. Engl.*, 2001, **40**, 3135.
70. W. Fraenk and T. M. Klapoetke, Recent Developments in the Chemistry of Covalent Main Group Azides, in ‘Inorganic Chemistry Highlights’, eds. G. Meyer, D. Naumann, and L. Wesemann, Wiley-VCH, Weinheim, 2002, p. 259.

71. D. Adam, K. Karaghiosoff, G. Holl, M. Kaiser, and T. M. Klapötke, *Propell. Explos. Pyrot.*, 2002, **27**, 7.
72. E. Wiberg and H. Micheaud, *Z. Naturforsch.*, 1954, **B9**, 500.
73. A. C. Filippou, P. Portius, and G. Schnakenburg, *J. Am. Chem. Soc.*, 2002, **124**, 12396.
74. C. Moberg and H. Adolfsson, *Sci. Synth.*, 2002, **4**, 435.
75. K. Karaghiosoff, T. M. Klapötke, B. Krumm, H. Nöth, T. Schütt, and M. Suter, *Inorg. Chem.*, 2002, **41**, 170.
76. M.-J. Crawford and T. M. Klapötke, *Inorg. Chem.*, 1999, **38**, 3006.
77. T. M. Klapötke, B. Krumm, H. Piotrowski, K. Polborn, and I. Schwab, *Z. Anorg. Allg. Chem.*, 2002, **628**, 1831.
78. T. M. Klapötke, B. Krumm, P. Mayer, and O. P. Ruscitti, *Inorg. Chem.*, 2000, **39**, 5426.
79. A. Hammerl, G. Holl, M. Kaiser, T. M. Klapötke, and H. Piotrowski, *Propell. Explos. Pyrot.*, 2001, **28**, 161.
80. A. Schulz, I. C. Tornieporth-Oetting, and T. M. Klapötke, *Angew. Chem.*, 1993, **105**, 1697; *Angew. Chem., Int. Ed. Engl.*, 1993, **32**, 1610.
81. T. M. Klapötke and A. Schulz, *Chem. Ber.*, 1995, **128**, 201.
82. R. Engelke, N. C. Blais, and R. K. Sander, *J. Phys. Chem. A*, 1999, **103**, 5611.
83. T. M. Klapötke, A. Schulz, and I. C. Tornieporth-Oetting, *Chem. Ber.*, 1994, **127**, 2181.
84. R. D. Harcourt and N. Hall, *J. Mol. Struct. (THEOCHEM)*, 1995, **342**, 59.
85. W. N. Lipscomb, F. E. Wang, R. May, and E. L. Lippert, *Acta Cryst.*, 1961, **14**, 1100.
86. L. P. Olson, K. T. Kuwata, M. D. Bartberger, and K. N. Houk, *J. Am. Chem. Soc.*, 2002, **124**, 9469.
87. G. B. Richter-Addo and P. Legzdins, ‘Metal Nitrosyls’, Oxford University Press, New York, 1992.
88. J. Horakh, H. Borrmann, and A. Simon, *Chem. Eur. J.*, 1995, **1**, 389.
89. K. B. Borisenko, M. Kolonits, B. Rozsondai, and I. Hargittai, *J. Mol. Struct.*, 1997, **413–414**, 121.
90. A. Obermeyer, H. Borrmann, and A. Simon, *Z. Kristallog.*, 1991, **196**, 129.
91. L. H. Jones, B. I. Swanson, and S. F. Agnew, *J. Chem. Phys.*, 1985, **82**, 4389.
92. D. A. Pinnick, S. F. Agnew, and B. I. Swanson, *J. Phys. Chem.*, 1992, **96**, 7092.
93. Y. Song, M. Somayalazulu, H.-k. Mao, R. J. Hemley, and D. R. Herschbach, *J. Chem. Phys.*, 2003, **118**, 8350.
94. X. Zhang and K. Seppelt, *Z. Anorg. Allg. Chem.*, 1998, **624**, 667.
95. C. C. Addison, Chemistry in Liquid Dinitrogen Tetroxide, in ‘Chemistry in Nonaqueous Ionizing Solvents’, eds. G. Jander, H. Spandau, and C. C. Addison, Pergamon, Oxford, 1967, Vol. III.
96. B. M. McClelland, A. D. Richardson, and K. Hedberg, *Helv. Chim. Acta*, 2001, **84**, 1612.
97. I. Wängberg, T. Etzkorn, I. Barnes, U. Platt, and K. H. Becker, *J. Phys. Chem. A*, 1997, **101**, 9694.
98. W. Eisfeld and K. Morokuma, *J. Chem. Phys.*, 2003, **119**, 4682.
99. F. Cacace, G. de Petris, M. Rosi, and A. Troiani, *Chem. Eur. J.*, 2002, **8**, 5684.
100. D. Trinschek and M. Jansen, *Angew. Chem.*, 1999, **111**, 234; *Angew. Chem., Int. Ed. Engl.*, 1999, **38**, 133.
101. M. Jansen, *Angew. Chem.*, 1976, **88**, 410; *Angew. Chem., Int. Ed. Engl.*, 1976, **15**, 376.
102. R. W. Rasmussen, *Acta Chem. Scand.*, 1958, **12**, 578.
103. V. Shafirovich and S. V. Lymar, *J. Am. Chem. Soc.*, 2003, **125**, 6547.
104. G. Maier, H. P. Reisenauer, and M. De Marco, *Angew. Chem.*, 1999, **111**, 1113; *Angew. Chem., Int. Ed. Engl.*, 1999, **38**, 108.
105. S. L. Laursen, J. E. Grace Jr, R. L. deKock, and S. A. Sprunk, *J. Am. Chem. Soc.*, 1998, **120**, 12583.
106. W. E. Wentworth, C. F. Batten, and E. C. M. Chen, *J. Phys. Chem.*, 1994, **98**, 11902.
107. L. Andrews, X. Wang, M. Zhou, and B. Liang, *J. Phys. Chem. A*, 2002, **106**, 92.
108. N. Arulsamy, D. S. Bohle, J. A. Imonigie, and E. S. Sagan, *Inorg. Chem.*, 1999, **38**, 2716.
109. C. Feldmann and M. Jansen, *Z. Anorg. Allg. Chem.*, 1997, **623**, 1803.
110. N. Arulsamy, D. S. Bohle, J. A. Imonigie, and S. Levine, *Angew. Chem.*, 2002, **114**, 2477; *Angew. Chem., Int. Ed. Engl.*, 2002, **41**, 2371.
111. M. J. Akthar, C. A. Lutz, and F. T. Bonner, *Inorg. Chem.*, 1979, **18**, 2369.
112. B. Liang and L. Andrews, *J. Am. Chem. Soc.*, 2001, **123**, 9848.
113. M. Wöhrle, P. Latal, R. Kissner, R. Nesper, and W. H. Koppenol, *Chem. Res. Toxicol.*, 1999, **12**, 305.
114. S. V. Lymar, R. F. Khairutdinov, and J. K. Hurst, *Inorg. Chem.*, 2003, **42**, 5259.
115. D. S. Bohle, B. Hansert, S. C. Paulson, and B. D. Smith, *J. Am. Chem. Soc.*, 1994, **116**, 1423.
116. S. V. Lymar and J. K. Hurst, *J. Am. Chem. Soc.*, 1995, **117**, 8867.
117. N. Lebrun, F. Mahe, J. Lamiot, M. Foulon, J. C. Petit, and D. Prevosta, *Acta Cryst.*, 2001, **B57**, 27.
118. G. Mark, H.-G. Korth, H.-P. Schuchmann, and C. von Sonntag, *J. Photochem. Photobiol.*, 1996, **101**, 89.
119. F. Cacace, G. dePetris, and A. Troiani, *Chem. Phys. Chem.*, 2003, **4**, 1128.
120. Th. Bremm and M. Jansen, *Z. Anorg. Allg. Chem.*, 1992, **608**, 49.
121. L. P. Olson, M. D. Bartberger, and K. N. Houk, *J. Am. Chem. Soc.*, 2003, **125**, 3999.

122. A. Häußler, T. M. Klapötke, and H. Piotrowski, *Z. Naturforsch.*, 2002, **57b**, 151.
123. J. C. Bottaro, P. E. Penwell, and R. J. Schmitt, *J. Am. Chem. Soc.*, 1997, **119**, 9405.
124. A. A. Pinkerton and J. P. Ritchie, *J. Mol. Struct.*, 2003, **657**, 57.
125. S. Alavia and D. L. Thompson, *J. Chem. Phys.*, 2003, **119**, 232.
126. H. J. Emeléus, J. M. Shreeve, and R. D. Verma, *Adv. Inorg. Chem.*, 1989, **33**, 139.
127. I. C. Tornieporth-Oetting and T. M. Klapötke, *Comments Inorg. Chem.*, 1993, **15**, 137.
128. R. D. Harcourt and T. M. Klapötke, *J. Fluorine Chem.*, 2003, **123**, 273.
129. J. Demaison, L. Marulés, and J. E. Boggs, *Chem. Phys.*, 2000, **260**, 65.
130. M. F. Klapdor, H. Willner, W. Poll, and D. Mootz, *Angew. Chem.*, 1996, **108**, 336; *Angew. Chem., Int. Ed. Engl.*, 1996, **35**, 320.
131. H. F. Bettinger, Pv. R. Schleyer, and H. F. Schaefer, *J. Am. Chem. Soc.*, 1998, **120**, 11439.
132. K. O. Christe and C. J. Schack, *Inorg. Chem.*, 1978, **17**, 2749.
133. K. O. Christe, R. D. Wilson, W. W. Wilson, R. Bau, S. Sukumar, and D. A. Dixon, *J. Am. Chem. Soc.*, 1991, **113**, 3795.
134. H. W. Roesky, O. Glemser, and D. Bormann, *Angew. Chem.*, 1964, **76**, 713; *Angew. Chem., Int. Ed. Engl.*, 1964, **3**, 181.
135. M. Knothe and W. Hasenpusch, *Inorg. Chem.*, 1996, **35**, 4529.
136. R. Minkwitz, D. Bernstein, and W. Sawodny, *Angew. Chem.*, 1990, **102**, 185; *Angew. Chem., Int. Ed. Engl.*, 1990, **29**, 181.
137. M. Gazda, K. Kumar, and D. W. Margerum, *Inorg. Chem.*, 1995, **34**, 3536.
138. J. Jander, J. Knackmuss, and K.-U. Thiedemann, *Z. Naturforsch.*, 1975, **30b**, 464.
139. I. C. Tornieporth-Oetting and T. M. Klapötke, *Angew. Chem.*, 1990, **102**, 726; *Angew. Chem., Int. Ed. Engl.*, 1990, **29**, 677.
140. J. S. Thrasher and D. D. Desmarteau, *J. Fluorine Chem.*, 1991, **52**, 51.
141. D. B. Exton, S. A. Williams, and J. V. Gilbert, *J. Phys. Chem.*, 1993, **97**, 4326.
142. M. A. Clyne and J. Connor, *J. Chem. Soc., Faraday Trans. 2*, 1972, **68**, 1220.
143. T. M. Klapötke, *Chem. Ber./Recueil*, 1997, **130**, 443.
144. I. C. Tornieporth-Oetting and T. M. Klapötke, *Angew. Chem.*, 1995, **107**, 559; *Angew. Chem., Int. Ed. Engl.*, 1995, **34**, 511.
145. M. Hargittai, I. C. Tornieporth-Oetting, T. M. Klapötke, M. Kolonitz, and I. Hargittai, *Angew. Chem.*, 1993, **105**, 773; *Angew. Chem., Int. Ed. Engl.*, 1993, **32**, 759.
146. P. Buzek, T. M. Klapötke, Pv. R. Schleyer, I. C. Tornieporth-Oetting, and P. S. White, *Angew. Chem.*, 1993, **105**, 289; *Angew. Chem., Int. Ed. Engl.*, 1993, **32**, 275.
147. Y. Zeng, L. Meng, S. Zheng, and D. Wang, *Chem. Phys. Lett.*, 2003, **78**, 128.
148. K. Dehnicke, *Angew. Chem.*, 1979, **91**, 527; *Angew. Chem., Int. Ed. Engl.*, 1979, **18**, 507.
149. I. C. Tornieporth-Oetting, P. Buzek, Pv. R. Schleyer, and T. M. Klapötke, *Angew. Chem.*, 1992, **104**, 1391; *Angew. Chem., Int. Ed. Engl.*, 1992, **31**, 1338.
150. I. C. Tornieporth-Oetting, T. M. Klapötke, A. Schulz, P. Buzek, and Pv. R. Schleyer, *Inorg. Chem.*, 1993, **32**, 5640.
151. K. Dehnicke, *Adv. Inorg. Chem. Radiochem.*, 1983, **26**, 169.
152. A. Obermeyer, H. Borrmann, and A. Simon, *J. Am. Chem. Soc.*, 1995, **117**, 7887.
153. A. Ellern and K. Seppelt, *Z. Anorg. Allg. Chem.*, 2001, **627**, 234.
154. R. D. Harcourt and T. M. Klapötke, *J. Fluorine Chem.*, 2003, **123**, 5.
155. H. Feilchenfeld, J. Kenat, and S. Manor, *Trans. Faraday Soc.*, 1969, **65**, 2350.
156. G. Maier, H. P. Reisenauer, and M. deMarco, *Chem. Eur. J.*, 2000, **6**, 800.
157. B. J. Finlayson-Pitts, F. E. Livingston, and H. N. Berko, *J. Phys. Chem.*, 1989, **93**, 4397.
158. K. O. Christe, *J. Am. Chem. Soc.*, 1995, **117**, 6136.
159. A. Vij, X. Zhang, and K. O. Christe, *Inorg. Chem.*, 2001, **40**, 416.
160. M.-J. Crawford, R. D. Harcourt, and T. M. Klapötke, *J. Phys. Chem.*, 2000, **104A**, 3406.
161. B. Casper, P. Lambotte, R. Minkwitz, and H. Oberhammer, *J. Phys. Chem.*, 1993, **97**, 9992.
162. W. W. Wilson and K. O. Christe, *Inorg. Chem.*, 1987, **26**, 1573.
163. R. R. Friedl, S. P. Sander, and Y. L. Yung, *J. Phys. Chem.*, 1992, **96**, 7490.
164. M. A. Tolbert, *Science*, 1994, **264**, 527.
165. B. J. Allan and J. M. C. Plane, *J. Phys. Chem. A*, 2002, **106**, 8634.
166. E. Lehmann, D. Naumann, and H.-H. Heinsen, *Z. Anorg. Allg. Chem.*, 1977, **431**, 233.
167. F. Bernardi, F. Cacace, G. de Petris, F. Pepi, and I. Rossi, *J. Phys. Chem. A*, 1998, **102**, 5831.

Acknowledgments

We are indebted to Dr. M.-J. Crawford, Carmen Novak, Gunnar Spieß, and Angelika Häußler and thank them for their help with improving this chapter. We also thank the Fonds der chemischen Industrie (FCI) for financial support.

Nitrogenase: Metal Cluster Models

Frédéric Barrière
Université de Rennes 1, Institut de Chimie, Rennes, France

1 Introduction 1
2 Models for the Fe_4S_4 Cluster of Nitrogenase 3
3 Models for the Fe_8S_7 P-cluster 5
4 Structural Models for the $MoFe_7S_9$ FeMo-cofactor 7
5 Conclusions 12
6 Related Articles 12
7 References 12

1 INTRODUCTION

Reduced nitrogen is essential to all forms of life for it is present in many important and universal biological molecules such as nucleotides and amino acids, the building blocks of DNA and proteins. Although abundant in its molecular state in today's earth atmosphere (78%), dinitrogen is very difficult to reduce. Indeed, the N≡N triple bond dissociation energy, as high as $940\,\mathrm{kJ\,mol^{-1}}$, and the unstability of some reduced intermediates make N_2 kinetically very stable. Thermodynamically, however, its reduction is generally favorable: for instance ΔG^0 for $N_2 + 3H_2 \rightarrow 2NH_3$ is $-32\,\mathrm{kJ\,mol^{-1}}$ in the gas phase.[1] Hence, dinitrogen is often referred to as an inert medium, as inferred by the Greek root of its name in French: *azote* (without life). Nevertheless, a restricted class of microorganisms called diazotrophs, comprising different archaea and bacteria, are able to overcome this relative inertness thanks to the nitrogenase enzyme, which catalyzes the biological reduction of dinitrogen to ammonia (*see* ***Nitrogenase Catalysis & Assembly***). Ammonia, in the protonated form of ammonium, is indeed the primary entry point of fixed nitrogen into the living world, mainly via the glutamate/glutamine biosynthesis pathway of plants. Before the advent of an efficient artificial ammonia synthesis (the Haber–Bosch process) at the beginning of the twentieth century,[2] dinitrogen reduction by nitrogenases was even the major (and almost the sole) provider of primary assimilable nitrogen for living organisms.[3]

The most extensively studied nitrogenase enzyme contains two kinds of transition metals, that is, iron and molybdenum, and is called molybdenum nitrogenase.[4–7] In growth conditions where molybdenum concentration is low, a nitrogenase depending on iron and vanadium is expressed.[8–11] When both molybdenum and vanadium are unavailable, a third type of nitrogenase is expressed that contains iron as the only transition metal.[8,12,13] The vanadium–nitrogenase and iron-only nitrogenases, also known as alternative nitrogenases, are related to the molybdenum nitrogenase but are all genetically distinct. A fourth and completely different 'nonconventional' type of nitrogenase is known; it also contains iron and molybdenum, but couples dinitrogen reduction to the oxidation of superoxide and carbon monoxide.[14]

Mo-nitrogenase is the only one for which both detailed structural and mechanistic data are available.[4–7,15–17] The enzymatic complex comprises two proteins: the iron-protein and the molybdenum iron-protein. The Fe-protein is an α_2 homodimer with a Fe_4S_4 cluster (*see* ***Iron–Sulfur Models of Protein Active Sites***; ***Iron–Sulfur Proteins***) bridging the two α-subunits via four iron-cysteinate ligations. Each α-monomer of the iron-protein possesses a nucleotide-binding site (ATP or ADP). The Fe-protein is a specific reductant of the MoFe-protein, an event that depends on, and is coupled to, the hydrolysis of MgATP. The MoFe-protein is an $\alpha_2\beta_2$ tetramer and contains two types of metal–sulfur centers: the so-called P-cluster of Fe_8S_7 stoichiometry that is located at the interface of each homologous $\alpha-\beta$ subunit, and the FeMo-cofactor ($MoFe_7S_9$) found in each α-subunit.

Two different structures are known for the P-cluster and are assigned to different cluster core oxidation states. In the reduced or P^N (native) state, the Fe_8S_7 cluster can be described as two Fe_4S_4 cubes sharing one common hexacoordinate sulfur atom, the iron atoms being linked to the protein by cysteinate ligands, two of them bridging the subcubes. In the P^{OX} state, oxidized by two electrons relative to P^N, the central sulfur atom loses two bonds with two iron atoms in one of the subcubes, thus becoming more open. The tetrahedral coordination of these two iron atoms is then completed by extra ligations from neighboring cysteine or serine residues.

The FeMo-cofactor structure can be viewed as the assembly of two incomplete $Fe_4(\mu_3\text{-S})_3$ and $MoFe_3(\mu_3\text{-S})_3$ subcubes, linked together by three central μ_2-S bridging sulfide ligands. The six central iron atoms form an approximate trigonal prism centered on a light atom 'Y' that has only been structurally recognized recently.[17] The identity of the light atom has been proposed to be nitrogen although carbon or oxygen have not been ruled out, while sulfur seems to be less likely. Theoretical investigations from different authors also concluded that 'Y' is most likely a nitrogen atom.[18–20] The pseudooctahedral coordination of molybdenum is completed by the exogenous bidentate (R)-homocitrate ligand and by imidazole from a neighboring histidine residue. A cysteine residue, covalently bound to the tetrahedral apical iron atom, provides the cofactor with its other protein ligation. The structure and location of the Mo-nitrogenase metal clusters are depicted in Figure 1.

The electrons transferred from the Fe_4S_4 cluster of the iron-protein to the molybdenum–iron protein are believed to shuttle through the P-cluster before eventually reaching

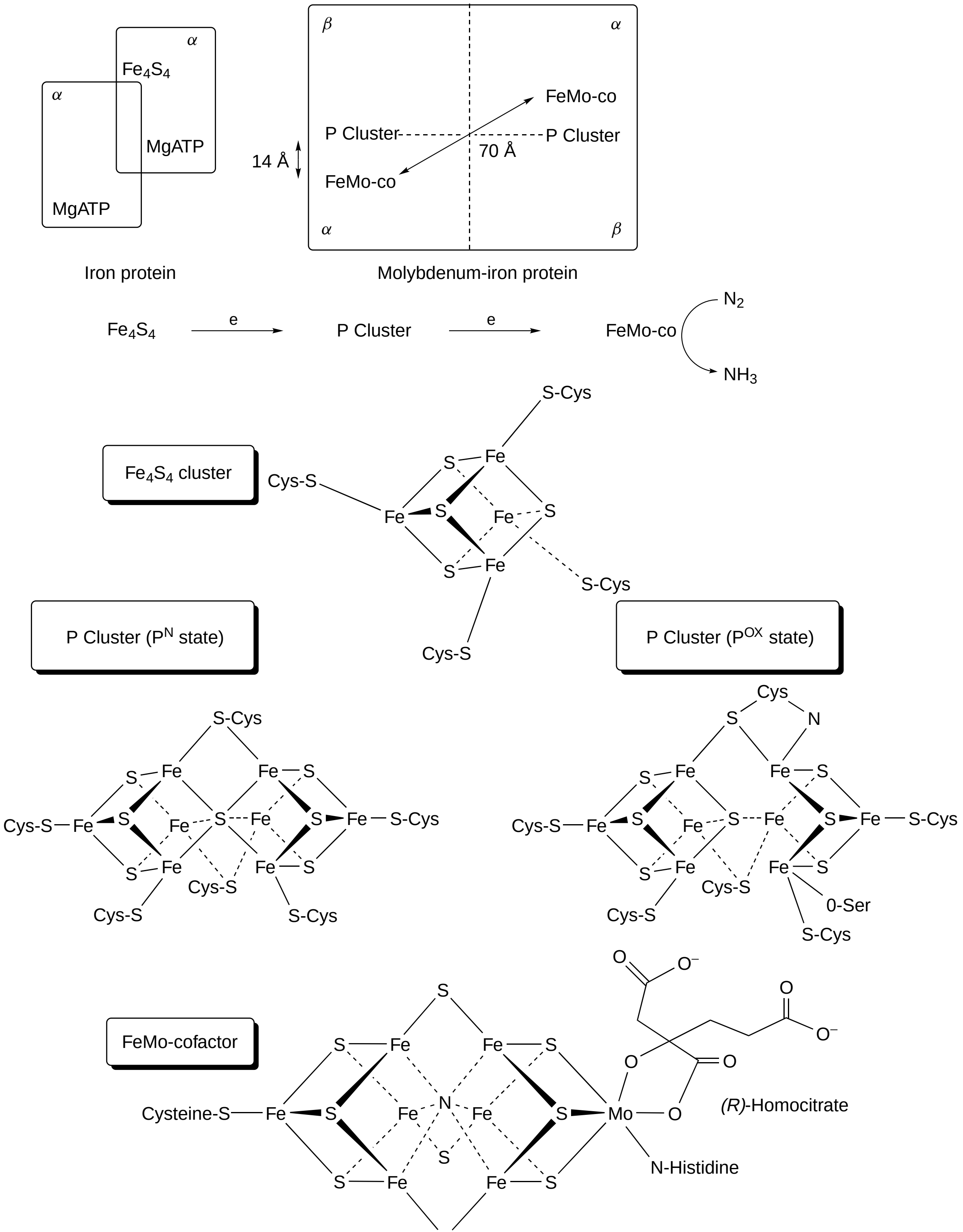
α
Fe4S4
α
MgATP
MgATP
Iron protein
β
α
FeMo-co
P Cluster
P Cluster
70 Å
14 Å
FeMo-co
α
β
Molybdenum-iron protein
Fe4S4
e
P Cluster
e
FeMo-co
N2
NH3
Fe4S4 cluster
S-Cys
Cys-S
S-Cys
Cys-S
P Cluster (PN state)
P Cluster (POX state)
S-Cys
Cys-S
S-Cys
Cys-S
Cys-S
S-Cys
Cys
N
Cys-S
S-Cys
Cys-S
Cys-S
0-Ser
S-Cys
FeMo-cofactor
Cysteine-S
Mo
N
(R)-Homocitrate
N-Histidine

$$N_2 + 8H^+ + 16MgATP + 8e^- \longrightarrow 2NH_3 + H_2 + 16MgADP + 16P_i$$

Figure 1 Schematic representation of the Fe-protein (60 kD, α_2 dimer) and the MoFe-protein (250 kD, $\alpha_2\beta_2$ tetramer) of the Mo-nitrogenase. Outline of the electron transfer path through the metal clusters. Structure of the Fe_4S_4 cluster of the Fe-protein. Structure of the P-cluster (in two oxidation states) and of the FeMo-cofactor in the MoFe-Protein. Limiting stoichiometry for the function of Mo-nitrogenase

the FeMo-co where N_2 binding, reduction, and protonation occurs.

The limiting stoichiometry for the reduction of one equivalent of dinitrogen by Mo-nitrogenase to two equivalents of ammonia involves the hydrolysis of 16MgATP and the production of one molecule of dihydrogen, as outlined in Figure 1. The three metal clusters found in Mo-nitrogenase belong to the diverse class of iron–sulfur prosthetic centers largely distributed in all living organisms.[21–24] However, while the Fe_4S_4 center is a common cluster found in many other iron–sulfur proteins, the P-cluster and the FeMo-cofactor represent to date unique structures in biology.

The complexity of the enzyme system, together with the extraordinary ambient conditions of transition metal-assisted dinitrogen reduction, have long fascinated inorganic chemists, still left with the high-temperature and high-pressure Haber–Bosch process for the artificial synthesis of ammonia from molecular nitrogen and hydrogen.

The current status of nitrogenase metal-cluster modeling by synthetic inorganic clusters and complexes is reported here. Modeling is to be understood not only in terms of structure and associated spectroscopic properties, but also in terms of function, that is, how well the models reproduce, or help to understand, the biological role of the metal–sulfur assemblies in nitrogenase, that is, electron transfer and the reduction of substrates.

The sequential electron transfer path in nitrogenase is followed: first models of the Fe_4S_4 cluster of the iron-protein are discussed, then mimics of the P-cluster in the molybdenum–iron protein, and finally structural and functional models of the FeMo-cofactor are summarized.

2 MODELS FOR THE Fe_4S_4 CLUSTER OF NITROGENASE

Fe_4S_4 clusters with cysteinate ligation at iron, in their $[Fe_4S_4]^{1+/2+/3+}$ redox states, are of pervasive occurrence in iron–sulfur proteins, functioning mostly as electron transfer relays as in ferredoxins (1+/2+) and high-potential iron proteins (2+/3+) (*see* ***Iron–Sulfur Proteins***). Examples are also known where they are implied in catalysis.[21,22] In Mo-nitrogenase,[4] the Fe-protein specifically reduces the MoFe-protein with its Fe_4S_4 cluster cycling between the $[Fe_4S_4]^{1+}$ and $[Fe_4S_4]^{2+}$ redox states at a potential of −0.31 V versus the normal hydrogen electrode (NHE), that is lowered by about 0.1 V upon nucleotide binding. The Fe_4S_4 cluster is symmetrically bridged between the α-subunits of the iron-protein and is accessible to solvent molecules (H_2O). Vicinal amino acid residues provide NH-S hydrogen bonds from amide groups to the iron–sulfur center. The $[Fe_4S_4]^0$ state can be artificially generated as a stable center within the protein (−0.79 V vs. NHE), however it is not known if this state is biologically relevant.[25,26]

The iron–sulfur cluster of the iron-protein in its $[Fe_4S_4]^{1+}$ redox state exists in a mixture of spin states of similar energy in frozen solution ($S = 3/2$) and ($S = 1/2$). However, proton NMR analysis suggests that in standard conditions only one spin state is populated ($S = 1/2$). Proton NMR spectroscopy is useful for the analysis of paramagnetic iron–sulfur clusters (those with the $[Fe_4S_4]^{1+}$ and $[Fe_4S_4]^{3+}$ core). Indeed, significant low- or high-field hyperfine isotropic shifts for the resonance of the protons bound at the carbon β to an iron center greatly simplify the analysis of the chemical environment of each iron center of the protein even if the signal is usually broad. ^{57}Fe Mössbauer spectroscopy is a method of choice to assign the overall core oxidation state of a native or synthetic iron–sulfur cluster. There exists an empirical linear relationship between the ^{57}Fe Mössbauer spectroscopy isomer shift (i.s.) and the oxidation state (or mean oxidation state) of an iron center (or a cluster of iron centers) in a pseudo-tetrahedral sulfur environment.[27]

Synthetic structural models for the Fe_4S_4 clusters have been known for three decades now.[27] They are readily prepared by self-assembly from ferric or ferrous chloride, a source of reduced sulfur and thiolates, acting as ligands to the iron sites (Figure 2). Ligand-substitution reactions at the iron centers allow the tuning over a large window of their redox potential that is linearly linked to the electron donor/acceptor properties of the ligands, usually an alkyl or phenyl thiolate, or a halide (Figure 2). Crystal structures of model Fe_4S_4 clusters with thiolate ligands are available for all $[Fe_4S_4]^{1+/2+/3+}$ redox states, the $[Fe_4S_4]^0$ state being only transiently generated in solution.

It has been shown that the Fe_4S_4 cluster of the Fe-protein can be further reduced with nonbiological reductants from the $[Fe_4S_4]^{1+}$ to the $[Fe_4S_4]^0$ (all ferrous) redox state, which suggests that the Fe-protein could transfer two electrons per reduction cycle to the MoFe-protein.[25] Although there is no precedence for a functional $[Fe_4S_4]^0$ state in biology, this is an attractive proposal considering that (1) substrates of nitrogenase can be reduced by multiple of two electrons, (2) the dicubane structure of both the P-cluster and the FeMo-cofactor is perhaps tailored to accept two electrons at once and (3) the homodimeric structure of the Fe-protein that may bind two donor molecules at a time.[26,28] Moreover, the redox potential originally reported for the $[Fe_4S_4]^{1+/0}$ redox couple (−0.46 V vs. NHE) was well within physiological range and only 150 mV negative of that of the $[Fe_4S_4]^{2+/1+}$ redox couple. The biological relevance of the $[Fe_4S_4]^0$ oxidation state however is contentious. In synthetic models with thiolate ligands, the all-ferrous redox state ($[Fe_4S_4]^0$) is only detected transiently in some instances at the cyclic voltammetry timescale, and has only been generated, but not isolated, as a persistent species in solution in the case of $Fe_4S_4(PR_3)_4$ bearing less relevant phosphine ligands, known to stabilize reduced oxidation states of metal complexes. Such a narrow potential separation ($\Delta E = 0.15$ V) between the 2+/1+ and

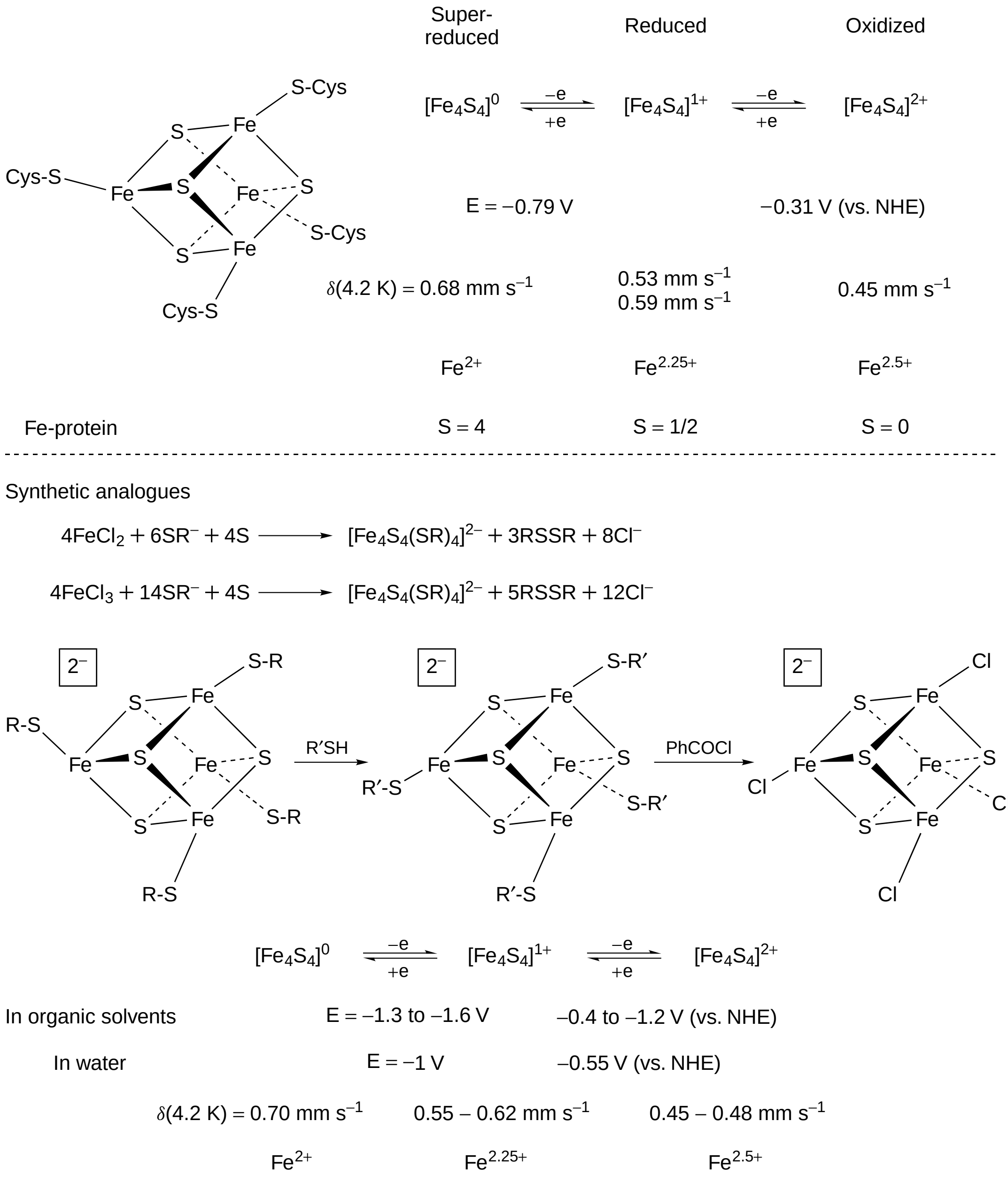
Super-reduced
Reduced
Oxidized
S-Cys
Cys-S
S-Cys
Cys-S
[Fe4S4]0
−e
+e
[Fe4S4]1+
−e
+e
[Fe4S4]2+
E = −0.79 V
−0.31 V (vs. NHE)
δ(4.2 K) = 0.68 mm s−1
0.53 mm s−1
0.59 mm s−1
0.45 mm s−1
Fe2+
Fe2.25+
Fe2.5+
Fe-protein
S = 4
S = 1/2
S = 0
Synthetic analogues
4FeCl2 + 6SR− + 4S → [Fe4S4(SR)4]2− + 3RSSR + 8Cl−
4FeCl3 + 14SR− + 4S → [Fe4S4(SR)4]2− + 5RSSR + 12Cl−
2−
S-R
R-S
S-R
R-S
R′SH
2−
S-R′
R′-S
S-R′
R′-S
PhCOCl
2−
Cl
Cl
Cl
Cl
[Fe4S4]0
−e
+e
[Fe4S4]1+
−e
+e
[Fe4S4]2+
In organic solvents
E = −1.3 to −1.6 V
−0.4 to −1.2 V (vs. NHE)
In water
E = −1 V
−0.55 V (vs. NHE)
δ(4.2 K) = 0.70 mm s−1
0.55 – 0.62 mm s−1
0.45 – 0.48 mm s−1
Fe2+
Fe2.25+
Fe2.5+

Figure 2 Electron transfer series in native and synthetic model clusters of the Fe_4S_4 center in the Fe-protein. Redox potential versus NHE, ^{57}Fe Mössbauer isomer shift (δ at 4.2 K vs. iron), mean iron oxidation state, and spin state are indicated for each redox state. Syntheses and ligand-substitution reactions are indicated for synthetic clusters

1+/0 redox couples of the iron-protein Fe_4S_4 cluster, was hard to reconcile with redox potentials of synthetic models. Indeed, a range of models with ligands differing by their charge, structure, and electron-withdrawing properties, has been studied electrochemically in dipolar aprotic organic solvent electrolytes (MeCN, DMF, DMSO) in order to assess the effect of the direct environment of the cluster core on its redox potentials.[29] The measured Δ E between the 2+/1+ and 1+/0 redox potentials of model clusters remains consistently in the range ca. 0.70 ± 0.05 V in organic solvent electrolytes, and ca. 0.40 ± 0.02 V in water. The reported absolute potential for the one-electron reduction of $[Fe_4S_4]^{1+}$ in nitrogenase was also too high compared to model system values generally reported to be in the range −1.50 to −1.85 V (saturated calomel electrode (SCE)) in organic solvent electrolytes and ca. −1.2 V (SCE) in water. Recently, the redox potential for the $[Fe_4S_4]^{1+/0}$ couple of the iron-protein has been measured at −0.79 V (NHE; i.e. ca. −1.03 V SCE), corresponding to a ΔE of 0.48 V between the two redox couples, more in line with experimental and theoretical redox potential and associated ΔE in model clusters.[29,30]

The polypeptide environment of the iron-protein Fe_4S_4 cluster appreciably stabilizes the $[Fe_4S_4]^0$ state compared to corresponding model clusters. This can be assigned to the network of hydrogen bonds between the protein residues and the cluster sulfide groups, and, to some extent, to the accessibility of water molecules to the cluster. However, the iron-protein iron–sulfur cluster in its $[Fe_4S_4]^{1+}$ state does not appear to be reducible in vivo by known physiological electron donors, unless a currently unknown mechanism, such as a protein conformation change, stabilizes the $[Fe_4S_4]^0$ state even more. Accurate synthetic models have helped to understand the structural, spectroscopic, and electronic properties of the Fe_4S_4 cluster, particularly that of the iron-protein of nitrogenase. Whether or not the $[Fe_4S_4]^0$ state is implied in the physiological electron transfer chain in nitrogenase remains to be proven. However, the sole fact that this latter state can be generated as a stable center within the protein encourages the quest for stable synthetic models in the all-ferrous state. These future models might bear a ligand scaffold mimicking the immediate stabilizing protein environment of the native cluster. In particular, it would be interesting to study the effect in terms of structure and associated electronic properties (electron transfer) of specific hydrogen bonds to the bridging sulfides as a function of the oxidation state of the cluster core. The modeling of a dielectric medium similar to the polarity and Lewis acidity experienced by iron–sulfur centers within proteins might be imposed by ligands sharing both covalent and noncovalent bonds to the cluster core. For recent progress towards the stabilization of the $[Fe_4S_4]^0$ state and the measurement of the hydrogen bonding effect on the redox potential of Fe_4S_4 clusters see references 73 and 74 respectively.

3 MODELS FOR THE Fe_8S_7 P-CLUSTER

Simple synthetic models for the active site of iron–sulfur proteins bearing centers of low nuclearity (one to four iron centers) have been relatively promptly synthesized and studied (*see* ***Iron–Sulfur Models of Protein Active Sites***).[27] Centers of higher nuclearity however, such as the P-cluster or the FeMo-cofactor of the nitrogenase MoFe-protein, present a greater synthetic challenge not only because of their higher metal–sulfur content and structural complexity but also because faithful structural models were obtained only recently by protein crystallography. Recent progress in the artificial synthesis of the P-cluster core of nitrogenase is now discussed.[31]

The Fe_8S_7 inorganic core of the P-cluster has been synthesized from tetramethylthiourea, 2,4,6-triisopropylbenzenethiol, elemental sulfur, and iron(II)bis(ditrimethylsilylamide) in toluene, in the respective 3/12/7/8 ratio (Figure 3a).[32] The differences between the model and the native P-cluster lie within the nature of the ligands to the iron–sulfur sites, the iron atoms' oxidation states, and the shorter bond distances in the model around the central hexacoordinated sulfur. While the iron atoms are terminated or bridged by cysteinate ligands in the P-cluster, different ligations are involved in the model. Indeed, the two opposite apical iron sites of the synthetic cluster have a terminal bis-amide ligation, thiourea completes the tetrahedral coordination of two opposite central iron atoms, and the two remaining pairs of opposite iron centers are linked by a bis-amide bridge, as shown in Figure 3. The tighter amide bridge of the model compared to the cysteinate bridge found in the MoFe-protein explains the shorter μ_6S-Fe bonds and shorter distance between opposite central iron atoms in the model. ^{57}Fe Mössbauer spectroscopy of the model compound distinguishes two iron sites in a 3/1 ratio: each quadrupole doublet's isomer shift and quadrupole splitting are consistent respectively with 6 Fe(II) and 2 Fe(III), the former assigned to the six central iron atoms and the latter assigned to the two opposite apical iron centers. The oxidation state of the model (6 ferrous/2 ferric) is therefore directly related to that of the P-cluster in the P^{OX} state. Nevertheless, the structure of the Fe_8S_7 core of the model resembles closely that of the P^N state, probably because the bridging amide prevents a more open structure similar to that of P^{OX}.

The model cluster has been reported to be very sensitive to oxygen and heat. This is consistent with the known instability of the P-cluster toward extraction from the MoFe-protein. Perhaps, for this reason no redox potentials were reported for the model. However, the current synthetic model (despite its different terminal and bridging ligands) provides the missing link for understanding the basic energetics of the electron transfer chain between the Fe_4S_4 cluster, the P-cluster, and FeMo-co. Indeed, the redox potentials of Fe_4S_4 clusters are well known both in vivo for the iron-protein Fe_4S_4 cluster and in accurate synthetic or theoretical models.[27,29,30] The electrochemistry of the extracted FeMo-cofactor has also been studied in depth.[33,34] The knowledge of the detailed electrochemical properties of each metallo-cluster would also help to assess the extent of redox potential control by the surrounding supramolecular protein interactions and possible associated structural changes.

While the former model has been obtained by self-assembly from its basic components, the detailed step-by-step synthesis of topological analogues of the P-cluster has been reported (Figure 3c).[31,35–38] Cubane-like clusters with the $[MoFe_3S_4]^{3+}$ or $[VFe_3S_4]^{2+}$ core oxidation state and chloro ligands at Fe (see Section 4 for their synthesis) react respectively with phosphine and $NaBPh_4$, or phosphine only, to yield the phosphine-substituted $[MoFe_3S_4]^{2+}$ and $[VFe_3S_4]^{2+}$ clusters. Reduction of these phosphine-substituted cubane-like clusters yield edge-bridged double cubanes with the $[M_2Fe_6S_8]^{2+}$ core (M = Mo or V). Upon exposure to 3 or 4 equivalents of $[Et_4N][HS]$, the edge-bridged double cubanes rearrange into topological analogues of the Fe_8S_7 P-cluster with the $[Mo_2Fe_6S_7]^{5+}$ or

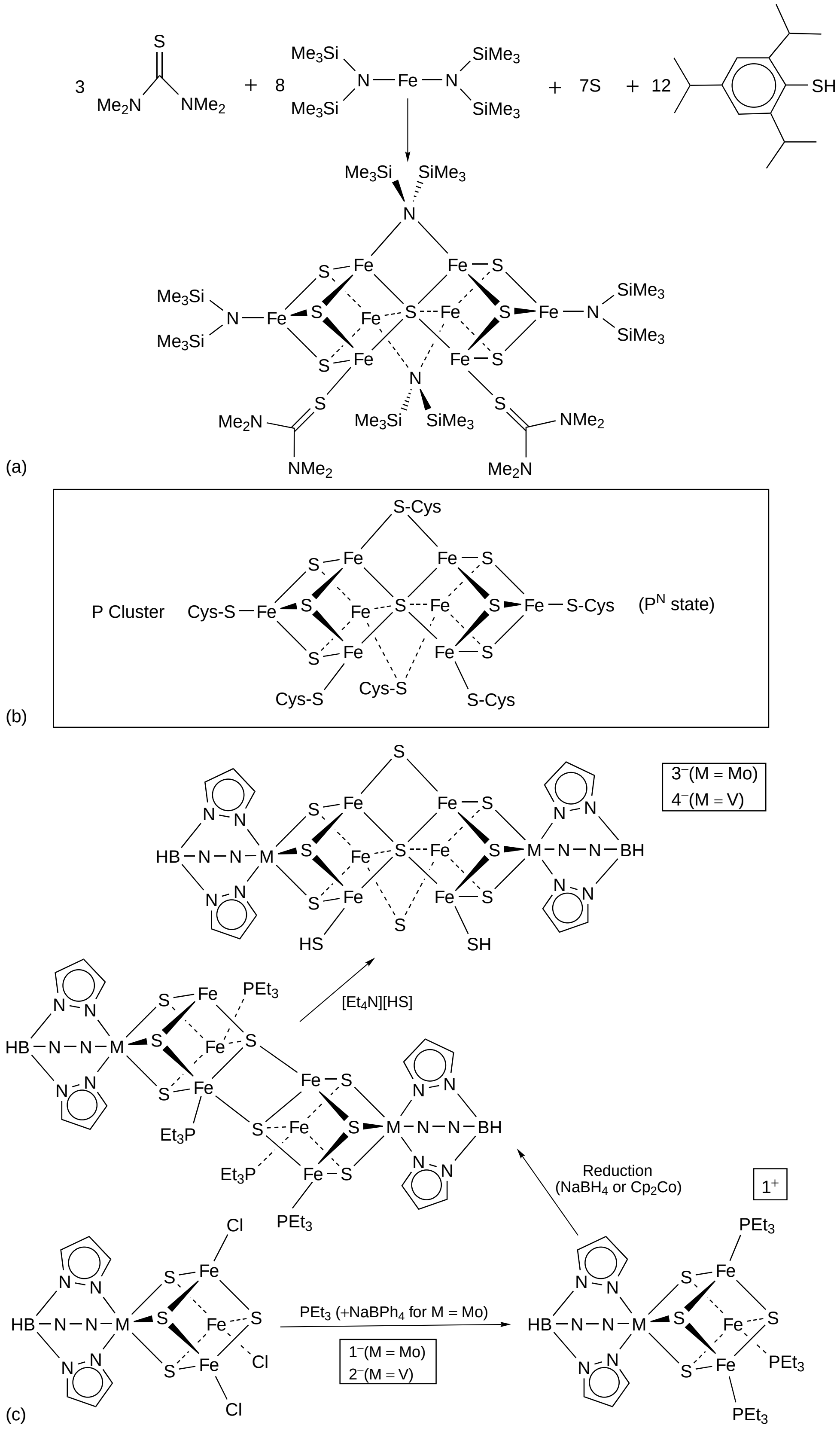
3
+ 8
+ 7S
+ 12
(a)
P Cluster
(P^N state)
(b)
[Et4N][HS]
3⁻(M = Mo)
4⁻(M = V)
Reduction
(NaBH4 or Cp2Co)
1+
PEt3 (+NaBPh4 for M = Mo)
1⁻(M = Mo)
2⁻(M = V)
(c)

Figure 3 (a) Synthesis of a P-Cluster analogue by self-assembly. (b) The structure of the P-Cluster in its native oxidation state (P^N state). (c) Stepwise synthesis of topological analogues of the P-cluster

$[V_2Fe_6S_7]^{4+}$ core respectively. Despite the heterogeneity of the metal content in the models, their inorganic cores are almost isostructural with the Fe_8S_7 P-cluster in the P^N state. In addition, the bridging sulfides or terminal hydrosulfide ligands are closer analogues to the natural cysteinate ligations found in the MoFe-protein. It is proposed that such a rearrangement (of an all-iron edge-bridged double cubane) could be of relevance to the biosynthesis of the P-cluster of nitrogenase. A similar biosynthesis might be envisaged as well for the FeMo-cofactor provided two different cubes are condensed ($MoFe_3S_4$ and Fe_4S_4). However, according to the recent crystallographic analysis of the MoFe-protein, the central light atom is unlikely to be a sulfur atom.

4 STRUCTURAL MODELS FOR THE $MoFe_7S_9$ FeMo-COFACTOR

As mentioned in the introduction, the crystallographic model of FeMo-co has been recently revised to include a light atom ‘Y’ at the center of the Fe_6 trigonal prism.[17] Among the possible candidates for the light atom, nitrogen fits most closely to the experimental X-ray diffraction data,[17] and is also the choice of theoreticians.[18–20] If ‘Y’ is a nitrogen atom, a question remains as to whether it is a permanent structural component of FeMo-co or originates from dinitrogen itself and is included into the cluster framework at some stage of catalysis. It has been argued that if the interstitial nitrogen had to be released as ammonia before a new N_2 molecule could bind to FeMo-co, then stoichiometric ammonia release should be detected after the transfer of three electrons. This is not consistent with available presteady state kinetic data.[39] In addition, spectroscopic investigations (by electron-nuclear double resonance and electron spin-echo envelope modulation) of both a wild type and a site-specifically altered nitrogenase MoFe-protein turning over $^{14}N_2$ and $^{15}N_2$, led to the conclusion that, if the central atom in FeMo-co is N, then it is not an exchangeable nitrogen.[40]

These observations point toward a permanent structural role of an interstitial nitrogen atom at the center of FeMo-co, although this is not yet proven.

The revised version of the crystallographic FeMo-co model implies an obvious reappraisal of the synthetic structural modeling toward iron–sulfur nitride chemistry, a field that does not currently exist as such.[41]

It would be far from fair however, to say that structural modeling has to start from scratch again. Of course, the quest for tricoordinate iron–sulfur metal centers is no longer relevant to the biological catalysis,[42] although some of the low-coordinate complexes may be promising as abiological catalysts for dinitrogen reduction.[43] Many of the impressive array of MoFeS clusters, first developed long before the publication of the first crystallographic FeMo-co model remain highly pertinent to structural modeling.[31,44–46] Lessons from the biosynthesis of FeMo-co should also in principle help to define a synthetic strategy toward a cofactor model cluster. This process is however very complicated and not fully understood.[47] It is known that the cluster is assembled outside the MoFe-protein before being inserted. The maturation of FeMo-co goes through the mobilization of iron and sulfur (encoded by the NifU and NifS genes) and rearrangement to a Fe–S cluster called NifB-co (encoded by the NifB genes) of unknown structure. Mo (or V) and a homocitrate are inserted (or substituted) in this cluster at a later stage of maturation. A speculative proposal on the structure of NifB-co and its biosynthesis by cluster rearrangement has been put forward and is shown in Figure 4 (*see also* ***Nitrogenase Catalysis & Assembly***).

The fragment of FeMo-co that has been most accurately modeled by synthetic clusters is its molybdenum cap. Indeed, cubane-like $MoFe_3S_4$ clusters reproduce very well the first and second coordination sphere of molybdenum in nitrogenase. $MoFe_3S_4$ clusters are usually synthesized from the double cubane $[Mo_2Fe_7S_8(SEt)_{12}]^{3-}$ (Figure 5) whose central iron bridge can be cleaved to yield independent $MoFe_3S_4$ monocubes.[31,44–46,48,49] As shown in Figure 6, the use of encumbered chelators (e.g. tetrachlorocatecholate or dimethylphosphino ethane) is required to isolate independent cubes.[48] If less bulky chelators like catecholate or π-acceptor ligands like carbon monoxide or isocyanides are used, the

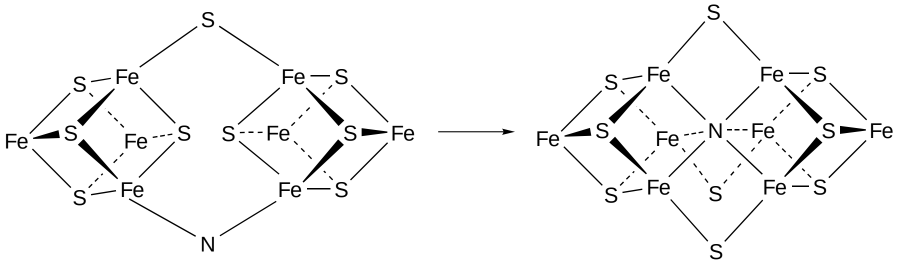

Figure 4 Proposed core rearrangement of the NifB-cofactor (within a protein) intermediate in the biosynthesis of the FeMo and FeV-cofactor. The heterometal and homocitrate ligands are inserted at a later stage of biosynthesis, in a different protein

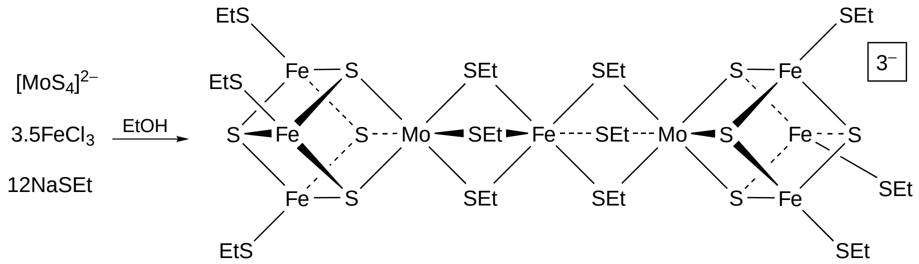

Figure 5 Self-assembly synthesis of the iron-bridged double cubane $[Mo_2Fe_7S_8(SEt)_{12}]^{3-}$

iron-bridged double cubane is heterolytically cleaved to yield a $MoFe_3S_4$ cube linked via Mo and thiolate bridges to an *exo*-Fe center.[49] When $[Mo_2Fe_7S_8(SEt)_{12}]^{3-}$ is left in solution (acetonitrile), it thermally evolves to the $[Mo_2Fe_6S_8(SEt)_9]^{3-}$ double cubane, demonstrating the inherent lability of the central iron bridge in $[Mo_2Fe_7S_8(SEt)_{12}]^{3-}$ and its great value as a synthon.

Alternatively, direct synthesis of $MoFe_3S_4$ clusters is also possible from $TpMoS(S_4)$, $FeCl_2$, and $NaSEt/PPh_3$ (Tp is hydro(trispyrazolyl)borate(1-)) (Figure 7).[50] In addition to being a simpler synthetic procedure, the trigonal symmetry imposed at Mo by the Tp ligand also avoids isomeric mixtures when bridged $MoFe_3S_4$ cubes are synthesized by the reaction of two single $MoFe_3S_4$ cubes (see Section 2 on P-cluster modeling and references 31, 35–38 and 50).

Similarly, VFe_3S_4 clusters are obtained by direct self-assembly from simple chemicals (ferrous chloride and tetrathiovanadate (Figure 7)).

Although the $MoFe_3S_4$ cubes have not been found to interact with dinitrogen, some partial functional chemistry relevant to nitrogenase has been developed. First, in some examples where the Mo site is coordinated by a labile solvent molecule, it has been shown that the solvent ligand could be displaced by different unsaturated nitrogenase substrates. Examples with cyanide, azide, hydrazine, phenylhydrazine, or piperidine bound at Mo have been characterized by X-ray crystallography and/or by NMR spectroscopy.[48] Furthermore, these $MoFe_3S_4$ with a labile solvent molecule at Mo catalyze the reduction of hydrazine to ammonia, of acetylene to ethylene and ethane, of *cis*-dimethyldiazene to methylamine, methane, and ammonia, or the disproportionation of hydrazine.[44,51–54] The involvement of the heterometal as the site of hydrazine reduction catalysis is strongly supported by: (1) inhibition experiments with inert ligands that bind to Mo like triethylphosphine, cyanide, or chloride; (2) much poorer catalysis results with related homometallic Fe_4S_4 clusters; and (3) structural characterization of cubanes with hydrazine or phenylhydrazine bound at Mo. Likewise, $[VFe_3S_4]^{2+}$ clusters catalyze the reduction of hydrazine to ammonia, and the rates of reduction correlate well with the availability of labile sites at the V atom.[44,51,55] Similar studies could also be envisioned with subsite-differentiated Fe_4S_4 clusters to probe the catalytic properties of a single Fe-site of an all-iron metal–sulfur cube in relation to the modeling of the all-iron nitrogenase.[56] Other $MoFe_3S_4$ clusters with polycarboxylate ligation at molybdenum (e.g. citrate) were found to be even better catalysts than those with a more readily accessible metal site by labile solvent decoordination. This implies that the polydentate ligand partially decoordinates during catalysis and may further play the role of a proton shuttle for the bound substrate. It is tempting to relate these experimental observations to the presence of the bidentate homocitrate ligand at molybdenum in nitrogenase. More generally, this raises the question of the possible direct involvement in the biological reduction of dinitrogen (or at least at a later stage of catalysis, e.g. at the diazene or hydrazine reduction level), of the heterometal in FeMo-co and FeV-co, and perhaps as well of the corresponding apical iron atom in FeFe-co.[44,51] The possibility of partial decoordination of homocitrate from Mo, preceding N_2 coordination at this metal, has been examined by molecular mechanics studies where the surrounding protein was taken into account.[57] It was found that *R*-homocitrate in its alkoxy monodentate form, is just of the right size to hydrogen bond via its longer (C_3) free carboxylate arm to a neighboring lysine residue and to the imidazole ring from the histidine residue bound to Mo. The corresponding shorter (C_2) arm of the closely related citrate ligand would not achieve this crucial interaction. Besides, (*R*)-homocitrate is known to be highly specific for biological nitrogen fixation, and mutated strains with a nitrogenase having citrate in place of (*R*)-homocitrate are much less efficient in reducing dinitrogen. The molecular mechanics study also showed that the medium (C_2) free carboxylate arm of (*R*)-homocitrate interacts with a glycine residue, which creates a hydrogen bond path between the P-cluster and FeMo-co.[34,57] These theoretical and graphical studies of the X-ray structure of the MoFe-protein came in support of experimental stopped-flow kinetic studies of substrates binding to different types of the extracted FeMo-cofactor. One type is extracted from a wild bacterial strain where FeMo-co bears (*R*)-homocitrate at Mo. The other type is extracted from a mutated bacterial strain ($NifV^-$) with citrate at Mo. The apical iron site of the extracted cofactors is coordinated by one solvent molecule (N-methyl formamide, NMF). This site binds a thiolate ligand (PhS^-) with kinetics depending on what other ligands bind to the cluster. When cyanide, azide, or proton bind

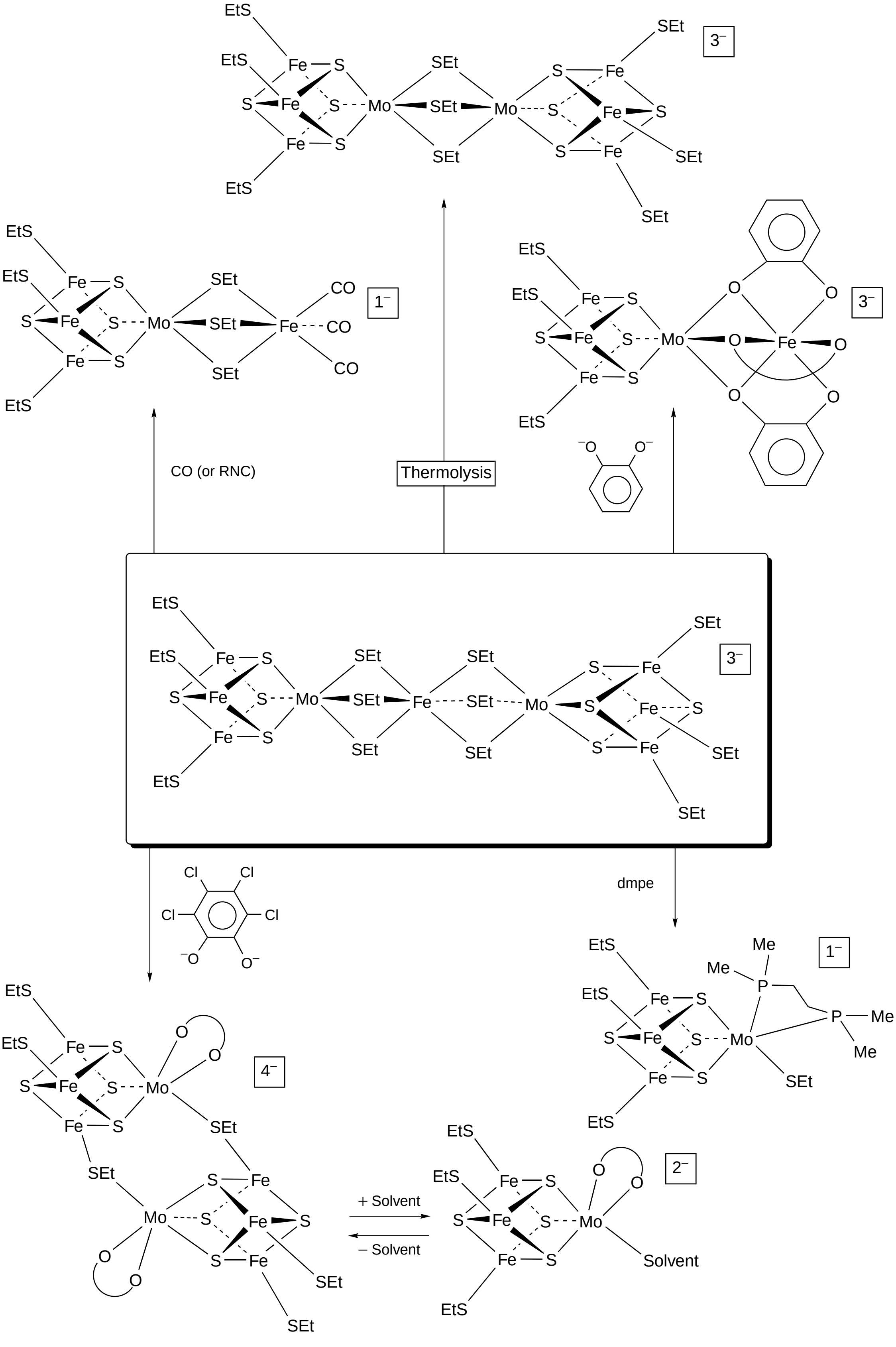
3−
1−
CO (or RNC)
Thermolysis
3−
1−
dmpe
4−
+ Solvent
− Solvent
2−
Solvent

Figure 6 Reactivity of $[Mo_2Fe_7S_8(SEt)_{12}]^{3-}$. Synthesis of $MoFe_3S_4$ monocubes from $[Mo_2Fe_7S_8(SEt)_{12}]^{3-}$(bottom)

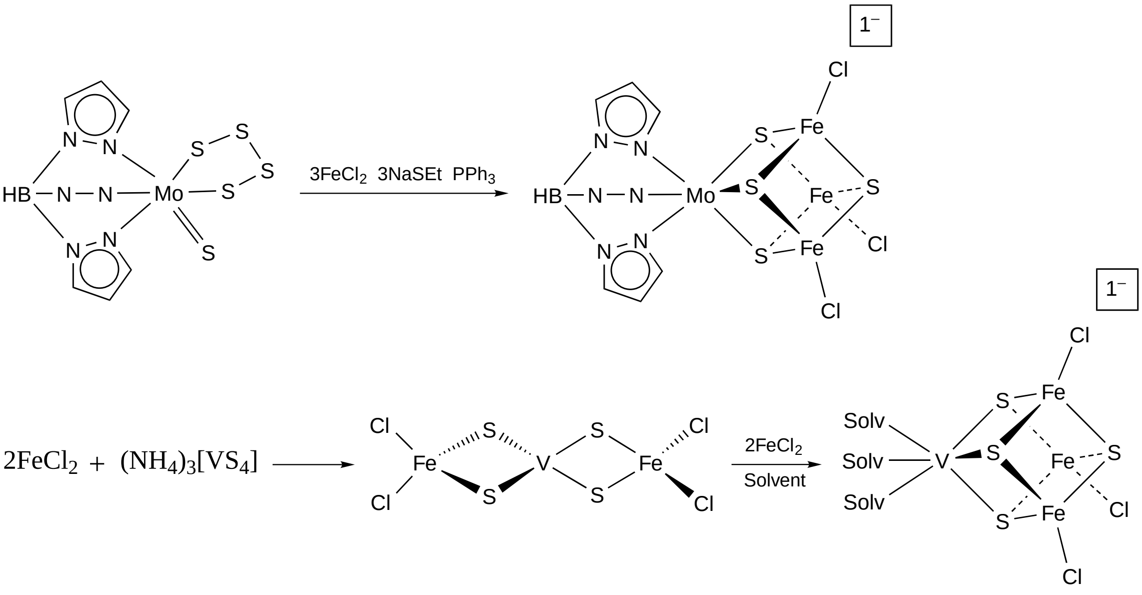

Figure 7 Direct synthesis of $MoFe_3S_4$ and VFe_3S_4 monocubes

to the cluster core, thiolate-binding kinetics to both types of cofactors are indistinguishable. However when imidazole binds to Mo, very different behaviors are observed. This was explained by specific H-bonding between (*R*)-homocitrate and imidazole. The binding of dinitrogen at the free Mo site has not been observed experimentally and remains a speculative proposal. It builds on earlier model studies with mononuclear molybdenum or tungsten phosphine dinitrogen complexes.[58] In some of these model complexes, a carboxylate ligand may act as a leaving group that opens a substrate binding site which coordinates N_2.[58]

When such molybdenum-dinitrogen complexes exist, the activation of N_2 is always stronger for the tungsten analogue. Then, if the cofactor heterometal is indeed the site of dinitrogen activation, a FeW-cofactor may be even more efficient with respect to biological nitrogen fixation. Testing this hypothesis requires the isolation of a tungsten nitrogenase. This is not an easy task because of the presence of a highly specific Mo storage protein (in *Azotobacter vilnelandii*) that contaminates with FeMo-co preparations grown on a tungstate medium, even when only traces of Mo are present. Besides, under Mo-deficient conditions, alternative nitrogenase systems may be expressed. Nevertheless, a tungsten (Mo-free) nitrogenase has recently been isolated under tungstate growth conditions from *Rhodobacter capsulatus*, that lacks a Mo-storage protein and whose mutated strain (anfA) is incapable of expressing the iron-only nitrogenase under molybdenum-deficient growth conditions.[59] The isolated tungsten-substituted nitrogenase was found to be only marginally active in reducing acetylene, and dinitrogen reduction was not observed. However, appreciable dihydrogen evolution was obtained, corresponding to a rate of ca. 25% of that observed for the native MoFe-protein. Redox titration of both proteins showed the tungsten-substituted protein midpoint potential to be at least 150 mV more negative (<-200 mV NHE) compared to that of the MoFe-protein (-50 mV NHE). Hence, the FeW-co appears to be at least partially reducible to a state where hydrogen evolution occurs (but to a lesser extent than for FeMo-co), whereas the more reduced state where substrate activation occurs is not accessed. Considering thermodynamics alone, it is interesting to note that a functional iron-protein with a $[Fe_4S_4]^0$ cluster would be a sufficiently strong reductant (ca -0.8 V NHE) to reduce a tungsten−iron protein with $E_{1/2}$ of approximately -0.3 V NHE. Decreased hydrogen evolution would be advantageous for nitrogen fixation as discussed next, however the apparent impossibility of physiologically reducing the WFe-protein to a state where N_2 would bind precludes any nitrogen fixation. This can be rationalized by two features of molybdenum and tungsten chemistry: (1) tungsten complexes or clusters are more difficult to reduce than their molybdenum analogues; (2) ligands are less labile at a tungsten center. Hence, even if FeW-co was reducible to the corresponding substrate binding redox state of FeMo-co, the partial decoordination of homocitrate from W might not occur because the breaking of a W–O bond requires more energy than for the corresponding Mo–O bond in FeMo-co.

Whether or not N_2 binds at Mo, a possible role for this metal at the active site of the enzyme has been recently pointed out and is now discussed.[60] In the absence of N_2, all conventional nitrogenases reduce protons to dihydrogen. In the presence of N_2, only a fraction of electrons are used to reduce dinitrogen while the other fraction is still involved in dihydrogen formation, and is therefore wasted. The limiting stoichiometries for all three types of nitrogenase are as follows (equivalent of dihydrogen formed per equivalent of reduced dinitrogen): Mo(1), V(3), and Fe(7.5). Hence, notwithstanding differences in the reduction mechanism and different protein structures, the presence of a heterometal in the iron–sulfur cofactor appreciably improves the efficiency of biological dinitrogen reduction, especially when this metal is molybdenum. The effect of Mo within a Fe–S cluster has been addressed experimentally by comparing the kinetics of proton binding to a Fe_4S_4 cluster, $[Fe_4S_4Cl_4]^{2-}$, and a thiolate-bridged double $MoFe_3S_4$ cluster: $[\{MoFe_3S_4Cl_3\}(\mu\text{-}SR_3)]^{3-}$ (R = Et or Ph).[60] The chloride ligands of these clusters are labile and can be substituted by nucleophiles such as thiolates. Protonation of Fe–S clusters, probably at the basic sulfide centers, is a known common reaction of such inorganic species. In the presence of a weak acid and a strong nucleophile such as thiophenolate, protonation of the cluster following thiolate binding is the rate-limiting step of the reaction with a similar rate constant for both types of MFe_3S_4 clusters (M=Fe or Mo). The rate of proton transfer to the cluster prior to nucleophile binding can be determined by measuring the kinetics of the reaction between the MFe_3S_4 cluster and a poor nucleophile such as bromide, in the presence of a weak acid. Results show that proton transfer to any Fe–S cluster is slower in the absence of a bound nucleophile, and is about two orders of magnitude slower for $MoFe_3S_4$ compared to Fe_4S_4. A simple electron-withdrawing effect of the heterometal seems excluded as the pKa of protonated clusters falls into the narrow range of 18.9–17.9 and is little affected by the structure of the cluster. Rather, energetically more demanding bond length changes in Mo–Fe–S cluster are proposed as a possible explanation. Very interesting implications for biological dinitrogen fixation are then put forward. Because any dinitrogen binding site needs to be electron rich to ensure the ligand–metal σ-bonding and metal–ligand π-back bonding interactions, such sites may be easily protonated, which would then either decrease their affinity for dinitrogen or labilize an already bound N_2 molecule. This could be avoided if electron transfer is also coupled to protonation, however this could also favor dihydrogen formation. Since proton transfer to Mo–Fe–S clusters is appreciably slower than to Fe–S clusters, the presence of molybdenum in the FeMo-cofactor could favor nitrogen fixation by enhancing the affinity of the binding site for dinitrogen and by slowing down the protonation of the cluster, which would also diminish or suppress unwanted dihydrogen evolution. Besides, model studies have shown that Mo–Fe–S clusters have a higher affinity than Fe–S cluster for binding species such as thiolates, halides, CO, or N_2O. Irrespective of the precise N_2-binding site at FeMo-co, molybdenum would make the enzyme a good nitrogenase and a poor hydrogenase, in agreement with the limiting stoichiometries reported for the Mo- and the all Fe-nitrogenase. It would be interesting to know if similar studies with VFe_3S_4 clusters would yield a protonation rate constant in between those observed with $MoFe_3S_4$ and Fe_4S_4 clusters, which would be consistent with the known relative N_2-reduction efficiency of all three types of conventional nitrogenases (Mo > V > Fe).

Current available cofactor models are hence only partially relevant in terms of structure: only the molybdenum/heterometal end of the cluster has been accurately modeled. In terms of functional relevance, no interactions with N_2 have been obtained despite catalytic activation of reduced diazo species (e.g. hydrazine) or alternative substrates (e.g. acetylene). Considering the available biochemical data as well, one can only speculate on the precise site of N_2 binding and reduction at FeMo-co, and on the exact role of the heterometal in this reaction. Electron-rich mononuclear molybdenum and tungsten complexes have been developed that bind dinitrogen and sometimes also support ammonia synthesis.[34,58,61,62] They are however structurally very different from FeMo-co for they are mononuclear and possess abiological ligands such as phosphine, permethylated cyclopentadienyl, or triamido amine. When more relevant sulfur ligands and/or metal–metal interactions were introduced, the key interaction with dinitrogen was lost in most cases although in some instances the activation of reduced diazo species was retained.[34,62–66] Theoretical assessments of possible N_2 binding sites at FeMo-co can assist this debate, with the limitation that it is difficult to take into account theoretically the full structure of the active site (cluster, protein, and solvent molecules) and the afferent mechanistic complexity and subtleties of nitrogenase.[18–20,34,62,67] Irrespective of the N_2 binding site considered, a general trend of theoretical calculations seems to be that FeMo-co is a rather weak N_2 activator compared to well understood and efficient mononuclear systems. One must also keep in mind that the extracted FeMo-co itself does not interact with dinitrogen, which underlines the important role of the protein for N_2 reduction by this center.

Given the current absence of interaction of any synthetic metal–sulfur cluster with dinitrogen, the binding of other and more reactive substrates or inhibitors of nitrogenase, like acetylene or carbon monoxide, are of interest. We have already pointed out that the heterometal site of $MoFe_3S_4$ or VFe_3S_4 cubes can support the reduction of acetylene. However, biochemical studies have established that acetylene is reduced on a specific Fe_4 face of the central Fe_6 trigonal prism of FeMo-co.[68,75] Besides, it is not known if acetylene and dinitrogen bind to the same site at FeMo-co, and these molecules probably bind with different FeMo-cofactor redox states. In any case, the current lack of structural models of the light atom–centered Fe_6 trigonal prism precludes functional modeling of this site for the moment. Recent iron–sulfur imido chemistry might be of relevance to the activation of nitrogenous substrates by the central iron–sulfur core, but the development of iron–sulfur nitride chemistry is awaited.[31,41,69]

The future synthetic models of FeMo-co will have to closely resemble the now more accurate $MoFe_7S_9Y$ crystallographic model (with ‘Y’ probably being N). The progress made in the synthesis of P-cluster analogues, discussed in the previous section, is encouraging since the P-cluster has a similar size and metal–sulfur content as FeMo-co, although a bit less complex. The next challenge will be the development of some functional chemistry of relevance to nitrogenase at these future accurate FeMo-co models. Interaction of dinitrogen with these centers, a property that few molecular cluster have shown so far,[3,70–72] would be a breakthrough. It is evident that the task is not obvious taking into account: (1) the original and complex FeMo-co structure; (2) the rather weak affinity of FeMo-co for N_2 compared to model systems; (3) the complex mechanism of N_2 biological reduction coupled to the evolution of H_2; and (4) the strong dependence of FeMo-co catalytic activity on the surrounding protein and specific amino acid residues, and on the (R)-homocitrate ligand. A synthetic functional peptide-FeMo-co center possessing the minimum structural and supramolecular requirements to activate N_2 could be a midterm goal.

5 CONCLUSIONS

Considerable progress in the synthesis of model clusters of nitrogenase has been made in recent years thanks to the continuous development in the laboratory of a rational and diverse iron–sulfur chemistry and to the increased knowledge of the natural systems themselves. The fact that biophysical and biochemical techniques now yield more detailed mechanistic and structural data on the enzymes may question the need for synthetic models. However, the advancement of the understanding of the mechanistic and structural complexity of the nitrogenase enzymes requires a multidisciplinary approach. Interactions and scientific debates between geneticists, biophysicists, biochemists, inorganic chemists, and theoretical chemists benefit all disciplines and scientists, and allow the knowledge of nitrogenases to advance at a faster pace. While the understanding of the enzyme advances, nitrogenase seems to challenge synthetic chemists regularly and the standards are set high. As discussed in this article, the scientific community has always taken up the challenge, sometimes brilliantly. For example, the $[Fe_4S_4]^{2+/1+}$ center of the iron-protein was thought to be well understood and modeled until this cluster was found to be stable in the $[Fe_4S_4]^0$ state within the protein. $[Fe_4S_4]^0$ synthetic models with thiolate ligands are all very unstable. Whether or not the $[Fe_4S_4]^0$ state is biologically relevant, which has to be clarified, the natural system gives the impetus to synthesize stable low-valent iron–sulfur centers and control their redox potentials by covalent and noncovalent binding. The two known structures of the P-cluster of nitrogenase show the importance of redox-linked structural flexibility of iron–sulfur clusters and the importance of the protein to stabilize them. The structure of the P-cluster in the native state can now be obtained in the laboratory by self-assembly, or topologically, in a stepwise and well-understood fashion. Taking into account its astonishing structure and function alone, the FeMo-cofactor represents evidently the greatest challenge to modeling chemistry. This cluster is now known to be centered on a light atom that is probably a nitrogen atom, waiting to be identified with certainty. FeMo-co reduces dinitrogen with the help of the protein and its heterogeneous (R)-homocitrate ligand with an unknown intimate mechanism that also produces dihydrogen. Catalytic properties are retained when molybdenum is substituted with vanadium or iron in alternative nitrogenases. Considering these facts and, despite their inherent weaknesses, the prolific synthetic structural and functional models of the metal–sulfur centers of nitrogenases developed over the years, one could sum up the work in nitrogenase model clusters by ‘a lot done, more to do.’

6 RELATED ARTICLES

Iron: Models of Proteins with Dinuclear Active Sites; Iron: Organometallic Chemistry; Iron–Sulfur Models of Protein Active Sites; Iron–Sulfur Proteins; Molybdenum: Inorganic & Coordination Chemistry; Molybdenum: Organometallic Chemistry; Nitrogenase Catalysis & Assembly; S-donor Ligands; Vanadium in Biology; Vanadium: Inorganic & Coordination Chemistry; Vanadium: Organometallic Chemistry.

7 REFERENCES

1. T. A. Bazhenova and A. E. Shilov, *Coord. Chem. Rev.*, 1995, **144**, 69.
2. R. Schlögl, *Angew. Chem., Int. Ed. Engl.*, 2003, **28**, 2004.
3. M. D. Fryzuk and S. A. Johnson, *Coord. Chem. Rev.*, 2000, **200–202**, 379.
4. B. K. Burgess and D. J. Lowe, *Chem. Rev.*, 1996, **96**, 2983.
5. B. E. Smith, *Adv. Inorg. Chem.*, 1999, **47**, 159.
6. J. Christiansen, D. R. Dean, and L. C. Seefeldt, *Annu. Rev. Plant Physiol. Plant Mol. Biol.*, 2001, **52**, 269.
7. R. Y. Igarashi and L. C. Seefeldt, *Crit. Rev. Biochem. Mol. Biol.*, 2003, **38**, 351.
8. R. R. Eady, *Chem. Rev.*, 1996, **96**, 3013.
9. R. R. Eady, *Coord. Chem. Rev.*, 2003, **237**, 23.
10. D. Rehder, *Inorg. Chem. Commun.*, 2003, **6**, 604.
11. D. C. Crans, J. J. Smee, E. Gaidamauskas, and L. Yang, *Chem. Rev.*, 2004, **104**, 849.
12. E. Krahn, B. J. R. Weiss, M. Kröckel, J. Groppe, G. Henkel, S. P. Cramer, A. X. Trautwein, K. Schneider, and A. Müller, *J. Biol. Inorg. Chem.*, 2002, **7**, 37.

13. S. Siemann, K. Schneider, M. Dröttboom, and A. Müller, *Eur. J. Biochem.*, 2002, **269**, 1650.
14. M. Ribbe, D. Gadkari, and O. Meyer, *J. Biol. Chem.*, 1997, **272**, 26627.
15. J. B. Howard and D. C. Rees, *Chem. Rev.*, 1996, **96**, 2965.
16. S. M. Mayer, D. M. Lawson, C. A. Gormal, S. M. Roe, and B. E. Smith, *J. Mol. Biol.*, 1999, **292**, 871.
17. O. Einsle, F. A. Tezcan, S. L. A. Andrade, B. Schmid, M. Yoshida, J. B. Howard, and D. C. Rees, *Science*, 2002, **297**, 1696.
18. I. Dance, *Chem. Commun.*, 2003, 324.
19. B. Hinnemann and J. K. Norskov, *J. Am. Chem. Soc.*, 2003, **125**, 1466.
20. T. Lovell, T. Liu, D. A. Case, and L. Noodleman, *J. Am. Chem. Soc.*, 2003, **125**, 8377.
21. R. H. Holm, P. Kennepohl, and E. I. Solomon, *Chem. Rev.*, 1996, **96**, 2239.
22. H. Beinert, R. H. Holm, and E. Münck, *Science*, 1997, **277**, 653.
23. D. C. Rees, *Annu. Rev. Biochem.*, 2002, **71**, 221.
24. C. L. Drennan and J. W. Peters, *Curr. Opin. Struct. Biol.*, 2003, **13**, 220.
25. G. D. Watt and K. R. N. Reddy, *J. Inorg. Biochem.*, 1994, **53**, 281.
26. M. Guao, F. Sulc, M. W. Ribbe, P. J. Farmer, and B. K. Burgess, *J. Am. Chem. Soc.*, 2002, **124**, 12100.
27. P. Venkateswara Rao and R. H. Holm, *Chem. Rev.*, 2004, **104**, 527.
28. D. C. Rees and J. B. Howard, *Curr. Opin. Chem. Biol.*, 2000, **4**, 559.
29. C. Zhou, J. W. Raebiger, B. M. Segal, and R. H. Holm, *Inorg. Chim. Acta*, 2000, **300–302**, 892.
30. R. A. Torres, T. Lovell, L. Noodleman, and D. A. Case, *J. Am. Chem. Soc.*, 2003, **125**, 1923.
31. S. C. Lee and R. H. Holm, *Chem. Rev.*, 2004, **104**, 1135.
32. Y. Ohki, Y. Sunada, M. Honda, M. Katada, and K. Tatsumi, *J. Am. Chem. Soc.*, 2003, **125**, 4052.
33. C. J. Pickett, K. A. Vincent, S. K. Ibrahim, C. A. Gormal, B. E. Smith, and S. P. Best, *Chem. Eur. J.*, 2003, **9**, 76.
34. F. Barrière, M. C. Durrant, and C. J. Pickett, Chemical Models, Theoretical Calculations, and the Reactivity of the Isolated Iron-Molybdenum Cofactor, in ‘Catalysts for Nitrogen Fixation, Nitrogenases, Relevant Chemical Models and Commercial Processes’, Nitrogen Fixation: Origins, Applications, and Research Progress eds. B. E. Smith, R. L. Richards, and W. E. Newton, Kluwer Academic Publishers, The Netherlands, 2004, Vol. 1, Chap. 7, p. 161.
35. Y. Zhang, J.-L. Zuo, H.-C. Zhou, and R. H. Holm, *J. Am. Chem. Soc.*, 2002, **124**, 14292.
36. Y. Zhang and R. H. Holm, *J. Am. Chem. Soc.*, 2003, **125**, 3910.
37. J.-L. Zuo, H.-C. Zhou, and R. H. Holm, *Inorg. Chem.*, 2003, **42**, 4624.
38. Y. Zhang and R. H. Holm, *Inorg. Chem.*, 2004, **43**, 674.
39. B. E. Smith, *Science*, 2002, **297**, 1654.
40. H.-I. Lee, P. M. C. Benton, M. Laryukhin, R. Y. Igarashi, D. R. Dean, L. C. Seefeldt, and B. M. Hoffman, *J. Am. Chem. Soc.*, 2003, **125**, 5604.
41. S. C. Lee and R. H. Holm, *Proc. Natl. Acad. Sci. U.S.A.*, 2003, **100**, 3595.
42. Y. Sanakis, P. P. Power, A. Stubna, and E. Münck, *Inorg. Chem.*, 2002, **41**, 2690.
43. T. A. Betley and J. C. Peters, *J. Am. Chem. Soc.*, 2003, **125**, 10782.
44. D. Coucouvanis and S. M. Malinak, *Prog. Inorg. Chem.*, 2001, **49**, 599.
45. R. H. Holm, *Adv. Inorg. Chem.*, 1992, **38**, 1.
46. R. H. Holm and E. D. Simhon, Molybdenum-tungsten-iron-sulfur Chemistry: Current Status and Relevance to the Native Cluster of Nitrogenase, in ‘Molybdenum Enzymes’, ed. T. G. Spiro, Wiley, New York, 1985, p. 1.
47. P. C. Dos Santos, D. R. Dean, Y. Hu, and M. W. Ribbe, *Chem. Rev.*, 2004, **104**, 1159.
48. R. E. Palermo, R. Singh, J. K. Bashkin, and R. H. Holm, *J. Am. Chem. Soc.*, 1984, **106**, 2600.
49. F. Barrière, D. J. Evans, D. L. Hughes, S. K. Ibrahim, J. Talarmin, and C. J. Pickett, *J. Chem. Soc., Dalton Trans.*, 1999, 957.
50. D. V. Fomitchev, C. C. McLauchlan, and R. H. Holm, *Inorg. Chem.*, 2002, **41**, 958.
51. D. Coucouvanis, *J. Biol. Inorg. Chem.*, 1996, **1**, 594.
52. K. D. Demadis, S. M. Malinak, and D. Coucouvanis, *Inorg. Chem.*, 1996, **35**, 4038.
53. D. Coucouvanis, K. D. Demadis, S. M. Malinak, P. E. Mosier, M. A. Tyson, and L. J. Laughlin, *J. Mol. Catal. A: Chem.*, 1996, **107**, 123.
54. S. M. Malinak, A. M. Simeonov, P. E. Mosier, C. E. McKenna, and D. Coucouvanis, *J. Am. Chem. Soc.*, 1997, **119**, 1662.
55. S. M. Malinak, K. D. Demadis, and D. Coucouvanis, *J. Am. Chem. Soc.*, 1995, **117**, 3126.
56. R. H. Holm, S. Ciurli, and J. A. Weigel, *Prog. Inorg. Chem.*, 1990, **49**, 599.
57. K. L. C. Grönberg, C. A. Gormal, M. C. Durrant, B. E. Smith, and R. A. Henderson, *J. Am. Chem. Soc.*, 1998, **120**, 10613.
58. C. J. Pickett, *J. Biol. Inorg. Chem.*, 1996, **1**, 601.
59. S. Siemann, K. Schneider, M. Oley, and A. Müller, *Biochemistry*, 2003, **42**, 3846.
60. J. Bell, A. J. Dunford, E. Hollis, and R. A. Henderson, *Angew. Chem., Int. Ed. Engl.*, 2003, **42**, 1149.
61. R. R. Schrock, *Chem. Commun.*, 2003, 2389.
62. F. Barrière, *Coord. Chem. Rev.*, 2003, **236**, 71.
63. D. Sellmann, B. Hautsch, A. Rösler, and F. W. Heinemann, *Angew. Chem., Int. Ed. Engl.*, 2001, **40**, 1505.

64. D. Sellmann, A. Fürsattel, and J. Sutter, *Coord. Chem. Rev.*, 2000, **200–202**, 545.
65. D. Sellmann, A. Hille, F. W. Heinemann, M. Moll, A. Rösler, J. Sutter, G. Brehm, M. Reiher, B. A. Hess, and S. Schneider, *Inorg. Chim. Acta*, 2003, **348**, 194.
66. N. Le Grand, K. W. Muir, F. Y. Pétillon, C. J. Pickett, P. Schollhammer, and J. Talarmin, *Chem. Eur. J.*, 2002, **8**, 3115.
67. L. Noodleman, T. Lovell, W.-G. Han, J. Li, and F. Himo, *Chem. Rev.*, 2004, **104**, 459.
68. D. R. Dean, I. G. Dance, and L. C. Seefeldt, *Biochemistry*, 2004, **43**, 1401.
69. J. S. Duncan, T. M. Nazif, A. K. Verma, and S. C. Lee, *Inorg. Chem.*, 2003, **42,**,1211.
70. B. A. MacKay and M. D. Fryzuk, *Chem. Rev.*, 2004, **104**, 385.
71. M. D. Fryzuk, *Nature*, 2004, **427**, 498.
72. J. A. Pool, E. Lobkovsky, and P. J. Chirik, *Nature*, 2004, **427**, 527.
73. T. A. Scott and H.-C. Zhou, *Angew. Chem., Int. Ed*, 2004, **43**, 5628.
74. X. Yang, S. Niu, T. Ichiye, and L.-S. Wang, *J. Am. Chem. Soc.*, 2004, **126**, 15790.
75. B. M. Barney, R. Y. Igarashi, P. C. Dos Santos, D. R. Dean, and L. C. Seefeldt, *J. Biol. Chem.*, 2004, **279**, 53621.

Nitrogenase Catalysis & Assembly

Yilin Hu,[1] Benedikt Schmid[2] & Markus W. Ribbe[1]
[1] *University of California-Irvine, Irvine, CA, USA*
[2] *University of Erlangen-Nürnberg, Erlangen, Germany*

Based in part on the article Nitrogenases & the Iron–Molybdenum Cofactor by Paul W. Ludden which appeared in the Encyclopedia of Inorganic Chemistry, First Edition.

1 Introduction 1
2 Molybdenum Nitrogenase 1
3 Nitrogenase Catalysis 6
4 Nitrogenase Assembly 8
5 Alternative Nitrogenases 12
6 Summary 14
7 Related Articles 14
8 References 14

Abbreviations

MgATP = the magnesium complex of adenosine 5′-triphosphate; MgADP = the magnesium complex of adenosine 5′-diphosphate; P_i = inorganic phosphate; MoFe protein = the molybdenum–iron protein of molybdenum nitrogenase; Fe protein = the iron protein of molybdenum nitrogenase; $MgADP{\cdot}AlF_4^-$ = the magnesium complex of adenosine 5′-diphosphate and aluminum tetrafluoride; Cys = cysteine; FeMo cofactor = the iron–molybdenum cofactor of nitrogenase; P cluster = the [8Fe–7S] cluster of nitrogenase; P^N = the dithionite-reduced state of P cluster; P^{OX} = the two-electron oxidized state of P cluster; EPR = electron paramagnetic resonance; NMF = *N*-methylformamide; C_2H_2 = acetylene; CS_2 = carbon disulfide; CO = carbon monoxide; Val = valine; Arg = arginine; *nif* = a molybdenum nitrogenase gene; VFe protein = the vanadium–iron protein of vanadium nitrogenase; *vnf* = a vanadium nitrogenase gene; MCD = magnetic circular dichroism; EXAFS = extended X-ray absorption fine structure spectroscopy; FeVa cofactor = the iron–vanadium cofactor of nitrogenase; FeFe protein = the iron–iron protein of iron-only nitrogenase; *anf* = an iron-only nitrogenase gene; FeFe cofactor = the iron–iron cofactor of nitrogenase; CO_2 = carbon dioxide; $O_2^{\bullet-}$ = superoxide radical; H_2O_2 = hydrogen peroxide.

1 INTRODUCTION

Nitrogenases represent a class of complex metalloenzymes that catalyze the process of biological N_2 fixation, during which dinitrogen is reduced to ammonia in a nucleotide-dependent process.[1–12] The ammonia produced is subsequently used for cell growth or maintenance. The overall reaction catalyzed by nitrogenases is usually depicted as follows:[8,11,12]

$$N_2 + 8H^+ + 16MgATP + 8e^- \longrightarrow 2NH_3 + H_2 + 16MgADP + 16P_i \quad (1)$$

Nitrogenases are unique to bacteria, and animals or plants that fix N_2 must do so in association with bacteria.[13] Interest in nitrogenases arises from the importance of these enzymes to agriculture. Biological N_2 fixation provides roughly 90 million tons of N for agricultural soil each year and represents a major contributor of new N to agriculture and the food supply.[8,10] Meanwhile, attention has been drawn to the interesting chemistry involved in breaking the triple bond of the dinitrogen molecule under biological N_2 fixation conditions. How nitrogenases can carry out such an energy-demanding process under mild temperatures and pressures remains yet another driving force for research on these fascinating enzymes.

Four classes of nitrogenases have been described. They are the molybdenum nitrogenase (Sections 2–4), the vanadium nitrogenase (Section 5.1), the iron-only nitrogenase (Section 5.2), and the nitrogenase from *Streptomyces thermoautotrophicus* (Section 5.3). The major distinctive feature of the first three classes of nitrogenases, which are otherwise very similar, is the heterometal atom in the active site of the metal cluster (molybdenum, vanadium, or iron).[5,8,10] The fourth nitrogenase, however, is superoxide-dependent and apparently different from the other nitrogenase classes.[14,15]

Most of the current knowledge concerning the mechanism of nitrogenases is based upon extensive studies of the molybdenum nitrogenase; hence this enzyme will be the focus of discussion in this article. The general properties of the molybdenum nitrogenase are described in Section 2, and the catalytic and assembly mechanism of this enzyme system will be dealt with in Sections 3 and 4. The alternative nitrogenase systems will also be briefly discussed in Section 5.

2 MOLYBDENUM NITROGENASE

The molybdenum nitrogenase, undoubtedly the best-characterized form of nitrogenase, has been isolated from a number of different microorganisms such as *Azotobacter vinelandii*, *Klebsiella pneumoniae*, and *Clostridium pasteurianum*.[9,10,16] Figure 1(a) is a schematic representation of the enzyme, which comprises two separately purifiable, oxygen-sensitive, metallosulfur proteins: the molybdenum-iron (MoFe) protein and the iron (Fe) protein, both of which are essential for enzymatic activity.[1–12] Figure 1(b) illustrates the substrate-reduction reaction of the molybdenum nitrogenase, a process in which the Fe protein forms a complex with the MoFe protein and acts as an obligate, MgATP-activated, electron donor for the MoFe protein, where the substrate is reduced (see also Section 3).[2,3,7,9]

2.1 The Fe Protein

The Fe protein, a member of the family of nucleotide-utilizing proteins (e.g. myosin, ras p21, recA),[4,9] is a homodimer of $M_r \sim 60\,\mathrm{kDa}$. The two identical subunits are encoded by the *nifH* gene, and there is a high degree of homology among the Fe proteins from a wide range of bacteria.[10] Each subunit of the Fe protein has a binding site for MgATP, and the two subunits are bridged by a [4Fe−4S] cluster (*see* ***Iron–Sulfur Proteins***).[1–4,6–9,17–20]

2.1.1 Protein Structure

The X-ray crystal structures of several conformations of the Fe protein, either alone or in complex with the MoFe protein, have been solved.[21–27] Figure 2 shows the MgADP-bound conformational state of the Fe protein of *A. vinelandii*,[10,26] where each subunit folds as a single α/β-type domain and the subunits together symmetrically ligate the surface-exposed [4Fe−4S] cluster through two cysteines from each subunit. Two MgADP molecules are

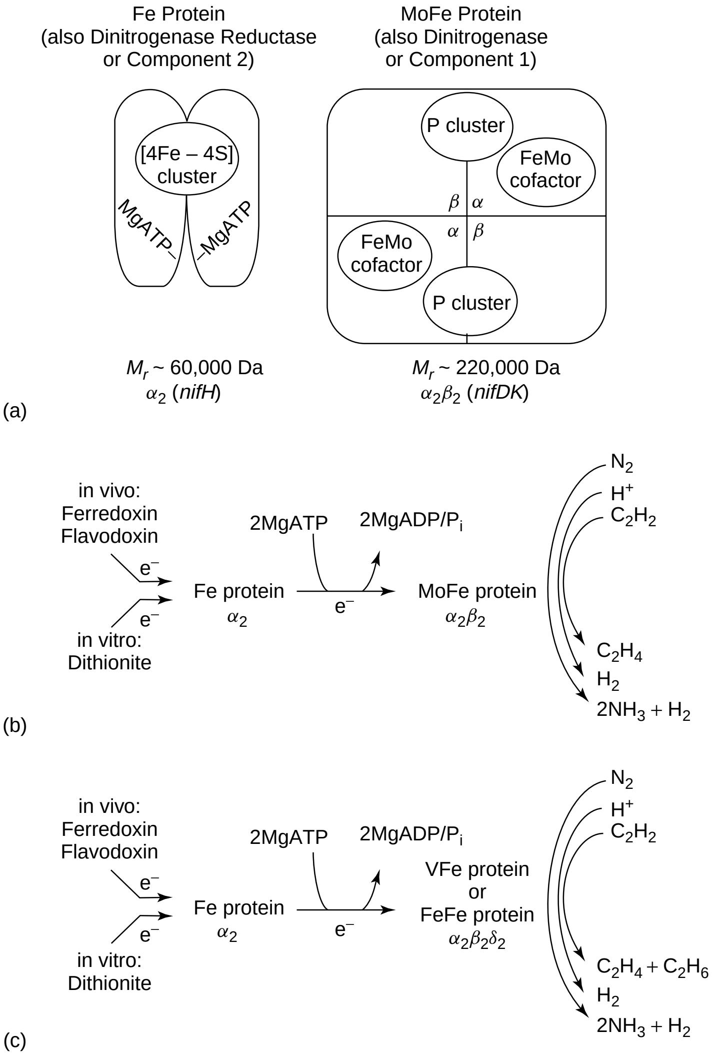
Fe Protein
(also Dinitrogenase Reductase
or Component 2)
[4Fe – 4S]
cluster
MgATP
MgATP
MoFe Protein
(also Dinitrogenase
or Component 1)
P cluster
FeMo
cofactor
β
α
α
β
FeMo
cofactor
P cluster
M_r ~ 60,000 Da
α_2 (*nifH*)
M_r ~ 220,000 Da
$\alpha_2\beta_2$ (*nifDK*)
(a)
in vivo:
Ferredoxin
Flavodoxin
e⁻
e⁻
in vitro:
Dithionite
Fe protein
α_2
2MgATP
2MgADP/P_i
e⁻
MoFe protein
$\alpha_2\beta_2$
N_2
H^+
C_2H_2
C_2H_4
H_2
$2NH_3 + H_2$
(b)
in vivo:
Ferredoxin
Flavodoxin
e⁻
e⁻
in vitro:
Dithionite
Fe protein
α_2
2MgATP
2MgADP/P_i
e⁻
VFe protein
or
FeFe protein
$\alpha_2\beta_2\delta_2$
N_2
H^+
C_2H_2
$C_2H_4 + C_2H_6$
H_2
$2NH_3 + H_2$
(c)

Figure 1 Schematic representation of the molybdenum nitrogenase (a) and the substrate-reduction reaction of the molybdenum nitrogenase (b) and alternative nitrogenases (c)

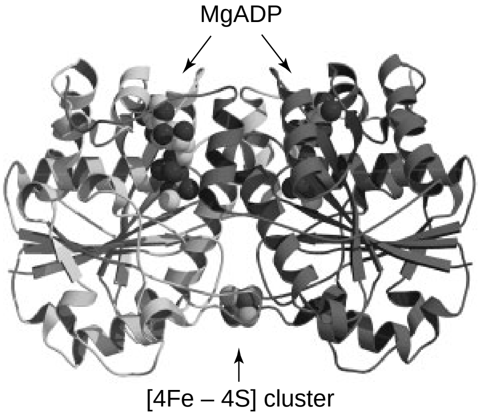

Figure 2 Structure of the α_2 homodimeric Fe protein of *A. vinelandii*, with the subunits colored in light and dark gray. The polypeptide chains are shown in ribbon presentation, and the [4Fe–4S] cluster and the two bound MgADP are shown in space-filling representation. PDB entry 1FP6 and programs MOLSCRIPT[29] and RASTER3D[30] were used to generate this figure

bound in a parallel orientation relative to each other near the dimer interface, one on each subunit. The nucleotide binding sites are located approximately 15 Å away from the [4Fe–4S] cluster and the docking surface between the Fe protein and the MoFe protein, indicating that the bound nucleotides need to exert their effects on the nitrogenase catalytic cycle from a distance through conformational changes.[6,9,19] The exact structure of the Fe protein in the MgATP-bound conformation is unknown, though X-ray scattering data have shown that the conformational changes of the Fe protein upon MgATP binding cause a contraction of the protein by 2.0 Å on average.[28] The same contraction is observed in the structure of the Fe protein in complex with the MoFe protein and MgADP·AlF_4^-,[21] suggesting that the MgATP-bound conformation of the isolated Fe protein is similar to that of the Fe protein in this complex structure. The structural details of the Fe protein involved in the catalytic mechanism will be discussed in Section 3.1.

2.1.2 *The [4Fe–4S] Cluster*

The [4Fe–4S] cluster is exposed to solvent and is symmetrically bridged between the two subunits of the Fe protein by the side chains of Cys97 and Cys132 (Figure 3).[3,10] The cluster ligands are located near the N termini of α-helices that are directed toward the cluster, permitting favorable electrostatic interactions between the terminal amide groups of the helices and the anionic cluster.[10] The [4Fe–4S] cluster of the Fe protein can exist in three different oxidation states,[10,25] that is, $[4Fe{-}4S]^{2+}$, $[4Fe{-}4S]^{1+}$, and $[4Fe{-}4S]^0$ (*see* ***Iron–Sulfur Proteins***). The physiological relevance of the various oxidation states of the [4Fe–4S] cluster will be discussed in greater detail in Section 3.1.

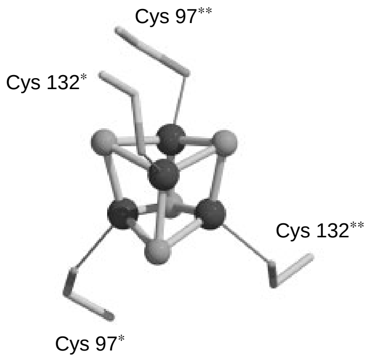

Figure 3 Structure of the [4Fe–4S] cluster of the *A. vinelandii* Fe protein including the coordinating ligands Cys97 and Cys132 from both subunits of the Fe protein (indicated as * and **). Iron and sulfur atoms are colored in dark and light gray, respectively. PDB entry 2NIP and programs MOLSCRIPT[29] and RASTER3D[30] were used to generate this figure

2.2 The MoFe Protein

The MoFe protein is an $\alpha_2\beta_2$ tetramer of $M_r \sim 220$ kDa, and its α and β subunits are encoded by the *nifD* and *nifK* gene, respectively (Figure 1(a) and Table 1).[7,9,10] It contains, in preparations with the highest activity, 2 molybdenum (Mo), ~30 to 34 iron (Fe), and an approximately equivalent number of acid-labile sulfur (S^{2-}) atoms (Table 1).[5,16] This metal content is consistent with the presence of two different types of unique metal clusters in the protein, that is, the [8Fe–7S] cluster (P cluster), which is bridged between each $\alpha\beta$ subunit pair, and the [Mo–7Fe–9S–homocitrate] cluster (FeMo cofactor or FeMoco), which is located within each α subunit (Figure 1a).[9,10,17]

2.2.1 *Protein Structure*

The X-ray crystal structures of MoFe protein, alone or in complex with the Fe protein, have been reported for *A. vinelandii*,[21,22,37–43] *C. pasteurianum*,[44,45] and *K. pneumoniae*,[46,47] and all of these structures are highly conserved on the basis of both primary sequence and three-dimensional structure. The MoFe protein of *A. vinelandii* is an $\alpha_2\beta_2$ heterotetramer consisting of a pair of $\alpha\beta$ dimers related by a molecular twofold rotation axis (Figure 4).[3,37,38] The homologous α and β subunits include three domains, designated αI, αII, and αIII and βI, βII, and βIII, respectively, all of which exhibit parallel β-sheet/α-helical type of polypeptide folds. Domains of both subunits contribute ligands to the P cluster. These ligands are located in a common core of a four-stranded, parallel β-sheet flanked by α-helices and additional β-strands.[7] The P clusters are located between

Table 1 Comparison of the catalytic and biophysical properties of MoFe, VFe, and FeFe proteins[5,8,16,31–36]

	MoFe protein		VFe protein			FeFe protein		
	Av	Kp	Av		Ac	Av	Rc	Rr
Subunits								
Structure	$\alpha_2\beta_2$	$\alpha_2\beta_2$	$\alpha\beta_2(\delta)$	$\alpha_2\beta_2(\delta)$	$\alpha_2\beta_2\delta_2$	$\alpha_2\beta_2(\delta)$	$\alpha_2\beta_2\delta_2$	$\alpha_2\beta_2\delta_2$
Encoding genes	*nifD* *nifK*	*nifD* *nifK*	*vnfD* *vnfK* *vnfG*	*vnfD* *vnfK* *vnfG*	*vnfD* *vnfK* *vnfG*	*anfD* *anfK* *anfG*	*anfD* *anfK* *anfG*	*anfD* *anfK* *anfG*
Metal and S^{2-} content[a]								
Mo	2	2	ND[b]	ND[b]	0.06	0.085	0.21	<0.05
V	ND[b]	0.06	0.7 ± 0.2	1.4 ± 0.2	2 ± 0.3	0.01	0.02	<0.05
Fe	33	32 ± 3	13	21.4	21 ± 1	24	20–29	16.5
S^{2-}	27	ND[b]	13	24	19 ± 0.2	18	31	ND[b]
Specific activities[c]								
NH_3 formation	1040–1270	990	ND[b]	ND[b]	350	30–110	350	4[d]
H_2 evolution under N_2	867	648	ND[b]	ND[b]	928	145–220	1300	67[d]
H_2 evolution under Ar	2220–3520	2100	ND[b]	ND[b]	1348	203–350	2400	71[d]
C_2H_4 formation from C_2H_2	2000	1693	184	245	608	18–58	160–260	6[d]
C_2H_6 formation from C_2H_2	ND[b]	0	ND[b]	ND[b]	15	26	5	0.2[d]

[a]Metal content in mol metal/mol protein. [b]ND = not determined. [c]Specific activities in nmol/min/mg protein. [d]These activities were originally reported in nmol/assay. The conversion of these values for the table are based on the reported assay conditions (assay time: 1 h; amount of FeFe protein: 0.92 mg).[33] Av = *Azotobacter vinelandii*; Kp = *Klebsiella pneumoniae*; Ac = *Azotobacter chroococcum*; Rc = *Rhodobacter capsulatus*; Rr = *Rhodospirillum rubum*. Note that the component proteins of the nitrogenase are often designated by the initials of the organism from which they were isolated and the arabic numeral of the component. For example, Av1 is the MoFe protein of *A. vinelandii* and Kp2 is the Fe protein from *K. pneumoniae*.[3,5,10] This nomenclature is also applied to the alternative nitrogenases, with the addition of a superscript ''V'' or ''Fe'' to indicate whether the component protein is from the vanadium or iron-only nitrogenase system. For example, $Av1^V$ is the VFe protein of *A. vinelandii* and $Rr2^{Fe}$ is the Fe protein from *R. rubum*. For the purpose of simplicity, this nomenclature is not used in this article, though readers may find it useful when reading some of the nitrogenase-related literature.

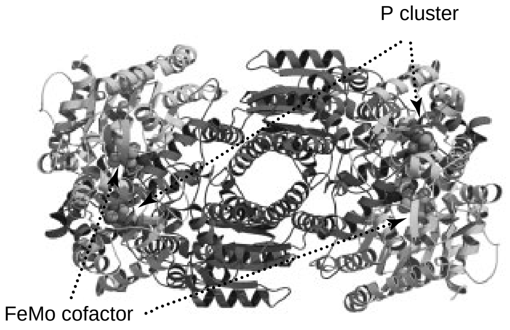

Figure 4 Structure of the $\alpha_2\beta_2$ tetrameric MoFe protein of *A. vinelandii*, with the α and β subunits colored in light and dark gray, respectively. The polypeptide chains are shown in ribbon presentation, and the FeMo cofactors and P clusters are shown in space-filling representation. PDB entry 1M1N and programs MOLSCRIPT[29] and RASTER3D[30] were used to generate this figure

domains αI and βI, whereas the FeMo cofactor occupies a cavity within the MoFe protein, formed among domains αI, αII, and αIII.

2.2.2 P Cluster

The P cluster is found at the interface between the α and β subunits, 10 Å below the surface of the protein.[7,10,48] When the MoFe protein is isolated in the presence of excess dithionite, its P cluster is in an $S = 4$, diamagnetic state (designated P^N).[4,49,50] All of the iron atoms of the P^N state are believed to be ferrous. There is some indication of the possible presence of some ferric character in this diamagnetic state, though there is no experimental evidence that the P cluster can be reduced further to an oxidation state below P^N. On the other hand, the P^N state of the P cluster can be two-electron oxidized to the P^{2+} state (designated P^{OX}) with dye oxidants thionine or indigodisulfonate (IDS).[51] This stable $S =$ integer (3 or 4) state can be recognized by a $g = 11.8$ signal observed in the parallel mode EPR.[49,52] In addition to P^N and P^{OX}, a mixed $S = 1/2 : S = 5/2$ state of the P cluster has been characterized[53] and is believed to represent P^{1+}, the one-electron oxidation product of P^N. The P cluster is proposed to be involved in the electron transfer during the substrate-reduction reaction (see also Section 3.2), though its exact function in this process is not clear (*see* ***Iron–Sulfur Proteins***).

Figure 5 shows the structures of P^N and P^{OX}. Both states of the P cluster contain eight iron and seven sulfur atoms, which are covalently coordinated to the MoFe protein by six cysteinyl ligands, three from the α-subunit, that is, Cys α62, Cys α88, and Cys α154, and three from the β-subunit, that is, Cys β70, Cys β95, and Cys β153. In both cases, Cys α62, Cys α154, Cys β70, and Cys β153 coordinate one iron atom each,

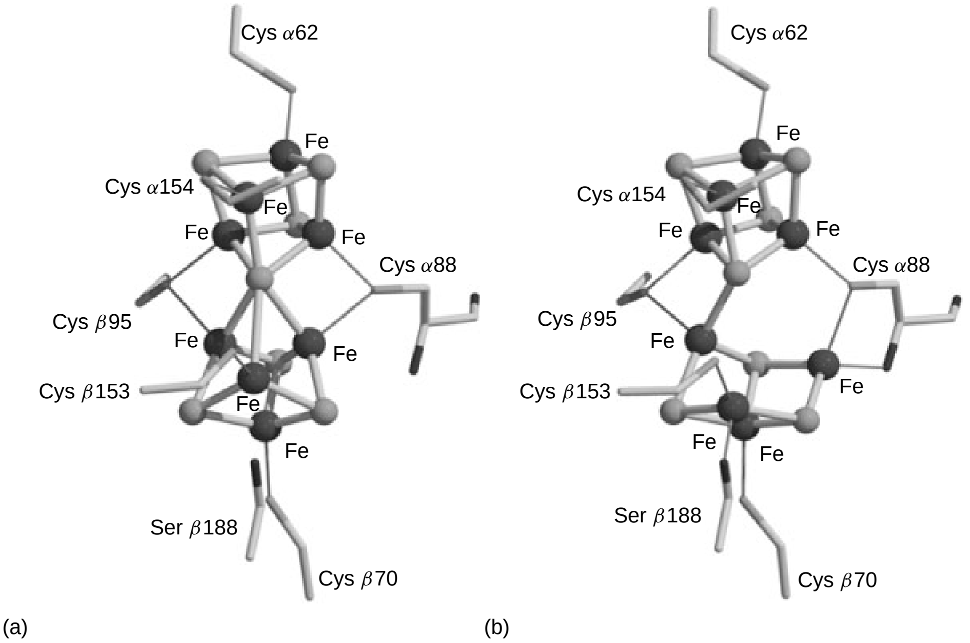

Figure 5 Structure of the (a) dithionite-reduced (P^N) and (b) two-electron–oxidized (P^{OX}) state of the P cluster of the *A. vinelandii* MoFe protein including the coordinating ligands. Iron and sulfur atoms are colored in dark and light gray, respectively. PDB entries 1M1N (P^N) and 2 MIN (P^{OX}) and programs MOLSCRIPT[29] and RASTER3D[30] were used to generate this figure

whereas Cys α88 and Cys β95 coordinate two iron atoms each.[37,38,40] However, P^N and P^{OX} are structurally different in that one half of the P cluster in the P^{OX} state is present in a more open conformation.[10] The interconversion between P^N and P^{OX} involves two iron atoms of the P cluster, and the changes in the core structure of the cluster are accompanied by the changes in the ligation between the cluster and the protein.[40] Two additional protein ligands are present in the P^{OX} state, one is the Oγ of Ser β188 that coordinates the same iron atom as the cysteinyl group of Cys β153, whereas the other is the Cys α88 that coordinates an iron with a backbone amide nitrogen ligand in addition to providing a cysteinyl ligand to the same iron atom (Figure 5).[40]

2.2.3 FeMo Cofactor

The FeMo cofactor is located within the α subunit of the MoFe protein, 14 Å away from the P cluster. It can be studied when it is buried within the MoFe protein or extracted into *N*-methylformamide (NMF).[3,4,18,54] The FeMo cofactor can undergo reversible one-electron oxidation and reduction,[4] and it is generally accepted that the FeMo cofactor provides the site for substrate reduction. The redox properties of the FeMo cofactor and their physiological relevance will be discussed further in Section 3.2.

Figure 6 shows the structure of the FeMo cofactor.[42] It has the overall stoichiometry of Mo : Fe_7 : S_9 : homocitrate and is composed of a [4Fe–3S] cluster and a [Mo–3Fe–3S] cluster bridged by three inorganic sulfide atoms.[37–39,42,44–46,48]

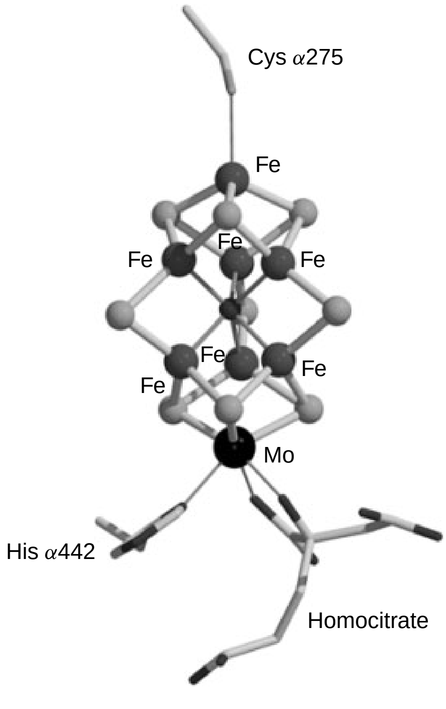

Figure 6 Structure of the FeMo cofactor of the *A. vinelandii* MoFe protein including the coordinating ligands Cys α275 and His α442. Molybdenum, iron, and the central ligand (plausibly nitrogen) are colored in dark gray, with a decrease in atomic radii in the order of Mo > Fe > central ligand. Sulfur is colored in light gray. PDB entry 1M1N and programs MOLSCRIPT[29] and RASTER3D[30] were used to generate this figure

A recently resolved high-resolution (1.16 Å) structure of the *A. vinelandii* MoFe protein revealed the possible presence of a nitrogen atom that is coordinated to six iron atoms in the center of the FeMo cofactor (Figure 6),[42] though conclusive evidence for the identity of this atom remains to be obtained. The core charge of the metals in the FeMo cofactor is proposed to be $+1$[55] or $+3$[56] in the resting state, yet the isolated FeMo cofactor is known to be anionic.[4] The overall negative charge of the FeMo cofactor is supplied by homocitrate, an organic terminal ligand of molybdenum, which is -4 if the –OH is deprotonated. The cofactor is ligated to the α subunit of the MoFe protein by just two ligands, His α442 and Cys α275 (Figure 6).

3 NITROGENASE CATALYSIS

The most comprehensive model for the function of molybdenum nitrogenase in the reduction of N_2 is that of Lowe and Thorneley, which was developed almost two decades ago.[57] This model describes two aspects of nitrogenase catalysis, the Fe protein cycle and the MoFe protein cycle.

3.1 Fe Protein Cycle: Electron Transfer from the Fe Protein to the MoFe Protein in the Nitrogenase Complex

Figure 7 shows what is believed to occur during the one-electron Fe protein cycle of the molybdenum nitrogenase, the process in which the Fe protein serves as an obligate electron donor for the MoFe protein.[4,8,10,57,58] In order to carry out the catalytic function of nitrogenase, the reduced Fe protein first binds two molecules of MgATP and undergoes a conformational change before forming a complex with the MoFe protein. Then, coupled with the hydrolysis of 2MgATP molecules to 2MgADP and $2P_i$, one electron is transferred from the $[4Fe-4S]^{1+}$ cluster of the Fe protein to the MoFe protein within the complex. This process is followed by complex dissociation, re-reduction of the oxidized Fe protein, and the dissociation of MgADP, which allows the enzyme complex to start the next cycle of electron transfer.

The distances between the nucleotide binding sites of the Fe protein, the [4Fe–4S] cluster, and the Fe protein/MoFe protein interface (Section 2.1.1) suggest that conformational changes are involved in the catalytic mechanism of the nitrogenase.[6,9,19] Mutagenic studies show that the initial conformational change of the Fe protein, which occurs upon MgATP binding, involves the Walker A motif or the phosphate-binding loop (P-loop), two switch regions (Switch I and II), and a region around residue A157. The Walker A motif and Switch I and II are characteristic of the G-protein family, whereas the area around A157 is unique to the Fe protein.[6,10,19,59–61] In the MgADP-bound conformation of the *A. vinelandii* Fe protein, the Walker A motif (residues 9–16, G̲KGGIG̲K̲S̲, consensus residues underlined) forms a loop that wraps around the phosphate groups of the nucleotide, with the hydroxyl of residue 16 coordinating the Mg^{2+} ion and the invariant lysine forming a salt bridge with the β phosphate. It is therefore proposed that Switch I (residues 38–44) provides direct communication links between the nucleotide binding site and the MoFe protein docking interface, whereas Switch II (residues 125–129) is responsible for signal transduction between the nucleotide binding site and the [4Fe–4S] cluster.[9,10]

Three oxidation states (0, $+1$, and $+2$) have been reported for the [4Fe–4S] cluster of Fe protein (Section 2.1.2).[10,25] Figure 8(a) shows the EPR spectrum of the dithionite-reduced $[4Fe-4S]^{1+}$ cluster of the Fe protein in the absence of nucleotides that exhibits an $S = 1/2$ signal in the $g = 2$ region with a rhombic line shape,[4,62,63] whereas Figure 8(b) shows the EPR-silent spectrum that arises from the diamagnetic IDS-oxidized $[4Fe-4S]^{2+}$ cluster of the Fe protein.[64] The $E^{0'}$ of the $[4Fe-4S]^{2+/1+}$ couple of Fe protein is -310 mV versus NHE, which becomes ca. 100 mV more negative in

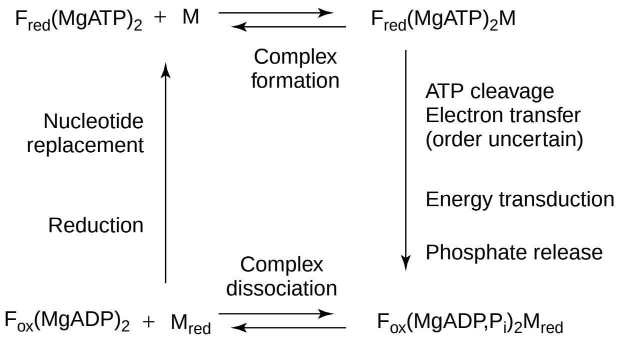

Figure 7 The Fe protein cycle of the molybdenum nitrogenase.[4,8,10,57,58] The cycle describes the MgATP-dependent electron transfer from the Fe protein (F) to one $\alpha\beta$ half of the MoFe protein (M), which is accompanied by the hydrolysis of 2MgATP to 2MgADP and $2P_i$. Subscripts: ox = oxidized and red = reduced

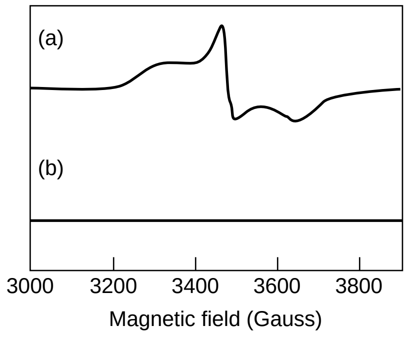

Figure 8 EPR spectra of (a) dithionite-reduced and (b) IDS-oxidized Fe protein in the absence of nucleotide.[4,62–64] The spectra were recorded at 13 K. Note that the dithionite-reduced Fe protein exists in a mixture of $S = 1/2$ and $S = 3/2$ spin states.[18] Only the $S = 1/2$ EPR signal in the $g = 2$ region is shown in the figure

the presence of MgATP.[4] It has been shown that ferredoxin or flavodoxin in vivo or dithionite in vitro can reduce the [4Fe–4S] cluster of the Fe protein to the +1 state (Figure 1b), and the $[4Fe–4S]^{2+/1+}$ couple is believed to be utilized in the Fe protein cycle under physiological conditions. However, it has also been demonstrated that the [4Fe–4S] cluster can be further reduced, reversibly, to the all-ferrous $[4Fe–4S]^0$ state[25,64] and that two electrons can be transferred from this state to the MoFe protein concomitant with the hydrolysis of two molecules of MgATP,[65] leading to the suggestion that the $[4Fe–4S]^{2+/0}$ couple is utilized in vivo at least under some circumstances. In addition to that, a midpoint potential of −800 mV versus NHE has been described recently for the $[4Fe–4S]^{1+/0}$ couple.[66] Nevertheless, the physiological relevance of the all-ferrous state of the Fe protein is yet to be established.

3.2 The MoFe Protein Cycle: Electron Transfer within the MoFe Protein and the Substrate-reduction Reaction

Figure 9 shows the MoFe protein cycle, which consists of eight one-electron transfer steps, each of which corresponds to one Fe protein cycle.[4,8,10,57,58] The reactions shown in Figure 9 are consistent with the overall stoichiometry of the enzymatic N_2 reduction, that is, $N_2 + 8H^+ + 8e^- \rightarrow 2NH_3 + H_2$.[10]

Following the transfer of one electron from the Fe protein to the MoFe protein, the FeMo cofactor, which is present in an $S = 3/2$ state with unique features at $g = 3.65$ and 2.01 (Figure 10a), is reduced to an EPR-silent but paramagnetic state.[4] The disappearance of this EPR signal, which can also be accomplished chemically by oxidation with thionine (Figure 10b),[4,64] occurs after the addition of one electron to one FeMo cofactor, indicating that the FeMo cofactor is the final location for the first electron that enters the MoFe protein from the Fe protein. The MgADP·AlF_4^--stabilized complex between the Fe protein and the MoFe protein, which is believed to represent the transition state during MgATP hydrolysis, provides some compelling evidence that the electrons are transferred from the Fe protein to first the P cluster and then the FeMo cofactor (Figure 11).[21] Following that, it is believed that electrons are transferred from the FeMo cofactor to the bound substrate, and the substrate reduction subsequently takes place. Interestingly, it has been observed that all products leaving the nitrogenase are reduced by multiples of two electrons. Therefore, the MoFe protein must be able to accumulate several electrons before products are released. Currently, it is not known whether the electrons are stored in the P cluster, the FeMo cofactor, or the enzyme-bound intermediate of substrate reduction. Also, direct evidence that suggests how

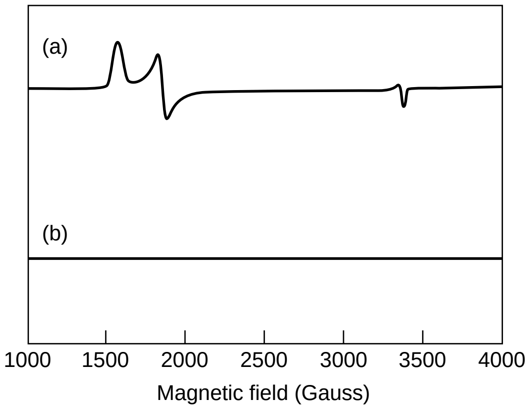

Figure 10 EPR spectra of (a) dithionite-reduced and (b) thionine-oxidized MoFe protein of *A. vinelandii*. The $S = 3/2$ EPR signal arises from the FeMo cofactor center of the protein.[4,8,10,18,64,67–69] The spectra were recorded at 10 K

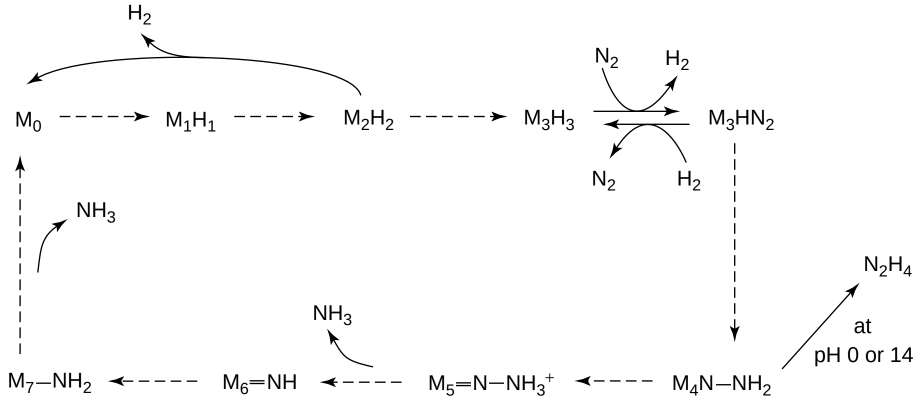

Figure 9 The MoFe protein cycle of the molybdenum nitrogenase.[4,8,10,57,58] The cycle describes a plausible sequence of events during the reduction of N_2 to $2NH_3$ and H_2. M represents one functional half of the MoFe protein, which is composed of one $\alpha\beta$ subunit pair plus one FeMo cofactor and one P cluster. Subscripts 0 to 7 indicate the number of electrons transferred to M from the Fe protein via the Fe protein cycle. It is plausibly assumed that each transferred electron is neutralized by the addition of one proton. Each dotted arrow corresponds to one completed Fe protein cycle (shown in Figure 7)

Table 2 Substrates and inhibitors of nitrogenase[4,8,58,83]

Substrate/inhibitor	Reaction catalyzed by nitrogenase
N_2	$N_2 + 8H^+ + 8e^- \longrightarrow 2NH_3 + H_2$
H^+	$2H^+ + 2e^- \longrightarrow H_2$
C_2H_2	$C_2H_2 + 2H^+ + 2e^- \longrightarrow C_2H_4$ (plus 1–5% C_2H_6 with V and Fe nitrogenases)
C_2H_4	$C_2H_4 + 2H^+ + 2e^- \longrightarrow C_2H_6$
HCN	$HCN + 6H^+ + 6e^- \longrightarrow CH_4 + NH_3$
	$HCN + 4H^+ + 4e^- \longrightarrow CH_3 + NH_2$
CH_3NC	$CH_3NC + 6H^+ + 6e^- \longrightarrow CH_3NH_2 + CH_4$
$N{\equiv}CNH_2$	$N{\equiv}CNH_2 + 8H^+ + 8e^- \longrightarrow CH_4 + 2NH_3$
	$N{\equiv}CNH_2 + 6H^+ + 6e^- \longrightarrow CH_3NH_2 + NH_3$
Cyclopropene	3 Cyclopropene $+ 6H^+ + 6e^- \longrightarrow$ Cyclopropane + 2 Propene
N_2O	$N_2O + 2H^+ + 2e^- \longrightarrow N_2 + H_2O$
NO_2^-	$NO_2^- + 7H^+ + 6e^- \longrightarrow NH_3 + 2H_2O$
N_2H_4	$N_2H_4 + 2H^+ + 2e^- \longrightarrow 2NH_3$
N_3^-	$N_3^- + 3H^+ + 2e^- \longrightarrow N_2 + NH_3$
O_2	$O_2 + 2H^+ + 2e^- \longrightarrow H_2O_2$
COS	$COS + 2H^+ + 2e^- \longrightarrow CO + H_2S$
CO_2	$CO_2 + 2H^+ + 2e^- \longrightarrow CO + H_2O$
CO	Inhibitor of all substrate reductions except H^+
H_2	Inhibitor of N_2 reduction.

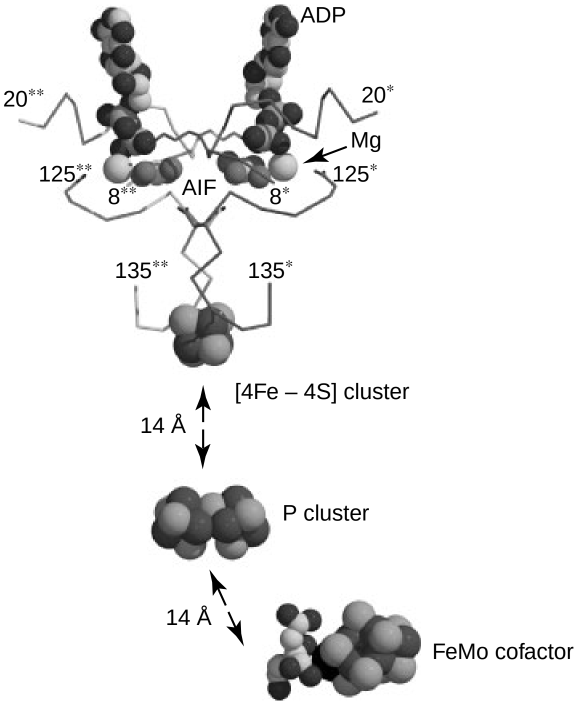

Figure 11 The relative positions of the components of the ADP·AlF_4^--stabilized complex that are involved in the electron flow during the substrate-reduction reaction. PDB entry 1M34 and programs MOLSCRIPT[29] and RASTER3D[30] were used to generate this figure. Metal clusters and ADP·AlF_4^- are shown in space-filling representation. In addition, residues 8 to 20 (including the Walker A motif) and 125 to 135 (including Switch II) from both subunits of the Fe protein are shown (indicated as * and **). Electrons flow in a MgATP-dependent reaction from the [4Fe–4S] cluster of Fe protein to first the P cluster and then the FeMo cofactor of the MoFe protein, where the reduction of dinitrogen to ammonia occurs

the substrate might bind to the FeMo cofactor site of the enzyme, where substrate reduction takes place, is limited. Furthermore, though it is known that the substrate-reduction reaction involves an equal number of electrons and protons and that the P cluster might be involved in this process,[9,40] how protons are transferred from the solvent to the FeMo cofactor site has not been established.

What is known, though, is that in addition to its physiological substrates, that is, N_2 and H^+, nitrogenase is able to reduce a large variety of small doubly and triply bonded substrates (Table 2). Progress has been made in understanding the interaction of the FeMo cofactor site with such substrates or inhibitors as C_2H_2, CS_2, or CO,[55,70–75] as well as that of the isolated FeMo cofactor with CN^- and CO.[76–80] Also, on the basis of a molecular biology approach, it has been suggested that the substrate might bind to the [4Fe–4S] face of the FeMo cofactor, which is capped by Val α70 and Arg α96 of the MoFe protein.[81,82] In addition, as mentioned in Section 2.2.3, a high-resolution (1.16 Å) structure of the nitrogenase MoFe protein has been obtained recently, which indicates the possible presence of a nitrogen atom that is coordinated to six iron atoms in the center of the FeMo cofactor.[42] This interesting finding may in time provide us with significant insight into the mechanism of dinitrogen reduction.

4 NITROGENASE ASSEMBLY

The biosynthesis of nitrogenase is arguably one of the most complex processes in the field of bioinorganic chemistry, requiring the participation of at least 15 different gene products. Like Section 3, this section will only discuss the assembly mechanism of the molybdenum nitrogenase, which is the best-characterized nitrogenase system.

4.1 Fe Protein Assembly

The assembly of the Fe protein involves the biosynthesis of the structural polypeptides and the biosynthesis and insertion of the [4Fe–4S] cluster into the Fe protein. Substantial progress has been made in understanding the assembly of the molybdenum nitrogenase Fe protein and its [4Fe–4S] cluster, a process that involves the *nifH* gene that encodes for the subunits of the Fe protein and at least *nifS*, *nifU*, and *nifM* gene products that are implicated in the [4Fe–4S] cluster assembly (Table 3 and Figure 12).[8,11,84] It was initially proposed that NifS (*nifS* gene product) and NifU (*nifU* gene product) have complementary functions related to the general mobilization of S and Fe for nitrogenase metallocluster formation. This suggestion was supported by experiments that demonstrated that NifS is a pyridoxal-dependent cysteine desulfurase and that NifU provides an in vitro scaffold for the formation of [2Fe–2S] clusters destined for nitrogenase metallocluster formation.[85–87] A likely pathway involves the formation of a protein-bound cysteine persulfide on NifS that is subsequently donated to NifU, upon which, in the presence of Fe, a labile [2Fe–2S] cluster is formed.[88] The exact mechanism concerning the assembly of [2Fe–2S] units on the NifU scaffold is not clear, nor is the issue of whether [2Fe–2S] or [4Fe–4S] units are ultimately formed on the NifU scaffold prior to their release for Fe protein maturation. In contrast to the emerging information of the role of NifS and NifU in the Fe protein assembly, little is known about the function of NifM (*nifM* gene product), which has been shown to be essential for the process.[8]

4.2 MoFe Protein Assembly

The assembly of the MoFe protein involves the biosynthesis of the FeMo cofactor, and in a separate pathway, the biosynthesis of a P cluster–containing yet FeMo cofactor–deficient species of the MoFe protein and the insertion of the completed FeMo cofactor into the FeMo cofactor–deficient MoFe protein.[2,8,18,67,69,89]

4.2.1 Biosynthesis of the FeMo Cofactor

Figure 12 illustrates the current model of FeMo cofactor biosynthesis, a process independent of the production of MoFe protein polypeptides,[91–93] which starts with the mobilization of iron and sulfur and the assembly of Fe/S fragments by NifS and NifU.[11] These Fe/S fragments are transferred to NifB (*nifB* gene product),[84] which is subsequently involved in the production of the Fe/S core of the FeMo cofactor (designated NifB cofactor) that probably contains all of the iron and sulfur that ends up in the FeMo cofactor (Table 3).[94,95] Following that, the NifB cofactor, probably bound to an ‘escort’ protein designated NifX (*nifX* gene product), binds to a scaffold $NifN_2E_2$ protein (encoded by the *nifN* and *nifE* gene products).[84,96–100] It is possible that molybdenum and homocitrate could be incorporated into the NifB cofactor while it is attached to NifX in a process that possibly involves NifW and NifV[84,101,102] (*nifW* and *nifV* gene products, respectively). Subsequently, at the transient $NifN_2E_2$ scaffold, the NifB cofactor is rearranged by an unknown mechanism and forms the completed FeMo cofactor. The process of FeMo cofactor formation also requires the Fe protein, MgATP, and reductant,[103–105] though their exact functions in the process have not been established. The completed FeMo cofactor is then transferred to another ‘escort’ protein, probably NifY that is encoded by the *nifY* gene in *K. pneumoniae*[106] or the non-*nif*–encoded protein called gamma (γ) in *A. vinelandii*,[107] which delivers the FeMo cofactor to the FeMo cofactor–deficient MoFe protein (see also Section 4.2.3). However, the exact function of γ in the MoFe protein assembly remains unknown, and the essential role of γ in the process was questioned very recently.[108]

4.2.2 Biosynthesis of a P Cluster–containing, FeMo Cofactor–deficient MoFe Protein

As shown in Figure 12, the biosynthesis of the P cluster–containing yet FeMo cofactor–deficient MoFe protein involves *nifD* and *nifK*, which encode the α and β subunit of the MoFe protein, respectively, and at least the *nifS* and *nifU* gene products, in addition.[8] Expression of the molybdenum nitrogenase is activated by molybdenum and regulated by *nifA* and *nifL* (Table 3). Little is known about the assembly mechanism of the P cluster. Nonetheless, such a P cluster–containing but FeMo cofactor–deficient MoFe protein is obtained from a *nifB* deletion strain of *A. vinelandii*, and an isolated FeMo cofactor can be readily inserted into this MoFe protein.[109] The X-ray crystal structure of this cofactor-deficient protein provides interesting insights into the FeMo cofactor insertion and MoFe protein maturation process[43] and will be discussed in greater detail in the following section.

4.2.3 Insertion of the FeMo Cofactor into the FeMo Cofactor–deficient MoFe Protein

Like the biosynthesis of the FeMo cofactor (Section 4.2.1), the insertion of the FeMo cofactor into the FeMo cofactor–deficient form of the MoFe protein also requires the presence of the Fe protein.[2,4,8,18,67,69,89] This final maturation process of the MoFe protein most likely occurs in a series of steps, which are shown in Figure 12. Initially, the FeMo cofactor site is not accessible to FeMo cofactor insertion (‘closed’ conformation).[105,110,111] The conversion of this site to another form with the FeMo cofactor site accessible to

Table 3 The *nif* gene products and functions[1,4,8,10,11,69,82–84,87,89,90]

Gene	Product/function
(a) Structural genes	
nifH	Product: Fe protein subunit. Forms homodimer ($M_r \approx 60\,000$ Da). A single [4Fe–4S] cluster is bridged between the two identical subunits. Binds two molecules of MgATP. Function: ATP-dependent electron transfer to the MoFe protein, FeMo cofactor biosynthesis, and insertion of the FeMo cofactor into the MoFe protein. Possible function: P cluster assembly and regulation of the alternative nitrogenases.
nifD	Product: MoFe protein α subunit. Forms $\alpha_2\beta_2$ tetramer ($M_r \approx 220\,000$ Da) with β subunit. Holoprotein contains two FeMo cofactors and two P clusters. Function: Contains substrate-reduction site (FeMo cofactor).
nifK	Product: MoFe protein β subunit. Function: See *nifD*.
(b) Processing genes	
nifQ	Product: NifQ. Function: Involved in FeMo cofactor biosynthesis, maybe at an early step. The *nifQ*$^-$ phenotype can be suppressed by elevated levels of Mo or cysteine.
nifB[a]	Product: NifB. Function: NifB is involved in the production of an Fe/S-containing FeMo cofactor precursor, designated NifB cofactor.
nifV[a]	Product: Homocitrate synthase. Function: Formation of homocitrate, which is the organic component of the FeMo cofactor.
nifX	Product: NifX. Possible function: NifX can bind the FeMo cofactor or NifB cofactor. Might be an intermediate carrier in FeMo cofactor biosynthesis.
nifY	Product: NifY. Possible function: NifY attaches to the FeMo cofactor-deficient, NifB$^-$ MoFe protein in case of Kp. Might be an intermediate carrier in FeMo cofactor biosynthesis.
nifN	Product: NifN. Forms $\alpha_2\beta_2$ tetramer ($M_r \approx 210\,000$ Da) with the *nifE* gene product ($NifN_2E_2$). Each tetramer contains two identical redox-active [4Fe–4S] clusters. NifN bears significant sequence identity when compared with the β subunit of the MoFe protein. Function: Required for FeMo cofactor biosynthesis. $NifN_2E_2$ appears to provide a transient site upon which one or more events related to FeMo cofactor assembly occurs.
nifE	Product: NifE. Forms $\alpha_2\beta_2$ tetramer ($M_r \approx 210\,000$ Da) with the *nifN* gene product ($NifN_2E_2$). NifE bears significant sequence identity when compared with the α subunit of the MoFe protein. Function: See *nifN*.
nifM[a]	Product: NifM. Function: Required for activation of the Fe protein.
nifU[a]	Product: NifU. Provides an in vitro scaffold for the formation of [2Fe–2S] clusters destined for nitrogenase metallocluster assembly. Functions: Complements NifS in the mobilization of Fe and S for metallocluster assembly. Required for the activity of the Fe protein and the MoFe protein.
nifS[a]	Product: Pyridoxal-dependent cysteine desulfurase. Functions: Complements NifU in the mobilization of Fe and S for metallocluster assembly. Required for the activity of Fe protein and MoFe protein.
nifW	Product: NifW. Function: Required for full activity of the MoFe protein. Possible function: Might be related in coupling Mo and homocitrate.
nifZ	Product: NifZ. Function: Required for full activity of the MoFe protein. Possible function: Related to FeMo cofactor formation or insertion.
nifT	Product: NifT. Function: Unknown.
(c) Electron transfer genes	
nifF	Product: Flavodoxin. Function: Physiological electron donor of the Fe protein.
nifJ	Product: Pyruvate: flavodoxin oxidoreductase. Composed of two identical $M_r \approx 120\,000$ Da subunits. Function: Couples the oxidation of pyruvate to the reduction of flavodoxin.
(d) Regulatory genes	
nifA	Positive regulatory element.
nifL	Negative regulatory element.

[a] Also required for the vanadium and iron-only nitrogenases, which are encoded by *vnf* and *anf* genes, respectively.

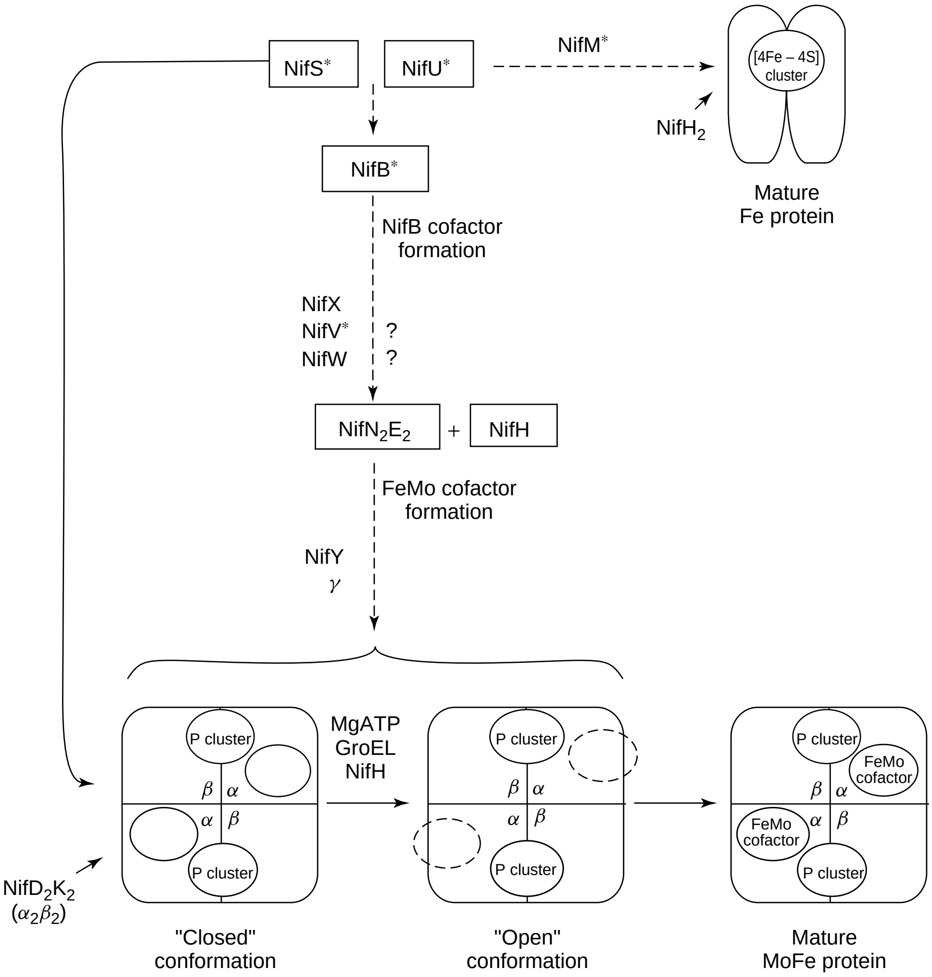

Figure 12 Assembly of the molybdenum nitrogenase. Pathways of FeMo cofactor biosynthesis, Fe protein maturation, and MoFe protein assembly are indicated in dotted, dashed, and solid arrows, respectively. The *nif* gene products that are also required for the vanadium and iron-only nitrogenase systems are indicated by *

FeMo cofactor insertion (‘open’ conformation) involves at least the combined action of Fe protein, GroEL, MgATP, and possibly γ.[106–108,110,112] Once the FeMo cofactor site is accessible, the FeMo cofactor is inserted, γ dissociates, and the assembly process of the mature nitrogenase is completed.

As mentioned above, a FeMo cofactor–deficient MoFe protein was obtained from a *nifB* deletion strain of *A. vinelandii*, and its X-ray crystal structure has been resolved at 2.3 Å.[43] Like the wild-type *A. vinelandii* MoFe protein (see Section 2.2), this MoFe protein (designated NifB^- MoFe protein)[43] is an $\alpha_2\beta_2$ tetramer consisting of a pair of $\alpha\beta$ dimers that are related by a molecular twofold rotation axis, and each subunit consists of three domains, designated αI, αII, and αIII and βI, βII, and βIII, respectively. In the dithionite-reduced state, the P cluster of the NifB^- MoFe protein, like that of its wild-type counterpart, is assigned to the P^{N} state and is located between domains αI and βI. However, the FeMo cofactor of the wild-type MoFe protein, which occupies a cavity formed between domains of the α subunit, is not present in the NifB^- MoFe protein (Figure 13). Accompanying the absence of the FeMo cofactor, domain αIII of the NifB^- MoFe protein undergoes substantial structural rearrangements, whereas domains αI and αII as well as the β subunit of the NifB^- MoFe protein remain mostly unchanged relative to those of the wild-type MoFe protein. The structural rearrangements of domain αIII in the NifB^- MoFe protein create a FeMo cofactor insertion funnel, which is not present in its wild-type counterpart. Despite the prevailing negative surface charge of the NifB^- MoFe protein, there is an evident accumulation of positive surface charge lining the funnel the entire way from the entrance down to the FeMo cofactor binding site.[43] Since the FeMo cofactor is overall negatively charged owing to the dominant contribution of homocitrate,[4] this electrostatic feature of the insertion funnel presumably helps to steer the FeMo cofactor down the funnel into its correct position in the holoprotein. Given the instability of the isolated FeMo cofactor, the biosynthetic pathway likely involves the protein-bound FeMo

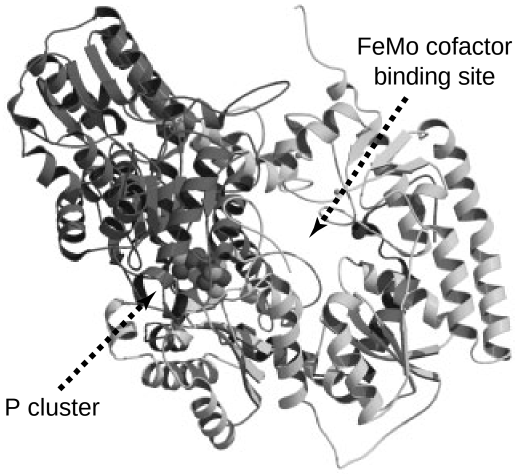

Figure 13 Front-side view of one $\alpha\beta$ subunit pair of the NifB$^-$ MoFe protein of *A. vinelandii*, with the α and β subunits colored in light and dark gray, respectively. The polypeptide chains are shown in ribbon presentation, and the P cluster is shown in space-filling representation. The FeMo cofactor binding site is indicated. PDB entry 1L5H and programs MOLSCRIPT[29] and RASTER3D[30] were used to generate this figure

cofactor instead of the free cofactor. Although the penultimate carrier of the FeMo cofactor preceding its incorporation into the MoFe protein has not been conclusively identified, the rearrangement of the αIII domain might create a potential interaction domain for the docking of the FeMo cofactor donor, in addition to generating the opening for FeMo cofactor insertion.

5 ALTERNATIVE NITROGENASES

5.1 Vanadium Nitrogenase

5.1.1 General Properties

The vanadium nitrogenase has been isolated from *A. vinelandii* and *A. chroococcum* (Table 1). With the molybdenum in the protein replaced by vanadium, the vanadium nitrogenase resembles its molybdenum counterpart.[5,8,10,16] It has the molybdenum–iron (MoFe) protein equivalent in the vanadium–iron (VFe) protein, as well as the iron (Fe) protein equivalent.

In contrast to the $\alpha_2\beta_2$ tetrameric MoFe protein, the VFe protein isolated from *A. chroococcum* is an $\alpha_2\beta_2\delta_2$ hexamer under optimal experimental conditions.[5,16] The VFe protein from *A. vinelandii*, however, shows variable subunit composition.[32] Two species of the *A. vinelandii* VFe protein, that is, $\alpha\beta_2(\delta)$ and $\alpha_2\beta_2(\delta)$, have been characterized[32] (Table 1). The exact stoichiometry between the α, β, and δ subunits has not been established in this case, and the suboptimal subunit composition was speculated to be a result of the weak interactions between the subunits.[36] Other than the subunit composition, the VFe proteins from *A. vinelandii* and *A. chroococcum* have similar properties, which is consistent with the sequence homology of their structural genes. The α and β subunits of the VFe protein, encoded by *vnfD* and *vnfK* genes, respectively, are homologous to the *nifD*-encoded α and *nifK*-encoded β subunits of the MoFe protein;[8,10] whereas the additional small δ subunit of the VFe protein is encoded by *vnfG* (Table 3).[5,8,16,31–36] The VFe protein contains, in preparations with the highest activity, up to 2 vanadium (V) atoms, ~20 iron atoms, and ~20 acid-labile sulfur atoms (Table 1). These metal contents are lower than those typically determined in MoFe protein preparations, which is most likely not significant since comparable values were commonly obtained in earlier studies of the MoFe proteins, but have increased with time.[36] Although no X-ray crystallographic data are currently available for the VFe proteins, EPR, MCD, Mössbauer, EXAFS, and cofactor extrusion studies indicate that the VFe proteins from both *A. vinelandii* and *A. chroococcum* contain redox centers that are respective homologues to the P cluster and FeMo cofactor,[5,8,36] leading to the hypothesis that the structure of the VFe protein resembles that of the MoFe protein apart from the presence of the additional δ subunit in the VFe protein. The homologue of the FeMo cofactor in the VFe protein is the designated FeVa cofactor or FeVaco.

The Fe protein of the vanadium nitrogenase, encoded by *vnfH*, shares a high degree of homology with the *nifH*-encoded Fe protein of the molybdenum nitrogenase.[8] Like its counterpart in the molybdenum enzyme, the Fe protein of the vanadium nitrogenase has an α_2 homodimeric composition and contains an [4Fe–4S] cluster.

5.1.2 Catalysis and Assembly

The requirements for vanadium nitrogenase activity are very similar to those of the molybdenum nitrogenase in that both the Fe protein and the VFe protein are essential, MgATP hydrolysis is required, dioxygen needs to be absent, and a reductant like ferredoxin or flavodoxin in vivo or dithionite in vitro is necessary (Figure 1c).[5,8,16] However, there are clear differences in the substrate-reducing profiles of the two enzymes.[5,8,10,16] First, the vanadium nitrogenase fixes N_2 less efficiently than the molybdenum nitrogenase at 30 °C (Table 1). This relationship is reversed at low temperatures. Secondly, in contrast to the molybdenum nitrogenase, hydrazine is a side product of N_2 reduction in the case of the vanadium nitrogenase. Thirdly, the vanadium nitrogenase reduces acetylene, relatively poorly than the molybdenum enzyme, to not only ethylene, which is the only product generated by the molybdenum enzyme, but also to small amounts of ethane (Tables 1 and 2).

As indicated in Table 3 and Figure 12, some *nif* gene products, for example, NifS, NifU, NifM, NifB, and NifV are also required for the biosynthesis of the vanadium nitrogenase of *A. vinelandii*. However, the expression of the vanadium nitrogenase is regulated by a different activator (i.e. *vnfA*) than the molybdenum enzyme.**[8]** Molybdenum inhibits the expression of the vanadium nitrogenase. Therefore, in the presence of molybdenum, only the molybdenum nitrogenase is expressed, whereas in the absence of molybdenum, vanadium activates the expression of the vanadium nitrogenase.

In the case of the molybdenum nitrogenase, $\mathrm{NifN_2E_2}$ is believed to be critical for the biosynthesis of the FeMo cofactor and functions as a transient scaffold on which modifications of the NifB cofactor occur (Section 4.2.1). Since the vanadium nitrogenase contains respective homologues to the *nifN* and *nifE* genes of the molybdenum nitrogenase, namely, *vnfN* and *vnfE*,**[8,84]** it is possible that *vnfN* and *vnfE* encode a similar transient scaffold protein complex for the biosynthesis of FeVa cofactor. Given that NifB is also required for the assembly of the vanadium nitrogenase, it is likely that the NifB cofactor binds to $\mathrm{VnfN_2E_2}$ during the biosynthesis of FeVa cofactor in a fashion similar to that when it binds to $\mathrm{NifN_2E_2}$. In addition, homocitrate synthesized by NifV might be added to the FeVa cofactor at a similar step in the biosynthesis pathway that is analogous to the FeMo cofactor biosynthesis (see Figure 12). Furthermore, NifS and NifU are most likely important for the mobilization of iron and sulfur and the assembly of Fe/S fragments for the vanadium nitrogenase, and NifM is likely required for the maturation of VnfH.

5.2 Iron-only Nitrogenase

5.2.1 *General Properties*

The iron-only nitrogenase has been isolated from *A. vinelandii*, *R. rubum*, and *R. capsulatus* (Table 1). It is also similar to the molybdenum nitrogenase except that the molybdenum is replaced by iron in the protein.**[5,8,10,16]** It has the molybdenum–iron (MoFe) protein equivalent in the iron–iron (FeFe) protein and the iron (Fe) protein equivalent.

As shown in Table 1, like the VFe protein, the FeFe protein has an $\alpha_2\beta_2\delta_2$ hexameric subunit composition under optimal conditions. The α, β and δ subunits of the FeFe protein are encoded by *anfD, anfK*, and *anfG*, respectively. Earlier efforts to purify the FeFe protein suffered from low activities, though progress has been made and recent preparations of the FeFe protein from *R. capsulatus* have activities comparable to that of the VFe protein and do not contain molybdenum or vanadium but high levels of iron (Table 1).

Recent EPR,**[35]** Mössbauer, and EXAFS**[113]** studies of the FeFe protein from *R. capsulatus* have provided spectroscopic evidence that the metal clusters of the FeFe protein bear a certain degree of structural homology to those present in the MoFe and VFe proteins. Therefore, it is likely that the FeFe protein contains redox centers that are homologous to the P cluster and FeMo or FeVa cofactor, respectively. The FeMo or FeVa cofactor homologue in the FeFe protein is termed FeFe cofactor or FeFeco.

The *anfH*-encoded Fe protein of the iron-only nitrogenase is very homologous to the *nifH*-encoded Fe protein of the molybdenum nitrogenase and the *vnfH*-encoded Fe protein of the vanadium nitrogenase.**[8]** This Fe protein also has an α_2 homodimeric composition and contains a [4Fe–4S] cluster.

5.2.2 *Catalysis and Assembly*

The requirements for the substrate-reduction activity of the iron-only nitrogenase are similar to those of the vanadium nitrogenases (Figure 1c).**[8,10]** The expression of the iron-only nitrogenase is only activated in the absence of both molybdenum and vanadium and regulated by a different activator (i.e. *anfA*) than the molybdenum or vanadium enzyme.**[8]** In contrast to the vanadium nitrogenase, the iron-only nitrogenase does not contain homologues to the *nifN* and *nifE* genes. Therefore, the biosynthesis of FeFe cofactor relies on not only the *nif* gene products (i.e. NifS, NifU, NifM, NifB, and NifV), but also on the *vnf* gene products (i.e. VnfN and VnfE). The $\mathrm{VnfN_2E_2}$ complex might act as a transient scaffold for the biosynthesis of both the FeVa cofactor and the FeFe cofactor.**[8]**

5.3 *Streptomyces thermoautotrophicus* Nitrogenase

S. thermoautotrophicus was isolated from the covering soil of a burning charcoal pile.**[14,15]** The bacterium uses gases as sources of energy, carbon, and nitrogen (hence designated gasotrophy) and is able to fix $\mathrm{N_2}$ with CO or $\mathrm{H_2}$ plus $\mathrm{CO_2}$ as growth substrate under aerobic conditions.**[14]** $\mathrm{N_2}$ fixation by *S. thermoautotrophicus* exhibits features that are not present in other nitrogen-fixing bacteria. $\mathrm{N_2}$ reduction in this case is coupled with the oxidation of carbon monoxide (CO) by a molybdenum-containing CO dehydrogenase (designated ST3) that transfers the electrons derived from CO oxidation to $\mathrm{O_2}$, thereby producing superoxide anion radicals ($\mathrm{O_2}^{\bullet-}$). A manganese-containing superoxide oxidoreductase (designated ST2) reoxidizes $\mathrm{O_2}^{\bullet-}$ to $\mathrm{O_2}$ and transfers the electrons to a MoFeS-dinitrogenase (designated ST1), where the reduction of $\mathrm{N_2}$ occurs. Among the most striking properties of the *S. thermoautotrophicus* nitrogenase system are the dependence of the enzyme on $\mathrm{O_2}$ and $\mathrm{O_2}^{\bullet-}$, the complete insensitivity of all components involved toward $\mathrm{O_2}$ and $\mathrm{H_2O_2}$, the inability of the enzyme to reduce ethyne or ethene, and a low MgATP requirement for enzymatic activities. In addition, the subunit structure of the *S. thermoautotrophicus* nitrogenase components and the polypeptides involved seem to be dissimilar from the known nitrogenases.**[15]**

6 SUMMARY

Nitrogenases are a class of metalloenzymes that catalyze biological N_2 fixation, the overall reaction of which is usually depicted as: $N_2 + 8H^+ + 16MgATP + 8e^- \longrightarrow 2NH_3 + H_2 + 16MgADP + 16P_i$. Four classes of nitrogenases, that is, the molybdenum nitrogenase, the vanadium nitrogenase, the iron-only nitrogenase, and the *S. thermoautotrophicus* nitrogenase, have been described. The first three classes of nitrogenases are very similar except for the heterometal atom in the active site of the metal cluster (molybdenum, vanadium, or iron), whereas the fourth is superoxide-dependent and apparently different from the other nitrogenases.

The best-characterized molybdenum nitrogenase comprises two metallosulfur proteins, that is, the molybdenum-iron (MoFe) protein and the iron (Fe) protein, both of which are essential for the enzymatic activity. The Fe protein is an α_2 homodimer (encoded by *nifH*) of $M_r \sim 60$ kDa. The two subunits are bridged by a [4Fe–4S] cluster and each has a MgATP binding site. The MoFe protein is an $\alpha_2\beta_2$ tetramer (encoded by *nifD* and *nifK*) of $M_r \sim 220$ kDa. It contains the [8Fe–7S] cluster (P cluster) that is bridged between each $\alpha\beta$ subunit pair and the [Mo–7Fe–9S–homocitrate] cluster (FeMo cofactor or FeMoco) that is located within each α subunit.

The catalysis of molybdenum nitrogenase occurs in a series of steps. First, the reduced Fe protein binds two molecules of MgATP and undergoes a conformational change before forming a complex with the MoFe protein. Then, coupled with the hydrolysis of two MgATP molecules to 2MgADP and $2P_i$, one electron is transferred from the Fe protein to the MoFe protein within the complex. This is followed by complex dissociation, re-reduction of the oxidized Fe protein, and the dissociation of MgADP, which allows the enzyme to start the next cycle of electron transfer. Once a sufficient amount of electrons is accumulated in the MoFe protein, reduction of the bound substrate takes place.

The assembly of the molybdenum nitrogenase Fe protein involves the *nifH* gene and at least the *nifS, nifU*, and *nifM* gene products that are implicated in the [4Fe–4S] cluster assembly, while the assembly of MoFe protein requires at least 15 *nif* gene products and involves the biosynthesis of FeMo cofactor and FeMo cofactor–deficient MoFe protein in separate pathways and the insertion of FeMo cofactor into the MoFe protein.

7 RELATED ARTICLES

Iron–Sulfur Proteins; Nitrogenase: Metal Cluster Models.

8 REFERENCES

1. R. M. Allen, R. Chatterjee, M. S. Madden, P. W. Ludden, and V. K. Shah, *Crit. Rev. Biotechnol.*, 1994, **14**, 225.
2. J. W. Peters, K. Fisher, and D. R. Dean, *Annu. Rev. Microbiol.*, 1995, **49**, 335.
3. J. B. Howard and D. C. Rees, *Chem. Rev.*, 1996, **96**, 2965.
4. B. K. Burgess and D. J. Lowe, *Chem. Rev.*, 1996, **96**, 2983.
5. R. R. Eady, *Chem. Rev.*, 1996, **96**, 3013.
6. L. C. Seefeldt and D. R. Dean, *Acc. Chem. Res.*, 1997, **30**, 260.
7. D. C. Rees and J. B. Howard, *Curr. Opin. Chem. Biol.*, 2000, **4**, 559.
8. B. E. Smith, *Adv. Inorg. Chem.*, 1999, **47**, 159.
9. J. Christiansen, D. R. Dean, and L. C. Seefeldt, *Annu. Rev. Plant Physiol. Plant Mol. Biol.*, 2001, **52**, 269.
10. D. M. Lawson and B. E. Smith, *Met. Ions Biol. Syst.*, 2002, **39**, 75.
11. J. Frazzon and D. R. Dean, *Met. Ions Biol. Syst.*, 2002, **39**, 163.
12. R. R. Eady, *Coord. Chem. Rev.*, 2003, **237**, 23.
13. J. R. Postgate, ‘The Fundamentals of Nitrogen Fixation’, Cambridge University Press, Cambridge, 1982.
14. D. Gadkari, G. Mörsdorf, and O. Meyer, *J. Bacteriol.*, 1992, **174**, 6840.
15. M. Ribbe, D. Gadkari, and O. Meyer, *J. Biol. Chem.*, 1997, **272**, 26627.
16. R. R. Eady, *Met. Ions Biol. Syst.*, 1995, **31**, 363.
17. D. C. Rees, *Annu. Rev. Biochem.*, 2002, **71**, 221.
18. B. K. Burgess, *Chem. Rev.*, 1990, **90**, 1377.
19. J. B. Howard and D. C. Rees, *Annu. Rev. Biochem.*, 1994, **63**, 235.
20. R. N. F. Thorneley and D. J. Lowe, *J. Biol. Inorg. Chem.*, 1996, **1**, 576.
21. H. Schindelin, C. Kisker, J. L. Schlessman, J. B. Howard, and D. C. Rees, *Nature*, 1997, **387**, 370.
22. H. Chiu, J. W. Peters, W. N. Lanzilotta, M. J. Ryle, L. C. Seefeldt, J. B. Howard, and D. C. Rees, *Biochemistry*, 2001, **40**, 641.
23. M. M. Georgiadis, H. Komiya, P. Chakrabarti, D. Woo, J. J. Kornuc, and D. C. Rees, *Science*, 1992, **257**, 1653.
24. J. L. Schlessman, D. Woo, L. Joshua-Tor, J. B. Howard, and D. C. Rees, *J. Mol. Biol.*, 1998, **280**, 669.
25. P. Strop, P. M. Takahara, H. Chiu, H. C. Angove, B. K. Burgess, and D. C. Rees, *Biochemistry*, 2001, **3**, 651.

26. S. B. Jang, L. C. Seefeldt, and J. W. Peters, *Biochemistry*, 2000, **48**, 14745.
27. B. Schmid, O. Einsle, H. J. Chiu, A. Willing, M. Yoshida, J. B. Howard, and D. C. Rees, *Biochemistry*, 2002, **41**, 15557.
28. L. Chen, N. Gavini, H. Tsuruta, D. Eliezer, B. K. Burgess, S. Doniach, and K. O. Hodgson, *J. Biol. Chem.*, 1994, **269**, 3290.
29. P. J. Kraulis, *J. Appl. Crystallogr.*, 1991, **24**, 946.
30. E. A. Merritt and D. J. Bacon, *Methods Enzymol.*, 1997, **277**, 505.
31. P. E. Bishop and R. Premakumar, Alternative Nitrogen Fixation Systems, in 'Biological Nitrogen Fixation', eds. G. Stacey, R. H. Burris, and H. J. Evan, Chapman & Hall, New York, 1992, p. 736.
32. C. Z. Blanchard and B. J. Hales, *Biochemistry*, 1996, **35**, 472.
33. R. Davis, L. Lehman, R. Petrovich, V. K. Shah, G. P. Roberts, and P. W. Ludden, *J. Bacteriol.*, 1996, **178**, 1445.
34. K. Schneider, U. Gollan, M. Dröttboom, S. Selsemeier-Voigt, and A. Müller, *Eur. J. Biochem.*, 1997, **244**, 789.
35. S. Siemann, K. Schneider, M. Dröttboom, and A. Müller, *Eur. J. Biochem.*, 2002, **269**, 1650.
36. R. R. Eady, *Coord. Chem. Rev.*, 2003, **237**, 23.
37. J. Kim and D. C. Rees, *Science*, 1992, **257**, 1677.
38. J. Kim and D. C. Rees, *Nature*, 1992, **360**, 553.
39. M. K. Chan, J. Kim, and D. C. Rees, *Science*, 1993, **260**, 792.
40. J. W. Peters, M. H. Stowell, S. M. Soltis, M. G. Finnegan, M. K. Johnson, and D. C. Rees, *Biochemistry*, 1997, **36**, 1181.
41. M. Sorlie, J. Christiansen, B. J. Lemon, J. W. Peters, D. R. Dean, and B. J. Hales, *Biochemistry*, 2001, **40**, 1540.
42. O. Einsle, F. A. Tezcan, S. L. A. Andrade, B. Schmid, M. Yoshida, J. B. Howard, and D. C. Rees, *Science*, 2002, **297**, 1696.
43. B. Schmid, M. W. Ribbe, O. Einsle, M. Yoshida, L. M. Thomas, D. R. Dean, D. C. Rees, and B. K. Burgess, *Science*, 2002, **296**, 352.
44. J. Kim, D. Woo, and D. C. Rees, *Biochemistry*, 1993, **32**, 7104.
45. J. T. Bolin, A. E. Ronco, T. V. Morgan, L. E. Mortenson, and N. H. Xuong, *Proc. Natl. Acad. Sci. U.S.A.*, 1993, **90**, 1078.
46. S. M. Mayer, D. M. Lawson, C. A. Gormal, S. M. Roe, and B. E. Smith, *J. Mol. Biol.*, 1999, **292**, 871.
47. S. M. Mayer, C. A. Gormal, B. E. Smith, and D. M. Lawson, *J. Biol. Chem.*, 2002, **277**, 35263.
48. J. T. Bolin, N. Campobasso, S. W. Muchmore, W. Minor, T. V. Morgan and L. E. Mortenson, Structure and environment of metal clusters in the nitrogenase molybdenum-iron protein from Clostridium pasteurianum, in 'Molybdenum Enzymes, Cofactors and Model Systems', eds. E. I. Stiefel, D. Coucouvanis, and W. E. Newton, American Chemical Society, Washington, DC, 1993, p. 186.
49. K. K. Surerus, M. P. Hendrich, P. D. Christie, D. Rottgardt, W. H. Orme-Johnson, and E. Münck, *J. Am. Chem. Soc.*, 1992, **114**, 8579.
50. R. Zimmermann, W. H. Orme-Johnson, E. Münck, V. K. Shah, W. I. Brill, M. T. Henzl, and J. Rawlings, *Biochim. Biophys. Acta*, 1978, **537**, 185.
51. G. D. Watt, A. Burns, S. Lough, and D. L. Tennent, *Biochemistry*, 1980, **19**, 4926.
52. A. J. Pierik, H. Wassink, H. Haaker, and W. R. Hagen, *Eur. J. Biochem.*, 1993, **212**, 51.
53. R. C. Tittsworth and B. J. Hales, *J. Am. Chem. Soc.*, 1993, **115**, 9763.
54. V. K. Shah and W. J. Brill, *Proc. Natl. Acad. Sci. U.S.A.*, 1977, **74**, 3249.
55. H.-I. Lee, B. J. Hales, and B. M. Hoffman, *J. Am. Chem. Soc.*, 1997, **119**, 11395.
56. S. J. Yoo, H. C. Angove, V. Papaefthymiou, B. K. Burgess, and E. Münck, *J. Am. Chem. Soc.*, 2000, **122**, 4926.
57. R. N. F. Thorneley and D. J. Lowe, Kinetics and mechanism of nitrogenase enzyme system, in 'Molybdenum Enzymes', ed. T. G. Spiro, John Wiley & Sons, New York, 1985, p. 221.
58. M. G. Yates, The enzymology of molybdenum-dependent nitrogen fixation, in 'Biological Nitrogen Fixation', eds. G. Stacey, R. H. Burris, and H. J. Evan, Chapman & Hall, New York, 1992, p. 685.
59. N. Gavini and B. K. Burgess, *J. Biol. Chem.*, 1992, **267**, 21179.
60. E. H. Bursey and B. K. Burgess, *J. Biol. Chem.*, 1998, **273**, 16927.
61. E. H. Bursey and B. K. Burgess, *J. Biol. Chem.*, 1998, **273**, 29678.
62. G. Palmer, J. S. Multani, W. C. Cretney, W. G. Zumft, and L. E. Mortenson, *Arch. Biochem. Biophys.*, 1972, **153**, 325.
63. W. G. Zumft, G. Palmer, and L. E. Mortenson, *Biochim. Biophys. Acta*, 1973, **292**, 413.
64. H. C. Angove, S. J. Yoo, E. Münck, and B. K. Burgess, *J. Biol. Chem.*, 1998, **273**, 26330.
65. A. C. Nyborg, J. L. Johnson, A. Gunn, and G. D. Watt, *J. Biol. Chem.*, 2000, **275**, 39307.
66. M. Guo, F. Sulc, M. W. Ribbe, P. J. Farmer, and B. K. Burgess, *J. Am. Chem. Soc.*, 2002, **124**, 12100.
67. W. E. Newton, Isolated iron-molybdenum cofactor of nitrogenase, in 'Biological Nitrogen Fixation', eds. G. Stacey, R. H. Burris, and H. J. Evan, Chapman & Hall, New York, 1992, p. 877.
68. W. E. Newton and D. R. Dean, Role of the iron-molybdenum cofactor polypeptide environment in azotobacter vinelandii-nitrogenase catalysis, in 'Molybdenum Enzymes, Cofactors and Model Systems', eds. E. I. Stiefel, D. Coucouvanis, and

W. E. Newton, American Chemical Society, Washington, DC, 1993, p. 216.

69. P. W. Ludden, V. K. Shah, G. P. Roberts, M. Homer, R. Allen, T. Paustian, J. Roll, R. Chatterjee, M. Madden and J. Allen, Biosynthesis of the iron-molybdenum cofactor of nitrogenase, in ‘Molybdenum Enzymes, Cofactors and Model Systems’, eds. E. I. Stiefel, D. Coucouvanis, and W. E. Newton, American Chemical Society, Washington, DC, 1993, p. 196.
70. R. C. Pollock, H. I. Lee, L. M. Cameron, V. I. Derose, B. J. Hales, W. H. Orme-Johnson, and B. M. Hoffman, *J. Am. Chem. Soc.*, 1995, **117**, 8686.
71. P. D. Christie, H. I. Lee, L. M. Cameron, B. J. Hales, W. H. Orme-Johnson, and B. M. Hoffman, *J. Am. Chem. Soc.*, 1996, **118**, 8707.
72. H. I. Lee, L. M. Cameron, B. J. Hales, and B. M. Hoffman, *J. Am. Chem. Soc.*, 1997, **119**, 10121.
73. H. I. Lee, M. Sorlie, J. Christiansen, R. T. Song, D. R. Dean, B. J. Hales, and B. M. Hoffman, *J. Am. Chem. Soc.*, 2000, **122**, 5582.
74. S. J. George, G. A. Ashby, C. W. Wharton, and R. N. F. Thorneley, *Am. Chem. Soc.*, 1997, **119**, 6450.
75. M. J. Ryle, H. I. Lee, L. C. Seefeldt, and B. M. Hoffman, *Biochemistry*, 2000, **39**, 1114.
76. S. K. Ibrahim, K. Vincent, C. A. Gormal, B. E. Smith, S. P. Best, and C. J. Pickett, *Chem. Commun.*, 1999, **11**, 1019.
77. S. D. Conradson, B. K. Burgess, S. A. Vaughn, A. L. Roe, B. Hedman, K. O. Hodgson, and R. H. Holm, *J. Biol. Chem.*, 1989, **264**, 15967.
78. H. I. Liu, A. Filipponi, N. Gavini, B. K. Burgess, B. Hedman, A. Dicicco, C. R. Natoli, and K. O. Hodgson, *J. Am. Chem. Soc.*, 1994, **116**, 2418.
79. A. J. M. Richards, D. J. Lowe, R. L. Richards, A. J. Thomson, and B. E. Smith, *Biochem. J.*, 1994, **297**, 373.
80. K. L. C. Grönberg, C. A. Gormal, B. E. Smith, and R. A. Henderson, *Chem. Commun.*, 1997, **7**, 713.
81. P. M. C. Benton, S. M. Mayer, J. L. Shao, B. M. Hoffman, D. R. Dean, and L. C. Seefeldt, *Biochemistry*, 2001, **40**, 13816.
82. P. M. C. Benton, M. Laryukhin, S. M. Mayer, B. M. Hoffman, D. R. Dean, and L. C. Seefeldt, *Biochemistry*, 2003, **42**, 9102.
83. B. K. Burgess, Nitrogenase structure, function and genetics, in ‘Molybdenum Enzymes, Cofactors and Model Systems’, eds. E. I. Stiefel, D. Coucouvanis, and W. E. Newton, American Chemical Society, Washington, DC, 1993, p. 144.
84. P. C. Dos Santos, D. R. Dean, Y. Hu, and M. W. Ribbe, *Chem. Rev.*, 2004, **104**, 1159.
85. L. Zheng, R. H. White, V. L. Cash, R. F. Jack, and D. R. Dean, *Proc. Natl. Acad. Sci. U.S.A.*, 1993, **90**, 2754.
86. L. Zheng and D. R. Dean, *J. Biol. Chem.*, 1994, **269**, 18723.
87. L. Zheng, R. H. White, V. L. Cash, and D. R. Dean, *Biochemistry*, 1994, **33**, 4714.
88. P. Yuvaniyama, J. N. Agar, V. L. Cash, M. K. Johnson, and D. R. Dean, *Proc. Natl. Acad. Sci. U.S.A.*, 2000, **97**, 599.
89. D. R. Dean and M. R. Jacobson, Biochemical genetics of nitrogenase, in ‘Biological Nitrogen Fixation’, eds. G. Stacey, R. H. Burris, and H. J. Evan, Chapman & Hall, New York, 1992, p. 763.
90. M. W. Ribbe, Y. Hu, M. Guo, B. Schmid, and B. K. Burgess, *J. Biol. Chem.*, 2002, **277**, 23469.
91. R. A. Ugalde, J. Imperial, V. K. Shah, and W. J. Brill, *J. Bacteriol.*, 1984, **159**, 888.
92. W. A. Fuller, R. M. Kemp, J. C. Ng, T. R. Hawkes, and B. E. Smith, *Eur. J. Biochem.*, 1986, **160**, 371.
93. A. C. Robinson, B. K. Burgess, and D. R. Dean, *J. Bacteriol.*, 1986, **166**, 180.
94. V. K. Shah, J. R. Allen, N. J. Spangler, and P. W. Ludden, *J. Biol. Chem.*, 1994, **269**, 1154.
95. R. M. Allen, R. Chatterjee, P. W. Ludden, and V. K. Shah, *J. Biol. Chem.*, 1995, **270**, 26890.
96. P. Rangaraj, M. J. Ryle, W. N. Lanzilotta, P. J. Goodwin, D. R. Dean, V. K. Shah, and P. W. Ludden, *J. Biol. Chem.*, 1999, **274**, 29413.
97. P. J. Goodwin, J. N. Agar, J. T. Roll, G. P. Roberts, M. K. Johnson, and D. R. Dean, *Biochemistry*, 1998, **37**, 10420.
98. P. Rangaraj, C. Ruttimann-Johnson, V. K. Shah, and P. W. Ludden, *J. Biol. Chem.*, 2001, **276**, 15968.
99. J. T. Roll, V. K. Shah, D. R. Dean, and G. P. Roberts, *J. Biol. Chem.*, 1995, **270**, 4432.
100. V. K. Shah, P. Rangaraj, R. Chatterjee, R. M. Allen, J. T. Roll, G. P. Roberts, and P. W. Ludden, *J. Bacteriol.*, 1999, **181**, 2797.
101. L. M. Zheng, R. H. White, and D. R. Dean, *J. Bacteriol.*, 1997, **179**, 5963.
102. T. R. Hoover, A. D. Robertson, R. L. Cerny, R. N. Hayes, J. Imperial, V. K. Shah, and P. W. Ludden, *Nature*, 1987, **329**, 855.
103. R. M. Allen, R. Chatterjee, P. W. Ludden, and V. K. Shah, *J. Biol. Chem.*, 1996, **271**, 4256.
104. R. Chatterjee, R. M. Allen, V. K. Shah, and P. W. Ludden, *J. Bacteriol.*, 1994, **176**, 2747.
105. A. C. Robinson, D. R. Dean, and B. K. Burgess, *J. Biol. Chem.*, 1987, **262**, 14327.
106. M. J. Homer, T. D. Paustian, V. K. Shah, and G. P. Roberts, *J. Bacteriol.*, 1993, **175**, 4907.
107. M. J. Homer, D. R. Dean, and G. P. Roberts, *J. Biol. Chem.*, 1995, **270**, 24745.
108. L. M. Rubio, P. Rangaraj, M. J. Homer, G. P. Roberts, and P. W. Ludden, *J. Biol. Chem.*, 2002, **277**, 14299.
109. J. Christiansen, P. J. Goodwin, W. N. Lanzilotta, L. C. Seefeldt, and D. R. Dean, *Biochemistry*, 1998, **37**, 12611.
110. A. C. Robinson, T. W. Chun, J.-G. Li, and B. K. Burgess, *J. Biol. Chem.*, 1989, **264**, 10088.
111. S. Tal, T. W. Chun, N. Gavini, and B. K. Burgess, *J. Biol. Chem.*, 1991, **266**, 10654.

112. M. W. Ribbe and B. K. Burgess, *Proc. Natl. Acad. Sci. U.S.A.*, 2001, **98**, 5521.

113. E. Krahn, B. J. R. Weiss, M. Kröckel, J. Groppe, G. Henkel, S. P. Cramer, A. X. Trautwein, K. Schneider, and A. Müller, *J. Biol. Inorg. Chem.*, 2002, **7**, 37.

Acknowledgments

Work in our laboratory is supported by the National Institute of Health, GM-67626 (MWR).

Noble Gases: Inorganic Chemistry

David A. Atwood
University of Kentucky, Lexington, KY, USA

Based in part on the article Noble Gases: Inorganic Chemistry by Boris Žemva which appeared in the Encyclopedia of Inorganic Chemistry, First Edition.

1 Introduction 1
2 The Noble Gas Elements 1
3 Weakly Bonded Species of Noble Gases 1
4 The Preparation of the First True Chemical Compound of a Noble Gas 2
5 The Chemistry of Xenon 2
6 The Chemistry of Krypton 14
7 The Chemistry of Radon 16
8 The Chemistry of the Lighter Noble Gases 16
9 Explosion Hazards with Noble Gas Compounds 16
10 Bonding in Noble Gas Compounds 16
11 Recent Developments in Transition Metal Derivatives 17
12 Applications 17
13 Related Articles 17
14 Further Reading 18
15 References 18

1 INTRODUCTION

In the early 1890s, Lord Rayleigh discovered that nitrogen obtained by removal of the gases O_2, CO_2, H_2O from an air sample was denser than nitrogen obtained by chemical procedures. Among other theories for this discrepancy was the idea that some heavier unknown gas was present in the air. In 1894, Lord Rayleigh and William Ramsay discovered that this unknown gas was a new element.[1] Because the gas was shown to be chemically inert, they named it argon, from Greek, *argon*, meaning inactive. The other members of the noble gas (Ng) series were discovered and isolated in the subsequent years up to 1900 by William Ramsay and his assistant Morris Travers. They used a new experimental technique, low-temperature distillation.

The element helium, from Greek *helios*, the sun, had already been noted in the Sun's spectrum in 1868, but was not isolated as a terrestrial element until 1895, when Ramsay obtained it by heating the mineral uraninite in which the helium was physically trapped. With an improved technique of liquid air distillation, Ramsay and Travers isolated neon (Greek, *neos*, new), krypton (Greek, *kryptos*, hidden), and xenon (Greek, *xenon*, stranger). An excellent account of the discovery of the noble gases and the early controversy regarding the discovery of argon is given by Travers.[2]

The last of the family of the noble gases was found in 1900 by Owens and Rutherford. This was radon-220, a product of the *Radioactive Decay* of thorium. Also in the same year, radon-222, which is a product of the radioactive decay of radium, was discovered by Dorn.

This article will cover the general chemistry of some of the more common noble gas species, including fluorides, oxides, transition metal salts, and derivatives of carbon and nitrogen.

2 THE NOBLE GAS ELEMENTS

Helium is the second most abundant element in the universe. In the Earth, it is continuously formed by radioactive decay, mostly of uranium and thorium. Its present concentration in the atmosphere is probably the equilibrium concentration between the amount being released from the Earth's crust and the amount of helium escaping from the atmosphere into space. The atmosphere represents the major source for neon, argon, krypton, and xenon. They are produced as by-products during fractional distillation of liquid air. Radon is obtained from the radioactive decay of radium.

The noble gases have closed-shell electronic structures ($1s^2$ for helium and ns^2np^6 for the other noble gases) (*see* ***Electronic Structure of Main-group Compounds***) and are extremely stable, as shown by the high ionization energies, especially of the lighter members: He, 24.58; Ne, 21.56; Ar, 15.76; Kr, 14.00; Xe, 12.13; Rn, 10.75 eV. They are all colorless, odorless, tasteless, low-boiling, monoatomic gases whose physical properties vary systematically with atomic number.[3] The boiling point of helium is the lowest of any known substance. The weak forces between noble gas atoms are proportional to the *Polarizability* element and increase with the increasing size of the electron clouds.

The ability of these gases to form true chemical compounds with other atoms is limited to the heavier members of the group, krypton, xenon, and radon, where the first ionization energies are reduced to a level comparable with other chemically active elements. Theoretical studies, however, have indicated that it may be possible to isolate helium derivatives, such as MeBeHe.[4] Many of the compounds are prepared at low temperature and characterized through spectroscopic techniques. More recently, multinuclear NMR has emerged as an extremely useful characterization technique.[5]

3 WEAKLY BONDED SPECIES OF NOBLE GASES

The species known before 1962 that contained noble gases combined with other elements and molecules were cationic species, observed only in the gas phase, or inclusion compounds. The latter involve noble gas atoms held in host crystal lattices, with only weak London exchange interactions helping to fix the gases in the lattice cage.

Emission spectra from discharge tubes or from mass spectrometric studies containing a single gas or mixtures of pure noble gases give evidence for the presence of diatomic molecules. Usually, it is not clear if these are neutral molecules or ions. Ions are more likely to exist because chemical bond formation seems more likely when the closed-shell arrangement is destroyed by removal of an electron. There is also spectroscopic evidence for diatomic molecules between noble gas atoms and other atoms (e.g. H, O, N, Hg) or molecules (e.g. CO_2, N_2, SF_6, etc.). All these species have exceedingly short lifetimes.

Inclusion compounds, or clathrates, are known where the noble gas is present within a crystalline framework of water (general ideal formula $8\,Ng{\cdot}46H_2O$) or hydroquinone ($Ng{\cdot}3C_6H_4(OH)_2$). There are no chemical bonds holding the guest atoms or molecules to the host molecules. Because it is difficult to define exactly what is and what is not a chemical bond, it is better to compare the energies involved.**[6]** The energies with which noble gas atoms are bound in clathrates are 10 times higher than the van der Waals energies between the noble gas atoms probably owing to the permanent dipoles possessed by the host molecules. By comparison, the energies in common chemical bonds are 10 times higher than bonding energies in clathrates. There are extensive reviews of weakly bound species of noble gases by Holloway**[7]** and Bartlett and Sladky.**[8]**

4 THE PREPARATION OF THE FIRST TRUE CHEMICAL COMPOUND OF A NOBLE GAS

After argon was isolated as the first member of the noble gas group in 1894 by Rayleigh and Ramsay, they tried various chemical reagents to form compounds of the new element, but without success. Ramsay also sent a 100-mL sample of the gas to his friend Moissan, the discoverer of fluorine, so that he could attempt to prepare a fluoride. His unsuccessful experiment was considered the ultimate test for the chemical inertness of argon. Unfortunately, some years later, the electronic theory of valence reinforced the notion of the chemical inertness of the noble gases. The noble gas valence-electron configuration was defined as the configuration to which other elements tend in their chemical bonding.

In 1933, besides some theoretical speculations that noble gas compounds should exist, some new reports of unsuccessful experiments to prepare noble gas compounds were published. The most promising experiment was carried out by Yost and Kaye**[9]** at the suggestion of Pauling, who was convinced that at least the heavier noble gases, for example, xenon, should react with the most electronegative elements, for example, fluorine (*see* ***Fluorine: Inorganic Chemistry***). The failure of Yost and Kaye was really very unfortunate, since a similar experiment, carried out 32 years later, using sunlight in place of their electrical discharge, was successful.

Bartlett and Lohmann proved that an oxyfluoride of platinum, made by fluorination in the presence of oxygen, was the salt $O_2{}^+PtF_6{}^-$. This indicated that PtF_6 was an oxidizer of unexpected power. Bartlett immediately noted that the ionization potential of the xenon atom is almost identical to that of the oxygen molecule ($I(O_2) = 12.2\,eV$, $I(Xe) = 12.13\,eV$). He tried the reaction of xenon gas with PtF_6 vapors. Yellow–orange xenon fluoroplatinate(V) was obtained.**[10]** This and the subsequent studies at Argonne National Laboratory, where PtF_6 had first been prepared in 1957, started a new era of inorganic chemistry. Interest was so wide that a special meeting on noble gas compounds was organized at Argonne eight months after the first preparation of the true xenon compound.**[11]** Since then, many books and reviews treating the developments in noble gas chemistry have been published.**[8,12–16]**

5 THE CHEMISTRY OF XENON

5.1 Xenon Fluorides

Three binary fluorides of xenon are known: XeF_2, XeF_4, and XeF_6. XeF_8 is not known (*see* ***Fluorides: Solid-state Chemistry***). The fluorides are readily prepared from the elements and are thermodynamically stable. Full characterization data is available for these compounds, including gas-phase ^{129}Xe and ^{19}F NMR data.**[17]** The commercial availability of XeF_2 has greatly increased the study and use of this reagent.**[18]**

5.1.1 Xenon Difluoride

Xenon difluoride was prepared for the first time from a xenon–fluorine gas mixture using an electric discharge.**[19]** Other kinds of energy, such as heat, UV light, sunlight, high-intensity γ-radiation, irradiation by electrons from a van de Graaff accelerator, irradiation by 10 MeV protons and so on, are also effective. A convenient preparation using very simple apparatus, and affording a pure product, is the exposure of a xenon–fluorine gas mixture to sunlight. Very pure XeF_2 in greater quantities (up to 1 kg) can be best prepared by UV irradiation (*see* ***Photosynthesis***) of a gaseous xenon–fluorine mixture in the mole ratio 1:2, with addition of about 1 mol% of HF in the fluorine as a catalyst. The thermal reaction between xenon and fluorine to form xenon difluoride is heterogeneous and takes place on the prefluorinated walls of the reaction vessel and/or the surface of an added fluoride, such as NiF_2. In the presence of NiF_2, it is possible to synthesize even XeF_6 at

393 K, starting with the gaseous mixture $Xe:F_2 = 1:5$. Xenon difluoride is colorless as solid, liquid, or gas. The vapor pressure of the solid at 298 K is 6.0×10^2 Pa, and therefore at room temperature large crystals are usually formed. The ΔH_f (solid) is $-163\,kJ\,mol^{-1}$.

In crystalline XeF_2, the linear molecules are aligned parallel in a body-centered tetragonal array (Figure 1). Each xenon atom has two bound fluorine atoms at 2.00 Å and eight fluorine atoms from fluorine ligands of the eight nearest XeF_2 neighbors at 3.42 Å. It is evident that there are strong interactions between XeF_2 molecules. This structural arrangement is compatible with the high enthalpy of sublimation of XeF_2 ($55.7\,kJ\,mol^{-1}$) and the assumed charge distribution in each molecule ($^{-05}F–Xe^{+1}–F^{-05}$). It is further evident from the packing arrangement that the equatorial region of each XeF_2 molecule is avoided by fluorine ligands of neighboring molecules because the nonbonding valence electrons of the xenon atom effectively shield the positive charge on the xenon.

Xenon difluoride dissolves in the halogen fluorides BrF_3, BrF_5, and IF_5 and in AHF (anhydrous hydrogen fluoride) as monomolecular species geometrically similar to the gas-phase species. XeF_2 sometimes forms complexes with the solvents (e.g. BrF_3 and IF_5). XeF_2 is also soluble in MeCN and other organic solvents.

XeF_2 is potentially a strong oxidizer, but is frequently unreactive for kinetic reasons. Its stability in aqueous solution is an example of this kinetic inertness. XeF_2 dissolves in water ($\approx 25\,g\,L^{-1}$ at 273 K) with only slight decomposition. XeF_2 may be recovered by extraction with CCl_4 or by fractional distillation. The equilibrium constant for equation (1) has been estimated to be about 10^{40}. This explains the observation that the fluorination of uranium and zirconium oxides by XeF_2 is initiated by the addition of water to the reaction mixture.[20] XeF_2 is, generally, a very good fluorinating agent for a wide range of substrates.[21]

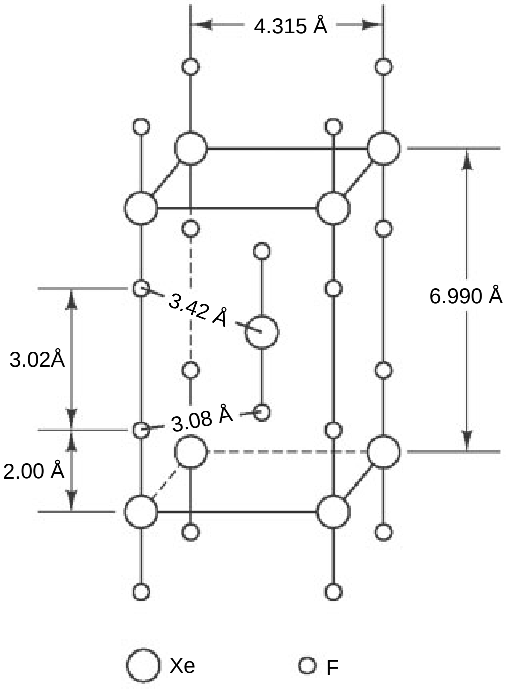

Figure 1 Unit cell of xenon difluoride

$$XeF_2(aq) + H_2O \longrightarrow Xe(g) + 0.5\,O_2(g) + 2HF(aq) \qquad (1)$$

Neutral and acid aqueous solutions of XeF_2 decompose rather slowly (half-life being ≈ 7 h at 273 K), while the decomposition in basic solution is fast, the base catalytic effect being roughly in the order of the base strength. XeF_2 is stable in dried propylene carbonate.[22]

5.1.2 *Xenon Tetrafluoride*

Xenon tetrafluoride was the first noble gas binary fluoride to be synthesized. It was prepared by heating a gaseous mixture of xenon and fluorine in the mole ratio 1:5 at a total pressure of 0.6 MPa at 673 K in a closed nickel can.[23] These conditions are close to the optimum for XeF_4 preparation.[24] Low temperatures and high-fluorine pressures favor XeF_6 formation, while low fluorine pressures and high temperatures favor XeF_2 formation. If high purity XeF_4 is desired, it is necessary to purify it by chemical methods because it is nearly impossible to separate xenon difluoride from the tetrafluoride by physical means (the two have similar vapor pressures and also form a 1:1 adduct). A general chemical purification method that can be used for any mixture of xenon fluorides exploits the inferior fluoride ion donor ability of XeF_4 compared to XeF_2 or XeF_6 (equation 2).[25]

$$\left.\begin{array}{l} XeF_2 \\ XeF_4 \\ XeF_6 \end{array}\right\} \text{in } BrF_5 \text{ soln.} + AsF_5(\text{excess}) \xrightarrow[273\,K]{-AsF_5,\ -BrF_5}$$

$$XeF_4 + (Xe_2F_3)^+AsF_6^- + XeF_5^+AsF_6^- \xrightarrow[293\,K]{\text{vacuum}} XeF_4 \qquad (2)$$

Other preparative methods include the photochemical reaction between xenon and excess of fluorine in the presence of NiF_2 as catalyst, thermal decomposition of XeF_6 in the presence of NaF (this method is also convenient for the preparation of pure fluorine) and the pyrolysis of some XeF^+ salts such as $XeF^+PtF_6^-$ or $XeF^+Pd_2F_9^-$ at 423 K (equations 3 and 4).

$$2XeFPtF_6(c) \longrightarrow XeF_4(g) + XePt_2F_{10}(c) \qquad (3)$$

$$XePd_2F_{10}(c) \longrightarrow XeF_4(g) + Pd_2F_6(c) \qquad (4)$$

XeF_4 is colorless as crystals, liquid, or vapor. The vapor pressure of the solid at 298 K is 3.4×10^2 Pa and the ΔHf is $-266\,kJ\,mol^{-1}$. Vibrational spectroscopic and electron diffraction data have proven that the $XeF_4(g)$ molecule is

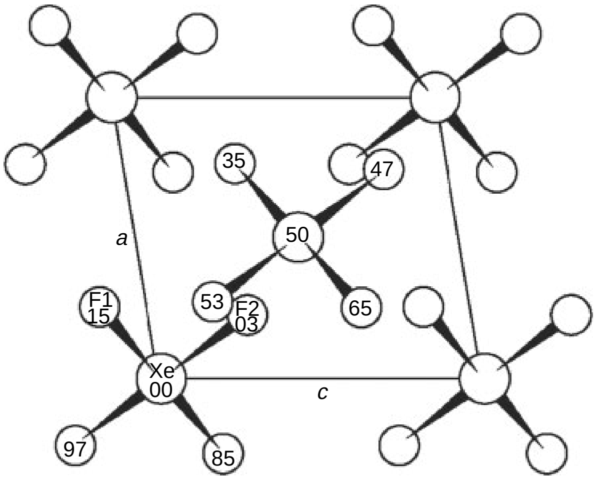

Figure 2 Molecular packing in XeF_4 as seen in projection down the *b* axis. The numbers on some of the atoms are *b* coordinates (×100)

square-planar (D_{4h}) with a Xe–F bond length of 1.94 Å (*see* ***Diffraction Methods in Inorganic Chemistry***). The size and the shape of XeF_4 in the crystal is not significantly different from the gas-phase molecule (see Figure 2). The Xe–F bond length in the solid is 1.953 Å and the F–Xe–F angle is 90.0°. The enthalpy of sublimation of XeF_4 (61 kJ mol^{-1}) indicates strong electrostatic interactions between XeF_4 molecules, as in the case of XeF_2.

XeF_4 can be kept in thoroughly dried glass or quartz and can be stored indefinitely in Kel-F (polyfluorotrichloroethylene), nickel, or monel containers. XeF_4 hydrolyzes very rapidly, with one-third of the xenon remaining in the solution as the trioxide (equation 5).

$$3XeF_4 + 6H_2O \longrightarrow XeO_3 + 2Xe + 1.5O_2 + 12HF \qquad (5)$$

The low bond energy of XeF_4 causes it to be a strong oxidative fluorinator (comparable with BrF_3), but it has high-kinetic inertness like XeF_2.

5.1.3 *Xenon Hexafluoride*

The first synthesis of XeF_6 was also reported in 1962.[26] All syntheses are best carried out in nickel or monel reaction vessels. From the equilibrium constants for the formation of xenon fluorides,[24] it is evident that an excess of fluorine is necessary to minimize the formation of XeF_4. In addition, the reaction temperature should be as low as possible, yet consistent with a reasonable reaction rate. In the presence of NiF_2 as catalyst the activation energy for the xenon–fluorine reaction is lowered and the reaction proceeds rapidly at 393 K, in contrast to 523 K without catalyst.

XeF_6 may be purified from other xenon fluorides and $XeOF_4$ by its complexation with sodium fluoride at 323 K. Impurities ($XeOF_4$, XeF_2, XeF_4) may be removed under vacuum at 323 K, the Na_2XeF_8 complex being stable at that temperature. XeF_6 is recovered by decomposing the complex at 398 K. Solid XeF_6 is colorless below the melting point, while the liquid and vapor are yellow–green. XeF_6 is much more volatile than XeF_2 or XeF_4, although much less so than other hexafluorides. Its ΔH_f is −338 kJ mol^{-1}.

The crystal structure of solid XeF_6 is complex. The solid assumes at least four distinct crystalline polymorphic forms (*see Polymorph*). The existence of three modifications was shown by heat capacity measurements.[27] These polymorphic phases were designated I, II, and III in order of decreasing temperature, with transitions at 291.8 K and 253.8 K. The phase IV is a cubic phase that exists from the melting point of XeF_6 to at least 93 K. Phase I is a high-temperature monoclinic modification, phase II is the orthorhombic form, and phase III is a low-temperature monoclinic form. The phases I, II, and III all contain tetrameric rings that approximate to F^--bridged $XeF_5{}^+$ clusters. Transformations between these three phases occur relatively easily, since all contain only tetramers. Solid–solid transformations seem to occur only when both phases contain the same structural units. Solid–solid transformations are not observed between these tetramer-based phases and the cubic phase, which contains both tetramers and hexamers. The crystal structure of the cubic modification (phase IV)[28] is shown in Figure 3. The hexameric clusters, like the tetramers, can also be viewed as F^--bridged clusters of $XeF_5{}^+$ species. Clearly, this phase cannot transform to the tetramer-based forms without breakup of the hexameric units, which must require considerable reorganization energy.

A comparison of the density of liquid XeF_6 with the densities of all the other hexafluorides shows that its density is unexpectedly high. This is linked with the association of the molecules in the liquid phase and may well involve aggregations similar to those observed in the crystal phases. The unusually large heat capacity of the liquid is in accord with this. Near the melting point the heat capacity of the liquid is almost twice as great as that of the solid. This places XeF_6 not only in a unique position among the other hexafluorides, but also among all other liquids in general. The entropy of vaporization of XeF_6 at its boiling point has the extraordinarily high value of 136.9 J K^{-1} mol^{-1}. This seems to be the highest entropy of vaporization observed for any known liquid. The association of molecules in the liquid phase must be caused by intermolecular forces beyond those of the van der Waals type. Strongly interacting $XeF_5{}^+$ and F^- species in tight clusters may be the cause. The gas-phase XeF_6 molecule has no dipole moment, but the autoionization observed in the solid state provides for the required strong association.

XeF_6 is a much more powerful oxidizer and fluorinator than the lower xenon fluorides. It also has lower kinetic stability than XeF_2 and XeF_4. Thus XeF_6 cannot be stored in glass or quartz, but reacts with them by exchanging fluorine for oxygen to yield initially $XeOF_4$, subsequently XeO_2F_2, and finally xenon trioxide (see Sections 5.2.1 and 9).

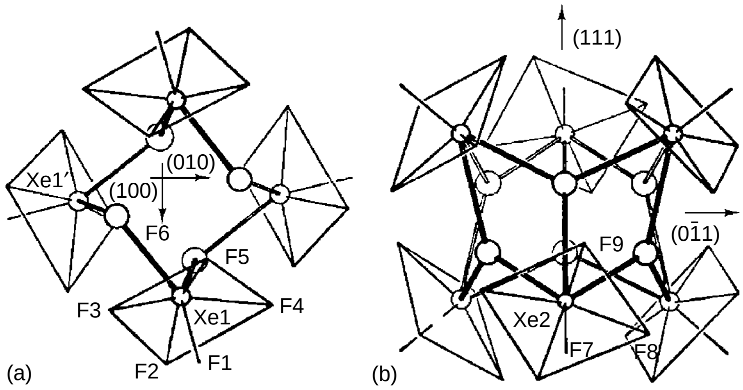

Figure 3 (a) Tetramer of $XeF_5{}^+F^-$, (b) hexamer of $XeF_5{}^+F^-$. Xenon atoms are indicated by small circles and bridging fluoride ions by large circles; $XeF_5{}^+$ ions are drawn in skeletal form

5.2 Xenon Oxides

Among xenon oxides only XeO_3 and XeO_4 have been definitively isolated and characterized. XeO is known, as a gas-phase species, to be bound with respect to a $^1D(0)$ atom but not with respect to ground-state $^3P(0)$. There is no evidence for a condensed phase XeO species. Recently, however, the unique radical, HXeO, has been isolated by UV photolysis of either H_2O/Xe or N_2O/HBr/Xe solid mixtures as 7 K. The compound was characterized by IR and its intrinsic stability supported by ab initio calculations.[29]

5.2.1 *Xenon Trioxide*

XeO_3 may be prepared by controlled hydrolysis of XeF_6 at low temperature (equation 6).[30] It can also be derived from XeF_4 as already described. The best hydrolysis is performed in the presence of sufficient magnesium oxide (MgO) to rapidly neutralize all the hydrogen fluoride (HF) produced. Aqueous XeO_3 solutions are indefinitely stable if reducing impurities and light are excluded. If the solution is evaporated to dryness the solid oxide may detonate.

$$XeF_6(g) + 3H_2O(l) \longrightarrow 6HF(aq) + XeO_3(aq) \qquad (6)$$

XeO_3 is a colorless, hygroscopic, detonatable solid with a low vapor pressure at room temperature. Its ΔH_{sub} is 126 (42) kJ mol^{-1} and ΔH_f is 402 kJ mol^{-1}.

5.2.2 *Xenon Tetroxide*

XeO_4 was first prepared by the reaction of concentrated sulfuric acid with xenates(VIII) at room temperature or lower.[31] When the reaction is carried out slowly, about one-third of the xenon is converted to XeO_4. The tetroxide is purified by vacuum sublimation. XeO_4 is a pale yellow solid that, at 273 K, has a vapor pressure of about 33×10^2 Pa, while at 195 K its volatility is still high enough for mass spectrometric detection. Usually, decomposition to xenon and oxygen occurs before the sample reaches 273 K. The decomposition is often violent in accord with the enthalpy of formation of XeO_4 (642 kJ mol^{-1}). XeO_4 is an oxidizing agent of great power. Its structure has been investigated in the gas phase by electron diffraction and shown to be tetrahedral with Xe–O = 1.74 Å.

5.3 Xenon Oxyfluorides

All possible xenon(IV) and xenon(VI) oxyfluorides are known. Among the xenon(VIII) oxyfluorides, only $XeOF_6$ is not yet isolated.

5.3.1 *Xenon Oxide Difluoride*

$XeOF_2$ has been prepared in the reaction of XeF_4 with water in HF solvent at 210 K.[32] $XeOF_2$ presumably decomposes slowly even at 210 K to yield XeF_2 and oxygen. After the reaction is completed, the product is washed with HF at 195 K to remove traces of unreacted water and XeF_2. $XeOF_2$ is a light-yellow solid that decomposes explosively at ca. 273 K On slow warming from 210 to 273 K over a period of 20 h, $XeOF_2$ decomposes to XeF_2 and XeO_2F_2. The solid $XeOF_2$ is characterized by its Raman spectrum (in cm^{-1}) (relative intensities in parentheses): 732 (8), 496 (100), 285 (4), 186 (8), 197 (1).

5.3.2 *Xenon Oxide Tetrafluoride*

$XeOF_4$ was first detected as an impurity by mass spectrometry among the xenon fluorides prepared by thermal methods. It was obtained in macroscopic quantities by the partial hydrolysis of xenon hexafluoride (equation 7).[33] Unreacted XeF_6 and HF formed in the reaction are removed by treatment with NaF.

$$XeF_6 + H_2O \longrightarrow XeOF_4 + 2HF \qquad (7)$$

$XeOF_4$ is known from NMR, vibrational, and *Microwave Spectroscopy* to be a square-based pyramid with an oxygen ligand at the apex (C_{4v}). The microwave data show the xenon and four fluorine atoms to be nearly in the same plane. The Xe–F bond length (1.903 Å) is very similar to that found for XeF_6 (1.890 Å). The Xe–O bond length (1.706 Å) is shorter than in XeO_3 (1.76 Å) or XeO_4 (1.74 Å). The observed geometry is consistent with location of the nonbonding electron pair on the fourfold molecular axis trans to the oxygen atom.

$XeOF_4$ is colorless as solid, liquid, and gas. It has a low-melting point (226.95 K) and is quite volatile (11×10^2 Pa at 273 K). The liquid is nonassociated and the low-electrical conductivity of the pure liquid indicates that autoionization is not significant. The liquid has, at 297 K, a dielectric constant of 24.6 and dissolves alkali fluorides with considerable enhancement of its electrical conductivity. $XeOF_4$ is the most stable molecular compound containing a Xe–O bond. It is thermally stable to nearly 573 K, where it starts to decompose slowly to XeF_4 and oxygen.

5.3.3 Xenon Dioxide Difluoride

XeO_2F_2 was observed in the early mass spectra of xenon fluorides and can be obtained by hydrolysis of XeF_6. The best method for its preparation in macroscopic quantities is by the reaction of XeO_3 and $XeOF_4$.**[34]** The $XeOF_4$ and XeF_2 impurities may be removed by fractional distillation. Xenon dioxide difluoride forms colorless crystals at room temperature, which have a vapor pressure between that of XeO_3 and $XeOF_4$ and melts at 303.95 K to give a colorless liquid. It can decompose to XeF_2 and O_2.

5.3.4 Xenon Dioxide Tetrafluoride

XeO_2F_4 was made by the reaction of XeO_3F_2 (see Section 5.3.5) and XeF_6 in $XeOF_4$ as solvent.**[35]** It was identified by *Mass Spectrometry*. XeO_2F_4 is the most volatile of all known xenon compounds and may therefore possess the symmetrical, nonpolar, D_{4h} symmetry.

5.3.5 Xenon Trioxide Difluoride

XeO_3F_2 was the first oxyfluoride of octavalent xenon to be prepared. It was made by reaction of XeF_6 with sodium perxenate solid at room temperature.**[36]** XeO_3F_2 is, like XeO_4, sufficiently volatile to distil at 195 K. The much greater volatility of XeO_3F_2 as compared to XeO_2F_2 indicates that the molecule of XeO_3F_2 is more symmetrical and probably nonpolar (D_{3h}).

XeO_3F_2 can be prepared in much better yield by the reaction of XeF_6 with XeO_4. Because XeO_3F_2 is rapidly destroyed by XeF_6 with formation of $XeOF_4$, special care must be taken to remove XeO_3F_2 (under vacuum) from the reaction vessel at 195 K immediately after all XeO_4 has been consumed. Structural information has been derived only from vibrational spectroscopy. On this basis, it has been concluded that the molecule XeO_3F_2 has the symmetry D_{3h}. The melting point of XeO_3F_2 is 219.05 ± 0.5 K. The vapor pressure of XeO_3F_2 as a function of temperature is (in 10^2 Pa) 5 at 222.75 K, 7 at 222.35 K, 16 at 236.25 K, 13 at 236.35 K, 29 at 243.85 K, and 32 at 245.15 K.**[37]** Its heat of vaporization is 33.0 ± 3.0 kJ mol^{-1}. The extrapolated boiling point is 313 K.

5.4 The Dixenon Cation

Green $Xe_2{}^+$ is formed either by oxidation of gaseous xenon, for example, with $O_2{}^+Sb_2F_{11}{}^-$ salt, or by reduction of XeF^+ salt with water or other reducing agents.**[38]** $Xe_2{}^+$ was also identified by the resemblance of its spectrum to the spectrum of the isoelectronic $I_2{}^-$ anion. The $Xe_2{}^+$ cation has a Raman band at 123 cm^{-1}.

5.5 Xenon(II) Compounds

XeF_2 forms many compounds with binary fluorides, oxide tetrafluorides, and some anhydrous acids. Strong fluoride ion acceptors, for example, such as AsF_5 and SbF_5, can withdraw a fluoride ion from XeF_2 forming XeF^+ species**[38,39]** or, in the case of excess XeF_2, also $Xe_2F_3{}^+$ species. The increase in the Xe–F bond energy in the cation formation (133.9 kJ mol^{-1} in XeF_2, 195.9 kJ mol^{-1} in the cation) contributes to the fluoride ion donor ability of the difluoride. A study focusing on the Lewis acid reactivity of XeF+ with various bases in the gas phase determined the bond dissociation enthalpy to be 188 kJ mol 1.**[39]** Xenon difluoride also forms molecular adducts in which the negatively charged F ligands of XeF_2 are attracted by the positive center of the partner molecule of the adduct.

Xenon(II) compounds can be prepared by fusing stoichiometric amounts of the component fluorides in an atmosphere of a dry inert gas or by dissolving them in a nonoxidizing or reducing solvent. One component can also be used in excess and removed by vacuum distillation to constant weight. Some reactions between binary fluorides in lower oxidation states and XeF_2 have also been carried out in a melt of XeF_2. Under these conditions, the oxidizing as well as the fluorobasic properties of XeF_2 are revealed, and Xe^{II} complexes of higher oxidation state fluorides are formed.

5.5.1 Compounds with Hexafluorides

In the system XeF_2–MF_6, only the adducts XeF_2MoF_6, XeF_2WF_6, and XeF_2UF_6 have been claimed. The existence of these adducts was established only from the melting point–composition diagrams. They are not stable at room temperature and they decompose readily into their component compounds.

5.5.2 Compounds with Pentafluorides

This type of xenon(II) compound is the most common. With pentafluorides, XeF_2 forms three types of compounds: $2XeF_2{\cdot}MF_5$, $XeF_2{\cdot}MF_5$, and $XeF_2{\cdot}2\,MF_5$. It is also possible that compositions richer or poorer in XeF_2 content exist. Both saltlike and fluorine-bridged formulations were suggested to explain the bonding in these compounds. The degree of ionic character in the compounds varies depending on the Lewis acid properties of the pentafluorides involved (*see Lewis Acids & Bases*). The stronger the Lewis acid, the more ionic the compound. $XeF^+Sb_2F_{11}^-$ (Figure 4) is considered to be the most ionic compound. Xenon(II) compounds with pentafluorides, claimed in the literature, are given in Table 1.

Table 1 Xenon(II) compounds with pentafluorides

$2XeF_2{\cdot}VF_5$	$XeF_2{\cdot}VF_5$	–
–	$XeF_2{\cdot}NbF_5$	$XeF_2{\cdot}2NbF_5$
$2XeF_2{\cdot}TaF_5$	$XeF_2{\cdot}TaF_5$	$XeF_2{\cdot}2TaF_5$
$2XeF_2{\cdot}RuF_5$	$XeF_2{\cdot}RuF_5$	$XeF_2{\cdot}2RuF_5$
$2XeF_2{\cdot}OsF_5$	$XeF_2{\cdot}OsF_5$	–
$2XeF_2{\cdot}RhF_5$	$XeF_2{\cdot}RhF_5$	$XeF_2{\cdot}2RhF_5$
$2XeF_2{\cdot}IrF_5$	$XeF_2{\cdot}IrF_5$	$XeF_2{\cdot}2IrF_5$
$2XeF_2{\cdot}PtF_5$	$XeF_2{\cdot}PtF_5$	$XeF_2{\cdot}2PtF_5$
$2XeF_2{\cdot}AuF_5$	–	–
$2XeF_2{\cdot}PF_5$	$XeF_2{\cdot}PF_5$	–
$2XeF_2{\cdot}AsF_5$	$XeF_2{\cdot}AsF_5$	–
$2XeF_2{\cdot}SbF_5$	$XeF_2{\cdot}SbF_5$	$XeF_2{\cdot}2SbF_5$
$2XeF_2{\cdot}BiF_5$	$XeF_2{\cdot}BiF_5$	$XeF_2{\cdot}2BiF_5$
–	–	$XeF_2{\cdot}2BrF_5$
–	$XeF_2{\cdot}IF_5$	$XeF_2{\cdot}2IF_5$

The isolation of the compounds $2XeF_2{\cdot}VF_5$ and $2XeF_2{\cdot}TaF_5$ was not confirmed. Stable 2:1 compounds were not obtained either in the XeF_2–NbF_5 nor in the XeF_2–TaF_5 systems.**[40]** The compound $XeF_2{\cdot}2OsF_5$ was not prepared. Even the 1:1 compound is thermally unstable at room temperature and decomposes to $2XeF_2{\cdot}OsF_5$, xenon, and osmium hexafluoride.

In the case of AuF_5, other compounds with a higher content of AuF_5 could probably also be synthesized. Probably because PF_5 is a relatively weak fluoroacid the compounds $2XeF_2{\cdot}PF_5$ and $XeF_2{\cdot}PF_5$ were not established with certainty. All efforts to prepare a phase richer in AsF_5 than $XeF_2{\cdot}AsF_5$ failed. Even the 1:1 compound loses AsF_5 at room temperature to yield $2XeF_2{\cdot}AsF_5$. In the system XeF_2–SbF_5 a set of additional compounds was postulated ($2XeF_2{\cdot}3SbF_5$, $XeF_2{\cdot}3SbF_5$, $XeF_2{\cdot}6SbF_5$) on the basis of the melting point–composition diagram. The molecular adducts, $XeF_2{\cdot}2BrF_5$ and $XeF_2{\cdot}9BrF_5$, were also postulated on the basis of the melting point–composition diagram. The compound $XeF_2{\cdot}IF_5$ is a molecular adduct. The compound $XeF_2{\cdot}2IF_5$ was not confirmed.

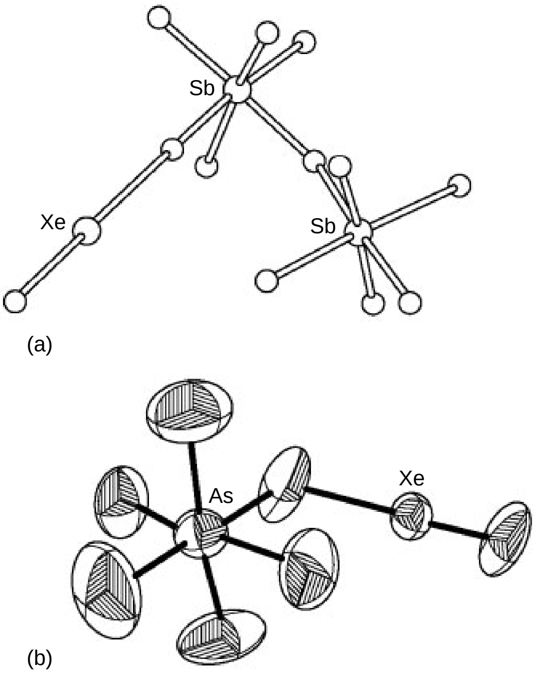

Figure 4 The molecular structures of (a) $XeF^+Sb_2F_{11}^-$, and (b) $XeF^+AsF_6^-$

Single-crystal structures of the types $XeF^+MF_6^-$ and $XeF^+M_2F_{11}^-$ are shown in Figure 4. The structures in Figure 4 confirm that xenon difluoride donates a fluoride ion to the metal pentafluoride to generate the MF_6^- or $M_2F_{11}^-$ salt, depending on the mole ratio of the reactants. When XeF_2 is in excess, the $Xe_2F_3^+$ cation (Figure 5) is formed. The V-shaped $[F–Xe–F–Xe–F]^+$ cation is planar and symmetrical about the bridging fluorine atom. The intermolecular separations suggest that $F–Xe^+F^-Xe–F^+$ is the major canonical form in the cation.

XeF^+ species in the $XeF^+MF_6^-$ and $XeF^+M_2F_{11}^-$ salts are characterized by a band or pair of bands in the Raman spectrum in the 596–619 cm^{-1} region, and in the IR spectrum in the 600–626 cm^{-1} region. $Xe_2F_3^+$ is characterized by strong Raman bands in the Xe–F stretching region at $\approx$593 and 580 cm^{-1}, and in the bending region at 160 cm^{-1}.

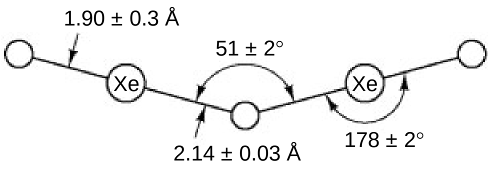

Figure 5 Bond lengths and angles in $Xe_2F_3^+$

5.5.3 Compounds with Tetrafluorides

In the system XeF_2–tetrafluorides, the set of compounds in Table 2 was claimed to exist. The existence of the compounds $2XeF_2{\cdot}MF_4$ (M = Ti, Zr, Hf, Sn) was not confirmed.[40] Tetrafluorides are not sufficiently strong Lewis fluoroacids to stabilize compounds of the type $(Xe_2F_3{}^+)_2MF_6{}^{2-}$. There is some evidence in the case of palladium of the possible existence of such a salt,[41] but it readily loses XeF_2. Even compounds of the type $(XeF^+)_2MF_6{}^{2-}$ have not been isolated. There are several stable polymeric compounds of the type $(XeF^+)_x(MF_5{}^-)_x$ (see Figure 6) and the type $(XeF^+)_x(M_2F_9{}^-)_x$.

Crystal structures have been determined only in the case of $XeF_2{\cdot}CrF_4$ (Figure 6) and $XeF_2{\cdot}XeF_4$. Vibrational spectra show $XeF_2{\cdot}CrF_4$ to be only partially on the ionization pathway towards an XeF^+ salt. The $XeF_2{\cdot}XeF_4$ is an adduct in which the component molecules closely resemble the molecules in the component fluoride crystals.

5.5.4 Compounds with Trifluorides, Difluorides, and Monofluorides

The compounds $2XeF_2{\cdot}BF_3$ and $XeF_2{\cdot}BF_3$ were reported in the literature, but they have not been confirmed.

Table 2 Xenon(II) compounds with tetrafluorides

$2XeF_2{\cdot}TiF_4$	$4XeF_2{\cdot}PdF_4$
$3XeF_2{\cdot}2TiF_4$	$3XeF_2{\cdot}PdF_4$
$XeF_2{\cdot}TiF_4$	$2XeF_2{\cdot}PdF_4$
$XeF_2{\cdot}2TiF_4$	$XeF_2{\cdot}PdF_4$
$2XeF_2{\cdot}ZrF_4$	$XeF_2{\cdot}2PdF_4$
$2XeF_2{\cdot}HfF_4$	$XeF_2{\cdot}2PtF_4$
$XeF_2{\cdot}CrF_4$	$2XeF_2{\cdot}SnF_4$
$XeF_2{\cdot}MnF_4$	$3XeF_2{\cdot}4SnF_4$
$XeF_2{\cdot}2MnF_4$	$XeF_2{\cdot}2SnF_4$
$XeF_2{\cdot}RhF_4$	$XeF_2{\cdot}XeF_4$

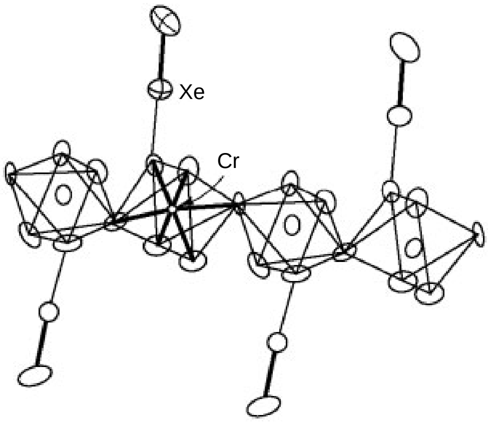

Figure 6 Crystal structure of polymeric $XeF_2{\cdot}CrF_4$

5.5.5 Compounds with Oxide Tetrafluorides

XeF_2 adducts with the weak fluoride ion acceptor species WOF_4 and $MoOF_4$ have been prepared with the stoichiometry $XeF_2{\cdot}MOF_4$ and $XeF_2{\cdot}2MOF_4$ (M = Mo, W). Fluorine-19 NMR spectroscopy has been used to investigate their solution structures in different solvents. In SO_2ClF solution, $XeF_2{\cdot}nMOF_4$ ($n = 1–4$) species were observed at low temperatures. The structures contain Xe–FL·M bridges that are nonlabile on the NMR timescale at low temperatures. In the adduct $XeF_2{\cdot}nWOF_4$ (n = 2, 3), isomerization between oxygen and fluorine-bridged Xe–F groups was observed for the first time. $XeF_2{\cdot}MOF_4$ adducts solvolyze in HSO_3F at 193 K, yielding a new species, the fluorosulfate-bridged structure $FXeSO_3FMOF_4$, which is in equilibrium with $FXeSO_3F$ and MOF_4.[42]

A molecular adduct $XeF_2{\cdot}XeOF_4$ is formed by the reaction between XeF_2 and $XeOF_4$.[43] It is a white solid with a melting point of 302 K. The 'semi-ionic' lattice is similar to that of $XeF_2{\cdot}IF_5$.

5.5.6 Compounds with Fluorosulfate and Related Groups

The preparation of monosubstituted XeF_2 derivatives has generally involved the reaction between XeF_2 and an appropriate anhydrous acid, according to equation (8). The driving force for equation (8) is the considerable exothermicity of formation of HF ($\Delta H_f^\circ = -271.6\,\text{kJ mol}^{-1}$). The first compound of this type was $FXeSO_3F$, but later a whole set of these compounds was isolated. The ligands involved were $-OTeF_5$, $-OSeF_5$, $-OC(O)CF_3$, $-OPOF_2$, and $-OClO_3$. The pentafluorotellurate is the most stable, but the perchlorate and the trifluoroacetate are kinetically unstable and detonate readily.

$$XeF_2 + HL \longrightarrow FXeL + HF \tag{8}$$

Disubstituted derivatives of XeF_2 have also been isolated. These compounds are obtained by treating XeF_2 with two moles of an anhydrous acid or by reacting FXeL with one mole of acid. The bis compounds are less stable than the monosubstituted species.

The bonding in $FXeOSO_2F$ is essentially covalent, with little ionic contribution to the bonding. Mixed compounds of the type $R^2O–Xe–OR^1$ have been detected in the ^{129}Xe NMR spectra. The compound $F_5SeO–Xe–OTeF_5$ exists only in equilibrium with the derivatives $Xe(OSeF_5)_2$ and $Xe(OTeF_5)_2$.

Some monosubstituted derivatives of XeF_2 can also form salts with strong Lewis acids. Unusual cations have been formed using this synthetic route. The reaction between xenon(II) fluoride orthopentafluorotellurate ($FXeOTeF_5$) and AsF_5 yields a bright-yellow solid $XeOTeF_5{}^+AsF_6{}^-$ melting at 433 K. $FXeOTeF_5$ is a poorer donor of F^- than XeF_2.

By reacting $XeF^+AsF_6{}^-$ with KSO_3F in the mole ratio 2:1, the salt $(FXe)_2SO_3F^+AsF_6{}^-$ was formed. The $(FXe)_2SO_3F^+$

cation is not stable in excess HSO_3F at room temperature and slowly decomposes, liberating xenon gas.

5.5.7 *Molecular Adducts of* XeF_2

Several adducts of XeF_2 have been prepared in which the XeF_2 molecule is indistinguishable from the molecule in crystalline XeF_2. The following adducts were isolated: $XeF_2{\cdot}XeF_4$, $XeF_2{\cdot}IF_5$, $XeF_2{\cdot}XeOF_4$, $XeF_2{\cdot}(XeF^+Sn_2F_9^-)_2$, $2XeF_2{\cdot}XeF_5^+AsF_6^-$, $XeF_2{\cdot}XeF_5^+AsF_6^-$, and $XeF_2{\cdot}(XeF_5^+AsF_6^-)_2$. The adducts may be prepared by mixing the starting compounds in the appropriate molar proportions, or by fusing their mixture, or dissolving them in a suitable solvent.

All XeF_2 molecular complexes owe their existence to appreciable coulombic interactions between the negatively charged F ligands and the positive center of the partner molecule.

5.6 Xenon(IV) Compounds

The fluorine ion donor ability of XeF_4 has been shown to be less than that of XeF_2 and XeF_6: $XeF_6 > XeF_2 \gg XeF_4$.**[25]** These findings are in agreement with the enthalpies of ionization**[44]** derived from photoionization studies (equations 9–11).

$$XeF_2(g) \longrightarrow XeF^+(g) + F^-(g) \qquad (9)$$

$$\Delta H^\circ = 9.45\,\text{eV}$$

$$XeF_4(g) \longrightarrow XeF_3^+(g) + F^-(g) \qquad (10)$$

$$\Delta H^\circ = 9.66\,\text{eV}$$

$$XeF_6(g) \longrightarrow XeF_5^+(g) + F^-(g) \qquad (11)$$

$$\Delta H^\circ = 9.24\,\text{eV}$$

The enthalpy of ionization of XeF_6 is more than 0.6 eV lower than that anticipated on the basis of XeF_2 and XeF_4 data. This is compatible with the greater stability of XeF_5^+ salts compared with XeF^+ and XeF_3^+. It seems that the pseudooctahedral geometry of the XeF_5^+ ion is especially favorable.

Although there is no doubt that XeF_6 is the strongest fluoride ion donor, there is disagreement as to the relative fluoride ion donor abilities of XeF_2 versus XeF_4. On the basis of the length, direction, and number of fluorine bridges in XeF^+ and XeF_3^+ salts, it has been concluded that the order of fluoride ion donor ability is $XeF_2 < XeF_4 < XeF_6$. That very few XeF_3^+ salts have been isolated, and that those known are thermally less stable than their XeF_2 relatives, contradicts this conclusion and supports the F^- donor strength being in the sequence $XeF_4 < XeF_2 < XeF_6$.

5.6.1 *Compounds with* XeF_4

XeF_4 only forms compounds with the strongest Lewis acids (SbF_5 and BiF_5). The compounds $XeF_4{\cdot}MF_5$ and $XeF_4{\cdot}2\,MF_5$ (M = Sb, Bi) have been isolated at room temperature, while the existence of the compound $XeF_4{\cdot}AsF_5$ has been claimed at low temperatures and in the presence of an excess of AsF_5. The compounds can be presented as XeF_3^+ salts on the basis of the first crystal structure obtained in this system (Figure 7). The XeF_3^+ cation is T-shaped and coordinated to the anion via a fluorine bridge, the length and polar character of which is determined by the Lewis acidity of the anion. The totally symmetric stretching vibration ν_1 of XeF_3^+ is $\approx$643 cm^{-1}.

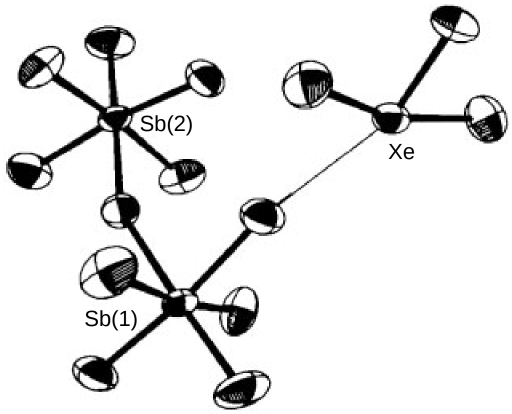

Figure 7 The $XeF_3^+Sb_2F_{11}^-$ structural unit

5.6.2 *Compounds with* $XeOF_2$

Cesium fluoride (CsF) was added at 77 K to solid $XeOF_2$ under a layer of HF. CsF dissolved upon warming to 195 K, forming $Cs^+\,(HF)_xF^-$, which reacted with $XeOF_2$ upon slow warming to 273 K. Under a dynamic vacuum to remove HF, the bright-yellow salt $Cs^+XeOF_3^-$ was obtained. It is stable at room temperature for several hours. The Raman spectrum of $XeOF_3^-$ has been assigned on the basis of C_{2v} symmetry.**[32]** Attempts to prepare the $XeOF^+$ cation have failed. Addition of AsF_5 to $XeOF_2$ under a layer of HF resulted in the decomposition to O_2 and $XeF^+AsF_6^-$.**[32]**

5.7 Xenon(VI) Compounds

The compounds obtained by the reaction of XeF_6 or xenon(VI) oxide fluorides with Lewis acids and bases are described here.

5.7.1 XeF_5^+ *and* $Xe_2F_{11}^+$ *Salts*

Many synthetic routes have been used for the preparation of xenon(VI) fluoro complexes.

1. *Direct method*. The interaction of a binary fluoride with an excess of XeF_6 in its melt. Several compounds have been prepared by using XeF_6 not only as a fluorobase but

also as an oxidizing and fluorinating agent. In some cases, the xenon(VI) compounds have been prepared by mixing the component fluorides in a nonreducing solvent.

2. *Indirect method*. The corresponding binary fluoride is synthesized in situ in a very reactive ‘molecular form’. In this case, XeF_6 acts as a fluorinating agent by fluorine/oxygen exchange ($XeOF_4$ formed) and in some cases also as an oxidizing agent. Hydrazinium or ammonium salts or oxides have been used as starting materials.
3. *Combined method*. In this case, KrF_2 and XeF_6 have been used simultaneously. This synthetic route is efficient in cases where the parent binary fluoride acceptor is itself thermodynamically unstable in the oxidation state in which the xenon(VI) fluoro compound is expected (e.g. $(XeF_5^+)_2NiF_6^{2-}$), or in cases where the binary fluoride exists in the appropriate oxidation state but XeF_6 is not strong enough to oxidize it to this state (e.g. $XeF_5^+AgF_4^-$).

Xenon hexafluoride forms compounds with monomeric and polymeric anions. In the case of monomeric anions we have the following set of compounds: $Xe_2F_{11}^+MF_6^-$, $XeF_5^+MF_6^-$, $XeF_5^+M_2F_{11}^-$, $(Xe_2F_{11}^+)_2MF_6^{2-}$, $(XeF_5^+)_2MF_6^{2-}$, $(Xe_2F_{11})_3^+MF_6^{3-}$ and $(XeF_5^+)_3MF_6^{3-}$. In the case of polymeric anions, with tetravalent fluorides, we have the following mole ratios: XeF_6: MF_4 = 4:3, 3:4, 1:2, 1:4, and with MF_3 1:1 and 1:2. The compounds between XeF_6 and F^- acceptors are given in Table 3. Estimates of stability, reaction activity, and solubility of (XeF_5^+) (MF_6^-) (M = P–Bi, V–Ta) have been made based upon ab initio calculations.[45]

The adducts $2XeF_6{\cdot}MoF_6$ and $XeF_6{\cdot}MoF_6$ were established only from melting point–composition diagrams. The 4:1 compounds are $Xe_2F_{11}^+$ salts, while the 1:4 compounds are XeF_5^+ salts with polymeric anions. The compounds $XeF_6{\cdot}MF_4$ (M = Zr, Hf), $XeF_6{\cdot}MF_3$ (M = Sc, Fe, Ga, In), and $XeF_6{\cdot}2MF_3$ (M = Al) are derived by the indirect synthetic route. The compounds $6XeF_6{\cdot}MF_3$ (M = Y, Ho, Er, Tm, Yb, Lu) and $3XeF_6{\cdot}MF_3$ (M = Y, Dy, Ho) are the first known monomeric salts of $Xe_2F_{11}^+$ and XeF_5^+, respectively, with a metal in the 3+ valence state. The compound $XeF_6{\cdot}AuF_3$,[46] together with $XeF_6{\cdot}AuF_5$, represents the first instance of XeF_5^+ occurring with two different valence states of a metal.

Table 3 Xenon(VI) compounds with F^- acceptors

$2XeF_6{\cdot}MF_6$ (M = Mo)
$XeF_6{\cdot}MF_6$ (M = Mo)
$2XeF_6{\cdot}MF_5$ (M = V, Nb, Ta, Ru, Ir, Pt, Au, P, As, Sb, Bi, U)
$XeF_6{\cdot}MF_5$ (M = V, Nb, Ta, Ru, Ir, Pt, Au, As, Sb, Bi, U)
$XeF_6{\cdot}2MF_5$ (M = V, Sb)
$4XeF_6{\cdot}MF_4$ (M = Ti, Mn, Ni, Pd, Ge, Sn, Pb, Ce, Pr, Tb)
$2XeF_6{\cdot}MF_4$ (M = Mn, Ni, Pd, Ge, Sn)
$4XeF_6{\cdot}3MF_4$ (M = Sn)
$XeF_6{\cdot}MF_4$ (M = Ti, Zr, Hf, Cr, Mn, Ge)
$3XeF_6{\cdot}4MF_4$ (M = Sn, Pb)
$XeF_6{\cdot}2MF_4$ (M = Ti, Mn, Ce, Pr, Tb)
$XeF_6{\cdot}4MF_4$ (M = Sn, Pb, Pr)
$6XeF_6{\cdot}MF_3$ (M = Y, Ho, Er, Tm, Yb, Lu)
$3XeF_6{\cdot}MF_3$ (M = Y, Dy, Ho)
$XeF_6{\cdot}MF_3$ (M = Sc, Ag, Au, Fe, Co, B, Ga)
$XeF_6{\cdot}2MF_3$ (M = Al)

As may be seen from the structures of $(Xe_2F_{11}^+)$ AuF_6^- and $(Xe_2F_{11}^+)_2NiF_6^{2-}$ (Figure 8), the group $Xe_2F_{11}^+$ consists of two similar XeF_5^+ groups linked by a bridging F species (formally F^-). It should be noted that the XeF_5^+ species occurring in the structures of $Xe_2F_{11}^+$ or XeF_5^+ salts are similar in shape but the total coordination of the cation varies from one salt to another. The xenon atom in XeF_5^+ retains a nonbonding valence-electron pair that is evidently sterically active so that the Xe atom is pseudooctahedrally coordinated with five fluorine atoms and the sterically active valence-electron pair. Negatively charged species are attracted most strongly when positioned off axis, as shown in Figure 9.

This model does not explain why certain anions (like RuF_6^-, AuF_6^-, and PtF_6^-) provide four F ligands (Figure 10) to coordinate to XeF_5^+, whereas PdF_6^{2-}, NiF_6^{2-}, and AsF_6^- provide only three, and NiF_6^{2-} in the structure $(Xe_2F_{11}^+)_2NiF_6^-$ (Figure 8) only two. When XeF_5^+ makes three bridging linkages to two different anions, the ring

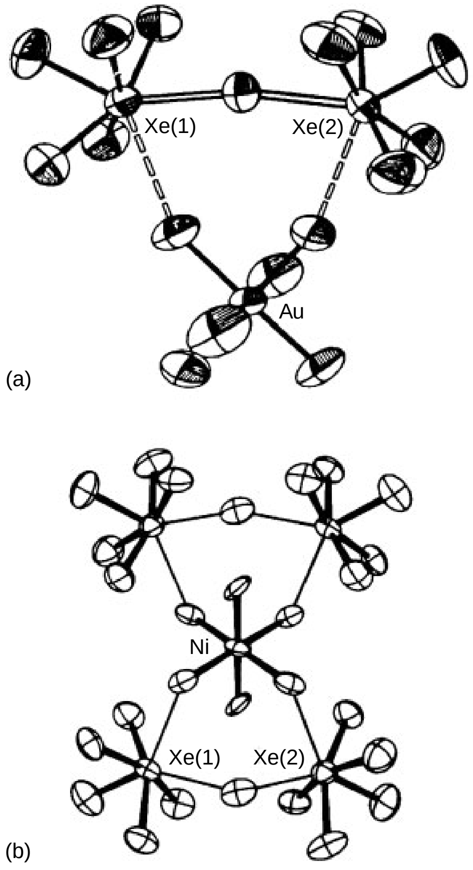

Figure 8 The structural units of (a) $Xe_2F_{11}^+AuF_6^-$, and (b) $(Xe_2F_{11}^+)_2NiF_6^{2-}$

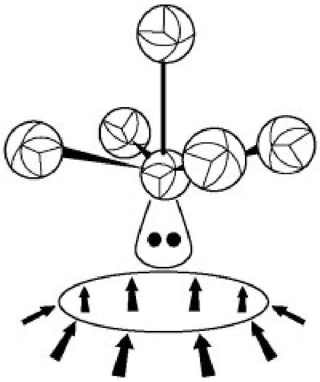

Figure 9 Shape of the XeF_5^+ ion based on steric activity of the nonbonding xenon valence-electron pair. Arrows indicate directions of maximum polarizing effect

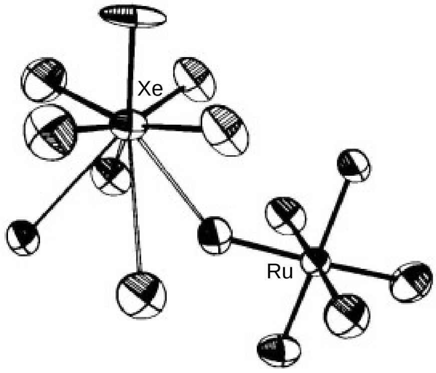

Figure 10 The XeF_5^+ and RuF_6^- structural units and the coordination of XeF_5^+

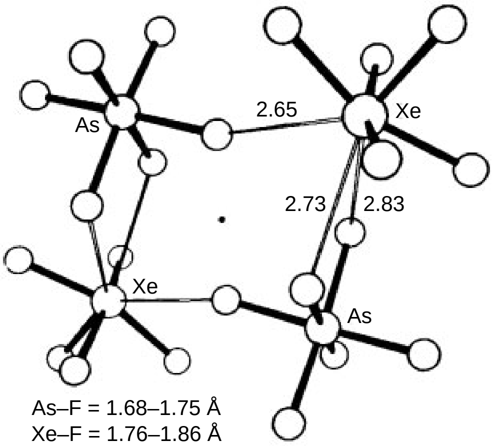

Figure 11 Configuration and bond distances for $XeF_5^+AsF_6^-$

system shown for $XeF_5^+AsF_6^-$ in Figure 11 occurs. That same ring appears repeatedly in the $(XeF_5^+)_2PdF_6^{2-}$ structure (Figure 12a), where each XeF_5^+ is similarly connected to two separate anions. In the $(XeF_5^+)_2NiF_6^{2-}$ structure (Figure 12b), however, one of the cations is coordinated to two separate anions to again generate the $XeF_5^+AsF_6^-$-type ring, but the other XeF_5^+ makes its three bridge bonds to one octahedral face of one anion. This creates discrete $(XeF_5)_4(NiF_6)_2$ clusters. The structure of $(XeF_5^+CrF_5^-)_4XeF_4$ shows that this is an XeF_4 molecular adduct of a XeF_5^+ salt (Figure 13). This

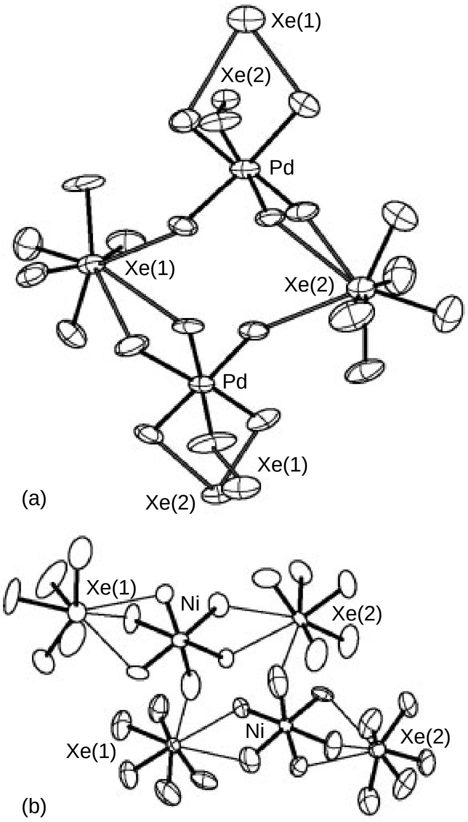

Figure 12 The structural units (a) $(XeF_5^+)_2PdF_6^{2-}$ and (b) $(XeF_5^+)_2NiF_6^{2-}$

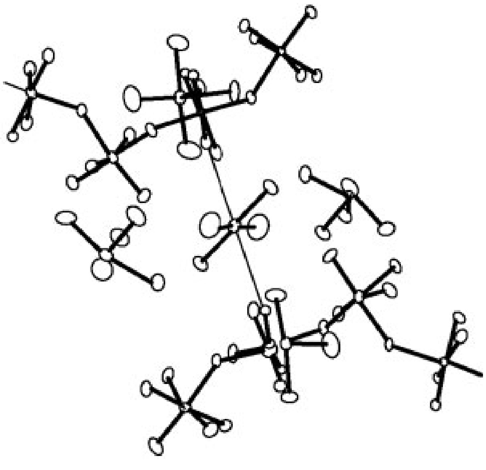

Figure 13 XeF_4 environment in $(XeF_5^+CrF_5^-)_4XeF_4$

structure is of particular interest in showing for the first time an appreciable deformation of the XeF_5^+ cation. In addition, the anion consists of an infinite chain of distorted $CrF_4(F_{0.5})_2^-$ octahedra that alternately share *cis* and *trans* vertices.

Vibrational spectroscopy (especially Raman) has been an important tool in the characterization of $Xe_2F_{11}^+$ and XeF_5^+ salts. The $Xe_2F_{11}^+$ species behave vibrationally like two weakly coupled XeF_5^+ species. The F bridging of the two XeF_5^+ groups in the $Xe_2F_{11}^+$ cation is characterized by a 'bridge stretch' at $\approx 360\,cm^{-1}$. The full assignments for the fundamentals is available.[47,48]

5.7.2 XeF_7^- and XeF_8^{2-} Salts

Complexes of XeF_6 with fluoride ion donors, for example, NO_2F, NOF, and alkali metal fluorides (with the exception of LiF), are listed in Table 4. On the basis of Raman spectroscopy, the compound $2NOF{\cdot}XeF_6$ could be written as $(NO^+)_2XeF_8^{2-}$. This is supported by its crystal structure. The anion XeF_8^{2-} can be described as a slightly distorted Archimedean antiprism with Xe–F distances ranging from 1.946 to 2.099 Å. The steric activity of the nonbonding xenon valence-electron pair is not convincingly present. $NF_4^+XeF_7^-$ decomposes to NF_3, F_2, and XeF_6. Evidence for $(NF_4^+)_2XeF_8$ as an intermediate has been given.

5.7.3 Xenon(VI) Oxyfluoro Cations: $XeOF_3^+$, XeO_2F^+

$XeOF_4{\cdot}2SbF_5$ was prepared by the reaction of $XeOF_4$ with an excess of SbF_5 at temperatures higher than room temperature, followed by removal of volatiles to constant weight at room temperature. A colorless solid with mp 334–338 K was obtained. $XeOF_4{\cdot}SbF_5$ was obtained by the reaction of $XeOF_4{\cdot}2SbF_5$ with an excess of $XeOF_4$ at temperatures a little above room temperature and removal of volatiles to constant weight at room temperature. A colorless solid with mp 377–378 K was obtained.[49] On the basis of their Raman spectra, it has been concluded that the compounds are ionic and contain the $XeOF_3^+$ cation. The structure of $XeOF_3^+$ is represented on a trigonal bipyramidal model with the nonbonding valence-electron pair and the oxygen ligand in equatorial sites. It is a geometric relative of XeF_3^+.

SbF_5 and XeO_2F_2 in the mole ratio 2:1 were allowed to react in HF solution. A white solid was obtained after removal of the solvent. $XeO_2F_2{\cdot}2SbF_5$, is unstable at room temperature, decomposing to $XeF^+Sb_2F_{11}^-$ and oxygen. The Raman spectrum of the compound $XeO_2F_2{\cdot}2SbF_5$ is consistent with the 'ionic' formulation $XeO_2F^+Sb_2F_{11}^-$. Vibrational spectroscopic evidence is consistent with the cation XeO_2F^+ having a pyramidal (pseudotetrahedral) geometry. No direct evidence for fluorine bridging was obtained. The Raman spectrum is available.[50]

Table 4 Xenon(VI) compounds with F^- donors

$2NaF{\cdot}XeF_6$	$NO_2F{\cdot}XeF_6$
$2KF{\cdot}XeF_6$	$(NO^+)_2{\cdot}XeF_8^{2-}$
$2RbF{\cdot}XeF_6$	$NF_4^+{\cdot}XeF_7^-$
$RbF{\cdot}XeF_6$	$(NF_4^+)_2{\cdot}XeF_8^{2-}$
$2CsF{\cdot}XeF_6$	
$CsF{\cdot}XeF_6$	

5.7.4 Xenon(VI) Oxyfluoro Anions: $XeOF_5^-$, $(XeOF_4)_3F^-$, $XeO_2F_3^-$, and XeO_3X^- (X = F, Cl, Br)

CsF reacts with an excess of $XeOF_4$ at room temperature yielding $CsF{\cdot}3XeOF_4$, a white solid. This product is stable in a dynamic vacuum at 273 K when the excess $XeOF_4$ is pumped away, but decomposes at room temperature in a static vacuum to $CsF{\cdot}XeOF_4$ and $XeOF_4$.[51] On the basis of the Raman spectra, $CsF{\cdot}XeOF_4$ is best formulated as the salt $Cs^+XeOF_5^-$. The presence of a single, sharp Xe=O stretching mode at ca. $900\,cm^{-1}$ in $CsF{\cdot}3XeOF_4$ indicates that all three $XeOF_4$ molecules are equivalently bonded to a central fluorine ion, thus implying an anion $(XeOF_4)_3F^-$.

On slow warming of a solution of $XeOF_2$ in HF from 210 to 273 K over a period of 20 h, pure $XeOF_2$ decomposes to XeF_2 and XeO_2F_2, which can further react with Cs^+ $(HF)_xF^-$ dissolved in HF yielding $Cs^+XeO_2F_3^-$. The probable structure of $XeO_2F_3^-$ is pseudooctahedral, with both oxygens in the axial positions and with the three fluorine atoms and the sterically active lone pair in equatorial positions.[32]

Hydrolysis of $Cs^+XeOF_5^-$ or $CsXeF_7^-$ leads to the compound $CsF{\cdot}XeO_3$. Single-crystal structure analysis of $KFXeO_3$ showed that the compound is a polymer, $[K^+]_n[XeO_3F^-]_n$. A more convenient method of preparation mixes appropriate amounts of the aqueous solutions of XeO_3 and metal fluoride (MF), subsequent evaporation yielding crystals of the salts. A series of compounds of the type M^+ $[XeO_3X^-]$ with M = Cs, Rb, K and X = F, Cl, Br is known. The thermal stability of these salts decreases with increasing atomic weight of the halogen. The fluoride salts are stable to 473 K, but decompose to xenon, oxygen, and alkali fluoride above 533 K. The chloride xenates begin to decompose at 423 K, while the bromo salt is unstable even at room temperature.

5.8 Xenon(VIII) Compounds

Xenon(VIII) oxyfluoro anions or cations have not yet been isolated.

5.9 Xenon Compounds with Bonds to Nitrogen and Carbon

5.9.1 Xe–N Bonding

The reaction of XeF_2 with $HN(SO_2F)_2$ proceeds at 273 K, yielding $FXeN(SO_2F)_2$ and HF.[52] $FXeN(SO_2F)_2$ was the first compound prepared with a Xe–N bond. The Xe–N and Xe–F distances are 2.200(3) and 1.967(3) Å, respectively with an F–Xe–N angle of 178.1(1)°. Like its XeF_2 precursor, the molecule exhibits fluoride ion donor properties. In reactions with Lewis acids, for example, AsF_5, SbF_5, and so on, the following salts have been obtained: $XeN(SO_2F)_2{}^+AsF_6{}^-$, $XeN(SO_2F)_2{}^+Sb_3F_{16}{}^-$, and $F[XeN(SO_2F)_2]_2{}^+AsF_6{}^-$. These cations are less stable than their XeF^+ and $Xe_2F_3{}^+$ counterparts. The reaction to prepare the disubstituted compound $Xe[N(SO_2F)_2]_2$ is much slower and should be performed at lower temperatures because $Xe[N(SO_2F)_2]_2$ decomposes rapidly near room temperature to xenon and $[N(SO_2F)_2]_2$.

A new class of Xe–N bonded compounds is obtained by the interaction of the electron lone pair of a nitrile with the Lewis acid XeF^+.[53] The cationic adducts $RC\equiv N–XeF^+$ with R = H, Me, CH_2F, Et, C_2F_5, C_3F_7, and Ph have been isolated by the reaction of the appropriate nitrile with $XeF^+AsF_6{}^-$ or $Xe_2F_3{}^+AsF_6{}^-$ in AHF at low temperatures.

Two additional xenon–nitrogen bonded cations represent unique examples of noble gas atoms functioning as aromatic ring substituents.[54] Equimolar amounts of $XeF^+AsF_6{}^-$ and 4-RC_5F_4N (R = F or CF_3) react in AHF at 243–253 K, yielding 4-$RC_5F_4N–XeF^+AsF_6{}^-$. Low-temperature Raman and ^{129}Xe, ^{19}F, and ^{14}N NMR spectroscopic results are consistent with planar cations in which the xenon atom is coordinated to the aromatic ring through the lone pair of electrons on the nitrogen ligand.

5.9.2 Xe–C Bonding

Compounds with bonding between carbon and Xe (II, IV) rely upon the maintenance of a partial positive charge on the Xe atom. A recent review detailed the full range and reactivity of these compounds so only a representative group will be described here.[55,56] The first established stable system with a xenon–carbon bond is the salt $[C_6F_5Xe]^+$ $[C_6F_5BF_3]^-$.[57] It can be prepared by nucleophilic displacement of fluorine in XeF_2 using $B(C_6F_5)_3$ as an aryl-transfer reagent. The product is a colorless solid, stable at temperatures lower than 243 K. Other aryl groups (e.g. monosubstituted phenyl groups, XC_6H_4) can be used to synthesize salts of the type $[XC_6H_4Xe]^+$ $[(XC_6H_4)_2BF_2]^-$. However, salts with the $[C_6F_5Xe]^+$ cation are significantly more stable and useful than those with $[XC_6H_4Xe]^+$.[58] The stability of the latter salts increases with decreasing F^- donor ability of the anion. In the absence of nucleophilic aryl groups in the anion, the thermal stability increases significantly. $[C_6F_5Xe]^+AsF_6{}^-$ melts without decomposition at 370–371 K and the viscous melt is stable to 398 K. Recently, $C_6F_5XeO_2CC_6F_5$ was reported.[59] Xe is linearly bonded by C (2.122 Å) and O (2.367 Å) and an intramolecular Xe–O contact of 3.142 Å is formed by the acyloxy group. Intermolecular Xe–O bridges (3.237 Å) form pairs of the molecules in the solid.

Of related interest is a recent study indicating that $SiF_3{}^+$ combines with Xe, Kr, and Ar in the gas phase to form the complexes $FNgSiF_3$.[60] Experimental and theoretical results indicated that $FXeSiF_3$ might be stable. Interestingly, similar reactions with $CF_3{}^+$ did not form noble gas compounds.

5.10 Xenates and Perxenates

Xenates are salts of xenic acid, (hypothetically $Xe(OH)_6$). Aqueous XeO_3 solutions (xenic acid) are prepared by hydrolysis of XeF_6 (see Section 5.2.1). XeO_3 is one of the strongest known oxidants in aqueous media. The monoalkali xenates $MHXeO_4\cdot1.5H_2O$ (M = Na, K, Rb, Cs) are prepared by titration of xenic acid with alkali hydroxide solution. Species such as $HXeO_4{}^-$ and $H_5XeO_6{}^-$ are possibly produced in this titration. The xenates(VI) are reported to be stable at room temperature in an inert atmosphere, but they disproportionate to xenon(0) and xenon(VIII) in air. They are thermally stable up to 373 or even 423 K. In some cases, they detonate.

$CsHXeO_4$ has been prepared by the reaction of xenon trioxide with aqueous cesium hydroxide in the presence of fluoride ion. The role of the fluoride ion in the preparation of $CsHXeO_4$ is not clear, but it seems that it prevents the formation of perxenate. In the absence of the fluoride ion, xenon trioxide and cesium hydroxide form a mixed perxenate and xenate salt. $CsHXeO_4$ is stable in air.

Perxenates were not prepared by oxidizing xenon with powerful oxidizers in aqueous media. The only preparative routes are by way of the xenon fluorides (XeF_6 or XeF_4). Hydrolysis of XeF_6 in strongly alkaline media generates xenon gas and hydrated perxenate as a precipitated solid (equation 12). The most efficient synthesis of perxenate was by using ozone to oxidize XeO_3 in a solution of 1 M alkali hydroxide. Na_4XeO_6 is a colorless solid, nearly insoluble in water. It contains 0.6 to 9 molecules of H_2O per xenon atom, depending on the drying procedure.

$$\begin{aligned} 2XeF_6 + 4Na^+ + 16OH^- &\longrightarrow Na_4XeO_6 \\ &+ Xe + O_2 + 12F^- + 8H_2O \end{aligned} \tag{12}$$

The perxenates are colorless, thermally stable solids. Anhydrous sodium perxenate can be obtained at 373 K. It decomposes at 633 K. The corresponding barium salt decomposes at about 570 K. Perxenate solutions are powerful and rapid oxidizing agents. Xenon(VIII) is reduced to xenon(VI). Oxidation processes in acid media are more effective, but they must be fast enough to compete with decomposition of the perxenate, which is also rapid in acid.

The crystal structures of $Na_4XeO_6\cdot6H_2O$, $Na_4XeO_6\cdot8H_2O$, and $K_4XeO_6\cdot9H_2O$ have been determined. The perxenate ion is octahedral. The water of the hydrates is coordinated to the cations and hydrogen-bonded to the perxenate oxygen ligands. The Xe–O bond lengths in the octahedra are in the range 1.84–1.88 Å. This is much longer than in tetrahedral XeO_4 (1.74 Å) or pseudotetrahedral XeO_3 (1.76 Å).

5.11 Xenon Chlorides and Bromides

$XeCl_2$ has been prepared by high-frequency discharge of the mixture of Xe, F_2, and $SiCl_4$ or CCl_4 in the mole ratio 1:1:1 at 193 K.[61] The compound has also been prepared using the matrix-isolation technique and microwave discharge of a xenon–chlorine mixture.[62] $XeCl_2$ is characterized by IR absorption at 313 cm^{-1} (ν_3, asymmetric Xe–Cl stretch), observed in the spectrum of the matrix-isolated material at 20 K, and matrix Raman at 253 cm^{-1} (ν_1, symmetrical Xe–Cl stretch). The greater bond energy of Cl_2 relative to F_2 (242 vs. 158 kJ mol^{-1}) and the lower thermochemical bond energy of chlorides relative to fluorides account for the low thermodynamic stability of $XeCl_2$.

Xenon tetrachloride and xenon dibromide have been detected by (*see Mössbauer Spectroscopy*) as products of the β-decay of their ^{129}I relatives (equation 13).

$$\begin{aligned} {}^{129}ICl_4^- &\xrightarrow{-\beta} {}^{129}XeCl_4 \\ {}^{129}IBr_2^- &\xrightarrow{-\beta} {}^{129}XeBr_2 \end{aligned} \qquad (13)$$

More recently, the matrix isolation of the linear, centrosymmetric, compounds, HNgX (where Ng = Xe, Kr, Ar and X = halide) has been achieved.[63,64] A theoretical study reveals that HF hydrogen bonding will be fairly strong to the fluoride of HNgF.[65]

6 THE CHEMISTRY OF KRYPTON

Compounds of Kr are currently only known for the 2+ oxidation state.[66]

6.1 Krypton Difluoride

Krypton difluoride was first prepared by Turner and Pimentel[67] by UV photolysis of fluorine suspended in a solid mixture of argon and krypton at 20 K. Because krypton difluoride is thermodynamically unstable, all effective syntheses have to be carried out at low temperatures (e.g. 77 K). Methods used for the preparation of KrF_2 in the laboratory include electric discharge of a gaseous mixture of krypton and fluorine at low temperature and pressure (yield 250 mg h^{-1}), high-frequency discharge in a mixture of krypton and CF_2Cl_2, irradiation of fluorine–krypton mixtures with 1.5 MeV electrons, or 10 MeV protons, thermal decomposition of F_2 at 950 K on a nickel wire (yield 6 g h^{-1}), and, less efficiently, by exposure to sunlight.

A very efficient method for the preparation of KrF_2 on a larger scale has been developed (30–40 g per batch).[68] It is based on the irradiation of a liquified mixture of fluorine and krypton with near-UV light at 77 K. The mole ratio of the krypton–fluorine mixture is 4:1 and the yield about 1 g h^{-1} of KrF_2.

Krypton difluoride is colorless in the solid and vapor phase and it decomposes at temperatures above 250 K. The rate of decomposition is dependent upon the pretreatment of the reaction vessel. Because KrF_2 has some vapor pressure even at temperatures between 220 and 230 K, it will start to react if the reaction vessel has not been thoroughly pretreated with KrF_2. Krypton difluoride has the lowest average bond energy of any known fluoride. The atomization energy of KrF_2 ($\Delta H_{at} = 98$ kJ mol^{-1}) is smaller than the dissociation energy of elemental fluorine ($\Delta H_{diss} = 158$ kJ mol^{-1}), thus indicating that krypton difluoride is closest in activity to atomic fluorine. Its $\Delta Hf = 60$ kJ mol^{-1}.

KrF_2 is a symmetrical linear molecule ($D_{\infty h}$). In the crystal, KrF_2 molecules are aligned in planes perpendicular to the tetrad axes of the unit cell. Within these sheets, nearest neighbor molecules are aligned roughly perpendicular to one another, thus placing the negatively charged F ligands close to the positively charged krypton atoms of neighboring molecules (Figure 14).

Hydrolysis of KrF_2 proceeds analogously to the hydrolysis of XeF_2 in basic solution (equation 14). This same reaction occurs rapidly in acid solution, in contrast to the behavior of XeF_2, which dissolves and may persist unhydrolyzed for an extended period of time. No ionic species containing krypton remain in solution after hydrolysis.

$$KrF_2 + H_2O \longrightarrow Kr + 0.5O_2 + 2HF \qquad (14)$$

6.2 Krypton Oxide

No krypton oxide has yet been isolated and characterized. When KrF_2 is hydrolyzed slowly with moist air, it is possible

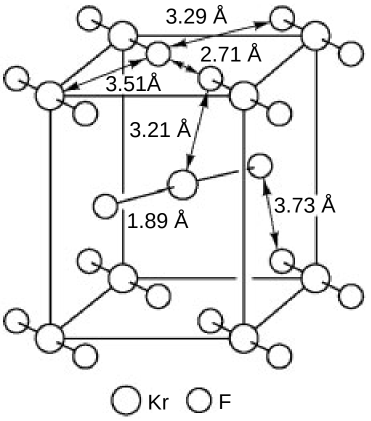

Figure 14 Unit cell of KrF_2

that some very unstable KrO is formed, which decomposes explosively.

6.3 Krypton(II) Compounds

Krypton(II) compounds are those krypton–fluorine compounds which exhibit a significant amount of ionic character and can be described either as KrF^+ and $Kr_2F_3^+$ salts, KrF_2 adducts with these salts, or molecular adducts of KrF_2 with certain binary fluorides. All known krypton(II) compounds are listed in Table 5.

Krypton complexes may be prepared directly by the reaction of KrF_2 with the appropriate binary fluoride, neat or in solution. In some cases, binary fluorides have been prepared in situ using KrF_2 as the fluorinating agent. So far, no X-ray crystal structure of any KrF_2 complex has been determined, and the characterization of the complexes has rested largely on vibrational spectroscopy. Raman spectroscopy has been especially valuable in studies of these compounds, all of which are of low thermal stability.

Observed Raman and IR frequencies for Kr^{II} compounds are best assigned on the basis of ionic formulations: $KrF^+M_2F_{11}^-$, $KrF^+MF_6^-$, and $Kr_2F_3^+MF_6^-$. The appearance of KrL·F and ML·F bridge-stretching and F–KrL·F bending modes points to a strong interaction between the cation and anion, indicative of some covalent character in that bonding. For the KrF^+ salts, the stretching vibration is in the range from 626 cm^{-1} (in the case of $KrF^+Sb_2F_{11}^-$) to 597 cm^{-1} (in the case of $KrF_2{\cdot}2NbF_5$).

The spectra of the $Kr_2F_3^+$ cation have been correlated with those of the $Xe_2F_3^+$ species, but additional peaks, which have no equivalents in the xenon spectra, suggest that $Kr_2F_3^+$ is less symmetrical than its xenon analog, with one longer and weaker Kr–F bond and one shorter and stronger Kr–F bond. An alternative interpretation is that this cation involves a distorted KrF_2 molecule fluorine-bridged to a KrF^+ cation.[20]

Table 5 Krypton(II) compounds

$2KrF_2{\cdot}TiF_4$
$2KrF_2{\cdot}MnF_4$
$KrF_2{\cdot}MnF_4$
$2KrF_2{\cdot}SnF_4$
$KrF_2{\cdot}VF_5$
$KrF_2{\cdot}9BrF_5$
$KrF_2{\cdot}2BrF_5$
$KrF_2{\cdot}BrF_5$
$KrF_2{\cdot}XeF_6$
$KrF^+RuF_6^-$
$KrF^+Ru_2F_{11}^-$
$KrF^+RhF_6^-$
$KrF^+PdF_6^-$
$KrF^+PtF_6^-$
$KrF^+Pt_2F_{11}^-$
$KrF^+AuF_6^-$
$KrF^+BiF_6^-$
$KrF^+BF_4^-$
$(xKrF_2{\cdot}KrF)^+Nb_2F_{11}^-$
$KrF^+Nb_2F_{11}^-$
$(xKrF_2{\cdot}KrF^+){\cdot}Ta_2F_{11}^-$
$Kr_2F_3^+TaF_6^-$
$KrF^+TaF_6^-$
$KrF^+Ta_2F_{11}^-$
$(xKrF_2{\cdot}Kr_2F_3^+)\ AsF_6^-$
$Kr_2F_3^+AsF_6^-$
$KrF^+AsF_6^-$
$(xKrF_2{\cdot}Kr_2F_3^+)\ SbF_6^-$
$(xKrF_2{\cdot}KrF^+)\ SbF_6^-$
$Kr_2F_3^+SbF_6^-$
$KrF^+SbF_6^-$
$KrF^+Sb_2F_{11}^-$

Krypton difluoride forms complexes mostly with Lewis acid pentafluorides in the mole ratio 2:1, 1:1, and 1:2. In addition, there are a number of compounds in which additional KrF_2 appears to be weakly associated, probably with the cationic part of the compound. Recently, the first adducts of KrF_2 with tetravalent fluorides have also been isolated and characterized: $2KrF_2{\cdot}MnF_4$ and $KrF_2{\cdot}MnF_4$. The 1:1 compound is most probably $KrF^+MnF_5^-$ with a polymeric anion.[69] Claims for the compounds $2KrF_2{\cdot}TiF_4$ and $2KrF_2{\cdot}SnF_4$ have not been supported by any characterizational evidence.

The highly polar bonds of KrF_2 also give rise to adducts with other molecules possessing highly polar bonds; compounds include $KrF_2{\cdot}BrF_5$ and $KrF_2{\cdot}XeF_6$.

The first krypton difluoride–metal oxide fluoride adducts have been prepared by reaction of KrF_2 with MOF_4 ($M = Mo$, W) in SO_2ClF solution at low temperatures. Raman spectra of the solid $KrF_2{\cdot}MoOF_4$ and $KrF_2{\cdot}WOF_4$ indicate that these compounds are not KrF^+ salts, but are more covalent fluorine-bridged structures. The ^{19}F NMR spectra of $KrF_2{\cdot}nMoOF_4$ ($n = 1$–3) and $KrF_2{\cdot}WOF_4$ indicate also that these complexes are best formulated as essentially covalent structures containing KrL·FL·M bridges and mononuclear or polynuclear metal oxide fluoride species.

6.4 Krypton Compounds with Bonds to Oxygen and Nitrogen

$Kr(OTeF_5)_2$ is the first krypton compound containing a krypton–oxygen bond. It was prepared by the reaction between KrF_2 and $B(OTeF_5)_3$ at 183–161 K in SO_2ClF as solvent.[70]

It is interesting that the compound containing the first krypton–nitrogen bond was synthesized before a compound with a krypton–oxygen bond. The first compound with a krypton–nitrogen bond was synthesized at low temperatures in BrF_5 solvent according to a general synthetic approach (equation 15). Each nitrogen base found capable of bonding with KrF^+ is oxidatively resistant and possesses a first adiabatic ionization potential close to or exceeding the estimated *Electron Affinity* of KrF^+ (13.2 eV). The first adiabatic ionization potential of $HC\equiv N$ is 13.59 eV. The low basicity of the nitrogen atoms in these bases gives the krypton–nitrogen bond significant ionic character. This is important for the thermal stability of such a cation.[71] Compounds with krypton–carbon bonds have not yet been isolated.

$$R_fC\equiv N\text{–}AsF_5 + KrF_2 \longrightarrow R_fC\equiv N\text{–}KrF^+AsF_6^- \qquad (15)$$

$$R_f = H, CF_3, C_2F_5, n\text{-}C_3F_7$$

7 THE CHEMISTRY OF RADON

There are no stable isotopes of radon and the longest lived 'natural' isotope, ^{222}Rn, has a half-life of only 3.83 days. Experimental difficulties arise not only from the radiation hazard, but also from the decomposition caused by the radiation. The most detailed review of radon chemistry, to early 1981, was written by Stein.**[72]**

Radon forms a series of clathrate compounds similar to those of krypton, xenon, and argon (e.g. $Rn{\cdot}6H_2O$, $Rn{\cdot}3C_6H_5OH$, $Rn{\cdot}3p\text{-}ClC_6H_4OH$).

^{222}Rn decays by α emission and exhibits only slight γ activity when freshly separated from radium. The short-lived β- and γ-emitting daughters ^{214}Pb and ^{214}Bi, as well as the short-lived α-emitting daughters ^{218}Po and ^{214}Po, grow into equilibrium with ^{222}Rn within 4 h. The energetic (1.8 MeV) γ-ray of ^{214}Bi is frequently used to trace ^{222}Rn.

Millicurie and curie amounts of radon react spontaneously with gaseous fluorine at room temperature and with liquid fluorine at 77 K. ^{222}Rn, owing to its intense α-radiation, produces large numbers of ions and excited atoms. Therefore, for fixation of radon as the fluoride it is necessary to mix a millicurie or larger amounts of the element with gaseous or liquid fluorine in a small volume (25–50 cm^3) and let the mixture stand for 0.5 h. Radon behaves as activator and reactant. In this way, RnF_2 is produced.

The first ionization potential of radon (10.7 eV) is smaller than the first ionization potential of xenon, and therefore similar reactions are expected. Thus radon reacts with a number of oxidizing cations such as $ClF_2{}^+$, $BrF_2{}^+$, $BrF_4{}^+$, $O_2{}^+$, N_2F^+, $N_2F_3{}^+$, $IF_6{}^+$, and so on, and it is believed that it forms RnF^+ salts. Radon also reacts to some extent with compounds that contain oxidizing anions such as $ClF_4{}^-$, $BrF_4{}^-$, and $BrF_6{}^-$.

Stable solutions of RnF_2 have been prepared through spontaneous reactions of ^{222}Rn with liquid ClF, ClF_3, ClF_5, BrF_3, BrF_5, and IF_7 at 298 K or lower temperatures.

RnF_2 is hydrolyzed by water in a reaction analogous to the reactions of KrF_2 and XeF_2 with water. Higher-valent xenon compounds, such as XeF_4 and XeF_6, yield soluble oxygenated xenon species (XeO_3 and $XeO_6{}^{4-}$) on hydrolysis with solutions of appropriate acidity. No corresponding radon species have been observed after hydrolysis of simple or complex radon fluorides. In all cases, only gaseous radon was obtained. Reported preparations of RnF_4 and RnF_6 and, by hydrolysis, also RnO_3 have not been sustained. Because of the chemical similarity of radon with xenon and its lower first ionization potential, a number of other compounds such as RnF_4, RnF_6, $RnCl_2$, $RnCl_4$, RnO, RnO_2, RnO_3, and $RnOF_4$ might be expected. The characterization of these compounds is very difficult because of their radioactivity, decay, short-lived isotopes, and so on. So far, no complex compounds of RnF^+, $Rn_2F_3{}^+$, or Rn^{2+} have been fully characterized.

8 THE CHEMISTRY OF THE LIGHTER NOBLE GASES

The first ionization potentials of the lighter noble gases Ar (15.76 eV), Ne (21.56 eV), and He (24.59 eV) show that these gases will remain difficult to incorporate into compounds. Nevertheless, the first stable neutral argon compound, HArF, has been isolated in a solid argon matrix, characterized by IR, and analyzed by ab initio calculations.**[63]** The calculations indicate that the compound is 'intrinsically stable' with ionic and covalent contributions to the bonding. Furthermore, a wide range of helium compounds, $[XBeHe]^+$ (where $X = NH_2$, CH_3, Ph, etc.) are calculated to be thermodynamically stable.**[4]** This is likely due to the presence of the covalency-inducing beryllium cation.

9 EXPLOSION HAZARDS WITH NOBLE GAS COMPOUNDS

Some noble gas compounds are explosive, so special care should be taken during their manipulation. The most dangerous is XeO_3, which can be obtained from XeF_4, XeF_6, any $XeF_3{}^+$ or $XeF_5{}^+$ salts when moisture is present, or by the reaction between XeF_6 and oxides. XeO_3 is comparable in detonation sensitivity to nitrogen triiodide and in explosive force to TNT. Detonation may be induced by mild heating, by mild mechanical disturbance, by pouring, or may take place spontaneously.

Beside XeO_3 and XeO_4, some xenon oxyfluorides are also thermally unstable compounds. They may detonate, particularly at higher temperatures. Other derivatives of the xenon and krypton fluorides involving ligands less electronegative than fluorine should also be assumed to be of low thermodynamic stability. Many derivatives such as perchlorates and trifluoroacetates are known to be explosive.

10 BONDING IN NOBLE GAS COMPOUNDS

For xenon fluorides and oxides, for example, the same models can be applied as for interhalogen and halogen oxy species. Furthermore, the very successful valence shell electron pair repulsion (VSEPR) rules**[73]** for molecule and ion shapes are as effective for noble gas compounds and their relatives as for classical 'octet' compounds.

All acceptable theories should account for the following facts: only the heavier, more readily ionizable noble gases form compounds and only the most electronegative atoms or groups are satisfactory ligands for the noble gases. Two theories of bonding in noble gas compounds are discussed here (*see also* ***Molecular Orbital Theory*** and *Valence Shell Electron Pair Repulsion Model*).

10.1 Molecular Orbital Theory

This model does not involve the outer, or higher valence shell orbitals of the noble gas atom, at least not to an extent that could significantly affect the bond energy. The xenon atom orbitals of prime importance are 5p, and less importantly 5s, and for fluorine 2p. It is interesting that Pimentel's[74] bonding model of 1951 for trihalide ions can be extended to the noble gas dihalides without modification. In this case, we have three three-center MOs generated from the Xe $5p_x$ and two fluorine $2p_x$ orbitals. The best net bonding for the three atoms occurs when the arrangement is centrosymmetric. The molecular symmetry of XeF_2 ($D_{\infty h}$) is in agreement with this requirement. The xenon atom contributes two electrons and each fluorine ligand one electron to this σp molecular orbital (MO) system. Two electrons are in the bonding MO and two in the nonbonding MO. The antibonding MO is empty. The xenon does not contribute to the nonbonding orbital; therefore the electrons of this orbital are concentrated on the fluorine ligands, thus restoring the fluorine ligand electron density. The bonding electron pair is responsible for binding together all three atoms. Delocalization of the electron pairs of this orbital results in a net negative charge on each fluorine ligand and a positive charge on the Xe atom. The charge distribution is close to the representation $F^{0.5-}-Xe^{1+}-F^{0.5-}$. This representation fits most of the physical and chemical properties of XeF_2.

Bonding in XeF_4 can be described in a similar way, having two such three-center systems at right angles. This simple three-center four-electron MO approach is in accord with the near equality of mean thermochemical bond energy in the three xenon fluorides and with the greater bond energy in XeF^+, but it predicts XeF_6 to be octahedral, which it is not.

10.2 Valence Shell Electron Pair Repulsion Theory

This theory implies outer orbital involvement in the bonding. It assumes that each bond between the ligand and the central atom involves an electron pair. A double bond involves four electrons. Further, it assumes that all nonbonding valence electrons have a steric effect. These lone pairs repel other electron pairs more than do bonding electron pairs and have about the same steric requirements as a double bond. Gillespie[75] predicted the shape of unknown species using this theory; all later isolated species conformed to his predictions.

The three-center, four-electron MO approach is as successful as the VSEPR approach for less than six coordination. The VSEPR correctly predicted that XeF_6 should be nonoctahedral and applies straightforwardly to seven and higher coordination numbers, in a way that the simple MO theories cannot.

11 RECENT DEVELOPMENTS IN TRANSITION METAL DERIVATIVES

Beyond the relatively simple transition metal salts described previously, many more interesting and esoteric compounds have been discovered in combinations of the noble gases with the transition metals. The broad range of these exciting new compounds warrants a separate in-depth review, so only representative examples will be provided here. Matrix isolation has been used to create the new class of organometallic compounds, $M(CO)_xNg$ where Ar and Xe act as weakly bound ligands.[76] Another emerging class of compounds are of formula NgMX, (Ng = Ar or Kr, M = Cu, Ag, Au, X = F, Cl, Br), prepared by laser ablation of the metal followed by reaction with the noble gas and halide source.[77] In these linear compounds, the Ng–M bonds are short and range from 2.3 Å for Ar–Cu to 2.7 Å for Kr–Ag. Theoretical calculations have been used to predict the bond lengths of the compounds for which no experimental data is available.[78] The laser ablation of uranium with CO in the presence of Ar, Kr, and Xe lead to the formation of the compounds, (C)U(O)(Ng), which have been characterized by IR spectra and CO and Ng isotopic substitution.[79] The compound, $[AuXe_4]^{2+}\ 2[Sb_2F_{11}]^-$, was discovered in a study aimed at creating AuF.[80] In the crystal structure, the cation forms a regular square, with Au–Xe bond lengths ~2.7 Å. This compound is a clear indication of the remarkable discoveries waiting to be made in combinations of the noble gases with transition metals.

12 APPLICATIONS

In addition to the synthetic uses mentioned previously, such as in oxidizing[81] and fluorinating agents, the noble gases and their compounds have a very broad, and growing, range of applications. With two NMR-active nuclei, ^{129}Xe and ^{131}Xe, xenon has found increasing use as an indirect structural probe in a broad range of substances.[82–86] Xenon has been found to prevent hypoxia-induced neuronal damage.[87] Additionally, it has been proposed as a replacement for nitrous oxide, once an economic means of providing the gas is found.[88] Dating methods are being developed using 20Ne/22Ne ratios[89] and the fractional yield of ^{136}Xe produced by the spontaneous fission of ^{238}U.[90] Jets of Ne and Ar are used to help tokamak nuclear reactors run more efficiently.[91]

13 RELATED ARTICLES

Fluorides: Solid-state Chemistry; Fluorine: Inorganic Chemistry.

14 FURTHER READING

I. H. Krouse and P. G. Wenthold, *Inorg. Chem.*, 2003, **42**, 4293.

J. F. Lehmann, H. P. A. Mercier, and G. J. Schrobilgen, *Coord. Chem. Rev.*, 2002, **233–234**, 1.

15 REFERENCES

1. Lord Rayleigh (J. W. Strutt) and W. Ramsay, *Proc. R. Soc.*, 1895, **57**, 265.
2. M. W. Travers, ‘A Life of Sir William Ramsay’, Arnold, London, 1956.
3. G. A. Cook, in ‘Argon, Helium and the Rare Gases’, ed. G. A. Cook, Interscience, New York, 1961, Vols. I and II.
4. P. Antoniotti, P. Facchini, and F. Grandinetti, *Int. J. Mass Spectrom.*, 2003, **228**, 415.
5. M. Gerken and G. J. Schrobilgen, *Coord. Chem. Rev.*, 2000, **197**, 335.
6. H. H. Claassen, ‘The Noble Gases’, Heath, Boston, 1966.
7. J. H. Holloway, ‘Noble Gas Chemistry’, Methuen, London, 1968.
8. N. Bartlett and F. O. Sladky, in ‘Comprehensive Inorganic Chemistry’, eds. J. C. Bailar and A. F. Trotman-Dickenson, Pergamon, Oxford, 1973, Vol. 1.
9. D. M. Yost and A. L. Kaye, *J. Am. Chem. Soc.*, 1933, **55**, 3890.
10. N. Bartlett, *Proc. Chem. Soc.*, 1962, 218.
11. H. H. Hyman ed., ‘Noble Gas Compounds’, University of Chicago Press, Chicago, IL, 1963.
12. H. H. Hyman, in ‘Physical Chemistry. An Advanced Treatise’, eds. H. Eyring, D. Henderson, and W. Yost, Academic Press, New York, 1970, Vol. 5, Chap. 11, p. 589.
13. F. O. Sladky, in ‘MTP International Review of Science, Inorganic Chemistry, Series One’, ed. V. Gutmann, Butterworths, London, 1972, Vol. 3, p. 1.
14. D. T. Hawkins, W. E. Falconer, and N. Bartlett, ‘Noble Gas Compounds, A Bibliography 1962–1976’, IFI/Plenum, New York, 1978.
15. K. Seppelt and D. Lentz, *Prog. Inorg. Chem.*, 1982, **29**, 167.
16. H. Selig and J. H. Holloway, *Top. Curr. Chem.*, 1984, **124**,.
17. M. Gerken, P. Hazendonka, J. Nieboera, and G. J. Schrobilgen, *J. Fluorine Chem.*, 2004, **125**, 1163.
18. K. O. Christe, *Angew. Chem., Int. Ed. Engl.*, 2001, **40**, 1419.
19. R. Hoppe, W. Dähne, H. Mattauch, and K. M. Rödder, *Angew. Chem., Int. Ed. Engl.*, 1962, **1**, 599.
20. P. A. Mayhewa and L. D. Boylea, *J. Fluorine Chem.*, 1998, **87**, 97.
21. M. Tamura, Y. Matsukawa, H. Quan, J. Mizukado, and A. Sekiya, *J. Fluorine Chem.*, 2004, **125**, 705.
22. T. Hirashige, R. Hagiwara, and Y. Ito, *J. Fluorine Chem.*, 2000, **106**, 205.
23. H. H. Claassen, H. Selig, and J. G. Malm, *J. Am. Chem. Soc.*, 1962, **84**, 3593.
24. B. Weinstock, E. E. Weaver, and C. P. Knop, *Inorg. Chem.*, 1966, **5**, 2189.
25. N. Bartlett and F. O. Sladky, *J. Am. Chem. Soc.*, 1968, **90**, 5316.
26. J. Slivnik, B. S. Brcic, B. Volavsek, J. Marsel, V. Vrscaj, A. Smalc, B. Frlec, and A. Zemljič, *Croat. Chem. Acta*, 1962, **34**, 253.
27. F. Schreiner, D. W. Osborne, J. G. Malm, and G. N. McDonald, *J. Chem. Phys.*, 1969, **51**, 4838.
28. R. D. Burbank and G. R. Jones, *Science*, 1970, **168**, 248.
29. L. Kriachtchev, M. Pettersson, J. Lundell, H. Tanskanen, T. Kiviniemi, N. Runeberg, and M. Rasanen, *J. Am. Chem. Soc.*, 2003, **125**, 1454.
30. E. H. Appelman and J. G. Malm, *J. Am. Chem. Soc.*, 1964, **86**, 2141.
31. H. Selig, H. H. Claassen, C. L. Chernick, J. G. Malm, and J. L. Huston, *Science*, 1964, **143**, 1322.
32. R. J. Gillespie and G. J. Schrobilgen, *J. Chem. Soc., Chem. Commun.*, 1977, 595.
33. D. F. Smith, *Science*, 1963, **140**, 899.
34. J. L. Huston, *J. Phys. Chem.*, 1967, **71**, 3339.
35. J. L. Huston, *J. Am. Chem. Soc.*, 1971, **93**, 5255.
36. J. L. Huston, *Inorg. Nucl. Chem. Lett.*, 1968, **4**, 29.
37. J. L. Huston, *Inorg. Chem.*, 1982, **21**, 685.
38. J. F. Liebman and C. A. Deakyneb, *J. Fluorine Chem.*, 2003, **121**, 1.
39. G. J. Schrobilgen, *Synth. Fluorine Chem.*, 1992, 1.
40. B. Žemva, *Croat. Chem. Acta*, 1988, **61**, 163.
41. N. Bartlett, B. Žemva, and L. Graham, *J. Fluorine Chem.*, 1976, **7**, 301.
42. J. H. Holloway and G. J. Schrobilgen, *Inorg. Chem.*, 1980, **19**, 2632.
43. N. Bartlett and M. Wechsberg, *Z. Anorg. Allg. Chem.*, 1971, **385**, 5.
44. J. Berkowitz, W. A. Chupka, P. M. Guyon, J. H. Holloway, and R. Spohr, *J. Phys. Chem.*, 1971, **75**, 1461.
45. A. V. Tsvetkov, M. F. Bobrov, and V. G. Tsirelson, *J. Mol. Struct. (THEOCHEM)*, 2003, **624**, 145.
46. K. Lutar, A. Jesih, I. Leban, B. Zemva, and N. Bartlett, *Inorg. Chem.*, 1989, **28**, 3467.
47. C. J. Adams and N. Bartlett, *Isr. J. Chem.*, 1978, **17**, 114.
48. K. O. Christe, C. C. Curtis, and R. D. Wilson, *Top. Curr. Chem.*, 1984, **124**, 159.
49. D. E. McKee, C. J. Adams, and N. Bartlett, *Inorg. Chem.*, 1973, **12**, 1722.

50. R. J. Gillespie, B. Landa, and G. J. Schrobilgen, *Inorg. Chem.*, 1976, **15**, 1256.
51. G. J. Schrobilgen, D. Martin-Rovet, P. Charpin, and M. Lance, *J. Chem. Soc., Chem. Commun.*, 1980, 894.
52. D. D. DesMarteau, R. D. LeBlond, S. F. Hossain, and D. Nothe, *J. Am. Chem. Soc.*, 1981, **103**, 7734.
53. A. A. A. Emara and G. J. Schrobilgen, *J. Chem. Soc., Chem. Commun.*, 1987, 1644.
54. A. A. A. Emara and G. J. Schrobilgen, *J. Chem. Soc., Chem. Commun.*, 1988, 257.
55. V. K. Brel, N. Sh. Pirkuliev, and N. S. Zefirov, *Russ. Chem. Rev.*, 2001, **70**, 231.
56. H. J. Frohn and V. V. Bardin, *Organometallics*, 2001, **20**, 4750.
57. H. J. Frohn and S. Jakobs, *J. Chem. Soc., Chem. Commun.*, 1989, 625.
58. H. J. Frohn and M. Theissen, *Chem. Phys. Lett.*, 2004, **393**, 448.
59. H. J. Frohn, A. Klose, and G. Henkel, *Angew. Chem., Int. Ed. Engl.*, 1993, **32**, 99.
60. A. Cunje, V. I. Baranov, Y. Ling, A. C. Hopkinson, and D. K. Bohme, *J. Phys. Chem. A*, 2001, **105**, 11073.
61. H. Meinert, *Z. Chem.*, 1966, **6**, 71.
62. L. Y. Nelson and G. C. Pimentel, *Inorg. Chem.*, 1967, **6**, 1758.
63. L. Khriachtchev, M. Pettersson, N. Runeberg, J. Lundell, and M. Rasanen, *Nature*, 2000, **406**, 874.
64. M. Pettersson, J. Lundell, and M. Rasanen, *Eur. J. Inorg. Chem.*, 1999, 729.
65. J. Lundell, L. Kriachtchev, M. Pettersson, and M. Rasanen, *J. Low Temp. Phys.*, 2000, **26**, 680.
66. S. Y. Yen, C. H. Mou, and W. P. Hu, *Chem. Phys. Lett.*, 2004, **383**, 606.
67. J. J. Turner and G. C. Pimentel, *Science*, 1963, **140**, 974.
68. A. Smalc, K. Lutar, and B. Zemva, *Inorg. Synth.*, 1992, **29**, 11.
69. K. Lutar, A. Jesih, and B. Žemva, *Polyhedron*, 1988, **7**, 1217.
70. J. C. P. Sanders and G. J. Schrobilgen, *J. Chem. Soc., Chem. Commun.*, 1989, 1576.
71. G. J. Schrobilgen, *J. Chem. Soc., Chem. Commun.*, 1988, 1506.
72. L. Stein, *Radiochim. Acta*, 1983, **32**, 163.
73. R. J. Gillespie and R. S. Nyholm, *Rev., Chem. Soc.*, 1957, **11**, 339.
74. G. C. Pimentel, *J. Chem. Phys.*, 1951, **19**, 446.
75. R. J. Gillespie, *Chem. Soc. Rev.*, 1992, **21**, 59.
76. D. C. Grills, X. Z. Sun, G. I. Childs, and M. W. George, *J. Phys. Chem. A*, 2000, **104**, 4300.
77. J. M. Thomas, N. R. Walker, S. A. Cooke, and M. C. L. Gerry, *J. Am. Chem. Soc.*, 2004, **126**, 1235.
78. C. C. Lovallo and M. Klobukowski, *Chem. Phys. Lett.*, 2003, **368**, 589.
79. B. Liang, L. Andrews, J. Li, and B. E. Bursten, *Inorg. Chem.*, 2004, **43**, 882.
80. S. Seidel and K. Seppelt, *Science*, 2000, **290**, 117.
81. H. P. A. Mercier, M. D. Moran, G. J. Schrobilgen, C. Steinberg, and R. J. Suontamo, *J. Am. Chem. Soc.*, 2004, **126**, 5533.
82. C. J. Jameson, ‘Multinuclear NMR’, Plenum Press, New York, 1987, p. 463.
83. J. Reisse, *New J. Chem.*, 1986, **10**, 665.
84. C. Dybowski and N. Bansal, *Annu. Rev. Phys. Chem.*, 1991, **42**, 433.
85. J. Jokisaari, *Prog. Nucl. Magn. Reson. Spectrosc.*, 1994, **26**, 1.
86. D. Raftery and B. F. Chmelka, in ‘NMR Basis Principles and Progress. Solid-State NMR I: Methods’, Springer-Verlag, Berlin, 1994, Vol. 30, p. 111.
87. C. Petzelta, P. Blomb, W. Schmehlb, J. Mullera, and W. J. Koxa, *Life Sci.*, 2003, **72**, 1909.
88. P. H. Tonner, K. Bangert, and J. Scholz, *Baillieres Best Pract. Res. Clin. An.*, 2001, **15**, 491.
89. F. Peeters, U. Beyerle, W. Aeschbach-Hertig, J. Holocher, M. S. Brennwald, and R. Kipper, *Geochim. Cosmochim. Acta*, 2002, **67**, 587.
90. R. A. Ragettlia, E. H. Hebedab, P. Signera, and R. Wielecra, *Earth Planet. Sci. Lett.*, 1994, **128**, 653.
91. D. G. Whyte, T. C. Jernigan, D. A. Humphreys, A. W. Hyatt, C. J. Lasnier, P. B. Parks, T. E. Evans, P. L. Taylor, A. G. Kellman, D. S. Gray, and E. M. Hollmann, *J. Nucl. Mater.*, 2003, **313–316**, 1239.

Noncrystalline Solids

Jean-Luc Adam & Jacques Lucas
University of Rennes, Chimie de la Matière Condensée (CNRS), Rennes, France

1 The Glassy State 1
2 Oxide Glasses 3
3 Chalcogenide Glasses 7
4 Halide Glasses 11
5 Metallic Glasses 15
6 Related Articles 17
7 References 17

Glossary

Critical cooling rate, R_c: minimum quenching rate of a melt that results in a glassy product
Glass transition temperature, T_g: temperature at which the viscosity of a glass begins to decrease continuously
Optical attenuation: continuous decrease of light intensity when propagating in a glass

1 THE GLASSY STATE

1.1 Introduction

Solids originating from the three-dimensional regular repetition of an elementary cell are described as crystalline. This situation can lead to poorly crystalline solids when the final size of the crystal is very small. This is the case for fine grain materials having nanometer or submicron dimension sizes, often called amorphous because the coherently X-ray diffracting domains are very small. Crystals can also be grown to centimeter size, for example, for jewelry or optoelectronics applications. In both cases, those solids have reached their thermodynamic equilibrium. In contrast, there is a limited but important class of materials that, when prepared from the melt, have no time to arrange and to connect periodically when crossing the strategic liquidus to solidus line. Solids that are obtained in this way are not in equilibrium. They are regarded as frozen liquids because they retain the structure of this disordered state. The corresponding materials are then in the 'glassy' or 'vitreous' state.

The metastable solids discussed in this article will correspond to this definition; the word glass is preferred to noncrystalline solids that have a connotation that is too negative and inexact. It must also be appreciated that this state of matter suffers in that it is without a clear descriptive image as is possible, for example, for the crystalline state. Nevertheless, vitreous materials research has become an increasingly active field since the emergence of high technology applications of glasses; examples are fiber optics for telecommunication and medicine, glass lasers, sophisticated optics for telescopes and ophthalmology, and sunglasses.

1.2 Conditions of Glass Formation

Noncrystalline solids formation needs to be clarified by reference to the nature of the final product. Several methods lead to amorphous fine particles, for instance, in solution by controlled precipitation. Through gel formation, poorly crystalline TiO_2 can be obtained according to the process $Ti(OR)_4 + H_2O \rightarrow Ti(OH)_4$ gel $\rightarrow$ amorphous $TiO_2 + H_2O$. In this case, the compound obtained is thermodynamically stable, as when amorphous films are obtained by chemical vapor deposition, sputtering, flash evaporation, and so on.

The noncrystalline solids described here are amorphous and metastable. This specific thermodynamic property is because they all originate from the liquid state. The corresponding glassy or vitreous materials are not very common in solid-state chemistry, and only a limited number of molten salts or molten alloys have the characteristics necessary to produce glasses when cooling.

The formation of glass is a kinetically controlled phenomenon and is directly associated with atomic or ionic diffusion within the melt. This controls the formation and growth of microcrystals when the temperature of the liquid reaches the solidus line (i.e. the crystallization temperature).

Some melts show unexpectedly high viscosities, indicating a large degree of association within this disordered state. This is due to the formation of strong chemical bonds in the liquid, leading to polymerized forms where individual atoms are no longer free to move. The effect of thermal agitation is to maintain the disordered state by bending or rotating the bonds linking the different building elements. Cooling the melt results in an increase of the viscosity and makes the formation of individual small crystallites difficult, owing to poor atomic diffusion. Finally, the melt becomes sufficiently viscous that a point is reached where it has to be considered as a solid, but retains the structure of the mother melt. Such a metastable solid is a glass.

Glass formation or the absence of crystallite nucleation and growth is also dependent on the 'confusion principle'. This is an empirical observation which suggests that, in a multicomponent melt, several crystalline forms are in competition in the crystallization process; the confused situation that results acts as a barrier to microcrystal growth and enhances the formation of the vitreous state.

Although glasses have been known for more than 4000 years, the number of chemical combinations leading to stable vitreous solids is very limited. In addition, most glasses have a poor behavior towards devitrification and humidity corrosion and are not suitable for industrial applications.

The most interesting glass compositions are derived from the elements of groups 6 and 7 of the periodic table, that is, the oxides, chalcogenides, and halides. A very specific class of vitreous materials is represented by a new family of noncrystalline solids, the so-called ‘metglasses’ or metallic glasses; their production is special in the sense that they require very rapid quenching of an alloy melt.

In the oxide family of glasses, the situation is largely dominated by silica (SiO_2): however, the oxides P_2O_5, B_2O_3, Al_2O_3, and so on are also known to generate vitreous phosphates, borates, and aluminates. Commercial glasses as used in everyday applications always have complex compositions involving several of these oxides.

The general feature of all chemical combinations that give rise to glass formation is that they correspond to a composition very close to the eutectic region, leading to a liquidus with a low-melting point.

1.3 Glass: A Very Special Solid

As previously mentioned, a glass is a liquid which has reached an infinite viscosity without crystallizing. In this sense, this solid is out of equilibrium and will have very specific and unique properties.

In optics, for instance, a glass is an ideal medium for photon propagation. This is because glass is a homogeneous solid without grains and grain boundaries, so that the scattering of light is minimized. For telecommunications, optical fiber technology has been developed to such a degree that the SiO_2 glasses used can propagate light for more than a hundred kilometers with weak attenuation.

The thermal behavior of a glassy solid is also unique in the sense that all the glasses are characterized by their so-called glass transition temperature, T_g. Above T_g a glass cannot be considered as a real solid with infinite viscosity. The relaxation phenomena happening at T_g correspond to an abrupt change in the viscosity η. This decreases linearly with temperature from T_g where η is typically 10^{13} P. From this point, the glass becomes a plastic solid that possesses unique properties, allowing shaping such as glass blowing, fiber drawing, and so on. The composition of a glass is often characterized by the softening temperature T_s, which corresponds to a viscosity of about 10^7 P, while the drawing temperature for optical fiber preparation corresponds to a viscosity close to 10^5 P.

Another property, characteristic of glassy materials, takes place above T_g when individual atoms begin to have a certain mobility owing to the decrease in viscosity and increase in thermal agitation. From this point, the solid tends towards its thermodynamic equilibrium by generating ordered crystalline phases; this is the domain of microcrystallite nucleation and crystal growth. The control of this phenomenon is essential in glass technology: devitrification can be detrimental, in optics for instance, because this generates scattering centers that are a major cause of optical loss. In other cases, the precise control of microcrystallization leads to very interesting composite materials, the vitroceramics, which consist of a glassy matrix in which submicronic crystals of consistent size are nucleated. The Vision range of cookware developed by Corning is a good example of this kind of product, characterized by an acceptable transparency in the visible region together with a high resistance to thermal shock. In this application, the presence of microparticles is also beneficial in decreasing and attenuating the propagation of mechanical and thermal phonons. The control of glass ceramics preparation at an industrial scale is a difficult challenge, especially when additional nucleating agents such as nanosize ZrO_2 have to be dispersed inside the silica-based matrix. This has been accomplished by Schott with the development of the Zerodur glass ceramic that is insensitive to temperature and is used as substrate for the very large mirrors of the astronomical telescopes. Recently complex silicate compositions containing a significant amount of rare earth and fluorine have been investigated with the aim of taking advantage of a glassy matrix containing low phonon RE doped fluorides crystallites, for laser or optical amplification.[1]

The glass–crystal competition, which is a permanent phenomenon in glass technology, is illustrated in Figure 1 by a typical thermal analysis, recorded for a fluoride glass.

More complex phenomena can also occur, especially when the glass is prepared from complex melt compositions containing several glass-forming components. In this event, subliquidus immiscibility is possible, giving rise to phase separation between two interconnecting glass frameworks usually of very different chemical compositions. One of them can be leached, for example, while the other forms a 3-D porous skeleton. The Vycor® glass developed by Corning is based on this phenomenon. As a frozen liquid, the vitreous state is a unique, homogeneous medium for light transmission. The absence of scattering loss due to grains, grains boundaries,

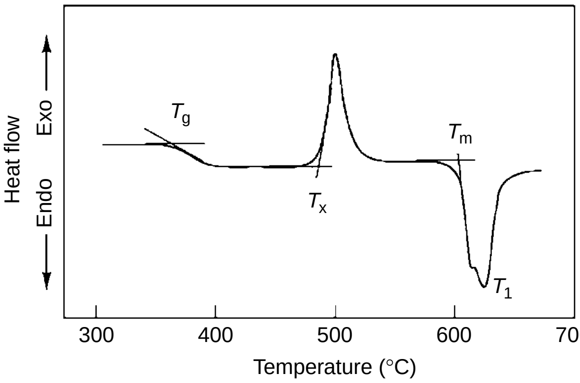

Figure 1 Thermal analysis of a fluoride glass showing characteristic temperatures: T_g is the glass transition temperature; T_x corresponds to the beginning of the crystallization; T_m is where the crystalline phase starts to melt; T_l is the liquidus temperature corresponding to the end of the melting process

the easy shaping above Tg explains why glass is a dominating materials for windows, bottles, optical fibers, and so on.

2 OXIDE GLASSES

2.1 Glass Formation in Oxide Systems

Oxide glass is one of the oldest materials made by man and vitreous objects are associated with the oldest civilizations. Halfway between art and technology, the development of glass making has been for many centuries essentially empirical. Most glasses have been of the soda-lime–silica type, SiO_2 being the major component. The conditions of glass formation in SiO_2-based systems have been extensively investigated and the generally recognized key factors are (1) formation of a 3-D aperiodic framework of SiO_4 tetrahedra sharing corners, (2) thermal motion easily causing rotation or bending of the strong Si–O–Si covalent bond leading to lack of periodicity, and (3) the skeleton can also be a giant negative anion if glass modifier oxides, such as Na_2O, CaO, and so on, are combined with SiO_2. In the latter case, the SiO_4 unit can contain two kinds of oxygen environment: bridging and covalently connected with two Si atoms; nonbridging, bonded on one side to Si atoms and having an ionic interaction on the other side, with the alkali ions statistically distributed inside the framework. Figure 2 illustrates a two-dimensional representation of a SiO_2-based glass.

The same type of strong covalent network with a large degree of freedom between the connected units is also found in a few other glass-forming oxides such as B_2O_3, P_2O_5, As_2O_3, GeO_2, and so on. The vitreous oxides strongly dominate glass science because they offer a large variety of materials with good thermomechanical properties, high resistance to devitrification, and good chemical durability.

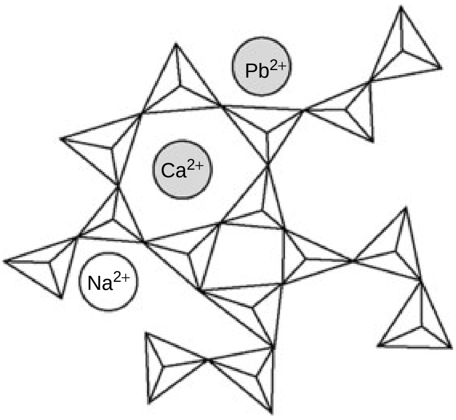

Figure 2 Structural representation of a SiO_2-based glass. The giant 3-D aperiodic skeleton is formed by SiO_4 tetrahedra sharing corners. The addition of glass modifier oxides such as PbO, Na_2O, and CaO results in nonbridging oxygen atom sites and a statistical distribution of the cations Pb^{2+}, Na^+, or Ca^{2+} throughout the lattice

2.2 Vitreous Silica and Silicate Glasses

2.2.1 Vitreous Silica

Silica glass, SiO_2, was initially prepared by fusion of natural crystalline SiO_2, such as quartz or sand. At temperatures above 1750 °C the melt is viscous enough to prevent any crystallization upon cooling. Much purer material, made to meet the requirements of optical fiber technology (e.g. ultralow-loss waveguides) is produced by the vapor phase oxidation[2] of ultrapure $SiCl_4$, following the reaction $SiCl_4 + O_2 \rightarrow SiO_2 + 2Cl_2$. The recent structural information obtained by Elliot[3] and Wright[4] confirms the initial model of Warren.[5] The basic unit of the framework is a very regular tetrahedron with an Si–O bond of 1.608 Å and an O–Si–O angle of 109.7°. Instead of being collinearly connected, the tetrahedra form a spectrum of intertetrahedral angles distributed around the average value of Si–O–Si ~150°. With a very low thermal expansion coefficient ($\alpha = 5 \times 10^{-7}\ °C^{-1}$), SiO_2 glass shows a strong resistance to thermal shock. On the other hand, with a T_g close to 1200 °C, this glass necessitates a very high temperature (>1700 °C) for blowing or fiber drawing. However, silica is highly resistant to devitrification, so that shaping and fiber drawing at such high temperature do not induce any crystallization. Silica is also highly resistant to corrosion, which makes this glass of large interest for long-term applications such as in optical fiber telecommunications.

As far as optical properties are concerned, vitreous silica is highly transparent from nearly 160 nm (8 eV) in the UV to 3 µm in the infrared (IR), as shown in Figure 3.

In the fiber form, silica exhibits a minimum optical loss of nearly 0.2 dB km^{-1} at 1.55 µm, that is far away from the UV and IR absorption edges. Attaining such a low attenuation is possible because of the use of the modified chemical vapor deposition (MCVD) process that eliminates metallic impurities during preform preparation. The usable transmission range of silica fibers utilized in telecommunications is typically from 1.3 µm to 1.6 µm as shown in the attenuation curve in Figure 4. In that range, the remaining losses are due to intrinsic factors: Rayleigh scattering combined with multiphonon absorption, and to extrinsic absorption due to the presence of residual hydroxyl OH groups responsible for the band at 1400 nm. This band corresponds actually to the first overtone of the fundamental O–H vibration. (see also Section 4.3.1)

The typical constitution of an optical fiber is shown in Figure 5. Determined by the initial preform geometry, the core diameter is a few micrometers while the cladding is ≈125 µm. The overall diameter for coated fibers is around 250 µm. With core diameters of the order of magnitude of the propagating wavelength, only the fundamental mode is

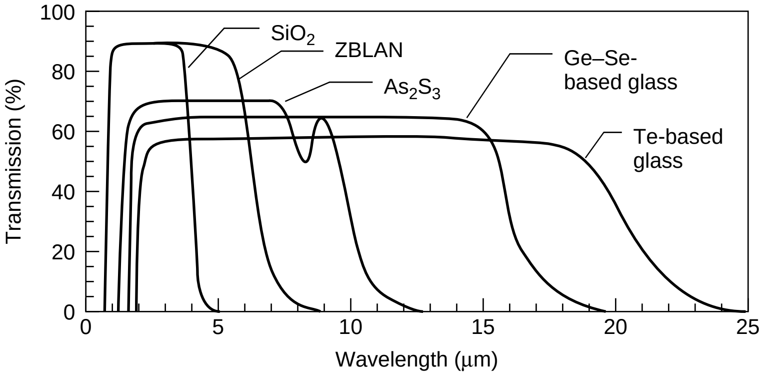

Figure 3 Optical transmission spectra of silica and nonoxide glasses. ZBLAN glass composition is given in Figure 12

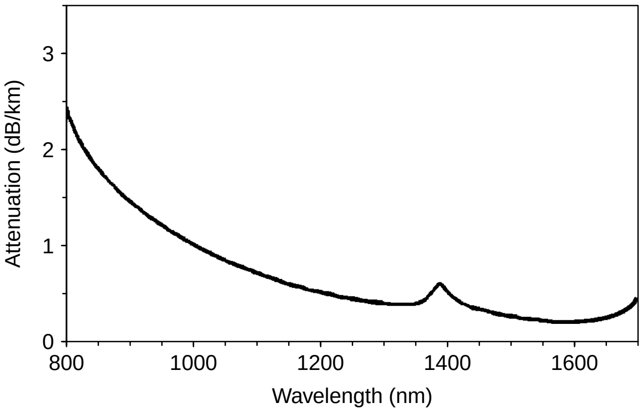

Figure 4 Optical attenuation curve of a single-mode commercial silica fiber

guided in fibers, which are then designated as single-mode fibers.

Because of basic optical principles, the light injected into the fiber must belong to a geometrical acceptance cone in order to be guided within the core. This condition is given by the numerical aperture, defined as $\mathrm{NA} = \sin\theta_m = (n_1{}^2 - n_2{}^2)^{1/2}$ with θ_m, the maximum angle of the cone, and n_1 and n_2 the refractive indices of the core and cladding, respectively. Numerical apertures are usually between 0.1 and 0.3 for telecommunication applications, with the refractive index of pure silica equal to 1.4586 at sodium D-line.

For further reading and references on the preparation of silica preforms and fibers, on light propagation and optical losses in fibers, see Ref. 6.

Recently, large-scale research has been devoted to a novel type of silica optical fiber, named photonic crystal fiber, whose structure is very different from that of the conventional fiber described above. The cross section of a photonic crystal fiber is shown in Figure 6. The cladding is made of glass with periodic air holes surrounding a full glass-core. This results in a cladding region with average refractive index lower than that of the core, and light can propagate by total internal reflection, like in a conventional fiber. Among other advantages, photonic crystal fibers possess the potential for broad-band single-mode guiding and high nonlinearities. Further reading is available in Ref. 7

2.2.2 Alkali and Other Binary Silicate Glasses

Glasses can be made in all the alkali silicate systems over a range of composition, from SiO_2 itself up to about 30 mol % Li_2O, 50 mol % Na_2O, or 50 mol % K_2O. The first observation is a large drop in the liquidus temperature and a drastic modification of some properties. For example, T_g falls from 1200 °C for SiO_2 to 350 °C for the 45% Na_2O-containing glass. Over the same composition range the thermal expansion increases almost linearly, from $\alpha = 5 \times 10^{-7}\ {}^\circ C^{-1}$ to $\alpha = 200 \times 10^{-7}\ {}^\circ C^{-1}$. For comparison, a typical commercial container glass has an α of $90 \times 10^{-7}\ {}^\circ C^{-1}$ and a T_g around 520 °C. The second tendency of alkali silicate glasses is to give rise to subliquidus immiscibility, leading to glass-phase separation; the same materials are also sensitive to moisture and water corrosion, especially in the alkali-rich region.

In most of the other binary silicate systems, involving oxides such as BaO, CaO, MgO, Al_2O_3, and so on, the liquidus temperature is very high and glass formation is limited by immiscibility in the melt; rapid quenching is needed to obtain glasses. The SiO_2–PbO system is of particular interest because of the low liquidus temperatures; these render glass formation easier and lead to heavy glasses due to the high atomic weight of lead.

The alkali silicate glasses are easily corroded by aqueous acids and the main reaction is an exchange between H_3O^+ of the solution with the alkali M^+ of the glass; the corrosion rate increases with the ionic radii of M^+, that is, $K^+ > Na^+ > Li^+$. The chemical durability is greatly increased by addition of divalent CaO or trivalent Al_2O_3 oxides, leading to commercial soda-lime–silica compositions.

The presence of modifier ions in silicate glasses make it possible to create optical guiding structure by ion exchange at

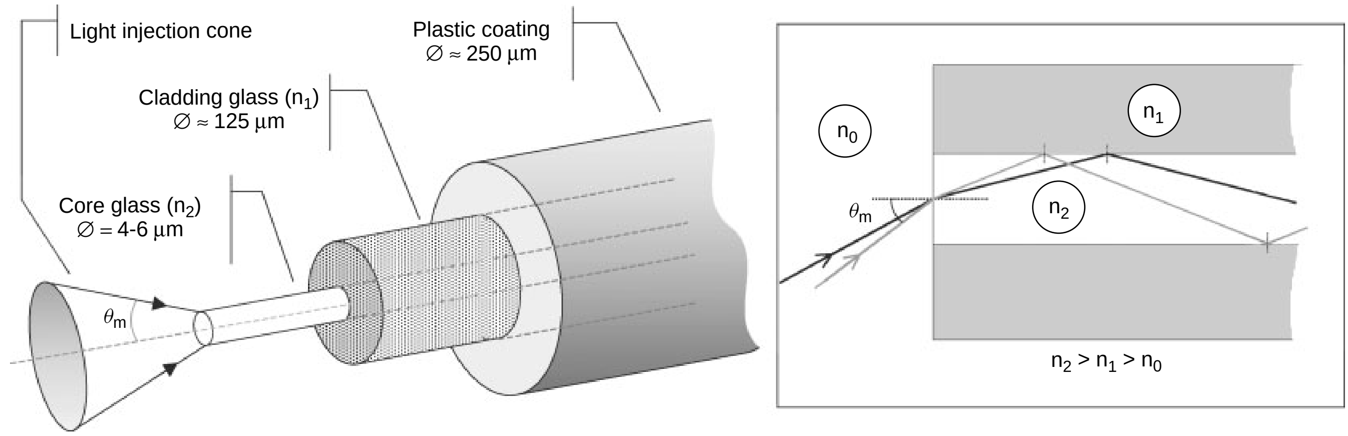

Figure 5 Typical structure of a silica fiber for telecommunication. Frame: Principle of light propagation in a multimode optical fiber

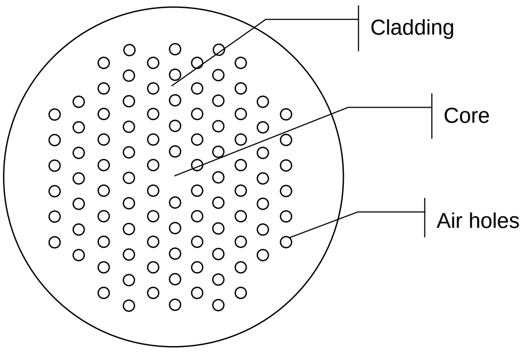

Figure 6 Cross section of a photonic crystal fiber

the glass surface. For example, Na^+ ions in the glass can be exchanged for more polarizable ions like Cs^+, Rb^+, K^+, or for small ions like Li^+ that generates collapsing and consequent densification of the glass matrix. Higher polarizability or material densification result in an increase of the refractive index.[8]

2.2.3 *Commercial SiO_2-based Glasses*

Commercial glass compositions change from one manufacturer to another, even for a given product. The selection given in Table 1 is taken from the article by Rawson[9] and indicates the general tendency in composition for a given application.

Glasses 1, 2, and 3 are, respectively, float glass for windows, container glass such as for bottles, and the glass used to make incandescent lamp bulbs. They have been optimized to achieve the viscosity–temperature characteristics required by the shaping process, and they are low cost. Glasses 4 and 5 are very rich in PbO and correspond to the traditional lead crystal composition having a high refractive index, $n = 1.6$, giving a brilliant appearance when cut. Glass 5 has the highest content of PbO and has a value of $n = 1.85$. These glasses are also strongly absorbing towards X ray and γ radiation.

Glasses 6, 7, and 8 represent the large and important group of borosilicate glasses including Pyrex, used for chemical apparatus and domestic cookwares.

Glass 9 is rich in alumina (Al_2O_3) and is a high-melting material suitable for glass fibers as used in composite reinforcement or thermal isolation. Glass 10 is used for cathode-ray tubes, glass 11 is an optical glass, and glass 12 is a solder glass used because of its high fluidity at about 550 °C to seal soda-lime glasses.

2.3 Boric Oxide and Borate Glasses

2.3.1 *Boric Oxide Glass*

B_2O_3 is very easily contaminated by OH and this significantly affects thermal properties, such as the melting point around 450 °C, leading to a melt with a rather low viscosity which vitrifies easily; the corresponding glass has a T_g close to 260 °C.

The building units in B_2O_3 glasses are triangular, owing to the three bonding electrons on the boron atom and sp^2 hybridization. Their association by corner sharing leads to a 2-D aperiodic network. As shown in Figure 7, the interchain connections generate boroxol groups, $B_3O_3O_{3/2}$.

2.3.2 *Borate Glasses*

Glass formation in the alkali borate system is characterized by an increase in the liquidus temperature, a high tendency to crystallize compared to B_2O_3 itself, and to give subliquidus immiscibility.[10,11] The phase separation phenomena can markedly affect the properties of borate glasses such as viscosity. The origin of this immiscibility can be found in the formation of two independent glassy networks during the addition of alkali oxides, M_2O.[12] The additional oxygen atoms brought by M_2O lead to a BO_4 tetrahedra-based

Table 1 Composition of some commercial glasses[a]

No.	SiO_2	Al_2O_3	B_2O_3	Na_2O	K_2O	Li_2O	MgO	CaO	BaO	PbO	ZnO
1	72.8	0.7	–	13.8	–	–	3.6	8.8	–	–	–
2	72	1.3	–	14.3	–	–	3.5	8.2	–	–	–
3	71.5	2.0	–	15.5	1.0	–	2.8	6.5	–	–	–
4	56.0	–	–	2.0	13.0	–	–	–	–	29.0	–
5	26.9	0.5	–	1.0	–	–	–	–	–	71.3	–
6	80.8	2.2	12.0	4.2	0.6	–	0.3	0.3	–	–	–
7	67.5	2.5	21.7	3.2	4.2	–	–	–	–	–	–
8	75.5	2.6	16.0	3.7	1.7	–	–	–	–	–	–
9	52.9	14.5	9.2	1.1	1.1	–	4.4	17.4	–	–	–
10	67.0	5.0	–	7.0	8.3	0.6	–	–	11.7	–	–
11	68.3	0.2	2.2	14.4	7.0	–	4.6	–	–	2.9	–
12	5.0	–	17.0	–	–	–	–	–	–	64.0	14.0

[a] In wt %.

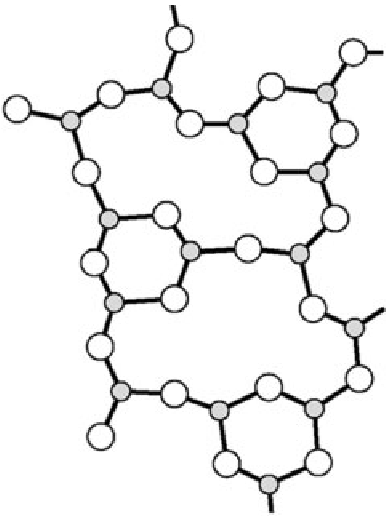

Figure 7 Structural representation of boron oxide (B_2O_3) glass. The giant 2-D skeleton is formed by BO_3 triangles sharing corners. Specific $B_3O_3O_{3/2}$ boroxol groups can be present in the structure

framework which is separated from the initial BO_3 triangular-based structure.

2.3.3 *Borosilicate Glasses*

While the practical applications of borate glasses are very limited, the glasses derived from Na_2O–B_2O_3–SiO_2 systems are of considerable technological importance. They include the glass commonly known as Pyrex, used for chemical apparatus and ovenware.

The addition of B_2O_3 to a silicate glass markedly reduces the thermal expansion coefficient and consequently enhances the resistance to thermal shock. At the same time, the chemical durability, especially the resistance to acid attack, is greatly improved.

Several borosilicate glass compositions exhibit immiscibility; they separate into two interconnecting phases, one rich in sodium borates, the other being almost pure silica. The first phase can be leached out by immersing the material in acid. The densified remaining glassy phase gives so-called Vycor® glass. The porous silica skeleton can also be used as a host for enzymatic and catalytic reactions.

2.4 Phosphate Glasses

The higher phosphorus oxide, P_2O_5, is a highly hygroscopic material. On melting it gives a very viscous liquid which can be readily supercooled to give a glass. This particular material has no practical interest owing to its rapid corrosion by water and moisture.

Information on binary phosphate glasses has to be regarded with some care owing to the variable amount of water retained in the glass and which varies with composition, time, and temperature of melting. The glass-forming ability and properties are very dependent on OH content, which introduces strong hydrogen bonds and which varies according to the equilibrium $2OH^- \rightleftharpoons O^{2-} + H_2O$.

The most interesting phosphate glasses for practical applications are multicomponent materials, often containing fluorides. They have been developed as optical glasses for laser applications; for instance, the Nd^{3+}-doped phosphate glasses of high optical quality used in large, high-power laser fusion have been selected because of their low nonlinear refractive index which attenuates the risk of beam self-focusing.

Er^{3+}-doped phosphate glasses are also very efficient lasers operating at 1.54 μm. In order to improve the resistance of the material to thermal shocks due to intense light pumping, phosphate glasses can be chemically strengthened by an ion-exchange process – Na^+ or K^+ for Li^+ – at the glass surface. Thus, laser output as high as 600 mJ at 1.54 μm could be achieved with 100 J pump energy.[13]

It must be noticed that Ca rich phosphate glasses and glass ceramics having a composition very close to apatite, the main component of bones are bioactive materials capable of bonding to natural bones and then used for surgery implantation.[14]

2.5 Miscellaneous Oxide Glasses

Several other oxides, such as GeO_2, Al_2O_3, TeO_2, and V_2O_5, containing small highly charged polarizing cations, are also able to form glasses when undercooling the melt. In these cases, the tendency for crystal formation upon cooling is very high and fast quenching is necessary.

GeO_2 is used in small quantities in the core of optical fibers for increasing the refractive index of SiO_2 in order to achieve the optical guiding conditions.

The only interest in this expensive oxide is its better IR transparency owing to a shift of the multiphonon edge; glasses of optical quality are therefore difficult to achieve even in multicomponent compositions. Addition of modified oxides such as alkali to GeO_2 contributes to the formation of GeO_6 octahedra in addition to the existing GeO_4 tetrahedra. Lead germanate glasses are commercial IR products.

The situation is very similar for Al_2O_3-based glasses. In the Al_2O_3–CaO system, where the two starting components have high-melting points, glasses can be prepared by fast quenching of the melt in the eutectic regions where the liquidus is around 1400 °C. The stability of Al_2O_3-based glasses is improved by making the composition more complex, but SiO_2 addition is detrimental to IR transparency.

A homogeneous TeO_2 glass is obtained only by quenching the melt when it is viscous above the melting point. The most stable tellurite glasses are formed in systems such as TeO_2–PbO, BaO, and so on. These glasses are of some interest because of their high refractive index, which can reach values up to 2.3. As far as phonon energies are concerned, tellurites are classified as intermediate glasses, between silicates and halides.[15]

V_2O_5 melts at 660 °C and forms a glass only by fast quenching. Therefore complex compositions belonging to the system V_2O_5–BaO–K_2O–ZnO enhance glass-forming ability. The most notable characteristic of these glasses is due to the easy mixed valence V^{4+}/V^{5+} situation, leading to semiconducting properties and coloration arising from charge transfer absorption.

The rigidity of the silicate or phosphate glass network can be markedly enhanced by substituting some oxygen atoms by nitrogen. The corresponding oxynitride glasses are characterized by a general modification of their thermal properties such as a sharp decrease in the expansion coefficient α and an increase in glass transition temperature. In the Y–Si–Al–O–N system,[16] when the nitrogen atomic percentage is increased from 0 to 6%, α varies from 70×10^{-7} to 35×10^{-7} $°C^{-1}$ and T_g moves from 800 to 900 °C. Both observations indicate an increase in the degree of cross-linking when the trivalent N atoms substitute the divalent O atoms in the glass-forming skeleton.

The most effective way of making nitrogen-containing silicate glasses is to melt together mixtures of oxides and nitrides in a nitrogen or inert atmosphere. A maximum of 10% atomic substitution is generally attained and it has been observed that the nitrogen solubility is increased if the glass composition contains Al_2O_3. This is attributed to the fact that the $Si(O,N)_4$ and AlO_4 tetrahedra are of similar size.

2.6 Glasses from Ionic Salts

Vitreous materials can be formed by undercooling certain molten salts consisting of mixtures of nitrates, acetates, and sulfates, which contain discrete anions such as NO_3^-, $C_2O_4^{2-}$, SO_4^{2-}, and so on.

As discussed by Angell,[17] the conditions for glass formation in such unusual systems are not very well understood, especially because of a lack of information about contamination of these molten salt mixtures by water.

As expected, the absence of crystallization upon cooling is especially marked when the melt is close to the eutectic region, having a low liquidus temperature. For example, the region of glass formation in the binary system KNO_3–$Ca(NO_3)_2$ is for 60 mol % KNO_3, corresponding to a eutectic temperature of 146 °C, while the melting points of the two constituents are 337 °C (KNO_3) and 561 °C ($Ca(NO_3)_2$).

Several sulfate mixtures such as $KHSO_4$–$NaHSO_4$ are also glass formers with good resistance to crystallization.

The fact that many crystalline hydrates melt, such as $Ca(WO_3)_2{\cdot}4H_2O$, while more complex binary hydrated systems have a tendency to form glasses is an indication of the critical role of the water molecule and the hydrogen bond.

It is clear that the polymerization process in these low-melting melts involves strong hydrogen bonding between the OH^- group and the O^{2-} atom of the neighboring anions. Rotation as well as bending of the hydrogen bond is rather easy, making possible a system with a lack of periodicity.

There are no commercial applications for these unconventional glasses.

3 CHALCOGENIDE GLASSES

3.1 Introduction: Definition

Chalcogenides are compounds containing elements of group 6 of the periodic table, with the exception of oxygen. Chalcogens such as sulfur, selenium, and tellurium are characterized by the typical six-electron outer shell $s^2p_x{}^2p_y{}^1p_z{}^1$. In most of the vitreous combinations described in this article, the chalcogen atom will be divalent, using its two odd electrons in twofold coordination. The two remaining nonbonding pairs will be considered as localized lone pairs having a strong stereochemical effect around the chalcogen and introducing nonbonding atomic levels in the energy diagram.

Most of the metallic chalcogenides are found as crystalline materials, often with 2-D character and only a very limited number of them are able to form glasses from the melt.

Consequently, the chalcogenide glass family is essentially represented by polymer-type compounds in which the chemical bond is highly covalent. The chalcogen atom is then bonded to neighboring elements of the periodic table with similar electronegativity, such as As, P, Ge, Si, Cl, Br, and Bi. The conditions of glass formation and the physics of amorphous chalcogenides have been discussed and reviewed by Elliot.[18,19]

These materials are generally semiconductors with small band gaps in the range of 1–3 eV, owing to the specific character of the chemical bonds, that is, covalence plus nonbonding electrons. The band-gap edge is then located in the visible or near-IR region and most of those glasses are black. Owing to the high atomic weights of the constituent elements, these glasses have IR absorption edges located in the long wavelength region, which renders these materials very attractive for IR light transmission.

3.1.1 Classification of Chalcogenide Glasses

The noncrystalline chalcogen-containing materials can be distinguished according to the nature of the accompanying elements. As presented in Table 2, four general families of glasses can be identified.

Category 1 is represented by pure chalcogen, solid solutions of different chalcogens, or association with a pseudochalcogen such as As or P having a very similar electronegativity. Crystalline sulfur or selenium on melting give very viscous melts, indicating that the liquid phase is highly polymerized. Since the elemental chalcogens are twofold coordinated, the structural configuration of the resulting polymer is limited to rings or chains bonded together by van der Waals or dipole–dipole forces. A sulfur glass can be made by quenching the melt above a temperature of about 440 K, when the high viscosity is due to long polymeric chains.

In the case of Se, the chains already exist in the crystalline form and, just above the melting point ($T_m = 490\,K$), the liquidus is viscous enough to lead to easy glass formation even with a moderate cooling rate.

Tellurium, which has more metallic character, is not able to support a polymeric arrangement in its liquid phase, which has a low viscosity like a molten metal. Glass formation is only possible from $Te_{1-x}Se_x$ solutions, and even then very fast quenching such as melt spinning is needed.

Table 2 Categories of chalcogen-based glasses[a]

No. Category	Examples of glass former
1. Pure chalcogen (6–6)	S, Se, Se_{1-x}, Te_x
or pseudochalcogen (5–6)	Se_{1-x}, S_x, As_2S_3, As_2Se_3
2. Semimetallic chalcogenides	$SiSe_2$, GeS_2
3. Metallic chalcogenides	Al_2S_3, Ga_2S_3
4. Chalcogen halides	Te–Cl, Te–Br

[a] 5 and 6 represent elements from group 5, except N, or group 6, except O, of the periodic table.

The most interesting materials in this group of glasses are the arsenic sulfide and selenide, As_2S_3 and As_2Se_3. This combination of groups 15 and 16 elements gives rise to a very strong covalent 2-D framework, rendering these materials stable to devitrification and chemical attack. Glass formation has also been discovered in the $P_{1-x}Se_x$ system[20] close to $x = 0.2$ and $x = 0.75$, but the corresponding glasses have no application due to poor chemical durability.

Category 2 corresponds to chemical combinations of groups 4 and 6 elements. In this particular case the group 4 atoms, such as Si and Ge, will be fourfold coordinated and form SiS_4 or GeS_4 tetrahedra. From this elementary, symmetric module, a 3-D aperiodic framework is expected similar to that in SiO_2 glass, except that the large size of the tetrahedron will allow edge sharing in addition to corner sharing.

This classification is of course arbitrary, and it must be noted that the very stable chalcogenide glasses are often ternary or quaternary compounds corresponding to mixed complex compositions of categories 1 and 2. For instance, the commercial glass called AMTIR (Amorphous Materials Transmitting Infrared) is the multicomponent glass $As_{12}Ge_{33}Se_{55}$. Figure 8 represents the region of glass formation in the system As–Ge–Se.[20]

Category 3 corresponds to combinations of a real metal such as aluminum or gallium with a chalcogen such as S. The simple sulfides, Al_2S_3 or Ga_2S_3, cannot form glasses by themselves and need to be combined with glass modifiers such as rare earth sulfides La_2S_3. For some other glasses, stabilizers are also necessary and ternary glasses have been isolated in the system Ga_2S_3–MnS–La_2S_3,[21] for instance. The glass-forming units here are also tetrahedral AlS_4 or GaS_4, and probably octahedral MnS_6.

The last group of glasses, corresponding to category 4, are similar to those of class 1 in the sense that they have a Se-type chain structure. A decade ago, glasses were discovered[22] in the Te–X system (X = Cl, Br, I), leading to glassy polymeric materials with very low phonon energies and excellent IR-transmitting properties.

3.2 Structure and Bonding in Chalcogenides Glasses

3.2.1 The Building Units

For most of the chalcogenides in categories 1–4, three types of building unit (Figure 9) can be distinguished, giving rise to so-called short-range order.

1. The angular unit is illustrated by the Se atom: among the six outer electrons, only two are bonding, the two other pairs being localized and giving, by repulsion with the bonding pairs, a pseudotetrahedral arrangement around Se.
2. The distorted triangular unit observed around group 5 elements such as As: in this case the three bonding

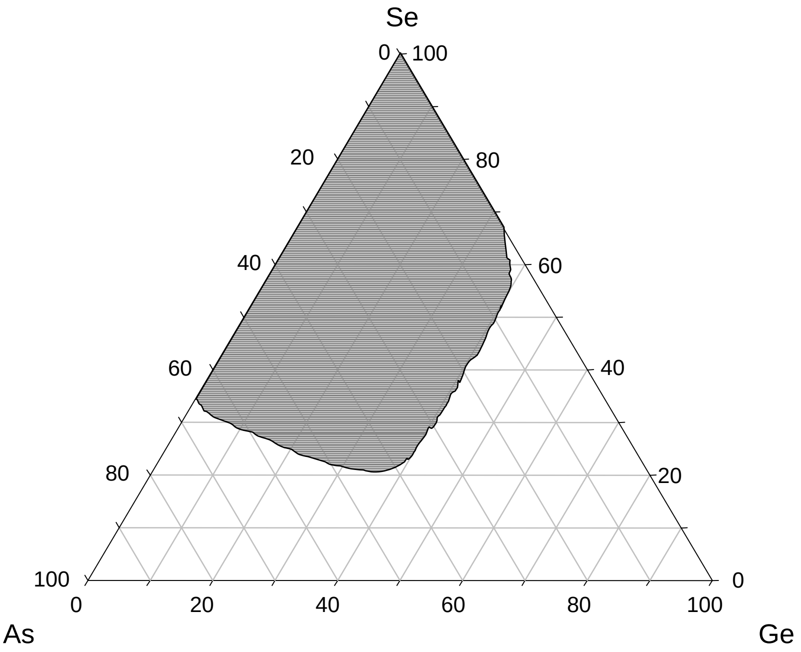

Figure 8 Glass-forming zone (approximate, since it depends on the quenching rate) in the Ge–Se–As system. The three components Se, $GeSe_2$, and As_2S_3 alone are able to form glasses

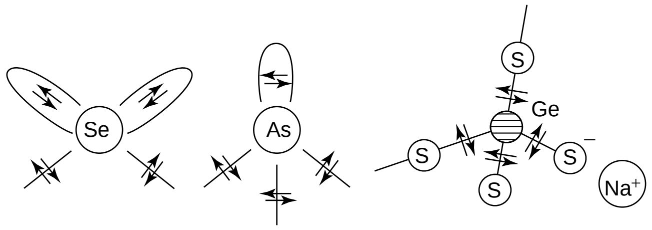

Figure 9 Building units found in most of the chalcogenide glasses: the angular unit existing in Se-type glasses; the pyramidal unit of the As-based glasses; and the tetrahedron of the GeS_2 glass

electrons lead to three bonding pairs which complement the remaining lone pair.

3. From the analysis of the corresponding crystalline materials the tetrahedron is the basic unit in the SiS_2-, $GeSe_2$-, Al_2S_3-, and Ga_2S_3-based glasses. When the glasses are stabilized by modifiers such as Na_2S, BaS, and La_2S_3, the tetrahedra are formed by bridging and nonbridging chalcogen.

3.2.2 The Nonperiodic Skeleton of Chalcogen-based Glasses

From the elementary units previously described, several 1-D, 2-D, or 3-D frameworks can be constructed, as shown in Figure 10. One-dimensional chains are found in Se by connecting the angular units. In sulfur, it has been observed that the unit can be rotated along the covalent σ-bond, giving rise to an equilibrium between chains and S_8 rings. The same situation occurs in SiS_2 glass, but here the chains are formed by connecting SiS_4 tetrahedra by sharing edges. In this $SiS_{4/2}$ chain, the distorted Si–S–Si bond reflects the strong stereochemical effect of the S electronic lone pairs.

In both 1-D-based glasses, the interactions between the chains being of the van der Waals type, are weak, and allow easy rotation or bending. Two-dimensional configurations, giving rise to distorted layer structures, are found in As_2S_3- or GeS_2-type glasses. The connection of pyramidal and angular units in As_2S_3 lead to an infinite distorted 2-D framework. The periodicity in this orpiment-related structure can be easily destroyed because the layers are bonded by van der Waals forces and because rotation and bending are possible around the S–As–S σ-bond without costing too much energy.

In GeS_2-based glasses, examination of the parent crystalline materials indicates that GeS_2 tetrahedra, connected by corner and edge sharing, also form a layered 2-D structure.

A 3-D framework analogous to the SiO_2 cristobalite structure is of course easy to build from elementary tetrahedra. Notice that, in the Ge/S system, the glass-forming ability is maximum for the composition GeS_4 which corresponds to tetrahedra connected by a S–S pairs bonds.

In all of these giant skeletons, the glassy state arises from the easy lack of periodicity. This means that a small rotation or bending of the bonds does not markedly affect the free enthalpy of the system because of framework flexibility.

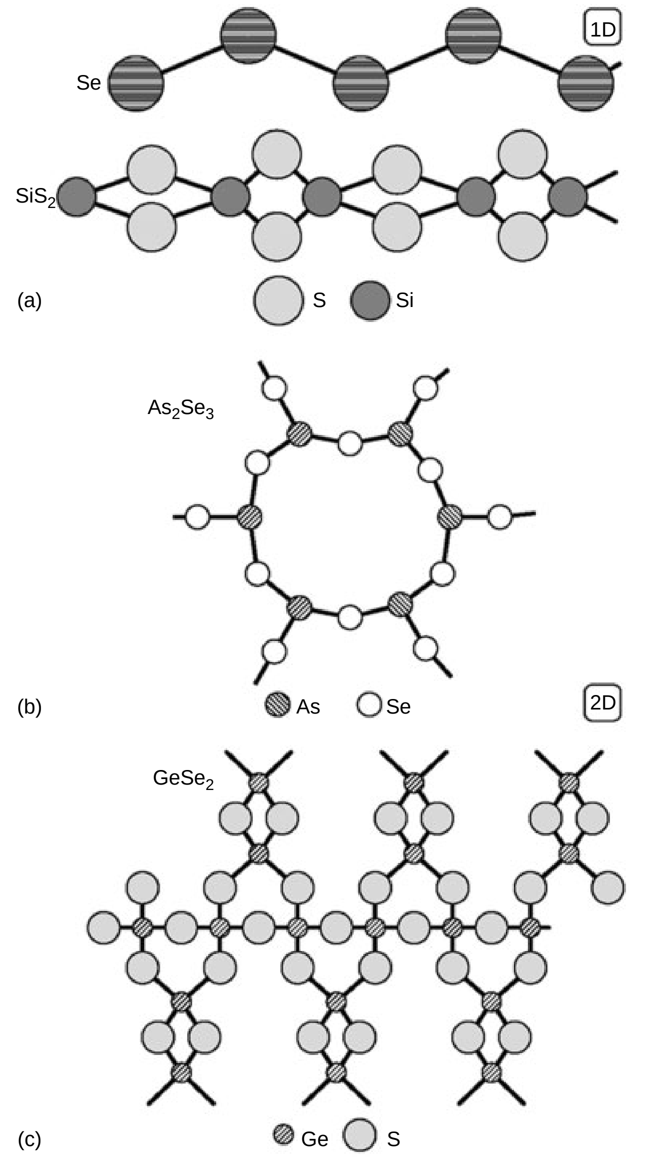

Figure 10 The different frameworks formed in chalcogen-based glasses: (a) a chain-like structure in Se or SiS_2; (b) 2-D skeleton in As_2S_3 formed by linking Se angular and As pyramidal units; (c) by sharing corners and edges, the tetrahedra of the GeS_2-based glasses also form a 2-D framework

3.3 Properties of Chalcogen-based Glasses

3.3.1 Thermal Properties

The glass transition temperatures give a good indication of the thermal stability of chalcogen-based glasses. Below T_g the glass is a real solid with infinite viscosity while above T_g the viscosity begins to decrease linearly, rendering the glass first plastic and then similar to a viscous liquid. Knowledge of these data is essential to allow comment on the thermal capabilities and for shaping the glass. Operations such as annealing, for relaxing the local stresses, and fibering, for optical waveguide preparation, need a precise determination of T_g. Table 3 gives T_g values for several glasses.

Table 3 Glass transition temperatures for several chalcogen-based glasses

Glass	T_g (°C)
S	−27
Se	35
Te_3Cl_2	82
As_2S_3	205
As_2Se_3	195
$As_{12}Ge_{33}Se_{55}$	362
$GeSe_2$	422
GeS_2	492

The glass transition temperature is directly related to the dimensionality of the glass and can be considered as an indication of the rigidity of the framework. For instance, the low T_g glasses are 1-D chain-like materials such as Se or Te_3Cl_2, while the high T_g glasses belong to families having a 2-D or 3-D configuration.

The same situation is found when wrong-bond[23] nonbridging anions are introduced in a glass by way of chalcogen–halogen substitution or sulfides are added as modifiers. For instance, T_g falls rapidly when xS atoms are substituted by $2x$I atoms to preserve electroneutrality in GeS_2 glass. The result of this substitution, when $x = 1$, is the formation of a chain-like glass $GeSI_2$, containing tetrahedral GeS_2I_2 units connected by corners and sharing only S atoms ($GeS_{2/2}I_2$), the I atoms being terminal.

When Na_2S is added to GeS_2 the same phenomenon is observed, the additional S atoms break the dimensionality of the skeleton by the transformation of the bridging bonds $\cdots$Ge–S–Ge$\cdots$ into two nonbridging $\cdots$Ge–$S^-Na^+S^-$–Ge$\cdots$ bonds, as indicated in Figure 9.

Chalcogen-based glasses can be deposited to form thin amorphous films by thermal evaporation or sputtering, owing to their low thermal characteristics. This technique is widely used in the deposition of Se-rich glasses on to cylindrical drums used as the photosensitive surface in Xerography.

3.3.2 Electrical and Optical Properties

A simplified picture of the density of states in a chalcogenide material comprises a low-energy σ valence bond and, at higher energy, the σ^* antibonding level corresponding to the conduction band. The novelty of chalcogen-based glasses comes from the existence of a nonbonding (nb) level arising from the lone pair electrons situated above the σ level, as depicted in Figure 11. The optical band gap E_g is due to the transition from the nb level to the σ^* level and it is observed that E_g varies from about 1 to 2.5 eV. The corresponding optical absorption edges follows Urbach-edge behavior and

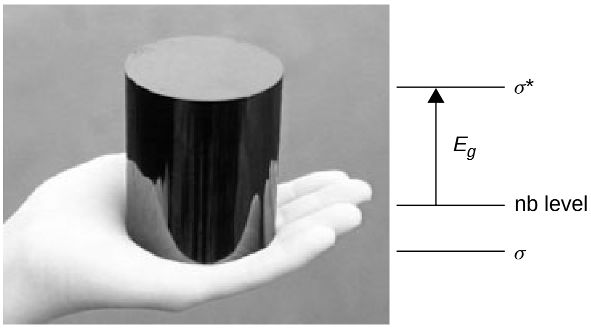

Figure 11 Optical band gap in chalcogen-based glasses. The optical band gap E_g is due to the transition from the nonbonding level to the antibonding level σ^*, which results in black-color glasses

give high values of the absorption coefficient α in the visible part of the spectrum. Consequently, most of the chalcogen-based glasses are black, as shown in Figure 11 except As_2S_3 that has a reddish color. (Recall the relationship λ_max (μm) E_g(eV) $= 1.24$ giving the correspondence between the band gap (electron volts) and the corresponding light wavelength and note that the optical absorption edge is not sharp but exhibits a long tail in the gap region.)

The chalcogenide glasses transmit light from the Urbach edge until the IR region where a second mechanism generates photon absorption. This phenomenon takes place in the low-energy region and arises from multiphonon processes associated with fundamental phonon vibrations of the material. In most of the chalcogen-derived glasses that contain heavy elements, the vibrational modes are at low energy and they exhibit excellent IR-transmitting properties. Most of the commercial chalcogen-based glasses such as AMTIR therefore have their IR cutoff after the 12 μm region and consequently cover the very strategic region 8–12 μm, corresponding to the second atmospheric window. This IR window is used for military and civil applications such as missile guidance, thermal imaging, and thermal detection, and so on. Chalcogen-based glasses can be shaped for making IR lenses and windows, and so on, as well as optical fibers used for carrying IR laser light from CO or CO_2 lasers and for local thermal imaging of room temperature black-body emitters.

Recently, chalcogenide glass IR fibers have been used as optical sensors for recording, in situ, the IR signatures of all kind of molecules in chemistry and biology. The principle is based on the absorption of the evanescent light circulating on the surface of the fiber, by the materials entering into contact with the fiber especially in the part which has been tapered.[24]

Noncrystalline chalcogenides are semiconductors with an activation energy about half of the optical band gap. The glass As_2S_3 taken as a prototype has the following characteristics: $W_\mathrm{e} = 1.14\,\mathrm{eV}$, $E_\mathrm{g} = 2.32\,\mathrm{eV}$, and $\sigma(300\,\mathrm{K}) \sim 10^{-17}\Omega^{-1}\,\mathrm{cm}^{-1}$.

Irradiation of chalcogenide films with light having an energy comparable to the band gap induces a variety of changes, such as photoluminescence and photoconductivity. Some of these are reversible and some are not, such as the chemical changes involved in lithography applications. Among the most peculiar photoinduced phenomena is the photodarkening corresponding to a reversible shift of the band-gap edge towards lower energy under illumination.

The electron–hole pairs created by illuminating the surface of a Se film is the basis of the xerography process. If the Se film is already positively charged, the photon from the ‘image’ of the page results in the excitation of an electron. This neutralizes a corresponding positive charge and leads to the formation of a positive electronic image. Carbon black particles are then deposited to give a black image of the documents.

As shown by Tanaka,[25] chalcogenide glasses are prone to photoinduced phenomena such as photorefractivity, photoexpansion, photofluidity, and so on which indicate that the local structure can be easily modified under suitable light irradiation.

4 HALIDE GLASSES

4.1 Introduction

Halide materials usually exist in the crystalline state when cooled from the liquidus. When the halogens are bound to small and highly charged cations, volatile molecular species such as $SiCl_4$ are easily formed. Consequently, a very limited number of halide systems lead to glass formation and the glass to crystal or glass to molecular vapor competition is severe.

Considerable progress has been made during the last two decades in the discovery of new glass-forming compositions, based on group 7 elements (F, Cl, Br, I), characterized by the outer electronic shell $s^2p_x{}^2p_y{}^2p_z{}^1$, showing one bonding electron.

The optical properties, and especially the possibility of extending the IR transparency domain, have been the main motivation for investigating such exotic glasses. Three intrinsic factors limit the technological development of such vitreous materials. Like other halides, they suffer from ready corrosion by moisture or water driven by stronger $M–OH_2$, M–OH, or M–O bonds. The relative weakness of the M–X bond also results in poor thermal capability, leading to low T_g glasses with high thermal expansion coefficients and sensitivity to thermal shock. Finally, the high electronegativity of the fluorine atom results in the easy formation of ionic bonding and leads to ionic microcrystal formation when crossing the strategic liquidus–solidus line. The optical properties, and especially the scattering losses, therefore suffer from the tendency to devitrify.

In addition to the development of very large IR optics, often difficult to accomplish with crystalline materials, an important property of halide glasses is the potential for the development of very transparent IR optical fibers. With its unique viscosity–temperature dependence the glassy state represents an ideal situation for transforming a bulk material into a very long waveguide. Several articles reviewing the chemistry and optical properties of these materials have been published.[26–28]

4.2 Glass Formation in Halide Systems

Because of its size, $r(\mathrm{F}^-) \sim r(\mathrm{O}^{2-}) \sim 1.40$ Å, fluorine is a rather special halogen leading to materials which are generally less sensitive to water corrosion and which are more suitable for practical applications. Consequently, among all the halide compounds which have been claimed to form glasses, only a very limited number are stable enough to be considered as optical materials and this is the case for several fluoride glass compositions. The heavy halide glasses, that is, the chlorides, bromides, and iodides, are all characterized by a high hygroscopicity and, despite their scientific interest, have to be considered as technological curiosities.

4.2.1 Fluoride Glasses

Fluoride glasses can be classified according to structural considerations and although glass-forming ability has been observed in many fluorides they cannot be considered of equal interest because of the high tendency for most of them to devitrify.

In most of these systems, the tendency to ionicity is high, leading to strong glass to crystal competition. This article is restricted to the compositions that are stable enough to make bulk samples, having a significant optical quality either for fundamental investigations or practical applications.

In all the following systems, the polymerization process arises from the twofold coordination of the F atoms which connect the elementary polyhedra in a 3-D manner. The F^- ions situated between two highly charged M^{n+} cations appear to be strongly sp hybridized, with a strong delocalization of the electrons located in the sp_x orbitals towards the empty orbitals of the M^{n+} cation. The formation of long polymerized chains, $\cdots\mathrm{M} \leftarrow \mathrm{F}^- \rightarrow \mathrm{M} \leftarrow \mathrm{F}^- \rightarrow \mathrm{M} \leftarrow \mathrm{F}^- \rightarrow \mathrm{M}\cdots$, contributes to the increase in the viscosity in the melt.

MF_2- and MF_3-based Glasses. One of the oldest fluoride materials prepared in the glassy state is beryllium fluoride, BeF_2. This compound, isotypic with SiO_2, shows a strong resistance to crystallization and is based structurally on a giant aperiodic corner-sharing BeF_4 tetrahedral framework. The main difference between the two glasses comes from the comparison between the bond strengths, Be–F and Si–O, which shows up in the difference in the glass transition temperatures, $T_g(\mathrm{SiO_2}) = 1100\,°\mathrm{C}$, $T_g(\mathrm{BeF_2}) = 250\,°\mathrm{C}$. Despite the unique optical properties of BeF_2-based glasses owing to their very low refractive index ($n = 1.27$) and low optical dispersion, these materials suffer from high hygroscopicity and toxicity. Several mixed compositions containing AlF_3 have been developed for high-power laser applications. This research has been pursued because of the interesting property that the low nonlinear refractive index reduces the risk of self-focusing and glass breaking.

The MF_3-based glass category is represented by AlF_3 and the transition metal MF_3 group with M = Fe, Co, Ga, and so on. By themselves the MF_3 compounds do not give glasses; they need to be combined with glass modifiers and stabilizers[29,30] such as PbF_2. For instance, an interesting glass composition $PbFeMnF_7$ is found in the ternary system FeF_3–MnF_2–PbF_2 and this material, rich in magnetic ions, exhibits remarkable spin-glass properties at low temperature. It has also been recently demonstrated that a glass composition belonging to the PbF_2–GaF_3–ZnF_2 system can be deposited as a thin layer on a cold substrate by physical vapor deposition.

The structural building units of these glasses are octahedral MF_6 units which, by sharing corners, generate a skeleton related to the ReO_3 structure. Most of these MF_3-based glasses show a great tendency to devitrify owing to the ionic character of the M–F bond.

ZrF_4-based Fluoride Glasses: ZBLAN glasses. The fluorozirconate glasses, based on the glass-forming ability of ZrF_4 when combined with other appropriate fluorides, have attracted considerable interest because of their promising optical properties in the mid-IR. Their discovery[31,32] resulted from a systematic investigation of ternary systems such as ZrF_4–LaF_3–BaF_2 as shown in Figure 12.

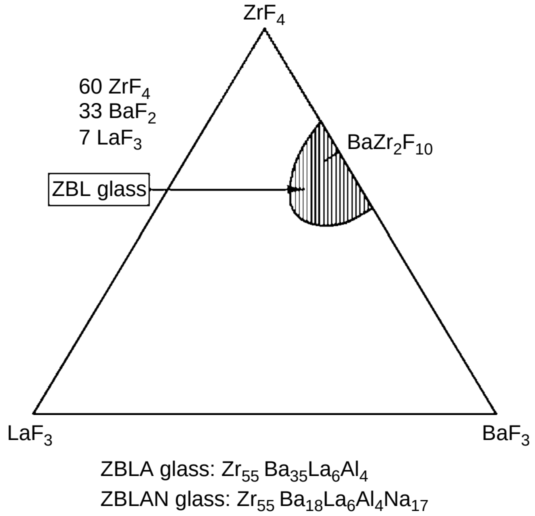
ZrF_4
60 ZrF_4
33 BaF_2
7 LaF_3
$BaZr_2F_{10}$
ZBL glass
LaF_3
BaF_3
ZBLA glass: $Zr_{55}\,Ba_{35}La_6Al_4$
ZBLAN glass: $Zr_{55}\,Ba_{18}La_6Al_4Na_{17}$

Figure 12 Glass-forming domain in the ternary diagram ZrF_4–BaF_2–LaF_3. The center of the vitreous area is represented by the ZBL glass. The composition $BaZr_2F_{10}$ corresponds to a very unstable glass while ZBLA and ZBLAN (composition in molar % of fluoride) are the acronyms of two very stable glasses

The optimized composition corresponding to the glass having the lowest critical cooling rate R_c, in the range $R_c \sim 1\,^\circ\mathrm{C\ min}^{-1}$, is the five-component glass ZBLAN: $55ZrF_4$–$18BaF_2$–$6LaF_3$–$4AlF_3$–$17NaF$. In this glass, the modifier cation Ba^{2+} has been partially replaced by Na^+ and this introduces an interdiffusion barrier to devitrification because of the competition between Na and Ba fluorozirconate microcrystal formation. From this ZBLAN composition, large pieces of optical glasses of several kilograms, as well as low-loss optical fibers, have been prepared. The good behavior versus devitrification can be also understood by examining the differential scanning calorimetry (DSC) trace of a ZBLAN glass. The glass transition temperature at 280 °C is far from the crystallization temperature ($T_x \sim 400\,^\circ$C), marked by a small exothermic peak. The liquidus temperature is around 550 °C.

The structural modeling of such glasses has been based on X-ray diffraction, molecular dynamics, and X-ray investigations of the parent crystalline materials[33] such as $BaZr_2F_{10}$. The 3-D skeleton as indicated in Figure 13 is built up from ZrF_7 and ZrF_8 polyhedra connected by corners or edges. The large Ba^{2+} cations are ionically bonded to the nonbridging fluorines and play the role of lattice modifiers.

Glass-forming ability has been also observed in several Zr-free fluoride systems, like in In-based glass systems whose IR edge is shifted towards longer wavelengths, as compared to ZBLAN.

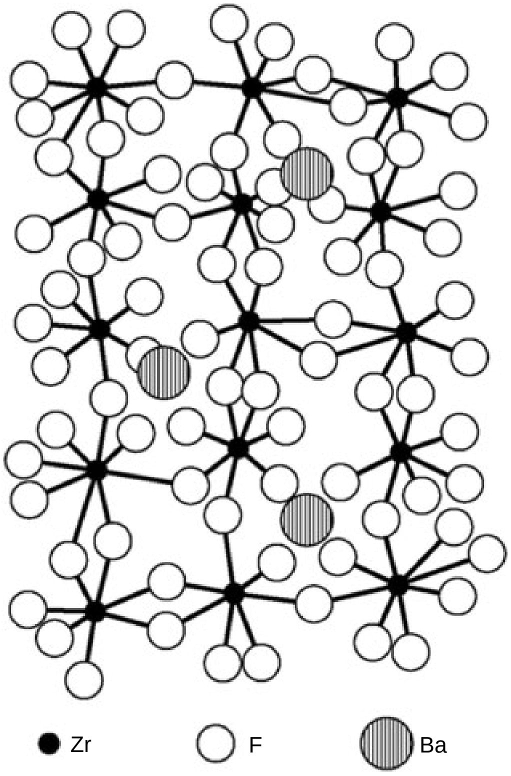

Figure 13 Structural model for the binary glass $BaZr_2F_{10}$. The polyhedra ZrF_7 and ZrF_8 are connected by corners and edges to form the 3-D aperiodic framework where Ba^{2+} ions are statistically distributed

4.2.2 Glasses Based on Heavy Halides

This terminology refers to glasses in which the electronegative part is a heavy halogen X (X = Cl, Br, I). Most of these materials suffer from strong moisture corrosion, low softening temperature, and a tendency to devitrify. The fundamental interest in such glasses is motivated by the fact that from a simple consideration of the masses of the anions, the heavy halide glasses would be expected to be more transparent in the IR than fluoride glasses.

4.3 Optical Properties of Halide Glasses

Considerable progress has been made during the last two decades in the discovery and investigation of halide glasses. The main justification of this research effort is the unusual and critical optical properties of these glasses. Unfortunately, the technical applications for most of them have been severely curtailed by their hygroscopicity and low thermal properties.

4.3.1 Passive Optical Properties

The total intrinsic optical loss in an optical glass is due to three factors, and the corresponding attenuation coefficient α can be expressed as:

$$\alpha = A \exp\left(\frac{-a}{\lambda}\right) + B\lambda^{-4} + C \exp\left(\frac{C}{\lambda}\right) \tag{1}$$

The first term is associated with multiphonon absorption mechanisms and is dependent on the IR edge. The second term represents the Rayleigh scattering and is due to electronic fluctuations on a microscopic scale. At long λ, this term is negligible. The third term, the Urbach tail, is related to the band-gap absorption and describes the limitation of transmission in the UV and visible part of the spectrum. In most of the halide glasses, the value of the band gap is high ($E_g > 3$–4 eV), making these glasses transparent in the visible. This is in contrast to chalcogenide glasses that are always colored or black.

The most important feature of the halide glasses is associated with the possibility of controlling the phonon edge absorption mechanism by shifting the IR edge towards longer wavelengths. By combining all the intrinsic attenuation factors it can be seen in Figure 14 that a limited part of the optical spectrum corresponds to very low optical loss. This ultratransparency region is located close to 1.55 µm for SiO_2 glass with a minimum loss of $0.16\,\mathrm{dB\,km}^{-1}$, while the same minimum of the V-shaped curve is around 3 µm for fluoride glasses with predicted ultralow-loss performance in the range of $0.01\,\mathrm{dB\,km}^{-1}$. To take advantage of this ultra

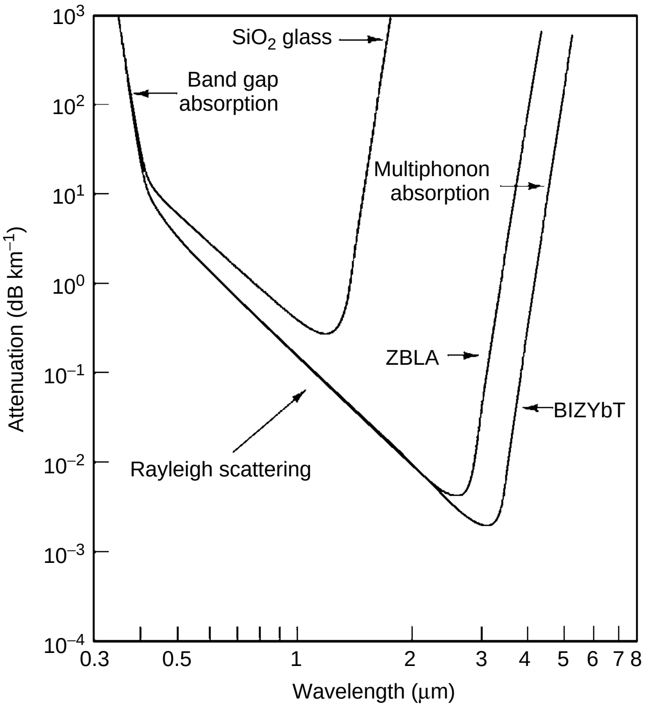

Figure 14 Intrinsic optical loss versus wavelength for SiO_2 and two fluoride glasses (Zr based and In–Ba based). The high transparency region for SiO_2 glass is around 1.5 μm with attenuation of 0.2 dB km^{-1}. The same ultrahigh transparency region is around 3 μm for the fluoride glasses with the theoretical optical loss as low as 0.01 dB km^{-1}

low-loss potential, optical losses of extrinsic nature should to be drastically reduced. The major two factors affecting the intrinsic glass transparency are:

1. colored impurities such as the transition metal ions of Fe, Cu, Co, Ni, and so on, or rare earths, characterized by parasitic absorption bands depending on λ;
2. the scattering defects arising from glass imperfections such as microbubbles, microcrystals, inhomogeneities, metallic particles, microphase separation, and so on, related to the glass making technology.

To date, the best experimental results in terms of fluoride fiber attenuation is 0.45 ± 0.15 dB km^{-1} at 2.35 μm, measured for a 60-m-long ZBLAN fiber.

4.3.2 *Fluoride Glass Fiber Lasers*

Fluoride glasses have a rather high capacity to accept doping elements such as rare earth ions, owing to their unusual structure. Several spectroscopic investigations conducted with doped glasses show unambiguously that the 4f ions substitute for Zr^{4+} in the glass-forming framework and are consequently subject to a rather well-defined ligand field corresponding to the usual coordination of Zr^{4+} which can vary from ZrF_6 to ZrF_8. Analysis of spectroscopic data indicates that rare earth ions are eightfold coordinate as in the corresponding parent crystalline materials.

As a new optical host for active properties[34] fluoride glasses have the following characteristics.

1. The doping concentrations can be rather high.
2. The broadening of the emission or absorption spectra owing to the glassy state is very limited and the envelope of the peak is in the range of the Stark decomposition.
3. Excitation and emission can be observed in a large spectral domain, 0.3–4 μm.
4. Compared to oxide glass matrices, such as silicates with a phonon energy at $W_\text{p} = 1100\,\text{cm}^{-1}$, the value of $W_\text{p} \sim 500\,\text{cm}^{-1}$ in fluoride glasses corresponds to much lower nonradiative relaxation and consequently higher quantum efficiency for laser emission.
5. It is also observed that in these glasses up-conversion mechanisms are quite efficient, allowing the population of high energy levels with red or IR pumping.

One of the most spectacular results in the field of active optical properties have been obtained with fluoride glasses shaped into an optical fiber configuration. Indeed, rare earth–doped fluoride glass fibers have been shown to be excellent laser materials.[35,36] Core-doped fibers represent a unique optical geometry that offers high optical power confinement and thus efficient interaction between light and matter over long lengths. In addition, the fiber geometry is adequate for releasing the heat generated by possible nonradiative processes concomitant to lasing. More than 40 lasing wavelengths which range from the mid-IR at 3.5 μm to the near-UV at 0.45 μm have been observed. Blue or green lasers are obtained by up-conversion processes and diode pumping has been achieved, allowing the miniaturization of such a new source of light. Details on the lasing characteristics of rare earth–doped fluoride glass fibers can be found in Ref. 37.

4.3.3 *Fluoride Glass Optical Amplifiers*

Optical amplifiers are essential components for the development of high capacity telecommunication networks. Silica fibers are characterized by a low-loss optical window that ranges from 1.2 to 1.7 μm, as shown in Figure 4. That window is divided into the ultrashort (XS), short (S), conventional (C) and long (L) bands. The first two bands are centered at 1.3 and 1.47 μm, while the C- and L-bands are equal to 1530–1565 nm and 1565–1625 nm, respectively. Amplification in the C- and L-bands is commonly achieved with Er^{3+}-doped silica fibers. On the other hand, amplification at 1.47 μm and 1.3 μm with Tm^{3+} and Pr^{3+} ions requires the use of materials with lower phonon energy than silica. High gain optical amplification was demonstrated in the XS, S, and C, telecommunication windows with rare earth–doped fluoride glass fibers. With an estimated lifetime of more than 25 years in normal conditions, state-of-the-art fluoride fiber are compatible with long-term applications such as telecommunications, and *Real-world* amplifiers have been constructed and commercialized. Performances of nonoxide glass amplifiers can be found in Ref. 37.

4.3.4 Fluoride Glass Channel Waveguides

Planar and channel waveguides can be obtained by ion-exchange technique with fluoride glasses. The experiment is carried out with Er^{3+}-doped ZBLA fluoride glass samples, treated by HCl gas at a temperature below the glass transition temperature T_g ($T_g = 307\,°C$ for ZBLA). The chemical reaction at the glass surface is:

$$MF_n + xHCl \rightleftarrows MF_{n-x}Cl_x + xHF \qquad (2)$$

where M represents all the cations in the glass.

Chloride ions, which substitute for part of the fluoride ions, modify locally the composition at the glass surface. The polarizability of Cl^- ions is greater than that of fluorides, and its introduction increases the refractive index. Then, ionic diffusion of Cl^- ions within the glass generates a gradient-index fluorochloride guiding structure.[38] Internal gain of $3.9\,dB\,cm^{-1}$ has been demonstrated at $1.53\,\mu m$ with such amplifying system.

5 METALLIC GLASSES

5.1 Introduction

As defined by Cahn,[39] a solid alloy with a liquid-like atomic arrangement is called a metallic glass, also called a metglass. Most of the metallic materials, which have been cooled to a state of rigidity without crystallization, are alloys and most of them have complex and well-defined compositions. As mentioned by Johnson in a well-documented article,[40] significant progresses have been made in the field, during the last decades and these noncrystalline solids, which were laboratory curiosities in the seventies, are now materials entering the market. This fast and spectacular evolution was due to the mastery of liquid alloy compositions exhibiting excellent resistance towards crystallization during the cooling process. For instance, in the sixties, the first liquid-metal alloys in the Au–Si system were vitrified in the Duwez group[41] by using ultrafast quenching techniques with very high rate of $10^6\,K\,s^{-1}$, while for the last generation of multicomponent Zr–Ti–Cu–Ni–Be alloys, the critical cooling rate is only $1\,K\,s^{-1}$, very similar to silicates or fluoride glasses. Consequently, the size of the glass samples has increased from a thickness of submillimeters to several centimeters.

As mentioned, the first glass-forming systems where fast quenching of the liquid was successfully applied were Au–Si and Pb–Si and it has also been observed that the most favorable region is close to a deep eutectic near 25 atom % Si. This observation is true for all the bulk glass-forming alloys and low-melting liquids are necessary to maintain a low thermal agitation which does not destroy the chemical bonds which take place in the melt and which is materialized by a significant increase of the melt viscosity. The nature of these chemical bonds is not yet well understood. However, clearly it ensures, in cooling, the formation of real out-of-equilibrium metallic glasses, exhibiting glass transition temperatures when reheated.

5.2 Glass-forming Alloy Systems

5.2.1 Development of Bulk Metallic Glasses (BMG)

Turnbull[42] had predicted that the ratio of the glass transition temperature T_g to the melting point or liquidus temperature Tl of an alloy, was the essential factor. When the ratio T_g/Tl increases from value near 1/2 to values near 2/3, the homogeneous nucleation of crystallites in the undercooled melt is expected to become more sluggish. This assumption is verified by the work on Au/Si, Pd/Si, and Pd/Cu/Si and is still one of the best rules for predicting the alloys glass-forming ability. A ratio of 2/3 observed in the Pd/Ni/P system was in agreement with the easy glass formation of this alloy leading to bulk ingots of centimeter size for a cooling rate of about $10\,K\,s^{-1}$.

Inoue and his group investigated the aluminum alloys combined with rare earth and transition metals such as the ternary alloys La/Al/Ni or La/Al/Cu. From there, they investigated more complicated alloys and demonstrated that the fabrication of glass samples having a thickness of about 1 cm was possible, for instance, in the alloys La/Al/Cu/Ni.

A similar family of excellent glass-forming materials was found in the alloys Zr/Cu/Ni/Al.

Zirconium-based alloys have received special attention, leading to the discovery, by Johnson group,[40] of several stable glasses and among them the complex composition $(Zr_3Ti)_{0,55}(Cu_5Ni_4)_{0,225}Be_{0,225}$. This material called Vitreloy 1 (V1) is a commercial product used, for instance, for the fabrication of golf clubs.

Attention has been also paid to Fe/Co/Ni rich alloys owing to their magnetic properties. Bulk glass cylinders of 6 mm diameter has been prepared in the system Fe/Co/Ni/Zr/B.[43]

5.2.2 Glass-forming Conditions

To make bulk glasses, one must frustrate the process of crystallization in introducing a kind of chemical disorder into the melt in order to avoid the dominant formation of one crystal species. This can be realized in mixing atoms having different sizes and electronegativities, as well as dissimilar valence electrons configurations. In this situation, solid solutions exhibit critical maximum solubility and become topologically unstable. This destabilization is reflected in the phase diagram by a falling of the liquidus curve which results in a lower melting point which indicate that the liquid phase is stabilized relative to the crystalline phase.

These principles are well illustrated by one of the most stable metallic glasses, which has been discovered in the Zr/Ti/Ni/Cu/Be alloy and which contains four transition metals with very different chemistry and associated to Be, which is considered to be one of the most original elements because of its small size and valence electrons. Both Zr/Be and Ti/Be alloys show deep eutectic valleys in the transition metal-rich region. The same observation is made in the Zr/Ni and Cu/Ti binary alloys where the competing crystalline forms Zr_2Ni and Ti_2Cu limit the glass-forming ability.

It is not surprising that in the Zr/Ti/Ni/Cu/Be system, the five elements acts almost independently, each species preferring different nonequivalent crystallographic sites in the competing crystals. In this case, the alloys appear to be exceedingly frustrated leading in the best glass-forming region to liquidus temperature as low as 700 °C, with glasses having their T_g in the range 360–400 °C. This situation has permitted the fabrication of bulk glassy rods with thicknesses ranging between 5 and 10 cm.

5.2.3 Crystallization, Phase Separation

To better characterize the bulk glass-forming ability of metallic alloys, one needs to study crystallization kinetics in detail. An elegant method has been developed to examine nucleation and growth of crystals in the undercooled liquid. Container-less processing using high vacuum and electrostatic levitation provides a means of diminishing the influence of heterogeneous nucleation and facilitates the drawing up of the time-temperature-transformation (TTT) curve which give information on the nucleation and critical cooling rate.[44]

This method, when applied to the V1 alloy, indicates a critical cooling rate in the order of 1 to 2 K/s. For the same alloys the existence of liquid–liquid phase separation into beryllium-rich and poor liquids was also demonstrated. The knowledge of this complex phenomenon is important since it governs the nano-crystallization process and is, consequently, a good guide to select the suitable accurate glass composition. Phase separated domains have been also observed by transmission-electron-microscopy in the Mg/Y/Cu/Li alloys of the Inoue type, showing Cu-poor and Cu-rich regions.

It is also interesting to notice that the crystallization kinetics are also strongly affected by the presence of impurities, especially oxygen at a level below one percent molar. This contamination can alter the critical cooling rate by two order of magnitude. For instance, the glassy alloy V105, which has the composition $Zr_{52,5}Ti_5Cu_{17,9}Ni_{14,6}Al_{10,}$ is characterized by a critical cooling rate of $1\,K\,s^{-1}$ when pure. If contaminated by 1 at % of Oxygen, the glass formation requires rapid solidification, owing to a critical cooling rate which is increased to hundred of $K\,s^{-1}$.

It is also well known that one parameter preventing glass devitrification is associated to the presence of nonmetallic elements, such as Si, P, B, Be, and C, which play an essential role to slow down nucleation during cooling. It is very probable that these elements form clusters containing several metal atoms linked by a directed (partly) covalent bond. This phenomenon introduces a diffusion barrier to long-range organization, which decreases microcrystallite formation during cooling. The metallic radius mismatch between the constituent atoms improves the glass-forming ability by preventing the formation of extensive ordered solid solutions.

5.2.4 Viscosity of Metallic Glasses

The exceptional stability of the glass-forming compositions discovered during the last two decades has permitted far more extensive investigation of the temperature dependence of the viscosity for a deeply undercooled metallic system than possible previously. For example, in the 1970s, Chen[45] was limited in measurements to temperatures of only 20–30 K above T_g, by the lack of stability against crystallization of the Pd/Cu/Si alloy that he was studying.

As shown in the article by Johnson,[40] viscosity measurements on the Vitreloy glasses such as the V1, have been obtained, using various methods, in almost all the temperature domain, covering 15 orders of magnitude in viscosity.

The interesting news was in the comparison of these metallic glasses with the other glass-forming systems when introduced in the, now famous Angell[46] diagram, which represents the evolution of the viscosity of many glass-forming liquids versus temperature, more precisely T_g/T. From this universal diagram which allows the classification between strong and fragile glass-forming liquid, it is concluded that a glass such as the industrial alloy V1, exhibits a strong liquid behavior, similar to some silicate or fluoride glasses.

5.3 Properties and Applications of Metallic Glasses

5.3.1 Chemical Properties

Metallic glasses exhibit corrosion resistance that can be spectacular, owing to the absence of grain boundaries, with their frequent forms of chemical heterogeneity. The Fe-based glasses have been more extensively investigated and it has been observed that addition of Cr or Mo is particularly effective in increasing corrosion protection against acidic solutions. A glass such as $Fe_{72}Cr_8P_{13}C_7$ passivates immediately in concentrated HCl solution. Metallic glasses, especially when partially crystallized on a surface, can play the role of catalysts for gas-phase reactions such as the hydrogenation of CO or methanol synthesis. Owing to their excellent corrosion resistance, metallic glasses are good candidates for protective coatings against aggressive environments. Laser amorphization of the container surface as well as glass alloy sputtering have been used to produce corrosion resistant layers. This technology has been successfully applied for developing electrodes having a good electrocatalytic activity for Cl_2 production while being resistant to oxidation by chlorine.

To avoid reaction between the Si substrate and Al metallizations during the manufacture of integrated circuits at high temperatures, diffusion barriers are necessary. It has been demonstrated that high crystallization-temperature glasses such as Ta–Ir glasses make excellent diffusion barriers in many microelectronics applications.

5.3.2 Magnetic Properties

For about two decades, amorphous iron based alloys are well known as good soft magnetic materials and alloys belonging in the Fe/Co/Ni/Zr/B system are among the best candidates owing to their interesting ferromagnetic properties. Their tendency to crystallize is such that their technological applications are limited, owing to the ribbon form in which they are commonly produced, in using fast quenching techniques such as the melt spinning or the twin-roller process represented in Figure 15.

As already mentioned, the optimization of the composition has allowed the fabrication of cylinders of a few millimeters diameters. Another alternative method has been recently developed in using successively ball milling of the thin alloy ribbons followed by a hot pressing operation in order to consolidate bulk samples.[47] Examination of the hysteresis loops reveal low coercive fields and fairly large saturation magnetization.

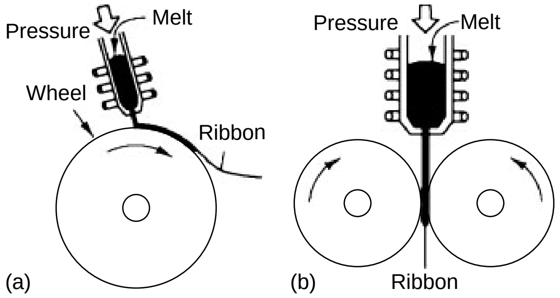

Figure 15 Two selected methods for metallic glass preparation: (a) in the melt-spinning process the molten alloys are projected against a spinning wheel; (b) in the twin-roller quenching technique the melt is cooled between two rotating wheels. In both processes, the aim is to achieve ultrafast cooling

5.3.3 Mechanical Properties

The distinctive features of bulk metallic glasses (BMG) are their exceptional mechanical characteristics such as very high yield strengths and high elasticity limits. The elastic strain that a metallic glass can support in tension or bending is at least double that of ordinary commercially crystalline alloys and are therefore premier 'spring' materials because they can store high densities of elastic energy.

A variety of composite materials has been obtained by the direct introduction of a reinforcing crystalline solid phase into the glass-forming melt. In many cases, the resistance of the glass to crystallization is good enough to avoid any heterogeneous nucleation at the interface. As an example, the V1 alloy has been used as a glassy matrix to fabricate composite structures with diamond, SiC particles as well as tungsten metal powder or wires. In the case of the W/glass composites, it is proved that the glassy matrix induce localized shear deformation.

The capability to store elastic-energy density in a range of about four time the traditional alloy finds utility in the design of certain types of sporting equipment such as the golf club. This particular application exploits the high strength, favorable density, and ideal elastic behavior of a glass such as the vitreloy V1, which significantly allows to improve the performances of these new generation of iron-free golf clubs.

6 RELATED ARTICLES

Borates: Solid-state Chemistry; Fluorides: Solid-state Chemistry; Luminescence; Sol–Gel Synthesis of Solids; Zeolites.

7 REFERENCES

1. M. J. Dejneka, *J. Non-Cryst. Solids*, 1998, **239**, 149.
2. P. C. Schultz and H. T. Smyth, in 'Amorphous Materials', eds. R. W. Douglas and B. E. Ellis, Wiley, New York, 1972, p. 435.
3. S. R. Elliott, 'Glass 99, XVth Int. Congr. Glass', Nauk, Leningrad, 1989, p. 65.
4. A. C. Wright, 'Glass 99, XVth Int. Congr. Glass', Nauk, Leningrad, 1989, p. 30.
5. B. E. Warren, *J. Am. Ceram. Soc.*, 1941, **24**, 256.
6. D. Hewak, ed., 'Glass and Rare-earth-doped Glasses for Optical Fibers', EMIS Datareviews Series, INSPEC, London, 1998, N° 22, p. 55.
7. J. Broeng, D. Mogilevstev, S. E. Barkou, and A. Bjarklev, *Opt. Fiber Technol.*, 1999, **5**, 305.
8. R. V. Ramaswamy and R. Srivastava, *J. Lightwave Technol.*, 1988, **6**, 984.

9. H. Rawson, in ‘Materials Science and Technology’, ed. J. Zarzycki, VCH, Weinheim, 1991, Vol. 9, p. 279.
10. R. R. Shaw and D. R. Uhlman, *J. Am. Ceram. Soc.*, 1968, **37**, 377.
11. P. B. Macedo and J. H. Simmons, *J. Res. Natl. Bur. Stand.*, 1974, **78A**, 53.
12. D. L. Griscom, in ‘Borate Glasses’, eds. L. D. Pye, V. D. Frechette, and N. J. Kreidl, Plenum Press, New York, 1978, p. 11.
13. S. Jiang, J. D. Myers, R. Wu, G. M. Bishop, D. L. Rhonehouse, and M. J. Myers, *S.P.I.E. Proc.*, 1995, **2379**, 17.
14. T. Kitsugi, T. Yamamura, T. Nakamura, T. Oha, and H. Takeuchi, *Biomaterials*, 1995, **16**, 1101.
15. S. Shen, A. Jha, E. Zhang, and S. J. Wilson, *C. R. Chimie*, 2002, **5**, 921.
16. R. E. Loehman, in ‘Treatise on Materials Science and Technology’, eds. M. Tomozawa and R. H. Doremus, Academic Press, New York, 1985, Vol. 26, p. 119.
17. C. A. Angell, in ‘Glass Science and Technology’, eds. D. R. Uhlman and N. J. Kreidl, Academic Press, New York, 1983, Vol. 1, p. 209.
18. S. R. Elliot, in ‘Materials Science and Technology’, ed. J. Zarzycki, VCH, Weinheim, 1991, Vol. 9, p. 375.
19. S. R. Elliot, ‘Physics of Amorphous Materials’, Longman, London, 1990.
20. Z. U. Borosiva, ‘Glassy Semiconductors’, Plenum Press, New York, 1981.
21. S. Barnier, M. Guittard, and J. Flahaut, *Mater. Res. Bull.*, 1984, **19**, 837.
22. J. Lucas and X. H. Zhang, *J. Non-Cryst. Solids*, 1990, **125**, 1.
23. P. Boolchand, in ‘Defects in Glasses’, eds. F. L. Galeener, D. Griscom, and M. T. Weber, Materials Research Society, Boston, 1986, Vol. 61, p. 57.
24. D. Lecoq, K. Michel, J. Keirsse, C. Boussard-Plédel, G. Fonteneau, B. Bureau, J. M. Lequéré, O. Sire, and J. Lucas, *C. R. Chimie*, 2002, **5**, 907.
25. K. Tanaka, *C. R. Chimie*, 2002, **5**, 805.
26. M. G. Drexhage, in ‘Materials Science and Technology’, eds. M. Tomozawa and R. H. Doremus, Academic Press, New York, 1985, Vol. 26, p. 151.
27. J. Lucas, in ‘Material Science and Technology’, ed. J. Zarzycki, VCH, Weinheim, 1991, Vol. 9, p. 455.
28. C. M. Baldwin, R. M. Almeida, and J. D. Mackenzie, *J. Non-Cryst. Solids*, 1981, **43**, 309.
29. K. H. Sun, *J. Am. Ceram. Soc.*, 1947, **30**, 277.
30. C. Jacoboni, A. Lebail, and R. Depape, *Glass Technol.*, 1983, **24**, 164.
31. J. Lucas, *J. Mater. Sci.*, 1989, **24**, 1.
32. M. Poulain, M. Poulain, P. Brun, and J. Lucas, *Mater. Res. Bull.*, 1975, **10**, 242.
33. C. C. Phifer, C. A. Angell, J. P. Laval, and J. Lucas, *J. Non-Cryst. Solids*, 1987, **94**, 315.
34. J. Lucas and J. L. Adam, *J. Alloys Compd.*, 1992, **180**, 27.
35. P. W. France, in ‘Materials Science Forum’, Trans. Tech. Publications, 1991, Vols. 67–68, p. 503.
36. M. Monerie, *Proc. SPIE-Int. Soc. Opt. Eng.*, 1991, **1581**, 2.
37. J. L. Adam, *Chem. Rev.*, 2002, **102**, 2461.
38. H. Haquin, G. Fonteneau, and J. L. Adam, *J. Non-Cryst. Solids*, 2003, **326 & 327**, 460.
39. R. Cahn, in ‘Materials Science and Technology’, ed. J. Zarzycki, VCH, Weinheim, 1991, Vol. 9, p. 493.
40. W. L. Johnson, *MRS Bulletin*, 1999, **24**, 42.
41. P. Duwez, *Prog. Solid State Chem.*, 1967, **3**, 377.
42. D. Turnbull, *J. Chem. Phys.*, 1950, **18**, 198.
43. A. Inoue, *Mater. Sci. Eng*, 1997, **A 226–228**, 357.
44. Y. F. Kim, R. Busch, W. L. Johnson, A. J. Rulison, and W. K. Rhim, *Appl. Phys. Lett.*, 1996, **68**, 1057.
45. H. S. Chen and M. Goldstein, *J. Appl. Phys.*, 1971, **43**, 1642.
46. C. A. Angell, *Science*, 1995, **267**, 1924.
47. A. Grabias, D. Oleszak, M. Kopcewicsk, J. Latuch, T. Kulik, and F. Stobiecki, *J. Non-cryst. Solids*, 2003, **330**, 75.

Nucleic Acid–Metal Ion Interactions

Sergei A. Kazakov[1] & Sidney M. Hecht[2]
[1]Somagenics, Inc, Santa Cruz, CA, USA
[2]University of Virginia, Charlottesville, VA, USA

1 Introduction 1
2 Properties of Nucleic Acids Essential for Binding with Metal Ions 2
3 Possible Effects of Polynucleotide Structures on Metal-Ion Binding 3
4 Properties of Metal Ions Essential for Interaction with Nucleic Acids 10
5 Metal-Binding Modes and Structure of Metal–Nucleic Acid Complexes 16
6 Metal Binding Can Induce Conformational Changes of Polynucleotide Structures 24
7 Metal Binding Can Induce Hydrolysis and Cleavage of Nucleic Acids 26
8 Conclusion 27
9 Related Articles 27
10 Further Reading 27
11 References 27

1 INTRODUCTION

Why would people be interested in metal-nucleic acid interactions? Perhaps because life as we know it is dependent on these interactions. Nucleic acids (DNA and RNA) are actually salts (or complexes) of metal ions from a chemical point of view. Therefore, it is difficult, if not impossible, to separate the behavior of DNA and RNA from their interactions with metal ions. We must also take into account specifically bound water molecules since they frequently mediate interactions between polynucleotides and metal ions.[1,2]

Metal ions are usually required to promote and stabilize functionally active or native conformations of nucleic acids, as well as to mediate nucleic acid–protein interactions. However, metal ions can also cause structural transformation of nucleic acids, or denature their native structures. In addition to structural roles, some metal compounds can induce cleavage (i.e. scission, fragmentation, or depolymerization) and modification (without cleavage) of nucleic acids. Metal–nucleic acid interactions can be either nonspecific or dependent on the chemical nature of nucleotide residues, nucleic acid sequence, or secondary and/or tertiary structure of nucleic acids. The specificity of these interactions is dependent on structural and chemical properties of both the nucleic acids and the metal ions. There are two extreme views of such interactions. The first, among biochemists and molecular biologists, is that properties of metal ions are primitive in comparison with the properties of nucleic acids (presumably because of their smaller size); and the opposite one, common among inorganic chemists, who regard nucleic acids simply as big organic ligands. In reality, both nucleic acids and metal ions exhibit considerable complexity in their interactions, and such interactions could affect the chemical and biochemical properties of both participants.

The involvement of metal-containing species in nucleic acid-dependent processes, including nucleotide biochemistry; genetic information storage and transfer, and control of gene expression (Mg^{2+});[3–7] mutagenesis (e.g. Mn^{2+}, Cu^{2+}, Co^{2+}, and Ni^{2+});[8–10] chromosomal abnormalities (e.g. Be^{2+} and Hg^{2+});[11,12] and carcinogenesis (e.g. Ni^{2+}, Cd^{2+}, Cu^{2+}, Co^{2+}, Fe^{3+}, and Be^{2+})[8,13–16] is well documented (*see* ***Metal Ion Toxicity*** and ***Metal-related Diseases of Genetic Origin***). There are only a few processes for which it is clear that the nucleic acid is the primary target of metal action.[11] In most cases, it is not clear whether the observed effects actually result from direct metal ion–nucleic acid interaction, since other species, such as specific proteins (*see* ***Zinc: DNA-binding Proteins***), may be mediators between the metal ion and the nucleic acid in these processes *in vivo*.[7,11,17,18] To better understand mechanisms of metal–nucleic acid interactions occurring *in vivo*, numerous *in vitro* studies of model reactions and structures of metal–nucleic acid complexes have been carried out (see reviews[19–37]). The interactions of nucleic acids with so-called 'biological' metal ions, that is, K^+, Na^+, Mg^{2+}, Ca^{2+}, Mn^{2+}, $Fe^{2+/3+}$, $Co^{2+/3+}$, $Cu^{+/2+}$, and Zn^{2+}, result in unstable, short-lived complexes with nucleic acids in which ligands bound to metal ions can undergo fast exchange.[37–41] That sometimes creates problems in structure determination of such labile complexes. In contrast, some nonbiological metal ions, for example, $Pt^{2+/4+}$, Pd^{2+}, $Ru^{2+/3+}$, Au^{3+}, Hg^{2+}, and Ag^+, form inert complexes with nucleic acids, which are convenient for isolation and investigation; numerous structural studies of such complexes have been described.[26,42,43] Such studies have also led to an interesting body of chemical knowledge, independent of the biological relevance of the species involved.

Eight general research areas can be argued to have contributed the most to what is known today about metal–nucleic acid interactions. The first involves studies of the mechanisms of antitumor activity of certain platinum compounds (*see* ***Platinum-based Anticancer Drugs***), which are believed to have nucleic acids as a critical target.[43–47] The second is concerned with studies of the binding of biological and nonbiological metal ions with nucleobases, nucleosides, and nucleotides.[25,30,35,42,48–50] The third involves studies of metal-binding centers in tRNA molecules,[51–54] catalytic RNAs (ribozymes),[53,55–58] and synthetic oligonucleotides that constitute fragments of natural nucleic acids.[53,59–66]

The fourth area involves studies of the role of metal ions (including Mg^{2+}, Ca^{2+}, Mn^{2+}, Cd^{2+}, Co^{2+}, Zn^{2+}, and Pb^{2+}) in mechanisms of chemical reactions catalyzed by ribozymes, which could play a key role in the origin of life (RNA World hypothesis).[39–41,57,67–69] The fifth involves the same metal ions (as well as Ni^{2+} and Cu^{2+}) as catalysts in reactions that could have resulted in prebiotic synthesis of nucleotides and oligonucleotides.[70–74] The sixth involves the use of certain metal ions and complexes as heavy-atom labels (e.g. for electron microscopy and X-ray crystallography), as well as chemical and spectroscopic probes of nucleic acid structure and function.[75–86] The seventh involves the use of metal compounds as biological diagnostic tools in nucleic acid-based assays and biosensors.[46,87–92] Finally, the eighth area is concerned with the development of applications of metal-nucleic acid complexes in nanotechnology (i.e. microarrays and biochips).[87,91–95]

2 PROPERTIES OF NUCLEIC ACIDS ESSENTIAL FOR BINDING WITH METAL IONS

2.1 Chemical Structures of Nucleic Acids

The chemical structure of nucleic acids[96] provides wide varieties of metal-binding centers that can be involved in the formation of ionic, coordinative (donor–acceptor), hydrogen (H-), and covalent bonds. The term ‘nucleic acid’ is usually used to refer to polynucleotides. The monomeric unit (a nucleotide) consists of a single heterocyclic nucleobase, which can be a purine (adenine or guanine) or pyrimidine (cytosine, uracil, or thymine), attached through an N-glycosyl bond to a pentose sugar (a nucleoside), which in turn is attached to a phosphate by a phosphodiester bond at the 5′- or 3′-terminus (Figure 1). Nucleotides (NMP, where is N = adenosine, A; guanosine, G; inosine, I; cytidine, C; thymidine, T; or uridine, U) can be linked together through $5' \rightarrow 3'$ phosphodiester bonds to produce linear oligonucleotides (usually <100 nt in length) and polynucleotides (>100 nt), or conjugated to additional phosphate groups to form nucleoside di- and triphosphates (NDPs and NTPs, respectively). Phosphate groups can be attached to a nucleoside through 5′- and 3′-hydroxyl groups of the pentose rings. There are two classes of nucleic acids; those in which the sugar residue bears a hydroxyl group at the 2′-position (ribonucleic acid, RNA) and those in which it does not (deoxyribonucleic acid, DNA). In DNA, the commonly occurring heterocyclic bases are adenine, guanine, cytosine, and thymine, whereas in RNA, thymine is replaced by uracil. The heterocyclic bases are essentially planar, with exocyclic groups lying in the plane of the rings and lone-pair electrons delocalized into the π-systems of the rings. The tautomeric forms of the bases (imino forms for guanine, adenine, and cytosine or enol forms for guanine, cytosine, uracil, and thymine), which are alternatives to the structures

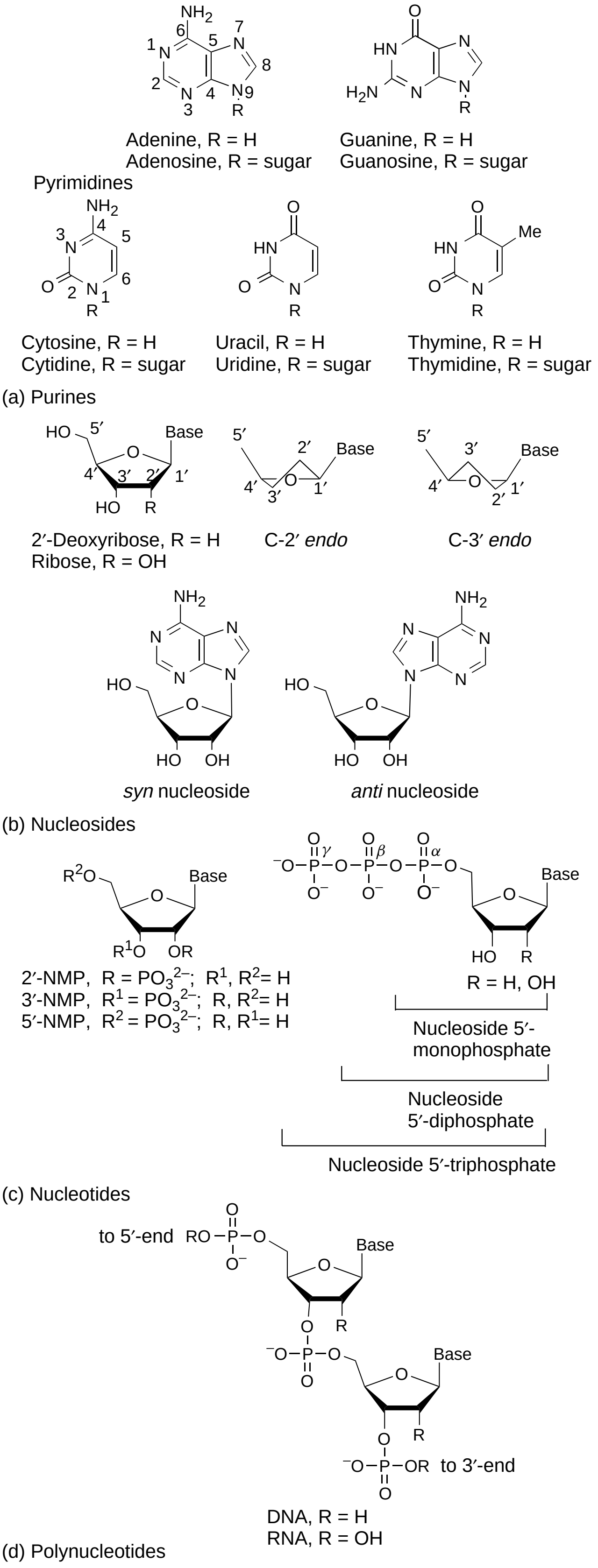
Adenine, R = H
Adenosine, R = sugar
Guanine, R = H
Guanosine, R = sugar
Pyrimidines
Cytosine, R = H
Cytidine, R = sugar
Uracil, R = H
Uridine, R = sugar
Thymine, R = H
Thymidine, R = sugar
(a) Purines
2′-Deoxyribose, R = H
Ribose, R = OH
C-2′ endo
C-3′ endo
syn nucleoside
anti nucleoside
(b) Nucleosides
2′-NMP, R = PO3 2−; R1, R2 = H
3′-NMP, R1 = PO3 2−; R, R2 = H
5′-NMP, R2 = PO3 2−; R, R1 = H
R = H, OH
Nucleoside 5′-monophosphate
Nucleoside 5′-diphosphate
Nucleoside 5′-triphosphate
(c) Nucleotides
to 5′-end
to 3′-end
DNA, R = H
RNA, R = OH
(d) Polynucleotides

Figure 1 Structures of the nucleic acids and their constituents

presented in Figure 1, do not ordinarily exist in significant concentrations in solution.[97] In comparison to DNA, RNA molecules also have a 2′- OH group that may provide more structural complexity at polynucleotide level and more options for metal binding, as well as higher chemical stability under acid pH conditions. However, the 2′-OH group also makes RNA subject to depolymerization through transesterification catalyzed by many polyvalent metal ions ($M^{\geq 2+}$) at neutral and alkali pH, while such reactions do not normally occur with DNA (see Section 7).

Nucleic acid residues are highly hydrated in water solutions and crystals: two H_2O per phosphate diester and up to six per base pair in DNA and RNA.[2,98,99] There are at least two different types of water molecules bound to nucleic acids. The first involves a highly ordered hydration shell, which is a layer of water molecules interacting via H-bonds primarily with hydrogen bond donor and acceptor groups of nucleic acid residues. These water molecules play important roles in both intra- and intermolecular interactions between nucleic acid residues as well as in metal–nucleic acid interactions that require the interacting surfaces (of both nucleic acids and metal ions) to be partially dehydrated so that either direct (inner-sphere) bonds or bonds through water molecule (outer-sphere) can form.[1,57,99–104] The second water layer is only partially ordered and weakly bound to nucleic acids (through secondary H-bonds or induced dipole–dipole interactions) making it easily exchangeable with bulk water molecules and metal ions. The polarization capability of water molecules can weaken electrostatic interactions between nucleic acids and metal ions.[104]

2.2 Potential Metal-binding Sites in Nucleotides and Nucleosides

Many donor and acceptor atoms in nucleic acids are capable of participating in indirect (outer-sphere) binding through H-bonds with water molecules or other ligands coordinated to metal ions. To understand the direct (inner-sphere) binding between nucleic acid residues and metal ions, both the nucleophilicity and basicity[28] of potential metal-binding sites must be considered. At neutral pH, the principal metal-binding sites in nucleotides (with $\mathrm{p}K_a$'s at ionic strength $I = 0.1$ in parentheses) include: terminal phosphate oxygens (1.0 and 6.6), internucleotide phosphate oxygens (1.0), and endocyclic atoms in guanosine (N-7, 2.0), adenosine (N-7 or N-1, 3.8), and cytidine (N-3, 4.2).[28,42] The purine N-3 nitrogen is generally sterically hindered by the sugar and does not bind metal ions, but changing the relative orientation of the nucleic acid base and sugar can make this site available for metal-ion binding. The exocyclic O^2 atom of cytidine is well established as a metal donor atom and constitutes the most important exocyclic metal-ion binding site at neutral pH. The carbonyl groups of other nucleic acid bases, in comparison, are relatively weak donors and usually only bind metal ions if other functional groups participate as well. Upon deprotonation, some endocyclic nitrogen atoms, notably guanosine N-1 ($\mathrm{p}K_a = 9.3$), uridine N-3 (9.5), and thymidine N-3 (9.9) become binding sites as well. The exocyclic NH_2 groups in adenosine and cytidine, as well as the ribose 2′-OH group, are poor ligands even when deprotonated ($\mathrm{p}K_a > 12$). However, for some metals, binding at specific secondary binding sites can be favorable enough that binding takes place at a pH considerably lower than the nominal $\mathrm{p}K_a$.

There are also metal interactions that do not involve coordination chemistry. For example, cytidine and uridine can form covalent bonds with Hg via C-5.[105,106] Another metal-binding site is the 5,6-alkenic bond in thymidine, which can be oxidized by hexavalent Os or by heptavalent Mn.[105]

All transfer RNAs (tRNAs) contain a number of modified nucleobases and typically 2′-*O*-methylated nucleosides.[107,108] DNA also contains a more limited number of such species. Some of these modifications, for example, N-7 methylation of guanosine, diminish the metal-binding ability of the bases. A few functional groups, such as the exocyclic S in 4-thiouridine and 2-thiocytidine and the exocyclic substituent in 5-carboxymethylaminomethyluridine, enhance the ambivalent nature of the bases.[35] Some of these modifications change the basicity of primary metal-binding sites.

To create new metal-binding centers or affect the stability and specificity of existing metal–nucleic acid bonds, certain nonnatural derivatives of nucleic acid bases, sugars, and phosphates have been artificially designed. One example is the thiophosphate moiety, in which one nonbridging or bridging oxygen of the normal phosphate diester is substituted by a sulfur atom (see Figure 1).[109,110] To remove or shield specific metal-binding sites, selected nucleic acid residues can also be modified (e.g. by ethylation of phosphate ester oxygens or methylation of ring nitrogen atoms in purine nucleotides).[111,112]

3 POSSIBLE EFFECTS OF POLYNUCLEOTIDE STRUCTURES ON METAL-ION BINDING

3.1 Polyelectrolyte Effect

The initial interaction between positively charged metal ions and the negatively charged phosphate groups of nucleotides and polynucleotides involves a fast electrostatic interaction that is weak and nonspecific.[37,103,104,113] For example, the increasing phosphate content (and hence negative charge) in the series A < AMP < ADP < ATP governs the increase in affinity toward alkaline earth metal ions, which bind predominantly to the phosphate groups of nucleotides.[114,115] The cation concentration in proximity to the polynucleotide polyanions is far higher than in the bulk solvent.[116] For low ionic strength solutions of DNA, the ratios of these concentrations (‘the polyelectrolyte effect’) for Na^+ and

Mg^{2+} were estimated to be roughly 3×10^3 and 9×10^6, respectively,[22] reflecting the greater attraction of divalent cations.[116] However, at a high ratio of monovalent to divalent cations, a competition for the available phosphate anion binding sites occurs, in addition to the dielectric effects of single charged cations; in some cases, this can effectively shield the negatively charged sites from polyvalent cations.[10] The electric field produced by a polyanion in association with that of the compensating counterions increases the pK_a values of the nucleic acid bases slightly and promotes polarization of water molecules bound both to the nucleic acid and metal ions.[98]

The negative charge density, and hence the polyelectrolyte effect, is smaller for single-stranded polynucleotides than for multistrand species (see below).[22] Nonspecific binding of metal ions with nucleic acid phosphates exhibits negative cooperativity, because bound cations reduce the net charge of the polyanion.

Nucleic acids usually bind alkali monovalent metal ions only in an 'atmospheric manner' (in which the M^+–phosphate distance is larger than 7 Å).[37,117] For polyvalent metal ions, two additional types of binding have been characterized: outer-sphere binding, in which a water molecule coordinated to the metal ion produces a hydrogen bond with the phosphate oxygen, and inner-sphere binding, in which the metal ion is bound directly to the phosphate oxygen (the M^+–phosphate distances associated with these two mechanisms are about 6 and 3 Å, respectively).[117] Because the ionic radii of divalent metal ions (Table 1) are about 10-fold smaller than the distance between adjacent phosphates in stacked polynucleotide chains, divalent metal ions generally do not bind with two phosphates simultaneously by an inner-sphere mechanism.[118] As was demonstrated for the interaction between Mg^{2+} and oligoriboadenylates, short flexible oligonucleotides may more easily bend to afford a loop structure in which two phosphate residues can provide full charge compensation by binding directly to a single metal ion.[118]

For many metal ions, the initial electrostatic interaction can be followed by stronger and more specific binding with nucleic acids via the formation of outer- and inner-sphere complexes. The formation of such complexes may be strongly accelerated (in comparison to binding to nucleosides and nucleotides) because of the polyelectrolyte effect.

3.2 Internucleotide Interactions

In addition to the polyelectrolyte effect, nucleotide sequence (or primary structure), and secondary and tertiary

Table 1 Basic features of hydrated metal ions involved in metal–nucleic acid interactions

Ion	Ionic radius[119,120]	Coordination number[120]	Typical geometry of inner-sphere complex[120]	First pK_a of $[M(H_2O)_n]^{M+a}$,[121,122]
Ag^+	1.26	2 > 4	Linear	9.8–11.7
Al^{3+}	0.51	6 > 4	Octahedral	4.3–5.0
Ba^{2+}	1.34	8	Square antiprism	13.4–14.0
Be^{2+}	0.35	4	Tetrahedral	5.7–6.7
Bi^{3+}	0.96	6	Octahedral	Unstable
Ca^{2+}	0.99	8	Square antiprism	12.6–13.4
Cd^{2+}	0.97	6 > 4	Octahedral	7.6–10.2
Co^{2+}	0.72	6	Octahedral	7.6–9.9
Co^{3+}	0.63	6	Octahedral	0.9–2.0
Cr^{2+}	0.89	6	Octahedral	8.7–11
Cr^{3+}	0.63	6	Octahedral	3.8–4.4
Cu^+	0.96	4	Tetrahedral	Unstable
Cu^{2+}	0.72	4 > 6	Square planar	6.8–8.5
Eu^{3+}	0.95	9	Variable	4.8–8.5
Fe^{2+}	0.74	6	Octahedral	5.9–6.7
Fe^{3+}	0.64	6	Octahedral	≈2.5
Hg^{2+}	1.10	2 > 4.6	Linear	2.4–3.7
In^{3+}	0.81	6	Octahedral	≈3.7
Mg^{2+}	0.66	6	Octahedral	11.4–12.8
Mn^{2+}	0.80	6	Octahedral	10.6–10.9
Ni^{2+}	0.69	6	Octahedral	6.5–10.2
Pb^{2+}	1.20	6 > 9	Octahedral	6.5–8.4
Sn^{2+}	0.93	3 > 6	Pyramidal	3.7–6.8
Sr^{2+}	1.12	6	Octahedral	13.2–13.8
$UO_2{}^{2+}$	0.80 (U^{6+})	6 > 8	Octahedral	≈5.7
VO^{2+}	0.63(V^{4+})	6	Octahedral	≈5.4
Zn^{2+}	0.74	4 > 6	Tetrahedral	8.2–9.8

[a] Dependent on ionic strength.

structures of single-stranded polynucleotides may dramatically affect the kinetics, mode, and affinity of metals ion binding through internucleotide interactions (base stacking, H-bonds) and the spatial arrangement of potential metal-binding centers (steric effects). These characteristics also vary among different types of polynucleotides. For example, the affinity of Mg^{2+} for individual types of polynucleotides is in the order tRNA $>$ poly(I) $\gg$ poly(A) $\sim$ poly(A)·poly(U) $\sim$ poly(I)·poly(C) $\sim$ DNA $\geq$ denatured DNA $>$ poly(C) $>$ poly(U).[123]

3.2.1 Base Stacking

In solutions of ordered polynucleotides, the heterocyclic bases are stacked, that is, packed vertically one upon the next. The greatest stability is for purine–purine base-stacking interactions. The next are purine–pyrimidine interactions, which in turn impart greater stability than pyrimidine–pyrimidine stacking interactions.[124,125]

Base-stacking interactions may strain or disrupt metal binding. This can occur in the plane of the nucleobase heterocycles, owing to the absence of proper geometry for chelation of neighboring nucleobases (e.g. binding of *cis*-$(NH_3)_2PtCl_2$ with neighbor purine bases),[47] and also for binding from above or below the plane (e.g. for the 5,6-double bond of T), because of steric hindrance.[96,125] Alternatively, base stacking can actually favor metal π-complex formation where the metal ion is inserted between two stacked bases.[125]

3.2.2 Hydrogen Bonds

The main factor determining the specificity of intra- and intermolecular interactions of polynucleotide chains is interbase H-bonding interactions, which occur between the amidate or exocyclic amine nitrogen donors of one nucleobase and the keto oxygen or heterocyclic nitrogen acceptors of another base.[97,125] The common H–bonding schemes involve Watson–Crick base pairs: A·T (A·U) and G·C or I·C in DNA (RNA) duplexes; T·A·T (or U·A·U) and C^+·G·C in triplexes; and G_4 in quadruplexes (Figure 2). There is also evidence for a few other types of interbase arrangements, for example, Hoogsteen and reverse Hoogsteen base pairs.[126] In some cases, nonWatson–Crick interactions may occur as frequently as Watson–Crick base pairs and play an important role in stabilizing the structure of RNA, for example, for G·U base pairs and tertiary (nonduplex) A·G pairs in tRNAs (Figure 2b)[124] and the active center of the hairpin ribozyme.[127]

As a consequence of base pairing, only a limited number of possible metal-binding sites in the bases are available in duplexes;[37,130] even fewer sites are accessible in triplex and quadruplex structures (Figure 2). The electron density of donor atoms that remain available for metal binding also differs from the electron density in isolated base residues.[32] For example, the affinity of purine N-7 and N-3 atoms for metal ions is greater in DNA duplexes than for the free nucleotides.[125]

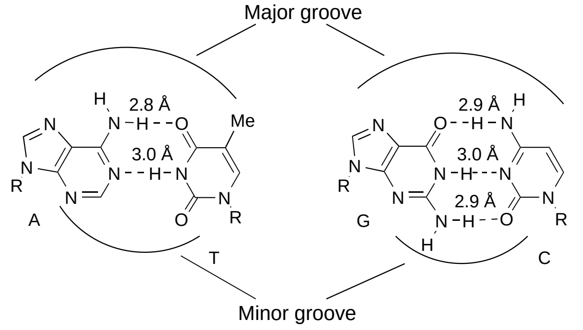

(a) Watson–Crick base pairs

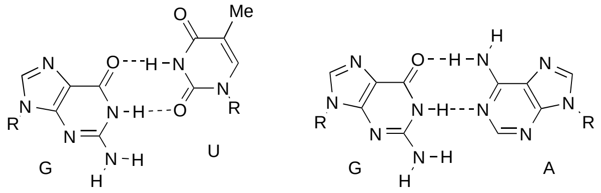

(b) Non-Watson–Crick base pairs

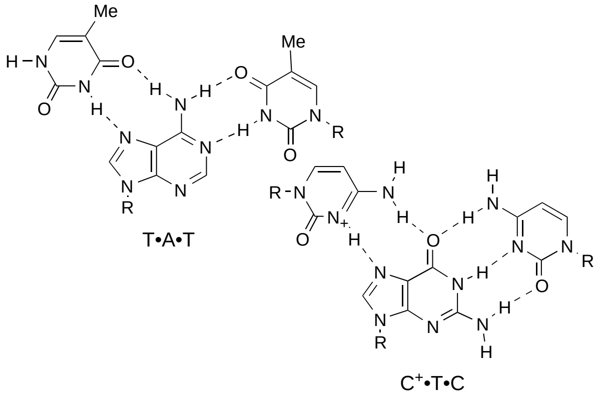

(c) Triplex cross-section

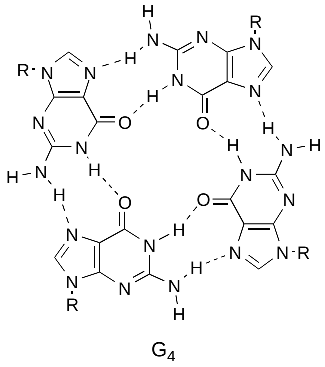

(d) Quadruplex cross-section

Figure 2 Structures illustrating cross-sections of nucleic acid duplexes, triplexes, and quadruplexes[76,128,129]

There are a few additional types of H-bonds in nucleic acids. For example, the sugar 2′-OH group in RNA can act as a H-bond donor to the neighboring 3′-phosphate oxygen anion.[97,125] The hydrogen atoms of water molecules interact with phosphate oxygen anions and sugar OH groups; water oxygen atoms form bonds with donor (N–H and C–NH_2) atoms in the nucleobases, while water hydrogen atoms interact with acceptor (N and C=O) atoms/groups. The hydrogen atoms of pentose 2′-OH groups in RNA also can interact with water oxygens. Such complex arrangement of internucleotide interactions between bases, sugar, and phosphate residues occurring in a GAAA tetranucleotide loop of a hairpin RNA is illustrated in Figure 3.

Interactions of the same water molecules with RNA nucleotides (via H-bonding) and metal ions (via inner-sphere coordination) could stabilize specific metal ion–nucleic acid complexes (e.g. in Mg^{2+}–tRNA chelates)[52] and also create the possibility for direct proton transfer through a 'water chain' that could play a role in ribozyme–metal ion catalysis[133] and in the mechanism of metal-dependent nucleases and polymerases.[134] Similar types of H-bonds between different nucleotide residues have been found in tRNA tertiary structures, where they provide additional stabilization of tertiary interactions.

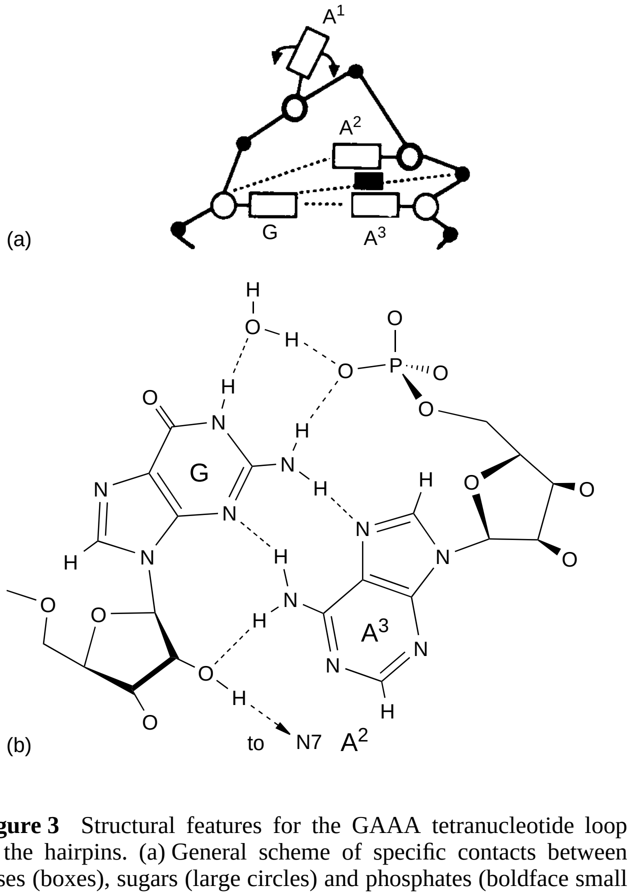

Figure 3 Structural features for the GAAA tetranucleotide loop in the hairpins. (a) General scheme of specific contacts between bases (boxes), sugars (large circles) and phosphates (boldface small circles). Hydrogen bonds and stacking interaction are shown by dotted lines and by a black box, respectively. (b), Putative hydrogen bonding network with the guanosine residue in the GAAA tetraloop structure. The N7 atom of the A^2 residue can make a hydrogen bond with 2′-hydroxyl group of G[131,132]

3.3 Intra- and Intermolecular Structures Formed by Polynucleotides

3.3.1 *Secondary Structures*

Single-stranded regions exist in most of the naturally occurring single-stranded RNAs, and in a few viral DNAs, as well as in denatured (see below) double-stranded DNAs. The single polynucleotide chains in solution may assume flexible right-handed helical structures as a result of base stacking and intramolecular H-bonds.[124] However, there are mostly short single–stranded regions present in single-stranded polynucleotides. As a result of folding back of the single polynucleotide strands, complementary H-bonds may form between bases, producing intramolecular duplexes and triplexes (see below) as well as internal loops, hairpin loops, and bulges (Figure 4a). Such structures, whether formed intra- or intermolecularly, are secondary structure elements.

The most prominent motif, which binds together all other secondary structure elements, is duplex (double helix). Most natural DNAs and a few viral RNAs are double-stranded and normally present in solution as duplexes, which are antiparallel (in terms of strand orientation), right-handed double helixes (Figure 5, A-B), stabilized through base–base interactions by both stacking and Watson–Crick H-bonding (see Figure 2). Double-stranded structures are less flexible than single-stranded ones, which limits the number of nucleic acid ligands that may participate in chelation of metal ions. In addition to the specific interbase (stacking and complementary) interactions, the restricted conformational freedom of pentose rings (involving C-2′ and C-3′-*endo* conformational isomers) and rotation about single bonds (see Figure 1), as well as steric (i.e. nonbonding) interactions between the bases and sugars, and electrostatic repulsion between phosphate groups, result in a limited variation in double helical structures. The conformational flexibility of double-stranded RNA is even more limited because of the added bulkiness of the 2′-OH group in ribose residues, which stiffens the sugar–phosphate backbone. In normal B-form DNA (Figure 5, B) the base pairs, intersecting at the helix axis and stacking perpendicular to it, form a central hydrophobic pillar surrounded by the hydrophilic sugar–phosphate backbone. In the usual A-form RNA double helix, the base pairs are located away from the center and tilted about 15° from the helical axis (Figure 5, A). There are other significant differences between these forms, such as the diameter of the backbone cylinder (which is slightly narrower in B-form than in A-form duplexes), the number of base pairs per helix turn (approximately 10 vs. 11), and the axial rise per base pair (3.4 vs. 2.8 Å for DNA and RNA duplexes, respectively). These structural features produce a major groove that is deep and narrow in A-form duplexes and a shallow, wider minor groove. In contrast, B-form duplexes have a wide major groove and narrow minor groove; both are of comparable depth (Figure 5). In the major groove of B-form DNA, potential metal-binding centers – atoms N-7 and

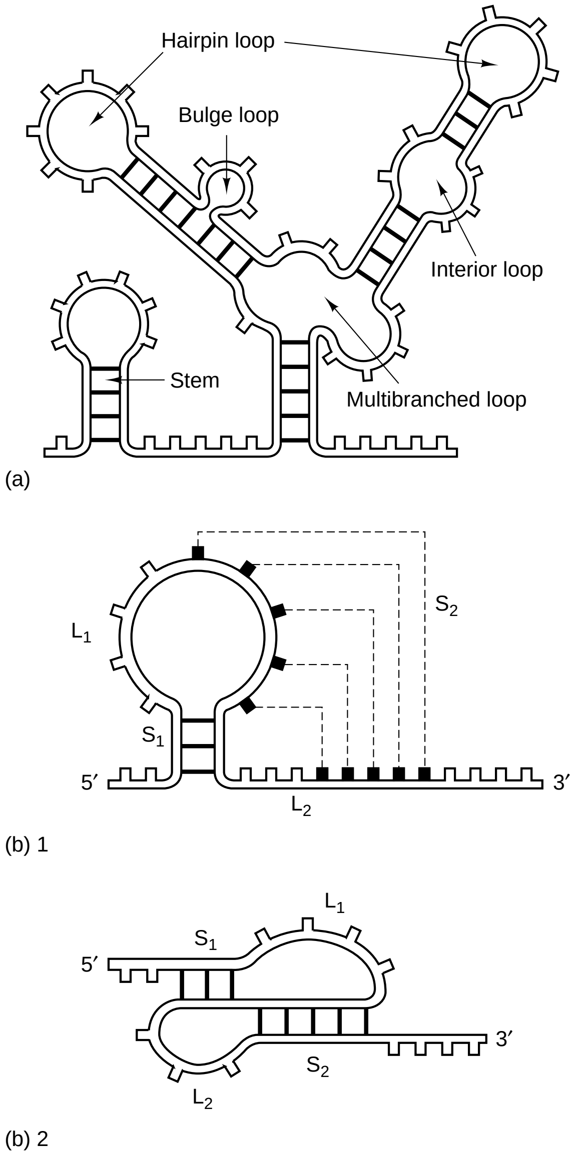

Figure 4 Tertiary structures of RNA's including (a) various stems, loops, and bulges, (b) an RNA pseudoknot. (Reprinted from Ref. 135, © 1990, with permission from Elsevier)

$O^6(N^6)$ of the purines and $O^4(N^4)$ of the pyrimidines are quite accessible; this is also true for N-3 of purines in the minor groove of DNA.[136,137]

Under conditions of reduced hydration, for example, in the presence of either high salt (of certain monovalent cations) or ethanol concentrations, or in crystals, DNA may adopt the A-form.[99] DNA–RNA hybrids (an intermediate in both forward and reverse transcription) exist as A-form duplexes.[126] Alteration of a duplex conformation can dramatically affect the accessibility of potential metal-binding sites.[37,139]

The most striking structure that has been observed for a DNA duplex is the left-handed Z-form DNA having Watson–Crick base pairing and a 'zigzag' sugar phosphate backbone (Figure 5, Z); this structure forms in alternating pyrimidine–purine sequences (e.g. CGCGCG) in the presence of appropriate polyvalent metal ions. The transition from B- to Z-form DNA is facilitated enormously by certain divalent metal ions, reflecting the importance of this metal ion to the stabilization of Z-DNA structure.[140,141] Z-form DNA is believed to exist in specific regions of DNA *in vivo*, and may play an important role in functions such as regulation of gene expression.[124]

Covalently closed circular DNAs exist in nature in a variety of organisms. Such topologically constrained DNAs can form both negatively supercoiled structures, which create a torsional stress on the double helix and favor its unwinding, and positively supercoiled molecules, which enforce tighter winding of the double helix. When the sugar–phosphate backbone of even one strand is broken, the supercoils are relaxed, forming an open circle of duplex DNA. Such backbone cleavage reactions can result from the action of metal compounds on DNA.[12]

DNA is prone to structural polymorphism: its structure can differ markedly from the classical double helix. For example, under superhelical stress, circular closed DNA can adopt an unusual structure, denoted H-DNA, in which homopurine–homopyrimidine tracts unwind and utilize the pyrimidine-rich strand to form an intramolecular triplex with another homopurine–homopyrimidine tract; the remaining purine single strand is left unpaired. The formation of H-DNA requires the presence of metal ions such as Mg^{2+} or Ca^{2+}.[142,143]

The great interest in triple-helix formation relates less to its possible physiological significance (which is currently unclear) than to potential applications (e.g. in gene-targeted therapy and genetic engineering) that can exploit the ability of single-stranded oligonucleotides to bind selected double-stranded DNA sites.[144] In triplexes composed of one polypurine and two polypyrimidine strands, the polypyrimidine 'third' strand lies in the major groove parallel to the purine strand of an A-form double helix. This additional strand interacts with the Watson–Crick duplex via Hoogsteen base pairing to form T·A·T and C^+·G·C triplets (see Figure 2c). The formation of the latter triplet is optimal at acid pH and markedly decreased at $pH > 6$ because of the need for cytidine protonation. However, the use of certain base analogs and phosphodiester backbone modifications allows triplex formation at physiological pH.[144] There are a few others type of triplexes that have been observed including G-rich pyrimidine–purine–purine structures.[144] Not surprisingly, triplex formation affects accessibility of potential metal-binding sites and requires certain divalent metal ions to stabilize the repulsion resulting from the negatively charged backbones of polynucleotide strands brought into close proximity. However, metal ions may both stabilize and destabilize the formation of triplex structures (see Section 6).

Both natural and synthetic polynucleotides containing repeats of G-rich sequences can also form quadruplexes (see

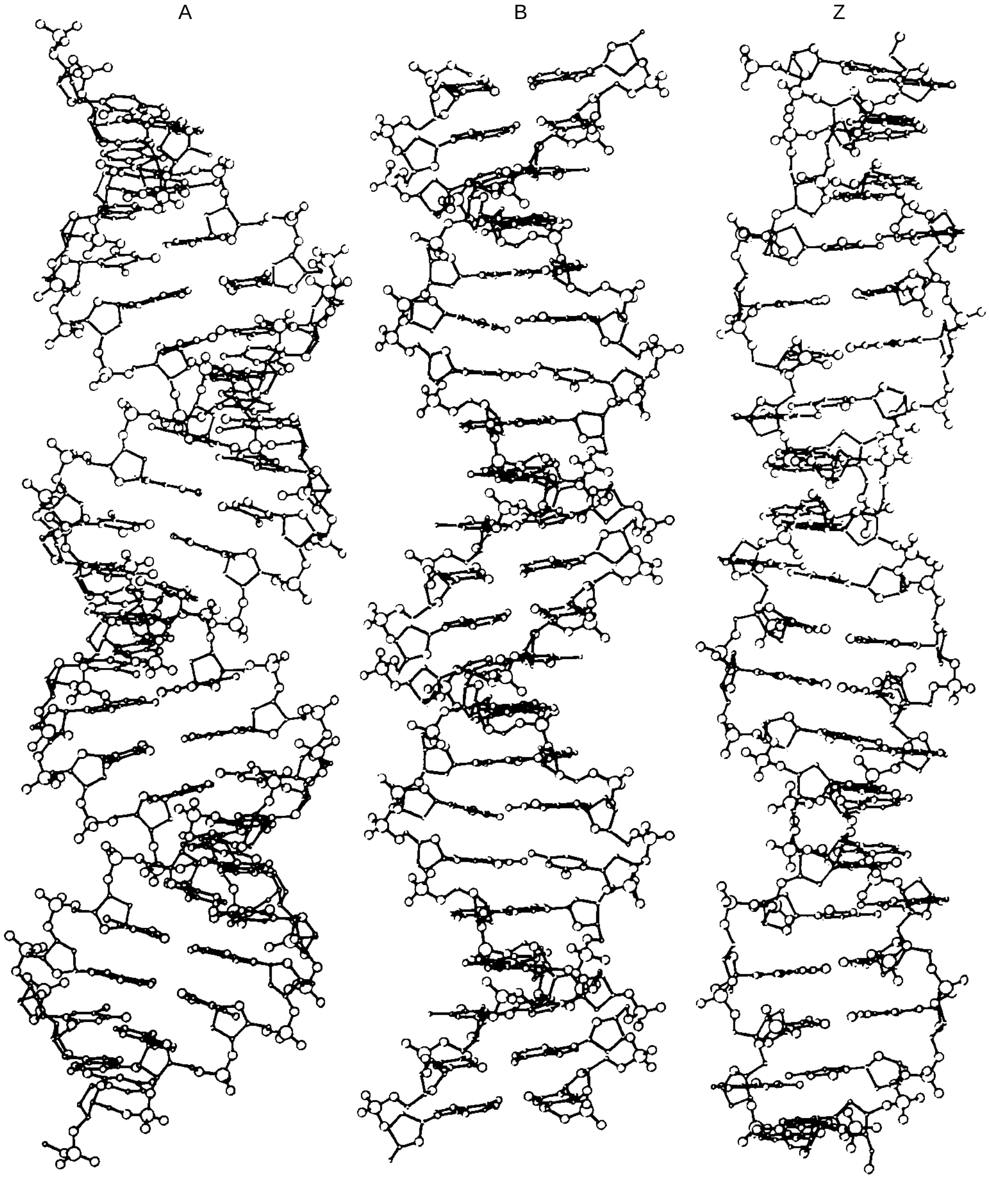

Figure 5 Structures of A, B, and Z-form DNAs[138]

Figure 2d), including parallel interstrand (most stable) and antiparallel intrastrand (fold-back) structures in DNA and RNA. These types of multistranded DNA structures have been proposed to be important in chromosomal telomer formation, immunoglobulin gene switching, and genetic recombination.[129] The large hydrophilic channel within the quadruplex structure is stabilized by monovalent metal ions such as $K^+ > Rb^+ \sim Na^+ > Li^+$ (in order of their effectiveness)[129,145–147] (also see Section 6).

3.3.2 Tertiary Structures

The structures described above, whether formed intra- or intermolecularly, are secondary structure elements. Additional interactions between these secondary structure elements, for example, base pairing between two loops or between a loop and a single-strand region, constitute tertiary structure (Figures 4b and 6). Most known tertiary interactions (including base triples, intercalation (insertion) of a base from one secondary structure element between two neighboring bases in another, and pseudoknots) have been found in RNA molecules, including tRNA.[124,148] DNA supercoiling (see above) is a feature of tertiary structure as well.

Single-stranded regions of nucleic acids provide metal ions with access to all possible binding sites in the nucleotide residues. In contrast, nucleic acid tertiary structure, while creating some restrictions on metal binding in certain regions, may also provide other sites at which donor atoms located in appropriate orientations chelate selected metal ions very specifically. The best-known examples of such complexes are also found in tRNAs (Figure 6). Metal binding, in turn, may stabilize such structural elements of nucleic acids (see below), which would otherwise assume a number of different conformations in solution.

One more interesting structure, also representing an unusual metal-binding center, is the DNA cruciform (or four-way junction) structure.[11,151] This type of structure results from rearrangement of palindromes (inverted repeat sequences) and may be formed reversibly under certain conditions (e.g. to relax strain in supercoiled DNA). The relative efficiency of different divalent metal ions in promoting the formation of DNA cruciform structures is $Mg^{2+} > Mn^{2+} > Co^{2+} > Ni^{2+} \sim Cu^{2+}$.[152,153]

Another class of tertiary structures involving nucleic acids comprises complexes between nucleic acids and proteins. Some of these complexes, whose structure and function are under the control of metal ions, are described in ***Zinc: DNA-binding Proteins***. Specific interactions between certain amino acid residues in proteins with nucleotide residues (e.g. via H-bonds, stacking, and electrostatic interaction with phosphate anions) in nucleic acid–protein complexes may also restrict metal-binding sites on the nucleic acid. Structural rearrangement of nucleic acids upon interaction with proteins, in turn, can also lead to the formation of new metal-binding sites (e.g. as a result of local denaturation of a duplex).[11] There is also evidence for the formation of metal-binding sites in nucleoprotein complexes that involve both the nucleic acid and protein residues (such as imidazole, –SH, $-SCH_3$, NH_2, and CO_2^-)[17] (*see* ***Peptide–Metal Interactions***).

3.3.3 Denaturation and Renaturation of Polynucleotide Structures

Complete disruption (unfolding) of specific, functionally important ('native') conformations of single-stranded and multistranded polynucleotides (as well their complexes with proteins) is called denaturation. Denaturation (or 'melting') of DNA is the simplest example of the unwinding of the double helix resulting in partial or complete separation of polynucleotide strands. Triplex melting proceeds in two steps: the first involves dissociation of the 'third' strand from the intact Watson–Crick duplex; the second involves duplex denaturation, which occurs under more stringent conditions.[154] Reassembly of the separated strands is called renaturation, or else hybridization (annealing) if the DNA strands were originally from different sources or if a DNA strand is matched with a complementary RNA strand.

The stability of multistrand nucleic acid secondary structures depends both on internal and external factors. Since the G·C base pair contains three H-bonds compared with two for the A·T (or A·U) base pair (Figure 2a), and because stacking interactions decrease in the order G > A > C > U, a duplex with greater GC content is expected to be more stable.

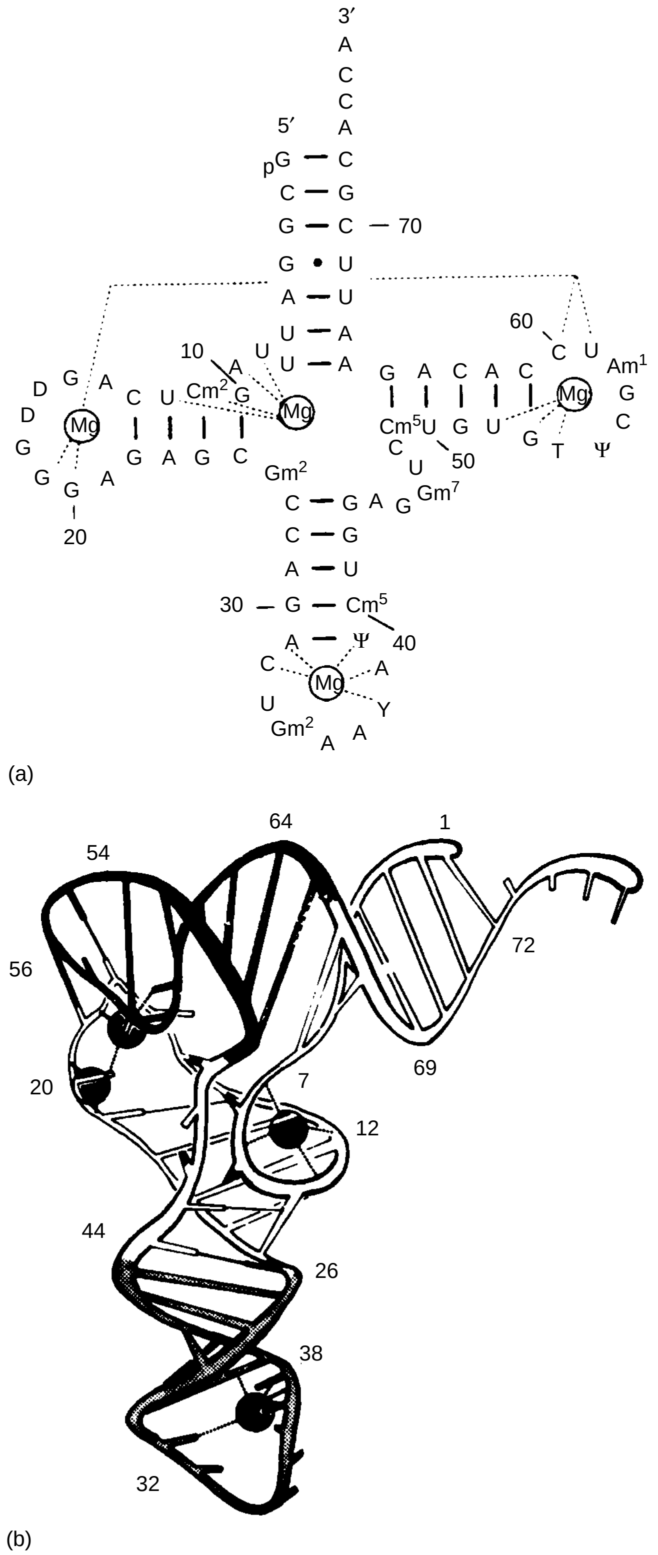

Figure 6 Sites of specific binding of Mg^{2+} ions in yeast $tRNA^{Phe}$. (a) secondary structure. (Ref. 149. Reproduced by permission of American Society for Biochemistry & Molecular Biology) (b) tertiary structure. (Ref. 150. Reproduced by permission of Oxford University Press)

Likewise, duplex stability tends to increase as the number of base pairs increases. Because there is electrostatic repulsion between negatively charged oxygens in the sugar–phosphate backbone, the structures of multistrand polynucleotides are unstable in pure water at temperatures above 0 °C; their stabilities increase with increasing concentrations of monovalent metal cations that act as counterions for the phosphate oxygens.[154] The influence of di- and trivalent metal ions on the stability of nucleic acids is more complicated and may be both stabilizing and destabilizing (see below).[7] Usually, the relative stability of nucleic acid hybrids increases in the order DNA–DNA $<$ DNA–RNA $<$ RNA–RNA.[155] In addition to elevated temperature, extremes of pH also may be used to disrupt multihelical polynucleotide structures, since protonation or deprotonation of bases involved in H-bonding destabilizes base pairing. Alkaline conditions (pH $>$ 11.5) are suitable for denaturation of DNAs, but not for RNAs, which are cleaved at high pH. In comparison, acidic conditions (pH $<$ 2.5) are suitable for denaturation of RNA, but cause depurination of DNA.[154] Some proteins can also induce local denaturation of DNA.[156] When the temperature or pH is restored smoothly to the 'biological' range (25–45 °C and pH 7–8, respectively), the denatured strands can renature to restore the intact duplex, but fast cooling (e.g. in ice) or shifting to neutral pH typically results in intrastrand collapse without proper interstrand base pairing. Denaturation of multistrand polynucleotide structures usually increases accessibility of potential metal-binding sites but may decrease or change the specificity of metal binding (see below).

The difference between native and denatured forms of RNA tertiary structures[124,157] are not quite as simple (or clear) as in the case of multistrand DNA structures. Stabilization of the RNA tertiary structures by metal ions and changes in metal-binding modes upon denaturation are based on a similar principle as for DNA but apparently are more complex processes.[57,104,157–163] For example, specific tertiary structures of tRNA molecules can exist at high concentration of Na^+, but are very unstable in the absence of divalent metal ions.[159] The tRNA tertiary structure provides the specific binding sites for divalent metal ions (naturally – Mg^{2+}) (Figure 6), which disappear with the liberation of the bound metal ions as a result of the tertiary structure unfolding under denaturing conditions.[158] However, if all endogenous Mg^{2+} ions were removed from a tRNA molecule (e.g. by heating the solution in the presence of excess of strong chelating agents such as EDTA) and then added back to solution in exactly the original amount, the native tertiary structure can be restored, but not for each tRNA molecule,[160] presumably because Mg^{2+} ions can stabilize both native RNA structures and also can trap RNA in relatively stable 'alternative' structures.[164] Interestingly, some RNA complexes containing certain metal ions (e.g. Mg^{2+} and Mn^{2+}) can survive under ambient temperatures even in the presence of EDTA (despite the strong metal affinity of EDTA: log K stability for [Mg^{2+}-EDTA] and [Mn^{2+}-EDTA] are 9.1 and 14.0, respectively[121]) presumably because of the electrostatic repulsion and steric inaccessibility of EDTA to some metal ions bound in internal pockets of RNA tertiary structure.[158,161,165] For this reason, to most effectively remove divalent (or trivalent) ions bound to RNA, the RNA should be heat-denatured in the presence of chelating agents and high concentrations of monovalent cations to accelerate ligand-exchange reactions if possible.[161]

3.4 Structure-Specific Binding of Metal Compounds to Polynucleotides

The specificity of metal ion/compound binding to a polynucleotide depends on its nucleotide sequence and structure as well as presence of modified nucleotides and reaction conditions (e.g. metal concentration, pH, and temperature). The specific binding always involves the formation of comparatively thermodynamically stable or kinetically inert (see below) metal–nucleic acid bonds. The term 'comparatively' means that the relative (not absolute) stability or inertness of the different bonds constitute the principal determinant of the specificity of interaction. There are different kinds of metal-binding selectivity, including (1) 'atom-specific' interactions, involving individual donor atoms in the nucleic acid residues; (2) 'group-specific' interactions, involving combinations of nucleotide residues such as phosphate, sugar, and nucleic acid bases; (3) 'base-specific' interactions in polynucleotides; (4) 'sequence-specific' interactions; (5) interactions specific to secondary structure, that is, involving binding to single-stranded or double-stranded polynucleotides; and (6) 'tertiary structure-specific' interactions, which are usual for RNA molecules and nucleoprotein macromolecular complexes. As the complexity of the structure of a nucleic acid increases, so does the probability of highly specific metal binding because of the greater opportunity for formation of unique ligand environments. In general, different metal ions bind to different sites in the same polynucleotide and vice versa – the same or closely located (see below) metal-binding centers of polynucleotides would bind different metal ions. For example, many specific metal-binding sites for different metal ions (for Mg^{2+} - see Figure 6) have been found within the $tRNA^{Phe}$ molecule.[51,53,54] (also see Section 5.5).

4 PROPERTIES OF METAL IONS ESSENTIAL FOR INTERACTION WITH NUCLEIC ACIDS

4.1 Metal-nucleic Acid Bond Formation Occurs Through Ligand-exchange Reactions

As mentioned above, metal ions and nucleic acids are equal partners in metal–nucleic acid interactions. Surprisingly, the number of potential bonds (both inner- and outer-sphere) that

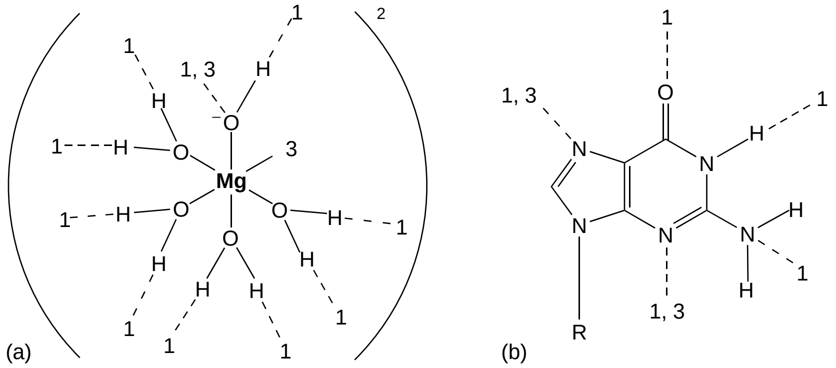

Figure 7 Types of specific bonds that can be formed by hydrated metal ion (a) as compared to guanine (b). The bond types are designated as follows: 1 – hydrogen, 2 – ions, and 3 – coordinative (donor–acceptor)[166]

can be formed by metal ions may even exceed this number for nucleic acid bases – as schematically shown in Figure 7 comparing $[Mg(H_2O)_6]^{2+}$ and the guanine residue.

In aqueous solutions, most metal ions (M^+, M^{2+} and M^{3+}) exist as aqua complexes $[M(OH_2)_x]^{n+}$, which tend to act as acids to form aqua-hydroxo complexes $[M(OH_2)_{x-1}(OH)]^{(n-1)+}$ (see Table 1 for pK_a values) owing to the influence of the positive charge and electron acceptor property of the metal ion that facilitates deprotonation. In buffered solutions the behavior of metal ions is affected by many factors. The acidity constants for the same metal-aqua complexes may vary with ionic strength and temperature.[121] While $pH < pK_a$ (Table 1) favors aqua-complex ($M\text{-}OH_2$) formation, $pH > pK_a$ favors formation of M–OH, which is resistant to ligand substitution[28] and also decreases or even neutralizes the positive charge of the metal complex, resulting in precipitation of metal hydroxides.[167] For instance, both $Pb(OH)_2$ and $Fe(OH)_2$ begin to precipitate at pH 7.5 and are almost completely insoluble ($\sim 10^{-5}$ M) at pH 9.0 and 9.7, respectively.[168] In contrast, $Mg(OH)_2$ doesn't begin to precipitate until pH 10.4.[168] Therefore, it is important to optimize the solution pH depending on the metal ions to be used. The formation of hydroxy forms also can result in oxidation (see Section 4.5) of metal ions as, for example, Mn^{2+} and Co^{2+} at $pH \geq 8.5$.[169]

In addition to H_2O and hydroxide anion (^-OH), other neutral (e.g. NH_3, imidazole, and nucleobases) or negatively charged ligands (e.g. RS^-, Cl^-, $CH_3CO_2^-$ or PO_4^{3-}) can be bound simultaneously to the same metal cations. Some ligands, such as ClO_4^- and NO_3^-, have no tendency to coordinate to metal ions even in rather concentrated aqueous solutions but most others (e.g. Cl^-, $MeCO_2^-$, and PO_4^{3-}) can substitute coordinated H_2O molecule(s).[170] Some commonly used biological buffers (e.g. polyamines, Tris, and phosphates) also can form metal-ion complexes of varying degrees of stability.[122] Moreover, cationic buffer components may also compete with metal ions for electrostatic and outer-sphere metal-binding sites in nucleic acids. In aqueous, buffered solutions, coordination compounds undergo exchange reactions, wherein inert ligands are retained while labile ones are substituted by water (aquation) or by ionic buffer constituents (*see* ***Coordination & Organometallic Chemistry: Principles***). Beyond its dependence on the nature and concentrations of metal ions and buffer solutions, the composition of the internal coordination spheres of dissolved metal ion complexes depends on pH (see above) and temperature. High temperature accelerates exchange processes, whereas low temperature (without freezing) usually slows it down.

Inner-sphere (direct) metal-nucleic acids bonds can be both formed and dissociated as result of preexisting ligand substitution (exchange) reactions, wherein inert ligands keep their places while labile ones are substituted. Mechanistically, there are generally considered to be three main classes of ligand-substitution (replacement) reactions: dissociative (1), associative (i.e. going through a transition state involving an inner-sphere complex) (2), and interchange (exchange of ligand X and Y between inner and outer coordination spheres of the metal) (3), as illustrated by the following equations:[120,170]

$$M\text{–}X + Y \longrightarrow [M + X] + Y \longrightarrow M\text{–}Y + X \quad (1)$$

$$X\text{–}M + Y \longrightarrow [X\text{–}M\text{–}Y] \longrightarrow M\text{–}Y + X \quad (2)$$

$$X\text{–}M + Y \longrightarrow [X\text{–}M\text{–}Y] \longrightarrow [X\text{–}M\text{–}Y] \longrightarrow M\text{–}Y + X \quad (3)$$

Since coordination positions are available on square-planar complexes from above or below the plane, and the fifth ligand can be added to form an inner-sphere intermediate (activated complex), an associative mechanism is generally observed for ligand substitution of such complexes. In contrast, six-coordinate complexes can form inner-sphere, seven-coordinated intermediates only with difficulty, owing to interligand steric constraints. Therefore these complexes are generally observed to react by dissociative or interchange mechanisms. Because dissociation of M–X is generally rate limiting in the dissociative mechanism, a first-order rate law obtains for such reactions; accordingly, such reactions do not depend on the concentration of nucleic acid. In contrast, reactions that proceed by an associative mechanism are bimolecular and do depend on nucleic acid concentration.

Ligand-substitution reactions in aqueous solutions rarely proceed directly. Instead, the leaving ligand is first replaced by H_2O, which is present in aqueous solution at a concentration of ∼55 M, the entering ligand then substitutes the metal-bound H_2O (M–OH_2) in the so-called anation reaction.**[120]** Therefore, the rate constant of forward reactions, which could be considered as the *reactivity* of aquo-metal species, will parallel the order of water substitution in the inner coordination sphere of the corresponding metal ions: $Cs^+ > Ba^{2+} > Hg^{2+} > K^+ > Cr^{2+} \sim Cu^{2+} > Na^+ > Sr^{2+}$ $Li^+ > Ca^{2+} > Cd^{2+} > Mn^{2+} \sim Zn^{2+} > Fe^{2+} > Co^{2+} > Mg^{2+} > Ni^{2+} > Pd^{2+} > Pt^{2+} > Cr^{3+}$.**[120,170,171]** In most cases, the interactions between hydrated metal ions and nucleic acids are fast with $t_{1/2}$ in the range 10^{-9}–10^{-3} sec.**[171–174]** However, if the limiting step of a substitution reaction is dissociation of a relatively stable bond(s), for example, AMP in the reaction with Pt–Cl**[175]** or Pt–OH,**[176]** the rate of this reaction could be quite slow ($t_{1/2}$ up to several hours or even days).

The general factors affecting the ability of coordination compounds to participate in substitution reactions include the nature of the central metal ion, the leaving and entering ligands (e.g. size, charge, nucleophilicity, and basicity), as well as the effects of other coordinated ligands, especially those in *trans* and *cis* positions to the leaving group.**[66]** The *trans* effect of donor atoms (i.e. the tendency to facilitate substitution in the position *trans* to themselves) has proven very useful for directed synthesis of model metal–nucleic acid complexes, especially in the cases of Pt^{2+}, Pt^{4+}, and Pd^{2+} complexes.

Because of the polyelectrolyte effect (Section 3.1), the rate of metal–polynucleotide reaction to form 'coordinative-covalent' bonds will depend on the positive charge of the metal species; accordingly, the rate can be increased significantly by introduction of additional positive charge to the reagent, for example, $[(NH_3)_2PtCl(H_2O)]^+ \rightarrow [(NH_3)_2Pt(H_2O)_2]^{2+}$. The rates of selected metal–nucleic acid reactions are given in Table 2.

Table 2 Kinetic parameters of selected metal–nucleic acid interactions[a]

System	k_f ($M^{-1}\,s^{-1}$)	$t_{1/2}$	k_r (s^{-1})
Ni^{2+} + 5′-CMP[b] **[171]**	1.9×10^5	–	2×10^3
Ni^{2+} + 5′-CDP[b] **[171]**	6.2×10^5	–	1.8×10^2
Ni^{2+} + 5′-CTP[b] **[171]**	1.4×10^6	–	5×10^1
Ni^{2+} + 5′-ATP[c] **[171]**	4.1×10^6	–	$>4 \times 10^4$
Mg^{2+} + 5′-ATP[c] **[171]**	1.2×10^7	–	1.2×10^3
Co^{2+} + 5′-ATP[c] **[171]**	9.2×10^7	–	2×10^3
Mn^{2+} + 5′-ATP[c] **[171]**	$>10^9$	–	$>10^4$
Ca^{2+} + 5′-ATP[c] **[171]**	$>10^9$	–	$>10^5$
Hg^{2+} + poly(U)[d] **[173]**	1.4×10^6	–	–
Hg^{2+} + poly(A)[d] **[173]**	1.2×10^5	–	–
Hg^{2+} + poly(A)·poly(U)[d] **[173]**	2.7×10^4	–	–
Hg^{2+} + UTP[e] **[172]**	–	20 min[h]	–
$[Pt(NH_3)_2Cl_2]$ + AMP[f] **[175]**	9.3×10^{-3}	–	–
$[Pt(NH_3)_2Cl_2]$ + ADP[f] **[175]**	$7.8 \times 10^{-}3$	–	–
$[Pt(NH_3)_2Cl_2]$ + ATP[f] **[175]**	6.3×10^{-3}	–	–
$[Pt(NH_3)_2(H_2O)Cl]^+$ + DNA[g] **[176]**	$2 \times 10^{-3}\,s^{-1}$[g]	6 min[h]	–
$[Pt(NH_3)_2Cl_2]$ + DNA[g] **[176]**	$10 \times 10^{-5}\,s^{-1}$[g]	120 min[h]	–

[a] k_f is the rate constant for the forward reaction and k_r for the reverse one; $t_{1/2}$ is the half-time of the forward reaction. [b] The metal ion concentrations were equimolar and ranged from 10^{-4} to 2×10^{-2} M nucleic acid in 0.1 M KNO_3, pH 6–7, at 15 °C. [c] The nucleotide and metal-ion concentrations were equimolar and ranged from 10^{-5} to 10^{-4} M in 0.1 M KNO_3, pH 5.5–7.5, at 25 °C. [d] The rates of coordination complex formation were determined at 15 °C at polynucleotide concentrations of about 10^{-4} M, $[Hg^{2+}]$/[nucleotide] = 0.25, in 10 mM Na phosphate buffer, pH 5.6–7.0, containing 0.25 M $NaClO_4$. [e] The rate of covalent mercuration of UTP was determined at 50 °C at a nucleotide concentration of 6×10^{-4} M ($[Hg^{2+}]$/[nucleotide] = 6.5) in 0.1 M Na phosphate buffer, pH 6.0, containing 0.25 M $NaClO_4$. [f] The nucleotide concentration ranged from 1.2 to 2.4 mM ([Pt]/[nucleotide] ≤ 0.1) in 0.5 M $NaClO_4$, pH 7.0, and 40 °C. [g] The pseudo first-order rate constant for monofunctional binding to N-7 of G in chicken erythrocyte DNA was determined at a nucleotide concentration of 0.46 M ([Pt]/[nucleotide] = 0.07) in 1 mM Na phosphate, pH 6.5, containing 3 mM NaCl at 37 °C. [h] Since the half-life for a second-order reaction is dependent on the concentration of the reactants, the significance of these entries is not entirely clear.

4.2 Thermodynamic Stability of Metal–Nucleic Acid Bonds

Consistent with the definition of 'hard and soft' metal ions (*see* ***Hard & Soft Acids and Bases***) based on the nature of the stable complexes that they form with different ligand donor atoms,**[170,177]** these metal ions behave similarly toward donor atoms of nucleic acids and their derivatives (Figure 8).**[178]**

'Hard' monovalent cations (M^+) usually interact with nucleic acid polyanions only in a diffuse 'ion atmosphere' manner, whereas 'hard' and 'borderline' polyvalent ($M^{\geq 2+}$) cations can form both outer- and inner-sphere complexes. 'Soft' metal ions tend to form inner-sphere complexes, however. 'Hard' metal ions (class A) prefer O-donor ligands (usually phosphate oxygens), while 'soft' ones (class B) prefer N-donor atoms of the nucleic acid bases as well as S atoms in thio derivatives of nucleic acids (*see* ***Ammonia & N-donor Ligands***; and ***S-donor Ligands***).

The first-row transition metal ions have borderline 'hard–soft' properties. Therefore, there is no simple rule to predict comparative complex stabilities for a given metal ion with the different donor atoms. In contrast, the stability of complexes of these metal ions with a given ligand does follow a general trend. Thus the stability constants for complexes with NTP increase with the metal ion in the order $Co^{2+} < Mn^{2+} < Zn^{2+} < Ni^{2+} < Cu^{2+}$,**[49,178]** which is the usual Irving–Williams order,**[170]** except for the reversal of cobalt and manganese. The usual decrease in stability with increasing atomic number is observed for the complexes with metal ions of the alkaline earth series.**[21,49]** The stability of the

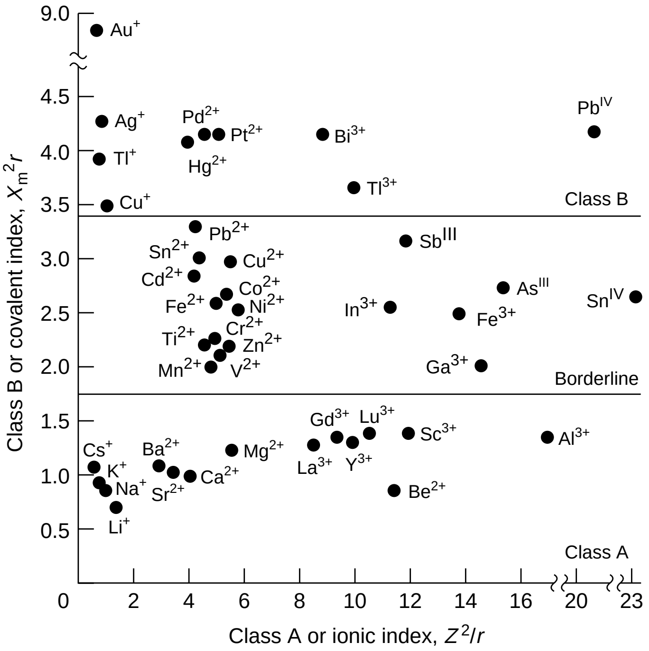

Figure 8 Classification of metal ions according to binding preferences[177]

complexes of these metal ions (other than Cu^{2+}) is largely independent of the nature of the nucleic acid base in NTPs, NDPs, and NMPs because the phosphate groups constitute the most favorable ligands.[115] The small differences in the stability of these complexes has been interpreted as resulting from predominant outer-sphere coordination of the phosphate oxygens to the metal ions.

The tendency to favor N- over O-donors for selected ‘hard’ and ‘borderline’ metal ions is in the order Mg^{2+} $\ll$ Mn^{2+} $<$ Fe^{2+} $<$ Zn^{2+} $<$ Co^{2+} $<$ Cd^{2+} $<$ Ni^{2+} $<$ Cu^{2+}.[170] Some metal ions in this group preferentially form mixed ternary complexes (involving phosphate oxygens and nucleic acid base nitrogens or oxygens as ligands), which are significantly more stable than those containing only one kind of donor atom.[28]

The relative stabilities of the metal complexes of nucleosides are generally considered to be in the order G $>$ A, C $\gg$ U, T;[49] however, this order does not obtain universally.[21,42] Thus the relative base affinities of Hg^{2+} and of Pb^{2+} appear to be T $>$ C $>$ A $>$ G and C $>$ G $>$ A, respectively.[21,49,179] This difference results from the variety of sites to which metal ions can bind on the nucleic acid bases. Stability constants of the complexes between selected metal ions and nucleic acids (from nucleosides to nucleoside triphosphates) are shown in Table 3.

Metal binding to polynucleotides that exist as duplexes is weaker than to single-stranded or denatured, double-stranded nucleic acids, reflecting the added binding capabilities of unpaired nucleic acid bases. Metal–nucleic acid binding could result in formation of a single bond as well as by chelation, involving multiple bonds between a metal ion and several available, appropriately located nucleic acid ligands. In some cases, one or more of the participating ligands alone may not have a particularly high affinity for the metal ion, but they get bound anyway because of the incremental gain in free energy that can be realized following initial metal-ion binding with more favorable ligands.

Thus Mg^{2+}, which binds only to phosphate oxygen anions in DNA, has a higher affinity for duplex DNA ($K_a = 2 \times 10^5\,\mathrm{M}^{-1}$) than species such as Mn^{2+} and Cu^{2+}

Table 3 Logarithms of the stability constants of metal–nucleic acid complexes in aqueous solutions at 25 °C

	Metal Ion									
Nucleos(t)ide	Mg^{2+}	Ca^{2+}	Mn^{2+}	Fe^{3+}	Zn^{2+}	Co^{2+}	Cd^{2+}	Ni^{2+}	Cu^{2+}	Pb^{2+}	Hg^{2+}
Adenosine									0.16[180]		4.25[19]
5′-AMP[181]	1.60	1.46	2.23		2.38	2.23	2.68	2.49	3.14		
3′-AMP[182]	1.49	1.36	2.06		1.98	1.80	2.32	1.89	2.75		
2′-AMP[182]	1.53	1.43	2.14		2.10	1.93	2.41	1.94	3.01		
5′-ADP	3.17[23]	2.86[23]	4.24[20]	4.30[23]	4.30[20]	4.30[20]		4.50[20]	6.00[20]		
5′-ATP[183]	4.29	3.91	5.01	5.40	5.16	4.97	5.34	4.86	6.34		
Guanosine					0.80[184]	1.0[184]		1.40[180]	1.90[180,184]	3.50[20]	4.00[19]
5′-GMP[34]	1.67	1.50	2.33		2.67	2.71	2.95	3.22	3.62		
5′-GTP	4.02[20]	3.58[20]	4.73[20]	5.60[23]		4.63[20]					
Cytidine					0.56[180]			0.95[180]	2.04[180]	0.97[20]	9.50[19]
5′-CMP[181]	1.54	1.40	2.10		2.06	1.86	2.40	1.94	2.84		
5′-CTP[183]	4.20	3.85	4.90	5.80	5.03	4.78	5.05	4.52	6.03		
Uridine										3.38[20]	9.00[19]
5′-UMP[181]	1.56	1.44	2.11		2.02	1.87	2.38	1.97	2.77		
5′-UTP[183]	4.27	3.94	4.91		5.01	4.73	5.10	4.47	5.87		
Thymidine										3.70[20]	10.60[19]
5′-TMP[181]	1.55	1.40	2.11		2.10	1.89	2.42	1.92	2.87		
5′-TTP[183]	4.23	3.85	5.01		5.03	4.78	5.09	4.52	5.83		

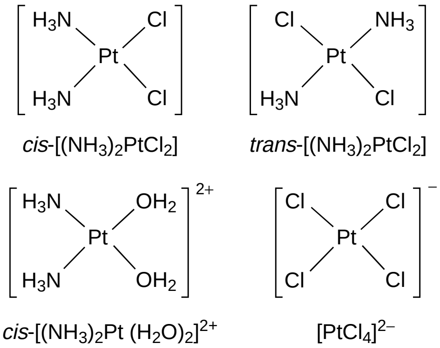

Figure 9 Structures of platinum(II) complexes

($K_a = 10^4\,M^{-1}$), but a lower affinity than these metal ions (which also bind to nucleic acid bases while Mg^{2+} does not) for single-stranded DNA. In addition, two classes of divalent cation binding sites in tRNA have been reported.[53,185] The first form complexes with stability constants between 2×10^4 and $5 \times 10^6\,M^{-1}$; the second involve weaker complexes with constants ranging from 5×10^2 to $10^4\,M^{-1}$, depending upon experimental conditions. For example, there are four strong and ‘intermediate’ magnesium-binding sites in yeast $tRNA^{Phe}$ (see Figure 6) as well as about 20 weak ones that still have structure-specific binding sites.[53,54,163,185,186]

4.3 Kinetic Lability of Metal–Nucleic Acid Bonds

In addition to the thermodynamic stability of metal–nucleic acid complexes, the rates at which nucleic acid ligands dissociate from a metal-ion coordination sphere are as important as the thermodynamic stability of the metal–nucleic acid bond.

The relative rates of reaction of the nucleic acid bases with heavy transition metal ions at neutral pH are in the same order as the relative nucleophilicites of the bases, that is $G > A > C \gg U$ or T.[79] This order parallels the relative rates of reactions for *cis*-$[(NH_3)_2Pt(OH_2)_2]^{2+}$ (see Figure 9), while the equilibrium constants for the same reactions are very close in magnitude.[79] In contrast, H_3CHgOH, which is more labile to substitution, undergoes more favorable binding with deprotonation at N-3 of thymine residues in nucleic acids.[79] Thus the relative facilities of individual reactions can lead to differences in initial product formation (kinetic control). Subsequent changes in the metal–nucleic acid complexes can be under kinetic or thermodynamic control.

The fact that a specific ligand is considered to be kinetically inert does not necessarily mean that the metal complex will persist in solution under ordinary conditions for an indefinite length of time. Clearly, complexes that are both thermodynamically stable and kinetically inert will tend to persist for the greatest length of time. A good example is Pt^{2+}, which forms complexes with nucleic acids containing single Pt–N bonds that are very stable thermodynamically and kinetically inert. Investigations of Pd^{2+} complexes with nucleic acids have been very useful in establishing a thermodynamic baseline for certain Pt^{2+} complexes, which undergo ligand substitution 10^5 times more slowly than the corresponding Pd^{2+} complexes.[170] Owing to the kinetic and thermodynamic properties of platinum complexes (*see* ***Platinum: Inorganic & Coordination Chemistry***), the unforced cleavage (dissociation) of a Pt–N bond with a nucleic acid base is not expected within a reasonable time (e.g. 100 h at 37 °C).[33] In comparison, the lifetime for Mg^{2+} bound to DNA is ≈ 4 ms at room temperature.[187] Indeed, the rate of ligand exchange is about 10^3 times slower for Mg^{2+} than for Ca^{2+}, and increases in the order $Ni^{2+} < Mg^{2+} < Co^{2+} < Fe^{2+} < Mn^{2+} < Zn^{2+} < Ca^{2+}$.[171] Mn^{2+} forms thermodynamically stronger complexes than Mg^{2+}, especially when nitrogen is a ligand or with multidentate ligands, but undergoes ligand exchange about 100 times faster than Mg^{2+}.[171]

Complexes of platinum group metals, which are more substitution labile than platinum, can undergo isomerization, which involves cleavage of the N–metal bond formed initially under kinetic control, and formation of a more thermodynamically stable complex. For example, $[(dien)Pd]^{2+}$ migrates from N-7 to N-1 in A and from N-3 to N^4 in C; likewise $[(NH_3)_5Ru]^{2+/3+}$ moieties migrate from N-1 to N^6 in A and from N-3 to N^4 in C.[33] Adenosine is of special interest, because both highly reactive donor atoms N-1 and N-7 are unprotonated at neutral pH and available for metal binding, in contrast to the situation in guanosine. In spite of the fact that N-1 of A is intrinsically 320 times more basic than N-7, the ratios of stability constants, $[M,\ \text{N-1}]/[M,\ \text{N-7}]$, for protons and selected metal ions have been determined as follows: $H^+(320) \gg [(dien)Pd]^{2+}(4) > Ni^{2+}(3) \geq Cu^{2+}(2.5) > Zn^{2+}\ (1)$.[32]

In the presence of millimolar concentrations of stronger nucleophiles such as CN^- and thiourea for Pt^{2+} complexes, or molar concentrations of Cl^- for Hg^+ complexes, nucleic acid base substitution takes place. However, steric constraints can lead to surprising inertness, as demonstrated for N-3-platinated T and U.[33] In contrast to coordination bonds of Hg^{2+} to heterocyclic N-atoms of nucleic acid bases, the covalent bond of mercury ion to C-5 of pyrimidines (*see* ***Mercury: Organometallic Chemistry***) is stable even in the presence of 1 M NaCl.[172]

4.4 Coordination Numbers and Geometry of Metal–Nucleic Acid Complexes

Most compounds containing metal–nucleic acid bonds are *Coordination Complexes* (*see* ***Coordination Numbers & Geometries***),[170] in which a central metal cation is bound (or coordinated) to a number of donor atoms that contain electron pairs (e.g. N, O, or S). In addition to the nucleic acids, many simple or sophisticated, negatively charged or neutral ligands can be bound to the same central metal ions. Water and hydroxyl anion also act as ligands (*see* ***Water & O-donor Ligands***). The total charge carried by

Table 4 Stoichiometries of Pt and Pt, M complexes with nucleic acid bases[33]

Number of bases per metal ion	Chemical composition
4	[Pt(9-methylguanine)$_4$]$^{2+}$
3	[Pt(NH$_3$)(1-methylcytosine)$_3$]$^{2+}$
	cis-[(NH$_3$)$_2$Pt(1-methylcytosine)$_2$]$^{2+}$·1-methylcytosine[a]
	cis-(NH$_3$)$_2$Pt(9-ethylguanine$^-$)$_2$·9-ethylguanine[b]
2	*cis*-[(NH$_3$)$_2$Pt(9-ethylguanine)$_2$]$^{2+}$
1.5	*cis*-[(NH$_3$)$_4$Pt$_2$(9-ethylguanine$^-$)(9-ethylguanine)$_2$]$^{3+}$
1.33	*cis*-[(NH$_3$)$_4$Pt$_2$Ag(1-methyluracil)$_4$]$^+$
1	*cis*-[(NH$_3$)$_2$Pt(1-methylcytosine)Cl]$^+$
	cis-[(NH$_3$)$_2$Pt(1-methyluracil)]$_2$$^{2+}$[c]
0.80	*cis*-[(NH$_3$)$_8$Pt$_4$Ag(1-methyluracil)$_4$]$^{5+}$
0.66	*cis*-[(NH$_3$)$_4$Pt$_2$Ag(1-methyluracil)$_2$]$^{3+}$
0.50	*Trans*-[Cl$_2$Pt(*I*-Pr)$_2$SO]$_2$(9-methyladenine)

[a] The third nucleic acid base is stacked upon a metal-coordinated base. [b] The third nucleic acid base is H-bonded to a metal-coordinated nucleic acid base. [c] Binuclear complex.

the coordination complex, being the sum of the charges possessed by a metal cation and its ligands, depends on the mode of binding (e.g. with or without proton dissociation or substitution in a nucleotide ligand) and pH, because of the ability of coordinated ligands to undergo deprotonation. The known coordination complexes of transition metals with nucleic acid constituents far outnumber those of the A group metals such as Na^+, Mg^{2+}, or Ca^{2+}.

Metal binding to the nucleic acid bases may formally be considered in terms of number of bases N bound per metal M ($n = N/M$, e.g. $n = 4$, 3, 2, 1, or less for Pt^{2+}) (Table 4). While the maximum number of nucleic acid bases that can be bound by single bonds to the metal ion is given by its nominal coordination number (values 2, 4, and 6 are the most common), low n values in multinuclear complexes can result from the binding of more than one metal at separate donor atoms in a single nucleic acid base.

Despite the fact that metal cation binding to a neutral nucleic acid base usually reduces its overall basicity (proton affinity),[33] this effect is not sufficient to prevent attachment of more than one metal species per nucleic acid base in the presence of an excess of the metal species. An example is the diplatination of G (via atoms N-7 and N-1) (Table 4). The N-1 atom in purine nucleosides and nucleotides is frequently identified as a binding site in solution, in spite of the fact that it has been documented less frequently in X-ray structural studies.[29] In N-7-platinated guanosine, the acidity of the N-1 proton is increased from $\mathrm{p}K_\mathrm{a}$ 9.3 to $\mathrm{p}K_\mathrm{a}$ 7.8,[188] thus making the N-1 site more susceptible to additional metal binding at neutral pH. Pt^{2+} behaves similarly to many other transition metals in this respect.[34] It is also possible that a coordinated metal may increase the basicity of a nucleic acid base through charge back-donation from the metal into the heterocyclic ring.[33] For example, substitution of the protons at N-1 and N-7 of G as well as N-3 of U or T by Pt^{2+}, having a smaller polarizing effect relative to H^+, actually increases the basicity of atoms N-3 in diplatinated G and O^4 in monoplatinated U or T. As a consequence, an additional metal ion can be bound to these sites, leading to a large class of multinuclear complexes, for example, triplatinated G.[33] Formation of multinuclear complexes with the participation of exocyclic amino groups has been observed for complexes of 1-methylcytosine and H_3CHg^+ or $Pt^{2+/4+}$; the metal–N bonds are formed in a condensation reaction between a M–OH moiety and an amino proton. The increased metal affinity of singly metalated base anions was also found for some heteronuclear metal complexes, for example, for Pt^{2+} and Ag^+ bound to 1-methyluracil.[33]

The coordination number and geometry of complexes (Table 1) is thought to be dictated by the valency (i.e. oxidation state of the central metal ion – also see Section 4.5), the number of electrons possessed by the metal to be shared with ligands, the relative sizes of metal ions and ligands, as well as symmetry considerations.[120] Small metal ions and large ligands favor low-coordination numbers and vice versa.

Consistent with the assumption that ligands repel one another, they tend to separate from each other spatially in a fashion that minimizes ligand–ligand repulsion, while remaining bound to the central metal ion.[170] Accordingly, two unidentate (i.e. having one donor atom) ligands should give rise to a linear arrangement, four to a tetrahedral arrangement, and six to an octahedral arrangement. Most metal complexes conform to these geometries, but there are also many exceptions (Table 1), which are believed to result from interligand nonrepulsive interactions and chelation geometry. In particular, the metal ions of Groups 8–11 of the periodic table often form square planar, rather than tetrahedral, complexes (Table 1). Some four-coordinate Ni^{2+} and Cu^{2+} complexes are tetrahedral, others are planar. In six-coordinate Cu^{2+} complexes, four ligands are strongly bound in square-planar geometry, while two weakly coordinated ligands (with longer internuclear distances) occupy axial positions that result in overall pseudooctahedral geometry of such complexes.[170]

There are some correlations between coordination number of metal ions (as well as geometry of the derived complexes) and metal-binding site in nucleic acid bases. Unhindered donor atoms (e.g. N-7 of purines) can be involved in octahedral complexes, while atoms that are in sterically hindered environments (e.g. N-3 of C, which is adjacent to the bulky N^4H_2 and O^2 groups, or N-1 of A, which is influenced sterically by the adjacent N^6H_2 substituent) prefer to form complexes in which the metal ion has coordination numbers of four or two.[27]

Strong binding between metal ions and ligands precludes their exchange and permits the resolution of geometric isomers: *cis*, in which the relevant ligands are adjacent to each other, and *trans*, in which the ligands are opposed. The dependence of metal–nucleic acid reactions on the geometrical arrangement of ligands about the metal ion is important when the reaction results from substitution of labile ligands with retention of inert ones.[189] These requirements are met in the case of the reactions of the isomers of $[(NH_3)_2PtCl_2]$, in which only Cl^- ions are substituted, and the bond positions available for nucleic acid base binding are 90° apart in the *cis* isomer and 180° apart in the *trans* isomer (see Figure 9). Geometrical isomers would also be formed as a result of the interaction of $[PtCl_4]^{2-}$ (see Figure 9) with nucleic acid bases because the reactivity of a Pt–Cl bond is strongly dependent on the nature of the ligands in the *trans* position.[189]

4.5 Oxidation State of Metal Ions in Complexes with Nucleic Acids

A metal oxidation state of a metal ion usually does not change as a result of binding to nucleic acids; however, there are some exceptions for the metals in high oxidation state (see below). Some metal ions in nonstable oxidation states can be stabilized in complexes with nucleic acids; examples include $[Cr^{3+}-ATP]$,[190] $[Co^{3+}-tRNA]$,[191] and $[Cu^{+}-DNA]$.[192] Metal ions at higher oxidation states are usually stabilized by ‘hard’ ligands, those at lower oxidation states by ‘soft’ ligands (see above and ***Hard & Soft Acids and Bases***).[38] Following coordination to a nucleic acid, certain metal ions having more than one oxidation state could be oxidized (e.g. tRNA-bound Co^{2+} was oxidized to Co^{3+})[191] or reduced (e.g. DNA-bound Cu^{2+} was reduced to Cu^{+}, and bound Fe^{3+} was reduced to Fe^{2+})[192] under mild conditions without obvious alteration of the binding sites or integrity of the nucleic acid. However, the oxidation of $[(NH_3)_5Ru]^{2+}$ bound to DNA via N-7 of G[193] as well as of Cu^{2+} and Fe^{2+} bound to DNA or RNA resulted in site-specific modification and cleavage (also see Section 7) of the bound nucleic acids, presumably by generation of reactive oxygen species.[166,194–197]

The oxidation state of some metal ions can be reduced as a result of binding to nucleic acids. For example, certain complexes of Pt^{4+} species attached to purine residues of DNA underwent reduction to Pt^{2+} without direct damage to the platinated DNA.[43] However, complexes of Pt^{4+}, which are stable in high oxidation states, can act as alkylation agents. These complexes kinetically prefer binding at the N7 atom of guanine residues. A transfer of positive charge from the metal cation to the platinated guanine residue results in the formation of abasic sites that could be determined by the site-specific cleavage of DNA via a β-elimination reaction.[166,198] Interestingly, the guanine platination and formation of the abasic sites is highly specific for single-stranded DNA and does not occur in duplexes. In contrast, the complexes of Pt^{2+}, which have substantially less electron acceptor capacity than Pt^{4+}, cannot promote the oxidative removal of guanine residues.[199]

Amino complexes of Ru^{3+}/Ru^{4+} act similarly to their platinum relatives, Pt^{2+}/Pt^{4+} (*see* ***Ruthenium: Inorganic & Coordination Chemistry***). Although coordination of $[(NH_3)_5Ru]^{3+}$ to N7 of guanine residues in DNA does not promote efficient depurination, after disproportionation of Ru^{3+} the corresponding complex of Ru^{4+} is able to carry out this reaction.[200] Base-specific N7-guanine modification by tetramine-Ni^{2+} complexes in the presence of $KHSO_5$ also results in Ni^{3+}-mediated oxidative guanine alkylation and removal of the modified guanine residue.[196] A possible ‘template’ role for nickel ions is to bridge guanine and oxidant species. This reaction is also highly specific for single-stranded or mismatched regions in polynucleotides, and has been successfully used as a structural probe for both DNA and RNA molecules.[196]

Reaction between DNA/RNA and MnO_4^- or OsO_4^{2-}, where the formal metal oxidation states are Mn^{7+} and Os^{6+}, results in base-specific modification of thymidine/uridine residues. These anionic metal species can oxidize the pyrimidine C5-C6 double bond, which results in formation of *cis*-5,6-dihydroxy-5,6-dihydro-pyrimidine.[96] This reaction is followed by opening of the pyrimidine ring and its subsequent removal from the polynucleotide chain. Permanganate can also oxidize and remove guanine residues (but not adenine) while osmium tetroxide acts much more specifically on pyrimidine residues with the following kinetic preferences (relative rates shown in parenthesis): $T\ (45) \gg U(4.5) > dU(2.8) > C(1.8) > dC\ (1)$.[96] The relatively bulky permanganate and osmium tetroxide anions are very sensitive to secondary structure and react preferentially with pyrimidines in single-stranded regions, single-base mismatches, bulges, loops, unstacked nucleobases in four-way junctions, curved $(A\text{-}T)_n$ tracts, B–Z and Z–Z junctions, H-DNA, and premelting of AT-rich sequences in supercoiled DNA.[201,202] This feature makes them very useful probes for detection of local distortions in DNA molecules under different conditions and upon binding of other molecules including small drugs and proteins.

5 METAL-BINDING MODES AND STRUCTURE OF METAL–NUCLEIC ACID COMPLEXES

5.1 Problems in Relating Crystal Structures and Solution Composition

Most available (and most detailed) information on the mode of metal binding to nucleic acid molecules is provided by X-ray structural studies. Until recently, diffraction-quality crystals of nucleic acids with bound metal ions were generally obtained most readily for molecules of limited size (from nucleosides to oligonucleotides).[30,37,60,64,137,203] Interestingly, crystallization of metal complexes with nucleotides and oligonucleotides was generally found to be more facile relative to the nucleoside complexes, which may be attributed to several factors including (1) the lower stability generally observed for nucleoside complexes, (2) the presence of the phosphate group(s) in (oligo)nucleotides, which can compensate for the charge of the metal ion and thereby facilitate crystallization of the complexes as neutral species, and (3) the greater opportunity for hydrogen bonding between water molecules coordinated to metal ions and the phosphate oxygen anions, thereby supporting specific intra- and intermolecular contacts in the crystals.[30] Newly developed techniques can now provide crystallization of large RNA from ribozymes[55,204,205] to subunits of ribosomal RNA,[206] allowing the study of structures of biological metal binding inside these RNA structures.

X-ray crystallographic analyses usually provide structural information that correctly represents the actual structures of metal ion–nucleic acid complexes in the crystal; this usually represents an environment that is drastically different from normal solution conditions. Obviously, such analyses are limited to complexes that are both stable and amenable to crystallization.[37] In comparison, solution NMR spectroscopy data are much more generally applicable to the analysis of metal ion–nucleic acid structure,[53,84,148,207] but can be more easily misinterpreted owing to factors such as the distribution of metal ions among several binding sites and the intrinsically weaker nature of some of the interactions that are studied. Also, nucleic acid crystallization requires the formation of ordered and uniform intermolecular interactions between nucleic acids.[208,209] These intermolecular interactions may either compete or interfere with the formation of certain metal–nucleic complexes and promote the formation of unnatural metal binding centers.[210]

Often, more than one structure of a metal–nucleic acid complex of a given nucleic acid will exist in solution at the same time, and these complexes may well be in dynamic equilibrium.[36,37] When multiple complexes are present, crystals are less likely to form; there are, for example, a dearth of examples of crystalline ambidentate isomers that have been characterized structurally. In principle, some of these isomers could be isolated as discrete species and crystallized separately, but this is possible only for thermodynamically stable and kinetically inert complexes. Therefore, the definition of the mode of binding of metal species to nucleic acids is usually very difficult, since many complexes of (biological) interest lack sufficient stability to permit their study as single species. Conditions favorable to crystal growth include high concentrations of the species of interest and also of organic solvents (and, therefore, low hydration) that can facilitate crystallization. Because both the specific intermolecular contacts in the crystals and the special environment from which the crystals are produced do not ordinarily exist in solution, some atom–atom interactions determined by X-ray crystallography may not occur in dilute aqueous solution where binding to (or through) water molecules would predominate.[210] For example, in solid-state structures, the formation of polymeric species in which each metal ion is bound to two or more nucleotide ligands is a common phenomenon. The relevance of such structures to solution geometry is also unclear. Likewise, in the highly concentrated solutions needed for crystal formation the pH, which can dramatically affect the mode of metal-ion binding, is generally not well controlled and could also change as a result of metal ion–nucleic acid interactions. Also, the low water activity inside the crystals of nucleic acids may promote formation of unusual direct (inner-sphere) bonds between dehydrated metal ions and nucleic acids. For example, in crystals, even monovalent ions (such as Li^+, Na^+ and Tl^+) can exhibit direct coordination with nucleobases and ribose residues.[24,211] Such interactions do not normally occur in dilute solutions.[37,103,212]

Interestingly, specific M^{2+}–nucleic acid interactions determined in solution for the hairpin ribozyme by spectroscopic and chemical interference methods were not later found in their X-ray crystal structures.[127,213] Even more confusing were results of X-ray crystallography[214,215] and initial solution experiments,[216–218] which both determined up to two, presumably functionally important Mg^{2+} ions in the catalytic center of the hammerhead ribozyme. However, as demonstrated recently in biochemical experiments in solution, neither of these ribozymes require either inner- or outer-sphere interactions with particular metal ions for catalysis.[56,57,219,220]

All of these factors dictate that great care must be exercised in relating well-defined crystal structures to the predominant structures that exist in solution.[30] Moreover, it is important to remember that there is a wide range of microenvironments present *in vivo*, each of which would also be expected to affect the metal–nucleic acid interactions in a fashion (superficially) analogous to a specific solvent or the absorption of the metal ions to a particular surface.[221]

5.2 Suggested Classification of Metal–Nucleic Acid Binding

According to the number of labile ligands bound to a metal ion that can be substituted by donor atoms of the nucleic acid ligand, metal species (ions and compounds) may be classified as *mono-, bi-, tri-, or multifunctional* reagents, up to the maximum limited by the metal coordination number.[40] Monofunctional attachment of a metal reagent to a nucleic acid is often followed by multifunctional binding, *chelating,* or *cross-linking,* which may occur both *intramolecularly* and *intermolecularly*. Since, in the initial monofunctional adduct, the effective local concentrations of the resulting metal species and the next potential ligand(s) can be very high (up to a few moles per liter), the rate of subsequent reactions can be much higher than the initial reaction where an associative mechanism is involved. The acceleration does not occur if a dissociative mechanism of ligand substitution obtains or if potential donor atoms are either not sterically accessible or not situated favorably.

5.3 Metal Binding to Nucleic Acid Bases

5.3.1 *Monofunctional Binding*

Monofunctional metal–nucleobase bonds constitute the usual mode of metal binding to nucleotides and polynucleotides. Most known metal-binding modes involve derivatives of nucleic acid bases in which chemically unreactive groups are attached to pyrimidine N-1 and purine N-9 atoms to mimic the N-glycosyl bond. This results in nucleic acid base models that behave in a fashion reasonably similar to that of the actual naturally occurring nucleosides, at least at the level of metal coordination to the heterocyclic bases. In contrast, metal-ion binding to free nucleic acid bases often gives products that are more complex and may bear less relevance biochemically. Despite obvious limitations, work with nucleic acid base models is meaningful in that fundamental questions such as binding patterns and ligand rotation processes may be studied conveniently.**[25,42,48]**

'Pure' monofunctional, inner-sphere binding to metal species usually obtains only when some chemical or structural restriction applies. Binding of this type generally results from (1) the use of monofunctional metal reagents having only one labile ligand, for example, $[(dien)PtCl]^{2+}$, $[(NH_3)_5RuCl]^{2+}$, and H_3CHgOH;**[26]** (2) transformations carried out at low pH, where additional metal-binding sites are 'blocked' via protonation;**[32]** or (3) modification of highly reactive S atoms in thio-substituted nucleic acid bases, for example, 6-thio-G and 4-thio-U.**[79]**

The mercury complexes of neutral uracil and dihydrouracil, the latter being a minor base found in tRNAs, reveal an unusual mode of coordination, wherein Hg^{2+} is bound not to the endocyclic N-3, which is blocked by a proton, but rather to the exocyclic atom O^4, which is a stronger donor atom than O^2.**[222,223]** The 'usual' binding to N-3 of deprotonated U and T residues proceeds slowly in buffered solution at neutral or slightly alkaline pH with heavy metals (e.g. in reactions with H_3CHgOH, Hg^{2+}, or Pt^{2+} species).**[223]** Although both purine and pyrimidine bases can form coordination bonds with mercury ion, U and C alone can form covalent bonds between C-5 and Hg.**[172]**

The rare nucleic acid base tautomers, ordinarily present to the extent of ~0.01% relative to the preferred tautomers, can be stabilized by metals via coordination of lone-pair electrons. For example, the 4-imino-2-oxo tautomer of cytosine has Pt^{4+} bound to its N^4 group, while the 4-hydroxy-2-oxo tautomer of U and T bases is platinated at N-3.**[33]**

5.3.2 *Bifunctional Binding*

The study of intrabase chelation can be effected most readily using model compounds that lack additional binding sites. Such intrabase chelates are usually obscured by the formation of 'macrochelates' in nucleotides and polynucleotides involving phosphates or neighboring nucleic acid bases. Such intrabase chelates may, nonetheless, sometimes be of importance biochemically.

Direct (inner-sphere) chelates involving donor atoms of the nucleic acid base heterocycles have only been observed for complexes of $[bis(cyclopentadienyl)Ti^{3+}]$ with derivatives of guanine (involving atoms N-7 and O^6), xanthine (N-1, O^2), and theophylline (N-7 and O^6), as well as for a complex of Pt^{4+} and 1-methylcytosine (N-3 and N^4).**[33]** In these chelates the angles about the metals can deviate strongly from the normal 90°, which implies considerable variation of the geometry of metal-centered chelate rings. For both Cu^{2+} and Hg^{2+} there is also evidence of binding to cytosine via a strong bond to N-3 and a weaker one to the O^2 carbonyl oxygen.**[25]**

As demonstrated for the 1-methylcytosine chelate, nucleic acid base deprotonation can be achieved intramolecularly under mild conditions by a Pt–OH group already coordinated via N-3. Similar reactions might be anticipated for a large series of metal–nucleic acid base complexes, including chelates of adenine (N-1 and N^6) and guanine (N-1 and N^2 or N-1 and O^6).**[33]** However, the existence of a (N-7 and O^6) chelate of guanine and *cis*-$[(NH_3)_2Pt]^{2+}$, whose possible role as a key DNA adduct in the mechanism of antitumor action of *cis*-diclorodiammineplatinum has been controversial for some time and has not yet been proven unequivocally (*see* ***Platinum-based Anticancer Drugs***).**[33,47]** In contrast, there are reliable data that 6-mercaptopurines bind soft metal ions such as Pd^{2+} and Cu^{2+} via both N-7 and S^6 atoms.**[25]**

5.4 Metal Binding to Nucleosides, Nucleotides, and Polynucleotides

5.4.1 *Metal–Ribose Binding*

There are only a few complexes known in which the ribose hydroxyl groups are involved in coordination to metal ions.**[27,42]** One of these is the bis(pyridine)osmate ester of adenosine, in which Os^{6+} chelates adenosine through deprotonated 2′- and 3′-OH groups; another is polymeric $[Cd_2(5'\text{-IMP})_3(H_2O)]_n$, in which one Cd^{2+} ion binds simultaneously to N-7 of one IMP molecule and to the protonated 2′- and 3′-OH groups of another IMP. These compounds may be considered somewhat atypical since they are prepared using extreme conditions. However, the complexes of VO_2^{2+} and 5′-ATP, the solution structure of which is pH dependent (Figure 10), includes bonds to the protonated 3′-OH group (at pH 3) or to the deprotonated 2′- and 3′-hydroxyl groups (at pH 7–12).**[224]** For Cu^{2+} the chelation of ribose *cis* hydroxyl groups in nucleosides has been detected only in solution owing to difficulties encountered in crystallization of the complexes.**[29]** One can speculate that RNA tertiary structure could favor inner-sphere coordination of a metal ion to the 2′-OH group, in spite of its intrinsically low affinity for metal ions, by the appropriate arrangement of potential ligands in specific metal-binding pockets.**[218]**

5.4.2 *Intranucleotide Chelation*

In reflection of the fact that the purine N-7 is the most favorable metal-binding site in nucleic acids, a number of different metal chelate structures involving this atom can be formed with purine nucleoside 5′-phosphates.**[34,42]** This

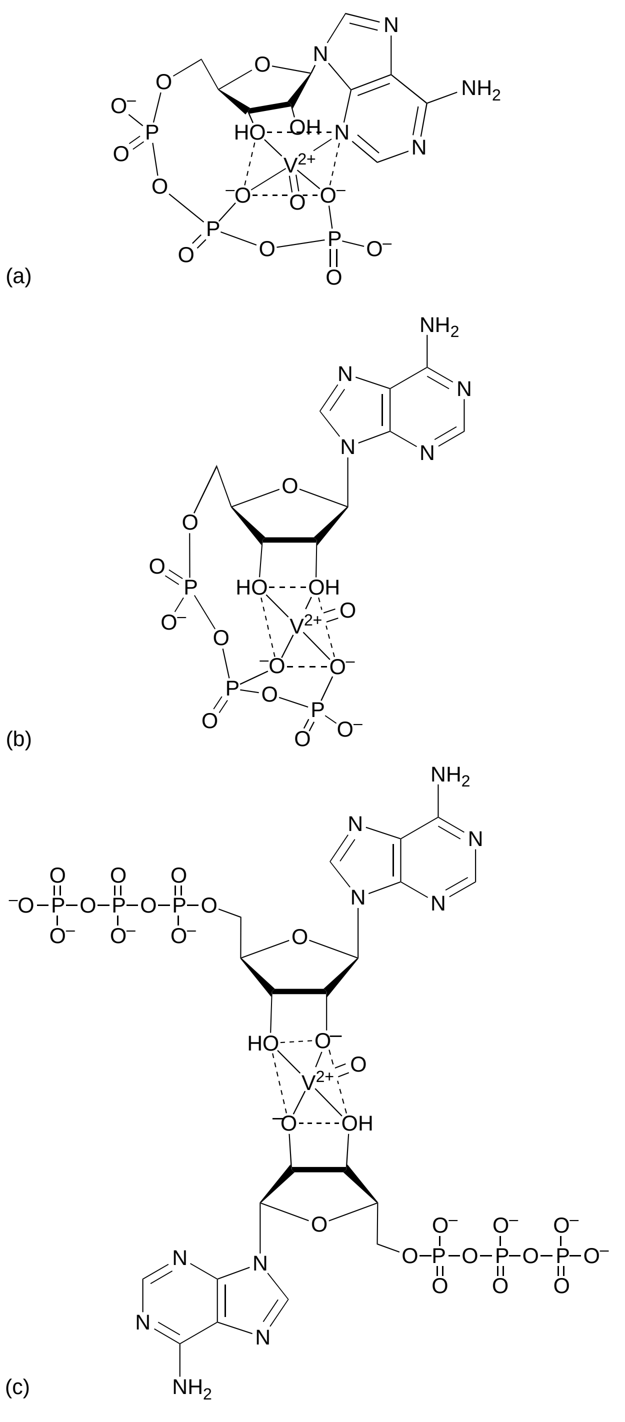

Figure 10 Possible structures of three types of ATP–vanadyl complex: (a) 1:1 complex at low pH, (b) 1:1 complex at neutral pH, (c) 2:1 complex at high pH[224]

includes chelates in which the metal ion participates in (1) inner-sphere binding to both the N-7 atom and phosphate group (Figure 11a); (2) inner-sphere binding to the N-7 atom and outer-sphere binding, that is, via water, to the phosphate group (Figure 11b); (3) outer-sphere binding to the N-7 group, but inner-sphere binding to the phosphate group (Figure 11c); and (4) outer-sphere binding to both sites (Figure 11d). The proportion of complexes having these structures will differ for individual purine residues and metal ions. For example, inner-sphere binding has been confirmed for [*cis*-$(NH_3)_2Pt(GMP)$] and [$(\eta^5$-$C_5H_5)_2Mo(dAMP)$] and predominates for [$Cu(GMP)(H_2O)_4$] and [$Ni(AMP)(H_2O)_4$], where molybdenum is tetravalent and the other metal ions are divalent.[34,35] [$Ni(IMP)(H_2O)_5$] is representative of the largest class of structures that bind to N-7 via an inner-sphere mechanism and to the phosphate group via an outer-sphere mechanism.[34,35] For complexes of GMP and Mg^{2+}, Ca^{2+}, Sr^{2+}, or Ba^{2+}, the most probable structures involve inner-sphere binding to the phosphate group and outer-sphere binding to N-7.[34,35] Chelates involving outer-sphere binding to the N-7 and phosphate groups are probably best exemplified for the alkaline earth elements.[34,35,103]

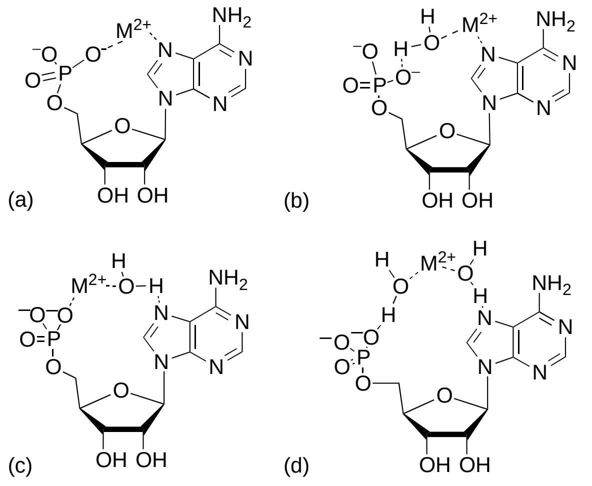

Figure 11 Four types of metal complexes involving N-7 of purine nucleosides[34]

In contrast to the relatively simple structures incorporating one of the first three binding motifs, the polymeric complex [$Cu_3(5'$-$GMP)_3(H_2O)_8]_n$ has three distinct coordination environments about different Cu^{2+} ions.[225] While this complex is unusually sophisticated, the polymeric nature of the material is common for many metal complexes with GMP or IMP, in which inner-sphere binding occurs to both the N-7 atom and phosphate oxygens of a single nucleotide residue, but does not involve the same metal ion.[29] As described in Section 5.5, there are also unusual structures ('open complexes') of Cu^{2+} species and GMP, which involve only inner-sphere metal binding to the phosphate group.

The anti conformation preferred by the adenine residue in 5′-AMP (Figure 1b) disposes this nucleotide to simultaneous inner-sphere binding of metal ions both to the phosphate oxygen and N-7 atoms. As would be expected, neither 2′- nor 3′-AMP (Figure 1c) is able to participate in forming the same type of complex for steric reasons. As was shown in experiments involving Mg^{2+}, Mn^{2+}, Cd^{2+}, Co^{2+}, and Cu^{2+}, intramolecular interactions of a phosphate-coordinated metal ions are possible for all three positional isomers of AMP, but the stability of these bonds decreases in the order 5′-AMP > 2′-AMP ≫ 3′-AMP (see Table 3).[34,35] Perusal of the structures shown in Figure 1 illustrates the fact that the most likely candidate for an additional binding site is the N-3 atom in both the anti conformational isomer of 2′-AMP and the *syn* isomer of 3′-AMP, although chelates involving the adjacent 3′-OH (or 2′-OH) groups might also exist.[34,35]

The results of model building suggest the probable formation of different chelates for purine nucleoside 5′-di- and triphosphates (Figure 1c). Inner-sphere coordination of the N-7 nitrogen and both the β- and γ-phosphate oxygens makes direct coordination of the α-phosphate oxygen improbable, but this group is coordinated via outer-sphere binding.[34,35] Potentially, there are many different combinations of inner- and outer-sphere bonds that are possible for metal–NTP complexes, involving both participation of heterocyclic donor atoms and for phosphate groups alone.[19,34,35,226] Metal binding to the α- and β-phosphate oxygens also creates new chiral centers and can lead to the formation of diastereomeric complexes.[227] One particularly interesting complex, derived from VO^{2+} and ATP, contains inner-sphere bonds to the metal ion V^{4+} and also involves all three structural components of the nucleotide, that is, the N-3 atom of the nucleic acid base, the β- and γ-phosphate oxygens, and the 3′-OH group of ribose (Figure 10a).[224]

Metal complexes of pyrimidine nucleotides have been studied much less intensively than those involving purines, undoubtedly reflecting the weaker coordination ability of the pyrimidine N-3 atom, relative to atoms N-7 and N-1 of purines. Nonetheless, the principal structures of such complexes have been determined.[27,29,42,50] Some of these are described below.

Although inner-sphere coordination of both N-3 and phosphate has been documented for at least four metal–5′-CMP complexes (involving Pt^{2+}, Co^{2+}, Zn^{2+}, and Cd^{2+}), dimeric $[(en)Pt(5'\text{-CMP})]_2\cdot 2H_2O$ is the only example of a nonpolymeric complex in which the metal ion (Pt^{2+}) is bonded to N-3 of one CMP and to the phosphate oxygen of another.[27]

In the structure of the polymeric complex of Mn^{2+} and 5′-CMP, an unusual cytosine inner-sphere coordination complex has been demonstrated involving O^2, rather than N-3, as well as four phosphate oxygen atoms of three different nucleotides and one water oxygen atom.[50] Thus, in the case of CMP binding, it seems clear that O^2 can act as a significant metal-binding site alone, or together with N-3 in chelate structures.

Exclusive binding via phosphate oxygens at neutral pH, including both inner- and outer-sphere modes, has been documented for dimeric complexes of Cu^{2+}, as well as polymeric complexes involving Co^{2+} and 5′-UMP.[27]

Many enzymes use [Mg–NTP] complexes as substrates and effectors, where the Mg^{2+} is coordinated exclusively to the oxygens of the triphosphate group forming mono-, bi-, and tridentate complexes.[114] In solution, Mg^{2+} can be replaced by several other metal ions in these complexes with NTPs and their thiophosphate analogs. The alternatives include both soft (e.g. Cd^{2+}) and intermediate (e.g. Mn^{2+}, Co^{2+} and Zn^{2+}) metal ions that, in contrast to the hard Mg^{2+} ion, can chelate both through O and S atoms.[227] The preference for O relative to S coordination in the complexes is estimated to be about 3×10^4 for Mg^{2+}, 3×10^3 for Ca^{2+}, and 2×10^2 for Mn^{2+}. In a similar complex, Cd^{2+} is bound to S atom 60-times more strongly than to O atom.[228] These differences are reflected in the structural nature of the metal-ion complexes formed with ligands such as ATPβS (Figure 12a).

The S_p and R_p stereoisomers of the nonbridging phosphorothioate group also provide the wherewithal for different modes of metal binding (Figure 12a,b). The positions of the phosphorothioate groups (α, β, or γ) (Figure 12c) affect both the stability of the formed M–S bonds (e.g. there is a

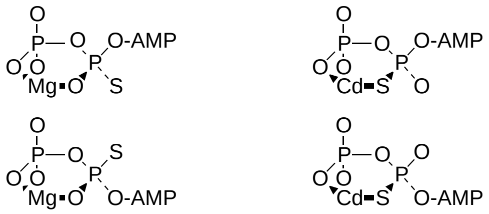

(a) Metal ion–ATPβS complexes

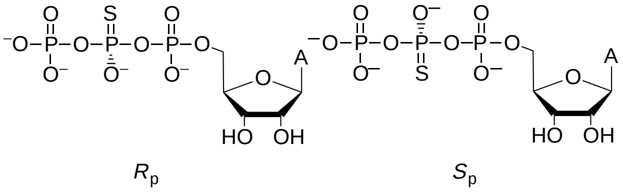

(b) Diastereomers of ATPβS

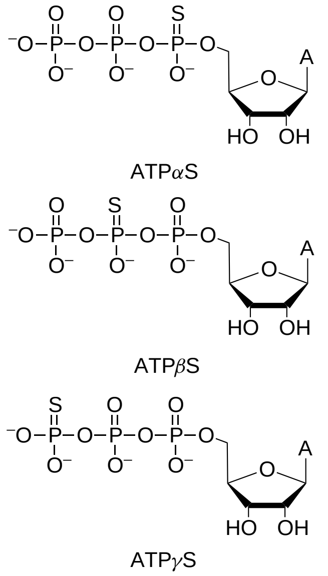

(c) Positional isomers of ATPS

Figure 12 Structures of S analogs of ATP and representative metal complexes[227]

10-fold lower preference for Cd–S interaction in ATPαS as compared to ATPβS[227]) and the type of coordination. Thus complexes of Cd^{2+} with ATPαS, in contrast to those with ATPβS, do not include inner-sphere coordination of atom N-7, because of favorable α, β, γ-phosphate tridentate chelation.[228] In fact, the release of inner-sphere N-7 in complexes involving Zn^{2+} or Cd^{2+} and ATP upon addition of a second ligand, L (e.g. imidazole, NH_3, or OH^-), to form $[M(ATP)(L)]^{2-}$, suggests that N-7 coordination is the 'weak' point in such macrochelates.[34,35]

In contrast to phosphate oxygen atoms, the negative charge in the phosphorothioate is largely localized on the more polarizable sulfur.[229] Hard divalent metal ions (e.g. Mg^{2+}) prefer to bind only the phosphorothioate oxygen, whereas softer metal ions, for example, Co^{2+}, Mn^{2+}, and Zn^{2+}, can bind (chelate) both oxygen and sulfur, while Cd^{2+} ions have stronger affinity toward sulfur (*see* ***Hard & Soft Acids and Bases***).[228,230] The difference in affinity of these metal ions toward phosphorothioate O and S atoms (both bridging and nonbridging S_p or R_p stereoisomers) have been used in 'rescue' experiments to determine whether direct interaction of a particular phosphate oxygen(s) with the metal ion(s) is essential for promotion of the specific RNA cleavage, and the stereochemical course of the cleavage reaction.[231–236]

5.4.3 Internucleotide Binding: Intra- and Interstrand Cross-linking

Different types of bifunctional binding of metal species that form bridges between two base residues in single- and double-stranded nucleic acids have been identified. There are two main types of interbase binding. In the first, the metal ion is bridging two bases in the same (intrastrand cross-linking) in ether single- or double-stranded polynucleotides. In other words, the metal ion is bound bi-functionally to nucleic acid bases, which are not in the same plane as the metal ion. The *cis* orientation of labile ligands in the coordination sphere of a bifunctional metal reagent is more favorable to intrastrand cross-linking of DNA than the corresponding *trans* isomer.

It has been suggested that Cu^{2+}, bound to duplex DNA in a nondenaturing fashion, may afford a charge-transfer, π-complex between adjacent purines on the same strand, with the purine aromatic ring playing the role of donor and the metal ion acting as the acceptor.[22] A recent model of interstrand binding of one Cu^{2+} ion between adjacent GC pairs has also been described.[237] This type of binding between metal ions and nucleic acid bases has also been proposed for Ag^+ and Fe^{2+}.[125]

In the second type of internucleotide binding, the metal ion acts as a bridge between two bases that belong to opposite strands paired in a double helix. The 'bridging' process is favorable for ions able to form stable, linear chelates (e.g. Ag^+, Cu^+, Hg^{2+}, and Au^{3+}).[238,239]

To form interstrand or intrastrand bonds in a duplex, a mononuclear metal species has to open (form internal loop) or bend the duplex structure. In contrast, dinuclear metal reagents with sufficiently long bridging groups connecting the reactive metal centers may be able to cross-link complementary polynucleotide strands without denaturation.[240–243] Owing to the presumed biochemical significance of metal-mediated cross-links in nucleic acids, numerous model complexes with nucleic acid bases,[25,48] synthetic oligonucleotides, and polynucleotides[43,238,239,244] have been characterized in detail.

Most of the data concerning bifunctional binding to nucleic acids involve platinum reagents, because of its possible relationship to the molecular mechanism of their anticancer activity. The major DNA products formed by *cis*-$[(NH_3)_2PtCl_2]$ (see Figure 9) *in vitro* are 1,2-intrastrand cross-links between the N-7 atoms in GG (about 70% of the total products) and AG (about 25%) sequences.[43,47,245] The ability of the *cis* isomer to chelate AG but not GA sequences in DNA is a result of different distances between the platinum and purine N-7 atoms in the two isomers.[43,246] Most intrastrand cross-links formed in linear duplex DNA by *cis*-$[(NH_3)_2PtCl_2]$ occur at G·C sites.[43,47,247] Intrastrand cross-links are generally more abundant than interstrand ones. The formation of the Pt-mediated interstrand cross-links requires partial disruption of the Watson–Crick base pairing,[43,248] and one could, therefore, expect such cross-linking to be rather slow. Surprisingly, kinetic measurements indicate that interstrand cross-linking is as fast as intrastrand cross-linking, or even faster.[249] These results suggest that the low occurrence of interstrand cross-links in *cis*-platinated DNA is due to slow initial platination of guanines involved in d(GCGC) sequences.[249]

Trans-$[(NH_3)_2PtCl_2]$ (see Figure 9) forms predominantly interstrand cross-links that are 1,3- and, to a lesser extent, 1,4-adducts. Adducts form at XNG and XNNG sequences (where $X = $ A or C and N is any intervening nucleotide) via purine N-7 and cytosine N-3 atoms.[43] DNA interstrand cross-linking by the platinum reagents occurs predominantly between two N-7 atoms of G residues on opposite strands. The 5′GC3′ sequence within a miniduplex is better able than the 5′GC3′ sequence to form a bridge with *cis*-$[(NH_3)_2Pt^{2+}]$, because the former has the more appropriate spatial orientation of donor atoms.[43]

T–Hg^{2+}–T interstrand cross-linking can occur in the alternating copolymer poly(dA-T)·poly(dA-T), but not within or between homopolymeric strands in poly(dA)·poly(T).[250] The related complex $[Hg(1\text{-methyl-}T)_2]$ in which Hg^{2+} ion coordinates the deprotonated N-3 atoms of two pyrimidine residues, has been described as well.[251]

Metal ion-binding modes, that compete with H-bonds for the donor and acceptor atoms of nucleic acids, normally destabilize the base pairs or prevent their formation, and thus promote melting (dissociation) of DNA at elevated temperatures.[125,252,253] However, some of these metal ions, for example, Cu^{2+}, Mn^{2+} and Al^{3+}, can also promote renaturation of the dissociated DNA strands upon cooling presumably via cross-linking between complementary polynucleotide strands.[239,252,254]

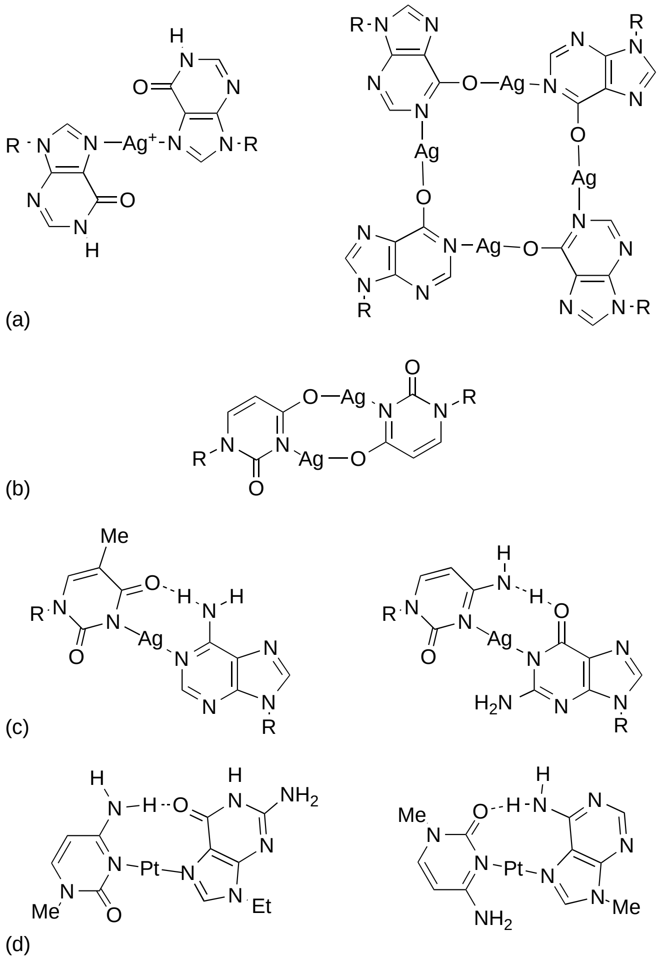

Figure 13 Examples of interstrand metal ion cross-links in polynucleotides[238,257,258]

A few helical polynucleotide structures containing interstrand metal cross-links in place of hydrogen bonds between natural bases have been described.[255,256] The structures of the complexes depends both on the nature of the cross-linked nucleic acid base and pH. Thus Ag^+ ions form a linear (N-7)–Ag–(N-7) 'bridge' between two poly(I) strands at low pH without base deprotonation, while at high pH a 'square' complex forms via (N-1)–Ag–(O^6) coordination that involves four Ag^+ ions and four polynucleotide strands and requires deprotonation of the N-1 proton on each strand (Figure 13a).[238] With poly(U) at high pH, a (N-3)–Ag–(N-3) complex forms with loss of the N-3 protons, but at neutral or low pH, two silver ions produce a centro-symmetric dimer via (N-3)–Ag–(O^4) coordination (Figure 13b).[238] A similar structure, wherein two 1-methylcytosines are bound by two (N-3)–Ag–(O^2) 'bridges', has been described.[257] The structures of related complexes in DNA, which involve one silver ion per A·T or G·C base pair and replacement of one proton by Ag^+, have been proposed (Figure 13c).[258]

It has been demonstrated that the *trans*-$[(NH_3)_2PtCl]^+$ adduct of 1-methylcytosine, bound via N-3, can form cross-links with either 9-ethylguanine or 9-methyladenine as a result of Cl^- substitution by purine N-7 atoms.[33] Additional H-bonds between exocyclic groups of cross-linked nucleic acid bases provide additional stabilization of the individual complexes (Figure 13d). Binding of the related complex $[(NH_3)_2Pt(N\text{-}3\text{-}cytosine)Cl]^+$ with d(GG) leads to the formation of a major product in which the platinum is bound only to N-7 of the 5′-nucleotide.[44]

Recent reports indicate that divalent transition metal ions, such as Cu^{2+}, forming links between two artificial hydroxypyridone nucleobases can efficiently replace the hydrogen bonding between natural nucleobases, A-T and G-C, in oligonucleotides.[259–262] Such artificial metal-mediated base pairs results in a moderate increase in the thermal stability of the duplex. They could lead to nucleic acid materials with novel chemical and physical properties. Such oligonucleotide derivatives are of interest for the design of biosensors, nanomolecular wires, and switches.

Despite the fact that complexes containing more than two (e.g. 3–6) coordinated nucleic acid bases have been synthesized,[33,263] as yet no examples of this type of binding have been found in natural polynucleotides, presumably due to structural constraints.

5.5 Outer-sphere Complexes and Ligand–Ligand Interactions

Some ligands (X and Y) in ternary inner-sphere ([X–M–Y]) and outer-sphere ([M – W···Y]) or ([M – X···Y]) complexes, where M is the metal ion and W is a water molecule, may interact directly with each other, forming noncovalent bonds (e.g. H-bonds and ion pairs) or undergo steric or electrostatic repulsion, depending on the ligands and the geometry of the complex.

Outer-sphere complexes at the nucleoside and nucleotide[50,103,264] are more favorable than intermolecular chelating because the indirect binding ligands to metal ion provide fewer geometrical and steric constraints for a larger number of ligands.

Typical examples of the mixed outer-sphere interactions are present in the crystal structure of yeast $tRNA^{Phe}$.[51,52,54] In contrast to a number of outer-sphere H-bonds between the metal-coordinated ligands and tRNA residues, these site-specific complexes contain only a few direct, inner-sphere bonds either to phosphate alone (Mg^{2+}),[52,54,57] to phosphate and bases (Mn^{2+}),[51] or to guanine alone (Pt^{2+})[51] (Figure 14).

Recently, high-resolution crystal structure of many RNAs other than tRNAs have been published, providing detailed information about different binding modes of the hydrated metal ions.[53,57,103,205] Strikingly, for each divalent metal ion, different binding patterns within the same RNAs have been found. Moreover, even if two similar (e.g. Mg^{2+} and Mn^{2+})

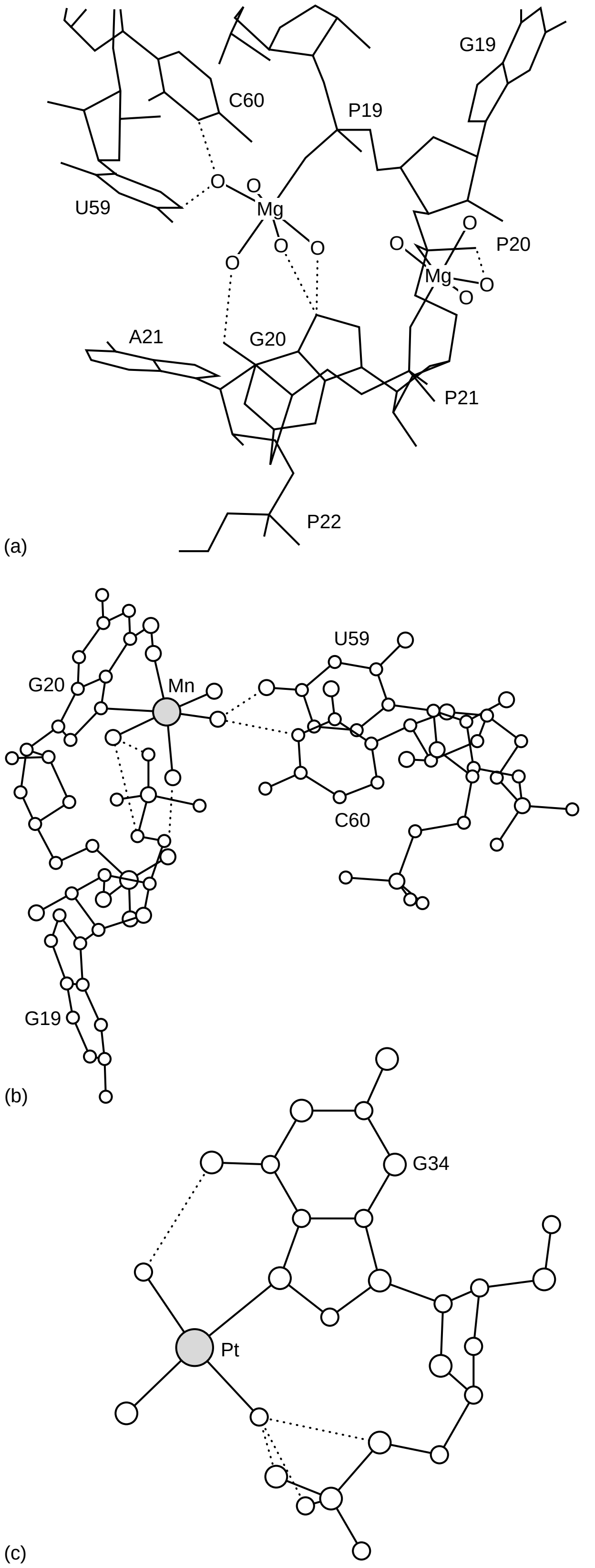

Figure 14 Binding of (a) Mg^{2+}, (b) Mn^{2+}, and (c) *trans*-$[(NH_3)_2PtCl_2]$ to $tRNA^{Phe}$[51,52]

metals both occupied the same 'binding pocket', their RNA coordination partners were different. For example, although Mn^{2+} has been thought to mimic Mg^{2+} in biochemical experiments,[265] in $tRNA^{Phe}$ crystals only one of three strongly bound Mg^{2+} ions could be substituted by Mn^{2+}.[51,52,54] Structural elements providing a wide diversity of potential ligands, such as bulges, loops, and pockets in tertiary structures of RNA molecules (Figures 4a and 6a), have been found as primary centers for specific and strong binding of metal ions.[53,57,62] Surprisingly, specific metal-binding sites have been also identified in RNA and DNA duplexes.[60,174,175,197,266–269]

In contrast to *cis*-$[(NH_3)_2PtCl_2]$, *trans*-$[(NH_3)_2PtCl_2]$ (see Figure 9) binds very strongly and specifically to a single site in $tRNA^{Phe}$. The reason for this difference is presumably that only the *trans* isomer allows the formation of hydrogen bonds between one NH_3 ligand and atom O^6 of G-34, and between another NH_3 and the 5′-phosphate group of the same nucleotide residue (Figure 14c).[51]

Interaction of *cis*-$[(NH_3)_2PtCl_2]$ or $[(en)PtCl_2]$ with DNA gives intrastrand cross-linking via atoms N-7 of adjacent guanine residues in about 65% yield.[270] The high percentage of intrastrand GG cross-links cannot be explained by an initial random, monofunctional reaction of these platinum reagents with any G in DNA, followed by a bifunctional reaction with a second G adjacent to the first one. One hypothesis, which posits the recognition of the GG sequence by Pt prior to covalent binding via specific interligand interactions between *cis* coordinated amino ligands and H-acceptor atoms of G (N-7 and O^6) and phosphate O, has been proposed to explain this observed phenomenon.[33]

Ligand–ligand H-bond interactions can be employed to design base-specific metal reagents.[271] The chelating ligands in metal reagents, which play a key role in the specificity of interaction with nucleic acids, can be divided into three major categories: (1) ligands having only H-bond donor sites, such as en and trien; (2) ligands having only H-bond acceptor sites, such as acac; and (3) ligands having both types of sites, such as glycylglycinate. In model reactions of Co^{3+} complexes of *cis*-β-$[Co(trien)Cl_2]^+$ and $[Co(acac)_2(NO_2)_2]^-$ with nucleosides,[271] the relative affinities for these metal reagents was dT > dG > dC, and A ≫ C, respectively. No binding was observed to the remaining nucleosides. Representations of the possible interactions between coordinated trien and the bases are shown in Figure 15. The interligand interactions between the bases and coordinated acac oxygens, which are substantially different from those in the trien system, result in the reverse order of reactivity.

There are also a few examples of interligand stacking interactions to give complexes of the form [M(L)(nucleotide)], where L is a π-aromatic base such as bipy, phen, or tryptophanate (Trp^-) (Figure 16).[34,35,272] Metal–phosphate bonding, rather than bonding direct to the heterocyclic bases, becomes the dominant interaction in these complexes.

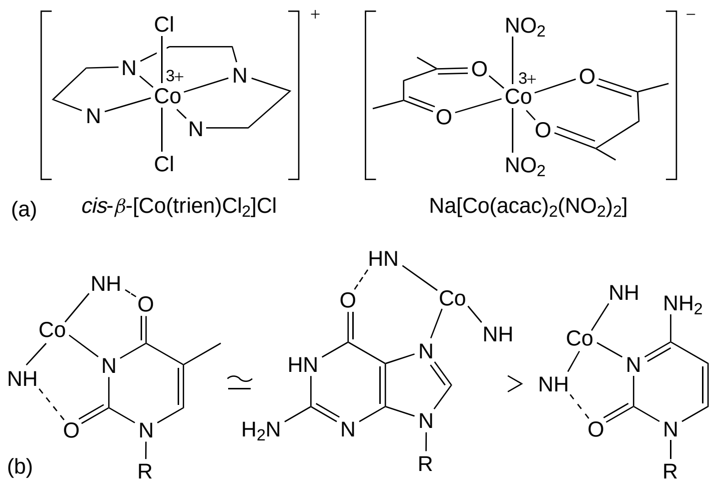

Figure 15 Structure of (a) *cis*-*β*-$[Co(trien)Cl_2]Cl$ and $Na[Co(acac)_2(NO_2)_2]$, and (b) putative complexes between *cis*-*β*-$[Co(trien)Cl_2]Cl$ and nucleosides[271]

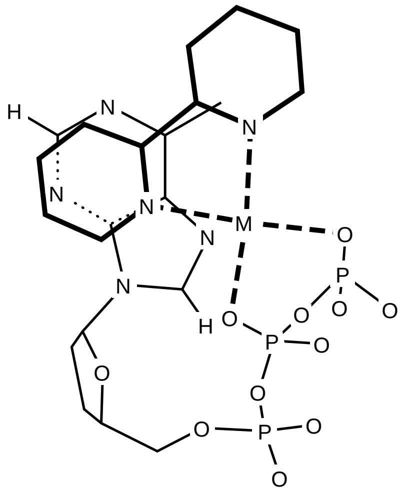

Figure 16 Simplified structural representation of the ternary complex formed between $Cu(2,2'\text{-bipyridyl})^{2+}$ and ATP^{4-} or ITP^{4-}[273]

The extent of intramolecular stacking interactions depends strongly on both the nature of the bases involved (i.e. purines stack better than pyrimidines) and the steric features of the nucleotides. For example, the stability of Cu^{2+} complexes of the type [Cu(phen)(AMP)] decreases in the order 2′-AMP > 5′-AMP > 3′-AMP. $[Cu(5'\text{-AMPH})(bipy)(H_2O)]_2{}^{2+}$ and $[Cu(3'\text{-GMP})(phen)(H_2O)]_2$ are the only known Cu–purine complexes in which N-7 is not involved in coordination to Cu^{2+}.[27]

There is evidence for interligand interactions, without inner-sphere metal–nucleic acid binding, in three different types of complexes. In the first, the potential metal-binding sites are blocked by a proton, for example, in ‘saltlike’ structures of the complexes of protonated bases 9-ethylguanine, hypoxanthine, and cytosine with $[PtCl_4]^{2-}$, $[AuCl_4]^{-}$, and $[PdCl_4]^{2-}$, respectively.[25] In the second type of complex, metal ions occur as constituents of inert complexes in which the small ligands cannot participate in exchange reactions. For example, in $[(NH_3)_6Co]^{3+}$ the ability of the amino groups to freely rotate, and thereby easily accommodate to the unique arrangement(s) of phosphates in structured polynucleotides, makes it useful as a probe for metal-binding sites in RNA molecules and mechanisms of RNA catalysis.[148,274] In the third type of the inert complexes, such as $[Cu(phen)_2]^{2+}$,[275–278] $[Pt(terpyridine)(SCH_2CH_2OH)]^{+}$,[77,279,280] metalloporphyrins[82,281–283] and metal complexes with different class of macrocyclic ligands[284] have been shown to bind primarily via stacking of the aromatic ligand with nucleic acid bases. Steric nonbinding restrictions in addition to wide types of engineered interligand interactions[285] make the latter complexes powerful probes for structural and physical properties of RNA and DNA molecules.

6 METAL BINDING CAN INDUCE CONFORMATIONAL CHANGES OF POLYNUCLEOTIDE STRUCTURES

An interaction of metal ions with phosphates usually leads to stabilization of polynucleotide secondary and tertiary structures, depending on the metal ions and their concentrations, whereas base binding or chelating base and phosphate by the same metal ion may result in destabilization, conformational change, or denaturation of the polynucleotide structures[238,286] (see also Sections 3.3.1 and 3.3.2). However, phosphate–specific binding can also induce significant conformational changes in DNA structure. The mechanisms of the latter structural interconversions are presumably based on the stabilization (by metal ions) of DNA conformations in which the phosphate groups can come closer together than in usual B-form of DNA duplex.[37,287]

For example, the interaction of some divalent (e.g. Zn^{2+} and Ni^{2+}) and trivalent (e.g. Cr^{3+} and Tb^{3+}) metal ions as well as polycationic inert metal species (e.g. $[Co(NH_3)_6]^{3+}$ and $[Ru(NH_3)_6]^{3+}$) could lead to dramatic changes in conformation of the double helical structure, namely transition from the right-handed B- to A- or C-forms and even to the left-handed Z-form.[140,141,286–297]

Metal ions are also known to play important roles in the formation of unusual DNA structures, the exact configuration of which is sometime difficult to elucidate. Such a delicate structural change of DNA, for example, that adopted by a single 5′-AGC-3′/5′-GCT 3′ trinucleotide under physiological conditions in the presence Zn^{2+} or Co^{2+} ions, may contribute to some genetic diseases[298] (*see* ***Metal-related Diseases of Genetic Origin***).

Certain divalent metal ions, such as Zn^{2+}, Co^{2+}, Ba^{2+}, and Mn^{2+}[299,300] as well as *cis*-$[(NH_3)_2PtCl_2]$[43] can promote sequence-directed bending of normally straight DNA duplexes. The efficacy of divalent metal ions required for the correct folding of four-way DNA cruciform junctions (yet another form of conformational polymorphism in DNA duplex) could be placed in the order as follows: $Mg^{2+} > Mn^{2+} > Co^{2+} > Ni^{2+} \sim Cu^{2+}$.[152]

Most trivalent metal cations would be anticipated to cause DNA collapse (aggregation) into condensed toroidal structures that are considered to be a model for DNA packaging in viruses and chromosomes.[238,301] $[Co(NH_3)_6]^{3+}$ induces this effect at five times lower concentration than spermidine, $[^+H_3N\text{-}(CH_2)_4\text{-}NH_3{}^+\text{-}(CH_2)_3\text{-}NH_3{}^+]$, whereas divalent metal ions and putrescine, $[^+H_3N\text{-}(CH_2)_4\text{-}NH_3{}^+]$, are incapable of causing DNA condensation in aqueous solution.[301,302] Some polyvalent metal compounds, including Al^{3+} ions,[303] also can relax supercoiled DNA, probably through single-strand DNA cleavage (see Section 7).

Triplexes are usually less stable than related double-strand structures because of the stronger electrostatic repulsion of the third chain. However, certain metal cations at appropriate concentrations can favor the formation of such structures by neutralization of the repulsive phosphate negative charges by the metal cations.[304] For example, at Na^+ concentrations about or less than 0.2 M, duplex poly(A)·poly(U) is predominant, but at higher concentrations of monovalent cations or in the presence of certain divalent metal cations (e.g. Mg^{2+} and Mn^{2+} at concentrations ≥ 10 mM), the duplex disproportionates to form poly(A)·2poly(U) triplex and a free poly(A) strand.[21,154]

Similar intramolecular processes are known for homopurine–homopyrimidine tracts in circular covalently closed DNA. Under the superhelical stress in such circular DNA, half the pyrimidine strand is unpaired and forms Hoogsteen base pairs with the remaining polypurine-polypyrimidine duplex, whereas the other half of the purine strand is left single-stranded (H-DNA) or vice versa toward purine and pyrimidine strands (*H-DNA). Such unusual structural transitions depend on the level of supercoiling, pH, and the presence of divalent metal ions. For example, Mg^{2+} is strictly required at neutral pH to support the H-type, $(dA)_n\cdot 2(dT)_n$, structure in plasmid DNA.[305] In supercoiled DNA, $(dG)_n\cdot(dC)_n$ sequences fold into halves from the center of this tract forming *H-type, (dG)·(dG)·(dC) triplex in the presence of Mg^{2+}, Ca^{2+}, or Mn^{2+}, whereas Zn^{2+} ions cannot support this particular triplex structure.[304,306] Moreover, Zn^{2+} can inhibit this structural conversion, if Zn^{2+} and Mg^{2+} are both present, via interfering with the magnesium binding to the $(dG)_n\cdot(dC)_n$ tract.

For heterogeneous polypurine–polypyrimidine tracts, the effect of various divalent metal ions on the transition to and stability of the *H-DNA triplexes can be very different depending on the sequence of such tracts.[142,143,175,307–309] For example, Cd^{2+}, Co^{2+}, Mn^{2+}, Ca^{2+}, and Zn^{2+} ions can stabilize the intramolecular triplex $(dTC)_n\cdot(dGA)_n\cdot(dAG)_n$, whereas Mg^{2+}, Ca^{2+}, Ba^{2+}, and Hg^{2+} cause destabilization.[309] For the sequence $(dCT)_{22}\cdot(dAG)_{22}$, the efficiency of promoting the corresponding duplex-triplex transition was found to be: $Zn^{2+} > Cd^{2+} \gg Mn^{2+}$, whereas Mg^{2+} was without effect in this system.[142] In another set of experiments, the formation of intermolecular Pu-Pu-Py triplex between a synthetic oligonucleotide and a fragment of the human papilloma virus DNA, occurred in the presence of Mn^{2+}, but not Mg^{2+} or Zn^{2+} ions.[309] Generally, the types of unusual structures adopted by long Pu-Py repeats in DNA are complex and heterogeneous with multiple different conformers.[307] Some monovalent cations were found to inhibit intermolecular Pu-Pu-Py triple-helical DNA conformation (with K^+ and Rb^+ being most effective, followed by Na^+), presumably via promotion of other multistrand structures.[310]

Triple-helix formation by G-rich oligonucleotides is supported by Mg^{2+} but strongly inhibited by physiological concentrations of certain monovalent cations, especially K^+, most likely due to oligonucleotide self-association in competitive structures such as guanine-quadruplexes.[311–313] Variation of the cation environment can differentially promote the assembly of multistranded nucleic acid structural alternatives. For example, by specifically counteracting the induction/stabilization of quadruplex structures by potassium ions, certain divalent ions (i.e. Mn^{2+}, Co^{2+}, and Ni^{2+} but not Mg^{2+}) at low millimolar concentrations allow triplex formation in the presence of 150 mM K^+.[313] In contrast, certain mono- and divalent metal ions can promote the transition from Watson–Crick duplexes to G_4 quadruplex structures relatively efficiently: $K^+ > Ca^{2+} > Na^+ > Mg^{2+} > Li^+$.[146,147,314]

The tertiary structure of single-stranded RNA molecules is affected by metal ions even more dramatically because of the complexity and flexibility of such species.[157] By stabilizing one RNA structure and destabilizing others, metal ions can promote structural transformations. Such conformational changes, induced by different (primarily biological) metal ions, have been studied extensively for several classes of RNA molecules, including tRNAs,[104,158–161,315] ribosomal RNAs,[157,316–318] and ribozymes.[57,319–322]

Certain complexes of platinum metals (such as Pt^{2+} and Ru^{2+}), containing planar aromatic ligands, bind DNA through intercalation between base pairs without distorting them. However, such metallo-intercalation agents can induce changes in the superhelical shape of DNA, producing extension, unwinding, and stiffening of the DNA helix.[279,280,284]

In addition to the formation of inner- and outer-sphere complexes, high concentrations of metal ions can affect RNA and DNA hydration through binding water molecules and affecting their activity and properties (polarization, orientation, and mobility) of adjacent water molecules.[323–325] Through effects on the local ordering of water molecules near and in the polynucleotide first hydration shell,[2,253] structure-promoting (kosmotropic)[325] ions and structure-breaking (chaotropic)[325] ions may indirectly alter the structure and stability of nucleic acids.

7 METAL BINDING CAN INDUCE HYDROLYSIS AND CLEAVAGE OF NUCLEIC ACIDS

Metal ions can catalyze the cleavage of nucleic acids through different mechanisms, which are discussed in detail elsewhere.[40,166,326] Briefly, these metal-dependent mechanisms may involve direct interaction of metal ion catalysts with either the atoms flanking the cleavable bonds or the nucleic acid functional groups participating in the cleavage chemistry. The hydrated metal ions can act either as general acids ($M–OH_2$) or general bases (M–OH). Alternatively, metal ions can stabilize the transition states of cleavable bonds. In addition, metal ions can promote cleavage through modification of nucleobase or sugar residues, resulting in destabilization of the N-glycosidic bond between these moieties (see Section 4.5). Oxygen radicals generated by some metal ions can also cleave both RNA and DNA (see Section 4.5).

However, not all cleavage reactions of nucleic acids promoted by metal ions occur through direct involvement of metal ions in cleavage chemistry. For example, metal ion cofactors stabilize the catalytically active conformations of several ribozymes, but do not participate directly in catalysis.[56]

Cleavage of nucleic acids refers to a reaction that results in the breakage of bonds in the phosphodiester backbone of a polynucleotide chain. There are two types of reactions resulting in the cleavage of either P–O or C–O bonds in the nucleic acid backbone (see Figure 1d).[96] Cleavage of the P–O bond occurs as a result of nucleophilic attack on the phosphorus atom via either an *inter*molecular reaction with a H_2O molecule (*hydrolysis*) or an *intra*molecular reaction involving the ribose 2′-OH (*transesterification*). Of these two reactions, transesterification is specific to RNA (since DNA lacks a 2′-OH moiety) and can be catalyzed by many $M^{\geq 2+}$ ions albeit with different efficiencies (see below), generating 5′-OH and intermediate 2′,3′-cyclic phosphate ends. The same metal ions can then promote subsequent hydrolysis of the 2′,3′-cyclic phosphate[96] resulting in an equimolar mixture of 2′- and 3′-phosphates (see Figure 1c). It is a common mistake to use the term ‘hydrolysis’ when referring to RNA cleavage by the transesterification mechanism. Only the postcleavage opening of the 2′,3′-cyclic phosphate proceeds via a hydrolytic mechanism.

A large variety of metal ions catalyze the cleavage of RNA through the transesterification mechanism, and some of them can also catalyze hydrolysis of cyclic phosphates (e.g. Pb^{2+}, Zn^{2+}, and Cd^{2+}) and nucleoside phosphomonoesters (e.g. Pb^{2+}, La^{3+}, and Th^{3+}).[96] The most efficient cleavage of RNA in aqueous solutions by free metal ions is achieved by the action of rare metal ions (e.g. Eu^{3+}, La^{3+}, and Tb^{3+}), Pb^{2+}, and Zn^{2+}.[39,96] Zn^{2+} is only about 4% as efficient as Pb^{2+},[327] but other catalytically active metal ions (e.g. Al^{3+}, Cd^{2+}, Mn^{2+}, Cu^{2+}, Co^{2+}, Ni^{2+}, or Mg^{2+}) are 1–2 orders of magnitude less efficient than Zn^{2+}.[328] As a rule, RNA cleavage has a maximum rate at pH values around the pK_as of the first metal-bound H_2O (see Table 1), that is, when the hydroxo-metal species still bear positive charge.[329]

Just as metal ions can bind nucleic acids both specifically and nonspecifically, they can promote both specific and nonspecific cleavage of nucleic acids. The rate and specificity of the cleavage reactions varies markedly with the identity of both metal ions and nucleic acid structures, as well as with the conditions of experiments. Higher pH, temperature, and concentrations of metal ions could enhance the rate of the polynucleotide cleavage but would decrease the specificity.

Numerous studies of metal-induced cleavage of RNA provide considerable insight into the relationship between nucleic acid structure and the specificity of polynucleotide cleavage. A higher rate of phosphodiester bond cleavage promoted by metal ions is observed for polynucleotides than for short oligonucleotides.[330] In RNA oligomers, the nature of the adjacent phosphate group can affect the rate and primary position of metal-dependent cleavage of internal phosphodiester bonds.[330] The nucleotide composition and the nature of the nearest-neighbor base of RNA molecules also affects the rate of metal-promoted cleavage.[252] This sequence specificity is presumably determined by specific interactions (e.g. stacking and H-bonds) between adjacent bases that determine the local conformation of the ribose–phosphate backbone at the site of cleavage.[331]

Secondary structure also affects the cleavage specificity. RNA duplexes are more resistant to cleavage by metal ions than single-stranded RNAs.[327,332,333] One of the principal reasons for this could be that base pairing interactions stabilize the conformation of the dinucleoside phosphate moiety such that the phosphorus atom is moved away from the sugar 2′-OH group and rotation about the C3′-O bond is restricted, which can interfere with the conversion of the polynucleotide to a conformation suitable for the transesterification reaction.[334]

Metal ions bound site-specifically within the RNA tertiary structure could induce cleavage of the phosphodiester backbone near the binding sites. One group of metal ions, including Eu^{3+},[335–338] Pb^{2+},[62,321,329,339–348] Zn^{2+},[335,349,350] Fe^{2+},[351,352] and Mn^{2+}[350,353,354] can induce specific nonenzymatic cleavage of different RNAs at neutral pH. Another group, which includes Mg^{2+}, Ca^{2+}, Ba^{2+}, Sr^{2+}, and Cu^{2+}, requires higher pH (8.5–9.5) to promote the specific cleavage of RNA molecules efficiently.[62,329,335–338,344,348,349,355,356]

Because of their high efficiency of RNA cleavage, Pb^{2+} ions have been used routinely as a probe of RNA structure.[332,357] Pb^{2+}-induced cleavage occurs preferentially in single-stranded regions of RNA, which include loops, bulges, and single-base mismatches, while stable double-stranded stems and highly structured tetraloops are partially resistant.[358] However, cleavage may also occur in destabilized base-paired regions. Similar to Pb^{2+}, lanthanide metal ions (e.g. Eu^{3+} and Tb^{3+}) have been used as probes of RNA folding as well as to map metal-binding sites in RNA molecules.[332,347,359–362]

There are three general approaches based on metal-induced cleavage of RNA to identify (map) metal-binding sites. In the first approach, the location of strongly bound $Mg^{2+}$and Ca^{2+} ions can be revealed by inducing cleavage at pH 9–9.5.[336,344,347,349,356] The second approach, is based on the assumption that certain metal ions (e.g. $Fe^{2+}$and Pb^{2+}) can replace Mg^{2+} at the same binding sites and induce RNA cleavage upon binding.[329,332,344,352] The third technique takes advantage of the fact that metal-induced cleavage of RNA (e.g. by Pb^{2+} or Zn^{2+}) can be inhibited when the reaction mixture is treated with increasing concentrations of Mg^{2+}, owing to substitution of the cleaving metal at the particular sites with Mg^{2+}.[186,332,344] However, the metal-dependent cleavage of RNA at a particular site does not automatically implicate the involvement of these nucleotides in the binding of this metal ion. Also, some specifically bound metal ions may not be able to induce cleavage at their binding sites because of the restricted flexibility or steric accessibility of the surrounding polynucleotide backbone, or unfavorable spatial orientation between metal ion and the relevant internucleotide bond. Moreover, different metals most probably will have different binding patterns even if they bound within the same metal-binding pocket.

8 CONCLUSION

This article does not attempt to be comprehensive, but rather presents selected examples to illustrate key facets of metal ion–nucleic acid interaction. The focus is on the chemical and structural properties of nucleic acids and metal ions relevant to their interactions, and in illustrating that both contribute as equal partners to the complexity of their interactions.

9 RELATED ARTICLES

Ammonia & N-donor Ligands; Coordination & Organometallic Chemistry: Principles; Mercury: Organometallic Chemistry; Metal Ion Toxicity; Metal-related Diseases of Genetic Origin; Peptide–Metal Interactions; Platinum-based Anticancer Drugs; Platinum: Inorganic & Coordination Chemistry; Ruthenium: Inorganic & Coordination Chemistry; S-donor Ligands; Water & O-donor Ligands; Zinc: DNA-binding Proteins..

10 FURTHER READING

C. Metcalfe and J. A. Thomas, *Chem. Soc. Rev.*, 2003, **32**, 215.

J. Reedijk, *Proc. Natl. Acad. Sci. USA*, 2003, **100**, 3611.

J. A. Subirana and M. Soler-Lopez, *Annu. Rev. Biophys. Biomol. Struct.*, 2003, **32**, 27.

S. D. Wettig, C. Z. Li, Y. T. Long, H. B. Kraatz, and J. S. Lee, *Anal. Sci.*, 2003, **19**, 23.

11 REFERENCES

1. V. A. Buckin, B. I. Kankiya, D. Rentzeperis, and L. A. Marky, *J. Am. Chem. Soc.*, 1994, **116**, 9423.
2. E. Westhof, *Annu. Rev. Biophys. Chem.*, 2001, **17**, 125.
3. G. L. Eichhorn, *Met. Ions Biol. Syst.*, 1980, **10**, 1.
4. M. Grunberg-Manago, G. H. B. Hoa, P. Douzou, and A. Wishina, in 'Metal Ions in Genetic Information Transfer', eds. G. L. Eichhorn and L. G. Marzilli, Elsevier/North-Holland, New York, 1981, p. 193.
5. A. S. Mildvan and L. A. Loeb, in 'Metal Ions in Genetic Information Transfer', eds. G. L. Eichhorn and L. G. Marzilli, Elsevier/North-Holland, New York, 1981, p. 103.
6. I. Bertini, L. Messori, and M. S. Viezzoli, *Coord. Chem. Rev.*, 1992, **120**, 163.
7. T. V. O'Halloran, *Science*, 1993, **261**, 715.
8. M. A. Sirover and L. A. Loeb, *Science*, 1976, **194**, 1434.
9. K. M. Downey and A. G. So, *Met. Ions Biol. Syst.*, 1989, **25**, 1.
10. V. G. Bregadze, *Met. Ions Biol. Syst.*, 1996, **32**, 419.
11. I. Sissoëff, J. Grisvard, and E. Guillé, *Prog. Biophys. Mol. Biol.*, 1976, **31**, 165.
12. N. T. Christie and M. Costa, *Biol. Trace Elem. Res.*, 1983, **5**, 55.
13. E. L. Andronikashvili and L. M. Mosulishvily, *Met. Ions Biol. Syst.*, 1980, **10**, 167.
14. C. P. Flessel, A. Furst, and S. B. Radding, *Met. Ions Biol. Syst.*, 1980, **10**, 23.
15. H. J. Issaq, *Met. Ions Biol. Syst.*, 1980, **10**, 55.

16. J. Anastassopoulou and T. Theophanides, *Crit. Rev. Oncol. Hematol.*, 2002, **42**, 79.
17. M. Sabat, *Met. Ions Biol. Syst.*, 1996, **32**, 521.
18. T. Mordasini, A. Curioni, and W. Andreoni, *J. Biol. Chem.*, 2003, **278**, 4381.
19. U. Weser, *Struct. Bonding*, 1968, **5**, 41.
20. R. M. Izatt, J. J. Christensen, and J. H. Rytting, *Chem. Rev.*, 1971, **71**, 439.
21. G. L. Eichhorn, in 'Inorganic Biochemistry', ed. G. L. Eichhorn, Elsevier, Amsterdam, 1973, Vol. 2, p. 1191.
22. M. Daune, *Met. Ions Biol. Syst.*, 1974, **3**, 1.
23. A. T. Tu and M. J. Heller, *Met. Ions Biol. Syst.*, 1974, **1**, 1.
24. V. Swaminathan and M. Sundaralingam, *Crit. Rev. Biochem.*, 1979, **6**, 245.
25. D. J. Hodgson, *Prog. Inorg. Chem.*, 1977, **23**, 211.
26. L. G. Marzilli, *Prog. Inorg. Chem.*, 1977, **23**, 255.
27. R. W. Gellert and R. Bau, *Met. Ions Biol. Syst.*, 1979, **8**, 1.
28. R. B. Martin and Y. H. Mariam, *Met. Ions Biol. Syst.*, 1979, **8**, 57.
29. L. G. Marzilli, T. J. Kistenmacher, and G. L. Eichhorn, in 'Metal Ions in Biology', ed. T. G. Spiro, Wiley, New York, 1980, Vol. 1, p. 180.
30. L. G. Marzilli, in 'Metal Ions in Genetic Information Transfer', eds. G. L. Eichhorn and L. G. Marzilli, Elsevier, New York, 1981, p. 47.
31. W. Saenger, 'Principles of Nucleic Acid Research', Springer-Verlag, New York, 1984, p. 201.
32. R. B. Martin, *Acc. Chem. Res.*, 1985, **18**, 32.
33. B. Lippert, J. Arpalabti, O. Kirzanovic, W. Micklitz, F. Schwarz, and G. Trötscher, in 'Platinum and Other Metal Coordination Complexes in Cancer Chemotherapy', ed. M. Nicolini, Nijhoff, Boston, MA, 1988, p. 564.
34. H. Sigel, in 'Metal–Nucleotide Interactions (ACS Symp. Ser.)', ed. T. D. Tullius, American Chemical Society, Washington, DC, 1989, Vol. 402, p. 159.
35. H. Sigel, *Chem. Soc. Rev.*, 1993, **22**, 255.
36. H. Sigel and B. Song, *Met. Ions Biol. Syst.*, 1996, **32**, 135.
37. N. V. Hud and M. Polak, *Curr. Opin. Struct. Biol.*, 2001, **11**, 293.
38. D. R. Williams, 'The Metals of Life. The Solution Chemistry of Metal Ions in Biological Systems', Van Nostrand Reinhold, London, 1971.
39. T. Pan, D. M. Long, and O. C. Uhlenbeck, in 'The RNA World', eds. R. F. Gesteland and J. F. Atkins, CSHL Press, New York, 1993, p. 271.
40. S. Kazakov, in 'Bioorganic Chemistry: Nucleic acids', ed. S. M. Hecht, Oxford University Press, New York, 1996, p. 244.
41. A. L. Feig and O. C. Uhlenbeck, in 'The RNA World', 2nd edn., eds. R. F., Gesteland, T. R. Cech, and J. F. Atkins, CSHL Press, New York, 1999, p. 287.
42. B. Lippert, *Coord. Chem. Rev.*, 2000, **200–202**, 487.
43. V. Brabec, *Prog. Nucleic Acid Res. Mol. Biol.*, 2002, **71**, 1.
44. S. J. Lippard, in 'Platinum and Other Metal Coordination Compounds in Cancer Chemotherapy', ed. S. B. Howell, Plenum Press, New York, 1991, p. 1.
45. J. Reedijk, in 'Platinum and other Metal Coordination Compounds in Cancer Chemotherapy', ed. S. B. Howell, Plenum Press, New York, 1991, p. 13.
46. M. J. Abrams and B. A. Murrer, *Science*, 1993, **261**, 725.
47. E. R. Jamieson and S. J. Lippard, *Chem. Rev.*, 1999, **99**, 2467.
48. B. Lippert, G. Frommer, O. Renn, O. Krizanovic, I. Dieter, M. Krumm, G. Trötscher, F. Schwarz, S. Menzer, and E. Hillgeris, in 'Platinum and Other Metal Coordination Compounds in Cancer Chemotherapy', ed. S. B. Howell, Plenum Press, New York, 1991, p. 25.
49. R. M. Smith, A. E. Martell, and Y. Chen, *Pure Appl. Chem.*, 1991, **63**, 1015.
50. K. Aoki, *Met. Ions Biol. Syst.*, 1996, **32**, 91.
51. A. Jack, J. E. Ladner, D. Rhodes, R. S. Brown, and A. Klug, *J. Mol. Biol.*, 1977, **111**, 315.
52. M. M. Teeter, G. J. Quigley, and A. Rich, in 'Metal Ions in Biology', ed. T. Spiro, Wiley, New York, 1980, Vol. 1, p. 147.
53. T. Hermann and E. Westhof, *Structure*, 1998, **6**, 1303.
54. H. Shi and P. Moore, *RNA*, 2000, **6**, 1091.
55. A. R. Ferre-D'Amare and J. A. Doudna, *Annu. Rev. Biophys. Biomol. Struct.*, 1999, **28**, 57.
56. R. Hanna and J. Doudna, *Curr. Opin. Chem. Biol.*, 2000, **4**, 166.
57. A. M. Pyle, *J. Biol. Inorg. Chem.*, 2002, **7**, 679.
58. V. J. DeRose, *Curr. Opin. Struct. Biol.*, 2003, **13**, 317.
59. S. Steinkopf, A. Garoufis, W. Nerdal, and E. Sletten, *Acta Chem. Scand.*, 1995, **49**, 495.
60. N. G. Abrescia, L. Malinina, L. G. Fernandez, T. Huynh-Dinh, S. Neidle, and J. A. Subirana, *Nucleic Acids Res.*, 1999, **27**, 1593.
61. B. Andersen and E. Sletten, *J. Inorg. Biochem.*, 2000, **79**, 353.
62. M. Olejniczak, Z. Gdaniec, A. Fischer, T. Grabarkiewicz, L. Bielecki, and R. W. Adamiak, *Nucleic Acids Res.*, 2002, **30**, 4241.
63. M. Soler-Lopez, L. Malinina, V. Tereshko, V. Zarytova, and J. A. Subirana, *J. Biol. Inorg. Chem.*, 2002, **7**, 533.
64. E. Ennifar, P. Walter, and P. Dumas, *Nucleic Acids Res.*, 2003, **31**, 2671.
65. S. Redon, S. Bombard, M. A. Elizondo-Riojas, and J. C. Chottard, *Nucleic Acids Res.*, 2003, **31**, 1605.
66. J. Vinje, J. A. Parkinson, P. J. Sadler, T. Brown, and E. Sletten, *Chemistry*, 2003, **9**, 1620.

67. A. M. Pyle, *Science*, 1993, **261**, 709.
68. M. Yarus, *FASEB J.*, 1993, **7**, 31.
69. M. J. Fedor, *Curr. Opin. Struct. Biol.*, 2002, **12**, 289.
70. L. E. Orgel and R. Lohrmann, *Acc. Chem. Res.*, 1974, **7**, 368.
71. E. Kanaya and H. Yanagawa, *Biochemistry*, 1986, **25**, 7423.
72. R. Rohatgi, D. P. Bartel, and J. W. Szostak, *J. Am. Chem. Soc.*, 1996, **118**, 3332.
73. A. Kanavarioti, P. A. Monnard, and D. W. Deamer, *Astrobiology*, 2001, **1**, 271.
74. M. Franchi, J. P. Ferris, and E. Gallori, *Orig. Life Evol. Biosph.*, 2003, **33**, 1.
75. J. M. Wolfson and D. R. Kearns, *Biochemistry*, 1975, **14**, 1436.
76. A. Rich and U. L. RajBhandary, *Annu. Rev. Biochem.*, 1976, **45**, 805.
77. S. J. Lippard, *Acc. Chem. Res.*, 1978, **11**, 211.
78. A. H.-J. Wang, G. J. Quigley, F. J. Kolpak, J. L. Crawford, J. H. van Boom, G. van der Marel, and A. Rich, *Nature*, 1979, **282**, 680.
79. J. K. Barton and S. J. Lippard, in ‘Nucleic Acid–Metal Ion Interactions’, ed. T. G. Spiro, Wiley, New York, 1980, p. 31.
80. D. Gersanovski, P. Colson, C. Houssier, and E. Fredericq, *Biochim. Biophys. Acta*, 1985, **824**, 313.
81. L. A. Basile and J. K. Barton, *Met. Ions Biol. Syst.*, 1989, **25**, 31.
82. A. M. Pyle and J. K. Barton, *Prog. Inorg. Chem.*, 1990, **38**, 413.
83. S. L. Klakamp and W. D. Horrocks, Jr *J. Inorg. Biochem.*, 1992, **46**, 175.
84. J. Feigon, S. E. Butcher, L. D. Finger, and N. V. Hud, *Methods Enzymol.*, 2001, **338**, 400.
85. C. F. Geraldes and C. Luchinat, *Met. Ions Biol. Syst.*, 2003, **40**, 513.
86. R. K. O. Sigel and A. M. Pyle, *Met. Ions Biol. Syst.*, 2003, **40**, 477.
87. M. E. Napier, C. R. Loomis, M. F. Sistare, J. Kim, A. E. Eckhardt, and H. H. Thorp, *Bioconjug. Chem.*, 1997, **8**, 906.
88. S. Seetharaman, M. Zivarts, N. Sudarsan, and R. R. Breaker, *Nat. Biotechnol.*, 2001, **19**, 336.
89. K. Maruyama, Y. Mishima, K. Minagawa, and J. Motonaka, *Anal. Chem.*, 2002, **74**, 3698.
90. Y. Lu, J. Liu, J. Li, P. J. Bruesehoff, C. M. Pavot, and A. K. Brown, *Biosens. Bioelectron.*, 2003, **18**, 529.
91. H. Cai, N. Zhu, Y. Jiang, P. He, and Y. Fang, *Biosens. Bioelectron.*, 2003, **18**, 1311.
92. K. Glynou, P. C. Ioannou, T. K. Christopoulos, and V. Syriopoulou, *Anal. Chem.*, 2003, **75**, 4155.
93. J. J. Storhoff and C. A. Mirkin, *Chem. Rev.*, 1999, **99**, 1849.
94. K. A. Browne, *J. Am. Chem. Soc.*, 2002, **124**, 7950.
95. A. C. Syvanen and H. Soderlund, *Nat. Biotechnol.*, 2002, **20**, 349.
96. N. K. Kochetkov and E. I. Budovskii, ‘Organic Chemistry of Nucleic Acids’, Plenum Press, New York, 1972, Part B, p. 496.
97. P. O. P. Ts’o, in ‘Basic Principles in Nucleic Acid Chemistry’, ed. P. O. P. Ts’o, Academic Press, New York, 1974, p. 453.
98. H. Eisenberg, in ‘Basic Principles in Nucleic Acid Chemistry’, ed. P. O. P. Ts’o, Academic Press, New York, 1974, Vol. 3, p. 171.
99. W. Saenger, *Annu. Rev. Biophys. Biophys. Chem.*, 1987, **16**, 93.
100. I. D. Kuntz, T. S. Brassfield, G. D. Law, and G. V. Purcell, *Science*, 1969, **163**, 1329.
101. T. Lundback and T. Hard, *Proc. Natl. Acad. Sci. U.S.A.*, 1996, **93**, 4754.
102. C. Mundoma and N. L. Greenbaum, *Biopolymers*, 2003, **69**, 100.
103. J. A. Subirana and M. Soler-Lopez, *Annu. Rev. Biophys. Biomol. Struct.*, 2003, **32**, 27.
104. D. E. Draper, *RNA*, 2004, **10**, 335.
105. T. R. Jack, *Met. Ions Biol. Syst.*, 1979, **8**, 159.
106. E. Sletten and W. Nerdal, *Met. Ions Biol. Syst.*, 1997, **34**, 479.
107. S. Nishimura, in ‘Transfer RNA: Structure, Properties, and Recognition’, eds. P. R. Schimmel, D. Söll, and J. N. Abelson, CSHL Press, New York, 1979, p. 547.
108. P. F. Agris, *Prog. Nucleic Acid Res. Mol. Biol.*, 1996, **53**, 79.
109. K. G. Strothkamp and S. J. Lippard, *Proc. Natl. Acad. Sci. U.S.A.*, 1976, **73**, 2536.
110. D. J. Szalda, F. Eckstein, H. Sternbach, and S. J. Lippard, *J. Inorg. Biochem.*, 1979, **11**, 279.
111. U. von Ahsen and H. F. Noller, *EMBO J.*, 1993, **12**, 4747.
112. S. A. Strobel, *Curr. Opin. Struct. Biol.*, 1999, **9**, 346.
113. M. Egli, *Chem. Biol.*, 2002, **9**, 277.
114. C. A. Klevickis and C. M. Grisham, *Met. Ions Biol. Syst.*, 1996, **32**, 1.
115. E. M. Bianchi, S. A. Sajadi, B. Song, and H. Sigel, *Chemistry*, 2003, **9**, 881.
116. R. Das, T. T. Mills, L. W. Kwok, G. S. Maskel, I. S. Millett, S. Doniach, K. D. Finkelstein, D. Herschlag, and L. Pollack, *Phys. Rev. Lett.*, 2003, **90**, 188103.
117. J. Granot and D. Kearns, *Biopolymers*, 1982, **21**, 219.
118. D. Pörschke, in ‘Structure and Dynamics of RNA’, eds. P. H. van Knippenberg and C. W. Hilbers, Plenum Press, New York, 1986, p. 77.
119. R. C. Weast, D. R. Lide, M. J. Astle, and W. H. Beyer, ‘CRC Handbook of Chemistry and Physics’, CRC Press, Boca Raton, FL, 1990, p. F.
120. F. A. Cotton and G. Wilkinson, ‘Advanced Inorganic Chemistry’, 5th edn., Wiley, New York, 1988, p. 1285.
121. J. Burgess, ‘Metal Ions in Solution’, Ellis Horwood, Chichester, 1978, p. 259.

122. D. D. Perrin and B. Dempsey, ‘Buffers for pH and Metal Ion Control’, Chapman & Hall, London, 1974.

123. C. Sander and P. O. P. Ts’o, *J. Mol. Biol.*, 1971, **55**, 1.

124. I. Tinoco Jr, P. W. Davis, C. C. Hardin, J. D. Puglisi, G. T. Walker, and J. Wyatt, *Cold Spring Harbor Symp. Quant. Biol.*, 1987, **LII**, 135.

125. J. Sponer, J. Leszczynski, and P. Hobza, *Biopolymers*, 2002, **61**, 3.

126. U. Nagaswamy, M. Larios-Sanz, J. Hury, S. Collins, Z. Zhang, Q. Zhao, and G. E. Fox, *Nucleic Acids Res.*, 2002, **30**, 395.

127. P. B. Rupert and A. R. Ferre-D’Amare, *Nature*, 2001, **410**, 780.

128. G. E. Plum, Y.-W. Park, S. F. Singleton, P. B. Dervan, and K. J. Breslauer, *Proc. Natl. Acad. Sci. U.S.A.*, 1990, **87**, 9436.

129. P. V. Scaria, S. J. Shire, and R. H. Shafer, *Proc. Natl. Acad. Sci. U.S.A.*, 1992, **89**, 10336.

130. J. V. Burda, J. Sponer, J. Leszczynski, and P. Hobza, *J. Phys. Chem. B*, 1997, **101**, 9670.

131. H. A. Heus and A. Pardi, *Science*, 1991, **253**, 191.

132. J. SantaLucia Jr, R. Kierzek, and D. H. Turner, *Science*, 1992, **256**, 217.

133. C. Guerrier-Takada, K. Haydock, L. Allen, and S. Altman, *Biochemistry*, 1986, **25**, 1509.

134. A. S. Mildvan and C. M. Grisham, *Struct. Bonding*, 1974, **20**, 1.

135. C. W. A. Pleij, *Trends Biochem. Sci.*, 1990, **15**, 143.

136. N. A. Froystein, J. T. Davis, B. R. Reid, and E. Sletten, *Acta Chem. Scand.*, 1993, **47**, 649.

137. Y.-G. Gao, M. Sriram, and A. H.-J. Wang, *Nucleic Acids Res.*, 1993, **21**, 4093.

138. D. M. J. Lilley, *Chem. Soc. Rev.*, 1989, **18**, 53.

139. G. R. Clark, C. J. Squire, L. J. Baker, R. F. Martin, and J. White, *Nucleic Acids Res.*, 2000, **28**, 1259.

140. R. V. Gessner, G. J. Quigley, A. H. Wang, G. A. van der Marel, J. H. van Boom, and A. Rich, *Biochemistry*, 1985, **24**, 237.

141. M. Gueron, J. Demaret, and M. Filoche, *Biophys. J.*, 2000, **78**, 1070.

142. J. Bernues, R. Beltran, J. M. Casasnovas, and F. Azorin, *Nucleic Acids Res.*, 1990, **18**, 4067.

143. S. Kang and R. D. Wells, *J. Biol. Chem.*, 1992, **267**, 20887.

144. M. D. Frank-Kamenetskii and S. M. Mirkin, *Annu. Rev. Biochem.*, 1995, **64**, 65.

145. D. Sen and W. Gilbert, *Nature*, 1990, **344**, 410.

146. C. C. Hardin, T. Watson, M. Corregan, and C. Bailey, *Biochemistry*, 1992, **31**, 833.

147. N. Nagesh, P. Bhargava, and D. Chatterji, *Biopolymers*, 1992, **32**, 1421.

148. R. L. Gonzalez Jr and I. Tinoco Jr, *J. Mol. Biol.*, 1999, **289**, 1267.

149. A. Hüttenhofer, S. Hudson, H. F. Noller, and P. K. Mascharak, *J. Biol. Chem.*, 1992, **267**, 24471.

150. S. R. Holbrook, J. L. Sussman, R. W. Warrant, G. M. Church, and S. H. Kim, *Nucleic Acids Res.*, 1977, **4**, 2811.

151. B. N. van Buuren, T. Hermann, S. S. Wijmenga, and E. Westhof, *Nucleic Acids Res.*, 2002, **30**, 507.

152. K. M. Sullivan and D. M. Lilley, *J. Mol. Biol.*, 1987, **193**, 397.

153. D. M. Lilley and R. M. Clegg, *Q. Rev. Biophys.*, 1993, **26**, 131.

154. G. Felsenfeld and H. T. Miles, *Annu. Rev. Biochem.*, 1967, **36**, 407.

155. N. Sugimoto, S. Nakano, M. Katoh, A. Matsumura, H. Nakamuta, T. Ohmichi, M. Yoneyama, and M. Sasaki, *Biochemistry*, 1995, **34**, 11211.

156. J. J. Champoux, *Annu. Rev. Biochem.*, 1978, **47**, 449.

157. I. Tinoco Jr and C. Bustamante, *J. Mol. Biol.*, 1999, **293**, 271.

158. G. Rialdi, J. Levy, and R. Biltonen, *Biochemistry*, 1972, **11**, 2472.

159. A. Stein and D. M. Crothers, *Biochemistry*, 1976, **15**, 160.

160. J. C. Thomas, J. M. Schurr, B. R. Reid, N. S. Riberto, and D. R. Hare, *Biochemistry*, 1984, **23**, 5414.

161. C. P. H. Vary and J. N. Vournakis, *Nucleic Acids Res.*, 1984, **12**, 6783.

162. W. Bujalowski, E. Graeser, L. W. Laughlin, and D. Pörschke, *Biochemistry*, 1986, **25**, 6365.

163. S. S. Reid and J. A. Cowan, *Biochemistry*, 1990, **29**, 6025.

164. S. L. Heilman-Miller, J. Pan, D. Thirumalai, and S. A. Woodson, *J. Mol. Biol.*, 2001, **309**, 57.

165. W. E. C. Wacker, M. P. Gordon, and J. W. Huff, *Biochemistry*, 1963, **2**, 716.

166. A. Dallas, A. V. Vlassov, S. A. Kazakov, in ‘Artificial Nucleases’, ed. M. A. Zenkova (‘Nucleic Acids and Molecular Biology Ser.’, ed. H. J. Gross), Springer-Verlag, Heidelberg, 2003, p. 61.

167. C. F. Baes Jr and R. E. Mesmer, ‘The Hydrolysis of Cations’, Wiley, New York, 1976.

168. J. A. Dean, ‘Lange’s Handbook of Chemistry’, 13th edn., McGraw-Hill, New York, 1985.

169. S. A. C. Dahm and O. C. Uhlenbeck, *Biochemistry*, 1991, **30**, 9464.

170. F. Basolo and R. G. Pearson, ‘Mechanism of Inorganic Reactions. A Study of Metal Complexes in Solution’, 2nd edn., Wiley, New York, 1967.

171. C. M. Frey and J. Stuehr, *Met. Ions Biol. Syst.*, 1974, **1**, 51.

172. R. M. K. Dale, E. Martin, D. C. Livingston, and D. C. Ward, *Biochemistry*, 1975, **14**, 2447.

173. N. Williams and D. M. Crothers, *Biochemistry*, 1975, **14**, 1944.

174. G. Ott, L. Arnold, and S. Limmer, *Nucleic Acids Res.*, 1993, **21**, 5859.

175. R. N. Bose, R. D. Cornelius, and R. E. Viola, *J. Am. Chem. Soc.*, 1986, **108**, 4403.

176. D. P. Bancroft, C. A. Lepre, and S. Lippard, *J. Am. Chem. Soc.*, 1990, **112**, 6860.

177. E. Nieboer and W. E. Sanford, *Rev. Biochem. Toxicol.*, 1985, **7**, 205.

178. R. J. Angelici, in ‘Inorganic Biochemistry’, ed. G. L. Eichhorn, Elsevier, Amsterdam, 1973, Vol. 1, p. 63.

179. H. Sigel and C. P. Da Costa, *Coord. Chem. Rev.*, 2001, **219–221**, 435.

180. S.-H. Kim and R. B. Martin, *Inorg. Chim. Acta*, 1984, **91**, 19.

181. S. S. Massoud and H. Sigel, *Inorg. Chem.*, 1988, **27**, 1447.

182. S. S. Massoud and H. Sigel, *Eur. J. Biochem.*, 1989, **179**, 451.

183. H. Sigel, R. Tribolet, R. Malini-Balakrishnan, and R. B. Martin, *Inorg. Chem.*, 1987, **26**, 2149.

184. H. Scheller and H. Sigel, *J. Am. Chem. Soc.*, 1983, **105**, 5891.

185. P. R. Schimmel and A. G. Redfield, *Annu. Rev. Biophys. Bioeng.*, 1980, **9**, 181.

186. D. Labuda, K. Nicoghosian, and R. Cedergren, *J. Biol. Chem.*, 1985, **260**, 1103.

187. E. Berggren, L. Nordenskiöld, and W. H. Braunlin, *Biopolymers*, 1992, **32**, 1339.

188. N. P. Johnson, J. P. Macquet, J. L. Wiebers, and B. Monsarrat, *Nucleic Acids Res.*, 1982, **10**, 5255.

189. M. E. Howe-Grant and S. J. Lippard, *Met. Ions Biol. Syst.*, 1980, **11**, 63.

190. J. I. Legg, *Coord. Chem. Rev.*, 1978, **125**, 103.

191. A. Danchin, *Biochimie*, 1972, **54**, 333.

192. L. E. Minchenkova and V. I. Ivanov, *Biopolymers*, 1967, **5**, 615.

193. K. A. Marx, R. Kruger, and M. J. Clarke, *Mol. Cell. Biochem.*, 1989, **86**, 155.

194. A. Samuni, J. Aronovitch, D. Godinger, M. Chevion, and G. Chapski, *Eur. J. Biochem.*, 1983, **137**, 119.

195. S. A. Kazakov, T. G. Astashkina, S. V. Mamaev, and V. V. Vlassov, *Nature*, 1988, **335**, 186.

196. C. J. Burrows and S. E. Rokita, *Met. Ions Biol. Syst.*, 1998, **33**, 537.

197. E. S. Henle, Z. Han, N. Tang, P. Rai, Y. Luo, and S. Linn, *J. Biol. Chem.*, 1999, **274**, 962.

198. T. G. Astashkina, V. V. Vlasov, and S. A. Kazakov, *Dokl. Akad. Nauk SSSR*, 1998, **301**, 234.

199. M. H. Baik, R. A. Friesner, and S. J. Lippard, *J. Am. Chem. Soc.*, 2002, **124**, 4495.

200. M. Clarke and M. Stubbs, *Met. Ions Biol. Syst.*, 1996, **32**, 727.

201. E. Palecek, *Methods Enzymol.*, 1992, **212**, 139.

202. C. T. Bui, K. Rees, A. Lambrinakos, A. Bedir, and R. G. Cotton, *Bioorg. Chem.*, 2002, **30**, 216.

203. B. H. Geierstanger, T. F. Kagawa, S.-L. Chen, G. J. Quigley, and P. S. Ho, *J. Biol. Chem.*, 1991, **266**, 20185.

204. J. A. Doudna, C. Grosshans, A. Gooding, and C. E. Kundrot, *Proc. Natl. Acad. Sci. U.S.A.*, 1993, **90**, 7829.

205. J. A. Doudna and J. H. Cate, *Curr. Opin. Struct. Biol.*, 1997, **7**, 310.

206. N. Ban, P. Nissen, J. Hansen, P. B. Moore, and T. A. Steitz, *Science*, 2000, **289**, 905.

207. E. Sletten and N. A. Froystein, *Met. Ions Biol. Syst.*, 1996, **32**, 397.

208. N. B. Leontis and E. Westhof, *RNA*, 1998, **4**, 1134.

209. J. P. Rife, S. C. Stallings, C. C. Correll, A. Dallas, T. A. Steitz, and P. B. Moore, *Biophys. J.*, 1999, **76**, 65.

210. N. Gresh, J. E. Sponer, N. Spackova, J. Leszczynski, and J. Sponer, *J. Phys. Chem. B*, 2003, **107**, 8669.

211. S. Basu, R. P. Rambo, J. Strauss-Soukup, J. H. Cate, A. R. Ferre-D’Amare, S. A. Strobel, and J. A. Doudna, *Nat. Struct. Biol.*, 1998, **11**, 986.

212. V. Tereshko, C. J. Wilds, G. Minasov, T. P. Prakash, M. A. Maier, A. Howard, Z. Wawrzak, M. Manoharan, and M. Egli, *Nucleic Acids Res.*, 2001, **29**, 1208.

213. S. P. Ryder and S. A. Strobel, *Nucleic Acids Res.*, 2002, **30**, 1287.

214. H. W. Pley, K. M. Flaherty, and D. B. McKay, *Nature*, 1994, **372**, 68.

215. W. G. Scott, J. B. Murray, J. R. Arnold, B. L. Stoddard, and A. Klug, *Science*, 1996, **274**, 2065.

216. T. Hermann, P. Auffinger, W. G. Scott, and E. Westhof, *Nucleic Acids Res.*, 1997, **25**, 3421.

217. D. M. Zhou, L. H. Zhang, and K. Taira, *Proc. Natl. Acad. Sci. U.S.A.*, 1997, **94**, 14343.

218. W. B. Lott, B. W. Pontius, and P. H. von Hippel, *Proc. Natl. Acad. Sci. U.S.A.*, 1998, **95**, 542.

219. E. A. Curtis and D. P. Bartel, *RNA*, 2001, **7**, 546.

220. J. M. Zhou, D. M. Zhou, Y. Takagi, Y. Kasai, A. Inoue, T. Baba, and K. Taira, *Nucleic Acids Res.*, 2002, **30**, 2374.

221. D. H. Brown and W. E. Smith, in ‘Enzyme Chemistry. Impact and Applications’, ed. C. J. Suckling, Chapman & Hall, London, 1984, p. 162.

222. J. A. Carrabine and M. Sundaralingam, *Biochemistry*, 1971, **10**, 292.

223. M. Goodgame and D. A. Jakubovic, *Coord. Chem. Rev.*, 1987, **79**, 97.

224. H. Sakurai, T. Goda, and S. Shimomura, *Biochem. Biophys. Res. Commun.*, 1982, **108**, 474.

225. R. Cini and G. Giorgi, *Inorg. Chim. Acta*, 1987, **137**, 87.

226. R. Phillips, *Chem. Rev.*, 1966, **66**, 501.

227. F. Eckstein, *Annu. Rev. Biochem.*, 1985, **54**, 367.

228. V. L. Pecoraro, J. D. Hermens, and W. W. Cleland, *Biochemistry*, 1984, **23**, 5262.

229. P. A. Frey and R. D. Sammons, *Science*, 1985, **228**, 541.

230. P. M. J. Burgers and F. Eckstein, *Biochemistry*, 1979, **18**, 592.

231. D. E. Ruffner and O. C. Uhlenbeck, *Nucleic Acids Res.*, 1990, **18**, 6025.

232. D. Herschlag, J. A. Piccirilli, and T. Cech, *Biochemistry*, 1991, **30**, 4844.

233. D. M. Zhou, Q. C. He, J. M. Zhou, and K. Taira, *FEBS Lett.*, 1998, **431**, 154.

234. S. Shan, A. Yoshida, S. Sun, J. A. Piccirilli, and D. Herschlag, *Proc. Natl. Acad. Sci. U.S.A.*, 1999, **96**, 12299.

235. M. L. Hamm, D. Nikolic, R. B. van Breemen, and J. A. Piccirilli, *J. Am. Chem. Soc.*, 2000, **122**, 12069.

236. S. O. Shan and D. Herschlag, *RNA*, 2000, **6**, 795.

237. Z. Prasal, *Acta Biochim. Pol.*, 1986, **33**, 153.

238. G. L. Eichhorn, in 'Metal Ions in Genetic Information Transfer', eds. G. L. Eichhorn and L. G. Marzilli, Elsevier, New York, 1981, p. 1.

239. S. J. Karlik and G. L. Eichhorn, *J. Inorg. Biochem.*, 1989, **37**, 259.

240. V. V. Vlassov, V. V. Gorn, E. M. Ivanova, S. A. Kazakov, and S. V. Mamaev, *FEBS Lett.*, 1983, **162**, 286.

241. N. Farrell, T. G. Appleton, Y. Qu, J. D. Roberts, A. P. Fontes, K. A. Skov, P. Wu, and Y. Zou, *Biochemistry*, 1995, **34**, 145480.

242. R. Zaludova, A. Zakovska, J. Kasparkova, Z. Balcarova, V. Kleinwachter, O. Vrana, N. Farrell, and V. Bravec, *Eur. J. Biochem.*, 1997, **246**, 508.

243. C. Hofr, N. Farrell, and V. Brabec, *Nucleic Acids Res.*, 2001, **29**, 2034.

244. L. G. Marzilli, S. Mukundan, Y. Xu, G. Zon, A. Bergman, P. Yohannes, and M. D. Reilly, in 'Platinum and Other Metal Coordination Compounds in Cancer Chemotherapy', ed. S. B. Howell, Plenum Press, New York, 1991, p. 101.

245. C. A. Lepre and S. J. Lippard, in 'Nucleic Acids and Molecular Biology', eds. F. Eckstein and D. M. J. Lilley, Springer-Verlag, Berlin, 1990, Vol. 4, p. 9.

246. A. Eastman, *Biochemistry*, 1985, **24**, 5027.

247. V. Monjardet-Bas, M. A. Elizondo-Riojas, J. C. Chottard, and J. Kozelka, *Angew. Chem., Int. Ed. Engl.*, 2002, **41**, 2998.

248. V. V. Vlasov and S. A. Kazakov, *Bioorg. Khim.*, 1982, **8**, 499.

249. V. Monjardet-Bas, J. C. Chottard, and J. Kozelka, *Chemistry*, 2002, **8**, 1144.

250. M. W. Lieberman, D. J. Harvan, D. E. Amacher, and J. B. Patterson, *Biochim. Biophys. Acta*, 1976, **425**, 265.

251. L. D. Kosturco, C. Folzer, and R. F. Stewart, *Biochemistry*, 1974, **13**, 3949.

252. G. L. Eichhorn, in 'Inorganic Biochemistry', ed. G. L. Eichhorn, Elsevier Scientific, Amsterdam, 1973b, Vol. 2, p. 1210.

253. A. M. Polyanichko, V. V. Andrushchenko, E. V. Chikhirzhina, V. I. Vorob'ev, and H. Wieser, *Nucleic Acids Res.*, 2004, **32**, 989.

254. A. P. Yurgaitis and Yu. S. Lazurkin, *Biopolymers*, 1981, **20**, 967.

255. M. Sabat and B. Lippert, *Met. Ions Biol. Syst.*, 1996, **33**, 143.

256. J. Sponer, M. Sabat, J. V. Burda, J. Leszczynski, P. Hobza, and B. Lippert, *J. Biol. Inorg. Chem.*, 1999, **4**, 537.

257. L. G. Marzilli, T. J. Kistenmacher, and M. Rossi, *J. Am. Chem. Soc.*, 1977, **99**, 2797.

258. H. Arakawa, J. F. Neault, and H. A. Tajmir-Riahi, *Biophys. J.*, 2001, **81**, 1580.

259. S. Atwell, E. Meggers, G. Spraggon, and P. G. Schultz, *J. Am. Chem. Soc.*, 2001, **123**, 12364.

260. H. Weizman and Y. Tor, *J. Am. Chem. Soc.*, 2001, **123**, 3375.

261. K. Tanaka, A. Tengeiji, T. Kato, N. Toyama, M. Shiro, and M. Shionoya, *J. Am. Chem. Soc.*, 2002, **124**, 12494.

262. N. Zimmermann, E. Meggers, and P. G. Schultz, *Bioorg. Chem.*, 2004, **32**, 13.

263. R. K. O. Sigel, S. M. Thompson, E. Freisinger, and B. Lippert, *Chem. Commun.*, 1999, 19.

264. G. Y. H. Chu, S. Mancy, R. E. Duncan, and R. S. Tobias, *J. Am. Chem. Soc.*, 1978, **100**, 593.

265. A. L. Feig, *Met. Ions Biol. Syst.*, 2000, **37**, 157.

266. K. J. Baeyens, H. L. De Bondt, A. Pardi, and S. R. Holbrook, *Proc. Natl. Acad. Sci. U.S.A.*, 1996, **93**, 12851.

267. M. Montrel, V. P. Chuprina, V. I. Poltev, W. Nerdal, and E. Sletten, *J. Biomol. Struct. Dyn.*, 1998, **16**, 631.

268. P. Rai, T. D. Cole, D. E. Wemmer, and S. Linn, *J. Mol. Biol.*, 2001, **312**, 1089.

269. T. Zuleeg, R. K. Hartmann, R. Kreutzer, and S. Limmer, *J. Mol. Biol.*, 2001, **305**, 181.

270. S. L. Bruhn, J. H. Toney, and S. J. Lippard, *Prog. Inorg. Chem.*, 1990, **38**, 477.

271. L. G. Marzilli and T. J. Kistenmacher, *Acc. Chem. Res.*, 1977, **10**, 146.

272. O. Yamauchi, A. Odani, H. Masuda, and H. Sigel, *Met. Ions Biol. Syst.*, 1996, **32**, 207.

273. C. F. Naumann and H. Sigel, *J. Am. Chem. Soc.*, 1974, **96**, 2750.

274. R. L. Karpel, N. S. Miller, A. M. Lesk, and J. R. Fresko, *J. Mol. Biol.*, 1975, **97**, 519.

275. D. S. Sigman, *Biochemistry*, 1990, **29**, 9097.

276. A. Mazumder, C. B. Chen, R. Gaynor, and D. S. Sigman, *Biochem. Biophys. Res. Commun.*, 1992, **187**, 1503.

277. D. S. Sigman, R. Landgraf, D. M. Perrin, and L. Pearson, *Met. Ions Biol. Syst.*, 1996, **33**, 485.

278. J. Gallagher, C. H. Chen, C. Q. Pan, D. M. Perrin, Y. M. Cho, and D. S. Sigman, *Bioconjug. Chem.*, 1996, **7**, 413.

279. K. W. Jennette, S. J. Lippard, G. A. Vassiliades, and W. R. Bauer, *Proc. Natl. Acad. Sci. U.S.A.*, 1974, **71**, 3839.

280. M. E. Howe-Grant and S. J. Lippard, *Biochemistry*, 1979, **18**, 5762.

281. B. Meunier, *Chem. Rev.*, 1992, **92**, 1411.

282. R. F. Pasternack and E. J. Gibbs, *Met. Ions Biol. Syst.*, 1996, **33**, 367.

283. E. Di Mauro, R. Saladino, P. Tagliatesta, V. De Sanctis, and R. Negri, *J. Mol. Biol.*, 1998, **282**, 43.

284. K. E. Erkkila, D. T. Odom, and J. K. Barton, *Chem. Rev.*, 1999, **99**, 2777.

285. M. Milkevitch, H. Storrie, E. Brauns, K. J. Brewer, and B. W. Shirley, *Inorg. Chem.*, 1997, **36**, 4534.

286. H. A. Tajmir-Riahi, M. Langlais, and R. Savoie, *Nucleic Acids Res.*, 1988, **16**, 751.

287. M. P. Kladde, Y. Kohwi, T. Kohwi-Shigematsu, and J. Gorski, *Proc. Natl. Acad. Sci. U.S.A.*, 1994, **91**, 1898.

288. N. A. Floro and K. E. Wetterhahn, *Biochem. Biophys. Res. Commun.*, 1984, **124**, 106.

289. D. Chatterji, *Biopolymers*, 1988, **27**, 1183.

290. Y. A. Shin, J. J. Butzow, L. D. Sinsel, P. Clark, R. P. Pillai, W. C. Johnson, and G. L. Eichhorn, *Biopolymers*, 1988, **27**, 1415.

291. T. J. Thomas and R. P. Messner, *Biochimie*, 1988, **70**, 221.

292. K. Nejedly, J. Klysik, and E. Palecek, *FEBS Lett.*, 1989, **243**, 313.

293. G. L. Eichhorn, *Coord. Chem. Rev.*, 1993, **128**, 167.

294. D. M. Loprete and K. A. Hartman, *Biochemistry*, 1993, **32**, 4077.

295. T. Schoenknecht and H. Dieblewr, *J. Inorg. Biochem.*, 1993, **50**, 283.

296. Q. Xu, S. R. B. Jampani, and W. H. Braunlin, *Biochemistry*, 1993, **32**, 11754.

297. F. E. Rossetto and E. Nieboer, *J. Inorg. Biochem.*, 1994, **54**, 167.

298. Y. Kohwi, H. Wang, and T. Kohwi-Shigematsu, *Nucleic Acids Res.*, 1993, **21**, 5651.

299. C. H. Laundon and J. D. Griffith, *Biochemistry*, 1987, **26**, 3759.

300. T. K. Chiu and R. E. Dickerson, *J. Mol. Biol.*, 2000, **301**, 915.

301. S. He, P. G. Arscott, and V. A. Bloomfield, *Biopolymers*, 2000, **53**, 329.

302. J. Widom and R. L. Baldwin, *Biopolymers*, 1983, **22**, 1595.

303. K. S. J. Rao, B. S. Rao, D. Vishnuvardhan, and K. V. S. Prasad, *Biochim. Biophys. Acta*, 1993, **1172**, 17.

304. J. Sponer, M. Sabat, J. V. Burda, A. M. Doody, J. Leszczynski, and P. Hobza, *J. Biomol. Struct. Dyn.*, 1998, **16**, 139.

305. K. R. Fox, *Nucleic Acids Res.*, 1990, **18**, 5387.

306. Y. Kohwi, *Nucleic Acids Res.*, 1989, **17**, 4493.

307. D. A. Collier and R. D. Wells, *J. Biol. Chem.*, 1990, **265**, 10652.

308. V. I. Lyamichev, O. N. Voloshin, M. D. Frank-Kamenetskii, and V. N. Soyfer, *Nucleic Acids Res.*, 1991, **19**, 1633.

309. V. A. Malkov, O. N. Voloshin, V. N. Soyfer, and M. D. Frank-Kamenetskii, *Nucleic Acids Res.*, 1993, **21**, 585.

310. A. J. Cheng and M. W. Van Dyke, *Nucleic Acids Res.*, 1993, **21**, 5630.

311. W. M. Olivas and L. J. Maher, *Nucleic Acids Res.*, 1995, **23**, 1936.

312. F. Svinarchuk, D. Cherny, A. Debin, E. Delain, and C. Malvy, *Nucleic Acids Res.*, 1996, **24**, 3858.

313. S. W. Blume, V. Guarcello, W. Zacharias, and D. M. Miller, *Nucleic Acids Res.*, 1997, **25**, 617.

314. Q. Xu, H. Deng, and W. H. Braunlin, *Biochemistry*, 1993, **32**, 13130.

315. V. M. Shelton, T. R. Sosnick, and T. Pan, *Biochemistry*, 2001, **40**, 3629.

316. R. T. Batey and J. R. Williamson, *RNA*, 1998, **8**, 984.

317. G. L. Conn, A. G. Gittis, E. E. Lattman, V. K. Misra, and D. E. Draper, *J. Mol. Biol.*, 2002, **318**, 963.

318. P. Auffinger, L. Bielecki, and E. Westhof, *J. Mol. Biol.*, 2004, **335**, 555.

319. S. E. Butcher and J. M. Burke, *J. Mol. Biol.*, 1994, **244**, 52.

320. M. Menger, T. Tuschl, F. Eckstein, and D. Porschke, *Biochemistry*, 1996, **35**, 14710.

321. M. Brannvall, N. E. Mikkelsen, and L. A. Kirsebom, *Nucleic Acids Res.*, 2001, **29**, 1426.

322. S. O. Shan and D. Herschlag, *RNA*, 2002, **8**, 861.

323. C. F. Anderson and M. T. Record Jr, *Annu. Rev. Phys. Chem.*, 1995, **46**, 657.

324. J. Barciszewski, J. Jurczak, S. Porowski, T. Specht, and V. A. Erdmann, *Acta Biochim. Pol.*, 1999, **46**, 133.

325. E. A. Vogler, in 'Water in Biomaterials Science', ed. M. Morra, John Wiley, New York, 2001, p. 3.

326. J. R. Morrow, *Met. Ions Biol. Syst.*, 1996, **33**, 561.

327. W. R. Farkas, *Biochim. Biophys. Acta*, 1968, **155**, 401.

328. J. J. Butzow and G. L. Eichhorn, *Biopolymers*, 1965, **3**, 95.

329. N. Polacek and A. Barta, *RNA*, 1998, **4**, 1282.

330. J. J. Butzow and G. L. Eichhorn, *Biochemistry*, 1971, **10**, 2019.

331. A. C. Dock-Bregeon and D. Moras, *Cold Spring Harbor Symp. Quant. Biol.*, 1987, **LII**, 113.

332. J. Ciesiolka, in 'RNA Biochemistry and Biotechnology', ed. B. F. C. Clark, Kluwer Academic Publishers, Dordrecht, 1999, p. 111.

333. K. A. Kolasa, J. R. Morrow, and A. P. Sharma, *Inorg. Chem.*, 1993, **32**, 3983.

334. G. A. Soukup and R. D. Breaker, *RNA*, 1999, **5**, 1308.

335. B. F. Rordorf and D. R. Kearns, *Biopolymers*, 1976, **15**, 1491.

336. J. Ciesiolka, J. Wrzesinski, P. Grniki, J. Podkowinski, and W. J. Krzyzosiak, *Eur. J. Biochem.*, 1989, **186**, 71.

337. T. Marciniec, J. Ciesiolka, J. Wrzesinski, and W. J. Krzyzosiak, *FEBS Lett.*, 1989, **243**, 293.

338. D. Michalowski, J. Wrzesinski, and W. Krzyzosiak, *Biochemistry*, 1996, **35**, 10727.

339. M. Sundaralingam, J. R. Rubin, and J. F. Cannon, *Int. J. Quantum Chem.*, 1984, **11**, 355.

340. R. S. Brown, J. C. Dewan, and A. Klug, *Biochemistry*, 1985, **24**, 4785.

341. K. Zito, A. Hüttenhofer, and N. R. Pace, *Nucleic Acids Res.*, 1993, **21**, 5916.

342. J. Ciesiolka, W. D. Hardt, J. Schlegl, V. A. Erdmann, and R. K. Hartmann, *Eur. J. Biochem.*, 1994, **219**, 49.

343. T. Pan, B. Dichtl, and O. C. Uhlenbeck, *Biochemistry*, 1994, **33**, 9561.

344. B. Streicher, E. Westhof, and R. Schroeder, *EMBO J.*, 1996, **15**, 2556.

345. D. Winter, N. Polacek, I. Halama, B. Streicher, and A. Barta, *Nucleic Acids Res.*, 1997, **25**, 1817.

346. J. Kufel and L. A. Kirsebom, *RNA*, 1998, **4**, 777.

347. S. Dorner and A. Barta, *Biol. Chem.*, 1999, **380**, 243.

348. M. Matysiak, J. Wrzesinski, and J. Ciesiolka, *J. Mol. Biol.*, 1999, **291**, 283.

349. S. Kazakov and S. Altman, *Proc. Natl. Acad. Sci. U.S.A.*, 1991, **88**, 9193.

350. M. Hertweck and M. W. Mueller, *Eur. J. Biochem.*, 2001, **268**, 4610.

351. C. P. H. Vary and J. N. Vournakis, *Proc. Natl. Acad. Sci. U.S.A.*, 1984, **81**, 6978.

352. C. Berens, B. Streicher, R. Schroeder, and W. Hillen, *Chem. Biol.*, 1998, **5**, 163.

353. J. Wrzesinski, D. Michalowski, J. Ciesiolka, and W. J. Krzyzosiak, *FEBS Lett.*, 1995, **374**, 62.

354. T. C. Kuo and D. L. Herrin, *Nucleic Acids Res.*, 2000, **28**, 4197.

355. M. Matsuo, T. Yokogawa, K. Nishikawa, K. Watanabe, and N. Okada, *J. Biol. Chem.*, 1995, **270**, 10097.

356. D. A. Lafontaine, S. Ananvoranich, and J. P. Perreault, *Nucleic Acids Res.*, 1999, **27**, 3236.

357. M. Lindell, P. Romby, and E. G. H. Wagner, *RNA*, 2002, **8**, 534.

358. J. Ciesiolka, D. Michalowski, J. Wrzesinski, J. Krajewski, and W. J. Krzyzosiak, *J. Mol. Biol.*, 1998, **275**, 211.

359. F. U. Gast, D. Kempe, R. L. Spieker, and H. L. Sanger, *J. Mol. Biol.*, 1996, **262**, 652.

360. M. R. S. Hargittai and K. Musier-Forsyth, *RNA*, 2000, **6**, 1672.

361. R. K. Sigel, A. Vaidya, and A. M. Pyle, *Nat. Struct. Biol.*, **7**, 1111.

362. N. G. Walter, N. Yang, and J. M. Burke, *J. Mol. Biol.*, 2000, **298**, 539.

Nutritional Aspects of Metals & Trace Elements

Katsuhiko Yokoi
Seitoku University Graduate School, Matsudo, Chiba, Japan

Based in part on the article Nutritional Aspects of Metals & Trace Elements by Paul Saltman which appeared in the Encyclopedia of Inorganic Chemistry, First Edition.

1	Introduction	1
2	Regulation	2
3	The Pathology of Metal Overload	6
4	Selenium and Nickel as Essential Ultratrace Elements	6
5	Summary	7
6	Related Articles	7
7	References	7

1 INTRODUCTION

All organisms including humans require essential minerals for survival, reproduction, and other physiological functions. As Underwood and Mertz stated,[1] the number of elements recognized as essential reflects the knowledge at a certain time point. Essentiality is established when a further reduction of a certain mineral intake (exposure) below the range of tolerable levels results in a consistent and reproducible impairment of a physiological function.[1] The essential inorganic nutrients consist of the major elements and the trace elements. The major elements include sodium, potassium, calcium, magnesium, chlorine, phosphorus, and sulfur. The trace elements include iron, copper, zinc, manganese, cobalt, chromium, molybdenum, vanadium, nickel, arsenic, selenium, iodine, fluorine, silicon, and boron. Tin, cadmium, lead, rubidium, and lithium can be added to the list of essential trace elements. Evidence of essentiality is limited for arsenic, boron, cadmium, fluorine, lead, lithium, nickel, rubidium, silicon, tin, and vanadium. Recently, noncorrin function of cobalt as a cofactor of methionine aminopeptidase in humans was found in addition to the well-known function as a metal center of vitamin B_{12} (*see* ***Cobalt: B_{12} Enzymes & Coenzymes***).[2] Ultratrace elements can be defined as trace elements whose requirements are approximately less than $1\,\mathrm{mg\,day^{-1}}$ for humans or $1\,\mathrm{mg\,kg^{-1}}$ diet for animals. In this context, most trace elements except for iron, zinc, copper, and manganese are classified as ultratrace elements.

For simplicity and brevity, this review will focus on human nutrition, but will also discuss other systems, where appropriate. The nature and amount of each element required by a given organism has been painstakingly determined by trial-and-error using purified (historically, synthetic or semisynthetic) diets to measure both essentiality and required amounts. For microorganisms and plants in hydroponic culture, such studies are a relatively easy matter once the difficulties of trace element contamination have been conquered. Investigations of endemic diseases revealed the essentiality of inorganic nutrients for humans such as zinc (dwarfism with hepatosplenomegaly in Egypt and Iran)[3] and selenium (Keshan disease in China).[4] Because the essentiality of minerals is the basic principle, occurrence of deficiencies of inorganic nutrients including zinc and selenium has been found to be worldwide rather than restricted in local areas. The technical ability to provide complete nutrient supplements intravenously, through total parenteral nutrition, has permitted the precise determination of how much of each element is required. The inadvertent omission of one or more trace elements led to serious pathological consequences that could be reversed by administration of the missing element(s).

Optimal dietary intake is difficult to determine. Dietary Reference Intakes (DRIs) in the US are reference values that are quantitative estimates of nutrient intakes to be used for planning and assessing diets for apparently healthy people.[5] DRIs are composed of reference values including Estimated Average Requirements (EARs), Recommended Dietary Allowances (RDAs), Adequate Intakes (AIs) and Tolerable Upper Intake Levels (ULs). Most nations have established the equivalent of the US DRIs. These are consensus and statistical values obtained from retrospective public health dietary studies, controlled experiments on metabolic wards, epidemiological surveys, isotopic tracer investigations, and extrapolation from animal models.

The values are a function of age, sex, and pregnancy. RDA is defined as the average daily dietary intake level that is sufficient to meet the nutrient requirement of nearly all (97 to 98%) healthy individuals in a particular life stage and gender group. AI is defined as a recommended intake value based on observed or experimentally determined approximations or estimates of nutrient intake by a group (or groups) of healthy people that are assumed to be adequate. AIs are used when an RDA cannot be determined. UL is defined as the highest level of daily nutrient intake that is likely to pose no risk of adverse health effects for almost all individuals in the general population. As intake increases above the UL, the risk of adverse effects may increase. EAR is defined as a daily nutrient intake value that is estimated to meet the requirement of half of the healthy individuals in a life stage and gender group. One may notice that EAR is defined as ‘median’ although it literally means ‘average’.

The prevalence (***D***) of the deficiency of the particular nutrient is the proportion of the individuals with the deficiency of the particular nutrient in the population.

$\boldsymbol{D} = \boldsymbol{\Sigma}$(Individuals whose dietary intake $<$ requirement) / (total number of individuals).

For the continuous distribution, the following equation with double integrals is obtained, where x is the dietary intake, y is the requirement, Ro is EAR, and p is the distribution function of the dietary intake and the requirement:

$$D = \int_{-\infty}^{+\infty} \int_{x}^{+\infty} p(x, y; R_o)\mathrm{d}y\mathrm{d}x \qquad (1)$$

When the distribution function of the dietary intake and the requirement follows the specific form, the above equation is used to estimate the prevalence of deficiency or inadequacy under the given condition and to evaluate the average requirement from the population data of the nutritional status.[6]

Values of RDAs and AIs for several minerals and trace elements from the current US DRIs are shown in Table 1.

All living systems require the major cations and anions: Na^+, K^+, Ca^{2+}, Mg^{2+}, Cl^-, $PO_4{}^{3-}$ and $SO_4{}^{2-}$. These ions are involved in the (1) regulation of intra- and extracellular electrolyte balance, (2) maintenance of bioelectric potentials and function of bioexcitable membranes, (3) control of pH, (4) stabilization of membrane structure and integrity, (5) mineralization of endo- and exoskeletons, (6) metabolic regulation and control as ‘second messengers’, (7) biomechanical contractility, (8) modulation of various ion channels and receptors, (9) activity of metallo-cofactors for various enzymes, (10) generation and utilization of energy as phosphate esters, and (11) structure and function of sulfo- and phospho-organic molecules. These major ions must be continually supplied in adequate amounts to maintain homeostasis.[7]

The trace elements comprise about 0.01% of the total wet weight of an organism. They serve six principal functions: (1) catalytic centers for enzymatic reactions, (2) oxidation–reduction centers, (3) oxygen binding and transport, (4) structural integrity of macromolecules, and (5) metabolic regulation and control, (6) modulation of various ion channels and receptors.[7] Modulation of various ion channels and receptors is added to the original lists in the second edition of this chapter for the major and trace elements based on the recent advancement in this field such as zinc finger proteins (*see* ***Zinc: DNA-binding Proteins***)[8] and cyclic nucleotide-gated (CNG) cation channels with nickel.[9]

Frequently, a given metal may be operative in two or more modes. Thus, iron can serve as a metallo-cofactor of an enzyme (uteroferrin; *see* ***Iron Proteins with Dinuclear Active Sites***), as a redox electron carrier (cytochrome; *see* ***Iron: Heme Proteins & Electron Transport***), in oxygen transport (hemoglobin; *see* ***Iron: Heme Proteins & Dioxygen Transport & Storage***), for structural integrity of a protein (transferrin; *see* ***Iron Proteins for Storage & Transport & their Synthetic Analogs***), and as a regulator of a metabolic reaction (aconitase; *see* ***Iron–Sulfur Proteins***; ***Metalloregulation***).

2 REGULATION

The regulation and control of all required inorganic nutrients are a function of eight coherent parameters:[7]

- availability of the total amount of the nutrient in the diet, soil or medium;
- solubility of the element;
- permeability of the element across membranes;
- ligand exchange rates of the metal ions among potential binding sites;
- transport of the element in cell and organs;
- assimilation of the element into its cellular or tissue target molecule;
- storage of the element for depot reserve or detoxification;
- excretion of excess nutrient to maintain homeostasis and prevent toxicity.

Examples of how each of the above operates in mineral nutrition may serve to illustrate the principles involved.

2.1 Availability

The proverbial ‘well-balanced diet’ should be able to provide adequate amounts of all of the necessary inorganic elements the body requires. The balancing act is not as simple as it may seem. Dietary restriction both in quantity and diversity is frequently encountered for economic, social, ethnic, esthetic, and religious reasons, as well as ignorance.

In both the developing and developed nations, inadequate intake of iron, calcium, zinc, and iodine gives rise to the most widespread and serious nutritional deficiencies. Iron and zinc are present in greatest abundance in red meats and organ meats. Oyster is a special source of zinc and copper. Milk and dairy products are the best source of calcium. Legumes and unrefined grains are good sources of copper, nickel, and chromium. The practice of fortifying flour and breakfast cereals with iron is widely used. Fortification of table salt with iodine has been widely employed (iodinated salt). Dietary supplements, either individual nutrients or multivitamin/multimineral preparations, are effective. A perspective of the amounts of iron, copper, and zinc in a few foods is shown in Table 2.

Diets low in meats and high in grains and legumes do not provide adequate available iron. The preparation of food in cast-iron utensils can significantly increase iron availability. Iron deficiency anemia is manifest as low hemoglobin concentrations, reduced myoglobin, and loss of activity of respiratory enzymes (*see* ***Cytochrome Oxidase***). Impaired growth, lethargy, and reduced exercise performance and attention span have been observed.[10]

Prospective studies in postmenopausal women have demonstrated that manganese, copper, zinc, magnesium, and boron are involved in the maintenance of bone density.[11] These trace elements appear to be essential for the synthesis of the organic matrix of bone.

Table 1 Dietary reference intakes: recommended intakes for individuals, Food, and Nutrition Board, The Institute of Medicine, National Academies

Life stage Group	Calcium (mg d^{-1})	Chromium (µg d^{-1})	Copper (µg d^{-1})	Fluoride (mg d^{-1})	Iodine (µg d^{-1})	Iron (mg d^{-1})	Magnesium (mg d^{-1})	Manganese (mg d^{-1})	Molybdenum (µg d^{-1})	Phosphorus (mg d^{-1})	Selenium (µg d^{-1})	Zinc (mg d^{-1})
Infants												
0–6 months	210*	0.2*	200*	0.01*	110*	0.27*	30*	0.003*	2*	100*	15*	2*
7–12 months	270*	5.5*	220*	0.5*	130*	**11**	75*	0.6*	3*	275*	20*	**3**
Children												
1–3 years	500*	11*	**340**	0.7*	**90**	**7**	**80**	1.2*	**17**	**460**	**20**	**3**
4–8 years	800*	15*	**440**	1*	**90**	**10**	**130**	1.5*	**22**	**500**	**30**	**5**
Males												
9–13 years	1300*	25*	**700**	2*	**120**	**8**	**240**	1.9*	**34**	**1250**	**40**	**8**
14–18 years	1300*	35*	**890**	3*	**150**	**11**	**410**	2.2*	**43**	**1250**	**55**	**11**
19–30 years	1000*	35*	**900**	4*	**150**	**8**	**400**	2.3*	**45**	**700**	**55**	**11**
31–50 years	1000*	35*	**900**	4*	**150**	**8**	**420**	2.3*	**45**	**700**	**55**	**11**
51–70 years	1200*	30*	**900**	4*	**150**	**8**	**420**	2.3*	**45**	**700**	**55**	**11**
>70 years	1200*	30*	**900**	4*	**150**	**8**	**420**	2.3*	**45**	**700**	**55**	**11**
Females												
9–13 years	1300*	21*	**700**	2*	**120**	**8**	**240**	1.6*	**34**	**1250**	**40**	**8**
14–18 years	1300*	24*	**890**	3*	**150**	**15**	**360**	1.6*	**43**	**1250**	**55**	**9**
19–30 years	1000*	25*	**900**	3*	**150**	**18**	**310**	1.8*	**45**	**700**	**55**	**8**
31–50 years	1000*	25*	**900**	3*	**150**	**18**	**320**	1.8*	**45**	**700**	**55**	**8**
51–70 years	1200*	20*	**900**	3*	**150**	**8**	**320**	1.8*	**45**	**700**	**55**	**8**
>70 years	1200*	20*	**900**	3*	**150**	**8**	**320**	1.8*	**45**	**700**	**55**	**8**
Pregnancy												
≤18 years	1300*	29*	**1000**	3*	**220**	**27**	**400**	2.0*	**50**	**1250**	**60**	**13**
10–30 years	1000*	30*	**1000**	3*	**220**	**27**	**350**	2.0*	**50**	**700**	**60**	**11**
31–50 years	1000*	30*	**1000**	3*	**220**	**27**	**360**	2.0*	**50**	**700**	**60**	**11**
Lactation												
≤18 years	1300*	44*	**1300**	3*	**290**	**10**	**360**	2.6*	**50**	**1250**	**70**	**14**
19–30 years	1000*	45*	**1300**	3*	**290**	**9**	**310**	2.6*	**50**	**700**	**70**	**12**
31–50 years	1000*	45*	**1300**	3*	**290**	**9**	**320**	2.6*	**50**	**700**	**70**	**12**

Note: This table presents RDAs in bold type and Adequate Intakes (AIs) in ordinary type followed by an asterisk (*). RDAs and AIs may both be used as goals for individual intake. RDAs are set to meet the needs of almost all (97 to 98%) individuals in a group. For healthy breastfed infants, the AI is the mean intake. The AI for other life stage and gender groups is believed to cover needs of all individuals in the group, but lack of data or uncertainty in the data prevent being able to determine RDA. Sources: Dietary Reference Intakes for Calcium, Phosphorus, Magnesium, Vitamin D, and Fluoride (1997), Dietary Reference Intakes for Vitamin C, Vitamin E, Selenium, and Carotenoids (2000), and Dietary Reference Intakes for Vitamin A, Vitamin K, Arsenic, Boron, Chromium, Copper, Iodine, Iron, Manganese, Molybdenum, Nickel, Silicon, Vanadium, and Zinc (2001). These reports may be accessed via www.nap.edu.

Table 2 Iron, copper, and zinc in selected foods

	Serving (g)	Iron (mg)	Copper (mg)	Zinc (mg)
Calves' liver, pan-fried	67	4.01	10.0	7.97
Ground beef, 75% lean meat, pan-browned	85	2.24	0.068	5.24
Chicken breast, roasted	98	1.05	0.049	1.00
Pacific cod, raw	116	0.30	0.030	0.46
Oyster, eastern, farmed, raw	84	4.86	0.620	31.9
Broccoli, raw	88	0.64	0.043	0.36
Bread, white, commercially prepared	25	0.94	0.063	0.18

Table 3 Calcium in selected foods

	Serving (g)	Calcium (mg)
Milk, whole, 3.25% milk fat	244	276
Cheese, cheddar	28	202
Yogurt, plain, whole milk	245	296
Broccoli, raw	88	41
Bread, white, commercially prepared	25	38

Goiter is the human pathology of hyperplasia of the thyroid gland induced by the deficiency of dietary iodine. The disease is localized in those regions where soils are low in iodine or where seafood is not consumed. Fortification of table salt with sodium iodide, where applied, has practically eradicated this disease. Unfortunately, many regions of the world do not practice this public health policy.

Inadequate amounts of dietary calcium contribute to loss of bone mineral density and increased rates of fracture observed in osteoporosis, a disease which afflicts over 40% of postmenopausal women in the developed nations.[12] The primary source of dietary calcium is dairy products (Table 3). The preparation of corn meal using calcium hydroxide 'fortifies' this grain. Because the intake of dairy products by adult females is low, their average calcium consumption (550 mg) is well below the recommended 1000–1200 mg. Supplementation with various forms of calcium is prudent. Fortification of fruit juices and soft drinks with calcium complexed with citric and malic acids has been achieved.

Amounts of dietary sodium in excess of the kidney's ability to dilute and to excrete it in the urine leads directly to hypertension and indirectly to coronary heart disease and stroke.[13] Although sodium chloride is required at about 1 g day^{-1}, a typical Western diet, in fact, may contain from 8 to 12 g day^{-1}. If renal transport is impaired, sodium ion accumulates and the osmotic pressure of the blood rises. Dietary reduction of salt can ameliorate some but not all of the problems. A wide variety of low-salt food products is now available.

2.2 Solubility

The total amount of a given element in the diet is not always the measure of its nutritional availability. Many trace metals readily hydrolyze to form polynuclear, frequently insoluble, hydroxides. Some metals, particularly iron, demonstrate dramatic differences in solubility as a function of their redox state. The maximum solubility of Fe^{II} at pH 7.0 is 10^{-2} M, while Fe^{III} is 10^{-17} M (*see* ***Iron Proteins for Storage & Transport & their Synthetic Analogs***; ***Iron Transport: Siderophores***). It is not surprising that Fe^{II} is more bioavailable than Fe^{III}. However, Fe^{II} readily autoxidizes and cannot be used to fortify foods because it causes rancidity.[7] Most di- and trivalent metals form insoluble complexes with inorganic and organic phosphates.

Iron pyrophosphate, both insoluble and inert, has been used to fortify foods. Phytic acid, hexaphosphoinositol, a constituent of many grains and vegetables, precipitates many metals. Precipitation of zinc is severe when calcium coexists with phytic acid.[14] Several naturally occurring fibers and polyphenols form insoluble complexes and render a metal less available. A remarkable example of this phenomenon is the recognition that a form of human dwarfism found in the Middle East was attributable to zinc deficiency. Individuals consuming some forms of whole grain containing high concentrations of fiber and phytic acids could not solubilize and absorb their dietary zinc. The ensuing metal deficiency prevented normal genital development. The condition could be reversed with proper diets and zinc supplementation.[15]

Low-molecular weight chelates, either secreted endogenously or provided exogenously in food, solubilize metals and facilitate their uptake. Sugars, amino acids, and organic acids can enhance metal solubility. Fructose and other reducing sugars and polyols bind Fe^{III}, lactose binds Ca^{II}, histidine complexes Cu^{II}, citrate, malate, and succinate complex Fe^{III}, Ca^{II}, Mg^{II}, Cu^{II}, and other metals. Ascorbic acid is unique for iron metabolism in that it both reduces Fe^{III} to Fe^{II} and becomes a powerful chelator, diketogulonic acid, as well. Plants secrete organic acids from their roots to solubilize and mobilize iron from the soil.[16] Frequently soluble complexes of metals with ethylenediamine-N,N,N',N'-tetraacetic acid (EDTA) or similar chelators are applied to soil or leaves to prevent iron deficiencies.[17]

The acid environment of the stomach provides a mechanism for solubilizing finely divided metallic iron as well as metal hydroxides prior to their entry into the small intestine. There, neutralization in the presence of suitable ligands makes the iron bioavailable. The oldest form of iron fortification employed iron filings added to sweet wine. Today, colloidal metallic iron, ferrum reductum, is still a widely used fortificant in food.

2.3 Permeability

Several mechanisms for the transport of ions are operative: (1) active transport of the ion against a concentration gradient by an ATP-driven membrane carrier, (2) passive carrier facilitated transport, (3) passive diffusion dependent upon the ability of the ion or complex to pass the membrane. Sodium, potassium, calcium, and magnesium are actively transported across intestinal and cellular membranes. Calcium and magnesium can also passively diffuse as low-molecular weight complexes bound to membrane proteins. Movement of iron in microbial systems involves the active membrane transport of the Fe^{III} hydroxamate, followed by the intracellular removal of the metal and recycling of the chelator.[18] Many complexes of iron move passively across the intestinal membrane as a function of their size and permeability coefficient. Large polynuclear complexes of iron, manganese, chromium, and copper are impermeable.

2.4 Ligand Exchange

The observed inhibition of Cu^{II} and Zn^{II} uptake by large amounts of Ca^{II} suggests a competition of these metal ions for limiting amounts of solubilizing chelators in the intestinal lumen. Wilson's disease, a heritable disorder of copper overload, is treated by feeding high levels of zinc to block copper uptake (*see* ***Metal-related Diseases of Genetic Origin***).[19] The presence of adequate amounts of a metal in a soluble and permeable form is not sufficient to insure nutritional efficacy. Thus Fe^{III}–EDTA, an excellent source of iron for plants, is nutritionally less effective in mammalian systems. Although dietary Fe^{III}–EDTA readily enters the blood, it readily passes through the kidney tubules and into the urine. The rate of Fe^{III}–EDTA exchange with apotransferrin in the serum or with intracellular sites is slow.[20]

2.5 Transport

The bulk of monovalent elements are ionic and are localized in extra- and intracellular water. Some divalent metals, particularly Ca^{II} and Mg^{II}, exist both as free ions and bound to low- and high-molecular weight ligands. Transferrin, a serum β_1-globulin, has two highly selective binding sites with affinity constants of about 10^{36} for Fe^{III} (*see* ***Iron Proteins for Storage & Transport & their Synthetic Analogs***). This protein solubilizes the Fe^{III} salt and transports it to the sites of assimilation. Absence of transferrin in a genetic disorder leads to pathological iron overload.[21] Serum albumin serves to bind and transport Cu^{II} and Zn^{II}. However, low-molecular weight chelators, including amino acids, may effectively transport these metals.[22–24]

2.6 Assimilation

Many metals are incorporated by equilibrium binding into their specific sites on their apoproteins. The rate of synthesis of the apoprotein by the cells or tissues controls the rate of incorporation. Most zinc and some copper proteins exhibit such behavior. The process of iron incorporation is far more complicated.[25] Uptake of heme into enterocytes occurs as an iron-protoporphyrin complex in an endosome process. Iron is released from heme by heme oxygenase to enter plasma from cytoplasm as inorganic iron. Ferric iron is absorbed via a β_3 integrin and mobilferrin pathway (IMP) specific for iron. Ferrous iron uptake is facilitated by a divalent cation transporter 1/divalent metal ion transporter 1 (DCT1/DMT1). DCT1/DMT1 has a broad substrate range that includes Fe^{II}, Zn^{II}, Mn^{II}, Co^{II}, Cd^{II}, Cu^{II}, Ni^{II}, and Pb^{II}. Many nutritional factors influence iron assimilation. Deficiencies in copper and vitamins B_{12} and B_6 inhibit cellular iron incorporation.

Intestinal absorption of copper is mediated by copper-transporting P-type ATPase 7A (ATP7A) or Menkes disease protein. Mutations in the ATP7A gene lead to Menkes disease in humans that is characterized by congenital impairment in intestinal transport of copper (*see* ***Metal-related Diseases of Genetic Origin***).[26]

2.7 Storage

A striking example of mineral storage is the skeleton. The apparent abundance of calcium available for mobilization is deceiving since loss of relatively little bone mineral density can lead to an increased incidence of serious fractures.[27] Significant amounts of magnesium are stored in bone and available for utilization.

Redox metals, particularly iron and copper, must be stored in a fashion to provide both available reserves of the metal and to sequester the metal in a form which prevents oxidative damage to the cells by Fenton-like reactions (*see Fenton Chemistry*; ***Iron Proteins for Storage & Transport & their Synthetic Analogs***). For iron this is accomplished with the ubiquitous protein, ferritin. Polynuclear iron(III) hydroxide polymer containing from $2-4 \times 10^3$ iron atoms is surrounded by 24 protein subunits. Iron atoms can be mobilized from or enter into the core. The mechanisms governing iron movement are not definitively elucidated. Liver and spleen are the primary organs for ferritin storage. The concentration of serum ferritin can be used as a readily measurable indicator of adequate nutritional iron status. When iron concentrations exceed the ability of the cell to synthesize apoferritin subunits, iron(III) hydroxide polymers aggregate and precipitate, partially surrounded by protein. This material, hemosiderin, is a histological sign of iron pathology, and becomes a focus for oxygen-free radical generation (*see* ***Iron Proteins for Storage & Transport & their Synthetic Analogs***).[28]

The primary organs for copper storage are the liver and spleen, where the metal is found in the cytosol in superoxide dismutase (*see* ***Copper Proteins with Type 2 Sites***) or metallothionein (*see* ***Metallothioneins***).[29] In response to a copper challenge, yeast adaptively synthesizes metallothionein to detoxify the metal.[30] Copper is also bound, transported, and assimilated into tissues by ceruloplasmin.

Although metallothionein in liver binds zinc, there seems no apparent zinc storage in the body according to the kinetic analysis.[31]

2.8 Excretion

The primary organ for the regulation of sodium, potassium, calcium, and magnesium is the kidney. An intricate series of physiological sensing elements and hormonal response mechanisms maintains homeostasis. A variety of diuretic drugs can be used to enhance urinary output of various soluble salts, primarily sodium and potassium chloride. Profuse sweating is also a pathway of excretion for soluble salts and occasionally zinc.[32]

The trace elements iron, copper, zinc, and manganese, however, are excreted via the feces. Not only do the insoluble and unabsorbed dietary metals pass through the gastrointestinal tract, but also continual sloughing off of intestinal cells removes significant amounts of metal from the organism.

Biliary excretion of copper and iron is important. Major losses of iron can be caused by internal bleeding. Thus women during their menstrual periods will be in negative iron balance unless proper nutrition is observed. Blood loss via the gastrointestinal tract, as in ulcers or some forms of cancer, leads quickly to loss of utilizable or stored iron.[10]

Defects in the copper-transporting ATPase 7B (ATP7B) causes Wilson's disease. The ATP7B transporter eliminates copper through the bile and also transports copper into plasma ceruloplasmin (*see* ***Metal-related Diseases of Genetic Origin***).[26]

3 THE PATHOLOGY OF METAL OVERLOAD

As trace element deficiencies give rise to impaired growth and development, excessive uptake or aberrant deposition of some metals can be pathological. Iron storage diseases are of three primary origins: (1) genetic predisposition to increased absorption of dietary iron, hemochromatosis (*see* ***Metal-related Diseases of Genetic Origin***), (2) repeated transfusions of blood, transfusion siderosis, (3) nutritional iron overload. The pathological consequences of each are quite similar. Iron is deposited in liver, spleen, heart, skin, and other tissues. Free radical damage to the tissues is manifest in increased incidence of tumors and heart muscle damage.[33] In the majority of hereditary hemochromatosis cases, mutations in HFE gene (the approved gene symbol responsible for hereditary hemochromatosis by the HUGO Gene Nomenclature Committee) were identified. HFE proteins were found from the small intestine, liver, and placenta in humans. A possible function of HFE protein is the modulation of the transferrin receptor activity.[34]

Conventional treatments for hemochromatosis and for nutritional iron overload include reduction of dietary iron and periodic removal of blood (phlebotomy) until iron stores are reduced. In transfusion siderosis, it is necessary to eliminate iron via the urine by the intravenous infusion of highly specific chelating agents such as desferral (*see* ***Iron Transport: Siderophores***). This process is painful, laborious, and costly. The development of new orally effective iron chelators is expected.

An epidemiological study in a Finnish population indicated an association between moderate iron overload (measured by serum ferritin; *see* ***Iron Proteins for Storage & Transport & their Synthetic Analogs***) and increased incidence of coronary heart disease. This remarkable association has not been confirmed[35] and further investigation will be necessary to determine whether excessive iron storage may relate to coronary heart disease.[10]

One of the most common forms of accidental chemical poisoning is found among young children who swallow iron(II) sulfate pills, their mother's iron supplements, in the mistaken belief that they are candy. Such poisoning demands immediate response with emetic, gastric lavage, and treatment with desferral.

Copper toxicity has been observed, although it is not a function of dietary overload. Abnormally low levels of ceruloplasmin associated with the genetic disorder, Wilson's disease, lead to excessive deposition of copper in the central nervous system, ocular tissue, liver, and other organs. Severe psychotic symptoms are observed. Urinary excretion of the copper can be achieved with specific chelating agents such as British anti-lewisite (BAL, 2,3-dimercaptopropanol) or penicillamine, orally administered. Symptoms of the disease are reversed as the copper levels return to normal. Reduction of dietary copper uptake by competition with relatively high levels of oral zinc is also effective.[19]

Manganese toxicity has been observed in miners exposed to high levels of MnO_2 dust. The neurological symptoms mimic Parkinson's disease. Major changes were observed in the biogenic amines, dihydroxyphenylalanine (DOPA), and phenylalanine. Restoration of appropriate levels of these bioamines alleviated the symptoms. Chelation therapy has not been demonstrated as an effective strategy.[36]

4 SELENIUM AND NICKEL AS ESSENTIAL ULTRATRACE ELEMENTS

Selenium is an amphoteric element whose chemistry and biochemistry has much in common with sulfur. The essentiality of selenium in experimental animals was demonstrated in 1957. It was necessary that the animals be vitamin E deficient to manifest selenium deficiency. Selenium manifests antioxidant activity by its incorporation into selenocysteine and its subsequent participation at the active site of glutathione peroxidase, a key enzyme in the detoxification of H_2O_2. Selenium is also found as selenomethionine, which is also incorporated into the peptide chain of proteins. Dietary selenium is present as the two seleno-amino acids and as inorganic selenite, which can be reduced and assimilated.[37] The nutritional status of selenium is best determined by measuring glutathione peroxidase levels in the blood.[38] Other important selenium-containing proteins include thioredoxin reductases (protein thiol redox regulation), iodothyronine deiodinases (thyroxin activation and triiodothyronine inactivation), selenoprotein P (selenium transport and antioxidant). Human selenium deficiency has been identified as the causal agent in Keshan disease. In some areas of China, soil selenium concentrations are so low that women of child-bearing age and children suffer cardiomyopathy.

Nickel belongs to the iron–cobalt group of metals and is found as a constituent in most meteorites and the nucleus of the Earth. The clear signs of nickel deficiency in experimental animals were demonstrated in 1975.[39] Nickel is decisive for life. Nickel occupies a metal center of urease as well as hydrogenase, carbon monoxide dehydrogenase and other enzymes in the primitive life forms, which have crucial roles in obtaining energy from hydrogen and carbon monoxide, presumably abundant in the primordial solar system (*see* ***Nickel Enzymes & Cofactors***). Nickel is believed to be essential for a chemoautotrophic origin of life.[40] Early studies of the essentiality of nickel indicated that nickel is beneficial for reproductive performance of experimental animals. Nickel deprivation during reproduction in rats is known to increase perinatal mortality.[41] Nickel deprivation of breeding goats significantly decreased the success rate of first insemination and conception rate, and increased the abortion rate.[42] The recent research in rats revealed that nickel deprivation decreased spermatozoa motility and density in the epididymides, epididymal transit time of spermatozoa, and testicular sperm production rate.[43] These findings can explain some parts of the decreased reproduction of nickel-deficient animals. Physiological concentration of nickel is known to potentiate CNG cation channels in the rod outer segments of retinae and to desensitize CNG cation channels of olfactory receptor cells.[9] Decreased spermatozoa motility of nickel-deficient rats may be attributable to the spermatic CNG channels that have a key role in activating flagellar movements. Further investigations of nickel functions in higher organisms including humans are awaited.

5 SUMMARY

In Greek mythology, when Phylacus was gelding rams, his son Iphyclus was frightened by his father's knife. After growing up, Iphyclus could not have children. The seer Melampus cured Iphyclus's male infertility or sexual impotency by having him drink rust scraped from his father's knife stuck on the sacred oak.[44] Perhaps this was one of the first manifestations of the belief system 'You are what you eat'. According to Guggenheim,[45] Thomas Sydenham (1624–1689) of London in 1661 treated chlorotic maidens with an iron syrup or a steel tonic, which he prepared from soaking steel filings in wine. This process presumably produced ferrous potassium tartrate. Hippocrates of Cos, in the fifth century BC, recommended the use of roasted flower of copper or copper ore ('chalcitis') with natron and other ingredients soaked in sweet wine for treatments of fistulae, ulcers, hemorrhoids, and other diseases.[46] Not long ago, table salt was a luxury item, heavily taxed and greatly coveted. Now some treat salt as a nutritional pariah. Paracelsus, one of the great alchemists, was a true believer in the efficacy of metal ions to cure and prevent disease. Paracelsus recognized 'sal' (salt or ash) as the active principle always found in all organisms as well as inanimate matters. He wrote one of the most prescient observations that serves us well today 'Only the dose makes the poison'.[47] It is our challenge to understand the optimal human mineral requirements and apply dietary strategies to ensure optimal health for all.

6 RELATED ARTICLES

Metal Ion Toxicity; Metal-related Diseases of Genetic Origin.

7 REFERENCES

1. E. J. Underwood, W. Mertz, Introduction, in 'Trace Elements in Human and Animal Nutrition', 5th edn., ed. W. Mertz, Academic Press, New York, 1987, Vol. 1, p. 1.
2. M. Kobayashi and S. Shimizu, *Eur. J. Biochem.*, 1999, **261**, 1.
3. H. H. Sandstead, *Nutrition*, 1995, **11**, 87.
4. R. A. Sunde, Selenium, in 'Present Knowledge in Nutrition', 8th edn., eds. B. A. Bowman and R. M. Russel, International Life Science Institute, Washington, DC, 2001, Chap. 33, p. 352.
5. Food and Nutrition Board, Institute of Medicine, 'Dietary Reference Intakes for Vitamin A, Vitamin K, Arsenic, Boron, Chromium, Copper, Iodine, Iron, Manganese, Molybdenum, Nickel, Silicon, Vanadium, and Zinc (2000)', National Academy Press, Washington, DC, 2001.
6. K. Yokoi, *Biol. Trace Elem. Res.*, 2003, **95**, 155.
7. P. Saltman, Nutritional Aspects of Metals & Trace Elements, in 'Encyclopedia of Inorganic Chemistry', ed. R. B. King, John Wiley & Sons, Chichester, 1994, Vol. 5, p. 2721.
8. J. M. Matthews and M. Sunde, *IUBMB Life*, 2002, **54**, 351.
9. J. P. Johnson Jr, and W. N. Zagotta, *Nature*, 2001, **412**, 917.

10. R. Yip, Iron, in ‘Present Knowledge in Nutrition’, 8th edn., eds. B. A. Bowman and R. M. Russel, International Life Science Institute, Washington, DC, 2001, Chap. 30, p. 311.
11. F. H. Nielsen, *Magnes. Trace Elem*, 1990, **9**, 61.
12. L. J. Melton III, E. A. Chrischilles, C. Cooper, A. W. Lane, and B. L. Riggs, *J. Bone Miner. Res.*, 1992, **7**, 1005.
13. H. G. Preuss, Sodium, Chloride, and Potassium, in ‘Present Knowledge in Nutrition’, 8th edn., eds. B. A. Bowman and R. M. Russel, International Life Science Institute, Washington, DC, 2001, Chap. 29, p. 302.
14. H. H. Sandstead, *J. Nutr.*, 2000, **130**, 347S.
15. A. Prasad, A. Miale, Z. Farid, H. H. Sandstead, and A. Schulert, *J. Lab. Clin. Med.*, 1963, **61**, 537.
16. D. Staiger, *Angew. Chem., Int. Ed. Engl.*, 2002, **41**, 2259.
17. J. C. Brown and L. D. Tiffen, *Plant Phys.*, 1965, **40**, 395.
18. G. Winkelmann, *Biochem. Soc. Trans.*, 2002, **30**, 691.
19. H. H. Sandstead, *J. Lab. Clin. Med.*, 1989, **114**, 615.
20. G. W. Bates, C. Billups, and P. Saltman, *J. Biol. Chem.*, 1967, **242**, 2810.
21. S. Sheth and G. M. Brittenham, *Annu. Rev. Med.*, 2000, **51**, 443.
22. I. Gyasi, R. G. Harper, and R. A. Wapnir, *Biochem. Mol. Med.*, 1995, **56**, 70.
23. P. Z. Neumann and A. Sass-Kortsak, *J. Clin. Invest.*, 1967, **46**, 646.
24. H. Faure, A. Favier, M. Tripier, and J. Arnaud, *Biol. Trace Elem. Res.*, 1990, **24**, 25.
25. M. E. Conrad and J. N. Umbreit, *Blood Cells Mol. Dis.*, 2002, **29**, 336.
26. D. W. Cox and S. D. Moore, *J. Bioenerg. Biomembr.*, 2002, **34**, 333.
27. W. C. Hayes, E. R. Myers, J. N. Morris, T. N. Gerhart, H. S. Yett, and L. A. Lipsitz, *Calcif. Tissue Int.*, 1993, **52**, 192.
28. G. W. Richter, *Am. J. Pathol.*, 1978, **91**, 362.
29. J. E. Hoadley, A. S. Leinart, and R. J. Cousins, *J. Nutr.*, 1988, **118**, 497.
30. D. H. Hamer, *Annu. Rev. Biochem.*, 1986, **55**, 913.
31. K. Yokoi, N. G. Egger, V. M. Ramanujam, N. W. Alcock, H. H. Dayal, J. G. Penland, and H. H. Sandstead, *Am. J. Physiol. Endocrinol. Metab.*, 2003, **285**, E1010.
32. K. C. DeRuisseau, S. N. Cheuvront, E. M. Haymes, and R. G. Sharp, *Int. J. Sport. Nutr. Exerc. Metab.*, 2002, **12**, 428.
33. R. S. Britton, K. L. Leicester, and B. R. Bacon, *Int. J. Hematol.*, 2002, **76**, 219.
34. C. S. Cardoso and M. de Sousa, *Tissue Antigens*, 2003, **61**, 263.
35. D. Claeys, M. Walting, F. Julmy, W. A. Wuillemin, and B. J. Meyer, *Eur. J. Clin. Invest.*, 2002, **32**,(Suppl. 1), 3.
36. J. Donaldson, *Neurotoxicology*, 1987, **8**, 451.
37. R. F. Burk, K. E. Hill, and A. K. Motley, *J. Nutr.*, 2003, **133**, 1517S.
38. K. E. Hill, R. F. Burk, and J. M. Lane, *J. Nutr.*, 1987, **117**, 99.
39. F. H. Nielsen, Nickel, in ‘Trace Elements in Human and Animal Nutrition’, 5th edn., ed. W. Mertz, Academic Press, New York, 1987, Chap. 8, Vol. 1, p. 245.
40. C. Huber, W. Eisenreich, S. Hecht, and G. Wachtershauser, *Science*, 2003, **301**, 938.
41. F. H. Nielsen, D. R. Myron, S. H. Givand, T. J. Zimmerman, and D. A. Ollerich, *J. Nutr.*, 1975, **105**, 1620.
42. M. Anke, B. Groppel, and U. Krause, Further Data on the Biological Essentiality of Nickel, in ‘Trace Elements in Man and Animals 6’, eds. L. S. Hurley, C. L. Keen, and B. Lonnerdal, Plenum Publishing, New York, 1988, p. 467.
43. K. Yokoi, E. O. Uthus, and F. H. Nielsen, *Biol. Trace Elem. Res.*, 2003, **93**, 141.
44. Apollodorus ‘Apollodorus, The Library’, with an English Translation by Sir James. G. Frazer, F. B. A., F. R. S. Harvard University Press, William Heinemann, Cambridge, MA, London, 1921.
45. K. Y. Guggenheim, ‘Nutrition and Nutritional Diseases’, DC Heath and Company, Lexington, MA, 1981.
46. P. T. Paul, ‘Hippocrates, Vol. VIII: Places in Man, Glands, Fleshes, Prorrhetic 1-2, Physician, Use of Liquids, Ulcers, Haemorrhoids and Fistulas’, Harvard University Press, Cambridge, MA, 1995.
47. W. C. Krieger, Forword on Paracelsus-Dose Response, in ‘Handbook of Pesticide Toxicology’ 2nd edn., ed. R. Krieger, Academic Press, San Diego, CA, 2001, Vol. 1–2, p. xxvii.

Oligomerization & Polymerization by Homogeneous Catalysis

Gregory G. Hlatky
Equistar Chemicals LP, Cincinnati, OH, USA

1	Introduction	1
2	Background	1
3	Group 4 Metals	4
4	Group 3 Metals, Lanthanides and Actinides	9
5	Group 5 Metal Complexes	10
6	Group 6 Metal Complexes	10
7	Iron and Cobalt	11
8	Nickel and Palladium	12
9	Other Metals	14
10	Related Articles	14
11	References	15

Abbreviations

Cp′ = Substituted or unsubstituted cyclopentadienide; Cp* = η^5-C_5Me_5; L = Ancillary ligand; MMA = Methyl methacrylate; Pn = Polymer chain.

1 INTRODUCTION

The 1963 Nobel Prize in Chemistry was awarded to Karl Ziegler and Giulio Natta for their research on catalysts (*see Catalysis*) for the oligomerization (*see Oligomer*) and polymerization (*see Polymerization*) of alkenes under mild conditions of temperature and pressure. Their discoveries have grown into a multibillion dollar industry for the production of plastics, elastomers, and inexpensive feedstock chemicals for copolymers, surfactants, and other useful additives.[1,2]

Homogeneous oligomerization and polymerization catalysts were for many years in the shadows of their heterogeneous counterparts but began to attract the interest of industrial and academic chemists since the late 1970s. The term 'homogeneous', when applied to polyalkene catalysis, does not necessarily mean that catalysts, reactants, and products are in a single phase; soluble polymerization catalysts, for example, become heterogeneous if the polymer precipitates from solution. Instead, we define a 'homogeneous' polymerization as one having a single type of active site, resulting in far more uniform products than those possible with, in the case of polymerization, multisited heterogeneous Ziegler–Natta catalysts (*see Ziegler–Natta Catalysts*).

As economics and demands of the marketplace require more tailored preparations of polyalkenes, researchers continue to work toward turning the 'art' of polyalkene catalysis into a science. Understanding and controlling the active catalyst species and the processes by which alkene-based macromonomers are formed offers the opportunity for preparing products of targeted characteristics or with greater selectivity. This article examines the more important homogeneous polymerization and oligomerization catalysts, emphasizing well-characterized systems.

2 BACKGROUND

Oligomerization and polymerization are processes by which a monomer M or monomers M and N are coupled into higher molecular weight molecules consisting of repeating units (equation 1).

$$\begin{gathered} x\,\mathrm{M} \longrightarrow (\mathrm{M})_x \\ x\,\mathrm{M} + y\,\mathrm{N} \longrightarrow (\mathrm{M})_x(\mathrm{N})_y \end{gathered} \qquad (1)$$

Dimerization occurs when x or $x + y = 2$. The products are considered oligomers when x or $x + y =$ from about 2 to 100. Molecules of more than about 100 monomer units are considered polymers. Homo-oligomers or -polymers result when one monomer is used. Co-oligomers or -polymers are formed from two or more different monomers. The distribution of comonomers in a co-oligomer or copolymer may be random (NMMNMMNMNMMNN), alternating (NMNMNMNMNMNMN), or blocked (NNNNNNNMMMMMM).

Branching can result from the chain-growth process or from branching groups in the monomers. For example, ethylene can be polymerized by a radical process to a highly branched low-density polyethylene (LDPE) or copolymerized with small amounts of α-alkenes like 1-hexene or 1-octene using a metal-mediated catalyst; the result is a linear polyethylene punctuated by short-chain branches and known as linear-low-density polyethylene (LLDPE).

Oligomerization and polymerization catalysis by metal complexes comprises three steps: initiation, propagation, and termination. Chain growth proceeds at a coordinatively unsaturated (*see Coordinative Saturation & Unsaturation*) center having a metal–carbon or metal–hydride (*see **Hydride Complexes of the Transition Metals***) bond, usually generated by the interaction of a metal complex with an activating species such as an alkylaluminum cocatalyst. The first insertion of an alkene monomer into the metal–carbon or metal–hydride bond (chain initiation) is followed by repeated insertions (propagation) until the chain is eliminated (termination), causing the cycle to start again (equation 2). Alkenes (cyclic olefins and α-olefins), dienes, and alkynes with terminal unsaturation make the most suitable monomers; internal alkenes are more difficult to polymerize, though certain nickel catalysts will polymerize *trans*-2-butene to poly(*trans*-2-butene).[3]

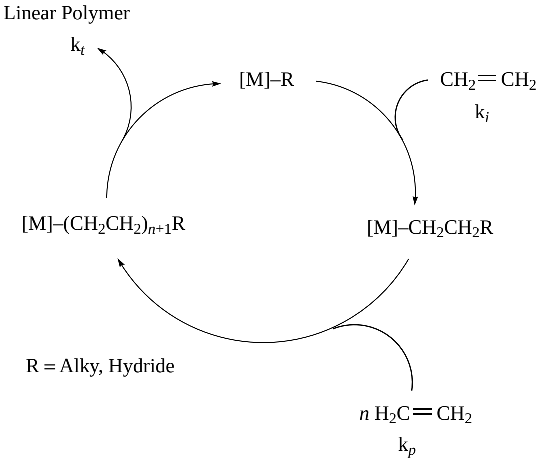

(2)

The mechanism of chain propagation now seems to be clear, following the Cossee (*see Cossee–Arlman Mechanism*) suggestion of chain growth by stepwise cis migratory insertion of the alkene into the metal–carbon bond.[4] Homogeneous catalysis has been invaluable in elucidating the chain-growth process, both in experimentation with model systems[5,6] and in theoretical calculations based on these complexes.[7] For example, the stepwise initiation and growth of a chain was observed by NMR spectroscopy using a precisely defined zirconium-based catalyst $1,2\text{-Et(Indenyl)}_2\text{Zr}^+\text{Me(MeB}^-(\text{C}_6\text{F}_5)_3)$ (equation 3);[8] such observations would have been impossible with the classic Ziegler–Natta catalyst systems.

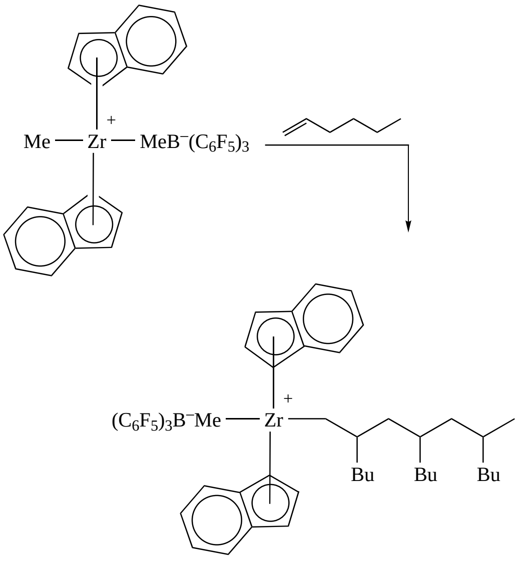

(3)

The predominant chain termination mechanisms are (i) β-hydride elimination (*see Polymerization*), giving a chain with a terminal alkene; (ii) reaction with hydrogen, frequently used to control chain length; (iii) chain transfer to monomer by σ-bond metathesis (*see σ-Bond Metathesis*); and (iv) chain transfer to cocatalyst (equation 4).

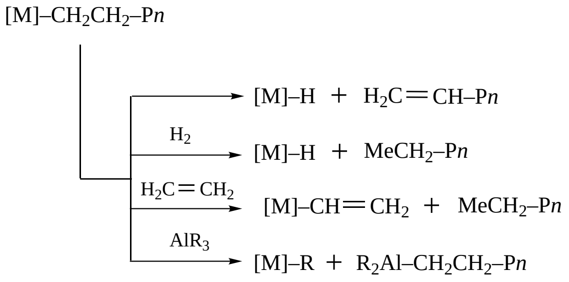

(4)

The ratio of the rate of propagation (k_p) to the rate of termination (k_t) determines the molecular weight of the polyalkene:

- $k_p \gg k_t$ high polymers
- $k_p \approx k_t$ oligomers
- $k_p \ll$ kt dimers

Catalysts based on high-valent compounds of the early transition series (groups 3–5) and the lanthanides and actinides generally form high polymers; these electron-deficient (*see Electron Deficient Compound*) metal complexes are poor π-bases and have little ability to bond either into the σ^* orbital on the β-C–H bond or into the π^* of the bound alkene. The later transition metals (groups 9–10) are far more electron-rich; β-elimination (*see β-Elimination*) is much faster and dimers and oligomers are produced.

Chains with monodisperse molecular weight distribution ($Mw/Mn = 1.00$) can occur in idealized conditions when all polymerizing centers initiate instantaneously and chain termination is absent. In these cases the catalyst is actually an initiator. These 'living' polymerizations are quite rare among transition metal catalysts. More often, random chain termination leads to many chains formed per metal atom. A Schulz–Flory 'most probable' distribution of polyalkene molecular weights ($Mw/Mn = 2.00$) is the result.[9] In cases when more than one type of active site is present, bimodal or multimodal distributions of molecular weights result ($Mw/Mn > 2.00$).

Branched α-alkenes, most notably propylene, can insert in either a Markovnikov (secondary or 2,1) fashion or anti-Markovnikov (primary or 1,2) fashion (equation 5). Depending on the regioorientation of the next inserting monomer, this can lead to head-to-tail sequences (the most frequent in polypropylene), head-to-head or tail-to-tail. An illustration of the possible structures is shown in the catalytic dimerization of propylene by nickel catalysts (Figure 1). n-Hexenes, methylpentenes, and 2,3-dimethylbutene can be formed by the nickel hydride catalyst

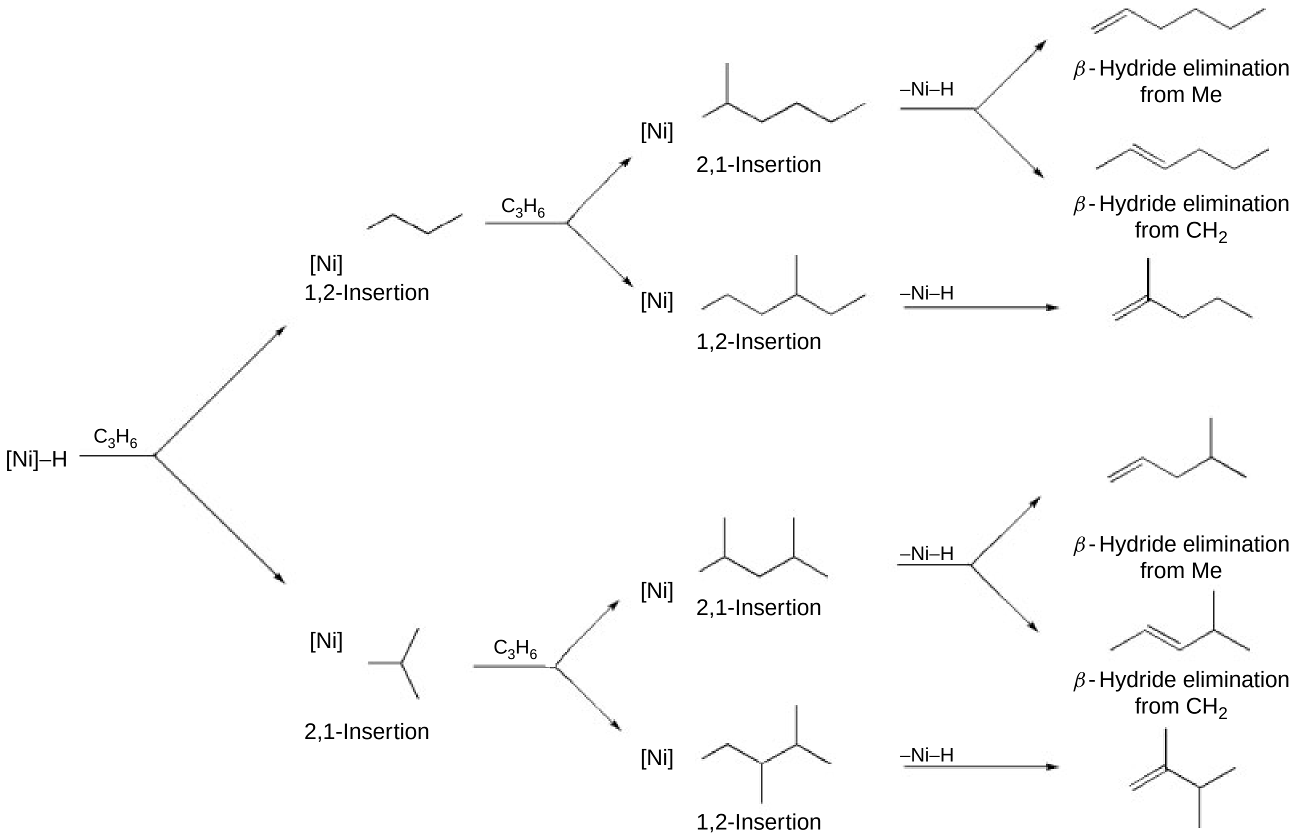
[Ni]–H
C_3H_6
[Ni]
1,2-Insertion
[Ni]
2,1-Insertion
C_3H_6
[Ni]
2,1-Insertion
[Ni]
1,2-Insertion
–Ni–H
β-Hydride elimination from Me
β-Hydride elimination from CH_2
C_3H_6
[Ni]
2,1-Insertion
[Ni]
1,2-Insertion
–Ni–H
β-Hydride elimination from Me
β-Hydride elimination from CH_2
–Ni–H

Figure 1 Regioisomerism in the dimerization of propylene

depending on the sequence of 2,1 and 1,2 insertions (*see Insertion*).

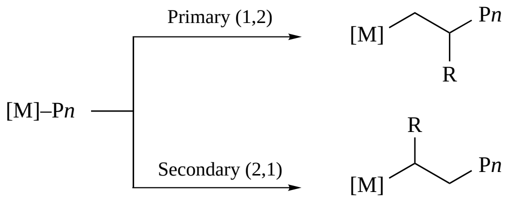
Primary (1,2)
[M]–P*n*
[M]
P*n*
R
Secondary (2,1)
R
[M]
P*n*

(5)

The regularity with which the branch groups of poly(α-olefins) are oriented leads to products of different properties. Propylene, for example, is prochiral and can polymerize with the methine carbons in either an (R) or (S) configuration. Two adjacent units with similar orientations are called a meso or m dyad while two adjacent units with different configurations are called rac or r dyads. Propylene in which the methyl groups are randomly oriented (random r and m dyads) is referred to as atactic, a rubbery material with limited commercial value (Figure 2). Isotactic polypropylene, where the methyl groups all have the same stereoorientation (all m dyads), is a crystalline material with many important applications. Syndiotactic polypropylene, with alternating sterocenters (all r dyads), can only be produced from homogeneous catalysts.

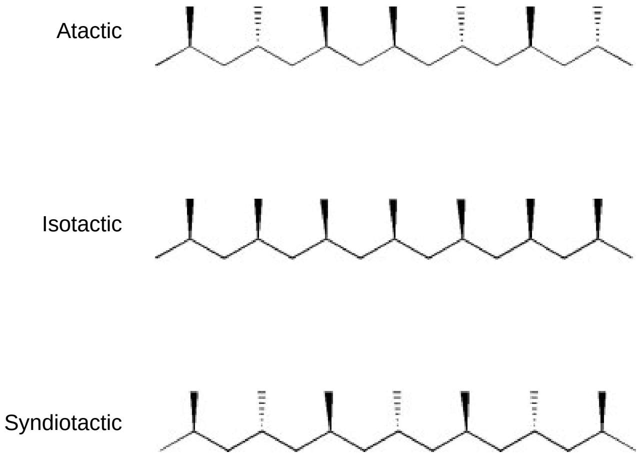
Atactic
Isotactic
Syndiotactic

Figure 2 Structures of propylene polymers (with Bovey dyad notation)

1,3-Butadiene can be polymerized to four different microstructures: *cis*-1,4, *trans*-1,4, isotactic 1,2 and syndiotactic 1,2 (Figure 3). All four microstructures can be prepared

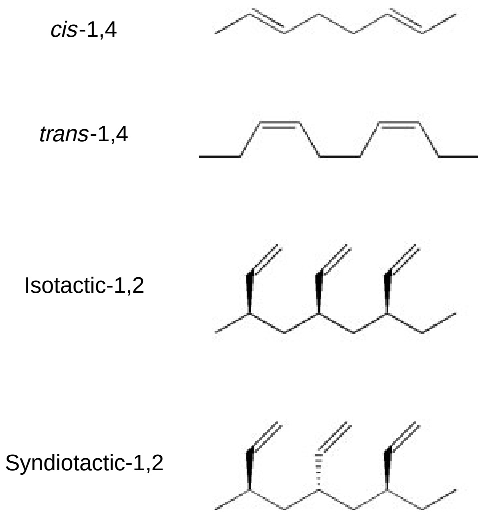

Figure 3 Structures of poly(1,3-butadiene)

to >95% selectivity using a wide variety of transition metal catalysts.[10]

Conventional heterogeneous catalysts have several drawbacks. Frequently a multiplicity of active sites (*see Active Site*) are generated by the interaction of the transition metal catalyst and the cocatalyst. Each type of active site has its own rates of initiation, propagation, termination, regio- and stereoregularity, and copolymerizing ability. The formation of complex mixtures of products containing undesirable species (chains with too many or too few branches, internal alkenes, high or low-molecular weight fractions, noncrystalline polymers) can give unwanted by-products, requiring costly separations or affording materials with inferior properties for a given application. Furthermore, the complexity of these catalysts limits our ability to understand and control their behavior.

Homogeneous polyalkene catalysts have three basic components: 1) a metal center; 2) a set of ligands (*see Ligand*) which react with cocatalyst and/or incoming monomer, and 3) a nonreactive ancillary ligand or ligands to limit the formation of multiple active catalyst species and control the electronic and steric environment around the active site. These catalysts afford much more uniform products than can be made from traditional heterogeneous systems. Alterations in the ancillary ligand set can be done rationally and molecular modeling can give insights into the response of the catalyst to the change.[7,11] An impressive array of instrumental techniques can be brought to bear in characterizing catalyst structures, catalytic mechanisms and products. High-throughput experimentation using automated process and data handling now allows researchers to screen a diverse array of catalysts far more quickly than serial testing.[12]

The ancillary ligands used in homogeneous polyalkene catalysis have become extraordinarily diverse, partly to exploit hitherto uninvestigated metals and partly to avoid the legal tangles associated with the industrial development of these systems. However, these ancillary ligands largely fall into three basic classes:

- Pi-bonded ligands, principally cyclopentadienyl (*see Cyclopentadienyl*) (especially in the earlier group metals) but also isolobal equivalents (*see Isolobal Analogy*) such as phospholes, boratabenzenes, and azaborolinyls.
- Sigma-bonded anionic ligands, usually chelating (*see Chelating Ligands*) ones such as β-diketenimides.
- Neutral ligands, which may be chelating or nonchelating.

All this does not suggest that homogeneous catalysts are prisoners of the laboratory. Homogeneous oligomerization and polymerization catalysts are now widely used industrially and new developments are constantly being brought into the commercial sphere.

3 GROUP 4 METALS

It was with the group 4 metals that homogeneous alkene polymerization catalysts began, almost contemporaneously with the discovery of Ziegler–Natta polymerization catalysts and cyclopentadienyl metal complexes. The Cp_2TiCl_2–$AlEt_2Cl$ catalyst discovered by Natta[13] and Breslow[14] was used extensively as a model system for heterogeneous polymerization catalysts, yielding many valuable insights into the mechanism of polymerization and active-site characterization. For example, electrochemical studies suggested the active polymerizing species was a $[Cp_2TiR]^+$ cation.[15] Subsequently, this species was characterized after trapping with a nonpolymerizable alkyne (equation 9).[16]

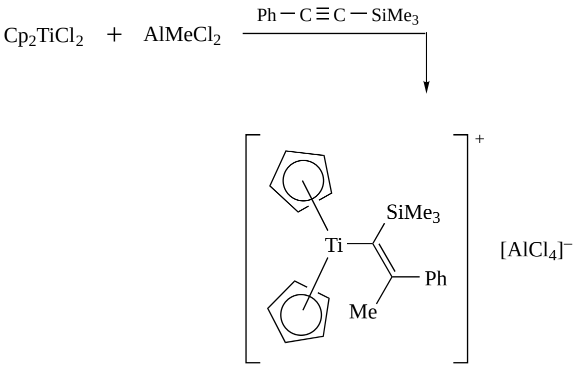

(6)

This catalyst is unsuitable for commercial applications because of its facile reduction to inactive Ti^{III} species in hydrocarbon solvents, its sluggish polymerization activity compared to conventional Ziegler–Natta catalysts, and its inability to polymerize propylene.

A breakthrough in the field took place in the mid-1970s when these group 4 metallocenes were combined with methylalumoxane, the product of the partial hydrolysis of trimethylaluminum (equation 7), to afford catalysts of vastly higher activity, especially of

$$AlMe_3 + CuSO_4(H_2O)_5 \xrightarrow{\text{Toluene}} [AlOMe]_n \qquad (7)$$
$$n = 5\text{–}25$$

zirconocenes.[17] The subsequent discovery[18] that substitutions on the cyclopentadienyl ring had a profound influence on activity, polymer molecular weight (from waxes to ultrahigh molecular weight materials), reactivity toward comonomer (from elastomers to high-density polyethylene), and stereospecificity in α-olefin polymerization began the great industrial development of homogeneous polymerization catalysts of the group 4 metals. These have long been dominated by metallocenes (*see Metallocene Complexes*), but highly effective catalysts with novel ancillary ligands are now coming on stream.

Catalysts of the group 4 metals are much used in the commercial production of high olefin polymers, principally ethylene and propylene homo- and copolymers. When the polymer is particularly rich in comonomer (ethylene-propylene copolymers, ultra low-density ethylene copolymers), it is of low crystallinity and usually soluble in a hydrocarbon medium. For polymers of greater crystallinity (high-density polyethylene, isotactic polypropylene), the catalysts must be heterogenized on an inert support such as silica to ensure uniform morphology of the polymer particles, essential to smooth process operations. Many supports and supporting techniques have been developed to ensure high catalyst activity and good particle morphology without alteration of polymer properties.[19]

Almost all group 4 metal complexes require a cocatalyst to generate an active metal–alkyl cationic species.[20] Ordinary alkylaluminums – used in conventional Ziegler–Natta catalysts – are insufficient to activate these compounds on their own. The principal activator used is methylalumoxane (MAO), a structurally enigmatic material with a mixture of nuclearities.[21] Its purpose is to alkylate the metal dichloride and to abstract one of the reactive ligands to form the ion pair active catalyst. The interaction is dynamic and a large excess of MAO is needed for effective catalyst performance, thus inhibiting a comprehensive characterization of these catalysts.

By switching from $AlMe_3$ to $Al(t\text{-}Bu)_3$, alumoxanes of discrete nuclearities can be isolated. $(t\text{-}BuAlO)_6$ was structurally characterized and its interaction with Cp_2ZrMe_2 studied spectroscopically, indicating that the alumoxane abstracted a methyl group to generate a catalytically active tight ion pair with the oxygen atom of the alumoxane coordinated to the zirconium cation (equation 8).[22]

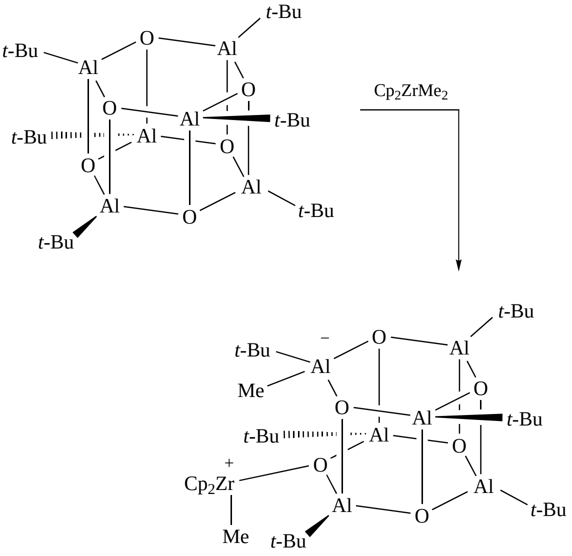

(8)

Highly active, yet completely characterizable catalysts are formed from Cp'_2MMe_2 and perfluorinated arylborates such as $B(C_6F_5)_3$[23] and $[Ct][B(C_6F_5)_4]$ ($[Ct]^+ = [HNMe_2Ph]^+$[24] or $[Ph_3C]^+$[25]). These form ion pairs with noncoordinating anions (*see Noncoordinating Anion or Cation*), which are largely resistant chemically to degradation by the strongly Lewis acidic metal cation. The neutral $B(C_6F_5)_3$ activator abstracts an alkyl group from Cp'_2ZrMe_2 to form $[Cp'_2ZrMe][Me(B(C_6F_5)_3)]$, adducts of which can be isolated and characterized crystallographically (*see X-ray Crystallography*).[23] The borane and borate cocatalysts also have the advantage of being used in near stoichiometric quantities with respect to the metal complex. In a further refinement, simple alkylaluminums can be used to alkylate the metal dichlorides before reaction with the activating boron cocatalysts (equation 9).[26]

$$\begin{tikzcd}
 & {[Cp'_2MR][RB(C_6F_5)_3]} \\
Cp'_2MCl_2 + AlR_3 \arrow[r] & Cp'_2MR_2 + AlRCl_2 \arrow[u, "B(C_6F_5)_3"'] \arrow[d, "{[Ct][B(C_6F_5)_4]}"] \\
 & {[Cp'_2MR][B(C_6F_5)_4]}
\end{tikzcd} \qquad (9)$$

The extent to which the metallocene framework can be modified is extraordinary indeed, with from one to four different substituents on each ring or a covalent bridging group like 1,2-ethylene or dimethylsilyl to lock the rings into one particular conformation and open the active site to varying degree. All these factors have an influence on catalyst performance and polymers produced.[27] An example

Table 1 Ethylene polymerization by 1,2-Et(Flu′)(Flu′)$ZrCl_2$–MAO catalysts

(Flu′)(Flu′)	Activity (kg mmol Zr^{-1} hr^{-1})	MW ($\times 10^{-3}$)
(4,5-dimethylfluorenyl)$_2$	2601	444
(4-methylfluorenyl)$_2$	2408	610
(4,5-dimethylfluorenyl)(fluorenyl)	1965	240
(4-benzylfluorenyl)$_2$	1464	610
(3,4-benzofluorenyl)(fluorenyl)	941	430
(2,7-dinapthylfluorenyl)(fluorenyl)	693	760
(2,7-dinapthylfluorenyl)$_2$	666	270
(2,7-di-*t*-butylfluorenyl)$_2$	613	93
(4-benzylfluorenyl)(fluorenyl)	561	510
(4,5-benzofluorenyl)$_2$	485	570
(fluorenyl)$_2$[a]	420	620
(2-napthylfluorenyl)$_2$	375	620
(4,5-benzofluorenyl)(fluorenyl)	279	1050
(1-methylfluorenyl)$_2$	221	270
(2-methylfluorenyl)$_2$	217	610
(2,7-dimethylfluorenyl)$_2$	214	680
(1,8-dimethylfluorenyl)(fluorenyl)	210	200
(2,7-diethylfluorenyl)$_2$	189	830
(2,7-dimethylfluorenyl)(fluorenyl)	125	575

[a] Reference compound.

with just one class of substituted 1,2-ethylene bridged bis(fluorenyl)zirconium dichlorides is shown in Table 1, with catalyst activities and polymer molecular weights ranging over an order of magnitude.[28]

Metallocene group 4 catalysts are now used for the commercial production of ethylene/α-olefin copolymers with superior properties (clarity, tear strength, extractables) to those from conventional Ziegler–Natta catalysts. Metallocenes also excel in the copolymerization of ethylene with olefin monomers generally not reactive with Ziegler–Natta systems. For example, copolymers of ethylene with cyclic olefins like norbornene have desirably high glass transition temperatures (>100 °C). Conventional Ziegler–Natta catalysts produce copolymers with unwanted unsaturation from ring opening. Metallocene catalysts afford high molecular weight products with high T_g without residual unsaturation (equation 10).[29]

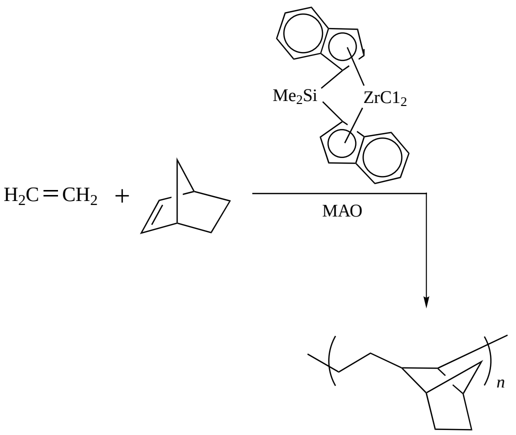

(10)

It is in the stereospecific polymerization of propylene that metallocene complexes display their astonishing versatility.[30] Commercial Ziegler–Natta catalysts for isotactic polypropylene – based on combinations of $TiCl_4$, $MgCl_2$, Lewis bases and aluminum alkyls – depend on a metal-centered chirality which exists at specific edge and defect sites on the crystal lattice to direct the incoming monomer in a particular orientation. These catalysts produce small amounts of undesirable atactic material due to the presence of achiral active sites.

Until the mid-1980s, no homogeneous catalyst for the stereospecific polymerization of propylene existed: Cp_2ZrCl_2-MAO produces only atactic material. Isospecific polymerization in which the stereoorientation of the monomer is caused by the active polymerizing site can be induced by stereorigid metallocenes which have chirality centered at the transition metal. Such metallocenes have groups bridging the two cyclopentadienyl rings and substituents in the β-positions of the cyclopentadienyl groups. The steric constraints exerted by the ring substituents on the polymer chain force the chain into one particular orientation, which serves to direct the incoming monomer (Figure 4). The achiral meso complex has no orienting ability and gives atactic material. It is quite interesting that detailed mechanistic studies have established that stereoerrors (. . .mmrrmm. . .) are not the result of insertion of the wrong enantioface of the monomer but are caused by epimerization of the chiral center at the chain-end near the metal.[31]

The first catalyst to produce isotactic polypropylene at meaningful temperatures was the C_2-symmetric

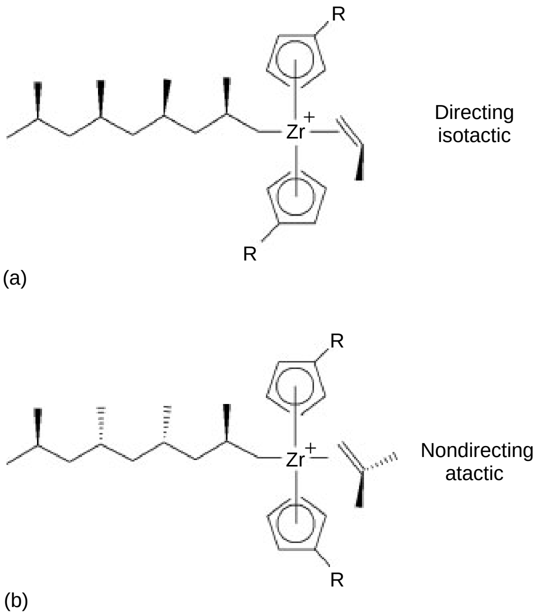

Figure 4 Polymer chain and monomer orientation in rac (a) and meso (b) isomers of stereorigid substituted zirconocene catalysts

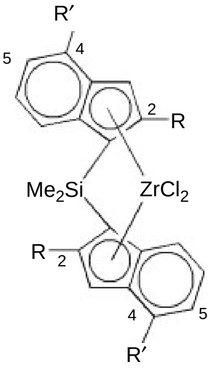

(**1**)

Figure 5 Structure of substituted dimethylsilyl-bridged bis(indenyl)zirconium dichlorides

complex *rac*-1,2-Et(4,5,6,7-tetrahydroindenyl)$_2$ZrCl$_2$ activated by MAO.[32] The polypropylene produced from this catalyst is of only modest molecular weight and isotacticity, but this disclosure served to set off a detailed search for more active catalysts to produce polypropylene of melting points and molecular weights produced by conventional Ziegler–Natta catalysts (mp = 165 °C, Mw = 900 000). This research effort, largely undertaken at Hoechst, made serial changes to the metallocene framework to improve its performance as a catalyst.[33] The use of a dimethylsilyl bridge (**1**, Figure 5) makes preparation of the complexes simpler and slightly improves activity, molecular weight, and stereospecificity. Adding a methyl group in the 2-position of the indenyl ring significantly increases the regioregularity of propylene insertions, increasing the melting point as well as the molecular weight. Substituents in the 4-position (or 4,5-benzoindenyl) have an enormous influence on catalyst performance (Table 2).

Syndiotactic polypropylene arises from the coordination of alternating enantiofaces of the incoming monomer. This can be induced by metallocene catalysts through the use of C$_s$ symmetric metallocene catalysts such as Me$_2$C(Cp)(Fluorenyl)ZrCl$_2$–MAO (equation 11).[34] This material is now sold commercially, though the long crystallization time from the melt has limited its applications.

Table 2 Propylene polymerization by Me$_2$Si(Ind′)$_2$ZrCl$_2$-MAO catalysts

Ind′	Activity (kgPPmmol^{-1} Zr^{-1})	Mw ($\times10^{-3}$)	M.p. (°C)
Indenyl	190	36	137
2-Methylindenyl	99	195	145
4-Isopropyl-2-methylindenyl	250	210	150
4-Phenyl-2-methylindenyl	550	730	157
4-(1-Naphthyl)-2-methylindenyl	880	920	161

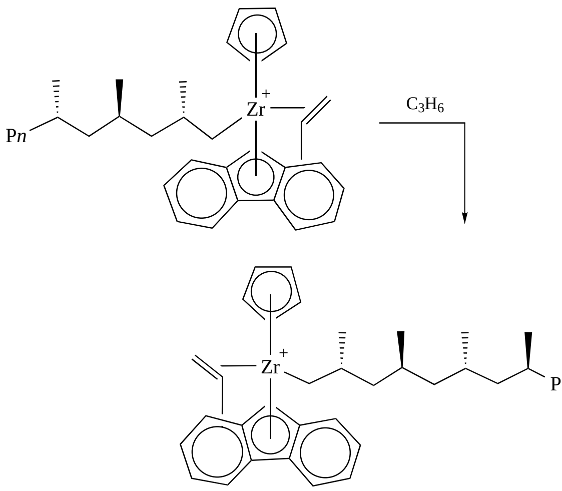

(11)

Substituents in the distal position of the cyclopentadienyl ring in these cyclopentadienyl-fluorenyl catalysts has a profound effect on the polymer product produced. A small substituent like methyl produces a novel material, hemiisotactic polypropylene, in which methine carbons of specific conformation alternate with methine carbons of random conformation.[35] A larger substituent like *t*-butyl makes isotactic polypropylene (Figure 6).

Elastomeric polypropylenes with thermoplastic behavior can be prepared from conformationally dynamic metallocenes such as bis(2-arylindenyl)zirconium dichlorides.[36] These can exist in two conformations in the course of the chain lifetime: a chiral rac isomer which is stereodirecting and an achiral meso isomer which is aspecific. The resulting polymer consists of blocks of isotactic polypropylene alternating with runs of atactic material (equation 12).

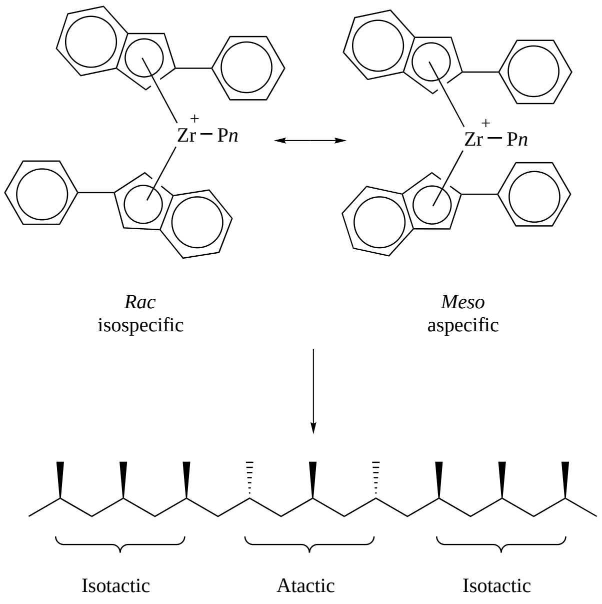

(12)

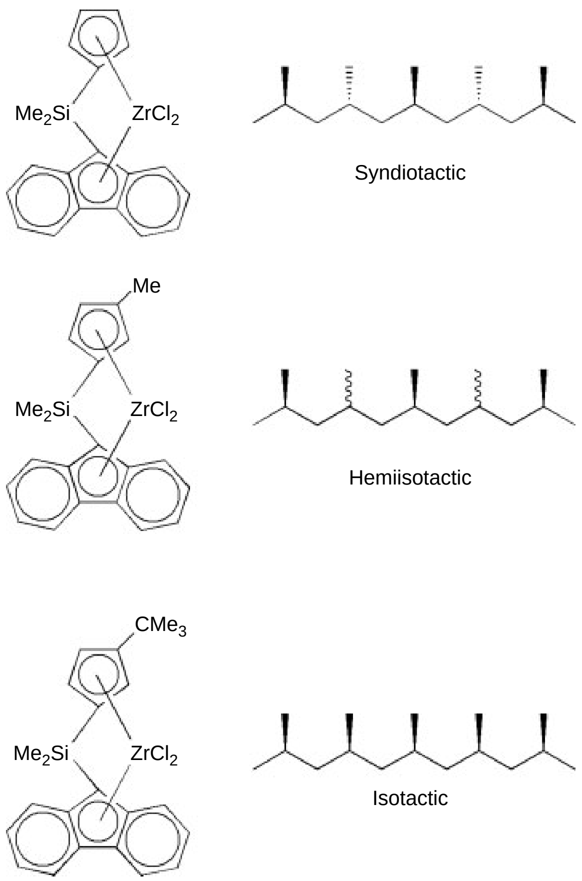

Figure 6 Effect of substituents on the tacticity of polypropylene

Group 4 metal complexes without two cyclopentadienyl rings have figured more prominently in polyolefin catalysis in recent years. Substituting an amide for one cyclopentadienyl ring in a bridged complex form the family of ‘constrained geometry’ catalysts discovered by Exxon and Dow.[37,38] Unlike in bis(cyclopentadienyl) complexes, where zirconium is preferred to titanium or hafnium, in these cyclopentadienyl-amide catalysts, titanium complexes like (**2**) in Figure 7 are preferred, yielding catalysts of high activity and high reactivity toward α-olefins, producing high molecular weight low-density copolymers ($<0.88\,\mathrm{g\,cm^{-3}}$). These catalysts can reincorporate chains with terminal olefins, leading to polymers with long-chain branching, which is valuable in improving the processablity of the material.[39]

Monocyclopentadienyl complexes of titanium ($\mathrm{Cp'TiX_3}$) perform poorly as catalysts for ethylene or propylene polymerization, but in the presence of MAO, they polymerize styrene to stereo- and regioregular syndiotactic polystyrene,[40] a crystalline material with very high melting point (273 °C) and glass transition temperature (100 °C).[41] In this case, the active polymerizing species is a $\mathrm{Ti^{III}}$ complex (Figure 8). Each styrene monomer inserts in a secondary manner and the stereoregularity is maintained by the conformation of the last inserted unit (chain-end control).

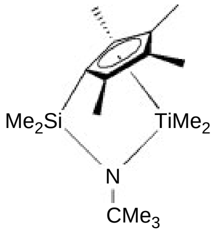

(**2**)

Figure 7 ‘Constrained geometry’ titanium complex $\mathrm{Me_2Si(N\text{-}\mathit{t}\text{-}Bu)(C_5Me_4)TiMe_2}$

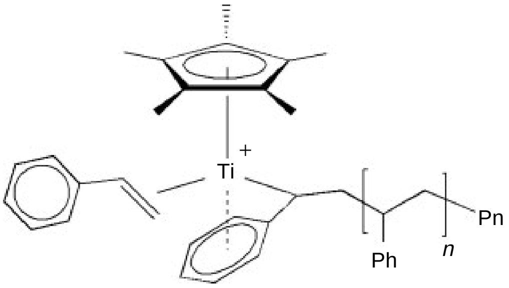

Figure 8 Active-site structure in syndiotactic polymerization of styrene

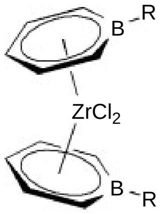

(**3**)

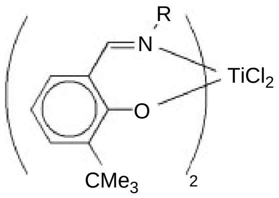

(**4**)

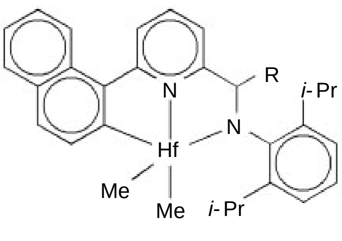

(**5**)

Figure 9 Nonmetallocene single-site catalysts of the group 4 metals

Nonmetallocene homogeneous catalysts of the group 4 metals have received no small amount of attention in recent years.[42] These largely fall into two main categories. One of them is isolobal equivalents to cyclopentadienyl, such as the boratabenzene complex (**3**) (Figure 9);[43] this catalyst can form chains from oligomers to high polymers depending on the nature of the substituent R. The second class is chelating sigma-bonded anions. Two of the more commercially interesting of these are the class of phenoxyimine titanium and zirconium complexes (**4**), some of which exhibit high activities and, suitably substituted, are capable of polymerizing propylene to syndiotactic polypropylene.[44] The family of pyridine amide compounds (**5**) has also received considerable attention; the hafnium complex polymerizes propylene to isotactic polypropylene.[45]

4 GROUP 3 METALS, LANTHANIDES AND ACTINIDES

The d^0 group 3 and lanthanide complexes $\mathrm{Cp}'_2\mathrm{MR}$ are isoelectronic with the $[\mathrm{Cp}'_2\mathrm{MR}]^+$ catalysts discussed in the previous section. These nonionic complexes are soluble in most hydrocarbons and as one-component systems make ideal models for many of the fundamental processes in polymerization catalysis.[5] For example, an alkyl–alkene complex can be observed by NMR when $\mathrm{Cp^*{}_2YH}$ is allowed to react with an α,ω-diene (equation 13).[46]

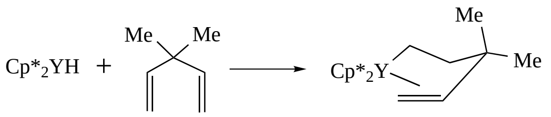

(13)

Neutral lanthanide-series metallocenes exhibit the remarkable ability to polymerize polar monomers such as methyl methacrylate to highly stereoregular polymers of extremely narrow molecular weight distribution (Mw/Mn $\approx$ 1) (equation 14).[47] It is possible to prepare block copolymers of ethylene and poly(methyl methacrylate) by first adding MMA to $\mathrm{Cp^*{}_2SmMe}$ to produce a PMMA segment followed by addition of ethylene; the reverse order of addition fails to give block materials because the ethylene monomer cannot insert into the enolate.

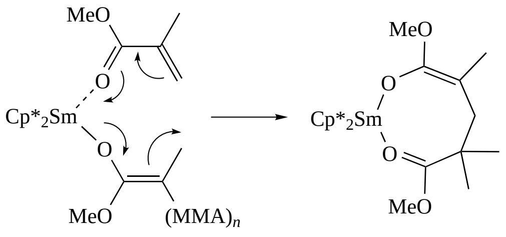

(14)

Such bis(pentamethylcyclopentadienyl) complexes exhibit extremely high activities in ethylene homopolymerization but the steric constraint of the permethylated rings does not allow insertion by higher α-olefins. Less constraining ligand environments like that in (**6**) (Figure 10) result in dimerization with consequent loss of activity. Compound (**6**) is a more versatile catalyst, polymerizing styrene to atactic polystyrene and t-butyl acrylate.[48]

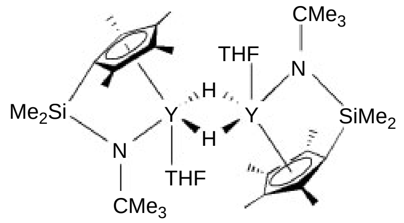

(**6**)

Figure 10 Cyclopentadienyl-amide hydride complex of yttrium

Ionic systems – less susceptible to deleterious dimerization – are accessible with a judicious choice of ancillary ligand. The β-diketoiminate scandium dimethyl complex (**7**) (Figure 11; Ar = 2,6-diisopropylphenyl), activated by $\mathrm{B(C_6F_5)_3}$ leads to a structurally characterizable ionic complex which polymerizes ethylene.[49] The neutral 1,4,7-triazocyclononane ligand was used to prepare a scandium trimethyl complex (**8**), which polymerizes ethylene when $\mathrm{B(C_6F_5)_3}$ is used as a cocatalyst.[50] A derivative pendant amide arm leads to the yttrium bis(trimethylsilylmethyl) compound (**9**), which exhibits modest activity in the presence of $\mathrm{[HNMe_2Ph][B(C_6F_5)_4]}$.[51]

The actinide dimethyl complexes $\mathrm{Cp^*{}_2MMe_2}$ (M = Th, U) are virtually inert in ethylene polymerization but are far more active when adsorbed on dehydroxylated alumina (*see Alumina*).[52] Solid-state ^{13}C NMR studies suggest that surface bound $[\mathrm{Cp^*{}_2MMe}]^+$ species are generated (Figure 12).

Because of the larger ionic radius of the actinide metals versus the group 4 metals ($\mathrm{Th^{4+}}$ = 1.08 Å vs. $\mathrm{Zr^{4+}}$ = 0.79 Å), organoactinides make good test compounds for the relative noncoordination of ionic activator anions.

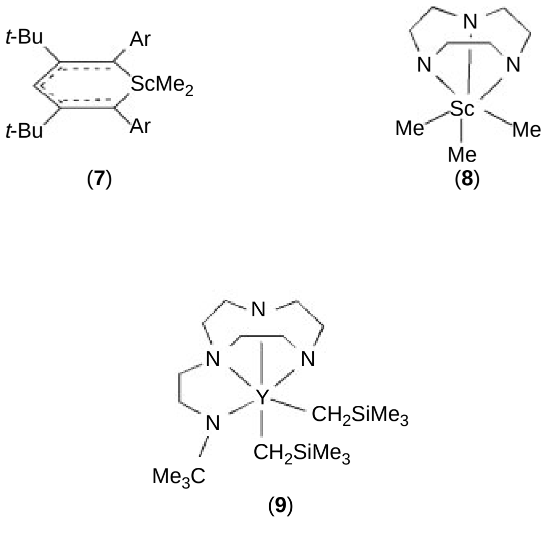

(**7**) (**8**)

(**9**)

Figure 11 Nonmetallocene single-site catalysts of the lanthanides

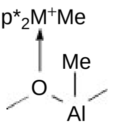

Figure 12 Proposed structure of $Cp^*_2MMe_2$ (M = Th, U) adsorbed on alumina

For example, the compound $[Cp^*_2ThMe]_2[(C_2B_9H_{11})_2Fe]$ is completely inactive in ethylene polymerization owing to strong coordination of the anion to each thorium center (the zirconium analog is an active catalyst)[53] but $[Cp^*_2ThMe][B(C_6F_5)_4]$ rapidly polymerizes ethylene.[54]

5 GROUP 5 METAL COMPLEXES

Vanadium-based homogeneous catalysts have found their greatest value in the commercial production of elastomeric ethylene-propylene copolymers.[55] Dienes such as dicyclopentadiene, 1,4-hexadiene, and ethylidenenorbornene are frequently used as termonomers for cross-linking, reducing the degree of unsaturation and making the material more resistant to environmental attack. While not highly active and prone to decomposition at elevated temperatures, these catalysts produce desirable copolymers owing to their lack of selectivity with respect to the individual monomers. Regio- and stereoirregularities produce a product with very little crystallinity arising from block distribution of comonomers and isotactic propylene segments.

$VOCl_3$ or V(β-diketonate)$_3$ in conjunction with alkylaluminums like $Al_2Et_3Cl_3$ appears to function as a single-site catalyst, giving a polymer with a low polydispersity. The paramagnetic (*see Paramagnetism*) nature of these systems and their low stability have inhibited their comprehensive characterization.

At −78 °C, the soluble catalyst system $VCl_4/AlEt_2Cl$ polymerizes propylene to a predominantly syndiotactic polymer.[56] A secondary insertion of propylene into the V–C bond was invoked to explain this phenomenon, a hypothesis subsequently confirmed experimentally.[57]

These catalysts display less stereo- and regiospecificity than their isospecific counterparts and the directing effect is lost at higher temperatures, where atactic polymer is produced.

Recently, efforts have been made to expand the number of homogeneous vanadium catalysts using ancillary, nonreactive ligands. These catalysts may be in the +5, +4 or +3 oxidation states. The dianionic imido ligand is isolobal with cyclopentadienide and has been used to prepare diamagnetic, formally d^0 metal compounds like (**10**) (Figure 13) which, when activated by MAO, display modest activity for ethylene polymerization.[58] VCl_3 complexes of α-diimines like (**11**) display well-resolved ^1H NMR spectra, their paramagnetism notwithstanding.[59] They polymerize ethylene in the presence of $AlEt_2Cl$, but MAO degrades the catalysts rapidly.

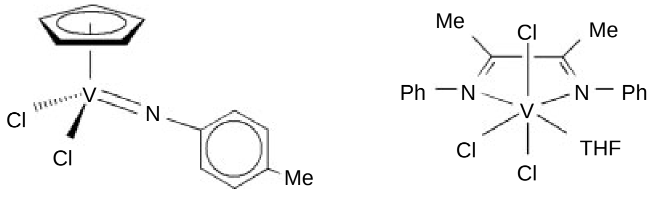

(**10**) (**11**)

Figure 13 Nonmetallocene single-site catalysts of vanadium

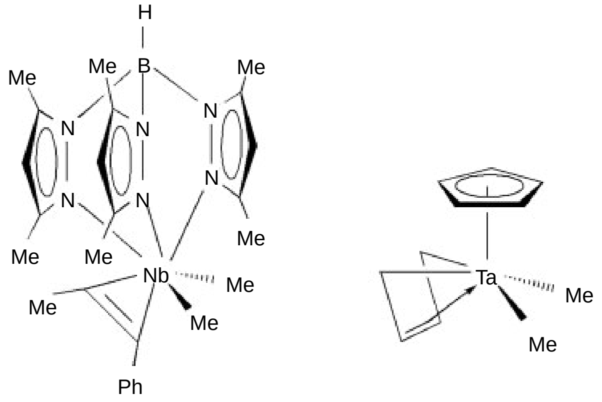

(**12**) (**13**)

Figure 14 Single-site catalysts of niobium and tantalum

Just as imido ligands (*see Imide Complexes*) have been used as cyclopentadienyl surrogates in group 5 and 6 metals, the alkyne ligand can be used as an imido surrogate in a series of niobium catalyst precursors such as (**12**) (Figure 14). These can be activated by $B(C_6F_5)_3$ to generate active systems for ethylene polymerization.[60] The isolobal concept also allowed investigators to move down the group 5 series to tantalum. The formally dianionic η^4-1,3-butadiene fragment is isolobal to cyclopentadienyl and has been used to prepare tantalum systems like (**13**) for use as catalysts in ethylene, norbornene, or methyl methacrylate polymerizations.[61]

6 GROUP 6 METAL COMPLEXES

While molybdenum and tungsten catalysts are associated with metathesis polymerization (*see* ***Organic Synthesis Using Metal-mediated Metathesis Reactions***), chromium catalysts are widely used in the production of polymers. The best-known system is the so-called Phillips catalyst, Cp_2Cr (*see*

Chromocene) deposited on silica; reaction of the metallocene with hydroxyl groups on the silica surface generates the active catalyst (equation 15). These ill-defined heterogeneous systems give high-density polyethylene with broad molecular weight distributions, indicative of multisited catalysts.

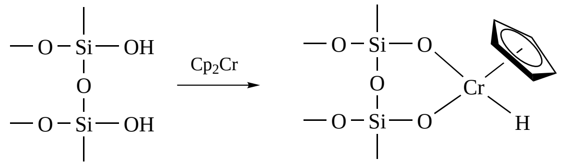

(15)

The commercial importance of chromium-based catalysts has inspired researchers to develop homogeneous systems that model the heterogeneous catalysts.[62] The cationic monomethyl complex (**14**) (Figure 15) represented the first working homogeneous analog for the Phillips catalyst, slowly polymerizing ethylene to linear polyethylene;[63] displacement of one tetrahydrofuran (THF) donor must take place for ethylene to react. The amino-substituted monocyclopentadienyl complex (**15**) activated by MAO exhibits high activity over a short polymerization time.[64] It also is capable of polymerizing propylene and 1-hexene, albeit at much lower rates. Complex (**17**), with a boratabenzene ligand (isolobal to Cp), is nearly as active as Cp_2ZrCl_2 under similar reaction conditions.[65] Strikingly, the activity of some of these 'model' systems is greatly increased when properly heterogenized; (**14**) [BPh_4] has an activity of just 510 g PE/g Cr·hr by itself but supported on $Al_2O_3{\cdot}2AlPO_4$ increases to 233 000 g PE/g Cr·hr![66]

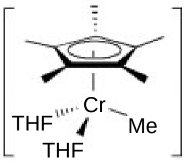

(**14**)

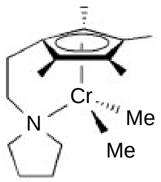

(**15**)

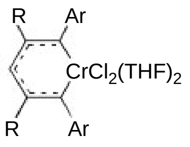

(**16**)

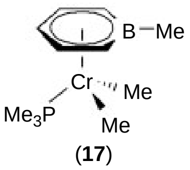

(**17**)

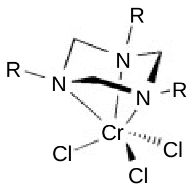

(**18**)

Figure 15 Homogeneous polymerization catalysts of chromium

Noncyclopentadienyl chromium complexes have also figured in polyolefin catalysis. The β-diketiminato chromium complexes like (**16**) polymerize ethylene and copolymerize ethylene and α-olefins in the presence of MAO.[67] The 1,3,5-triazacyclohexane complexes of $CrCl_3$ (**18**) polymerize ethylene in the presence of MAO or $[HNMe_2Ph][B(C_6F_5)_4]$/Al-*i*-Bu_3.[68] Some trimers are formed, resulting in butyl branches in the chain; higher α-olefins are trimerized.

7 IRON AND COBALT

Cobalt complexes have been used as model systems for some of the chain-growth processes in olefin polymerization. Protonation of the ethylene complex $(C_5Me_5)Co(PR_3)(C_2H_4)$ with HBF_4 forms an ethyl cation with an agostic (*see Agostic Bonding*) interaction between the metal and the β-C–H bond, which can isolated and the structure determined crystallographically (equation 16); successive insertions of ethylene can be observed by NMR spectroscopy.[69]

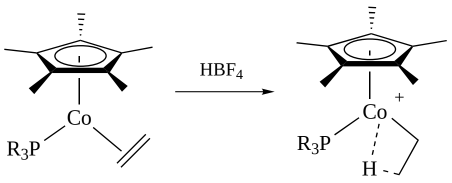

(16)

Research into iron and cobalt compounds as oligomerization and polymerization catalysts has increased enormously since the disclosure that complexes of the metals with tridentate 2,6-diiminopyridine ligands (**19**; Figure 16) function as catalysts.[70,71] Fe(II) compounds with no substituents on the N-aryl rings ($R_1 = R_2 = H$) are inactive, those with one substituent ($R_1 = Me$, $R_2 = H$) yield oligomers and those with substituents in the 2- and 6- positions ($R_1 = R_2 = Me$) polymerize ethylene to high molecular weight material.

The Co(II) analogs are about an order of magnitude less active than the Fe(II) systems. They undergo reduction to Co(I) when alkylated and the actual active species appears to

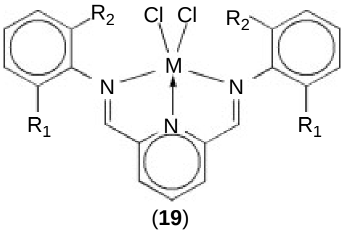

(**19**)

Figure 16 2,6-diiminepyridine complexes (M = Fe, Co) be an alkyl-free cobalt cation (equation 17).[72]

$$[\text{Lig}]\text{-CoCl}_2 \xrightarrow{\text{RMgX}} [\text{Lig}]\text{-CoMe} \xrightarrow{\text{B(C}_6\text{F}_5)_3} [\text{Lig-}]\overset{+}{\text{Co}}\text{-L}$$

$$\text{L} = \text{N}_2, \text{C}_2\text{H}_4 \qquad (17)$$

The performance of the catalysts is quite sensitive to the ligand environment.[73,74] For example, in the Fe(II) system, substituting pyrimidine for pyridine alters the activity only slightly while putting a furan or pyrrole group as the central donor almost completely shuts down activity.[75]

8 NICKEL AND PALLADIUM

Many MX_2, ML_2X_2, and ML_4 complexes (M = Ni or Pd; L = ancillary ligand; X = reactive ligand), activated by Lewis (*see Lewis Acids & Bases*) or Brønsted acids, or acting as single-component systems, are active for alkene oligomerization and polymerization.[76] Complexes with anionic ancillary ligands are usually single-component catalysts while those with neutral ancillary ligands exist as ion pairs (Figure 17). A judicious choice of ligands, solvents and conditions strongly influences chain lengths, linearity and α-alkene content. Polyalkenes ranging from dimers to ultrahigh molecular weight polyethylene can be prepared from suitably modified nickel and palladium catalysts of the same generic family.

Cationic allylnickel catalysts of the general formula $[(\eta^3\text{-}C_3H_5)NiL_2][X]$ have found wide use for studying ligand and anion effects in the polymerization of 1,3-butadiene.[77] Chain propagation occurs via *cis*-η^4 coordination of the butadiene monomer with insertion into a chain coordinated to the metal by an η^3 allyl. *Cis*-1,4- and *trans*-1,4-polybutadiene are formed from the η^3 allyl complexes in which the pendant chain is syn (thermodynamically preferred) or anti with respect to the metal (Figure 18). Large donors like ($L = P(OPh)_3$) favor the anti configuration with formation of *trans*-1,4-polybutadiene while smaller donors (L = MeCN) or no donor leads to selectivity for the syn configuration and the formation of *cis*-1,4-polybutadiene. Similarly weakly coordinating anions (PF_6^-, SbF_6^-) lead to the cis polymer while more strongly coordinating anions ($CF_3SO_3^-$) make the anti configuration preferable with trans polymer the product.

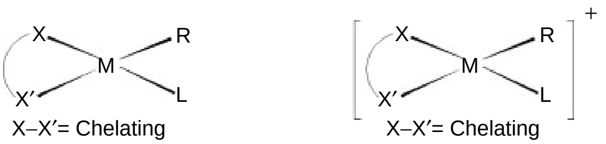

X–X′= Chelating anionic ligand

X–X′= Chelating neutral ligand

Figure 17 Structures of nickel and palladium complexes with neutral or anionic ligands

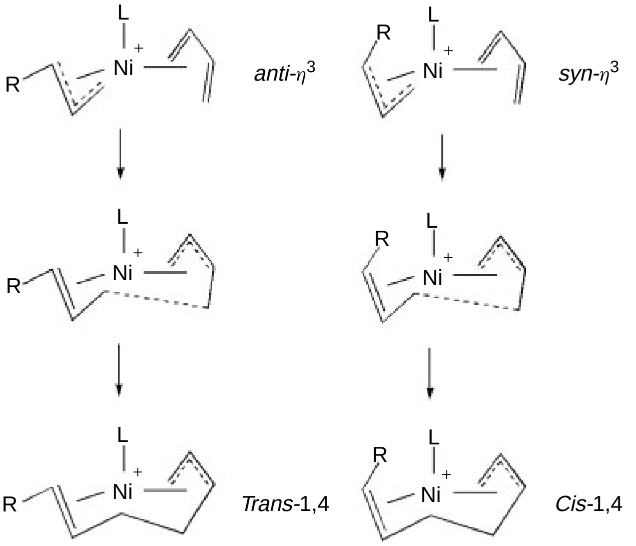

Figure 18 Transition states for formation of *cis*- and *trans*-poly(1,3-butadiene)

In the Shell Higher Olefin Process (SHOP), ethylene is oligomerized by single-component nickel catalysts which make α-alkenes of very high linearity (almost 99%) and high content of 1-olefin (96–98%). A mixture of C_4 to C_{40} alkenes is produced with the C_{12} to C_{20} fraction the most desirable. The light and heavy alkenes are removed and isomerized to internal alkenes in a separate reactor. The mixture is metathesized over a heterogeneous catalyst to desirable chain lengths.

The catalysts comprise a chelating ligand such as diphenylphosphinobenzoic or – acetic acid combined with nickel sources like $(\eta^4\text{-}1,5\text{-cyclooctadiene})_2Ni$ (equation 18) or $NiCl_2/NaBH_4$. A nickel hydride species is presumed to be the active catalytic species. On an industrial scale, the reaction is run in a polar solvent such as 1,4-butanediol, in which the catalyst is soluble but the olefin products are insoluble. Addition of $B(C_6F_5)_3$ to these systems converts them from neutral to zwitterionic (*see Zwitterion*) with a large increase in activity (equation 19).[78]

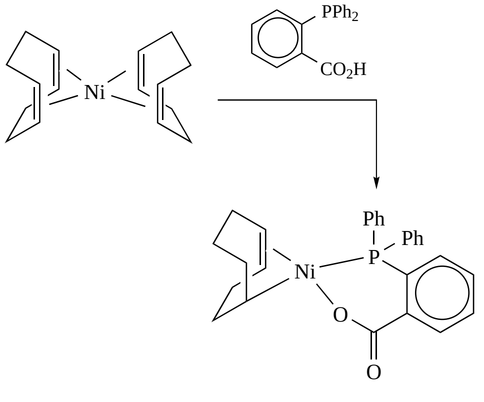

(18)

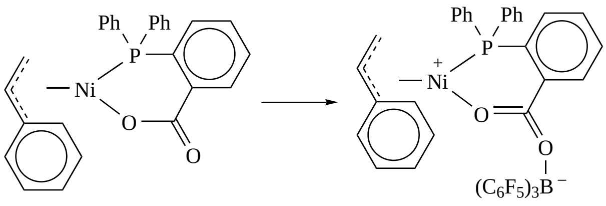

(19)

When phosphorus ylides (*see Ylide*) such as $Ph_3P{=}CH{-}C({=}O)R$ are allowed to react with (η^4-1,5-cyclooctadiene)$_2$Ni or Ni(PR$_3$)$_4$ single-component catalysts are formed which polymerize ethylene to polyethylenes with molecular weights ranging from waxes (MW $\approx$ 1500) to ultrahigh molecular weight materials (MW $> 10^6$) and which are active even in polar solvents, including water (equation 20).**79** The molecular weight of the polymer can be modulated by choice of ligands and the use of phosphorus ylides affords particularly active catalysts.

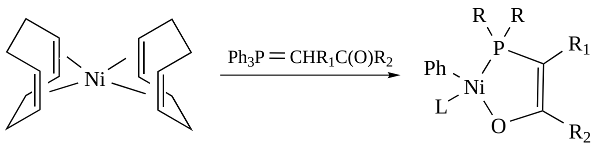

(20)

Another family of single-component catalysts uses salicylaldimides as ligands for nickel catalysts (equation 21).**80** Bulky groups like 9-phenanthryl in the 6- position on the phenyl ring inhibit chain termination and chain loss and encourage the formation of higher molecular weight polymer while using groups of smaller size (R = H) leads to the formation of waxes.

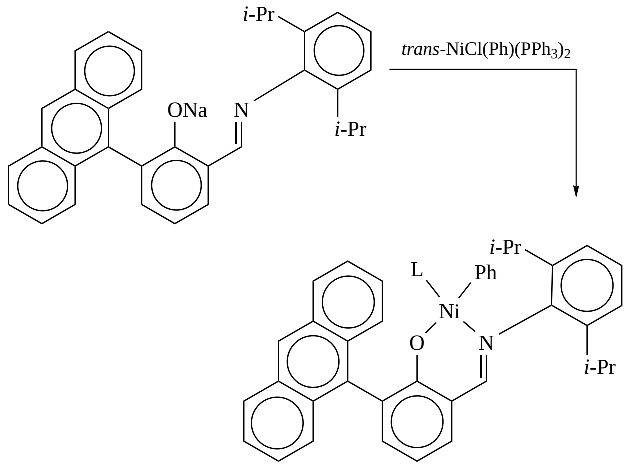

(21)

One of the more extraordinary recent developments in nickel and palladium polyalkene catalysis has been the development of α-diimines with bulky substituents as ligands in nickel and palladium complexes.**81** When bulky aryl groups are used (R′ = isopropyl), these catalysts polymerize ethylene with high activities to high molecular weight highly branched homopolyethylene (equation 22). In these catalysts, chain transfer is slowed by the large size of the axial aryl groups. The highly branched nature of the polyethylene is ascribed to a ‘chain walking’ mechanism with occasional β-hydride elimination without chain loss followed by insertion of an incoming monomer (equation 23). The molecular weight of the polymer and branching are dependent on monomer concentration and axial substituents: polymers ranging from highly branched to highly linear can be produced. When the bulk of the axial substituents is reduced (R′ = H), oligomers are produced.**82**

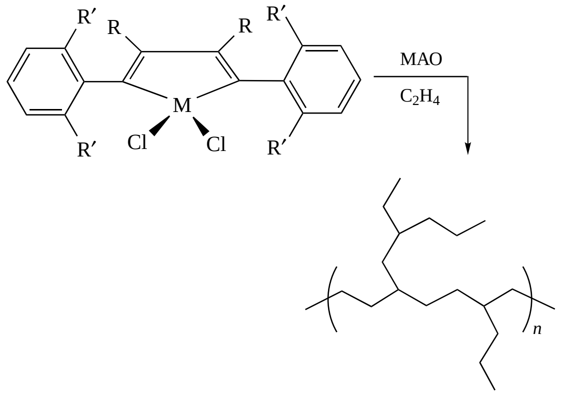

(22)

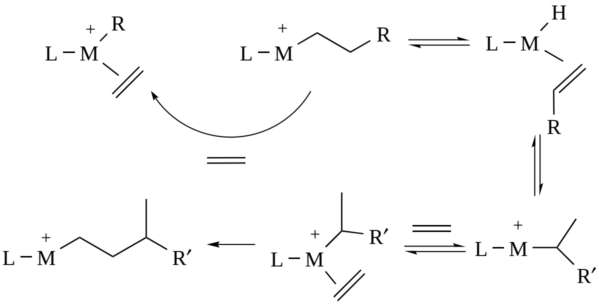

(23)

Because of the relative rates of chain propagation versus chain walking, polymers from the bis(imine) catalysts can be quite different depending on the metal. Nickel complexes form polymers with mostly shorter-chain branches and more crystallinity while polyethylene from the palladium analogs is more highly branched, to the point it can be amorphous. The palladium complexes also have the ability to incorporate remarkably high (1–10 mole percent) amounts of polar monomers such as methyl acrylate and methyl vinyl ketone, though at considerable loss in activity.**83**

Palladium complexes figure prominently as well in the copolymerization of α-olefins with carbon monoxide.**84** Unlike the low molecular weight photodegradable random copolymers of ethylene and CO produced from a free-radical process, olefin/carbon monoxide copolymers produced from homogeneous palladium catalysts are perfectly alternating, the result of successive insertions of olefin and CO (Figure 19). Consecutive insertion of two similar monomers is either slow

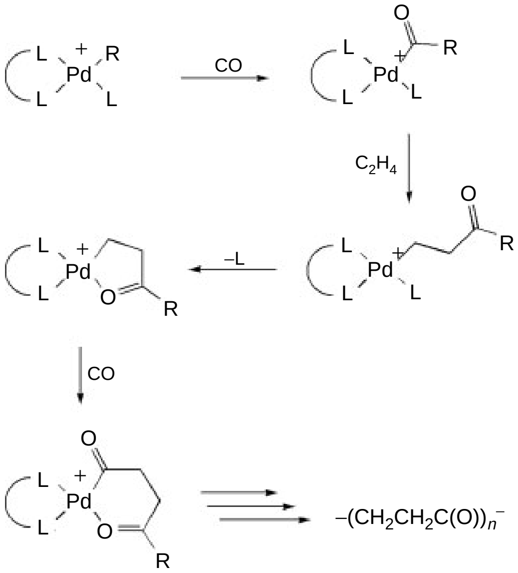

Figure 19 Alternating ethylene–CO polymerization by palladium catalysts

or nonexistent with respect to CO insertion into a metal–alkyl bond or olefin into a metal acyl linkage.

Neutral chelating bidentate ligands are used as ancillary ligands in these systems and greatly affect the catalyst performance and products. For ethylene/CO copolymerizations, bidentate arylphosphines such as 1,3-bis(diphenylphosphino)propane give the highest activities and polymer molecular weights. In the copolymerization of propylene and CO, catalysts with this ligand produce copolymer of low regioregularity, but this is much improved when alkylphosphines such as 1,3-(diisopropylphosphino)propane is used. The preferred ancillary ligand in styrene/CO copolymerization are N–N ligands such as 1,10-phenanthroline or 2,2′-bipyridine; the styrene/CO copolymers are not only highly regioregular but can also be made largely isotactic or syndiotactic depending on the choice of N–N ligand.[85]

9 OTHER METALS

Homogeneous polyalkene catalysis has progressed to the point where metals not generally associated with coordination polymerization can now be made to promote olefin chain growth and metals long ago associated with polyalkene catalysis have been given new life.

Copper complexes, which have never figured in coordination olefin polymerization, can be induced to polymerize ethylene by a judicious choice of ligand. The α-diimine compound (**20**) (Figure 20) in the presence of MAO shows modest activity in ethylene polymerization when R = Ph but not with R = i-Pr.[86] Cocatalyzed by MAO, the bis(benzimidzole) copper complex (**21**) homopolymerizes ethylene to polyethylene without detectable branches.[87]

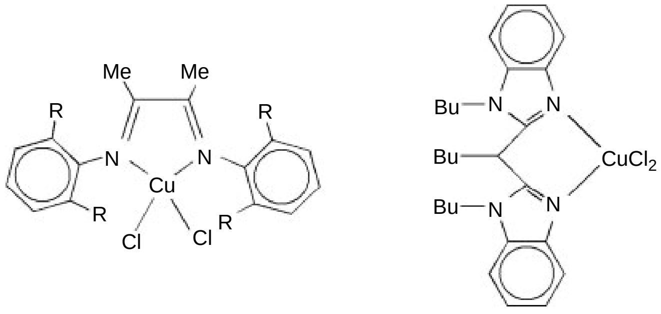

(**20**) (**21**)

Figure 20 Homogeneous polymerization catalysts based on copper

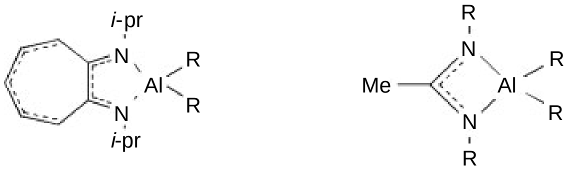

(**22**) (**23**)

Figure 21 Homogeneous polymerization catalysts based on aluminum

Aluminum alkyls were first used by Ziegler in the early 1950s as olefin oligomerization catalysts (the ‘Aufbau’ catalyst). Within the last few years, aluminum is again receiving attention as a chain-growth system. Simple aluminum alkyls like $AlEt_3$, allowed to react with $B(C_6F_5)_3$, promote the polymerization of ethylene and propylene.[88] Aminotroponiminate complexes of aluminum such as (**22**) (Figure 21) are activated by $B(C_6F_5)_3$ or $[Ph_3C][B(C_6F_5)_4]$ to generate aluminum cations which polymerize ethylene with low activity.[89] The alkylaluminum and -gallium amidinates (**23**) similarly activated exhibit polymerization activity toward ethylene.[90]

10 RELATED ARTICLES

Actinides: Inorganic & Coordination Chemistry; Aluminum: Organometallic Chemistry; Chromium: Organometallic Chemistry; Cobalt: Organometallic Chemistry; Copper: Organometallic Chemistry; Iron: Inorganic & Coordination Chemistry; Metathesis Polymerization Processes by Homogeneous Catalysis; Nickel: Organometallic Chemistry; Niobium & Tantalum: Organometallic Chemistry; Palladium: Organometallic Chemistry; Paramagnetic Organometallic Complexes; Scandium, Yttrium & the Lanthanides: Inorganic

& Coordination Chemistry; Supported Organotransition Metal Compounds; Titanium: Organometallic Chemistry; Vanadium: Organometallic Chemistry; Zirconium & Hafnium: Organometallic Chemistry.

11 REFERENCES

1. R. Blom, A. Follestad, E. Rytter, M. Tilset, and M. Ystenes eds, 'Organometallic Catalysts and Olefin Polymerization: Catalysts for a New Millennium', Springer Verlag, Berlin, 2001.
2. D. Vogt, in 'Applied Homogeneous Catalysis with Organometallic Compounds', eds. B. Cornils and W. A. Herrmann, VCH Publishers, New York, 1996, Vol. 1, p. 245.
3. M. D. Leatherman and M. Brookhart, *Macromolecules*, 2001, **34**, 2748.
4. P. Cossee, *J. Catal.*, 1964, **3**, 80; E. J. Arlman and P. Cossee, *J. Catal.*, 1964, **3**, 99.
5. B. J. Burger, W. D. Cotter, E. B. Coughlin, S. T. Chacon, S. Hajela, T. A. Herzog, R. Köhn, J. Mitchell, W. E. Piers, P. J. Shapiro, and J. E. Bercaw, in 'Ziegler Catalysts', eds. G. Fink, R. Mülhaupt, and H. H. Brintzinger, Springer Verlag, 1995, p. 317.
6. J.-F. Carpentier, Z. Wu, C. W. Lee, S. Strömberg, J. N. Christopher, and R. F. Jordan, *J. Am. Chem. Soc.*, 2000, **122**, 7750.
7. A. K. Rappé, W. M. Skiff, and C. J. Casewit, *Chem. Rev.*, 2000, **100**, 1435.
8. C. R. Landis, K. A. Rosaaen, and D. R. Sillars, *J. Am. Chem. Soc.*, 2003, **125**, 1710.
9. L. H. Peebles Jr, 'Molecular Weight Distributions in Polymers', John Wiley & Sons, New York, 1971.
10. R. Taube, H. Windisch, and S. Maiwald, *Macromol. Symp.*, 1995, **89**, 393.
11. S. M. Nagy, M. P. Mack, and G. G. Hlatky, *Adv. Chem. Ser.*, 2003, **857**, 76.
12. G.-J. M. Gruter, A. Graham, B. McKay, and F. Gilardoni, *Macromol. Rapid Commun.*, 2003, **24**, 73.
13. G. Natta, P. Pino, G. Mazzanti, and U. Gianinni, *J. Am. Chem. Soc.*, 1957, **79**, 2975.
14. D. S. Breslow and N. R. Newburg, *J. Am. Chem. Soc.*, 1957, **79**, 5072.
15. F. S. Dyachkovski, A. K. Shilova, and A. E. Shilov, *J. Polym. Sci., Part C*, 1967, **16**, 2333.
16. J. J. Eisch, A. M. Piotrowski, S. K. Brownstein, E. J. Gabe, and F. L. Lee, *J. Am. Chem. Soc.*, 1985, **107**, 7219.
17. H. Sinn and W. Kaminsky, *Adv. Organomet. Chem.*, 1980, **18**, 99.
18. H. C. Welborn Jr and J. A. Ewen, Eur. Pat. Appl. 129,368, 1984; *Chem. Abstr.*, 1985, **102**, 114142.
19. G. G. Hlatky, *Chem. Rev.*, 2000, **100**, 1347.
20. E. Y.-X. Chen and T. J. Marks, *Chem. Rev.*, 2000, **100**, 1391.
21. E. Zureck and T. Ziegler, *Prog. Polym. Sci.*, 2004, **29**, 107.
22. C. J. Harlan, S. G. Bott, and A. R. Barron, *J. Am. Chem. Soc.*, 1995, **117**, 6465.
23. X. Yang, C. L. Stern, and T. J. Marks, *J. Am. Chem. Soc.*, 1991, **113**, 3623.
24. H. W. Turner and G. G. Hlatky, Eur. Pat. Appl. 277,004, 1988; *Chem. Abstr.*, 1988, **110**, 58290.
25. J. A. Ewen and M. J. Elder, Eur. Pat. Appl.426,637, 1991; *Chem. Abstr.*, 1991, **115**, 136998.
26. R. Sugimoto, T. Asanuma, T. Iwatani, K. Takeuchi, and O. Uchida, Eur. Pat. Appl. 500,944, 1992; *Chem. Abstr.*, 1992, **117**, 131719.
27. H. G. Alt and A. Köppl, *Chem. Rev.*, 2000, **100**, 1205.
28. P. Schertl, H. G. Alt, and M. B. Welch, U.S. Patent 5,668,230, 1997; *Chem. Abstr.*, 1997, **127**, 278622.
29. M.-J. Brekner, J. Rohrmann, W. Spaleck, and M. Antberg, U.S. Patent 5,087,677, 1992; *Chem. Abstr.*, 1991, **114**, 247975.
30. L. Resconi, L. Cavallo, A. Fait, and F. Piemontesi, *Chem. Rev.*, 2000, **100**, 1253.
31. M. K. Leclerc and H. H. Brintzinger, *J. Am. Chem. Soc.*, 1995, **117**, 1651.
32. W. Kaminsky, K. Külper, H. H. Brintzinger, and F. R. W. P. Wild, *Angew. Chem., Int. Ed. Engl.*, 1985, **24**, 507.
33. W. Spaleck, M. Antberg, M. Aulbach, B. Bachmann, V. Dolle, S. Haftka, F. Küber, J. Rohrmann, and A. Winter, in 'Ziegler Catalysts', eds. G. Fink, R. Mülhaupt, and H. H. Brintzinger, Springer Verlag, Berlin, 1995, p. 83.
34. J. A. Ewen, R. L. Jones, A. Razavi, and J. D. Ferrara, *J. Am. Chem. Soc.*, 1988, **110**, 6255.
35. J. A. Ewen, M. J. Elder, R. L. Jones, L. Haspeslagh, J. L. Atwood, S. G. Bott, and K. Robinson, *Makromol. Chem., Macromol. Symp.*, 1991, **253**, 48.
36. S. Lin and R. M. Waymouth, *Acc. Chem. Res.*, 2002, **35**, 765.
37. J. M. Canich, Eur. Pat. Appl. 420,436, 1991; *Chem. Abstr.*, 1991, **115**, 184145.
38. J. C. Stevens, F. J. Timmers, D. R. Wilson, G. F. Schmidt, P. N. Nickias, R. K. Rosen, G. W. Knight, and S. Y. Lai, Eur. Pat. Appl. 416,815, 1991; *Chem. Abstr.*, 1991, **115**, 93163.
39. P. S. Chum, W. J. Kruper, and M. J. Guest, *Adv. Mater.*, 2000, **12**, 1759.
40. J. Schellenberg and N. Tomotsu, *Prog. Polym. Sci.*, 2002, **27**, 1925.
41. M. Malanga, *Adv. Mater.*, 2000, **12**, 1869.
42. V. C. Gibson and S. K. Spitzmesser, *Chem. Rev.*, 2003, **103**, 283.
43. G. C. Bazan, G. Rodriguez, A. J. Ashe III, S. Al-Ahmad, and J. W. Kampf, *Organometallics*, 1997, **16**, 2492.
44. H. Makio, N. Kashiwa, and T. Fujita, *Adv. Synth. Catal.*, 2002, **344**, 477.

45. J. C. Stevens and D. D. Vanderlende, PCT Int. Appl. 2003/040201, 2003; *Chem. Abstr.*, 2003, **138**, 385930.
46. C. P. Casey, S. L. Hallenbeck, D. W. Pollock, and C. R. Landis, *J. Am. Chem. Soc.*, 1995, **117**, 9770.
47. H. Yasuda and E. Ihara, *Adv. Polym. Sci.*, 1997, **133**, 53.
48. S. Arndt, P. Voth, T. P. Spaniol, and J. Okuda, *Organometallics*, 2000, **19**, 4690.
49. P. G. Hayes, W. E. Piers, L. W. M. Lee, L. K. Knight, M. Parvez, M. R. J. Elsegood, and W. Clegg, *Organometallics*, 2001, **20**, 2533.
50. S. Hajela, W. P. Schaefer, and J. E. Bercaw, *J. Organometal. Chem.*, 1997, **532**, 241.
51. S. Bambirra, D. van Leusen, A. Meetsma, B. Hessen, and J. H. Teuben, *J. Chem. Soc., Chem. Commun.*, 2001, 637.
52. M.-Y. He, G. Xiong, P. J. Toscano, R. L. Burwell Jr, and T. J. Marks, *J. Am. Chem. Soc.*, 1985, **107**, 641.
53. H. W. Turner and G. G. Hlatky, Eur. Pat. Appl. 277,003, 1988.
54. X. Yang, C. L. Stern, and T. J. Marks, *Organometallics*, 1991, **10**, 840.
55. R. Karpeles and A. V. Grossi, in 'Handbook of Elastomers', eds. A. K. Bhownick and H. L. Stephens, Marcel Dekker, New York, 2001, p. 845.
56. G. Natta, I. Pasquon, and A. Zambelli, *J. Am. Chem. Soc.*, 1962, **84**, 1488; Y. Doi, M. Takada, and T. Keii, *Macromolecules*, 1979, **180**, 57.
57. A. Zambelli, P. Longo, S. Terenghi, D. Recupero, and G. Zannoni, *J. Mol. Catal. A*, 2000, **152**, 25.
58. D. J. Crowther, R. A. Fisher, J. M. Canich, G. G. Hlatky, and H. W. Turner, U.S. Patent 5,504,409, 1996.
59. S. Milione, G. Cavallo, C. Tedesco, and A. Grassi, *J. Chem. Soc., Dalton Trans.*, 2002, 1839.
60. J. Jaffart, C. Nayral, R. Choukroun, R. Mathieu, and M. Etienne, *Eur. J. Inorg. Chem.*, 1998, 425.
61. K. Mashima, *Macromol. Symp.*, 2000, **159**, 69.
62. K. H. Theopold, *Eur. J. Inorg. Chem.*, 1998, 15.
63. B. J. Thomas and K. H. Theopold, *J. Am. Chem. Soc.*, 1988, **110**, 5902.
64. A. Döhring, J. Göhre, P. W. Jolly, B. Kryger, J. Rust, and G. P. J. Verhovnik, *Organometallics*, 2000, **19**, 388.
65. J. S. Rogers, X. Bu, and G. C. Bazan, *Organometallics*, 2000, **19**, 3948.
66. M. J. Carney and D. L. Beach, U.S. Patent 5,418,200, 1995.
67. V. C. Gibson, C. Newton, C. Redshaw, G. A. Solan, A. J. P. White, and D. J. Williams, *Eur. J. Inorg. Chem.*, 2001, 1895.
68. R. D. Köhn, D. Smith, D. Lilge, S. Mihan, F. Molnar, and M. Prinz, *Adv. Chem. Ser.*, 2003, **857**, 88.
69. R. B. Cracknall, A. G. Orpen, and J. L. Spencer, *J. Chem. Soc., Chem. Commun.*, 1984, 326.
70. B. L. Small, M. Brookhart, and A. M. A. Bennett, *J. Am. Chem. Soc.*, 1998, **120**, 4049.
71. G. J. P. Britovsek, V. C. Gibson, B. S. Kimberley, P. J. Maddox, S. J. McTavish, G. A. Solan, A. J. P. White, and D. J. Williams, *J. Chem. Soc., Chem. Commun.*, 1998, 849.
72. V. C. Gibson, M. J. Humphries, K. P. Tellmann, D. F. Wass, A. J. P. White, and D. J. Williams, *J. Chem. Soc., Chem. Commun.*, 2001, 2252.
73. G. J. P. Britovsek, V. C. Gibson, B. S. Kimberley, S. Mastroianni, C. Redshaw, G. A. Solan, A. J. P. White, and D. J. Williams, *J. Chem. Soc., Dalton Trans.*, 2001, 1639.
74. G. J. P. Britovsek, S. Mastroianni, G. A. Solan, S. P. D. Baugh, C. Redshaw, V. C. Gibson, A. J. P. White, D. J. Williams, and M. R. J. Elsegood, *Chem. – Eur. J.*, 2000, **6**, 2221.
75. G. J. P. Britovsek, V. C. Gibson, O. D. Horau, S. K. Spitzmesser, A. J. P. White, and D. J. Williams, *Inorg. Chem.*, 2003, **42**, 3454.
76. S. D. Ittel, L. K. Johnson, and M. Brookhart, *Chem. Rev.*, 2000, **100**, 1169.
77. R. Taube, U. Schmidt, J.-P. Gehrke, P. Böhme, J. Langlotz, and S. Wache, *Makromol. Chem., Macromol. Symp.*, 1993, **66**, 245.
78. Z. J. A. Komon, X. Bu, and G. C. Bazan, *J. Am. Chem. Soc.*, 2000, **122**, 1830.
79. W. Keim, *Stud. Surf. Sci. Catal.*, 1986, **25**, 201.
80. C. M. Wang, S. Friedrich, T. R. Younkin, R. Li, R. H. Grubbs, D. A. Bansleben, and M. W. Day, *Organometallics*, 1998, **17**, 3149.
81. L. K. Johnson, C. M. Killian, and M. Brookhart, *J. Am. Chem. Soc.*, 1995, **117**, 6414.
82. C. M. Killian, L. K. Johnson, and M. Brookhart, *Organometallics*, 1997, **16**, 2005.
83. L. K. Johnson, S. Mecking, and M. Brookhart, *J. Am. Chem. Soc.*, 1996, **118**, 267.
84. E. Drent and P. H. M. Budzelaar, *Chem. Rev.*, 1996, **96**, 663.
85. A. Aeby and G. Consiglio, *Inorg. Chim. Acta*, 1999, **296**, 45.
86. V. C. Gibson, A. Tomov, D. F. Wass, A. J. P. White, and D. J. Williams, *J. Chem. Soc., Dalton Trans.*, 2002, 2261.
87. R. T. Stibrany, A. O. Patil, and S. Zushma, *Adv. Chem. Ser.*, 2003, **857**, 194.
88. J. S. Kim, L. M. Wojcinski II, S. Liu, J. C. Sworen, and A. Sen, *J. Am. Chem. Soc.*, 2000, **122**, 5668.
89. A. V. Korolev, E. Ihara, I. A. Guezi, V. G. Young Jr, and R. F. Jordan, *J. Am. Chem. Soc.*, 2001, **123**, 8291.
90. S. Dagorne, I. A. Guezi, M. P. Coles, and R. F. Jordan, *J. Am. Chem. Soc.*, 2000, **122**, 274.

Organic Synthesis using Transition Metal Carbonyl Complexes

Björn C. G. Söderberg
West Virginia University, Morgantown, WV, USA

1 Introduction 1
2 Metal Carbonyl–Carbene Complexes 1
3 Metal Carbonyl–Arene Complexes 19
4 Iron Tricarbonyl Complexesof Conjugated Dienes 30
5 Dicobalt Hexacarbonyl Alkyne Complexes 43
6 Related Articles 62
7 References 62

Abbreviations

AIBN = 2,2′-azobisisobutyronitrile; 9-BBN = 9-borabicyclo[3.3.1]nonane; Bn = benzyl; BOC = *t*-butoxycarbonyl; Bz = benzoyl; CAN = ceric ammonium nitrate; Cp = cyclopentadienyl; Cy = cyclohexyl; DAST = diethylaminosulfur trifluoride; DBA = 1,3-dibromo-5,5-dimethylhydantoin; DDQ = 2,3-dichloro-5,6-dicyano-1,4-benzoquinone; DET = diethyl tartrate; DIAD = diisopropyl acetylene dicarboxylate; DIBAL-H = diisobutylaluminum hydride; DIPEA = diisopropyl ethyl amine; DMDO = dimethyldioxirane; HMPA = hexamethylphosphortriamide; LDA = lithium diisopropylamide; Ms = methylsulfonyl; MOM = methoxymethyl; NBS = *N*-bromosuccinimide; NMO = *N*-methylmorpholine *N*-oxide; PDC = pyridinium dichromate; PMP = *p*-methoxyphenyl; THP = tetrahydropyranyl; TIPS = trisisopropylsilyl; TMANO = trimethylamine *N*-oxide; TBDMS = *t*-butyldimethylsilyl; Tf = trifluoromethanesulfonyl; TMP = 2,2,6,6-tetramethylpiperidyl; TMS = trimethylsilyl; Ts = *p*-toluenesulfonyl.

1 INTRODUCTION

Synthetically important reactions employing transition metal–carbonyl complexes (*see* ***Carbonyl Complexes of the Transition Metals***) have been extensively developed and applied in total synthesis of complex organic molecules. Stoichiometric amounts of metal carbonyl complexes are usually employed, but the often significant increase in complexity going from starting material to product and the high stereoselectivity observed makes them very attractive reagents. In addition, reactions of transition metal–carbonyl complexes are frequently unique without any related reaction available for 'pure' organic compounds.

The following four types of complexes will be discussed in detail: (1) metal carbonyl–carbene complexes, (2) chromium tricarbonyl arene complexes, (3) iron tricarbonyl diene complexes, and (4) dicobalt hexacarbonyl alkyne complexes. A few examples of related transition metal–carbonyl complexes will be discussed under each heading. Only reactions of proven synthetic utility in which stoichiometric amounts of transition metal–carbonyl complexes have been used to mediate the reactions are included. Synthesis of the starting transition metal–carbonyl complexes will only be briefly discussed. Because of the vast amount of work published, the reactions selected for discussion will frequently be those that have been employed in total syntheses of natural products but important observations taken from methodological studies will also be discussed. Mechanistic considerations will be minimized to accommodate a larger number of examples of each reaction or complex type described (*see* ***Mechanisms of Reaction of Organometallic Complexes***). Reactions involving transient intermediates containing a metal–carbonyl bond or carbonylations of organometallic intermediates will not be covered. Reactions involving nucleophilic attack (*see Nucleophilic Addition: Rules for Predicting Direction*) on π-bonded alkene or alkyne metal–carbonyl complexes are discussed in an accompanying article (*see* ***Osmium: Inorganic & Coordination Chemistry***). In addition, catalytic reactions of transition metal–carbonyl complexes, such as hydroformylation (*see Hydroformylation*), reduction (*see Reduction*), alkoxycarbonylation (*see Alkoxycarbonylation*), hydrosilation (*see Hydrosilation*), hydrocyanation (*see Hydrocyanation*), and polymerization (*see Polymerization*) are covered elsewhere (*see* ***Carbonylation Processes by Homogeneous Catalysis***; ***Hydrocyanation by Homogeneous Catalysis***, and ***Oligomerization & Polymerization by Homogeneous Catalysis***).

2 METAL CARBONYL–CARBENE COMPLEXES

A very rapid growth of novel and synthetically useful reactions of Fischer-type carbene complexes (*see Fischer-type Carbene Complexes*) has occurred over the last decade. Reactions leading to cyclic and polycyclic compounds of high complexity and reactions wherein chirality has been transferred from the starting material to the product are of particular importance. A number of recent reviews on the chemistry of Fischer carbene complexes and their application in organic synthesis are available.[1–7]

2.1 Formation and Elaborations of Fischer Carbene Complexes

Metal carbonyl–carbene complexes with a stabilizing heteroatom substituent on the carbene carbon (Fischer carbenes) can be prepared and further elaborated via a variety of methods. Methoxy- and ethoxy-substituted Fischer carbenes are generally prepared by reaction of metal carbonyl complexes with organolithium (*see* ***Alkali Metals: Organometallic Chemistry***) or dialkylzinc[8] (*see* ***Zinc: Organometallic Chemistry***) reagents forming a metal acylate. The metal acylate is usually unstable and is therefore directly alkylated with trimethyl- or triethyloxonium- tetrafluoroborates or methyl triflate (Scheme 1). This methodology is limited to methoxy- and ethoxy-substituted carbenes. Alkyl iodides can be used under phase-transfer catalysis conditions for the preparation of more substituted alkoxychromium carbenes. Other heteroatom substituents can be introduced via facile nucleophilic substitution of the alkoxy group upon reaction with thiols, selenols, primary and secondary amines, and aryllithiums. For example, carbene (**1**) reacts with pyrrole to give the pyrrole-substituted carbene (**2**) (Scheme 2).[9]

Lithium acylates are readily transformed to the substantially more thermally stable tetramethylammonium acylates by lithium-tetramethylammonium ion exchange. Reaction of tetramethylammonium salts with acid halides, usually acetyl chloride or bromide or pivaloyl chloride, affords thermally unstable acyloxycarbenes. These versatile complexes are transformed into alkoxy-, amino-, thio-, or seleno-substituted carbene complexes upon reaction with alcohols, primary and secondary amines, thiols, or selenols respectively (Scheme 3). In addition, direct alkylation of tetramethylammonium acylates can be achieved using alkyldiphenylsulfonium salts (Scheme 4).[10]

N,*N*-Disubstituted aminocarbenes can be prepared directly by reaction of chromium, tungsten, molybdenum pentacarbonyl, and iron tetracarbonyl dianions with tertiary amides in the presence of chlorotrimethylsilane (Scheme 5).

Reaction of 4-hydroxy-1-alkynes or 5-hydroxy-1-alkynes with chromium or tungsten pentacarbonyl compounds having a readily displaced ligand furnishes 2-tetrahydrofuranyl- and 2-tetrahydropyranylcarbenes respectively. This type of reaction was used in the synthesis of a number of natural products, including andirolactone and salinomycin[11] (Scheme 6). Related reactions of 4-amino- and 4-thiol-substituted alkynes furnishes dihydropyrroles, indoles, and dihydrothiophens. In contrast, the corresponding annulation using molybdenum carbonyls only affords dihydrofurans and dihydropyranes via elimination of the transition metal

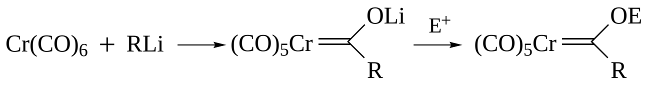

Scheme 1

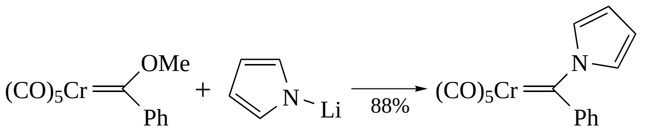

(**1**) (**2**)

Scheme 2

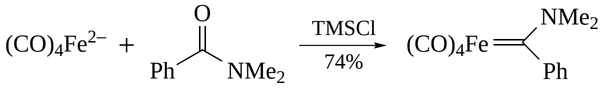

Scheme 5

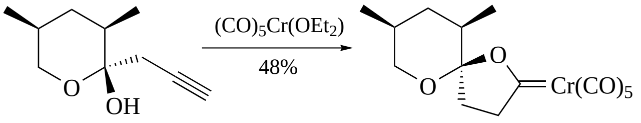

Scheme 6

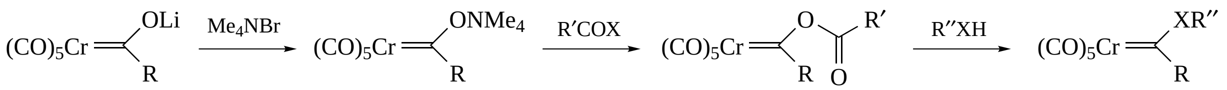

Scheme 3

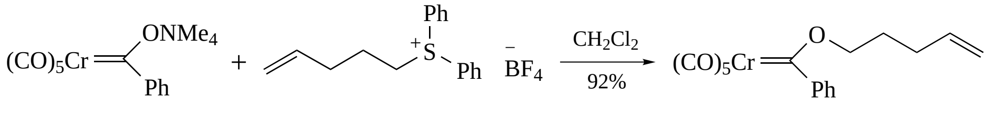

Scheme 4

moiety.[12] The intermediately formed carbene is apparently not stable under the reaction conditions. The direct formation of cyclic ethers can be made catalytic in molybdenum (Scheme 7).

Reaction of enyne-esters and -amides and 2-alkynyl-substituted aromatic ketones in a related fashion led to pyrranylidene complexes (Scheme 8).[13] Compounds with a stabilized anion or a trialkylsilyl enolate in the 4- or 5-position relative to the alkyne can be used in related reactions to give carbocyclic products (Scheme 9).

The relatively acidic α hydrogens of amino- and alkoxy-substituted Fischer carbenes are readily removed and the 'metal-enolate' formed participates in a number of carbon–carbon bond forming reactions. They can be alkylated using alkyl triflates, iodides, and tosylates, or benzyl bromides. Dialkylation of 'metal-enolates' is at times a competitive side reaction and can be used advantageously to introduce a cyclopropyl group α to the carbene carbon (Scheme 10). Alkylation of carbene anions with epoxides gives five-membered oxacyclic carbenes via an epoxide ring-opening-intramolecular alkoxy-exchange sequence. Reaction of optically active epoxides furnishes optically active carbene complexes. Allylic anions formed from α,β-unsaturated carbenes are alkylated with alkyl halides to give mixtures of α- (minor) and γ-alkylation (major) products. The same anion is exclusively or predominantly quenched in the α position using proton, deuterium, or chlorotrimethylsilane. It is interesting to note that N,N-dialkylhydrazino carbene complexes can readily be stepwise mono- and dialkylated in the α position (Scheme 11).[14] N,N-Dimethylamino-substituted tungsten and chromium acetylides undergo 1,2-additions to cyclohexenones.

Anions formed from group 6 and manganese Fischer carbene complexes undergo aldol condensations with aldehydes and ketones. Allylic carbenes exclusively react in the γ position with aldehydes affording dienyl-substituted carbenes. For alkoxy-substituted carbenes, the presence of an excess Lewis acid (*see Lewis Acids & Bases*), such as boron trifluoride etherate, titanium tetrachloride, or tin tetrachloride is required for the reaction to proceed in reasonable yield. The initial aldol product can be isolated without elimination (Scheme 12).[15]

Anions of amino-substituted complexes are sufficiently reactive and do not require a Lewis acid in order

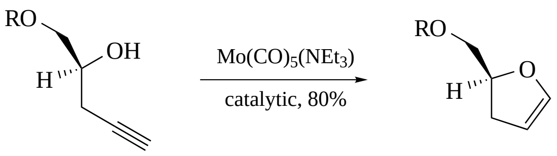
RO
OH
H
Mo(CO)5(NEt3)
catalytic, 80%
RO
O
H

Scheme 7

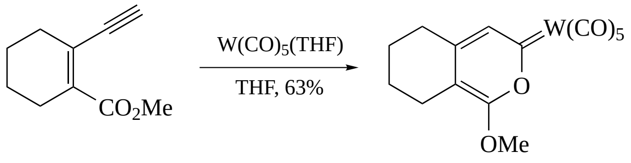
CO2Me
W(CO)5(THF)
THF, 63%
W(CO)5
O
OMe

Scheme 8

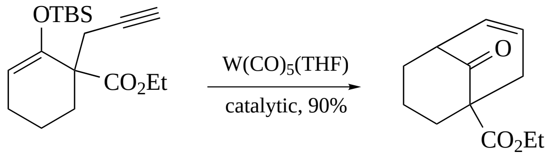
OTBS
CO2Et
W(CO)5(THF)
catalytic, 90%
O
CO2Et

Scheme 9

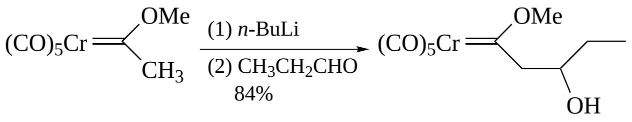
(CO)5Cr
OMe
CH3
(1) n-BuLi
(2) CH3CH2CHO
84%
(CO)5Cr
OMe
OH

Scheme 12

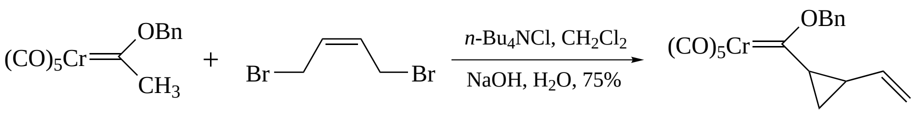
(CO)5Cr
OBn
CH3
+
Br
Br
n-Bu4NCl, CH2Cl2
NaOH, H2O, 75%
(CO)5Cr
OBn

Scheme 10

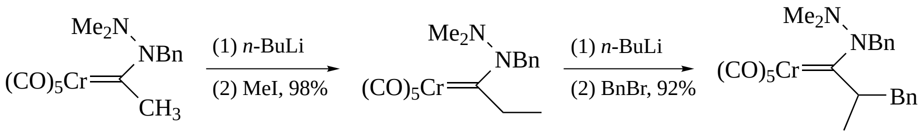
Me2N
NBn
(CO)5Cr
CH3
(1) n-BuLi
(2) MeI, 98%
Me2N
NBn
(CO)5Cr
(1) n-BuLi
(2) BnBr, 92%
Me2N
NBn
(CO)5Cr
Bn

Scheme 11

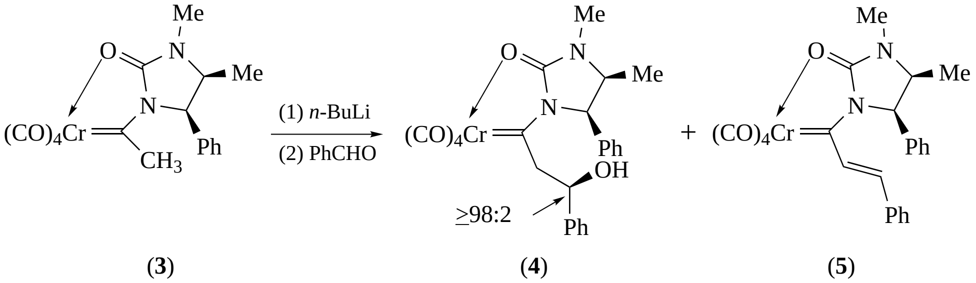

Scheme 13

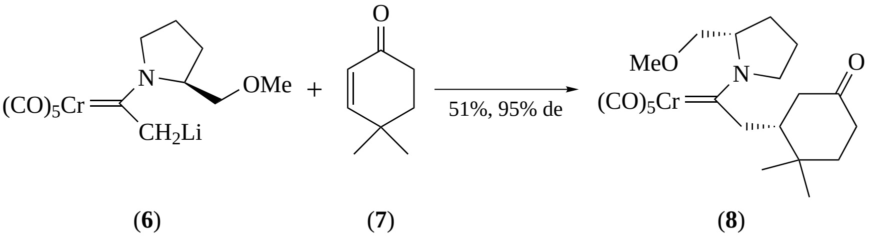

Scheme 14

to undergo aldol reactions with ketones and aldehydes. Highly diastereoselective reactions of chiral aminocarbenes are observed. For example, complex (**3**) reacts with benzaldehyde to give an essentially pure aldol product (**4**) together with the elimination product (**5**) (Scheme 13). 3-Hydroxy-substituted amino- and alkoxycarbenes are readily dehydrated by treatment with base, to give α,β-unsaturated carbenes of considerable synthetic value.

Deprotonation of carbene complexes followed by treatment with electron-deficient alkenes affords Michael addition products in fair to good yield. Reaction of the chiral pyrrolidine-substituted carbene (**6**) with 4,4-dimethyl-2-cyclohexen-1-one (**7**) furnishes the alkylkated product (**8**) in 95% de (Scheme 14).

α,β-Unsaturated complexes undergo a number of facile cycloaddition reactions to produce more elaborate complexes. For example, cycloadditions using diazoalkanes, nitrileimines, alkylnitrones, azomethine ylids (*see Ylide*), and imines are feasible. For example, reaction of the chiral carbene (**9**) with trimethylsilyldiazometathane gave the heterocyclic-substituted carbene (**10**) (Scheme 15).[16]

Alkene- and alkyne-substituted Fischer carbenes participate as dienophiles in Diels–Alder reactions. The conditions are usually mild and the reaction proceeds smoothly at room temperature. Similar isomeric ratio and rate acceleration is observed to that of Lewis acid–promoted Diels–Alder reactions between methyl acrylates and dienes when compared to the uncatalyzed reactions. The reactions are endo-selective. Asymmetric Diels–Alder reactions are observed using alkyne carbene complexes having a chiral amino group (Scheme 16)[17] or using a chiral diene (Scheme 17). Intramolecular Diels–Alder reaction can also be performed forming more complex bicyclic carbenes (Scheme 18).

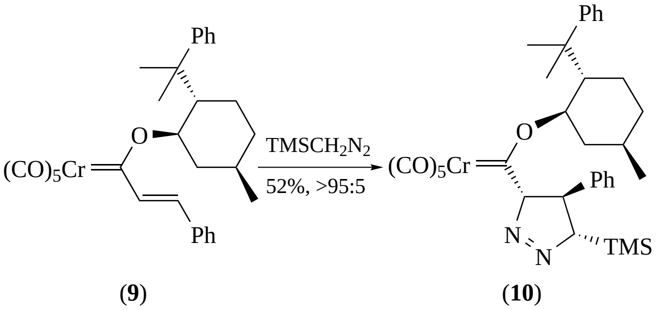

Scheme 15

Depending on the size of the nucleophile, α,β-unsaturated carbene complexes either undergo 1,4-addition and/or 1,2-addition of the nucleophile. Michael addition is observed using relatively large carbanion nucleophiles, such as the enolates of cyclopentanone, isobutyrophenone, or dimethyl malonate. Enamines can also be employed as nucleophiles affording Michael-type adducts. Reaction of alkenyl (methoxy) carbene complexes with enolates derived from methylketones gave five- and seven-membered carbocycles under mild reaction conditions. For example, reaction of (**11**) with (**12**) gave cycloheptanone (**13**) or cyclopentane (**14**), depending on the nucleophile (Scheme 19).[18] Triethyl boron can be used to

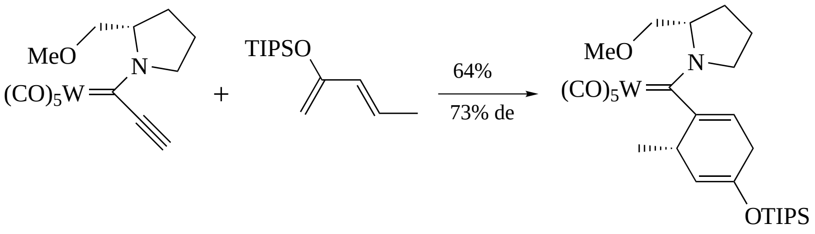
MeO
N
(CO)5W
+
TIPSO
64%
73% de
MeO
N
(CO)5W
OTIPS

Scheme 16

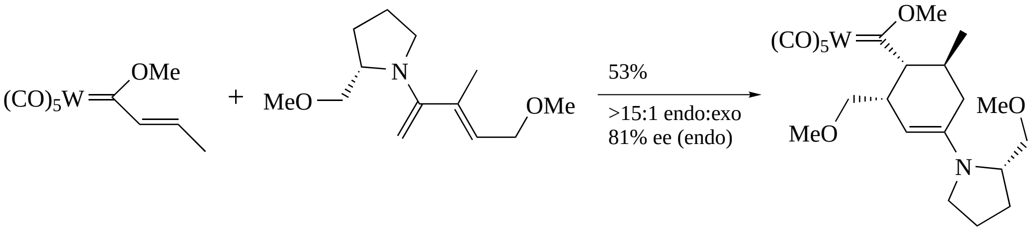
OMe
(CO)5W
+
MeO
N
OMe
53%
>15:1 endo:exo
81% ee (endo)
OMe
(CO)5W
MeO
MeO
N

Scheme 17

deliver an ethyl group to α,β-unsaturated alkoxy-chromium carbenes in a radical-type reaction using oxygen as the initiator. Asymmetric conjugate addition of organolithiums to aryl group of aryl-carbene complexes (Scheme 20) and to alkenyl-substituted carbenes can be achieved (Scheme 21). In the latter reaction, the addition reaction was accompanied by elimination of the metal carbonyl fragment. Hydrolysis of the enol ether affords an optically active aldehyde.

Several heteroatom nucleophiles, for example, amines, alcohols, thiols, carboxylates, and dialkylphosphines, undergo Michael addition reactions with alkene- and alkyne-substituted carbene complexes. Reaction of alkyne-substituted chromium carbenes with urea affords products derived from Michael addition and amine-alkoxy exchange (Scheme 22).[19] A Michael addition cyclization is observed upon reaction of hydrazine acetamide with alkynyl-substituted carbenes producing substituted pyrazoles (Scheme 23).

Chromium and tungsten carbene complexes containing an alkynyl or alkenyl substituent afford moderate to high yields of cyclobutene or cyclobutane complexes respectively via formal [2 + 2]cycloaddition with

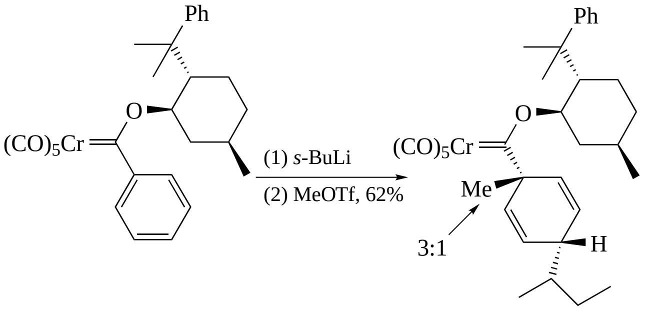
Ph
O
(CO)5Cr
(1) s-BuLi
(2) MeOTf, 62%
Ph
O
(CO)5Cr
Me
3:1
H

Scheme 20

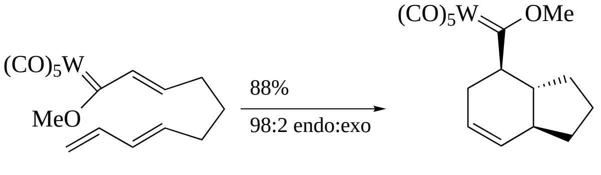
(CO)5W
MeO
88%
98:2 endo:exo
(CO)5W
OMe

Scheme 18

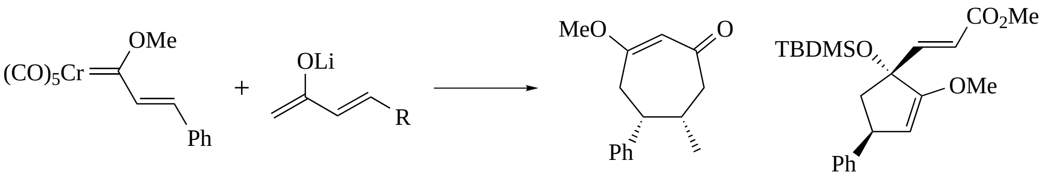
OMe
(CO)5Cr
Ph
+
OLi
R
MeO
O
Ph
CO2Me
TBDMSO
OMe
Ph

(**11**) (**12**) (R = Me, 51%, **13**) (R = CO_2Me, 72%, **14**)

Scheme 19

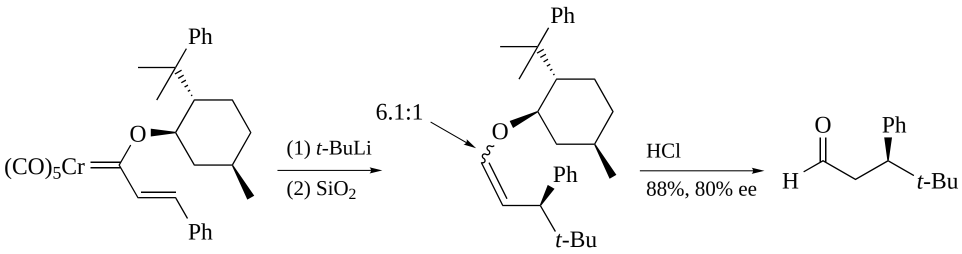
(CO)$_5$Cr
O
Ph
Ph
(1) t-BuLi
(2) SiO$_2$
6.1:1
O
Ph
Ph
t-Bu
HCl
88%, 80% ee
O
Ph
H
t-Bu

Scheme 21

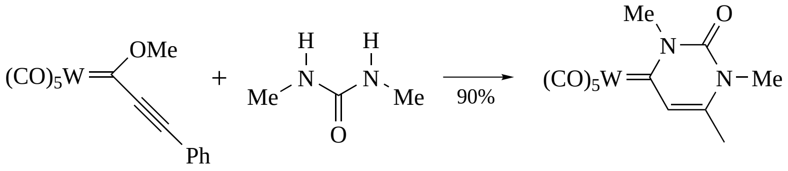
(CO)$_5$W
OMe
Ph
+
H
H
Me
N
N
Me
O
90%
Me
O
N
(CO)$_5$W
N−Me

Scheme 22

enol ethers and enamines (Scheme 24). In some cases, the ene reaction is a competitive pathway. This reaction path is exclusively seen using 1-substituted enol ethers and α-exomethyleneoxacyclopentylidene complex (**15**) (Scheme 24).[20]

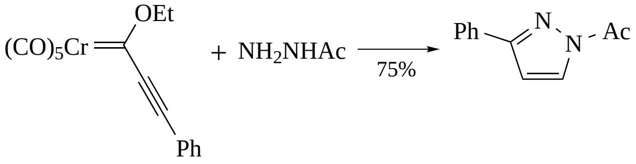
(CO)$_5$Cr
OEt
Ph
+ NH$_2$NHAc
75%
Ph
N
N
Ac

Scheme 23

Fischer-type carbenes can also be modified via transition metal catalyzed reactions. Fischer chromium aminocarbene complexes can be used as nucleophiles in palladium-catalyzed allylic substitution reactions with allylic acetates and carbonates, affording the corresponding allyl-substituted aminocarbenes. For example, reaction of the lithiated carbene (**15**) gives (**16**) in good yield (Scheme 25).[21]

Six- and seven-membered 2-oxacycloalkenylidene chromium complexes can be prepared via a ruthenium-catalyzed ring-closing metathesis using Grubb's catalyst (Scheme 26, *see* ***Organic Synthesis Using Metal-mediated Metathesis Reactions***). However, β-alkylated vinylcarbene complexes do not readily participate in the metathesis reaction.[22] Ene-yne functionalized carbenes undergo Pauson–Khand reactions (*see Pauson–Khand Reaction*) to

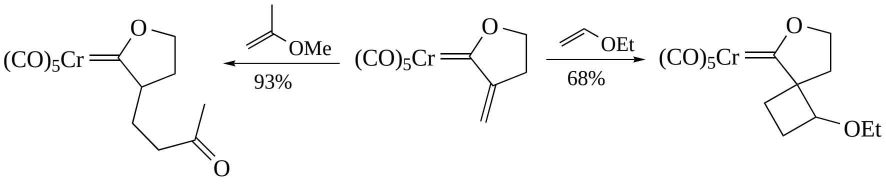
(CO)$_5$Cr
O
O
OMe
93%
(CO)$_5$Cr
O
OEt
68%
(CO)$_5$Cr
O
OEt

Scheme 24

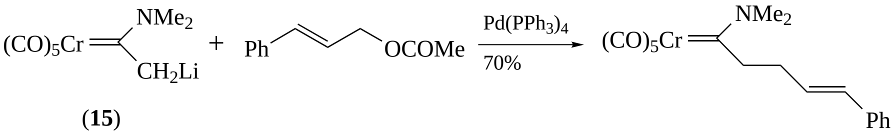
(CO)$_5$Cr
NMe$_2$
CH$_2$Li
+
Ph
OCOMe
Pd(PPh$_3$)$_4$
70%
(CO)$_5$Cr
NMe$_2$
Ph

(**15**)

(**16**)

Scheme 25

give bicyclic complexes under mild reaction conditions (Scheme 27).

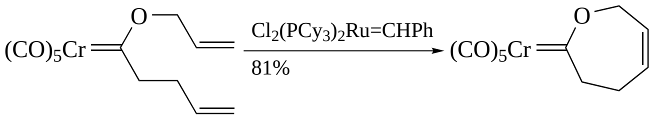

Scheme 26

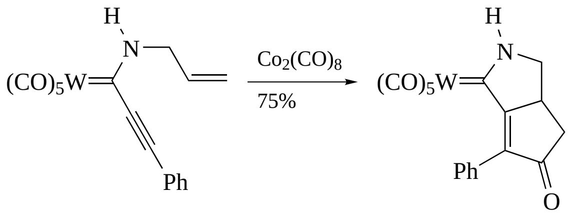

Scheme 27

2.2 Photolytic Reactions

Irradiation of Fischer carbene complexes generates, by insertion of carbon monoxide, a metal-bound ketene intermediate. Photolytic reactions of carbene complexes are synthetically attractive, in that the reaction conditions are mild and the reactions of ketene intermediates with a variety of reagents is of significant scope. A low concentration of metal-bound ketene is probably obtained and in the absence of a nucleophile, the starting material can usually be recovered even after prolonged irradiation. The ketene intermediates are readily trapped with nucleophiles; for example, dipeptides are formed in excellent yield and with very high diastereoselectivity upon irradiation of optically active carbenes in the presence of natural or ‘unnatural’ α-amino acids (Scheme 28). Dipeptides and PEG-supported amino acids and dipeptides can also be used as nucleophiles.

Photolysis of chiral amino carbene complexes in the presence of alcohols gives amino acid esters, again with a very high diastereoselectivity. Irradiation of aminocarbenes in the presence of 2,4,5-trichlorophenol produced optically active, activated, α-amino 2,4,5-trichlorophenoxide esters. Related intramolecular reactions of carbenes having a pendant alcohol afford lactones. For example, aldol condensation of (**17**) followed by photolysis give (**18**) (Scheme 29). α-Hydroxy esters are prepared by irradiation of in situ generated hydroxy-substituted Fischer carbenes in the presence of an alcohol.

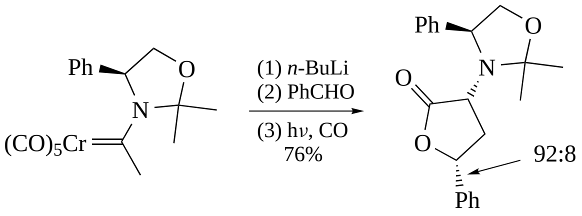

(**17**) (**18**)

Scheme 29

Photolytic reaction of chromium carbene complexes in the presence of cyclic and acyclic imines and iminodithiocarbonates produce β-lactams. This reaction is closely related to the well-precedented Staudinger reaction and the stereochemical outcome is the same. A large selection of free imines or the corresponding trimers, 1,3,5-triazines, can be used to form β-lactams. Several different classes of β-lactams can be synthesized using this methodology, including monocyclic β-lactams, cephams, oxacephams, carbacephams, penams, carbapenams, oxapenams, and azapenams. A wide range of optically active β-lactams can be made, in good to excellent yield with high diastereoselectivity, by photolysis of optically active aminocarbene complexes in the presence of imines or by reaction of achiral carbenes with optically active imines (Scheme 30).

Irradiation of alkoxycarbene complexes in the presence of alkenes and carbon monoxide produces cyclobutanones. A variety of inter- and intramolecular [2 + 2]cycloadditions have been reported. The regioselectivity is comparable with those obtained in reactions of ketenes generated from carboxylic acid derivatives. Cyclobutanones can be obtained with a high degree of diastereoselectivity upon reaction of alkoxycarbenes with chiral N-vinyloxazolidinones. For example, photolysis of (**19**) in the presence of (**20**) gives cyclobutanone (**21**) (Scheme 31).[23] In addition to alkoxycarbenes, carbenes having a thioether or pyrrole substituent can also be employed. Related intramolecular cycloadditions of γ,δ-unsaturated chromium carbenes afford bicyclo[2.1.1]hexanones (Scheme 32).

Nonstabilized phosphorus ylids (*see Ylide*) either deprotonate the relatively acidic α-position of chromium alkoxycarbenes or produce enol ethers by a formal metathesis reaction

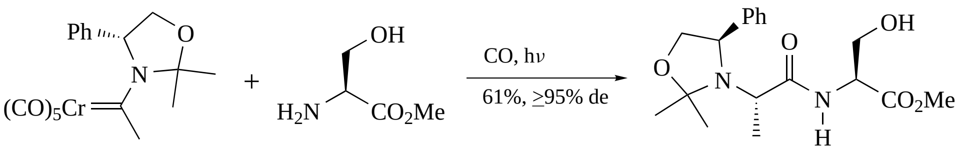

Scheme 28

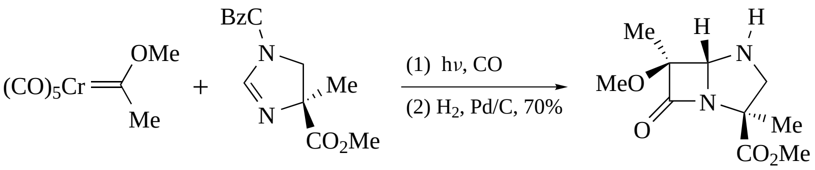
BzC
OMe
(CO)5Cr
Me
N
N
Me
CO2Me
(1) hν, CO
(2) H2, Pd/C, 70%
Me
H
H
N
MeO
N
O
Me
CO2Me

Scheme 30

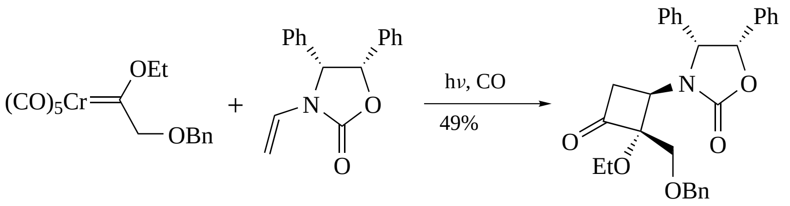
OEt
(CO)5Cr
OBn
Ph
Ph
N
O
O
hν, CO
49%
Ph
Ph
N
O
O
O
EtO
OBn

(**19**) (**20**) (**21**)

Scheme 31

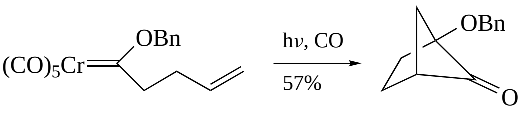
OBn
(CO)5Cr
hν, CO
57%
OBn
O

Scheme 32

with carbene complexes lacking α-protons. Photolytic reactions of alkoxycarbenes in the presence of carbonyl-stabilized sulfur ylids produce trisubstituted alkenes (Scheme 33).

Polycyclic aromatic compounds are obtained upon irradiation of diaryl-substituted chromium carbenes under a carbon monoxide atmosphere. The reaction probably proceeds via the formation of a biaryl-alkoxy ketene followed by cyclization. For example, the pyrrole-substituted carbene (**22**) gave the tricyclic compound (**23**) (Scheme 34).[24] Related intramolecular Friedel–Crafts-type reactions of carbenes having tethered electron-rich aromatic rings are feasible, usually in moderate yields (Scheme 35). A Lewis acid catalyst such as zinc dichloride is required for optimum yields.

Photolysis of chromium alkoxycarbene complexes with aldehydes in the presence of a Lewis acid or base, and carbon monoxide, affords β-lactones in low to moderate yield. The intramolecular variation of this [2 + 2]cycloaddition using carbene complexes having a pendant aldehyde are considerably more efficient (Scheme 36).

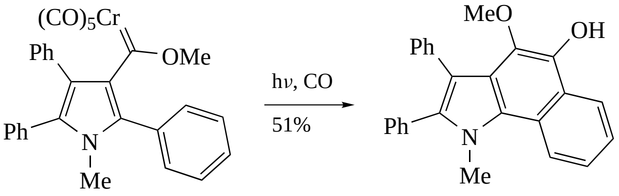
(CO)5Cr
Ph
OMe
Ph
N
Me
hν, CO
51%
MeO
OH
Ph
Ph
N
Me

(**22**) (**23**)

Scheme 34

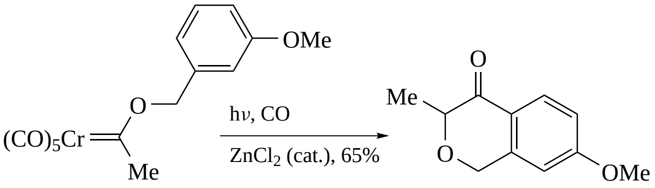
OMe
O
(CO)5Cr
Me
hν, CO
ZnCl2 (cat.), 65%
O
Me
O
OMe

Scheme 35

2.3 Metal–Carbon Double Bond Cycloaddition and Further Reactions

Thermal reactions of Fischer carbenes with alkynes afford a variety of products depending on the substrates. The reactions can be visualized mechanistically as a [2 + 2]cycloaddition

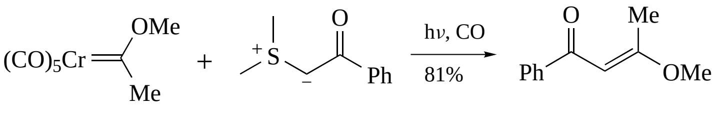
OMe
(CO)5Cr
Me
+
S
O
Ph
hν, CO
81%
O
Me
Ph
OMe

Scheme 33

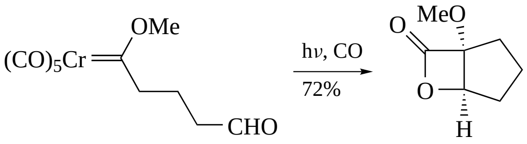

Scheme 36

between the alkyne and the carbon–metal double bond. The intermediately formed metallacyclobutene then undergoes a variety of reactions. Common ‘termination’ reactions include β-hydride elimination (*see β-Hydride Elimination*), insertion of carbon monoxide (*see CO Insertion*), forming a ketene, and reaction with nucleophiles. For example, dienes and trienes can be obtained from alkynes and Fischer carbenes via β-hydride elimination (Scheme 37). Alkynes having a pendant hydroxy group afford β- and γ-lactones (Scheme 38). Coupling of carbenes with 2-alkynylbenzaldehydes furnish isobenzofuran derivatives (Scheme 39).**[25]** Related reactions of 2-ene-4-yne-imines and 2-ene-4-yne-aldehydes give substituted pyrroles and furans respectively.

2.4 Benzannulation Reactions

Thermal reaction of alkoxy-substituted Fischer carbenes of group 6 metals with alkynes has been applied to the syntheses of a variety of polycyclic aromatic compounds. The reaction has been extensively developed into one of the more powerful reactions employing Fischer carbenes. Aryl-, alkenyl-, and alkynyl-substituted carbenes undergo benzannulation reaction furnishing cyclized products upon heating in the presence of an alkyne. A probable mechanism for the benzannulation involves [2 + 2] cycloaddition between the alkyne and the carbon–metal double bond forming a metallacyclobutene, metathesis to give a vinyl carbene, insertion of carbon monoxide to form a ketene followed by cyclization–aromatization. The regiochemistry of the initial cycloaddition puts the terminal end of the alkyne next to the initial carbene carbon. For internal alkynes, both cycloadducts are possible but the alkyne terminus containing the more sterically demanding group is usually connected to the metal. Oxidation of the 1,4-hydroxy-ether benzannulation products affords 1,4-quinones (Scheme 40). While the benzannulation of alkoxycarbenes results in the formation of new six-membered rings by insertion of carbon monoxide, as described above, aminocarbenes produce primarily indene derivatives, however this reaction has found little synthetic use. Cyclohexadienones are formed when tautomerization to an aromatic ring is not possible (Scheme 41).

The benzannulation reaction can be promoted in a variety of ways including ultrasound, microwaves, and irradiation using a xenon lamp. Reactions are also possible on solid support such as, silica gel, magnesium sulfate, and aluminium

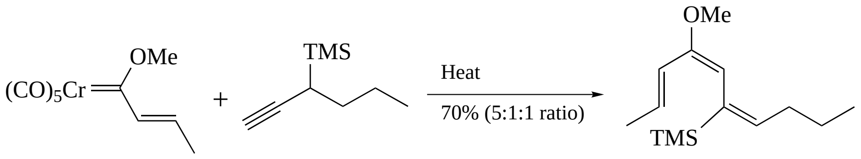

Scheme 37

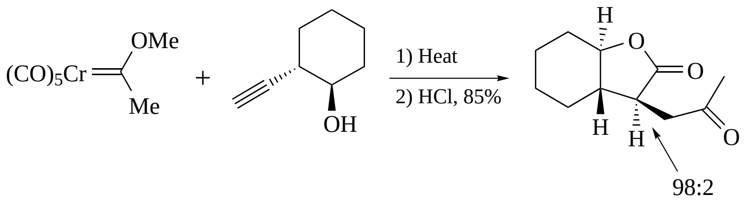

Scheme 38

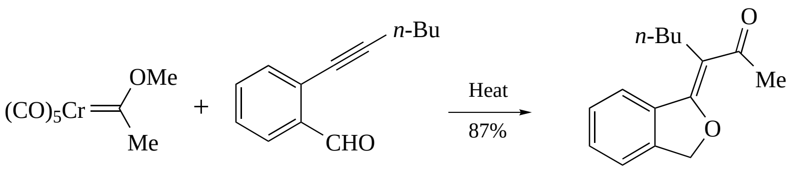

Scheme 39

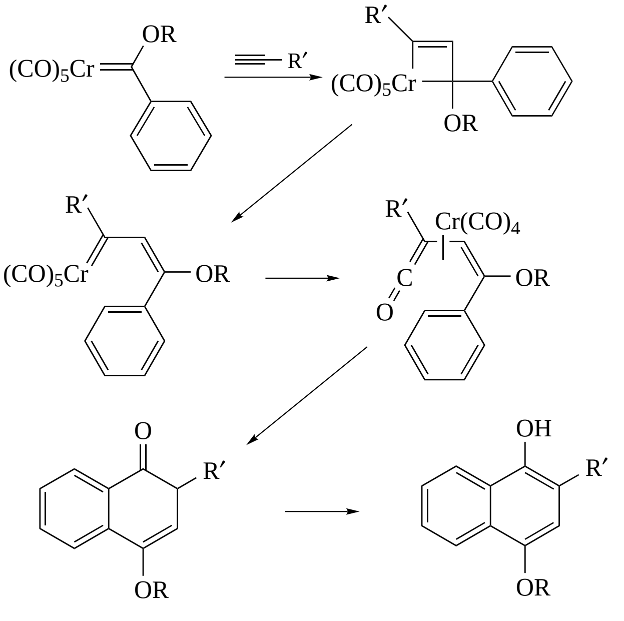

(CO)$_5$Cr
OR
R′
(CO)$_5$Cr
OR
R′
(CO)$_5$Cr
OR
R′
Cr(CO)$_4$
C
O
OR
O
R′
OR
OH
R′
OR

Scheme 40

trioxide in the absence of a solvent. By tethering the alkyne via a silicon linkage, reversal of regiochemistry can be obtained (Schemes 42 and 43).

The aromatic products often contain an arene-complexed chromium tricarbonyl unit. The metal-free product is obtained by oxidation commonly using CAN or air under irradiation. The formation of complexed adducts can be used to prepare chiral chromium tricarbonyl arene complexes (Scheme 44, *see Arene Complexes*).

Many reactions afford, in addition to the naphthalene derivatives, mixtures of products. One of the major side reactions is the formation of indene derivatives directly from the metathesis intermediate without insertion of carbon monoxide. Other products frequently isolated as minor components are furans, cyclobutanones, and cyclopentenediones. The product distribution is dependent on numerous factors, including solvent, reaction temperature, concentration of the alkyne, and the nature of the aryl substituent. Molybdenum carbenes give, depending on the alkyne, either naphthols or indenes exclusively. The molybdenum Fischer carbenes can be tuned to give naphthoquinones by replacing one of the carbon monoxide ligands with a phosphine (Scheme 45).

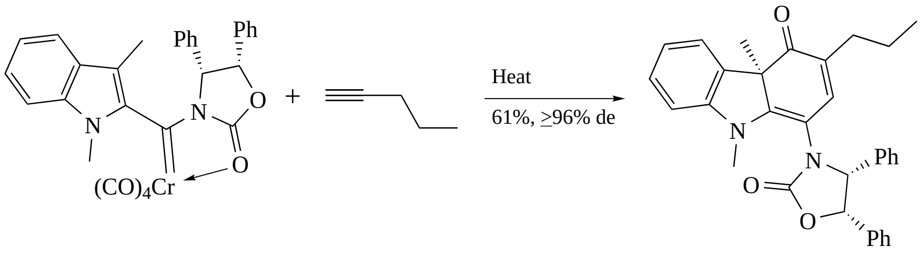

N
Ph
Ph
N
O
O
(CO)$_4$Cr
+
Heat
61%, ≥96% de
O
N
N
Ph
O
O
Ph

Scheme 41

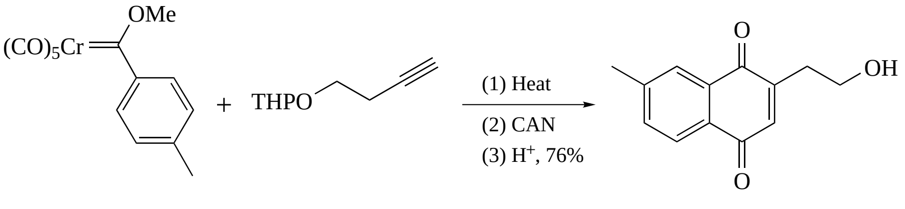

OMe
(CO)$_5$Cr
+
THPO
(1) Heat
(2) CAN
(3) H$^+$, 76%
O
OH
O

Scheme 42

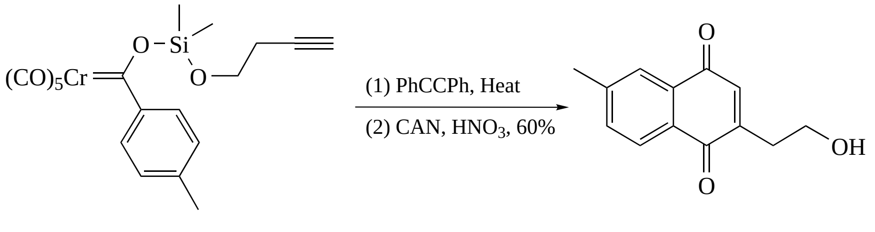

O
Si
O
(CO)$_5$Cr
(1) PhCCPh, Heat
(2) CAN, HNO$_3$, 60%
O
OH
O

Scheme 43

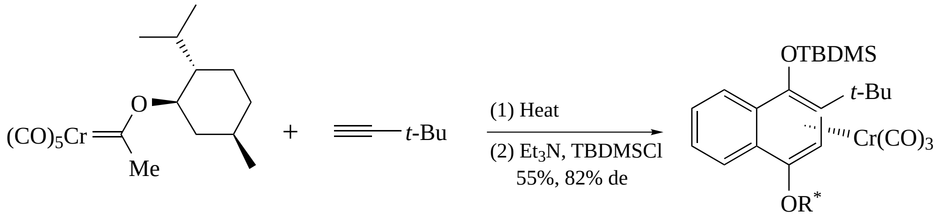
(CO)5Cr
O
Me
+
t-Bu
(1) Heat
(2) Et3N, TBDMSCl
55%, 82% de
OTBDMS
t-Bu
Cr(CO)3
OR*

Scheme 44

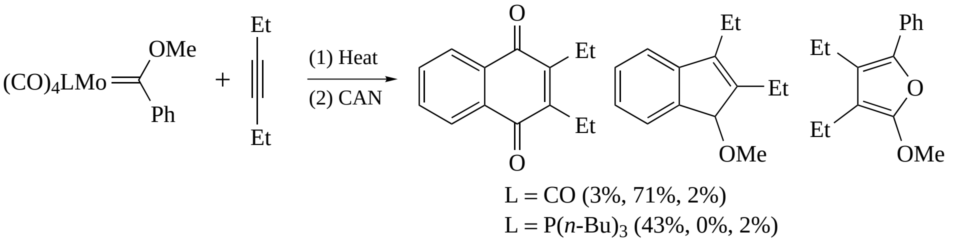
(CO)4LMo
OMe
Ph
+
Et
Et
(1) Heat
(2) CAN
O
O
Et
Et
Et
Et
OMe
Ph
Et
Et
O
OMe
L = CO (3%, 71%, 2%)
L = P(n-Bu)3 (43%, 0%, 2%)

Scheme 45

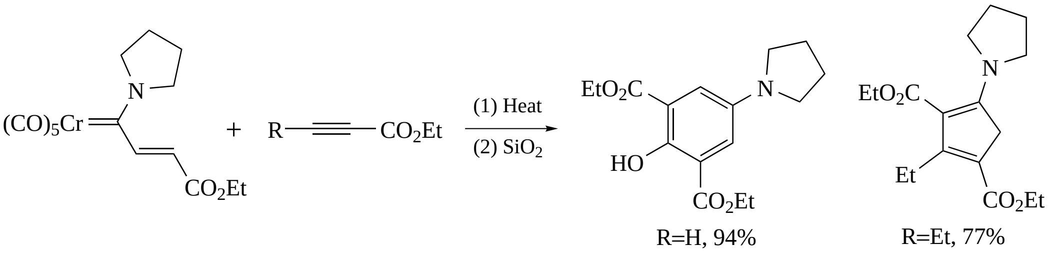
(CO)5Cr
N
CO2Et
+
R
CO2Et
(1) Heat
(2) SiO2
EtO2C
HO
N
CO2Et
R=H, 94%
EtO2C
N
Et
CO2Et
R=Et, 77%

Scheme 46

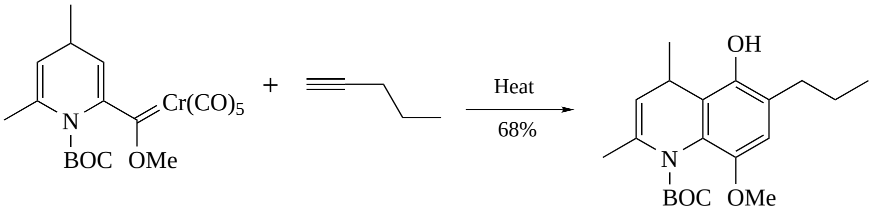
N
BOC
OMe
Cr(CO)5
+
Heat
68%
OH
N
BOC
OMe

Scheme 47

Depending on the alkyne, both six- and five-membered rings may be obtained upon reaction of ß-carbomethoxy-alkenyl-amino carbenes (Scheme 46).[26] Dihydropyridine and indole carbene complexes participate in benzannulation reactions (Scheme 47). Alkynes containing boronic esters may be used, affording boronic ester-functionalized quinones that can be used in palladium-catalyzed coupling reactions (Scheme 48).[27]

The benzannulation reaction of aryl- and alkenyl-substituted Fischer carbenes with alkynes has been used in several total syntheses. Some recent examples of benzannulation reactions used to synthesize advanced intermediates include, for example, allocolchicinoids[28] and menogaril (Schemes 49 and 50).[29]

Related benzannulation reactions are also observed using isocyanides in place of carbon monoxide. It should be noted that the regiochemistry is opposite to that previously described. Reaction of complex (**24**) with *t*-butylisocyanide under thermal conditions produced naphthalene (**25**) used in total synthesis of the calphostins (Scheme 51).[30] Benzannulations

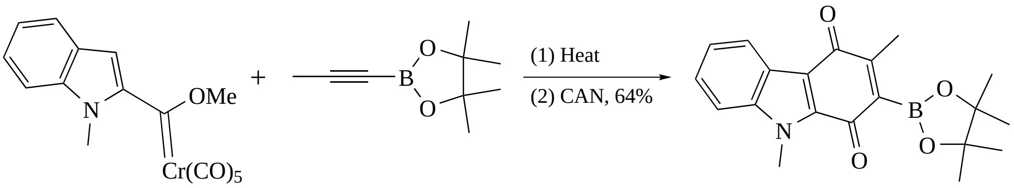
N
OMe
Cr(CO)5
+
B
O
O
(1) Heat
(2) CAN, 64%
O
O
N
B
O
O

Scheme 48

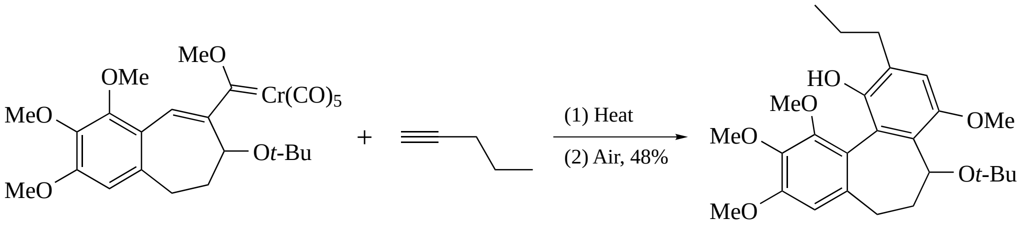
MeO
OMe
MeO
Cr(CO)5
Ot-Bu
MeO
+
(1) Heat
(2) Air, 48%
HO
MeO
MeO
OMe
Ot-Bu
MeO

Scheme 49

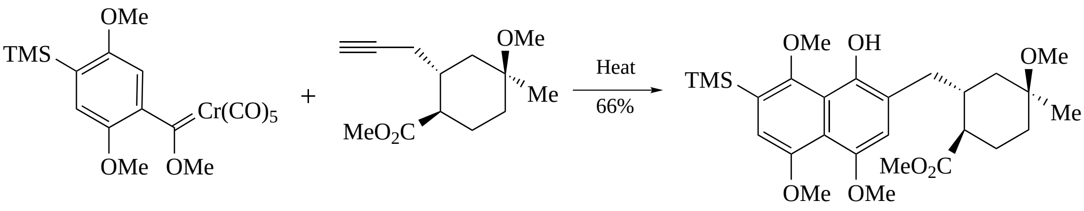
OMe
TMS
Cr(CO)5
OMe
OMe
+
OMe
Me
MeO2C
Heat
66%
OMe
OH
TMS
OMe
Me
MeO2C
OMe
OMe

Scheme 50

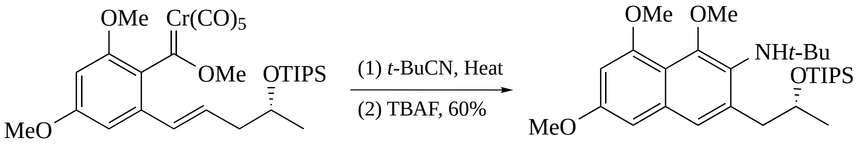
OMe
Cr(CO)5
OMe
OTIPS
MeO
(1) t-BuCN, Heat
(2) TBAF, 60%
OMe
OMe
NHt-Bu
OTIPS
MeO

(**24**) (**25**)

Scheme 51

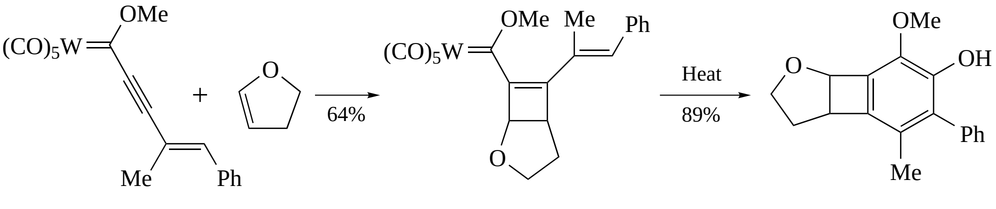
OMe
(CO)5W
Me
Ph
+
O
64%
OMe
Me
Ph
(CO)5W
O
Heat
89%
OMe
O
OH
Ph
Me

Scheme 52

of cyclobutenyl-substituted complexes, derived from [2 + 2]cycloaddition of alkyne-substituted complexes with enol ethers is also possible (Scheme 52).[31] A somewhat unusual annulation was employed to prepare the steroid skeleton (**27**) from (**26**) (Scheme 53).

2.5 Cyclopropanations

Several useful inter- and intramolecular reactions of chromium, molybdenum, tungsten, iron, or manganese Fischer carbenes with alkenes to form cyclopropanated products have

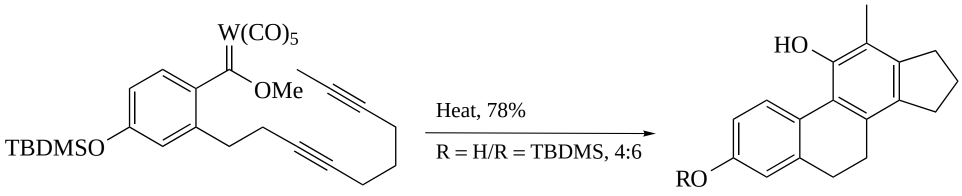

(**26**) (**27**)

Scheme 53

been developed. Thermal reaction of electron-deficient alkenes with group 6 carbenes affords donor–acceptor-substituted cyclopropanes. The geometry of the alkene is retained to a very high degree in the cyclopropane. Aminocarbenes usually do not produce cyclopropanated products upon thermolysis in the presence of alkenes. However, intramolecular reactions and the reaction of pyrrole-substituted carbenes give satisfactory yields of cyclopropanated products (Scheme 54). This is probably a result of a lower electron-donating ability, compared to amines, of the pyrrole nitrogen. Alkoxycarbonyldialkylaminocarbenes also cyclopropanate alkenes to give cyclopropane products in a high diastereomeric ratio (Scheme 55).[32] Reaction of carbenes with dihydropyridines transferring a hydride to the carbene carbon followed by cyclopropanation of alkenes, enol ethers, and enamines can be achieved (Scheme 56).[33]

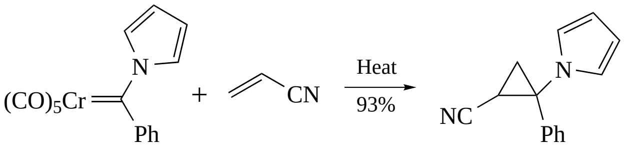

Scheme 54

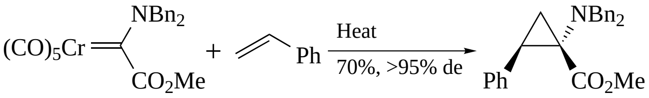

Scheme 55

Diastereoselective and enantioselective (*see Enantioselectivity*) cyclopropanations of chiral alkenes can be achieved (Scheme 57).[34] Unactivated alkenes usually do not participate in cyclopropanation reactions of Fischer carbenes. However, alkenyl- and heteroaryl-substituted group 6 alkoxy carbene complexes cyclopropanate unactivated alkenes in good yield (Scheme 58).[35]

Intramolecular cyclopropanations of pendant alkenes are more favorable. Heteroatom-substituted 2-aza- and 2-oxabicyclo[3.1.0]hexanes, together with 2-oxabicyclo[4.1.0] heptanes, can be prepared from chromium and tungsten Fischer carbenes having a tethered alkene chain. An interesting carbene formation via a cationic alkylidene intermediate, nucleophilic addition (*see Nucleophilic Addition: Rules for Predicting Direction*), and intramolecular cyclopropanation is shown in Scheme 59. An intramolecular cyclopropanation via reaction of alkenyl Fischer carbene complex (**28**) and propyne was used in a formal synthesis of carabrone (Scheme 60).

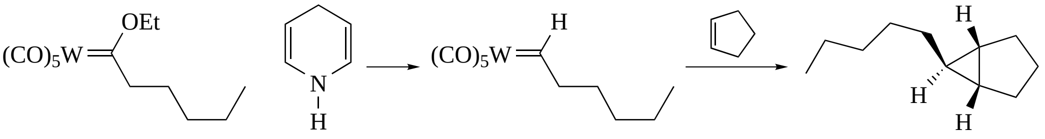

Scheme 56

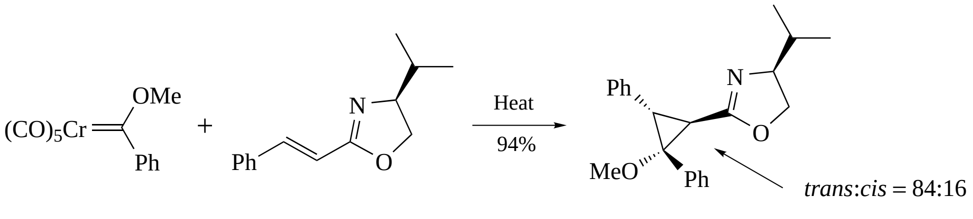

Scheme 57

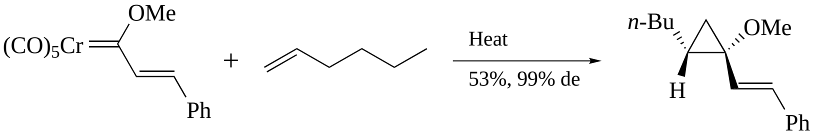

Scheme 58

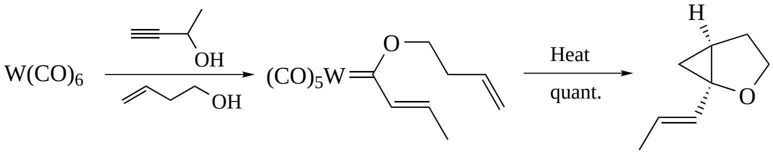

Scheme 59

Cyclopropanation reactions of nonheteroatom-stabilized carbenes have also been developed. The most versatile are the cationic iron carbenes that cyclopropanate alkenes with high stereospecificity under very mild reaction conditions. The cyclopropanation reagents are available from a number of iron complexes, for example, *O*-alkylation of cyclopentadienyl dicarbonyliron alkyl or acyl complexes using Meerwein salts affords cationic Fischer carbenes. Cationic iron carbene intermediates can also be prepared by reaction of $CpFe(CO)_2^-$ with aldehydes followed by treatment with TMS-chloride. Chiral intermolecular cyclopropanation using a chiral iron carbene having a complexed chromium tricarbonyl unit is observed (Scheme 61).

2.6 Miscellaneous Reactions of Fischer Carbenes

Fischer carbenes react with silanes and stannanes to form alkoxy- or amino-stannanes and -silanes. For example, diastereoselective reaction of the chiral aminocarbene (**29**) with triphenylsilane or tri-*n*-butyltin hydride gave (**30**) and (**31**), respectively (Scheme 62).[36] Tin-substituted ethers can be prepared from α,β-unsaturated cyclic carbenes by treatment with tri-*n*-butyltin triflate in the presence of triethylamine (Scheme 63).[37] Reaction with lithiumdibromomethane and α-halo enolates affords carbonyl compounds (Schemes 64 and 65).[38]

A variety of annulations leading to ring systems other than benzenes can be isolated from reactions of Fischer carbenes. Cyclopentenone derivatives are formed from a reaction of *Z*-ß-amino-α,β-unsaturated chromium carbenes with alkynes (Scheme 66). In contrast, *E*-ß-amino-α,β-unsaturated chromium carbenes reacts with alkynes to give cyclopentadienes (Scheme 67).

Formation of polycyclic ring systems via intermolecular reactions of Fischer carbenes with alkynes can be achieved. In a metathesis-type reaction, reactions of 1,6-enynes afford

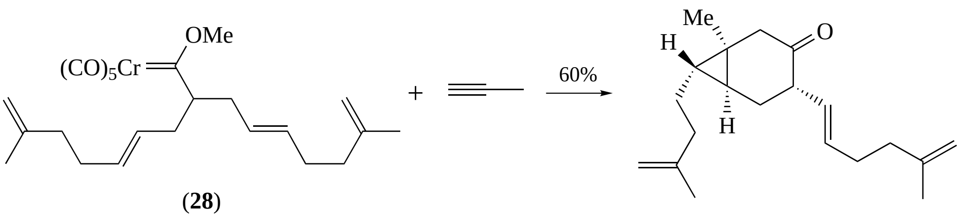

(**28**)

Scheme 60

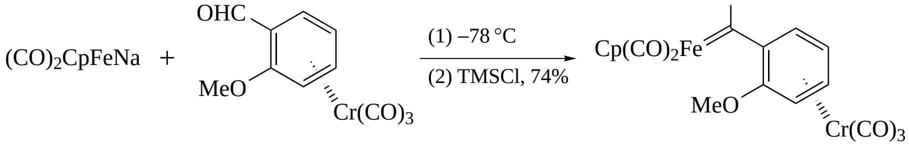

Scheme 61

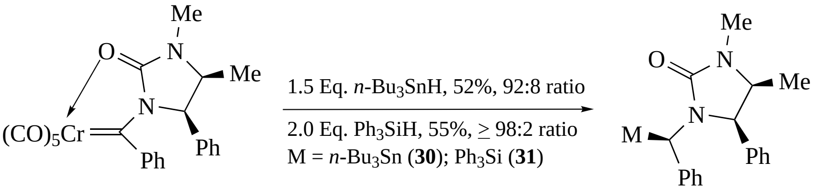
Me
O
N
Me
N
(CO)5Cr
Ph
Ph
1.5 Eq. n-Bu3SnH, 52%, 92:8 ratio
2.0 Eq. Ph3SiH, 55%, ≥ 98:2 ratio
M = n-Bu3Sn (30); Ph3Si (31)
Me
O
N
Me
N
M
Ph
Ph

(**29**)

Scheme 62

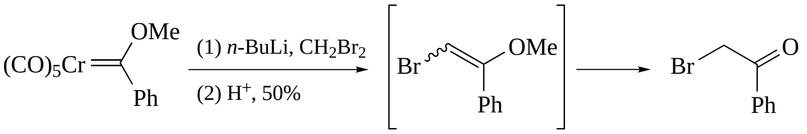
OMe
(CO)5Cr
Ph
(1) n-BuLi, CH2Br2
(2) H+, 50%
Br
OMe
Ph
Br
O
Ph

Scheme 64

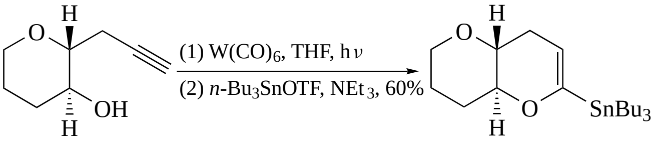
H
O
OH
H
(1) W(CO)6, THF, hν
(2) n-Bu3SnOTF, NEt3, 60%
H
O
O
SnBu3
H

Scheme 63

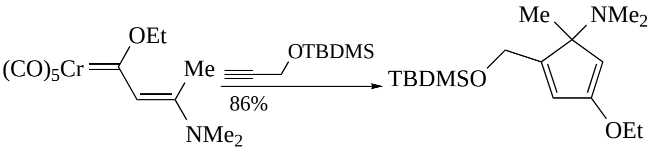
OEt
(CO)5Cr
Me
NMe2
OTBDMS
86%
TBDMSO
Me
NMe2
OEt

Scheme 67

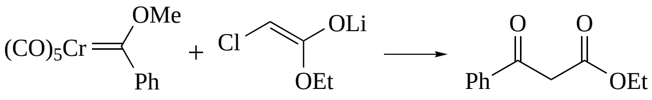
OMe
(CO)5Cr
Ph
+
Cl
OLi
OEt
O
O
Ph
OEt

Scheme 65

bicyclic ketones (Scheme 68). Related reactions of 3-ene-1,5-diynes afford polycyclic compounds (Scheme 69).[39] Reactions of other polyunsaturated compounds leading to complex molecules have also been reported (Scheme 70). Chromium-mediated β-lactone synthesis using ultrasonication or thermal reactions has been reported (Scheme 71).[40] The reactions are most likely initiated by a [2 + 2]cycloaddition.

Interesting reactions wherein two carbon monoxides have been inserted into the final product have been described. For example, reaction of carbene (**32**) with N-phenyl-1,4-dihydropyridine affords the bicyclic lactone (**33**) (Scheme 72).[41] A possible mechanism is hydride transfer to the carbene carbon, carbon monoxide insertion, [2 + 2] and cycloaddition to give (**34**). Metathesis and ketene formation would form (**35**) followed by intramolecular lactone formation to give (**33**). Reaction of β-vinyl-cyclobutenyl-substituted carbenes with alkynes gives cyclooctatriene (Scheme 73).[42]

Fischer carbene complexes undergo elimination reactions under thermal conditions to form enol ethers, enol acetates, or enamines, depending on the heteroatom substituent on the carbene carbon and, depending on the conditions, aldehydes. High (Z) to (E) ratios of isomers are obtained in most cases. Although thermal reactions have been reported, this formal 1,2-hydrogen shift is in most cases facilitated by tertiary

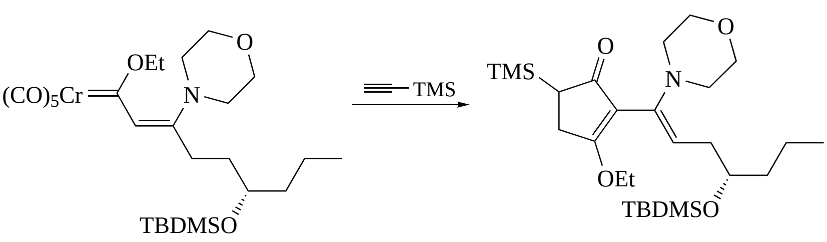
OEt
O
(CO)5Cr
N
TBDMSO
TMS
TMS
O
O
N
OEt
TBDMSO

Scheme 66

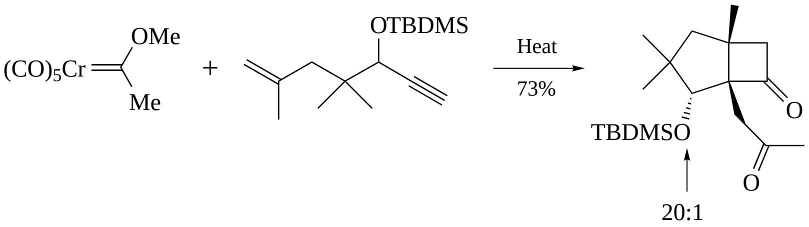

Scheme 68

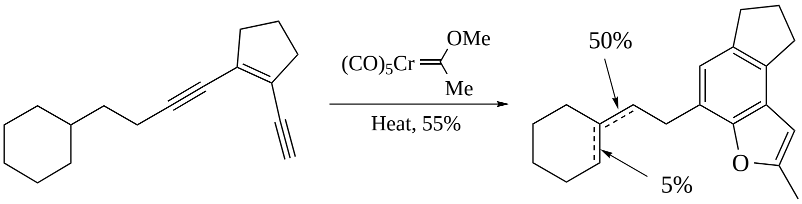

Scheme 69

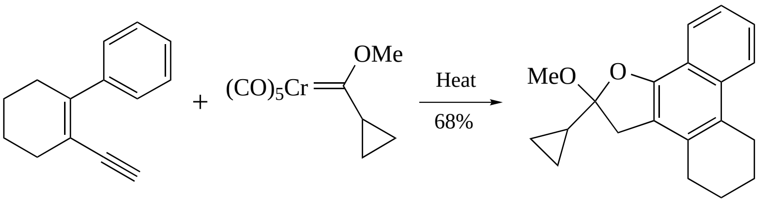

Scheme 70

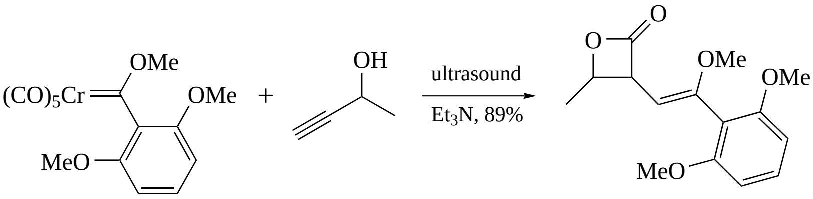

Scheme 71

amines, pyridine, or alkoxides. An example of α-acylation-elimination forming an enol ether can be seen in Scheme 74.

Fischer carbene complexes are smoothly transformed by oxidation to esters or amides without racemization of α-substituents. Oxidizing agents frequently used includes, pyridine *N*-oxide, oxygen, dimethyloxirane, dimethyl sulfoxide, $[FeCl_2(DMF)_2][FeCl_2]$, hydrogen peroxide, and CAN. For example, cyclopropanation of (**36**) with chloroiodomethane to give (**37**) followed by oxidation give the trans-substituted cyclopropane (**38**) (Scheme 75).

Thermally induced ring-expansions of cyclopropyl-substituted chromium carbene affording 2-alkoxy-cyclopentenones or cyclopentadienones have been developed (Scheme 76). Reaction of a cyclopropylcarbene having a tethered alkoxyalkyne gives bicyclic systems (Scheme 77).[43]

Reactions of σ-alkynyltungsten complexes forming cationic carbene intermediates have been developed. Treatment of (**39**) with acetaldehyde in the presence of borontrifluoride etherate affords carbene (**40**) (Scheme 78). Treatment of (**40**) with base forms a new σ-alkynyltungsten complex (**41**). The σ-complexes are readily prepared from cyclopentadienyl(dicarbonyl)tungsten chloride and acetylides. A variety of potentially useful transformations can be made, for example, oxidation, reduction–oxidation, Michael addition, cyclopropanation–oxidation, and double alkylation (Scheme 79).[44]

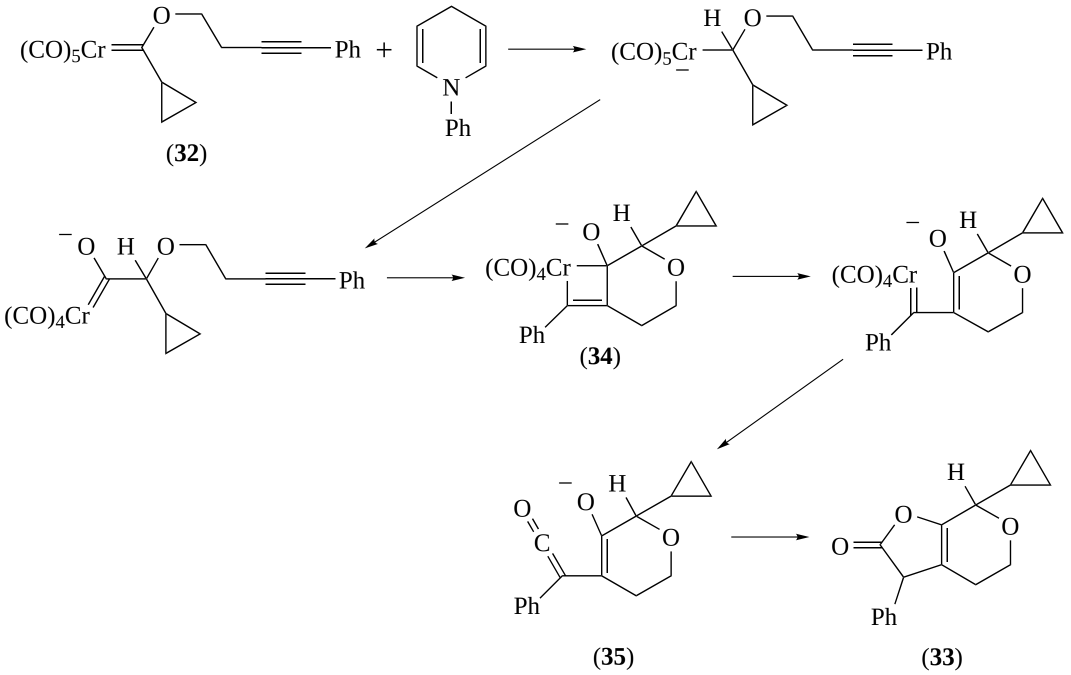
(CO)$_5$Cr
Ph
N
Ph
(CO)$_4$Cr
(CO)$_5$Cr
O
H

(**32**) (**34**) (**35**) (**33**)

Scheme 72

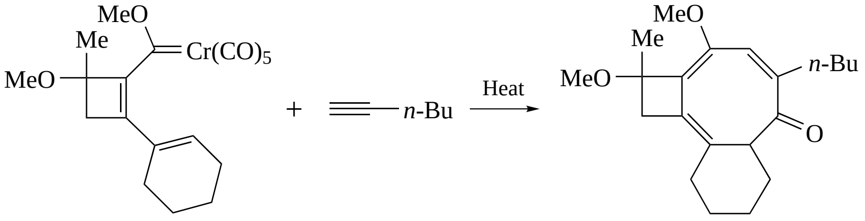
MeO
Me
MeO
Cr(CO)$_5$
n-Bu
Heat
O

Scheme 73

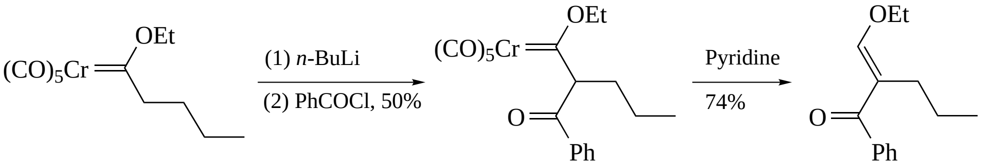
(CO)$_5$Cr
OEt
(1) n-BuLi
(2) PhCOCl, 50%
Pyridine
74%
O
Ph

Scheme 74

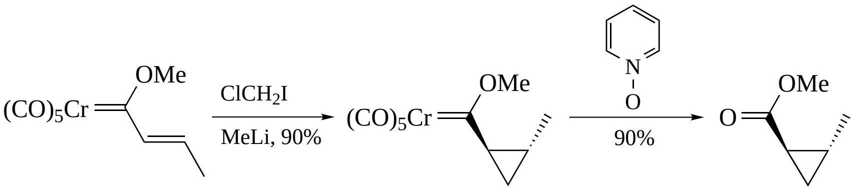
(CO)$_5$Cr
OMe
ClCH$_2$I
MeLi, 90%
N
O
90%
O

(**36**) (**37**) (**38**)

Scheme 75

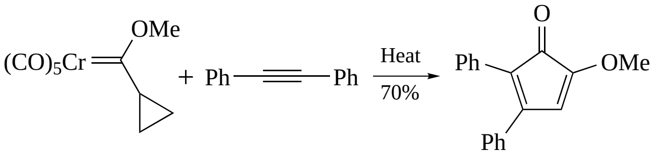
OMe
$(CO)_5Cr$
+ Ph—Ph
Heat
70%
Ph
O
OMe
Ph

Scheme 76

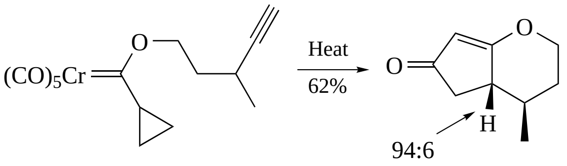
$(CO)_5Cr$
O
Heat
62%
O
O
H
94:6

Scheme 77

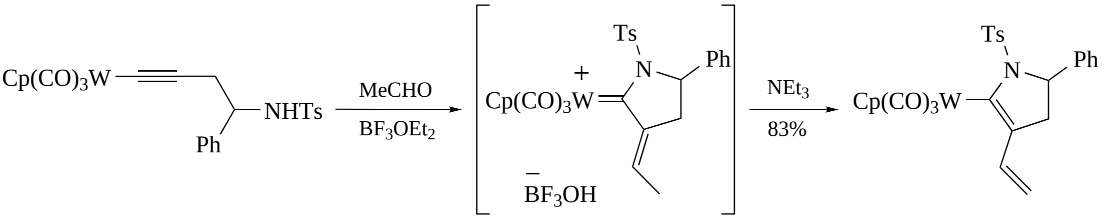
$Cp(CO)_3W$
NHTs
Ph
MeCHO
BF_3OEt_2
Ts
+
N
Ph
$Cp(CO)_3W$
$\bar{B}F_3OH$
NEt_3
83%
Ts
N
Ph
$Cp(CO)_3W$

(**39**) (**40**) (**41**)

Scheme 78

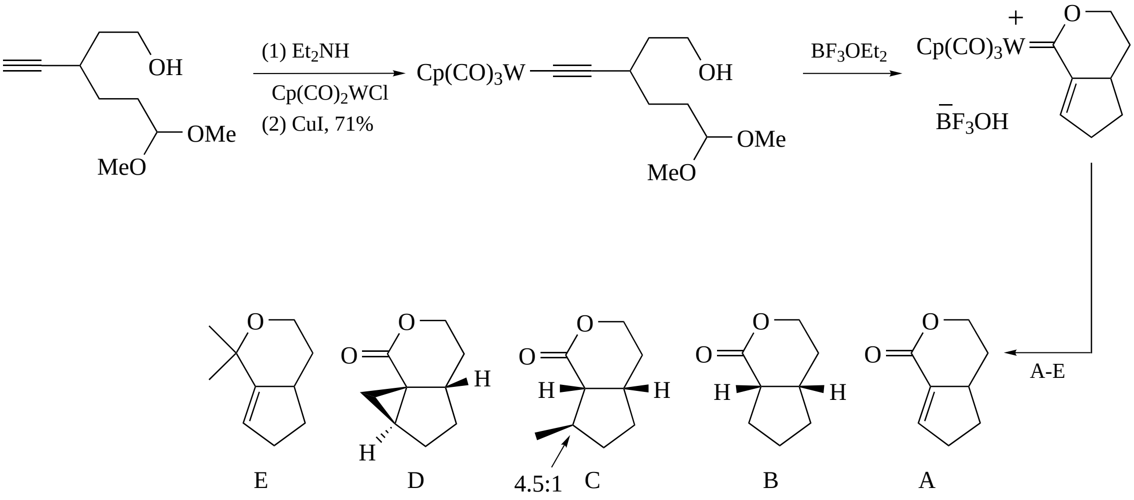
OH
OMe
MeO
(1) Et_2NH
$Cp(CO)_2WCl$
(2) CuI, 71%
$Cp(CO)_3W$
OH
OMe
MeO
BF_3OEt_2
+
$Cp(CO)_3W$
O
$\bar{B}F_3OH$
A-E
O
O
O
H
H
O
O
H
H
4.5:1
O
O
H
H
O
O
O
O
E
D
C
B
A

A = Air, H_2O, 81%; B = a) Et_3SiH, b) Air, H_2O, 64%; C = a) Me_2CuLi, air, H_2O, 71%; D = CH_2N_2, 62%;
E = MeMgBr, 71%.

Scheme 79

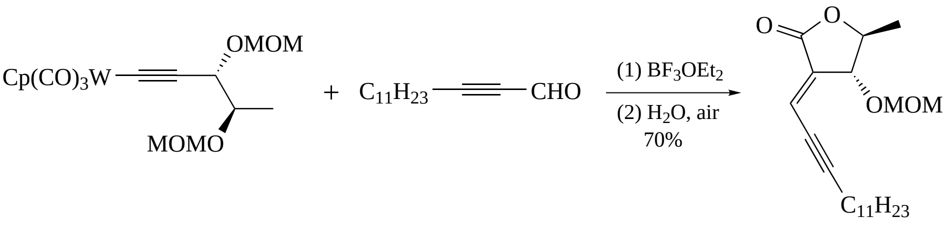
OMOM
$Cp(CO)_3W$
MOMO
+ $C_{11}H_{23}$
CHO
(1) BF_3OEt_2
(2) H_2O, air
70%
O
O
OMOM
$C_{11}H_{23}$

Scheme 80

This methodology has been used to prepare a variety of natural products such as (+)-blastomycinone, (−)-listenolide C_1, and related lactones. The cyclization step for (−)-listenolide is seen in Scheme 80.[45]

Intramolecular C–H insertion reactions of (η^5-cyclopentadienyl)dicarbonyliron carbene complexes can be used to prepare complex polycyclic compounds. Carbon–hydrogen bond insertion using an iron carbene was used as a key step in the synthesis of sterpurene and pentalene (Scheme 81).[46]

3 METAL CARBONYL–ARENE COMPLEXES

A variety of transition metals, for example, chromium, molybdenum, tungsten, iron, vanadium, manganese, and rhodium can be used to prepare relatively stable η^6-arene complexes (*see Arene Complexes*). Reactions of η^6-arene chromium tricarbonyl complexes have been extensively examined, and numerous reviews are available.[47,48] Although chromium complexes are by far the most utilized in organic synthesis, complexes of iron and manganese are emerging as potentially useful alternatives.

A number of substituted benzenes, naphthalenes, indans, pyridines, and indoles form arene(tricarbonyl)chromium complexes upon thermolysis under an inert atmosphere, usually in a high boiling ether, or by irradiation of the arenes in the presence of chromium hexacarbonyl. The complexes are relatively air-stable and can usually be stored for long periods in the absence of light. Somewhat milder conditions can be used by transfer of the chromium tricarbonyl group from preformed naphthalene(tricarbonyl)chromium, tris(L)tricarbonyl chromium (L = acetonitrile, ammonia, pyridine), or tricarbonyl(η^5-1-methylpyrrole)chromium. Enantiomerically pure arene(tricarbonyl)chromium complexes having two different substituents, either ortho or meta can be prepared conveniently by classical resolution of racemic mixtures. Resolution of *ortho*-substituted benzaldehyde complexes has been achieved by formation of the aminal with chiral diamines, enamine from chiral amino alcohols, or from chiral semioxamazones, all followed by chromatographic separation and mild acid hydrolysis. Columns with chiral stationary phases can be used to directly separate enantiomers. Hydroquinone chromium tricarbonyl complexes can be prepared from Fischer carbene complexes via a benzannulation reaction (Scheme 82).

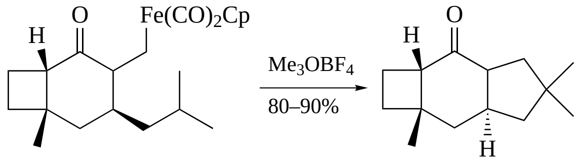

Scheme 81

Arene(tricarbonyl)chromium complexes undergo a number of synthetically important transformations not usually observed for uncomplexed arenes. The chromium tricarbonyl moiety facilitates nucleophilic, electrophilic, and radical reactions at the benzylic position. Upon complexation, one side of the aromatic ring and adjacent functionalities is blocked by the metal carbonyl moiety and highly stereoselective reactions are usually observed even at relatively remote positions. In addition, the protons of the complexed aromatic ring have a substantially higher acidity and are readily removed and further substituted by electrophiles. Finally, the aromatic ring is activated toward addition reactions using a variety of nucleophiles.

Decomplexation to liberate the organic ligand is usually achieved by oxidation of the metal employing hydrogen peroxide, iodine, CAN, or photolysis in the presence of oxygen.

3.1 Arene Chromium Tricarbonyl Complexes as a Stereodirecting Group

The large chromium tricarbonyl ligand is a powerful stereodirecting group and nucleophilic, electrophilic, and radical reactions occur exclusively or with a very high selectivity from the *exo* side, relative to the metal, of the complexed ring. Nucleophilic addition to benzaldehyde complexes with a high degree of stereoselectivity is observed using silyl enol ethers, trimethylsilyl ketene acetals, hydrides, stabilized nucleophiles, and a variety of organometallic nucleophiles. High erythro selectivity is observed in aldol reactions of complexed benzaldehydes.

In a similar fashion, chromium tricarbonyl complexes of aryl ketones are exclusively alkylated and reduced from the *exo* face relative to the metal. For example, addition of vinyl magnesium chloride to the substituted tetralone complex (**42**) affords the alcohol (**43**) exclusively with an antirelationship between the incoming nucleophile and the chromium tricarbonyl group (Scheme 83).[49] This was used in a synthesis of 11-epi-helioporin B. 2-Trimethylsilyl-substituted benzaldehyde complexes undergo an interesting

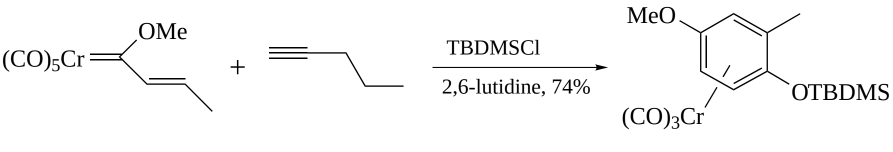

Scheme 82

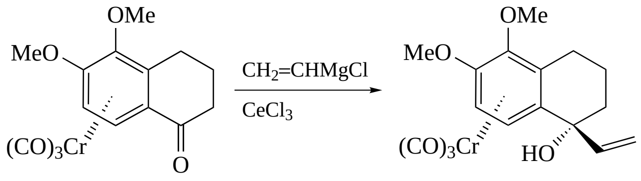

(**42**) (**43**)

Scheme 83

alkylation-silyl-migration and cyclization upon reaction with ester enolates (Scheme 84).[50]

Enantiomerically enriched or pure benzaldehydeimine complexes react with nucleophiles such as Grignard (*see Grignard Reagents*) and organozinc reagents, and they participate in a number of cycloaddition reactions. Enantiopure tricyclic β-lactams can be obtained from stereoselective $[2+2]$cycloaddition between a complexed chiral benzaldehyde imine and a ketene (Scheme 85).[51] For example, reaction of (**44**) with acetoxyketene gives (**45**). The acetoxy group was hydrolyzed using hydrazine to give (**46**). Nucleophilic substitution of the fluorine atom produced the tricyclic β lactam (**47**). A diastereoselective aza-Diels–Alder reaction was used in a synthesis of (−)-lasubine (I). Tin tetrachloride–mediated reaction of complex (**48**) with Danishefsky's diene afford 2,3-dihydro-4-pyridone (**49**) as a single diastereomer (Scheme 86).[52] Chiral benzaldehyde imines can be allylated with high diastereoselectivity to give optically active homoallylic amines (Scheme 87).

Stereoselective, conjugate allylation of more remote positions using allyl trimethylsilane and $TiCl_4$ is possible. Further transformation by nucleophilic addition and ring-closing metathesis affords fused polycyclic ring systems (Scheme 88).[53] Stabilized anions and organocopper (*see* ***Copper: Organometallic Chemistry***) reagents also participate in Michael-type additions to complexed α,β-unsaturated aromatic enones.

The stereodirecting power of the chromium ligand does not only apply to reactions at the benzylic position or using rigid ring systems, but also to more remote sites. Reaction of mesylate complex (**50**) with sodium acetate affords (**51**) with

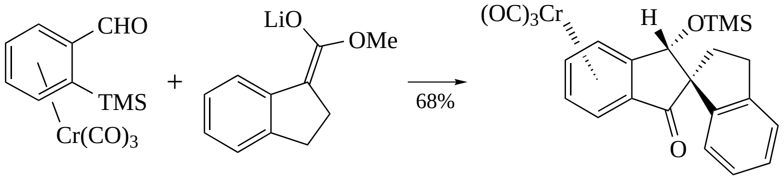

Scheme 84

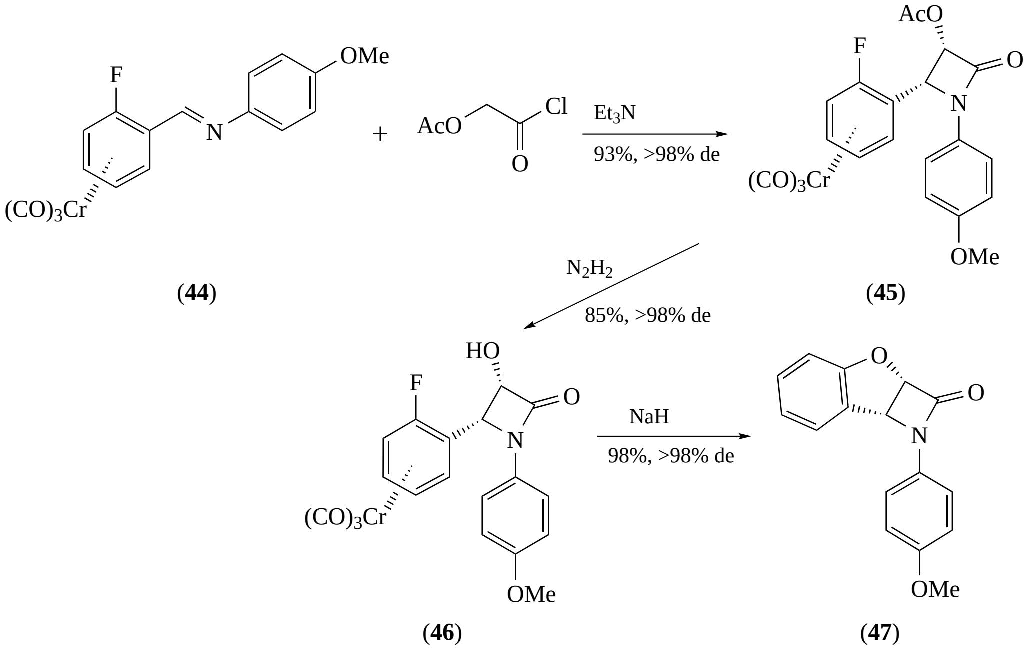

(**44**) (**45**)

(**46**) (**47**)

Scheme 85

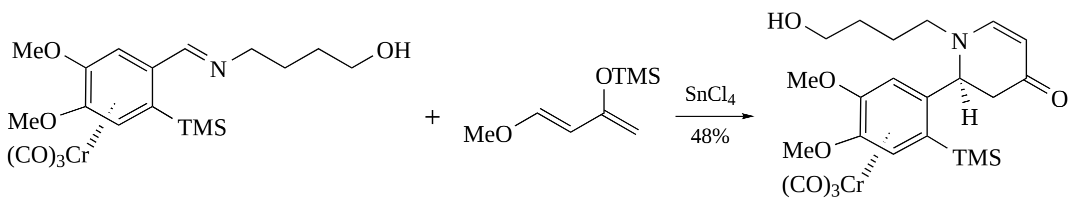
MeO
MeO
(CO)3Cr
N
OH
TMS
+
MeO
OTMS
SnCl4
48%
HO
N
MeO
MeO
(CO)3Cr
H
O
TMS

(**48**) (**49**)

Scheme 86

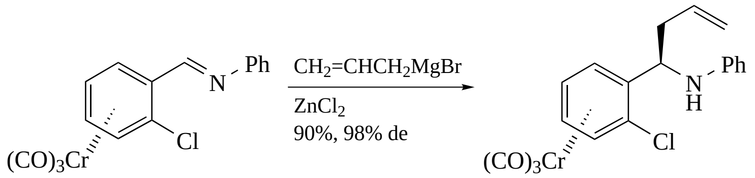
N
Ph
Cl
(CO)3Cr
CH2=CHCH2MgBr
ZnCl2
90%, 98% de
N
H
Ph
Cl
(CO)3Cr

Scheme 87

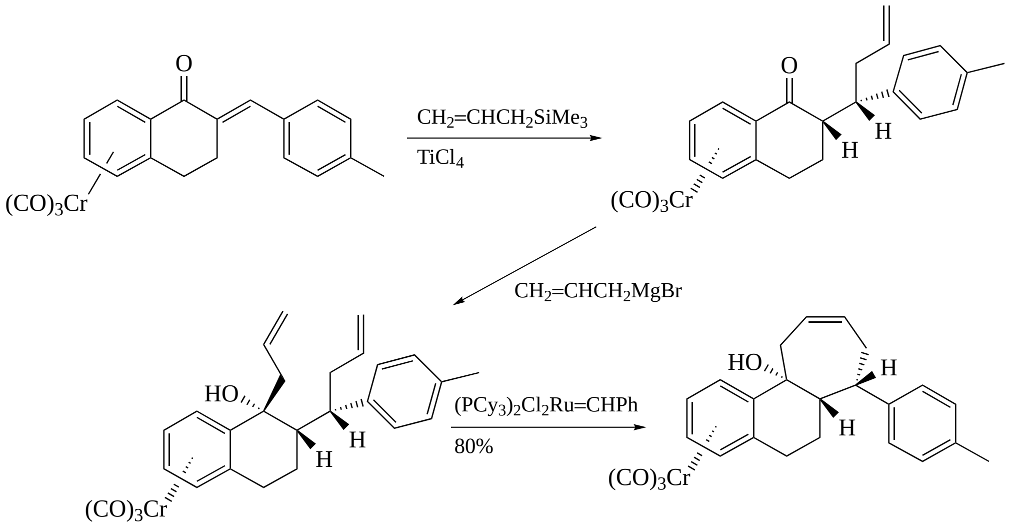
O
(CO)3Cr
CH2=CHCH2SiMe3
TiCl4
O
H
H
(CO)3Cr
CH2=CHCH2MgBr
HO
H
H
(CO)3Cr
(PCy3)2Cl2Ru=CHPh
80%
HO
H
H
(CO)3Cr

Scheme 88

retention of stereochemistry (Scheme 89). In contrast, the uncomplexed substrate gave mostly inversion (Scheme 90).[54] A quinolizidinone (**53**) was obtained as a single diastereomer in an intramolecular radical cyclization reaction (Scheme 91).

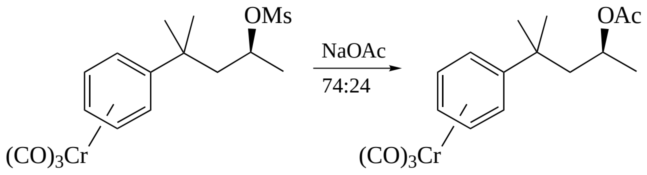
OMs
(CO)3Cr
NaOAc
74:24
OAc
(CO)3Cr

(**50**) (**51**)

Scheme 89

3.2 Stabilization of Benzylic Anions and Cations

A synthetically very powerful property of chromium tricarbonyl arene complexes is the ability to stabilize a negative charge at both the α- and β-positions of an alkyl side-chain. Deprotonation of the benzylic position using sodium hydride, *t*-butyl lithium, or potassium *t*-butoxide followed by addition of an electrophile affords alkylated products. The steric requirement of the chromium tricarbonyl group again forces the incoming electrophile to be added from the *exo* face of the complex. Only one diastereomer is isolated upon reaction of complexes wherein the benzylic position is part of a ring such as indans, 1,3-dihydroisobenzofuran, 1,2,3,4-tetrahydroisoquinoline and tetrahydrobenzazepine, and 1,3-dihydroisobenzothiophen. Furthermore, acyclic systems are commonly alkylated with a high diastereoselectivity.

A variety of common electrophiles can be used in conjunction with deprotonation of the benzylic position of complexed alkylbenzenes. This includes alkyl iodides, aldehydes, ketones, and epoxides. Mitosanes can be prepared by deprotonation of the tricyclic complex (**52**) followed by addition of oxirane (Scheme 92). Depending on the substituent on the complexed aromatic ring, both regio- and stereoselective benzylic alkylations are observed. For example, deprotonation and alkylation of the benzylic position meta to the dimethylamino group of (**53**) is exclusively observed (Scheme 93).

Chromium tricarbonyl complexed to benzaldehyde acetals can be reduced using lithium 4,4′-di(*t*-butyl)biphenyl to give benzyllithium complexes that can be further functionalized using electrophiles (Scheme 94).

Examples of benzylic alkylation, aromatic ring deprotonation, and nucleophilic addition to a β-position were used in a synthesis of (+)-20-methoxy-serrulat-14-en-7,8-diol.[55] Deprotonation of the optically active complex (**54**) followed by reaction with chloromethyl methyl ether affords (**55**) (Scheme 95). The trimethyl silyl-protecting group was removed using tri-n-butylammonium fluoride (TBAF) followed by lithiation and methylation forming (**56**). Addition of phenyl methyllithium sulfone gave a 94% de after decomplexation (**57**).

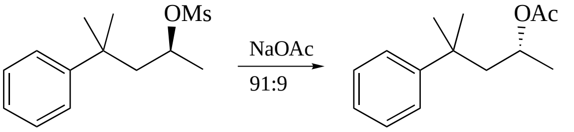

Scheme 90

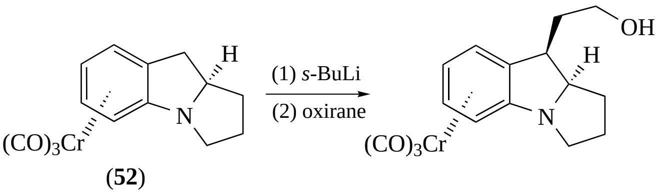

(**52**)

Scheme 92

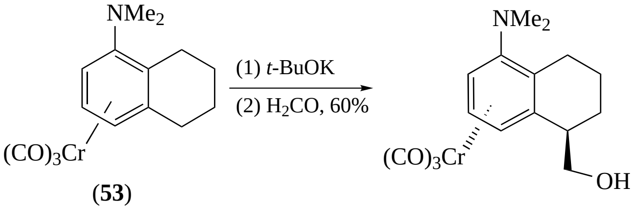

(**53**)

Scheme 93

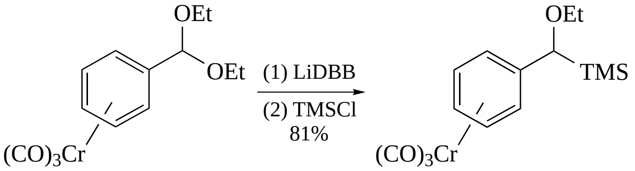

Scheme 94

Benzylic carbocations are also stabilized by complexation to chromium and a number of interesting reactions have been reported. Again, reaction of the carbocations with nucleophiles occurs from the *exo* face of the complex, relative to the metal. Carbocations are readily formed by treatment of benzylic alcohols with a strong acid, such as sulfuric acid, tetrafluoroboric acid, or borontrifluoride etherate. The cation can be trapped with water, alcohols, nitriles, and mono- or disubstituted amines to form alcohols, ethers, amides, and di- or trisubstituted amines respectively. Scheme 96 illustrates the formation of a benzylic carbocation followed by intramolecular trapping, resulting in a net inversion of stereochemistry. Benzylic acetates react with trimethyl aluminium introducing a methyl group from the opposite face of the metal.

A dimethylamino group can be transformed into a chloride using 2-chloropropionylchloride (Scheme 97). The chloride in turn is readily replaced by a diphenyl

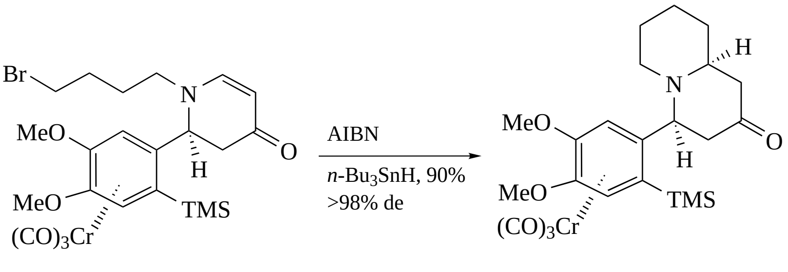

Scheme 91

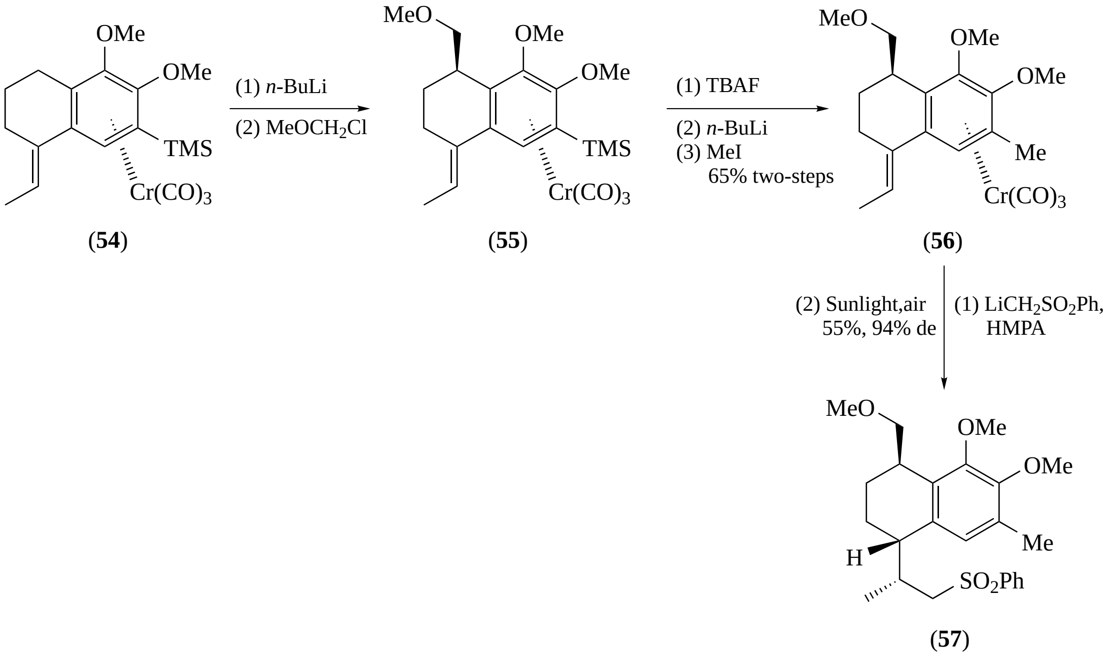
OMe
OMe
TMS
Cr(CO)3
(54)
(1) n-BuLi
(2) MeOCH2Cl
MeO
(55)
(1) TBAF
(2) n-BuLi
(3) MeI
65% two-steps
Me
(56)
(1) LiCH2SO2Ph, HMPA
(2) Sunlight,air
55%, 94% de
H
SO2Ph
(57)

Scheme 95

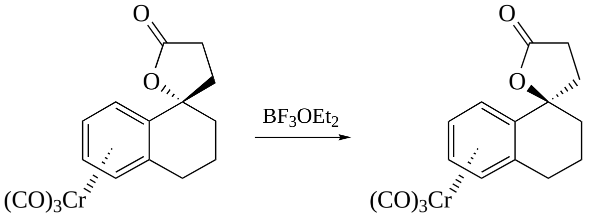
O
O
BF3OEt2
(CO)3Cr

Scheme 96

phosphino group using thallium hexafluorophosphate. These transformations are again highly stereospecific due to the stereodirecting power of the bulky chromium tricarbonyl group.

Acetals and ethers can also be used to produce benzylic carbocations by reacting with a Lewis acid. Treatment of acetals derived from chiral 2-substituted benzaldehyde chromium tricarbonyl complexes with trimethylsilyl triflate followed by reaction with a silyl enol ether give diastereomerically pure alkylation products (Scheme 98).[56] Benzylic alcohols can be

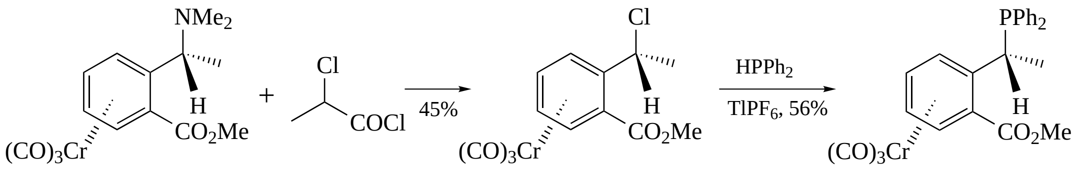
NMe2
H
CO2Me
(CO)3Cr
+
Cl
COCl
45%
Cl
HPPh2
TlPF6, 56%
PPh2

Scheme 97

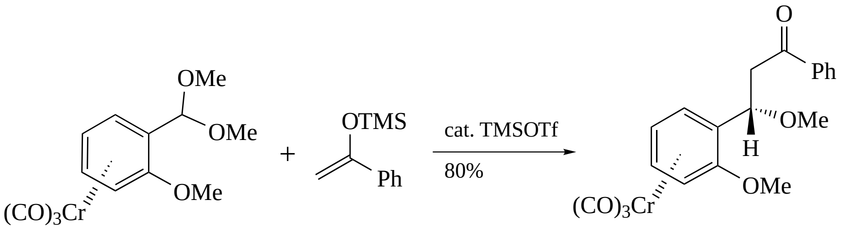
OMe
OMe
OMe
(CO)3Cr
+
OTMS
Ph
cat. TMSOTf
80%
O
Ph
OMe
H
OMe

Scheme 98

readily reduced using triethylsilane and trifluoro acetic acid (Scheme 99).

Asymmetric benzylic functionalization using a chiral base can be achieved. For example, reaction of complex (**58**) with the chiral base (**59**) and methyl iodide produce complex (**60**) in high yield and enantiomeric excess (Scheme 100).[57] Asymmetric benzylic alkylation can also be obtained using the chiral complex (**62**) derived from enantioselective deprotonation of (**61**) (Scheme 101).[58] High enantiomeric excess is observed upon deprotonation and alkylation of isobenzothiophen complexes with a chiral base (Scheme 102).

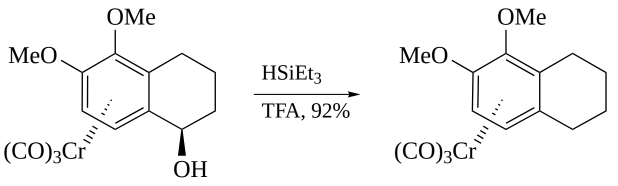

OMe
MeO
(CO)3Cr
OH
HSiEt3
TFA, 92%
OMe
MeO
(CO)3Cr

Scheme 99

3.3 Lithiation of the Aromatic Ring

The ring protons of arenes, when complexed to a chromium tricarbonyl group, have enhanced acidity and are readily deprotonated to form, for example, lithiated (η^6-arene) complexes. Reaction of these anions with electrophiles affords substituted arene tricarbonyl complexes. A wide range of common electrophiles can be used including ketones, iodomethane, iodine, carbon dioxide, trialkyltin chlorides, trimethylsilyl chloride, chloro triphenylphosphine, disulfides, chloroformates, sulfur, diphenyldiselenide, and 1,2-dibromoethane. The latter reagent introduces a bromine atom. Lithiation of the chiral dimethylamine–substituted complex (**63**) with *t*-butyllithium followed by addition of Mander's reagent affords the ester-functionalized complex (**64**) (Scheme 103). Depending on the base and the amount of base used, *t*-butylsulfonylbenzene chromium tricarbonyl affords a variety of substituted products (Scheme 104).

Substituted aromatic rings usually produce mixtures of products upon lithiation-electrophilic addition. Fluorine, chlorine, and alkoxy groups in monosubstituted chromium

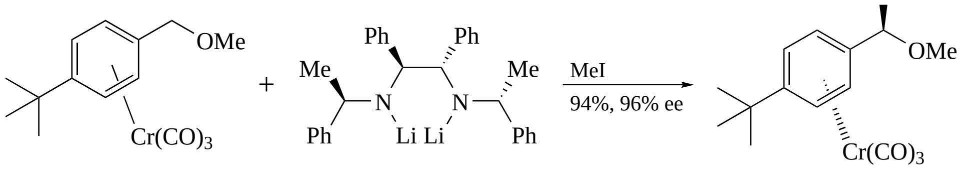

OMe
Cr(CO)3
+
Ph
Ph
Me
Me
N
N
Ph
Li Li
Ph
MeI
94%, 96% ee
OMe
Cr(CO)3

(**58**) (**59**) (**60**)

Scheme 100

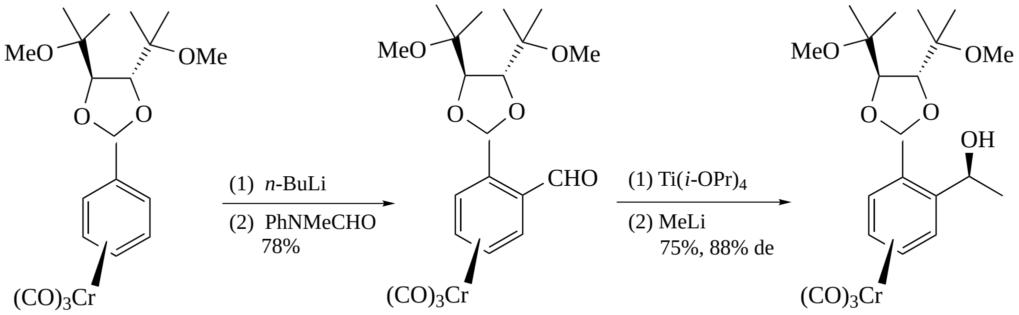

MeO
OMe
O
O
(CO)3Cr
(1) n-BuLi
(2) PhNMeCHO
78%
MeO
OMe
O
O
CHO
(CO)3Cr
(1) Ti(i-OPr)4
(2) MeLi
75%, 88% de
MeO
OMe
O
O
OH
(CO)3Cr

(**61**) (**62**)

Scheme 101

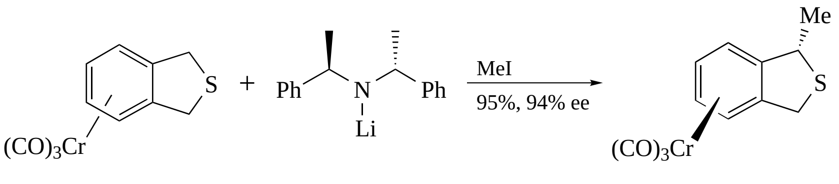

S
(CO)3Cr
+
Ph
N
Li
Ph
MeI
95%, 94% ee
Me
S
(CO)3Cr

Scheme 102

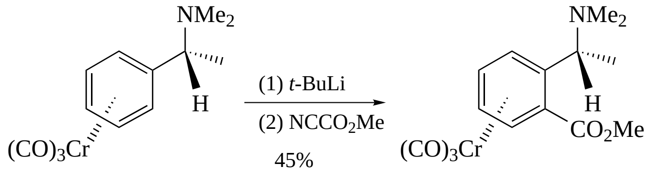
NMe2
H
(CO)3Cr
(1) t-BuLi
(2) NCCO2Me
45%
NMe2
H
CO2Me
(CO)3Cr

(**63**) (**64**)

Scheme 103

benzene complexes direct lithiation to the ortho position, and alkylation occurs exclusively in this position. Alkyl groups afford lithiation predominantly at the meta position. Lithiation using a chiral base, such as butyllithium/(−)-spartein, give in some cases products in high enantiomeric excess (Scheme 105).[59]

Optically active chromium tricarbonyl complexes can be lithiated and subsequently functionalized by a wide array of electrophiles with high diastereoselectivity. For example, reaction of (**65**) with a base and benzophenone gave (**66**) (Scheme 106).[60] The sugar-derived complex (**67**) was lithiated and reacted with diphenyldisulfide to give the chiral complex (**68**) (Scheme 107).

3.4 Miscellaneous Reactions of Arene Chromium Tricarbonyl Complexes

Although many oxidizing reagents remove the chromium tricarbonyl group, benzylic alcohols can be oxidized to benzaldehydes using dimethyl sulfoxide with acetic anhydride, trifluoroacetic anhydride, or sulfurtrioxide with minimal decomplexation. Asymmetric oxidation of alkylthio-substituted complexes can be achieved using titanium tetraisopropoxide and an optically active tartrate ester (Scheme 108). Dimethyloxirane can also be used to oxidize sulfides to sulfoxides.

Fluoro- and chloro-substituted tricarbonyl chromium arene complexes can be reductively coupled with ketones, in the presence of samarium iodide, to give tertiary alcohols (Scheme 109).[61] A related reaction of a tethered alkoxyimine furnished a tricyclic compound (Scheme 110).[62] Samarium also promotes the formation of a benzylic ketyl

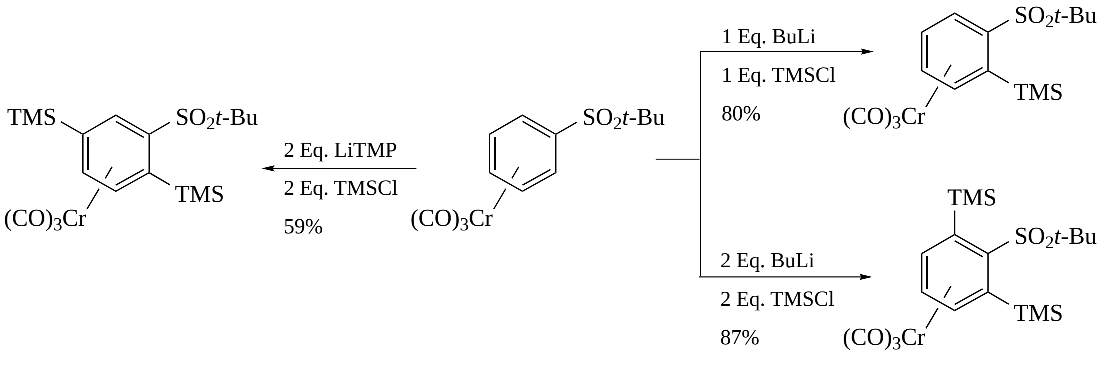
TMS
SO2t-Bu
TMS
(CO)3Cr
2 Eq. LiTMP
2 Eq. TMSCl
59%
SO2t-Bu
(CO)3Cr
1 Eq. BuLi
1 Eq. TMSCl
80%
SO2t-Bu
TMS
(CO)3Cr
2 Eq. BuLi
2 Eq. TMSCl
87%
TMS
SO2t-Bu
TMS
(CO)3Cr

Scheme 104

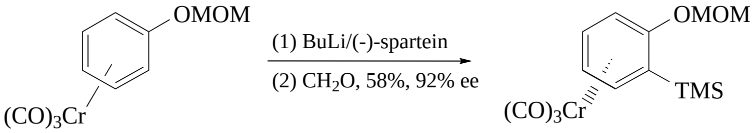
OMOM
(CO)3Cr
(1) BuLi/(-)-spartein
(2) CH2O, 58%, 92% ee
OMOM
TMS
(CO)3Cr

Scheme 105

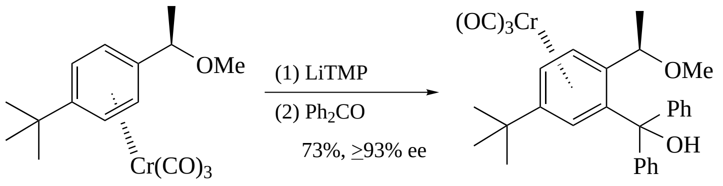
OMe
Cr(CO)3
(1) LiTMP
(2) Ph2CO
73%, ≥93% ee
(OC)3Cr
OMe
Ph
OH
Ph

(**65**) (**66**)

Scheme 106

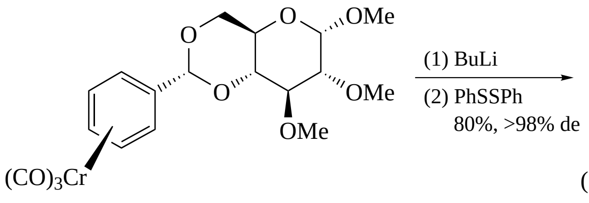
(1) BuLi
(2) PhSSPh
80%, >98% de
OMe
SPh
(CO)3Cr

(**67**) (**68**)

Scheme 107

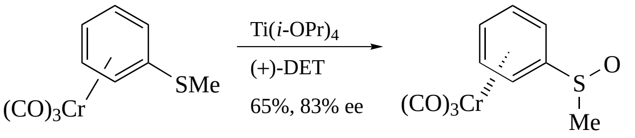
Ti(i-OPr)4
(+)-DET
65%, 83% ee
SMe
(CO)3Cr

Scheme 108

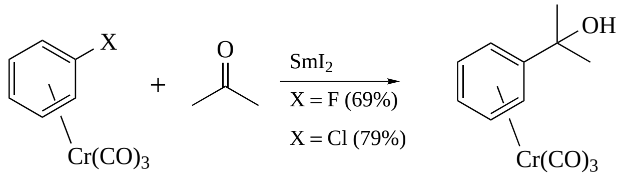
SmI2
X = F (69%)
X = Cl (79%)
OH
Cr(CO)3

Scheme 109

radical followed by Michael-type addition-lactone formation (Scheme 111).[63]

Iodo-, bromo-, and chloro-substituted chromium-complexed benzenes undergo a variety of palladium-catalyzed reactions. Complexed aryl halides readily react with alkynes, organoboron, organotin, organofluorosilane, and organozinc reagents under palladium catalysis. A significant enhancement in reactivity of the otherwise fairly unreactive chlorobenzenes is obtained upon complexation. Sterically hindered aryl bromides are readily coupled with arylboronic acids. Diastereoselective coupling of chiral chromium-complexed aryl bromides can be achieved (Scheme 112). In addition to reactions of transmetallating reagents, the aryl halides can be carbonylated to form benzoic acids, esters, and amides. Intramolecular alkene insertion followed by carbonylation furnishes substituted indanes (Scheme 113).[64] Aryl ketones are formed upon reaction of chromium tricarbonyl–complexed trialkylstannylbenzene. It is interesting to note that no external carbon monoxide is required.

An interesting [6 + 4]cycloaddition of thiephin-1,1-dioxide chromium tricarbonyl complex (**69**) with diene (**70**) was used in a synthesis of (+)-estradiol (Scheme 114).[65]

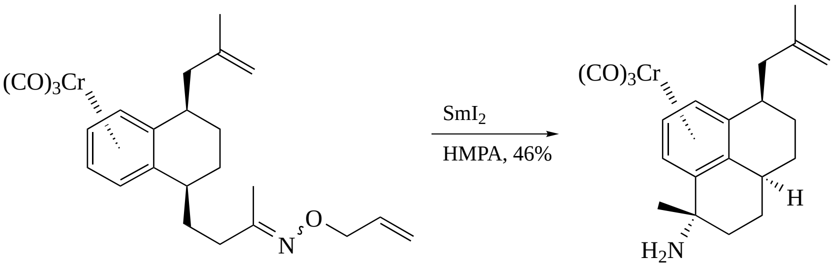
SmI2
HMPA, 46%
(CO)3Cr
H
H2N

Scheme 110

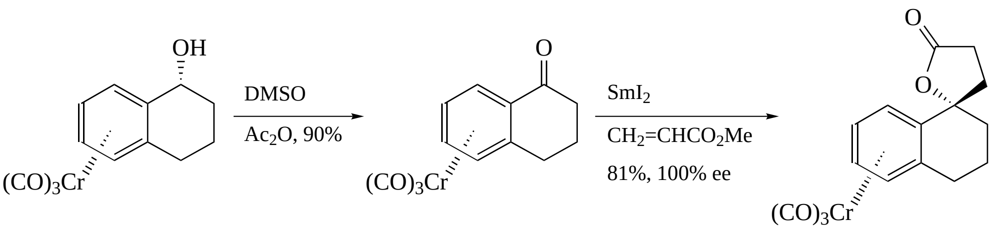
DMSO
Ac2O, 90%
SmI2
CH2=CHCO2Me
81%, 100% ee
OH
(CO)3Cr

Scheme 111

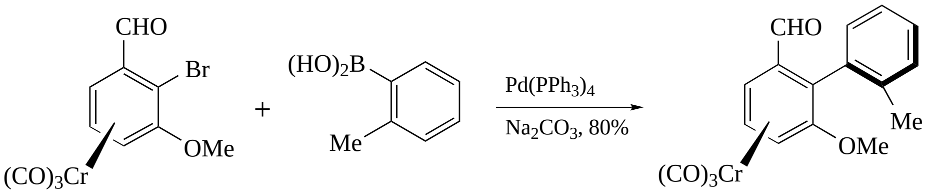
CHO
Br
OMe
(CO)3Cr
+
(HO)2B
Me
Pd(PPh3)4
Na2CO3, 80%
CHO
Me
OMe
(CO)3Cr

Scheme 112

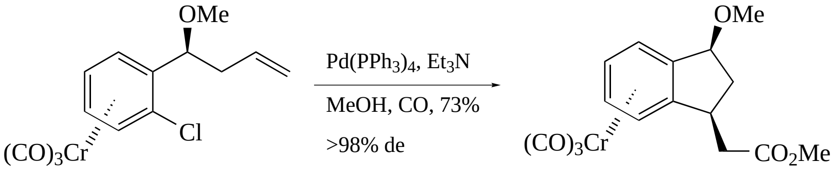
OMe
(CO)3Cr
Cl
Pd(PPh3)4, Et3N
MeOH, CO, 73%
>98% de
OMe
(CO)3Cr
CO2Me

Scheme 113

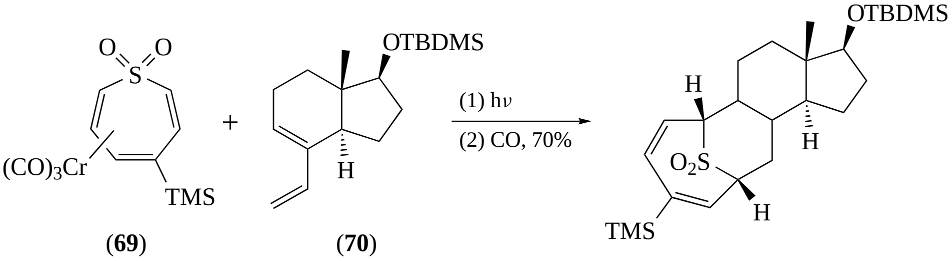
O
O
S
(CO)3Cr
TMS
+
OTBDMS
H
(1) hν
(2) CO, 70%
OTBDMS
H
H
O2S
H
TMS

(**69**) (**70**)

Scheme 114

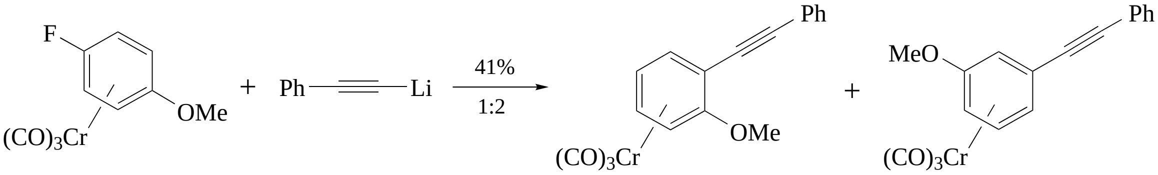
F
(CO)3Cr
OMe
+
Ph
Li
41%
1:2
Ph
(CO)3Cr
OMe
+
Ph
MeO
(CO)3Cr

(**71**) (**72**) (**73**) (**74**)

Scheme 115

3.5 Nucleophilic Addition to the Aromatic Ring

Chromium tricarbonyl–complexed aryl fluorides undergo nucleophilic substitution reactions. The substitution is not a straightforward S_NAr mechanism as can be seen using, for example, 4-methoxy-1-fluorobenzene complex (**71**). Reaction of (**71**) with acetylide (**72**) gives a 1:2 mixture of the 1,2 and 1,3 products (**73**) and (**74**) (Scheme 115). Other leaving groups include halogens, alkoxides, and amines. Indazoles can be prepared by reaction with hydrazine followed by acidic deprotection–decomplexation (Scheme 116).

Sequential addition of organolithium reagents to enantiomerically pure tricarbonyl chromium arene complexes having a chiral oxazoline, hydrazone, ether, or imine functionality, followed by quenching with an electrophile form highly substituted, optically active cyclohexadienes (Scheme 117).[66] Depending on the conditions, two or three alkyl groups can be introduced.

The chemistry outlined above was used in a synthesis of (+)-ptilocaulin (Scheme 118). Lithiation of (**75**) followed by addition of copper chloride and an electrophile gave (**76**). Highly diastereoselective nucleophilic addition of 2-lithio-1,3-dithiane followed by treatment with TMS-chloride, oxidation, and hydrolysis produced the intermediate (**77**).

Cationic arene tricarbonylmanganese complexes of phenols can be deprotonated to give neutral η^5-cyclohexadienyl

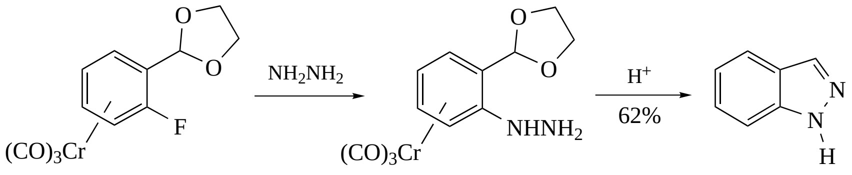

Scheme 116

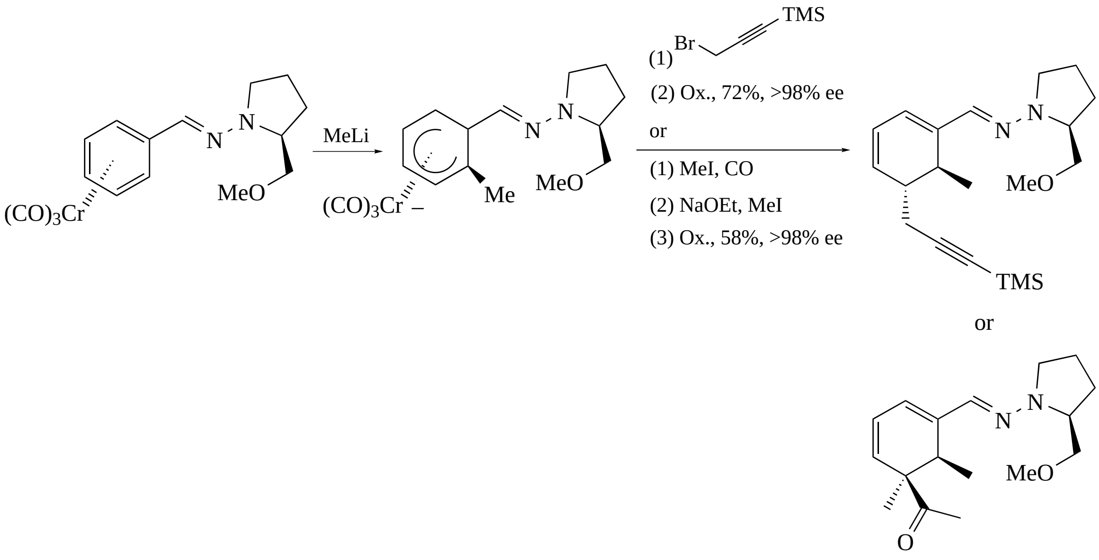

Scheme 117

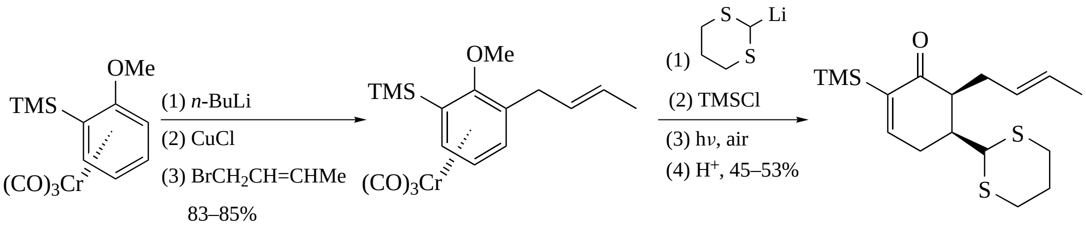

(75) (76) (77)

Scheme 118

complexes. These complexes undergo nucleophilic addition reactions (*see Nucleophilic Addition: Rules for Predicting Direction*) to give a new η^5-complex that can be decomplexed to form substituted phenols (Scheme 119).[67] It is noteworthy that the nucleophile does not add to the carbonyl carbon. Chiral arene-manganese complexes can be obtained by addition of the nucleophile in the presence of a chiral ligand. For example, reaction of (**78**) with phenyl magnesium bromide in the presence of (S)-binaphthol produced (**79**) after acetylation (Scheme 120).

Organozinc reagents can also be added to the cationic manganese arene complexes. Neutral η^5-1-chlorocyclohexadienyl manganese complexes undergo palladium-catalyzed couplings with organotin compounds (Scheme 121, *see Stille Coupling*). Alkylation of cationic manganese complexes of amino-substituted arenes affords neutral cyclohexadienyl complexes. The latter complexes can be further transformed into substituted cyclohexenones by ligand exchange, hydrolysis, and hydride reduction (Scheme 122). 2-Lithio-2-chloro- and 2-lithio-2-bromopropanoates can be used as nucleophiles in alkylations of cationic manganese arene complexes. Only the complex resulting from meta alkylation was observed using toluene and anisol complexes. Alkylation of chiral cationic manganese complexes having a 2,5-dimethylpyrrolidine group

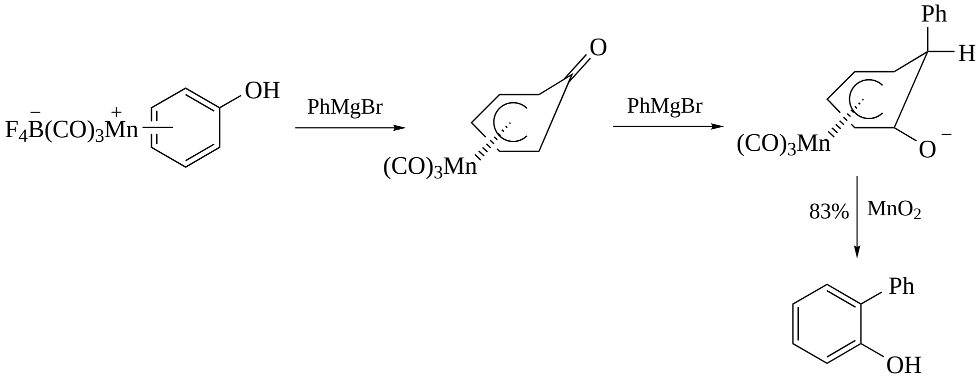
$F_4\bar{B}(CO)_3\overset{+}{M}n$
OH
PhMgBr
O
$(CO)_3Mn$
PhMgBr
Ph
H
$(CO)_3Mn$
O^-
83%
MnO_2
Ph
OH

Scheme 119

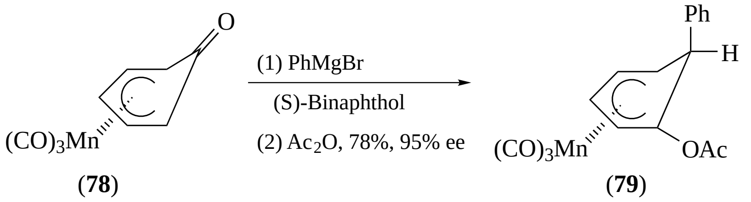
O
$(CO)_3Mn$
(78)
(1) PhMgBr
(S)-Binaphthol
(2) Ac_2O, 78%, 95% ee
Ph
H
$(CO)_3Mn$
OAc
(79)

Scheme 120

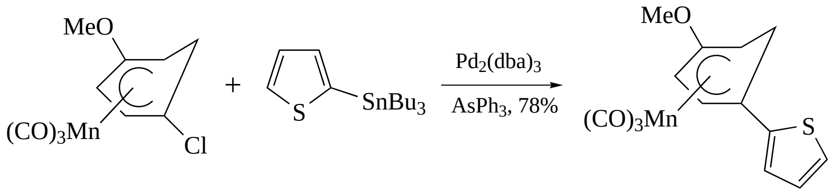
MeO
$(CO)_3Mn$
Cl
+
S
$SnBu_3$
$Pd_2(dba)_3$
$AsPh_3$, 78%
MeO
$(CO)_3Mn$
S

Scheme 121

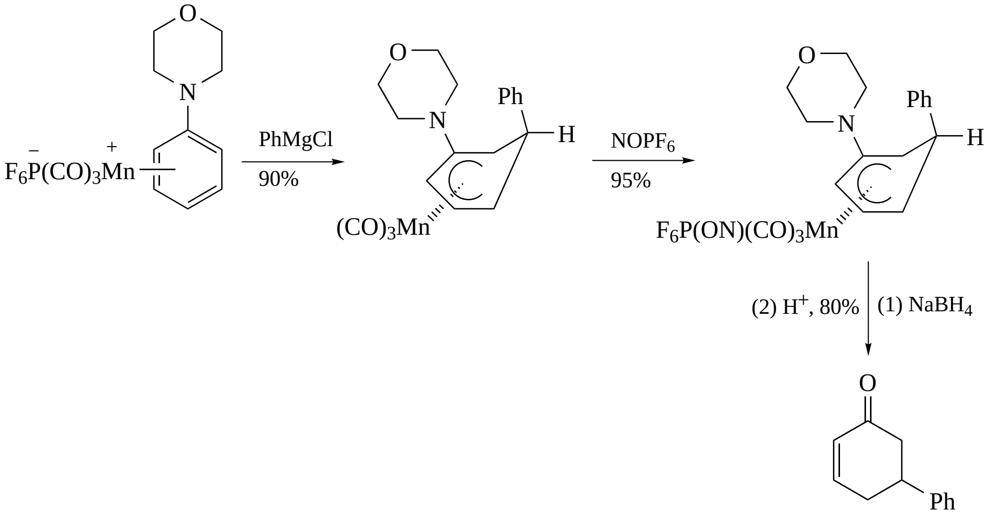
O
N
$F_6\bar{P}(CO)_3\overset{+}{M}n$
PhMgCl
90%
O
N
Ph
H
$(CO)_3Mn$
$NOPF_6$
95%
O
N
Ph
H
$F_6P(ON)(CO)_3Mn$
(2) H^+, 80%
(1) $NaBH_4$
O
Ph

Scheme 122

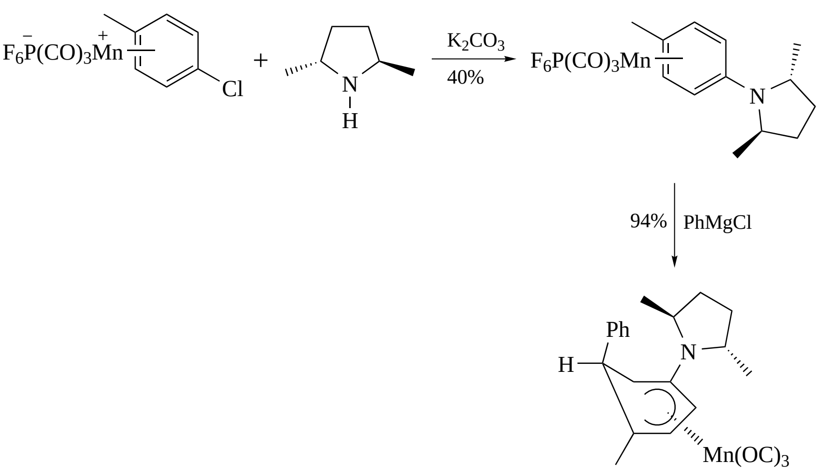

Scheme 123

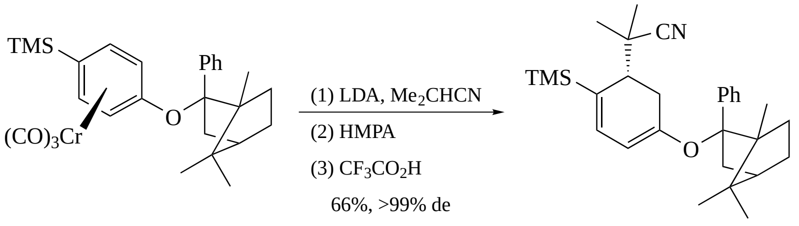

(**80**) (**81**)

Scheme 125

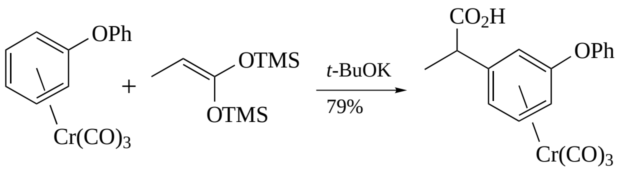

Scheme 124

produce products with diastereoselectivities up to 94% (Scheme 123).

Direct nucleophilic addition of potassium enolates derived from bis(trimethylsilyl)ketene acetals to aromatic chromium-complexed aromatic ethers affords meta substituted products (Scheme 124).[68] A very high degree of asymmetric induction is obtained upon reaction of chiral arene chromium tricarbonyl complexes. For example, alkylation of complex (**80**) gave (**81**) after decomplexation (Scheme 125).[69]

4 IRON TRICARBONYL COMPLEXESOF CONJUGATED DIENES

The use of cyclic and acyclic diene iron tricarbonyl complexes (*see Diene Complexes*) in organic synthesis of complex molecules has continued to grow over the last decade.[70,71] The relatively stable iron tricarbonyl diene complexes are easily prepared on a multigram scale from readily available starting materials. Other transition metals, such as molybdenum, cobalt, iridium, and rhodium also form complexes of this type but still remain relatively unexplored. The significant synthetic utility of iron tricarbonyl diene complexes relies heavily on four important features: (1) the stereodirecting power of the bulky iron tricarbonyl group; (2) optically active complexes can be prepared by fractional crystallization or chromatography of diastereomeric mixtures; (3) through complexation, the diene system is stable towards a large number of reagents and the iron tricarbonyl fragment can be used as a protecting group for diene systems; and (4) the metal can be removed from the dienes in high yields under mild conditions.

Diene iron tricarbonyl complexes are prepared by thermal or photochemical reaction of conjugated dienes with iron pentacarbonyl in the presence of TMANO, triiron dodecacarbonyl, (η^4-benzylidenacetone)iron tricarbonyl, diiron nonacarbonyl, or diiron nonacarbonyl absorbed on silica gel in the absence of solvent. The latter method is particularly useful for the preparation of complexes from polar electron-rich dienes and heterodienes. A reductive complexation of cycloheptatrienes using iron tricarbonyl and sodium borohydride to give cycloheptadiene iron tricarbonyl has been developed (Scheme 126).

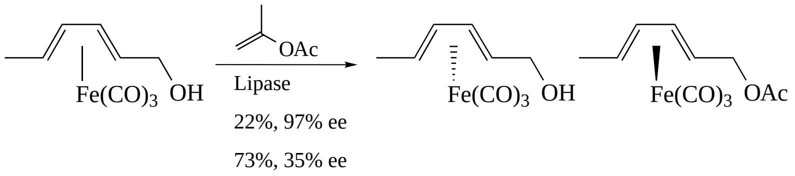

Scheme 127

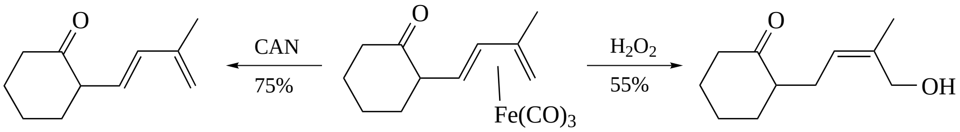

Scheme 128

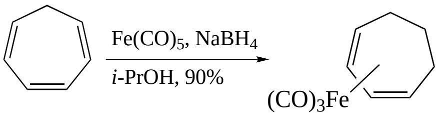

Scheme 126

Unsymmetrically substituted diene iron tricarbonyl complexes are formed as racemic mixtures of compounds having planar chirality. Optically pure diene iron tricarbonyl complexes can been prepared by classical chromatographic separation of diastereomeric mixtures of α-methylbenzylamine and ephedrine salts, and of semioxamazones and oxazolidines derivatives. Direct asymmetric complexation to cyclic dienes can be achieved 73% ee using iron pentacarbonyl in the presence of a chiral 1-aza-1,3-butadiene.

Kinetic resolution of racemic dienal iron tricarbonyl complexes by reduction using baker's yeast has been developed. Porcine pancreatic lipase-catalyzed transesterification of hydroxymethyl-substituted complexes have also been used to kinetically resolve diene complexes (Scheme 127).

Oxidative removal of the iron tricarbonyl group can be achieved using iron trichloride, copper dichloride, CAN, hydrogen peroxide under basic conditions, 3-chloroperbenzoic acid, or TMANO. The latter oxidant is frequently the reagent of choice. Depending on the reagent, decomplexation may occur with or without concomitant transformation (Scheme 128). It is important to note that no racemization of optically active compounds is detected upon decomplexation. Reductive decomplexation to form an alkene is observed upon UV irradiation in acetic acid. Tricarbonyl complexes with a pendant carboxylic acid undergo decomplexation to form lactones containing an unsaturated aldehyde (Scheme 129).

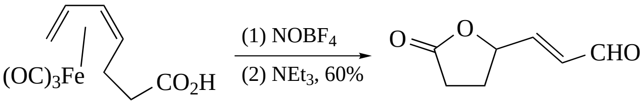

Scheme 129

4.1 Reductions and Oxidations

Conjugated dienes are protected toward a variety of reagents by coordination to an iron tricarbonyl moiety. For example, diene iron tricarbonyl complexes are stable to a number of reducing reagents, such as lithium aluminium hydride (LAH), diborane, diisobutylaluminum hydride (DIBAL-H), zinc in hydrochloric acid, heterogenous hydrogenation, Raney-nickel hydrogen gas, and borohydrides. For example, cycloheptatrienone complex (**82**) was reduced to the corresponding cycloheptadienone complex (**83**) using Raney-nickel hydrogen gas (Scheme 130). Stereoselective Luche-type reduction of the ketone in (**84**) is observed using, for example, sodium borohydride in the presence of cerium trichloride (Scheme 131).

Epoxidation of allylic and homoallylic alcohols not part of the diene complex can be achieved using the Sharpless t-butyl hydroperoxide/vanadium acetylacetonate protocol. Dihydroxylation of alkenes adjacent to the diene complex using osmium tetraoxide-t-butyl peroxide has been reported

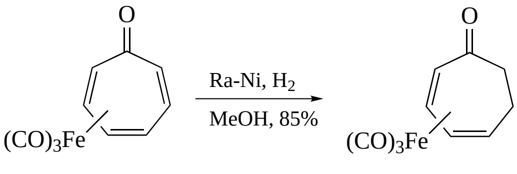

(82) **(83)**

Scheme 130

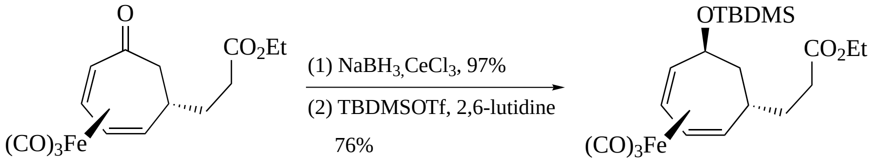
O
CO2Et
(CO)3Fe
(1) NaBH3,CeCl3, 97%
(2) TBDMSOTf, 2,6-lutidine
76%
OTBDMS
CO2Et
(CO)3Fe

(**84**)

Scheme 131

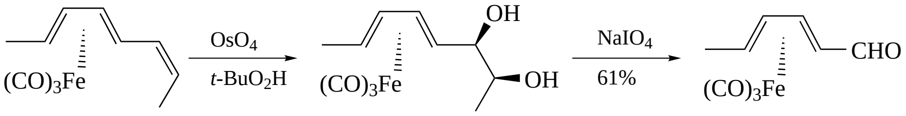
(CO)3Fe
OsO4
t-BuO2H
OH
(CO)3Fe
OH
NaIO4
61%
CHO
(CO)3Fe

Scheme 132

(Scheme 132). Sodium periodate oxidatively cleaves the diol without decomplexation of the diene moiety.

A number of oxidizing reagents can also be used to modify side-chain groups. For example Swern oxidation, pyridinium dichromate (PDC), and sulfur trioxide-pyridine/dimethyl sulfoxide (DMSO)/triethylamine oxidations are all possible without affecting the complexed diene (Scheme 133). Remote alkenes can be transformed to epoxides using DMDO (Scheme 134) and to allylic alcohols using photooxygenation and triphenylphosphine reduction. This again exemplifies the protective ability of the diene–iron tricarbonyl complex.

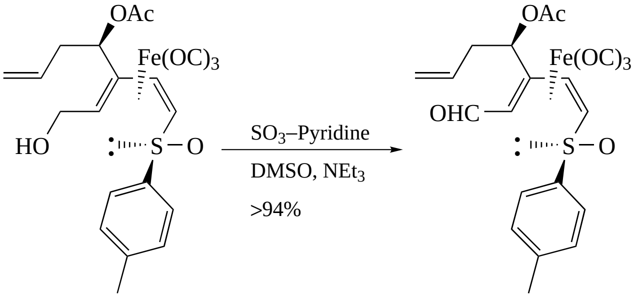
OAc
Fe(OC)3
HO
S
O
SO3–Pyridine
DMSO, NEt3
>94%
OAc
Fe(OC)3
OHC
S
O

Scheme 133

4.2 Reactions with Nucleophiles

Because of the stability of iron tricarbonyl diene complexes, conjugated dienals are protected from polymerization when complexed, while other reactions can be carried out at the aldehyde functionality. A number of synthetically attractive nucleophilic transformations of the aldehyde can be performed on these complexes. These include, aldol reactions, Michael additions, reactions with organozinc, -silicon, -boron, and -tin reagents, or Wittig-type reactions. Stereospecific reduction of adjacent ketones to give alcohols with very high stereoselectivity is observed (Scheme 135).

Aldol reaction of dienal complexes usually gives diastereomeric mixtures of readily separated *exo*- and *endo*-alcohols in good yields. The diastereoselectivity is highly dependent on the reaction temperature, the metal counterion of the nucleophile, and the presence

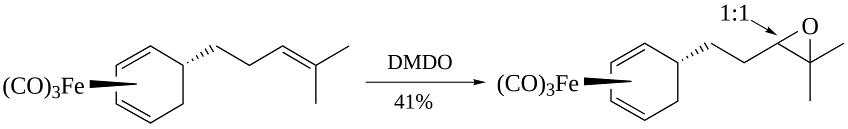
(CO)3Fe
DMDO
41%
(CO)3Fe
1:1
O

Scheme 134

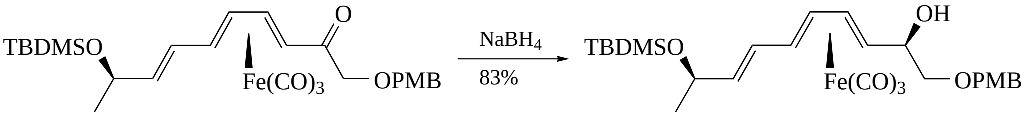
TBDMSO
O
Fe(CO)3
OPMB
NaBH4
83%
TBDMSO
OH
Fe(CO)3
OPMB

Scheme 135

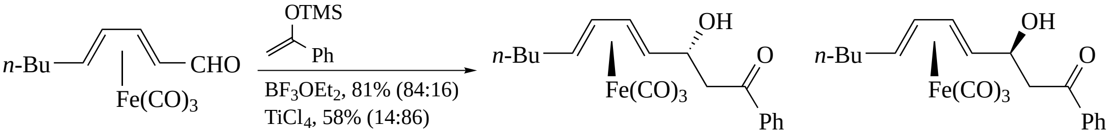
n-Bu
CHO
Fe(CO)3
OTMS
Ph
BF3OEt2, 81% (84:16)
TiCl4, 58% (14:86)
n-Bu
OH
O
Fe(CO)3
Ph
n-Bu
OH
O
Fe(CO)3
Ph

Scheme 136

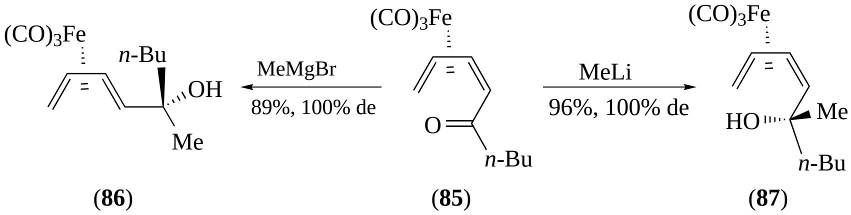
(CO)3Fe
n-Bu
OH
Me
MeMgBr
89%, 100% de
(CO)3Fe
O
n-Bu
MeLi
96%, 100% de
(CO)3Fe
HO
Me
n-Bu
(86)
(85)
(87)

Scheme 137

or absence of electrophiles. The diastereoselectivity can be reversed using nucleophiles containing the second-row metals copper, titanium, and aluminum, in contrast with that observed with lithium and magnesium reagents. In addition to the nucleophile, reversal of selectivity can be obtained depending on the Lewis acid used (Scheme 136).

Reactions of the corresponding ketones have been much less studied, but alkylation reactions appear to be highly antiselective relative to the metal. Some alkylations resulting in the isomerization of the diene geometry have been observed. For example, reaction of (**85**) with methyl magnesium bromide gives (**86**) but reaction with methyl lithium affords (**87**) (Scheme 137). Related reductions of dienone iron complexes with sodium borohydride are also highly antiselective.

Diastereoselective allylation of optically pure sulfinyl dienal complexes using tributyl allyltin can be obtained (Scheme 138). 2,4-Hexadien-1,6-dial iron tricarbonyl complex (**88**) undergoes nucleophilic addition reactions with dialkylzincs in the presence of a catalytic amount of an optically active amino alcohol (Scheme 139). Very high enantio- and diastereoselectivity is observed. Related reactions of (**88**) with chiral allyl boronic esters give allylated alcohols in very high enantiomeric excess.

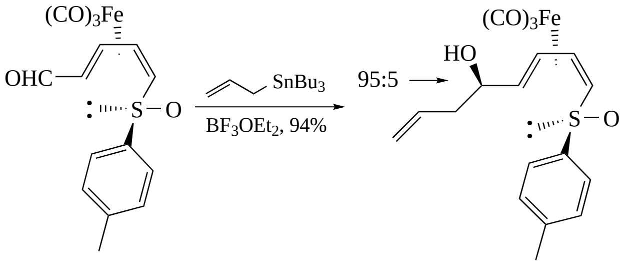
(CO)3Fe
OHC
S
O
SnBu3
BF3OEt2, 94%
95:5
(CO)3Fe
HO
S
O

Scheme 138

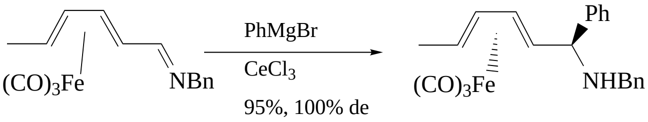
(CO)3Fe
NBn
PhMgBr
CeCl3
95%, 100% de
Ph
(CO)3Fe
NHBn

Scheme 140

Imines formed from dienal complexes not surprisingly undergo stereoselective nucleophilic additions. Particularly selective nucleophiles are organocerium and Grignard reagents (Scheme 140). An intramolecular Mannich-type cyclization was used in a synthesis of dienomycins (Scheme 141). Imine complexes also undergo Diels–Alder reactions with Danishefsky's diene (Scheme 142).

Isomeric products are obtained upon complexation of polyenes. Instead, these complexes are usually prepared

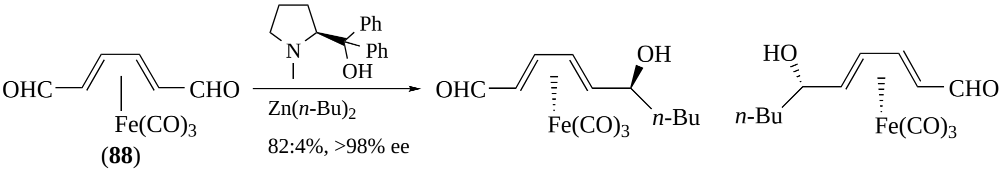
OHC
CHO
Fe(CO)3
(88)
N
Ph
Ph
OH
Zn(n-Bu)2
82:4%, >98% ee
OHC
OH
Fe(CO)3
n-Bu
HO
n-Bu
CHO
Fe(CO)3

Scheme 139

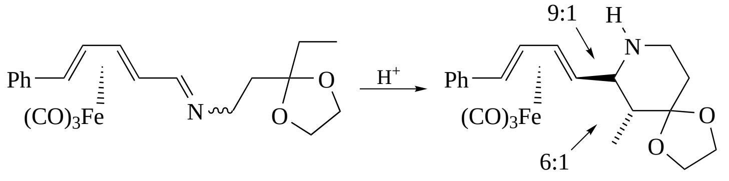

Scheme 141

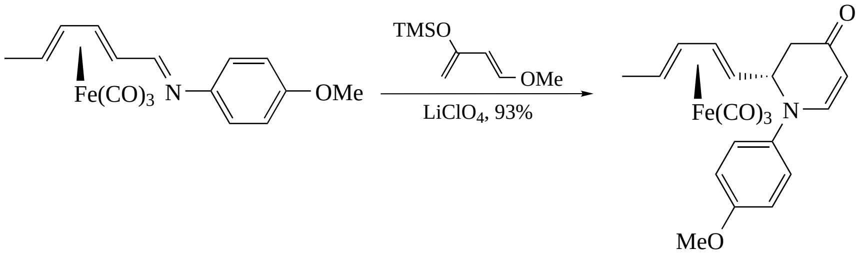

Scheme 142

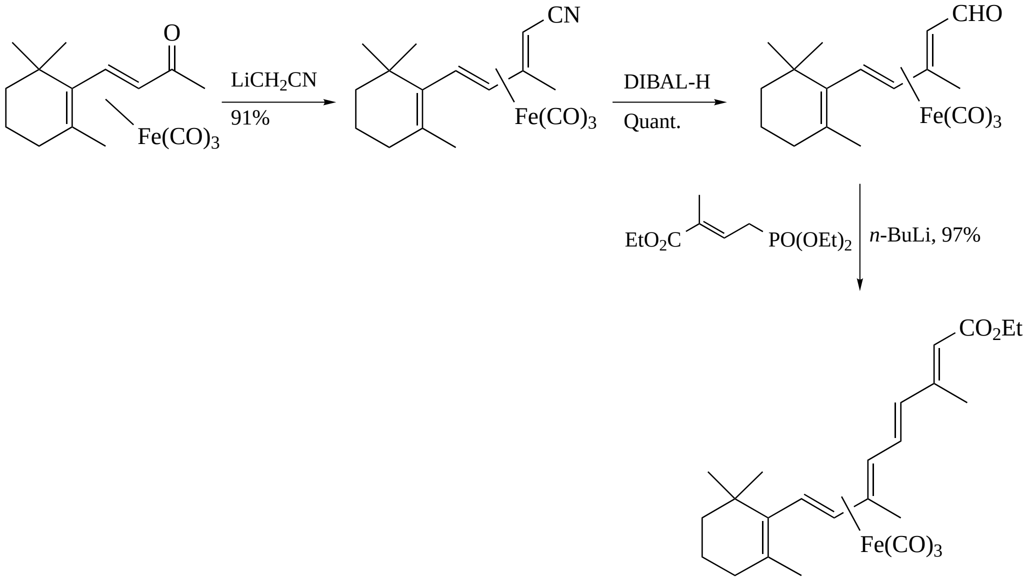

Scheme 143

via standard alkenation procedures of dienal complexes. The most useful reactions in this context are Wittig-type reactions (*see Wittig Reagent*). Complexed dienals react readily with both stabilized and nonstabilized phosphoranes, as well as with phosphonate carbanions, to give *E*-alkenes. The inverse reaction, that is, adding aldehydes to diene complexes containing phosphorane groups, also affords the corresponding alkenes. Reactions of complexed dienals with ketone and ester enolates or $LiCH_2CN$ afford alkenation products in which the iron tricarbonyl moiety has shifted towards the electron-withdrawing group. This type of shift occurs both in the presence of a strong base or a Lewis acid. A synthesis of retinoic acids utilized the migration of iron followed by reduction and a Horner–Emmons reaction (Scheme 143). It should be noted that the migration of iron does not occur in the last phosphorous-based olefination. Petersen olefination also afford products without migration of the metal (Scheme 144).

Alkylidene malonate substitute complex (**89**) undergoes diastereoselective Michael-type additions with a number of nucleophiles including organolithiums, Grignards (*see Grignard Reagents*), allyl tributylstannane, and ketene silyl

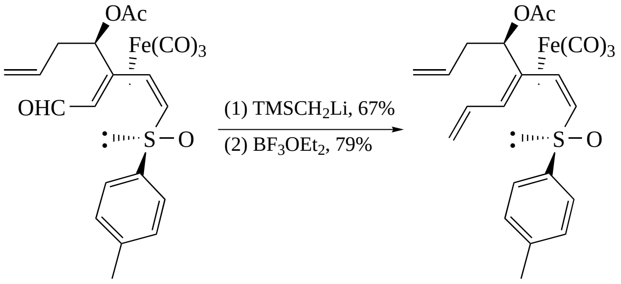
OAc
Fe(CO)3
OHC
S
O
(1) TMSCH2Li, 67%
(2) BF3OEt2, 79%
OAc
Fe(CO)3
S
O

Scheme 144

acetals (Scheme 145). Related conjugate addition reactions using dialkylzinc reagents is also possible.

Stereoselective Michael addition of functionalized zinc–copper reagents to cycloheptatrienone iron tricarbonyl complexes is observed (Scheme 146). A pendant nitrile can participate in an alkylation reaction of the intermediate enolate forming a fused bicyclic ring system (Scheme 147). Addition in a 1,2- or 1,4-fashion depends on the nucleophile. Harder nucleophiles tend to form 1,2-adducts (Scheme 148).

Reaction of complex (**90**) with methyllithium followed by acid and carbon monoxide affords a mixture of acylated complexes (Scheme 149). Reaction of an oxime complex with organocuprates followed by acetic anhydride, carbon monoxide, and potassium carbonate gives *meta*-acylaniline derivatives (Scheme 150). In both cases, the nucleophile probably initially adds to the metal followed by an acyl transfer.

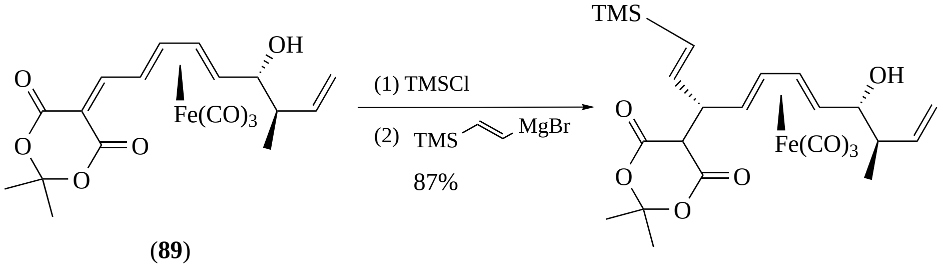
O
O
O
O
OH
Fe(CO)3
(1) TMSCl
(2) TMS MgBr
87%
TMS
O
O
O
O
OH
Fe(CO)3

(**89**)

Scheme 145

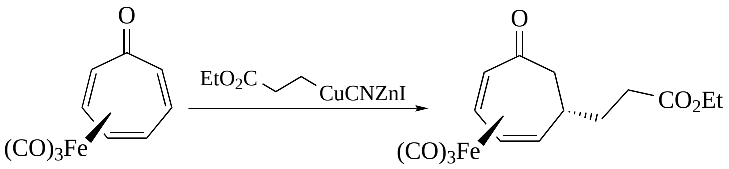
O
(CO)3Fe
EtO2C CuCNZnI
O
CO2Et
(CO)3Fe

Scheme 146

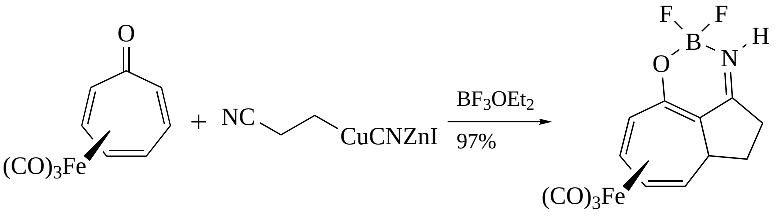
O
(CO)3Fe
+ NC CuCNZnI
BF3OEt2
97%
F F
B
O N H
(CO)3Fe

Scheme 147

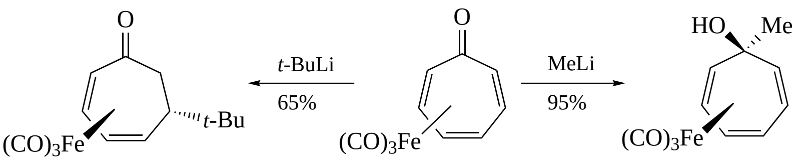
O
(CO)3Fe
t-Bu
t-BuLi
65%
O
(CO)3Fe
MeLi
95%
HO Me
(CO)3Fe

Scheme 148

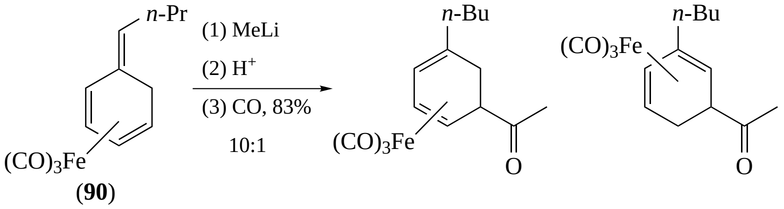
n-Pr
(1) MeLi
(2) H^+
(3) CO, 83%
10:1
$(CO)_3Fe$
(90)
n-Bu
$(CO)_3Fe$
O
n-Bu
$(CO)_3Fe$
O

Scheme 149

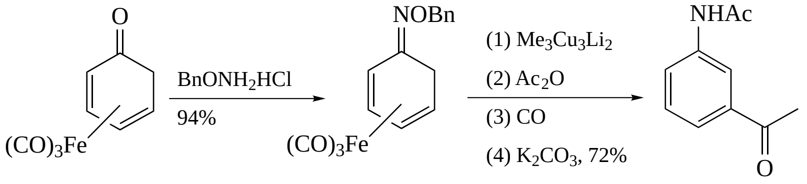
O
$BnONH_2HCl$
94%
$(CO)_3Fe$
NOBn
$(CO)_3Fe$
(1) $Me_3Cu_3Li_2$
(2) Ac_2O
(3) CO
(4) K_2CO_3, 72%
NHAc
O

Scheme 150

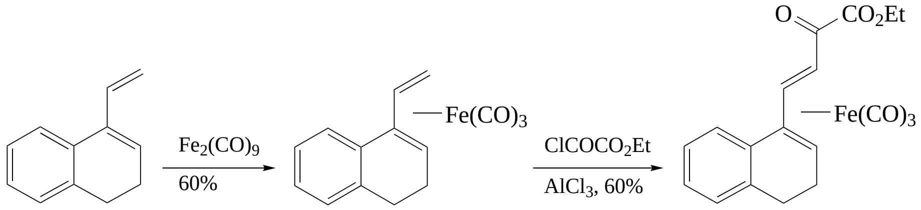
$Fe_2(CO)_9$
60%
$Fe(CO)_3$
$ClCOCO_2Et$
$AlCl_3$, 60%
O
CO_2Et
$Fe(CO)_3$

Scheme 151

4.3 Reactions with Electrophiles

Friedel–Crafts acylation of complexed dienes can be accomplished on the nonsubstituted terminus without isomerization. An example of a complexation–acylation can be seen in Scheme 151. The cis–trans complex is often obtained as the major product from Friedel–Crafts acylations (Scheme 152). Acid-catalyzed isomerization furnishes the thermodynamically more stable trans–trans complexes.

Highly enantioselective alkylations α to acyclic diene complexes have been developed. Deprotonation of (**91**) with LDA to form an ester enolate, followed by reaction with iodomethane, gives the alkylated product (**92**) in excellent yield with 82% ee (Scheme 153). Stereospecific remote alkylation was used in a synthesis toward macrolactin A (Scheme 154).[72] In the synthetic sequence, the primary alcohol of (**93**) is oxidized to an aldehyde. Reaction of the formed acetal with methyl trisopropoxytitanium furnishes the alkylation product (**94**). The α-hydroxy group is removed using sodium borohydride in the presence of boron trifluoride etherate to give (**95**). Cycloheptadienone complex (**96**) is readily deprotonated to form an enolate followed by stereospecific alkylation to give (**97**) (Scheme 155). Treatment of 1-aza-1,3-diene iron tricarbonyl complexes with a strong base followed by addition of methyl iodide, allyl bromide, or benzyl bromide affords N-alkylated 1,3-diene complexes (Scheme 156).

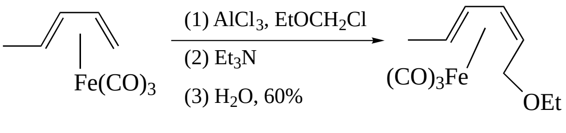
$Fe(CO)_3$
(1) $AlCl_3$, $EtOCH_2Cl$
(2) Et_3N
(3) H_2O, 60%
$(CO)_3Fe$
OEt

Scheme 152

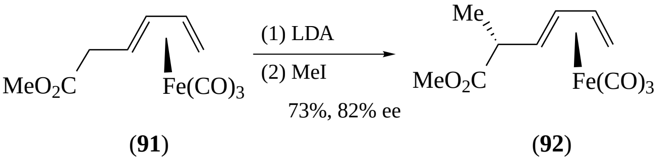
MeO_2C
$Fe(CO)_3$
(91)
(1) LDA
(2) MeI
73%, 82% ee
Me
MeO_2C
$Fe(CO)_3$
(92)

Scheme 153

Regioselective deprotonation of ironphosphonate complexes have been reported. Depending on the phosphonate, 1,3-migration of phosphonate or ring alkylation of the anion is observed (Schemes 157–158).

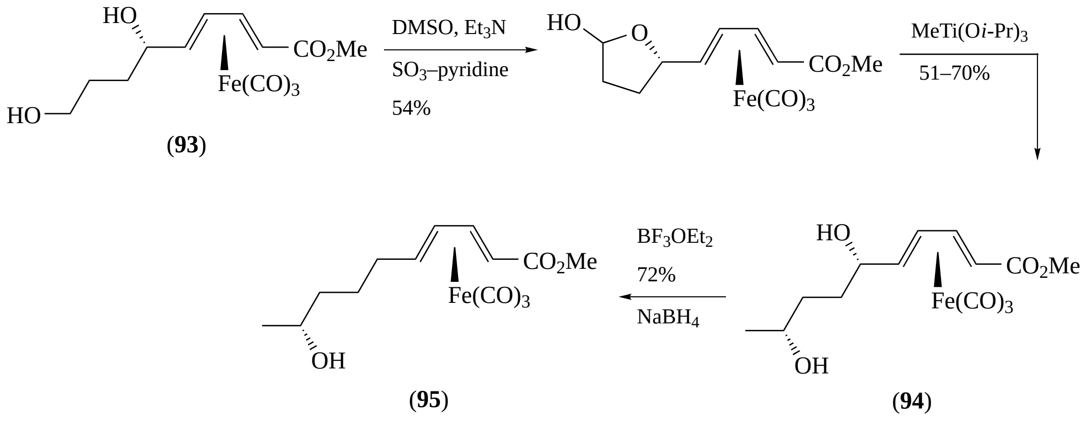
HO
HO
CO$_2$Me
Fe(CO)$_3$
(93)
DMSO, Et$_3$N
SO$_3$–pyridine
54%
HO
O
CO$_2$Me
Fe(CO)$_3$
MeTi(O*i*-Pr)$_3$
51–70%
HO
CO$_2$Me
Fe(CO)$_3$
OH
(94)
BF$_3$OEt$_2$
72%
NaBH$_4$
CO$_2$Me
Fe(CO)$_3$
OH
(95)

Scheme 154

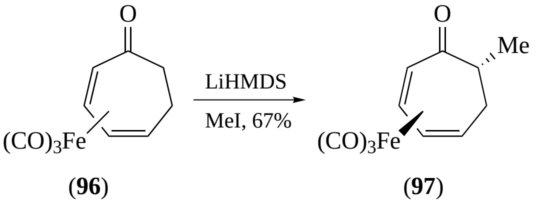
O
(CO)$_3$Fe
(96)
LiHMDS
MeI, 67%
O
Me
(CO)$_3$Fe
(97)

Scheme 155

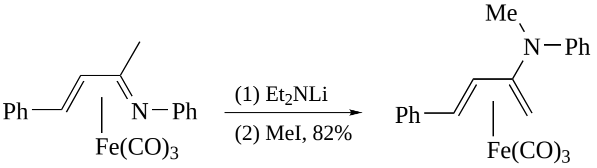
Ph
N−Ph
Fe(CO)$_3$
(1) Et$_2$NLi
(2) MeI, 82%
Me
N−Ph
Ph
Fe(CO)$_3$

Scheme 156

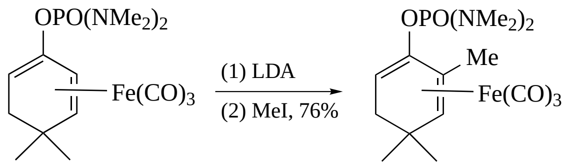
OPO(NMe$_2$)$_2$
Fe(CO)$_3$
(1) LDA
(2) MeI, 76%
OPO(NMe$_2$)$_2$
Me
Fe(CO)$_3$

Scheme 157

A number of the reactions discussed above were used in a synthetic sequence. Friedel–Crafts acylation of (**98**) gives (**99**) after isomerization of the diene geometry using sodium methoxide. Bromination of aTMS-enol ether, formed from (**99**), with DBA was nonstereospecific; however, the isomers were readily separated (Scheme 159). The pure α-bromoketone is stereospecifically methylated and transformed into an epoxide. Lewis acid–mediated isomerization of the epoxide affords an optically pure ketone (**100**).

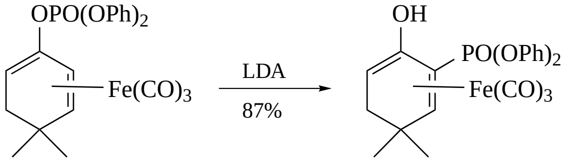
OPO(OPh)$_2$
Fe(CO)$_3$
LDA
87%
OH
PO(OPh)$_2$
Fe(CO)$_3$

Scheme 158

4.4 Annulations

Dienes coordinated to iron tricarbonyl do not undergo Diels–Alder reactions and a number of interesting annulation reactions of groups attached to iron tricarbonyl diene complexes have been developed. Cyclohexadiene iron tricarbonyl complexes having a pendant alkene undergo annulation reactions to form spirocyclic compounds (Scheme 160). Related reactions of allylic thioesters afford spirocyclic thialactones.

Double bonds adjacent to complexed dienes can be cyclopropanated using diazomethane, methyl diazoacetate, or sulfur-based ylids. Cycloheptatriene iron tricarbonyl undergo a $[2+2]$cycloaddition with chloroketene derived from trichloroacetyl chloride (Scheme 161).

Diene complexes containing alkene or diene substituents undergo Diels–Alder reactions in good yields. Hetero-Diels–Alder reactions have also been reported. Chirality transfer is observed upon reaction of chiral diene iron tricarbonyl complexes.^{73} Reaction of the chiral complex (**101**) with cyclopentadiene in the presence of a Lewis acid give (**102**) with a relatively high chirality transfer from the metal complex (Scheme 162).

Alkene-functionalized 1,3-diene complexes undergo regio- and stereoselective 1,3-dipolar cycloaddition reactions with nitrile *N*-oxides. Related cycloadditions of nitroalkanes in the presence of triethyl amine and phenylisocyanate afford dihydroisoxazoles. This type of cycloaddition was used in a synthesis toward macrolactin A (Scheme 163).

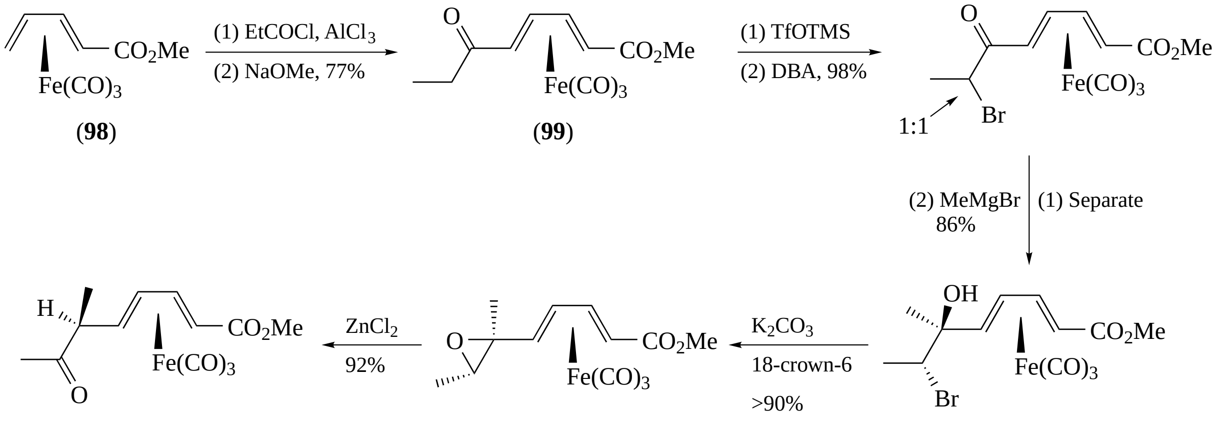
CO2Me
Fe(CO)3
(1) EtCOCl, AlCl3
(2) NaOMe, 77%
O
CO2Me
Fe(CO)3
(1) TfOTMS
(2) DBA, 98%
O
CO2Me
Fe(CO)3
1:1
Br
(2) MeMgBr
86%
(1) Separate
OH
CO2Me
Fe(CO)3
Br
K2CO3
18-crown-6
>90%
O
CO2Me
Fe(CO)3
ZnCl2
92%
H
CO2Me
Fe(CO)3
O

(**98**) (**99**) (**100**)

Scheme 159

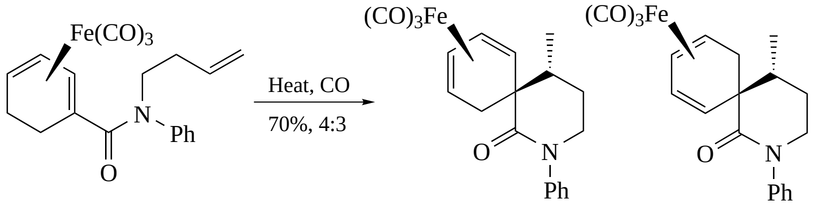
Fe(CO)3
N
Ph
O
Heat, CO
70%, 4:3
(CO)3Fe
O
N
Ph
(CO)3Fe
O
N
Ph

Scheme 160

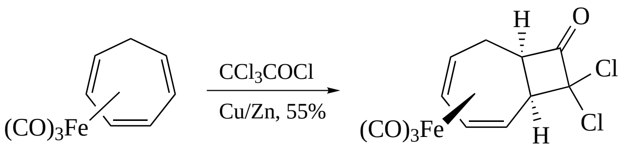
(CO)3Fe
CCl3COCl
Cu/Zn, 55%
H
O
Cl
Cl
(CO)3Fe
H

Scheme 161

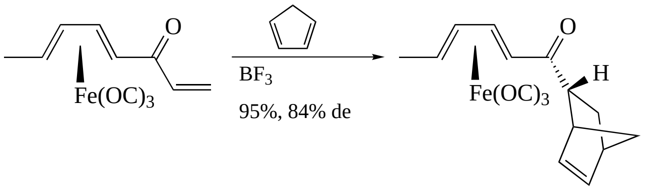
O
Fe(OC)3
BF3
95%, 84% de
O
Fe(OC)3
H

(**101**) (**102**)

Scheme 162

Cyclobutadiene iron tricarbonyl complexes can be isolated and have been utilized in organic synthesis. Both intra- and intermolecular [2 + 2]cycloadditions of alkenes with cyclobutadiene complexes are observed upon decomplexation using CAN or TMANO (Schemes 164–165).[74] The stereochemistry of the alkene is retained in the product. Iron tricarbonyl diene complexes are compatible with metathesis reactions using ruthenium catalysts (Scheme 166, *see* ***Organic Synthesis Using Metal-mediated Metathesis Reactions***).

Benzannulated products are obtained via thermolysis of α-diazo ester-substituted complexes. For example, formation of diazo ketone complex (**103**) via a tosyl hydrazone followed by thermolysis gave (**104**) (Scheme 167).[75]

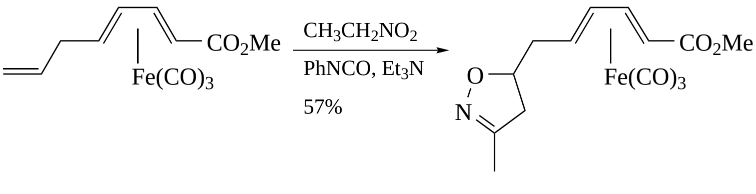
CO2Me
Fe(CO)3
CH3CH2NO2
PhNCO, Et3N
57%
O
N
CO2Me
Fe(CO)3

Scheme 163

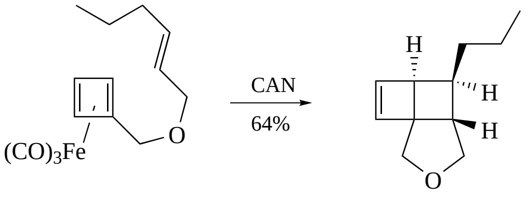

Scheme 164

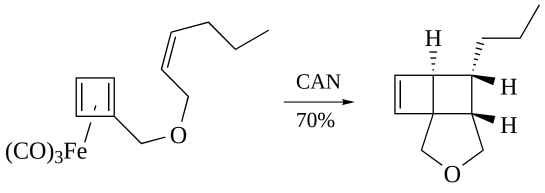

Scheme 165

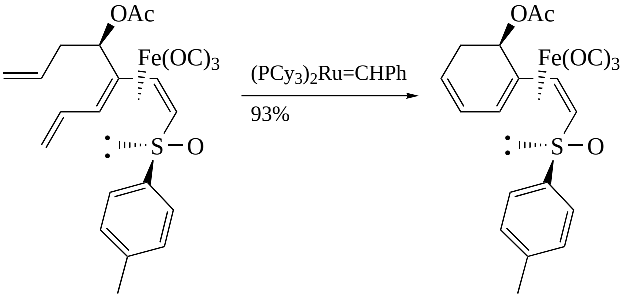

Scheme 166

The chemistry of diene iron tricarbonyl complexes described above has been in a number of total syntheses. An iterative stereospecific 1,3-migration of the iron tricarbonyl moiety was used to prepare compounds with multiple chiral centers. An example of one iteration can be seen in Scheme 168.[76] Ester hydrolysis of (**105**) and protection of the resulting alcohol gives (**106**). Reduction of the nitrile with DIBAL-H followed by olefination furnished (**107**). Treatment of (**107**) with a base resulted in the migration of iron toward the nitrile to give (**108**). The uncomplexed double bond can be dihydrolylated and transformed to ketal (**109**). Triethylsilane–Lewis acid reduction of the carbon adjacent to the diene system affords a new complex (**110**) completing the sequence.

A synthesis of α-lipoic acid and derivatives has been reported. The pendant alkene of complex (**111**) was transformed to a primary alcohol (**112**) via hydroboration-oxidation sequence. Mitsunobu coupling of (**112**) with thiobenzoic acids to give (**113**), followed by desilylation and nucleophilic substitution again employing thiobenzoic acid gave the advanced intermediate (**114**) (Scheme 169).

4.5 Cationic η^5-dienyl Iron Complexes

Hydride abstraction from dienyl tricarbonyl iron complexes furnishes cationic dienyl tricarbonyl iron complexes. For example, reaction of the diene–iron tricarbonyl complex (**115**) with triphenylmethyl hexafluorophosphate followed by trimethylsilyl cyanide furnished with excellent regio- and stereoselectivity a new diene–iron tricarbonyl complex (**116**) (Scheme 170). Excellent regio- and stereoselectivity is seen upon reaction of the cationic complex (**116**) with trimethylsilyl cyanide (TMS-CN) (Scheme 170). Reduction of the nitrile affords a spirocyclic lactam complex. Intramolecular cyclization of in situ formed enols furnishes spirocyclic compounds again with excellent stereocontrol (Scheme 171). An interesting example of hydride transfer from a cyclohexadiene ring to a pendant aldehyde followed by nucleophilic addition is seen in Scheme 172.

Addition of stabilized nucleophiles to complex (**117**) affords (**118**) via addition of the nucleophile to the face opposite the metal (Scheme 173).[77] Oxidative decomplexation of (**118**) results in the formation of a stereodefined vinylcyclopropane (**119**). Vinyl ketene complexes insert electron-deficient alkenes and undergo related cyclopropanations upon oxidation (Scheme 174). Harder nucleophiles such as Grignard reagents (*see Grignard Reagents*) usually add to the terminal carbon of the dienyl system (Scheme 175). Depending on the cation and ligand on iron, either addition of a stabilized nucleophile to the ring or a Michael-type reaction is observed (Schemes 176–177).

Cationic complexes formed from acyclic diene iron complexes react in a fashion very similar to dicobalt hexacarbonyl stabilized propargylic cations. The cations can

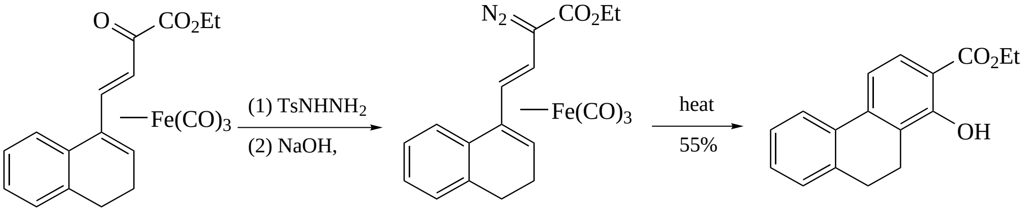

(**103**) (**104**)

Scheme 167

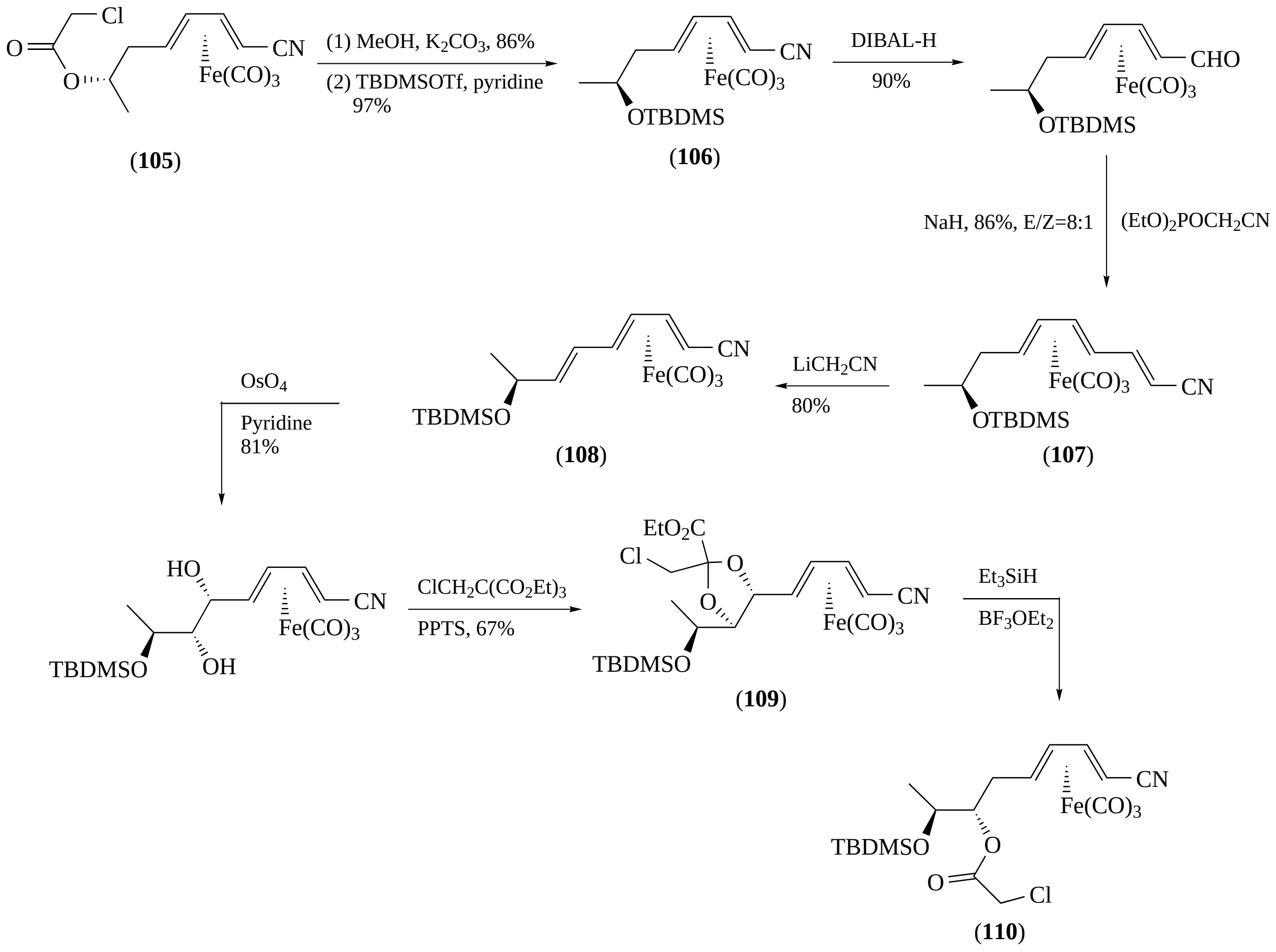
Cl
O
O
CN
Fe(CO)3
(105)
(1) MeOH, K2CO3, 86%
(2) TBDMSOTf, pyridine
97%
CN
Fe(CO)3
OTBDMS
(106)
DIBAL-H
90%
CHO
Fe(CO)3
OTBDMS
NaH, 86%, E/Z=8:1
(EtO)2POCH2CN
Fe(CO)3
CN
OTBDMS
(107)
LiCH2CN
80%
CN
Fe(CO)3
TBDMSO
(108)
OsO4
Pyridine
81%
HO
CN
Fe(CO)3
TBDMSO
OH
ClCH2C(CO2Et)3
PPTS, 67%
EtO2C
Cl
O
O
CN
Fe(CO)3
TBDMSO
(109)
Et3SiH
BF3OEt2
CN
Fe(CO)3
TBDMSO
O
O
Cl
(110)

Scheme 168

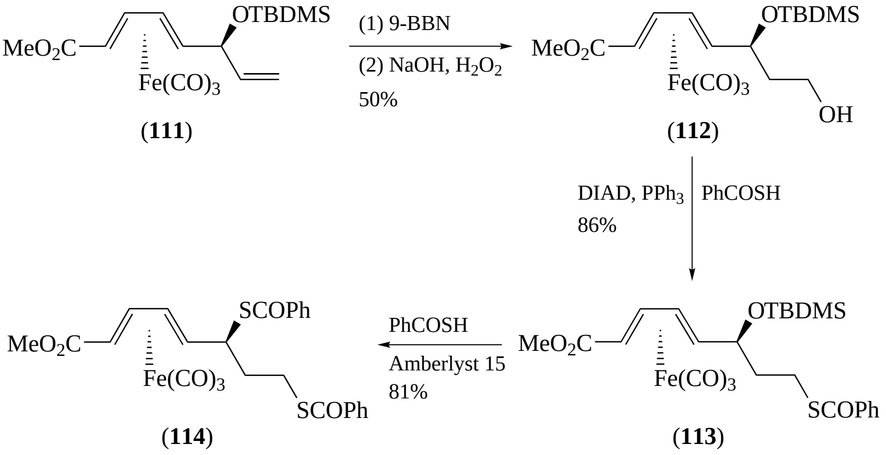
MeO2C
OTBDMS
Fe(CO)3
(111)
(1) 9-BBN
(2) NaOH, H2O2
50%
MeO2C
OTBDMS
Fe(CO)3
OH
(112)
DIAD, PPh3
86%
PhCOSH
MeO2C
OTBDMS
Fe(CO)3
SCOPh
(113)
PhCOSH
Amberlyst 15
81%
MeO2C
SCOPh
Fe(CO)3
SCOPh
(114)

Scheme 169

be formed by reaction of an adjacent alcohol or an ester group with a Lewis acid. The cationic species undergo reactions with a variety of nucleophiles to give products from addition to the face opposite the metal. Nucleophiles include trialkylaluminum, ketene silylacetals, allyltributyltin, allyltrimethylsilane, and trimethylsilylazide (Scheme 178).

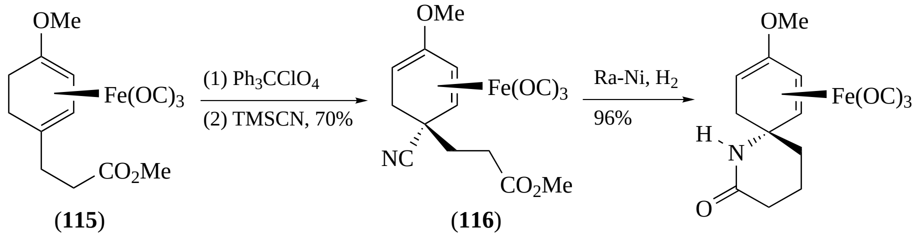
OMe
Fe(OC)3
CO2Me
(1) Ph3CClO4
(2) TMSCN, 70%
OMe
Fe(OC)3
NC
CO2Me
Ra-Ni, H2
96%
OMe
Fe(OC)3
H
N
O

(**115**) (**116**)

Scheme 170

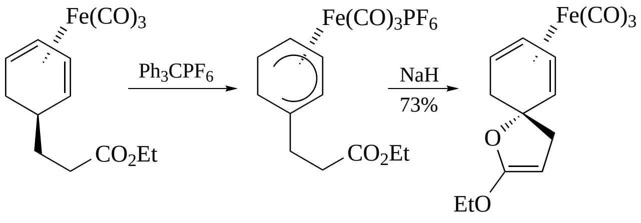
Fe(CO)3
CO2Et
Ph3CPF6
Fe(CO)3PF6
CO2Et
NaH
73%
Fe(CO)3
O
EtO

Scheme 171

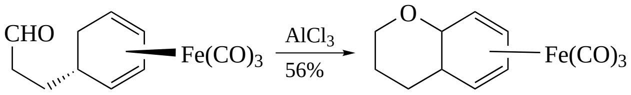
CHO
Fe(CO)3
AlCl3
56%
O
Fe(CO)3

Scheme 172

Highly stereospecific additions of thio-groups are also seen and this was used as a key step in the synthesis of halicholactone (Scheme 179).[78] Treatment of dienol iron tricarbonyl complexes with DAST introduces a fluorine atom with complete retention of stereochemistry. Stereospecific cyclization reactions involving pendant alkenes or electron-rich aromatic rings can be achieved (Scheme 180).[79] The incorporation of a fluoride atom from boron trifluoride is usually observed from reaction with alkenes. The carbocation can also be generated from a double bond adjacent to the diene moiety. For example, reaction of (**120**) with formic acid gave (**121**) via stereoselective interception of an intermediately formed secondary carbocation (Scheme 181).[80]

A very high stereoselectivity is observed upon formation of a dienyl carbocation (**123**) from the enantiomerically pure complex (**122**) followed by nucleophilic addition. An

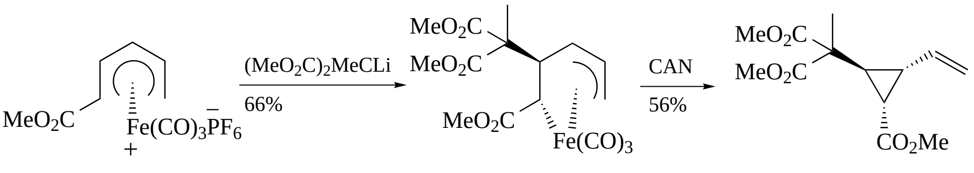
MeO2C
Fe(CO)3PF6
−
+
(MeO2C)2MeCLi
66%
MeO2C
MeO2C
MeO2C
Fe(CO)3
CAN
56%
MeO2C
MeO2C
CO2Me

(**117**) (**118**) (**119**)

Scheme 173

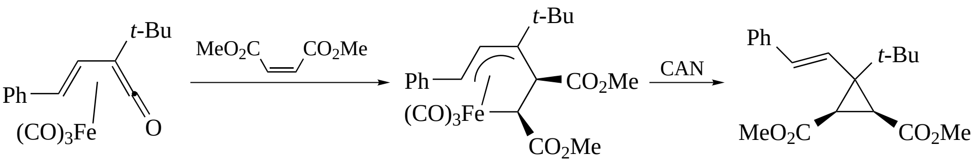
t-Bu
Ph
(CO)3Fe
O
MeO2C
CO2Me
t-Bu
Ph
CO2Me
(CO)3Fe
CO2Me
CAN
Ph
t-Bu
MeO2C
CO2Me

Scheme 174

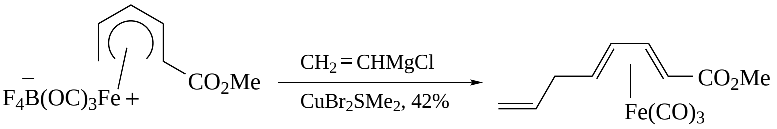
−
F4B(OC)3Fe +
CO2Me
CH2 = CHMgCl
CuBr2SMe2, 42%
CO2Me
Fe(CO)3

Scheme 175

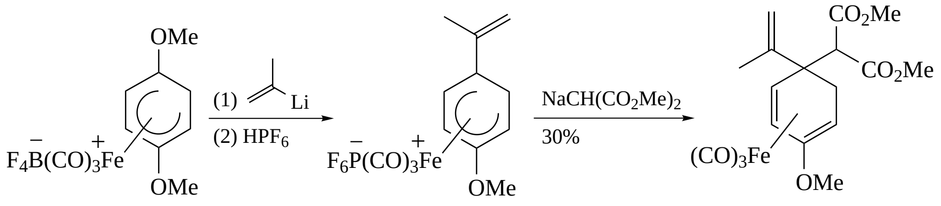
OMe
F4B(CO)3Fe
OMe
(1) Li
(2) HPF6
F6P(CO)3Fe
OMe
NaCH(CO2Me)2
30%
CO2Me
CO2Me
(CO)3Fe
OMe

Scheme 176

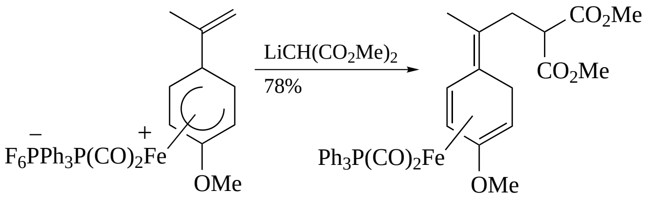
F6PPh3P(CO)2Fe
OMe
LiCH(CO2Me)2
78%
CO2Me
CO2Me
Ph3P(CO)2Fe
OMe

Scheme 177

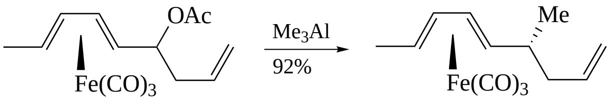
OAc
Fe(CO)3
Me3Al
92%
Me
Fe(CO)3

Scheme 178

E, Z product is formed via reaction of the u-form (**123**) (Scheme 182). In contrast, more reactive nucleophiles react with the s-form (**122**) to give E, E geometry of the double bond (Scheme 183).

Cycloheptadienylcations are readily alkylated. The regioselectivity of the addition depends on the substituents on the ring. For example, the methoxy-substituted complex (**124**) is alkylated on the methoxy bearing carbon (Scheme 184). In contrast, complex (**125**) having a methyl group in place of the methoxy group affords complex (**126**).

Of particular synthetic importance are the reactions of cyclohexadienyl cations with aromatic amines under oxidative conditions (Scheme 185). This type of reaction has been utilized as the key step in highly convergent synthetic relays to a variety of carbazole alkaloids. Enamines can be used

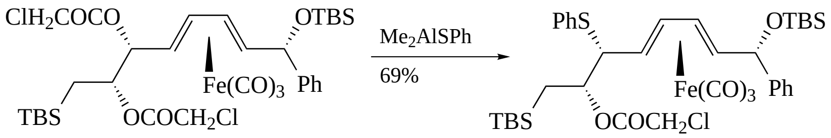
ClH2COCO
OTBS
Fe(CO)3
Ph
TBS
OCOCH2Cl
Me2AlSPh
69%
PhS
OTBS
Fe(CO)3
Ph
TBS
OCOCH2Cl

Scheme 179

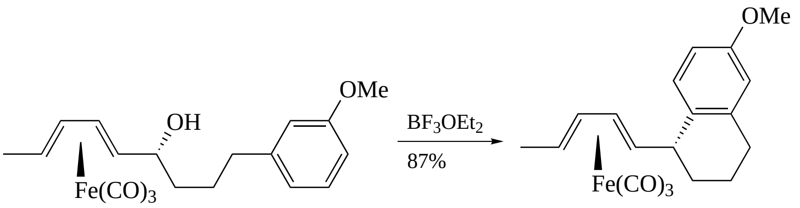
OH
OMe
Fe(CO)3
BF3OEt2
87%
OMe
Fe(CO)3

Scheme 180

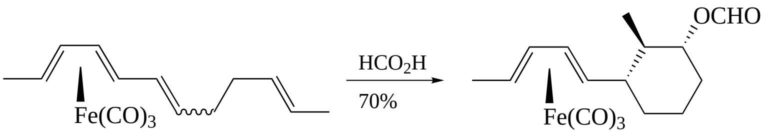
Fe(CO)3
HCO2H
70%
OCHO
Fe(CO)3

(**120**) (**121**)

Scheme 181

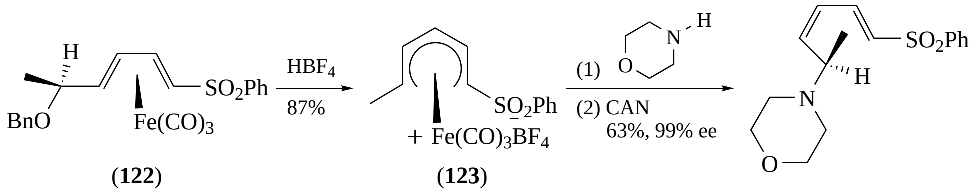
H
BnO
Fe(CO)3
SO2Ph
HBF4
87%
SO2Ph
+ Fe(CO)3BF4
(1) morpholine
(2) CAN
63%, 99% ee
SO2Ph
H
N
O

(**122**) (**123**)

Scheme 182

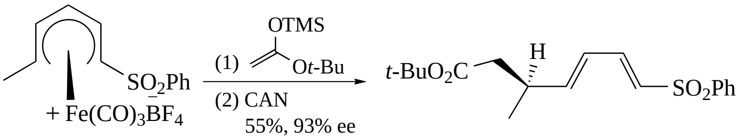
SO2Ph
+ Fe(CO)3BF4
OTMS
(1)
Ot-Bu
(2) CAN
55%, 93% ee
t-BuO2C
H
SO2Ph

Scheme 183

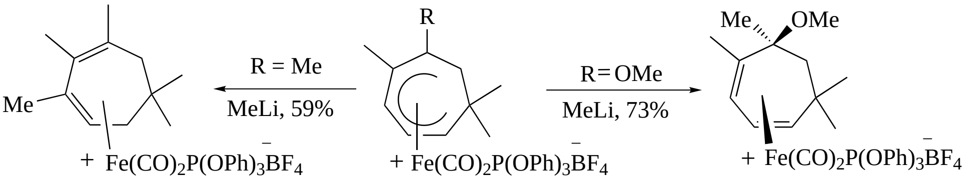
Me
+ Fe(CO)2P(OPh)3BF4
R = Me
MeLi, 59%
R
+ Fe(CO)2P(OPh)3BF4
R=OMe
MeLi, 73%
Me
OMe
+ Fe(CO)2P(OPh)3BF4

(**126**) (**124–125**)

Scheme 184

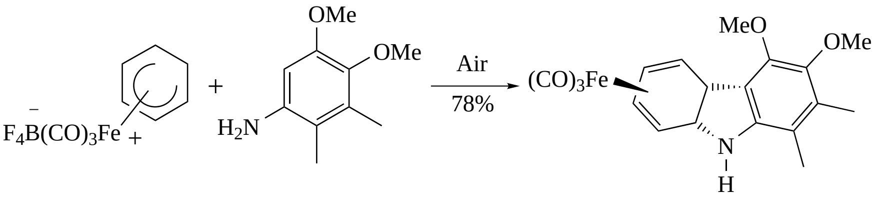
F4B(CO)3Fe +
+
OMe
OMe
H2N
Air
78%
(CO)3Fe
MeO
OMe
N
H

Scheme 185

as the nucleophile affording cyclic adducts after oxidative amination (Scheme 186).

Cyclobutadiene iron tricarbonyl complexes also stabilized carbocations on an adjacent carbon. The cation reacts with silyl enol ethers to afford alkylated complexes such as (**127**) (Scheme 187). A samarium diiodide–mediated intermolecular radical cyclization of iron tricarbonyl complex (**128**) is depicted in Scheme 188. An excellent stereocontrol at three contiguous centers is observed.

5 DICOBALT HEXACARBONYL ALKYNE COMPLEXES

Alkyne complexes (*see Alkyne Complexes*) of almost all transition metals have been isolated and characterized. By far, the most studied and synthetically versatile are dicobalt hexacarbonyl alkyne complexes. The relative stability of cobalt–alkyne complexes, compared to related complexes of other transition metals, and their ability to further react with a number of reagents makes them ideal intermediates in organic synthesis. Alkyne dicobalt hexacarbonyl complexes are usually prepared by thermolysis of a solution of $Co_2(CO)_8$ in the presence of an alkyne. Alkyne cobalt complexes can also be prepared by reaction of alkynes with cobalt dibromide in the presence of zinc and carbon monoxide.

The bridged complex between two cobalt tricarbonyl units and all four π-electrons of the alkyne distorts the alkyne from being linear to being bent in a 150°C angle. For simplicity, all $Co_2(CO)_6$ complexes will be represented by a single bond from the $Co_2(CO)_6$ fragment to the alkyne (Scheme 189).

The cobalt moiety can be removed to give the free alkyne in high yields using, for example, CAN, TBAF, iron trinitrate,

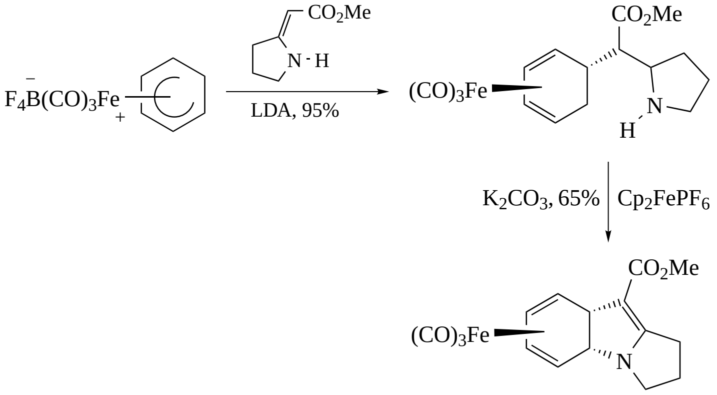

$F_4\bar{B}(CO)_3Fe^+$
CO_2Me
N - H
LDA, 95%
$(CO)_3Fe$
CO_2Me
N
H
K_2CO_3, 65%
Cp_2FePF_6
$(CO)_3Fe$
CO_2Me
N

Scheme 186

iodine, or trimethylamine *N*-oxide, sodium methylthiolate, and 1,2-diaminoethane. A carbonylative decomplexation in the presence of a primary or secondary amine can be achieved. For example, reaction of phenylethyne dicobalt hexacarbonyl with *N*,*N*-dibenzylamine gave (**129**) (Scheme 190). Also of synthetic interest is the oxidative decomplexation of (**130**) furnishing an anhydride (**131**) (Scheme 191).

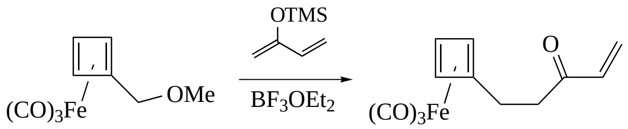

$(CO)_3Fe$
OMe
OTMS
BF_3OEt_2
76%
$(CO)_3Fe$
O

(**127**)

Scheme 187

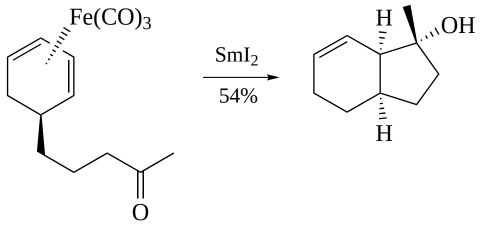

$Fe(CO)_3$
O
SmI_2
54%
H
OH
H

(**128**)

Scheme 188

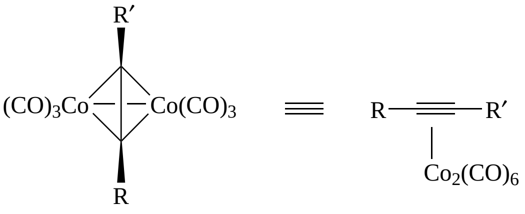

R′
$(CO)_3Co$
$Co(CO)_3$
R
R
R′
$Co_2(CO)_6$

Scheme 189

A number of reductive decomplexation methods are available. A reductive removal using tributyltin hydride to give the saturated hydrocarbon has been reported (Scheme 192). Reductive decomplexation has also been observed using trifluoro acetic acid to afford a cis-alkene as the major product (Scheme 193).

5.1 Alkyne Cobalt Complexes as a Protecting Group

Dicobalt hexacarbonyl−alkyne complexes are stable to a number of electrophilic reagents, and uncomplexed multiple

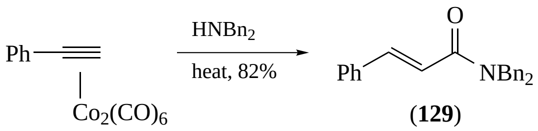

Ph
$Co_2(CO)_6$
$HNBn_2$
heat, 82%
O
Ph
NBn_2

(**129**)

Scheme 190

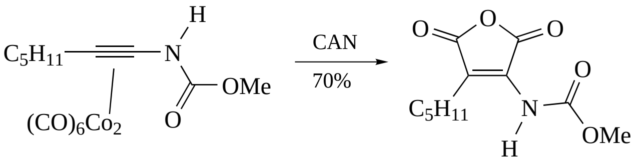

H
C_5H_{11}
N
OMe
$(CO)_6Co_2$
O
CAN
70%
O
O
O
O
C_5H_{11}
N
H
OMe

(**130**) (**131**)

Scheme 191

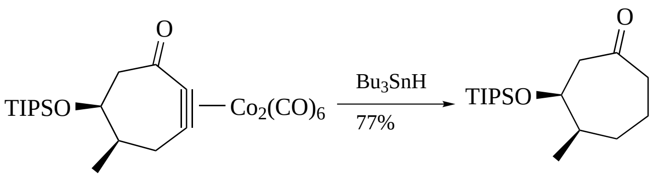

O
TIPSO
$Co_2(CO)_6$
Bu_3SnH
77%
TIPSO
O

Scheme 192

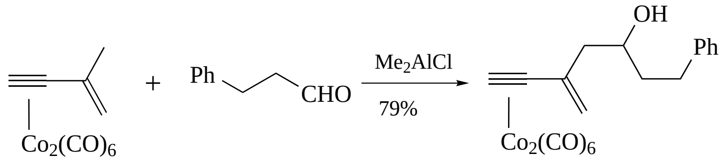

Scheme 194

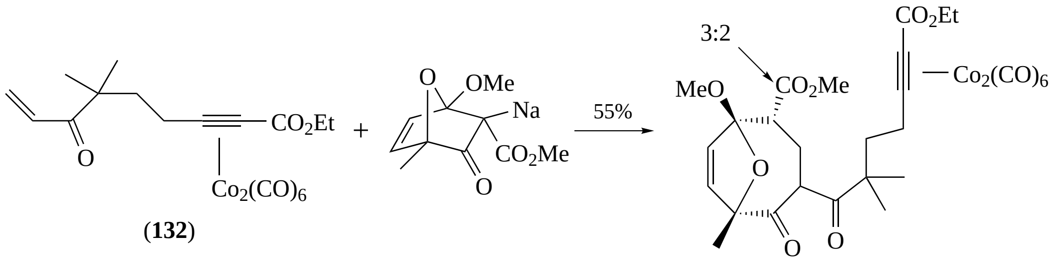

(**132**)

Scheme 195

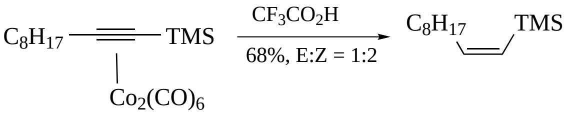

Scheme 193

bonds present within these molecules can be manipulated. For example, pendant alkenes can be reduced using hydrazine or oxidized using hydroboration-peroxide oxidation. It is noteworthy to observe that hydrogen peroxide does not result in demetallation of the complex.

Alkynols complexed to cobalt can be oxidized to alkynals without decomplexation. Propargyl aldehydes are protected from polymerization upon complexation with $Co_2(CO)_6$. These aldehydes smoothly undergo Wittig-type reactions. Carbonyl-ene reactions have been demonstrated (Scheme 194). Complexation to cobalt protected the enyne in complex (**132**) from Michael-type reactions (Scheme 195). Alkenyl-substituted complexes undergo [3 + 2]cycloadditions with nitrile N-oxides (Scheme 196).

Cobalt-complexed propargylic aldehydes can be alkylated using both cyclic and acyclic trimethylsilyl enol-ethers and -esters in the presence of a Lewis acid. Boron trifluoride etherate is the most frequently employed Lewis acid. Other nucleophiles include organolithiums and Grignard reagents.

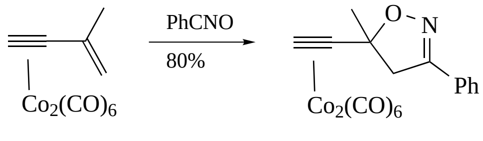

Scheme 196

Aldol-type reactions of complexed propargylic aldehydes afford mixtures of syn/anti aldol products. Double alkylation can be obtained using butynedial complex (**133**) (Scheme 197). Reaction of complexed aldehydes with diethyl zinc in the presence of a chiral ligand takes place with high enantioselectivity (Scheme 198).[81] Very high diastereoselectivities are observed upon reaction of Grignard reagents to phosphine-substituted complexes (Scheme 199). Optically active allylboranes also react with complexed propargylic aldehydes and afford propargylic alcohols in high enantiomeric excess. For example, reaction of the chiral γ-alkoxyborane (**134**) with (**135**) affords the allylation product (**136**) with an excellent degree of diastereoselectivity (Scheme 200, $R^* =$ isocampheyl).

Mukaiyama-type reaction of cobalt-alkyne complexes with ketene acetals gives the *syn* product exclusively, a reaction used as a key in a relay to bengamide E (Scheme 201). Total synthesis of blastomycinone utilizing a Mukaiyama-type reaction has been reported (Scheme 202). It is interesting to note the complete reversal of selectivity compared to the uncomplexed aldehyde (Scheme 203).

Highly strained cyclic compounds containing an alkyne group can be prepared upon complexation to $Co_2(CO)_6$. The success of these reactions relies on the severely bent nature of the alkyne triple bond when complexed to cobalt. Cyclization of (**137**) to form bicyclo[7.3.0]tridecane (**138**), a calichiamycinone derivative has been reported (Scheme 204). The nine-membered enyne complex (**140**) was prepared by ring-closing metathesis of (**139**) (Scheme 205). A related reaction was used to give complex (**141**) (Scheme 206).[82] It should be noted that no cyclization occurs without prior complexation to cobalt in the latter case. A complexation-initiated

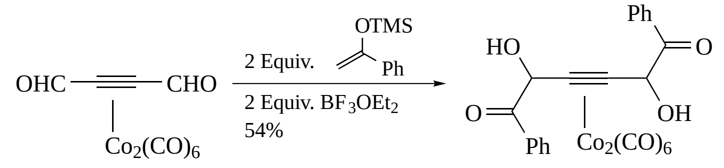
OHC
CHO
Co2(CO)6
OTMS
2 Equiv.
Ph
2 Equiv. BF3OEt2
54%
HO
Ph
O
O
Ph
OH
Co2(CO)6

(**133**)

Scheme 197

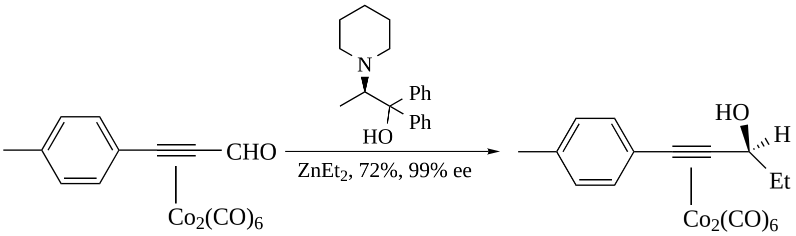
N
Ph
Ph
HO
CHO
Co2(CO)6
ZnEt2, 72%, 99% ee
HO
H
Et
Co2(CO)6

Scheme 198

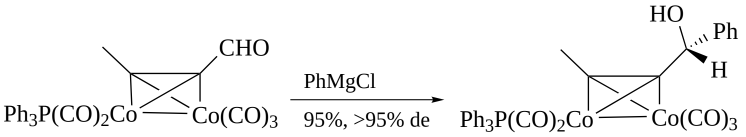
CHO
Ph3P(CO)2Co
Co(CO)3
PhMgCl
95%, >95% de
HO
Ph
H
Ph3P(CO)2Co
Co(CO)3

Scheme 199

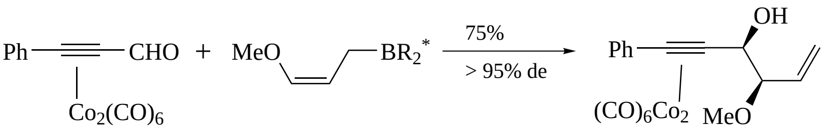
Ph
CHO
Co2(CO)6
+
MeO
BR2*
75%
> 95% de
OH
Ph
(CO)6Co2
MeO

(**135**) (**134**) (**136**)

Scheme 200

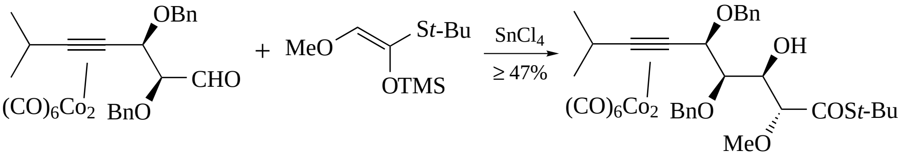
OBn
CHO
(CO)6Co2
BnO
+
MeO
St-Bu
OTMS
SnCl4
≥ 47%
OBn
OH
(CO)6Co2
BnO
COSt-Bu
MeO

Scheme 201

Diels–Alder reaction of (**142**) was described. The equilibrium was shifted toward the product upon complexation of the alkyne (Scheme 207).[83]

Ring expansion of complexed cycloalkynones using TMS-diazomethane is possible (Scheme 208). It should be noted that both product- and starting-material compounds are highly unstable in the absence of the cobalt carbonyl moiety.

5.2 Propargylic Activation

Complexation of dicobalt octacarbonyl to alkynes not only protects the triple bond against a number of reagents, but stabilization of propargylic cations, anions, and radicals is also observed. The carbocations are readily obtained as dark–red, thermally stable solids by treatment of propargylic alcohols,

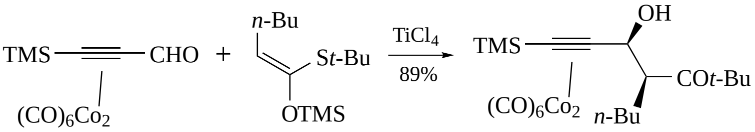
TMS
CHO
(CO)6Co2
n-Bu
St-Bu
OTMS
TiCl4
89%
OH
COt-Bu
n-Bu

Scheme 202

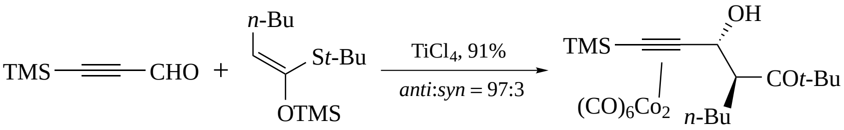
TMS
CHO
n-Bu
St-Bu
OTMS
TiCl4, 91%
anti:syn = 97:3
OH
COt-Bu
(CO)6Co2
n-Bu

Scheme 203

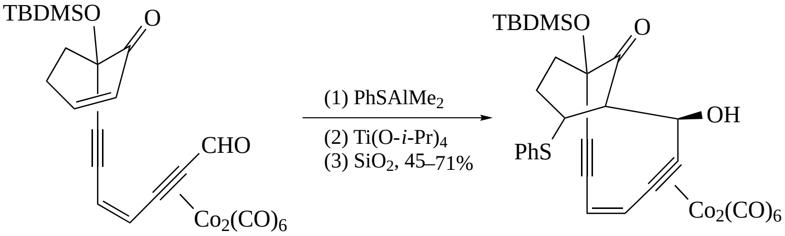
TBDMSO
O
CHO
Co2(CO)6
(1) PhSAlMe2
(2) Ti(O-i-Pr)4
(3) SiO2, 45–71%
PhS
OH

(**137**) (**138**)

Scheme 204

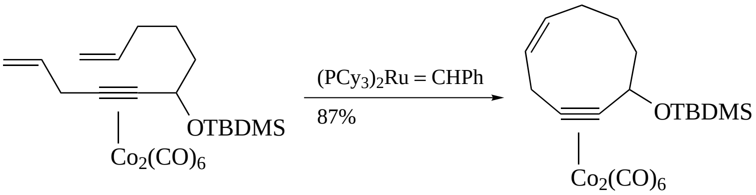
OTBDMS
Co2(CO)6
(PCy3)2Ru = CHPh
87%

(**139**) (**140**)

Scheme 205

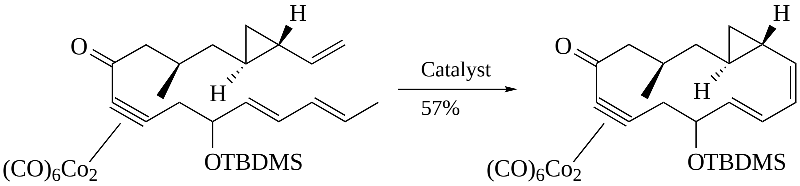
O
H
H
(CO)6Co2
OTBDMS
Catalyst
57%

(**141**)

Scheme 206

ethers, epoxides, acetals, or acetates with Lewis acids. Stability similar to the triphenylmethyl carbenium ion is observed.

The Nicholas reaction, that is, the addition reaction of nucleophiles to cobalt-complexed propargylic cations, formed in situ, has been extensively developed.[84–87] The nucleophilic addition occurs exclusively at the α-carbon without competing formation of allenic products. Nucleophiles include amines, water, alcohols, trialkylaluminum reagents, sodium borohydride, diethylaluminum cyanide, trialkylsilyl enol ethers, enol acetates, furans, stabilized anions, and

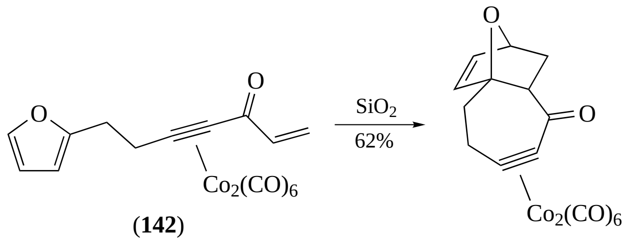
O
O
SiO$_2$
62%
O
O
$Co_2(CO)_6$
$Co_2(CO)_6$
(142)

Scheme 207

allylsilanes and -boranes. Isomerization from the α-anomer to the more stable β-anomer of furanoses can be achieved in the presence of an acid (Scheme 209).

Electron-rich aromatic compounds are readily alkylated at room temperature with propargyl complexes to form, after demetallation, 2-propyne-substituted aromatic compounds. Depending on the substitution pattern of the alkyne complex and the aromatic substrate, alkylation occurs at times with very high regioselectivity. This type of annulation was used in a synthesis of pseudoipterosin

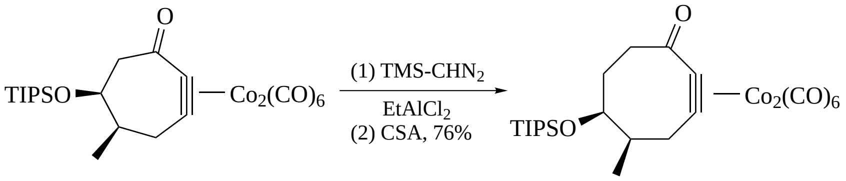
O
TIPSO
$Co_2(CO)_6$
(1) TMS-CHN$_2$
EtAlCl$_2$
(2) CSA, 76%
O
TIPSO
$Co_2(CO)_6$

Scheme 208

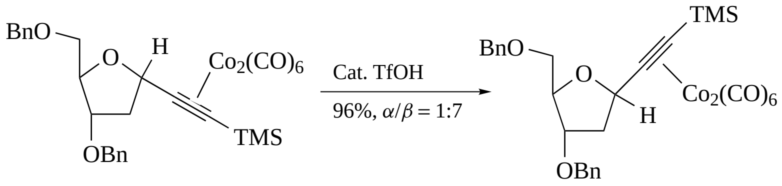
BnO
O
H
$Co_2(CO)_6$
TMS
OBn
Cat. TfOH
96%, $\alpha/\beta = 1:7$
BnO
O
TMS
$Co_2(CO)_6$
H
OBn

Scheme 209

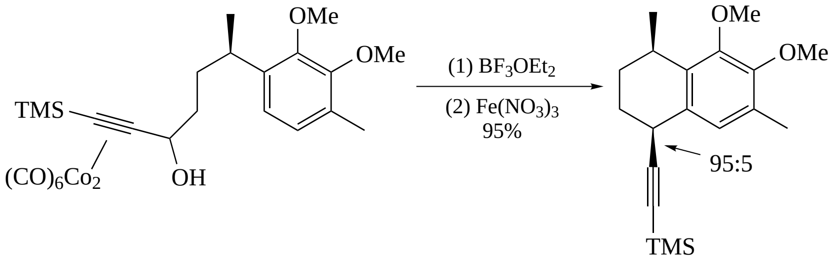
OMe
OMe
TMS
$(CO)_6Co_2$
OH
(1) BF$_3$OEt$_2$
(2) Fe(NO$_3$)$_3$
95%
OMe
OMe
95:5
TMS

Scheme 210

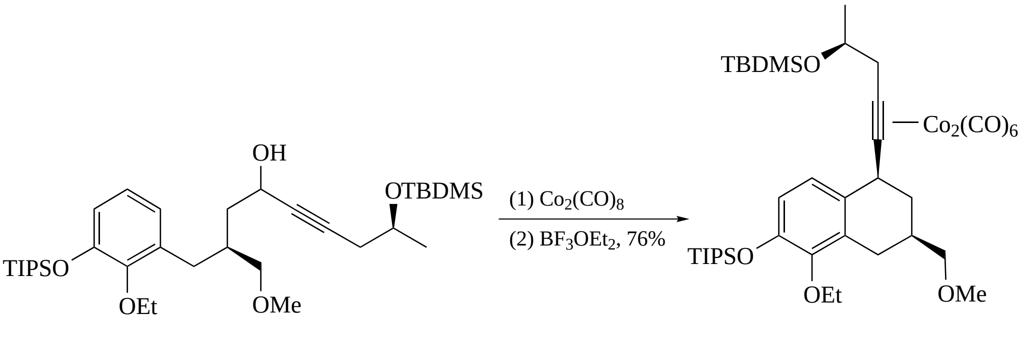
OH
OTBDMS
TIPSO
OEt
OMe
(1) $Co_2(CO)_8$
(2) BF$_3$OEt$_2$, 76%
TBDMSO
$Co_2(CO)_6$
TIPSO
OEt
OMe

Scheme 211

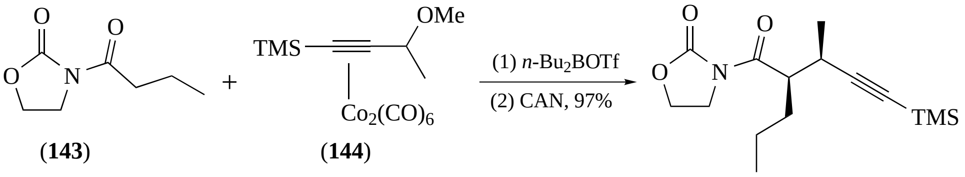

OMe
TMS
$Co_2(CO)_6$
(1) n-Bu_2BOTf
(2) CAN, 97%
TMS
(143)
(144)

Scheme 212

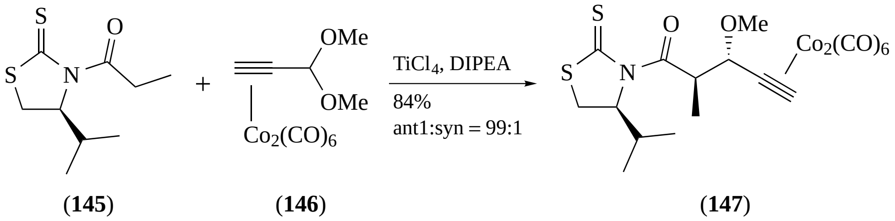

OMe
OMe
$Co_2(CO)_6$
$TiCl_4$, DIPEA
84%
ant1:syn = 99:1
OMe
$Co_2(CO)_6$
(145)
(146)
(147)

Scheme 213

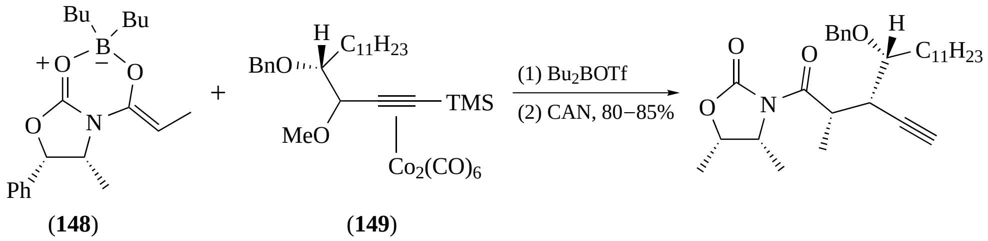

Bu
Bu
Ph
H
$C_{11}H_{23}$
BnO
MeO
TMS
$Co_2(CO)_6$
(1) Bu_2BOTf
(2) CAN, 80–85%
BnO
H
$C_{11}H_{23}$
(148)
(149)

Scheme 214

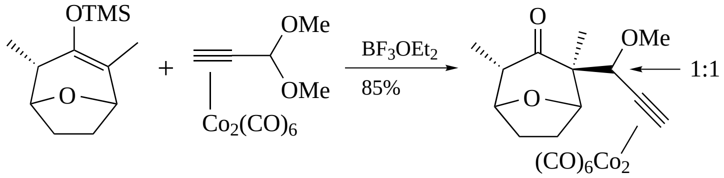

OTMS
OMe
OMe
$Co_2(CO)_6$
BF_3OEt_2
85%
OMe
1:1
$(CO)_6Co_2$

Scheme 215

aglycones (Scheme 210)[88] and toward daphnanes and (+)-resiniferatoxine (Scheme 211).

High diastereoselectivity is observed upon reaction of the boron enolate of (**143**) with complex (**144**) (Scheme 212). This reaction was utilized in a synthesis of pyrromethenone. Chiral Evans'-type enolates can be alkylated with very high stereoselectivity. For example, reaction of the chiral 1,3-thiazolidine-2-thione (**145**) and complex (**146**) gave (**147**) with excellent selectivity (Scheme 213).[89] Enantioselective synthesis of (+)- and (−)-nephrosteranic acid has been also been reported using the chiral boron enolate (**148**) with propargylic ether (**149**) (Scheme 214).[90] A low degree of diastereoselectivity was observed at the propargylic position upon the Nicholas reaction of cyclic silyl enol ethers with propargylic acetals (Scheme 215).

Allylic transfer from a pendant allylic silane to a propargylic cation is seen in Scheme 216. Allylic silanes

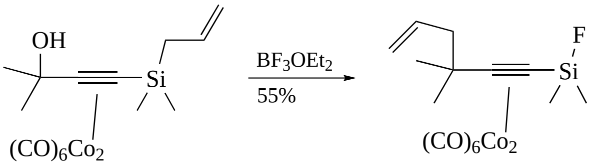

OH
Si
$(CO)_6Co_2$
BF_3OEt_2
55%
F
Si
$(CO)_6Co_2$

Scheme 216

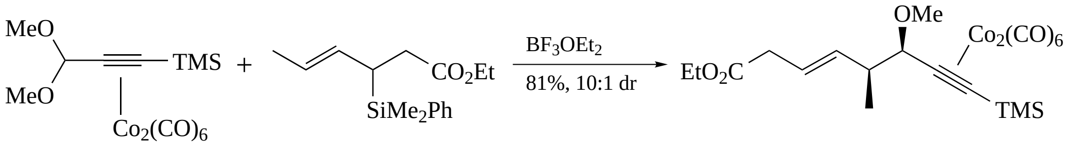

Scheme 217

undergo reactions with propargylic acetals to form products with relatively high distereoselectivity (Scheme 217).

Intramolecular alkylation reactions employing allylsilanes have been developed. A taxoid bicyclo[9.3.1]pentadecane ring system was prepared via intramolecular alkylation of (**150**). It is interesting to note that the alkylation occurred in the γ-position relative to the alkyne (Scheme 218).[91] A Nicholas reaction was used in the synthesis of (+)-epoxydictymene (Scheme 219).

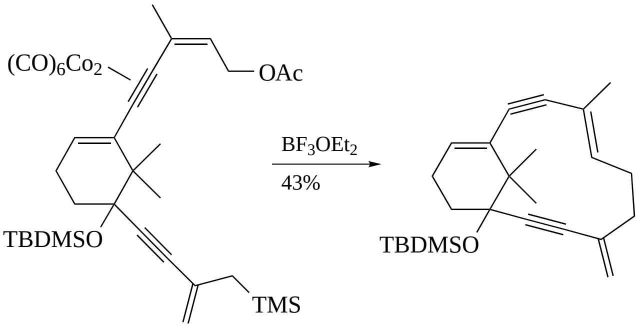

(**150**)

Scheme 218

Reduction of the propargylic cation is observed upon reaction of γ-benzylprotected-α-hydroxy complexes. A hydride shift from the benzyl group to the intermediately formed carbocation is observed. For example, deuterium-labeled complex (**151**) gave alkyne (**152**) with a deuterium in the α-position (Scheme 220).[92] Benzaldehyde is observed as the side product.

Cationic cascade-type reactions of appropriately substituted complexes were used to prepare spirocyclic compounds (Scheme 221). Intramolecular variations on the carbocation theme discussed above can be employed to form macrocyclic compounds. This general strategy of propargylic activation has been used to prepare ingenol. The highly strained ring system of ingenol was obtained by intramolecular trapping of the formed propargylic cation with a pendant alkene (Scheme 222).[93] A variation of the intramolecular reaction is seen in Scheme 223, wherein an alkene reacts with the formed propargylic cation. The secondary cation undergoes nucleophilic addition reactions with the present anion. It is interesting to note that an elimination product is formed using titanium tetraiodide. Alkene-substituted complexes react with benzhydryl carbocations to form a propargylic cation that can be alkylated using an allylic silane (Scheme 224).

The complexed propargylic carbocation intermediates also react with nucleophiles to form, in some cases, a

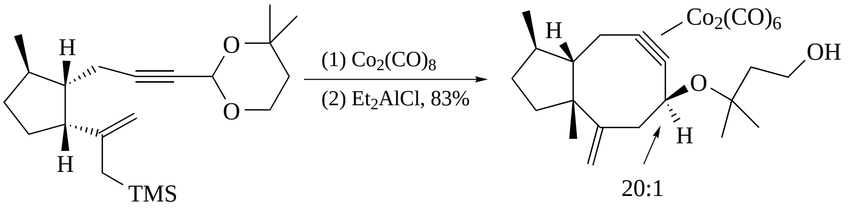

Scheme 219

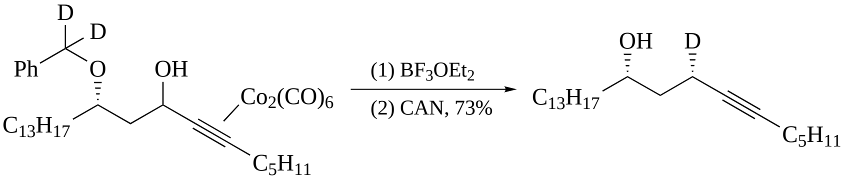

(**151**) (**152**)

Scheme 220

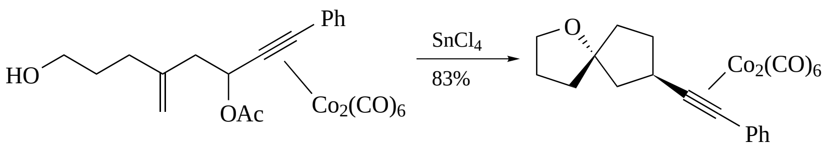
HO
OAc
Ph
Co2(CO)6
SnCl4
83%
O
Co2(CO)6
Ph

Scheme 221

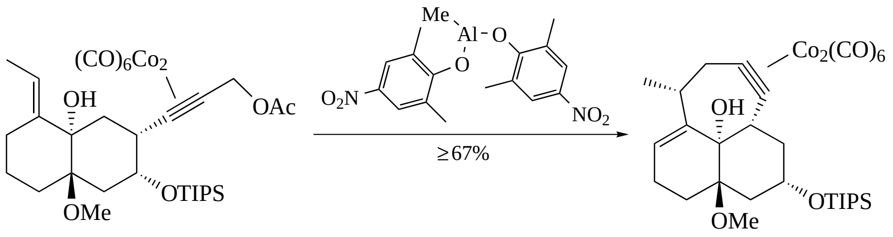
(CO)6Co2
OH
OAc
OTIPS
OMe
Me
Al
O
O
O2N
NO2
≥67%
Co2(CO)6
OH
OTIPS
OMe

Scheme 222

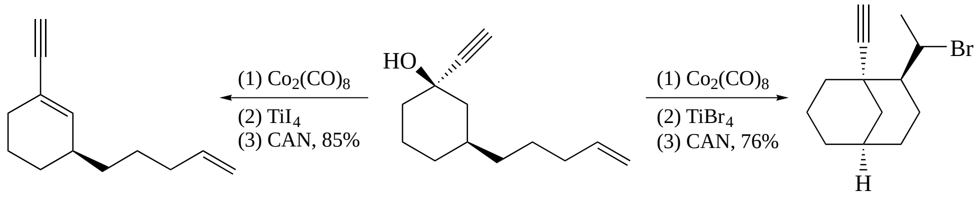
(1) Co2(CO)8
(2) TiI4
(3) CAN, 85%
HO
(1) Co2(CO)8
(2) TiBr4
(3) CAN, 76%
Br
H

Scheme 223

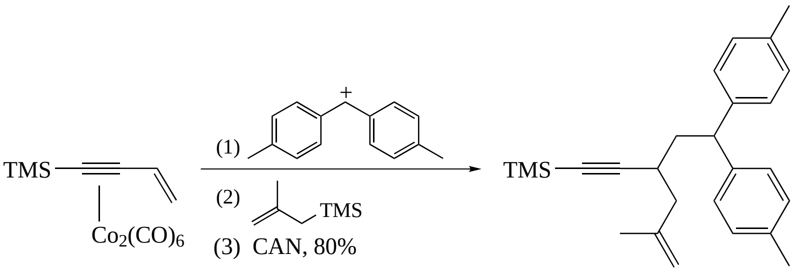
TMS
Co2(CO)6
+
(1)
(2)
TMS
(3) CAN, 80%
TMS

Scheme 224

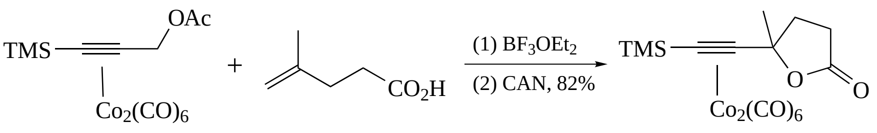
OAc
TMS
Co2(CO)6
+
CO2H
(1) BF3OEt2
(2) CAN, 82%
TMS
O
O
Co2(CO)6

(**153**) (**154**) (**155**)

Scheme 225

new carbocation that can undergo further reaction. For example, reaction of (**153**) with the unsaturated acid (**154**) gave (**155**) after addition of the alkene and intramolecular esterification (Scheme 225). Lewis acid treatment of γ-mesylated complexes having an adjacent alkene and a remote phenyl group has been studied. Depending on the substitution pattern, cyclobutane formation or migration of a remote alkyl group is observed (Scheme 226–227).[94]

Cyclic ethers (5–10 membered) can be prepared by reaction of the formed carbocation with pendant alcohols.[95] The reaction is usually stereospecific at the propargylic carbon (Scheme 228). Intramolecular formation of ethers has been

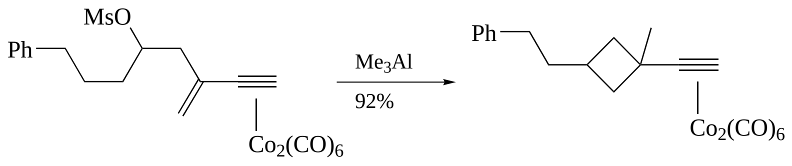
MsO
Ph
Co2(CO)6
Me3Al
92%
Ph
Co2(CO)6

Scheme 226

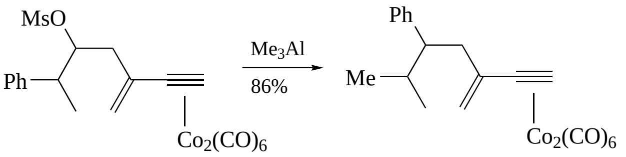
MsO
Ph
Co2(CO)6
Me3Al
86%
Ph
Me
Co2(CO)6

Scheme 227

utilized extensively in the total synthesis of polycyclic ethers such as ciguatoxin and gabiertoxin. For example, the seven-membered ether (**157**) was obtained upon treatment of (**156**) with a Lewis acid (Scheme 229).[96] The organic fragment was liberated using a reductive decomplexation that used tributyltin hydride and 1,2-bis-TMS-ethyne to give a cis double bond (**158**). A synthesis of (+)-secosyrins and (+)-syributins utilized the intramolecular trapping of an intermediately formed carbocation. High diastereoselectivity was observed (Scheme 230).

Propargylic epoxides can be used as precursor for the carbocations. For example, complexation of (**159**) and reaction of the complex with borontrifluoride etherate give, stereoselectively, complex (**160**) (Scheme 231). This sequence was used in a synthesis of (−)-ichthyothereol.[97]

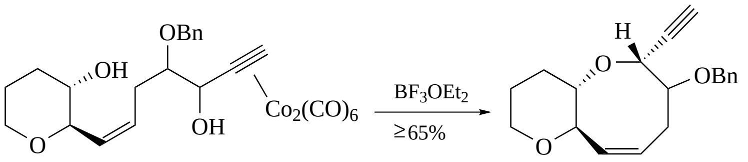
OBn
OH
OH
O
Co2(CO)6
BF3OEt2
≥65%
H
O
OBn
O

Scheme 228

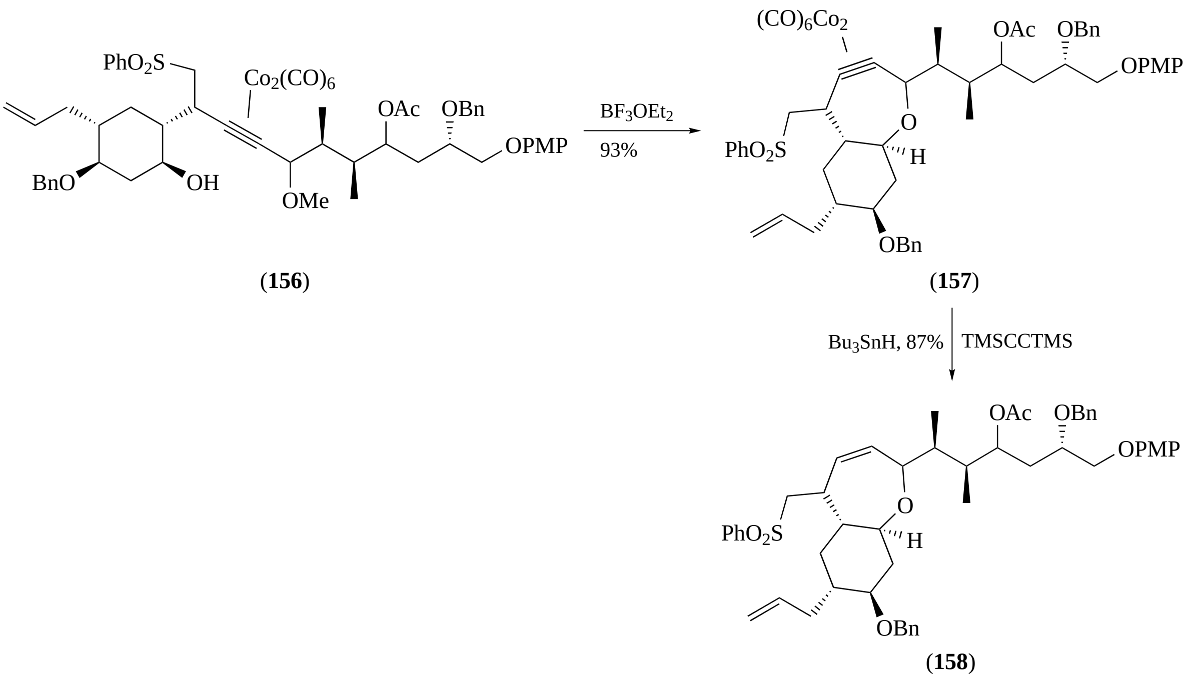
PhO2S
Co2(CO)6
OAc
OBn
OPMP
BnO
OH
OMe
BF3OEt2
93%
(CO)6Co2
OAc
OBn
OPMP
O
PhO2S
H
OBn
Bu3SnH, 87%
TMSCCTMS
OAc
OBn
OPMP
O
PhO2S
H
OBn

(**156**)

(**157**)

(**158**)

Scheme 229

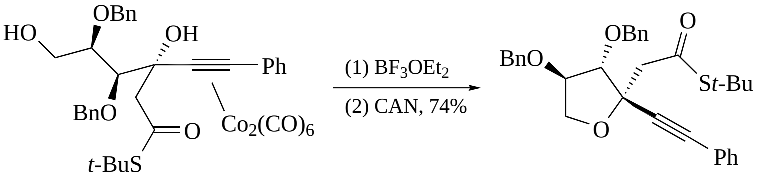
HO
OBn
OH
Ph
BnO
O
Co2(CO)6
t-BuS
(1) BF3OEt2
(2) CAN, 74%
BnO
OBn
O
St-Bu
O
Ph

Scheme 230

A related ring expansion forming a seven-membered ring has been reported (Scheme 232). Ring expansion of a tetrahydrofuran-tethered alkyne complexes to give (**161**), and (**162**) can also be achieved (Scheme 233).[98]

Lewis acid–mediated rearrangement of enol ethers affords 1,2-disubstituted cycloalkanones with high stereoselectivity (Scheme 234).[99] Related reactions of dichloro-substituted enol ethers afford 2,2-dichloro-substituted cycloalkanones (Scheme 235). When titanium tetrachloride was used as the Lewis acid, a carbonyl-ene Prince-type reaction can take place (Scheme 236).

An interesting stereospecific 1,2-shift is observed upon treatment of complex (**163**) with trimethyl aluminium and a nucleophile (Scheme 237). Direct fluorination of chiral-complexed propargylic alcohols using DAST can be achieved in good diastereomeric excess (Scheme 238).

Ethyl aluminum dichloride mediates a formal [5 + 2]cycloaddition of complex (**164**) and (**166**) with enol silyl ethers to produce the highly strained seven-membered rings (**165**) and (**167**) respectively (Schemes 239–240).[100] Excellent stereoselectivity is observed in both cases. A related double alkylation affords complexed seven-membered rings via a formal [4 + 3]cycloaddition. Incorporation of fluorine is observed using boron trifluoride etherate (Scheme 241). ABCDE-ring analog of fredericamycin A was prepared using an intramolecular [4 + 2]cycloaddition of a cobalt-complexed alkyne (Scheme 242).

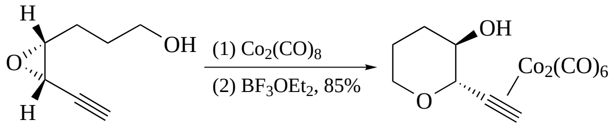
H
O
H
OH
(1) Co2(CO)8
(2) BF3OEt2, 85%
OH
Co2(CO)6
O

(**159**) (**160**)

Scheme 231

A reductive removal of a propargylic hydroxy group using triethyl silane followed by a reductive decomplexation

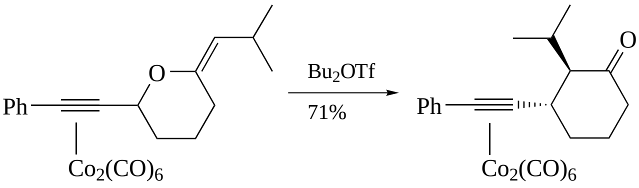
O
Ph
Co2(CO)6
Bu2OTf
71%
O
Ph
Co2(CO)6

Scheme 234

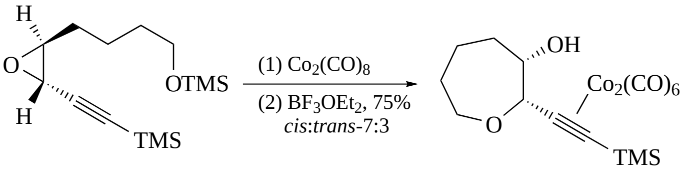
H
O
H
OTMS
TMS
(1) Co2(CO)8
(2) BF3OEt2, 75%
cis:trans-7:3
OH
Co2(CO)6
O
TMS

Scheme 232

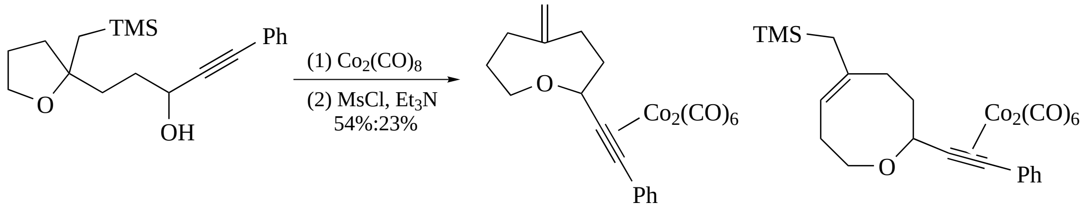
TMS
Ph
O
OH
(1) Co2(CO)8
(2) MsCl, Et3N
54%:23%
O
Co2(CO)6
Ph
TMS
Co2(CO)6
O
Ph

(**161**) (**162**)

Scheme 233

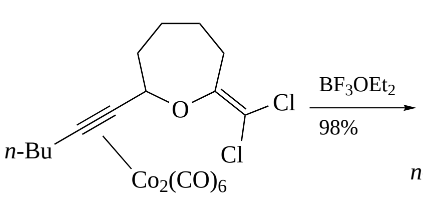
n-Bu
O
Cl
Cl
Co2(CO)6
BF3OEt2
98%
O
Cl
Cl
n-Bu
Co2(CO)6

Scheme 235

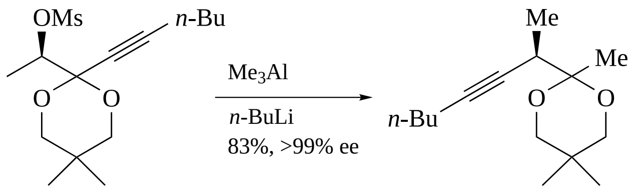
OMs
n-Bu
O
O
Me3Al
n-BuLi
83%, >99% ee
Me
Me
n-Bu
O
O

(**163**)

Scheme 237

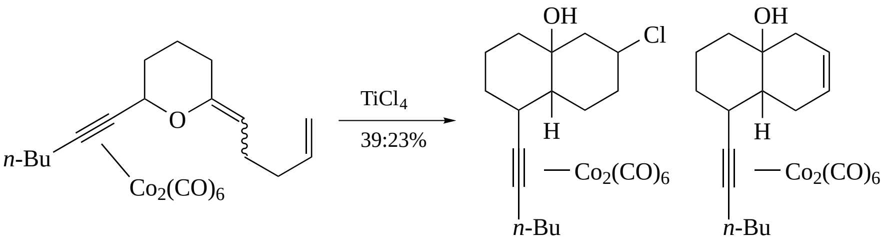
n-Bu
O
Co2(CO)6
TiCl4
39:23%
OH
Cl
H
Co2(CO)6
n-Bu
OH
H
Co2(CO)6
n-Bu

Scheme 236

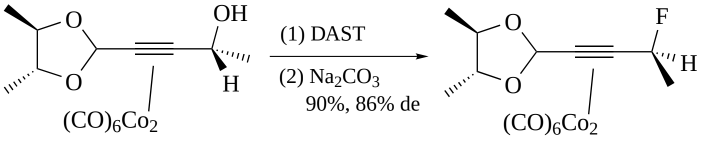
O
O
OH
H
(CO)6Co2
(1) DAST
(2) Na2CO3
90%, 86% de
O
O
F
H
(CO)6Co2

Scheme 238

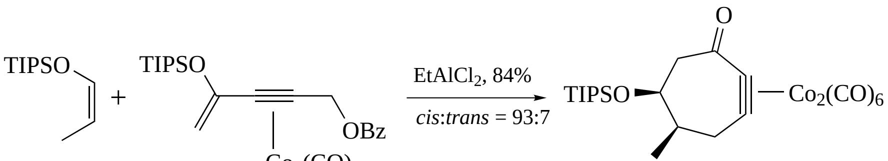
TIPSO
+
TIPSO
OBz
Co2(CO)6
EtAlCl2, 84%
cis:trans = 93:7
O
TIPSO
Co2(CO)6

(**164**) (**165**)

Scheme 239

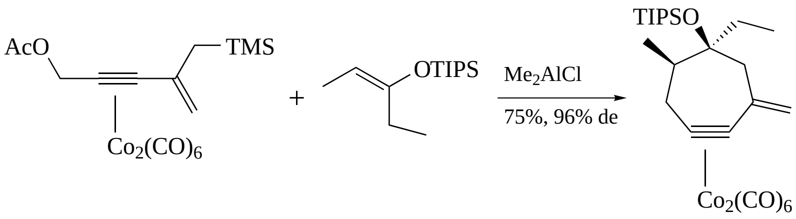
AcO
TMS
Co2(CO)6
+
OTIPS
Me2AlCl
75%, 96% de
TIPSO
Co2(CO)6

(**166**) (**167**)

Scheme 240

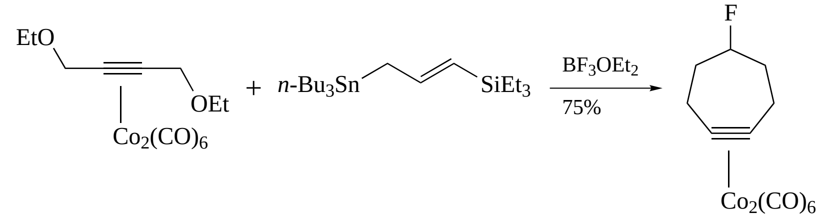
EtO
OEt
Co2(CO)6
+ n-Bu3Sn
SiEt3
BF3OEt2
75%
F
Co2(CO)6

Scheme 241

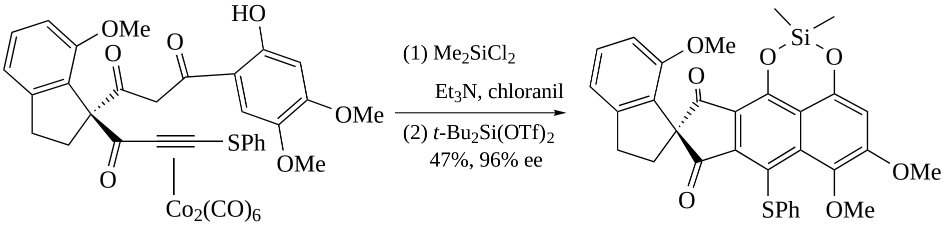
OMe
O
O
HO
OMe
SPh
OMe
O
Co2(CO)6
(1) Me2SiCl2
Et3N, chloranil
(2) t-Bu2Si(OTf)2
47%, 96% ee
OMe
Si
O
O
O
O
OMe
SPh
OMe

Scheme 242

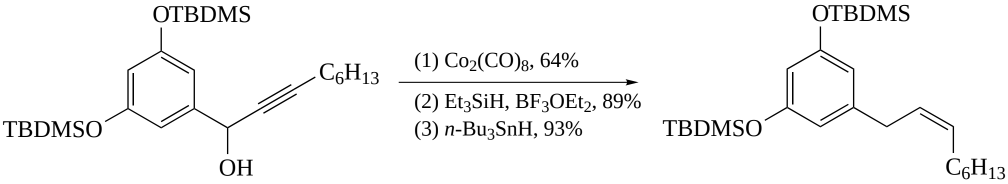
OTBDMS
TBDMSO
OH
C6H13
(1) Co2(CO)8, 64%
(2) Et3SiH, BF3OEt2, 89%
(3) n-Bu3SnH, 93%
OTBDMS
TBDMSO
C6H13

Scheme 243

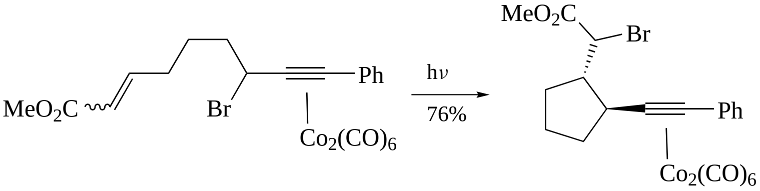
MeO2C
Br
Ph
Co2(CO)6
hν
76%
MeO2C
Br
Ph
Co2(CO)6

Scheme 244

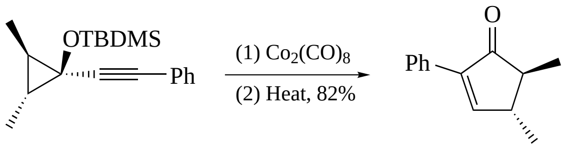
OTBDMS
Ph
(1) Co2(CO)8
(2) Heat, 82%
O
Ph

Scheme 245

was used in a synthesis of climacostol. Exclusive formation of the cis-alkene is observed (Scheme 243).[101] α-Bromo-substituted alkyne complexes undergo stereoselective radical cyclizations (Scheme 244). Finally, a rearrangement of 1-(1-alkynyl)cyclopropanol derivatives to 2-cyclopentenones via the corresponding dicobalt hexacarbonyl complex has been described (Scheme 245).

5.3 The Pauson–Khand Reaction (*See Pauson–Khand Reaction*)

The cocyclization of alkyne dicobalt hexacarbonyl with alkenes is probably one of the most straightforward methods for the formation of cyclopentenones.[102–105] This formal [2 + 2 + 1]cycloaddition reaction was first reported by Khand

and Pauson in 1973 and has since been extensively developed. In general, $Co_2(CO)_8$ reacts with alkynes to generate thermally very stable, readily characterized metal–alkyne complexes (see Section 5.1). The complexes can subsequently be made to react, under thermal conditions, with alkenes and carbon monoxide from the cobalt ligand to form cyclopentenones. Although a number of catalytic Pauson–Khand reactions have been published, only reactions using stoichiometric amounts of cobalt are discussed herein.

The Pauson–Khand reaction is compatible with a wide variety of functionalities, such as ethers, alcohols, tertiary amines, thioethers, ketones, ketals, esters, tertiary amides, carbamates, and benzene, furan, and thiophen rings. Disubstituted alkynes, alkenes with bulky allylic substituents, and trisubstituted alkenes frequently afford reduced yields of products. Because of the reduced ability of sterically hindered alkenes to coordinate and undergo insertion, insertion of one or more molecules of alkyne occurs instead.

Water can be used as the solvent in the presence of added surfactants. Reactions in ionic liquids and supercritical fluids are also feasible. A variety of reagents promote cyclization, which can be achieved at room temperature. Examples of compounds that promote and accelerate the reaction include *N*-methylmorpholine *N*-oxide, trimethylamine *N*-oxide, phosphine oxides, dimethylsulfoxide, alkyl methyl sulfides, molecular sieves, and lithium perchlorate. A comparison of a few promoters is seen in Scheme 246. Promoters attached to a solid support and ultrasounds, microwaves, and UV irradiation can also been used to facilitate the annulation.

Intramolecular Pauson–Khand reactions usually afford 2-substituted 2-cyclopentenones from terminal alkynes. Mixtures of products are often seen from reactions of internal alkynes with little or no stereo- or polarity differentiation between the two sides of the alkyne. Electron-rich and hydrocarbon-substituted alkynes are usually employed but electron-deficient alkenes such as esters, sulfones, and nitriles also participate in the Pauson–Khand reaction.

Cycloaddition of 7-oxanorbornadiene derivatives has been reported (Scheme 247). 5-Bromo-7-azanorbornenes undergo regioselective Pauson–Khand reaction to give (**168**). The bromine is lost during the reaction (Scheme 248). *N*-Protected alkynylamides undergo intramolecular reactions with alkenes to give 2-amidocyclopentenones (Scheme 249).

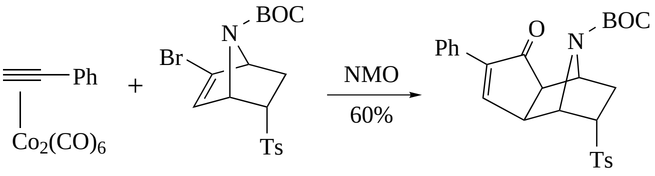

(**168**)

Scheme 248

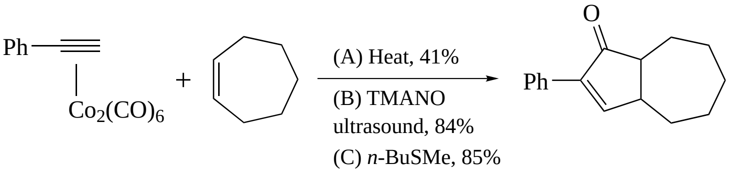

Scheme 246

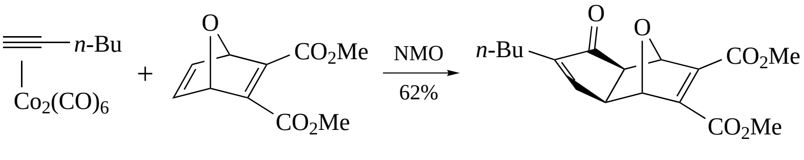

Scheme 247

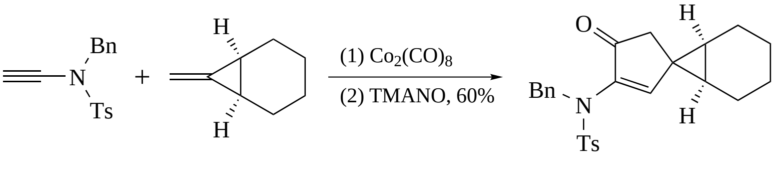

Scheme 249

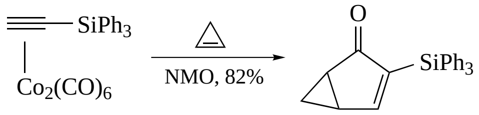

Scheme 250

Cyclopropene can also be used as the alkene component and affords bicyclo[3.1.0]hexen-2-ones upon reaction with alkyne dicobalt octacarbonyl complexes in the presence of NMO (Scheme 250). Vinyl ethers and vinyl esters serve as ethene equivalents in Pauson–Khand reactions. For example, reaction of vinyl benzoate with complex (**169**) furnished cyclopentenone (**170**) (Scheme 251). This reaction was used in a synthesis of (+)-taylorine and nortaylorine.[106] Allenes participate in intermolecular Pauson–Khand reactions affording alkylidene-substituted cyclopentenones (Scheme 252).[107]

Asymmetric intermolecular Pauson–Khand reactions have been realized using a number of chiral auxiliaries chelating to the metal and/or attached to the alkyne. One example using a camphor-derived ligand is seen in Scheme 253. Moderate asymmetric induction has been observed using chiral amine *N*-oxides as the promoter. For example, (+)-indolizino[3,4-b]quinoline *N*-oxide gave up to 53% ee.

A few applications of intramolecular Pauson–Khand reactions in organic synthesis have been reported. For example, total syntheses of asteriscanolide (Scheme 254)[108] and cis-9-retinoic acid and tagretin analogs have been completed (Scheme 255).

Intramolecular Pauson–Khand reactions are synthetically more useful compared to their intermolecular counterparts. Enynes separated by either three or four atoms (1,6- or 1,7-enynes) cyclize in an intramolecular fashion upon complexation with $Co_2(CO)_8$, and subsequent heating to form bicyclic enones. Angular tricyclic ring systems have been prepared in

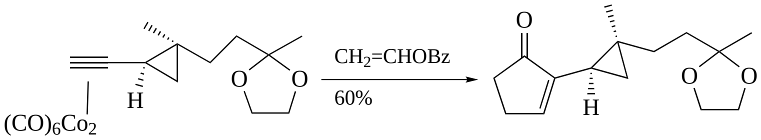

(**169**) (**170**)

Scheme 251

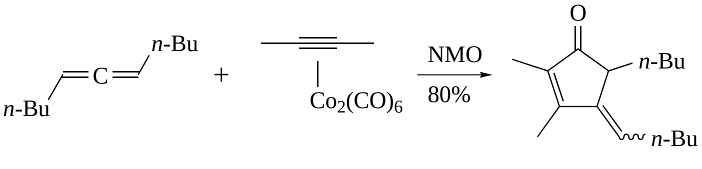

Scheme 252

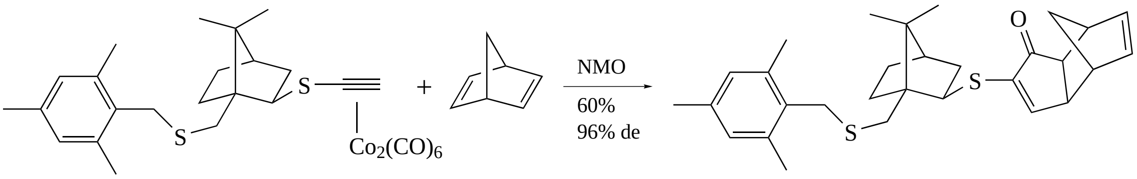

Scheme 253

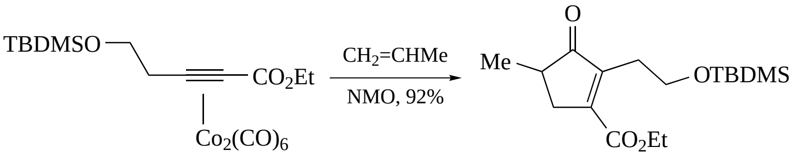

Scheme 254

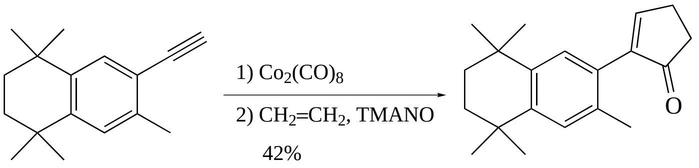
1) $Co_2(CO)_8$
2) CH_2=CH_2, TMANO
42%
O

Scheme 255

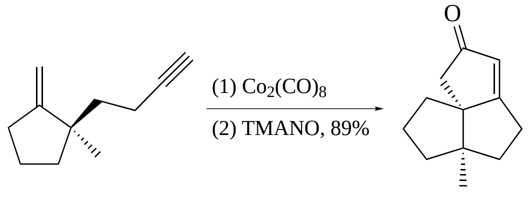
(1) $Co_2(CO)_8$
(2) TMANO, 89%
O

(**171**) (**172**)

Scheme 256

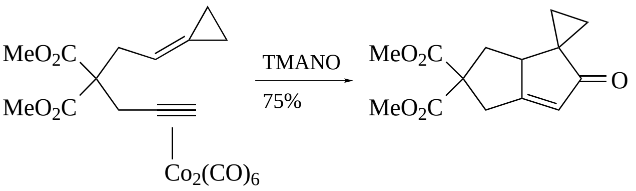
MeO$_2$C
MeO$_2$C
$Co_2(CO)_6$
TMANO
75%
MeO$_2$C
MeO$_2$C
O

Scheme 257

good yields (Scheme 256). For example, a single isomer of the tricyclic compound (**172**) was isolated from complexation and thermolysis of (**171**). Spirocyclopropyl-substituted bicyclic compounds can be obtained from methylenecyclopropane containing enynes (Scheme 257). *N*-Alkynylsulfonamides participate in intramolecular Pauson–Khand reactions (Scheme 258). Microwave-promoted intramolecular reactions have also been developed (Scheme 259).

Intramolecular allene–alkyne cyclizations using cobalt complexes are nonspecific and both double bonds of the allene participate in the reaction affording [4.3.0] and [3.3.0]ring systems (Scheme 260).[109] Both inter- and intramolecular Pauson – Khand-type reactions have been reported using molybdenum hexacarbonyl in place of dicobalt octacarbonyl. For example, only the bicyclo[3.3.0]ring system was observed using molybdenum hexacarbonyl (Scheme 261). In contrast, only the bicyclo[4.3.0]nonadienone was obtained using allenyne (**173**) (Scheme 262).

Cyclopentenones-fused indoles and quinolines can be prepared via intramolecular annulations (Scheme 263).[110]

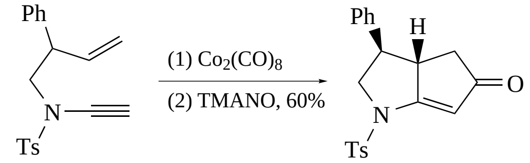
Ph
N
Ts
(1) $Co_2(CO)_8$
(2) TMANO, 60%
Ph
H
N
Ts
O

Scheme 258

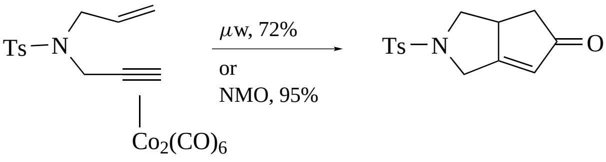
Ts—N
$Co_2(CO)_6$
μw, 72%
or
NMO, 95%
Ts—N
O

Scheme 259

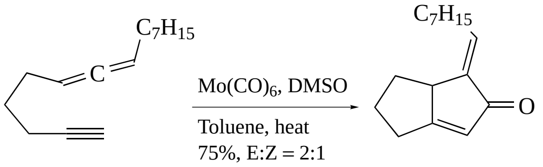
C_7H_{15}
C
Mo(CO)$_6$, DMSO
Toluene, heat
75%, E:Z = 2:1
C_7H_{15}
O

Scheme 261

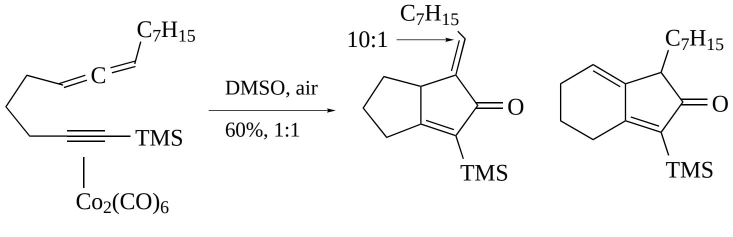
C_7H_{15}
C
TMS
$Co_2(CO)_6$
DMSO, air
60%, 1:1
10:1
C_7H_{15}
O
TMS
C_7H_{15}
O
TMS

Scheme 260

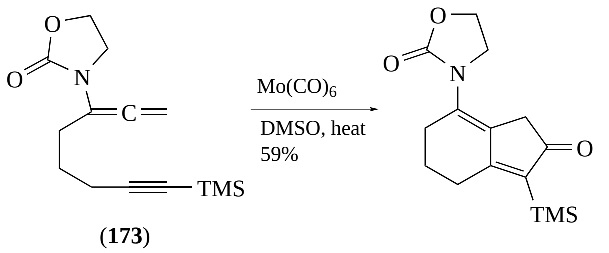

(**173**)

Scheme 262

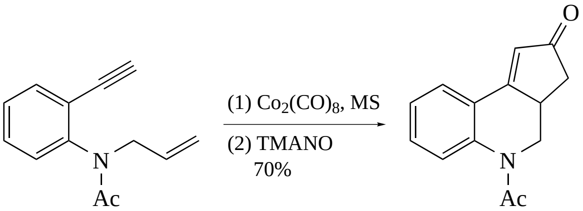

Scheme 263

Seven-membered rings can be fused onto the cyclopentenone using heteroaromatic enyne-starting materials. A high stereoselectivity is observed in some cases (Scheme 264).

Steric effects are probably the main contributor to the high stereoselectivity observed in most intramolecular reactions. No chirality transfer was observed upon thermolysis of the chiral enynamide (**174**) (Scheme 265). In contrast, optically active sulfoxides are excellent chiral auxiliaries in intramolecular reactions (Scheme 266). Amino acid–derived enynes have been used with excellent enantioselectivity (Scheme 267). A lower selectivity is observed using optically active enol ethers in place of the vinyl sulfoxide.

Combination of the propargyl activation chemistry discussed in Section 5.2 has been utilized in conjunction with the Pauson–Khand reaction. Alkylation of enol ether (**175**) with complex (**176**) followed by Pauson–Khand reaction gave the tricyclic diketone (**177**) (Scheme 268).[111]

The intramolecular Pauson–Khand reaction has been extensively used as a key step in total synthesis of fairly complex polycyclic natural products. The [2 + 2 + 1]cycloaddition was, for example, used in recent syntheses of magellanine (Scheme 269),[112] tecomanine, toward palau'amines and styloguanidines (Scheme 270), 8α-hydroxystreptazolone (Scheme 271),[113] ceratopicanol (Scheme 272), 13-deoxyserratine (Scheme 273), ABC-rings of nakadomarin and manzamine (Scheme 274), cedrone (Scheme 275), (−)-dendrobine (Scheme 276),[114] toward kalmanol (Scheme 277), and (+)-epoxydictymene (Scheme 278).

Under some reaction conditions, cycloadditions without insertion of carbon monoxide have been observed. Reaction of complex (**178**) having an electron-deficient alkene under thermal conditions furnished the expected bicyclic enone (**179**) (Scheme 279).[115] However, reaction promoted by TMANO gave cyclopentadiene (**180**). This

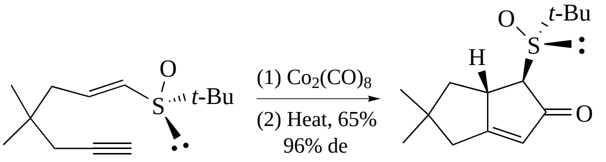

Scheme 266

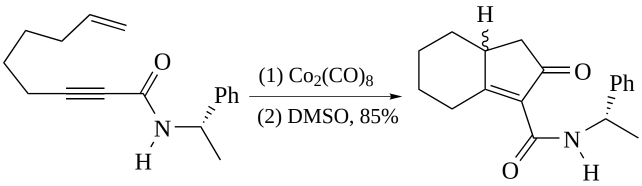

(**174**)

Scheme 265

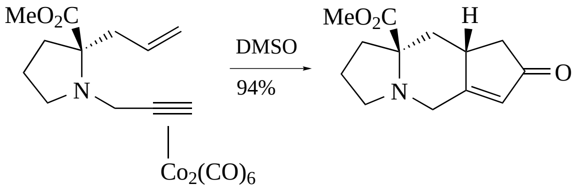

Scheme 267

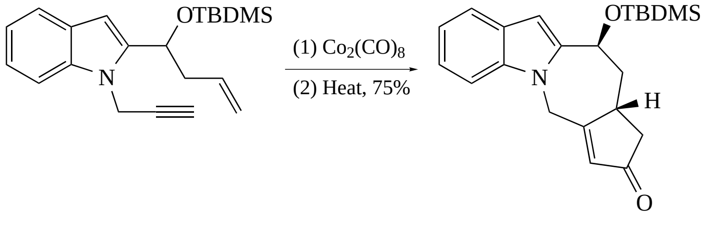

Scheme 264

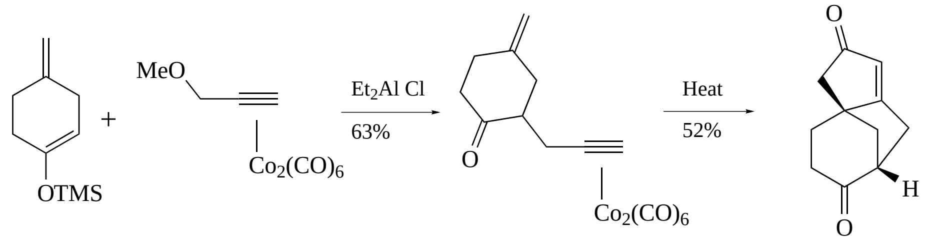

OTMS
+
MeO
Co2(CO)6
Et2Al Cl
63%
O
Co2(CO)6
Heat
52%
O
H
O

(**175**) (**176**) (**177**)

Scheme 268

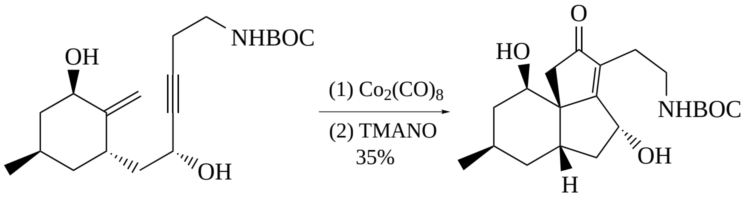

OH
NHBOC
OH
(1) Co2(CO)8
(2) TMANO
35%
O
HO
NHBOC
OH
H

Scheme 269

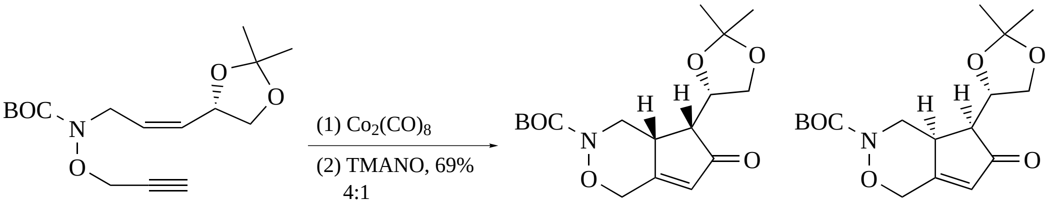

BOC
N
O
O
O
(1) Co2(CO)8
(2) TMANO, 69%
4:1
BOC
N
O
H
H
O
O
O
BOC
N
O
H
H
O
O
O

Scheme 270

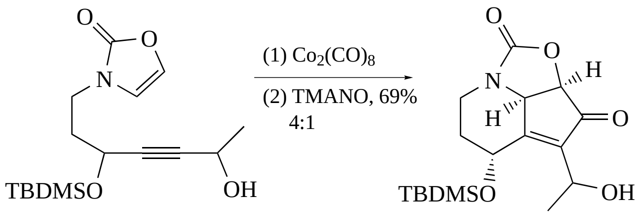

O
O
N
TBDMSO
OH
(1) Co2(CO)8
(2) TMANO, 69%
4:1
O
O
N
H
H
O
TBDMSO
OH

Scheme 271

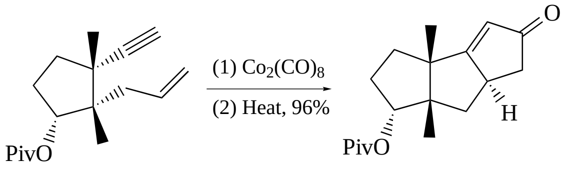

PivO
(1) Co2(CO)8
(2) Heat, 96%
O
PivO
H

Scheme 272

type of ‘abnormal’ reactivity is often observed using electron efficient alkenes. Some examples have been reported and the product formed is highly dependant on the conditions used, as can be seen in Scheme 280. Related reactions of (**181**) under thermal reactions and hydrogen gas gave the bicyclic enone (**182**); while in the presence

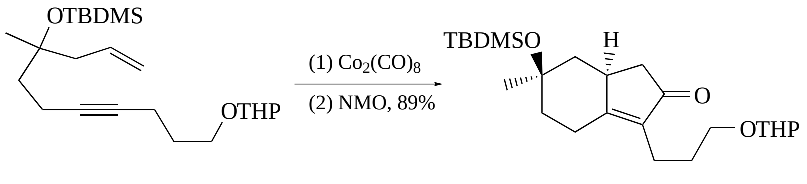

OTBDMS
OTHP
(1) Co2(CO)8
(2) NMO, 89%
TBDMSO
H
O
OTHP

Scheme 273

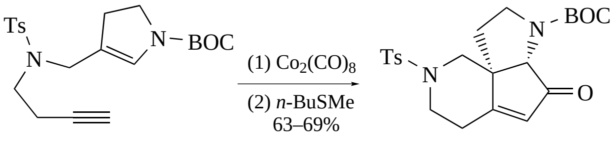
Ts
N
N
BOC
(1) Co2(CO)8
(2) n-BuSMe
63–69%
Ts
N
N
BOC
O

Scheme 274

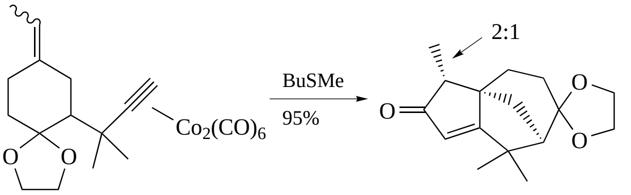
Co2(CO)6
O
O
BuSMe
95%
2:1
O
O
O

Scheme 275

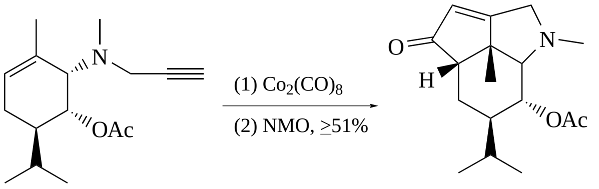
N
OAc
(1) Co2(CO)8
(2) NMO, ≥51%
O
H
N
OAc

Scheme 276

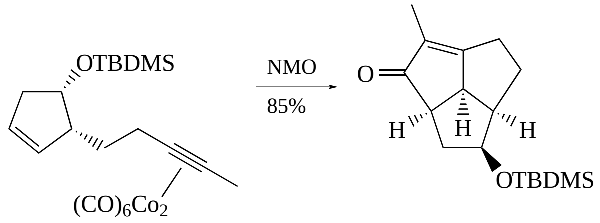
OTBDMS
(CO)6Co2
NMO
85%
O
H
H
H
OTBDMS

Scheme 277

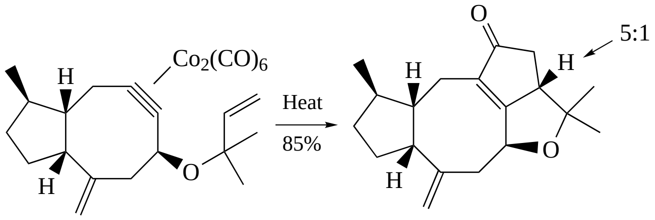
H
H
Co2(CO)6
O
Heat
85%
O
H
H
5:1
H
O

Scheme 278

of triethylsilane, the monocyclic diene (**183**) was obtained (Scheme 281). Performing the same reaction but using $Co_4(CO)_{12}$ in 2-hydroxypropane gave a reduced bicyclic ketone (Scheme 282).

Silyloxy-tethered enones undergo a reductive process in wet nitrile solvent to give cyclopentenones. For example, complexation and thermolysis of (**183**) results both in loss of the silicon and oxygen atoms (Scheme 283).[116] As was the case for intramolecular reactions, alkoxy- and acyloxy-groups are also lost during the intramolecular Pauson–Khand reaction (Scheme 284). Carbon–oxygen bond cleavage was also observed using (**184**) (Scheme 285).[117] Performing the reaction in the presence of ammonium hydroxide gave an interesting hydroxylated product (**185**) (Scheme 285). An aminocarbonylation Pauson–Khand reaction is observed using the cobalt complex of 1-chloro-2-phenylethyne (Scheme 286).[118]

Intermolecular reductive Pauson–Khand reaction in the presence of trifluoroacetic acid is also observed (Scheme 287). Reaction in the presence of silica gel also produced reduced compounds in some cases.

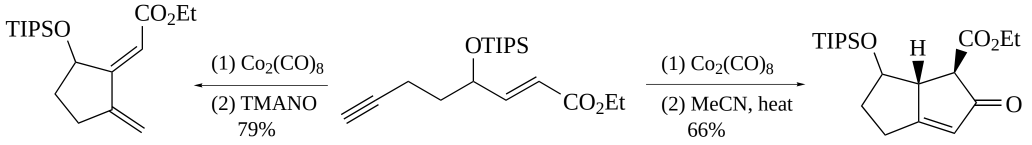
TIPSO
CO2Et
(1) Co2(CO)8
(2) TMANO
79%
OTIPS
CO2Et
(1) Co2(CO)8
(2) MeCN, heat
66%
TIPSO
H
CO2Et
O

(**180**) (**178**) (**179**)

Scheme 279

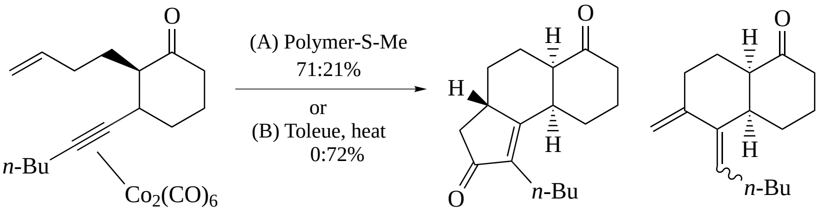
O
n-Bu
Co2(CO)6
(A) Polymer-S-Me
71:21%
or
(B) Toleue, heat
0:72%
H
O
H
H
O
n-Bu
H
O
H
n-Bu

Scheme 280

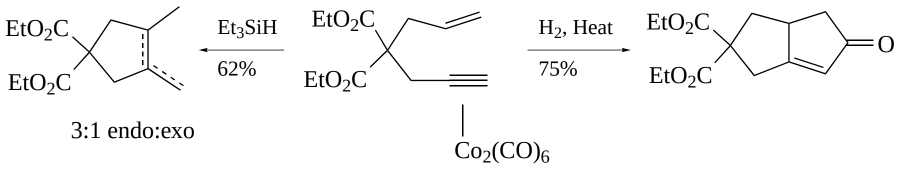
EtO2C
EtO2C
Et3SiH
62%
3:1 endo:exo
EtO2C
EtO2C
Co2(CO)6
H2, Heat
75%
EtO2C
EtO2C
O

(**183**) (**181**) (**182**)

Scheme 281

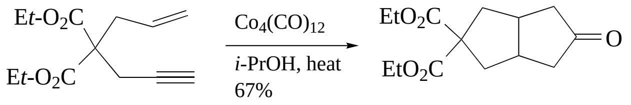
Et-O2C
Et-O2C
Co4(CO)12
i-PrOH, heat
67%
EtO2C
EtO2C
O

Scheme 282

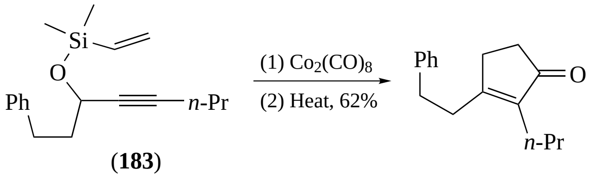
Si
O
Ph
n-Pr
(1) Co2(CO)8
(2) Heat, 62%
Ph
O
n-Pr

(**183**)

Scheme 283

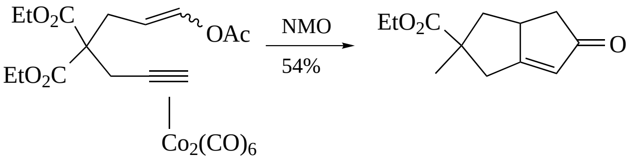
EtO2C
EtO2C
OAc
Co2(CO)6
NMO
54%
EtO2C
O

Scheme 284

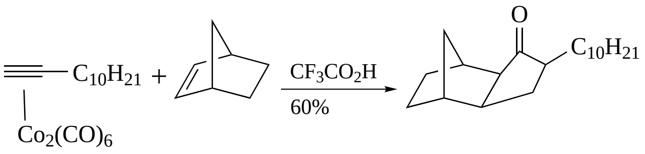
C10H21
Co2(CO)6
+
CF3CO2H
60%
O
C10H21

Scheme 287

6 RELATED ARTICLES

Carbonylation Processes by Homogeneous Catalysis; Hydrocyanation by Homogeneous Catalysis; Mechanisms of Reaction of Organometallic Complexes; Oligomerization & Polymerization by Homogeneous Catalysis; Osmium: Inorganic & Coordination Chemistry.

7 REFERENCES

1. J. Barluenga, *Pure Appl. Chem.*, 2002, **74**, 1317.
2. J. Barluenga, J. Florez, and F. J. Fananas, *J. Organomet. Chem.*, 2001, **624**, 5.

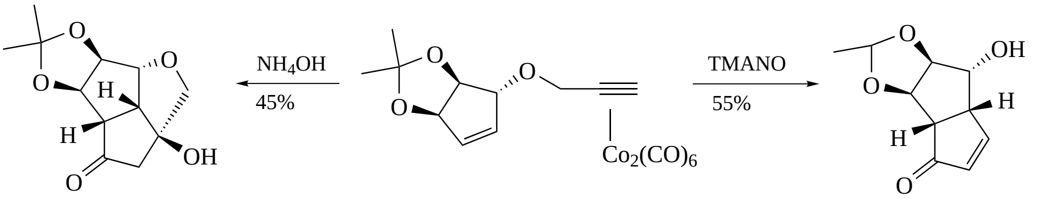
O
O
H
O
H
OH
O
NH4OH
45%
O
O
O
Co2(CO)6
TMANO
55%
O
O
OH
H
H
O

(**185**) (**184**)

Scheme 285

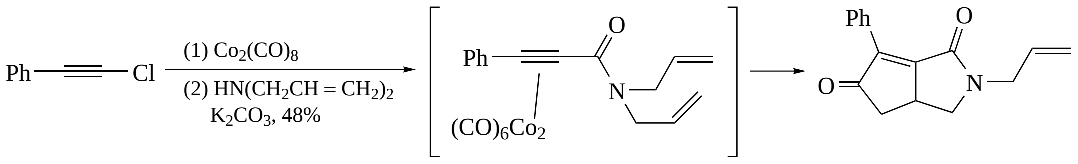
Ph
Cl
(1) Co2(CO)8
(2) HN(CH2CH = CH2)2
K2CO3, 48%
Ph
O
N
(CO)6Co2
Ph
O
O
N

Scheme 286

3. A. De Meijere, H. Schirmer, and M. Duetsch, *Angew. Chem., Int. Ed. Engl.*, 2000, **39**, 3964.
4. A. De Meijere, H. Schirmer, and M. Duetsch, *Angew. Chem., Int. Ed. Engl.*, 2000, **39**, 3964.
5. J. Barluenga and F. J. Fananas, *Tetrahedron*, 2000, **56**, 4597.
6. J. W. Herndon, *Tetrahedron*, 2000, **56**, 1257.
7. K. H. Dötz and P. Tomuschat, *Chem. Soc. Rev.*, 1999, **28**, 187.
8. H. Stadtmueller and P. Knochel, *Organometallics*, 1995, **14**, 3163.
9. I. Merino and L. S. Hegedus, *Organometallics*, 1995, **14**, 2522.
10. H. Matsuyama, T. Nakamura, and M. Iyoda, *J. Org. Chem.*, 2000, **65**, 4796.
11. P. J. Kocienski, R. C. D. Brown, A. Pommier, M. Proctor, and B. Schmidt, *J. Chem. Soc., Perkin Trans. 1*, 1998, 9.
12. F. E. McDonald and M. M. Gleason, *J. Am. Chem. Soc.*, 1996, **188**, 6648.
13. K. Ohe, K. Miki, T. Yokoi, F. Nishino, and S. Uemura, *Organometallics*, 2000, **19**, 5525.
14. E. Licandro, S. Maiorana, D. Perdicchia, C. Baldoli, C. Graiff, and A. Tiripicchio, *J. Organomet. Chem.*, 2001, **617–618**, 399.
15. H. Wang, R. P. Hsung, and W. D. Wulff, *Tetrahedron Lett.*, 1998, **39**, 1849.
16. J. Barluenga, F. Fernandez-Mari, A. L. Viado, E. Aguilar, and B. Olano, *J. Chem. Soc., Perkin Trans. 1*, 1997, 2267.
17. A. Rahm, A. L. Rheingold, W. D. Wulff, and D. William, *Tetrahedron*, 2000, **56**, 4951.
18. M. Hoffmann, M. Buchert, and H.-U. Reissig, *Angew. Chem., Int. Ed. Engl.*, 1997, **36**, 283.
19. R. Polo, J. M. Moreto, U. Schick, and S. Ricart, *Organometallics*, 1998, **17**, 2135.
20. K. H. Dötz, A. W. Koch, B. Weyershausen, H. Hupfer, and M. Nieger, *Tetrahedron*, 2000, **56**, 4925.
21. V. Drahonovsky, D. Borgo, and D. Dvorak, *Tetrahedron Lett.*, 2002, **43**, 7867.
22. J. Sultemeyer, K. H. Dötz, H. Hupfer, and M. Nieger, *J. Organomet. Chem.*, 2000, **606**, 26.
23. B. Brown and L. S. Hegedus, *J. Org. Chem.*, 1998, **63**, 8012.
24. C. A. Merlic, A. Baur, and C. C. Aldrich, *J. Am. Chem. Soc.*, 2000, **122**, 7398.
25. D. Jiang and J. W. Herndon, *Org. Lett.*, 2000, **2**, 1267.
26. J. Barluenga, L. A. Lopez, S. Martinez, and M. Tomas, *Tetrahedron*, 2000, **56**, 4967.
27. M. A. Davis, C. N. Johnson, and J. P. A. Harrity, *J. Org. Chem.*, 2001, **66**, 3525.
28. A. V. Vorogushin, W. D. Wulff, and H.-J. Hansen, *Org. Lett.*, 2001, **3**, 2641.
29. J. Su, W. D. Wulff, and R. G. Ball, *J. Org. Chem.*, 1998, **63**, 8440.
30. C. A. Merlic, C. C. Aldrich, J. Albaneze-Walker, A. Saghatelian, and J. Mammen, *J. Org. Chem.*, 2001, **66**, 1297.
31. J. Barluenga, F. Aznar, and M. A. Palomero, *J. Org. Chem.*, 2003, **68**, 537.
32. J. Barluenga, F. Aznar, I. Gutierrez, S. Garcia-Granda, and M. A. Llorca-Baragano, *Org. Lett.*, 2002, **4**, 4273.
33. H. Rudler, A. Parlier, T. Durand-Reville, B. Martin-Vaca, M. Audoin, E. Garrier, V. Certal, and J. Vaissermann, *Tetrahedron*, 2000, **56**, 5001.
34. J. Barluenga, A. L. Suarez-Sobrino, M. Tomas, and S. Garcia-Granda, *J. Am. Chem. Soc.*, 2001, **123**, 10494.
35. J. Barluenga, S. Lopez, A. A. Trabanco, A. Fernandez-Acebas, and J. Florez, *J. Am. Chem. Soc.*, 2000, **122**, 8145.
36. M. Parisi, A. Solo, W. D. Wulff, I. A. Guzei, and A. L. Rheingold, *Organometallics*, 1998, **17**, 3696.
37. J. L. Bowman and F. E. McDonald, *J. Org. Chem.*, 1998, **63**, 3680.
38. J. M. Concellon, P. L. Berard Jr, *Tetrahedron Lett.*, 1998, **39**, 7967.
39. Y. Zhang and J. W. Herndon, *Tetrahedron*, 2002, **56**, 2175.
40. J. J. Caldwell, J. P. A. Harrity, N. M. Heron, W. J. Kerr, S. McKendry, and D. Middlemiss, *Tetrahedron Lett.*, 1999, **40**, 3481.
41. H. Rudler, A. Parlier, V. Certal, and J. Vaissermann, *Angew. Chem., Int. Ed. Engl.*, 2000, **39**, 3417.
42. J. Barluenga, F. Aznar, and M. A. Palomero, *Angew. Chem., Int. Ed. Engl.*, 2000, **39**, 4346.
43. J. W. Herndon, J. Yan, J. Zhu, and J. J. Matasi, *J. Org. Chem.*, 1999, **64**, 1291.
44. K.-W. Liang, M. Chandrasekharam, C.-L. Li, and R.-S. Liu, *J. Org. Chem.*, 1998, **63**, 7289.
45. M. J. Chen, C. Y. Lo, C. C. Chin, and R. S. Liu, *J. Org. Chem.*, 2000, **65**, 6362.
46. S. Ishii, S. Zhao, G. Mehta, C. J. Knors, and P. Helquist, *J. Org. Chem*, 2001, **66**, 3449.
47. A. Berger, J.-P. Djukic, and C. Michon, *Coord. Chem. Rev.*, 2002, **225**, 215.
48. S. E. Gibson and E. G. Reddington, *Chem. Commun.*, 2000, 989.
49. F. Dehmel and H.-G. Schmalz, *Org. Lett.*, 2001, **3**, 3579.
50. W. H. Moser, J. Zhang, C. S. Lecher, T. L. Frazier, and M. Pink, *Org. Lett.*, 2002, **4**, 1981.
51. P. Del Buttero, C. Baldoli, G. Molteni, and T. Pilati, *Tetrahedron: Asymmetry*, 2000, **11**, 1927.
52. H. Ratni and E. P. Kündig, *Org. Lett.*, 1999, **1**, 1997.
53. B. C. Maity, V. M. Swamy, and A. Sarkar, *Tetrahedron Lett.*, 2001, **42**, 4373.
54. C. A. Merlic and M. M. Miller, *Organometallics*, 2001, **20**, 373.
55. F. Dehmel, J. Lex, and H.-G. Schmalz, *Org. Lett.*, 2002, **4**, 3915.

56. V. M. Swamy, M. M. Bhadbhade, V. G. Puranik, and A. Sarkar, *Tetrahedron Lett.*, 2000, **41**, 6137.
57. S. E. Gibson, H. Ibrahim, C. Pasquier, and J. W. Steed, *Tetrahedron*, 2002, **58**, 4617.
58. M. K. McKay and J. R. Green, *Can. J. Chem.*, 2000, **78**, 1629.
59. R. Wilhelm, I. K. Sebhat, A. J. P. White, D. J. Williams, and D. A. Widdowson, *Tetrahedron: Asymmetry*, 2000, **11**, 5003.
60. S. E. Gibson, H. Ibrahim, C. Pasquier, and J. W. Steed, *Tetrahedron*, 2002, **58**, 4617.
61. H.-G. Schmalz, O. Kiehl, and B. Gotov, *Synlett*, 2002, 1253.
62. O. Schwarz, R. Brun, J. W. Bats, and H.-G. Schmalz, *Tetrahedron Lett.*, 2002, **43**, 1009.
63. C. A. Merlic and J. C. Walsh, *J. Org. Chem.*, 2001, **66**, 2265.
64. P. E. Kündig, H. Ratni, B. Crousse, and G. Bernardinelli, *J. Org. Chem.*, 2001, **66**, 1852.
65. J. H. Rigby, N. C. Warshakoon, and A. J. Payen, *J. Am. Chem. Soc.*, 1999, **121**, 8237.
66. G. Bernardinelli, S. Gillet, E. P. Kündig, R. Liu, A. Ripa, and L. Saudan, *Synthesis*, 2001, 2040.
67. H. Seo, S.-G. Lee, D. M. Dong, B. K. Hong, S. Hwang, D. S. Chung, and Y. K. Chung, *Organometallics*, 2002, **21**, 3417.
68. H. Rudler, V. Comte, E. Garrier, M. Bellassoued, E. Chelain, and J. Vaissermann, *J. Organomet. Chem.*, 2001, **621**, 284.
69. J. Dudones and A. J. Pearson, *Tetrahedron Lett.*, 2000, **41**, 8037.
70. H.-J. Knölker, *Chem. Soc. Rev.*, 1999, **28**, 151.
71. L. R. Cox and S. V. Ley, *Chem. Soc. Rev.*, 1998, **27**, 301.
72. H. Bärmann, V. Prahlad, C. Tao, Y. K. Yun, Z. Wang, and W. A. Donaldson, *Tetrahedron*, 2000, **56**, 2283.
73. S. Nakanishi, K. Kumeta, Y. Sawai, and T. Takata, *J. Organomet. Chem.*, 1996, **515**, 99.
74. J. Limanto, J. Tallarico, J. R. Porter, K. S. Kelli, K. N. Houk, and M. L. Snapper, *J. Am. Chem. Soc.*, 2002, **124**, 14748.
75. M. Franck-Neumann, P. Geoffroy, and D. Gassmann, *Synlett*, 2002, 2054.
76. Y. Takemoto, K. Ishii, T. Ibuka, Y. Miwa, T. Taga, S. Nakao, T. Tetsuaki, Y. Kai, and N. Kanehisa, *J. Org. Chem.*, 2001, **66**, 6116.
77. Y. K. Yun, K. Godula, Y. Yeyu, and W. A. Donaldson, *J. Org. Chem.*, 2003, **68**, 901.
78. Y. Takemoto, Y. Baba, S. Yasutaka, N. Goutum, I. Syusuke, T. Tanaka, and T. Ibuka, *Tetrahedron Lett.*, 2000, **41**, 3653.
79. A. J. Pearson, A. R. Alimardanov, and W. D. Kerber, *J. Organomet. Chem.*, 2001, **630**, 23.
80. A. J. Pearson and V. P. Ghidu, *Org. Lett.*, 2002, **4**, 4069.
81. M. Fontes, X. verdauer, L. Sola, and A. Vidal-Ferran, *Org. Lett.*, 2002, **4**, 2381.
82. Z.-Q. Yang and S. J. Danishefsky, *J. Am. Chem. Soc.*, 2003, **125**, 9602.
83. N. Iwasawa, F. Sakurada, and M. Iwamoto, *Org. Lett.*, 2000, **2**, 871.
84. B. J. Teobald, *Tetrahedron*, 2002, **58**, 4133.
85. J. R. Green, *Curr. Org. Chem.*, 2001, **5**, 809.
86. T. J. J. Muller, *Eur. J. Org. Chem.*, 2001, **11**, 2021.
87. M. E. Welker, *Curr. Org. Chem.*, 2001, **5**, 785.
88. R. Chow, P. J. Kocienski, A. Kuhl, J.-Y. LeBrazidec, K. Muir, and P. Fish, *J. Chem. Soc., Perkin Trans. 1*, 2001, 2344.
89. A. Cosp, P. Romea, P. Talavera, F. Urpi, J. Vilarrasa, M. Font-Bardia, and X. Solans, *Org. Lett.*, 2001, **3**, 615.
90. P. A. Jacobi and P. Herradura, *Can. J. Chem.*, 2001, **79**, 1727.
91. T. Shibata, T. Ohta, and K. Soai, *Tetrahedron Lett.*, 1998, **39**, 5785.
92. D. Diaz and V. S. Martin, *Org. Lett.*, 2000, **2**, 335.
93. K. Tanino, K. Onuki, K. Asano, M. Miyashita, N. Masaaki, T. Nakamura, Y. Takahashi, and I. Kuwajima, *J. Am. Chem. Soc.*, 2003, **125**, 1498.
94. M. Kitamura, K. Ohmori, and K. Suzuki, *Tetrahedron Lett.*, 1999, **40**, 4563.
95. J. M. Betancourt, T. Martin, J. M. Palazon, and V. S. Martin, *J. Org. Chem.*, 2003, **68**, 3216.
96. T. Baba and M. Isobe, *Synlett*, 2003, 547.
97. C. Mukai, N. Miyakoshi, and M. Hanaoka, *J. Org. Chem.*, 2001, **66**, 5875.
98. C. Mukai, H. Yamashita, T. Ichiryu, and M. Hanaoka, *Tetrahedron*, 2000, **56**, 2203.
99. D. A. Carbery, S. Reignier, N. D. Miller, H. Adams, and J. P. A. Harrity, *J. Org. Chem.*, 2003, **68**, 4392.
100. K. Tanino, F. Kondo, S. Fumikatsu, and M. Tadashi, *Org. Lett.*, 2002, **4**, 2217.
101. H. Wack, W. J. Drury III, A. E. Taggi, D. Ferraris, T. Lecthka, *Org. Lett.*, 1999, **1**, 1985.
102. M. R. Rivero, J. Adrio, and J. C. Carretero, *Eur. J. Org. Chem.*, 2002, 2881.
103. R. Fryatt and S. D. R. Christie, *J. Chem. Soc., Perkin Trans. 1*, 2002, 447.
104. K. M. Brummond and J. L. Kent, *Tetrahedron*, 2000, **56**, 3263.
105. K. C. Young, *Coord. Chem. Rev.*, 1999, **188**, 297.
106. W. J. Kerr, M. McLaughlin, P. L. Pauson, and S. M. Robertson, *J. Organomet. Chem.*, 2001, **630**, 104.
107. H. C. Hailes, B. Isaac, and M. H. Javaid, *Synth. Commun.*, 2003, **33**, 29.
108. M. E. Krafft, Y. Y. Cheung, and K. A. Abboud, *J. Org. Chem.*, 2001, **66**, 7443.
109. K. M. Brummond, A. D. Kerekes, and H. Wang, *J. Org. Chem.*, 2002, **67**, 5156.
110. G. Dominguez, L. Casarrubios, J. Rodriguez-Noriega, and J. Perez-Castells, *Helv. Chim. Acta*, 2002, **85**, 2856.

111. M. R. Rivero, J. Adrio, and J. C. Carretero, *Eur. J. Org. Chem.*, 2002, 2881.

112. M. Ishizaki, Y. Niimi, and O. Hoshino, *Tetrahedron Lett.*, 2003, **44**, 6029.

113. I. Nomura and C. Mukai, *Org. Lett.*, 2002, **4**, 4301.

114. J. Cassayre and S. Z. Zard, *J. Organomet. Chem.*, 2001, **624**, 316.

115. M. Rodriguez Rivero and J. C. Carretero, *J. Org. Chem.*, 2003, **68**, 2975.

116. J. F. Reichwein, S. T. Iacono, and B. L. Pagenkopf, *Tetrahedron*, 2002, **58**, 3813.

117. R. Muto and K. Ogasawara, *Tetrahedron Lett.*, 2001, **42**, 4143.

118. J. Balsells, A. Moyano, A. Riera, and M. A. Pericas, *Org. Lett.*, 1999, **1**, 1981.

Organic Synthesis using Transition Metal Complexes Containing π-Bonded Ligands

W. H. Morris III, Lisa M. Sullivan, Matthew S. Wellons & C. M. Lukehart
Vanderbilt University, Nashville, TN, USA

Based in part on the article Organic Synthesis using Transition Metal Complexes Containing π-Bonded Ligands by Martin F. Semmelhack which appeared in the Encyclopedia of Inorganic Chemistry, First Edition.

1 Scope of this Article 1
2 Introduction 1
3 Alkene Insertion/Elimination: The Heck Reaction 2
4 Nucleophilic Addition to Metal-Activated Alkenes 9
5 Nucleophilic Addition to Allyl Ligands: Allylic Alkylation 14
6 Nucleophilic Addition to 1,3-Diene Ligands 22
7 Nucleophile Addition to η^5-Cyclohexadienyl Ligands 26
8 Nucleophilic Addition to Arene–Metal Complexes 30
9 Coupling of Allyl–Ni^{II} Complexes with Organic Halides 46
10 Related Articles 50
11 References 50

Glossary

π-Bonded: coordination to a metal via π-orbitals, as with ethylene
Chemoselectivity: selectivity in reaction of one functional group in the presence of one or more other similar groups
Conjugating substituents: functional groups interacting through π-bonds with a reactive center
Electrophile: electron-deficient species that reacts by accepting a pair of electrons to form a covalent bond
Enolate anion: a carbanion obtained by deprotonation of the position adjacent to a carbonyl group
Heteroaromatics: aromatic rings with a heteroatom in the π-system
Macrolides: natural organic compounds with large lactone rings
Nucleophile: electron-rich species that reacts by donating a pair of electrons to form a covalent bond
Regioselectivity: selectivity in reaction of one site of a functional group with two or more reactive sites
Spectator ligand: ligand not involved in a relevant process around the metal center
Stereoselectivity: selectivity in generation of a stereocenter
Transmetalation: transfer of an organic unit from one metal to another
Triflate: an ester of trifluoromethanesulfonic acid, a good leaving group

1 SCOPE OF THIS ARTICLE

The focus of this article is on organic synthesis methodologies that involve transition metal complexes containing π-bonded ligands. For this discussion, π-bonded ligands are limited to those with only carbon atoms involved in the coordinating unit, such as alkenes and not, for example, imines. In addition, because some useful methods involve metal complexes with both π-bonded ligands and CO ligands, some arbitrary decisions were necessary in distributing the topics between this article and ***Organic Synthesis using Transition Metal Carbonyl Complexes***. For example, the major topics of alkyne trimerization to form arenes (Vollhardt reaction),[1] the coupling of an alkyne with CO and an alkene unit to give cyclopentenones (Pauson–Khand reaction),[2] and the coupling of alkynes and CO with vinylcarbene ligands (Doetz reaction)[3] are excluded from this discussion. Excellent coverage of related topics has appeared in compendia.[4,5] Space limitations prevent the presentation of synthesis methods that are of limited scope or not yet well developed.

2 INTRODUCTION

π-Bonded ligands can be closed shell, $2n$ electron donors ($n = 1 - 3$) such as alkenes, allenes, alkynes, arenes, and polyenes; these have been termed 'even' polyene ligands.[6] They may also be open shell, 'odd' polyene ligands such as allyl, pentadienyl, cyclopropenyl, and cyclopentadienyl, which are formally viewed as anionic ligands, donating $2n$ electrons ($n = 1 - 3$).

2.1 Nonpolar Coupling Reactions

Even π-bonded ligands can undergo coupling reactions within the ligand sphere of the metal following the mechanistic types shown for an alkene in Scheme 1. These mechanisms are appropriately viewed as nonpolar, relatively independent of polar functional groups on the ligands, and not sensitive to polar driving forces. An analogy in traditional organic chemistry is the set of concerted electrocyclic mechanisms, the Diels–Alder reaction being a prototype.

Each of these mechanisms is the basis of a major envelope of synthetic methods. The first has appeared as the *Heck*

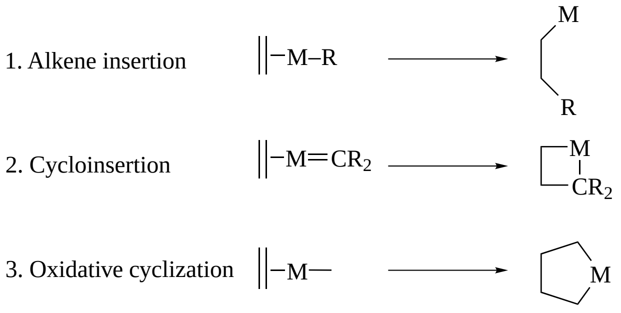

Scheme 1 Nonpolar coupling mechanisms

Reaction,[7] and will be reviewed below. The second mechanism is the first stage of the Doetz reaction,[3] while the third (operating with alkynes) is the first stage of the Vollhardt reaction[1] and of the *Pauson–Khand Reaction*.[2]

2.2 Polar Coupling Reactions

The metal and spectator ligands can influence the reactivity of a π-bonded ligand by changing the polarization or polarizibility. An increase in polarizibility is obvious for the alkene in an η^2-alkene metal complex, making it easier both to add electron density (e.g. in nucleophilic addition) and remove electron density (electrophilic addition). Depending on the oxidation state of the metal and the donor/acceptor characteristics of the spectator ligands, the coordinated alkene might be polarized and be viewed as distinctly electrophilic or nucleophilic. Key features of the activation process are: (a) the driving forces are based on polar factors and (b) the reactant (nucleophile or electrophile) need not interact with the metal, but can couple with the π-ligand directly. The metal–ligand system is a functional group, influencing the rate and selectivity of a polar addition to a π-system.

A complete survey of polar coupling reactions might include all types of organic ligands, π- and σ-bonded, and both nucleophilic and electrophilic additions. However, the only generally useful synthesis methodology based on polar activation by transition metals is nucleophile addition to coordinated alkenes and polyenes, both even and odd systems. Two prototypes are presented in Scheme 2: nucleophile addition to an alkene (even π-ligand) and nucleophile addition to an η^3-allyl ligand (odd). The first has a close analogy in the Michael reaction of traditional organic synthesis, while the second can be viewed as a special case of S_N2 reaction of allyl–X species. In both cases, the transition metal activation leads to new opportunities in control of reaction rate and selectivity, including stereo-, regio-, and chemoselectivity.

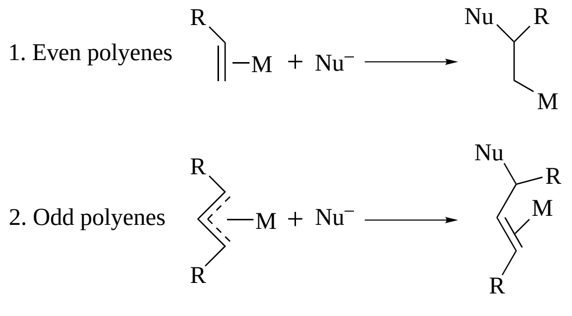

Scheme 2 Polar coupling mechanisms

3 ALKENE INSERTION/ELIMINATION: THE HECK REACTION

3.1 Basic Reaction

The basis for the Heck Reaction is the process shown in equation (1),[8] the coordination of an alkene to a σ-organopalladium(II) species, followed by alkene *Insertion* and then *β-Elimination*. The products are the 1,2-disubstituted alkene, HX, and Pd^0. The power of the process for organic synthesis is due to the existence of several general techniques for preparing the required R–Pd–X reactant and that the β-elimination of hydrogen can be fast. Overall substitution of a vinyl hydrogen by a carbon unit has no general analogy in traditional synthesis methodology.

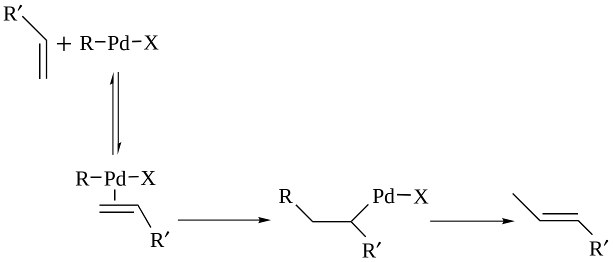

(1)

For a catalytic process, the product Pd^0 must be used to regenerate the R–Pd–X reactant. Two techniques are known (Scheme 3). In the first, Pd^0 can undergo *Oxidative Addition* with R–X to give R–Pd–X directly. This requires R–X be a good substrate for oxidative addition, and many electronegative functional groups serve as effective X units. Alternatively, the Pd^0 can be reoxidized to Pd^{II}, and then direct transfer of an organic unit to the Pd^{II} can be arranged.[7] The transfer might be electrophilic aromatic substitution (aromatic palladation), giving Ar–Pd–X + HX, or *Transmetalation* from an organo-main group derivative such as R–Hg–X. Important limitations include: (a) the group R must be stabilized toward β-hydride elimination in R–Pd–X, generally meaning no β-H on an sp^3-carbon and (b) the efficiency decreases rapidly with addition of substituents to the alkene; the process is generally efficient only for monosubstituted alkenes.

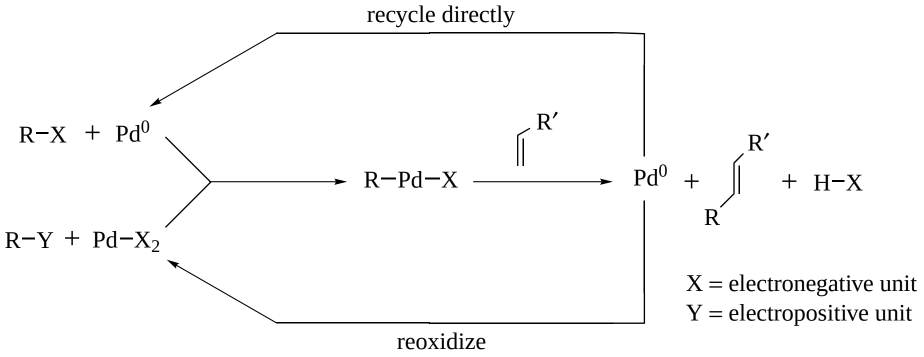

Scheme 3 Two pathways for the Heck reaction

3.2 The Alkene and Selectivity Issues

Ethylene is the most reactive alkene, and the rates of reaction can decrease with the size and number of alkene substituents.**[8]** However, the rate-limiting step can be the initial oxidative addition of R–X with Pd^0, making alkene structure less important in the overall rate. Successful substitution is general for monosubstituted alkenes and common even with 1,2-disubstituted alkenes. Trisubstituted alkenes are largely useless in the Heck reaction; the intermediate R–Pd–X species undergo side reactions such as homocoupling instead of vinyl substitution.

The geometry of the product 1,2-disubstituted alkene is determined to be (E) (trans) by the mechanism of β-hydrogen elimination, if two β-hydrogens are available (Scheme 4). If only one β-H is available (from 1,2-disubstituted alkene substrates), then the geometry of the product is determined by kinetic control following the syn conformation for alkene insertion and syn conformation for β-H elimination.

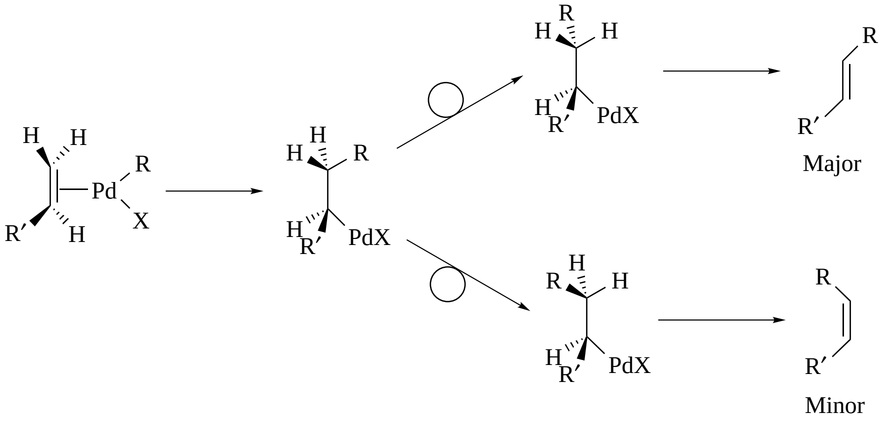

Scheme 4 Conformational alternatives in the β-elimination

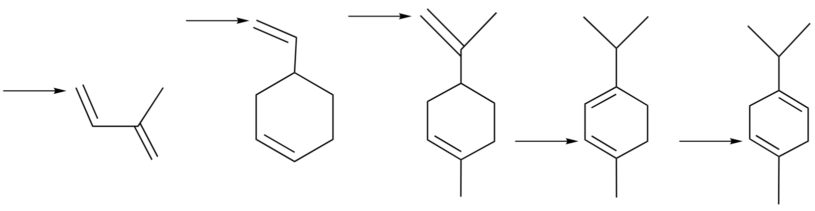

Figure 1 Regioselectivity in Heck vinylation reactions; arrows show the site of C–C bond formation

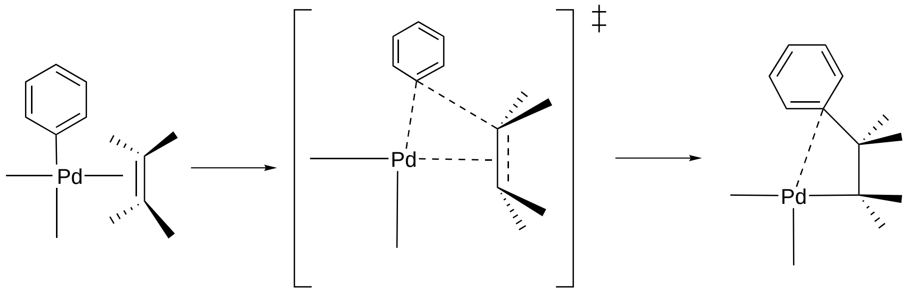

Figure 2 Transition state for alkene insertion

The regioselectivity of the vinyl substitution with monosubstituted alkenes shows a strong trend toward addition of the new carbon substituent at the less-substituted end, primarily attributed to a substituent steric effect, as shown in Figure 1.[3,8,9] With a simple alkyl group (propylene, 1-hexene, 3-hydroxy-1-butene), the selectivity is relatively low. Electron donors, conjugating substituents, and electron-withdrawing groups (EWG) produce the same trend, in some cases with perfect selectivity as in the case of styrene. The selectivity with enol ethers and enamines is more complex, and can favor coupling of the organic unit at the carbon-bearing oxygen. Unsymmetrical 1,2-disubstituted alkenes can give useful selectivity with substitution at a methyl-bearing carbon being strongly preferred over substitution at alkene carbon atoms bearing carboalkoxy or phenyl substituents. *Cis*-β-methylstyrene gives significantly higher selectivity compared to the trans isomer.

While there is obviously some electronic effect influencing regioselectivity, the dominant effect is steric. A simple rationale for the regioselectivity takes into account a syn transition state (Figure 2) for the alkene insertion, with a shorter distance for C–H compared to C–Pd, as the bonds develop. The shorter distance could be due to a differential degree of bond making or the intrinsically longer C–Pd bond distance. Additional examples of regioselectivity will be taken up in the appropriate section below.

3.3 Vinyl Substitution with R–H: Direct Palladation

The primary method of direct palladation begins with Pd^{II} and proceeds by either electrophilic aromatic substitution or oxidative addition of an arene C–H bond (equation 2).[10] In both cases, loss of H–X leads to an aryl–Pd–X derivative. Simple arenes can undergo palladation, but lead to isomers in the absence of a strongly directing substituent. The process is usually done in a stepwise manner, with isolation of the aryl–Pd–X intermediate. It is not easily made catalytic; various reoxidation recipes are used for conversion of Pd^0 to Pd^{II} in other applications,[7] but none has been found satisfactory here.

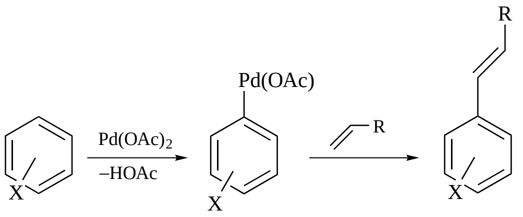

(2)

Heteroaromatics have high reactivity toward electrophilic palladation and show good regioselectivity. Reactions with pyrrole,[11] thiophene,[11] furan,[11] and indole[12] have been reported (equation 3). The use of stoichiometric copper(II) ion gives a process catalytic in Pd.

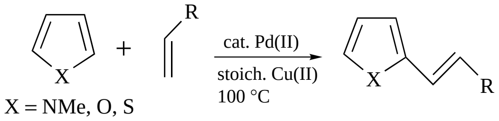

(3)

3.4 Vinyl Substitution via Transfer from a Main Group Metal

One of the earliest examples of Pd-promoted vinyl substitution involved transfer of an aryl group from Hg^{II} to Pd^{II}, followed by insertion/elimination (equation 4).[13–15] The general process requires reoxidation of the Pd for catalysis, and this is generally possible by using excess of Cu^{II}. While the method is applicable to alkyl–Hg–X reactants, it is limited to those alkyl groups that cannot undergo β-hydride elimination after transfer to Pd, such as Me and alkoxycarbonyl.

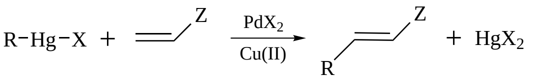

(4)

For organic synthesis applications, C–C bond formation between the R group and an alkene carbon atom is of paramount importance and Pd-catalyzed R–R coupling is to be avoided. Equation (5) displays a palladium-catalyzed Mizorki-Heck-type (MH) reaction using tellurium salts.[16]

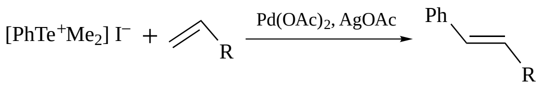
[PhTe+Me2] I−
+
R
Pd(OAc)2, AgOAc
Ph
R

(5)

One general approach takes advantage of the *Hydroboration* of alkynes to give vinylboron compounds.[17] As shown in equation (6), Heck vinylation occurs using a variety of aryl-boron reagents.[18–20]

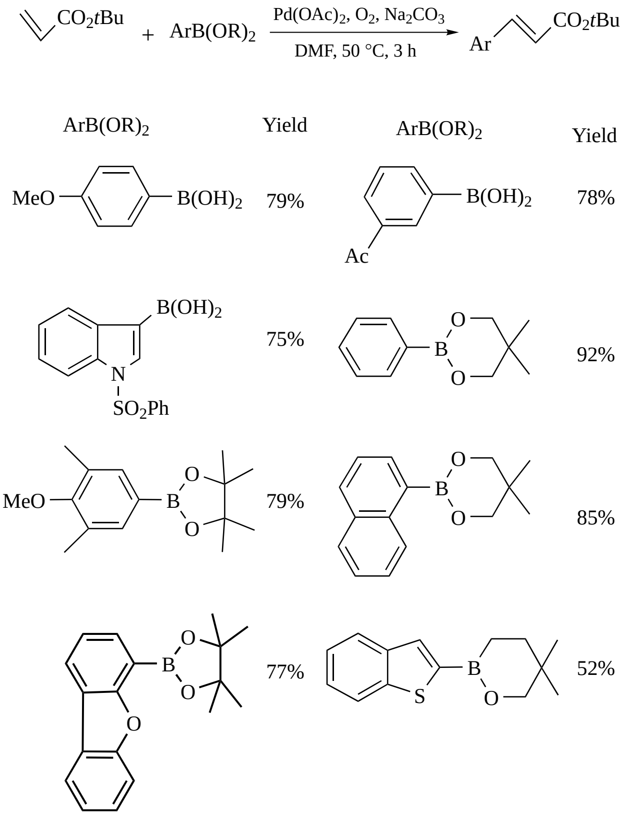
CO2tBu
+ ArB(OR)2
Pd(OAc)2, O2, Na2CO3
DMF, 50 °C, 3 h
Ar
CO2tBu
ArB(OR)2
Yield
ArB(OR)2
Yield
MeO
B(OH)2
79%
B(OH)2
Ac
78%
B(OH)2
N
SO2Ph
75%
O
B
O
92%
MeO
O
B
O
79%
O
B
O
85%
O
B
O
O
77%
S
B
O
52%

(6)

Recently, it was found that organometallic compounds, such as silicon (equation 7),[21,22] tin (equation 8),[23] antimony (equation 9),[24] and lead (equation 10),[25] instead of organic halides, react with olefins to produce the same products as obtained by the MH reaction.

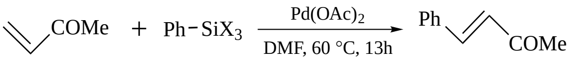
COMe
+ Ph−SiX3
Pd(OAc)2
DMF, 60 °C, 13h
Ph
COMe

$SiX_3 = SiMe_2OH$ (64%), $SiEt_2OH$ (66%), SiPhMeOH (80%), SiF_3 (79%)

(7)

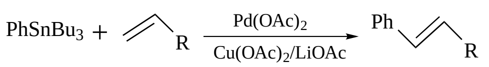
PhSnBu3 +
R
Pd(OAc)2
Cu(OAc)2/LiOAc
Ph
R

(8)

$R = CO_2Bu$ (77%), COMe (64%), CN (59%), CHO (58%), Ph (73%)

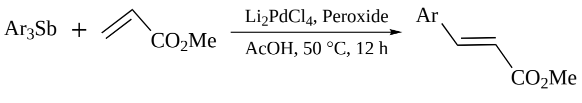
Ar3Sb +
CO2Me
Li2PdCl4, Peroxide
AcOH, 50 °C, 12 h
Ar
CO2Me

Ar = Ph; $4\text{-}MeC_6H_4$; $3\text{-}MeC_6H_4$; $2\text{-}MeC_6H_4$; $2,4,6\text{-}Me_3C_6H_2$; $4\text{-}MeOC_6H_4$

(9)

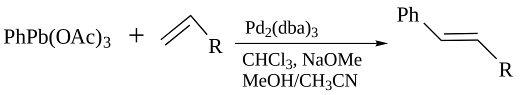
PhPb(OAc)3 +
R
Pd2(dba)3
CHCl3, NaOMe
MeOH/CH3CN
Ph
R

(10)

R = Ph (75%), CO_2Me (71%), $CH(OH)CH(OH)CH_2OBn$ (54%)

Other main group metals (or nonmetals) also serve as the agents for transfer of organic units to Pd for the Heck reaction; these include lead,[13] lithium,[26] magnesium,[13,26,27] sodium,[28] and boronic acids.[29]

3.5 Vinyl Substitution via Oxidative Addition of an Organic Halide or Equivalent

The second general mechanism of the Heck reaction involves oxidative addition of an organic species to Pd^0 to give the key organo-Pd^{II} intermediate, and then the usual final stage with an alkene to produce vinyl substitution and generate Pd^0.[7] This mechanism allows for spontaneous recycling of the Pd; no reoxidation is necessary. A base is present as buffer since strong acid is generated from the leaving group on the organic substrate.

Aryl and vinyl bromides and iodides have been employed most commonly, with 1–5 mol% Pd^0, and reaction temperatures ranging from ambient to 125 °C (equation 11). The Pd catalyst can be $Pd(Ph_3P)_4$ or the Pd^0 species produced by in situ reduction of Pd^{II}. The alkene itself can serve as the reducing agent for Pd^{II}, but the catalyst can also be produced by deliberate addition of a reducing agent, such as sodium borohydride, formic acid, or hydrazine.[30]

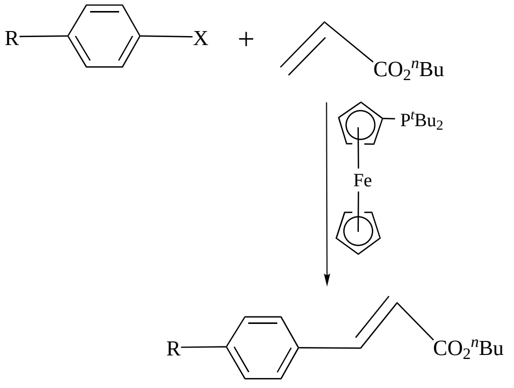
R
X
+
CO2nBu
PtBu2
Fe
R
CO2nBu

(11)

R	X	Time (h)	Temp (°C)	Yield
CO_2Me	Br	2	75	92%
MeO	Br	2	75	91%
CO_2Me	Cl	4	110	97%

As before, the reaction is best with monosubstituted alkenes; regioselectivity is not high with 1,2-disubstituted alkenes, and the yields are less impressive (equation 12).[31]

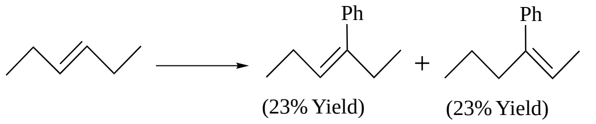
Ph
Ph
+
(23% Yield)
(23% Yield)

(12)

In another stoichiometric process, 1,2-dibromobenzene combines directly with propene to give a divinyl substitution product in 79% yield (equation 13).[32]

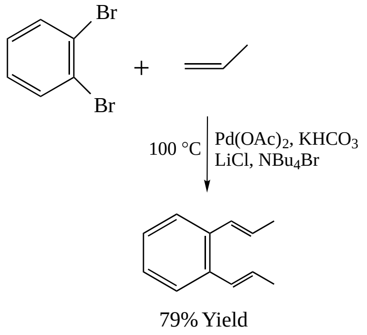
Br
Br
+
100 °C
Pd(OAc)₂, KHCO₃
LiCl, NBu₄Br
79% Yield

(13)

Intramolecular versions are generally successful. The position of the newly formed π-bond in the product can be the result of equilibration, especially in cases where a particularly stable position is available, as for indole in equation (14).[33]

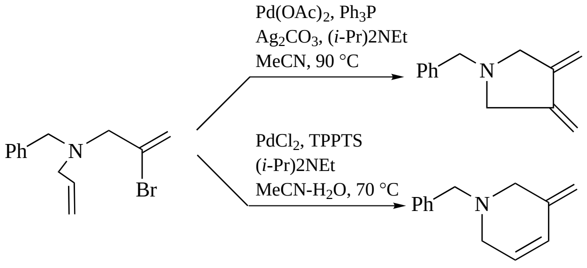
Pd(OAc)₂, Ph₃P
Ag₂CO₃, (i-Pr)2NEt
MeCN, 90 °C
Ph
N
Ph
N
Br
PdCl₂, TPPTS
(i-Pr)2NEt
MeCN-H₂O, 70 °C
Ph
N

(14)

Vinyl substitution has been developed and applied in many examples. A simple intermolecular example summarizes the power of this technique in the formation of unsymmetrical (or symmetrical) 1,3-dienes (equation 15).[34]

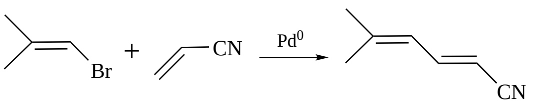

(15)

Aryl diazonium salts are effective aryl transfer agents, as shown in equation (16).[35] Divinylation of a biphenyl nucleus is achieved.

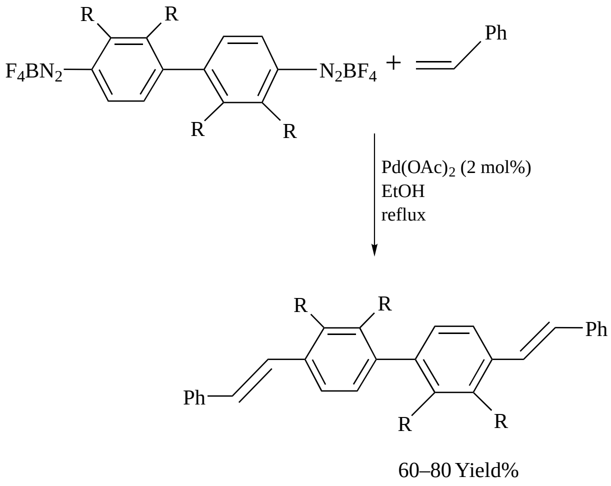
R
R
F₄BN₂
N₂BF₄
+
Ph
R
R
Pd(OAc)₂ (2 mol%)
EtOH
reflux
R
R
Ph
Ph
R
R
60–80 Yield%

(16)

Electron withdrawing group (EWG) have been found to serve as leaving groups for C–C coupling as seen in equation (17).[36]

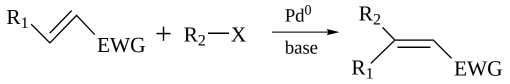
R₁
EWG
+
R₂—X
Pd⁰
base
R₂
R₁
EWG

(17)

EWG = CO_2R, COR, CN, SOAr
R_1 = Alkyl, Aryl
R_2 = Aryl, Alkenyl

The intramolecular version of vinyl–vinyl coupling has been less often applied, but the potential should be clear from one example of macrolide formation. This example also demonstrates the use of formic acid as an in situ reducing agent and the high reactivity of vinyl iodides; 25 °C is an unusually low temperature for the Heck reaction (equation 18).[37]

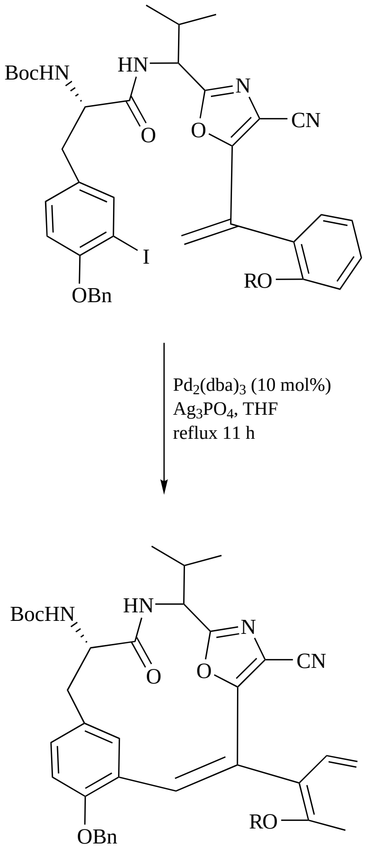
BocHN
HN
N
O
O
CN
I
OBn
RO
$Pd_2(dba)_3$ (10 mol%)
Ag_3PO_4, THF
reflux 11 h
BocHN
HN
N
O
O
CN
OBn
RO

(18)

R = H 66% Yield
R = Me 2% Yield

The use of alkyl halides is much more restricted. Only those alkyl groups that cannot allow β-hydride elimination are useful for intermolecular examples, but the restrictions on intramolecular examples are fewer. Both five- and six-membered rings are formed in good yield (equation 19).[38]

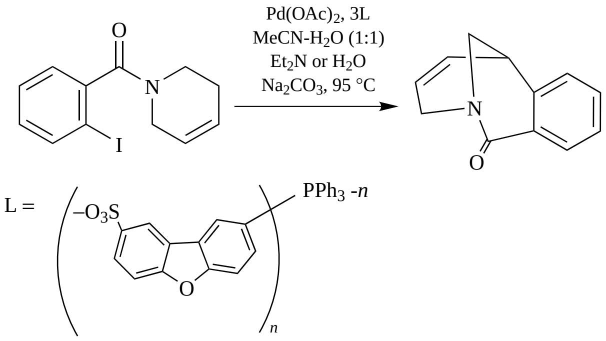
O
N
I
$Pd(OAc)_2$, 3L
$MeCN-H_2O$ (1:1)
Et_3N or H_2O
Na_2CO_3, 95 °C
N
O
L =
$-O_3S$
O
PPh_3 -n
n

(19)

Other leaving groups are effective in the oxidative addition with Pd^0, and can lead to efficient Heck reactions. An attractive possibility is an aniline as starting material, with in situ generation of a diazonium salt. While the oxidation of the amino group can occur with Pd^{II} alone at elevated temperatures, deliberate addition of t-butyl nitrite leads to higher yields (equation 20).[39]

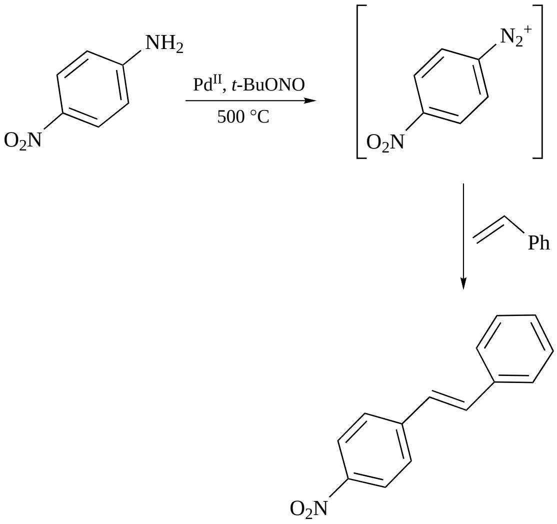
NH_2
O_2N
Pd^{II}, t-BuONO
500 °C
N_2^+
O_2N
Ph
O_2N

(20)

Aryl and vinyl sulfonate esters are reactive toward oxidative addition, and the perfluoroalkyl versions are useful substrates in the Heck reaction. Conditions can be mild, comparable to those for vinyl iodide reactions. The enol (vinyl) triflates are particularly attractive, since they are prepared directly from the corresponding ketone (equation 21).[40–42]

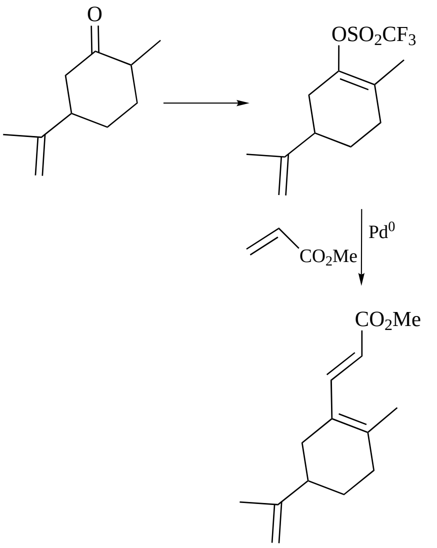
O
OSO_2CF_3
Pd^0
CO_2Me
CO_2Me

(21)

Conversion of phenols to triflate esters followed by vinylation constitutes one of the few general methods for the direct substitution of a carbon unit for a phenolic hydroxyl. Relatively few examples are known,[43] but high generality is easy to predict.

Carboxylic acid halides present interesting alternative processes (Scheme 5). Oxidative addition of acid chlorides to Pd^0 occurs under mild conditions, and the resulting acyl–Pd^0 complex will undergo decarbonylation upon heating. The decarbonylated product, an organo-Pd^0 species, can undergo

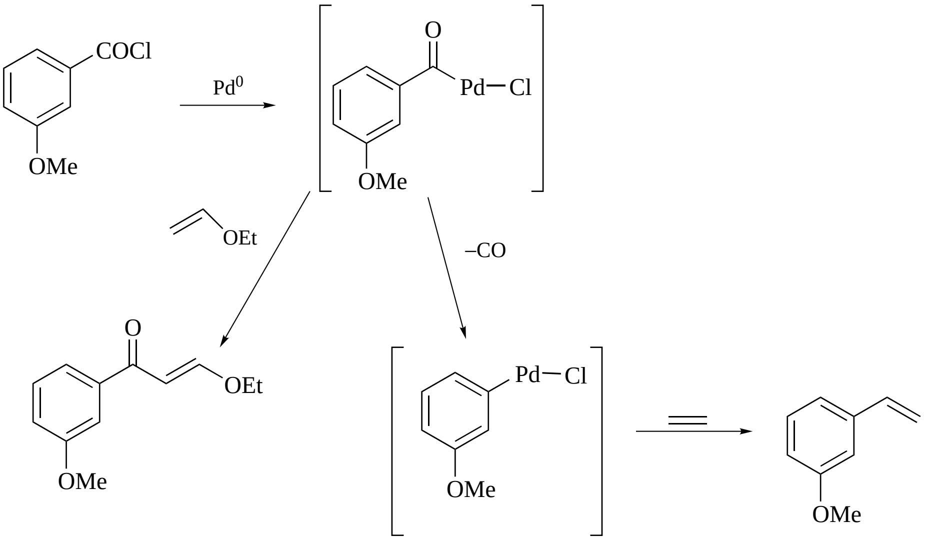
COCl
Pd⁰
OMe
O
Pd—Cl
OMe
OEt
−CO
O
OEt
OMe
Pd—Cl
OMe
OMe

Scheme 5 Heck coupling with and without CO incorporation

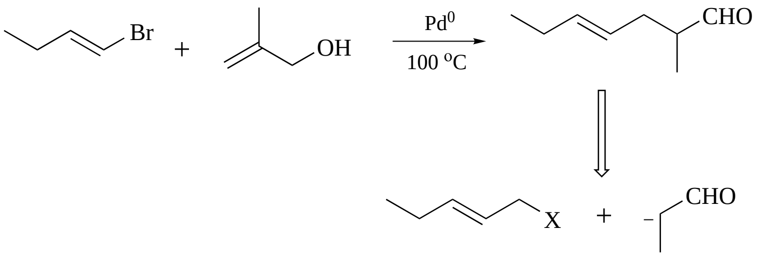
Br
+
OH
Pd⁰
100 °C
CHO
X
+
−
CHO

Scheme 6 Synthetic equivalency of Heck coupling with allylic alcohols and enolate alkylation

vinylation in the usual way. However, with very reactive vinyl derivatives, the vinylation can occur with the acyl unit intact. The two possibilities are illustrated with *m*-methoxybenzoyl chloride.[44,45]

Heck reactions without Pd or Pt (equation 22).[46]

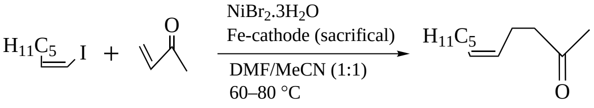
H11C5
I
+
O
NiBr2.3H2O
Fe-cathode (sacrifical)
DMF/MeCN (1:1)
60–80 °C
H11C5
O

(22)

3.6 Special Applications

Two transformations require special note because of their very high potential in organic synthesis. First, the use of allylic alcohols as substrates has been shown to result in β-hydride elimination toward the OH group, and the resulting enol tautomerizes to the aldehyde. This overall conversion, illustrated for 2-methallyl alcohol and 1-bromobutene, opens a new strategy for the synthesis of carbonyl-containing compounds, and is equivalent (with very different selectivities) to the allylation of an enolate anion by traditional techniques (Scheme 6).[47–49]

The second general transformation is the intramolecular version with multiple vinyl substitution steps (equations 23 and 24). There is high potential for synthesis of complex rings in a very efficient manner.[50,51]

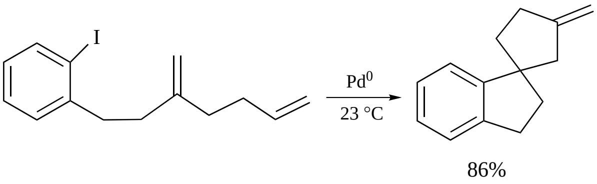

(23)

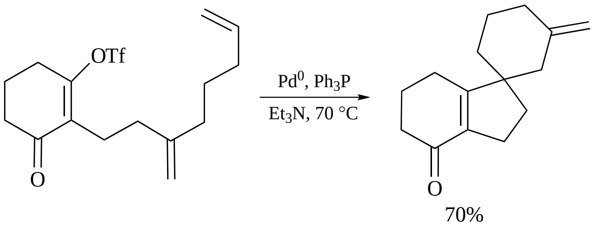
OTf
O
Pd⁰, Ph3P
Et3N, 70 °C
O
70%

(24)

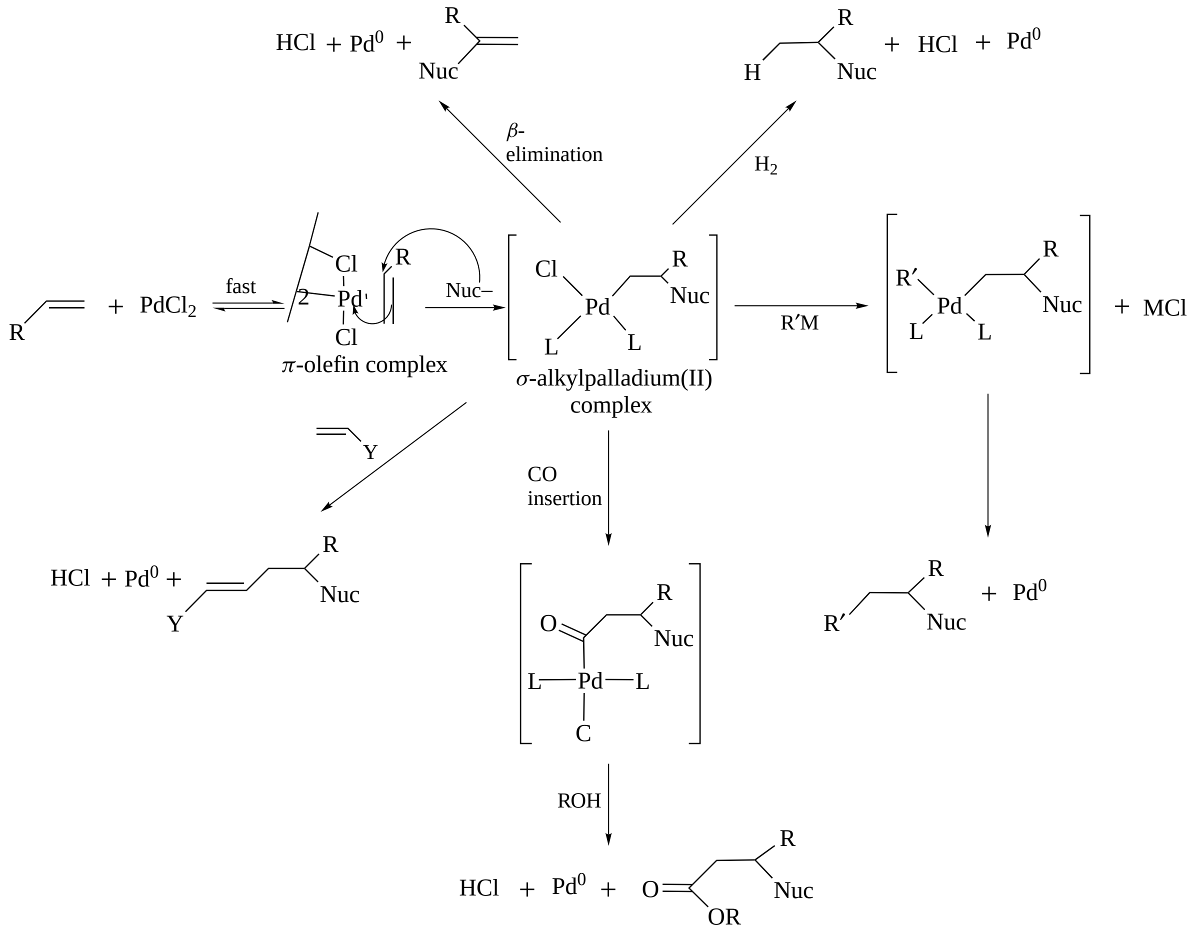

Scheme 7

3.7 Summary

The Heck reaction is a powerful process for vinyl substitution by a carbon unit, with no direct analogy with traditional organic synthesis methodology. While it has not seen many applications in complex synthesis, it has been adapted to the preparation of a variety of ‘value added’ organic intermediates.

4 NUCLEOPHILIC ADDITION TO METAL-ACTIVATED ALKENES

4.1 Basic Reaction

The addition of EWG to alkenes promotes nucleophilic addition to the alkene, an activation that is the basis of powerful general methodology in organic synthesis (e.g. the Michael reaction).[52] Coordination of a metal–ligand unit to an alkene via the π-orbitals can also enhance nucleophile addition, leading to a σ-organometal species without a change in the oxidation state of the metal.[53–60] The organometal bond can then be led into characteristic processes, such as *Carbonylation*, β-hydride elimination, or others, as illustrated by several examples in Scheme 7. Overall, the process leads to addition of a nucleophilic species to one end of an alkene and one further elaboration at the other end. The fundamental difference between the traditional addition to electron-deficient alkenes (conjugate addition) and the metal-promoted process is that the metal activation does not dominate the regioselectivity. To a first approximation, the activation influence is independent of the orientating influence. In the traditional addition to electron-deficient alkenes, the activating group also dominates the regioselectivity factors.

Two systems have been developed to the level of useful organic synthesis methodology: spontaneous coordination of the alkene to Pd^{II} and the preparation of discrete $Cp(CO)_2Fe$–alkene cationic complexes. With the Pd system, efficient catalytic processes have been developed for the addition of heteroatom nucleophiles, while the coupling with carbon nucleophiles is mainly relegated to stoichiometric reactions: these two topics will be presented separately. In the iron series, the reactions involve stable intermediates and are invariably not amenable to catalysis.

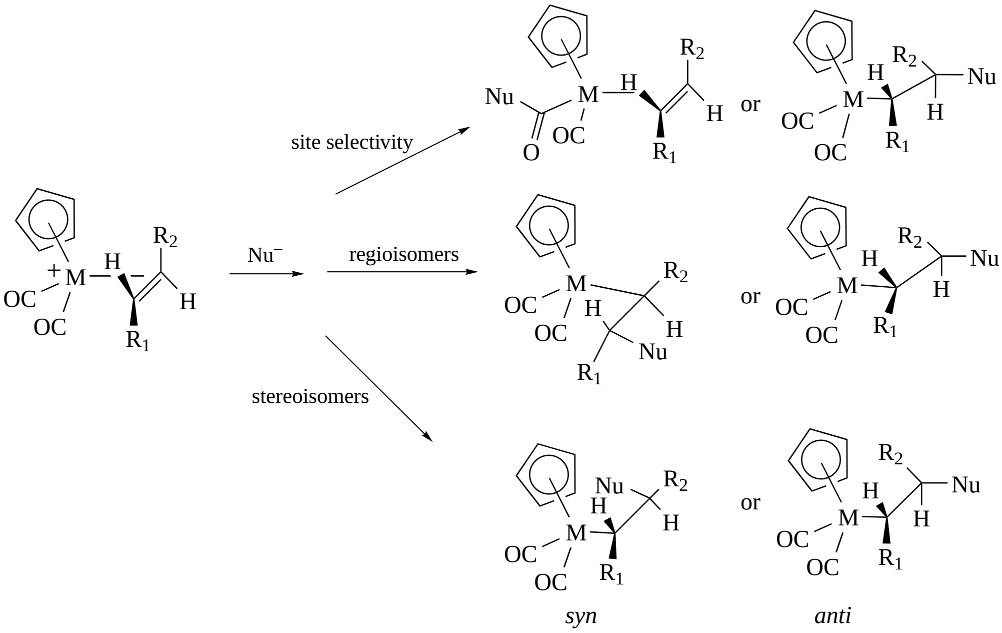

Scheme 8 Three selectivity issues in nucleophilic addition to alkene–metal complexes

There are three primary issues of selectivity. (1) Site selectivity: which of several electrophilic ligands will add to the nucleophile? In Scheme 8, the alkene, the CO, and the Cp ligands are all candidates. (2) In an unsymmetrical polyene, which end or position of the π-system will be more reactive? In Scheme 8, either end of the alkene might be attacked, giving rise to two regioisomers. (3) The metal is coordinated to one face of the polyene. Which face will be attacked by the nucleophile? Addition from the face opposite the metal is anti addition, while attack from the same face as the metal is syn addition. Syn addition is generally thought to involve initial coordination of the nucleophile to the metal and then conventional alkene insertion, as for the Heck reaction. A coordinatively unsaturated metal is required for syn addition, and the configurations of the new sp^3 centers in the product would be opposite to that for anti addition.

The issue of site selectivity has been considered,[6] and a simple pattern was identified and analyzed. The guidelines are useful, but typically the activation energies for addition to the various electrophilic ligands depend on a number of parameters, such as the type of nucleophile. It is not possible to predict from a set of rules whether, in a new complex, an alkene ligand will be more or less reactive toward nucleophiles compared to a CO ligand. However, the higher reactivity of noncyclic polyenes (alkene, η^3-allyl) compared to pseudoaromatic ligands (cyclopentadienyl, cyclobutadiene, arene) is quite general; in the example of Scheme 8 the Cp ring is unlikely to be the preferred site of addition.

Regioselectivity is quite predictable, and consistent in a simple way with typical electrophilic activation of an alkene (Markovnikov's rule). Just as in bromination of an unsymmetrical alkene, initial coordination of an electrophile (M^+, Br^+) activates the alkene toward nucleophilic addition of a nucleophile, the addition is preferred at the end of the alkene that best stabilizes a cation. Electronic effects dominate over steric effects. An molecular orbital (MO) analysis has been put forward ('the slip mechanism') to rationalize the activating effect of the metal and, in a secondary way, the regioselectivity.[61] It focuses on the reactants and products, and notes that the metal moves during the reaction from the approximate midpoint of the alkene to one end. As that 'slip' occurs toward one end of the alkene, the lowest unoccupied molecular orbital (LUMO) for the complex changes and a large coefficient develops at the other end.

Stereoselectivity is largely predictable, as most examples involve coordinatively saturated reactants and initial coordination of the nucleophile with the metal is inhibited. Anti addition is prevalent, addition from the face opposite the metal. Especially with Pd^{II}, as summarized below, the preference for syn or anti addition depends on the nucleophile, and an MO analysis has been advanced.[62]

4.2 Activation with Pd^{II}

Nucleophilic addition to metal-activated alkenes as a synthetic method can be traced to the *Wacker Process*, the oxidation of ethylene to acetaldehyde with Pd^{II} and

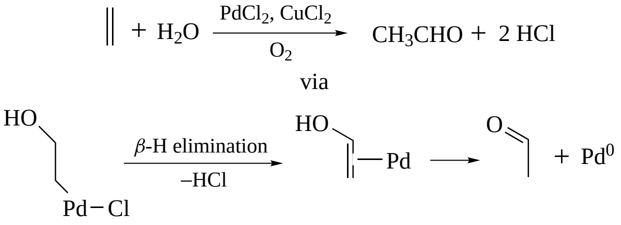

Scheme 9 The Wacker process

oxygen (Scheme 9).[7,63] This process includes all of the basic features of the Pd^{II} activation and has now been greatly extended with regard to substrate type and generality. The alkene spontaneously coordinates with the Pd^{II} species, even at low temperature, but in a rapidly reversible process. Initial addition of the water nucleophile has been shown to occur by anti addition, although stereoselectivity is not an issue in this case.[63,64] The resulting β-hydroxyethyl–PdCl intermediate is unstable with respect to β-elimination of a vinyl hydrogen, and produces the new alkene complex (an enol complex in this case). Ligand dissociation after successive β-hydride rearrangements leads to acetaldehyde and Pd^0. Typical of reactions in this series, a stoichiometric reoxidant for the Pd^0 is necessary in order to be able to use catalytic amounts of Pd^{II}. Copper offers the possibility of reoxidation using catalytic Cu^{II} and stoichiometric oxygen. There are numerous other techniques for reoxidation, as given in the examples below.[63] The problem of reoxidation of the Pd in order to have an efficient catalytic process has no general solution.

A direct extension of the Wacker process is the general conversion of α-alkenes into methyl ketones (equations 25 and 26).[65] The regioselectivity shown in many examples (strong preference for the methyl ketone over the aldehyde) is consistent with the regioselectivity rule of attack at the more substituted carbon of the alkene (Markovnikov's rule). Functional group compatibility is high. The method is very general and efficient for monosubstituted alkenes, but gives lower yields (lower rates) and mixtures of regioisomers with more substituted substrates.

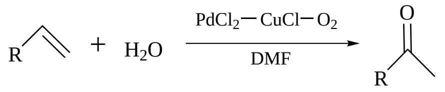

(25)

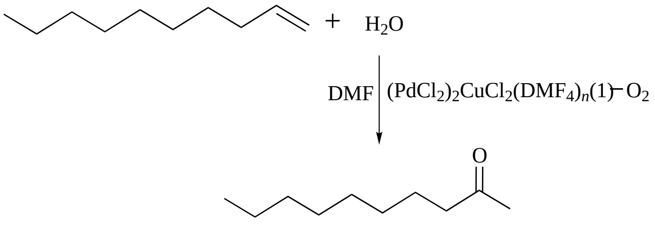

(26)

Selective oxidation of styrene to acetophenone by a Pd(II) catalyst in the presence of ionic liquids has been achieved (equation 27). Electronic effects on the site of Pd(II) oxidation of substituted styrenes are indicated in equation (28).[66,67] Strong pi-donation from the phenyl substituent favors oxidation at the alkene carbon alpha to the aromatic ring.

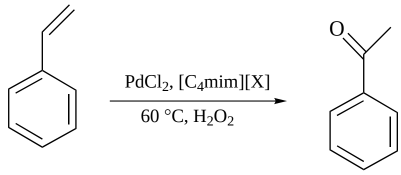

(27)

X = PF6 or BF4
[C_4mim] = 1-butyl-3-methylimidazolium

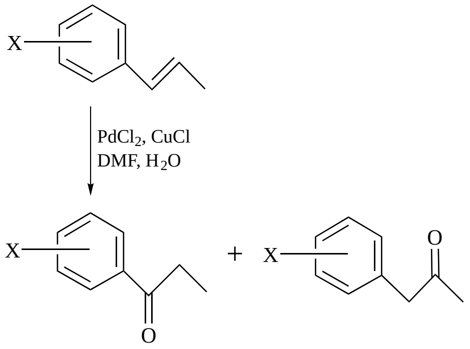

(28)

Position and Composition of X	Product 1	Product 2
4-CF_3		Dominant
4-H		Dominant
4-CH_3		Dominant
2-OCH_3		Dominant
4-OCH_3		Dominant
2,4-OCH_3	Dominant	
2,4,6-OCH_3	Dominant	

An interesting case in the β-lactam series gave selective anti-Markovnikov addition, attributed to the directing effect of the lactam carbonyl group (equation 29).[68]

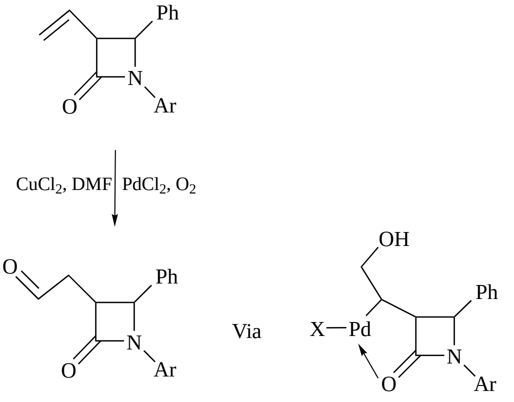

(29)

Other oxygen nucleophiles are also effective, from alcohols to carboxylic acids. The conversion of ethylene to vinyl acetate and vinyl ethers is well documented, but applications in synthesis with more complex alkenes are few.

The intermolecular addition of nitrogen nucleophiles has been shown to lead to interesting products, with remarkable control based on the reaction conditions (Scheme 10).[68,69] Carbonylation of the organo-Pd intermediate can also be efficient, leading to β-amino esters.[69] Unfortunately, these processes require stoichiometric Pd^{II}; no reoxidation scheme has been developed.

Much more general and efficient is the intramolecular version, the formation of tetrahydrofuran and tetrahydropyran rings from oxygen nucleophiles, and pyrrolidine and indole rings from amine nucleophiles. The general reaction in Scheme 11 summarizes the questions: regioselectivity now includes a question of ring size preference, and the relative configuration of existing stereocenters might be expected more strongly to influence the newly formed sp^3 carbons. Several recent examples of these and related cyclizations are shown in equations (30–44).[70–86]

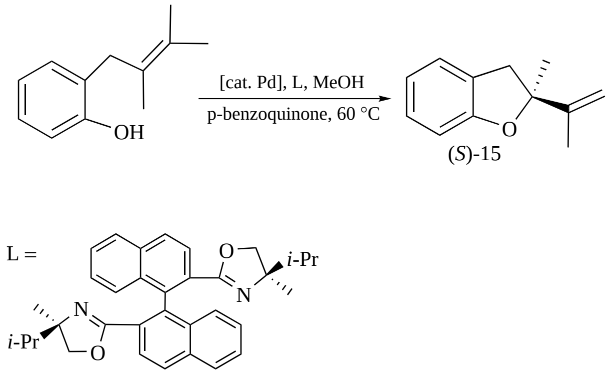
OH
[cat. Pd], L, MeOH
p-benzoquinone, 60 °C
O
L =
O
N
i-Pr
N
O
i-Pr

(*S*)-15

[cat. Pd] = $Pd(O_2CCF_3)_2$ - 75% yield
[cat. Pd] = $[Pd(MeCN)_4](BF_4)_2$ - 88% yield

(30)[70]

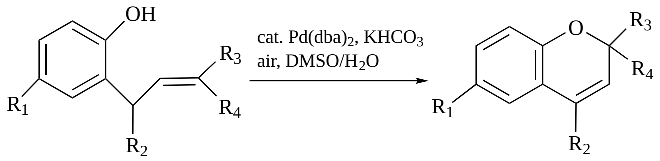
OH
R_3
R_1
R_4
R_2
cat. $Pd(dba)_2$, $KHCO_3$
air, $DMSO/H_2O$
O
R_3
R_4
R_1
R_2

R_1 = H, OMe, Ac, CN
R_2 = H, Me, Ph
R_3 = H, Me
R_4 = H, Me, Ph

(31)[71]

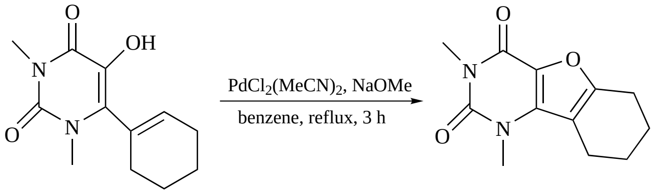
O
OH
N
O
N
$PdCl_2(MeCN)_2$, NaOMe
benzene, reflux, 3 h
O
O
N
O
N

82% Yield

(32)[72]

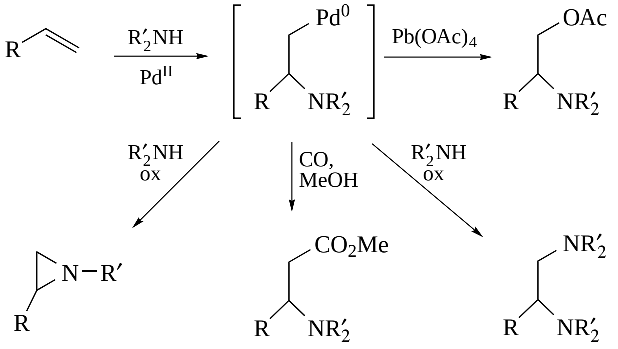
R
R'_2NH
Pd^{II}
Pd^0
R
NR'_2
$Pb(OAc)_4$
OAc
R
NR'_2
R'_2NH
ox
CO,
MeOH
R'_2NH
ox
N−R′
R
CO_2Me
R
NR'_2
NR'_2
R
NR'_2

Scheme 10 Generalized pathways for nitrogen nucleophiles

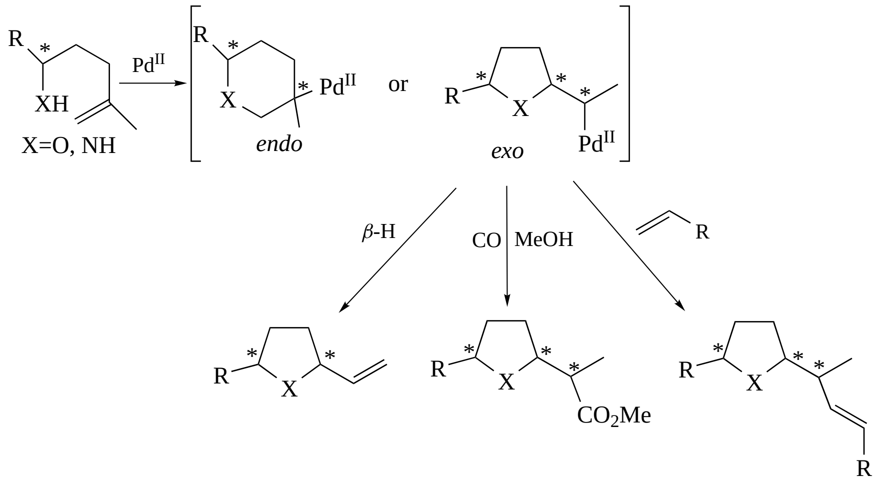
R
*
XH
X=O, NH
Pd^{II}
R
*
X
*
Pd^{II}
endo
or
R
*
X
*
*
Pd^{II}
exo
β-H
CO
MeOH
R
R
*
X
*
R
*
X
*
*
CO_2Me
R
*
X
*
*
R

Scheme 11 Selectivity issues in ring formation

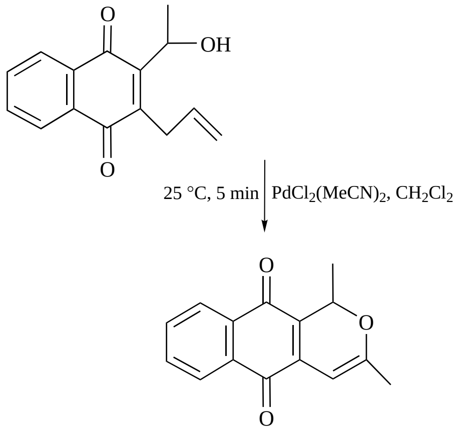
O
OH
O
25 °C, 5 min
PdCl2(MeCN)2, CH2Cl2
O
O
O

60% Yield

$(33)^{73}$

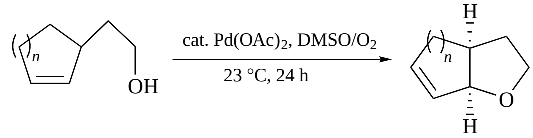
n
OH
cat. Pd(OAc)2, DMSO/O2
23 °C, 24 h
H
n
O
H

$(34)^{74}$

$n = 0, 1, 2$

90–96 % Yield

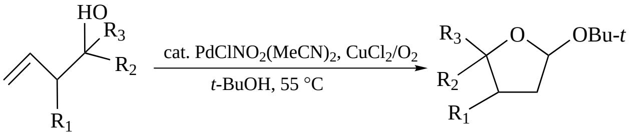
HO
R3
R2
R1
cat. PdClNO2(MeCN)2, CuCl2/O2
t-BuOH, 55 °C
R3
O
OBu-t
R2
R1

$R_1 = H, CH_3$

$R_2 = H, CH_3, C_6H_5$

$R_3 = H, CH_3, CH_3CH_2, C_6H_5$

$(35)^{75}$

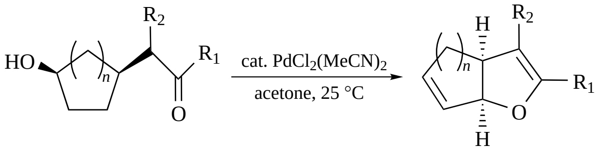
R2
HO
n
R1
O
cat. PdCl2(MeCN)2
acetone, 25 °C
H
R2
n
R1
O
H

$R_1 = Me, Ph, n\text{-}Bu, CH_2CO_2Me, OEt, OMe$

$R_2 = COMe, COPh, CO_2Me, NO_2$

$(36)^{76}$

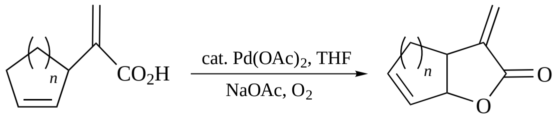
n
CO2H
cat. Pd(OAc)2, THF
NaOAc, O2
n
O
O

$n = 1,2,3$

$(37)^{77}$

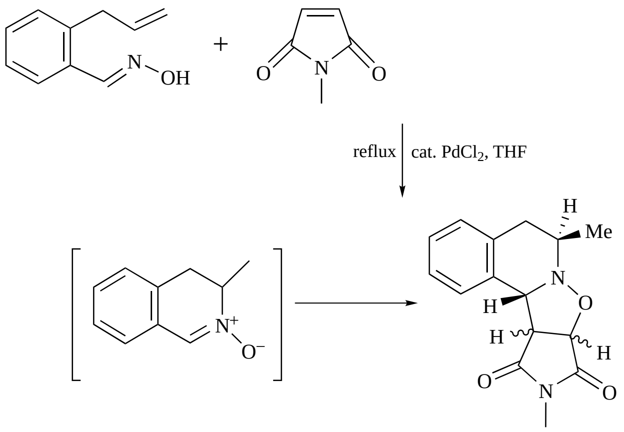
N
OH
+
O
N
O
reflux
cat. PdCl2, THF
N+
O−
H
Me
N
O
H
H
H
O
N
O

$(38)^{78–80}$

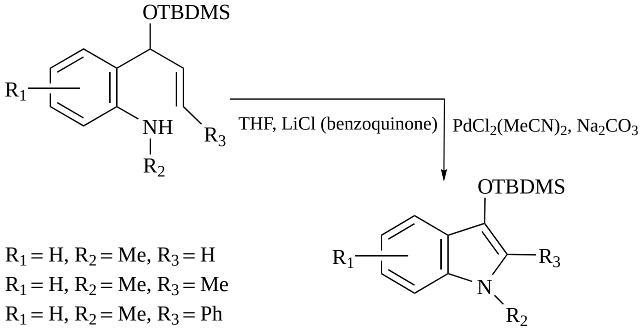
OTBDMS
R1
NH
R2
R3
THF, LiCl (benzoquinone)
PdCl2(MeCN)2, Na2CO3
OTBDMS
R1
R3
N
R2

$R_1 = H, R_2 = Me, R_3 = H$

$R_1 = H, R_2 = Me, R_3 = Me$

$R_1 = H, R_2 = Me, R_3 = Ph$

$R_1 = 4\text{-}OMe, R_2 = C_6H_4Br\text{-}p, R_3 = H$

$R_1 = H, R_2 = CH_2CH = CH_2, R_3 = H$

$(39)^{81}$

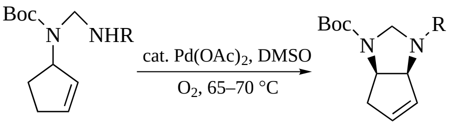
Boc
N
NHR
cat. Pd(OAc)2, DMSO
O2, 65–70 °C
Boc
N
N
R

$(40)^{82}$

$R = Ts, CHO, COCH_3, CONH_2, CO_2Me, CO_2Bn$

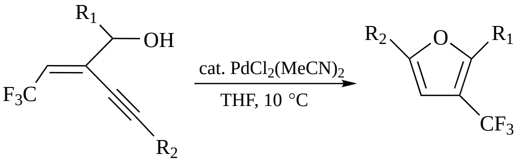
R1
OH
F3C
R2
cat. PdCl2(MeCN)2
THF, 10 °C
R2
O
R1
CF3

$(41)^{83}$

64–77% Yield

$R_1 = Ph, n\text{-}C_3H_7, H; R_2 = Ph, n\text{-}C_6H_{13}, p\text{-}CH_3OC_6H_4$

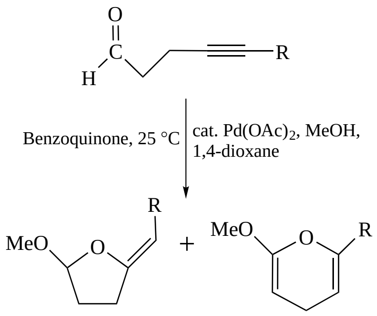
O
C
H
R
Benzoquinone, 25 °C
cat. Pd(OAc)2, MeOH,
1,4-dioxane
R
MeO
O
+
MeO
O
R

$(42)^{84}$

13–66% 0–17%

$R = Ph, p\text{-}MeC_6H_4, p\text{-}CF_3C_6H_4, n\text{-}C_8H_{17}$

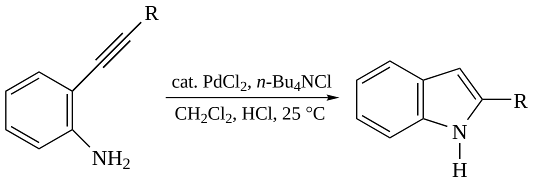

(43)[85]

R = vinyl, aryl

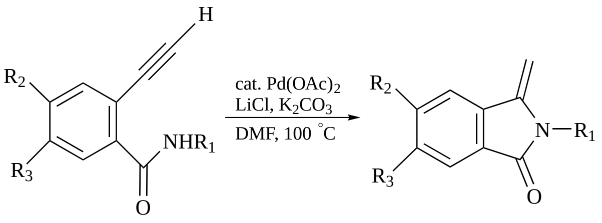

$R_1 = p\text{-}MeC_6H_4$, $m\text{-}ClC_6H_4$, $p\text{-}MeOC_6H_4$, CH_3, Ph, CH_2Ph, H
$R_2 = H$, OMe
$R_3 = OH$, NO_2, OMe

(44)[86]

4.3 Summary

The activating effect of Pd^{II} and Fe^{II} toward nucleophilic addition to alkenes is powerful and allows addition of stabilized anions to simple alkenes at low temperatures. However, the only efficient catalytic processes are based on the addition of oxygen nucleophiles to alkenes activated by spontaneous coordination with Pd^{II}, extensions of the Wacker process.

5 NUCLEOPHILIC ADDITION TO ALLYL LIGANDS: ALLYLIC ALKYLATION

5.1 Introduction

Oxidative addition of an allylic σ-bond can lead to η^3-allyl ligands. The allyl ligand can behave as a nucleophile (M = Ni, X = halide) or as an electrophile, depending on the metal–ligand system. The electrophilic allyl ligand can couple with a nucleophile to produce an alkene (equation 45). There are several issues of selectivity as well as reactivity. The addition can be syn or anti, resulting in opposite configurations of the newly formed chiral center. There are three potentially reactive sites in the typical allyl ligand; either terminus and the central carbon (C-2). The useful methodology has been developed around addition at a terminal position. Finally, the alkene unit in the product can be (E) or (Z), depending on the configuration of the terminus not undergoing coupling.

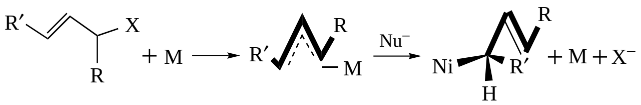

(45)

There are a number of metal–ligand systems that will provide the proper activation for nucleophile coupling, but the Pd^{II} system is by far the most well developed and useful. In recent years, asymmetric allylic alkylation reactions have received the most interest for organic synthesis applications (*see* ***Asymmetric Synthesis by Homogeneous Catalysis***). Metals other than Pd have also received some additional attention.

5.2 Allylic Alkylation with Allyl–Pd^{II} Complexes

What should be the nature of the group X undergoing oxidative addition in equation (46) In the initial formulation of the possibilities, there was a focus on X = H, relying on spontaneous insertion of Pd^{II} into a C–H bond (equation 46). The overall process would be very powerful, analogous to the synthetic methods depending on the reactive site adjacent to a C=O π-bond.[87]

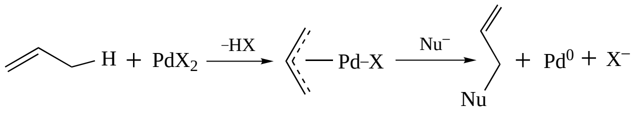

(46)

While good procedures are available for the initial oxidative addition to give allyl–PdX complexes, and the nucleophile addition has been fully developed, this process has not been amenable to catalysis. The Pd^{II} is reduced to Pd^0 during the basic pathway, and no compatible reoxidation system has been defined.

The useful procedures began to be developed with the recognition that by initial activation of the allylic position with an electronegative atom, direct oxidative addition with Pd^0 can give the key η^3-allyl intermediate.[87] Spontaneous recycling then leads to an efficient catalytic process (equation 47).

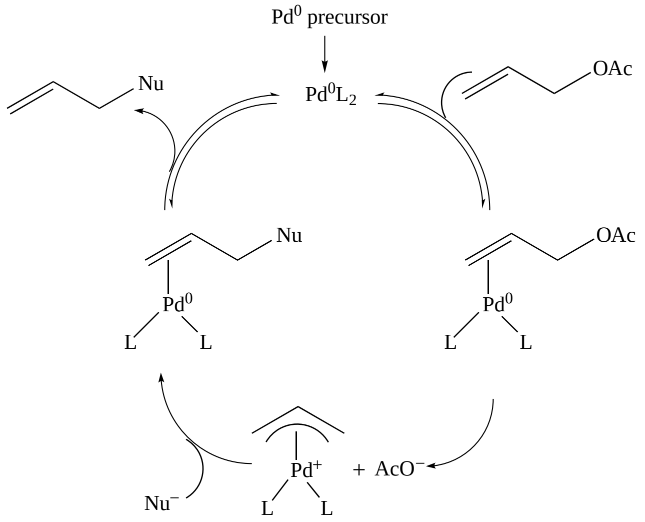

(47)

The overall process is illustrated by the reaction of a homochiral allylic acetate (Scheme 12). With ‘soft’ anions, derived from carbon acids of pK_a 8–15, the addition is very efficient, exclusively anti, and can occur at either end of the allyl system (1:1 in the symmetrical case). In contrast to the addition to alkene ligands, the primary influence on regioselectivity is steric and not electronic. The less-substituted end of the allyl ligand is preferentially attacked.

The acetate unit is particularly convenient, since it is obtained from the corresponding alcohol and is relatively stable toward solvolysis, S_N2 reactions, and so on. Many other electronegative units are also effective, including halide and tosylate. Less obvious is the high reactivity of allylic sulfones and allylic nitro compounds toward the oxidative addition. Three special cases are outlined here. First, an allylic epoxide can undergo rapid oxidative addition of the allylic C–O bond under mild conditions, leading to the zwitterion or equivalent (Scheme 13).**[87,88]** Proton abstraction can lead to the anion form of the nucleophile, and then nucleophilic addition gives the final product. The process requires no base. For example, a mixture of the allylic epoxide with dimethyl malonate can react with a small amount of Pd^0 in the absence of solvent or base to give rapid and efficient conversion to the nucleophile adduct.

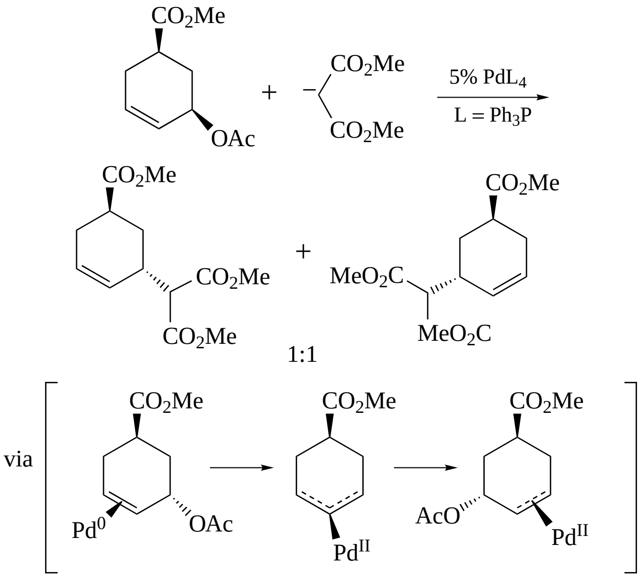

Scheme 12

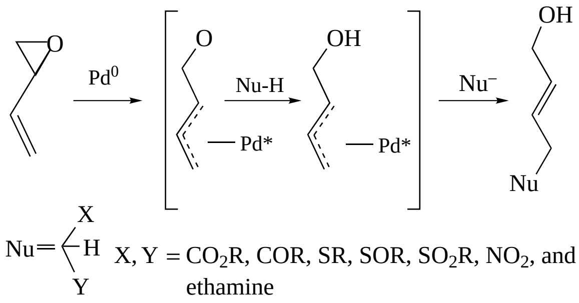

X, Y = CO_2R, COR, SR, SOR, SO_2R, NO_2, and ethamine

Scheme 13

Allylic carbonates also undergo oxidative addition, cleavage of the allyl–O bond, and loss of CO_2 can occur to give a species formulated as the allyl–Pd–alkoxide (equation 48). In the presence of a suitably acidic carbon acid (pK_a15 or lower), the carbanion is generated and nucleophile addition can occur. The overall process requires only a catalytic amount of Pd^0; no base or other stoichiometric reagents is necessary.**[87]**

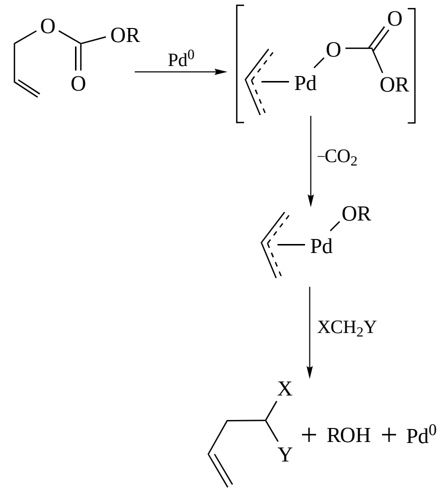

(48)

The oxidative addition of allylic esters is also gaining popularity as a means of deprotecting a carboxylic acid or alcohol (concomitant loss of CO_2 from a carbonate).**[89]**

Allylic sulfones show a reactivity toward oxidative addition that seemed remarkable when first defined, being much higher than other conditions for breaking the carbon–sulfur bond (e.g. an S_N2 process). This reactivity, together with the well known stabilizing effect of the SO_2 group on an adjacent carbanion, allows a strategy for double functionalization of the allyl unit with opposite polarization for each operation. For example, proton abstraction followed by α-electrophile trapping gives monosubstitution; then treatment with catalytic Pd^0 and a soft nucleophile gives γ-substitution by allylic alkylation (equation 49). The electrophile can be a simple alkyl group (S_N2) or conjugated carbonyl compound (1,4-addition) (equation 50).**[87,90]**

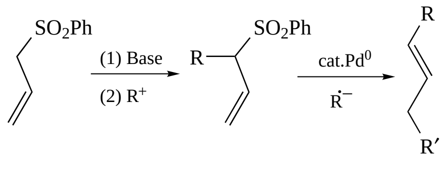

(49)

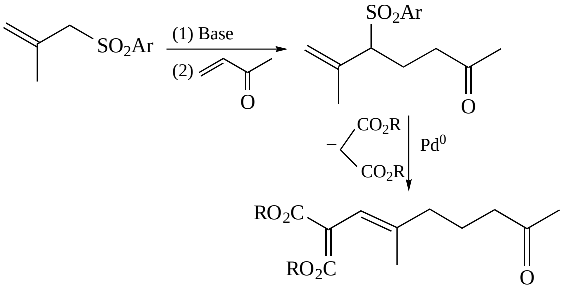
SO2Ar
(1) Base
(2)
O
SO2Ar
O
CO2R
CO2R
Pd0
RO2C
RO2C
O

(50)

A similar strategy is available with allylic nitro compounds, but the applications are less well developed. It is interesting to note that both alkene isomers of the nitro species react smoothly by oxidative addition of the carbon–nitro bond, presumably by rapid equilibration of the alkene isomers under the allylic alkylation conditions (equation 51).

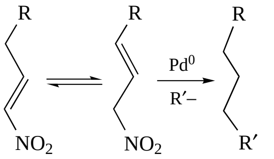
R
R
R
Pd0
R′–
NO2
NO2
R′

(51)

More reactive anions, such as the very well studied enolate anions from ketones and esters, do not undergo allylic alkylation except in special cases. Tin enolate derivatives are generally effective (equation 52).

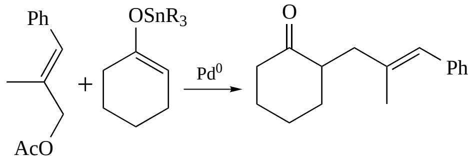
Ph
OSnR3
+
Pd0
O
Ph
AcO

(52)

The enolate can be ‘built-in’ in the allyl esters of β-keto esters (equation 53).[87] The chemoselectivity is excellent, as shown by selective reaction of an allylic acetate in the presence of a simple ketone, using a tin enolate anion (equation 54).[87] Even mildly nucleophilic species, such as allylic–tin$^{\text{IV}}$ derivatives, react at room temperature, the method of choice for cross coupling of allylic units (equation 55).

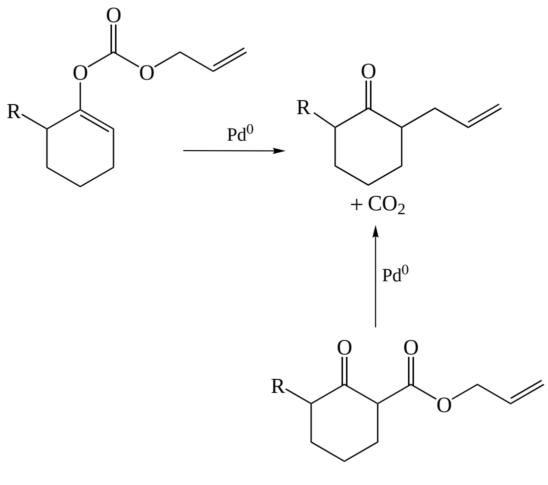
O
O
O
R
Pd0
O
R
+ CO2
Pd0
O
O
R
O

(53)

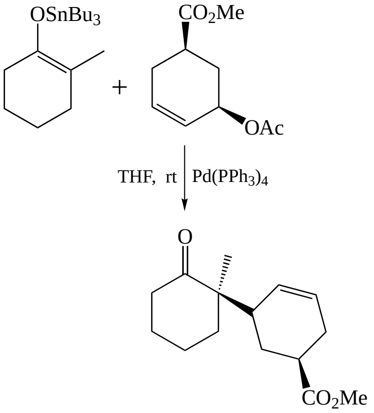
OSnBu3
CO2Me
+
OAc
THF, rt
Pd(PPh3)4
O
CO2Me

(54)

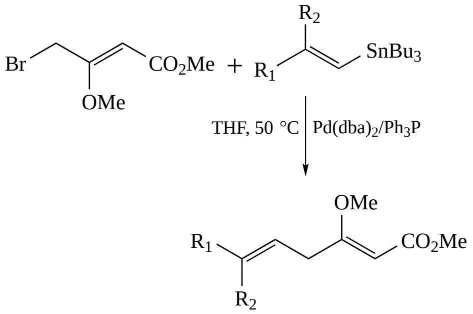
R2
Br
CO2Me
+
R1
SnBu3
OMe
THF, 50 °C
Pd(dba)2/Ph3P
OMe
R1
CO2Me
R2

(55)

Intramolecular couplings have been among the more impressive applications, with macroring structures prepared in good yield without using high dilution conditions (equations 56 and 57). In the case of the allylic epoxide example (equation 57), the Pd^0 catalyst is attached to polystyrene beads, apparently important in producing the high yields at normal concentrations.

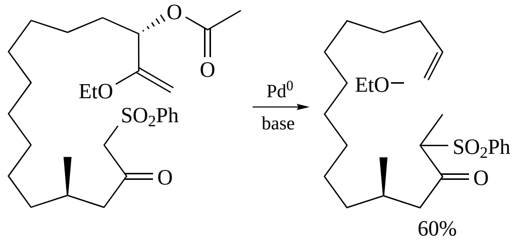
O
O
EtO
SO2Ph
O
Pd0
base
EtO–
SO2Ph
O
60%

(56)

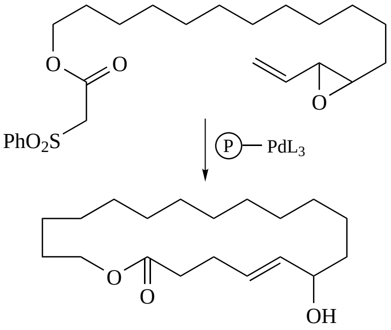
O
O
PhO2S
O
P
PdL3
O
O
OH

60–80% at 0.5 M

(57)

Heteroatom nucleophiles have not been developed extensively. Amine nucleophiles behave well if derivatized

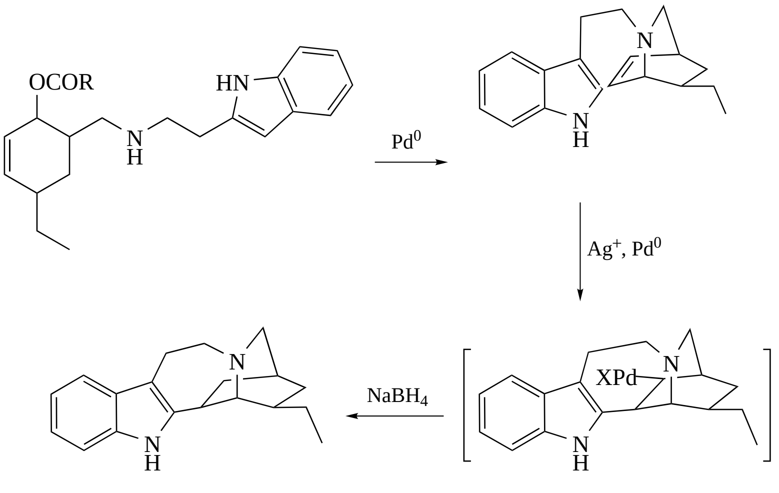
OCOR
HN
N
H
Pd0
Ag+, Pd0
XPd
NaBH4

Scheme 14

as a benzylamine or sulfonamide (equation 58).[87] The intramolecular version with indole nitrogen as nucleophile was used in a simple and elegant construction of the ibogamine alkaloid skeleton (Scheme 14).

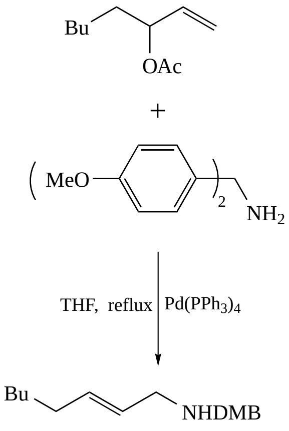
Bu
OAc
+
MeO
2
NH2
THF, reflux
Pd(PPh3)4
Bu
NHDMB

(58)

The direction of addition (syn or anti) with amine nucleophiles has been tested and found to be dependent on the reaction conditions. The situation is clearest with the homochiral cyclohexane derivative (Scheme 15). In this example, a simple Pd^0 catalyst gives a mixture of isomers owing to competitive syn and anti addition, while the polymer-supported catalyst produces only the (usual) anti addition.[87]

The transfer of main group metal derivatives can be achieved efficiently using aluminum derivatives, but the stereoselectivity is now *syn*, suggesting initial transfer of the metalloid to the Pd (Scheme 16).

A particularly clear example of syn versus anti addition was carried out in stoichiometric fashion using vinyl–zirconium reagents, in direct comparison with the stereochemical outcome of the catalytic allylic alkylation with soft anions (Scheme 17). The zirconium reagent gives the natural steroid configuration, while the malonate anion gives the opposite epimer.[91]

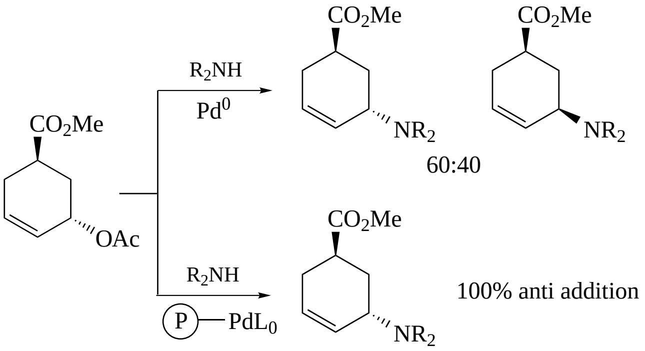
CO2Me
OAc
R2NH
Pd0
CO2Me
NR2
CO2Me
NR2
60:40
R2NH
P
PdL0
CO2Me
NR2
100% anti addition

Scheme 15

Regioselectivity is primarily driven by steric factors. A systematic comparison is available with Me and other alkyl groups (equation 59). The sensitivity is obviously high, with a change from 77:23 to >99 by a change from primary alkyl to secondary alkyl.

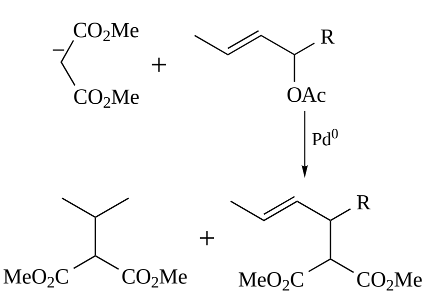
CO2Me
CO2Me
+
R
OAc
Pd0
MeO2C
CO2Me
+
R
MeO2C
CO2Me

(59)

R = *i*-Pr	77	23
R = *i*-Bu	93	7
R = *i*-Pr	>99	0

In the competition between Ph and CN, the selectivity is high for addition to the carbon-bearing Ph (equation 60).

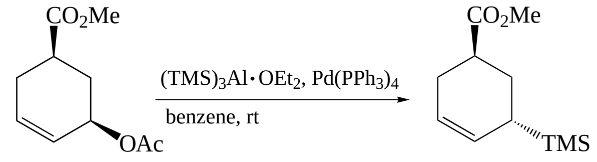
CO2Me
OAc
(TMS)3Al·OEt2, Pd(PPh3)4
benzene, rt
CO2Me
TMS

Scheme 16

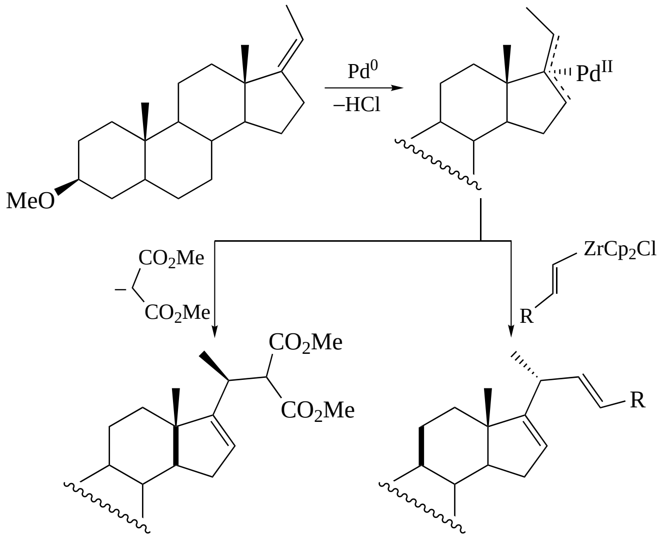
MeO
Pd0
–HCl
PdII
CO2Me
CO2Me
ZrCp2Cl
R
CO2Me
CO2Me
R

Scheme 17

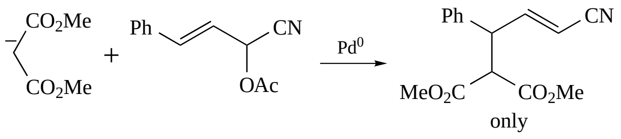
CO2Me
CO2Me
Ph
CN
OAc
Pd0
Ph
CN
MeO2C
CO2Me
only

(60)

Allylsilanes lead to vinylsilanes by the usual allylic rearrangement mechanism, and the example in equation (61) nicely demonstrates the equilibration of the alkene unit to the more stable (E) version.

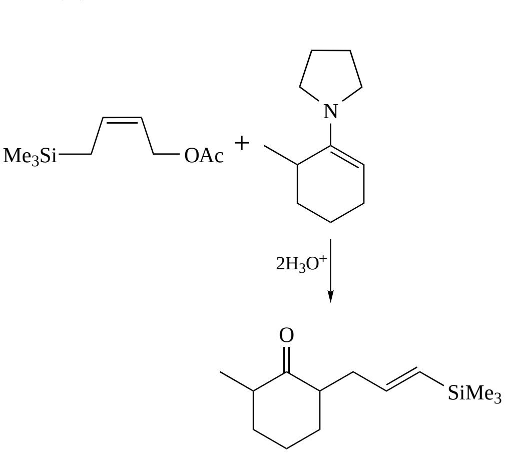
Me3Si
OAc
N
2H3O+
O
SiMe3

(61)

The vitamin E side chain can be prepared stereoselectively by addition to an homochiral vinyl lactone (equation 62). The product is the result of selective anti addition.

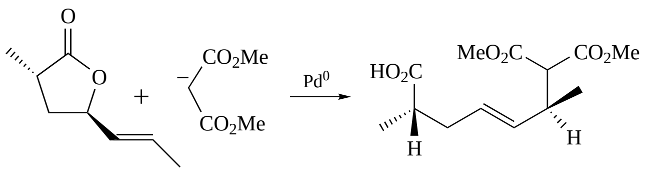
O
O
CO2Me
CO2Me
Pd0
HO2C
MeO2C
CO2Me
H
H

(62)

The Heck reaction with 1,3-dienes can lead to in situ generation of allyl–Pd complexes, with nucleophile coupling in a second step (equation 63).

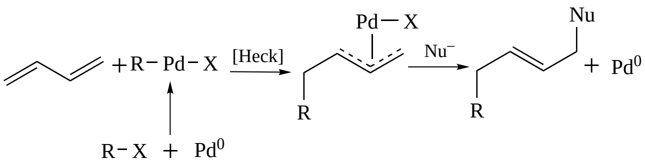
+R−Pd−X
[Heck]
Pd−X
Nu−
Nu
+ Pd0
R
R
R−X + Pd0

(63)

An example of the overall strategy is the coupling of bromopyridine and a secondary amine across 1,3-butadiene (equation 64). The conditions employ Pd^{II} and rely on in situ reduction to the effective catalyst, a version of Pd^0.

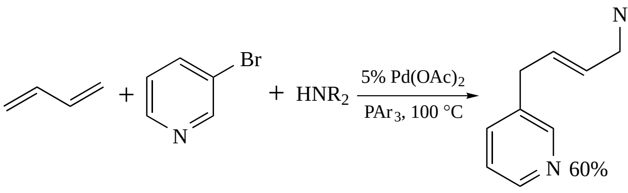
Br
N
+ HNR2
5% Pd(OAc)2
PAr3, 100 °C
NR2
N 60%

(64)

The selectivity of the Heck reaction shows up with unsymmetrical dienes, leading to initial coupling at the less-substituted alkene and then nucleophile addition at the other end (equation 65). The intramolecular Heck reaction also is efficient, leading in equation (66) to dihydrofurans.

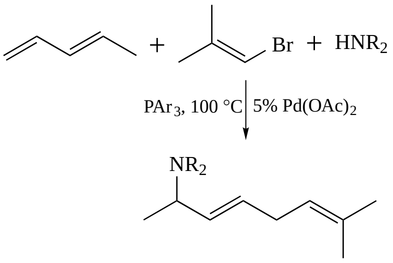
Br + HNR2
PAr3, 100 °C
5% Pd(OAc)2
NR2

(65)

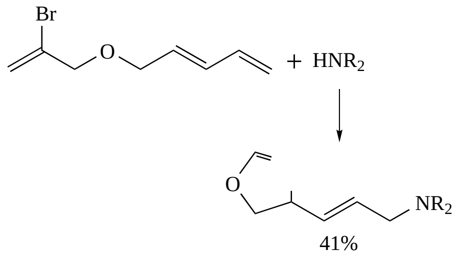
Br
O
+ HNR₂
O
NR₂
41%

(66)

5.3 Variations: Other Metals

The simple metal hexacarbonyls of molybdenum and tungsten will catalyze allylic alkylation, with dramatic effects on the regioselectivity.[92] The comparison of $Mo(CO)_6$ with Pd^0 shows a remarkable contrast in regioselectivity (equation 67).[92] The basis for the selectivities is somewhat mysterious, especially considering another dramatic reversal of selectivity with change in anion, from malonate, using $Mo(CO)_6$ and the same conditions. This regioselectivity of Mo carbonyl catalysts has been used to synthesize (*R*)-baclofen, as shown in equation (68).

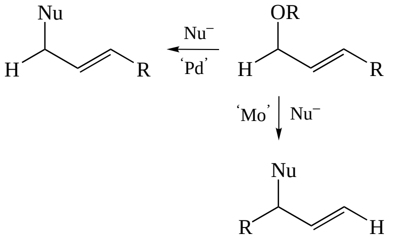
Nu
H
R
Nu⁻
'Pd'
OR
H
R
'Mo'
Nu⁻
Nu
R
H

(67)

Parent Ligand: bis(pyridylamide)

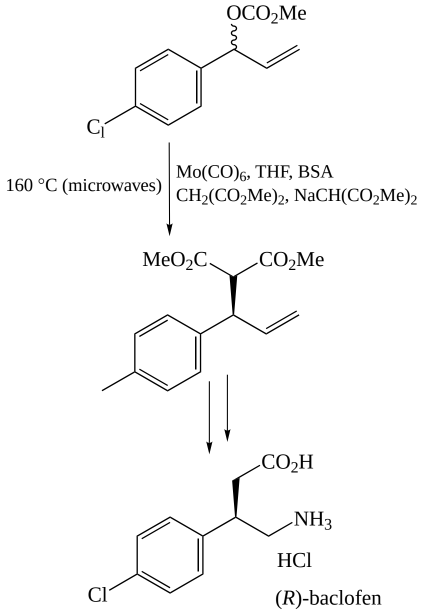
OCO₂Me
Cl
160 °C (microwaves)
Mo(CO)₆, THF, BSA
CH₂(CO₂Me)₂, NaCH(CO₂Me)₂
MeO₂C
CO₂Me
CO₂H
NH₃
HCl
Cl
(R)-baclofen

(68)

Tungsten carbonyl complexes are also effective catalysts, showing some preference for nucleophile addition at the more hindered position of an unsymmetrical allyl ligand (equations 69 and 70).[93] Other allylic alkylation reactions have been reported.[94]

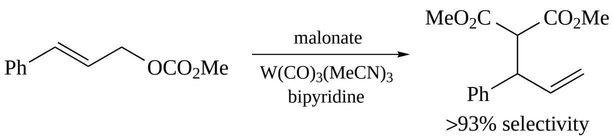
Ph
OCO₂Me
malonate
W(CO)₃(MeCN)₃
bipyridine
MeO₂C
CO₂Me
Ph
>93% selectivity

(69)

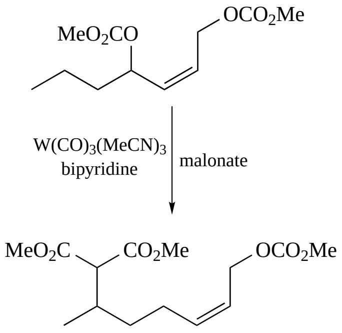
MeO₂CO
OCO₂Me
W(CO)₃(MeCN)₃
bipyridine
malonate
MeO₂C
CO₂Me
OCO₂Me

(70)

A number of π-allylmetal complexes react with nucleophiles resulting in transfer of the allyl group from the metal to the nucleophile.[95–100] As previously shown the most developed are the π-allylpalladium complexes. However, π-allyltricarbonylcoblat(I) complexes also react with carbanions to produce allylic alkylation products in good yield. Acylated π-allylcobalt complexes when reacted with a nucleophile result in an overall acylation/alkylation of 1,3-dienes, (equation 71).

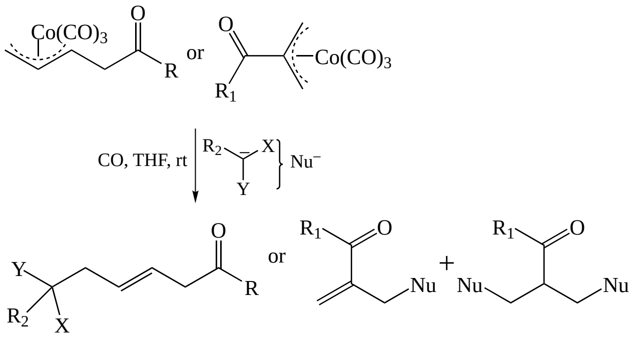
Co(CO)₃
O
R
or
O
R₁
Co(CO)₃
CO, THF, rt
R₂
X
Y
Nu⁻
Y
R₂
X
O
R
or
R₁
O
Nu
+
R₁
O
Nu
Nu

$R_1 = Me, P$
$R_2 = H, Me$
$X = CO_2Me, CO_2Et, Ac, CN$
$Y = CO_2Me, CO_2Et$

(71)

Unsubstituted malonate esters and ethyl acetonate give highest yields, while methyl substituted analogs are less effective. Esters and ketones enolates are do not undergo allylic alkylation, and instead induce proton abstraction, generating acyldienes. There seems to be competition between nucleophilic attack and proton abstraction when utilizing unstable carbanions.[95]

Copper-catalyzed asymmetric allylic alkylations with organometallic reagents used for small-ring openings, such as epoxides and aziridines, have gained interest. Illustrating the differences between palladium and copper is the ring opening of oxabicycles alkenes, (equation 72), where the regioselectivity found with the unsymmetrical palladium-catalyzed product rules out the formation of π-allyl palladium intermediate. In contrast the copper-catalyzed products configuration points to a π-allyl pathway followed by reductive elimination at the less-hindered secondary terminus with retention of overall structure.[96]

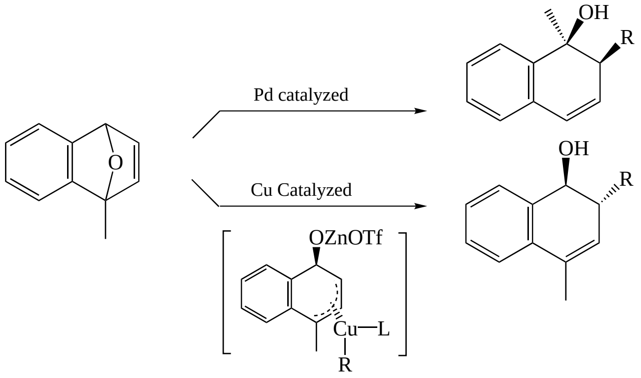

(72)

An in-depth study of platinum allylic alkylation and subsequent comparison to ligand-identical palladium catalysts was done by Blacker *et al*. The allylic alkylation of diphenyl-2-enyl acetate with dimethyl malonate, (equation 73), reveals activity for a variety of complexes with activity restricted by the source of zerovalent platinum (Table 1). Nonactive complexes are thought to be less prone to dissociation into coordinatively unsaturated catalytical active species.

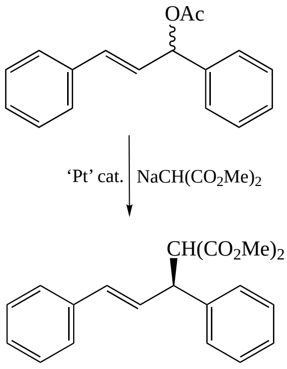

(73)

Table 1 Types of platinum complexes that catalyze allylic alkylation at room temperature

	Catalyst	Conversion	Isolated yield
1	$[(Ph_3P)_4Pt]$	100	82
2	$[(Ph_3P)_2Pt$-ethylene]	100	88
3	$[(dppe)_2Pt]$	0	0
4	$[(Ph_3P)_2Pt$-stilbene]	100	N/A
5	$[\{(PhO)_3P\}_4Pt]$	0	0
6	$[(dppe)PtC_3H_5]BF_4$	100	78
7	$[(Ph_3P)_2PtCl_2]$ and $NaBH(OMe)_3$	100	85

A phosphinooxazoline ligand has been utilized to control enantioselectivity with success. It is determined that overall platinum catalyst generally give better regioselectivity than palladium towards products containing more electron-deficient double bonds.[97]

Rhodium-catalyzed allylic alkylation demonstrates excellent regioselectivity provided there is a strong π-acidic ligand present on the metal center (equation 74). In a unique approach, Evans *et al*. demonstrated a tandem allylic alkylation and Pauson–Khand annulation reaction using the same Rh catalysis with high regio- and diastereoselectivity. Initially product (**1**) is produced in excess (37:1, **1:2**) and the following annulation is highly enantioselective (7:1, **3:4**) resulting in one major product (**3**).[98]

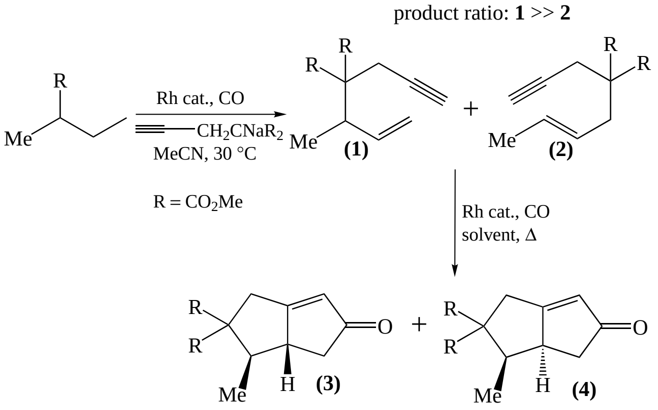

(74)

Ruthenium-catalyzed allylic alkylation falls between known catalysis with respect to regioselectivity and chirality of products. Like Pd, Mo, and W – but unlike Rh – regioselectivity is not highly dependent on the nature of the starting carbonate. However, unlike Pd and Mo, but similar to Rh and W, substitution of the chiral substrate occurs with high retention of configuration, (equation 75). Hence the Ru system compliments other metal-catalyzed allylic systems well.[99]

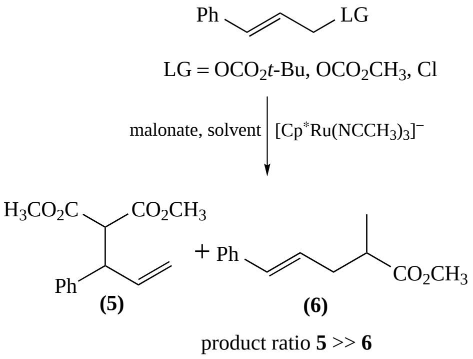

(75)

Though largely unstudied, it has recently been shown that Ir-catalyzed allylic substitution reactions where a strong π-acceptor ligand, for example, triphenylphosphite, is present in situ will give rise to excellent regioselectivity in favor of the branch product (equation 76) for both aryl and alkyl-substituted substrates. When a chiral π-acceptor ligand, for example, phosphinooxazoline, is used, high enantioselectivity can be achieved as well.[100]

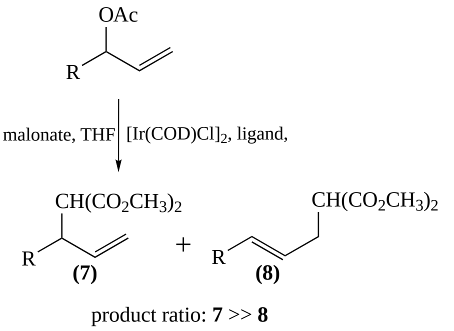

(76)

5.4 Variations: Propargyl–Metal Complexes

While little is known about the reactivity of simple propargyl–metal complexes toward nucleophiles, the special case of alkyne coordination with $Co_2(CO)_6$ leads to stable propargyl cations that can react smoothly with nucleophiles. The overall process begins with spontaneous coordination of the cobalt unit, added as $Co_2(CO)_8$, with the alkyne in a pseudotetrahedral arrangement. If there is an electronegative atom in the propargyl position, ionization is strongly enhanced; the metal-coordinated propargyl cation can be directly observed and is comparable in stability to the trityl cation. Nucleophile addition produces a coordinated alkyne with the nucleophile in the propargylic position; oxidative cleavage releases the newly substituted alkyne – sometimes referred to as the Nicholas reaction (Scheme 18). The process is stoichiometric, primarily because of the stability of the alkyne–cobalt complexes; simple ligand exchange to release the alkyne unit has not been demonstrated. The overall result, replacement of an electronegative atom from an activated position by nucleophile displacement, does not appear to justify the elaborate intermediates compared to easy direct displacement. However, the direct displacement is often complicated by appearance of allene substitution products, while the metal-promoted process gives 100% selectivity for the alkyne derivative. The reactivity is high, as illustrated by direct reaction with an enol silyl ether (equation 77). After cation generation by acid treatment and nucleophile coupling, the intermediate substituted alkyne complex can be isolated, purified by chromatography, and the cobalt detached by oxidation.[101]

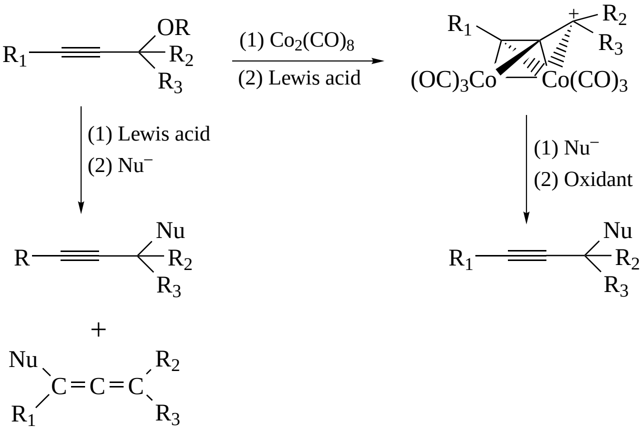

Scheme 18

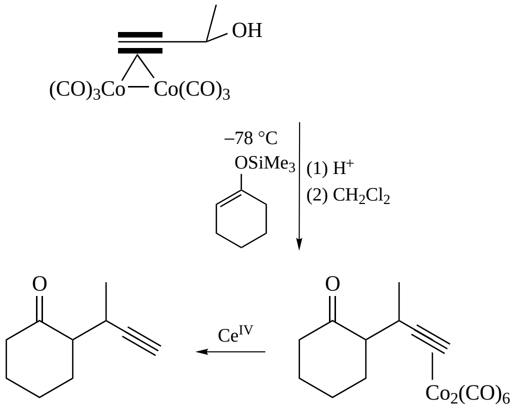

(77)

The method is limited because of the requirement for stoichiometric reagents, but impressive applications in the preparation of complex molecules have appeared. For example, a model system for ene–diyne antibiotics has been prepared by an intramolecular route (Scheme 19).[102] Added versatility arises from the electophilic coupling of vinyl–propargyl complexes, such as in Friedel–Crafts acylation conditions.

Coupling of silyl enol ethers or boron enolates with $Co_2(CO)_6$-stabilized carbocations, generated via Lewis acid treatment of the appropriate propargyl ethers or aldehydes (aldol reaction), via the Nicholas reaction has been used to obtain large, highly strained, ring ketones.

5.5 Summary

Catalytic allylic alkylation with Pd^0 is one of the most powerful techniques to come out of the development of organotransition metal reagents for organic synthesis. Especially powerful is the versatility in the reactants; a wide range of allyl species with electronegative allylic substituents and essentially every type of nucleophile. Allylic alkylation using metals other than Pd are known but have been less commonly applied to organic synthesis.

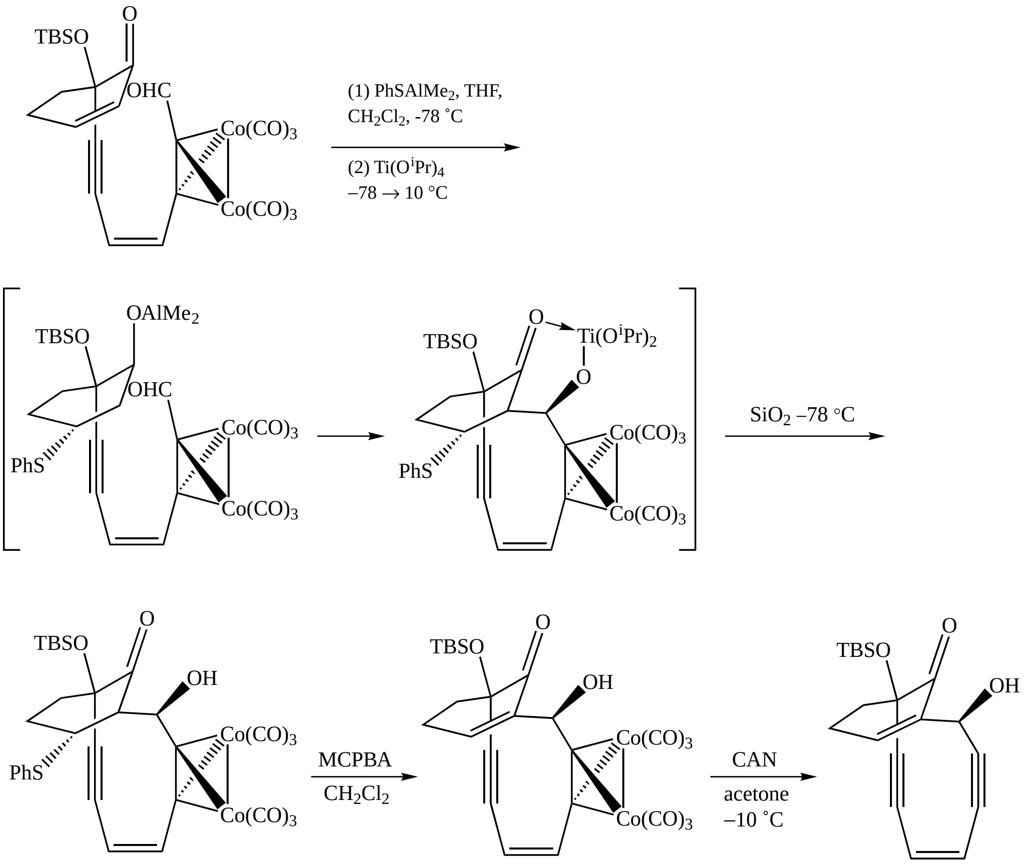

Scheme 19

6 NUCLEOPHILIC ADDITION TO 1,3-DIENE LIGANDS

6.1 Introduction

Complexes of 1,3-dienes in the η^4-arrangement with metals can be formed by direct ligand displacement, and are known for many metals. The η^2-arrangement is also possible, and is probably the preferred mode of coordination with Pd^{II} in the examples below. Even with the simplest diene ligand, from 1,3-butadiene, questions of regioselectivity arise. Addition at the terminal position leads to an allyl–metal complex, while internal addition produces a homoallyl complex (equation 78). The early correlation of regioselectivity in all types of nucleophile addition to ligands in metal complexes suggested that terminal addition would be preferred for cationic complexes.**6** The general rule of anti addition again applies. Two systems have been studied more: the complexes formed in situ from Pd^{II} and a 1,3-diene, and the stable diene complexes of $Fe(CO)_3$.

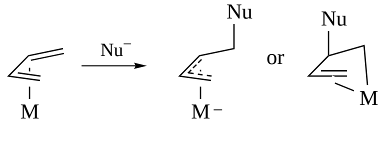

(78)

6.2 Oxidation of 1,3-Dienes with Palladium(II) Catalysis[103]

This process takes advantage of the fact that coordination of a 1,3-diene with Pd^{II}, presumably in the η^2-mode, can activate the diene toward nucleophile addition. The product is an allyl–Pd^{II} complex, which, as described in the previous section, is also reactive toward nucleophiles, also at the less-substituted position, and eventually leads to a 1,4-disubstituted 2-alkene. The Pd ends up as Pd^0 and must be reoxidized in order to operate a smooth catalytic cycle (equation 79). The optimum conditions for the process have been worked out in fine detail.**103**

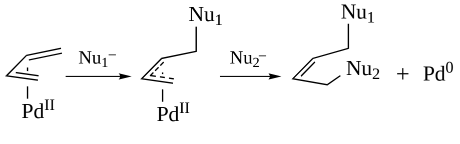

(79)

An interesting example of Pd-catalyzed oxidation of a 1,3-conjugated diene is shown in Scheme 20. This reaction type produces stero-defined 1,4-functionalized dienes, which are useful synthetic building blocks and reaction intermediates. Benzoquinone oxidation of an η^3-allyl–Pd intermediate is a key step in releasing the organic product.**104**

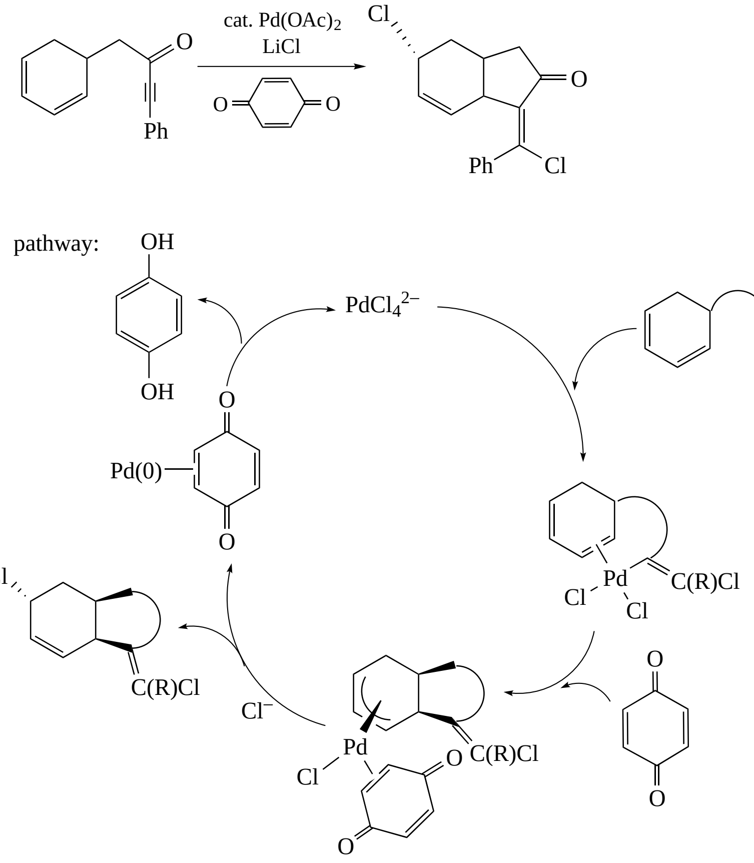
cat. Pd(OAc)2
LiCl
Ph
Cl
O
pathway:
OH
PdCl4 2−
Pd(0)
R
Pd
Cl
C(R)Cl
Cl−
Cl
O

Scheme 20 Pd(II) catalyzed intramolecular 1,4-oxidation of 1,3-conjugated diene

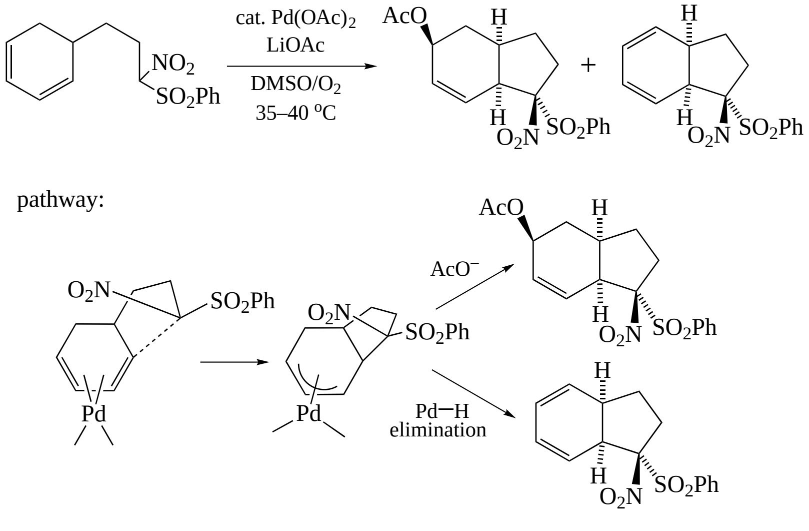
cat. Pd(OAc)2
LiOAc
DMSO/O2
35–40 °C
NO2
SO2Ph
AcO
H
O2N
+
pathway:
AcO−
Pd
Pd—H
elimination

Scheme 21

An example of cis-addition of two nucleophiles to a 1,3-diene catalyzed by Pd(II) is shown in Scheme 21.[105] Pd–H elimination is competitive with addition of the second nucleophile affording either mono or di-unsaturated bicyclic products.

With a limited amount of chloride anion (0.2 mol. equiv.; twice the amount of Pd^{II}), the coordination of acetate is inhibited, and the key intermediate is presumably an allyl–Pd^{II} with chloride attached to the Pd (Scheme 22).[106] Then *syn* addition of an acetate is unlikely,

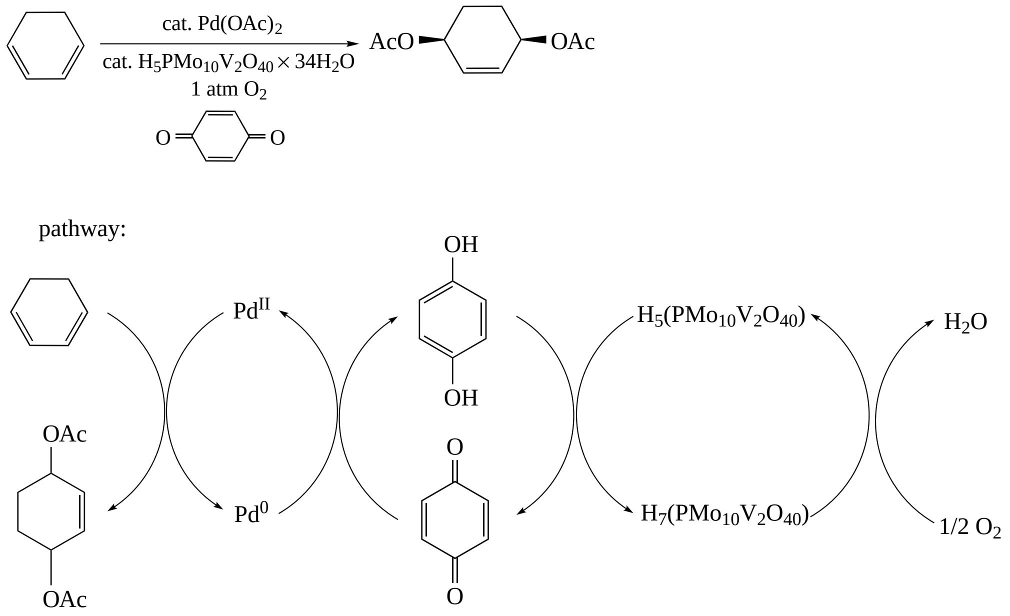
cat. Pd(OAc)$_2$
cat. H$_5$PMo$_{10}$V$_2$O$_{40}$ × 34H$_2$O
1 atm O$_2$
AcO
OAc
O
O
pathway:
Pd^{II}
Pd^0
OH
OH
OAc
OAc
O
O
H$_5$(PMo$_{10}$V$_2$O$_{40}$)
H$_7$(PMo$_{10}$V$_2$O$_{40}$)
H$_2$O
1/2 O$_2$

Scheme 22 Pd(II) catalyzed 1,4-diacetoxylation of 1,3-dienes

and the product results from anti (external) addition of acetate.

With excess chloride anion, not only is the syn acetate addition mechanism blocked, but the chloride competes effectively with external acetate as the primary nucleophile in anti addition (Scheme 23).[107]

The versatility of the 1,4-disubstituted cyclohexene derivatives as synthesis intermediates, with emphasis on stereo control, was demonstrated by substitution procedures. Direct S$_N$2 with malonate anion proceeds selectively for Cl with inversion, and Pd^0-catalyzed substitution also proceeds selectively at Cl, but with retention. A second substitution, Pd^0-catalyzed, using dimethylamine in this case, leads to replacement of the acetate with retention (Scheme 24).[103]

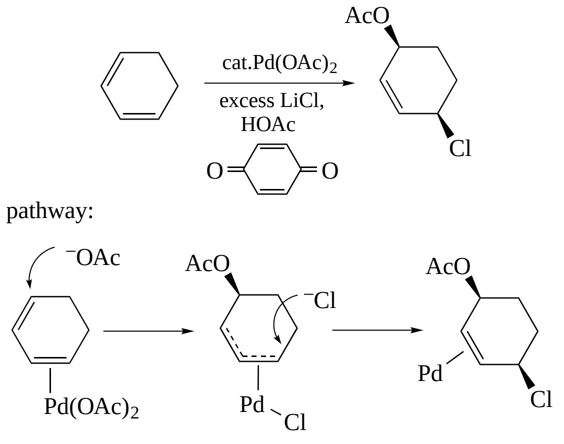

Scheme 23 Formation of *cis*-1-acetoxy-4-chlorocyclohex-2-ene

6.3 Nucleophilic Addition to 1,3-Diene–Fe(CO)$_3$ Complexes

Iron tricarbonyl forms exceptionally stable complexes with 1,3-dienes. The complexes are uncharged, readily soluble species, chromatographable and, for the simpler versions, distillable. They are formed by direct reaction of the 1,3-diene with Fe(CO)$_5$, Fe$_2$(CO)$_9$, or Fe$_3$(CO)$_{12}$. These iron–diene complexes are known to be reactive toward electrophiles, undergoing the analogous reaction to electrophilic aromatic substitution under Friedel–Crafts conditions. However, it is clear that the metal–ligand unit increases the polarizibility of the diene unit, and, with a sufficiently reactive nucleophile, can provide a sink for electron density. How reactive does the nucleophile need to be? The other important selectivity question for 1,3-dienes concerns the regioselectivity.

It was determined that carbon nucleophiles derived from carbon acids with p$K_a > 22$ or so are sufficiently reactive to combine with the diene ligand rapidly at $-78\,°$C to produce an anionic intermediate (Scheme 25).[108–110] With a few exceptions, the regioselectivity favors formation of the homoallyl anionic complex from addition at C-2, by kinetic control. This intermediate can be quenched with protons to give the terminal alkene, or can react with excess CO to produce an acyl iron intermediate. Following the recipes of Collman's reaction, the acyl iron intermediate can lead to methyl ketones, aldehydes, or carboxylic acids. The processes are illustrated with the 1,3-cyclohexadiene complex (Scheme 25).[111]

The carbon nucleophiles which will add to 1,3-diene-Fe(CO)$_3$ complexes include LiCH$_2$–X (where X = CO$_2$Me, CN, SPh) as well as the cyanohydrin acetal carbanions and

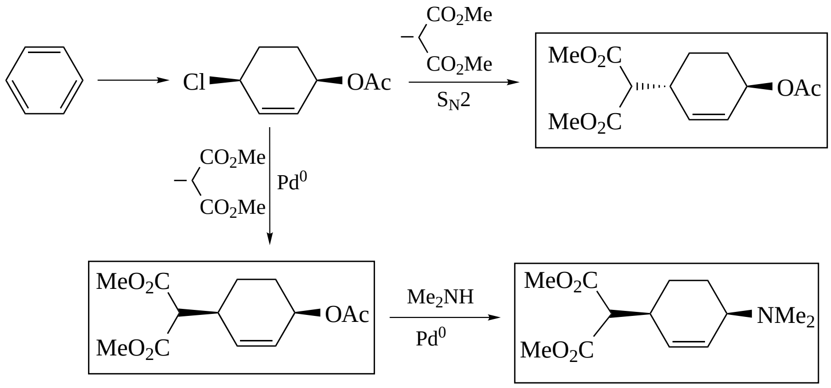

Scheme 24 Substitution procedures to elaborate the 1,4-disubstituted-2-cyclohexenes

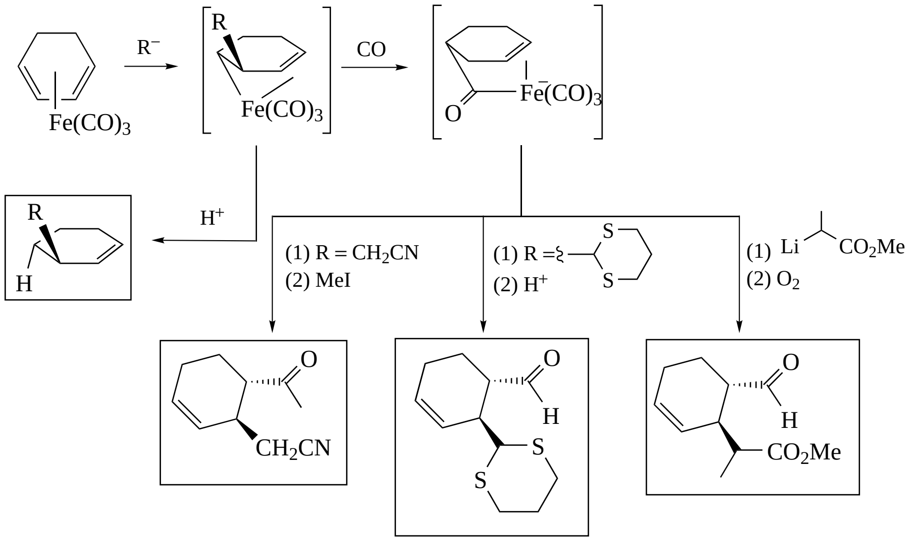

Scheme 25 Pattern of reactions of 1,3-cyclohexadiene–Fe(CO)$_3$

2-lithio-1,3-dithiane. Simple ketone enolate anions are of borderline reactivity; with activation, such as the use of a potassium counterion and a crown ether additive, 50% yields or better are observed. With more reactive anions, such as PhLi, alkyl–Li, and alkyl–MgX, addition is preferred at a CO ligand.

Addition of carbon nucleophiles to an internal carbon atom of a diene ligand, even with highly reactive nucleophiles such as diphenylmethyllithium, is reversible at higher temperatures, around 0 °C.[112] Equilibration allows slower but more favorable addition at a terminal position, to give (irreversibly) the allyl–Fe(CO)$_3$ anionic complex. The process is illustrated in Scheme 26. Intermediate (**9**) can be trapped with electrophiles at – 78 °C and undergoes transformation to the thermodynamically stable η^3-allyl structure, (**10**), at elevated temperatures.

The example shown in Scheme 25 of 1,3-cyclohexadiene undergoing nucleophile addition and then CO insertion and trapping is not, in fact, the general case. With most open-chain 1,3-dienes, the intermediate acyl–Fe anionic complex undergoes CO insertion and then intramolecular rearrangement by alkene insertion (Scheme 27).[113] The resulting cyclopentanone undergoes a set of β-H eliminations/readditions to

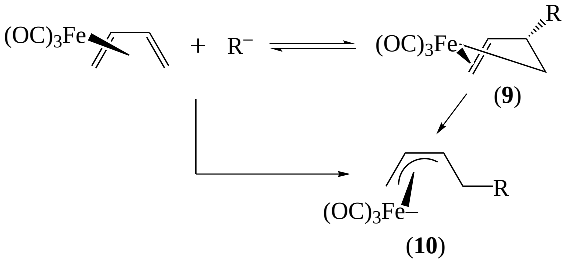

Scheme 26 Reversible addition at an internal carbon of (1,3-diene)Fe(CO)$_3$ complexes

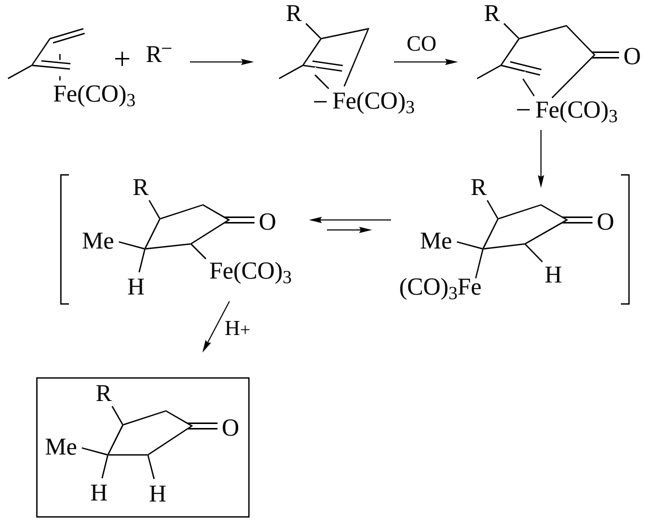

Scheme 27 Mechanism of cyclopentanone formation

give a stable iron enolate. This species is resistant to further CO insertion and is simply protonated during the isolation procedure to produce a cyclopentanone. The overall anti stereoselectivity is revealed with isoprene as the substrate, giving a 3,4-*cis* disubstituted cyclopentanone.

There is no exception to the regioselectivity rule that nucleophile addition proceeds by kinetic control at the unsubstituted internal position of the diene ligand. With 1-methoxy-1,3-cyclohexadiene, the addition/CO insertion/MeI quenching leads to a latent 1,4-dicarbonyl derivative (equation 80). With 2-methoxy-1,3-butadiene, the same conditions (but with protons instead of MeI) lead to a 3-methoxycyclopentanone that is very sensitive to acid, and can be readily converted to the corresponding cyclopentenone (equation 81).

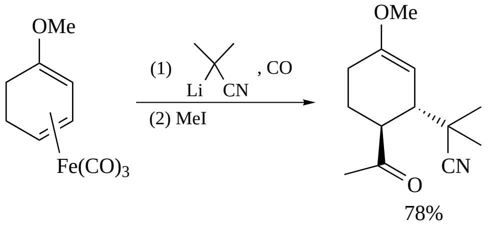

(80)

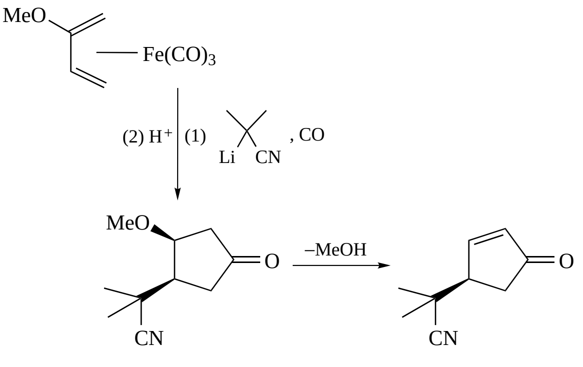

(81)

The selectivity demonstrated by these examples is potentially very attractive in synthesis problems; the stoichiometric use of iron carbonyl should not be a serious limitation. The reactivity of the nucleophile is required to be quite high, and perhaps this lends a significant limitation.

6.4 Nucleophilic Addition to Cationic 1,3-Dienyl–Mo(CO)$_2$Cp Complexes

Cationic complexes of Mo^{II} have an intrinsically higher reactivity compared to the Fe^0 analogs. For example, the complex of 1,3-cycloheptadiene reacts with nucleophiles ranging from simple enamines to organomagnesium reagents.**114** The stereoselectivity verifies the expected anti addition. The product is an allyl–Mo^{II} complex, which can be converted back into a 1,3-diene cationic complex by abstraction of an anti-hydride using, for example, trityl cation. A second addition leads to overall 1,4-substitution with complete control over the two new stereocenters (cis). However, detachment of the ligand from the Mo requires further reaction, such as oxidative decomplexation.

Related chemistry of a cationic η^4-α-pyran Mo(II) complex is shown in Scheme 28. Hydride addition to the cationic reactant complex gives a neutral allyl–Mo that is oxidized by pyridinum dichromate (PDC) to a cation. Nucleophilic addition of water and oxidative decomplexation of the Mo fragment gives an enone. Substituted α-pyran ligands follow one of two paths depending on the electronic and steric effects of the substituent, as shown.

6.5 Summary

The addition of oxygen and chloride nucleophiles to dienes transiently activated by catalytic Pd^{II} is a practical process for production of 1,4-disubstituted 2-alkenes from 1,3-dienes; however, it is not useful with carbon nucleophiles. Examples of carbon nucleophile addition to Fe^0 and Mo^{II} complexes show useful selectivity, but only in stoichiometric processes, and few applications have appeared.

7 NUCLEOPHILE ADDITION TO η^5-CYCLOHEXADIENYL LIGANDS

7.1 Introduction

As the complexity of the ligand increases and as additional carbon atoms are included, the restrictions on starting material availability and potential applications increase rapidly. The

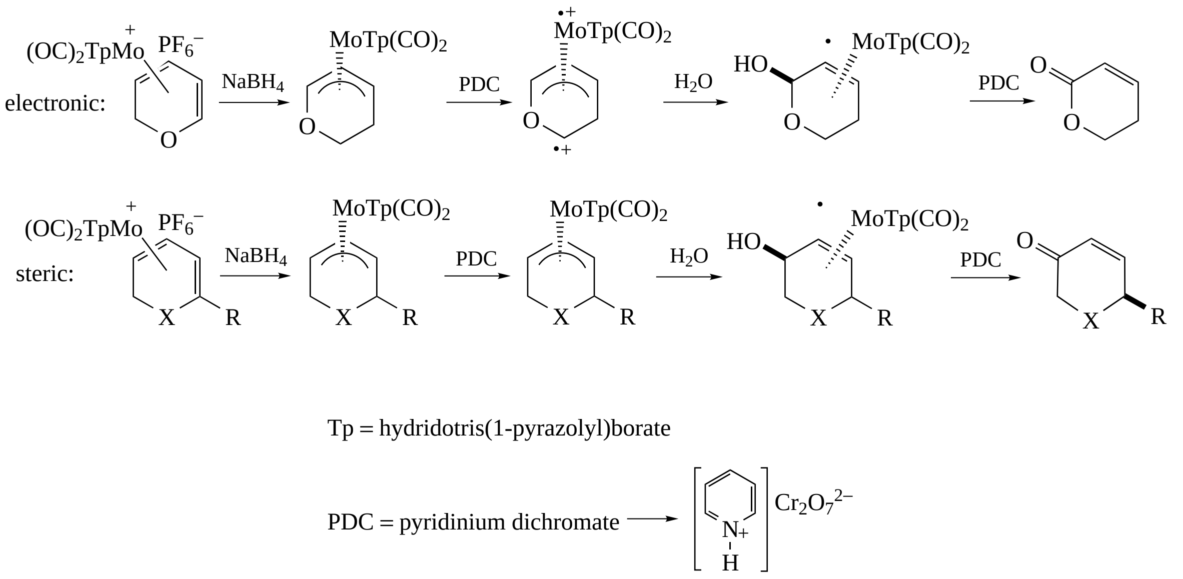

Scheme 28

selectivity questions also increase, as suggested by the general process (equation 82). There are relatively few different types of η^5-pentadienyl ligands.

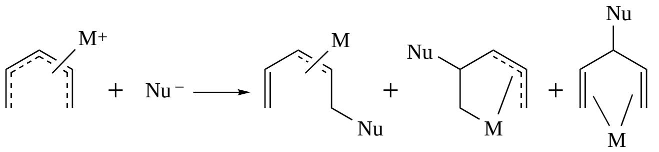

(82)

7.2 Cyclohexadienyl–M(CO)$_3$ Cation Complexes[115–119]

7.2.1 Basic Process

One type of η^5-pentadienyl ligand is easily available, and many substituted variations are simple to arrange. This is the η^5-cyclohexadienyl-Fe(CO)$_3$ set of cationic complexes, which are obtained from Birch reduction products of arenes in a thermal reaction, followed by loss of a substituent with a pair of electrons. Equation (83) oversimplifies the process for the preparation of η^5-cyclohexadienyl-Fe(CO)$_3$ cation, typically, the leaving group is a hydride, pulled off with agents such as trityl cation. In special cases, the leaving group is a heteroatom such as methoxy; key questions include how to position the X group in the proper position (adjacent to the 1,3-diene system) to leave smoothly. Similar synthetic strategies have been employed to prepare the corresponding η^5-cyclohexadienyl cation complexes of the following metals, Cr,[120–123] Mo,[120] W,[120] and Mn.[120,124]

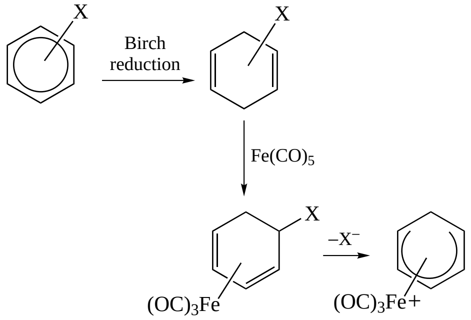

(83)

The cationic complex is highly electrophilic, reacting even with simple electron-rich arenes as nucleophiles. The range of successful nucleophiles extends across the complete range of nucleophile reactivity, up to n-BuLi, under the proper reaction conditions (see below). The addition is from the anti direction, without exception, and at a terminal position. The product 1,3-diene−metal complex is very stable, and the ligand can be obtained only by deliberate oxidation; trimethylamine N-oxide is a gentle oxidants, but I_2 is often used. The stability of the reactants and products, together with the oxidative detachment methods means that the process is not a reasonable candidate for catalysis (equation 84).[124] At the same time, the metal system is convenient, inexpensive, and has minimal toxicity problems, so that a large-scale batch process is not unreasonable.

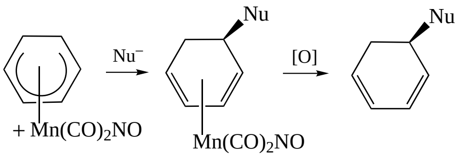

(84)

7.2.2 Range of Effective Nucleophiles

In the initial development of the methodology, using standard conditions in tetrahydrofuran (THF), for example, a wide range of carbon and heteroatom nucleophiles was successful (Scheme 29).**119**

A special case is the use of dichloromethane with organolithium reagents. This solvent is not the obvious choice for RLi reactions, but it has a strong effect in minimizing electron-transfer side reactions and/or promoting the simple nucleophile addition. Similarly, the reaction of the cyclohexadienyl cationic complexes with Grignard reagents leads to homocoupling of the cyclohexadienyl ligand (Scheme 30). There is obviously a delicate balance between the pathway for two-electron transfer, with bond formation of the nucleophile with the cyclohexadienyl ligand, and one-electron transfer to give the 19-electron cyclohexadienyl–$Fe(CO)_3$ complex, which then dimerizes. Replacing a CO ligand with the more electron-donating phosphine ligand should clearly slow both processes, but it turns out that the one-electron transfer reduction is more strongly inhibited and good yields of coupling with Grignard reagents is the general rule for the monophosphine complexes.

7.2.3 Regioselectivity

There are three nonequivalent positions on the simplest η^5-pentadienyl ligand. In the parent case (η^5-cyclohexadienyl) and in every other case that has been studied, the addition is at a terminal position to give a 1,3-diene–$Fe(CO)_3$ complex. Questions immediately arise regarding the effect of substituents on the reactivity of the cyclohexadienyl ligand: how does an original arene substituent influence the regioselectivity in the nucleophile addition? From examples with strong perturbations, such as alkoxy and carbomethoxy substituents, rules for regioselectivity have been formulated: addition is at the terminal position away from the more electron-donating substituent (such as methoxy). This is true even when the predicted position is already substituted with an alkyl group. The 2-methoxycyclohexadienyl complex is readily available, since it is the preferred isomer from hydride abstraction from the complex of the Birch reduction product of anisole (Scheme 31). In this example, cyanide anion adds under mild conditions, and the iron is decomplexed oxidatively while the enol ether spontaneously hydrolyzes to the ketone. The overall transformation is equivalent to nucleophilic aromatic substitution with the

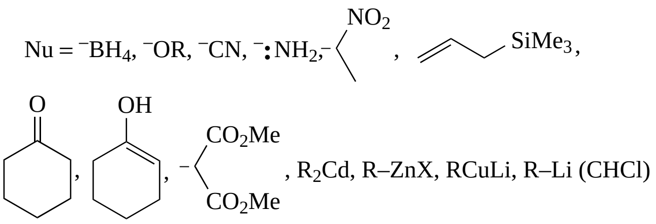
Nu = $^-BH_4$, ^-OR, ^-CN, $^-$:NH_2,
NO_2
$SiMe_3$,
O
OH
CO_2Me
CO_2Me
, R_2Cd, R–ZnX, RCuLi, R–Li (CHCl)

Scheme 29 Range of nucleophiles that add successfully

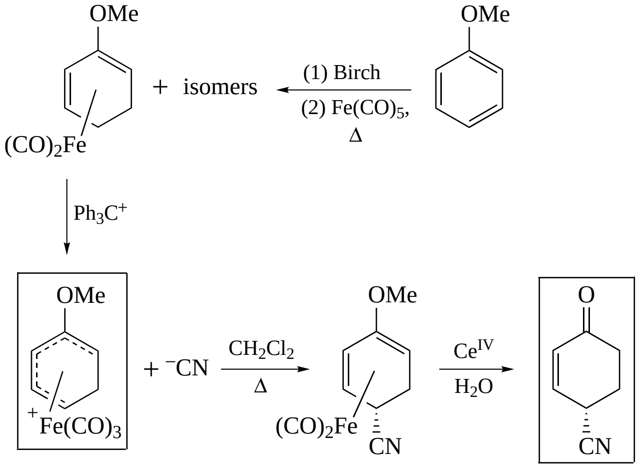

Scheme 31 Application of anisole

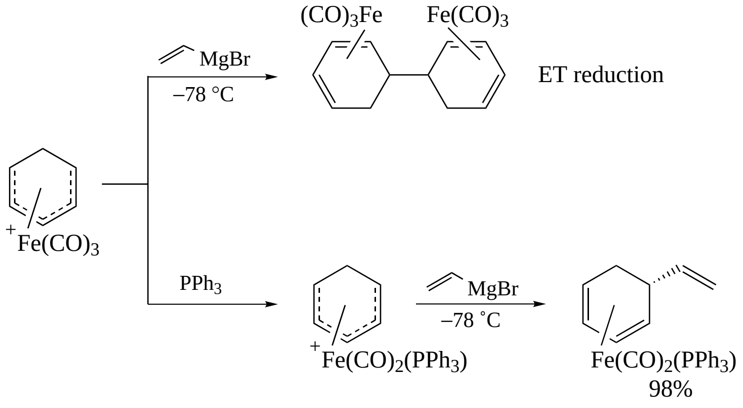

Scheme 30 Electron transfer versus nucleophile addition

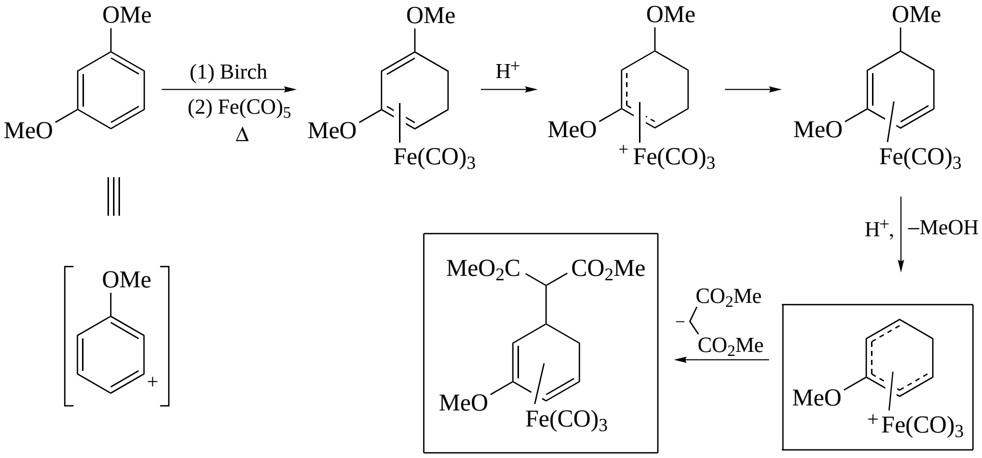

OMe
MeO
(1) Birch
(2) Fe(CO)5
Δ
H+
Fe(CO)3
+ Fe(CO)3
H+, –MeOH
MeO2C
CO2Me
CO2Me
CO2Me

Scheme 32 Generation of the 3-methoxycyclohexadienyl complex

methoxy group serving as a para-directing group. This same regioselectivity can be seen in the application of anisole using the corresponding η^5-cyclohexadienyl $Cr(CO)_3$ complex.[121–123]

At the same time, the 3-methoxycyclohexadienyl complex (Scheme 32) can also be prepared, presumably under kinetic conditions that do not allow isomerization of the double bonds. The key technique is acid-induced elimination of an alkoxy group, and the starting material is *m*-dimethoxybenzene. The addition of the malonate anion is at one of the two equivalent terminal positions, and from a direction anti to the iron. The product is a stable complex that may be purified by chromatography or may be decomposed oxidatively to free the organic ligand.

The strong directing effect of a 2-methoxy group is evident in the nucleophilic addition to the 2-methoxy-5-methylcyclohexadienyl ligand. Addition is strongly selective for the position pseudopara to the methoxy group, even in the presence of the steric hindrance provided by the Me group (equation 85). As the steric hindrance grows, addition can shift to the other terminal position.

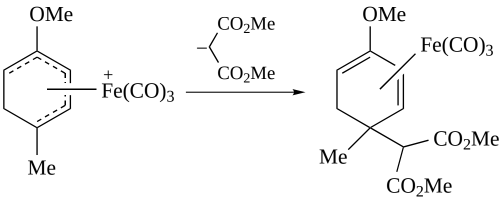

OMe
+ Fe(CO)3
Me
CO2Me
CO2Me
OMe
Fe(CO)3
Me
CO2Me
CO2Me

(85)

The more stable position for a electron-withdrawing group, such as carbomethoxy, is at C-3 of the starting cyclohexadienyl complexes, and terminal addition is again observed. Even the weak nucleophile, allylsilane, reacts at room temperature at the less-hindered terminal position (equation 86).

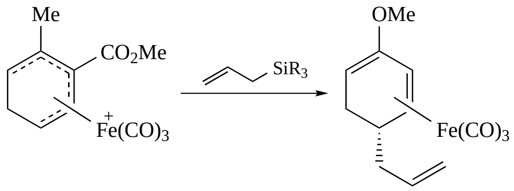

Me
CO2Me
+ Fe(CO)3
SiR3
OMe
Fe(CO)3

(86)

Silicon acts as an electron acceptor and stabilizes the 3-silylcyclohexadienyl ligand during hydride abstraction (equation 87).

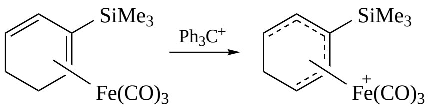

SiMe3
Fe(CO)3
Ph3C+
SiMe3
+ Fe(CO)3

(87)

A particularly attractive starting material is the homochiral carboxylic acid derivative, obtained by conventional resolution. Esterification and then simple amine addition and oxidative decomplexation produces a precursor of (−)-gabaculine (Scheme 33).

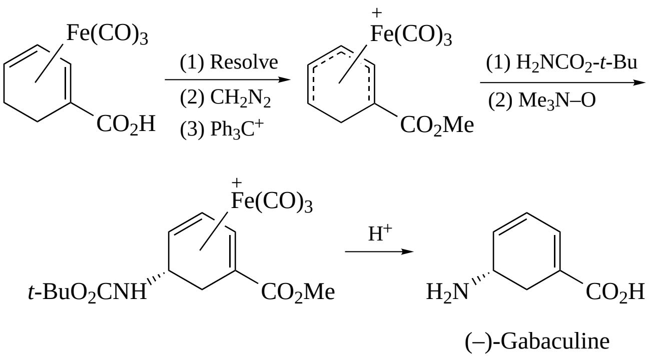

Fe(CO)3
CO2H
(1) Resolve
(2) CH2N2
(3) Ph3C+
+ Fe(CO)3
CO2Me
(1) H2NCO2-t-Bu
(2) Me3N–O
+ Fe(CO)3
t-BuO2CNH
CO2Me
H+
H2N
CO2H
(–)-Gabaculine

Scheme 33 Homochiral complexes

There is an opportunity for multiple substitution, via regeneration of the cyclohexadienyl cationic complex, after the initial nucleophile addition. Unfortunately, the required *exo* hydride abstraction is severely retarded by the exo substituent (nucleophile unit) (equation 88).

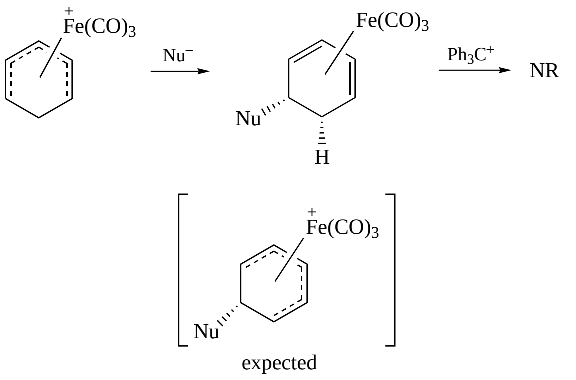

(88)

7.3 Cycloheptatrienyl–Fe(CO)$_3$ Cationic Complexes[125–127]

Cycloheptadiene complexes are useful synthetic building blocks in the preparation of complex organic and natural products. A variety of substituted cycloheptadiene complexes can be prepared via catalytic hydrogenation of the respective cycloheptatriene–Fe(CO)$_3$ complex. Subsequent oxidation liberates the iron carbonyl moiety affording the uncomplexed substituted cycloheptadiene complex (Scheme 34).

7.4 Summary

A number of substituted cyclohexadienyl–Fe(CO)$_3$ cationic complexes are readily available and will add nucleophiles with a wide range of reactivity. The addition can be highly regioselective and always stereospecific (exo addition). This methodology leads to useful and complex intermediates, but is limited by the need for stoichiometric application of the metal and deliberate synthesis of the starting iron complexes.

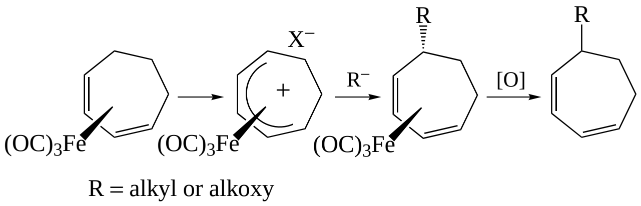

Scheme 34 Synthesis of substituted cycloheptadiene complexes

8 NUCLEOPHILIC ADDITION TO ARENE–METAL COMPLEXES

8.1 Introduction

The coordination of the metal to the π-orbital system of an arene ring makes the system much more polarizable and can generate a large permanent dipole moment, with the ring being electron poor. The arene ring can then be reactive toward nucleophiles, and provide 'umpolung' of the usual reactivity of arenes.[128] Most of the transition metals have been observed to form such π-complexes,[129] and the reactivity depends on the formal charge, oxidation state, and the spectator ligands. The initial addition produces a cyclohexadienyl complex, and three processes have been worked out from this intermediate (Scheme 35).[130] First, if there can be an electronegative atom at the ipso position, elimination of that atom can occur, usually slowly, to give a substituted arene. Alternatively, an electrophile can add to the electron-rich dienyl intermediate and produce a disubstituted 1,3-cyclohexadiene. Finally, and uniquely, oxidation leads to removal of an ipso hydrogen and detachment of the metal.

The reactions are related mechanistically to traditional nucleophilic aromatic substitutions (S$_N$Ar),[131] but offer several unique features. With suitable electron-withdrawing substituents attached to the arene via σ-bonds, nucleophiles may add to produce the corresponding anionic intermediate, a cyclohexadienyl anion, stabilized by interaction with the substituents (Scheme 36). Attack is kinetically favored at a position bearing a hydrogen (path a), but the intermediate thus formed cannot proceed directly to substitution (by loss of a hydride ion). In the general version of the S$_N$Ar reaction, an electronegative atom (usually halide) is attached to the arene ortho or para to an activating group, and the addition of the nucleophile is reversible. A slower addition occurs at the carbon bearing the electronegative atom, to produce an anionic intermediate that can lose the electronegative atom in an irreversible step and give the product from nucleophilic

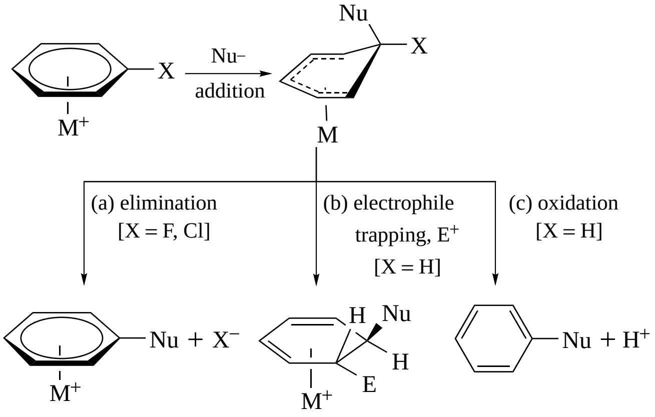

Scheme 35 General reactions of arene metal complexes after initial nucleophilic addition

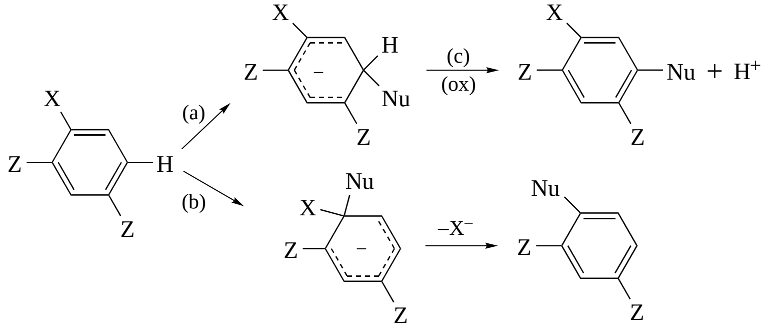

Z = electron-withdrawing group
X = electronnegative atom (group)

Scheme 36 Comparison with traditional nucleophilic aromatic substitution

substitution for halide (path b). In a few cases, loss of hydrogen from the cyclohexadienyl anionic intermediates has been induced by oxidation, which presumably allows departure of a proton, as shown in step c.[12] The overall addition/oxidation pathway of nucleophilic aromatic substitution for hydrogen is too limited to be considered synthesis methodology.

The first arene–transition metal complexes were prepared in the 1950s,[129,132] and it was immediately recognized that the added polarizibility or electron deficiency would promote addition of nucleophiles to the arene ligand. A number of cyclohexadienyl complexes were characterized following nucleophilic addition, but the question of inducing the ipso hydrogen to depart was not answered (equation 89).

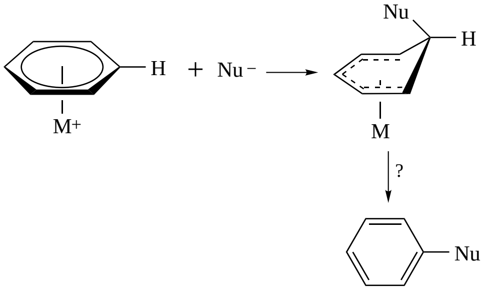

(89)

The isolation of the first halobenzene complex, (η^6-chlorobenzene)tricarbonyl Cr^0, allowed a test for a direct analog of classical S$_N$Ar reactivity.[133] The activating effect of the Cr(CO)$_3$ unit was found to be comparable to a single p-nitro substituent in reaction with methoxide in methanol, and the substituted arene ligand was detached with mild oxidation. The regiochemistry of nucleophilic addition to substituted arenas can be controlled by electronic factors, as shown in equation (90).[134] Resonance donor R groups attack at the meta position, while bulky R groups and resonance acceptor R groups attack at the para position. R groups that can coordinate to the incoming organolithium reagent direct attack to an ortho position.

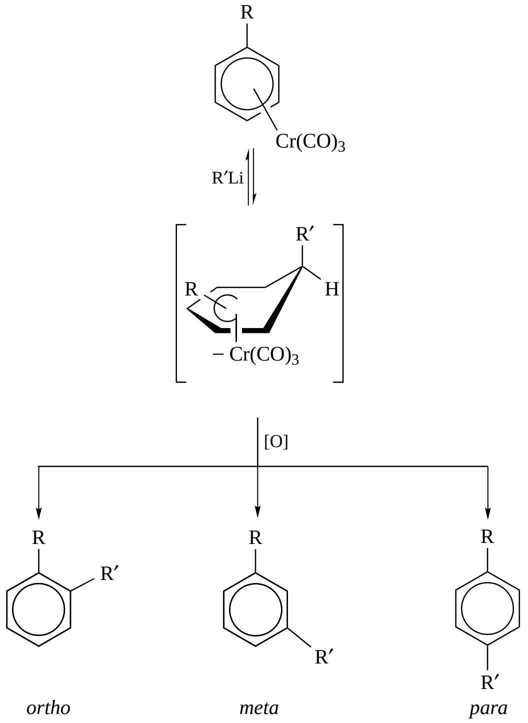

(90)

Three types of arene π-complexes have seen significant development in synthesis methodology: neutral η^6-arene–Cr(CO)$_3$,[135–138] the isoelectronic cationic η^6-arene–Mn(CO)$_3$,[139] and the cationic (η^6-arene)(η^5-cyclopentadienyl)iron(II) complexes (Figure 3).[140,141] The arene–Cr(CO)$_3$ species are formed by simple displacement of neutral ligands (L) from Cr(CO)$_3$L$_3$ by the arene, and a large number of variously substituted arene–Cr(CO)$_3$ complexes

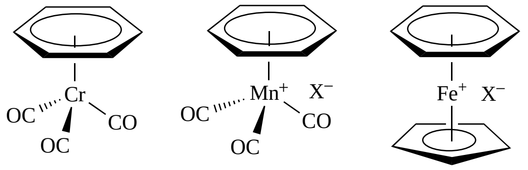

Figure 3 Examples of electrophilic arene–metal complexes

are available.[129] Gentle and general syntheses of the cationic complexes are only recently available, and the development of these complexes as synthesis intermediates is far less advanced.

8.2 Preparation of Arene–Cr(CO)$_3$ Complexes

The general process begins with Cr(CO)$_3$L$_3$, in which the L unit can be CO (most common),[142] MeCN,[143] *o*-alkylpyridine,[144] ammonia,[145] and other donor ligands (equation 91). The rate (reaction temperature) is related to the nature of L; the most reactive readily available source of Cr(CO)$_3$ is (η^6-naphthalene)Cr(CO)$_3$, which undergoes favorable arene exchange under mild conditions with many substituted arenes.[146] The most general and convenient procedure employs a mixture of THF and di-*n*-butyl ether at reflux.[147] A variety of polar and nonpolar aprotic solvents has been used; and, for some purposes such as complexation of α-amino acids with aromatic side chains, water–THF mixtures are effective.[142]

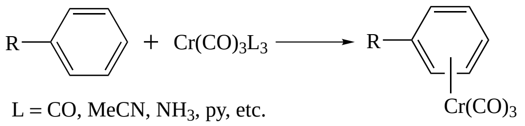

L = CO, MeCN, NH$_3$, py, etc.

(91)

After complexation, the yellow to red arene–Cr(CO)$_3$ complex can be purified by crystallization from nonpolar organic solvents or chromatographed on silica gel. Most common synthesis operations, such as acid and base hydrolysis, hydride reduction, and carbanion addition to ketones, can be carried out on side-chain functional groups without disturbing the arene–Cr bond.[128,148] However, even very mild oxidation conditions will detach the arene by oxidizing the metal. An important aspect of the complexation procedure is diastereoselectivity. Complexes of disubstituted (and more highly substituted) arenes can have molecular asymmetry; a stereogenic center in a side chain leads to diastereoisomers. Under favorable conditions, especially with low-temperature conditions for complexation, significant diastereoselectivity is observed in the complexation step. Arene–Cr(CO)$_3$ complexes can also be formed under very mild thermal conditions by the ligand displacement reaction shown in equation (92).[149]

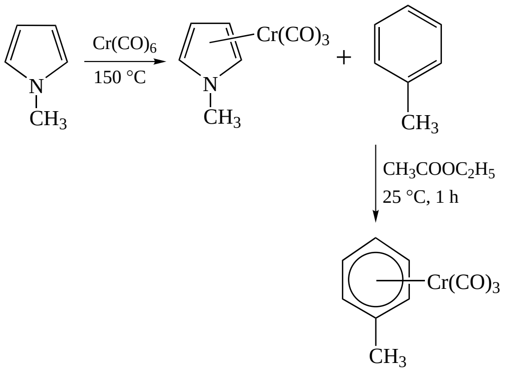

(92)

8.3 Preparation of Arene–Mn(CO)$_3$ Complexes

A gentle procedure has made these complexes available with a variety of substituted arenes.[150] Direct displacement of CO from the perchlorate salts of $^+$Mn(CO)$_5$ or $^+$Mn(CO)$_3$(acetone)$_3$ with the arene in dichloromethane at reflux leads to precipitation of the arene–Mn(CO)$_3$ salt. The conditions are milder than the AlCl$_3$-promoted procedure employed earlier.[151] Only a handful of substituted arenes have been attached to Mn(CO)$_3{}^+$, but the general synthesis method suggests few limitations (equation 93).

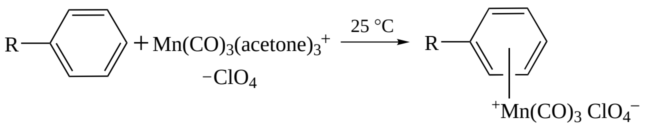

(93)

The complexes are air stable; indeed, a limitation is the need for powerful oxidizing agents, such as Jones reagent [Cr^{IV}], to detach the arene ligand.[152] They are highly reactive toward nucleophiles, which limits the number of compatible synthesis manipulations that can be carried out in the presence of the arene–Mn(CO)$_3$ unit, but broadens the scope of effective nucleophiles.

8.4 Preparation of Arene–FeCp$^+$ Complexes

One of the few useful reactions of ferrocene is the AlCl$_3$-catalyzed exchange of one Cp group for an arene ligand (equation 94).[153] The requirement for AlCl$_3$ adds some obvious limitations, but a modest number of substituted arenes have been successfully coordinated to the FeCp$^+$ unit. The charged complexes are not purified by conventional organic techniques such as chromatography, but recrystallization is possible. The complexes are very air and heat stable; again, methods of removal of the arene from the Fe are few. The simplest is pyrolysis at >200 °C.[154]

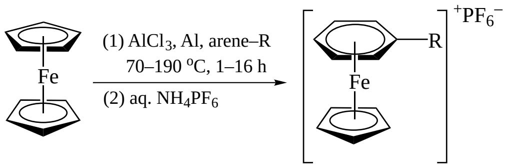

ferrocene:AlCl$_3$:Al = 1:2:1

(94)

8.5 Nucleophilic Substitution for Heteroatoms on Arene Ligands: S$_N$Ar Reaction

8.5.1 *The Basic Process*

The smooth replacement of a heteroatom (usually halide) from arene ligands requires reversible addition of the nucleophile, since the kinetic site of addition

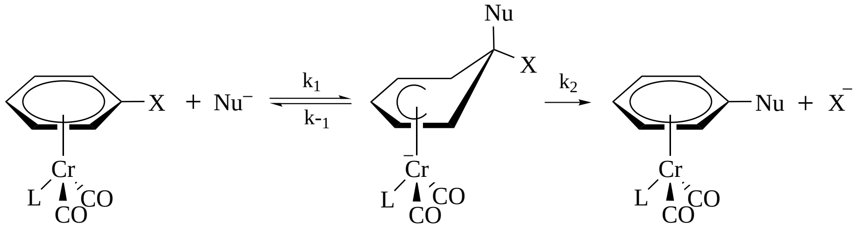

Scheme 37 Pathway for substitution of halides

is usually at a position bearing a hydrogen substituent (path k_1) (Scheme 37).[155] The relative rates of each step depend critically on the nature of M and of the nucleophile. More reactive nucleophiles and more reactive complexes disfavor equilibration ($k_1 \gg k_{-1}$), and the process can stop with formation of the first cyclohexadienyl intermediate. Equilibration leads through to the substitution product. The overall order of reactivity for electron-deficient arenes is (arene)(CO)$_3$Mn$^+$ > 2,4-(NO$_2$)$_2$C$_6$H$_3$Cl > (arene)CpFe$^+$ $\gg$ 4-(NO$_2$)$_2$C$_6$H$_4$Cl > (arene)(CO)$_3$Cr.[128,155]

8.5.2 Halobenzene–Cr(CO)$_3$ Complexes

Intermolecular Nucleophilic Substitution with Heteroatom Nucleophiles. A patent issued in 1965 claims substitution for fluoride on fluorobenzene–Cr(CO)$_3$ in dimethyl sulfoxide (DMSO) by a long list of nucleophiles including alkoxides (from simple alcohols, cholesterol, ethylene glycol, pinacol, and dihydroxyacetone), carboxylates, amines, and carbanions (from triphenylmethane, indene, cyclohexanone, acetone, cyclopentadiene, phenylacetylene, acetic acid, and propiolic acid).[156] In the reaction of methoxide with halobenzene–Cr(CO)$_3$, the fluorobenzene complex is ca. 2000 times more reactive than the chlorobenzene complex.[155] The difference is taken as evidence for a rate-limiting attack on the arene ligand followed by fast loss of halide; the concentration of the cyclohexadienyl anion complex does not build up. In the reaction of fluorobenzene–Cr(CO)$_3$ with amine nucleophiles, the coordinated aniline product appears rapidly at 25 °C, and a careful mechanistic study suggests that the loss of halide is now rate limiting.[157]

Hydroxide, alkoxide, and phenoxide nucleophiles react with chlorobenzene–Cr(CO)$_3$ at 25–50 °C in polar aprotic media to give high yields of the phenol or aryl ether chromium complexes; oxidation with excess iodine at 25 °C for a few hours releases the free arene, CO, chromium(III), and iodide anion.[133,158] Only the arene remains in the organic layer after a conventional aqueous extraction (equation 95). An alternative general procedure for detaching the arene ligand from the Cr(CO)$_3$ unit is to expose a solution of the complex to air in the presence of normal room light or sunlight.

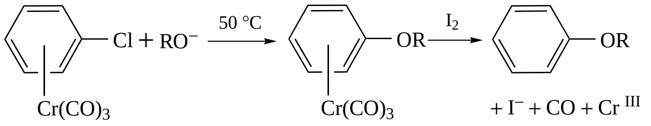

(95)

The reaction proceeds almost exclusively by direct substitution (ipso), as shown by reactions of isomeric chlorotoluene complexes (Scheme 38). While polar protic solvents, such as MeOH, strongly retard reaction,[159] phase transfer catalysis (*see Phase Transfer Catalyst*) using benzene[158] or addition of *Crown Ethers* to potassium alkoxides in benzene[160] allows reaction at 25 °C. Even with strong electron donors such as alkyl, methoxy, or dialkylamino in the ortho, meta, or para positions, substitution for chloride by potassium methoxide proceeds smoothly using the crown ether activation in benzene (equation 96).[160]

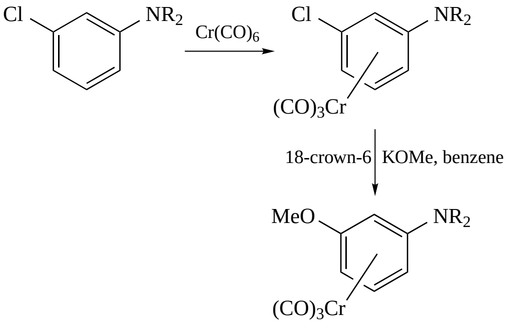

(96)

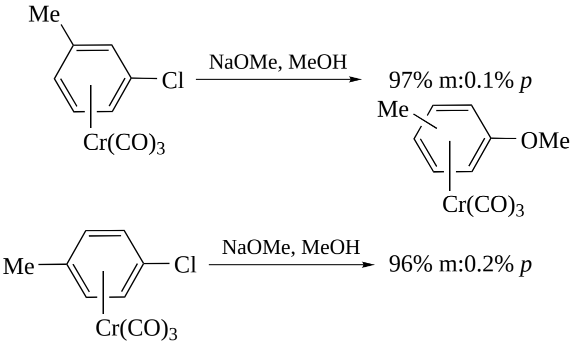

Scheme 38 Selective reactions of chlorotoluenes

In general, replacement of fluoride occurs under milder conditions and in higher yield than chloride; however, compared to chloride, a fluoride substituent slows the complexation of arenes and often leads to lower yields in the formation of the starting arene–Cr complexes. An excellent procedure for formation of the parent fluorobenzene–$Cr(CO)_3$ complex has been reported.[161] The bromo- and iodoarene complexes are known, but generally are not effective in the S_NAr reaction.[162] Direct replacement of oxygen leaving groups, such as tosylate, is not effective, perhaps owing to steric retardation of the departure of the endo leaving group.

Thiolate anions[163] and oxime alkoxides[163] react under phase transfer conditions to give aryl thio ethers and *O*-aryl oximes, respectively; the *o*-dichlorobenzene complex can be converted selectively to the monosubstitution product (equation 97).

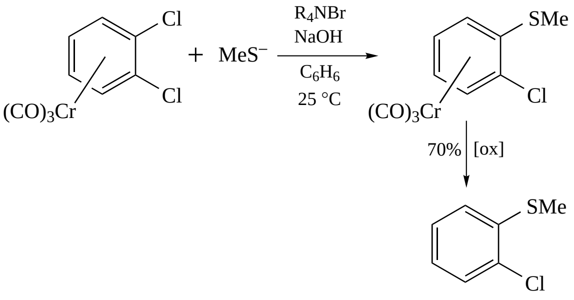

(97)

The arylation of oximes leads to a simple process for benzofuran formation. Simple primary and secondary amine nucleophiles react smoothly in the absence of added base, in a very general and efficient process for aniline derivatives (equation 98).[157]

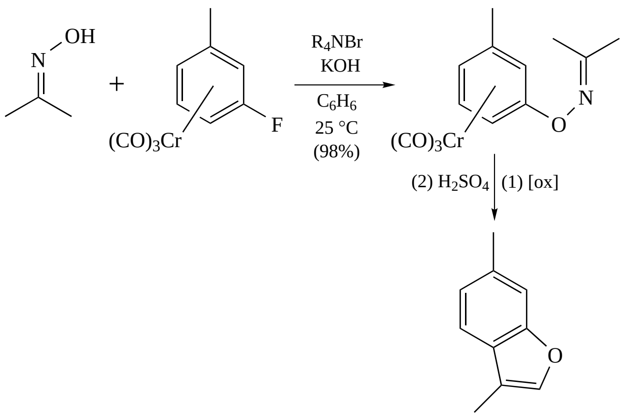

(98)

Chromium activation allows a strategy for aryl ether synthesis in four stages: (a) electrophilic chlorination, (b) chromium coordination, (c) alkoxide substitution for chloride, and (d) oxidative decomplexation.[159] The process is effective for the synthesis of 6-methoxytetrahydroquinoline and 5-methoxydihydroindole derivatives, for example. Chlorination of *N*-acetyltetrahydroquinoline with SO_2Cl_2 followed by deacetylation provides 6-chlorotetrahydroisoquinoline in 77% yield.[159] The complexed amine is moderately acidic and must be protected (in situ) as the benzyl ether before methoxide treatment (equation 99). The overall yield for protection, substitution, and oxidative decomplexation is 80%.

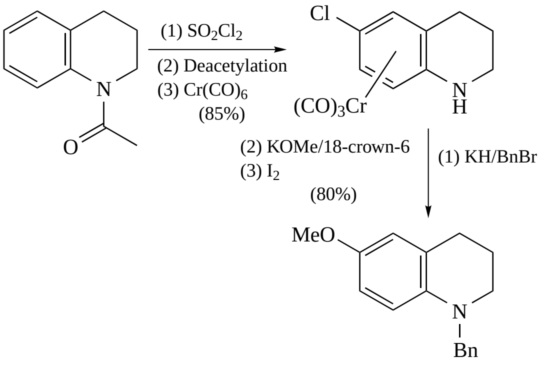

(99)

Intramolecular Heteroatom Substitution for Halide. Intramolecular substitution for chloride or fluoride is particularly effective. Oxygen heterocycles with fused benzo rings are obtained from $Cr(CO)_3$ complexes of fluorobenzene with an *o*-(hydroxyalkyl) side chain (equation 100). Efforts to produce the dihydrobenzofuran under the same conditions failed; only intermolecular substitution products were obtained.[164]

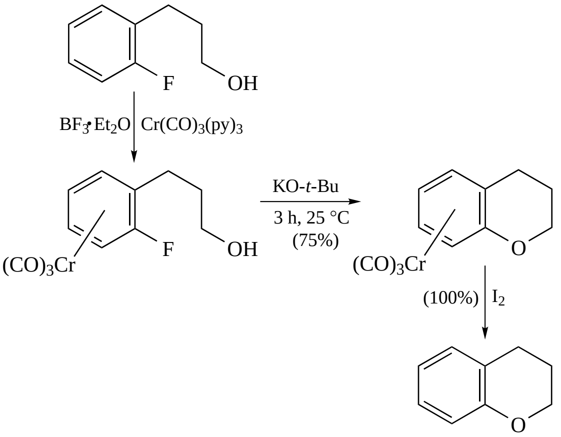

(100)

Coordination of arenes with $Cr(CO)_3$ also activates the ring hydrogens toward abstraction with strong base (metalation).[164,165] Simple arene ligands can be metalated with alkyllithium reagents; alkoxy, amino, and halo substituents on the arene direct the metalation to the ortho position with rates and regioselectivity higher than with the corresponding free arene (see equation 101).[134,161,166,167] This allows a strategy for annulating aromatic rings via ortho-lithiation, trapping with a bifunctional electrophile, and finally nucleophilic substitution for the electronegative substituent.

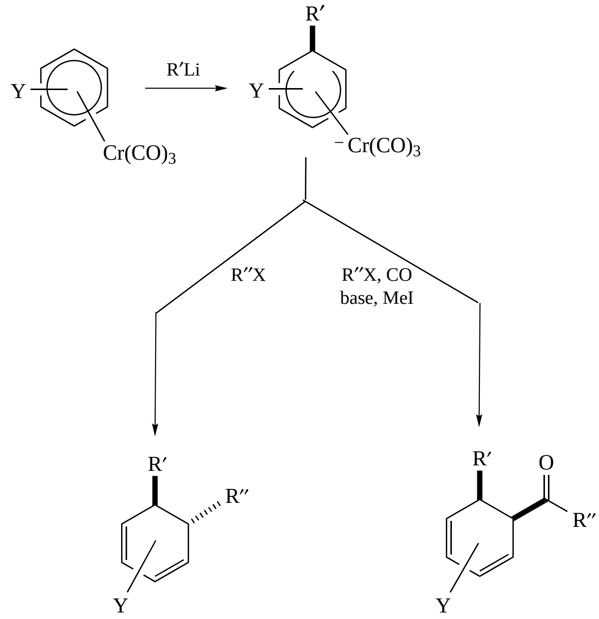

(101)

Although chlorobenzene–$Cr(CO)_3$ undergoes lithiation to give a moderately stable species that can be trapped with electrophiles to produce *ortho*-substituted chloroarene–$Cr(CO)_3$ complexes,[168] the fluoro analog appears to be more efficient, in the same way. The *ortho*-lithio haloarene complexes are highly basic, and the electrophilic trapping species is restricted to those with low kinetic acidity and high electrophilicity. Good results are obtained with isocyanates, ketenes, and acyl derivatives with α-protons of low acidity.[161,166] Examples include phenyl isocyanate, which reacts twice to give a six-membered heterocycle, while the dimethyl-N-carboxyanhydride proceeds directly to the five-membered ring after spontaneous decarboxylation (equation 102).

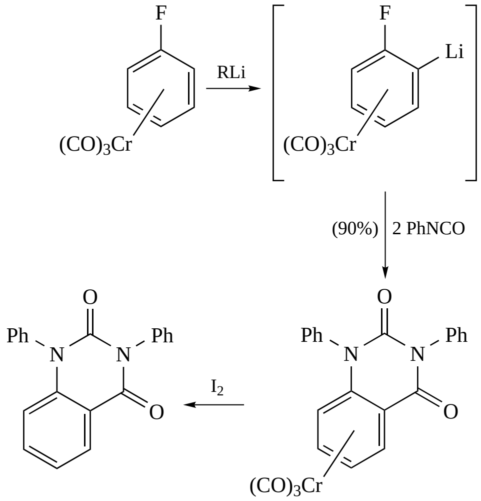

(102)

A variation involves an aryl cuprate coupled with a vinyl halide, leading eventually to the β-methylenedihydrobenzofuran complex (equation 103). Cyclization occurs spontaneously upon fluoride-induced removal of the silyl protecting group.[166] The complex is much more stable than the free ligand, and can be used to advantage as a synthesis equivalent of 3-methylenedihydrobenzofuran.

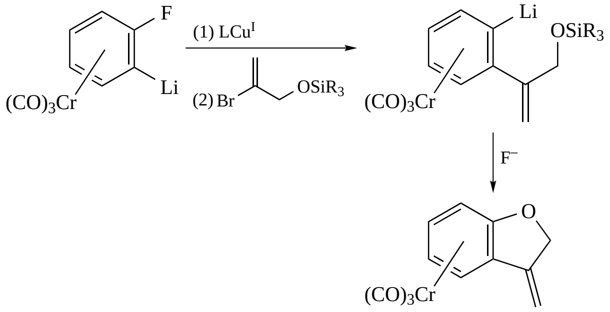

(103)

8.5.3 Substitution with Carbon Nucleophiles

While carbon nucleophiles were suggested to be efficient in substitution for fluoride in the 1966 patent,[156] the first examples in the primary literature appeared in 1974.[162,169] It is now clear that there are three reactivity classes of carbon nucleophiles (Scheme 39): (a) stabilized carbanions (from carbon acids with $pK_a <$ ca. 18); (b) more reactive carbanions ($pK_a > 20$), which give complete conversion to cyclohexadienyl addition products prior to slow equilibration via reversible anion addition; and (c) more reactive carbanions ($pK_a > 20$), which give irreversible addition to the arene ligand.[170]

Diethyl sodiomalonate is an example of type (a). Reaction with fluorobenzene–$Cr(CO)_3$ proceeds to completion after 20 h at 50 °C in HMPA to give the diethyl phenylmalonate complex in over 95% yield. Monitoring the reaction by NMR gave no evidence for an intermediate (e.g. the cyclohexadienyl anion complex); interruption of the reaction by addition of iodine at less than 20 h gave significant amounts of unreacted fluorobenzene. A satisfactory picture is the simple one, that the anion adds reversibly and unfavorably ($k_1 < k_{-1}$), slowly finding itself at the ipso position, then irreversible loss of fluoride gives the substitution product.

Lithio isobutyronitrile is an example of anion type (b). The initial addition to chlorobenzene–$Cr(CO)_3$ is over within minutes at −78 °C, but the substitution product does not appear until the mixture is warmed to 25 °C. Quenching with iodine after a short reaction time leads to a mixture of phenylisobutyronitrile and o- and (m-chlorophenyl)isobutyronitrile. This appears to be a case of fast addition ortho and meta to the chloride to give cyclohexadienyl anionic complexes, followed by slow rearrangement to the ipso intermediate. Quenching with iodine before equilibration is complete leads to oxidation of the intermediates and formal substitution for hydrogen.

Carbon nucleophiles of type (c) add to the arene ligand and do not rearrange; examples include the very reactive anions such as 2-lithio-2-methyl-1,3-dithiane and less sterically encumbered anions such as lithioacetonitrile and t-butyl lithioacetate. In these cases, the anion adds to an unsubstituted position (mainly ortho or meta to Cl) and does not rearrange.

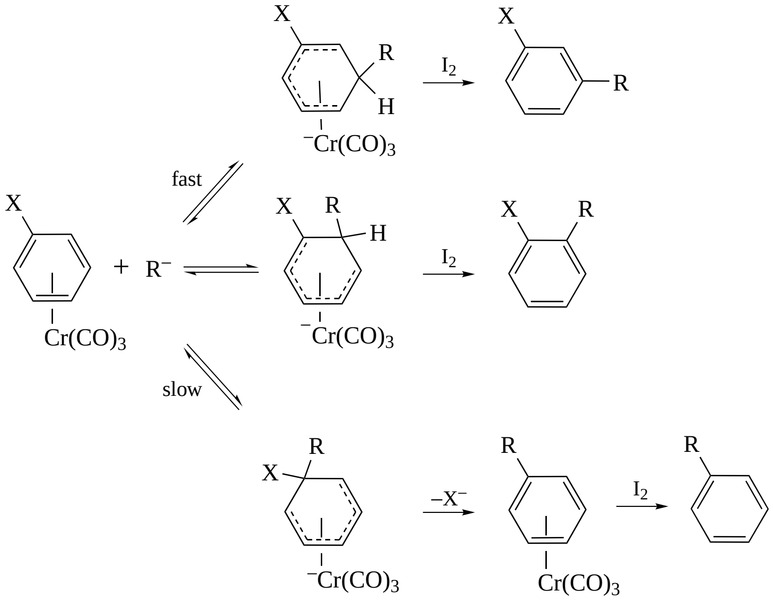

Scheme 39 Pathways for reaction of carbon nucleophiles with arene ligands

Then iodine quenching, even after a long period at 25 °C, gives almost exclusively the products from formal substitution for hydrogen.

Successful substitution for halogen by carbanions requires reversible addition and that sets upper limits on the reactivity of the anion, although steric effects can also favor equilibration (the more substituted equilibrate faster). As before, fluoride is a better leaving group than chloride. An example is shown in equation (104), leading to methyl 2-phenyl-2-(*t*-butylthio)propionate in 94% yield after 15 h at 25 °C. There is an important solvent effect on the rate of equilibration of the carbanions,[171] and the conditions chosen for these early experiments are not necessarily the best; there may be room to expand the scope of useful anions by careful choice of media (less polar solvents should favor equilibration).

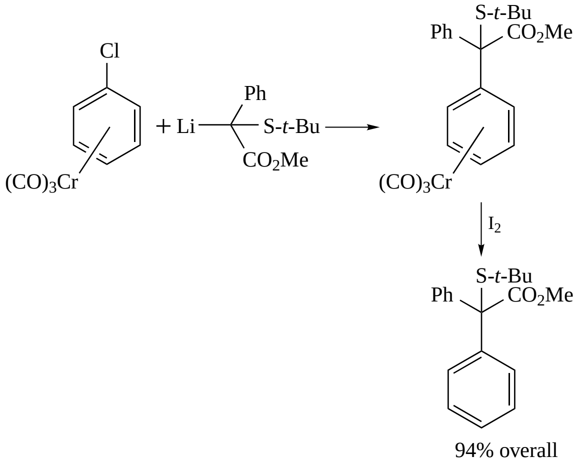

(104)

Except in the formation of minor side products, the replacement of halogen by hydride as nucleophile is not observed. Halide exchange is also not a general process with haloarene–Cr(CO)$_3$ species.

There is an alternative mechanism for halide replacement, following the sequence of nucleophile addition, protonation, and elimination of HX. In this pathway, the addition of the nucleophile need not be at the ipso position; it can be ortho to halide leading to ‘*cine*’ substitution or it can be at the meta or para positions, leading to ‘*tele*’ substitution.[172] The processes depend on the formation of the cyclohexadienyl anion intermediates in a favorable equilibrium (carbon nucleophiles from carbon acids with $pK_a > 22$ or so), protonation (which can occur at low temperature with even weak acids such as acetic acid), and hydrogen shifts in the proposed diene–chromium intermediates. Hydrogen shifts lead to an isomer that allows elimination of HX and regeneration of an arene–chromium complex, now with the carbanion unit indirectly substituted for X (Scheme 40).[173,174]

An important example of indirect substitution utilizes alkoxy leaving groups; the intermediate from the reaction of the diphenyl ether–Cr(CO)$_3$ complex and the 2-methyl-1,3-dithiane anion can be induced to eliminate phenol by protonation at low temperature; the result is tele substitution (Scheme 41).[174]

An impressive example is the reaction of 2,6-dimethyl-1-fluorobenzene–Cr(CO)$_3$ with 2-lithio-2-methyl-1,3-dithiane at −78 °C, followed by treatment with trifluoroacetic acid at −78 °C (equation 105).[174] Loss of HF leads to the 1,2,4 (tele)

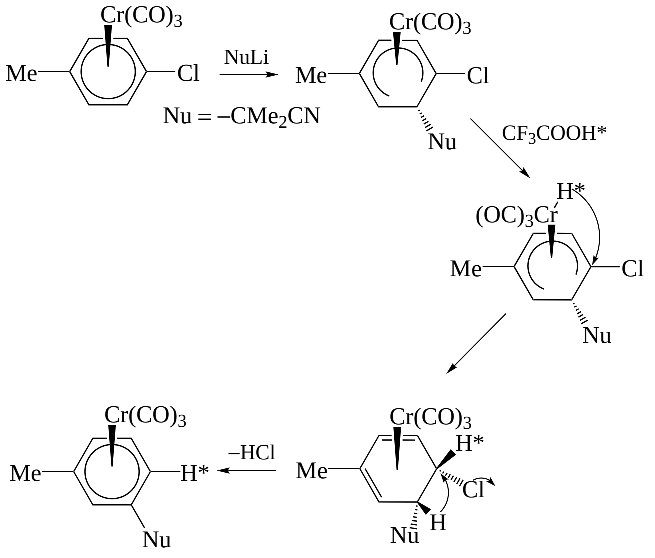
Cr(CO)3
Me
Cl
NuLi
Nu = –CMe2CN
Nu
CF3COOH*
H*
(OC)3Cr
–HCl
H*

Scheme 40 Indirect cine nucleophilic aromatic substitution

substitution product, in 62% yield.

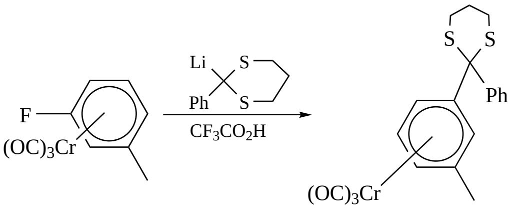
F
(OC)3Cr
Li
S
Ph
CF3CO2H
Ph

(105)

The directing effects of F (strong meta) versus Cl (weak, o/m; discussed below) allow control over the site of tele substitution; the chloro analog leads to the 1,3,5-substitution pattern (equation 106).[175]

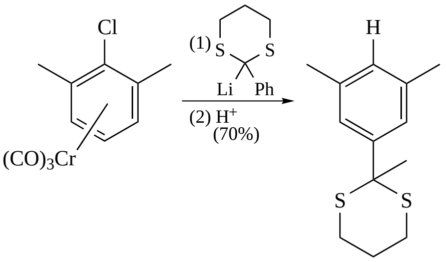
Cl
(CO)3Cr
(1)
S
Li
Ph
(2) H+
(70%)
H

(106)

Under certain conditions, apparently when the $Cr(CO)_3$ unit is spontaneously displaced from the product by a weak donor ligand (solvent), the simple addition product (1,3-cyclohexadiene derivative) can be the major product (equation 107).[175]

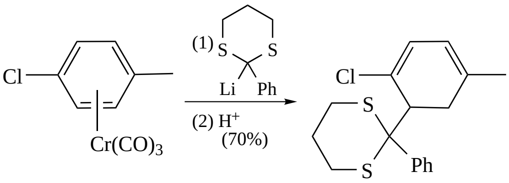
Cl
Cr(CO)3
(1)
S
Li
Ph
(2) H+
(70%)

(107)

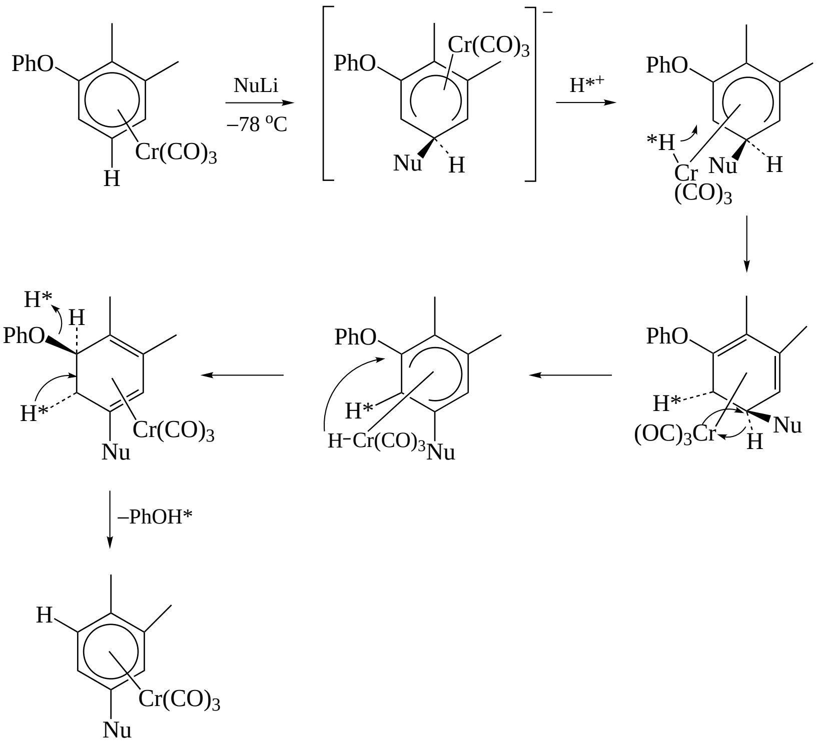
PhO
H
Cr(CO)3
NuLi
–78 °C
Nu
H*+
*H
Cr
(CO)3
H*
(OC)3Cr
H-Cr(CO)3
–PhOH*

Scheme 41 Indirect *tele* nucleophilic aromatic substitution

8.5.4 Halide Substitution using Activation with Other Metal–Ligand Systems

While the potential for other metal–ligand activation of arenes in nucleophile substitution for chloride has been demonstrated, the processes have not been fully developed nor applied. The two-stage process of addition/substitution for chloride and arene detachment is exemplified for the iron system in equation (108).

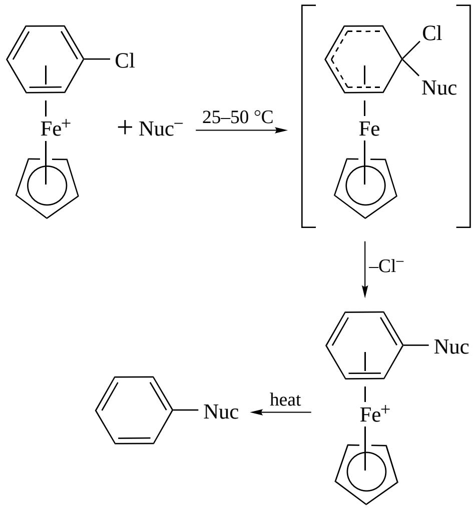

(108)

The first stage (addition/elimination) is well known with CN^- and a variety of N, O, and S nucleophiles.[140,176] The detachment of the product arene from the Fe is more difficult. The conversion in equation (109) demonstrates the stability of the arene–Fe bond toward oxidation, as a side-chain methyl is converted to a carboxylic acid, and suggests the generality of heteroatom substitution under mild conditions.[177]

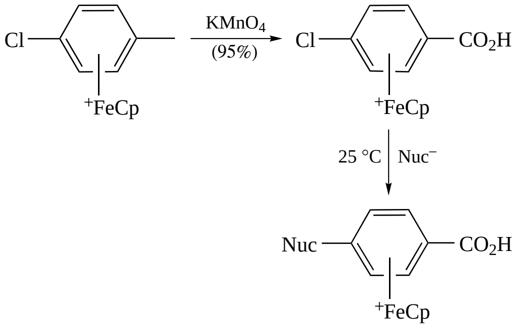

(109)

Nuc = PhS (51%) and EtO (68%)

The analogous *p*-dichlorobenzene complex will react rapidly with phenoxide and alkoxide nucleophiles in the first substitution and more slowly in the second; monosubstitution can be readily achieved (equation 110).[178] Simple amines give only monosubstitution, even in the presence of excess amine.

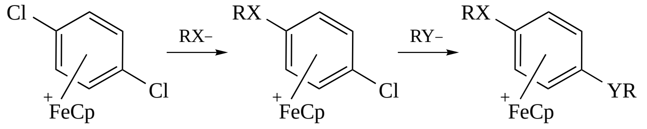

(110)

Substitution with amine nucleophiles in the series of chlorotoluene complexes showed that the substitution is direct; no cine or tele substitution was observed.[176] The analogous (fluoroarene)FeCp$^+$ complexes are known, but less well developed. Kinetics studies show that the fluoro derivatives are more reactive compared to the chloro analogs.

A special example is the replacement of a nitro group on η^6-nitrobenzene–FeCp$^+$.[178,179] Reaction with O, S, N, and stabilized C nucleophiles gives overall addition/elimination (equation 111). The nitroarene complexes are prepared by oxidation of the corresponding aniline complexes and are readily available.

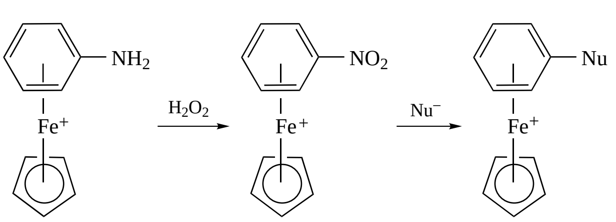

(111)

Stabilized carbon nucleophiles (e.g. from β-diketones, β-keto esters, malonate esters, etc.) can be arylated by substitution for chloride on the arene in arene–Fe–Cp cation complexes (equation 112).[179,180] A base is necessary, and two heterogeneous systems are favored: potassium carbonate in dimethyl formamide (DMF) or potassium fluoride prepared on Celite-545. As usual in the CpFe$^+$ system, detachment of the substituted arene requires somewhat extreme conditions, usually pyrolytic sublimation at 200 °C.[140]

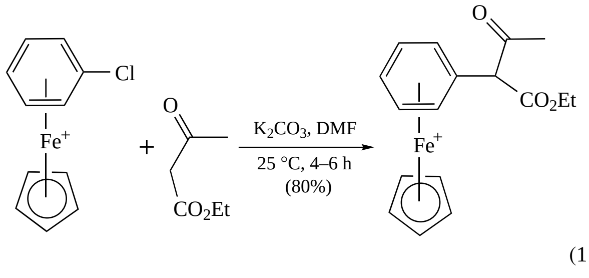

(112)

The most reactive of the common arene–metal complexes has been the least developed with regard to nucleophilic substitution for halide. It is only an improved, gentler method of complexation that allowed isolation of the fluorobenzene complex with $Mn(CO)_3{}^+$.[150] The chlorobenzene analog is easily prepared and undergoes substitution with alkoxy, phenoxy, thiolate, amine, and azide nucleophiles.[150,181] Reaction is complete with aniline (a weak nucleophile) within 3 min at room temperature. In examples with a methyl substituent on the arene as a label, the substitution is shown to be direct (equation 113). The detachment of the substituted arene ligand from the $Mn(CO)_3$ unit is still limited by the requirement for strong oxidizing conditions, a serious limitation if this series is to be put forward in synthesis methodology.

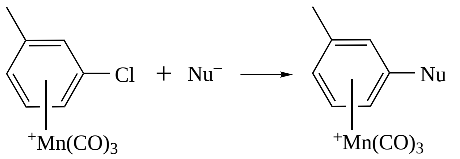

(113)

Nuc⁻ = alkoxy, phenoxy, thiolate, amine, and azide

8.6 Nucleophile Addition/Oxidation: Substitution for Hydrogen

8.6.1 Basic Process and Intermolecular Examples

Once it is recognized that cyclohexadienyl anionic complexes of chromium can be generated by addition of sufficiently reactive nucleophiles and that simple oxidizing techniques convert the anionic intermediates to free substituted arenes, a general substitution process becomes available, which does not depend on a specific leaving group on the arene (equation 114).[169] While no heteroatom nucleophile has been successfully utilized, the process is general for carbanions derived from carbon acids with $pK_a > 22$ or so. Exceptions among the very reactive anions include organolithium reagents (deprotonation of the arene ligand and addition to the CO ligand are favored) and Grignard reagents (addition to the CO ligand is favored). With anions such as ester enolate anions, reaction occurs within minutes at −78 °C and the intermediate cyclohexadienyl complex can be observed spectroscopically.[148] The intermediates are exceedingly air sensitive and are generally quenched directly, without purification. In one case, from the addition of 2-lithio-1,3-dithiane, the adduct has been crystallized and fully characterized by X-ray diffraction analysis. Oxidation with excess iodine (at least 2.5 mol. equiv. of I_2) also proceeds at −78 °C and is complete within hours below room temperature. The products are the substituted arene, HI, Cr^{III}, and CO. Table 2[182] provides a representative sample of the carbanions that have been tested with (η^6-benzene)$Cr(CO)_3$.

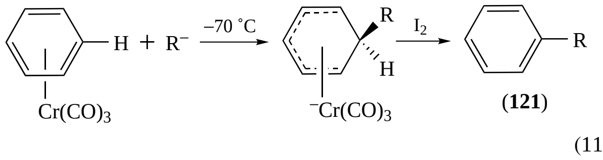

(121)

(114)

Table 2 Reactivity of carbanions (R–Li) toward benzene–$Cr(CO)_3$

Unreactive	Successful	Metalation
$LiCH(CO_2R)_2$	$LiCH_2CO_2R$	${}^{n}BuLi$
$LiCH_2COR$	$LiCH_2CN$	$LiCH_3$
CH_3MgBr	$KCH_2COC(CH_3)_3$	${}^{s}BuLi$
$(CH_3)_3CMgBr$	$LiCH(CN)(OR)$	
$(CH_3)_2CuLi$	$LiCH_2SPh$	
$LiC(OR)(CN)Ph$	2-Li-1,3-dithianyl	
	$LiCH{=}CH_2$	
	LiPh	
	$LiC{\equiv}CR$	
	$LiCH_2CH{=}CH_2$	
	${}^{t}BuLi$	

Regioselectivity has been the subject of numerous studies with a variety of mono- and polysubstituted arene ligands. The addition of synthetically interesting carbanions to the typical arene ligand, especially those bearing electron-donating substituents, can be reversible at rates comparable to the rate of addition: it is not always obvious whether to assume kinetic or thermodynamic control.[171,183] However, correlations have been suggested that allow prediction or rationalization of regioselectivity with a modest degree of confidence. With some significant exceptions as discussed below, the difference between the kinetic and thermodynamic selectivity has not been determined or is small.

With arenes bearing a single resonance donor substituent (NR_2, OMe, F), the addition is strongly preferred at the meta position, with small amounts of ortho substitution (0–10%).[184] The meta acylation of anisole, using a carbonyl anion equivalent as the nucleophile, illustrates the unique regioselectivity available with the $Cr(CO)_3$ activation (equation 115).[185]

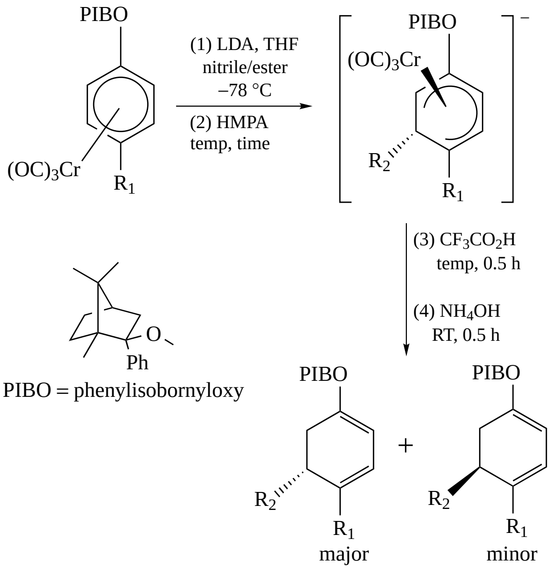

(115)

However, the selectivity is more complicated with a methyl or chloro substituent (equation 116). Again, meta substitution

Table 3 Addition/oxidation with chlorobenzene and toluene $Cr(CO)_3$ (equation 116)

Entry	X	LiY	Ratio (o:m:p)	Combined yield (%)
1.	Me	$LiCH_2CN$	35:63:2	88
2.	Me	$LiCMe_2CN$ (−100 °C/1.5 min)	2:96:2	52
3.	Me	$LiCMe_2CN$ (−78 °C/1.5 min)	1:97:2	95
4.	Me	$LiCMe_2CN$ (0 °C/20 min)	1:97:2	86
5.	Me	$LiCH_2CO_2 - t$-Bu	28:72:0	89
6.	Me	$LiCMe_2CO_2 - t$-Bu	3:97:0	96
7.	Me	2-lithio-1,3-dithiane	52:46:2	94
8.	Cl	$LiCH_2CO_2 - t$-Bu	54:45:1	98
9.	Cl	$LiCHMeCO_2 - t$-Bu	53:46:1	88
10.	Cl	$LiCMe_2CO_2 - t$-Bu	5:95:0	84
11.	Cl	$LiCH_2COCMe_3$	76:24:0	87
12.	Cl	$LiCMe_2CN$	10:89:1	84
13.	Cl	2-Lithio-1,3-dithiane	46:53:1	56
14.	CF_3	LiC(CN)(Me)(OR)[a]	0:30:70	33
15.	$SiMe_3$	$LiCMe_2CN$	0:2:98	65

[a] The R group is –CH(Me)(OEt).

is always significant, but ortho substitution can account for 50–70% of the mixture in some cases.[184,186] More reactive anions (1,3-dithianyl) and less-substituted carbanions (e.g. *t*-butyl lithioacetate) tend to favor ortho substitution. Representative examples are shown in Table 3. Entries 2–4 show that variation of reaction temperatures from −100 to 0 °C has no significant effect in that highly selective system. The added activating effect of the Cl substituent allows addition of the pinacolone enolate anion (entry 11), whereas no addition to the anisole or toluene ligand is observed with the same anion. Table 3 also includes results with para-directing substituents, CF_3 and Me_3Si (entries 14 and 15).[186] In general, electron-withdrawing substituents, such as acyl and cyano, are also activated toward nucleophile addition to the substituent (C=O or CN), and this process competes with addition to the ring itself.

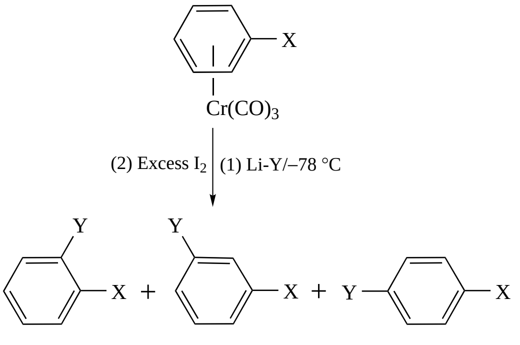

(116)

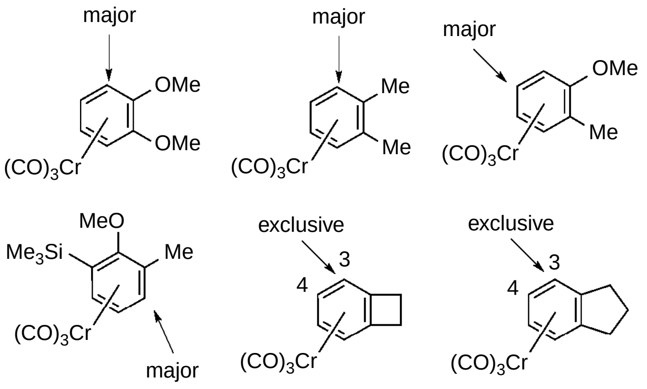

Figure 4 Summary of regioselectivity in addition to substituted arene ligands

Regioselectivity in *o*-disubstituted arenes is often high and useful. A series of examples is summarized in Figure 4. The resonance donor substituent (OMe) appears to dominate the directing influences, favoring addition at the less-hindered position meta to itself.[186] But with two identical substituents, the addition is preferred in the adjacent position.[186] For example, with the complex of benzocyclobutene, six carbon nucleophiles were tested and each gave addition exclusively at C-3.[183,186] With the complex of indan, selective addition at C-3 was observed with dithianyl anions, but cyano-stabilized anions gave up to 20% of the isomeric product from addition at C-4.[183,186] Substituents at the benzylic carbons in the indan ligand have a strong effect on selectivity, and can lead to the 1,2,4-substitution product.[183]

Indole is a particularly interesting case of regioselectivity, because the $Cr(CO)_3$ unit selectively activates the six-membered ring,[187] while in free indole the five-membered ring dominates the (electrophilic addition) reactivity. The selectivity in addition to the $Cr(CO)_3$ complexes of indole derivatives shows a preference for addition at C-4 (indole numbering) and C-7, with steric effects owing to substituents at C-3 (Y in Scheme 42) and N-1 (X in Scheme 42) as well as anion type influencing the selectivity.[187,188] In Scheme 42 example A, a hydrogen substituent at Y and a tertiary carbanion leads to selective C-4 substitution. In example B, the same substrate adds trimethyl(1-propenyl)silane predominantly at C-7. With a trimethylsilylmethyl substituent at Y, the addition is preferred at C-7 (example C). A sufficiently large sterically protecting group as X can disfavor addition at C-7 (example D).

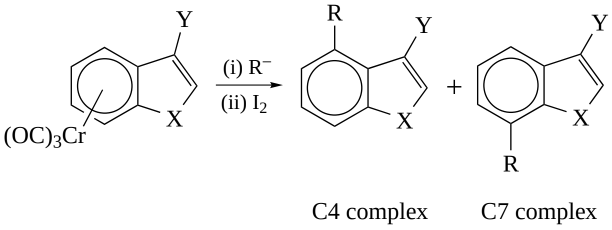
Y
(OC)3Cr
X
(i) R⁻
(ii) I2
R
Y
X
+
Y
X
R
C4 complex
C7 complex

	X	Y	R	C4:C7	Yield
A	NMe	H	CMe_2CN	97:3	73%
B	NMe	H	$CH_2CH{=}CHSi(Me)_3$	16:84	43%
C	NMe	CH_2SiMe_3	CMe_2CN	17:83	82%
D	NCH_2Ph	H	CMe_2CN	100:0	82%

Scheme 42 Selectivity in addition to indole ligands

An example in which the regioselectivity of addition is different under kinetic versus thermodynamic control is the naphthalene series. In the addition of $LiC(Me)_2CN$ to naphthalene–$Cr(CO)_3$, a mixture of products is observed from addition at C-α and C-β in the ratio 42:58 under conditions where equilibration is minimized (0.3 h, −65 °C, THF/HMPA). With the same reactants, but in THF and at 0 °C, the product is almost exclusively the α-substituted naphthalene (equation 117).[183,189]

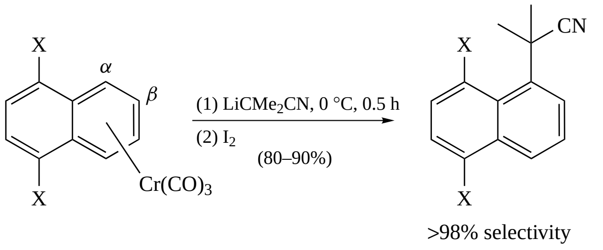
X
α
β
X
Cr(CO)3
(1) LiCMe2CN, 0 °C, 0.5 h
(2) I2
(80–90%)
CN
X
X
>98% selectivity

(117)

Using the standard procedures, 1,4-dimethoxynaphthalene is complexed at the less-substituted ring with high selectivity.[171] Again, under conditions of minimum equilibration of anion addition, $LiC(Me)_2CN$ gave a mixture (after iodine oxidation) of the 1,4-dimethoxy-β-substituted and 1,4-dimethoxy-α-substituted products in the ratio 78:22. After equilibration, the α-substitution product was essentially the only product found (equation 118).

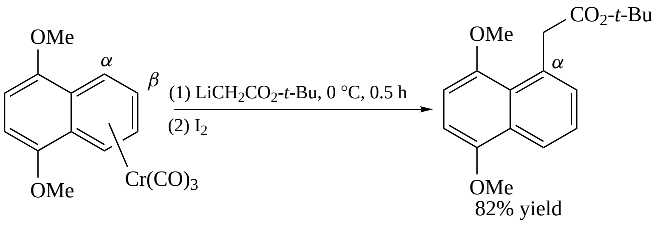
OMe
α
β
OMe
Cr(CO)3
(1) LiCH2CO2-t-Bu, 0 °C, 0.5 h
(2) I2
CO2-t-Bu
OMe
α
OMe
82% yield

(118)

With the 1,4-dimethoxynaphthalene ligand, cyano-stabilized anions (including cyanohydrin acetal anions) and ester enolates equilibrate even at low temperature and strongly favor addition at the α-position (C-5). The kinetic site of addition is also generally C-α. However, the 2-lithio-1,3-dithiane anion and phenyllithium do not equilibrate over the temperature range −78 to 0 °C. The sulfur-stabilized anions favor addition at C-β (equation 119),[134,190] while phenyllithium gives a mixture favoring C-α (equation 120).

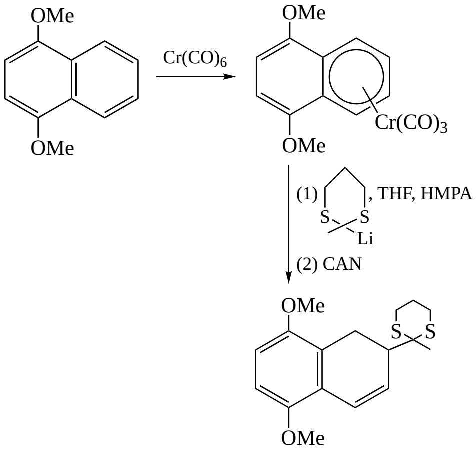
OMe
OMe
Cr(CO)6
OMe
OMe
Cr(CO)3
(1)
, THF, HMPA
S
S
Li
(2) CAN
OMe
S
S
OMe

(119)

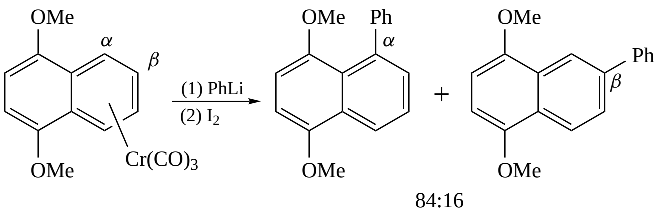
OMe
α
β
OMe
Cr(CO)3
(1) PhLi
(2) I2
OMe
Ph
α
OMe
+
OMe
Ph
β
OMe
84:16

(120)

Selectivity in polar reactions can be discussed in terms of two features: charge control and orbital control.[191]

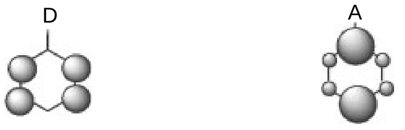

A. LUMO for D = donor (Me, Cl, OMe, NR_2)

B. LUMO for A = acceptor (RCO, NC, Me_3Si, F_3C)

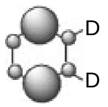

C. LUMO for *ortho*-D (*o*-di-Me, *o*-di-OMe)

Figure 5 Orbital distributions for substituted benzenes

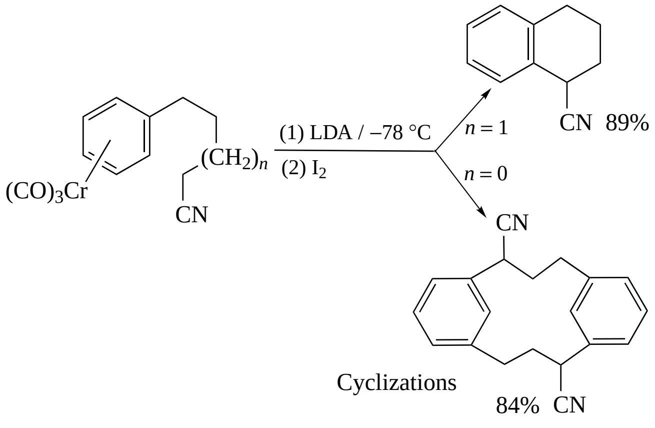

Scheme 43 Cyclizations

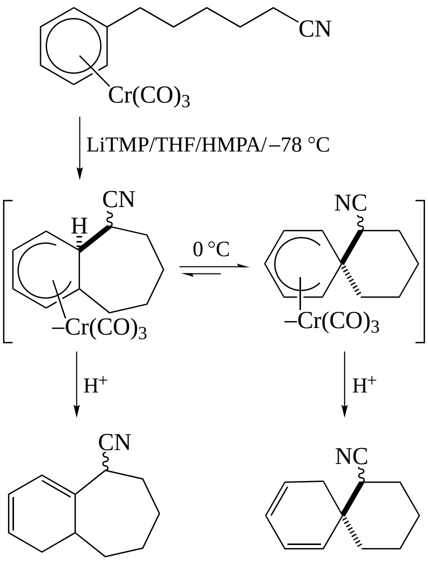

Scheme 44 Intramolecular nucleophilic addition to Arene–$Cr(CO)_3$ complexes

Analysis of charge control requires knowledge of charge distribution within the arene ligand. Analysis of orbital control can be approximated by emphasizing interaction of the frontier molecular orbitals: highest occupied molecular orbital (HOMO) for the nucleophile and lowest unoccupied molecular orbital (LUMO) for the arene complex. It was recognized early that the ortho/para selectivity observed with weakly polar substituents, such as Me and Cl, correlated with the LUMO for the free arene, and the assumption was made that the LUMO for the arene ligand has a distribution of coefficients similar to the free arene.[186] This has been supported by computation at the level of extended Huckel theory.[183,192] LUMOs for (uncoordinated) toluene and chlorobenzene are distributed nearly equally at the ortho and meta positions, and show small density at the para position (Figure 5).[193] Similarly for the case of two donor substituents arranged ortho, the LUMO is predicted to be localized at adjacent positions, consistent with the observed selectivity. With electron acceptor substituents (R_3Si, CF_3), LUMO has large coefficients ipso and para, consistent with para-addition selectivity.

However, the frontier orbital picture based on the free arene does not account for nearly exclusive meta selectivity in addition to anisole–$Cr(CO)_3$; the LUMO for anisole shows essentially the same pattern as for toluene.[193] With a strong resonance electron donor, the traditional electronic picture (deactivation of the ortho and para positions) is sufficient to account for the observed meta selectivity. In this case the balance of charge control and orbital control is pushed toward charge control by strong polarization. The same argument applies to the aniline and fluorobenzene complexes.

8.6.2 Intramolecular Examples

Intramolecular addition/oxidation with reactive carbanions is generally successful; most of the examples involve cyano-stabilized carbanions. Formation of a six-membered fused ring is efficient, but five-membered fused-ring formation is not.[194] The only addition/oxidation product is a cyclic dimer, [3,3]-metacyclophane (Scheme 43).[194]

Reversibility again is apparent with higher homologs, as shown in Scheme 44.[195] At low temperature, a mixture of cyclohexadienyl anionic intermediates is formed. An alternative quenching procedure, using trifluoroacetic acid produces the fused-ring diene shown. If the initial adduct is allowed to warm to 0 °C, rearrangement to the fused-ring spiro adduct occurs, and oxidative quenching gives the spiro[5.5]cyclohexadiene product.

8.6.3 Addition/Oxidation with Other Complexes

It has been recognized for many years that nucleophiles will add to (η^6-benzene)–$FeCp^+$ complexes.[196] The nucleophiles range from cyanide anion[197] to metal hydrides and methyllithium; the intermediate neutral [η^5-(6-substituted) cyclohexadienyl]−FeCp complexes can be isolated and characterized. The regioselectivity has been determined for a number of monosubstituted arene ligands. Chloro[196] and carbomethoxy[196] substituents are ortho-directing, while methoxy[196] is a meta director, and a methyl group leads to similar amounts of addition at the o, m, and p positions.[196] In general, electron-withdrawing groups (nitro, halo, benzoyl, cyano, and sulfonyl) favor ortho addition, as exemplified for the addition of the acetone enolate (equation 121).[196,198]

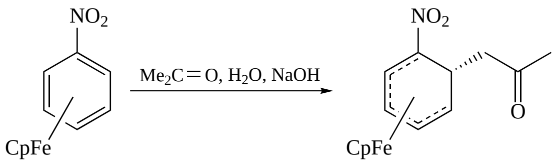

(121)

The primary limitations in applying these complexes are the two-stage detachment of the endo C-6 hydrogen and the detachment of the FeCp unit. Direct abstraction with trityl cation has been employed for the first stage,[196] and oxidation with N-bromosuccinimide completes both stages, leading to the substituted arene in the few cases tested.[199] In the cases with electron-withdrawing substituents on the starting arene, Ce^{IV} has been employed to aromatize and detach the arene unit after addition (equation 122).[198] Because of the high reactivity of the arene−FeCp$^+$ complexes, it can be expected that further developments and definition of selectivity features will be forthcoming.

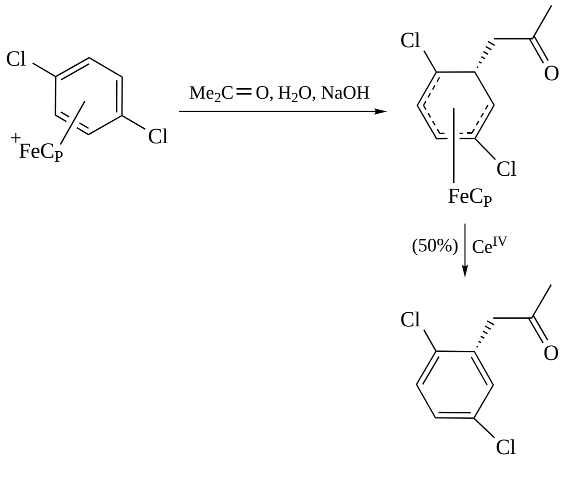

(122)

The reactivity of the (η^6-arene)−Mn(CO)$_3{}^+$ complexes toward addition of nucleophiles is high and general, leading to neutral, isolable [η^6-(6-substituted) cyclohexadienyl]−Mn(CO)$_3$ derivatives (equation 123).[200] The addition of Grignard reagents to anisole and aniline ligands shows good meta selectivity.[201,202] Addition to the chlorobenzene ligand gives similar amounts of ortho and meta (orbital control), while the toluene ligand favors addition at all three positions (o, m, p).[201,202]

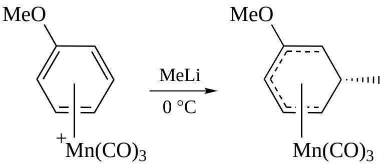

(123)

The completion of the substitution process to produce a substituted arene free of the metal has not been worked out in general. Direct abstraction of the endo hydride of the η^5-cyclohexadienyl intermediate with trityl cation is not effective, but an interesting thermal rearrangement has been observed at 130–150 °C to create an isomeric cyclohexadienyl ligand that bears an exo (easily abstracted) hydrogen substituent (equation 124).[202,203]

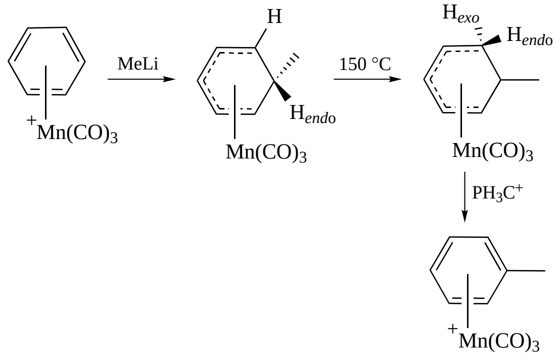

(124)

A general process for double addition to arene−Mn(CO)$_3{}^+$ complexes is shown in Scheme 45.[134,204] The neutral, η^5-cyclohexadienyl−Mn(CO)$_3$ complex obtained from an initial exo nucleophilic addition undergoes a second exo nucleophilic addition with very reactive nucleophiles. Oxidative decomplexation gives a syn disubstituted cyclohexadiene product. Ligand substitution of a CO ligand by NO$^+$ generates a cationic η^5-cyclohexadienyl−Mn(CO)$_3$ complex that undergoes a second nucleophilic addition to give either a syn disubstituted cyclohexadiene product or an anti disubstituted cyclohexadiene product containing an acylated substituent when using organolithium nucleophiles. In the latter case, nucleophilic attack likely occurs on a CO ligand with subsequent endo transfer of the resulting acyl ligand to the pi-ligand.

The arene−Mn(CO)$_3{}^+$ system is very promising, but more development work is necessary in order to assess the full possibilities for overall addition/oxidation and substitution for hydrogen.

8.7 Addition/Protonation: Synthesis of Substituted 1,3-Cyclohexadienes

The intermediate η^5-cyclohexadienyl anionic species from nucleophilic addition to the arene−Cr(CO)$_3$ complexes are

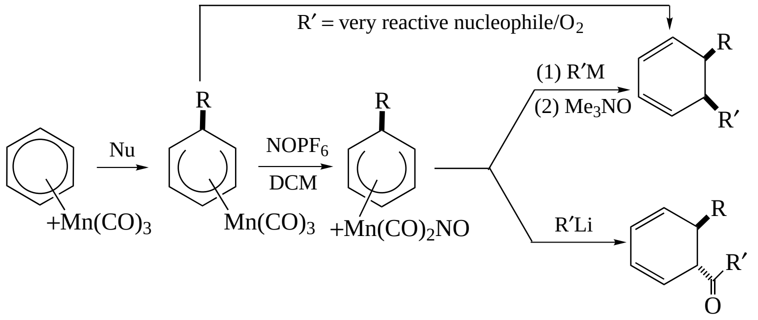

Scheme 45 Double addition to arene-Mn(CO)3 complexes

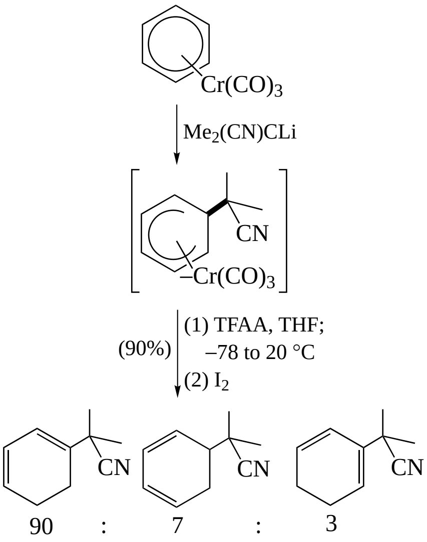

Scheme 46

obviously highly electron rich, and should be susceptible to reactions with electrophiles. Protonation is efficient at low temperature, and is suggested to produce a labile η^4-1,3-cyclohexadiene complex that can undergo H-migration to give the more stable 1,3-cyclohexadiene isomer; in simple systems, the major product is the 1-substituted 1,3-cyclohexadiene (Scheme 46).[134,205]

The reaction appears to be general, although a limited number of examples have been reported. A particularly useful process begins with meta addition to anisole–Cr(CO)$_3$, followed by protonation and hydrolysis of the enol ether unit. The result is a 5-substituted cyclohex-2-en-1-one.[206] This dienol ether can be isolated in high yield before the aqueous hydrolysis.

Other alkene positional isomers of the product enone can be obtained selectively, depending on the conditions of the acid treatment and the acid hydrolysis.[206] The addition/protonation process does not change the oxidation state of the chromium, and a procedure has been defined for recovery of the Cr^0 in order to allow direct recycling.[207]

The intramolecular version of addition/protonation with (m-cyanoalkyl)anisole ligands produces spirocyclic enones (equation 125).[207]

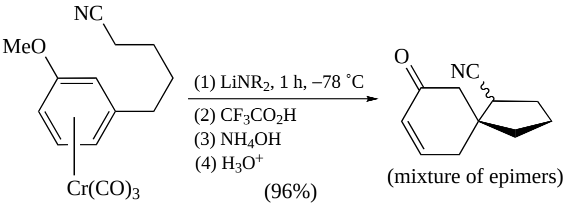

(125)

8.8 Addition/Acylation: Synthesis of Disubstituted 1,3-Cyclohexadienes

The efficient trapping of the cyclohexadienyl anionic intermediates with protons raises the possibility of quenching with carbon electrophiles. The process is not as general as the proton quench. However, when the nucleophile adds essentially irreversibly, quenching with a limited set of carbon electrophiles is successful.[183,208] For example, addition of 2-lithio-1,3-dithiane to benzene–Cr(CO)$_2$L, followed by addition of ethyl iodide and then oxidation or addition of a donor ligand (CO, Ph$_3$P), produces a cyclohexa-1,3-diene substituted by both acetyl (Me + CO) and the nucleophile (Scheme 47).[134,209] The insertion of CO occurs, without exception, with a variety of electrophiles. The insertion is efficient without added CO, but gives somewhat higher yields under a modest pressure (<4 bar) of CO during electrophile coupling. The attachment of the electrophile is from the *endo* direction, consistent with initial addition to the metal following by CO insertion and migration up to the arene unit; the products then have the trans arrangement of the new substituents.

More reactive anions such as the 2-lithio-1,3-dithiane derivatives, phenyllithium, and t-butyllithium do not require a special solvent and proceed in high yield in THF. While HMPA is known to suppress the migratory insertion to CO in anionic complexes, it does not deter the CO insertion in these cases; no example of direct alkylation is reported. The only electrophile that adds without CO insertion is the proton,

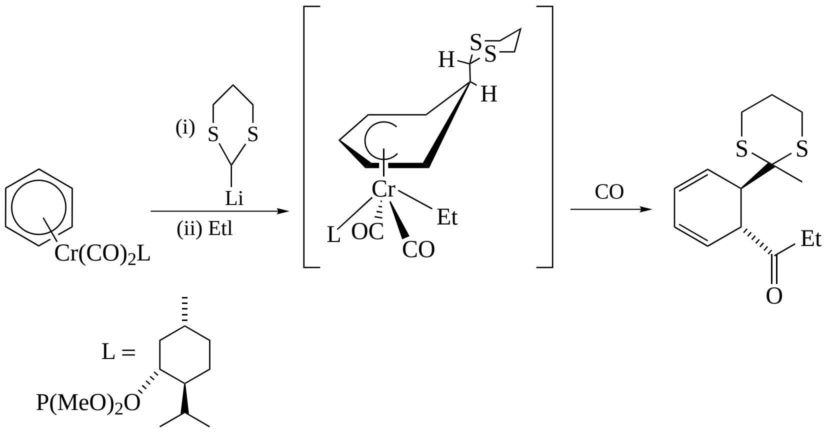

Scheme 47 Nucleophilic addition to Arene–Cr(CO)$_3$ complexes

as discussed above. Good alkylating agents (primary iodides and triflates, allyl bromide, benzyl bromide) react below 0 °C, but ethyl bromide requires heating at 50 °C. The reaction is selective for a primary alkyl iodide in the presence of an ester or a ketone unit.

While the addition/oxidation and the addition/protonation procedures are successful with ester enolates as well as more reactive carbon nucleophiles, the addition/acylation procedure requires more reactive anions and the addition of a polar aprotic solvent (HMPA has been used) to disfavor reversal of anion addition. Under these conditions, cyano-stabilized anions and ester enolates fail (simple alkylation of the carbanion), but cyanohydrin acetal anions are successful. The addition of a cyanohydrin acetal anion to 1,4-dimethoxynaphthalene–Cr(CO)$_3$ occurs by kinetic control at C-β in THF/HMPA and leads to the α,β-diacetyl derivative after methyl iodide addition and hydrolysis of the cyanohydrin acetal. Monoacylation of 1,4-dimethoxynaphthalene–Cr(CO)$_3$ has been achieved using the sequence of reactions shown in equation (126).**[134,210]**

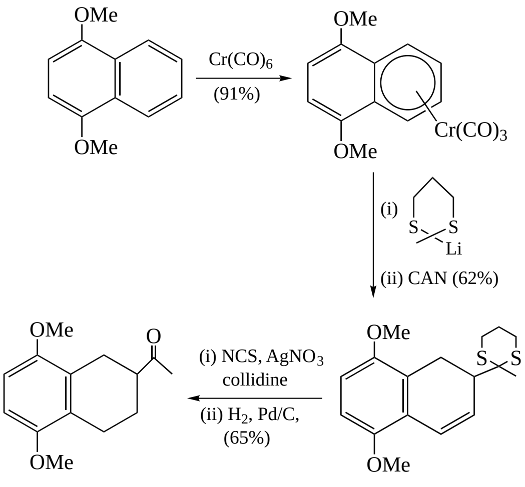

(126)

Addition of a cyanohydrin acetal anion to benzene–Cr(CO)$_3$ followed by reaction with allyl bromide produces the cyclohexadiene derivative in 94% yield, which undergoes a Diels–Alder reaction rapidly to give the tricyclic framework. After quenching with methyl iodide and disassembling of the cyanohydrin group, the diketone is obtained in 50% yield overall (equation 127).**[208]**

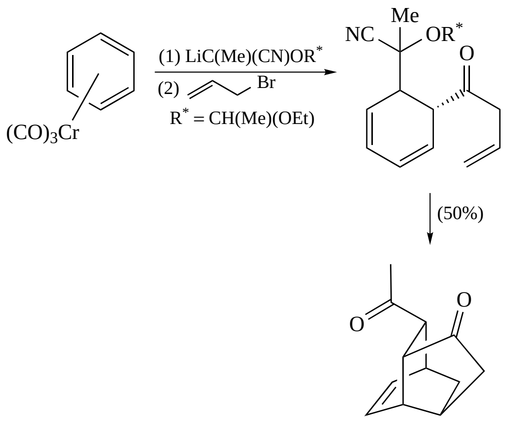

(127)

8.9 Summary

Coordination of a metal to the π-orbitals of an arene opens pathways for nucleophile addition to the arene. The power of the effect is related to the oxidation state (Cr^0, Mn$^\mathrm{I}$, Fe$^\mathrm{II}$) and peripheral ligands (Cp or CO). Under suitable conditions, both heteroatom and carbon-based nucleophiles add rapidly under mild conditions. The fate of the cyclohexadienyl intermediate depends on the conditions of the next stage of the batch-wise process. Loss of an electronegative leaving group leads to an analog of conventional nucleophilic aromatic substitution, but there are procedures for oxidation/loss of a hydrogen substituent, protonation to give a monosubstituted 1,3-diene, and acylation to give a disubstituted 1,3-diene.

9 COUPLING OF ALLYL–Ni^{II} COMPLEXES WITH ORGANIC HALIDES

9.1 Basic Reaction

Before the modern era of organotransition metal reactivity, it was observed that nickel carbonyl reacted with 2-methallyl chloride in methanol to give methyl 3-methyl-3-butenoate and 2,5-dimethyl-1,5-hexadiene as a by-product.[211] In THF at 25 °C, the diene was the exclusive product. This mild formation of a carbon–carbon bond, and the interest in the synthesis of terpene-based natural products led to efforts to test the scope and limitations of the process. An obvious pathway involves stepwise oxidative addition of each allyl unit followed by *Reductive Elimination*. As discussed below, the key intermediates (left vague in Scheme 48) are likely to involve Ni^{I}–Ni^{III} couples.

This pathway suggests that unsymmetrical coupling and perhaps coupling with other types of organic halides might be possible if the process could be interrupted after the first oxidative addition and allow isolation of the allyl–Ni complex. A remarkable solvent effect began to be delineated when it was reported that in benzene, reaction of allylic halides with nickel carbonyl leads to the η^3-allyl–NiBr species as a bridged dimer. Subsequently, it has been reported that many of forms of Ni^0, including bis(1,5-cyclooctadiene)Ni^0 and ‘Rieke’ nickel, react at room temperature or below in many solvents to produce the same allyl–nickel complexes in high yield. Such η^3-allyl–NiBr dimers dissociate into monomeric complexes when treated with Lewis bases like PPh$_3$ (equation 128).[212]

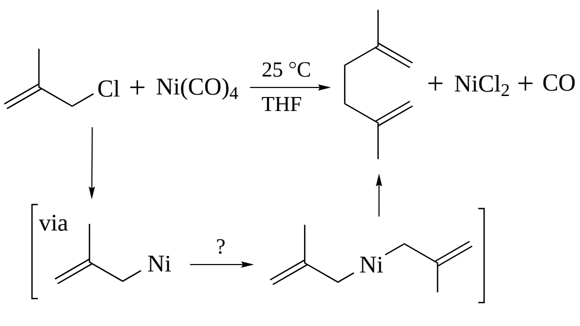

Scheme 48

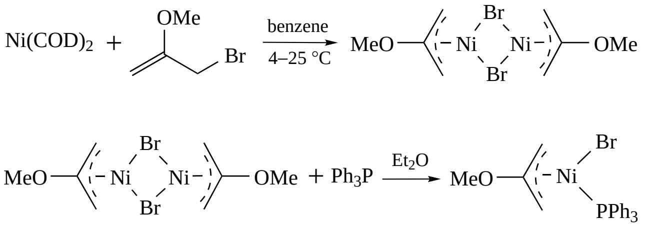

(128)

The complexes are typically deep red, soluble in organic solvents, and moderately air sensitive. The solids can be handled in air for short periods, but routine manipulations should be done under inert atmosphere conditions. The coupling reactions are strongly inhibited by oxygen. It is not generally possible to carry out organic transformations on the organic ligand, and they are simply used directly in coupling with organic halides. Complexation can be accomplished in the presence of numerous functional groups, including ester, alkoxy, and so on, and it is unlikely that the list has been fully elaborated. The allyl–Ni^{II} complexes are relatively inert toward all common functional groups, including acyl halides and phenolic hydroxyl. Stronger acid will protonate the ligand to give the propene derivative.

The symmetrical coupling of allylic halides (Scheme 48) is very general and compatible with most common functional groups.[211] It is limited by rapid equilibration of the configuration of the allyl double bond during coupling and production of the more stable diene configuration. For simple allyl units, a mixture of the possible geometrical isomers results. Symmetrical coupling does not lead to a versatile synthesis method, but intramolecular applications have been impressively successful (equation 129).[213,214] Medium-sized rings can be formed, although there is no significant evidence for features that favor such rings and high dilution is generally employed.

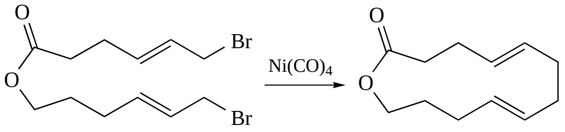

(129)

Attempts to bring about cross coupling of different allylic halides invariably led to mixtures suggesting exchange of the allylic units before coupling. This problem in synthesis is better solved by cross coupling of an allylic halide and an allylic derivative of a main group metal.[212,215] However, electrophilic alkylation of η^3-allyl–NiBr dimers by simple alkyl halides is successful (equations 130 and 131).

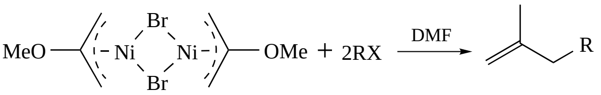

(130)

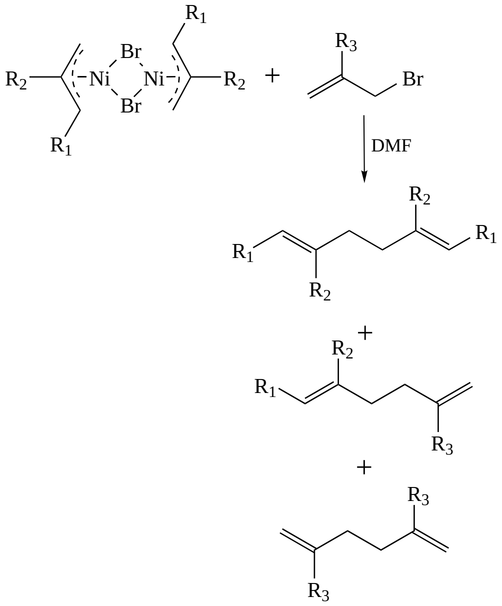

(131)

The utility of the allyl–Ni^{II} complexes lies in that fact that nonallylic halides undergo cross coupling with high selectivity.[211,212] Moreover, the pattern of reactivity of organic halides was unlike any other synthesis methodology available at that time (1967), and opened new opportunities. The method is summarized by the general equation (132). It is a stoichiometric process, but easy to carry out. The first step is most economically done with excess nickel tetracarbonyl in toluene (80 °C, 0.5 h) and most conveniently with bis(1,5-cyclooctadiene)nickel (0 °C in ether). After the complex is formed, the volatile material can be removed and the residue taken up in DMF, a strongly activating solvent for the next step. Alternatively, the residue can be crystallized, typically from ether, and isolated by filtration as usual.[216]

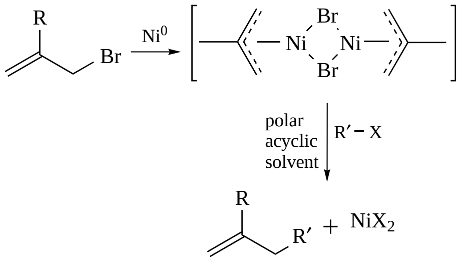

(132)

9.2 Pattern of Reactivity in the Organic Halide

The reactivity series for R′–X is summarized in Figure 6 and the special case is exemplified in equation (133).[212]

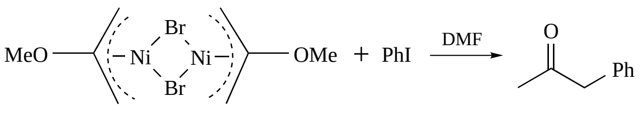

(133)

Structure of R′: allyl > benzyl > aryl > vinyl > methyl > alkyl
R′: = Alkyl: primary > secondary > tertiary
Leaving group: I > Br > Cl (OTs unreactive)

Figure 6 Reactivity series for organic electrophiles in reaction with allyl–Ni^{II} complexes

The relatively high reactivity of the allyl–Ni^{II} complexes toward aryl halides, especially bromides, is unusual among traditional organic mechanisms and represented one of the first observations of this special feature in transition metal reactions. An S_N2 mechanism for activation of the halide is clearly ruled out, and the reactivity correlates better with an electron-transfer mechanism. The rates are roughly correlated with ease of reduction of the organic halide. This also is consistent with the low reactivity of *p*-toluenesulfonate esters, compared to bromides.[211]

9.3 Selectivity Issues

A revealing example is the reaction of 4-iodocyclohexanol with 2-methallyl–NiBr.[211] The product is a mixture of epimers, symbolizing the general result that the configuration of the halide undergoing coupling is equilibrated during the reaction. The hydroxyl group is not protected and does not interfere. This is a secondary halide, very prone to β-hydride elimination, and yet no elimination is observed. Presumably, the key intermediates bearing a σ-cyclohexyl unit are coordinatively saturated or undergo intramolecular processes faster than β-elimination. The process must involve an intermediate related to the allyl–Ni–cyclohexyl species shown in equation (134).

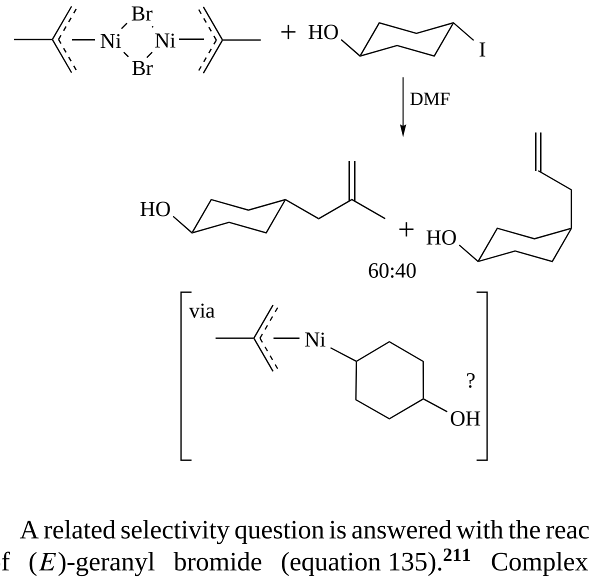

(134)

A related selectivity question is answered with the reactions of (*E*)-geranyl bromide (equation 135).[211] Complexation gives a noncrystalline residue that couples with cyclohexyl iodide on heating in DMF, but the coupled product shows evidence of equilibration of the double bond in the starting halide. Isomerization of the allylic π-bond is a general feature of the allyl–Ni coupling process. The difference in reactivity of the halides is large.[211] Selective reaction of iodide in the presence of either chloride or bromide is easy to predict (equation 136). Even neopentyl halides, normally very resistant to coupling by any mechanism, will react under forcing conditions and with good efficiency (equation 137).[211]

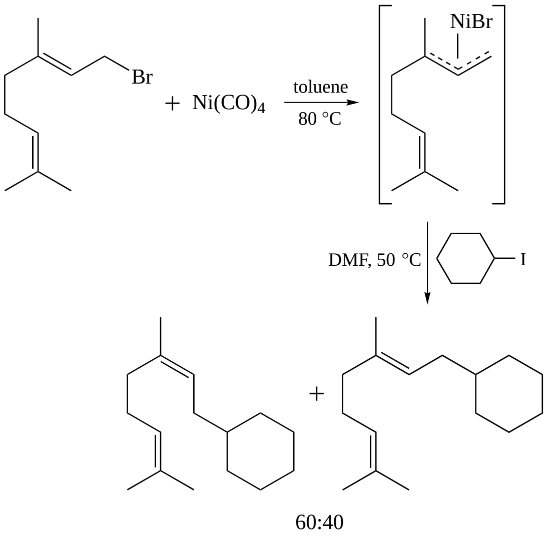

(135)

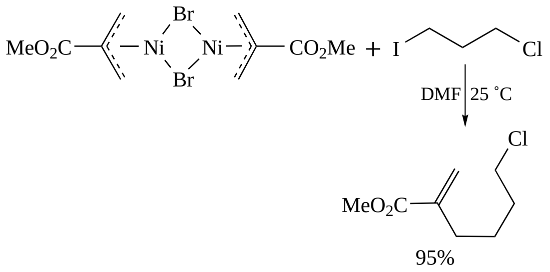

(136)

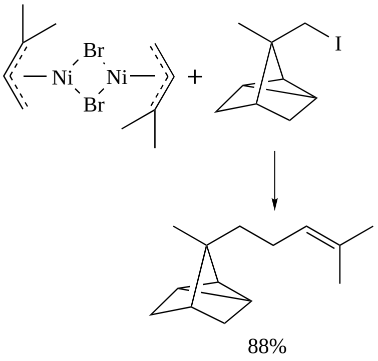

(137)

9.4 Mechanism

A simple mechanism for the process was proposed in the original papers, involving oxidative addition to give a $\mathrm{Ni^{IV}}$ species. However, it did not explicitly account for a number of observations, and difficult questions continued to accumulate.[217] In summary, mechanistically significant observations are:

1. Complete equilibration of configuration of the halide undergoing coupling. This has been verified with the racemization of 2-octyl bromide during coupling.
2. Inhibition of the coupling reaction by oxygen, *m*-dinitrobenzene, and other conventional radical chain inhibitors.
3. None of the typical products of radicals (R· from R–X) have been observed (coupling or elimination).
4. Radical rearrangement products from, for example, 6-hexenyl iodide and vinyl iodide are minimal, although the cyclopropylcarbinyl example (Scheme 49) shows the nearly complete rearrangement typical of a cyclopropylcarbinyl radical.

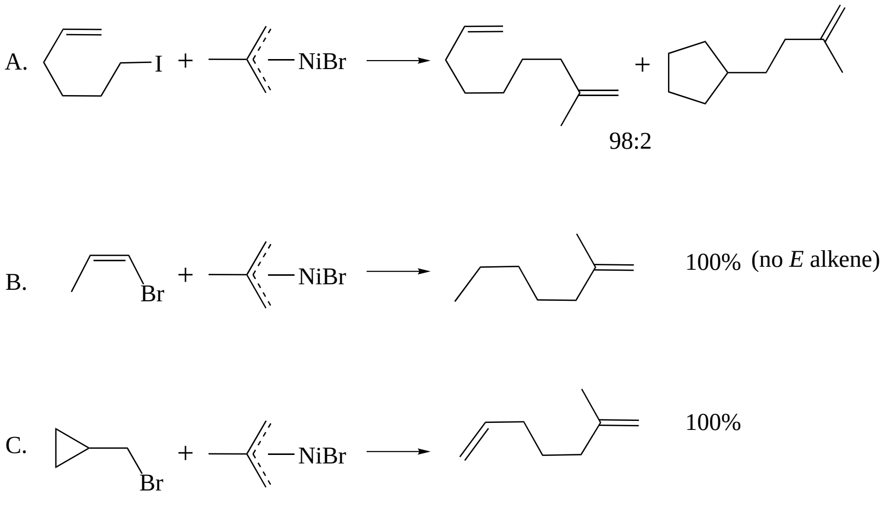

Scheme 49 Radical clock experiments to detect radical intermediates

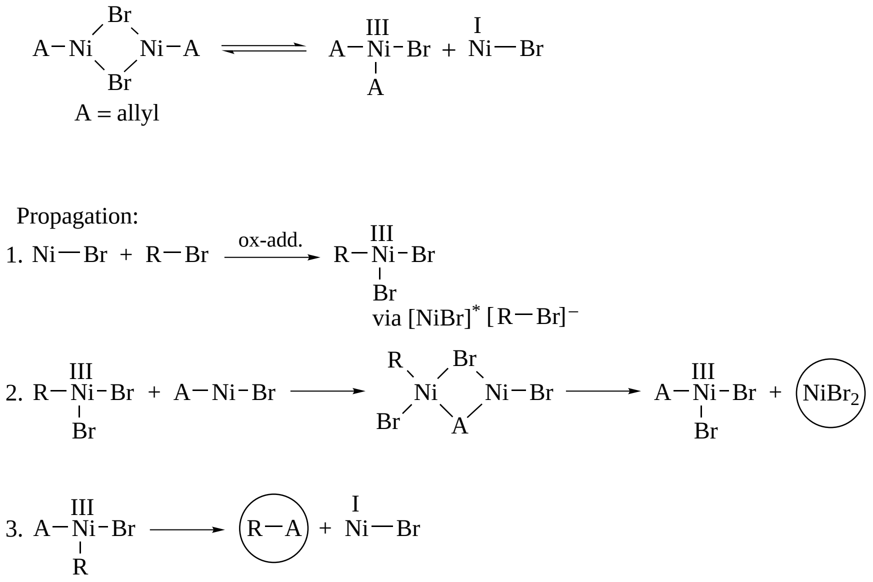

Scheme 50 Mechanism of the allyl–Ni coupling reaction

In these ‘radical clock’ experiments, the observations are somewhat contradictory: a vinyl radical should rearrange to the other geometrical isomer (Z to E in this case) at least as rapidly as the cyclopropylcarbinyl radical rearranges to the allylcarbinyl radical. A simple explanation is that the putative cyclopropylcarbinyl–nickel intermediate has a low-energy pathway for rearrangement to the allylcarbinyl ligand, not involving radicals. Overall, the reactions in Scheme 50 are taken as evidence against radical intermediates generated from R–Br.[217]

A consistent picture is presented in Scheme 50.[217] Initial formation of a Ni^{I} species occurs by an unspecified mechanism (initiation); one possibility is ‘redox disproportionation’ with the dimer Ni^{II} complex giving rise to Ni^{I} and Ni^{III} species. The Ni^{I} derivative is expected to be a good electron donor, and can transfer an electron to the organic halide. Then the radical anion of the organic halide can fragment rapidly to produce the organic radical, now coordinated with the Ni, and the halide anion. The resulting Ni^{III} species can undergo a ligand exchange through a bridging interaction with the starting Ni^{II} allyl species, leading to a Ni^{III} unit with both the R group and the allyl group attached. Then reductive elimination gives the coupled product, R–allyl, as well as a new Ni^{I} unit. This scheme does not involve R· and can be shown to operate at a very high rate in the absence of radical inhibitors. The loss of configuration is not readily apparent from this scheme; it requires some mechanism for racemization of the carbon attached to Ni during the coupling.[217]

Trihapto-allyl–Ni complexes have been used in Pauson–Khand cycloadditions to form cyclopentenones (see equations 138 and 139).[218,219] In the reactions shown, Ni(COD)$_2$ is the source of Ni^0 to give allyl–Ni intermediates through oxidative addition of an allylic halide or silylation of a coordinated enone. Carbonylation reactions of allyl halides by Ni(CO)$_4$ have also been examined theoretically.[220]

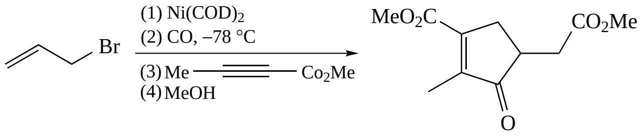

(138)

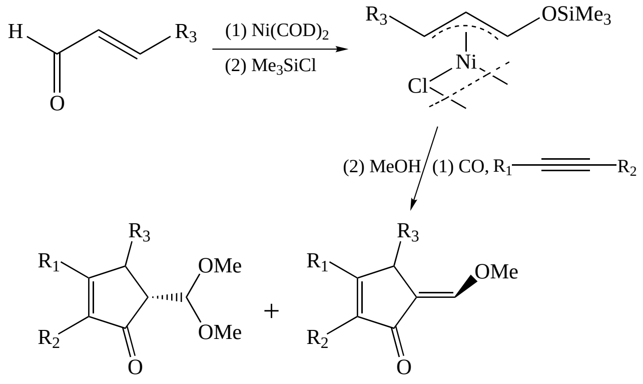

(139)

9.5 Applications

A particularly interesting combination of allyl ligand structure and the high reactivity toward aryl halides leads to the synthesis equivalent of nucleophilic aromatic substitution by enolate anions, but under completely different conditions (Scheme 51).[221] In this example, the 2-methoxyallyl ligand is equivalent to an acetone enolate anion, but reacts with very different functional group compatibility (no polar

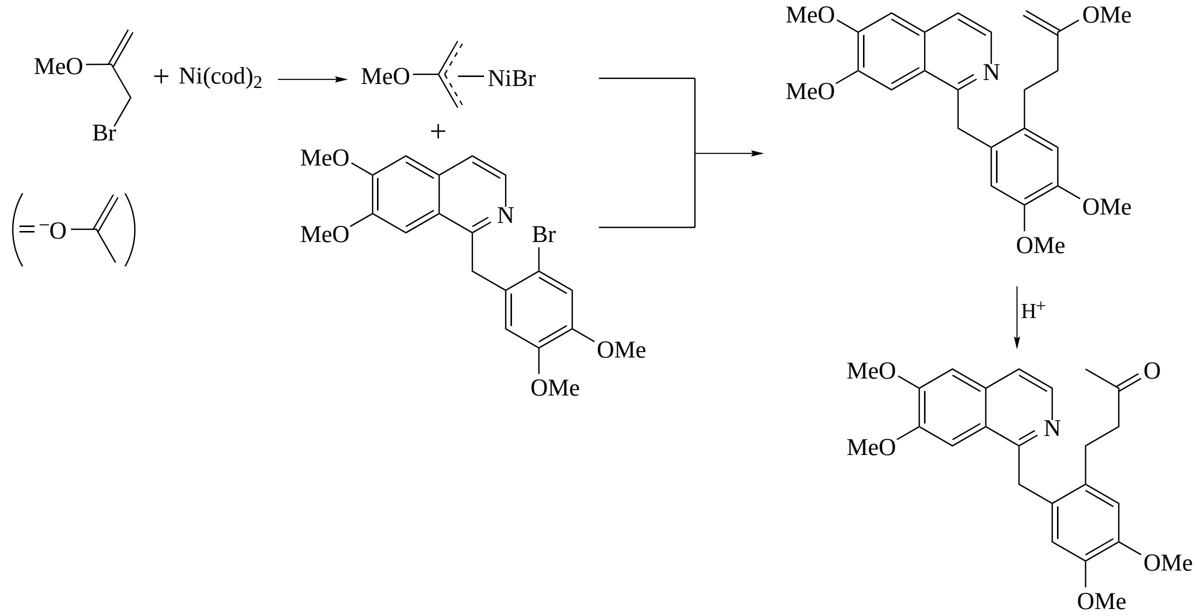

Scheme 51 Synthesis equivalent of nucleophilic aromatic substitution

reactions) and with aromatic halides, even if electron rich. The selective coupling of an allyl ligand in the presence of a free amino group and an ester demonstrates the chemoselectivity of these reagents, and leads to an intermediate that can be oxidatively cyclized with Pd^{II} to give indoles (equation 140).[222]

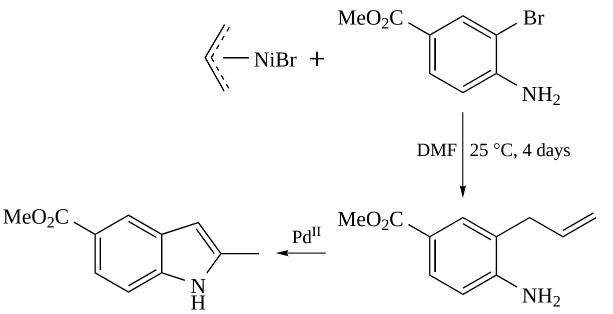

(140)

The discussion above emphasizes that the allyl–Ni^{II} reagents are quite selective for carbon–halogen bonds, especially allyl, vinyl, and aryl halides. At the same time, modest reactivity as nucleophiles toward reactive carbonyl derivatives has been reported.[211,219,223] Simple aldehydes, the more reactive ketones (such as cyclopentanone and benzoquinone), and certain epoxides will undergo 1,2-addition of the allyl ligand to the carbonyl group. Esters, amides, and, most remarkably, acyl halides are inert toward the allyl–Ni^{II} reagents under conditions where the reagents do not decompose thermally ($<80\,^\circ$C or so).

9.6 Summary

The coupling of the allyl–Ni^{II} reagents with organic halides opens special reactivity patterns not available by traditional organic methods. The high reactivity of aryl and vinyl halides is particularly useful. The functional group compatibility is very high, although rapid epimerizations and double bond inversions limit the selectivity. There is no catalytic version, but the processes are convenient to carry out on a large scale stoichiometrically, and the Ni^{II} by-products can be recycled or disposed of easily.

10 RELATED ARTICLES

Chromium: Organometallic Chemistry; Cobalt: Organometallic Chemistry; Iron: Organometallic Chemistry; Mercury: Organometallic Chemistry; Nickel: Organometallic Chemistry; Organic Synthesis using Transition Metal Carbonyl Complexes; Palladium: Organometallic Chemistry.

11 REFERENCES

1. K. P. C. Vollhardt, *Angew. Chem., Int. Ed. Engl.*, 1984, **23**, 539.
2. P. J. Harrington, 'Transition Metals in Total Synthesis', Wiley, New York, 1990, p. 259.

3. W. Wulff, *Adv. Metal-Org. Chem.*, 1989, **1**, 209.
4. B. Trost and I. Fleming eds, 'Comprehensive Organic Synthesis', Pergamon, Oxford, 1992, (especially Vol. 4).
5. G. Wilkinson ed., 'Comprehensive Organometallic Chemistry', Pergamon, Oxford, 1982, (especially Vol. 8).
6. S. G. Davies, M. L. H. Green, and R. Wade, *Tetrahedron*, 1978, **34**, 3047; F. R. Hartley and S. Patai eds, For a general review on nucleophilic attack on transition metal complexes see 'Chemistry of the Metal Carbon Bond', Wiley, New York, 1985, Vol. 2, p. 401.
7. R. Heck, *Org. React.*, 1982, **27**, 345; R. Heck, in 'Comprehensive Organic Synthesis', eds. B. Trost and I. Fleming, Pergamon, Oxford, 1992, Vol. 4, p. 834; R. F. Heck, 'Palladium Reagents in Organic Synthesis', Academic Press, London, 1985, Chap. 6; S. E. Gibson and R. J. Middleton, *Org. Synth.*, 1996, **3**, 447; N. J. Whitcombe, K. K. Hii, and S. E. Gibson, *Tetrahedron*, 2001, **57**, 7449; I. P. Beletskaya and A. V. Cheprakov, *Chem. Rev.*, 2000, **100**, 3009.
8. R. F. Heck, *Acc. Chem. Res.*, 1979, **12**, 146.
9. A. C. Albeniz, P. Espinet, and Y.-S. Lin, *Organometallics*, 1995, **14**, 2977.
10. Y. Fujiwara, R. Asano, I. Moritani, and S. Teranishi, *J. Org. Chem.*, 1976, **41**, 1681.
11. Y. Fujiwara, O. Maruyama, M. Yoshidomi, and H. Taniguchi, *J. Org. Chem.*, 1981, **46**, 851.
12. T. Itahara, M. Ikeda, and T. Sakakibara, *J. Chem. Soc., Perkin Trans. 1*, 1983, 1361.
13. R. F. Heck, *J. Am. Chem. Soc.*, 1968, **90**, 5518.
14. R. F. Heck, *J. Am. Chem. Soc.*, 1968, **90**, 5535.
15. R. F. Heck, *J. Am. Chem. Soc.*, 1971, **93**, 6896.
16. K. Hirabayashi, Y. Nara, T. Shimizu, and N. Kamigata, *Chem. Lett.*, 2004, **33**, 1280.
17. R. C. Larock and M. A. Mitchell, *J. Am. Chem. Soc.*, 1978, **100**, 180.
18. Y. C. Jung, R. K. Mishra, C. H. Yoon, and K. W. Jung, *Org. Lett.*, 2003, **5**, 2231.
19. X. Du, M. Suguro, K. Hirabayashi, A. Mori, T. Nishikata, N. Hagiwara, K. Kawata, T. Okeda, H. F. Wang, K. Fugami, and M. Kosugi, *Org. Lett.*, 2001, **33**, 3313.
20. C. S. Cho and S. Uemura, *J. Organomet. Chem.*, 1994, **465**, 85.
21. K. Hirabayashi, J. Ando, J. Kawashima, Y. Nishihara, A. Mori, and T. Hiyama, *Bull. Chem. Soc. Jpn.*, 2000, **73**, 1409.
22. J. Yoshida, K. Tamao, H. Yamamoto, T. Kakui, T. Uchida, and M. Kumada, *Organometallics*, 1982, **1**, 542.
23. K. Hirabayashi, J. Ando, Y. Nishihara, A. Mori, and T. Hiyama, *Synlett*, 1999, **1**, 99.
24. D. V. Moiseev, V. A. Morugova, A. V. Gushchin, and V. A. Dodonov, *Tetrahedron Lett.*, 2003, **44**, 3155.
25. S. K. Kang, S. C. Choi, H. C. Ryu, and T. Yamaguchi, *J. Org. Chem.*, 1998, **63**, 5748.
26. L. S. Hegedus and M. A. McGuire, *Organometallics*, 1982, **1**, 1175.
27. N. Luong-Thi and H. Riviere, *J. Chem. Soc., Chem. Commun.*, 1978, 918.
28. T. Hayashi and L. S. Hegedus, *J. Am. Chem. Soc.*, 1977, **99**, 7093.
29. H. Dieck and R. F. Heck, *J. Org. Chem.*, 1975, **40**, 1083.
30. K. H. Shaughnessy, P. Kim, and J. F. Hartwig, *J. Am. Chem. Soc.*, 1999, **121**, 9550.
31. N. Cortese, C. Ziegler Jr, B. Hrnjez, and R. F. Heck, *J. Org. Chem.*, 1978, **43**, 2952.
32. S. Brase, J. Rumper, K. Voigt, S. Albecq, G. Thurau, R. Villard, B. Waegell, and A. de Meijere, *Eur. J. Org. Chem.*, 1998, **1**, 671.
33. S. Lemaire-Audoire, M. Savignac, C. Dupuis, and J. P. Genet, *Tetrahedron*, 1996, **37**, 2003.
34. B. Patel and R. F. Heck, *J. Org. Chem.*, 1978, **43**, 3898.
35. S. Sengupta, S. Bhattacharyya, and S. K. Sadhukhan, *J. Chem. Soc., Perkin Trans.*, 1998, **1**, 275.
36. P. Mauleon, A. A. Nunez, I. Alonso, and J. C. Carretero, *Chem. – Eur. J.*, 2003, **9**, 1511.
37. S. Jeong, X. Chen, and P. G. Harran, *J. Org. Chem.*, 1998, **63**, 8640.
38. A. E. S. Gelpke, J. J. N. Veerman, M. S. Goedheijt, P. C. J. Kamer, P. W. N. Mv. Leeuwen, and H. Hiemstra, *Tetrahedron*, 1999, **55**, 6657.
39. K. Kikukawa, K. Maemura, Y. Kliseki, F. Wada, and T. Matsuda, *J. Org. Chem.*, 1981, **46**, 4885.
40. Q. Chen and Z. Yang, *Tetrahedron Lett.*, 1986, **27**, 1171.
41. S. Cacchi, E. Morera, and G. Ortar, *Tetrahedron Lett.*, 1984, **25**, 2271.
42. W. Scott, M. Pena, K. Sward, A. Stoessel, and J. Stille, *J. Org. Chem.*, 1985, **50**, 2302.
43. Q. Chen and Z. Yang, *Tetrahedron Lett.*, 1986, **27**, 1171.
44. C. Anderson and A. Hallberg, *Tetrahedron Lett.*, 1983, **24**, 4215.
45. A. Spencer, *J. Organomet. Chem.*, 1984, **265**, 323.
46. M. Webel and H.-U. Reissig, *Synlett*, 1997, **10**, 1141.
47. L. Kao, F. G. Stakem, B. Patel, and R. F. Heck, *J. Org. Chem.*, 1982, **47**, 1267.
48. J. Melpolder and R. F. Heck, *J. Org. Chem.*, 1976, **41**, 265.
49. A. Chalk and S. Magennis, *J. Org. Chem.*, 1976, **41**, 1206.
50. J. Melpolder and R. F. Heck, *J. Org. Chem.*, 1976, **41**, 265.
51. M. M. Abelman, L. E. Overman, and V. D. Tran, *J. Am. Chem. Soc.*, 1990, **112**, 6959.
52. B. Trost and I. Fleming eds, For a comprehensive review see 'Comprehensive Organic Synthesis', Pergamon Press, Oxford, 1992, Vol. 4, p. 1.
53. G. Zeni and R. C. Larock, *Chem. Rev.*, 2004, **104**, 2285.

54. P. M. Maitlis, 'The Organic Chemistry of Palladium', Academic Press, New York, 1971, Vol. 1 and 2.
55. J. Tsuji, 'Organic Synthesis with Palladium Compounds', Springer-Verlag, New York, 1980.
56. R. F. Heck, 'Palladium Reagents in Organic Synthesis', Academic Press, New York, 1985.
57. R. C. Larock, 'In Advances in Metal-Organic Chemistry', JAI Press, London, 1994, Vol. V.
58. J. Tsuji, 'Palladium Reagents and Catalysts', Wiley & Sons, New York, 1995.
59. E. Negishi, 'Handbook of Organopalladium Chemistry for Organic Synthesis', Wiley & Sons, New York, 2002, Vol. 1 and 2.
60. J. J. Li and G. W. Gribble, 'Palladium in Heterocyclic chemistry', Pergamon, New York, 2000.
61. O. Eisenstein and R. Hoffman, *J. Am. Chem. Soc.*, 1981, **103**, 4308.
62. J. Backvall, *J. Am. Chem. Soc.*, 1984, **106**, 4369.
63. P. M. Henry, 'Palladium Catalyzed Oxidation of Hydrocarbons', Reidel, Dordrecht, 1980; R. F. Heck, 'Palladium Reagents in Organic Synthesis', Academic Press, New York, 1985.
64. P. M. Henry, *Adv. Organomet. Chem.*, 1975, **13**, 363.
65. T. Hosokawa, T. Nomura, and S.-L. Murahashi, *J. Organomet. Chem.*, 1998, **551**, 387.
66. V. V. Namboodiri, R. S. Varma, E. Sahle-Demessie, and U. R. Pillai, *Green Chem.*, 2002, **4**, 170.
67. M. J. Gaunt, J. Q. Yu, and J. B. Spencer, *Chem. Commun.*, 2001, **18**, 1844.
68. A. J. K. Bose, L. Krishnan, D. R. Wagle, and M. S. Manhas, *Tetrahedron Lett.*, 1986, **27**, 5955.
69. J. Backvall and E. E. Bjorkman, *J. Org. Chem.*, 1980, **45**, 2893.
70. Y. Uozumi, K. Kato, and T. Hayashi, *J. Am. Chem. Soc.*, 1997, **119**, 5063.
71. R. C. Larock, L. Wei, and T. R. Hightower, *Synlett*, 1998, 522.
72. K. C. Majundar, U. Das, U. K. Kundu, and A. Bandyopadhyay, *Tetrahedron*, 2001, **57**, 7003.
73. R. G. Giles, I. R. Greem, and C. P. Taylor, *Tetrahedron Lett.*, 1999, **40**, 4871.
74. M. Ronn, J.-E. Backvall, and P. G. Andersson, *Tetrahedron Lett.*, 1995, **36**, 7749.
75. T. M. Meulemans, N. H. Kiers, B. L. Feringa, and W. N. M. Van Leeuwen, *Tetrahedron Lett.*, 1994, **35**, 455.
76. A. Tenaglia and F. Kammerer, *Synlett*, 1996, 576.
77. S. Jabre-Truffert and B. Waegell, *Tetrahedron Lett.*, 1997, **38**, 835.
78. M. Frederickson, R. Grigg, J. Markandu, and J. Redpath, *J. Chem. Soc., Chem. Commun.*, 1994, 2225.
79. K. Narasaka, *Pure Appl. Chem.*, 2002, **74**, 143.
80. H. Tsutsui, M. Kitamura, and K. Narasaka, *Bull. Chem. Soc. Jpn.*, 2002, **75**, 1451.
81. M. Gowan, A. S. Caille, and C. K. Lau, *Synlett*, 1997, 1312.
82. Y. Hirai, J. Watanabe, T. Nozaki, H. Yokoyama, and S. Yamaguchi, *J. Org. Chem.*, 1997, **62**, 776.
83. F.-L. Qing, W.-Z. Gao, and J. Ying, *J. Org. Chem.*, 2000, **65**, 2003.
84. N. Asao, T. Nogami, K. Takahashi, and Y. Yamamoto, *J. Am. Chem. Soc.*, 2002, **124**, 764.
85. A. Arcadi, S. Cacchi, and F. Marinelli, *J. Organomet. Chem.*, 1994, **475**, 289.
86. N. G. Kundu and M. W. Khan, *Tetrahedron*, 2000, **56**, 4777.
87. M. Lautens, 'Science of Synthesis', Georg Thieme Verlag, New York, 2001, Vol. 1, p. 11; E. Negishi, 'Handbook of Organopalladium Chemistry for Organic Synthesis', Wiley-Interscience, New-York, 2002, Version 2; B. M. Trost and M. L. Crawley, *Chem. Rev.*, 2003, **103**, 2921; B. M. Trost and C. Lee, Asymmetric Allylic Alkyaltion Reactions, 'Catalytic Asymmetric Synthesis', Wiley-VCH, 2000, p. 593; A. Pfaltz and M. Lautens, Allylic Substitution Reactions, 'Comprehensive Catalysis I-III', Springer, 1999, Vol. 2, p. 833.
88. J. Tsuji, *Pure Appl. Chem.*, 1982, **54**, 197; E. Negishi, 'Handbook of Organopalladium Chemistry for Organic Synthesis', Wiley Interscience, New York, 2002, Vol. 2.
89. T. W. Greene and P. G. M. Wuts, 'Protective Groups in Organic Synthesis', 2nd edn., Wiley, New York, 1991, p. 248.
90. B. M. Trost, N. R. Schmuff, and M. J. Miller, *J. Am. Chem. Soc.*, 1980, **102**, 5981.
91. J. S. Temple and J. Schwartz, *J. Am. Chem. Soc.*, 1980, **102**, 7382.
92. O. Belda and C. Moberg, *Acc. Chem. Res.*, 2004, **37**, 159.
93. B. M. Trost and M.-H. Hung, *J. Am. Chem. Soc.*, 1983, **105**, 7757.
94. G. C. Lloyd-Jones and A. Pfatz, *Angew. Chem. Int. Ed. Engl.*, 1995, **34**, 462.
95. M. Lautens, 'Science of Synthesis', Georg Thieme Verlag, New York, 2001, Vol. 1, p. 480.
96. M. Pineschi, *New J. Chem.*, 2004, **28**, 657.
97. A. J. Blacker, M. L. Clarke, M. S. Loft, M. F. Mahon, M. E. Humphries, and J. M. J. Williams, *Chem. – Eur. J.*, 2000, **6**, 353.
98. P. A. Evans and J. E. Robison, *J. Am. Chem. Soc.*, 2001, **123**, 4609.
99. B. M. Trost, P. L. Fraisse, and Z. T. Ball, *Angew. Chem. Int. Ed. Engl.*, 2002, **41**, 1059.
100. B. Bartel and G. Helmchen, *Chem. Commun.*, 1999, **8**, 741.
101. B. Toebald, *Tetrahedron*, 2002, **58**, 4133.
102. P. Magnus, G. F. Miknis, N. J. Press, D. Grandjean, G. M. Taylor, and J. Harling, *J. Am. Chem. Soc.*, 1997, **119**, 6739.
103. J. Backvall, *Adv. Metal-Org. Chem.*, 1989, **1**, 136.

104. (a) J. Backvall, Y. I. M. Nilsson, P. G. Andersson, R. G. P. Gatti, and J. Wu, *Tetrahedron Lett.*, 1994, **35**, 5713; (b) J. Backvall, *Pure Appl. Chem.*, 1996, **68**(3), 535.

105. M. Ronn, P. G. Andersson, and J. Backvall, *Tetrahedron Lett.*, 1997, **38**, 3603.

106. K. Bergstad, H. Grennberg, and J. Backvall, *Organometallics*, 1998, **17**, 45.

107. (a) J. Backvall, J. E. Nystrom, and R. E. Nordberg, *J. Am. Chem. Soc.*, 1985, **107**, 3876; (b) E. Hupe, K. Itami, A. Aranyos, K. J. Szabo, and J. E. Backvall, *Tetrahedron*, 1998, **54**, 5375.

108. L. S. Hegedus, 'Comprehensive Organic Synthesis', Pergamon, Oxford, 1992, Vol. 4, p. 551.

109. M. F. Semmelhack, C. M. Bodurow, E. Fewkes, J. W. Herndon, G. Knaus, H. T. M. Le, and M. Sanner, *Chem. Scr.*, 1985, **25**, 131.

110. M. F. Semmelhack and J. W. Herndon, *Organometallics*, 1983, **2**, 363.

111. M. F. Semmelhack, J. W. Herndon, and J. P. Springer, *J. Am. Chem. Soc.*, 1983, **105**, 2497.

112. J. Fan and R. Liu, *Organometallics*, 1998, **17**, 1002.

113. M. F. Semmelhack, J. W. Herndon, and J. K. Liu, *Organometallics*, 1983, **2**, 1885.

114. A. Akudia, R. G. Arrayas, and L. S. Liebeskind, *J. Org. Chem.*, 2002, **67**, 5773.

115. A. J. Birch, *J. Organomet. Chem.*, 1985, **285**, 267.

116. A. Pearson, *Acc. Chem. Res.*, 1980, **13**, 463.

117. A. J. Pearson, *Tetrahedron*, 1985, **42**, 5765.

118. A. J. Pearson, *Adv. Metal-Org. Chem.*, 1989, **1**, 1.

119. A. J. Pearson, in 'Comprehensive Organic Chemistry', eds. B. Trost and I. Fleming, Pergamon, Oxford, 1992, Vol. 4, p. 663.

120. W. Chen, J. B. Sheridan, M. L. Cote, and R. A. Lalancette, *Organometallics*, 1996, **15**, 2700.

121. H. Rudler, V. Comte, M. Bellassoued, E. Garrier, J. Vaissermann, and J.-C. Daran, *C. R. Acad. Sci. Chim.*, 2000, **3**, 113.

122. A. J. Pearson and A. V. Gontcharov, *J. Org. Chem.*, 1998, **63**, 152.

123. E. P. Kundig, A. Ripa, R. Liu, and G. Bernardinelli, *J. Org. Chem.*, 1994, **59**, 4773.

124. B. C. Roell Jr, K. F. McDaniel, W. S. Vaughan, and T. S. Macy, *Organometallics*, 1993, **12**, 224.

125. (a) Y. Coquerel, J. Depres, A. E. Greene, P. Cividino, and J. Court, *Synth. Commun.*, 2001, **31**, 1291; (b) J. H. Rigby and C. O. Ogbu, *Tetrahedron Lett.*, 1990, **31**(24), 3385.

126. A. R. Pape, K. P. Kaliappan, and E. P. Kundig, *Chem. Rev.*, 2000, **100**, 2917.

127. F. Rose-Munch, V. Gagliardini, C. Renard, and E. Rose, *Coord. Chem. Rev.*, 1998, **178–180**, 249.

128. J. P. Collman, L. Hegedus, J. R. Norton, and R. G. Finke, 'Principles and Applications of Organotransition Metal Chemistry', University Science Books, Mill Valley, CA, 1987, pp. 424, p. 921; W. E. Watts, in 'Comprehensive Organometallic Chemistry', ed. G. Wilkinson, Pergamon, Oxford, 1982, Vol. 8, p. 1013; L. A. P. Kane-Maguire, E. D. Honig, and D. A. Sweigart, *Chem. Rev.*, 1984, **84**, 525.

129. W. E. Silverthorn, *Adv. Organomet. Chem.*, 1975, **13**, 47.

130. M. F. Semmelhack, in 'Comprehensive Organic Synthesis', eds. B. Trost and I. Fleming, Pergamon, Oxford, 1992, Vol. 4, p. 517.

131. C. Paradisi, in 'Comprehensive Organic Synthesis', eds. B. Trost and I. Fleming, Pergamon, Oxford, 1992, Vol. 4, p. 423.

132. H. Zeiss, P. J. Wheatley, and H. J. S. Winkler, 'Benzenoid-Metal Complexes', Ronald Press, New York, 1966.

133. B. Nichols and M. C. Whiting, *J. Chem. Soc.*, 1959, 551.

134. A. R. Pape, K. P. Kaliappan, and E. P. Kundig, *Chem. Rev.*, 2000, **100**, 2917.

135. M. F. Semmelhack, *J. Organomet. Chem. Libr.*, 1976, **1**, 361.

136. M. F. Semmelhack, *Ann. N. Y. Acad. Sci.*, 1977, **295**, 36.

137. M. F. Semmelhack, G. R. Clark, J. L. Garcia, J. J. Harrison, Y. Thebtaranonth, W. Wulff, and A. Yamashita, *Tetrahedron*, 1981, **37**, 3957.

138. M. F. Semmelhack, *Pure Appl. Chem.*, 1981, **53**, 2379.

139. P. J. C. Walker and R. J. Mawby, *Inorg. Chim. Acta*, 1973, **7**, 621.

140. R. G. Sutherland, M. Iqbal, and A. Piorko, *J. Organomet. Chem.*, 1986, **302**, 307.

141. D. Astruc, *Tetrahedron*, 1983, **39**, 4027.

142. W. Strohmeier, *Chem. Ber.*, 1961, **94**, 2490; M. F. Semmelhack, L. Keller, and Y. Thebtaranonth, *J. Am. Chem. Soc.*, 1977, **99**, 959; C. A. L. Mahaffy and P. L. Pauson, *Inorg. Synth.*, 1979, **19**, 154; S. Top and G. Jaouen, *J. Organomet. Chem.*, 1979, **182**, 381; C. Sergheraert, J.-C. Brunet, and A. Tartar, *J. Chem. Soc., Chem. Commun.*, 1982, 1417.

143. K. Ofele and E. Dotzauer, *J. Organomet. Chem.*, 1971, **30**, 211; G. R. Knox, D. G. Leppard, P. L. Pauson, and W. E. Watts, *J. Organomet. Chem.*, 1972, **34**, 347.

144. K. Ofele, *Chem. Ber.*, 1966, **99**, 1732.

145. M. D. Rausch, *Pure Appl. Chem.*, 1972, **30**, 523.

146. E. P. Kundig, C. Perret, S. Spichiger, and G. Bernardinelli, *J. Organomet. Chem.*, 1985, **286**, 183.

147. C. A. L. Mahaffy and P. L. Pauson, *Inorg. Synth.*, 1979, **19**, 154; S. Top and G. Jaouen, *J. Organomet. Chem.*, 1979, **182**, 381.

148. A. Meyer and G. Jaouen, *J. Chem. Soc., Chem. Commun.*, 1974, 787.

149. A. Goti and M. F. Semmelhack, *J. Organomet. Chem.*, 1994, **470**, C4; K. Ofele and E. Dotzauer, *J. Organomet. Chem.*, 1971, **30**, 211.

150. K. K. Bhasin, W. G. Balkeen, and P. L. Pauson, *J. Organomet. Chem.*, 1981, **204**, C25.

151. T. H. Coffield, V. Sandel, and R. D. Closson, *J. Am. Chem. Soc.*, 1957, **79**, 5826; J. D. Jackson, S. J. Villa, D. S. Bacon, R. D. Pike, and G. B. Carpenter, *Organometallics*, 1994, **13**, 3972, and references therein.

152. Y. K. Chung, P. G. Williard, and D. A. Sweigart, *Organometallics*, 1982, **1**, 1053.

153. E. P. Kundig, P. Jeger, and G. Bernardinelli, *Inorg. Chim. Acta*, 2004, **357**, 1909.

154. R. G. Sutherland, W. J. Pannekock, and C. C. Lee, *Can. J. Chem.*, 1978, **56**, 1782.

155. M. F. Semmelhack, G. Hilt, and J. H. Colley, *Tetrahedron Lett.*, 1998, **39**, 7683.

156. M. C. Whiting (Ethyl Corp.), US Patent 3,225,071, 1966; *Chem. Abstr.*, 1966, **64**, 6694h.

157. J. F. Bunnett and H. Hermann, *J. Org. Chem.*, 1971, **36**, 4081.

158. M. F. Semmelhack and H. T. Hall Jr, *J. Am. Chem. Soc.*, 1974, **96**, 7092; T. Oishi, M. Fukui, and Y. Endo, *Heterocycles*, 1977, **7**, 947; A. Alemagna, C. Baldoli, P. Del Buttero, E. Licandro, and S. Maiorana, *J. Chem. Soc., Chem. Commun.*, 1985, 417.

159. T. Oishi, M. Fukui, and Y. Endo, *Heterocycles*, 1977, **7**, 947.

160. S. I. Rosca and S. Rosca, *Rev. Chem. (Bucharest)*, 1964, **25**, 461.

161. M. Ghavshou and D. A. Widdowson, *J. Chem. Soc., Perkin Trans. 1*, 1983, 3065.

162. M. F. Semmelhack and H. T. Hall Jr, *J. Am. Chem. Soc.*, 1974, **96**, 7091.

163. A. Alemagna, P. Del Buttero, C. Gorini, D. Landini, E. Licandro, and S. Maiorana, *J. Org. Chem.*, 1983, **48**, 605; A. Alemagna, P. Cremonesi, P. Del Buttero, E. Licandro, and S. Maiorana, *J. Org. Chem.*, 1983, **48**, 3114.

164. (a) F. Rose-Munch and E. Rose, *Curr. Org. Chem.*, 1999, **3**(5), 445; (b) J. L. Kiplinger, T. G. Richmond, and C. E. Osterberg, *Chem. Rev.*, 1994, **94**(2), 373; (c) M. F. Semmelhack, P. Del Buttero, C. Gorini, D. Landini, E. Licandro, and S. Maiorana, *J. Org. Chem.*, 1983, **48**, 605; R. R. Houghton, M. Voyle, and R. Price, *J. Organomet. Chem.*, 1983, **259**, 183.

165. R. J. Card and W. S. Trayhanovsky, *J. Org. Chem.*, 1980, **45**, 2560.

166. J. P. Gilday and D. A. Widdowson, *Tetrahedron Lett.*, 1986, **27**, 5525; P. J. Beswick and D. A. Widdowson, *Synthesis*, 1985, 492; J. P. Gilday and D. A. Widdowson, *J. Chem. Soc., Chem. Commun.*, 1986, 1235.

167. (a) S. Maiorana, C. Baldoli, P. Del Buttero, M. Di Ciolo, and A. Papagni, *Synthesis*, 1998, **5**, 735; (b) K. Kirschke, J. Deutsch, and H. J. Niclas, *Phosphorus Sulfur Relat. Elem.*, 1996, **117**, 293.

168. M. F. Semmelhack and C. Ullenius, *J. Organomet. Chem.*, 1982, **235**, C10.

169. M. F. Semmelhack and H. T. Hall Jr, *J. Am. Chem. Soc.*, 1974, **96**, 7092.

170. A. R. Pape, K. P. Kaliappan, and E. P. Kundig, *Chem. Rev.*, 2000, **100**, 2917.

171. E. P. Kundig, V. Desobry, D. P. Simmons, and E. Wenger, *J. Am. Chem. Soc.*, 1989, **111**, 1804.

172. F. Rose-Munch, E. Rose, A. Semra, L. Mignon, J. Garcia-Oricain, and C. Knobler, *J. Organomet. Chem.*, 1989, **363**, 297; F. Rose-Munch, E. Rose, and A. Semra, *J. Chem. Soc., Chem. Commun.*, 1987, 942; F. Rose-Munch, V. Gagliardini, C. Renard, and E. Rose, *Coord. Chem. Rev.*, 1998, **178–180**, 249.

173. H. G. Schmalz, S. Siegel, and A. Schwarz, *Tetrahedron Lett.*, 1996, **37**, 2947.

174. F. Rose-Munch, V. Gagliardini, C. Renard, and E. Rose, *Coord. Chem. Rev.*, 1998, **178–180**, 249.

175. F. Rose-Munch, E. Rose, A. Semra, Y. Jeannin, and F. Robert, *J. Organomet. Chem.*, 1988, **353**, 53.

176. R. M. Moriarty and U. S. Gill, *Organometallics*, 1986, **5**, 253; A. N. Nesmeyanov, N. A. Vol'kenau, and I. N. Bolesova, *Dokl. Akad. Nauk, SSSR*, 1967, **175**, 606; R. G. Sutherland, A. Piorko, U. S. Gill, and C. C. Lee, *J. Heterocycl. Chem.*, 1982, **19**, 801; C. C. Lee, U. S. Gill, M. Iqbal, C. I. Azogu, and R. G. Sutherland, *J. Organomet. Chem.*, 1982, **231**, 151.

177. A. N. Nesmeyanov, N. A. Vol'kenau, E. I. Sirorkina, and V. V. Deryabin, *Dokl. Akad. Nauk, SSSR*, 1967, **177**, 1110.

178. C. C. Lee, A. S. Abd-El-Aziz, R. L. Chowdhury, A. Piorko, and R. G. Sutherland, *Synth. React. Inorg. Met.-Org. Chem.*, 1986, **16**, 541.

179. R. L. Chowdhury, C. C. Lee, A. Piorko, and R. G. Sutherland, *Synth. React. Inorg. Met.-Org. Chem.*, 1985, **15**, 1237.

180. R. G. Sutherland, A. S. Abd-El-Aziz, A. Piorko, and C. C. Lee, *Synth. Commun.*, 1987, **17**, 393.

181. P. L. Pauson and J. A. Segal, *J. Chem. Soc., Dalton Trans.*, 1975, 1677.

182. A. R. Pape, K. P. Kaliappan, and E. P. Kundig, *Chem. Rev.*, 2000, **100**, 2917.

183. E. P. Kundig, V. Desobry, and D. P. Simmons, *J. Am. Chem. Soc.*, 1983, **105**, 6962; E. P. Kundig, A. F. Cunningham Jr, P. Paglia, and D. P. Simmons, *Helv. Chim. Acta*, 1990, **73**, 386; B. Ohlsson and C. Ullenius, *J. Organomet. Chem.*, 1984, **267**, C34; B. Ohlsson and C. Ullenius, *J. Organomet. Chem.*, 1988, **350**, 3588; B. Ohlsson, C. Ullenius, S. Jagner, C. Grivet, E. Wegner, and E. P. Kundig, *J. Organomet. Chem.*, 1989, **365**, 243 and references therein.

184. M. F. Semmelhack and G. Clark, *J. Am. Chem. Soc.*, 1977, **99**, 1675.

185. J. Dudones and A. J. Pearson, *Tetrahedron Lett.*, 2000, **41**, 8037.

186. M. F. Semmelhack, G. R. Clark, R. Farina, and M. Saeman, *J. Am. Chem. Soc.*, 1979, **101**, 217.

187. M. F. Semmelhack, W. Wulff, and J. L. Garcia, *J. Organomet. Chem.*, 1982, **240**, C5; A. P. Kozikowski and K. Isobe, *J. Chem. Soc., Chem. Commun.*, 1978, 1076.

188. S. Maiorana, C. Baldoli, P. D. Buttero, M. D. Ciolo, and A. Papagni, *Synthesis*, 1998, 735.

189. E. P. Kundig, *Pure Appl. Chem.*, 1985, **57**, 1855.

190. E. P. Kundig, V. Desobry, and D. P. Simmons, *J. Am. Chem. Soc.*, 1983, **105**, 6962.
191. G. Klopmann, ‘Chemical Reactivity and Reaction Paths’, Wiley, New York, 1974.
192. M. F. Semmelhack, J. L. Garcia, D. Cortes, R. Farina, R. Hong, and B. K. Carpenter, *Organometallics*, 1983, **2**, 467.
193. K. W. Bowers, in ‘Radical Ions’, eds. E. T. Kaiser and L. Kevan, Interscience Publishers, New York, 1968, p. 211.
194. M. F. Semmelhack, L. Keller, and Y. Thebtaranonth, *J. Am. Chem. Soc.*, 1977, **99**, 959.
195. A. R. Pape, K. P. Kaliappan, and E. P. Kundig, *Chem. Rev.*, 2000, **100**, 2924.
196. I. U. Khand, P. L. Pauson, and W. E. Watts, *J. Chem. Soc. C*, 1968, 2257, 2261; I. U. Khand, P. L. Pauson, and W. E. Watts, *J. Chem. Soc. C*, 1969, 116, 2024; F. Haque, J. Miller, P. L. Pauson, and I. B. P. Tripathi, *J. Chem. Soc. C*, 1971, 743; J. F. McGreer and W. E. Watts, *J. Organomet. Chem.*, 1976, **110**, 103.
197. R. G. Sutherland, R. L. Chowdhury, A. Piorko, and C. C. Lee, *J. Organomet. Chem.*, 1987, **319**, 379.
198. R. G. Sutherland, R. L. Chowdhury, A. Piorko, and C. C. Lee, *J. Chem. Soc., Chem. Commun.*, 1985, 1296.
199. A. Zimniak, *Bull. Acad. Pol. Sci., Ser. Chim.*, 1979, **27**, 743; J. C. Boutonnet and E. Rose, *J. Organomet. Chem.*, 1981, **221**, 157.
200. R. C. Cambie, G. R. Clark, S. R. Gallagher, P. S. Rutledge, M. J. Stone, and P. D. Woodgate, *J. Organomet. Chem.*, 1988, **342**, 315.
201. Y. K. Chung, P. G. Williard, and D. A. Sweigart, *Organometallics*, 1982, **1**, 1053.
202. P. L. Pauson and J. A. Segal, *J. Chem. Soc., Dalton Trans.*, 1975, 1683; G. A. M. Munro and P. L. Pauson, *J. Chem. Soc., Chem. Commun.*, 1976, 134.
203. G. A. M. Munro and P. L. Pauson, *Z. Anorg. Allg. Chem.*, 1979, **458**, 211.
204. B. C. Roell, K. F. McDaniel, W. S. Vaughan, and T. S. Macy, *Organometallics*, 1993, **12**, 224; T.-Y. Lee, Y. K. Kang, Y. K. Chung, R. D. Pike, and D. A. Sweigart, *Inorg. Chim. Acta*, 1993, **214**, 125.
205. M. F. Semmelhack, G. R. Clark, J. L. Garcia, J. J. Harrison, Y. Thebtaranonth, W. Wulff, and A. Yamashita, *Tetrahedron*, 1981, **37**, 3957.
206. M. F. Semmelhack, J. J. Harrison, and Y. Thebtaranonth, *J. Org. Chem.*, 1979, **44**, 3275.
207. J. C. Boutonnet, J. Levisalles, J. M. Normant, and E. Rose, *J. Organomet. Chem.*, 1983, **255**, C21.
208. E. P. Kundig and D. P. Simmons, *J. Chem. Soc., Chem. Commun.*, 1983, 1320; E. P. Kundig, N. P. Do Thi, P. Paglia, D. P. Simmons, S. Spichiger, and E. Wenger, in ‘Organometallics in Organic Synthesis’, eds. A. de Meijere and H. tom Dieck, Springer-Verlag, Berlin, 1987, p. 265; R. C. Cambie, G. R. Clark, S. R. Gallagher, P. S. Rutledge, M. J. Stone, and P. D. Woodgate, *J. Organomet. Chem.*, 1988, **342**, 315.
209. E. P. Kundig, A. Quattropani, M. Inage, A. Ripa, C. Dupre, A. F. Cunningham Jr, and B. Bourdin, *Pure Appl. Chem.*, 1996, **68**, 97.
210. E. P. Kundig, V. Desobry, and D. P. Simmons, *J. Am. Chem. Soc.*, 1983, **105**, 6962.
211. M. F. Semmelhack, *Org. React.*, 1972, **2**, 89.
212. M. Lautens, ‘Science of Synthesis’, Georg Thieme Verlag, New York, 2001, Vol. 1, p. 680.
213. E. J. Corey and E. Hamanaka, *J. Am. Chem. Soc.*, 1967, **89**, 2758; W. G. Dauben, G. H. Beasley, M. D. Broadhurst, B. Muller, D. J. Peppard, P. Pesnelle, and C. Suter, *J. Am. Chem. Soc.*, 1975, **97**, 4724.
214. E. J. Corey and H. A. Kirst, *J. Am. Chem. Soc.*, 1972, **94**, 667.
215. E. Negishi, *Adv. Metal-Org. Chem.*, 1989, **1**, 178.
216. R. Rieke, A. Kavaliunas, and L. Rhyne, *J. Am. Chem. Soc.*, 1979, **101**, 246.
217. L. Hegedus and D. Thompson, *J. Am. Chem. Soc.*, 1985, **107**, 5663.
218. G. G. Gomez, X. Camps, A. J. Cayuela, and J. M. Moretó, *Inorg. Chim. Acta*, 1999, **296**(1), 94.
219. G. Garcia-Gomez and J. M. Moreto, *J. Am. Chem. Soc.*, 1999, **121**(4), 878.
220. A. Bottoni, G. P. Miscione, J. J. Novoa, and X. Prat-Resina, *J. Am. Chem. Soc.*, 2003, **125**(34), 10412.
221. L. Hegedus, G. Allen, J. Bozell, and E. Waterman, *J. Am. Chem. Soc.*, 1978, **100**, 5800.
222. L. Hegedus and S. Varaprath, *Organometallics*, 1982, **1**, 259.
223. L. Hegedus and B. Evans, *J. Am. Chem. Soc.*, 1978, **100**, 3461; L. Hegedus, S. Wagner, E. Waterman, and K. Siirala-Hansen, *J. Org. Chem.*, 1975, **40**, 593; G. P. Chiusoli and L. Cassar, *Angew. Chem., Int. Ed. Engl.*, 1967, **6**, 124.

Osmium: Inorganic & Coordination Chemistry

Simon R. Collinson & Martin Schröder
University of Nottingham, Nottingham, UK

1	Introduction	1
2	General Features	1
3	Osmium(VIII)	2
4	Osmium(VII)	4
5	Osmium(VI)	4
6	Osmium(V)	8
7	Osmium(IV)	8
8	Osmium(III)/(II)	10
9	Low Oxidation States	21
10	Related Articles	21
11	References	21

Abbreviations

[9]aneS_3 = 1,4,7-trithiacyclononane; bq = Benzoquinone; cat = Catechol (1,2-dihydroxybenzene); hp = 2-hydroxypyridine; imid = Imidazole; OEL = Occupational exposure limit; OEP = Octaethylporphyrin; Pc = Phthalocyanine; porph = Porphyrin; TLV = Threshold limit value; Tp = Hydrotris(pyrazol-1-yl)borate; tz = Tetrazine.

1 INTRODUCTION

Osmium (Os) was first isolated as the tetraoxide, OsO_4, by Smithson Tennant**[1]** in 1803 by distillation of a mixture of platinum group metals (Ru, Os, Rh, Ir, Pd, Pt) oxidized with aqua regia. This reflects the general feature that Os and many of its compounds can be readily oxidized to form the pungent, highly volatile OsO_4 (osmium: from $o\sigma\mu\acute{\eta}$, osme: a smell). Os has *Atomic Number* 76, *Atomic Mass* 190.2 with *Electron Configuration* [Xe]$4f^{14}6s^2 5d^6$, and has seven naturally occurring isotopes, ^{184}Os 0.02%, ^{186}Os 1.58%, ^{187}Os 1.6%, ^{188}Os 13.3%, ^{189}Os 16.1%, ^{190}Os 26.4%, and ^{192}Os 41.0%. Os is a rare element with an estimated abundance in the Earth's crust of some 0.005 ppm. It is found with other platinum group metals in ores in South Africa, the Urals, and Canada.

2 GENERAL FEATURES

Several reviews and texts on the coordination chemistry (*see* ***Coordination & Organometallic Chemistry: Principles***) of Os have been published. The works of Gmelin**[2]** give comprehensive coverage of the literature up to 1980, with the review of Griffith**[3]** giving an excellent account of Os coordination chemistry up to 1987, with updated reviews published in 2003.**[4]** For organometallic chemistry of Os, *see* ***Osmium: Organometallic Chemistry***, and for its cluster chemistry, *see Metal Clusters*; several inorganic texts dealing with aspects of Os chemistry have been published.**[5]** Review articles on specific areas of Os chemistry are cited in the text.

The coordination chemistry of Os features a very wide variety of oxidation states (*see Oxidation Number*) from high oxidation state VIII d^0 Os^{VIII} to low oxidation state −II d^{10} Os^{-II}. High oxidation state metal complexes are associated with strong σ-donor and π-donor (*see* π*-Base*) ligands such as O^{2-} ($Os^{VIII}O_4$), N^{3-} ($[Os^{VIII}O_3N]^-$), and F^- ($Os^{VII}F_7$), while low oxidation state species are stabilized by strong π-acceptor ligands such as CO (e.g. $[Os^0(CO)_5]$), NO^+, and PPh_3 (e.g. $[Os^{-II}(NO)_2(PPh_3)_2]$). The most common oxidation states for Os are II, III, and IV, with the stability of each oxidation state controlled by the types of ligand bound to the metal. Thus π-acceptor ligands such as bipy, phen, terpy, CN^-, and CO will tend to stabilize Os^{II}, for example, $[Os^{II}(bipy)_3]^{2+}$ and $[Os^{II}(bipy)_2(CN)_2]$, while ligands such as Cl^-, NH_3, en, and H_2O will tend to stabilize III and IV as in $[Os(NH_3)_6]^{3+}$ and $[OsCl_6]^{3-/2-}$.

Associated with these oxidation states are a variety of coordination geometries (*see* ***Coordination Numbers & Geometries***), among which octahedral coordination (*see Octahedral*) dominates overwhelmingly. Tetrahedral coordination (*see Tetrahedral*) is rare, although it is observed for the very important OsO_4. There are examples of five-coordinate, square-based pyramidal or trigonal bipyramidal complexes, for example, $[OsNCl_4]^-$, $[OsO_2(OAc)_3]^-$, $[OsCl_2(PPh_3)_3]$, and $OsO_4\cdot py$ (*see Square Pyramidal*; *Trigonal Bipyramidal*). Seven and eight coordination, although rare, have been observed in OsF_7, $[Os(EDTA)(H_2O)]$, and certain polyhydrides such as $[OsH_4(PMe_2Ph)_3]$, $[OsH_3(PPh_3)_4]^+$, and $[OsH_6(PPhR_2)_2]$ (R = *i*-Pr). Table 1 illustrates the oxidation states observed for some Os coordination compounds.

Os shares the group 8 triad with Fe and Ru. The highest available oxidation state for Fe is usually regarded as VI in the ferrate dianion $[FeO_4]^{2-}$, while the VIII oxidation state for Ru in RuO_4 is much more oxidizing than OsO_4. This reflects the stabilization of high oxidation states for the third-row transition element (Os) compared to its second- (Ru) and first-row (Fe) congeners. Likewise, Os^{VI} complexes tend to be more stable and are therefore more common than Ru^{VI} analogs. Thus, compared with Ru, the higher oxidation states are more stable for Os, while the lower oxidation states

Table 1 Examples of coordination compounds of osmium

Oxidation state	Complex
VIII	OsO_4, $[OsO_3N]^-$, $OsO_4\cdot py$, $[OsO_2F_4]^{2-}$, $[OsO_4Cl]^-$
VII	OsF_7, $[Os(EDTA)(H_2O)]$[a]
VI	$[OsO_2(en)_2]^{2+}$, $[OsO_2(OEP)]$, $Os_2O_6(py)_4$, $[OsO_2(OAc)_3]^-$, OsF_6, $[OsNX_5]^{2-}$, $[OsNX_4]^-$
V	$[OsCl_6]^-$, $[OsF_6]^-$, Os_2Cl_{10}
IV	$[OsCl_6]^{2-}$, $[OsCl_5(H_2O)]^-$, $[Os_2OCl_{10}]^{4-}$, $[Os(OEP)(OR)_2]$.
III	$[Os(NH_3)_6]^{3+}$, $[OsCl_6]^{3-}$, $[Os(NH_3)_5Cl]^{2+}$, $[Os(bipy)_2(OH)_2]^+$
II	$[Os(bipy)_3]^{2+}$, $[Os(CN)_6]^{4-}$, $[Os(bipy)_2(CN)_2]$, $[Os(NH_3)_5(N_2)]^{2+}$, $[Os(OEP)CO(py)]$, $[Os(NH_3)_5(NO)]^{3+}$, $[OsCl_2(PPh_3)_3]$
I	$[OsCl_2(NO)(PPh_3)_2]$
0	$[Os(CO)_5]$, $[Os_3(CO)_{12}]$, $[OsCl(NO)(PPh_3)_2]$, $[Os(NO)H(PR_3)_2]$
−I	$[Os(NO)(depe)_2]$
−II	$[Os(NO)_2(PPh_3)_2]$

[a] EDTA = Ethylenediaminetetraacetic acid.

are relatively less stable. All Os complexes are low-spin species, reflecting the large ligand field splittings expected for complexes of a third-row transition element (*see Transition Metals*). There is much interest in the use of platinum group metals in catalysis, and the area of homogeneous catalysis by osmium complexes, including the reduction of aldehydes, the selective reduction of alkynes to alkenes, asymmetric dihydroxylation and catalysis by carbonyl clusters, has been reviewed.**[6]**

3 OSMIUM(VIII)

3.1 Oxo Complexes

OsO_4 (Figure 1) is an extremely important Oxo Complex of Os. It is used industrially for the cis-hydroxylation of alkenes to cis-diols, and in biology for the fixation of biological tissue. OsO_4 is tetrahedral with the $Os{=}O = 1.711(3)$ Å in the gas phase,**[7]** and 1.684(7), 1.710(7) Å, $O{=}Os{=}O = 106.7(4)$, 110.7(3)° in the solid state.**[8]** It can be prepared by oxidation of the metal or of simple Os salts, and its high volatility allows it to be readily sublimed. It is a yellow solid which is soluble in water and CCl_4 to give pale yellow solutions. OsO_4 is highly oxidizing and is readily reduced, particularly in alcoholic solutions, to give insoluble OsO_2 and other reduced forms of Os. OsO_4 is toxic (TLV 2.5 ppm; OEL 0.002 mg m^{-3}) and is usually stored in sealed ampoules at reduced temperatures.

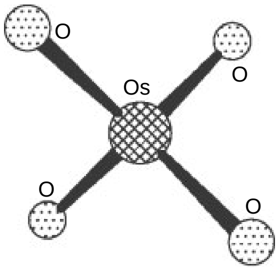

Figure 1 The structure of osmium tetroxide

OsO_4 is formally a 16-electron species and can therefore form five-coordinate, 18-electron adducts (*see Eighteen Electron Compounds*) $OsO_4\cdot L$ with certain tertiary N-donor ligands (L) such as py and quinuclidine (equation 1). The structure of the 2:1 hexamethylenetetramine adduct (*see Addition Compound*) $[OsO_4]_2\cdot N_4C_6H_{12}$ (**1**) shows each Os to be five-coordinate, with a distorted trigonal bipyramidal (TBP) structure in which the N-donor of the tetramine occupies an apical site.**[9]** This complex has a much lower vapor pressure than that of OsO_4 but, importantly, retains the reactivity of OsO_4 itself. The complex can, therefore, be regarded as a safer form of OsO_4 and one that can be stored easily and used as a biological preservation and staining agent when required.**[10]** The action of OsO_4 in biological tissues is complicated with interactions with unsaturated phospholipids, proteins, catechols, and alkaloids being proposed.

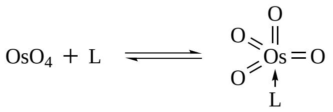

$$OsO_4 + L \rightleftharpoons O_3Os{=}O \leftarrow L \qquad (1)$$

Reaction of OsO_4 with alkali metal hydroxides affords the *cis*-perosmate salts $M_2[OsO_4(OH)_2]$ ($M = Li, Na, K, Rb, Cs$) (**2**) and $M[OsO_4(OH)_2]$ ($M = Ca, Sr, Ba$). Reaction of OsO_4 with CsF affords $[OsO_4F_2]^{2-}$, while with Ph_4PCl the complex $[OsO_4Cl]^-$ can be isolated. Reaction of OsO_4 with KrF_2 gives the Os^{VIII} oxide $[OsO_2F_4]$ (**3**).**[11]** Os^{VIII} oxofluorocations have

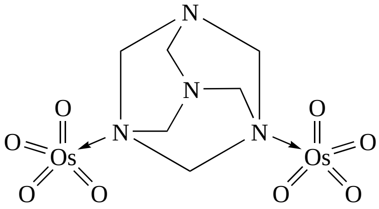

(**1**)

been investigated via the reaction of *cis*-$[OsO_2F_4]$ with strong fluoride acceptors such as AsF_5 and SbF_5. An X-ray structure of one complex shows discrete fluoride bridging between $[(cis\text{-}OsO_2F_3)_2]^+$ and $Sb_2F_{11}{}^-$ ions.[12]

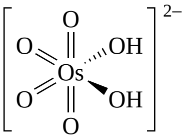

(**2**)

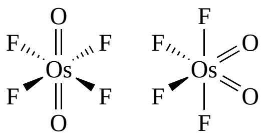

(**3**)

3.2 Cis-hydroxylation of Alkenes

OsO_4 can be used stoichiometrically or catalytically for the cis-dihydroxylations of alkenes to cis-diols (equation 2).[13] The ester species (**4**) represents an Os^{VI} intermediate, which can be hydrolyzed to afford the corresponding cis-diol in fair to good yield. The structures of Os^{VI} ester complexes are discussed in Section 5. Hydrolysis of intermediate Os^{VI} esters can be achieved reductively, for example with $SO_3{}^{2-}$, to form insoluble Os–sulphito species. Oxidative hydrolysis can occur with $IO_4{}^-$, organic peroxides, or N-oxides to regenerate OsO_4, thus making the process catalytic in terms of OsO_4. The X-ray structures of OsO_4 with the cooxidant N-methylmorpholine N-oxide and its reduced form N-methylmorpholine confirm coordination via the N-oxide oxygen and amine N-donor, respectively.[14] Addition of tertiary amines L leads to a marked increase in the rate of Os^{VI} osmyl ester formation, and an overall increase in rate of cis-hydroxylation. Through the addition of N,N,N',N'-tetramethylethylenediamine (TMEDA) to OsO_4 a directed dihydroxylation reaction can be realised with a range of homoallylic alcohols and amides. The course of the reaction appears to be influenced by hydrogen-bonding between the oxo group of the active intermediate and an alcohol or an amide of the substrate.[15]

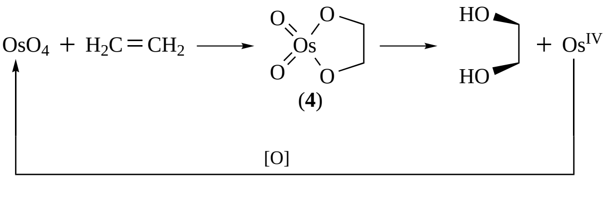

(2)

By using OsO_4 in the presence of chiral auxiliaries such as (**5**) the asymmetric dihydroxylation of a range of organic substrates can be achieved.[16] Kinetic studies on the Sharpless enantioselective dihydroxylation of terminal olefins support a [3 + 2] cycloaddition pathway and a U-shaped binding pocket to favor one enantiomer of the product.[17] In recent work, Sharpless and coworkers have demonstrated[18] that certain alkenes, for example, unsaturated carboxylic acids, can be rapidly converted almost quantitatively by a second cycle of asymmetric dihydroxylation, which has traditionally been avoided. Indeed, using N-toluene sulfonyl derivatives of α, β-hydroxyamino acids, ee's of up to 42% have been achieved using the second cycle, where the ligand remains bound throughout.[18]

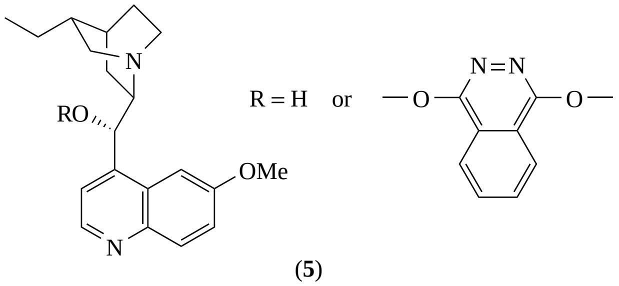

(5)

3.3 Nitrido and Imido Complexes

Treatment of OsO_4 with concentrated KOH (to form $[OsO_4(OH)_2]^{2-}$) followed by addition of NH_4OH affords a unique nitrido complex containing the osmiamate anion, $[OsO_3N]^-$. The structure of $Cs[OsO_3N]$ (Figure 2) shows Os=O = 1.739(8) and Os≡N = 1.676(15)Å.[19] Reaction of OsO_4 with amines under controlled conditions affords the Os^{VIII}–imido complexes $[OsO_3(NR)]$ (**6**), $[OsO_2(NR)_2]$ (**7**), $[OsO(NR)_3]$ (**8**), and $[Os(NR)_4]$ (**9**) (R = for example, *t*-Bu, *t*-oct, 1-adamantyl).[20] The structure of $[OsO_3(N\text{-}1\text{-adamantyl})]$ (Figure 3) shows the complex to be tetrahedral with Os=O = 1.714(4), Os=N = 1.697(4)Å.[21] The relatively short Os=N bond length may suggest some triple bond character.

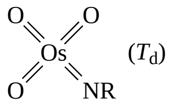

(**6**)

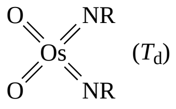

(**7**)

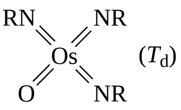

(**8**)

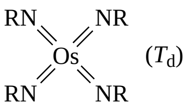

(**9**)

The oxyamination (equation 3) and diamination (equation 4) of alkenes using these imido complexes have been

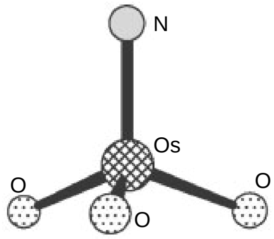

Figure 2 The structure of the osmiamate anion

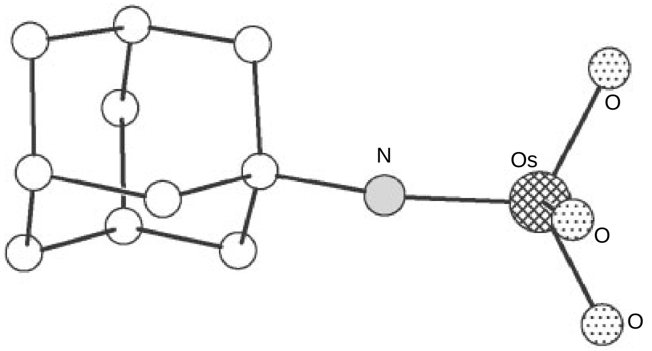

Figure 3 The structure of $[OsO_3(N\text{-}1\text{-adamantyl})]$

reported; these reactions can be made catalytic in the presence of argentocarbamates and chloramine-T.[22] Asymmetric aminohydroxylation reactions using Os substrates has been recently reviewed.[23]

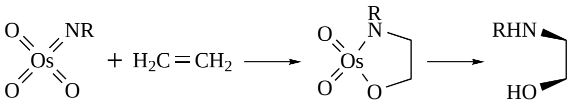

(3)

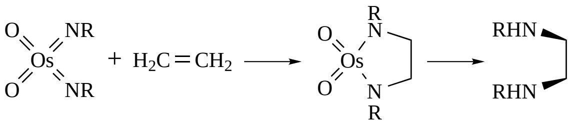

(4)

4 OSMIUM(VII)

Osmium(VII) complexes are rare and would be expected to be paramagnetic (*see Paramagnetism*), having a d^1 configuration. OsF_7 (**10**) can be made by fluorination of osmium metal with F_2 at elevated temperatures and high pressure. It shows a magnetic moment (*see Magnetic Susceptibility*) of $\mu_{\text{eff}} = 1.08\,\text{BM}$, and is proposed to have a pentagonal bipyramidal structure (*see Pentagonal Bipyramid*).[24] Reaction of osmium metal with a mixture of F_2 and O_2 at 300 °C at 5 atm pressure affords the green, paramagnetic ($\mu_{\text{eff}} = 1.47\,\text{BM}$ at 298 K) complex $[OsOF_5]$ (Figure 4), which has a C_{4v} structure with Os=O = 1.74(3), Os–F = 1.78(3), 1.72(3) Å.[25] Chemical or electrochemical reduction of OsO_4 under controlled conditions affords $[OsO_4]^-$ ($\mu_{\text{eff}} = 1.37\,\text{BM}$ at 298 K).[26]

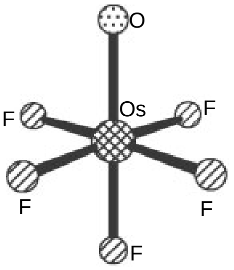

Figure 4 The structure of $[OsOF_5]$

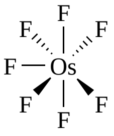

(**10**)

The crystal structure of $[Os(NBu^t)_2(\mu\text{-}NBu^t)]_2{}^{n+}$ ($n = 0$ or 2) has been reported in both the (VII) and (VI) oxidation states; the Os–Os separation is 2.68 Å in the former and 3.1 Å in the latter. This is consistent with the formation of an Os–Os single bond in this rare osmium(VII) dimer.[27]

5 OSMIUM(VI)

5.1 Oxo Complexes

A wide range of d^2 Os^{VI} complexes has been prepared and characterized. These complexes are usually diamagnetic (*see Diamagnetism*) and often incorporate the osmyl *trans*-O=Os=O dioxo unit or the monooxo Os=O unit, often with halide, N-, or O-donor ligands. They are more stable and less oxidizing than their Ru analogs, and are often prepared by reduction of OsO_4 or, in certain cases, by controlled oxidation of Os^{IV} and Os^{V} precursors.

Reaction of $[OsO_4(OH)_2]^{2-}$ (**2**) with EtOH as a reducing agent affords the Os^{VI} *trans*-dioxo complex $[OsO_2(OH)_4]^{2-}$. A range of related complexes of type $[Os^{VI}O_2(X)_4]^{x-}$ incorporating the *trans*-dioxo O=Os=O unit have been prepared by controlled reduction of OsO_4 in the presence of X (X = for example, Cl, OMe, OAc, $\frac{1}{2}$OX, $\frac{1}{2}$cat, CN). Neutral species such as $[OsO_2Cl_2(PPh_3)_2]$ and cationic species such as $[OsO_2(NH_3)_4]^{2+}$ and $[OsO_2(en)_2]^{2+}$ have also been reported. These osmyl complexes typically show bands in the IR spectrum (*see Infrared Spectroscopy*) in the regions 840–820

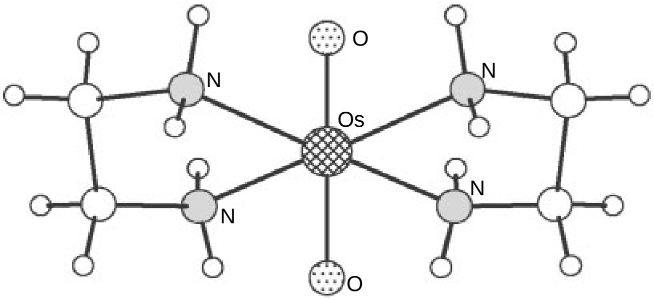

Figure 5 The structure of *trans*-$[OsO_2(en)_2]^{2+}$

and 290–310 cm^{-1}, assigned to the asymmetric O=Os=O stretching vibration and the O=Os=O bending mode, respectively. The symmetric O=Os=O stretching vibration is also observed in the Raman spectrum (*see Raman Spectroscopy*) in the region 860–910 cm^{-1}, at higher frequency than the asymmetric vibration. The assignment of these complexes as trans-dioxo complexes has been confirmed by structural studies. For example, the single crystal X-ray structure of *trans*-$[OsO_2(en)_2]^{2+}$ (Figure 5) shows**[28]** Os=O = 1.74(1) Å with a linear O=Os=O unit. A similar structure is observed for *trans*-$[OsO_2(OEP)]$ (OEP = octaethylporphyrin) (Figure 6), which shows**[29]** Os=O = 1.745(5) Å; reduction of OsO_4·py affords the binuclear species $Os_2O_6py_4$ (**11**), which incorporates an OsO_2Os bridging unit.**[30]** The synthesis and photophysics of a range of dioxo–Os^{VI} complexes of tetraaza macrocyclic ligands have been reviewed.**[31]** A cis-dioxo complex $[OsO_2(OAc)_3]^-$ (Figure 7) has also been reported.**[32]**

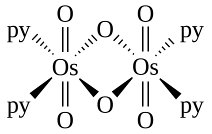

(**11**)

A range of Os^{VI} oxo ester complexes can be isolated from the reaction of OsO_4 with alkenes, dienes, and alkynes. These ester complexes represent the Os^{VI} intermediates in the cis-hydroxylation of alkenes to cis-diols by OsO_4. In the absence of tertiary amines, reaction of OsO_4 with alkenes affords the oxo ester complexes (**12**), (**13**), and (**14**). In the presence of tertiary amines (L), oxo ester complex formation is rapid, and trans-dioxo complexes of type (**15**; L = py) and the binuclear species (**16**; L = quinuclidine) can be isolated.**[33]** The dioxosmium(VI) cation (**17**) has been stabilized via complexation to a tetra-deprotonated amide ligand, which also serves to stabilize the dioxo unit through the formation of weak hydrogen-bonds to the urea NH groups. The complex shown displays reversible oxidative chemistry, whereas the related complex with one N–H hydrogen-bonding group removed displays an irreversible oxidative wave by cyclic voltammetry.**[34]**

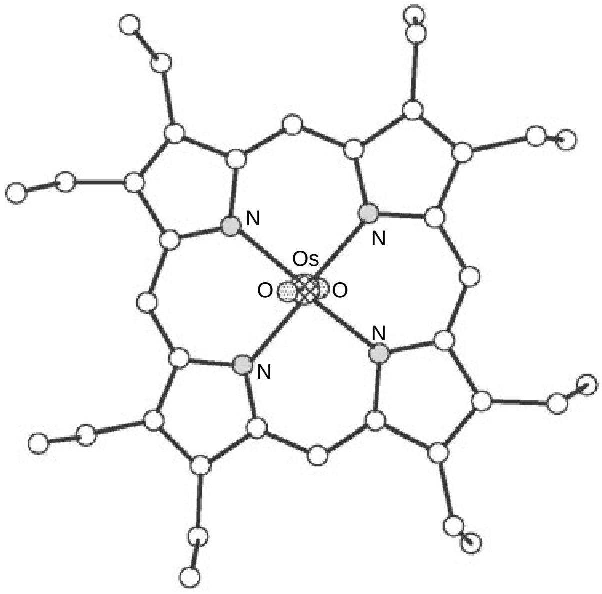

Figure 6 The structure of *trans*-$[OsO_2(OEP)]$

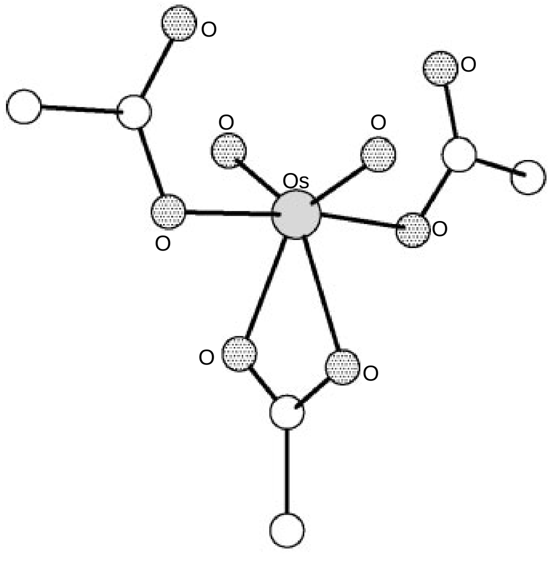

Figure 7 The structure of the *cis*-dioxo complex $[OsO_2(OAc)_3]^-$

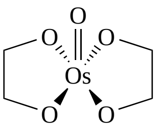

(**12**)

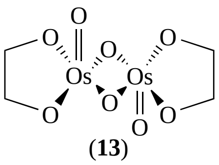

(**13**)

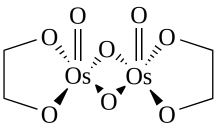

(**14**)

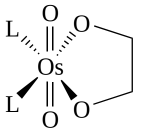

(**15**)

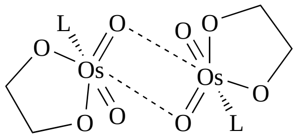

(**16**)

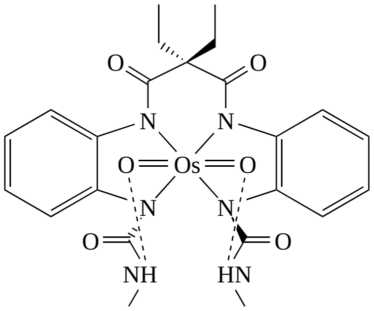

(**17**)

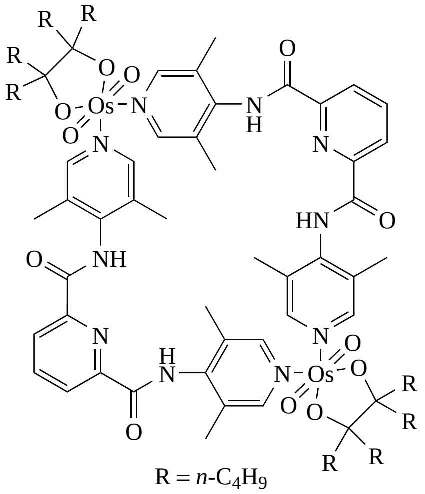

R = n-C_4H_9

(**21**)

The reaction of OsO_4 with Buckminsterfullerene C_{60} gives the corresponding osmyl ester species[35] (*see **Carbon: Fullerenes***).

Analogous Os^{VI} imido esters such as (**18**) can be isolated from the reactions of $[OsO_3(NR)]$ with alkenes. Reaction of $[OsO_3(N\text{-}t\text{-}Bu)]$ with alkylating agents such as MgR_2 affords the unusual Os^{VI} alkyl species OsO_2R_2,[36] while related oxoalkyl complexes of Os^{VI} have also been prepared.[37] Alkyl Os^{VI} species including $[OsO(Me)_4]$ (**19**) and an unusual trinuclear species $[OsO_2(Me)_2py]_3$ (**20**) have been isolated.[38]

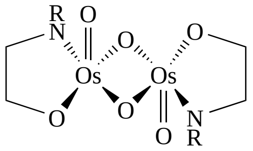

(**18**)

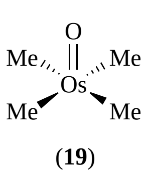

(**19**)

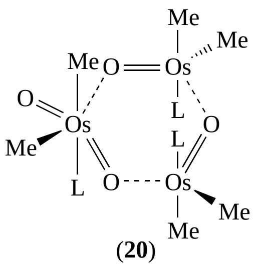

(**20**)

Os^{VI}-bridged macrocycles (**21**) have been assembled via reaction of OsO_4, alkenes, and L-shaped bispyridyl ligands. The resulting osmate ester-bridged binuclear macrocycles act as hosts for guests such as adipamide and terephthalamide, but not for guests such as benzamide and isophthalamide.[39]

Nonoxo containing Os^{VI} species of the type $[Os(L)_3]$ (L = catechol and substituted catechol) (**22**) showing D_{3h} symmetry can be prepared by reaction of OsO_4 with L.[40] $[Os(L)_3]$ can be reduced electrochemically to $[Os(L)_3]^-$ and $[Os(L)_3]^{2-}$.

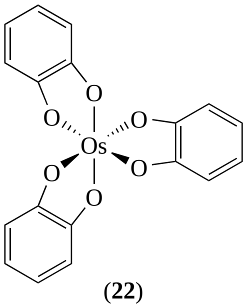

(**22**)

5.2 Nitrido and Imido Complexes

A range of Os^{VI} nitrido species incorporating the Os≡N unit can be synthesized including $[OsNX_5]^{2-}$ (**23**; X = Cl, Br) and $[OsNX_4]^-$ (**24**; X = Cl, Br, I). $[OsNX_5]^{2-}$ (X = Cl, Br) can be prepared by reaction of osmiamate $[OsO_3N]^-$ with HX, the product reacting with water to give $[OsNX_4(H_2O)]^-$. The complexes $[OsNX_5]^{2-}$ are six-coordinate while the species $[OsNX_4]^-$ (X = Cl, Br, I) show square-based pyramidal structures with the Os≡N occupying the apical site; Os≡N = 1.640(10), 1.583(15), 1.626(17) Å for X = Cl, Br, I, respectively.[41]

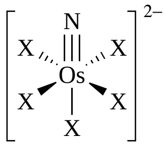

(**23**)

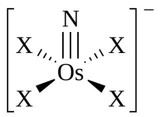

(**24**)

The complexes $[OsNX_5]^{2-}$ (X = Cl, Br) and $[OsNX_4]^-$ (X = Cl, Br, I) are very useful starting materials for the synthesis of a wide range of substituted Os^{IV} and Os^{III} halophosphine complexes, and species incorporating phosphineiminato, $Os{=}N{-}PR_3$, functionalities. The electrochemical oxidation of *cis*- and *trans*-$[Os(terpy)(Cl)_2NH_3](PF_6)$ and $[Os(terpy)(bpy)(NH_3)](PF_6)_2$ is metal based at low pH. However, at high pH proton loss and oxidation of bound ammonia occurs to yield either $[Os(terpy)(Cl)_2(N)](PF_6)$ via a four-electron process or $[Os(terpy)(bpy)(NO)](PF_6)_3$ by a six-electron process.[42]

The hydrazido complexes *trans*-$[Os(terpy)(Cl)_2(NNR_2)]^{n+}$ (NR_2 = morpholide, terpy = 2,2′:6′,2″-terpyridine) have been structurally characterised in the (VI), (V), and (IV) oxidation states. The systematic structural changes observed are accounted for by a generalized bonding model in which Os^{IV} is converted to Os^{VI} and then the ligand is converted from a four-electron to a six-electron donor, with the Os^{V} complex being intermediate between the two.[43] Osmium hydrazido complexes have been reported to display oxo-like reactivity related to Ru^{IV}-oxo chemistry. For example, *trans*-$[Os(terpy)(Cl)_2(NNR_2)]^{2+}$ (NR_2 = morpholide) is able to oxidize benzylalcohol to benzaldehyde.[44] Furthermore, under remarkably mild conditions, a number of ring substituted terpy products have been obtained from the reaction of *trans*-$[Os(terpy)(Cl)_2(NNR_2)]^{2+}$ with a series of nitrogen and oxygen bases. One example *trans*-$[Os(4'\text{-}O(CH_2CH_2)_2Nterpy)(Cl)_2(NNR_2)]^{2+}$ has been characterised crystallographically and further substitution at both the 4- and 4″-positions is possible in this system.[45] Additionally, in MeCN the Os^{VI} complex *trans*-$[Os(terpy)(Cl)_2(N)]^+$ reacts with excess azide to form the Os(III) product $[Os(terpy)(Cl)_2(5\text{-}CH_3\text{-tetrazolate})]$ which has been structurally characterised as the first osmium-tetrazolato complex.[46]

The Os^{VI} nitrido complex $TpOs(N)Cl_2$ [Tp = hydrotris (pyrazol-1-yl)borate] reacts rapidly with either PhMgCl or arylboranes to transfer one organic group to the nitrogen center to afford $TpOs[N(Ph)(BPh_2)]Cl_2$. It was suggested that there may be a general preference for nucleophiles to add directly to the metal-ligand multiple bond rather than binding to the metal first followed by a migration.[47]

Reaction of OsO_4 with ArNCO affords the highly unusual Os^{VI} imido complex $[Os(NAr)_3]$ (Ar = 2,6-*i*-PrC_6H_3) (Figure 8), the crystal structure of which shows Os–N distances of 1.736(5), 1.736(5), and 1.738(7) Å.[48] Reduction of $[Os(N\text{-}t\text{-}Bu)_4]$ affords a series of imido bridged complexes such as $[Os_2(N\text{-}t\text{-}Bu)_4(\mu\text{-}N\text{-}t\text{-}Bu)_2]$ (Figure 9).[49] Related Os^{VI} complexes $[Os(porph)(O)(N\text{-}t\text{-}Bu)]$ and $[Os(porph)(N\text{-}t\text{-}Bu)_2]$ (*see Porphyrin*) have been isolated.[50]

The heterobimetallic complex $[Os(N)Me(CH_2SiMe_3)(\mu\text{-}O)CrO_2]^-$ has been characterised structurally and shown to be active in the catalysis of the oxidation of benzyl alcohol by molecular oxygen. Kinetic data are consistent with a mechanism involving initial binding of the alcohol to Os, followed by a proton transfer to a bridging oxo and finally a β-hydrogen elimination.[51] A mixed valence Os^{VIII}-Os^{VI} dimer $[OsN\{N(SPPh_2)_2\}]_2(\mu\text{-}N)(OsO_3)$ can be isolated from the reaction of *trans*-$[OsN\{N(SPPh_2)_2\}]_2(Cl)$ and $[NBu_4][OsO_3N]$ in the presence of $AgBF_4$.[52] Furthermore, *trans*-$[OsN\{N(SPPh_2)_2\}]_2(Cl)$ can be used to synthesize the first osmium(VI)-polyoxometallate complexes, *trans*-$[OsN\{N(SPPh_2)_2\}]_2(M_6O_{19})$ (M = Mo or W).[53]

Generally high-valent Os complexes are less oxidizing than their Ru analogs; however, the oxidizing power of Os-oxo and Os-nitride complexes can be enhanced by excitation

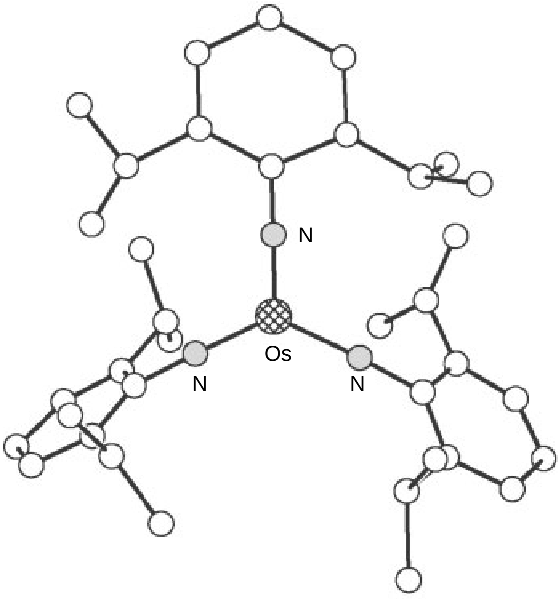

Figure 8 The structure of $[Os(NAr)_3]$ (Ar = 2,6-*i*-PrC_6H_3)

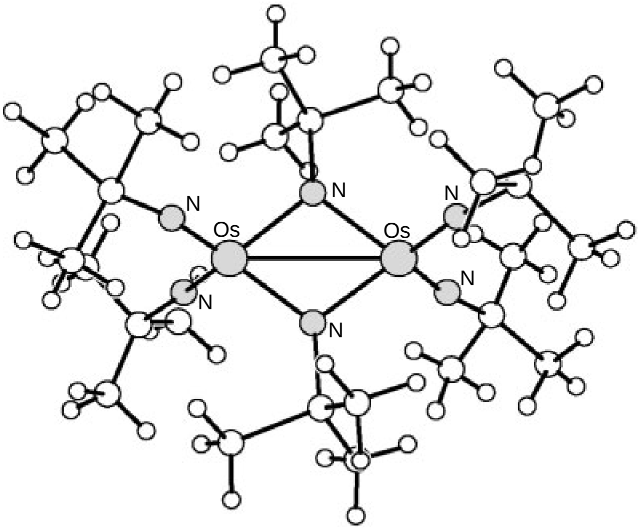

Figure 9 The structure of $[Os_2(N\text{-}t\text{-}Bu)_4(\mu\text{-}N\text{-}t\text{-}Bu)_2]$

with UV-vis light. Consequently, the rich redox chemistry of the $^3[(d_{xy})^1(d_{xz},d_{yz})^1]$ excited states of some Os(VI)-oxo and Os(VI)-nitrido complexes has been reported.[35]

5.3 Halide and Hydrido Complexes

OsF_6 (**25**) is prepared by fluorination of OsO_4 and has been shown to be octahedral in the gas phase, with Os–F = 1.831(8) Å. Treatment of OsF_6 with FNO affords $[OsF_7]^-$.

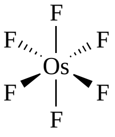

(**25**)

Hydrido complexes such as $[OsH_6(PR_3)_2]$ (*see* ***Hydride Complexes of the Transition Metals***) can be prepared by reaction of $[OsO_2Cl_2(PR_3)_2]$ with $LiAlH_4$, and are related to the Os^{IV} hydrido complexes $[OsH_4(PR_3)(\eta^2\text{-dppm})]$ and $[OsH_4(PR_3)_2(\eta^1\text{-dppm})]$.[54]

6 OSMIUM(V)

Coordination complexes of d^3 Os^V are relatively rare and are generally limited to certain simple halide and mixed halide complexes of the type $[OsF_6]^-$ and $[OsF_5]_4$ (**26**), the magnetic moment of the latter complex being 1.73 BM at 102 K and 2.06 BM at 295 K. $[OsX_6]^-$ can be prepared by oxidation of $[OsX_6]^{2-}$ (X = Cl, Br); the structure of $[OsCl_6]^-$ shows an average Os–Cl distance of 2.284 Å compared to a value of 2.332 Å for $[OsCl_6]^{2-}$.[55] Reaction of OsF_6 with BCl_3 or OsO_4 with SCl_2 affords $[Os_2Cl_{10}]$ (**27**).[56] $[Os_2Cl_{10}]$ ($\mu_{eff} = 2.54$ BM per Os) is a chloro bridged dimer (*see Bridging Ligand*) with an Os–Os distance of 3.63 Å. The stabilization of the Os^V oxidation state has been achieved electrochemically in tetraaza macrocyclic complexes.

The Os^V-imido complex $[Os(Tp)(Cl)_2(NH)]$ (Tp = hydrotris(pyrazol-1-yl)borate) has been synthesized in MeCN by the one-electron reduction of $[Os(Tp)(Cl)_2(N)]$. The complex $[Os(Tp)(Cl)_2(NH)]$ disproportionates in aqueous solution to form $[Os(Tp)(Cl)_2(N)]$ and $[Os(Tp)(Cl)_2(NH_3)]$.[57]

7 OSMIUM(IV)

Os^{IV} has a d^4 configuration and its coordination chemistry is dominated by polyhalide complexes.

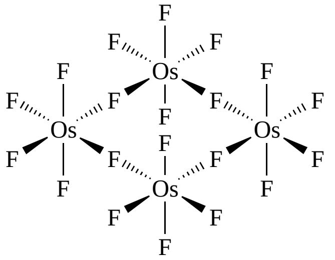

(**26**)

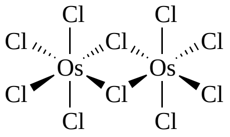

(**27**)

7.1 O-donor Complexes

Oxo complexes containing the terminal Os=O linkage are relatively rare for Os^{IV}, the tendency for this oxidation state being the formation of Os–O–Os bridged species. A wide range of such complexes has been prepared, a good example being the diamagnetic $[Os_2OCl_{10}]^{4-}$ anion (Figure 10). The structure of $[Os_2OCl_{10}]^{4-}$ shows a linear Os–O–Os unit with Os–O = 1.778(15) Å.[58] The Os–Cl distance for the Cl^- *trans* to O is elongated compared to the *cis*-Cl^- ligands, reflecting the trans influence of the μ^2-O bridge. A similar type of μ^2-O bridge, Os–O–Os = 1.808(3) Å, is observed in $[Os_2O(OEP)_2(OMe)_2]$ (**28**).[59] Related oxo bridged Os^{IV}/Os^{IV} complexes have been prepared with related porphyrin and polydentate ligands.

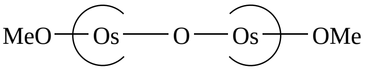

(**28**)

Mononuclear Os^{IV} porphyrin complexes of type $[Os(porph)L_2]$ (L = OR, SR, Br) have been prepared and their

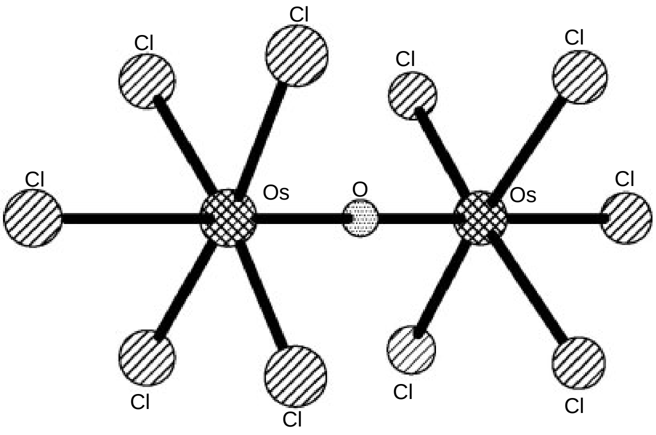

Figure 10 The structure of the diamagnetic anion $[Os_2OCl_{10}]$

electrochemical oxidation to Os^{V} species assessed.[60] The convenient synthesis of bis(aliphatic amine)osmium(II), bis(arylamido)osmium(IV), and bis(imido)- and oxo(imido) osmium(VI) tetraphenylporphyrins have been reported. The latter two types of complexes were structurally characterised for the *t*-butylimido derivatives.[61]

The first X-ray structure of an Os^{IV} oxo complexes, *trans*-$[OsCl(O)(dcpe)_2]^+$ (dcpe = 1,2-bis(dicyclohexylphosphino) ethane), has been reported. Its formation proceeds via the activation of O_2 to form $[OsCl(\eta^2\text{-}O_2)(dcpe)_2]^+$, which then reacts with HCl gas. Although the complex $[OsCl(\eta^2\text{-}O_2)(dcpe)_2]^+$ readily displays oxo-transfer chemistry, for example, with phosphines, the oxo complex *trans*-$[OsCl(O)(dcpe)_2]^+$ is surprisingly stable and unreactive towards standard reducing agents such as phosphines.[62]

Trans-$[Os(en)_2(\eta^2\text{-}H_2)H_2O]^{2+}$ is readily converted in water to *trans*-$[Os(en)_2(\eta^2\text{-}H_2)\ Fe(CN)_6]^{2-}$, an Os^{II}–Fe^{II} species, which oxidises in air to afford $[Os(en)_2(H)H_2O\ Fe(CN)_6]$, an $Os^{IV-}Fe^{II}$ complex, in which it was suggested that the Os center can assume a coordination number of 7. The characteristics of the absorption spectrum indicate that the mixed valence molecule is localized and the absorption bands are associated with a $Fe(CN)_6{}^{4-} \rightarrow Os(IV)$ electron transfer.[63]

7.2 N-donor Complexes

The most studied Os^{IV} complexes with N-donors are binuclear species incorporating linear Os–N–Os units. A range of complexes $[Os_2N(NH_3)_8X_2]^{3+}$ (**29**; X = Cl, Br, I, N_3, NO_3, NCS) and $[Os_2NX_8(H_2O)_2]^{3-}$ (**30**; X = Cl, Br, I) has been prepared and related to their Ru analogs. These complexes can be prepared conveniently from $[OsX_6]^{2-}$ (X = Cl, Br, I). Highly colored (violet) trinuclear species (**31**) incorporating a linear Os–N–Os–N–Os backbone can also be prepared by similar routes. As for the binuclear analogs, the ligands trans to the μ^2-N bridge are more labile than those at *cis* positions reflecting the high trans influence of μ^2-N bridges.[64]

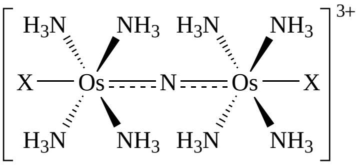

(**29**)

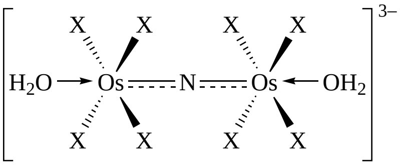

(**30**)

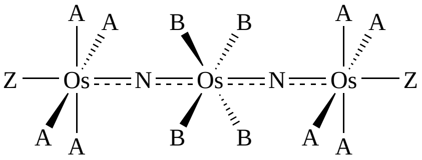

(**31**)

Mononuclear Os^{IV} complexes of amines have been reported although they remain, in general, ill-defined since deprotonation of the coordinated amine(s) occurs very readily. This reflects the relatively high positive charge at Os^{VI} and Os^{IV} and the resultant high pK_a of N–H protons in this environment. For example, $[Os(en)_3]^{4+}$ has been reported, although it is unstable with respect to deprotonation. A very unusual dihydrido complex thought to be $[Os(en)_2(H)_2]^{2+}$ (*see* ***Hydride Complexes of the Transition Metals***) can be prepared by reduction of the dioxo–Os^{VI} species $[OsO_2(en)_2]^{2+}$ (Figure 5) with Zn and HCl;[65] however, this complex was subsequently reassigned as $[Os(en)_2(\eta^2\text{-}H_2)Cl]^+$ (see below).

A novel example of oxygen activation based upon the ligand reactivity has been described in the Os^{IV}-sulfoximido complex, *cis*-$[(terpy)(Cl)_2Os{=}NSOC_6H_3Me_2]$. Upon addition of acid oxygen evolution is observed to form *cis*-$[(terpy)(Cl)_2Os{=}NSHC_6H_3Me_2]$, which, upon addition of bipyridine as base, reforms the initial complex in the presence of air.[66]

7.3 Halide and Hydride Complexes

A large literature has built up describing the synthesis, spectroscopic, and magnetic properties of the Os^{IV} hexahalo and mixed halo complexes $[OsX_6]^{2-}$ (X = Cl, Br, I). The complexes $[OsX_6]^{2-}$ (X = Cl, Br, I), in particular $Na_2[OsCl_6]$, are useful starting materials for a very wide range of Os^{II} and Os^{III} complexes.[3,4] Hydrolysis of $[OsX_6]^{2-}$ affords $[OsX_5(H_2O)]^-$ and $[OsX_5(OH)]^{2-}$ with other mixed aqua/hydroxy species postulated to exist in solution. The synthesis of the binuclear species $[Os_2X_{10}]^{2-}$ and $[Os_2X_8]$ (X = Cl, Br, I) from mononuclear precursors has been reported. The structure of $[Os_2X_{10}]^{2-}$ (X = Cl, **32**) shows an Os–Os distance of 3.626(1) Å, which increases to 3.788(3) Å for X = Br.[67] Electrochemical interconversion of $[Os_2Br_{10}]^{2-}$, $[Os_2Br_{10}]^{3-}$, $[Os_2Br_{10}]^{4-}$, and $[Os_2Br_{10}]^{5-}$ has been monitored; the latter species is unstable via loss of Br^- to afford $[Os_2Br_9]^{4-}$.[68]

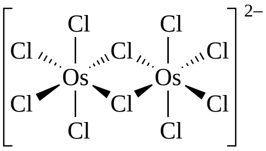

(**32**)

Although tertiary phosphines PR_3 tend to stabilize lower valent states, particularly Os^{III} and Os^{II}, a number of Os^{IV} hydrido phosphine complexes are known. These include $[OsH_4(PR_3)_3]$, $[OsH_4(PR_3)(\mu^2\text{-dppm})]$, and $[OsH_4(PR_3)_2(\mu^1\text{-dppm})]$. The assignment of these complexes as terminal hydride or H_2 complexes is an important aspect of these systems. A series of Os^{IV} species $[OsX_4(L)_2]$ (X = Cl, Br; L = PEt_3, PPh_3, $PPhEt_2$, PPh_2Et, $AsPh_3$, $SbPh_3$, $SeMe_2$, py) has been reported.[69]

8 OSMIUM(III)/(II)

The vast majority of the coordination compounds of Os that have been prepared are in the oxidation states II and III. Moreover, many of these compounds show reversible or well defined $Os^{II/III}$ couples in which the electronic and redox properties at the metal are controlled by the σ-donor, π-acceptor, and π-donor properties of the ligands. Indeed, the study of the redox behavior in $Os^{II/III}$ and $Ru^{II/III}$ species, metal ions in which octahedral coordination is almost universally retained in both redox partners, has been central in recent developments to parameterize metal centered redox processes as a function of ligand donor and acceptor capacity.[70] The chemistries of Os^{II} and Os^{III} are, therefore, intimately linked, and have been extended to studies of important mixed valence $Os^{II/III}$ binuclear and polynuclear species (*see* ***Mixed Valence Compounds***). For the purposes of brevity and convenience, this section will deal with Os^{III} and Os^{II} complexes together. The extensive literature on $Os^{III/II}$ complexes has been developed with a very wide range of donor ligands; a comprehensive assessment of this work is beyond the scope of this article, and the reader is directed to published comprehensive reviews.[3,4]

In general, paramagnetic d^5 Os^{III} is stabilized by relatively good π-donor ligands such as halides, together with O-donor and certain thiolate S-donor ligands, while π-acceptor ligands such as bipy, phen, terpy, CN^-, thioethers, nitriles, and tertiary phosphines stabilize diamagnetic d^6 Os^{II}. The coordination geometries about Os^{III} and Os^{II} are almost invariably octahedral with electronic configurations $t_{2g}{}^5$ and $t_{2g}{}^6$ respectively.

8.1 Cyanide Complexes

The CN^- ligand is a good π-acceptor and therefore stabilizes Os^{II} as in $[Os(CN)_6]^{4-}$. The 10 *Dq* value for $[Os(CN)_6]^{4-}$ is $>34\,000\,\text{cm}^{-1}$, significantly greater than for the Ru and Fe analogs. Interestingly the $M^{II/III}$ couples for the low-spin $t_{2g}{}^6$ complexes $[M(CN)_6]^{4-/3-}$ follow the order +0.12 (M = Fe), +0.62 (M = Ru), +0.36 V (M = Os) vs. Fc/Fc^+. The observation that the $Ru^{II/III}$ couple occurs at the most anodic potentials has also been observed for other homoleptic low-spin complexes (*see Homoleptic Compound*) of bipy, phenanthroline, and [9]aneS_3 (see below) and reflects the spatial and energy matches between the metal ion and the ligand donor sets.[71] CN^- coordination is also found in higher oxidation state species such as $[Os(CN)_6]^{3-}$, $[OsO_2(CN)_4]^{2-}$, and $[OsN(CN)_4(H_2O)]^-$.

8.2 N-donor Complexes

There is a large literature based on the coordination of ammines, monodentate and chelate amines (*see Monodentate Ligand*; *Chelating Ligands*), monodentate and chelate heterocycles, and porphyrin and mixed N/O and N/S donor ligands (*see* ***Mixed Donor Ligands***) to Os^{II} and Os^{III}. This is only surpassed by the even larger body of work on Ru^{II} and Ru^{III} analogs. Indeed, studies on N-donor complexes of Os parallel the work on Ru coordination compounds, particularly with respect to the photophysics of $[Ru(bipy)_3]^{2+}$ and electron transfer in Ru^{II}–Ru^{III} mixed valence complexes (*see also* ***Ammonia & N-donor Ligands***).[50]

8.2.1 Ammine Complexes

Reduction of Os^{IV} salts such as $[OsCl_6]^{2-}$ in the presence of NH_3 affords the stable $[Os(NH_3)_6]^{3+}$ (**33**); the analogous Os^{II} species $[Os(NH_3)_6]^{2+}$ is unstable with respect to oxidation to the Os^{III} complex. Thus for Os, the NH_3 ligand stabilizes the $t_{2g}{}^5$ rather than $t_{2g}{}^6$ configuration. This contrasts with the chemistry of Ru where $[Ru(NH_3)_6]^{2+}$ is a stable isolable complex. In order to stabilize Os^{II} in the presence of ammine ligands, π-acceptor ligands must also be present; thus $[Os(NH_3)_5(L)]^{2+}$ (L = CO, N_2, H_2, alkene) and $[Os(NH_3)_5NO]^{3+}$ (a complex containing formally NO^+ as a ligand) can be prepared. The complex $[Os(NH_3)_5(\eta^2\text{-}H_2)]^{2+}$ (**34**) is particularly intriguing and has been compared to the related H_2 complexes *trans*-$[Os(en)_2X(\eta^2\text{-}H_2)]^+$ (X = Cl, Br) and *trans*-$[Os(en)_2(\eta^2\text{-}H_2)py]^{2+}$.[72] The hydrogenation of naphthalene is catalyzed by the $[Os(NH_3)_5]^{2+}$ fragment under H_2[73] (*see* ***Hydrogenation & Isomerization of Alkenes***). Some coordination chemistry of Os–ammine complexes is summarized in Scheme 1.

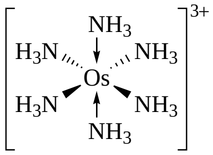

(**33**)

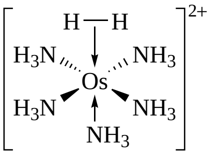

(**34**)

Substituted Os^{III} complexes of type $[Os(NH_3)_5X]^{2+}$ (X = Cl, Br, I, OH) and $[Os(NH_3)_5(H_2O)]^{3+}$ can also be prepared. Oxidation to Os^{IV} species such as $[Os(NH_3)_3Cl_3]^+$ and $[Os(NH_3)_4Cl_2]^{2+}$ has been reported, although these relatively high oxidation state materials tend to deprotonate

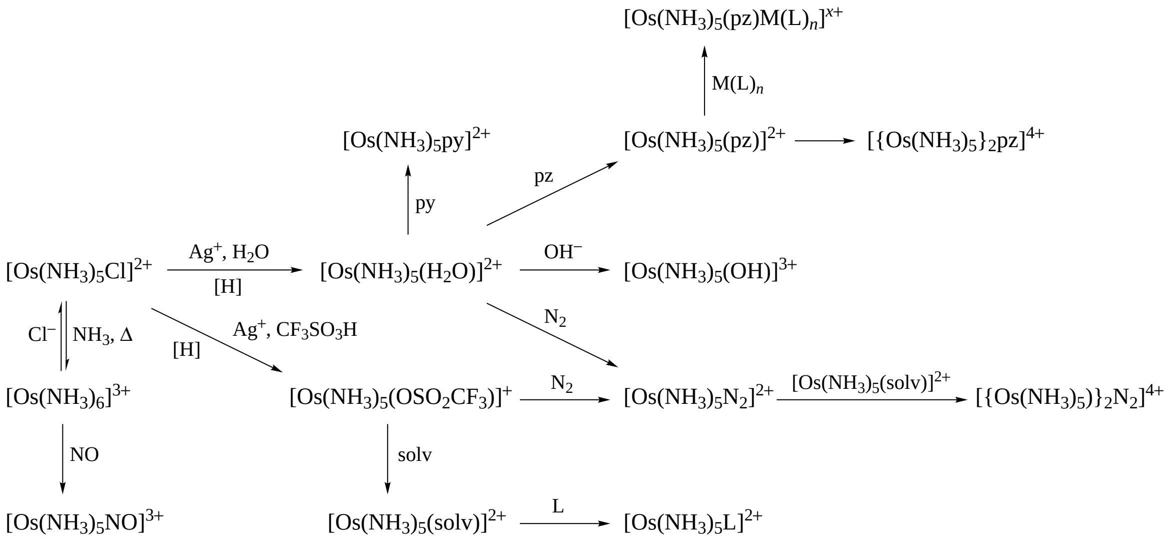
[Os(NH3)5(pz)M(L)n]x+
M(L)n
[Os(NH3)5py]2+
[Os(NH3)5(pz)]2+
[{Os(NH3)5}2pz]4+
py
pz
[Os(NH3)5Cl]2+
Ag+, H2O
[H]
[Os(NH3)5(H2O)]2+
OH−
[Os(NH3)5(OH)]3+
Cl−
NH3, Δ
Ag+, CF3SO3H
[H]
N2
[Os(NH3)6]3+
[Os(NH3)5(OSO2CF3)]+
N2
[Os(NH3)5N2]2+
[Os(NH3)5(solv)]2+
[{Os(NH3)5)}2N2]4+
NO
solv
[Os(NH3)5NO]3+
[Os(NH3)5(solv)]2+
L
[Os(NH3)5L]2+

Scheme 1

at the coordinated ammine and therefore are stabilized by acidic media.

8.2.2 Amine Complexes

Like NH_3, amine ligands, RNH_2, tend to stabilize Os^{III} rather than Os^{II}, for example, $[Os(en)_3]^{3+}$ (**35**). Oxidation of $[Os(en)_3]^{3+}$ affords Os^{IV} species which tend to be unstable, owing to deprotonation of the coordinated amine to give deprotonated en (en-H) complexes such as $[Os(en)_2(en\text{-}H)]^{3+}$ and $[Os(en\text{-}H)_2(en)]^{2+}$ (equation 5). The resultant amido ligands are strong π-donors, reflecting the net stabilization of Os^{IV} in these species. One such complex, $[Os^{IV}(en\text{-}H)_2(en)]^{2+}$ (Figure 11), has been structurally characterized and shows shortened Os–N(amido) bond lengths, suggesting multiple M=N bond character.**74** Additionally, imino and diimino complexes incorporating C=N linkages can be isolated. These species are formed via oxidative dehydrogenation of coordinated amines; this reactivity is paralleled in Ru chemistry.

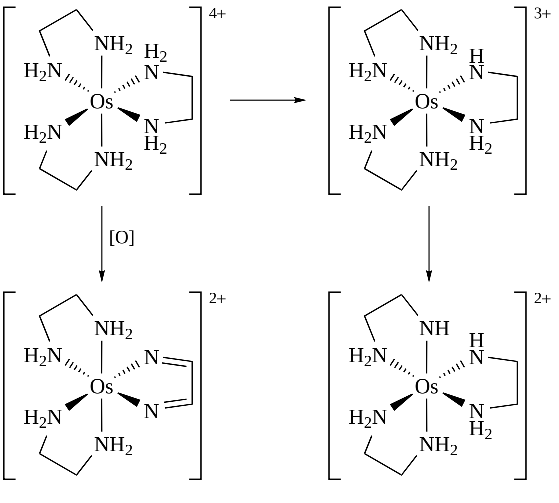
4+
3+
[O]
2+
2+
NH2
H2N
Os
N
H2
NH

(5)

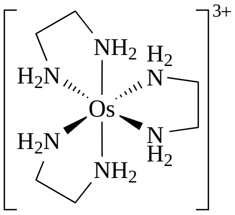

(**35**)

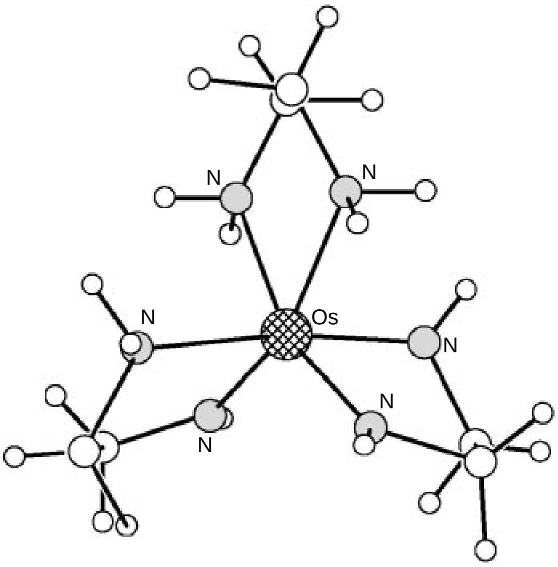

Figure 11 The structure of $[Os(en\text{-}H)_2(en)]^{2+}$

In general, Os complexes are highly effective for the oxidative dehydrogenation of coordinated amine and alcohol ligands. This is due to their ability to attain oxidation states that are two electrons apart. This is stabilized by deprotonation and formed by disproportionation to provide a low-energy route for even-electron transfer required in ligand dehydrogenation processes.**75**

8.2.3 Heterocyclic Complexes

A wide range of mixed ligand Os^{II} and Os^{III} complexes incorporating py, substituted py, and related heterocyclic amines have been reported. These include $[OsCl_2(py)_2(CO)_2]$, $[Os(NH_3)_5py]^{2+/3+}$, $[OsX_2py_4]$ (X = Cl, Br), and $[OsCl_2py_3(PPh_3)]$. Mononuclear pyrazine, pyrimidine, and pyridazine (L) complexes of type $[Os(NH_3)_5(L)]^{2+}$ and the protonated forms $[Os(NH_3)_5(LH)]^{3+}$ have been reported, the pK_a of LH being higher in the complex than for the free protonated heterocycle.**76**

The formation of binuclear complexes using bifunctional ligands has been an important area in Os chemistry. The pyrazine bridged complexes $[(H_5N)_5Os(pz)Os(NH_3)_5]^{4+/5+/6+}$ represent the Os analogs of the famous Ru^{II}–Ru^{III} mixed valence Creutz–Taube ion $[(H_5N)_5Ru(pz)Ru(NH_3)_5]^{5+}$ (*see* ***Ruthenium: Inorganic & Coordination Chemistry***). $[(H_5N)_5Os(pz)Os(NH_3)_5]^{4+/5+/6+}$ can be readily prepared from the highly labile mononuclear precursor $[Os(NH_3)_5(OSO_2CF_3)]^{2+}$ (Scheme 1), $[(H_5N)_5Os(pz)Os(NH_3)_5]^{5+}$ (**36**) being categorized as a delocalized Class III mixed valence complex with formal oxidation state $Os^{II.5}Os^{II.5}$.**77**

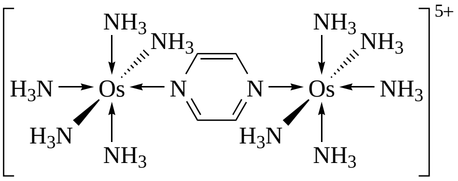

(**36**)

Another class of binuclear complexes are those incorporating bridging chelate ligands. For example, reaction of $OsCl_3$ with 2-hydroxypyridine (hp) gives a dinuclear species $[Os_2(hp)_4Cl_2]$ (**37**) ($\mu_{eff} = 1.44\,BM$) with hp bridging two Os centers, Os–Os = 2.344(2) Å; in the complex $[Os_2(hp)_4Cl_2(NCMe)_2]$ the Os–Os distance is elongated to 2.357(1) Å.**78**

Bidentate heterocyclic chelate ligands (*see Bidentate Ligand*) such as bipy, phen, and their substituted derivatives (LL) form tris-chelate complexes of the type $[Os(LL)_3]^{2+}$, the Os^{II} oxidation state being stabilized by these π-acceptor ligands. A wide variety of methods can be employed to

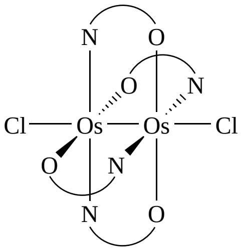

(**37**)

prepare these species, one of the best being the reaction of LL with $[OsCl_6]^{2-}$ at elevated temperatures. The main interest in these types of complex derives from the use of the Ru^{II} analogs $[Ru(LL)_3]^{2+}$ as photosensitizers, the excited state of $[Ru(bipy)_3]^{2+*}$ being relatively long lived ($t_{1/2} = 6.0\,\mu s$). The excited state complex can be assigned as a Ru^{III}–bipy radical anion species in which an electron has been excited via irradiation within the metal-to-ligand charge transfer manifold to form an oxidized metal and reduced ligand center (equation 6). This principle of ‘charge separation’ is the basis of potential solar traps and photochemical catalysts. As a result of this interest in Ru chemistry, there is an extensive literature based on the coordination chemistry, spectroscopy, and photophysics of tris-chelate Os^{II} complexes $[Os(LL)_2]^2$.

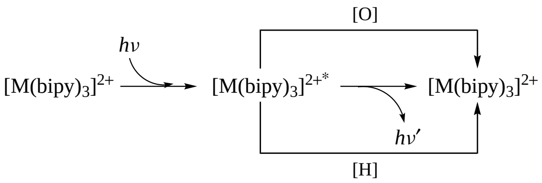

(6)

Although many tris-chelate complexes of Os^{II}, $[Os(LL)_3]^{2+}$, are luminescent, the lifetimes of the Metal to Ligand Charge Transfer (MLCT) excited state species $[Os(LL)_3]^{2+*}$ are, in general, substantially shorter than those of the Ru analogs. This reflects the efficient quenching of the third-row metal radical via spin–orbit coupling, leading to enhanced radiative and nonradiative decay rates for the triplet–singlet transitions.**79** Interestingly, the lifetimes of the excited state species $[Os(LL)_3]^{3+*}$ (LL = bipy, phen) are some 10^6 times less than for $[Ru(LL)_3]^{2+*}$. Quenching of this excited state species by a variety of electron transfer agents such as Fe^{III} and Co^{III} ions has been reported. The luminescent and redox properties of supramolecular polynuclear transition metal complexes have been comprehensively reviewed.**3,4,80**

The complex $\{\Lambda\text{-}[Ru(bpy)_3]\Delta\text{-}[Os(bpy)_3]\}(PF_6)_4$ exhibits alternating layers of $\Lambda\text{-}[Ru(bpy)_3]^{2+}$ and $\Delta\text{-}[Os(bpy)_3]^{2+}$. Interestingly, this novel hetero-racemic material is characterized by the specific property that the excitation energy is efficiently transferred to and accumulated at the site of lowest energy, that is, the $\Delta\text{-}[Os(bpy)_3]^{2+}$ complex and this is the only site which emits. Furthermore, the emission spectrum is completely altered under the application of a magnetic field.[81]

The complexes $[Os(LL)_3]^{2+}$ can be oxidized chemically or electrochemically to $[Os(LL)_3]^{3+}$, the $Os^{II/III}$ couples being related to the photophysical behavior of the 2+ complexes. A substantial amount of work has been carried out on the outer-sphere electron transfer to $[Os(LL)_3]^{3+}$ (a good one-electron oxidant that is co-ordinatively stable) with a range of reductants such $[Fe(CN)_6]^{4-}$ (*see* ***Electron Transfer in Coordination Compounds***).

The substitution chemistry of Os–bipy complexes is illustrated in Scheme 2. A wide variety of mixed ligand Os^{II} and Os^{III} (and some Os^{IV}) bipy species can be prepared. Many of the complexes $[Os(bipy)_2X_2]^{x+}$ have *cis* geometries in order to minimize steric interactions (*see Steric Effect*) between the bipy ligands.

One of the more important aspects of complexes of the type *cis*-$[Os(bipy)_2(L_2)]^{2+}$ (L = vinylpyridine) is their use as derivatives to form electroactive polymer films. Thus polypyridine films containing redox-active $Os^{II/III}$ centers can be generated by electropolymerization of the coordinated vinylpyridine ligands of the parent complex from homogeneous solution.[82] Importantly, these polypyridyl films contain redox-active Os fragments at each unit.

The electrochemical reduction of CO_2 by *cis*-$[Os(bipy)_2(CO)Cl]^+$ has been the subject of much interest. Under anhydrous conditions CO is formed, while in the presence of H_2O formate ion is formed additionally.[83] The Os^{II} complex *cis*-$[Os(bipy)_2(H_2O)_2]^{2+}$ can be oxidized via a series of steps to the corresponding Os^{VI} species *cis*-$[Os(bipy)_2(O)_2]^{2+}$ (equation 7).[84]

$$\begin{aligned} &[Os^{II}(bipy)_2(H_2O)_2]^{2+} \longrightarrow [Os^{III}(bipy)_2(OH)(H_2O)]^{2+} \longrightarrow \\ &[Os^{IV}(bipy)_2(O)(H_2O)]^{2+} \longrightarrow [Os^{V}(bipy)_2(O)(OH)]^{2+} \\ &\longrightarrow [Os^{VI}(bipy)_2(O)_2]^{2+} \end{aligned} \tag{7}$$

A range of Os complexes of terpy has been prepared. Like bipy and phen, terpy tends to stabilize Os^{II}, and so reaction of $[OsCl_6]^{2-}$ with terpy at high temperature affords the highly stable complex $[Os(terpy)_2]^{2+}$. Aspects of the substitution chemistry of Os–terpy complexes are summarized in Scheme 3.

As for the bipy analogues, the interconversion of aqua to oxo ligand can occur on oxidation of $[Os(terpy)(bipy)(H_2O)]^{2+}$ (equation 8).[85] The formation of asymmetric complexes $[Os(LL)_2]^{2+}$ (LL = substituted terpy) has been accomplished; these species incorporate a donor substituent on one terpy and an acceptor substituent on the other, thus facilitating intramolecular electron transfer in MLCT excited state, $[Os(LL)_2]^{2+*}$.[86]

$$\begin{aligned} &[Os^{II}(terpy)(bipy)(H_2O)]^{2+} \longrightarrow [Os^{III}(terpy)(bipy)(OH)]^{2+} \\ &\longrightarrow [Os^{IIV}(terpy)(bipy)(O)]^{2+} \end{aligned} \tag{8}$$

Heterobimetallic complexes of Os^{II} and Ru^{II} bipy have been covalently linked via peptide-bridges derived from L-proline and L-leucine. Efficient intramolecular quenching of the Ru^{II} excited state by the Os^{II} complex was observed.[87] Heterobimetallic complexes of Os^{II} and Ru^{II} have been prepared with 2,2′:3′,2″:6″,2‴-quaterpyridine where two bipy ligands are directly linked together, and efficient intramolecular photo-induced electron transfer observed (Figure 12). Attachment of nucleobases to bipy ligands has afforded heterobimetallic complexes of Os^{II} and Ru^{II} via Watson–Crick base pair formation, and efficient intramolecular electron transfer is observed across the hydrogen-bonded interface. Also, attachment of two bipyridyl ligands by poly(oxoethylene) chains yields complexes whose conformation is solvent dependent. Consequently, by control of the solvent polarity the Os-Ru distance can be modulated and correspondingly the Ru → Os energy transfer rate.[88]

In a related manner, bipyridyl units have been linked by a redox-active benzoquinone (bq) spacer, which acts as a redox switch in the Ru-bq-Os complex.[89]

Os^{II} and Ru^{II} bis(terpyridine) complexes have been covalently linked (Figure 13) and their electrochemical, absorption spectra, photochemical and photophysical properties have been studied. The strong electronic interaction decreases as the one or two phenylene spacers are added but remains large enough to allow fast electron transfer.[90]

A series of Ru-Os terpy complexes have been reported with the terpy ligands separated by an a 1,4-diethynylene-2,5-dialkoxybenzene connector. Each additional 1,4-diethynylene-2,5-dialkoxybenzene unit in the bridge contributes about 8.1 Å to the length and decreases the rate of electron transfer by a factor of three.[91] An Os bis(terpyridine) complex has been designed where one terpy ligand incorporating a hydrophobic biphenylene tail inserts into a cyclodextrin which in turn is attached to a ruthenium terpyridine complex. It has been shown that this supramolecular complex displays fast electron transfer with a rate of $9.5 \times 10^9\ s^{-1}$.[92] Similarly, Os and Ru phenanthroline complexes have been linked by an adamantane spacer, the life-time of the Ru^{III}–Os^{II} intermediate being particularly long (130 µs) with the electron transfer rate from Ru^{II} to Os^{II} being faster than for Ru^{II} to Os^{III}.[93]

Two short reviews on the chemistry of mixed Ru^{II} and Os^{II} dendrimers $[M(L)_n(BL)_{3-n}]^{2+}$ (L = 2,2′-bipyridine or 2,2′-biquinoline; BL = 2,3- or 2,5-di-pyrindin-2-yl pyrazine; $n = 0$ or 2) have been published.[94,95] The energy transfer between units is very fast due to sufficiently strong electronic interaction; for the complexes of 2,3-dpp this takes place within 200 fs. Therefore, these dendrimers can be used to perform valuable functions such as light harvesting and the controlled storage or release of a given number of electrons at a certain potential.[94,95] This work has been further extended to include decanuclear dendrimers bearing three different metal ions for example, $Os\{(\mu\text{-}2,3\text{-}dpp)Ru\text{-}[(\mu\text{-}2,3\text{-}dpp)PtCl_2]_2\}_3(PF_6)_8$. Also, tetranuclear dendrimers with Os^{II}

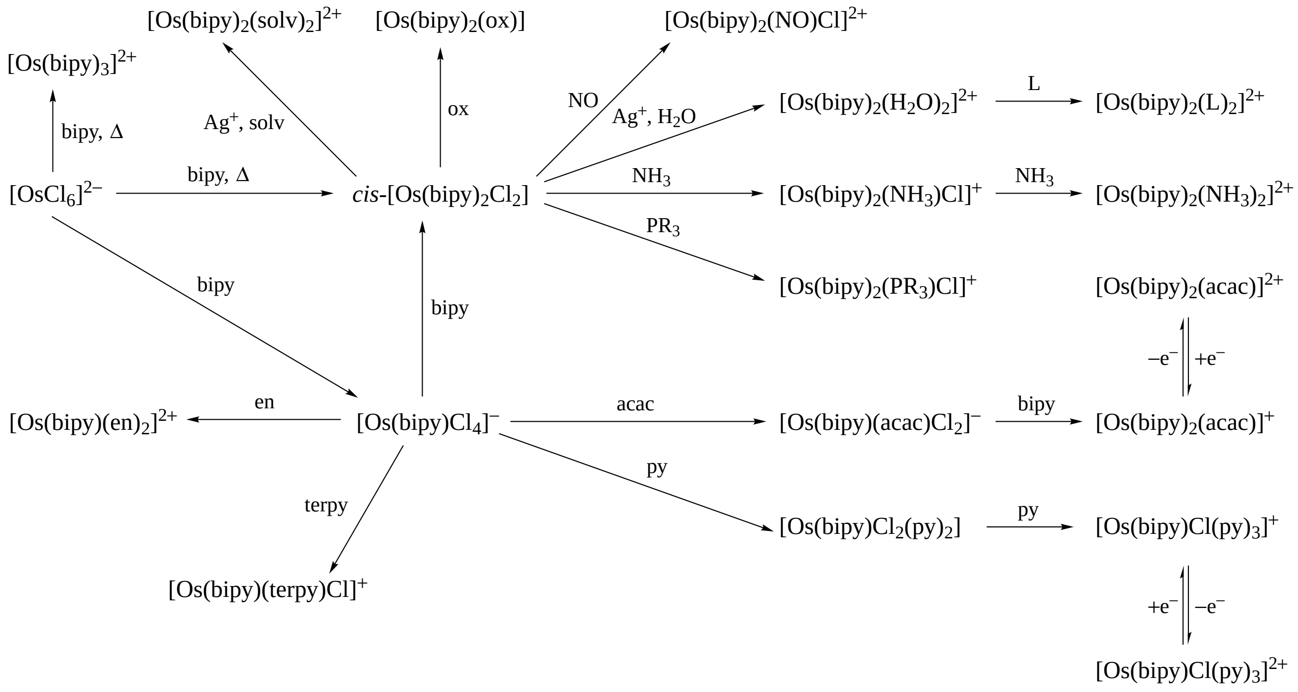
[Os(bipy)2(solv)2]2+
[Os(bipy)2(ox)]
[Os(bipy)2(NO)Cl]2+
[Os(bipy)3]2+
bipy, Δ
Ag+, solv
ox
NO
Ag+, H2O
[Os(bipy)2(H2O)2]2+
L
[Os(bipy)2(L)2]2+
[OsCl6]2–
bipy, Δ
cis-[Os(bipy)2Cl2]
NH3
[Os(bipy)2(NH3)Cl]+
NH3
[Os(bipy)2(NH3)2]2+
PR3
[Os(bipy)2(PR3)Cl]+
[Os(bipy)2(acac)]2+
bipy
bipy
−e−
+e−
[Os(bipy)(en)2]2+
en
[Os(bipy)Cl4]−
acac
[Os(bipy)(acac)Cl2]−
bipy
[Os(bipy)2(acac)]+
py
terpy
[Os(bipy)Cl2(py)2]
py
[Os(bipy)Cl(py)3]+
[Os(bipy)(terpy)Cl]+
+e−
−e−
[Os(bipy)Cl(py)3]2+

Scheme 2

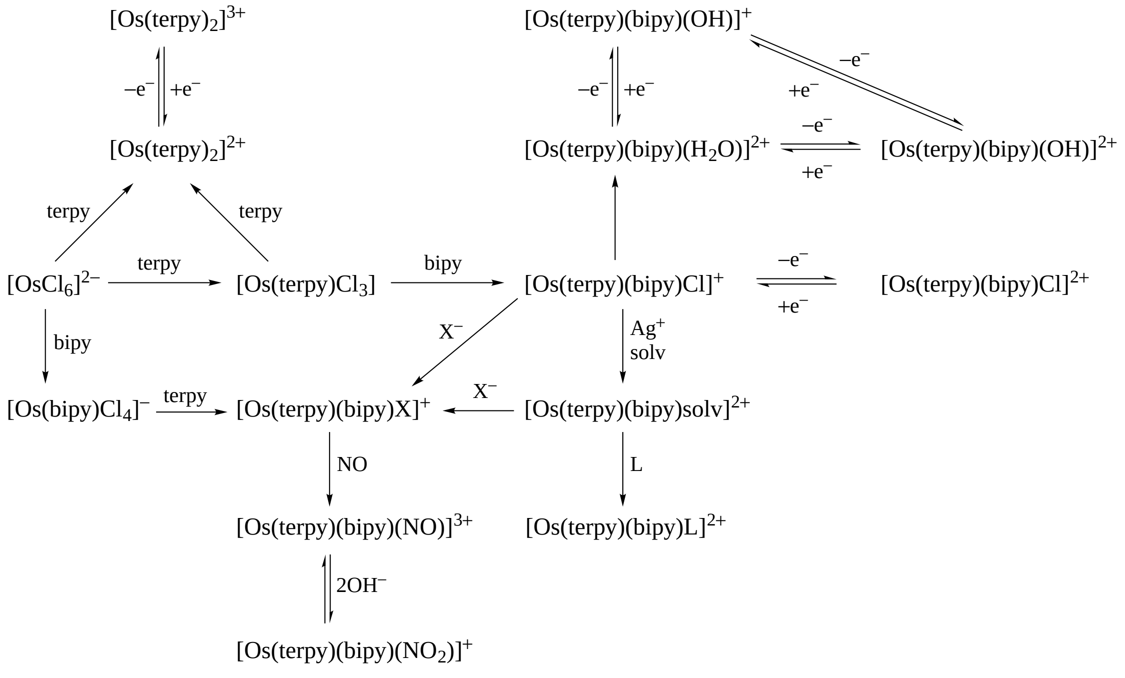
[Os(terpy)2]3+
−e−
+e−
[Os(terpy)2]2+
terpy
terpy
[Os(terpy)(bipy)(OH)]+
−e−
+e−
−e−
+e−
[Os(terpy)(bipy)(H2O)]2+
−e−
+e−
[Os(terpy)(bipy)(OH)]2+
[OsCl6]2–
terpy
[Os(terpy)Cl3]
bipy
[Os(terpy)(bipy)Cl]+
−e−
+e−
[Os(terpy)(bipy)Cl]2+
bipy
X−
Ag+
solv
[Os(bipy)Cl4]−
terpy
[Os(terpy)(bipy)X]+
X−
[Os(terpy)(bipy)solv]2+
NO
L
[Os(terpy)(bipy)(NO)]3+
[Os(terpy)(bipy)L]2+
2OH−
[Os(terpy)(bipy)(NO2)]+

Scheme 3

at the core and three external Ru^{II} complexes associated with six pyrenyl chromophores attached to the periphery have been described. The aim here is to harvest light and promote a periphery to core energy transfer.**[96]**

The intercalation of several Os^{II} complexes such as $[Os(Phen)_2(dppz)]^{2+}$ dppz = dypyrido[3,2-a:2′,3′-c]phenazine and charge transfer through the DNA base stack has been reviewed.**[97]** Os^{II} complexes have also been tethered

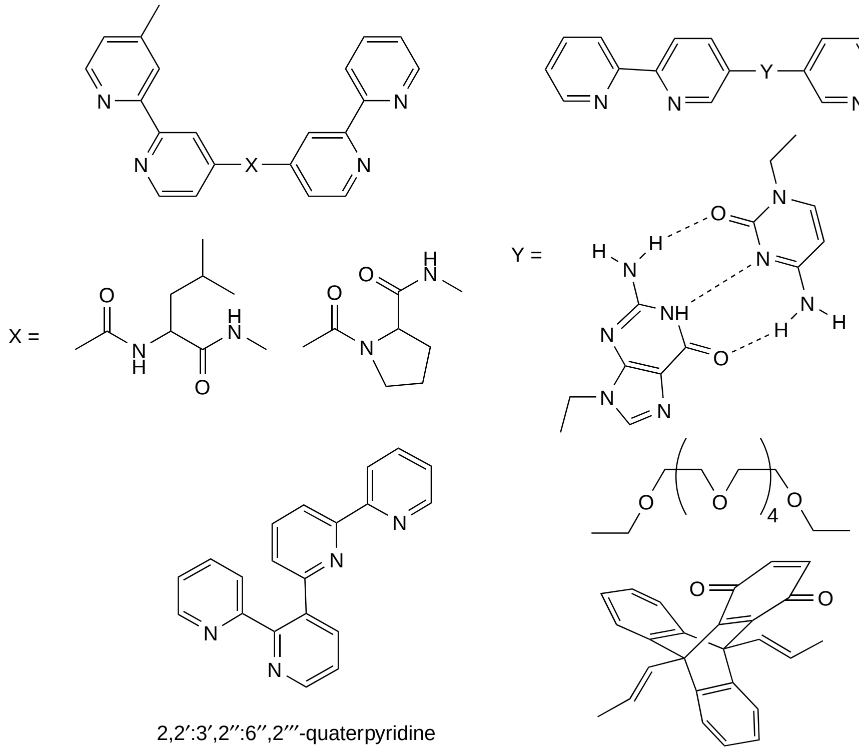

Figure 12 Bipyridyl ligands used to form heterobimetallic complexes of Os^{II} and Ru^{II}

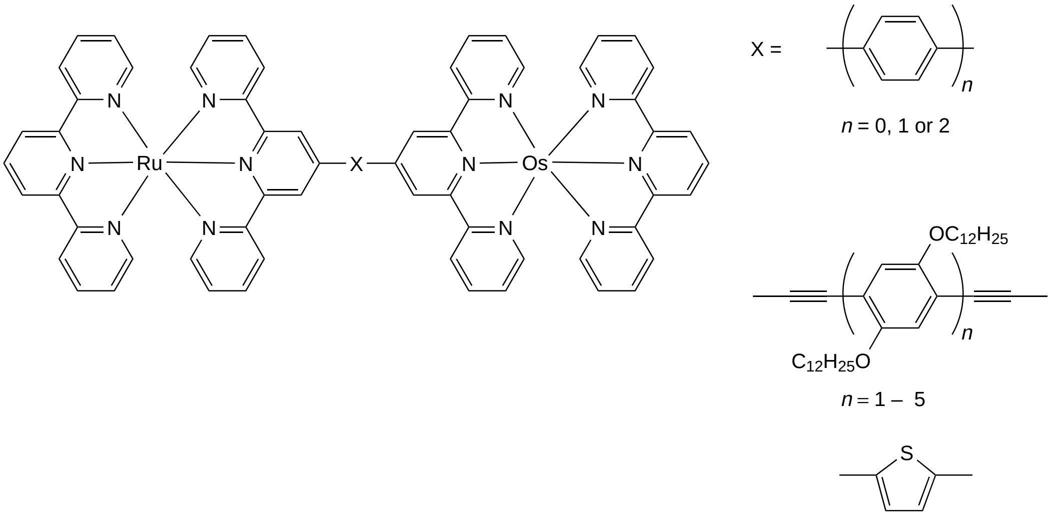

Figure 13 Terpyridyl heterobimetallic complexes of Os^{II} and Ru^{II}

to DNA to study the triplet energy transfer between metallointercalators.**[98]**

8.2.4 N_2 Complexes

Coordination of the π-acceptor N_2 ligand is most often found for Os^{II}, although some dinitrogen complexes of Os^{III} are known (*see Dinitrogen & Dinitrogen Complexes*). These complexes are generally prepared by substitution reaction at Os^{II} with N_2, or by controlled oxidation of coordinated NH_3 ligands with KNO_2 under acidic conditions. In the complex $[Os(NH_3)_5(N_2)]^{2+}$ (Figure 14), the N_2 ligand is bound terminally, Os–N = 1.842(13) Å, with Os–N(NH_3) = 2.144(15), 2.151(15) Å,**[99]** the shorter bond to N(N_2), reflecting the strong π-back donation (*see Back Bonding*) from Os^{II} to N_2. Other N_2 complexes include $[Os(NH_3)_4(N_2)(CO)]^{2+}$,

$[Os(NH_3)_4(N_2)_2]^{2+}$, $[OsCl(N_2)(PMe_2Ph)_3(SC_6F_5)]$ (Figure 15),[100] and $[Os(H)_2\ (N_2)(PEtPh_2)_3]$.

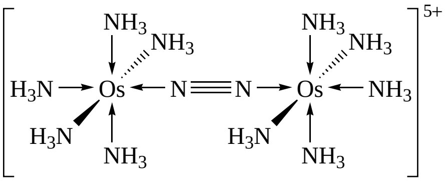

(**38**)

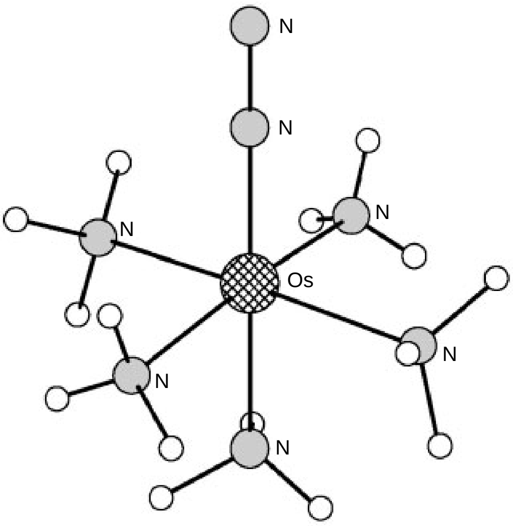

Figure 14 The structure of $[Os(NH_3)_5(N_2)]^{2+}$

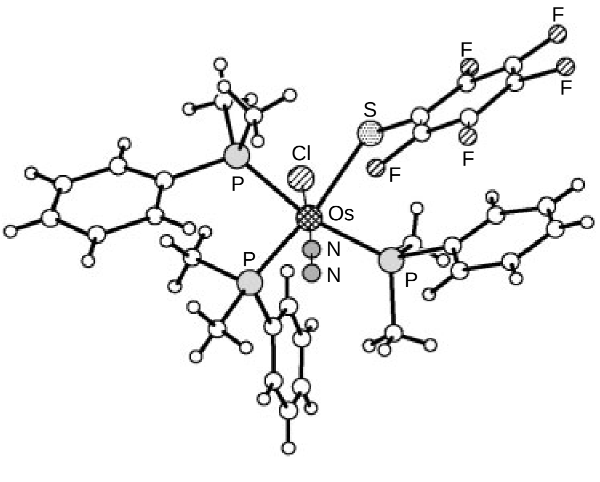

Figure 15 The structure of $[OsCl(N_2)(Pme_2Ph)_3(SC_6F_5)]$

Bridging N_2 complexes can also be prepared. Thus reaction of $[Os(NH_3)_5(N_2)]^{3+}$ with $[Os(NH_3)_5(H_2O)]^{2+}$ affords the mixed valence Os^{II}–Os^{III} dimer $[(H_3N)_5Os(\mu^2\text{-}N_2)Os(NH_3)_5]^{5+}$ (**38**), which can be reduced to the 4+ and oxidized to the 6+ ions.[101] Other μ^2-N_2 complexes include $[(H_3N)_4(OC)Os(\mu^2\text{-}N_2)Os(CO)(NH_3)_4]^{4+}$ and $[(H_3N)_4ClOs(\mu^2\text{-}N_2)OsCl(NH_3)_4]^{3+}$.

8.2.5 Nitrosyl Complexes

The chemistry of metal nitrosyls has been reviewed.[102] Most NO complexes of Os are regarded as formally NO^+ complexes with terminal, linear coordination of the ligand (*see Nitrosyl Complexes*). Most of the complexes are of d^6 Os^{II}, although there are examples of d^5, d^7, d^8, d^9, and d^{10} Os centers with NO^+ and related ligands. The stabilization of low oxidation state Os species reflects the very strong π-acceptor properties of NO^+, NO^+ being isoelectronic with CO and one of the strongest π-acceptor ligands known. The coordination chemistry of NO^+ with Ru is much better developed than that with Os, but there are clear similarities and parallels between them. Coordinated NO^+ can be readily characterized by IR spectroscopy, the $\nu_{N\equiv O}$ stretching vibration occurring in the range $1900-1800\ cm^{-1}$. Most of the Os–NO^+ complexes incorporate other ligands and are commonly prepared either by substitution reactions with NO or by reactions with NO_2^-, NH_2OH, or N_2H_4, or by oxidative reactions (*see Oxidative Addition*) of substrates to formal Os^0 and Os^{-II} species such as $[OsCl(NO)(PR_3)_2]$ and $[Os(NO)_2(PPh_3)_2]$ (see Section 9). Common examples of Os–NO^+ complexes include $[Os(NO)X_5]^{2-}$ (**39**) (X = F, Cl, Br, I), $[Os(NO)Cl_4]^-$ (**40**), $[Os(NH_3)_5NO]^{3+}$ (**41**), and $[OsX_2(OH)(NH_3)_2(NO)]$ (**42**).

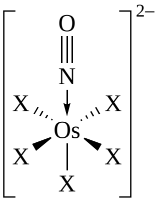

(**39**)

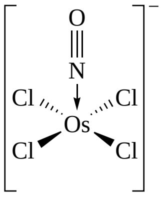

(**40**)

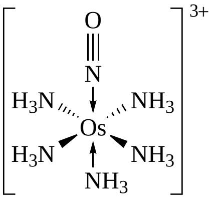

(**41**)

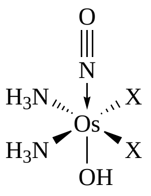

(**42**)

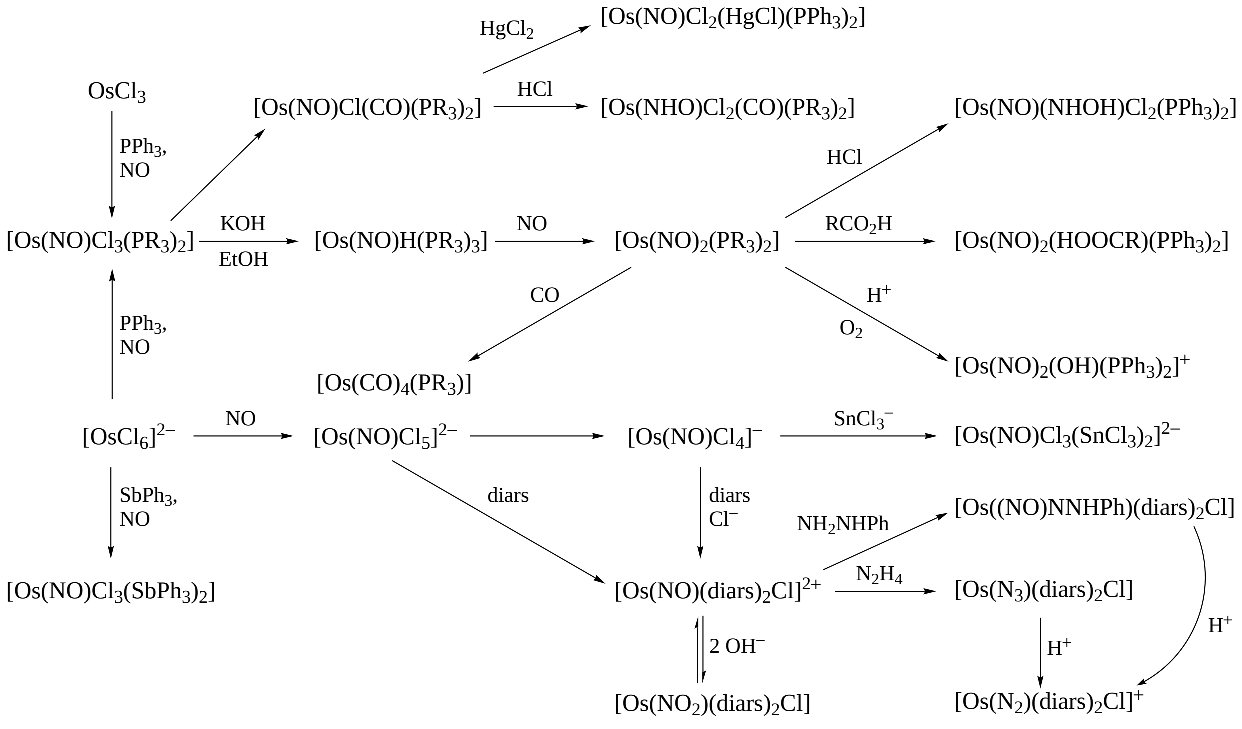

OsCl3
PPh3, NO
[Os(NO)Cl3(PR3)2]
KOH
EtOH
[Os(NO)H(PR3)3]
NO
[Os(NO)2(PR3)2]
RCO2H
[Os(NO)2(HOOCR)(PPh3)2]
[Os(NO)Cl(CO)(PR3)2]
HgCl2
[Os(NO)Cl2(HgCl)(PPh3)2]
HCl
[Os(NHO)Cl2(CO)(PR3)2]
HCl
[Os(NO)(NHOH)Cl2(PPh3)2]
CO
[Os(CO)4(PR3)]
H+
O2
[Os(NO)2(OH)(PPh3)2]+
PPh3, NO
[OsCl6]2–
NO
[Os(NO)Cl5]2–
[Os(NO)Cl4]–
SnCl3–
[Os(NO)Cl3(SnCl3)2]2–
SbPh3, NO
[Os(NO)Cl3(SbPh3)2]
diars
diars
Cl–
NH2NHPh
[Os((NO)NNHPh)(diars)2Cl]
[Os(NO)(diars)2Cl]2+
N2H4
[Os(N3)(diars)2Cl]
H+
H+
2 OH–
[Os(NO2)(diars)2Cl]
[Os(N2)(diars)2Cl]+

Scheme 4

A complication in NO^+ coordination chemistry is that reactions can occur at the metal center or at the NO^+ center to afford other N-containing ligands such N_2, $NO_2{}^-$, or NH_2OH. Some of the reactions of coordinated NO^+ are illustrated in Scheme 4.

Examples of complexes incorporating hydrazine (NH_2NH_2), HNO, RN_2, NS, and NSCl have also been reported.

8.2.6 *Macrocyclic Complexes*

The chemistry of Os with macrocycles (*see Macrocycle*) is dominated by complexes of OEP, tetraphenylporphyrin (TPP), and related porphyrins. Insertion of Os into these ligands occurs under vigorous conditions (typically using Os_3CO_{12} or related CO containing low-valent Os starting material, *see Metal Carbonyls*) in the presence of py to give [Os(OEP)(CO)(py)] and [Os(TPP)(CO)(py)]. These complexes can be converted to $[Os(porph)(L)_2]$ (L = py, PR_3, tetrahydrofuran (THF), imid, MeCN) by photolytic removal of CO. Thermolysis of $[Os(OEP)py_2]$ affords the highly novel Os=Os bonded dimer $[Os(OEP)]_2$ (equation 9).[103] The complex $[Os(OEP)(\eta^2\text{-}H_2)]$ has been reported[104] as have binucleating porphyrins which insert H_2 into the Os=Os bond (equation 10).[105] Complexes of octaethylporphyrin complexes with Os^{II} have been dimerised to form homometallic and heterobimetallic (the latter with Ru porphyrins) complexes. The electrochemical and magnetic properties have been studied to illustrate the bonding in various oxidation states, particularly relating to the formation of δ-bonds.[106]

By comparison, the chemistry of Os phthalocyanins (Pc) is less well developed, mainly because of their much lower solubility. Reaction of $OsCl_3$ with *o*-cyanobenzamide in naphthalene at 290 °C followed by extended extraction affords '[OsPc]'. Reaction with ligands L affords the complexes $[Os(Pc)(L)_2]$ (L = py, pz, tz). Addition of one equivalent of L affords the polymers $[Os(Pc)(L)]_n$ (L = pz, tz).[107] Examples of Os complexes with saturated polyaza macrocycles have been reported.

$$[Os(OEP)(CO)py] \xrightarrow[py]{h\nu} [Os(OEP)py_2] \xrightarrow{\Delta} (OEP)Os{=}Os(OEP) \tag{9}$$

$$(L)(\overline{porph)Os{=}Os(porph})(L) \xrightarrow{H_2} (L)(\overline{porph)Os\text{–}H_2\text{–}Os(porph})(L) \tag{10}$$

A novel Os^{II} and Ru^{II} bis(bipyridyl) containing an amide macrocyclic receptor has been shown to detect the presence of anions by both electrochemical and optical methodologies. Photophysical studies have clearly shown that the rate constants of the energy transfer process responsible for the quenching of the luminescent ruthenium excited state significantly decreases in the presence of chloride ions.[108]

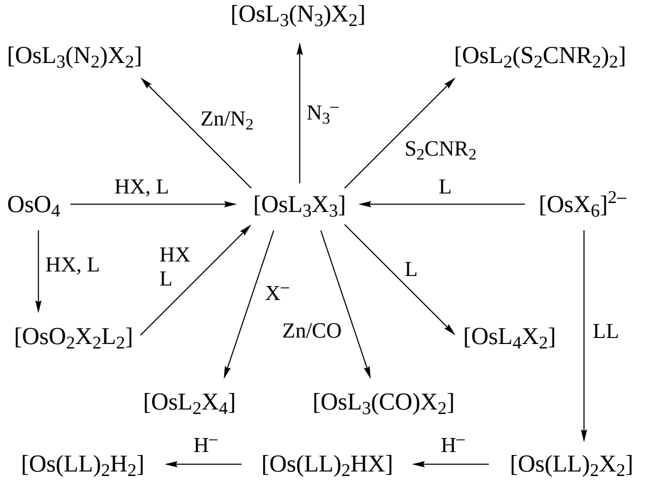

Scheme 5

8.3 P-, As-, and Sb-donor Complexes

The chemistry of Os with PR_3, AsR_3, and SbR_3 ligands is very extensive and rich, and is based largely about the substitution chemistry of octahedral, mixed ligand Os^{II} complexes, although there are examples extending from Os^{-II}, for example, $[Os(NO)_2(PPh_3)_2]$, to Os^{VI}, for example, $[OsO_2(en)(PR_3)_2]^{2+}$.[3,4] Scheme 5, in which reactivity depends upon L (= tertiary phosphine) and LL (= chelate phosphine), illustrates aspects of the substitution chemistry of Os–phosphine complexes.

An interesting series of Os–phosphine hydride and polyhydride complexes spanning formal oxidation states of Os^{II} to Os^{VI} has been prepared. Scheme 6, in which reactivity depends upon L (= tertiary phosphine), illustrates the synthesis of some of the more important polyhydrides including complexes of type $[Os(L)_2(dppe)H_2]$, $[Os(L)H_4]$, $[Os(L)_4H_3]^+$, and $[Os(L)_3H_6]$ ($L = PR_3$). The question of whether these complexes should be regarded as genuine η^1-polyhydrido (H^-) or η^2-dihydrogen (H_2) complex has caused controversy, the precise formulation being very sensitive to the types of ligand present.[109] *Trans*-$[Os(H\cdots H)(H)(depe)_2]^+$ is a fascinating case of an η^2-dihydrogen ligand with a long $H\cdots H$ distance on the brink of homolytic cleavage,[110] the corresponding dppe complex being assigned as *trans*-$[Os(H_2)(H)(dppe)_2]^+$ with a short H–H bond. $[OsH_6\{P(i\text{-}Pr)_3\}_2]$ shows relatively short but nonbonding $H\cdots H$ distances as determined by neutron diffraction, and is assigned as a hexahydride.[111]

8.4 O-donor Complexes

The chemistry of Os with O-donors (*see* ***Water & O-donor Ligands***) is dominated by high-valent Os^{VI}–Os^{VIII} oxo complexes incorporating the Os=O and osmyl O=Os=O units. Although H_2O ligation occurs readily in mixed ligand complexes of Os^{III} and Os^{II}, the chemistry of $[Os(H_2O)_6]^{3+}$ is ill-defined with the formation of oxo–Os^{IV} species being prevalent. Surprisingly few alkoxide, diketonate, oxalate, nitro, sulfato, and carboxylate complexes have been well characterized. An interesting peroxo complex, $[Os(O_2)(CO)_2(PPh_3)_2]$ (*see Peroxo Complexes*), has been reported as the product of the reaction of O_2 with $[Os(CO)_2(PPh_3)_2]$.[112] An important series of binuclear complexes incorporating bridging carboxylates and other bifunctional ligands has been characterized. Thus reaction of $[OsCl_6]^{2-}$ with acetic anhydride and acetic acid affords the Os^{III}–Os^{III} complex $[Os_2(OCOMe)_4Cl_2]$ in good yield; reaction of $[Os_2(OCOMe)_4Cl_2]$ with other acids, RCOOH, yields $[Os_2(OCOR)_4Cl_2]$ (R = typically Pr, Bu). The structure of $[Os_2(OCOMe)_4Cl_2]$ (Figure 16) confirms an Os–Os distance of 2.316(2) Å[113]. The complexes $[Os_2(OCOR)_4Cl_2]$ are paramagnetic at room temperature (μ_{eff} = approx 1.2 BM per Os). Diosmium tetracarboxylates have been the subject of a recent review discussing their synthesis, physical properties and applications. Such complexes have been isolated as $Os^{II}Os^{II}$, $Os^{III}Os^{III}$ and mixed valence $Os^{II}Os^{III}$ dimers.[114]

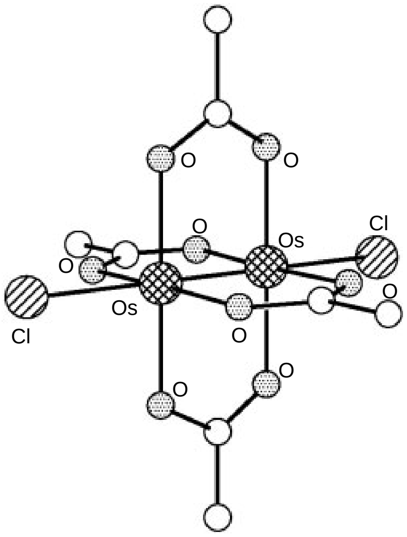

Figure 16 The structure of $[Os_2(OCOMe)_4Cl_2]$

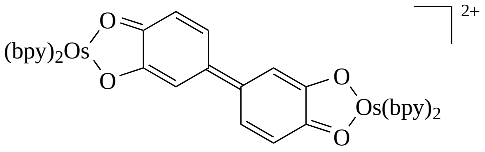

(43)

The redox noninnocence of Os^{II} and Ru^{II} dioxolene complexes and of their nitrogen donor analogues has

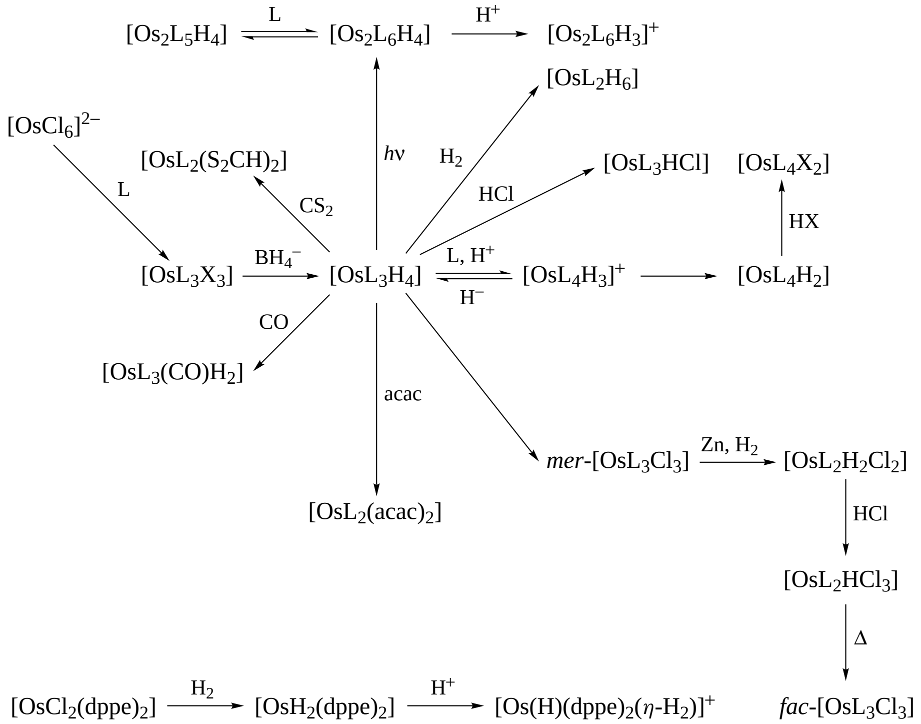
[Os2L5H4]
L
[Os2L6H4]
H+
[Os2L6H3]+
[OsL2H6]
[OsCl6]2–
[OsL2(S2CH)2]
hν
H2
[OsL3HCl]
[OsL4X2]
L
CS2
HCl
HX
BH4–
L, H+
[OsL3X3]
[OsL3H4]
[OsL4H3]+
[OsL4H2]
H–
CO
[OsL3(CO)H2]
acac
mer-[OsL3Cl3]
Zn, H2
[OsL2H2Cl2]
[OsL2(acac)2]
HCl
[OsL2HCl3]
Δ
[OsCl2(dppe)2]
H2
[OsH2(dppe)2]
H+
[Os(H)(dppe)2(η-H2)]+
fac-[OsL3Cl3]

Scheme 6

recently been discussed in a short review. The complex (**43**) is best described as a Os^{III}(catecholate–catecholate)Os^{III} species with cyclic voltammetry displaying two metal based reduction peaks and two ligand based oxidation peaks. In contrast, the Ru analogue is best described as a Ru^{II}(semiquinone–semiquinone)Ru^{II} complex.**[115]**

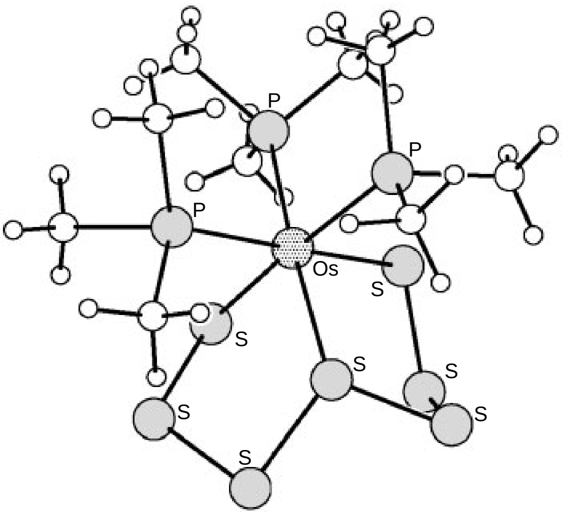
P
P
P
Os
S
S
S
S
S
S
S

Figure 17 The structure of $[Os(PMe_3)_3(S_2)]$

8.5 S-donor Complexes

The chemistry of Os with S-donors is not well established. This is surprising, considering the expected match between soft Os^{II} and soft S-thioether and thiolate donors. Reaction of $[Os(PMe_3)_3(H)(CH_2PMe_2)]$ with elemental S (S_8) (*see* ***S-donor Ligands***; ***Sulfur: Inorganic Chemistry***) affords two products, $[Os(PMe_3)_3(S_6)]$ and $[Os(PMe_3)_3(S_7)]$ (Figure 17), the latter incorporating a tridentate $S_7{}^{2-}$ ligand.**[116]** The homoleptic thioether complex $[Os([9]aneS_3)_2]^{2+}$ (Figure 18) has been prepared and shows Os–S = 2.3313(18)–2.3408(20) Å.**[71]** Furthermore, a mixed sandwich complex $Os(4\text{-}MeC_6H_4Pr^i)([9]aneS_3)$ has been structurally characterised.

Trans-$[OsCl_2(Me_2SO)_4]$ reacts with excess hydrazine hydrochloride to form *mer*-$[OsCl_3(NH_3)_4(Me_2S)]$ in a concerted reaction. Overall this reaction involves oxidation of Os, deoxygenation of dimethylsulfoxide (DMSO), disproportion of hydrazine, and substitution by ammonia. In contrast, *cis*-$[RuCl_2(Me_2SO)_4]$ reacts to give *mer*-$[RuCl_3(N_2H_5)_4(Me_2SO)_2]$.**[117]**

A range of *Dithiocarbamate* complexes including the tris-chelate species $[Os(S_2CNR_2)_3]$ has been prepared by reaction of $[OsCl_6]^{2-}$ with the corresponding ligand. Additionally, an unusual dimeric species $[Os_2(S_2CNR_2)_3(S_3CNR_2)_2]^+$ (Figure 19) has been isolated from the above reaction, while reaction of $[Os(S_2CNR_2)_3]$ with elemental S_8 affords $[Os_2(S_5)(S_3CNR_2)(S_2CNR_2)_5]$ (Figure 20).**[118]** Various, mostly ill-defined, complexes of

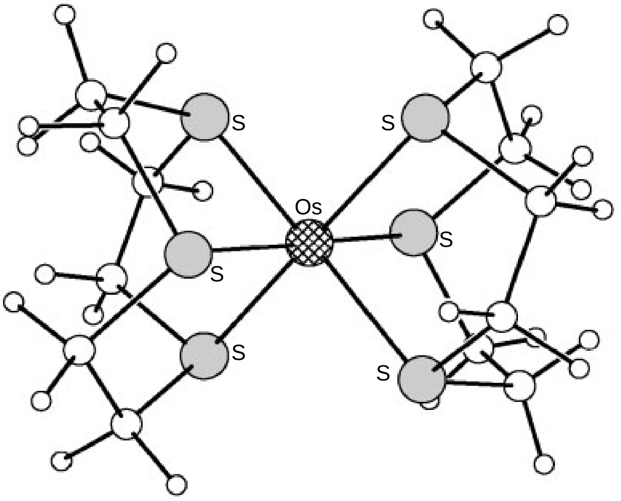

Figure 18 The structure of $[Os([9]aneS_3)_2]^{2+}$

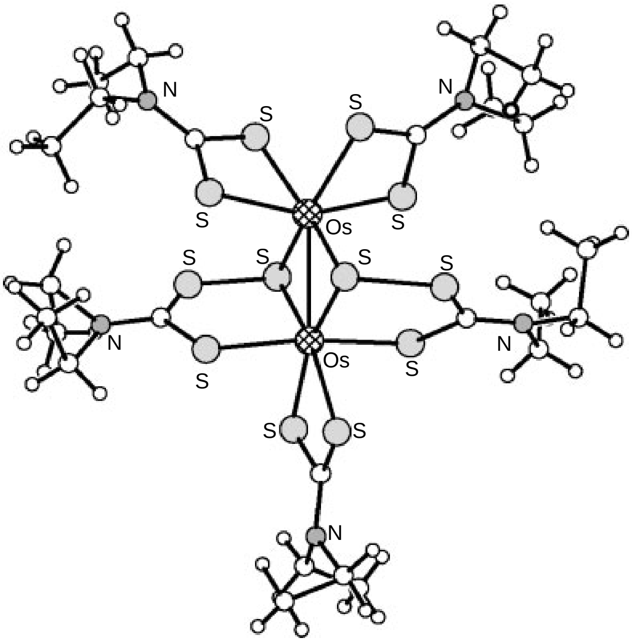

Figure 19 The structure of $[Os_2(S_2CNR_2)_3(S_3CNR_2)_2]^+$

thiones, dithiolenes, thioketonates, and thiourea derivatives have been reported.

8.6 Halogen Complexes

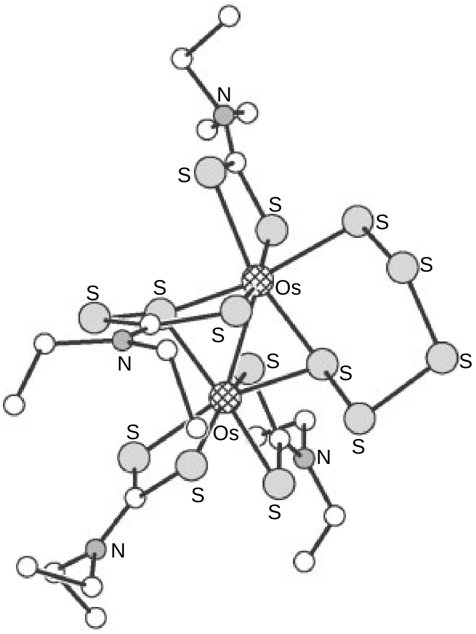

Figure 20 The structure of $[Os_2(S_5)(S_3CNR_2)_3(S_2CNR_2)_5]$

Halides tend to stabilize the higher valent states of Os and so their chemistry has been described in previous sections. The interconversion of $Os^{V/IV/III/II}$ oxidation states in a series of halo–pyridine complexes $[OsX_npy_{6-n}]^{x+}$ $(n = 0–6)$ has been assessed. It was found that py tends to stabilize Os^{II}, with Cl^- stabilizing the higher oxidation states Os^{IV} and Os^V.**119** Reduction of $[Os_2X_9]^{2-}$ affords the Os^{III} anion $[Os_2X_9]^{3-}$, which loses X^- to give $[Os_2X_8]^{2-}$. Interestingly, the Os–Os distance in staggered $[Os_2X_8]^{2-}$ increases on going from X = Cl (2.182), Br (2.196), I (2.217 Å), while the Os–Os distance of 2.209(1) Å is observed in eclipsed $[Os_2Cl_8]^{2-}$.**120**

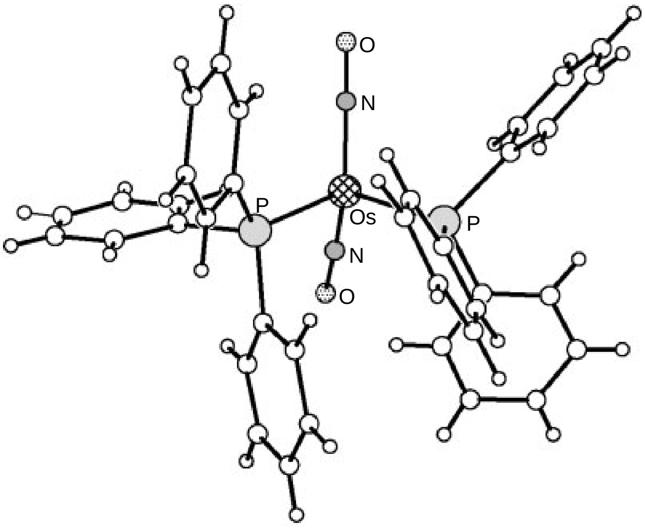

Figure 21 The structure of $[Os^{-II}(NO)_2(PPh_3)_2]$

9 LOW OXIDATION STATES

Coordination compounds of Os^{I} and Os^{-I} are very rare,**[4]** and when detected are often intermediates in redox reaction. Os^{0} and Os^{-II} complexes have d^8 and d^{10} electron configurations respectively, and are often associated with organometallic clusters.

The d^8 complex $[Os^{0}(NO)H(PR_3)_3]$ can be prepared from $[Os^{II}(NO)Cl_3(PR_3)_2]$ in KOH, and can be reduced further to the d^{10} nitrosyl complexes $[Os^{-II}(NO)_2(PPh_3)_2]$ by reaction with *N*-methyl-*N*-nitroso-*p*-toluenesulfonamide. The structure of $[Os^{-II}(NO)_2(PPh_3)_2]$ (Figure 21) is tetrahedral, with linear Os–N–O linkages.**[121]** The $\nu_{N\equiv O}$ stretching vibration occurs near 1600 cm^{-1} consistent with very strong π-back donation to NO^+ from the highly electron rich Os^{-II} center (*see Electron Rich Compound*). $[Os^{0}(NO)Cl(PPh_3)_3]$ can be prepared from $[Os^{0}(NO)(CO)Cl(PPh_3)_2]$.**[122]** Ligand substitution occurs in $[OsCl(NO)(PPh_3)_3]$ to afford $[OsCl(NO)(PPh_3)_2(L)]$ (L = alkene, PR_3, SO_2). Further, $[Os^{0}(NO)Cl(PPh_3)_3]$ reacts with P(*i*-Pr)$_3$ to give *trans*-$[Os^{0}(NO)Cl\{P(i\text{-Pr})_3\}_2]$ (Figure 22), which shows a square planar stereochemistry.**[123]** Since $[Os^{0}(NO)Cl\{P(i\text{-Pr})_3\}_2]$ is a 16-electron species and is also co-ordinatively unsaturated, it undergoes a range of oxidative addition reactions to give the octahedral Os^{II} products illustrated in Scheme 7.

Oxidation of $[Os(NO)_2(PPh_3)_2]$ by O_2 in the presence of H^+ affords $[Os^{0}(NO)_2(OH)(PPh_3)_2]^+$ (Figure 23), which shows a square based pyramid (SQPY) structure with one linear and one bent Os–N–O linkage.**[124]**

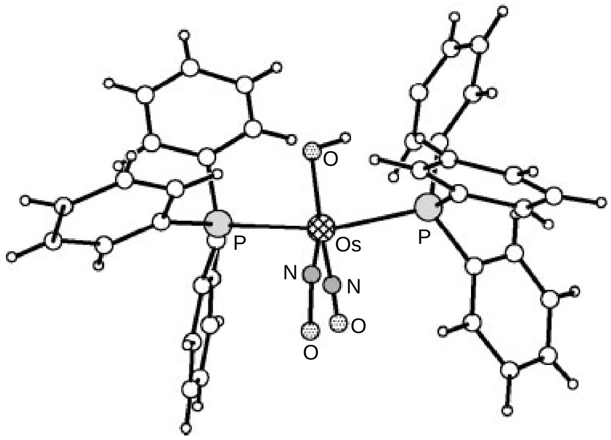

Figure 23 The structure of $[Os^{0}(NO)_2(OH)(PPh_3)_2]^+$

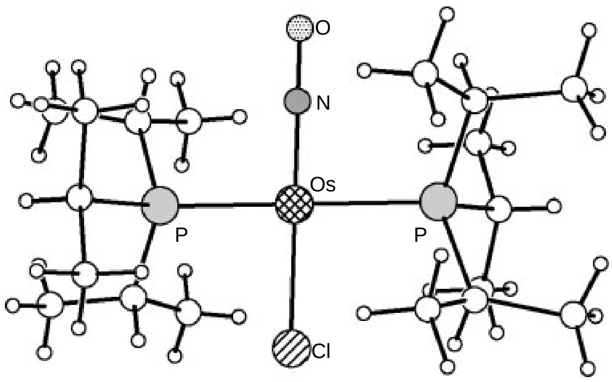

Figure 22 The structure of *trans*-$[Os^{0}(NO)Cl\{P(i\text{-Pr})_3\}_2]$

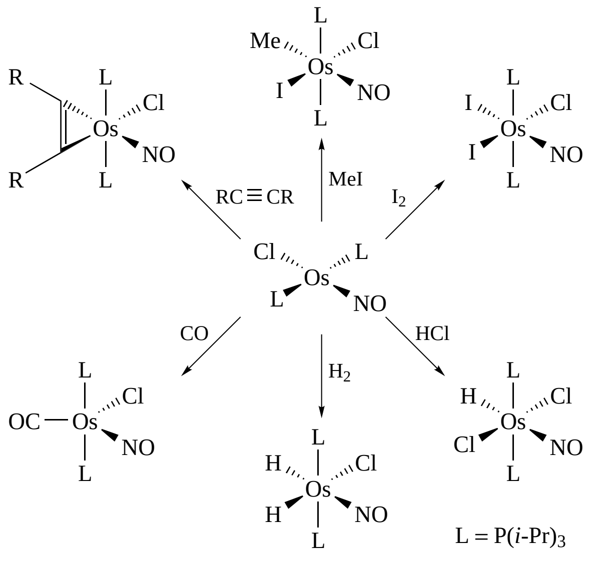

Scheme 7

10 RELATED ARTICLES

Ammonia & N-donor Ligands; Coordination Numbers & Geometries; Coordination & Organometallic Chemistry: Principles; Cyanide Complexes of the Transition Metals; Electron Transfer in Coordination Compounds; Hydride Complexes of the Transition Metals; Hydrogenation & Isomerization of Alkenes; Macrocyclic Ligands; Osmium: Organometallic Chemistry; Ruthenium: Inorganic & Coordination Chemistry; S-donor Ligands; Sulfur: Inorganic Chemistry; Water & O-donor Ligands.

11 REFERENCES

1. S. Tennant, *Phil. Trans. Roy. Soc.*, 1804, **94**, 411; *Nicholson's J. Nat. Philos., Chem. Arts*, 1805, **10**, 24.
2. 'Gmelin's Handbuch der Anorganische Chemie', Supplement Volume, Springer Verlag, Berlin, 1980, Vol. 1, (No. 66).

3. G. Wilkinson, R. D. Gillard, and J. A. McCleverty eds, ‘Comprehensive Coordination Chemistry’, Pergamon, Oxford, 1987, Vol. 4.
4. J. A. McCleverty and T. J. Meyer eds, ‘Comprehensive Coordination Chemistry’, 2nd edn., Pergamon, Oxford, 2003, Vol. 4.
5. F. A. Cotton, G. Wilkinson, C. A. Murillo, and M. Bochmann, ‘Advanced Inorganic Chemistry’, 6th edn., Wiley Interscience, New York, 1999.
6. R. A. Sanchez, M. Rosales, M. A. Esteruelas, and L. A. Oro, *J. Mol. Catal. A*, 1995, **96**, 231.
7. H. M. Seip and R. Stolevik, *Acta Chem. Scand.*, 1966, **20**, 385.
8. B. Krebs and K. D. Hasse, *Acta Crystallogr., Sect. B*, 1976, **32**, 1334.
9. W. P. Griffith, A. C. Skapski, K. A. Woode, and M. J. Wright, *Inorg. Chim. Acta*, 1978, **31**, L413.
10. J. S. Hanker, D. K. Romanovicz, and H. Padykula, *J. Histochem. Cytochem.*, 1976, **49**, 263.
11. K. O. Christie and R. Bougon, *J. Chem. Soc., Chem. Commun.*, 1992, 1056.
12. W. J. Casteel, D. A. Dixon, H. P. A. Mercier, and G. J. Schrobilgen, *Inorg. Chem.*, 1996, **35**, 4310.
13. M. Schröder, *Chem. Rev.*, 1980, **80**, 187; W. P. Griffith, *Transition Met. Chem.*, 1990, **15**, 251.
14. A. J. Bailey, M. G. Bhowon, A. G. F. Shoair, A. J. P. White, and D. J. Williams, *J. Chem. Soc., Dalton Trans.*, 1997, 3245.
15. T. J. Donohoe, *Synlett*, 2002, **8**, 1223.
16. H. C. Kolb, M. Van Nieuwhenze, and K. B. Sharpless, *Chem. Rev.*, 1994, **94**, 2483.
17. E. J. Corey and M. C. Noe, *J. Am. Chem. Soc.*, 1996, **118**, 319.
18. M. A. Andersson, R. Epple, V. V. Fokin, and K. B. Sharpless, *Angew. Chem., Int. Ed. Engl.*, 2002, **41**, 472.
19. P. R. Pastuszak, P. L’Haridon, R. Marchand, and Y. Laurent, *Acta Crystallogr., Sect. B*, 1982, **38**, 1427.
20. W. A. Nugent, *Coord. Chem. Rev.*, 1980, **31**, 123.
21. W. A. Nugent, R. L. Harlow, and R. J. McKinney, *J. Am. Chem. Soc*, 1979, **101**, 7265.
22. E. Herranz and K. B. Sharpless, *Org. Synth.*, 1983, **61**, 85.
23. J. A. Bodkin and M. D. McLeod, *J. Chem. Soc., Perkin Trans. 1*, 2002, 2733.
24. O. Glemser, H. W. Roesky, J. H. Hellberg, and H. U. Werther, *Chem. Ber.*, 1966, **99**, 2652.
25. N. Bartlett and J. Trotter, *J. Chem. Soc.*, 1968, 543.
26. E. Bilger, J. Pebler, R. Webber, and K. Dehnicke, *Z. Naturforsch., Teil B*, 1984, **39**, 259.
27. A. A. Danopoulos, G. Wilkinson, B. Hussain-Bates, and M. B. Hursthouse, *J. Chem. Soc., Dalton Trans.*, 1991, 269.
28. J. M. Malin, E. O. Schlemper, and R. K. Murmann, *Inorg. Chem.*, 1977, **16**, 615.
29. H. Nasri and W. R. Scheidt, *Acta Crystallogr., Sect. C*, 1990, **46**, 1096; J. W. Buchler and P. D. Smith, *Angew. Chem., Int. Ed. Engl.*, 1974, **13**, 341.
30. A. M. R. Galas, M. B. Hursthouse, E. J. Behrman, W. R. Midden, G. Green, and W. P. Griffith, *Transition Met. Chem.*, 1981, **6**, 194.
31. V. W.-W. Yam and C.-M. Che, *Coord. Chem. Rev.*, 1990, **97**, 93.
32. T. Behling, M. V. Capparelli, A. C. Skapski, and G. Wilkinson, *Polyhedron*, 1982, **1**, 840.
33. M. Schröder, A. J. Nielson, and W. P. Griffith, *J. Chem. Soc., Dalton Trans.*, 1979, 1607.
34. A. S. Borovik, J. Dubois, and K. N. Raymond, *Angew. Chem. Int. Ed. Engl.*, 1995, **34**, 1359.
35. J. M. Hawkins, A. Meyer, T. A. Lewis, U. Bunz, R. Nunlist, G. A. Ball, T. W. Ebbesen, and K. Tanigaki, *J. Am. Chem. Soc.*, 1992, **114**, 7955.
36. B. S. McGilligand, J. Arnold, G. Wilkinson, B. Hussain-Bates, and M. B. Hursthouse, *J. Chem. Soc., Dalton Trans.*, 1990, 2465.
37. R. W. Marshman, W. S. Bigham, S. R. Wilson, and P. A. Shapley, *Organometallics*, 1990, **9**, 1341.
38. W. A. Hermann, S. J. Eder, P. Kiprof, K. Rypdal, and P. Watzlowik, *Angew. Chem., Int. Ed. Engl.*, 1990, **29**, 1445.
39. K.-S. Jeong, Y. L. Cho, S.-Y. Chang, T.-Y. Park, and J. U. Song, *J. Org. Chem.*, 1999, **64**, 9459.
40. S. Bhattacharya, S. R. Boone, G. A. Fox, and C. G. Pierpoint, *J. Am. Chem. Soc.*, 1990, **112**, 1088.
41. D. Collison, C. D. Garner, F. E. Mabbs, J. A. Salthouse, and T. J. King, *J. Chem. Soc., Dalton Trans.*, 1981, 1812; P. A. Belmonte and Z.-Y. Own, *J. Am. Chem. Soc.*, 1984, **106**, 7493.
42. G. M. Coia, K. D. Demadis, and T. J. Meyer, *Inorg. Chem.*, 2000, **39**, 2212.
43. M. H. V. Huynh, E.-S. El-Samanody, K. D. Demadis, P. S. White, and T. J. Meyer, *Inorg. Chem.*, 2000, **39**, 3075.
44. M. H. V. Huynh, E. S. El-Samanody, K. D. Demadis, T. J. Meyer, and P. S. White, *J. Am. Chem. Soc.*, 1999, **121**, 1403.
45. M. H. V. Huynh, D. G. Lee, P. S. White, and T. J. Meyer, *J. Am. Chem. Soc.*, 1999, **121**, 10446.
46. K. D. Demadis, T. J. Meyer, and P. S. White, *Inorg. Chem.*, 1998, **37**, 3610.
47. T. J. Crevier, B. K. Bennett, J. D. Soper, J. A. Bowman, A. Dehestani, D. A. Hrovat, S. Lovell, W. Kaminsky, and J. M. Mayer, *J. Am. Chem. Soc.*, 2001, **123**, 1059.
48. J. T. Anhaus, T. P. Kee, M. H. Schofield, and R. R. Schrock, *J. Am. Chem. Soc.*, 1990, **112**, 1642.
49. A. A. Danopoulos, G. Wilkinson, B. Hussain-Bates, and M. B. Hursthouse, *J. Chem. Soc., Dalton Trans.*, 1991, 1855.
50. J.-S. Huang, C.-M. Che, and C.-K. Poon, *J. Chem. Soc., Chem. Commun.*, 1992, 161.

51. P. A. Shapley, N. J. Zhang, J. L. Allen, D. H. Pool, and H. C. Liang, *J. Am. Chem. Soc.*, 2000, **122**, 1079.
52. Q. F. Zhang, K. K. Lau, J. L. C. Chim, T. K. T. Wong, W. T. Wong, I. D. Williams, and W. H. Leung, *J. Chem. Soc., Dalton Trans.*, 2000, 3027.
53. C. Che, *Pure Appl. Chem.*, 1995, **67**, 225.
54. S. W. Carr, E. H. Fowles, X. L. R. Fontaine, and B. L. Shaw, *J. Chem. Soc., Dalton Trans.*, 1990, 573.
55. R. H. Magnuson, *Inorg. Chem.*, 1984, **23**, 387; E. E. Kim, K. Eriks, and R. Magnuson, *Inorg. Chem.*, 1984, **23**, 393.
56. R. C. Burns and T. A. O'Donnell, *Inorg. Chem.*, 1979, **18**, 3081.
57. M. H. V. Huynh, P. S. White, K. D. John, and T. J. Meyer, *Angew. Chem., Int. Ed. Engl.*, 2001, **40**, 4049.
58. K. F. Tebbe and H. G. van Schnering, *Z. Anorg. Allg. Chem.*, 1973, **396**, 66.
59. H. Masuda, T. Taga, K. Osaki, H. Sugimoto, and M. Mori, *Bull. Chem. Soc. Jpn.*, 1984, **57**, 2345.
60. C.-M. Che, W.-H. Leung, and W. C. Chung, *Inorg. Chem.*, 1990, **29**, 1841.
61. Z.-Y. Li, J.-S. Huang, M. C.-W. Chan, K.-K. Cheung, and C.-M. Che, *Inorg. Chem.*, 1997, **36**, 3064.
62. P. Barthazy, M. Worle, H. Ruegger, and A. Mezzetti, *Inorg. Chem.*, 2000, **39**, 4903.
63. Z.-W. Li, A. Yeh, and H. Taube, *Inorg. Chem.*, 1994, **33**, 2874.
64. S.-H. Kim, B. A. Moyer, A. Azam, G. M. Brown, A. L. Olins, and D. P. Allinson, *Inorg. Chem.*, 1989, **28**, 4648.
65. J. Malin and H. Taube, *Inorg. Chem.*, 1971, **10**, 2403.
66. M. H. V. Huynh, D. E. Morris, P. S. White, and T. J. Meyer, *Angew. Chem., Int. Ed. Engl.*, 2002, **41**, 2330.
67. F. A. Cotton, S. A. Duraj, C. C. Hinkley, M. Matusz, and W. J. Roth, *Inorg. Chem.*, 1984, **23**, 3080.
68. G. A. Heath and D. G. Humphrey, *J. Chem. Soc., Chem. Commun.*, 1990, 672.
69. R. A. Cipriano, W. Levason, R. A. S. Mould, D. Pletcher, and M. Webster, *J. Chem. Soc., Dalton Trans.*, 1990, 339.
70. A. P. B. Lever, in 'Molecular Electrochemistry of Inorganic, Bioinorganic and Organometallic Compounds', eds. A. J. L. Pombeiro and J. A. McCleverty, NATO ASI Series, 1993, Vol. 385, p. 41; B. E. Bursten and M. R. Green, *Prog. Inorg. Chem.*, 1988, **36**, 474.
71. M. N. Bell, A. J. Blake, R. M. Christie, R. O. Gould, A. J. Holder, T. I. Hyde, M. Schröder, and L. J. Yellowlees, *J. Chem. Soc., Dalton Trans.*, 1992, 2977.
72. Z.-W. Li and H. Taube, *J. Am. Chem. Soc.*, 1991, **113**, 8947.
73. W. D. Harman, W. P. Schaefer, and H. Taube, *J. Am. Chem. Soc.*, 1990, **112**, 2682.
74. P. Lay, A. M. Sargeson, B. W. Skelton, and A. H. White, *J. Am. Chem. Soc.*, 1984, **104**, 6161.
75. F. R. Keene, *Coord. Chem. Rev.*, 1999, **187**, 121.
76. J. Sen and H. Taube, *Acta Chem. Scand., Ser. A*, 1979, **33**, 125.
77. A. Bino, P. A. Lay, H. Taube, and J. F. Wishart, *Inorg. Chem.*, 1985, **24**, 3969.
78. F. A. Cotton and J. L. Thompson, *J. Am. Chem. Soc.*, 1980, **102**, 6437.
79. E. M. Kober, B. P. Sullivan, W. J. Dressick, J. V. Caspar, and T. J. Meyer, *J. Am. Chem. Soc.*, 1980, **102**, 7383.
80. V. Balzani, A. Juris, M. Venturi, S. Campagna, and S. Serroni, *Chem. Rev.*, 1996, **96**, 759.
81. H. Yersin and C. Kratzer, *Coord. Chem. Rev.*, 2002, **229**, 75.
82. J. C. Jernigan and R. W. Murray, *J. Am. Chem. Soc.*, 1990, **112**, 1034.
83. M. R. M. Bruce, E. Megehee, B. P. Sullivan, H. H. Thorp, T. R. O'Toole, A. Downhard, J. R. Pugh, and T. J. Meyer, *Inorg. Chem.*, 1992, **31**, 4864.
84. K. J. Takeuchi, G. J. Samuels, S. W. Gersten, J. A. Gilbert, and T. J. Meyer, *Inorg. Chem.*, 1983, **22**, 1407.
85. D. W. Pipes and T. J. Meyer, *J. Am. Chem. Soc.*, 1984, **106**, 7654.
86. J.-P. Collin, S. Guillerez, and J.-P. Sauvage, *J. Chem. Soc., Chem. Commun.*, 1990, 776.
87. M. Furue, M. Ishibashi, A. Satoh, T. Oguni, K. Maruyama, K. Sumi, and M. Kamachi, *Coord. Chem. Rev.*, 2000, **208**, 103.
88. M. Ward and F. Barigelletti, *Coord. Chem. Rev.*, 2001, **216**, 127.
89. A. Beyeler and P. Belser, *Coord. Chem. Rev.*, 2002, **230**, 28.
90. J. P. Sauvage, J. P. Collin, J. C. Chambron, S. Guillerez, C. Coudret, V. Balzani, F. Barigelletti, L. De Cola, and L. Flamigni, *Chem. Rev.*, 1994, **94**, 993.
91. A. Harriman, A. Khatyr, R. Ziessel, and A. C. Benniston, *Angew. Chem., Int. Ed. Engl.*, 2000, **39**, 4287.
92. J. M. Haider, M. Chavarot, S. Weidner, I. Sadler, R. M. Williams, L. De Cola, and Z. Pikramenou, *Inorg. Chem.*, 2001, **40**, 3912.
93. P. Belser, S. Bernard, C. Blum, A. Beyeler, L. De Cola, and V. Balzani, *Coord. Chem. Rev.*, 1999, **190**, 155.
94. V. Balzani, S. Campagna, G. Denti, A. Juris, S. Serroni, and M. Venturi, *Acc. Chem. Res.*, 1998, **31**, 26.
95. S. Serroni, S. Campagna, F. Puntoriero, C. Di Pietro, N. D. McClenaghan, and F. Loiseau, *Chem. Soc. Rev.*, 2001, **30**, 367.
96. S. Campagna, C. Di Pietro, F. Loiseau, B. Maubert, N. D. McClenaghan, R. Passacqua, F. Puntoriero, V. Ricevuto, and S. Serroni, *Coord. Chem. Rev.*, 2002, **229**, 67.
97. R. E. Homlin, P. J. Dandliker, and J. K. Barton, *Angew. Chem. Int. Ed. Engl.*, 1997, **36**, 2714.
98. R. E. Homlin, R. T. Tong, and J. K. Barton, *J. Am. Chem. Soc.*, 1998, **120**, 9724.

99. J. E. Fergusson, J. L. Love, and W. T. Robinson, *Inorg. Chem.*, 1972, **11**, 1662.
100. D. Cru-Garritz, H. Torrens, J. Leal, and R. L. Richards, *Transition Met. Chem.*, 1983, **8**, 127.
101. P. H. Lay, R. H. Magnuson, H. Taube, J. Ferguson, and R. E. Krausz, *J. Am. Chem. Soc.*, 1985, **107**, 2551.
102. J. A. McCleverty, *Chem. Rev.*, 1979, **79**, 53.
103. J. P. Collman, C. E. Barnes, and L. K. Woo, *Proc. Natl. Acad. Sci. U.S.A.*, 1983, **80**, 7684.
104. J. P. Collman, P. S. Wagenknecht, R. T. Hambre, and N. S. Lewis, *J. Am. Chem. Soc.*, 1990, **112**, 1294.
105. J. P. Collman, P. S. Wagenknecht, J. E. Hutchison, N. S. Lewis, M. A. Lopez, R. Guilard, M. L'Her, A. A. Bothner-By, and P. K. Mishra, *J. Am. Chem. Soc.*, 1992, **114**, 5654.
106. J. P. Collman and H. J. Arnold, *Acc. Chem. Res.*, 1993, **26**, 586.
107. M. Hanack and P. Vermehren, *Inorg. Chem.*, 1990, **29**, 134; M. Hanack, A. Gül, and L. R. Subramanian, *Inorg. Chem.*, 1992, **31**, 1542.
108. P. D. Beer, F. Szemes, V. Balzani, C. M. Salsa, M. G. B. Drew, and M. Maestri, *J. Am. Chem. Soc.*, 1997, **119**, 11864.
109. G. J. Kubas, *Acc. Chem. Res.*, 1988, **21**, 120; R. H. Crabtree, *Acc. Chem. Res.*, 1990, **23**, 95.
110. K. A. Earl, G. Jia, P. A. Maltby, and R. H. Morris, *J. Am. Chem. Soc.*, 1991, **113**, 3027.
111. J. A. K. Howard, O. Johnson, T. F. Koetzle, and J. L. Spencer, *Inorg. Chem.*, 1987, **26**, 2930.
112. B. E. Cavit, K. R. Grundy, and W. R. Roper, *J. Chem. Soc., Chem. Commun.*, 1972, 60.
113. F. A. Cotton, A. K. Chakravarty, D. A. Tocher, and T. A. Stephenson, *Inorg. Chim. Acta*, 1984, **87**, 115.
114. M. A. S. Aquino, *Coord. Chem. Rev.*, 1998, **170**, 141.
115. M. D. Ward and J. A. McCleverty, *J. Chem. Soc., Dalton Trans.*, 2002, 275.
116. J. Götzig, A. L. Rheingold, and H. Werner, *Angew. Chem., Int. Ed. Engl.*, 1984, **23**, 814.
117. M. F. C. Da Silva, A. J. L. Pombeiro, S. Geremia, E. Zangrando, M. Calligaris, A. V. Zinchenko, and V. Y. Kukushkin, *J. Chem. Soc., Dalton Trans.*, 2000, 1363.
118. L. J. Maheu and L. H. Pignolet, *Inorg. Chem.*, 1979, **18**, 3626; *J. Am. Chem. Soc.*, 1980, **102**, 3626.
119. K. J. Taylor and L. J. Yellowlees, in 'Molecular Electrochemistry of Inorganic, Bioinorganic and Organometallic Compounds', eds. A. J. L. Pombeiro and J. A. McCleverty, NATO ASI Series, 1993, Vol. 385, p. 69.
120. F. A. Cotton and K. Vidyasagar, *Inorg. Chem.*, 1990, **29**, 3197.
121. B. L. Haymore and J. A. Ibers, *Inorg. Chem.*, 1975, **14**, 2610.
122. A. F. Hill, W. R. Roper, J. M. Waters, and A. H. Wright, *J. Am. Chem. Soc.*, 1983, **105**, 5939.
123. H. Werner, A. Michenfelder, and M. Schulz, *Angew. Chem., Int. Ed. Engl.*, 1991, **30**, 596.
124. G. R. Clark, J. M. Waters, and K. R. Whittle, *J. Chem. Soc., Dalton Trans.*, 1975, 463.

Osmium: Organometallic Chemistry

Patricia A. Shapley
University of Illinois, Urbana, IL, USA

1 Introduction 1
2 Alkyl Complexes and Related Species of Os(II), Os(III), Os(IV) 1
3 Pi Complexes 5
4 Osmium Carbene and Carbyne Complexes 8
5 High Oxidation State Complexes 11
6 Carbonyl Complexes 13
7 Catalysis with Osmium Complexes 17
8 Related Articles 17
9 References 17

Abbreviations

$\mathrm{Otf}^- = \mathrm{CF_3S(O)_2O}$; $\mathrm{Cp} = \eta^5\text{-}\mathrm{C_5H_5}$; $\mathrm{Cp}^* = \eta^5\text{-}\mathrm{C_5Me_5}$; Tp = hydrido tris(pyrazolyl)borate; Tp^* = hydrido tris(3,5-dimethylpyrazolyl)borate; $\mathrm{pz_3CH}$ = tris-pyrazoylmethane; phpy = 2-phenylpyridine; Bcat = catecholborane; por = porphyrin; (*S*,*S*)-Chiraphos = (*S*,*S*)-$\mathrm{Ph_2PCHMeCHMePPh_2}$.

1 INTRODUCTION

Organometallic complexes consist of a metal bonded to one or more carbon atoms of an organic molecule. The bond can be a sigma bond, as with metal–alkyl complexes (*see Alkyl Complexes*), or a π bond, as with metal–alkene (*see Alkene Complexes*) complexes. This section covers representative organometallic complexes of osmium along with a discussion of carbonyl complexes. It does not include cyanide complexes (*see* ***Cyanide Complexes of the Transition Metals***) or complexes of organic ligands, such as amines or alkoxides, bonded to osmium through an element other than carbon. General reviews of the organometallic chemistry of osmium can be found in annual surveys of the *Journal of Organometallic Chemistry* or *Coordination Chemistry Reviews*. Textbooks on aspects of organometallic chemistry such as 'The Organometallic Chemistry of the Transition Elements' or 'Metal–Ligand Multiple Bonds' typically include the organometallic chemistry of osmium.[1,2]

Osmium and ruthenium frequently form analogous complexes (*see* ***Ruthenium: Organometallic Chemistry***). The chemistry of iron is quite different (*see* ***Iron: Organometallic Chemistry***). Osmium forms stronger metal–metal bonds and stronger metal–carbon bonds than either iron or ruthenium. Osmium, like other third row transition elements, is more stable in its higher oxidation states. It is much less 'oxophilic' than the early transition metals so oxygen and nitrogen ligands bind reversibly to this metal. Unlike metals in the nickel and copper triads, osmium forms many complexes with terminal oxo, imido, and nitrido ligands.

Because it forms stronger bonds with ligands, osmium complexes are generally less active catalysts than analogous ruthenium complexes. The exception is in oxidation chemistry where certain osmium complexes are better and more selective catalysts. Because of this, osmium tetroxide and other osmium oxo complexes are widely used in the synthesis of complex organic molecules.

A variety of techniques are used to characterize organometallic osmium complexes. Particularly important are X-ray crystallography, for a three-dimensional picture of the placement of atoms within a molecule, NMR spectroscopy (^{1}H, ^{13}C, ^{31}P, and ^{183}Os), for information on the structure and symmetry of ligands in diamagnetic complexes, and IR spectroscopy, for the identification of multiple bonds between osmium and a ligand or within a ligand. Electrochemical studies and photoelectron spectroscopy provide information on the oxidation state of osmium and the relative electron density of the complex.

2 ALKYL COMPLEXES AND RELATED SPECIES OF Os(II), Os(III), Os(IV)

Osmium forms a wide variety of alkyl and aryl complexes including homoleptic alkyl and aryl complexes and many complexes with ancillary carbonyl (*see* ***Carbonyl Complexes of the Transition Metals***), cyclopentadienyl (*see Cyclopentadienyl*), arene (*see Arene Complexes*), and alkene ligands (*see Alkene Complexes*). It forms stronger bonds to carbon and other ligands than do the lighter elements of the triad. Because of this, most reactions of alkyl and aryl osmium complexes are slower than the reactions of the corresponding ruthenium complexes. However, because osmium is more stable in higher oxidation states, the oxidative addition (*see Oxidative Addition*) of C–H bonds is favored for osmium complexes. The rate of oxidative addition reactions decreases in the order Os $>$ Ru $\gg$ Fe.

2.1 Simple Alkyl and Aryl Complexes

Alkyl and aryl carbonyl complexes of osmium result from the reactions of anionic carbonyl complexes with organic electrophiles. The reactions between $\mathrm{Na_2Os(CO)_4}$ or $\mathrm{NaOsH(CO)_4}$ and ROTf, or RI (R = Me, Et) produce

$OsR_2(CO)_4$ or $OsR(H)(CO)_4$. The alkyl hydrido complexes are prone to reductive elimination (*see Reductive Elimination*). A bimolecular reductive elimination of CH_4 from $OsMe(H)(CO)_4$ forms $Os_2(CO)_8Me(H)$. The reaction between $Os_2(CO)_8Me(H)$ and $OsMe(H)(CO)_4$ gives CH_4 and a linear trimetallic $\{Os(CO)_4Me\}\{Os(CO)_4\}\{Os(CO)_4Me\}$.

Other alkyl and aryl complexes are prepared by reactions between osmium halides and main group alkyl complexes. The reaction between $OsHCl(CO)(PPh_3)_3$ and $CH_2{=}C(CH_3)CH_2MgCl$ gives a sigma bonded allyl complex. Loss of PPh_3 causes isomerization to a π-allyl $OsH(\eta^3\text{-}CH_2CMeCH_2)(CO)(PPh_3)_2$.

The first homoleptic tetraalkyl and tetraaryl complexes of the platinum group metals, Os(*cyclo*-$C_6H_{11})_4$ and Os(*o*-$C_6H_4Me)_4$, were reported in 1985 (Scheme 1). These tetrahedral complexes were prepared by treatment of the appropriate Grignard reagents with OsO_4 or with $Os_2(\mu\text{-}O_2CMe)_4Cl_2$. Lewis bases CO, PMe_3, and Me_3CNC react with Os(*o*-$C_6H_4Me)_4$ to form Os(II) aryl complexes via reductive coupling (*see Reductive Coupling*) of the aryl ligands. Silver(I) salts oxidize Os(*o*-$C_6H_4Me)_4$ to [Os(*o*-$C_6H_4Me)_4]^+$ in dichloromethane.**3**

2.2 Alkenyl and Alkynyl Complexes

The insertion of alkynes into Os–H bonds produces vinyl complexes. For example, $OsH(O_2CCF_3)(CO)(PPh_3)_2$ reacts with $PhC{\equiv}CR$ (R = Me, Ph) to give $Os\{C(Ph){=}CHR\}(O_2CCF_3)(CO)(PPh_3)_2$. These complexes are catalysts for the oligomerization of phenyl acetylene. Terminal alkynes insert into the Os–H bond of $OsHCl(CO)(P^iPr_3)_2$ to give $Os(CH{=}CHR)Cl(CO)(P^iPr_3)_2$. This complex is coordinatively unsaturated (*see Coordinative Saturation & Unsaturation*) and can react with CO to form the six-coordinate complex $Os(CH{=}CHR)Cl(CO)_2(P^iPr_3)_2$ (Scheme 2).

Alkynyl and alkenyl complexes can also be prepared by treating osmium halides with main group metal alkynyl or alkenyl complexes. However, the main group reagent can also act as a base. The reaction between $Os(PNP)Cl_2(PPh_3)$, where PNP is 2,6-$(CH_2PPh_2)C_5H_3N$, and lithium phenyl acetylide gives an alkenyl complex through an indirect route. The acetylide deprotonates an acidic C–H bond of the ligand. This forms an alkyne and a carbon nucleophile that combine. Successive addition of base, H_2 and acid results in the formation of a dihydrogen complex (*see **Hydrogen Bonding & Dihydrogen Bonding***) (Scheme 3).**4**

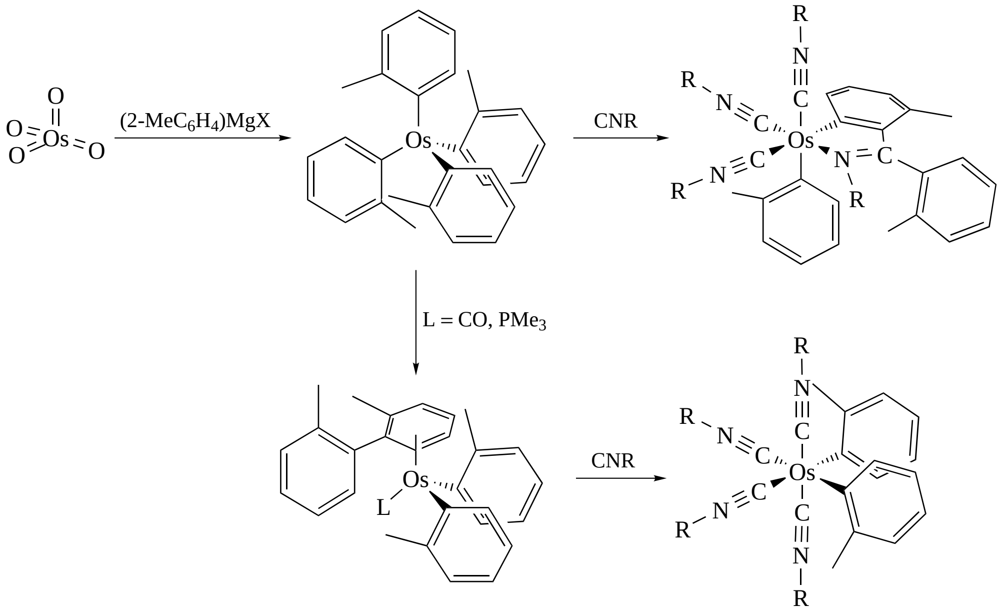

Scheme 1

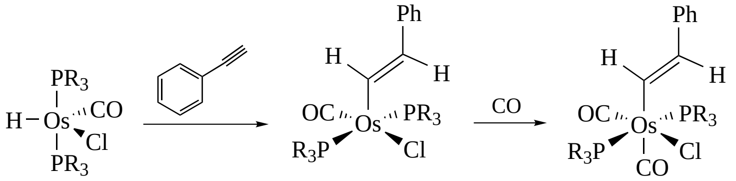

Scheme 2

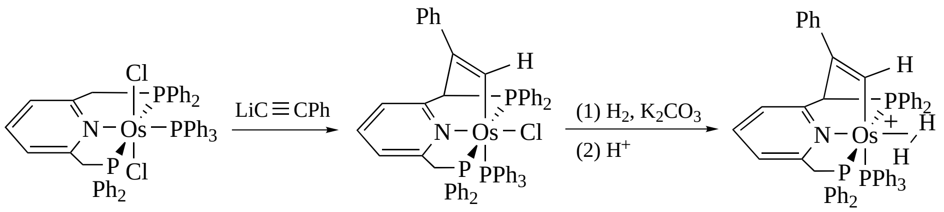

Scheme 3

2.3 Reactions of Alkyl Complexes

In general, organometallic complexes with both hydrido and alkyl ligands are unstable due to facile reductive elimination. Because of the greater strength of the Os–C and Os–H and the greater stability of this metal in higher oxidations states, osmium alkyl hydrides eliminate alkane more slowly than ruthenium or iron complexes. The reaction of $[Os(CO)_3(PMe_3)_2(CH_3)][BPh_4]$ with borohydrides in acetonitrile gives $Os(CO)_2(PMe_3)_2(CH_3)H$ while the analogous iron complex reacts with borohydride to form $Fe(CO)_2(PMe_3)_2(NCMe)$ after reductive elimination of acetone.[5]

The rate of migratory insertion (*see Migratory Insertion*) reactions is usually lower for osmium complexes than for analogous ruthenium or iron complexes. In comparing CO insertion (*see CO Insertion*) into M–C bonds, the rate of insertion depends on metal according to $Ru > Fe \gg Os$ or $Fe > Ru \gg Os$, depending on the ligand set.[6]

As a result of a stronger metal-iodide bond, the osmium complex of formula *trans*-$[MI(Me)(CO)_2(PMe_3)_2]$ does not spontaneously ionize in polar solvents. The ruthenium and iron complexes dissociate I^- in these solvents. Silver(I) salts are required to abstract the iodide from the osmium complex. When tris-pyrazoylmethane is added along with the silver salt, the methyl ligand migrates to a coordinated carbonyl ligand and $[Os(COMe)(pz_3CH)(CO)(PMe_3)_2]^+$ forms.

Typically, electrophiles react with osmium alkyl and aryl complexes at the metal−carbon bond. In a few cases, electrophiles add to the aromatic ligand instead. The aryl group in the osmium complexes $Os(Ar)Cl(CO)(PPh_3)_2$ undergoes electrophilic substitution reactions. The chelated 2-pyridylphenyl complex $Os(C_6H_4\text{-}2\text{-}C_5H_4N)Cl(CO)(PPh_3)_2$ is also activated toward electrophilic attack (*see Electrophilic Reaction*) at the phenyl ligand. Coordination of the pyridyl nitrogen stabilizes the complex and prevents attack at the Os–C bond even with reactive electrophiles (Scheme 4).[7]

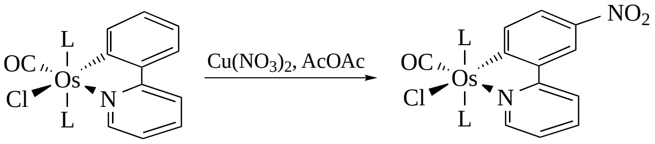

Scheme 4

2.4 Cyclometallation

The oxidative addition of C–H bonds of ligands is very common and this reaction forms metal−alkyl or metal−aryl complexes. In osmium triarylphosphine complexes, orthometallation gives four-membered metallocycles. When the ortho positions are blocked with alkyl groups, oxidative addition can form five-membered osmacycles. For example, the reaction of $PPh_2(2,6\text{-}Me_2C_6H_3)$ with either $[OsCl_6]^{2-}$ or $OsCl_2(PPh_3)_3$ gives a cyclometallated products and couples two of the phosphine ligands. The reaction could occur either through a simple coupling reaction or through a carbene intermediate. A similar double C–H activation takes place between $[OsCl_6]^{2-}$ and $(Bu^t_2P)CH_2CH_2CH_2\ CH_2CH_2(PBu^t_2)$.[8] Metallation of the phenyl ring occurs when $1,3\text{-}(Pr^i_2PCH_2)_2C_6H_4$ coordinates to $OsCl_2(PPh_3)_3$ in the presence of a base.[9] The reaction between $1,3\text{-}(CH_2P^tBu_2)_2C_6H_4$ and $OsCl_2{}^{2-}$ gives the metallated product in methanol or 2-propanol solvent/reducing agent. The products react with borohydride to give hydrido and dihydrogen complexes (*see* ***Hydrogen Bonding & Dihydrogen Bonding***) (Scheme 5).

When *trans*-$OsCl_2(PMe_3)_4$ is reduced with Na/Hg it oxidatively adds a C–H bond of PMe_3 and forms $OsH(\eta^2\text{-}CH_2PMe_2)(PMe_3)_3$. Hydrolysis of $OsH(\eta^2\text{-}CH_2PMe_2)(PMe_3)_3$ yields $OsH(OH)(PMe_3)_4$. A related complex $OsH(R)(PMe_3)_4$ (where $R = Me, CH_2CMe_3, CH_2SiMe_3$) activates C–H bonds in benzene after dissociation of a phosphine ligand. There is a rapid γ-hydrogen activation with loss of H_2 in the neopentyl and (trimethylsilyl)methyl derivatives. Kinetic and isotopic labeling studies support an Os(IV) intermediate in the activation of benzene C–H bonds.

The C–H activation of nitrogen ligands such as pyridines, hydroxamates, and azido complexes results in the formation of osmium−carbon bonds. Cyclometallation of 2-phenylpyridine by $[Os(\eta^6\text{-benzene})Cl_2]_2$ gives $Os(\eta^6\text{-benzene})Cl(phpy)$ and HCl. Substitution by phenanthroline produces $[Os(phen)_2(phpy)]^+$. Both complexes show reversible electrochemical behavior (Os^{II}/Os^{III}) and can mediate electron transfer with glucose oxidase.[10] Cyclometallation of a hydroxamic acid to $Os(bpy)_2Cl_2$ gives an osmium(III) organometallic complex with N–C coordination to the hydroxamate ligand, $[Os(bpy)_2\{N(Ar)C(O)C_6H_3R\}]^+$.

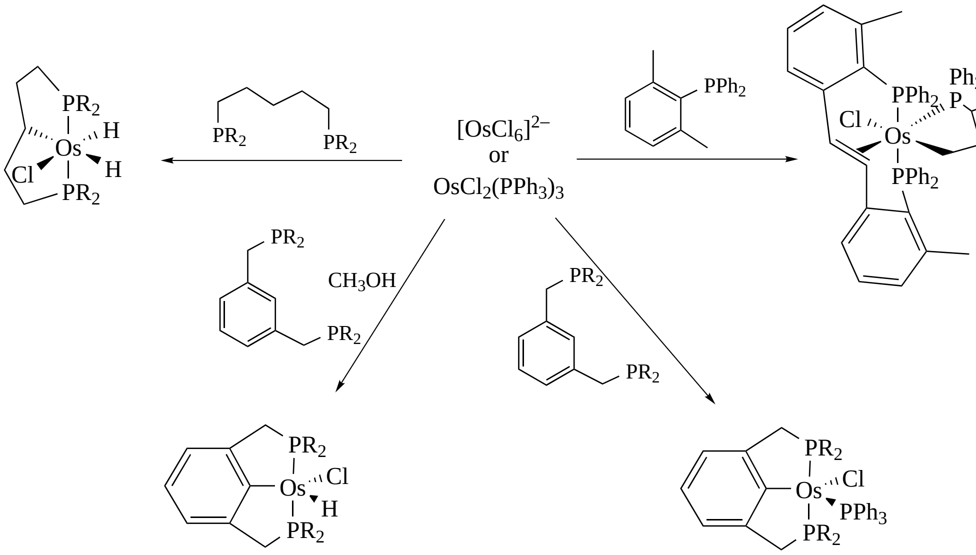

Scheme 5

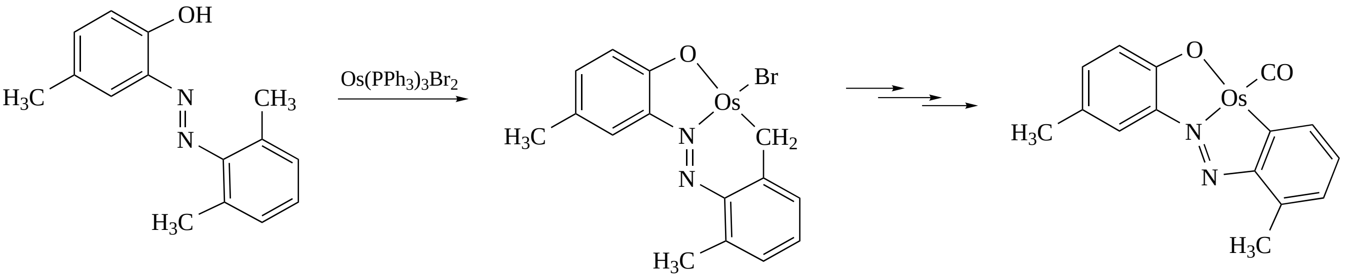

Scheme 6

Simple C–H activation of several arylazaphenols produces osmium complexes with tridentate O–N–C coordination to the arylazaphenolate ligand, $[Os^{II}(PPh_3)_2(CO)(L)]$. One electron oxidation of these complexes produces stable osmium(III) complexes that can function as mild, 1 electron oxidants. An internal C–C activation takes place with a phenylazido ligand, 2-(2′,6′-dimethylphenylazo)-4-methylphenol, and $Os(PPh_3)_3Br_2$. The carbonyl ligand in the product is derived from one methyl group on the ligand (Scheme 6).**[11]**

The hexahydride complex $OsH_6(PPr^i_3)_2$ reacts with ketones to give products resulting from C–H activation in the position adjacent to the carbonyl group of the ketone. The reaction with cyclohexylmethyl ketone to gives $OsH_3(PPr^i_3)_2(C_6H_8C(O)Me)$ and 3 equivalents of H_2. This probably results from metallation of the cyclohexyl ring at the 2 position followed by beta-hydride elimination (*see β-Hydride Elimination*), and metallation of the alkene. This means that three hydrogen atoms are removed from the ketone.**[12]** This same hydrido osmium complex reacts with aromatic ketones to give orthometallated (*see Orthometalation*) products $OsH_3(PPr^i_3)_2(C_6H_4C(O)R)$. When the aromatic group is fluorinated in both ortho positions, there is C–F activation to give $OsH_3(PPr^i_3)_2(C_6H_xF_yC(O)R)$, $2H_2$, and HF. When only one ortho position is fluorinated, C–H bond activation is preferred over C–F bond activation.

2.5 Boryl and Stannyl Complexes

Boryl and stannyl complexes are similar in some ways to alkyl complexes. Both are important because of their relationship to intermediates in the catalytic borylation and stannylation of alkenes. The reaction of catecholborane complex of osmium, $Os(Bcat)Cl(CO)(PPh_3)_3$ with tolyllithium gives a molecule with both Os–B and Os–C sigma bonds. This reductively eliminates when the borane and aryl ligand are cis to one another to give (tolyl)Bcat and an orthometallated product. A B–Cl bond in the simple borane complex $Os(BCl_2)Cl(CO)(PPh_3)_2$ reacts with 2-hydroxypyridine to give a bidentate pyridylborane complex $Os\{–B(Cl)OC_5H_4N–\}Cl(CO)(PPh_3)_2$. With 2-aminopyridine in ethanol, $Os(BCl_2)Cl(CO)(PPh_3)_2$ reacts to give either $Os\{–B(Cl)NHC_5H_4N–\}Cl(CO)(PPh_3)_2$, with the amino group

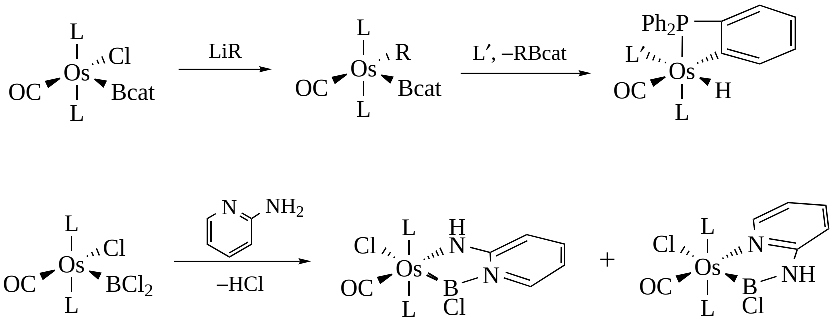

Scheme 7

bonded to boron, or Os{–B(OEt)NC$_5$H$_4$–hNH–}Cl(CO)(PPh$_3$)$_2$, with the pyridine nitrogen bonded to boron (Scheme 7).**[13]**

The coordinatively unsaturated stannyl complexes Os(SnR$_3$)Cl(CO)(PPh$_3$)$_2$ reacts with Na[Me$_2$NCS$_2$] to give the dithiocarbamate complex Os(SnR$_3$)(S$_2$CNMe$_2$)(CO)(PPh$_3$)$_2$. This reacts with I$_2$ at the Sn–C bonds.**[14]**

3 PI COMPLEXES

3.1 Alkene and Alkyne Complexes

Alkenes and alkynes add to coordinatively unsaturated (*see Coordinative Saturation & Unsaturation*) osmium complexes to form η^2-alkene and alkyne complexes. Ethene accelerates the reductive elimination of methane from OsH(CO)$_4$Me and forms Os(η^2-CH$_2$=CH$_2$)(CO)$_4$. Photochemical displacement of a phosphine ligand in Os(CO)$_2$(PPh$_3$)$_3$ gives an unsaturated complex that is trapped by ethene to give Os(η^2-CH$_2$=CH$_2$)(CO)$_2$(PPh$_3$)$_2$. An unsaturated species results from abstraction of chloride by Ag(I) in OsCl(NO)(CO)(PPh$_3$)$_2$. Either ethene or a number of different alkynes can add to form [Os(η^2-CH$_2$=CH$_2$)(NO)(CO)(PPh$_3$)$_2$]$^+$ or [Os(η^2-RC≡CR′)(NO)(CO)(PPh$_3$)$_2$]$^+$. Diphenyl acetylene displaces two ligands in Os(CS)(CO)(PPh$_3$)$_3$ to give Os(CS)(PhC≡CPh)(PPh$_3$)$_2$.

Photolysis of Os$_3$(CO)$_{12}$ in the presence of a diene (1,3-butadiene, 1,3-pentadiene, 1,3-cyclooctadiene, or 1,3-cyclohexadiene) gives the mononuclear diene complexes Os(CO)$_3$(η^4-diene). The 1,3-cyclooctadiene complex OsCl$_2$(COD)(PEtPh$_2$)$_2$ was prepared by the reduction of [OsCl$_6$]$^{2-}$ in the presence of the diene followed by treatment with PEtPh$_2$.

Alkene and η^2-ketone complexes can be prepared by reduction of [Os(NH$_3$)$_5$(OSO$_2$CF$_3$)]$^{2+}$ in the presence of substrate. The acetone complex [Os(NH$_3$)$_5$(η^2-O=CMe$_2$)]$^{2+}$ undergoes substitution reactions only very slowly at room temperature. the acetone is not labile. Upon thermolysis, it decomposes to a carbonyl complex [Os(NH$_3$)$_5$(CO)]$^{2+}$. The propenoic acid ligand in [Os(NH$_3$)$_4$(CH$_2$=CHCO$_2$H)]$^{2+}$ coordinates to the metal through the double bond and through one oxygen atom of the acid moiety. The pK_a of the coordinated propenoic acid is 3.20, demonstrating that the coordinated alkene substituent is electron withdrawing. The complex can be reversibly oxidized to the Os(III) state. Selenophene, *cyclo*-C$_4$H$_4$Se, coordinates to osmium(II) through one C=C in the complex [Os(NH$_3$)$_5$(η^2-selenophene)][OSO$_2$CF$_3$]$_2$. Electrophilic addition to the unsaturated ligand is dramatically affected by coordination to osmium (Scheme 8).**[15]**

Substitution reactions at Os(CO)$_4$(η^2-alkene) or Os(CO)$_4$(η^2-alkyne) take place through initial dissociation of a ligand. The complexes Os(CO)$_4$(η^2-alkyne), where the alkyne is CF$_3$C≡CCF$_3$ or HC≡CH, compounds are more reactive than Os(CO)$_5$ in substitution and insertion reactions. The acetylene complex is 10 times more reactive than the hexafluoro-2-butyne complex. This is probably due to the ability of the alkyne to act as a four electron donor and stabilize electron-deficient intermediates. The reaction of Os(CO)$_4$(η^2-HC≡CH) with excess PMe$_3$ gives a CO insertion product Os(CO)$_2$(PMe$_3$)$_2${C(H)=C(H)-C(O)} while reaction with the bulkier phosphine PBu$^t_3$ gives a double insertion product, Os(CO)$_3$(PBu$^t_3$){C(O)–C(H)=C(H)–C(O)} (Scheme 9).**[16]**

3.2 Arene Complexes

Arene complexes of osmium(0) or osmium(II) can be prepared by co-condensation of osmium atoms with arenes at low temperature or by the reduction of osmium halides in the presence of the arene. An osmium complex with a tetrahapto- and hexahapto-benzene, Os(η^6-C$_6$H$_6$)(η^4-C$_6$H$_6$), results when osmium atoms are condensed with benzene at low temperature. NMR studies show that this molecule is fluxional (*see Fluxional Molecule* and ***Structure & Property Maps for Inorganic Solids***) and the two arene rings interconvert. Acids protonate one arene ring in Os(η^6-C$_6$H$_6$)(η^4-C$_6$H$_6$) and form the cyclohexadienyl cation [Os(η^6-C$_6$H$_6$)(η^5-C$_6$H$_7$)]$^+$, while addition of trimethylphosphine gives an arene C–H addition product Os(η^6-C$_6$H$_6$)Ph(H)(PMe$_3$).

The benzene complex [OsCl$_2$(η^6-C$_6$H$_6$)]$_x$ is polymeric. Similar complexes of *p*-cymene (*p*-MeC$_6$H$_4$Pr^i)

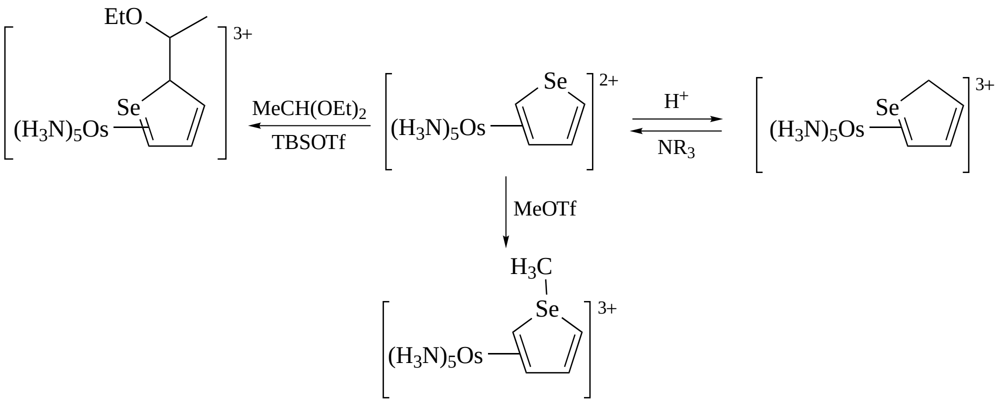
EtO
3+
Se
(H3N)5Os
MeCH(OEt)2
TBSOTf
Se
2+
(H3N)5Os
H+
NR3
Se
3+
(H3N)5Os
MeOTf
H3C
Se
3+
(H3N)5Os

Scheme 8

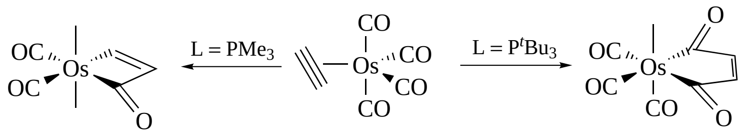
OC
OC
Os
O
L = PMe3
CO
Os
CO
CO
CO
L = PtBu3
OC
OC
Os
CO
O
O

Scheme 9

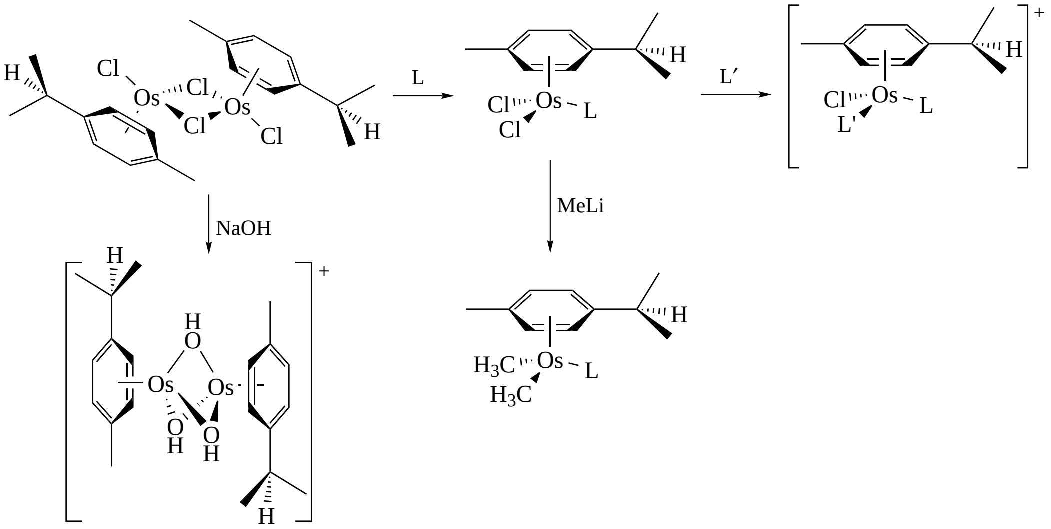
H
Cl
Os
Cl
Os
Cl
Cl
H
L
H
Cl
Os
L
Cl
L′
H
Cl
Os
L
L′
+
NaOH
MeLi
H
H
O
Os
Os
O
H
O
H
H
+
H
H3C
Os
L
H3C

Scheme 10

and mesitylene (1,3,5-$Me_3C_6H_3$) are dimeric complexes $[OsCl_2(\eta^6\text{-arene})]_2$. The osmium arene unit is relatively inert in the *p*-cymene and mesitylene complexes. The reaction between $[OsCl_2(\eta^6\text{-}p\text{-}MeC_6H_4Pr^i)]_2$ and NaOH gives the bridging hydroxide complex $[\{Os(\eta^6\text{-}p\text{-}MeC_6H_4Pr^i)\}_2(\mu\text{-}OH)_3]^+$. This complex is catalytically active for the oxidation of acetaldehyde and propionaldehyde to the carboxylic acids in water. The reactions of $[OsCl_2(\eta^6\text{-arene})]_2$ with CO, nitriles, isonitriles, trialkylphosphines, triarylphosphines, or phosphites yields complexes with the formula $OsCl_2(\eta^6\text{-arene})L$. The *p*-cymene complexes add a second donor ($L'{=}CO$, $CH_2{=}CH_2$, $CH_2{=}CHCH_3$) to form cationic complexes $[OsCl_2(\eta^6\text{-}p\text{-}MeC_6H_4Pr^i)LL']^+$ (Scheme 10). One or both of the chloride ligands in $OsCl_2(\eta^6\text{-arene})L$ can exchange for alkyl (or aryl) groups by reaction with alkyllithium or alkylmagnesium halide compounds.

The synthesis of chiral-at-metal complexes may lead to the development of more selective asymmetric catalysts (*see*

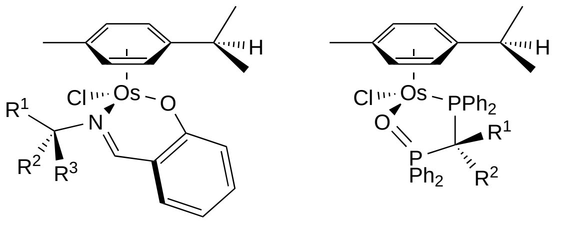

Figure 1 Chiral, half-sandwich complexes of osmium(II)

Asymmetric Synthesis by Homogeneous Catalysis). Two chiral-at-metal osmium complexes, (η^6-cymene)OsCl(κ^2-(S))–($R^1R^2R^3$)N=CH(o-C_6H_4(OH)-N,O), were prepared from [$OsCl_2$(η^6-p-cymene)]$_2$ and Schiff bases as mixtures of diastereomers (Figure 1). The complexes are configurationally stable in the solid state but isomerize in solution.**[17]** The reaction of [$OsCl_2$(η^6-p-cymene)]$_2$ with a diphenylphosphine monooxide and $AgSbF_6$ ligand gave [(η^6-p-cymene)OsCl(κ^2-$Ph_2PCH(Me)P(O)Ph_2$-P,O)][SbF_6].**[18]**

The triphenylmethyl carbocation, [CPh_3][PF_6], abstracts a hydride from a methyl group in $OsMe_2(\eta^6\text{-}C_6H_6)(PR_3)$ and $Os(H)Me(\eta^6\text{-}C_6H_6)(P^iPr_3)$. With $OsMe_2(\eta^6\text{-}C_6H_6)(PR_3)$, the intermediate methyl methylene complex forms a stable ethene complex $Os(\eta^2\text{-}CH_2{=}CH_2)(\eta^6\text{-}C_6H_6)(PR_3)$ after loss of a proton. A deuterium labeling study indicates that a hydrido methylene complex is intermediate in hydride abstraction from $Os(H)Me(\eta^6\text{-}C_6H_6)(P^iPr_3)$ but the final product $OsMe(\eta^6\text{-}C_6H_6)(\kappa^2\text{-}CH_2CHMeP^iPr_2)$ is derived from C–H activation of the phosphine ligand. Cationic arene complexes such as $[OsI(\eta^6\text{-}C_6H_6)(PMe_3)_2][PF_6]$ react with alkyllithium reagents or sodium borohydride at the arene ring to produce cyclohexadienyl complexes $OsI(\eta^5\text{-}C_6H_6R)(PMe_3)_2$ or $OsI(\eta^5\text{-}C_6H_7)(PMe_3)_2$.

Binuclear (*see* ***Dinuclear Organometallic Cluster Complexes***) and polynuclear (*see* ***Polynuclear Organometallic Cluster Complexes***) arene complexes can be prepared from $[OsCl_2(\eta^6\text{-arene})]_2$. The reaction of [$OsCl_2$($\eta^6$-$p$-cymene)]$_2$ with $[PPh_4]_2[WS_4]$ forms a trimetallic [OsCl(η^6-p-cymene)]$_2WS_4$ with two pseudooctahedral osmium atoms bridged by a tetrahedral tetrathiotungstate.**[19]** An (arene)metal sulfido cluster [(η^6-p-cymene)$_3Os_3S_2$]$^{2+}$ results from the reaction of [$OsCl_2$(η^6-p-cymene)]$_2$ with $S(SiMe_3)_2$, methanolic NaSH, or aqueous Na_2S. The 1:1 reaction between the arene complexes $[OsCl_2(\eta^6\text{-arene})]_2$ and $[NEt_2H_2][Pt(S_2CNEt_2)(Ph_2PS)_2]$ produced the heterobimetallic complexes $(\eta^6\text{-arene})ClOs(SPPh_2)_2Pt(S_2CNEt_2)$. With additional quantities of the platinum complex, tri- and pentametallic complexes are produced.

3.3 Cyclopentadienyl Complexes

The cyclopentadienyl ligand is a good π-donor and π-acceptor ligand. Stable cyclopentadienylosmium complexes are known for the metal in oxidation states 0 through VI.

Osmacene, $Os(\eta^5\text{-}C_5H_5)_2$, is prepared in low yield from the reaction of $OsCl_4$ with sodium cyclopentadienide in refluxing THF and decamethylosmacene is prepared similarly from lithium pentamethylcyclopentadienide and $[OsCl_6]^{2+}$. The cyclopentadienyl rings in osmacene are eclipsed. The cyclopentadienyl rings can be monoacylated under Friedel–Crafts conditions and can be lithiated. Oxidation of osmacene gives a dimer with a metal–metal bond. The reaction with ferric ammonium sulfate produces $[Cp_2Os(OH)]^+$ while oxidation with I_2 in sulfuric acid gives $[Cp_2OsI]^+$.

Due to the greater metal–metal bond strength of the third row metal, the carbonyl complex $[CpOs(CO)_2]_2$ has an osmium–osmium bond that is unbridged by carbonyl ligands. In the iron analog, the metal–metal interaction is very weak and the dimer owes its integrity mainly to the bridging carbonyl groups. The reaction between $OsCl_2(CO)_4$ and sodium cyclopentadienide produces $[CpOs(CO)_2]_2$. Oxidation of $[CpOs(CO)_2]_2$ with Br_2 gives $CpOs(CO)_2Br$ (Scheme 11). The reaction of OsO_4 with cyclopentadiene in HBr, followed by the addition of PPh_3 gives $CpOs(PPh_3)_2Br$. The pentamethylcyclopentadienyl dimer $[Cp^*OsBr_2]_2$ is prepared in a series of steps from OsO_4.**[20]**

The halide complexes CpOsL(CO)X and Cp*OsL(CO)X (L = CO, PMe_3, PPh_3; X = Cl, Br, I) are precursors to alkyl, aryl, alkene, and alkyne complexes. For example, The reaction of $Cp^*Os(CO)_2I$ with LiMe give a methyl complex, $Cp^*Os(CO)_2(CH_3)$. Photolysis results in the loss of methane, probably thorough intermediate oxidative addition of a C–H bond from the Cp* group, and activation of benzene to give $Cp^*Os(CO)_2Ph$. Ethene displaces a carbonyl ligand in $Cp^*Os(CO)_2(CH_3)$ to give $Cp^*Os(CO)(\eta^2\text{-}CH_2{=}CH_2)(CH_3)$. Oxidation of $Cp^*Os(PMe_2Ph)(CO)(CH_3)$ with Br_2 gives the osmium(VI) methyl complex $[Cp^*Os(PMe_2Ph)(CO)Br(CH_3)][Br]$, which eliminates CH_3Br. Silver(I) salts abstract I^- from $Cp^*Os(PPh_3)(CO)I$ in the presence of internal alkynes to give the alkyne complexes $[Cp^*Os(PPh_3)(CO)(\eta^2\text{-}RC{\equiv}CR)]^+$ (Scheme 12).

Certain metalloboranes are structurally and electronically related to osmium cyclopentadienyl complexes. Metalloboranes (*see* ***Cluster Compounds: Inorganometallic Compounds Containing Transition Metal & Main Group Elements***) with arachno, nido, and closo type geometries with four, five, six, ten, and eleven vertices have been synthesized from $[OsCl_2(\eta^6\text{-}C_6H_6)]_2$ or from $OsCl_3(PPhMe_2)_3$.

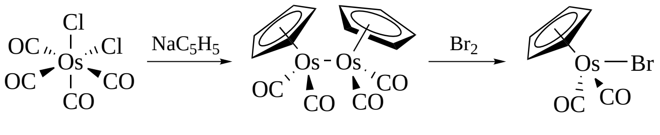

Scheme 11

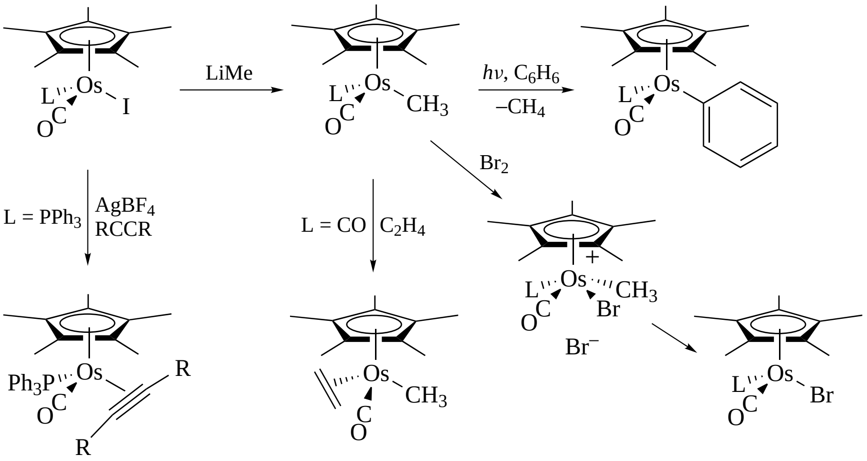

Scheme 12

4 OSMIUM CARBENE AND CARBYNE COMPLEXES

Carbene ligands can be classified as singlet carbenes (Fischer carbenes, *see Fischer-type Carbene Complexes*) or triplet carbenes (Schrock carbenes or alkylidene, *see Schrock-type Carbene Complexes*). Singlet carbenes bond to osmium, usually in low oxidation states, in a way that is very similar to bonding between the metal and CO. Typically, there is a heteroatom or phenyl substituent to the carbene carbon and the degree of multiple bonding between the metal and carbene carbon is low. The bond between a triplet carbene and osmium is similar to the double bond between carbon atoms in ethene. There are only hydrogen or carbon substituents on the carbene carbon and the osmium center is usually in higher oxidation states.

Osmium carbyne (*see Carbyne Complexes*) or alkylidyne complexes have a triple bond between the metal and the carbon atom of the ligand. Carbyne complexes are related to singlet carbenes. They are analogous to linear nitrosyl (*see Nitrosyl Complexes*) complexes and the osmium is usually in a lower oxidation state. Alkylidyne complexes are related to triplet carbenes and the bonding between the osmium and the carbon atom is similar to the C–C bond in an alkyne.

The chemistry of osmium carbene and carbyne complexes is rich owing to the high Os–C bond strength that stabilizes these species. Alkyl and vinyl complexes can convert to carbene and vinylidene complexes. They can interconvert with carbyne complexes. In similar systems, the osmium(VI) carbyne $OsHCl_2(CR)L_2$ and the ruthenium(IV) carbene $RuCl_2(CHR)L_2$ form. This demonstrates the tendency for osmium to react to form higher oxidation state species. Osmium carbyne complexes are usually more stable than ruthenium carbyne complexes. Other π-acceptor ligands, such as CO, favor the conversion of the carbyne–hydrido complex to a carbene complex.**[21]**

4.1 Carbenes

Carbene complexes with heteroatom substituents can be prepared by adding electrophiles to coordinated imidoyl, acyl, thioacyl, dithioester, or diselenoester ligands. Protonating the nitrogen atom of $Os(CH{=}NMe)Cl(CO)_2(PPh_3)_2$ gives the cationic carbene complex $[Os({=}CHNHMe)Cl(CO)_2(PPh_3)_2]^+$. The addition of HCl to $OsEtCl(CO)_2(PPh_3)_2$ promotes migration of the ethyl group to CO. The acyl ligand is protonated to give the hydroxycarbene $Os\{{=}C(OH)Et\}Cl_2(CO)(PPh_3)_2$ (Scheme 13). Alkylation of the thioformyl complex $Os(CHS)Cl(CO)_2(PPh_2)_2$ with $CH_3OSO_2CF_3$ gives $[Os\{{=}C(SCH_3)H\}Cl(CO)_2(PPh_3)_2][SO_3CF_3]$.

There are several other methods for the synthesis of carbene complexes of osmium. The reaction of a nucleophile with isocyanide complexes can result in the formation of osmium carbene complexes. Certain electron-rich alkenes add to osmium to form carbene complexes. For example,

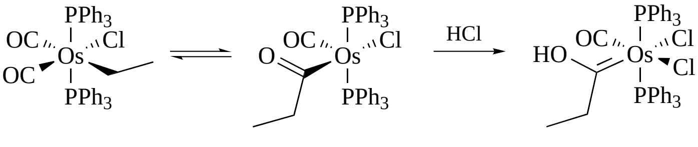

Scheme 13

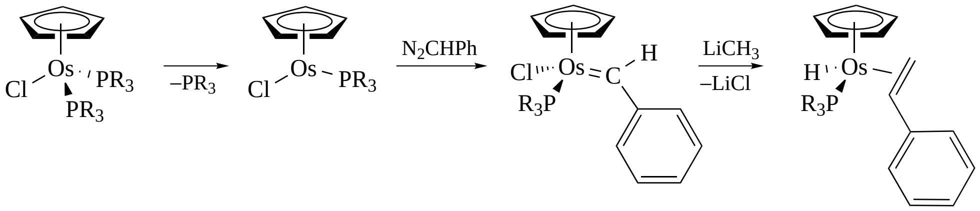

Scheme 14

the reaction of $\{(\textit{cyclo}\text{-}CH_2NMe)_2C\}{=}\{C(NMeCH_2\text{-})_2\}$ with $OsCl_2(PBu_2Ph)_4$ gives the tetracarbene complex $OsCl_2(\textit{cyclo}\text{-}CNMeCH_2CH_2NMe)_4$. The elimination of halide from the haloalkyl complex $OsCl(CCl_3)(CO)(PPh_3)_3$ gives $OsCl_2(CCl_2)(CO)(PPh_3)_2$. Nitrogen, oxygen, and sulfur-containing nucleophiles react with halocarbenes to give substituted carbene complexes. Dimethylamine reacts with $OsCl_2(CCl_2)(CO)(PPh_3)_2$ to produce $OsCl_2\{C(Cl)NMe_2\}(CO)(PPh_3)_2$.

A common method for the preparation of carbene complexes without heteroatom substituents is the reaction of a coordinatively unsaturated metal complex with a diazoalkane. This method is effective for the preparation of $CpOsCl(P^iPr_3)({=}CHPh)$ from $CpOsCl(P^iPr_3)_2$. The carbene in this complex is electrophilic and reacts with alkyl and aryl lithium compounds and with Grignard reagents (*see Grignard Reagents*) (Scheme 14).[22]

The reaction between diphenyldiazomethane and the osmium porphyrin complexes Os(por)(CO) in air produces oxo-bridged carbene complexes $[Os(por)({=}CPh_2)]_2(\mu\text{-}O)$. When the porphyrin is highly electron deficient, a bis-carbene complex $Os(por)({=}CPh_2)_2$ is formed instead. The oxo carbene complexes catalyze the cyclopropanation of styrene and cyclohexane with ethyl diazoacetate.[23] Diphenyldiazomethane also reacts with $(\eta^6\text{-arene})Os\kappa^1\{\text{-}OC(O)CF_3\}\kappa^2\{\text{-}O_2CCF_3\}$ to give diphenylcarbene complexes $(\eta^6\text{-arene})Os\kappa^1\{\text{-}OC(O)CF_3\}_2({=}CPh_2)$. Coupling products result when the carbene complex is treated with vinylmagnesium bromide or with ethylvinyl ether in the presence of a proton-acceptor.[24]

Carbene complexes can also form via the abstraction of an alpha hydrogen atom from an alkyl ligand. The abstraction of a methylimido ligand on an osmium(VI) complex $[CpOs(NCH_3)(CH_2SiMe_3)_2]^+$ with PPh_3 leads to the formation of Ph_3PNMe, alpha elimination of $SiMe_4$, and trapping of the resulting alkylidene complex with additional PPh_3 to give $[CpOs\{CH(SiMe_3)PPh_3\}]^+$. Cyclometallation of the ylide (*see Ylide*) gives the isolated product.

4.2 Carbynes

There are two principle methods for the synthesis of osmium carbyne complexes: (1) modification of a halocarbene, or (2) reaction of a hydride with a terminal alkyne. The reaction of $OsCl_2(CCl_2)(CO)(PPh_3)_2$ with p-tolyllithium produces $OsCl({\equiv}CC_6H_4CH_3)(CO)(PPh_3)_2$. The alpha carbon of the carbyne ligand is nucleophilic. Electrophiles such as HCl and Cl_2 add to this carbon to form carbene complexes.

Osmium hydrido and dihydrogen complexes (*see* ***Hydrogen Bonding & Dihydrogen Bonding***) react with terminal alkynes to form carbene, vinylidene, and carbyne complexes. The simple dihydride $OsH_2Cl_2(P^iPr_3)_2$ reacts with certain terminal alkynes, $HC{\equiv}CR$, to give the carbyne complex $OsHCl_2({\equiv}CCH_2R)(P^iPr_3)_2$. The dihydrogen complex $Os(H_2)(CO)Cl_2(P^iPr_3)_2$ reacts with phenyl acetylene to give the carbene complex $OsCl_2({=}CHCH_2Ph)(CO)(P^iPr_3)_2$. Carbene complexes also results from the addition of CO to $OsHCl_2({\equiv}CCH_2R)(P^iPr_3)_2$. The π-acid ligand induces migration of the hydride to the unsaturated hydrocarbon ligand in an intramolecular reductive elimination.

The acetate derivative, $OsH_2(OAc)_2(P^iPr_3)_2$ reacts with $HC{\equiv}CCMe{=}CH_2$ to give a vinylidene $OsH(OAc)({=}C{=}CHCMe{=}CH_2)$. The monoacetate cation $[OsH_2(OAc)(H_2O)(P^iPr_3)_2][BF_4]$ reacts with $HC{\equiv}CR$ to give either the osmacylopropene $[OsH(OAc)({=}CR\text{–}CH_2\text{–})(P^iPr_3)_2][BF_4]$ or the carbyne complex $[OsH(OAc)({\equiv}C\text{–}CH_2R)(P^iPr_3)_2][BF_4]$ depending on the nature of R. The reaction of $[OsH_2(OAc)(H_2O)(P^iPr_3)_2][BF_4]$ with acetylene gives $[Os(CH{=}CH_2)(OAc)({\equiv}C\text{–}CH_3)(P^iPr_3)_2][BF_4]$. The complex catalytically polymerizes acetylene (Scheme 15). The aquo dihydrido complex $[OsH_2(OAc)(H_2O)(P^iPr_3)_2][BF_4]$ reacts with ethene to form a bimetallic complex, $[\{(P^iPr_3)(\eta^2\text{-}C_2H_4)_2Os\}_2(\mu\text{-}OH)_2(\mu\text{-}O_2CCH_3)][BF_4]$, with bridging hydroxides along with ethane.

A dihydrido osmium(IV) complex of a P–C–P chelating ligand $\{2,6\text{-}(CH_2PBu^t_2)_2C_6H_5\}OsH_2Cl$ reacts with terminal alkynes to give vinylidenes $\{2,6\text{-}(CH_2PBu^t_2)_2C_6H_5\}OsCl({=}C{=}CHR)$. The reaction of $HC{\equiv}CCMe_3$ with $OsCl_2(PPh_3)_3$ gives a mixture of carbyne and vinylidene complexes. The products result from a series of steps beginning with the oxidative addition of the terminal alkyne to the Os(II) center, forming $OsCl_2H(PPh_3)_3(C{\equiv}CCMe_3)$ followed by either reductive elimination of HCl or by rearrangement to the vinylidene $OsCl_2(PPh_3)_2({=}C{=}CHCMe_3)$.

Protonation of the oximate complexes $OsHCl_2(ON{=}CR_2)(P^iPr_3)_2$ produces $OsHCl_2({=}N{=}CR_2)(P^iPr_3)_2$. An X-ray crystal structure of one derivative shows that it has a short osmium–nitrogen bond distance. This complex reacts with

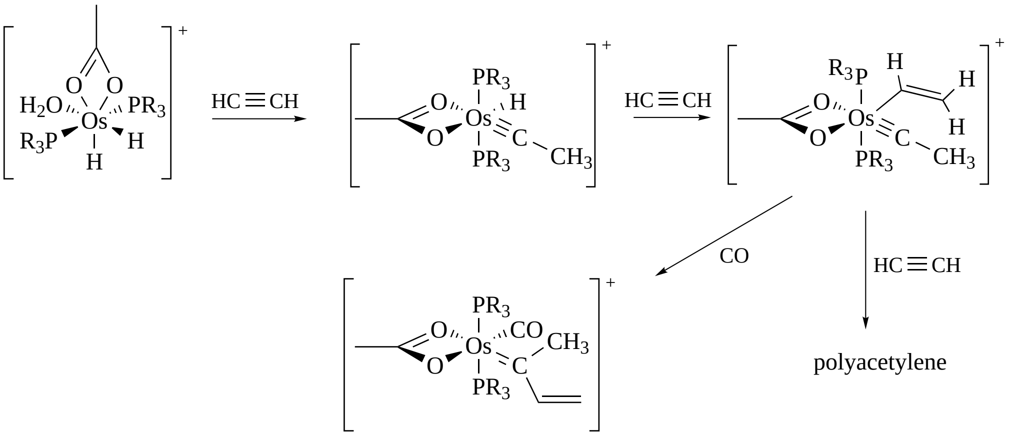

Scheme 15

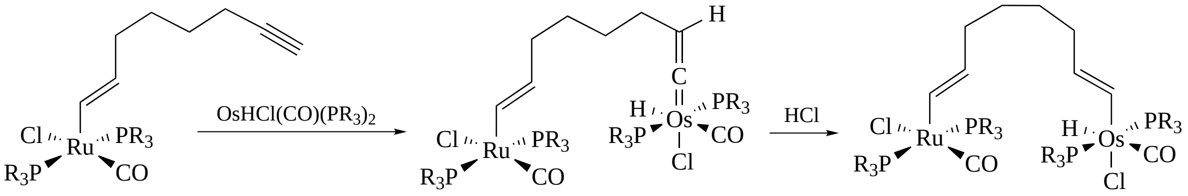

Scheme 16

terminal alkynes to give carbyne complexes. Studies of reaction intermediates show that the transformation involves a series of hydrogen transfer reactions among the metal center, the acetylene, and the coordinated nitrogen atom.[25]

The reactivity of osmium with terminal alkynes can be used to prepare bimetallic complexes. When an osmium hydride reacts with a terminal alkyne that is part of a ruthenium complex, the product is a Ru–Os bimetallic complex with a hydrocarbon bridge (Scheme 16). Another bimetallic complex, $[Cp(PPh_3)_2Os{=}C{=}C{=}CH{-}C{\equiv}C{-}Os(PPh_3)_2Cp]^+$, resulted from the reaction between $[CpOs(PPh_3)_2]^+$ with $HC{\equiv}CCH(OH)C{\equiv}CH$ followed by alumina. The unsaturated C_5 bridging group is V-shaped.

Several groups have completed computational studies on the relative stabilities of osmium carbyne, carbene, and vinylidene species. DFT calculations on the relative thermodynamic stability of the possible products from the reaction of $OsH_3Cl(P^iPr_3)_2$ with a vinyl ether $CH_2{=}CH(OR)$ showed that the carbyne was favored.[26] Ab initio calculations indicate that the vinylidene complex $[CpOs({=}C{=}CHR)L]^+$ is more stable than the acetylide, $CpOs({-}C{\equiv}CR)L$, or acetylene, $[CpOs(\eta^2\text{-}HC{\equiv}CR)L]^+$, complexes but it doesn't form from these complexes spontaneously. The unsaturated osmium center in $[CpOsL]^+$ oxidatively adds terminal alkynes to give $[CpOsH({-}C{\equiv}CR)L]^+$. Deprotonation of the metal followed by protonation of the acetylide ligand gives the vinylidene product.

Carbynes and vinylidenes interconvert. Deprotonation of $OsHCl_2({\equiv}CCH_2Ph)(P^iPr_3)_2$ converts the carbyne to a vinylidene ligand. In the presence of pyrazole, the vinylidene complex $OsH(pz)(Hpz)({=}C{=}CHPh)(P^iPr_3)_2$ can be isolated. A related complex, $OsH_3Cl(PPh_3)_2$, reacted with an internal alkyne, $CH_3C{\equiv}CPh$, to give the allenyl–vinyl complex $OsCl(CMe{=}CHPh)(CH_2{=}C{=}CHPh)(PPh_3)_2$. Deprotonation of one of the methylene protons on the carbyne ligand of $[CpOs(H)({\equiv}CCH_2Ph)(P^iPr_3)][BF_4]$ converts it to a vinylidene complex that is in equilibrium with an orthometallated metallocycle. Trimethylphosphite traps a vinyl complex and reprotonation of this gives a carbene. The reaction of $[CpOs(H)({\equiv}CCH_2Ph)(P^iPr_3)][BF_4]$ with KBr results in the formation of an alkene complex $CpOsBr(\eta^2\text{-}CH_2{=}CHPh)(P^iPr_3)$ rather than a vinylidene complex (Scheme 17). Labeling studies indicate that bromide induces hydride migration in an intermediate vinylidene hydride complex.[27]

4.3 Phosphinidene and Silylene Complexes

An aminophosphinidene complex $Cp^*Os(CO)_2\{PCl(N\text{-}^iPr_2)\}$ was prepared by reaction of $[Cp^*Os(CO)_2]^-$ with $^iPr_2NPCl_2$. As with Fischer carbenes (*see Fischer-type Carbene Complexes*), the nitrogen group stabilizes the electron-deficient phosphorus atom of the phosphinidene ligand. Based on a crystal structure of the ruthenium analog, there is likely

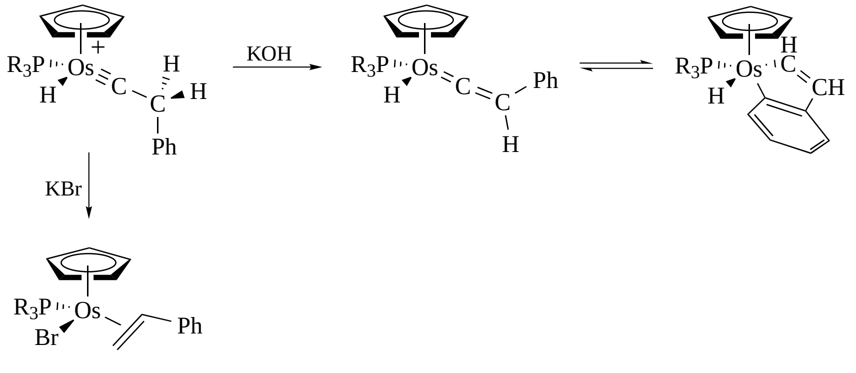

Scheme 17

an osmium–phosphorus single bond in this complex.[28] An unstabilized silylene complex $(C_5Me_5)Os(PMe_3)_2(=SiMe_2)$ results from the reaction of $Cp^*Os(PMe_3)_2(SiMe_2X)$, where $X = Cl$, OTf, with $LiB(C_6F_5)_4$ in fluorobenzene solution. The product is unstable in dichloromethane, probably owing to Cl abstraction by the silicon center.[29]

5 HIGH OXIDATION STATE COMPLEXES

While inorganic complexes of osmium in oxidation states +4 through +8 have been known for many years, the study of high-valent alkyl and aryl complexes of osmium is much more recent. The organometallic complexes include homoleptic (*see Homoleptic Compound*) alkyls and aryls, oxo alkyls and aryls, nitrido/imido alkyls and aryls, and cyclopentadienyl (*see Cyclopentadienyl*) alkyls and aryls. The majority of these are complexes of osmium(VI).

Organometallic osmium(IV) complexes are readily characterized by NMR spectroscopy because they are either diamagnetic or, depending on their symmetry, paramagnetic but with sharp NMR signals. Unlike most Os(IV), six-coordinate porphyrin complexes, the dialkylporphyrin complex of osmium(IV) $Os(TPP)(CH_2SiMe_4)_2$ is diamagnetic and has a distorted geometry with a C–Os–C angle of 140°. Calculations indicate that this distortion in the environment removes the degeneracy of the d_{xz} and d_{yz} orbitals on osmium and is responsible for the diamagnetism.[30]

5.1 Nitrido and Imido Complexes

The nitrido osmium(VI) alkyl and aryl complexes constitute the largest group of high oxidation state organometallic complexes of this metal. Five-coordinate complexes are square pyramidal with an apical nitrido ligand. Examples include anionic complexes $[N(n\text{-}Bu)_4][Os(N)Ph_4]$, cationic complexes $[Os(N)(CH_2SiMe_3)_2(NCMe)_2][BF_4]$, and neutral species $Os(N)(CH_3)_3(PMe_3)_2$. The acetylide complexes $[N(n\text{-}Bu)_4][Os(N)(C{\equiv}CR)_4]$ are similar to the alkyl and aryl derivatives but somewhat less sensitive to moisture. The chiral-at-metal osmium complex $[N(n\text{-}Bu)_4][cis\text{-}Os(N)(CH_2SiMe_3)PhCl_2]$ results from series of alkylation and protonation reactions from $[N(n\text{-}Bu)_4][Os(N)Cl_4]$. (*S*,*S*)-Chiraphos displaces a chloride from this complex to produce two isomers of $Os(N)(CH_2SiMe_3)PhCl((S,S)$-chiraphos) with different configurations at osmium (Scheme 18). One isomer reversibly loses an additional chloride ion and can be separated from the isomer with the opposite configuration by the careful addition of $AgSbF_6$. The diastereomers

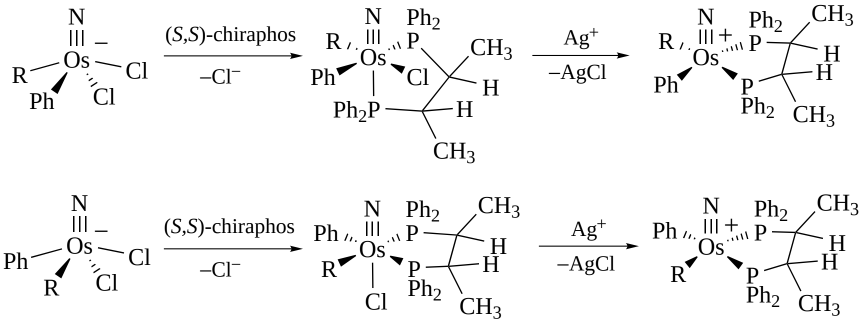

Scheme 18

[(*S*)-Os(N)(CH_2SiMe_3)Ph((*S*,*S*)-chiraphos)][SbF_6] and [(*R*)-Os(N)(CH_2SiMe_3)Ph((*S*,*S*)-chiraphos)] [SbF_6] can be isolated separately.

Nitridoosmium complexes with sulfur-containing ligands are electron rich because of the strong π donation from the ligands to the metal. Metal–alkyl complexes with thiolate or dithiolate ligands show a lowered Os≡N stretching vibration in the IR spectrum.[31] The nitridoosmium(VI) complex with four coordinated sulfur atoms in Os(N)Cl(κ^2-$SPPh_2NPPh_2S)_2$ reacts with $(CF_3CO)_2O$, and other acylating agents gave a product resulting from chloride substitution Os(N)($OCOCF_3$)(κ^2-$SPPh_2NPPh_2S)_2$ rather than rather than acylation of the nitrido group.

Simple alkyl and arylimido complexes of osmium(VI), such as $Os(NAr)_2R_2$ or $Os(NMe)R_4$, can be prepared by reacting oxo complexes with primary amines or arylcyanates, or by alkylating nitrido ligands. In general, the imido ligands are weaker π -donors than nitrido or oxo ligands.

5.2 Cyclopentadienyl, Indenyl, and Poly(pyrazolyl)borato Complexes

Cyclopentadienyl (*see Cyclopentadienyl*) and pentaalkylcyclopentadienyl osmium complexes have a very rich reaction chemistry and there has been a recent increase in reports of high oxidation state osmium cyclopentadienyl complexes. Poly(pyrazolyl)borates (*see Tris(pyrazolyl)borates*) and alkyl-substituted poly(pyrazolyl)borates are often used as cyclopentadienyl ligand analogues because of the facial coordination that each ligand type usually exhibits, the number of electrons it donates to the metal, and its charge. The bimetallic complex $Cp^*_2Os_2Br_4$ is a precursor for osmium(IV) allyls such as Cp*Os(η^3-allyl)Br_2.[32] The carbyne complex CpOs(≡$CCMe_3$)($CH_2CMe_3)_2$ results from the reaction of Os(≡$CCMe_3$)($CH_2CMe_3)_2(py)_2(O_3SCF_3)$ with NaCp.

As with $[Os(N)R_4]^-$, the nitrido ligand in CpOs(N)($CH_2SiMe_3)_2$ is nucleophilic. This complex reacts with BF_3 to form an adduct, CpOs(NBF_3)($CH_2SiMe_3)_2$, with $AgBF_4$ to form a silver(I)-bridged adduct, {[CpOs($CH_2SiMe_3)_2]_2$(μ-N–Ag–N)}[BF_4] and with [Me_3O][BF_4] or $MeOSO_2CF_3$ to yield cationic methyl imido complexes [CpOs(NMe)($CH_2SiMe_3)_2$][X]. The isoelectronic indenyl and hydrotris(3,5-dimethylpyrazolyl)borate complexes are less reactive with electrophiles. A study of the electrochemistry of isoelectronic oxo, imido, and nitrido complexes Tp*M(E)(X)(Y) [M = Re, Os; Tp* = HB(3,5-$Me_2pz)_3$; Tp = HB$(pz)_3$] shows that the osmium nitrido complexes are the most electron poor. The oxidation potentials follow simple trends, Os(N) > Re(O) > Re(Ntolyl) and Tp > Tp*. Within each series, the oxidation potential trend correlates with the Hammett parameters of the ligands X and Y.

The osmium methylimido complex [CpOs(NCH_3)($CH_2SiMe_3)_2$][SO_3CF_3] reacts with PPh_3 to give both a methyleneamido complex CpOs(NCH_2)($CH_2SiMe_3)_2$ and the unique osmium(IV) metallocycle [CpOs(H)(PPh_3){$CHSiMe_3PPh_2$(C_6H_4)}][SO_3CF_3]. The imido group transfers to PPh_3 to produce Ph_2P=NMe. The imido complex reacts with ethylene to give oligomers of [–N(Me)CH_2CH_2–] (Scheme 19).

The nitrido ligands in nitridoosmium(VI) complexes that lack strongly electron-donating alkyl ligands are electrophilic. The nitrido complexes *cis*- and *trans*-[(tpy)$OsNCl_2]^+$ react with 1,3-diphenylisobenzofuran to form azavinylidene complexes. The *trans* terpyridyl complex also reacts with secondary amines, such as morpholine, to give azido complexes *trans*-[Os(tpy)$Cl_2(NNR_2)$][PF_6] along with a reduced, μ-dinitrogen complex [(tpy)$Cl_2Os]_2$(μ-N_2). Trialkyl and triarylphosphines also react at the electrophilic nitrido ligand in [Os(tpy)Cl_2(N)][PF_6]. The reaction with triphenylphosphine is first order in both phosphine and metal complex and gives [Os(tpy)$Cl_2(NPPh_3)$][PF_6]. Related nitridoosmium(VI) complexes of Schiff-base ligands also form phosphoranimato complexes by attack of PPh_3 on the electrophilic nitrido group.

Grignard reagents (*see Grignard Reagents*), organoboranes (*see* ***Boron: Organoboranes***), and other nucleophilic reagents add to the electrophilic nitrido ligand in the hydrotris(1-pyrazolyl)borate (*see Tris(pyrazolyl)borates*) complex TpOs(N)Cl_2. The reactions with phenylmagnesium chloride or phenyllithium give the anilino complex after workup. Other aryl Grignard reagents react similarly. Boranes, such as BPh_3, also add to the nitrido group. Water, in the absence

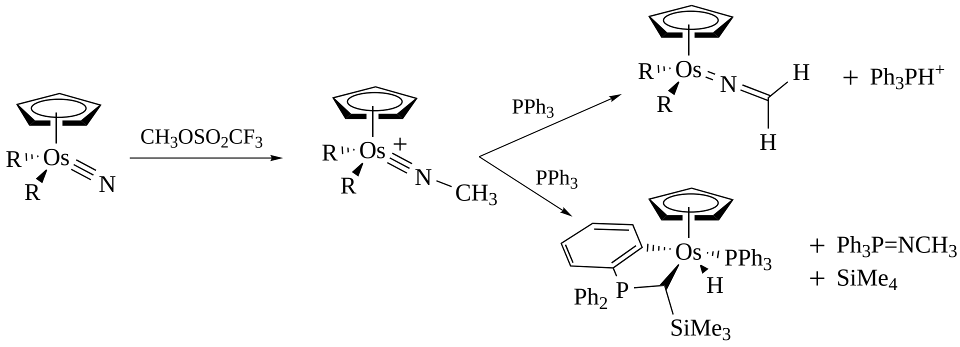

Scheme 19

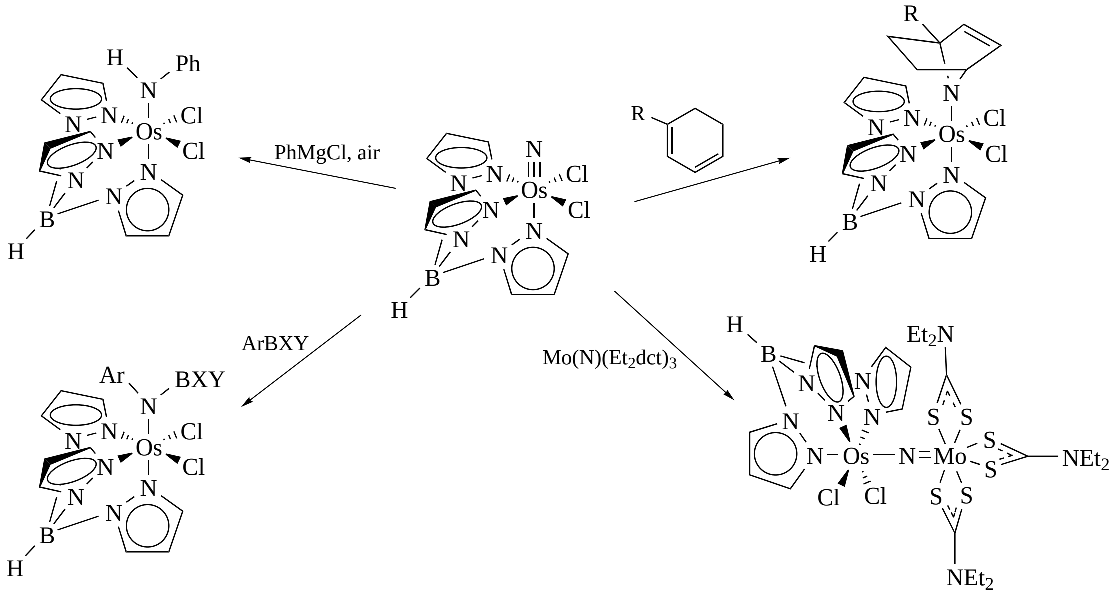

Scheme 20

of O_2, reacts with the addition product to form an anilino derivative of osmium(IV). It reacts with 1,3-cyclohexadienes at the nitride to form a azanorbornene derivatives. With a nucleophilic molybdenum nitrido complex, $(Et_2NCS_2)_3MoN$, $TpOs(N)Cl_2$ produces dinitrogen along with a bridging nitrido complex $(Et_2NCS_2)_3Mo(\mu\text{-}N)OsCl_2Tp$ and an osmium thionitrosyl complex $TpOsCl_2(NS)$ (Scheme 20). Labeling studies show that the dinitrogen results from the mixed-metal coupling reaction.[33] Derivatives of $TpOs(N)X_2$, where X is a halide, nitrato, or carboxylate ligand, react with PPh_3 to give reduced complexes $TpOs(NPPh_3)X_2$ and with BPh_3 to give $TpOs\{(NPh)BPh_2\}X_2$. The rate of reactions with phosphine correlates with the reduction potential of the nitrido complexes (*see Nitride Complexes*).[34] The nitrido ligand in $TpOs(N)Cl_2$ abstracts an oxygen from nitric oxide to form N_2O and $TpOs(NO)Cl_2$. A similar reaction occurs between $TpOs(N)Cl_2$ and $ONMe_3$.

Several new trimetallic complexes containing osmium in high oxidation state have been reported. The thermolysis of $Os(N)Cl_3L_2$, where L is a substituted pyridine ligand, produces linear triosmium complexes with bridging nitrido groups $Os_3(N)_2Cl_8L_6$.[35] The polynuclear osmium sulfido complexes $[N(n\text{-}Bu)_4][\{Os(N)(CH_2SiMe_3)_2\}_3(\mu_3\text{-}S)_2]$ and $\{Os(N)(CH_2SiMe_3)_2\}_2(\mu_3\text{-}S)_2(Pt)(dppe)$ were prepared by the reaction of $[N(n\text{-}Bu)_4][Os(N)(CH_2SiMe_3)_2Cl_2]$ with LiS or with $Pt(SSiMe_3)_2(dppe)$.[36]

5.3 Oxo Complexes and O_2 Activation

Oxo ligands help to stabilize high oxidation state alkyl complexes. Some oxo alkyl and aryl complexes of osmium(VI) can be prepared from OsO_4. A mesityl complex, $OsO_2(2,3,5\text{-}C_6H_2Me_3)_2$, and a (trimethylsilyl)methyl complex, $OsO(CH_2SiMe_3)_4$, each result from the direct reaction of the Grignard reagent and OsO_4. The methyl complex $OsO(CH_3)_4$ can be prepared by alkylation of OsO_4 with $ZnMe_2$ or with $MeTi(OCHMe_2)_3$, or by methylation of $OsO(OCH_2CH_2O)_2$ (Scheme 21). Similar reactions result in $Os(O)Et_4$ and $Os(O)Me_2(CH_2SiMe_3)_2$. The reaction between $Os(O)_2(py)_2(OCH_2CH_2O)$ and dialkylzinc compounds produces $Os(O)_2(py)_2R_2$ (R = CH_3, CH_2SiMe_3). Except for $Os(O)Et_4$ which decomposes by ß-hydrogen elimination (*see β-Hydride Elimination*), the oxoalkyl complexes are remarkably stable to air and water.

The reaction of molecular oxygen with osmium complexes is significant because of the importance of osmium-containing selective oxidation catalysts. Dioxygen adds to $OsCl_2H_2(P^iPr_3)_2$ to give an osmium(VI) dioxo complex *trans*-$Os(O)_2Cl_2(P^iPr_3)_2$. Reduction of this complex with n-butyllithium produces a unique square-planar d^4 complex *trans*-$OsO_2(P^iPr_3)_2$ (Scheme 22).[37] The osmium(II) complexes of chelating diphosphines $[OsCl(P\text{–}P)_2][PF_6]$ react quantitatively with O_2 to give peroxide complexes, $[OsCl(P\text{–}P)_2(\eta^2\text{-}O_2)][PF_6]$. The peroxo complex oxidizes iodide to I_3^- and PPh_3 to $OPPh_3$ in the presence of acid. The osmium-containing product is an osmium(IV) oxo complex.

6 CARBONYL COMPLEXES (*See Carbonyl Complexes of the Transition Metals*)

Carbon monoxide is a relatively poor Lewis base. The strength of the Os–CO bond depends on both the overlap

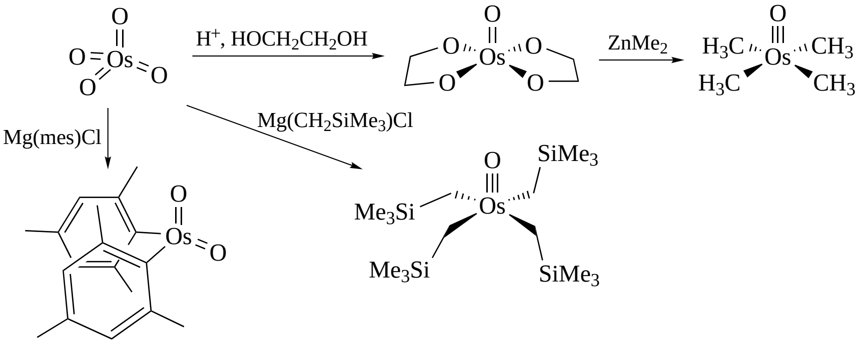

Scheme 21

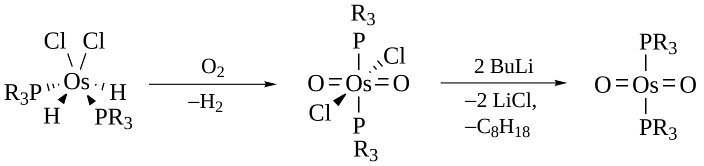

Scheme 22

of the CO orbital containing the lone pair of electrons with an empty osmium orbital and the back donation of electron density from a filled osmium d orbital to the empty CO π^* orbital. This and the other π-acid ligands CS, CNR, NO, and PF_3 bond most strongly with electron rich, low oxidation state transition metals.

6.1 Simple Carbonyl Complexes

Osmium pentacarbonyl, a volatile, colorless liquid, has a trigonal bipyramidal structure. It loses CO to form the air stable yellow solid $Os_3(CO)_{12}$ (Figure 2). Photolysis of $Os(CO)_5$ at low temperature produces $Os_2(CO)_9$. Thermolysis of osmium carbonyl produces $Os_5(CO)_{16}$, $Os_6(CO)_{18}$, $Os_7(CO)_{21}$, and $Os_8(CO)_{23}$. At higher temperatures, the carbido clusters $Os_5C(CO)_{15}$ and $Os_8C(CO)_{21}$ are formed from $Os_3(CO)_{12}$. Reduction of either $Os(CO)_5$ or $Os_3(CO)_{12}$ with sodium produces the anionic carbonyl complex $Na_2Os(CO)_4$. This reacts with CO_2 to give the dimer $Na_2Os_2(CO)_8$. A cationic carbonyl complex $[Os(CO)_6][AlCl_4]$ has been characterized spectroscopically.

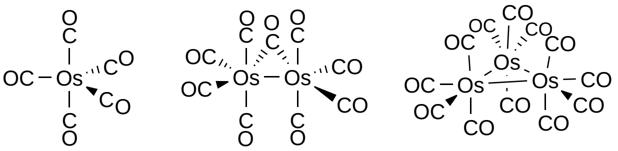

Figure 2 Osmium carbonyl complexes

Osmium pentacarbonyl is a convenient precursor to other osmium carbonyl complexes. Hydrogenation gives the dihydride $OsH_2(CO)_4$. This hydride is not acidic with a pK_a of 18.5 but it can be deprotonated by strong bases to give $[OsH(CO)_4]^-$ and reduced by sodium (Scheme 23). Substitution of CO on $Os(CO)_5$ by trialkyl or triarylphosphines, arsines, or stibenes gives $Os(CO)_4L$ or $Os(CO)_3L_2$. Other carbonyl phosphine complexes result from the reduction of osmium halides by alcohols in the presence of the tertiary phosphine.

Neutral carbonyl halides $Os(CO)_4X_2$, $[Os(CO)_3X_2]_2$, $[Os(CO)_2X_2]_n$, and $[Os(CO)_4X]_2$ can be prepared from $Os(CO)_5$ or from $OsH_2(CO)_4$. The anionic carbonyl halides *trans*-$[OsX_4(CO)_2]^-$, *cis*-$[OsX_4(CO)_2]^-$, and *mer*-$[OsX_3(CO)_3]^-$ result from carbonylation of Na_2OsX_6 (X = Cl, Br) under different conditions. The reaction between $NaOsBr_4(CO)_2$ and HX (X = Cl, Br, I) produces $[OsX_5(CO)]^{2-}$.

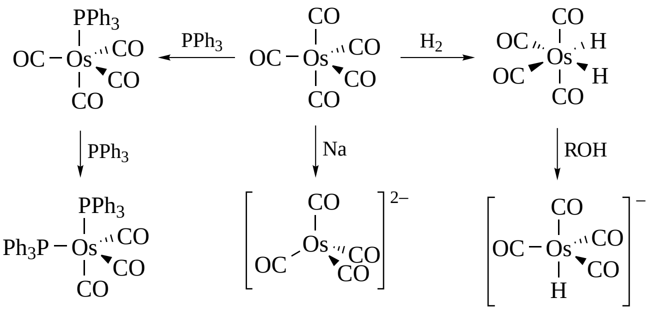

Scheme 23

6.2 Complexes of Other Pi Acid Ligands

Isonitriles are isoelectronic with carbon monoxide but homoleptic (*see Homoleptic Compound*) isonitrile complexes are more difficult to prepare than carbonyl complexes. The reduction of OsX_6^{2-} with ethanol in the presence of methylisonitrile gives $OsX_2(CNMe)_4$. The osmium(II) isonitrile complex $[Os(CNMe)_6]^{2+}$ results from the alkylation of $[Os(CN)_6]^{4-}$ with $MeOSO_2CF_3$. More generally, $[Os(CNR)_6]^{2+}$ can be prepared by reaction of $Os_2(O_2CMe)_4Cl_2$ with alkyl isonitriles.

The reaction between osmium carbonyl complexes and $NO_{(g)}$ produces nitrosyl complexes. Photolysis of $Os(CO)_5$ with NO in an inert gas matrix at low temperature generates $Os(CO)_2(NO)_2$ but this complex is thermally unstable. The phosphine complex $Os(PPh_3)_2(NO)_2$ results from the reaction of $Os(PPh_3)_2(CO)_2Cl_2$ with $NaNO_2$. The reaction of $Os(PPh_3)_2(NO)_2$ with perfluoroacetic acid produces a hydroximate $Os\{ON{=}C(O)CF_3\}(O_2CCF_3)(NO)(PPh_3)_2$ and a hydride $OsH(O_2CCF_3)(NO)(PPh_3)_2$.

Substitution reactions of CS_2 for alkene, carbonyl, or phosphine ligands gives either carbon disulfide complexes or thiocarbonyl complexes. The reaction of $Os(CO)_2(\eta^2\text{-}C_2H_4)(PPh_3)_2$ with CS_2 forms $Os(CO)_2(\eta^2\text{-}CS_2)(PPh_3)_2$. This reacts with PPh_3 to give the thiocarbonyl complex $Os(CO)(CS)(PPh_3)_3$ and $S{=}PPh_3$. The reaction between $OsCl_2(PPh_3)_3$ with CS_2 gives $OsCl_2(CS)(PPh_3)_2$ and $S{=}PPh_3$ directly. The carbon disulfide complex $Os(CO)_2(\eta^2\text{-}CS_2)(PPh_3)_2$ reacts with methyl iodide to give a dithiocarbene complex and with sodium borohydride to give a thioester (Scheme 24).

6.3 Carbonyl Clusters

Osmium forms stronger metal–metal bonds than either iron or ruthenium; consequently, there are a large number of osmium carbonyl clusters (*see Cluster*) and these complexes have a large body of reaction chemistry. The triosmium cluster are prepared from $Os_3(CO)_{12}$. Most are diamagnetic and air-stable materials. Additional information can be found in a review by Deeming.**[38]**

The triosmium carbonyl $Os_3(CO)_{12}$ is a saturated complex in that all of the osmium centers achieve an 18 electron count and the molecule is relatively unreactive. By heating to temperatures over 120 °C or photolysis, various two-electron donor molecules can substitute for carbonyl ligands and form mixtures of $Os_3(CO)_{11}L$, $Os_3(CO)_{10}L_2$, $Os_3(CO)_9L_3$ and other complexes. Bulky phosphine and phosphite ligands usually take equatorial positions in the cluster while less sterically demanding isonitrile ligands can bond in axial positions. More selective carbonyl substitution reactions occur when the cluster is treated with amine-N-oxides or phosphine oxides. Nucleophilic attack by $ONMe_3$, for example, on one carbonyl ligand of $Os_3(CO)_{12}$ results in the formation of CO_2 and $Os_3(CO)_{11}(NMe_3)$. The amine is weakly bonded and can be displaced by a variety of other donors.

The acetonitrile complexes $Os_3(CO)_{11}(NCMe)$ and $Os_3(CO)_{10}(NCMe)_2$ are particularly reactive species and are useful precursors to other triosmium cluster complexes. Aldehydes react with $Os_3(CO)_{11}(NCMe)$ to give $Os_3(CO)_{10}(\mu\text{-}H)(COR)$. Phosphines, phosphites, and arsines cleanly substitute for the acetonitrile ligands.

Alkenes and alkynes can substitute for carbonyl ligands on $Os_3(CO)_{12}$. Carbon monoxide slowly dissociates from $Os_3(CO)_{11}(\eta^2\text{-}PhC{\equiv}CPh)$ and a cluster with a bridging alkyne ligand forms, $Os_3(CO)_{10}(\mu\text{-}PhC{\equiv}CPh)$. The addition of ethene to the cluster gives a bridging vinylidene complex, $Os_3(CO)_9(\mu\text{-}H)_2(\mu\text{-}C{=}CH_2)$. The oxidative addition of terminal alkynes to $Os_3(CO)_{12}$ gives $Os_3(CO)_9(\mu\text{-}H)(\mu_3\text{-}CCR)$. Nucleophiles add to the bridging alkyne unit.

The reaction of $Os_3(CO)_{12}$ with H_2 at 110 °C. produces a reactive, unsaturated hydrido cluster $Os_3(\mu\text{-}H)_2(CO)_{10}$. This dark purple complex is analogous to diborane and has the two hydrides bridging a very short Os–Os bond. It can add phosphines, phosphites, arsines, pyridine, and isocyanides to form $Os_3H_2(CO)_{10}L$ (Scheme 25). The hydrido cluster adds alkenes and alkynes. Initially, an addition complex with a π-bonded alkene or alkyne is formed. Hydride addition to the unsaturated ligand follows.

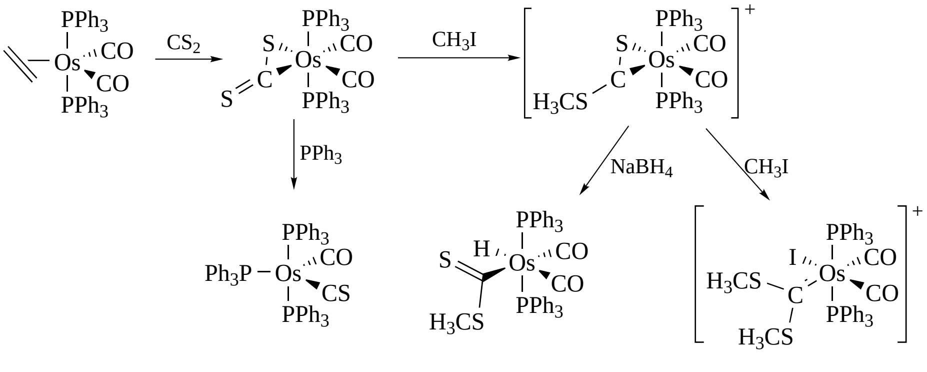

Scheme 24

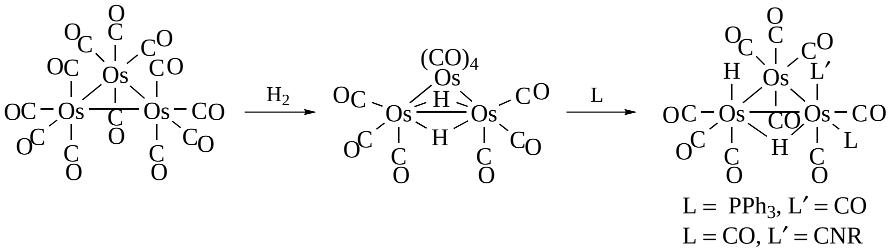

Scheme 25

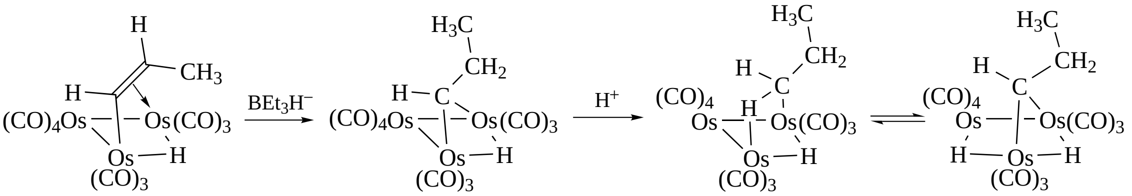

Scheme 26

While much of the efforts in osmium cluster chemistry are on synthesis and structural characterization, there have been a number of important studies on reactions in solution, particularly on isomerization reactions. The reaction between diazomethane and $Os_3(\mu\text{-}H)_2(CO)_{10}$ produces a mixture of a methyl complex $Os_3(\mu\text{-}H)(CH_3)(CO)_{10}$ and a methylene complex $Os_3(\mu\text{-}H)_2(\mu\text{-}CH_2)(CO)_{10}$. Variable-temperature NMR studies showed that these two isomers are in equilibrium and that the methyl group interacts with a second osmium center through a C–H–Os bridge.[39] Two isomers of the substituted vinyl compound $Os_3(CO)_9L(\mu\text{-}H)(\mu\text{-}CH{=}CH_2)$ are in equilibrium in solution. The position of the equilibrium depends on the size of the phosphine ligand, L. There is a similar steric effect in the equilibration of methyl and methylene tautomers of $Os_3(\mu\text{-}H)_2(\mu\text{-}CH_2)(CO)_9L$ and $Os_3(\mu\text{-}H)(CH_3)(CO)_9L$ with larger ligands favoring the methylene complex.

The propyl compound $Os_3(\mu\text{-}H)_2(\mu\text{-}CHCH_2CH_3)(CO)_{10}$ equilibrates with a propylidene tautomer $Os_3(\mu\text{-}H)(CH_2CH_2CH_3)(CO)_{10}$ at −25 °C (Scheme 26). It decomposes to propene and $Os_3(\mu\text{-}H)_2(CO)_{10}$ near room temperature. Information from this and other studies shows that the alkyl/alkylidene equilibrium shifts toward the alkylidene form with greater chain length of the alkyl. The rate of β-hydride elimination (*see β-Hydride Elimination*) is four times greater for the propyl compound versus the ethyl compound $Os_3(\mu\text{-}H)R(CO)_{10}$ at room temperature.[40]

The monophosphine complexes $Os_3(\mu\text{-}H)_2(CO)_9L$ react with diazomethane to give N_2 and a wide range of homologous alkenes. The rates of diazomethane decomposition correlate well with the electronic nature of L rather than its size, with less donating ligands showing higher rates.

Roberto and coworkers have developed a high-yield synthesis of $Os_3(CO)_{10}(\mu\text{-}H)(\mu\text{-}OH)$ by hydrolysis of the silica supported intermediate $Os_3(CO)_{10}(\mu\text{-}H)$(OSi-silica) in a biphasic water/toluene mixture.[41] The hydroxy compound undergoes ready substitution by a variety of HOR compounds to give new $Os_3(CO)_{10}(\mu\text{-}H)(OR)$ derivatives. This suggests the use of the triosmium compound as a labeling agent for specific sites in biomolecules.

The face-bonded triosmium cluster of buckminsterfullerene $Os_3(CO)_9(\mu_3\text{-}\eta^2;\eta^2;\eta^2\text{-}C_{60})$ has been prepared and phosphine substituted derivatives were structurally characterized.

Larger osmium clusters result from the pyrolysis of $Os_3(CO)_{12}$ or by the addition of mononuclear fragments to unsaturated clusters. A by-product of the hydrogenation of $Os_3(CO)_{12}$ is $Os_4(CO)_{12}H_2$. The thermal reaction between $OsH_2(CO)_4$ and Os_3 clusters gives tetraosmium hydrido clusters. The addition of sulfur, selenium, or tellurium to $Os_3(CO)_{12}$ produces clusters with bridging chalogenide ligands such as $Os_4(CO)_{12}(\mu_3\text{-}S)$. The raft-like (*see Raft Clusters*) clusters $Os_6(CO)_{20}(NCMe)$ and $Os_6(CO)_{19}(NCMe)_2$ were formed by the coupling of $Os_3(CO)_{10}(NCMe)_2$ in the presence of $PdCl_2$. Mercury(II) induces the coupling of two triosmium clusters to $Os_6(\eta^6\text{-}Hg)(\mu\text{-}PR_2)_2(CO)_{20}$ (Scheme 27).[42]

Silica has been used as a reaction medium for improved syntheses of higher nuclearity clusters by reduction of supported $[Os(CO)_3Cl_2]_2$ in the presence of adsorbed sodium or potassium carbonate. In this manner $K_2[H_2Os_4(CO)_{12}]$ is prepared in yields greater than 85% by carbonylation at 200 °C, and $Na_2[Os_{10}C(CO)_{24}]$ is generated in 75% yield by reduction with H_2 at a similar temperature. Treatment of silica supported $[Os(CO)_3Cl_2]_2$ with Na_2CO_3 in ethylene glycol at

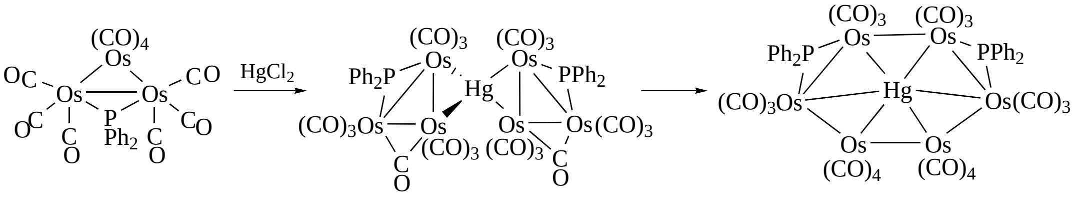

Scheme 27

160 °C. and 1 atmosphere H_2 gives $Na_2[H_4Os_{10}(CO)_{24}]$ in up to 80% yield.

7 CATALYSIS WITH OSMIUM COMPLEXES

Osmium complexes catalyze a large number of reaction of organic molecules including the reduction of alkenes, alkyne, carbon monoxide, aldehydes, and ketones with molecular hydrogen.[43] The osmium catalysts are used less often than corresponding ruthenium catalysts. Because the Os-ligand bonds are stronger than Ru-ligand bonds, catalytic reactions are usually slower with osmium. Also, the greater cost of osmium over ruthenium disfavors its use in most catalytic reactions.

In oxidation reactions, however, osmium is significantly more selective than catalysts derived from other transition metals. Osmium-based catalysts for the hydroxylation and amination of alkenes are very widely used in organic synthesis.[44] With alkaloid-derived ligands, the hydroxylation and amination reactions are highly enantioselective (*see Enantioselectivity*). The use of bleach, hydrogen peroxide, ferric cyanide, and oxygen have been reported as secondary oxidants for some of these reactions.

The heterobimetallic complexes $[N(n\text{-Bu})_4]$ $[Os(N)R_2(\mu\text{-}O)_2CrO_2]$ catalyze the selective oxidation of alcohols with molecular oxygen.[45] A mechanism in which alcohol coordinates to the osmium center and is oxidized by ß-hydrogen elimination (*see β-Hydride Elimination*) is consistent with the data. The hydroxide adduct of OsO_4, $[Os(OH)_2O_4]^{2-}$, with ferric cyanide and other co-oxidants catalyzes the oxidative dehydrogenation of primary aromatic and aliphatic amines to nitriles, the oxidation of primary alcohols to carboxylic acids, and of secondary alcohols to ketones. Osmium derivatives such as $OsCl_3$ catalyze the effective oxidation of saturated hydrocarbons in acetonitrile through a radical mechanism.[46]

Much of the current research focuses on improving the selectivity of the oxidation reactions while making them more atom efficient. Oxidation of single functional groups with high stereoselectivity (*see Stereoselectivity*) is important for applications of osmium catalysis in organic synthesis. The use of molecular oxygen or hydrogen peroxide as secondary oxidants improves the atom economy of the reactions, and the development of supported analogs of osmium catalysts will improve their ease of use.

8 RELATED ARTICLES

Asymmetric Synthesis by Homogeneous Catalysis; Carbonyl Complexes of the Transition Metals; Dihydrogen Complexes & Related Sigma Complexes; Dinuclear Organometallic Cluster Complexes; Hydride Complexes of the Transition Metals; Iron: Organometallic Chemistry; Mechanisms of Reaction of Organometallic Complexes; Polynuclear Organometallic Cluster Complexes; Ruthenium: Organometallic Chemistry.

9 REFERENCES

1. R. H. Crabtree, ‘The Organometallic Chemistry of the Transition Metals’, 3rd edn, John Wiley, New York, 2001.
2. W. A. Nugent and J. M. Mayer, ‘Metal-Ligand Multiple Bonds’, John Wiley & Sons, New York, 1988.
3. J. Arnold, G. Wilkinson, B. Hussain, and M. B. Hursthouse, *Chem. Commun.*, 1988, 1349.
4. S. H. Liu, S. T. Lo, T. B. Wen, Z. Y. Zhou, C. P. Lau, and G. Jia, *Organometallics*, 2001, **20**, 667.
5. G. Bellachioma, G. Cardaci, A. Macchioni, and C. Zuccaccia, *J. Organomet. Chem.*, 2001, **628**, 255.
6. G. R. Andersen and J. A. M. Moss, *J. Organomet. Chem.*, 1995, **505**, 131.
7. A. M. Clark, C. E. F. Rickard, W. R. Roper, and L. J. Wright, *Organometallics*, 1999, **18**, 2813.
8. D. G. Gusev and A. J. Lough, *Organometallics*, 2002, **21**, 2601.
9. R. M. Gauvin, H. Rozenberg, L. J. W. Shimon, and D. Milstein, *Organometallics*, 2001, **20**, 1719.
10. A. D. Ryabov, V. S. Soukharev, L. Alexandrova, R. Le Lagadec, and M. Pfeffer, *Inorg. Chem.*, 2003, **42**, 6598.
11. R. Acharyya, S.-M. Peng, G.-H. Lee, and S. Bhattacharya, *Inorg. Chem.*, 2003, **42**, 7378.

12. P. Barrio, R. Castarlenas, M. A. Esteruelas, and E. Onate, *Organometallics*, 2001, **20**, 2635.
13. C. E. F. Rickard, W. R. Roper, A. Williamson, and L. J. Wright, *Organometallics*, 2002, **21**, 4862.
14. A. M. Clark, C. E. F. Rickard, W. R. Roper, T. J. Woodman, and L. J. Wright, *Organometallics*, 2000, **19**, 1766.
15. M. L. Spera and W. D. Harman, *Organometallics*, 1999, **18**, 1559.
16. T. Mao, Z. Zhang, J. Washington, J. Takats, and R. B. Jordan, *Organometallics*, 1999, **18**, 2331.
17. H. Brunner, T. Zwack, M. Zabel, W. Beck, and A. Böhm, *Organometallics*, 2003, **22**, 1741.
18. J. W. Faller and J. Parr, *Organometallics*, 2000, **19**, 3556.
19. K. E. Howard, J. R. Lockemeyer, M. A. Massa, T. B. Rauchfuss, S. R. Wilson, and X. Yang, *Inorg. Chem.*, 1990, **29**, 4385.
20. C. L. Gross, S. R. Wilson, and G. S. Girolami, *J. Am. Chem. Soc.*, 1994, **116**, 10294.
21. H. Jacobsen, *J. Organomet. Chem.*, 2003, **674**, 50.
22. M. A. Esteruelas, A. I. Gonzélez, A. M. López, and E. Oñate, *Organometallics*, 2003, **22**, 414.
23. Y. Li., J.-S. Huang, Z.-Y. Zhou, and C.-M. Che, *Chem. Commun.*, 2003, 1362.
24. B. Weberndörfer, G. Henig, D. C. R. Hockless, M. A. Bennett, and H. Werner, *Organometallics*, 2003, **22**, 744.
25. R. Castarlenas, M. A. Esteruelas, and E. Oñate, *Organometallics*, 2001, **20**, 3283.
26. K. G. Caulton, *J. Organomet. Chem.*, 2001, **617–618**, 56.
27. M. Baya, M. A. Esteruelas, and E. Oñate, *Organometallics*, 2002, **21**, 5681.
28. B. T. Sterenberg, K. A. Udachin, and A. J. Carty, *Organometallics*, 2003, **22**, 3927.
29. P. W. Wanandi, P. B. Glaser, and T. D. Tilley, *J. Am. Chem. Soc.*, 2000, **122**, 972.
30. S.-Y. Yang, W.-H. Leung, and Z. Lin, *Organometallics*, 2001, **20**, 3198.
31. W. A. Reinerth and P. A. Shapley, *Inorg. Chim. Acta.*, 1998, **267**, 335.
32. H. D. Mui, J. L. Brumaghim, C. L. Gross, and G. S. Girolami, *Organometallics*, 1999, **18**, 3264.
33. S. B. Seymore and S. N. Brown, *Inorg. Chem.*, 2002, **41**, 462.
34. A. Dehestani, W. Kaminsky, and J. M. Mayer, *Inorg. Chem.*, 2003, **42**, 605.
35. C. Newton, K. D. Edwards, J. W. Ziller, and N. M. Doherty, *Inorg. Chem.*, 1999, **38**, 4032.
36. P. A. Shapley, H. C. Liang, and N. C. Dopke, *Organometallics*, 2001, **20**, 4700.
37. M. A. Esteruelas, F. J. Modrego, E. Oñate, and E. Royo, *J. Am. Chem. Soc.*, 2003, **125**, 13344.
38. A. J. Deeming, *Adv. Organomet. Chem.*, 1986, **26**, 1.
39. R. B. Calvert and J. R. Shapley, *J. Am. Chem. Soc.*, 1978, **100**, 7726.
40. M. E. Cree and J. R. Shapley, *Inorg. Chim. Acta*, 2003, **345**, 345.
41. E. Lucente, D. Roberto, C. Roveda, R. Ugo, and E. Carieti, *J. Cluster Sci.*, 2001, **12**, 113.
42. H. Egold, M. Schraa, U. Flörke, and J. Partyka, *Organometallics*, 2002, **21**, 1925.
43. R. A. Sanchez-Delgado, M. Rosales, M. A. Esteruelas, and L. A. Oro, *J. Mol. Catal. A*, 1995, **96**, 231.
44. K. B. Sharpless, *Angew. Chem., Int. Ed. Engl.*, 2002, **41**, 2024.
45. P. A. Shapley, N. Zhang, J. L. Allen, D. H. Pool, and H. C. Liang, *J. Am. Chem. Soc.*, 2000, **122**, 1079.
46. G. B. Shul'pin, G. Suss-Fink, and L. S. Shul'pina, *Chem. Commun.*, 2000, 1131.

Oxidation Catalysis by Transition Metal Complexes

Robert H. Crabtree
Yale University, New Haven, CT, USA

1	Introduction	1
2	Reagents and Conditions	1
3	Autoxidation	3
4	Oxidation Pathways	3
5	Bioinorganic Model Oxidation Catalysts	3
6	Oxidation Catalysts for Organic Synthesis	4
7	Oxidation Catalysts for Green Chemistry	4
8	Organometallic Oxidation Catalysts	5
9	Conclusion	5
10	References	5

1 INTRODUCTION

Oxidation catalysis[1–7] by transition metals holds a special place in chemistry. It forms a part of bioinorganic chemistry[1,2,5,6] in that biological oxidations are catalyzed by metalloenzymes. It relates to organic chemistry[3] in that organic reactions are the ones often catalyzed. It poses hard mechanistic problems, as shown by the sharp disagreements that have arisen on this issue over the years on matters such as the intermediacy of radical versus nonradical pathways. Oxidation is often also harder to control in terms of selectivity than most reductive pathways. A few highly selective catalysts like the Sharpless and Jacobsen oxidations have been developed, and they have proved so useful that they have been widely adopted as organic methods. Selective oxidation also has great importance for industrial applications.[7] Many potentially useful conversions, such as methane to methanol, remain elusive yet a broad spectrum of valuable catalytic transformations has been discovered, including the Wacker process and terephthalic acid syntheses. Suppression of oxidation catalysis by transition metals with sequestering agents such as sodium EDTA is also of practical importance, for example, in the food industry. Environmental applications[8] include oxidative environmental remediation, as in the Collins catalyst.

So vast and disparate is the range of topics involved that we can only touch on selected individual aspects. Severe selection is therefore necessary, and the reader interested in following up particular areas in greater detail is referred to the appropriate monographs.[1–6] In particular, Meunier's book[2] is good for mechanistic detail and biomimetic applications, and Comprehensive Organic Chemistry[3] has an extensive discussion of reagents, catalysts, and their reactions in the context of organic methods.

2 REAGENTS AND CONDITIONS

Some general points hold for all catalytic oxidations. In any catalytic reaction, we need a stoichiometric source of oxidizing power, the primary oxidant. In biology this is typically air, in large-scale commercial applications, air or oxygen, but in organic chemistry, a wide range of more sophisticated oxidants tends to be used, often *t*BuOOH, MCPBA or some other peroxy species. Commercially, only the cheaper oxidants are possible for large-scale work while higher value fine chemical products can justify more expensive oxidants.

Where O_2 or air is used as primary oxidant, both oxygen atoms may be introduced into substrate, in which case we have a dioxygenase (equation 1). This pathway tends to occur for substrates that are most readily oxidized. The harder substrates, notably unactivated CH bonds, require the presence of a 2e reductant to help activate the O_2. In this case one O atom of the O_2 molecule is reduced to H_2O while the other is incorporated into substrate, Q. This is the monooxygenase pathway.[1,2]

$$2Q + O_2 = 2Q{=}O \tag{1}$$

$$Q + 2e^- + 2H^+ + O_2 = Q{=}O + H_2O \tag{2}$$

Each major class of oxygenase and monooxygenase enzyme has a vast literature. A general pattern, however, is that most such enzymes have either Fe or Cu as active site metals, often in multinuclear cluster centers. For iron, the Fe(II)/(III) couple is often accessed with Fe(IV) present in certain cases. For copper, the typical states are Cu(I)/(II) with Cu(III) also present in some cases. Since O_2 is a 4e oxidant, while the low-valent metals are 1 or 2e reductants, a cluster site can help attain compatibility of oxidant and reductant by allowing the site to take up more than one electron.

The initial interaction of O_2 with a reduced metal in a metalloenzyme commonly goes with 1e or 2e metal-to-ligand electron transfer to give coordinated superoxide ($O_2{}^-$) as in hemoglobin or peroxide ($O_2{}^{2-}$) as in hemocyanin (Figure 1). Reversibility of O_2 binding is possible in this way as in oxygen transport proteins. In an oxygenase reaction the initial $O_2{}^-$ or $O_2{}^{2-}$ metal adduct can react directly with the substrate to go on to product. In the case of a monooxygenase, 2e reduction cleaves the O–O bond to form a highly reactive metal-oxo intermediate that is the active oxidant.

Typical examples of enzymes and their properties appear in the articles ***Copper Proteins: Oxidases***; ***Iron: Heme Proteins, Peroxidases, Catalases & Catalase-peroxidases***; ***Iron: Heme***

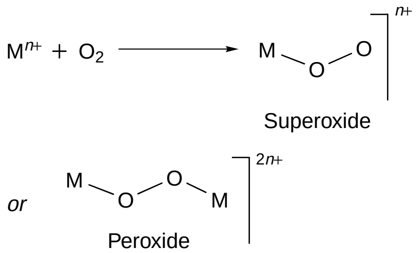

Figure 1 Two of the commonest ways in which O_2 can bind to a metal

Proteins, Mono- & Dioxygenases; oxygen as a ligand is discussed in ***Dioxygen & Related Ligands***.

Air and dioxygen are desirable primary oxidants where they are effective; a stoichiometric coreductant may have to be present for oxidation to occur if a monooxygenase pathway is adopted.

A very broad class of primary oxidants act as oxygen atom transfer agents, the most widely used oxidants in oxidation catalysis. These include peracids or their anion forms, such as MCPBA or oxone ($O\text{-}OSO_3{}^{2-}$) as well as *N*-oxides such as *N*-methyl morpholine *N*-oxide or hypochlorite ion. They all have general structure XO, where X is a good leaving group.

Peroxides, typically *t*BuOOH and H_2O_2 itself, form another very important class of oxidant. These can act as O transfer agents but more commonly undergo metal-catalyzed O–O homolysis to yield radicals. A typical reaction sequence is shown in (equation 3–4). These oxidants are favored because of their cheapness and, for H_2O_2, its benign character. Electron transfer oxidants, including Ce(IV) and $[FeCp_2]^+$, are less often involved in catalytic chemistry.

$$\mathrm{Fe(II)} + \mathrm{H_2O_2} \Longrightarrow \bullet\mathrm{OH} + \mathrm{Fe(III)\text{-}OH} \qquad (3)$$

$$\mathrm{Fe(III)\text{-}OH} + \mathrm{H_2O_2} \Longrightarrow \bullet\mathrm{O_2H} + \mathrm{Fe(II)} + \mathrm{HOH} \qquad (4)$$

Mayer[9] has given the best discussion of thermodynamic issues at stake in oxidation. Primary oxidants differ greatly in their thermodynamic driving force given by the Mayer classification, for example: O_3/O_2, 25 kcal mol^{-1}; H_2O_2/H_2O, 34 kcal mol^{-1}; N_2O/N_2, 40 kcal mol^{-1}; $1/2O_2$, 60 kcal mol^{-1}; C_6H_5NO/C_6H_5N, 72 kcal mol^{-1}. Lower numbers are associated with more powerful oxidants. Ozone is so powerful an oxidant it does not need a catalyst, but all the others mentioned are commonly used with catalysis.

Likewise, substrates differ in their ease of oxidation. Mayer's figures are: Ph_3P/Ph_3PO, −135 kcal mol^{-1}; CO/CO_2, −127 kcal mol^{-1}; RH/ROH, −90 to −102 kcal mol^{-1}; Me_2S/Me_2SO, −87 kcal mol^{-1}; alkene/epoxide, −85 to −92 kcal mol^{-1}. PPh_3 is so easily oxidized, both thermodynamically and kinetically, that it is often used as a probe for minimal oxidation activity. If it is not oxidized then the catalytic system in question will probably be inactive for all substrates. Obviously, in order to catalyze a given oxidation, an oxidant with an adequate driving force needs to be chosen and the Meyer numbers provide a rational basis to make this choice.

A related problem is selectivity for partial oxidation. For example, in the oxidation of methane to methanol, one needs to avoid over-oxidation. This is hard because the intermediate oxidation products between CH_4 and CO_2 become progressively more kinetically reactive as the reaction proceeds, as suggested by Mayer's figures:

$$\mathrm{CH_4} + \mathrm{O} \longrightarrow \mathrm{CH_3OH} \qquad \Delta H^\circ = -89.8\ \mathrm{kcal/mol} \qquad (5)$$

$$\mathrm{CH_3OH} + \mathrm{O} \longrightarrow \mathrm{CH_2O} + \mathrm{H_2O} \qquad -95.3\ \mathrm{kcal/mol} \qquad (6)$$

$$\mathrm{CH_2O} + \mathrm{O} \longrightarrow \mathrm{HCOOH} \qquad -124.1\ \mathrm{kcal/mol} \qquad (7)$$

$$\mathrm{HCOOH} + \mathrm{O} \longrightarrow \mathrm{CO_2} + \mathrm{H_2O} \qquad -120.9\ \mathrm{kcal/mol} \qquad (8)$$

Of course, kinetics rather than thermodynamics is the key factor in selectivity so the Meyer figures only provide a rough guide.

In hydrogen atom transfer (HAT) oxidations, a common mechanistic type, a metal-oxo species abstracts an H atom from an X–H bond. In so doing the oxo acts as the base and takes the proton and the metal acts as the reductant and takes the electron. Thus HAT can be seen as the simultaneous transfer of H^+ and e^-. The main determinant of relative reactivity is the C–H (or X–H) bond energy. For example, tertiary CH bonds react before secondary and primary in line with the bond energies (CH_3–H, 105 kcal mol^{-1}; Et-H, 101 kcal mol^{-1}; *i*Pr-H, 98.6 kcal mol^{-1}). Once again, kinetic factors are relevant, for example, polar effects,[10] but where radical intermediates, X•, carry out a HAT, an important factor in understanding reactivity trends is the H–X bond energy of the corresponding product:

H–OH, 119 kcal mol^{-1}; RO–H, 105 kcal mol^{-1}; Cl–H, 103 kcal mol^{-1}; ROO–H, 89 kcal mol^{-1}; Br–H, 88 kcal mol^{-1}; I-H, 71 kcal mol^{-1}. Higher bond energies are associated with more reactive radicals.

Mayer[9] has also shown some of the best examples in which an effective HAT can occur by coupled transfer of a proton and an electron. For example, in the case of $MnO_4{}^-$ as oxidant, a proton can be transferred to an oxo group while an electron reduces Mn(VII) to Mn(VI). Although it is diamagnetic, $MnO_4{}^-$ acts as if it were an X• reagent with reactivity corresponding to an X–H bond energy of 80 kcal mol^{-1}. Phenol substrates are much more kinetically reactive than their PhO–H bond energy (87 kcal mol^{-1}) would suggest, presumably as the result of polar effects.

Alkyl hydroperoxides, very common primary oxidants, raise difficult mechanistic issues. Either free radical reactions can follow from peroxide homolysis, or metal-oxo chemistry can follow from O atom transfer to the metal. A peroxide that has proved useful in distinguishing the two cases is $PhCH_2CMe_2(OOH)$. If homolysis occurs, the resulting $PhCH_2CMe_2O\bullet$ radical fragments to $PhCH_2\bullet$ and Me_2CO at a rate of ca. 2×10^8 sec^{-1}, fast enough to avoid most bimolecular traps. Likewise, the substrate may be chosen to rearrange rapidly: cyclopropylmethyl radical rearranges to homoalkyl radical at a rate of *ca*. 10^8 sec^{-1}. Ingold**[11]** has taken this analysis furthest and 'unmasked' several systems originally thought to involve metal-oxo chemistry but in fact going by a radical route.

Careful choice of solvent is usually required. Typical oxidation-resistant solvents include AcOH, MeCN, H_2O, $PhNO_2$, and $CHCl_3$.

The ligands also have to be oxidation resistant. This means that ligands, such as ethylenediamine, with weak, reactive CH bonds usually need to be avoided.

Strongly electron-donating ligands are often preferred as they stabilize high oxidation states. Deprotonated amides combine this feature with oxidation resistance and have seen numerous applications, such as the Collins catalyst.**[12]** In contrast, phosphines are not useful, being neither particularly strong donors, nor oxidation resistant. Most of the ligands that have proved useful in oxidation are chelates, no doubt to avoid ligand dissociation which would normally be followed by ligand oxidation.

3 AUTOXIDATION

Autoxidation, the oxidation of organic compounds by air, normally occurs via a radical chain mechanism. For example, cyclohexene undergoes allylic CH abstraction by an initiator, and the resulting cyclohexenyl radical reacts with O_2 to give the corresponding hydroperoxy radical that abstracts an H from cyclohexene. In this case the final product is the allylic hydroperoxide. Conversion of ethers to the hydroperoxides is another familiar example. The conversion of cumene to phenol and acetone is a commercial application of the reaction (equation 9).

$$\text{Ph-CHMe}_2 \Longrightarrow \text{Ph-C(OOH)Me}_2 \Longrightarrow \text{Ph}-\text{OH} + \text{Me}_2\text{CO} \quad (9)$$

$$\text{Q}\bullet + \text{RH} \longrightarrow \text{R}\bullet + \text{QH} \quad (10)$$

$$\text{R}\bullet + \text{O}_2 \longrightarrow \text{RO}_2\bullet \quad (11)$$

$$\text{RO}_2\bullet + \text{RH} \longrightarrow \text{R}\bullet + \text{RO}_2\text{H} \quad (12)$$

$$2\text{RO}_2\bullet \longrightarrow \text{RO}_4\text{R} \longrightarrow \text{products} + \text{O}_2 \quad (13)$$

A schematic autoxidation pathway involves initiation (equation 10), propagation (equation 11–12) and termination (equation 13). Since hydroperoxides easily undergo metal-catalyzed decomposition, the addition of a metal can both speed up an air oxidation and avoid the formation of a hydroperoxide, which is rarely the desired final product. This is perhaps the simplest type of metal catalysis. The metal is normally capable of 1e redox behavior, hence typically a 3d transition metal. As shown in equations (14–15), it can decompose the RO_2H to give the highly reactive RO• radical in a manner resembling equation (3–4). RO• radical can abstract H from RH and provide R• radical that in turn reacts with O_2 to form RO_2•; in this way, R plays the role of Q• in equation (10).

$$\text{RO}_2\text{H} + \text{M}^+ \longrightarrow \text{RO}\bullet + \text{M}^{2+} + \text{HO}^- \quad (14)$$

$$\text{RO}_2\text{H} + \text{M}^{2+} \longrightarrow \text{RO}_2\bullet + \text{M}^+ + \text{H}^+ \quad (15)$$

Fe(II)/(III) is the best known such redox couple, but numerous other catalysts are common, including Cu(I)/(II) and Co(II)/(III).

4 OXIDATION PATHWAYS

Metals that are capable of 2e redox changes, typically main group elements and 4d and 5d transition metals, can give heterolysis of a peroxide to form a diamagnetic oxidant that may avoid the radical pathways seen in the case of equation (14–15). O atom transfer to the substrate is possible in this way. Sharpless**[13]** epoxidation provides an excellent example. In this case *t*BuOOH is the primary oxidant, Ti(*i*-OPr)$_4$ is the catalyst precursor and a tartrate ester is the ligand that induces a high ee in the epoxy alcohol formed from an allylic alcohol. This reaction has been successfully developed on an industrial scale.

Meunier**[14]** has reviewed recent advances in asymmetric oxidation. Jacobsen's**[15]** asymmetric epoxidation catalysts are some of the most successful. These use Mn(III) in a chiral salen ligand with NaOCl as primary oxidant. The intermediacy of Mn(V) oxo species has been proposed as the active species formed after O atom transfer from the hypochlorite. Enantiomeric excesses of 97–98% are seen in the epoxide product on a consistent basis across a wide variety of alkene substrates.

Radical clock substrates,**[12]** such as methylcyclopropane, are also useful. Because the ring CH bonds are particularly strong, the methyl CH bonds are subject to H atom abstraction by radicals such as RO• or •OH. The resulting cyclopropyl methyl radical rearranges via ring opening with a rate of ca. $2 \times 10^8\ \text{s}^{-1}$. Seeing ring opened products can be a good test for a radical oxidation pathway. These tests refer to radicals that are genuinely free. If they are constrained in some way, anomalous results could be seen. It is not yet clear how constraints such as reversible trapping by metal species, or the presence of a constrained cavity such as an enzyme active site, could affect the outcome of such tests.

5 BIOINORGANIC MODEL OXIDATION CATALYSTS

The earliest homogeneous oxidation catalyst was Fenton's reagent**[16]** of 1898, which used H_2O_2 as primary oxidant and

Fe salts as the catalyst for alkane oxidation. These and many related later systems are believed to go by metal-catalyzed decomposition of H_2O_2 generating reactive radicals such as •OH in the process. A typical cycle of reactions often proposed is shown as (3)–(4). Once •OH is formed, it can abstract an H atom from an alkane C–H bond and lead to a hydroxylated product (equation 10–14).

Of the monooxygenase type of model, some use O_2 and a reducing agent, much like the enzymes themselves, some use H_2O_2, which can be regarded as prereduced O_2, and some use oxo-transfer agents such as PhIO. Porphyrins of Fe and Mn have been studied most extensively as catalysts.[17] The presumption has been that all these classes go through metal-oxo intermediates, although in reality, the mechanisms may be more complicated. The H_2O_2 type have their enzyme analogue in peroxidases, and the oxo-transfer type has its enzyme analogue in the fact that several monooxygenases accept oxo-transfer agents as viable primary oxidants *in vitro*.

A feature of many monooxygenases that hydroxylate arenes is the 1,2-migration of an H (D) atom during the oxidation, denoted the NIH shift.[18] This may be a result of the presence of an intermediate carbocation at the 2-position, following epoxidation of the 1,2-C=C multiple bond of the ring and subsequent ring opening.[19]

The Udenfriend[20] system of 1954 was perhaps the first to be specifically presented as a model of a biological process. In this system, Fe(II) is the catalyst, EDTA the ligand, air is the primary oxidant and ascorbic acid provides the reducing equivalents called for in this ‘monooxygenase’ system. Arenes can be hydroxylated to phenols, alkanes to alcohols, and alkenes to epoxides, although with modest efficiency. The NIH shift was not observed in the model, however.

Groves[21] has shown how a variety of model complexes, notably iron porphyrins, can catalyze a series of oxidation reactions of the monooxygenase type with oxo donors such as PhIO as primary oxidants. The intermediacy of metal-oxo species is indicated.

Meunier[22] has developed model chemistry for peroxidases such as ligninase with $KHSO_5$ as oxo-transfer oxidant and Fe or Mn-tetrasulfoporphyrin in aq. MeCN. These catalysts oxidize lignin models such as veratryl alcohol (3,4-methoxybenzyl alcohol) to give biologically relevant products such as quinones.

Another biologically inspired problem is water oxidation to dioxygen,[23] modeling Photosystem II (PSII) of green plants. The oxygen evolving center of PSII consists of a Mn_4Ca oxo-cluster that stores up four oxidizing equivalents before using them to release O_2. These storage steps may well be Mn(III) to Mn(IV) oxidations but the final O_2 forming step is still somewhat mysterious. A model system is known that uses oxone as oxidant and $[(\mathrm{terpy})(H_2O)\mathrm{Mn(III)}(\mu\text{-}O)_2\mathrm{Mn(IV)}(H_2O)(\mathrm{terpy})]$ as catalyst. Isotope labeling shows that the oxygen that appears in the O_2 formed comes, at least in part, from water.[24]

6 OXIDATION CATALYSTS FOR ORGANIC SYNTHESIS

The main goal of recent research in this area has been to find efficient asymmetric versions of nonradical metal-catalyzed epoxidation and hydroxylation reactions. The Sharpless epoxidation[25] converts allyl alcohols to the epoxides with exceptionally high e.e.s. and with predictable absolute configuration. The catalyst dictates the configuration independent of the substitution pattern.

Sharpless also introduced the catalytic asymmetric dihydroxylation of cis-disubstituted olefins with osmium tetroxide.[26] Jacobsen’s catalyst,[15] mentioned earlier, is also much used in synthesis.

7 OXIDATION CATALYSTS FOR GREEN CHEMISTRY

The rise of green chemistry[8,27] is likely to greatly modify the practice of chemical science in the twenty-first century, as climate change obliges governments to mandate a move to renewable resources. This will undoubtedly involve a reliance on catalysis to convert the available feedstock to useful chemical products.

One of the goals of green chemistry is the destruction of pollutants, an area in which oxidation chemistry can play a major role. Collins[12] has developed an extremely robust, efficient Fe-based catalyst that uses H_2O_2 as oxidant to oxidize a variety of pollutant materials. The ligand set features deprotonated amide, a very strong electron donor ligand, with extensive alkyl substitution to protect what would otherwise be sensitive CH bonds. The result is an extremely oxidation-resistant catalyst which has proved useful in commercial applications, such as oxidative degradation of dyes.

Another goal is to develop the use of benign primary oxidants such as hydrogen peroxide for commercial oxidations. Neumann and coworkers[28] have reported an H_2O_2-based oxidation of alcohols to aldehydes and ketones that involving a benign medium, H_2O, a nontoxic catalyst, an early transition-metal polyoxometalate, and green work-up conditions – separation of the aqueous phase containing the catalyst from the organic-solvent-free aldehyde/ketone phase. Hill has useful catalysts of a similar type.[29] Many related catalysts exist: Sheldon’s review is a useful resource.[30]

Ideally, air or oxygen would be able to act as primary oxidant. Bäckvall *et al.*[31] used a $\mathrm{RuCl(OAc)(PPh_3)_3}$/hydroquinone/ $\mathrm{Co(salophen)(PPh_3)}$ system, for aerobic oxidation of benzylic and allylic alcohols. A modified Ru/quinone/Co system catalyzed the aerobic oxidation of secondary aliphatic alcohols.[32] Quinone can be used as an intermediate carrier of the oxidizing equivalents from oxygen or air. The regeneration of the quinone being performed directly with molecular oxygen, without the need for an extra catalyst.[33]

A number of systems consist of a palladium salt, typically $PdCl_2$ or $Pd(OAc)_2$, with a base. For example, $PdCl_2$–NaOAc catalyzes the aerobic oxidation of secondary alcohols in ethylene carbonate under mild conditions.[34] Sheldon has carried out mechanistic investigations on a number of related Pd systems and shown that water-soluble complexes of Pd(II) with phenanthrolines are stable, recyclable catalysts for the selective aerobic oxidation of a wide range of alcohols to aldehydes, ketones, and carboxylic acids in a biphasic liquid–liquid system. The active catalyst is a dihydroxy-bridged palladium dimer.[35]

Sheldon[36] and Trost[37] have both emphasized the importance of atom efficiency and catalysis in organic synthesis.

8 ORGANOMETALLIC OXIDATION CATALYSTS

Several important nonradical catalytic oxidations go via organometallic mechanisms. The commercially useful Wacker process[38] converts ethylene to acetaldehyde with air as oxidant, using Pd(II) and Cu(II) catalysts. The Pd(II) binds to the ethylene to give an organometallic intermediate, the alkene complex. This complex subsequently uses water as the O source to oxidize the ethylene to acetaldehyde, the Pd being reduced in the process. The resulting Pd(0) is reoxidized to Pd(II) with two equivalents of Cu(II) and the Cu(I) so formed is then reoxidized by air to close the cycle.

Shilov chemistry,[39] developed from 1970, employs $[Pt(II)Cl_4]^{2-}$ salts to oxidize alkanes RH to ROH or RCl with modest efficiency. Pt(IV) is an efficient (but economically impractical) primary oxidant that makes the process catalytic. This discovery strongly contributed to the continuing activity in CH activation. Periana developed a related and much more efficient system for methane oxidation to methanol using 2,2′-bipyrimidine ligands and sulfuric acid as solvent. In this case, the sulfuric acid is the primary oxidant and the methanol formed is protected by being converted in situ to $MeOSO_3H$, an ester that strongly resists further oxidation. This area is more fully described under the entry ***Alkane Carbon–Hydrogen Bond Activation***.

9 CONCLUSION

Oxidation is still less well developed than other metal-catalyzed reactions but the application is a very important one practically, so efforts are continuing. The mechanisms are hard to decipher, often being radical in character, but selective nonradical oxidations are becoming much more common. Asymmetric versions of oxidation catalysts have now appeared that have become very useful in organic synthetic and commercial applications.

10 REFERENCES

1. O. de Montellano ed., ‘Cytochromes’, Plenum, New York, 1995, p. 450.
2. B. Meunier ed., ‘Biomimetic Oxidations Catalyzed by Transition Metal Complexes’, ICP, London, 2000.
3. M. Hudlicky ed., ‘Oxidations in Organic Chemistry’, ACS Monograph 186, Washington, DC, 1990, ‘Comprehensive Organic Chemistry’, ed. B. M., Trost, Pergamon, Oxford, 1991 Vol. 7.
4. K. I. Goldberg, A. S. Goldman, eds, ‘Activation and Functionalization of C–H Bonds’, American Chemical Society, Washington DC, 2004.
5. ‘Metalloproteins in Catalytic Oxidations’, RA Sheldon; Marcel Dekker, New York, 1994.
6. F. Montanari, L. Casella, eds, ‘Metalloporphyrin Catalysed Oxidations’, Kluwer, Dordrecht, 1994.
7. W. Buijs, *Top. Catal.*, 2003, **24**, 73; J. H. Clark and D. J. Macquarrie, *Org. Proc. Res. Devel.*, 1997, **1**, 149.
8. P. T. Anastas and M. M. Kirchhoff, *Acc. Chem. Res.*, 2002, **35**, 686.
9. J. M. Mayer, Chap. 1 in B. Meunier ed., ‘Biomimetic Oxidations Catalyzed by Transition Metal Complexes’, ICP, London, 2000.
10. B. P. Roberts, *Chem. Soc. Rev.*, 1999, **28**, 25.
11. K. U. Ingold and P. A. MacFaul, Chap. 2 in B. Meunier ed., ‘Biomimetic Oxidations Catalyzed by Transition Metal Complexes’, ICP, London, 2000.
12. T. J. Collins *Acc. Chem. Res.*, 2002, **35**, 782.
13. R. A. Johnson, K. B. Sharpless, in ‘Catalytic Asymmetric Synthesis’, ed. I. Ojima, VCH Weinheim, 1993.
14. A. Robert, B. Meunier, Chap. 12 in B. Meunier ed., ‘Biomimetic Oxidations Catalyzed by Transition Metal Complexes’, ICP, London, 2000.
15. E. N. Jacobsen, *Acc. Chem. Res.*, 2000, **33**, 431.
16. H. S. H. Fenton, *J. Chem. Soc.*, 1898, 808.
17. J. T. Groves, R. C. Haushalter, M. Nakamura, T. E. Nemo, and B. J. Evans, *J. Am. Chem. Soc.*, 1981, **103**, 2884.
18. D. M. Jerina, J. W. Daly, W. Landis, B. Witkop, and S. Udenfriend, *J. Am. Chem. Soc.*, 1967, **89**, 3347.
19. D. R. Boyd, J. T. G. Hamilton, N. D. Sharma, J. S. Harrison, W. C. McRoberts, and D. B. Harper, *Chem. Commun.*, 2000, (16), 1481.
20. S. Udenfriend, C. T. Clark, J. Axelrod, and B. B. Brodie, *J. Biol. Chem.*, 1954, **208**, 731.
21. J. T. Groves, *Proc. Natl. Acad. Sci. USA*, 2003, **100**, 3569.
22. B. Meunier, Chap. 4 in B. Meunier ed., ‘Biomimetic Oxidations Catalyzed by Transition Metal Complexes’, ICP, London, 2000.
23. W. Ruttinger and G. C. Dismukes, *Chem. Rev.*, 1997, **97**, 1.
24. G. Brudvig, J. Vrettos, D. Stone, J. Limburg, H. Y. Chen, and R. H. Crabtree, *J. Inorg. Biochem.*, 2001, **86**, 27.

25. M. G. Finn, K. B. Sharpless, *J. Am. Chem. Soc.*, 1991, **113**, 113; S. S. Woodard, M. G. Finn, K. B. Sharpless, *J. Am. Chem. Soc.*, 1991, **113**, 106.
26. L. Wang and K. B. Sharpless, *J. Am. Chem. Soc.*, 1992, **114**, 7568.
27. P. Anastas and J. Warner, 'Green Chemistry: Theory and Practice', Oxford University Press, Oxford, 1998.
28. D. Sloboda-Rozner, P. L. Alsters, and R. Neumann, *J. Am. Chem. Soc.*, 2003, **125**, 5280.
29. C. L. Hill and I. A. Weinstock, *Nature*, 1997, **388**, 332.
30. R. A. Sheldon, I. W. C. E. Arends, and A. Dijksman, *Catal. Today*, 2000, **57**, 157.
31. J.-E. Bäckvall, R. L. Chowdhury, and U. Karlsson, *Chem. Commun.*, 1991, 473.
32. G.-Z. Wang, U. Andreasson, and J.-E. Bäckvall, *Chem. Commun.*, 1994, 1037.
33. A. Hanyu, E. Takezawa, S. Sakaguchi, and Y. Ishii, *Tetrahedron Lett.*, 1998, **39**, 5557.
34. T. F. Blackburn and J. Schwartz, *Chem. Commun.*, 1977, 157.
35. G. J. ten Brink, I. W. C. E. Arends, and R. A. Sheldon, *Adv. Synth. Catal.*, 2002, **344**, 355.
36. R. A. Sheldon, *Pure Appl. Chem.*, 2000, **72**, 1233.
37. B. M. Trost, *Acc. Chem. Res.*, 2002, **35**, 695.
38. R. H. Crabtree, 'The Organometallic Chemistry of the Transition Metals', 4th edn., Wiley, New York, 2005.
39. A. E. Shilov and A. A. Shteinman, *Acc. Chem. Res.*, 1999, **32**, 763.

Oxide Catalysts in Solid-state Chemistry

Toshio Okuhara & Yuichi Kamiya
Hokkaido University, Sapporo, Japan

Based in part on the article Oxide Catalysts in Solid State Chemistry by Toshio Okuhara & Makoto Misono which appeared in the Encyclopedia of Inorganic Chemistry, First Edition.

1	Introduction	1
2	General Aspects Pertinent to Catalysis	1
3	Mixed Oxide Catalysts	3
4	References	19

1 INTRODUCTION

Metal oxides containing single metallic elements (binary oxides) and more than two metallic elements (double oxides and salts of oxoacids) are commonly used as catalysts in a variety of chemical reactions.[1] Oxide and metallic catalysts are two major groups of industrial catalysts. In practice, most catalysts are produced from mixtures of more than two phases; the phase primarily responsible for the catalysis is called the active component.

The components, which are added to enhance or modify catalytic functions, are called promoters or additives. In general, the active components are dispersed on the surface of materials, called supports or carriers, to increase the surface area and/or stability of the active components. Typical supports include metal oxides, such as alumina, silica, and titania, and zeolites that possess micropores. The categorization of catalyst materials into three components – active, additive, and support – is a convenient classification method.

Metal oxide catalysts can be classified as oxides of transition elements or as oxides of other typical metals. Typical transition elements include Cr, Fe, Co, Mo, and V, whose oxides catalyze oxidation and reduction reactions by changing the oxidation state of the metal ion. For selective oxidation of hydrocarbons, mixed oxides containing Mo and V are widely used. Oxides of other metals (acidic oxides such as silica and silica-alumina, basic oxides such as CaO and MgO, and amphoteric oxides such as alumina) catalyze acid or base reactions such as alkylation, isomerization, and hydration-dehydration.

Table 1 classifies catalysts according to reaction type, and shows typical oxide catalysts used in practical processes.

2 GENERAL ASPECTS PERTINENT TO CATALYSIS

Catalyst design involves both chemical and reaction engineering aspects in a rational and efficient methodology for the development of practical catalysts. Catalytic activity, selectivity, and durability are the main gauges of catalyst performance, while redox capability and acid-base properties are the most important chemical properties. The first two relationships shown in Scheme 1 for oxide catalysts will be described briefly. The factors controlling catalyst performance may be categorized into geometric (crystal plane and surface defects) and material-intrinsic factors that are intrinsic to the oxide material constituting the catalyst. The bulk structure is more closely reflected in the surface for oxide catalysts than for metal catalysts, as in the case of zeolites, heteropoly compounds, and perovskites.[2,3]

2.1 Geometric Factors

Even for the oxide catalysts consisting of the same elements and composition, the activity and selectivity vary depending on surface geometry. For example, the basal (010) plane of MoO_3 crystal (dispersed on graphite) is not selective, whereas the side (100) planes are highly selective for the oxidation of propene to acrolein (Table 2).[4] Another example is the anisotropic oxidation of n-butane to maleic anhydride over microcrystallites of $(VO)_2P_2O_7$.[5] The basal plane on which the $V^{4+}(=O)–O–V^{4+}$ sites are located are highly selective, but the side planes are less selective.

Vacancies in solid bulk influence oxidation activity in several ways. Allylic oxidation over multicomponent Bi–Mo oxide catalysts[6] is accelerated by cation vacancies by the rapid supply of oxygen from inside the bulk to active surface sites. Rapid oxygen diffusion in the bulk[7] as well as its correlation with catalytic activity[8] has been reported for Bi–Mo oxide (the oxygen diffusion becomes significant only in the presence of reductant). The redox cycle (see below) is accelerated by diffusion of metal ions in the case of iron oxide, $Fe_3O_4 \longleftrightarrow \gamma\text{-}Fe_2O_3$, in which the oxide ion packing remains unchanged during the reduction-oxidation process.[9]

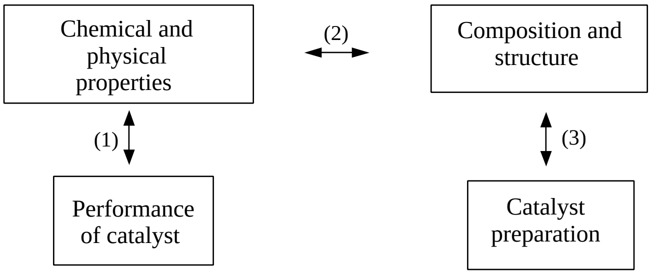

Scheme 1 Useful relations for catalyst design

Table 1 Typical reactions catalyzed by oxide catalysts

Reaction	Catalyst
Oxidation	
Selective oxidation	
Propene $\rightarrow$ acrolein (acrylonitrile)	Mo–Bi–O, Fe–Sb–O
Propane $\rightarrow$ acrylic acid (acrylonitrile)	Mo–V–Te(Sb)–Nb–O
n-Butane $\rightarrow$ maleic anhydride	$(VO)_2P_2O_7$
Naphthalene $\rightarrow$ phthalic anhydride	V_2O_5/TiO_2
Isobutene $\rightarrow$ methacrylic acid	Mo–V–O(1st stage) + heteropolyacids (2nd stage)
Complete oxidation	
Catalytic combustion	Mn–Ba–Al_2O_3, La(Ce,Sr)CoO_3, Co_2MnO_4
Hydrogenation	
Ph–COOH $\rightarrow$ Ph–CHO	ZrO_2–Cr, In, etc.
$CO + H_2 \rightarrow CH_3OH$	Cu–ZnO, CuO–Cr_2O_3
Dehydrogenation	
Oxidative dehydrogenation	
Ethylbenzene $\rightarrow$ styrene	Fe_2O_3 – (K–Cr or –Ce, –Mo)
Simple dehydrogenation	
2-butanol $\rightarrow$ methyl ethyl ketone	Cu–ZnO
Acid catalysis	
Cracking (FCC)	Zeolite (USY)+ amorphous silica-alumina
Alkylation, isomerization	Zeolite, silica – alumina, Pt–$SO_4{}^{2-}/ZrO_2$, etc.
Methanol $\rightarrow$ gasoline	Zeolite (H-ZSM-5)
Hydration	$H_3PW_{12}O_{40}$, H-ZSM-5
Esterifiation	$H_4SiW_{12}O_{40}/SiO_2$
Ethylene + $H_2O + O_2 \rightarrow$ acetic acid + H_2O	Pd(–Te)–$H_4SiW_{12}O_{40}/SiO_2$
Base catalysis	
Isomerization(e.g. double bond shift)	Na/NaOH/alumina
Polymerization of alkene	CrO_2/Al_2O_3
Metathesis of alkene	WO_3/SiO_2
Denitrification	
$NO + NH_3 + (1/4)O_2 \rightarrow N_2 + (3/2)H_2O$	V_2O_5/TiO_2
Other reactions	
Anode of solid-state fuel cell	La(Sr)Co(Mn)O_3

Table 2 Oxidation of propene over different crystal planes of MoO_3 crystal dispersed on graphite

	Rate of oxidation		
	Basal plane (010)	Side plane (100)	Apical plane (101), etc.
To acrolein	0.06	2.26	0.73
To CO_x	1.00	0	0
Total	1.06	2.26	0.73

For valency-controlled perovskite-type mixed oxides, such as $La_{1-x}Sr_xCoO_3$, the ease with which they form oxide vacancies increases the catalytic activity for hydrocarbon oxidation.[2]

2.2 Material-Intrinsic Factors

General trends exist between the catalytic activity (or selectivity) and the intrinsic nature of the metallic components, which depend on the type of catalysis. General correlations for three typical cases and the promotion effects of mixing more than two metal oxides are described below.

Most oxidation reactions over oxide catalysts are well understood in terms of the redox mechanism, for example, repeated reduction and oxidation of the surface layer or bulk of the oxide catalyst. In the first step, a metal oxide catalyst oxidizes reactant molecules, such as carbon monoxide to carbon dioxide (equation 1; reduction of catalyst). In the second step, the reduced catalyst is oxidized back to its initial state by oxygen molecules supplied by the gas phase (equation 2; reoxidation of catalyst). The catalytic oxidation (equation 3) proceeds by repetition of this redox cycle.

$$CO + MO \longrightarrow CO_2 + M \tag{1}$$

$$M + \tfrac{1}{2}O_2 \longrightarrow MO \tag{2}$$

$$CO + \tfrac{1}{2}O_2 \longrightarrow CO_2 \tag{3}$$

During selective oxidation of alkenes, hydrogen abstraction and oxygen-addition reactions are usually key steps, in which different oxygen species participate. The rate of hydrogen abstraction increases, in general, with an increase in the basicity of oxide ion, whereas oxygen addition is facilitated by oxygen bonded to high-valence metal ions as in $Mo^{VI}{=}O$ and $V^{V}{=}O$. For the selective oxidation of alkanes, the Lewis acid site or Lewis acid-base pair site on oxide catalysts are considered to play an important role for activation of alkane through dehydration from methylene group. Oxygen species on the surface are formed as expressed by equation (4); the formation and reactivity of these species have been reviewed.[10]

$$O_2(\text{ads}) \longrightarrow O_2^-(\text{ads}) \longrightarrow O_2^{2-}(\text{ads}) \longrightarrow O^-(\text{ads}) \longrightarrow O^{2-}(\text{lattice}) \quad (4)$$

In acid–base catalysis,[11] proton addition to or abstraction from reactant molecules (with Brønsted acids or bases), or formation of coordination bonds (with Lewis acids), and subsequent bond breaking and rearrangement are the key reaction processes. Most cases involve ionic reaction intermediates bound to the surface by electrostatic interactions.

In the case of binary oxides (single metallic elements), the surface tends to change from basic to acidic as the electronegativity of the metal ion increases (decrease in ionic radii and increase in the positive charge), for example, from BaO and CaO to SiO_2 and MoO_3. Thomas[12] and Tanabe[13] predicted the acidic properties of mixed oxides containing two kinds of cations, on the basis of differences in the coordination number and positive charge of the cation species introduced in the framework of the major component oxide. In the case of aluminosilicate zeolites, the isomorphic substitution of Si in the framework of Si^{IV} oxide by Al^{III} creates cation-exchange sites.

The acid strength of metallic salts of oxoacids in the solid state (and hence the catalytic activity by acid catalysis) increases with electronegativity of the metal ion.[14]

2.3 Promotion Effects of Mixed Oxides

As described above, most industrial catalysts are mixed oxides of at least two oxide phases, because catalyst performance is greatly improved by mixing different oxides, according to be following mechanisms: (i) stabilization, (ii) control of redox properties, (iii) creation of acidity and basicity, (iv) control of electronic and coordination state of the metal ion, and (v) combination of more than two functions to evolve acid-oxidation and acid–base bifunctional catalysts. Examples are provided in the following sections.

3 MIXED OXIDE CATALYSTS

3.1 Bi–Mo Oxides

Bismuth molybdates having a Bi/Mo ratio in the range of 0.67–2.0 catalyze the selective oxidation of propene to acrolein, and the ammoxidation of propene to acrylonitrile (equations 5 and 6). Both reactions proceed through an allylic intermediate. Three typical active phases – α-$Bi_2Mo_3O_{12}$, β-$Bi_2Mo_2O_9$, and γ-Bi_2MoO_6 – exist in this Mo/Bi ratio range. Their structural characteristics are summarized in Table 3.[15] The α-phase has a structure similar to that of scheelite (AMO_4).[16] The structure of the γ-phase is related to koechlinite with layers of $[Bi_2O_2]^{2+}$ and $[MoO_2]^{2+}$ connected by O^{2-} ions. The β-phase structure possesses Bi vacancies in addition to the two structures described above.

$$CH_2{=}CH\text{-}CH_3 + O_2 \longrightarrow CH_2{=}CH\text{-}CHO + H_2O \quad (5)$$

$$CH_2{=}CH\text{-}CH_3 + NH_3 + \tfrac{3}{2}O_2 \longrightarrow CH_2{=}CH\text{-}CN + 3H_2O \quad (6)$$

The catalytic activities of these phases for the oxidation of propene are α-$Bi_2Mo_3O_{12}$ (37), β-$Bi_2Mo_2O_9$ (16), and γ-Bi_2MoO_6 (8), where the figures in parentheses are measures of activity in units of 10^{-8} mol m^{-2} s^{-1} at 660 K.[17] The selective oxidation rate on bismuth molybdate is higher than that for iron molybdate by approximately two orders of magnitude, while these gave similar rates for complete oxidation.[17] Selectivity for acrolein over bismuth molybdates and other catalysts is given in Table 4.[18] The selectivity toward acrolein over these bismuth molybdates and bismuth iron molybdate is greater than 90%. When the partial pressure of oxygen is greater than that of propene, selectivity decreased.

The reaction proceeds via a redox mechanism. Evidence exists for involvement of bulk oxygen in the partial oxidation of propene over bismuth molybdates, suggested by the independence of the reaction rate from the partial pressure of oxygen in the feed gas over these catalysts. The percentage of oxygen atoms that can exchange with ^{18}O during the reaction of $^{18}O_2$ + propene are 9.4, 100, and 100 layers for α-$Bi_2Mo_3O_{12}$, β-Bi_2MoO_6, and γ-$Bi_3FeMo_2O_{12}$, respectively,

Table 3 Crystal structures of Bi–Mo oxides

Formula	Number of oxygen atoms bound only to Bi (per formula)	Number of Bi^{3+} vacancies	Degree of clustering of MoO_4
$\alpha-Bi_2Mo_3O_{12}$	–	1	2
$\beta-Bi_2Mo_2O_9$	1	0.5	4
$\gamma-Bi_2MoO_6$	2	–	Infinite

Table 4 Acrolein selectivities in partial oxidation of propene

Catalyst	Selectivity (%)	Temp. (K)	Reaction feed (%) C_3H_6	O_2	Inert
α-$Bi_2(MoO_4)_3$	88–95	623–723	10	10	80
	88	703	50	50	0
β-$Bi_2Mo_2O_9$	85–93	623–743	30	30	40
	65	660	13	26	61
γ-Bi_2MoO_6	91	623–723	10	10	80
	66	660	12	26	61
$Bi_3FeMo_2O_{12}$	82–86	623–723	10	10	80
	83	703	50	50	0
Thermal oxidation	0	698	50	37	13

indicating that the partial oxidation involves lattice rather than gas-phase oxygen and that diffusion of oxygen in the bulk is rapid.[19] The roles of MoO_3 and Bi_2O_3 are assumed to be as follows. Initial α-hydrogen abstraction during the partial oxidation of propene over bismuth molybdates proceeds via oxygen atoms associated, at least partially, with bismuth molybdate catalysts acting as centers for the second abstraction of hydrogen and subsequent insertion of oxygen into acrolein.[18] A proposed mechanism for the partial oxidation of propene to acrolein is shown in Figure 1.[20]

A range of important multicomponent catalysts has the general formula $Bi_aMo_bM_c^{2+}\ M_d^{3+}\ O_n$, where M^{2+} is Ni, Co, Mg, or Mn, and M^{3+} is Fe, Cr, Al, or Ce. Proposed models of unsupported multicomponent catalysts are shown in Figure 2.[21,22] M^{2+} ions are essential and constitute the fundamental structure of the catalyst systems. Their catalytic activity is attributed to γ-Bi_2MoO_6 and α-$Bi_2Mo_3O_{12}$ phases on the surface.

More complex Bi–Mo oxide catalysts are claimed in patents, such as Bi–Mo–M^{2+}–M^{3+}–M^{+}–X–Y–O, where M^{+} is an alkali metal, X=Sb, W, and Y=P, B, and so on. In multicomponent catalysts, the metal molybdates $M^{2+}MoO_4$ and $M_2^{3+}(MoO_4)_3$ serve as supports for the active phase, α-$Bi_2Mo_3O_{12}$. Bulk migration of O^{2-} ions through lattice vacancies plays an important role in enhancing catalytic activity. In this complex system, the multifunctional nature promotes activation of oxygen, migration of oxygen species, and consecutive dehydrogenation and oxygenation. Tracer experiments using a model catalyst, α-$Bi_2Mo_3O_{12}$ supported on $Co_{11/12}Fe_{1/12}MoO_n$, whose lattice oxide was labeled by ^{18}O, led to the conclusion that the activation of molecular oxygen and oxidation of propene take place on different active sites; oxygen species activated by the support oxide involving iron and/or cobalt cations spill over through bulk diffusion to the reaction site of propene on bismuth molybdate.[23]

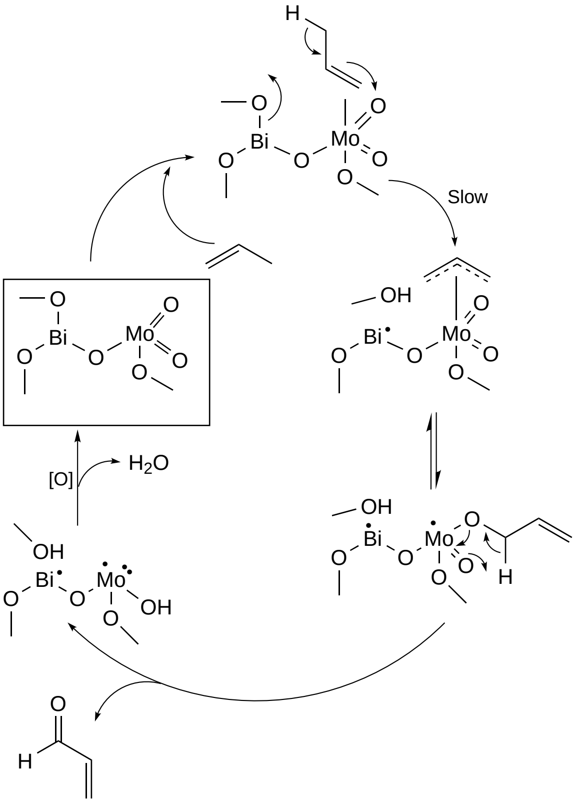

Figure 1 Mechanism for the selective oxidation of propene to acrolein over bismuth molybdate catalysts

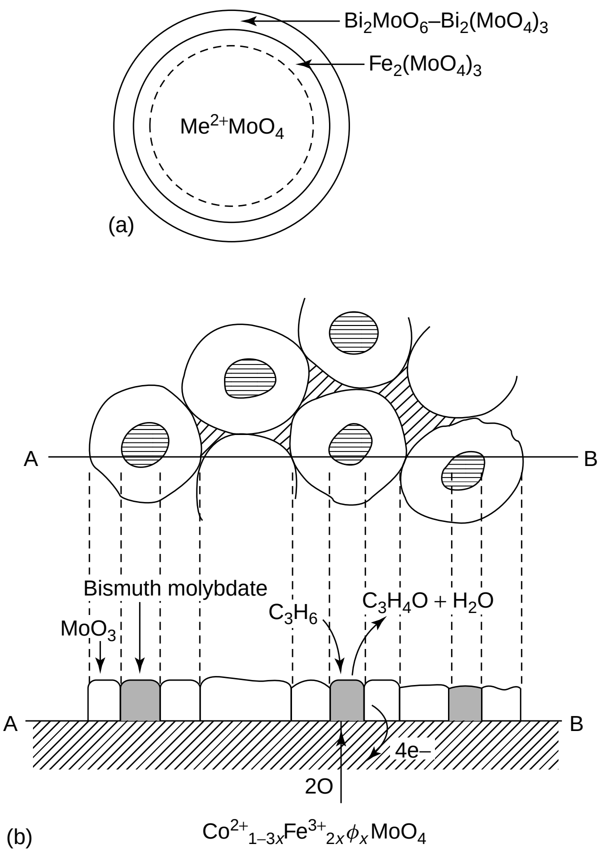

Figure 2 Model of multicomponent Bi–Mo oxide catalysts: (a) Wolf's model, and (b) Matsuura's model

Typical ammoxidation catalysts include $Bi_2O_3 + MoO_3$, $Fe_2O_3 + Sb_2O_4$ ($FeSbO_4$), $UO_3 + Sb_2O_4$ (USb_3O_{10}), and $SnO_2 + Sb_2O_4$.[15] In the $UO_3-Sb_2O_4$ catalyst, only USb_3O_{10} is the active and selective oxidation catalyst. Sb_2O_4 is inactive, and $USbO_5$ and UO_3 are active only for complete combustion. $FeSbO_4$ is also effective for ammoxidation and has been applied commercially.

3.2 Mo–V–Te–Nb Oxides

Among various mixed oxide catalysts supposedly active for the oxidation of propane to acrylic acid (equation 7) in patents and literature (Table 5),[24–29] Mo–V–Te–Nb oxides

Table 5 Mixed oxide catalysts for propane oxidation to acrylic acid

Catalyst	Conversion (%)	Selectivity (%)	Yield (%)	Temperature (K)	Feed
$MoSnO_n$	4	48	2	633	$C_3H_8/O_2/N_2$
$Mo_{1.51}Ni_1Te_{0.01}P_{0.02}O_n$	12	23	3	733	$C_3H_8/O_2/H_2O/He$
$Mo_1V_{0.4}Nb_{0.04}Bi_{0.08}Sb_{0.08}K_{0.08}O_n$	19	29	6	673	$C_3H_8/O_2/H_2O/N_2$
$Mo_1V_{0.3}Te_{0.23}Nb_{0.12}O_n$	80	60	48	653	$C_3H_8/air/H_2O$
$Mo_1V_{0.25}Te_{0.17}Nb_{0.20}O_n$	69	67	46	705	$C_3H_8/O_2/H_2O/N_2$
$Mo_1V_{0.3}Sb_{0.16}Nb_{0.05}O_n$	50	32	16	653	$C_3H_8/air/H_2O$
$Mo_1V_{0.3}Sb_{0.17}Nb_{0.07}O_n$	62	55	34	700	$C_3H_8/O_2/H_2O/N_2$

appear most promising. When Te of Mo–V–Te–Nb oxides is substituted with Sb, catalytic performance remains good, although these catalysts are less active and selective than the corresponding Te-containing catalysts.[28,29] As shown in Table 6, Mo–V–Te–Nb oxides are concurrently effective catalysts for the ammoxidation of propane to acrylonitrile (equation 8).[27,28,30] Two reactions, propane oxidation and ammoxidation, share fundamental reaction steps such as propane activation and propane dehydration, while ammonia activation and steps involving nitrile formation are present only for ammoxidation. Selective propane oxidation and ammoxidation are more difficult compared to propene oxidation and ammoxidation because the highly stable propane C–H bonds must be activated, and at the same time further oxidation of more reactive products to undesirable products or to carbon oxides must be suppressed. The highest yield of acrylic acid for propane oxidation over Mo–V–Te–Nb oxide catalysts (less than 60%) is much lower than that for propene oxidation followed by acrolein to acrylic acid (total yield greater than 90%).

$$CH_3\text{-}CH_2\text{-}CH_3 + 2O_2 \longrightarrow CH_2{=}CH\text{-}COOH + 2H_2O \qquad (7)$$

$$CH_3\text{-}CH_2\text{-}CH_3 + NH_3 + 2O_2 \longrightarrow CH_2{=}CH\text{-}CN + 4H_2O \qquad (8)$$

Mo is the essential element of effective catalysts for propene oxidation to acrolein and acrolein oxidation to acrylic acid, while V is an essential element for effective catalysis of acrolein oxidation to acrylic acid. Mo–V–Nb oxide catalysts are capable of activating propane even at 573 K, but yields products of acetic acid, acetaldehyde, and carbon oxides.[31] The addition of Te or Sb to Mo–V–Nb oxides induces certain structural changes leading to the formation of acrylic acid.[27,28]

The role of Nb in Mo–V–Te–Nb oxide catalysts has been clarified using model oxides, for example, mono-phasic crystalline Mo–V–Te oxide and Mo–V–Te–Nb oxide with the same orthorhombic layered structure.[32] Figure 3 shows a structural model of the orthorhombic phase of Mo–V–Te–(Nb) oxide in the *a*-*b* plane. Mo and V occupy octahedral sites and pentagonal bipyramidal sites, and Te is located in the hexagonal channels exclusively, but the heptagonal channels remain empty. Researchers have speculated that Nb is partially substituted with V.[32] As shown in Table 7, both catalysts show the same catalytic activity for propane oxidation and propene oxidation. However, selectivity for acrylic acid in both reactions increases by about 20% in the Nb-containing catalyst, while selectivities toward acetic acid and carbon oxides decrease. In addition, selectivity toward acrylic acid at low conversion for the propane oxidation is almost the same for both catalysts (Figure 4). These results indicate that the main role of Nb is not propane activation and formation of acrylic acid but is suppression of further oxidation of acrylic acid formed on the catalyst surface.

Few reports have discussed the structures of Mo–V–Te–Nb oxide catalysts in relation to propane oxidation and ammoxidation. Some reports indicate that not only the elemental composition but also preparative variables greatly affect the structure and performance of Mo–V–Te–Nb oxide catalysts. Among the preparative variables, methods for precursor preparation appear to be critical. One example is Mo–V–Te–Nb oxide, which when prepared by a solid-state method from corresponding oxides of each element is a mixture of MoO_3 and $(Mo-X)_5O_{14}$ (X is other cations) and is inactive for the propane ammoxidation. However, Mo–V–Te–Nb oxide prepared by a hydrothermal reaction method from the same oxide by the solid-state method is a mono-phasic oxide with an orthorhombic layered structure, which selectively catalyzes propane to acrylonitrile.[33]

Table 6 Catalytic results in propane oxidation and ammoxidation over Mo–V–Te–Nb oxide catalyst[a]

Reaction	Conversion (%)	Selectivity (%)	Yield (%)	Temperature (K)
Oxidation	80	60 (acrylic acid)	48 (acrylic acid)	653
Ammoxidation	89	64 (acrylonitrile)	58 (acrylonitrile)	693

[a] Composition of catalyst is $Mo_1V_{0.3}Te_{0.23}Nb_{0.12}O_n$.

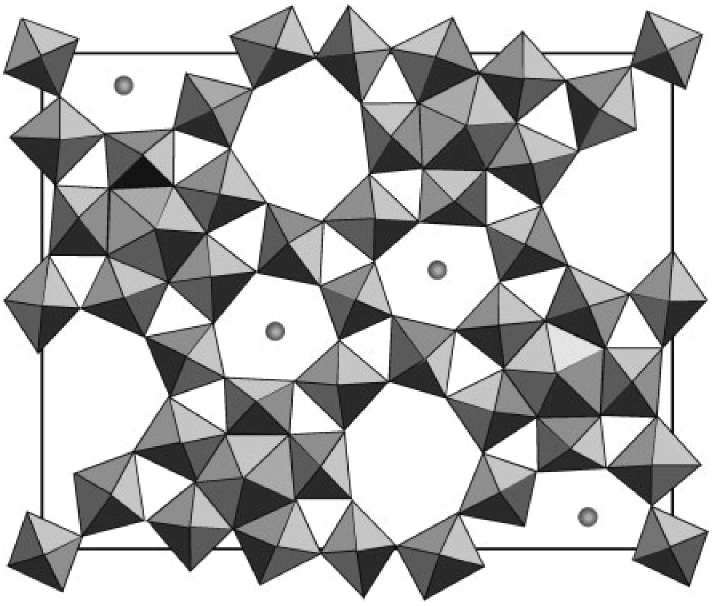

Figure 3 Structural model of the orthorhombic phase of Mo–V–Te–(Nb) oxide catalysts. Mo, V, and Nb are located in octahedral positions and in pentagonal channels. Te (•) is located in hexagonal channels

Table 7 Catalytic activity and selectivity for propane oxidation and propene oxidation over Mo–V–Te–(Nb) oxide catalysts

Catalyst	Temperature (K)	Conversion (%)		Selectivity (%)				
		C_3H_8	C_3H_6	acrylic acid	C_3H_6	acetone	acetic acid	CO_x
$Mo_1V_{0.44}Te_{0.10}O_n$	653	36.2	–	46.6	7.7	1.3	16.5	27.9
$Mo_1V_{0.25}Te_{0.11}Nb_{0.1}O_n$	653	33.4	–	62.4	8.7	0.4	7.3	21.2
$Mo_1V_{0.44}Te_{0.10}O_n$	615	–	56.5	55.6	–	17.3	14.2	12.9
$Mo_1V_{0.25}Te_{0.11}Nb_{0.1}O_n$	613	–	61.1	81.7	–	6.2	6.7	5.4

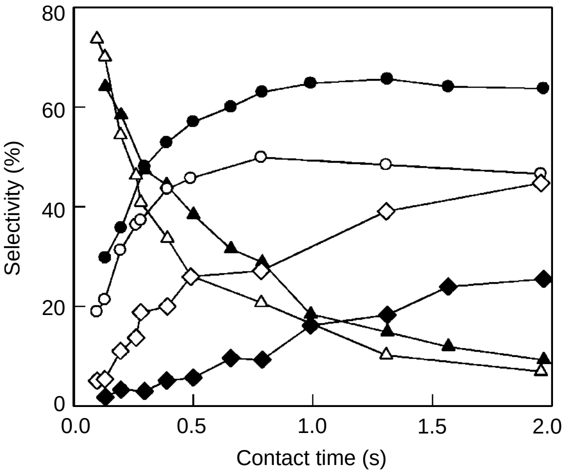

Figure 4 Selectivity changes of acrylic acid (circle), propene (triangle), and further oxidation products (lozenge) as a function of contact time in the oxidation of propane over Mo–V–Te oxide (open symbol) and Mo–V–Te–Nb oxide (closed symbol) catalysts

Catalyst calcination conditions are additional critical preparative variables that have a significant impact on the structure as well as the catalytic performance of Mo–V–Te–Nb oxide catalyst. From one precursor, two catalysts of very different crystal phases are obtained under different calcination atmospheres.[34] The catalyst calcined in nitrogen flow exhibits a high catalytic performance. In contrast, catalyst calcined in air is inactive toward propane oxidation.

3.3 V–P Oxides

3.3.1 *V-P-O with Different Structures and Catalysis*

V_2O_5 promoted by P or Mo is widely used for selective oxidation. V–P oxide catalysts are effective for the selective oxidation of *n*-butane to maleic anhydride.[35,36] The reaction is a 14-electron oxidation involving the abstraction of eight hydrogen atoms and insertion of three oxygen atoms (equation 9).

$$C_4H_{10} + \tfrac{7}{2}O_2 \longrightarrow C_4H_2O_3 + 4H_2O \qquad (9)$$

Among several crystalline phases of V–P oxides, crystalline phases having P/V ratios near unity are important for the selective oxidation of n-butane. The presence of a short V=O bond in the vanadyl group in its oxidized (V^{5+}) or reduced (V^{4+}) form, brings about structural anisotropy.[37] In most cases, the distorted octahedra are linked together to produce a chain of alternating short and long V–O bonds. The four corners are generally shared with single or double tetrahedra as in orthophosphates (PO_4) and pyrophosphates (P_2O_7), respectively. The structures of β-$VOPO_4$ and $(VO)_2P_2O_7$ are illustrated in Figure 5. β-$VOPO_4$ is composed of chains of highly distorted VO_6 octahedra sharing four oxygen atoms with four PO_4 groups. $(VO)_2P_2O_7$ comprises chains of V polyhedra linked by pyrophosphate groups. The V atoms are linked through oxygen atoms of vanadyl groups in V–O–V chains, and the V octahedra are linked into pairs through a common edge, forming a double chain. Although the structural determination of the X_1-phase (V^{5+}, P/V $= 1.0$) has not been accomplished, its structure is proposed to be similar to that of orthorhombic $(VO)_2P_2O_7$ having V–O–V chains.

Table 8 shows a comparison of selectivities toward maleic anhydride during the oxidation of n-butane. $(VO)_2P_2O_7$ is selective for the formation of maleic anhydride, while α-$VOPO_4$ and β-$VOPO_4$ are nonselective.[38] The bulk structure of $(VO)_2P_2O_7$ is retained during the n-butane oxidation, whereas the surface structure changes with the redox state of V between V^{4+} and V^{5+} during the n-butane oxidation.[39,40]

3.3.2 Catalytic Properties of $(VO)_2P_2O_7$

The catalytic properties of $(VO)_2P_2O_7$ are summarized as follows. 1) Ability of selective activation of alkanes. $(VO)_2P_2O_7$ is superior for the selective dehydrogenation of n-butane to butene to other crystalline V–P oxides, while few differences exist between the oxidation of butene and butadiene, which are considered reaction intermediates.[38] The abstraction of methylene hydrogen from n-butane is the slowest step. Hence this step determines the overall catalytic activity.[41] 2) Selectivity in forming anhydride from C_4 and C_5 alkanes, but not in selective oxidation of lower (C_2 and C_3) or higher (C_6–C_8) alkanes.[42] 3) The number of surface layers involving the catalytic reactions is limited to 2–3[38] in contrast to Bi–Mo–O catalysts.

Table 8 Oxidation of butane oxidation over V–P oxides

Catalyst	Activity[a] (10^{-4} mol g^{-1} h^{-1} at 713 K)	Selectivity (%) to maleic anhydride at 70% conversion
$(VO)_2P_2O_7$	11	71
α-$VOPO_4$	25	10
β-$VOPO_4$	15	9

$(VO)_2P_2O_7$ is prepared generally by the calcination of vanadyl hydrogen phosphate, $VOHPO_4{\cdot}0.5H_2O$. Preparation methods of $VOHPO_4{\cdot}0.5H_2O$ are classified into three types:[42] (1) Preparation in organic media (organic solvent method), such as the utilization of alcohols as solvents and as reducing agents for V^{5+} starting compounds, has a rose petal-like shape of the particles and is more active than the catalysts prepared by (2) and (3); (2) Preparation by a reduction of V_2O_5 followed by H_3PO_4 addition in aqueous solution, showing block-like morphology; and (3) Preparation by reduction of $VOPO_4{\cdot}2H_2O$, showing high selectivity to maleic anhydride. Most commercial catalysts are obtained by the organic solvent method. Good catalytic performance is achieved with a catalyst possessing a bulk P/V ration of 1.1;[42] the excess phosphorus is necessary to stabilize the V^{4+} ion in the active surface phase.

3.3.3 Mechanism and Anisotropy

$(VO)_2P_2O_7$ catalysis proceeds via a redox mechanism. The oxidation state of highly active and selective $(VO)_2P_2O_7$ catalysts for n-butane oxidation is close to 4+.[43] Temporal analysis of product (TAP) studies suggest that at least two types of surface oxygen species exist which are essential for maleic anhydride formation. The first type is strongly chemisorbed oxygen, which is responsible for n-butane activation and furan oxidation. The second is lattice oxygen in the surface layers, which is concerned with the allylic

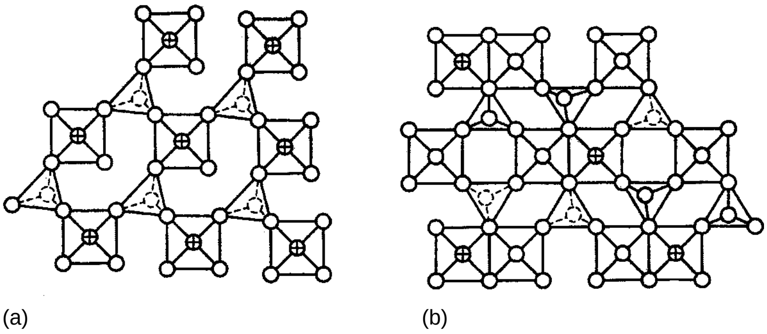
(a) (b)

Figure 5 Crystal structures of (a) β–$VOPO_4$ and (b) $(VO)_2P_2O_7$. ($\oplus$) shows a vanadyl group (V=O)

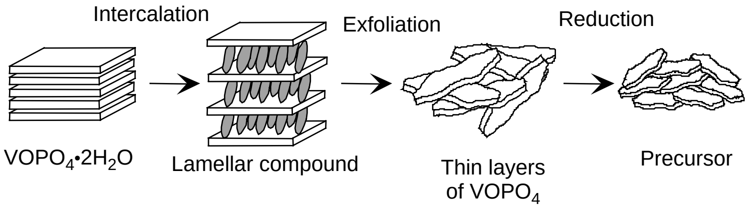

Figure 6 Concept of exfoliation–reduction method for preparation of $VOHPO_4{\cdot}0.5H_2O$ with thin microcrystallites

oxydehydrogenation of alkenes and oxygen insertion to form furan.[42,44]

The (100) plane of $(VO)_2P_2O_7$ is the active plane for formation of maleic anhydride. The side faces, such as the (001) plane, are nonselective for the reaction, that is, are active only for the formation of CO and CO_2. $V^{4+}(=O)–O–V^{4+}$ sites, located on the (100) plane, are probably part of the active site for the formation of maleic anhydride.[5] The anisotropic transformation of $(VO)_2P_2O_7$ also is observed by XRD and Raman spectrometry; the oxidation of the (100) plane results in X1-phase, but side planes are oxidized to the nonselective β-phase,[40] in accord with the structure-sensitive behavior of $(VO)_2P_2O_7$ in its selectivity.

On the basis of this anisotropic selectivity, the control of the shape of $(VO)_2P_2O_7$ crystallites, that is, expansion of the (100) plane, is a promising approach to obtaining a selective catalyst. It is well known that $VOPO_4{\cdot}2H_2O$ possesses a layered structure with high capability for intercalation of various molecules.[45] Exfoliation techniques have been developed from intercalation of various layered materials, in which exfoliation occurs by delaminating stacked inorganic sheets in solvent by infinite swelling of their interlayer space. Previous studies report the preparation of precursor $VOHPO_4{\cdot}0.5H_2O$ by exfoliation of $VOPO_4{\cdot}2H_2O$ in alcohol, followed by reduction (Figure 6).[46,47] Stepwise thermal treatment of a suspension of $VOPO_4{\cdot}2H_2O$ crystallites in 2-butanol caused subsequent processes (intercalation, exfoliation, and reduction) leading to the formation of $VOHPO_4{\cdot}0.5H_2O$ crystallites, which were approximately $1 \sim 2\,\mu m$ in length and roughly $0.1\,\mu m$ in thickness with leaf-like shapes. The catalyst derived from this process was more active and selective than well-known rose petal–like crystallites ($\sim 1\,\mu m$) by the organic solvent method using isobutanol and benzyl alcohol. The higher activity of the catalyst prepared by the exfoliation technique is attributed to the high surface area (approximately $30\,m^2\,g^{-1}$ after the reaction for 200 h), and the higher selectivity is attributable to the preferential exposure of the basal (100) plane of $(VO)_2P_2O_7$ owing to the leaf shape as well as the pure phase of $(VO)_2P_2O_7$.

Disorder within the structure of $(VO)_2P_2O_7$ has been identified with catalytic activity. The number of V^{4+} defects in $(VO)_2P_2O_7$, as measured by magnetic susceptibility, correlates with the rate of n-butane oxidation. The structural disorder can enhance the oxidation and reduction of $(VO)_2P_2O_7$. The catalyst with high redox ability is effective for the operation under the high n-butane concentrations.[48]

3.4 Perovskite-Type Mixed Oxides

3.4.1 *Structure*

The perovskite-type mixed oxides have a general formula of ABO_3. The structure of the ideal cubic ABO_3 perovskite structure is illustrated in Figure 7. Cations with a large ionic radius have 12 coordination to oxygen atoms and occupy A-sites, while cations with small ionic radius have 6 coordination and occupy B-sites.[49] Ideally, A and O form a cubic closest packing, and B is contained in the octahedral voids in the packing. If the ionic radii of r_A, r_B, and r_O are to form a perovskite crystal structure, the tolerance factor (t) (equation 10) must lie within the range $0.8 < t < 1.0$, as well as $r_A > 0.090\,nm$, $r_B > 0.051\,nm$.[49] Thus, a great number of elements can form ideal or modified perovskites, depending

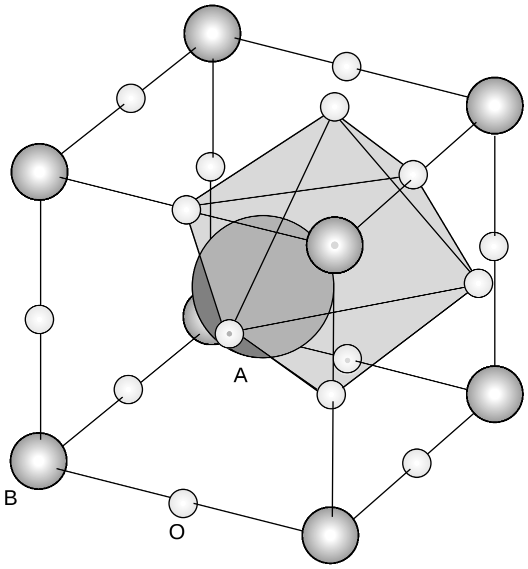

Figure 7 The structure of ABO_3 ideal perovskite. A-site; B-site; oxide ion

on the tolerance factor.

$$t = \frac{(r_{\mathrm{A}} + r_{\mathrm{O}})}{\sqrt{2}(r_{\mathrm{B}} + r_{\mathrm{O}})} \qquad (10)$$

Deviations from the ideal structure with orthorhombic, rhombohedral, tetragonal, monoclinic, and triclinic symmetry are known, although the latter three are scarce and poorly characterized.[50–52] The cubic cell of $LaAlO_3$, $LaNiO_3$, or $LaCoO_3$ often has a small deformation from rhombohedral symmetry. The distorted structure usually exists at room temperature, but transforms to a cubic structure at high temperature.

Besides the ionic radii requirements, another condition that must be fulfilled is electroneutrality, which is attained by means of appropriate charge distribution of the form $A^{1+}B^{5+}O_3$, $A^{2+}B^{4+}O_3$, or $A^{3+}B^{3+}O_3$. Incorporating two cation types of different size and charge into B-sites (e.g. $AB_{0.5}B'_{0.5}O_3$) can modify the simple perovskite structure.

3.4.2 *Nonstoichiometry in Perovskites*

Partial substitution of A and B ions is allowed, yielding a plethora of compounds while preserving the perovskite structure. This brings about deficiencies of cations at the A- or B-sites or of oxygen anions (e.g. defective perovskites). Introduction of abnormal valency causes a change in electric properties, while the presence of oxide ion vacancies increases the mobility of oxide ions and, therefore, the ionic conductivity. Thus, perovskites have found wide application as electronic and catalytic materials.

Oxygen vacancies are more common than cationic vacancies (oxygen-excess perovskite). $LaCuO_{3-\delta}$ perovskite is an example. This compound is stable over a remarkably wide oxygen stoichiometry range, that is, $0.5 \geq \delta \geq 0.0$.[53] The stoichiometric $LaCuO_3$, containing 100% Cu^{3+}, loses oxygen upon heating under ambient oxygen pressure, yielding several $LaCuO_{3-\delta}$ oxygen deficient phases.[54] In contrast, few examples of oxygen-excess nonstoichiometry in perovskite oxides exist, such as $LaMnO_{3+\lambda}$, $Ba_{1-\lambda}La_{\lambda}TiO_{3+\lambda/2}$, and $EuTiO_{3+\lambda}$. In the case of $LaMnO_{3+\lambda}$, calcination of the individual oxides in air at 1473 K produces $LaMnO_{3.12}$.[55]

3.4.3 *Effects of A- and B-Sites on Catalysis*

Perovskite oxides are effective catalysts for various reactions, such as CO oxidation,[56,57] total[58,59] and partial oxidation[60,61] of hydrocarbons, NO_x decomposition,[62,63] hydrogenation,[64,65] hydrogenolysis,[66,67] and photocatalysis.[68–70] Two types of catalytic processes are proposed for the catalysis of perovskites, namely, suprafacial and intrafacial catalysis.[49] During suprafacial catalysis, the reactions between adsorbed species on the surface are much faster than reactions involving lattice oxygen, as in low-temperature oxidation of CO. In this case, the reaction rate appears to be correlated primarily with the electronic configurations of the surface transition metal ions.

During intrafacial catalysis, the removal of oxygen from the lattice of the catalyst or the reverse process, can occur at a comparable or higher rate than in other catalytic processes. High-temperature oxidations as well as reduction of NO are good examples. In these cases, the bond strength between metal and oxygen in the lattice becomes important. Over $(A, A')MnO_3$ catalysts, the production rate of N_2 from N_2O increases in the order (La, Sr) < (La, K) < (La, La) < (Bi, K), in line with the decrease in the calculated binding energy of oxygen.[55]

When A-site elements in ABO_3 are rare earths and B-site elements are transition metals of the first row in the periodic table, the catalytic activity for oxidation is determined mainly by the transition metal.[56,71,72] In the case of propane oxidation (Figure 8), activity patterns show two peaks at Mn and Co regardless of the rare earth elements at the A-site.[73] This reaction is considered to proceed through a suprafacial process. According to crystal field theory, the octahedral (truncated octahedron at the surface) environment of the M^{3+} ions splits into two levels: the lower one (t_{2g}) contains orbitals that are repelled less by negative point charges than are the orbitals in the higher energy (e_g) level. Co and Mn perovskites have e_g levels occupied by fewer than one electron and t_{2g} levels that are half-filled or fully occupied, owing to the preferred adsorption on B cations with unfilled e_g levels and occupied t_{2g} levels (such as Mn and Co). The decomposition of N_2O on titanates is also suprafacial in nature, that is, the catalyst surface acts as a template, providing orbitals of suitable or proper symmetry and energy for the adsorption of N_2O.[74,75]

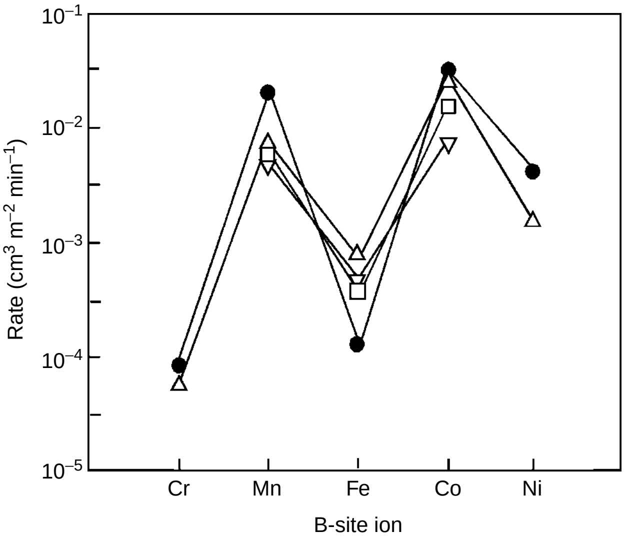

Figure 8 Catalytic activities of perovskites and B-site oxides for propane oxidation at 500 K. (●) oxides of B-site metals; (△) $LaBO_3$, (□) $SmBO_3$, (▽) $GdBO_3$

3.4.4 Designing Perovskite Catalysts

When trivalent A cations in $A^{3+}B^{3+}O_3$ are partially replaced by divalent A′ cations, charge compensation can be achieved by stoichiometric formation of either tetravalent B cations or positive holes. Valency change and nonstoichiometry are possible in perovskites without changing the fundamental structure. For example, in the case of families of $La_{1-x}A'_xBO_3$ (B=Co, Fe, Ni) oxides, substitution of A-site with a bivalent cation (A′=Sr, Eu) or a tetravalent cation (A′=Ce) led to a decrease or an increase, respectively, of methane combustion activity.[76] Eu or Sr substitution for La leads to higher oxidation states for Co, so that a higher amount of Sr results in a higher concentration of Co^{4+}, which is abnormal. However, Co^{4+} is unstable, therefore oxygen release can occur, ending in the formation of oxygen vacancies. In contrast, insertion of Ce^{4+} leads to a large amount of active sites for oxygen adsorption from the gas phase, causing higher catalytic activity for methane combustion.

The oxidation state of a B-site ion in La_2CuO_4 can be controlled by substitution at both A- and B-sites. The catalytic activity for the NO–CO reaction shows a maximum when Cu is in the $+2$ state. The rate of $CO–O_2$ reaction over $LaMn_{1-x}Cu_xO_3$ is very sensitive to the extent of Cu for Mn substitution. For $x = 0.4$, the rate is greater than that for either $LaMnO_3$ or La_2CuO_4 (note that $LaCuO_3$ cannot be prepared under ordinary conditions) by more than a factor of 10^2 for the initial activity, and a factor of 10 for the stationary activity. This large synergistic effect probably is due to an appropriate combination of the activation of CO by Cu and the high reactivity of the Mn–oxide oxygen.

Perovskites usually have small surface areas ($<10\,m^2\,g^{-1}$) because they are prepared by calcination at high temperatures (>1073 K). To increase the catalytic activity, various attempts to enhance surface area have been made using methods such as mist-drying, chelating, and metal-citric-cellulose complexing.[77,78] Although a surface area as high as $50\,m^2\,g^{-1}$ is obtained by these methods, it diminishes rapidly when the substance is exposed to high temperatures.

Another possible method for enhancing surface area is spreading perovskite as a thin layer or nano-particles on an appropriate high surface area support.[79] The major problem of this method is a solid-state reaction between the precursors of perovskite and the support, brought about by the high-temperature calcination to form perovskite. In the case of $LaCoO_3$, Co easily forms a spinel with Al_2O_3, but $LaCoO_3$ is highly dispersed on the surface of ZrO_2 as fine particles or thin over-layers when La–Co/ZrO_2 is calcined at 1123 K. The reaction between the substance (La–Co oxide) and ZrO_2 to form $La_2Zr_2O_7$ and Co_3O_4 occurred by calcination above 1123 K.

3.5 Heteropoly Compounds

Heteropolyacids are condensates of different types of oxoacids and involve inorganic metal-oxygen clusters (polyoxometalates). Among these acids, those with Keggin-type anions are widely used as catalysts because of their stability in solution and in the solid state.[80–83] Important properties of the Keggin-type heteropolyacids include: (1) high solubility in water and polar organic solvents; (2) a polybasic strong acidity (completely dissociative in water); (3) high oxidizing ability of Mo- and V-containing compounds; (4) formation of soluble or insoluble salts having unique functions; and (5) high thermal stability in the solid state.

3.5.1 Synthesis of Heteropolyanions and Structures

The formation of a typical Keggin-type heteropolyacid, $H_3PW_{12}O_{40}$, is given by equation (11).[84] As shown in Figure 9, the structure has overall tetrahedral symmetry and is based on a central PO_4 tetrahedron surrounded by $12WO_6$ octahedra arranged in four groups of three edge-shared octahedra, W_3O_{13}. These W_3 triplets are linked by corners shared with each other and the central PO_4. The Keggin structure has been characterized by X-ray diffraction, UV, NMR, and IR spectroscopy.

$$23H^+ + HPO_4^{2-} + 12WO_4^{2-} \longrightarrow PW_{12}O_{40}^{3-} + 12H_2O \qquad (11)$$

Heteropolyanions with W or Mo atoms as a polyatom (addenda atom) are listed in Table 9.[85] The thermal stability increases in the sequence of $H_4SiMo_{12}O_{40} < H_3PMo_{12}O_{40} < H_4SiW_{12}O_{40} < H_3PW_{12}O_{40}$, where $H_3PW_{12}O_{40}$ decomposes when heated higher than 673 K.[86]

In aqueous solution, the Keggin structure, for example, $PW_{12}O_{40}^{3-}$, is stable at about pH 1.0.[84] At pH 1.5–2.0,

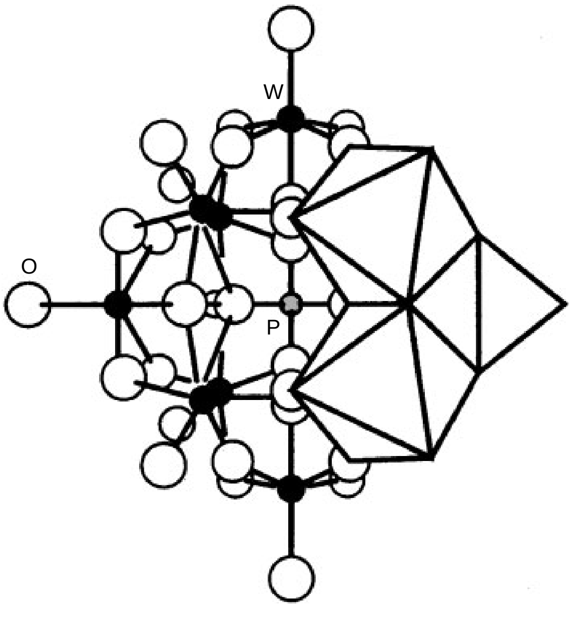

Figure 9 Structure of Keggin-type anion

Table 9 Heteropolyanions having Mo and V as addenda atoms

Formula type	M = Mo	M = W
Keggin structure $X^{n+}M_{12}O_{40}{}^{(8-n)-}$	Si^{4+}, Ge^{4+}, P^{5+}, As^{5+}, Ti^{4+}, Zr^{4+}	B^{3+}, Si^{4+}, Ge^{4+}, P^{5+}, As^{5+}, l^{3+}, Fe^{3+}, Co^{2+}, Co^{3+}, Cu^{+}, Cu^{2+}, Zn^{2+}
Lacunary Keggin $X^{n+}M_{11}O_{40}{}^{(12-n)-}$	Si^{4+}, Ge^{4+}, P^{5+}, As^{5+},	B^{3+}, Si^{4+}, Ge^{4+}, P^{5+}, As^{5+}, l^{3+}, Ga^{3+}, Fe^{3+}, Co^{2+}, Co^{3+}, n^{2+}, Sb^{3+}, Bi^{3+}
Dawson structure	P^{5+}, As^{5+},	P^{5+}, As^{5+}

the Keggin structure is converted to a lacunary anion, $H_xPW_{11}O_{39}{}^{(7-x)-}$, which can act as a ligand in compounds with metal cations and metal complexes.[87]

3.5.2 Acidic Properties

Heteropolyacids are strong acids that dissociate completely in aqueous solution. The acidity of nonaqueous solutions of $H_3PW_{12}O_{40}$ is higher by 1–1.5 units of the Hammett acidity function than the acidity of $HClO_4$ or H_2SO_4.[80,88] As a liquid acid in CH_3CN, $H_3PW_{12}O_{40}$ has been characterized as a superacid by calorimetry.[89] The order of acid strength is estimated to be $H_3PW_{12}O_{40} > CF_3SO_3H >$ PTS $> H_2SO_4 > CF_3COOH > ClC_6H_4COOH$.

Indicator color changes demonstrate that solid $H_3PW_{12}O_{40}$ possesses acidity greater than −13.16 in H_0.[90] As solid acids, microcalorimetry of NH_3 adsorption and temperature programmed desorption (TPD) of NH_3 reveal that acid strength is in the order; $H_3PW_{12}O_{40} > Cs_{2.5}H_{0.5}PW_{12}O_{40} >$ H-ZSM-5 (Si/Al = 40) $> SiO_2-Al_2O_3$.[91] This indicates that the acid strength of anhydrous solid $H_3PW_{12}O_{40}$ is higher than that of zeolites including H-ZSM-5 and can be classified as super acidity.[92,93] Protons of $H_3PW_{12}O_{40}$ are localized on the bridging oxygen atoms (e.g. W–O–W) of the polyanions in the crystal lattice. The acid centers are considered to be at the bridging oxygen on the surface of anion. The studies using ^{13}C NMR spectroscopy with mesityl oxide as indicator shows that the three protons of $H_3PW_{12}O_{40}$ have the same strength.

Supporting heteropoly acids on other solids with high surface areas is a useful method for improving catalytic performance. In general, strong interactions of heteropoly acids with supports are observed at low loadings and the intrinsic properties of heteropoly acids prevail at high loadings. The supports promote changes in acid strength and the structure of the aggregates. Basic solids such as Al_2O_3 and MgO tend to decompose heteropolyacids.[94–97]

3.5.3 Solid Heteropolyacids

Acid Form – Pseudoliquid Phase Behavior.[80,98] Owing to a high affinity for polar molecules, large quantities of molecules such as alcohols and ether are absorbed within the bulk phase of crystalline heteropolyacids. The amounts of pyridine, methanol, and 2-propanol absorbed correspond to 50–100 times that which can be adsorbed on the surface, while nonpolar molecules like ethylene and benzene are adsorbed at the surface only. Catalytic reactions of polar molecules occur both on the surface and in the bulk, so that the solid heteropolyacid behaves as a highly concentrated solution, called a ‘pseudoliquid phase’. The dehydration of alcohols, various conversions of methanol and dimethyl ether to hydrocarbons in gas–solid systems, and the alkylation of phenol and pinacol rearrangements can all occur in the pseudoliquid.[80,99] The transient response using isotopically labeled 2-propanol provides evidence for the pseudoliquid phase behavior of $H_3PW_{12}O_{40}$. This behavior influences the selectivity, for example, the alkene/alkane ratio, in the conversion of dimethyl ether.

Acidic Salts of Heteropolyacids. Although the acid form of heteropolyacid itself is a useful solid acid, the number of acidic sites on the surface is relatively small because of the low surface area (about $5\,m^2\,g^{-1}$). Substitution of the proton by an alkaline cation produces interesting effects on the surface area and pore structures. Salts with large monovalent ions, such as Cs^+, are insoluble in water and possess high surface areas,[93,100] while the acid forms are highly soluble in water. Partial substitution of protons with Cs^+ ions results in unique changes in the surface area and hence in the number of acidic sites on the surface. As shown in Figure 10, surface area increased when the Cs content, x in $Cs_xH_{3-x}PW_{12}O_{40}$, changed from $x = 2$ ($1\,m^2\,g^{-1}$) to $x = 3$ ($156\,m^2\,g^{-1}$), although it decreased

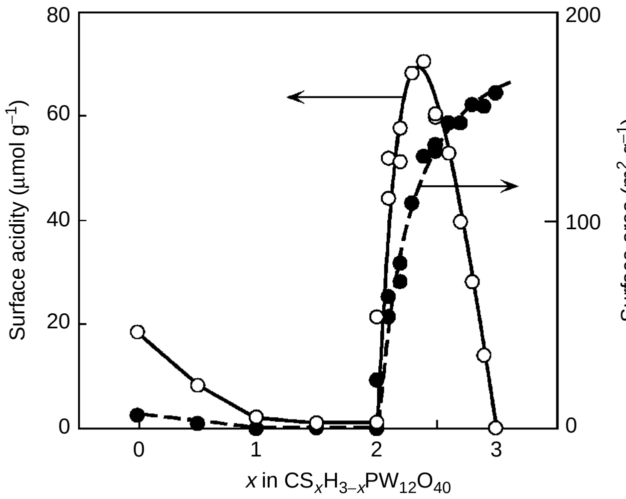

Figure 10 Changes in the surface area and surface acidity of $Cs_xH_{3-x}PW_{12}O_{40}$ as a function of the Cs content

slightly from $x = 0$ ($6\,\mathrm{m^2\,g^{-1}}$) to $x = 2$. The acid amount on the surface (surface acidity), estimated from the surface area and the formal concentration of protons attached to the polyanion, decreased initially with the Cs content, but sharply increased when x exceeded 2, with a maximum at $x = 2.5$. Salts of heteropolyacids with Rb and K give changes in the surface area similar to those of Cs salts.[101] A marked increase in the surface area is observed at $x = 1.8$ for the Rb salts. In the case of K salts, the change in the surface area is rather arbitrary.

As shown in Figure 11, the pore sizes of $Cs_{2.5}H_{0.5}PW_{12}O_{40}$ (abbreviated as Cs2.5) are bimodal distributions in the range from micropore to mesopore.[91,102] The mesopores (about 4 nm) correspond to the voids between the primary particles (crystallites; about 10 nm in size), and the micropores correspond to the spaces between the crystal planes formed by misaligned fragments.[102–104] $Cs_{2.1}H_{0.9}PW_{12}O_{40}$ (abbreviated as Cs2.1) possesses only micropores, for which the peak is 0.51 nm.[102–104] Adsorptions of various molecules, such as N_2 (molecular size (MS) = 0.36 nm), n-butane (MS = 0.43 nm), isobutane (MS = 0.50 nm), benzene (MS = 0.59 nm), 2,2-dimethylpropane (MS = 0.62 nm), and 1,3,5-trimethylbenzene (MS = 0.75 nm) reveal that the pore-width of $Cs_{2.1}H_{0.9}PW_{12}O_{40}$ is in the range of 0.43–0.50 nm. Proposed models for Cs2.5 and Cs2.1 are illustrated in Figure 12.

During a titration preparation method, $Cs_3PW_{12}O_{40}$ crystallites are formed initially, followed by epitaxial adsorption of $H_3PW_{12}O_{40}$ on the surface of $Cs_3PW_{12}O_{40}$ crystallites.[91] When the Cs content, x, is low, ultrafine particles of $Cs_3PW_{12}O_{40}$ (8–10 nm in diameter) are thickly covered by $H_3PW_{12}O_{40}$ upon drying the solution. Heat treatment converts them to particles having a nearly uniform composition and a size similar to what existed before heat treatment. At $x = 2.5$, $H_3PW_{12}O_{40}$ forms very thin films or small islands on $Cs_3PW_{12}O_{40}$ crystallites after drying. Heat treatment produces fine particles having a uniform composition of $Cs_{2.5}H_{0.5}PW_{12}O_{40}$. The unusual increase in the surface area for $x = 2$–3 can be understood by this mechanism.

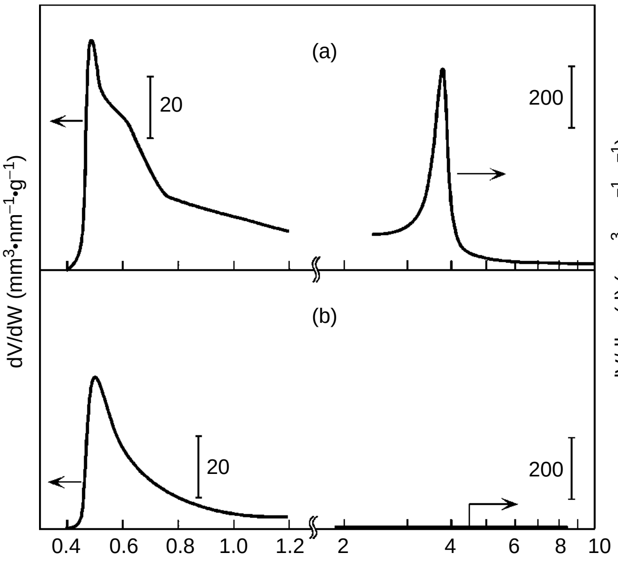

Figure 11 Pore-size distributions of $Cs_{2.5}H_{0.5}PW_{12}O_{40}$ (a) and $Cs_{2.1}H_{0.9}PW_{12}O_{40}$ (b)

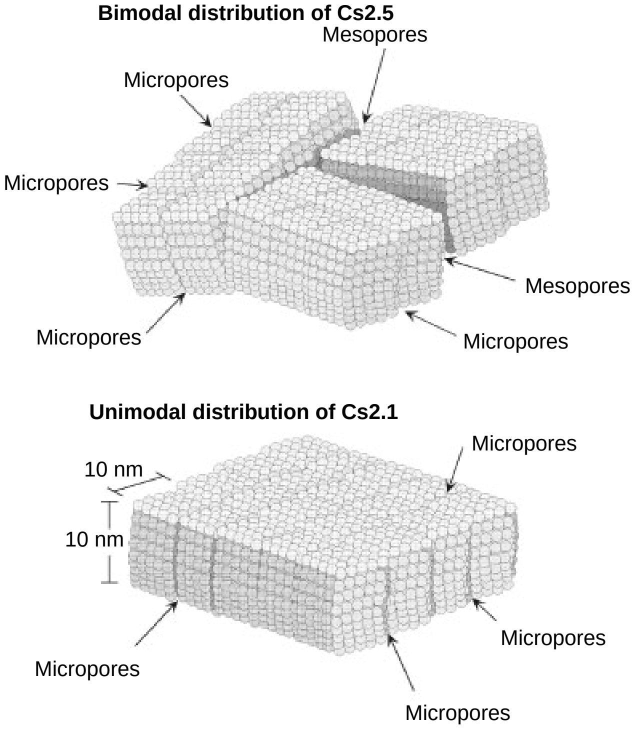

Figure 12 Model of pores for $Cs_{2.5}H_{0.5}PW_{12}O_{40}$ and $Cs_{2.1}H_{0.9}PW_{12}O_{40}$

3.5.4 *Acid Catalyzed Reactions*

Table 10 summarizes examples of acid-catalyzed reactions over heteropoly compounds. Supporting and composite catalysts consisting of silica or MCM-41 and $H_3PW_{12}O_{40}$ or $H_4SiW_{12}O_{40}$ possess excellent catalytic performance.[105–109] Well-dispersed heteropoly acids show high catalytic activities during liquid-phase alkylation of aromatics. $H_3PW_{12}O_{40}$ supported on MCM-41 is highly active for alkylation of aromatics with added shape selectivity. $H_3PW_{12}O_{40}/SiO_2$ catalyzes Diels–Alder reactions of quinones. This catalyst is active under mild conditions and can be easily recovered and reused. $H_3PW_{12}O_{40}$ subsumed in a silica matrix by an in situ sol-gel method shows higher activity than Amberlyst and zeolite H-ZSM-5.

The acidic salts of heteropolyacids, in which the protons are partially substituted with Cs^+, are active for acid-catalyzed reactions such as Friedel–Crafts reactions,[110] Ritter-type reactions,[111] and skeletal isomerization of alkanes.[112–118] The

Table 10 Acid catalysis by heteropoly compounds

Reaction	Catalyst
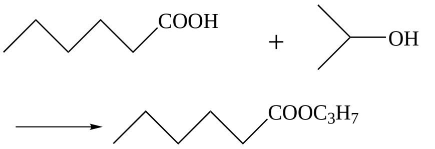 COOH OH $COOC_3H_7$	$H_3PW_{12}O_{40}$, $H_4SiW_{12}O_{40}$/MCM-41
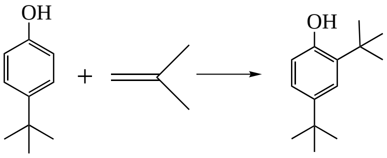	$H_3PW_{12}O_{40}$/MCM-41
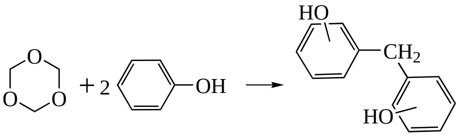 O O O 2 OH HO CH_2 HO	Silica-included $H_3PW_{12}O_{40}$
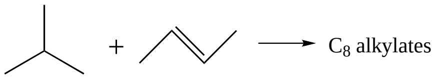 C_8 alkylates	$H_3PW_{12}O_{40}$/MCM-41, $K_{2.6}H_{0.4}PW_{12}O_{40}$
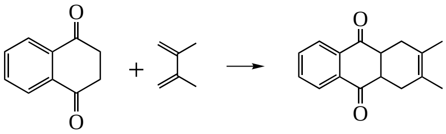	$H_3PW_{12}O_{40}/SiO_2$
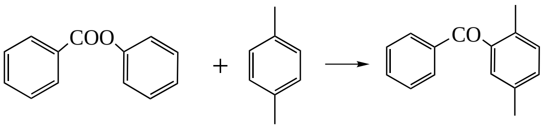	$Cs_{2.5}H_{0.5}PW_{12}O_{40}$
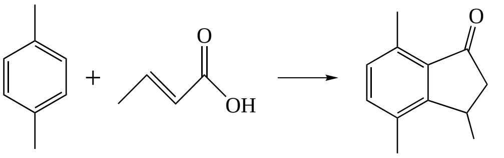	$Cs_2HPW_{12}O_{40}$
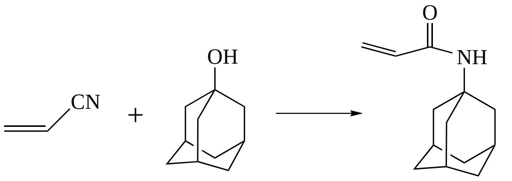	$Cs_{2.5}H_{0.5}PW_{12}O_{40}$
$C_2H_5OCOCH_3 + H_2O \rightarrow C_2H_5OH + CH_3COOH$	$Cs_{2.5}H_{0.5}PW_{12}O_{40}/SiO_2$
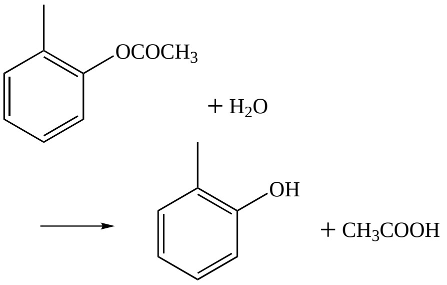 $OCOCH_3$ $+ H_2O$ OH $+ CH_3COOH$	$Cs_{2.5}H_{0.5}PW_{12}O_{40}$
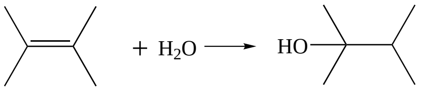	$Cs_{2.5}H_{0.5}PW_{12}O_{40}$

(cont'd overleaf)

Table 10 cont'd

Reaction	Catalyst
Pinacol rearrangement of 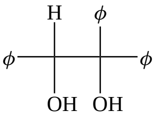	$Cs_{2.5}H_{0.5}PW_{12}O_{40}$ $Cs_{2.5}H_{0.5}PW_{12}O_{40}$
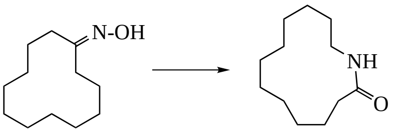	
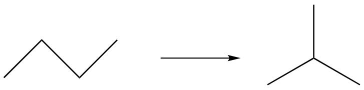	$(NH_4)_{2.4}H_{0.6}PW_{12}O_{40}$, $Cs_{1.9}H_{1.1}PW_{12}O_{40}$, $Cs_{2.5}H_{0.5}PW_{12}O_{40}$, $Cs_2HPW_{12}O_{40}$, Pt–$Cs_{2.5}H_{0.5}PW_{12}O_{40}$
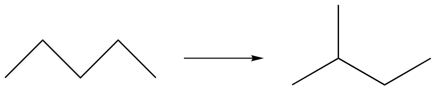	$Cs_2HPW_{12}O_{40}$
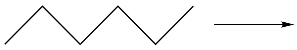 *iso*-C_6	Pt–$Cs_{2.5}H_{0.5}PW_{12}O_{40}$, Pt–$Cs_{2.5}H_{0.5}PW_{12}O_{40}/SiO_2$, Pt–$Cs_2HPW_{12}O_{40}/SiO_2$
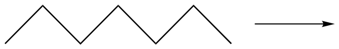 *iso*-C_7	Pt–$Cs_{2.5}H_{0.5}PW_{12}O_{40}$ + SiO_2
$C_2H_4 + O_2 + H_2O \rightarrow CH_3COOH$	Pd–Se(0.02)–$H_4SiW_{12}O_{40}$
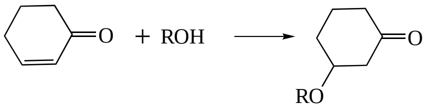	$H_3PW_{12}O_{40}$
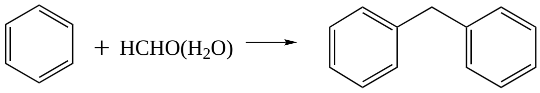	$H_3PW_{12}O_{40}$

specific catalytic properties of the Cs salts are attributed to a hydrophobic surface and porosity as well as strong acidity.

3.5.5 *Water-tolerant Catalysis by $Cs_{2.5}H_{0.5}PW_{12}O_{40}$*[119]

Generally, solid acids are severely poisoned by water and lose their catalytic activities in aqueous solution. An important feature of Cs2.5 is its high activity for acid-catalyzed reactions, even in the presence of a large excess of water. The activity of Cs2.5 (per weight) toward hydrolysis of ethyl acetate in excess water is 3 and 35 times higher than those of H-ZSM-5 (Si/Al = 40) and H-ZSM-5 (Si/Al = 628), respectively,[120] while SiO_2–Al_2O_3 and Al_2O_3 are inactive. The specific activity of Cs2.5 (per unit of acid amount) was seven times higher than those of the two H-ZSM-5 catalysts, which are commercial water-tolerant solid acid catalysts used for a liquid-phase hydration of cyclohexene.

Hydrophobicity of a solid surface can be evaluated semiquantitatively by comparison of water and benzene adsorption.[121] Figure 13 shows the ratio of the adsorption area of benzene to that of water as a function of the relative pressure of the adsorbates, where the adsorption area is defined as the product of the adsorption amount and molecular cross sectional area. From the ratio of adsorption area of benzene to that of water, the hydrophobicity of solid acid surface is evaluated to occur in the order: H-ZSM-5 (Si/Al = 628) > $Cs_3PW_{12}O_{40}$ (Cs3) > H-ZSM-5 (Si/Al = 40) > $Cs_{2.5}H_{0.5}PW_{12}O_{40}$ (Cs2.5) > SiO_2–Al_2O_3 > Al_2O_3.[122] Thus, it is concluded that the surface of Cs2.5 has a hydrophobic nature similar to that of H-ZSM-5 (Si/Al = 40). The hydrophobic character of the Cs2.5 surface probably prevents the acidic protons from becoming poisoned by water. The hydrophobic surface as well as the strong acidity of Cs2.5 are reasons for the high activity toward the water-related reactions.

A feature of Cs2.5 is its mesopores, in which bulky molecules can access the active sites. Thus, potential of Cs2.5 as a water-tolerant catalyst is especially evident in reactions involving large size reactants and products. Table 11 shows catalytic activity for hydrolysis of 2-methylphenyl acetate. Cs2.5 exhibits significantly superior activity against other

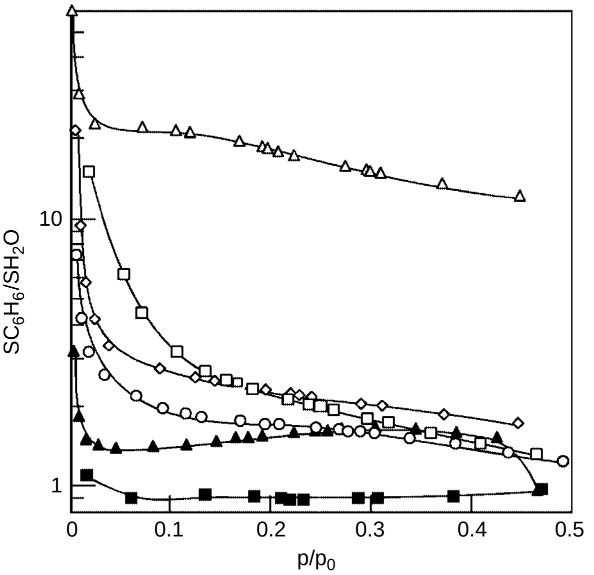

Figure 13 Hydrophobicity of solid acids evaluated from the adsorptions of benzene and water: $Cs_{2.5}H_{0.5}$ $PW_{12}O_{40}$ (○), Cs_3 $PW_{12}O_{40}$ (□), H-ZSM-5 (Si/Al = 628) (△), H-ZSM-5 (Si/Al = 40) (◇), Al_2O_3 (■), and $SiO_2-Al_2O_3$ (▲). S_{C6H6} and S_{H2O} are adsorption areas of benzene and water, respectively

solid acids. H-ZSM-5, which is active for the hydrolysis of ethyl acetate, is inactive for hydrolysis of 2-methylphenyl acetate, because the large reactant cannot approach the acid sites located in the micropores.

3.5.6 Bifunctional Catalysts of Heteropolyacids and Cs Salts

Pd modified $H_4SiW_{12}O_{40}/SiO_2$ (bifunctional catalyst) is effective for skeletal isomerization of n-pentane in the presence of hydrogen.[123] The catalyst optimized in Pd and $H_4SiW_{12}O_{40}$ loadings exhibits very high selectivity toward branched heptanes (>95%). The space-time yield of this catalyst is three times greater than that found for Pd–H-β zeolite, which is one of the best catalysts known for this reaction. A mechanism based on a classical bifunctional catalysis is proposed, involving an acid-catalyzed reaction and dehydrogenation-hydrogenation.[115]

Pt-promoted Cs2.5 catalyst also is efficient for the skeletal isomerization of n-butane,[121] n-pentane,[116] n-hexane,[117,118] and n-heptane.[117] Pt–Cs2.5 supported on silica is effective for isomerization of cyclohexane and the hydroisomerization of benzene to methylcyclopentane.[122]

Several acid-catalyzed reactions are used as test reactions to demonstrate the shape selectivity of the microporous heteropoly compound, Cs2.1, having only micropores. Catalytic activities of Pt–Cs2.1 and Pt/SiO_2 toward the oxidation of various molecules are summarized in Table 12.[124] Two catalysts are active for the oxidation of CH_4, CO, and n-butane. In contrast, Pt–Cs2.1 is relatively inactive for the oxidation of isobutene, 2,2-dimethyl pentane, and benzene, while Pt/SiO_2 shows high catalytic activity. This result clearly demonstrates that the ultramicropores of Pt–Cs2.1 can distinguish n-butane from isobutane; only n-butane is adsorbed into the pores and subsequently oxidized. The pore-width of Cs2.1 is in the range of $0.43 \sim 0.50$ nm, demonstrated by the adsorption of various molecules (See Section 3.5.3).

Another example of catalysis over a bifunctional heteropolyacid is the direct synthesis of acetic acid from ethene.

Table 11 Catalytic activities of solid and liquid acids for hydrolysis of 2-methylphenyl acetate

	Reaction rate	
Catalyst	Per weight (μmol g^{-1} min^{-1})	Per acid amount [mmol (acid-mol)$^{-1}$ min^{-1}]
Solid acids		
$Cs_{2.5}H_{0.5}PW_{12}O_{40}$	10.7	71.3
H-ZSM-5(Si/Al = 40)	0.0	0.0
SO_4^{2-}/ZrO_2	0.4	2.0
H–Y	0.0	0.0
H-mordenite	0.0	0.0
Nb_2O_5	0.5	1.7
$SiO_2-Al_2O_3$	0.0	0.0
γ-Al_2O_3	0.0	0.0
TiO_2-SiO_2	0.0	0.0
Organic resins		
Amberlyst-15	32.7	6.9
Nafion-H	44.5	55.6
Liquid acids		
H_2SO_4	55.3	2.7
PTS	27.7	4.8
$H_3PW_{12}O_{40}$	5.6	5.6
Sc(Of)$_3$	14.4	7.2

Reaction Conditions: 2-Methylphenyl acetate 4.03 mmol, H_2O 3.3 mol, at 353 K.

Table 12 Stationary catalytic activities for oxidation of various molecules over 0.5 wt% Pt–$Cs_{2.1}H_{0.9}PW_{12}O_{40}$ and 0.5 wt% Pt/SiO_2

		Catalytic activity (μmol min^{-1} g^{-1})	
Molecules	MS[a]	0.5 wt% Pt–$Cs_{2.1}H_{0.9}PW_{12}O_{40}$	0.5 wt% Pt/SiO_2
CH_4[b]	0.38	22.5	22.8
CO[c]	0.38	49.7	132.8
n-Butane	0.43	12.7[d]	18.0[e]
Isobutane	0.50	0.6[d]	18.7[e]
2,2-Dimethyl pentane[d]	0.62	2.8	28.6
Benzene[f]	0.59	0.0	49.0

[a] Molecular size is in nm. [b] At 573 K. [c] At 493 K. [d] At 493 K. [e] At 453 K. [f] At 473 K.

Pd-promoted $H_4SiW_{12}O_{40}/SiO_2$ is effective for this reaction in a mixture of ethene, water, and oxygen; this process has been commercialized since 1997.[125] The reaction is proposed to proceed through hydration of ethene, followed by oxidation of ethanol. The selectivity toward acetic acid reaches 86% over $Pd/H_4SiW_{12}O_{40}$–SiO_2.

3.5.7 Redox Properties and Oxidation Catalysis

Mo-heteropolyanions with a Keggin structure are readily reduced to give heteropoly blue in solution. A trend exists toward anions with X of higher charge (small value of n) being more easily reduced, while the reduction potential decreases in the order V > Mo > W. In the case of $XMnW_{11}O_{40}H_2{}^{n-}$, the Mn^{2+} in the anion is oxidized by O_2.

The oxidizing ability of the alkali salt is estimated from the rate of its reduction by H_2 and CO.[126] The rate of reduction by H_2, normalized to catalyst weight, represents the oxidizing ability of the catalyst bulk. Similarly, the rate of reduction by CO, divided by the surface area, expresses the oxidizing ability of the surface. The oxidizing ability in both cases decreases monotonically with an increase in neutralization by alkali, except for the reduction by H_2 of $Cs_{2.5}PMo_{12}O_{40}$, for which a higher value than the monotonous change was observed. This high value is due to a very high surface area and rigid secondary structure.

Table 13, presents a summary of oxidation reactions catalyzed by heteropoly compounds.[127–129] Vapor-phase oxidation of methacrolein to methacrylic acid has been commercialized using heteropoly compounds (220×10^3 tonnes/year).[130] Heteropoly compounds exhibit high catalytic performance for this reaction, different from simple single oxides such as MoO_3 and V_2O_5. The main component of the catalyst is $H_3PMo_{12}O_{40}$ or its salts, in which V is substituted for one or two Mo atoms. Cs salts increase the stability of the catalysts; the acidic salts are the active components. In the oxidation of acrolein to acrylic acid over $K_xH_{3-x}PMo_{12}O_{40}$, maximum selectivity is obtained at $x = 2.5$. A drop in selectivity at lower values of x is associated with increasing concentrations of decomposition products from the thermally unstable $H_3PMo_{12}O_{40}$ component[131]

Table 13 Oxidation reactions catalyzed by heteropoly compounds

Reaction	Catalyst
Homogeneous oxidation	
Alkyl sulfide + O_2 → sulfone	$H_{3+n}PMo_{12-n}V_nO_{40}$
Ketone + O_2 → acid and aldehyde	$H_5PMo_{10}V_2O_{40}$
Alkylcyclohexadiene + O_2 → alkylbenzene	$H_5PMo_{10}V_2O_{40}$
1-Octene + H_2O_2 → octane oxide	$(CP)_3PW_{12}O_{40}{}^a$
1-Octene + H_2O_2 → heptanoic acid	$(CP)_3PW_{12}O_{40}{}^a$
Cyclohexene + H_2O_2 → adipic acid	$H_3PMo_6W_6O_{40}$
Tetramethylphenol + H_2O_2 → tetramethylquinone	$H_3PMo_{12}O_{40}$
Heterogeneous oxidation with O_2	
Methacrolein → methacrylic acid	$CsH_3PVMo_{11}O_{40}$
Isobutylic acid → methacrylic acid	$H_4PV_{12}Mo_{10}O_{40}$
Isobutene → methacrolein	$PbFeBiMo_{12}O_{40}$
Butene → maleic anhydride	$Cs_{2.5}H_{0.5}PMo_{12}O_x + VO^{2+}$
Butane → maleic anhydride	$BiPMo_{12}O_x + VO^{2+}$
Isobutane → methacrylic acid	$H_3PMo_{12}O_{40}$
Pentane → maleic anhydride	$H_5PV_2Mo_{10}O_{40}$

[a] CP = cetylpyridinium ion.

A possible mechanism for oxidation of methacrolein over $H_3PMo_{12}O_{40}$ is given by equation (12). The first step, in which a diol or ester-type intermediate forms from methacrolein and $H_3PMo_{12}O_{40}$, is reversible and rapid, being catalyzed by the acidic sites. The dehydrogenation of a diol or ester is the likely rate-determining step, because the rates correlate not to the acid strength but to the oxidizing ability.[127]

$$H_2C{=}C(Me)CHO \longrightarrow H_2C{=}C(Me)CH(OM)_2 \longrightarrow H_2C{=}C(Me)CO_2H \qquad M = H \text{ or } Mo \qquad (12)$$

Another route to methacrylic acid is via oxidative dehydrogenation of isobutyric acid (equation 13). This reaction is catalyzed by molybdovanadophosphoric acid ($H_{3+n}PMo_{12-n}V_nO_{40}$; $n = 0$–3), whose redox potential and acidity are well-balanced for effecting this reaction. The acidity is necessary, although excess acidity accelerates the decomposition of isobutyric acid into CO and propene.

$$Me_2CHCO_2H + \tfrac{1}{2}O_2 \longrightarrow H_2C{=}C(Me)CO_2H \qquad (13)$$

The acidity and oxidizing ability work cooperatively for oxidation of methacrolein, while they function competitively for oxidative dehydrogenation of isobutyric acid.[127] These two reactions also differ in that the former is a surface-type and the latter a bulk-type. From this standpoint, different considerations in effective catalyst design are necessary.

3.6 Solid Acid and Base Catalysts

3.6.1 Acid and Basic Properties of Oxides

Aluminum oxide is a widely used catalyst, mainly as a support. The surface of Al_2O_3 possesses both acidic and basic sites after heat treatment above 670 K. The acid sites are mainly Lewis acid sites; strong Brønsted sites are absent. The Lewis acid site is visualized as a coordinatively unsaturated Al atom formed by dehydroxylation, and the weak Broønsted sites act as acidic surface hydroxyls, while the basic sites are considered to be basic hydroxyls and oxide ions. Three OH groups are present: loosely adsorbed water, surface hydroxyl groups, and other OH types that interact weakly with neighboring functional groups.[14,132]

Al_2O_3 catalyzes various kinds of reactions, such as dehydrohalogenation, dehydration, hydration, deamination, and aldol condensation. During the dehydrohalogenation of 1,1,2-trichloroethane, Al_2O_3 yields different products from acidic $SiO_2-Al_2O_3$ and basic $KOH-SiO_2$, probably because of a concerted mechanism both acid- and base-catalyzed. The importance of the acid-base pair sites has been proposed in dehydration reactins as well.[14] It is remarkable that Al_2O_3 is effective for the activation of H–H and C–H bonds at low temperatures. The C–H bond probably is dissociated as $RH \rightarrow R^- + H^+$, because the rate decreases with an increase in the pK_a value of alkanes.

Niobium pentoxide ($Nb_2O_5 \cdot 5H_2O$) has acidity corresponding to 70% $H_2SO_4(H_0 = -5.6)$ and exhibits high catalytic activity, selectivity, and stability for acid-catalyzed reactions in which water molecules participate. For the hydration of ethylene, the activity of niobium pentoxide is higher than that of H_3PO_4/SiO_2.[133] For the esterification of ethanol with acetic acid, niobium pentoxide possesses a higher activity than do resin and $SiO_2-Al_2O_3$. Synthesis of 2,5-dimethyl-2,4-hexadiene (an intermediate for an agricultural chemical) from isobutene and isobutyraldehyde has been performed using Nb_2O_5. MoO_3 and WO_3 are weak acids and active for the isomerization of n-butene.[14]

Alkaline earth oxides are well-known basic oxides. MgO and CaO possess basic sites, created by heat treatment above 673 K. Most (90%) of the basic sites on CaO are surface species O^{2-} that are strongly basic, together with a small quantity of OH groups. The order of basic strength of alkaline earth metal oxides is $BaO > SrO > CaO > MgO$.[14]

In 1-butene, isomerization with a high *cis* to *trans* ratio to 2-butene is characteristic of basic oxides such as MgO and CaO, owing to the high stability of *cis*-allyl anion intermediates, as compared to *trans*-allylic anions. For the double bond isomerization of ethers, activity is in the order $CaO > SrO > La_2O_3 > MgO \gg ThO_2, ZrO_2$[134] (in agreement with base strength).

MgO, modified with a metal ion, is useful for the formation of unsaturated compounds by the reaction of methanol with ketones, esters, and nitriles (equation 14). The reaction is initiated by dehydrogenation of methanol followed by aldol addition and subsequent dehydration. The dehydrogenation activity of MgO is enhanced by the addition of Cr^{3+}, Fe^{3+}, and Mn^{2+}.[135]

$$RCH_2X + MeOH \longrightarrow H_2C{=}CRX + H_2 + H_2 \qquad (14)$$

$$X = CN, COR, CO_2R; R = H, Me$$

ZrO_2 contains both acidic and basic sites and its bifunctional nature is pronounced compared with Al_2O_3. The highest acid strength of ZrO_2 is $H_0 = 1.5$. The highest base strength of ZrO_2 is $H- = 18.4$.[14] Although the strengths are rather weak, the bifunctional nature of ZrO_2 makes it highly selective for the formation of 1-butene from 2-butanol. ZrO_2 also catalyzes dehydration of 1-cyclohexylethanol and the elimination of ammonia from 2-butanamine.[136] The reactions probably are initiated by the abstraction of H^+ by basic sites; the acidic sites then stabilize the carbanion formed. ZrO_2 will hydrogenate dienes or CO, with isobutene being the main product from the hydrogenation of CO.[132] Direct hydrogenation of aromatic carboxylic acids to the corresponding aldehydes is selectively catalyzed by ZrO_2.

ThO_2 shows catalytic behavior similar to ZrO_2. The selectivity of ThO_2 (prepared by hydrolysis of the nitrate) for the formation of 1-octene from 2-octanol is very high (99%).[14]

The acid strength of oxoacid salts in the solid state increases with the electronegativity of the metal ion, and hence catalytic activity increases with electronegativity. Figure 14 shows an example of selectivity, in which the selectivity of double bond isomerization of butene over metal sulfates changes with the electronegativity.[14]

The maximum acid strength of mixed oxides increases with average electronegativity (Figure 15).[14] However, no general rule about the basicity of mixed oxides has been formulated. The acid sites on $SiO_2-Al_2O_3$ are more strongly acidic than $H_0 = -8.2$, and involve both Brønsted and Lewis acids. $SiO_2-Al_2O_3$ catalyzes a wide variety of reactions such as propene polymerization, cumene cracking, and o-xylene isomerization. SiO_2-TiO_2 also is strongly acidic. SiO_2-MgO possesses a large number of acidic as well as basic sites

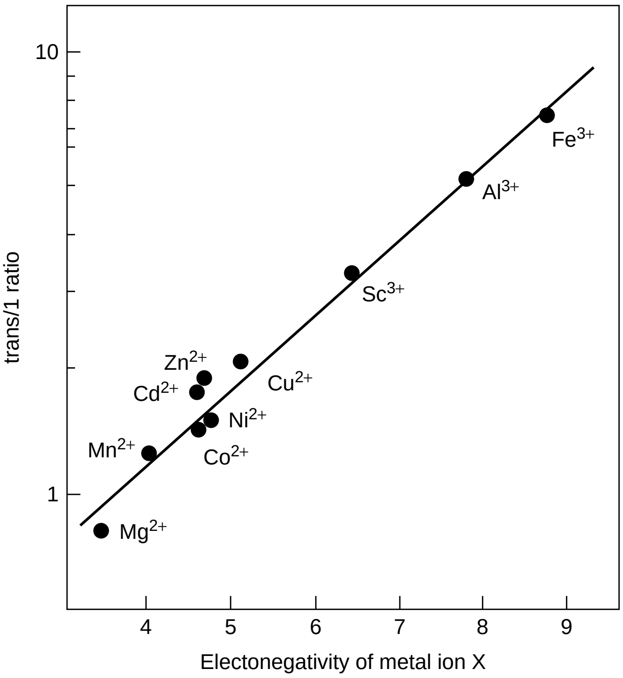

Figure 14 Effect of acid strength on the selectivity observed for isomerization of *cis*-2-butene over metal sulfates

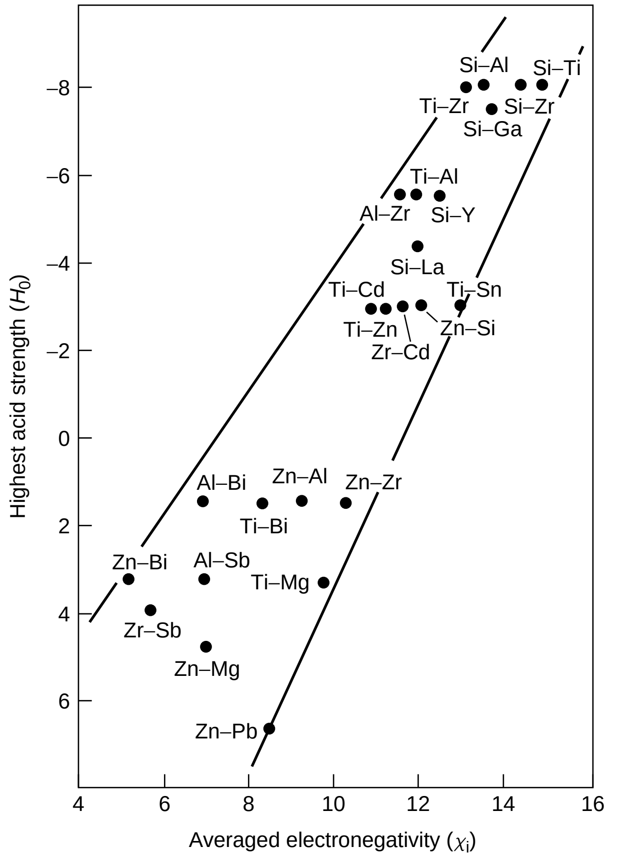

Figure 15 Highest acid strength versus average electronegativity of metal ions of mixed oxides (molar ratio = 1)

and catalyzes bifunctionally the conversion of ethanol to butadiene.[137]

WO_3-ZrO_2 is active in various acid-catalyzed reactions involving skeletal isomerization of alkanes,[138,139] xylene isomerization,[140] and hydration of olefins.[141,142] Catalytic activity is heavily dependent on calcination temperature. Maximum activity for ethene hydration and isomerization of *n*-butane is obtained when the catalyst is calcined at 1073 and 923 K, respectively.[138,142] Calcination at high temperatures leads to the formation of two-dimensional polytungstate domains, which is proposed to be essential for formation of strong acid sites. In addition, calcination at high temperatures induces surface hydrophobicity,[142] which is an important factor influencing catalytic activity in water-participating reactions,[119] because hydrophobicity either increases the access of olefins to the acid sites[143] or suppresses the poisoning effect of water.[119] The hydrophobicity as well as the strong acidity of WO_3-ZrO_2 calcined at high temperature is responsible for the high activity toward the hydrolysis of ethene.[142]

MoO_3-ZrO_2 is active in acid-catalyzed reactions. In addition, this catalyst possesses an unique acidic function that reversibly accelerates acid-catalyzed reactions such as dehydration of 2-butanol in the gas phase by addition of water vapor when the catalyst is calcined at temperatures higher than 773 K.[144] Conventional solid acids like $SiO_2-Al_2O_3$ are rapidly deactivated by water.

3.6.2 Solid Superacids and Superbases

A superacid is an acid whose acidity (acid strength) is greater than that of 100% H_2SO_4 ($H_0 = -11.94$). $SO_4{}^{2-}/ZrO_2$ and $SO_4{}^{2-}/TiO_2$ have acid strengths near $H_0 = -14.52$.[1498] These catalysts are active for skeletal isomerization of *n*-butane at room temperature, but the deactivation is significant. $SO_4{}^{2-}/ZrO_2$ also catalyzes acylation, while $SO_4{}^{2-}/TiO_2$, $SiO_2-Al_2O_3$, and H-ZSM-5 are inactive.[145]

Catalytic activity of $SO_4{}^{2-}/ZrO_2$ is sensitive to pretreatment. By heating $Zr(OH)_4$ at 373–673 K, active catalysts were obtained, but their activities are greatly decreased by treatment at 723 K. Crystallization temperature of ZrO_2 is 683 K and leads to undesirable effects.[146]

$SO_4{}^{2-}/ZrO_2$ catalyzes reactions such as cracking, skeletal isomerization, acylation, esterification, and polymerization. In the alkylation of isobutane with butenes, $SO_4{}^{2-}/ZrO_2$ is highly active and gives alkylates analogous to cases involving H_2SO_4. The structure of the catalytically active species or of the species responsible for the highly acidic properties involves an organic sulfate structure with a metal cation.[145,146]

The addition of Pt to $SO_4{}^{2-}/ZrO_2$ resulted in a drastic increase in catalytic activity and catalyst life for the skeletal isomerization of pentane in the presence of hydrogen. The roles of Pt include: (1) dissociated hydrogen on Pt which spills over to the $SO_4{}^{2-}/ZrO_2$ surface to form H^+; (2) dissociated hydrogen that hydrogenates the carbonaceous residue; and (3) the addition of Pt that suppresses acid strength to prevent the formation of carbonaceous materials.[147]

The solid superbase $Na/NaOH/Al_2O_3$ has been synthesized. This catalyst, prepared by treating Al_2O_3 with NaOH followed by addition of metallic Na, possesses basic sites stronger than $H_0 = 35$.[148] $Na/NaOH/Al_2O_3$ is used in an industrial process for the selective double bond isomerization of 5-vinylbicyclo-[2,2,l]heptene. When prepared by the addition of NaN_3 to MgO followed by heat treatment, the catalyst exhibits strong basicity and possesses high catalytic activity for decomposition of methyl formate to CO and methanol.[149]

4 REFERENCES

1. J. Haber, in ‘Catalysis. Science and Technology’, eds. J. R. Anderson and M. Boudart, Springer, Berlin, 1981, Vol. 2, p. 13; T. Seiyama, ‘Kinzokusankabutsu to Sono Shokubaisayou (Metal Oxides and Their Catalysis)’, Kodansha, Tokyo, 1978.

2. M. Misono, in ‘Future Opportunities in Catalytic and Separation Technology’, eds. M. Misono, Y. Moro-oka, and S. Kimura, Elsevier, Amsterdam, 1990, p. 13.
3. M. Thomas, *Angew. Chem., Int. Ed. Engl.*, 1988, **27**, 1673.
4. J. C. Volta, I. M. Tatibouet, C. Phichitkul, and J. E. Germain, ‘Proceedings of the 8th Int. Congress on Catalysis, 1984’, Springer, Berlin, 1984, Vol. 4, p. 451.
5. T. Okuhara, K. Inumaru, and M. Misono, *ACS Symp. Ser.*, 1993, **523**, 156.
6. Y. Moro-oka, De.-Hua. He, and W. Ueda, in ‘Structure-Activity and Selectivity Relationships in Heterogeneous Catalysis’, eds. R. K. Grasselli and A. W. Sleight, Elsevier, Amsterdam, 1991, p. 57.
7. G. W. Keulks, *J. Catal.*, 1970, **19**, 232; R. D. Wragg, P. G. Ashmore, and J. A. Hockey, *J. Catal.*, 1971, **22**, 49; 1973, **28**, 337.
8. G. W. Keulks and L. D. Krenzke, ‘Proceedings of the 6th Int. Congress on Catalysis, 1976’, The Chemical Society, London, 1976, p. 806.
9. M. Misono, Y. Nozawa, and Y. Yoneda, ‘Proceedings of the 6th Int. Congress on Catalysis, 1976’, The Chemical Society, London, 1977, p. 386.
10. J. H. Lunsford, *Catal. Rev. Sci. Eng.*, 1973, **8**, 135; M. Che and A. J. Tench, *Adv. Catal.*, 1982, **31**, 77; 1983, **32**, 1.
11. B. C. Gates, ‘Catalytic Chemistry’, John Wiley & Sons, New York, 1992, p. 19.
12. C. L. Thomas, *Ind. Eng. Chem.*, 1949, **41**, 2564.
13. K. Tanabe, ‘Solid Acid and Bases’, Kodansha, Tokyo, Academic Press, New York, 1970.
14. K. Tanabe, M. Misono, Y. Ono, and H. Hattori, ‘New Solid Acids and Bases’, Elsevier, Amsterdam, 1989.
15. B. C. Gates, J. R. Katzer, and G. C. Schuit, ‘Chemistry of Catalytic Processes’, McGraw-Hill, New York, 1979.
16. A. W. Sleight, in ‘Advanced Materials in Catalysis’, eds. J. J. Burton and R. L. Garten, Academic, New York, 1977, p. 181.
17. V. D. Sokolovskii, *Catal. Rev.*, 1990, **32**, 1.
18. T. P. Snyder and C. G. Hill Jr, *Catal. Rev.*, 1989, **31**, 43.
19. L. D. Krenzke and G. W. Keulks, *J. Catal.*, 1980, **61**, 316.
20. R. K. Grasselli and J. D. Burrington, *Adv. Catal.*, 1981, **30**, 133; R. K. Grasselli, *Appl. Catal.*, 1985, **15**, 127.
21. I. Matsuura, R. Schut, and K. Hirakawa, *J. Catal.*, 1980, **63**, 152.
22. M. W. J. Wolfs and P. A. Batist, *J. Catal.*, 1974, **32**, 25.
23. Y. Moro-oka, De.-Hua. He, and W. Ueda, in ‘Structure-Activity and Selectivity Relationships in Heterogeneous Catalysis’, eds. R. K. Grasselli and A. W. Sleight, Elsevier, Amsterdam, 1991, p. 57.
24. J. Bartek, A. Ebner, and J. Brazdil, US Patent 5198580, 1993.
25. G. Blanchard and G. Ferre, EP Patent 609122-A1, 1994.
26. C. Mazzocchia, E. Tempesti, R. Anouchinsky, and A. Kaddouri, FR Patent 2693384, 1994.
27. T. Ushikubo, H. Nakamura, Y. Koyasu, and S. Wajiki, US Patent 5380933, 1995.
28. T. Ushikubo, Y. Koyasu, H. Nakamura, and S. Wajiki, JP Patent 98045664, 1998.
29. H. Tsuji and Y. Koyasu, *J. Am. Chem. Soc.*, 2002, **124**, 5608.
30. M. Hatano and A. Kayo, EP Patent 0318295-B1, 1992.
31. E. Thorsteinson, T. Wilson, F. Young, and P. Kasai, *J. Catal.*, 1978, **52**, 116.
32. D. Vitry, Y. Morikawa, J. L. Dubois, and W. Ueda, *Appl. Catal., A*, 2003, **251**, 411.
33. H. Watanabe and Y. Koyasu, *Appl. Catal., A*, 2000, **194/195**, 479.
34. M. M. Lin, *Appl. Catal. A*, 2001, **207**, 1.
35. G. Centi, F. Trifiro, J. R. Ebner, and V. M. Franchetti, *Chem. Rev.*, 1988, **88**, 55.
36. B. K. Hodnett, *Catal. Rev.*, 1985, **27**, 373.
37. E. Bordes, *Catal. Today*, 1987, **1**, 499.
38. M. Misono, K. Miyamoto, K. Tsuji, T. Goto, N. Mizuno, and T. Okuhara, in ‘New Developments in Selective Oxidation’, eds. G. Centi and F. Trifiro, Elsevier, Amsterdam, 1990, p. 605.
39. T. P. Moser and G. L. Schrader, *J. Catal.*, 1987, **104**, 99.
40. G. Koyano, T. Okuhara, and M. Misono, *J. Am. Chem. Soc.*, 1998, **120**, 767.
41. M. A. Pepera, J. L. Callahan, M. J. Desmond, E. C. Milberger, P. R. Blum, and N. J. Bremer, *J. Am. Chem. Soc.*, 1985, **107**, 4883.
42. G. Centi, F. Trifiro, J. R. Ebner, and V. M. Franchetti, *Chem. Rev.*, 1988, **88**, 55.
43. T. Shimoda, T. Okuhara, and M. Misono, *Bull. Chem. Soc. Jpn.*, 1985, **58**, 2163.
44. G. Gleaves, J. R. Ebner, and T. C. Kuechier, *Catal. Rev.*, 1988, **30**, 49.
45. L. Benes, K. Melanova, V. Zima, J. Kalousova, and J. Votinsky, *Inorg. Chem.*, 1997, **36**, 2850.
46. N. Hiyoshi, N. Yamamoto, N. Ryumon, Y. Kamiya, and T. Okuhara, *J. Catal.*, 2004, **221**, 225.
47. N. Yamamoto, N. hiyoshi, and T. Okuhara, *Chem. Mater.*, 2002, **14**, 3882.
48. Y. Kamiya, E. Nishikawa, T. Okuhara, and T. Hattori, *Appl. Catal., A*, 2001, **206**, 103.
49. R. J. H. Voorhoeve ed., ‘Advanced Materials in Catalysis’, Academic press, 1997, p. 129.
50. C. P. Khattak and F. F. Wang, in ‘Handbook pf Physics and Chemistry of Rare Earth’, K. A. Gschneider Jr and L. Eyring eds. North-Holland Publisher, Amsterdam, 1979, p. 525.
51. J. B. Goodenough, J. M. Longo, in ‘Landolt-Bronstein New Series’, K. H. Hellwege and A. M. Helwege eds. Springer-Verlag, Berlin, Vol. 4, part a, p. 126.
52. J. B. Goodenough, in ‘Solid State Chemistry’, ed. C. N. R. Rao, Marcel Dekker, New York, 1974, p. 215.

53. J. F. Bringley, B. A. Scott, S. J. La Placa, R. F. Boehme, T. M. Shaw, M. W. McElfresh, S. S. Trail, and D. E. Cox, *Nature*, 1990, **347**, 263.
54. J. F. Bringley, B. A. Scott, S. J. La Placa, T. R. McGuire, F. Mehran, M. W. McElfresh, and D. E. Cox, *Phys. Rev. B*, 1993, **47**, 15269.
55. B. C. Tofield and W. R. Scott, *J. Solid State Chem.*, 1974, **10**, 183.
56. L. G. Tejuca, J. L. G. Fierro, and J. M. D. Tascon, *Adv. Catal.*, 1898, **36**, 237.
57. M. R. Balasubramanian, R. Natesan, and P. Rajendran, *J. Sci. Ind. Res.*, 1984, **34**, 500.
58. W. F. Libby, *Science*, 1975, **171**, 499.
59. H. Arai, T. Yamada, K. Eguchi, and T. Seiyama, *Appl. Catal.*, 1986, **26**, 265.
60. J. E. Ten Elshof, H. J. M. Bouemeester, and H. Verweij, *Appl. Catal., A*, 1995, **130**, 195.
61. T. Hayakawa, A. G. Anderson, H. Orita, M. Shimizu, and K. Takehira, *Catal. Lett.*, 1992, **16**, 373.
62. R. J. H. Voorhoeve, J. P. Remeika, and L. E. Trimble, *Ann. N.Y. Acad. Sci.*, 1976, **272**, 3.
63. J. Happel, M. Hnatow, and L. Bajars, ‘Base Metal Oxide Catalysts’, Dekker, New York, 1977, p. 117.
64. P. R. Watson and G. A. Somorjai, *J. Catal.*, 1982, **74**, 282.
65. M. A. Ulla, R. A. Migone, J. O. Petuchi, and E. A. Lombardo, *J. Catal.*, 1987, **105**, 107.
66. M. A. Ulla and E. A. Lombardo, *Bull. Chem. Soc. Jpn.*, 1982, **55**, 2311.
67. J. H. Sinfelt, *Adv. Catal.*, 1973, **23**, 91.
68. K. Domen, S. Naito, T. Onishi, K. Tamura, and M. Soma, *J. Phys. Chem.*, 1982, **86**, 3657.
69. M. S. Wrighton, A. B. Ellis, P. T. Wolczanski, D. L. Morse, H. B. Abrahamson, and D. S. Ginley, *J. Am. Chem. Soc.*, 1976, **98**, 277.
70. M. A. Pena and J. L. G. Fierro, *Chem. Rev.*, 2001, **101**, 1981.
71. M. Misono, *Stud. Surf. Sci. Catal.*, 1990, **54**, 13.
72. M. Misono and N. Mizuno, ‘Catalyst Materials for High-temperature Processes’, American Ceramic Society, 1997, p. 67.
73. T. Nitadori, T. Ichiki, and M. Misono, *Bull. Chem. Soc. Jpn.*, 1988, **61**, 621.
74. G. Nagasubranian, B. Viswanthan, and M. V. C. Sastri, *Indian J. Chem.*, 1978, **16A**, 642.
75. C. S. Swamy and J. Christopher, *Catal Rev.*, 1992, **34**, 409.
76. D. Ferri and L. Forni, *Appl. Catal., B*, 1998, **16**, 119.
77. Z. Shao, G. Xiong, S. Sheng, H. Chen, and L. Li, *Stud. Surf. Sci. Catal.*, 1998, **118**, 431.
78. N. Mizuno, H. Fujii, and M. Misono, *Chem. Lett.*, 1986, 1333.
79. R. Bradow, *Ind. Eng. Chem. Res.*, 1995, **34**, 1929.
80. M. Misono, *Catal. Rev.*, 1987, **29**, 269.
81. Y. Izumi, K. Urabe, and M. Onaka, ‘Zeolite, Clay, and Heteropolyacid in Organic Reactions’, VCH, Weinheim, 1992.
82. Y. Ono, ‘Perspectives in Catalysis’, Blackwell, London, 1992, p. 431.
83. I. V. Kozhevnikov, *Russ. Chem. Rev.*, 1987, **56**, 811.
84. M. T. Pope, ‘Heteropoly and Isopoly Oxometalates’, Springer, Berlin, 1983.
85. T. J. R. Weakely, *Struct. Bonding*, 1974, **18**, 131.
86. G. A. Tsigdinos, *Top. Curr. Chem.*, 1978, **76**, 1.
87. M. T. Pope and A. Muller, *Angew. Chem., Int. Ed. Engl.*, 1991, **30**, 34.
88. I. V. Kozhevnikov and K. I. Matveev, *Appl. Catal.*, 1983, **5**, 135.
89. R. S. Drago, J. A. Dias, and T. O. Maier, *J. Am. Chem. Soc.*, 1997, **119**, 7702.
90. T. Okuhara, T. Nishimura, H. Watanabe, and M. Misono, *J. Mol. Catal.*, 1992, **74**, 247.
91. T. Okuhara, H. Watanabe, T. Nishimura, K. Inumaru, and M. Misono, *Chem. Mater.*, 2000, **12**, 2230.
92. F. Lefebvre, F. X. Liu-Cai, and A. Auroiux, *J. Mater. Chem.*, 1994, **4**, 125.
93. T. Okuhara, T. Nishimura, and M. Misono, *Stud. Surf. Sci. Catal.*, 1996, **101**, 559.
94. K. Nowinska, R. Fiedorow, and J. Adamiec, *J. Chem. Soc., Faraday Trans.*, 1991, **87**, 749.
95. W.-C. Chemg and N. P. Luthra, *J. Catal.*, 1988, **109**, 163.
96. K. M. Rao, R. Gebetto, A. Lannibello, and A. Zecchina, *J. Catal.*, 1989, **119**, 512.
97. J. A. R. van Veer, P. A. J. M. Hendriks, R. R. Andrea, E. J. M. Romers, and A. E. Wilson, *J. Phys. Chem.*, 1990, **94**, 1831.
98. M. Misono, ‘Proceedings of the 10th Int. Congress on Catalysis, 1992’, Akademiai Kiado, Budapest, 1992, p. 69.
99. T. Nishimura, T. Okuhara, and M. Misono, *Chem. Lett.*, 1991, 1695.
100. T. Okuhara, T. Nishimura, H. Watanabe, and M. Misono, ‘Acid-Base Catalysis II’, Kidansha, Tokyo-Elsevier, Amsterdam, 1994, p. 419.
101. M. Yoshimune, Y. Yoshinaga, and T. Okuhara, *Microporous Mesopor. Mater.*, 2002, **51**, 165.
102. Y. Yoshinaga, T. Suzuki, M. Yoshimune, and T. Okuhara, *Top. Catal.*, 2002, **19**, 170.
103. Y. Yoshinaga and T. Okuhara, *J. Chem. Soc., Faraday Trans. 1*, 1998, **94**, 2235.
104. T. Yamada, Y. Yoshinaga, and T. Okuhara, *Bull. Chem. Soc. Jpn.*, 1998, **71**, 2727.
105. I. V. Kozhevnikov, A. Sinneme, R. J. J. Jansen, K. Pamin, and H. van Bekkum, *Catal. Lett.*, 1995, **30**, 241.
106. M. J. Verhoef, P. J. Kooyman, J. A. Peters, and H. van Bekkum, *Microporous Mesopor. Mater.*, 1999, **27**, 365.

107. Y. Wang, A. Y. Kim, X. S. Li, L. Wang, C. H. F. Peden, and B. C. Bunker, *ACS Symp. Ser.*, 2000, **738**, 353.
108. S. Choi, Y. Wang, Z. Nie, J. Liu, and C. H. F. Peden, *Catal. Today*, 2000, **55**, 117.
109. W. Chu, X. Yang, Y. Shan, X. Ye, and Y. Wu, *Catal. Lett.*, 1996, **42**, 201.
110. C. Castro, J. Primo, and A. Corma, *J. Mol. Catal. A*, 1998, **134**, 215.
111. T. Okuhara, X. Chen, and M. Matsuda, *Appl. Catal., A*, 2000, **200**, 109.
112. A. corma, A. Martinez, and C. Martinez, *J. Catal.*, 1996, **164**, 422.
113. N. Essayem, S. Kieger, G. Coudurier, and J. C. Verdrine, *Stud. Surf. Sci. Catal.*, 1996, **101**, 591.
114. B. B. Bardin and R. Davis, *Topics Catal.*, 1998, **6**, 77.
115. K. Na, T. Okuhara, and M. Misono, *J. Catal.*, 1997, **170**, 96.
116. Y. Liu, K. Na, and M. Misno, *J. Mol. Catal. A*, 1999, **141**, 145.
117. Y. Liu, G. Koyano, and M. Misono, *Topics Catal.*, 2000, **11/12**, 239.
118. C. Travers, N. Essayem, M. Delage, and S. Quelen, *Catal. Today*, 2000, **65**, 355.
119. T. Okuhara, *Chem. Rev.*, 2002, **102**, 3641.
120. M. Kimura, T. Nakato, and T. Okuhra, *Appl. Catal. A*, 1997, **165**, 227.
121. T. Yamada and T. Okuhara, *Langmuir*, 2000, **16**, 2321.
122. R. Watanabe, T. Suzuki, and T. Okuhara, *Catal. Today*, 2001, **66**, 119.
123. A. Miyaji, R. Ohnishi, and T. Okuhara, *App. Catal., A*, 2004, **262**, 143.
124. T. Okuhara, N. Mizuno, and M. Misono, *Appl. Catal., A.*, 2001, **222**, 63.
125. K. Sano and H. Uchida, *Shokubai (Catal Catal)*, 1999, **41**, 290.
126. N. Mizuno, T. Watanabe, and M. Misono, *J. Phys. Chem.*, 1985, **89**, 80.
127. M. Misono, *Catal. Rev.*, 1987, **29**, 269.
128. Y. Izumi, K. Urabe, and M. Onaka, ‘Zeolite, Clay, and Heteropolyacid in Organic Reactions’, VCH, Weinheim, 1992.
129. Y. Ono, ‘Perspectives in Catalysis’, Blackwell, London, 1992, p. 431.
130. M. Misono, ‘Proceedings of the 10th Int. Congress on Catalysis, 1992’, Akademiai Kiado, Budapest, 1992, p. 69.
131. J. B. Black, N. J. Chayden, P. L. Gal, J. P. Scott, E. M. Serwicka, and J. B. Goodenough, *J. Catal.*, 1987, **106**, 1.
132. H. Knozinger and P. Ratnasamy, *Catal Rev.*, 1978, **17**, 52.
133. K. Tanabe, *CHEMTECH*, 1991, 628.
134. H. Matauhashi and H. Hattori, *J. Catal.*, 1984, **85**, 457.
135. H. Kurokawa, W. Ueda, Y. Morikawa, Y. Moro-oka, and T. Ikawa, in ‘Acid-Base Catalysis’, eds. K. Tanabe, H. Hattori, T. Yamaguchi, and T. Tanaka, VCH, Weinheim, 1989, p. 93.
136. A. Satoh, H. Hattori, and K. Tanabe, *Chem. Lett.*, 1983, 497.
137. H. Niiyama and E. Echigoya, *Bull. Chem. Soc. Jpn.*, 1972, **45**, 655.
138. M. Hino and K. Arata, *J. Chem. Soc., Chem. Commun.*, 1988, 1259.
139. R. A. Comelli, S. A. Canavese, and N. S. Figoli, *Catal. Lett.*, 1998, **55**, 177.
140. R. D. Wilson, D. G. Barton, C. D. Baertsch, and E. Iglesia, *J. Catal.*, 2000, **194**, 175.
141. S. Wakamatsu, M. Shimamura, S. Asaoka, and Y. Shirato, ‘Preprints of the Annual Meeting of the Japan Petroleum Institute’, Tokyo, 1995, p. B34.
142. W. Chu, T. Echizen. Y. Kamiya, and T. Okuhara, *Appl. Catal., A*, 2004, **259**, 199.
143. H. Kochkar and F. Figueras, *J. Catal.*, 1997, **171**, 420.
144. L. Li, Y. Yoshinaga, and T. Okuhara, *Phys. Chem. Chem. Phys.*, 2002, **4**, 6129.
145. T. Yamaguchi, *Appl. Catal.*, 1990, **61**, 1.
146. K. Arata, *Adv. Catal.*, 1990, **37**, 165.
147. K. Ebitani, J. Konishi, and H. Hattori, *J. Catal.*, 1991, **130**, 257.
148. G. Suzukamo, M. Fukao, T. Hibi, K. Tanaka, and K. Chikaishi, in ‘Acid-Base Catalysis’, eds. K. Tanabe, H. Hattori, T. Yamaguchi, and T. Tanaka, VCH, Weinheim, 1988, p. 405.
149. T. Ushikubo, H. Hattori, and K. Tanabe, *Chem. Lett.*, 1984, 649.

Oxides: Solid-state Chemistry

William H. McCarroll[1] **& Kandalam V. Ramanujachary**[2]
[1]*Rider University, Lawrenceville, NJ, USA*
[2]*Rowan University, Glassboro, NJ, USA*

1 Introduction 1
2 Trends in the Properties of Binary Oxides 2
3 Oxide Crystal Structures 3
4 Structure-property Relationships in Oxides 23
5 Preparative Methods for Oxides 30
6 Some Applications of Oxides 38
7 Related Articles 44
8 References 44

Abbreviations

BST = $BaTiO_3$-$SrTiO_3$ Solid Solutions; CP = Close packed; CCP = Cubic close packing; CDW = Charge density wave; CMR = Colossal magnetoresistance; DMS = dilute magnetic semiconductors; $DPTB_h$ = Diphosphate tungsten bronzes with hexagonal tunnels; $DPTB_p$ = Diphospahte tungsten bronzes with pentagonal tunnels; DRAM = Dynamic Random Access Memory; FeRAM = Ferroelectric Random Access Memory HCP = Hexagonal close packed; HREM = High-resolution electron microscopy; HTB = Hexagonal tungsten bronze; $MPTB_h$ = Monophosphate tungsten bronzes with hexagonal tunnels; $MPTB_p$ = Monophosphate tungsten bronzes with pentagonal tunnels; NASICON = Sodium super ionic conductor; NLO = Nonlinear Optical; PLZT = Lead lanthanum zirconium titanate; PZT = Lead zirconium titanate; SBT = Strontium Bismuth Tantalate, $SrBi_2Ta_2O_9$; SOFC = Solid oxide fuel cell; TTB = Tetragonal tungsten bronze; YAG = Yttrium iron garnet; 3D = Three-dimensional; TEOS = Tetraethylorthosilicate.

1 INTRODUCTION

Oxygen comprises approximately 21% of the Earth's atmosphere and nearly 47% of its crust, thus making it the most abundant terrestrial element. By far, the greatest amount of this oxygen is found in combination with silicon and aluminum in the form of complex aluminosilicates that make up the vast proportion of igneous rocks. Smaller amounts are found as concentrated deposits of anhydrous oxides, hydroxides, carbonates, sulfates, or other oxyanions, which can be exploited commercially for their elemental components. Indeed, the earlier studies by mineralogists and chemists who elucidated the compositions and structures of these naturally occurring compounds of oxygen provided the basis for the rich and varied solid-state chemistry that has evolved in the modern laboratory.

This article will be concerned with the chemistry of inorganic solid compounds or composites with interesting and useful properties in which the valence of oxygen is -2. Readers interested in molecular oxides, oxyhalides, molecular oxygenyl complexes, peroxides, superoxides, or ozonides should consult established publications[1–6] and the index of this encyclopedia.

Oxygen is a highly reactive element, forming at least one binary oxide with virtually all of the known elements (the exceptions being Radon and the lighter noble gases) as well as a wide variety of interesting and useful ternary and quaternary compounds. Although many gaseous oxides are known at standard temperatures and pressures, particularly those of the lighter members of groups 15–17 as well a few liquids (e.g. P_4O_6 and Mn_2O_7), by far the largest number are solids. Within this latter class the physical properties vary greatly, depending upon the position of the combining element in the periodic table and its formal valence. Thus we find, for instance, refractory, electrically insulating oxides such as ZrO_2 and Cr_2O_3 with melting points of 2670 and 2450 °C, highly reactive low-melting oxides such as CrO_3 (mp 190 °C) or V_2O_5 (mp 685 °C) as well as partially reduced oxides such as MoO_2 or ReO_3 whose electrical conductivities rival those of conventional metals.

The ability of oxygen to form this wide variety of compounds results from a number of favorable factors. One is a high electronegativity, 3.5 on the Pauling scale, which is a measure of its desire to acquire negative electronic charge and is second only to fluorine in this respect. A second very important factor is that it has a high electron affinity, which can be looked upon as the ability or capacity to acquire an electron. A third factor is its ability to form strong chemical bonds with most elements that may be ionic or covalent in nature depending upon the electronegativity of the combining element. In covalently bonded environments, oxygen may adapt coordination numbers of 2, 3, or 4. This is the result of the ability of oxygen to hybridize sp, sp^2, or sp^3, allowing it to form strong σ type covalent bonds in three dimensions leading to the extended network structures that characterize so many oxides. Further, when one or more p orbitals are not utilized in hybridization, they may be used to form weaker, but nonetheless important, metal-oxygen π bonds by overlap of oxygen 2p orbitals with properly oriented d orbitals of transition metal ions. Such interactions may dramatically affect the electrical and magnetic properties of the material.

2 TRENDS IN THE PROPERTIES OF BINARY OXIDES[1–3,7]

This section gives a brief overview of some of the more important properties of the binary oxides of the elements. Some of the more important aspects that must be considered in evaluating a compound are its thermodynamic stability and chemical reactivity, particularly with respect to oxidation or reduction as well as reactivity with such constituents of the atmosphere as dioxygen, water vapor, and carbon dioxide, since these factors will determine the commercial availability of the compound and the need for any particular precautions in its handling or storage in the laboratory.

2.1 Acid–Base Properties

The reactivity of oxides towards water follows well-defined trends based upon the electronegativity, size, oxidation number, and position in the periodic table. Thus elements of groups 1 and 2, with the exception of Be, are strongly basic, being converted to their respective hydroxides on contact with water, which absorb carbon dioxide from the air or liberate ammonia from ammonium salts. In the case of the alkali hydroxides, thermal dehydration to form the oxide takes place only at very high temperatures except for LiOH, which can be decomposed to the oxide above 925 °C. The somewhat less basic properties of the divalent alkaline-earth oxides from Mg to Ba is illustrated by the fact that the oxides can be regenerated from their hydroxides at temperatures progressively increasing from 400 to 700 °C as the size of the alkaline-earth metal increases. The situation is further complicated by the fact that both the alkali and alkali earth hydroxides readily absorb carbon dioxide from the air to form extremely stable carbonates. Thus, alkali metal oxides are not likely to be found in the chemical stockroom, while those of the alkaline earths that are should always be looked upon with suspicion. In the case of Mg and Ca, ignition at 500 and 1000 °C respectively is normally sufficient to destroy any hydroxide or carbonate present while in the case of Ba and Sr, heating in the presence of H_2 or C at temperatures above 1200 °C is required to break the strong C–O bond and regenerate the pure oxide:

$$BaCO_3 + H_2 = BaO + H_2O + CO \qquad (1)$$

A similar but less formidable trend is observed for the group 3 metals and the trivalent rare earths where hydroxide and/or carbonate removal from the commercially available materials is assured by heating at 800–1000 °C for the lighter members of the series while progressively lower temperatures are required for the heavier members. The tendency of small charge, large size cations to yield basic oxides is illustrated by the fact that Ag_20 and Tl_20 are strongly basic in all their reactions.

Quite different behavior is found for the oxides of groups 15 through 17. Here these covalent, molecular oxides react with water to form some of the strongest acids known, many of which are strongly oxidizing. In general, the acid behavior becomes less pronounced as one proceeds down a given group or when the oxide has a valence less than the group valence. Thus, nitric and sulfuric acids are much stronger acids than phosphoric or selenic acids. On the other hand, these two latter acids are much stronger than phosphorus acid, H_3PO_3, or selenous acid, H_2SeO_3. Often the reaction with water takes place readily but there are some exceptions. Thus, P_2O_5 is an effective desiccant for the removal of trace quantities of water from gas streams but the reaction of SO_3 with water is kinetically limited and commercially, sulfuric acid is manufactured from SO_3 by passing the latter through concentrated H_2SO_4 to form pyrosulfuric acid, $H_2SO_4{\cdot}SO_3$, which is then diluted with water to form sulfuric acid of the desired concentration.

With regard to the rest of the periodic table, the acid-base behavior is usually less pronounced. Indeed, many of these oxides, particularly those in the trivalent state, are amphoteric, reacting readily with stronger acids or bases. Typically, however, many of these oxides are kinetically inhibited and will not react easily with water or with aqueous reagents. Thus, Cr_2O_3 is immune to concentrated aqueous acids or bases but will react readily with solid oxides at elevated temperatures. Similar behaviors are noted for the oxides of group 4 and for Nb and Ta in the group valency. NiO, which on the basis of size and charge would be expected to have pronounced basic characteristics, reacts slowly if at all with concentrated aqueous acids but does display basic properties in high-temperature solid-state reactions. On the other hand, there are many acidic oxides that are essentially insoluble in water but will react readily with aqueous hydroxide solutions, or in some cases alkali carbonates, to form oxyanion salts. These are typically high-valent oxides such as V_2O_5, MoO_3, and CrO_3.

2.2 Valence State Trends

A well-known property of oxygen is that it tends to stabilize the higher valencies of the elements with which it combines. Indeed, while fluorine may have a higher electronegativity and is noted for its ability to stabilize high oxidation states, the highest valence known for a given binary compound of a transition metal is often an oxide. Thus, one finds Mn(VII) Mn_2O_7 but MnF_5 is the highest valent fluoride. Similarly, OsO_4 is well established but the highest valent fluoride is OsF_6. A general trend among the transition metals is that the higher oxidation states will tend to be more stable as one goes down a given periodic group while the group valence will become less accessible as one goes from group 3 to group 12. Thus, for group 4, the dioxide is the most stable and lower valent oxides can be prepared only for titanium. Further, one notes that the relative ease of reduction of Ti(IV) can be responsible for the bluish cast found in some titania based white pigments. Similarly, CrO_3 is highly oxidizing while WO_3 is the most stable binary oxide of tungsten. Although higher oxidation states of Fe and Ni can be stabilized in mixed-metal oxides, Fe_2O_3 and NiO represent the highest valent binary oxides of these two members. For osmium, OsO_2 can be prepared by the reduction of the volatile, molecular OsO_4, which is well known for the preparation of stained biological slides. All oxides of Pt are easily decomposed although it is possible to prepare PtO_3. Cu_2O and Ag_2O are well established but the existence of Au_2O is not. The only divalent group 11 oxide is CuO, AgO being a mixture of the mono- and trivalent states. The existence of Cu_2O_3 is questionable but Au_2O_3 is well established but again unstable with respect to decomposition to the elements at temperature above 160 °C. Cu(III) is stabilized by mixed oxide formation, the best-known example being $YBa_2Cu_3O_7$ and related compounds, which form the recently discovered class of high-temperature superconducting cuprate oxides. Except for the metal–metal bonded Hg_2O, only the divalent state is known for group 12 oxides.

In the case of right-hand main group oxides, the general observation is that compounds with a valence two less than the group valence will be thermodynamically more stable as one goes down the group. Thus while Al_2O_3 and Ga_2O_3 are the only known solid binary oxides of these two elements, an unstable In_2O has been observed while Tl_2O, PbO, and Bi_2O_3 are the stable oxides for the heaviest members of groups 13 through 15. Indeed, Bi_2O_5 is not well established and PoO_3 does not exist, in contrast to the well-known SO_3.

The halogens form a variety of binary compounds, all of which are highly unstable and, with the exception of gaseous ClO_2, of little economic value. Here the oxygen chemistry is dominated by oxyhalogen acids and their salts. Two binary oxides of xenon are known, both of which are highly unstable. White crystals of XeO_3 are obtained by the careful evaporation of dilute solution of $Xe(OH)_6$ produced by the hydrolytic decomposition of XeF_4.

$$6XeF_4 + 18H_20 = 2Xe(OH)_6 + 4Xe + 3O_2 + 24HF \qquad (2)$$

XeO_4, like the trioxide, is highly unstable and explosive. This gaseous oxide is obtained by the action of concentrated sulfuric acid on Ba_2XeO_6 solutions.

3 OXIDE CRYSTAL STRUCTURES

3.1 Oxide Structures Derived from Closest Packing of Spheres[8–10]

The high electronegativity of oxygen imparts a significant ionic character to the bonds formed by it with metals in formal valences of four or less, the effect being particularly pronounced for the lower values. The omni-directional character of ionic bonds mandates that the structures be 3D in nature and this in fact is found to be the case even where there may be significant covalent character to the bonds. However, as the electronegativity of the positive end of the dipole increases, the structures tend to become more anisotropic in nature. In this case, one sees clear evidence for chains or sheets of strongly bonded atoms whose properties are one or two dimensional. Finally, in the cases of the nonmetallic main group elements and transition metals in high valence states, a definite trend towards molecular bonding is observed. This may be either in the form of neutral molecules held together by van der Waals forces or, more often, as small covalently bound oxyanions in combination with group 1 and 2 cations (e.g. Na_2SO_4), where the extended interactions are essentially ionic.

An elegant description of the most common 3D oxide structures can be given in terms of space filling models derived from the closest packing of spheres. The assumption is made that ions can be treated as hard spheres with well-defined ionic radii. When they come in contact with one another, the repulsive forces rise exponentially owing to the interaction of the respective electron shells. The model postulates that the most stable arrangements of equal sized spheres will be those that fill space most efficiently leading to maximum density. In two dimensions, the most efficient way to pack equal sized spheres is to form equilateral triangles of spheres, which are then stacked side by side to form a layer in which each sphere is now surrounded by six other spheres to form a layer with hexagonal symmetry (Figure 1(a)).

Note that for each close-packed (CP) atom there exist also two triangular shaped interstices. These interstices form two sublattices labeled P and R, either of which (but not both at the same time) may serve as a nesting spot so that similar layers of close-packed spheres can be stacked one on top of the other to generate a three-dimensional CP lattice. Figure 1(b) shows a two-layer arrangement in which the P positions have been utilized. Note that if the R position had been chosen, the arrangement would look the same except for the translation. The bottom layer is designated as the A layer and the top the B layer. When one proceeds to add a third layer, there are two choices, which lead to spatially different arrangements. If the nesting spot is chosen that lies directly above the A layer, then so-called ABA packing results. If this motif is continued

...... ABABABABA ......

a lattice is generated with hexagonal symmetry that is referred to as hexagonal closest packing (HCP). On the other hand, if the R interstice sublattice is chosen for the nesting, this layer is labeled as C (Figure 1(c)). The arrangement is spatially different and is called ABC. By placing a fourth layer over the original A layer, this motif can be continued indefinitely

...... ABCABCABCABC ......

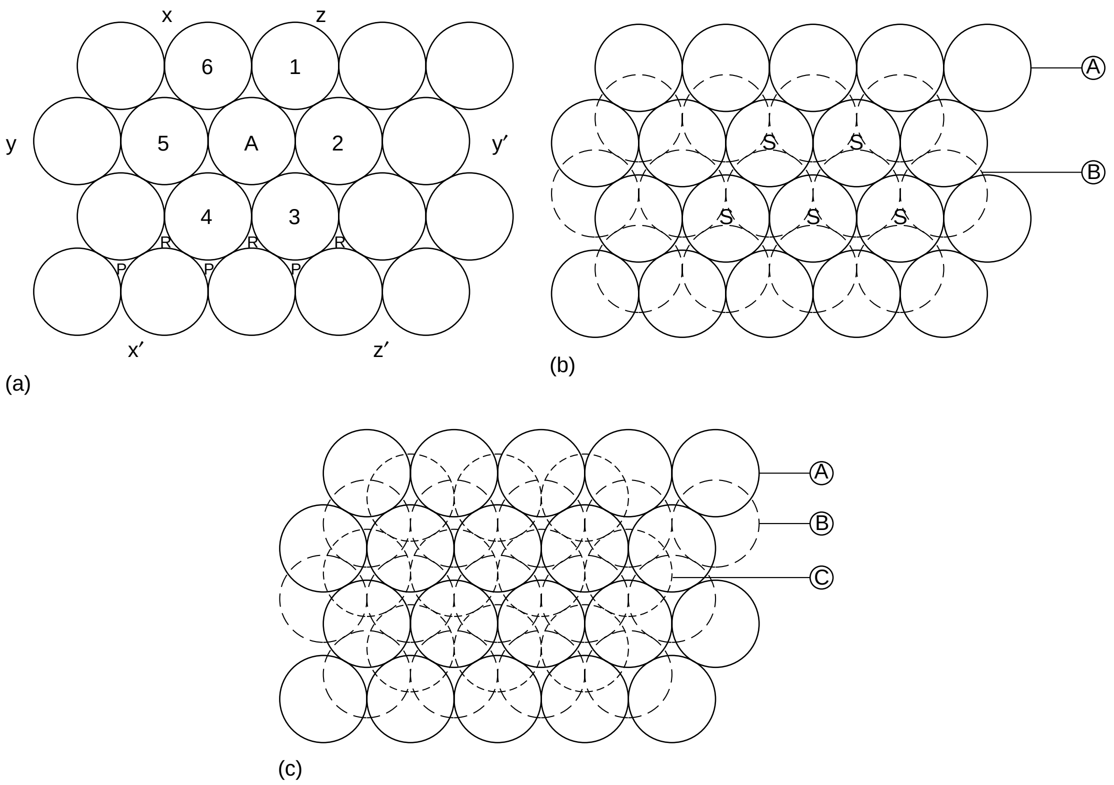

Figure 1 (a) A close-packed layer of equal sized spheres. (b) The layer labeled B is added below A and nests in the P positions shown in (c)

and a lattice is generated that has face-centered cubic symmetry. The stacking arrangement is referred to as cubic close packing (CCP).

These two packing schemes form the basis for the most common structures derived from the closest packing of spheres. Many other arrangements that are a mixture of the two sequences are possible and are seen in nature, such as . . ..ABAC. . .. or . . ..ABCAC. . . or others with larger repeat motifs (see Section 3.11), but these occur with less frequency than the simple ABA and ABCA arrangements. However, all conserve space with the same efficiency, approximately 74% of the volume being filled by spheres. Further, each sphere is surrounded by 12 other spheres leading to a regular icosahedral coordination symmetry for each close-packed atom. The efficacy of this simple model is shown by the fact that hexagonal and cubic CP structures are adopted by 67% of the group 1 through 11 and lanthanide metals while another 28% adopt the simple body-centered cubic arrangement, which is quasi-close packed with a 68% space filling efficiency.

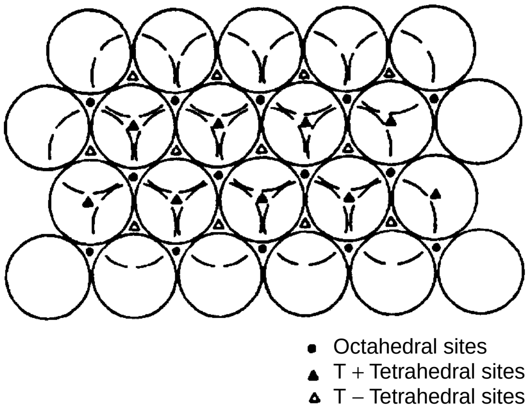

Figure 2 Three close-packed layers in a CCP sequence

For metallic elements, only one type of sphere is needed. However, in compound oxides two or more ‘spheres’ of different sizes must be accommodated. To do this, the interstices of the hard sphere lattice are utilized and since O^{-2} is normally the larger ion, it is generally considered to comprise the close-packed array. Within any such array, there are two types of interstices; those with tetrahedral symmetry and those with octahedral symmetry, which are distributed as shown in Figure 2. These are commonly referred to as ‘tetrahedral holes’ and ‘octahedral holes’. There are two tetrahedral holes per CP atom but only one octahedral hole per CP atom. Within each layer there are two types of tetrahedral holes, one forming a sublattice with their apices pointing up and the other with their apices pointing down as viewed normal to the stacking direction. These are labeled T+ and T− respectively in Figure 2. The centers of the octahedral holes are midway between the two CP layers while tetrahedral sites lie off center, one sublattice being nearer to one layer and vice-versa.

The structures will have the greatest stability when the cations can be inserted into the structure and just be in contact with the anions. Thus, in a hard sphere model, cations entering a tetrahedral hole must have a radius 0.224 times that of the anion while the octahedral hole will be most stable when the radius ratio of the cation to anion is exactly 0.414. Since these conditions will be met only by chance, in practice what is observed is that the anions are moved apart to accommodate the larger cation and will continue to do so until a larger coordination number can be achieved, either by a switch from the tetrahedral to the octahedral site or to a nonclose-packed structure with a larger coordination number. For instance, the center of a cube anion can just accommodate a cation whose radius is 0.732 that of the anion leading to eightfold cuboidal coordination. Finally, a close-packed array can be maintained when the cation and anion have similar sizes. Here, a metallic sublattice is formed by partial replacement of the anions in an ordered fashion. Some examples of simple structures derived from the closest packing of spheres are described in more detail below.

If, on the other hand, the radius ratio rules are violated on the downside, that is to say the hard sphere cation and anion no longer touch, the structure is longer stable and another structure should be adopted. For instance, if $r^+/r^- < 0.224$, then tetrahedral coordination is no longer possible but a threefold planar triangular coordination can be found by locating the cation in the trigonal hole centered in the plane of the close-packed layer. Such coordination should be stable for $0.15 \leq r^+/r^- \leq 0.224$. In fact, however, trigonal coordination is rare in chemical systems other than those of boron.

In order to use these concepts to predict structures, one needs a listing of radii and it should be recalled that a crystal radius cannot be measured directly. Rather, one measures an interatomic distance from which a decision has to be made as to the relative contribution of the interacting species. However, a number of compilations of ionic radii have been made, the most notable being those of Pauling, and were based upon semiempirical calculations. These largely have been replaced by the 'experimental' radii of Shannon and Prewitt.[11] The data set is based upon the assignment of a radius of 1.19 Å to F^-, and from this deriving the best radii for other ions based upon their extensive study of the crystallographic literature. A further complication in applying these rules is that the ionic radius of a given atom is dependent to some extent upon its coordination number. Thus, the tetrahedral radius of a cation is about 6% smaller than its octahedral radius, while its cubic or eightfold radius is expected to be about 3% larger, which is borne out experimentally (*see* ***Bond Lengths in Inorganic Solids & Liquids***).

It should be pointed out that the application of the radius rules to the prediction of structure often fails. The theory is strictly applicable to only the most ionic of chemical systems and the introduction of covalent effects will inevitably lead to modifications of the ideal structure and oftentimes what will be seen are structures distantly related to the actual hard sphere model. However, the model provides a convenient basis for visualizing the structure. What is remarkable is that it works as well as it does in predicting what type of oxides should form in a given system. It is particularly useful for predicting the structures of transition metal binary and ternary oxide systems and in a sense explains the instability of alkali and alkaline-earth oxides with respect to moisture, carbon dioxide, and their further reaction with oxygen. On the other hand, it is of limited value in predicting the structure of complex silicates or for the more covalent main group oxides.

3.2 Binary Oxide Structures Based upon Close Packing[8,10]

3.2.1 MO Structures

One of the simplest structures is the sodium chloride or rock salt structure shown in Figure 3(a). Here the anions are CCP and all of the octahedral holes are filled leading to perfect octahedral coordination for both the cation and anion. This is a highly 3D structure and is found for oxides formed with a wide variety of medium and large divalent cations. These include the oxides of the alkaline earths except beryllium (which is too small), CdO, and the divalent oxides of Mn, Fe, Co, and Ni.

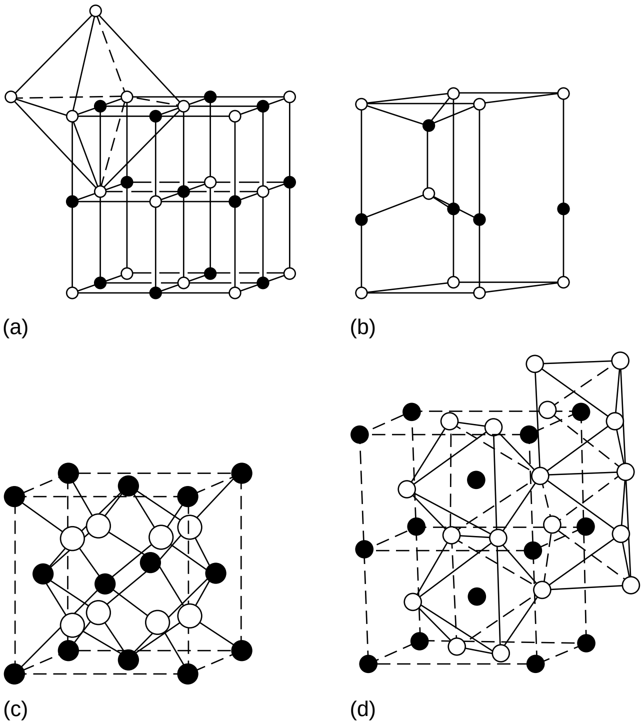

Figure 3 Unit cells for (a) Rock salt, (b) Wurtzite, (c) Fluorite (d) Rutile

With several other transition metal monoxides, covalent and special electronic effects that are not compatible with the ideal structure manifest themselves. As examples, PdO and PtO display the characteristic tendencies of heavier d^8 ions for square-planar coordination by adopting different structures while a severe Jahn–Teller distortion yields essentially fourfold planar coordination in CuO. In the cases of TiO, VO, and NbO, formation of weak metal to metal bonds are seen as defect variants of the rock salt structure.

So-called ternary or mixed oxide systems based on the rock salt structure are well established. Thus $LiFeO_2$ exists both in a disordered form in which Li and Fe are randomly distributed on the metal sites, and as an ordered variant with tetragonal symmetry. Rhombohedral distortions are found for $LiNiO_2$, $LiVO_2$, and $NaFeO_2$ in which the cations are ordered on different sublattices. The HCP counterpart of the sodium chloride structure, the so-called Nickel Arsenide stucture (*see* ***Chalcogenides: Solid-state Chemistry***), is found only for the heavier members of the Oxygen family.

Both ZnO and the low-temperature form of BeO have the wurtzite structure (Figure 3(b)) in which the cations occupy one half of the tetrahedral sites in an ordered three-dimensional fashion in an HCP arrangement of oxygens. This small cation structure and its CCP analog, the zinc blende structure, are found for small metallic elements, which tend to form strong sp^3 covalent bonds. Indeed, these structures are much more common for sulfides and the heavier chalcogenides (*see* ***Chalcogenides: Solid-state Chemistry***). $LiBO_2$ and $LiGaO_2$ have superstructures based on wurtzite (ZnS) in which the cations are ordered on tetrahedral sites. β-BeO has a wurtzite related structure but here the cations are ordered in tetrahedral sites such that the BeO_4 tetrahedra share faces leading to an anomalously short Be–Be distance of 2.24 Å.

3.2.2 *MO_2 and M_2O Structures*

The Fluorite (CaF_2) structure is shown in Figure 3(c). This is a structure for large cations and as such can be described in terms of a cubic closest packing of cations in which all of the tetrahedral holes are filled by the anions. In so doing, a cubic, eightfold coordination of the cation is achieved. The structure is found for cerium dioxide, hafnium dioxide, and the high-temperature form of ZrO_2 as well for as a number of actinide dioxides such as ThO_2, UO_2, and AmO_2. PrO_2 at high pressures also has this structure. Again, the bonding in this structure extends uniformly in three dimensions and has a strong covalent component owing to the high formal charge on the cation. As a result, fluorite type oxides tend to be extremely refractory with those of Ce, Zr, Hf, U and Th all having melting points in excess of 2500 °C.

In the antifluorite structure, the positions of the cation and anions in the fluorite structure are juxtaposed with the cations being tetrahedrally coordinated. One might expect this structure to be stable for small cations. However, all monovalent cations, with the exception of Li^+, are quite large and normally would be expected to be in six or eightfold coordination in oxygen. Nonetheless this is the stable structure for all of the monoxides of the alkali metals except Cs_2O. Although this may seem surprising from the point of view of the arguments present here, it is entirely consistent with the fact that the oxides cannot be prepared by direct combination of the elements; instead peroxides or superoxides are formed that do have distorted versions of the rock salt structure. The monoxides also react with moisture in the air to form hydroxides that also have distorted versions of the rock salt structure.

The structure of Cs_2O deserves mention. It can be considered as derived from a CCP of the large cesium ions in which 100% of the octahedral holes are filled in alternate layers by oxygens leading to a layer structure. The layers are pushed away from each other so that the Cs–Cs distances are about 4.2 Å but collapse upon the oxygens to yield extremely short Cs–O lengths. The structure is effectively that of $CdCl_2$ with the cation and anion positions interchanged. The bizarre nature of this structure is underscored by the fact that cesium reacts with oxygen to form not only a peroxide and superoxide but several suboxides as well.

The rutile structure is characteristic of a number of transition metal dioxides (rutile is a polymorphic form of TiO_2). Cassiterite (SnO_2), PoO_2, and one modification of both GeO_2 and PbO_2 also have this structure, given in Figure 3(d). Here the oxygens are in hexagonal closest packing and one half of the octahedral holes in each layer are filled in an ordered fashion. The oxide ions are in trigonal planar coordination with the metal ions. The overall lattice type is tetragonal. Again the structure is three-dimensionally cross-linked with strong M–O bonds and as a result most binary oxides with this structure have very high melting points. Rutile-type oxides containing one or more d electrons often display remarkable electronic and magnetic properties. Some of them undergo electronically driven distortions (see Section 4.3.2). In rutile itself, the Ti atoms are at the center of the edge-sharing octahedra and are equidistant from one another. However, when one or more d electrons are present, the metal atoms may move off center along the chain direction to form an alternating pattern of short and long metal–metal distances, the short distance being as short or shorter than that expected for a metal–metal bond as shown in Figure 4. Such distortions occur in MoO_2, WO_2, and

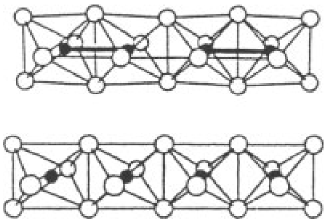

Figure 4 Sequence of edge-sharing TiO_6 octahedral in rutile showing equal spacing of Ti (a). Distorted chains seen in VO_2 and MoO_2 with metal–metal bonds (b)

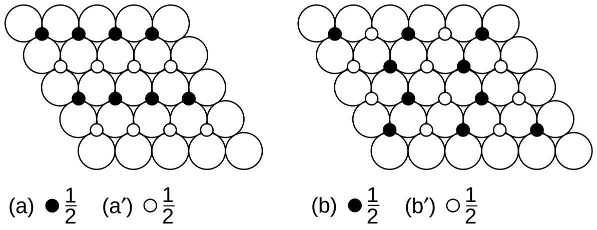
(a) ● $\frac{1}{2}$ (a′) ○ $\frac{1}{2}$
(b) ● $\frac{1}{2}$ (b′) ○ $\frac{1}{2}$

Figure 5 Pattern of octahedral site occupancies between pairs of close-packed layers in (a) rutile and (b) wolframite. Small shaded circles are octahedral sites above the plane of paper. Small open circles are sites below the plane

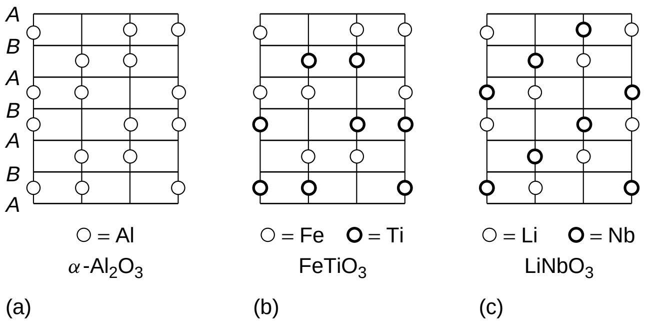

Figure 6 Elevations along hexagonal *c* axis for (a) corundum, (b) ilmenite, (c) lithium niobate

the low-temperature form of VO_2. In MoO_2, the short Mo–Mo distance is 2.51 Å, considerably less than the Mo–Mo distance of 2.725 Å in molybdenum metal itself. A different but related distortion is found in NbO_2.

The structure and distorted variants of it are also found for a number of mixed transition metal oxides. In the trirutile structure, the tetragonal *c* axis of the simple unit cell is tripled and the titanium sites are no longer equivalent. The mineral tapiolite, $FeTa_2O_6$, has this structure in which the Fe and Ta occupy separate crystallographic positions. The ferrous ion can be replaced by Mg^{+2} and other divalent transition metal cations such as Co^{+2} and Ni^{+2}. Antimonates of the form MSb_2O_6 ($M^{+2} =$ Mg, Fe, Co, Ni, Zn) also form with the trirutile structure. Examples are known in which the transition metals are mixed on the two sites. This occurs for WCr_2O_6, which might more correctly be formulated $Cr(Cr_{0.5}W_{0.5})_2O_6$.

The arrangement of the filling of half of the octahedral holes to form the rutile structure is only one of several possible. Figure 5 shows two possible fillings for 50% occupancy. If sites represented by small black circles are filled by metal atoms above the plane of the paper while the small white circles are filled below the plane as shown in Figure 5(a), a rutile lattice is generated where chains are formed in alternate layers. Figure 5(b) shows a different ordering found in the mineral $FeWO_4$, wolframite, which is a common structure for a variety of transition metal tungstates, molybdates, and vanadates (see Section 3.4.5). The cations in the mineral columbite (niobite), $(Fe,Mn)Nb_2O_6$, also utilize the positions shown in Figure 5(b). A three-layer sequence is required to complete the unit cell. More detailed discussion of these and other variants can be found in Wells.[12]

3.2.3 *M_2O_3 Type Structures and Related Ternarys*

One of the most common structures for sesquioxides of small to medium sized cations that favor sixfold coordination with oxygen is the corundum structure (α-Al_2O_3). Here, the oxygens are placed in an HCP array but only 2/3 of the octahedral sites are occupied following the motif shown in Figure 6(a). Strong Al–O–Al cross linking takes place in three dimensions in which AlO_6 octahedra share not only corners but edges and faces as well. These properties are reflected in the fact that the mineral corundum is the second hardest substance known, is chemically inert, and has a melting point above 2000 °C. Other corundum type oxides include Ti_2O_3, V_2O_3, Cr_2O_3, α-Fe_2O_3, Rh_2O_3, α-Ga_2O_3, and one form of In_2O_3.

A well-known ternary structure derived from the corundum arrangement is the ilmenite ($FeTiO_3$) structure where Al sites are now occupied exclusively by Fe and Ti in alternate layers (Figure 6(b)). The structure is stable for cations that have similar sizes. Typically, one cation is divalent and the other tetravalent (2:4 ilmenites) but $NaSbO_3$ is an example of a 1:5 ilmenite. While size considerations might lead one to expect that $LiNbO_3$ would have this structure, it turns out that it adopts the somewhat different but related arrangement shown in Figure 6(c) where ordering of Li and Nb takes place in each layer.

Trivalent group 3 and rare earth cations are larger on average than those of the transition metals and the lighter main group metals. However, the effects of the *lanthanide contraction* result in a considerable difference in the octahedral radii of La^{+3} and Lu^{+3}, for example, 1.17 versus 1.00 Å. The lightest member of the trivalent group 3 elements, Sc^{+3}, has an octahedral radius of 0.88 Å, 0.07 to 0.20 Å larger than those of the trivalent first period transition metals and Al^{+3}, which typically form oxides with the corundum or ilmenite structures. As a result these elements have a greater tendency to form compounds in which higher coordination can be achieved. While sixfold coordination is observed, eightfold coordination is more common, while in mixed oxide systems coordination numbers of 7, 9, 10, and 12, particularly for the larger members of this series, are not unusual.

Three principal types of structure are noted for the rare earth oxides designated as the A, B, and C rare earth structures. The A rare earth structure is the stable room temperature structure for the lighter rare earths from La to Nd while the C rare earth structure is the stable polymorphs for Sm through Lu. The B form is seen for several oxides at intermediate temperatures and/or high pressures. All polymorphic forms have been observed for several of the rare earths. Other structures are also observed for temperatures above 2000 °C. A comprehensive review of binary oxide chemistry of the lanthanides, including other oxidation states, is given by Eyring.**[13]**

The dominant feature of the A rare earth structure is a distorted MO_6 octahedron in which one of the faces is capped by a 7th oxygen. The metal-oxygen bond distances vary from about 2.35 to 2.45 Å for the octahedral bonds while the face-capping bond is about 0.3 Å longer. Thus, while this structure cannot really be described in terms of closest packing of spheres, the C rare earth structure can be. It is related to that of CaF_2 but the edges of the unit cell must be doubled yielding the composition $M_{16}O_{32}$. Then 8 anions are removed from the structure in an ordered fashion and the remaining oxygens are moved off of their idealized positions. The net effect is to destroy the cubic metal coordination by oxygen of the fluorite structure and replace it with what might be called a distorted octahedral arrangement, which has shared edges. The lower coordination number of this structure as compared with the 7 coordinate A structure is consistent with the smaller size of the cations for which it is stable. The C rare earth structure is also adopted by α-Mn_2O_3 (Bixbyite), In_2O_3 and Tl_2O_3. The latter two adopt the corundum structure at high pressures.

In the corundum structure, the metal atoms are in crystallographic sites with variable coordinates. Because edge and face sharing of MO_6 octahedra can result in an abnormally close approach of the metal atoms to one another, such interactions can be minimized if the atoms move off center away from one another. However, in Ti_2O_3, the Ti atoms are only 2.58 Å apart in face-shared octahedra and the d^1 electrons are used to form a metal–metal bond. This compound is a semiconductor, but between 125 to 325 °C a broad structural transition takes place where this bond is broken, thus providing free electrons for electrical conduction and the compound now displays metallic conductivity.**[14]** V_2O_3 also has this structure but has a more complex temperature dependence of its conductivity.

3.2.4 MO_3 Structures

The ReO_3 structure is an interesting application of the concept of closest packing of spheres. The unit cell of the structure is shown in Figure 7(a). The basic building block is a cubic closest packing of oxygens in which one-quarter of the octahedral holes are filled in an ordered fashion while one-quarter of the oxygens are removed in a similar fashion. As a result, a three-dimensional network of ReO_6 octahedra is formed in which all vertices are shared with other octahedra (Figure 7(b)). Although the cubic structure is unique to ReO_3 in oxide systems (WO_3 has a distorted version of it, however), ternary structures derived from this 3D octahedral network are among the most important in oxide chemistry and will be discussed in Section 3.4.1. ReO_3 is a bright red, lustrous, metallic looking material and in fact displays excellent metallic conductivity. The electronic aspects of this structure are very important and may in part explain why the structure is so unusual for binary oxide systems (see Section 4.3.1).

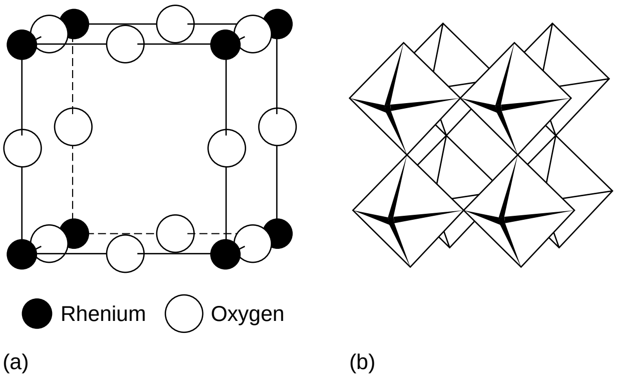

Figure 7 Unit cell of the ReO_3 structure (a). Diagram showing the 3D corner sharing of ReO_6 octahedra (b)

Indeed, in species with +6 oxidation states, high degrees of covalency are expected, high coordination numbers are unusual, and corner sharing of polyhedra does not occur to any extent unless mitigated by the presence of other cations. A good example of this is the structure of CrO_3 where the structure is built up of infinite chains of corner-sharing tetrahedra. Thus, with considerably fewer bonds to be broken, CrO_3 melts at 197 °C while WO_3 melts at nearly 1500 °C although it does have a significant vapor pressure at 1000 °C. The structure of MoO_3 is intermediate between these two. Basic building blocks are double chains of MoO_6 octahedra that share edges and corners to form a layer structure in which the layers are held together by van der Waals forces. Thus, MoO_3 has a significant vapor pressure above 550 °C and melts at 795 °C.

3.3 Other Transition Metal Oxides

This is meant to be a limited overview of some of the more interesting or representative oxides, which because of increased covalency usually cannot be described in terms of structures derived from closest packing of spheres.

3.3.1 Monovalent Oxides of Copper, Silver, and Thallium

Isostructural Cu_2O and Ag_2O illustrate the tendency of these group 12 d^{10} ions to be two-coordinate. While higher coordination numbers of 4 or 6 might be expected, it appears that a stronger bond can be obtained as a result of the hybridization of ns and np_z orbitals with the $(n-1)d_z{}^2$ orbitals of the metal atoms. Figure 8 shows one of the two interpenetrating Cu–O sublattices that form the cuprite structure found for both Cu_2O and Ag_2O. The linear coordination of Cu by O and the tetrahedral coordination of oxygen by Cu is clearly seen. Two-coordinate copper is seen in mixed oxides, the most important being the ‘123’

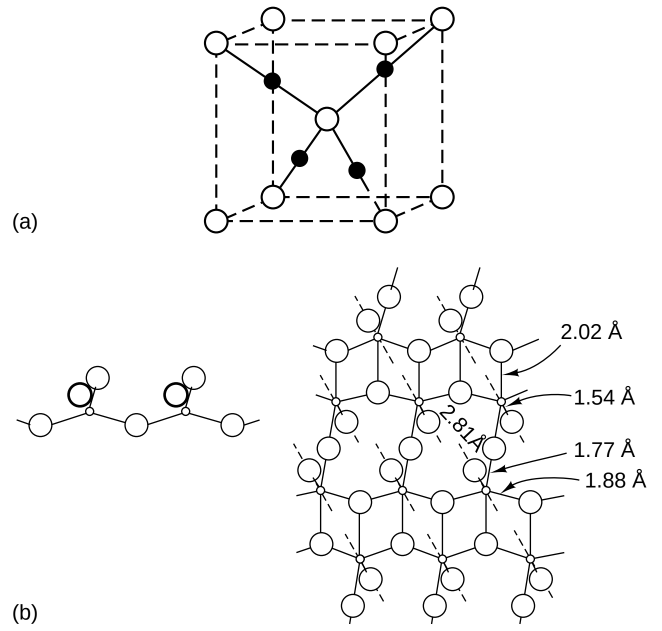

Figure 8 Unit cell (a) and structure (b) of Cu_2O. Note linear coordination of Cu (black circles) by oxygen

superconducting oxides such as $YBa_2Cu_3O_{7-\delta}$, which lose their superconductivity as the result of oxygen loss (i.e. $\delta > 0.5$) in which a portion of the copper becomes linearly coordinated.

Tl_2O is a variant of the anti-CdI_2 structure, which is the HCP counterpart to the anti-$CdCl_2$ structure discussed in connection with Cs_2O (Section 3.2.2). For the thallium compound, there is a 12 layer stacking sequence in which the lone pair plays an important role.

3.3.2 *Group 5 and 15 Pentoxides*

The basic building blocks of V_2O_5 are double chains of badly distorted VO_4 tetrahedra that share 3 vertices with other tetrahedra similar to those found in the polymeric metavanadate ion, $(VO_3)_n{}^{-n}$. These chains are then connected to one another to form V_2O_5 layers. Thus, the complete oxygen coordination of each vanadium is a distorted square pyramid. The bond distances range from 1.59 to 2.02 Å with the short distance being that of the unshared vertex, which points into the gap. A sixth oxygen on vanadiums in the neighboring layer at 2.81 Å is much too long to be considered as bonding. However, it does seem to play a role in limiting what species can be intercalated into this phase and sometimes descriptions of its structure are given in terms of an 'idealised' octahedral coordination.**[14,15]**

Both Nb_2O_5 and Ta_2O_5 have a complex crystal chemistry, each with several polymorphic forms, two of which will be described here. The high-temperature form of Nb_2O_5 utilizes two different sized corner-sharing ReO_3-like blocks that are joined by edge sharing to form infinite planar slabs. The details of the structure are described in Section 3.5. The H form of Ta_2O_5 is formed by edge-sharing TaO_6 octahedra, which also share edges with corner-sharing pentagonal bipyramidal TaO_7 groups, illustrating the tendency of pentavalent Ta to enter into sevenfold coordination. We note in summary that the crystal chemistry of V_2O_5 is strikingly different from the other two members and that overall it is extremely complex. Further, these basic characteristics of their crystal chemistry are often maintained when they enter into mixed oxide formation.

Sb_2O_5 has a structure similar to one of the Nb_2O_5 polymorphs in which distorted SbO_6 octahedra share edges and corners to build a complicated 3D framework. Pure Bi_2O_5 has not been prepared. As_2O_5 may be prepared by the careful dehydration of its hydrate $As_2O_5{\cdot}4H_20$. It has a complex 3D structure formed by the sharing of edges and corners of both AsO_4 tetrahedra and AsO_6 octahedra. The three polymorphic forms of solid P_2O_5 are all based on the linking of tetrahedral PO_4 groups through three of their four corners. One form has P_4O_{10} molecules, identical to those found in the gaseous state. A second consists of layers having the composition P_2O_5 and the third is a 3D structure containing rings built from ten PO_4 groups.

3.3.3 *Mercury(II) Oxides*

The stable orthorhombic form of HgO can be prepared by the gentle heating of mercury(I) or (II) nitrate in air. The structure (**1**) can be described as consisting of zig-zag Hg–O–Hg chains in which Hg is in linear twofold coordination with oxygen and the Hg–O–Hg angle is 109°.

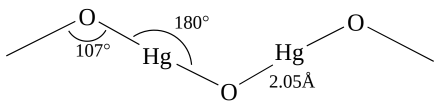

(**1**)

The Hg–O distances within the chains is 2.03 Å while the closest interchain distance is 2.82 Å. If a Hg^{+2} salt solution is treated with warm, aqueous NaOH for several hours, metastable crystals of HgO form that have the hexagonal cinnabar (HgS) structure. Again the basic building blocks are O–Hg–O chains but now they wrap in a helical fashion and are cross-linked to other chains by Hg–O bonds to form a highly distorted octahedron of oxygens about each mercury with the motif of 2 short linear Hg–O bonds being maintained.

3.3.4 *Heavier Group 14 Oxides*

The stable, dark blue form of SnO is isostructural with the tetragonal form of PbO that is shown in Figure 9. It is a layer structure in which a square array of oxygens is

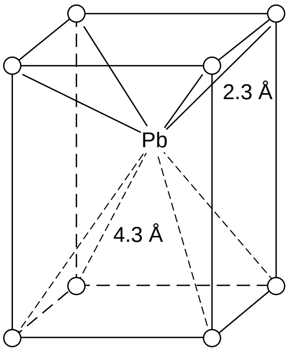

Figure 9 Unit cell of PbO illustrating inert pair effect

sandwiched between two partially occupied lead layers with a van der Waals gap between each Pb–O–Pb unit. The Pb (or Sn) sits at the apex of a square pyramid having an oxide ion base. This unusual coordination is believed to arise from a sterochemically active electron pair on the metal, which is directed out into the gap.

Other unstable monoxides of these two elements have been reported. Tin also forms the very stable SnO_2 found in nature as the mineral cassiterite. This compound has the rutile structure as discussed previously. PbO_2 also has a rutile isomorph while α-PbO_2 has a columbite structure (Section 3.2.2). If PbO is oxidized in air between 300 and 570 °C, the stable oxide Pb_3O_4 is obtained, commonly referred to as 'red lead'. This is a mixed-valence oxide in which the positions of Pb(II) and Pb(IV) are clearly defined and thus one might consider it to be a ternary structure. Indeed, $MgSb_2O_4$ is isomorphous to Pb_3O_4 as is $NiAs_2O_4$. Here one finds chains of essentially regular PbO_6 octahedra that share opposite edges. These chains are linked to one another by Pb(II) in a roughly pyramidal coordination. In the arsenic and antimony isomorphs, the Mg^{+2} and Ni^{+2} occupy the Pb(IV) positions. The unusual pyramidal coordination is again due to the stereochemically active lone electron pair on the group 14 and 15 ions.

3.4 Major Ternary Oxide Structures[8–10,16]

3.4.1 Perovskite Structure

Ternary oxides of the type ABO_3 in which A is a large cation such as an alkali, alkaline earth, or rare earth ion and B is a medium sized ion with a preference for octahedral coordination, typically a transition metal, are often found with the perovskite structure shown in Figure 10. Alternate spellings such as perowskite or perewskite are sometimes seen. The structure can be looked upon as a rhenium oxide type lattice in which the ordered vacancy in the cubic close-packed oxygen lattice is now filled by the large A cation. A large variety of oxides adopt this structure, either in the simple cubic symmetry shown or with varying degrees of distortion to lower symmetry as is the case with the mineral perovskite ($CaTiO_3$) itself. In addition, many more complex oxides form structures in which perovskite-like slabs or layers can be identified sandwiched between other basic structural units. For the ideal perovskite structure, the A and B cations should just be in contact with their oxygen nearest neighbors and deviations from the ideal symmetry might be expected when this condition is not met. In fact, a considerable leeway exists that can be empirically quantified by the so-called Goldschmidt tolerance factor t, which can be derived from the geometry of the ideal cell:

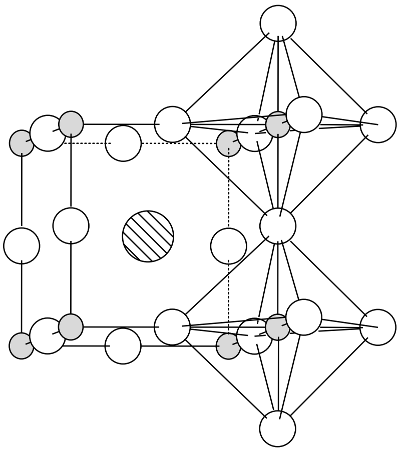

Figure 10 Perovskite structure, ABO_3 (large cross hatched circle is A, small shaded circles are B)

$$t = \frac{R_A + R_O}{\sqrt{2}(R_B + R_O)} \tag{3}$$

where R_A, R_B, and R_O are the ionic radii of the A, B and oxygen atoms. The value of t is 1 for the ideal structure. In general, the cubic structure is maintained for t greater than about 0.95 but below that distortions to tetragonal, rhombohedral, or orthorhombic symmetry usually take place, which have been reviewed by S. Geller[17] and more recently by Attfield[18] and Woodward.[19] So-called double perovskites of the type $A_2BB'O_6$, where the unit cell is doubled and cations of two types are found ordered on the B sites, are quite common. In particular, Sr_2FeMoO_6 and related compounds are of current interest because they are both ferrimagnetic at room temperature and show large magnetoresistive effects.[20] In fact, however, most perovskites are distorted, the most common one being the orthorhombic $GdFeO_3$ type. The net effect here is that the coordination number of Gd with oxygen is lowered to 8 by distortion of the Fe–O octahedron.

The large number of compounds found with perovskite based structures arises from several factors other than the great stability implied by the permitted variation in t and the subsequent distortions that take place with the maintenance of the basic framework. One factor is that the A and B sites are relatively insensitive to charge distributions and the structure is found for valence combinations of 1:5, 2:4, and 3:3 of the A and B cations. In addition, the structure can withstand considerable departures from ideal stoichiometry, particularly with respect to the A cation and the oxide ion. For example, the so-called tungsten oxide bronzes A_xWO_3 exist with the cubic perovskite structure for $0.3 \leq x \leq 1$, while $LaTiO_3$ can be rendered deficient in oxygen without loss of structure by replacing 50% of the La^{+3} by Sr^{+2} to form $La_{0.5}Sr_{0.5}TiO_{2.5}$. Reaction of CaO and Fe_2O_3 in air yields the oxygen deficient perowskite $CaFeO_{2.5}$.**[21]**

This structure has been utilized by solid-state chemists as a template to stabilize transition metals in so-called unusual valence states $SrMoO_3$, $LaTiO_3$, $LaMnO_3$, $CaMnO_3$, $BaCrO_3$ (perovskite related), $Sr_{1-x}Nb0_3$, and so on. In addition, perovskites and perovskite related phases in which the transition metal contains 1 or more d electrons often have interesting electrical and magnetic properties including, semiconducivity, metallic conductivity, superconductivity, and antiferro-, ferri-, and ferromagnetic behavior. Those having no d electrons such as $BaTiO_3$, $NaNbO_3$, and $KTaO_3$ are useful ferroelectric materials that have distorted perovskite structures at room temperature but become cubic at higher temperatures (see Section 6.8 and *see Ferroelectricity*). A variety of structure-property relationships in perovskites have been reviewed recently by Pena and Fiero.**[22]**

3.4.2 The Spinel Structure

This is a structure for small to medium sized cations whose ideal composition takes the form AB_2O_4. The basic structure is derived from a cubic closest packing of spheres with a doubled face-centered cubic unit cell. Such a cell contains 32 octahedral holes and 64 tetrahedral holes, which can be broken down into a number of crystallographically different sublattices. Thus, in the spinel structure 50% of the octahedral holes are designated as B positions and one eighth of the tetrahedral holes as A sites, yielding the composition $A_8B_{16}O_{32}$ for the unit cell. The structure is difficult to view in three dimensions and is shown here as a projection down one of the cubic axes with the atom elevations with respect to that direction given in parentheses in Figure 11.

The A and B cations can have valences between 1 and 6, the only requirement being that their sum adds up to 8. Although typically thought of as a structure for transition metal ions, spinels form with a number of the smaller alkali and alkaline-earth cations as well as post-transition metals such as Zn^{+2}, Cd^{+2}, Ga^{+3}, In^{+3}, Ge^{+4}, and Sn^{+4}. Some examples include $TiCo_2O_4$, $CdCr_2O_4$, $FeCr_2O_4$, Fe_3O_4, $ZnAl_2O_4$, $FeGa_2O_4$, NiV_2O_4.

Assignment of A or B sites to cations in spinel type oxides based upon their chemical formulae can often be misleading. Thus, for the mixed-valence oxide $NiFe_2O_4$, we might conclude that the Ni^{+2} ions are on the tetrahedral A

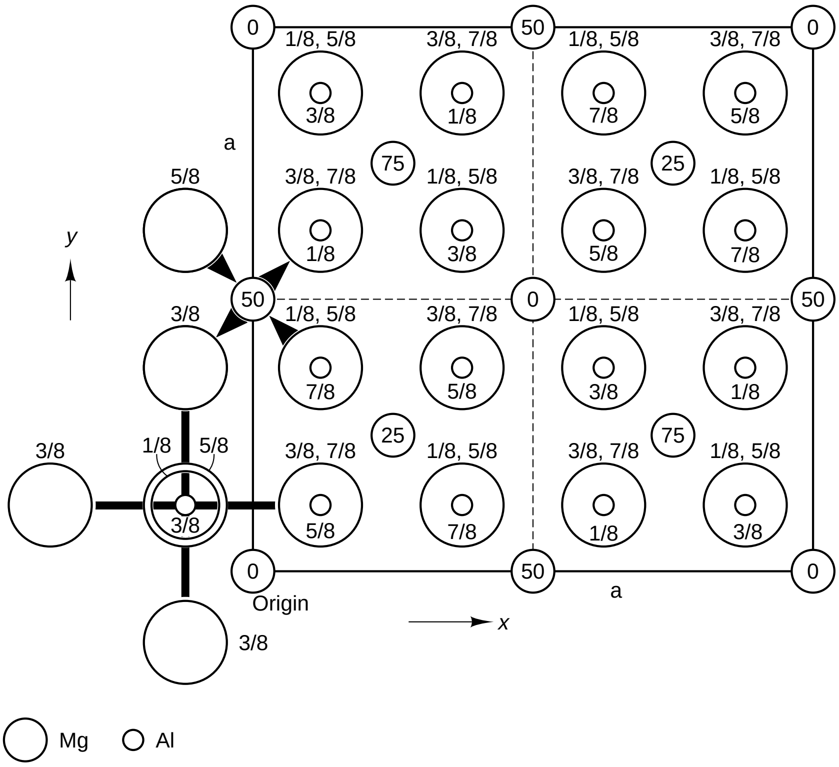

Figure 11 Projection of the spinel structure down one of the fourfold cube axes showing representive octahedral and tetrahedral sites. Fractions represent relative elevations of ions

sites while the Fe^{+3} ions were on the B sites as implied by the formula. In fact, the actual distribution places all the Ni^{+2} on octahedral sites and half of the iron in tetrahedral sites giving a site preference formula of $Fe^{+3}[Ni^{+2}{}_{0.5}Fe^{+3}{}_{0.5}]_2O_4$. Such an arrangement is referred to as an *inverse* spinel. On the other hand, the mineral spinel, $MgAl_2O_4$ and $Ni^{+2}Cr_2{}^{+3}O_4$, have the site distributions predicted by the chemical formula and are referred to as *normal* spinels.

The factors that determine whether or not a spinel is normal or inverse are complex. Moreover, the actual distribution may be only partially inverse. Thus, $MgFe_2O_4$ has a structure that is 90% inverse, while $NiAl_2O_4$ is about 75% inverse. Large differences in ion charge seem to favor a normal site distribution and inverse structures are most often found in 2:3 spinels, although inverse 4:2 spinels are known. One factor that appears to play a role is an ion's site preference energy for octahedral sites, which can be estimated from *crystal field theory* considerations. Although easy to apply, the method yields the correct result only about 2/3 of the time. Another, more complex explanation based upon phase field, size, and charge relationships has been given by Burdett and is much more accurate.**[23]** Inverse spinels, particularly those containing iron, are by far the most intensively studied of the two forms because of their useful magnetic properties and are often referred to as ferrites (*see* ***Magnetic Oxides*** and ***Magnetism of Extended Arrays in Inorganic Solids***).

Oxides with spinel-like superstructures can be produced by partially replacing atoms in the A or B sites with a third species or by removing A or B cations to produce an ordered superstructure. Thus, the spinel $LiFe_5O_8$ forms where all of the normal tetrahedral sites are filled by Fe^{+3} while the octahedral sites are broken into fourfold sublattices, one of which is occupied exclusively by Li. Such changes result in small movements of the oxygens from their ideal positions. In γ-Fe_2O_3, 2/3 of the octahedral sites occupied by Li in $LiFe_5O_8$ are vacant and the remainder filled by iron yielding the composition $Fe_{21.33}O_{32}$ for the basic spinel unit. In such systems, structures that are ordered at room temperature may become randomized by heating. Thus, $LiFe_5O_8$ becomes disordered above 755 °C.

3.4.3 The Garnet Structure

The garnet group of minerals have the general formula $A_3B_2(SiO_4)_3$ where, in naturally occurring substances, A typically will be Ca^{+2}, Fe^{+2}, Mg^{+2} or Mn^{+2} while $B = Al^{+3}$, Cr^{+3}, Fe^{+3}, Mn^{+3}, Ti^{+4}, V^{+4} or Zr^{+4}. In the 1950s, it was found that rare earth iron oxides having this structure behaved as *ferrimagnets* with commercially useful properties. They are also of interest because of their optical properties. The garnet structure can be rewritten as $A_3B_2T_3O_{12}$ to represent its three-dimensional nature. Typically, A is a large cation preferring a coordination number higher than 6, B is a typical octahedral cation, while T is a small cation, such as Al^{+3}. The basic building blocks of the structure are BO_6 octahedra and TO_4 tetrahedra. Each octahedron shares its six corners with individual TO_4 groups while the latter share each of their corners with BO_6 units. The result is a $B_2T_3O_{12}$ framework with eightfold dodecahedral cavities that can accommodate the large A cations. Some typical examples of compounds with the garnet structure are $Y_5Fe_3O_{12}$, $Dy_5Al_3O_{12}$, $Ca_3Cr_2Si_3O_{12}$, and $Mg_3Al_2Si_3O_{12}$.

As with spinel-type oxides, the chemical formula of compounds with the garnet structure can sometimes be misleading. For instance, in the normal pressure form of $CaGeO_3$, calcium is in sixfold and Ge in fourfold coordination with oxygen but at high pressures it transforms to the garnet structure where Ca is now in eightfold coordination and the sixfold sites are occupied by equal amounts of Ca and Ge, viz. $Ca_3[Ca_{0.5}Ge_{0.5}]_2Ge_3O_{12}$.

3.4.4 The Pyrochlore Structure

The mineral pyrochlore has the chemical formula $CaNaNb_2O_6F$. Since the fluoride and oxide ions have similar sizes as is also the case with Na^+ and Ca^{+2}, it is not surprising that this structure is adopted by a number of ternary oxides and reformulated as $A_2B_2O_7$. Ideal pyrochlores have a cubic structure whose dimensions correspond to a doubled fluorite cell. The structure may be derived from the fluorite structure by removing one eighth of the anions in an ordered fashion and then moving a portion of the remaining O^{-2} off of their ideal positions to provide a distorted octahedral environment for the B cations. The remaining cation sites retain their eightfold cuboidal coordination and are occupied by the larger A cations. Pyrochlore oxides have been of interest because of the variety of interesting properties they display, which may include high electrical or ionic conductivity, catalytic activity, and ferroelectric behavior.

The most common pyrochlores have 3:4 charge arrangements such as $La_2Ti_2O_7$ or 2:5 arrangements exemplified by $Cd_2Nb_2O_7$, which is of interest as a ferroelectric material. Pyrochlores, like perovskite oxides, are of interest owing to their ability to stabilize unusual oxidation states (e.g. $Cd_2Re_2O_7$ and $Sc_2Pt_2O_7$) and owing to their interesting electrical and magnetic properties as well. OH^- and F^- may substitute for O^{-2} to yield cation deficient pyrochlores such as $BiTa_2O_6F$ and $Sb^{+3}(Sb^{+5})_2O_6OH$. Defect pyrchlores have been studied for possible applications as solid electrolytes. Normally, the structure is stable for 3:4 pyrochlores when r_A^{+3}/r_B^{+4} is between 1.2 and 1.6. However, high-pressure synthesis will raise the upper limit to about 1.90 as exemplified by $Gd_2Ge_2O_7$.**[24]**

3.4.5 The Scheelite, Wolframite and Related Structures

The mineral Scheelite, $CaWO_4$, was named after the famous nineteenth century chemist Carl Wilhelm Scheele. The ideal structure, shown in Figure 12, has tetragonal

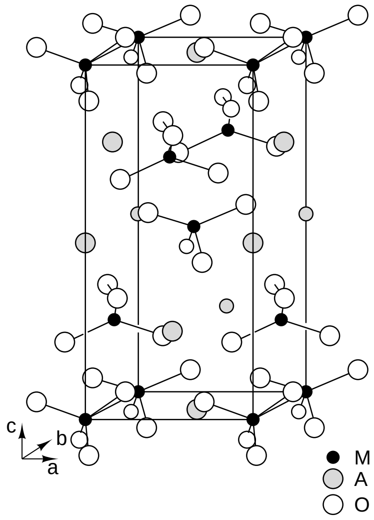

Figure 12 Unit cell of the sheelite structure

symmetry in which discrete $WO_4{}^{-2}$ tetrahedra are found arranged in a nearly perfect cubic packing in which the corners of the tetrahedra point towards the center to provide a slightly distorted cubic coordination for the large Ca^{+2} ion. $CaMoO_4$ and $PbMoO_4$ are isomorphic. Monoclinically distorted versions of this structure are found for a number of rare earth niobates and tantalates, which in themselves form an interesting chemistry. Zircon, $ZrSiO_4$, in which Zr is in eightfold coordination has a different structure.

A medium to small cation counterpart to the Scheelite structure is that of wolframite, $(Fe,Mn)WO_4$. Here both the tungsten and the divalent metal cations are in octahedral coordination. This ABO_4 structure can be derived from a hexagonal closest packing of oxygens in which two sublattices, each comprising 25% of the octahedral holes are occupied by the A and B cations, the B cations typically being smaller and higher charged than the A cations. The A cations have nearly regular octahedral coordination while the BO_6 groups are distorted considerably (see Section 3.2.2.).

A variety of related structures can be identified with 6,8, and 12-fold coordination of the A cation and four or sixfold coordination of the anion. In fact, the chemistry of ABO_4 ternarys is extremely complicated with solid solutions and phase transitions being common. Lattice defects may be introduced easily by appropriate dopings. Scheelites and its relatives have been studied intensively for their properties as heterogeneous catalysts, as host materials for impurity activated luminescent materials, and for specialized optical uses (*see* ***Oxide Catalysts in Solid-state Chemistry*** and Section 4.4).

3.4.6 Beta Alumina and Nasicon Structures

β-Alumina, originally believed to be a polymorph of Al_2O_3, actually has the composition $Na_{1+x}Al_{11}O_{17(1+x/2)}$. The interest in this compound arises from the very high mobilities found for the sodium ions and as a result this and related compounds have been studied for use as solid electrolytes in high energy density batteries, which operate under extremely corrosive conditions (*see* ***Ionic Conductors***). The Al–O framework of the structure is related to that of spinel and exists as slabs that are held together by Na^+ ions and occasional oxygen atoms as shown in Figure 13. The connecting oxygens have been likened to pillars in a parking garage as shown in the diagram. The interlayer distances are about 4 Å wide. The fact that the Na–O bonds are quite long and not all their positions are occupied, the ideal value of x being 2, results in abnormally high ionic conductivities since the Na^+ ions are relatively free to move. β''-alumina is a derivative of β-alumina stabilized by the presence of magnesium, $Na_{1+y}Mg_yAl_{11-y}O_{17}$, where the value of y is typically about 0.66. These materials have ionic conductivities that surpass those of the β analogs. Na may be also be replaced by other alkali metals as well as alkaline earths and lanthanides.[25,26]

Sodium zirconium phosphate $NaZr_2(PO_4)_3$ has a three-dimensional structure with hexagonal symmetry formed by a framework of corner-sharing tetrahedral PO_4 groups and octahedral ZrO_6 groups. A set of ordered octahedral sites are found along the hexagonal c axis occupied by Na^+. There also exist empty octahedral sites within the CP layers that are filled in the otherwise isomorphous compound, $Na_4Zr_2(SiO_4)_3$. Both compounds are poor sodium ion conductors but the solid solutions $Na_{1+x}Zr_2P_{3-x}Si_xO_{12}$ have high Na^+ mobility and have been given the acronym NASICON (Sodium Superionic Conductor).[9]

3.5 Crystallographic Shear Structures[27]

Mo_9O_{26} is sometimes written as $MoO_{2.89}$ and $Mo_{10}O_{29}$ as $MoO_{2.90}$, which might imply that these oxides are part of a solid solution series. They are not; rather their structures are those of a well-defined homologous series based upon the principle of crystallographic shear. The latter is a term used to describe the generation of complex structures from fairly simple ones by the translation of one or more portions of the structure with respect to the remainder. It has been applied with great success to describe a series of reduced oxides of molybdenum and tungsten having general formulas such as M_nO_{3n-1} ($n = 8-12, 14$) and M_nO_{3n-2}, a similar homologous series of titanium oxides of the type Ti_nO_{2n-1}, ($n = 4$ to 10), binary oxides of niobium(V) and niobium(IV) as well as a variety of complex mixed transition metal and mixed-valence oxides such as $TiNb_2O_7$, $Nb_{25}O_{62}$, $W_3Nb_{14}O_{44}$, and $Ti_2Nb_{10}O_{29}$. The molybdenum and tungsten oxides are derived from an idealized ReO_3 lattice by introducing edge sharing between MoO_6 octahedra while the TiO_{2n-1} series is derived from the rutile structure by introducing face sharing as a result of the shear operation.

The process is illustrated for Mo_9O_{26}, which is part of the series Mo_nO_{3n-1} with $n = 9$. The crystallographic

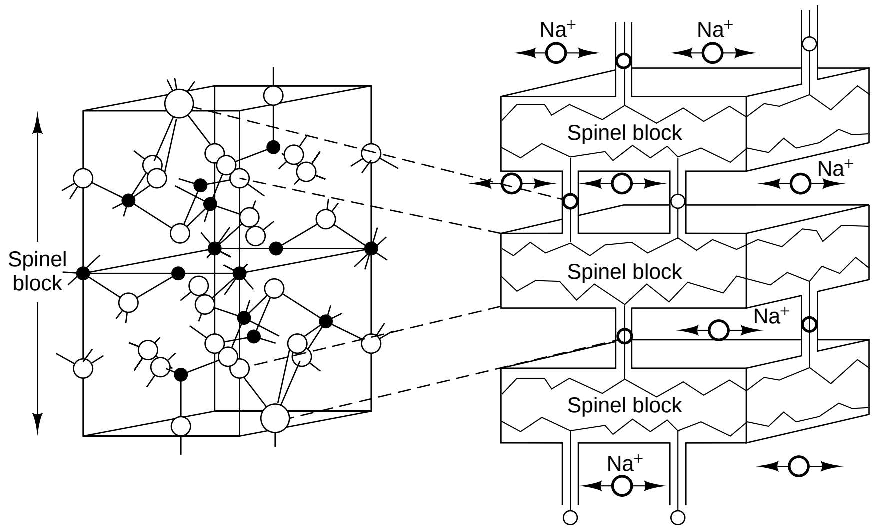

Figure 13 Layering of β-alumina

shear operation takes place along planes of ordered oxygen vacancies introduced into the ReO_3-like idealized MoO_3 lattice as a result of reduction (Figure 14(a)). These vacancies are eliminated by the shear operation with the result that blocks of the ideal ReO_3 structure are now separated by regions containing four MoO_6 octahedra sharing edges (Figure 14(b)). The ReO_3-like blocks extend infinitely in two dimensions but their length in the third is determined by the value of n. $Mo_{10}O_{29}$ is similar in structure; however, the ReO_3 block is longer.

The simplest member of a shear structure derived from rutile is that found for Ti_5O_9 where $n = 5$. A block of the structure is shown in Figure 15. Here, edge and corner-sharing TiO_6 blocks of the rutile type, five octahedra thick, are joined by face sharing to similar five unit blocks. As the level of reduction decreases, the size of the rutile block increases but the crystallographic shear remains the same.

Reduction need not occur in order for crystallographic shear to take place. All that is required is that an oxygen deficiency be introduced as is the case in the H form of Nb_2O_5. Here, 3×4 ReO_3-like blocks, one layer thick, and infinite blocks 3×5 octahedra thick result from a double shear operation along directions approximately 90 degrees apart. In addition, one out of every 27 Nb is located in a tetrahedral hole leading to an extremely complicated structure. The H structure is one of at least 14 polymorphic forms of Nb_2O_5, 10 of which are based on crystallographic shear.

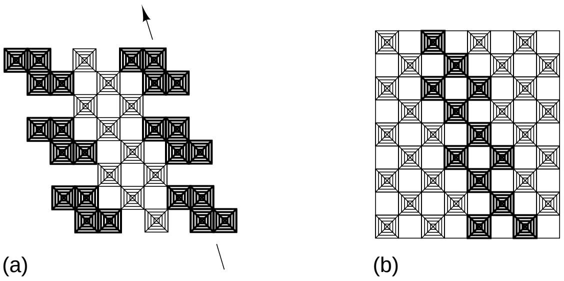

Figure 14 Corner-sharing ReO_3 like layer (a). Same layer after having undergone crystallographic shear (b)

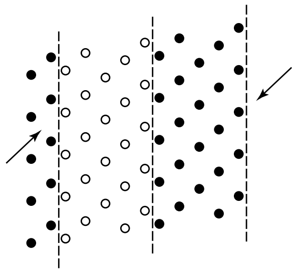

Figure 15 Layer of the crystallographic shear Ti_5O_9 structure

3.6 Tetragonal and Hexagonal Tungsten Bronzes[8–10,16]

Oxide bronzes are ternary transition metal oxides of the type $A_xM_yO_z$ in which A is typically a large cation and M is a transition metal, some or all of which are in a reduced valence state. They often are brightly colored, have metallic luster, display a range of stoichiometry, and have high electrical conductivity. Although for particular systems exceptions to one or more of the above properties can be cited, their structures, without exception, are derived from corner-sharing MO_6 octahedra of the ReO_3-type. The structure may be modified by the insertion of a large cation into a vacancy in the lattice to form the perovskite structure, or more likely by some distortion of the ideal structure by crystallographic shear or internal rotation.

As mentioned in Section 3.4.1, a simple perovskite is found for the series Na_xWO_3 for $0.30 \leq x \leq 1.0$. However, there is a second structure found for $x \leq 0.40$, or if Na is replaced by K and x is between approximately 0.45 and 0.57. Here, a tetragonal distortion occurs that yields the so-called tetragonal tungsten bronze (TTB) structure. This can be considered as being derived from a normal perovskite (Figure 16(a)) by an internal rotation of a 2×2 block of the perovskite structure as shown in Figure 16(b). The result is the formation of four large pentagonal shaped tunnels where the large cations reside and four small triangular tunnels, which are empty. The structure requires that the value of x be no larger than 0.60, otherwise there would not be enough vacant sites present to permit the formation of the empty triangular tunnels. Studies of potassium TTBs of lower K content indicate that the occupancy of the pentagonal sites is favored over the 12-fold perovskite-like sites. where the K–O bond distance is only 2.72 Å. This is much shorter than the expected 2.99 Å, based on Shannon–Prewitt radii. The potassium atoms in the pentagonal tunnels have an irregular 15-fold coordination derived from a pentagonal prism in which the sides are capped by oxygen atoms. The K–O bond distances range from 2.8–3.35 Å, six of which are formed with oxygens at the corners of a distorted trigonal prism 2.8–2.9 Å distant inscribed within the pentagonal prism.[28]

Phases formed in the WO_3 rich portion of the WO_3-Nb_2O_5 system have complex structures that display blocks of the TTB type intergrown with ReO_3-like blocks. $K_6Li_4Nb_{10}O_{30}$ has a TTB-related structure where the small Li^+ is found in the triangular tunnels in ninefold coordination. A derivative structure is shown by $Ba_{0.15}WO_3$, which contains ribbons of pentagonal tunnels condensed so that the square perovskite channels are eliminated. The value of x is limited to ≤ 0.167 by the structure.[29]

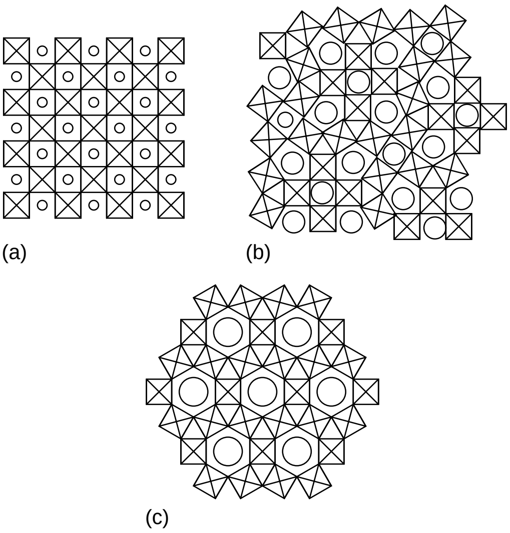

Figure 16 Normal perovskite layer. Circles represent A cations (a). Tetragonal tungsten bronze layer (b). Hexagonal tungsten bronze layer

Alkali tungsten bronzes of the type M_xWO_3, M = K, Rb, or Cs with $0.16 \leq x \sim 0.3$ may adopt the hexagonal tungsten bronze (HTB) structure in which the large Cs atoms reside in hexagonal tunnels formed by six WO_6 octahedra in 12-fold coordination. The limit of x, as determined by the structure is 1/3. The structure is of interest since these compounds display superconductivity with T_c values between 1 and 7 K. It is also found for several mixed oxides of Nb and Ta with large A cations.

3.7 Molybdenum Oxide Bronzes[30–32]

Alkali molybdenum oxide bronzes with the cubic perovskite or TTB structure are unstable and can only be prepared at high pressures. The more common normal pressure structures are derived from ReO_3 by crystallographic shear and are of interest because of their quasi-low dimensional electrical and magnetic properties. Like their perovskite tungsten counterparts, they may be brightly colored and display metallic conductivity, However, their structures are more complex with a higher degree of MO_6 edge sharing where layers are formed in which the large A cations reside. Three of the more interesting types will be described here.

$K_{0.30}MoO_3$ is the prototype for the so-called blue bronzes of the type $A_{0.3}MoO_3$ where A = K, Rb, Tl. All possess a monoclinic C-centered unit cell. Although the compound is actually stoichiometric with a formula $K_3Mo_{10}O_{30}$, the general practice is to use the decimal formulation in keeping with the nonstoichiometric tungsten bronzes. The basic building blocks are clusters of ten MoO_6 octahedra that share edges as shown in Figure 17(a). These then share corners in two dimensions to build layers of composition MoO_3 that are held together by K^+.

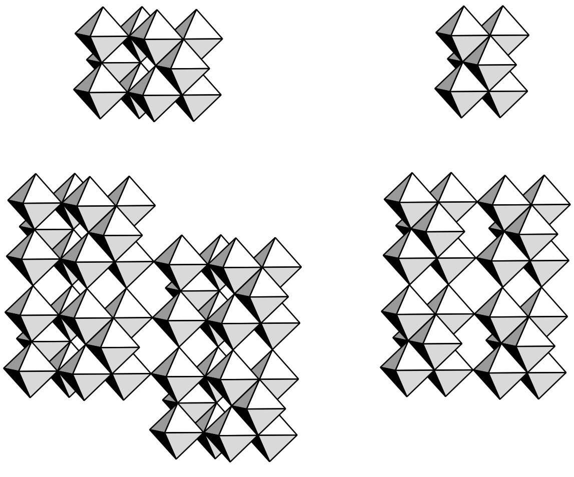
(a) Blue $K_3Mo_{10}O_{30}$
(b) Red $K_2Mo_6O_{18}$

Figure 17 Mo–O slabs in $K_{0.30}MoO_3$ (a) and for $K_{0.33}MoO_3$ (b)

Although the structure is three dimensional overall, the MoO_3 network is two dimensional. Further, effective overlap of molybdenum t_{2g} and oxygen p_z orbitals occurs along the monoclinic *b* directions, which provides for effective delocalization of electrons in this direction. Electronically then, this compound behaves as a quasi-one-dimensional material. Furthermore, bond valence calculations based upon observed bond distances indicate that over 80% of the d electron density is associated with Mo atoms that run along the *b* axis. This is confirmed by measurements of electrical conductivity performed on large single crystals prepared by fused salt electrolysis, which show that the conductivity is metallic at room temperature and two orders of magnitude higher along the *b* parallel to the layers than perpendicular to them.

A broad transition to semiconducting behavior is observed at 180 K in $K_{0.30}MoO_3$, which is attributed to a *charge density wave* (CDW) predicted as a mechanism by Peierls and H. Fröhlich as a means of lowering the electronic energy of a one-dimensional metal.**[31]** A specific heat change is also associated with the transition and X-ray diffuse scattering has shown that the transition at 180 K leads to an incommensurate, semiconducting CDW state with a wave vector equal to 0.26b*.**[33]** The rubidium and thallium analogs appear to behave similarly.

The ‘purple’ molybdenum bronzes have the general formula AMo_6O_{17}, where A = Li, Na, K or Tl. The potassium and thallium members have trigonal structures while the Li and Na compounds show different types of distortions, which result in monoclinic symmetry. The ideal value of A in this structure should be 1.0; however, it seems to be closer to 0.9 for all members except Tl. Only for the Na compound has a slight stoichiometry range ($0.84 \leq x \leq 0.96$) been observed. The origin of this behavior is not clear although it may be electronic in nature.

The idealized structure of $K_{0.9}Mo_6O_{17}$ is shown in Figure 18. The structure consists of infinite slabs of MoO_6 octahedra, four units thick, sharing corners in a ReO_3-like fashion and terminated by MoO_4 tetrahedra to form a six-unit layer having the composition Mo_6O_{17}. These units are held together by K^+. The Mo–O arrangement is similar to that of the monoclinic form of Mo_4O_{11}. Although the Tl and Na compounds have different symmetries, the basic structure remains essentially unchanged.

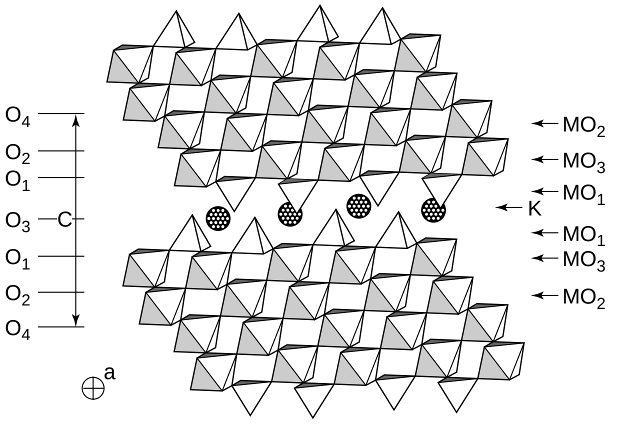

Figure 18 $K_{0.9}Mo_6O_{17}$ structure

The structure of the Li compound shown in Figure 19 is noticeably different. The layered ReO_3-like Mo–O network has been partially destroyed. It is now only three units thick and the surfaces are a combination of corner-sharing tetrahedra and octahedra. Octahedra in adjacent layers are then bridged by other MoO_4 tetrahedra to form a weakly cross-linked Mo–O network. The lithium ions are coordinated by 9 oxygens and reside in cavities created as a result of the cross linking. Although the Mo–O network is truly three dimensional, the d electrons remain confined to the ReO_3-like layers and the material displays quasi-two dimensional electronic properties.**[32,34]** Low-temperature anomalies in the electrical and magnetic properties of these compounds exist with the Na, K, and Tl compounds behaving in a quite similar fashion showing metal to metal transitions between 70 and 100 K. In contrast, the Li compound retains its metallic conductivity down to 24 K where it undergoes a relatively sharp transition to semiconducting behavior followed by a transition to the superconducting state at 1.9 K.**[35]** In all cases, the conductivity is several orders of magnitude higher parallel to the layers than perpendicular to them.

A final class of Mo oxide bronzes are the ‘red’ bronzes, which have the general formula $A_{0.33}MoO_3$, A = Li, K, Rb, Cs, and Tl. Like the blue bronze $K_{0.3}MoO_3$, they are stoichiometric and might more correctly be formulated $K_2Mo_6O_{18}$. The heavier members are monoclinic and isostructural while the triclinic Li compound has a different structure, which will not be discussed here.**[36]** The basic building block of the $K_{0.33}MoO_3$ structure is a cluster of six edge-sharing MoO_6 octahedra Figure 17(b), which link corners in one dimension to form chains. These chains then link by partial corner sharing to form infinite MoO_3 slabs, which are separated by K^+ in an irregular eightfold coordination with oxygen. In this compound, the Mo–O distances along the monoclinic *b* axis are too long for effective Mo–O $d_{t_{2g}}$-p_π overlap for electron delocalization to occur. As a result, the compounds are semiconductors with conductivities several orders of magnitude lower than the metallic blue or purple bronzes.

3.8 Vanadium Bronzes

Like molybdenum and tungsten, vanadium forms a variety of nonstoichiometric oxides with the alkali metals and other cations, for example, Cu^+, Ag^+, Zn^{+2}, or Al^{+3}, which have bronze-like properties.**[37–39]** These compounds can be made by heating appropriate mixtures of V_2O_5 and the desired alkali metal carbonate or oxide in platinum vessels under argon at 700–800 °C and then cooling slowly over

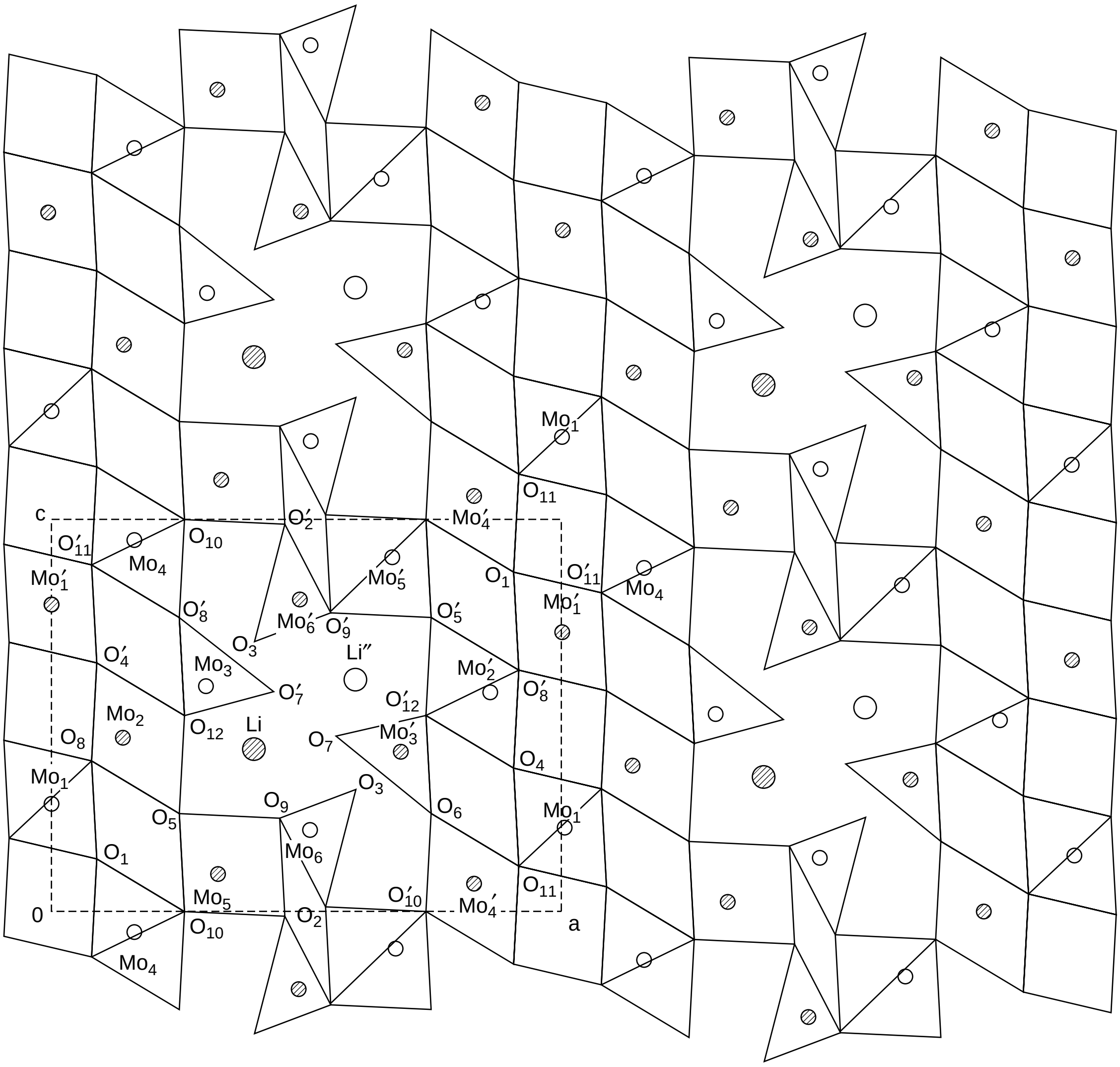

Figure 19 $Li_{0.9}Mo_6O_{17}$ layer

a period of several days. The sodium system illustrates the complexity of these bronzes, which are discussed here as examples. Four distinct structure types are noted for $Na_xV_2O_5$: Unlike the molybdenum bronzes, they display wide ranges of stoichiometry but like them they display complex quasi-low dimensional structures.

α-orthorhombic,	$0 < x \leq 0.02$
β-monoclinic,	$0.22 \leq x \leq 0.40$
α'-monoclinic,	$0.65 \leq x \leq 0.69$
β'-orthorhombic,	$0.70 \leq 0.70 \leq 1.0$

The α-orthorhombic phase has the layer structure of V_2O_5 itself with the alkali metals inserted in between the layers. For Na^+, the substitution of what appears to be an inappropriately large cation into a small trigonal prismatic hole is quite limited. However, the smaller Li^+ ion may substitute up to $x \leq 0.13$. A diagram of the structure of the β form is shown in Figure 20. Here layers are formed by corner-sharing distorted square pyramidal VO_5 groups. The layers overlap one another in such a fashion to form tunnels in which the Na^+ reside. Various sites in the tunnels are available but not all can be occupied simultaneously.**[40]** The most stable phase appears to have a composition $Na_{0.33}V_2O_5$ but the value of x can be extended to about 0.40 for Na^+ by the utilization of alternate sites for the alkali ions. In the case of Li, values of x up to 0.49 have been observed with slight modifications of the V–O layer arrangement.

The electrical conductivity of the material is complex behaving partly like an anisotropic semiconductor and partly like a metal. The metal to semiconductor transition appears to be sample dependent since various workers have reported transition temperatures ranging from 130 to 340 K for samples

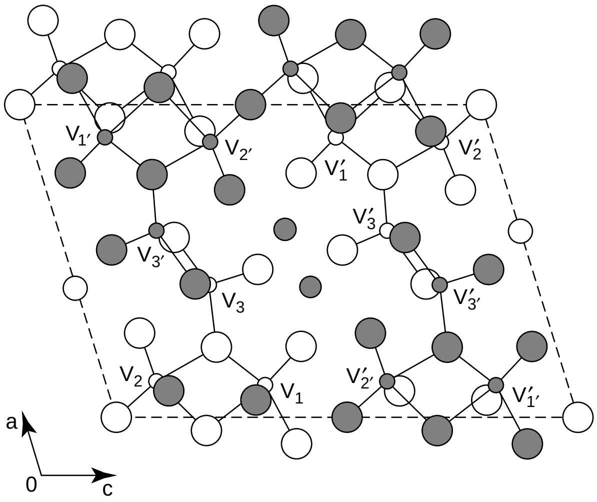

Figure 20 Projection of the β-$Na_xV_2O_5$ structure

of apparently similar composition, while others have reported seeing semiconducting behavior only from room temperature to 500 °C.[41] Because of the partial occupancy of the available cation sites and the relatively well-defined path for ion migration within the tunnels, high cation mobility is to be expected for these compounds. Lithium ion conductivities of the order of 10^{-4} S cm^{-1} are observed at 500 °C for $Li_xV_2O_5$. This conductivity decreases as Li is added ostensively because of the resultant decrease in the number of sites available for ion migration.[42]

3.9 Silica, Silicates, Borates, and Phosphates[8,43–46]

The chemistry of boron, silicon, and phosphorus with oxygen is not only one of the richest in terms of chemical diversity but also among the most commercially important. It is discussed in detail under ***Borates: Solid-state Chemistry***; ***Phosphates: Solid-state Chemistry*** and ***Silicon: Inorganic Chemistry***. However, there is a commonalty of a number of factors that affects their chemistry and distinguishes them from other oxide systems that should be noted. The first is that their chemistry is essentially that of the group valency. Although a limited phosphite (P(III)) chemistry exists, only an ill-defined amorphous silicon ‘monoxide’ is known and conventional boron chemistry is limited to the trivalent state. The second is that they all possess small coordination numbers with well-defined coordination polyhedra, typically triangular planar or tetrahedral in the case of boron, which cannot expand its octet. While Si and P can expand their octet, this rarely happens in oxides, although 6 coordinate Si is occasionally seen in a few high-pressure polymorphs and certainly is important as a short-lived reaction intermediate. However, these basic MO_3 and MO_4 building blocks easily condense by corner sharing in all three systems to form M–O–M complex anions, infinite chains, sheets, and ultimately 3 dimensional cross-linked framework structures. Thirdly, the flexibility of the interconnects between these coordination polyhedra is evidenced by the fact that the M–O–M angles varies from about 115 to essentially linear, which provides for easy accommodation of a wide range of ternary cations and for structures with a varying degree of openness.[44] This flexibility leads to the formation of a number of polymorphic forms, particularly those sensitive to pressure.

Not surprisingly, these small differences in bonding energetics leads to the formation of noncrystalline materials, that is, glasses in which entropy is the deciding factor in determining the form of the stable phase. The tendency towards glass formation is particularly evident with alkali phosphates. Boric oxide itself is difficult to crystallize and while silica glasses form easily they are subject to recrystallization (devitrification) at high temperatures. The glasses known to the ancients were silicate-based materials but the twentieth century has seen increasing needs for glasses with different properties for a variety of applications, which utilize not only borate or phosphates but also a variety of other elements as well. Oxide glasses are discussed in depth under ***Noncrystalline Solids***.

Silica, SiO_2, is an extremely important industrial chemical and exists is several forms. The classical view of silica is that the three principal crystalline forms of silica are quartz, tridymite, and cristobelite, each of which undergoes a *martensitic transformation*, which involves minor structural changes without the breaking of Si–O bonds. In all three structural types, the basic building blocks are the SiO_4 tetrahedra, which share their corners with other tetrahedra. Of these three forms, the most open structure is that of cristobelite while the densest is quartz as shown in Figure 21. There are also two very dense forms of silica that occur at high pressures; coesite (d $=$ 3.01 gm cc^{-1}), which retains

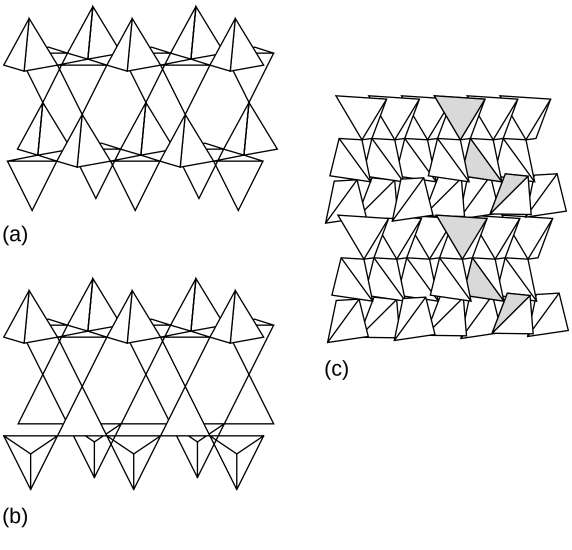

Figure 21 Relative openness of silica polymorphs as illustrated by packings of SiO_4 tetrahedra. $\beta\beta$-cristobelite (a). β-tridymite (b). β-quartz. Shaded tetrahedra shows helical nature of the structure (c)

the tetrahedral coordination of Si by O, and stishovite, which is formed above 150 K bar, in which the Si is now in sixfold coordination with oxygen and displays the rutile structure.

There is a considerable amount of evidence that quartz and cristobelite are the only normal pressure forms of silica while tridymites are considered to be defect structures stabilized by impurities. However this view has been questioned by Hill and Roy, who were able to prepare tridymite from very pure silicon and water.[47]

There are a variety of other silicas. These include the metastable silica-W, which has a very low density (1.97 g cm^{-3}), and whose structure consists of edge-sharing chains of SiO_4 tetrahedra, the microcrystalline diatomaceous earths, various forms of noncrystalline silica including vitreous silica (glassy silica), and the finely divided amorphous silicas such as dry silica gel, fumed silicas, and colloidal silicas.

Silicates and aluminosilicates represent the largest class of inorganic compounds known comprising more than three quarters of the earths crust. Although their study as naturally occurring materials is normally considered to be the purview of the discipline of mineralogy or geochemistry, their rich chemistry has been exploited by chemists to produce a variety of useful materials derived from silicate-based compounds. The basic building block of silicates is the SiO_4 tetrahedron, which, by various combinations of corner sharing, can create a vast variety of structures ranging from materials that contain simple orthosilicate anions, $SiO_4{}^{-4}$, to more complicated structures containing Si–O networks in the form of chains, sheets, multilayer slabs, and finally complex, cross-linked, three-dimensional structures containing tunnels and cavities that can accommodate a variety of organic and inorganic species. The complexity and variety of these structures is increased by the partial replacement of silicon by trivalent Al in the SiO_4 tetrahedra to produce aluminosilicates that include not only the vast majority of igneous rocks but also the layered clays, micas, and the complex zeolite 3D and zeolite related materials (*see* ***Zeolites***).

Because of its small size and s^2p^1 electronic ground state, boron is unique among the elements with its predilection for sp^2 hybridized trigonal planar coordination. However, given the acidic character of the unfilled octet, hybridization to tetrahedral BO_4 configurations is also important. These simple elementary units may be found as discrete anions but more often they are utilized as building blocks of more complicated ions or as part of extended two and three-dimensional structures.

An extensive chemistry of phosphorus and oxygen exists, the preponderance of which deals with aqueous chemistry with great interest focused upon those of biological importance. A broad review of phosphorus oxygen chemistry is given in ***Phosphates***. Reduced transition metal oxide phosphates and silicates are discussed in Section 3.12.

Alkali phosphates are typically prepared by the dehydration of crystalline orthophosphates. The phosphate building block is the PO_4 tetrahedron, which shares corners to form discrete anion units the simplest being the diphosphate (or pyrophosphate) ion $P_2O_7{}^{-4}$ and the well-known linear triphosphate ion $P_30_{10}{}^{-5}$ widely found in detergents and water softeners. Pyrophosphates and related pyrovanadates formed with di- tri- and tetravalent cations have been the object of intense study since they display a variety of polymorphic forms where the P–O–P angle is particularly sensitive to the size and coordination requirements of the ternary ion. Polyphosphates of general formula $M_n(PO_3)_n$ exist as infinite chains of PO_4 tetrahedra sharing two corners or as ring type members with 3 to 10 P, the most common being the trimer and the tetramer. Polyphosphate ions of general formula $[(PO_3)_nO]^{(n+2)-}$ with n up to 16 are well established. Finally, there are framework structures in which PO_4 tetrahedra share three or more corners. For example, $AlPO_4$ has three polymorphs, each an ordered variant of the three forms of silicon dioxide. YPO_4 on the other hand contains discrete $PO_4{}^{-3}$ anions.

3.10 Oxides with Defect Structures[9,19,31,48]

Nonstoichiometry is a pervasive aspect of oxide chemistry, particularly where the cation can assume two or more valences or aliovalent cation substitutions are facile. These can be classified into three rather broad ranges. Class I includes systems where the nonstoichiometry approaches or exceeds that which cannot be detected by classical methods of chemical analysis (i.e., less than 1 part in 1000) but may manifest itself in dramatic changes in electrical or optical properties. Class II includes systems where the nonstoichiometry is of the order of several mole % and readily discernible by chemical analysis, density measurements, or X-ray diffraction measurements of unit cell constants. Class III are those systems with broad ranges of nonstoichiometry such as the alkali metal tungsten bronzes.

The nonstoichiometry may be found on the oxygen sites as is the case with stabilized zirconia $(Y_xZr_{1-x})O_{2-x/2}$, metal deficient oxides such as $Fe_{1-x}O$, anion excess oxides such as UO_{2+x} and systems that display combinations of these effects. The vacancies in such systems may cluster or ultimately may order by some mechanism such as crystallographic shear. Catlow has discussed such systems in detail.[49]

As an example of the first type of nonstoichiometry, pellets of TiO_2 were heated in hydrogen at temperatures between 500 to 700 °C. Thermogravimetric analysis established that the oxygen stoichiometry decreased slightly from $TiO_{2.000}$ to $TiO_{1.993}$, the resistivity of the samples decreased by over five orders of magnitude.[50] An alternate method of introducing mobile d electrons is to replace a portion of the oxygen by fluorine, viz., $TiO_{2-x}F_x$. Samples of TiO_2 that were heated at 700 °C in HF diluted with an Ar/H_2 mixture were found to have the composition $TiO_{1.998}F_{0.002}$ had a resistivity of only 2.5 ohm-cm.[50]

FeO, in contrast to TiO_2, is very difficult to prepare in an Fe:O ratio equal to 1 and apparently does not exist at normal pressures.[50] Stoichiometric FeO reportedly can be prepared by heating ferrous oxalate in vacuo but the finely divided product picks up oxygen rapidly in air. As the oxygen content of the wustite phase of FeO increases from $FeO_{1.06}$ to $FeO_{1.19}$, the observed density and the lattice constant of the cubic rock salt unit cell decrease, indicating that the compound is deficient in iron rather than containing an excess of oxygen. Therefore, it should be formulated as $Fe_{1-x}O$ where it is found that $0.06 \leq x \leq 0.14$. X-ray and neutron diffraction studies suggest that, rather than the vacant cation sites in the NaCl-like lattice being randomly distributed, a significant portion of the Fe^{+3} occupies tetrahedral interstices that are stabilized by a cluster of 4 octahedral cation vacancies designated as a (4:1) cluster. More complex defect arrays such as the 6:2, 8:3, or 16:5 clusters shown in Figure 22 also form. The binding energy due to coulomb interactions between the vacancies and interstitials in these clusters has been calculated to be between 2.0 and 2.5 eV, which serves in part to explain the stability of these defect phases. More complex defect clusters have been postulated and are discussed by Catlow.[49]

TiO has a defect sodium chloride superstructure in which 5/6 of both the Ti and O sites are occupied in an ordered fashion. The defect nature of structure allows for both cation and anion deficiency and as a result it is stable for Ti:O ratios between 0.75 and 1.4 with the percentage of Ti sites filled approaching unity at high Ti:O ratios while at low ratios the oxygen sites approach complete filling.

Fluorite type oxides are particularly prone to nonstoichiometric effects. This most commonly occurs in the form of cation nonstoichiometry induced by partial reduction of the cation or by replacement of a portion of the oxide by fluoride. Anion excess phases can occur as a result of cation oxidation or by replacement with higher valence impurities. The dominant defect in this structure involves the migration of oxygen to the large cuboidal interstice resulting in the formation of a vacancy at a normal lattice site. A vacancy of this type is called a Frenkel defect.

These large cuboidal interstices play an important role in gross anion excess fluorites such as UO_{2+x}, $x \leq 0.25$. However, the excess oxygen is not found at the centers of these sites but is displaced along the $\langle 110 \rangle$ and $\langle 111 \rangle$ directions while two near neighbor lattice oxygens are displaced towards neighboring cubic interstices. As in $Fe_{1-x}O$, defect clustering is also postulated to occur. In this case, clusters of 6 or 9 defect units are postulated. Such clusters have been found by diffraction studies of anion excess alkaline-earth fluorides, which have this structure.[51]

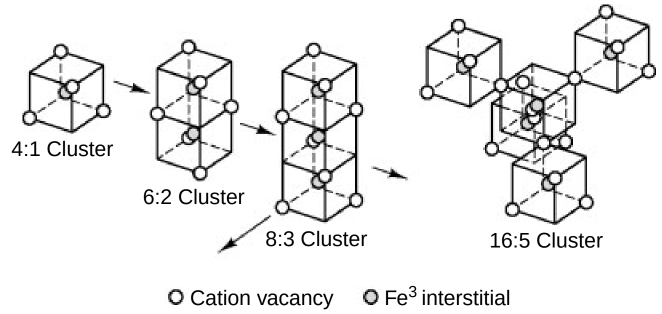

Figure 22 Defect clustering in $Fe_{1-x}O$

Anion deficient fluorite oxides of the rare earths and actinide elements are well established as are those based on hafnia or zirconia. The latter is of particular interest since the cubic fluorite structure in pure ZrO_2 exists only above 870 °C, transforming at lower temperatures to a denser monoclinic form. However, the cubic form can be stabilized by doping with several mole percent of CaO or Y_2O_3 so that the phase transition does not take place upon cooling. This permits the manufacture of so-called stabilized zirconia containers, valued for their chemical inertness and refractory properties. Further, stabilized zirconias are part of a class of solid materials called fast ion conductors (or superionic conductors), which have unusually high oxide ion mobilities and display electrical conductivities above 600 °C, which approach those of fused salts (*see* ***Ionic Conductors***). Stabilized zirconias are used as oxygen sensors and as solid electrolytes in fuel cells. Defect clustering plays an important role in the ion movement that is discussed in more detail in ***Defects in Solids***.

The perovskite based tungsten oxide bronzes are examples of a third class of nonstoichiometric materials where there is a broad range of defect composition. The properties of these cation deficient materials were discussed in Section 3.4.1. In addition, anion deficient perovskites are well established. The X-ray powder diffraction patterns for the $SrTiO_{3-x}$ and $SrVO_{3-x}$ systems show only the lines of a simple perovskite over the range $0 \leq x \leq 0.5$ indicating that the anion vacancies are not ordered. In other cases, such as $SrFeO_{3-x}$, distortion of the simple perovskite structure occurs when $x \geq 0.12$ while a mixture of phases is seen for nominal values of $x \geq 0.28$. Oxides of the type $LaBO_3$ (B = Cr, Mn, Fe, Co) are known to have mobile oxide ions at high temperatures whose mobility is defect mediated.[52] An ordering of vacancies occurs in $Ca_2Fe_2O_5$, which has a superstructure related to perovskite. The ordering is accompanied by movement of some Fe ions so that layers of octahedral FeO_6 and tetrahedral FeO_4 can be identified. Vacancy ordering occurs in $LaNiO_{3-x}$ in which definite line phases have been observed for $La_nNi_nO_{3-1}$ with $n = 7, 9, 13$ and 30.[53]

A phase that was once thought to have an excess of oxygen is $LaMnO_{3+x}$ where the 'excess' oxygen was believed to be accommodated at interstitial sites. Tofield and Scott[54] studied a phase of nominal composition $LaMnO_{3.12}$ using neutron diffraction. Although they considered interstitial models, their results show that the compound is actually $La_{0.94}\square_{0.06}Mn_{0.98}\square_{0.02}O_3$, where $\square$ represents lattice vacancies. The level of nonstoichiometry is much less in $LaVO_{3-x}$ ($x < 0.05$) and not determinable for the Cr and Fe analogs.[55]

3.11 Intergrowth Structures

Intergrowth phases occur when slabs of two or more well-defined structural sequences can interface with one another to form an ordered or disordered sequence. A good example of a simple ordered intergrowth structure is that of K_2NiF_4. One way to view this structure, shown in Figure 23, is as a series of perovskite cells stacked one on top of the other but displaced by a translation of 1/2 in both the tetragonal a and b directions. The structure is a common one for oxides of the transition metals with the larger alkaline earth and rare earth cations. An alternate description of the structure is one that contains alternating layers of the perovskite (ABO_3) and rock salt (AO type).

Many systems that form perovskites also form K_2NiF_4 type oxides, for example, $SrTiO_3$ and Sr_2TiO_4. The latter can be considered as the first member of a general homologous series $\mathrm{A}'_2[\mathrm{A}_{n-1}\mathrm{Bn0}_{3n+1}]$ where $n \leq 4$ and A′ and A may or may not be the same. Here a perovskite slab can be looked upon as a TiO_2 layer sandwiched between two SrO layers that are in register with each other. The ideal, ordered structure of $Sr_3Ti_2O_7$ ($n = 2$) should contain a double perovskite layer separated by an SrO layer, as shown in Figure 23(b), but in fact high-resolution electron microscopy HREM studies of a typical sample of $Sr_3Ti_2O_7$ show intergrowth regions where $n = 2$, 3, 4, 5, 7, and 8 are clearly evident. Other areas of the crystal show large domains with the composition $SrTiO_3$ so that the average composition is $Sr_3Ti_2O_7$.[55]

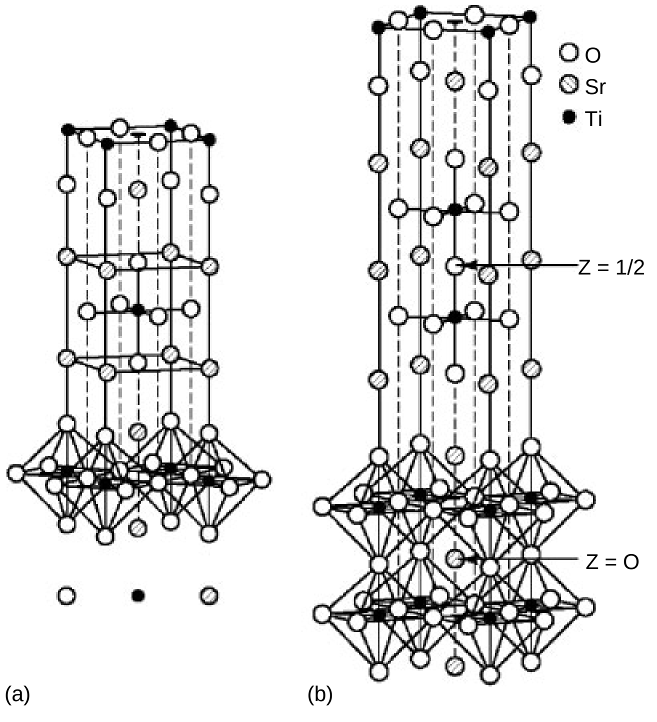

Figure 23 Unit cell of Sr_2TiO_4 (K_2NiF_4 type) at right. Unit cell of $Sr_3Ti_2O_7$

La_2CuO_4 also has the K_2NiF_4 structure at high temperatures. However, La^{+3} is too small to fit comfortably into the close-packed cavities and upon cooling, it transforms to an orthorhombically distorted variant in which there are four short Cu–O bonds in the ab plane and two long bonds along the c axial direction. In addition, the distorted CuO_6 octahedra are tilted slightly with respect to the unit cell edges and a slight excess of oxygen is introduced, $La_2CuO_{4+\delta}$, $\delta < 0.03$. However, if a small amount of Sr is substituted for La, then the normal tetragonal K_2NiF_4 form is stabilized for $La_{2-x}Sr_xCuO_4$ ($0.10 \leq x \leq 0.27$) with a stoichiometric oxygen content. These phases were found to be superconducting between $T = 25-40$ K with the maximum value of T_c being for $X = 0.15$.[56] Shortly thereafter the now famous yttrium barium copper oxide, $YBa_2Cu_3O_{7-\partial}$, was discovered with a $T_c = 93$ K.[57] This can be looked upon as a tripled perovskite unit in which Ba and Y occupy the A cation positions in an ordered fashion. The ideal oxygen stoichiometry of 7 is then achieved by removal all of the oxygen in the 001 plane about Y and along 2 opposite edges of Cu(1) as seen in Figure 24(a). This results in a pyramidal coordination of Cu(2), which exists as an infinite planar net perpendicular to the c axis, and a square coordination of Cu(1) in the form of chains running along the b axis.

The structure is conveniently described as an intergrowth structure of the following layers stacked along the orthorhombic c axis

$$\text{–Cu(1)O–BaO–Cu(2)O}_2\text{–Y–Cu(2)O}_2\text{–BaO–}$$

Oxygen may be removed progressively by heating under controlled partial pressures of O_2 between 400 and 950 °C. As oxygen is removed disrupting the CuO_2 planes, T_c decreases. The orthorhombic phase is stable up to $\delta = 0.5$. Here a transformation to the tetragonal form takes place and is stable for $0.5 \leq \delta \leq 1.0$, the end member of which is shown in

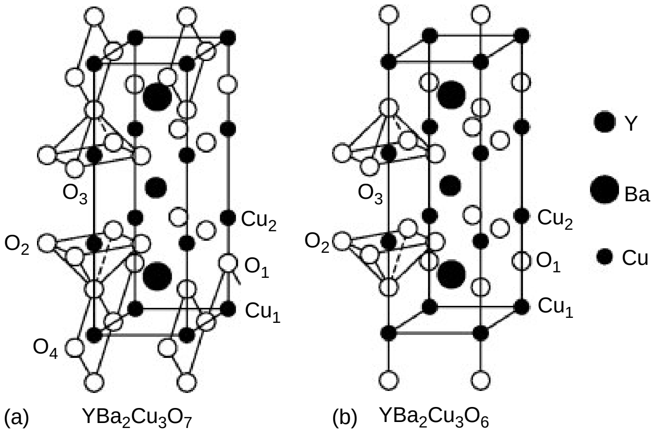

(a) $YBa_2Cu_3O_7$ (b) $YBa_2Cu_3O_6$

Figure 24 Unit cells of $YBa_2Cu_3O_7$ (a) and $YBa_2Cu_3O_6$ (b) Pyramidal, planar, and linear coordination of Cu by O is highlighted

Figure 24(b) where Cu(1) is now in linear coordination with oxygen. This phase is not superconducting. Thus for the $YBa_2Cu_3O_{7-\delta}$, $0 \leq \delta \leq 01.0$, the intergrowth sequence might be reformulated

$$-CuO_{1-x}-BaO-CuO_2-Y-CuO_2-BaO-.$$

If a second CuO chain is inserted into $YBa_2Cu_3O_7$, the compound $YBa_2Cu_4O_8$ is obtained with $T_c = 80\,K$, while $Y_2Ba_4Cu_7O_{14}$ ($T_c = 40\,K$) is an intergrowth of these two structures. $Tl_2Ba_2Ca_2Cu_3O_{10}$ with a $T_c = 125\,K$ is a member of the homologous intergrowth series $(TlO)_nBa_2Ca_{m-1}Cu_mO_{2+m}$ with $n = 1$ and $m = 1-4$ or $n = 2$ and $m = 1-3$. Such intergrowth structures in layered cuprates have been studied extensively by HREM, which reveals a variety of complex nonrecurrent intergrowth features. These structures have been reviewed by Raveau and coworkers.[58,59,60] The relationships between intergrowths and superconducting behavior are discussed in ***Superconductivity***.

Closely related in structure to the RP phases are the so-called Dion–Jacobsen (DJ) phases that have the general formula $A'[A_{n-1}B_n0_{3n+1}]$, where n is typically 2 or 3. These phases have one half the number of cations between the perovskite layers as do RP and they are typically alkali metal cations, an example of which would be $CsCa_2Nb_3O_{10}$. Aurivillius phases, such as $Bi_2W_2O_9$, are intergrowths of two dimensional perovskite slabs and $Bi_2O_2{}^{+2}$ layers. An interesting feature of RP, DJ, and Aurivillius phases is that the layered cations can often be replaced easily by ion-exchange or intercalation methods and thus are templates for preparing new materials with controlled properties (see Section 5.6 and 5.7).[61]

An interesting example of intergrowth structures are a series of magnetic oxides based upon the structure of $PbFe_{12}O_{19}$, magnetoplumbite. The structure can be described in terms of five HCP layers of 4 oxygens each, in which one of the layers has one-quarter of its oxygen replaced by the large Pb^{+2} ion to yield a PbO_{19} framework. The iron then fill octahedral and tetrahedral holes in a spinel-like fashion. The layer sequencing is BABAB. A closely related compound is $BaFe_{12}O_{19}$, which differs from magnetoplumbite in that the sixth layer of the structure has been translated so that the 10 layer stacking sequence

$$BABABCACAC$$

now occurs. Phases of the type $Ba_2M_2Fe_{12}O_{22}$, ($M = Zn^{+2}$, Mg^{+2}, or a divalent transition metal cation) are formed when a second BaO_3 layer is inserted into a five-layer magnetoplumbite cell along with two small cations to maintain electro-neutrality. A great variety of intergrowth structures utilizing these two sequences along with that of spinel have been observed.[62] Some of these may have extremely long repeat distances (up to 1600 Å) along the CP direction that are best observed by HREM. Magnetic interactions in these structures appear to be important since they do not form if an attempt is made to replace Fe^{+3} by nonmagnetic ions such as Al^{+3} (*see **Magnetic Oxides***).

The compound $La_5Mo_4O_{16}$ is of interest since is one of the few examples of 4d oxides that display strong ferromagnetic-like interactions, being a so-called metamagnet below 180 K. The structure consists of perovskite-like layers of corner-sharing MoO_6 octahedra sandwiched between insulating Mo_2O_{10} clusters that have an extremely short Mo–Mo bond of 2.406 Å (see Section 4.2). The Mo in the perovskite layers have valences of 4 and 5 and are ordered in alternate MoO_6 octahedra.[63] Partial replacement of the tetravalent Mo by divalent 3d transition metal ions and Mg^{+2} can be achieved resulting in reduction or elimination of the metamagnetic properties.[64] A rhenium analog, $La_5MnRe_3O_{16}$, has also been reported.[65]

A homologous series of cesium tungsten oxides having the formula $Cs_{2n}W_{4n-1}O_{12n}$ has been reported. The general structure consists of slabs composed of layers of the hexagonal tungsten bronze and the pyrochlore type. The alkali cations reside in between the layers and in the tunnels formed within the slabs.[66]

3.12 Reduced Transition Metal Phosphates

The fact that boron, silicon, or phosphorus will not normally enter into sixfold coordination with oxygen offers chemists the possibility of using these elements to interrupt the formation of high density three-dimensional transition metal oxide structures based on octahedral coordination and isolate them with the more flexible polyhedra of the main group elements. Two relatively new classes of reduced transition metal oxides are phosphates of molybdenum and tungsten in reduced valence states. While one might expected that they would be similar, they are not. The structure of the tungsten analogs are built up of ReO_3-like slabs of WO_6 octahedra in which monophosphate (PO_4) or diphosphate (P_2O_7) groups bridge the WO_3 layers. In the process, the d electrons of tungsten are confined to the slabs creating the opportunity for quasi-low dimensional electrical and magnetic behavior.

Large channels exist between the phosphate-terminated slabs, which may accommodate ternary ions. These bronzes can be divided into the following categories according to the phosphate bridging group used and the nature of the principal channel created in the structure. (1) Monophosphate tungsten bronzes ($MPTB_p$) contain pentagonal tunnels and have the general formula $(PO_4)_4(WO_3)_{2m}$ where $m = 2$, $4 \leq m \leq 10$ and also represents the number of WO_3 layers between the terminating phosphate groups as shown in Figure 25(a). (2) Monophosphate tungsten bronzes containing hexagonal tunnels ($MPTB_h$) of the type $A_x(PO_2)_4(WO_3)_{2m}$. Here the channels are large enough to accept moderately large cations, ($A = Na$, K) where $x = 1.75-3$, the limit being 2 for K and about 3 for Na. Values for m

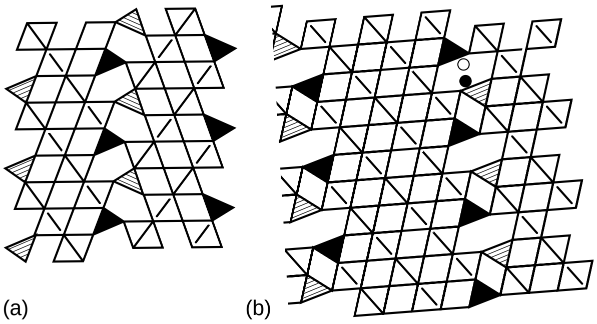

Figure 25 $MPTB_p$ layer with $m = 4$ (a). $MPTB_h$ with $m = 7$, $K_{1.4}P_4W_{14}O_{50}$ (b). PO_4 groups in black. Note pentagonal and hexagonal tunnels

are between 4 and 13. (3) Diphosphate tungsten bronzes containing P_2O_7 units and having pentagonal channels, ($DPTB_p$). These have the formula $(PO_2)_4(WO_3)_{2m}$, $m = 4-16$. (4) Diphosphate tungsten bronzes with hexagonal tunnels ($DPTB_h$). These have the general composition $A_x(P_2O_4)_2(WO_3)_{2m}$ ($A = Na^+$, K^+, Rb^+, Tl^+, Ba^{+2}) and values of m between 4 and 20, depending in part on the nature of the A cation. The structures and properties have been reviewed by Borel,[67] Greenblatt[68,69] and more recently by Labbé.[70]

In contrast, the phosphate molybdenum oxides contain MoO_6 octahedra or limited groups of edge and corner-sharing MoO_6 octahedra. These are isolated from one another by mono- or diphosphate ions that share corners or edges with the oxygens of the MoO_6 octahedra such that structures are formed that contain large voids or tunnels that can accommodate large guest ions. Since the MoO_6 octahedra do not form a continuous Mo–O network, electronic conduction is prevented and the materials are insulators. A large variety of these phases exist that are discussed in detail elsewhere.[67]

3.12.1 Other Reduced Transition Metal Phosphates

Mixed-valence transition metal phosphates have been found for Ti, V, and Nb. Their crystal chemistry and properties are more closely related to those of the Mo analogs in that they have mixed frameworks of MO_6 octahedra that are partially or wholly isolated from one another by intervening phosphate groups and the d electrons do not appear to be delocalized. A particularly rich chemistry exists for the vanadium analogs. Details of their structural properties have been reviewed by Borel and coworkers.[67,70]

If silica is introduced into a reduced phospho-molybdate system, Mo can be stabilized in the trivalent state. The structure of MoP_3SiO_{11} is built from MoO_6 octahedra that share all six corners with diphosphate groups, which in turn share their remaining corners with disilicate units.[71] A number of mixed-valence Mo(III),Mo(IV) oxides of the type $AMo_3P_6O_{12}Si_2O_{25}$ have also been reported.

4 STRUCTURE-PROPERTY RELATIONSHIPS IN OXIDES

4.1 Introduction

The relationship between the structure of a solid and its resultant physical properties have made oxides the object of intense activity from both a practical and theoretical point of view. Several examples of structure-property relationships are discussed briefly below, many of which are discussed in detail elsewhere. Three examples will be discussed in somewhat greater detail.

Main group oxides with three-dimensional structures or transition metal oxides with d^0 or d^{10} configurations are wideband gap materials and are colorless when pure. As such they may serve as transparent optical materials or hosts for such applications as lasers or luminescent materials when properly doped. Others that lack a center of symmetry may have ferroelectric or ferroic properties that make them useful for a variety of device applications. Some of these may have nonlinear optical properties so important to modern communication networks (see Sections 6.3 and 6.5 and *see* ***Luminescence*** and *see Ferroelectricity*).

On the other hand, transition metals with unpaired d electrons and main group oxides with mixed valences or with defect structures often display high electrical conductivity. In some cases, this conductivity may be metallic in nature provided the structure allows for proper overlap of the atomic orbitals of the metals, either with each other, or more often, with oxygen. Some examples of this behavior are given in Section 4.2. Low-valent electron-rich oxides often have structures with metal–metal bonds. Certain structures will be stable for localized cluster interactions resulting in insulating materials while other structures stabilize extended systems of metal–metal bonds that are often highly conducting. These structures are discussed in Section 4.2.

Cooperative magnetic effects are one of the most sensitive of structure-property relationships (*see* ***Magnetism of Extended Arrays in Inorganic Solids***). While useful magnetic oxides are limited to only a few structure types (*see* ***Magnetic Oxides***), anomalous magnetic behavior is observed in a number of metallic and narrow band semiconductors, which are of great interest since they often are not well understood. Anomalous magnetic effects are often associated with quasi-low dimensional, considered by some to be a precursor to superconductivity. Indeed, the strong diamagnetism associated with the superconducting state could be considered to be an extreme case of an anomalous magnetic effect. Although the origins of high-temperature superconductivity are still a matter of intense debate, it is generally agreed that the phenomenon is extremely structure sensitive (*see* ***Superconductivity***).

One final effect of unpaired d electrons is the formation of intensely colored materials particularly when defects or mixed valences are involved. This, coupled with the valence stabilization often imparted by the structure, causes oxides to be highly valued as pigments (see Section 6.3.6).

Oxides with layered structure or those whose structures contain large tunnels or cavities may display abnormal ion movement or serve as templates for heterogeneous catalysis (*see* ***Ionic Conductors***; ***Intercalation Chemistry***; ***Oxide Catalysts in Solid-state Chemistry***; and ***Zeolites***). Many oxides are stabilized by the formation of structures that are highly defective nature and have similar properties to those listed above (*see* ***Defects in Solids***). The strong bonds, which result in three-dimensional cross-linked structures, give rise to inert, refractory materials that have a variety of uses (see Section 5.3.6 and *Ceramics*).

4.2 Oxides with Strong Metal–Metal Bonds

For many years, strong metal–metal interactions were largely regarded as chemical curiosities of little interest exemplified by some suboxides of the heavier alkali metals and a few 4 or 5d elements, principally Mo, Nb, and Re. However, research since 1978 has shown that the phenomenon is much more widespread than previously thought. A few reviews covering work through about 1985 on Mo and Nb cluster oxides exist.[72–75]

The chemistry of the alkali metals suboxides such as Rb_6O, Cs_7O, Rb_9O_2, and $Cs_{11}O_3$ has been reviewed by Simon[76,77] and will not be discussed here. Rather, this section will concentrate on transition metal compounds where d electrons are utilized in bonding.

Diagonal M_2 clusters are quite common being found for several rutile and NaCl variants as discussed previously, which include Ti, V, Nb, Mo, and W as well as other oxides of Re, Ru, Os, Ir, Pt, and Ag. Larger, isolated clusters containing 3,4,6,7,8,10 or more atoms have been discovered in a variety of low-valent molybdenum and niobium oxides. For instance, trigonal clusters in which the metal atoms are 2.51 Å apart are found in $Zn_2Mo_3O_8$ and related compounds. This compound is an electrical insulator and is diamagnetic in support of the idea that the Mo d electrons are localized in forming three strong metal–metal bonds. Approximate molecular orbital calculations have shown that Mo_3O_{13} clusters (Figure 26(a)) should be stable for 4, 6, and 8 electrons.[78] Subsequently, 7 and 8 electron containing clusters were found for $LiZn_2Mo_3O_8$ and $Zn_3Mo_3O_8$.[72,79] Butterfly Mo_4 clusters are found in $K_2Mo_8O_{16}$, isolated octahedral Nb_6 clusters are found in $Mg_3Nb_6O_{11}$ and $Na_3Al_2Nb_{34}O_{64}$ (Figure 26(b)), while a unique cis-edge shared Mo_8 cluster (Figure 26(c)) was found in $LaMo_{7.7}O_{14}$ and subsequently in stoichiometric $LnMo_8O_{14}$ ($Ln^{+3} =$ La, Ce, Pr, Nd, Sm, and Gd).[80,81] Here two Mo cap edge-sharing faces of a Mo_6 octahedron (Figure 32(c)) in the so-called *cis* configuration. Subsequently, it was found that the *cis*-Mo_8 cluster can exist in enantiomorphic forms as well as in the isomeric *trans* form. The result is a group of diverse, complex phases.[82]

Linear, cross-linked double chains of bonded Mo are found in $NaMo_2O_4$.[74] The fact that these chains can accommodate a variable number of electrons is shown by the fact that a series of solid solutions can be obtained for $Na_{2-x}Mo_2O_4$.[83] The conducting nature of this material coupled with easily exchangeable alkali ions makes the Li analog a promising cathode material for secondary lithium cells (see Section 5.7). The double-chain units of bonded Mo are shown in Figure 27. Hexagonal $LiMoO_2$, prepared by a solid-state reaction, also forms an extended metallic bonded system but here hexagonal

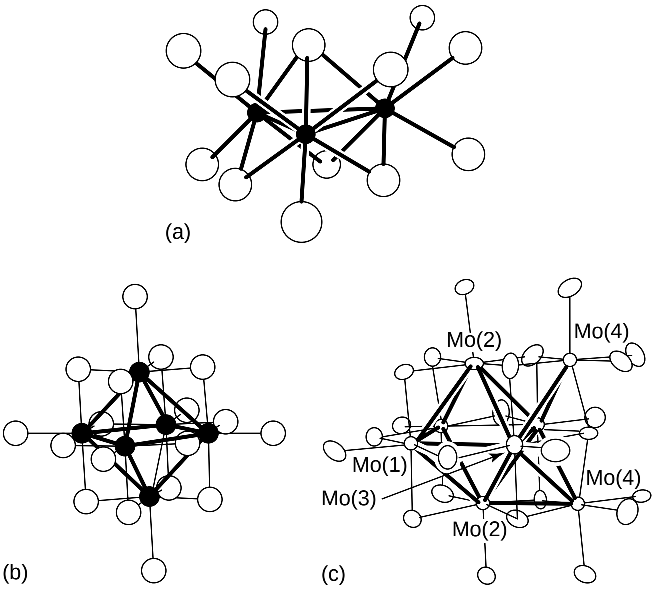

Figure 26 Some examples of metal-atom clusters in oxides. M_3O_{13} cluster (a). Nb_6O_{18} cluster (b). Mo_8O_{24} cluster (c)

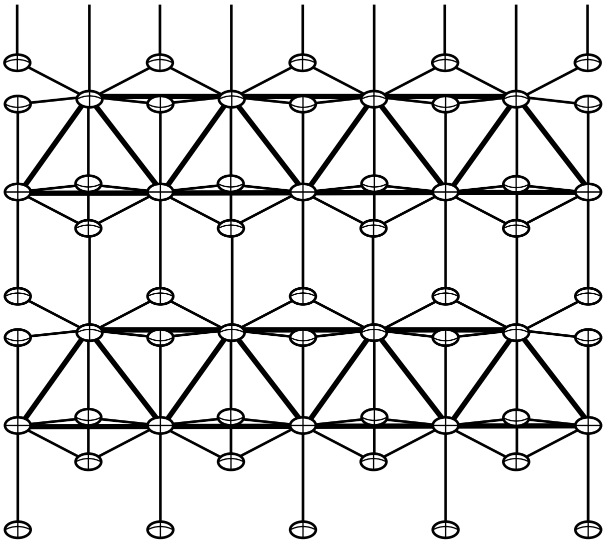

Figure 27 Double cross-linked chains of bonded Mo shown in $NaMo_2O_4$ shown in bold face. Intra and interchain Mo–O linkages indicated in light lines

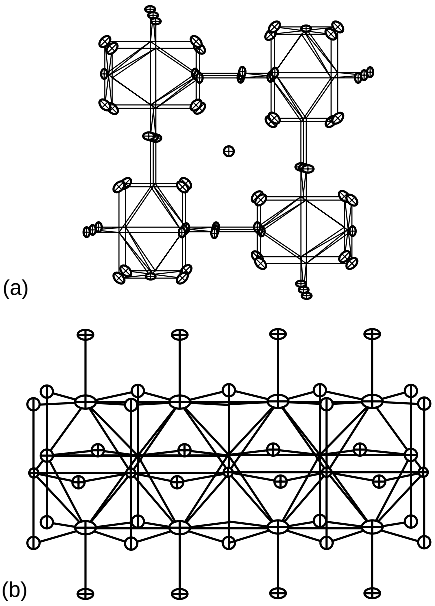

Figure 28 Structure of $NaMo_4O_6$. View down the tetragonal *c* axis showing Mo–O linages between trans edge-sharing Mo_6 units. Na^+ resides in center of tunnel (a). Trans edge-sharing chain of bonded Mo (bold) viewed perpendicular to the chain axis (b)

sheets of weakly bonded Mo, 2.866 Å distant, are formed by placing Mo in the interstices of a CP oxide ion lattice.[84]

Mo_6 octahedra may condense to form oligomers containing up to 6 units. Here the basic building block is an Mo_6O_{18} cluster in which the Mo_6 octahedra share trans-edges to form linear oligomeric units. $LaMo_5O_8$ contains the dimeric $Mo_{10}O_{16}$ unit with Mo–Mo bond lengths ranging from 2.676 to 2.836 Å. These cluster units are then linked to each other by two additional Mo–Mo bonds forming infinite chains. $In_{11}Mo_{40}O_{62}$ contains the 4 and 5 member oligomers, $Mo_{18}O_{28}{}^{-7}$ and $Mo_{22}O_{34}{}^{-8}$.[75–77] This compound also contains In–In metal bonds.

A variety of extended metal–metal bonded systems are also found for molybdenum and niobium based on M_6 clusters. In the case of molybdenum, the repeat motif is formed by trans-edge-sharing Mo_6 octahedra while corner-sharing Nb_6 groups form the primary mode in the niobium oxides. In $NaMo_4O_6$, infinite trans edge-sharing Mo_6O_{18} units, similar to those shown in Figure 26(b), are linked through their oxygens to form tunnels in which the Na reside.[85] The structure is shown in Figure 28. The basic repeat unit, Mo_4O_6, contains 13-d electrons delocalized in the metal–metal framework. The metal bonded chain provides for electron delocalization and the compound is a metallic conductor. Mo–Mo bonds range in length from 2.751 to 2.860 Å with an average distance of 2.801 Å, slightly longer than the 2.725 Å length found in Mo metal itself. Similar chains based are found in a variety of other compounds including $InMo_4O_6$, $Ba_{0.62}Mo_4O_6$, $Mn_{1.5}Mo_8O_{11}$, and $ZnMo_8O_{10}$.[72–74] The number of metal-cluster electrons in the Mo_4O_6 unit is between 13 and 15, which is consistent with the values estimated from bond length-bond strength calculations. Delocalization of these electrons along the chains would be expected to make these compounds metallic conductors. This has been found to be the case for the isomorphic AMo_4O_6 phases, ($A^+ = $ Na, K, In).

Layers of corner-sharing Nb_6 clusters sandwiched between perovskite-like layers formed by NbO_6 octahedra are found in $SrNb_5O_9$ and KNb_4O_6 while double layers of corner-sharing Nb_6 octahedra are found in $BaNb_7O_9$.[76] These oxides often contain more than one type of cluster. For example, $Ca_{5.45}Mo_{18}O_{32}$ contains discrete Mo_2O_{10} and Mo_3O_{13} type clusters in addition to infinite chains based on the Mo_4O_6 repeat. $BaSiNb_{10}O_{19}$ contains both octahedral Nb_6 and trigonal Nb_3 units. Most of the niobium compounds containing discrete clusters for which resistivity measurements have been made are found to be semiconductors although $NaNb_{10}O_{18}$ has been found to be metallic. Here the cluster-electron count is formally fifteen, one above the stable limit of 14 (*see* ***Electronic Structure of Clusters***), and the extra electron is expected to be delocalized through the Nb–O network.[75,86]

The niobium cluster oxides can be quite complex. For instance, $Na_3Al_2Nb_{34}O_{64}$ has a 30 layer repeat unit with four different types of Nb units. There are discrete Nb_6 clusters coordinated as Nb_6O_{18}, bonded Nb_2 clusters, Nb_3O_{13} units in which the Nb–Nb interactions are nonbonding ($d_{Nb-Nb} = 3.17$ Å), and discrete Nb, which fill octahedral holes in the oxide layers. $K_4Al_2Nb_{11}O_{21}$ contains an $Nb_{11}O_{30}$ unit in which two Nb_6 clusters share corners to form an Nb_{11} dimer. One-dimensional corner-sharing $(Nb_4)_\infty$ chains are found in $Ba_{0.2}Nb_5O_8$ while triple chains composed of 3 cross-linked Nb_6 clusters are found in $Ba_4Nb_{14}O_{23}$. In NbO,

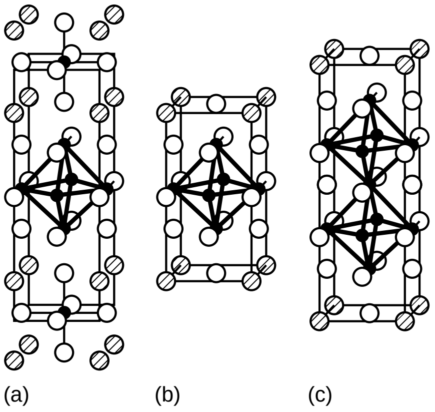

Figure 29 Unit cells of $Ba_2Nb_5O_9$ (a), $BaNb_4O_6$ (b), and $BaNb_7O_9$ (c) showing Nb_6 cluster building block

each Nb_6 cluster shares corners with similar clusters to form a three-dimensional metallic array. Layers of Nb_6 octahedra sharing four corners are found in $Ba_2Nb_5O_9$, $BaNb_4O_6$ and $BaNb_7O_9$ whose unit cells are shown in Figure 29. These structures can be considered as simple intergrowths of NbO-like layers and perovskite-like $BaNbO_3$ slabs. More complex intergrowth structures are reviewed by Kohler, Svensson, and Simon.[75] Because of the delocalized nature of the metal–metal bonding in these structures, metallic conductivity might be expected. Recent measurements of the electrical conductivity and magnetic susceptibility would seem to confirm this for $Sr_2Nb_5O_9$ while the behavior of $Ba_2Nb_5O_9$ is more complex.[87]

A number of Mo oxides containing chains are formed by two different cluster units sharing corners. In $Sr_4Al_3Mo_{26}O_{48}$, there exist chains from mono-faced-capped Mo_7 clusters and dioctahedral edge-sharing Mo_{10} clusters to form Mo_7-Mo_{10}-Mo_7 groups that repeat to form chains.[88] Mo_3, Mo_7, Mo_{13}, and Mo_{19} clusters are found in $PrMo_9O_{18}$. The Mo_7 cluster here is planar and formed by triangular Mo_3 groups sharing a central Mo. Mo_{13} and Mo_{19} groups are formed by condensation of Mo_6 octahedra. These clusters have C_{3v} symmetry and each form separate slabs in the structure.[89] $Sn_{0.4}Mo_{24}O_{38}$ contains tri-octahedral trans-edge-sharing Mo_{14} clusters as well as bioctahedral Mo_{10} clusters linked through corners to form chains.[90]

While clusters with two, three, or more metal atoms are largely confined to early transition metals, an increasing number of such clusters have been found for both late transition metals such as Re, Ru, Rh, and Ir. The typical building unit is an M_2O_9 unit built from to MO_6 octahedra by sharing a face. A rich chemistry derives from this group. The M_2O_9 unit may share may share faces to form infinite chains or finite oligimers. The oligimers may share faces with trigonal prismatic MO_6 units or share corners with one another to form infinite zig-zag chains.[91–93] The metal–metal distances in the oligimeric units can be quite short, of the order of 2.5 to 2.7 Å. However, it is clear that in some instances these are nonbonded interactions, while in others electron bonding appears likely.[94,95]

4.3 Electronic Conduction in Oxides[9,96–100]

The electrical conductivity of a solid may be defined by the following relationship

$$\sigma = ne\mu_- + pe\mu_+ \tag{4}$$

where σ is the electrical conductivity in $(\text{ohm-cm})^{-1}$. The number of charge carriers per unit volume are given by n for electrons and by p for holes while the respective carrier mobilities in cm^2/V-sec are given by μ_- and μ_+ respectively (*see* ***Semiconductors***). In oxides, the conductivity may vary from 10^{-8} $(\text{ohm-cm})^{-1}$ or less for high purity oxides containing an empty d manifold such as CaO or TiO_2 to values of the order of 10^4 to 10^5 $(\text{ohm-cm})^{-1}$ found for MoO_2, Na_xWO_3, or ReO_3, which contain one or more d electrons. Main group oxides of high purity are normally insulating but may show a modest conductance as a result of impurity doping or other defects. In the case of mixed valences, for example, In_2O_{3-x} or $Pb_xBi_{1-x}O_3$, very high conductivities may be observed.[101]

The conductivity mechanisms in many oxides are often complex and obscure. Details of the quantitative physical models will not be discussed here. There are some elementary classifications and some simple arguments based on qualitative band theory (*see* ***Semiconductors*** and ***Electronic Structure of Clusters***). Some examples that apply to transition metal oxides are discussed here. In this case, insulators are stoichiometric d^0 oxides with a large forbidden energy gap of several electron volts between the filled valence band (usually predominantly oxygen 2p in character) and the next highest empty band (conduction band) as shown in Figure 30(a). Such oxides may be made semiconducting by introducing impurities that create states that lie close to either the valence or conduction band, the latter being p-type and the former being n-type (Figures 30b,c). An example of such behavior was given in Section 3.10 for TiO_{2-x}.

A second class of semiconducting oxides are those of the late transition metals, for example, Cr_2O_3 or NiO,

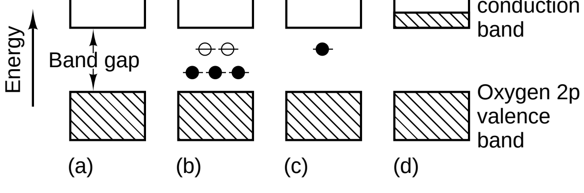

Figure 30 Simplified band diagrams. Insulator or intrinsic semiconductor (a). Extrinsic semiconductors (b) and (c). Metallic conductor (d)

which contain localized d electrons that function very much like impurity levels shown in Figure 35(c). Because these compounds have unpaired electrons, they are sometimes called as magnetic insulators. MnO is an insulator at room temperature and has a measurable semiconductivity at elevated temperatures.[102] A complex behavior is observed for samples of MnO heated between 1100–1400 °C in controlled partial pressures of oxygen formed by CO_2/O_2 mixtures. Conductivities are in the range 1 to $10^{-2}\,(\text{ohm-cm})^{-1}$. At low partial pressures of oxygen, the phase is n-type and conductivity increases with decreasing partial pressure. As the partial pressure of oxygen is increased, the conductivity goes through a minimum for a given isotherm and as the O_2 pressure is increased, the majority carriers are holes resulting from the removal of electrons by the oxidation of Mn^{+2} to form $Mn_{1-x}O$.

Semiconductors are characterized by low carrier densities 10^{16}–10^{20} carriers cm^{-3} and low mobilities, typically 10^{-5} to $1.0\,V\,cm^{-2}$-sec. Semiconductors display an increase in conductivity with increasing temperature as the result of thermal excitation of electrons located either at the top of the valence band (intrinsic carriers) or from impurity sites in the forbidden gap, or from the filling of low lying acceptor levels in the case of p-type materials. In many cases, the temperature dependence is of the Ahrrenius form

$$n = n_0 e^{-(E_a/kT)} \tag{5}$$

where E_a is the energy difference between the impurity state and the conduction band. For narrow band semiconducting oxides, E_a could represent the band gap. More often however, a more complex nonlinear behavior is found whose particular form depends upon the conductivity mechanism. These have been discussed in detail.[96–98] Metals, in contrast to semiconductors, typically have high carrier densities close to $10^{22}\,cm^{-3}$ and high mobilities. In the free electron theory, metallic electrons reside in a partially filled conduction band (delocalized) and are free to move through the lattice. Resistance to electron flow arises primarily from electron-lattice interactions, which are increased by increased vibrations of the atoms. A metal's conductivity will therefore decrease with increasing temperature. In transition metal oxides, metallic conductivity will be achieved if a means can be found to delocalize the highest energy d electrons. This occurs in a variety of compounds and usually involves either (1) the formation of a weakly bonded extended metal–metal network in which the resulting band is only partially filled or more often (2) the formation of a continuous metal d orbital-oxygen p π bonding network.

Materials that are formally insulating such as WO_3 may become semiconducting by appropriate doping; for example, Na_xWO_3 where $x < 0.3$. Upon further doping, what had been W(V) localized impurity states coalesce into a band and the bronze phase becomes metallic for $x > 0.3$.

4.3.1 ReO_3 and Perovskite Tungsten Bronzes

A qualitative diagram of the sigma and pi bonding for ReO_3 is given in Figure 31. In this structure, each Re is oriented so that its s, p and e_g orbitals can overlap with oxygen s and p orbitals (or sp hybridized orbitals) to form 6 strong σ bonds pointing towards the corners of an octahedron, (Figure 31(b)). Each oxygen is two coordinated by the metal. At the same time, the t_{2g} orbitals of the metal are oriented so that they can form an overlapping pi network with the p_x and p_y orbitals of oxygen (Figure 31(c)). The fillings of the electronic bands thus formed are given in the qualitative band diagram shown in Figure 32, proposed by Goodenough.[98] The low lying 12 electron σ band represents the 6σ bonds formed by each Re with six oxygens while the six electron Re–O π band is next. The lone pair on each oxygen is represented by the localized p_π levels. Because the sigma overlap is stronger than the pi overlap, the σ^* bands lie at higher energy than the π^* band.

The largely metallic 6 electron π^* band is now the conduction band and is only partially filled by the d^1 electrons of Re^{+6}. Hence, metallic conductivity is expected. The basic tenets of this simple qualitative model are confirmed by theoretical calculations.

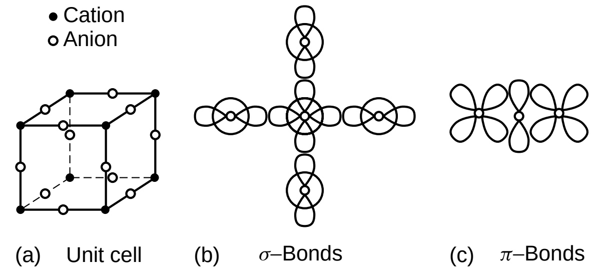

Figure 31 Unit cell of ReO_3 (a). Re–O sigma bonding arrangement. Each O bonds with a second Re (not shown) (b). Re–O–Re pi bonding arrangement (c)

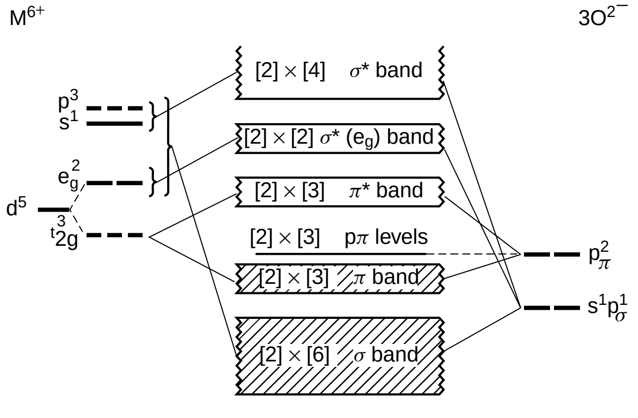

Figure 32 Qualitative band diagram for ReO_3. Electron filling indicated by shading

This diagram can also be applied to the sodium tungsten bronzes, Na_xWO_3, which adopt the cubic perovskite structure for $x > 0.3$. WO_3 is an insulator with a slightly distorted ReO_3 type structure. If a small amount of Na is added, localized electron donor sites are created having energies that lie between the π and π^* bands in Figure 32. With increasing doping, these localized impurity states coalesce into a band and the bronze phase becomes metallic for $x > 0.3$.

4.3.2 Conduction in Rutile and Rutile Related Oxides[103]

In rutile-type oxides, enormous differences in conductivity can occur that depend upon electronically induced distortions of the structure. The structure has been discussed previously (Section 3.2.2). Here the important thing to note are the chains of trans edge-sharing octahedra, which run parallel to the tetragonal c axis (Figures 3 and 4 (a)). In TiO_2, the metal atoms are located at the centers of the octahedra, 2.96 Å distant from one another. TiO_2, having no d electrons, is an insulator but the high-temperature form of VO_2, which also has this structure, is a metal.

Below 341 K the structure undergoes a distortion in which the V atoms move off center to form a chain with alternating long and short V–V distances (see Figure 4). The short V–V distance is 2.62 Å and corresponds to a metal–metal covalent single bond. This form is semiconducting. This behavior may also be explained by the one-electron band energy diagrams shown in Figure 33.[98] In the normal rutile structure, two of the three t_{2g} orbitals overlap oxygen p orbitals to form a metal-oxygen π band, which can contain up to 8e per V_2O_4 unit. The remaining t_{2g} orbital, which lies along the tetragonal c direction, that is, perpendicular to the edge shared oxygens, forms a nonbonding cation sublattice band. This represents the conduction band, which may also overlap the π^* band. In TiO_2 (Figure 33(a)), this band is empty and the compound is an insulator. The low lying σ and π bands represent the M–O bonding and contain 32 e with primarily O character. In the normal rutile form of VO_2, the two d electrons of a V_2O_4 unit partially fill the conduction band and the compound is a metal (Figure 33(b)). In the monoclinically distorted polymorph, the d electrons are localized in V–V bonds and the t_{2g} sublattice band is split into localized bonding and antibonding levels as shown in Figure 33(c). This compound is an insulator.

MoO_2 also has a monoclinic rutile distortion similar to that in the high-temperature form of VO_2 in which the Mo–Mo distances alternate between 2.51 and 3.11 Å. Here, one might expect that two of the four electrons per Mo_2O_4 unit would be used to form the Mo–Mo bond and the remainder occupy the conduction band and the compound would be a metal, in conformance with observation. This model can only be considered to be approximate since the observed Mo–Mo distance is more nearly that of a double bond. However, this would require the localization of all Mo d electrons, with one of the Mo t_{2g} orbitals in the ab plane being used to form metal–metal π bonds, and the compound would be a semiconductor. The true situation must be a combination of metal σ, π (and perhaps δ) contributions combined with band delocalization, a picture not easily represented in a one-electron band diagram.

In normal rutile oxides based on Figure 33(a), one might expect that elements with up to 5 d electrons would be metals and this appears to be borne out although accurate measurements of the conductivity have been limited by the quality of the samples available. In addition, CrO_2 is a ferromagnetic insulator and α-ReO_2 has a somewhat more complex distortion of the simple rutile structure. However according to the simple model, d^6 metals which can contribute 12 electrons per M_2O_4 unit would have a filled conduction band and be semiconductors. This has been shown experimentally to be the case for PtO_2.[103]

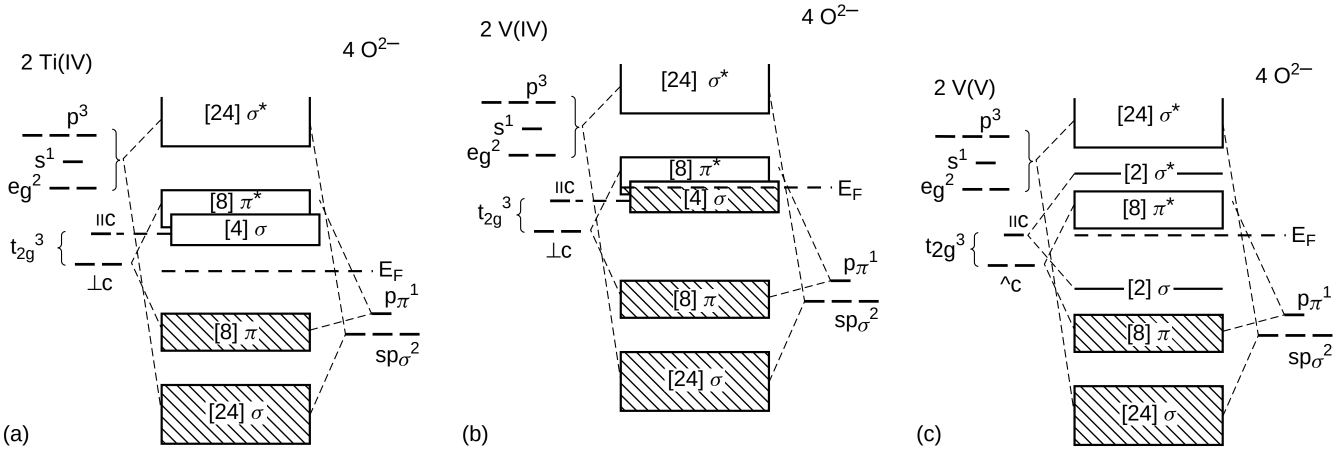

Figure 33 Qualitative band diagrams. TiO_2 (a). Tetragonal VO_2 (V_2O_4) (b). Mononclinic distorted VO_2 (V_2O_4). V–V bond indicated by 2σ level (c)

A somewhat different behavior is shown in the rutile related oxide $Y_5Mo_2O_{12}$. This compound contains chains of edge-sharing MoO_6 octahedra similar to those found in the distorted rutile type of MoO_2. In the ternary compound, the alternating long and short Mo–Mo distances are 2.496 and 3.221 Å and the chains are linear. In MoO_2 the chains are slightly puckered, the Mo–Mo–Mo angle being 173 degrees, and the Mo–Mo distances alternate between 2.511 and 3.112 Å.

The structure can be considered as containing rutile-like slabs in which certain octahedral interstices are now occupied by Y. These rutile-like planes are then interconnected by a second set of Y in sevenfold coordination. Given the mixed valence of this compound and its rutile-like nature, metallic conductivity might have been expected. Instead, the compound is a semiconductor with a room temperature resistivity of 4×10^3 ohm-cm. This is attributed to the fact that the bridging oxygens in the octahedral chains now bond to Y and are in approximate sp^3 hybridization. The p orbital that is used for Mo–O π bonding in metallic MoO_2 is no longer available and, as a result, the d electrons are localized between molybdenums and the compound is a semiconductor.[104]

4.3.3 *Electronic Conduction in Rock Salt Related Oxides*

TiO has a rock salt related superstructure discussed in Section 3.2.1. Here the t_{2g} orbitals of Ti can overlap to form a continuous Ti–Ti array, shown in Figure 34, leading to a partially filled t_{2g} band. The Ti–Ti distance is considerably longer than that in Ti metal but short enough to allow for electron delocalization. As one moves across a given period of divalent transition metals, the increasing effective nuclear charge tends to localize these electrons and metal–metal interactions are no longer important. VO behaves similarly to TiO while MnO and NiO have the normal rock salt structure and are insulating.

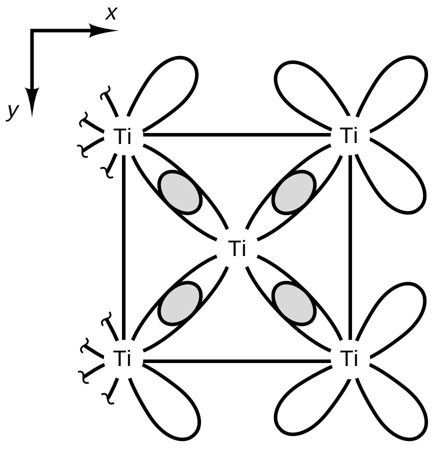

Figure 34 Diagram of sigma Ti–Ti bonding in TiO

4.4 Scheelite Based Catalysts[105,106]

Scheelite oxides are a good example of how structure-property relationships have been used to create a modern catalyst. More detailed descriptions of these and other catalysts are given in ***Oxide Catalysts***. The scheelite structure was discussed in Section 3.4.5. Scheelite based oxides are of interest as catalytic materials because of their ability to form with transition elements in high but easily reducible valence states and to form a variety of defects and defect structures that provide numerous sites for selective catalytic activity.

Molybdate based scheelites have been intensively studied in this respect, one reason being that they are found with molybdenum in both the penta- and hexavalent state. Bismuth molybdates in particular are useful catalysts for selective oxidation of propylene to acrolein, propylene ammoxidation to acrylonitrile and the oxidative dehydrogenation of butene to butadiene.

Gross cation vacancies can be introduced into a scheelite such as $PbMoO_4$ by the addition of a trivalent rare earth or bismuth to form solid solutions of the type $Pb_{1-3x}Bi_{2x}\square_xMoO_4$. When $x = 0$, no catalytic activity towards olefin oxidation is observed but for $x > 0$ increasingly significant activity is observed, reaching a maximum at about $x = 0.06$ for the oxidation of both propylene and 1-butene. Thereafter activity progressively decreases until the end member; $Bi_2(MoO4)_3$ is reached where the catalytic activity is about one-quarter of that of the optimum phase. $Bi_2(MoO4)_3$ has a distorted scheelite type structure in which 2/3 of the A cation sites are filled in an ordered fashion. The ordering of vacancies, shown in Figure 35, is believed to be the principal cause of its reduced activity.

The A cation defects in $Pb_{1-3x}Bi_2MoO_4$ are believed to function as hydrogen acceptor sites during the formation of an allyl intermediate. Oxidation of the intermediate, as established by ^{18}O studies, is accomplished through lattice oxygen at the surface, which is then replenished, by bulk lattice oxygen. This is consistent with the observation that catalytic activity is independent of oxygen partial pressure. Bismuth containing catalysts are rapidly reoxidised. Here the lone pair of electrons on Bi^{+3} are postulated to be directed towards the surface of the catalyst and behave as donor sites for the reduction of O_2 in the gas stream. The A cation defects

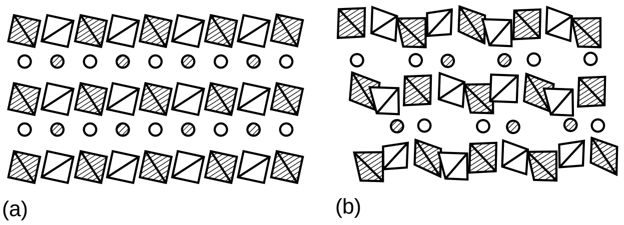

Figure 35 Structure of a regular tetragonal scheelite (a) compared with the distorted, defected structure in $Bi_2Mo_3O_{12}$ (b)

must also play a role in the high mobility of lattice oxygen and its replenishment by the gas stream.

Modern day bismuth molybdate catalysts, in addition to $A_{1-3x}Bi_{2x}MoO_4$ phases, contain other compounds such as Bi_2MoO_6 and $Bi_2Mo_2O_9$ as well as small amounts transition metal molybdates that not only increase conversion rates and selectivity but also increase catalyst lifetime and allow operation at lower temperatures.[107]

5 PREPARATIVE METHODS FOR OXIDES[9,21,50,108–111]

5.1 Direct Synthesis from the Elements

Although the majority of elements will react readily with oxygen, particularly when heated, this method is not used frequently because of the added expense of obtaining the element in a pure and usable form when compared to more convenient and less expensive alternatives. The method is also useful for those metals that do not easily form salts or whose hydrous oxides are difficult to solubilize or purify. Thus, the preferred method for the preparation of Ta_2O_5 is by burning the pure metal in oxygen. Nb_2O_5 can also be prepared in this fashion but less expensive methods are also possible. The highest valent binary oxides known are OsO_4 and RuO_4. The former is readily prepared by heating powdered osmium to red heat in the presence of oxygen. The highly toxic, volatile molecular oxide is collected as a colorless solid (mp 41 °C) in a cold trap. The stable product of the reaction of Ru with oxygen is the dioxide, the tetroxide being best prepared by passing Cl_2 through an alkaline ruthenate solution.

5.2 Decomposition Methods

Oxalates, carbonates, ammonium salts, and related materials often have the advantage that they can be obtained in high purity and the decomposition coproducts are gases. Such reactions may be carried out in air if there is no danger of mixed valency formation. The method is particularly convenient for the preparation of ZnO and CdO, trivalent rare earth oxides, and the lighter alkaline-earth oxides. High purity gallium oxide is prepared by dissolving gallium metal in hydrochloric acid, diluting the solution and adding an excess of oxalic acid to precipitate the highly crystalline gallium oxalate, which is then filtered, washed, and ignited at red heat to give pure Ga_2O_3.

Mg and Ca oxide are easily prepared by igniting the carbonates in air. However, for the Sr and Ba carbonates breaking the C–O is particularly difficult and decomposition of the carbonate is best accomplished by heating in the presence of hydrogen at temperatures above 1200 °C, thus attacking the C–O bond directly.

Decomposition of a mixture of nitrates is often a convenient method for the preparation of mixed transition metal oxides. The success of the method depends upon the fact that typically, the decomposition of the nitrates results in an intimate oxide mixture that readily reacts at higher temperatures to form a homogeneous, complex oxide. Oftentimes nitrate mixtures can be formed as precursors by dissolving a stoichiometric mixture of the oxides or carbonates in nitric acid and evaporating to dryness. This method is one of the options used to prepare the superconducting $YBa_2Cu_3O_{7-\delta}$ and isotypes.

In the case of transition metal oxides, mixed-valence compounds may result if the decomposition is carried out in air. Thus, highly pure NiO and MnO can be obtained by heating the respective carbonates in vacuo while nearly stoichiometric FeO is obtained by the decomposition of its oxalate but it will rapidly pickup oxygen when exposed to air. Conversely, decomposition of $Fe_2(Ox)_3$ yields Fe_2O_3.

More acidic acids, which form oxyanions when reacted with bases, can be prepared in high purity by the decomposition of their ammonium salts. V_2O_5, MoO_3, and WO_3 are conveniently prepared by this method. Zirconium dioxide is obtained by heating the hydrated oxychloride at 600 °C.

5.3 Precipitation Methods

Although precipitation of hydrous oxides from basic solutions might appear to be attractive such materials are often difficult to handle because of their gelatinous nature (*see* ***Sol–Gel Synthesis of Solids*** and see Section 5.5.2). In such cases, one must be sure to use highly pure reactants that yield only volatile electrolytes. High ignition temperatures may be required to obtain the pure oxide. However, there are some notable exceptions. Titanium can be isolated in pure form as $TiCl_4$ or $TiOSO_4$. The chloride reacts spontaneously with water to form hydrous titanium dioxide, which can be ignited to yield pure TiO_2 while $TiOSO_4$, which is soluble in cold water, yields gelatinous TiO_2 when its solutions are heated. Very pure, hydrous aluminum oxide can be obtained from bauxite ore by taking advantage of the amphoteric nature of Al^{+3}. This is subsequently heated to red heat to obtain the anhydrous oxide.

The adverse properties of colloidal precipitates of hydrous oxides can sometimes be avoided by using the technique of homogeneous precipitation whereby high local supersaturations are avoided by slowly generating the precipitating agent, in this case hydroxide ion, in situ. For instance, if urea is added to a solution of a soluble ion salt and the solution warmed to just below boiling, hydroxide ion is slowly generated according to the reaction

$$(NH_2)_2CO + 3H_2O = CO_2 + 2NH_4^+ + 2OH^- \qquad (6)$$

Under these conditions, the formation of the hydrous oxide takes place slowly, which results in a precipitate with an order of magnitude less volume than those formed by direct precipitation methods. Such materials are much easier to filter and wash, thus yielding a purer product upon ignition. The method has been used successfully for the preparation of the sesquioxides of Al, Ga, Fe, and Bi, and the dioxides of Th and Sn.

Some of the more acidic oxides, such as MoO_3, WO_3, As_2O_3, As_2O_5, and Sb_2O_3 can be obtained from solution as well-defined hydrates or acids, which lose water at low heat to give the pure oxide. Similarly, the hydrous oxides of tetravalent germanium and tin can be ignited at red heat to obtain the pure oxide.

5.4 Flux and Melt Growth Methods[108,111–113]

These are techniques that are commonly used to produce high quality crystals, usually of millimeter size but sometimes several grams or hundreds of grams in weight. Flux growth usually refers to those methods in which a molten salt acts as solvent for the reactant oxides. In some cases, the flux may take part in the reaction. Melt growth usually refers to the growth of crystals from a melt of the same composition. Fluxes may be used in small amounts, for example, 1–5 percent by weight, to promote crystal growth by providing a liquid-solid interface where the crystals can form. More details of these methods can be found elsewhere.[108,109,111–113]

A desirable flux is one that can provide a significant solubility for the starting oxides, melts below 1000 °C and can be handled conveniently at temperatures up to 1500 °C. Crystallization of the desired product may result from a chemical reaction in the melt but more often will be induced by slow cooling. If the flux is volatile at the temperatures used, this property may sometimes be used to promote crystal growth. One of the problems associated with this method is that the superior solvent abilities of the flux often result in attack of refractory oxide containers, thus introducing undesirable foreign ions into the melt, which can adversely affect crystal quality. Such attack can be minimized by operating at as low a temperature as possible, consistent with other growth parameters. More often however, a noble metal crucible such a gold or platinum is used.

The flux method has been used with great success to prepare several high melting refractory oxides that are difficult to prepare by other means. For example, PbF_2 (mp 855 °C) and PbO-PbF_2 mixtures have been used to prepare large, pure α-Al_2O_3 crystals (mp ca. 2050 °C) as well as synthetic rubies and sapphires by suitable melt dopings.[114] PbO and PbO-PbF_2 mixtures have also been used to prepare crystals of many other refractory oxides such as MgO (mp 2800 °C), ZnO (mp 1975 °C), and Y_2O_3 (mp 2475 °C) as well as a variety of ternary oxides such as $BaTiO_3$, $CaMoO_4$, iron spinels of the type MFe_2O_4 ($M =$ a divalent transition metal cation such as Mn, Ni, Fe, Zn, etc.) as well as rare earth iron and aluminum garnets, for example, YFe_5O_{12} and $GdAl_5O_{12}$. Lithium molybdate, Li_2MoO_4 with and without additions of MoO_3 has been used to grow crystals of ThO_2 (mp 3210), BeO (mp 2550 °C), and CeO_2 (mp 2600 °C). A sodium tetraborate flux, $Na_2B_4O_7$ has been used for the growth of UO_2 (mp 2870 °C), HfO_2 (mp 2780 °C), and Cr_2O_3.

One of the drawbacks to flux growth methods is that the crystals may entrap flux so it is desirable where possible to grow crystals from pure melts. Melt methods for growing single crystals were originally developed for low-melting materials (<1500 °C) where crystal growth is initiated by slow cooling of the melt, crystal pulling techniques, or liquid displacement methods. However, these techniques have been adapted so that they can be can be applied to refractory oxides as well. A few of the more important methods are described here.

One of the most widely used techniques is the Bridgeman–Stöckbarger method in which the crucible containing the melt is slowly cooled by passing it down through a vertical furnace (Figure 36(a)). In other variations of the method, the crucible may rest on a grooved pedestal that is mobile. The bottom of the crucible is tapered to a fine point to limit the number of nuclei formed in the crystallization process. The furnace is usually multizoned so that the temperature gradient may be carefully controlled and postsolidification annealing can be carried out. Although the method can be applied conveniently to the growth of such low-melting compounds as $NaNO_3$ (mp 271 °C), it can be adapted for use at much higher temperatures as well. Examples include the growth of $CaWO_4$ and $CaMoO_4$, which melt around 1500 °C, Al_2O_3, Fe_3O_4, U_3O_8, as well as stabilized zirconia single crystals.

The Verneuil method was developed in the early part of this century for the production of precious gems and other high melting oxides such as those of the rare earths. The apparatus is shown in Figure 36(b). Here, a fine powder of the starting material is dispensed from a hopper at a controlled rate and passes through an oxy-hydrogen flame at which the temperatures are in excess of 200 °C. Melting takes place in the flame and the small liquid droplets are deposited on a moving pedestal so that the top of the deposit can be kept at a fixed distance from the flame. Often a seed crystal is used whose top is slightly melted in the process. The introduction of more powerful heat sources, such as the electric arc, arc imaging devices, plasma emission sources, and laser imaging devices, has increased the temperatures available so that it is now possible to produce single crystals of such high melting compounds as CaO and HfO_2.

In the Kyropoulos method, the top of the melt is only slightly above its melting temperature and a seed crystal, which is cooled externally by attaching it to a water cooled heat sink, is placed in contact with the liquid to induce crystallization. The crystal may be rotated and continues to grow in the melt (Figures 37a and b). The size and quality of the crystal produced depends on the temperature gradient induced by the external coolant and the degree to which the temperature of the furnace can be controlled.

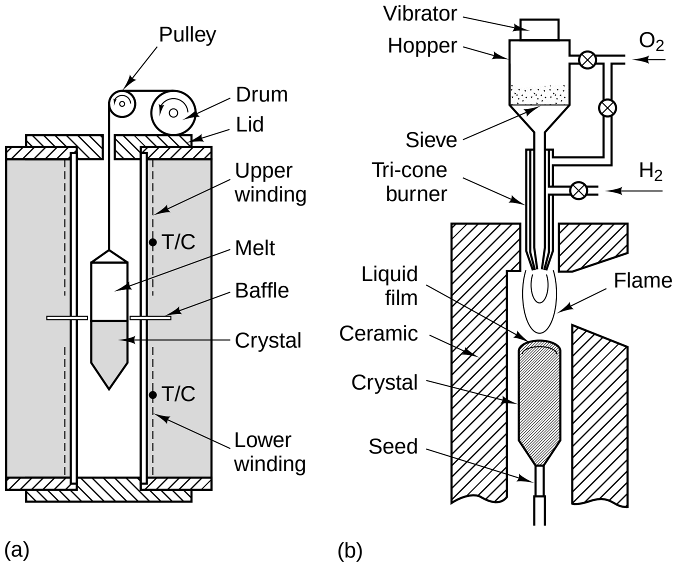

Figure 36 Schematic of the Bridgeman crystal growth method (a). Verneuil crystal growth method (b)

The Czochralski method is an adaptation of the Kyropoulos method in which the rod holding the crystal is allowed to rotate while it is slowly pulled from the melt as shown in the schematic in Figure 37. The method has been exploited for the growth of large single-crystal boules of silicon and germanium for the production of various semiconducting devices but has been applied successfully to the preparation of a variety of complex oxides including Ti_2O_3 $Ln_2Mo_3O_{12}$ (Ln = Gd, Lu), $ZnWO_4$, $Bi_{12}GeO_{20}$, $LiNbO_3$, $LiTiO_3$, $MnFe_2O_4$, $Y_3Al_5O_{12}$ and other rare earth garnets at temperatures from about 1000 °C to over 2000 °C.

For high melting oxides, where container attack is a problem, vertical zone methods have been developed where a vertically held bar of the compound is heated by a moving furnace with a very narrow temperature zone above the melting point of the sample, the liquid region being held in place by surface tension. Provision is made for rotating either end of the sample. For materials melting above 1500 °C, radiation focusing or induction methods may be employed. The former method is preferred for highly resistive materials such as alumina and Ga_2O_3. In some apparatus, provision is also made for pulling the upper portion of the boule. Other ‘crucibleless’ methods make provisions for the sample itself to serve as the container. One is the so-called skull method where the sample, contained in a water cooled copper vessel is heated by a high intensity radio frequency field such that only the interior of the sample is melted while a thick, solid coating is maintained on the walls of the container. Temperatures up to 3330 °C have been obtained by this method, permitting the growth of single crystals of ThO_2, ZrO_2.[115] Growth can be carried out in reducing atmospheres to produce lower valent binary and mixed-metal oxide crystals.

5.5 Precursor Methods

5.5.1 *Mixed Crystal Method*

One of the difficulties with the classical solid-state reaction is that mechanical mixing methods are relatively ineffective in bringing the solid reactants in contact with one another. Diffusion lengths, on an atomic scale, are still enormous and the temperatures required may preclude the formation of phases that might be stable at intermediate temperatures. One method, called a precursor method, involves the formation of a mixed-metal salt of a volatile organic oxyanion such as oxalate by wet chemical methods, which result in mixing essentially on the atomic level. The salt is then ignited at relatively low temperatures to form the mixed-metal oxide. The method has been applied successfully to the preparation of a number of ternary transition metal oxides with the spinel structure.[109]

5.5.2 *Sol–Gel Methods*[110–112,116–119]

Sol–gel methods are those in which a semirigid gel is formed either by the polymerization of a partially hydrolyzed organometallic compounds such as aluminum alkoxide or by the formation of a colloidal sol, which is then induced to form a gel where the colloidal particles randomly cross-link with one another and entrap great quantities of solvent in the process. The gel product may be a polymer or an amorphous material with particle sizes on the nanometer scale offering numerous advantages provided no foreign ions are present. A popular method, called the citrate or Pecini method has been used to prepare a variety of fine particle sized transition metal oxides containing two or more metal ions. A mixture of citric acid and ethylene glycol is rapidly stirred into a solution of

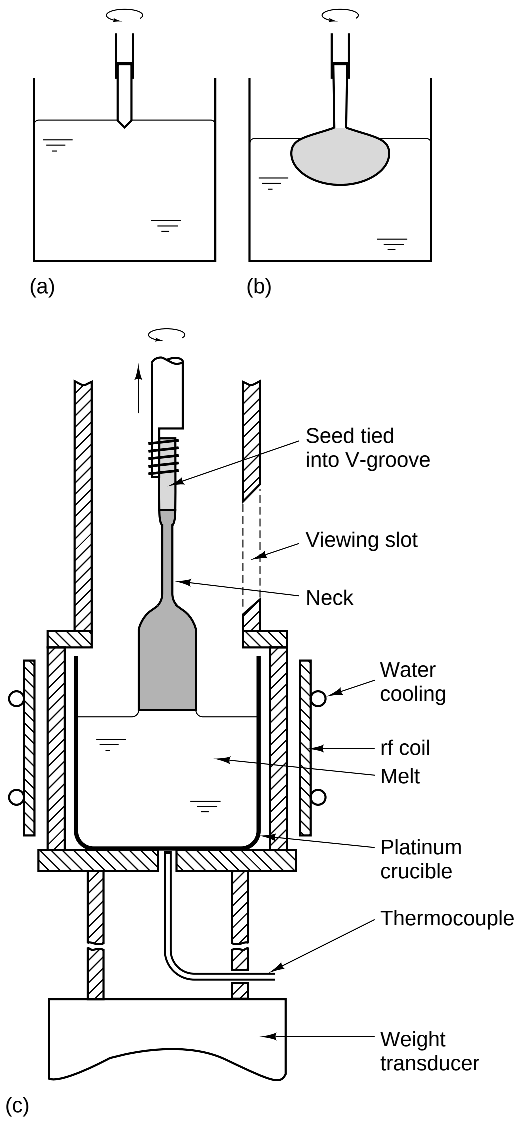

Figure 37 Kyropolis crystal growth method (a), (b). Czochralski crystal growth method (c)

the metal nitrates and lightly heated to dispel nitrogen oxides and to form a gel. The dried material is a complex polymeric material that contains uniform mixture of metal ions. This is then fired at higher temperatures to produce the desired solid.

Typically, much lower firing temperatures can be used to produce a crystalline material than is the case where the starting materials have particles sizes of several microns or more and are mechanically mixed. Since lower temperatures are required to induce reactions, new, metastable phases may be formed that might not form at higher temperatures. A low-temperature route to high density materials offers a route to low defect, high strength ceramics that are inherently impossible to prepare by standard high-temperature methods. Further, the fact that the gels may be spun into wires or precasted into shapes before firing offers a whole host of engineering possibilities (see Section 5.6). A comprehensive description of sol–gel methods for a variety of chemical systems is given in ***Sol–Gel Synthesis of Solids***, while the discussion here is limited to a few examples involving oxide systems.

An important application of the polymerized alkoxide precursor process is the formation of silica gels, carried out in water-ethyl alcohol solutions to which tetraethylorthosilicate Tetraethylorthosilicate TEOS, is added. A small amount of a mineral acid such as HCl or HNO_3 serves as a catalyst for the reaction that involves the formation of hydroxy-orthosilicate intermediate.

$$\mathrm{Si(OC_2H_5)_4} + x\mathrm{H_2O} = \mathrm{Si(OC_2H_5)_{4-x}(OH)_x} + x\mathrm{C_2H_5OH} \qquad (7)$$

The partially hydrolyzed species then condense to form a $(SiO_2)_n$ polymer in the form of a gel along with the elimination of ethyl alcohol. By varying the relative amounts of TEOS, water, and alcohols, different gels may be produced, and they may be spinable, useful for coatings, or able to form monoliths.**[117]** Silica glasses useful for optical applications are prepared by sintering such gels at 1150 °C. These glasses are relatively free of impurities such as Al, Fe, Cl, or OH as compared to conventional fused quartz prepared at 2000 °C. It is these impurities that limit the transparency and homogeneity of the material.

Transparent, porous semicrystalline aluminium oxide has been prepared by this method as well as coatings of a variety of binary oxides including TiO_2, ZrO_2, Y_2O_3, and SnO_2. The alkoxide method has also been used to prepare such mixed oxides as the fast ion conductor $Na_3Zr_2Si_2PO_{12}$, the ferroelectrics $LiNbO_3$, $BaTiO_3$, and $Sr_xBa_{1-x}Nb_2O_6$ as well as a variety of other perovskite and perovskite based oxides. WO_3 gels may be prepared from sodium tungstate solutions by passing them through an acidified cation-exchange resin. After standing for several hours, a polymeric species of high molecular weight is formed. Thin films of WO_3 have interesting photo- and electrochromic properties that make them attractive candidates for large area display devices. The sol–gel process offers a cheap, rapid, and convenient alternative to vacuum deposition for their preparation.

Colloidal sols of certain transition and inner transition metal hydroxides can be formed by peptization of the precipitated hydroxide by washing it with distilled water to break up the electrical double layer that holds the coagulated colloidal precipitate together. These sols are then concentrated and added dropwise into an alcohol that partially dehydrates them and causes gellation of the droplet. This process has been used, for example, as a precusor to form small spheres of Pr_6O_{11} with 100% theoretical density and for the formation of easily sinterable, finely divided powders of $PbZrO_3$. Dispersed colloidal particles of ThO_2 are treated with a solution of $UO_2(NO_3)_2$ to which ammonia is added slowly, forming a uranium oxide coating on the ThO_2 colloid. This then can be processed to form highly dense nuclear fuel fragments.

Sol–gel methods are used to prepare a heterogeneous, nanometer composite of calcium zirconium phosphate and strontium zirconium phosphate, $Ca_{0.5}Sr_{0.5}Zr_6O_{13}$. In this composite, individual domains both expand and contract upon heating, leading to a material with virtually zero thermal expansion over the range 0–500 °C.

5.6 Intercalation in Oxides[15,111]

Intercalation reactions involve the reversible insertion of foreign ions or molecules into a host species in which, ideally, the basic structure of the host is not disrupted. As the name implies such reactions were once considered to be confined to layered structures where the guest species was inserted into the van der Waals gap. However, modern intercalation chemistry includes numerous examples of three-dimensional host structures flexible enough to accommodate the guest.[119–122]

Intercalation is usually carried out under mild conditions and at relatively lowtemperatures (0–300 °C). Thus, the process offers the opportunity to synthesize new phases that might not be stable at the temperatures required for classical solid-state reactions in oxide systems. Because of the reversible nature of the process, intercalated oxides have also attracted attention for use as reversible electrodes in high energy density batteries (Lithium batteries) and as catalysts for a variety of reactions where selective organic chemistry can be carried out within the host. Intercalation has also been found to induce superconductivity in layered materials or increase T_c where it already existed.[15,122] For example, the intercalation of *Chevrel Phases* has led to a new class of superconductors. Indeed, some look upon the formation of superconducting $YBa_2Cu_3O_7$ and related phases to be the result of the intercalation of oxygen into the insulating phase $YBa_2Cu_3O_6$. For a more general discussion of intercalation and intercalates, (*see* ***Intercalation Chemistry***).

Alkali metal intercalation reactions have been intensively studied for systems involving lithium. Host oxides are those of elements in high oxidation states that possess lower valence states that are also stable in oxides. Lithium intercalation may be carried out by LiI solutions for easily reducible systems, for example,

$$x\text{LiI} + V_2O_5 = \text{Li}_xV_2O_5 + I_2 \qquad (8)$$

while more difficultly reducible oxides will require treatment with lithium organics, the typical choice being n-butyl lithium (n-BuLi)

$$2x(n\text{-BuLi}) + 2WO_2 = 2\text{Li}_xWO_2 + xC_8H_{18} \qquad (9)$$

The reactions are carried in an organic solvent such as hexane using controlled amounts of the lithiating agent.

Crystalline V_2O_5 is somewhat difficult to intercalate but a gel form can be intercalated easily. On the other hand, crystalline $VOPO_4$ has a structure that is more clearly two dimensional than V_2O_5 and forms a variety of intercalates. As in V_2O_5, the V are well off center in the octahedra and their coordination is more square pyramidal than octahedral. This and related compounds of the type $MOXO_4$ (M = V, Nb, Ta, Mo; X = P, As, S) undergo a variety of intercalation reactions under soft conditions with the larger alkali and alkaline earths as well as a variety of organic molecules with electron donors such as long chain alcohols and heterocyclic amines.[120]

$LiBH_4$ has been used for the intercalation of MoO_2 while ReO_3 also undergoes a complex series of intercalation and deintercalation reactions with Li. Other types of intercalations are also possible. MoO_3 has been intercalated successfully to form new hydrogen oxide bronzes H_xMoO_3 with four distinct solid solution ranges for $0.23 \le x \le 1.72$ as well as a phase with the composition $H_{1.99}MoO_3$. They can be prepared by electrolysis of an acidic molybdate solution or by hydrogen 'spillover' reduction with a Pt catalyst.[14] These phases are metallic. Hydrogen molybdenum bronzes may react with strong Lewis bases L, to give layered intercalation compounds $L_nH_xMo_3$.[120] Hydrogen vanadium bronzes can be prepared by similar techniques but these are amorphous semiconductors.

Electrochemical insertion of Li has been intensively studied for use in rechargeable high energy density batteries principally on transition metal disulfides (*see* ***Intercalation Chemistry***). However, the process is also important in the common MnO_2 dry cell where H^+ intercalation occurs, as well as in so-called nickel oxide batteries. Manthiram and Kim have reviewed insertion materials for lithiated batteries and the current status of lithiated batteries is discussed by Takamura.[122,123]

Quasi-layered oxides of the type AMO_2 (A = Li, Na; M = trivalent Ti, V, Cr, Mn, Fe, Co, Ni) prepared by high-temperature solid-state reactions have also been studied as possible cathodes since these materials undergo loss of alkali metal upon treatment with I_2 or Br_2 in acetonitrile. Of these, $LiCoO_2$ is the material of choice in the current generation of lithium batteries. A practical problem here is the expense of Co. However, $LiNiO_2$ doped with 10–30 mole% $LiCoO_2$ shows promise as a replacement.[123]

5.7 Ion Exchange

Ion-exchange methods are those in which a compound containing a mobile ion, usually a cation, is placed in contact with a solution containing a high concentration of another ion of similar size or charge, which is exchanged for an ion in the original solid.

Such reactions can be carried out with those solid-state systems that have large tunnels in them established by the crystallographic architecture or layer compounds in which covalently bound layers are linked to one another by ions inserted between them (*see* ***Intercalation Chemistry***).

β-aluminas such as $Na_2Al_{16}O_{25}$ contain exchangeable sodium ions between weakly connected Al–O slabs. Exchange can be achieved by placing the compound in molten salt baths containing cations such as Li^+, K^+, Ag^+, Cu^+, NH_4^+, Mg^{+2}, Ca^{+2}, and so on.[124,125] Sodium in $Na_xMo_2O_4$ may be completely exchanged for Li by treatment with excess LiI at 340 °C.[126] This compound is of interest as a possible cathode material for rechargeable lithium batteries. Layered α-$Zr(HPO_4)\cdot 2H_2O$ and related compounds will exchange their phosphate hydrogens for alkali metals by titration with MCl–MOH mixtures.[127,128]

An interesting variation of ion exchange was reported recently where nanometer sized particles of γ-Fe_2O_3 were obtained embedded in a sulfonated polystyrene resin. The resin in its hydrogen form was exchanged with an aqueous solution of Fe, which was subsequently soaked for several hours in a strongly basic NaOH solution. The composite formed is magnetic and transparent. Its magnetization is more than an order of magnitude higher than other known transparent magnetic materials and could find application in magnetic inks for photocopiers, information storage, and magnetic refrigeration.[129]

5.8 Solid-state Reactions

This method is the most common one used for the preparation of mixed-metal oxides. Accurately weighed, stoichiometric amounts of the constituent binary oxides are intimately mixed by grinding or ball milling and heated at high temperatures in refractory containers for several hours or days to produce the desired product. Since the reactions take place by a diffusion mechanism, intimate contact between reactant particles is essential. Reactivity will also be promoted by using finely divided powders with large surface areas. Typically, it is necessary to make intermittent regrindings of the products to promote homogeneity among the particles of any unreacted or partially reacted starting materials since the reactions take place by diffusion. Often, the reactants are pressed into pellets to promote internal reaction and to minimize contact with the container. Ternary oxides such as $BaZrO_3$, $MgAl_2O_4$, $LiNbO_3$, garnets, and so on are prepared in this fashion as are the high-temperature superconductors $YBa_2Cu_3O_{7-x}$ but here the oxygen stoichiometry depends upon the temperature and partial pressure of oxygen.

5.9 Chemical Vapor Transport Methods[21,130,131]

This is one of several specialized methods designed to obtain small quantities of well-formed single crystals of a few tenths to several millimeters in largest dimension. Typically, a charge of polycrystalline material, either the desired material itself or a mixture of oxides, is sealed off in an evacuated silica tube along with a small amount of a volatile transporting agent such as $TeCl_4$, NH_4Cl, Cl_2, I_2, O_2, or water vapor. In some cases, the transporting agent promotes a reaction such as

$$Ru(s) + O_2(g) = RuO_2(s) \tag{10}$$

The tube is heated in a two or three zone furnace, the charge being placed in the hottest zone. The transporting agent reacts with the charge to form one or more gaseous species that then diffuse to the colder end of the tube where decomposition takes place to form the desired compound. Considerable experimentation is often required to determine the optimum parameters for growth. The method has been applied successfully to the preparation of binary oxides such as MoO_2, NbO_2, RuO_2, IrO_2, V_2O_3, Fe_3O_4, ReO_3, Nb_2O_5, and Mo_4O_{11}. In certain circumstances, crystals have been grown of mixed-metal oxides such as $MgTiO_3$, $A_2Mo_3O_8$ (A^{+2} = Zn, Mn, Ni, Fe), ATa_2O_6 (A^{+2} = Mg, Mn, Co, Ni), AWO_4 (A^{+2} = Mg, Mn, Fe, Co, Ni, Zn), ACr_2O_4, and AFe_2O_4 (A^{+2} = Mn, Co, Ni, Fe). In some cases, more than one transporting agent is used.

A primary advantage of this method is that it produces extremely well-formed crystals and, because the transport action is also a method of purification, the products are often of high purity. The principal disadvantages are that the crystals are usually no larger than a few millimeters in largest dimension and the yields are small. The success of the method depends on optimizing the partial pressure of the transport agent and rigorous control of the gradient temperatures to insure stability of growth conditions at the solid-vapor interface.

5.10 Deposition as Thin Films[112]

The deposition of oxides in the form of thin films is essential for the manufacture of electronic devices. These take the form of either physical or chemical methods. Physical methods include evaporation and sputtering either by a plasma discharge, reactive magnetron sputtering or by laser ablation. Sputtering methods are used to make coatings of group 4 and group 5 refractory transition metal oxides for use in optical communication filters.[132] Chemical vapor deposition involves the decomposition of a gas to form a thin-film layer. An example is the decomposition of silane to form a layer of Si, which then can be oxidized to form a thin film of SiO_2. MOCVD methods use volatile organometallic compounds to accomplish the same purpose.[133,134] Numerous oxide films have been prepared by this method including ZrO_2, HfO_2, V_2O_5, superconducting $YBa_2Cu_3O_7$, Lead zirconium titanate PZT, Strontium Bismuth Tantalate SBT ferroelectrics, and conducting ZnO.

5.11 Electrochemical Reduction

Electrochemical reduction of high-temperature solvents to which solute compounds have been added has long been an important method for the large scale commercial preparation of aluminum, the lighter alkali metals, the alkaline earths, and lanthanides. It is also used to prepare crystal specimens of a variety of low-valent transition metal oxides that cannot be prepared easily by other means. The method is applied with great success to the preparation of reduced, mixed, nonstoichiometric oxides of tungsten with the alkali metals, known as tungsten bronzes, because of their bright colors, metallic luster, and high electrical conductivity. The bronzes have the general formula Na_xWO_3 where $O < x < 1$ and the color depends on the value of x. Typically, WO_3 is added to Na_2WO_4 to form a melt at 700–900 °C in a high density alumina or noble metal crucible. The electrolysis is carried out for several days at low current densities (typically <10 ma cm^{-2}) using platinum electrodes. The crystals grow on the cathode and single crystals, usually of cubic habit, up to several grams in size can be obtained. The stoichiometry of the crystals obtained depends upon the melt composition. The method has been extended to other tungsten bronze systems and to the related molybdenum oxide bronzes such as $K_{0.30}MoO_3$, $A_{0.9}Mo6O_{17}$, ($A^+ = Li$, Na, K, Tl) and $K_{0.33}MoO_3$. A more detailed description of electrochemical oxide bronze preparation by this method has been given by Wold and coworkers.[135] In more recent years, the method has been applied successfully to the preparation of a wide variety of low-valent ternary transition metal oxides including vanadium bronzes of the type $Na_xV_2O_5$, a number of vanadium spinel-type oxides, MV_2O_4 ($M^{+2} = Mg$, Mn, Fe, Co, Zn, Cd), some nonstoichiometric rhenium oxides such as $Na_{0.6}ReO_3$ and $K_{0.3}ReO_3$ as well as stoichiometric $LiReO_3$ and Li_2ReO_3. In addition, a variety of apparently stoichiometric, low-valent molybdenum oxides containing strong metal–metal bonds including $Y_5Mo_2O_{12}$, $La_2Mo_2O_7$, $La_5Mo_4O_{16}$, and $LaMo_8O_{14}$ have been prepared by this method. A more general review of oxide prepared by fused salt electrolysis is given by DeRoy and Besse;[136] (*see also* ***Intercalation Chemistry***).

Examples of electrochemical oxidation for oxide synthesis are far less numerous than its reductive counterpart. However, the method is regularly used for the production of commercial grade lead dioxide, PbO_2, and for the tough oxide coating found on aluminum siding. It has been used successfully to prepare α-Mn_2O_3, Co_3O_4 as well as Na and Sr doped Colossal magnetoresistance (CMR) oxomanganates phases using a M_2MoO_4-MoO_3 (M = Na, Cs) solvents.[137,138] Well-formed crystals of superconducting ($T_c = 18$ K) $K_xBa_{1-x}BiO_3$, $0.6 \leq x \leq 0.8$, have been prepared from KOH melts containing Bi_2O_3 as a solute.[139]

5.12 Hydrothermal Methods[21,50,140–142]

Hydrothermal methods provide a specialized synthesis technique where aqueous solutions are placed in a sealed system and then heated above the normal boiling point of water, often near or slightly above the critical temperature of the solvent (374 °C). Usually, the charge has a low solubility in water that sometimes can be enhanced by adjusting the pH. The success of the method hinges upon establishing a suitable temperature gradient, usually between 10 and 50 °C with the cold end being the growth region, over which mass transfer and growth can take place. Seed crystals are normally used to initiate growth. For oxide systems, strongly basic solutions are usually preferred but weakly basic mineralizers such as KF and NH_4Cl have been used for the preparation of $PbTiO_3$ and $NiFe_2O_4$ respectively.

Hydrothermal synthesis methods have been in use for over 150 years to prepare a wide variety of compounds including oxides, sulfates, carbonates, sulfides, and oxyhalides. The primary use of hydrothermal synthesis is to produce good quality single crystals of few millimeters in size but it is also used for the preparation of large amounts of polycrystalline powders. However, considerably larger crystals may also be grown. Without a doubt its most spectacular application has been in the production of high quality single-crystal quartz required for a variety of electronic and optical device applications. Here large autoclaves are used in which single crystals a kilogram or more in weight are produced over a several week period. For other oxides, the results are less spectacular in terms of crystal size and its use is largely limited to laboratory scale preparations, the notable exceptions being the commercial production of zinc oxide and certain zeolitic materials.

Other examples of the types of phases produced include TiO_2, Fe_3O_4, spinels such as $NiFe_2O_4$ and $ZnFe_2O_4$, the ferrimagnetic garnet $Y_5Fe_3O_{12}$, semiprecious stones such as zircon ($ZrSiO_4$) and tourmaline, and such ternary oxides as $AlPO_4$ and $AlAsO_4$.[140,141] A variety of scheelite and wolframite based molybdates and tungstates of the transition metals and rare earths have also been prepared.[143] Although hydrothermal methods are usually considered as a means for the preparation of high-valent oxides, there have been numerous reports of the synthesis of reduced oxides also, such as V_2O_3, V_2O_4, LiV_2O_4, and $K_2Mo_8O_{16}$.[140,144]

One of the problems with the method is that growth rates are extremely slow, often between a 0.01 and 0.1 mm per day (quartz is an exception where rates of 1 mm day^{-1} are obtained). However, the slow rates are usually offset by the quality of the materials obtained, which in turn is a consequence of the slow growth rate.

Details of the synthesis of zeolites and quartz are given below as examples of two important commercial methods. Large crystals of quartz may be grown hydrothermally from a solution 1 molar in NaOH in which the charge region is held at 400 °C while the growth region is at 360 °C. Pressures of the order of 1.7 kbar are developed. The quartz charge dissolves in the hot region and is transported to the colder region where its solubility is lowered by the convection currents set up by the temperature gradient. The silica then deposits on a high quality single-crystal seeds placed in the cold region.[141,142]

Zeolites are normally prepared under alkaline conditions using a charge of silica, alumina, and a base, typically an alkali metal hydroxide or organic base that have been prereacted to form a gel. The reactions are carried out at fairly low temperatures, rarely approaching 200 °C and sometimes less than 100 °C. Precipitation methods are often used to prepare large quantities of commercially important zeolites. In a typical zeolite A synthesis, hydrated alumina is dissolved in a concentrated sodium hydroxide solution and upon cooling, a measured amount of sodium metasilicate solution, $Na_2SiO_3{\cdot}9H_2O$, is added to give the desired ratio of Na, Al, and Si such as $2.1Na_2O{\cdot}Al_2O_3{\cdot}2.1SiO_2{\cdot}60H_20$. The mixture reacts to form a white gel, which is then collected and sealed in a plastic bottle, which is then heated for several hours at around 90 °C to induce crystallization. If the heating is allowed to go on for a longer period of time, the zeolitic structure may break down and other materials will be produced. The use of different bases, both inorganic and organic, and different ratios of reactants lead to different classes of zeolites.[143]

Hydrothermal autoclaves are usually placed in a furnace where a temperature gradient can be established between the charge or nutrient region and the growth area. A baffle between the two regions restricts convective flow and sharpens the temperature gradient. Provision may be made to allow adjustments in baffle openings. Seed crystals may or may not be used. Design of the autoclave depends on the internal pressures that are generated, most being made for operation below 600 atm. The typical laboratory autoclave has a working volume of about 100 cm^3 or less but those designed for commercial operations may have diameters of 1 m and heights of 2 m or more. The reaction chamber may be lined with an inert material such as Teflon, gold, or platinum.

5.13 High-Pressure Methods

High-pressure methods are discussed in detail under ***High Pressure Synthesis of Solids***. Hydrothermal methods are discussed in the previous Section. A few examples relative to oxide synthesis are given here. Descriptions of the equipment used are given by Rao and Gopalkrishnan and by Rooymans.[145,146]

An important use of high mechanical pressures is to force solids to assume crystal structures and coordination numbers in which they are normally unstable. Thus, four-coordinate Si in SiO_2, typified by quartz or trydimite, can be forced to assume the six-coordinate rutile structure under very high pressures. Once formed, these structures are kinetically stable. The high-pressure polymorph of silica, called stishovite is found terrestrially as the result of meteor impact.

The same principles can be applied in the laboratory. Goodenough, Longo, and Kafalas have described the application of high pressure to obtain mixed oxides with high coordination numbers.[147] Thus, wurtzite-like $NaAlO_2$ is transformed to a spinel at high pressures while the olivine types phases Ca_2GeO_4 and Sr_2CrO_4, where the transition metal is in fourfold coordination, adopt the K_2NiF_4 structure. $PbRuO_3$ and $BiScO_3$, which have defect pyrochlore structures at atmospheric pressure, adopt the denser perovskite structure at 90 and 70 kbars respectively.

Novel oxidation states can also be achieved by the use of high pressures. The apparently stoichiometric oxides $Sr_{0.5}La_{1.5}Li_{0.5}Fe_{0.5}O_4$ and La_2LiFeO_6 can be prepared under 60 Kbar pressure. These remarkable oxides contain tetravalent and pentavalent iron in an unexpected sixfold coordination with oxygen.[148] Pentavalent chromium, which is extremely difficult to stabilize, is prepared in mixed-valence oxides of the type A_xCrO_3, ($A^+ = Na$, K, Rb) by heating under 25–65 kbar pressure. These nonperovskite type phases contain both tetrahedral and octahedrally coordinated Cr with an apparent site preference of Cr^{+5} for the octahedral sites.[147]

Tetravalent chromium oxides are not easily prepared at atmospheric pressures but form readily under pressure. Examples include the cubic perovskites $SrCrO_3$, a metal and $PbCrO_3$, a semiconductor. $BaCrO_3$ forms a perovskite related hexagonal phases in several different polytypic intergrowth forms. Cubic alkali molybdenum oxide bronzes, similar to those of tungsten, can only be prepared at high pressures.[149]

High gas pressures of oxygen are used where high oxidation states are difficult to achieve and in systems where the normal pressure phase is substoichiometric with respect to oxygen. These include several alkaline and rare earth oxides of iron, cobalt, nickel, and copper. For instance, $NdNiO_3$ and several other rare earth isotypes were prepared at 950 °C under 60 Kbar of oxygen generated in situ by the decomposition of $KClO_3$ while others have used 150–200 bars of oxygen at 1000 °C with several intermittent regrinding and repelleting steps.[149]

5.14 Chemical Oxidation/Reduction Methods

Many elements form oxides in a number of different valence states whose synthesis requires the use of oxidizing or reducing conditions. Low-valent oxides can often be obtained by heating a higher valent oxide in hydrogen. Careful attention must be paid to the purity of the gas, the temperature, and partial pressure of water vapor. Otherwise a mixture of oxides may result or reduction to the metal takes place. Thus, MoO_2 is produced by hydrogen reduction of MoO_3 at 600–650 °C but Mo metal is the product at 800 °C. Below 600 °C, one gets a variety of mixed-valence oxides. Reduction with carbon can be used for the preparation of many transition metal oxides but the products are usually contaminated with various amounts of carbide, unreacted carbon, or mixed oxides. CO has been used successfully for the preparation of various di- and trivalent oxides of the first period of transition metals.

A common method for preparation of small quantities of reduced oxides is a solid-state reaction of stoichiometric quantities of a higher valent oxide and a lower valent oxide or the metal. The reaction is carried out in an evacuated sealed container, which may be glass, quartz, or metal, but dynamic vacuums or inert gas blankets are also used. The latter method is especially useful in the preparation of intermediate phases where careful control of the oxygen partial pressure is necessary. The sealed capsule method is one of the more reliable means of obtaining a pure product providing complete reaction can be obtained. Since this requires careful mixing of reactants, usually by grinding, the method is usually limited to the preparation of small quantities.

Often, the highest valent oxide cannot be obtained by the direct combination of the elements and special methods must be used. A general rule of thumb is that basic conditions tend to stabilize high oxidation states. Thus, potassium permanganate is prepared by fusion of MnO_2 in KOH while the unusual 4 and 6 valence states of iron are stabilized by ternary oxide formation in basic media. Potassium nitrate is often used to assist the oxidation. Thus, the hexavalent ferrate K_2FeO_4 is prepared by heating Fe_2O_3 with a mixture of K_2O_2 and KNO_3.

Higher valent oxides of nickel with Ba can be made by basic fusion of NiO to which sodium or barium peroxide has been added. Excess oxygen can be added to $LaNiO_3$ by high-pressure oxygenation. Holland has reported the preparation of $Sr_5Ni_4O_{11}$ by reaction of $SrCO_3$ and NiO in KOH at 700 °C.[150] Low-melting NaOH/KOH mixtures have been used recently to prepare superconducting $La_{(2-x)}Sr_xCuO_4$.[151] These caustic mixtures are saturated with H_2O and melt at temperatures below 200 °C, thus offering a low-temperature route to the synthesis of metastable phases.

5.15 Synthesis of Multiple Perovskites by Metathesis

Several oxides with a double, triple, and even quadrupled perovskite formula units, $(AA')_n(BB')_nO3_n$ ($n = 2$, 3 and 4), have been known for some time. In the ideal formulation, the B and B′ cations, of necessity, should be ordered although the degree of ordering may vary depending on the synthetic conditions, oxide ion defects, and chemical compatibility between the B-site ions. In the absence of an ordered B-site sublattice, these compounds should be regarded as simple perovskites. In general, the ordering of B-site ions is rock-salt-like although there are examples showing a layered-order. An excellent compilation of the work carried out up to 1970 detailing the structure and properties of multiple perovskites is available in the literature.[152] A critical survey of nearly 300 oxides with double perovskite structure has illustrated the importance of chemical, geometrical, and valence factors that influence the ordering of the B and B′ cations.[153]

An interesting aspect of the multiple perovskites is their ability to accommodate mono- and divalent cations at the B-site, which is not possible with a simple perovskite formulation.

In the last decade, study of double perovskites has accelerated with the discovery of tunneling magnetoresistive (TMR) effects in $Sr_2FeMoO_{6.156}N$. Both the magnetism and transport in these oxides is strongly influenced by the cationic nature and the order/disorder of the ions at the B-site. Ferromagnetism and half-metallic properties are often observed in the $A_2BB'O_6$ oxides with $BB' = CrW$, CrRe, FeMo, or FeRe and $A = Ca$, Sr or Ba. The simultaneous presence of magnetism and transport also make these materials attractive for spintronics applications.

Recently, the synthesis of truly triple and quadruple perovskites has been reported in the literature by way of metathesis reactions. The low temperatures routes are necessary to realize the formation of otherwise meta-stable phases. Articles describing the utility of topotactic methods for the synthesis of several perovskite and related phases can be found elsewhere.[154,155,156]

6 SOME APPLICATIONS OF OXIDES[157–159]

Oxides are among the most useful compounds known and find a wide variety of applications in all walks of life from heavy construction to microelectronic circuits. Oxide based minerals along with sulfides are often the primary source of most metallic elements and their compounds but, for the most part, their extraction and purification will not be a part of this discussion. Other high volume oxides such as Al_2O_3, CaO, and TiO_2, and particularly SiO_2 have important applications in their own right.[157]

6.1 Applications of Magnetic Oxides

The useful properties of magnetic materials depend upon the existence of a net magnetic moment beyond that predicted by the Curie–Weiss Law (*see Curie Constant*) as the result of spin interactions between ions with unpaired electrons. For a discussion of the origins and types of cooperative magnetic effects observed in oxide systems, *see* ***Magnetic Oxides*** and ***Magnetism of Extended Arrays in Inorganic Solids***.

Most commercially useful magnetic oxides are (*see Ferrimagnetism*) often called ‘ferrites’ and contain Fe^{+3} as a major component. A notable exception is ferromagnetic CrO_2, which is used in high quality magnetic tapes (*see Ferrimagnetism*). Ferrites can be divided into three main classifications: (1) Spinel-type oxides (Section 3.4.2); (2) Hexagonal ferrites based on the magnetoplumbite structure (Section 3.11); and (3) Rare earth ion garnets (Section 3.4.3). These phases are particularly useful because, unlike most conventional magnetic materials, they can be prepared with very high electrical resistances, resulting in low-energy loss properties. Rare earth iron garnets can be prepared with resistivities exceeding 10^{12} ohm-cm, making them particularly valuable for high frequency (microwave) applications.

Most spinel ferrites used in device applications are not simple ternary oxides but rather contain proprietary mixtures of several different magnetic ions tailor made for specific applications.[160] So-called (Mn, Zn) ferrites of general formula ${Zn^{+2}}_x\ {Fe^{+3}}_{1-x}[{Mn^{+2}}_{1-x\mathrm{F}}\ ]O_4$ and related (Ni, Zn) ferrites are used as cores for inductors or transformers and in TV deflector yokes. (Mg, Mn) ferrites and yttrium iron garnets including those partially substituted by Al or Gd find numerous applications in microwave circuitry.[161]

One of the biggest applications of magnetic oxides is for information storage. Computer memories typically utilize (Mn, Mg) based spinels. Hexagonal barium ferrites are used in floppy discs. Fe_3O_4 is used as a magnetic toner in photocopiers and as a magnetic printing ink while the defect spinel γ-Fe_2O_3 and γ-Fe_2O_3/Fe_3O_4 mixtures compete with ferromagnetic CrO_2 for the audio and video magnetic tape market.[162] In addition to composition, the shape and size of the particles plays a crucial role in the quality and performance of the tape. In this respect CrO_2 is superior because of its normal, needle-like crystal habit.

6.2 Oxide Sensors

Sensors are materials that produce a reversible and reproducible electrical response to various physical or chemical changes that can be used to automatically control a given process. There is an expanding list of processes that could be controlled with inexpensive microprocessors if the right sensor was available. There exist a variety of oxides with sensitive responses to changes in temperature, pressure, or gas ambient.[160] A few examples will be given here.

Temperature sensors include thermistors such as doped $BaTiO_3$ and $Ni_{0.6}Mn_{2.4}O_4$ that have large temperature coefficients of resistance. $BaTiO_3$ and $PbZrO_3$-$PbTiO_3$ solid solutions (PZT) show anomalously large changes in resistivity as their ferroelectric-paraelectric transition is approached, which makes them useful as switches. Switching temperatures can be adjusted by varying the solid solution composition and by the addition of other dopants (*see Ferroelectricity*). Stabilized, cubic zirconia acts as an oxygen sensor since changes in O_2 partial pressure affect its ionic conductivity. Ti^{+4} doped $MgCr_2O_4$ (a p-type semiconductor) acts as a humidity sensor. Suitably doped SnO_2 responds to the presence of hydrocarbon gases. Piezoelectric materials, such as lead zirconate $PbZrO_3$, PZT, and α-quartz, are substances that produce an electrical signal under pressure. Long established as acoustical pickups in hydrophones and phonographs, they now find application as micromechanical positioners, ultrasonic cleaners, small high quality loud speakers ('piezo speakers'), gas igniters, sensors in automobile suspension systems, transformers, and filters.[163]

6.3 Luminescent Materials[164]

Luminescent oxides (or phosphors) play an important role in television receivers and other cathode ray tube (CRT) applications, fluorescent lamps, scintillation counters, and information display devices including CRT and flat panel display (FPD) as well as the emerging plasma display panels (PDP). Although some materials exhibit intrinsic luminescence, most phosphors are obtained by doping suitable hosts with small amounts of a foreign substance (called the activator), which provides the necessary defect levels to produce luminescence when stimulated by shorter wavelength light (photoluminescence) or by bombardment with electrons in vacuo (cathodoluminescence). The mechanisms of these interactions are discussed in ***Luminescence***.

Production of good phosphors requires rigorous attention to synthesis or activation conditions. Careful control of activator concentrations, usually measured in parts per million, is essential. Multiple activators may be necessary to achieve the desired color, brightness, response or decay times. Virtually unmeasurable, trace amounts of unwanted substances may have such severe deleterious effects on phosphor performance that the materials are usually produced under clean room conditions rivaling those used in the production of silicon based integrated circuits.[164]

Some examples of commercial luminescent oxides are Mn doped willemite, Zn_2SiO_4:Mn, a standard green phosphor with wide application, $CaSiO_3$:Pb, Mn, an orange phosphor used in radar screens because of its long persistence, $Ca_2MgSi_2O_7$:Ce, an ultraviolet emitting phosphor used in flying spot scanners and photography, and $Zn_3(PO_4)_2$:Mn, an old, standard red phosphor for color TV. Other red phosphors developed specifically for color TV include YVO_4, Y_2O_3 and Gd_2O_3 as well as the oxysulfides R_2O_2S ($R^{+3} = Y$, La, Gd), all of which must be doped with small amounts of europium. A very short persistence yellow–green phosphor can be obtained by doping the yttrium aluminum garnet $Y_3Al_5O_{12}$ with cerium.[165]

In fluorescent lamps, an electrical discharge produces UV emission, which stimulates the emission of visible light from a phosphor coated on the walls of the tube. Early 'white' lamps used Mn doped willemite resulting in an orange cast and were replaced by a heavily Be^{+2} doped material. The highly toxic nature of beryllium salts eventually led to their replacement by materials such as the halophosphate $Ca_5(PO_4)_3X$:Mn,Sb ($X^- = Cl$, F). In these multiply activated phosphors, the color balance may be varied by changing the relative amount of each activator. Other important host materials include $CaWO_4$, YVO_4, $Cd_2B_2O_5$, and $MgGa_2O_4$.

A relatively new class of luminescent materials are the β''-aluminas. Sodium β'' alumina when doped with approximately 10^{19} Cu^{+2} cm^{-3} has a visible emission in the green, which can be tuned from the blue to the red by the addition of codopants such as Ca^{+2}, Ba^{+2}, or Ag^{+}.[166]

Europium doped barium aluminates of the type $Ba_{1-x}Eu_xMg_2Al_{16}O_{27}$ are used as a blue component in fluorescent lamps, and are also being investigated for possible use in flat panel displays.[167] The crystal structure of this material is characterized by an intergrowth of spinel and magnetoplumbite units (See 3.4.2 and 3.11).

A historical review of the development of luminescent materials is given by Chen and Lockwood.[168]

6.4 Colossal Magnetoresistive Perovskites

Lanthanide oxomanganates attracted renewed attention in the 1990s because of the discovery of an anomalously high magnetoresistance in several of these perovskite related phases, referred to as colossal magnetoresistance (CMR).[169,170] The phenomenon of magnetoresistance, a change in the resistance of a material in the presence of a magnetic field, forms the basis for current devices used in data retrieval and recording technology such phase are potentially of great practical interest provided certain processing problems related to mass production can be overcome.

$LaMnO_3$ is a prototype for a wide range of rare earth oxomanganates whose physical properties can be radically altered by partial substitution of alkaline earths for La or by similar replacement of Mn by a 3d or other small to medium sized cation. $La_{1-x}A_xMnO3$ (A = Ca, Sr, Ba) constitutes one of the more interesting systems for CMR applications. Pure stoichiometric $LaMnO_3$ is an insulator that orders antiferromagnetically at 135 K and it is only by introducing a critical amount of Mn^{+4} into the structure that the CMR effect can be observed. Thus, some comment about the nature of the defect chemistry of $LaMnO_3$ is in order.

The actual stoichiometry of nominal $LaMnO_3$ is strongly dependant upon the method of preparation. Samples can be made by solid-state reactions of constituent oxides but sol–gel or other precursor precipitation reactions are preferred where the products are subsequently fired at high temperatures in atmospheres having various partial pressures of oxygen.[170–172] As mentioned in Section 3.11, the variable oxygen stoichiometry of $LaMnO_3$ is often represented by a chemical formula such as $LaMnO_{3+\delta}$ implying an 'excess' of oxygen where, in fact, the actual vacancies are on the cation sites. Unfortunately, the simplicity of the oxygen excess formula has resulted in its continued use in spite of its incorrect implications. However, defect stoichiometries in lanthanide oxomanganates are not limited to oxygen. Indeed, $LaMnO_3$ could fairly be called 'Daltons nightmare' since nonstoichiometry can exist not only on the oxygen sites but also on the La and Mn sites as well. In fact, all three may simultaneously exist in the same compound at the same time. Thus, to produce materials with the desired properties, careful control of synthesis conditions is essential.

The effects of firing conditions on samples whose La:Mn ratio is fixed at 1 is illustrated by the following data reported by Hauback and coworkers.[170] If the sample is fired in Ar at 1000 °C, it has the composition $LaMnO_{3.00}$ and a structure that is an orthorhombic distortion of the cubic perovskite. If the sample is heated in air at 750 °C, a sample with a rhombohedral perovskite structure results that becomes ferromagnetic at low temperatures before transforming at 9 K to the ORTH 1 variant of the $GdFeO_3$ structure. On the other hand if the firing temperature is lowered to 900 °C, δ increases to 0.09 and a phase with a rhombohedral modification of perovskite is formed. If the La/Mn ratio is lowered to 0.88, firing at 750 °C results in a rhombohedral phase with $\delta = -0.08$ that becomes ferromagnetic at 248 K. Ferromagnetism is believed to occur in these systems via the so-called double exchange mechanism, which requires that a critical amount of Mn^{+3} be replaced by Mn^{+4}, the amount of which also affects the critical temperature, T_c, at which the transition occurs.

While CMR is observed at low temperatures in metal deficient $LaMnO_3$, the highest T_c observed is only around 250 K for phases with compositions $La_{0.94}Mn_{0.98}O_3$ and $La_{0.90}MnO_{3-\delta}$. However, partial replacement of La by Sr in $La_{1-x}A_xMnO_3$ in bulk samples with $x = 0.20–0.30$ results in a material that is ferromagnetic at room temperature and above. It typically displays MR values between 30 and 45%, depending upon the method of preparation, in 5 to 7 tesla fields. These samples have rhombohedral structures are essentially stoichiometric with respect to oxygen.[171,172] Near room temperature CMR can also be achieved by doping $LaMnO_3$ with approximately 10 mole% Na.[137] The crystal chemistry and properties of $Ln_{1-x}A_xMnO_3$ materials are described by Raveau and coworkers.[173] In order for CMR materials to be useful for device applications, they must be able to be prepared reproducibly in the form of thin films. Various techniques for such thin-film deposition have been explored such as molecular beam epitaxy (MBE), pulsed laser deposition (PLD), and metal organic chemical vapor deposition.[174] So-called charge ordering, where Mn^{+3} and Mn^{+4} order on crystallographic sites, is prevalent in $La_{1-x}A_xMnO_3$ phases and can have dramatic effects on CMR properties.[175,176]

The observation of room temperature CMR in the ordered double perovskite Sr_2FeMoO_6 has sparked renewed interest in this class of compounds.[177] Similar effects are seen when Fe is replaced by Fe, Co or Mn, or Mo partially replaced by W.[178,179]

6.5 Materials for Solid Oxide Fuel Cells[180]

There is great interest in fuel cells since they offer the possibility of nonpolluting power sources of high efficiency that use methane, or preferably, hydrogen as a fuel.

One of the more important fuel cells is the solid oxide fuel cell Solid oxide fuel cell (SOFC), since they offer a realistic opportunity for use in electric utility operations. A schematic of a fuel cell is shown in Figure 38. These can be developed in stacks having 5–10 kW capacity that would be suitable for both stationary and mobile power units.

The basic elements of a SOFC are (1) a cathode, typically a rare earth transition metal perovskite oxide, where oxygen from air is reduced to oxide ions, which then migrate through a solid electrolyte (2) into the anode, (3) where they combine electrochemically with to produce water if hydrogen is the fuel or water and carbon dioxide if methane is used. Carbon monoxide may also be used as a fuel. The solid electrolyte is typically a yttrium or calcium stabilized zirconia fast oxide ion conductor. However, in order to achieve acceptable anion mobility, the cell must be operated at about 1000 °C. This requirement is the main drawback to SOFCs. The standard anode is a Nickel–Zirconia cermet.

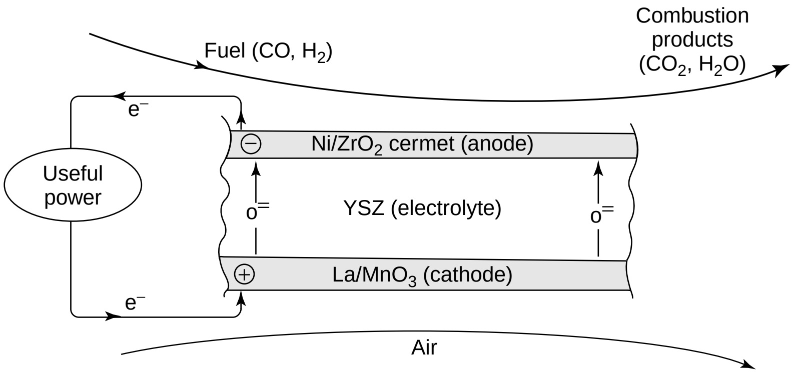

Figure 38 Schematic of a Solid Oxide Fuel Cell

Strontium substituted lanthanum oxomanganates, $La_{1-x}Sr_x$ MnO_3 ($x = 0.1-0.3$) (LSM) are the current cathode materials of for choice in SOFCs. These phases have excellent electronic conductivity but their ionic conductivity is poor even at 1000 °C so that attempts to operate at lower temperatures give unacceptably high resistive effects. This can, in part, be ameliorated by forming a composite with yttrium stabilized zirconia, but even these cannot operate below 800 °C. Other perovskite oxides that have higher ionic conductivities are strontium doped lanthanum oxocobaltates and oxoferrates, which have conductivities 2 to 3 order of magnitude higher than LSM. Unfortunately, cobaltates react with the zirconia electrolytes and the electronic conductivity of the ferrate based materials is too low. However, the use of gadolinium doped CeO_2 electrolyte in combination with a Sr and Fe doped lanthanum cobaltate is being explored, which may overcome these problems.[181]

The interconnecting material used in building a stack of fuel cells must have a high electrical conductivity and a coefficient of expansion similar to that of the electrolyte. The perovskite oxide $LaCrO_3$ meets these requirements nicely and is widely used although ferritic stainless steels have been used successfully in certain fuel cell geometries.[182,183]

6.6 Ferroelectric Materials[184–186]

Ferroelectrics are high dielectric materials that are easily polarized in an electric field and can remain polarized to some degree after the field is removed. Such properties make them ideal candidates for computer memory applications and they have been used in the form of thin films as ferroelectric random access memories (FeRAMs) and as high permittivity dielectrics for Dynamic Random Access Memory DRAMs. They have also been looked at as a replacement for silicon dioxide in certain MOS applications.

Materials of particular interest are the perovskite oxides $BaTiO_3$-$SrTiO_3$ (BST) and $PbZrO_3$-$PbTiO_3$ (PZT) solid solutions as well as the layered perovskites based upon $SrBi_2Ta_2O_9$ (SBT). Since the ferroelectric effect requires a lack of a center of symmetry, all of these phases must necessarily have a structure that is distorted from the ideal cubic structure described previously. No one material has the ideal properties and current research centers on achieving optimal performance by modifying existing materials while also search for new ones. To be useful for memory applications, the materials must be prepared in the form of thin films. This appears to be well worked out for PZT where the chemical vapor deposition method is routinely used.

Films with 47 mole% $PbTiO_3$ have optimal properties. BST containing about 70 mole% $BaTiO_3$ appears to be the an attractive material for DRAMs where large dielectric constants can be achieved that are necessary for high storage capacities, provided a satisfactory method for preparing thin films can be found. SBT is of interest because of its remarkably high resistance to polarization fatigue. In addition, lead-free SBT also offers an environmentally friendly alternative to PZT but its efficacy remains to be proved.

6.7 Optical Materials

While silicate-based glasses and quartz still play an important role in the optics industry, there has been a dramatic growth in the use of Nonlinear Optical (NLO) materials for use with high intensity beams of radiation generated by laser sources (*see* ***Noncrystalline Solids***; and Section 6.5). NLO materials provide an effective means of doubling the frequency of an incident light beam and electronically processing optical signals of high intensity such as those generated by lasers. NLO materials play an important role in the development of optically based computers.

Nonlinear optical oxides are typically d^0, acentric compounds. Useful materials include $LiIO_3$, KH_2PO_4, $KB_5O_8{\cdot}4H0$, and $KTiOPO_4$, which are used as harmonic generators, frequency mixers, and parametric oscillators in the UV, visible and near IR regions. Another class of oxides is the so-called electro-optic materials in which electric fields may be used to control light beams.[187] Such materials need not be acentric but they often are. La doped lead lanthanum zirconium titanates (PLZT) are transparent electro-optic materials for the 0.4 to 6 µm region. Other electro-optic oxides are $K(Ta,Nb)O_3$, $LiTaO_3$ and $BaNaNb_5O_{15}$. $LiNbO_3$ finds many uses in optical communications. Its primary use is as an optical modulator but it can also be used as a laser, waveguide, or light emitting diode.[188] SiO_2 coatings doped with refractory oxides such as HfO_2 or Nb_2O_5 are an important material for optical communication filters.[132]

Oxide lasers include the Cr doped Al_2O_3 ruby laser, Nd doped Yttrium iron garnet (Nd:YAG), and the Nd doped silicate and phosphate glass lasers. Nd:YAG lasers have high radiant power outputs and are used for pumping tunable dye lasers. SiO_2 coatings doped with refractory oxides such as HfO_2 or Nb_2O_5 are an important material for optical communication flters.[132]

6.8 Dilute Magnetic Semiconductors

Materials that exhibit ferromagnetism and semiconductivity simultaneously at room temperature are important for magneto-optoelectronics and spintronics applications.[189,190] The rationale here seems to integrate the functionality of the magnetic storage and semiconductor driven processor technologies into one single material. Although there are many materials that are either ferromagnetic or semiconducting, there are very few that display both. Until recently, the study of DMS has been limited to III to IV pnictides doped with transition metals such as Mn. However, currently the search has been extended to oxides and led to the development of Co doped anatase form of TiO_2 and Mn doped ZnO.[191,192] In the Co doped TiO_2, the question of whether the magnetism is intrinsic (carrier-induced) or due to elemental cobalt atom-clustering has not been resolved unambiguously. In the case of Mn doped ZnO, ferromagnetic ordering seems to be intrinsic although the exact composition of this phase is unclear. While the precise origin of ferromagnetism is currently debated, the hope for discovering new oxide systems however remains high.

6.9 Other Electronic Applications of Oxides

By this term, we mean other uses of oxides such as insulating substrates, capacitors, resistors, and conductors in electronic circuits. Insulating oxides are used in electrical circuits for such jobs as the separation of conductors, mechanical supports, heat sinks, and capacitor materials. Classical materials include naturally occurring minerals or manufactured composites such as zircon, steatite, mica, quartz, porcelain, and glass. The latter was particularly useful in low stress situations because of its low cost and the ease of forming it into desired shapes.

While these materials still find some application, such materials as alumina, beryllia, and single-crystal corundum find increasing use in high-power applications for heat dissipation because of their relatively high thermal conductivity. Classical ceramic capacitors with dielectric constants of the order of 10 largely have been replaced by $BaTiO_3$ based materials that can have combined dielectric constants of a 1000 or more (10^5 in composite, grain boundary barrier layer capacitors) and exceptionally low dielectric loss. Useful composites include $(Ba,Mg)(Ti,Sn)O_3$, $(Ba,Sr,Ca)TiO_3$ and $BaTiO_3/Bi_2(SnO_3)_3$. $BaTiO_3$ shows a large increase in its resistance near 130 °C, which allows it to function as a surge protector in electrical devices. $Ba_2Ti_9O_{20}$ finds use as a microwave filter for radio communications networks.[193]

Certain semiconductor device fabrication methods require the formation of a single-crystal deposit of the semiconductor on an insulating substrate. In epitaxial methods, the semiconductor is deposited on a single-crystal piece of substrate chosen, in part, on the basis of the match of the lattice parameters, thermal expansion coefficients and chemical compatibility of the substrate and deposit. Single-crystal substrates include those of Al_2O_3, $MgAl_2O_4$, α-quartz and $ZrSiO_4$.[194]

ZnO varistors are high resistance, semiconducting devices that, because of their highly nonlinear current-voltage characteristics, are used to mitigate power surges in electronic circuits and electric power transmission lines by providing an emergency conduit to ground. Their electrical behavior appears to be determined by grain boundary effects. Optimum characteristics are obtained by the addition of small amount of various transition metal and main group oxides.[195,196]

Conducting RuO_2 and the pyrochlore $BiRu_2O_7$ are used in the formation of conductive thick films on substrates where conventional conductors would be destroyed under the conditions required to achieve suitable bonding between the two. RuO_2, IrO_2, Tl_2O_3, $Bi_2Ru_2O_7$, and $Pb_2Ru_2O_6$ are also in the preparation of glass composite resistors.

Transparent, conducting, tin oxide coatings are used in applications where light must pass through the substrate in order to strike the active element such as a photoconductive or photoelectric material. Chemically deposited films of silicon dioxide serve as masks on semiconductor materials for selective doping in the preparation of integrated circuits that can later be removed by chemical etching.

6.10 Ceramics and Refractories[197]

These areas represent another huge market for oxide based materials. Traditional silicate-based materials are those stable to about 1000–1100 °C and that are used for porcelain chinas, dishware, electric insulators, and other low stress industrial applications.

More specialized ceramics include refractory silicates such as mullite, $Al_6Si_2O_{13}$, or binary oxides such as MgO, Al_2O_3, TiO_2, or stabilized zirconia, which are fired and sintered, sometimes under pressure at 1500–2000 °C. A great deal of this refractory production involves the fabrication of low and medium density fire-bricks for ovens and furnaces.

These include inexpensive, high silica content fire clay bricks produced from silica and clays used in glass making furnaces and alumina-rich bricks ranging from 50 to 85% Al_2O_3 that are used as furnace linings for making steel. Because of their resistance to basic slags, they are also employed in certain cement and glassmaking operations. Sintered magnesia bricks containing up to 80% MgO, and fosterite bricks (approximately 50% fosterite, $(Mg, Fe)_2SiO_4$ and 50% MgO) are used as liners in steel making furnaces and in nonferrous metallurgy.[197]

High purity binary oxides such as BeO, MgO, Al_2O_3, TiO_2, And stabilized zirconia are sintered under pressure to produce high density ceramic ware, particularly crucibles and other containers for use in nonferrous metallurgy and other specialized applications where temperature resistance and corrosion are a problem. Titania is also formed in honeycomb arrays for use as catalyst supports.

In all of these materials, the ceramic consists of grains or crystallites having dimensions of 10^2 to 10^4 nm. It is in the grain boundary regions where impurity phases, formed at high temperatures, tend to congregate and form a glass-like binder. It is this type of defect that gives the classical ceramics their notorious brittleness and poor mechanical properties that limit their usefulness.

Modern ceramic materials with microstructures in the 1–100 nm region are precast into desired shapes as sol–gel precursors (see Section 5.5) and then crystallized at high temperatures. Alternatively, the gel may be prepared as a low-temperature glass and machined or spun into wires or fibres. These are then crystallized by firing at higher temperatures. Because of the small particle size of the colloidal precursor, grain size is greatly reduced and much lower firing temperatures are possible, reducing or even eliminating grain boundary problems and yielding materials with superior mechanical properties. Applications already exist in the production of flaw-free optical materials and fuel-efficient ceramic prototype engines have been made for operation at high temperatures. Glass ceramic techniques show some promise for the preparation of flexible wires of the new high-temperature superconducting cuprate oxides.

6.11 Miscellaneous Specialized Applications[157,187]

In addition to its use as a specialized refractory, great quantities of CaO are used for the fabrication of construction materials and the manufacture of concrete also serves as a trap for desulfurization of flue gases. CaO is obtained by the decomposition of calcite, $CaCO_3$, at 1000 °C. Much of it is converted to slaked lime, $Ca(OH)_2 \cdot 2H2_O$. Slaked lime is used as a whitewash for buildings. BeO is used as an admixture in nuclear fuels because of its superior properties as a neutron moderator.

Yttria and the rare earths find a variety of specialized applications. Y_2O_3 is used to produce yttria stabilized zirconia ceramics. Cerium, neodynium, and didymium oxides (a mixture of the heavier rare earth oxides) are used to reduce discoloration in glass screens of color television sets caused by small amounts of iron(III) oxide. Ceric oxide is also used as an opacifier in white porcelain enamels and as a optical polishing agent. Other rare earths are used as core materials for arc carbons to increase luminosity and spectral balance. A number are used as coloring agents in ceramics, the more notable being praseodymium oxide, which imparts a brilliant yellow to zirconium silicate glazes. Small amounts are used in the manufacture of rare earth iron garnet magnets. There is also some demand for rare earth-borate glasses because of their high refractive indices. Certain rare earth transition metal oxides are used as hosts for luminescent materials (see Section 6.3).[198]

A large multibillion dollar market ($2.5 billion in the United States alone in 2002) exists for inorganic metal oxides for use as pigments for paints and coatings, printing inks, and coloring agents for plastics, enamels, and ceramics. Most pigments produced today are synthetic, tailor made to meet exacting standards with respect to color, application, and weathering. Natural pigments, mainly iron oxides, account for only about 3% of world production. White titanium dioxide accounts for over 2/3 of the pigment market world wide, while iron based pigments account for another 1/6 of the market. The latter are relatively cheap and are used in construction where color is secondary. White zinc oxide is used as a colorant and antifungal agent in polymer composites. Other important colored oxide pigments are Cr_2O_3 (green), $PbCrO_4$ (chrome yellow), $Pb(Cr,Mo,S)O_4$ (molybdate red), $(Fe_{1-x}Mn_x)_2O_3$ (black to red–brown), and $CoAl_2O_4$ (cobalt blue).[157] Mica is an important component in the production of the currently popular bright, pearlescent coatings. Ultramarines, particularly the blue often found in fine porcelain china, are valued by artists for their bright, vivid hues.[198]

TiO_2, beyond its use in paints and coatings, is also used as an additive for the production of glossy paper. Doped with group 5 and 6 oxides it serves as an effective ceramic substrate for the catalytic removal of NO_x from flue gases.

The worldwide production of bauxite (unrefined alumina) in 1999 was 127 million tons. Approximately 85% was used for the production of the metal. The remainder was used in the fabrication of refractory materials, abrasives, ‘hard’ concretes, aluminum-based chemicals and as a filler for plastics and toothpaste. Activated alumina is used as a desiccant, filtering media, chromatographic column packing, and as an inert support for finely divided catalytic materials. Many applications exist for boron oxide, B_2O_3, such as in the manufacture of borosilicate glasses, welding and soldering fluxes, water softeners, and detergents. It is the product of ignition of boric acid, obtained by the addition of strong acids to borates, principally sodium tetraborate (borax) found in large natural deposits (*see* ***Borates: Solid-state Chemistry***).

Pure vitreous silica has important laboratory applications as containers in the 1000–1300 °C range and is used for optics in the ultraviolet region. The grades may vary widely depending upon the method of preparation. Silica glasses made by flame fusion may contain significant amounts of hydroxyl impurity, which has a deleterious effect on its optical properties. The sol–gel method of synthesis (Section 5.5.2) offers a means of overcoming impurity and structural problems associated with high-temperature processing. Quartz is valued for its piezoelectric properties and finds use in quartz crystal oscillators and various electro-mechanical transducers. Amorphous silicas are used as drying agents, catalyst supports, fillers, binders, and stiffeners in waxes and fibers. So-called food grade silica may be used as an additive but finely divided crystalline silica dusts are a lethal hazard and are cited as the main cause of the lung disease known as silicosis. Sodium silicates are used for detergents. Their solutions are important precursors for the synthesis of zeolites.

Many oxides and oxide mixtures are used as catalysts and catalyst supports (*see* ***Oxide Catalysts in Solid-state Chemistry***).

7 RELATED ARTICLES

Bond Lengths in Inorganic Solids & Liquids; Borates: Solid-state Chemistry; Defects in Solids; Electronic Structure of Solids; Electronic Structure of Clusters; High Pressure Synthesis of Solids; Intercalation Chemistry; Ionic Conductors; Luminescence; Magnetic Oxides; Magnetism of Extended Arrays in Inorganic Solids; Noncrystalline Solids; Oxide Catalysts in Solid-state Chemistry; Oxygen: Inorganic Chemistry; Phosphates: Solid-state Chemistry; Polyoxometalates; Semiconductors; Silicon: Inorganic Chemistry; Sol–Gel Synthesis of Solids; Structure & Property Maps for Inorganic Solids; Superconductivity; Zeolites.

8 REFERENCES

1. F. A. Cotton, G. Wilkinson, C. A. Murillo, and M. Bachmann, ‘Advanced Inorganic Chemistry’, 6th edn., Wiley, New York, 1999.
2. C. E. Housecroft and A. G. Sharpe, ‘Inorganic Chemistry’, Prentice Hall, Harlow, England, 2001.
3. D. Shriver and P. Aitkins, ‘Inorganic Chemistry’, 3rd. edn., W. H. Freeman, New York, 1999.
4. C. Ebel, ‘Kirk-Othmer Encyclopedia of Chemical Technology’, 3rd edn., Wiley, New York, 1981, Vol 16, p. 683.
5. S. Patai ed., ‘The Chemistry of Peroxides’, Wiley, New York, 1983.
6. J. A. Conner and E. A. V. Ebsworth, in ‘Advances in Inorganic Chemistry and Radiochemistry’, eds. H. G. Emeléus and A. G. Sharpe, Academic Press, New York, 1964, Vol. 6, p. 279.
7. N. N. Greenwood and A. Earnshaw, ‘Chemistry of the Elements’, Pergamon Press, New York, 1984.
8. A. F. Wells, ‘Structural Inorganic Chemistry’, 5th edn., Clarendon Press, Oxford, l984.
9. A. R. West, ‘Basic Solid State Chemistry’, 2nd edn., Wiley, West Sussex, l999.
10. G. M. Clark, ‘The Structures of Non-Molecular Solids’, Applied Science, London, l972.
11. R. D. Shannon, ‘The Structures of Non-Molecular Solids’, Applied Science, London, l976, Vol. A32, p. 75l.
12. A. F. Wells, ‘Structural Inorganic Chemistry’, 5th edn., Clarendon Press, Oxford, l984, p. 267.
13. L. Eyring, in ‘Handbook on The Chemistry and Physics of Rare Earths’, eds. K. A. Geschneidner and L. Eyring, North Holland, Amsterdam, l979, Vol. 3, Chap. 27, p. 337.
14. A. Jacobson, in ‘Solid State Chemistry, Compounds’, eds. A. K. Cheetham and P. Day, Clarendon Press, Oxford, 1992, p. 182ff.
15. D. W. Murphy, in ‘Advances in the Synthesis and Reactivity of Solids’, ed. T. Mallouk, JAI Press, London, 1991, Vol. 1, p. 237.
16. R. Ward, in ‘Progress in Inorganic Chemistry’, ed. F. A. Cotton, Interscience, New York, l959, Vol. l, p. 465.
17. S. Geller, *Acta Crystallogr.*, l957, **10**, 248.
18. J. P. Attfield, *Int. J. Inorg. Mat.*, 2001, **3**, 1147.
19. P. M. Woodward, T. Vogt, D. E. Cox, A. Arulaj, C. N. R. Rao, P. Karen, and A. K. Cheetham, *Chem. Mater.*, 1998, **10**, 3562.
20. D. D. Sarma, *Curr. Opin. Solid State Mater. Sci.*, 2001, **5**, 261.
21. C. N. R. Rao and J. Gopalakrishnan, ‘New Directions in Solid State Chemistry’, Cambridge Press, Cambridge, l986, p. 262.
22. M. A. Pena and J. L. G. Fiero, *Chem. Rev.*, 2001, **101**, 1981.
23. J. K. Burdett, G. D. Price, and S. L. Price, *J. Am. Chem. Soc.*, l982, **104**, 95.
24. R. D. Shannon and A. W. Sleight, *Inorg. Chem.*, 1968, **7**, 1649.
25. G. Farrington and J. L. Briant, *Science*, 1979, **204**, 1371.
26. K. J. H. Buschow and H. H. Van Mal, in ‘Intercalation Chemistry’, eds. M. S. Whittingham and A. J. Jacobson, Academic press, New York, 1982, p. 405.
27. J. S. Anderson, in ‘Intercalation Chemistry’, eds. M. S. Whittingham and A. J. Jacobson, Academic press, New York, 1982, Chap. 15, p. 405.
28. L. Kihlborg and A. Klug, *Chem. Scr.*, 1973, **3**, 207.
29. C. Michel, M. Hervieu, R. J. D. Tilly, and B. Raveau, *J. Solid State Chem.*, 1984, **52**, 281.
30. M. Greenblatt, *Chem. Rev.*, l988, **88**, 31. references cited therein.
31. P. A. Cox, ‘Transition Metal Oxides’, Clarendon Press, Oxford, l992.

32. C. Schlenker ed., ‘Low Dimensional Electronic Properties of Molybdenum Bronzes and Oxides’, Kluwer, Dordrecht, l989.
33. C. Schlenker, J. Dumas, C. Escribe-Filippini, and H. Guyot, in ‘Low Dimensional Electronic Properties of Molybdenum Bronzes and Oxides’, ed. C. Schlenker Kluwer, Dordrecht, l989, p. 159.
34. E. Canadel and M. H. Wangbo, *Chem. Rev.*, l991, **91**, 965.
35. M. Greenblatt, W. H. McCarroll, R. Niefeld, M. Croft, and J. V. Waszczak, *Solid State Commun.*, l984, **51**, 67l.
36. P. P. Tsai, J. A. Potenza, M. Greenblatt, and H. J. Schugar, *J. Solid State Chem.*, l986, **64**, 47.
37. E. Banks and A. Wold, in ‘Preparative Inorganic Chemistry’, ed. W. L. Jolly, Wiley, New York, l969, Vol. 4, p. 252.
38. J. Galy, J. Darriet, A. Casalot, and J. B. Goodenough, *J. Solid State Chem.*, l970, **1**, 339.
39. I. D. Raistrick, *Rev. Chem. Miner.*, 1984, **21**, 456.
40. J. B. Goodenough, *J. Solid State Chem.*, 1970, **1**, 349.
41. M. J. Sienko, in ‘Nonstoichiometric Compounds’, ed. R. S. Gould, Amer. Chem. Soc., Washington, DC, 1963, p. 224.
42. K. Kuwabara, M. Itoh, and K. Sugiyama, *Solid State Ionics*, 1986, **20**, 135.
43. J. Emsley and D. Hall, ‘The Chemistry of Phosphorus’, Wiley, New York, 1976.
44. F. Liebau, ‘Structural Chemistry of Silicates’, Springer-Verlag, Berlin, l985.
45. J. B. Farmer, in ‘Advances in Inorganic Chemistry and Radio-Chemistry’, eds. H. J. Emeléus and A. G. Sharpe, Academic Press, New York, l982, Vol 25, p. 187.
46. R. K. Iler, ‘The Chemistry of Silica’, Wiley, New York, 1979.
47. V. G. Hill and R. Roy, *Trans. Brit. Ceram. Soc.*, 1958, **57**, 496.
48. O. Toft, in ‘Nonstoichiometric Oxides’, ed. O. T. Sorenson, Academic Press, New York, 1981, p. 1.
49. C. R. A. Catlow, in ‘Nonstoichiometric Oxides’, ed. O. T. Sorenson, Academic Press, New York, 1981, p. 61.
50. A. Wold and K. Dwight, ‘Solid State Chemistry’, Chapman-Hall, New York, 1993, p. 93ff.
51. A. K. Cheetham, in ‘Nonstoichiometric Oxides’, ed. O. T. Sorenson, Academic Press, New York, 1981, p. 399.
52. M. Cherry, M. S. Islam, and C. R. A. Catlow, *J. Solid State Chem.*, 1995, **118**, 125.
53. C. N. R. Rao ‘New Directions in Solid State Chemistry’, Cambridge Press, Cambridge, l986, p. 259.
54. B. Tofield and W. Scott, *J. Solid State Chem.*, 1974, **10**, 183.
55. R. J. Tilly, *J. Solid State Chem.*, 1977, **21**, 293.
56. J. G. Bednorz and G. Müller, *Z. Phys. B*, 1986, **64**, 189.
57. M. K. Wu, J. R. Ashburn, C. J. Torng, P. H. Hor, R. L. Meng, L. Gao, Z. J. Huang, Y. Q. Wang, and C. W. Chu, *Phys. Rev. Lett.*, 1987, **58**, 908.
58. B. Raveau, M. Hervieu, C. Michel, D. Groult, and J. Provost, *Eur. J. Solid State Inorg. Chem.*, 1990, **27**, 25.
59. K. K. Singh and P. Edwards, ‘Advances in Solid State Chemistry’, ed. C. R. A. Catlow, JAI Press, London, 1982, p. 99.
60. T. Vanderah, ‘Chemistry of Superconductor Materials’ Noyes Publications, Park Ridge, NJ (1992).
61. R. E. Schaak and T. E. Mallouk, *Chem. Mater.*, 2002, **14**, 1455.
62. P. H. La Corre, M. Hervieu, and B. Raveau, *Rev. Inorg. Chem.*, 1984, **6**, l95.
63. M. Lesdesert, Ph. Labbé, W. H. McCarroll, H. Leligny, and B. Raveau, *J. Solid State Chem.*, 1993, **105**, 143.
64. K. V. Ramanujachary, S. E. Lofland, W. H. McCarroll, T. J. Emge, M. Greenblatt, and M. Croft, *J. Solid State Chem.*, 2002, **164**, 60.
65. C. R. Wiebe, A. Gourrier, T. Langet, J. F. Britten, and J. E. Greedan, *J. Solid State Chem.*, 2000, **151**, 31.
66. R. J. Cava, R. S. Roth, T. Siegrist, B. Hessen, J. J. Krajewski, and W. F. Peck, *J. Solid State Chem.*, 1993, **103**, 359.
67. M. M. Borel, M. Goreaud, A. Grandin, P. Labbe, A. Leclaire, and B. Raveau, *Eur. J. Solid State Inorg. Chem.*, 1991, **28**, 93.
68. M. Greenblatt, *Acc. Chem. Res.*, 1996, **29**, 219.B.
69. M. Greenblatt, *Int. J. Mod. Phys. B*, 1993, **7**, 3937.
70. P. Roussel, O. Perez, and Ph. Labbé, *Acta Crystallogr.*, 2001, **B57**, 603.
71. A. Leclaire and B. Raveau, *J. Solid State Chem.*, l987, **71**, 283.
72. R. E. McCarley, in ‘Inorganic Chemistry Towards the 21st Century’, ed. M. Chisholm, ACS, Washington, DC, 1983, p. 273.
73. R. E. McCarley, *Polyhedron*, 1986, **5**, 51.
74. J. Corbett and R. E. McCarley in ‘Crystal Chemistry and Properties of Materials with Quasi-One-Dimensional Structures’, ed. J. Rouxel and D. Reidel, 1986, p. 179.
75. J. Köhler, G. Svensson, and A. Simon, *Angew. Chem., Int. Ed. Engl.*, 1992, **31**, 1437.
76. A. Simon, in ‘Solid State Chemistry, Compounds’, eds. A. K. Cheetham and P. Day, Clarendon Press, Oxford, 1992, p. 112.
77. A. Simon, *Angew. Chem., Int. Ed. Engl.*, l988, **27**, 159.
78. F. A. Cotton and T. Haas, *Inorg. Chem.*, l964, **3**, 1217.
79. C. C. Torardi and R. E. McCarley, *J. Solid State Chem.*, 1981, **37**, 393.
80. H. Leligny, M. Ledesert, P. Labbé, B. Raveau, and W. H. McCarroll, *J. Solid State Chem.*, 1990, **87**, 35.
81. P. Gougeon and R. E. McCarley, *Acta Crystallogr.*, 1991, **C47**, 241.
82. R. Gautier, O. K. Andersen, P. Gougeon, J.-F. Halet, E. Candadell, and J. D. Martin, *Inorg. Chem.*, 2002, **41**, 4689.
83. J. M. Tarascon and G. W. Hull, *Solid State Ionics*, 1986, **22**, 85.

84. L. E. Aleandri and R. E. McCarley, *J. Solid State Chem.*, l988, **27**, 1041.
85. C. C. Torardi and R. E. McCarley, *J. Am. Chem. Soc.*, 1979, **101**, 3963.
86. G. V. Vajenine and A. Simon, *Inorg. Chem.*, 1999, **38**, 3463.
87. C. E. Michelson, P. E. Rauch, and F. DiSalvo, *Mater. Res. Bull.*, 1990, **25**, 971.
88. J. Tortelier, P. Gougeon, K. V. Ramanujachary, and M. Greenblatt, *Mater. Res. Bull.*, 1998, **33**, 1151.
89. J. Tortelier and P. Gougeon, *Inorg. Chem.*, 1998, **36**, 6229.
90. N. Barrier, J. Tortelier, and P. Gougeon, *Acta Crystallogr.*, 2000, **C56**, 269.
91. P. D. Battle, G. R. Blake, J. Sloan, and J. F. Vente, *J. Solid State Chem.*, 1998, **136**, 103.
92. K. E. Stitzer, J. Darriet, and H.-C. zur Loye, *Curr. Opin. Solid State Mater. Sci.*, 2001, **5**, 535.
93. Z. Serpil, J. Gopalakrishnan, B. W. Eichhorn, and R. L. Greene, *Inorg. Chem.*, 2001, **40**, 4996.
94. A. Santoro, I. N. Sora, and Q. Huang, *J. Solid State Chem.*, 1999, **143**, 69.
95. C. Feiser and R. J. Cava, *Phys. Rev.*, 2000, **B61**, 10006.
96. R. N. Vest and J. M. Honig, in ‘Electrical Conductivity in Ceramics and Glass’, ed. N. M. Tallan, Dekker, New York, l974, Part B, Chap. 6, p. 343.
97. D. Adler, in ‘Electrical Conductivity in Ceramics and Glass’, ed. N. M. Tallan, Dekker, New York, l974, Part A, Chap. 1, p. 1.
98. J. G. Goodenough, *Prog. Solid State Chem.*, 1971, **5**, 149.
99. A. Wold and K. Dwight, ‘Solid State Chemistry’, Chapman-Hall, New York, 1993, p. 90ff.
100. C. N. R. Rao, *Annu. Rev. Phys. Chem.*, l989, **40**, 291.
101. Z. Teweldemedhin, K. V. Ramujachary, and M. Greenblatt, *J. Solid State Chem.*, 1990, **86**, 109.
102. P. Kofstad, ‘Nonstoichiometry, Diffusion and Electrical Conductivity in Binary Metal Oxides’, Wiley-Interscience, New York, 1972, p. 213.
103. D. B. Rogers, R. D. Shannon, A. W. Sleight, and J. L. Gillson, *Inorg. Chem.*, 1969, **8**, 841.
104. C. C. Torardi, C. Fecketter, W. H. McCarroll, and F. DiSalvo, *J. Solid. State Chem.*, 1985, **60**, 332.
105. A. W. Sleight, in ‘Advanced Materials in Catalysis’, eds. J. Burton and R. L. Garten, Academic Press, New York, 1977, Chap. 6, p. 181.
106. A. W. Sleight, in ‘Solid State Chemistry, Compounds’, eds. A. K. Cheetham and P. Day, Clarendon Press, Oxford, 1992, Chap. 5, p. 166.
107. S. C. Stinson, *Chem. Eng. News*, 1983, **61**, 19.
108. J. C. Brice, ‘Crystal Growth Processes’, Wiley, New York, 1986.
109. P. Hagenmuller, ed., ‘Preparative Methods in Solid State Chemistry’, Academic Press, New York, 1972.
110. A. Wold and K. Dwight, in ‘Advances in the Synthesis and Reactivity of Solids’, ed. T. Mallouk, JAI Press, London, 1991, Vol. 1, p. 133.
111. U. Schubert and N. Husing, ‘Synthesis of Inorganic Materials’, Wiley VCH, Weinheim, 2000.
112. T. W. Swaddle, ‘Inorganic Chemistry’, Academic press, New York, 1997.
113. P. J. van der Put, ‘The Inorganic Chemistry of Materials’, Plenum Press, New York, 1998, Chap. 8.
114. J. P. Remeika, *J. Am. Chem. Soc.*, 1956, **78**, 4259.
115. J. M. Honig, in ‘Preparation and Characterization of Materials’, eds. J. M. Honig and C. N. R. Rao, Academic Press, New York, l98l, p. 339.
116. D. W. Johnson, Jr, *Am. Ceram. Soc., Bull.*, 1985, **64**, 1597.
117. L. C. Klein, *Ann. Rev. Mater. Sci.*, 1985, **15**, 227.
118. C. D. Chandler, C. Roger, and M. J. Hammpden-Smith, *Chem. Rev.*, 1993, **93**, 1205.
119. M. S. Whittingham and A. J. Jacobson eds, ‘Interculation Chemistry’, Academic Press, New York, l982.
120. A. Jacobson, in ‘Solid State Chemistry, Compounds’, eds. A. K. Cheetham and P. Day, Clarendon Press, Oxford, 1992, p. 211. cited refs.
121. R. Schöllhorn, *Angew. Chem., Int. Ed. Engl.*, 1980, **19**, 983.
122. A. Manthiram and J. Kim, *Chem. Mater.*, 1998, **10**, 2895.
123. T. Takamura, *Solid State Ionics*, 2002, **152–153**, 19.
124. G. Farrington and J. L. Briant, *Mater. Res. Bull.*, 1978, **13**, 763.
125. B. C. Tofield, in ‘Interculation Chemistry’, eds. M. S. Whittingham and A. J. Jacobson, Academic Press, New York, l982, Chap. 6, p. 181.
126. J. M. Tarascon, *J. Electrochem. Soc.*, 1987, **134**, 1345.
127. A. Clearfield, ‘Inorganic Ion Exchange Materials’, CRC Press, Boca Raton, FL, l982.
128. A. Clearfield, in ‘Preparation and Characterization of Materials’, eds. J. M. Honig and C. N. R. Rao, Academic Press, New York, l98l, p. 283.
129. R. F. Ziolo, E. P. Giannelis, B. A. Weinstein, M. P. O’Horo, B. N. Ganguly, V. Mehrotra, M. W. Russell, and D. R. Huffman, *Science*, l992, **257**, 219.
130. H. Schafer, in ‘Preparative Methods in Solid State Chemistry’, ed. P. Hagenmuller, Academic Press, New York, 1972, p. 252.
131. H. Schafer, ‘Chemical Transport Reactions’, Academic Press, New York, 1964.
132. R. B. Sargent and N. A. O’Brien, *MRS Bull.*, 2003, **28**, 372.
133. J. T. Spencer, *Prog. Inorg. Chem.*, 1994, **41**, 145.
134. A. C. Jones, *J. Mater. Chem.*, 2002, **12**, 2516.
135. A. Wold and D. Bellevance, in ‘Preparative Methods in Solid State Chemistry’, ed. P. Hagenmuller, Academic Press, New York, 1972, p. 279.
136. M. E. DeRoy and J. P. Besse, *Rev. Int. Haute Temp. Refract.*, 1987, **24**, 71.

137. W. H. McCarroll, I. D. Fawcett, M. Greenblatt, and K. V. Ramanujachary, *J. Solid State Chem.*, 1999, **146**, 88.

138. W. H. McCarroll, C. Darling, and G. Jakubicki, *J. Solid State Chem.*, 1983, **48**, 189.

139. M. L. Norton and H. Y. Tang, *Chem. Mater.*, 1991, **3**, 431.

140. J. Etourneau, in ‘Solid State Chemistry, Compounds’, eds. A. K. Cheetham and P. Day, Clarendon Press, Oxford, 1992, p. 90.

141. R. A. Laudise, *Int. J. Inorg. Mat.*, 2001, **3**, 1.

142. A. M. Anthony and R. Collongues, in ‘Preparative Methods in Solid State Chemistry’, ed. P. Hagenmuller, Academic Press, New York, 1972, p. 208.

143. J. M. Newsam, ‘Advances in Solid State Chemistry’, ed. C. R. A. Catlow, Chap. 7, JAI Press, London, 1982, p. 251.

144. C. C. Torardi and J. C. Calbrese, *Inorg. Chem.*, 1984, **23**, 3281.

145. C. J. M. Rooymans, in ‘Preparative Methods in Solid State Chemistry’, ed. P. Hagenmuller, Academic Press, New York, 1972, p. 72.

146. C. N. R. Rao and J. Gopalakrishnan, ‘New Directions in Solid State Chemistry’, Cambridge Press, Cambridge, l986, Chap. 3, p. 124.

147. J. Goodenough, J. A. Kafalas and J. M. Longo, in ‘Preparative Methods in Solid State Chemistry’, ed. P. Hagenmuller, Academic Press, New York, 1972, p. 2.

148. G. Demazeau, A. Marbeuf, M. Pouchard, and P. Hagenmuller, *J. Solid State Chem.*, 1971, **3**, 582.

149. G. Demazeau, B. Bouffat, M. Pouchard, and P. Hagenmuller, *J. Solid State Chem.*, 1982, **45**, 88.

150. W. K. Ham, G. F. Holland, and A. M. Stacy, *J. Am. Chem. Soc.*, 1988, **119**, 5214.

151. J. Lee and G. Holland, *J. Solid State Chem.*, 1991, **93**, 267.

152. J. B. Goodenough and J. M. Longo, ‘Landolt-Bornstein, New Series’, Springer-Verlag, New York, 1970, Group III/, Vol. 4a.

153. M. T. Anderson, K. B. Greenwood, G. A. Taylor, and K. R. Poeppelmeier, *Prog. Solid State Chem.*, 1993, **22**, 197.

154. W. Sugimoto, M. Shirata, Y. Sugahara, and K. Kuroda, *J. Am. Chem. Soc.*, 1999, **121**, 11601.

155. T. A. Kodenkandath, J. N. Lalena, W. L. Zhou, E. E. Carpenter, C. Sangregorio, A. U. Falster, W. B. Simons Jr, C. J. O’Connor, and J. B. O’Connor, *J. Am. Chem. Soc.* 1999, **121**, 10743.

156. T. Sivakumar, K. Ramesha, S. E. Lofland, K. V. Ramanujachary, G. N. Subbanna, and J. Gopalakrishnan, *Inorg. Chem.*, 2004, **43**(6), 1857.

157. W. Büchner, R. Schliebs, G. Winter, and K. H. Büchel, ‘Industrial Inorganic Chemistry’, VCH, New York, 1989, p. 556.

158. R. C. Buchanan ed., ‘Ceramic Materials for Electronics’, 2nd edn., Marcel Dekker, New York, l991.

159. R. A. Laudise, in ‘Solid State Chemistry, A Contemporary Overview’, eds. S. M. Holt, J. B. Milstein, and M. Robbins, American Chem. Soc., Washington, DC, l980, p. 95.

160. D. C. Hill and H. L. Tuller, *Prog. Solid State Chem.*, 1993, **22**, 249.

161. W. Büchner, R. Schliebs, G. Winter and K. H. Büchel, ‘Landolt-Bornstein, New Series’, Springer-Verlag, New York, 1970, Group III, Vol. 4a, p. 557.

162. T. G. Reynolds and R. C. Buchanan, ‘Industrial Inorganic Chemistry’, Chap. 4, VCH, New York, 1989, p. 207.

163. G. H. Hartling, *J. Am. Chem. Soc.*, 1999, **121**, 129.

164. G. Blass and B. C. Grabmaier, ‘Luminescent Materials’, Springer Verlag, Berlin, 1994.

165. W. Büchner, R. Schliebs, G. Winter and K. H. Büchel, ‘Industrial Inorganic Chemistry’, VCH, New York, 1989, Sect. 5.9, p. 553.

166. B. Dunn, G. C. Farrington, and J. O. Thomas, *MRS Bull.*, 1989, **14**, 22.

167. C. F. Bacalski, M. A. Cherry, G. A. Hirata, J. M. McKittrick, J. Mourant, *J. Soc. Inf. Disp.*, Suppl. 1, 2000, 93.

168. R. Chen and D. J. Lockwood, *J. Electrochem. Soc.*, 2002, **149**, S69.

169. M. Kusters, J. Singleton, D. A. Keon, R. M. Greedy, and W. Hayes, *Physica B*, 1989, **155**, 362.

170. B. C. Hauback, H. Fjellvag, and N. Sakai, *J. Solid State Chem.*, 1996, **124**, 43.

171. Y. Tokura, A. Urushibara, Y. Morimoto, T. Arima, A. Asamitsu, G. Kido, and N. Furukawa, *J. Phys. Soc. Jpn.*, 1994, **63**, 3931.

172. A. Urushibara, Y. Morimoto, T. Arima, A. Asamitsu, G. Kido, and Y. Tokura, *Phys. Rev.*, 1995, **B51**, 14104.

173. B. Raveau, A. Maignan, C. Martin, and M. Hervieu, *Chem. Mater.*, 1998, **10**, 2641.

174. B. Mercey, J. Wolfman, and B. Raveau, *Curr. Opin. Solid State Mater. Sci.*, 1999, **4**, 27.

175. B. Raveau, M. Hervieu, A. Maignan, and C. Martin, *J. Mater. Chem.*, 2001, **11**, 29.

176. P. M. Woodward, D. E. Cox, T. Vogt, C. N. R. Rao, and A. K. Cheetham, *Chem. Mater.*, 1999, **11**, 3528.

177. K.-I. Kovayashi, T. Kimura, H. Sawada, K. Terakura, and Y. Tokura, *Nature*, 1998, **395**, 877.

178. S. Li and M. Greenblatt, *J. Alloys Compd.*, 2002, **338**, 121.

179. R. I. Dass and J. B. Goodenough, *Phys. Rev.*, 2001, **B63**, 64417.

180. W. A. Surdoval, S. C. Singhai, and G. L. McVay, in ‘Proc. 7th Int. Symp. On Solid Oxide Fuel Cells’, eds. H. Yokokawa and S. C. Singhal, Electrochemical Society, 2001, Vol. 16 PV, p. 53.

181. J. P. P. Huijsmans, *Curr. Opin. Solid State and Mater. Sci.*, 2001, **5**, 317.

182. K. Keqin, P. Hou, and J. B. Goodenough, *Solid State Ionics*, 2000, **143**, 237.

183. T. Brylewski, M. Nanko, T. Maruyama, and K. Pzybylski, *Solid State Ionics*, 2000, **143**, 13.

184. A. I. Kingdon and S. K. Streiffer, *Curr. Opin. Solid State Mater. Sci*, 1999, **4**, 39.

185. U. Schubert and N. Hüsing, 'Synthesis of Inorganic Materials', Wiley-VCH, New York, 2000, p. 194.

186. H. N. Al-Shareef, D. Dimos, T. J. Boyle, W. L. Warren, and B. A. Tuttle, *Appl. Phys. Lett.*, 1996, **68**, 690.

187. K. F. Hulme, in 'Modern Oxide Materials', eds. B. Cockayne and D. W. Jones, Academic press, New York, 1972, p. 53.

188. P. Guenot, *MRB Bull.*, 2003, **28**, 360.

189. H. Ohno, *Science*, 1998, **281**, 951.

190. G. Prinz, *Science*, 1998, **282**, 1660.

191. Y. Matsumoto, M. Murakami, T. Shono, T. Hasegawa, T. Fukumura, M. Kawasaki, P. Ahmet, T. Chikyow, Sh. Koshihara, and H. Koinuma, *Science*, 2001, **291**, p854.

192. P. Sharma, A. Gupta, K. V. Rao, F. J. Owens, R. Sharma, R. Ahuja, J. M. O. Guillen, B. Johansson, and G. A. Gehring, *Nature Materials*, 2003, **2**, 673.

193. G. Goodman, in 'Ceramic Materials for Electronics', 2nd edn., ed. R. C. Buchanan, Marcel Dekker, New York, l991, p. 69.

194. J. D. Filby, in 'Modern Oxide Materials', eds. B. Cockayne and D. W. Jones, Academic press, New York, 1972, p. 203.

195. R. Einzinger, *Ann. Rev. Mater. Sci.*, 1987, **17**, 299.

196. L. M. Levenson and H. R. Philipp, in 'Ceramic Materials for Electronics', 2nd edn., ed. R. C. Buchanan Marcel Dekker, New York, l991, p. 349.

197. D. I. Makin, K. F. Hulme, in 'Modern Oxide Materials', eds. B. Cockayne and D. W. Jones, Academic press, New York, 1972, p. 235.

198. M. M. Woyski and W. J. Silvernail, in 'The Rare Earths', eds. F. H. Spedding, and A. H. Deane, Kreiger Publications, NY, 1971, p. 512.

Oxygen: Inorganic Chemistry

Mohan S. Bharara & David A. Atwood
University of Kentucky, Lexington, KY, USA

Based in part on the article Oxygen: Inorganic Chemistry by Donald T. Sawyer which appeared in the Encyclopedia of Inorganic Chemistry, First Edition.

1 Introduction 1
2 Redox Thermodynamics for Oxygen Species (O_2, O_3, HOO•, O_2^{-}•, HOOH, HOO^{-}, O, and HO•) 4
3 Chemical Bonds for Oxygen 5
4 Reactivity and Activation of Hydrogen Peroxide (HOOH) and Hydroperoxides (ROOH) 11
5 Reactivity of Oxygen Radicals (HO•, RO•, HOO•, and ROO) 19
6 Reactivity and Activation of Dioxygen (•O_2•) 22
7 Reactivity of Superoxide Ion (O_2^{-}•) 28
8 Reactivity of Oxyanions (HO^{-}, RO^{-}, HOO^{-} and ROO^{-}) 34
9 Related Articles 42
10 References 42

1 INTRODUCTION

Dioxygen, produced by photosynthetic bacteria more than two billion years ago, makes up 21% of the atmosphere of the earth. Oxygen is ubiquitous both in inorganic minerals and in all living things, where it is a key component of proteins and carbohydrates, for example. Unlike any other molecule in the atmosphere, oxygen, in its ozone allotrope protects the earth by filtering out harmful UV-C and UV-B radiation. The many disparate uses for oxygen rely on the fact that the molecule is reactive and can be converted into many other reactive oxygen species. This review will describe how these additional oxygen species are formed, give some basic chemical information, and offer a brief description of the important reactions these species participate in.

1.1 Water

The HOH molecule (oxygenated hydrogen) is the most important oxygen-containing molecule and is fundamental to the realm of oxygen chemistry. It possesses exceptional ruggedness and thermal stability by virtue of strong chemical bonds (equation 1).

$$\mathrm{HOH\,(g)} \xrightarrow[\Delta H_{\mathrm{DBE}} = 119\ \mathrm{kcal\ mol^{-1}}]{} \mathrm{H\bullet\,(g)} + \mathrm{HO\bullet(g)} \xrightarrow[\Delta H_{\mathrm{DBE}} = 103\ \mathrm{kcal\ mol^{-1}}]{} \mathrm{H\bullet} + \bullet\mathrm{O}\bullet \qquad (1)$$

DBE = dissociative bond energy

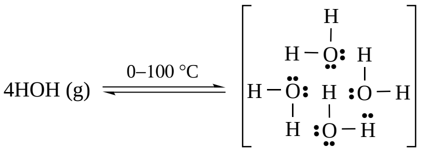
(2)

Thus, 222 kcal mol^{-1} must be transferred to HOH to produce atomic oxygen, which is a measure of the deactivation and stabilization of atomic oxygen in the formation of a water molecule. Another important and unique characteristic of water molecules is their tendency to cluster through intermolecular *hydrogen bonds* (more properly hydrogen–oxygen bonds) (equation 2). In contrast, for ambient conditions, BH_3, CH_4, NH_3, and HF are monomeric gas molecules (as are CO, CO_2, H_2S, and SO_2).

Liquid water also has exceptional solvation energies for small ions and thereby promotes the dissolution and heterolytic dissociation (ionization) of salt, acid, and base molecules, for example, NaCl (s), HCl (g), and NaOH (s) (equation 3).

This ability to interact strongly with positively and negatively charged ions is consistent with water's unique amphoteric (acid–base) properties, and is why it is fundamental to the Brønsted acid–base theory (equations 4 and 5).

$$\mathrm{NaCl(s)} \xrightarrow{H_2O} \underset{[\mathrm{Na^+(aq)}]}{[\mathrm{Na(OH_2)_{4-6}}]^+} + \underset{[\mathrm{Cl^-(aq)}]}{[\mathrm{Cl(H_2O)_{4-6}}]^-} \qquad (3)$$

$$\mathrm{HCl(g) + H_2O(l)} \xrightarrow{H_2O} \mathrm{H_3O^+(aq) + Cl^-(aq)} \qquad (4)$$

$$\mathrm{Na_2O(s) + H_2O(l)} \xrightarrow{H_2O} \mathrm{2Na^+(aq) + 2HO^-(aq)} \qquad (5)$$

$$\mathrm{Cl_2(aq) + 2H_2O(l)} \xrightleftharpoons{H_2O} \mathrm{HOCl(aq) + H_3O^+(aq) + Cl^-(aq)} \qquad (6)$$

$$\mathrm{SO_3(g) + 2H_2O(l)} \xrightleftharpoons{H_2O} \mathrm{H_3O^+(aq) + HOSO_2O^-(aq)} \qquad (7)$$

$$\mathrm{2Na(s) + 2H_2O} \longrightarrow \mathrm{H_2(g) + 2Na^+(aq) + 2HO^-(aq)} \qquad (8)$$

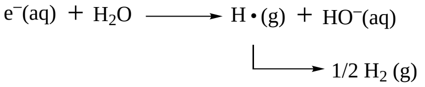
$$\mathrm{e^-(aq) + H_2O} \longrightarrow \mathrm{H\bullet(g)} + \mathrm{HO^-(aq)};\quad \mathrm{H\bullet(g)} \longrightarrow \tfrac{1}{2}\,\mathrm{H_2\,(g)} \qquad (9)$$

Although the water molecule is exceptionally rugged, it is a reductant (nucleophile) of strong oxidants (electrophiles) (equations 6 and 7) and an oxidant (electrophile) of strong reductants (nucleophiles) (equations 8 and 9).

Water is the essential matrix for (C, N, O, H)-based life. Thus, all living biopolymers have a water–carbohydrate surface component with hydrogen–oxygen bonding. The inter- and intracellular aqueous phases are essential for the dissolution and transport of sugars, salts, nutrients, and some enzymes and cofactors for homogeneous, solution-phase metabolism and respiration.

1.2 Metals and Nonmetals

When the Earth first formed from a condensed cloud of gases and dust, those elements and molecules that are unstable in the presence of water reacted to form oxygenated products through the reduction of water to molecular hydrogen (equations 10–14).

$$\begin{tikzcd}
\mathrm{Ca\,(g)} + \mathrm{H_2O\,(g)} \arrow[r] & \mathrm{H_2\,(g)} + \mathrm{(CaO)}_n\,\mathrm{(s)} \arrow[d, "\mathrm{H_2O\,(l)}"] \\
 & \mathrm{Ca^{2+}\,(aq)} + \mathrm{2HO^-\,(aq)}
\end{tikzcd} \qquad (10)$$

$$2\mathrm{Al(g)} + 3\mathrm{H_2O(g)} \longrightarrow 3\mathrm{H_2(g)} + (\mathrm{Al_2O_3})_n\mathrm{(s)} \qquad (11)$$

$$\begin{tikzcd}
\mathrm{Fe\,(g)} + \mathrm{H_2O(g)} \arrow[r] & \mathrm{H_2(g)} + \mathrm{FeO\,(s)} \arrow[d, "\mathrm{H_2O(l)}"] \\
 & \mathrm{Fe^{2+}\,(aq)} + \mathrm{2HO^-\,(aq)}
\end{tikzcd} \qquad (12)$$

$$2\mathrm{P(g)} + 6\mathrm{H_2O(g)} \longrightarrow 3\mathrm{H_2(g)} + 2\mathrm{HPO(OH)_2(aq)} \qquad (13)$$

$$n\,\mathrm{Si(g)} + 2n\mathrm{H_2O(g)} \longrightarrow 2n\mathrm{H_2(g)} + (\mathrm{SiO_2})_n\mathrm{(s)} \qquad (14)$$

The transformation of the Earth's atmosphere to an oxidizing environment through the photosynthetic oxidation of water to dioxygen (O_2) (photosystem II of green plants; *see Photosystem I*) resulted in the autoxidation of the reduced forms of the molecules of the Earth's crust, oceans, and atmosphere (over a period of about 750 million years) (equations 15–19).[1–3]

$$4\mathrm{FeO(s)} + \mathrm{O_2} \longrightarrow 2\mathrm{Fe_2O_3(s)} \xrightarrow{\mathrm{FeO}} \mathrm{Fe_3O_4(s)} \qquad (15)$$

$$2\mathrm{HPO(OH)_2(aq)} + \mathrm{O_2} \xrightarrow{\mathrm{H_2O}} 2\mathrm{(HO)_3PO(aq)} \qquad (16)$$

$$2\mathrm{Cu(s)} + \mathrm{O_2} \longrightarrow 2\mathrm{CuO(s)} \qquad (17)$$

$$2\mathrm{C} + \mathrm{O_2} \longrightarrow 2\mathrm{CO} \xrightarrow{\mathrm{O_2}} 2\mathrm{CO_2} \qquad (18)$$

$$4\mathrm{NH_3} + 3\mathrm{O_2} \longrightarrow 2\mathrm{N_2} + 6\mathrm{H_2O} \qquad (19)$$

Another unique characteristic of oxygen-containing molecules is their exceptionally strong X–O bonds. For example, the gas-phase enthalpies for homolytic bond dissociation (ΔH_{DBE}) are: H–O•, 103 kcal mol^{-1}; HO–H, 119 kcal mol^{-1}; CO, 257 kcal mol^{-1}; BaO, 134 kcal mol^{-1}; FeO, 93 kcal mol^{-1}.

1.3 Dioxygen

The discovery and isolation of molecular oxygen (dioxygen, O_2) was first reported in 1774 by Joseph Priestley, but was independently codiscovered by Scheele in Sweden, who gave it the name *fire air* (reported in 1777).[1] Because it did not support combustion in a manner equivalent to other fuels, Priestley named the substance 'dephlogisticated air' ('air that does not burn'). He also discovered that green plants generate dioxygen. In 1777, Antoine L. Lavoisier identified dioxygen as a component of air, and named it *oxygen* on the basis that its reaction with other elements generated oxy acids (his alternative designation was *vital air*). He established that dioxygen is the oxidant of fuels in combustion, and that it is the essential oxidant for biological respiration. Because science was a hobby rather than a vocation with Lavoisier, his contributions were limited by available time and by a foreshortened life. Prior to the French Revolution, he made a living as a tax collector. He was beheaded during the French revolution. Scheele observed that pure dioxygen (1 atm) is toxic to plants; Priestley made similar observations.[1]

Thus, in the late 18th century, Priestley, Scheele, and Lavoisier had established that dioxygen comprises about 21% (by volume) of the Earth's atmosphere, that it is essential for aerobic life and toxic to plant life at high concentrations, and that it is the essential oxidant for the combustion of organic molecules (fuels). Priestley also noted that nitric oxide reacts with O_2 to produce NO_2 and N_2O_4, which react with water to form HON(O) and $HON(O)_2$ (nitrous acid and nitric acid).

About 2.5 billion years before dioxygen was chemically identified and characterized, it was added to the Earth's atmosphere as a natural product through photosynthetic oxidation of water by primitive green plants (blue–green algae). Life, which evolved on Earth in the absence of dioxygen some 3.5 billion years ago, was restricted to hydrogen sulfide as a source of hydrogen atoms for bacterial photosynthetic energy transfer.[2,3] With the development of blue–green algae and photosystem II some one billion years later, water replaced hydrogen sulfide as a source of reducing equivalents with dioxygen a by-product. Prior to the development of these primitive marine plants, photosynthetic life was limited to bacteria that could avail themselves of hydrogen sulfide from marine sources. Although extensive production of dioxygen occurred with the appearance of blue–green algae, biological utilization of dioxygen (aerobic life and oxidative metabolism) had to await another 750 million years for significant quantities of dioxygen to become available. This amount of time was required to produce sufficient dioxygen to titrate the immense amount of reduced iron (Fe^{II}) present in the Earth's oceans. Until this was precipitated as iron(III) oxide, the atmospheric concentration of oxygen was less than 1%. Thus, about 1.7 billion years ago there was an almost instant transformation of the atmosphere to 17–21% dioxygen.[2] Until then, life was restricted to the aquatic environment of the ocean. The absence of atmospheric oxygen precluded the photosynthetic production of ozone, which is the essential shield from the solar UV radiation that is sufficiently energetic to break the chemical bonds of organic compounds.

1.4 Biosynthesis of Dioxygen

Green-plant photosynthesis utilizes water as a source of reducing equivalents (hydrogen atoms). As a result, there is a parallel evolution of dioxygen from the plant cells (chloroplasts) with the photosynthetic 'fixing' of carbon dioxide as carbohydrate. The conventional wisdom for the mechanism of photosynthesis includes two independent photosystems that pump reducing equivalents from water (photosystem II)[4–7] through a cascade of steps controlled by enzymes to a CO_2 reduction center (photosystem I).[8] The essential components for the dehydrogenation of water include manganese,[4–6] chloride ion, calcium ion, and bicarbonate ion. Green plants that are deprived of manganese in the chloroplast cells of the leaves cease to evolve oxygen. Full photosynthetic activity and oxygen evolution can be restored by the administration of manganese.

Photosystem II (PS II) within higher plants represents a solar-energy-driven process that removes hydrogen atoms from water to form molecular oxygen (O_2, dioxygen) through an overall four-electron transfer reaction (equation 20),[9–12]

$$2H_2O \longrightarrow O_2 + 4[H^+ + e^- \equiv H] \qquad (20)$$
$$E^{\circ\prime}(\text{pH } 5) = +0.93 \text{ V vs. NHE}$$

where NHE is the normal hydrogen electrode. The mechanistic sequence that facilitates this reaction involves an initial photoactivation process in which light is trapped and converted to chemical energy. This energy is subsequently transferred to other protein complexes within the lipoprotein membrane, where the chemical transformation of water to dioxygen occurs. The almost instantaneous increase in the concentration of dioxygen in the oceans had revolutionary consequences for the existent anaerobic life. The vast majority of species could not adapt rapidly enough and were destroyed (or retreated to an oxygen-free environment). Some species adapted and others evolved to oxygen-utilizing aerobes. With dioxygen present in the atmosphere, solar radiation transformed a small fraction of it to ozone and thereby provided a protective shield against short-wavelength UV light (equation 21).

$$3O_2 \xrightarrow{h\nu} 2O_3 \qquad (21)$$

In turn, this made it possible for the newly evolved aerobes to leave the marine environment and establish terrestrial life, and the subsequent evolutionary development of higher forms of life. Aerobic life had to develop and make effective use of dioxygen as an energy source through oxidation of organic molecules. This required the biosynthesis of a series of metalloproteins to facilitate the transport and the selective reactivity of dioxygen and its activated forms ($O_2^{-}\cdot$, HOO•, HOOH, HOO^-, and HO•) in respiration, metabolic, and detoxification processes. Although dioxygen is vital for biological oxidations and oxygenation reactions, the mechanisms and energetics for its reduction, and for the interconversion of the various dioxygen species, have been characterized to a reasonable degree only during the past two decades.

In the chemical realm, the dioxygen molecule (•O• triplet ground state) is a unique reagent with two unpaired electrons (biradical) and a bond order of two. With its introduction into the oceans of the planet as a by-product of green-plant photosynthesis, the transformation of the reducing environment into an oxidized state began. Those transition metals that were present autoxidized ($Fe^{II} \rightarrow Fe_2O_3$ (s), Fe_3O_4 (s); $Mn^{II} \rightarrow MnO_2$ (s), etc.) and, in most cases, precipitated as metal oxides. The same was true for the reduced forms of organic molecules (MeCH(O) $\rightarrow$ MeC(O)OH, RSH $\rightarrow$ RSSR, $H_2S \rightarrow S_8$, etc.).

Aerobic life makes use of dioxygen as an oxidant in all of its respiration and oxidative metabolic processes. These are processes whereby the reducing equivalents of food (carbohydrates, fats, and proteins) are oxidized by dioxygen to give water, carbon dioxide, and urea. Although the transformation is equivalent to combustion, biology uses catalysts known as enzymes and cofactors (*see Enzyme* and *Coenzyme*) to control the reaction pathway in specific steps that release and/or store energy. Combustion is a radical autoxidation process that requires a high-temperature initiation step. For example, the efficient transformation of the oxidizing energy of dioxygen into heat and stored chemical energy is accomplished in eukaryotic cells with a protein known as **Cytochrome Oxidase**.[13,14] This system contains two iron–porphyrin (heme) groups and at least two copper atoms, and is able to transform about 80% of the redox energy stored in dioxygen (chemists and engineers have not been able to achieve a comparable efficiency with synthetic catalysts). Aerobic life also makes use of a vast array of metalloproteins for the selective catalysis of processes that produce useful biomolecules from the reaction of dioxygen and hydrogen peroxide with specific substrates.[15] In most cases, these biological catalysts include one or more transition metals (iron, copper, manganese, and molybdenum) at their active sites. Although oxidases and peroxidases accomplish their chemistry by hydrogen-atom transfer (or electron–proton transfer), there are other catalysts (oxygenases) that transform substrates by the addition of one or two oxygen atoms from the dioxygen molecule.

1.5 Activation and Reactivity of Dioxygen Species (•O_2•, HOO•, $O_2^{-}\cdot$, HOOH)

Because the ground state of dioxygen is a triplet with two unpaired electrons with parallel spins, its reactivity with organic molecules in the singlet state is severely restricted, particularly at room temperature. Dioxygen's limited reactivity as a product is undoubtedly an essential feature of biosynthetic processes. A product with high reactivity would have destroyed the 'maker'. Although dioxygen is a strong oxidant at pH 7 when utilized as a concerted four-electron transfer agent, it is an extremely weak one-electron oxidant ($O_2 + e^- \rightarrow O_2^-\cdot$; $E°$, -0.16 V vs. NHE (unit molarity for standard states)).

Because approximately 15% of the O_2 that is respired by mammals appears to go through the superoxide state, the biochemistry and reaction chemistry of this species is of interest to those concerned with oxygen toxicity, carcinogenesis, and aging.[16] The most general and universal property of $O_2^-\cdot$ is its tendency to act as a strong Brønsted base. Although the acidity of hydroperoxy radical (HOO•) in water (pK_a 4.9) is the same as acetic acid, the strong proton affinity of $O_2^-\cdot$ is due to its redox-driven propensity to be O_2 and HOOH (equation 22).

$$2O_2^-\cdot + H_2O \rightleftharpoons O_2 + HOO^- + HO^- \qquad (22)$$
$$K = 2.5 \times 10^8 \text{atm}$$

Thus, two superoxide ions plus a water molecule are converted to two strong bases. This strong proton affinity manifests itself in any media and is exemplified by the ability of $O_2^-\cdot$ to deprotonate butanol.

The existence of proteins such as *Superoxide Dismutase*[17] and *Catalase*[18,19] in aerobes often is cited in support of the conclusion that $O_2^-\cdot$ and HOOH are biological toxins. The present understanding of the biological utilization of hydrogen peroxide includes enzyme-facilitated processes that involve its disproportionation, the dehydrogenation of organic molecules, and the production of hypochlorous acid in neutrophils (equations 23–25).

$$\text{HOOH} + \text{HOOH} \xrightarrow{\text{catalase}} O_2 + 2H_2O \qquad (23)$$

$$RCH_2OH + \text{HOOH} \xrightarrow{\text{peroxidase}} RCHO + 2H_2O \qquad (24)$$

$$HCl + \text{HOOH} \xrightarrow{\text{myeloperoxidase}} HOCl + H_2O \qquad (25)$$

Given that the myeloperoxidase enzyme[20] (*see Peroxidases*) within the neutrophils produces hypochlorous acid, an intriguing possibility is that it may combine with another hydrogen peroxide molecule. Such a reaction in the laboratory produces a stoichiometric quantity of singlet dioxygen ($^1O_2$), which is selectively reactive with conjugated polyenes.

Although the introduction of O_2 into the Earth's atmosphere revolutionized biology and gave birth to oxidative metabolism and the associated biochemistry (oxidases, peroxidases, superoxide dismutases, monooxygenases, dioxygenases, lipid peroxidation and autoxidation, and antioxidants (ascorbic acid, α-tocopherol, glutathione, and thiols)), the chemistry of dioxygen and hydrogen peroxide has not enjoyed the attention of most chemists. However, process engineers appreciate an essentially free reagent (air) and have developed major processes that are based on the catalytic activation of O_2:

1. Sulfuric acid production from H_2S and SO_2 with V_2O_5 (s) as the catalyst;
2. Ethylene oxide production from ethylene with supported Ag (s) as the catalyst;
3. Cyclohexanol and cyclohexanone from cyclohexane with supported Co (s) as the catalyst.
4. Catalysis with transition-metal complexes.[21]

Likewise, hydrogen peroxide, perborates, and peracids are used as bleaches and decolorizing agents, disinfectants, and general oxidizing agents. There is increasing interest in the use of ozone (O_3) for water purification (in place of chlorine), and as a clean oxygenating reagent. Nature for the past 1.7 billion years has devised highly selective catalysts for the constructive use of dioxygen and hydrogen peroxide to synthesize molecules. Through an understanding of the chemistry for these biological oxygen-activation processes, new catalyst systems can be designed.

2 REDOX THERMODYNAMICS FOR OXYGEN SPECIES (O_2, O_3, HOO•, $O_2^-\cdot$, HOOH, HOO^-, O, AND HO•)

The reaction thermodynamics for oxygen species are influenced by the solution matrix and its acidity. Thus, the redox thermodynamics of O_2 are directly dependent upon hydronium ion activity,

$$O_2 + 4H_3O^+ + 4e^- \longrightarrow 6H_2O \qquad (26)$$

which, in turn, depends upon the reaction matrix. In acetonitrile, the activity values for pK_a' range from -8.8 for $(H_3O)ClO_4$ to 30.4 for H_2O.[22] This means that the formal potential ($E°'$) for equation (26) in acetonitrile (MeCN) is $+1.79$ V versus NHE in the presence of 1 M $(H_3O)ClO_4$ and -0.53 V in the presence of 1 M $(Bu_4N)OH$.

Another limiting factor with respect to chemical energy flux for oxidative metabolism and respiration is the solubility of O_2. Because of its nonpolar character, dioxygen is much more soluble in organic solvents than in H_2O.

The reduction potentials for O_2 and various intermediate species in H_2O at pH 0, 7, and 14 are summarized in Table 1;[23–26] similar data for O_2 in MeCN at pH -8.8, 10.0, and 30.4 are presented in Table 2.[27–29] Potentials for the reduction of ozone (O_3) in aqueous and acetonitrile solutions are presented in Table 3.[26,28]

The reduction manifolds for O_2 (Tables 1 and 2) indicate that the limiting step (in terms of reduction potential) is the first electron transfer to O_2, and that an electron source

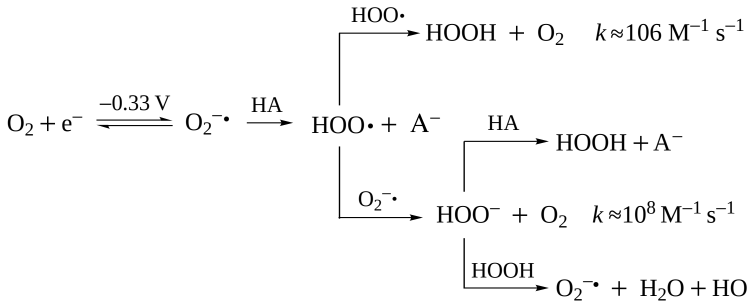
HOO•
HOOH + O2 k≈106 M−1 s−1
O2 + e− −0.33 V O2−• HA HOO• + A−
HA HOOH + A−
O2−• HOO− + O2 k≈108 M−1 s−1
HOOH O2−• + H2O + HO

Scheme 1 Formation and degradation of the superoxide ion ($O_2^{-}\bullet$)

adequate for the reduction of O_2 will produce all of the other reduced forms of dioxygen ($O_2^{-}\bullet$, HOO•, HOOH, HOO^-, •OH) through reduction, hydrolysis, and disproportionation steps (Scheme 1).[30,31] Thus, the most direct means to activate O_2 is the addition of an electron (or hydrogen atom), which results in significant fluxes of several reactive oxygen species.

The dominant characteristic of $O_2^{-}\bullet$ in any medium is its ability to act as a strong Brønsted base to form HOO•,[32,33] which reacts with itself or a second $O_2^{-}\bullet$ (Scheme 1). Within water, superoxide ion is rapidly converted to dioxygen and peroxide (equation 27).

$$2O_2^{-}\bullet + H_2O \rightleftharpoons O_2 + HOO^- + HO^- \qquad (27)$$

$$K \approx 2.5 \times 10^8 \text{atm}$$

$$(DMF)^+Fe^{III}TPP + O_2^{-}\bullet \longrightarrow Fe^{II}TPP + O_2 \qquad (28)$$

$$\Delta E = +0.7\ \text{V}$$

Such a proton-driven disproportionation process means that $O_2^{-}\bullet$ can deprotonate acids much weaker than water (up to $pK_a \sim 23$).[34] The data of Tables 1 and 2 indicate that $O_2^{-}\bullet$ is a moderate one-electron reducing agent. Thus, cytochrome *c* (Fe^{III}) is reduced in H_2O[35,36] and iron(III) porphyrins in DMF (equation 28).

Superoxide ion reacts with proton sources to form HOO•, which disproportionates through a second $O_2^{-}\bullet$ or itself (Scheme 1). However, with limiting fluxes of protons to control the rate of HOO• formation from $O_2^{-}\bullet$, the rate of decay of HOO• is enhanced by reaction with the allylic hydrogens of excess 1,4-cyclohexadiene (1,4-CHD).[37] Because HOO• disproportionation is a second-order process, low concentrations favor hydrogen-atom abstraction from 1,4-CHD. This is especially so for Me_2SO, in which the rate of disproportionation for HOO• is the slowest (PhCl > MeCN > H_2O > DMF > DMSO).[37]

2.1 Atomic Oxygen

The electron-transfer potentials for the reduction of ground-state atomic oxygen in water and in acetonitrile are directly related to hydronium ion concentration (equations 29–31).[23,24,38]

$$O(g) + H_3O^+ + e^- \longrightarrow HO\bullet + H_2O \qquad (29)$$

$$(E^\circ)_{H_2O} = +2.14\ \text{V},\ (E^\circ)_{MeCN} = +2.66\ \text{V}$$

$$HO\bullet + H_3O^+ + e^- \longrightarrow 2H_2O \qquad (30)$$

$$(E^\circ)_{H_2O} = +2.72\ \text{V},\ (E^\circ)_{MeCN} = +3.24\ \text{V}$$

$$O(g) + 2H_3O^+ + 2e^- \longrightarrow 3H_2O \qquad (31)$$

$$(E^\circ)_{H_2O} = +2.43\ \text{V vs. NHE},\ (E^\circ)_{MeCN} = +2.95\ \text{V}$$

$$2H_3O^+ + 2e^- \longrightarrow 2H\bullet + 2H_2O \qquad (32)$$

$$E^\circ = -2.10\ \text{V vs. NHE}$$

Because the oxygen atom in a water molecule is essentially without charge, these reduction processes represent the facilitated reduction of hydronium ions by stabilization of the product H atom through strong covalent bond formation with atomic oxygen. Thus, the standard state reduction of protons to hydrogen atoms (equation 32) is shifted to a much more favored process in the presence of atomic oxygen (equation 31).

3 CHEMICAL BONDS FOR OXYGEN

The bonding for oxygen atoms in heteratomic molecules is viewed as essentially covalent (*see Covalent Bonds*) (e.g. MeOH, $Me_2C{=}O$, MeCHO, and MeC(O)OOH) and similar to that for carbon, nitrogen, and chlorine atoms. In contrast, a Lewis acid–base formalism often is used for metal–oxygen compounds with ionic interactions by dianionic oxo groups (e.g. $[Ba^{2+}\ O^{2-}]$, $[Fe^{6+}\ (O^{2-})_4]^{2-}$, $[Mn^{7+}\ (O^{2-})_4]^-$, and $[(Cu^+)_2O^{2-}]$). This results from the thermodynamic relations for ionic solution equilibria, and the inference that the combination of ions results in molecules and complexes held together by electrostatic interactions (equations 33–35).

$$H_3O^+ + HO^- \rightleftharpoons 2H_2O \qquad K_f = 10^{14} \qquad (33)$$

$$Zn^{2+} + 4HO^- \rightleftharpoons Zn(OH)_4^{\;2-} \qquad K_f = 10^1 \qquad (34)$$

$$Fe^{3+} + 3HO^- \rightleftharpoons Fe(OH)_3(s) \qquad K_f = 10^{36} \qquad (35)$$

Table 1 Standard reduction potentials for dioxygen species in water[a]

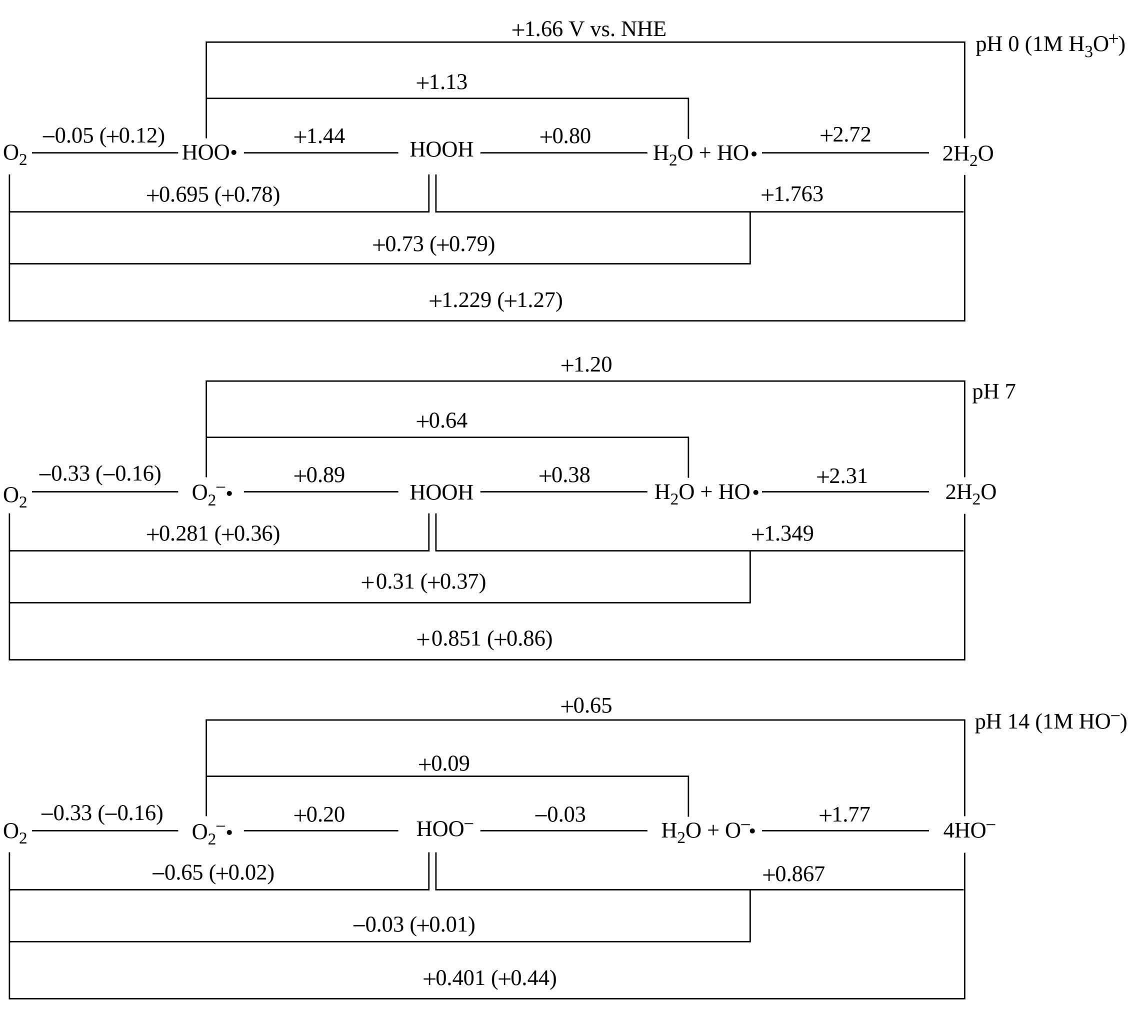
+1.66 V vs. NHE
pH 0 (1M H_3O^+)
+1.13
O_2
−0.05 (+0.12)
HOO•
+1.44
HOOH
+0.80
H_2O + HO•
+2.72
$2H_2O$
+0.695 (+0.78)
+1.763
+0.73 (+0.79)
+1.229 (+1.27)
+1.20
pH 7
+0.64
O_2
−0.33 (−0.16)
O_2^-•
+0.89
HOOH
+0.38
H_2O + HO•
+2.31
$2H_2O$
+0.281 (+0.36)
+1.349
+0.31 (+0.37)
+0.851 (+0.86)
+0.65
pH 14 (1M HO^-)
+0.09
O_2
−0.33 (−0.16)
O_2^-•
+0.20
HOO^-
−0.03
H_2O + O^-•
+1.77
$4HO^-$
−0.65 (+0.02)
+0.867
−0.03 (+0.01)
+0.401 (+0.44)

[a] O_2, 1 atm (1.0 mM). Formal potentials for O_2 at unit activity in parentheses.

However, the bonding in the H_2O molecule is essentially covalent [H–OH (1s−2p)] with a charge excess of 0.12+ per hydrogen atom (0.25− for oxygen), and *not* [$H^{+-}OH$].**[39,40]** The same is true for all of the molecular products in equations (33−35).

Thus, the bonding in metal compounds and complexes has traditionally been viewed as ionic, with a positive metal center interacting with negative ions, such as HO^-, O^{2-}, Cl^-, AcO^-, and coordinate donor, Lewis acid−base interactions with a positive metal center interacting with negative ions and electron-pair Lewis bases, such as $:NH_3$, $:PPh_3$, $H\underset{\cdot\cdot}{\ddot{O}}H$. Examples of ionic versus covalent bonding illustrate the tradition: H^+Cl^- versus H–Cl (1s−3p), $C^{4+}(Cl^-)_4$ versus $C(–Cl)_4$ [$2sp^3–(3p)_4$], $Fe^{3+}(Cl^-)_3$ versus $Fe(–Cl)_3$ [$3d^5sp^2–(3p)_3$], $H^{+-}OH$ versus H–OH (1s−2p), $C^{4+}(O^{2-})_2$ versus O=C=O [$2sp^3–(2p^2)_2$], and $Fe^{2+}(O^{2-})$ versus Fe=O [$3d^6sp–(2p^2)$]. Such ionic formulations for these molecules in an inert matrix are not consistent with their physical and chemical properties. For example, ferrate ion (FeO_4^{2-}) is formulated as an ionic salt $Fe^{6+}(O_2^{2-})_4$ ($3d^2$, $S = 2/2$, tetrahedral). This is in spite of the fact that O^{2-} is unattainable with electron beams in a vacuum, which would make it a stronger reducing agent than the electron (electrons transform all oxidized iron to Fe^0 or Fe^-).

3.1 Covalent Bonding in Oxygen-containing Molecules

With simple organic compounds, covalent bonds result from the combination of the four unpaired electrons in the sp^3 hybridized orbitals of carbon with the unpaired electrons of hydrogen or oxygen (equations 36 and 37). Likewise, atomic hydrogen forms covalent bonds with atomic oxygen (without charge transfer) (equations 38 and 39). An additional electron, added to HOH or HO•, goes to the atom with the greatest electron affinity (O, 1.46 eV and H, 0.75 eV) (equations 40 and 41).

Table 2 Formal reduction potentials for dioxygen species in acetonitrile[a]

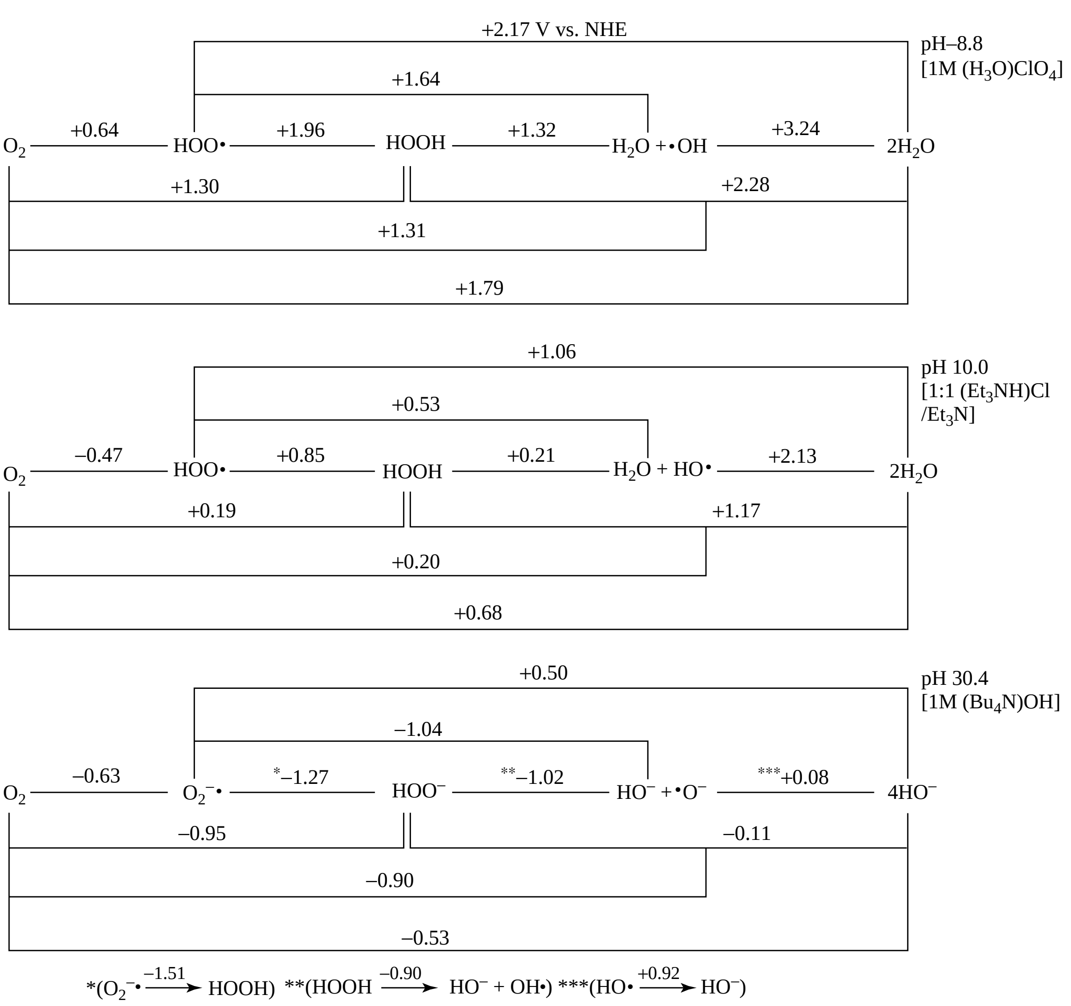
+2.17 V vs. NHE
pH–8.8
[1M (H_3O)ClO_4]
+1.64
O_2
+0.64
HOO•
+1.96
HOOH
+1.32
H_2O + •OH
+3.24
$2H_2O$
+1.30
+2.28
+1.31
+1.79
+1.06
pH 10.0
[1:1 (Et_3NH)Cl
/Et_3N]
+0.53
O_2
−0.47
HOO•
+0.85
HOOH
+0.21
H_2O + HO•
+2.13
$2H_2O$
+0.19
+1.17
+0.20
+0.68
+0.50
pH 30.4
[1M (Bu_4N)OH]
−1.04
O_2
−0.63
O_2^{-}•
*−1.27
HOO^-
**−1.02
HO^- + •O^-
***+0.08
$4HO^-$
−0.95
−0.11
−0.90
−0.53
*(O_2^{-}• $\xrightarrow{-1.51}$ HOOH) **(HOOH $\xrightarrow{-0.90}$ HO^- + OH•) ***(HO• $\xrightarrow{+0.92}$ HO^-)

[a] O_2, 1 atm (8.1 mM).

Table 3 Standard reduction potentials for ozone in water and in acetonitrile

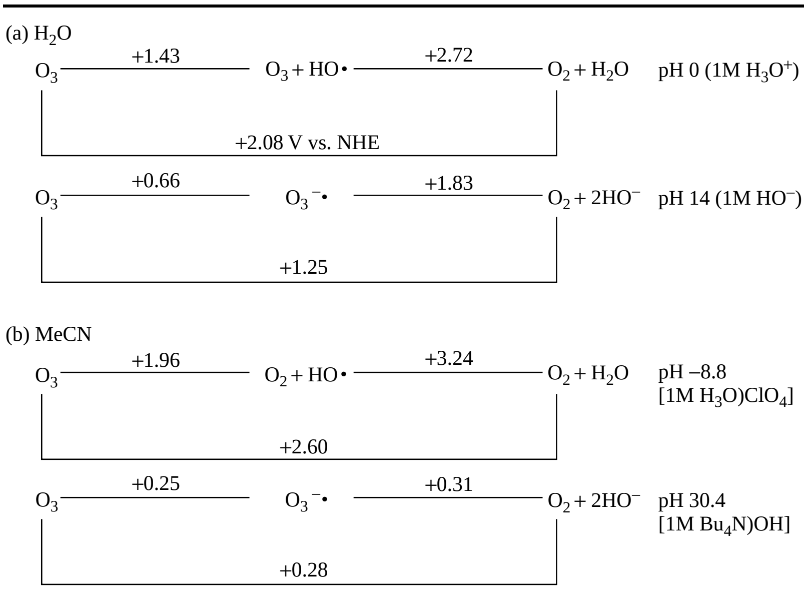
(a) H_2O
O_3
+1.43
O_3 + HO•
+2.72
O_2 + H_2O
pH 0 (1M H_3O^+)
+2.08 V vs. NHE
O_3
+0.66
O_3^{-}•
+1.83
O_2 + $2HO^-$
pH 14 (1M HO^-)
+1.25
(b) MeCN
O_3
+1.96
O_2 + HO•
+3.24
O_2 + H_2O
pH −8.8
[1M H_3O)ClO_4]
+2.60
O_3
+0.25
O_3^{-}•
+0.31
O_2 + $2HO^-$
pH 30.4
[1M Bu_4N)OH]
+0.28

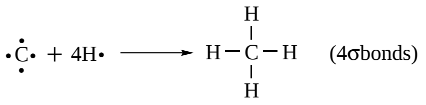

$$\cdot\dot{\underset{\bullet}{C}}\cdot + 4H\cdot \longrightarrow H{-}\overset{\displaystyle H}{\underset{\displaystyle H}{C}}{-}H \quad (4\sigma\text{bonds}) \qquad (36)$$

$$\cdot\dot{\underset{\bullet}{C}}\cdot + 2\cdot O\cdot \longrightarrow O{=}C{=}O \ (2\sigma \text{ bonds and } 2\pi \text{ bonds}) \qquad (37)$$

$$2H\cdot + \cdot O\cdot \longrightarrow H{-}O{-}H \qquad (38)$$

$$H\cdot + \cdot O\cdot \longrightarrow H{-}O\cdot \qquad (39)$$

$$HOH + e^- \longrightarrow HO^- + H\cdot \qquad (40)$$

$$E^\circ = -2.9 \text{ V vs. NHE}$$

$$HO\cdot + e^- \longrightarrow HO^- \qquad (41)$$

$$E^\circ = +1.9 \text{ V vs. NHE}$$

The covalent bonding of atomic oxygen (·O·, $2s^2p^4$) with carbon and hydrogen is representative of its bonding to all elements. In neutral molecules without an oxygen-centered radical (HO· and MeO·), the covalence of oxygen is two (e.g. H–O–H, H–O–O–H, ·N=O, H–O–Cl, O=C=O, Me–O–H). In contrast, the covalence of oxygen in the hydronium ion (H_3O^+) is three, and in hydroxide ion (HO^-) is one. The valence bond approach can be extended to molecular oxygen (dioxygen, $\cdot O_2\cdot$, **1**), which has a bond order of two, nitric acid (**2**), pyridine *N*-oxide (**3**), and carbon dioxide (O=C=O).

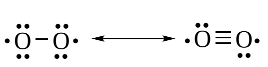

(1)

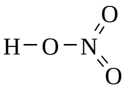

(2)

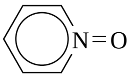

(3)

The C–O bond energy (ΔH_{DBE}) in CO_2 is 130 kcal mol^{-1}, and the N–N bond energy in N≡N is 227 kcal mol^{-1}. Hence, the bond energy for CO (isoelectronic with N_2), 257 kcal mol^{-1}, prompts the formulation of an eight-electron covalent bond (C≡O: or two three-electron bonds plus a σ bond).

The bond orders for ground-state molecular oxygen (dioxygen, $^3O_2$), for superoxide ion ($O_2^-\cdot$), and for (HOOH) are 2, 1.5, and 1, respectively. Table 4 provides molecular orbital diagrams for dioxygen ($^3\Sigma_g^-$, $^1\Delta_g$, and $^1\Sigma_g^+$) and superoxide ion, which illustrates the biradical character of $^3O_2$ ($\cdot O_2\cdot$) and the delocalized spin density of $O_2^-\cdot$ (one-half spin per oxygen).

Table 4 Molecular orbital diagrams for O_2 and $O_2^-\cdot$

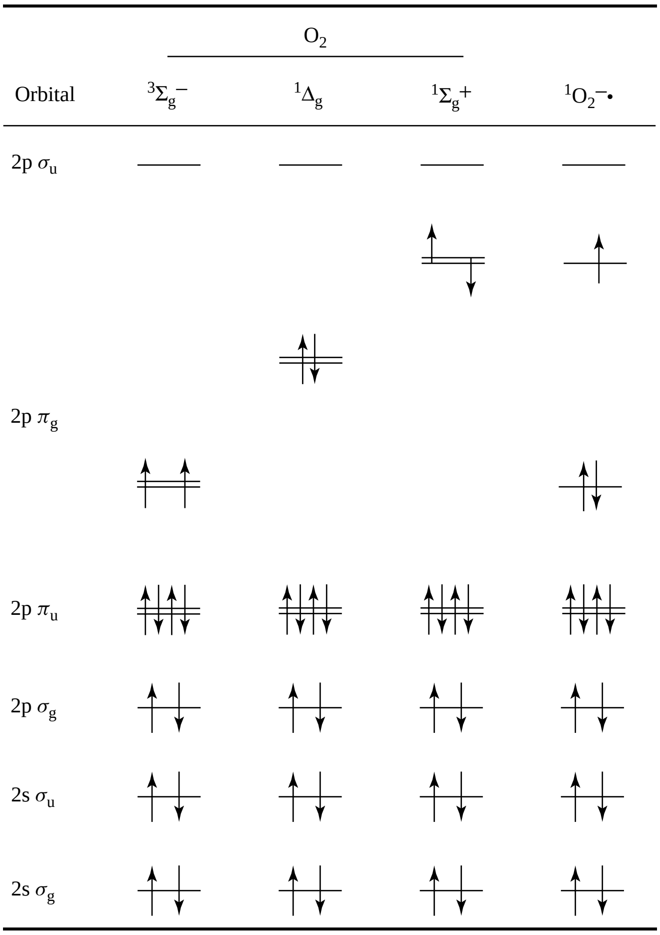

	O_2			
Orbital	$^3\Sigma_g^-$	$^1\Delta_g$	$^1\Sigma_g^+$	$^1O_2^-\cdot$
2p σ_u	—	—	—	—
			↑ ↓	↑
		↑↓		
2p π_g				
	↑ ↑			↑↓
2p π_u	↑↓ ↑↓	↑↓ ↑↓	↑↓ ↑↓	↑↓ ↑↓
2p σ_g	↑↓	↑↓	↑↓	↑↓
2s σ_u	↑↓	↑↓	↑↓	↑↓
2s σ_g	↑↓	↑↓	↑↓	↑↓

The bonding of an oxygen atom in a water molecule H–$\ddot{\underset{\bullet\bullet}{O}}$–H involves an octet of electrons about the oxygen atoms (closed valence-electron shell) with two covalent sigma (σ) H–O bonds ($1s{-}2p_{x,y}$) at a dihedral angle of 104° (≈90° for the $p_{x,y}$ orbital geometry of ground-state atomic oxygen (·O·)). This bivalent bond order for oxygen is general in its compounds with nonmetals and metals. The addition of covalently bonded $Na^I{}_2O$ (s) to water results in the transfer of an electron from each sodium atom to the oxygen of a water molecule and internally to the oxygen atom (equation 42). Likewise, the reaction of $Na^I{}_2O$ (s) with CO_2 (s) yields covalently bonded sodium carbonate, which dissociates heterolytically in aqueous solutions (equation 43). Metal–oxygen compounds can be directly synthesized by atom–atom reactions, especially when sources of atomic oxygen are utilize (equations 44–48).

$$Na^I{}_2O(s) + HOH \xrightarrow{H_2O} 2Na^+(aq) + 2HO^-(aq) \qquad (42)$$

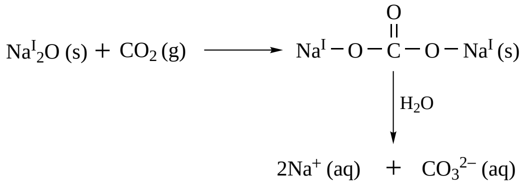

$$\begin{array}{c} Na^I{}_2O\,(s) + CO_2\,(g) \longrightarrow Na^I{-}O{-}\overset{\displaystyle O}{\overset{\|}{C}}{-}O{-}Na^I\,(s) \\ \Big\downarrow H_2O \\ 2Na^+\,(aq) + CO_3^{2-}\,(aq) \end{array} \qquad (43)$$

$$m\text{-}ClC_6H_4C(O)OOH \longrightarrow m\text{-}ClC_6H_4CO_2H + [O] \qquad (44)$$

$$HOOH \longrightarrow HOH + [O] \qquad (45)$$

$$O_3 \longrightarrow O_2 + [O] \qquad (46)$$

$$HOCl \longrightarrow HCl + [O] \qquad (47)$$

$$HOIO_3 \longrightarrow HOIO_2 + [O] \qquad (48)$$

The dissolution and oxidation of the elemental manganese in steel alloys to permanganate ($HOMn^{VII}O_3$) by $HOIO_3$

illustrates such oxygen-atom transfer chemistry and the associated increase in the covalence of Mn (equations 49 and 50).

$$\mathrm{Mn(s)} + [\mathrm{O}] \longrightarrow \mathrm{Mn^{II}{=}O(s)} \xrightarrow{[\mathrm{O}]} \mathrm{O{=}Mn^{IV}{=}O(s)} \qquad (49)$$

$$2\mathrm{Mn^{IV}O_2(s)} + 3[\mathrm{O}] \longrightarrow \mathrm{O_3Mn^{VII}OMn^{VII}O_3} \xrightarrow{\mathrm{H_2O}}$$
$$2\mathrm{H_3O^+(aq)} + 2\mathrm{O_3Mn^{VII}O^-}\ \mathrm{(aq)} \qquad (50)$$

3.2 Covalent Bond Energies for Oxygen in Molecules

Although the gas-phase dissociative X–O bond energies (ΔH_{DBE}) are known for many diatomic and nonmetallic molecules (see Table 5 for illustrative examples),[41] the metal–oxygen bond energetics for transition-metal complexes, organometallics, and metalloproteins in the condensed phase are not understood. With the latter systems, the traditional thermochemical methods of evaluation are tedious and imprecise.

The need for quantitative bond energy data for oxygen-containing molecules in the condensed phase has prompted the development of an evaluation procedure that is based on electron-transfer thermodynamics. The approach is illustrated for H–O bonds and for Fe–O bonds, but is applicable to any X–O bond for which appropriate electron-transfer potentials are available. Table 6(a) summarizes the one-electron standard reduction potentials for $\mathrm{H_3O^+}$, HO•, HOH, $\mathrm{O_2}$, HOO•, $\mathrm{O_2^-}$•, •O•, and $\mathrm{O^-}$• in aqueous solutions (see Table 1).

Combination of the appropriate electron-transfer half-reactions (Table 6a) provides an expression for the free energy of bond formation [$-\Delta G_{\mathrm{BF}} = nF(\Delta E°)_{\mathrm{reac}}$]. For example, in the case of the H–OH bond the energetics for the reduction of a hydronium ion in the absence and presence of HO• are given by (equations 51 and 52). Subtraction of equation (51) from equation (52) gives equation (53). This provides a measure of the H–OH bond energy (equation 54).

Table 5 Gas-phase dissociative bond energies for oxygen-containing molecules

Bond	ΔH_{DBE} (kcal mol^{-1})	Bond	ΔH_{DBE} (kcal mol^{-1})
O=O	119	H–OH	119
HO–OH	51	H–O•	102
t-BuO–OBu-*t*	52	H–OOH	89
$\mathrm{PhCH_2O}$–Me	67		
OC=O	127	H–OO•	47
CO	257	H–$\mathrm{O^-}$	115
$\mathrm{Ba^{II}{=}O}$	134	H–$\mathrm{OO^-}$	63
$\mathrm{Mn^{II}{=}O}$	96		
$\mathrm{^+Mn^{II}{=}O}$	57	H–OMe	104
$\mathrm{Fe^{II}{=}O}$	93	H–OAc	106
$\mathrm{^+Fe^{II}{=}O}$	71	H–OBu-*t*	105
$\mathrm{^+Fe^{I}}$–OH	73		
$\mathrm{Fe^{I}}$–Cl	84		
$\mathrm{(CO)_4Fe^{VIII}}$–CO	41		
$\mathrm{•Co^{II}{=}O}$	92		
$\mathrm{Ni^{II}{=}O}$	91		

$$\mathrm{H_3O^+} + \mathrm{e^-} \longrightarrow \mathrm{H•} + \mathrm{H_2O} \qquad (51)$$
$$E° = -2.10\ \mathrm{V\ vs.\ NHE}$$

$$\mathrm{HO•} + \mathrm{H_3O^+} + \mathrm{e^-} \longrightarrow 2\mathrm{H{-}OH} \qquad (52)$$
$$E° = +2.72\ \mathrm{V}$$

$$\mathrm{HO•} + \mathrm{H•} \longrightarrow \mathrm{H{-}OH} \qquad (53)$$
$$(\Delta E°)_{\mathrm{reac}} = +4.82\ \mathrm{V}$$

$$-\Delta G_{\mathrm{BF}} = nF(\Delta E°)_{\mathrm{reac}} = [(4.82)][23.1\ \mathrm{kcal\,mol^{-1}(eV)^{-1}}]$$
$$= 111\ \mathrm{kcal\,mol^{-1}} \qquad (54)$$

Analogous arguments are used to evaluate the free energies

Table 6 Standard aqueous reduction potentials for protons, water, and oxygen species; and the free energy of bond formation for several hydrogen – oxygen species

(a) Reduction potentials in $\mathrm{H_2O}$ (standard states, unit molality) Redox couple	$E°$ (V vs. NHE)	Redox couple	$E°$ (V vs. NHE)
$\mathrm{HO•} + \mathrm{H_3O^+} + \mathrm{e^-} \rightarrow \mathrm{H{-}OH} + \mathrm{H_2O}$	+2.72	$\mathrm{•O^-} + \mathrm{HOH} + \mathrm{e^-} \rightarrow \mathrm{H{-}O^-} + \mathrm{HO^-}$	+1.77
$\mathrm{•O•} + \mathrm{H_3O^+} + \mathrm{e^-} \rightarrow \mathrm{H{-}O•} + \mathrm{H_2O}$	+2.14	$\mathrm{O_2^-•} + \mathrm{HOH} + \mathrm{e^-} \rightarrow \mathrm{H{-}OO^-} + \mathrm{HO^-}$	+0.20
$\mathrm{HOO•} + \mathrm{H_3O^+} + \mathrm{e^-} \rightarrow \mathrm{H{-}OOH} + \mathrm{H_2O}$	+1.44	$\mathrm{H_3O^+} + \mathrm{e^-} \rightarrow \mathrm{H•} + \mathrm{H_2O}$	−2.10
$\mathrm{•O_2•} + \mathrm{H_3O^+} + \mathrm{e^-} \rightarrow \mathrm{H{-}OO•} + \mathrm{H_2O^+}$	+0.12	$\mathrm{HOH} + \mathrm{e^-} \rightarrow \mathrm{H•} + \mathrm{HO^-}$	−2.93

(b) Free energies of bond formation ($-\Delta G_{\mathrm{BF}}$) Bond	Redox evaluation $-\Delta G_{\mathrm{BF}}$ (kcal mol^{-1} eV^{-1})	$-\Delta G_{\mathrm{BF}}$ (kcal mol^{-1})
H–OH	[2.72 – (−2.10)] 23.1	111
H–O•	[2.14 – (−2.10)] 23.1	98
H–$\mathrm{O^-}$	[1.77 – (−2.93)] 23.1	109
H–OOH	[1.44 – (−2.10)] 23.1	82
H–$\mathrm{OO^-}$	[0.20 – (−2.93)] 23.1	72
H–OO•	[0.12 – (−2.10)] 23.1	51

of bond formation ($-\Delta G_{BF}$) for the H–O•, H–O$^-$, H–OOH, H–OO$^-$, and H–OO• bonds, which are summarized in Table 6(b).

An equivalent approach has been used to evaluate metal–ligand covalent bond-formation free energies ($-\Delta G_{BF}$) for metal complexes (ML_n)[42] and metal–oxygen compounds.[43] Thus, for ML_3 complexes the differential redox potentials ($\Delta E^{\circ\prime}=E^{\circ\prime}{}_{\cdot L/L^-} - E^{\circ\prime}{}_{ML3/ML3^-}$) of their ligand-centered electron-transfer processes provide a measure of the L_2M–L bond energy ($-\Delta G_{BF} = (\Delta E^{\circ\prime})23.1\ \text{kcal mol}^{-1}$).[42] Table 7 illustrates such an approach for iron complexes and summarizes their apparent free energies of covalent bond formation (M–L, $-\Delta G_{BF}$).[26,42–44]

Although the uncharged tris(3,5-di-*t*-butylcatecholate) complex of iron [Fe(DTBC)$_3$] has been extensively studied,[44–46] the proposed bonding in these reports is unclear. The most common formulation is as an ionic salt between iron(III) and three semiquinone anion radicals, $Fe^{3+}(DTBSQ^-\cdot)_3$. However, the magnetic moment is 2.9 BM (consistent with an $S = 2/2$ spin state)[44,46] and the electrochemistry indicates a ligand-centered reduction.[29] Both of these characteristics are analogous to ferrate dianion, $Fe^{VI}(O)_4{}^{2-}$ (d^5sp^2; $S = 2/2$; covalence, 6). Thus, the iron center (d^5sp^2, eight unpaired electrons) forms six covalent Fe–O bonds with three catechols (equivalent to the six H–O bonds in three $DTBCH_2$ molecules), which leaves two unpaired electrons at the iron center ($S = 2/2$) (Table 7).

Additional X–O dissociative bond energies (ΔH_{DBE}; XO → X + O) for oxygen-containing molecules are summarized in Table 8.[26,41] These provide a thermodynamic measure of the propensity for oxygen-atom transfer. For example, the dissociative bond energies (ΔH_{DBE}) of the oxygen atom in the compound I model [$(Cl_8TPP^{+}\cdot)Fe^{IV}{=}O$] and in ethylene oxide (CH_2-CH_2O) are 54 and 84 kcal mol^{-1}, respectively. Hence, the transfer of an oxygen atom from compound I to ethylene is an exothermic process ($-\Delta H_{reac} = 30\ \text{kcal mol}^{-1}$) (equation 55).

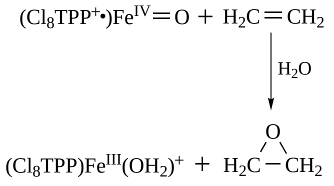

$$(Cl_8TPP^{+}\cdot)Fe^{IV}{=}O + H_2C{=}CH_2 \xrightarrow{H_2O} (Cl_8TPP)Fe^{III}(OH_2)^+ + H_2C\overset{O}{-}CH_2 \qquad (55)$$

In summary, the bond energies for atomic oxygen (•O•) and dioxygen (•O$_2$•) with transition metals are much smaller than with either carbon or hydrogen (Tables 5–8), and hereby provide the means to stabilize active forms of oxygen [•O• → MO; •O$_2$• → M(O$_2$); •O$_2$• → MOOM]. Although the weak metal–oxygen bonds attenuate the reactivity of atomic oxygen, this is more than compensated by its increased lifetime in condensed phase reactors (the reaction of equation (55) is a good example). In some cases, the stabilization by transition metals can enhance the reactivity through a change in the spin state of atomic oxygen (•O• → MO) (equation 56). This appears to be the approach that has been utilized by Nature for the activation of •O$_2$• and HOOH for the dehydrogenation, monooxygenation, and dioxygenation of organic substrates.

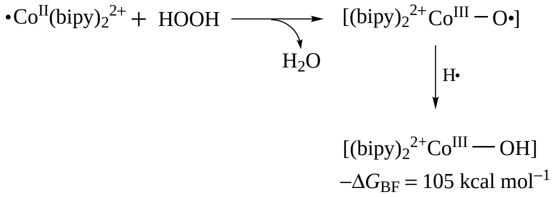

$$\cdot Co^{II}(bipy)_2{}^{2+} + HOOH \xrightarrow[H_2O]{} [(bipy)_2{}^{2+}Co^{III}-O\cdot] \xrightarrow{H\cdot} [(bipy)_2{}^{2+}Co^{III}-OH] \qquad (56)$$

$-\Delta G_{BF} = 105\ \text{kcal mol}^{-1}$

Table 7 Redox potentials for iron complexes and ligands, and their apparent metal–ligand covalent bond-formation free energies

	$E_{1/2}$ (V vs. NHE^b)			
Complex (FeL_n)^a	•L/L$^-$	$FeL_n/FeL_n{}^-$	Bond	$-\Delta G_{BF}$ (kcal mol^{-1})^c
(a) MeCN^d				
$Fe^{III}Cl_3$ (d^5sp^2)	+2.11	+0.34	Cl_2Fe–Cl	41
$Fe^{III}(8Q)_3{}^e$	+0.21	−0.41	$(8Q)_2Fe$–O (of 8Q)	14
$Fe^{III}(acac)_3{}^e$	+0.55	−0.42	$(acac)_2Fe$–O (of acac)	18
$Fe^{III}(PA)_3{}^e$	+1.50	+0.20	$(PA)_2Fe$–O (of PA)	30
$Fe^{III}(OPPh_3)$				
$Fe^{VI}(DTBC)_3{}^f$ (d^5sp^2; $S = 2/2$)	+0.12	−0.29	$(DTBC)_2Fe$–O (of DTBC)	
(b) Aqueous, pH14^{d,g}				
$Fe^{VI}(O)_2(O^-)$ (d^5sp^2; $S = 2/2$)	+1.43 (•O•/O$^-$•)	+0.55		
$Fe^{III}(O)(O^-)^-$ (d^5sp^2)	+1.77 (O$^-$•/2$^-$OH)	−0.7	(O)Fe–O$^-$	57
$Fe^{II}(OH)(O^-)^-$ (d^6sp)	+1.89 (•OH/$^-$OH)	−0.8	($^-$O)Fe–OH	62
(c) Aqueous, pH 0^{d,g}				
$(H_2O)_2{}^{2+}$ $Fe^{III}(OH)$ (d^5sp^2)	+2.72 (•OH,H_3O^+/H_2O)	+0.77	$^{2+}(H_2O)_2Fe$–OH	45

[a] 8Q, 8-quinolinate; acac, acetylacetonate; PA, picolinate; DTBC, 3,5-di-*t*-butylcatecholate. [b] $E_{NHE}=E_{SCE} + 0.24$ V. [c] Richert *et al.*[30] [d] The superscript Roman numerals indicate the covalence (number of covalent bonds) for the metal; not the oxidation state. [e] Richert *et al.*[30] [f] Jones *et al.*[32] [g] Bard *et al.*[14]

Table 8 Dissociative bond energies ($XO \rightarrow X + O$) for oxygen-containing molecules

Compound	ΔH_{DBE} (kcal mol^{-1})
$O_2 \rightarrow 2O$	119
$O_3 \rightarrow O_2 + O$	25
$1,2\text{-}(CO_2H)(CO_2OH)C_6H_4 \rightarrow 1,2\text{-}(CO_2H)_2C_6H_4 + O$	31
$BrO_4^- \rightarrow BrO_3^- + O$	35
$N_2O \rightarrow N_2 + O$	39
$HOOH \rightarrow HOH + O$	39
$ClO^- \rightarrow Cl^- + O$	41
$t\text{-BuOOH} \rightarrow t\text{-BuOH} + O$	44
$(HO)_5IO \rightarrow HOIO_2 + 2H_2O + O$	46
$BrO^- \rightarrow Br^- + O$	47
$ClO_2^- \rightarrow ClO^- + O$	51
$HOCl \rightarrow HCl + O$	52
$IO^- \rightarrow I^- + O$	61
$ClO_4^- \rightarrow ClO_3^- + O$	65
$ClO_3^- \rightarrow ClO_2^- + O$	68
$MeONO_2 \rightarrow MeONO + O$	72
$HOSe(O)_2O^- \rightarrow HOSe(O)O^- + O$	73
$NO_3^- \rightarrow NO_2^- + O$	83
$H_2\overline{C{-}CH_2{-}O} \rightarrow H_2C{=}CH_2 + O$	84

4 REACTIVITY AND ACTIVATION OF HYDROGEN PEROXIDE (HOOH) AND HYDROPEROXIDES (ROOH)

The reactivity of hydroperoxides is primarily dependent upon their unique bond energies (e.g. H–OOH, 90 kcal mol^{-1}; HO–OH, 51 kcal mol^{-1}; H–OOBu-*t*, 91 kcal mol^{-1}, HO–OBu-*t*, 47 kcal mol^{-1}),[41] which allow low-energy rearrangements to give (HO•) and (•O•) (equations 57–60).[43]

$$HOOH \longrightarrow HOH + [O] \qquad -\Delta H = 39\ \text{kcal mol}^{-1} \tag{57}$$

$$HOOH + Fe^{II}L_2 \longrightarrow L_2Fe^{III}\text{–}OH + HO\bullet \qquad \Delta H_{H_2O} = -2\ \text{kcal mol}^{-1} \tag{58}$$

$$m\text{-}ClC_6H_4C(O)OOH \longrightarrow m\text{-}ClC_6H_4CO_2H + [O] \qquad \Delta H = 31\ \text{kcal mol}^{-1} \tag{59}$$

$$HOOH \xrightarrow{Fe^{III}Cl_3} HOH + [Cl_3Fe{=}O] \qquad \Delta H_{MeCN} = -11\ \text{kcal mol}^{-1} \tag{60}$$

Thus, m-ClC$_6$H$_4$C(O)OOH in acetonitrile will epoxidize alkenes without a catalyst, but the presence of an iron complex accelerates the process by several orders of magnitude.[47]

In water, the Brønsted acidity of HOOH and HO• are essentially the same (pK_a = 11.8 and 11.9, respectively). Electrochemical reduction of HOOH in acetronitrile yields molecular hydrogen (rather than cleavage of the HO–OH bond) (equation 61)[29] and oxidation of HOOH yields hydroperoxyl radical (HOO•) (equation 62).

$$HOOH + e^- \xrightarrow[\text{GC, MeCN}]{-1.7\ \text{V vs. SCE}} \tfrac{1}{2}H_2 + HOO^- \tag{61}$$

$$HOOH + HOH \xrightarrow[\text{GC, MeCN}]{+2.1\ \text{V vs. SCE}} HOO\bullet + H^+ + e^- \tag{62}$$

Hydrogen peroxide is formed from (a) the dimerization of hydroxyl radicals (equation 63), (b) the proton-induced decomposition of superoxide ions (equation 64), (c) the reductive electrolysis of O$_2$ in acidic media (equation 65), and (d) the base-induced reduction of O$_2$ by 1,2-disubstituted hydrazines (equation 66).[48]

$$2HO\bullet \longrightarrow HOOH \qquad k = 1 \times 10^9\,M^{-1}s^{-1} \tag{63}$$

$$2O_2^-\bullet + 2H_3O^+ \longrightarrow HOOH + O_2 \tag{64}$$

$$O_2 + H_3O^+ + 2e^- \xrightarrow[\text{MeCN, Pt}]{+0.4\ \text{V vs. SCE}} HOOH + 2H_2O \tag{65}$$

$$O_2 + PhNHNHPh \xrightarrow{:B} HOOH + PhN{=}NPh \tag{66}$$

Hydrogen peroxide is produced industrially by (a) the base/anthraquinone-catalyzed chemical reduction of O$_2$ by water and (b) the palladium-catalyzed hydrogenation of O$_2$. In aerobic biology, many oxidases (dehydrogenases) produce HOOH as a by-product along with oxidized substrate (e.g. glucose oxidase, O$_2$ + glucose → gluconic acid + HOOH; xanthine oxidase, O$_2$ + xanthine → uric acid + HOOH (*see Oxidoreductase*)). Alkyl hydroperoxides and peroxy acids are formed via the reaction of HOOH with alkyl halides and acid chlorides, respectively.

4.1 Elementary Reaction Chemistry

Hydrogen peroxide is (a) a modest electron-transfer oxidant that requires a one-electron catalyst (usually iron or copper) (equation 67) and (b) a weak two-equivalent reductant that also requires a one-electron catalyst (equation 68).

$$HOOH + 2I^- + 2HA \xrightarrow{\text{cat}} I_2 + 2HOH + 2A^- \tag{67}$$

$$2Mn^{VII}O_4^- + 5HOOH + 6H_3O^+ \xrightarrow{\text{cat}} 5O_2 + 2Mn^{II}(OH_2)_6^{\,2+} + 2HOH \tag{68}$$

The hydroperoxide ion (HOO$^-$) in aprotic media is an effective nucleophile that (a) oxygenates sulfoxides (equation 69),[49] (b) hydrolyzes nitriles and amides (equations 70–71) and (c) reacts with HOOH to form superoxide ions and hydroxyl radicals (equations 72 and 73).[31]

$$HOO^- + Me_2SO \longrightarrow Me_2SO_2 + HO^- \tag{69}$$

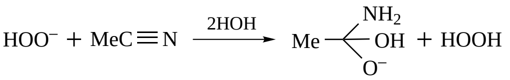

$$HOO^- + MeC{\equiv}N \xrightarrow{2HOH} Me{-}C(NH_2)(OH)(O^-) + HOOH \quad (70)$$

$$HOO^- + Me_2NCHO \xrightarrow{HOH} Me_2NH + HCO_2^- + HOOH \quad (71)$$

$$HOO^- + HOOH \longrightarrow O_2^{-}\bullet + HOH + HO\bullet \quad (72)$$

$$2HOO^- + HOOH \longrightarrow 2O_2^{-}\bullet + 2HOH \quad (73)$$

4.2 Fenton Chemistry

Although the activation of hydrogen peroxide by reduced transition metals has been known for almost 100 years as Fenton chemistry (equations 74–77)[50] there is uncertainty as to whether this chemistry produces free hydroxyl radicals (HO•). There is clear kinetic evidence[51,52] that free HO• is not the dominant reactive intermediate in Fenton chemistry, but rather an HOOH/$Fe^{II}L$ adduct that results from nucleophilic addition.[53,54]

$$HOOH + LFe^{II} \xrightarrow{pH\ 2} LFe^{III}OH + HO\bullet \quad (74)$$
$$k = {\sim}100\ M^{-1}s^{-1}$$

$$HO\bullet + LFe^{II} \longrightarrow LFe^{III}OH \quad (75)$$
$$k = 3 \times 10^8 M^{-1}s^{-1}$$

$$HO\bullet + RH \longrightarrow R\bullet + H_2O \quad (76)$$
$$k = 10^7 - 10^{10} M^{-1}s^{-1}$$

$$HO\bullet + HOOH \longrightarrow HOO\bullet + H_2O \quad (77)$$
$$k = 1 \times 10^7 M^{-1}s^{-1}$$

The bis(picolinate)iron(II) complex [$Fe^{II}(PA)_2$; PAH = picolinic acid, 2-pyridinecarboxylic acid] in combination with hydrogen peroxide (HOOH) is an effective Fenton reagent for organic substrates, and has reactivities and product profiles that are closely similar to those for traditional aqueous Fenton reagents.[55] This system reacts with hydrocarbon substrates (c-C_6H_{12}) via an intermediate that results from the nucleophilic addition by HOOH to the electrophilic $Fe^{II}(PA)_2$ center (equation 78).[56]

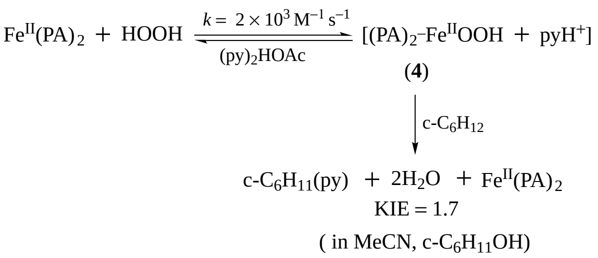

$$\begin{array}{c} Fe^{II}(PA)_2 + HOOH \underset{(py)_2HOAc}{\overset{k = 2\times10^3 M^{-1}s^{-1}}{\rightleftharpoons}} [(PA)_2\text{-}Fe^{II}OOH + pyH^+] \\ (\mathbf{4}) \\ \downarrow \text{c-}C_6H_{12} \\ \text{c-}C_6H_{11}(py) + 2H_2O + Fe^{II}(PA)_2 \\ KIE = 1.7 \\ (\text{ in MeCN, c-}C_6H_{11}OH) \end{array} \quad (78)$$

The resulting adduct (**4**) is the reactive intermediate for this Fenton system and reacts directly with substrates (the observed kinetic isotope effect (KIE, $k_{c-C_6H_{12}}/k_{c-C_6D_{12}}$) is 1.7; aqueous Fenton systems produce c-$C_6H_{11}OH$ with a KIE of 1.1[51] and free HO• (pulse radiolysis) produces c-$C_6H_{11}\bullet$ with a KIE of 1.0).

4.3 Nucleophilic Character of HOOH

Because the HO–OH bond in hydrogen peroxide is weak ($\Delta H_{DBE} = 51\ kcal\ mol^{-1}$ vs. $90\ kcal\ mol^{-1}$ for the H–OOH bond), there has been a tendency to assume homolytic cleavage in the reactivity and activation of HOOH. However, a pioneering study[57] established that sulfur dioxide is converted to sulfuric acid through a nucleophilic addition mechanism (equation 79).

$$HO^*O^*H + SO_2 \longrightarrow [HO^*O^*S(O)OH] \longrightarrow HO^*S(O^*)(O)OH \quad (79)$$

A subsequent investigation[58] of this system with anhydrous HOOH in dry MeCN demonstrated that there is no net reaction in the absence of H_2O. The reaction is first order with respect to H_2O up to a 100 mM concentration, and becomes second and third order at higher concentrations. The reactivity of *t*-BuOOH and SO_2 also exhibits a similar first-order dependence on H_2O concentration, but *t*-BuOOBu-*t* is unreactive under all conditions (the *t*-BuO–OBu-*t* bond energy is essentially the same as that for the HO–OH bond). Thus, water induces HOOH ($pK_a = 11.8$) to act as a nucleophile towards SO_2 ($pK_a = 1.9$) with the reaction rate fastest at pH 1.9 (equation 80).

$$HOOH + SO_2 + H_2O \longrightarrow [HOOS(O)O^- + H_3O^+] \longrightarrow$$
$$(HO)_2S(O)_2{\bullet}H_2O \longrightarrow HOS(O)_2O^- + H_3O^+ \quad (80)$$

If HOOH can act as a nucleophile in aqueous solutions at pH 1.9, then stronger bases in aprotic media (e.g. pyridine (py) in py_2(HOAc) and MeCN solvents) should facilitate similar pathways. Hence, the Fenton process in H_2O (at pH 2–10) and in aprotic media [py_2(HOAc)] must involve nucleophilic addition to the iron(II) center (equation 81).

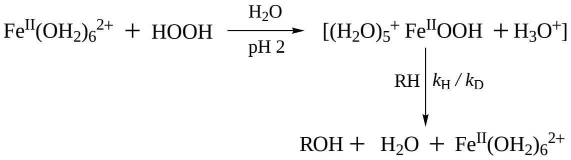

$$\begin{array}{c} Fe^{II}(OH_2)_6^{2+} + HOOH \xrightarrow[pH\ 2]{H_2O} [(H_2O)_5^{+} Fe^{II}OOH + H_3O^+] \\ \downarrow RH\ k_H/k_D \\ ROH + H_2O + Fe^{II}(OH_2)_6^{2+} \end{array} \quad (81)$$

4.4 Hydroperoxide Adducts of Copper(I) and Iron(II) Activate Dioxygen

In acetonitrile/pyridine, bis(bipyridine)copper(I) [$Cu^I(bipy)_2^+$] activates HOOH and *t*-BuOOH for the selective ketonization of methylenic carbons.[59,60] With 5 mM $Cu^I(bipy)_2^+$/100 mM HOOH(Bu), the conversion efficiencies [product per 2 HOOH(Bu)] for c-C_6H_{12} are 31% (HOOH) and 59% (*t*-BuOOH, argon atmosphere), and for $PhCH_2Me$ are 24% (HOOH) and 64% (*t*-BuOOH, argon). With 5 mM $Cu^I(bipy)_2$ and 10 mM *t*-BuOOH under argon, the conversion efficiency for c-C_6H_{12} is 10% and for $PhCH_2Me$ is 140%. However, in the presence of O_2 (1 atm, 7 mM) the conversion efficiency for c-C_6H_{12} increases to 67%, and for $PhCH_2Me$ to 440% [all PhCOMe (22 mM)], respectively. The latter result

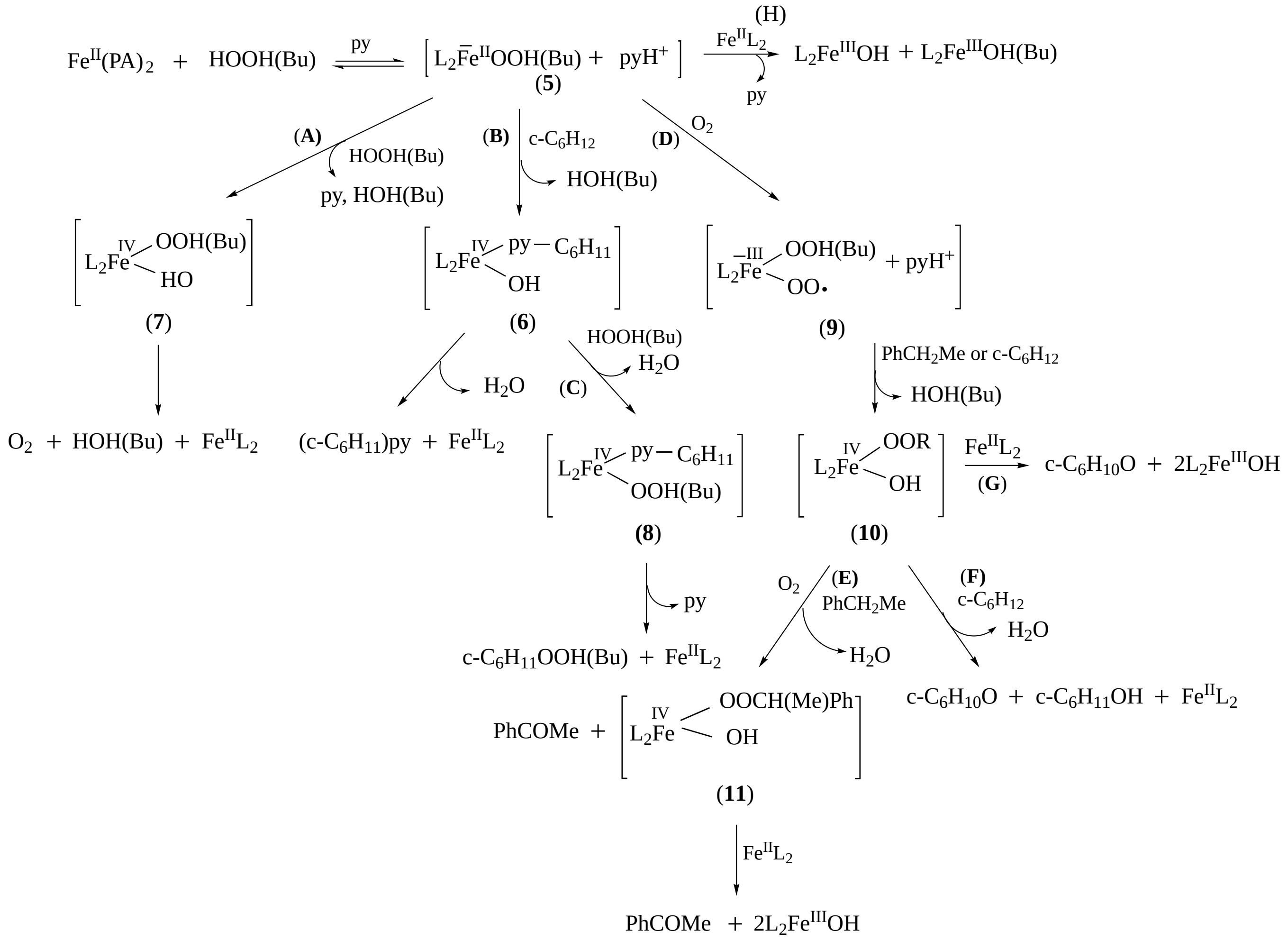

Scheme 2 Iron/HOOH(t-Bu) induced activation of dioxygen (O_2) for the oxygenation of hydrocarbons

represents a $Cu^I(bipy)_2/t$-BuOOH induced autooxygenation with at least 2.2 O_2/catalyst turnovers. The first-formed intermediate is a one-to-one adduct [$(bipy)_2Cu^IOOBu$-$t + pyH^+$], which reacts with (a) excess $Cu^I(bipy)_2{}^+$ to give 2 $(bipy)_2{}^+Cu^{II}OH$, (b) excess t-BuOOH to give O_2 and t-BuOH, (c) excess c-C_6H_{12} to give c-$C_6H_{11}OH$, (d) excess c-C_6H_{12} and excess t-BuOOH to give c-$C_6H_{11}OOBu$-t, and (e) O_2 to form an adduct [$(bipy)_2Cu^{III}(O_2)(OOBu$-$t)$ $+pyH^+$] that reacts with (i) c-C_6H_{12} to give c-$C_6H_{10}O$ and c-$C_6H_{11}OH$ and (ii) $PhCH_2Me$ to give PhCOMe.

Via closely similar pathways, iron complexes [$Fe^{II}(PA)_2$ (PA = picolinate), $Fe^{II}(bipy)_2{}^{2+}$, $Fe^{II}(OPPh_3)_4{}^{2+}$, $Fe^{II}(MeCN)_4{}^{2+}$, $(Cl_8TPP)Fe^{II}(py)_2$ (Cl_8TPP = tetrakis(2,6-dichlorophenyl)porphyrin), and $Fe^{III}Cl_3$] in combination with HOOH or t-BuOOH in MeCN, $(MeCN)_4py$, or $(py)_2HOAc$ solution matrices catalytically activate O_2 to oxygenate hydrocarbons {e.g c-C_6H_{12} → c-$C_6H_{10}O$ [9O_2 turnovers per $Fe^{II}(PA)_2$ or $Fe^{II}(bipy)_2{}^{2+}$, and 13 per $(Cl_8TPP)Fe^{II}(py)_2$]; $PhCH_2Me$ → PhCOMe (up to 25O_2 turnovers per FeL_x); c-C_6H_{10} → c-C_6H_8O (up to 9O_2 turnovers per FeL_x); $PhCHMe_2$ → PhCOMe, $PhCMe_2OH$, and $Ph(Me)C{=}CH_2$ (up to 5O_2 turnovers per FeL_x); and *cis*-PhCH=CHPh → 2 PhCHO (up to 2O_2 turnovers per FeL_x)}.**[61]** With large t-BuOOH (or HOOH)/FeL_x ratios, spontaneous decomposition occurs to give free O_2 that is incorporated into the substrates. The product profiles for the various FeL_x/t-BuOOH, O_2/RH systems and their electrochemical characterization during steady-state turnover confirm that the first-formed intermediate is a one-to-one t-BuOOH/FeL_x adduct (e.g. [$(PA)_2Fe^{II}OOBu$-t (**5**) $+pyH^+$]) (Scheme 2), which reacts with (a) excess t-BuOOH to give O_2 and t-BuOH (path A), (b) excess $Fe^{II}(PA)_2$ to give $(PA)_2Fe^{III}OH(Bu$-$t)$ (path H), (c) excess c-C_6H_{12} to give (c-C_6H_{11})py (path C, Fenton chemistry) (kinetic isotope effect, [KIE] = $k_{c-C_6H_{12}}/k_{c-C_6D_{12}}$, 4.6 with t-BuOOH and 1.7 with HOOH), and (d) O_2 to form an adduct (path D) [$(PA)_2{}^-Fe^{III}(O_2)(OOBu$-$t)$ (**9**) $+pyH^+$], that reacts with c-C_6H_{12} to form c-$C_6H_{10}O$ (paths F and G), [KIE] = 8.7. When $PhCH_2Me$ or c-C_6H_{10} are the substrates (RH), (**9**) reacts to form [$(PA)_2Fe^{IV}(OH)(OOR)$] (**10**), which in turn reacts with RH and O_2 in a catalytic cycle to give

PhCOMe or c-C_6H_8O (path E) (up to 7 O_2 turnovers per iron with $Fe^{II}(OPPh_3)_4{}^{2+}$).

4.5 Activation of HOOH by Lewis Acids

In a rigorously nonbasic solution matrix (e.g. dry acetonitrile), reduced iron without basic ligands (e.g. $[Fe^{II}(MeCN)_4](ClO_4)_2$) is not oxidized by hydroperoxides (HOOH, *t*-BuOOH, or *m*-$ClC_6H_4C(O)OOH$). Table 9 summarizes the reactivity and products from the combination of iron(II) and hydrogen peroxide in MeCN with a series of organic substrates.[62,63] Whereas Fenton chemistry in aqueous solutions produces a diverse group of products through the radical processes that are induced by (**5**, Scheme 2), the products in a nonbasic matrix such as acetonitrile are characteristic of dehydrogenations, monooxygenations, and dioxygenations. That traditional Fenton chemistry does not occur is confirmed by the complete retention of the reduced oxidation state for iron.

The slow addition of dilute HOOH [pure HOOH (98%) in dry acetonitrile (MeCN)], *t*-BuOOH, or *m*-$ClC_6H_4C(O)OOH$ to a solution that contains $[Fe^{II}(MeCN)_4](ClO_4)_2$ and an organic substrate (RH) in dry MeCN ($<0.004\%$ H_2O) results in the dehydrogenation (oxidation) or monooxygenation of RH. The net reactions and the conversion efficiencies (moles of substrate per mole of HOOH) for 1:0.5:0.5 RH/Fe^{II}/HOOH combinations of several organic substrates are summarized in Table 10. The results from studies with *t*-BuOH and *m*-$ClC_6H_4C(O)OOH$ as the oxidant in place of HOOH also are included. In sharp contrast to aqueous Fe^{II}/HOOH radical chemistry, the products from the RH/Fe^{II}/ROH combination in dry acetonitrile are characteristic of oxidase (dehydrogenation) and monooxygenation reactions. The total absence of products from (HO•) radical chemistry, and of any Fe^{III} in the product solutions, confirms that classical Fenton chemistry does not occur.

In the absence of substrate, the combination of Fe^{II} and HOOH in dry MeCN results in the latter's rapid disproportionation to O_2 and H_2O, but the Fe^{II} remains unoxidized. Similar combinations of Fe^{II} and *t*-BuOOH or *m*-$ClC_6H_4C(O)OOH$ do not promote their rapid disproportionation, but facilitate a slow hydrolysis process ($ROOH + H_2O \rightarrow ROH + HOOH$, assayed by ROH). Because all of the HOOH is consumed in the experiments of Table 10, the reaction efficiency for the Fe^{II}–HOOH system represents a crude measure of the relative rate of reaction for the adduct with substrate and HOOH. Scheme 3 outlines an activation cycle that is based on the argument that within an aprotic matrix the iron(II) center is a strong Lewis acid that weakens the O–O bond of HOOH.

The results of Table 10 confirm that the $Fe^{II}(ROOH)^{2+}$ adducts are effective dehydrogenation agents for substrates such as cyclohexadienes, substituted hydrazines, catechols, and thiols. For PhNHNHPh and 3,5-*t*-Bu_2-1,2-$(OH)_2C_6H_2$, the reaction efficiencies are comparable for HOOH and *m*-$ClC_6H_4C(O)OOH$ as the oxidant but somewhat reduced for *t*-BuOOH. This may indicate that the oxene complex (**13**, Scheme 3) is the dominant reactive form and that *t*-BuOOH is hindered from assuming this configuration. Thus, the end-on configuration (**13**) with its oxene character is favored for HOOH and *m*-$ClC_6H_4C(O)OOH$.

1,4-Cyclohexadiene yields only benzene for the three $Fe^{II}(ROOH)^{2+}$ adducts. Either the bound substrate induces the homolytic scission of the RO–OH bond to give bound RO• and •OH (**12**, Scheme 3) for the concerted removal of two H atoms from the substrate or the oxene-like character of the end-on configuration (**13**) results in the same concerted removal of two H atoms. Although H_2S is oxygenated to H_2SO_4 by the $Fe^{II}(HOOH)^{2+}$ adduct (four HOOH molecules per H_2S), thiols (both aromatic and aliphatic) are dehydrogenated by the $Fe^{II}(ROOH)^{2+}$ complex to give disulfides as the only product. The reaction stoichiometry of two RSH molecules per ROOH is the same as for the dimerization of 1,3-c-C_6H_8; a similar bis adduct for the reaction complex probably is formed (equation 82).

$$2RSH + Fe^{II} + ROOH \longrightarrow [(RSH)_2(\mathbf{12})]^{2+} \longrightarrow RSSR + Fe^{II}(H_2O)(ROH)^{2+} \qquad (82)$$

Because the side-on configuration (**12**) of the $Fe^{II}(ROOH)^{2+}$ adduct appears to be the reactive form, the lower yields for the *m*-$ClC_6H_4C(O)OOH$ oxidant indicate that the oxene configuration (**13**) is dominant for the peroxy acid.

The monooxygenation of methylstyrene (PhCH=CHMe) to form the epoxide (Table 9) appears to involve an O-atom transfer from the end-on configuration (**13**) of the $Fe^{II}(ROOH)^{2+}$ complex (equation 83).

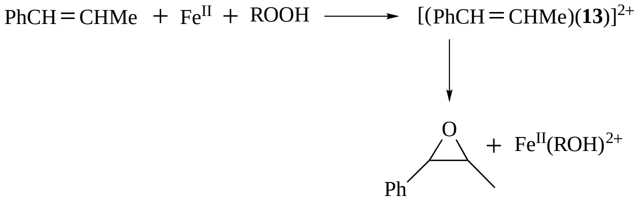

(83)

However, a significant fraction of the products from this substrate (75% for HOOH and 80% for *t*-BuOOH, Table 10) is the result of a dioxygenation to give PhCHO and MeCHO. When *m*-$ClC_6H_4C(O)OOH$ is the oxidant, only 10% of the PhCH=CHMe that reacts is dioxygenated. These results are consistent with the proposition that the end-on configuration of the $Fe^{II}[m\text{-}ClC_6H_4C(O)OOH]^{2+}$ adduct has the most oxene character and favors O-atom transfer to PhCH=CHMe and that the $Fe^{II}(HOOH)^{2+}$ and $Fe^{II}(t\text{-}BuOOH)^{2+}$ adducts react via a biradical mechanism (**12**, Scheme 3).

The formulations of Scheme 3 for the reactive forms of the $Fe^{II}(ROOH)^{2+}$ adducts represent unique electrophilic centers that are consistent with reasonable dehydrogenase (**12**), monooxygenase (**12** and **13**), and dioxygenase (**14**) reaction

Table 9 Products from the iron(II)-induced monooxygenation, dehydrogenation, and dioxygenation of organic substances (RH) by HOOH in dry acetonitrile[a]

Substrate	Reaction efficiency (%)[b]	Products
Monooxygenation		
Blank (H_2O_2)	100	O_2, H_2O, Fe^{II}
PPh_3	100	PPh_3O
Me_2SO	100	Me_2SO_2
Ph_2SO	100	Ph_2SO_2
EtOH	70	MeCHO (90%), $MeCO_2H$ (10%), O_2
$PhCH_2OH$	100	PhCHO
Cyclohexanol	47	Cyclohexanone, O_2
MeCHO	20	$MeCO_2H$, O_2
Me_2CO	NR	O_2
PhCHO	28	$PhCO_2H$, O_2
Dehydrogenation and oxidation		
Cyclohexane	NR	O_2
1,4-c-C_6H_8	59	PhH, O_2
PhNHNHPh	100[c]	PhN=NPh
H_2S	100	H_2SO_4
H_2O (56 mM)	100	Fe^{III}
Dioxygenation		
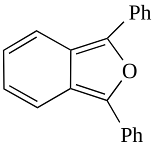	100	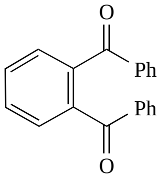
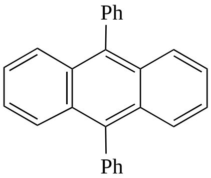	69	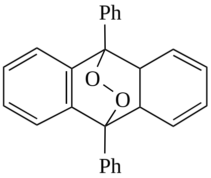
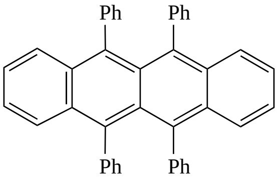	83	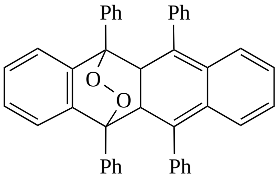
$Ph_2C{=}CPh_2$	22	Ph_2CO, O_2
$PhC\equiv CPh$	42	PhCOCOPh, O_2
$PhC\equiv CMe$	26	PhCOCOMe, O_2
$PhC\equiv CH$	11	PhCOCHO, O_2
c-PhCH=CHPh	52	PhCHO (98%), $PhC\equiv CPh$ (2%), O_2
t-PhCH=CHPh	28	PhCHO, O_2
PhCH=CHMe	32	PhCHO + MeCHO (85%), 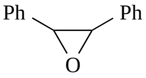 (15%), O_2

[a] Product solution (from the slow addition (∼5 min to give a final 100 mM or 200 mM concentration) of 1 M HOOH (98% HOOH in MeCN) to a solution that contained 100 mM $[Fe^{II}(MeCN)_4](ClO_4)_2$ plus 200 mM substrate) analyzed by gas chromatography, and assayed for residual Fe^{II} by MnO_4^- titration and by colorimetry with 1,10-phenanthroline. [b] 100% represents one substrate oxygenation or dehydrogenation per HOOH added. For dioxygenations, 100% represents one substrate converted per two HOOH added. [c] 100% represents one H_2S converted to H_2SO_4 per four HOOH added.

Table 10 Conversion efficiencies for Fe^{II}–ROOH (R = H, *t*-Bu, *m*-ClC_6H_4CO) induced dehydrogenations and monooxygenations of organic substrates (RH) in acetonitrile[a]

	Oxidants		
Substrate reaction	HOOH	*t*-BuOOH	*m*-$ClC_6H_4CO_2OH$
(a) Dehydrogenation			
HOOH → O_2	100[b]	–	–
1,4-c-C_6H_8 → PhH	59	100	53
1,3-c-C_6H_8 → [PhH/$(C_6H_7)_2$]	86 [1/2][c]	89 [1/2][c]	41 [1/2.5][c]
PhNHNHPh → PhN=NPh	100	75	100
3,5-*t*-Bu_2-1,2-$(OH)_2C_6H_2$ → 3,5-*t*-Bu_2-*o*-benzoquinone	100	70	90
$2PhCH_2SH$ → $PhCH_2SSCH_2Ph$	34/2	32/2	10/2
2PhSH → PhSSPh	68/2	32/2	10/2
(b) Monooxygenations			
c-$C_6H_{11}OH$ → c-$C_6H_{10}O$	47	27	45
$MeCH_2OH$ → MeCHO	70	20	10
$PhCH_2OH$ → PhCHO	100	72	48
$PhCH_2OBu$-*t* → PhCHO + *t*-BuOH	30	70	60
MeCHO → $MeCO_2H$	20	10	27
PhCHO → $PhCO_2H$	28	9	28
t-PhCH=CHMe → PhPh$\overline{\text{CH–CHPh–O}}$/(PhCHO + MeCHO)	16 [1/3][c]	13 [1/4][c]	29 [9/1][c]
Ph$\overline{\text{CH–CHMe–O}}$ → dioxame (dimer) + (PhCHO + MeCHO)	80 [7/3][c]	80 [4/1][c]	85 [19/1][c]
$PhCH_3$ → $PhCH_2OH$ (+PhCHO, $CH_3C_6H_4OH$)	0.3	2	0
$(c\text{-}C_6H_{11})_2S$ → $(c\text{-}C_6H_{11})_2SO$	35	0	15
Ph_2S → Ph_2SO	27	7	51
Ph_2SO → Ph_2SO_2	100	1	71
Ph_3P → Ph_3PO	100	100	47

[a] To 1.0 mmol of substrate and 0.5 mmol of $[Fe^{II}(MeCN)_4](ClO_4)_2$ in 10 mL of MeCN was added slowly 0.5 mmol of hydroperoxide (1 M ROOH in MeCN). Reaction time and temperature: 23 °C for 5 min (1,4-c-C_6H_8, 1,3-c-C_6H_8, PhNHNHPh, $PhCH_2SH$, PhSH, c-$C_6H_{11}OH$, MeCHO, PhCHO, $PhCH_3$, Ph_2SO and Ph_3P); 5 °C for 10 min (3,5-*t*-Bu_2-1,2-$(OH)_2C_6H_2$, $MeCH_2OH$). [b] 100% represents one substrate dehydrogenation or oxygenation per ROOH. [c] Product ratio.

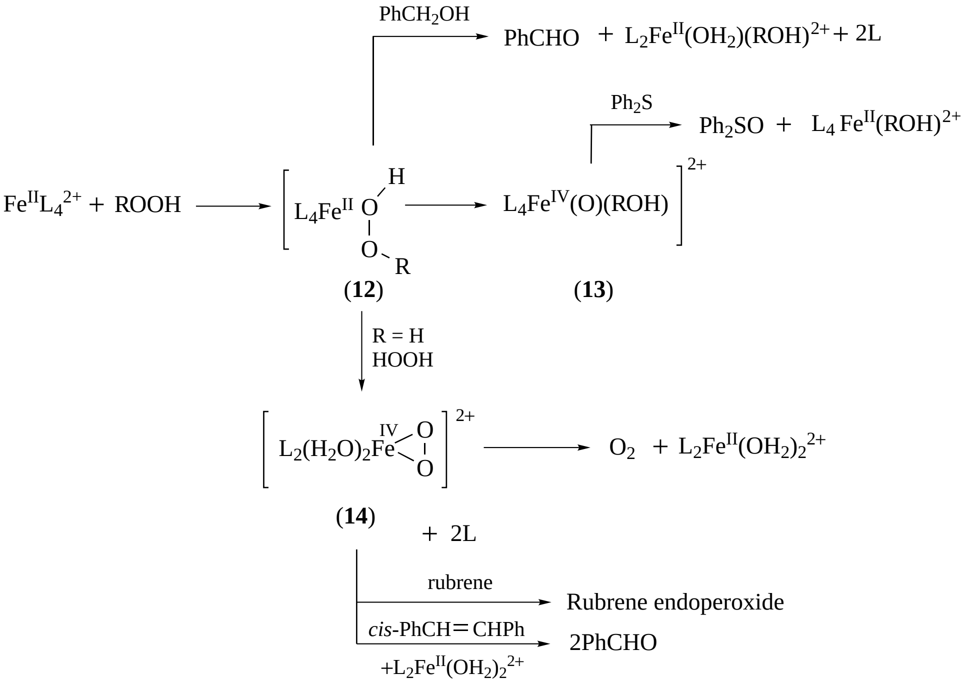
PhCH2OH
PhCHO + L2FeII(OH2)(ROH)2+ + 2L
Ph2S
Ph2SO + L4 FeII(ROH)2+
FeIIL42+ + ROOH
L4FeII O H O R
L4FeIV(O)(ROH)
2+
(12)
(13)
R = H
HOOH
L2(H2O)2FeIV O O
2+
O2 + L2FeII(OH2)22+
(14)
+ 2L
rubrene
Rubrene endoperoxide
cis-PhCH=CHPh
+L2FeII(OH2)22+
2PhCHO

Scheme 3 Activation of ROOH by Iron(II) Lewis acids mechanisms. The monooxygenase formulations also are consistent with the redox stoichiometry of the cytochrome P-450 cycle[64] and represent a form of oxygen activation that promotes electrophilic abstraction of a hydrogen atom (or O-atom transfer) to give radical (or oxene) activated intermediates[65] and the monooxygenation of cytochrome P-450 substrates (Table 10).[66]

In the presence of excess HOOH, the $Fe^{II}(MeCN)_4{}^{2+}$ catalyst forms a reactive adduct (**14**) that reacts with diphenylbenzofuran, arylalkenes, 9,10-diphenylanthracene, or rubrene to form exclusively dioxygenated products (Table 9). Such reactivities parallel those of dioxygenases with this group of substrates.

In a base-free medium (dry MeCN), $Fe^{III}Cl_3$ activates HOOH to form a reactive intermediate that oxygenates alkanes, alkenes, and thioethers, and dehydrogenates alcohols and aldehydes.[67] Table 11 summarizes the conversion efficiencies and product distributions for a series of alkene substrates subjected to the $Fe^{III}Cl_3$/HOOH/MeCN system. The extent of the $Fe^{III}Cl_3$-induced monooxygenations is enhanced by higher reaction temperatures and increased concentrations of the reactants (substrate, $Fe^{III}Cl_3$, and HOOH). For 1-hexene (representative of all of the alkenes), a substantial fraction of the product is the dimer of 1-hexene oxide, a disubstituted dioxane. With other organic substrates (RH), $Fe^{III}Cl_3$ activates HOOH for their monooxygenation; the reaction efficiencies and product distributions are summarized in Tables 11(b). In the case of alcohols, ethers, and cyclohexane, a substantial fraction of the product is the alkyl chloride, and with aldehydes, for example, PhCHO, the acid chloride represents one-half of the product. In the absence of substrate the $Fe^{III}Cl_3$/MeCN system catalyzes the rapid disproportionation of HOOH to O_2 and H_2O.

Because $Fe^{III}Cl_3$ is an exceptionally strong Lewis acid and electrophilic center, it activates HOOH (which acts as a nucleophile) for the dehydrogenation of a second HOOH. On the basis of the disproportionation process, as well as the monooxygenation and dehydrogenation reactions of Table 11, the activation of HOOH by $Fe^{III}Cl_3$ probably involves the initial formation of at least two reactive forms (**15** and **16**) of an $Fe^{III}Cl_3$(HOOH) adduct (Scheme 4).

The disproportionation of HOOH occurs via a concerted transfer of the two hydrogen atoms from a second HOOH to the $Fe^{III}Cl_3$(HOOH) adduct. This dehydrogenation of HOOH is a competitive process with the $Fe^{III}Cl_3$/substrate/HOOH reactions. The controlled introduction of dilute HOOH into the $Fe^{III}Cl_3$/substrate solution limits the concentration of HOOH and ensures that the substrate/HOOH reaction can be competitive with the second-order disproportionation process. The substrate reaction efficiencies in Table 11 are proportional to the relative rates of reaction (k_{RH}/k_{HOOH}). The mode of activation of HOOH by $Fe^{III}Cl_3$ is analogous to that of $Fe^{II}(MeCN)_4{}^{2+}$; both are strong electrophiles in ligand-free dry MeCN and induce HOOH to monooxygenate organic substrates.

The epoxidation of alkenes (Table 11(a)) appears to involve an O-atom transfer from the oxene configuration of the $Fe^{III}Cl_3$(HOOH) adduct (**16**). The resulting epoxides are rapidly dimerized to dioxanes. Hence, the complete conversion of an alkene to its epoxide is precluded; the more complete the conversion, the higher the fraction of dioxane in the product mixture.

The results in Table 11 indicate that the $Fe^{III}Cl_3$(HOOH) adduct monooxygenates alkanes, alcohols, and aldehydes. A mechanism that is consistent with this involves the homolytic scission of the HO–OH bond in the side-on configuration (**15**), induced by the bound substrate, and the subsequent abstraction by one •OH of an H atom from the α-carbon and addition of the second •OH to the resulting carbon radical (Scheme 4). An analogous process appears to occur for the oxygenation of benzaldehyde by the $Fe^{III}Cl_3$(HOOH) adduct, but 50% of the product is the acid chloride. Occurrence of the latter indicates that the activated side-on complex (**15**) has some hypochlorous acid (HOCl) character and can add a chlorine atom to the carbon radical that results from the H-atom abstraction by the •OH group. This also occurs with alkanes, alcohols, and ethers (Table 11). Such chemistry is similar to the activation of chloride ion and HOOH to HOCl by heme-centered myeloperoxidase.[68,69] Phosphines, dialkyl sulfides, and sulfoxides are monooxygenated by the $Fe^{III}Cl_3$(HOOH) adduct in a manner that appears to be analogous to that for the epoxidation of alkenes via species (**16**).

Anhydrous $Fe^{III}Cl_3$ catalyzes the stereospecific epoxidation of norbornene, the demethylation of *N*,*N*-dimethylaniline, and the oxidative cleavage of PhCMe(OH)CMe(OH)Ph (and other α-diols) by hydrogen peroxide (Table 11 and Scheme 4).[67] For each class of substrate, the products parallel those that result from their enzymatic oxidation by cytochrome P-450. The close congruence of the products indicates that the reactive oxygen in the $Fe^{III}Cl_3$/HOOH model system and in the active form of cytochrome P-450 is essentially the same, with strong electrophilic oxene character (stabilized singlet atomic oxygen).

4.6 Formation and Reactivity of Atomic Oxygen from Hydroperoxides [HOOH, ROOH, R′C(O)OOH]

The function of peroxidase enzymes is the activation of HOOH to provide two oxidizing equivalents for the oxidation of a variety of substrates. The interaction of horseradish peroxidase (HRP, an iron(III) heme that has a proximal imidazole) with HOOH results in the formation of a green reactive intermediate known as Compound I. It is reduced by one electron to give a red reactive intermediate, Compound II.[70] Both of these intermediates contain a single oxygen atom from HOOH, and Compound I is two oxidizing equivalents above the iron(III)−heme state with a magnetic moment equivalent to three unpaired electrons ($S = 3/2$). A recent extended X-ray-absorption fine-structure (EXAFS) study[71] summarizes the physical data in support of $(por^{+}\bullet)Fe^{IV}{=}O$ as a

Table 11 Products and conversion efficiencies for the $Fe^{III}Cl_3$ induced oxygenation–dehydrogenation of alkenes and organic substrates (RH) by HOOH in dry acetonitrile[a]

Substrate	Reaction efficiency (%)[b]	Products[c]
(a) Alkenes (−5 °C, 10 min reaction times)		
Blank (HOOH)	100	O_2, H_2O
1-Hexene	10	Epoxide (1-hexene oxide) (71%), dimer (dioxane) (10%), others (19%)
1-Hexene (+5 °C)	23	Epoxide (55%), dimer (15%), others (30%)
1-Octene	60	Epoxide (53%), dimer (10%)
Cyclohexene	25	Epoxide (45%), dimer (30%)
Norbornene	52	*exo*-Epoxide (80%), non-epoxide products (20%)
1,4-Cyclohexadiene	39	PhH (76%), epoxide (17%)
cis-Stilbene	63	PhCHO (50%), epoxides (50%) (cis:trans ratio, 2.5:1)
(b) Other substrates (+5 °C, 20 min reaction times)		
Cyclohexanol	52	Cyclohexanone (88%)
$PhCH_2OH$	63	PhCHO (51%), $PhCH_2Cl$ (21%), $PhCO_2H$ (14%), PhCOCl (14%)
$PhCH_2OBu$-*t*	56	PhCHO (72%), $PhCH_2Cl$ (11%), $PhCO_2H$ (3%), PhCOCl (14%)
PhCH(O)	75	$PhCO_2H$ (55%), PhCOCl (45%)
$PhCH_3$ (25 °C)	2	$PhCH_2OH$, PhCHO, PhCOCl, $PhCO_2H$, cresols
Cyclohexane	22	Cyclohexyl chloride (45%), cyclohexanol (40%), cyclohexanone (15%)
PhC(Me)(OH)C(Me)(OH)Ph	30	PhCOMe (100%)
$PhNMe_2$	39	PhNHMe (95%), PhN(CHO)Me (5%)
Ph_2S	58	Ph_2SO (100%)
Ph_2SO	60	Ph_2SO_2 (100%)
Ph_3P	80	Ph_3PO (100%)

[a] RH and $Fe^{III}Cl_3$ (1.0 mmol of each) combined in 10–20 mL of dry MeCN, followed by the slow addition of 1 mmol HOOH (1 M HOOH (98%) in MeCN). [b] Percentage of substrate converted to products. [c] After the indicated reaction time, the product solution was quenched with water, extracted with diethyl ether, and analyzed by capillary gas chromatography and GC–MS.

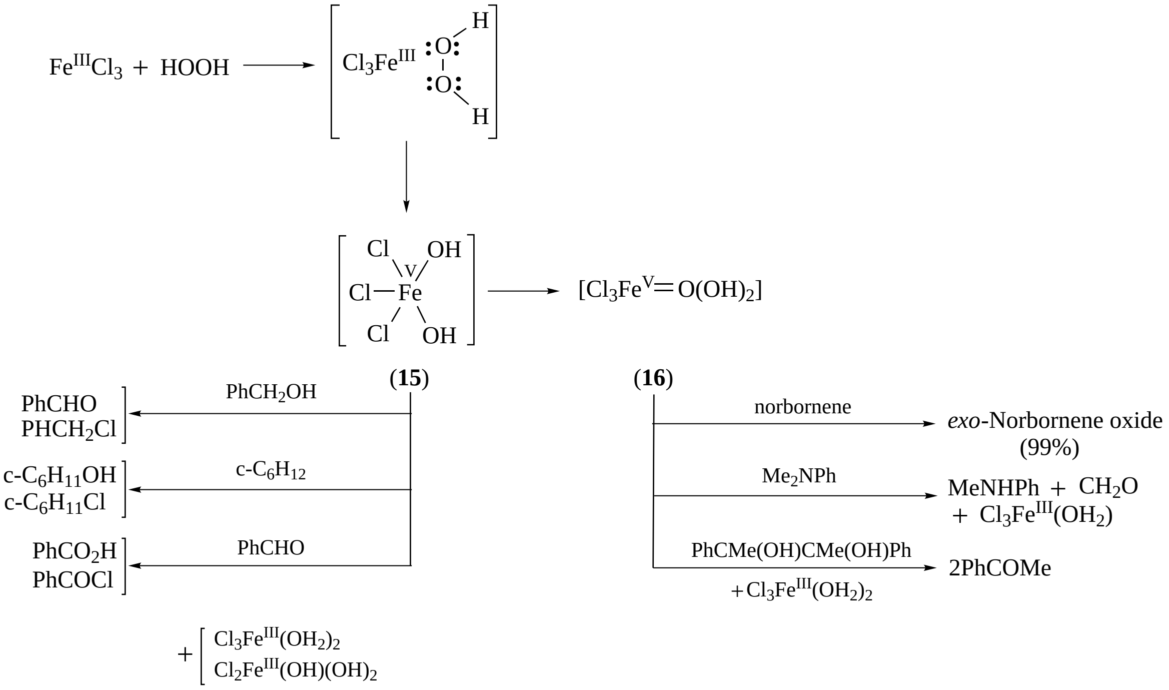

$Fe^{III}Cl_3$ + HOOH
Cl_3Fe^{III}
H
:O:
:O:
H
Cl
OH
V
Cl—Fe
Cl
OH
$[Cl_3Fe^V{=}O(OH)_2]$
(15)
(16)
$PhCH_2OH$
PhCHO
$PHCH_2Cl$
$c\text{-}C_6H_{12}$
$c\text{-}C_6H_{11}OH$
$c\text{-}C_6H_{11}Cl$
PhCHO
$PhCO_2H$
PhCOCl
$+ \left[\begin{array}{l} Cl_3Fe^{III}(OH_2)_2 \\ Cl_2Fe^{III}(OH)(OH)_2 \end{array}\right.$
norbornene
exo-Norbornene oxide (99%)
Me_2NPh
MeNHPh + CH_2O + $Cl_3Fe^{III}(OH_2)$
PhCMe(OH)CMe(OH)Ph
$+Cl_3Fe^{III}(OH_2)_2$
2PhCOMe

Scheme 4 Proposed pathways for activation of HOOH by $Fe^{III}Cl_3$in MeCN

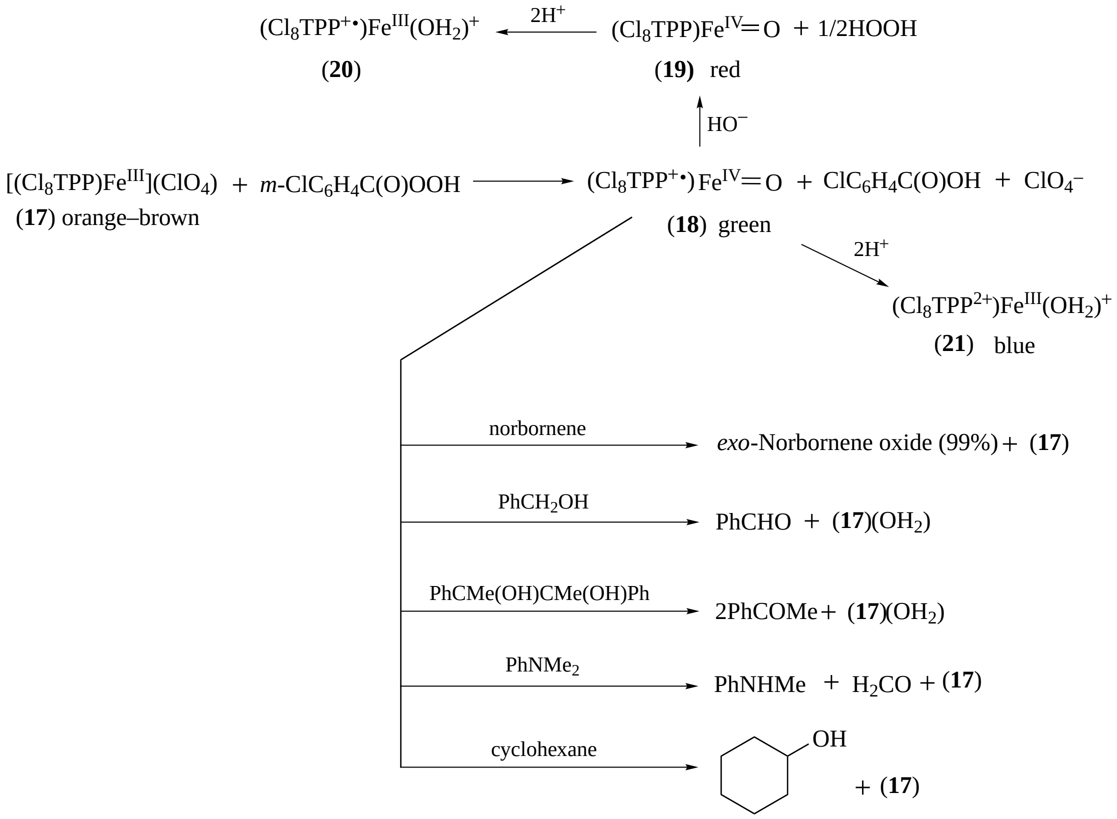
$(Cl_8TPP^{+\bullet})Fe^{III}(OH_2)^+$
(**20**)
2H+
$(Cl_8TPP)Fe^{IV}{=}O$ + 1/2HOOH
(**19**) red
HO−
$[(Cl_8TPP)Fe^{III}](ClO_4)$ + m-$ClC_6H_4C(O)OOH$
(**17**) orange–brown
$(Cl_8TPP^{+\bullet})Fe^{IV}{=}O$ + $ClC_6H_4C(O)OH$ + ClO_4^-
(**18**) green
2H+
$(Cl_8TPP^{2+})Fe^{III}(OH_2)^+$
(**21**) blue
norbornene
exo-Norbornene oxide (99%) + (**17**)
$PhCH_2OH$
PhCHO + (**17**)(OH_2)
PhCMe(OH)CMe(OH)Ph
2PhCOMe + (**17**)(OH_2)
$PhNMe_2$
PhNHMe + H_2CO + (**17**)
cyclohexane
OH
+ (**17**)

Scheme 5 Model for Compounds I and II horseradish peroxidase

formulation for Compound I, and (por)$Fe^{IV}{=}O$ for Compound II, and concludes that both species contain an oxene–ferryl group (Fe=O) with a bond length of 1.64 Å.

Model systems provide compelling evidence that stabilized atomic oxygen is present in Compound I and Compound II of HRP.[47] Thus, the combination of tetrakis(2,6-dichlorophenyl)porphinatoiron(III) perchlorate (**17**, Scheme 5) with pentafluoroiodosobenzene, *m*-chloroperbenzoic acid, or ozone in acetonitrile at −35 °C yields a green porphyrin–oxene adduct (**18**). This species, which has been characterized by spectroscopic, magnetic, and electrochemical methods, cleanly and stereospecifically epoxidizes olefins (>99% *exo*-norborneneoxide). The reaction chemistry of Scheme 5 illustrates how (**18**) acts as an oxygen-atom transfer agent towards alkenes. The stereospecificity for the epoxidation of norbornene is consistent with the concerted insertion[72] of a singlet oxygen atom into the π bond which is analogous to the stereospecific transfer of a singlet oxygen atom from uncatalyzed m-$ClC_6H_4C(O)OOH$ to norbornene.

The spectroscopy, electrochemistry, and magnetic properties of (**18**) indicate that its iron center is equivalent to that of Compound I of HRP. The spectroscopic and electrochemical properties of (**19**), and its reduced reactivity with alkenes, indicate that the electronic structure of its iron–oxygen center is analogous to that of Compound II of HRP.

5 REACTIVITY OF OXYGEN RADICALS (HO•, RO•, HOO•, AND ROO)

Oxygen radicals are defined as those molecules that contain an oxygen atom with an unpaired, nonbonding electron (e.g. HO•). Although triplet dioxygen ($\bullet O_2\bullet$) and superoxide ion ($O_2^{-}\bullet$) come under this definition, their nonradical chemistry dominates their reactivity. The hydroxyl radical (HO•) is the most reactive member of the family of oxygen radicals (HO•, RO•, •O•, HOO•, ROO•, and RC(O)O•), and is the focus of most oxygen radical research. In the gas phase, the dramatic example of oxygen-radical reactivity with hydrocarbon substrates is combustion, which is initiated by HO• (or RO• or MO•) and propagated by $\bullet O_2\bullet$ and •O• (equation 84).

$$\begin{tikzcd} CH_4 + HO\bullet \arrow[r] & HOH + Me\bullet \arrow[r, "\bullet O_2\bullet"] \arrow[dr, "\bullet O\bullet"'] & MeOO\bullet \\ & & MeO\bullet \end{tikzcd} \qquad (84)$$

These initial steps are highly exothermic, which accelerates the autoxidation cycle to an explosive rate to give CO, CO_2, and H_2O as the stable products. Within biological matrices the autoxidation and peroxidation of lipids and fats from foodstuffs are important examples of oxygen radical chemistry. In general, the initiator is HO• (or HOO•) and the autoxidation cycle is carried by •O_2• (equation 85).

$$\begin{tikzcd}
\underset{(\mathbf{22})}{RCH{=}CHCH_2(CH_2)_nCO_2R'} + HO\bullet \arrow[r] & \underset{(\mathbf{23})}{RCH{=}CH\dot{C}H(CH_2)_nCO_2R'} \arrow[d, "\bullet O_2\bullet"] \\
& RCH{=}CHCH(OO\bullet)(CH_2)_nCO_2R' \arrow[d, "(\mathbf{22})"] \\
& (\mathbf{23})\bullet + RCH{=}CHCH(OOH)(CH_2)_nCO_2R'
\end{tikzcd} \qquad (85)$$

Both combustion and lipid autoxidation are initiated through the creation of a carbon radical (abstraction of a hydrogen atom by HO• from a C–H bond). The rate is inversely proportional to the C–H bond energy. The C–H bond energies of aromatic carbons are so large that the reaction of HO• with benzene usually goes by addition. Thus, conjugated systems can stabilize radicals by delocalization throughout the π-electron system. However, with saturated σ-bonded substrates the only pathway for oxygen-radical reactions is by hydrogen-atom abstraction (equation 86).

$$\text{R–H} + \text{YO}\bullet \longrightarrow \text{YO–H} + \text{R}\bullet \qquad (86)$$

The driving force for such a reaction is the difference between the free energy of bond formation for YO–H ($-\Delta G_{\mathrm{BF}}$), and the enthalpy of bond dissociation for R–H (ΔH_{DBE}). Table 12 summarizes the YO–H bond-formation energies for oxygen radicals (YO•), as well as dissociative bond energies for several R–H substrates.[41,73] Reference to these data indicates that t-BuO• will react exothermally with toluene ($PhCH_3$), but will be essentially unreactive with methane.

5.1 Reactivity of HO•

Gas-phase HO• is generated by photolysis of HOOH and by cosmic radiation and solar radiation of O_2/H_2O in the atmosphere. The latter process is an important contributor to the atmospheric chemistry associated with organic pollutants. The gas-phase reactions of HO• with organic molecules have been exhaustively reviewed and summarized in a recent compendium.[74] In aqueous solutions, HO• is produced by radiolysis (continuous and pulsed) (equation 87),[75]

$$\begin{tikzcd}
HOH \arrow[r, "h\nu"] & H\bullet + HO\bullet \arrow[d, "N_2O"] \\
& N_2 + HO\bullet
\end{tikzcd} \qquad (87)$$

and has been the basis for a massive compilation of reactivity data for HO• with organic and inorganic substrates.[76] Although sophisticated measuring techniques provide precise kinetic data for the primary (HO•/R–H) reaction with hydroxyl radicals generated by pulse radiolysis, the limited yields of terminal products preclude identification and assay. For this reason, much of the characterization of HO• chemistry with organic substrates has made use of the Fenton process.

Fenton chemistry is the use of reduced transition metal ions (Fe^{II}, Mn^{II}, V^{III}, and Ti^{III}) in stoichiometric combination with HOOH to generate HO• in situ at a slow rate (equation 88).[50] The dynamics of (HO•) reactivity with organic substrates are assessed as relative rates vis-à-vis the fate of the Fenton-generated hydroxyl radical in these competitive reactions (equations 89–91).[51,60]

$$\begin{tikzcd}
{[Fe^{II}(OH)_2)_6]^{2+}} + HOOH + H_2O \arrow[r, "k", "\text{pH } 2"'] & {[(H_2O)_5{}^{+}Fe^{II}OOH + H_3O^{+}]} \arrow[d] \\
& (H_2O)_5{}^{2+}Fe^{III}OH + HO\bullet
\end{tikzcd}$$

$$k = 42\ M^{-1}s^{-1} \qquad (88)$$

Table 12 Radical strength of oxygen radicals (YO•) in terms of their YO–H bond formation free energies, and dissociative bond energies for H–R molecules

Oxy radical (YO•)	Bond (YO–H)	($-\Delta G_{\mathrm{BF}}$)(aq)[a] (kcal mol^{-1})	Bond (H–R)	(ΔH_{DBE})(g)[b] (kcal mol^{-1})
HO•	HO–H	111	H–CH_3	105
O^{-}•	$^{-}$O–H	109	H–(n-C_3H_7)	100
•O•	•O–H	98	H–(c-C_6H_{11})	95
t-BuO•	t-BuO–H	97	H–(t-C_4H_9)	93
MeO•	MeO–H	96	H–CH_2Ph	88
PhO•	PhO–H	79	H–(c-C_6H_7)(CHD)	73
HOO•	HOO–H	82	H–C(O)Ph	87
$O_2{}^{-}$•	$^{-}$OO–H	72	H–Ph	111
•O_2•	•OO–H	51	H–SH	91
t-BuOO•	t-BuOO–H	83	H–SMe	89
MeOO•	MeOO–H	82	H–SPh	83
MeC(O)O•	MeC(O)O–H	98	H–OPh	86

[a]Sawyer.[58] [b]Lide.[29]

$$\mathrm{Fe^{II}L}_n + \mathrm{HO\bullet} \longrightarrow \mathrm{L}_n\mathrm{Fe^{III}OH} \qquad k = 2 \times 10^8 \mathrm{M^{-1}s^{-1}} \tag{89}$$

$$\mathrm{RH} + \mathrm{HO\bullet} \longrightarrow \mathrm{R\bullet} + \mathrm{HOH} \qquad k = 10^8\text{–}10^{10} \mathrm{M^{-1}s^{-1}} \tag{90}$$

$$\mathrm{HOOH} + \mathrm{HO\bullet} \longrightarrow \mathrm{HOO\bullet} + \mathrm{HOH} \qquad k = 1 \times 10^7 \mathrm{M^{-1}s^{-1}} \tag{91}$$

With a 1:1 $\mathrm{Fe^{II}L}_n$/HOOH ratio at modest concentrations in the presence of excess substrate, the attack of substrate is favored. Although H-atom abstraction is the common path for most substrates, the large bond energy of aromatic C–H bonds (ΔH_{DBE}, 111 kcal mol^{-1}; Table 12) precludes this as a facile process. However, addition to the conjugated π-electron system is energetically favored (equation 92).

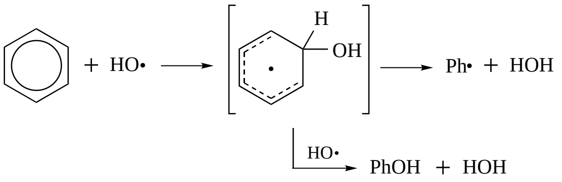

(92)

5.2 Reactivity of HOO•

The hydroperoxyl radical (HOO•) is the conjugate acid of superoxide ion ($\mathrm{O_2}^{-}\bullet$) (equation 93) and constitutes about 1% of the $\mathrm{O_2}^{-}\bullet$ that is formed in aqueous systems at pH 7.[77] Although the O–O bond of HOO• traditionally is viewed to be the same as the single σ bond of HO–OH (ΔH_{DBE}, 51 kcal mol^{-1}), its bond energy (ΔH_{DBE}) is about 85 kcal mol^{-1}, which is more consistent with the 1.5 bond order of $\mathrm{O_2}^{-}\bullet$. However, HOO• is unstable in protic media (such as water and alcohols) and rapidly decomposes via heterolytic and homolytic disproportionation (equations 94 and 95).[78]

$$\mathrm{HOO\bullet} + \mathrm{H_2O} \rightleftharpoons \mathrm{H_3O^+} + \mathrm{O_2}^{-}\bullet \qquad \mathrm{p}K_\mathrm{a} = 4.9 \tag{93}$$

$$\mathrm{HOO\bullet} + \mathrm{O_2}^{-}\bullet \xrightarrow{\mathrm{H_2O}} \mathrm{HOOH} + \mathrm{HO^-} + \mathrm{O_2} \qquad k = 1 \times 10^8 \mathrm{M^{-1}s^{-1}} \tag{94}$$

$$\mathrm{HOO\bullet} + \mathrm{HOO\bullet} \longrightarrow \mathrm{HOOH} + \mathrm{O_2} \qquad k = 8.3 \times 10^5 \mathrm{M^{-1}s^{-1}} \tag{95}$$

Another route to the formation of HOO•/$\mathrm{O_2}^{-}\bullet$ is UV irradiation of HOOH in aqueous solutions.[79] Aerobic organisms produce minor fluxes of superoxide ion ($\mathrm{O_2}^{-}\bullet$, and thereby HOO•) during respiration and oxidative metabolism; for example, possibly up to 10–15% of the $\mathrm{O_2}$ reduced by cytochrome *c* oxidase and by xanthine oxidase passes through the HOO•/$\mathrm{O_2}^{-}\bullet$ state.[80] Thus, the chemistry of HOO• (and of $\mathrm{O_2}^{-}\bullet$) may be important to an understanding of oxygen toxicity in biological systems. In aprotic media, the rate of protonation of $\mathrm{O_2}^{-}\bullet$ is proportional to the acidity of the associated Brønsted acids (equation 96).[81] Electrolytic oxidation of HOOH in acetonitrile yields stoichiometric fluxes of HOO• (equation 97).[29] Reduction of $\mathrm{O_2}$ in MeCN at a platinum electrode in the presence of excess protons yields adsorbed Pt(HOO•) (equation 98) which forms [HOOOOH] via radical coupling at the surface and homolytically dissociates to $^1\mathrm{O_2}$ and HOOH.[67]

$$\mathrm{O_2}^{-}\bullet + \mathrm{HA} \xrightarrow[k \,\propto\, K_{\mathrm{HA}}]{k} \mathrm{HOO\bullet} + \mathrm{A^-} \tag{96}$$

$$\mathrm{HOOH} \xrightarrow[\mathrm{MeCN}]{\mathrm{H_2O}} \mathrm{HOO\bullet} + \mathrm{H_3O^+} + \mathrm{e^-}$$
$$\mathrm{HOO\bullet} \xrightarrow[\mathrm{MeCN}]{\mathrm{HOO\bullet}} \mathrm{HOOH} + \mathrm{O_2} \qquad k = 1 \times 10^7 \mathrm{M^{-1}\,s^{-1}} \tag{97}$$

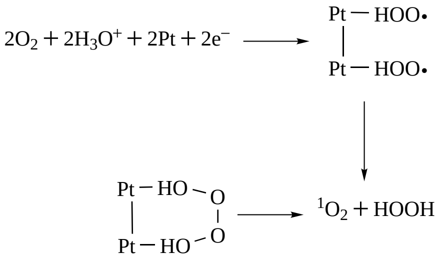

(98)

The homogeneous disproportionation of HOO• in aprotic solvents does not yield $^1\mathrm{O_2}$ and appears to involve a 'head-to-tail' dimer intermediate that undergoes H-atom transfer (equation 99).[37,82]

$$2\mathrm{HOO\bullet} \longrightarrow [\mathrm{HOO\bullet\,HOO\bullet}] \longrightarrow \mathrm{HOOH} + \bullet\mathrm{O_2}\bullet\, k_\mathrm{d} \tag{99}$$

The rate constants (k_d) for the homogeneous disproportionation of HOO• in various solvent systems range from 1.7×10^4 M^{-1} s^{-1} (DMSO) to 6.3×10^8 M^{-1} s^{-1} (PhCl) and 8.3×10^5 M^{-1} ($\mathrm{H_2O}$).[29,37,77,81,83] This second-order parameter limits the steady-state concentration (flux) of HOO• in a given solvent and thereby its reactivity with substrates. Hence, DMSO provides a matrix that stabilizes HOO• better than the other solvents.

An early study[83] used radical-initiated autoxidation experiments in acetonitrile (MeCN) and in chlorobenzene (PhCl) to demonstrate that HOO• abstracts hydrogen atoms from allylic hydrocarbons, for example, 1,4-cyclohexadiene (1,4-CHD). Subsequent investigations[37] have used $\mathrm{O_2}^{-}\bullet$ in DMSO with limiting fluxes of protons to generate HOO• at a controlled rate (equation 96). Because the disproportionation of HOO• is a second-order process, such limiting conditions favor H-atom abstraction by HOO• from excess 1,4-CHD (especially true for DMSO solvent in which HOO• disproportionation is slower than in other solvents). Hence, the presence of 1,4-CHD (1,4-c-$\mathrm{C_6H_8}$) enhances the rate of disappearance of HOO• because of its parallel oxidation of an allylic hydrogen to give a radical that disproportionates to 1,3-CHD and benzene:

$$\mathrm{HOO\bullet} + 1,4\text{-c-}\mathrm{C_6H_8} \longrightarrow 1,3\text{–}\dot{\mathrm{C}}_6\mathrm{H_7} + \mathrm{HOOH}$$

$$k_{ox} = 1.6 \times 10^2 M^{-1} s^{-1} \tag{100}$$

Analysis of the kinetic data for the decay of the HOO• concentration in such systems provides evaluations of k_{ox}.

Table 13 summarizes values of k_{ox} in three solvents (DMSO, MeCN, and PhCl) for the oxidation of 1,4-CHD by HOO•,**[37,83]** as well as for several other substrates in water/alcohol solvents.**[37,83–87]** A reasonable reaction sequence for the formation and reaction of HOO• is outlined in Scheme 6. Initial formation of HOO• (at diffusion-controlled rates for strong acids) is followed by its disproportionation (k_d) or attack of 1,4-CHD (k_{ox}). As with the rates of dehydrogenation for HOO•, its relative rate of oxidation of 1,4-CHD in the three solvents is in the same order, PhCl > MeCN > DMSO. For DMSO, the value of k_{ox} is slightly greater than ${k_d}^{1/2}$, but with MeCN and PhCl the values of k_{ox} are an order of magnitude smaller than their ${k_d}^{1/2}$ values. Hence, the propensity of HOO• to initiate the autoxidation of allylic groups is greater in DMSO and occurs at much lower concentrations of substrate. The rate constants (k_{ox}) for the allylic hydrogen oxidation of linoleic acid and arachidonic acid in protic media also are slightly greater than $({k_d}^{1/2})_{H_2O}$ (Table 13). The large rate constants (k_{ox}) for the reaction of HOO• with antioxidants (α-tocopherol, cysteine, and ascorbic acid) are consistent with their protective role in biology.

The reactivity of ROO• radicals parallels that of HOO•, and is essentially equivalent because its bond energy (ROO–H; $-\Delta G_{BF}$, 83 kcal mol^{-1}) is the same as that for the HOO–H bond ($-\Delta G_{BF}$, 82 kcal mol^{-1}). However, the 'head-to-tail' mechanism for the disproportionation of HOO• (via H-atom transfer, equation 99) is not possible. Instead, ROO• radicals dimerize via radical–radical coupling to form a dialkyl tetraoxide (equation 101).**[88]**

$$2ROO\bullet \xrightarrow{k_d} [ROOOOR] \longrightarrow ROOR + {}^1O_2 \tag{101}$$

The [ROOOOR] intermediate decomposes to dialkyl peroxide and singlet dioxygen, but also reacts more vigorously than $^1O_2$ with '$^1O_2$ substrates' (1,4-CHD, 1,3-diphenylisobenzofuran, rubrene).

Table 13 Rate constants for the second-order oxidation by HOO• of allylic and other X–H functions of organic substrates

Substrate	Solvent	k_{ox} ($M^{-1} s^{-1}$)
1,4-CHD	Me_2SO	1.6×10^2
	MeCN	3.5×10^2
	PhCl	1.4×10^3
Linoleic acid	85:15 EtOH/H_2O	1.2×10^3
Arachidonic acid	85:15 EtOH/H_2O	3.0×10^3
α-Tocopherol	85:15 EtOH/H_2O	2.0×10^5
Cysteine	H_2O	1.8×10^4
Ascorbic acid	H_2O	1.6×10^4

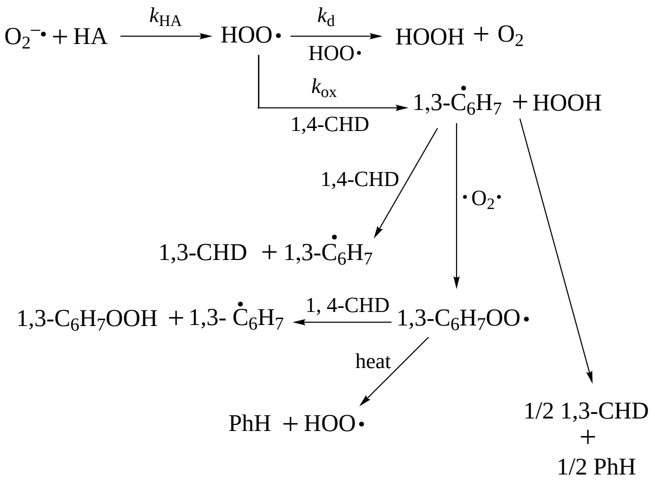

Scheme 6 Formation and reactivity of HOO•

6 REACTIVITY AND ACTIVATION OF DIOXYGEN (•O₂•)

Ground-state dioxygen has two unpaired electrons (•O_2•), which makes it a biradical with a triplet electronic state (see Table 4). Its radical character is limited because the H–OO• bond is weak ($-\Delta G_{BF}$, 51 kcal mol^{-1}), and the triplet state precludes direct reaction with singlet-state substrate molecules with saturated σ bonding.

Perhaps the most important (but nonproductive) reaction chemistry for $^3O_2$ is its reversible binding by metalloproteins: hemoglobin, myoglobin, hemerythrin, and hemocyanin. Nature developed such systems to obviate the limited solubility of O_2 in water ($\approx$1 mM at 1 atm O_2), which restricts the energy flux from oxidative metabolism in aerobic organisms. In the case of myoglobin (a reduced heme protein with an axial histidine base; B), the reversible binding of •O_2• causes the paramagnetic iron(II) center (S = 4/2) of the heme to become diamagnetic via the formation of two covalent Fe–(O_2) bonds (the estimated charge transfer for the iron to the bound O_2 is about 0.1 electron) (equation 102).**[89]**

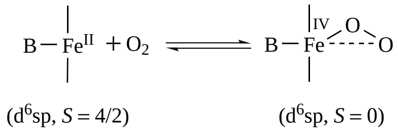

$$B{-}Fe^{II} + O_2 \rightleftharpoons B{-}Fe^{IV}(O{-}O) \tag{102}$$

(d^{6}sp, S = 4/2) (d^{6}sp, S = 0)

$$K_{O_2} = \frac{1}{(P_{1/2})_{O_2}} \approx 10^3\ atm^{-1}$$

where $(P_{1/2})_{O_2}$ represents the partial pressure of O_2 when one-half of the heme centers have an O_2 adduct. Carbon monoxide is more strongly bound, with a K_{CO} value of about 10^6 atm^{-1} via an analogous nucleophilic interaction by the reduced imidiazole-liganded iron–porphyrin center (**24**, d^{6}sp, $S = 0$).

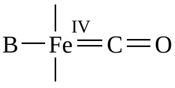

(24)

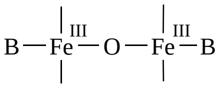

(25)

Although the function of the O_2-binding proteins is the enhancement of the O_2 concentration for transport and storage, there is an inevitable degradation of the oxy–heme system, primarily via interaction with nonoxygenated reduced hemes to give (**25**). The kinetics and mechanism for this irreversible process have been characterized through the use of hindered ('picket-fence') iron–porphyrin models for myoglobin (equation 103).[90]

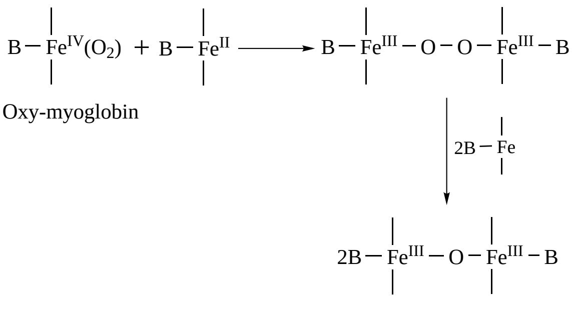

$$\text{B}-\text{Fe}^{IV}(O_2) + \text{B}-\text{Fe}^{II} \longrightarrow \text{B}-\text{Fe}^{III}-\text{O}-\text{O}-\text{Fe}^{III}-\text{B} \xrightarrow{2\text{B}-\text{Fe}} 2\text{B}-\text{Fe}^{III}-\text{O}-\text{Fe}^{III}-\text{B} \quad (103)$$

Oxy-myoglobin

Met-myoglobin

The 'picket fence' hinders the face-to-face approach of the two hemes, but less effectively than the polypeptide chains of the heme protein. The autoxidation pathway for the heme in myoglobin (equations 102 and 103) is sufficiently slow to give the protein a useful life of several weeks, but is analogous to that for all reduced-iron systems.

Biological systems overcome the inherent unreactive character of $^3O_2$ by means of metalloproteins (enzymes) that activate dioxygen for selective reaction with organic substrates. For example, the cytochrome P-450 proteins (thiolated protoporphyrin IX catalytic centers) facilitate the epoxidation of alkenes, the demethylation of N-methylamines (via formation of formaldehyde), the oxidative cleavage of α-diols to aldehydes and ketones, and the monooxygenation of aliphatic and aromatic hydrocarbons (RH) (equation 104).[91] The methane monooxygenase proteins (MMO, dinuclear nonheme iron centers) catalyze similar oxygenation of saturated hydrocarbons (equation 105).[92,93]

$$O_2 + (2H^+ + 2e^-) + RH \xrightarrow{\text{cyt P-450}} ROH + H_2O \quad (104)$$

cytochrome P-450 reductase

$$O_2 + (2H^+ + 2e^-) + CH_4 \xrightarrow{\text{MMO}} MeOH + H_2O \quad (105)$$

reductase

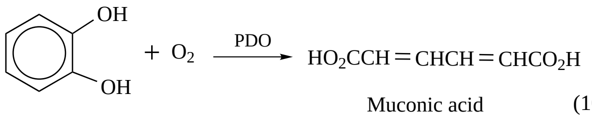

$$\text{C}_6\text{H}_4(\text{OH})_2 + O_2 \xrightarrow{\text{PDO}} HO_2CCH{=}CHCH{=}CHCO_2H \quad (106)$$

Muconic acid

$$^3O_2 \xrightarrow[\text{Rose Bengal}]{h\nu} {}^1O_2$$

$$^3O_2 \xrightarrow[\text{Rose Bengal}]{h\nu} {}^1O_2 \quad (107)$$

Both of these systems activate O_2 via a two-equivalent reduction (without the protein catalysts this would give HOOH). In contrast, pyrocatechol dioxygenase (PDO) (a nonheme iron protein)[94] activates $^3O_2$ without a reductive cofactor (equation 106).

The most direct means to activate $^3O_2$ is by reduction with electrons or hydrogen atoms to give $O_2^-\bullet$, HOO•, HOOH, and HOO^-. Ground-state dioxygen ($^3O_2$) also can be activated by photochemical energy transfer to yield singlet dioxygen ($^1O_2$) (equation 107).[95]

6.1 Radical–Radical Coupling and Autoxidation

Although $^3O_2$ is unreactive with singlet substrates and is unable to abstract hydrogen atoms from hydrocarbon substrates, it is a biradical and as such can undergo coupling with other radicals (carbon and nonmetals as well as transition metals). Such radical–radical coupling reactions usually have zero activation energy. Thus, an HO• radical can initiate the reaction of organic substrates with $^3O_2$:

Initiation

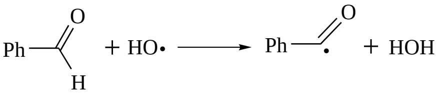

(108)

Propagation

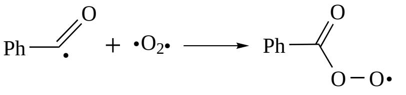

(109)

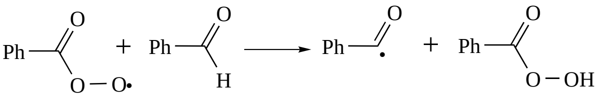

(110)

Termination

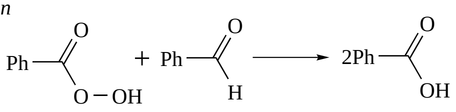

(111)

Propagation in such autoxidation cycles by $^3O_2$ requires that the ROO• intermediate be a sufficiently strong radical to break a C–H bond of the substrate. Allylic, aldehydic, and benzylic C–H bonds are examples that meet this limitation.

Reduced transition metals with unpaired electrons also undergo autoxidation via radical–radical coupling. For example, reduced-iron porphyrins are rapidly converted to dinuclear

μ-oxo dimers (equation 112).[96] Similar heterogeneous radical–radical coupling occurs at the solution–surface interface of metallic iron (equation 113).

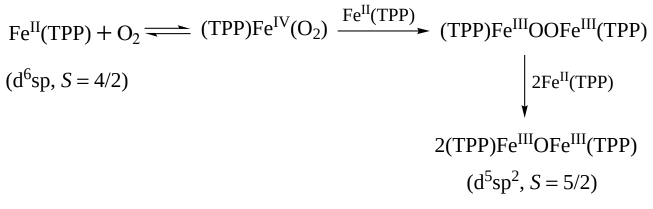

(112)

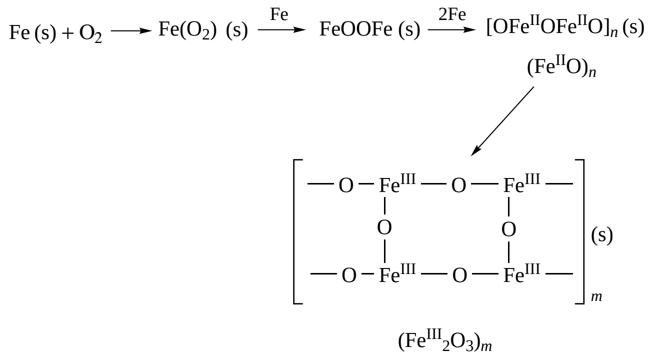

(113)

6.2 Metal-induced Activation of $^3O_2$ for the Initiation of Autoxidation

Reduced transition metal complexes are traditionally implicated as the initiators for the autoxidation of fats, lipids, and foodstuffs.[97] However, whether this involves direct activation of O_2 or of reduced dioxygen ($O_2^{-}\bullet$, HOO•, and HOOH) is unclear. Reduced metal plus HOOH yields HO• via Fenton chemistry and probably is the pathway for initiation of autoxidation in many systems. Although there has been an expectation that one or more of the intermediates from the autoxidation of reduced transition metals (equation 112) can act as the initiator for the autoxidation of organic substrates, direct experimental evidence has not been presented.

The addition of trace levels ($>10^{-6}$ M) of bis(bipyridine)cobalt(II) to O_2-saturated solutions of aldehydes in acetonitrile initiates their rapid autoxidation to carboxylic acids.[83] The initial reaction rates appear to be first order in catalyst concentration, first order in substrate concentration, and first order in O_2 concentration. However, within one hour the autoxidation process is almost independent of catalyst concentration.

6.3 Metal-induced Activation of $^3O_2$ for Dehydrogenation and Oxygenase Chemistry

The addition of $Co^{II}(bipy)_2^{2+}$ to dioxygen-saturated acetonitrile solutions of N-methylanilines catalyzes their demethylation via a monooxygenase pathway to give formaldehyde and demethylated aniline.[98] This is analogous to the chemistry facilitated by cytochrome P-450 proteins with N-methylanilines.[91] The $Co^{II}(bipy)_2^{2+}$ /O_2/MeCN system also dehydrogenates benzylamines and basic benzyl alcohol:

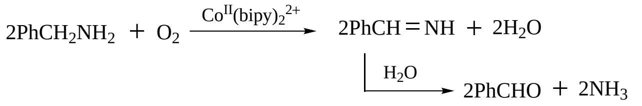

(114)

$$2PhCH_2OH + O_2 \xrightarrow{(HO)Co^{II}(bipy)_2^{+}} 2PhCHO + 2H_2O \qquad (115)$$

The rates of transformation are first order in $Co^{II}(bipy)_2^{2+}$ concentration, first order in O_2 concentration, and first order in substrate concentration. In the case of the dehydrogenation of benzyl alcohols, the $Co^{II}(bipy)_2^{2+}$ catalyst is inactive and must be neutralized with one equivalent of HO^- (equation 116).

$$\bullet Co^{II}(bipy)_2^{2+} + HO^- \longrightarrow HO\underset{\bullet}{Co}^{II}(bipy)_2^{+} \qquad (116)$$

Either $HOC(O)O^-$ or Et_3N can be used in place of HO^-, but the reaction rates are slower. In the absence of substrate, the neutralized catalyst is autoxidized via residual water in the solvent to generate HOOH (equation 117).

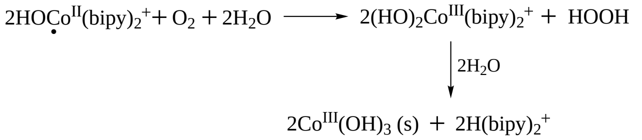

(117)

6.4 Metal-induced Reductive Activation of $^3O_2$ for Monooxygenation

Diphenylhydrazine (PhNHNHPh) is an effective reaction mimic for the flavin cofactors in xanthine oxidases and

Table 14 Monooxygenation and dehydrogenation of organic substrates via a model system for the cytochrome P-450 monooxygenase/reductase enzymes[a]

Substrate (RH)	Product	% Reaction efficiency
Ph_3P	Ph_3PO	100 ± 5
$PhCH_2OH$	PhCH(O)	30 ± 4
Ph_2SO	$Ph_2S(O)_2$	25 ± 3
1,4-Cyclohexadiene	PhH	10 ± 2

[a] Solution conditions: 1 mM $Fe^{II}(MeCN)2+:4$, 1.6 mM O_2, 1 mM PhNHNHPh, 0.1 mM HO^-, and 3 mM substrate in MeCN. Reaction time, 0.5 h.

cytochrome P-450 reductases, and in combination with O_2 yields HOOH (equation 118).[48]

$$\mathrm{PhNHNHPh} + O_2 \xrightarrow{\text{base}} \mathrm{PhN{=}NPh} + \mathrm{HOOH} \qquad (118)$$

Table 14 summarizes the product yields from the combination of substrate (Ph_3P, Ph_2SO, $PhCH_2OH$, or 1,4-cyclohexadiene) with O_2, PhNHNHPh, and $Fe^{II}(MeCN)_4{}^{2+}$ in DMF.[99] The system acts as an effective monooxygenase/dehydrogenase, and as such mimics the reaction cycle of the cytochrome P-450 monooxygenase/reductase system:

$$\begin{aligned} &\mathrm{Ph_2SO} + O_2 + \mathrm{PhNHNHPh} \xrightarrow{[\mathrm{Fe^{II}(MeCN)_4}]^{2+}} \\ &\qquad \mathrm{Ph_2SO_2} + H_2O + \mathrm{PhN{=}NPh} \qquad (119) \end{aligned}$$

The activation of dioxygen for the monooxygenation of saturated hydrocarbons by the methane monooxygenase enzyme systems (MMO; hydroxylase/reductase) represents an almost unique biochemical oxygenase, especially for the transformation of methane to methanol.[92,93,100] The basic process involves the insertion of an oxygen atom into the C–H bond of the hydrocarbon via the concerted reduction of O_2 by the reductase cofactor (equation 120).

$$CH_4 + O_2 \xrightarrow{\mathrm{MMO/H_2}} \mathrm{MeOH} + H_2O \qquad (120)$$

The combination of bis[(2,6-carboxyl-carboxylato)pyridine]iron(II) [$Fe^{II}(DPAH)_2$] and O_2 results in the rapid autoxidation of the iron complex and is essentially unreactive with hydrocarbon substrates (e.g. c-C_6H_{12}). However, the presence of excess PhNHNHPh gives a system that is a hydrocarbon monooxygenase (c-$C_6H_{12} \rightarrow$ c-$C_6H_{11}OH$).[101] The distribution of R–OH isomers from 2-Me-butane indicates a selectivity in the order $\equiv CH > {=}CH_2 > {-}CH_3$; the relative reactivities per C–H bond are 1.00, 0.29, and 0.05, respectively. With $Fe^{II}(PA)_2$/HOOH Fenton chemistry in 1.8:1 py/HOAc, the relative reactivities are 1.00, 0.43, and 0.07,[53] and the values for aqueous HO• are 1.00, 0.48, and 0.10.[102] Thus, the reactive intermediate from the $Fe^{II}(DPAH)_2/O_2$/PhNHNHPh system is more selective than Fenton-derived and free HO•.

The ability of the $Fe^{II}(DPAH)_2/O_2$/PhNHNHPh system (where PhNHNHPh is a mimic for flavin reductases)[48,100] to monooxygenate saturated hydrocarbons closely parallels the chemistry of the methane monooxygenase proteins.[92,93,101] However, the enzyme oxygenates 2-Me-butane with an isomer distribution of 82% primary alcohol, 10% secondary, and 8% tertiary.[103] The present model gives a distribution of 21% primary, 29% secondary, and 50% tertiary. Clearly the protein affords a cavity that is selective for $-CH_3$ groups.

6.5 Metal Surface Induced Activation of Dioxygen for Oxygenase Chemistry

Supported silver is used for the activation of the O_2 in ambient air for the gas-phase selective epoxidation of ethylene (equation 121).[104]

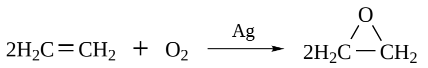

(121)

Although the mechanism for O_2 activation is not known, the model for Compound I of horseradish peroxidase, $[(Cl_8TPP)^{+}\bullet]Fe^{IV}{=}O$, is an especially effective epoxidation reagent. The bond energy ($-\Delta G_{BF}$) for the Fe=O bond in this model is 46 kcal mol^{-1}, which is in accord with its facile epoxidation of alkenes ($-\Delta G_{BF}$, 77 kcal mol^{-1}). Because the gas-phase bond energy (ΔH_{DBE}) for the Ag=O bond is about 53 kcal mol^{-1} ($-\Delta G_{BF} \sim 45$ kcal mol^{-1}),[41] this entity should be an effective O-atom transfer agent for alkene epoxidation.

If the silver surface is an infinite oligomer of trivalent Ag atoms $(Ag^{III})_n$, then a reasonable O_2-activation reaction should lead to $(Ag^{III})_{n-1}{-}Ag^{III}{=}O$ groups on the surface (equation 122).

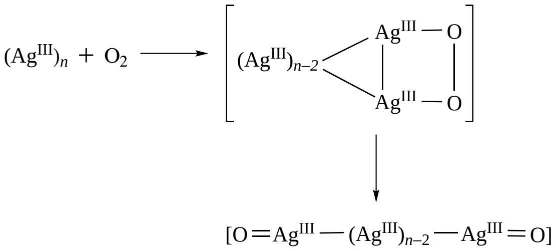

(122)

Such groups will have Ag=O bond energies ($-\Delta G_{BF}$) that are less than 45 kcal mol^{-1}, and should be effective epoxidation agents.

Another heterogeneous O_2-activation system uses supported cobalt metal to catalyze the gas-phase oxygenation of cyclohexane to cyclohexanol and cyclohexanone, which are intermediates for the production of adipic acid ($HO_2C(CH_2)_4CO_2H$) (equation 123).

$$\text{c-}C_6H_{12}(g) + O_2 \xrightarrow{(\mathrm{Co})_n} \text{c-}C_6H_{11}OH + \text{c-}C_6H_{10}O + H_2O \qquad (123)$$

As in the case of silver, the cobalt surface probably is an infinite oligomer of trivalent cobalt atoms $(Co^{III})_n$ that may activate O_2 to give reactive intermediates such as (**26**) and (**27**).

$$(Co^{III})_{n-1}{-}Co^{III}{=}O$$

(**26**)

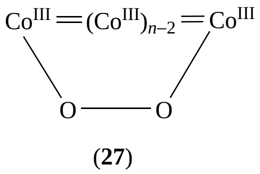

(**27**)

Dioxygen appears to form similar M–O–O–M groups on all transition metal surfaces, but most systems rapidly degrade to M–O–M (equation 124).

This is especially true for manganese, iron, and coinage metal (Cu, Ag, Au) surfaces,[105] but apparently is not favored with cobalt.

$$(\mathrm{M})_{n-1}\text{–M–O–O–M–}(\mathrm{M})_{n-1} \longrightarrow (\mathrm{M})_{n-2}\text{–M–O–M–O–M–}(\mathrm{M})_{n-1} \qquad (124)$$

6.6 Biological Systems

Nature uses a variety of metalloproteins and flavoproteins to activate (or catalyze) dioxygen for useful chemistry.[106–109] These can be subdivided into (a) oxidases (electron-transfer oxidation by O_2, e.g. cytochrome *c* oxidase); (b) dehydrogenases (removal of two hydrogen atoms from the substrate by O_2; many so-called oxidases actually dehydrogenate substrates, for example, glucose oxidase and xanthine oxidase); (c) monooxygenases (oxygen-atom transfer to substrate from O_2; usually have a reductase (hydrogenase) cofactor to reduce the second oxygen atom of O_2 to H_2O (hence the archaic name of 'mixed function' oxidases), e.g. cytochrome P-450 and methane monooxygenase); and (d) dioxygenases (transfer of the two oxygen atoms of O_2 to a substrate molecule, e.g. pyrocatechol dioxygenase). Each class of O_2-activating systems includes a variety of proteins and functions.

Within aerobic biology, the 'harvesting' of the oxidative energy of O_2 is fundamental to oxidative metabolism. Because this is accomplished via the electron-transfer oxidation of four cytochrome $c(\mathrm{Fe^{II}})$ molecules ($E^{\circ\prime}_{\mathrm{pH7}}$, $+0.3$ V vs. NHE) per O_2, the challenge is to facilitate the reduction of O_2 via four one-electron steps, each with a potential greater than $+0.4$ V versus NHE at pH 7 (equation 125). The thermodynamics for the uncatalyzed electron-transfer reduction of O_2 does not meet this criterion (equation 126) especially for the initial pH-independent electron transfer to O_2.

$$\begin{aligned}&O_2 + 4(H_3O^+)_{\mathrm{pH7}} + 4\mathrm{cyt}\ c(\mathrm{Fe^{II}}) \xrightarrow{\mathrm{cyt}\ c\ \mathrm{oxid}}\\ &\quad 4\mathrm{cyt}\ c(\mathrm{Fe^{III}})^+ + 6H_2O \end{aligned} \qquad (125)$$

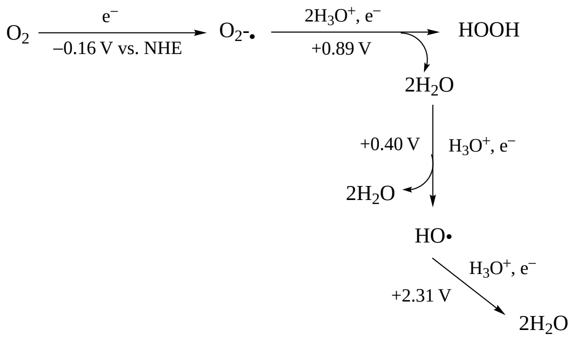

(126)

The cytochrome *c* oxidase protein is thought to consist of two heme–iron centers (heme *a* with two axial histidines and heme a_3 with one axial histidine (analogous to myoglobin)) and two copper centers ($\mathrm{Cu_A}$ with two histidine, two cysteine, and one water/tyrosine ligand in its oxidized state; and $\mathrm{Cu_B}$ with three histidine, one methionine, and one H_2O/HO^- ligands).[110,111] The $\mathrm{Cu_A}$/heme *a* pair constitute two coupled, one-electron redox couples (low potential, ≈0.4 V) that facilitate (a) electron transfer from cytochrome $c(\mathrm{Fe^{II}})$ at the matrix side of the inner mitochondrial membrane as well as (b) proton transfer from the mitochondrial matrix across the inner membrane to the cytosol. At the cytosol side of the inner mitochondrial membrane, the $\mathrm{Cu_B}$/heme a_3 pair constitute the binding site for O_2 as well as the conduit for its high-potential four-electron, four-proton reduction to two H_2O molecules.

Cytochrome P-450, which is the most extensively studied of the monooxygenase proteins, has a heme–iron active center with an axial thiol ligand (a cysteine residue). However, most chemical model investigations[91,106] use simple iron(III) porphyrins without thiolate ligands. As a result, model mechanisms for cytochrome P-450 invoke a reactive intermediate that is formulated to be equivalent to Compound I of horseradish peroxidase, $(\mathrm{por}^{+}\bullet)\mathrm{Fe^{IV}}{=}\mathrm{O}$, with a high-potential porphyrin cation radical. Such a species would be reduced by thiolate, and therefore is an unreasonable formulation for the reactive center of cytochrome P-450.

Again, on the basis of (a) the chemistry for O_2 in the presence of transition metals and reducing agents and (b) reasonable bonding energetics for the components of the cytochrome P-450 monooxygenase/reductase system ($(\mathrm{por})\mathrm{Fe^{III}}\text{–SR}/O_2/(\mathrm{NADH},\ H_3O^+/\mathrm{flavin})/\mathrm{substrate}$), a self-consistent mechanism is proposed and outlined in Scheme 7. The presence of an axial Fe–SR bond enhances the covalence of the iron, reduces the Fe–O bond energy, and thereby increases the radical character and reactivity of the ($\mathrm{RS–Fe^{IV}–OOH}$) group, and precludes formation of a high-potential porphyrin cation-radical one-electron oxidant.

Another example of a monooxygenase, *p*-hydroxybenzoate hydroxylase (HBH), makes use of a flavin cofactor in combination with a reductase (equation 127).[112]

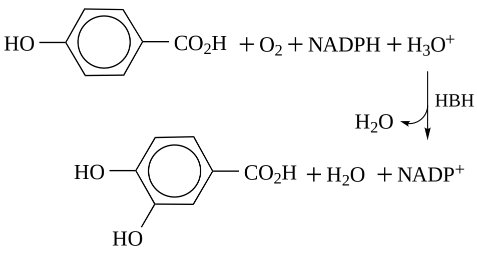

(127)

Spectral studies of rapid-quench experiments indicate that the substrate/oxidized flavin/O_2/reductase combination forms an initial reactive intermediate that subsequently oxygenates

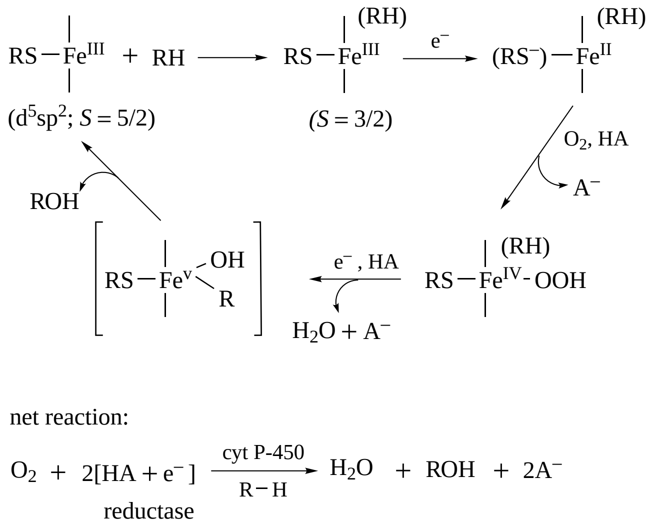

RS—Fe^III + RH
(d^5sp^2; S = 5/2)
(RH)
RS—Fe^III
(S = 3/2)
e^−
(RS^−)—Fe^II
(RH)
O2, HA
A^−
ROH
RS—Fe^V OH R
e^−, HA
H2O + A^−
RS—Fe^IV-OOH
(RH)
net reaction:
O2 + 2[HA + e^−] reductase
cyt P-450
R−H
H2O + ROH + 2A^−

Scheme 7 Proposed mechanism for the activation of O_2 for the monooxygenation of substrates (RH) by cytochrome P-450

the substrate.[113,114]

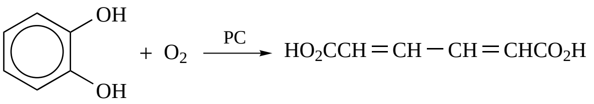

OH
OH
+ O2
PC
HO2CCH=CH−CH=CHCO2H

(128)

Pyrocatechase (PC) is representative of a class of proteins that facilitates the transfer of both atoms of O_2 to a substrate molecule. With this particular dioxygenase, pyrocatechol is transformed to muconic acid (equation 29).

There is agreement that the enzyme contains nonheme iron at the active site with N or O ligands (probably histidine, tyrosine, and/or aspartate residues),[115,116] but there is less certainty as to the oxidation state, coordination sphere, and mode of O_2 binding and activation for the iron center. Because the $Fe^{II}(DPAH)_2/O_2$/pyrocatechol system[117] parallels the chemistry of the enzyme (equation 128), some of the essential elements of O_2 binding and activation may be the same. On the basis of what is known for the enzymatic process and the $Fe^{II}(DPAH)_2/O_2$/pyrocatechol system, a nonionic oxygen-atom transfer mechanism for O_2 activation by pyrocatechol dioxygenase is proposed and outlined in Scheme 8. Key elements of the mechanism include recognition that (1) only reduced-iron binds dioxygen, (2) the net process is two O-atom transfers per substrate and not electron transfer, and (3) only a single dioxygenated product is formed. The latter requires a reactive intermediate (**28**) with two equivalent oxygen atoms that can be transferred in a concerted manner.

6.7 Singlet Dioxygen ($^1O_2$)

Ground-state dioxygen ($^3O_2$) can be activated by photolytic energy transfer to the singlet state ($^1O_2$) (equation 129) and this may be duplicated at the surface of biomembranes by solar radiation. In the laboratory, singlet dioxygen is conveniently produced by the stoichiometric oxidation of hydrogen peroxide by hypochlorous acid (equation 130).

$$^3O_2 \xrightarrow[\text{Rose Bengal}]{h\nu} {}^1O_2 \qquad (129)$$

$$\text{HOOH} + \text{HOCl} \longrightarrow {}^1O_2 + H_2O + \text{HCl} \qquad (130)$$

Singlet dioxygen in biological systems is highly selective; $^1O_2$ is unreactive with most organic functional groups (e.g. saturated σ bonds, simple alkenes, and carbonyl groups). In part, this is due to its limited lifetime (2 μs in H_2O, 58 μs in ^2H_2O, 16 μs in DMF, 65 μs in MeCN, and 610 μs in d_3-MeCN),[118,119] to its paired valence-electron shell, and to its

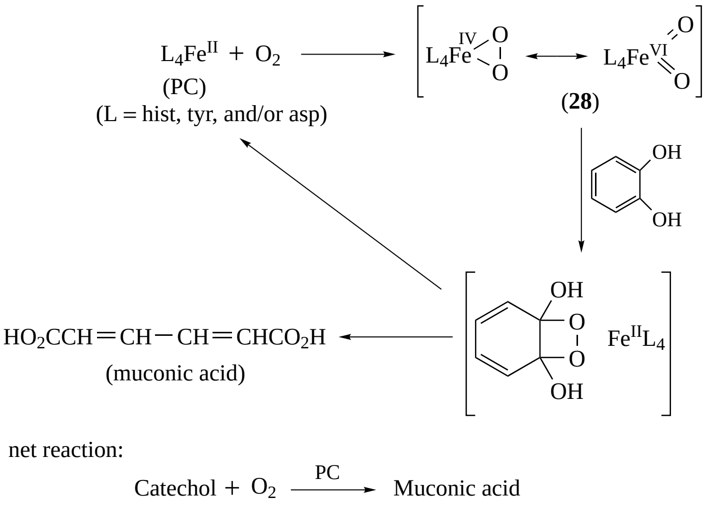

L4Fe^II + O2
(PC)
(L = hist, tyr, and/or asp)
L4Fe^IV O O
L4Fe^VI O O
(28)
OH
OH
OH
O
O
OH
Fe^II L4
HO2CCH=CH−CH=CHCO2H
(muconic acid)
net reaction:
Catechol + O2
PC
Muconic acid

Scheme 8 Proposed mechanism for the activation of O_2 by pyrocatechase (PC) for the dioxygenation of catechols strong O–O bond (ΔH_{DBE}, $119\,\text{kcal mol}^{-1}$). The suspected biological hazard of $^1O_2$ has prompted extensive research with a substantial literature in several disciplines. A recent review[120] provides a comprehensive overview of the reactivity for $^1O_2$ in various phases and matrices. The most facile chemistry for $^1O_2$ is addition to conjugated polymers and polynuclear aromatic molecules (equations 131–133).[121,122]

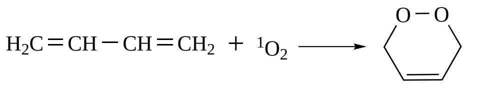

(131)

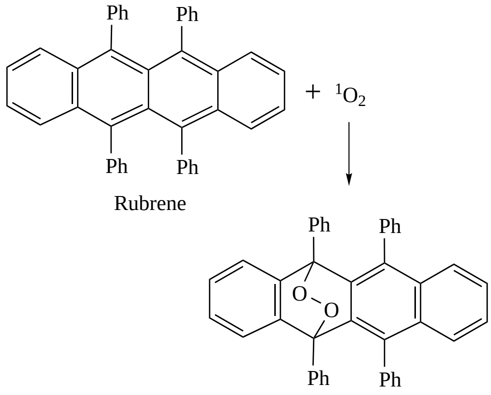

Rubrene

(132)

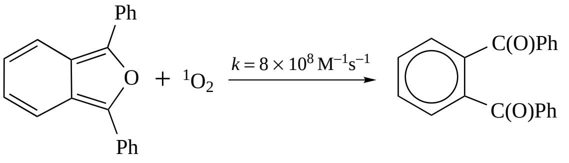

1, 3-Diphenylisobenzofuran
(DPBF)

o-Dibenzoylbenzene
(DBB)

(133)

Unfortunately, much of the chemistry attributed to $^1O_2$ actually is due to a precursor in its generation cycle. Thus, many have used *cis*-stilbene (c-PhCH=CHPh) to indicate the presence of $^1O_2$ via the production of PhCHO. Careful experiments with authentic photochemically generated $^1O_2$ (equation 129) have established that c-PhCH=CHPh has a small reaction rate.[123] Hence, the large yields of PhCHO that are attributed to $^1O_2$ may result from oxygenation by an $^1O_2$ precursor molecule.

7 REACTIVITY OF SUPEROXIDE ION ($O_2^{-}\bullet$)

Reduction by electron transfer yields superoxide ion ($O_2^{-}\bullet$),[31] which has its negative charge and electronic spin density delocalized between the two oxygens. As such, it has limited radical character (H–OO$^-$ bond energy ΔG_{BF}, $72\,\text{kcal mol}^{-1}$)[73] and is a weak Brønsted base in water (equation 134).[124]

$$\text{HOO}\bullet \xrightarrow{H_2O} H_3O^+ + O_2^{-}\bullet \qquad k_{\text{diss}} = 2.0 \times 10^{-5} \tag{134}$$

The dynamics for the hydrolysis and disproportionation of $O_2^{-}\bullet$ in aqueous solutions have been characterized by pulse radiolysis.[124–128] For all conditions, the rate-limiting step is second order in $O_2^{-}\bullet$ concentration, and the maximum rate occurs at a pH that is equivalent to the pK_a for HOO• (it decreases monotonically with further decreases in the hydrogen-ion concentration) (equations 135–137).

$$\text{HOO}\bullet + O_2^{-}\bullet \xrightarrow{H_3O^+} \text{HOOH} + O_2 \qquad k_2 = 1.0 \times 10^{8}\,\text{M}^{-1}\text{s}^{-1} \tag{135}$$

$$\text{HOO}\bullet + \text{HOO}\bullet \longrightarrow \text{HOOH} + O_2 \qquad k_2 = 8.6 \times 10^{5}\,\text{M}^{-1}\text{s}^{-1} \tag{136}$$

$$O_2^{-}\bullet + O_2^{-}\bullet + 2H_2O \longrightarrow \text{HOOH} + O_2 + 2\text{HO}^- \qquad k_4 < 0.3\,\text{M}^{-1}\text{s}^{-1} \tag{137}$$

7.1 Brønsted Base

In water, at pH 7 the disproportionation equilibrium is far to the right[129] and even at pH 14 it is complete (equation 139).

$$2O_2^{-}\bullet + 2H_3O^+ \rightleftharpoons \text{HOOH} + O_2 \qquad K = 4 \times 10^{20} \tag{138}$$

$$2O_2^{-}\bullet + H_2O \rightleftharpoons \text{HOO}^- + {}^-\text{OH} + O_2 \qquad K = 9.1 \times 10^{8} \tag{139}$$

Thus, the dominant characteristic of $O_2^{-}\bullet$ in any medium is its ability to act as a strong Brønsted base via formation of HOO•, which reacts with allylic hydrogens, itself, or a second $O_2^{-}\bullet$ (Scheme 9). Such a proton-drive disproportionation process means that $O_2^{-}\bullet$ can deprotonate acids much weaker than water (up to p$K_a \sim 23$).[34]

The propensity of $O_2^{-}\bullet$ to remove protons from substrates accounts for its reactivity with acidic reductants and their overall oxidation. Thus, combination of $O_2^{-}\bullet$ with protic substrates (α-tocopherol, hydroquinone, 3,5-di-*t*-butylcatechol, L(+)-ascorbic acid) yields products that are consistent with an apparent one-electron oxidation of the substrate and the production of HOOH. However, the results of electrochemical studies[130] provide clear evidence that these substrates are not oxidized in aprotic media by direct one-electron transfer to $O_2^{-}\bullet$. The primary step involves abstraction of a proton from the substrate by $O_2^{-}\bullet$ to give substrate anion and the disproportionation products of HOO• (HOOH and O_2). In turn, the substrate anion is oxidized by O_2 in a multistep process to yield oxidation products and HOOH. Thus, by continuously purging the O_2 that results from the

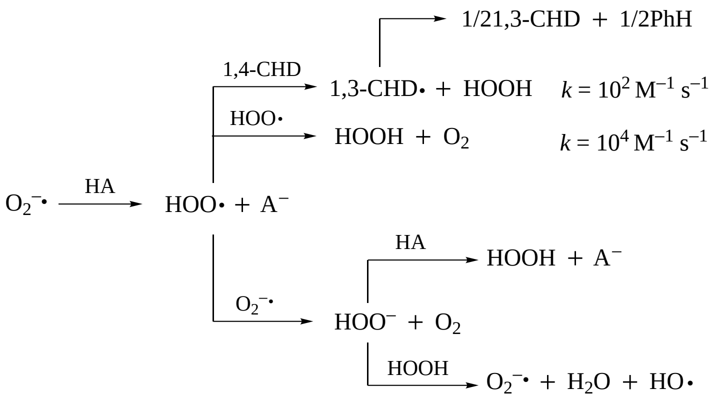

Scheme 9 Proton-induced activation of $O_2^{-}\bullet$ in Me_2SO

disproportionation of $O_2^{-}\bullet$ when it is combined with α-tocopherol (by vigorous Ar bubbling through the solution), quantitative yields of substrate anion are obtained without significant oxidation.

7.2 Nucleophilicity

Although superoxide ion is a powerful nucleophile in aprotic solvents, it does not exhibit such reactivity in water, presumably because of its strong solvation by that medium ($\Delta H_{\text{hydration}}$, $100\,\text{kcal mol}^{-1}$) and its rapid hydrolysis and disproportionation. The reactivity of $O_2^{-}\bullet$ with alkyl halides via nucleophilic substitution was first reported in 1970.[131,132] These and subsequent kinetic studies[133–135] confirm that the reaction is first order in substrate, that the rates follow the order primary $>$ secondary $\gg$ tertiary for alkyl halides and tosylates, and that the attack by $O_2^{-}\bullet$ results in inversion of configuration (S_N2).

The nucleophilicity of $O_2^{-}\bullet$ toward primary alkyl halides (Scheme 10) results in an S_N2 displacement of halide ion from the carbon center. The normal reactivity order, benzyl $>$ primary $>$ secondary $>$ tertiary, and leaving group order, I $>$ Br $>$ OTs $>$ Cl, are observed, as are the expected stereoselectivity and inversion at the carbon center.[136–141] In DMF, the final product is the dialkyl peroxide. The peroxy radical (ROO•), which is produced in the primary step and has been detected by spin trapping,[142] is an oxidant that is readily reduced by $O_2^{-}\bullet$ to form the peroxy anion (ROO^-). Because the latter can oxygenate Me_2SO to its sulfone, the main product in this solvent is the alcohol (ROH) rather than the dialkyl peroxide.

Although formation of the dialkyl peroxide is shown in the prototype reaction (Scheme 9), hydroperoxides, alcohols, aldehydes, and acids also have been isolated. The extent of these secondary paths depends on the choice of solvent and reaction conditions. Secondary and tertiary halides also give substantial quantities of alkenes from dehydrohalogenation by $O_2^{-}\bullet/HOO^-/HO^-$.

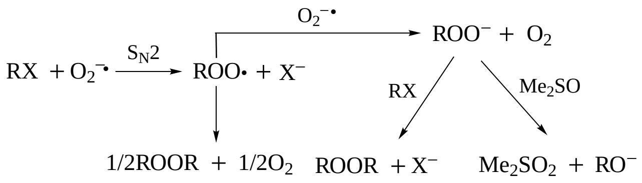

Scheme 10 Nucleophilic displacement of alkyl halides by $O_2^{-}\bullet$

The reaction of $O_2^{-}\bullet$ with CCl_4 and $RCCl_3$ compounds almost certainly cannot occur via an S_N2 mechanism because the carbon-atom center is inaccessible. Rather, superoxide ion appears to attack a chlorine atom with a net result that is equivalent to an electron transfer from $O_2^{-}\bullet$ to chlorine (equation 140).

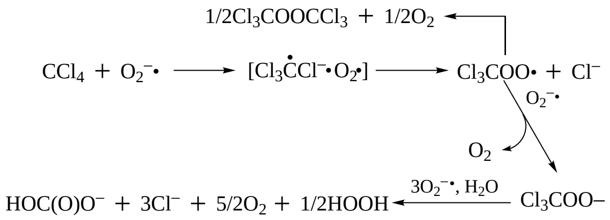

(140)

This step is analogous to the 'single-electron-transfer' (SET) mechanism that has been proposed for many nucleophilic reactions, that is, an initial transfer of an electron followed by the collapse of a radical pair (equation 141).[143]

$$E^+ + Nu^- \longrightarrow [E\bullet\,\bullet Nu] \longrightarrow E\text{–}Nu \qquad (141)$$

The initiation step for the $(O_2^{-}\bullet)/CCl_4$ reactions must be followed by rapid combination in the solvent cage of $\bullet O_2\bullet$ and $Cl_3C\bullet$ to form the $Cl_3COO\bullet$ radical. This radical is thought to initiate lipid peroxidation,[144] which could account for the hepatoxicity of CCl_4.[145] The rates of reaction for $O_2^{-}\bullet$ with $RCCl_3$ compounds are proportional to their reduction potentials, which is consistent with the SET mechanism.[136] A plot of log $k_1/[S]$ against the reduction potentials of $RCCl_3$ compounds is approximately linear with a slope of -4.9 decade per volt.

Polyhalogenated aromatic hydrocarbons (e.g. hexachlorobenzene (HCB, C_6Cl_6) and polychorobiphenyls (PCBs)) are rapidly degraded by superoxide ion in DMF to bicarbonate and halide ions.[140] Because halogen-bearing intermediates are not detected, the initial nucleophilic attack is the rate-determining step. The rates of reaction exhibit a direct correlation with the electrophilicity of the substrate (reduction potential) (e.g. C_6Cl_6, $E^{\circ\prime} = -1.48\,\text{V}$ vs. SCE; $k_1/[S] = 1 \times 10^3\,\text{M}^{-1}\,\text{s}^{-1}$; and 1,2,4-$C_6H_3Cl_3$, $E^{\circ\prime} = -2.16$ V; $k_1/[S] = 2 \times 10^{-2}\,\text{M}^{-1}\,\text{s}^{-1}$).

Although polyhaloaromatics are degraded by $O_2^{-}\bullet$ in MeCN and DMSO, the rates of reaction are about one-tenth as great in MeCN and 20 times slower in DMSO. A reasonable initial step for these oxygenations is nucleophilic addition of $O_2^{-}\bullet$ to the polyhalobenzene (e.g. C_6Cl_6; Scheme 11).

Subsequent loss of chloride ion will give a benzoperoxy radical, which will close on an adjacent aromatic carbon center and add a second $O_2^{-}\bullet$ to become a peroxo nucleophile that can attack the adjacent carbochlorine center with displacement of chloride ion and a highly electrophilic tetrachloro center. The latter undergoes facile reactions with $O_2^{-}\bullet$ to displace the remaining chloro atoms.

When Aroclor 1268 (a commercial PCB fraction that contains a mixture of Cl_7, Cl_8, Cl_9, and Cl_{10} polychlorobiphenyls) is combined with excess $O_2^{-}\bullet$, the entire mixture is degraded. Samples taken during the course of the reaction confirm that (a) the most heavily chlorinated members react first (the initial nucleophilic addition is the rate-determining step) and (b) all components are completely dehalogenated. Tests with other PCB mixtures establish that those components with three or more chlorine atoms per phenyl ring are completely degraded by $O_2^{-}\bullet$, within several hours.

Superoxide ion reacts with esters, diketones, and carbon dioxide.[34,146–148] Initial reaction occurs via a reversible

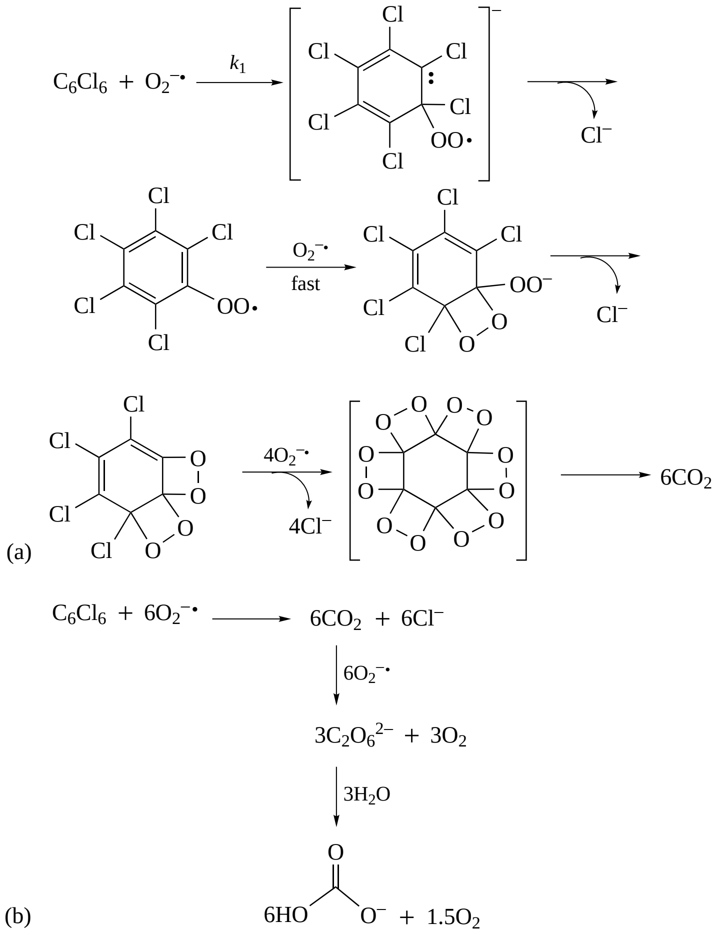

Scheme 11 Nucleophilic degradation of hexachlorobenzene (HCB) by $O_2^{-}\bullet$

addition–elimination reaction at the carbonyl carbon (equation 142).

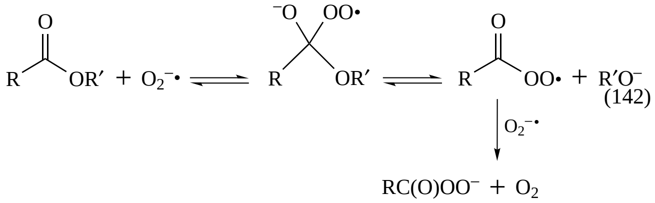
(142)

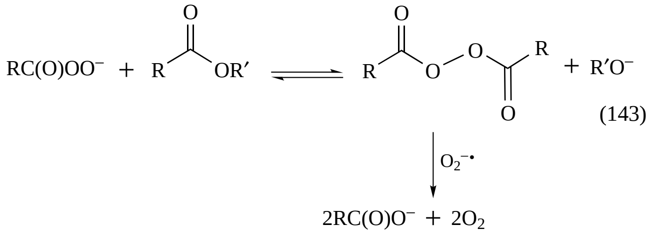
(143)

This conclusion is supported by the products that are observed in the gas-phase reaction of $O_2^{-}\cdot$ with phenyl acetate and phenyl benzoate, which has been studied by Fourier transform mass spectrometry.**149** In effect, there is a competition between loss of $O_2^{-}\cdot$ and loss of the leaving group. Carbanions are poor leaving groups, so that simple ketones without acidic α-hydrogen atoms are unreactive.

Simple diketones such as 2,3-butanedione are rapidly deprotonated by $O_2^{-}\cdot$, but the original diketone is recovered upon acidification (equation 144). However, benzil (PhCO-COPh) cannot enolize and is dioxygenated by $O_2^{-}\cdot$ to give two benzoate ions (equation 145). Carbon dioxide reacts rapidly with $O_2^{-}\cdot$ in aprotic solvents with a net stoichiometry in acetonitrile (equation 146) and the proposed reaction path involves an initial nucleophilic addition (equation 147).

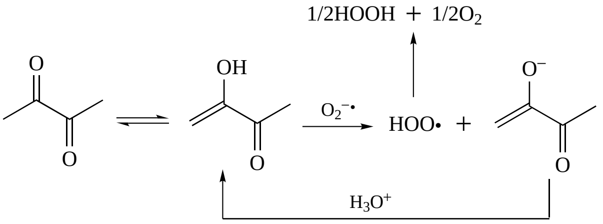
(144)

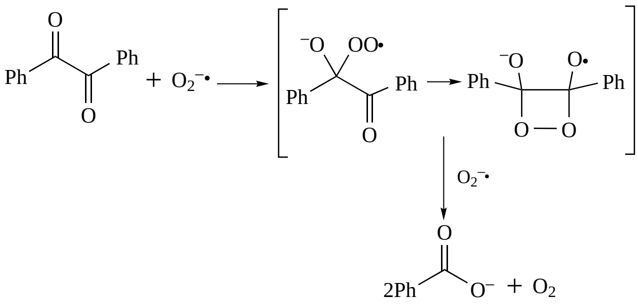
(145)

$$2CO_2 + 2O_2^{-}\cdot \longrightarrow C_2O_6^{2-} + O_2 \qquad (146)$$

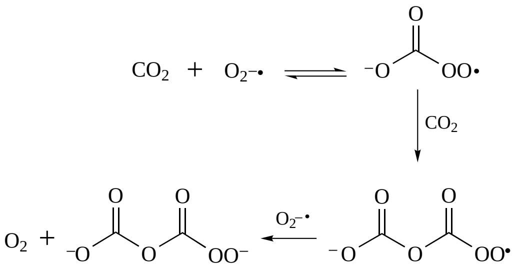
(147)

The primary product from the nucleophilic addition of $O_2^{-}\cdot$ to electrophilic substrates with leaving groups (RX) is a peroxy radical (ROO•). The presence of a large excess of substrate often precludes the diffusion-controlled reduction of ROO• by $O_2^{-}\cdot$, and results in the reaction manifold that is outlined in Scheme 12. The limits on the rate constants are consistent with the observed reactivities and product profiles for the indicated substrates.**150** Thus, the dimerization of ROO• to give ROOOOR is a radical–radical coupling and should be close to a diffusion-controlled process. The lifetime of [ROOOOR] is related to its O–O bond energies, which are smaller when R is an electron-withdrawing group (Cl_3C). A recent study of singlet dioxygen ($^1O_2$) production by these systems confirms that the ROOOOR intermediates decompose to ROOR and $^1O_2$,**151** while a separate investigation**150** indicates that ROOOOR is more reactive than $^1O_2$ and is a dioxygenase of rubrene and *cis*-stilbene.

7.3 One-electron Reductant

Another characteristic of $O_2^{-}\cdot$ is its ability to act as a moderate one-electron reducing agent. For example, combination of $O_2^{-}\cdot$ with 3,5-di-*t*-butylquinone (DTBQ) in DMF yields the semiquinone anion radical DTBSQ$^{-}\cdot$ as the major product.**152** The relevant redox potentials in DMF are $O_2/O_2^{-}\cdot$, $E^{\circ\prime} = -0.60$ V versus NHE, and DTBQ/DTBSQ$^{-}\cdot$, $E^{\circ\prime} = -0.25$ V versus NHE, which indicate that the equilibrium constant K for the reaction of $O_2^{-}\cdot$ with DTBQ has a value of 0.8×10^6 (equation 148). Electrochemical studies of sulfur dioxide**153** ($SO_2/SO_2^{-}\cdot$, $E^{\circ\prime} = -0.58$ V vs. NHE) and of molecular oxygen**130** in DMF indicate that the equilibrium constant (K) for the reaction of SO_2 with $O_2^{-}\cdot$ has a value of 1.1 (equation 149).

$$O_2^{-}\cdot + \text{DTBQ} \rightleftharpoons \text{DTBSQ}^{-}\cdot + O_2 \qquad (148)$$

$$SO_2 + O_2^{-}\cdot \rightleftharpoons O_2 + SO_2^{-}\cdot \qquad (149)$$

However, the reaction goes to completion because $SO_2^{-}\cdot$ is complexed by SO_2 and also dimerizes to dithionite ion.**154** Thus, $O_2^{-}\cdot$ is a stronger and more effective reducing agent than dithionite ion in aprotic solvents. In aqueous media, the equilibrium constant for the reduction of [iron(III)]–cytochrome *c* by $O_2^{-}\cdot$ has a value of 3.7×10^4.**155** Within DMF, the reduction of [iron(III)]–porphyrin is even

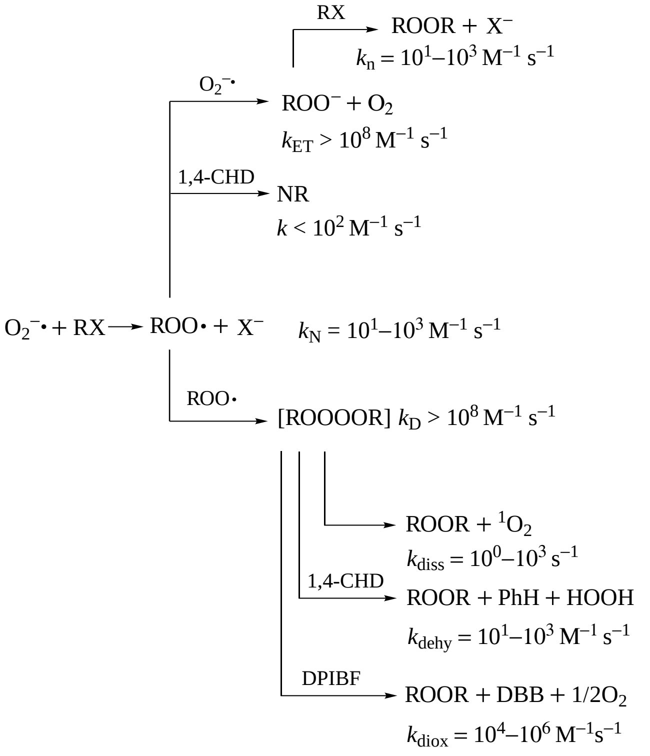
RX
ROOR + X⁻
$k_n = 10^1$–10^3 M⁻¹ s⁻¹
O₂⁻•
ROO⁻ + O₂
$k_{ET} > 10^8$ M⁻¹ s⁻¹
1,4-CHD
NR
$k < 10^2$ M⁻¹ s⁻¹
O₂⁻• + RX → ROO• + X⁻ $k_N = 10^1$–10^3 M⁻¹ s⁻¹
ROO•
[ROOOOR] $k_D > 10^8$ M⁻¹ s⁻¹
ROOR + ¹O₂
$k_{diss} = 10^0$–10^3 s⁻¹
1,4-CHD
ROOR + PhH + HOOH
$k_{dehy} = 10^1$–10^3 M⁻¹ s⁻¹
DPIBF
ROOR + DBB + 1/2O₂
$k_{diox} = 10^4$–10^6 M⁻¹s⁻¹

(RX = CCl_4, F_3CCCl_3, $PhCCl_3$, PhCOCl, BuBr, BuCl;1,4-CHD = 1, 4-cyclohexadiene; DPIBF = diphenylisobenzofuran; DBB = dibenzoylbenzene)

Scheme 12 ($O_2^{-}\bullet$)-induced formation of ROO• and its reaction paths

more complete (equation 150).

$$(\mathrm{TPP})\mathrm{Fe^{III}}(\mathrm{DMF})^+ + \mathrm{O_2}^{-}\bullet \longrightarrow \mathrm{O_2} + (\mathrm{TPP})\mathrm{Fe^{II}} \qquad K = 7 \times 10^{11} \tag{150}$$

7.4 Sequential Deprotonation–Dehydrogenation of Dihydro Groups

The direct transfer of an electron to $O_2^{-}\bullet$ is an unlikely process because of the extreme instability of the O_2^{2-} species. As a result, most of the reported electron-transfer oxidations by $O_2^{-}\bullet$ actually represent an initial proton abstraction to give substrate anion and HOO•, which disproportionates (or reacts with $O_2^{-}\bullet$) to give O_2 and HOOH (or HOO^{-}). One or more of these species oxidizes the substrate anion.

Superoxide ion is an effective hydrogen-atom oxidant for substrates with coupled heteroatom (O or N) dihydro groups such as 3,5-di-*t*-butylcatechol ($DTBCH_2$), ascorbic acid (H_2Asc), 1,2-disubstituted hydrazines, dihydrophenazine (H_2Phen), and dihydrolumiflavin (H_2Fl).[48,156,157]

The general mechanism involves the rapid sequential transfer to $O_2^{-}\bullet$ of a proton and a hydrogen atom to form HOOH and the anion radical of the dehydrogenated substrate (equations 151–153).

$$\mathrm{O_2}^{-}\bullet + \mathrm{DTBCH_2} \longrightarrow \mathrm{DTBC}^{-}\bullet + \mathrm{HOOH} \tag{151}$$

$$\mathrm{O_2}^{-}\bullet + \mathrm{H_2Asc} \longrightarrow \mathrm{Asc}^{-}\bullet + \mathrm{HOOH} \tag{152}$$

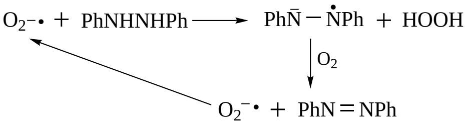

(153)

With 1,2-diphenylhydrazine (PhNHNHPh), the azobenzene anion radical is rapidly oxidized by dioxygen to azobenzene, which also is true for the phenazine and lumiflavin anion radicals. Hence, $O_2^{-}\bullet$ acts as an initiator for the autoxidation of these compounds (equation 153). For 1,2-diphenylhydrazine, turnover numbers in excess of 200 substrate molecules per $O_2^{-}\bullet$ have been observed. The 1,2-diphenylhydrazine autoxidation cycle can be initiated by HO^{-}, which indicates that $O_2^{-}\bullet$ is formed in the HO^{-} initiated process. Superoxide ion also initiates the autoxidation of dihydrophenazine, which is a model for dihydroflavin. For example, the addition of 1 mM $(Me_4N)O_2$ in DMF to 10 mM H_2Phen in an O_2-saturated DMF solution results in the complete oxidation of the substrate (about 80% recovered as phenazine) and the production of 9–10 mM HOOH.

Support for the general mechanism outlined in equation (153) is provided by gas-phase Fourier transform mass spectrometric studies of the anionic reaction products of several substrates with $O_2^{-}\bullet$ (produced by electron impact with O_2; HO^{-} can be produced by electron impact with H_2O).[149] In these experiments, neutral products are not detected. Both $O_2^{-}\bullet$ and HO^{-} react rapidly with 1,2-diphenylhydrazine in the gas phase ($P \sim 10^{-7}$ Torr) to give the anion radical of azobenzene ($PhN^{-}\bullet NPh$; $m/e = 182$) and the anion from deprotonation ($PhN^{-}NHPh$; $m/e = 183$), respectively. When $O_2^{-}\bullet$ is ejected from the experiment, the peak at $m/e = 182$ disappears. In contrast to the exponential decay that is observed for the HO^{-} peak with time, the ion current for $O_2^{-}\bullet$ decays to a steady-state concentration.

Analogous FTMS studies with 1,2-dihydroxybenzenes also provide support for the general mechanism. Superoxide ion reacts rapidly with 3,5-di-*t*-butylcatechol ($DTBCH_2$) in the gas phase to give the anion ($DTBCH^{-}$; $m/e = 221$) and the anion radical of 3,5-di-*t*-butyl-*o*-benzoquinone ($DTBSQ^{-}\bullet$ $m/e = 220$) in an approximate ratio of 3:1. With hydroquinone (p-$C_6H_4(OH)_2$), the dominant product (ca. 70%) is the anion radical ($SQ^{-}\bullet$ $m/e = 108$). When HO^{-} is the gas-phase reagent, the only product for $DTBCH_2$ (and for o-$C_6H_4(OH)_2$) is the anion from deprotonation. The fact that the anion radicals of the dehydrogenated substrates are produced in the gas phase as well as in aprotic solvents confirms that the reaction sequence of deprotonation/hydrogen-atom abstraction to form HOOH must either be a rapid sequence or a nearly concerted process. Because $O_2^{-}\bullet$ is expected to abstract hydrogen atoms much less easily than HOO•, the initial step is deprotonation

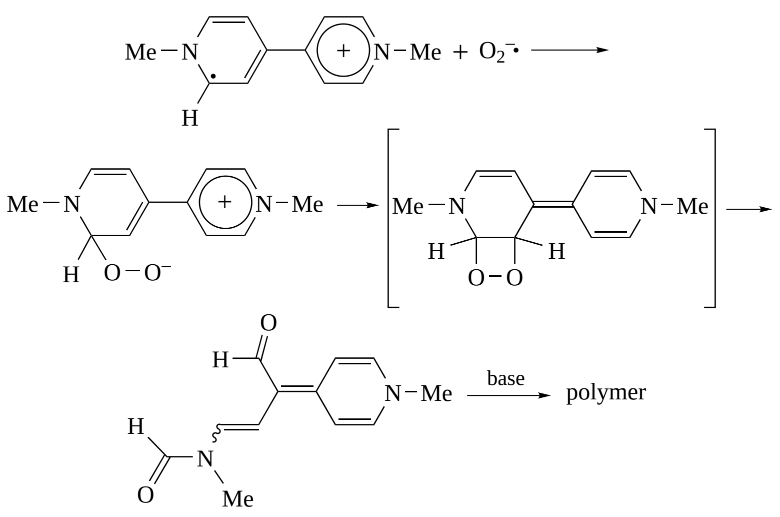

Scheme 13 Oxygenation of methyl viologen cation radical via radical–radical coupling with $O_2^{-}\cdot$

of the substrate by $O_2^{-}\cdot$ to form HOO•; the latter (contained within the solvent cage or weakly bonded to the substrate in a 'sticky collision' in the gas phase) then abstracts a hydrogen atom from the substrate anion to form HOOH and the anion radical of the dehydrogenated substrate.

Thus, the $O_2^{-}\cdot$ induced autoxidations of 1,2-disubstituted hydrazines, dihydrophenazines, and dihydroflavins in aprotic media provide a simple pathway for rapid conversion of dioxygen to HOOH, and one that does not involve catalysis by metal ions or metalloproteins. This is exemplified by the net reaction for dihydrolumiflavin:

$$H_2Fl + O_2 \xrightarrow{O_2^{-}\cdot,\ HO^{-}} Fl + HOOH \qquad (154)$$

7.5 Radical–radical Coupling

Combination of superoxide ion with the cation radical ($MV^{+}\cdot$) of methyl viologen (1,1′-dimethyl-4,4′-bipyridinium ion, Paraquat) is one of the best-documented examples of a stoichiometric $O_2^{-}\cdot$ radical coupling reaction.**[158,159]** The initial addition to give an unstable diamagnetic product is assumed to be at α-carbon atoms (which possess the maximum unpaired spin density in the cation radical), followed by formation of a dioxetane-like intermediate that decomposes to a complex mixture of products (Scheme 13). This process may provide a means to explain the mechanism of Paraquat toxicity. Several other reports have proposed direct coupling of $O_2^{-}\cdot$ to cation radicals.**[160]**

Although superoxide ion reacts with reduced transition metal complexes (Fe^{II}, Mn^{II}, Co^{II}, Fe^{II}(EDTA), Fe^{II}(TPP))**[161,162]** to give oxidized products, for simple solvated cations the reaction sequence is a Lewis acid catalyzed disproportionation (equation 155)**[161]** with subsequent Fenton chemistry (equation 156).

$$[Fe^{II}(OH_2)_6]^{2+} + 2O_2^{-}\cdot \longrightarrow O_2 + HOOH + Fe^{II}(OH)_2 + 4H_2O \qquad (155)$$

$$2Fe^{II}(OH)_2 + HOOH \longrightarrow 2Fe^{III}(OH)_3(s) \qquad (156)$$

In the cases of Fe^{II}(EDTA) and Fe^{II}(TPP), the peroxide products (Fe^{III}(EDTA)(O_2^{-})**[162]** and Fe^{III}(TPP)(O_2^{-})**[163]**) were believed to result from an outer-sphere electron transfer from the metal to $O_2^{-}\cdot$ with subsequent coordination of the oxidized metal by O_2^{2-}. However, the reduction of $O_2^{-}\cdot$ to 'naked' O_2^{2-} requires an exceptionally strong reducing agent (e.g. sodium metal), and is precluded for Fe^{II}(EDTA) and Fe^{II}(TPP).

Investigations**[164]** of the interaction of $O_2^{-}\cdot$ with sterically protected metalloporphyrins ((Cl_8TPP)Fe^{II}, (Cl_8TPP)Mn^{II}, and (Cl_8TPP)Co^{II}; Cl_8TPP=tetrakis(2,6-dichlorophenyl)-*meso*-porphyrin) establish that adducts are formed via radical–radical coupling to form a metal–oxygen covalent bond (analogous to H• + $O_2^{-}\cdot$ → H–OO⁻) (equation 157).

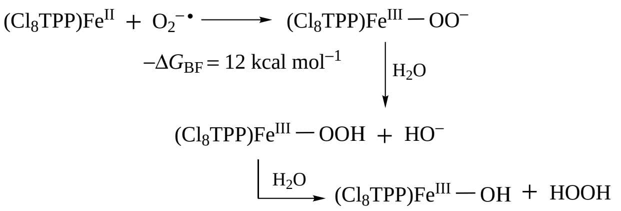

$$\begin{array}{l}
(Cl_8TPP)Fe^{II} + O_2^{-}\cdot \longrightarrow (Cl_8TPP)Fe^{III}-OO^{-} \\
\quad -\Delta G_{BF} = 12\ \text{kcal mol}^{-1} \quad \big\downarrow H_2O \\
(Cl_8TPP)Fe^{III}-OOH + HO^{-} \\
\quad \xrightarrow{H_2O} (Cl_8TPP)Fe^{III}-OH + HOOH
\end{array} \qquad (157)$$

Similar reactivities occur with the manganese and cobalt porphyrins to give (Cl_8TPP)Mn^{III}–OO^{-} ($-\Delta G_{BF}$, 17 kcal mol^{-1}) and (Cl_8TPP)Co^{III}–OO^{-} ($-\Delta G_{BF}$, 8 kcal mol^{-1}). Such radical–radical coupling is favored for all reduced transition metal complexes with unpaired electrons and probably is the reaction path for $O_2^{-}\bullet$ with Fe^{II}(EDTA)[162] and Fe^{II}(TPP).[163]

Thus, the radical–radical coupling reaction path is favored under neutral conditions with reduced transition metal complexes, and provides insight to the mechanisms for superoxide ion disproportionation that are catalyzed by the iron and manganese superoxide dismutase proteins. The combination of $(Cl_8TPP)Fe^{II}$ or $(Cl_8TPP)Mn^{II}$ with $O_2^{-}\bullet$ does not result in electron transfer from the metal; instead they couple to form $(Cl_8TPP)Fe^{III}$–OO^- and $(Cl_8TPP)Mn^{III}$–OO^-. The latter abstract protons from the medium, and the $(Cl_8TPP)Fe^{III}OOH$ and $(Cl_8TPP)Mn^{III}OOH$ products react with a second $O_2^{-}\bullet$ and a proton to give HOOH and O_2 (equation 158).

$$\begin{array}{l} (Cl_8TPP)Fe^{II} + O_2^{-\bullet} + HA \longrightarrow (Cl_8TPP)Fe^{III}{-}OOH + A^- \\ \qquad\qquad\qquad\qquad\qquad\qquad \Big\downarrow{\scriptstyle O_2^{-\bullet},\ HA} \\ \qquad\qquad\qquad (Cl_8TPP)Fe^{II} + O_2 + HOOH + A^- \end{array} \tag{158}$$

Hence, $(Cl_8TPP)Fe^{II}$ and $(Cl_8TPP)Mn^{II}$ facilitate the disproportionation of $O_2^{-}\bullet$, which is equivalent to the function of the iron and manganese superoxide dismutase proteins.

8 REACTIVITY OF OXYANIONS (HO^-, RO^-, HOO^- AND ROO^-)

The preceding section describes the primary reaction chemistry of superoxide ion ($O_2^{-}\bullet$) to be that of (a) a Brønsted base (proton transfer from substrate), (b) a nucleophile (via displacement or addition), (c) a one-electron reductant, and (d) a dehydrogenase of secondary amine groups. The chemistry is characteristic of all oxyanions (HO^- (RO^-), HOO^- (ROO^-), and $O_2^{-}\bullet$), but the relative reactivity for each is determined by its pK_a and one-electron oxidation potential, which are strongly affected by the anionic solvation energy of the solvent matrix. The present focus is on the reactivity of hydroxide ion (HO^-), but the principles apply to all oxyanions and permit assessments of their relative reactivity.

The reactivity of hydroxide ion (and that of other oxyanions) is interpreted in terms of two unifying principles: (a) the redox potential of the $YO^-/YO\bullet$ ($Y = H$, R, HO, RO, and O) couple (in a specific reaction) is controlled by the solvation energy of the YO^- anion and the bond energy of the R–OY product ($RX + YO^- \rightarrow R{-}OY + X^-$), and (b) the nucleophilic displacement and addition reactions of YO^- occur via an inner-sphere *single-electron* shift.[165] The electron is the ultimate base and one-electron reductant which, upon introduction into a solvent, is transiently solvated before it is 'leveled' (reacts) to give the conjugate base (anion reductant) of the solvent. Thus, in water the hydrated electron $(e^-)_{H_2O}$ yields HO^- via addition to the H–OH bond of water (equation 159).

$$(e^-)_{H_2O} + H{-}OH \longrightarrow H\bullet + (HO^-)_{H_2O} \qquad E^\circ = -2.93\ \text{V vs. NHE} \tag{159}$$

The product combination ($H\bullet + HO^-$) represents the ultimate thermodynamic reductant for aqueous systems. In the absence of an H• atom (and the stabilization afforded to HO• by formation of the 119 kcal mol^{-1} H–OH bond), the hydroxide ion becomes a much less effective reductant (equation 160).

$$(e^-)_{H_2O} + HO\bullet \longrightarrow (HO^-)_{H_2O} \qquad E^\circ = +1.89\ \text{V vs. NHE} \tag{160}$$

8.1 Solvent Effects on the Redox Chemistry of HO^-

Table 15 summarizes the redox potentials in water and in acetonitrile for the single-electron oxidation of HO^- and other bases.[23,26,38] In MeCN, the $HO\bullet/HO^-$ redox potential is more negative by about 1.0 V and the $O_2/O_2^{-}\bullet$ redox potential by about 0.5 V relative to their values in H_2O. Most of this is due to the decrease in the energy of solvation for HO^- and $O_2^{-}\bullet$ in MeCN (compared to water, where each has an estimated energy of hydration of about 100 kcal mol^{-1}).[166] The increase in the ionization energy for HO^- from 1.8 eV in the gas phase to 6.2 eV in water[166] attests to its large solvation energy and to its dramatic deactivation as a base and nucleophile in water.

Hydroxide ion is a stronger base and a better one-electron donor in MeCN and DMSO than in water, because these organic solvents have solvation energies for HO^- that are 20–25 kcal mol^{-1} ($\approx$1 eV) less than water.[22] Thus, reduced solvation of HO^- decreases its ionization energy and causes it to have a more negative redox potential and to be a stronger electron donor. This dramatically enhances the reactivity of HO^- toward the electrophiles shown in Table 15 and reveals a facet of HO^- chemistry that is effectively quenched by water, namely, its ability to function as a one-electron reducing agent.

The redox potentials for the electron acceptors that react with HO^- (Table 15) are such that a pure outer-sphere single-electron transfer (SET) step would be endergonic (the $HO\bullet/HO^-$ redox potential is more positive than the redox potential of the electron acceptor). Hence, the observed net reactions must be driven by coupled chemical reactions, particularly bond formation by the HO• to the electrophilic atom of the acceptor molecule that accompanies a single-electron shift. (The formation of the bond provides a driving force sufficient to make the overall reaction thermoneutral or exergonic: 1.0 V per 23.1 kcal mol^{-1} of bond energy.) The effect of various transition metal complexes on the oxidation potential for HO^- in MeCN illustrates some of these effects; the results are summarized in Table 16.[38]

Table 15 Redox potentials for the single-electron (a) oxidation of HO^- and other oxyanion bases and (b) reduction of electrophilic substrates in water and in acetonitrile

(a) Oxidation of Oxyanion Bases Base (B^-)	$(pK_{HB})_{H_2O}{}^a$	$(E^{\circ\prime}{}_B)_{H_2O}{}^b$ (V vs. NHE)	$(pK_{HB})_{MeCN}{}^{a,c}$	$(E^{\circ\prime}{}_B)_{H_2O}{}^d$ (V vs. NHE)
$Cl^- \rightarrow Cl\cdot + e^-$		+2.41	–	+2.24
$HO^- \rightarrow HO\cdot + e^-$	15.7	+1.89	30.4	+0.92
$PhO^- \rightarrow PhO\cdot + e^-$	9.2	≈+0.7	16.0	+0.30
$O_2{}^-\cdot \rightarrow \cdot O_2\cdot + e^-$	4.9	−0.16[e]	≈13	−0.63[e]
$HOO^- \rightarrow HOO\cdot + e^-$	11.8	+0.20	≈22	−0.34
$H^- \rightarrow H\cdot + e^-$	–	−2.20	–	−3.2
$[e^-(H_2O)\ H\cdot + HO^-] \rightarrow H_2O + e^-$	–	−2.93	–	−3.90

(b) Reduction of Electrophiles Electrophile (YX)	$(-\Delta G)_{Y\text{–}OH}$ (kcal mol^{-1})^f	$(E^{\circ\prime}{}_E)_{H_2O}$ (V vs. NHE)	$(E^{\circ\prime}{}_E)_{MeCN}$ (V vs. NHE)
$Au^+ + e^- \rightarrow Au\cdot$	31	+1.7	+1.58
$Ag^+ + e^- \rightarrow Ag\cdot$	24	+0.80	+0.54
$(TPP)Fe^{III}(py)$			
$MV^{2+} + e^- \rightarrow MV^{+}\cdot$	72	−0.45	−0.18
$AQ + e^- \rightarrow AQ^-\cdot$	72	–	−0.58
$CCl_4 + e^- \rightarrow Cl_3C\cdot + Cl^-$	80	–	−0.91
$C_6Cl_6 + e^- \rightarrow \cdot C_6Cl_5 + Cl^-$	84	–	−1.26
$BuCl + e^- \rightarrow Bu\cdot + Cl^-$	83	–	−2.5
$H_3O^+ + e^- \rightarrow H\cdot + H_2O$	111	−2.10	−1.58

[a] pK_a of the conjugate acid.[150] [b] Parsons.[11] [c] Barette *et al.*[10] [d] Tsang *et al.*[26] [e] Standard state for O_2 is 1 M. [f] Lide.[29]

Table 16 Oxidation potentials for HO^- in H_2O and MeCN, and in the presence of metal complexes

		$E^{\circ\prime}$ (V vs. NHE)	
(a)	Free base	H_2O	MeCN
	$HO^- \rightarrow HO\cdot + e^-$	+1.89	+0.92
	$2HO^- \rightarrow O^-\cdot + H_2O + e^-$	+1.77	+0.59
	$2HO^- \rightarrow O(g) + H_2O + 2e^-$	+1.60	+0.63
	$3HO^- \rightarrow HOO^- + H_2O + 2\ e^-$	+0.87	−0.11
(b)	Metal/porphyrin complexes		
	$(TPP)Zn^{II}(^-OH)^- + HO^- \rightarrow (TPP)Zn^{II}(O^-\cdot)^- + H_2O + e^-$	+0.73	
	$(TPP)Co^{II}(^-OH)^- \rightarrow (TPP)Co^{III}\text{–}OH + e^-$	+0.02	
	$(TPP)Fe^{II}(^-OH)^- \rightarrow (TPP)Fe^{III}\text{–}OH + e^-$	−0.48	
	$(TPP)Mn^{II}(^-OH)^- \rightarrow (TPP)Mn^{III}\text{–}OH + e^-$	−0.35	
(c)	Metal/(Ph_3PO) complexes		
	$(Ph_3PO)_4Zn^{II}(OH)_2 + HO^- \rightarrow (Ph_3PO)_4Zn^{II}(OH)(O\cdot) + H_2O + e^-$	+0.67	
	$(Ph_3PO)_4Ni^{II}(OH)_2 + HO^- \rightarrow (Ph_3PO)_4Ni^{III}(O)(OH) + H_2O + e^-$	−0.01	
	$(Ph_3PO)_4Co^{II}(OH)_2 + HO^- \rightarrow (Ph_3PO)_4Co^{III}(O)(OH) + H_2O + e^-$	−0.05	
	$(Ph_3PO)_4Fe^{II}(OH)_2 + HO^- \rightarrow (Ph_3PO)_4Fe^{III}(O)(OH) + H_2O + e^-$	+0.12	
	$(Ph_3PO)_4Mn^{II}(OH)_2 + HO^- \rightarrow (Ph_3PO)_4Mn^{III}(O)(OH) + H_2O + e^-$	+0.31	

8.2 Reaction Classifications (Single-electron Shift Mechanism)

The reaction continuum for HO^- can be subdivided into three discrete categories that are outlined in Scheme 14: (a) displacement reactions in which the leaving group departs with an electron supplied by HO^- (polar-group transfer), (b) addition reactions in which a covalent bond is formed (polar-group addition), and (c) simple electron-transfer reactions in which HO^- acts as an electron donor (single-electron transfer). This view of the chemistry of HO^- also applies to the reactions of superoxide ion ($O_2{}^-\cdot$) and other nucleophilic oxyanions (Table 16).

The polar pathways are formally equivalent to a discrete electron-transfer step, that is, a pure SET step that is followed by a chemical step. If a hypothetical SET step is followed by coupling of a radical pair that is produced in the SET step, the overall reaction is the equivalent of a polar-group coupling reaction (Scheme 14(b)). If the coupling is accompanied by the elimination of a leaving group, a polar-group transfer reaction results (Scheme 14(a)).

The 'single-electron shift' mechanism appears to be general and applicable for electron, proton, atom, and group transfer reactions. The assumptions for this proposition include: (a) polar and SET pathways share a common feature, a single-electron shift from an electron donor to an electron acceptor; (b) the barrier heights for the exchange of an electron, proton, atom, or group of atoms can be described by the same general equation;[167] (c) for an unsymmetrical polar-group transfer reaction the net energy change, $-\Delta G$ (the thermodynamic component of the energy barrier), is proportional to the sum of (i) the difference of the redox potentials for the electron

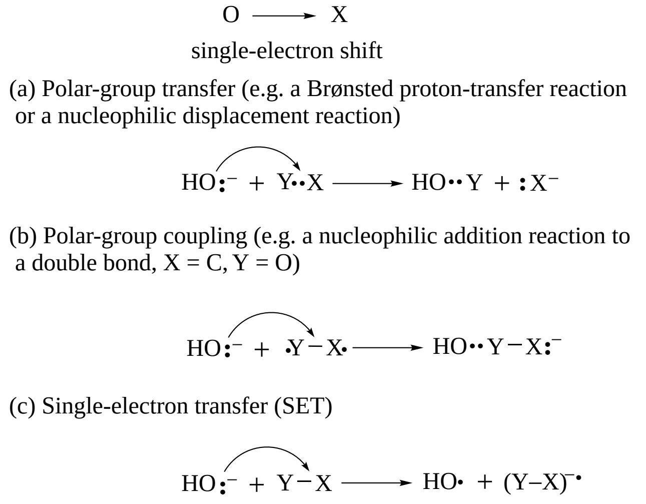

O → X
single-electron shift
(a) Polar-group transfer (e.g. a Brønsted proton-transfer reaction or a nucleophilic displacement reaction)
HO:⁻ + Y••X → HO••Y + :X⁻
(b) Polar-group coupling (e.g. a nucleophilic addition reaction to a double bond, X = C, Y = O)
HO:⁻ + •Y−X• → HO••Y−X:⁻
(c) Single-electron transfer (SET)
HO:⁻ + Y−X → HO• + (Y–X)⁻•

Scheme 14 Single-electron shift (equivalent to the transfer of an electron from O to X)

Energy change (J mol^{-1})

Electron donor

$$HO:^- \longrightarrow HO + e^- \qquad -(E^\circ_{HO\bullet/HO-})nF$$

Electron acceptor

$$X{-}Y + e^- \longrightarrow Y{-}X \longrightarrow Y\bullet + X:^- \qquad -(E^\circ_{XY\bullet/XY})nF$$

Bond formation

$$HO + Y\bullet \longrightarrow HO{-}Y \qquad (-\Delta G_{BF})_{HO-Y}nF/23.1$$

Polar-group transfer

$$HO:^- + Y{-}X \longrightarrow HO{-}Y + X:^-$$

$$(-\Delta G_{reac} = nF[E^\circ_{YX/YX\bullet-} - E^\circ_{HO\bullet/HO-}) + (-\Delta G_{BF})_{HO-X}/23.1] = nF(\Delta E^\circ_{reac} + (-\Delta G_{BF})_{HO-X}/23.1)$$

Polar-group coupling

$$HO:^- + Y{-}X \longrightarrow HO:Y:X^-$$

$$-\Delta G_{reac} = nF[\Delta E^{\circ\prime}_{reac} + (-\Delta G_{BF})_{HO-YX-}/23.1)]$$

Single-electron transfer (SET)

$$HO:^- + Y{-}X \longrightarrow HO\bullet + Y{-}X^{-\bullet}$$

$$-\Delta G_{reac} = nF\Delta E^{\circ\prime}_{reac}$$

Scheme 15 Redoc energetics for single-electron shift reactions

acceptor (Y–X) and the electron donor (HO$^-$) and (ii) the bond energy (BE) for the group transfer product (HO–Y; see Scheme 15).

Table 17 lists a number of reactions of hydroxide ion and, for comparison, superoxide ion with electron donors. These reactions are classified conventionally and according to the categories shown in Scheme 14. When water is replaced by a dipolar aprotic solvent (e.g. MeCN or DMSO), many of these electron donor–electron acceptor reactions proceed at dramatically faster rates and produce much larger yields of free-radical products. (DMF is generally avoided because of the possible hydrolysis of the amide bond by hydroxide ion).[168]

Although Brønsted proton transfer reactions appear to belong to a unique category not described by Scheme 14, they are examples of polar-group transfer reactions and are not different in principle from nucleophilic displacement reactions. Deprotonation by hydroxide ion can be regarded as the shift of an electron from HO$^-$ to the Brønsted acid synchronously with the transfer of a hydrogen atom from the Brønsted acid to the incipient HO• radical, with the reaction driven by covalent bond formation between the HO• radical and the H• atom to form water (equation 161).

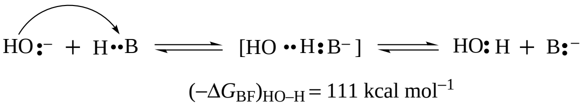

$$HO:^- + H{\bullet\bullet}B \rightleftharpoons [HO{\bullet\bullet}H:B^-] \rightleftharpoons HO:H + B:^- \qquad (161)$$

$$(-\Delta G_{BF})_{HO-H} = 111\ \text{kcal mol}^{-1}$$

Consistent with the idea that the single-electron shift is a fundamental process is the notion that the electron distribution (or partial charge) on atoms near the reaction site changes during the course of the reaction. This is so obvious as to seem trivial, but bears repeating because our thinking often is misdirected by the assignment of oxidation numbers (or oxidation states) to atoms via arbitrary rules. For example, by convention the oxidation state +1 is assigned to the hydrogen and −2 is assigned to the oxygen in hydronium ion, water, and hydroxide ion. However, the partial charges on the hydrogen and oxygen atoms change substantially in this series: H_3O^+ (+0.35, −0.05); H_2O (+0.12, −0.25); and HO$^-$ (−0.35, −0.65).[169]

From Scheme 14 and the notion of the charge number (or partial charge on an atom), the reaction of hydroxide ion (oxygen charge −1) with a proton (charge +1) to form H_2O (H and O zero charge) involves a single-electron shift from HO$^-$ to H$^+$ (H_2O) to form HO• and •H(H_2O) that form a covalent bond (HO–H) with a bond energy ($-\Delta G_{BF}$) of 111 kcal mol^{-1}. This reaction does not result in the formation of a detectable radical, but is an example of a polar-group transfer reaction (Scheme 14(b)) in which an atom transfer occurs synchronously with the electron shift.

Thus, the reaction of H_3O^+ with HO$^-$ is a prototype example of a charge transfer or redox reaction that is also a polar-group transfer reaction. It can be resolved into three component reactions (see Scheme 16) (equations 162–164) and combined (equations 165 and 166).

$$H^+(aq) + e^- \longrightarrow H\bullet(aq) \qquad (162)$$

$$E^{\circ\prime}_{162} = -2.10\ \text{V vs. NHE}$$

Table 17 Reactions of hydroxide ion and superoxide ion with electrophiles

---

1. Polar-group transfer reactions
   (a) Deprotonation by hydroxide ion

$HO^- + H_3O^+ \rightarrow 2H_2O$
$HO^- + MeOH \rightarrow H_2O + MeO^-$
$HO^- + HOC(O)R \rightarrow H_2O + {}^-OC(O)R$
$O_2^{-\bullet} + NH_4^+ \rightarrow HOO\bullet + NH_3$
$O_2^{-\bullet} + MeOH \rightarrow HOO\bullet + MeO^-$

   (b) Nucleophilic substitution reactions

$HO^- + RCl \rightarrow ROH + Cl^-$
$O_2^{-\bullet} + RCl \rightarrow ROO\bullet + Cl^-$
$HO^- + RCO_2R' \rightarrow RCO_2H + R'O^- \rightarrow RCO_2^- + R'OH$
$O_2^{-\bullet} + RCO_2R' \rightarrow RC(O)OO\bullet + RO^-$
$4HO^- + CCl_4 \rightarrow 3Cl^- + ClCO_2^- + 2H_2O$
$5O_2^{-\bullet} + CCl_4 + H_2O \rightarrow 4Cl^- + HOCO_2^- + 7/2O_2 + 1/2HOOH$
$HO^- + C_6Cl_6 \rightarrow C_6Cl_5OH + Cl^-$

2. Polar-group coupling reactions
   (a) Nucleophilic addition reactions

$HO^- + CO_2 \rightarrow HOCO_2^-$
$O_2^{-\bullet} + CO_2 \rightarrow \bullet OOC(O)O^-$

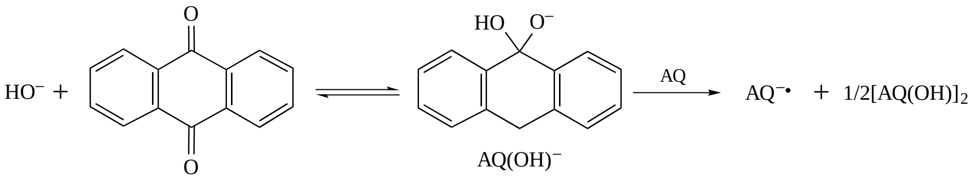

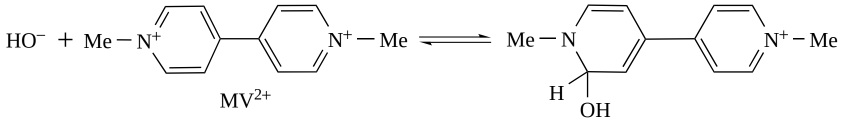

   (b) Reductive addition reactions

$HO^- + Au^+ \rightarrow AuOH$
$HO^- + Fe^{III}(TPP)^+ \rightarrow (TPP)Fe^{III}OH$
$HO^- + Fe^{III}(TPP)(py)_2^+ \rightarrow Fe^{II}(TPP) + (1/n)[py(\bullet OH)]_n$
Other $M^{III}/{}^-OH$ reactions

3. Single-electron transfer reactions

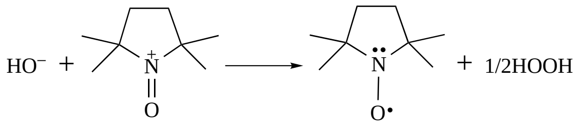

$HO^- + O_2 \rightarrow pyO_2^{-}\bullet + (1/n)[py(\bullet OH)]_n$
$HO^- + (CN)_2C{=}C(CN)_2 \rightarrow [(CN)_2C{=}C(CN)_2]^{-\bullet} + 1/2HOOH$

$$\begin{tikzcd}
HO^- + S_8 \arrow[r] & HOS_5\bullet + S_3^-\bullet \arrow[d, "HO^-"] \\
& HOSSOH + S_3^-\bullet \arrow[d] \\
& HOOH + 1/4S_8
\end{tikzcd}$$

$$\mathrm{HO{\bullet}\,(aq)} + e^- \longrightarrow \mathrm{HO^-\,(aq)} \qquad (163)$$

$$E^{\circ\prime}_{163} = +1.89\ \mathrm{V}$$

$$\mathrm{H{\bullet}\,(g)} + \mathrm{HO{\bullet}\,(g)} \longrightarrow \mathrm{HOH(g)} \qquad (164)$$

$$-\,\Delta G^{\circ\prime}_{164} = 111.4\ \mathrm{kcal\,mol^{-1}}(+4.83\ \mathrm{V})$$

$$\mathrm{H^+(aq)} + \mathrm{HO^-\,(aq)} \xrightarrow{K_f} \mathrm{HOH(aq)} \qquad (165)$$

$$-\,\Delta G^{\circ\prime}_{165} = nE^{\circ\prime}_{165}F$$

$$-\,\Delta G^{\circ\prime}_{165} = -(\Delta G^{\circ\prime}_{162} - \Delta G^{\circ\prime}_{163} + \Delta G^{\circ\prime}_{164}) = 19.2\ \mathrm{kcal\,mol^{-1}}\ (+0.83\ \mathrm{V}) \qquad (166)$$

The evaluation of $-\Delta G^{\circ\prime}_{165}$ neglects the small differences in the hydration energies of H•, HO•, and H_2O, but provides a reasonable measure of the formation constant (K_f) (equation 167).

$$\log K_f = \frac{+0.83}{0.059} = 14 \qquad (167)$$

In the net reaction (equation 165), the energy from bond formation (equation 164) provides a driving force of nearly 5 V, which is more than sufficient to overcome the unfavorable electron-transfer energy (−3.89 V).

The reaction of superoxide ion ($O_2^{-\bullet}$), a radical anion, with water also can be viewed as a polar-group transfer reaction (equation 168). The product HOO• is a radical that reacts bimolecularly to form hydrogen peroxide and dioxygen (equation 169).

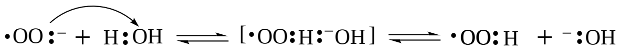

(168)

$$2\mathrm{HOO{\bullet}} \longrightarrow \mathrm{HOOH} + O_2 \qquad (169)$$

The formation of the stable covalent bonds in the product molecules provides the driving force that allows superoxide ion to deprotonate Brønsted acids that are much weaker acids than HOO•.

Most accept the view that many nucleophilic displacement reactions occur by a SET mechanism.[170] In a number of cases, radical intermediates have been identified, which is consistent with a discrete SET step. Only a slight extension of this concept is required to encompass all nucleophilic reactions within the categories described in Scheme 14.

The reactions of HO^- and O_2^-• with alkyl halides exhibit the same general pattern (Scheme 16), with second-order kinetics and inversion of configuration.[134,135] Radicals are not detected in the reactions with hydroxide ion, which indicates that there probably is not a discrete SET step, but rather that the transfer of the entering and leaving groups is synchronous with a single-electron shift.

The reaction of superoxide ion with alkyl halides produces a radical in the primary step, because the spin angular momentum of the unpaired electron of the superoxide anion radical is conserved. Again, the transfer of the entering and leaving group is presumed to be synchronous with the single-electron shift. The alternative mechanism, a discrete SET step followed by expulsion of the leaving group and coupling of the radical with dioxygen, is implausible because the reduction potentials of most alkyl halides are at least 0.8 V more negative than the O_2/O_2^-• redox potential and the formation of alkyl radicals has not been observed.

Thus, the reaction of HO^- with BuBr is another example of a redox reaction that involves a polar-group transfer. This can be resolved into three component reactions (in MeCN) (equations 170–174).

$$\mathrm{BuBr} + e^- \longrightarrow \mathrm{Bu{\bullet}} + \mathrm{Br^-} \qquad (170)$$

$$E^{\circ\prime}_{170} = -1.45\ \mathrm{V\ vs.\ NHE}$$

$$\mathrm{HO{\bullet}} + e^- \longrightarrow \mathrm{HO^-} \qquad (171)$$

$$E^{\circ\prime}_{171} = +1.89\ \mathrm{V}$$

$$\mathrm{Bu{\bullet}(g)} + \mathrm{HO{\bullet}(g)} \longrightarrow \mathrm{BuOH(g)} \qquad (172)$$

$$-\,\Delta G^{\circ\prime}_{172} = 86\ \mathrm{kcal\,mol^{-1}}(+3.72\mathrm{V})$$

$$\mathrm{BuBr} + \mathrm{HO^-} \longrightarrow \mathrm{BuOH} + \mathrm{Br^-} \qquad (173)$$

$$-\,\Delta G^{\circ\prime}_{172} = nE^{\circ\prime}_{173}F$$

$$-\,\Delta G^{\circ\prime}_{173} = -(\Delta G^{\circ\prime}_{170} - \Delta G^{\circ\prime}_{169} + \Delta G^{\circ\prime}_{172}) = \begin{array}{c} 8.8\ \mathrm{kcal\,mol^{-1}} \\ (+0.38\ \mathrm{V}) \end{array} \qquad (174)$$

Similar analyses are possible for the initial polar-group transfer step for CCl_4 ($E^{\circ\prime}_{\mathrm{red}}$, −0.91 V vs. NHE), C_6Cl_6 ($E^{\circ\prime}_{\mathrm{red}}$, −1.26 V), and $C_{12}Cl_{10}$ (PCB; $E^{\circ\prime}_{\mathrm{red}}$, −1.30 V). Each of these substrates undergoes a net exergonic redox reaction with HO^-; the initial step is analogous to that of equation (173).

The reactions of HO^- and O_2^-• with the carbonyl group of esters[34,171] and quinones[172,173] share a common feature, the addition of the nucleophile to the carbonyl carbon. When a suitable leaving group is present, there is an essentially concerted elimination to give products, as shown

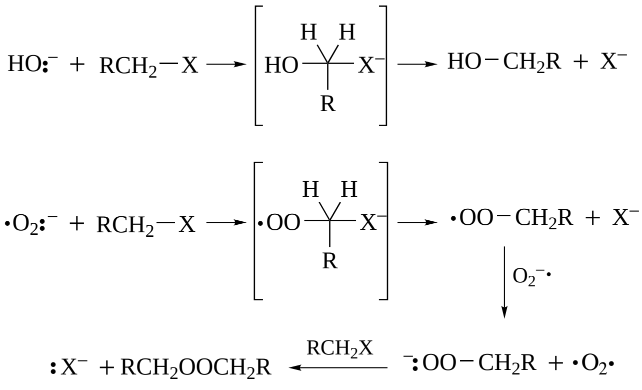

Scheme 16 Nucleophilic substitution

in Scheme 17. The addition of HO^- to a carbonyl group in quinones, which have no leaving group, yields an adduct that is sufficiently stable to characterize.[172]

The most common addition reaction is to a carbonyl group without an adequate leaving group. Examples include the reaction of HO^- and $O_2^{-}\cdot$ with CO_2 and quinones.[172] A common feature of these reactions is the formation of an adduct that is sufficiently stable to be isolated or characterized (see Scheme 18). The same orange-colored species results from the reaction of solid tetramethylammonium superoxide with gaseous CO_2 and with neat CCl_4,[174] and is believed to be an anion radical, $\cdot OOC(O)O^-$.[150]

The reaction of HO^- with 9,10-anthraquinone in MeCN produces an adduct (stable at −20 °C),[156] which reacts further at room temperature to yield the semiquinone anion radical ($AQ^-\cdot$). The equilibrium constants for the formation of the adducts and the rate constants for the reaction of the adduct with a second quinone molecule are given in Table 18 (see Scheme 18).

Several examples of reduction by HO^- of transition metal complexes are known (see Table 17).[38,164,175–178] The reaction of Au^+ with HO^- in MeCN is believed to be a prototype of reactions that involve a single-electron shift and the formation of a metal atom/hydroxyl radical bond (equation 175).

$$HO{:}^- + Au^+ \longrightarrow [HO\cdot\cdot Au] \longrightarrow HO{:}Au^I(s) \qquad (175)$$

The $E^{\circ\prime}$ for the Au^+/Au redox couple in MeCN is +1.58 V versus NHE compared to +0.9 V for the $HO\cdot/HO^-$ couple;[38,175] hence electron transfer is an exergonic process. Electrochemical oxidation of HO^- at a gold electrode in MeCN occurs at −0.19 V versus NHE, which indicates an Au–OH bond energy of 26 kcal mol^{-1} ($-\Delta G_{BF}$). (However, a Au–Au bond must be broken (54 kcal mol^{-1}); this gives a value of 53 kcal mol^{-1} (26 + 54/2) for the Au–OH bond[41]).

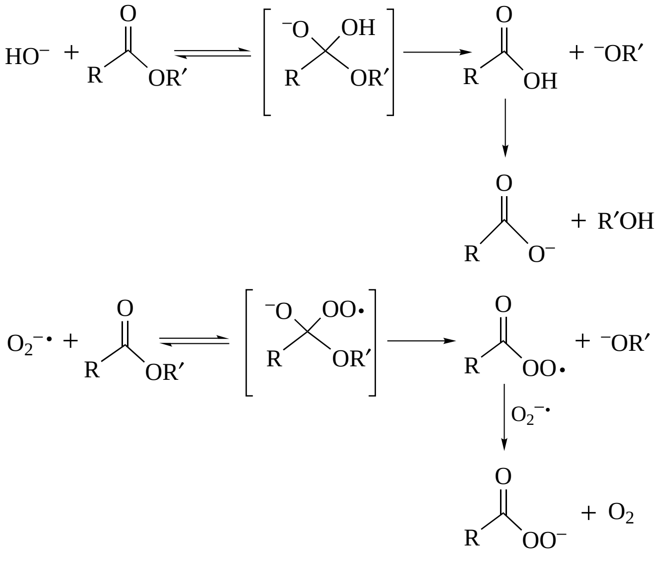

Scheme 17 Polar group transfer; HO^- and $O_2^{-}\cdot$ reactions with esters

The addition of HO^- to manganese(III) complexes ($Mn^{III}(O_2{-}bipy)_3{}^{3+}$, $Mn^{III}(TPP)^+$, $Mn^{III}(PA)_3$, and $Mn^{III}(OAc)_3$) in aprotic media results in the rapid precipitation of the same inorganic manganese oxide (equation 176).[38]

$$Mn^{III}L_3 + 3HO^- \longrightarrow 3L^- + Mn^{III}(OH)_3(s) + H_2O \qquad (176)$$

The ligands of $Mn^{III}L_3$ are reduced by electron transfer from three HO^- ions. The resulting $HO\cdot$ radicals are stabilized via three $d^5sp{-}p$ covalent metal–oxygen bonds (equation 178). Similar electron-transfer reductions by HO^- have been reported for Ru^{III} complexes[160] and for $(py)_2Fe^{III}TPP(ClO_4)$ (equation 179).[177] The direct reduction of X within $[(TPP)Fe^{III}X]$ via addition of HO^- has been demonstrated by electrochemical measurements[164] and an NMR titration.[178]

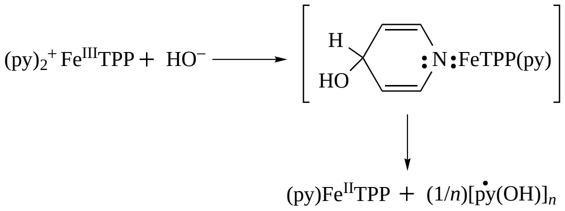

(177)

$$\begin{tikzcd}
{[Mn^{III}(T\dot{P}P)]ClO_4 + HO^-} \arrow[r] & {(TPP)Mn^{III}-OH + ClO_4^-} \\
{Mn^{II}(TPP) + HO^-} \arrow[r] \arrow[u, "{\begin{array}{l}-e^- \\ +0.1\ V\ vs.\ NHE\end{array}}"'] & {(TPP)Mn^{II}(OH)^-} \arrow[u, "{\begin{array}{l}-e^- \\ -0.3\ V\ vs.\ NHE\end{array}}"']
\end{tikzcd}$$

$$Mn-OH\ BE = 25\ kcal\ mol^{-1}$$

(178)

$$(TPP)Fe^{III}X + HO^- \longrightarrow (TPP)Fe^{III}\text{–}OH + X^- \qquad (179)$$

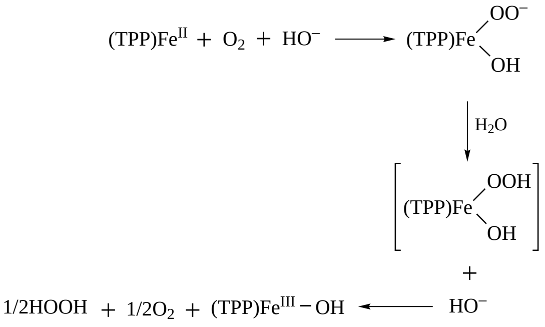

$$\begin{array}{c}
(TPP)Fe^{II} + O_2 + HO^- \longrightarrow (TPP)Fe\begin{matrix}OO^-\\OH\end{matrix} \\
\downarrow H_2O \\
\left[(TPP)Fe\begin{matrix}OOH\\OH\end{matrix}\right] \\
+ \\
1/2HOOH + 1/2O_2 + (TPP)Fe^{III}-OH \longleftarrow HO^-
\end{array}$$

(180)

Another example of reductive addition by HO^- is its termolecular reaction with reduced $Fe^{II}(TPP)$ in the presence of dioxygen (equation 180).[171] The net effect is the reduction of O_2 to bound superoxide ion, which hydrolyzes to bound

HOO•; the latter dissociates from the iron center and disproportionates to HOOH and O_2.

The most striking and unexpected reactions of HO^- are those that produce anion radicals when hydroxide is added to solutions of aromatic ketones, quinones, paraquats, and strong electron acceptors such as tetracyanoethylene.[170] If the primary reaction is a SET reaction, a radical pair will be produced (equation 181).

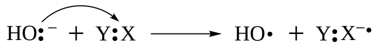

$$HO{:}^- + Y{:}X \longrightarrow HO\cdot + Y{:}X^{-\cdot} \qquad (181)$$

Because HO• is a strong oxidant (although about 1 V weaker in MeCN than in water), a single-electron transfer would be greater than 1 V endergonic for quinones, paraquats, and ketones. All of these compounds, unless substituted with electron-withdrawing groups, are reduced at potentials less negative than −0.3 V versus NHE in MeCN, compared to +0.9 V for the HO•/HO^- redox couple. Hence, the reactions of quinones, paraquats, and ketones with HO^- are unlikely examples of the SET process. Only synchronous coupling of the electron transfer to a chemical reaction that results in covalent bond formation of the HO• can account for the spontaneous reactivity. Although the coupling of two HO• to form HOOH is one possibility, a more likely primary step for reactants is attack by HO^- of an unsaturated center (aromatic or carbonyl carbon compound) or, in the case of the paraquats, a dequaternization reaction initiated by addition. The observed radicals are then produced in subsequent reactions that involve the intermediates from the primary step. Thus, the production of a radical is not adequate evidence that the primary step is a SET reaction.

In aprotic solvents, HO^- reacts with elemental sulfur (S_8) via a net SET process to give the trisulfide anion radical ($S_3^{-}\cdot$) and HOOH (equation 182).[179]

Perhaps this is the most compelling example that HO^- represents a stabilized electron and can affect the electron-transfer reduction of a nonmetal to give an anion radical.

$$3S_8 + 8HO^- \longrightarrow 8S_3^{-}\cdot + 4HOOH \qquad (182)$$

8.3 Relative Reactivity of $HOO^-/O_2^{-}\cdot/HO^-$ with Electrophilic Substrates

The nucleophilicity of oxyanions (YO^-) is directly related to their oxidation potentials ($E^{\circ\prime}{}_{B/B^{-}\cdot}$, Table 15) and the bond energies of their products (YO–R) with electrophilic substrates (RX) (equation 183).

$$YO^- + RX \longrightarrow YO\text{–}R + X^- \qquad (183)$$

Hence, the more negative the oxidation potential and the larger the YO–R bond energy, the proportionally greater nucleophilic reactivity that will result. The shift in the oxidation potential of HO^- from +1.89 V versus NHE in H_2O to +0.92 V in MeCN reflects the 'leveling effect' of protic solvents on the nucleophilicity of oxyanions. Likewise, the shift in potential for HOO^- [+0.20 V (H_2O) to −0.34 V (MeCN)] is in accord with the exceptional reactivity of HOO^- in aprotic solvents. In aqueous media, the reactivity of HOO^- is leveled by extensive anionic solvation,[180] but remains significant with many substrates owing to its unique orbital energies[181] and the presence of an unshared pair of electrons on the atom adjacent to the nucleophilic center (α effect).[182]

The reactivity of $O_2^{-}\cdot$ with alkyl halides in aprotic solvents occurs via nucleophilic substitution. Kinetic studies confirm that the reaction order is primary > secondary >>> tertiary and I > Br > Cl >>> F for alkyl halides, and that the attack by $O_2^{-}\cdot$ results in inversion of configuration (S_N2). Superoxide ion also reacts with CCl_4, $Br(CH_2)_2Br$, C_6Cl_6, and esters in aprotic media. The reactions are via nucleophilic attack by $O_2^{-}\cdot$ on carbon, or on chlorine with a concerted reductive displacement of chloride ion or alkoxide ion. As with all oxyanions, water suppresses the nucleophilicity of $O_2^{-}\cdot$ (hydration energy, 100 kcal mol^{-1}) and promotes its rapid hydrolysis and disproportionation. The reaction pathways for these compounds produce peroxy radical and peroxide ion intermediates (ROO• and ROO^-).

Hydroperoxide ion (HOO^-) is unstable in most aprotic solvents, but persists for several minutes in pyridine (k_{decomp}, $4.6 \times 10^{-3}\ s^{-1}$), which allows studies of its nucleophilic reactivity. In pyridine, HOO^- is oxidized in a one-electron transfer to give HOO•, which

Table 18 Equilibrium and rate constants for the reactions of quinones with hydroxide ion

Quinone	K_1 (M^{-1})	K_2 ($M^{-1}s^{-1}$)	$Q(OH)^-$ adduct λ_{max} (nm)	log ε
p-Benzoquinone monosulfonate[a]	125	–	253	3.86
Chloro-*p*-benzoquinone[a]	364	–	267	4.00
2,5-Dichloro-*p*-benzoquinone[a]	1.7×10^3	–	250	4.00
Trichlorohydroxy-*p*-benzoquinone[a]	210	–	250	3.75
			365	3.70
Tetrachloro-*p*-benzoquinone[b] (chloroanil)	1×10^5	–	285	3.83
9,10-Anthraquinone[c]	4.3×10^4	1.2	268	4.3
2-Ethyl-9,10-anthraquinone[c]	4×10^4	4.2	268	–

[a] Aqueous phosphate buffer, ionic strength 0.375.[157] [b] 50% aqueous ethanol.[157] [c] MeCN/tetra-*n*-butylammonium hydroxide.[156]

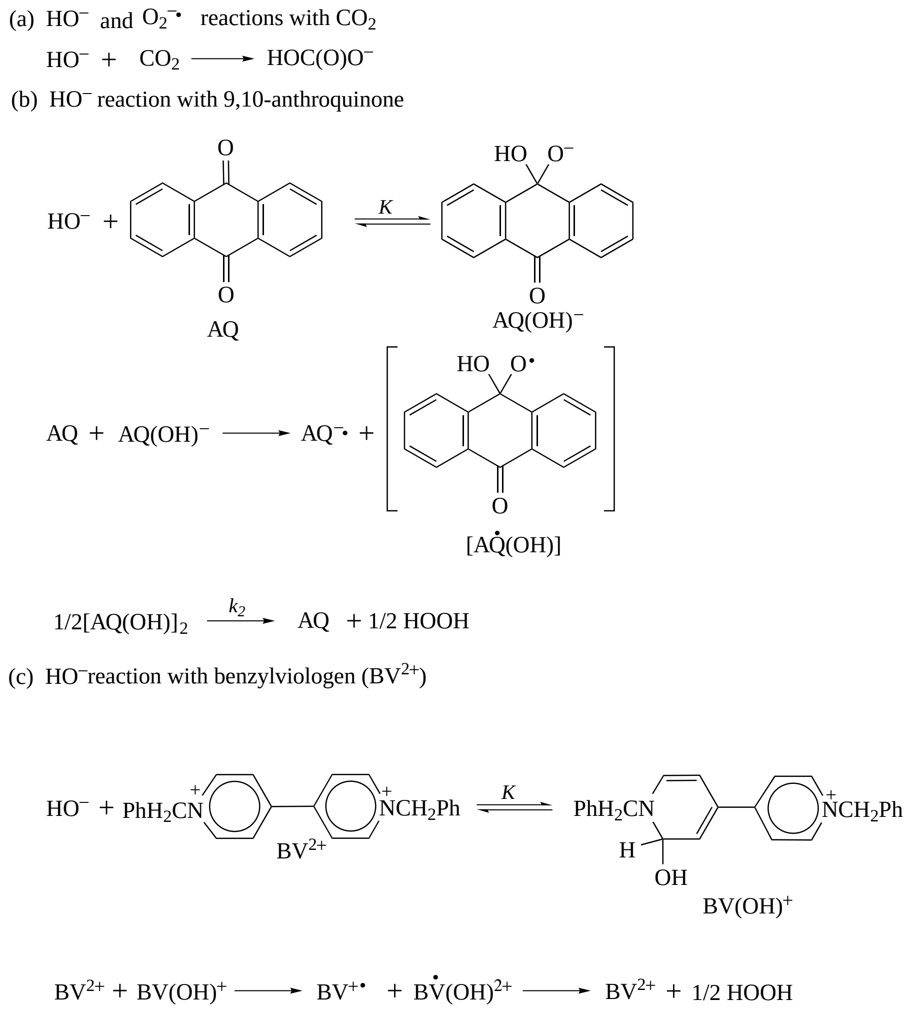
(a) HO⁻ and O₂⁻• reactions with CO₂
HO⁻ + CO₂ → HOC(O)O⁻
(b) HO⁻ reaction with 9,10-anthroquinone
HO⁻ +
K
AQ
AQ(OH)⁻
AQ + AQ(OH)⁻ → AQ⁻• +
[AQ•(OH)]
1/2[AQ(OH)]₂ →k₂ AQ + 1/2 HOOH
(c) HO⁻reaction with benzylviologen (BV²⁺)
HO⁻ + PhH₂CN NCH₂Ph
BV²⁺
K
PhH₂CN NCH₂Ph
H OH
BV(OH)⁺
BV²⁺ + BV(OH)⁺ → BV⁺• + BV•(OH)²⁺ → BV²⁺ + 1/2 HOOH

Scheme 18 Polar group coupling

Table 19 The relative reactivities of $HO^-(MeOH)/HOO^-/O_2^{-}\bullet$ with halocarbons and esters in pyridine [0.1 M $(Et_4N)ClO_4$], and the kinetics for the reaction of $O_2^{-}\bullet$ with substrates[184]

	$[k_{YO^-}/k_{O_2^-\bullet}]^a$				
Substrate (1–10 mM)	$YO^-{=}HO^-(MeOH)^c$	$HO^-(H_2O)$	HOO^{-d}	$O_2^-\bullet$	$k_{O_2^-\bullet}/[S]^b$ ($M^{-1}\,s^{-1}$)
CCl_4	0.6 ± 0.3	0.4 ± 0.2	1.8 ± 0.6 (1.2)^e	1.0	(1.4 ± 0.5) $\times 10^3$
n-BuBr	0.3 ± 0.2	0.2 ± 0.1	3.0 ± 1.0 (2.1)^e	1.0	(1.0 ± 0.1) $\times 10^3$
CH_2Br_2	0.3 ± 0.2	–	3.1 ± 1.0	1.0	(2.3 ± 0.5) $\times 10^2$
$BrCH_2CH_2Br$	0.3 ± 0.2	–	2.7 ± 1.0	1.0	(1.8 ± 0.3) $\times 10^3$
$PhCH_2Br$	0.3 ± 0.2	0.2 ± 0.1	3.0 ± 1.0	1.0	$>3 \times 10^3$
Br(Me)CHCN	0.3 ± 0.2	–	2.8 ± 1.0	1.0	(1.4 ± 0.3) $\times 10^{3f}$
C_6Cl_6	0.15 ± 0.1	0.0	5.0 ± 1.5 (2.9)^e	1.0	(1.0 ± 0.2) $\times 10^{3g}$
$MeCO_2Ph$	0.2 ± 0.1	–	4.5 ± 1.5	1.0	(1.6 ± 0.5) $\times 10^{2h}$
$MeCO_2Et$	0.2 ± 0.15	–	4.7 ± 2.0	1.0	(1.1 ± 0.2) $\times 10^{-2h}$

[a] Determined from the impact of YO^- upon the rate of disappearance of $O_2^-\bullet$ in the presence of excess substrate; rate of disappearance of $O_2^-\bullet$ monitored by linear-sweep voltammetry. [b] Determined from the ratio of $i_{p,a}/i_{p,c}$ for the cyclic voltammogram of O_2 in DMF in the presence of excess substrate. [c] $HO^-(MeOH)$ from $(Bu_4N)OH$ in MeOH. [d] HOO^- prepared either from $O_2^-\bullet$ plus $PhNHNH_2$ or HOOH plus HO^-. [e] *t*-$BuOO^-$. [f] $k/[S] = 3.5 \times 10^2\ M^{-1}\,s^{-1}$ in MeCN. [g] The primary product is Cl_5C_6OMe. [h] Kinetics in pyridine.

is in accord with previous studies in MeCN (equation 184).

$$\mathrm{HOO^-} \longrightarrow \mathrm{HOO\bullet} + \mathrm{e^-} \qquad (184)$$

$$E_{\mathrm{p,a}} = -0.34\ \mathrm{V\ vs.\ NHE(MeCN)}$$

In the case of HOO^- (and t-$BuOO^-$), the general 'leveling' of nucleophilic reactivity by protic solvents (water and alcohols) enhances its lifetime such that the net reactions for HOO^- with electrophilic substrates usually are most efficient and complete in H_2O or t-BuOOH. Almost all other solvents react with HOO^- or facilitate its decomposition. The relative lifetime of HOO^- in various solvents is in the order: $H_2O \gg$ MeOH $>$ EtOH $\gg$ diglyme $>$ pyridine $\sim$ PEGM 350 $\gg$ MeCN $>$ DMF $\gg$ DMSO.[183]

Table 19 summarizes the relative reactivities of $HO^-(H_2O)/HO^-(MeOH)/HOO^-/O_2^{-}\bullet$ with halocarbons and esters in pyridine and the kinetics for the reaction of $O_2^{-}\bullet$ with the substrates in aprotic solvents.[183] The relative reactivity with primary halides (n-BuBr and $PhCH_2Br$) in pyridine is HOO^- (3.0) $>$ t-$BuOO^-$ (2.1) $>$ $O_2^{-}\bullet$ (1.0) $>$ $HO^-(MeOH)$ (0.3) $>$ $HO^-(H_2O)$ (0.2). For CCl_4 the relative reactivities are HOO^- (1.8) $>$ t-$BuOO^-$ (1.2) $>$ $O_2^{-}\bullet$ (1.0) $>$ $HO^-(MeOH)$ (0.6) $>$ $HO^-(H_2O)$ (0.4), and for $PhCl_6$ are HOO^- (5.0) $>$ t-$BuOO^-$ (2.9) $>$ $O_2^{-}\bullet$ (1.0) $>$ $HO^-(MeOH)$ (0.2) $>$ $HO^-(H_2O)$ (0.0).

Although Br(Me)CHCN has two active sites for reaction with HOO^- (Br and CN), its relative rate is similar to that for n-BuBr and it reacts with HOO^- at the bromo carbon to yield Br^-, NCO^-, and MeCHO. In contrast, Br(Me)CHCN reacts with HO^- to give HO(Me)CHCN. The apparent reaction rate (k/[S]) between HOO^- and Br(Me)CHCN is $9.8 \times 10^2\ M^{-1}\ s^{-1}$ in MeCN, which is almost 10^4 times faster than the apparent rate for the reaction of HOO^- with MeCN ($k/[S] = 2.1 \times 10^{-1}\ M^{-1}\ s^{-1}$).[183]

The relative reactivity of $HOO^-/HO^-(MeOH)$ with primary halocarbons (n-BuBr, $PhCH_2Br$, $BrCH_2CH_2Br$) is about 10 in pyridine (Table 19), which compares with a ratio of 13 for their reaction with $BrCH_2CO_2H$ in H_2O[184] and 35 for reaction with $PhCH_2Br$ in 50% acetone/water.[185] Although $O_2^{-}\bullet$ is a powerful nucleophile in aprotic media, it does not exhibit such reactivity in water, presumably because of its strong solvation by that medium and its rapid hydrolysis and disproportionation. Kinetic and electrochemical studies for the reaction of $O_2^{-}\bullet$ with primary halocarbons confirm that the initial step is rate limiting and first order with respect to substrate and $O_2^{-}\bullet$, and occurs via a nucleophilic reductive displacement of halide ion with inversion of configuration (S_N2). The other oxyanions of Table 19 are believed to react via an analogous nucleophilic displacement.

The reactions of hexachlorobenzene (C_6Cl_6) with the oxyanions are unique. Thus, HOO^- is five times as reactive as $O_2^{-}\bullet$ and 33 times as reactive as $HO^-(MeOH)$ (Table 19). Superoxide ion reacts with C_6Cl_6 via an initial nucleophilic addition followed by displacement of Cl^-. The other oxyanions probably follow the same pathway. In the case of HOO^- the displacement of Cl^- gives C_6Cl_5OOH, which is deprotonated by a second HOO^- (or HO^-) to give $C_6Cl_5OO^-$. The latter displaces an adjacent chlorine to give the o-quinone.

The relative rates of reaction between esters and oxyanions (HOO^- (4.5) $>$ $O_2^{-}\bullet$ (1.0) $>$ $HO^-(MeOH)$ (0.2)) are similar to those for C_6Cl_6, which indicates that both substrates undergo an initial nucleophilic addition to an unsaturated carbon (carbonyl and aryl chlorine, respectively).[183] When a suitable leaving group is present, there is a net nucleophilic substitution.

The reactivity of oxyanions with nitriles relative to that for $O_2^{-}\bullet$ cannot be measured because the latter does not give a net reaction. However, the reaction between MeCN and HOO^- is rapid (k_{HOO^-}/[S], $0.21\ M^{-1}\ s^{-1}$) via nucleophilic addition to the unsaturated carbon (equation 185).[183]

$$\begin{aligned} &\mathrm{MeC{\equiv}N + HOO^-} \longrightarrow \mathrm{[(Me)(HOO)C{=}N^-]} \\ &\qquad\qquad\qquad\quad \longrightarrow \mathrm{[(Me)(^-OO)C{=}NH]} \\ &\xrightarrow{\mathrm{H_2O}} \mathrm{[(Me)(HOO)(^-O)CNH_2]} \xrightarrow{\mathrm{H_2O}} \mathrm{MeC(OH)(O^-)NH_2 + HOOH} \end{aligned} \qquad (185)$$

Intramolecular rearrangement and hydrolysis yield the (HO^-) adduct of acetamide. The (k_{HOO^-}/k_{HO^-}) ratio for p-$NCPhCO_2H$ in water[184] is about 10^3 and for PhCN in 50:50 H_2O/Me_2CO[185] is $10^{4.6}$.

9 RELATED ARTICLES

Copper Proteins: Oxidases; Cytochrome Oxidase; Dioxygen & Related Ligands; Iron: Heme Proteins & Dioxygen Transport & Storage; Iron: Heme Proteins & Electron Transport; Iron: Heme Proteins, Mono- & Dioxygenases; Iron: Heme Proteins, Peroxidases, Catalases & Catalase-peroxidases; Iron Porphyrin Chemistry; Manganese: The Oxygen-evolving Complex & Models; Oxidation Catalysis by Transition Metal Complexes.

10 REFERENCES

1. D. L. Gilbert ed., 'Oxygen and Living Processes: An Interdisciplinary Approach', Springer Verlag, New York, 1981, p. 1.
2. W. Day, 'Genesis on Planet Earth', 2nd edn., Yale University Press, New Haven, CT, 1984.
3. R. J. P. Williams, *Chem. Scr.*, 1986, **26**, 513.
4. P. Glatzel, W. Bergmann, J. Yano, H. Visser, J. H. Robblee, W. Gu, F. M. F. de Groot, G. Christou, V. L. Pecararo, S. P. Cramer, and V. K. Yachandra, *J. Am. Chem. Soc.*, 2004, **126**, 9946.

5. S. Mukhopadhyay, S. K. Mandai, S. Bhaduri, and W. H. Armstrong, *Chem. Rev.*, 2004, **104**, 3981.
6. J. Yano, K. Sauer, J.-J. Girerd, and V. K. Yachandra, *J. Am. Chem. Soc.*, 2004, **126**, 7486.
7. S. H. Kim, W. Gregor, J. M. Peloquin, M. Brynda, and R. D. Britt, *J. Am. Chem. Soc.*, 2004, **126**, 7228.
8. H. Metzner ed., ‘Photosynthetic Oxygen Evolution’, Academic Press, New York, 1978.
9. T. A. Ono, H. Kajikawa, and Y. Inoue, *Plant Physiol.*, 1986, **80**, 85.
10. A. J. Hoff, in ‘Light Reaction Path of Photosynthesis’, ed. F. K. Fong, Springer-Verlag, Heidelberg, 1982, p. 80.
11. C. Critchley and A. M. Sargeson, *FEBS Lett.*, 1984, **177**, 2.
12. G. C. Dismukes, D. A. Ambramowicz, K. F. Ferris, P. Mathur, Y. Siderer, B. Upadrashjta, and P. Watnick, in ‘The Oxygen Evolving System of Photosynthesis’, eds. Y. Inoue, A. R. Crofts, G. Govindjee, N. Murata, G. Renger, and K. Satoh, Academic Press, New York, 1983, p. 145.
13. H. S. Carr and D. R. Winge, *Acc. Chem. Res.*, 2003, **36**, 309.
14. M. Wikstrom, *Biochim. Biophys. Acta*, 2004, **1655**, 241.
15. O. Hayaishi ed., ‘Molecular Mechanisms of Oxygen Activation’, Academic Press, New York, 1974.
16. J. S. Valentine, D. L. Wertz, T. J. Lyons, L.-L. Liou, J. J. Goto, and E. B. Gralla, *Curr. Op. Chem. Biol.*, 1998, **2**, 253.
17. G. N. Landis and J. Tower, *Mech. Ageing Dev.*, 2005, **126**(3), 365.
18. A. J. Wu, J. E. Penner-Hahn, and V. L. Pecararo, *Chem. Rev.*, 2004, **104**, 903.
19. A. E. M. Boelrijk and G. C. Dismukes, *Inorg. Chem.*, 2000, **39**, 3020.
20. A. J. Kettle and C. C. Winterbourn, *Biochemistry*, 2001, **40**, 10204.
21. B. G. Jacob, D. S. Laitur, L. Pu, M. F. Wargocki, A. G. DiPasquale, K. C. Fortner, S. M. Schuck, and S. N. Brown, *Inorg. Chem.*, 2002, **41**, 4815.
22. W. C. Barrette Jr, H. W. Johnson Jr, and D. T. Sawyer, *Anal. Chem.*, 1984, **56**, 1890.
23. R. Parsons, ‘Handbook of Electrochemical Constants’, Butterworths, London, 1959.
24. H. A. Schwarz and R. W. Dodson, *J. Phys. Chem.*, 1984, **88**, 3643.
25. J. Wilshire and D. T. Sawyer, *Acc. Chem. Res.*, 1979, **12**, 105.
26. A. J. Bard, R. Parsons, and J. Jordon eds, ‘Standard Potentials in Aqueous Solution’, Dekker, New York, 1985.
27. D. T. Sawyer, G. Chiericato Jr, C. T. Angelis, E. J. Nanni Jr, and T. Tsuchiya, *Anal. Chem.*, 1982, **54**, 1720.
28. P. Cofré and D. T. Sawyer, *Anal. Chem.*, 1986, **58**, 1057.
29. P. Cofré and D. T. Sawyer, *Inorg. Chem.*, 1986, **25**, 2089.
30. D. T. Sawyer, J. L. Roberts Jr, T. Tsuchiya, and G. S. Srivatsa, in ‘Oxygen Radicals in Chemistry and Biology’, eds. W. Bors, M. Saran, and D. Tait, de Gruyter, Berlin, 1984.
31. J. L. Roberts Jr, M. M. Morrison, and D. T. Sawyer, *J. Am. Chem. Soc.*, 1978, **100**, 329.
32. J. L. Roberts Jr and D. T. Sawyer, *Isr. J. Chem.*, 1983, **23**, 430.
33. D.-H. Chin, G. Chiericato Jr, E. J. Nanni Jr, and D. T. Sawyer, *J. Am. Chem. Soc.*, 1982, **104**, 1296.
34. M. J. Gibian, D. T. Sawyer, T. Ungerman, R. Tangpoonpholvivat, and M. M. Morrison, *J. Am. Chem. Soc.*, 1979, **101**, 640.
35. I. Fridovich, in ‘Oxygen and Oxy Radicals’, eds. M. A. J. Rodgers and E. L. Powers, Academic Press, New York, 1981.
36. J. A. Fee, in ‘Oxygen and Oxy Radicals’, eds. M. A. J. Rodgers and E. L. Powers, Academic Press, New York, 1981.
37. D. T. Sawyer, M. S. McDowell, and K. S. Yamaguchi, *Chem. Res. Toxicol.*, 1988, **1**, 97.
38. P. K. S. Tsang, P. Cofré, and D. T. Sawyer, *Inorg. Chem.*, 1987, **26**, 3604.
39. J. Mullay, *J. Am. Chem. Soc.*, 1986, **108**, 1770.
40. K. Jung, N. D. Epiotis, and S. Buss, *J. Am. Chem. Soc.*, 1986, **108**, 3640.
41. D. R. Lide ed., ‘CRC Handbook of Chemistry and Physics’, 71st edn., CRC, Boca Raton, FL, 1990, p. 9.
42. S. A. Richert, P. K. S. Tsang, and D. T. Sawyer, *Inorg. Chem.*, 1989, **28**, 2471.
43. D. T. Sawyer, *Comments Inorg. Chem.*, 1990, **10**, 129.
44. S. E. Jones, L. E. Leon, and D. T. Sawyer, *Inorg. Chem.*, 1982, **21**, 3692.
45. S. R. Sofen, D. C. Ware, S. R. Cooper, and K. N. Raymond, *Inorg. Chem.*, 1979, **18**, 234.
46. S. R. Boone, G. H. Purser, H.-R. Chang, M. D. Lowery, D. N. Hendrickson, and G. G. Pierpont, *J. Am. Chem. Soc.*, 1989, **111**, 2292.
47. H. Sugimoto, H.-C. Tung, and D. T. Sawyer, *J. Am. Chem. Soc.*, 1988, **110**, 2465.
48. T. S. Calderwood, C. L. Johlman, J. L. Roberts Jr, C. L. Wilkins, and D. T. Sawyer, *J. Am. Chem. Soc.*, 1984, **106**, 4683.
49. A. D. Goolsby and D. T. Sawyer, *Anal. Chem.*, 1968, **40**, 83.
50. C. Walling, *Acc. Chem. Res.*, 1975, **8**, 125.
51. D. H. R. Barton, E. Csuhai, D. Doller, N. Ozbalik, and N. Senglet, *Tetrahedron Lett.*, 1990, **31**, 3097.
52. I. Yamazaki and L. H. Piette, *J. Am. Chem. Soc.*, 1991, **113**, 7588.
53. B. Ensing, F. Buda, and E. J. Baerends, *J. Phys. Chem.*, 2003, **107**, 5722.
54. M. L. Kremer, *J. Phys. Chem.*, 2003, **107**, 1734.

55. C. Sheu, A. Sobkowiak, L. Zhang, N. Ozbalik, D. H. R. Barton, and D. T. Sawyer, *J. Am. Chem. Soc.*, 1989, **111**, 8030.
56. H.-C. Tung and D. T. Sawyer, *J. Am. Chem. Soc.*, 1992, **114**, 3445.
57. J. Halperin and H. Taube, *J. Am. Chem. Soc.*, 1952, **74**, 380.
58. A. Sobkowiak and D. T. Sawyer, unpublished results, 1993.
59. A. Sobkowiak, A. Qiu, X. Liu, A. Llobet, and D. T. Sawyer, *J. Am. Chem. Soc.*, 1993, **115**, 609.
60. D. T. Sawyer, A. Sobkowiak, and T. Matsushita, *Acc. Chem. Res.*, 1996, **29**, 409.
61. C. Kang, C. Redman, V. Cepak, and D. T. Sawyer, *Bioorg. Med. Chem.*, 1993, **1**, 125.
62. H. Sugimoto and D. T. Sawyer, *J. Am. Chem. Soc.*, 1985, **107**, 5712.
63. H. Sugimoto and D. T. Sawyer, *J. Am. Chem. Soc.*, 1984, **106**, 4283.
64. P. Nicholls, *Biochim. Biophys. Acta*, 1972, **279**, 306.
65. F. P. Guengerich and T. L. MacDonald, *Acc. Chem. Res.*, 1984, **17**, 9.
66. J. T. Groves, G. A. McClusky, R. E. White, and M. J. Coon, *Biochem. Biophys. Res. Commun.*, 1978, **81**, 154.
67. H. Sugimoto and D. T. Sawyer, *J. Org. Chem.*, 1985, **50**, 1785.
68. H. Rosen and S. Klebanoff, *J. Biol. Chem.*, 1977, **252**, 4803.
69. A. M. Held and J. K. Hurst, *Biochem. Biophys. Res. Commun.*, 1978, **81**, 878.
70. (a) P. George, *Adv. Catal.*, 1952, **4**, 367; (b) P. George, *Biochem. J.*, 1953, **54**, 267; (c) P. George, *Biochem. J.*, 1953, **55**, 220.
71. J. E. Penner-Hahn, K. E. Eble, T. J. McMurry, M. Renner, A. L. Balch, J. T. Groves, J. H. Dawson, and K. O. Hodgson, *J. Am. Chem. Soc.*, 1986, **108**, 7819.
72. M. Chance, L. Powers, T. Poulos, and B. Chance, *Biochemistry*, 1986, **25**, 1266.
73. D. T. Sawyer, *J. Phys. Chem.*, 1990, **93**, 7977.
74. R. Atkinson, *Chem. Rev.*, 1986, **86**, 69.
75. M. S. Matheson and L. M. Dorfman, ‘Pulse Radiolysis’, MIT Press, Cambridge, MA, 1969.
76. (a) L. F. Dorfman and G. E. Adams, *Natl. Stand. Ref. Data Serv. (US Natl. Bur. Stand.)*, 1973, NSRDS-NBS46, 20 (SD catalog No. C13.48:46); (b) G. V. Burton, C. Greenstock, W. D. Helman, and A. B. Ross, *J. Phys. Chem. Ref. Data*, 1988, **17**, 513.
77. B. H. J. Bielski, D. E. Cabelli, R. L. Arudi, and A. B. Ross, *J. Phys. Chem. Ref. Data*, 1985, **14**, 1041.
78. D. T. Sawyer and J. S. Valentine, *Acc. Chem. Res.*, 1981, **14**, 393.
79. A. Nadezhdin and H. B. Dunsford, *J. Phys. Chem.*, 1979, **83**, 1957.
80. I. Fridovich, in ‘Advances in Inorganic Biochemistry’, eds. G. L. Eichhorn and D. L. Marzilli, Elsevier, New York, 1979, p. 67.
81. D.-H. Chin, G. Chiericato Jr, E. J. Nanni Jr, and D. T. Sawyer, *J. Am. Chem. Soc.*, 1982, **104**, 1296.
82. H. Sugimoto, M. Matsumoto, J. R. Kanofsky, and D. T. Sawyer, *J. Am. Chem. Soc.*, 1988, **22**, 1182.
83. J. A. Howard and K. V. Ingold, *Can. J. Chem.*, 1967, **45**, 785.
84. B. H. J. Bielski, R. L. Arudi, and M. W. Sutherland, *J. Biol. Chem.*, 1983, **258**, 4759.
85. T. L. Arudi, M. W. Sutherland, and B. H. J. Bielski, in ‘Oxy Radicals and Their Scavenger Systems’, eds. G. Cohen and R. A. Greenwald, Elsevier, New York, 1983, Vol. 1, p. 26.
86. A. A. Al-Thannon, J. P. Barton, J. E. Packer, R. J. Sims, C. N. Trumbore, and R. V. Winchester, *Int. J. Radiat. Phys. Chem.*, 1974, **6**, 233.
87. D. E. Cabelli and B. H. J. Bielski, *J. Phys. Chem.*, 1983, **87**, 1809.
88. J. R. Kanofsky, M. Matsumoto, H. Sugimoto, and D. T. Sawyer, *J. Am. Chem. Soc.*, 1988, **110**, 5193.
89. B. D. Olafson and W. A. Goddard III, *Proc. Natl. Acad. Sci. U.S.A.*, 1977, **74**, 1315.
90. J. P. Collman, R. R. Gagné, C. A. Reed, T. R. Halbert, G. Lang, and W. T. Robinson, *J. Am. Chem. Soc.*, 1975, **97**, 1427.
91. P. R. Ortiz de Montellado ed., ‘Cytochrome P-450’, Plenum, New York, 1985.
92. A. Ericson, B. Hedman, K. O. Hodgson, J. Green, H. Dalton, J. G. Bentsen, S. J. Beer, and S. J. Lippard, *J. Am. Chem. Soc.*, 1988, **110**, 2330.
93. B. G. Fox, K. K. Surerus, E. Munck, and J. D. Lipscomb, *J. Biol. Chem.*, 1988, **263**, 10553.
94. L. Que Jr, *J. Chem. Educ.*, 1985, **62**, 938.
95. C. S. Foote, *Free Radic. Biol.*, 1976, **2**, 85.
96. D.-H. Chin, A. L. Balch, and G. N. LaMar, *J. Am. Chem. Soc.*, 1990, **102**, 1446.
97. M. G. Simic and M. Karel eds, ‘Autoxidation in Food and Biological Systems’, Plenum, New York, 1980.
98. A. Sobkowiak and D. T. Sawyer, *J. Am. Chem. Soc.*, 1991, **113**, 9520.
99. D. T. Sawyer, H. Sugimoto, and T. S. Calderwood, *Proc. Natl. Acad. Sci. U.S.A.*, 1981, **81**, 8025.
100. H. Dalton, *Adv. Appl. Microbiol.*, 1980, **26**, 71.
101. C. Sheu and D. T. Sawyer, *J. Am. Chem. Soc.*, 1990, **112**, 8212.
102. A. F. Trotman-Dickenson, *Adv. Free-Radical Chem.*, 1965, **1**, 1.
103. J. D. Lipscomb, University of Minnesota, personal communication, March 30, 1990.
104. J. Hagen, L. D. Socaciu, J. Le Roux, D. Popolan, T. M. Bernhardt, L. Woste, R. Mitric, H. Noack, and V. Bonacic-Koutecky, *J. Am. Chem. Soc.*, 2004, **126**, 3442.

105. D. T. Sawyer, P. Chooto, and P. K. S. Tsang, *Langmuir*, 1989, **5**, 84.
106. T. E. King, H. S. Mason, and M. Morrison eds, 'Oxidases and Related Redox Systems', Liss, New York, 1988.
107. O. Hayaishi ed., 'Oxygenases', Academic Press, New York, 1962.
108. J. V. Bannister and W. H. Bannister eds, 'The Biology and Chemistry of Active Oxygen', Elsevier, New York, 1974.
109. L. L. Ingraham and D. L. Meyer, 'Biochemistry of Dioxygen', Plenum, New York, 1985.
110. S. I. Chan, S. N. Witt, and D. F. Blair, *Chem. Scr.*, 1988, **28A**, 51.
111. S. I. Chan, P. M. Li, T. Nilson, D. F. Blair, and C. T. Martin, in 'Oxidases and Related Redox Systems', eds. T. E. King, H. S. Mason, and M. M. Morrison, Liss, New York, 1988, p. 731.
112. V. Massey and P. Hemmerick, in 'The Enzymes', ed. P. Boyer, Academic Press, New York, 1975, Vol. XII, p. 191.
113. B. Entsch, V. Massey, and D. P. Ballou, *Biochem. Biophys. Res. Commun.*, 1974, **57**, 1018.
114. V. Massey, L. M. Schopfer, and R. F. Anderson, in 'Oxidases and Related Redox Systems', eds. T. E. King, H. S. Mason, and M. Morrison, Liss, New York, 1988, p. 147.
115. L. Que Jr, *Struct. Bonding*, 1980, **40**, 39.
116. M. Nozaki and O. Hazaishi, in 'The Biology and Chemistry of Active Oxygen', eds. J. V. Bannister and W. H. Bannister, Elsevier, New York, 1984, p. 68.
117. C. Sheu, A. Sobkowiak, S. Jeon, and D. T. Sawyer, *J. Am. Chem. Soc.*, 1990, **112**, 879.
118. H. Sugimoto, D. T. Sawyer, and J. R. Kanofsky, *J. Am. Chem. Soc.*, 1988, **110**, 8707.
119. P. R. Ogilly and C. S. Foote, *J. Am. Chem. Soc.*, 1983, **105**, 3423.
120. A. A. Frimer ed., 'Singlet O_2', CRC Press, Boca Raton, FL, 1985, Vols. 1–4.
121. C. S. Foote, in 'Biochemical and Clinical Aspects of Oxygen', ed. W. S. Caughey, Academic Press, New York, 1979, p. 603.
122. P. B. Merkel and D. R. Kearns, *J. Am. Chem. Soc.*, 1972, **94**, 7244.
123. W. Adam, K. J. Roschmann, C. R. Saha-Moller, and D. Seebach, *J. Am. Chem. Soc.*, 2002, **124**, 5068.
124. B. H. J. Bielski, *Photochem. Photobiol.*, 1978, **28**, 645.
125. B. H. J. Bielski and A. O. Allen, *J. Phys. Chem.*, 1977, **81**, 1048.
126. Y. A. Ilan, D. Meisel, and G. Czapski, *Isr. J. Chem.*, 1974, **12**, 891.
127. D. Behar, G. Czapski, J. Rabini, L. M. Dorfman, and H. A. Schwartz, *J. Phys. Chem.*, 1970, **74**, 3209.
128. J. Rabini and S. O. Nielsen, *J. Phys. Chem.*, 1969, **73**, 3736.
129. D. T. Sawyer and E. J. Nanni Jr, in 'Oxygen and Oxy Radicals in Chemistry and Biology', eds. E. J. Powers and M. A. J. Rodgers, Academic Press, New York, 1981.
130. E. J. Nanni Jr, M. D. Stallings, and D. T. Sawyer *J. Am. Chem. Soc.*, 1980, **102**, 4481.
131. R. Dietz, A. E. J. Forno, B. E. Larcombe, and M. D. Peover, *J. Chem. Soc., B* 1970, **816**,.
132. M. V. Merritt and D. T. Sawyer, *J. Org. Chem.*, 1970, **35**, 2157.
133. F. Magno, R. Seeber, and S. Valcher, *J. Electroanal. Chem.*, 1977, **83**, 131.
134. J. San Fillipo Jr, C.-I. Chern, and J. S. Valentine, *J. Org. Chem.*, 1975, **40**, 1678.
135. R. A. Johnson and E. G. Nidy, *J. Org. Chem.*, 1975, **40**, 1680.
136. J. L. Roberts Jr, T. S. Calderwood, and D. T. Sawyer, *J. Am. Chem. Soc.*, 1983, **105**, 7691.
137. T. S. Calderwood, R. C. Neuman Jr, and D. T. Sawyer, *J. Am. Chem. Soc.*, 1983, **105**, 3337.
138. T. S. Calderwood and D. T. Sawyer, *J. Am. Chem. Soc.*, 1984, **106**, 7185.
139. M. Hojo and D. T. Sawyer, *Chem. Res. Toxicol.*, 1989, **2**, 193.
140. H. Sugimoto, S. Matsumoto, and D. T. Sawyer, *J. Am. Chem. Soc.*, 1987, **109**, 8081.
141. H. Sugimoto, S. Matsumoto, D. T. Sawyer, J. R. Kanofsky, A. K. Chowdhury, and C. L. Wilkins, *J. Am. Chem. Soc.*, 1988, **110**, 5193.
142. M. V. Merritt and R. A. Johnson, *J. Am. Chem. Soc.*, 1977, **99**, 3713.
143. L. Eberson, *Adv. Phys. Org. Chem.*, 1982, **18**, 79.
144. R. P. Mason, in 'Free Radicals in Biology', ed. W. A. Pryor, Academic Press, New York, 1982, Vol. 6, p. 161.
145. T. F. Slater, in 'Free Radicals, Lipid Peroxidation and Cancer', eds. D. C. H. McBrien and T. F. Slater, Academic Press, New York, 1982, p. 243.
146. J. L. Roberts Jr, and D. T. Sawyer, *J. Am. Chem. Soc.*, 1984, **106**, 4667.
147. F. Magno and G. Bontempelli, *J. Electroanal. Chem.*, 1976, **68**, 337.
148. D. T. Sawyer, J. J. Stamp, and K. A. Menton, *J. Org. Chem.*, 1983, **48**, 3733.
149. C. L. Johlman, R. L. White, D. T. Sawyer, and C. L. Wilkins, *J. Am. Chem. Soc.*, 1983, **105**, 2091.
150. S. Matsumoto, H. Sugimoto, and D. T. Sawyer, *Chem. Res. Toxicol.*, 1988, **1**, 19.
151. J. K. Kochi, in 'Free Radicals', ed. J. K. Kochi, Wiley, New York, 1973, p. 698.
152. D. T. Sawyer, D. T. Richens, E. J. Nanni Jr, and M. D. Stallings, *Dev. Biochem.*, 1980, **11A**, 1.
153. R. P. Martin and D. T. Sawyer, *Inorg. Chem.*, 1972, **11**, 2644.
154. M. D. Stallings and D. T. Sawyer, *J. Chem. Soc., Chem. Commun.*, 1979, 340.
155. P. S. Rao and E. Hazen, *J. Phys. Chem.*, 1975, **79**, 397.
156. D. T. Sawyer, T. S. Calderwood, C. L. Johlman, and C. L. Wilkins, *J. Org. Chem.*, 1985, **50**, 1409.

157. D. T. Sawyer, G. Chiericato Jr, and T. Tsuchiya, *J. Am. Chem. Soc.*, 1982, **104**, 6273.
158. E. J. Nanni Jr and D. T. Sawyer, *J. Am. Chem. Soc.*, 1980, **102**, 7591.
159. E. J. Nanni Jr, C. T. Angelis, J. Dickson, and D. T. Sawyer, *J. Am. Chem. Soc.*, 1981, **103**, 4268.
160. W. Ando, Y. Kabe, S. Kobayashi, C. Takyu, A. Yamagishi, and H. Inoda, *J. Am. Chem. Soc.*, 1980, **102**, 4527.
161. E. J. Nanni Jr, Ph.D. Dissertation, University of California, Riverside, CA, 1980.
162. G. J. McClure, J. A. Fee, G. A. McCluskey, and J. T. Groves, *J. Am. Chem. Soc.*, 1977, **99**, 5220.
163. E. McCandlish, A. R. Miksztal, M. Nappa, A. Q. Sprenger, J. S. Valentine, J. D. Strong, and T. G. Spiro, *J. Am. Chem. Soc.*, 1980, **102**, 4268.
164. P. K. S. Tsang and D. T. Sawyer, *Inorg. Chem.*, 1990, **29**, 2848.
165. A. Pross, *Acc. Chem. Res.*, 1985, **18**, 212.
166. R. G. Pearson, *J. Am. Chem. Soc.*, 1986, **108**, 6109.
167. J. R. Murdoch, *J. Am. Chem. Soc.*, 1983, **105**, 2159.
168. E. Buncel, S. Kesmarky, and E. A. Symons, *Chem. Commun.*, 1971, 120.
169. R. T. Sanderson, ‘Polar Covalence’, Academic Press, New York, 1983, p. 181.
170. M. Chanon and M. L. Tobe, *Angew. Chem., Int. Ed. Engl.*, 1982, **21**, 1.
171. A. R. Forrester and V. Purushotham, *J. Chem. Soc., Chem. Commun.*, 1984, 1505.
172. J. L. Roberts Jr, H. Sugimoto, W. C. Barrette Jr, and D. T. Sawyer, *J. Am. Chem. Soc.*, 1985, **107**, 4556.
173. C. A. Bishop and L. K. Tong, *Tetrahedron Lett.*, 1964, 3043.
174. J. L. Roberts Jr, T. S. Calderwood, and D. T. Sawyer, *J. Am. Chem. Soc.*, 1984, **106**, 4667 and references therein.
175. A. D. Goolsby and D. T. Sawyer, *Anal. Chem.*, 1968, **40**, 1978.
176. D. M. Hercules and F. E. Lytle, *J. Am. Chem. Soc.*, 1966, **88**, 4745.
177. G. S. Srivatsa and D. T. Sawyer, *Inorg. Chem.*, 1985, **24**, 1732.
178. K. Shin, S. K. Kramer, and H. M. Goff, *Inorg. Chem.*, 1987, **26**, 4103.
179. M. Hojo and D. T. Sawyer, *Inorg. Chem.*, 1989, **28**, 1201.
180. C. D. Ritchie, *Acc. Chem. Res.*, 1972, **5**, 348.
181. S. S. Shaik and A. Pross, *J. Am. Chem. Soc.*, 1982, **104**, 2708.
182. J. O. Edwards and R. G. Pearson, *J. Am. Chem. Soc.*, 1962, **84**, 16.
183. P. K. S. Tsang, S. Jeon, and D. T. Sawyer, in ‘Industrial Environmental Chemistry’, eds. D. T. Sawyer and A. E. Martell, Plenum, New York, 1992, p. 181.
184. J. E. McIssac Jr, L. R. Subbaraman, J. Subbaraman, H. A. Hulhausen, and E. J. Behrman, *J. Org. Chem.*, 1972, **37**, 1037.
185. R. G. Pearson and D. N. Edgington, *J. Am. Chem. Soc.*, 1962, **84**, 4607.

P-donor Ligands

Annette Schier & Hubert Schmidbaur
Technische Universität München, Munich, Germany

Based in part on the article P-Donor Ligands by Charles A. McAuliffe & Anthony G. Mackie which appeared in the Encyclopedia of Inorganic Chemistry, First Edition.

1	Introduction	1
2	The Effect of Substituents R on R_3P Donor Ligands	1
3	P-donor–Metal Bonding	4
4	The Structural Diversity of P-donor Ligands	11
5	Elemental Phosphorus as a Ligand	19
6	Phosphorus Oxides and Sulfides as P-donor Ligands	20
7	Phosphaalkynes RC≡P as Ligands	20
8	Phosphinidenes RP and Diphosphenes RP=PR as P-donor Ligands	21
9	Phosphaalkenes $R_2C{=}PR'$ as P-donor Ligands	22
10	Phosphinines (Phospha-Benzenes) as Ligands to Metals	22
11	Phosphenium Cations as P-bound Ligands	23
12	Related Articles	23
13	Further Reading	23
14	References	23

Glossary

Donor: an atom or assemblage of atoms that is a net donor of electrons to another atom or assemblage of atoms
Ligand: a moiety that is bound to a central atom, usually a metal
Phosphorus: a nonmetal, the second member of group 15, collectively called the pnictogens

PART I
Ligands with Three-coordinate Phosphorus Atoms

1 INTRODUCTION

Why use P-donor ligands instead of, for example, N-donor ligands? Prominent among the reasons is their ability to form a molecular complex that often stabilizes unusual valency states. Furthermore, though demanding, their syntheses are mainly straightforward using conventional laboratory techniques and apparatus. Also of interest is the fact that metal–phosphorus bonding has been factored into three components: σ-bonding, π-bonding, and steric effects (*see σ-Bond*; *π-Bond*; and *Steric Effect*). The ability to vary each component independently, or almost so, has found important uses in the development of homogeneous transition metal catalysts and their 'fine tuning' for optimum product yields. To this list may be added their ability to meet the recent demands for *chiral* synthesis by the pharmaceutical industry. Finally, but by no means least, there are the enormous advantages in analysis of ^{31}P NMR and P-specific GC detectors in following complex reactions. While none of these reasons is unique to phosphorus, the combination makes P-donor phosphorus ligands highly attractive.

For the purpose of Part I of the article, we consider P-donor ligands of the type R_3P that are neutral molecules with a *Lone Pair* of electrons available for complex formation. Therefore this is essentially tervalent phosphorus chemistry. Anionic species such as PPh_2^- are excluded, but the simple inorganic compounds such as the phosphorus trihalides are included.

Part I of this article has been divided into four sections. The introduction is followed by a description of the variety of P-donor ligands available. The third section is devoted to the bonding of P-donor ligands with metals. Finally, an attempt is made to show the enormous structural diversity of P-donor ligands, ranging from simple phosphines to those with sophisticated and elaborate architecture.

It was about a decade after the first preparation of a tertiary phosphine, PMe_3, in 1847,[1] that the coordinating power of phosphorus was appreciated. Hoffman[2] and later Cahours[3] prepared the first P-donor complexes in the 1850s. The exponential growth of P-donor chemistry started with the pioneering work of Mann[4] and Jensen[5] in the 1930s and was continued in the immediate postwar era by Dwyer,[6] Chatt,[7] and Nyholm,[8] to name but three.

2 THE EFFECT OF SUBSTITUENTS R ON R_3P DONOR LIGANDS

The P-donor ligands we consider in this Part I are phosphorus(III) compounds. We avoid the classification difficulties of phosphine, PH_3, as based on P-oxidation state −III by referring throughout to tervalent phosphorus. Low-coordination number phosphorus species, such as RP, RCP, $R_2C{=}PR'$, and P_n, are presented in Part II. The P-donor ligands considered in Part I are covered by the generalized formula PR_3 for a P-donor ligand. The PR_3 ligands have a pyramidal shape due to their sterically active lone pair of electrons. In terms of a *Valence Shell Electron Pair Repulsion Model* model, the lone pair occupies the 'vacant' tetrahedral site of the phosphorus center.

The elements bonded to the P-Atom commonly found in R_3P ligands are E = H, C, Si, N, O, S, F, and Cl; other elements are known but are rare. Driven by the quest for ever more sophisticated semiconductor devices, material scientists are constantly extending the range of precursors for MOCVD processes (*see Metal–Organic Chemical Vapor Deposition*), and inter alia compounds with P–Al/Ga/In linkages are rapidly gaining importance. All the common elements bound to P-donor ligands, except hydrogen, are members of the p-block.

It will be seen later (Part I, Section 3) that the π acidity of P-donor ligands is primarily a function of the σ^* antibonding orbital of the ligand molecules. In general, the greater the e*lectronegativity* difference between E and P (Table 1), the lower is the energy of the σ^* orbital and the stronger the π acidity of the ligand (*see π-Acid Ligand*). The elements, E, will be discussed briefly group by group.

2.1 Phosphorus Hydrides as P-donor Ligands

Phosphine and its derivatives containing P–H bonds, the primary (RPH_2) and secondary (R_2PH) phosphines, do not have a well-developed coordination chemistry. The greater the number of hydrogen substituents, the more modest is the steric requirement of the ligand (see Section 3.1.3). PH_3, with a *Cone Angle* of 87°, is the least sterically demanding phosphine. The majority of transition metal complexes formed with hydrogen-containing phosphines is used to prepare phosphide bridged species (see, for example, equation 1).

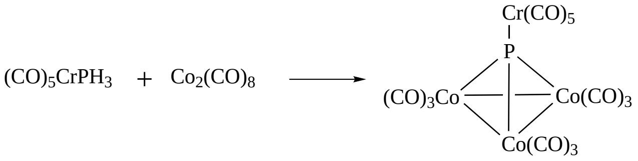

(1)

Homoleptic phosphine complexes with transition metals, such as $[Ni(PH_3)_4]$ or $[Ni(PPh_2H)_4]$, have been prepared.[10,11] The main group Me_3GaPH_3 coordination compound can be pyrolyzed to afford GaP in Na^+/H^+ exchanged zeolite Y.[12]

Table 1 Selected electronegativities of the elements[9]

Element	Pauling	Allred–Rochow	Mulliken	Spectroscopic data
P	2.19	2.06	2.39	2.25
H	2.20	2.20	3.06	2.30
C	2.55	2.50	2.67	2.54
Si	1.90	1.74	2.03	1.92
N	3.04	3.07	3.08	3.07
O	3.44	3.50	3.21	3.61
F	3.98	4.10	4.42	4.19
Cl	3.16	2.83	3.54	2.87

2.2 Phosphorus–Group 14 Compounds as P-donor Ligands

2.2.1 *Carbon*

Tertiary phosphines (PR_3) are, by a large margin, the commonest of the P-donor ligands and, as such, are constantly referred to throughout this article. Their bonding is discussed in detail in Section 3 and their structural aspects in Section 4. Since this section is primarily describing electronegativity effects, it is appropriate to include here the effect of electron-withdrawing substituents on organo groups, which effectively increases electronegativity. The effect of using perfluoroalkyl substituents is to increase the π acidity of the phosphine; $P(CF_3)_3$ is comparable to CO in π acceptor properties. Although these compounds were prepared in the 1960s,[13] the preparative difficulties restricted their use. Improved preparative procedures have resulted in a renaissance in perfluoroalkylphosphine coordination chemistry; examples include $(CF_3)_2PCF_2CF_2P(CF_3)_2$ and $(CF_3)_2P(CH_2)_nP(CF_3)_2$ ($n = 2, 3$), prepared by Cavell and coworkers,[14] and $(C_2F_5)_2PCH_2CH_2P(C_2F_5)_2$, prepared by Roddick and Ernst.[15] The analysis of the CO stretching frequencies of the nickel $[(CF_3)_2PCX_2CX_2P(CF_3)_2Ni(CO)_2]$[13] and molybdenum $[(CF_3)_2PCX_2CX_2P(CF_3)_2Mo(CO)_2]$[14] complexes (X = H, F) clearly indicates that these bidentate fluorine-containing ligands are strong π acceptors. Brookhart and coworkers[16] noted that the CO stretching frequencies of $[\{(C_2F_5)_2PCH_2CH_2P(C_2F_5)_2\}Fe(CO)_3]$ are substantially higher than those of the dppe analog $[(Ph_2PCH_2CH_2PPh_2)Fe(CO)_3]$ and comparable to those of $[(PF_3)_2Fe(CO)_3]$.

2.2.2 *Silicon*

Silylphosphines, $(R_3Si)_3P$, are well known. On the basis of electronegativity (Table 1) they are weaker π acids than organophosphines. With the isolation of $R_2Si{=}PR'$ compounds,[17,18] an increased variety of structures is available. Six-membered silicon–phosphorus heterocycles (**1**) have been proposed as ligands for catalyst candidates, owing to the steric accessibility of the transition metal.

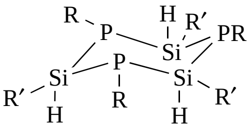

(**1**) R′ = Mes*; R = Cy

It has been shown by Schumann and Benda[19] that, while molybdenum coordinated to all three phosphorus sites, chromium used only two. Driess and coworkers[20] characterized the ligand (**1**; R = Cy, R′ = Mes), and its $M(CO)_3$ complexes (M = Cr, Mo).

2.3 Phosphorus–Group 15 Compounds as P-donor Ligands

2.3.1 Nitrogen

Aminophosphines, $P(NR_2)_3$, are well known and form a part of a wide variety of structural types including heterocycles and P–N cage compounds. In terms of π acidity, aminophosphines (other substituent effects being equal) lie between organophosphines (PR_3) and the phosphites ($P(OR)_3$).

Of the aminophosphines, tris(dimethylamino)phosphine is the most widely used. It has the feature of combining three hard nitrogen and the soft phosphorus sites, thus being potentially an eight-electron donor ligand. In complexes such as $[M(CO)_5P(NMe_2)_3]$, it is a two-electron P-donor ligand.[21]

The cage ligand $P(N(Me)CH_2)_3CMe$ is often studied in relation to the phosphite and carbocyclic analogs.[22] Cyclic amines such as (**2**), potentially a six-electron pair donor,[23] are available but are not often used as ligands.

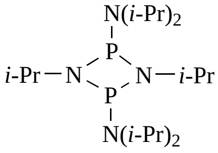

(**2**)

2.4 Phosphorus–Group 16 Compounds as P-donor Ligands

2.4.1 Oxygen

Of the P-donor ligands the triorganophosphites $P(OR)_3$, together with the phosphonites $R'P(OR)_2$ and phosphinites R'_2POR, are second only to the organophosphines in number. They are often contrasted with the organophosphines in ligating properties because of their increased π acidity, together with their ready availability. Their steric requirements are less than those of the analogous phosphines; for example, $P(OMe)_3$ and PMe_3 have cone angles of 107° and 115° respectively (see Section 3.1.3). The diphenylphosphinic methyl, ethyl, and phenyl esters have cone angles of 132°, 133°, and 139°, respectively, showing the lowering of cone angle by oxygen insertion; compare the cone angles of the corresponding phosphines: Ph_2PMe 132°, Ph_2PEt 140°, and Ph_3P 145°.

A stereoelectronic effect shown particularly by phosphites is the so-called α-effect. This is the enhanced nucleophilicity of phosphorus (or other nucleophilic center) when the adjacent atom has free lone pairs of electrons. Steric constraints such as ring systems can reduce the α-effect;[24,25] (**3**) is a weaker nucleophile than (**4**).

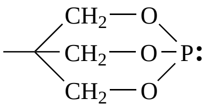

(**3**)

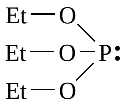

(**4**)

The biphosphite ligands, (**5**) and (**6**), react with $[(cod)_2Ni]$ to form nickel complexes of type (**7**). Nickel phosphite complexes are catalysts in the hydrocyanation of butadiene; complex (**7**) is more robust than the monodentate phosphite analogs.[26,27]

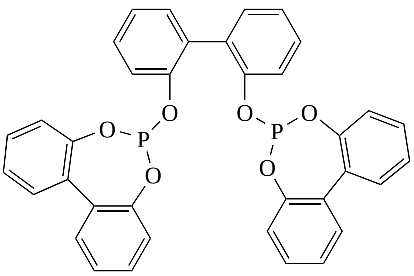

(**5**)

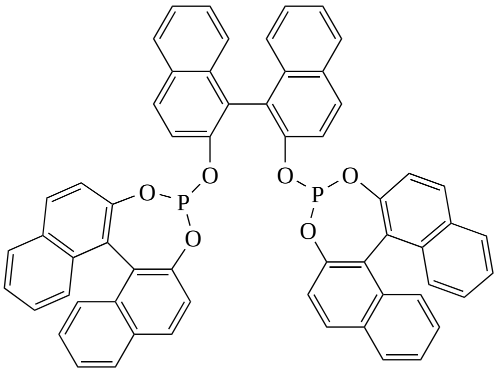

(**6**)

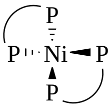

(**7**)

The reactions of phosphite esters with transition metal centers are usually unexceptional, but in some cases an oxidative cleavage of one of the O–C bonds is observed (see, for example, equation 2).

$$L_nMX + P(OMe)_3 \longrightarrow [L_{n-1}M(X)P(OMe)_3] \longrightarrow [L_{n-1}MP(O)(OMe)_2] + MeX \qquad (2)$$

These Arbuzov-like reactions (*see Arbuzov Rearrangement*) of phosphite ester transition metal complexes have been reviewed by Brill and Landon.[28]

2.5 Phosphorus–Group 17 Compounds as P-donor Ligands

2.5.1 Fluorine

PF_3 is the strongest of the P-donor π acids and its ability to replace carbon monoxide in a zerovalent transition metal complex was realized in the 1940s by Chatt.[29] However, Wilkinson[30] was the first to isolate a homoleptic PF_3 complex, viz. $[Ni(PF_3)_4]$ (*see Homoleptic Compound*), which turned out to be more thermally stable than $[Ni(CO)_4]$; subsequent research into the PF_3 complexes of transition metals was carried out by Nixon.[31] Bidentate ligands with two PF_2 moieties have been prepared; an example is $F_2P(1,2\text{-cyclo-}C_6H_{10})PF_2$.[32] The volatility of the homoleptic PF_3 transition metal species together with their relative stability has led to their use in MOCVD processes; $[Pt(PF_3)_4]$, for instance, has been used to deposit platinum films.[33]

2.5.2 The Remaining Halogens

Chlorine, bromine, and iodine are considered here together because of their relative rarity in P-donor ligands. A selection of homoleptic PX_3 complexes is given in Table 2. Edwards and Fawcett,[34] in their analysis of the vibrational spectra of $[Ni(PX_3)_4]$ (X = F, Cl, Br, and Me), show that the force constant k_R(P–X) decreases as the stability of the complex decreases (Table 3). This reflects the fall in electronegativity down the group.

Table 2 Mononuclear homoleptic transition metal PX_3 complexes (X = F, Cl, Br, or I)

Ligand	Complex
PF_3	$Cr(PF_3)_6$[35]
	$Fe(PF_3)_5$[35]
	$Ni(PF_3)_4$[30,35]
	$Mo(PF_3)_6$[36]
	$Ru(PF_3)_5$[37]
	$Pd(PF_3)_4$[35]
	$W(PF_3)_6$[38]
	$Os(PF_3)_5$[38]
	$Pt(PF_3)_4$[39]
	$U(PF_3)_6$[40]
PCl_3	$[Ni(PCl_3)_4]$[30,41]
PBr_3	$[Ni(PBr_3)_4]$[30,42]
PI_3	$[Ni(PI_3)_4]$[43]

Table 3 Nickel–phosphorus stretching force constants for $[Ni(PX_3)_4]$ complexes[34]

Compound	k_R (10^{-8} N Å $^{-1}$)
$[Ni(PF_3)_4]$	3.45
$[Ni(PCl_3)_4]$	1.67
$[Ni(PMe_3)_4]$	1.62
$[Ni(PBr_3)_4]$	1.27

3 P-DONOR–METAL BONDING

P-donor ligands usually form phosphorus–metal bonds with a main group or transition metal that are essentially covalent and in which the phosphorus is the lone pair donor. Despite the vast number of complexes prepared, often with elaborate architecture, the nature of the phosphorus–metal bond remains elusive and controversial, in particular, for transition metals. The simple statement of the bond as a neutral donor–acceptor complex has been elaborated by identifying the many contributing factors. We will discuss the steric factor and the electronic component of the P–M bond separately. The separation of the electronic component into σ and π factors is a formal exercise, the reality being *Synergic Bonding*, wherein these electronic factors are mutually dependent.

3.1 The Influence of Basicity on σ-Bonding

The measure of basicity of phosphine ligands most widely quoted in the literature is pK_a (aqueous), which is a measure of Brønsted basicity or proton affinity. A selection of pK_a values for various phosphines is given in Table 4. Angelici and coworkers[44] have established a method for determining proton affinities from enthalpies of protonation using the extremely powerful acid CF_3SO_3H. The enthalpy values (ΔH_{HP}) and pK_a values are related by the empirical equation (3):

$$\Delta H_{HP} = 1.82\ pK_a + 16.3\ (\text{kcal mol}^{-1}) \qquad (3)$$

They extended the method[52] to obtain values for bisphosphines for the first and second equilibrium constants (Table 5).

Reliable pK_a values are not often available, although reasonable estimates (±1 unit) can be calculated. Kabachnik and Mastryukova[53] showed that the Hammett equation is applicable to organophosphorus acids, deriving σ^{ϕ} substituent constants for substituents on phosphorus. These σ^{ϕ} are claimed[54] to be superior to Hammett/Taft parameters.[55]

The basicity of phosphines is affected by the bulk of the substituents. Increasing bulk increases the R–P–R angle, which in turn increases the p character of the lone pair. The highest reported pK_a is that of tris(*t*-butyl)phosphine, 11.4. In general, alkylphosphines are stronger bases than arylphosphines. However, in the case

Table 4 pK_a and ΔH_{HP} values for tertiary phosphines[a]

Tertiary phosphine	pK_a	$-\Delta H_{HP}$ (kcal mol^{-1})[45]
$P(t\text{-}Bu)_3$	11.40[46]	36.6
$P\{2,4,6\text{-}(MeO)_3C_6H_2\}_3$	$<$11.2[47]	–
$P\{2,6\text{-}(MeO)_2C_6H_3\}_3$	$\approx$10.7[47]	–
PCy_3	9.65[46,48]	33.2
PEt_3	8.69[48]	33.7
PMe_3	8.65[48]	31.6
$P(4\text{-}Me_2NC_6H_4)_3$	8.65[48]	–
$P(n\text{-}Pr)_3$	8.64[48]	–
Me_2PEt	8.62[48]	–
Et_2PMe	8.62[48]	–
$P(n\text{-}Bu)_3$	8.43[48]	–
$P(n\text{-}C_5H_{11})_3$	8.33[48]	–
$P(\{CH_2CH_2O(n\text{-}Bu)\}_3$	8.03[48]	–
$P(i\text{-}Bu)_3$	7.97[48]	–
$Cy_2PCH_2CH_2CN$	7.13[48]	–
$PhP\{2,6\text{-}(MeO)_2C_6H_3\}_2$	$\approx$7.0[47]	–
$P(CH_2CH_2Ph)_3$	6.60[48]	–
$(n\text{-}Bu)_2PCH_2CH_2CN$	6.49[48]	–
Me_2PPh	6.49[48]	28.4
$Me_2PCH_2CH_2CN$	6.35[48]	–
$(n\text{-}C_8H_{17})_2PCH_2CH_2CN$	6.27[48]	–
Et_2PPh	6.25[48]	–
$4\text{-}Me_2NC_6H_4PEt_2$	5.08[49]	–
Ph_2PMe	4.59[50]	24.7
$P(4\text{-}MeOC_6H_4)_3$	4.57[46] 3.15[49]	24.1
$P(4\text{-}MeC_6H_4)_3$	3.84[46]	23.2
$4\text{-}MeOC_6H_4PEt_2$	3.88[51]	–
$(CNCH_2CH_2)_2PEt$	3.80[48]	–
$(CNCH_2CH_2)_2PMe$	3.61[48]	–
$Ph_2P\{2,6\text{-}(MeO)_2C_6H_3\}$	3.5[47]	–
$(PhCH_2CH_2)_2PCH_2CH_2CN$	3.43[48]	–
$P(3\text{-}MeC_6H_4)_3$	3.30[46]	–
$4\text{-}FC_6H_4PEt_2$	3.02[51]	–
$PhP(CH_2CH_2CN)_2$	3.20[48]	–
$4\text{-}Me_2NC_6H_4PPh_2$	2.95[49]	–
$(4\text{-}ClC_6H_4)_3P$	2.86[49]	–
$4\text{-}ClC_6H_4PEt_2$	2.79[51]	–
PPh_3	2.73[46,48] (2.30)[49]	21.2
$4\text{-}BrC_6H_4PEt_2$	2.70[51]	–
$Ph_2P(n\text{-}Pr)$	2.64[51]	–
Ph_2PEt	2.62[51]	–
$(4\text{-}ClC_6H_4)_2P(n\text{-}Pr)$	2.59[51]	–
$4\text{-}MeOC_6H_4PPh_2$	2.58[49]	–
$4\text{-}ClC_6H_4PPh_2$	2.18[49]	–
$4\text{-}BrC_6H_4PPh_2$	2.09[49]	–
$(4\text{-}FC_6H_4)_3P$	1.97[46]	19.6
$P(CH_2CH_2CN)_3$	1.37[48]	–
$P(4\text{-}ClC_6H_4)_3$	1.03[46]	17.9

[a] The methodology of the various workers varied so the interested reader should refer to the original paper for experimental details.

of tris(2,4,6-trimethyoxyphenyl)phosphine, where electron-donating OMe groups reinforce the effect of the bulk of the substituted aryl rings, a pK_a of 11.2 has been recorded.[56]

It is often stated that the stability of the metal–phosphorus σ bond decreases in the series $P(t\text{-}Bu)_3 > P(OR)_3 > PR_3 \sim PPh_3 > PH_3 > PF_3 > P(OPh)_3$,[57] on the basis of, for example, ligand-substitution experiments (equation 4):[58]

$$[(RNH_2)W(CO)_5] + PR_3 \longrightarrow [(R_3P)W(CO)_5] + RNH_2 \qquad (4)$$

The rate of substitution of a given amine has been found to reflect the phosphine basicity: $PBu_3 \sim PCy_3 > P(OCH_2)_3CEt > P(SCH_2)_3CMe > P(OBu)_3 > PPh_3 > P(OPh)_3$.

Questions have been raised concerning the relevance of pK_a values, based on the hard acid H^+ interactions, to bonding of the soft acids, that is, low-valent transition metals. The large electric field created by a proton is not generated in the case of, for example, a zerovalent transition metal carbonyl. These deficiencies have subsequently generated interest in gas-phase basicities as a measure of electron availability (Section 3.1.1).

3.1.1 *Basicities of Phosphines in the Gas Phase*

The availability of the electron pair in the isolated ligand can be directly measured by photoelectron spectroscopy. The comparative ionization potentials show a reverse of the proton affinities in aqueous systems. For example, the gas-phase basicity of PPh_3 (lower ionization energy) is greater than that of PMe_3;[45] a selection of values is given in Table 6. These differences between solution based gas-phase basicities are ascribed to solvation effects.

Some recent quantum mechanical calculations[63] show that all P-donor ligands, PX_3, are good σ donors, including PF_3. These calculations estimate that the σ donor contribution to the proton affinity is only 10% larger in PMe_3 than in PF_3. Thus, the controversy about the significance of phosphine basicities is far from settled.

3.1.2 *π-Bonding in Phosphorus–Transition Metal Complexes*

An empirical π acid series may be compiled[64] from experimental data, mainly spectroscopic, and P-donor ligands are notable members covering a wide range. The π acid series that emerges is: $NO > CO \sim RNC \sim PF_3 > PCl_3 > PCl_2(OR) > PCl_2R > PBr_2R > PCl(OR)_2 > PClR_2 > P(OR)_3 > PR_3 \sim SR_2 > RCN >$ *o*-phenanthroline $> RNH_2 \sim R_2O$.

The explanation of the transition metal carbonyl bonding in terms of π *Back Bonding* led to its application to phosphorus–transition metal bonding, notably by Chatt.[65] Pidcock has outlined the early development of Chatt's theories.[66] The symmetry requirements for π back bonding between transition metals and phosphorus d orbitals appear to be met. The d orbitals of a transition metal in an octahedral field are split into bonding e_g orbitals and nonbonding t_{2g} orbitals. The e_g orbitals form σ-bonds with the six ligands, leaving the nonbonding t_{2g} orbitals directed between the six metal–ligand bonds. The σ-bond is formally between a transition metal

Table 5 ΔH_{HP1}, ΔH_{HP2}, and pK_{a1}, pK_{a2} values for bidentate phosphines[52]

Phosphine	$-\Delta H_{HP1}$ (kcal mol^{-1})	pK_{a1}	$-\Delta H_{HP2}$ (kcal mol^{-1})	pK_{a2}
$Ph_2PCH_2PPh_2$	22.0	3.81	14.9	−2.73
$Ph_2P(CH_2)_2PPh_2$	22.8	3.86	20.2	0.99
$Ph_2P(CH_2)_3PPh_2$	23.4	4.50	22.4	2.53
$Ph_2P(CH_2)_4PPh_2$	24.6	4.72	23.8	4.28
$Ph_2P(CH_2)_5PPh_2$	24.8	4.84	24.5	4.67
$Ph_2P(CH_2)_6PPh_2$	25.2	5.05	24.9	4.89
cis-$Ph_2P(CH{=}CH)PPh_2$	19.9	2.27	10.0	–
trans-$Ph_2P(CH{=}CH)PPh_2$	21.7	2.74	12.7	–
$Ph_2P(1,2\text{-}C_6H_4)PPh_2$	21.3	2.91	10.7	–
$Ph_2P(CH_2)_2AsPh_2$	23.2	3.96	8.2	–
$Me_2PCH_2PMe_2$	31.0	8.24	25.8	
$Et_2P(CH_2)_2PEt_2$	31.3	8.41		5.04

Table 6 Gas-phase ionization energies of phosphines

Compound	Ionization energy (eV)
$P(NMe_2)_3$	7.58[59]
$P(t\text{-Bu})_3$	7.70[60]
PPh_3	7.80[45]
$P\{S(i\text{-Pr})_3\}$	7.91[59]
PPh_2Me	8.28[45]
$PPhMe_2$	8.32[45]
$P(SMe)_3$	8.33[59]
$PH(t\text{-Bu})_2$	8.35[60]
$PCl(t\text{-Bu})_2$	8.44[60]
$PF(t\text{-Bu})_2$	8.50[60]
PMe_3	8.63[60]
	8.62[45]
	8.60[61]
$P(NMeCH_2)_3CMe$	9.03[59]
$PHMe_2$	9.08[60]
	9.10[61]
$PClMe_2$	9.19[60]
$P(OMe)_3$	9.22[59]
$PH_2(t\text{-Bu})$	9.32[60]
$PCl_2(t\text{-Bu})$	9.32[60]
$PFMe_2$	9.37[60]
$PF_2(t\text{-Bu})$	9.63[60]
$P(SCH_2)_3CMe$	9.65[59]
PH_2Me	9.70[61]
	9.72[60]
PCl_2Me	9.83[60]
$P(OCH_2)_3CH$	9.9[59]
$P(OCH_2)CMe$	9.95[59]
PF_2Me	10.34[60]
PH_3	10.58[60]
PCl_3	10.59[61]
	10.7[60]
PF_2H	11.0[61,62]
PF_2I	11.2[62]
PF_2Br	11.8[62]
$PF_2(NCS)$	11.9[62]
$PF_2(CN)$	11.9[62]
$PF_2(NCO)$	12.2[62]
PF_3	12.23(±0.02)[62]
	12.3[60]
PF_2Cl	12.8[62]

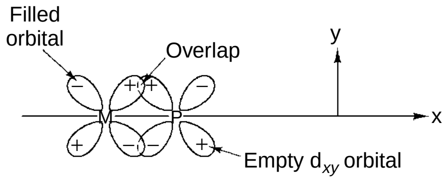

Figure 1 Back bonding to an empty $3d_{xy}$ phosphorus orbital from a filled metal orbital of complementary symmetry. This is repeated in the *yz* plane

d^2sp^3 hybrid orbital and an sp^3 hybrid phosphorus orbital (*see* ***Coordination & Organometallic Chemistry: Principles***). Thus the π back bonding between the empty d orbitals of phosphorus and the filled t_{2g} orbitals of the transition metal (Figure 1) is intuitively appealing and has been widely used in descriptive inorganic chemistry. However, it was pointed out[67,68] that the phosphorus 3d orbitals are too diffuse and also energetically unfavorable to participate in metal–phosphorus bonding. Quantum mechanical calculations[69] have shown that, for the frontier orbitals of PH_3, PF_3, and PMe_3, the *LUMO* has most 3p character:

PX_3	%3p	%3d
PH_3	36	23
PF_3	44	23
PMe_3	14	10

Marynick and coworkers[70,71] made the more extreme assumption, finding no need to include 3d orbitals in the phosphorus basis set. Their results for zerovalent Cr–PH_3 bonding in $[Cr(NH_3)_5PH_3]$ are shown in Figure 2. They suggest that the empty P–X σ^* antibonding orbital is the π acceptor for metal back bonding electronic charge.

The previously held view was that the greater π acidity of PF_3 and PH_3 (see the π acidity series described above) was due to an electronegativity effect, thus lowering the energy

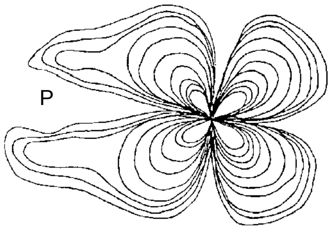

Figure 2 The electron density plot of one of the two π donating orbitals in $Cr(NH_3)_5PH_3$, omitting the phosphorus d orbitals from the calculations. (Reprinted with permission from Ref. 70. © 1984 American Chemical Society)

of the 3d phosphorus orbitals and making them accessible to the metal back bonding charge. Marynick's radical alternative paradigm is that the highly polar P–F bonds have low lying antibonding σ^* orbitals of suitable symmetry for overlap with the metal d orbitals and, further, that they would be superior acceptors than the higher energy P–H σ^* orbitals. In other words, the greater is the polarity $P \rightarrow E$ of the σ-bond because of electronegativity differences, the greater the σ^* 'reverse polarity' to phosphorus (increased π acidity), resulting in increased σ^*–metal d–π overlap. Giordan and coworkers[72] measured the attachment energy for the formation of negative ions by electron transmission spectroscopy, that is, a direct estimation of the phosphine LUMO. They found that the orbital energies of PR_3 are sensitive to substitution. If the LUMO were 3d in character, or predominately 3d, then it would be insensitive, or relatively so, to substitution effects.

Indeed, Orpen and Connelly,[73] in their analysis of bond length data derived from X-ray crystallography (Table 7), support the σ^* theory but in modified form, reintroducing a 3d orbital contribution from phosphorus. This revisionist view, maintaining a role for the phosphorus 3d orbitals, albeit diminished, has received support from quantum mechanics calculations of Pacchioni and Bagus.[63] They find that the phosphorus d orbital basis functions are essential for an accurate description of the length and strength of the phosphorus–metal bond. The phosphorus d orbital role is that of polarization functions. The vacant antibonding P–X orbitals of PX_3 are π acids even without d orbital mixing, although the π acidity is enhanced by the inclusion of the d orbital equations. In the case of alkylphosphines, the π acidity is appreciable in the presence of the phosphorus 3d orbitals, but modest if these are omitted.

Various authors have proposed schemes that claim to distinguish between phosphorus σ donor and π acceptor contributions to the transition metal–phosphorus bond. Alyea and Song[74] have suggested ^{95}Mo NMR analysis of $Mo(CO)_{6-n}(PR_3)_n$ complexes, together with Kabachnik $\Sigma\sigma^{\phi}$ parameters (see Section 3.1) as a probe of the nature of phosphorus(III) ligands. A plot of $\Sigma\sigma^{\phi}$ against $\delta(^{95}Mo)$ affords a quantitative differentiation of the σ and π bonding effects (Figure 3).

Giering and coworkers[50,75] have combined electrochemical and spectroscopic analyses to develop a method, the quantitative analysis of ligand effects (QALE), for the separation of P-donor ligands into pure σ donors and those with a significant degree of phosphorus π acceptor character (Figure 4).

3.1.3 *The Influence of Steric Factors*

Tolman[76,77] introduced the concept of the cone angle in 1970 to separate and quantify steric and electronic factors in the reactions of phosphines with transition metals. The original measurements were made from simple physical models, and this approach has been extended to mathematical and computer modeling. Other workers have used X-ray diffraction data to observe and measure cone angles directly. These various approaches are outlined below.

Table 7 Metal–phosphorus and phosphorus–substituent bond lengths[73]

Complex	Charge	Counterion	M–P^a (Å)	P–X^a (Å)
$[Fe(CO)\{P(OMe)_3\}_2(\eta^4\text{-}C_4Ph_4)]$	0	–	2.146(1)	1.598(3)
	+1	BF_4	2.262(2)	1.579(6)
$[\{Rh(CO)(PPh_3)\}_2(\eta^5, \eta'^5\text{-fulvalene})]$	0	–	2.255(2)	1.844(5)
	+2	PF_6	2.322(4)	1.813(15)
$[\{Rh(CO)(PPh_3)\}_2\{\mu\text{-}N\text{-(tolyl)-}N,N\text{-(tolyl)}\}_2]$	0	–	2.290(5)	1.855(12)
	+1	PF_6	2.335(1)	1.825(5)
$[Co(PEt_3)_2(\eta\text{-}C_5H_5)]$	0	–	2.218(1)	1.846(3)
	+1	BF_4	2.230(1)	1.829(3)
$[Fe(\eta^3\text{-}C_8H_{13})\{P(OMe)_3\}_3]$	0	–	2.138(1)	1.621(1)
	+1	BF_4	2.153(2)	1.600(2)
$[Re_2Cl_4(\mu\text{-}Cl)_2(Ph_2PCH_2PPh_2)_2]$	0	–	2.475(2)	1.828(8)[Ph] 1.843(8)[CH_2]
	+1	H_2PO_4/H_3PO_4	2.524(3)	1.82(1) [Ph] 1.84(1) [CH_2]

^{a}M–P and P–X distances are mean values.

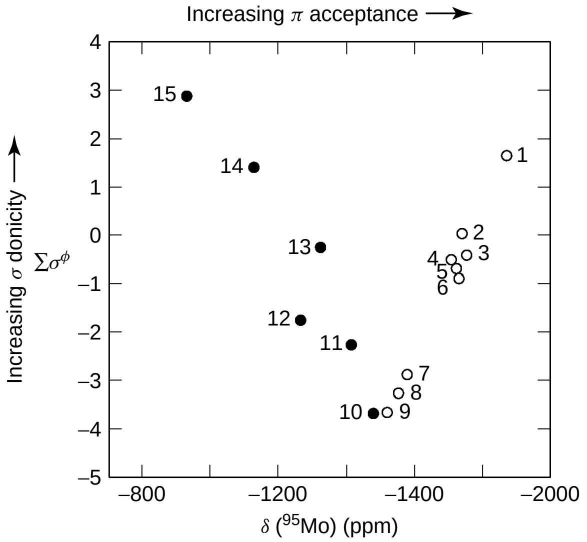

Figure 3 A plot of $\delta(^{95}\mathrm{Mo})$ versus Kabachniyk's parameter $\Sigma\sigma^{\phi}$ for the phosphorus substituents of the ligands, L, in [*fac*-$\mathrm{Mo(CO)_3L_3}$]. L: 1, PF_3; 2, $P(OCH_2CH_2Cl)_3$; 3, $P(OMe)_3$; 4, PH_2Ph; 5, $P(OEt)_3$; 6, $P(O\text{-}i\text{-}Pr)_3$; 7, PMe_3; 8, PEt_3; 9, PBu_3; 10, $P(NMe_2)_3$; 11, $PEtPh_2$; 12, PPh_3; 13, $PClPh_2$; 14, PCl_2Ph; 15, PCl_3. (Reprinted with permission from Ref. 74. © 1992 American Chemical Society)

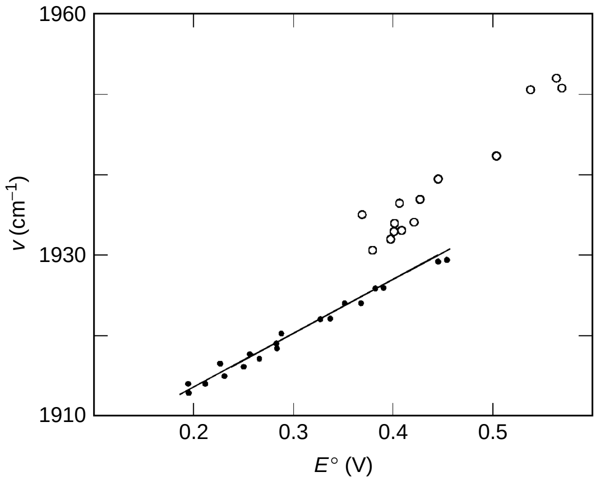

Figure 4 A plot of the terminal CO stretching frequencies of CpFe(CO)LCOMe versus the reduction potential. The open circles are σ donor ligands and the solid circles σ donor/π acceptor ligands and are clearly in different populations. (Reprinted with permission from Ref. 75. © 1989 American Chemical Society)

Tolman's Cone Angle. The model Tolman used[77] to define the cone angle is shown in Figure 5. In order to make the cone angles comparable, he chose an arbitrary value for d, the M–P bond length, of 2.28 Å. The phosphine depicted in Figure 5(a), PR_3, is a symmetrical model. In order to accommodate unsymmetrical ligands, the model was developed to include a measure of each substituent's contribution to the steric bulk, its half cone angle, $\theta_i/2$ (Figure 5b). The cone angle θ of a chiral ligand is given by two-thirds of the half cone angles, that is, $\theta = \frac{2}{3}\sum \phi_i/2$. Thus, if the cone angles for PR'_3, PR''_3 and PR'''_3 are known, then that of $PR'R''R'''$ may be calculated. In the cases of complex or long chain substituents, the conformer chosen is that which gives the minimum cone angle.

Tolman found a slight increase in cone angle with the increase in chain length with the other features unchanged. Thus, for the bidentate phosphine sequence $Ph_2P(CH_2)_nPPh_2$, cone angles for $n = 1$, 2, and 3 were 121°, 125°, and 127°, respectively; when the chain length was held constant, the variation with substituent for the bidentate sequence $R_2PCH_2PR_2$ was 107°, 115°, 125°, and 142° for R = Me, Et, Ph, and Cy, respectively,

Mathematical Modeling of Cone Angles. In what amounts to a pencil and paper conversion of Tolman's molecular models, Imyanitov[78] devised a technique of estimating cone angles from atomic radii, van der Waals radii, and molecular geometry. He combined the mathematical formula for θ, above, with graphical methods (Figure 6a) that are applicable to any ligand. In the case of complex substituents, a more sophisticated geometrical construction (Figure 6b) is necessary to convert the substituent into a sphere equivalent to R in Figure 8(a). In choosing a M–P distance of 2.23 Å, Imyanitov's cone angles are systematically 5° higher than Tolman's,[77] which are based on d(M–P) of 2.28 Å.

In their study of lanthanide and actinide complexes, Bagnall and Zing-Fu[79,80] investigated the steric demands of a wide variety of ligands. They defined first- and second-order steric crowding. First-order steric crowding is a measure of the steric demands of the coordinating atom. Second-order steric crowding is due to the substituents of the coordinating atom. In the case of a single coordinating atom, such as a chloride anion, there is no second-order crowding. They quantified these effects by two terms: the *cone angle factor* (CAF), which is the solid angle of the cone, comprising the apical center and the coordinating atom or ligand divided by 4 (Figure 7a), and the *fan angle*, which describes the crowding in the plane and is the angle subtended by the atom or group in the various symmetry planes (Figure 7b). This is equivalent

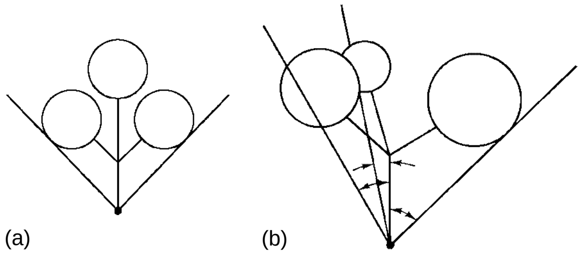

Figure 5 Tolman's cone angle: (a) simple symmetrical tertiary phosphine and (b) chiral phosphine

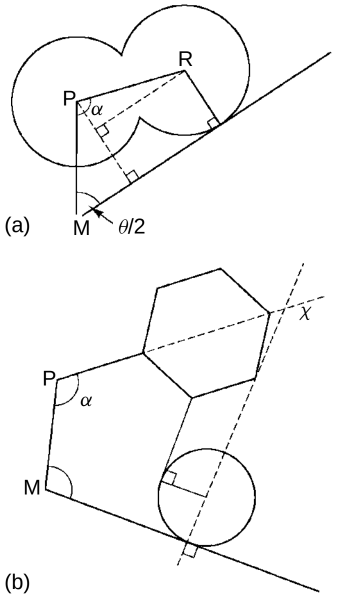

Figure 6 Imyanitov's methodology: (a) simple substituents and (b) complex substituents

to the *ligand profile* defined by Ferguson *et al.*,[81a] and to *ligand angular encumbrance* defined by Immirzi and Musco (Figure 8).[81b]

Mingos[82] applied the cone angle concept to metal clusters stabilized by P-donor ligands. This led him to define a *plane of coverage* for the ligand (Figure 9a). For the idealized ligand shown, this plane is a circle of diameter d. However, in actual systems, the projection would be coglike.[80,81] Further, since the significance of the ligand geometry is the cluster rather than the specific atom to which it is coordinated, Mingos defined a *cluster cone angle* δ (Figure 9b). This is similar to the cone angles of phosphine oxides described by Bagnall and Zing-Fu.[79] The M′–P bond length is by definition longer than the M–P distance. Since, for a given system, a cone angle is inversely proportional to the length of the metal–ligand bond, cluster cone angles are smaller than the corresponding ligand cone angles.

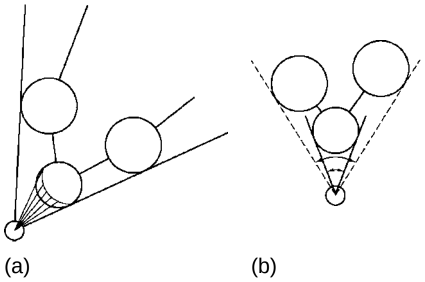

Figure 7 (a) First- and second-order cone angles and (b) fan angles. Irregularly shaped ligands have various fan angles in different planes

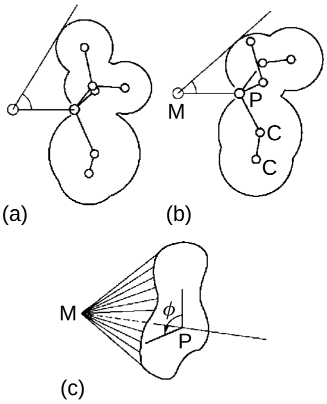

Figure 8 The geometry used by Immirzi and Musco[81b] to show the variations of the angular encumbrance of the orientation of, for example, PEt_3. In (a) and (b), the metal–ligand tangent angle is seen to vary with orientation and (c) shows the summation of all the tangents

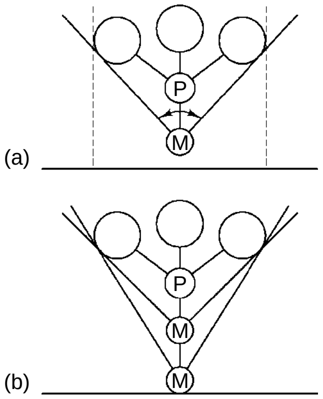

Figure 9 (a) Tolman's cone angle used in mononuclear complexes, indicating the 'plane of coverage' and (b) a diagram showing the parameters of the cluster cone angle

Cone Angles and Molecular Mechanics. The explosion in the availability of computer power in the last decades has made molecular mechanics calculations a common laboratory tool. P-donor ligands were investigated by Mosbo and coworkers,[83] who used semiempirical molecular orbital calculations (MINDO/3). They used the following bond lengths and angles: (P–H) 1.4 Å, (P–C) 1.8 Å, (C–C)alkyl 1.5 Å, (C–C)aryl 1.4 Å, (C–H) 1.1 Å, (R–P–R) 109.5°, (R–C–C)alkyl 109.5°, and (R–C–R)aryl 120°; all the low-energy conformations of the ligands were calculated. The energy minima of the conformers of H_2PR (R = Et, *i*-Pr, and 2-MeC_6H_4) were computed. The group used Tolman's M–P distance of 2.28 Å on the vector through P normal to the plane defined by the three points 1.00 Å from P to the substituent R. The rotation ϕ about the M–P axis through 360° in 1° increments generated the half cone angles $\theta/2$ of the outermost atoms. The g_rg_l conformer of H_2P–*i*-Pr is shown in

Figure 10. The weighted average of all conformations was the optimum value for the cone angle; these are listed in Table 8.

Cone Angles and X-ray Studies. The large and growing database of X-ray crystal structures has attracted several workers into systematizing steric effects by the direct observation of real systems.

Ferguson, Alyea, and coworkers,[81,84,85] in their studies of bulky phosphine ligands and their transition metal complexes, noted a limitation in Tolman's cone angle concept in the solid state. Essentially Tolman describes ligands as if they were solid cones, but Ferguson and coworkers noted the uneven shape given by the phosphine substituents and the gaps between them, which they describe as the 'depth of tooth' of the 'conic cog'. In their graphical analyses of the data they refer to 'ligand profiles'. These profiles are obtained by rotating the ligand about the axis of the M–P bond (ϕ is the angle of rotation), thus obtaining the half cone angle $\theta/2$ from the tangent to the maximum van der Waals radius through M (Figure 11).[81]

The ligand profile is the graph of the angle of rotation ϕ versus the half cone angle $\theta/2$; some of their measured cone angles, together with selected crystallographic data, are shown in Table 9. Ferguson defined the cone angle as the maximum value shown in the profile. Using this approach, the cone angle for a given ligand varies with the complex; for example, for tri(cyclohexyl)phosphine (Tolman 170°), Ferguson's group calculates a cone angle of 181° in $[Hg(NO_3)_2(PCy_3)]_2$ and 163° in $[PtI_2(PCy_3)_2]$.

Other workers noted the intermeshing of ligands in crystal structures and proposed various graphical representations. Oliver[86] suggested using circular coordinates (Figure 12) to show the intermeshing of PCy_3 ligands in $[Pt(C_3H_5)(PCy_3)_2]PF_6$. Cone angles for other phosphorus compounds are listed in Tables 10–12.

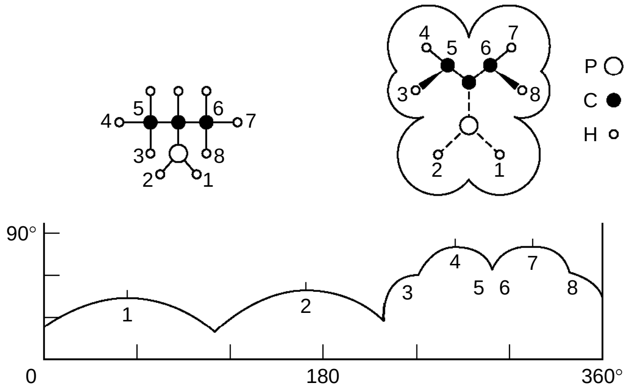

Figure 10 Ligand profile plot for the g_rg_l conformer of H_2P–*i*-Pr. The van der Waals contact surface is shown in the upper right figure and the atom numbering in the upper left figure. (Reprinted with permission from Ref. 83. © 1980 American Chemical Society)

Table 8 Weight-average cone angles from MINDO 3 optimized geometries[83]

Compound	MINDO calculated cone angles (°)
PH_3	91.2
PH_2Me	103.4
PH_2Et	108.0
PH_2(*i*-Pr)	111.6
PH_2(*t*-Bu)	116.4
PH_2Ph	106.3
PH_2(*o*-Tol)	110.2
$PHMe_2$	117.7
$PHEt_2$	126.8
PH(*i*-Pr)$_2$	135.3
PHMePh	117.5
PHEtPh	121.5
PMe_3	134.4
PEt_3	148.2
PMe_2Ph	139.3

3.2 The Effect of Soft and Hard Acids and Bases on the Transition Metal–Phosphorus Bond

The generalizations of the soft and hard acids and bases (SHAB) principle are extremely useful in rationalizing the facts of inorganic chemistry. However, they are guidelines rather than 'laws'. On the basis of SHAB theory, complex formation between hard Mn^{II} and soft R_3P would not be favored nor predicted. In fact, an extensive series of MnX_2L[92] and MnX_2L_2[93] (X = halogen, pseudohalogen; L = PR_3, R = organyl) complexes have been synthesized. Further, the

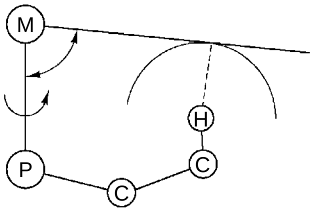

Figure 11 Details of the calculation of the maximum semicone angle, $\phi/2$. The point of contact of the cone generating vector M → X from the metal, with the van der Waals sphere of the hydrogen atom, is coplanar with the metal, phosphorus, and hydrogen atoms

Table 9 Cone angles obtained from crystallographic data[81,84,85]

Complex	Cone angle (°)	
	From X-ray data	Tolman's value from models
$[Cy_3PHg(SCN)_2]_n$	177	170
$[Cy_3PHg(NO_3)_2]_2$	181	170
(*t*-Bu)$_3$PHg(OAc)$_2$	187	182
$[(2\text{-}MeC_6H_4)_3PHg(Cl)ClO_4]_2$	198	194

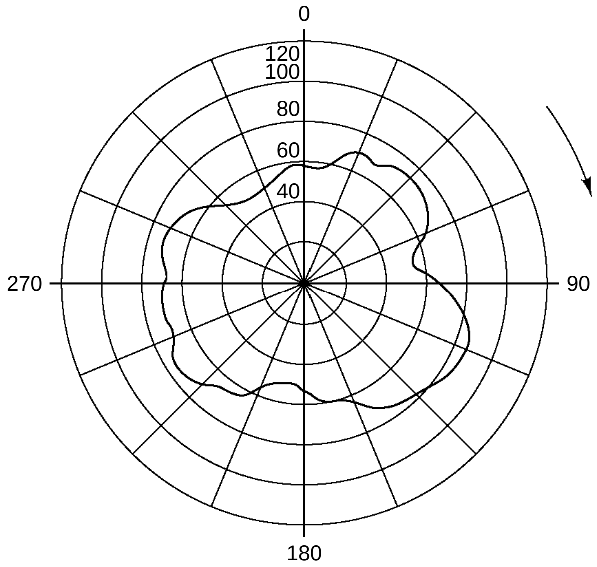

Figure 12 Oliver and Smith's[86] presentation of a ligand profile showing the variation of van der Waals contacts with the rotation (ϕ) about the M–P bond resulting in cone angle (θ) variations. (Reprinted with permission from Ref. 86. © 1978 American Chemical Society)

even harder Mn^{III} has also formed a phosphine complex, $MnI_3(PMe_3)_2$, with a trigonal bipyramidal structure.[94]

This is not to say that there are no SHAB problems of donor–acceptor incompatibility. Several groups have adopted the strategy of synthesizing ligands that have hard and soft moieties, such as (**8**). For example, Fryzuk and coworkers[95] use ligands with a hard center to anchor to the hard metal, in this case Zr^{IV} or Hf^{IV} enabling the phosphorus chelating moieties to form a stable complex (**9**).

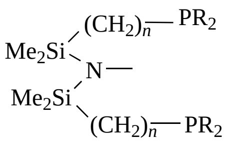

(**8**)

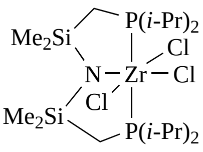

(**9**)

The deliberate mixing of hard and soft centers has been extended to macrocyclic systems (Part I, Section 4.6).

4 THE STRUCTURAL DIVERSITY OF P-DONOR LIGANDS

Within the format of this contribution, only a brief outline of the vast range of P-donor ligand architecture can be given. Most of the examples given are based upon P–C bonding, which reflects the historical development of the subject. Attention has already been drawn to the effect on π acidity of p-block substituents on phosphorus. It should also be noted that p-block elements may be introduced into a structure remote from phosphorus to provide a variation in ligand texture (hard

Table 10 Phosphine cone angles

Cone angle (°)	Phosphine (PR_3)
76 (87)[a]	PH_3[77,83]
82 (101)	$PhPH_2$[77,83]
87	$MePH_2$[83]
91	$EtPH_2$[83]
97	$(i\text{-}Pr)PH_2$[83]
99	$2\text{-}MeC_6H_4PH_2$[83]
100	Me_2PH[83]
102	PTA[b,87]
103	$t\text{-}BuPH_2$[83]
104	PF_3[77]
108	$PhP(H)Me$[83]
108	$P(CH_2CH_2)_3N$[77]
109	Et_2PH[83]
112	$PhP(H)Et$[83]
115 (118)	PMe_3[77,83]
120	$(i\text{-}Pr)_2PH$[83]
122 (123)	$PhPMe_2$[77,83]
122	$PhP(H)Et$[83]
124	PCl_3[77]
128	Ph_2PH[77]
128 (132)	PEt_3[77,83]
131	PBr_3[77]
132	$P(n\text{-}Bu)_3$[77]
132	$P(CH_2CH_2CN)_3$[77]
132 (139)	$P(n\text{-}Pr)_3$[77,88]
136	Ph_2PMe[77]
136	$PhPEt_2$[77]
137	$P(CF_3)_3$[77]
140	Ph_2PEt[77]
141 (143)	$Ph_2P(n\text{-}Bu)$[50,89]
143	$P(i\text{-}Bu)_3$[77]
145	PPh_3[77]
145	$(4\text{-}RC_6H_4)_3P$ (R = F, Cl, Me, OMe)
145	$(3\text{-}FC_6H_4)_3P$[77]
157	$P(NMe_2)_3$[77]
157	$PPh_2(t\text{-}Bu)$[77]
160 (165)	$P(CH_2Ph)_3$[77,88]
160	$P(s\text{-}Bu)_3$[77]
160	$P(i\text{-}Pr)_3$[77]
162	$PhPCy_2$[87]
164	$Ph_2P(i\text{-}Pr)$[50]
167	$(i\text{-}Pr)_2P(t\text{-}Bu)$[90]
170	PCy_3[77]
170	$PhP(t\text{-}Bu)_2$[77]
171	$Cy_2P(t\text{-}Bu)$[90]
180	$P(neopentyl)_3$[77]
182	$P(t\text{-}Bu)_3$[77]
184	$P(C_6F_5)_3$[77]
194	$(2\text{-}MeC_6H_4)_3P$[77]
212	$PMes_3$[77]

[a] The alternative value in brackets is from the second reference. [b] PTA = phosphatriazaadamantane.

Table 11 Phosphorous acid ester cone angles

Cone angle (°)	Phosphite ester $P(OR)_3$
107	$P(OMe)_3$[77]
109	$P(OEt)_3$[77]
110	$P(OCH_2CH_2Cl)_3$[77]
112	$P(O\text{-}n\text{-}Bu)_3$[88]
115	$P(OCH_2CCl_3)_3$[77]
128	$(3\text{-}MeC_6H_4O)_3P$[77]
128	$P(OPh)_3$[77]
130	$P(O\text{-}i\text{-}Pr)_3$[77]
135	$P(OCy)_3$[91]
140	$P(OC_{10}H_{20})_3$[a][90]
141	$(2\text{-}MeC_6H_4O)_3P$[77]
148	$\{2\text{-}(i\text{-}Pr)C_6H_4O\}_3P$[77]
152	$(2\text{-}PhC_6H_4O)_3P$[77]
172	$P(O\text{-}t\text{-}Bu)_3$[77]
190	$(2,5\text{-}Me_2C_6H_3O)_3P$[77]

[a] 1-Menthyl.

Table 12 Phosphonic acid ester cone angles

Cone angle (°)	Phosphonite ester $RP(OR')_2$
115	$PhP(OMe)_2$[77]
115	$EtP(OMe)_2$[77]
116	$PhP(OEt)_2$[77]
118	$PhP(O\text{-}n\text{-}Bu)_2$[88]
142	$PhP(OC_{10}H_{20})_2$[a][90]
209	$(i\text{-}Pr)P(OC_{10}H_{20})_2$[a][81b]

[a] 1-Menthyl.

and/or soft sites) in order to generate cooperative effects in catalytic systems.

4.1 Simple P-donor Ligands

The ‘simple’ R_3P phosphine is the workhorse of P-donor chemistry. The preparative aspects are dealt with elsewhere (*see* ***Phosphorus: Organophosphorus Chemistry***) and they have been reviewed extensively.[96–100]

New resources are constantly being found in the superficially simple phosphine–transition metal chemistry. For example, West and coworkers[101] reacted the phosphorus(V) compound Et_3PTe with $[Mn(CH_2Ph)(CO)_5]$, which resulted in the redox (*see Redox Properties & Processes*) insertion of Te into the Mn–C bond. The phosphorus was reduced to the phosphine ligand, forming the complex $[Mn(TeCH_2Ph)(CO)_3(PEt_3)_2]$. McAuliffe and coworkers[102] have developed a new synthetic approach to the synthesis of phosphine–transition metal complexes that also involves a redox reaction. For example, the reaction between cobalt powder and trimethyldiiodophosphorane affords a trimethylphosphine complex, $[Co(PMe_3)_2I_3]$.[102] The reaction is quite general and a number of metal powders have been used, such as Fe,[103] Ni,[103] Zn,[104] and Mn.[105,106b] The same reaction can even be carried out with gold powder, which is dissolved by Me_3PI_2 to give $(Me_3P)_2AuI_3$.[106,106c] The products are not always those anticipated; indeed, several unique or rare complexes have been prepared by this route. Trivinylphosphine $(CH_2{=}CH)_3P$ has for some time been excluded from most studies with tertiary phosphines, but has recently become readily accessible and employed for coordination chemistry.[106d]

The electron-rich ligand[107a] tris(tetrathiafulvalenyl)phosphine (**10**) (*see Electron Rich Compound*) is one of the more recently available phosphines with great potential in materials science.

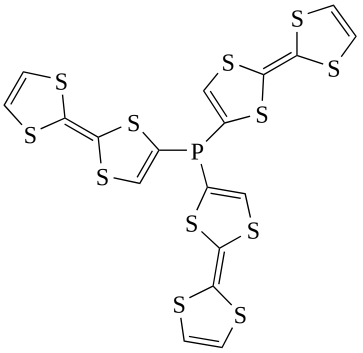

(**10**)

It is important to note that simple PR_3 ligands may also function as bridging units between two metal atoms with the P-atom becoming five coordinate as shown in Figure 13.[107b]

4.2 Bidentate P-donor Ligands

4.2.1 Methylene Bridged Bidentate P-donor Ligands

Bidentate (*see Bidentate Ligand*) methylene bridged bisphosphine ligands, $R_2P(CH_2)_nPR_2$ ($n = 1–16$), have ligating properties that characteristically depend on chain length. As with other P-donor ligands, of course, their behavior is also governed by the nature of R. Short chain ligands

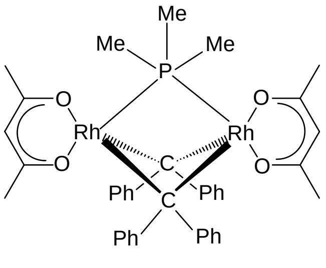

Figure 13 The PR_3 ligand functioning as bridging unit between two rhodium centers, with the P-atom becoming five coordinate[107b]

($n = 1$) have been excellently reviewed by Puddephatt[108] and Chaudret *et al.*[109] Because of ring strain, complexes such as (**11**) are formed rather than cyclic species (**12**).

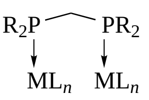

(**11**)

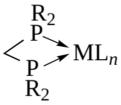

(**12**)

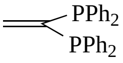

(**13**)

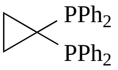

(**14**)

The bite angle and other properties can be varied by altering the substituents on the methylene bridge. Much interest has been shown in ligands such as (**13**) and (**14**). With chain lengths $n = 2$ or 3, the thermodynamically favored (the chelate effect) five- and six-membered rings are commonly formed [(**15**) and (**16**)]. Large *dinuclear* rings have also been isolated (**17**).

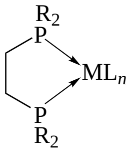

(**15**)

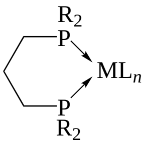

(**16**)

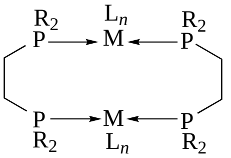

(**17**)

These dinuclear ring structures may be 'forced' by constraining the ligand; (**18**), for example, affords (**19**).[110]

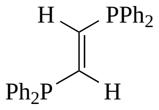

(**18**)

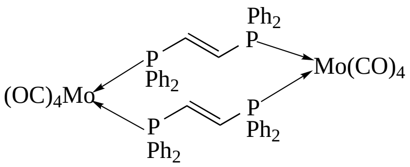

(**19**)

With long chain bis(phosphines) ($n = 4 - 16$), trans chelate rings become possible, although with the longest chains bridged dinuclear species would be expected.

4.2.2 Bidentate Phosphine Ligands with Ring Bridging

1,2-di(phosphino)benzenes (**20**) are the most widely used of this type of ligand, and many chiral ligands (see Section 4.3) are bidentate. Much interest has been shown in the phosphorus analog (**21**)[111] of 2,2′-bipyridyl and the mixed nitrogen/phosphorus ligand (**22**).[112]

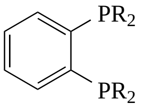

(**20**)

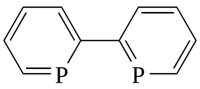

(**21**)

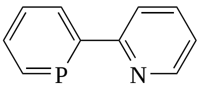

(**22**)

4.2.3 Polydentate P-donor Ligands

Increasing the number of ligating sites greatly increases the structural possibilities both of the ligand and of the complexes. Tridentate ligands may be either linear $R_2P(CH_2)_nP(R)(CH_2)_mPR_2$, or of the so-called tripod type (**23**) (*see Tripodal Ligand*).

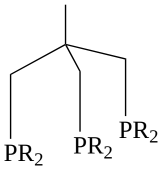

(**23**)

Metal catalysts containing tripod phosphine ligands have been reviewed.[113] The limiting value for molecular polydentate ligands in practice is a hexakisphosphine such as $(Et_2PCH_2CH_2)_2PCH_2CH_2P(CH_2CH_2PEt_2)_2$; such compounds usually complex with two metal centers. There is no barrier to more complex structures, however.

4.3 Chiral Phosphines

These compounds are important in asymmetric catalysis, in which a prochiral substrate is converted into a chiral product. There are basically three types of chiral phosphines. Firstly, there are phosphines of the type PRR′R″, where the chiral center is the phosphorus atom. Secondly, the substituent(s) or the molecule as a whole may be chiral. Finally, a coordinated phosphine complex may be chiral at the metal center.

4.3.1 Phosphines with Chiral Phosphorus Centers

Simple chiral phosphines have already been mentioned (Section 3.1.3) and the macrocycle enantiomers are discussed below (Section 4.6). Current research in this area is concentrated on bidentate chiral phosphines, such as the ligands (**24**)–(**27**). Although their transition metal complexes are normally used for stereospecific synthesis, Whitmire and coworkers[114] used the molybdenum complexes to resolve their racemic bisphosphines via flash chromatography. The phosphines were 'decomplexed' by reductive cleavage at low temperatures (−78 °C) using sodium naphthalenide (Scheme 1).

More complex chiral phosphines have also been prepared, for example, (**24**).[115a]

4.3.2 Phosphines with Chiral Substituents

Phosphines that owe their chirality to their substituents or to general molecular asymmetry include (*S*)-BINAP (**28**),[116,117]

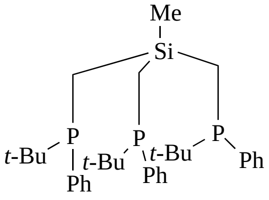

(**24**)

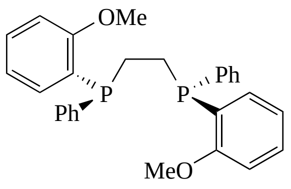

(**25**)

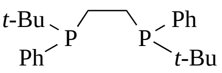

(**26**)

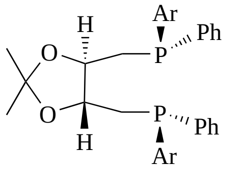

(**27**)

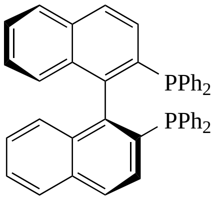

(**28**) (*S*)-BINAP

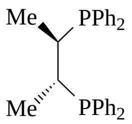

(**29**) (*R,R*)-CHIRAPHOS

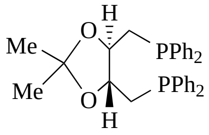

(**30**) (*R,R*)-DIOP

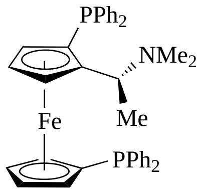

(**31**)

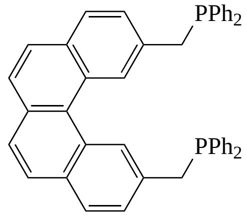

(**32**)

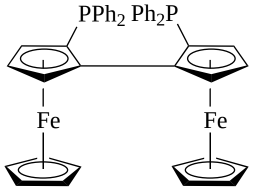

(**33**)

(*R*, *R*)-CHIRAPHOS (**29**),[118] (*R*, *R*)-DIOP (**30**),[119] (*S*, *R*)-BPPFA (**31**),[120] (**32**),[121] and (**33**).[122] Such compounds are much more numerous than those with a chiral phosphorus atom. This is because the synthetic methods are much simpler, the readily obtainable R_2P^- (usually Ph_2P^-) being grafted into an optically active substrate. The pioneering work was summarized by Peterson *et al.*[123] Some more recent examples of enantiospecific reactions catalyzed by chiral phosphines are given in equations (5–7),[124–126] with the enantiomeric excess (ee) for the reaction. In equation (7), (**36**) = NEt_4 $[Ru_2\{(R)\text{-BINAP}\}_2Cl_4]$.

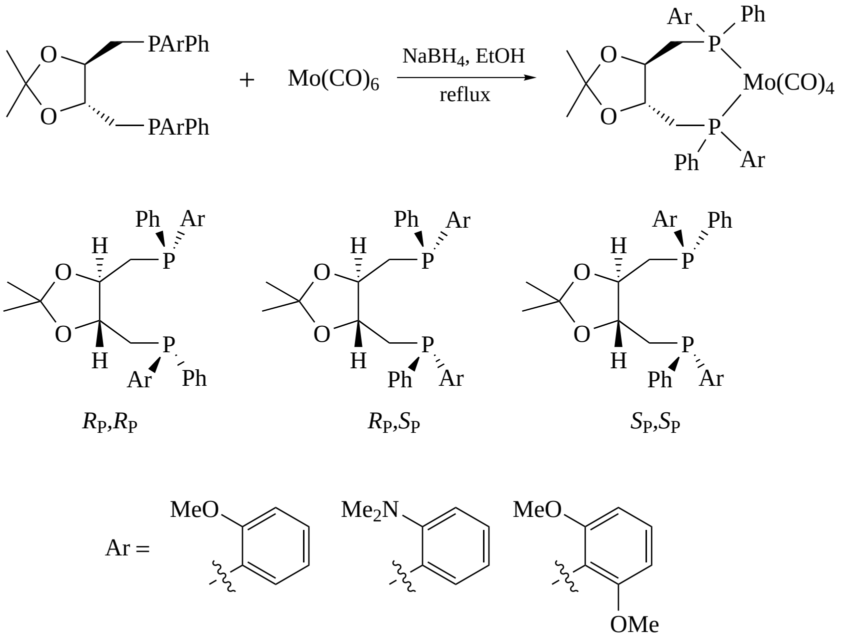

R_P and S_P refer to *R* and *S* configurations at phosphorus

Scheme 1

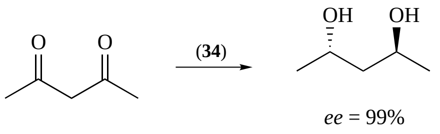

(5)

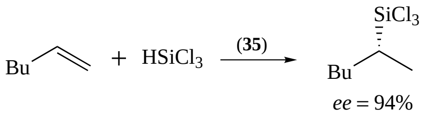

(6)

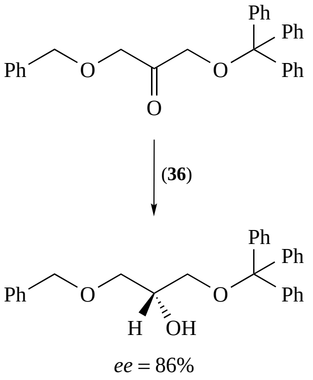

(7)

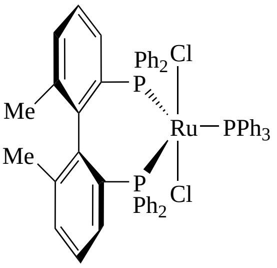

(**34**)

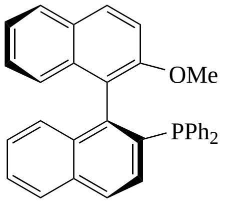

and Pd^0

(**35**)

$[Ru_2\{(R)\text{-BINAP}\}_2Cl_4]NEt_4$

(**36**)

4.3.3 *Transition Metal Complexes with a Chiral Metal Center*

In principle, steric control may be exercised by a chiral transition metal catalyst in which the metal center is the asymmetry origin rather than the phosphine or its substituents. Gladysz and coworkers[127] have separated the enantiomers of rhenium complexes using HPLC.

4.4 Solubility Effects

Here, we are not alluding to changes in a reaction induced by the use of aprotic as opposed to aqueous solvents, but to the means of achieving solubility in the desired solvent. Organophosphines and -phosphites are usually soluble in organic solvents and so enhance the hydrophobic solubility of the transition metal moiety in their complexes. If necessary, the organic groups used may be large; for example, R = n-$C_{10}H_{21}$ to n-$C_{19}H_{39}$ in PR_3 and R = Et to n-C_9H_{19} in $P(4\text{-}RC_6H_4)_3$ have been used by Chipperfield.[128] Hartley and Franks[129] synthesized phosphines with the chains in the para position, that is, $(4\text{-}RC_6H_4)_3P$ (R = Et to C_9H_{19}), and used them to prepare complexes[130] soluble in hydrocarbon solvents.

The importance of water as a solvent has led to the development of water-soluble phosphines. This has been achieved by the incorporation of hydrophilic substituents into the phosphine structure. The choice of substituents, whether anionic, cationic, or neutral, depends on the exigencies of the end use. The anionic species $[Ph_2P(3\text{-}C_6H_4SO_3)]^-Na^+$ has been used to afford a water-soluble palladium catalyst (**37**) by Du Pont workers.[131a]

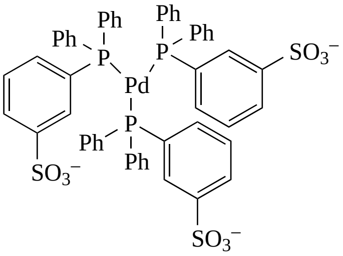

(**37**)

Variations on this theme, produced by varying the steric and electronic properties of sulfonated phosphines, have been carried out by Hanson and coworkers.[131b] They inserted alkyl chains between phosphorus and the sulfonated aryl group to give the series $P[(CH_2)_n(4\text{-}C_6H_4SO_3Na)]_3$ ($n = 1$, 2, 3, and 6). An investigation of the nickel complexes $[(CO)_3NiP\{(CH_2)_n(4\text{-}C_6H_4SO_3Na)\}_3]$ using Tolman's electronic parameter χ showed that the effect of the sulfonation is greater when $n = 0$, 1, or 2 and the electronic parameter approaches that of $P(n\text{-}Bu)_3$ when $n > 3$.

An example of the alternative cationic species is provided by $[Ph_2PCH_2NMe_3]^+I^-$. Baird and coworkers[132,133] developed this theme in preparing the all-phosphorus cationic phosphonium phosphines $[Ph_2P(CH_2)_nPMe_3]X^-$ ($n = 2, 3, 6, 10$; X = NO_3, Cl, PF_6), to which they gave the trivial names II-, III-, VI-, and X-phosphos. These ligands form water-soluble transition metal complexes such as $[(nbd)RhCl(\text{II-phosphos})][PF_6]$.[134]

The neutral triazaadamantane phosphine PTA (**38**) has been used by Darensbourg's group[135] to solubilize rhodium and ruthenium catalysts without impairing their selectivity (Scheme 2).

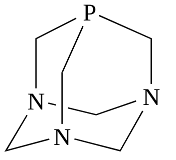

(**38**)

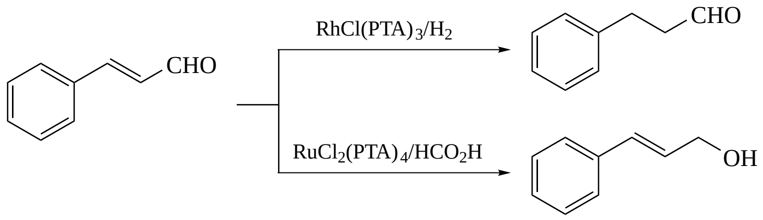

Scheme 2

Pringle and coworkers[136] have developed a neutral (in the sense of uncharged) hydrophilic phosphine, $P(CH_2OH)_3$, for use in catalysis. The palladium(0) and nickel(0) complexes $[M\{P(CH_2OH)_3\}_4]$ are soluble in water and polar organics such as MeOH and DMSO, but insoluble in halocarbon or hydrocarbon solvents. The analogous nominally platinum(0) complex $[Pt\{P(CH_2OH)_3\}_4]$ illustrates the fascinating unpredictability of chemistry. This complex gives a strongly alkaline aqueous solution, which Pringle ascribes to the equilibrium in equation (8), the species (**40**) being stabilized by the intramolecular hydrogen bonding of the phosphine hydroxyl groups to form a structure analogous to the tripod tetradentate ligand $P(CH_2CH_2PPh_2)_3$ (see Section 4.2.3), which is known to stabilize platinum trigonal bipyramidal geometry.

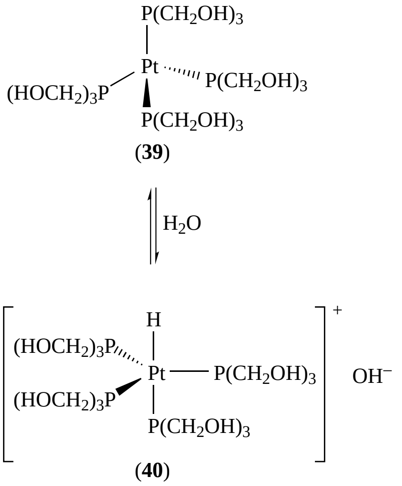

(**39**)

(**40**)

(8)

4.5 Polymer Supported Phosphines

The anchoring of homogeneous transition metal catalysts to polymers via anchored phosphine ligands combines the advantages of homogeneous and heterogeneous catalysis. Ideally there is ease of separation of the product and no loss of expensive metal, which is recycled. Several books outline the synthetic methods available[137–139] and illustrate two basic routes to functionalized polymers. Firstly, the phosphine may be polymerized or copolymerized to give the polyphosphine. Alternatively, the phosphine may be grafted on to an existing polymer. In each case the phosphine may be complexed to a transition metal. The useful polymers are insoluble, cross-linked resins, usually styrene–divinylbenzene copolymers. We use the representation [Res] for these resins rather than P, which is also commonly used, because of the ready confusion with the symbol for phosphorus.

The highly toxic osmium complex $Os_3(CO)_8(\mu\text{-Cl})_2PPh_3$ was immobilized via an anchored phosphine ligand as $Os_3(CO)_8(\mu\text{-Cl})_2Ph_2P\text{-[Res]}$.[140] The bonding may be more complex, for example, Kalck and coworkers[141] have proposed that each rhodium atom of the dinuclear carbonyl is anchored to the resin (equation 9):

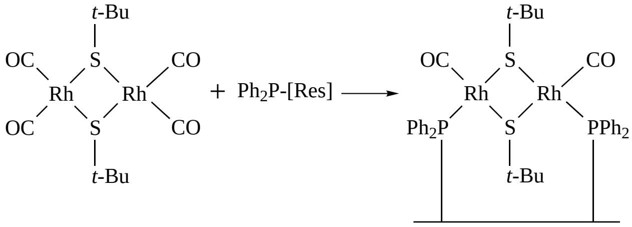

(9)

Unfortunately, in practice these anchored polymer systems often underperform owing to leaching of the metal and even the phosphine, especially under the conditions in continuous flow reactors. Critical accounts of these problems have been given by Garrou and Gates[142] and Garrou.[143] However, there are compelling environmental arguments[144] for the continued development of these polymeric ligands, inter alia minimizing toxic emissions to the biosphere.

An alternative approach to anchoring complexes is to embed them in a polymer. The complex is incorporated in the cross-linked polymer using a solvent that produces the maximum swelling. The solvent is evaporated and the surface washed free of excess complex. A second solvent that causes minimum swelling is used for reactions, so that the catalyst is effectively ‘caged’ in the polymer.[145]

4.6 P-donor Macrocyclic Ligands

Phosphorus-containing macrocycles have not proved to be popular ligands owing, in part, to their difficult multistage synthesis. We arbitrarily define phosphorus macrocycles as those with 10 or more ring members, at least one of which is phosphorus. It should be noted that the usual purpose of using macrocyclic ligands is to encapsulate a metal and that rings with less than 12 members are thought to be too small for this purpose. Meso rings (seven to ten members) may act as multidentate ligands depending on their geometry; for example, Musker and coworkers**[146]** employed the ligand (**41**) to prepare complexes with platinum(II) in which it acted as a bidentate ligand (Figure 14). Melson's short form of macrocycle nomenclature is used in this article, and two examples, (**42**) and (**43**), are shown to indicate his method.

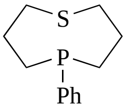

(**41**)

It is not within the scope of this article to detail the preparative aspects of organophosphorus chemistry (*see* ***Phosphorus: Organophosphorus Chemistry***). We limit ourselves to indicating the two basic routes to phosphorus macrocycles. The first route utilizes the conventional synthetic methods of organometallic chemistry and is illustrated by Ciampolini and coworkers**[147–149]** here, but others could have been chosen.**[150–153]** They reacted two moles of a dilithiophosphide in THF with two moles of bis(chloroethyl) ether in THF at low temperature, which gave a 12% yield of [18]aneP_4O_2 (Scheme 3a). The five diastereoisomers are separable by chromatographic methods. [18]aneP_4S_2 is produced in a similar way using a thioether. The nitrogen analog [18]aneP_4N_2 required the more vigorous potassium reagent (Scheme 3b).

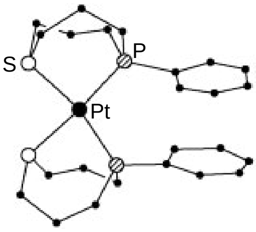

Figure 14 Structure of the *cis*-bis(5-phenyl-1-thia-5-phosphacyclooctane)platinum(II) dication[146]

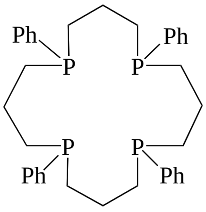

(**42**) [16]aneP_4

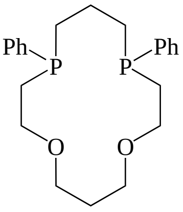

(**43**) [14]aneP_2O_2

The alternative route to phosphorus macrocycles uses the coordinating properties of phosphine ligands to assemble the macrocycle precursors in favorable conformations using a transition metal as a template. The general principles are illustrated in Scheme 4, developed by Cooper and coworkers.**[154]** This template synthesis of macrocycles may occur fortuitously; for example, Musker and coworkers**[146]** fortuitously dimerized their ligand (**41**) to afford the macrocycle [16]aneP_2S_2 (**44**).

4.6.1 *The Macrocyclic Effect*

Quantitative data are sparse for phosphorus macrocycle complex stabilities. However, the broad thermodynamic principles that apply to nitrogen systems should apply to those of phosphorus. The macrocylic effect is the net effect of a number of factors, inter alia changes in entropy, enthalpy, pH, solvent effects, ring size, and conformation, that results

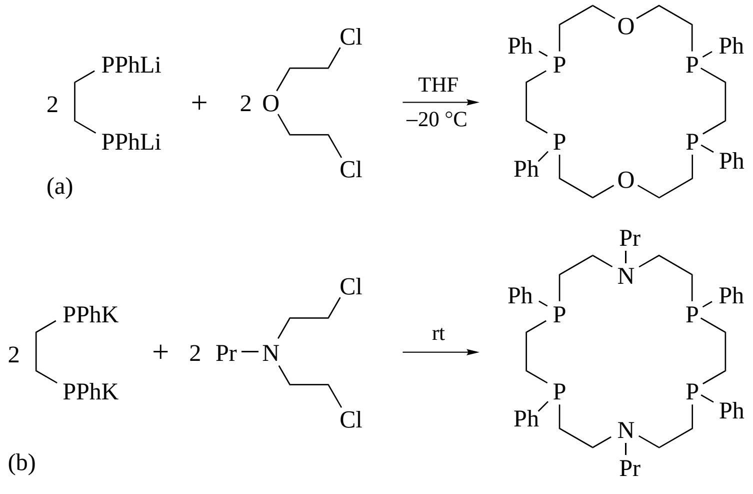

Scheme 3

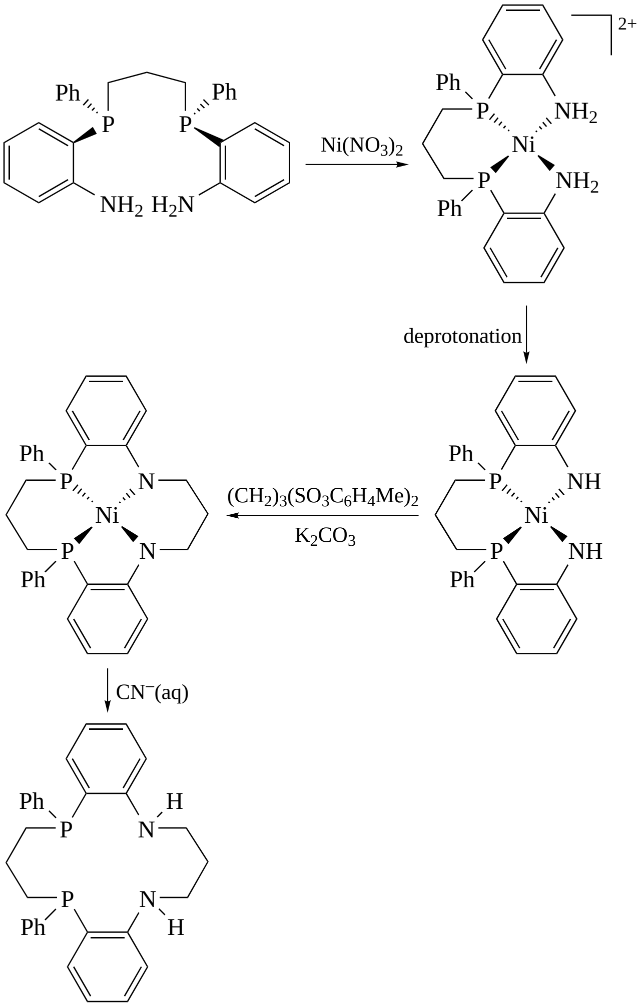

Scheme 4

in enhanced stability vis à vis their noncyclic analogs. The effect was neatly demonstrated in the case of the copper(II) complex in equation (10), where the macrocycle displaced the open-chain analog.[155]

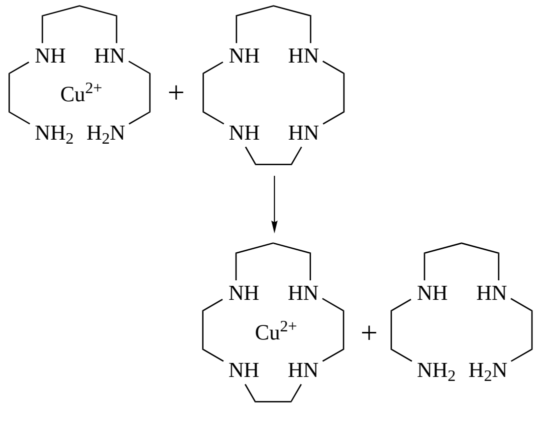

(10)

log $K = 5.2$ at 27 °C

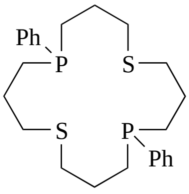

(**44**)

4.6.2 *Ring Size Consideration for P-donor Macrocycles*

The size of the ligating macrocycle chosen is governed by end use. If a stable mononuclear complex is required, then size is critical if the full macrocycle effect is to be harnessed. Kyba and coworkers[156] found that the [11]aneP_3 ring is too small to encapsulate a transition metal ion, which in this case ‘sits’ on top of the ring. They showed that [14]aneP_4 contained the optimum sized ring for metal binding.

There is interest in macrocycles capable of binding two metals independently with sufficient space between the sites to bind and activate substrate molecules, for example, 22[ane]$P_2O_2N_3$ (**45**) and 21[ane]P_2O_5 (**46**).[157] These ligands were designed to form heteronuclear bimetallic complexes sufficiently flexible to enable the adjacent metal centers to bind small molecule substrates. In terms of texture (hard or soft) these ligands are asymmetric, containing the hard oxygen and the soft phosphorus pockets, thus in principle selecting the sites of the metal. Both nickel and palladium form mono complexes with the soft P-center.[158]

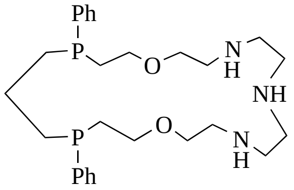

(**45**)

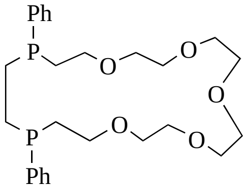

(**46**)

4.6.3 *Stereochemistry of Phosphorus Macrocycles and Their Complexes*

Phosphorus macrocyclic isomerization is complex but the isomers are relatively stable, the barrier to phosphorus(III) pyramidal inversion being $\approx 30\,\mathrm{kcal\,mol^{-1}}$, enabling room temperature isolation of the isomers. In the case of 18[ane]P_4O_2 there are five diastereoisomers (Figure 15). These isomers occur in nearly statistical amounts in the reaction mixture or upon thermal equilibration of a pure isomer. These macrocycles are flexible, but the preferred conformation with the metal will vary between the diastereoisomers; for example, the cobalt complexes of ε-18[ane]P_4S_2 (Figure 16)[159] and γ-18[ane]P_4S_2 are quite distinctive, the former being green and the latter orange, one of the sulfur atoms being uncoordinated. Increasing the size of

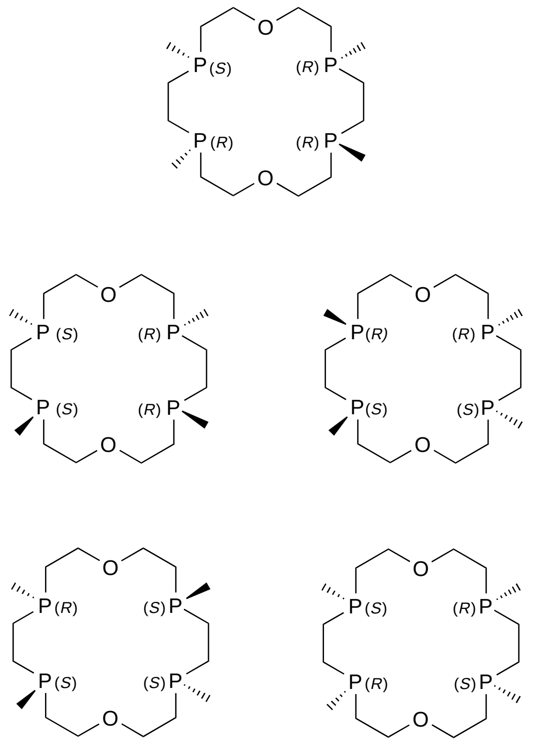

Figure 15 The five diastereoisomers of 18[ane]P_4O_2

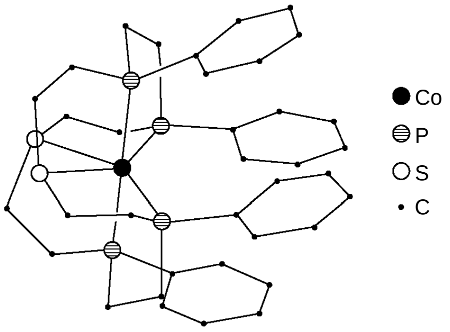

Figure 16 Structure of the complex cation of the green complex [Co(ε-18[ane]P_4S_2)][BF_4]$_2$[159]

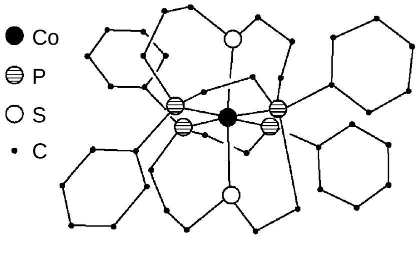

Figure 17 Structure of the low-spin complex cation [Co(δ-22[ane]P_4S_2)][BF_4]$_2$·$0.5H_2O$[160]

the ring enables the formation of complexes accommodating longer M–S bonding, for example, the low-spin Co^{II} complex with δ-22[ane]P_4S_2 (Figure 17).[160] Very recently, tripodal ligands of the 1,4,7-triphospha-cyclononane type have also been prepared with metal atoms as a template.[161] A review on related systems is available.[162]

PART II
Other P-donor Ligands

5 ELEMENTAL PHOSPHORUS AS A LIGAND

It was first demonstrated in exploratory work by the groups of Dahl,[163] Ginsburg,[164] Sacconi[165] and Huttner[166] that elemental phosphorus can play a role as a ligand for transition metals. These early contributions were followed by extremely successful systematic studies by Scherer and his collaborators, the results of which have been summarized in several review articles.[167–170] The work was also put into perspective referring to the isolobal principle (CH/P)[171] and to cluster theories.[172,173]

As a ligand, elemental phosphorus not only appears in the oligomeric forms present in its polymorphs (like P_4), but as P_n with n covering a large range from $n = 1$ to at least $n = 16$, and as the corresponding cations and anions (the polyphosphides).

The ‘natural’ tetrahedral P_4 molecule can function as a monohapto two-electron donor at each of its four vertices, as, for example, in Sacconi’s neutral $(L_3)Ni(P_4)$ complexes (**47**),[165] where (L_3) represents a triopodal auxiliary ligand, or as an edge-on dihapto four-electron donor as in Ginsburg’s $Cl(L)_2Rh(P_4)$ compounds (**48**).[164] Upon photochemical or thermal cage-opening, P_4 can also be accommodated as a square-planar cyclic unit (**49**) or as a bicyclobutane- or butterfly-type ligand (**50**), respectively.[174,175]

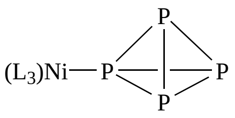

(**47**)

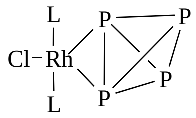

(**48**)

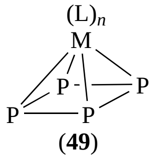

(**49**)

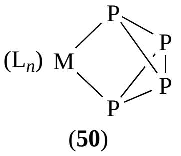

(**50**)

The oligomer P_3 has been trapped in a cobalt complex $(L_3)CoP_3$, in which it caps one face of an octahedron as a triangular six-electron donor ligand (**51**),[165] and ring-opening of the P_3 triangle can lead to clusters with angular triatomic P-P-P units.[176,177]

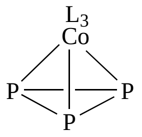

(**51**)

A fascinating analogy between cp$^-$ and P_5^- became apparent by the isolation of the mixed ferrocene cp*Fe(P_5), where cp* represents pentamethylcyclopentadienyl and (P_5) the planar, strictly pentagonal phosphorus unit (**52**). The compound is prepared in the thermolysis of $[\text{cp}^*\text{Fe(CO)}_2]_2$ in the presence of white phosphorus. The P_5^- unit, which clearly acts as a six-electron donor in this mononuclear complex, can also function as a central unit in a cationic triple-decker cation $[(\text{cp})\text{Fe}(P_5)\text{Fe}(\text{cp}^*)]^+$ (**53**).[178]

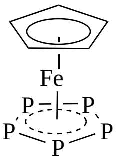

(**52**)

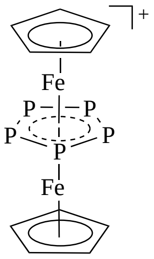

(**53**)

P_6 has been found as a planar middle-deck ligand in dinuclear complexes of niobium, for example, $[(\text{cp}^*)\text{Nb}(P_6)\text{Nb}(\text{cp}^*)]$ (**54**),[179] or – in a chair conformation – between titanium atoms in $(\text{cp}^*)\text{Ti}(P_6)\text{Ti}(\text{cp}^*)$ (**55**).[166] P_7 is present in $(P_7)[\text{Fe(cp)(CO)}_2]_3$ as a bicyclic cage reminiscent of P_4S_3.[180] The P_7 unit can also be introduced, by using K_3P_7 as a reagent, into complex anions of the type $[(P_7)\text{M(CO)}_3]^{3-}$ (**56**), in which it has a norbornane structure.[181] For information on larger P_n oligomers as ligands to transition elements and on the rich coordination chemistry of diatomic P_2, the reader is directed to reviews on the subject.[166–169]

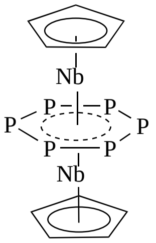

(**54**)

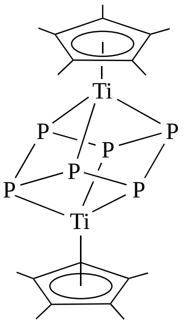

(**55**)

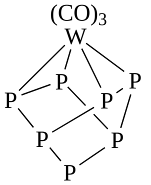

(**56**)

Finally, *single phosphorus atoms* have recently been detected as multiply bonded ligands to a variety of transition metals. Triply bonded terminal phosphorus atoms were discovered in complexes of metals in higher oxidation states and with electronegative auxiliary ligands, mainly N-donors. Thus, there are tungsten complexes of the type $(\text{NN}_3)\text{W}{\equiv}\text{P}$ with (NN_3) representing a tripodal eight-electron ligand, or molybdenum complexes of the type $(R_2N)_3\text{Mo}{\equiv}\text{P}$.[182,183] Substituent-free, two-coordinate phosphorus atoms are found as linear bridges in dinuclear complexes of the type $(R_2N)_3\text{Mo}{=}\text{P}{=}\text{Mo}(NR_2)_3$.[184] P atoms may also play the role of triply bridging units, as in $(\text{cp}_2\text{Zr})_3\text{Cl}_2(\text{P})$.[185]

6 PHOSPHORUS OXIDES AND SULFIDES AS P-DONOR LIGANDS

In oxides or sulfides of low-valent phosphorus with their cage-type structures, like P_4O_6 or P_4S_3, the phosphorus atoms have very significant donor character and consequently the molecules can be introduced as ligands into metal complexes. Classical examples are the 1:1 complexes with nickel carbonyls, $(P_4O_6)\text{Ni(CO)}_3$ (**57**) or $(P_4O_6)[\text{Ni(CO)}_3]_2$, in which one or two P-donor sites are occupied by Ni(CO)_3 acceptors.[186]

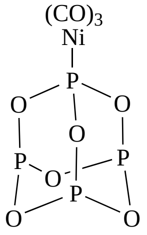

(**57**)

Apart from these traditional examples, the two-atomic unit PO has recently been detected as a P-bound ligand in metal complexes. Because of the direct analogy with NO, these results are of great current interest. PO can appear as a simple terminal ligand as in $(R_2N)_3\text{Mo(PO)}$,[182,183] or as triply bridging group as in $(\text{cp}'\text{Co})_3(\text{PO})_2$ or $(\text{cp}'\text{Ni})_2[\text{W(CO)}_4](\text{PO})_2$.[166,187] Analogous complexes with diatomic PS are also known.[166]

7 PHOSPHAALKYNES RC≡P AS LIGANDS

Phosphaalkynes RC≡P have become popular reagents and ligands ever since a few simple, stable compounds of this type have become readily available.[188,189] The molecules can behave as terminal monohapto (**58**), side-on dihapto (**59**) or side-on bridging ligands in mono- and dinuclear complexes, respectively. The terminal coordination is still rare, as in the type $(PP)_2Mo(P\equiv CR)_2$, where (PP) is a chelating ditertiary phosphine.[190] Side-on coordination has been observed in prototypes like $(R_3P)_2Pt(RC\equiv P)$[31] or $(cp)_2(Me_3P)Mo(RC\equiv P)$.[189] Bridging RCP units can be placed between two cobalt atoms in compounds $(CO)_3Co(RC\equiv P)Co(CO)_3$ with a tetrahedral core structure reminiscent of the analogous alkyne complexes (**60**).[191] In these complexes the P-atom can again function as a donor center.[189]

$R-C\equiv P-M(L)_n$

(**58**)

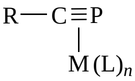

$R-\underset{|\atop M(L)_n}{C}\equiv P$

(**59**)

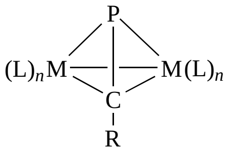

(**60**)

Phosphaalkyne molecules $RC\equiv P$ can undergo oxidative coupling to form 1,3-diphospha-cyclobutadienes as new ligands in the coordination sphere of a metal. Numerous examples of this reaction have been reported leading to simple products like $(CO)_3Fe(C_2P_2R_2)$ (**61**).[192a] A different type of $(RCP)_2$ dimer is formed under reducing conditions, as in $(cp)_2Zr(C_2P_2R_2)$ (**62**). This ligand can be considered a 1,3-diphospha-cyclobutane-2,4-diyl unit with a folded structure as compared to the planar structure in the previous examples.[192b] Cocyclization of phosphaalkynes with alkynes to give four-membered ring ligands has also been observed.[189] More often than not, the metal atom may be incorporated into the phosphacycle to give a metalla-phospha-heterocyclic core unit.[189]

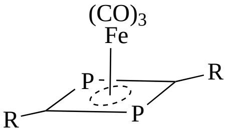

(**61**)

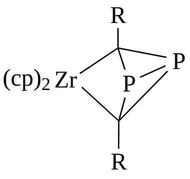

(**62**)

Cyclotrimerization has been achieved with a variety of metals. The products may contain the trimer as a flat 1,3,5-triphospha-benzene unit (**63**), or as a folded Dewar-benzene type ligand (**64**).[189] Recently, the pentamerization of a phosphaalkyne has also been reported.[193]

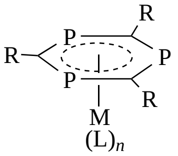

(**63**)

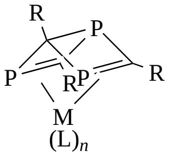

(**64**)

8 PHOSPHINIDENES RP AND DIPHOSPHENES RP=PR AS P-DONOR LIGANDS

Phosphinidenes RP (with a sextet of electrons at the P-atom) are isolobal with carbenes R_2C, and their dimers $(RP)_2$, with a P=P double bond, are the counterparts of the carbene dimers, the olefins $R_2C{=}CR_2$. The coordination chemistry of the two phosphorus species is far less developed, but the number of stable complexes is growing rapidly, as summarized in review articles.[194,195]

Phosphinidenes have been introduced into metal complexes as terminal and bridging ligands, M–PR and M–P(R)–M, respectively. Early examples are compounds of the terminal type $(cp)_2Mo{=}PR$ with R representing a bulky substituent like $CH(SiMe_3)_2$ or 2,4,6-$(^tBu)_3C_6H_2$.[196] $RP{=}ML_n$ fragments, where L_n are auxiliary ligands, are generally produced as reactive intermediates by elimination from 7-phospha-norbornadiene (**65**) or phospha-cyclopropane and -propene complexes. Conversely, phosphinidenes can be trapped by alkenes and alkynes to give phospha-cyclopropanes and -propenes (**66**), respectively.[194]

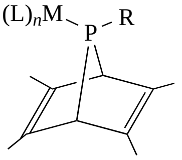

(**65**)

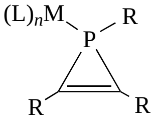

(**66**)

Dinuclear complexes with bridging phosphinidenes (**67**) can be prepared via various routes including, for example, the metallation of coordinated phosphine $M–PH_3$, primary phosphines $M–PRH_2$ or halophosphines $M–PRX_2$, and so on. Alternatively, alkali metal carbonylates can be reacted with organohalophosphines.[197] Two phosphinidenes may bridge two metal complex fragments to give four-membered ring arrays (**68**).[198]

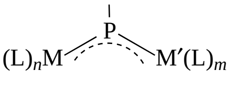

(**67**)

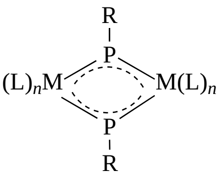

(**68**)

Phosphinidenes were finally found as units capping metal triangles and squares. The compounds were obtained upon thermolysis of dinuclear precursors.[197]

Diphosphenes R–P=P–R appear as P-donors in simple 1:1 and 1:2 complexes, an example for the former being the type R–P=P[Fe(CO)$_4$]R (**69**) with the substituents R = 2,4,6-(^{t}Bu)$_3$C$_6$H$_2$ in the trans (*E*) position. These complexes can be prepared using the free ligands as precursors, or by assembling the diphosphene in the coordination sphere of the metal atom(s), as demonstrated for *trans*-Ph[(CO)$_5$Cr]P=P[Cr(CO)$_5$]Ph (**70**). The diphosphene may finally also act as a π-donor via its P=P bond to give trinuclear complexes: (PhP=PPh)[Cr(CO)$_5$]$_3$. With Cr(CO)$_3$ groups, η^6-coordination to the arene rings has also been observed. A unique case demonstrating the diphosphene-alkene analogy is the tetrahedral cluster complex (^{t}Bu)$_2$P$_2$Fe$_2$(CO)$_6$ obtained from ^{t}BuPH$_2$ and Fe(CO)$_5$ in a multistep synthesis.[199]

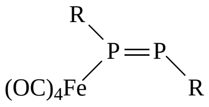
(**69**)

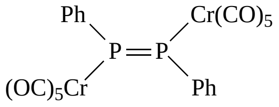
(**70**)

9 PHOSPHAALKENES $R_2C{=}PR'$ AS P-DONOR LIGANDS

Phosphaalkenes of the general formula R$_2$C=PR′ can function as P-bound monohapto and/or P=C-bound dihapto-ligands to metals.[200] The two modes (**71a,b**) are not always easily distinguished and the complexes may be fluxional in solution depending on the nature of the substituents and the solvent. This phenomenon was carefully investigated for the 1:1 complex (Ph$_2$C=PMes)Pt(PPh$_3$)$_2$ (Mes = mesityl).[201a] The dinuclear complex (RP=CH$_2$)[Fe(CO)$_4$]$_2$ is an example for a combination of both modes of coordination [R = 2,4,6-(^{t}Bu)$_3$C$_6$H$_2$].[202]

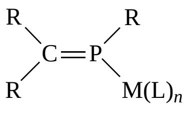
(**71a**)

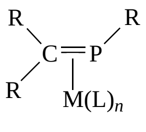
(**71b**)

Two independent phosphaalkenes can be coordinated in the dihapto-mode to the same metal center, as exemplified by [(Me$_3$Si)$_2$C=PCl]$_2$Ni(CO).[200] Similarly, α, ω-difunctional phosphaalkenes can form chelate complexes (**72**).[201b] From vinylphosphines, phospha-allyl metal complexes can be generated, but this mode of coordination is not yet very common. By contrast, with phosphinyl groups attached to the carbon atom of the phosphaalkene unit, neutral or cationic 1,3-diphospha-allyl ligands can be generated that were shown to appear in a large variety of stable complexes. The situation is similar for 1,4-diphospha-butadienes, for which a selection of open-chain and chelated metal complexes have been reported.[203]

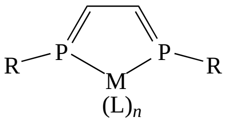
(**72**)

Transition metals complexes in which the metal atom is one of the substituents of the P-atom of a phosphaalkene, L$_n$M–P=CR$_2$, have been described. This chemistry was extended to dinuclear species of the types (L$_n$M)$_2$P=CR$_2$ and R$_2$C=P[ML$_n$]$_2$P=CR$_2$.[204]

10 PHOSPHININES (PHOSPHA-BENZENES) AS LIGANDS TO METALS

Phosphinines are a special group of phosphaalkenes in which the P=C double bond becomes integrated into the aromatic system of benzene and related arenes. The majority of examples are based on the mono-phospha-benzenes, but di- and triphospha-benzenes in various substitution patterns have also been employed as ligands. The coordination chemistry of this class of ligands has been reviewed.[205]

Phosphinines can act mainly as monohapto two-electron σ-donors through the phosphorus atom(s) or as polyhapto six-electron π-donors with metal atoms centered above the ring system (**73a,b**). The σ-mode has been observed, for example, with units Cr(CO)$_5$, Ni(PR$_3$)$_2$, Ni(C$_2$H$_4$)(PR$_3$), Mn(cp)(CO)$_2$, AuCl, and others. π-Complexation is achieved in most cases only after P-σ-complexation, as in (L′)[σ-Cr(CO)$_5$][π-Cr(CO)$_3$] with L′ = 4-Hex-C$_5$H$_4$P. A di(benzene)chromium analog was obtained with two molecules of 2,4,6-tri(^{t}butyl)phosphinine,[205] while a mixed complex (cp)Mn(L″) could be obtained for a phosphinine L″ with a different set of substituents.[206]

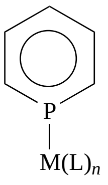
(**73a**)

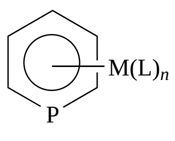
(**73b**)

There is also a rich and rapidly growing coordination chemistry of various other phosphorus heterocycles. The early work has been reviewed.[207,208]

11 PHOSPHENIUM CATIONS AS P-BOUND LIGANDS

Phosphenium cations of the general formula $[R–P–R]^+$ with an electron-sextet at the phosphorus atom can formally be generated by heterolytic cleavage of the P–X bond in precursor compounds R_2PX, and in many cases the synthesis follows this route.**[209]** The $[R_2P]^+$ species are analogs of the neutral carbenes $[R_2C]$ and hence of great current interest (**74a,b**).

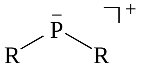
(**74a**)

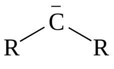
(**74b**)

Because of the high electron deficit at the two-coordinate phosphorus atom, phosphenium cations are only stable with electron-donating substituents R, predominantly with nitrogen donor atoms. This is an obvious parallel to the situation with 'stable carbenes' of the Wanzlick-Arduengo type. Therefore most complexes in this series are derived from diazaphospholes (**75a,b**).**[209]**

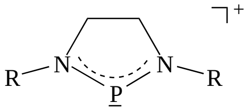
(**75a**)

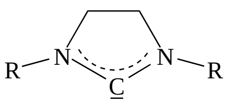
(**75b**)

A selection of typical examples includes the cations obtained from $Fe(CO)_5$ and the N,N'-dimethyl-diazaphospholenium cation, $\{[(CH_2NMe)_2P]Fe(CO)_4\}^+$ (**76**),**[210]** for which open-chain analogs are also known: $\{[(Me_2N)_2P]Fe(CO)_4\}^+$.**[211]** Related cationic complexes with the acceptor units $(CO)_3Ni$, $(bipy)(CO)_3Mo$, or $[(MeO)_3P]_5Mo$ are also known. Neutral complexes can have the formulae $[(CH_2NBz)_2P]Mo(cp)(CO)_2$ or $[(Mes)_2P]W(cp)(CO)_2$.**[209]**

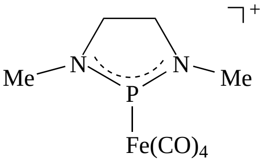
(**76**)

12 RELATED ARTICLES

Coordination & Organometallic Chemistry: Principles; Phosphorus: Inorganic Chemistry; Phosphorus: Organophosphorus Chemistry.

13 FURTHER READING

T. Imamoto, T. Oshiki, T. Kusumoto, K. Sato, and T. Onozawa, *J. Am. Chem. Soc.*, 1990, **112**, 5244.

B. D. Vineyard, W. S. Knowles, M. J. Sabacky, G. L. Bachman, and D. J. Weinkauff, *J. Am. Chem. Soc.*, 1977, **99**, 5946.

14 REFERENCES

1. P. Thenard, *C. R. Hebd. Seances Acad. Sci., Ser. C*, 1847, **25**, 892.
2. A. W. Hoffmann, *Justus Liebigs Ann. Chem.*, 1857, **103**, 357.
3. A. Cahours and A. W. Hoffman, *J. Chem. Soc.*, 1859, **11**, 56.
4. F. G. Mann and J. Chatt, *J. Chem. Soc.*, 1938, 1622.
5. K. A. Jensen, *Z. Anorg. Allg. Chem.*, 1936, **229**, 225.
6. F. P. Dwyer and D. M. Stewart, *J. Proc. R. Soc. NSW*, 1949, **83**, 177.
7. J. Chatt, *Nature (London)*, 1951, **167**, 652.
8. D. P. Craig, *Biogr. Mem. R. Soc.*, 1972, **18**, 445.
9. P. W. Atkins, 'Quanta: A Handbook of Concepts', 2nd edn., Oxford University Press, Oxford, 1991.
10. M. Bigorgne, A. Loutellier, and M. Trabelsi, *J. Organomet. Chem.*, 1977, **133**, 201.
11. H. B. Jonassen, C. W. Weston, A. W. Verstuyft, and J. H. Nelson, *Inorg. Chem.*, 1977, **16**, 1313.
12. a) D. Cox, J. E. MacDonald, G. D. Stucky, E. Eckert, N. Herron, Y. Wang, K. Moller, and T. Bein, *J. Am. Chem. Soc.*, 1989, **111**, 8006; b) M. G. Gardiner, C. L. Raston, *Coord. Chem. Rev.*, 1997, **166**, 1.
13. A. B. Burg and G. B. Street, *Inorg. Chem.*, 1966, **5**, 1532.
14. R. G. Cavell, I. G. Phillips, and R. G. Ball, *Inorg. Chem.*, 1988, **27**, 4038.
15. D. M. Roddick and M. F. Ernst, *Inorg. Chem.*, 1989, **28**, 1624.
16. M. Brookhart, W. A. Chandler, A. C. Pfister, C. C. Santini, and P. S. White, *Organometallics*, 1992, **11**, 1263.
17. V. D. Romanenko, A. V. Ruban, A. B. Drapailo, and L. N. Markovskii, *J. Gen. Chem. USSR (Engl. Transl.)*, 1985, **55**, 2486.
18. F. Bickelhaupt and C. N. Smit, *Organometallics*, 1987, **6**, 1156.
19. H. Schumann and H. Benda, *Angew. Chem., Int. Ed. Engl.*, 1970, **9**, 76.
20. M. Driess, M. Reisgus, and H. Pritzkow, *Angew. Chem., Int. Ed. Engl.*, 1992, **31**, 1510.
21. S. O. Grim, G. T. Andrews, I. J. Colquhoun, and W. McFarlane, *J. Chem. Soc., Dalton Trans.*, 1982, 2353.
22. J. G. Verkade, S. M. Socol, and R. A. Jacobson, *Inorg. Chem.*, 1984, **23**, 88.
23. O. J. Scherer and K. Andres, *Z. Naturforsch.*, 1978, **33B**, 467.

24. D. G. Gorenstein, K. Taira, and W. L. Mock, *J. Am. Chem. Soc.*, 1984, **106**, 7831.
25. D. G. Gorenstein and K. Taira, *J. Am. Chem. Soc.*, 1984, **106**, 7825.
26. P. G. Pringle and M. J. Baker, *J. Chem. Soc., Chem. Commun.*, 1991, 803.
27. P. G. Pringle, *J. Chem. Soc., Chem. Commun.*, 1991, 1292.
28. T. B. Brill and S. J. Landon, *Chem. Rev.*, 1984, **84**, 577.
29. J. Chatt, *J. Chem. Soc.*, 1949, 3340.
30. G. Wilkinson, *J. Am. Chem. Soc.*, 1951, **73**, 5501.
31. J. F. Nixon, *Adv. Inorg. Chem. Radiochem.*, 1985, **29**, 42.
32. D. L. Gallup and J. G. Morse, *Inorg. Chem.*, 1978, **17**, 3438.
33. P. B. Comita and R. Zhang, *Chem. Phys. Lett.*, 1992, **200**, 297.
34. H. G. M. Edwards and V. Fawcett, *Inorg. Chim. Acta*, 1992, **197**, 89.
35. P. L. Timms, *J. Chem. Soc. (A)*, 1970, 2526.
36. R. E. Hester and K. M. Lee, *J. Organomet. Chem.*, 1973, **57**, 169.
37. R. J. Clark and C. A. Udovich, *J. Organomet. Chem.*, 1972, **36**, 355.
38. T. Kruck, *Angew. Chem., Int. Ed. Engl.*, 1967, **6**, 53.
39. J. F. Nixon, *J. Chem. Soc. (A)*, 1967, 1136.
40. Y. V. Petrov, V. N. Prusakov, A. A. Terentev, and N. F. Simonov, *Radiokhimiya*, 1981, **23**, 319.
41. H. G. M. Edwards, *J. Mol. Struct.*, 1987, **156**, 137.
42. H. G. M. Edwards, *Spectrochim. Acta, Part A*, 1986, **42**, 431.
43. H. G. M. Edwards, *J. Mol. Struct.*, 1987, **158**, 153.
44. R. C. Bush and R. J. Angelici, *Inorg. Chem.*, 1988, **27**, 681.
45. R. J. Puddephatt, G. M. Bancroft, and T. Chan, *Inorg. Chim. Acta*, 1983, **73**, 83.
46. R. G. Goel and T. Allman, *Can. J. Chem.*, 1982, **60**, 716.
47. M. Wada, S. Higashizaki, and A. Tsuboi, *J. Chem. Res. (S)*, 1985, 38.
48. C. A. Streuli and W. Henderson, *J. Am. Chem. Soc.*, 1960, **82**, 5791; *Anal. Chem.*, 1960, **32**, 985.
49. H. Goetz and S. Sidhu, *Justus Liebigs Ann. Chem.*, 1965, **682**, 71.
50. W. P. Giering, M. N. Golovin, M. M. Rahman, and J. E. Belmonte, *Organometallics*, 1985, **4**, 1981.
51. H. Goetz and S. Domin, *Justus Liebigs Ann. Chem.*, 1967, **704**, 1.
52. R. J. Angelici and J. R. Sowa, Jr, *Inorg. Chem.*, 1991, **30**, 3534.
53. M. I. Kabachnik and T. A. Mastryukova, *Russ. Chem. Rev. (Engl. Transl.)*, 1969, **38**, 795.
54. W. H. Thompson and C. T. Sears, *Inorg. Chem.*, 1977, **16**, 769.
55. J. R. Chipperfield, in ‘Advances in Linear Free Energy Relationships’, eds. N. B. Chapman and J. Shorter, Plenum, London, 1972, p. 355, Chap. 7.
56. M. Wada, S. Higashizaki, and A. Tsuboi, *J. Chem. Res. (S)*, 1985, 38.
57. N. N. Greenwood and A. Earnshaw, ‘Chemistry of the Elements’, Pergamon, Oxford, 1984, p. 566.
58. R. J. Angelici and C. M. Ingemanson, *Inorg. Chem.*, 1969, **8**, 83.
59. A. H. Cowley, M. Lattman, P. M. Stricklen, and J. G. Verkade, *Inorg. Chem.*, 1982, **21**, 543.
60. M. F. Lappert, J. B. Pedley, B. T. Wilkins, O. Stelzer, and E. Unger, *J. Chem. Soc., Dalton Trans.*, 1975, 1207.
61. A. H. Cowley, R. A. Kemp, M. Lattman, and M. L. McKee, *Inorg. Chem.*, 1982, **21**, 85.
62. S. Cradock and D. W. H. Rankin, *J. Chem. Soc., Faraday Trans. 2*, 1972, **68**, 940.
63. G. Pacchioni and P. S. Bagus, *Inorg. Chem.*, 1992, **31**, 4391.
64. J. E. Huheey, ‘Inorganic Chemistry’, 3rd edn., Harper and Row, New York, 1983, p. 436.
65. J. Chatt, *Nature (London)*, 1950, **165**, 637.
66. A. Pidcock, in ‘Transition Metal Complexes of Phosphorus, Arsenic and Antimony Ligands’, ed. C. A. McAuliffe, Macmillan, London, 1977, p. 1.
67. L. M. Venanzi, *Chem. Br.*, 1968, **4**, 162.
68. D. A. Bochvar, N. P. Gambaryan, and L. M. Epshtein, *Russ. Chem. Rev. (Engl. Transl.)*, 1976, **45**, 660.
69. D. E. Ellis, W. C. Trogler, S. X. Xiao, and Z. Berkovitch-Yellin, *J. Am. Chem. Soc.*, 1983, **105**, 7033.
70. D. S. Marynick, *J. Am. Chem. Soc.*, 1984, **106**, 4064.
71. D. S. Marynick, S. Askari, and D. F. Nickerson, *Inorg. Chem.*, 1985, **24**, 868.
72. J. C. Giordan, J. A. Tossell, and J. H. Moore, *Inorg. Chem.*, 1985, **24**, 1100.
73. A. G. Orpen and N. C. Connelly, *J. Chem. Soc., Chem. Commun.*, 1985, 1310.
74. E. C. Alyea and S. Song, *Inorg. Chem.*, 1992, **31**, 4909.
75. W. P. Giering, M. M. Rahman, H. Y. Liu, K. Eriks, and A. Prock, *Organometallics*, 1989, **8**, 1.
76. C. A. Tolman, *J. Am. Chem. Soc.*, 1970, **92**, 2953.
77. C. A. Tolman, *Chem. Rev.*, 1977, **77**, 313.
78. N. S. Imyanitov, *Koord. Khim.*, 1985, **11**, 1041, 1181.
79. K. W. Bagnall and L. Zing-Fu, *J. Chem. Soc., Dalton Trans.*, 1982, 1365.
80. K. W. Bagnall, *J. Less-Common Met.*, 1984, **98**, 309.
81. (a) G. Ferguson, E. C. Alyea, S. A. Dias, and R. J. Restivo, *Inorg. Chem.*, 1977, **16**, 2329; (b) A. Immirzi and A. Musco, *Inorg. Chim. Acta*, 1977, **25**, L41.
82. D. M. P. Mingos, *Inorg. Chem.*, 1982, **21**, 464.
83. J. A. Mosbo, J. T. DeSanto, B. N. Storhoff, P. L. Block, and R. E. Bloss, *Inorg. Chem.*, 1980, **19**, 3086.
84. G. Ferguson, E. C. Alyea, and M. Khan, *Inorg. Chem.*, 1978, **17**, 2965.

85. G. Ferguson, E. C. Alyea, S. A. Dias, and M. Pavez, *Inorg. Chim. Acta*, 1979, **37**, 45.
86. J. D. Oliver and J. D. Smith, *Inorg. Chem.*, 1978, **17**, 2585.
87. D. J. Darensbourg and R. L. Kump, *Inorg. Chem.*, 1978, **17**, 2680.
88. P. Heimbach, J. Kluth, H. Schenkluhn, and B. Weimann, *Angew. Chem., Int. Ed. Engl.*, 1980, **19**, 570.
89. T. Bartik, C. Bianchini, and A. Meli, *J. Organomet. Chem.*, 1984, **276**, 412.
90. H. Schenkluhn, W. Scheidt, B. Weimann, and M. Zähres, *Angew. Chem., Int. Ed. Engl.*, 1979, **18**, 401.
91. F. Basolo and M. E. Rerek, *Organometallics*, 1983, **2**, 372.
92. C. A. McAuliffe, H. F. Al-Khateeb, D. S. Barratt, J. C. Briggs, A. Challita, A. Hosseiny, M. G. Little, A. G. Mackie, and K. Minten, *J. Chem. Soc., Dalton Trans.*, 1983, 2147.
93. C. G. Howard, G. Wilkinson, M. Thornton-Pett, and M. B. Hursthouse, *J. Chem. Soc., Dalton Trans.*, 1983, 2025.
94. B. Beagley, C. A. McAuliffe, K. Minton, and R. G. Pritchard, *J. Chem. Soc., Chem. Commun.*, 1984, 658.
95. M. D. Fryzuk, A. Carter, and A. Westerhaus, *Inorg. Chem.*, 1985, **24**, 642.
96. C. A. McAuliffe ed., 'Transition Metal Complexes of Phosphorus, Arsenic and Antimony Ligands', Macmillan, London, 1973.
97. C. A. McAuliffe and W. Levason, 'Phosphine, Arsine and Stibine Complexes of the Transition Elements', Elsevier, Amsterdam, 1979.
98. C. A. McAuliffe, in 'Comprehensive Coordination Chemistry', ed. G. Wilkinson, Pergamon, Oxford, 1986.
99. W. Levason, in 'The Chemistry of Organophosphorus Compounds', ed. F. R. Hartley, Wiley, New York, 1990, Vol. 1.
100. F. R. Hartley ed., 'The Chemistry of Organophosphorus Compounds. Vol. 1. Primary, Secondary and Tertiary Phosphines, Polyphosphines and Heterocyclic Organophosphorus(III) Compounds', Wiley, Chichester, 1990.
101. K. McGregor, G. B. Deacon, R. S. Dickon, G. D. Fallon, R. S. Rowe, and B. O. West, *J. Chem. Soc., Chem. Commun.*, 1990, 1293.
102. C. A. McAuliffe, A. G. Mackie, S. M. Godfrey, and R. G. Pritchard, *Angew. Chem., Int. Ed. Engl.*, 1992, **31**, 919.
103. S. M. Godfrey, D. G. Kelly, A. G. Mackie, P. P. MacRory, C. A. McAuliffe, R. G. Pritchard, and S. M. Watson, *J. Chem. Soc., Chem. Commun.*, 1991, 1447.
104. N. Bricklebank, S. M. Godfrey, C. A. McAuliffe, A. G. Mackie, and R. G. Pritchard, *J. Chem. Soc., Chem. Commun.*, 1992, 945.
105. C. A. McAuliffe, S. M. Godfrey, A. G. Mackie, and R. G. Pritchard, *J. Chem. Soc., Chem. Commun.*, 1992, 483.
106. a) S. M. Godfrey, N. Ho, C. A. McAuliffe, and R. G. Pritchard, *Angew. Chem. Int. Ed. Engl.*, 1995, **35**, 2344; b) S. M. Godfrey, C. A. McAuliffe, and R. G. Pritchard, *J. Chem. Soc., Dalton Trans.*, 1993, 371; c) D. Schneider, A. Schier, and H. Schmidbaur, *Dalton Trans.*, 2004, 1995; d) U. Monkowius, S. Nogai, and H. Schmidbaur, *Organometallics*, 2003, **22**, 145.
107. a) M. Fourmigué and P. Batail, *J. Chem. Soc., Chem. Commun.*, 1991, 1370; b) T. Pechmann, C. D. Brandt, H. Werner, *Angew. Chem. Int. Ed. Engl.* 2000, **39**, 3909.
108. R. J. Puddephatt, *Chem. Soc. Rev.*, 1983, **12**, 99.
109. B. Chaudret, B. Delavaux, and R. Polblanc, *Coord. Chem. Rev.*, 1988, **86**, 191.
110. B. L. Shaw, G. B. Jacobsen, and M. Thornton-Pett, *J. Organomet. Chem.*, 1987, **323**, 313.
111. F. Mathey, P. Le Flock, D. Carmichael, and L. Richard, *J. Am. Chem. Soc.*, 1991, **113**, 667.
112. F. Mathey, B. Schmid, L. M. Venanzi, T. Gerfin, and V. Gramlich, *Inorg. Chem.*, 1992, **31**, 5117.
113. L. Sacconi and F. Mani, *Transition Met. Chem.*, 1982, **8**, 179.
114. K. H. Whitmire, K. Burgess, and M. J. Ohlmeyer, *Organometallics*, 1992, **11**, 3588.
115. a) L. M. Venanzi, T. R. Ward, A. Albinati, F. Lianza, T. Gerfin, V. Gramlich, and G. M. R. Tombo, *Helv. Chim. Acta*, 1991, **74**, 983; b) P. G. Edwards, P. D. Newman, and K. M. A. Malik, *Angew. Chem. Int. Ed. Engl.*, 2000, **39**, 2922.
116. R. Noyori, A. Miyashita, H. Takaya, and T. Souchi, *Tetrahedron*, 1984, **40**, 1245.
117. R. Noyori, A. Miyashita, A. Yasuda, H. Takaya, K. Toriumi, T. Ito, and T. Souchi, *J. Am. Chem. Soc.*, 1980, **102**, 7932.
118. B. Bosnich and M. D. Fryzuk, *J. Am. Chem. Soc.*, 1977, **99**, 6262.
119. H. B. Kagan and T. P. Dang, *J. Am. Chem. Soc.*, 1972, **94**, 6429.
120. K. Yamamoto, J. Wakatsuki, and R. Sugimoto, *Bull. Chem. Soc. Jpn.*, 1980, **53**, 1132.
121. L. M. Venanzi, H. B. Bürgi, J. Murry-Rust, M. Camalli, and F. Caruso, *Helv. Chim. Acta*, 1989, **72**, 1293.
122. Y. Ito, M. Sawamura, A. Yamauchi, and T. Takegawa, *J. Chem. Soc., Chem. Commun.*, 1991, 874.
123. S. J. Peterson, L. R. Sita, W. Choy, and S. Masamune, *Angew. Chem., Int. Ed. Engl.*, 1985, **24**, 1.
124. A. Mezzetti and G. Consiglio, *J. Chem. Soc., Chem. Commun.*, 1991, 1675.
125. T. Hayashi and Y. Uozumi, *J. Am. Chem. Soc.*, 1991, **113**, 9887.
126. E. Cesarotti, P. Antognazza, A. Mauri, M. Pallavicini, and L. Villa, *Helv. Chim. Acta*, 1992, **75**, 2563.
127. J. A. Gladysz, J. A. Ramsden, and C. M. Garner, *Organometallics*, 1991, **10**, 1631.
128. J. R. Chipperfield, S. Franks, and F. R. Hartley, in 'Catalytic Aspects of Metal-Phosphine Chemistry', eds. E. C. Alyea and D. W. Meek, American Chemical Society, Washington, DC, 1982, Chap. 16.
129. F. R. Hartley and S. Franks, *J. Chem. Soc., Perkin Trans. 1*, 1980, 2233.

130. F. R. Hartley and S. Franks, *Inorg. Chim. Acta*, 1981, **47**, 235.

131. (a) A. L. Casalnuovo and J. C. Calabrese, *J. Am. Chem. Soc.*, 1990, **112**, 4324; (b) B. E. Hanson, T. Bartik, B. Bartik, I. Guo, and I. Toth, *Organometallics*, 1993, **12**, 164.

132. M. C. Baird, R. T. Smith, R. T. Ungar, and L. J. Sanderson, *Organometallics*, 1983, **2**, 1138.

133. M. C. Baird and R. T. Smith, *Inorg. Chim. Acta*, 1982, **62**, 135.

134. M. C. Baird, E. Renaud, R. B. Russell, S. Fortier, and S. J. Brunar, *J. Organomet. Chem.*, 1991, **419**, 403.

135. D. J. Darensbourg, F. Joo, M. Kannisto, A. Katho, and J. H. Reibenspies, *Organometallics*, 1992, **11**, 1990.

136. P. G. Pringle, J. W. Ellis, P. A. T. Hoye, K. N. Harrison, A. G. Orpen, and M. B. Smith, *Inorg. Chem.*, 1992, **31**, 3026 and refs. therein.

137. D. C. Sherrington and P. Hodge eds, 'Polymer Supported Reactions in Organic Synthesis', Wiley, New York, 1980.

138. L. H. Pignolet ed., 'Homogeneous Catalysis with Metal Phosphine Complexes', Plenum, New York, 1983.

139. P. Hodge and D. C. Sherrington eds, 'Syntheses and Separations using Functional Polymers', Wiley, New York, 1988.

140. B. C. Gates, M. Wolf, J. Lieto, B. A. Matrana, D. B. Arnold, and H. J. Knözinger, *J. Catal.*, 1984, **89**, 100.

141. P. Kalck, E. L. de Oliveira, R. Queau, B. Peyrille, and J. Molinier, *J. Organomet. Chem.*, 1992, **433**, C4.

142. P. E. Garrou and B. C. Gates, in 'Syntheses and Separations using Functional Polymers', eds. P. Hodge and D. C. Sherrington, Wiley, New York, 1988, Chap. 3.

143. P. E. Garrou, *Chem. Rev.*, 1985, **85**, 171.

144. D. C. Sherrington, *Chem. Ind. (London)*, 1991, 15.

145. D. Milstein, Y. Ben-David, and A. Patchornik, *J. Chem. Soc., Chem. Commun.*, 1990, 1090.

146. W. K. Musker, S. D. Toto, M. M. Olmstead, B. W. Arbuckle, and P. K. Bharadwaj, *Inorg. Chem.*, 1990, **29**, 691.

147. M. Ciampolini, P. Dapporto, A. Dei, N. Nardi, and F. Zanobini, *Inorg. Chem.*, 1982, **21**, 489.

148. M. Ciampolini, N. Nardi, and F. Zanobini, *Inorg. Chim. Acta*, 1983, **76**, L17.

149. M. Ciampolini, P. Dapporto, A. Dei, N. Nardi, and F. Zanobini, *J. Chem. Soc., Dalton Trans.*, 1984, 575.

150. A. van Zon, J. H. G. Frijns, and F. J. Torny, *Recl. Trav. Chim. Pays-Bas*, 1983, **102**, 326.

151. T. N. Kudyra, A. A. Chaikovskaya, Z. Z. Rozhkova, and A. M. Pinchuk, *Zh. Obshch. Khim.*, 1982, **52**, 1092.

152. E. P. Kyba, C. N. Clubb, S. B. Larson, V. J. Schueler, and R. E. Davis, *J. Am. Chem. Soc.*, 1985, **107**, 2141.

153. M. Vincens, J. T. G. Moron, R. Pasqualini, and M. Vidal, *Tetrahedron Lett.*, 1987, **28**, 1259.

154. M. K. Cooper, C. W. G. Ansell, K. P. Dancey, P. A. Duckworth, K. Hendrick, M. McPartlin, and P. A. Tasker, *J. Chem. Soc., Chem. Commun.*, 1985, **437**, 439.

155. P. H. Davis, *Inorg. Chem.*, 1975, **14**, 1753.

156. E. Kyba, A. M. John, B. Brown, C. W. Hudson, M. J. McPhaul, A. Hardin, K. Larsen, S. Niedzwiecki, and R. E. Davis, *J. Am. Chem. Soc.*, 1980, **102**, 139.

157. S. J. Lippard, L. Wei, A. Bell, K. H. Ahn, M. M. Holl, S. Warner, and I. D. Williams, *Inorg. Chem.*, 1990, **29**, 825.

158. M. Ciampolini, *Pure Appl. Chem.*, 1986, **58**, 1429.

159. M. Ciampolini, N. Nardi, P. L. Orioli, S. Mangani, and F. Zanobini, *J. Chem. Soc., Dalton Trans.*, 1985, 1425.

160. M. Ciampolini, N. Nardi, P. L. Orioli, S. Mangani, and F. Zanobini, *J. Chem. Soc., Dalton Trans.*, 1985, 1179.

161. P. G. Edwards, P. D. Newman, and K. M. A. Malik, *Angew. Chem., Int. Ed. Engl.*, 2000, **39**, 2922.

162. I. A. Fallis, *Annu. Rep. Prog. Chem., Sect. A*, 1999, **95**, 313.

163. A. S. Foust, M. S. Foster, and L. F. Dahl, *J. Am. Chem. Soc.*, 1969, **91**, 5633.

164. A. P. Ginsburg, W. E. Lindsell, K. J. McCullough, and A. J. Welch, *J. Am. Chem. Soc.*, 1986, **108**, 403.

165. M. Di Vaira and L. Sacconi, *Angew. Chem. Int. Ed. Engl.*, 1982, **21**, 330.

166. G. Huttner and K. Evertz, *Acc. Chem. Res.*, 1986, **19**, 406.

167. O. J. Scherer, *Acc. Chem. Res.*, 1999, **32**, 751.

168. O. J. Scherer, *Angew. Chem. Int. Ed. Engl.*, 1990, **29**, 1104.

169. K. H. Whitmire, *Adv. Organomet. Chem.*, 1998, **42**, 1.

170. K. B. Dillon, F. Mathey, and J. F. Nixon, 'Phosphorus, The Carbon Copy', Wiley, New York, 1998.

171. R. Hoffmann, *Angew. Chem. Int. Ed. Engl.*, 1982, **21**, 711.

172. K. Wade, *Adv. Inorg. Chem. Radiochem.*, 1976, **18**, 1.

173. D. M. P. Mingos and J. D. Wales, 'Introduction to Cluster Chemistry', Prentice-Hall, Englewood Cliffs, NJ, 1990, p. 249.

174. M. E. Barr, S. K. Smith, B. Spencer, and L. F. Dahl, *Organometallics*, 1991, **10**, 3983.

175. M. Scheer, E. Herrmann, J. Sieler, and M. Oehme, *Angew. Chem. Int. Ed. Engl.*, 1991, **30**, 969.

176. M. Herberhold, G. Frohmader, and W. Milius, *J. Organomet. Chem.*, 1996, **522**, 185.

177. O. J. Scherer, T. Mohr, and G. Wolmershäuser, *J. Organomet. Chem.*, 1997, **529**, 379.

178. O. J. Scherer, T. Brück, and G. Wolmershäuser, *Chem. Ber.*, 1989, **122**, 2049.

179. A. C. Reddy, E. D. Jemmis, and O. J. Scherer, *Organometallics*, 1992, **11**, 3894.

180. R. Ahlrichs, D. Fenske, K. Fromm, U. Krautscheid, H. Krautscheid, and O. Treutler, *Chem. Eur. J.*, 1996, **2**, 238.

181. S. Charles, J. A. Danis, J. C. Fettinger, and B. W. Eichhorn, *Inorg. Chem.*, 1997, **36**, 3772.

182. C. C. Cummins, *Chem. Commun.*, 1998, 1777.

183. M. Scheer, *Coord. Chem. Rev.*, 1997, **163**, 271.

184. M. J. A. Johnson, P. M. Lee, A. L. Odom, W. M. Davis, and C. C. Cummins, *Angew. Chem., Int. Ed. Engl.*, 1997, **36**, 87.

185. J. Ho, R. Rousseau, and D. W. Stephan, *Organometallics*, 1994, **13**, 1918.

186. J. G. Riess and J. R. van Wazer, *J. Am. Chem. Soc.*, 1966, **88**, 2168.

187. O. J. Scherer, J. Braun, P. Walther, G. Heckmann, and G. Wolmershäuser, *Angew. Chem., Int. Ed. Engl.*, 1991, **30**, 852.

188. a) G. Becker, G. Gresser, W. Uhl, *Z. Naturforsch.* 1981, **36b**, 16; b) T. Allspach, M. Regitz, G. Becker, W. Becker, *Synthesis*, 1986, 31.

189. a) P. Binger, in ‘Multiple Bonds and Low Coordination in Phosphorus Chemistry’, eds. M. Regitz and O. J. Scherer, Thieme, Stuttgart, 1990, p. 58; b) J. F. Nixon, *Chem. Rev.*, 1988, **88**, 1327; c) J. F. Nixon, *Coord. Chem. Rev.*, 1995, **145**, 201; d) J. F. Nixon, *Chem. Soc. Rev.* 1995, 319.

190. P. B. Hitchcock, M. J. Maah, J. F. Nixon, J. A. Zora, G. J. Leigh, and M. A. Bakar, *Angew. Chem., Int. Ed. Engl.*, 1987, **26**, 474.

191. J. C. T. R. Burckett-St. Laurent, P. B. Hitchcock, H. W. Kroto, and J. F. Nixon, *Chem. Commun.*, 1981, 1141.

192. a) P. Binger, B. Biedenbach, R. Schneider, M. Regitz, *Synthesis*, 1989, 960; b) P. Binger, B. Biedenbach, C. Krüger, M. Regitz, *Angew. Chem., Int. Ed. Engl.*, 1987, **26**, 764.

193. P. Kramkowski and M. Scheer, *Angew. Chem., Int. Ed.*, 1999, **111**, 3384.

194. a) F. Mathey, in ‘Multiple Bonds and Low Coordination in Phosphorus Chemistry’, eds. M. Regitz and O. J. Scherer, Thieme, Stuttgart 1990, p. 33; b) F. Mathey, *Chem. Rev.*, 1990, **90**, 997; c) F. Mathey, *Angew. Chem. Int. Ed. Engl.* 1987, **26**, 275; d) K. Lammertsma, M. J. M. Vlaar, A. W. Ehlers, F. J. J. de Kanter, M. Schakel, A. L. Spek, *Angew. Chem., Int. Ed. Engl.*, 2000, **39**, 2943.

195. a) M. Yoshifuji in ‘Multiple Bonds and Low Coordination in Phosphorus Chemistry’, eds. M. Regitz and O. J. Scherer, Thieme, Stuttgart 1990, p. 321; b) K. Lammertsma, *Top. Curr. Chem.*, 2003, **229**, 95.

196. P. B. Hitchcock, M. F. Lappert, and W.-P. Leung, *Chem. Commun.*, 1987, 1282.

197. G. Huttner and H. Lang, in ‘Multiple Bonds and Low Coordination in Phosphorus Chemistry’, eds. M. Regitz and O. J. Scherer, Thieme, Stuttgart, 1990, p. 48.

198. K. M. Flynn, R. A. Bartlett, M. M. Olmstead, and P. P. Power, *Organometallics*, 1986, **5**, 813.

199. H. Vahrenkamp and D. Wolters, *Angew. Chem., Int. Ed. Engl.*, 1983, **22**, 154.

200. R. Appel, in ‘Multiple Bonds and Low Coordination in Phosphorus Chemistry’, eds. M. Regitz and O. J. Scherer, Thieme, Stuttgart, 1990, p. 191.

201. a) H. W. Kroto, S. I. Klein, M. F. Meidine, J. F. Nixon, R. K. Harris, K. J. Parker, and R. Raams, *J. Organomet. Chem.*, 1985, **280**, 281; b) P. LeFloch, N. Maigret, L. Ricard, C. Charrier, and F. Mathey, *Inorg. Chem.* 1995, **34**, 5070.

202. R. Appel, C. Casser, and F. Knoch, *J. Organomet. Chem.*, 1985, **293**, 213.

203. R. Appel, W. Schuhn, and F. Knoch, *J. Organomet. Chem.*, 1987, **319**, 345.

204. A. M. Arif, A. H. Cowley, and S. Quashie, *Chem. Commun.*, 1985, 428.

205. G. Märkl, in ‘Multiple Bonds and Low Coordination in Phosphorus Chemistry’, eds. M. Regitz and O. J. Scherer, Thieme, Stuttgart, 1990, p. 247.

206. F. Nief, C. Charrier, F. Mathey, and M. Simalty, *J. Organomet. Chem.*, 1980, **187**, 277.

207. F. Mathey, J. Fischer, and J. H. Nelson, *Struct. Bonding*, 1983, **55**, 153.

208. C. A. McAuliffe, in ‘Comprehensive Coordination Chemistry’, eds. G. Wilkinson, R. D. Gillard, and Ja. McCleverty, Pergamon, Oxford, 1987, p. 1042.

209. M. Sanchez, M.-R. Mazieres, L. Lamande, and R. Wolf, in ‘Multiple Bonds and Low Coordination in Phosphorus Chemistry’, eds. M. Regitz, and O. J. Scherer, Thieme, Stuttgart, 1990, p. 129.

210. R. G. Montemayor, D. T. Sauer, S. Fleming, D. W. Bennett, M. G. Thomas, and R. W. Parry, *J. Am. Chem. Soc.*, 1978, **100**, 2232.

211. A. H. Cowley, R. A. Kemp, and J. C. Wilburn, *Inorg. Chem.*, 1981, **20**, 4289.

Palladium: Inorganic & Coordination Chemistry

Ana C. Albéniz & Pablo Espinet
Universidad de Valladolid, Valladolid, Spain

1 Introduction 1
2 General Properties of the Metal 1
3 Simple Compounds 2
4 Complexes of Palladium(0) 4
5 Complexes of Palladium(I) and Other Small Clusters 5
6 Complexes of Palladium(II) 9
7 Complexes of Palladium(III) 15
8 Complexes of Palladium(IV) 16
9 Related Articles 17
10 References 18

Abbreviations

acac = acetylacetonate; bipy = bipyridine; ^{t}Bu = *tert*butyl; Cp* = pentamethylcyclopentadienyl; dba = dibenzylideneacetone; DMF = dimethylformamide; DMSO = dimethylsulfoxide; dpma = bis(diphenylphosphinomethyl)phenylarsine; dppm = bis(diphenylphosphino)methane; dppe = 1,2-bis(diphenylphosphino)ethane; dppf = 1,1′-bis(diphenylphosphino) ferrocene; EPR = electron paramagnetic resonance; fcc = face-centered cubic; NMR = Nuclear Magnetic Resonance; phen = 1,10-phenantroline; quinquepy = 2,2′:6′,2″:6″,2‴:6‴, 2⁗-quinquepyridine; THF = tetrahydrofurane.

1 INTRODUCTION

Palladium was discovered in 1803 by Wollaston in the course of his studies on the refining of platinum. It was named after a newly discovered asteroid, Pallas, which bears the name of the Greek goddess of wisdom. Pd occurs associated with other platinum group metals and the extraction processes depend on the particular ore used. It is the second most abundant platinum group metal and its major sources are located in South Africa and Russia. Supplies of palladium in 2002 reached 5.25 million oz and sales amounted to 4.78 million oz, at an average price of $222 per ounce. The highest demand for palladium comes from the manufacturing of exhaust autocatalysts in the automobile industry, which uses a mixture of platinum group metals to effect the oxidation of hydrocarbons and CO (to CO_2) and the reduction of nitrogen oxides (to N_2). The relative demand of Pt, Pd, and Rh for this purpose is strongly affected by price and market considerations. In 2002, a total of 3.08 million oz of newly supplied Pd (56.70% of the total new demand) plus 0.37 million oz of exhaust recovered Pd were used in this manufacture. Dental palladium alloys accounted for a further 15.69%. The electronics industry represented 14.85% of the 2002 demand of Pd, used in the form of silver-palladium or pure palladium pastes for printing conductive tracks and in the production of multilayer ceramic capacitors. The rest of the supply satisfied the demand for jewelry alloys (7.43%) and the manufacture of industrial catalysts (5.33%).[1] Pd compounds are catalysts for the production of vinyl acetate monomer (VAM), and for purified terephthalic acid (PTA), while palladium catchment gauze is used in the manufacture of nitric acid.

Six naturally occurring isotopes have been found for palladium: ^{102}Pd (1.02%), ^{104}Pd (11.14%), ^{105}Pd (22.33%), ^{106}Pd (27.33%), ^{108}Pd (26.46%), and ^{110}Pd (11.72%).[2] Their nuclear properties ($I = 5/2$ for ^{105}Pd; $I = 0$ for the other isotopes) preclude the use of NMR as an observation technique for Pd. The only ^{105}Pd resonance recorded in $K_2[PdCl_6]$ has a bandwidth at half height of 25 000 Hz.

Palladium belongs to group 10 and has the ground-state electronic configuration: [Kr] $4d^{10}$. Pd chemistry bears similarity to that of Pt, its 3rd row congener, but the former is generally more reactive. Although the chemistry of palladium is dominated by the oxidation state +2 (the most stable for the element), it has also a well-established chemistry in oxidation states 0, +1, and +4. Examples of Pd(III) compounds are also known. An unstable Pd(V) complex, $[PdF_6]^-$, and a Pd(VI) compound, PdF_6,[3] have been reported but they have not been confirmed by other research groups. This reluctance to reach high oxidation states follows the observed trend in late transition metals, due to the increased stability of their d valence orbitals. The inorganic and coordination chemistry of palladium has been reviewed in several comprehensive works.[4–9]

Palladium exhibits a rich organometallic chemistry widely applied to organic syntheses, which is covered in other chapters in this encyclopedia (*see* ***Palladium: Organometallic Chemistry***; ***Organic Synthesis using Transition Metal Complexes Containing π-Bonded Ligands***; ***Oligomerization & Polymerization by Homogeneous Catalysis***; and ***Organic Synthesis Using Metal-mediated Coupling Reactions***).

2 GENERAL PROPERTIES OF THE METAL

Palladium metal is silvery-white, ductile, and malleable, crystallizing in the fcc structure (*see* ***Structure & Property Maps for Inorganic Solids***). The metal can be made into finely divided forms (including nanoparticles) that are catalytically

Table 1 Some properties of palladium

Property	Value
Abundance (earth's crust/ppm)	c. 6×10^{-4}
Electron affinity ($M \rightarrow M^-$/kJ mol^{-1})	53.7
Ionization energies (kJ mol^{-1})	
$M \rightarrow M^+$	805
$M^+ \rightarrow M^{2+}$	1875
$M^{2+} \rightarrow M^{3+}$	3177
Radii (pm)	
Metallic	137.6
Pd^{II} (six-coordinated)	86
Pd^{IV} (six-coordinated)	64
Electronegativity (Pauling)	2.2
Melting point (K)	1825
Boiling point (K)	3413
ΔH_{fusion} (kJ mol^{-1})	17.2
$\Delta H_{vaporization}$ (kJ mol^{-1})	393.3
Density (kg m^{-3})	12 020 (293 K)
Thermal conductivity (W m^{-1} K^{-1})	71.8 (300 K)
Electrical resistivity (Ωm)	10.8×10^{-8} (293 K)
Coefficient of linear thermal expansion (K^{-1})	11.2×10^{-6}

very active. Palladium on carbon is a widely used catalyst that contains dispersed Pd (Pd(0) but also Pd(II)) and variable amounts of water. Table 1 shows some properties of the element.

Perhaps, the most remarkable property of metallic palladium is its ability to absorb hydrogen, greater than for any other metal (up to 900 times its own volume). The absorption is reversible and highly selective for H_2 and D_2. The amount of gas absorbed decreases with temperature for a given pressure. This property provides a method to purify H_2 (used in the industrial production of this gas) just by passing the impure H_2 through a Pd membrane at a controlled temperature. As palladium absorbs H_2, its metallic conductivity falls and the material becomes a semiconductor for a composition close to $PdH_{0.5}$ (*see* ***Semiconductors***). However, its ductility is not lost until large quantities of H_2 have been absorbed. It seems that H_2 is first chemisorbed on the surface of the metal, but as the gas pressure increases, hydrogen enters the metallic lattice, forming a 'hydrogen dilute' or α-phase. As H_2 is added further, a hydride phase, called α' or β-phase, is formed. Inelastic neutron-scattering and vibrational techniques have been applied to the study of these phases and have shown that hydrogen atoms occupy octahedral holes in the metallic structure. A variety of Pd-rich alloys also absorb H_2. The most interesting one, Pd–Ag (20%), is utilized in the manufacture of industrial membranes as it does not undergo the volume expansion observed for pure Pd when forming the β-phase.[10]

Palladium is a noble metal, difficult to oxidize because of a combination of high sublimation energy and high ionization potential, although it is more reactive than the other platinum group metals. It is oxidized by O_2, F_2, and Cl_2 at red heat. It dissolves slowly in oxidizing acids (HNO_3 or H_2SO_4), and readily in aqua regia. Pd is also attacked by molten alkali metal oxides or peroxides.

3 SIMPLE COMPOUNDS

3.1 Hydrogen and Hydrides

In addition to the interaction between bulk palladium and hydrogen discussed in Section 2, spectroscopic studies have proved that Pd atoms react with H_2 on codeposition with H_2-doped Ar, Kr, and Xe matrices at very low temperatures. The ligand-free side-on bonded Pd(η^2-H_2) molecular–dihydrogen complex is found in Xe and Kr at 12 K, and in Ar at 9 K.[11] Some IR bands that had been assigned to the end-on bonded Pd(η^1-H_2) complex, were finally recognized to arise from $Pd(H_2)_n$ ($n = 2$, 3). The stable $(PdH)_2$ reaction product containing dissociated dihydrogen and Pd–Pd(H_2) were also detected.[11] Theoretical calculations have shown that the interaction between single Pd atoms and H_2 does not catalyze the cleavage of the H–H bond, but Pd_2 fragments (modeling a hydrogen-adsorbed palladium surface) do (*see* ***Hydride Complexes of the Transition Metals***).[12]

Complex hydrides of palladium have been synthesized with formally zerovalent Pd. Linear, trigonal planar, and tetrahedral 'PdH_n' units can be found in M_2PdH_2 (M = Li, Na), $NaBaPdH_3$, and M_2PdH_4 (M = Sr, Ba, Eu) respectively.[13,14] A square planar hydrido complex of Pd(II), Na_2PdH_4, has been prepared using extremely high H_2 pressure (1800 bar).[15]

3.2 Halides

Only fluorine, the most oxidizing halogen, gives binary combinations with Pd in oxidation states higher than II. The brick-red Pd(IV) fluoride, PdF_4, is formed by fluorination of 'palladium trifluoride' under strong reaction conditions (7 atm F_2, 150 °C) and is violently hydrolyzed by water. It is diamagnetic and its structure consists of edge-sharing $[PdF_6]$ octahedra.

A trifluoride of empirical formula 'PdF_3' is known. It is not a Pd(III) compound as the composition might suggest, but a mixed oxidation state derivative better represented as $Pd^{II}Pd^{IV}F_6$. It can be synthesized by treating $PdBr_2$ with BrF_3. This gives the adduct $Pd_2F_6{\cdot}2BrF_3$, which loses BrF_3 at 180 °C to yield $Pd^{II}Pd^{IV}F_6$. It is also hydrolyzed in water and its paramagnetism is due to the octahedral environment of Pd(II) (d^8), not due to the presence of Pd(III) (d^7) (*see* ***Magnetism of Transition Metal Ions***).

All divalent palladium halides are known. PdF_2, also easily hydrolyzable, is synthesized by refluxing $Pd^{II}Pd^{IV}F_6$ with SeF_4. It has a rutile type structure and Pd is six-coordinated, a situation very unusual for Pd(II). The compound shows the expected paramagnetism ($\mu = 1.90$ B.M.) for a $t_{2g}{}^6e_g{}^2$

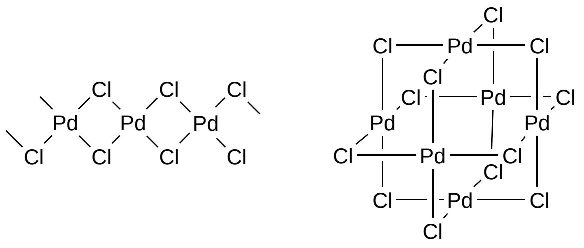

α-$PdCl_2$ β-$PdCl_2$

Figure 1 The two structures of $PdCl_2$

configuration. $PdCl_2$ is obtained by direct synthesis from the elements or by heating $H_2[PdCl_4]\cdot nH_2O$. At about 600 °C, $PdCl_2$ sublimes and then dissociates into its elements. Two different structures (Figure 1) have been found: (1) α-$PdCl_2$, red crystals containing infinite flat chains of four-coordinated square- planar Pd atoms sharing Cl atoms; and (2) β-$PdCl_2$, which consists of Pd_6Cl_{12} cubes in which the central points of the faces and edges are occupied by the Pd atoms and by the Cl atoms, respectively.**[16]** When synthesized by dry methods, $PdCl_2$ is insoluble in water, but the hydrate $PdCl_2\cdot 2H_2O$ can be obtained from an aqueous solution as dark red hygroscopic crystals. $PdCl_2$ is one of the most useful starting materials in the chemistry of Pd(II). It is also easily reduced to the metal by H_2 at room temperature, or by ethyl alcohol and ethylene in warm solutions. $PdBr_2$ is obtained by direct reaction with its elements. An alternative route (similar to the synthesis of $PdCl_2$) is the treatment of the metal with a mixture of HNO_3 and HBr to form $H_2[PdBr_4]\cdot nH_2O$, which on heating loses HBr to give $PdBr_2$. The water insoluble PdI_2 is easily accessible by addition of KI to a solution of $K_2[PdCl_4]$.

3.3 Chalcogenides

There is only one stable oxide of palladium, PdO. The black, anhydrous palladium(II) oxide is insoluble in acids and can be obtained by heating the metal in oxygen below 875 °C (it dissociates above this temperature). The hydrated oxide $PdO\cdot nH_2O$ can be obtained by addition of alkali to an aqueous solution of $Pd(NO_3)_2$. It is a yellowish-brown precipitate, soluble in acids, that cannot be completely dehydrated without loss of oxygen. A Pd(IV) oxide, $PdO_2\cdot nH_2O$, is said to precipitate when alkali is added to a solution of $K_2[PdCl_6]$. It is a dark red solid, strongly oxidizing, which evolves O_2 slowly at room temperature. At 200 °C, it decomposes to give PdO. Anhydrous PdO_2 has been obtained from PdO and $KClO_3$ at high temperature and pressure, and it also loses O_2 readily. A rich structural chemistry of mixed-metal oxides, such as $M^{I}{}_2PdO_3$, $M^{II}{}_2PdO_3$, or $M^{II}{}_4PdO_6$, has been reported.

Palladium(II) sulfide is readily formed as a brown precipitate by bubbling H_2S through a solution of $[PdCl_4]^{2-}$, or as a greyish-black crystalline powder if palladium and sulfur are heated together. In this compound, Pd is coordinated to four sulfur atoms in a slightly distorted square-planar arrangement. PdSe and PdTe are also known and can be synthesized following analogous procedures. The disulfide PdS_2, diselenide $PdSe_2$, and ditelluride $PdTe_2$, have also been prepared. They do not contain Pd(IV), as the formulas seem to indicate, but Pd(II) and $S_2{}^{2-}$, $Se_2{}^{2-}$, or $Te_2{}^{2-}$ groups, respectively.

3.4 Compounds with Other Nonmetals

The reactions of palladium with nonmetals such as boron, silicon, phosphorus, arsenic, and antimony have been investigated. The systems are complex and nonstoichiometry is frequent although some complexes of definite, stoichiometric composition have been reported.

3.5 Other Simple Compounds

A few palladium compounds with simple anions, some of them useful as starting materials, are discussed in this section.

3.5.1 Palladium Acetate

Palladium(II) acetate is usually prepared by the reaction of Pd sponge in hot glacial acetic acid with nitric acid as oxidant. A slight excess of Pd sponge must be used to make sure that all the HNO_3 is consumed. Several other palladium(II) carboxylates can be obtained similarly. The crystal-structure determination of the acetate reveals a trimeric structure with bridging acetates in the solid state (**1**).**[17]** Thus, the compound is better formulated as $[Pd(\mu\text{-}O_2CMe)_2]_3$.

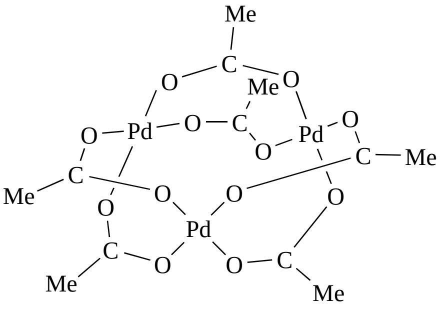

(**1**)

3.5.2 Palladium Acetylacetonate

$Pd(acac)_2$ can be made from acetylacetone and tetrachloropalladate salts or palladium acetate. It has a monomeric structure with a square-planar coordination of palladium to the four oxygens of two chelating acetylacetonates.

3.5.3 Palladium Nitrate

Nitrates are known for Pd(II) and Pd(IV). A hydrated Pd(II) nitrate can be prepared by dissolving the metal in nitric acid followed by crystallization. The composition of the brown crystals obtained is $Pd(NO_3)_2(H_2O)_2$ and IR studies indicate monodentate coordination for the nitrato groups. The anhydrous nitrate, $Pd(NO_3)_2$, contains bridging nitrato groups and can be prepared by reaction of $Pd(NO_3)_2(H_2O)_2$ and liquid N_2O_5 at room temperature. If the hydrated nitrate reacts with N_2O_4, the palladium(IV) nitrate $Pd(NO_3)_4$ is obtained.

4 COMPLEXES OF PALLADIUM(0)

4.1 Introduction

Palladium(0) (d^{10}) forms $[PdL_n]$ complexes with phosphines, arsines, phosphites, cyanide, isocyanides, and olefins. The reduction of $K_2[Pd(CN)_4]$ with potassium in liquid ammonia affords the stable palladium(0) cyanide $K_4[Pd(CN)_4]$. However, the isoelectronic palladium $[Pd(CO)_4]$ is not stable in spite of the excellent π-acceptor properties of the CO ligand. Since CN^- is a good σ-donor (in addition to π-acceptor), and CO is a very bad σ-donor, the presence of some σ-donation, in addition to π-acception, helps stabilize Pd(0). For instance, CO can stabilize Pd(0) in mixed complexes with σ-donor coligands, that is, $[Pd(CO)(PPh_3)_3]$. The high ionization energies of Pd and Pt (805 and 870 kJ mol^{-1} respectively) suggest that, in the absence of significant σ donation, the metal would be reluctant to π-back-donate to the acceptor ligand. Pure σ-donors such as amines or σ-, π-donors like halides can also stabilize Pd(0) if combined with π-acid ligands (olefins or phosphines).**[18]**

4.2 Synthesis

A common synthetic procedure is the reduction of a Pd(II) compound or complex in the presence of an excess ligand. $[PdL_n]$ complexes have been prepared for a large number of phosphines (mono and bidentate), phosphites, arsines, and stibines by procedures similar to those shown for the synthesis of $[Pd(PPh_3)_4]$ in Scheme 1.

The coordination number of palladium depends on L, very bulky phosphines (e.g. P^tBu_3, $P(C_6H_{11})_3$, P^tBu_2Ph, P^tBu_2Me, P(*o*-Tol)$_3$) favoring the species $[PdL_2]$ (linear or bent). These apparently 14-electron species show additional interactions in the solid state (C–H *Agostic Bonding* or Pd–C_{ipso}(aryl) contacts). Structurally characterized $[PdL_3]$ species (16-electron, trigonal planar) are well known. The tetrahedral $[PdL_4]$ complexes (18-electron) show a tendency to dissociate ligands in solution to give coordinatively unsaturated species $[PdL_3]$ and, in a very small extent, $[PdL_2]$. ^{31}P NMR studies have shown that the displacement of the equilibria represented in equations (1) and (2) depends on the size and basicity of the phosphine. Generally, not all three species are observed for a given phosphine.**[19]**

$$[PdL_4] \rightleftharpoons [PdL_3] + L \qquad (1)$$

$$[PdL_3] \rightleftharpoons [PdL_2] + L \qquad (2)$$

Most Pd(0) compounds are easily oxidized in the air, but the complexes $[Pd(dba)_2]$ (better formulated as $[Pd_2(dba)_3]\cdot dba$) or $[Pd_2(dba)_3]$ (**2**, dba = dibenzylideneacetone) are stable and easy to store. Moreover, they are excellent precursors to generate $[Pd(dba)L_2]$ and $[PdL_2]$ complexes in solution (L_2 = bidentate phosphines or two monodentate phosphines).

$[Pd_2(\mu\text{-dppm})_3]$ is a useful starting material for Pd-dppm derivatives in other oxidation states. Its luminescent properties have been studied and the distance between Pd atoms has been estimated to be 304.3 pm from spectroscopic studies. This suggests a weak metal–metal interaction.**[20]**

$[PdL_2(olefin)]$ complexes (L_2 = diphosphine, 2 monophosphines) are very common. The complex $[Pd(PPh_3)_2(\eta^2\text{-}C_{60})]$ (**3**) is formed by reaction of C_{60} with $[Pd\,(PPh_3)_4]$.**[21]**

Isocyanide complexes $[Pd(CNR)_2]_n$ are prepared by reduction of a Pd(II) isocyanide complex with RNC in the presence of a strong alkali (equation 3), or by treating $[Pd(\pi\text{-}C_5H_5)(\pi\text{-}C_3H_5)]$ with RNC. Their structure is unknown but that of the corresponding Pt complexes is a triangular

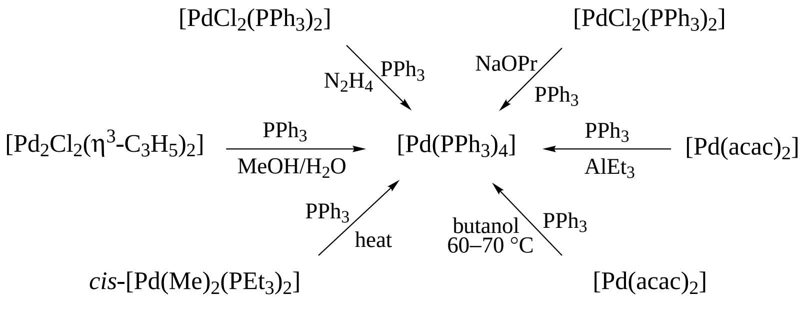

Scheme 1

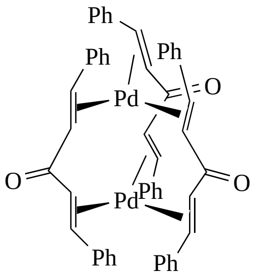

(**2**)

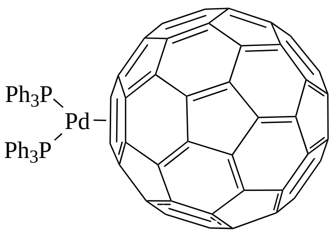

(**3**)

arrangement of three platinum atoms [Pt(μ-CNR)(CNR)]$_3$.

$$[PdI_2(CNR)_2] + 2KOH + 3RNC \longrightarrow [Pd(CNR)_2]_n + RNCO + H_2O + 2KI + 2RNC \qquad (3)$$

In addition, other forms of Pd(0) stabilized in less conventional ways should be cited. Catalytically active palladium colloids are obtained by reduction of palladium acetate in DMSO,**[22]** or in the presence of a number of polymers.**[23,24]** Some of the latter are easy to recycle and avoid the leaching of Pd during the catalytic runs.

4.3 Reactions

Palladium(0) complexes are prone to undergo ligand dissociation as it has already been noted. The lability of the ligands in [PdL$_n$] complexes can be used in the synthesis of mixed ligand complexes (equation 4).

$$[Pd(PPh_3)_4] + 2SbPh_3 \longrightarrow [Pd(PPh_3)_2\,(SbPh_3)_2] + 2PPh_3 \qquad (4)$$

[PdL$_2$L′] adducts are formed by reaction of [PdL$_4$] with small molecules such as NO, SO$_2$, CS$_2$, or O$_2$. [PdL$_2$(O$_2$)] species have shown to be active oxidizing agents reacting with CO$_2$, SO$_2$, NO$_2$, or NO to yield carbonato, sulfato, nitrato, and nitrito complexes respectively (equation 5).**[25]**

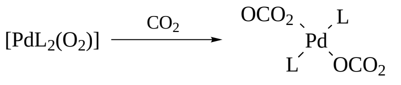

(5)

$$[PdL_2(O_2)] \xrightarrow{CO_2} [Pd(OCO_2)_2L_2] \qquad (5)$$

Oxidative Addition reactions that give palladium(II) complexes (Scheme 2) are also facile processes that occur on the coordinatively unsaturated species [PdL$_n$] with a variety of substrates (halogens, HCl, alkyl, and aryl halides, etc.) and are involved in catalytic processes where a Pd(0) complex is added as the catalyst or is formed in the course of the reaction (*see* ***Palladium: Organometallic Chemistry***; ***Asymmetric Synthesis by Homogeneous Catalysis***; ***Carbonylation Processes by Homogeneous Catalysis***; ***Organic Synthesis Using Metal-mediated Coupling Reactions***; ***Organic Synthesis using Transition Metal Complexes Containing π-Bonded Ligands***). Some of the formally dicoordinated [PdL$_2$] complexes with bulky ligands such as electron-rich phosphines, either isolated or formed as intermediates in Pd-catalyzed reactions, undergo easy oxidative addition reactions by RX reagents that do not work on conventional [PdL$_4$] complexes. The application of these ligands has revolutionized the use of catalytic C–C coupling reactions with less reactive organic electrophiles such as aryl tosylates and chlorides.**[26,27]** Reactions with main group halides or organometallics such as Cd(GePh$_3$)$_2$ or Ph$_3$PbPbPh$_3$ give palladium(II) complexes containing Pd–M bonds.

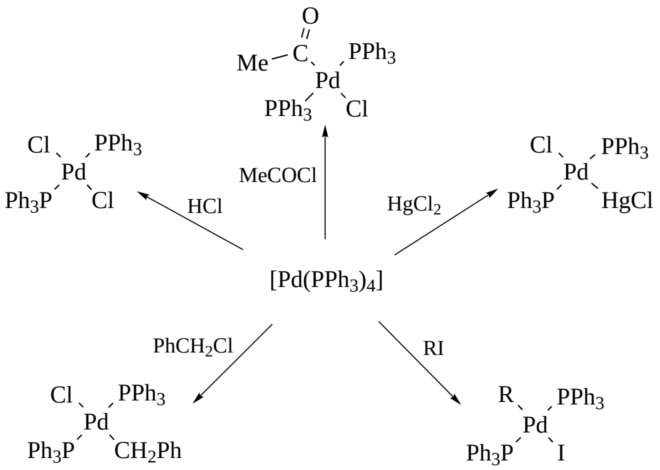

Scheme 2

5 COMPLEXES OF PALLADIUM(I) AND OTHER SMALL CLUSTERS

5.1 Introduction

All characterized Pd(I) compounds have Pd–Pd or Pd–M bonds. Accordingly, the paramagnetic behavior anticipated for a d^9 configuration is not found in these multinuclear diamagnetic complexes as the expected unpaired electron is in fact involved in the formation of a metal−metal bond. There are some palladium clusters in formal oxidation states ranging from 0 to +1 (metal−metal bonds do not count in the assignment of oxidation states) that will be considered here.

Their number, however, is small compared to the rich cluster chemistry found for other transition metals, possibly because of the lower stability of palladium carbonyls. High nuclearity clusters are dealt with in another article (*see* ***Polynuclear Organometallic Cluster Complexes***).

5.2 Complexes with Unsupported Palladium–Metal Bonds

Most of the compounds with palladium–metal bonds are complexes with both metal atoms held together by small bite bridging ligands. Exceptions are the isocyanide derivatives shown in Scheme 3. An X-ray crystal-structure determination of the cationic complex $[Pd_2(CNMe)_6](PF_6)_2$ (**4**) showed only terminal CNMe ligands that adopt a staggered arrangement.**[28]** The Pd–Pd distance is short, 253.1 pm. In the related cation $[Pd_2(PMe_3)_6]^{2+}$, the distance increases to 259.8 pm.**[29]** In the unusual trinuclear cluster with linear Pd arrangement $[Pd_3(CNMe)_6(PPh_3)_2](PF_6)_2$ (**5**), each palladium atom has a square-planar environment with short Pd–Pd distances (259.2 pm).**[30]**

A palladium(I) complex isostructural to (**4**) and synthetically very useful is $[Pd_2(CH_3CN)_6](BF_4)_2$. It can be considered as a 'naked' unsupported $[Pd–Pd]^{2+}$ unit since easy substitution of the acetonitrile ligands leads to a variety of Pd(I) compounds and small clusters.**[31]**

Another class of unsupported Pd–M compounds is that of complexes of the type *trans*-$[Pd(mCO)_2L_2]$ (L = neutral ligand; mCO = $Mn(CO)_5$, $Co(CO)_4$, $CrCp(CO)_3$, $MoCp(CO)_3$, $WCp(CO)_3$), obtained by reaction of *trans*-$[PdCl_2L_2]$ with the corresponding carbonylate. Note that formally they are palladium(0) complexes, although in this case the stability of the carbonylate anions in solution strongly suggests that the mCO moieties are playing a role not very different from that of the chloro ligands in the precursor, a typical palladium(II) complex. For L = NCPh, these complexes react with PR_2H to give heterobimetallic complexes stabilized by bridging phosphido groups (Scheme 4).**[32]**

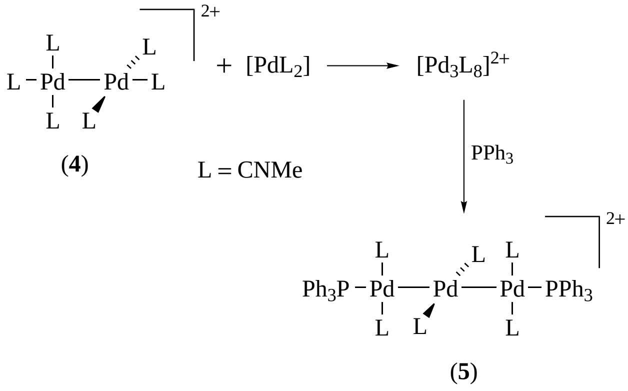

Scheme 3

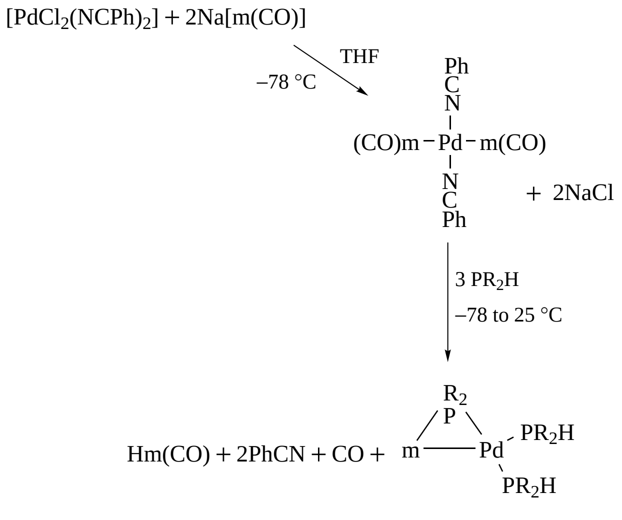

Scheme 4

5.3 Dimeric Complexes with Palladium–Metal Bonds Supported by Small Bite Ligands

A great deal of chemistry has been developed in the last three decades concerning complexes with binucleating ligands similar to 1,2-bis(diphenylphosphino)methane (dppm) and 2-pyridyldiphenylphosphine (PPh_2Py). They behave somewhat differently since a double bridge with two dppm ligands is rather flexible and can accommodate a range of Pd to Pd distances, whereas PPh_2Py ligand bridges are more rigid. The torsion angles shown by the two palladium coordination planes in the complexes also reflect this difference in flexibility and they change from 0° for the bridging PPh_2Py and related ligands, to a range of 37–72° for the dppm-type derivatives.

The derivative $[Pd_2Cl_2(\mu\text{-dppm})_2]$ (Pd–Pd bond length = 265.2 pm) can be prepared by a variety of methods including reduction of the palladium(II) complex $[PdCl_2(dppm)]$ and comproportionation of palladium(0) and palladium(II) complexes, for example, $[Pd(PPh_3)_4]$ and $[PdCl_2(PhCN)_2]$ in the presence of dppm. This method also applies to the synthesis of the heterodinuclear complex $[PdPtCl_2(\mu\text{-dppm})_2]$ from $[Pd(PPh_3)_4]$, $[PtCl_2(^t BuCN)_2]$, and dppm. For both the Pd–Pd and Pd–Pt derivatives, the metal–metal bond is very reactive and undergoes insertion of small molecules as shown in equation (6). Sulfur inserts into the M–M bond when the palladium(I) dimer (**6**, M = Pd) reacts with S_8 or $MeCHCH_2S$. The addition occurs at the expense of the metal–metal bond, producing the so-called A-frame complexes (**7**). These are formally Pd(II) complexes, where the Pd–Pd distance has increased to 325–350 pm, depending on the inserted group.

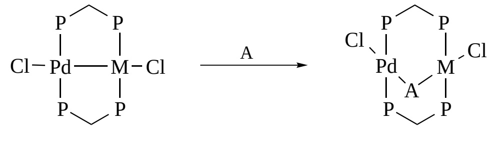

(**6**) (**7**)

(6)

P⌒P = $Ph_2PCH_2PPh_2$; M = Pd, Pt; A = CO, SO_2, $MeO_2CC_2CO_2Me$

2-Pyridyldiphenylphosphine forms a number of homo- and heteronuclear palladium dinuclear clusters with short Pd–M bonds (about 260 pm). They are usually made by comproportionation of a Pd(II) complex and a second complex in a low oxidation state, for example, Pd(0), Rh(I), Ru(0). For these derivatives, head-to-head and head-to-tail isomers are possible, but the latter seems to be preferred (Figure 2). The metal–metal bonds in these derivatives are not as reactive as in the corresponding dppm complexes and insertion reactions do not occur. Some single-bridged complexes, such as $[Cp(CNR)Rh(\mu\text{-}PPh_2Py)Pd(CNR)Cl]^+$ (Pd–Rh distance 263.1 pm) are also known.

Complexes with other ligands such as $R_2PCH_2AsR_2$ and R_2PCH_2SR are similar to the dppm or PPh_2Py complexes. A cationic complex displaying a particularly short Pd–Pd bond (250.0 pm) is formed by the ligand *o*-$(PPh_2)C_6H_4CH_2O(CH_2)_3\text{-}2\text{-}C_5H_4N$ (**8**).**33**

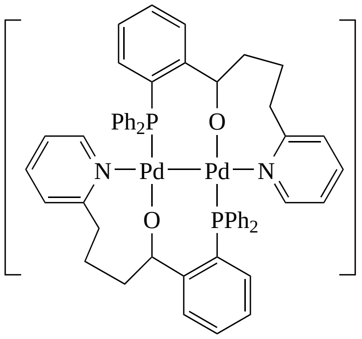

(**8**)

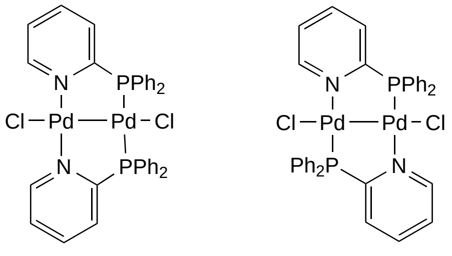

Head to head isomer Head to tail isomer

Figure 2 Isomers for two bridging 2-pyridyldiphenylphosphines

Thio- and selenophosphide complexes have also been synthesized according to Scheme 5. The Pd–Pd bond distance found for a thiophosphide complex (L = CNMe) is 260.8 pm.

The complexes $[Pd_2(\mu\text{-}P^tBu_2)_2(PMe_3)_2]$ (Pd–Pd distance 257.1 pm)**34** and $[Pd_2(\mu\text{-}P^tBu_2)_2(PH^tBu_2)_2]$ (Pd–Pd distance 259.4 pm)**35** are examples of Pd–Pd bonds supported by double phosphido bridges. The latter is a red solid easily prepared through the thermal reaction in equation (7).

$$2CpPd(\eta^3\text{-}C_3H_5) + 4P^tBu_2H \longrightarrow [Pd_2(\mu\text{-}P^tBu_2)_2(P^tBu_2H)_2] + 2C_5H_5CH_2CH{=}CH_2 + H_2 \tag{7}$$

Palladium(I) dimeric complexes are also known where the Pd–Pd bond is supported by electron-deficient hydrido or silyl ligands. In the case of SiR_2H bridges, an agostic interaction (*see Agostic Bonding*) of one of the Pd atoms with the Si–H bond is observed (**9**).**36** The same feature has been found for some phosphido-bridged Pd(I) dimers.

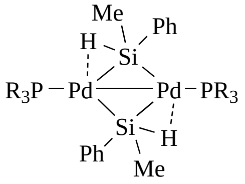

(**9**)

In sandwich-type complexes supported by s-*trans*-1,3-diene ligands, a remarkably large Pd–Pd distance is observed in $[Pd_2(\mu\text{-diene})_2(PPh_3)_2]^{2+}$ (Pd–Pd = 318.52 pm) compared to the usual range of Pd(I)–Pd(I) distances (250–285 pm). This was attributed to the fact that Pd–Pd lengthening decreases the steric congestion and the Pd–Pd weakening is compensated by both back donation and donation interactions between the diene and the Pd dinuclear unit. Contributions, to a large extent, of Pd(II) resonant structures where the diene would oxidatively add to the dimer to give a bridging enediyl ligand (with elimination of the Pd–Pd bond) were discarded.**37**

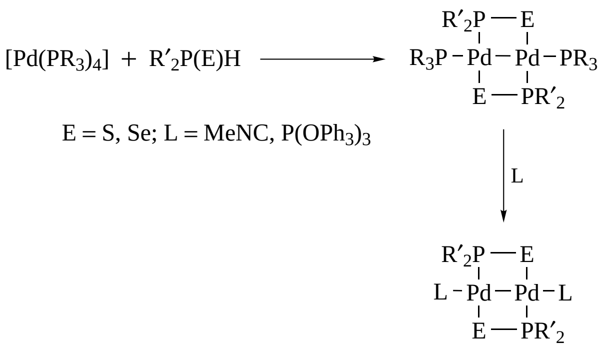

E = S, Se; L = MeNC, $P(OPh_3)_3$

Scheme 5

5.4 Small Clusters

Monodentate bridging ligands such as SO_2, PPh_2, and CO usually lead to nuclearities higher than two. Several examples of homo- and heteronuclear, three or four-member palladium clusters that adopt a variety of geometries are known.

A triangulo arrangement is the most common structure for trinuclear clusters. $[Pd_3(\mu\text{-}SO_2)_2({}^tBuNC)_5]\cdot 2C_6H_6$ (**10**), synthesized from $[Pd({}^tBuNC)_2]_n$ and SO_2, displays the triangular arrangement of Pd atoms. The Pd–Pd distances are 276 pm for the unsupported interaction and 273.4 pm for the other two.**38** Phosphido-bridged triangulo clusters (**11**) have also been prepared, with rather large Pd–Pd distances of 290 pm. Reaction of the palladium(I) dimer (**6**) with metaloanions gives heteronuclear clusters with triangular arrangement and short Pd–M distances (equation 8).**39**

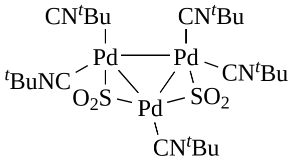
(**10**)

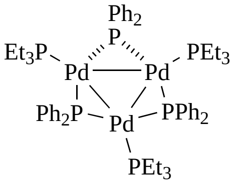
(**11**)

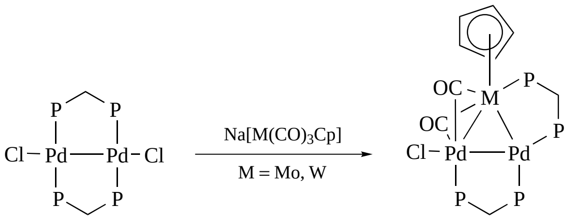

(**6**) (**12**)

(8)

The reaction of palladium acetate with dppm and CO affords the trinuclear dicationic cluster $[Pd_3(\mu\text{-}dppm)_3(\mu^3\text{-}CO)]^{2+}$ (**13**), which contains a planar triangular $Pd_3(\mu\text{-}dppm)_3$ framework. The selective attachment of halide ions gives (**14**) (equation 9),**40** closely related to (**15**), which is obtained by disproportionation of $[Pd_2Cl_2(\mu\text{-}dppm)_2]$ in the presence of PF_3.**41**

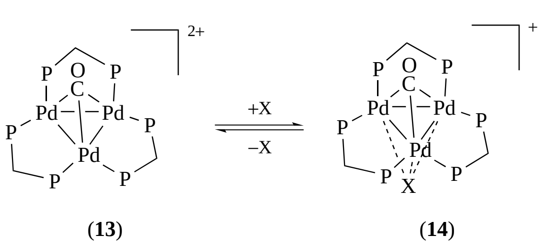

(**13**) (**14**)

(9)

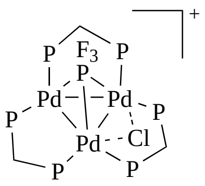
(**15**)

The tridentate ligand bis-(diphenylphosphinomethyl) phenylarsine (dpma) gives metallamacrocycles with Rh or Ir (**16**), which react with $[PdCl_2(NCPh)_2]$ to give (**17**) (equation 10). The X-ray structure of the Rh complex shows a Rh–Pd distance of 269.9 pm, whereas the Cl-bridged Rh···Pd distance of 316.6 pm is not indicative of a metal–metal bond.**42**

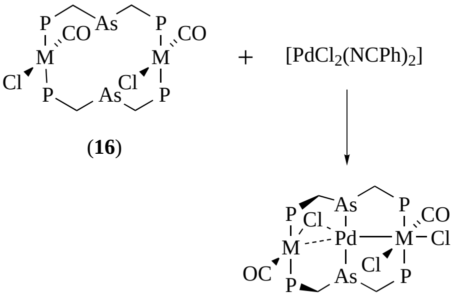

(**16**) (**17**)

(10)

Complexes with the formula $[Pd(O_2CR)(CO)]\cdot n RCO_2H$ ($n = 0$, 0.5; R = Me, Et, Ph) have been prepared from the Pd(II) carboxylates and CO in carboxylic acid/benzene solution. These compounds are actually tetrameric clusters (**18**) with two short (266.3 pm) and two long (290.9 pm) Pd–Pd distances, and are better regarded as two dimeric Pd(I) units linked by acetate bridges.**43** The structurally related (**19**) is also known.**44** The four palladium atoms in complexes $[Pd_4(\mu_3\text{-}S)(\mu\text{-}SO_2)_2L(PBz_3)_4]$ (L = CO, CNR) show a tetrahedral arrangement with a capping μ_3-sulfido and two bridging SO_2 ligands,**45** while a rectangular structure is found in $[Pd_4(\mu\text{-}Cl)_2(\mu\text{-}dppm)_4](ClO_4)_2\cdot bpe$.**46**

Carbonylation of different palladium complexes, often in the presence of phosphines, led to the synthesis of a variety of clusters including halocarbonyl clusters of unknown nuclearity $[PdX(CO)]_n$ (X = Cl, Br), and phosphine–carbonyl clusters from tetrameric $[Pd_4(CO)_5(PR_3)_4]$ to high nuclearity compounds such as $[Pd_{38}(\mu^3\text{-}CO)_4(\mu^2\text{-}CO)_{24}(PEt_3)_{12}]$.**47** From these preformed clusters, nanosized cluster compounds of higher nuclearity such as $[Pd_{69}(CO)_{36}(PEt_3)_{18}]$ can be prepared.**48**

When SO_2 is bubbled through a solution of $[Pd_8(CO)_8(PMe_3)_5]$, the cluster $[Pd_5(\mu^2\text{-}SO_2)_2(\mu^3\text{-}SO_2)_2(PMe_3)_5]$ is formed in high yield. Rather than being isostructural and isoelectronic with $[Pt_5H_8(PR_3)_5]$ (tbp arrangement for the platinum atoms), its structure consists of a rhombus of palladium atoms with a fifth palladium atom bridging the internal Pd–Pd bond of the rhombus. This is due to the fact that two of the SO_2 ligands are acting as four-electron bridging

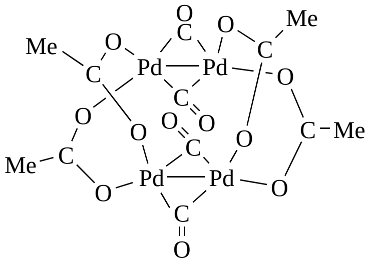

(**18**)

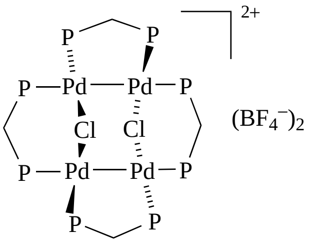

(**19**)

ligands using one oxygen lone pair (*see* ***Electronic Structure of Clusters***).[49]

6 COMPLEXES OF PALLADIUM(II)

6.1 Introduction

Pd(II) is a second row, d^8 transition metal center. Considering the splitting of the d orbitals in crystal fields of different symmetry (*see* ***Coordination & Organometallic Chemistry: Principles***), the four-coordinated square-planar geometry is energetically the most favorable. Indeed, it is by far the most frequently found geometry, and therefore the Pd(II) complexes are diamagnetic. However, there are exceptions to this behavior, depending on the ligands. In a few cases involving bulky ligands, the complex is apparently three-coordinated, but this initial impression is usually corrected when additional interactions (for instance, C–H agostic bonds, or Fe–Pd bonds) are considered.[50] One case of tetrahedral paramagnetic Pd(II) complex is known. The compound PdF_2 is a rare example of a six-coordinated Pd(II) (see Section 3.2). Finally, the formation of five-coordinated complexes is more frequent, either with a bpt structure, a square pyramidal structure or, very often, intermediate geometries. Five-coordinated complexes are the usual nonobserved intermediates in associative ligand substitution reactions, but a good number of stable compounds, both in solution and in the solid state, are also known.

Palladium(II) is a class b or a soft metallic center. Accordingly, it forms numerous stable complexes with soft ligands. A vast palladium(II) coordination chemistry is found for S-, N-, P-, and As-donor ligands. Pd(II) also shows a higher affinity for the heavier halogens. Ligand-exchange reactions with alkali metal salts are favorable when moving from $[PdX_nL_{4-n}]^{(2-n)+}$ to $[PdX'_nL_{4-n}]^{(2-n)+}$, provided X′ is heavier than X. The reverse exchange can be forced with silver or thallium salts, the formation of the more insoluble Ag or Tl halide (that with the heavier halide) being the driving force (equation 11).

$$[PdX_nL_{4-n}]^{(2-n)+} \underset{MX}{\overset{M'X'}{\rightleftharpoons}} [PdX'_nL_{4-n}]^{(2-n)+} \qquad (11)$$

X′heavier than X

M = Ag, Tl; M′ = alkaline metal

Complexes containing O–donor ligands are less abundant and monodentate ligands of this type readily undergo substitution reactions by other ligands. However, the *Chelate Effect* is important in favoring the final stability of a complex, and there is a well-developed chemistry for bidentate O-donors and also for chelating ligands that combine a soft and a hard-donor center.

Substitution reactions in palladium(II) complexes are a common preparative route to new types of derivatives. Halocomplexes are often employed as starting materials. These reactions are usually noticeably faster for palladium than for platinum and proceed through associative mechanisms whenever organometallic ligands are not present.[50] It has been proved that even in the case of sterically very hindered complexes, where the reaction rates can depart from the order predicted by the n_{Pt} scale, when this occurs, it is because of steric factors that overcome the usual electronic control, but the mechanism remains associative.[51] It is generally possible to predict the leaving ligand in a substitution reaction considering the relative *Trans Effects* of the different ligands in the complex. The lability of palladium(II) complexes makes it often difficult to isolate unstable isomers, and fast isomerization to the more stable isomer is frequently found. Therefore, few examples of kinetically stable pairs of cis and trans isomers are known.

In the following sections, the coordination chemistry of palladium(II) will be illustrated with selected examples. They are roughly organized according to the number of donor atoms in the ligand and the binding mode to the metal. More information can be found in the comprehensive works and monographs cited.[5–9] *Coordination Chemistry Reviews* often offers surveys of the recent palladium literature.

6.2 Complexes with Monodentate Ligands

Palladium(II) complexes with monodentate ligands are widespread. Table 2 illustrates the most important types. Besides, there are a large number of compounds that combine different L (neutral) or X (monoanionic) ligands, that is,

Table 2 Palladium (II) complexes with monodentate ligands

Stoichiometry	X	L
$[PdX_4]^{6-}$	$\underline{S}O_3{}^{2-}$	
$[PdX_4]^{2-}$	Cl, Br, I, CN, $\underline{S}CN$	
$[PdX_3L]^-$	Cl, Br	PR_3, SR_2
	Cl	NH_3
$[PdX_2L_2]$	Cl, Br	NR_3H_{3-n}, RCN, py, PR_3, $P(OR)_3$, $E = PPh_3$ (E = O, S, Se), ER_2 (E = S, Se), $DM\underline{S}O$,
	I	PR_3, $P(OR)_3$
	CN, N_3	PR_3
	$\underline{S}CN$	NH_3, py, PR_3, $AsPh_3$, $SbPh_3$,
	$SC\underline{N}$	PR_3, $AsPh_3$
	$GePh_3$, $PbPh_3$	PR_3
$[PdYL_3]$	$\underline{S}O_3$	NH_3
$[PdXL_3]^+$	Cl	NMe_3, $P(OR)_3$
	Cl, Br, I	PR_3
$[PdL_4]^{2+}$		H_2O, $DMS\underline{O}$ + $DM\underline{S}O$, $\underline{S}C(NH_2)_2$, NR_3H_{3-n}, MeCN, PR_3

$[PdXX'LL']$, although there is a strong tendency to give fast equilibria with their symmetrization compounds $[PdX_2L_2]$, $[PdX'_2L'_2]$, and so on.[52] Complexes of group 15 (specially P- and As-donors) and S-donor ligands are by far the most numerous.

$PdCl_2$ and halo complexes are useful starting materials for the preparation of Pd(II) complexes. $[PdCl_4]^{2-}$, easily prepared from $PdCl_2$ and a soluble chloride salt in MeOH or HCl(aq), is commonly used. When substitution of the halogen cannot be easily accomplished, it can be forced by creating a vacant coordination site on the metal. The use of soluble silver(I) salts ($AgBF_4$, $AgNO_3$) in a non or weakly coordinating solvent (CH_2Cl_2, acetone, THF) eliminates the halogen from the Pd coordination sphere in the form of an insoluble AgX salt. The 'vacant' coordination site (usually solvent coordinated) is then more available to the incoming ligand. Similarly, metathesis reactions, for example, treatment of the $[PdCl_nL_{4-n}]^{(2-n)+}$ derivatives with M^IX ($X^- = Br^-$, I^-, CN^-, SCN^-, etc.), provide access to other $[PdX_nL_{4-n}]^{(2-n)+}$ derivatives. The fluorocomplexes of palladium are scarce: $[PdF(PEt_3)_3](BF_4)$,[53] and $[PdF_2(diapp)]$ (diapp = dialkylphosphinopropane),[54] in addition to some organometallic derivatives $[PdFAr(PR_3)_2]$.[55] The latter are a convenient source of 'naked fluoride' and have proved to be interesting fluorinating reagents. Ultrasound-promoted reaction of AgF with the appropriate iodo precursor is a convenient preparation method for $[PdFAr(PR_3)_2]$. Reaction of XeF_2 with $[PdMe_2(diapp)]$ was used to prepare $[PdF_2(diapp)]$.

CN^- is probably the strongest anionic monodentate ligand toward palladium(II). The coordination mode of SCN^- has been extensively studied by infrared spectroscopy and X-ray crystallography.[56] Both N and S linked SCN^- complexes are found for Pd (see table 2 for a few examples). These forms are very similar in stability. Therefore electronic differences, introduced by other ligands coordinated to Pd, and steric effects (coordinated $\underline{N}CS$ is linear but $\underline{S}CN$ is bent, M–S–C angle about 105°) may determine which donor atom is attached to the metal. Linkage isomerism has been observed for nitro complexes as well. The fluxional behavior of $[Pd(NO_2)_2(diphos)]$ has been studied by ^{15}N NMR and is due to exchange between the N- (nitro) and O-bound (nitrito) forms of the NO_2 ligand.

Oxygen-containing solvents such as water, alcohols, ethers, or ketones are hard donors, and few palladium(II) complexes have been isolated although they are probably intermediates in substitution reactions carried out in these solvents. It is possible to isolate $[Pd(solv)_4]^{2+}$ complexes for solv = DMSO, H_2O and $[PdL_2(solv)_2]^{2+}$ for L_2 = bidentate phosphine and solv = H_2O, $DMS\underline{O}$, acetone. $[Pd(H_2O)_4]^{2+}$ has been used to selectively cleave polypeptides.[57] DMSO is capable of linkage isomerism and $[Pd(DMSO)_4]^{2+}$ is better represented as $[Pd(DM\underline{S}O)_2(DMS\underline{O})_2]^{2+}$. The solv ligands are easily replaced by other species. Attempts at isolating these species for EtOH produce reduction to the Pd metal. $[Pd(H_2O)_4]^{2+}$ is stable only in strongly acidic solutions of noncoordinating acids like $HClO_4$. The complex is acidic and it readily undergoes hydrolysis to give hydroxo species, rarely isolated. Studies on *trans*-$[Pd(H)(H_2O)(PCy_3)_2]X$, obtained by oxidative addition of strong acids $[H_3O^+][BF_3OH^-]$ or $[H_3O^+][BF_4{}^-]$ to $Pd(PCy_3)_2$ suggest that the acidity of the hydridic hydrogen is higher than that of the hydrogens of the coordinated water.[58]

Many Pd(II) complexes with amines, nitriles, and heterocyclic N-containing ligands (pyridines, imidazoles, etc.) are known, $[PdX_2L_2]$ being the commonest type. These are usually trans, although cis isomers can also be obtained by careful choice of the preparation procedure. Nitrile complexes $[PdCl_2(NCR)_2]$ (R = Me, Ph) and $[Pd(NCMe)_4]^{2+}$ are used as starting materials for other complexes, as they are soluble in most organic solvents and RCN ligands are easily substituted by other ligands. The complexes of Pd(II) derivatives with peptides and nucleosides–nucleotides have been reviewed,[59] and may be relevant to the mechanism of anticancer action of transition metal compounds such as *cis*-$[PtCl_2(NH_3)_2]$ (*see* ***Platinum-based Anticancer Drugs***).[60] Tetraamine complexes $[PdL_4]X_2$ are also common. Among them, the salts $[Pd(NH_3)_4][PdCl_4]$ and $[Pd(NH_3)_4][PtCl_4]$ are noteworthy for their solid-state structure, similar to $[Pt(NH_3)_4][PtCl_4]$, where the square-planar ions are stacked vertically. The short axial metal–metal distances (325 pm) seem responsible for the anomalous visible spectra and the semiconductivity and photoconductivity that arise from a filled and empty band structure created from the overlap between the p_z and d_z2 orbitals.[61]

Although amido palladium complexes are less abundant than amino complexes, they play an important role in the catalytic amination of organic compounds. The same applies to alkoxy ligands for the Pd-mediated synthesis of organic ethers. Terminal amido or alkoxy Pd complexes are usually rather reactive due to the high nucleophilicity associated with the lone pairs on the heteroatom. For this reason, bridging amido or alkoxy groups, where these lone pairs are involved in bonding, often lead to more stable complexes.

The numerous P-donor ligand complexes are found as cis and trans isomers. The relative stability of the two isomers depends on the actual ligands and on the solvent if the stability in solution is being considered.[62,63] Solvation effects are very important and favor the polar cis form in solution. Bulky ligands tend to favor the trans form. The cis–trans isomerization is favored by addition of excess PR_3. Phosphines play an important role in stabilizing organometallic palladium(II) derivatives, and hence PR_3 complexes are often used as catalyst precursors for the transformation of organic substrates. Most of the palladium hydrides known also contain phosphines as ancillary ligands, for example, $[PdHX(PR_3)_2]$ (X = Cl, OPh, $GePh_3$) or [PdHX(diphos)] (X = SiR_3, SnR_3), $[PdH(triphos)]^+$ (exception is the homoleptic $[PdH_4]^{2-}$, see Section 3.1).

In connection with the wide applicability of palladium in catalytic processes, much work has been devoted to the synthesis of palladium complexes with ligands attached to a support (silica or a polymer), which should combine the advantages of homogeneous and heterogeneous catalysis.[64] These ligands very often bind Pd through phosphine ends, although other types of donor atoms (N, As) have also been used (*see* ***Supported Organotransition Metal Compounds***).

A homoleptic square-planar palladium(II) carbonyl complex $[Pd(CO)_4](Sb_2F_{11})_2$ that displays ν(CO) at 2259 cm^{-1} (the value for free CO is 2143 cm^{-1}) has been recently prepared. This is an exceptional complex, dubbed by the authors as 'superelectrophilic metal carbonyl'. The very high value of ν(CO) shows that the carbonyl ligands behave as σ-donors (*see* ***Carbonyl Complexes of the Transition Metals***). Additional data (e.g. ν(M–C)) and stability data support that this ligand is very weakly coordinated as only a σ-donor.[65]

Isocyanides are excellent ligands for Pd(II) and Pt(II), to the point that they can be used in the synthesis of thermotropic liquid crystals. Some $[MX_2(isocyanide)_2]$ complexes are liquid crystals (discotic) at room temperature.[66] The thermal properties depend very much on the cis or trans geometry of the complex. For X = I, the trans geometry is favored, whereas for X = Cl, cis complexes are formed.

The complexes referred to so far are four-coordinated square planar, the normal geometry for Pd(II). As stated above, some palladium(II) complexes deviate from this trend. Since early times, conductimetric and electronic spectral measurements provided evidence for five-coordinated species of the type $[PdXL_4]X$ in solution for L = N, N' disubstituted thio- and seleno-ureas.[67] $[PdX_2(ER_3)_3]$ (E = P, As, Sb) have also been isolated when ER_3 is a ligand with suitable steric requirements (e.g. $PBzMe_2$ or 5-ethyl-5H-dibenzophosphole). The geometry of these derivatives is distorted tetragonal pyramidal with an apical X group. $[Pd\{P(OR)_3\}_5]^{2+}$ complexes have been synthesized in the presence of excess $P(OR)_3$, but recrystallization in the absence of phosphite results in the loss of the fifth ligand to give $[PdL_4]^{2+}$.

6.3 Complexes with Bi- or Polydentate Chelating Ligands

In mononuclear palladium derivatives with ligands bearing two or more donor atoms, the geometric and steric requirements of the ligand are determinant of the number of donor atoms that will coordinate, the final geometry and stability of the metallic species. For most bidentate ligands, a cis arrangement of their donor atoms is adopted, and the highest stability is reached for a five-membered metallacycle, although four- and six-membered rings are not uncommon.

The main general types of derivatives with bidentate ligands (representing as X a monoanionic donor, and as L a neutral donor end) are: 1) $[Pd(X-X)_2]^{2-}$ (X–X = oxalate; malonate; dithiooxalate; 1,1-dithiolate); 2) $[Pd(X-L)_2]$ (X–L = β-diketonate; glycinate-N,O-; dioximate-N,O-; *o*-aminophenolate-N,O-; salicylaldiminate-N,O-; thioether–thiolate; dithiocarboxylate; o-$C_6H_4(AsR_2)S^-$); 3) $[PdX_2(L-L)]$ and 4) $[Pd(L-L)_2]^{2+}$ (L–L = bidentate amine; α-diimine; 2,2′-bipy; phen; bidentate phosphine; substituted amines $Ph_2ECH_2CH_2NH_2$, E = P, As; bis-thioethers). Besides, many chiral and nonchiral bidentate ligands have been developed that combine two different donor atoms (N, O, P, As, S) and are either anionic or neutral. Many of their palladium complexes are useful in catalytic processes such as the polymerization of olefins,[68] and others.[69]

The influence of the ligand backbone on the geometry of the metal derivative is clearly seen for bidentate phosphines and arsines. Diphosphines $R_2P(CH_2)_nPR_2$ usually form cis complexes $[PdX_2(L-L)]$, if $n = 2, 3$. For $n = 1$, cis chelating ligand complexes are rare and dppm prefers to bridge two metals or to act as a pendant η^1-ligand, for example *trans*-$[Pd(CN)_2(\eta^1\text{-dppm})_2]$. Large values of n give *trans*-$[PdX_2(L-L)]$ derivatives (L–L = ${}^tBu_2P(CH_2)_nP^tBu_2$; $n = 10$) or dinuclear complexes with bridging phosphine.

Palladium(II) β-diketonates give a complex substitution chemistry due to the many coordination modes adopted by these ligands: O,O′-chelate, Pd–C through the γ-carbon, singly O-bonded, and so on. Some of this chemistry is summarized in Scheme 6. The use of acetylacetonate as an easy leaving group by protonation is noticeable. Thus, $M(acac)_2$ deprotonates diphosphines $Ph_2PCHRPPh_2$ to give $M(Ph_2PCRPPh_2)_2$, and $ArNH_2$ to give $[Pd_2(\mu\text{-NHAr})_2(acac)_2]$.

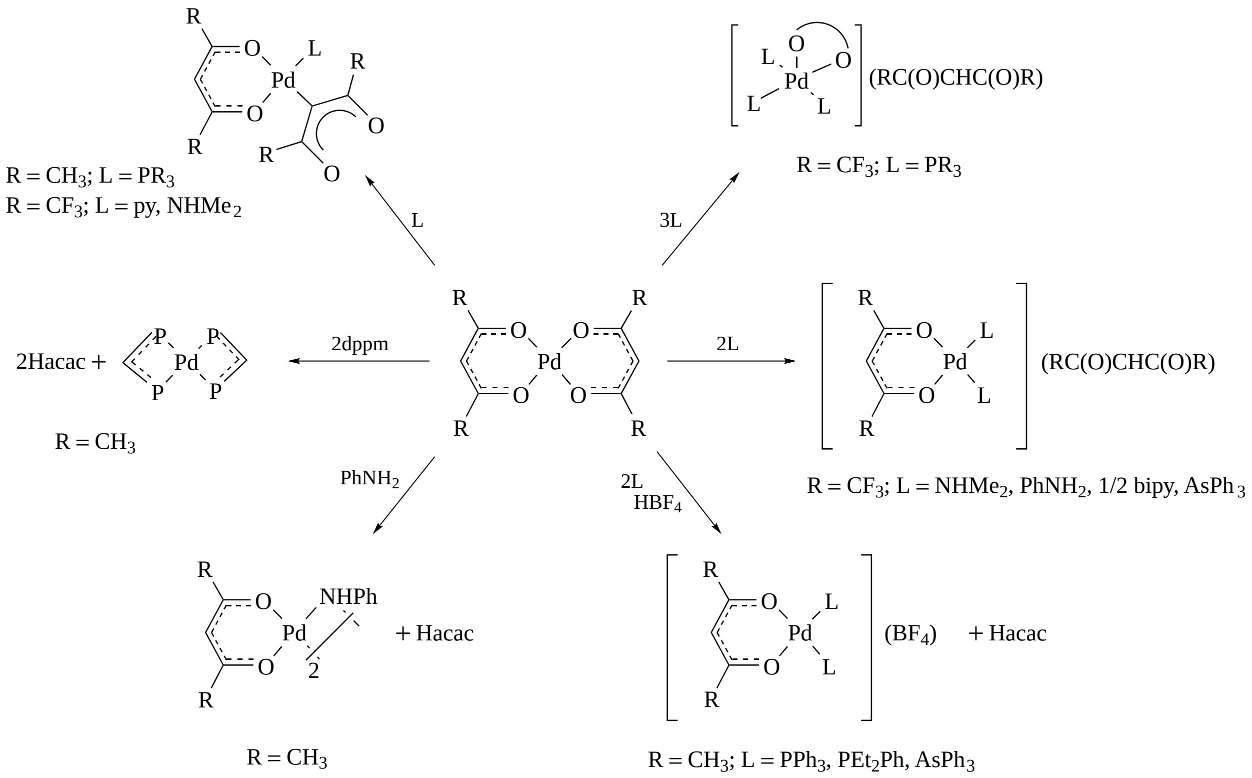

Scheme 6

The related volatile hexafluoroacetylacetonate, Pd(hfacac)$_2$, and several mixed allyl diketonates, including the liquid [Pd(C_3H_5)(Bu^{t}C(O)CH(CO)C_3F_7)], are used for chemical vapor deposition on surfaces (CVD) and subsequent reduction to Pd. The mechanism of formation of a Pd film on a copper surface by thermal decomposition of deposited Pd(hfacac)$_2$ has been studied in detail.[70,71] Reduction with H_2 can also be used and it produces polycrystalline Pd.

Among the numerous S-donor chelating ligand complexes, the 1,2-dithiolene derivatives are peculiar since these ligands are redox active and therefore easily and reversibly oxidized and reduced. This makes it often difficult to assign oxidation states to the metal (*see Dithiolenes* and Section 7).[72]

The preference for chelation in some bidentate ligands can lead to a departure from the normal square-planar coordination. Thus, a small distortion of the square-planar structure toward a tetrahedral geometry has been observed for [Pd(2,2′-bipy)(NO_3)$_2$]·H_2O due to steric constrain. The complex [PdX(L–L)$_2$]$^+$ (X = halogen; L–L = 2, 9-dimethyl-1, 10-phenantroline) has a trigonal bipyramidal structure, and [PdCl(*o*-phen)(PPh_3)$_2$]$^+$ has a distorted square pyramidal structure with a long apical Pd–N distance (268 pm).[73] An interesting family thoroughly investigated is that of the trigonal bipyramidal Pd or Pt compounds containing a coordinated alkene, [M(N–N)(C_2H_4)XY].[74] The reasons for their stability have been discussed on the basis of quantum-mechanical calculations. Six-coordination in the solid state is observed for the *o*-phenylene derivatives [PdX_2(L–L)$_2$] (X = halogen, L–L = *o*-C_6H_4(EMe_2)E′Me_2, E, E′ = P, As, Sb). The X-ray crystal-structure determination carried out for [PdI_2{*o*-C_6H_4(AsMe_2)$_2$}$_2$] shows an hexacoordinated Pd atom with long *trans*-Pd–I bonds. However, in solution five-coordinated species [PdX(L–L)$_2$]$^+$ are formed. Perhaps, the most extraordinary distortion is observed in [PdCl_2(dppfO_2-*O*,*O*′)]. This complex, bearing a chelating ligand with a large *bite angle*, is actually tetrahedral (**20**). The dihedral angle between the {PdCl_2} and {PdO_2} planes is 84.2°. According to its tetrahedral structure, the complex shows a magnetic moment of 2.48 μ_B, consistent with paramagnetic Pd(II) with two unpaired electrons and in sharp contrast with the diamagnetic behavior of other Pd(II) complexes.[75]

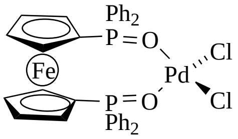

(**20**)

Tri- and tetradentate ligands coordinated to palladium usually contain group 15 donor atoms. The tridentate amine *N*-(2-aminoethyl)-1,2-diaminoethane (dien) gives [PdX(dien)]X and [PdL(dien)]X_2 complexes. *N*,*N′*-Di(2-aminoethyl)-1,2-diaminoethane (trien) acts as tetradentate in [Pd(trien)]X_2. The four N atoms bind palladium in a trapezoidal arrangement as shown in the structure determination of its PF_6^- derivative, with Pd–N distances between 1.95 and 2.08 Å. The tripod ligand tris[2-(dimethylamino)ethyl]amine is tetracoordinated in alkaline media to give the five-coordinated complex (**21**). A number of other five-coordinated palladium complexes containing N-donor atoms are known. Particularly remarkable is the double-helical dinuclear structure of $[Pd_2(\text{quinquepy})_2]^{4+}$ where each palladium is in an irregular five-coordinated environment with four short contacts to a terpyridyl fragment of one quinquepy and a terminal pyridine of a second quinquepy. The coordination sphere is completed by a long contact (260 pm) to the remaining pyridine of the second ligand (**22**).**[76]**

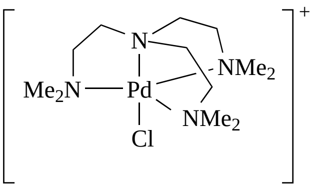

(**21**)

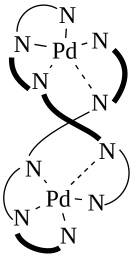

(**22**)

Symmetric pincer ligands take three positions of the square coordination plane in Pd, while the ligands in the fourth position can be varied. This allows complexes that are nonsusceptible to isomerization to be built, with a dipolar moment in the direction defined by the fourth ligand and the central donor atom of the pincer (equation 12).**[77]**

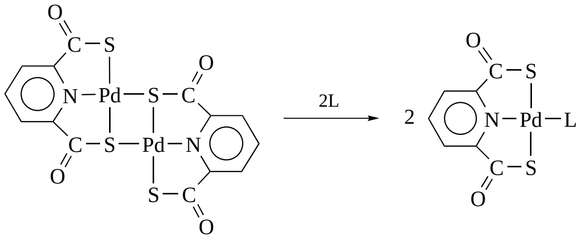

(12)

Tridentate phosphines and arsines are also known to give [PdXL]X complexes. Mixed P,N,N or P,S,S neutral ligands, however, form [PdX_2L] derivatives with one donor atom uncoordinated. The tetraphosphine $Ph_2PCH_2CH_2PPhCH_2CH_2PPhCH_2CH_2PPh_2$ forms a planar complex [PdL]$[PF_6]_2$ while the tripod ligand $P(CH_2CH_2PR_2)_3$ (R = neopentyl), which cannot adopt a planar structure, acts as tridentate in $[PdXL]^+$ with an uncoordinated PR_2 group. Five-coordinated complexes [PdXL]X are also formed for the tetraarsine ligands $Me_2AsCH_2CH_2AsPhCH_2CH_2AsPh$-$CH_2CH_2AsMe_2$ and $As(o\text{-}C_6H_4AsR_2)_3$ (R = Me, Ph).

Overall, the formation of pentacoordinated complexes is favored by chelating and particularly by polydentate macrocyclic ligands. A search in the Cambridge Structural Database reveals that many of the structurally characterized five-coordinated Pd(II) compounds contain macrocyclic or rigid polydentate ligands, S, N, and P donor atoms being dominant. Complexes (**23**), (**24**) and (**25**) are typical examples.

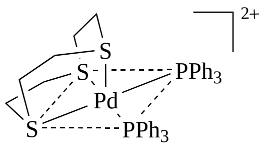

(**23**)

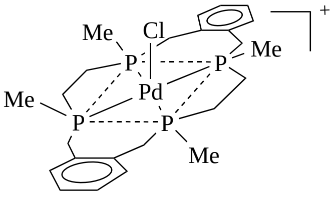

(**24**)

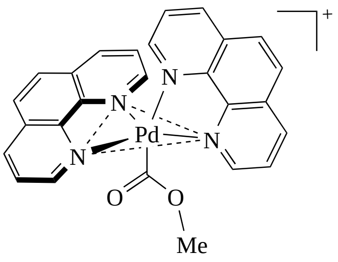

(**25**)

6.4 Complexes with Bridging Ligands and without Pd–Pd Bonds

Palladium atoms can be held together by ligands with a donor atom having at least two electron pairs or by a ligand containing at least two donor atoms. These cases lead to electron precise bridges, and to the absence of Pd–Pd interactions unless these are forced by severe steric constraints. When a bridging ligand shares a one-electron pair with both metals, an electron-deficient bridge is formed. This is possible for R (hydrocarbyl) and for H. Although few bridging R or hydrido palladium(II) complexes are known, they play an important role in some organometallic transformations. Only nondeficient bridges will be dealt with in this section.

Double bridges $Pd_2(\mu\text{-}X)_2$ are formed very frequently, but less stable single bridges $Pd_2(\mu\text{-}X)$ are also known. Dimeric compounds are the most abundant, but trimeric derivatives $[L_2Pd(\mu\text{-}X)_2Pd(\mu\text{-}X)_2PdL_2]^{2+}$ and compounds with higher nuclearity have been prepared.

Halogens and pseudohalogens are the simplest and most common bridging ligands. Complexes with $[Pd_2(\mu\text{-}X)_2X'_4]^{2-}$, $[Pd_2(\mu\text{-}X)_2X'_2L_2]$, and $[Pd_2(\mu\text{-}X)_2L_4]^{2+}$ stoichiometries (X = halogen or pseudohalogen; X′ = monoanionic ligand; L = neutral ligand) have been prepared. The only complex bearing bridging fluoride, $[Pd_2(\mu\text{-}F)_2Ph_2(PR_3)_2]$, has been recently reported.[78] Chelating ligands also give $[Pd_2(\mu\text{-}X)_2(L{-}L)_2]^{2+}$. Halogen bridge-splitting by an incoming ligand is a facile process and offers a synthetic way to monomer derivatives. There are some examples of monomer–dimer equilibrium (or terminal-bridging halogen equilibrium) in solution (equation 11). Labile dimeric compounds with unsupported halide single bridges are also known.

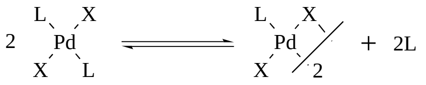

(13)

L = RCN, RSO_2; X = Cl, Br

Hydroxide can also behave as a bridging ligand, for example, in $[Pd(\mu\text{-}OH)_2L_4]^{2+}$, $[Pd(\mu\text{-}OH)_2(L{-}L)_2]^{2+}$, and so on. The OH group can be easily protonated and displaced by acidic ligands, and reacts with CO_2 to give hydrogen carbonato complexes.[79] Amines can also protonate hydroxo bridges leading to remarkably stable amido-bridged palladium compounds.

Thiolates have a very strong tendency to act as bridges. Simple thiolato palladium compounds $Pd(SR)_2$ (R = alkyl, aryl) are oligomers or polymers with bridging SR^- groups between metal atoms. Thiolato complexes containing ancillary ligands are rarely monomers, and dimeric derivatives analogous to the halogen-bridged derivatives are known. Thiolate bridges are very strong and bridge splitting is difficult to accomplish. Sulfide and selenide are also prone to act as bridging ligands binding two or even three palladium atoms.

Phosphido-bridged dimers $[Pd_2(\mu\text{-}PR_2)_2X_2(PR_2H)_2]$ can be obtained by reaction of secondary phosphine complexes $[PdX_2(PR_2H)_2]$ with a base. HX elimination is easier in the order $PPh_2H > PPhEtH > PEt_2H$.

Small bite bidentate ligands usually prefer to bridge two palladium(II) atoms, as this arrangement is more stable than the strained chelating form. The systems μ-$\underline{S}C\underline{N}^-$, μ-SO_3, μ-dppm, and μ-carboxylates are examples of these types of ligands. CN bridges act as a C,N-donor and the linearity of the two bonds produces tetrameric single-bridged complexes when these are forced to be cis, or polymers for trans complexes. In contrast to halide single bridges, cyanide single bridges are rather strong.

Double-bridged carboxylate derivatives adopt a butterfly conformation (**26**), which usually leads to Pd···Pd interactions.[80] Pyrazolate ligands form similar structures, although in this case, the higher rigidity of the boat shaped double bridge keeps the two Pd atoms apart. Polydentate species such as oxalate or biimidazolate can act as bridging and chelating ligands simultaneously (**27**).

6.5 Complexes with Macrocyclic Ligands

Palladium gives complexes with many macrocyclic ligands containing N, S, and O heteroatoms. Some have already been mentioned for their ability to stabilize five-coordinated Pd(II), and others will be mentioned in Section 7. In general, the strong preference of Pd (II) for square-planar coordination has to be balanced against the coordination ability and structural requirements of the ligand. Porphyrins and similar $(N_4)^{n-}$ ligands offer a square-planar bonding cavity and give very stable complexes (**28**), but other types of complexes are formed when this match does not occur and a compromise has to be reached, as in structure (**29**). Sometimes apparently minor changes in the ligand, such as replacing H (**30**) for Me (**31**), produce dramatic changes in the coordination mode, from $S_2N_2{+}S_2$ quasi-octahedral (two Pd to S distances are long, 295.4 and 300 pm) to S_4 square planar. In this case, space-filling models show that the steric bulk of the NMe groups is big enough to prevent the meridional S–N–S binding adopted in (**30**).[81]

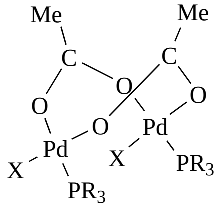

(**26**)

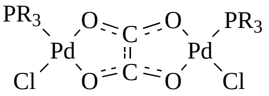

(**27**)

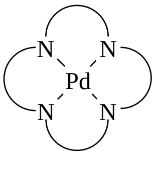

(**28**)

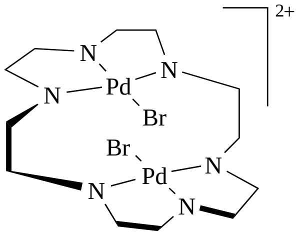

(**29**)

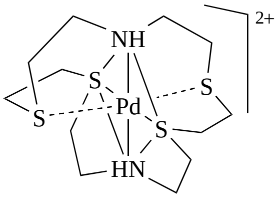

(**30**)

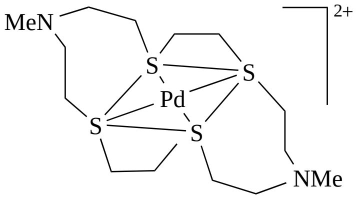

(**31**)

6.6 Pd(II) As a Tool for Self-assembly

In recent years, there has been an enormous development in the construction of extended self-assembled structures with the participation of metal atoms, either in the corner or in the edges of molecular triangles, squares, rectangles, and cages. *Cis*-'PdL_2' can be used to define corners in square and triangular structures, using the two available coordination sites, while *trans*-'PdL_2' moieties can participate to define linear edges. Excellent reviews of the topic are available.**[82,83]**

To give a simple example of this use, the linearity in the bonds formed by CN and by 4,4′-bipy leads to similar tetrameric structures for $[Pd_4(\mu\text{-}CN)_4(C_6F_5)_4(PEt_3)_4]$ (**32**),**[84]** and for$[\{Pd(en)(4,4'\text{-}bipy)\}_4][NO_3]_8$ (**33**).**[85]** The short length of the bridging ligands in (**32**) does not allow accommodating anything in the square cavity, whereas (**33**) recognizes organic molecules in aqueous media.

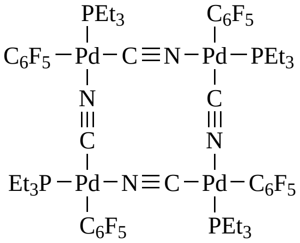

(**32**)

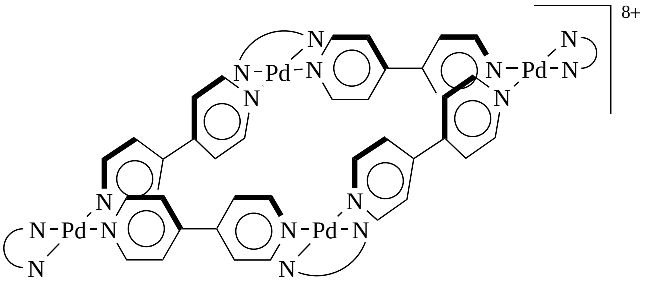

(**33**)

Planar exo-multidentate ligands (molecular panels, e.g. **34**) coordinate to palladium to give a variety of polyhedra.**[86]** Molecular cages have also been assembled using *cis*-'PdL_2' corners (*see* ***Self-assembled Inorganic Architectures***).

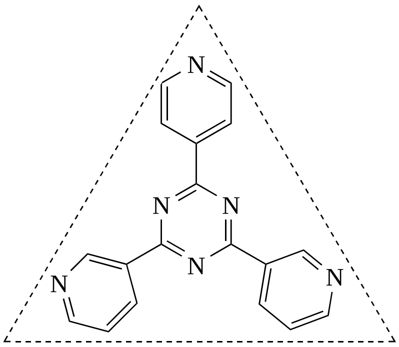

(**34**)

7 COMPLEXES OF PALLADIUM(III)

There is a certain reluctance to assign the oxidation number +3 to palladium, whereas there is not much trouble in assigning it +4 in other complexes. Thus, Pd(III) candidates are looked at with suspicion, not because it is difficult to accept that Pd can have charge densities midway between Pd(II) and Pd(IV), but probably because in many instances where a formal oxidation state +3 can be assigned, either the complex has some noninnocent ligands which do not allow a clear decision, or the complex is a dimer or a higher polymer and can be assigned mixed oxidation states.

The first case is best exemplified by the 1,2-dithiolene complexes (*see Dithiolenes*).**[72,87]** Bis(1,2-dithiolene) complexes of palladium of the types represented in Scheme 7 are known. The monoanionic complexes are assigned as Pd(III) complexes if (as applied in Scheme 7) the two ligands are considered in its reduced dianionic dithiolene form (**35**) (equation 14). However, very different oxidation states can be assigned to the metal if one or two ligands are considered in their oxidized neutral dithiabutadiene form (**36**) (equation 14). Obviously, the ambiguity in oxidation number affects the three complexes, and not only the Pd(III) candidates. Molecular orbital calculations favor the dithiolene structure (**35**). The EPR spectra of the monoanionic complexes, which are monomeric and paramagnetic, show hyperfine splitting (sextet) caused by the interaction of the unpaired electron with the ^{105}Pd nuclei. The stacking properties and solid-state systems involving these complexes have been reviewed.**[72]**

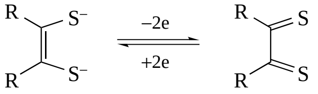

(**35**) (**36**) (14)

The paramagnetic complex $[Pd_2(\mu\text{-form})_4]PF_6$ (form = $(p\text{-Tol})NCHN(p\text{-Tol})$) (**37**), is obtained by oxidation of $[Pd_2(\mu\text{-form})_4]$ with $AgPF_6$, but the EPR spectrum indicates that the odd electron is located in a ligand-based orbital.**[88]** Similarly, for the mixed blues (*see* ***Mixed Valence***

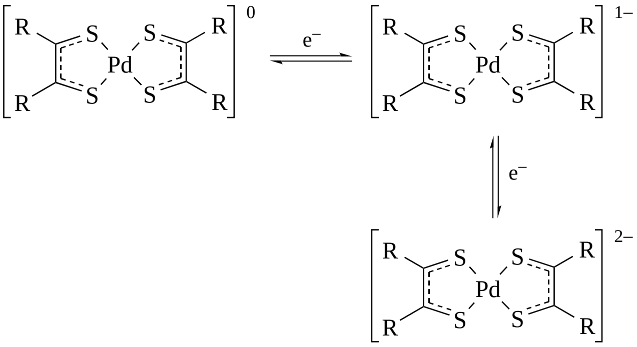

Scheme 7

Compounds) *cis*-$[\mathrm{A_2Pt}(\mu\text{-L})_2\mathrm{Pd}(\mu\text{-L})_2\mathrm{PtA_2}]\mathrm{X_3}$ (A = amine; L = 1-methyluracilato, 1-methylthyminato; $\mathrm{X^-} = \mathrm{NO_3}^-$, $\mathrm{ClO_4}^-$) (**38**), which can be formally considered $\mathrm{Pt^{II}}_2\mathrm{Pd^{III}}$, it is difficult to rule out the possibility of ligand oxidation rather than metal oxidation.[89]

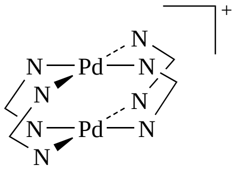

(**37**)

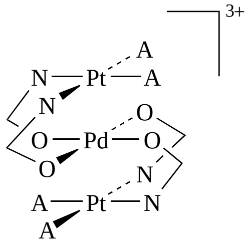

(**38**)

Complexes containing linear-chains $\cdots\mathrm{Pd}\cdots\mathrm{X}\cdots\mathrm{Pd}\cdots\mathrm{X}\cdots$(X = halide), for example, those formed by the partial oxidation of $[\mathrm{PdL}][\mathrm{ClO_4}]_2$ (L = tetradentate planar ligand, two bidentate ligands, or four monodentate ligands, usually amines) with $\mathrm{X_2}$, have Peierls-distorted structures (*see Peierls Distortion*) and are better regarded as having Pd atoms alternating in oxidation states and bridged by nonequidistant halogen atoms, that is, $[\mathrm{Pd^{II}L}][\mathrm{Pd^{IV}LX_2}][\mathrm{ClO_4}]_4$.[90]

The tridentate macrocyclic ligands 1,4,7-triazacyclononane and 1,4,7-trithiacyclononane (**39**, E = NH, S, respectively), act as bidentate chelates toward Pd(II) to give square-planar complexes $[\mathrm{Pd^{II}L_2}]^{2+}$ with two pendant E donor atoms (**40**). The complexes can be oxidized chemically or electrochemically to $[\mathrm{Pd^{III}L_2}]^{3+}$ (**41**) (equation 15), which show tetragonally elongated octahedral coordination, as expected for a Jahn–Teller distorted $\mathrm{d^7}$ complex.[91,92] Interestingly, electrochemical studies on the Pd(II) complexes (**30**) and (**31**) (Section 6.5) show that only the second can be reversibly oxidized to Pd(III).

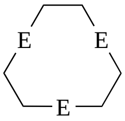

(**39**)

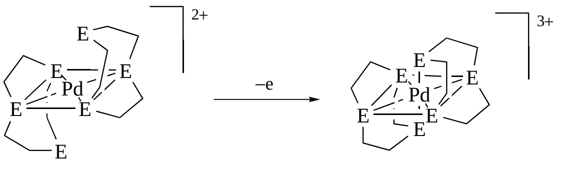

(**40**) (**41**)

(15)

The Pd(II) complex with mixed donor atoms $[\mathrm{Pd}([9]\mathrm{aneNS_2})_2](\mathrm{BF_4})_2$ ($[9]\mathrm{aneNS_2}$ = 1, 4-dithia,7−azacyclononane) has a primary NS coordination, but presents a purple–blue color due to long-range interactions to the two remaining S donors. Its cyclic voltammetry study shows two one-electron oxidations assigned to Pd(II)–Pd(III) and Pd(III)–Pd(IV) couples. Quantitative electrochemical oxidation affords orange solutions of $[\mathrm{Pd}\ ([9]\mathrm{aneNS_2})_2]^{3+}$ in MeCN, which is shown by electron spin resonance (ESR) to contain a $\mathrm{d^7}$ Pd center.[93]

The present overall picture seems to suggest that oxidation to Pd(III) requires to be electronically counterbalanced by an increase in coordination numbers to a distorted octahedral geometry, as found in the latter complexes discussed. In its absence, Pd(III) will withdraw more electron density from the ligands in a square-planar coordination (e.g. 1,2-dithiolenes), and the oxidation will become more ligand based.

A dinuclear complex of Pd(III), $[\mathrm{Pd_2(hpp)_4Cl_2}]$ (hpp = the anion of 1,3,4,6,7,8-hexahydro-2H-pyrimido[1,2-α]pyrimidine), has been reported. The four bridging hpp ligands describe a paddle wheel–type structure. This compound presents the shortest Pd–Pd distance ever reported (239.1 pm), shorter than all reported Pd(I)−Pd(I) bonds, and 36 pm shorter than the Pd–Pd distance in the metal itself (**42**, N^N = hpp).[94]

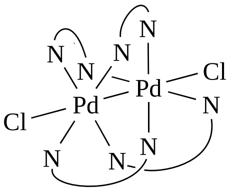

(**42**)

8 COMPLEXES OF PALLADIUM(IV)

8.1 Introduction

Palladium(IV) is a hard metal center and therefore it requires strong σ-donor ligands to give stable species that are six-coordinated and octahedral. Pd(IV) complexes are usually prepared by oxidation of the analogous Pd(II) derivatives and halogens or nitric acid are generally used as oxidants. Thus, the dissolution of Pd in aqua regia and subsequent treatment with alkaline chloride affords $\mathrm{M_2[PdCl_6]}$ complexes, which thermally decompose to give the stable Pd(II) chloropaladates. Although Pd(IV) compounds are not particularly difficult to attain, they are usually labile toward *Reductive Elimination*. Hence, species that have a trans-X configuration are easier to handle than the corresponding cis-X configuration, since the former are more resistant to the elimination of $\mathrm{X_2}$ and to give Pd(II) derivatives.

8.2 Palladium(IV) Complexes Containing Group 17 and 16 Donor Atoms

Besides PdF_4 and the mixed valence compound $Pd^{II}[Pd^{IV}F_6]$ (see Section 3.1), the known halogen derivatives of Pd(IV) are the halocomplexes $[PdX_6]^{2-}$ (X = F, Cl, Br, I). Obtained by halogen oxidation (or, for $[PdI_6]^{2-}$, addition of excess CsI to $[PdCl_6]^{2-}$), they have been crystallized with a variety of alkali metal cations. $Cs_2[PdI_6]$ has been also obtained in the solid state by application of pressure to samples of $Cs_2[PdI_4]\cdot I_2$.**95**

Some Pd(IV) complexes with oxoanions have been prepared, including the hydroxide $[Pd(OH)_6]^{2-}$ and periodate or tellurate derivatives. S-containing anionic ligands such as dithiocarbamates have generally been more efficient in giving stable Pd(IV) complexes than the neutral donors, because of their higher basicity. However, stable $(NR_4)[PdX_5(EMe_2)]$ derivatives (R = alkyl; X = Cl, Br; E = S, Se) have been prepared. ^{77}Se NMR studies support the presence of Pd(IV) by the high-field shifts of the Se resonances in comparison with the corresponding Pd(II) complexes.

8.3 Palladium(IV) Complexes Containing Group 15 Donor Atoms

Amines and heterocyclic N-donor ligands form palladium(IV) complexes that have the stoichiometry $[PdCl_4L_2]$ ($L = NMe_3$, $NMeH_2$, piperidine, pyridine, α-picoline, etc.; L_2 = bipy, phen, biguanidine). They are prepared by chlorine oxidation of the corresponding Pd(II) complexes. The bromo derivatives are also known for the amines, although they are more difficult to obtain for the heterocyclic ligands (py, bipy). These complexes are thermally unstable and eliminate X_2 on heating. An X-ray crystal-structure determination of $[PdCl_4(bipy)]$ confirmed the expected cis octahedral geometry for the complex. $[PdCl_2(NH_3)_4]Cl_2$ and $(NR_4)[PdX_5L]$ ($L = NMe_3$, Py) have also been prepared. See also Section 7 for mixed valence complexes of the type $[Pd^{II}L][Pd^{IV}LX_2]Y_4$.

Palladium(IV) complexes with ligands containing heavier group 15 donor atoms are less stable than those with the harder N-donor ligands. Careful control of the oxidation conditions enables the synthesis of a number of $[PdCl_4L_2]$ (L = monodentate phosphine or arsine) or *cis*-$[PdCl_4(L{-}L)]$ (L–L = bidentate phosphine or arsine) complexes. *Trans*-$[PdX_2(L{-}L)_2](ClO_4)_2$ (X = Cl, Br; L–L = o-$C_6H_4(AsMe_2)_2$, o-$C_6H_4(PMe_2)_2$, o-$C_6F_4(PMe_2)_2$, $Me_2PCH_2CH_2PMe_2$) complexes have also been prepared and their trans octahedral geometry has been confirmed for the diarsine derivative by an X-ray diffraction study. The anions $[PdX_5L]^-$ are also known for phosphine and arsine ligands, and as for the N-derivatives, they are more stable than the neutral compounds.

8.4 Palladium(IV) Complexes Containing Group 14 Donor Atoms

Organometallic Pd(IV) complexes are not dealt with in this section (*see* ***Palladium: Organometallic Chemistry***). $[Pd(CN)_6]^{2-}$ has been prepared by metathesis of $[PdCl_6]^{2-}$ with KCN. The crystal-structure determination of $Cd[Pd(CN)_6]$ shows a perfect octahedral environment for Pd with Pd–C distances of 2.07(2) Å.**96**

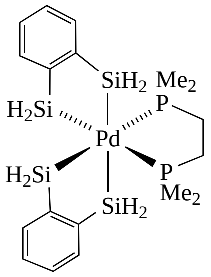

(**43**)

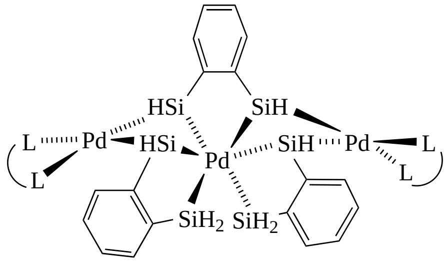

(**44**)

The silylpalladium(IV) complex (**43**), which has also been structurally characterized by X-ray diffraction, is obtained by reaction of $[PdMe_2(dmpe)]$ with three equivalents of 1,2-disilyl-benzene. This reaction must involve oxidative addition steps of Si–H to Pd(II).**97** Closely related to this complex is the unusual, formally Pd(VI) complex $[Pd_3(H_2SiC_6H_4SiH_2)_3(L{-}L)_2]$ (L–L = diphosphine) (**44**).**98** The X-ray diffraction study of this complex revealed two short Si–Si contacts. Thus, the complex can also be understood as a Pd(II) derivative, as supported by theoretical calculations.

9 RELATED ARTICLES

Asymmetric Synthesis by Homogeneous Catalysis; Carbonylation Processes by Homogeneous Catalysis; Coordination & Organometallic Chemistry: Principles; Electronic Structure of Clusters; Hydride Complexes of the Transition Metals; Hydrides: Solid State Transition Metal Complexes; Organic Synthesis using Transition Metal Complexes Containing π-Bonded Ligands; Oxidation

Catalysis by Transition Metal Complexes; Palladium: Organometallic Chemistry; Polynuclear Organometallic Cluster Complexes; Self-assembled Inorganic Architectures; Supported Organotransition Metal Compounds.

10 REFERENCES

1. T. Kendall, ‘Platinum’, Johnson Matthey, London, 2003.
2. J. Emsley, ‘The Elements’, 3rd edn., Oxford University Press, New York, 1998.
3. A. A. Timakov, V. N. Prusakov, and Yu. V. Drobyshevskii, *Russ. J. Inorg. Chem.*, 1982, **27**, 1704.
4. S. E. Livingstone, in ‘Comprehensive Inorganic Chemistry’, eds. J. C. Bailar, H. J. Eméleus, R. Nyholm, and A. F. Trotman–Dickenson, Pergamon, Oxford, 1973 Vol. 3, Chap. 43, p. 1274.
5. N. M. Kostic, L. M. Dutca, in ‘Comprehensive Coordination Chemistry II’, eds. J. A. McCleverty and T. J. Meyer, Elsevier, Oxford, UK, 2004, Vol 6.
6. C. F. J. Barnard and M. J. H. Russell, in ‘Comprehensive Coordination Chemistry’, eds. G. Wilkinson, R. D. Gillard, and J. A. McCleverty, Pergamon, Oxford, 1987, Vol 5, Chap. 51.
7. A. T. Hutton, in ‘Comprehensive Coordination Chemistry’, eds. G. Wilkinson, R. D. Gillard, and J. A. McCleverty, Pergamon, Oxford, 1987, Vol 5, Chap. 51.8.
8. A. T. Hutton and C. P. Morley, in ‘Comprehensive Coordination Chemistry’, eds. G. Wilkinson, R. D. Gillard, and J. A. McCleverty, Pergamon, Oxford, 1987, Vol 5, Chap. 51.9.
9. F. R. Hartley ed., ‘Chemistry of the Platinum Group Metals. Recent Developments’, Elsevier, Amsterdam, 1991.
10. T. B. Flanagan and Y. Sakamoto, *Platinum Met. Rev.*, 1993, **37**, 26.
11. L. Andrews, L. Manceron, M. E. Alikhani, and X. Wand, *J. Am. Chem. Soc.*, 2000, **122**, 11011.
12. H. Nakatsuji, M. Hada, and T. Yonezawa, *J. Am. Chem. Soc.*, 1987, **109**, 1902.
13. M. Olofsson–Mårtensson, M. Kritikos, and D. Noréus, *J. Am. Chem. Soc.*, 1999, **121**, 10908.
14. H. Kohlmann, H. E. Fischer, and K. Yvon, *Inorg. Chem.*, 2001, **40**, 2608.
15. W. Bronger and G. Auffermann, *J. Alloys Compd.*, 1995, **228**, 119.
16. D. B. Dell’Amico, F. Calderazo, F. Marchetti, and S. Ramello, *Angew. Chem., Int. Ed. Engl.*, 1996, **35**, 1331.
17. A. C. Skapski and M. L. Smart, *J. Chem. Soc. (D) Chem. Commun.*, 1970, 658.
18. A. M. Kluwer, C. J. Elsevier, M. Bühl, M. Lutz, and A. L. Spek, *Angew. Chem., Int. Ed. Engl.*, 2003, **42**, 3501.
19. B. E. Mann and A. Musco, *J. Chem. Soc., Dalton Trans.*, 1975, 1673.
20. P. D. Harvey and H. B. Gray, *J. Am. Chem. Soc.*, 1988, **110**, 2145.
21. V. V. Bashilov, P. V. Petrovskii, V. I. Sokolov, S. V. Lindeman, I. A. Gruzey, and Y. T. Struchkov, *Organometallics*, 1993, **12**, 991.
22. R. A. T. M. van Benthem, H. Hiemstra, P. W. N. M. Van Leeuwen, J. W. Geus, and W. N. Speckamp, *Angew. Chem., Int. Ed. Engl.*, 1995, **34**, 457.
23. S. Klingelhofer, W. Heitz, A. Greiner, S. Oestreich, S. Forster, and M. Antonietti, *J. Am. Chem. Soc.*, 1997, **119**, 10116.
24. R. Akiyama and S. Kobayashi, *J. Am. Chem. Soc.*, 2003, **125**, 3412.
25. P. J. Hayward, D. M. Blake, C. J. Nyman, and G. Wilkinson, *J. Am. Chem. Soc.*, 1970, **92**, 5873.
26. A. H. Roy and J. F. Hartwig, *J. Am. Chem. Soc.*, 2003, **125**, 8704.
27. A. F. Littke and G. C. Fu, *Angew. Chem., Int. Ed. Engl.*, 2002, **41**, 4176.
28. S. Z. Goldberg and R. Eisenberg, *Inorg. Chem.*, 1976, **15**, 535.
29. W. Lin, S. R. Wilson, and G. S. Girolami, *Inorg Chem.*, 1994, **33**, 2265.
30. A. L. Balch, J. R. Boehm, H. Hope, and M. M. Olmstead, *J. Am. Chem. Soc.*, 1976, **98**, 7431.
31. T. Murahashi, T. Nagai, T. Okuno, T. Matsutani, and H. Kurosawa, *Chem. Commun.*, 2000, 1689.
32. P. Braunstein, E. de Jesús, A. Dedieu, M. Lanfranchi, and A. Tiripicchio, *Inorg Chem.*, 1992, **31**, 399.
33. K. Tani, S. Nakamura, T. Yamagata, and Y. Katoaka, *Inorg. Chem.*, 1993, **32**, 5398.
34. A. M. Arif, D. E. Heaton, R. A. Jones, and M. Nunn, *Inorg. Chem.*, 1987, **26**, 4228.
35. P. Leoni, M. Sommovigo, M. Pasquali, P. Sabatino, and D. Braga, *J. Organomet. Chem.*, 1992, **423**, 263.
36. Y. J. Kim, S. C. Lee, J. I. Park, K. Osakada, J. C. Choi, and T. Yamamoto, *J. Chem. Soc., Dalton Trans.*, 2000, 417.
37. T. Murahashi, T. Otani, E. Mochizuki, Y. Kai, H. Kurosawa, and S. Sakaki, *J. Am. Chem. Soc.*, 1998, **120**, 4536.
38. S. Otsuka, Y. Tatsuno, M. Miki, T. Aoki, M. Matsumoto, H. Yasioka, and K. Nakatsu, *J. Chem. Soc., Chem. Commun.*, 1973, 445.
39. P. Braunstein, J. M. Jud, Y. Dusausoy, and J. Fischer, *Organometallics*, 1983, **2**, 180.
40. L. Manojlovic–Muir, K. W. Muir, B. R. Lloyd, and R. J. Puddephatt, *J. Chem. Soc., Chem. Commun.*, 1985, 536.
41. A. L. Balch, B. J. Davis, and M. M. Olmstead, *J. Am. Chem. Soc.*, 1990, **112**, 8592.
42. A. L. Balch, L. A. Fossett, M. M. Olmstead, D. E. Oram, and P. E. Reedy Jr, *J. Am. Chem. Soc.*, 1985, **107**, 5272.

43. I. I. Moiseev, T. A. Stromnova, M. N. Vargaftig, G. J. Mazo, L. G. Kuzmina, and Y. T. Struchkov, *J. Chem. Soc., Chem. Commun.*, 1978, 27.

44. P. Braunstein, M. A. Luke, A. Tiripicchio, and M. Tiripicchio–Camellini, *Angew. Chem., Int. Ed. Engl.*, 1987, **26**, 768.

45. A. M. Williamson, G. R. Owen, D. M. P. Mingos, R. Vilar, A. J. P. White, and D. J. Williams, *J. Chem. Soc., Dalton Trans.*, 2003, 2526.

46. M. Maekawa, M. Munakata, T. Kuroda–Sowa, and Y. Suenaga, *Anal. Sci.*, 1998, **14**, 451.

47. E. G. Mednikov, N. K. Eremenko, Y. L. Slovokhotov, and Y. T. Struchkov, *J. Chem. Soc., Chem. Commun.*, 1987, 218.

48. N. T. Tran and L. F. Dahl, *Angew. Chem., Int. Ed. Engl.*, 2003, **42**, 3533.

49. S. G. Bott, O. J. Ezomo, and D. M. P. Mingos, *J. Chem. Soc., Chem. Commun.*, 1988, 1048.

50. J. A. Casares, P. Espinet, and G. Salas, *Chem. Eur. J.*, 2002, **8**, 4843.

51. H. Krüger and R. van Eldik, *J. Chem. Soc., Chem. Commun.*, 1990, 330.

52. J. A. Arn, M. S. Holt, and J. H. Nelson, *Polyhedron*, 1989, **8**, 897.

53. N. M. Doherty and N. W. Hoffman, *Chem. Rev.*, 1991, **91**, 553.

54. A. Yahav, I. Goldberg, and A. Vigalok, *J. Am. Chem. Soc.*, 2003, **125**, 13634.

55. V. V. Grushin, *Chem. Eur. J.*, 2002, **8**, 1007.

56. A. H. Norbury, *Adv. Inorg. Chem. Radiochem.*, 1975, **17**, 231.

57. N. M. Milovic and N. M. Kostic, *Inorg. Chem.*, 2002, **41**, 7053.

58. P. Leoni, M. Sommovigo, M. Pasquali, S. Midollini, D. Braga, and P. Sabatino, *Organometallics*, 1991, **10**, 1038.

59. S. Kasselouri, A. Garoufis, M. Lamera–Hadjiliadis, and N. Hadjiliadis, *Coord. Chem. Rev.*, 1990, **104**, 1.

60. M. Krumm, I. Mutikainen, and B. Lippert, *Inorg. Chem.*, 1991, **30**, 884.

61. J. R. Miller, *Proc. Chem. Soc.*, 1960, 318.

62. A. W. Verstuyft and J. H. Nelson, *Inorg. Chem.*, 1975, **14**, 1501.

63. J. N. Harvey, K. M. Heslop, A. G. Orpen, and P. Pringle, *Chem. Commun.*, 2003, 278.

64. N. E. Leadbeater and M. Marco, *Chem. Rev.*, 2002, **102**, 3217.

65. H. Willner, M. Bodenbinder, R. Bröchler, G. Hwang, S. T. Rettig, J. Trotter, B. von Ahsen, U. Westphal, V. Jonas, W. Thiel, and F. Aubke, *J. Am. Chem. Soc.*, 2001, **123**, 588.

66. S. Coco, F. Díez–Expósito, P. Espinet, C. Fernández–Mayordomo, J. M. Martín–Álvarez, and A. M. Levelut, *Chem. Mat.*, 1998, **10**, 3666.

67. T. Tarantelli and C. Furlani, *J. Chem. Soc. (A)*, 1968, 1717.

68. S. D. Ittel, L. K. Johnson, and M. Brookhart, *Chem. Rev.*, 2000, **100**, 1169.

69. P. Espinet and K. Soulantica, *Coord. Chem. Rev.*, 1999, **193–195**, 499.

70. W. B. Lin, B. C. Wiegand, R. G. Nuzzo, and G. S. Girolami, *J. Am. Chem. Soc.*, 1996, **118**, 5977.

71. W. B. Lin, R. G. Nuzzo, and G. S. Girolami, *J. Am. Chem. Soc.*, 1996, **118**, 5988.

72. P. I. Clemenson, *Coord. Chem. Rev.*, 1990, **106**, 171.

73. Z. Taira and S. Yamazaki, *Bull. Chem. Soc. Jpn.*, 1986, **59**, 649.

74. V. G. Albano, G. Natile, and A. Panuzi, *Coord. Chem. Rev.*, 1994, **133**, 67.

75. J. S. L. Yeo, J. J. Vittal, and T. S. A. Hor, *Chem. Commun.*, 1999, 1477.

76. E. C. Constable, S. M. Elder, J. Healy, M. D. Ward, and A. Tocher, *J. Am. Chem. Soc.*, 1990, **112**, 4590.

77. P. Espinet, C. Lorenzo, J. A. Miguel, C. Bois, and Y. Jeannin, *Inorg. Chem.*, 1994, **33**, 2052.

78. V. V. Grushin and W. J. Marshall, *Angew. Chem., Int. Ed. Engl.*, 2002, **41**, 4476.

79. S. Ganguly, J. T. Mague, and D. M. Roundhill, *Inorg. Chem.*, 1992, **31**, 3831.

80. J. Powell and T. Jack, *Inorg. Chem.*, 1972, **11**, 1039.

81. G. Reid, A. J. Blake, T. I. Hyde, and M. Schröder, *J. Chem. Soc., Chem. Commun.*, 1988, 1397.

82. S. Leininger, B. Olenyuk, and P. L. Stang, *Chem. Rev.*, 2000, **100**, 853.

83. F. Hof, S. L. Craig, C. Nuckolls, and J. Rebek Jr, *Angew. Chem., Int. Ed. Engl.*, 2002, **41**, 148.

84. J. P. H. Charmant, P. Espinet, and K. Soulantica, *Acta Cryst.*, 2001, **E57**, m451.

85. M. Fujita, J. Yazaki, and K. Ogura, *J. Am. Chem. Soc.*, 1990, **112**, 5645.

86. M. Fujita, K. Umemoto, M. Yoshizawa, N. Fujita, T. Kusukawa, and K. Virada, *Chem. Commun.*, 2001, 509.

87. R. P. Burns and C. A. McAuliffe, *Adv. Inorg. Chem. Radiochem.*, 1979, **22**, 303.

88. F. A. Cotton, M. Matusz, R. Poli, and X. Feng, *J. Am. Chem. Soc.*, 1988, **110**, 1144.

89. W. Micklitz, G. Müller, B. Huber, J. Riede, F. Rashwan, J. Heinze, and B. Lippert, *J. Am. Chem. Soc.*, 1988, **110**, 7084.

90. R. J. H. Clark, D. J. Michael, and M. Yamashita, *J. Chem. Soc., Dalton Tans.*, 1991, 725.

91. A. J. Blake, A. J. Holder, T. I. Hyde, and M. Schröder, *J. Chem. Soc. Chem. Comm.*, 1987, 987.

92. A. J. Blake, L. M. Gordon, A. J. Holder, T. I. Hyde, G. Reid, and M. Schröder, *J. Chem. Soc., Chem. Commun.*, 1988, 1452.

93. A. J. Blake, R. D. Crofts, B. de Droot, and M. Schröder, *J. Chem. Soc., Dalton Trans.*, 1993, 485.

94. F. A. Cotton, J. Gu, C. A. Murillo, and D. J. Timmons, *J. Am. Chem. Soc.*, 1998, **120**, 13280.

95. B. Schüpp, P. Heines, A. Savin, and H. L. Keller, *Inorg. Chem.*, 2000, **39**, 732.

96. H. J. Buser, G. Ron, A. Ludi, and P. Engel, *J. Chem. Soc., Dalton Trans.*, 1974, 2473.

97. S. Shimada, M. Tanaka, and M. Shiro, *Angew. Chem., Int. Ed. Engl.*, 1996, **35**, 1856.

98. W. Chen, S. Shimada, and M. Tanaka, *Science*, 2002, **295**, 308.

Palladium: Organometallic Chemistry

J. William Suggs
Brown University, Providence, RI, USA

1 Introduction 1
2 Structure and Spectroscopy of Organopalladium Compounds 4
3 Stabilities of Organopalladium Compounds 7
4 Complexes with Pd–C σ-Bonds 9
5 Alkene and Alkyne Complexes of Palladium 20
6 Diene, Cyclobutadienyl, and Cyclopentadienyl Complexes 23
7 π-Allyl Palladium Complexes 26
8 Heterocyclic Compounds with Palladium–Carbon Bonds 30
9 Oxidation Reactions 34
10 Organic Synthesis with Organopalladium Compounds 36
11 Related Articles 39
12 References 40

Glossary

Heck reaction: the palladium-catalyzed reaction of an aryl or vinyl halide with an alkene to give an arylated or vinylated alkene
Stille reaction: the palladium-catalyzed reaction of an aryl or vinyl halide with an organotin reagent, where one of the organic groups is alkynyl, aryl, or vinyl, to give a cross coupled product
Suzuki reaction: the palladium-catalyzed reaction of an aryl or vinyl halide with an aryl boronic acid to give an arylated or vinylated arene. In some cases, primary alkyl halides can react in place of the aryl or vinyl halides
Wacker process: the palladium-catalyzed oxidation of ethene to acetaldehyde by oxygen

1 INTRODUCTION

The organometallic chemistry of palladium is one of the most extensive and varied fields of transition metal organometallic chemistry. In many respects, the chemistry of palladium parallels that of platinum, as one would expect from its place in the periodic table. However, where a given compound might be a stable species in platinum chemistry, it will often be a reactive intermediate in some palladium-catalyzed process. Many of the more than 1000 research articles that are published each year in organopalladium chemistry deal with applications of palladium complexes to organic synthesis. These applications arise because palladium complexes readily form reactive adducts with many common, inexpensive classes of organic molecules, such as alkenes, alkynes, dienes, CO, and alkyl, aryl, and, vinyl halides. The resulting compounds, in turn, can be used to introduce new functional groups into organic molecules or change the framework of the organic moiety through carbon–carbon bond formation.

Four oxidation states of palladium are encountered in organometallic chemistry (*see* ***Palladium: Inorganic & Coordination Chemistry***).**[1,2]** In order of importance, they are Pd^{II}, Pd^0, Pd^{IV}, and Pd^I. With the reduction of palladium from Pd^{II} to Pd^0, the metal changes its reactivity from electrophile to nucleophile. However, unlike main group nucleophiles such as thiolates or cyanide, Pd^0 complexes react with both alkyl halides and aryl or vinyl halides. Reactions of Pd^0 complexes with these latter sp^2 halides generate new Pd^{II} aryl or vinyl bonds through the process of oxidative addition.

Derivatives of Pd^{II} are normally prepared from $PdCl_2$. This salt is insoluble in organic solvents, and nearly so in water. Thus, it is normally used in a solubilized form. Addition of MCl to $PdCl_2$, where M = Li, Na, or K, gives M_2PdCl_4, which is soluble in water and low-molecular weight alcohols. The Li salt is also soluble in a number of organic solvents. For increased solubility in organic media, $PdCl_2(PhCN)_2$ is a common starting material. It can be prepared simply by heating palladium chloride in benzonitrile. Upon cooling the solution, yellow–brown crystals of the complex are deposited.

The more electrophilic reagent $Pd(OAc)_2$ is another useful reagent in organopalladium chemistry. It is monomeric in benzene at 80 °C, but is trimeric at room temperature in benzene. For even greater reactivity, $Pd(O_2CCF_3)_2$ can be used. Both the acetate and trifluoroacetate are soluble in organic solvents. Reaction of palladium acetate with acetylacetone produces $Pd(acac)_2$. This acetylacetonate and especially the hexafluoroacetylacetonate, $Pd(hfac)_2$, are useful as volatile sources of palladium in metalorganic chemical vapor deposition.

The organic derivatives of Pd^{II} include palladium alkyls, such as $PdMe_2(bpy)_2$ (bpy = 2,2′-bipyridine); π-allyl complexes, such as $Pd(\eta^3{-}C_3H_5)_2$ and $[Pd(\eta^3{-}C_3H_5)Cl]_2$; diene complexes including (1,5-cyclooctadiene)$PdCl_2$, cationic metal alkyls (**1**), and cyclometalated or cyclized diene complexes (*see Cyclometalation*) in which the palladium is in a chelate ring, bound to one or more ligand atoms such as N or P and also σ-bonded to a carbon, as typified by complex (**2**).

Pd^{II} is classified as a soft metal center.**[3]** Thus, it readily coordinates to polarizable ligands such as alkenes, dienes,

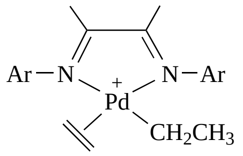

(**1**)

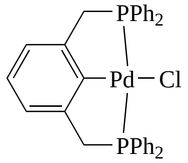

(**2**)

phosphines and phosphites, CO, σ-arenes, and σ-alkyls. In the case of alkene and π-allyl complexes, palladium coordination is able to reverse the reactivity profile of the organic ligand. While alkenes normally react with electrophiles such as H^+, Br_2, or R^+, when alkenes (or π-allyl complexes derived from alkenes) are coordinated to Pd^{II}, they undergo reactions with nucleophiles such as water, amines, and carbon nucleophiles including Pd^{II}-R groups and malonic ester anions (Scheme 1). This polarity reversal in the reactions of coordinated ligands is a major reason organopalladium compounds play such an important role in modern organic synthesis (*see* ***Organic Synthesis using Transition Metal Complexes Containing π-Bonded Ligands***).

The kinetics of reactions at Pd^{II} centers is an additional reason for the numerous synthetic applications of organopalladium complexes. The stereochemistry of Pd^{II} is almost exclusively square planar. When the rates of substitution at isostructural Ni^{II}, Pd^{II}, and Pt^{II} complexes are compared (equation 1), the relative rates of reaction are Ni^{II}, 5×10^6; Pd^{II}, 1×10^5; and Pt^{II}, 1.

$$\begin{aligned}&\textit{trans-}(Et_3P)_2M(\textit{o}\text{-tolyl})Cl + py \longrightarrow\\&\textit{trans-}(Et_3P)_2M(\textit{o}\text{-tolyl})py^+ + Cl^-\end{aligned} \tag{1}$$

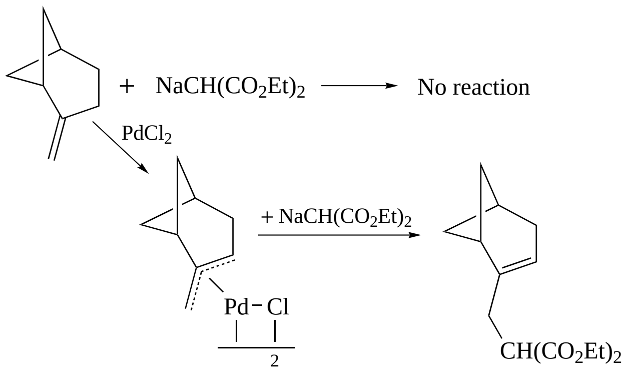

Scheme 1

Thus, for many systems, compounds that would be reactive intermediates in palladium chemistry are stable species in platinum chemistry (*see* ***Mechanisms of Reaction of Organometallic Complexes***). Coupled to the kinetic lability of palladium versus platinum complexes is the thermodynamic advantage of bonds to the heavier element. In at least one case, bond dissociation energies of Pd–CH_3 bonds in an isolable compound ([Pd(bpy)Me_2]) are estimated to be 10% lower than the bond dissociation energy of a Pt–CH_3 bond in an isostructural compound (approximately 130 kJ mol^{-1} for Pd^{II} vs 145 kJ mol^{-1} for Pt^{II}) (*see* ***Bonding Energetics of Organometallic Compounds***).**[4]**

Complexes of palladium in the zero oxidation state are easily prepared and are important catalysts for transformations in organic synthesis. The tetrakis(triphenylphosphine)Pd^0 complex is one of the most used Pd^0 reagents. It can be synthesized from $PdCl_2(PPh_3)_2$ and hydrazine hydrate in DMSO. The yellow solid can be handled briefly in air without extensive decomposition, but it is best handled under an inert atmosphere. Solutions are rapidly oxidized by exposure to air. A second important source of Pd^0 is 'bis(dibenzylideneacetone)palladium(0)'. In fact, the stoichiometry of this preparation is $[Pd_2(dba)_3]$dba. The alkenes of the dibenzylideneacetone ligands bridge the two Pd^0 sites in this complex, leading to a short Pd–Pd distance of approximately 324 pm. Molecules with such contacts are generally deeply colored, and $[Pd_2(dba)_3]$ is a brown solid that gives purple solutions. An advantage of this Pd^0 reagent is that, as a solid and in solution, it is relatively insensitive to oxygen, but the organic ligands are easily displaced by many different ligands. For example, rather than trying to isolate a species such as $Pd(P\textit{t}\text{-}Bu_3)_2$, one adds two equivalents of $P\textit{t}\text{-}Bu_3$ to a $Pd_2(dba)_3$ solution. Since many palladium-catalyzed organic reactions go through a Pd^0–Pd^{II} catalytic cycle, the Pd^0 species is generated in situ. For example, a reaction is charged with a Pd^{II} compound such as $Pd(OAc)_2$ and ligands. One of the substrates in the reaction acts as a reducing agent, transiently producing a L_nPd^0 species.

Unlike Ni^0, Pd^0 does not form a stable binary carbonyl. When $PdCl_2$ is carbonylated in acetic anhydride, reduction takes place to give the polymeric $[Pd(CO)Cl]_n$. However, $Pd(CO)_4$ can only be prepared and studied using matrix-isolation techniques.

There is continuing interest in the organometallic chemistry of Pd^{IV}.**[5]** This oxidation state has often been invoked as an intermediate in the reactions of Pd^{II} species with reactive acyl or alkyl halides. Spectroscopic evidence has been obtained for this hypothesis. When phenacyl bromide reacts with dimethylpalladium(II) complexes, such as $PdMe_2$(bpy), a complex can be isolated at 0 °C, which is shown, by ^{1}H NMR and X-ray crystallography, to be $PdBrMe_2(CH_2COAr)$(bpy) (equation 2). The same complex reacts with MeI to form $PdIMe_3$(bpy). The d^6 Pd^{IV} complexes are expected to exhibit octahedral geometries and to be kinetically inert.

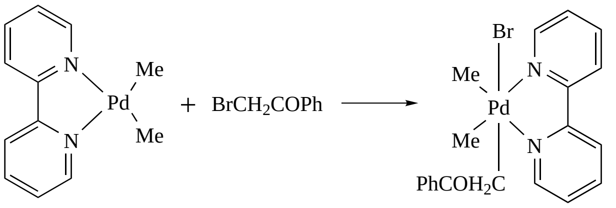

(2)

There is one report of a formally hexavalent Pd^{VI} complex.**6** Heating 1,2-$C_6H_4(SiH_3)Pd^{II}$(dmpe), where dmpe = 1,2-bis(dimetylphosphino)ethane, in toluene gives a trinuclear complex with the central palladium ligated to six silicon atoms. Two of the Pd–Si distances are normal, ∼240 pm, while four of the Pd–Si distances are considerably longer, ∼250 pm. This asymmetry could be explained if the central Pd atom is a bis σ-complex of Pd^{II} with two Si–Si bonds, instead of a Pd^{VI} derivative.

The organometallic chemistry of Pd^{I} has expanded considerably over the last few decades. Because Pd^{I} has the d^9 electronic configuration, a monomeric complex would be paramagnetic. However, the reported Pd^{I} organometallic complexes are dimeric, with Pd^{I}–Pd^{I} bond lengths on the order of 260 pm, twice the covalent radius of palladium. Many Pd^{I} compounds are synthesized by mixing an equimolar amount of a Pd^{II} and Pd^{0} compound. A number of Pd^{I} dimers exist with bridging Cp or π-allyl ligands. For example, the reaction of the $Pd^{II}\pi$-allyl compound $[CH_2C(Me)CH_2]_2Pd$ with the Pd^0 complex Pd(P-i-$Pr_3)_2$ gives the Pd^{I} dimer $\{[CH_2C(Me)CH_2](P\text{-}i\text{-}Pr)_3Pd\}_2$ (equation 3).

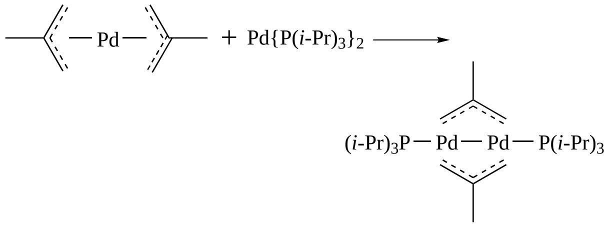

(3)

Isocyanide ligands have been found to promote the formation of Pd^{I} dimers. When an aqueous solution of $[Pd(MeNC)_4]^{2+}$ is prepared, disproportionation to produce $(MeNC)_3Pd$–$Pd(MeNC)_3{}^{2+}$ takes place (equation 4). Several different isocyanides can be used in this reaction, and PPh_3 will displace one or two of the isocyanide ligands. The unsupported metal–metal bond is not particularly reactive, but irradiation at 315 nm will generate the reactive metal radical $Pd(MeNC)_3{}^{+}$.

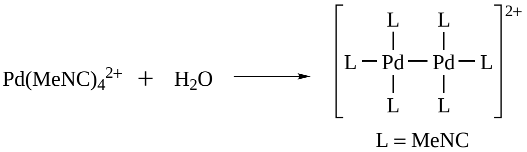

L = MeNC

(4)

Metal–metal bonded chains of $Pd_n{}^{2+}$ units form in good yield when a combination of one Pd^{II} species and $(n-1)Pd^0$ species are sandwiched between two polyene chains (equation 5). With the appropriate polyene, chains of three to five palladium atoms can be constructed.

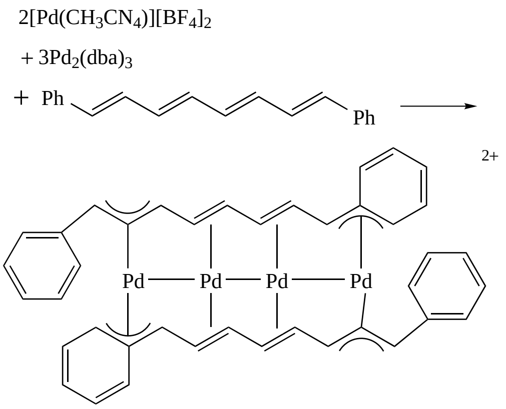

(5)

The numerous palladium-catalyzed organic reactions have a relatively small number of elementary steps. *Oxidative Addition*, *Reductive Elimination*, ligand coordination, and addition to coordinated ligands (either intramolecular or intermolecular) are the most important classes of transformations in most palladium catalytic cycles. The exact nature of the species within the coordination sphere of palladium and the order in which the steps take place are responsible for the variety of the organic products produced. Four representative and important palladium-catalyzed reactions are briefly discussed here to illustrate the range of organopalladium reactions.

The oxidation of ethene by palladium salts in water to give acetaldehyde has been known for 100 years (*see* ***Oxidation Catalysis by Transition Metal Complexes***). It is often called the *Wacker Process*, after Wacker Chemie GmbH, which first developed the process. The key steps in this oxidation are shown in Scheme 2.**7** Palladium catalyzes the nucleophilic addition of water to ethene, leading to the reduction of Pd^{II} to Pd^0. Then the palladium is reoxidized back to Pd^{II} with Cu^{II} salts, giving Cu^{I}, which in turn is oxidized by oxygen.

A more detailed catalytic cycle is shown in Scheme 3, which takes into account the other ligands on the metal. Even in a scheme as detailed as Scheme 3, some information is lacking. For example, it is not made clear whether attack of water on the ethene double bond is cis to the metal or trans.

$$\begin{array}{lcl}
H_2O + H_2C{=}CH_2 + Pd^{II} & \longrightarrow & MeCHO + Pd^0 + 2H^+ \\
Pd^0 + 2Cu^{II} & \longrightarrow & Pd^{II} + 2Cu^{I} \\
2Cu^{I} + \frac{1}{2}O_2 + 2H^+ & \longrightarrow & 2Cu^{II} + H_2O \\
\hline
H_2C{=}CH_2 + \frac{1}{2}O_2 & \longrightarrow & MeCHO
\end{array}$$

Scheme 2

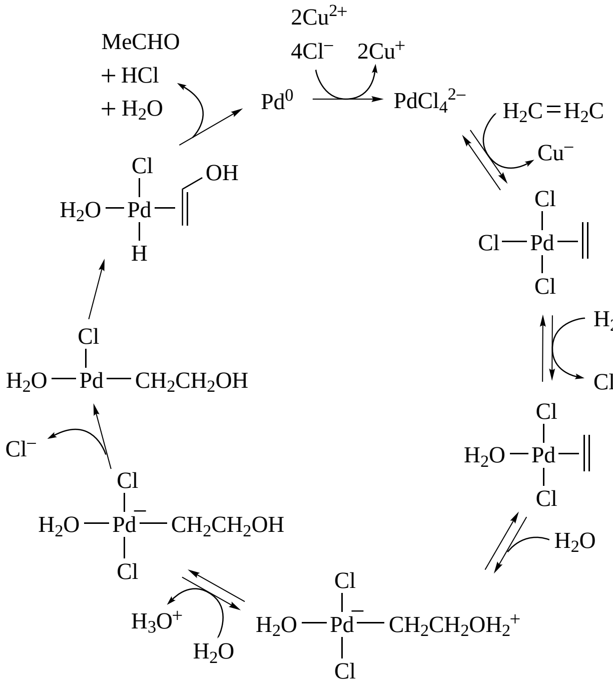

Scheme 3

Evidence exists for both possibilities, as will be discussed in Section 9.

A second important palladium-catalyzed process is cross coupling of an aryl or alkenyl tialkyltin reagent with an alkyl or aryl halide. In this reaction, one carbon–palladium bond is generated by transmetalation of Pd^{II}-X with Bu_3Sn-R, while the other carbon–palladium bond is formed by oxidative addition of an organic halide with a Pd^0L_n species. This reaction, which is tolerant of many organic functional groups, is normally known as the Stille Reaction (Scheme 4).[8]

The *Heck Reaction* is the name given to the palladium-catalyzed vinylation of organic halides.[9] It is applicable to a wide range of alkenes, although it is limited to aryl and vinyl halides or tosylates (equation 6). A simplified catalytic cycle is shown in Scheme 5. The reason for the limitation to aryl and vinyl halides is due to the facile *β-Elimination* of hydrogen from palladium alkyls. For many processes, β-elimination is competitive with reductive elimination of carbon groups.

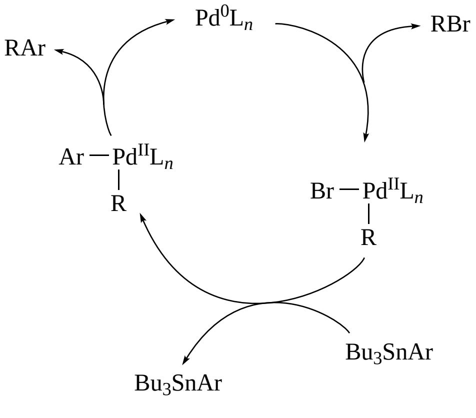

Scheme 4

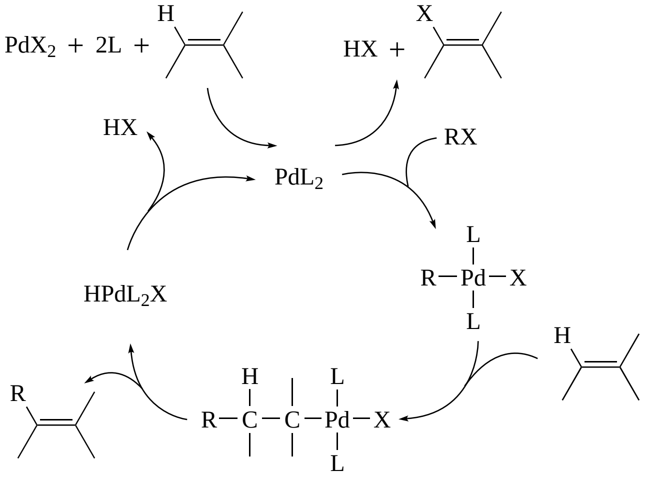

Scheme 5

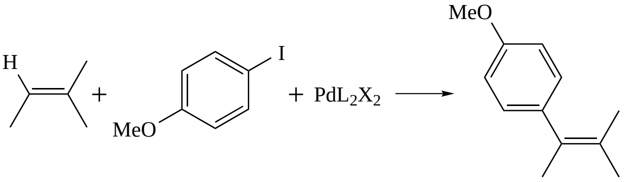

(6)

Palladium catalysts are increasingly used to make complex organic structures, where several framework carbon–carbon bonds are formed in one flask. Many of these processes are examples of 'atom economy' in synthesis, where a catalyst promotes addition reactions, and all of the atoms in the starting materials appear in the products.[10] The process in Scheme 6 illustrates this principle. A Pd^0 nucleophile reacts with a propargylic carbonate to give a σ-allenyl intermediate, where [Pd] indicates a Pd species with undetermined ligands. Sequential insertion of the [Pd]–C bond into coordinated alkenes leads to a σ-vinyl complex. Carbon monoxide inserts into the Pd–vinyl bond, giving a palladium acyl, which reacts with methanol to give the ester final product in 80%.

2 STRUCTURE AND SPECTROSCOPY OF ORGANOPALLADIUM COMPOUNDS

2.1 Structural Aspects of Organopalladium Compounds

The coordination geometry of organopalladium compounds is quite regular (*see* ***Coordination Numbers & Geometries***).

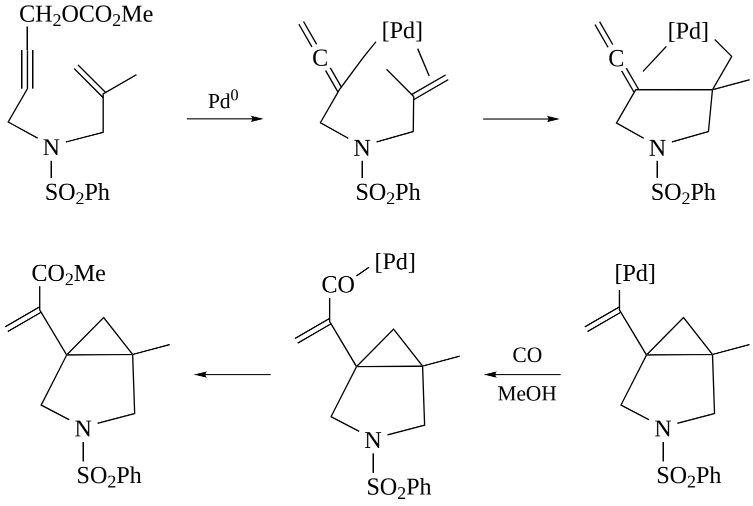

Scheme 6

Complexes of zero-valent palladium (d^{10}) are tetrahedral if the coordination number is four, trigonal if the coordination number is three, and linear if the coordination number is two. For Pd^{II} (d^8), the geometry is square planar, unlike Ni^{II}, which is normally octahedral, but like Pt^{II}. With a very bulky ligand, 14-electron three-coordinate T-shaped species can be stabilized and structurally characterized. For example, the complex $Pd(Ar)I[P(t\text{-}Bu)_3]$, where Ar = 2,4-xylyl, can be isolated and the aryl group is opposite the open coordination site.**[11]** For the few Pd^{IV} (d^6) complexes that have been structurally characterized, octahedral geometry is found.

Bonds between palladium and carbon groups are covalent, as their Pauling electronegativities would predict (Pd; 2.2; C; 2.5; H; 2.1). The covalent radius of palladium is 128 pm. This leads to expected bond lengths of 207 pm for Pd–C(sp^3) bonds, 196 pm for Pd–C(sp^2) bonds, and 190 pm for Pd–C(sp) bonds. In general, the experimentally determined bond lengths are within a few percent of these values. The bond lengths for Pd^{II}–Me bonds and Pd^{IV}–Me bonds are essentially the same, which suggests that the covalent radii for these two oxidation states are the same.

All carbon groups have a strong *Trans Influence*, which means groups trans to the Pd–C bond are lengthened relative to most other groups. For example, in the simple chelate (**3**), the Cl trans to the CH_2 group has a Pd–Cl bond length of 252 pm, while the Cl trans to the tertiary amine has a Pd–Cl length of 234 pm. Acyl groups are especially strong trans influence groups.

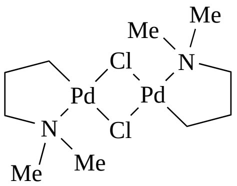

(**3**)

Alkene and diene complexes of Pd^{II} have the C–C axis of the double bond perpendicular to the palladium square plane, as in (**4**) and (**5**). Steric, rather than orbital factors, favor this coordination geometry for d^8 metals. With a properly designed ligand, such as 7-methylenebicyclo[2.2.1]hept-2-ene, one alkene can be constrained to lie in the coordination plane (**6**). Coordination lengthens the carbon–carbon alkene bond by 3–6%. Buckminsterfullerene, C_{60}, forms isolable complexes with up to six $Pd(PEt_3)_2$ units. The palladium atoms lie over a 6–6 ring junction, with the carbon and phosphorus atoms in the same plane and the C–C bond lengths increased ~7pm.

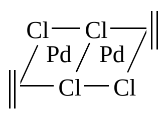

(**4**)

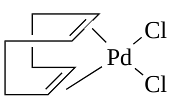

(**5**)

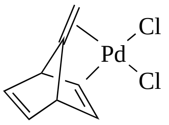

(**6**)

Most stable Pd–alkyne complexes are of Pd^0 species with electron-poor alkynes. Dimethyl acetylenedicarboxylate forms $Pd(MeO_2CC_2CO_2Me)(PPh_3)_2$, which has a trigonal geometry, with both P atoms and both alkyne carbons coplanar. The C–C–CO_2Me angle is decreased to 145° and the alkynic C–C bond is lengthened to 128 pm. The bridging alkyne complex $Pd_2(C_5Ph_5)_2(\mu\text{-}C_2Ph_2)$ has also been structurally characterized. Bridging by the alkyne group increases the C–C bond to 133 pm.

Palladium forms many complexes with η^3-allyl, or π-allyl, ligands. In these complexes, the π-allyl ligand and the other groups coordinated to palladium adopt a square-planar geometry (**7a**) as opposed to a tetrahedral geometry (**7b**). In symmetric complexes, such as $Pd_2Cl_2(\eta^3\text{-}C_3H_5)_2$, the carbon–carbon bonds have equivalent lengths of approximately 136 pm. The Pd–C1 and Pd–C3 distances in structure (**8**) are equal, at 212 pm, but in most cases C2 is closer to the metal. The plane containing the C_3H_5 group is not strictly perpendicular to the Cl_2Pd plane, but is tilted to make an angle of approximately 111°. The anti groups in (**8**) are tilted slightly toward the palladium center, as is the group on carbon C2. The syn groups are tilted slightly away from the metal.

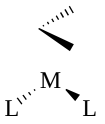

(**7a**)

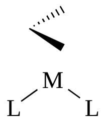

(**7b**)

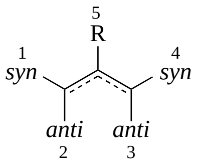

(**8**)

In the asymmetrically substituted π-allyls, such as $Pd(\eta^3\text{-}C_3H_5)Cl(PPh_3)$ (**9**), the greater trans influence of PPh_3 versus Cl leads to marked asymmetry in the bonding of the C_3H_5 group. The Pd–C bond trans to PPh_3 is lengthened, and the associated carbon–carbon bond length is shortened. Numerous structural and molecular mechanics studies have been carried out on π-allyl complexes with chiral ligands, such as CHIRAPHOS ($Ph_2PCHMeCHMePPh_2$). The object has been to establish the chiral environment around palladium in order to understand and develop new catalysts for enantioselective reactions.[12]

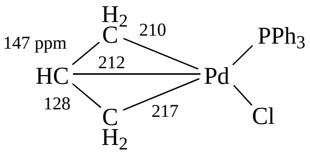

(**9**)

2.2 Infrared Spectroscopy of Organopalladium Compounds (*See Transition Metal Carbonyls: Infrared Spectra*)

Matrix-isolation techniques permit the isolation of $Pd(CO)_4$ in a CO matrix. This unstable species exhibits a ν_{CO} of 2066 cm^{-1}. The analogous $Pt(CO)_4$ gives ν_{CO} of 2044 cm^{-1} and the ν_{CO} of $Ni(CO)_4$ is 2037 cm^{-1}. The increase in ν_{CO} is further indication that $d_\pi - p_\pi$ bonding decreases in the order Ni > Pt > Pd. In general, platinum carbonyls have a lower ν_{CO} value than isostructural palladium complexes.

Terminal Pd–H groups will normally be observed in the range 2060–1950 cm^{-1}; however, the assignment of such a band should be confirmed by NMR or investigation of the analogous Pd–D compound, if carbonyl ligands are present. IR spectroscopy can aid in the identification of some Pd–C groups. Palladium acyls generally have a strong absorption between 1630 and 1720 cm^{-1}. σ-bonded palladium alkynes have an absorption band of variable intensity between 1950 and 2125 cm^{-1}, and σ-alkenes have $\nu_{C=C}$ between 1535 and 1630 cm^{-1}.

As with CO, coordination of an alkene to palladium lowers the stretching frequency of the unsaturated group, but to a lesser extent than in the analogous platinum compound. In $Pd_2Cl_4(C_2H_4)_2$, the coordinated ethene group has a $\nu_{C=C}$ of 1527 cm^{-1}, compared to 1623 cm^{-1} for free ethene and 1516 cm^{-1} for the analogous Pt complex.

2.3 NMR Spectroscopy of Organopalladium Compounds (*See Stereochemical Nonrigidity of Organometallic Complexes*)

The ^{105}Pd nucleus (22.2% natural abundance) is, unfortunately, not a useful nucleus for NMR measurements, given the fact that it is spin 5/2, with a large quadrupole moment. ^1H and ^{13}C NMR, however, have been used extensively in structural and mechanistic studies of organopalladium compounds. The NMR spectra of π-allyl complexes illustrate these applications. In $Pd_2Cl_2(\eta^3\text{-}C_3H_5)_2$, the proton at C_2 is seen at 5.42δ the syn protons (syn to C2 substituent) at 4.11δ, and the anti protons (anti to C2 substituent) at 3.06δ. In general, groups in the anti position of a π-allyl complex are more shielded. A σ-allyl is expected to produce an $ABCX_2$ spin system. If there is dynamic equilibrium, the protons on C1 and C3 can all exchange, leading to an AX_4 spin system (Scheme 7). If the π-allyl system is asymmetric, each proton can exhibit a distinct chemical shift.

Coupling constants are a valuable aid in structure assignment of π-allyls. $J_{1,2}$ is very small, less than 1 Hz. The trans coupling, $J_{2,5}$ or $J_{3,5}$, is larger, on the order of 12 Hz, compared to the cis coupling of $J_{1,5}$ or $J_{4,5}$, which is near 7 Hz. The ^{13}C NMR of the π-allyl carbons gives very different chemical shifts for C2 versus C1 and C3. In $Pd_2Cl_2(C_3H_5)_2$, for example, C1 and C3 occur at 55.8δ while C2 is at 113.5δ. The simplest rationale comes from resonance theory, where the π-allyl can be thought of as a resonance hybrid of two σ-allyl structures, which gives C1 and C3 some single bond character. 2-D NMR techniques such as NOESY can be used to establish the solution structure of organopalladium compounds. For complexes with phosphorus ligands, 2D ^{31}P-^1H correlation

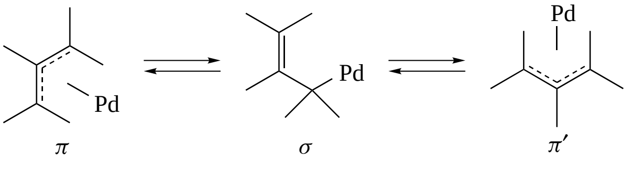

Scheme 7

spectroscopy is useful for resonance assignments in complex cases.

3 STABILITIES OF ORGANOPALLADIUM COMPOUNDS

3.1 Bond Dissociation Enthalpies[13]

Relatively few bond dissociation enthalpies for organopalladium compounds have been obtained. For (Pd–C_3H_5) in the dimer $[Pd(\eta^3\text{-}C_3H_5)Cl]_2$, a value of 105 kJ mol^{-1} was obtained using differential scanning calorimetry. In $Pd(Cl)_2$(1,5-cod), a Pd–Cl bond dissociation enthalpy of 215 kJ mol^{-1} was calculated, and Pd−(1,5-cod) was calculated to be 169 kJ mol^{-1}. An estimate for the mean Pd–CH_3 bond dissociation enthalpy in $PdIMe_3$(bpy) was 136 kJ mol^{-1}. Energetics of bond dissociation energies for fragments in the gas phase give values of 247 ± 21 kJ mol^{-1} in Pd–CH_3^+. The N-heterocyclic carbene *cyclo*-C[N*t*-BuCH]$_2$, NHC, dissociated from Pd(NHC)(Ac)Cl with an enthalpy of 107 kJ mol^{-1}. The average bond dissociation energy in $PdMe_2$ was calculated to be 158 kJ mol^{-1}, using the generalized valence bond approach. Most theoretical calculations on organopalladium bond dissociation enthalpies use simplified ligands, such as PH_3 or NH_3. Different levels of theory can produce qualitatively different results (*see* ***Bonding Energetics of Organometallic Compounds***).[14]

3.2 Reactions of Pd–C Bonds via Reductive Elimination and β-elimination

If inorganic palladium salts are treated with C_2H_5Li, one obtains a mixture of ethane, ethene, and butane. The ethane and ethene arise from β-elimination reactions, while the butane arises from reductive elimination. For β-elimination to take place, there must be a vacant coordination site on palladium to accept the β-hydrogen of the alkyl group. The nature of the ligands on palladium determine the stability and course of the decomposition of palladium alkyls. In addition, alkyl groups in a chelate ring are resistant to β-elimination. The ring prevents a conformation in which the metal and β-hydrogen can interact.

In the case of *trans*-$[PdEt_2(PR_3)_2]$, where the phosphines include PEt_3, PMe_2Ph, and $PEtPh_2$, warming to between 25 and 32 °C caused decomposition to equimolar amounts of ethane and ethene.[15] Essentially, no butane is formed. Added phosphines had little effect on the rate of the reaction. Kinetic studies are consistent with the mechanism shown in Scheme 8, in which β-elimination takes place predominately from the four-coordinate complex, with only minor reaction from the partially dissociated species $[PdEt_2(PR_3)]$.

Using the complex $[PdEt_2(bpy)]$, thermolysis at 80 °C also produces ethane and ethene. However, addition of methyl acrylate reverses the product composition, and leads to butane formation. In the absence of the alkene, the complex is 16-electron, and thus, a vacant coordination site is available for β-elimination. In the presence of the alkene, the complex is 18-electron, and C–C reductive elimination is the preferred reaction path. The greater steric bulk of the phosphine ligands in Scheme 8 prevents the formation of an 18-electron complex when excess phosphines are added.

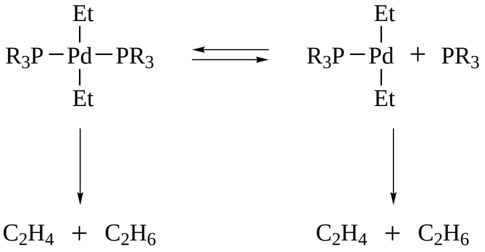

Scheme 8

The presence of halide ions can influence whether β-heteroatom or β-hydride elimination occurs. When palladium alkyls of the type $PhCH_2CH[Pd^{II}]CH_2OAc$ were generated by insertion of an allylic acetate into a $[Pd^{II}]$–Ph bond, β-hydride elimination to give $PhCH{=}CH{-}CH_2OAc$ was the exclusive product. However, in the presence of excess LiCl, the major product was $PhCH_2CH{=}CH_2$ from β-elimination of –OAc. The role of LiCl may be to form highly charged $RPdX_4^{3-}$ complexes that promote an E2-like mechanism for β-heteroatom elimination.

Theoretical studies of Pd^{II} dimethyl complexes indicate that reductive elimination of ethane requires a cis arrangement of alkyl groups on palladium. In the four-coordinate complexes, increasing the σ-donating capability (*see σ-Donor*) of the leaving groups promotes reductive elimination. Thus, reductive elimination of CH_3 groups should be more facile than CH_2F groups, for example. Stronger donor ligands trans to the leaving groups are predicted to increase the barrier to elimination. In addition, reductive elimination from a three-coordinate $[PdMe_2(PR_3)]$ species with adjacent methyl groups had a lower activation energy than reductive elimination from a four-coordinate complex, a result supported by experimental results.[16] The hybridization of the group undergoing reductive elimination affects the ease of reductive elimination. Formation of an R–H bond typically has a lower activation energy than formation of an R–R bond, and reductive elimination of two sp^2 groups is more facile than two sp^3 groups. This arises from the shape of the orbitals on the groups undergoing reductive elimination. The greater the *s* character to the orbital, the more spherical, less directional, it is. Thus, the orbital can have more multicentered bonding in the transition state, leading to lower activation energies for reductive elimination.

Reductive elimination in palladium complexes can take place through intermolecular exchange of organic groups.

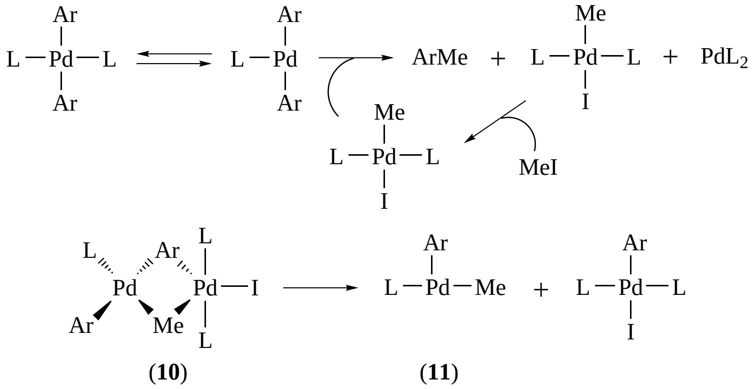

Scheme 9

Reaction of *trans*-[$PdAr_2(PEt_2Ph)_2$] with MeI gives good yields of ArMe. Mechanistic studies show that most of the elimination product arose not from a Pd^{IV} intermediate, but from a cis Pd^{II}-aryl methyl complex (**11**), which comes about from exchange in a complex such as (**10**), as shown in Scheme 9.

For palladium complexes with chelating diphosphine ligands, the bite angle of the ligand has a major influence on the rate of reductive elimination.[17] In $P_2PdMePh$ complexes where P_2 was either 1,3-(diphenylphosphino)propane (dppp), 1,1′-(diphenylphosphino)ferrocene (dppf), or 1,1′-(diphenylphosphino)ruthenocene (dppr), the species with the largest bite angle, the dppr complex, underwent reductive elimination the fastest (rapid decomposition above −5 °C). In contrast, the (dppp)PdMePh complex was stable for hours at room temperature. The nature of the $C_{sp}{}^3$ group also influenced stability, since the σ-vinyl complexes were less stable than the phenyl complexes.

The reagents used to generate a PdR_2L_2 species can have a controlling effect on the outcome of reductive elimination. A stoichiometric reaction between LiC_2-*t*-Bu and $PhPd(PPh_3)_2I$ gave the coupling product PhC_2-*t*-Bu via formation of the mixed Pd dialkyl followed by reductive elimination. However, when a catalytic reaction is attempted between PhI and LiC_2-*t*-Bu, using $Pd(PPh_3)_4$ in catalytic amounts, no coupling to give PhC_2-*t*-Bu occurs. Nevertheless, a catalytic reaction using $Pd(PPh_3)_4$, PhI, and $ClZnC_2$-*t*-Bu as the acetylide source gives PhC_2-*t*-Bu in 90% yield. An excess of the nucleophilic LiC_2-*t*-Bu caused the formation of $Li_2Pd(C_2$-*t*-$Bu)_4$. This complex does not readily decompose to give *t*-BuC_2–C_2-*t*-Bu. The less nucleophilic zinc reagent does not form the $PdR_4{}^{2-}$ species, which accounts for its successful use in the catalytic coupling reaction.

3.3 Decomposition Pathways for Pd^{II} Alkyls Lacking β-hydrogens

Several decomposition pathways exist for monoalkylpalladium(II) complexes, which lack β-hydrogens.[18] The compound *trans*-$Pd(CH_2Ph)(Cl)(PPh_3)_2$ (**12**) can be heated for 8 h in benzene at reflux. However, the addition of $PdCl_2(PhCN)_2$, which acts as a phosphine sponge, causes the quantitative formation of $PhCH_2Cl$. When Ag^I is used to abstract Cl^- from (**12**) in $CD_3C_6D_5$ solution at 85 °C, a 1:1 mixture of *o*- and *p*-$CD_3C_6D_4CH_2C_6H_5$ is produced. No radicals appear to be generated in this reaction. When the cationic complex $Pd(PPh_3)_2(CD_3CN)(CH_2Ph)^+$ $BF_4{}^-$ (**13**) is prepared and heated to 65 °C in C_6D_6−$CDCl_3$, a mixture of $C_6H_5CH_3$ and $C_6H_5CH_2CH_2C_6H_5$ is obtained, indicating that heating (**13**) generates benzyl radicals. Apparently, for arene alkylation to take place, it is necessary for the arene to be coordinated to the metal. Thus, the alkyl group in $Pd(PPh_3)_2(CD_3CN)(CH_2Ph)^+$ $BF_4{}^-$ behaves as a carbocation to coordinated arenes, but undergoes Pd–R bond homolysis in the absence of coordinated arene.

When the methyl complex $Pd(PPh_3)_2(I)(Me)$ is treated with Ag^I in C_6D_6 at 85 °C, the only product is PPh_3Me^+. No benzene alkylation takes place. Heating the cationic $Pd(PPh_3)_2(CD_3CN)(Me)^+$ also produces only PPh_3Me^+. The relative instability of methyl radical probably accounts for the different reaction paths of the benzyl and methyl cationic complexes. When phosphonium salt formation is not possible, for example, in the neopentyl complex

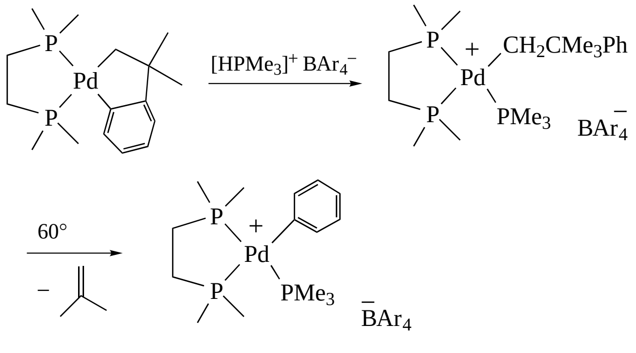

Scheme 10

cis-Pd(bpy)(CH_3CN)(CH_2CMe_3)$^+$ $BF_4{}^-$, heating at 70 °C gives only CMe_4. This product presumably arises from the neopentyl radical, since a carbocation would give rearrangement products.

Reductive elimination of C_{alkyl}–C_{aryl} bonds can take place when β-hydride elimination is blocked. As shown in Scheme 10, β-aryl reductive elimination occurs in neophyl, –CH_2CMe_2Ph, complexes. This reaction is a rare example of unstrained C–C bond activation in organopalladium chemistry.

4 COMPLEXES WITH Pd–C σ-BONDS

4.1 Formation of Pd–C Bonds

4.1.1 Transmetalation of Pd–X by R–M Reagents

A large number of basic R–M reagents, where M can be various metals, will transfer an alkyl, aryl, vinyl, or acetylide group to Pd (normally Pd^{II}), displacing a halide or pseudohalide group. Reagents most often used are R_3B, $RB(OH)_2$, R_4Sn, RMgBr, RLi, $LiCuR_2$, and aluminum alkyls. A sample of palladium complexes with Pd–C σ-bonds prepared in this way is given in Table 1.

Most transmetalations with basic organometallics are done in ether or THF solvents at 0 °C to −78 °C. In general, alkyl *Grignard Reagents* will displace only one halide from L_2PdX_2 complexes, while lithium reagents will replace both halides. Chelating ligands, such as $Ph_2PCH_2CH_2PPh_2$ or 2,2′-bipyridyl, favor the isolation of derivatives with alkyl groups possessing β-hydrogens, although such compounds will often slowly decompose in solution at or slightly above room temperature. R_4Sn and $RB(OH)_2$ transfer alkyl groups and are unreactive with most functional groups.

Many transmetalation reactions take place as part of a catalytic cycle. For example, aryl (as well as heterocyclic and vinyl) halides, tosylates, and triflates form biaryls with numerous aryl-metal partners.**[19]** The cross-coupling reactions (which are increasingly being used to prepare other products besides biaryls) are usually named after the chemists who developed the reaction. The most important of these name reactions are summarized in Table 2.

4.1.2 Cyclometalation

The reaction of palladium reagents with amines, phosphines, and other organic ligands to produce chelated complexes with Pd–C bonds is the *Cyclometalation* reaction (equation 7).**[20]** It has been used to synthesize thousands of complexes with Pd–alkyl and Pd–aryl bonds. These complexes are beginning to be used as very stable, high turnover number catalysts and as intermediates in the synthesis of complex natural products. The scope and limitations of this reaction are detailed in Section 8.

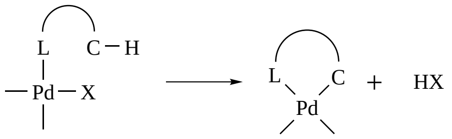

(7)

4.1.3 Oxidative Addition

The reaction of Pd^0 complexes (such as $Pd(Ph_3P)_4$) with organic halides and related compounds has been used to prepare a number of stable Pd^{II} alkyl and vinyl compounds. This reaction with alkyl halides has the characteristics of an S_N2 reaction. Primary halides react faster than secondary halides. Also, when a chiral halide is used, such as (*S*)-(+)-benzyl-α-D chloride, the benzyl palladium product is formed with inversion of configuration at the benzylic carbon (equation 8). With vinylic halides, retention of configuration at the double bond is observed

Table 2 Palladium-catalyzed biaryl couplings: ArM + Ar′X → Ar–Ar′

Aryl-metal source	Reaction name
ArMgBr	Kumada
$ArSnR_3$	Stille or Kosugi–Migita–Stille
ArZnX	Negishi
$ArB(OR)_2$	Suzuki or Suzuki–Miyaura
$ArSiR_3$	Hiyama

Table 1 Synthesis of isolable organopalladium compounds via transmetalation

Palladium reagent	RM	Product	Yield (%)
$(Ph_3P)_2PdCl_2$	CH_3Li	$(Ph_3P)_2Pd(CH_3)_2$	66
(1,5-cod)$PdCl_2$	$Mg(CH_2SiMe_3)Cl$	(1,5-cod)Pd $(CH_2SiMe_3)_2$	80
$(MePPh_2)_2PdBr_2$	$Mg(C_6F_5)Br$	$(MePPh_2)_2Pd(C_6F_5)Br$	84
(1,5-cod)$PdCl_2$	$LiCuMe_2$	(1,5-cod)$PdMe_2$	93
(diphos)$PdCl_2$	$EtAl(OEt)_2$	(diphos)$PdEt_2$	75
$(Ph_3P)_2PdBr_2$	PhC_2MgBr	$(Ph_3P)_2Pd(C_2Ph)_2$	66
$(Ph_3P)PdBr(Cp)$	$TlCH(COCH_3)_2$	$(Ph_3P)Pd[CH(COCH_3)_2](Cp)$	100

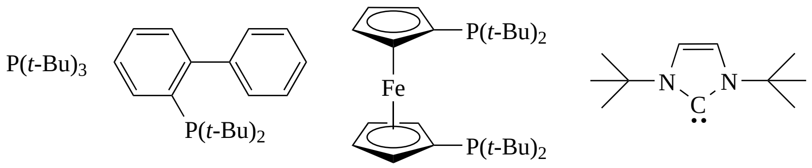

Scheme 11

(equation 9). Aryl halides reactivity with Pd^0 complexes is normally ArI > ArBr, ArOTf > ArCl.[21] Since aryl chlorides are much cheaper than the other derivatives, it was a major advance to find ligands for Pd^0 that promoted oxidative addition of ArCl at 25–100 °C. Major types of ligands that promote ArCl oxidative addition are electron-rich, bulky trialkylphosphines, dialkylbiphenylphosphines, and N-heterocyclic carbene ligands.[22] Pd^0 complexes of these phosphine ligands for catalytic reactions are often prepared by adding one or two equivalents of the ligand to $[Pd_2(dba)_3]$. Representative ligand structures are given in Scheme 11. It is usually assumed that L_2Pd^0 or LPd^0 species are the species undergoing oxidative addition with these bulky ligands in catalytic reactions. However, many reactions are carried out in the presence of strong bases, such as NaO-*t*-Bu. A $[LPd(OR)]^-$ anion can be the kinetically important species in such reactions. The aryl and vinyl Pd^{II} compounds that result from oxidative addition are useful reagents in organic synthesis for cross-coupling reactions, as described in Sections 4.2 and 10.

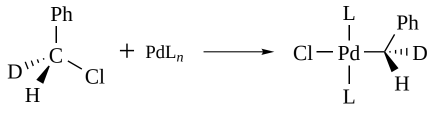

(8)

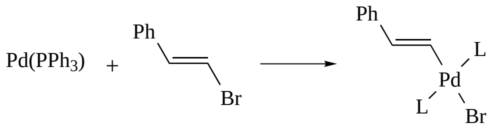

(9)

Acylpalladium complexes are readily prepared through oxidative addition of Pd^0 complexes to acid chlorides.[23] PdL_4 compounds, where L is a tertiary phosphine, react with acid chlorides at room temperature to give *trans*-$L_2Pd(COR)Cl$ complexes. Since carbon monoxide does not insert into palladium acyl bonds, $Pd(COCO_2R)$ complexes are made from oxidative addition of oxalyl chloride monoesters.

4.1.4 Addition of Nucleophiles to Palladium-coordinated Alkenes, Dienes, and Related Compounds

A reaction of considerable generality is the attack of a nucleophile (such as an alkoxide, alcohol, amine, or enolate) on an alkene–Pd^{II} complex. One example is given in equation (10). This reaction will be discussed in detail in Section 5.

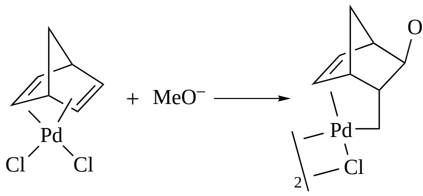

(10)

4.1.5 Addition of Pd–R to Alkenes and Alkynes

Complexes with a Pd–C bond will add across alkynes to form vinyl complexes. Alkynes with electron-withdrawing groups are the most reactive in such additions, such as dimethyl acetylenedicarboxylate and hexafluoro-2-butyne. The stereochemistry of addition is cis. Examples exist of alkyl, aryl, and alkynyl Pd^{II} complexes undergoing reaction (equation 11). The addition of a Pd–R group across an alkene can also be seen as the migratory insertion of an alkene into a Pd–C bond. The addition of palladium and carbon is cis and the alkyl group is added preferentially to the less-hindered carbon. Alkenes with electron-withdrawing groups tend to insert fastest (equation 12).[24]

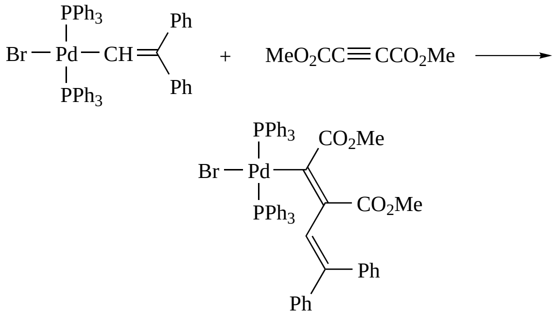

(11)

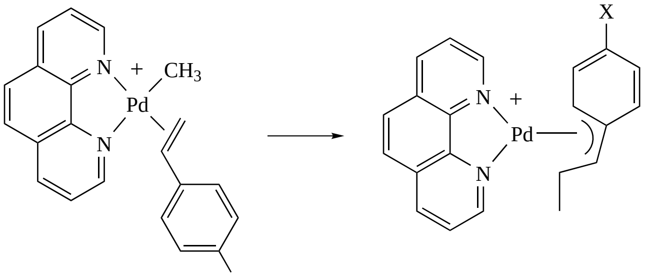

$\Delta G^{\ddagger}$ 73.5 X = CF_3
kJ mol^{-1} 76.0 X = H
76.9 X = CH_3

(12)

4.1.6 *Addition of Pd–H to Unsaturated Groups and Alkene Isomerization*

As with Pd–C bonds, Pd–H will add to unsaturated functional groups (*see* ***Hydride Complexes of the Transition Metals***). In the case of alkynes, the Pd–H addition is cis, to give vinyl complexes. The addition of a Pd–H bond to an alkene will normally generate a $\mathrm{Pd^{II}}$ alkyl with β-hydrogens, which can undergo further β-elimination. This process can lead to alkene isomerization. However, palladium complexes have not proved as useful as those of other transition metals for alkene isomerization. While 1,5-cyclooctadiene can be isomerized to 1,3-cyclooctadiene with $\mathrm{PdCl_2(PhCN)_2}$, palladium on charcoal is a more convenient and active catalyst for this isomerization.

4.1.7 *Insertion of CO and Isonitriles into Pd–C Bonds (See* ***Carbonylation Processes by Homogeneous Catalysis****)*

The insertion of CO into palladium–carbon bonds is a common step in many palladium-catalyzed carbonylation reactions and polymerizations.**[25]** This reaction takes place under moderate CO pressure (1–3 atm). From the range of compounds that can be carbonylated, it can be inferred that CO will insert into alkyl, aryl, and alkynic bonds (equation 13). One of the few types of Pd–C bonds inert to CO insertion is the Pd–acyl bond, thus only single carbonylations are normally observed. However, a few examples of double carbonylation have been reported. In the case of palladium-catalyzed formation of $\mathrm{PhCOCONEt_2}$ from PhI, CO, and $\mathrm{NHEt_2}$, reductive elimination from a bisacyl complex has been established as the mechanism, rather than CO insertion into a Pd–acyl bond.

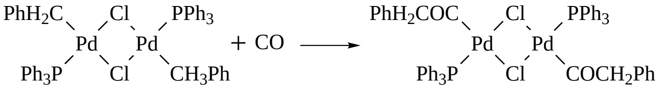

(13)

Unlike CO, isocyanides can insert into Pd–C bonds once, twice, or even three times, to give isolable complexes (equation 14). The Pd/RNC molar ratio, the nature of the ligands on palladium, and the isocyanide determine what product is formed

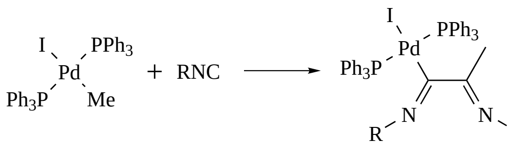

(14)

When CO inserts into a palladium–carbon bond, the resulting acyl can be hydrolyzed to an ester if methanol or another alcohol is present in the reaction. This overall reaction is termed hydroesterification when the alkyl is derived from an alkene. Alternatively, if ethene is present, and bidentate phosphine ligands are used, one can achieve alternating copolymerization of CO and $\mathrm{C_2H_4}$ to produce polyketones.

4.1.8 *Palladium Carbene Complexes*

Palladium isocyanide complexes react with amines and alcohols to give palladium ***Carbene Complexes*** (equation 15) in a reaction that is a nucleophilic attack on the isonitrile carbon. These complexes easily lose a halide if it is trans to the carbene ligand, since the carbene carbon has a high trans influence. The structures of these compounds have the carbene carbon and its two heteroatom groups in one plane, which is perpendicular to the coordination plane of the Pd.

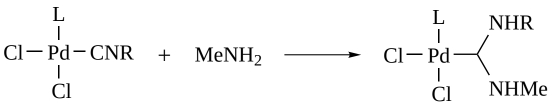

(15)

N-Heterocyclic carbenes are relatively stable, electron-rich ligands and can be made sterically demanding.**[26]** They are σ-donor ligands with little π-acid properties, like trialkylphosphines. These new ligands are readily available by deprotonation of azolium precursors, and the deprotonation can be carried out in the presence of palladium salts to generate the complexes directly (Scheme 12).

4.1.9 *Other Routes to Pd–C Bonds*

The C–H bonds of arenes can react with electrophilic palladium cations to generate new $\mathrm{Pd^{II}}$-Ar derivatives, in a process that is basically an electrophilic aromatic substitution.**[27]** For example, mixing $\mathrm{Pd(OAc)_2}$ in trifluoroacetic acid generates the powerful electrophile $\mathrm{[PdO_2CCF_3]^+}$ that reacts with electron-rich arenes at room temperature (equation 16). This reaction can form the basis for the conversion of benzene derivatives to benzoic acids. Mixing 10% $\mathrm{Pd(OAc)_2}$ in trifluoroacetic acid with chlorobenzene and $\mathrm{K_2S_2O_8}$ as an oxidant under 1 atm of CO at room temperature gave p-chlorobenzoic acid in 100% yield. The advantage of using arenes over aryl halides is that no HX is produced that must be disposed of.

$$\begin{aligned} \mathrm{Pd(OAc)_2 + CF_3CO_2H} &\longrightarrow \mathrm{[PdO_2CCF_3]^+ + ArH} \\ &\longrightarrow \mathrm{ArPdO_2CCF_3} \qquad (16) \end{aligned}$$

Strained carbon–carbon bonds can undergo reaction with electron-rich complexes such as $\mathrm{Pd(PEt_3)_3}$. Biphenylene reacts to form two new C–C bonds with $\mathrm{Pd(PEt_3)_3}$ in a reaction that is undoubtedly aided by the formation of two strong Pd–$\mathrm{C}_{sp}{}^2$ bonds as well as by the strain of the bond being broken (equation 17).**[28]**

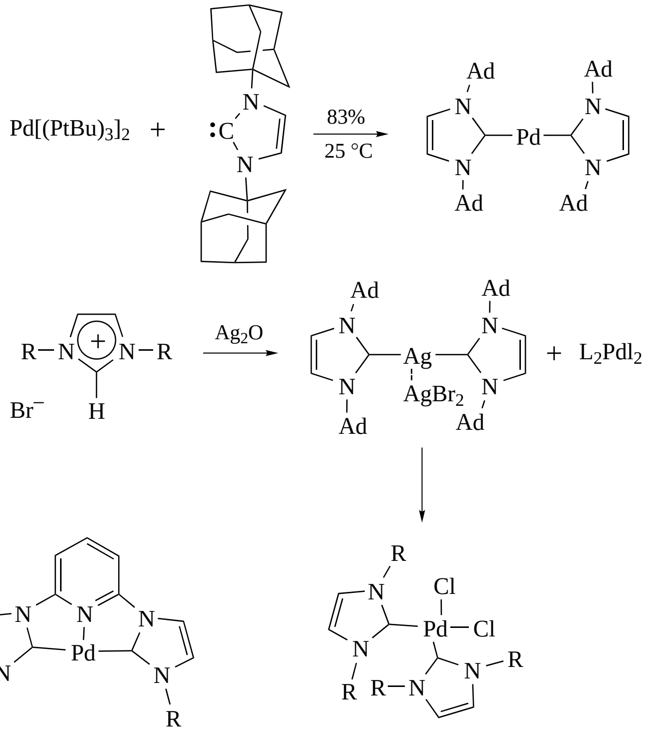

Scheme 12

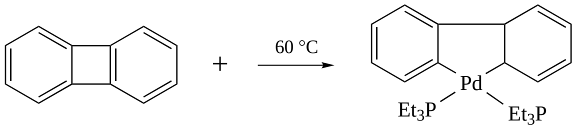

(17)

4.1.10 *Formation of Palladium Carbonyl and Isonitrile Complexes*

The reduction of $Pd(acac)_2$ with $AlEt_3$ in the presence of CO and PPh_3 gives the Pd^0 carbonyl complex $Pd(CO)(PPh_3)_3$. This spontaneously loses PPh_3 in solution to yield $Pd_3(PPh_3)_4(CO)_3$. In toluene, this trimer gives, reversibly, $Pd_3(PPh_3)_3(CO)_3$. Carbonylation of $Pd_3(PPh_3)_3(CO)_3$ at 500 atm of CO converts the complex into $Pd(CO)_3PPh_3$, which decomposes at atmospheric pressure.

As with Pd^0, there are relatively few examples of Pd^{II} carbonyl complexes that have been isolated. Since palladium is an active catalyst for scores of carbonylation reactions, this lack arises from facile insertion reaction of CO into Pd–C bonds, and the ease of displacement of CO from Pd^{II} centers by other ligands, rather than a lack of interaction between Pd^{II} and CO. Reaction of $Pd(\eta^5\text{-}C_5H_5)Cl(PPh_3)$ with $AgClO_4$ followed by CO gives $[Pd(\eta^5\text{-}C_5H_5)CO(PPh_3)]ClO_4$. This compound exhibits a ν_{CO} at $2113\,cm^{-1}$. Isostructural Ni and Pt complexes each give lower energy ν_{CO} bands at $2081\,cm^{-1}$ and $2093\,cm^{-1}$, respectively. This result is further evidence that Pd^{II} is less effective at π-donation to the CO ligand than either Ni^{II} or Pt^{II}.

A much wider range of palladium isonitrile complexes have been isolated compared to the palladium carbonyls. Isonitriles will displace both acetonitrile ligands from $Pd(CH_3CN)_2Cl_2$, which offers a convenient synthesis of $Pd(RNC)_2Cl_2$. The corresponding $Pd(RNC)_2I_2$ reacts with KOH in the presence of RNC to give the zero-valent $Pd(RNC)_4$. RNC is a better σ-donor ligand and a worse π-acceptor than CO, which accounts for the formation of $Pd(RNC)_4$.

4.1.11 *Organopalladium(IV) Compounds*

There are a relatively small number of organopalladium(IV) compounds isolated.**29** One of the first examples was prepared by oxidizing $PdCl(C_6F_5)(bpy)$ with Cl_2 to give $PdCl(C_6F_5)(bpy)$ (bpy $= 2, 2'$-bipyridyl). Subsequently, it was discovered that reactive halides such as methyl iodide or benzyl halides undergo oxidative addition to Pd^{II} complexes with chelating nitrogen ligands (especially 2,2′-bipyridine, 1,10-phenanthroline and tris(pyrazol-1-yl)methane). In this way, complexes such as $PdBrMePh(CH_2Ph)(bpy)$ can be prepared. These additions seem to be standard S_N2 reactions. Reductive elimination of alkyl groups requires a vacant coordination site, which is usually generated by ionization of a halide. Where different alkyl groups are present on the Pd^{II} atom, there is a preference for coupling of two methyl groups. In acetone solution, slightly above room temperature, $PdBrMePh(CH_2Ph)(bpy)$ decomposes to give toluene and $PdBr(CH_2Ph)(bpy)$. Differential scanning calorimetry of reductive elimination in solid Pd^{IV} alkyls, where one assumes the heat absorbed corresponds to the bond enthalpies being broken, suggests the $Pd^{IV}–CH_3$ bond enthalpy is ~130 kJ mol^{-1} and the $Pd^{IV}–CH_2Ph$ bond enthalpy is ~123 kJ mol^{-1}.

4.2 Reactions of the Pd^{II}-Carbon Bonds

4.2.1 Reduction

Compounds with Pd^{II}–C bonds will undergo reduction by H_2 or D_2, $NaBH_4$, $LiAlH_4$, or $NaCNBH_3$. This reaction provides a convenient way to remove palladium from an organometallic molecule formed from addition to a coordinated alkene or diene (equations 18 and 19). The hydride reagents work by replacing one of the halides with H, leading to reductive elimination of RH. Because of the stability of $Pd(CN)_4{}^{2-}$, aqueous cyanide solutions will break Pd–C bonds, releasing C–H. Basic alcohol solutions will also decompose organopalladium compounds, depositing palladium metal.

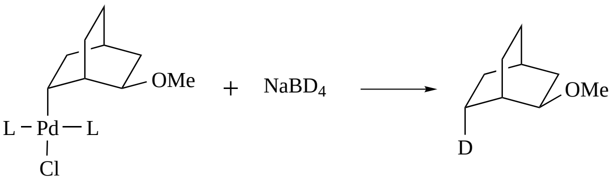

(18)

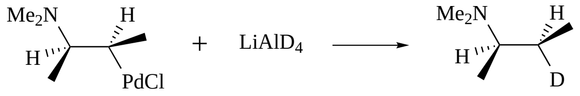

(19)

4.2.2 Reactions with Acids, Electrophiles, and Oxidants

Addition of HCl (as a solution in $CHCl_3$) to compounds with Pd–C bonds results in rapid cleavage to the corresponding RH and Pd–Cl species. Bromine will cleave Pd–C bonds at temperatures between −78 °C and 20 °C to produce the corresponding RBr (equation 20). In the case of palladium acyls, an acid bromide is produced, and running the cleavage reaction in the presence of alcohols or amines leads to the formation of esters or amides. Occasional reports have described the oxidations of palladium alkyls with peracids or C_6F_5IO to give alcohols. Hydrogen peroxide in the presence of an iron porphyrin catalyst (*meso*-tetrakis(pentafluorophenyl)porphyrinatoiron(III) chloride) is reported to oxidize Pd–C bonds as well.[30]

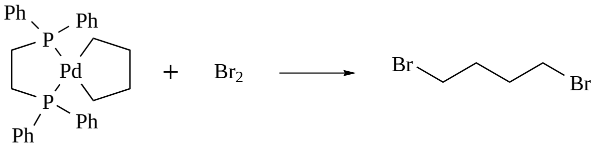

(20)

4.2.3 Reaction of Organopalladium Species with Alkenes

A number of important reactions involve the addition of R–Pd across an alkene double bond. The palladium-catalyzed vinylation or arylation of organic halides, the Heck reaction (also known as the Mizoroki–Heck reaction), was introduced in Scheme 5 (equation 21). In this reaction, an aryl, vinyl, or benzylic halide undergoes oxidative addition to a Pd^0 species, usually generated in the reaction from a catalytic quantity of $Pd(OAc)_2$, $PdCl_2$, or $(PR_3)_2PdX_2$. Other types of halides have β-hydrogens that lead to β-elimination products instead of vinylation. The reaction is run in solvents such as DMF or acetonitrile at temperatures of 70 to 150 °C. After addition of Pd–R across the double bond, reductive elimination of L_nPd–H regenerates the double bond. Since one equivalent of acid is generated, a base is required. Common choices are K_2CO_3, Cs_2CO_3, and tertiary amines. The orientation of addition of the R group to the alkene depends on the other groups, on the double bond, and the structure of the R group.[31]

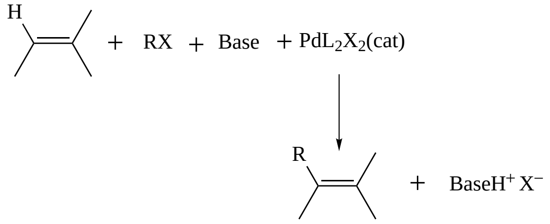

(21)

Under standard reaction conditions, the mechanism of the Heck reaction is more complicated than the textbook pathway shown in Scheme 5. The active catalyst responsible for oxidative addition of the ArX substrate is an anionic Pd^0 species, either L_2PdCl^- or $L_2Pd(OAc)^-$, depending on the starting palladium compound, where L is triphenylphosphine.[32] Reduction of the starting palladium salt to a Pd^0 species is carried out by the phosphine. A mechanism that is consistent with spectroscopic and electrochemical data is given in Scheme 13.

In general, the alkyl group is added to the less-substituted carbon atom of the double bond. If an electron-withdrawing group is attached to the alkene, the alkyl group usually attaches β to it. Changing from a monodentate to a bidentate ligand can sometimes reverse the regioselectivity of the addition. (Scheme 14).

The addition of R–Pd to the double bond and the elimination of Pd–H from it are both syn. Thus, the relative stereochemistry of the double bond is inverted (equation 22). Mixtures of stereoisomers are in fact produced, since the β-elimination reaction is reversible. Lower reaction temperatures and higher phosphine concentrations increase the stereoselectivity of the reaction.

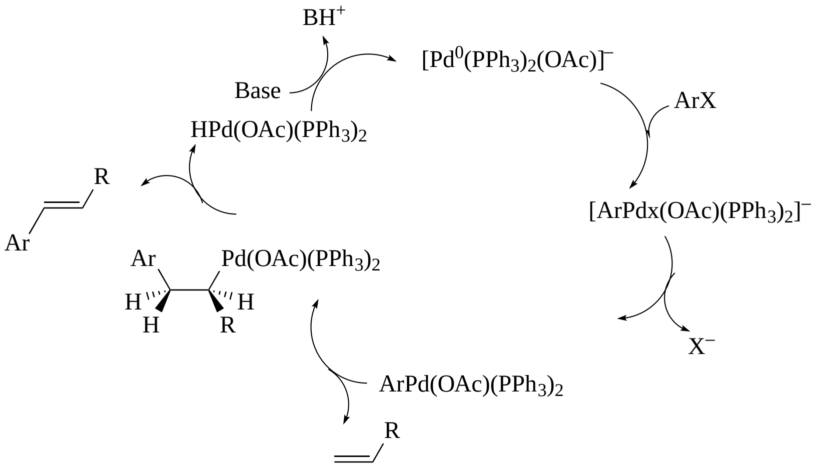
BH+
Base
[Pd0(PPh3)2(OAc)]−
ArX
HPd(OAc)(PPh3)2
R
Ar
[ArPdx(OAc)(PPh3)2]−
Ar
Pd(OAc)(PPh3)2
H
H
H
R
X−
ArPd(OAc)(PPh3)2
R

Scheme 13

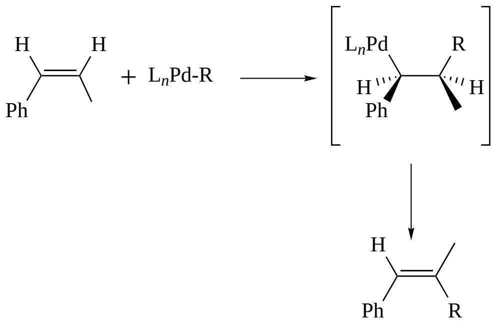
H
H
Ph
+ LnPd-R
LnPd
R
H
Ph
H
H
Ph
R

(22)

Steric hindrance is tolerated in the organic halide component of the reaction. The reaction of 2,5-diisopropyliodobenzene with methyl acrylate proceeds in 79% yield at 125 °C, for example. The alkene component, conversely, is sensitive to the number and size of the substituents on the alkene. Useful yields of product are only obtained for ethene and mono- and disubstituted alkenes. If the alkene is unreactive, the RX component is dimerized to R–R as the major reaction.

Intramolecular Heck reactions take place and can produce medium and large size rings. The new double bond can be formed exocyclic or endocyclic to the new ring, depending on the conformational freedom in the approach of the alkene to the Pd–C bond (Scheme 15). If one uses a chiral ligand, such as (S)-BINAP, chiral products can result (Scheme 16).**33**

Other reagents can serve as the source of Pd–R in addition to organic halides. Organomercurials readily transfer organic groups to Pd^{II} at 25 °C, permitting the vinylation to take place at a lower temperature, although the reaction is stoichiometric. In addition, a wider range of carbon groups can be transferred, including methyl, carboalkoxy, neopentyl, and neophyl. More sensitive compounds can thus be coupled to alkenes via mercurials. 5-Chloromercuricytosine can be converted to 5-allylcytosine in 77% yield. In this reaction, β-elimination of Pd–Cl takes place in preference to Pd–H elimination (equation 23).

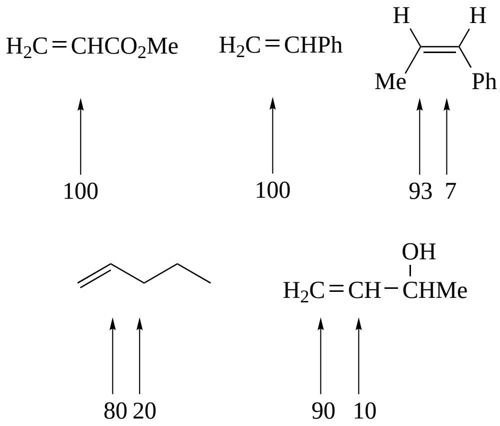
H2C=CHCO2Me
H2C=CHPh
H
H
Me
Ph
100
100
93
7
OH
H2C=CH−CHMe
80 20
90
10

Scheme 14

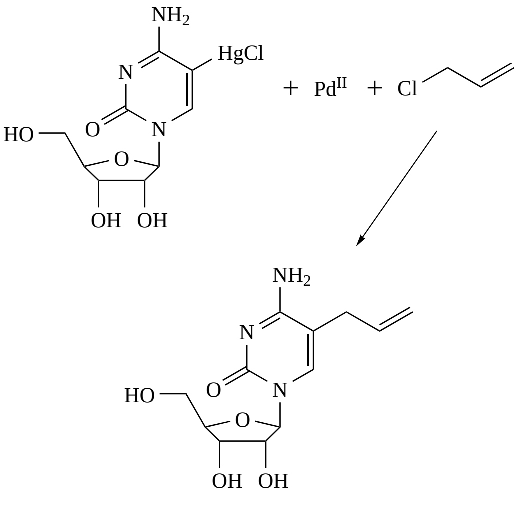
NH2
HgCl
N
+ PdII + Cl
HO
O
N
O
OH OH
NH2
N
HO
O
N
O
OH OH

(23)

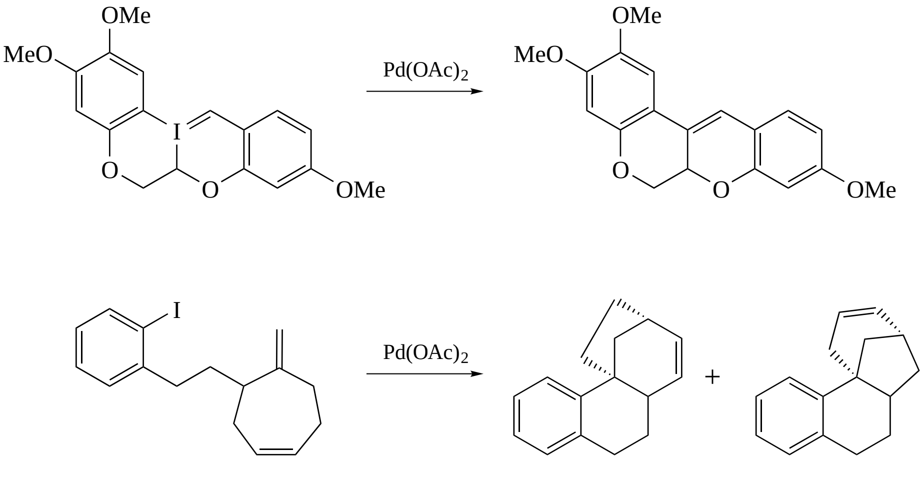
OMe
MeO
I
O
O
OMe
Pd(OAc)2
OMe
MeO
O
O
OMe
I
Pd(OAc)2
+

Scheme 15

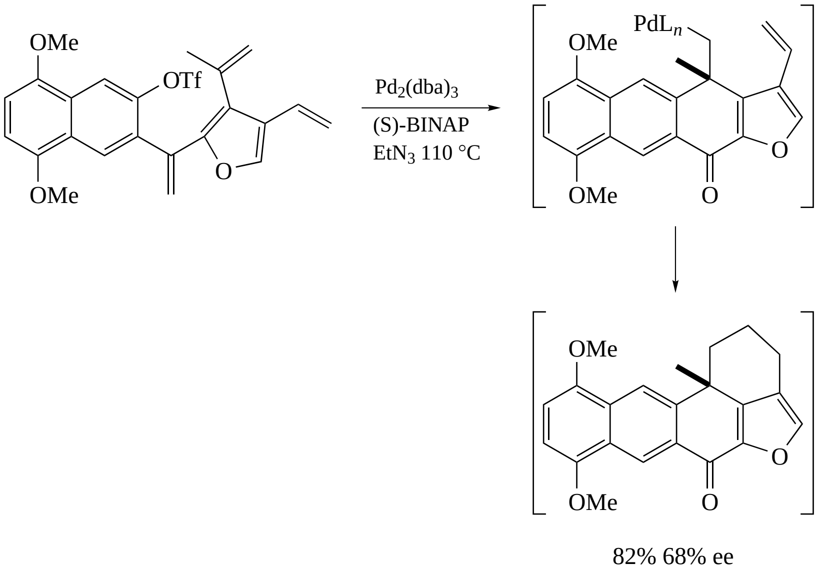
OMe
OTf
OMe
O
Pd2(dba)3
(S)-BINAP
EtN3 110 °C
PdLn
OMe
OMe
O
O
OMe
OMe
O
O
82% 68% ee

Scheme 16

The search for more stable or more reactive catalysts has produced many new leads. One of the most promising is represented by the palladacycle (**14**), known as Hermann's catalyst. This can be used in Heck reactions at high temperatures (above 140 °C), which leads to high turnover numbers of up to 10^6 with electron-poor aryl bromides.**34**

Because stoichiometric amounts of base-HX salts are produced in a Heck reaction, alternative sources of aryl groups have been investigated. Carboxylic acid anhydrides were found to react with a PdC_2/NaBr catalyst system, where the by-products were CO and a carboxylic acid. *p*-Nitrophenylbenzoates were also found to be aryl donors in a decarbonylative Heck reaction.**35** An arylation of cinnamates was discovered using $Pd(OAc)_2$ to activate the C–H bonds of electron-rich benzene derivatives. This reaction took place in toluene and used $Mn(OAc)_3/O_2$ to reoxidize the Pd^0 produced to close the catalytic cycle (equation 24).

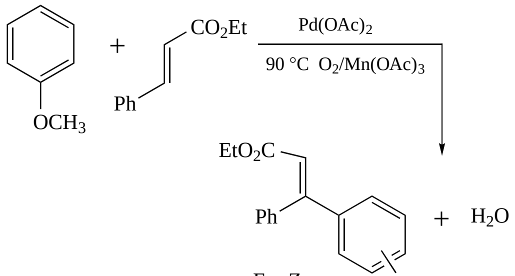
OCH3
+
CO2Et
Ph
Pd(OAc)2
90 °C O2/Mn(OAc)3
EtO2C
Ph
+ H2O
E + Z
OCH3

(24)

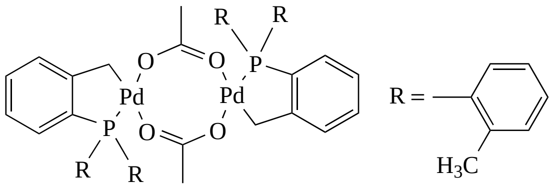
R
R
O
O
P
Pd
Pd
P
O
O
R
R
R =
H$_3$C

(**14**)

4.2.4 *Catalytic Cross Coupling with Organostannanes and Organosilanes, the Stille and Hiyama Reactions*

The general mechanism for the cross coupling of organostannanes and aryl halides (the Stille reaction) is given in Scheme 4.[36,37] The transmetalation step takes place through a cyclic, four-center transition state. In general, the rate of ligand transfer from tin to palladium is alkyne > vinyl > aryl > allyl, benzyl > methyl > butyl. Originally, acyl halides were used as the electrophile (equation 25). The major side reaction in that case is decarbonylation, but running the reaction under CO retards decarbonylation.

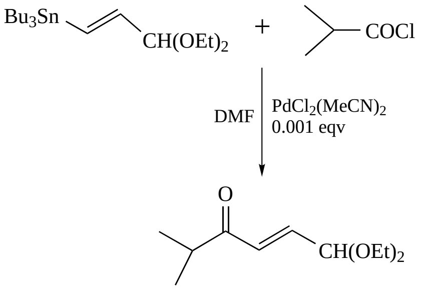
Bu$_3$Sn
CH(OEt)$_2$
+
COCl
DMF
PdCl$_2$(MeCN)$_2$
0.001 eqv
O
CH(OEt)$_2$

(25)

Subsequently, it was found that aryl and vinyl iodides, bromides, and triflates were excellent substrates in Stille couplings. In general, the rate for oxidative addition of ArX is X = I > Br > OTf > Cl. In addition, haloheterocycles such as 2- and 4-chloropyridines and 6-chloropurines react with standard Pd(PPh$_3$)$_4$ catalysts. Alkyl substrates tend to undergo β-elimination prior to coupling. Frequently an additive, such as Et$_4$NCl or CsF, is used. These, especially the fluoride salts, form transient five-coordinate R$_4$SnX$^-$ species, which are more reactive in the transmetalation step. Fluoride in the reaction mixture also leads to formation of insoluble Bu$_3$SnF, which makes the otherwise difficult removal of organotin residues easy (equation 26). Recently, the use of hindered phosphine Pd^0 catalysts in conjunction with CsF cocatalysts has been found to activate simple aryl chlorides for biaryl couplings (equation 27).

These PdL$_n$ complexes also have been found to couple vinylstannanes to alkyl bromides. Assaying a number of different hindered phosphines, including P(t-Bu$_3$)$_3$, PCy$_2$(t-Bu), and P(t-Bu)$_2$Et, only P(t-Bu)$_2$Me and PCy$_3$ gave coupled products instead of β-elimination.[38] This work illustrates the remarkable sensitivity individual catalytic reactions have to ligand size and electronic properties (equation 28).

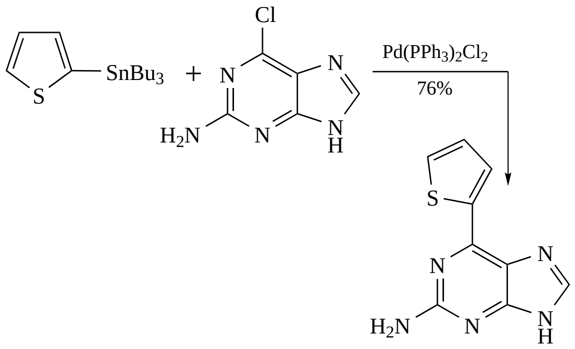
S
SnBu$_3$
+
Cl
N
N
H$_2$N
N
N
H
Pd(PPh$_3$)$_2$Cl$_2$
76%
S
N
N
H$_2$N
N
N
H

(26)

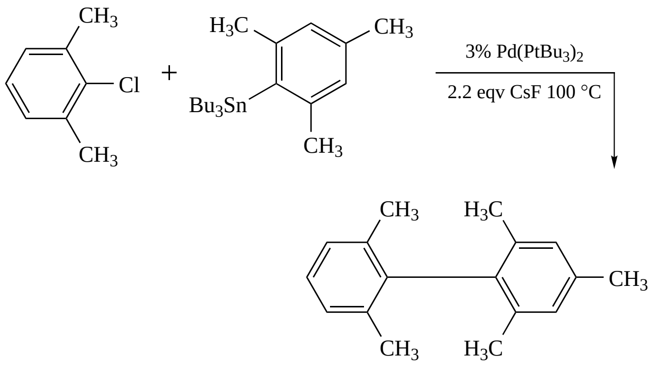
CH$_3$
Cl
CH$_3$
+
H$_3$C
CH$_3$
Bu$_3$Sn
CH$_3$
3% Pd(PtBu$_3$)$_2$
2.2 eqv CsF 100 °C
CH$_3$
H$_3$C
CH$_3$
CH$_3$
H$_3$C

(27)

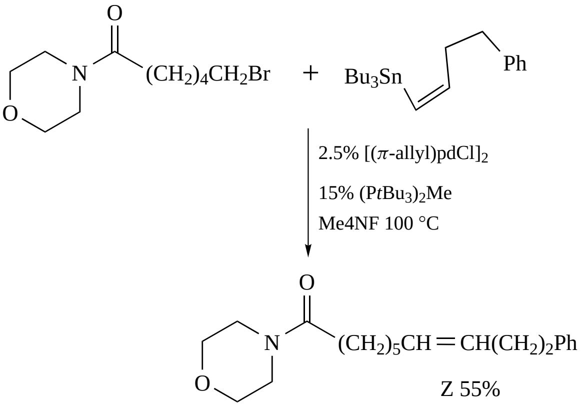
O
N
O
(CH$_2$)$_4$CH$_2$Br
+
Bu$_3$Sn
Ph
2.5% [(π-allyl)pdCl]$_2$
15% (PtBu$_3$)$_2$Me
Me4NF 100 °C
O
N
O
(CH$_2$)$_5$CH=CH(CH$_2$)$_2$Ph
Z 55%

(28)

Coupling of organosilane derivatives to RX species is known as the Hiyama reaction. This process is seen as more difficult to catalyze than the Stille reaction since a C–Si bond is less reactive than a C–Sn bond. However, addition of additives, such as Bu$_4$NF or CsF, that form hypervalent silicon intermediates, or the use of more reactive silane precursors, such as Me$_3$SiSiMe$_3$, ArSiMe$_2$OH, or Cl$_2$MeSi(vinyl), can overcome this limitation (equation 29).

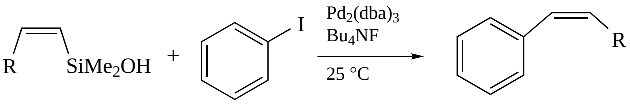
R
SiMe$_2$OH
+
I
Pd$_2$(dba)$_3$
Bu$_4$NF
25 °C
R

(29)

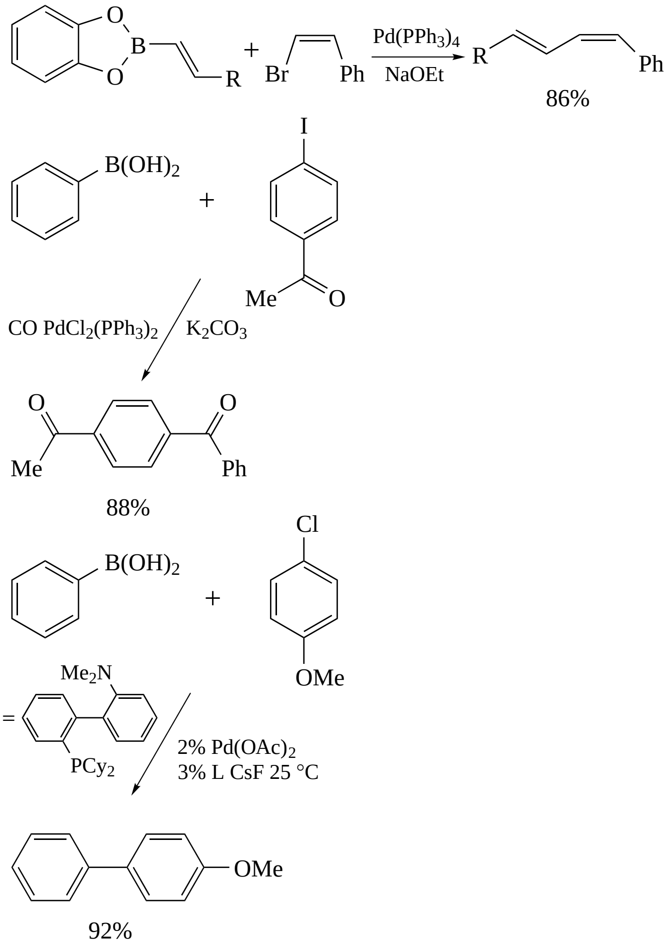

Scheme 17

4.2.5 *Catalytic Cross Couplings with Organoboranes, the Suzuki or Suzuki–Miyaura Reaction*

The palladium-catalyzed coupling of boronic acids (as well as other boron derivatives) with aryl and vinyl halides and pseudohalides is known as the Suzuki or Suzuki–Miyaura reaction.**[39]** Because boron is nontoxic, this reaction has been used in pharmaceutical syntheses. In addition, hydroboration or borate substitution allows for the synthesis of virtually any desired coupling partner. For these reasons, as well as the high yields and functional group compatibility, the Suzuki reaction is the first reaction to consider for carrying out a cross coupling. Representative substrates and catalysts are shown in Scheme 17. The various bases are used to generate four-coordinate boron ‘ate’ complexes that are more reactive in transmetalation.

An extremely useful variant of Suzuki reaction uses B-alkyl substrates with aryl or vinyl halides.**[40]** The B-alkyls are prepared by hydroboration of an alkene with 9-BBN-H. With appropriate palladium ligands, reductive elimination takes place faster than β-hydride elimination of alkyl groups. The major limitation is that alkyl groups must be primary, since secondary and tertiary alkyls undergo β-hydride elimination exclusively. Intermolecular and intramolecular examples are shown in Scheme 18.

4.2.6 *Catalytic Cross Couplings with Grignard, Organozinc and Related Reagents, the Kumada and Negishi Reactions*

The palladium-catalyzed coupling of Grignard reagents with aryl or vinyl halides is known as the Kumada, or alternatively, the Kharasch reaction. It is perhaps the original transition metal catalyzed cross-coupling reaction, and works with both Pd and Ni catalysts. This reaction is used extensively to synthesize biaryls. Because of the basicity of Grignard reagents, there is no need to add additional bases to this coupling reaction.

The Negishi reaction, which couples aryl and vinyl halides with organozinc reagents, is potentially more useful than the Kumada reaction because of the greater functional group tolerance of organozinc compounds.[41] If functional group compatibility is not a consideration, aryl zinc compounds can be made in situ from Grignards and catalytic quantities of $ZnCl_2$. The use of $PdCl_2$(dppf) (dppf = 1,1-bis(diphenylphosphino)ferrocene) or Pd(Pt-Bu_3)$_2$ permits coupling of ArZnX to ArCl at temperatures at or below 100 °C. Other organometallics that can be used in palladium-catalyzed cross couplings include RHgX, Cp_2RZrCl, AlR_3, and RCu.

4.2.7 *Catalytic Cross Couplings to Terminal Alkynes, the Sonogashira Reaction*

Coupling terminal alkynes with aryl or vinyl halides using palladium and copper cocatalysts is known as the Sonogashira reaction.[42] The copper is needed to activate the alkyne C–H. The industrial synthesis of the active ingredient in Lamisil®, the antimycotic agent Terbinofin, involves a Sonogashira coupling (equation 30).

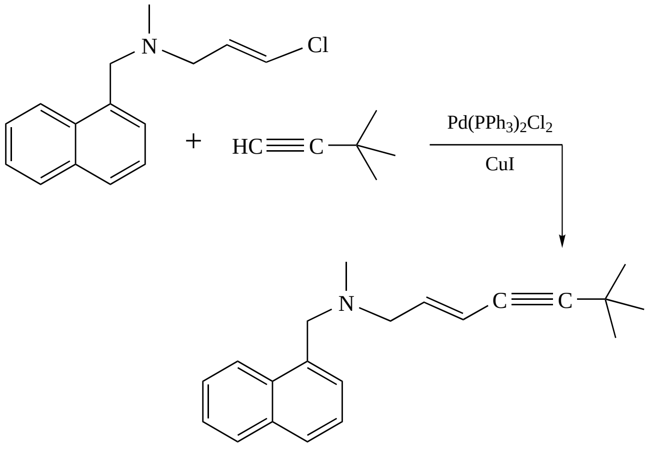

(30)

4.2.8 *Catalytic Cross Couplings of Aryl Halides with Enolates*

Active methylene compounds, such as malonates, malononitrile, and aliphatic nitro compounds are coupled efficiently to aryl and heteroaromatic halides.[43] The best ligands, as is the case for many other cross couplings, are bulky phosphines such as 2-(di-t-butylphosphino)-2′-methylbiphenyl (see Scheme 11). Enolates of less acidic carbonyl compounds, such as ketones, esters, and amides, also undergo α-arylation using these hindered ligands. This reaction depends on the base used to generate the enolate, as well as the phosphine, with NaO-t-Bu, KN(SiMe)$_2$, Cs_2CO_3, and K_3PO_4 being preferred. Characteristic examples are collected in Scheme 19.

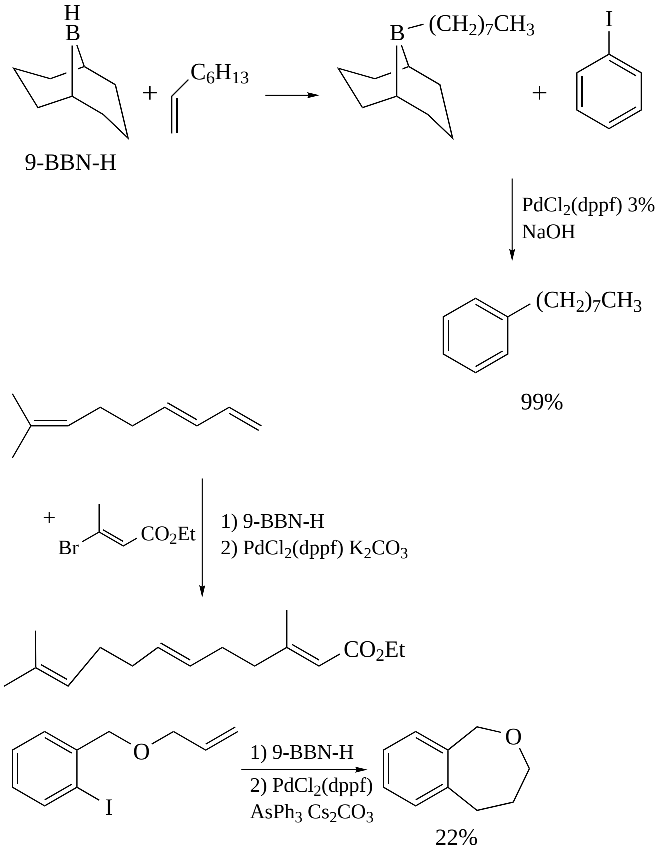

Scheme 18

4.2.9 *Catalytic Cross Couplings of Aryl Halides to Nitrogen and Oxygen Nucleophiles, the Buchwald–Hartwig Reaction*

Palladium-catalyzed amination and alkoxylation of aryl halides have been developed only since the mid-1990s.[44,45] The catalytic cycle is similar to other cross-coupling reactions (Scheme 20).

Two problems had to be solved for these reactions to be made useful. First, reductive elimination to form C–N and C–O bonds was not a well-known reaction with classical ligands such as PPh_3.[46] Second, β-hydride elimination is very facile for primary and secondary heteroatom substrates. As with other cross-coupling reactions, the use of hindered, basic phosphines turned out to be crucial. Amination reactions tend to give better yields, since reductive elimination is faster for more basic groups. For example, the base used in catalytic aminations is Na-O-t-Bu, but the product is the aryl amine.

For aromatic ether formation, electron-withdrawing groups on the arene accelerate the rate of reductive elimination. Further, the more basic alkoxide groups form ethers faster than phenoxides. These facts have led to the proposal that, in addition to the usual concerted reductive elimination mechanism, some substrates can undergo reductive elimination via a Meisenheimer type intermediate (equation 31).

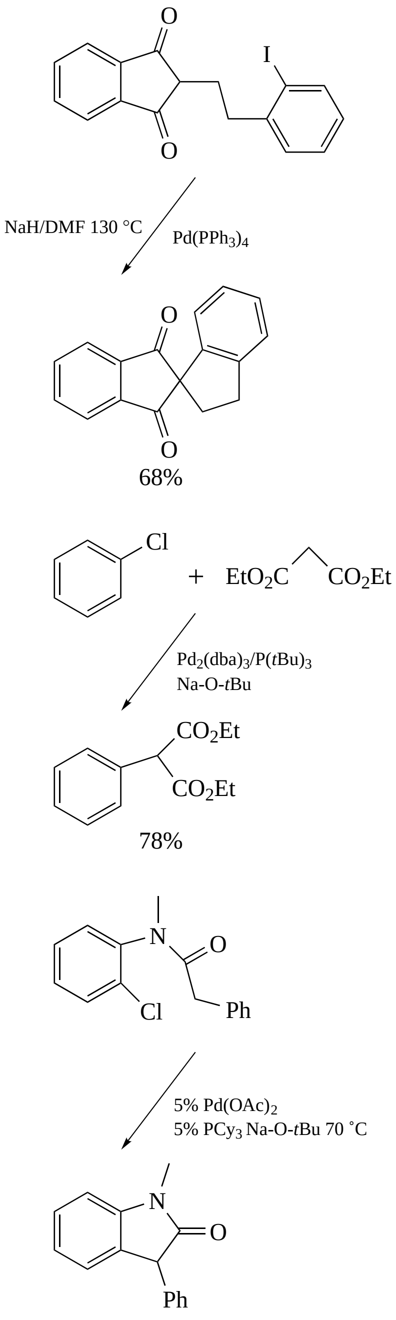
O
I
O
NaH/DMF 130 °C
Pd(PPh3)4
O
O
68%
Cl
+ EtO2C CO2Et
Pd2(dba)3/P(tBu)3
Na-O-tBu
CO2Et
CO2Et
78%
N
O
Cl
Ph
5% Pd(OAc)2
5% PCy3 Na-O-tBu 70 ˚C
N
O
Ph

Scheme 19

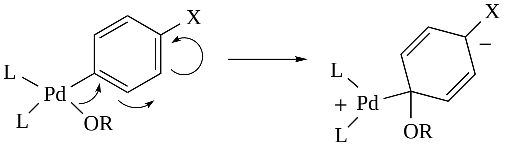
X
L
Pd
L
OR
X
−
L
+ Pd
L
OR

(31)

Examples of amination and alkoxylation reactions are given in Scheme 21. Synthetic equivalents of ammonia, such as $Ph_2C{=}NH$, can be used to prepare anilines and t-$BuMe_2SiONa$ reacts to give protected phenols.**47**

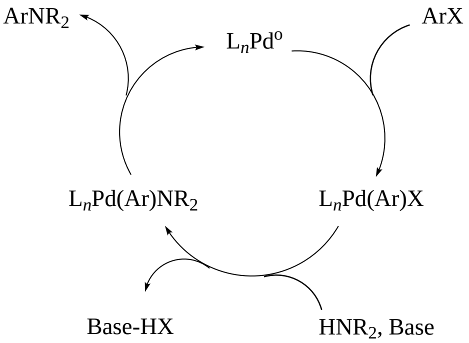
ArNR2
LnPdo
ArX
LnPd(Ar)NR2
LnPd(Ar)X
Base-HX
HNR2, Base

Scheme 20

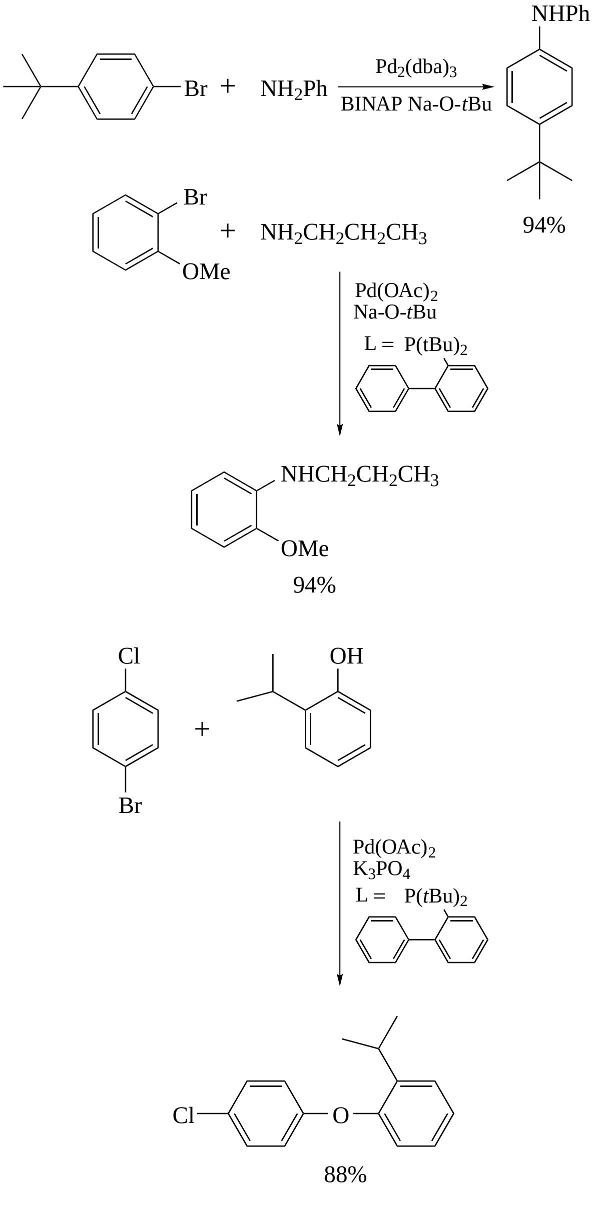
NHPh
Br +
NH2Ph
Pd2(dba)3
BINAP Na-O-tBu
94%
Br
+ NH2CH2CH2CH3
OMe
Pd(OAc)2
Na-O-tBu
L = P(tBu)2
NHCH2CH2CH3
OMe
94%
Cl
OH
+
Br
Pd(OAc)2
K3PO4
L = P(tBu)2
Cl
O
88%

Scheme 21

5 ALKENE AND ALKYNE COMPLEXES OF PALLADIUM

5.1 Synthesis of Monoalkene and Monoalkyne Complexes

Alkene complexes of Pd^0 are very unstable unless the double bond is substituted with electron-withdrawing groups. Condensation of palladium atoms with ethene gives $(\eta^2\text{-}C_2H_4)_3Pd$. Reduction of $[PdCl_2(1,5\text{-cod})]$ with $Li_2C_8H_8$ gives the unstable $Pd(1,5\text{-cod})_2$. The most commonly used Pd^0 alkene complex, and one that can be stored and handled in air, is Pd_2(dibenzylideneacetone)$_3$, which can be prepared from K_2PdCl_4, dibenzylideneacetone, and sodium acetate in ethanol.**48** The dibenzylideneacetone ligands are easily displaced by phosphines, and because of its stability, the complex serves as a useful precursor to PdL_4. Mixed phosphine/alkene complexes of Pd^0 have been prepared by reducing $Pd(acac)_2$ with Et_2AlOEt in the presence of phosphines (equation 32).

$$Pd(acac)_2 + Et_2AlOEt + PR_3 \longrightarrow Pd(C_2H_4)(PR_3)_2 \qquad (32)$$

Zero-valent complexes of palladium with both phosphine ligands and alkynes substituted with electron-withdrawing groups, $PdL_2(RC_2R)$, are known. Alkynes have been found to bridge two Pd^I centers in the dinuclear complex $[Pd_2(\mu\text{-}PhC_2Ph)(\eta^5\text{-}C_5Ph_5)_2]$, which is synthesized from $Pd(OAc)_2$ and diphenylacetylene in methanol. Unusual asymmetric alkyne-bridged complexes derived from the paramagnetic compound $[Pd_2(\mu\text{-}PhC_2Ph)(\eta^5\text{-}C_5Ph_5)_2]^+$ have been made, including $[Pd_2(bpy)(P(OPh)_3)(\mu\text{-}PhC_2Ph)(\eta^5\text{-}C_5Ph_5)_2]^+$.

Two general routes are used to synthesize isolable alkene complexes of Pd^{II}. In the first route, $(PhCN)_2PdCl_2$ is reacted with alkenes such as styrene, cyclohexene, isobutene, or ethene to give the monoalkene chlorine-bridged dimers $[(alkene)PdCl_2]_2$. The same starting material reacts with vinyl ethers and 1,2-dimethoxyethane to give the vinyl ether complexes (vinyl ether)$PdCl_2$. Because vinyl ethers are much better σ-donors than π-acceptors, this result supports the observation that σ-donation is more important than π-acceptor ability in determining the stability of Pd^{II}–alkene complexes. Alternatively, one alkene may displace a second from $[(alkene)PdCl_2]_2$. The stability of these alkene complexes decreases in the order *cis*-2-pentene > 1-pentene > *trans*-2-pentene. The ease with which nucleophiles add to alkenes coordinated to Pd^{II}, together with the tendency for palladium to form π-allyl complexes, accounts for the limited number of stable Pd^{II}–alkene complexes. There are also only few examples of Pd^{II}–alkyne complexes that have been isolated. The bulky alkyne di-*t*-butylacetylene reacts with $Pd_2Cl_4(C_2H_4)_2$ to displace both ethene ligands. Where possible, alkynes can be isomerized to π-allyl palladium complexes through addition–elimination of a palladium hydride.

5.2 Reactions of Coordinated Alkenes and Alkynes

Coordinated alkenes and alkynes undergo two kinds of reactions: substitution reactions and nucleophilic additions to the coordinated ligand.**49** While a relatively few examples of nucleophilic attack exist for stable Pd^{II}–alkene complexes, a far larger number of examples can be inferred from the palladium-catalyzed reactions of alkenes.

5.2.1 *Substitution Reactions of Coordinated Alkenes and Alkynes*

Most ligands will displace alkenes from $[Pd_2Cl_4(alkene)_2]$. However, the chelating alkene ligands derived from attack of nucleophiles on 1,5-cyclooctadiene complexes of Pd^{II} undergo bridge-splitting reactions with amine and phosphine ligands (equation 33).

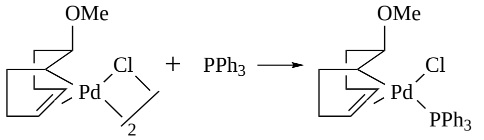

(33)

5.2.2 *Nucleophilic Attack on Coordinated Alkene Complexes*

There is an extensive chemistry of nucleophilic attack on one of the double bonds of coordinated 1,5-cyclooctadiene; this is outlined in Section 6. In addition, the attack of water on ethene coordinated to Pd^{II} is the key step in the Wacker process for the oxidation of ethene to acetaldehyde, which is discussed in Section 9. However, there are some examples of nucleophilic attack on stable Pd^{II}–alkene complexes. The addition of NaOEt to $Pd_2Cl_4(C_2H_4)_2$ gives the diethyl acetal of acetaldehyde (equation 34) along with trace quantities of ethyl vinyl ether. A possible mechanism for this oxidation is outlined in Scheme 22. Addition of methoxide gives a $Pd\text{–}CH_2CH_2OMe$ intermediate, which undergoes β-elimination to form a coordinated vinyl ether. The resulting double bond can insert into the Pd–H bond, and cleavage of the resulting Pd–C bond by methoxide gives the acetal. With acetate as nucleophile in place of alkoxide, the product is vinyl acetate. With butylamine, $Pd_2Cl_4(C_2H_4)_2$ gives MeCH=NBu (equation 35). This reaction undoubtedly proceeds via nucleophilic attack on the coordinated alkene and β-elimination, as in the case of methoxide; however, the subsequent steps may differ, as outlined in equation (36).

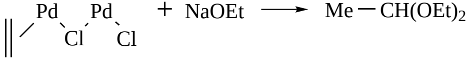

(34)

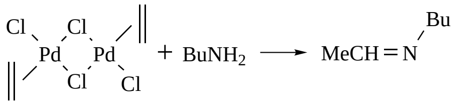

(35)

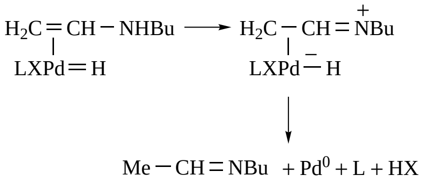

(36)

The geometry of alkene coordination appears to affect the reactivity toward nucleophiles. 7-Methylenenorbornene reacts with $PdCl_2$ to give the product from Pd–Cl addition across the *exo*-methylene double bond (equation 37). In the intermediate $PdCl_2$–diene complex, which could not be isolated, the 7-*exo* double bond would be coordinated so as to lie in the ring plane, while the other alkenic group would lie perpendicular to the palladium square plane, as is normal. From the structure of the product, trans addition of Pd and Cl occurs.

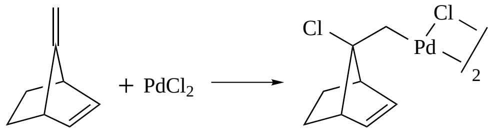

(37)

A general procedure for the addition of stabilized nucleophiles (such as diethyl malonate anion or the enolate of ethyl phenylacetate) to alkenes ($RCH{=}CH_2$) involves letting $PdCl_2(PhCN)_2$ react with an unhindered alkene at 25 °C to form $[PdCl_2(alkene)]_2$, followed by cooling to −78 °C and addition of two equivalents of Et_3N and the enolate ($R'Li$). Warming the reaction to room temperature leads to β-elimination, forming alkenes of the type $RR'C{=}CH_2$ from addition of the enolate anion to the more-substituted end of the alkene. If an H_2 atmosphere is added to the cold solution, no β-elimination takes place, and instead the newly formed Pd–C bond is hydrogenated, leading to $RR'CH{-}CH_3$. If HMPA is present in addition to Et_3N, less-stabilized carbanions can be used, such as phenyllithium. In this reaction, the nucleophile adds to the less-hindered carbon of the alkene. When the coordinated alkene has hydrogens α to the double bond that can be deprotonated to give a π-allyl complex, this deprotonation is facile as detailed in Section 7.

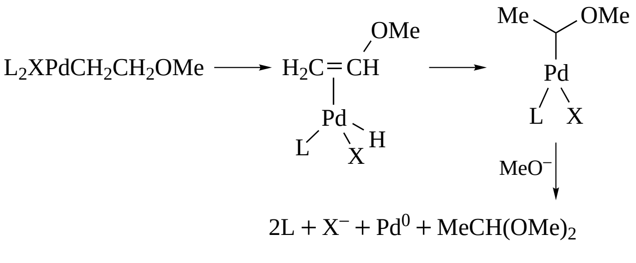

Scheme 22

5.2.3 *Dimerization and Polymerization of Alkenes Catalyzed by Palladium (See* ***Oligomerization & Polymerization by Homogeneous Catalysis****)*

Palladium complexes have been found to dimerize ethene to butenes under a variety of conditions.**[50]** In ethanol, the reaction can take place at 20 to 70 °C and ethene pressures of 1 to 40 atm, using $PdCl_4{}^{2-}$. Propene is dimerized to high proportions (65–90%) of straight chain hexenes with $PdCl_2$ in solvents such as $CHCl_3$. With the catalyst mixture $PdCl_2$, $EtAlCl_2$, and PPh_3, propene gives 2-hexene as the predominant product.

New cationic Pd^{II} (as well as Ni^{II}) complexes have been discovered that polymerize ethene, α-olefins, and cyclic olefins as well as copolymerize alkenes with functionalized monomers, such as methyl acrylate.**[51]** These catalysts use α-diimines as ligands and have been trademarked by DuPont as the Versipol catalyst system. The polyethylene produced by the palladium catalysts is unlike the one produced by the related nickel systems. It is an amorphous, highly branched (with branched branches) polymer having a glass transition temperature below −30 °C. The exact structure depends on the extent of ‘chain walking’ engaged in by the catalyst, which refers to the series of β-hydride elimination and readditions that take place between each ethene insertion step (Scheme 23). The rotation of the $Pd{-}C_\alpha$ bond, that breaks an agostic interaction with the β-H, is the process that controls the overall rate of chain walking. The barrier to β-H elimination is approximately 33 kJ mol^{-1}, while the $Pd{-}C_\alpha$ rotation barrier is approximately 42 kJ mol^{-1}.

Unlike early metal ethene polymerization catalysts, these catalysts have a cationic alkyl/ethene complex as the resting state. The turnover-limiting step is alkene insertion, resulting in an alkyl group stabilized by an agostic interaction with the β-C–H bond. Chain growth kinetics are thus zero order in ethene. Insertion of ethene has a barrier of approximately 71 kJ mol^{-1} for palladium and 54 kJ mol^{-1} for nickel. The use of bulky α-diimine ligands retards chain transfer, leading to high molecular weight polymers.

The specific catalysts that work the best are characterized by cationic palladium centers with bulky α-diimine ligands and noncoordinating counterions. Generation of a specific catalyst is shown in equation (38).

The palladium diimine catalysts can be used to prepare polymers of α-olefins as well as cyclic internal olefins. For α-olefins, the rate of polymerization is slower, compared to ethene, but high molecular weigh polymers are formed. Chain walking takes place with α-olefins, but the α-olefin does not insert into secondary methylene carbons. Copolymers of α-olefins and ethene give polymers with complex microstructures since ethene will insert into secondary

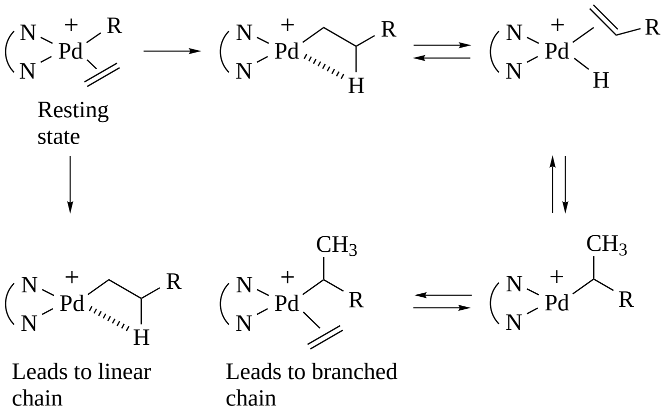

Scheme 23

Pd−alkyl bonds. Cyclic olefins are polymerized to high molecular weight polymers with useful processing properties. The resting state for the cyclopentene polymer has an agostic interaction with a ring β-H (**15**) as shown by ^{1}H NMR.

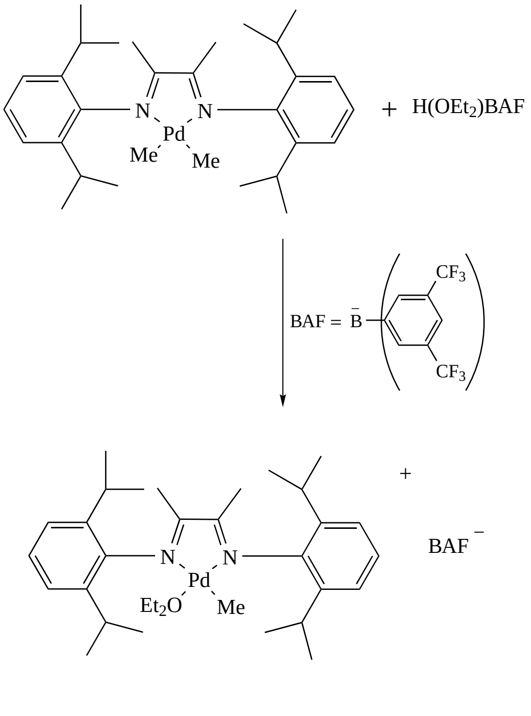

(38)

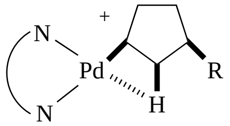

(**15**)

The cationic palladium α-diimine catalysts, much more so than their nickel analogs, are tolerant of polar functional groups. Emulsion polymerization in aqueous solvents can take place to give polymer microspheres useful as adhesives. Monomers such as acrylates, unsaturated ethers, and unsaturated alcohols can be added to ethene polymerization reactions to give random copolymers. Theoretical calculations suggest that oxygen-containing functional groups bind to the nickel catalysts in preference to ethene, while this binding is relatively weaker for palladium. The ethene/methyl acrylate copolymer has been extensively studied. The polymer possesses the highly branched polyethylene structure with ester groups distributed randomly through the branches, mostly at branch termini. The resting state for the ethene/methyl acrylate polymer is a six-membered C,O chelate ring with the palladium bound to the carbon chain and a carbonyl oxygen lone pair.

5.2.4 Coupling and Polymerization of Alkenes with Carbon Monoxide

Methoxycarbonylation of ethene and CO in methanol to give methyl propanoate is carried out with a catalyst prepared by adding methanesulfonic acid to Pd(1,2-$(CH_2P\textit{t}Bu_2)_2C_6H_4$)dba. All the intermediates in the catalytic cycle for this reaction could be seen using low-temperature NMR and ^{13}C labeling.**[52]** The pathway was found to follow the hydride catalytic cycle, where ethene inserts into a Pd–H bond as part of the mechanism, as shown in Scheme 24. The alternative catalytic cycle, known as the methoxycarbonyl cycle, where CO inserts into a Pd–OMe bond to give PdCOOMe, followed by ethene insertion to give $PdCH_2CH_2CO_2Me$ and finally reaction with methanol to give the ester and regeneration of PdOMe did not occur.**[53]**

Slightly different ligands can lead to the polymerization of alkenes and CO to give alternating, ‘polyketone’ polymers with interesting and useful properties.**[54,55]** A diphosphine ligand such as 1,3-bis(diphenylphosphino)propane, dppp, added to $Pd(OAc)_2$ in methanol with an acid having a weakly coordinating conjugate base, such as tosylate or tetrafluoroborate gives ethene/CO copolymers with an average molecular weight of ∼20 000 and total conversions of more

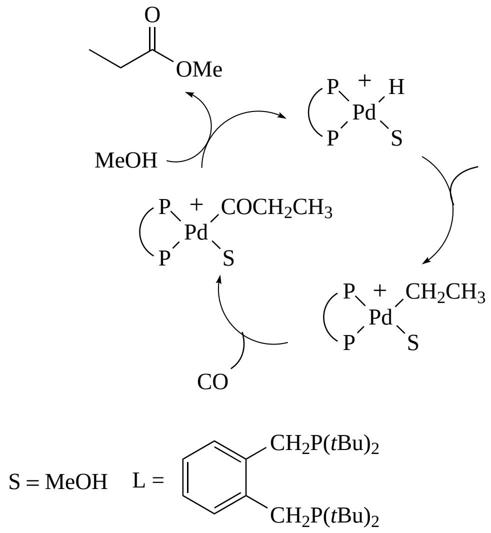

Scheme 24

than 10^6 mol of ethene per mole of Pd. When PPh_3 or similar monodentate ligands are used, the phosphine ligands can adopt a trans-geometry, and the intermediate $L_2Pd–COCH_2CH_3$ will react with methanol to give an ester product. With cis-ligands, the growing chain and a vacant (or solvent-occupied) coordination site are always cis to one another. Since only cis-ligands can undergo insertion, bidentate ligands favor polymer production. The probable reason strict alternation of ethene and CO insertion occurs is that the chain adopts a chelate structure (**16**) that is more readily broken up by CO, since CO is a better ligand than ethene.

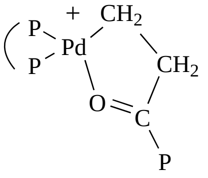

(**16**)

5.2.5 *Coupling of Alkynes*

Many zero-valent platinum group metals couple alkynes to metallacyclopentadienes or catalyze the trimerization to arenes. Normally, the alkynes are substituted with electron-withdrawing groups, such as dimethyacetylenedicarboxylate (dmad) or hexafluoro-2-buyne. When $Pd_2(dba)_3$ reacts with dmad, a 'base-free' palladacyclopentadiene polymer forms in addition to $C_6(CO_2Me)_6$ (Scheme 25). This complex reacts with ligands to generate discrete monomers. Addition of strained alkenes such as norbornene can give cyclohexadiene adducts.

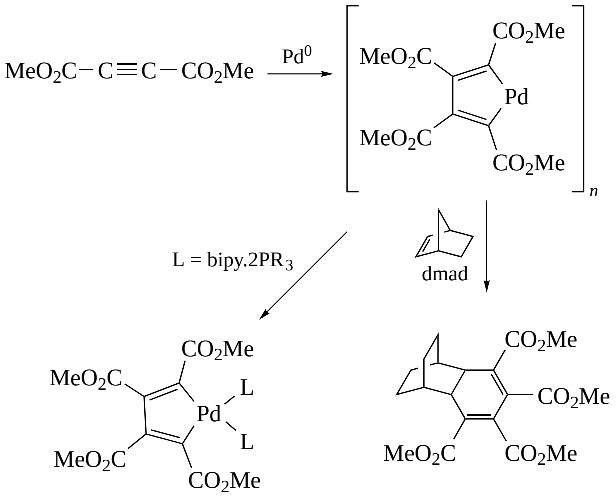

Scheme 25

6 DIENE, CYCLOBUTADIENYL, AND CYCLOPENTADIENYL COMPLEXES

6.1 Diene Complexes of Pd^{II}

Both 1,4- and 1,5-dienes form stable complexes with Pd^{II}. For most 1,3-dienes, such as 1,3-butadiene, reaction with Pd^{II} compounds leads to π-allyl formation. These reactions are described in Section 7. The coordinated double bonds in palladium diene complexes are reactive toward attack by many nucleophiles, and the resulting chelating alkene palladium alkyls are easily isolated. Many useful reactions of dienes were discovered by Jiro Tsuji in the 1960s and 1970s. These have been recently reviewed in a historical memoir.**[56]**

6.1.1 *Synthesis of Palladium(diene) Complexes*

A general route to Pd^{II}(diene) complexes is the reaction of the diene with $PdCl_2(PhCN)_2$. Norbornadiene, 1,5-cyclooctadiene, cyclooctatetraene, hexamethyl(Dewar benzene), and 1,6-cyclodecadiene all react to give $Pd(diene)Cl_2$ products (equation 39). For 1,5-dienes, the size of the organic ligand and the length of the palladium–alkene bond results in the two alkene groups subtending an angle of close to 90° at the metal, which is the favored angle for square-planar Pd^{II}. In the case of 1,4-dienes, the angle subtended is less, approximately 75°. However, the thermodynamic stabilities of $PdCl_2$(diene) complexes, measured via the enthalpy of the reaction of $PdCl_2(PhCN)_2$ with a diene, decrease in the order norbornadiene > 1,5-cyclooctadiene > 1,5-hexadiene > dipentene > cyclooctatetraene > dicyclopentadiene.

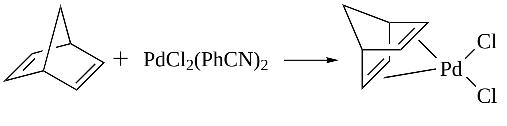

(39)

Cyclic dienes preorganize the geometry of the two double bonds, favoring chelation over π-allyl formation. Acyclic dienes tend to give π-allyl complexes. However, the reaction of allyl chloride with $PdCl_2(PhCN)_2$ at low temperatures in the absence of solvent gives the 1,5-hexadiene complex (equation 40).

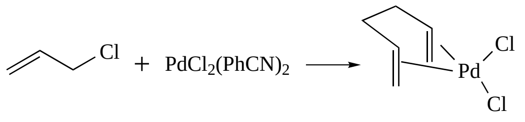

(40)

6.1.2 *Reactions of Palladium(diene) Complexes*

Many nucleophiles add to one of the double bonds of chelating palladium(diene) complexes to give a chelating Pd^{II}alkyl(alkene) derivative, as exemplified by the reaction of $PdCl_2$(1,5-cod) with methoxide (equation 41). In most cases, the direction of attack is exo. If the nucleophile is in a form that can undergo transmetalation with the Pd–Cl bond, such as Ph_2Hg, the nucleophilic group can be delivered endo. In this case, prior formation of a Pd–nucleophile bond accounts for the direction of attack (equation 42).

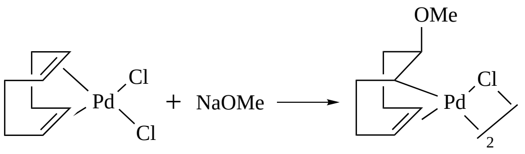

(41)

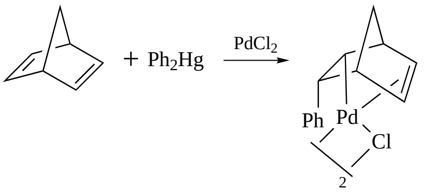

(42)

Among the nucleophiles that add exo to coordinated dienes are alkoxides, amines, azide, acetates, halides, and stabilized carbon enolates, such as malonates and β-diketones. The alkoxide addition is reversible if the product is treated with HCl. With a few nucleophiles, double addition reactions are observed. Acetate will react with 1,5-cod in the presence of $Pb(OAc)_4$ and palladium salts to give a bicyclic product from addition of two acetate groups, both exo (equation 43).

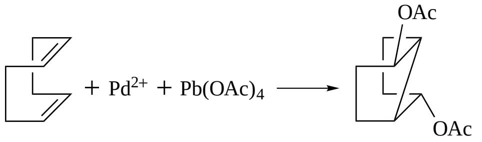

(43)

Reaction of 1,3-butadienes and Pd^{II} salts give numerous C_4 and C_8 products, depending on the exact reaction conditions. Either π-allyl C_4 complexes or bis-π-allyl C_8 dimers form, which can undergo further reactions with nucleophiles, CO, or solvent (Scheme 26).

The direct catalytic reaction of nucleophiles such as amines with 1,3-dienes to give allylic amines is difficult to achieve. A high-throughput assay was used to screen catalysts for the 1:1 hydroamination of aniline to 1,3-cyclohexadiene (equation 44).**[57]**

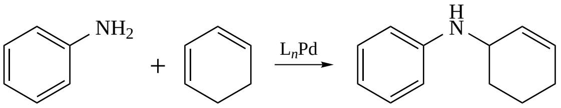

(44)

96-Well glass plates were loaded with different phosphines, metal complexes, aniline, and 1,3-cyclohexadiene. A colorometric assay for unreacted aniline (a red color arising from the acid catalyzed reaction of aniline with furfural) was used to screen successful catalysts, that is, those that did not turn red. Catalysts derived from $[Pd(\pi\text{-allyl})Cl]_2$ and PPh_3 were most active. Increasingly, such high-throughput methods are being used in catalyst discovery and optimization.

Nucleophiles that have a tendency to bind to soft metal centers will usually displace the diene ligand rather than add to the coordinated alkene bond. Among the nucleophiles that react in this way are phosphines, DMSO, and pyridine. The products from these reactions are $PdCl_2L_2$ and free diene. If a chelating phosphine or diamine, such as *o*-phenanthroline, is added to $PdCl_2$(1,5-cod) in the presence of the halide acceptor $AgPF_6$, the product is the cationic [Pd(1,5-cod)(*o*-phen)]$[PF_6]_2$. In addition to silver salts, $[Et_3O][BF_4]$ reacts with $PdCl_2$(1,5-cod) to remove Cl groups, leading to the formation of $[Pd_2Cl_2(1,5\text{-cod})_2]^{2+}$ $[BF_4]_2$.

The zero-valent palladium complex Pd(nbd)(ma), nbd = norbornadiene, ma = maleic anhydride, is a useful precursor to novel Pd^0 complexes with nitrogen σ-donor ligands. In THF, pyridine, diethyl amine, aniline, and even NH_3 displaced the nbd ligand to form L_2Pd(ma) complexes.**[58]**

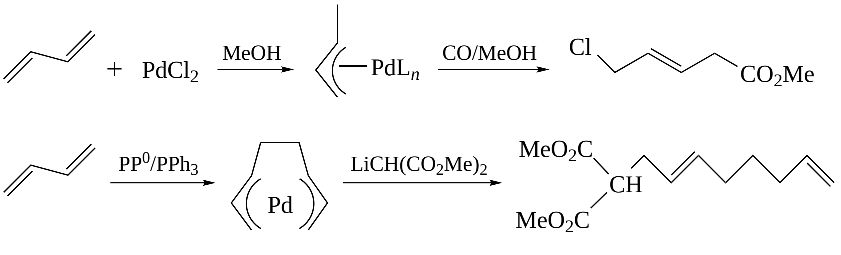

Scheme 26

6.2 Synthesis and Reaction of Cyclobutadiene Complexes

The reaction of alkynes substituted with bulky groups on both carbons with Pd^{II} complexes leads to complexes of substituted cyclobutadienes. Treatment of $PdCl_2(PhCN)_2$ with t-BuC_2Ph gives a cyclobutadiene complex (equation 45). A very interesting case of dimerization to a cyclobutadiene complex is provided by the strained seven-membered ring cyclic alkyne (equation 46).

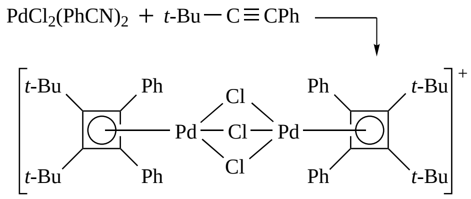

(45)

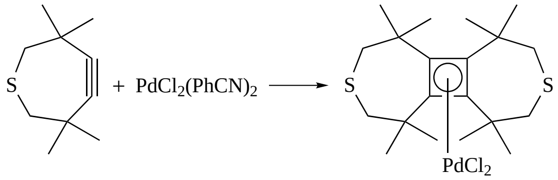

(46)

When alkynes such as diphenylacetylene are treated with $PdCl_2(PhCN)_2$ in ethanol, the product is a tetraphenylcyclobutadiene complex to which ethoxide has been added. Addition of HCl causes the alkoxycyclobutenyl ligand to eliminate alkoxide and reform the cyclobutadiene ligand (equation 47). Many of the palladium cyclobutadiene complexes isolated are 18-electron complexes rather than the 16-electron complexes that are common for square-planar Pd^{II}. It has been suggested that the small angle subtended at the metal by the cyclobutadiene ligand allows for three additional groups to bind to the Pd^{II} center.

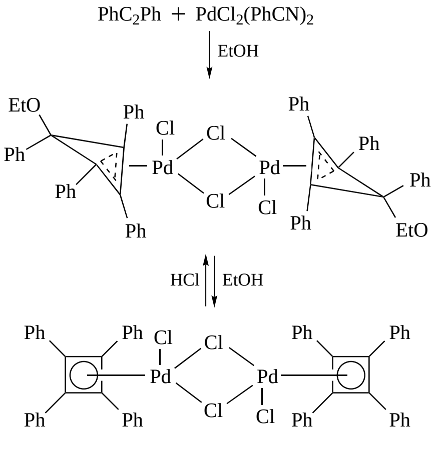

(47)

6.3 Synthesis and Reactions of Cyclopentadienyl Complexes

A number of cyclopentadienyl complexes of Pd^{II} are known. In most cases, the other groups are π-allyl, cyclobutadienyl, or a chelating dialkene. Reacting $[Pd(\eta^3\text{-}C_3H_5)Cl]_2$ with CpNa, for example, leads to the formation of $Pd(\eta^3\text{-}C_3H_5)(\eta^5\text{-}C_5H_5)$. Other sources of Cp^- that have been used are $CpFe(CO)_2Br$ and TlCp. This iron complex reacts with $Pd_2Br_4(C_4Ph_4)_2$ to produce a cationic cyclobutadiene cyclopentadienyl sandwich complex of palladium (equation 48). Unlike the case for Ni^{II}, there is no $PdCp_2$ sandwich complex known (*see Sandwich Compound*).

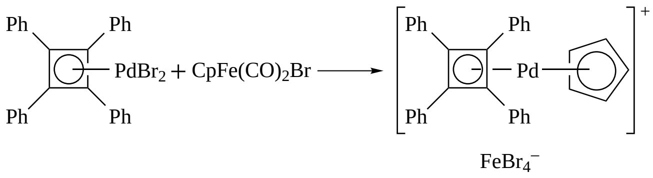

(48)

Notwithstanding the fact that $(\eta^5\text{-}C_5H_5)$ complexes of Pd^{II} are typically 18-electron complexes, they are often unstable toward substitution reactions, especially with phosphines. When $Pd(\eta^5\text{-}C_5H_5)Ph(PPh_3)$ is treated with excess PPh_3, decomposition takes place. It is probable that η^5 to η^3 to η^1 rearrangements are promoted by the addition of phosphines. The cyclopentadienyl ligand is also lost when $Pd(\eta^3\text{-}C_3H_5)(\eta^5\text{-}C_5H_5)$ is reacted with HCl, $HgCl_2$, or $FeCl_2$. In this case, the palladium-containing product is $[Pd(\eta^3\text{-}C_3H_5)Cl]_2$.

Indenyl complexes of Pd^{II} are prepared by the reaction of indenyl sodium with anhydrous $PdCl_2$. Alternatively, they are available by ring-opening reactions of aryl-substituted cyclopropenes with $PdCl_2(PhCN)_2$ (equation 49).

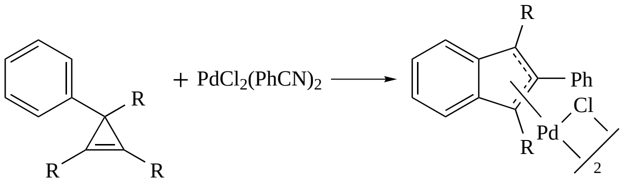

(49)

Finally, dinuclear Pd^{II} complexes can be prepared, which contain bridging cyclopentadienyl ligands (*see* ***Dinuclear Organometallic Cluster Complexes***). When $Pd(\eta^5\text{-}C_5H_5)(\eta^3\text{-}2\text{-}MeC_3H_5)$ is reacted with two equivalents of phosphines or phosphites, dinuclear species $Pd_2(\mu\text{-}C_5H_5)(\mu\text{-}2\text{-}MeC_3H_5)L_2$ are formed (equation 50).

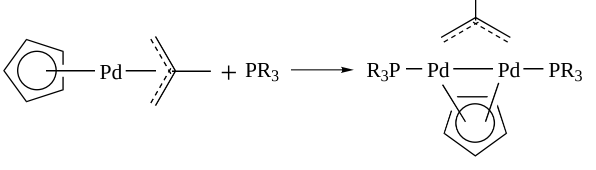

(50)

7 π-ALLYL PALLADIUM COMPLEXES

Palladium forms a more extensive series of π-allyl complexes than any other transition metal. In many cases these molecules are thermally stable, air-stable crystalline solids. In addition to stoichiometric π-allyl compounds, many palladium π-allyls are prepared under catalytic conditions as intermediates in palladium-catalyzed organic synthetic reactions.

7.1 Preparation of η^3-Allylic Palladium Complexes

7.1.1 From Allylic Precursors

A number of allylic compounds, including allyl chloride and bromide, diallyl ether, allyl acetate, allylmagnesium chloride, and allyltrimethylsilane react with $PdCl_2$ to give $[(\eta^3\text{-}C_3H_5)Pd(\mu\text{-}Cl)]_2$. For these reactions, the Pd^{II} salt must be reduced to Pd^0, either by an added reagent, such as CO or methanol, or by the substrate itself, as in the conversion of diallyl ether to acrolein. It has been established, using allylic carboxylates, that cleavage of the allylic C–O bond by a Pd^0 species takes place with inversion at the C–O bond.[59] In other words, the Pd^0 acts as a nucleophile in an S_N2 reaction.

In the preparation of π-allyl complexes from cyclic allylic chlorides, the stereochemistry of chloride displacement has been found to depend on the reaction conditions (Scheme 27).[60] When the allylic chloride (**17**) is reacted with $Pd_2(dba)_3$, the product from syn oxidative addition, (**18**)-trans, predominates in nonpolar solvents, while polar solvents give the product from inversion, (**18**)-*cis*. When the $Pd(PPh_3)_4$ complex is used as the source of Pd^0, the isomer from anti addition is isolated in essentially quantitative yield. Apparently, more powerful donor solvents or ligands favor anti attack.

In some cases, the cleavage of allylic oxygen bonds by Pd^0 is reversible. When $CD_2{=}CHCH_2OAc$ is treated with $Pd(PPh_3)_4$, which is a common reagent for catalytic generation of allylic palladium complexes, no π-allyl product is observed. However, the isolated allyl acetate is isomerized to a mixture of $CD_2{=}CHCH_2OAc$ and $CH_2{=}CHCD_2OAc$. The reversibility of π-allyl formation in acetates may be the reason that addition of sodium halides frequently improves the yields of Pd^0-catalyzed allylic substitution reactions of allylic acetates.

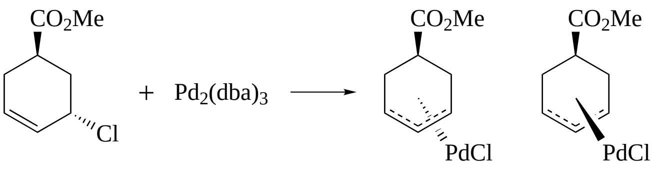

(**17**) (**18**)-*trans* (**18**)-*cis*

Benzene	100	0
Acetone	75	25
DMF	29	71
Acetonitrile	5	95

Scheme 27

Allylic carbonates undergo a useful conversion to π-allyl palladium complexes.[61] A Pd^0 reagent readily reacts with an allylic carbonate to form a cationic π-allyl palladium species. The alkyl carbonate anion loses CO_2 to generate a basic alkoxide anion, which is capable of deprotonating other species in the reaction medium.

Allylic trifluoroacetates are very reactive with Pd^0 reagents, generating η^3-allyl palladium trifluoroacetates (equation 51), which can react further to produce cationic π-allyl complexes when reacted with chelating amines (equation 52). The cationic complexes can also be synthesized from η^3-allyl palladium trifluoroacetates by treatment with HBF_4 and ligands, L, producing $PdL_2(\eta^3\text{-allyl})^+\ BF_4^-$ complexes.

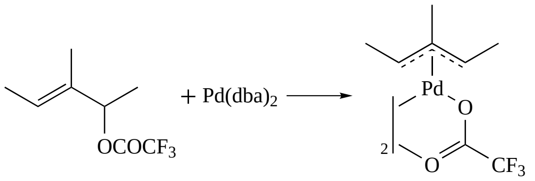

(51)

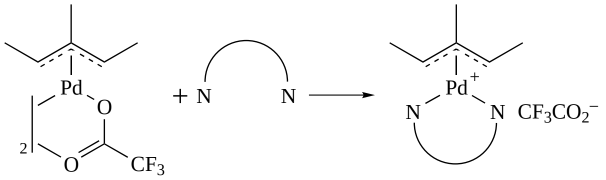

(52)

7.1.2 From Alkenes and $PdCl_2$

Many alkenes will react with $PdCl_2$, forming a π-allyl complex and one mole of HCl. A base is normally added to react with the HCl produced. Solvents that have proven useful include acetic acid, chloroform, methanol, and DMF. Where isomeric π-allyl palladium complexes can be formed, one often obtains a mixture of products. This is particularly true for reactions run in acetic acid. The addition of $CuCl_2$ causes an increase in regioselectivity, resulting in abstraction of the allylic C–H bond that leads to the more-substituted π-allyl complex (equation 53).

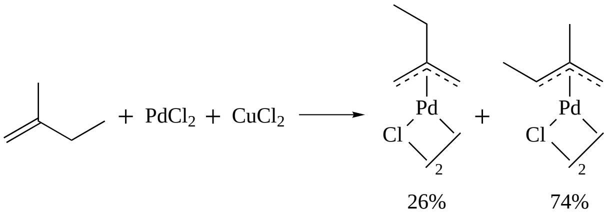

(53)

In general, 2-alkenes will form the more-substituted π-allylic complex, and 1-methylcycloalkanes react to give the π-allyl complex from abstraction of one of the $-CH_3$ hydrogens. If a given alkene is unreactive, use of the very electrophilic $Pd(O_2CCF_3)_2$ may result in reaction. When the alkene contains a particularly acidic C–H bond, such as one α to a carbonyl group, that C–H bond is normally the one abstracted to give the allylic complex (equation 54).

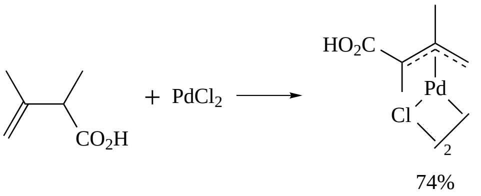

(54)

7.1.3 *From Dienes*

The addition of Pd–X groups to 1,3-dienes is an excellent route to η^3-allyl complexes (equation 55). For example, a 1,3-diene and palladium salt in the presence of a nucleophile, such as Cl^-, RO^-, or $RCOO^-$, will produce a π-allyl complex through addition of the nucleophile to a palladium-coordinated double bond (equation 56). Allenes commonly react with addition of nucleophiles at the central sp-hybridized carbon, producing 2-substituted π-allyls. However, because of the orthogonality of the π-orbitals, an η^3-allyl cannot form directly. First an η^1-allyl is generated, then C–C rotation gives the π-allyl.

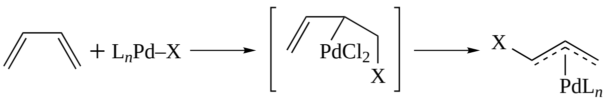

(55)

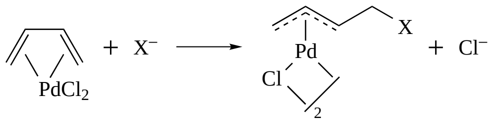

(56)

7.2 Reactions of π-Allyl Palladium Complexes

7.2.1 *Reactions at the Palladium Center*

Many ligands will cleave the chlorine-bridged dimer in $[Pd(\eta^3\text{-allyl})Cl]_2$ to give $PdL(\eta^3\text{-allyl})Cl$ (equation 57). Various types of exchange reactions can be followed in the NMR spectrum of π-allyl complexes, depending on the type of ligand added and the temperature of the exchange reaction (Scheme 28).

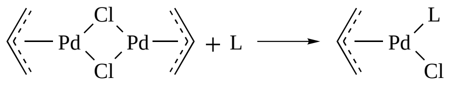

(57)

At lower temperatures, phosphine ligands will promote exchange of the syn protons (1 and 4) and the anti protons (2 and 3) through an associative mechanism. Subsequently, exchange can take place between the syn and anti protons (syn-4 and anti-3 as well as syn-1 and anti-2). Phosphines and other ligands promote this exchange through a complex, which is in equilibrium with an η^1-allyl intermediate. Rotation around the carbon–carbon single bond in the η^1-allyl intermediate exchanges protons 3 and 4, and analogously protons 1 and 2 exchange, leading to an NMR spectrum in which all four protons, 1, 2, 3, and 4, coalesce. A similar type of exchange changes the face of the allyl to which the palladium is bound (Scheme 29). A slightly different process can occur if the π-allyl complex is asymmetrically substituted (Scheme 28). With the 1,1-dimethallyl complex, addition of PPh_3 gives exchange of protons 3 and 4, as shown by coalescence of the NMR signals, but Me and Me′ do not exchange. This can be explained if a four-coordinate η^1-allyl intermediate forms, with the new phosphine ligand less tightly bound to palladium than the original phosphine, due to steric interactions with the methyl groups. Rotation around the carbon–carbon single bond exchanges 3 and 4, and loss of the less tightly bound phosphine returns the π-allyl complex. However, the other η^1-allyl isomer does not form to exchange Me and Me′. If two

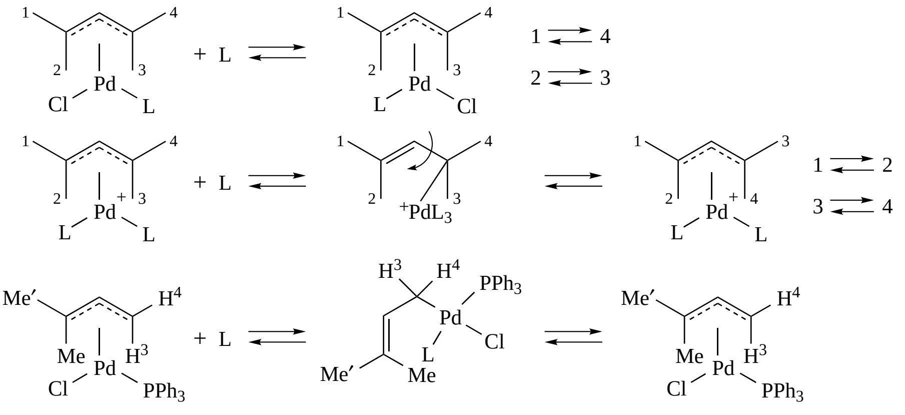

Scheme 28

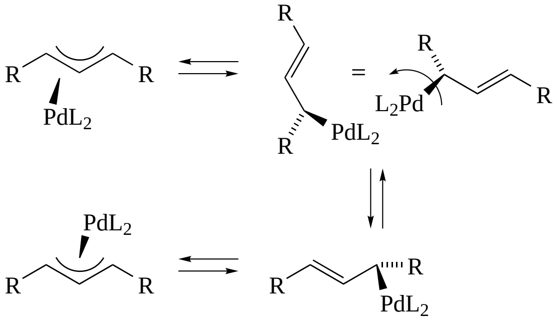

Scheme 29

equivalents of PPh_3 are added to the 1,1-dimethallyl palladium complex, the NMR spectra are consistent with the formation of two η^1-allyl complexes, $PdCl(CH_2CH{=}CMe_2)(PPh_3)_2$ and $PdCl(CMe_2CH{=}CH_2)(PPh_3)_2$, in the ratio 5:1.

Further reactions can take place at the metal with the monomeric $Pd(\eta^3\text{-allyl})ClL$, where L is a tertiary phosphine. Reaction of these complexes with MeLi at $-78\,°C$ produces the $Pd(\eta^3\text{-allyl})MeL$ species ($L = P(C_6H_{11})_3, PPh_3, PPh_2Me$). These yellow complexes are moderately stable in the air at room temperature for a few days. Thermolysis of these solids gives ethane as the major volatile product, rather than butenes from coupling of the allyl and methyl ligands. When an excess of phosphine ligands or maleic anhydride (which forms stable alkene complexes) is added to the thermolysis (50 °C) mixture, a mixture of butenes and ethane results. Only when allyl chloride is added, which presumably can undergo oxidative addition to give a Pd^{IV} intermediate, do butenes become the major product.

Cationic π-allyl palladium species of the type $[Pd(\eta^3\text{-allyl})L_2]^+$ are important reagents in palladium-promoted organic synthetic reactions.**62** While they can be generated in situ from an allylic acetate and $Pd(PPh_3)_4$, they are also available through the reaction of $[Pd(\eta^3\text{-allyl})(\mu\text{-}Cl)]_2$ with silver salts of noncoordinating anions in the presence of ligands, including PPh_3, diphos, 2,2′-bipyridine, and $AsPh_3$.

7.2.2 Oxidation and Reduction of Allylic Complexes

At elevated temperatures of 60–100 °C, π-allyl complexes will react with water to give aldehydes or ketones (equation 58). The mechanism probably involves attack of OH^- on the coordinated π-allyl, and elimination of Pd–H to generate the aldehyde group. Molecular bromine cleaves π-allyl–palladium bonds to give allylic bromides. Peracids have been reported to convert π-allyl complexes into allylic alcohols. Photolysis of π-allyl complexes in the presence of oxygen results in the conversion of an allylic group into an α,β-unsaturated ketone.

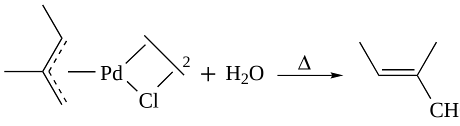

(58)

The reaction of π-allyl palladium complexes with hydrogen causes decomposition of the compounds, and produces either alkenes or alkanes, depending on the degree of substitution of the π-allyl complex and the reaction conditions. Hydride reagents, such as $NaBH_4$ and $LiAlH_4$, also reduce the allylic group to alkanes or alkenes.

7.2.3 Reactions of Nucleophiles at the π-Allyl Ligand

The addition of nucleophiles to the terminal carbons of the π-allyl group leads to allylation of the nucleophile (equation 59). The nucleophilic group normally bonds to the less-hindered terminal carbon. However, this preference depends on the other ligands coordinated to palladium. In the case of the π-allyl complex derived from methylenecyclohexane, the nucleophile $LiCH(SO_2Me)CO_2Me$ gives the product (**19**) from nucleophilic attack at the less-hindered carbon when the reaction is carried out in the presence of HMPA. Addition of the bulky phosphine tri-*o*-tolylphosphine gives the other regioisomer from bond formation at the more hindered site (**20**) (equation 60).

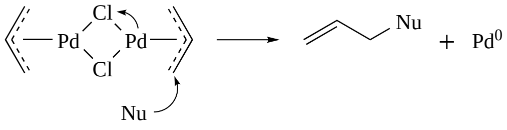

(59)

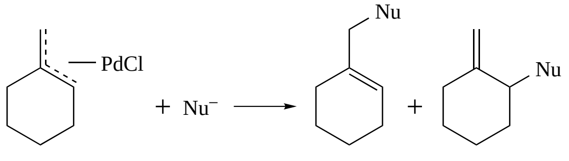

(60)

(**19**) (**20**)

Frequently, $Pd(PPh_3)_4$ (or another Pd^0 complex) is used as a catalyst for the displacement of allylic acetates or halides by nucleophiles. A general catalytic cycle is depicted in Scheme 30. If chloride ions are present, no $(\pi\text{-allyl})PdL_2^+$ forms. Instead, a $(\eta^1\text{-allyl})PdL_2Cl$ intermediate is formed. Thus, different precursors (such as allylic chlorides or allylic acetates) or different reaction conditions can lead to different reactivities, regioselectivities, and enantioselectivities.

The range of carbon nucleophiles that can be used in the catalytic allylic substitution reaction is not unlimited. The use of more basic reagents, such as alkyllithiums or cuprates, usually results only in reduction of the allylic substrate. Malonate derivatives, enol stannanes, enamines, and stable enols, however, can give allylation products.

With suitable additives, $Pd(OAc)_2$ can catalyze the allylation of even aldehydes using allyl alcohol as the allyl

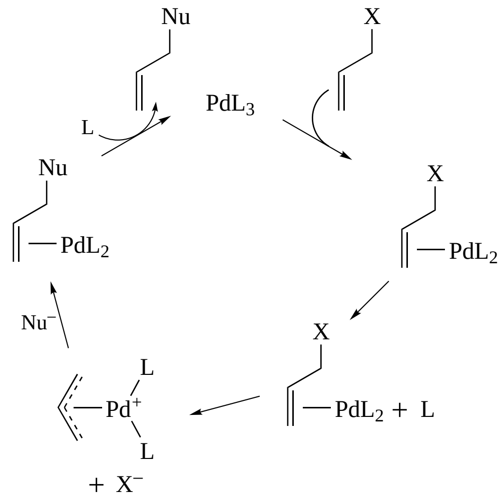

Scheme 30

source (equation 61).**63** Since aldehyde enolates undergo self-condensation and other reactions, this process is synthetically useful. No doubt procedures will be found to carry out allylation of other difficult substrates, such as ketone and ester enolates.

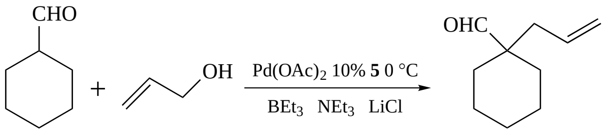

(61)

The stereochemistry of Pd^0-catalyzed allylic alkylation is net retention (equation 62). This arises from sequential inversion steps. Initially, the Pd^0 approaches from the face of the C3 unit opposite the leaving group, to form the π-allyl complex. Subsequently, the nucleophile adds to the face of the π-allyl opposite palladium. If a bulky or unreactive nucleophile is used with allylic acetates, the acetoxy group can add again to the complex. Ultimately, this results in the production of a mixture of stereoisomers upon nucleophilic addition. As an example of the range of allylic substrates that react, nitrogen nucleophiles, in particular primary and secondary amines, undergo palladium-catalyzed substitution with allylic alcohols, acetates, and ethers (equation 63).

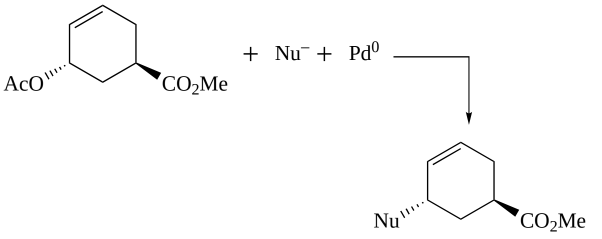

(62)

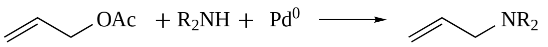

(63)

7.2.4 *Asymmetric Allylic Alkylation*

Essentially, any transition metal–catalyzed reaction that generates a product with a stereogenic center has been studied in an attempt to develop a version that is enantioselective. In general, chiral ligands are designed that favor one of two diastereomeric transition states, leading to new bond formation. The case of palladium-catalyzed allylic substitution is a particularly complex reaction to make enantioselective since any one of four steps, alkene complexation, leaving group ionization, nucleophilic attack at one of the allylic termini or exchange of the palladium group (via an η^1-allyl intermediate) between enantiotopic π-allyl cases can control enantioselectivity.**64** For *meso*-allyls, such as those derived from cycloalkyl acetates, it is the nucleophilic attack step that is enantioselective. Using *meso*-substrates, many ligands have been examined, with the bis-amide (**21**) (Scheme 31) being one of the most generally useful. The chirality of the backbone induces propeller twisting of the P(Ph)$_2$ groups, creating a chiral pocket for binding a palladium π-ally (Scheme 31).

The exact ee (enantiomeric excess) is very sensitive to reaction variables, such as solvent and additives (such as R$_4$NX salts), which influence the amount of ion pairing in the nucleophile. For substrates with enantiotopic leaving groups, the degree of asymmetric induction depends on the ionization step, and is relatively independent of the nucleophile (equation 64).

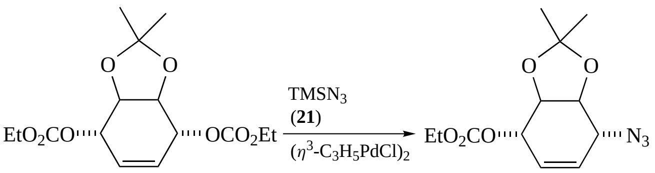

(64)

Proper choice of leaving group and nucleophile can produce deracemization of allylic carbonates.**65** When an allylic carbonate is treated with Pd$_2$(dba)$_3$ and (**21**), the loss

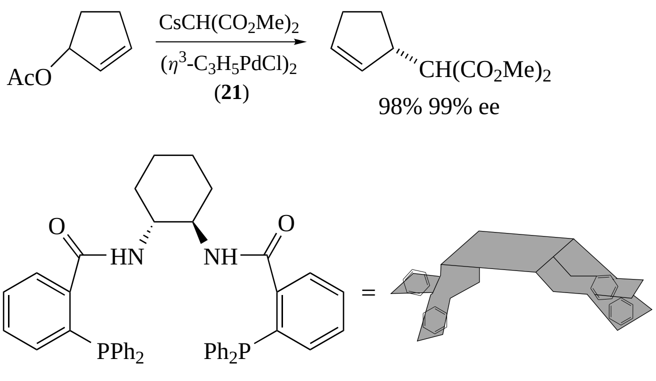

(**21**)

Scheme 31

of carbonate is reversible, but the anion can react with water to give bicarbonate. When bicarbonate adds to the π-allyl and CO_2 is then lost, the result is a chiral allylic alcohol (Scheme 32). For this process to work, loss of CO_2 from the allylic bicarbonate has to be faster than reformation of the π-allyl.

7.2.5 Reactions of π-Allyl Complexes Derived From 1,3-Dienes

Several palladium catalysts, including maleic anhydride bis(triphenylphosphine)Pd^0 and bis(π-allyl)Pd^{II}, will dimerize 1,3-butadiene to 1,3,7-octatriene. The mechanism of this reaction is believed to proceed by the formation of an octadienediylpalladium complex, which undergoes β-hydride elimination and transfer of the hydrogen atom to the other allyl group (Scheme 33).

Three-component additions, comprising two conjugated diene molecules and a nucleophile, can be catalyzed by palladium salts, such as palladium acetate. The major products are 1-substituted 2,7-octadienes, along with minor amounts of 3-substituted 1,7-octadienes (equation 65). Water, alcohols, phenols, carboxylic acids, and amines are some of the nucleophiles that have been used in this reaction.

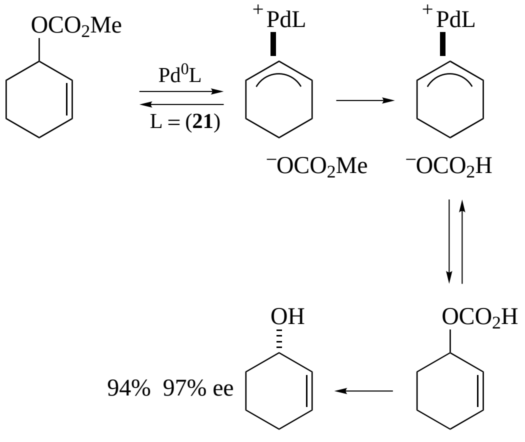

Scheme 32

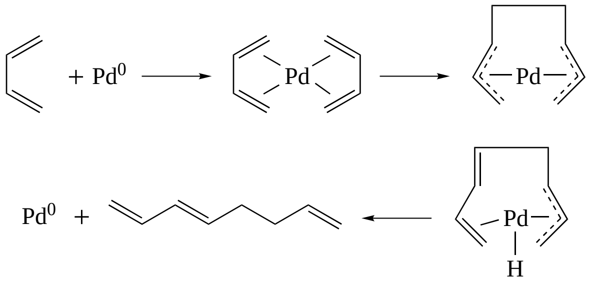

Scheme 33

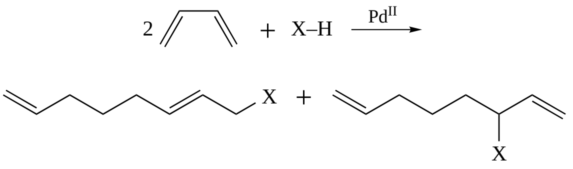

(65)

8 HETEROCYCLIC COMPOUNDS WITH PALLADIUM–CARBON BONDS

8.1 Cyclometalated Complexes: Introduction

Cyclometalation is one of the most reliable and versatile methods for the synthesis of stable Pd–C σ-bonds. In this reaction, a palladium (or other metal) complex is reacted with a ligand possessing a donor atom. The metal is directed by the donor atom to insert into a C–H bond, forming a chelate ring. This donor is usually the nitrogen of a tertiary amine, heterocyclic amine, or imine, or a phosphorus in a tertiary phosphine or phosphite. Other donor atoms, such as O and S, are occasionally encountered. The chelate ring size is normally five.**[66]**

The first report of cyclometalation in organopalladium chemistry was the reaction of azobenzene with potassium tetrachloropalladate to give the C,N-chelate (**22**) (equation 66). This reaction is characteristic of most cyclometalation reactions with palladium, in that it takes place with Pd^{II} in protic solvents with the loss of HCl, and the resulting chelate is stable to air and moisture.

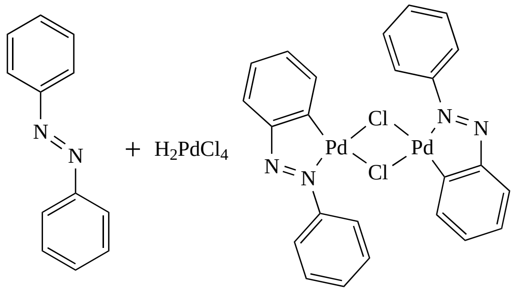

(66)

(**22**)

8.1.1 Scope of Cyclometalation

Many different palladium complexes have been used to form chelates via cyclometalation. Li_2PdCl_4 is preferred over $PdCl_2$ for solubility reasons. Also commonly used are $(PhCN)_2PdCl_2$, $Pd(OAc)_2$, $Pd(O_2CCF_3)_2$, and $Pd(acac)_2$. Where amines are the donor atom, dozens of different ligand types have reacted to form five-membered C,N-chelates. These include *N*,*N*-dimethylbenzylamines (**23**) and 3,2′-dimethylene-2-phenylpyridines (**24**).

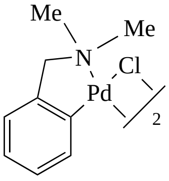

(**23**)

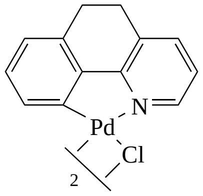

(**24**)

Where halogen or acetate is the counterion, the cyclometalated products are halide- or acetate-bridged dimers. Particularly in the case of halides, these dimers are easily cleaved by various ligands, such as pyridine, phosphines, phosphites, and acetylacetone, to give more soluble, monomeric species. Cyclometalation, especially with nitrogen atom donors, inserts into C–H bonds to form five-membered rings. However, formation of six-membered rings can occur (equation 67).

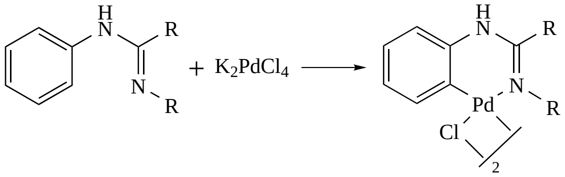

(67)

Cyclometalation directed by phosphorus is common. For example, in triaryl phosphite complexes of Pd^{II}, $PdX_2[P(OAr)_3]_2$ (X = Cl, Br, I; Ar = phenyl, *p*-chlorophenyl, *o*-, *m*-, or *p*-tolyl), react in decalin at reflux to give cyclometalated triaryl phosphite derivatives, $Pd[P(OC_6H_4)(OPh)_2][P(OPh)_3]X$, with loss of one molecule of HX. In these systems, the tendency to undergo cyclometalation is dependent upon the halide, and increases in the order Cl > Br > I. A feature of cyclometalation with phosphines is that bulky groups on the phosphine facilitate the reaction. The bulky diphosphine 1,3-bis[(di-*t*-butylphenylphosphino)methyl]benzene will cyclometalate with $(PhCN)_2PdCl$ in 2-methoxyethanol at reflux to give a tridentate P,C,P ligand (equation 68). These kind of tridentate complexes with one metal–carbon bond and trans donor ligands are known as pincer ligands.[67]

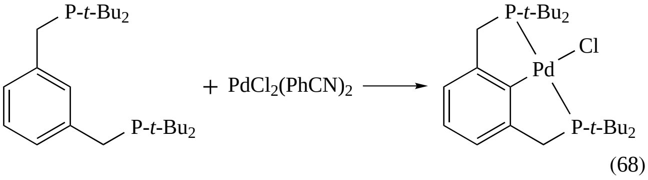

(68)

Cyclometalation occurs with other kinds of C–H bonds besides arene C–H bonds. The 8-methylquinoline ligand and its derivatives provide many such examples of metalation at sp^3-carbon atoms. Treatment of 8-methylquinoline with Li_2PdCl_4, followed by addition of PEt_3 to split the chlorine bridge, provides the cyclometalated complex (equation 69).

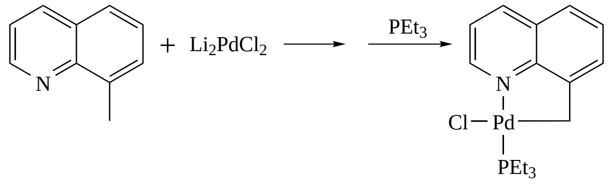

(69)

Other, less activated, sp^3 C–H bonds in addition to the benzylic C–H of 8-alkylquinolines will undergo cyclometalation. (*E*)-2,2-Dimethylcyclohexanone oxime will react with Na_2PdCl_4 to give metalation of the unactivated CH_3 group in 85% isolated yield (equation 70).

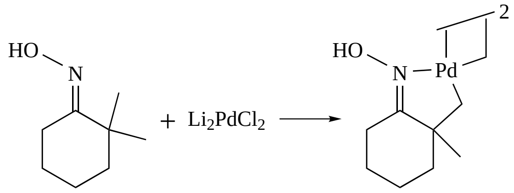

(70)

Unactivated C–H bonds can be functionalized if a suitable directing group can be incorporated into a substrate. For example, an *ortho-t*-butylaniline derivative will react with a substituted benzaldehyde to give an imine. This imine nitrogen then directs cyclometalation of the *t*−butyl methyl group (equation 71). The resulting Pd–C bond is then able to undergo further functionalization.

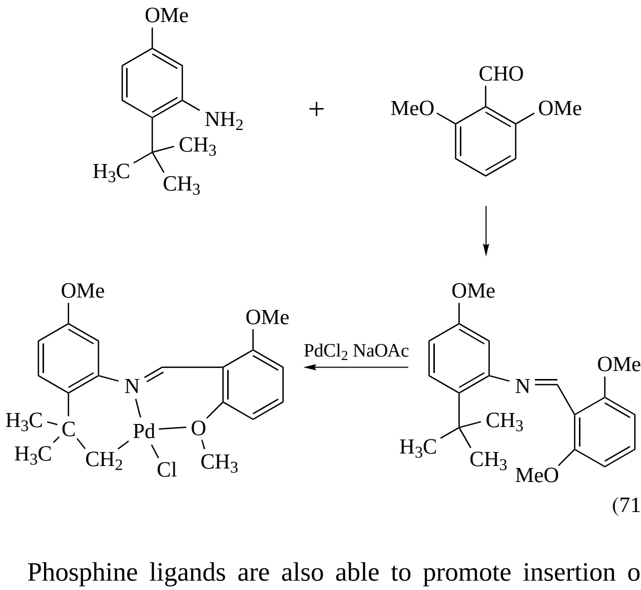

(71)

Phosphine ligands are also able to promote insertion of Pd^{II} into alkyl C–H bonds. For example, P-*t*-Bu_3 will react with $PdCl_2(cod)$ to generate, ultimately, a four-membered chelate ring (equation 72). The longer C–P and P–Pd bonds may be a factor in permitting a transition state, which leads to a four-membered ring. Bis-chelates can also be formed at sp^3 C–H bonds. The ligand P-*t*-$Bu_2(CH_2CH_2\underline{C}H_2CH_2CH_2)$P-*t*-$Bu_2$ undergoes cyclometalation at the underlined carbon, producing bicyclic chelates.

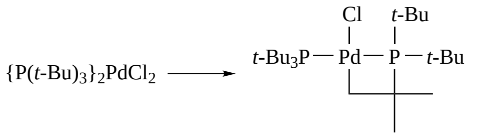

(72)

In some cases it is possible to control the site of palladation, choosing either an sp^3 or sp^2 C–H bond for insertion. When *N*-thiobenzoylpyrrolidine is treated with Pd^{II} in methanol, cyclometalation takes place at the aryl C–H, directed by one of the lone pairs on S (equation 73). When the same reaction is carried out in HMPA, an alkyl C–H bond reacts.**[1]** The reason for this change of reactivity with change of the solvent is not known. Certainly, different palladium complexes will be present in the two solvents.

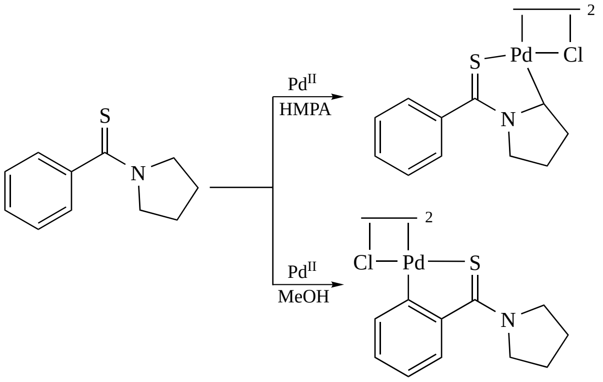

(73)

A limited number of cyclometalation reactions at alkene and related C–H bonds have been carried out. In part, this may have arisen because such ligands can form Pd–alkene π-complexes rather than give C–H insertion products. Nevertheless, examples can be found, as in the cyclometalation of vinylic oximes (equation 74).

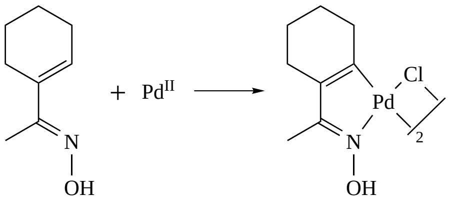

(74)

Aldehyde C–H bonds can also undergo cyclometalation with palladium salts. Reaction of 8-quinolinecarbaldehyde with $PdCl_4{}^{2-}$ gives a chloride-bridged dimer with a palladium–acyl bond (equation 75). No intermediates could be isolated in case of the palladium reaction, but when $[(PEt_3)PtCl_2]_2$ is reacted with 8-quinolinecarbaldehyde, a platinum complex is isolated with an intact aldehyde C–H bond. The nitrogen atom of the quinoline is coordinated to the platinum, and the aldehyde C–H bond occupies an axial site in the complex. Heating this material results in insertion into the aldehyde C–H bond and formation of a chelated platinum acyl.

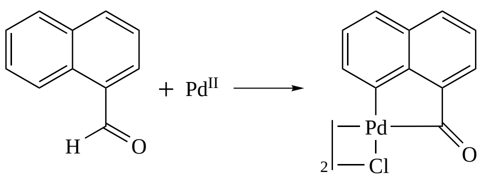

(75)

In addition to C–H bonds, cyclometalation can take place through the cleavage of other types of bonds. The ligands $n\text{-}Bu_3Sn(CH_2)_3NMe_2$ and $Ph_3Sn(CH_2)_3NMe_2$ react with $(PhCN)_2PdCl_2$ to give five-membered palladium chelates, in which the nitrogen atom is able to direct palladium insertion into a specific carbon–tin bond (equation 76). Normally, the Ph–Sn bond would be more reactive than the alkyl–tin bond, but the chelate formed from insertion into the Sn–CH_2 bond is isolated in 72% yield. Directing effects could not, however, lead to formation of four- or six-membered chelate rings via this strategy.

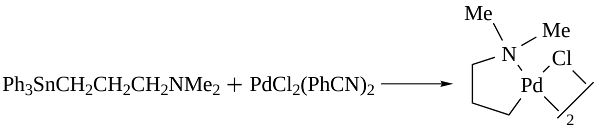

(76)

8.1.2 *Mechanism of Cyclometalation with Palladium*

Cyclometalation with Pd^{II} has the characteristics of an electrophilic substitution reaction.**[68]** With an unsymmetrically substituted azobenzene ligand, $(m\text{-}FC_6H_4)N{=}N(C_6H_5)$, Pd^{II} salts cyclometalate the more electron-rich ring preferentially. Similarly, in the unsymmetrically substituted benzyl sulfide $(p\text{-}MeC_6H_4)CH_2SCH_2(p\text{-}NO_2C_6H_4)$, palladium acetate reacts to give cyclometalation on the alkyl-substituted ring (equation 77).

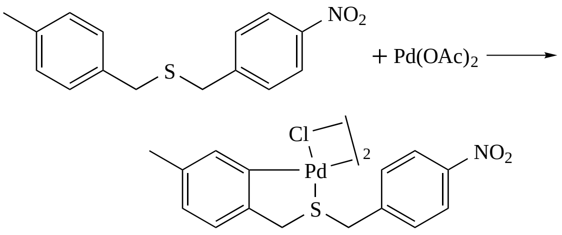

(77)

Studies of the cyclometalation of *N,N*-dimethylbenzylamines in chloroform solution with palladium acetate support the mechanism shown in Scheme 34 (N–R represents the benzyl amine). Two parallel routes to the cyclometalated product exist. One proceeds through a 16-electron complex, while the second route goes via a 14-electron complex with cis acetate groups. The Pd–C bond-forming step is approximately 10^2 faster for the 14-electron complex. It exhibits a kinetic isotope effect, k_H/k_D, of 2.2. Electron-donating substituents on the aromatic ring increase the rate of the Pd–C bond-forming step, consistent with Pd^{II} acting as an electrophile. The $\Delta S^{\ddagger}$

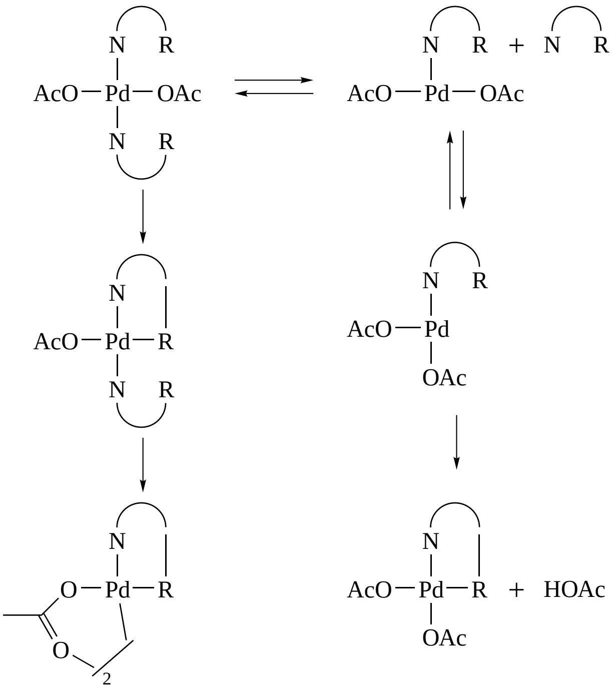

Scheme 34

for the rate-limiting step is $-254\,\mathrm{J\,K^{-1}\,mol^{-1}}$, which suggests a highly ordered transition state, in which one acetate group acts as an internal base to remove the proton from the carbon undergoing cyclometalation. Metalation is proposed to take place in the palladium coordination plane.

This mechanism suggests why cyclometalation is common for aliphatic tertiary amines and rare for primary and secondary amines. In general, a tertiary amine is expected to dissociate from $\mathrm{Pd^{II}}$ bis(amine) complexes, leaving behind a 14-electron complex, more readily than a less-hindered primary or secondary amine. In order for cyclometalation to take place with primary or secondary amines, a coordination site should be opened up by loss of an anionic group. This can be achieved in halide complexes using $\mathrm{Ag^{I}}$ salts. Using (R)-8-(α-deuterioethyl)quinoline, cyclometalation was shown to take place with retention of configuration at carbon, as expected for an electrophilic mechanism.**[69]**

8.1.3 Reactions of Cyclometalated Complexes

Many of the reactions outlined in Section 4 for Pd–C bonds occur in cyclometalated complexes. However, the existence of the Pd–C bond in a chelate ring imposes some kinetic stability on the bond. In general, mild acids and bases and oxygen are unreactive with cyclometalated palladium complexes. More vigorous reagents will lead to useful reactions, however.

Grignard and lithium reagents will alkylate or arylate the Pd–C bond in cyclometalated complexes. The mechanism involves Pd−halogen exchange with the anionic reagent and subsequent reductive elimination to produce the alkylated or arylated ligand (equation 78).

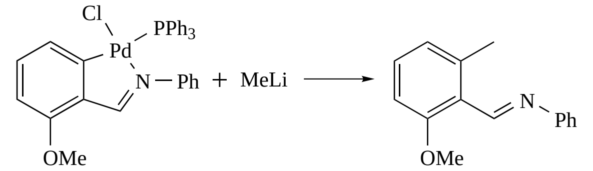

(78)

Hydride donors, such as $LiAlH_4$ or $NaBH_4$, will cleave Pd–C bonds, including those in cyclometalated complexes. If the molecule contains groups that will react with hydride reagents, the same transformation can be carried out using H_2 (equation 79). This reaction has been used with $LiAlD_4$ to establish the precise position of metalation.

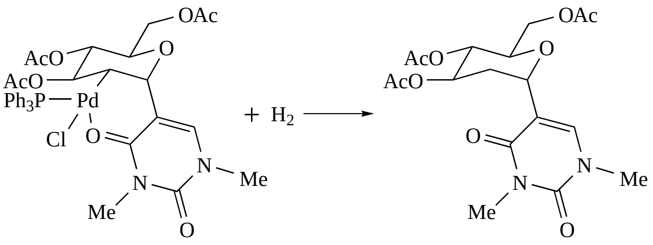

(79)

Electrophilic reagents, including Br_2, Cl_2, NCS–SCN, and I_2, will react rapidly and in high yield to add across the Pd–C bond. Mineral acids will cleave the bond in cyclometalated complexes as well. Since cyclometalation with palladium halide complexes generates HCl, frequently a weak base, such as sodium acetate, is added to prevent reversal of the cyclometalation reaction.

A characteristic reaction of the Pd–C bond in cyclometalated compounds is the insertion of alkynes and alkenes with electron-withdrawing groups. Hexafluoro-2-butyne is particularly reactive, but other alkynes, such as diphenylacetylene and dimethyl acetylenedicarboxylate will also insert into the cyclometalated Pd–C bond. When the chlorine-bridged dimer of cyclopalladated 8-methylquinoline is reacted with diphenylacetylene in refluxing chlorobenzene, two molecules of the alkyne insert to give a nine-membered chelate ring (equation 80). In contrast, hexafluoro-2-butyne produces the mono insertion product, in which the chlorine bridge is intact. Styrene and α,β-unsaturated carbonyl compounds will insert once into the chelate Pd–C bond, followed by β-hydride elimination to form HCl and regenerate the α,β-unsaturated carbonyl compound (equation 81).

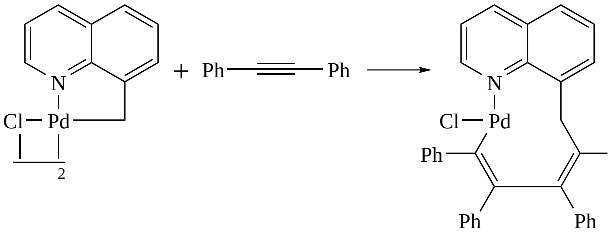

(80)

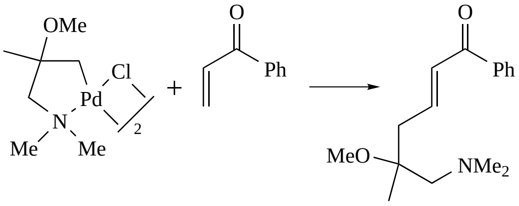

(81)

Cyclometalated complexes are effective catalysts for most of the common palladium-catalyzed reactions, including the Heck reaction, Suzuki and Stille couplings, the Buchwald–Hartwig amination reaction, and couplings of 1,3-butadienes with CO_2 and alcohols (Scheme 35). Some of these reactions have been suggested to take place through Pd^{IV} intermediates. However, involvement of anionic Pd^0 species, such as (**28**), is more likely. Advantages of palladacycles as catalysts include air and moisture stability, high turnover numbers and thermal stability (catalysts can be recovered and recycled).[70]

Because cyclometalated systems are rigid and stable, they can be used as building blocks for supramolecular assemblies. A 1,4-dipalladated aromatic ring can interact with pyrazine to give linear polymers (equation 82). With other nonlinear diamines, such as 4,7-phenanthroline, cyclic timers are formed.

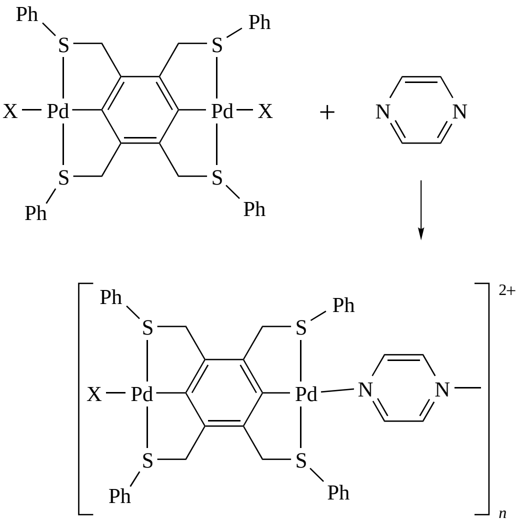

(82)

9 OXIDATION REACTIONS (*See Oxidation Catalysis by Transition Metal Complexes*)

9.1 Alkene Oxidations Related to the Wacker Process

The first important application of palladium compounds for industrial and laboratory syntheses was the oxidation of alkenes to carbonyl compounds, vinyl acetates, and related

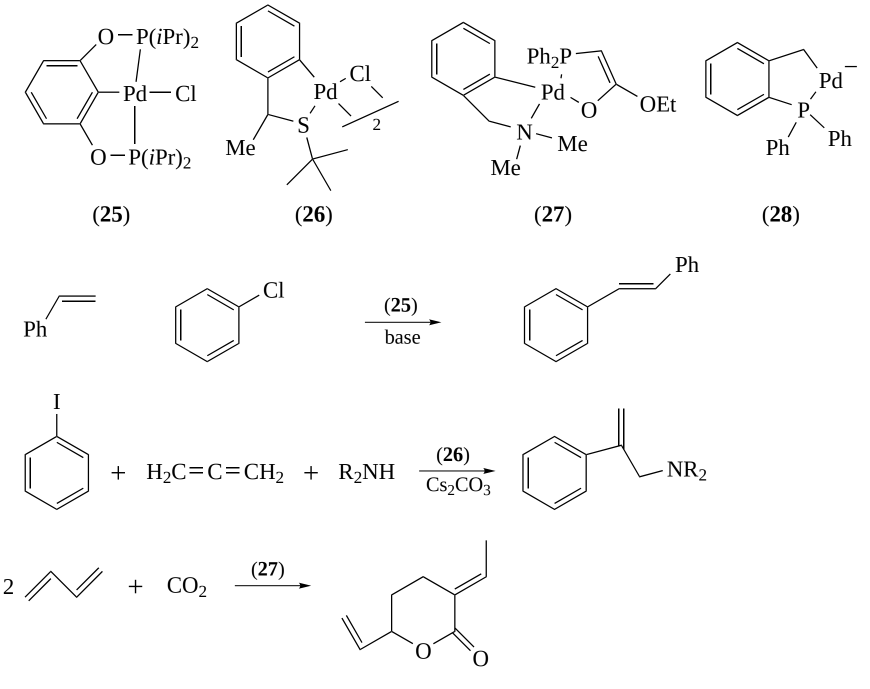

(**25**) (**26**) (**27**) (**28**)

Scheme 35

compounds. The classic example is the commercial process, the Wacker oxidation of ethene to acetaldehyde, which uses a Pd^{II} salt as catalyst, ethene, and water, with oxygen and Cu^{II} as oxidants (equation 83).[7] Under slightly different reaction conditions, ethene can be oxidized to $CH_2{=}CHOAc$, $CH_3CH(OR)_2$, $HOCH_2CH_2Cl$, and $ClCH_2CHO$, among other products. Terminal alkenes give excellent yields of methyl ketones.

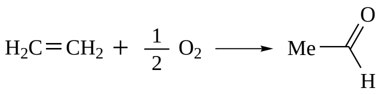

$$H_2C{=}CH_2 + \frac{1}{2}O_2 \longrightarrow MeCHO \qquad (83)$$

The mechanism for these oxidations involves addition of a nucleophile to an alkene–palladium complex, followed by a step that cleaves the Pd–C bond. While Cu^{II} salts have been used commercially for reoxidation of the Pd^0, many other oxidants have been recommended, such as benzoquinone. Benzoquinone has an advantage for mechanistic studies over $CuCl_2$ in that it does not affect the $[Cl^-]$ concentration.

The kinetics of the reaction have been extensively studied. The rate expression

$$-\,d[C_2H_4]/dt = k^1K_1[PdCl_4{}^{2-}][C_2H_4]/[H^+][Cl^-]^2$$

describes the overall kinetics of the reaction. With increasing amounts of $CuCl_2$, chlorine-containing by-products are formed, such as mono-, di-, and trichloroacetaldehyde, along with acetic acid. An interesting feature of the reaction is that when it is run in D_2O, the acetaldehyde product contains no deuterium. Thus, all four hydrogens of ethene are present in the final product. This implies that a vinyl alcohol π-complex of a Pd–H species is an intermediate in the reaction and that the Pd–H adds to the coordinated vinyl alcohol to give a species of the form $CH_3CH(PdL_n)OH$. This can eliminate Pd–H in the direction of the alcohol OH to produce acetaldehyde.

A long-standing controversy in the mechanism of the Wacker process has been the addition of water to the coordinated ethene. On the basis of kinetic arguments, a syn addition of coordinated hydroxide has been suggested. However, an anti attack of water from outside the coordination sphere can also fit the kinetic data. A stereochemical study used *trans*-1,2-dideuteroethylene. In the presence of $PdCl_2$, $CuCl_2$ (2.7 M), and LiCl (3.3 M) in water, β-chloroethanol is formed. The microwave spectrum of the product identified the product as the threo isomer, which would be the expected product if the attack of water on coordinated ethene were trans, and if cleavage of the Pd–C bond occurs with inversion of configuration (Scheme 36).[71]

The point has been made that the conditions of β-chloroethanol formation are not the same as used for the Wacker oxidation. Cu^{II}–Pd^{II} chlorine-bridged dimers are likely reactants under higher $[Cl^-]$ reaction conditions, which may lead to a different reaction mechanism. However, a second stereochemical study also obtained results consistent with trans hydroxypalladation. When *cis*-1,2-dideuteroethene is oxidized in water with $PdCl_2$ under a CO atmosphere, the product is *trans*-2,3-dideutero-β-propiolactone (Scheme 37). The reaction conditions were, once again, not identical with standard Wacker process conditions, since the solvent was acetonitrile–water, the temperature was −25 °C, the *bis*-ethene $PdCl_2$ complex was used, and there was no excess Cl^- present. Nevertheless, it is clear that, under many reaction conditions, a trans addition of water onto ethene coordinated to Pd^{II} is the favored reaction stereochemistry.

The rate of alkene oxidation depends on the substitution pattern of the alkene. For a series of alkenes oxidized in aqueous solution, with benzoquinone as oxidant for the $PdCl_2$, the relative rates are ethene (850) > propene(450) > 1-butene (380) > *trans*-2-pentene (90) > *cis*-2-pentene (80) > cyclohexene (8) > cycloheptene (1). Thus, selective oxidation of terminal alkenes to methyl ketones can occur in the presence of internal alkenes (equation 84).

When water is replaced by alcohols as the reaction solvent in Wacker oxidation, the primary products of ethene oxidation are acetals. If base is present, vinyl ethers and acetals

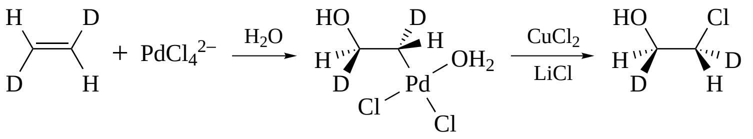

Scheme 36

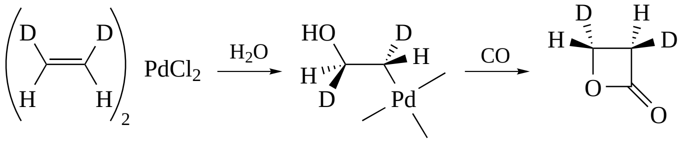

Scheme 37

are formed. For organic compounds with alkenes and OH groups in the same molecule, palladium salts can catalyze intramolecular cyclization (equation 85).

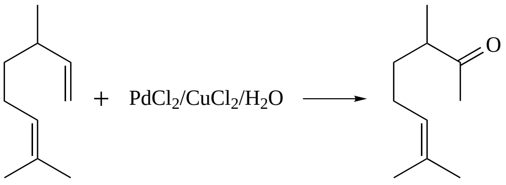

(84)

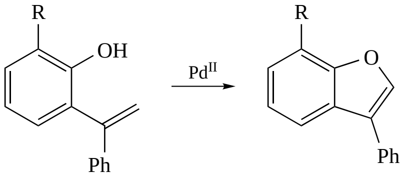

(85)

1,4-oxidation of 1,3-dienes is a useful reaction.[72] Nucleophiles such as carboxylic acids, halides, and amines add to the 1,4 positions and overall 1,4-*cis* stereospecificity is easy to achieve. The mechanism involves initial formation of a π-allyl complex that places a nucleophile at carbon 1. Delivery of the second nucleophile from the external direction gives the *cis*-1,4 products, while attack of a nucleophile coordinated to palladium gives the 1,4-*trans* isomer. The Pd^0 intermediates are reoxidized by added *p*-benzoquinone (equation 86).

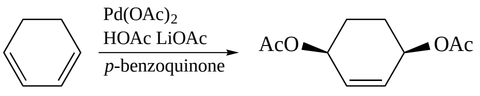

(86)

9.2 Oxidative Carbonylation of Alkenes and Alcohol Oxidation

In the presence of CO, terminal alkenes are oxidized by $PdCl_2$ to $RCH(Cl)CH_2COCl$. When the reaction is made catalytic in palladium by the addition of $CuCl_2$ and oxygen, and carried out in alcohols, the products are α,β-unsaturated esters, β-alkoxy esters, and, under some conditions, succinate derivatives (equation 87). Two mechanisms are possible for this reaction. In the first, an oxypalladation can produce a $Pd–CH_2–CH_2–X$ species, which can undergo CO insertion into the Pd–C bond. Alternatively, an $XCOPd^{II}$ species can form and add across the double bond. Loss of Pd–H can generate the α,β-unsaturated ester, or a second carbonylation step can lead to succinate derivatives.

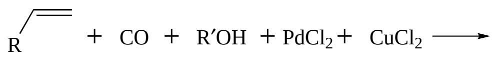

$$\text{R} + CO + R'OH + PdCl_2 + CuCl_2 \longrightarrow$$

$$RCH{=}CHCO_2R' + R'CHRCH_2CO_2R + (CO_2R')RHCCH_2CO_2R \qquad (87)$$

The catalytic oxidation of alcohols to carbonyl compounds using the oxygen in air as an oxidant is an example of Green Chemistry, since no toxic by-products, such as reduced chromium salts are generated and the reaction could take place in aqueous solvents.[73] A specific catalyst system that works in water with primary and secondary alcohols to give aldehydes and ketones uses an 1,10-pehenanthroline derived ligand (substituted with sulfonic acids to produce water solubility) with palladium acetate and NaOAc. The alcohol is used as a second phase or a cosolvent can be added. The oxidation mechanism involves formation of a L_nPd^{II}-$OCHR_2$ species that undergoes β-hydride elimination to form the carbonyl group and an L_nPd^0 intermediate, which is reoxidized with molecular oxygen.

9.3 Arene–Arene Oxidative Couplings

Benzene and related arenes will react with $PdCl_2$ to give good (40–80%) yields of biphenyl derivatives. If palladium acetate is the source of Pd^{II}, a second reaction is acetoxylation. The reaction has some of the characteristics of electrophilic aromatic substitution, in that electron-donating groups speed up the reaction and electron-withdrawing groups retard it. However, the isomer distribution is different from the standard electrophilic aromatic substitution reactions in that meta isomers are formed in substantial amounts from substituted benzene derivatives, and 4,4′-biphenyls are produced in much greater amounts than 2,2′-biphenyls. Intramolecular coupling to form fused heterocycles can take place in high yield (equation 88). Co-oxidants can be used to make the arene-coupling reaction catalytic in palladium. Mixed heteropolyacids of the composition $H_{3+n}PMo_{12-n}V_nO_{40}$ are interesting co-oxidants in that the possibility of chlorinated by-products is avoided.

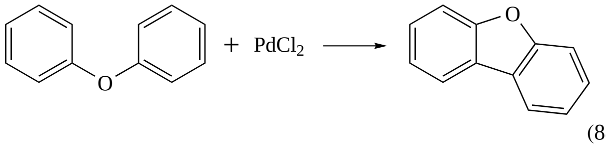

(88)

10 ORGANIC SYNTHESIS WITH ORGANOPALLADIUM COMPOUNDS

With the variety of transformations that can be promoted by organopalladium reagents, it is unfortunate that palladium is such a rare metal. Biochemical processes might be much more exotic if palladium had been more abundant in the earth's crust at the origin of life (although selenium, which is an essential trace nutrient, is only approximately five times as concentrated as palladium in the earth's crust). The discovery of high turnover number catalysts has allowed several palladium-catalyzed reactions to be used in fine chemical and pharmaceutical synthesis.[74,75] Naproxen (**29**) can be made using a Heck reaction. Ibuprofen's (**30**) synthesis

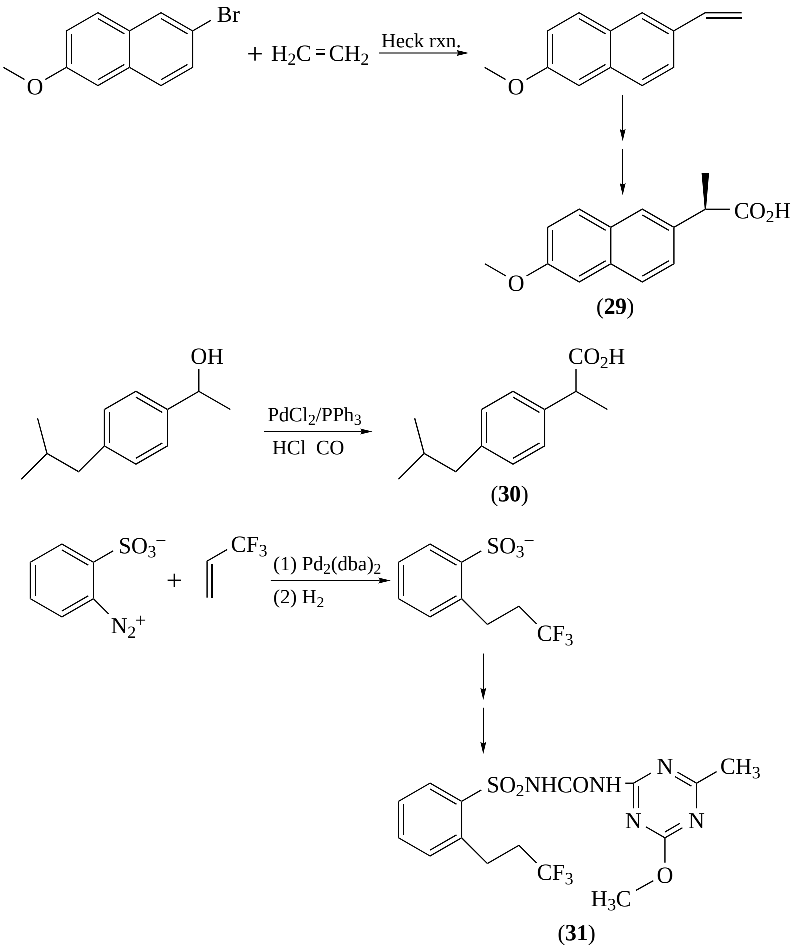
Br
+ H2C=CH2
Heck rxn.
O
CO2H
(29)
OH
PdCl2/PPh3
HCl CO
CO2H
(30)
SO3−
N2+
+
CF3
(1) Pd2(dba)2
(2) H2
SO3−
CF3
SO2NHCONH
N
CH3
N
N
O
H3C
CF3
(31)

Scheme 38

involves a palladium-catalyzed carbonylation. The herbicide Prosulfuron (**31**) has been synthesized on a multiton scale using a Heck reaction with a diazonium ion–leaving group (Scheme 38).

10.1 Trimethylenemethane Reactions

The reaction of $Pd(PPh_3)_4$ with 3-acetoxy-2-[(trimethyl silyl)methyl]-1-propene generates an organometallic *Ylide* complex (**32**), which adds to polarized alkenes (those attached to an electron-withdrawing group) to produce five-membered rings (equation 89).[76] The palladium complex is best described as a trimethylenemethane complex, which is bound in an η^3-fashion; however, this species has not been isolated in the case of palladium. The addition to conjugated alkenes is highly ordered, but stepwise, rather than concerted.

Substituted trimethylenemethane complexes can be prepared from the appropriate reagents. In general, any substituents on the trimethylenemethane group direct the attached carbon to the β-carbon of the acceptor alkene (equation 90). This directing effect is seen for both electron-donating and electron-withdrawing substituents.

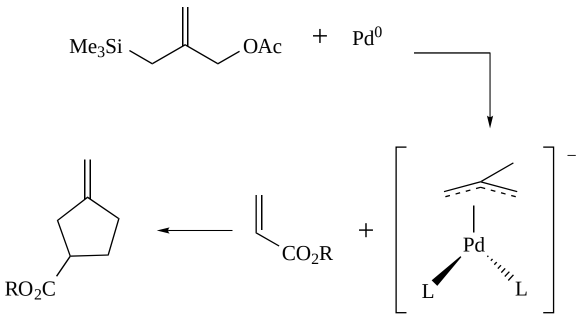
Me3Si
OAc
+
Pd0
−
Pd
L
L
+
CO2R
RO2C

(**32**)

(89)

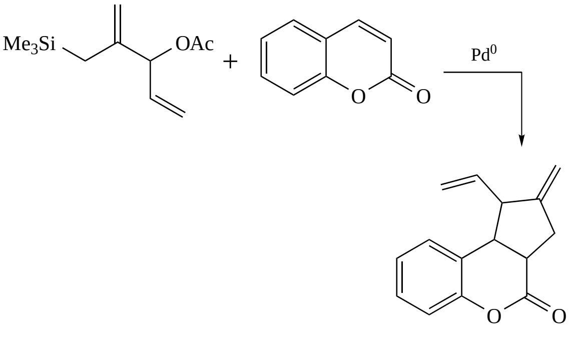
Me3Si
OAc
+
O
O
Pd0
O
O

(90)

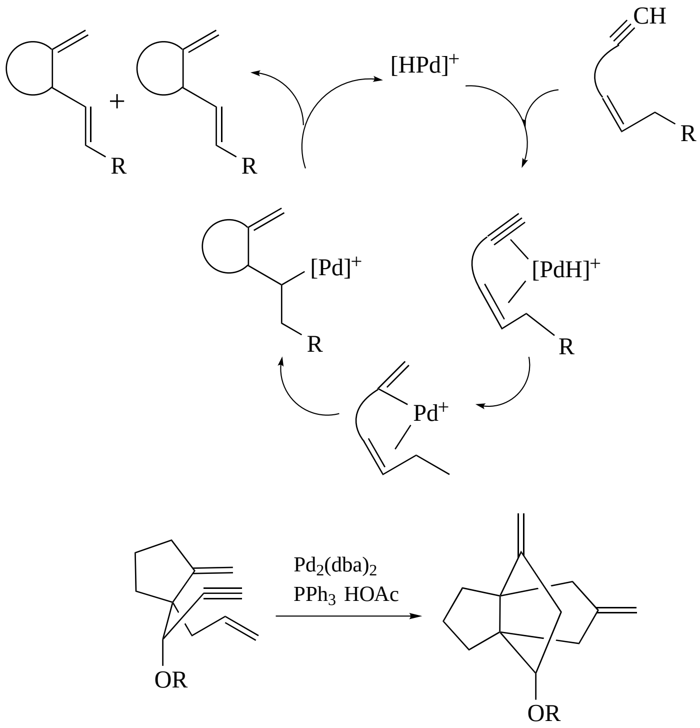

Scheme 39

10.2 Cascade Reactions of Alkenes and Alkynes

Depending on the organic framework, palladium complexes can initiate a series of additions and insertions with alkenes and alkynes, leading to polycyclic structures from linear or monocyclic starting materials.[77] A simple catalytic cycle for the cyclization of 1,6 and 1,7 enynes is given in Scheme 39.

A living oligomerization process can give linked spiro systems with the proper distance between alkene units (Scheme 40).

Generation of a σ-palladium species that can insert into alkene or alkyne bonds mimics [2.2.2] cyclization (equation 91).

10.3 Heterocyclic Synthesis via Organopalladium Intermediates

A number of different heterocyclic ring systems can be obtained through the use of palladium catalysts.[78] The facility with which CO, RNC, CO_2, and related unsaturated molecules insert into Pd–C bonds often leads to heterocyclic products. Many transition metal complexes can catalyze the formation of β-lactams. In the case of palladium, treatment of azirines with $Pd(PPh_3)_4$ under CO leads to a bicyclic β-lactam (equation 92).

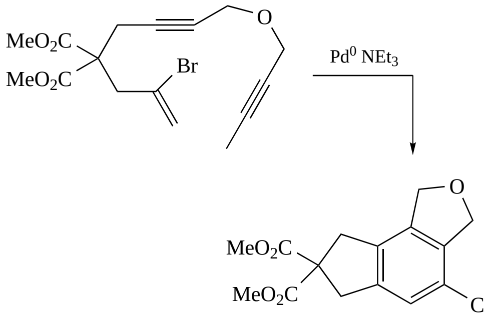

(91)

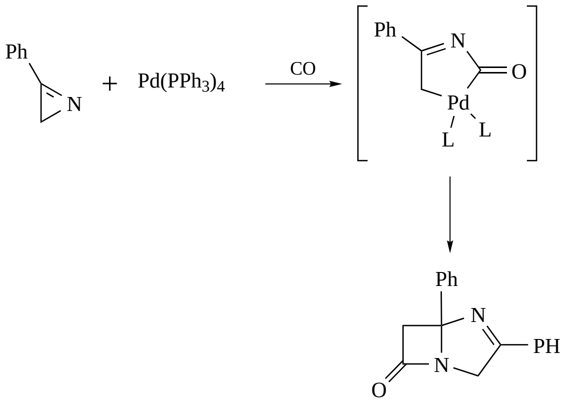

(92)

The palladium-catalyzed intramolecular addition of an amine to an alkene is an efficient route to nitrogen heterocycles. The products often undergo further dehydrogenation under the reaction conditions to form fully aromatic

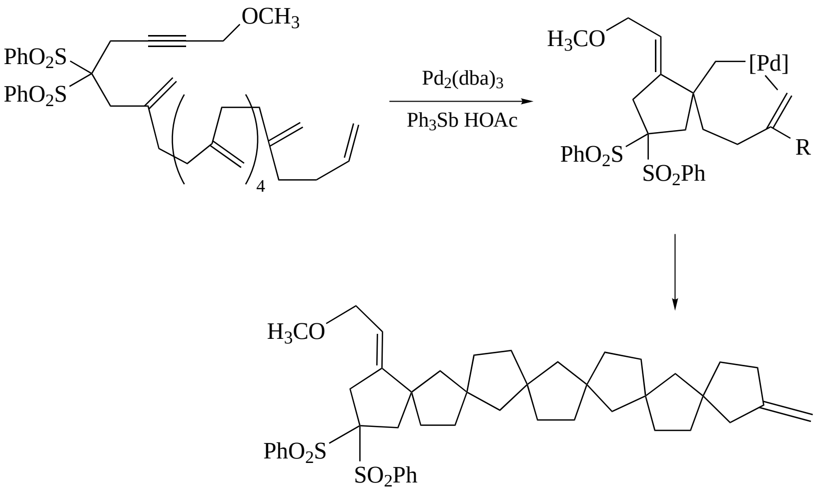

Scheme 40

products (equation 93). In many cases, running the reaction in the presence of CO can lead to insertion of CO into the transient Pd–C bond, and the resulting palladium acyl can react with an alcohol to give an ester (equation 94).

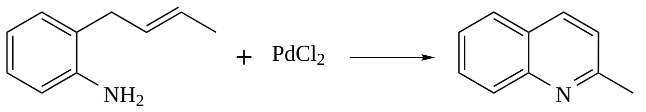

(93)

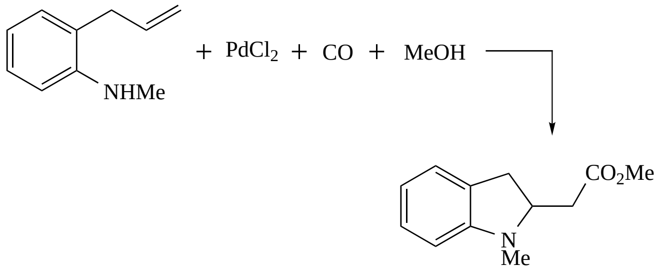

(94)

In these heterocyclization reactions, palladium can be used to introduce the alkene group as well as catalyze the cyclization. Reacting 2-bromoaniline with 1-alkenes and Li_2PdCl_4 at room temperature leads to the vinylamine. Upon heating this product with a Pd^0 reagent at 100 °C, an intramolecular Heck arylation follows to give the indole (equation 95).

Oxygen heterocycles can be prepared in several different ways via palladium catalysis, even though oxygen is a poorer nucleophile than nitrogen. For example, β,γ-alkynic ketones are cyclized to furans in the presence of $Pd(dba)_2$ and PPh_3 (equation 96).

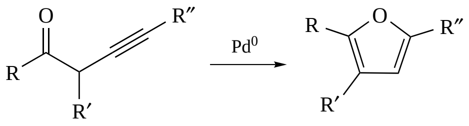

(96)

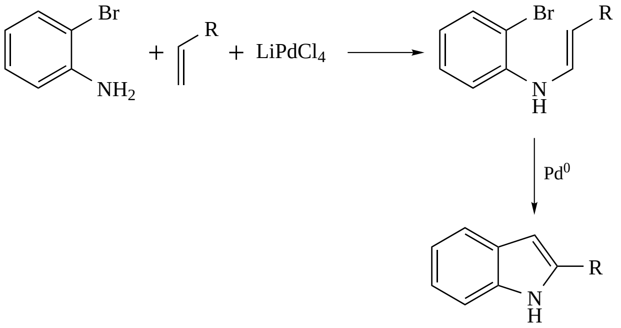

(95)

Intramolecular cyclization of alcohols to 1,3-dienes can lead to fused tetrahydrofurans and tetrahydropyrans. In this reaction, using 5 mol% $Pd(OAc)_2$, the first step involves a trans oxypalladation to form the heterocyclic ring and a π-allyl palladium complex. In the presence of 0.2 equiv. of LiCl, AcO^- adds trans to the π-allyl, leading to a net *cis*-1,4 addition of oxygen nucleophiles to the diene. When LiCl is omitted, the AcO^- adds to the same face of the π-allyl as the palladium, giving net *trans*-1,4-addition of oxygen groups to the diene (Scheme 41).

11 RELATED ARTICLES

Bonding Energetics of Organometallic Compounds
Carbonylation Processes by Homogeneous Catalysis
Mechanisms of Reaction of Organometallic Complexes;

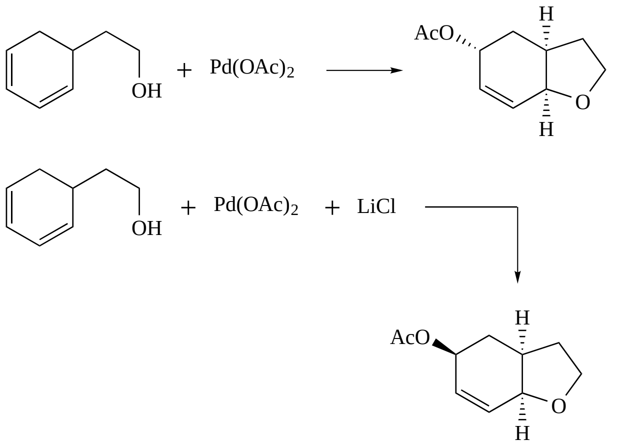

Scheme 41

Nickel: Organometallic Chemistry; Oligomerization & Polymerization by Homogeneous Catalysis; Organic Synthesis using Transition Metal Complexes Containing π-Bonded Ligands; Palladium: Inorganic & Coordination Chemistry; Platinum: Organometallic Chemistry; Stereochemical Nonrigidity of Organometallic Complexes.

12 REFERENCES

1. P. M. Maitlis, ‘The Organic Chemistry of Palladium’, John Wiley & Sons, New York, 1971.
2. J. Tsuji, ‘Palladium Reagents and Catalysts’, John Wiley & Sons, New York, 1995.
3. R. H. Crabtree, ‘The Organometallic Chemistry of the Transition Metals’, 3rd edn., John Wiley & Sons, New York, 2001, p. 8.
4. P. K. Byers, A. J. Canty, M. Crespo, R. J. Puddephatt, and J. D. Scott, *Organometallics*, 1988, **7**, 1363.
5. A. J. Canty, *Acc. Chem. Res.*, 1992, **25**, 83.
6. W. Chen, S. Shimada, and M. Tanaka, *Science*, 2002, **295**, 308.
7. P. M. Henry, ‘Palladium Catalyzed Oxidation of Hydrocarbons’, Reidel, Dordrecht, 1980.
8. J. K. Stille, *Angew. Chem., Int. Ed. Engl.*, 1986, **25**, 508.
9. R. F. Heck, *Org. React.*, 1982, **27**, 345.
10. B. M. Trost, *Acc. Chem. Res.*, 2002, **35**, 695.
11. J. P. Stambuli, M. Bühl, and J. F. Hartwig, *J. Am. Chem. Soc.*, 2002, **124**, 9346.
12. P. S. Pregosin and R. Salzmann, *Coord. Chem. Rev.*, 1996, **155**, 35.
13. J. A. Matinho Simões and J. L. Beauchamp, *Chem. Rev.*, 1990, **90**, 666.
14. A. Dedieu, *Chem. Rev.*, 2000, **100**, 543.
15. F. Ozawa, T. Ito, and A. Yamamoto, *J. Am. Chem. Soc.*, 1980, **102**, 6457.
16. A. Moravskiy and J. K. Stille, *J. Am. Chem. Soc.*, 1981, **103**, 4182.
17. J. M. Brown and P. J. Guiry, *Inorg. Chem. Acta*, 1994, **220**, 249.
18. E. Gretz and A. Sen, *J. Am. Chem. Soc.*, 1986, **108**, 6038.
19. S. P. Stanforth, *Tetrahedron*, 1998, **54**, 263.
20. M. I. Bruce, *Angew. Chem., Int. Ed. Engl.*, 1977, **16**, 73.
21. M. Pornoy and D. Milstein, *Organometallics*, 1993, **12**, 1665.
22. A. F. Litke and G. C. Fu, *Angew. Chem., Int. Ed. Engl.*, 2002, **41**, 4176.
23. R. K. Dieter, *Tetrahedron*, 1999, **55**, 4177.
24. F. C. Rix, M. Brookhart, and P. S. White, *J. Am. Chem. Soc.*, 1996, **118**, 2436.
25. J. Tsuji, ‘Organic Synthesis with Palladium Compounds’, Springer-Verlag, Berlin, 1980.
26. W. A. Herrmann, *Angew. Chem., Int. Ed. Engl.*, 2002, **41**, 1290.
27. C. Jia, T. Kitamura, and Y. Fujiwara, *Acc. Chem. Res.*, 2001, **34**, 633.
28. B. L. Edelbach, R. J. Lachicotte, and W. D. Jones, *J. Am. Chem. Soc.*, 1998, **120**, 2843.
29. A. J. Canty, in ‘Handbook of Organopalladium Chemistry for Organic Synthesis’, eds. E.-i. Negishi and A. Meijere, Wiley-Interscience, Hoboleen, 2002, Vol. 1, p. 189.
30. P. Wadhwani and D. Bandyopadhyay, *Organometallics*, 2000, **19**, 443.
31. I. P. Beletskaya and A. V. Cheprakov, *Chem. Rev.*, 2000, **100**, 3009.
32. C. Amatore and A. Jutand, *Acc. Chem. Res.*, 2000, **33**, 314.
33. A. B. Dounay and L. E. Overman, *Chem. Rev.*, 2003, **103**, 2945.
34. V. P. W. Böhm and W. A. Herrmann, *Chem. Eur. J.*, 2001, **7**, 4191.
35. L. J. Grossen and J. Paetzold, *Angew. Chem., Int. Ed. Engl.*, 2002, **41**, 1237.
36. A. L. Casado, P. Espinet, and A. M. Gallego, *J. Am. Chem. Soc.*, 2000, **122**, 11771.
37. J. A. Casares, P. Espinet, and G. Salas, *Chem. Eur. J.*, 2002, **8**, 4844.
38. K. Menzel and G. C. Fu, *J. Am. Chem. Soc.*, 2003, **125**, 3718.
39. N. Miyaura and A. Suzuki, *Chem. Rev.*, 1995, **95**, 2457.
40. S. R. Chemler, D. Trauner, and S. J. Danishefsky, *Angew. Chem., Int. Ed. Engl.*, 2001, **40**, 4544.
41. E. Erdik, *Tetrahedron*, 1992, **48**, 9577.
42. K. Sonogashira, in ‘Metal-Catalyzed Cross-Coupling Reactions’, eds. F. Diederich and P. J. Stang, Wiley-VCH, Weinheim, 1997, Chap. 5.
43. M. Miura and M. Nomura, *Top. Curr. Chem.*, 2002, **219**, 211.
44. J. P. Wolfe, S. Wagaw, J.-F. Marcoux, and S. L. Buchwald, *Acc. Chem. Res.*, 1998, **31**, 805.

45. J. F. Hartwig, *Acc. Chem. Res.*, 1998, **31**, 852.
46. G. Mann, Q. Shelby, A. H. Roy, and J. F. Hartwig, *Organometallics*, 2003, **22**, 2775.
47. D. Prim, J.-M. Campagne, D. Joseph, and B. Andrioletti, *Tetrahedron*, 2002, **58**, 2041.
48. R. J. Angelici, ‘Inorganic Synthesis’, John Wiley & Sons, New York, 1990, Vol. 28, p. 104.
49. L. S. Hegedus, *Tetrahedron*, 1984, **13**, 2415.
50. S. M. Pillai, M. Ravindranathan, and S. Sivaaram, *Chem. Rev.*, 1986, **86**, 353.
51. S. D. Ittel, L. K. Johnson, and M. Brookhart, *Chem. Rev.*, 2000, **100**, 1169.
52. G. R. Eastham, B. T. Heaton, J. A. Iggo, R. P. Tooze, R. Whyman, and S. Zacchini, *Chem. Commun.*, 2000, 609.
53. G. Kiss, *Chem. Rev.*, 2001, **101**, 3435.
54. E. Drent and P. H. M. Budzelaar, *Chem.Rev.*, 1996, **96**, 663.
55. C. J. Elsevier, *Coord. Chem. Rev.*, 1999, **185–186**, 809.
56. J. Tsuji, *New J. Chem.*, 2000, **24**, 127.
57. O. Löber, M. Kawatsura, and J. F. Hartwig, *J. Am. Chem. Soc.*, 2001, **123**, 4366.
58. A. M. Kluwer, C. J. Elsevier, M. Bühl, M. Lutz, and A. L. Spek, *Angew. Chem., Int. Ed. Engl.*, 2003, **42**, 3501.
59. A. Yamamoto, *Adv. Organomet. Chem.*, 1992, **34**, 111.
60. K. Fagnou and M. Lautens, *Angew. Chem., Int. Ed. Engl.*, 2002, **41**, 26.
61. C. Amatore, S. Gamez, A. Jutand, G. Meyer, M. Moreno-Mañas, L. Morral, and R. Pleixats, *Chem. Eur. J.*, 2000, **6**, 3372.
62. C. Amatore, A. Jutand, M. A. M’Barki, G. Meyer, and L. Mottier, *Eur. J. Inorg. Chem.*, 2001, 873.
63. M. Kimura, Y. Horino, R. Mukai, S. Tanaka, and Y. Tamaru, *J. Am. Chem. Soc.*, 2001, **123**, 10401.
64. B. M. Trost and D. L. Van Vranken, *Chem. Rev.*, 1996, **96**, 395.
65. B. J. Lüssem and H.-J. Gais, *J. Am. Chem. Soc.*, 2003, **125**, 6066.
66. J. Cámpora, P. Palma, and E. Carmona, *Coord. Chem. Rev.*, 1999, **193–195**, 207.
67. M. Albrecht and G. van Koten, *Angew. Chem., Int. Ed. Engl.*, 2001, **40**, 3750.
68. A. D. Ryabov, *Chem. Rev.*, 1990, **90**, 403.
69. H. L. Holcomb, S. Nakanishi, and T. C. Flood, *Organometallics*, 1996, **15**, 4228.
70. J. Dupont, M. Pfeffer, and J. Spencer, *Eur. J. Inorg. Chem.*, 2001, 1917.
71. J.-E. Bäckvall, B. Å kermark, and S. O. Ljunggren, *J. Chem. Soc., Chem. Commun.*, 1977, 264.
72. J.-E. Bäckvall, in ‘Metal-Catalyzed Cross-Couplings Reactions’, eds. F. Diederich and P. J. Stang, Wiley-VCH, Weinheim, 1998, p. 339.
73. R. A. Sheldon, I. W. C. E. Arends, G.-J. Ten Brink, and A. Dijksman, *Acc. Chem. Res.*, 2002, **35**, 774.
74. A. Zapf and M. Beller, *Top. Catal.*, 2002, **19**, 101.
75. C. E. Tucker and J. G. de Vries, *Top. Catal.*, 2002, **19**, 111.
76. B. M. Trost, *Angew. Chem., Int. Ed. Engl.*, 1986, **25**, 1.
77. G. Poli, G. Giambastiani, and A. Heumann, *Tetrahedron*, 2000, **56**, 5959.
78. J. J. Li and G. W. Gribble, ‘Palladium in Heterocyclic Chemistry’, Pergamon, Oxford, 2000.

Paramagnetic Organometallic Complexes

Daniel B. Leznoff & Garry Mund
Simon Fraser University, Burnaby, BC, Canada

1 Introduction 4189
2 Long-lived Paramagnetic Complexes 4190
3 Short-lived Paramagnetic Complexes 4194
4 Characterization of Paramagnetic Complexes 4195
5 Applications of Paramagnetic Organometallic Complexes 4197
6 Related Articles 4198
7 References 4198

Abbreviations

acac = acetylacetonate; COT = cyclooctatetraene; Cp = cyclopentadienyl; Cp^* = pentamethylcyclopentadienyl; dmit = 1,3-dithiole-2-thione-4,5-dithiolate; DFT = density functional theory; ESR = electron spin resonance; HOMO = highest occupied molecular orbital; LUMO = lowest unoccupied molecular orbital; Mes = mesityl; MO = molecular orbital; NMR = nuclear magnetic resonance; py = pyridine; R = alkyl or aryl moiety; S = spin quantum number; SQUID = superconducting quantum interference device; TCNE = tetracyanoethylene; THF = tetrahydrofuran; Tp = tris(pyrazolylborate); VSM = vibrating sample magnetometer; μ_{eff} = effective magnetic moment; μ_{B} = Bohr magneton.

1 INTRODUCTION

1.1 ‘Open-shell’ Organometallic Systems

Since the beginning of transition metal organometallic chemistry, the field has been and is still dominated by compounds that follow the effective atomic number (EAN) rule (*see Effective Atomic Number Rule*), also commonly known as the 18-electron rule. However, odd-electron organometallic compounds, once considered to be unstable (with a few exceptions) are no longer rare. In particular, for the first-row transition metals (*see Transition Metals*), stable paramagnetic organometallic complexes have been the focus of numerous synthetic, structural, and reactivity studies.[1] The general notion that open-shell molecules (paramagnetic metal compounds or ‘metalloradicals’) may be more reactive and thus potentially important as catalytic intermediates has added impetus to the study of these systems.[2,3] As a result, a field completely dominated by the idea that only diamagnetic even-electron (16 or 18) species (*see Eighteen Electron Compounds*) could be involved in catalytic processes, has been increasingly enlightened by the potential of paramagnetic systems.[4,5] The presence of the unpaired electrons also allows for completely different reactivity patterns to be observed (e.g. one-electron redox processes) compared with the more familiar diamagnetic systems. Despite this, the chemistry of paramagnetic organometallic complexes is still relatively unexplored versus that of the diamagnetic, even-electron counterparts, and is thus an exciting, current field of active research.

1.2 Exceptions to the 18-electron Rule

According to molecular orbital theory (*see* ***Molecular Orbital Theory***), maximum stability for a generic ML_n organometallic complex with n ligands results when all the valence shell orbitals are doubly occupied, giving rise to a closed-shell 18-electron configuration. Since the ligand field splitting (*see* ***Ligand Field Theory & Spectra***), Δ (or HOMO-LUMO gap *see HOMO–LUMO Gap*), is large for complexes with carbon-based, π-acidic ligands (*see π-Acid Ligand*) (e.g. CO, Cp, olefins etc.), such complexes readily adopt a diamagnetic (spin-paired) configuration. Still, paramagnetism (*see Paramagnetism*) can arise in 18-electron complexes if the ligand field splitting (*see Ligand Field Theory*) (Δ) is small. An example is the monomeric, paramagnetic, 18-electron, spin-equilibrium molecule Cp*Ni(acac), which is diamagnetic below 150 K but becomes paramagnetic with increasing temperature.[6] That said, paramagnetic organometallic complexes generally violate the 18-electron rule, with both odd- and even-electron stable compounds known. There are several reasons that can be invoked to justify this unexpected stability: (1) The complexes are stabilized with fewer ligands by use of π-donor ligands such as alkoxides, amides, and alkylthiolates that have lone pairs available for additional π donation to the paramagnetic metal center. (2) The complexes are kinetically stabilized with sterically demanding ligands. (3) In systems with fewer than 18 electrons, the incompletely filled molecular orbitals are nonbonding or only slightly bonding. (4) In systems with more than 18 electrons, the partially filled molecular orbitals are only slightly antibonding (*see* ***Molecular Orbital Theory*** and ***Electronic Structure of Organometallic Compounds***).

Open-shell organometallic compounds have electron counts spanning a range of 8–20 electrons. Low electron counts are less frequent, especially for the second and third-row transition metals. The 12-electron triamidoamine complex $MoR[N(CH_2CH_2NR)_3]$ (R = alkyl) is one such system, and is an example of the first factor above. Coordination numbers lower than four are also rare (*see* ***Coordination & Organometallic Chemistry: Principles***), although isolated examples of two- and three-coordinate complexes such as $Mn[C(SiMe_3)_3]_2$ and $[Mn(Mes)_3]^-$ have been reported with extremely bulky ligands (factor 2). Similarly, the 13-electron complex $Cp^*Cr(CH_2SiMe_3)_2$ (**1**) uses sterically demanding trimethylsilylmethyl ligands to stabilize the mononuclear chromium complex and prevent dimerization.[7] Chromocene (*see Chromocene*) (Cp_2Cr; 16-electron complex) and cobaltocene (*see Cobaltocene*) (Cp_2Co; 19-electron complex) are examples of paramagnetic organometallic complexes that do not obey the 18-electron rule [Cp_2M; M = Cr or Co (**2**)], based on factors 3 and 4 respectively. The other neutral, first-row metallocenes (with the exception of 18-electron ferrocene) also illustrate these two factors at work.

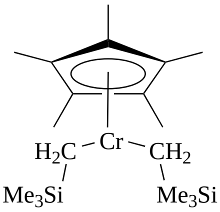

(**1**)

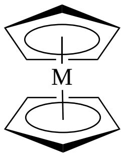

(**2**)

In addition to the synthesis of stable paramagnetic organometallic complexes, studies of radical-based reaction mechanisms have generated investigations of organometallic radical reactivity. Organometallic radicals, especially those characterized with a 17-electron configuration, are receiving a great deal of attention in view of their involvement as intermediates in a variety of fundamental processes.[8]

This article is divided into several parts, with long-lived organometallic complexes as the primary focus. Short-lived systems (*see* ***Short-lived Intermediates***), as well as techniques used to characterize paramagnetic systems, will also be discussed. In addition, potential applications of open-shell organometallic complexes, especially for catalysis and magnetic materials, will also be presented.

2 LONG-LIVED PARAMAGNETIC COMPLEXES

2.1 Paramagnetic Metallocene Derivatives

Modern transition metal organometallic chemistry can be said to have been invigorated by the discovery and subsequent bonding description of ferrocene (*see Ferrocene*) by Wilkinson and Fischer in 1951. As predicted by MO theory, all of the neutral first-row metallocenes (*see Metallocene Complexes*) (V–Ni) are paramagnetic, with the exception of ferrocene. Metallocenes probably represent the most studied of all paramagnetic organometallic complexes.

Paramagnetic 19-electron cobaltocene and 20-electron nickelocene (*see Nickelocene*) are stable despite their $>$ 18-valence electron count. These 'extra' electrons occupy metal–ligand antibonding molecular orbitals and cause a lengthening of the M–C bonds (*see* ***Bonding Energetics of Organometallic Compounds***). Some paramagnetic metallocenes are not stable and instead adopt diamagnetic electron configurations, as demonstrated by titanocene (*see Titanocene*) (Cp_2Ti) and rhenocene (Cp_2Re). The latter complex dimerizes via metal–metal bond formation, whereas the former complex C–H activates a ring (*see* ***Alkane Carbon–Hydrogen Bond Activation***) and dimerizes with hydride bridges (*see* ***Hydride Complexes of the Transition Metals***) to give isomeric $Cp_2(\mu\text{-}\eta^5\text{:}\eta^5\text{-}C_5H_4C_5H_4)Ti_2(\mu\text{-H})_2$. Niobocene and tantalocene also dimerize in a similar fashion. However, employing more sterically demanding moieties can stabilize the monomeric form of titanocene (and other paramagnetic metallocenes). The corresponding Cp* derivative of titanocene is thermally sensitive but is nevertheless an isolable compound, in which there is a tautomeric equilibrium (equation 1) between $Cp^*{}_2Ti$ (**3**) and $Cp^*(\eta^6\text{-}C_5Me_4CH_2)TiH$ (**4**).[1]

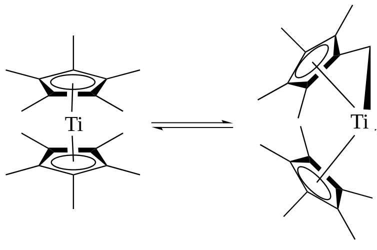

(1)

(**3**) (**4**)

Although analogous bis(pentadienyl) titanium complexes (also referred to as 'open titanocenes') are diamagnetic, paramagnetic 'open metallocenes', such as bis(pentadienyl) vanadocene (**5**) and 'half-open chromocene' (**6**), have also been reported (*see* ***Transition Metal Complexes with Bulky Allyl Ligands***).[1] Compared to Cp rings, the acyclic cyclopentadienyl system is a stronger electron acceptor for geometric and electronic reasons.[9]

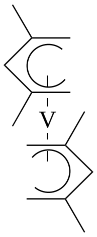

(**5**)

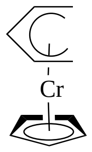

(**6**)

A few paramagnetic metallocene cations such as chromocinium ($Cp^*{}_2Cr^+$) have been reported but are only stable when sterically protected.

Recently, an effort has been made to develop 'maximum spin' transition metal Cp complexes of which high-spin

d^4 chromocenes and d^5 manganocenes, such as bis(1,3-dialkylindenyl)chromium and octaisopropylmanganocene would be examples. The effect of the eight isopropyl groups in the latter complex results in pure high-spin behavior ($\mu_{\text{eff}} = 5.87\,\mu_B$) even at 2 K. By altering the Cp-ligand, many such species are readily accessible, but are highly reactive and serve as versatile starting compounds for a broad range of products.[9] The high degree of reactivity is attributed to the large ionic contribution to metal–Cp bonding in high-spin systems compared to the corresponding low-spin metallocenes.

A related area of research involves the paramagnetic η^5-polyphospholyl complexes of the transition metals $[\eta^5\text{-}(C_nR_nP_{5-n})_2]M$ ($n = 0-3$), also referred to as 'phosphametallocenes.' Although the subject has been previously reviewed, several new trends have emerged, in particular, some promising applications in homogeneous catalysis.[10]

2.2 Cyclopentadienyl Ligands as Ancillary Ligands

As mentioned in Section 2.1, much of paramagnetic organometallic research is based on complexes containing Cp-type ligands (*see Cyclopentadienyl*). These ligands are often used as stabilizing ligands that are generally nonreactive (i.e. kinetically inert), and are thus referred to as spectator or ancillary ligands (*see Ancillary Ligand*). For example, so-called 'half-sandwich' compounds (*see Half-sandwich Complexes*), which contain one Cp-type ligand, are ubiquitous in organometallic chemistry. In particular, the group 5 metals (V, Nb, and Ta) form an extensive series of 17-electron, paramagnetic 'four-legged piano stool' complexes of the type $CpMX_2L_2$ (**7**); ($X =$ halide, $L =$ THF, py, PR_3 etc.).[1] The half-sandwich, 'three-legged piano stool' Cr(III) complexes also form a class of very well studied Cp-type systems, with general formulas of $[CpCrL_3]^{2+}$, $[CpCrXL_2]^+$, $CpMX_2L$ (**8**), and $[CpCrX_3]^-$.

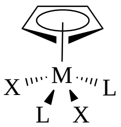

(**7**)

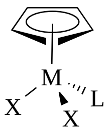

(**8**)

The half-sandwich compounds of the trivalent group 6 metals (Cr, Mo, and W) demonstrate how the structure and the reactivity of paramagnetic organometallic compounds are related to their spin state. While molybdenum and tungsten form four-legged piano stool structures (**7**) with 17-electron counts ($S = 1/2$), the chromium system usually adopts the three-legged piano stool structure (**8**) consisting of a 15-electron count ($S = 3/2$).[11] The lower electronic configuration for Cr(III) is not solely attributed to the different metal size and M–L bond strengths, but also to the greater energetic advantage for unpaired electrons in this system (i.e. high spin-pairing energy vs. Δ). Many other paramagnetic half-sandwich compounds are also known and can be pursued in an excellent review.[1]

2.3 σ-Alkyl Complexes

In addition to the ubiquitous Cp-fragment, other donor functionalities can be used to stabilize paramagnetic organometallic compounds. For example, the triamidoamine ligand $[N(CH_2CH_2NR)_3]^{3-}$ has been effectively used to develop a class of paramagnetic Mo(IV) and W(IV) alkyls, aryls, and hydrides of the type $MR'[N(CH_2CH_2NR)_3]$ (**9**).[12] Highly steric β-diketiminate ligands have stabilized isolable three-coordinate σ-alkyl complexes (**10**) of iron, cobalt, and nickel.[13,14] The mixed-donor tridentate diphosphineamido ligand $[N(SiMe_2CH_2PPh_2)_2]^-$ has also been used[15] to stabilize low-coordinate metal compounds of the form $MR[N(SiMe_2CH_2PPh_2)_2]$ (**11**) ($M =$ Co, Cr; $R =$ Me, CH_2Ph, CH_2SiMe_3; $M =$ Fe, $R = CH_2SiMe_3$, $CH(SiMe_3)_2$).[16–18] The chromium(II) σ-alkyl systems react with alkyl halides RX to give the unusual five-coordinate $Cr(R)X[N(SiMe_2CH_2PPh_2)_2]$ ($R =$ Me, CH_2SiMe_3; $X =$ Cl, Br, I).[18] This reaction also occurs with the simple $[Cr(H_2O)_6]^{2+}$ ion to give $[CrR(H_2O)_5]^{2+}$ cations that are used in organic synthesis (Scheme 1).[19] Such systems have relevance to radical-based organic transformations. This reaction route is also employed for the synthesis of vitamin B_{12} models.[20] The discovery that the active site of vitamin B_{12} contains a readily homolyzable Co(III)-carbon bond has fueled research into the preparation and reactivity of model species that can mimic the coenzyme's bioinorganic functions (*see* ***Cobalt: B₁₂ Enzymes & Coenzymes***).

While hindered tris(pyrazolyl)borate (Tp) ligands (*see Tris(pyrazolyl)borates*) have been used extensively as ancillary ligands in bioinorganic and coordination chemistry,

$$\begin{array}{lcl}
Cr(H_2O)_6^{2+} + RX & \longrightarrow & CrX(H_2O)_5^{2+} + H_2O + R\bullet \\
Cr(H_2O)_6^{2+} + R\bullet & \longrightarrow & CrR(H_2O)_5^{2+} + H_2O \\
\hline
2Cr(H_2O)_6^{2+} + RX & \longrightarrow & CrX(H_2O)_5^{2+} + CrR(H_2O)_5^{2+} + 2H_2O
\end{array}$$

Scheme 1

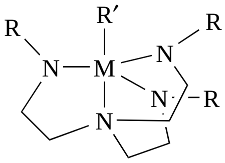

(**9**)

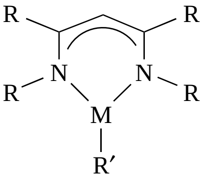

(**10**)

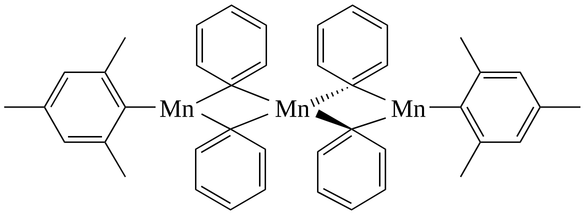

(**13**, central mesityl groups simplified)

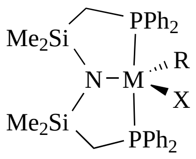

(**11**)

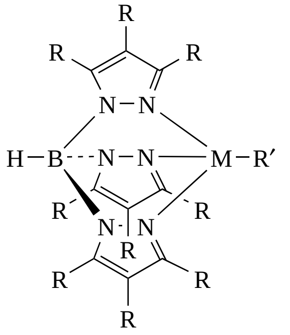

(**12**)

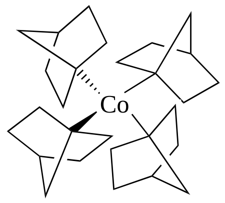

(**14**)

their use in the preparation of paramagnetic organometallic compounds has been more limited. One of the most significant features of facial Tp ligands in first-row organometallic complexes is their ability to act as ‘tetrahedral enforcers’, giving rise to highly coordinately unsaturated (*see Coordinative Saturation & Unsaturation*) organometallic species of the type (Tp)MR′ (**12**) (M = Fe (14-electron species), Co (15 electron species); R′ = alkyl, aryl). The formation of these coordinately unsaturated complexes are important from the point of view that they are suggested to be key intermediates in catalytic C–C bond formation.**[21]**

The use of very bulky alkyl groups has allowed for the isolation of highly coordinately and electronically unsaturated, homoleptic (*see Homoleptic Compound*) metal σ-alkyls, some of which are paramagnetic.**[22,23]** Examples include MR_3 ($R = CH(SiMe_3)_2$, M = Ti(III), d^1; V(III), d^2; Cr(III), d^3), $M(CH_2SiMe_3)_4$ (M = V(IV), d^1; Cr(IV), d^2), and $Mn(CH_2SiMe_3)_2$ (Mn(II), d^5). Homoleptic metal σ-aryls of the form $M(2,4,6\text{-}Me_3C_6H_2)_x$ ($M(x)$ = V(III) and Cr(IV), d^2; Cr(III), d^3; Cr(II), d^4; Mn(II), d^5; Fe(II), d^6; Co(II), d^7) have also been reported; the manganese(II) complex is trimeric (**13**).**[24]** The 15-electron species $[NBu_4][Ni(C_6Cl_5)_4]$ is the first example of a homoleptic, organometallic Ni(III) compound.**[25]** The pentachlorophenyl group has also been used to develop a series of homoleptic organochromium derivatives of the type $[Cr(C_6Cl_5)_4]^{n-}$ ($n = 0, 1, 2$) in three adjacent oxidation states: Cr(IV), Cr(III), and Cr(II).**[26]** Finally, the series of $M(1\text{-norbornyl})_4$ (M = V, Cr, Mn, Fe, Co) complexes deserve special mention since they include rare examples of highly oxidized iron(IV) and cobalt(IV) (**14**) metal-alkyl complexes, which also have the unique distinction of being tetrahedral and low spin (*see* ***Ligand Field Theory & Spectra***).**[27]**

In general, high-oxidation state complexes have far fewer than 18 electrons because extreme steric crowding would result if enough ligands were bonded to the metal center to form either a 17- or 19-electron species. Similarly, dimerization to generate cluster-type complexes is often prevented for steric reasons (*see* ***Dinuclear Organometallic Cluster Complexes***).

2.4 Ligand Localized Nineteen-electron Complexes

Nineteen-electron organometallic complexes are important intermediates in many organometallic radical reactions.**[28,29]** However, the short lifetime of many 19-electron species has inhibited a thorough study of their reactivity and electronic structure. On the other hand, ligand localized, or radical-anion ligand complexes are stable systems in which the ‘19th’ electron is localized on the π^* orbital of the ligand. Thus, one strategy for stabilizing such complexes is to introduce a ligand with a low-energy π^* orbital into the complex; such ligands include diazobutadienes, tetraazabutadienes, and quinones. In this case, the unpaired electron preferentially occupies the π^* orbital instead of a metal-centered orbital, which is higher in energy. Systems of this type are often referred to as $18 + \delta$ complexes as they can be described as 18-electron species with a partial electron density contribution to the metal (δ) via delocalization of the unpaired electron from the reduced ligand.**[30]** For example, the value of δ for compound (**15**) in CH_2Cl_2 (equation 2) is very low at only 0.01, whereas the analogous cobalt complex has a δ value of 0.25 in 2-MeTHF. Ranges of δ, as well as solvent, ligand, and metal effects on δ have also been discussed.**[31]** These $18 + \delta$ complexes are dissociatively labile, a feature that makes these molecules attractive candidates for catalysts in odd-electron processes. The ability of these systems to catalyze the cyclooligomerization of acetylenes has been investigated.[32]

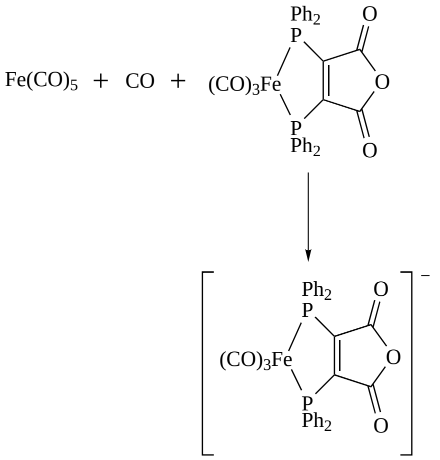

(15)

(2)

2.5 f Electron Organometallic Complexes

With the number of stable paramagnetic d element organometallic complexes increasing in the literature, the organometallic chemistry of the f elements is frequently overlooked. In fact, many paramagnetic organometallic lanthanide and actinide systems are also known (*see* ***Actinides: Organometallic Chemistry*** and ***Scandium, Yttrium & the Lanthanides: Organometallic Chemistry***). Organometallic complexes of the diamagnetic d^0f^0 actinides U(VI) and Th(IV),[33] and also the paramagnetic U(IV) and U(III) ions have been reported.[34]

As with their d element counterparts, many organometallic compounds of the f elements involve the use of Cp-type ligands, giving rise to many sandwich and half-sandwich complexes (*see Sandwich Compound* and *Half-sandwich Complexes*).[35,36] Thus, the monoanionic nature and steric flexibility of the Cp-type ligand has been widely exploited for the f elements, since Cp-ancillary groups provide electrostatic and steric stabilization while taking up only one valency of the metal (electrostatic charge balance is important for the f elements, since they have a tendency to form bonds with greater ionic character due to the limited extension of the 4f and 5f orbitals). Also, as the f-element metal centers are generally larger than their transition metal counterparts (*see* ***Actinides: Inorganic & Coordination Chemistry***), they can accommodate (or sometimes require) more sterically demanding ligand sets. For example, substituted cyclooctatetraenes are commonly used as ligands in f-element chemistry.[37] Another set of sterically demanding ligands that has been used to effectively stabilize f-element organometallic systems is the tris(pyrazolylborate)-based ligand framework.[38]

The interesting class of highly sterically congested, paramagnetic $(Cp^*)_3Ln$ complexes have contributed significantly to the advancement of lanthanide organometallic chemistry by introducing new types of reactions and complexes that are not typically observed in other f-element organometallic systems, and certainly not in the transition metal realm.[39] For example, $(Cp^*)_3Sm$ (**16**) has been found to (1) ring-open THF, (2) polymerize ethylene, and (3) react with hydrogen to form a hydride (**17**) with loss of Cp*H (equation 3). None of these processes are known to occur with $(Cp)_3Ln$ complexes.

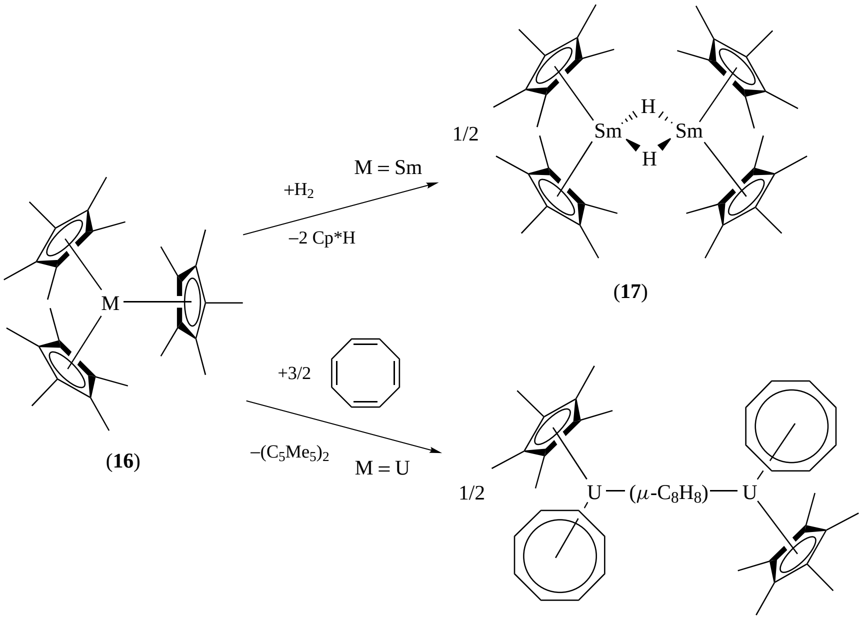

(16)

(17)

(18)

(3)

The analogous uranium(III) compounds also show unusual reactivity patterns. For example, addition of COT to $(Cp^*)_3U$ yields a mixed metallocene dimer (**18**) bridged by a COT^{2-} ligand; in this reaction, the $(Cp^*)_3U$ complex has effectively acted as a formal three-electron reductant (equation 3).[40] A variety of substituted $(Cp')_3U$ complexes form adducts with CO and CNR (isocyanides) – these are rare examples of actinide metals with π-acidic ligands.[41] Paramagnetic uranium alkyl complexes are active in a range of catalytic processes.[42]

2.6 Paramagnetic Organometallic Carbene Complexes

A relatively new area of organometallic research involves the use of carbene-type ligands (*see* ***Carbene Complexes***).[43] Carbenes are often viewed as alternatives to phosphine ligands as they are neutral, two-electron donor ligands, but they do not extensively π back-bond. An interesting example of an organometallic carbene system involves the reaction of carbenes with chromocene (Scheme 2) to generate the 14-electron species $(\eta^1\text{-}C_5H_5)(\eta^5\text{-}C_5H_5)Cr(carbene)$ (**19**) and/or a cationic Cr(II) system $[(\eta^5\text{-}C_5H_5)Cr(carbene)_2]^+$ (**20**).[44]

3 SHORT-LIVED PARAMAGNETIC COMPLEXES

Organometallic radicals are a topic of special interest due to their reactivity and potential activity in the catalytic realm. There are several methods used to generate short-lived organometallic radicals such as homolysis of metal–metal or metal–ligand bonds, electron transfer (*see* ***Electron Transfer in Coordination Compounds***), atom abstraction, or addition of organic radicals to closed-shell complexes.[2,29] In addition, chemical or electrochemical redox reactions can also be used (*see* ***Electrochemistry: Applications in Inorganic Chemistry***). These methods will not be discussed here but can be pursued in the very thorough review conducted in the previous edition of this series.[45]

3.1 17- and 19-electron Radicals and 'Super Reducing Agents'

Transient species (17- or 19-electron) are generally formed from the starting diamagnetic 18-electron (or 16-electron) complexes by the addition or loss of one electron.[2,29] These radicals are usually much more reactive than their diamagnetic counterparts. For example, substitution of the 17-electron organometallic radical $[Fe(CO)_3(PPh_3)_2]^+$ by pyridine nucleophiles occurs 10^9 faster than in its 18-electron analogue $[Fe(CO)_3(PPh_3)_2]$.[46] The kinetics and reactivity of 17-electron radicals have been conducted both in organic solvents and also in aqueous solution.[47] In the presence of electron-pair donor ligands, 17-electron organometallic radicals readily convert to 19-electron adducts.[48] Experimental measurements of K_{eq} show that in many systems, the formation of a 19-electron adduct is thermodynamically stabilizing.[48] Stable 19-electron (or $18+\delta$) systems were discussed in Section 2.4; genuine 19-electron metalloradicals are those in which the extra electron is localized in a

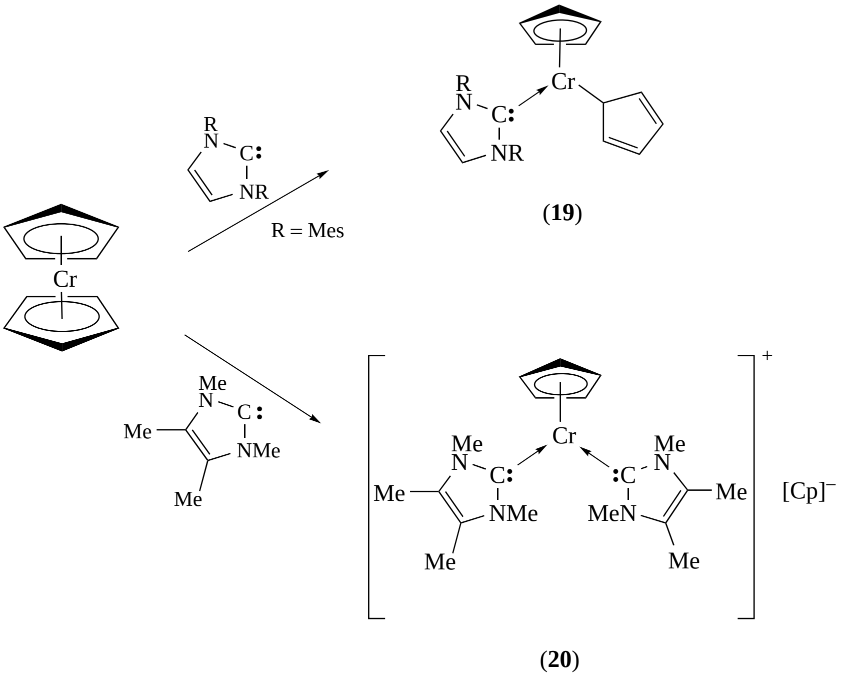

Scheme 2

metal–ligand antibonding orbital. The inherent instability of such species gives rise to 'super reducing agents', which are, in principle, capable of single electron transfer to a wide variety of substrates. An example of a highly reducing 19-electron radical is the L-$W(CO)_5{}^{\bullet -}$ species, which is formed from the reaction of photogenerated $W(CO)_5{}^{\bullet -}$ radicals (*see* ***Luminescence Behavior & Photochemistry of Organotransition Metal Compounds***), with donor solvents or phosphine ligands (L = THF, MeCN, PEt_3; equation 4 and 5).**49** Electrochemical reduction has also been used to generate 19-electron radicals, such as the bis-phosphine nickel(I) species $CpNi(PR_3)^{\bullet +}$. It should be noted that $CpM(CO)_3L^{\bullet}$ radicals are often referred to as 19-electron radicals, however, these systems might adopt 17- or 18-electron configurations in solution via 'slippage' (η^5 to η^4 or η^5 to η^3) of Cp rings.

$$[W_2(CO)_{10}]^{2-} \underset{}{\overset{h\nu}{\rightleftharpoons}} 2\,W(CO)_5{}^{\bullet -} \qquad (4)$$

$$W(CO)_5{}^{\bullet -} + PPh_3 \overset{k_f}{\rightleftharpoons} [W(CO)_5(PPh_3)]^{\bullet -} \qquad (5)$$

3.2 Reactions Involving Transient Organometallic Radicals

An organometallic radical may undergo several different types of reactions.**45** Scheme 3 illustrates some different reactions of $CpM(CO)_3{}^{\bullet}$ radicals (**21**)**50** including (i) dimerization; (ii) halide abstraction from an alkyl halide or metal halide; (iii) hydrogen atom abstraction from metal hydrides; (iv) electron-transfer reduction; (v) electron-transfer oxidation and ligand addition; (vi) electron-transfer induced disproportionation (*see* ***Electron Transfer in Coordination Compounds***).

Neutral 17-electron complexes tend to undergo metal-centered reactions, while reactivity of 19-electron complexes are typically ligand-centered. Scheme 4 displays an example of these reactivity differences within the same system.**51** Photolysis of the iron dimer results in homolysis of the metal–metal bond to form the neutral 17-electron species (**22**), whereas in the presence of PPh_3, the intermediate 19-electron radical (**23**) is produced, which then undergoes ligand oxidation to yield a 17-electron final product. Selected

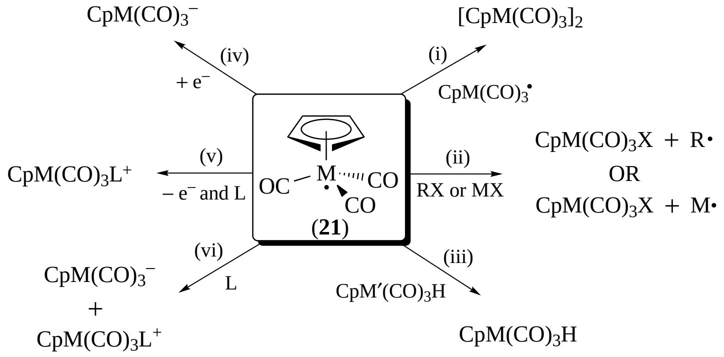

Scheme 3

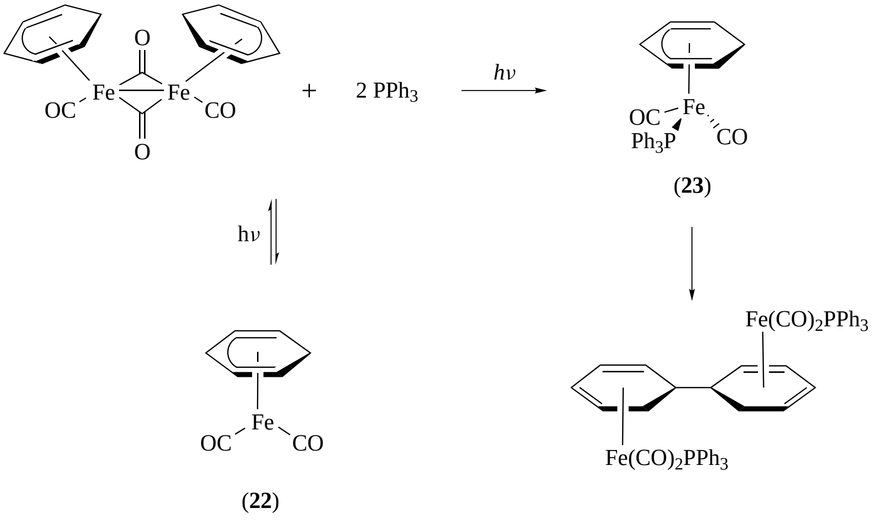

Scheme 4

aspects of metal radical reactivity have been previously reviewed.[52]

4 CHARACTERIZATION OF PARAMAGNETIC COMPLEXES

The study of paramagnetic organometallic complexes has been hampered by the difficulty of their characterization relative to diamagnetic systems. In particular, proton and multinuclear magnetic resonance spectroscopy are much less applicable to paramagnetic systems. Although ESR (or EPR) spectroscopy (*see Electron Paramagnetic Resonance*) is often considered a valuable tool in the study of paramagnetic systems, this technique can also be of limited use as many complexes are ESR-silent.

4.1 Paramagnetic NMR Spectroscopy

Paramagnetic complexes are characterized by the usual physical methods, however, the application of NMR spectroscopy usually yields resonances that are broadened and highly shifted from their diamagnetic values.[53] Furthermore, coupling information is usually lost. The unpaired electrons in a paramagnetic system can relax NMR-active nuclei via either dipole–dipole interactions or through-bond coupling resulting in broadened or even unobservable peaks. The shifting of resonances through either pseudo-contact shifting (through-space effects) or contact (Fermi) shifts (through-bond effects) can hinder resonance assignments. Despite these setbacks, assignments of a paramagnetic ^{1}H NMR spectrum can still be obtained using a combination of peak integration, broadness and shift patterns, and variable temperature studies.[54]

Generally, ^{1}H NMR peaks of paramagnetic molecules will sharpen and shift toward their diamagnetic values upon an increase in temperature. Consequently, plots of chemical shift (δ) versus 1/T are often useful as the y-intercept is the theoretical diamagnetic value of δ.

Unfortunately, nuclear relaxation effects in paramagnetic compounds are generally too strong to allow for the observation of spectra of other nuclei, such as ^{31}P or ^{13}C. However, ^{2}H NMR spectroscopy has been shown to be a useful procedure for obtaining sharper spectra as the deuterium nucleus relaxes at a substantially slower rate than the proton, allowing for sharper lines.[53,55] Solid-state NMR studies have also successfully been performed for paramagnetic organometallic complexes. The first 2D-correlation NMR experiment involving the detection of dilute spins (e.g. ^{13}C) in a nonlabeled paramagnetic solid Cu(II)(DL-alanine)$_2$·H$_2$O was recently observed.[56] Furthermore, solid-state NMR spectroscopy has also been applied toward the characterization of paramagnetic metallocenes and metallocenium ions.[57]

4.2 ESR Spectroscopy and DFT Calculations

ESR spectroscopy detects unpaired electrons and their coupling to nearby spin-active nuclei. However, due to fast relaxation of the unpaired electrons causing broadening of the resonances and zero-field splitting of integer spin states to yield a nonmagnetic $S = 0$ ground state, a large number of paramagnetic complexes are ESR-silent. Cooling the sample to liquid nitrogen or helium temperatures can sometimes reduce fast relaxation, and then in some cases, a signal can be observed. However, ESR spectroscopy is widely used in studying $18 + \delta$ complexes in order to identify the spin density and delocalization of the ligand-unpaired electron. When observable, ESR spectra are also used to study fluxional processes. The applications of ESR to organometallic chemistry have been reviewed.[2] The spin density distribution within organometallic compounds has also been examined via NMR spectroscopy.[58]

Density functional theory (DFT) has recently been employed in conjunction with ESR in order to determine where the ‘extra’ electron is in a 19-electron species (i.e. is it ligand localized, metal localized, or delocalized over the entire molecule). For example, this technique has been applied to determine that the 19th electron in both $[CpCo(CO)_2]^-$ and $[Mn(CO)_5Cl]^-$ is delocalized over the entire molecule.[59,60]

4.3 Magnetism

Paramagnetism typically results from magnetic effects due to the spin and orbital motion of unpaired electrons. A detailed theoretical explanation of magnetic behavior is well beyond the scope of this review (*see* ***Magnetism of Extended Arrays in Inorganic Solids*** and ***Magnetism of Transition Metal Ions***), and can be explored in various other treatises on the subject.[61,62] Solid-state magnetic susceptibilities (*see Magnetic Susceptibility*) of complexes may be obtained using VSM and SQUID magnetometers, while Evans’ method[63] (*see Evans Method*) is an NMR technique for the measurement of magnetic susceptibilities in solution. The measurement of the magnetic susceptibility and calculation of the magnetic moment can provide important information as to the oxidation state and spin state of the compound. For mononuclear systems, this determination can be straightforward, but in cases where two or more paramagnetic metal ions are bridged by diamagnetic ligands, their spins may interact giving rise to antiferromagnetic (spins-opposed) or ferromagnetic (spins-aligned) coupling (*see Antiferromagnetism* and *Ferromagnetism*). For example, the dinuclear complex $[Cp^*Cr(\mu\text{-}Me)]_2$ (**24**) has a magnetic moment smaller than that expected for a low-spin Cr(II) center ($S = 1$; $\mu_B = 2.87$), implying that the two chromium atoms of the dimer are strongly antiferromagnetically coupled.[64] However, ferromagnetic behavior is observed in (**25**), which is described as a mixed-valent Cr(I)/Cr(III) dimer. Thus, the spins of all the unpaired electrons are aligned with the magnetic

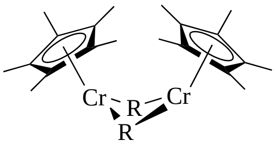

(**24**)

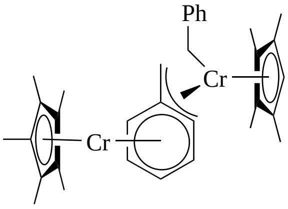

(**25**)

field (S = 3/2 for Cr(III) and S = 1/2 for Cr(I)), giving rise to a molecule with four unpaired electrons (S = 2) and a higher magnetic moment than expected.[65]

5 APPLICATIONS OF PARAMAGNETIC ORGANOMETALLIC COMPLEXES

The synthesis and reactivity of paramagnetic organometallic complexes (*see* ***Mechanisms of Reaction of Organometallic Complexes***), in particular reactions involving the metal–carbon bond, are of interest from both an industrial view (primarily catalysis) and from an academic view, in terms of the novelty of such compounds. The use of reactivity patterns (e.g. radical reactions) unique to the presence of unpaired electron density at the metal center is of interest to synthetic chemists. In addition to catalysis and organic synthesis, potential applications of paramagnetic organometallic complexes include their use as spin-labels,[66] as building blocks in supramolecular chemistry and crystal engineering,[67] and in the development of systems displaying optical limiting properties.[68]

5.1 Reactions and Catalytic Cycles Involving Paramagnetic Organometallic Species

One of the most useful applications of paramagnetic organometallic chemistry is in the area of catalysis. In addition to the development of diamagnetic zirconocene-based (Cp_2Zr) technology,[69] there has been intensive investigation into the study of the active site(s) of chromium-based catalysts, which produce approximately one-third of the world's polyethylene. A recent review examines several homogeneous, coordinatively unsaturated paramagnetic alkyl chromium complexes in intermediate oxidation states (II – IV) that have been studied with respect to their ability to act as catalysts for olefin polymerization (*see* ***Oligomerization & Polymerization by Homogeneous Catalysis***).[70] Diamagnetic group IV metallocene systems (and their related half-sandwich analogues) have typically dominated the field of olefin polymerization catalysis, but more recently focus has turned toward nonmetallocene paramagnetic species.[71] In particular, complexes of iron(II) and cobalt(II), featuring the bis(imino)pyridine ligand, have been shown to exhibit high activity rates (see complex (**26**) for the iron example), although the exact nature of the active site is still under investigation. In addition, vanadium(III) complexes, including substituted $V(acac)_3$ complexes, are widely employed in ethylene–propylene copolymerizations.[72] Paramagnetic organometallic species are also employed in other areas of catalysis – the 19-electron iron(I) complex $[FeCp(C_6Me_6)]$ has been effectively used as a catalyst to synthesize $Ru_3(CO)_{11}$-loaded dendrimers, which have potential applications as electron-transfer-chain catalysts.[73]

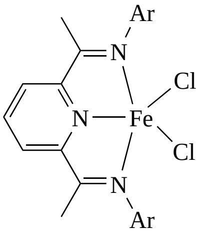

Ar = 2,6-$^i Pr_2C_6H_3$, 2,4,6-$Me_3C_6H_2$

(**26**)

Paramagnetic metallocenes, such as the titanocene(III) species, have been shown to be effective reagents to reduce aryl and alkyl halides, ketones, and aldehydes (*see* ***Organic Synthesis using Transition Metal Complexes Containing π-Bonded Ligands***). $[Cp_2MCl]_2$ (M = Ti and Zr) are useful in carbohydrate chemistry for the conversion of glycosyl halides to glycals, and for the stereoselective preparation of glycosides.[74] The mechanisms of these reactions are proposed to involve the generation of free radicals.[75] Equation (6) shows the clean deoxygenation of the alcohol (*R*,*R*)-2,3-epoxy-1-decanol to (*R*)-1-decen-3-ol with no loss of stereochemistry.

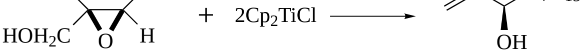

(6)

5.2 Magnetism and Metallocene-based Magnets

The synthesis of paramagnetic materials that have specifically tailored magnetic properties is gaining considerable interest (*see* ***Magnetism of Extended Arrays in Inorganic Solids*** and ***Magnetism of Transition Metal Ions***). For example, metallocenes and their derivatives are known to display molecular ferromagnetism, ferromagnetic, or antiferromagnetic exchange interactions and spin-crossover behavior. In addition, the 15-electron species vanadocene (*see Vanadocene*) has been used as a reducing agent in organic solution to generate a new method for the preparation of ultrafine iron powder and iron colloids. Such powders and colloids are of interest in areas such as catalysis, magnetic materials, and optics.**76** Recently, much effort has been made toward the synthesis of molecule-based magnetic materials. In these materials, the goal is to use open-shell molecules and arrange them in such a way that the magnetic exchange interactions between them give rise to spontaneous magnetization. Both organic radicals, open-shell molecules, and combinations of the two have been used as building blocks toward magnetic ordering.**77** Paramagnetic organometallic systems have also been employed in this field of research. Most notably, stacks of alternating radical anions such as TCNE (*see* ***Self-assembled Inorganic Architectures***) and metallocenium cations have been used to develop low-temperature magnets. An example is the electron-transfer salt $[(Cp^*)_2Fe]^{\bullet+}$ $[TCNE]^{\bullet-}$, which is a bulk ferromagnet below 4.8 K. Paramagnetic metallocenes have also been instrumental in developing higher temperature magnets.**77** The reaction of TCNE with the sandwich compound $V(C_6H_6)_2$ gives $V(TCNE)_z \cdot y$(solvent), which is a bulk ferrimagnet below its thermal decomposition temperature of 350 K. One potential application for this material is in magnetic shielding (i.e. the attenuation of magnetic fields found in many electronic applications such as high voltage lines or near cell phones).

Compared to organic or mixed organic/organometallic systems, as described above, attempts at developing 'pure' organometallic magnets have progressed less fruitfully. The fulvalene ligand has successfully been used as a link between two paramagnetic organometallic systems, giving rise to bimetallocenes (**27**).**78** While the magnetic properties that result invariably depend on the metal center, the cobalt system, for example, gives rise to ferromagnetic interactions between the organometallic fragments.

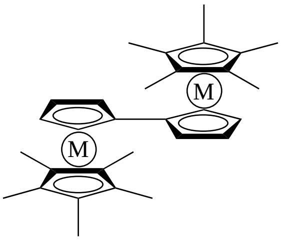

(**27**)

Antiferromagnets such as the organometallic dithiolene complexes $[Cp_2M(dmit)]^{\bullet+}$ $[X]^-$ (M = Mo, W; X = PF_6^-, AsF_6^-, SbF_6^-) offer a series of systems that have variable transition temperatures and magnetic anisotropy characteristics.**79** Interestingly, the $[Cp^*W(dmit)_2]^\bullet$ (**28**) system is a 15-electron neutral radical (d^1) with optical limiting properties in solution, and contains an antiferromagnetic ground state in the solid state.

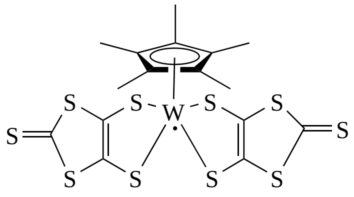

(**28**)

Recently, the first example of unusual spin glass behavior in a mesoporous material has been described.**80** The study of mesoporous niobium oxide with a variety of organometallic sandwich-type compounds has resulted in the formation of a series of mesostructured composites with mixed oxidation state molecular phases within the pores. These systems have the potential to give rise to nanowire technology as well as conducting and insulating behavior. Examples of sandwich-type systems used include bis(benzene)chromium and vanadium as well as cobaltocene. While the niobium oxide-cobaltocene material shows superparamagnetic behavior, the niobium oxide-bis(cyclopentadienyl)nickel system exhibits spin glass behavior.

6 RELATED ARTICLES

Bonding Energetics of Organometallic Compounds; Coordination & Organometallic Chemistry: Principles; Electrochemistry: Applications in Inorganic Chemistry; Electronic Structure of Organometallic Compounds; Magnetism of Extended Arrays in Inorganic Solids; Magnetism of Transition Metal Ions; Mechanisms of Reaction of Organometallic Complexes; Molecular Orbital Theory; Oligomerization & Polymerization by Homogeneous Catalysis; Short-lived Intermediates.

7 REFERENCES

1. R. Poli, *Chem. Rev.*, 1996, **96**, 2135.
2. W. C. Trogler, 'Organometallic Radical Processes', Elsevier, Amsterdam, NY, 1990.
3. J. K. Kochi, 'Organometallic Mechanisms and Catalysis', Academic Press, New York, 1978.
4. R. H. Crabtree, 'The Organometallic Chemistry of the Transition Metals', John Wiley & Sons, New York, 2000.
5. D. Astruc, *Acc. Chem. Res.*, 1991, **24**, 36.

6. M. E. Smith and R. A. Andersen, *J. Am. Chem. Soc.*, 1996, **118**, 11119.
7. R. A. Heintz, S. Leelasubcharoen, L. M. Liable-Sands, A. L. Rheingold, and K. H. Theopold, *Organometallics*, 1998, **17**, 5477.
8. M. C. Baird, *Chem. Rev.*, 1988, **88**, 1217.
9. H. Sitzmann, *Coord. Chem. Rev.*, 2001, **214**, 287.
10. D. Carmichael and F. Mathey, New Trends in Phosphametallocene Chemistry, 'Topics in Current Chemistry', Springer-Verlag, Berlin, 2002, Vol. 220, p. 27.
11. R. Poli, *Acc. Chem. Res.*, 1997, **30**, 494.
12. K.-Y. Shih, R. R. Schrock, and R. Kempe, *J. Am. Chem. Soc.*, 1994, **116**, 8804.
13. J. M. Smith, R. J. Lachicotte, and P. L. Holland, *Chem. Commun.*, 2001, 1542.
14. P. L. Holland, T. R. Cundari, L. L. Perez, N. A. Eckert, and R. J. Lachicotte, *J. Am. Chem. Soc.*, 2002, **124**, 14416.
15. M. D. Fryzuk, *Can. J. Chem.*, 1992, **70**, 2839.
16. M. D. Fryzuk, D. B. Leznoff, R. C. Thompson, and S. J. Rettig, *J. Am. Chem. Soc.*, 1998, **120**, 10126.
17. M. D. Fryzuk, D. B. Leznoff, E. S. F. Ma, S. J. Rettig, and V. G. Young-Jr, *Organometallics*, 1998, **17**, 2313.
18. M. D. Fryzuk, D. B. Leznoff, S. J. Rettig, and V. G. Young-Jr, *J. Chem. Soc., Dalton Trans.*, 1999, 147.
19. J. H. Espenson, *Acc. Chem. Res.*, 1992, **25**, 222.
20. D. Dolphin ed., 'B12', John Wiley & Sons, New York, 1982.
21. M. Akita and S. Hikichi, *Bull. Chem. Soc. Jpn.*, 2002, **75**, 1657.
22. P. J. Davidson, M. F. Lappert, and R. Pearce, *Chem. Rev.*, 1976, **76**, 219.
23. R. R. Schrock and G. W. Parshall, *Chem. Rev.*, 1976, **76**, 243.
24. S. U. Koschmieder and G. Wilkinson, *Polyhedron*, 1991, **10**, 135.
25. P. J. Alonso, L. R. Falvello, J. Forniés, A. Martín, B. Menjón, and G. Rodríguez, *Chem. Commun.*, 1997, 503.
26. P. J. Alonso, J. Forniés, M. A. García-Monforte, A. Martín, B. Menjón, and C. Rillo, *Chem. Eur. J.*, 2002, **8**, 4056.
27. E. K. Byrne and K. H. Theopold, *J. Am. Chem. Soc.*, 1989, **111**, 3887.
28. W. E. Geiger, *Acc. Chem. Res.*, 1995, **28**, 351.
29. D. Astruc, 'Electron Transfer and Radical Processes in Transition Metal Chemistry', VCH, New York, 1995.
30. D. R. Tyler and F. Mao, *Coord. Chem. Rev.*, 1990, **97**, 119.
31. D. M. Schut, K. J. Keana, D. R. Tyler, and P. H. Rieger, *J. Am. Chem. Soc.*, 1995, **117**, 8939.
32. F. Mao, D. M. Schut, and D. R. Tyler, *Organometallics*, 1996, **15**, 4770.
33. J.-Y. Hyeon and F. T. Edelmann, *Coord. Chem. Rev.*, 2003, **241**, 249.
34. T. J. Marks and I. L. Fragala eds, 'Fundamental and Technological Aspects of Organo-f-element Chemistry, NATO ASI Series', D. Reidal Publishing Company, Dordrecht, 1985.
35. S. Arndt and J. Okuda, *Chem. Rev.*, 2002, **102**, 1953.
36. F. T. Edelmann and V. Lorenz, *Coord. Chem. Rev.*, 2000, **209**, 99.
37. P. W. Roesky, *Eur. J. Inorg. Chem.*, 2001, 1653.
38. N. Marques, A. Sella, and J. Takats, *Chem. Rev.*, 2002, **102**, 2137.
39. W. J. Evans and B. L. Davis, *Chem. Rev.*, 2002, **102**, 2119.
40. W. J. Evans, G. W. Nyce, and J. W. Ziller, *Angew. Chem., Int. Ed. Engl.*, 2000, **39**, 240.
41. M. del-Mar-Conejo, J. S. Parry, E. Carmona, M. Schultz, J. G. Brennann, S. M. Beshouri, R. A. Andersen, R. D. Rogers, S. Coles, and M. Hursthouse, *Chem. Eur. J.*, 1999, **5**, 3000.
42. F. T. Edelmann, in 'Comprehensive Organometallic Chemistry II', eds. E. W. Abel, F. G. A. Stone, and G. Wilkinson, Pergamon, New York, 1995, Vol. 4, p. 11.
43. W. A. Herrmann and C. Köcher, *Angew. Chem., Int. Ed. Engl.*, 1997, **36**, 2162.
44. C. D. Abernethy, J. A. C. Clyburne, A. H. Cowley, and R. A. Jones, *J. Am. Chem. Soc.*, 1999, **121**, 2329.
45. D. R. Tyler and A. Avery, Paramagnetic Organometallic Complexes, 'Encyclopedia of Inorganic Chemistry', Wiley, Chichester, 1994, p. 3055.
46. C. Balzarek, T. J. R. Weakley, and D. R. Tyler, *Inorg. Chim. Acta*, 2001, **315**, 139.
47. I. T. Horváth and F. Joó eds, 'Aqueous Organometallic Chemistry and Catalysis', Kluwer, Dordrecht, 1995.
48. D. R. Tyler, *Acc. Chem. Res.*, 1991, **24**, 325.
49. I. S. Zavarine and C. P. Kubiak, *Coord. Chem. Rev.*, 1998, **171**, 419.
50. J. H. Espenson, *J. Mol. Liq.*, 1995, **65–66**, 205.
51. K. E. Torraca and L. McElwee-White, *Coord. Chem. Rev.*, 2000, **206–207**, 469.
52. C. D. Hoff, *Coord. Chem. Rev.*, 2000, **206–207**, 451.
53. G. N. Lamar, W. D. Horrocks, and R. H. Holm, 'NMR of Paramagnetic Molecules', Academic Press, New York, 1973.
54. R. S. Drago, 'Physical Methods for Chemists', W. B. Saunders, Orlando, 1992.
55. A. Johnson and G. W. Everett-Jr, *J. Am. Chem. Soc.*, 1972, **94**, 1419.
56. Y. Ishii, N. P. Wickramasinghe, and S. Chimon, *J. Am. Chem. Soc.*, 2003, **125**, 3438.
57. H. Heise, F. H. Köhler, M. Herker, and W. Hiller, *J. Am. Chem. Soc.*, 2002, **124**, 10823.
58. F. H. Köhler, Probing Spin Densities by Using NMR Spectroscopy, 'Magnetism: Molecules to Materials', Wiley-VCH, New York, 2001, p. 379.
59. D. A. Braden and D. R. Tyler, *J. Am. Chem. Soc.*, 1998, **120**, 942.

60. D. A. Braden and D. R. Tyler, *Organometallics*, 1998, **17**, 4060.

61. O. Kahn, ‘Molecular Magnetism’, VCH, New York, 1993.

62. R. L. Carlin, ‘Magnetochemistry’, Springer-Verlag, Heidelberg, 1986.

63. D. F. Evans, *J. Chem. Soc.*, 1959, 2003.

64. R. A. Heintz, R. L. Ostrander, A. L. Rheingold, and K. H. Theopold, *J. Am. Chem. Soc.*, 1994, **116**, 11387.

65. C. Pariya and K. H. Theopold, *Curr. Sci.*, 2000, **78**, 1345.

66. D. B. Leznoff, C. Rancurel, J.-P. Sutter, S. J. Rettig, M. Pink, and O. Kahn, *Organometallics*, 1999, **18**, 5097.

67. D. Braga and F. Grepioni, *Coord. Chem. Rev.*, 1999, **183**, 19.

68. B. Domercq, C. Coulon, P. Feneyrou, V. Dentan, P. Robin, and M. Fourmigué, *Adv. Funct. Mater.*, 2002, **12**, 359.

69. H. H. Brintzinger, D. Fischer, R. Mülhaupt, B. Rieger, and R. M. Waymouth, *Angew. Chem., Int. Ed. Engl.*, 1995, **34**, 1143.

70. K. H. Theopold, *Eur. J. Inorg. Chem.*, 1998, 15.

71. V. C. Gibson and S. K. Spitzmesser, *Chem. Rev.*, 2003, **103**, 283.

72. S. Gambarotta, *Coord. Chem. Rev.*, 2003, **237**, 229.

73. E. Alonso and D. Astruc, *J. Am. Chem. Soc.*, 2000, **122**, 3222.

74. R. P. Spencer and J. Schwartz, *Tetrahedron*, 2000, **56**, 2103.

75. T. V. RajanBabu and W. A. Nugent, *J. Am. Chem. Soc.*, 1994, **116**, 986.

76. R. Choukroun, D. de-Caro, S. Matéo, C. Amiens, B. Chaudret, E. Snoeck, and M. Respaud, *New. J. Chem.*, 1998, **22**, 1295.

77. J. S. Miller and A. J. Epstein, *Coord. Chem. Rev.*, 2000, **206–207**, 651.

78. H. Hilbig, P. Hudeczek, F. H. Köhler, X. Xie, P. Bergerat, and O. Kahn, *Inorg. Chem.*, 1998, **37**, 4246.

79. M. Fourmigué, *Acc. Chem. Res.*, 2004, **37**, 179.

80. M. Vettraino, X. He, M. Trudeau, and D. M. Antonelli, *J. Mater. Chem.*, 2001, **11**, 1755.

Peptide–Metal Interactions

Claude F. Meares
University of California, Davis, CA, USA

Based in part on the article Peptide–Metal Interactions by Justin K. Moran & Claude F. Meares which appeared in the Encyclopedia of Inorganic Chemistry, First Edition.

---

1 Introduction 1
2 Copper–Peptide Complexes 2
3 Nickel–Peptide Complexes 6
4 Palladium–and Platinum–Peptide Complexes 7
5 Zinc–Peptide Complexes 8
6 Metal-Mediated Hydrolysis of Amino Acid Esters and Peptides 9
7 Related Articles 12
8 References 12

Glossary

1N, 2N, 3N etc.: indicate the number of nitrogens coordinated to the metal ion

---

Abbreviations

Amino acid residues in peptides will be those recommended by IUPAC–IUB for the nomenclature of peptides.

---

1 INTRODUCTION

The condensation of two amino acids yields a dipeptide. The resulting amide bond is often referred to as a peptide bond or a peptide group (equation 1). Peptides can be effective ligands for a wide range of metal ions since they contain a variety of potential donor groups. In addition to the amino group of the N-terminus, and the carboxylate of the C-terminus, peptides can bind through the amide carbonyl, the deprotonated amide nitrogen, and through any functional groups on the side chains (*see* ***Ammonia & N-donor Ligands***). Metal–peptide complexes have aroused increasing interest in recent years. This attention is mainly because of the applications of such systems as models for the structures and reactions of metalloproteins, and the renewed interest in biologically active peptides such as peptide fragments of the prion protein. The reaction of copper(II) with proteins in strongly alkaline solutions to give a violet-red color, which was first noted by Wiedmann in the 1800s,[1] is one of the first examples of a metal ion reacting with a peptide. Schiff[2] also studied this reaction, which occurs with biuret and other compounds which contain two or more amide or peptide groups, and is now known as the biuret reaction. In the early 1900s, Kober and Sigiura studied the reactions of copper(II) with di-, tri-, and tetraglycine in basic solutions.[3] In later spectrophotometric investigations, Kober and Haw concluded that, in biuret reactions, the violet-red color was due to ring formation of the copper with the nitrogens of the peptide groups.[4] The isolation of the disodium salt of the copper–tetraglycine complex in 1934 by Rising *et al.* showed conclusively that the peptide hydrogens were replaced by copper.[5] Infrared studies by Chouteau later confirmed the existence of the metal–peptide linkage.[6] With the use of both potentiometric and spectrophotometric methods, the determination of the stability constants and pK_a values of several metal–oligopeptide complexes were made possible by the work of Dobbie and Kermack,[7] Martell *et al.*,[8] and Gurd and associates (*see* ***Stability Constants & their Determination***).[9]

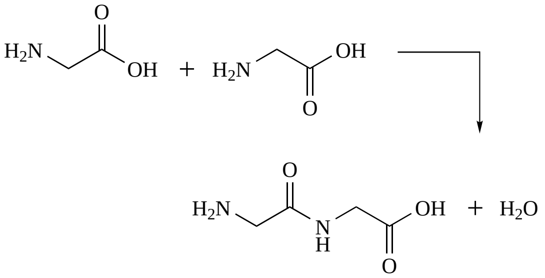

(1)

The hydrogen atom in the peptide linkage is not very acidic and, in the absence of metal ions, it is not ionized even in strongly alkaline solutions. This weak acidity makes quantitative equilibrium measurements difficult. The pK_a values for hydrogen loss of several peptides have been estimated to be 16.4 for *N*-methylacetamide, 14.1 for glycylglycinate, and 15.1 for triglycine with an estimated average value of 15.[10]

For H^+ addition, the amide group is a very weak base, and there once was considerable debate over whether the amide oxygen or the amide nitrogen was the most favorable protonation site. However, NMR experiments have decisively established that the oxygen atom serves as the main protonation site over the entire range of acidic solutions.[11,12] Several groups have estimated the ratio of the O- to N-protonated amide cations to be 10^7.[10]

The replacement of a nitrogen-bonded hydrogen by a metal ion should form a strong bond. However, due to the weak acidity of the peptide hydrogen it is improbable that alkali or alkaline-earth metal ions would be able to remove this hydrogen. Transition metal ions, however, should be more effective in substitution for the nitrogen-bound hydrogen. The problem with transition metal ions is that they are more susceptible to hydrolysis, and generally precipitation occurs in neutral and alkaline solutions. So simple amides in their neutral state form adducts with metal ions at the amide oxygen and not the amide nitrogen (equation 2). This has been confirmed by both experimental and theoretical results, which show an increase in double bond character in the C–N bond and a lengthening of the C=O bond.[13,14]

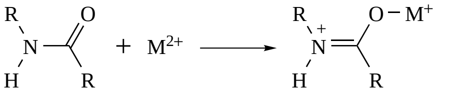
(2)

One possible way to prevent transition metal ions from precipitating, and thus allow them to coordinate to peptides, is to have a primary ligating site or anchor, which would allow the amide oxygen to chelate to the metal. This will allow for subsequent substitution of the amide hydrogen by the metal ion. This primary binding site reduces the importance of metal ion hydrolysis and permits attainment of pH values where substitution of a metal ion for an amide hydrogen may occur (equation 3).

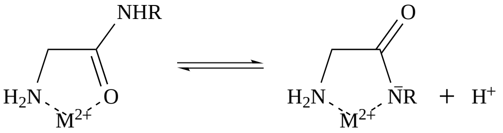
(3)

There are two possible primary ligating groups available in peptides. The first is the carboxylate oxygen on the C-terminus. However, chelation involving the carboxylate oxygen and the amide oxygen would form an unfavorable seven-membered ring. It is possible to form a more stable five-membered chelate ring with the carboxylate oxygen and the deprotonated amide nitrogen of the peptide group; however, due to the weak basicity of the carboxylate these complexes are not very stable and the metal ion is eventually hydrolyzed. The other primary binding site is the amino group on the N-terminus. If the amino group acts as the primary binding site, this allows for the formation of five-membered chelate rings with either the amide oxygen or the deprotonated amide nitrogen of the peptide linkage (equation 3). As will be seen for simple peptides, it is the amino group that acts as the primary binding site in metal–peptide complexes.

Early studies on metal–peptide complexes were generally concerned with polyglycines, and there are several reviews on these complexes.[15] In the first part of this article, we will discuss various metal–peptide complexes that have coordinating side chains. Comparison of these metal–peptide complexes will be made with their glycine analogs, and the differences will be noted. The second part of the article will deal with metal-mediated peptide-bond cleavage.

2 COPPER–PEPTIDE COMPLEXES

Copper–peptide complexes have been the most extensively studied of all the metal–peptide complexes.[16] Copper(II) is the most important oxidation state in copper–peptide complexes, although copper(III) can be stabilized by coordination to peptides. The deprotonated peptide nitrogens help stabilize the higher oxidation state of copper; therefore the more deprotonated peptide nitrogens, the more stable the copper(III) complex. Copper(III) complexes are generally prepared by electrochemical oxidation of the copper(II) complex at pH 10 or higher.

The coordination geometry around copper(II) peptide complexes is generally tetragonally distorted octahedral, although there are some cases where square planar and square pyramidal geometries can also be found. X-ray crystal structure determinations have shown that copper(III)–peptide complexes have square-planar geometry[17] (*see* ***Copper: Inorganic & Coordination Chemistry***). In this section, we discuss copper(II)–peptide complexes; copper(III)–peptide complexes are reviewed elsewhere.[18]

The type of complex formed between copper(II) and amino acids depends largely upon which amino acid is present. Amino acids that contain a free amino terminus form 1N complexes with copper(II), in which the amino acid acts as a bidentate ligand, binding through the amino nitrogen and the carbonyl oxygen. The stability constants for these complexes are directly related to the basicity of the amine. For amino acids that are substituted at the amino nitrogen, such as *N*-acetylglycinate, copper(II) complexes show only unidentate coordination via the carboxylate oxygen.[19]

Simple peptides initially coordinate copper(II) via the terminal amino nitrogen and to the carbonyl oxygen of the amide group (1N). As the pH is raised to about 5, copper(II) displaces the proton on the amide nitrogen to form a $CuH_{-1}L$ complex (2N). This is followed sequentially at the nitrogens of the second and third peptide linkages to give $CuH_{-2}L$ (3N) and $CuH_{-3}L$ (4N) complexes (Figure 1). However, as amino acid residues with coordinating side chains are added to the peptide, the types of complexes are changed.

Stability constants of copper(II) complexes can be calculated most accurately from pH titrations. In addition, stability constants can be derived from *electron spin resonance spectroscopy* (*see Electron Paramagnetic Resonance*), although the precision of this method is usually significantly lower.[20] *UV-Visible Spectroscopy* provides a simple method for identifying the number of nitrogens coordinated to copper. Generally as the number of coordinated nitrogens increases, the λ_{max} for the d–d transition increases. 1N complexes are usually deep blue in color, while 4N complexes tend to be red in color (as seen with biuret). Another spectroscopic tool used to determine the structure of metal–peptide complexes is circular dichroism (*see Cotton Effect*), and there is a good review of this subject elsewhere.[21]

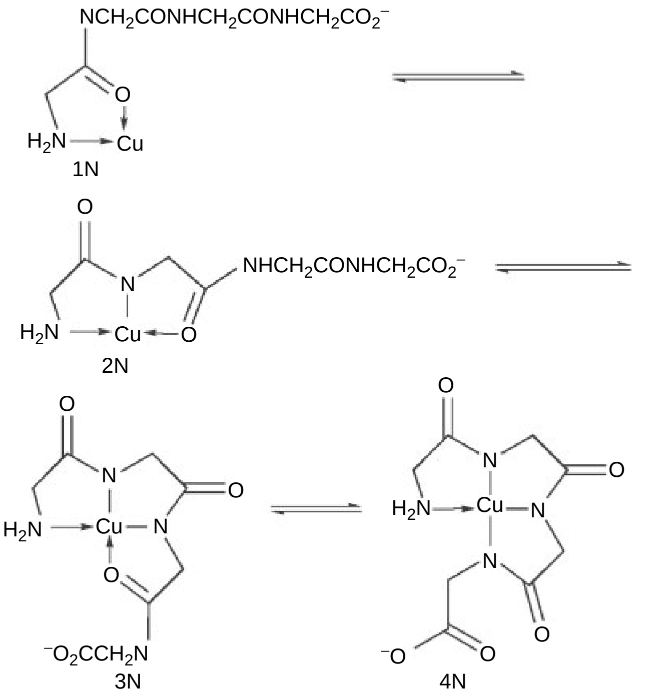

Figure 1 Stepwise complexation of copper(II) by tetraglycine

Copper(II) reacts with glycylglycine to form first a compound in which the copper is bound to the amino nitrogen and the carbonyl oxygen. As the pH is raised, the copper coordinates to the deprotonated amide nitrogen to form a complex that is bound through the amino nitrogen, the amide nitrogen and the carboxylate oxygen. The pK_a for this reaction is 3.99.[22] If the second glycine is modified at the amide nitrogen by methylation to form glycylsarcosine (glycyl-N-methylglycine), deprotonation of the peptide nitrogen cannot occur and a different complex is formed.[23]

2.1 Peptides with Noncoordinating Side Chains

Peptides that contain amino acid residues with noncoordinating side chains generally act like the polyglycine analogs. Those that contain aromatic rings such as phenylalanine are exceptional. The hydrophobic interactions or ring stacking of the phenylalanine residue can influence the structure as well as the stability of the copper(II) complexes that are formed. For example, a study was done with copper(II) and four optically pure dipeptides: L-Phe–L-Met, L-Met–L-Phe, L-Phe–L-Leu, and L-Leu–L-Phe.[24] The major complex formed in the pH range 5–8 was $CuH_{-1}L$. It was found that the formation constant for L-Leu–L-Phe was higher than that of L-Phe–L-Leu: there is an increase in stability when the aromatic ring is on the C-terminal residue. This enhanced stability is considered to be due to the interaction between the metal ion and the aromatic ring moiety. It is suggested that the weak carboxylate oxygen bond can be distorted by the metal ion–aromatic ring interaction when the phenyl ring is on the C-terminal residue. This interaction does not occur when the aromatic ring is on the N-terminal residue, because of the strong copper(II)–amine interaction. Such a difference is not seen for the dipeptides L-Phe–L-Met and L-Met–L-Phe. It is suggested that the copper(II)–sulfur and copper(II)–aromatic ring interactions have the same effect, so there is no significant difference resulting from switching the positions of the residues.

The proline residue is of interest for many reasons, even though it does not contain a coordinating side chain. Since the nitrogen of proline is secondary rather than primary, when it is incorporated into a peptide chain it does not have a dissociable hydrogen. So the proline residue acts as a break point for coordination. However, when proline is the N-terminus, it is able to coordinate through the nitrogen. A significant property of the proline residue is that it can induce β-turns within the peptide chain (*see Beta Turn*). This has importance since many biologically active peptides contain the proline residue. A study to determine the effect of a proline residue in a peptide chain was done with two sets of peptides.[25] The tetrapeptides Gly–Gly–Pro–Gly and Gly–Gly–Pro–Lys, and their octapeptide analogs $(\text{Gly–Gly–Pro–Gly})_2$ and $(\text{Gly–Gly–Pro–Lys})_2$, are models for dog tuftsinyltuftsin octapeptide. The copper(II) complexes of Gly–Gly–Pro–Gly and $(\text{Gly–Gly–Pro–Gly})_2$ are very similar. At low pH, both peptides bond through the amino nitrogen and carbonyl oxygen of the first peptide linkage. As the pH is raised, the first peptide hydrogen is displaced to give a 2N complex. Since the next peptide linkage does not contain an ionizable hydrogen due to the proline residue, the next ionizable hydrogen is on the C-terminal glycine. This hydrogen is deprotonated at pH above 9.5 for both peptides. This indicates that the peptide is bent around the copper atom. The peptides Gly–Gly–Pro–Lys and $(\text{Gly–Gly–Pro–Lys})_2$ initially form 1N complexes with copper(II). The most stable species in the pH range 6.5–10.0, however, is $CuH_{-1}L$ for the tetrapeptide and CuL for the octapeptide. These complexes have been determined to be coordinated by three nitrogens and are similar to those of the other two peptide complexes, except that the third nitrogen is from the ε-amino nitrogen of the lysine residue. It was determined from spectroscopic studies that it was the Lys^4 of the octapeptide that is coordinated to copper(II) rather than the Lys^8 residue.

2.2 Peptides Containing the Histidine Residue

Owing to the fact that imidazole (N^3-Im) forms very strong bonds with copper(II), peptides containing the histidine residue have been studied extensively. Histidine-containing peptides form a large range of complexes with copper(II), which include many polynuclear species. Whereas most peptides initially bind the metal through the amino nitrogen, it is possible for the imidazole nitrogen of a histidine residue to initiate coordination. When the C-terminal residue of a dipeptide is a histidine, initial coordination through the imidazole nitrogen facilitates the deprotonation of the peptide group, which allows for the formation of a Cu–N bond at pH 4, which is one pH unit less than with simple dipeptides.[16]

There is interest in the interaction of copper(II) with luteinizing hormone-releasing hormone (LHRH).[26] LHRH is a decapeptide amide (*p*Glu–His–Trp–Ser–Tyr–Gly–Leu–Arg–Pro–Gly–NH_2) which is the main mediator in the secretion of gonadotropins. The major copper(II) complex formed in the pH range of 5.5–9.5 is $CuH_{-1}L$, which means that it is the predominant species at physiological pH. The copper(II) is coordinated via the imidazole nitrogen and two deprotonated peptide nitrogens. This 3N complex is also seen with the copper(II) complex of the tripeptide *p*Glu–His–Pro–NH_2 (thyrotropin releasing factor) (TRF).[27]

A study done on three dipeptides containing the histidine residue, His–Gly, Gly–His, and Ala–His (carnosine), showed that various copper(II) complexes can be formed depending on the nitrogen atoms available and the metal-to-ligand ratio.[28] Coordination of carnosine and His–Gly was similar to that of Gly–Gly in which the dipeptides bond through the amino nitrogen, amide nitrogen, and carboxylate oxygen (2N). However, the main difference was that carnosine and His–Gly were able to form dimeric complexes of the form $Cu_2H_{-2}L$, in which the two copper atoms are bridged via the imidazole nitrogen donors. If an excess of His–Gly is present, the deprotonation of the peptide linkage is prevented owing to formation of the bis complex CuL_2 in which the ligands are bonded histamine-like. Carnosine was shown not to form any bis complex. The geometrical positions of the donor atoms in Gly–His make possible the coordination of the three nitrogen donors (amino, peptide, and imidazole). This results in a very stable monomeric complex $CuH_{-1}L$.

Initially, copper(II) coordinates to the octapeptide angiotensin II (Asp–Arg–Val–Tyr–Ile–His–Pro–Phe) at the imidazole nitrogen.[29] At neutral pH the main copper complex is CuL, which is a 3N complex (Figure 2). The copper(II) is bonded via the imidazole nitrogen of the histidine residue, and two deprotonated peptide nitrogens. As the pH is raised above 8.0, the coordination site changes to the N-terminus of the peptide chain, where the copper(II) is bonded by the terminal amino, and three deprotonated peptide nitrogens in a 4N complex (Figure 3).

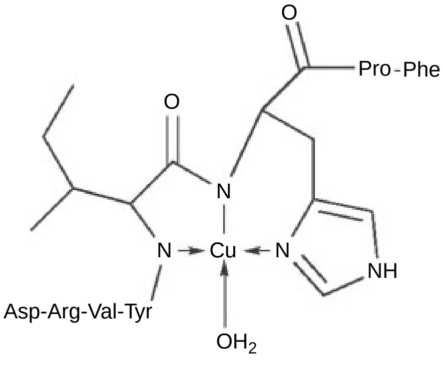

Figure 2 Copper(II)–angiotensin II 3N complex

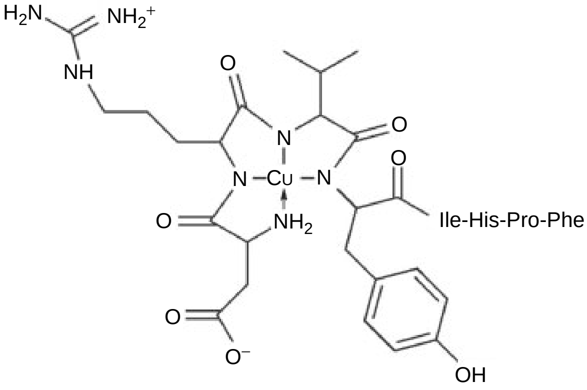

Figure 3 Copper(II)–angiotensin II 4N complex

Analogs of the metal-chelating center of bleomycin, which is a glycopeptide antibiotic, have been synthesized and the structures of their copper(II) complexes have been determined. These complexes show similar bonding as bleomycin.[30] The copper is in a highly distorted environment approaching square pyramidal, with 3N coordination that includes coordination by an imidazole nitrogen.

2.3 Peptides with Side Chains Containing Other Donor Groups

The oxygen atoms in Gln ($(CH_2)_2CONH_2$) and Ser (CH_2OH) do not coordinate to copper(II) appreciably.[31] However, the β-carboxylate oxygen of the Asp residue is able to bind copper(II) very effectively. When Asp is the N-terminal residue of a peptide, initial coordination is made more facile due to coordination by the β-carboxylate of the Asp residue rather than the peptide carbonyl. When Asp is in the second or third position of a peptide chain, such as the tetrapeptide fragment of fibrinopeptide A (Ala–Asp–Ser–Gly), or Ala–Ala–Asp–Ala,[32] the most stable copper(II) complexes formed are $CuH_{-1}L$ (2N) and $CuH_{-2}L$ (3N), respectively. The increased stability of these complexes due to the Asp residue delays or even prevents coordination of a fourth nitrogen. As can be seen in the structure of $CuH_{-2}L$ (3N), the β-carboxylate oxygen of the Asp residue prevents coordination of the last peptide nitrogen (Figure 4).

In addition to the carbonyl oxygen on the side chain of Gln, there is also an amide nitrogen. This only deprotonates and coordinates at pH greater than 10, so it does not play a large role in the coordination of copper(II) complexes at physiological pH.[31]

When a Lys residue occurs toward the C-terminus of a peptide, as in Gly–His–Lys or Gly–Gly–Pro–Lys, the ε-amino nitrogen of Lys is too far from the other donor sites

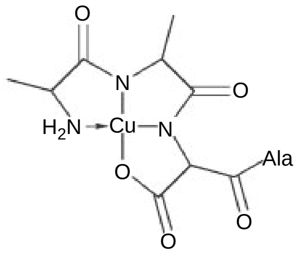

Figure 4 Copper(II)–(Ala–Ala–Asp–Ala) 3N complex

to allow it to coordinate effectively. However, if there is a proline residue in the peptide chain, then it is possible for the ε-amino nitrogen of Lys to coordinate due to the β-turn induced by the proline residue.[16]

When Tyr is the N-terminal residue, polynuclear copper(II) complexes can form, primarily because it is sterically impossible for the amino nitrogen and phenolic oxygen of the Tyr residue to bind the same copper(II) atom. A study done on β-casomorphin-5 (Tyr–Pro–Phe–Pro–Gly) and its fragments Tyr–Pro–Phe–Pro, Tyr–Pro–Phe, and Tyr–Pro,[33] showed that the dipeptide fragment Tyr–Pro (H_2L) acted as a simple amino acid, forming mono and bis complexes with copper(II). The dipeptide bonded copper(II) through the amino nitrogen and the peptide carbonyl. Since there was no ionizable hydrogen on the peptide nitrogen, there was no bonding by the peptide nitrogen. The major species of the other peptides at physiological pH were the dimeric species Cu_2L_2. In these complexes the copper(II) is bonded by the amino nitrogen and the peptide carbonyl of one ligand and the phenolic oxygen of a second ligand. If the pH is raised to above 8.0, then another species is formed, $Cu_2H_{-2}L_2$. In addition to being coordinated by the amino nitrogen and peptide carbonyl, as was seen with Cu_2L_2 species, the copper(II) atoms are also coordinated by the peptide nitrogens of the C-terminal residue of Tyr–Pro–Phe–Pro–Gly.

The coordination ability of several vasopressin-like peptides (AVP, D-VAVP, TMe-D-VAVP, AVT, and D-VAVT) (Figure 5) with copper(II) has been described.[34] With copper(II), AVT and AVP behave the same: the major species is $CuH_{-2}L$. Spectroscopic results have shown that the $CuH_{-2}L$ species is a 4N complex. The copper(II)–AVP complex is one of the most stable 4N copper–peptide complexes known. The high stability of both the AVP and AVT copper(II) complexes can be attributed to the disulfide bridge which makes the peptides resemble other macrocyclic ligands, and presents the nitrogen donor atoms in the correct conformation and at the right separations for coordination to copper(II). When the normal L-Gln residue is replaced with D-Val (a residue with the opposite chirality) there is a large difference in the stoichiometry of the complexes formed. The peptides D-VAVP and D-VAVT are the same as AVP and AVT except with a D-Val residue in place of Gln in position 4. The major complex formed with D-VAVT and D-VAVP is the $CuH_{-1}L$ species. Spectroscopic studies have shown this species to be a 3N complex.

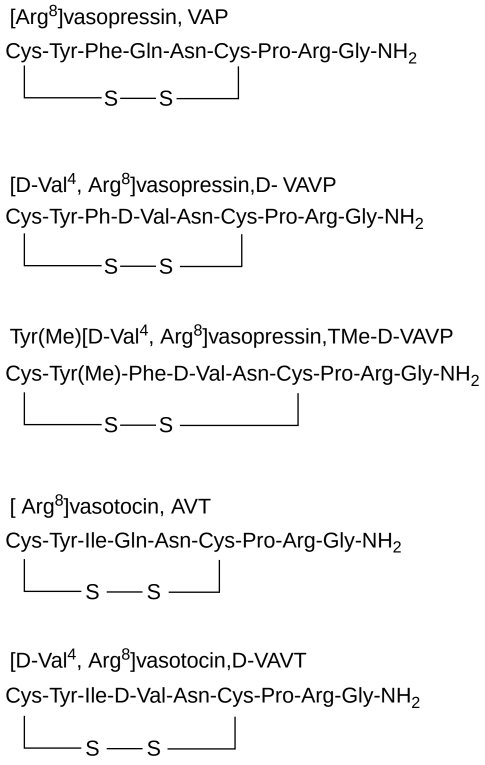
[Arg8]vasopressin, VAP
Cys-Tyr-Phe-Gln-Asn-Cys-Pro-Arg-Gly-NH2
S—S
[D-Val4, Arg8]vasopressin,D- VAVP
Cys-Tyr-Ph-D-Val-Asn-Cys-Pro-Arg-Gly-NH2
S—S
Tyr(Me)[D-Val4, Arg8]vasopressin,TMe-D-VAVP
Cys-Tyr(Me)-Phe-D-Val-Asn-Cys-Pro-Arg-Gly-NH2
S—S
[Arg8]vasotocin, AVT
Cys-Tyr-Ile-Gln-Asn-Cys-Pro-Arg-Gly-NH2
S—S
[D-Val4, Arg8]vasotocin,D-VAVT
Cys-Tyr-Ile-D-Val-Asn-Cys-Pro-Arg-Gly-NH2
S—S

Figure 5 AVP, D-VAVP, TMe-D-VAVP, AVT, and D-VAVT

Copper(II) usually does not form very stable complexes with the sulfur side chains in amino acid residues such as Cys or Met, owing to the fact that the SH group tends to oxidize very rapidly (*see* ***S-donor Ligands***). However, when a thiocarbonyl group is incorporated into a peptide chain, the resulting metal complexes are usually more stable. The dipeptide amide Alat–Ala–OMe (Alat is the thiocarbonyl analog of Ala) initially forms the complexes CuL and CuL_2, in which the copper(II) ion is bonded via the amino nitrogen and the thiocarbonyl sulfur.[35] The stability constants for these complexes are slightly higher than their nonthio analogs. However, the thiocarbonyl group is not able to prevent peptide deprotonation, and at high pH the complexes $CuH_{-1}L_2$ and $CuH_{-2}L_2$, which have one or two ligands bound via the amino nitrogen and deprotonated peptide nitrogen, dominate. The peptide Asp–Phet–NH_2 (Phet is the thiocarbonyl analog of Phe), initially bonds copper(II) through the amino nitrogen and thiocarbonyl sulfur. In the pH region of 4.5–8.0 the major species is $CuH_{-1}L$ in which the copper(II) is bonded via the amino and deprotonated peptide nitrogens, and thiocarbonyl sulfur. When the pH is raised, the terminal peptide nitrogen is deprotonated, resulting in the $CuH_{-2}L$ complex, which has 3N coordination similar to the nonthiocarbonyl analog.

3 NICKEL–PEPTIDE COMPLEXES

Owing to their similarities, nickel(II)–peptide complexes are usually studied along with copper(II) complexes. As was seen with copper, the most common oxidation state of nickel in nickel–peptide complexes is +2. Like copper(III), nickel(III) is also stabilized by coordination to deprotonated peptide nitrogens, and this chemistry is reviewed elsewhere.[36] Nickel(II), which is d^8, can exist in two distinct coordination geometries depending on the ligand field (*see* ***Nickel: Inorganic & Coordination Chemistry***). In neutral to acidic solutions, simple nickel(II)–dipeptide complexes behave the same as nickel(II) tri- and larger peptide complexes. The nickel is coordinated through the amino nitrogen and the carbonyl oxygen (1N). When the pH is raised to 9.0, nickel(II) substitutes for a peptide hydrogen, and the coordination changes. The dipeptide complexes are coordinated through the amino and deprotonated peptide nitrogens and the carboxylate oxygen (2N), while larger peptides are bound via the amino and deprotonated peptide nitrogens and the carbonyl oxygen of the peptide group.

Since larger peptides have several peptide nitrogens that can be deprotonated, the nickel(II) complexes change from an octahedral geometry to a square-planar geometry in which the nickel(II) is bonded via the amino nitrogen, and three deprotonated peptide nitrogens (4N). This abrupt change in coordination geometry, which has been termed the *cooperative effect*, makes it very difficult to detect the $NiH_{-1}L$ (2N) and $NiH_{-2}L$ (3N) complexes. The change is caused by the enforced planarity of the peptide after the second peptide nitrogen is deprotonated. The change in geometry is accompanied by a change in color, from blue for the octahedral complexes to yellow for square-planar complexes.

Dipeptides do not have a second peptide nitrogen, so they do not force this change in geometry. Instead they form octahedral bis complexes with each dipeptide acting as a tridentate ligand. Coordination is through the amino and deprotonated peptide nitrogens and the carboxylate oxygen (Figure 6).

Dinuclear nickel(II) complexes are formed with the dipeptide Gly–L-Cys. The nickel atoms are coordinated by the amino and deprotonated peptide nitrogens and the sulfur groups, with the sulfur atoms bridging the two nickel atoms (Figure 7).[37] This is in contrast to the dipeptide L-Cys–Gly where, due to the strong binding ability of the cysteine residue, nickel(II) is coordinated through the Cys residue only in a cysteine-like fashion, and no deprotonation of the peptide nitrogen is observed. Notably, copper(II) does not form stable complexes with sulfur-containing ligands. The NiL_2 species predominates at all metal-to-ligand ratios.[37] The dipeptides Ala–Cys and Phe–Cys form complexes similar to those of Gly–Cys.[38] The main difference is that the mono complex $NiH_{-1}L$, which is not seen with Gly–Cys, is seen with Ala–Cys and Phe–Cys owing to steric effects caused by the methyl and benzyl side chains. In the $NiH_{-1}L$ complexes the nickel is coordinated via the amino and deprotonated peptide nitrogens and the thiol group. This coordination is also seen in the dimer $Ni_2H_{-2}L_2$. At high pH and an excess of ligand, the dimer $Ni_2H_{-2}L_2$ is converted into the $NiH_{-1}L_2$ complex, which has one ligand coordinated through the amino, and deprotonated peptide nitrogens and thiol group, while the second ligand is coordinated through the thiol group only (Figure 8).

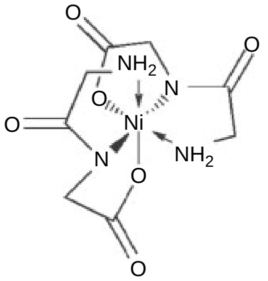

Figure 6 Ni(Gly–Gly)$_2$

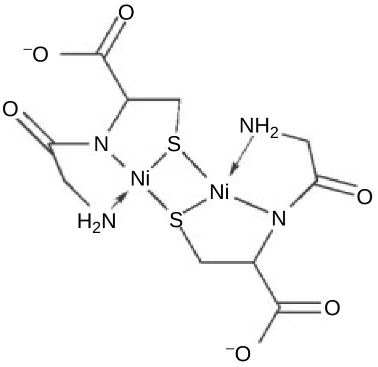

Figure 7 Ni_2(Gly–L-Cys)$_2$

With the tripeptide Gly–Gly–L-Cys, two species were found to form with nickel(II). At low pH the NiLH species was found to dominate, but as the pH is raised there is a simultaneous release of three protons from NiLH to give the major species $NiH_{-2}L$. Only monomeric complexes are formed because there are no available binding sites in the planar species for sulfur to create polynuclear complexes. This is also seen with the tripeptide Ala–Ala–Cys, where the major species at pH 6.25 and above is $NiH_{-2}L$.[39]

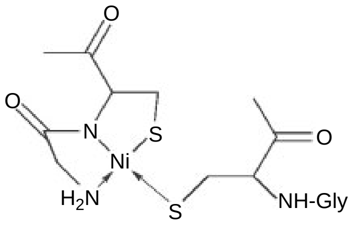

Figure 8 Ni(Gly–Cys)$_2$

The influence of the thiocarbonyl group on the coordination of nickel(II) by peptides was examined.[35] Initially Alat–Ala–OMe forms the bis octahedral NiL_2 complex which is coordinated via the amino nitrogen and thiocarbonyl sulfur. The thiocarbonyl group is not able to prevent deprotonation of the amide nitrogen, and the square-planar complex $NiH_{-2}L_2$, which is coordinated by the amino and deprotonated peptide nitrogens, forms at a lower pH than the corresponding non-thiocarbonyl analog. Similar nickel(II) complexes are formed with the dipeptide amide Asp–Phet–NH_2.

A study done with four optically pure dipeptides, L-Phe−L-Met, L-Met−L-Phe, L-Phe−L-Leu, and L-Leu−L-Phe, showed that the major species formed at physiological pH with nickel(II) is NiL. This is different from the complex with copper(II), in which the major product was $CuH_{-1}L$.[24] This difference is due to the fact that the first complexation with nickel(II) occurs at pH 4.5, while the copper(II) complexes begin to form between pH 2 and 3. It is this lesser ability of nickel(II) to deprotonate the peptide nitrogen that causes the difference. In the case of the $NiH_{-1}L$ complex the formation of L-Phe−L-Leu is more difficult than L-Leu−L-Phe. This suggests that the nickel(II)−aromatic ring interaction influences the stability, as was seen with the copper(II) complexes.

The dipeptide His–Gly coordinates to nickel(II) in the same manner as a substituted histidine would, that is through the amino and imidazole nitrogens (2N). This is another example of how the imidazole of the histidine residue effects the coordination of peptides when it is the N-terminal residue. However, the dipeptide Gly–His acts as a tridentate ligand, bonding through the amino, deprotonated peptide, and imidazole nitrogens (3N).[39] When the pH is increased to above 9.0, the imidazole pyrrole hydrogen is substituted by a nickel from another complex.[40] In the tripeptide Gly–Gly–His, coordination is through the amino nitrogen, two deprotonated peptide nitrogens, and the imidazole nitrogen (4N).[41] This complex is of interest because histidine is the third amino acid residue in both bovine and human serum albumins. Gly–Gly–L-His shows bonding similar to that of Asp–Ala–His–methylamide, which is the model for the N-terminus of human serum albumin.

With the biologically active peptide TRF (Gly–His–Pro–NH_2), two different types of complexes are formed.[27] At pH lower than 8.5 the major complex is the octahedral NiL, which is initially bonded through the imidazole nitrogen, not the amino nitrogen. At pH greater than 8.5 the major species is the planar $NiH_{-2}L$, which is bonded through the imidazole nitrogen and two deprotonated peptide nitrogens. A study done with angiotensin II (Asp–Arg–Val–Tyr–Ile–His–Pro–Phe) and two fragments, Asp–Arg–Val–Tyr (the N-terminal fragment) and MeCO–Tyr–Ile–His,[42] showed that, with nickel(II) at high pH, angiotensin II gave complexes closely similar to those formed with Asp–Arg–Val–Tyr (Figure 9). The imidazole nitrogen may play some role at lower pH, but comparison of the nickel(II) complexes of MeCO–Tyr–Ile–His with those of Asp–Arg–Val–Tyr indicate that the latter peptide forms complexes more readily.

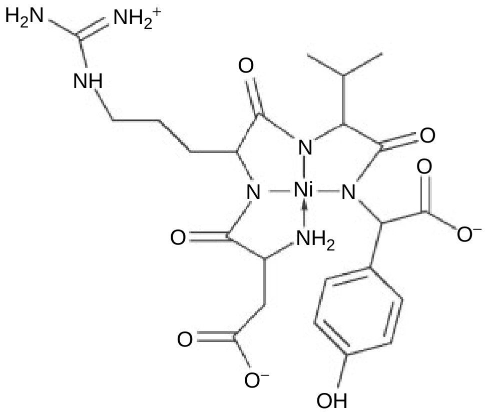

Figure 9 Ni(Asp–Arg–Val–Tyr) 4N complex

4 PALLADIUM–AND PLATINUM–PEPTIDE COMPLEXES

There is considerable interest in the cytotoxic activity of many platinum(II) complexes related to cisplatin $[Cl_2Pt(NH_3)_2]$ (*see* ***Platinum-based Anticancer Drugs***), and several analogs containing peptide ligands have been studied. Since platinum complexes are generally inert to substitution reactions, the palladium(II) analogs are generally used instead. Palladium(II) and platinum(II) complexes are similar to those of nickel(II) in that they all form square planar, four-coordinate complexes (*see* ***Palladium: Inorganic & Coordination Chemistry*** and ***Platinum: Inorganic & Coordination Chemistry***). Unlike copper(II), both palladium(II) and platinum(II) are soft acceptors and as such are expected to coordinate to soft donors like sulfur and aromatic nitrogen donors in residues such as Met and His, and deprotonated peptide nitrogens (*see* ***Hard & Soft Acids and Bases***). Palladium(II) has been found to promote the ionization of peptide hydrogens more easily than copper(II), nickel(II), and cobalt(II). Generally, the pK_a of deprotonation is 3.5,[43] although deprotonation has been observed at pH <2.0.[15] This value is 2, 5, and 7 pK units less than the values for copper, nickel, and cobalt respectively.

At low pH, dipeptides generally coordinate palladium(II) through the deprotonated peptide nitrogen in a monodentate manner. At high pH, the dipeptides act as bidentate ligands, coordinating through the amino nitrogen and the deprotonated peptide nitrogen. At intermediate pH values, dipeptides coordinate through the amino and deprotonated peptide nitrogens and the carboxylate oxygen.[44] Dipeptides in which the N-terminal residue is Met generally bond palladium(II) through the thioether sulfur and amino nitrogen at low pH. At pH values greater than 7, a dinuclear complex is formed where the palladium(II) is bonded via the amino and deprotonated peptide nitrogen, while the sulfur atom coordinates to a neighboring palladium atom. This explains why the deprotonation of the peptide nitrogen occurs at such a high pH. Palladium(II) complexes of the type Pd(Met–X), where X is another amino acid, form bis complexes where at low pH the peptides are bonded through the sulfur and amino nitrogen, while at high pH the palladium is coordinated by four nitrogen atoms.

In the cysteine-containing dipeptides Cys–Gly and Gly–Cys, palladium(II) is bonded by the amino nitrogen and sulfur in the first dipeptide and by the amino nitrogen, deprotonated peptide nitrogen, and sulfur in the second dipeptide.**[46]** This is an example where strong coordination by the thiol group in cysteine can prevent the deprotonation of the peptide nitrogen, even though palladium(II) deprotonates the peptide nitrogens at a low pH. Palladium(II) coordinates to oxygen donors only very weakly; that is why the dipeptide Gly–His coordinates to palladium(II) in a 3N fashion through the amino, deprotonated peptide, and imidazole nitrogens, without coordination through the carboxylate oxygen.**[47]** A recent study on dipeptides which contain protected cysteine residues, Gly–S-Me–Cys, S-Me–Cys–Gly, and S-Me–Cys–S-Me–Cys, show that the S-Me–Cys residue binds through both the amino nitrogen and sulfur, as was seen with just the protected amino acid.**[48]** When the thioether is coordinated, this causes the sulfur to become chiral, and in solution two diastereomers are observed.

The dipeptides Gly–L-His, L-Ala–L-His, and L-Ala–D-His initially form 3N complexes with palladium(II), bonding through the amino, deprotonated peptide, and imidazole nitrogens. When the pH is raised above 9.5, the pyrrole proton is ionized, resulting in a 4N tetramer formation.**[49]**

The tripeptide Gly–L-His–Gly coordinates to palladium(II) via the nitrogen atoms of the amino group, deprotonated peptide, and the imidazole (Figure 10). The coordination of the imidazole nitrogen over the second peptide nitrogen is expected, due to the fact that palladium(II) favors soft donor atoms (like aromatic nitrogens) over harder donor atoms. This same coordination is also seen in the tripeptide Gly–L-His–Lys. The fourth coordination site of this complex is occupied by a chloride ion.**[50]** In the 1:2 palladium(II)–Gly–Gly–L-Cys complex, the palladium is bonded through the amino nitrogen, two deprotonated nitrogens, and the sulfur of the cysteine side chain.**[45]** As the pH is increased to 10.0 and above, the two peptides coordinate the palladium through the amino nitrogen and one deprotonated peptide nitrogen. For the 1:1 complex at pH above 10.0, the palladium–sulfur bond breaks and is replaced by a hydroxide ion.

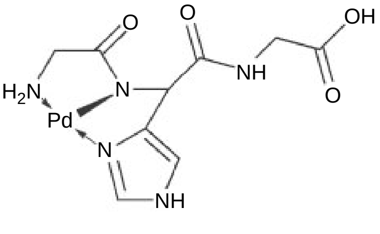

Figure 10 Pd(Gly–L-His–Gly) 3N complex

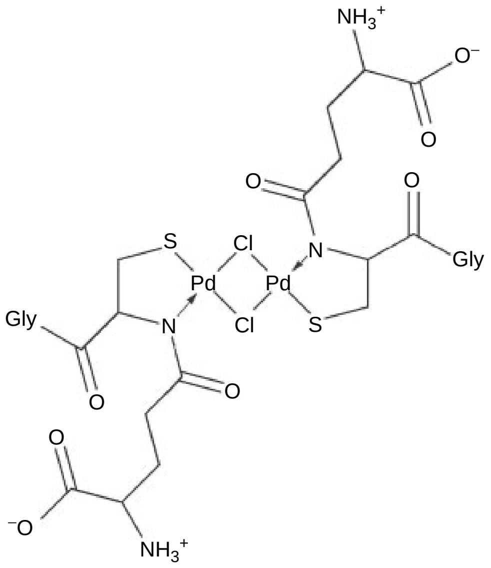

Figure 11 $[Pd(GluH_2)Cl]_2$

Glutathione (γ-Glu–L-Cys–Gly) has a large selection of possible donor atoms with which to complex palladium(II). A palladium–glutathione complex has been isolated with the formula $[Pd(GluH_2)Cl]\cdot 3H_2O$, where $GluH_3{}^+ = {}^+NH_3(CO_2{}^-)CHCH_2CH_2CONHCH(CH_2SH)CONHCH_2CO_2H$.**[51]** The IR spectrum showed a stretch for free CO_2H but no stretch for S–H, which implies coordination by the sulfur. In addition, there was a stretch in the region where a Pd–Cl–Pd bridge would appear. The suggested structure is a dimer with two bridging chlorines (Figure 11). Complexes with the formulae $[PdCl_2(GluH)]^{2+}$ and $[PdCl_2(GluH)_2]^+$ have also been isolated and their stabilities measured.

Palladium(II) and platinum(II) complexes as synthetic peptidases have been reviewed elsewhere.**[52]**

5 ZINC–PEPTIDE COMPLEXES

Zinc(II), unlike copper(II) and nickel(II), does not form very stable complexes with peptides. A study of 12 dipeptides containing the Gly, Ala, Leu, and Pro residues with zinc(II) showed that the only two species formed in detectable quantities were $[ZnLH]^+$ and ZnL_2H_2.**[53]** This is in contrast to copper(II) and nickel(II), in which the major species are $MH_{-1}L$ and $MH_{-3}L$. The main reason for the difference in the type of complexes formed is that zinc(II) does not induce peptide-bond deprotonation as effectively as copper(II) and nickel(II). To allow for deprotonation of the peptide nitrogen, the pH has to be raised above pH 8.0, at which point zinc precipitates out as $Zn(OH)_2$ (*see* ***Zinc: Inorganic & Coordination Chemistry***).

With the dipeptides Ala–His and Gly–His at high pH, zinc(II) was shown to form complexes coordinated through the amino nitrogen, deprotonated peptide nitrogen, and the imidazole nitrogen. However, in dipeptides in which the N-terminus is the His residue, zinc(II) does not cause deprotonation of the peptide nitrogen.[54] The only complexes that are formed are the mono and bis complexes where the dipeptide is coordinated to zinc(II) in a histidine-like fashion (that is, coordination through the amino and imidazole nitrogens only).

The complexes formed when zinc(II) is coordinated to peptides which contain the cysteine residue, depend on the location of the cysteine.[55] The dipeptide Cys–Gly forms mono and bis complexes, with the bis complexes being the most stable. The zinc(II) is coordinated only through the cysteine residue of the dipeptide. The strong cysteine-like coordination via the amino nitrogens and the thiol groups precludes the possibility of amide deprotonation and coordination. When cysteine is the C-terminus in the dipeptide as in Gly–Cys, coordination through the sulfur and nitrogen is not possible due to the formation of an unfavorable eight-membered chelate ring. Coordination through the sulfur and oxygen is possible, with the formation of a more stable six-membered chelate ring. As with the dipeptide Cys–Gly, the bis complexes are the most favored with zinc(II) and Gly–Cys. One of the differences between the two dipeptides is that, with Gly–Cys, no mono complexes were detected. Also, since there is a free amine in the zinc(II)–Gly–Cys complexes, this allows for the formation of the protonated species $ZnLH^+$ at low pH values.

The complexes formed between zinc(II) and the tripeptide His–Gly–His are strongly dependent on pH.[56] At pH >7.5 the major species present is the bis complex in which the tripeptides are bonded via the amino and imidazole nitrogens. At lower pH, the zinc(II) ion coordinates via the amino nitrogen, imidazole nitrogen, and the carbonyl of the peptide linkage. At pH 7.0, zinc(II) forms a mono complex which is coordinated to the tripeptide Gly–His–Lys through the amino nitrogen, deprotonated peptide nitrogen, and the imidazole nitrogen. The amino group on the Lys side chain remains protonated.[57]

Unlike both copper(II) and nickel(II), zinc(II) does not form very strong complexes with LHRH. Studies have shown that, at pH 7.0, only 20% of LHRH is complexed with zinc(II).[58] In addition to binding to the imidazole of the histidine residue, the zinc(II) ion is also weakly coordinated by a carbonyl of a peptide group. NMR studies have indicated that it is the carbonyl oxygen of the His–Trp peptide bond that coordinates the metal ion.

In recent years, there has been a lot of interest in the binding of zinc(II) by the peptide sequence (Tyr, Phe)–X–Cys–$X_{2,4}$–Cys–X_3–Phe–X_5–Leu–His–$X_{3,4}$–His where X is a relatively variable amino acid.[59] This peptide sequence has been termed a *Zinc Finger*. The zinc ion is coordinated tetrahedrally by the two cysteine and histidine residues. Proteins that contain these sequences have been shown to bind to specific sites on nucleic acids (*see* ***Zinc: DNA-binding Proteins***).[59]

6 METAL-MEDIATED HYDROLYSIS OF AMINO ACID ESTERS AND PEPTIDES

Hydrolysis of proteins and peptides is an important reaction in many biological processes. Amide bonds are extremely unreactive, with an estimated half-life for hydrolysis in neutral solution of about 9 years.[60] Hydrolytic procedures in biochemical work usually call for prolonged heating and high concentrations of strong acids or bases, and usually these esters have to first be activated. In the body, however, proteolytic enzymes hydrolyze even unactivated amide bonds rapidly and under mild conditions.[61] Studies have shown that certain proteolytic enzymes require metal ions for activity.[62] This fact has brought the inorganic chemist into the area of peptide-bond cleavage.

Early investigations of metals showed that divalent metals such as copper(II), cobalt(II), and nickel(II) could catalyze the hydrolysis of amino acid esters.[63] It was the work of Buckingham and Collman in the early 1960s that led to the investigation of using cobalt(III) to hydrolyze amino acid residues (*see* ***Cobalt: Inorganic & Coordination Chemistry***).[64] Cobalt(III) was selected because it was believed that if cobalt(III) could chelate the N-terminus of a peptide, it might enhance hydrolysis via direct polarization of the carbonyl oxygen of the peptide linkage, as was seen with the divalent metals. Cobalt(III) should strongly coordinate to the amino nitrogen, and form a favorable five-member chelate ring with the carbonyl oxygen. Unlike copper(II) and nickel(II), cobalt(III) does not induce deprotonation of peptide nitrogens until relatively high pH. This is important since coordination through the peptide nitrogen results in a complex that is more stable toward hydrolysis. Like the divalent metals which were studied early on, cobalt(III) is able to polarize and thus facilitate the reactions of coordinated ligands. The ligands are less labile, so it should be possible to identify reaction intermediates, helping to clearly differentiate various mechanisms.

There has been a lot of research done on cobalt(III)-mediated peptide-bond cleavage.[64] This section will discuss some of the basic features of the reactions and mechanisms. Also, the idea of metal-mediated peptide-bond cleavage will be extended to the relatively new area of metal–chelate mediated peptide-bond cleavage.

Two mechanisms of cobalt(III)-mediated peptide-bond cleavage have been investigated. The first one involves hydrolysis of a directly activated amino acid ester, or peptide (equation 4). The other mechanism involves the intramolecular attack of an amino acid ester or peptide by a *cis* coordinated hydroxide or water molecule (equation 5). In both cases, the cobalt(III) complex must have two open coordination sites *cis* to each other. For the directly activated mechanism, these sites are needed to bind the amino acid ester or peptide. The intramolecular reaction requires one site for coordination of the ester or peptide, and one site for the coordination of the hydroxy or water molecule. One of the initial cobalt(III) complexes to be investigated was $[Co(en)_2(OH_2)(OH)]^{2+}$.[65,66]

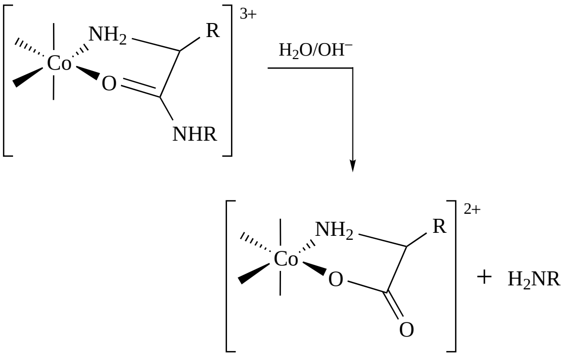

(4)

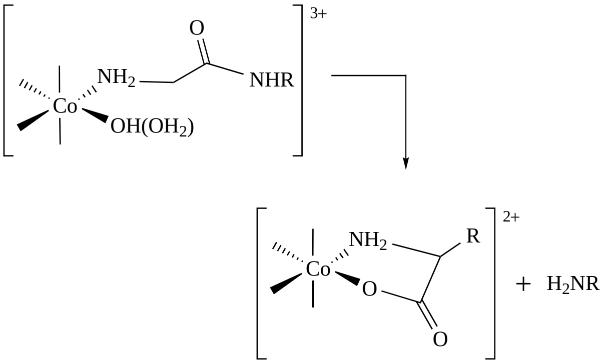

(5)

6.1 Directly Activated Amino Acid Esters

The rate of hydrolysis of esters is dependent upon whether the ester is activated (bound to the metal) or unactivated. For esters that are coordinated to cobalt(III) in a monodentate fashion (Figure 12), the rate of hydrolysis is only accelerated by about 100 times over that of an uncoordinated ester.[67] However, when the ester is coordinated in a bidentate fashion through the amino nitrogen and carbonyl oxygen (Figure 13), the rate of hydrolysis is accelerated by 10^6 times.[64] Compared to hydroxide, water does not cause a large increase in the rate of hydrolysis, and it is 10^{11} times slower.[68]

The hydrolysis reaction has been studied by using ^{18}O-labeled hydroxide. There was no evidence of any ring-opened species. This indicates that the chelate ring remains intact throughout the hydrolysis (equation 6).[69]

$[L_5Co\text{-}NH_2CHRCO_2R]^{3+}$

Figure 12 Monodentate coordination

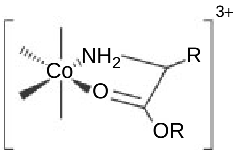

Figure 13 Bidentate coordination

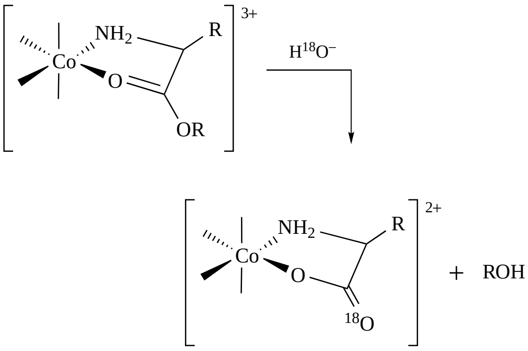

(6)

One of the main questions in the cobalt(III)-promoted hydrolysis of activated amino acid esters is whether the rate-determining step is addition of hydroxide to the carbonyl carbon, or loss of the alkoxide from the intermediate. Work with β-alanine ester showed that below pH 8.5 the rate-determining step was the elimination of alkoxide.[68] At pH 10 and above, the rate-determining step changes and the addition of hydroxide to the activated ester becomes the rate-controlling step. This is due to the fact that above pH 10 the hydroxyl group of the intermediate becomes deprotonated (equation 7). The deprotonation of the hydroxyl group accelerates the loss of alkoxide by 10^5 times.[68]

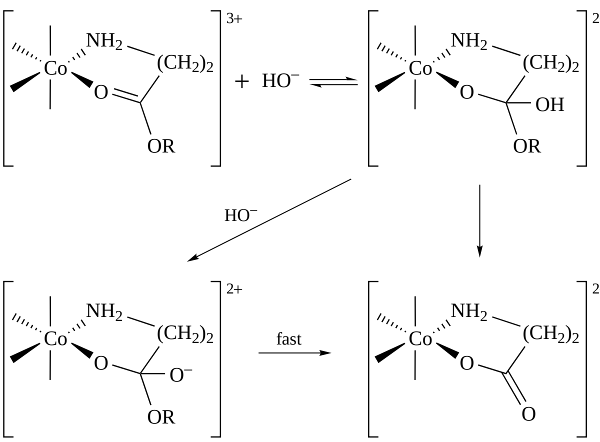

(7)

When amines are substituted for hydroxide as the base, there is no change in the rate of hydrolysis. This is because amines do not catalyze the hydrolysis of amino acid esters; instead they prefer to add directly to the carbonyl carbon to form the corresponding amides. In this reaction the rate-limiting step is not the addition of amine, but rather the deprotonation of the coordinated amine by another base (equation 8). The pK_a of the tetrahedral intermediate is approximately 7 since almost any nonsterically hindered base with a pK_a above 7 can deprotonate it.[64]

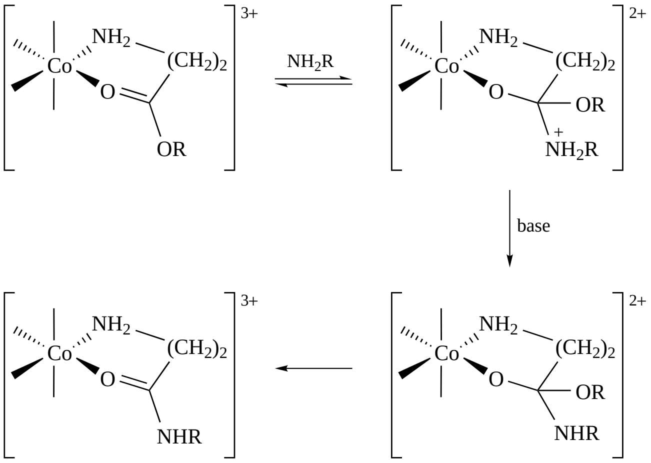

(8)

6.2 Directly Activated Peptides

Owing to the success of cobalt(III)-mediated hydrolysis of amino acid esters, the next step was to examine how these complexes reacted with peptides. If similar hydrolytic results could be obtained with peptides, then one of the potential uses of cobalt(III) complexes would be in the N-terminal determination and sequential analysis of polypeptides. This area has been investigated by several groups.[70] Peptides coordinate to cobalt(III) through the amino nitrogen of the N-terminal amino acid, and carbonyl oxygen of the first peptide linkage. The hydrolysis of peptides goes through a tetrahedral intermediate similar to the hydrolysis of amino acid esters (equation 9). The main difference is that the rate-limiting step in the hydrolysis of peptides is the attack on the peptide carbonyl carbon by hydroxide. This is true at all pH values except for 7.0–8.0, where the loss of hydroxide is comparable to the loss of amine. Above pH 11 the peptide nitrogen is deprotonated, forming a stable imidate which causes the reaction to no longer be first order in hydroxide.[71]

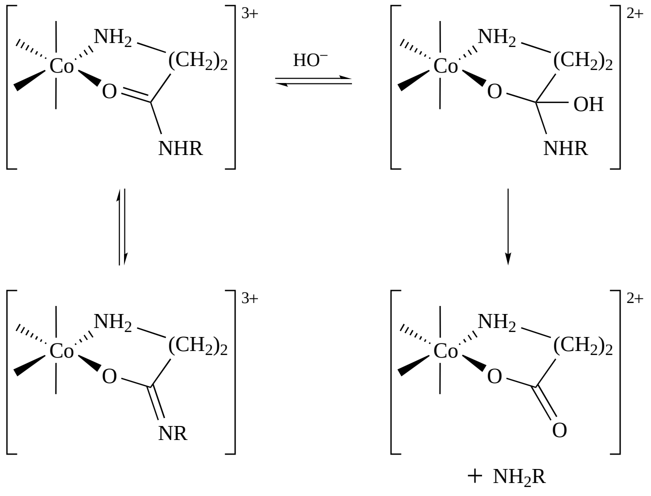

(9)

The rate of hydrolysis of peptides by cobalt(III) complexes is 10^4 times faster than hydrolysis with no metal present.[64] Unlike the hydrolysis of amino acid esters, where the rate of hydrolysis is dependent on how the ester is bonded to the cobalt(III) complex, peptides are hydrolyzed equally if they are bound to the cobalt(III) complex in a monodentate fashion (through the carbonyl oxygen) or in a bidentate fashion (through the amino nitrogen and carbonyl oxygen).

6.3 Intramolecular Hydrolysis of Amino Acid Esters

The second route for hydrolysis of amino acid esters involves water or hydroxide bonded directly to the cobalt(III) complex. Through the use of isotopically labeled oxygen it has been determined that the mechanism of hydrolysis involves an intramolecular attack of the carbonyl oxygen by a *cis* coordinated hydroxy or water molecule (cf. equation 10 for peptide hydrolysis).[72] The most important feature in this mechanism is that the carbonyl carbon must be held in close proximity to the metal center to allow the attack. This importance can be seen in the difference in rate of hydrolysis between glycine and β-alanine. Glycine is a shorter amino acid than β-alanine, and holds the carbonyl carbon in a more favorable position for attack by the hydroxy or water molecule. This results in a 10^3 increase in the rate of hydrolysis over that of β-alanine. In addition, glycine forms a five-membered chelate ring intermediate. The conformation of this ring compared to that of the six-membered chelate ring formed with β-alanine also adds to the increase in hydrolysis rate.

The importance of the ring size in the intramolecular reaction is the opposite from what was seen in the directly activated reaction, where the ring size has almost no effect on the rate of hydrolysis. In addition to the difference ring size plays in the intramolecular reaction, another major difference between the directly activated reaction and the intramolecular reaction is the importance of the buffer. For the directly activated ester reaction the buffer has no effect on the rate of hydrolysis, and in some cases causes a decrease in hydrolysis due to nucleophilic attack of the carbonyl carbon by the buffer. The intramolecular reaction, however, can be greatly affected by the buffer present, with CO_2^{2-} and PO_4^{3-} having the greatest influence.[68]

The hydrolysis of amino acid esters by directly coordinated hydroxy or water molecules is slower than the corresponding reactions involving the directly activated esters. The rate of hydrolysis for coordinated water is 30 times slower, while the rate for coordinated hydroxide is 10^5 times slower.**[64]**

6.4 Intramolecular Hydrolysis of Peptides

The hydrolysis of peptides by coordinated water or hydroxide follows a path similar to that of amino acid esters (equation 10). The rate of hydrolysis is 10^2 times faster for coordinated water compared to coordinated hydroxide.**[73]** As with the hydrolysis of amino acid esters, the attack of the coordinated water or hydroxy group is the rate-limiting step in the hydrolysis of peptides. However, it has been shown that the elimination of the amine group is an important feature in the mechanism.

At acidic to neutral pH, the hydrolysis of a peptide is faster via the attack of a coordinated water or hydroxide relative to that of the directly activated peptide. However, as the pH is raised to 9.0 and above, the hydrolysis of the directly activated peptide becomes the favored route. Also, if the metal binds strongly to the carbonyl oxygen, then the hydrolysis will follow the directly activated mechanism, not the intramolecular mechanism.

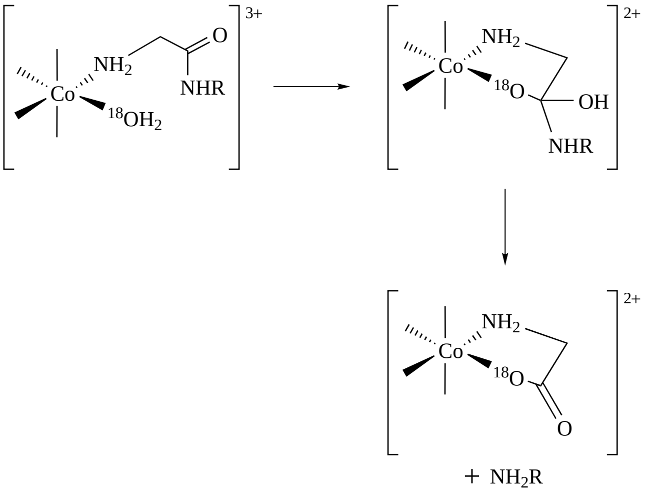

(10)

6.5 Metal–Chelate Mediated Peptide Hydrolysis

Because cobalt(III) complexes bind to the N-terminal amino acid residue of peptides, only the N-terminal peptide bond is hydrolyzed. It would be advantageous if the metal complex could coordinate to various parts of a peptide chain, thus allowing for cleavage of other areas of the peptide chain. Recently this has become an active area of research, and there have been several publications on the cleavage of the polypeptide backbone of proteins promoted by metal complexes.**[74–78]** The advantage that these complexes have over the cobalt(III) complexes is that they can be selectively introduced on to various amino acid side chains, allowing for cleavage of peptide bonds at locations other than the N-terminus. This is of interest because, by selectively incorporating the metal chelate on to the polypeptide backbone of a protein, it may be possible to learn structural features of the protein by analysis of the cleavage products.

One such experiment involved the introduction of an iron chelate on to a unique residue on the protein human carbonic anhydrase I (HCAI).**[77]** By labeling the free SH group of Cys-212 of HCAI with (*p*-bromoacetamidobenzyl)EDTA, in which the EDTA was loaded with iron(II), the HCAI peptide backbone was cleaved in one place. The cleavage takes place in the presence of ascorbate and hydrogen peroxide. It is believed that the mechanism for cleavage is by nucleophilic attack of an iron-coordinated peroxo group at the carbonyl carbon. This is similar to the hydrolysis of peptides by coordinated water or hydroxide.

The peptide bond that is cleaved is the bond between Leu-189 and Asp-190. There are two peptide bonds in close proximity to the iron chelate on Cys-212. The other peptide bond is between Ile-144 and Gly-145. The Cys-212 sulfur is 5.1 Å from the carbonyl carbon of Gly-145, and 5.3 Å from the carbonyl carbon of Leu-189. However, the main difference is that the peptide bond of Leu-189–Asp-190 is oriented parallel to Cys-212, while the peptide bond of Ile-144–Gly-145 is oriented away for Cys-212. As was seen with cobalt(III) hydrolysis of peptide bonds, the proximity and orientation of the carbonyl carbon is important for hydrolysis. This approach has been extended to the cleavage of multisubunit proteins.**[79]** Palladium(II) and platinum(II) complexes as synthetic peptidases have been reviewed elsewhere.**[52]**

7 RELATED ARTICLES

Ammonia & N-donor Ligands; Cobalt: Inorganic & Coordination Chemistry; Copper: Inorganic & Coordination Chemistry; Nickel: Inorganic & Coordination Chemistry; Palladium: Inorganic & Coordination Chemistry; Platinum: Inorganic & Coordination Chemistry; S-donor Ligands; Stability Constants & their Determination; Zinc: DNA-binding Proteins; Zinc: Inorganic & Coordination Chemistry.

8 REFERENCES

1. G. Wiedmann, *Annals.*, 1848, **68**, 323.
2. H. Schiff, *Annals.*, 1907, **73**, 352.
3. P. A. Kober and K. Sigiura, *Am. Chem. J*, 1912, **48**, 383.
4. P. A. Kober and A. B. Haw, *J. Am. Chem. Soc.*, 1916, **38**, 457.
5. M. M. Rising, F. M. Parker, and D. P. Gaston, *J. Am. Chem. Soc.*, 1934, **56**, 1178.

6. J. Chouteau, *C. R. Acad. Sci. Paris*, 1951, **232**, 3314.
7. H. Dobbie and W. C. Kermack, *Biochem. J.*, 1955, **59**, 257.
8. C. B. Murphy and A. E. Martell, *J. Biol. Chem.*, 1957, **37**, 226.
9. W. L. Koltun, M. Fried, and F. R. N. Gurd, *J. Am. Chem. Soc.*, 1960, **82**, 233.
10. H. Sigel and R. B. Martin, *Chem. Rev.*, 1982, **82**, 385.
11. (a) R. B. Martin, *J. Chem. Soc., Chem. Commun.*, 1972, 750; (b) R. B. Martin and W. C. Hutton, *J. Am. Chem. Soc.*, 1973, **95**, 4752.
12. R. A. McClelland and W. F. Reynolds, *J. Chem. Soc., Chem. Commun.*, 1972, 824.
13. W. Egan, T. E. Bull, and S. Gorgen, *J. Chem. Soc., Chem. Commun.*, 1972, 1096.
14. A. M. Armbrustrer and A. Pullman, *FEBS Lett.*, 1974, **49**, 20.
15. (a) H. Sigel and R. B. Martin, *Chem. Rev.*, 1982, **82**, 385; (b) S. H. Laurie, in ‘Comprehensive Coordination Chemistry’, ed. G. Wilkinson, Pergamon Press, Oxford, 1972, Vol. 2, p. 739.
16. L. D. Pettit, J. E. Gregor, and H. Kozlowski, in ‘Perspectives on Bioinorganic Chemistry’, eds. R. W. Hay, J. R. Dilworth, and K. B. Nolan, JAI Press, London, 1991 and references therein.
17. L. L. Diaddario, M. R. Robinson, and D. W. Margerum, *Inorg. Chem.*, 1983, **21**, 1021.
18. D. W. Margerum, *Pure Appl. Chem.*, 1983, **55**, 23.
19. M. R. Udupa and B. Krebs, *Inorg. Chim. Acta*, 1978, **31**, 251.
20. W. S. Kittl and B. M. J. Rode, *J. Chem. Soc., Dalton Trans*, 1983, 409.
21. R. B. Martin, in ‘Metal Ions in Biological Systems’, ed. H. Sigel, Marcel Dekker, New York, 1974, Vol. 1.
22. H. Sigel, *Inorg. Chem.*, 1975, **14**, 1535.
23. S. P. Datta and B. R. Rubin, *Trans. Faraday Soc.*, 1956, **52**, 1117.
24. L. Xiao, M. Jouini, B. T. Fan, G. Lapluye, and J. Huet, *J. Chem. Soc., Dalton Trans*, 1990, 1137.
25. M. Bataille, L. D. Pettit, I. Steel, H. Kozlowski, and T. Tatarowski, *J. Inorg. Biochem.*, 1985, **24**, 211.
26. K. Gerega, H. Kozlowski, E. Masiukiewicz, L. D. Pettit, S. Pyburn, and B. Rzeszotarska, *J. Inorg. Biochem.*, 1988, **33**, 11.
27. G. Formicka-Kozlowska, M. Bezer, and L. D. Pettit, *J. Inorg. Biochem.*, 1983, **18**, 335.
28. I. Sovago, E. Farkas, and A. Gagely, *J. Chem. Soc., Dalton Trans*, 1982, 2159.
29. B. Decock-LeReverend, F. Liman, C. Livera, L. D. Pettit, S. Pyburn, and H. Kozlowski, *J. Chem. Soc., Dalton Trans*, 1988, 887.
30. M. Maruyama, T. Kumagai, Y. Matoba, M. Hayashida, T. Fujii, Y. Hata, and M. Sugiyama, *J. Biol. Chem.*, 2001, **276**, 9992.
31. A. Gergely and E. Farkas, *J. Chem. Soc., Dalton Trans*, 1982, 381.
32. B. Decock-LeReverend, L. Andrianarijaona, C. Livera, L. D. Pettit, I. Steel, and H. Kozlowski, *J. Chem. Soc., Dalton Trans*, 1986, 2221.
33. G. Formicka-Kozlowska, L. D. Pettit, I. Steel, B. Hartrodt, K. Neubert, P. Rekowski, and G. Kupryszewski, *J. Inorg. Biochem.*, 1984, **22**, 155.
34. H. Kozlowski, B. Radomska, G. Kupryszewski, B. Lammek, C. Livera, L. D. Pettit, and S. Pyburn, *J. Chem. Soc., Dalton Trans*, 1989, 173.
35. K. Varnagy, H. Kozlowski, I. Sovago, T. Kowalik-Jankowska, M. Kruszynski, and J. Zboinska, *J. Inorg. Biochem.*, 1988, **34**, 83.
36. (a) R. B. Martin, in ‘Metal Ions in Biological Systems’, eds. H. Sigel and A. Sigel, Marcel Dekker, New York, 1988, Vol. 23; (b) S. F. Schadler, C. Sharp, and A. G. Lappin, *Inorg. Chem.*, 1992, **31**, 51.
37. H. Kozlowski, B. Decock-LeReverend, D. Ficheux, C. Loucheux, and I. Sovago, *J. Inorg. Biochem.*, 1987, **29**, 187.
38. K. Cherifi, B. Decock-Le Reverend, K. Varnagy, T. Kiss, I. Sovago, C. Loucheux, and H. Kozlowski, *J. Inorg. Biochem.*, 1990, **38**, 69.
39. E. Farkas and A. Gergely, *J. Chem. Soc., Dalton Trans*, 1983, 1545.
40. P. J. Morris and R. B. Martin, *J. Inorg. Nucl. Chem.*, 1971, **33**, 2913.
41. T. Salonria and A. Nakahara, *Inorg. Chem.*, 1980, **19**, 847.
42. L. D. Pettit, S. Pyburn, H. Kozlowski, B. Decock-LeReverend, and F. Liman, *J. Chem. Soc., Dalton Trans*, 1989, 1471.
43. E. W. Wilson and R. B. Martin, *Inorg. Chem.*, 1970, **9**, 528.
44. S. Kasselouri, A. Garoufis, and M. Lamera-Hadjiliadis, *Coord. Chem. Rev.*, 1990, **104**, 1.
45. B. Jezowska-Trzebiatowska, T. Kowalik, and H. Kozlowski, *Bull. Acad. Pol. Sci.*, 1978, **26**, 223.
46. T. Kowalik, H. Kozlowski, and B. Decock-LeReverend, *Inorg. Chim. Acta*, 1982, **67**, L39.
47. D. L. Rabenstein, A. A. Isaab, and M. M. Shoukry, *Inorg. Chem.*, 1982, **21**, 3234.
48. B. Decock-LeReverend, C. Loucheux, T. Kowalik, and H. Kozlowski, *Inorg. Chim. Acta*, 1983, **78**, 31.
49. L. R. Pettit and M. Bezer, *Coord. Chem. Rev.*, 1985, **61**, 97 and references therein.
50. J. Laussac, P. Pasdeloup, and M. Hadjiliads, *J. Inorg. Biochem.*, 1987, **30**, 227.
51. S. T. Chow, C. A. McAuliffe, and B. J. Sayle, *J. Inorg. Nucl. Chem.*, 1975, **37**, 451.
52. N. M. Milovic and N. M. Kostic, *Met. Ions Biol. Sys.*, 2001, **38**, 145.
53. W. S. Kill and B. M. Rode, *Inorg. Chim. Acta*, 1982, **63**, 47.
54. B. Radomska, T. Kiss, and I. Sovago, *J. Chem. Res. (S)*, 1987, 156.
55. I. Sovago, T. Kiss, K. Varnagy, and B. Decock-Le Reverend, *Polyhedron*, 1988, **7**, 1089.

56. J. Ueda, A. Hanaki, N. Yoshida, and T. Nakajima, *Chem. Pharm. Bull.*, 1985, **33**, 3096.
57. S. A. Daignault, A. P. Arnold, A. A. Isab, and D. L. Rabenstein, *Inorg. Chem.*, 1985, **24**, 3984.
58. B. Wojciech, H. Kozlowski, E. Masiukiewicz, B. Rzeszotarska, and I. Sovago, *J. Inorg. Biochem.*, 1989, **37**, 135.
59. B. A. Krizek, B. T. Amann, V. J. Kilfoil, D. L. Merkle, and J. M. Berg, *J. Am. Chem. Soc.*, 1991, **113**, 4518 and references therein.
60. D. Kahne and W. C. Still, *J. Am. Chem. Soc.*, 1988, **110**, 7529.
61. A. Fersht, ‘Enzyme Structure and Mechanism’, 2nd edn., Freeman, New York, 1985, p. 405.
62. B. W. Matthews, *Acc. Chem. Res.*, 1988, **21**, 333.
63. H. Krell, *J. Am. Chem. Soc.*, 1952, **74**, 2036.
64. P. A. Sutton and D. A. Buckingham, *Acc. Chem. Res.*, 1987, **20**, 357 and references therein.
65. J. P. Collman and D. A. Buckingham, *J. Am. Chem. Soc.*, 1963, **85**, 3039.
66. D. A. Buckingham and J. P. Collman, *Inorg. Chem.*, 1967, **6**, 1803.
67. D. A. Buckingham, D. M. Foster, and A. M. Sareson, *J. Am. Chem. Soc.*, 1969, **91**, 3451.
68. E. Baraniak, D. A. Buckingham, C. R. Clark, B. H. Meynihan, and A. M. Sargeson, *Inorg. Chem.*, 1986, **25**, 3466.
69. D. A. Buckingham, D. M. Foster, and A. M. Sargeson, *J. Am. Chem. Soc.*, 1968, **90**, 6032.
70. (a) E. Kimura, *Inorg. Chem.*, 1974, **13**, 951; (b) K. W. Bentley and E. K. Creaser, *Inorg. Chem.*, 1974, **13**, 1115.
71. D. A. Buckingham, C. E. Davis, D. M. Foster, and A. M. Sargeson, *J. Am. Chem. Soc.*, 1970, **92**, 5571.
72. D. A. Buckingham, D. M. Foster, and A. M. Sargeson, *J. Am. Chem. Soc.*, 1969, **91**, 4105.
73. C. J. Boreham, D. A. Buckingham, and R. R. Keene, *J. Am. Chem. Soc.*, 1979, **101**, 1409.
74. T. M. Rana and C. F. Meares, *J. Am. Chem. Soc.*, 1990, **112**, 2457.
75. A. Schepartz and B. Cuenoud, *J. Am. Chem. Soc.*, 1990, **112**, 3247.
76. D. Hoyer, H. Cho, and P. G. Schultz, *J. Am. Chem. Soc.*, 1990, **112**, 3249.
77. T. M. Rana and C. F. Meares, *J. Am. Chem. Soc.*, 1991, **113**, 1859.
78. T. M. Rana and C. F. Meares, *Proc. Natl. Acad. Sci. U.S.A.*, 1991, **88**, 10578.
79. S. A. Datwyler and C. F. Meares, *Trends Biochem. Sci.*, 2000, **25**, 408.

Periodic Table: Trends in the Properties of the Elements

G. P. Wulfsberg
Middle Tennessee State University, Murfreesboro, TN, USA

1 Introduction 1
2 Periodic Trends in Fundamental Atomic Properties 2
3 Acid–Base Reactivity of Ions of the Elements 3
4 Solubility and Complex-Ion Formation Tendencies of Metal Ions 5
5 Redox Reactivity of Elements and Their Ions 8
6 Physical Properties of Elements, Compounds, and Materials 10
7 Chemical Properties of Compounds 13
8 Conclusions 13
9 References 13

Glossary

Maximum total coordination number: the highest value of the total coordination number of the central atom likely to be encountered in a given period: for example, four in the second period

Penultimate total coordination number: the next-to-highest value of the total coordination number of the central atom likely to be encountered in a given period: for example, three in the second period

See also definitions of terms italicized in Tables 1 and 7

Total coordination number: the total number of atoms (and unshared electron pairs, if in the p-block) around a central atom

Abbreviations

HSAB = hard–soft acid–base (principle); HA = hard acid; HB = hard base; SA = soft acid; SB = soft base; χ_P = Pauling electronegativity; χ_{AR} = Allred–Rochow electronegativity; ΔH_{hyd} = hydration energy; ΔH_{atom} = atomization energy; $\Delta H(\mathrm{A{-}A})$ = bond dissociation energy of the bond between two atoms of element A; IE = ionization energy; pK_a = negative of the logarithm of the acid dissociation constant; pK_b = negative of the logarithm of the base dissociation constant.

1 INTRODUCTION

Inorganic chemistry is a field taught by inorganic chemists, largely for inorganic chemists, even though its content is also of serious interest to scientists in many allied fields of chemistry and science in general (e.g. analytical chemistry, biochemistry and medicinal chemistry, environmental science, agricultural and geochemistry, industrial chemistry and safety, metallurgy, materials science, surface chemistry). Students and research workers in these allied fields, who have limited time to take chemistry courses, find too little material they can profitably use in the typical one-semester Advanced Inorganic Chemistry course. A recent survey[1] shows that such courses in the United States place special emphasis on topics of relatively little use to such nonspecialists: symmetry and group theory, molecular orbital theory, and organometallic chemistry. Little time is spent on some areas that would meet their needs: redox chemistry and aqueous descriptive chemistry (and this limited coverage is diminishing with time). Some areas that are potentially useful to them are allocated little time, but are receiving increasing emphasis: bioinorganic and materials chemistry. Earlier we wrote a textbook which had, as one of its objectives, to capture the interest of, and serve students in, those allied sciences;[2] later we expanded it to cover these interests as well as the topics traditionally covered in an Advanced Inorganic Chemistry course for chemistry majors.[3] (When the French edition of the latter text appeared,[4] it was marketed specifically for an applied group, engineering students.)

It is, of course, challenging to present a generally useful survey of inorganic chemistry that is concise enough to serve chemistry majors and also fit into the curricula of nonspecialists: one must make potentially arguable choices on what to cover, how to cover it, and to what depth. We chose to look at a selection of inorganic reaction categories and property types that are broadly useful for diverse students. Great advances were made in the teaching of organic chemistry when it first began to focus on one type of chemical reactivity in one class of compounds (e.g. addition reactions of alkenes) at a time. The approach described here similarly looks at a given type of physical property or chemical reaction of a given class of inorganic species (e.g. trends in the acid–base reactivity of cations of all elements) across the entire periodic table at once.

The article then explains the periodic trends using the most accessible and generally applicable types of inorganic concepts. The most broadly applicable of all inorganic concepts is that of the periodic table and of chemical periodicity. The periodic table can be compared to a forest: it is a beautiful whole, which when examined more closely, consists of various zones (blocks of the periodic table), then further consists of a number of trees (18 or 32 groups), which each have components (elements). Unfortunately its complete study takes too much time for nonspecialists. Many presentations of the useful descriptive material are organized by groups of the periodic table (looking at the trees). But, considering that nonspecialists might then not be able to see the forest for the trees, we have attempted to see how much could be learned looking at the periodic table as a whole (a forest). This article attempts a brief summary of this way of looking at useful inorganic chemistry through the periodic table as a whole.

The physical and chemical property types considered can be grouped broadly into five categories familiar to the student from the General Chemistry course: acid–base reactivity, coordination chemistry, precipitation reactivity, redox reactivity, and physical properties. The inorganic species studied begins with the most important class of all for many applied fields: the ions of the elements (monatomic at first, then polyatomic ions such as oxo anions (*see Oxoanion*), and then complex ions). We begin with the acid–base reactivity of ions: trends in the reactivity of all monatomic cations with water to form hydrated cations, followed by their hydrolysis to give acidic solutions. This trend is examined for all of the approximately 150 known simple cationic forms of the elements, regardless of the block, period, or group in which they are found, since many important properties such as these do vary smoothly and predictably across the periods, groups, and blocks of the periodic table.

One of the goals of our first textbook[2] was to apply Occam's Razor to the proliferation of theories and rationalizations taught in the early study of inorganic chemistry: we strove to make do with the minimum number of theories and periodic trends in atomic properties necessary to explain and organize adequately the numerous physical properties and reactivity types covered. Many periodic trends can be simply related to just three atomic properties: the ionic radius (r) (*see Crystallographic Radius*), the charge (Z), and the Pauling electronegativity (χ_P, *see Electronegativity*) of the element in the ion. Other more sophisticated theories and properties become necessary from time to time, such as electron configurations, relativistic effects (*see Relativistic Effects*), ligand field (*see* ***Ligand Field Theory & Spectra***) and molecular orbital (*see* ***Molecular Orbital Theory***) theories, symmetry, and so on; these are included as needed in the text, but will not be described here.

2 PERIODIC TRENDS IN FUNDAMENTAL ATOMIC PROPERTIES

Since so much can be predicted or at least rationalized on the basis of the periodicity of a few simple atomic properties, especially Pauling electronegativity, size, and charge (or oxidation number) (*see Oxidation Number*) of the atoms or ions involved, we begin by looking at these trends in some detail (beyond that done in General Chemistry courses) and then look into the physical reasons for the periodic trends in these properties.

In probing the broad and finer trends of periodicity in these properties, we have found it advantageous to use the calculations of the effective nuclear charges of atoms, Z^*, as predicted by Slater's rules. Even though much more accurate calculations have since been done, Slater's rules have the advantage of having been verbalized as rules; hence they can be explained in terms of the shielding and penetration of atomic orbitals, which can in turn be understood in terms of the radial extension and nodal properties of atomic orbitals. Periodic trends in radii, for example, can be rationalized using the old Bohr equation for the radius of the orbit of an electron (even though the absolute values of radii obtained from this equation are poor):

$$r = \frac{a_0(n^*)^2}{Z^*} \tag{1}$$

Appropriate calculations using this equation (in which n^* is the effective principal quantum number of the orbital, also given by Slater's rules) reproduce the main horizontal and vertical periodic trends in ionic or covalent radii (*see Covalent Radii*), and illustrate the scandide contraction that follows the filling of the first set of d orbitals. The calculations do not catch the effects of the lanthanide contraction (*see Lanthanide Contraction*, but this is due to the fact that Slater, in pursuit of simplicity, did not write any rules to catch the poor shielding effects of inner f orbitals. A modification of Slater's rule 4 to give ($n-2$)f orbitals poorer shielding effects of 69% rather than the previous 100% has been proposed recently.[5] Slater's rules are based on nonrelativistic calculations, and so do not capture relativistic effects;[6–8] for example, the relativistic contraction of s orbitals with many inner lobes in very heavy atoms, in which the electrons are accelerated to near the speed of light, become more massive, and hence contract in radius. They also cannot include crystal or ligand field effects on d orbitals, which influence a number of properties in substances not traditionally thought of as complexes.

Slater's rules have these limitations, but are easily used to predict trends in electronegativities using the equation that gives Allred – Rochow electronegativities:

$$\chi_{AR} = \frac{3590(Z^* - 0.35)}{r_{cov}^2 + 0.74} \tag{2}$$

In most parts of the periodic table, Allred – Rochow electronegativities match Pauling electronegativities well; hence, trends in effective nuclear charges and shielding can be used to explain the main periodic trends in Pauling electronegativities, as well as the effect of the scandide contraction. Since Allred – Rochow electronegativities do not capture the effect of the lanthanide contraction, relativistic effects, or crystal-field effects, they are low in parts of the d-block and, in particular, in much of the sixth period, but modifications recently proposed[5] give substantially higher values for post-lanthanide elements such as Tl. Gold has the largest discrepancies between its Allred – Rochow and Pauling electronegativities ($\chi_{AR} = 1.44$; $\chi_P = 2.54$) since relativistic effects reach a maximum at the element.

Pauling electronegativities are based on experimental properties: bond energies and heats of formation, which are affected by the lanthanide contraction, crystal-field effects, and relativistic effects. Many other electronegativity scales are based on nonrelativistic calculations or properties that cannot be accurately determined for heavy atoms. Since we desire to correlate electronegativity with experimental properties of elements across all of the periodic table, including the heavy elements near gold, we have chosen to emphasize correlations with the Pauling scale of electronegativities; many other electronegativity scales give much poorer correlations with important periodic chemical trends. This is because many electronegativity scales do not correlate well with each other beyond the s and lighter p elements. Since each electronegativity scale is based on a different physical property with different problems of measurement or interpretation, and uses a different interpretation of Pauling's original definition of electronegativity, we suggest that 'electronegativity' is not one concept but is a family of related, but distinct concepts.

Besides charge, size, and Pauling electronegativity, other parameters such as valence electron configurations of atoms and ions are also important in predicting the periodicity of chemical properties. Since ions are more important than isolated gaseous atoms for nearly all atoms, and important ions have no anomalous electron configurations, there is little reason to worry students with anomalous electron configurations of atoms: we prefer to teach 'characteristic' electron configurations without anomalies in the occupancies of d and s orbitals in the transition elements or d, s, and f orbitals in the inner transition elements. Such characteristic electron configurations are most easily arrived at by considering the f-block of elements to begin with La and Ac and end with Yb and No, allowing Lu and Lr to be members of group 3 of the d-block, an adjustment of the periodic table that has been advocated on several chemical and physical grounds.[9–13]

3 ACID–BASE REACTIVITY OF IONS OF THE ELEMENTS

The first and most fundamental reaction of cations in the most common solvent, water, is the formation of hydrated ions; Latimer[14] gave an equation relating ΔH_{hyd} for this reaction to the charge and size of the cation, which we have updated to be compatible with the Shannon – Prewitt ionic radii in pm:

$$\Delta H_{\text{hyd}} = \frac{-60\,900 Z^2}{(r + 50)\ \text{kJ mol}^{-1}} \tag{3}$$

It is clear that the electronegativity of the cation also has an influence, but this has not been quantified.

Subsequently hydrated ions react as Lewis acids with solvent water molecules:

$$[\text{M(H}_2\text{O)}_6]^{z+} + \text{H}_2\text{O} \rightleftharpoons [\text{M(H}_2\text{O)}_5\text{(OH)}]^{(z-1)+} + \text{H}_3\text{O}^+ \tag{4}$$

This reaction and the corresponding one for anions turn out to be useful prototypes for a number of Lewis acid properties of fundamental importance in aquatic chemistry, bioinorganic chemistry, and inorganic chemistry itself. Six broadly applicable categories of the acid–base reactivity of cations and anions have been defined (Table 1):

Adding a soluble salt of a strongly or very strongly acidic cation to water can produce dramatic effects, as illustrated in a recently produced discovery video.[15] One of the most elementary applications of these categories and pK (*see Acidity Constants*) ranges is in predicting the pH conditions under which the cation or anion actually exist (and is the predominant form) in aqueous solutions (such as natural waters). To a rough approximation (neglecting effects such as those due to variations in concentrations), a cation will predominantly exist as the hydrated ion at pH values up to the pK_a of the cation; above a pH roughly equal to the pK_a of the cation, the hydroxide or oxide of the cation will predominate (and normally will precipitate). Correspondingly, an anion will predominate in hydrated forms at pOH values up to the pK_b of the anion; above that pOH (below the corresponding pH) the anion will mainly be protonated. Thus, nonacidic cations such as K^+ predominate at all pHs up to about 14, that is, at all practical pHs. Nonbasic anions such as Cl^- predominate at all pHs down to 0. The protonated form of Cl^-, HCl, is not the predominant form at any practical pH. In contrast, very strongly acidic cations such as 'P^{3+}' predominate only at pHs somewhere below −4, and very strongly basic anions such as O^{2-} predominate only somewhere above a pH of 18: these 'ions' are too reactive to exist in water.

These categories are useful for understanding the kinetics of exchange reactions (less acidic cations tend to exchange water or other ligands more rapidly), environmental persistence, and nutritional availability (*see* ***Nutritional Aspects of Metals & Trace Elements***). Thus, natural waters polluted by acid rain may have pHs as low as 2 or 3; in such waters and only in such waters do moderately acidic cations such as Fe^{3+} and

Table 1 Categories of acid–base reactivity

An ion is *nonacidic* or *nonbasic* if its pK_a or pK_b exceeds 14.
An ion is *feebly acidic* or *feebly basic* if its pK_a or pK_b lies between 11.5 and 14.
An ion is *weakly acidic* or *weakly basic* if its pK_a or pK_b lies between 6 and 11.5.
An ion is *moderately acidic* or *moderately basic* if its pK_a or pK_b lies between 1 and 6.
An ion is *strongly acidic* or *strongly basic* if its pK_a or pK_b lies between −4 and +1.
An ion is *very strongly acidic* or *very strongly basic* if its pK_a or pK_b is below −4.

Al^{3+} become predominant (through dissolution of $Fe(OH)_3$, etc.); the toxic effects of acid rain involve the leaching of such metal ions into the water. Correspondingly, the widespread nature of iron deficiency is related to the precipitation of the moderately acidic Fe^{3+} ion at the pHs found in the intestine.

The categories and pK values in Table 1 are related to the charge, size, and electronegativity (if it exceeds 1.50) of the cation:

$$\mathrm{p}K_a = 15.14 - 88.16\left[\frac{Z^2}{r + 0.096(\chi_P - 1.50)}\right] \tag{5}$$

In this relationship, the acidity is determined primarily by the charge-to-size ratio, Z^2/r, which is a useful way of characterizing the approximately 150 monatomic cations from across the periodic table (Table 2, Figure 1).

The basicity categories of Table 1 can not only be applied to simple monatomic anions (of which there are relatively few) but also to the far more abundant and practically important oxo anions (*see Oxoanion*) $MO_x{}^{y-}$; for the latter, the categories can be predicted from the number of oxo groups present, x, and the number of units of negative charge, y:

$$\mathrm{p}K_b \text{ of } MO_x{}^{y-} = 10.0 + 5.7x - 10.2y \pm 1 \tag{6}$$

Increasing the negative charge of an anion increases its basicity, while increasing the number of oxo groups decreases its basicity (since this increases the size and the number of electronegative atoms in the anion). Monatomic and oxo anions can thus be classified as in Table 3.

It is straightforward, using the concepts of conjugate acids and bases, to derive the familiar principles for the relative strengths of the oxo acids (*see Acids & Acidity*). Since these have no charge, their acidity depends only on the number of oxo groups (x in the formula $(HO)_yMO_x$): oxo acids with three oxo groups are very strong acids; those with two oxo groups are strong acids, those with one oxo group are moderately acidic, and those without oxo groups are (at best) weakly acidic.

Table 2 Acidity categories of metal ions[a]

Nonacidic cations have Z^2/r ratios *below 0.01*; examples include Na^+ through Cs^+, R_4N^+, and most complex cations.
Feebly acidic cations have Z^2/r ratios *between 0.01 and 0.04*, and include most +2 ions of the s and f-blocks.
Weakly acidic cations have Z^2/r ratios *between 0.04 and 0.10*, and include most +2 ions of the d-block and +3 ions of the f-block.
Moderately acidic cations have Z^2/r ratios *between 0.10 and 0.16*, and include most +3 ions of the d-block and +4 ions of the f-block.
Strongly acidic cations have Z^2/r ratios *between 0.16 and 0.22*, and include most +4 ions of the d-block.
Very strongly acidic cations have Z^2/r ratios *above 0.22*, and include the 'cations' of the nonmetals.

[a] Radius in pm; if the electronegativity of the metal exceeds 1.8, it is moved up one category in acidic strength.

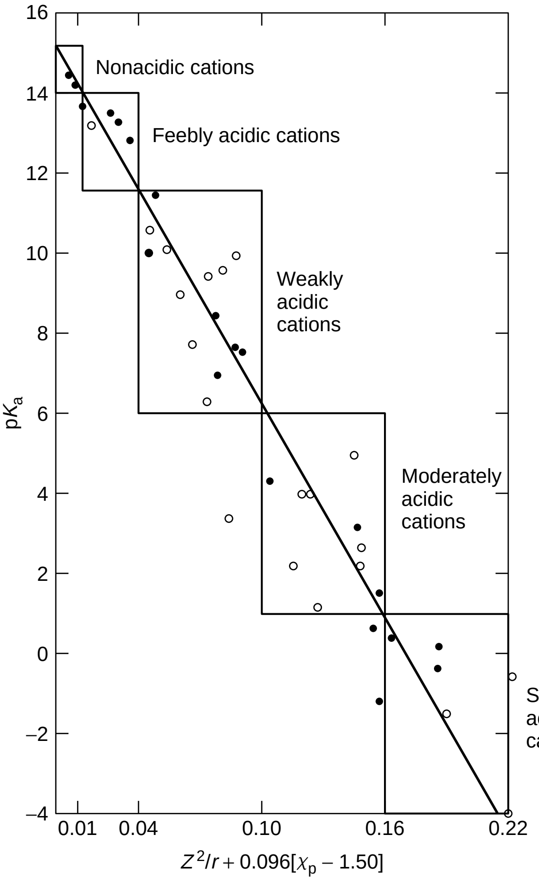

Figure 1 pK_a values of cations as a function of charge, size, and electronegativity. Closed circles equal metals of electronegativity (χ_P) less than 1.5, plotted as a function of Z^2/r. Open circles equal metals of electronegativity greater than 1.5, plotted as a function of $Z^2/r + 0.096(\chi_P - 1.50)$. (Ref. 3. Reproduced by permission of University Science Books)

Table 3 Basicity categories of anions

Nonbasic anions include Cl^-, Br^-, I^-, and oxo anions for which p$K_b > 14$ (e.g. $ClO_4{}^-$, $NO_3{}^-$), and most other complex anions.
Feebly basic anions include F^- and oxo anions for which $11{-}11.5 < \mathrm{p}K_b < 14$ (e.g. $SO_4{}^{2-}$, $NO_2{}^-$).
(*Weakly basic anions* are few; they fall at the margins of this category and have no clear special properties, so we do not usually invoke this category, transferring F^- and $MO_2{}^-$ to the feebly basic category, which they almost fit, and $MO_3{}^{2-}$ to the moderately basic category, which it almost fits.)
Moderately basic anions include Te^{2-} and oxo anions for which $1 < \mathrm{p}K_b < 6$ (e.g. $PO_4{}^{3-}$, $CO_3{}^{2-}$).
(*Strongly basic anions* are few, marginal, and have no clear special properties, so we do not usually invoke this category.)
Very strongly basic anions cannot exist as such in water, but must be (at least partially) protonated; this category includes O^{2-}, N^{3-}, and oxo anions for which p$K_b < -4$ (e.g. $SiO_4{}^{4-}$).

The formulas of oxo anions are seemingly aperiodical (e.g. $CO_3{}^{2-}$, $SiO_4{}^{4-}$, $SnO_6{}^{8-}$) but have profound effects: carbonate minerals bear no structural relationship to silicate minerals.

Fortunately the chemical formulas can be rationalized on the basis of the size of the central atoms involved; it is not necessary to memorize their formulas! In general, second-period atoms are limited to a maximum total coordination number (the total coordination number counts unshared electron pairs in the p-block) of four; third and fourth-period atoms can have maximum total coordination numbers of six; fifth and sixth-period atoms can exceed a total coordination number of six. These observations explain the hydrolytic inertness (and persistence in the atmosphere) of compounds such as CF_4 and SF_6, which contain very strongly acidic 'cations'; they also explain why the formulas of fluoro anions vary (e.g. BF_4^- in period 2; AlF_6^{3-} in period 3; WF_8^{2-} in period 6). Evidently, because of the influence of π bonding to oxygen, central atoms in oxo anions fail to exhibit these coordination numbers, but instead settle for lower penultimate total coordination numbers: 3 in the second period, for example, CO_3^{2-}; 4 in the third and fourth periods, for example, SiO_4^{4-} and $GeO4^{4-}$; 6 in the fifth and sixth periods.

Some of these categories of ions show distinctive structural and thermodynamic properties. The nonacidic metal cations and nonbasic anions are distinct from all of the other categories, in that there is a positive entropy change accompanying their hydration as they dissolve from the solid state (Figure 2); they are known to physical chemists as electrostatic structure breakers because these large ions break up the structure of liquid water (which is sometimes described in terms of 'icebergs'). The feebly acidic cations and feebly basic anions have small negative entropy changes ($T\Delta S$ between 0 and $-35\,\mathrm{kJ\,mol^{-1}}$ at room temperature) accompanying their hydration; these entropy changes are too small to govern their solution properties. All stronger categories of acidic and basic ions have larger, chemically significant negative entropy changes accompanying their hydration, and are among the electrostatic structure makers; these ions hydrate very strongly and extensively, forming multiple hydration spheres involving dozens or even hundreds of water molecules. Collectively we may call this group of cations, with strengths ranging from weakly acidic to very strongly acidic, the acidic cations; the corresponding group of anions we may call the basic anions.

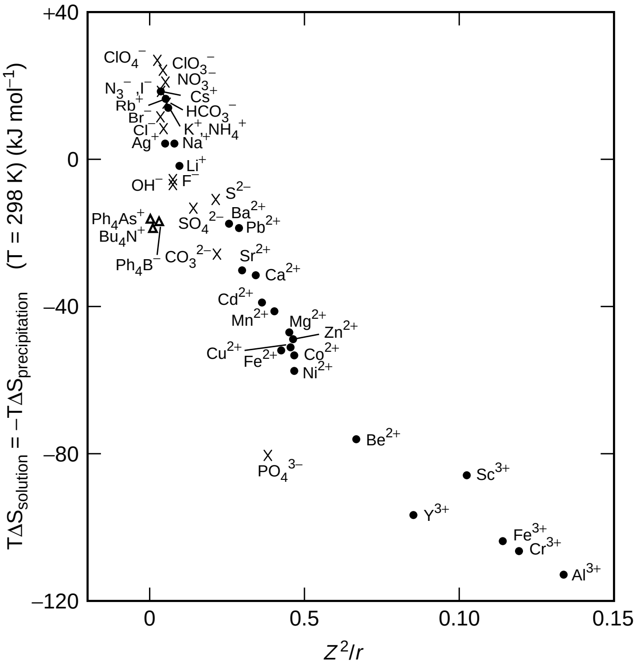

Figure 2 298 K entropy terms ($T\Delta S_{\mathrm{solution}} = -T\Delta S_{\mathrm{precipitation}}$) for cations and anions as a function of Z^2/r. Crosses equal anions; dots equal metal cations; triangles equal organic ions. (Ref. 3. Reproduced by permission of University Science Books)

4 SOLUBILITY AND COMPLEX-ION FORMATION TENDENCIES OF METAL IONS

The solubilities of salts in water (clearly of importance in aquatic, analytical, and geochemistry) can be fairly well predicted and explained using two principles; later we shall return to the more familiar of these, the hard–soft acid–base (HSAB) principle (*see* ***Hard & Soft Acids and Bases***). To control this principle, we must first consider only salts of anions that are hard bases, that is, salts of oxo and fluoro anions, and oxides, hydroxides, and fluorides. The solubilities of salts of these anions can be fairly well predicted and explained on the basis of the acidity classification of the cation and the basicity classification of the anion, that is, on a principle of acid–base strength. The numerous 'solubility rules' taught in General Chemistry could be replaced with four solubility principles (Table 4), two of which are quite reliable and two of which are less reliable, for known reasons.

The precipitation of salts according to Rule I is accompanied by a large favorable entropy change, as the strongly hydrated cations and anions release numerous waters of hydration. In contrast, the dissolution of salts according to Rule II is accompanied by very little entropy change, since one ion is a structure breaker, while the other is a structure maker; the dissolution occurs because the ions are mismatched

Table 4 Solubility principles for salts of hard-base anions

Rule I. Acidic cations and basic anions give insoluble salts (e.g. TiO_2, Mg_2SiO_4).

Rule II. Acidic cations and nonbasic anions, or nonacidic cations and basic anions ('cross-combinations'), give soluble salts (e.g. $Fe(NO_3)_3$, Na_3PO_4, NaOH).

Tendency III. Large nonacidic cations plus large nonbasic anions tend to give relatively insoluble salts (e.g. $KClO_4$, $[(CH_3)_4N][PF_6]$, $[Cr(NH_3)_6][Ni(CN)_5]$).

Tendency IV. Large feebly acidic cations and large feebly basic anions tend to give relatively insoluble salts (e.g. $BaSO_4$).

in size, and therefore give lattice energies that are smaller in magnitude than the combined hydration energies.

Tendencies III and IV are tendencies rather than rules because the effects of ΔH and $T\Delta S$ work in opposition to each other, giving varying, somewhat unpredictable results and moderate driving forces for precipitation; the smaller nonacidic cations (Na^+) and the smaller nonbasic anions (NO_3^-) tend not to show the predicted behavior. The mild insolubility that results when Tendency III holds favors good crystal growth, so Tendency III is often used by synthetic inorganic and organic chemists to isolate newly synthesized ions (which tend to be large, therefore nonacidic or nonbasic) in crystalline solids.[16] The prevailing driving force when Tendencies III and IV work is the formation of good crystal lattices because both the cation and anion are matched in size and charge; this force also favors thermal stability of the solid. It should be noted that unusual types of lattices and hydration are to be expected for grossly nonspherical complex cations and anions so that these rules and tendencies may not be reliable for these types of ions.[17] It is often important to dissolve metal salts in organic solvents (e.g. as catalysts); principles covering solubility of salts in organic solvents are given in our textbooks.[2,3] Room-temperature ionic liquids are a new class of organic solvents that should show distinctive properties as solvents for inorganic salts.[18]

The other principle that governs solubility across groups, periods, and blocks of the periodic table is the well-known Hard–Soft Acid–Base Principle (*see* ***Hard & Soft Acids and Bases***), which states that ‘Hard(er) (Lewis) acids tend to combine with hard(er) bases, while soft(er) acids prefer soft(er) bases.[19] Table 5 shows the classifications of the most common ions of the elements. Whereas the strength of cations and anions is primarily determined by their Z^2/r ratios and only secondarily by their electronegativities, the softness of cations and anions is primarily a function of the electronegativities of the donor or acceptor atoms and only secondarily of their charges (oxidation states) and sizes. Hard acids and hard bases characteristically have very disparate Pauling electronegativities (0.7–1.6 for hard acids, 3.4–4.0 for hard bases), so combinations of them benefit from strong ionic bonding; softer acids and softer bases characteristically have similar, more moderate electronegativities (1.9–2.54 for soft acids, 2.1–3.0 for soft bases), so combinations of them are good for covalent bonding. The softest acids are those closest to the metal with the highest Pauling electronegativity, Au ($\chi_P = 2.54$); the softest bases are those near the metal–nonmetal boundary, where electronegativities are in the vicinity of 2.1. Of recent interest are new classes of weak soft Lewis bases, the chlorocarbons, bromocarbons, and iodocarbons,[20] (*see Halocarbons & Halocarbon Complexes*)

Table 5 Hard and Soft Acids and Bases[a]

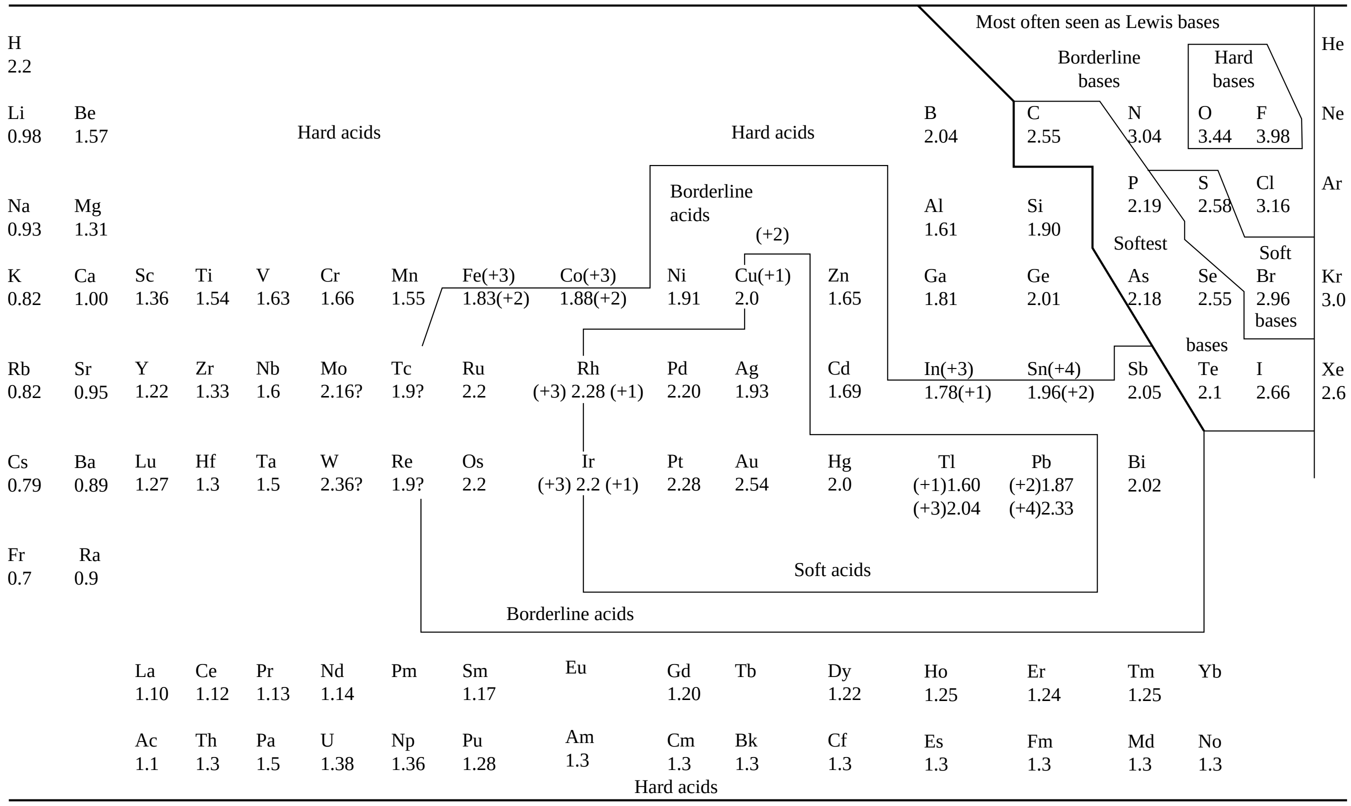
Most often seen as Lewis bases
Borderline bases
Hard bases
Hard acids
Hard acids
Borderline acids
(+2)
Softest
Soft bases
Soft acids
Borderline acids
Hard acids

H 2.2																	He
Li 0.98	Be 1.57											B 2.04	C 2.55	N 3.04	O 3.44	F 3.98	Ne
Na 0.93	Mg 1.31											Al 1.61	Si 1.90	P 2.19	S 2.58	Cl 3.16	Ar
K 0.82	Ca 1.00	Sc 1.36	Ti 1.54	V 1.63	Cr 1.66	Mn 1.55	Fe(+3) 1.83(+2)	Co(+3) 1.88(+2)	Ni 1.91	Cu(+1) 2.0	Zn 1.65	Ga 1.81	Ge 2.01	As 2.18	Se 2.55	Br 2.96	Kr 3.0
Rb 0.82	Sr 0.95	Y 1.22	Zr 1.33	Nb 1.6	Mo 2.16?	Tc 1.9?	Ru 2.2	Rh (+3) 2.28 (+1)	Pd 2.20	Ag 1.93	Cd 1.69	In(+3) 1.78(+1)	Sn(+4) 1.96(+2)	Sb 2.05	Te 2.1	I 2.66	Xe 2.6
Cs 0.79	Ba 0.89	Lu 1.27	Hf 1.3	Ta 1.5	W 2.36?	Re 1.9?	Os 2.2	Ir (+3) 2.2 (+1)	Pt 2.28	Au 2.54	Hg 2.0	Tl (+1)1.60 (+3)2.04	Pb (+2)1.87 (+4)2.33	Bi 2.02			
Fr 0.7	Ra 0.9																
		La 1.10	Ce 1.12	Pr 1.13	Nd 1.14	Pm	Sm 1.17	Eu	Gd 1.20	Tb	Dy 1.22	Ho 1.25	Er 1.24	Tm 1.25	Yb		
		Ac 1.1	Th 1.3	Pa 1.5	U 1.38	Np 1.36	Pu 1.28	Am 1.3	Cm 1.3	Bk 1.3	Cf 1.3	Es 1.3	Fm 1.3	Md 1.3	No 1.3		

[a]Numbers in parentheses are oxidation numbers. The number below each atomic symbol is the Pauling electronegativity of that element. (Ref. 3. Reproduced by permission of University Science Books)

and xenon atoms in complexes such as $[AuXe_4]^{2+}$ and $[Re(C_5H_5)(CO)_2(Xe)]$.[21]

Solubility rules for salts of the heavier halide and chalcogenide ions are primarily based on the HSAB principle, but also involve strength to some degree. The chloride, bromide, iodide, and many pseudohalide ions (*see Pseudohalide*) involve borderline-to-soft donor atoms and characteristically combine with (give insoluble salts with) soft-acid cations. The sulfide, selenide, telluride, and arsenide ions are also soft bases, but have greater basic strength than chloride, bromide, and iodide, and so give insoluble salts not only with the soft acids near gold but also with the borderline acids further from gold, which characteristically are either smaller or more highly charged than the soft acids, and hence have more acidic strength.

In geochemistry, these two principles resulted in the differentiation of the metallic elements as lithophiles (hard acids; *see Lithophiles*) and chalcophiles (borderline and soft acids; *see Chalcophiles*) during the formation of the earth, and continue to affect the chemistry that occurs in the black smokers at the midoceanic ridges; these are also the organizing principles behind the familiar qualitative analysis scheme of the cations.[22]

The two principles of acid/base strength and hardness/softness apply not only to the prediction of the results of solubility equilibria but also to the prediction of complex ion equilibria (*see* ***Coordination & Organometallic Chemistry: Principles***). In such equilibria, we also take into account the additional principles of the chelate (*see Chelate Effect*) and macrocyclic (*see* ***Macrocyclic Ligands***) effects: chelate (*see Chelating Ligands*) ligands tend to form more stable complexes than analogous monodentate ligands, and macrocyclic ligands tend to form more stable complexes than analogous chelate ligands.

Among many possible applications, we may mention the prediction of the toxicities of simple ionic species (*see* ***Metal Ion Toxicity*** and ***Metal-related Diseases of Genetic Origin***). Soft-acid metal ions (except Ag^+) are uniformly very toxic because they bind preferentially to sulfur donor atoms in the body, frequently rupturing the disulfide linkages in the cystine in enzymes and consequently disrupting the tertiary and quaternary structure of the enzyme. Soft bases are also often very toxic since they bond strongly to (borderline acid) metal ions such as Fe^{2+} in the body, displacing less soft but more essential ligands such as O_2 (in oxygen transport by heme); however, the very toxic soft donor atom, selenium, also has beneficial effects in that it is softer than sulfur, and hence can apparently successfully remove soft-acid metal ions such as Hg^{2+} from the sulfur atoms in enzymes. Medicinal chemistry often employs the proper degree of softness in the design of pharmaceuticals so as to remove toxic metal ions; to ensure selectivity and good formation constants, ligands generally chosen are also chelate (or macrocyclic) ligands (*see* ***Metal-based Drugs***).

Since the HSAB classifications seem to depend principally on the Pauling electronegativity of a donor or acceptor atom, and Pauling electronegativities are based on bond energies (*see Bond Dissociation Energy*); the HSAB principle is best explained by analyzing the strengths of the bonds broken and formed during a typical HSAB reaction, in which HA = hard acid, SB = soft base, and so forth:

$$\mathrm{HA{:}SB(g)} + \mathrm{SA{:}HB(g)} \rightleftharpoons \mathrm{HA{:}HB(g)} + \mathrm{SA{:}SB(g)} \qquad (7)$$

We evaluate the donor–acceptor bond energies of each of the reactants and products using the equation that defines the Pauling electronegativities, χ_P, of the acceptor and donor atoms A and B:

$$\Delta H(\mathrm{A{-}B}) = \frac{1}{2}[\Delta H(\mathrm{A{-}A}) + \Delta H(\mathrm{B{-}B})] + 96.5[\chi_P(\mathrm{A}) - \chi_P(\mathrm{B})]^2 \qquad (8)$$

This equation has recently been found to be much more accurate in predicting bond energies ($\pm 6\,\mathrm{kJ\,mol^{-1}}$) than was commonly thought, provided the equation is applied as originally intended.[23] When we take the sum of the bond dissociation energies of the reactants minus the sum of the bond dissociation energies of the products, all the terms involving element–element bond energies (ΔH(A-HA), etc.) drop out, leaving four terms:

$$\begin{aligned}\Delta H = 96.5\{&[\chi_P(\mathrm{HA}) - \chi_P(\mathrm{SB})]^2 + [\chi_P(\mathrm{SA}) - \chi_P(\mathrm{HB})]^2 \\ &- [\chi_P(\mathrm{HA}) - \chi_P(\mathrm{HB})]^2 - [\chi_P(\mathrm{SA}) - \chi_P(\mathrm{SB})]^2\}\end{aligned} \qquad (9)$$

Let us now take some typical electronegativity values for the donor and acceptor atoms of hard and soft acids and bases: $\chi_P(\mathrm{HA}) = 1.6$; $\chi_P(\mathrm{HB}) = 3.4$; $\chi_P(\mathrm{SA}) = \chi_P(\mathrm{SB}) = 2.5$. Substituting these values in equation (9) gives us

$$\Delta H = 96.5[0.81 + 0.81 - 3.24 - 0] = -156\,\mathrm{kJ\,mol^{-1}} \qquad (10)$$

This calculation indicates that the reaction to give the products HA-HB and SA-SB is accompanied by a favorable ΔH, which is supported by experimental data for a typical HSAB reaction (in which water, aq, is the hard acid and the hard base):

$$\begin{aligned}\mathrm{Hg^{2+}(aq)} + \mathrm{I^-(aq)} \rightleftharpoons \mathrm{HgI^+(aq)} + \mathrm{aq.aq}; \quad \Delta\mathrm{H} = -315\,\mathrm{kJ\,mol^{-1}};\\ -T\Delta\mathrm{S} = +10\,\mathrm{kJ\,mol^{-1}}\end{aligned} \qquad (11)$$

The calculation of equation (10) also indicates why the HSAB principle works so often: the driving force of the HSAB reaction lies in the formation of the very stable ionic hard acid–hard base product.

The chemical periodicity exhibited in the crystal or ligand field splitting of d-block metal-ion complexes, as a function of their d-electron configuration, is familiar and needs no elaboration here (*see* ***Ligand Field Theory & Spectra***;

Coordination & Organometallic Chemistry: Principles). Often cited are the effects of this periodicity on the hydration energies of metal ions, the lattice energies of simple salts, the enthalpies of formation of simple salts, complex-ion formation constants, and radii of d-block metal ions: all of these show double-humped curves when measured across a period for like-charged ions in high-spin octahedral complexes. Less well known is the fact that the Pauling electronegativities of the fourth-period d-block metal ions also show such a double-humped curve; this is because the Pauling electronegativities of the fourth-period d-block metals are obtained from the enthalpies of the formation of simple salts of these metals, which show high-spin octahedral coordination. And in fact, since appropriate ionic radii and Pauling electronegativities already incorporate crystal-field effects, the hydration energies of d-block metal ions, for example, do not show deviations from the Latimer-type equation (1).

For the benefit of nonspecialists with orientations toward biochemistry, the effects of crystal-field splitting are nicely illustrated using the Perutz model of the cooperative binding of O_2 as a ligand by the Fe^{2+} of hemoglobin, which undergoes a transition from high to low-spin upon binding O_2, which in turn triggers dramatic conformational changes in the protein of heme (*see* ***Iron: Heme Proteins & Dioxygen Transport & Storage***). The coordination of the strong-field ligand nitric oxide, NO, is very important biochemically (*see* ***Nitrogen Monoxide (Nitric Oxide): Bioinorganic Chemistry***) in triggering smooth-muscle relaxations such as are involved in penile erections, as well as in numerous other processes in the brain.**[24]**

5 REDOX REACTIVITY OF ELEMENTS AND THEIR IONS

The standard reduction potentials (*see Redox Potential*) of the elements and their compounds have many important applied implications for chemists, not the least of which is being aware when a compound or mixture of compounds they are handling has the potential for exploding. This should be considered as a possibility when the appropriate potentials differ by more than about one volt and appropriate kinetics considerations apply. A simply predictable case is the sometimes-violent reaction of metals with acids, as illustrated in a recently produced discovery video.**[15]** Redox activities of elements are most commonly (and most precisely) analyzed via thermochemical cycles such as the familiar Born–Haber cycle for the production of NaCl from Na and Cl_2. A similar analysis of the activities of different metals in their reactions with acids shows that the standard reduction potential for the metal (the quantitative measure of the activity of the metal) can be expressed in terms of the appropriate ionization energies of the metal, the atomization energies of the metal (*see Atomization Enthalpy of Metals*), and the hydration energies of the metal ion:

$$96.5E^{\mathrm{o}} = \frac{\Delta H_{\mathrm{atom}}}{z} + \frac{\Sigma \mathrm{IE(z)}}{z} + \frac{\Delta H_{\mathrm{hyd}}}{z} - 439\,\mathrm{kJ\,mol^{-1}} \qquad (12)$$

where z is the charge on the metal ion produced (this equation neglects the small contribution of $-T\Delta S$). By the time this equation is solved, however, the explosion may have occurred, so a more useful empirically based prediction of the metal's activity is based on the good correlation of metal standard reduction potentials and low Pauling electronegativities (Figure 3; Table 6).

Since Pauling electronegativities are stated in terms of bond energies, the theoretical derivation of the relationship of the activity of a metal to its Pauling electronegativity**[25]** requires analysis of the electronegativity differences in the bonds being broken and formed during the reaction of a metal (containing metal–metal bonds of variable bond order) with hydronium ions to form hydrogen and hydrated metal ions (containing variable numbers of coordinate-covalent metal-oxygen bonds). Applying the Pauling equation rigorously requires that the reaction conserve the total number of bonds (including consideration of their bond orders). This condition cannot be met generally for the dissolution of solid metals to give hydrated ions. Thus, the empirical relationship of Figure 3 cannot be derived exactly, but its form can be explained: if the metal is less electronegative than hydrogen, there is a greater electronegativity difference and ionic character in the M^+–OH_2 bond than in the H^+–OH_2 bond; hence, the total bond energies are maximized for the products rather than for the reactants.

Standard reduction potentials also relate to the commercial methods of production of the elements, to the methods of production and use of oxo anions as oxidizing agents, and to the oxidation states in which the elements will be found in natural waters and soils. Many of these tendencies depend both on the reduction potential and the pH of the system in which the elements are found, and can be shown graphically in Pourbaix

Table 6 Redox categories of elements

Very electropositive metals have low Pauling electronegativities ($\chi_P < 1.4$) and standard reduction potentials ($E^{\mathrm{o}} < -1.6$V), and include the very active metals such as Na whose cations are hard acids.

Electropositive metals have moderate Pauling electronegativities ($1.4 < \chi_P < 1.9$) and standard reduction potentials ($-1.6\mathrm{V} < E^{\mathrm{o}} < 0\mathrm{V}$), and include the moderately active metals such as Fe whose cations are borderline acids.

Electronegative metals have high Pauling electronegativities for metals ($1.9 < \chi_P < 2.55$) and high standard reduction potentials ($E^{\mathrm{o}} > 0$V), and include the inactive metals such as Au whose cations are soft acids.

Electronegative nonmetals have low Pauling electronegativities for metals ($1.9 < \chi_P < 2.8$) and include relatively inactive nonmetals such as S whose anions are soft bases.

Very electronegative nonmetals have high Pauling electronegativities ($\chi_P > 2.8$) and include active nonmetals such as fluorine whose anions are borderline or hard bases.

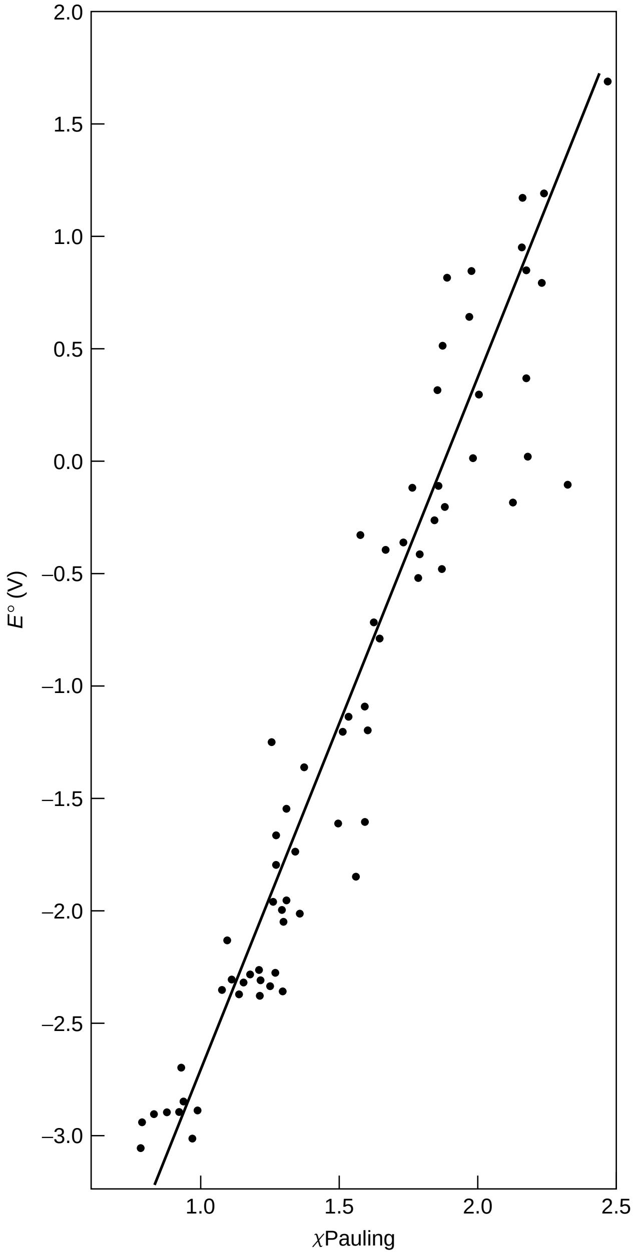

Figure 3 The standard reduction potential ($E°$) of the most common cation of each metallic element versus its Pauling electronegativity. (Ref. 3. Reproduced by permission of University Science Books)

($E°$/pH, pE/pH) diagrams[26] (*see Pourbaix Diagram*) of the elements (Figure 4), a form of expressing redox reactivity which is seldom taught by pure inorganic chemists,[1] but which is widely used by applied chemists such as environmental and soil scientists and corrosion engineers. With such diagrams, one does not have to remember the sign conventions of electrochemistry: the reaction of two species is favored thermodynamically if their predominance areas do not overlap; the further apart the predominance areas, the more exothermic or potentially explosive the reaction is.

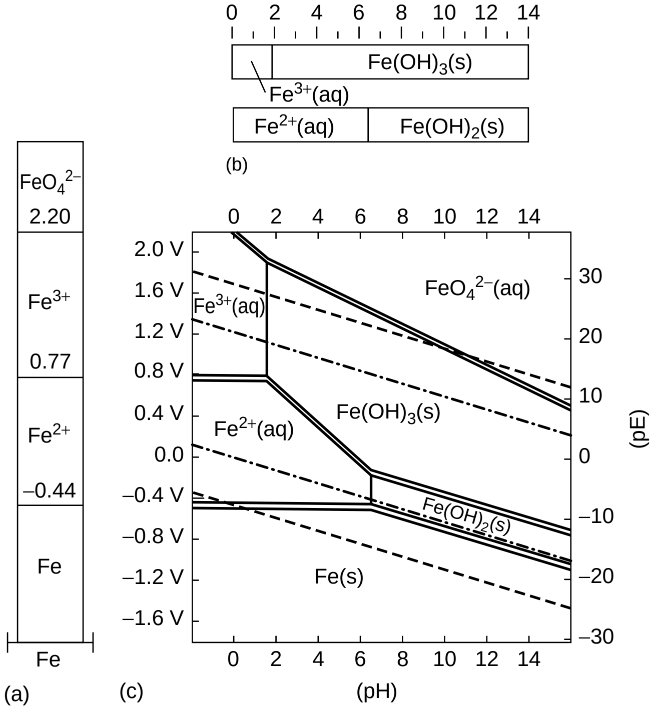

Figure 4 (a) At left, the redox predominance diagram for iron; (b) above, the acid–base predominance diagrams for Fe(III) and Fe(II); and (c) above right, the Pourbaix diagram showing the predominant form of iron at any given combination of redox potential and pH for 1 M iron solutions. Solid single lines (———) separate species related by acid–base equilibria; solid double lines (═══) separate species in different oxidation states. Dash-dotted lines (-·-·-·-) enclose the theoretical and dashed lines (- - - -) enclose the practical region of stability of water to oxidation or to reduction. (Ref. 3. Reproduced by permission of University Science Books)

Information is quite crowded in Pourbaix diagrams, so that students can benefit if reduction potentials are first provided at the standard pH of 0 in lower-dimensional vertical redox predominance diagrams (Figure 4). In these diagrams, strong oxidizing agents are confined to the top and strong reducing agents are confined to the bottom, which mirrors where they would be found in stratified natural waters that are well aerated at the top but oxygen-starved at the bottom. Thus, in the two predominance diagrams of Figure 5, the strongest oxidizing agent shown is FeO_4^{2-} and the strongest reducing agent is Mn(s). Since their (shaded) predominance areas do not overlap, MnO_4^- and Fe^{2+} are thermodynamically favored to react; but since the areas of MnO_4^- and Fe^{3+} do overlap, these two species do not react but instead can coexist in equilibrium.

Connections between the HSAB classifications of ions and their redox properties have long been noted: soft-acid cations tend to be good oxidizing agents and soft-base anions tend to be good reducing agents. It follows, of course, that the redox activities of the parent elements are also related to the HSAB classifications: the metals resulting from the reduction

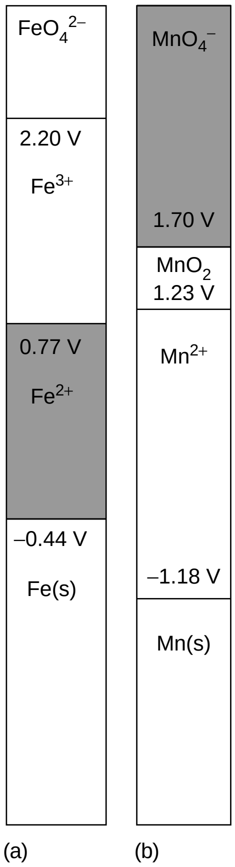

Figure 5 Redox predominance diagrams for iron (a) and manganese (b); boundaries represent the standard reduction potential for reduction of the (thermodynamically-stable) species above the boundary to the (thermodynamically-stable) species below the boundary. If the redox predominance regions of two species (e.g., the gray regions of Fe^{2+} and MnO_4^-) do not overlap along the y-axis when the two diagrams are superimposed, reaction between the two species is thermodynamically favored

of soft-acid cations are 'noble', that is, very poor reducing agents, which are geochemically also classified as siderophiles (*see Siderophiles*) since they are concentrated in the iron core of the molten earth and are depleted in the crust (but not in asteroids or in the deposits laid down on earth at the time the dinosaurs became extinct).

6 PHYSICAL PROPERTIES OF ELEMENTS, COMPOUNDS, AND MATERIALS

The major new area of materials science includes the study of the physical properties of solids and focuses on solids that have extended structures in at least one dimension (and thus usually excludes gases, liquids, and molecular solids containing small molecules); such solids are of importance not only to metallurgists and materials and surface scientists and workers in heterogeneous catalysis but also (especially when the structures are based on polysilicates) to geochemists, soil and agricultural chemists, and environmental chemists. Important materials fall among many classes of substances: elements and alloys, oxides, nitrides, sulfides, and so on. Many elements, oxides, and nitrides, however, are not of interest as materials because they consist of small molecules, which are not found in the solid state at a convenient temperature, or if they are, they lack extended structures to give rise to interesting bulk properties. A first question one would ask would be whether one could predict (from the simplest formula of a substance) if it would form a solid with an extended structure that might have interesting properties.

Extended structures of (at least) binary compounds EX_n most frequently involve covalent bonding between the simplest formula units E_1X_n via E and X atoms or groups that are bridging (two-coordinate or higher), rather than terminal (one-coordinate). Moderately accurate predictions of periodic trends in structural types for EX_n can be made using stoichiometry and radius-ratio calculations (starting with the premise that the compound can be formed, at least conceptually, from cations of E and anions of X). (1) If the radius ratio of the ions in the compound EX_n lies between 0.225 and 0.414, E is predicted to have a total coordination number of 4; if the ratio lies between 0.414 and 0.732, E should have a total coordination number of 6; if the ratio is above 0.732, E should have a total coordination number of 8. (2) Once the coordination number of E is predicted, the average coordination number of the 'anionic' element X can be predicted:

$$\begin{aligned}&(\text{Coordination number of E})(\text{Number of E in formula})\\&\quad = (\text{Coordination number of X})(\text{Number of X in formula}) \qquad (13)\end{aligned}$$

(3) If the coordination number of either atom (in practice, normally X) is 1.00, the structure is molecular and not extended. As the average coordination number of X increases, there are more and more bridging interactions involving X-atom bridges, so the structure becomes more extended, proceeding from one-dimensional polymerization through two-dimensional sheet and then to three-dimensional network (ionic or covalent) structures.

Among the halides (*see* ***Fluorides: Solid-state Chemistry*** and *see* ***Halides: Solid-state Chemistry***) and oxides (*see* ***Oxides: Solid-state Chemistry***) of the elements in their maximum oxidation states in a given period, on the left of the period, where oxidation states are low, the coordination numbers of both the metal ion and the halide or oxide ion are high, allowing the construction of three-dimensional network (ionic or polymeric covalent) structures (Table 7). As oxidation states rise to the right in a period, the average coordination number of the X (halide or oxide) atom or ion necessarily drops; when this falls below two, oligomeric and eventually monomeric molecular structures are adopted (e.g. Mn_2O_7 and PtF_6, OsO_4, RuO_4, and FeO_4 in the d-block; Cl_2O_7 and SF_6, IF_7, and XeO_4 in the p-block). This

Table 7 Predictions of physical properties and structures of some halides and oxides

Period 3:	NaF	MgF_2	AlF_3	SiF_4	PF_5	SF_6	(ClF_7)	
Radius ratio	0.975	0.723	0.563	0.454	0.437	0.361	0.345	
Predicted								
C.N. of metal	8	8 or 6	6	6 or 4	6 or 4	6 or 4	6 or 4	
C.N. of F	8	4 or 3	3	1.5 or 1	$\sim$1	$\sim$1	$\sim$1	
Observed								
C.N. of metal	6	6	6	4	5	6	6	
C.N. of F	6	3	2	1	1	1	0.857	
Lattice type:	NaCl	CaF_2	*	molec.	molec.	molec.	(ClF_6^+)	
Melting point:	1012	1263	1272	−86	−75	−64		
Period 3:	Na_2O	MgO	Al_2O_3	SiO_2	P_2O_5	SO_3	Cl_2O_7	
Radius ratio:	0.921	0.683	0.532	0.429	0.413	0.341	0.325	
Predicted								
C.N. of metal:	4	6	6	6 or 4	4	4	4	
C.N. of oxide:	8	6	4	3 or 2	1.6	1.33	1.14	
Observed:								
C.N. of metal:	4	6	6	4	4	4	4	
C.N. of oxide:	8	6	4	2	1.6	1.33	1.14	
Lattice type:	antifluorite	NaCl	corundum	beta-silica	oligomer	oligomer	molecular	
Melting point:	(1275)	2800	2050	1723	(300)	17	−91	
Period 6:	Cs_2O	BaO	Lu_2O_3	HfO_2	Ta_2O_5	WO_3	Re_2O_7	OsO_4
Radius ratio:	1.437	1.183	0.793	0.675	0.619	0.587	0.537	0.476
(Inverse ‘‘ ’’):	(0.696)	(0.846)						
Predicted								
C.N. of metal:	3	8	8	6	6	6	6	6
C.N. of oxide:	6	8	5.33	3	2.4	2	1.71	1.5
Observed								
C.N. of metal:	3	6	7	8	6	6	5	4
C.N. of oxide:	6	6	4.67	4	2.4	2	1.42	1
Lattice type:	ionic	NaCl	ionic	rutile	ionic	polymer	2-D polymer	molecular
Melting point:	490	1920	2487	2900	1870	1473	296	40

Melting points in °C; if in parentheses, these are sublimation temperatures. C.N. = average coordination number. (Ref. 3. Reproduced by permission of University Science Books)

trend in structures has drastic effects on the properties of the halides or oxides as materials: their volatility and gaseous, liquid, or solid status is affected, the possibilities for magnetic interactions (*see* ***Magnetism of Extended Arrays in Inorganic Solids***) and conductivity are completely changed, and so on. These differences in structure are often so pronounced as to form the bases of classification schemes for certain types of compounds: molecular or covalent hydrides (*see* ***Hydrogen: Inorganic Chemistry***) and organometallics are found to the right of the periodic table as contrasted to saltlike or polymeric hydrides and organometallics, found at the left.

Research workers in applied chemical fields are especially interested in the polysilicates and aluminosilicates, which are so important in geochemistry, soil chemistry, environmental chemistry, and in catalysts such as zeolites (*see* ***Zeolites***) and clays (*see Clay Minerals*) such as montmorillonite (on which, according to one heretical theory, life first originated).[27] These materials often contain polysilicate and polyaluminosilicate ions of varying degrees of polymerization, which can be rationalized from their stoichiometries. SiO_2 itself is a three-dimensional network solid, as are the zeolites in which the oxygen-to-(aluminum plus silicon) ratios in the framework are also 2:1. Polysilicates are produced by reaction of this acidic oxide with basic metal oxides; as the ratio of oxygen to silicon (or silicon plus aluminum) in the anion increases, the average (covalent bond) coordination number of the oxygen in the polyanion decreases, hence successively less polymeric ions are produced. Two-dimensional (layer) polymeric ions such as $[Si_4O_{10}]_n^{4-}$ are found in mica and clays; two-stranded, one-dimensional (needle) polymeric ions such as $[Si_4O_{11}]_n^{6-}$ are found in some forms of asbestos; one-dimensional (linear and cyclic) structures such as $[SiO_3]_n^{2-}$ are found in pyroxenes and beryl; finally oligomeric $[Si_2O_7]^{6-}$ and monomeric $[SiO_4]^{4-}$ ions are found in thortveitite and olivine. The less polymerized the polysilicate anion, the more readily minerals containing the ion are weathered to release their nutrient cations. Minerals such as olivine are generally found only in deserts or other ‘youthful’ soils; they readily release nutrient ions to water, accounting for the high productivity of desert soils upon irrigation. Conversely, only highly polymeric, insoluble oxides can persist in tropical soils exposed to high levels of heat and rainfall; in slash-and-burn agriculture the tropical soil is quickly reduced to a content of such hard, polymeric, infertile oxides known as laterite. Polysilicates and polyaluminosilicates also offer a fertile field in which one can introduce the concept of isomorphous (*see Isomorphous*) substitution of different ions of similar radii and the same total charge.

The same question of the building up of extended structures comes up among elements, but since they are not binary compounds, one cannot apply radius ratios. In contrast to oxides, halides, and so on, the most nonvolatile and high-melting elements are found in the middle of their periods (carbon in the second period; tungsten in the sixth period). The rules of Engle and Brewer[28,29] relate this trend to the average number of unpaired valence electrons per atom available for bonding, which reaches a maximum approximately in the middle of a block of the periodic table. As electrons pair in valence orbitals to the right in the p-block, the degree of polymerization of the element decreases, from two- or three-dimensional network polymeric structures (diamond, graphite) to one-dimensional structures (Se_x) to small molecules (Cl_2) and finally to individual atoms (He). Among metals at the left or right of the d-block, the degrees of polymerization and coordination numbers do not decrease, but the average bond order does: full explanation of this finally requires the use of the Molecular Orbital Theory (*see* ***Molecular Orbital Theory***) or band theory (*see Band Theory*), which are unlikely to be accessible to the nonspecialist. As bond orders decrease to the left or right in the d-block, so do the melting points and physical hardness of the metals.

While the argument continues of whether the bonding in metals is of a type distinct from ionic and covalent bonding, one point of view is that metallic bonding is not distinct from covalent bonding.[30–32] Clearly there are some important differences in physical properties of metallic substances from those of covalent (even covalent network) substances that need explanation; these include not only the obvious differences in conductivity but also such properties as malleability and ductility.[33] Density functional calculations[34] (*see Crossover Experiment*) point to a particular feature of the electronic distribution in metals: it is not concentrated on the most electronegative atom, as in ionic compounds, nor especially in the regions between neighboring atoms, as in molecular or network covalent substances, but is found in the regions between nonadjacent atoms so that the electron density has a nonlocalized ‘flatness’ of distribution across the space between all of the metal atoms (Figure 6). This flatness means that

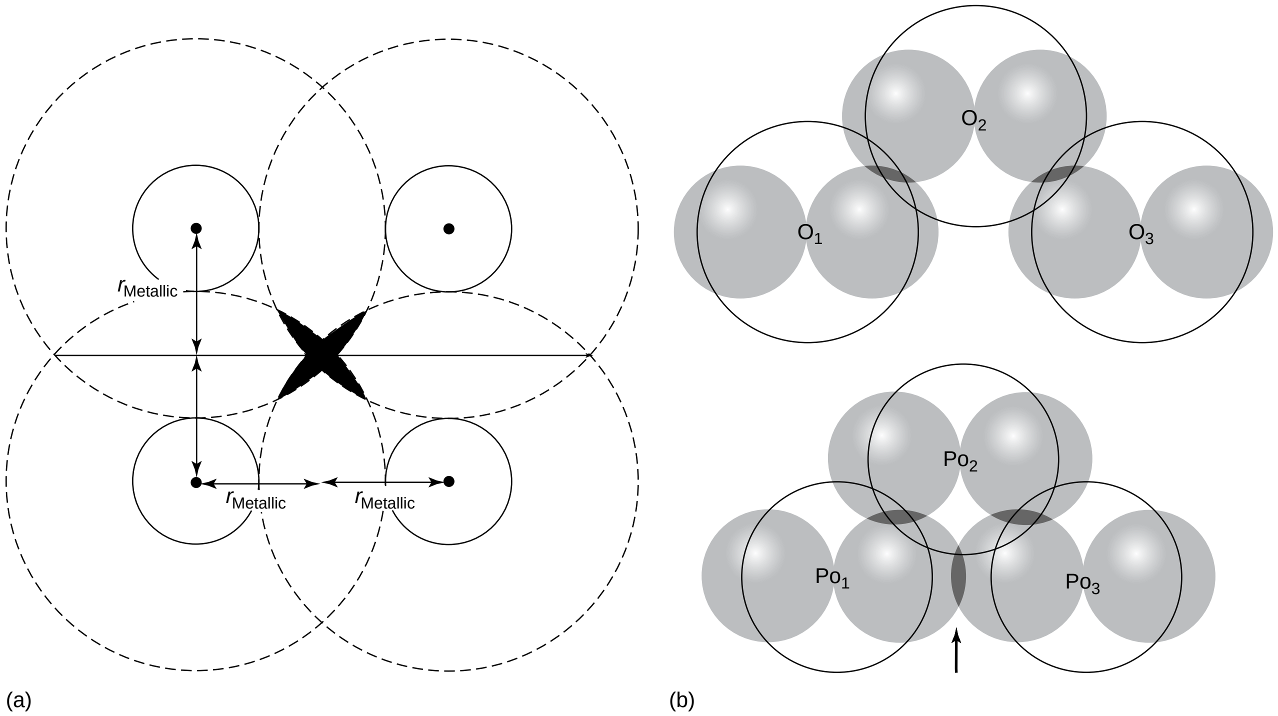

Figure 6 Two illustrations of overlap (shaded in darkest color) of nonadjacent orbitals that participate in ‘‘flat’’ molecular orbitals involved in metallic conduction. (a) Drawing of four atoms in a metallic solid. Inner solid circle = largest filled (core) orbital of a metal; outer (dashed - - - -) circle = partially occupied valence orbital. Note the overlap of the valence orbitals of the nonadjacent top left and bottom right atoms, and the overlap involving the top right and the bottom left atoms. (b) Drawing of three atoms of hypothetical chain polymeric allotropes of oxygen and polonium (selected to have the structure actually found for μ-sulfur, selenium, and tellurium). Inner solid circle = filled valence s orbital of the element; gray shaded double circles = partially occupied valence p orbital of the element. Overlap of the p orbitals of the nonadjacent first and third atoms occurs only for Po, since the p orbital extends further beyond the s orbital in the case of Po than in the case of O. (Ref. 3. Reproduced by permission of University Science Books)

bonding ability is not lost when atoms are displaced from their original positions during hammering or drawing a metal into a wire; it also gives a rationale for the classical description of metals as 'metal ions in a sea of electrons.'

Provided that there is a large 'radius ratio' between the partially filled atomic orbitals involved in conduction and the last filled atomic orbitals, and provided that the geometric arrangement of the atoms is appropriate, one can sketch situations as in Figure 6, in which partially filled atomic orbitals will overlap other such orbitals on nonadjacent atoms, giving rise to 'flat' molecular orbitals involved in conduction. This large radius ratio tends to be found among atoms early in the periodic table (especially groups 1 and 2) and, in the p-block, among atoms lower in a group.

Chemists have long tried to classify substances into the broad categories of ionic, metallic, and covalent (or covalent network and covalent molecular) on the basis of the fundamental atomic properties, in particular, electronegativity; the earliest of these attempts was the van Arkel triangle[35–37] (*see* ***Structure & Property Maps for Inorganic Solids***), which has been gradually refined by Sproul, most recently to a graph for elements and binary compounds comparing the electronegativities of the element of lowest electronegativity and the element of the highest electronegativity.[38] In such a graph, metallic elements and alloys are predicted when the element of higher electronegativity has an electronegativity less than about 2.2 (gold is clearly an exception). Electronegativities cannot explain, however, the great differences in conductivities of different allotropes (*see Allotrope*) of some elements (especially carbon); in different allotropes, the different arrangements of atoms may sometimes allow or exclude the overlap of orbitals of nonadjacent atoms to give 'flat' molecular orbitals.

7 CHEMICAL PROPERTIES OF COMPOUNDS

Space allows us to consider only one example. Even in General Chemistry courses, it is often pointed out that the acidity of metal oxides increases to the right in the periodic table. With the classification scheme for simple ions (Table 1), it is possible to rationalize and amplify this periodic trend: oxide ion is a very strongly basic anion; in combinations with nonacidic and feebly acidic cations, it is reasonable that the basic properties of the oxide ion should prevail, giving water-soluble basic oxides. Oxides of weakly and moderately acidic cations are insoluble according to Solubility Rule I, but it is reasonable that the basic properties of the oxide ion should still prevail so that these oxides dissolve in acid and are also generally classified as basic oxides. (Some are amphoteric oxides; unfortunately we have found no way to use our classification schemes with any high degree of accuracy to predict amphoterism.) At the other end of the periodic table, oxides of very strongly acidic 'cations' tend to be acidic oxides; they tend to be water-soluble if the oxo acid formed on hydrating them is very strongly, strongly, or moderately acidic. However, if the element has reached its penultimate total coordination number in its oxide, it is unable to add hydroxide or oxide ions, and hence is a neutral oxide. With these concepts, it is easy to explain the presence of acidic oxides (CrO_3, Mn_2O_7, OsO_4) and even a neutral oxide (FeO_4) in the middle of the d-block.

8 CONCLUSIONS

A systematic, across-the-periodic-table overview of reactivity trends, based primarily on simple concepts of the periodicity of charge or oxidation number, size, and electronegativity, provides benefits: (1) to nonspecialists, who will more readily grasp the inorganic aspects of their chosen fields, and in the future will more readily see opportunities for collaboration with inorganic chemists; (2) to inorganic chemists, who (a) will more readily grasp many of the properties of the compounds and materials that are the focus of modern 'pure' inorganic research and (b) will more readily see areas of applied chemistry to which they can direct their own research efforts later in their careers, as the tendency toward applied and interdisciplinary research continues.

9 REFERENCES

1. L. L. Pesterfield and C. H. Henrickson, *J. Chem. Educ.*, 2001, **78**, 677.
2. G. Wulfsberg, 'Principles of Descriptive Inorganic Chemistry', University Science Books, Mill Valley, CA, 1991.
3. G. Wulfsberg, 'Inorganic Chemistry', University Science Books, Sausolito, CA, 2000.
4. G. Wulfsberg, 'Chimie Inorganique: Théories et Applications', Dunod, Paris, 2002.
5. K. A. Waldron, E. M. Fehringer, A. E. Streeb, J. E. Trotsky, and J. J. Pearson, *J. Chem. Educ.*, 2001, **78**, 635.
6. K. S. Pitzer, *Acc. Chem. Res.*, 1979, **12**, 271.
7. P. Pyykkö and J.-P. Desclaux, *Acc. Chem. Res.*, 1979, **12**, 276.
8. P. Schwerdtfeger, *Heteroat. Chem.*, 2002, **13**, 578.
9. A. I. Cherkesov, *Radiokhimiya*, 1984, **26**, 53.
10. W. B. Jensen, *J. Chem. Educ.*, 1982, **59**, 634.
11. V. M. Chistyakov, *Vestsi Akad. Navuk BSSR, Seryya Khim. Navuk*, 1968, 50.
12. H. Merz and K. Ulmer, *Phys. Lett. A*, 1967, **26**, 6.
13. D. C. Hamilton, *Am. J. Phys.*, 1965, **33**, 637.
14. W. M. Latimer, K. S. Pitzer, and C. M. Slansky, *J. Chem. Phys.*, 1939, **7**, 108.
15. L. H. Laroche, G. Wulfsberg, and B. Young, *J. Chem. Educ.*, 2003, **80**, 962.

16. F. Basolo, *Coord. Chem. Rev.*, 1968, **3**, 213.
17. W. G. Van der Sluys, *J. Chem. Educ.*, 2001, **78**, 111.
18. J. D. Holbrey, A. E. Visser, and R. D. Rogers, Solubility and Solvation in Ionic Liquids, in 'Ionic Liquids in Synthesis', eds. P. Wasserscheid and T. Welton, Wiley, Weinheim, Germany 2003, p. 68.
19. R. G. Pearson, *J. Am. Chem. Soc.*, 1963, **85**, 3533.
20. R. J. Kulawiec and R. H. Crabtree, *Coord. Chem. Rev.*, 1990, **99**, 89.
21. D. C. Grills and M. W. George, *Adv. Inorg. Chem.*, 2001, **52**, 113.
22. C. S. G. Phillips and R. J. P. Williams, 'Inorganic Chemistry', Oxford University Press, New York, 1965, Vol. 2, Chap. 34.
23. N. Matsunaga, D. W. Rogers, and A. A. Zavistas, *J. Org. Chem.*, 2003, **68**, 3158.
24. S. H. Snyder, *Science*, 1992, **257**, 494.
25. G. Wulfsberg, 'Inorganic Chemistry', University Science Books, Sausolito, CA, 2000, p. 336.
26. M. Pourbaix, 'Atlas of Electrochemical Equilibria in Aqueous Solutions', National Association of Corrosion Engineers, Houston, TX, 1974.
27. J. P. Ferris, A. R. Hill Jr, R. Liu, and L. E. Orgel, *Nature*, 1996, **381**, 59.
28. L. Brewer, in 'Electronic Structure and Alloy Chemistry of the Transition Metals', ed. P. A. Beck, Interscience, New York, 1963.
29. L. Brewer, *J. Nucl. Mater.*, 1989, **167**, 3.
30. W. P. Anderson, J. K. Burdett, and P. T. Czech, *J. Am. Chem. Soc.*, 1994, **116**, 8808.
31. L. C. Allen and J. F. Capitani, *J. Am. Chem. Soc.*, 1994, **116**, 8810.
32. J. C. Schon, *Angew. Chem., Int. Ed. Engl.*, 1995, **34**, 1081.
33. J. J. Gilman, *J. Chem. Educ.*, 1999, **76**, 1330.
34. P. Mori-Sánchez, A. Martín Pendás, and V. Luaňa, *J. Am. Chem. Soc.*, 2002, **124**, 14721.
35. A. E. van Arkel, 'Moleculen en Kristallen', van Stockum, s'Gravenhage, 1941.
36. A. E. van Arkel, 'Molecules and Crystals', Butterworths, London, 1949.
37. W. B. Jensen, *J. Chem. Educ.*, 1995, **72**, 395.
38. G. Sproul, *J. Chem. Educ.*, 2001, **78**, 387.

Phosphates: Solid-state Chemistry

J. Paul Attfield
University of Edinburgh, Edinburgh, UK

1	Introduction	1
2	Phosphate Anions	1
3	Characterization	5
4	Synthesis	6
5	Structural Classes	8
6	Properties	12
7	Natural Phosphates	14
8	Related Articles	15
9	References	15

Glossary

Catenaphosphate: the infinite chain phosphate, $(PO_3{}^-)_\infty$
Cyclophosphates: cyclic anions of two-connected phosphate tetrahedra, $P_nO_{3n}{}^{n-}$
Diphosphate: the $P_2O_7{}^{4-}$ anion
Metaphosphates: cyclo and catenaphosphates
Orthophosphate: the $PO_4{}^{3-}$ anion
Polyphosphates: chain anions of two-connected phosphate tetrahedra, $P_nO_{3n+1}{}^{(n+2)-}$
Ultraphosphates: anions formed by two and three-connected phosphate tetrahedra, $P_nO_{3n-1}{}^{(n-2)-}$

Abbreviations

ADP = Ammonium Dihydrogen phosphate, $NH_4H_2PO_4$; AlPO = A framework aluminophosphate; HUP = Hydrogen uranyl phosphate; KDP = Potassium Dihydrogen phosphate, KH_2PO_4; KTP = Potassium Titanyl Phosphate, $KTiOPO_4$; NASICON = Sodium Superionic Conductor.

1 INTRODUCTION

Phosphates are compounds that contain oxyanions of phosphorus(V), ranging from the simple orthophosphate group to condensed chain, ring, and network anions.[1] Oxyanions of phosphorus in lower oxidation states such as phosphite, $HPO_3{}^{2-}$, are also known.

A very large number of solid phosphates have been prepared or found as minerals. Their diversity results from variations in the phosphate species, the large number of cations to which they may be coordinated, and the presence of other anions or molecules, notably H_2O. Their chemistry is similar to that of solid silicates (*see* ***Zeolites***) and borates (*see* ***Borates: Solid-state Chemistry***).

Attention will be focused on phosphates of metallic elements and other small cations (H^+, $NH_4{}^+$), although it should be noted that a variety of phosphate salts of large organic or inorganic coordination complex cations are also known. Background information of the chemistry of phosphates and related phosphorus species can be found in the texts by Corbridge[2] and Kanazawa[3] (*see also* ***Phosphorus: Inorganic Chemistry***).

Phosphate structures are generally rigid, resistant to chemical attack, and (when anhydrous) insoluble and thermally stable. This leads to some applications as nuclear waste immobilization hosts or negative thermal expansion materials. Many solid phosphate hosts permit diffusion of extra-framework species, leading to potential uses as ion exchangers (*see Ion Exchange*) and conductors (*see* ***Ionic Conductors***), and as microporous catalysts (*see* ***Porous Inorganic Materials*** and ***Zeolites***). Phosphate anions do not absorb significantly in the UV-visible region and so solid phosphates can also find use as optical materials such as glasses, phosphors (*see Phosphorescence*), nonlinear media (*see Nonlinear Optical Materials*) and lasers.

Solid phosphates constitute many minerals, notably Apatites, which are also found in living organisms as rigid components such as bones and teeth (*see* ***Biomineralization***). Amorphous Phosphorite deposits are important sources of phosphate fertilizers.

2 PHOSPHATE ANIONS

Solid phosphates are conveniently classified according to the anions they contain.

2.1 Orthophosphates

The orthophosphate group, $PO_4{}^{3-}$, (often shortened to 'phosphate') is the most ubiquitous oxyanion of phosphorus. In solid orthophosphates, all four oxygen atoms are usually coordinated to cations resulting in a strongly bonded three-dimensional framework, although layered or chain structures sometimes result.

The covalent bonding in the tetrahedral $PO_4{}^{3-}$ anion may be described as the average of four resonance hybrids such as (**1**), giving the average structure (**2**) with tetrahedral (T_d) symmetry. These two views of the bonding illustrate important features of phosphate chemistry. (**1**) shows that up to three

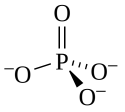

(**1**)

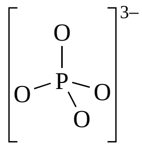

(**2**)

covalent (P)O–X bonds may be formed with high-valent elements X, notably P^V in condensed phosphates, whereas (**2**) shows that all four oxygen atoms are equally involved in predominantly ionic bonding in metal orthophosphates. In ionic phosphates, terminal P=O and $P–O^-$ bonds within the same tetrahedral group are equivalent and are strengthened by P:3d$_{\pi}$-O:2p$_{\pi}$ overlap (*see* π*-Bond*).

The orthophosphate group usually displays a near-regular tetrahedral geometry. Analysis of geometric data from 85 reliably determined crystal structures gives a mean P–O bond length (*see Bond Length*) of 1.536 Å with distances lying in the range 1.50–1.58 Å, and tetrahedral angles between 97 and 115°.**4** Distorted geometries can occur when the orthophosphate group acts as a bidentate ligand (*see Ligand*), resulting in a strained four-membered ring. (**3**) shows the geometry of the ring formed by phosphate tetrahedra and CrO_6 octahedra sharing a common edge in α-$CrPO_4$, as determined by low-temperature neutron diffraction.**5**

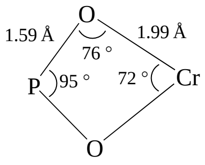

(**3**)

The acid orthophosphate anions, (mono)hydrogenphosphate $HPO_4{}^{2-}$ and dihydrogenphosphate $H_2PO_4{}^-$, also have extensive solid-state chemistries. Protonation lowers the bonding symmetry as the P–O(H) bonds have single bond character and the unprotonated oxygens are consequently bonded more strongly to phosphorus. Analysis of 21 acid orthophosphate structures gives P–O(H) distances in the range 1.56–1.62 Å,**4** whereas the average P–O_t bond distance (O_t = terminal oxygen) of 1.52 Å is slightly shorter than that in orthophosphates. The unprotonated oxygen atoms are readily coordinated to cations whereas the protonated sites are often uncoordinated, but are hydrogen bonded to nearby P–OH groups or other suitable species. This tends to result in more open structures with lower dimensionalities for acid orthophosphates than for orthophosphates.

The great diversity of orthophosphates is illustrated throughout this entry. Structural variety results from the large number of cations that form stable orthophosphates and the incorporation of additional molecules, notably water, or anions. Virtually every metallic element forms an orthophosphate, sometimes in a variety of oxidation states, for example, from V^{II} to V^V in $NaV^{II}V^{III}{}_2(PO_4)_3$, $V^{III}PO_4$, $V^{IV}O(H_2PO_4)_2$, and V^VOPO_4. The former compound is one of many mixed valent orthophosphates (*see* ***Mixed Valence Compounds***). A very large number of mixed cation orthophosphates are also known; a complex example is $Mg_{21}Ca_4Na_4(PO_4)_{18}$. Hydrated phosphates are common, and variation of the water content may be possible; $VO(HPO_4)\cdot nH_2O$ structures have been characterized for $n = 1/2$, 1, 2 (two forms), 3, and 4.**6** Orthophosphates containing additional anions include $Ca_2(PO_4)F$, $Fe_2(PO_4)O$, $Ca_{10}(PO_4)_6S$, $LiMn(PO_4)(OH)$, $Zr_2(WO_4)(PO_4)_2$, $Ca_5(PO_4)_2(SiO_4)$, $Pb_3Mn(PO_4)_2(SO_4)$, and $Na_3Ca(SiO_3)PO_4$(containing an infinite catenasilicate chain). Solid solutions involving substitutions of the cations or the orthophosphate group (e.g. for ortho- arsenate, vanadate, and silicate groups) further extend the range of possible phases.

2.2 Diphosphates

The diphosphate anion, $P_2O_7{}^{4-}$ (also known as pyrophosphate), is the simplest polyphosphate anion and is found in many solids. Variations in composition and structure are similar to those described above for the orthophosphates.

The bonding and consequent geometry of the O_b-PO_3 (O_b = bridging oxygen) group is very similar to that of the (H)O–PO_3 group. P–O_b distances are in the range 1.58–1.64 Å whereas the reported mean P–O_t distance for 17 diphosphates is 1.512 Å.**4** P–O–P angles lie in the range 120–160°. Unusually large values are a result of disorder of the bridging oxygen atom, notably in the 'linear', centrosymmetric diphosphate groups (**4**) present in Thortveitite type transition metal diphosphate structures, $M_2P_2O_7$. Disorder is evidenced by anomalous P–O_b distances and O_b-P–O_t angles, and a large amplitude of thermal vibration for the bridging oxygen. Careful refinement of $Mn_2P_2O_7$ using single crystal X-ray and powder neutron diffraction data shows that the bridging oxygens lie 0.2 Å on either side of the inversion center, giving a P–O–P angle of 166°, in better agreement with well ordered diphosphate groups.**7** In general, apparently linear P–O–P linkages in condensed phosphates arise from such disorder and do not reflect a stable geometry.

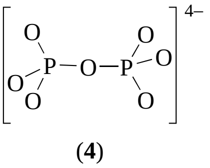

(**4**)

All three acid diphosphate anions have been found in the solid state, for example, $Mn(HP_2O_7)$, $Na_2(H_2P_2O_7)\cdot 6H_2O$, and $Cs(H_3P_2O_7)\cdot H_2O$. However, trihydrogendiphosphate salts are rare owing to the low pK_a (*see Acidity Constants*) of the doubly protonated phosphate group (*cf* H_3PO_4 has p$K_1 = 2.1$). The bridging oxygen is of very low basicity and does not coordinate even to highly charged cations. This is a universal feature in the chemistry of condensed phosphates.

2.3 Polyphosphates

Linking phosphate tetrahedra into chains through two vertices results in polyphosphate anions, $P_nO_{3n+1}{}^{(n+2)-}$, also known as oligophosphates.**[8]** Examples are shown in Table 1. Finite chains containing up to six tetrahedra have been found in the solid state. They become less common with increasing n.

A large number of anhydrous and hydrated triphosphates have been characterized, including structures containing the mono- and dihydrogentriphosphate anions. Only the terminal phosphate groups are protonated, as bridging –$OP(O_2H)O$– groups have lower pK_a's. The layered triphosphates $MH_2P_3O_{10}\cdot 2H_2O$ ($M = Al$, Cr, Mn, Fe) are intercalation hosts (*see* ***Intercalation Chemistry***) like the lamellar orthophosphates described in Section 5.3.

Tetraphosphates are less common than triphosphates, and the best-defined examples are crystalline, anhydrous materials. An acid tetraphosphate, $(NH_4)_4H_2P_4O_{13}$, has been reported. Pentaphosphate anions have been structurally characterized in $Mg_2Na_3P_5O_{16}$, $CsM_2P_5O_{16}$ ($M = V$, Fe) and the mixed phosphate $Rb_2Ta_2H(PO_4)_2(P_5O_{16})$. One hexaphosphate, $Ca_4P_6O_{19}$, has been reported, but the structure has not been determined. There is evidence for longer polyphosphate anions up to at least $P_8O_{25}{}^{10-}$ in solution, but no well-defined solid derivatives have yet been prepared.

A number of solid structures containing two polyphosphate anions have been reported. All have complex stoichiometries involving at least two cationic species, examples are $K_2Ni_4(PO_4)_2P_2O_7$, $CsTa_2(PO_4)_2P_3O_{10}$, $NH_4Cd_6(P_2O_7)_2P_3O_{10}$, and $CaNb_2O(P_2O_7)P_4O_{13}$. $KAl_2(H_2P_3O_{10})P_4O_{12}$ contains the dihydrogentriphosphate and cyclotetraphosphate anions

Table 1 Polyphosphates and cyclophosphates classified by the number of linked tetrahedra, n

n	Polyphosphates	Cyclophosphates
3	$Na_5P_3O_{10}$, $FeH_2P_3O_{10}\cdot H_2O$, $KEuHP_3O_{10}$	$K_3P_3O_9$, $Cd_3(P_3O_9)_2\cdot 7H_2O$, $LiFeP_3O_9$
4	$Gd_2P_4O_{13}$, $(NH_4)_6P_4O_{13}\cdot 2H_2O$, $(NH_4)_2SiP_4O_{13}$	UP_4O_{12}, $CoAg_2P_4O_{12}\cdot 5H_2O$, $KNdP_4O_{12}$, $Yb_4(P_4O_{12})_3$
5	$Na_3Mg_2P_5O_{16}$, $CsV_2P_5O_{16}$	$Na_4(NH_4)P_5O_{15}\cdot 4H_2O$
6	$Ca_4P_6O_{19}$	$K_6P_6O_{18}$, $Cu_3P_6O_{18}\cdot 14H_2O$, $Ag_4Li_2P_6O_{18}\cdot 2H_2O$
8	$Na8P_8O_{24}\cdot 6H_2O$,$Cu_3(NH_4)_2P_8O_{24}$, $Ag_9NaP_8O_{24}(NO_3)_2\cdot 4H_2O$	
10		$K_{10}P_{10}O_{30}\cdot 4H_2O$, $Ag_4K_6P_{10}O_{30}\cdot 10H_2O$
12		$Cs_3V_3P_{12}O_{36}$

2.4 Cyclophosphates

Previously known as cyclopolyphosphates, these rings may contain up to 12 tetrahedra, but those with three, four, and six units are most common (see Table 1). The cyclotri- and cyclotetraphosphate rings adopt puckered geometries typical of saturated six and eight atom rings. The predominance of even membered cyclophosphates reflects their ability to pack efficiently in the solid state, rather than any inherent stability over odd membered ones. This is often reflected by a high internal symmetry in the crystalline state; an analysis of thirty reliably determined cyclohexaphosphate structures shows that 18 have inversion symmetry and a further seven have threefold (D_{3d}) internal symmetry.**[9]**

Both hydrated and anhydrous cyclophosphates have been prepared, but no acid anions have been found in these solids owing to the low basicity of two-connected phosphate groups. A common structural feature, especially with large rings, is the formation of layers of cyclophosphate groups. This enables a large range of hydration numbers to be observed, as cations can be coordinated between two layers in anhydrous salts, or by cyclophosphate groups on one side and water molecules on the other in some hydrated compounds. Fully hydrated cations can also lie between the layers and further noncoordinated water molecules may occupy the intra-annular and interlamellar spaces. Examples of highly hydrated cyclohexaphosphates are $Nd_2P_6O_{18}\cdot 12H_2O$ and $Cu_3P_6O_{18}\cdot 14H_2O$.

2.5 Catenaphosphates

The infinite chain catenaphosphate anion $(PO_3{}^-)_\infty$ represents the infinite limit of the poly- and cyclophosphate series. Catenaphosphates are formed at high temperatures and so all reported structures are anhydrous, for example, $Al(PO_3)_3$, $UO_2H(PO_3)_3$, and $Cs_2Co(PO_3)_4$. $P–O_t$ and $P–O_b$ distances are ~ 1.48 and ~ 1.60 Å, respectively, similar to values for two-connected phosphate tetrahedra in other anions. The cations lie between parallel, infinite polyphosphate chains resulting in strongly bonded three-dimensional structures. Thermal decomposition of hydrogenphosphates has resulted in the acid catenaphosphates $Na_2H(PO_3)_3$, $BiH(PO_3)_4$ and $UO_2H(PO_3)_3$. In $BiH(PO_3)_4$, one of the terminal oxygens on every fourth phosphate tetrahedron is protonated; this is the only nonbridging oxygen not to coordinate to Bi^{3+}.

As cyclophosphates and the catenaphosphate anion (together termed metaphosphates) share the basic composition $(PO_3{}^-)_n$, crystal-structure analysis is often the only way to determine which species is present, although IR spectroscopy may be useful (see Section 3.2.1). Different isomers of the same metaphosphate composition are often found. Six crystal forms (A-F) of $M(PO_3)_3$ ($M = Al$, Cr, Mn, Fe, Ga) have been identified, three of which have been structurally characterized and found to contain cyclotetraphosphate (form A), cyclohexaphosphate (B), and catenaphosphate (C) anions.

However, structures containing two metaphosphate anions are very rare, an example is $Pb_2Cs_3(P_4O_{12})(PO_3)_3$ in which both cyclotetraphosphate and catenaphosphate groups are present.

2.6 Ultraphosphates

Possible ultraphosphate anions containing x two-connected and y three-connected tetrahedra have stoichiometry $P_{x+y}O_{3x+5y/2}{}^{x-}$. All observed anions have $y = 2$, and so may be written $P_nO_{3n-1}{}^{(n-2)-}$, where $n = 4$, 5, 6, and 8.**10** Solid ultraphosphates are anhydrous, as the P–O–P bridges between three-connected phosphate tetrahedra are susceptible to hydrolysis. The potential of lanthanide ultraphosphates MP_5O_{14} as laser materials has driven the exploration of ultraphosphate chemistry. The list of characterized ultraphosphates is now MP_4O_{11} (M = Mg, Ca, Mn, Co, Ni, Cu, Zn), MP_5O_{14} (M = Lanthanide, Y, Bi), $NiHP_5O_{14}$, $M_2P_6O_{17}$ (M = Ca, Cd, Sr), $(UO_2)_2P_6O_{17}$, $(TaO_2)_4P_6O_{17}$, and $Na_3MP_8O_{23}$ (M = Al, V, Cr, Fe, Ga). The structures of these anions vary from discrete anions to infinite ribbons, sheets, and three-dimensional frameworks.

The MP_4O_{11} structures contain infinite layers of fused eight- and twelve-membered rings, but the MP_5O_{11} structures vary with the cation radius and fall into three principal types. Types I (M = La-Ho, Bi) and III (M = Dy-Lu, Y) both contain infinite ribbons (**5**), while in type II materials (M = Tb-Lu, Y) a complex three-dimensional phosphate framework is formed. A unique polymorph of CeP_5O_{11} contains infinite sheet anions. Sheets of fused 14-membered rings are found in $M_2P_6O_{17}$ compounds, whereas $UO_2P_6O_{17}$ contains an infinite three-dimensional anionic network. The $Na_3MP_8O_{23}$ structure contains the unique cage phosphate anion $P_8O_{23}{}^{6-}$ (**6**), which has a threefold symmetry axis. This is the only molecular ultraphosphate anion to have been characterized.

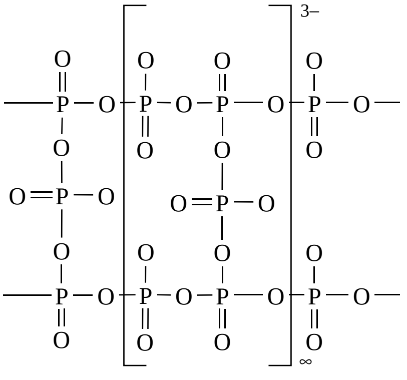

(**5**) $P_5O_{14}{}^{3-}$

Phosphorus pentoxide may be regarded as a neutral ultraphosphate containing only three-connected phosphate tetrahedra. Two extended forms of P_2O_5 are known, one containing infinite sheets, and the other a three-dimensional framework. The third form, molecular P_4O_{10} (**7**), consists of four tetrahedra each joined through three vertices and is the most highly condensed phosphate species.

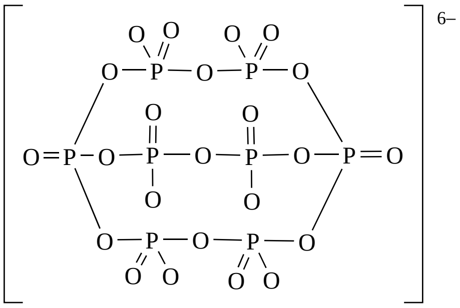

(**6**)

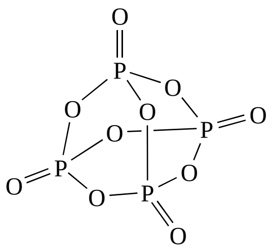

(**7**)

2.7 Substituted Anions

Condensing phosphate tetrahedra with other $XO_4{}^{n-}$ groups results in P-substituted anions such as the polyphosphate derivatives $Na_3PS_2O_{10}$, $Na_4P_2S_2O_{13}$, $Na_3PCr_3O_{13}\cdot 3H_2O$, and $Li_3PCr_4O_{16}$. The phosphate groups are found in the bridging positions of these chains. Infinitely extended tetrahedral anions formed by condensing phosphate and other tetrahedral groups are described in Section 5.1.

Electronegative nonmetals can substitute for oxygen in phosphate anions. Many fluoro- and difluoro-orthophosphates are known, for example, $CaPO_3F\cdot 2H_2O$, $Cu(PO_2F_2)_2$, and sodium salts of all the thioorthophosphate anions $PO_{4-n}S_n{}^{3-}$ ($n = 1$–4) have been crystallized. Condensed thiophosphates have also been reported, for example, $Cs_3P_3O_6S_3$ and $Na_4P_4O_8S_4\cdot 6H_2O$, and analogous cycloimidophosphate anions are found in $K_3P_3O_6(NH)_3$ and $Cs_4P_4O_8(NH)_4\cdot 6H_2O$. In the cyclothiophosphates, one terminal sulfur atom is present on each phosphate unit, however, the NH groups occupy the bridging positions in the cycloimidophosphate rings. Many monovalent and divalent cation salts of the $P_3O_6(NH)_3{}^{3-}$ anion have been prepared. $AgPO_2(NH_2)_2$ is a rare example of a diamidophosphate, the nitrogen analog of a dihydrogenphosphate.

3 CHARACTERIZATION

3.1 Diffraction Methods

These provide the most complete structural characterization for crystalline phosphates (*see* ***Diffraction Methods in Inorganic Chemistry***). Single crystal X-ray diffraction is used whenever possible, but powder X-ray diffraction (*see* ***Solids: Characterization by Powder Diffraction***) has been applied increasingly over the last decade to the many phosphates that can only be prepared in a polycrystalline form. Unknown structures determined using powder data include $KZrH(PO_4)_2$, $VOHPO_4{\cdot}2H_2O$, the framework aluminophosphates MCS-1 and SAPO-40, and the zeolitic nickel(II) phosphate VSB-5 using laboratory X rays, and α-$CrPO_4$,[5] $MnPO_4{\cdot}H_2O$, and $(VO)_3(PO_4)_2{\cdot}9H_2O$ from highly resolved synchrotron X-ray diffraction data.

Neutron diffraction is used to determine oxygen positions precisely and to locate hydrogen atoms in hydrated or acid phosphates, enabling hydrogen bonding arrangements to be elucidated. Electron diffraction and High-Resolution Electron Microscopy (*see Electron Microscopy*) imaging can be applied to structures that have at least one simple projection, such as the phosphate tungsten bronzes discussed in Section 6.1.

3.2 Spectroscopies

Vibrational and nuclear magnetic resonance (NMR) spectroscopies complement diffraction methods in the study of solid phosphates. They characterize the local environments around phosphate tetrahedra such as the number of bridges to other phosphate groups and the nature of local cations. They are particularly useful in the study of highly disordered or amorphous phosphates.

3.2.1 Vibrational

Infrared (*see Infrared Spectroscopy*) and Raman (*see Raman Spectroscopy*) spectroscopies are used to study the vibrations of P–O bonds in solid phosphates. The frequencies and splittings of the stretching and bending vibrations can be related to the local symmetry and connectivity of the phosphate groups. Coupling of the phosphate bending vibrations with low-frequency lattice modes may be significant for light or strongly bonded cations so that features in the P–O stretching region (700–1400 cm^{-1}) are of greatest diagnostic use (Table 2).[11] However, even these vibrations may be shifted when strong M–O(P) bonds are present so that they are no longer characteristic of the anion alone.

The IR spectrum of a tetrahedrally symmetric (T_d) orthophosphate anion is characterized by a strong transition in the stretching region (Table 2) and a strong bending mode at 500–600 cm^{-1}. The Raman spectrum is dominated by the totally symmetric stretch. These bands may be broadened or split if the anions are distorted from T_d symmetry. Both the IR and Raman spectra of orthophosphates are notable for an absence of bands in the 700–900 cm^{-1} region, unlike condensed phosphates, but hydrogenphosphate groups or other species (e.g. H_2O) may contribute in this region. Acid

Table 2 Infrared and Raman stretching frequency ranges (cm^{-1}) for phosphate anions in the solid state.[11] The intensities of the bands (s = strong, m = medium, w = weak) and their assignments (s = symmetric, as = antisymmetric vibrations) are shown

Anion	IR	Raman
$PO_4{}^{3-}$	1000–1070(s) as(PO_4)	930–970(s) s(PO_4)
$P_2O_7{}^{4-}$	720–750(w) s(POP)	720–750(s) s(POP)
	900–950(s) as(POP)	1010–1020(s) s(PO_3)
	1070–1120(s) as(PO_3)	
$P_nO_{3n+1}{}^{(n+2)-}$ (Polyphosphates)	900–940(s) as(POP)	1000(s) s(PO_3)
	1120–1150(s) as(PO_3)	1100–1160(s) s(PO_2)
	1200–1300(s) as(PO_2)	
$P_nO_{3n}{}^{n-}$ (Cyclophosphates)	$n = 3$ 760–780(s) s(POP)	$n = 3$ 620–650(m) s(POP)
	$n = 4$ 670–750(m)	
	$n = 3,4$ 970–1050(s) as(POP)	$n = 3,4$ 650–690(s) s(POP)
	$n \geq 6$ 910–940(s)	$n \geq 6$ 700–760(s)
	1250–1300(s) as(PO_2)	1150–1200(s) s(PO_2)
$(PO_3{}^{-})_\infty$ (Catenaphosphates)	670–780(m) s(POP)	650–750(s) s(POP)
	860–950(s) as(POP)	1150–1200(s) s(PO_2)
	1250–1300 as(PO_2)	
$P_nO_{3n-1}{}^{(n-2)-}$ (Ultraphosphates)	600–800(w) s(POP)	600–800(w) s(POP)
	950–1050(s) as(POP)	1150–1200(s) s(PO_2)
	1250–1300(s) as(PO_2)	
	1300–1400(s) (PO)	

phosphate groups are also distinguished by O–H stretches at 2300–2800 cm^{-1}.

Diphosphates are distinguished from orthophosphates by the vibrations of the P–O–P bridge. The antisymmetric P–O–P stretch (ν_{as}) gives a strong IR absorption at 900–950 cm^{-1}, whereas the symmetric stretch (ν_s) around 750 cm^{-1} is weak in the IR spectrum, and may not be apparent in near-linear diphosphates such as $Mn_2P_2O_7$, but is strong in the Raman spectrum. In the approximation that the P–O–P unit vibrates independently from the rest of the anion, the quantity Δ (equation (1)) is predicted to vary smoothly with the bridge angle. This has been verified using data from 15 diphosphates;**[11]** the resulting curve enables the P–O–P angle to be estimated from the vibrational spectrum.

$$\Delta = \frac{(\nu_{as} - \nu_s)}{(\nu_{as} + \nu_s)} \qquad (1)$$

Correlations between the structures and vibrational spectra of finite polyphosphate chains have not been widely investigated. The spectra are complex owing to the presence of, and coupling between, bridging PO_2 and terminal PO_3 groups. As the chain length increases the PO_2 group frequencies increase to approach those in catenaphosphates.

Metaphosphates are characterized by the high frequencies of the asymmetric and symmetric PO_2 stretches in their IR and Raman spectra, respectively. The $(\text{–P–O–})_n$ rings in cyclophosphates give diagnostic vibrations in the 600–850 cm^{-1} region, which can be used to identify cyclotri- and cyclotetraphosphates (Table 2). The antisymmetric stretch of the $(\text{–P–O–})\infty$ chain at ~900 cm^{-1} distinguishes catenaphosphates from the common small-ring cyclophosphates.

The short, strong P=O bond in ultraphosphates gives the highest IR absorption of all phosphates, at 1300–1400 cm^{-1}. Otherwise the spectra of ultraphosphates (which consist of fused rings) resemble those of cyclophosphates.

3.2.2 NMR

NMR spectroscopy is extremely useful for the study of phosphates,**[12]** as the ^{31}P nucleus has a spin of 1/2 and is 100% abundant. The magic angle spinning technique (MASNMR) is used to obtain highly resolved spectra from solid phosphates with linewidths of a few ppm, comparable to those of solution ^{31}P spectra. Information about the local environments in solid phosphates is derived from the number and intensities of ^{31}P signals, their anisotropies and mean (isotropic) chemical shifts, possible spin–spin couplings through asymmetric P–O–P bridges, and any line broadening interactions. MASNMR can also be used to study kinetic processes, such as the crystallization of the phosphates from solution.

The isotropic ^{31}P chemical shifts move to high-field values with increasing connectivity of phosphate tetrahedra and increasing charge on the coordinated cations. For orthophosphates and one-, two- and three-connected phosphate tetrahedra the isotropic shifts usually lie in the ranges -30 to $+15$, -35 to $+5$, -50 to -5, and -65 to -45 ppm, respectively. The sensitivity of the chemical shift to local cations can be used to resolve different local environments in disordered materials.

Paramagnetic cations can give a large contact or pseudo-contact shift and may broaden the ^{31}P resonance. Chemical shifts of up to 1650 ppm have been found in vanadyl phosphates and used to estimate the magnetic exchange constants between vanadyl electronic spins.**[6]**

The anisotropy of the chemical shift tensor reflects the asymmetry in the bonding to the four oxygens, and so increases with increasing connectivity of the phosphate tetrahedra. A MASNMR study of the crystalline forms of P_2O_5 reveals axially symmetric chemical shift tensors in all three cases. The shifts perpendicular and parallel to the principal axis lie in the ranges -52 to -24 and $+211$ to $+244$ ppm. This axis corresponds to the P=O direction as the double bond gives a strong shielding.

4 SYNTHESIS

Preparative routes for solid phosphates are typical of those used in solid-state chemistry. Reactions in which cations and phosphate anions are combined can take place in solution under atmospheric or hydrothermal pressures, or by direct combination at high temperatures. Transformations of phosphates into new structures can be achieved thermally or through topotactic exchange reactions. Hydrothermal and chemical vapor transport techniques are used to facilitate crystal growth.

4.1 Solution

Soluble phosphates can be deposited from aqueous solutions, and this method may also yield suitable single crystals for structure determination and physical measurements. This method is commonly used to obtain hydrated and acid phosphates of soluble cations, for example, alkali and alkaline earth metals, NH_4^+. Acid phosphates such as KDP (KH_2PO_4) may be prepared by partial neutralization of phosphoric acid with metal hydroxides or carbonates.

Insoluble phosphates can be precipitated by mixing cation and phosphate solutions, or by generating one species in situ, for example equation (2). Condensed phosphates can be prepared from polyphosphoric acids, made by adding a small amount of water to P_2O_5.

$$Mn^{2+}{}_{(aq)} + PO_4{}^{3-}{}_{(aq)} \xrightarrow{\text{c. HNO}_3} Mn^{III}PO_4{\cdot}H_2O_{(s)} \qquad (2)$$

4.2 Hydrothermal

Phosphates of divalent and more highly charged cations are usually insoluble at ambient pressures, and precipitated samples are often poorly crystalline. The solubility of such phosphates increases at higher temperatures and pressures, and so hydrothermal conditions are used to obtain more crystalline products, as well as many phases not observed at atmospheric pressure (*see* ***High Pressure Synthesis of Solids***). This method is also used to grow large single crystals of materials such as $KTiOPO_4$ (Section 5.2.2).

Hydrothermal bombs containing aqueous mixtures of a metal compound and phosphoric acid are typically heated to temperatures of 100–350 °C, generating autogenous pressures up to 300 bar. The pressure rises more rapidly above the critical temperature of water, 373 °C, and hydrothermal pressures of ~3000 bar are typically generated at 600–1000 °C in sealed metal tubes surrounded by a supporting pressure of an inert gas.

The products of such reactions depend upon the pressure, temperature, pH, phosphate, and cation concentrations, and may be difficult to predict or rationalize. For example, the equation (3) produces an acid phosphate and a phosphate hydroxide. Microporous aluminophosphates and related phases (see Section 5.1.2) are prepared in hydrothermal bombs using hydrated cations or molecular templates such as organic amines or ammonium cations to direct the porous framework. Many new structures with metal phosphate chains, layers, or three-dimensional networks have been prepared hydrothermally in recent years, for example, templated vanadium phosphates[13] and iron phosphates.[14]

$$\begin{aligned} Fe_2O_3 + {\sim}3H_3PO_4 &\xrightarrow{700\,^{\circ}C,\ 3\,\text{kbar}} Fe_2(P_2O_7)(HPO_4) \\ &\quad + Fe_4(OH)_3(PO_4)_3 \end{aligned} \tag{3}$$

4.3 Solid State

Heating intimate mixtures of a metal salt and P_2O_5 or an ammonium phosphate is a convenient route to many anhydrous phosphates. To minimize evaporation of P_2O_5, the reactants are often dissolved in dilute acid and the solution is heated to dryness, giving a precursor residue for firing. This method gives a good control of stoichiometry, for example, $CrPO_4$, $Cr_4(P_2O_7)_3$, or $Cr(PO_3)_3$ may be obtained by varying the Cr:P ratio in the initial solutions.

4.4 Ion Exchange

Ion-Exchange (*see Ion Exchange*) reactions in solution are used to produce phosphates of soluble cations, for example, equation (4). Solid-state reactions such as (5) and (6) may be used to exchange mobile cations and are usually topotactic (*see Topotactic*). In the notable equation (6), the exchange of Li^+ for H^+ is accompanied by a migration of the Mn^{3+} cations from one set of octahedral sites to another, within an unchanged $(PO_4)(OH)$ lattice.[15]

$$Ag_6P_6O_{18}\cdot H_2O + 6NaCl_{(aq)} \longrightarrow Na_6P_6O_{18} + 6AgCl \tag{4}$$

$$\alpha\text{-}Zr(HPO_4)_2 \xrightarrow{\text{NaCl, }200\,^{\circ}C} ZrNaH(PO_4)_2 + ZrNa_2(PO_4)_2 \tag{5}$$

$$MnPO_4\cdot H_2O \xrightarrow{LiNO_3,\ 200\,^{\circ}C,\ 4\text{ weeks}} LiMnPO_4(OH) \tag{6}$$

4.5 Thermal Transformations

Gentle dehydration gives many anhydrous phosphates. Further thermal decomposition often yields new phases; in particular, dehydration of acid phosphates can result in condensed phosphate anions. If neighboring hydrogenphosphate groups are present then the new structure may be related to the old, for example, the dehydration (**7**) is thought to form diphosphate bridges between the zirconium phosphate layers (see Section 5.3.1). The structures of the reactant and product in equation (8) are so closely related that a single crystal of the hydrogenphosphate may be thermally transformed into a crystal of the diphosphate.[16] Equations (9) and (10) exemplify the formation of more highly condensed phosphates.

$$\alpha\text{-}Zr(HPO_4)_2 \xrightarrow{\Delta} ZrP_2O_7 + H_2O \tag{7}$$

$$2Fe_2(P_2O_7)(HPO_4) \xrightarrow{\Delta} Fe_4(P_2O_7)_3 + H_2O \tag{8}$$

$$\begin{aligned} Ga(H_2PO_4)_3 &\xrightarrow{140\,^{\circ}C} GaH_2P_3O_{10}\cdot 2H_2O \xrightarrow{230\,^{\circ}C} GaH_2P_3O_{10} \\ &\longrightarrow Ga(PO_3)_3 \end{aligned} \tag{9}$$

$$NH_4GaHP_3O_{10} \xrightarrow{450\,^{\circ}C} Ga_2P_6O_{18} \tag{10}$$

4.6 Flux Growth

Slow cooling of phosphate-rich melts can be used to grow large crystals for optical characterization, for example, the lanthanide ultraphosphates, MP_5O_{14}, are grown from M_2O_3–P_2O_5–H_2O melts by cooling from 400–500 °C. Phosphate glasses are obtained by quenching melts.

4.7 Vapor Transport (*see Chemical Vapor Deposition*)

Anhydrous metal phosphates can be transported across thermal gradients at high temperatures (~1000 °C) using halogens as carrier gases. Transport takes place through the formation and decomposition of volatile metal and phosphorus halides and oxyhalides.[17] This method has been used to grow crystals of several phosphates, for example, $TiPO_4$, $Fe_2P_2O_7$, RhP_3O_9, and to prepare the new compounds such as the low-valent chromium diphosphates $Cr_2P_2O_7$ and $Cr_3(P_2O_7)_2$.

5 STRUCTURAL CLASSES

Solid phosphates show a huge variety of crystal structures, and it is not practical to classify them in terms of structural types as is done with simple oxides, halides, etc. However, some general classes of metal phosphate structures will be considered: three-dimensional frameworks of linked phosphate tetrahedra and tetrahedrally or octahedrally coordinated cations, layered phosphates, and phosphate glasses. In all of these materials the size and topology of pores within the structure are of importance, as these determine the ability of ions and molecules to move within the structure, giving rise to useful ion exchange, ionic conduction, or catalytic properties. Ion exchange can also be used to modify the properties of the host network, for example, the nonlinear optical behavior of potassium titanyl phosphate (KTP) derivatives.

5.1 Tetrahedral Networks

Phosphate tetrahedra can share up to three apices with each other or tetrahedral anions of high-valent elements. This limits the formation of infinite phosphate anions to the catena and ultraphosphates. However, with MO_4^{n-} groups of divalent or trivalent cations, in which there is a strong ionic component to the (P)O–M bonding, all four corners of the phosphate group may be shared. This enables infinite networks of alternating PO_4 and MO_4 tetrahedra to be prepared, analogous to highly connected silicate structures (*see* ***Zeolites***).

5.1.1 Silicophosphates

In well-defined silicophosphate anions, the phosphate groups are found to be one or two-connected owing to the covalent nature of the P–O–Si bonds. However, the silicate groups share all four corners enabling infinite anion networks to be built up in some cases. Simple columnar anions are found in $VO(P_2SiO_8)$ and $Cd_2(P_4SiO_{11})$ consisting of silicate tetrahedra bridged by phosphate (**8**) and diphosphate groups, respectively.

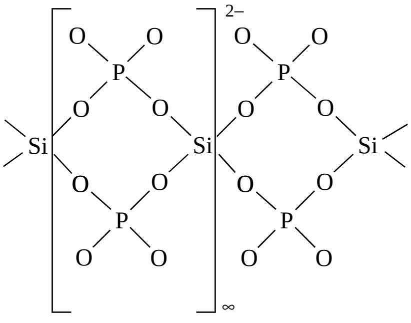

(**8**) $SiP_2O_8^{2-}$

The discrete $(P_6Si_2O_{25})^{12-}$ anion $[O(Si(OPO_3^{2-})_3)_2]$ is found in a large number of solids: $M_3P_6Si_2O_{25}$ (M = Si, Ge) $AM_3P_6Si_2O_{25}$ (A = K, Rb, Cs, Tl; M = Mo, Ti) and $M_3P_5SiO_{19}$ (M = V, Mo). The latter compounds may be written $M_6(P_6Si_2O_{25})(P_4O_{13})$ as they contain separate $(P_6Si_2O_{25})^{12-}$ and tetraphosphate anions. $Si_5P_6O_{25}$ is notable for containing two tetrahedrally coordinated and three octahedrally coordinated silicon atoms. In MP_3SiO_{11} (M = Fe, Mo, Ru), phosphate groups from different $P_6Si_2O_{25}$ units are linked through a shared apex to give an infinite three-dimensional silicophosphate framework of corner-sharing diphosphate and disilicate groups.

In addition to the above well-defined silicophosphates, there have been many attempts to substitute phosphate anions into four-connected silicate zeolites (*see* ***Zeolites***). Substitution of 5–25% phosphate into zeolites such as Faujasite have been reported, but these materials are less well-characterized than the aluminophosphates and silicon aluminophosphates described below.

5.1.2 Aluminophosphates and Metalloaluminophosphates

Tetrahedral networks containing equal amounts of M^{III} and P^V are silicate analogs. They are most common for M = Al, but tetrahedral structures with M = B, Ga, and Fe are also known, for example, the borophosphate $CsHB_2P_2O_9$.[18]

One-, two-, and three-dimensional aluminophosphate structures have been prepared.[19] An infinite chain anion is found in $MoOAlP_2O_8$ which is isomorphous to VOP_2SiO_8, with Al replacing Si in the anion (**8**). Sheet anions such as $Al_2P_3O_{12}^{3-}$ and $Al_3P_4O_{16}^{3-}$ have been prepared hydrothermally using various alkylammonium templates which lie between the layers.

$AlPO_4$ (the mineral Berlinite) is the aluminophosphate analog of SiO_2, and adopts a structure based on that of α-quartz, with Al and P atoms ordered in alternate layers. There has been considerable interest in making similar analogs of zeolitic silicates, known as aluminophosphates (AlPOs).[20] Many of these also display new microporous structures; a notable AlPO is the large pore material VPI-5 containing one-dimensional channels in which the connecting windows have diameters of 12 Å enabling the structure to reversibly sorb large molecules such as $(C_4F_9)_3N$.[21]

Further variation of the structural and catalytic properties of four-connected tetrahedral frameworks is obtained by the substitution of silicon or metal cations,[22] giving materials known as SAPO's and MeAPO's, respectively.[20] More than twenty metal aluminophosphate frameworks have been identified with Mg, Mn, Fe, Co, or Zn substituents. These give the possibility of framework redox activity (e.g. Fe^{2+}/Fe^{3+}) in catalysis as well as the usual Brønsted acidity. For further information about zeolitic and microporous phosphate frameworks (*see* ***Porous Inorganic Materials*** and ***Zeolites***) and recent reviews.[23,24]

5.1.3 *Divalent Metal Frameworks*

Be^{2+}, Mg^{2+}, Co^{2+}, and Zn^{2+} can form anionic tetrahedral networks, for example, the mineral Beryllonite, $NaBePO_4$, is isostructural with $NaAlSiO_4$. New microporous variants of $NaBePO_4$, $AgBePO_4$, and $AgZnPO_4$, in which the monovalent cations reside within the divalent metal phosphate framework, have been reported in recent years.

5.2 Octahedral-tetrahedral Frameworks

A vast number of transition metals and post-transition elements form phosphates in which the tetrahedral anions and octahedrally coordinated cations build up an infinite framework. Some notable examples follow.

5.2.1 *NASICON Types*

The framework of $NaZr_2(PO_4)_3$ consists of corner-sharing ZrO_6 octahedra and orthophosphate tetrahedra (Figure 1). Large cavities within the structure are linked by narrow passages to give a three-dimensional network of pores in which up to four cations per formula unit may be accommodated. In $NaZr_2(PO_4)_3$, Na^+ occupies the type I site in the cavities, and the three type II sites in the narrow connecting passages are vacant, whereas in the silicate analog $Na_4Zr_2(SiO_4)_3$, all four sites are filled. The two compounds form a complete series of solid solutions $Na_{1+x}Zr_2(PO_4)_{3-x}(SiO_4)_x$, $(0 < x < 3)$. The sodium ion conductivity of intermediate compositions is very much higher than those of the end members, owing to the expansion of the type II sites by substitution of silicate for phosphate, and the creation of sodium vacancies to compensate for the substitution of phosphate for silicate. Compositions in the range $1.8 < x < 2.2$ have very high ionic conductivities and have been named NASICON (NA Super Ionic CONductor) (*see* ***Ionic Conductors***).

$NaZr_2(PO_4)_3$ can be prepared by solid-state and hydrothermal reactions or grown as crystals from melts and ion-exchanged derivatives $AZr_2(PO_4)_3$ ($A = K$, NH_4, H) have been prepared. A large number of substituted NASICON frameworks are known, for example, $AM_2(PO_4)_3$ ($A = Na$, Ca, Sr, Ba; $M = Ti$, Mo), $Na_3M_2(PO_4)_3$ ($M = Sc$, Cr, Fe), $Na_3MgZr(PO_4)_3$, $NbTi(PO_4)_3$ and $Nb_2(PO_4)_3$. The channels are vacant in the latter two compounds.

5.2.2 *KTP Types*

$KTiOPO_4$, abbreviated to KTP, is an important nonlinear optical material (*see Nonlinear Optical Materials*).[25,26] Helical chains of TiO_6 octahedra are interlinked by orthophosphate groups to give a framework containing one-dimensional channels in which K^+ ions reside (Figure 2). The Ti^{4+} ions lie away from the centers of the octahedra owing to the formation of dipolar Ti=O 'titanyl' groups, and give rise to a net hyperpolarizability (a second order electric susceptibility), as the structure is acentric. KTP is an efficient second harmonic generator, converting the near-IR emission of Nd-YAG lasers (1064 nm) into blue–green light with twice the frequency (532 nm). It may also be used for optical frequency mixing, in electro-optic modulation devices and optical waveguides.

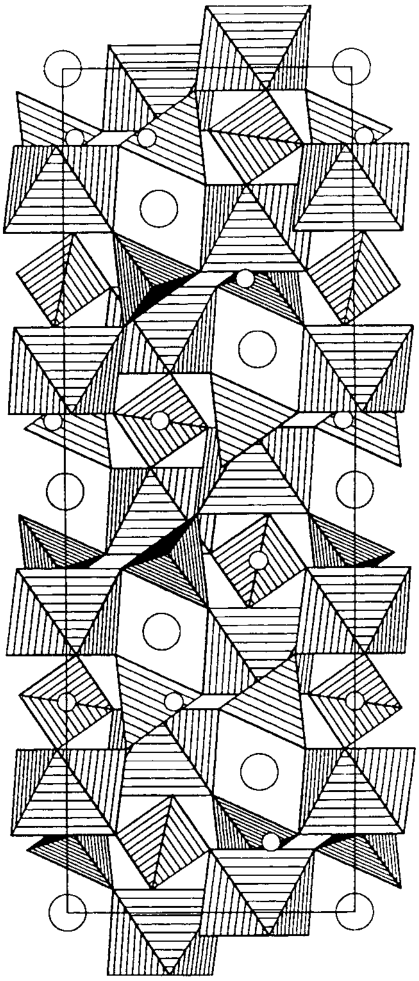

Figure 1 A polyhedral view of the NASICON unit cell containing linked ZrO_6 octahedra and PO_4 tetrahedra. Large and small circles represent type I and II Na^+ sites, respectively

KTP powders can be prepared by direct solid-state reactions, and single crystals are grown from K_2O–P_2O_5 fluxes or hydrothermally. The KTP structure permits a large number of cation substitutions. Attention has been focused on exchanging K for other cations to modify the nonlinear properties. $ATiOPO_4$ derivatives ($A = Rb$, Cs, Tl, NH_4) can be prepared directly and the $A = Na$ and Ag compounds are obtained by ion-exchange reactions of KTP with molten salts. KTP type frameworks can be prepared in which Ti is replaced by V, Ge, Sn, Zr, Ga or Nb, and P by As or Si. The phosphate fluorides NH_4MPO_4F ($M = Fe$, V) also adopt this structure.

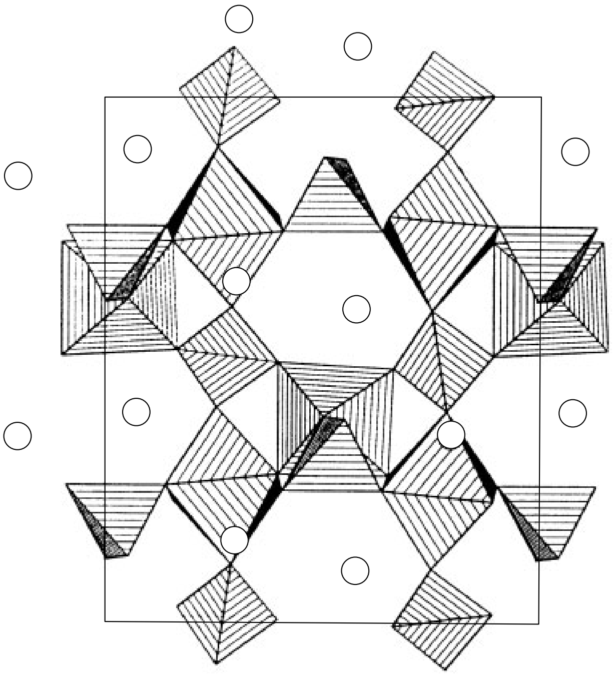

Figure 2 A projection of the cell of KTP showing the linking of TiO_6 octahedra by PO_4 tetrahedra and K^+ ions (circles) in the channels

5.2.3 Reduced Molybdenum Phosphates

Molybdenum forms a large number of phosphates, including Keggin ions such as $PMo_{12}O_{40}{}^{3-}$, and a large number of frameworks built from MoO_6 octahedra and phosphate tetrahedra. The Mo oxidation state in these solids is usually in the range $+3$ to $+5$ and the frameworks can vary from being densely packed, for example, MoP_2O_7, to layered and microporous structures containing large voids.**27** Similar framework structures are found in reduced phosphates of Ti, V, and Nb.**28**

The MoO_6 octahedra are often distorted owing to the formation of a strong Mo=O bond by Mo^V (*cf* Ti^{IV} in KTP above) and Mo–Mo bonds between face or edge-sharing octahedra. A single Mo^V–Mo^V bond is often found in dimeric units (**9**), and larger Mo–Mo bonded clusters or multiple bonds may result, for example, the triply bonded molybdenum dimer in $Cs_2[Mo^{III}{}_2(HPO_4)_4(H_2O)_2]$ (*see* ***Molybdenum: Inorganic & Coordination Chemistry***).

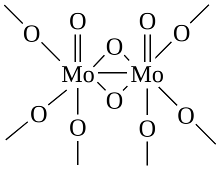

(**9**)

Dense octahedral-tetrahedral frameworks have been crystallized by heating alkali-metal, molybdenum, and phosphorus oxides with molybdenum metal in evacuated silica glass tubes at 900–1100 °C.**28** Many phases are formed as the Mo/P ratio and Mo oxidation state vary. For example, more than 15 compounds have been found in the Cs–Mo–P–O system; typical phases are $CsMoP_2O_7$, $CsMoP_2O_8$, $CsMo_2P_2O_{10}$, $CsMo_2P_3O_{13}$, $Cs_3Mo_4P_3O_{16}$, $Cs_3Mo_6P_{10}O_{38}$, and $Cs_4Mo_{10}P_{18}O_{66}$. Ortho- and diphosphate anions are found in these materials, and the latter phase contains both di- and triphosphate chains. Some of these structures, for example, $Cs_3Mo_4P_3O_{16}$, contain cubane-like Mo_4O_4 clusters of interpenetrating Mo_4 and O_4 tetrahedra in which the six Mo–Mo bonds are bridged by phosphate groups.

Open framework molybdenum phosphates with 15–40% micropore volumes can be prepared hydrothermally, providing further examples of phosphate-based porous inorganic materials (*see* ***Porous Inorganic Materials***). The $[Mo_2O_2(PO_4)_2H_nPO_4]^{(3-n)-}$ ($n = 1$, 2) framework (**10**) is particularly versatile; it is formed by inserting additional H_nPO_4 groups into the layered structure of $MoOPO_4$ (**11**), described in Section 5.3.2, and can accommodate Cs^+, H_3O^+, and $CH_3NH_3{}^+$ cations.

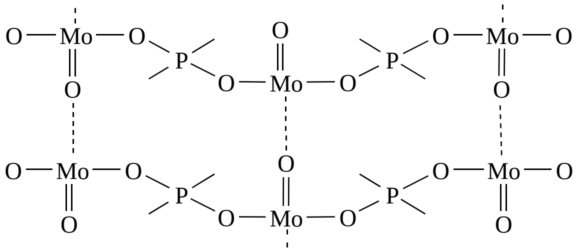

(**10**) $MoOPO_4$ layers

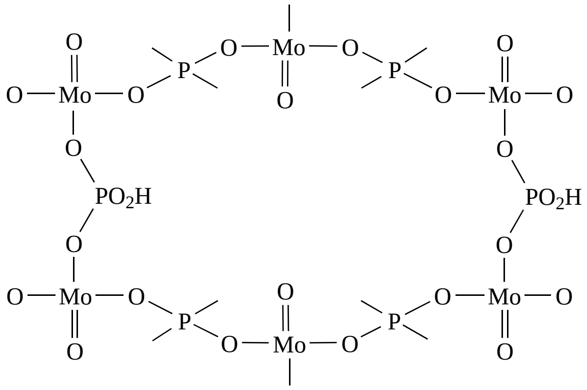

(**11**) $Mo_2O_2(PO_4)_2H_2PO_4{}^-$ framework

Hydrothermal preparations have also resulted in several layered materials such as $Na_3Mo_2O_4H(PO_4)_2{\cdot}2H_2O$ and alkylammonium derivatives of $Mo_4O_8(PO_4)_2{}^{2-}$. These show properties comparable to the materials described in the next section; the former material is a proton and sodium ion conductor and the latter can act as a host for intercalation and ion exchange chemistry.

5.3 Layered Phosphates

Lamellar materials can show similar ion exchange and conducting properties to the three-dimensional frameworks described above, but the additional ability to increase the interlayer spacing allows large molecules to be intercalated (*see* ***Intercalation Chemistry***). Pillaring the layers with large inorganic clusters or organic molecules can further enhance the intercalation of guest molecules. Many layered phosphates are known; three important examples are described below.

5.3.1 α-Zirconium Phosphate

The layered structure of α-$Zr(HPO_4)_2{\cdot}H_2O$ is shown in Figure 3. The hydrogenphosphate groups use three unprotonated oxygens to coordinated Zr^{4+} octahedrally, and the P–OH groups point into the interlamellar spaces and are hydrogen bonded to the water molecules. Successive layers are 7.6 Å apart, and are held together only by weak Van der Waals Forces (*see van der Waals Forces*). This enables the layers to adjust their spacing or stacking pattern to adjust to external conditions and any intercalated species, giving α-$Zr(HPO_4)_2{\cdot}H_2O$ a diverse chemistry.[29]

One or both of the hydrogens can be replaced by monovalent and divalent cations, and these phases can show various degrees of hydration. For example, eight different sodium-exchanged forms have been identified, in which the interlayer spacing varies from 7.6 Å in $ZrNa_2(PO_4)_2$ to 11.8 Å in $ZrNaH(PO_4)_2{\cdot}5H_2O$. Polar molecules such as amines can be reversibly intercalated into α-$Zr(HPO_4)_2{\cdot}H_2O$, which can act as an acid catalyst for their reactions. Amine-intercalated α-$Zr(HPO_4)_2{\cdot}H_2O$ and other layered phosphates can be pillared, for example, with the Keggin ion $Al_{13}O_4(OH)_{24}{\cdot}12H_2O^{7+}$ or chromium acetate polymers.[30]

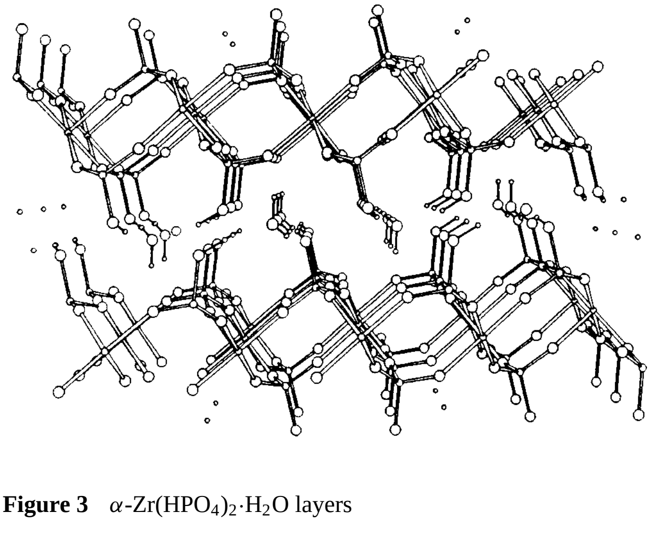

Figure 3 α-$Zr(HPO_4)_2{\cdot}H_2O$ layers

The diffusion of protons in the interlamellar regions results in ionic conductivities of 10^{-3}–$10^{-5}\,\Omega^{-1}\,cm^{-1}$ for α-$Zr(HPO_4)_2{\cdot}H_2O$ materials at room temperature. The dispersion in these values is due to variations in the water content, as proton exchange between H_3O^+ cations can enhance the conductivity.

Isostructural $M^{IV}(HPO_4)_2{\cdot}H_2O$ materials have been obtained with M = Ti, Hf, Ce, and Sn and $SbH(PO_4)_2{\cdot}H_2O$ also adopts this layered structure. In addition, a large number of layered phosphonates $M^{IV}(RPO_3)_2$ have been prepared in which the alkyl groups R lie between the inorganic layers in place of the OH groups in the hydrogenphosphates.

5.3.2 Vanadyl Phosphate

α-$VOPO_4$ is one of a series of layered oxysalts $MOXO_4$ (M = V, Nb, Ta, Mo; X = P, As, S),[31] shown schematically in (**11**) for $MoOPO_4$. Each vanadyl group is coordinated by four phosphate groups and vice versa. Weak $V{=}O{\cdots}V{=}O$ interactions hold the layers together, which enables one equivalent of Lewis base molecules to be intercalated through coordination to the vanadyl group. $VOPO_4{\cdot}L$ derivatives are formed with L = H_2O, ROH, py. In $VOPO_4{\cdot}2H_2O$ the second, uncoordinated, water molecule lies in the interlamellar space. Cross-linked layers are found in $VOPO_4$. $(4,4\text{-bipyridine})_{1/2}$, analogous to the pillaring of $MoOPO_4$ layers by hydrogenphosphate groups in the $[Mo_2O_2(PO_4)_2H_nPO_4]^{(3-n)-}$ frameworks described in Section 5.2.3. Cation insertion reactions occur under mildly reducing conditions giving a variety of $M_xVOPO_4{\cdot}nH_2O$ derivatives, for example, $Na_{0.2}VOPO_4{\cdot}2H_2O$. This results in a decrease in the interlayer spacing due to the electrostatic attraction between the anionic layers and the inserted cations.

5.3.3 HUP

Hydrogen uranyl phosphate (HUP), $HUO_2PO_4{\cdot}4H_2O$, consists of $UO_2PO_4^-$ planes similar to the $VOPO_4$ layers described above. The two dimensional network of hydrogen-bonded water molecules lying between the layers accommodates the extra proton, which gives rise to very high proton conductivities of $\sim 10^{-2}\ \Omega^{-1}cm^{-1}$ at 300 K. HUP and other members of the Torbenite group of minerals can undergo cation exchange, for example, Autunite, $Ca(UO_2PO_4)_2{\cdot}nH_2O$, can reversibly exchange Ca^{2+} for K^+, Ba^{2+}, Mn^{2+}, Cu^{2+}, and Mg^{2+} in aqueous solutions.

5.4 Phosphate Glasses

Rapid cooling of phosphate melts gives vitreous materials in which no long-range order is present, but with similar local environments and connectivity of phosphate tetrahedra to crystalline phases of comparable compositions (*see* ***Noncrystalline Solids***).[32]

Vitreous P_2O_5 and phosphate-rich glasses are difficult to prepare, owing to the volatility of P_2O_5, and are very moisture sensitive. Vibrational and MASNMR spectra show that they contain three-dimensional phosphate networks comparable to those in the extended forms of P_2O_5 and ultraphosphates.

M_2O–P_2O_5 glasses ($M = $ Li, Na, K, Rb, Cs, Ag) containing over 30% M_2O are straightforward to prepare and handle, and the ionic conductivities and optical properties of these materials have been studied extensively. Raman, MASNMR, and X-ray photoelectron spectroscopies have been used to study the proportions of n-connected ($n = 0-3$) tetrahedra in these glasses. The M_2O–P_2O_5 glasses can incorporate M halides giving materials with useful ionic conductivity. It has been proposed that microphase separation occurs in $AgPO_3$-AgI glasses, giving small regions of highly conducting α-AgI. The glassy matrix suppresses the structural phase change that drastically reduces the ionic conductivity of AgI below 150 °C.

Phosphate glasses have also been investigated as nuclear waste forms.[33] These are typically made with nonvolatile, high-valent metals such as Fe, Zr, lanthanides, or Th, sometimes with additions of lead to promote glass formation, for example, Fe–Pb-phosphate glasses. Crystalline waste forms based on the $NaZr_2(PO_4)_3$ NASICON structure (see Section 5.2.1) have also been studied as these can exchange Na for Cs, which is difficult to immobilize.

6 PROPERTIES

Notable chemical or physical properties of phosphates are usually not due to the phosphate group itself. However, the general stability associated with the strength of the P–O and M–O(P) bonds and the inertness of the phosphate group to chemical attack and redox reactions are important in determining the durability of these materials. Furthermore, a lack of electronic absorption bands in the UV-Visible–Near IR regions of the electromagnetic spectrum allows phosphates to be useful optical materials.

6.1 Electronic Conductors

Most metal phosphates are insulators; however, phosphate substitution has been demonstrated in some notable conducting oxides. For example, superconducting $MBaSrCu_{2.8}(PO_4)_{0.2}O_{6.2}$ ($M = $ La-Ho, Y) analogs of $YBa_2Cu_3O_7$ (*see* ***Superconductivity***) have been prepared, with critical temperatures up to 38 K.[34]

The largest series of electronically conducting materials are the phosphate tungsten bronzes.[35] These have similar properties to oxides bronzes such as Na_xWO_3 (*see* ***Oxides: Solid-state Chemistry***) and are strongly colored metals or semiconductors. They are formed by inserting planes of orthophosphate or diphosphate anions into the ReO_3 type WO_3 lattice, analogous to the formation of shear phases in the reduction of this structure (*see* ***Defects in Solids***). The stability of these reduced phases results from the good match between the shortest O–O distances in WO_6 octahedra and PO_4 tetrahedra. The lower connectivity of the phosphate groups results in the formation of small channels in the WO_3 structure.

Three principal families of phosphate tungsten bronzes have been identified, all of which have general composition $A_x(PO_2)_4(WO_3)_{2m}$. Orthophosphate bronzes with pentagonal tunnels are formed without additional cations ($x = 0$), for $m = 2, 4-16$, whereas orthophosphate tungsten bronzes with larger hexagonal tunnels are stabilized by $A = $ Na and K cations and have $1.75 < x < 3$ and $4 < m < 13$. Diphosphate bronzes containing hexagonal tunnels (Figure 4) are formed with larger cations, $A = $ K, Rb, Tl, and Ba, in which $m = 4-20$. The conductivities of these materials are highly anisotropic and are typically $\sim 10^{-3}\ \Omega^{-1}cm^{-1}$ in the optimum direction and $\sim 10^{-5}\ \Omega^{-1}cm^{-1}$ in perpendicular directions. The low-dimensional electronic properties of these materials have been studied in detail.

6.2 Fast Ion Conductors

Appreciable ionic conductivity is found in open framework or layered materials containing mobile cations (*see* ***Ionic Conductors***). Several phosphates have been found to be good ionic conductors and are described above: NASICON (Section 5.2.1), α-zirconium phosphates (Section 5.3.1), HUP (Section 5.3.3), and phosphate glasses[36] (Section 5.4). Current interest in lithium ion-conducting electrolytes for battery applications has led to many lithium-containing phosphate glasses and crystalline solids such as NASICON type titanium phosphate being studied.[37]

6.3 Ferroics

Ferroics can be switched between two or more oriented states under appropriate forces. The charge separation present

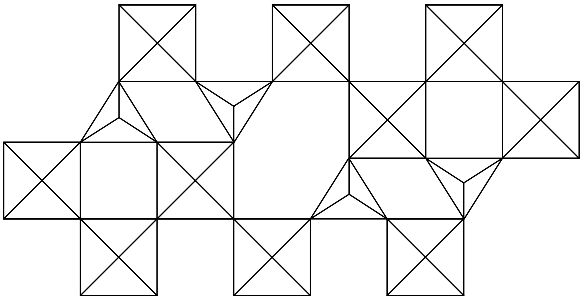

Figure 4 Idealized structure of a diphosphate tungsten phosphate bronze containing hexagonal channels formed by the insertion of diphosphate groups (projected down the P–P axis) into the WO_3 lattice of WO_6 octahedra (projected down a fourfold axis)

in metal phosphates gives rise to electric dipoles which can result in ferroic properties for which the switching forces are electrical or mechanical.[38]

6.3.1 Ferroelectrics

These (*see Ferroelectricity*) possess a net polarization due to parallel ordering of local dipoles; this requires a noncentrosymmetric crystal structure. Many solid phosphates are ferroelectrics,[39] the potassium dihydrogenphosphate (KDP) family, MH_2PO_4 (M = Na, K, Rb, Cs), are the best known examples. In KDP, a net polarization results from the ordering of asymmetric P–O–H···O–P hydrogen bonds below $T_c = 123$ K. Additional N–H···O–P hydrogen bonding in $NH_4H_2PO_4$(ammonium dihydrogen phosphate, ADP) gives a slightly different ordering of the acidic protons in which the dipoles cancel out; this is an antiferroelectric phase.

Ordering of orthophosphate anions results in ferroelectricity in $K_2Bi_3O(PO_4)_2$ whereas in $AM_2(PO_4)_3$ types (A = Li-Cs, Ag, Cu; M = Ce, Th, U) it results from the alignment of A cation displacements from the center of AO_8 polyhedra. $A^IM^{II}PO_4$ materials (e.g. A = Rb, Cs; M = Mg, Co, Zn) containing tetrahedral $MPO_4{}^-$ frameworks can undergo ferroelectric transitions due to the coupled rotations of the tetrahedra.

6.3.2 Piezoelectrics

Coupling of mechanic stress and electrical polarization results in piezoelectricity. KDP type materials are piezoelectrics at room temperature and ADP was formerly used in submarine applications to emit and receive ultrasonic waves. Berlinite, $AlPO_4$, is structurally related to the common piezoelectric α-SiO_2 (see Section 5.1.2) and has superior properties in some respects.

6.4 Optical Materials

6.4.1 Nonlinear Materials

Phosphates showing a bulk polarization (i.e. ferroelectric phases) may be used for nonlinear optical processes (*see Nonlinear Optical Materials*) such as second harmonic generation and electro-optic switching. KTP (Section 5.2.2) and related phases (NH_4TiOPO_4 and $KTiOAsO_4$) are very efficient nonlinear materials. The ferroic phosphates described above also show nonlinear properties. KDP materials are inferior to KTP types but they find use in electro-optics as they are very transparent over a wide frequency range.

6.4.2 Phosphors

Nonabsorbing phosphate hosts doped with impurities to act as absorption and emission centers provide useful phosphors (*see Phosphorescence*). In particular, Fluoroapatite ($Ca_5(PO_4)_3F$) doped with Sb and Mn is used as a coating in commercial fluorescent lamps to convert 254 nm mercury UV radiation into visible light. $Na_3(Ce_{0.65}Tb_{0.35})(PO_4)_2$ and lanthanide-doped $Zn_3(PO_4)_2$ are also efficient phosphors.

6.4.3 Laser Materials

The basic requirements for a laser material are similar to those for phosphors: a low concentration of active centers in a nonabsorbing host lattice. Both crystalline and glassy phosphate materials have been extensively researched as laser materials.[40] The low cation concentration in the lanthanide ultraphosphates MP_5O_{14} leads to large cation–cation separations, enabling stoichiometric NdP_5O_{14} to lase without excessive fluorescence quenching. Other self-activated neodymium phosphate laser crystals are the cyclotetraphosphates $MNdP_4O_{12}$ (M = Li, Na, K) and the orthophosphates $M_3Nd(PO_4)_2$ (M = Na, K).

Nd-doped phosphate glasses are also used in a variety of high-gain or high-power laser applications. These materials are typically metaphosphate glasses such as $NaPO_3$ or $Al(PO_3)_3$ containing <1% Nd. Vitreous NdP_5O_{14} can also be used.

6.5 Catalysis

The phosphate group has no inherent catalytic activity, but many phosphates are useful catalysts by virtue of the metals present and their structures.

6.5.1 Surface Oxidation Catalysis

Several transition metal phosphate systems are found to catalyze mild oxidations of organic molecules.[41] Catalytic activity is due to transition metal redox couples (*see* ***Oxidation Catalysis by Transition Metal Complexes*** and ***Oxide Catalysts in Solid-state Chemistry***), but the phosphate groups are important in determining the underlying and surface structures.

A variety of vanadium phosphates catalyze the selective oxidation of linear C_4 hydrocarbons to maleic anhydride through the in situ formation of $(VO)_2P_2O_7$. The catalytic sites are thought to be formed on surfaces perpendicular to the direction of the V=O bonds, and so the structure of the initial vanadium phosphate is important in determining the morphology and catalytic activity of the $(VO)_2P_2O_7$ particles. Highly active, platy microcrystallites can be prepared through the topotactic decomposition of layered precursors such as $VOHPO_4{\cdot}1/2H_2O$.

Iron phosphates catalyze the oxidative dehydrogenation of isobutyric acid to methacrylic acid. The initial Fe^{II} or Fe^{III} phase is converted to the mixed valent orthophosphate $Fe_7(PO_4)_6$, but the catalytically active phase may be a diphosphate $Fe_3(P_2O_7)_2$.

$CuTi_2(PO_4)_3$ and related NASICON type phases (see Section 5.2.1) catalyze the oxidation of propylene to acrolein and alcohol dehydrogenations. The open framework of this structure enables Cu ions to diffuse to the surface under oxidizing or reducing conditions (equations (11) and (12), respectively) giving surface growths of Cu or CuO. These redox properties and the ability of $Cu_{0.5}Ti_2(PO_4)_3$ to absorb hydrogen give rise to the catalytic activity.

$$Cu^{I}Ti_2(PO_4)_3 + \frac{1}{4}O_2 \rightleftharpoons Cu^{II}{}_{1/2}Ti_2(PO_4)_3 + \frac{1}{2}CuO \quad (11)$$

$$Cu^{I}Ti_2(PO_4)_3 + \frac{x}{2}H_2 \rightleftharpoons Cu^{II}{}_{1/2-x}Cu^{I}{}_{x}H_xTi_2(PO_4)_3 + \frac{1}{2}Cu \quad (12)$$

6.5.2 Lamellar, Microporous, and Mesoporous Catalysts

Phosphates having these types of open structures can act as shape-selective acid catalysts, for example, for the cracking and isomerization of hydrocarbons. For examples of lamellar materials, see Section 5.3 and (*see* ***Intercalation Chemistry***). Microporous catalysts are described above and in (*see* ***Porous Inorganic Materials*** and ***Zeolites***). Mesoporous AlPO materials have larger pores within a matrix of amorphous $AlPO_4$.[42]

6.6 Magnetism

Phosphates of transition metal and lanthanide cations possessing unpaired spins behave as paramagnets (*see Paramagnetism*; ***Magnetism of Transition Metal Ions***) at ambient temperatures. On cooling they can display a variety of magnetic ordering phenomena due to superexchange interactions through phosphate groups and other bridges between the cations (*see* ***Magnetism of Extended Arrays in Inorganic Solids***). M–O–P–O–M interactions are usually antiferromagnetic (*see Antiferromagnetism*) with exchange constants $J/k \sim -1$ to -10 K. The ease of preparation and structural variety of metal phosphates has resulted in the study of magnetic ordering phenomena in many compounds, for example, an incommensurate spiral of ordered Cr^{3+} moments is found in β-$CrPO_4$ below 25 K.[43] However, low ordering temperatures and the tendency of metal phosphates to order antiferromagnetically precludes their practical use as magnetic materials.

6.7 Battery Cathode Materials

Solids that can reversibly take up and lose lithium ions (accompanied by reduction or oxidation) can be used as cathode materials in rechargeable lithium batteries. Several transition metal phosphates, for example, $Li_3V_2(PO_4)_3$, $LiVOPO_4$, and $LiFePO_4$, that can undergo oxidative de-intercalation of lithium have been investigated in recent years.

6.8 Negative Thermal Expansion Ceramics

Useful zero thermal expansion composites are made by combining materials that show the unusual property of negative thermal expansion (i.e. contraction) with normal (positive) expansion materials. Examples of phosphates showing negative thermal expansion are the diphosphate-divanadate solid solutions $ZrP_{2-x}V_xO_7$ and the microporous aluminophosphate AlPO-17 which shows a particularly large effect.[44]

6.9 Biomaterials

Materials that are compatible with biomineralized phosphates (see Section 7.2) may be useful for implants.[45] A variety of synthetic calcium phosphates have been investigated. $Ca_3(PO_4)_2$ can be used as a biodegradable bone implant, which is gradually replaced by autogenous bone, and less degradable apatite implants can attach to natural bone without inflammation. Bioinert zinc phosphate cements are used in prosthetic dental applications.

7 NATURAL PHOSPHATES

Phosphate minerals are found in rocks and living systems, and many biologically important molecules are phosphate esters (*see* ***Phosphorus: Inorganic Chemistry***). The balance between insoluble and soluble phosphates in the biosphere has been adversely affected by the use of phosphate fertilizers, water softeners and detergents.

7.1 Minerals

Several hundred phosphate minerals (*see Mineralogy*) are known, virtually all of which are orthophosphates.[46] An exception is Canaphite, $CaNa_2P_2O_7{\cdot}4H_2O$. The important mineral Apatite, $Ca_5(PO_4)_3X$ is found in igneous pegmatite rocks and hydrothermal veins. Fluoro-, Chloro-, and Hydroxy-apatites are found ($X = F$, Cl, OH, respectively) as well as many substituted varieties.

Poorly crystalline or amorphous Phosphorite sediments made from the hard remains of marine organisms are the principal commercial source of phosphates, although Apatites are also mined. Treatment of phosphate minerals with sulfuric acid yields 'superphosphate' fertilizer, a mixture of $Ca(H_2PO_4)_2$, H_3PO_4 and $CaSO_4$. Phosphoric acid treatment gives 'triple superphosphate', rich in $Ca(H_2PO_4)_2$. Other soluble fertilizers such as ammonium phosphates are obtained from these products.

Many of the f-block elements are extracted from phosphate minerals. Monazite, MPO_4, can contain the lanthanide metals, Y and Th, at the cation sites M. The Torbenite and other groups of minerals related to HUP (see Section 5.3.3) are sources of uranium.

7.2 Biominerals

Phosphates are found in soft organic tissues as phosphate esters, and in hard tissues, notably bones and teeth, as solid calcium orthophosphates (*see* ***Biomineralization***).**[47]** Hard tissues are composites of Apatite and an organic matrix: collagen in bone, dentin, and dental cement, and keratin in dental enamel. The Apatite phases are defective with Ca/P ratios of 1.6–1.8 and can incorporate other cations (Na^+, K^+, Mg^{2+}) or anions (F^-, Cl^-, $CO_3{}^{2-}$, citrate).

8 RELATED ARTICLES

Intercalation Chemistry; Ionic Conductors; Phosphorus: Inorganic Chemistry; Porous Inorganic Materials; Zeolites.

9 REFERENCES

1. A. Durif, ‘Crystal Chemistry of Condensed Phosphates’, Plenum Publishing, New York, 1995.
2. D. E. C. Corbridge, ‘The Structural Chemistry of Phosphorus’, Elsevier, Amsterdam, NY, 1974.
3. T. Kanazawa ed., ‘Inorganic Phosphate Materials’, Vol. 52, Materials Science Monographs, Elsevier, Amsterdam, NY, 1989.
4. D. E. C. Corbridge, Proceedings of the Second International Congress on Phosphorus Compounds, 1980, 145.
5. J. P. Attfield, A. W. Sleight, and A. K. Cheetham, *Nature*, 1986, **322**, 620.
6. D. Beltran-Porter, A. Beltran-Porter, P. Amoros, R. Ibanez, E. Martinez, A. Le. Bail, G. Ferey, and G. Villeneuve, *Eur. J. Solid State Inorg. Chem.*, 1991, **28**, 131.
7. T. Stefanidis and A. G. Nord, *Acta Crystallogr., Sect. C*, 1984, **40**, 1995.
8. M. T. Averbuch-Pouchot and A. Durif, *Annu. Rev. Mater. Sci.*, 1991, **21**, 65.
9. M. T. Averbuch-Pouchot and A. Durif, *Eur. J. Solid State Inorg. Chem.*, 1991, **28**, 9.
10. M. T. Averbuch-Pouchot and A. Durif, *Z. Kristallogr.*, 1992, **201**, 69.
11. A. Rulmont, R. Cahay, M. Liegeois-Duyckaerts, and P. Tarte, *Eur. J. Solid State Inorg. Chem.*, 1991, **28**, 207.
12. R. J. Kirkpatrick and R. K. Brow, *Solid State Nucl. Magn. Reson.*, 1995, **5**, 9.
13. R. C. Finn, J. Zubieta, and R. C. Haushalter, *Prog. Inorg. Chem.*, 2003, **51**, 421.
14. K.-H. Lii, Y.-F. Huang, V. Zima, C.-Y. Huang, H.-M. Lin, Y.-C. Jiang, F.-L. Liao, and S.-L. Wang, *Chem. Mater.*, 1998, **10**, 2599.
15. M. A. G. Aranda, J. P. Attfield, and S. Bruque, *Angew. Chem., Int. Ed. Engl.*, 1992, **31**, 1090.
16. W. M. Rieff and C. C. Torardi, *Hyperfine Interact.*, 1990, **53**, 403.
17. R. Glaum, M. Walterpeter, D. Ozalp, and R. Gruehn, *Z. Anorg. Allg. Chem.*, 1991, **601**, 145.
18. R. Kneip, H. Engelhardt, and C. Hauf, *Chem. Mater.*, 1998, **10**, 2930.
19. J. H. Yu and R. R. Xu, *Acc. Chem. Res.*, 2003, **36**, 481.
20. S. T. Wilson and E. M. Flanigen, in ‘Zeolite Synthesis’, eds. M. L. Occelli and H. E. Robinson, Vol. 398, Symposium Series, American Chemical Society, 1989, p. 329.
21. M. E. Davis, C. Montes, and J. M. Garces, in ‘Zeolite Synthesis’, eds. M. L. Occelli and H. E. Robinson, Vol. 398, Symposium Series, American Chemical Society, 1989, p. 291.
22. B. M. Weckhuysen, R. R. Rao, J. A. Martens, and R. A. Schoonheydt, *Eur. J. Inorg. Chem.*, 1999, **4**, 565.
23. G. Ferey, *Chem. Mater.*, 2001, **13**, 3084.
24. A. Corma, *Chem. Rev.*, 1997, **97**, 2373.
25. M. E. Hagerman and K. R. Poeppelmeier, *Chem. Mater.*, 1995, **7**, 602.
26. M. N. Satyanarayan, A. Deepthy, and H. L. Bhat, *Crit. Rev. Solid State Mater. Sci.*, 1999, **24**, 103.
27. R. C. Haushalter and L. A. Mundi, *Chem. Mater.*, 1992, **4**, 31.
28. M. M. Borel, M. Goreaud, A. Grandin, P. Labbe, A. Leclaire, and B. Raveau, *Eur. J. Solid State Inorg. Chem.*, 1991, **28**, 93.
29. A. Clearfield, *Eur. J. Solid State Inorg. Chem.*, 1991, **28**, 37.
30. A. Clearfield and M. Kurchenmeister in ‘Supramolecular Architecture: Synthetic Control in Thin Films and Solids’, ed. T. Bein, Vol. 499, ACS Symposium Series, American Chemical Society, 1992, p. 128.
31. A. J. Jacobson, in ‘Solid State Chemistry: Compounds’, eds. A. K. Cheetham and P. Day, Oxford University Press, 1992, p. 218.
32. C. Mercier, G. Palavit, L. Montagne, and C. Follet-Houttemane, *Compt. Rend. Chim.*, 2002, **5**, 693.
33. R. C. Ewing and L. M. Wang, *Rev. Miner. Geochem.*, 2002, **48**, 673.
34. K. N. Marimuthu, M. S. R. Rao, and U. V. Varadaraju, *Physica C*, 1997, **280**, 327.
35. P. Roussel, O. Perez, and P. Labbe, *Acta Crystallogr., Sect. B*, 2001, **57**, 603.
36. S. W. Martin, *J. Am. Chem. Soc.*, 1991, **74**, 1767.
37. Z. S. Zheng, Z. T. Zhang, Z. L. Tang, and W. C. Shen, *Prog. Chem.*, 2003, **15**, 101.
38. M. Quarton, *Eur. J. Solid State Inorg. Chem.*, 1991, **28**, 289.
39. V. A. Isupov, *Ferroelectrics*, 2002, **274**, 203.

40. J. E. Marion and M. J. Weber, *Eur. J. Solid State Inorg. Chem.*, 1991, **28**, 271.
41. L. Monceaux and P. Courtine, *Eur. J. Solid State Inorg. Chem.*, 1991, **28**, 233.
42. F. Schuth, *Chem. Mater.*, 2001, **13**, 3184.
43. J. P. Wright, J. P. Attfield, W. I. F. David, and J. B. Forsyth., *Phys. Rev. B*, 2000, **62**, 992.
44. M. P. Attfield and A. W. Sleight, *Chem. Mater.*, 1998, **10**, 2013.
45. J. J. Videau and V. Dupuis, *Eur. J. Solid State Inorg. Chem.*, 1991, **28**, 303.
46. D. M. C. Huminicki and F. C. Hawthorne, *Rev. Miner. Geochem.*, 2002, **48**, 123.
47. J. C. Elliott, *Rev. Miner. Geochem.*, 2002, **48**, 427.

Phosphides: Solid-state Chemistry

Rainer Pöttgen,[1] Wolfgang Hönle[2] & Hans Georg von Schnering[3]

[1] *Institut für Anorganische und Analytische Chemie, Universität Münster, Germany*
[2] *Max-Planck-Institut für Chemische Physik fester Stoffe, Dresden, Germany*
[3] *Max-Planck-Institut für Festkörperforschung, Stuttgart, Germany*

1	Introduction	1
2	Compounds: General Relationships	1
3	Synthesis	12
4	Bond Lengths, Bond Angles, Coordination, Volumes	13
5	Chemical Reactions of Phosphides	18
6	Structure and Bonding	20
7	Phosphorus−Arsenic Substitution	39
8	Physical Properties and Applications	40
9	Related Articles	46
10	References	46

Abbreviations

A = Alkali metal; AE = Alkaline-earth metal; a-P = Amorphous phosphorus; $\overline{\mathrm{CN}}$ = Mean coordination number; d(M−P) = Distance between M and P atom; d(P–P) = Distances between P atoms; E = Element; E_g = Band gap; M = Metal; PBO = Pauling bond order; q(P) = Formal charge of a P atom; q(M) = Formal charge of a M atom; R = Zr, Hf, rare earth metal or actinoid metal; RE = Rare earth element; R_{cov} = Covalent radius; R_{met} = Metallic radius; R_{vdW} = Van der Waals radius; T = Transition metal; t_p = trigonal prism; VEC = Valence electron concentration; V_i = Volume increment; V_m = Molar volume; V_m^o = Observed molar volume; V_P = Volume increment of phosphorus; $V_{P(sm)}$ = Volume increment of phosphorus in semimetallic compounds; X = Halogen; Y = Skeleton atoms; τ = Translation period; ${}^{1}_{\infty}$ = One-dimensional infinite; ${}^{2}_{\infty}$ = Two-dimensional infinite; ${}^{3}_{\infty}$ = Three-dimensional infinite; (0b) = Homonuclear nonbonded; (1b) = Homonuclear onefold bonded; (2b) = Homonuclear twofold bonded; (3b) = Homonuclear threefold bonded; 1-D = One-dimensional; 2-D = Two-dimensional; 3-D = Three-dimensional.

1 INTRODUCTION

This article deals with metal phosphides in the solid state.[1–13] Since the first contribution to this Encyclopedia in 1994, a huge number of original publications on the synthesis, crystal growth, crystal chemistry, and the physical properties of phosphides have appeared. The largest field compromises the rare earth-transition metal phosphides. Most of this work was done in the groups of Guérin, Jeitschko, Kuz'ma, and Mewis and has been reviewed by Kuz'ma and Chykhrij.[14,15] Other recent research topics cover the crystal chemistry and chemical bonding of new metal-rich phosphides, phosphide oxides, and intensive studies of the largely varying physical properties of these intriguing materials. Compounds with a high phosphorus content are common and the polyphosphides are of particular interest because they exhibit an unexpected wealth of chemical composition, physical properties, and structural features.[16,17] No other element approaches phosphorus in the variety of homoatomic connected polyanions formed, as a result of its relatively low electronegativity and stereochemical features. The threefold bonded neutral P atom acts like a fragment of surface structures and, therefore, the structures of the different phosphorus modifications will be maintained in a large frame of redox steps down to very small ones: P_{15}^{-} (KP_{15}), $P_{12}^{\pm 0}$ (CuI charge transfer, $(CuI)_3P_{12}$) or P_{14}^{2+} ($P_{14}S$).

2 COMPOUNDS: GENERAL RELATIONSHIPS

It has long been known that binary compounds with phosphorus are formed by most elements; the few exceptions are Hg, Pb, Sb, Bi, Te, Po, and the noble gases. However, ternary compounds like $HgPbP_{14}$ are readily formed. The established compounds are listed in Tables 1−5, ordered from metal rich to phosphorus rich, and from main-group binary compounds to binary and ternary polyphosphides, and metal-rich phosphides.[1] The phosphides MP_x and $(M,M')P_x$ have been ordered according to ascending x(P) and ascending numbers of M and M′ (Tables 4 and 5, respectively), using the general formula and not the alphabetical order of M, M′ atoms. The crystal structures are characterized by structure type and Pearson code, and the phosphorus partial structures of the polyphosphides are classified by their linkage types. In some cases of site occupancy factors <1, the Pearson code for full occupancy minus the unoccupied part has been given. Because of the still increasing number of phosphides, the tables cannot be complete. Besides the books, reviews, and databases listed in Ref. 1−13, most literature on phosphides is easily accessible via the SciFinder Scholar data base.[18] The broad range of composition from $M_{15}P_2$ to MP_{15} is remarkable, as is the fact that some elements form only one distinct phosphide, while others form up to 10. The various phosphides differ greatly in their chemical and physical properties, which can be related

Table 1 Phosphides and polyphosphides of group 1–3 and 11–14 metals

Formula	Metal[a]	Structure type[b]	Pearson code	Anionic partial structure[c]
Group 1 metals				
M_3P	Li, Na, K,	Na_3As	*hP* 8	(P^{3-}) isolated anion
	$K_{3-x}P$ ($x \sim 1$)	Li_3Bi def.	*cF* $16 - 2x$	(P^{3-}) and $(P_2{}^{4-})$ stat dis.
M_4P_3	K	W_3CoB_3	*oC* 28	$(P_3{}^{4-})$ chain, radicalic
M_5P_4	K	Y_4GaCo_4	*mC* 18	$(P_4{}^{5-})$ chain, radicalic
MP	Li	LiAs	*mP* 16	${}^{1}_{\infty}(P^{-})$ helical chain
	Na, K	NaP	*oP* 16	${}^{1}_{\infty}(P^{-})$ helical chain
M_4P_6	K, Rb, Cs (α)	Rb_4P_6	*oF* 40	$(P_6{}^{4-})$ planar *cyclo*-P_6
	K (β)	β-K_4P_6	*oF* 80	$(P_6{}^{4-})$ planar *cyclo*-P_6
M_3P_7	Li (α)	α-Li_3P_7	*oP* 40	$(P_7{}^{3-})$ cage
	Na (α)	α-Na_3P_7	*oP* 80	$(P_7{}^{3-})$ cage
	K (α)	?	?	$(P_7{}^{3-})$ cage
	Rb, Cs (α)	α-Cs_3P_7	*tP* 40	$(P_7{}^{3-})$ cage
	Li (β)	β-Li_3P_7	*oP* 40	$(P_7{}^{3-})$ cage
	Na → Cs (β)	β-Rb_3P_7	*cF* 40	$(P_7{}^{3-})$ cage
$M_3P_{8.33}$	Li	$Li_3P_{8.33}$	*hP**	$(P_7{}^{3-})$:$(P_{11}{}^{3-}) = 2$:1
	Cs (β)	β-Rb_3P_7	*cF* 40/56	$(P_7{}^{3-})$:$(P_{11}{}^{3-}) = 2$:1
M_3P_{11}	Na, K, Rb (α)	α-Na_3P_{11}	*oP* 56	$(P_{11}{}^{3-})$ cage
	Cs (α)	?	?	$(P_{11}{}^{3-})$ cage
	Na (β)	β-Na_3P_{11}	*tP* 128	$(P_{11}{}^{3-})$ cage
	K (β)	β-K_3P_{11}	*cP* 28	$(P_{11}{}^{3-})$ cage
	Rb, Cs (β)	β-Rb_3P_7	*cF* 56	$(P_{11}{}^{3-})$ cage
MP_5	Li, Na	LiP_5	*oP* 24	${}^{3}_{\infty}(P_5{}^{-})$ cond. $cyclo$-$P_6 + cyclo$-P_{18}
MP_7	Li, Na	LiP_7	*tI* 128	${}^{1}_{\infty}(P_7{}^{-})$ helical tubes
	Rb, Cs	CsP_7	*oP* 32	${}^{1}_{\infty}(P_7{}^{-})$ cage polymer
$MP_{10.3}$	K, Rb	$KP_{10.3}$	*tP* 1488	Complex tubular superstructure
MP_{11}	Rb, Cs	RbP_{11}	*mP* 48	${}^{1}_{\infty}(P_7{}^{-}) + {}^{1}_{\infty}(P_{15}{}^{-})$ tubes (1:1)
MP_{15}	Li → Cs	KP_{15}	*aP* 32	${}^{1}_{\infty}(P_{15}{}^{-})$ tube
Group 2 metals				
M_3P_2	Be, Mg	Mn_2O_3	*cI* 80	(P^{3-}) isolated anion
	Be	Be_3P_2	*tI* 160	(P^{3-}) isolated anion
	Ca, Sr, Ba	Th_3P_4 def.	*cI* 28	(P^{3-}) isolated anion
M_4P_3	Ca, Sr, Ba	Ba_4P_3	*oP* 56	$(P^{3-}) + (P_2{}^{4-})$ dumbbells
M_5P_4	Ca, Sr, Ba(β)	Eu_5As_4	*oC* 36	$(P^{3-}) + (P_2{}^{4-})$ dumbbells
M_5P_4	Ba(α)	Sm_5Ge_4	*oP*36	$(P^{3-}) + (P_2{}^{4-})$ dumbbells
MP	Ca, Sr	Na_2O_2	*hP* 12	$(P_2{}^{4-})$ dumbbell
M_5P_8	Ca	Ca_5P_8	*mC* 26	$((P^{+})_2(P^{2-})_6)^{10-}$ ethane analogous
MP_2	Be	BeP_2	*tI* 12	${}^{1}_{\infty}(P^{-})$ chain with short-range order
		BeP_2	*mC* 48	
	Sr, Ba	$BaAs_2$	*mP* 18	${}^{1}_{\infty}(P_2{}^{2-})$ *cis*–*trans* helical chain
M_3P_4	Sr, Ba, Eu	Sr_3As_4	*oF* 56	$(P_4{}^{6-})$ chain
M_3P_5	Ca ?			
MP_3	Ca	CaP_3	*aP* 8	${}^{2}_{\infty}(P_3{}^{2-})$ cond. *cyclo*-P_{14} corr.
	Sr (β), Eu (β)	SrP_3	*mC* 32	${}^{2}_{\infty}(P_3{}^{2-})$ cond. *cyclo*-P_6 and *cyclo*-P_{22}
	Sr (α), Ba	BaP_3	*mC* 16	${}^{1}_{\infty}(P_3{}^{2-})$ linear chain of *cyclo*-P_6 (1,4)
MP_4	Mg, Cd	CdP_4	*mP* 10	${}^{2}_{\infty}(P_4{}^{2-})$ cond. *cyclo*-P_{14} corr.
M_3P_{14}	Sr, Ba	Ba_3P_{14}	*mP* 34	$(P_7{}^{3-})$ cage
MP_8	Ba	BaP_8	*aP*18	Cond. *cyclo*-P_6, *cyclo*-P_{10}, *cyclo*-P_{14},
MP_{10}	Ba	BaP_{10}	*oC* 44	${}^{2}_{\infty}(P_{10}{}^{2-})$ linked tubes; cf. TlP_5
Group 3 metals (including 4f and 5f elements and Th)				
M_3P	Sc	Fe_3C	*oP* 16	(P^{3-}) isolated anion
M_7P_3	Sc	Ru_7B_3	*hP* 20	(P^{3-}) isolated anion
M_3P_2	Sc	Cr_3C_2	*oP* 20	(P^{3-}) isolated anion
	Sc	Hf_3P_2	*oP* 20	(P^{3-}) isolated anion
	Eu	Ba_3P_2	*cI* 28	(P^{3-}) isolated anion

Table 1 cont'd

Formula	Metal[a]	Structure type[b]	Pearson code	Anionic partial structure[c]
M_4P_3	Eu	Th_3P_4 dist.	*cI* 28	(P^{3-}) isolated anion
M_5P_4	Eu	Eu_5As_4	*oC* 36	(P^{3-}) and $(P_2{}^{4-})$ dumbbell
MP	Sc, Y, La, Ce, Pr, Nd, Sm, Eu, Gd, Tb, Dy, Ho, Er, Tm, Yb, Lu, Th, U, Pu, Cm, Bk	NaCl	*cF* 8	(P^{3-}) isolated anion
M_3P_4	Th, Pa, U	Th_3P_4	*cI* 28	(P^{3-}) isolated anion
	Eu	Sr_3As_4	*oF* 56	$(P_4{}^{6-})$ chain
MP_2	U	UP_2	*tI* 24	(P^{3-}) isolated anion
	U (HT)	Cu_2Sb	*tP* 6	(P^{3-}) isolated anion
	Th	Ca_2Si	*oP* 12	(P^{3-}) and ${}^{1}_{\infty}(P^{-})$ chain
	Pa	Fe_2As	*tP* 6	(P^{3-}) isolated anion
	La, Ce (HT)	LaP_2	*mI* 48	$(P_3{}^{5-}) + (P_5{}^{7-})$ chains (1:1)
	Ce (LT), Pr, Nd	$NdAs_2$	*mP* 12	$(P_4{}^{6-})$ chain
	Eu	EuP_2	*mP* 18	${}^{1}_{\infty}(P^{-})$ *cis–trans* helical chain
MP_3	Eu (α)	$EuAs_3$	*mC* 16	${}^{2}_{\infty}(P_3{}^{2-})$ cond. *cyclo*-P_{14} corr.
	Eu (β)	SrP_3	*mC* 32	${}^{2}_{\infty}(P_3{}^{2-})$ cond. *cyclo*-P_6 and *cyclo*-P_{22}
MP_5	Y, La(α), Ce, Pr, Nd, Sm, Gd, Tb, Dy, Ho, Er, Tm, Yb (α), Lu	NdP_5	*mP* 12	${}^{2}_{\infty}(P_5{}^{3-})$ cond. *cyclo*-P_{12} corr.
	Yb (β)	β- YbP_5	*mP* 24	${}^{2}_{\infty}(P_5{}^{3-})$ cond. *cyclo*-P_{12} corr.
	La (β), Ce	LaP_5	*mP* 24	${}^{2}_{\infty}(P_5{}^{3-})$ cond. *cyclo*-P_{12} corr.
M_2P_{11}	Th	Th_2P_{11}	*mP* 156	${}^{1}_{\infty}(P_{16}{}^{10-})$ band (cond. *cyclo*-P_6,P_8) and *cyclo*-P_6 (chair)
MP_7	La, Ce, Pr	LaP_7	*mP* 32	${}^{3}_{\infty}(P_7{}^{3-})$ cond. *cyclo*-P_7 and *cyclo*-P_{20}
	Eu	EuP_7	*mP* 32	${}^{2}_{\infty}(P_7{}^{2-})$ cond. *cyclo*-P_6 and *cyclo*-P_8 corr.
	Th	ThP_7	*oP* 32	${}^{3}_{\infty}(P_7{}^{4-})$ cond. *cyclo*-P_6 and *cyclo*-P_{12}
Group 11–14 metals				
$M_{12}(P,B)_2$	B	$B_{12}(P,B)_2$	*hR* 42	(P^{3-}) isolated anion
M_6P	B	B_6P	*hR* 14	(P^{3-}) isolated anion
M_3P	Cu (LT)	Cu_3P (LT)	*hP* 24	(P^{3-}) isolated anion
	Cu (HT)	Cu_3P (HT)	*hP* 8	(P^{3-}) isolated anion
M_3P_2	Zn, Cd	Zn_3P_2	*tP* 40	(P^{3-}) isolated anion
M_4P_3	Sn	Bi_4Se_3	*hR* 7	(P^{3-}) isolated anion + ${}^{2}_{\infty}$cond. *cyclo*-Sn_6
MP	B, Al, Ga, In, Si (hp), Ge (hp)	ZnS	*cF* 8	(P^{3-}) isolated anion
	In (β), Sn (hp)	NaCl	*cF* 8	(P^{3-}) isolated anion
	Sn (hp)	GeAs	*tI* 4	(P^{3-}) isolated anion
	Si	SiP	*oC* 48	(P^{3-}) and M_2 dumbbell
	Ge	GaTe	*mC* 24	(P^{3-}) and M_2 dumbbell
	Sn	SnP	*hP* 4	$(P_2{}^{4-})$ dumbbell bonded to Sn^{II}
	Si (hp), Ge (hp)	–	–	Further high-pressure modifications Si (I–IV), Ge (I–VIII)
M_6P_7	Cd	?	*c***	
M_3P_4	Sn	?	*h***	
M_7P_{10}	Zn, Cd	Cd_7P_{10}	*oF* 126	P^{3-} and ${}^{1}_{\infty}(P^{-})$ helical chain
M_2P_3	Au	Au_2P_3	*mC* 20	${}^{1}_{\infty}(P_3{}^{2-})$ chain of *cyclo*-P_6(1,6)
MP_2	Zn, Cd	ZnP_2, red	*tP* 24	${}^{1}_{\infty}(P^{-})$ helical chain
	Zn	ZnP_2, black	*mP* 24	${}^{1}_{\infty}(P^{-})$ semispiral chain
	Cd	CdP_2	*oP* 12	${}^{1}_{\infty}(P^{-})$ helical chain
	Cu, Ag	CuP_2	*mP* 12	${}^{2}_{\infty}(P_4{}^{2-})$ cond. *cyclo*-P_{10}
	Si (β)	$GeAs_2$	*oP* 24	(P^{3-}) and ${}^{1}_{\infty}(P^{-})$ chain
	Si, Ge?	*p*-FeS_2	*cP* 12	$(P_2{}^{4-})$ dumbbell
MP_3	In, Ge (hp), Sn	SnP_3	*hR* 24	$(P_6{}^{6-})$ *cyclo*-P_6 (chair)

(cont'd overleaf)

Table 1 cont'd

Formula	Metal[a]	Structure type[b]	Pearson code	Anionic partial structure[c]
M_2P_7	Cu	Cu_2P_7	*mC* 72	$^{2}_{\infty}(P_7{}^{2-})$ tubular fragment $(P_{12}{}^{4-})$ and $(P_{16}{}^{4-})$
M_3P_{11}	Ag	Ag_3P_{11}	*mC* 28	$^{2}_{\infty}(P_{11}{}^{3-})$ tubular fragment $(P_{11}{}^{3-})$
MP_4	Cd	CdP_4	*mP* 10	$^{2}_{\infty}(P_4{}^{2-})$ cond. *cyclo*-P_{10}
	Zn?	ZnP_4	*tP* 20	CdP_4 analogous?
MP_5	Tl	TlP_5	*oP* 24	$^{2}_{\infty}(P_5{}^{-})$ linked tubes; cf. BaP_{10}
	Ge (hp)	?	*hR**	

[a] HT = high-temperature form; LT = low-temperature form; hp = high-pressure form. [b] def. = defect type; dist. = distorted type. [c] stat. dis. = statistically disordered; corr. = corrugated; cond. = condensed.

Table 2 Binary polyphosphides of the group 4–10 metals

Formula	Metal[a]	Structure type[b]	Pearson code	Polyanionic structure[b]
M_5P_4	Ni	Ni_5P_4	*hP* 30	(P^{3-}) and $(P_4{}^{6-})$ pyramidal
MP	Ni	NiP	*oP* 16	$(P_2{}^{4-})$ dumbbell
	Cr, W, Mn, Ru, Fe, Co,[c] (Cr,Fe), (Cr,Co), (Cr,Ni), (Mn,Co), (Mn,Fe), (Mn,V), (Mn,Ni), (Fe,W), (Cr,Mn), (Fe,Ni), (Ni,Co), (Co,W), $Fe(P_{1-x}Si_x)$ $(x = 0.5)$, $Co(P_{1-x}B_x)$ $(x \leq 0.1)$,	MnP	*oP* 8	$^{1}_{\infty}(P^{n-})$ chain with half bonds
	Fe	CoAs	*oP* 8	Acentric version of MnP type
M_3P_4	Re	Cr_3S_4	*mC* 14	$(P_2{}^{4-})$ dumbbell and chains, respectively
M_2P_3	Tc	Tc_2As_3	*aP* 20	(P^{3-}) and $(P_2{}^{4-})$ dumbbell
M_4P_7	V, Nb	V_4P_7	*hP* 29	(P^{3-}) and ?
MP_2	Ti, Zr, Hf (*Pnma*)	Co_2P	*oP* 12	(P^{3-}) and $^{1}_{\infty}(P^{-})$ chain
	V, Cr, W ($C2/m$)	$OsGe_2$	*mC* 12	(P^{3-}) and $(P_2{}^{4-})$ dumbbell
	Mo, W ($Cmc2_1$)	MoP_2	*oC* 12	$(P_2{}^{4-})$ dumbbell
	Nb, Ta ($C2$)	$NbSb_2$	*mC* 12	Perhaps $OsGe_2$ type?
	Fe, Ru, Os, Ni (*Pnnm*)	$FeS_2(m)$	*oP* 6	$(P_2{}^{4-})$ dumbbell
	Co, Rh, Ir ($P2_1/c$)	$CoSb_2/FeAsS$	*mP* 12	$(P_2{}^{4-})$ dumbbell
	Ni, Pd ($C2/c$) Ni, Pt (*Pa*)	NiP_2	*mC* 12	$^{1}_{\infty}(P^{-})$ chain
M_6P_{13}	Re	Re_6P_{13}	*hR* 38	(P^{3-}) and $(P_2{}^{4-})$ dumbbell and $(P_4{}^{6-})$ chain and *cyclo*-P_6 (chair)
M_2P_5	Nb	Nb_2P_5	*oP* 28	(P^{3-}) and $^{2}_{\infty}(P_3{}^{2-})$ cond. *cyclo*-P_8
	Re	Re_2P_5	*aP* 28	$2(P^{3-})$ and $(P_2{}^{4-})$ dumbbell and $(P_4{}^{6-})$ chain and $^{1}_{\infty}(P_{12}{}^{12-})$ branched chain
MP_3	Tc, Re	ReP_3	*oP* 16	$^{1}_{\infty}(P_3{}^{3-})$ branched chain
	Co, Rh, Ir, Pd, Ni, $Fe_{0.5}Ni_{0.5}$	$CoAs_3$	*cI* 32	$(P_4{}^{4-})$ plane *cyclo*-P_4
	Ru	RuP_3	*aP* 16	$^{1}_{\infty}(P_6{}^{6-})$ branched chain
MP_4	Cr, Mo, V	CrP_4	*mC* 20	$^{2}_{\infty}(P_4{}^{2-})$ cond. *cyclo*-P_{10}
	Tc, Re	ReP_4	*oP* 40	$^{2}_{\infty}(P_4{}^{2-})$ cond. *cyclo*-P_{10}
	Ru, Os	OsP_4 (β)	*aP* 15	$^{2}_{\infty}(P_4{}^{2-})$ cond. *cyclo*-P_{10}
	Ru, Os, (Cd) (Mg)	OsP_4 (α)	*mP* 10	$^{2}_{\infty}(P_4{}^{2-})$ cond. *cyclo*-P_{10}
	Mn	MnP_4 (2)	*aP* 10	$^{2}_{\infty}(P_4{}^{2-})$ cond. *cyclo*-P_{10}
	Mn	MnP_4 (6)	*aP* 30	$^{2}_{\infty}(P_4{}^{2-})$ cond. *cyclo*-P_{10}
	Mn (hp)	MnP_4 (8)	*mC* 80	$^{2}_{\infty}(P_4{}^{2-})$ cond. *cyclo*-P_{10}
	Fe	FeP_4 (α)	*mP* 30	$^{2}_{\infty}(P_4{}^{2-})$ cond. *cyclo*-P_{10}
	Fe	FeP_4 (β)	*oC* 20	$^{2}_{\infty}(P_4{}^{2-})$ cond. *cyclo*-P_{10}
	Fe	FeP_4 (γ)	*mC* 40	$^{2}_{\infty}(P_4{}^{2-})$ cond. *cyclo*-P_{10}
	W	WP_4	*tI* 20	?

[a] hp = high-pressure form. [b] cond. = condensed. [c] For substitution variants in M site see 10.

Table 3 Binary phosphides of group 4–10 metals MP_x with $x \leq 1$, all with isolated P atoms

Formula	Metal	Structure type	Pearson code
$M_{15}P_2$	Pd	$Pd_{15}P_2$	*hR* 17
M_6P	Pd	Pd_6P	*mC* 14, *mP* 28
M_4P	W	?	?
$M_3P_{0.8}$	Pd	Fe_3C	*oP* 16–0.8
$M_3P_{0.8}D_{0.15}$	Pd	Fe_3C, filled	*oP* 24–8.2
M_3P	Ti, V, Nb, Ta (α), Hf, Zr	Ti_3P	*tP* 32
	Ta (β)	V_3S	*tP* 32
	Ni, Cr, Mo, Mn, Fe, Tc	Fe_3P	*tI* 32
	Ti	Mn_5Si_3	*hP* 16
$M_3PH_{1/8}$	Zr, Hf	Ti_3P	*tP* 36–3
M_8P_3	Ni, $(Ni_{0.97}Fe_{0.03})/(Si_{0.79}P_{0.21})$	Pd_8Sb_3	*hR* 132
M_5P_2	Pd	Fe_3C	*oP* 16
	Pt	Pt_5P_2	*mC* 28
	Ni	Ni_5P_2	*hP* 169
$M_{12}P_5$	Ni	$Ni_{12}P_5$	*tI* 34
M_7P_3	Pd	Pd_7P_3	*hR* 20
M_2P	Co, Re, Ru, V, (Co, Mn): (Co_{1-x}/Mn_x) $(0.0 \leq x \leq 0.8)$	Co_2P	*oP* 12
	W	?	?
	Hf	Ta_2P	*oP* 36
	Nb	Nb_2P	*oP* 54
	Ta	Ta_2P	*oP* 32
	Fe, Ni, Mn	Fe_2P	*hP* 9($P\bar{6}\,2m$)
	(Mn,Rh)/$(As_{1-x}P_x)$ $(0.33 \leq x \leq 0.5)$, Cr	TiFeSi	*oI* 36
	$Mn_{1.88}$	Fe_2P	*hP* 9–0.36
	Ni, Mn	Ni_2P	*hP* 9 ($P321$)
	Rh, Ir	CaF_2	*cF* 12
M_7P_4	Nb, $(Ti_{6.77}Cu_{0.23})$ Hf	Nb_7P_4	*mC* 44
$M_{12}P_7$	Cr, (Cr_9W_3), (Mn_9W_3), V	$Cr_{12}P_7$	*hP* 19
	$(Co_{10}Ti_2)$, Cr, $(Cr_{10}Ni_2)$, (Cr_6Fe_6), (Cr_9Fe_3)	(Th_7Se_{12})	*hP* 20
M_5P_3	Ti, $(Ti_{4.99}Cu_{0.02})$	Yb_5Sb_3	*oP* 32
	$(Ti_{4.95}Cu_{0.06})$	Yb_5Sb_3 (β)	*oP* 32
	Ti	Mn_5Si_3	*hP* 16
	Nb, $(Ti_{4.88}Cu_{0.13})$	Nb_5As_3	*oP* 64 + 0.08
	Ta		*oP* 64
M_8P_5	Mo	Mo_8P_5	*mP* 13
	Nb	Nb_8P_5	*oP* 52
$M_5P_{3.16}$	Ti	Mn_5Si_3, filled	*hP* 16.32
$M_{14}P_9$	Zr, $(Ti_{13.86}Cu_{0.14})$, $(Zr_{2.7}Hf_{11.3})$	$Zr_{14}P_9$	*oP* 92
M_3P_2	Rh	*anti*-PbFCl	*tP* 5
	Hf	Sb_2S_3	*oP* 20
M_4P_3	Rh	Rh_4P_3	*oP* 28
	Mo	Mo_4P_3	*oP* 56
MP	V	NiAs	*hP* 4
	Ti, Hf, Zr (β)	TiAs	*hP* 8
	Nb, Ta	NbAs	*tI* 8
	Zr (α), Th	NaCl	*cF* 8
	Mo	WC	*hP* 2

to structure and bonding. However, there is a general lack of systematic physical data available, and in particular for hydrogen phosphides such as MPH_2 (M = Li, K, Rb). These compounds and higher derivatives such as KP_5H_2 and anions $P_9H_2^-$ are therefore only discussed marginally.

In principle, all phosphides are compounds with valence electrons in localized states, and even in 'metallic' compounds only a few valence electrons are substantially delocalized. Classification into metallic and semiconducting types is therefore a poor way to differentiate between these compounds. The name 'phosphide' defines the P atoms as the most electronegative ones in a compound MP_x, forming the anionic part with the mean oxidation state $q(P_x) = -q(M)$. A broad classification of phosphide types can be made using the oxidation states: (a) 'normal' phosphides with only heteroatomic bonds, $3x = q(M)$; (b) polyphosphides, $3x > q(M)$; and (c) metal-rich phosphides, $3x < q(M)$. With type (b), P–P bonds are expected, and with type (c), electrons are available for metal-to-metal bonds. The value for $q(P_x)$ may be derived from $q(M)$ or from the structural details. Whatever the real effective charges are, formal oxidation states (P^{3-}, P^{2-}, P^-, P^0, P^+, etc.) can be assigned from the homoatomic P–P bond numbers (i.e. twofold-linked = (2b) etc.) of the involved species (0b)P^{3-}, (1b)P^{2-}, (2b)P^-, (3b)P^0, (4b)P^+, according to $q(P_x) = -x(3A + 2B + C - E)/N$, with $N = (A + B + C + D + E)$. Here A, B, C, D, and E are the quantities of these species in the structure per formula unit. Another way is to count the number of P–P bonds, $\sum_b$, and to calculate $q(P_x) = -x(3 - 2\sum_b/N)$, or to calculate $\sum_b$ from $q(M)$ according to $\sum_b = N/2(3 - q(M)/x)$.

The inherent basis of these procedures is the Zintl–Klemm concept[19,20] and the Mooser–Pearson[21] extended $(8 - N)$ rule. Formerly applied only to classical two-center–two-electron bonds, the extended procedures comprise all varieties of bonding (multiple bonds, partial bonds, multicenter systems, radicals, and free electrons). Generally, for a compound A_mB_n, an electron transfer $A \twoheadrightarrow A^{p+}$, $B \twoheadrightarrow B^{q-}$ ($|mp| = |nq|$) to the more electronegative element B forms pseudoelements A^*, B^* that show the structural principles of the corresponding isoelectronic elements with the whole spread of homoatomic bond types. Alternatively, one can derive from the number of valence electrons e_A and e_B according to the equation $me_A + ne_B + k = 8n$ the term $k = -\sum e_{AA} + \sum e_{BB} - \sum e^*$, which accounts for the number of electrons involved in A–A and B–B bonds as well as the number of electrons e^* that are not involved in localized bonds. However, one cannot predict all structural details because k is composed of three independent terms.[5] This corresponds to the fact that the formal ions A^{p+} and B^{q-} do not need to use all remaining electrons to form covalent homonuclear bonds. Application of the $(8 - N)$ rule leads to the same result as obtained by looking at the phosphides as derivatives of phosphanes with the structural elements: (3b)P$\hat{=}$(3b)CH, (2b)PH$\hat{=}$(2b)$CH_2$$\hat{=}$(2b)S, (1b)$PH_2$$\hat{=}$(1b)$CH_3$$\hat{=}$(1b)Cl, (0b)$PH_3$$\hat{=}$(0b)$CH_4$$\hat{=}$(0b)Ne.

Table 4 Ternary and multinary metal-rich phosphides $(M/M')P_x$, all with isolated P atoms, ordered according the descending ratio $(M + M')/P$

Formula	Metals (M/M′)	Structure type[a]	Pearson code	(M + M′)/P
$M_{9+x}M'_{4-x}P$	Hf/Mo ($x = 0.29$), Hf/Re ($x = 0$)	Hf_9Mo_4Ni	*hP* 28	13.000
$M_{31}M'_{12-x}P_x$	Mn/Si ($0.86 \leq x \leq 3.44$)	?	?	11.000 upper limit
$M_{31}M'_8P_4$	Ni/Si	?	*hP* 129	9.750
$M_2M'_5M''_2P_{0.72}$	Mg/Ir/B	$Ti_3Co_5B_2$	*tP* 20−0.56	9.000
$MM'_{2-x}P_x$	Mn/Ni ($x = 0.3$)	$MgCu_2$	*cF* 24	8.000
$M_5M'P$	Pd/Ga, Pt/Ga	Pd_5TlAs	*tP* 7	6.000
MM'_4P	Fe/Ta, Fe/Nb, Co/Nb, Ni/Nb, Co/Hf, Co/Ta, Co/Zr	$CoNb_4Si$	*tP* 12	5.000
$M_2M'_3P$	Mo/Ni, Wo/Co	$MgZn_2$	*hP* 12	5.000
	Mg/Ni	$MgCu_2$	*hR* 18	
$M_3M'_2P_{1+x}$	Mo/Ni ($x = 0.18$)	Mn_3Ni_2Si	*cF* 96 + 2.68	5.000
$M_2M'_{12}P_5$	(La, Ce, Pr, Nd, Eu)/Ni	$La_2Ni_{12}P_5$	*mP* 38	4.800
$M_2M'_2P$	$Pd_{1.5}/Cu_{2.5}$	Pd_4Se	*tP* 10	4.000
$M_3M'_{20}P_6$	Mg/Ni, Mn/Ni	$Cr_{23}C_6$	*cF* 116	3.833
$M_{21}M'_2P_6$	Ni/In	$Cr_{23}C_6$	*cF* 116	3.833
$M_{10}M'P_3$	Ni/Si	?	?	
$MM'_{10}P_3$	Zn/Ni, Ga/Ni, Sn/Ni, Sb/Ni	$ZnNi_{10}P_3$	*hP* 42	3.667
MM'_6P_2	Ba/Cu	$BaCu_6P_2$	*tP* 9	3.500
$M_2M'_7M''P_3$	Eu/Pt/Al, Eu/Pt/Mg, Eu/Pt/Mn, Eu/Pt/Fe, Eu/Pt/Zn, Ca/Pt/Sc, Ca/Pt/Al	$Eu_2Pt_7AlP_3$	*tI* 26	3.333
$M_{16}M'_6P_7$	Ni/Mn	$Mn_{23}Th_6$	*cF* 116	3.143
$M_{3-x}M'_xP$	Mo/Ni ($x = 0.325$)	Mo_3P	*tI* 32	3.000
$M_{2-x}M'_{1+x}P$	Ti/Mo ($x = 0.4$)	Ti_3P	*tP* 32	3.000
$M_{2-x}M'_{1+x}P$	Mo/Ti ($x = 0.4$)	α-V_3S	*tP* 32	3.000
MM'_2P	Li/Cu, $Li_{0.96}/Cu_{1.88}$	Cu_3P	*hP* 8	3.000
	Ti/Cu	$TiCu_2P$	*tI* 32	
	Yb/Ni	?	?	
	$Li_{0.58}/(Li_{0.93}Zr_{0.07})$	Li_3Bi	*cF* 16	
	Mg/Ni	Fe_3C	*oP* 16	
$M_2M'P$	Na/Cu, K/Cu, K/Au	Na_2CuAs	*oC* 16	3.000
	Ni/Si	Ni_2SiP	*oP* 32	
	Li/Cu	Na_3As	16· *hP* 8	
	Ni/Sn	Ni_2SnP	*oP* 16	
	$Zr/Ni_{0.48}$	$Zr_2Ni_{1-x}P$	*oP* 32	
	Zr/Co, Zr/Ni, Hf/Co, Hf/Ni	Hf_2NiP	*mP* 8	
	Fe/Ni	Ni_3P	*tI* 32	
	V/C, Nb/C	$AlCr_2C$	*hP* 8	
$M_3M'_3P_2$	K/Cu	$K_3Cu_3P_2$	*hR* 24	3.000
	Cr/Fe, Cr/Mn, Fe/Ni	Ni_3P	*tI* 32	
$M_5M'P_2$	K/Au	K_5CuSb_2, stack. var.	*hP* 16	3.000
	Cr/Ni	Ni_3P	*tI* 32	
$MM'_{11}P_4$	Yb/Ni	?	?	3.000
$M_9M'_{26}P_{12}$	Ce/Ni, Nd/Ni, Sm/Ni, Eu/Ni, Yb/Ni	$Ce_9Ni_{26}P_{12}$	*hP* 47	2.917
$M_9M'_2P_4$	Zr/Co, Zr/Ni	$Zr_9Co_2P_4$	*tP* 30	2.750
$M_6M'_5P_4$	$Zr_{6.45}/Nb_{4.55}$	$Zr_{6.45}Nb_{4.55}P_4$	*oI* 30	2.750
$MM'_{10}P_4$	Ba/Cu	$BaCu_{10}P_4$	*mC* 60	2.750
$MM'_{10}P_4$	La/Ni, Ce/Ni	$LaNi_{10}P_4$	*oP* 60	2.750
$M_{10}M'P_4$	$Li_{9.8}/Zr_{0.6}$	$Li_{9.8}Zr_{0.6}P_4$	*cF* 14	2.750
$M_{9-x}M'_{7+x}P_6$	Mo/Ni ($x = 0.42$)	$Mo_{8.58}Ni_{7.42}P_6$	*aP* 22	2.667
$M_2M'_6P_3$	Mo/Ni	$Mo_2Ni_6P_3$	*oP* 22	2.667
$M_{5-x}M'_{5+x}M''_3P_5$	Hf/Nb/Ni ($x = 0.04$)	$Hf_5Nb_5Ni_3P_5$	*hP* 18	2.600
$M_{31}M'_{8.5}P_{3.5}$	Co/Si, Mn/Si	$Ni_{31}Si_{12}$	*hP* 43	2.583
MM'_4P_2	$Ca/Cu_{0.95}$, Ln/Cu (Ln = Y, La–Yb)	$CaCu_4P_2$	*hR* 7−0.2	2.500
	Th/Fe, Sm/Ni, $Nd/Cu_{3.8}$	$SmNi_4P_2$	*oP* 42	
	Ca/Cu	$CaCu_4P_2$	*tP* 14	
	Sc/Fe, Zr/Ni, Gd/Ni, Dy/Ni, Er/Ni, Yb/Ni, U/Ni	$ZrFe_4Si_2$	*tP* 14	

Table 4 cont'd

Formula	Metals (M/M′)	Structure type[a]	Pearson code	(M + M′)/P
$M_4M'P_2$	V/C	V_4CP_2	*hP* 21	2.500
	K/Be, Na/Zn, K/Zn, Na/Cd, K/Cd, Na/Hg, K/Hg	K_4BeP_2	*hR* 21	
	Li/Eu	Li_4EuP_2	*hR* 21	
$M_3M'_7P_4$	Er/Pd	$Er_3Pd_7P_4$	*mC* 28	2.500
$MM'_{11}P_5$	La/Ni, Ce/Ni, Nd/Ni, Eu/Ni	?	?	2.400
$M_{16}M'_{36}P_{22}$	Ln/Ni (Ln = Ce–Nd, Sm, Eu–Dy)	$Tb_{16}Ni_{36}P_{22}$	*hP* 74	2.364
MM'_6P_3	La/Ni, Ce/Ni	$LaNi_6P_3$	?	2.333
$M_5M'_{2-x}P_3$	Hf/Ni ($x = 0{-}0.87$)	$Hf_5Ni_{2-x}P_3$	*oP* $40 - x$	2.333
$M_6M'P_3$	K/In	K_6InP_3	*aP* 22−2	2.333
	Na/Ga	Na_6GaP_3	*aP* 40	
MM'_8P_4	Ba/Cu	$BaCu_8P_4$	*tI* 26	2.250
$M_2M'_7P_4$	Ca/Ni, Ce/Ni, Nd/Ni, Eu/Ni	$Nd_2Ni_7P_4$	*oP* 26	2.250
$M_2M'_{25}P_{12}$	La/Fe	$La_2Fe_{25}P_{12}$	*oP* 78	2.250
$M_5M'_4P_4$	Ta/Ni, Nb/Ni	$Nb_5Cu_4Si_4$	*tI* 26	2.250
$M_{25}M'_{49}P_{33}$	Ln/Ni (Ln = Ce–Sm, Gd–Er)	$Tb_{25}Ni_{49}P_{33}$	*hP* 107	2.242
$M_6M'_{32}P_{17}$	La/Rh, Ce/Rh	$La_6Rh_{32}P_{17}$	*hP* 165	2.235
$M_3M'_{12}P_7$	La/Ni	?	?	2.143
$M_6M'_{15}P_{10}$	U/Ni, Ce/Ni, Yb/Ni	$Ce_6Ni_{15}P_{10}$	*hP* 62	2.100
$M_{20}M'_{42}P_{30}$	Ce/Ni, Nd/Ni, Sm/Ni	$Ce_{20}Ni_{42}P_{30}$	*hP* 92	2.067
$M_{2-x}M'_xP$	Ti/Mo (x = 0.1)	?	?	2.000
$M_5M'_{1+x}P_{3-x}$	Hf/Co (x = 0.23)	$Hf_5Co_{1+x}P_{3-x}$	*oP* 36	2.000
$MM'P$	Li/Zn, Li/Mg, K/Mn	MgAgAs	*cF* 12	2.000
	Li/Mn	LiMnP	*tP* 6	
	Th/Cu, U/Cu, Cs/Mn, Rb/Mn, Na/Mn, Li/Be, K/Mn, K/Mg, K/Cd, Na/Zn, Co/Pd, Fe/Li	Cu_2Sb	*tP* 6	
	Ca/Au, Sr/Au, Sr/Pd, Ba/Au, Ce/Pd	ZrBeSi	*hP* 6	
	K/Zn, Rb/Zn, Ca/Cu, Sr/Cu, Sr/Ag, Ba/Cu, Ba/Ag, Zr/Ni, $(Eu_{1-x}Gd_x)$/Pt ($0.05 \leq x \leq 0.90$), $(Eu_{0.5}Sr_{0.5})$/Pt, Eu/Ag, Eu/Au, $(Eu_{0.5}Gd_{0.5})$/Pt, $(Eu_{0.8}Gd_{0.2})$/Pt Ln/Pd (Ln = La–Tb)	Ni_2In	*hP* 6	
	Eu/Pt (α, β)	Ni_2In, dist.	*hP* 6	
	Eu/Pt (γ)	Ni_2In, dist.	*hP* 6($P\bar{3}ml$)	
	Ce/Pt	YPtAs	*hP* 12	
	Fe/Zr, Ta/Fe, Fe/Cr, Fe/Mo, Zr/Co, Fe/Co, Co/Nb, Co/Mo, Co/W, Nb/Ni, Fe/Mn, Co/Ta, Ti/Co, Co/V, Cr/Nb, Fe/Nb, Fe/V	Co_2P	*oP* 12	
	Mg/Cu, Mn/Co, Zr/Ru, Nb/Mn, Mn/Cu, Li/Eu, Zr/Ti, Hf/Cr, Hf/Mn, Ta/V, Ta/Cr, Ta/Mn, Hf/Fe, Hf/Co, Hf/Ni, Ln/Pt (Ln = Dy–Lu)	TiNiSi	*oP* 12	
	Ca/Pt	AlB_2,dist.	*oP* 12	
	Ba/Pt, Eu/Ir, Ba/Ir	LaIrSi	*cP* 12	
	Ba/Pd	BaPdP	*oC* 24	
	Ni/Mo, Ni/W, Cr/Pd, Mn/Pd, Fe/Mn, Ca/Ag, Fe/Fe [P:B], Ni/Co, Cr/Ni, Fe/Ni, Zr/Mo, Hf/Mo	Fe_2P	*hP* 9	
	Eu/Ni	SrPtSb	*hP* 3	
	Y/Pt, Sm/Pt, Ln/Pt (Ln = Gd → Dy, Tm → Lu)	AlB_2	*hP* 3	
	Ln/Ni (Ln = La–Sm, Gd)	$Tb_{1-x}NiP$	*hP* 12	
	Sr/Sn, Eu/Sn	NbCrN	*tP* 6	
MM'_3P_2	Yb/Cu	$YbCu_3P_2$	*hR* 36	2.000
	Y/Li, La/Li, Nd/Li	$CaAl_2Si_2$, fill.	*hP* 6	
	U/Ni, Ln/Co (Ln = Gd → Lu), Y/Co	$HoCo_3P_2$	*oP* 36	

(cont'd overleaf)

Table 4 cont'd

Formula	Metals (M/M′)	Structure type[a]	Pearson code	(M + M′)/P
MM'_5P_3	Th/Fe, Y/Co, Er/Co, Tm/Co, U/Mn, Y/Fe, Ce/Co, Ln/Co (Ln = Gd → Lu)	YCo_5P_3	*oP* 36	2.000
	Sr/Ni, La/Co, Eu/Ni, La/Ni, Yb/Ni	$LaCo_5P_3$	*oC* 36	
	Ce/Ni	$CeNi_5P_3$	*mC* 70.88	
	Zr/Cr, U/Cr, U/V	UCr_5P_3	*mP* 18	
MM'_9P_5	Ba/Ni, Sr/Ni	$BaNi_9P_5$	*hP* 30	2.000
	Ni/Co	Co_2P	*oP* 12	
$M_2M'_4P_3$	Th/Fe, Hf/Co, Zr/Co, Nb/Co	$Hf_2Co_4P_3$	*hP* 36	2.000
$MM'M''_2P_2$	Li/Sm/Cu, Li/Tb/Cu, Li/Y/Cu, Li/Yb/Cu	Fe_2Si	*hP* 6	2.000
$M_2M'M''P_2$	K/Na/Ga, K/Na/In, K/K/In	Na_3AlAs_2	*oI* 24	2.000
	K/Na/B	K_2NaBP_2	*mC* 24	
$M_2M'_{12}P_7$	Zr/Fe, $Ca_{2.1}/Ni_{11.9}$, $Li_{3.4}/Ni_{10.6}$, U/Ni, $Mg_{2.5}/Ni_{11.5}$, Nb/Co, Li/Ni, Li/Co, $Li_{3.2}/Ni_{10.8}$, $Na_{2.3}/Ni_{11.7}$, Ca/Ir Ln/Fe (Ln = Pr → Sm, Gd → Lu), Ln/Co (Ln = Ce, Pr → Lu), Zr/Co, Y/Ni, Ca/Ni, Ti/Co, Sc/Ni, Ca/Co Ln/Ni (Ln = Ce → Nd, Sm, Eu → Lu), Ln/Mn (Ln = Sc, Sm, Gd → Lu), Th/Mn Zr/Ni, U/Ni, U/Ru, Mg/Co Th/Fe, Th/Co, U/Co, Th/Ni, Th/Ru, U/Fe	$Zr_2Fe_{12}P_7$	*hP* 21	2.000
	Dy/Rh, Er/Rh	$Zr_2Rh_{12}As_7$	*hP* 22−1	
	Sr/Rh	$Ho_2Rh_{12}As_7$	*hP* 21	
$M_3M'P_2$	Li/Al	CaF_2, supercell	*oI* 96	2.000
	Rb/Ga, $(Rb_{1-x}K_x)$/Ga ($x = 0.157$), $(Cs_{1-x}K_x)$/Ga ($x = 0.115$), $(Cs_{1-x}Rb_x)$/Ga ($x = 0.175$)	Rb_3GaP_2	*oP* 96	
	Na/B, K/B, Cs/B, $(Na_{7/3}K_{2/3})$/B	K_3BP_2	*mC* 24	
	Na/In	Na_3InP_2	*mP* 48	
	K/In, (K,Na)/In, (K,Na)/Ga	Na_3AlAs_2	*oI* 24	
	Li/Ga	CaF_2, supercell	*cI* 96	
$M_3M'_7P_5$	Ln/Ni (Ln = La, Pr, Nd, Sm, Gd, Tb)	$Nd_3Ni_7P_5$	*hP* 60	2.000
$M_5M'P_3$	Li/Si, Li/Ge, Li/Ti	CaF_2	*cF* 12	2.000
	$(Na_{0.6}K_{0.4})$/Si, Cs/Si, Rb/Ge, Cs/Ge	Cs_5SiP_3	*oP* 36	
$M_6M'_2P_4$	Na/In, Cs/Al, Cs/Ga	$Cs_6Al_2P_4$	*mP* 48	2.000
	Li/Mn	$Li_6Mn_2P_4$	*tP* 12	
$M_6M'_{20}P_{13}$	Th/Co, U/Co, Th/Ni, U/Ni, U/Rh, Zr/Ni, Ho/Ni, Y/Ni, Ce/Ni, Nd/Ni, Sm/Ni, Gd/Ni, Yb/Ni	$Th_6Co_{20}P_{13}$	*hP* 39	2.000
$M_7M'_{19}P_{13}$	Y/Ni, Dy/Ni, Er/Ni	$Y_6Ni_{20}P_{13}$	*hP* 39	2.000
$M_8M'_{42}P_{25}$	Th/Fe	$Th_8Fe_{42}P_{25}$	*hP* 75	2.000
$M_{10}M'_2P_6$	Na/Si, Na/Ge, Na/Sn	$Na_{10}Si_2P_6$	*mP* 36	2.000
$M_{12}M'_4P_8$	K/Al, Cs/In	$K_{12}Al_4P_8$	*aP* 48	2.000
$M_5M'_9P_7$	Zr/Pd, Hf/Pd	$Zr_5Pd_9P_7$	*oC* 42	2.000
$M_{12}M'_{30}P_{21}$	Th/Ni, (La,Ce)/Rh	$(La,Ce)_{12}Rh_{30}P_{21}$	*hP* 63	2.000
$M_{20}M'_{66}P_{43}$	Ho/Ni	$Ho_{20}Ni_{66}P_{43}$	*hP* 129	2.000
$M_5M'_{19}P_{12}$	Th/Fe	$Th_5Fe_{19}P_{12}$	*mC* 72	2.000
	U/Ru, Y/Co, Ln/Co (Ln = Gd → Lu), Sc/Co, Zr/Co, Ca/Rh, Ca/Ir, Ce/Cu, Nd/Ni Y/Ru, Ln/Ru (Ln = La → Nd, Sm, Gd → Yb), Th/Ru	$Sc_5Co_{19}P_{12}$	*hP* 37−1	
	Yb/Ni	$Yb_5Ni_{19}P_{12}$	*mC* 180	
$MM'_{1-x}P$	Hf/Ni ($x = 0.534$)	$HfNi_{0.426}P$	*hP* 10−0.296	1.941
$M_5M'_{19}P_{12}$	$Nd/Cu_{17.8}$	$Nd_5Cu_{17.8}P_{12}$	*hP* 37−1.2	1.900
$M_6M'_{30}P_{19}$	U/Fe, U/Ru, U/Co, Er/Co, Tm/Co, Yb/Co, Lu/Co, Ca/Rh, Eu/Rh, Yb/Rh	$Yb_6Co_{30}P_{19}$	*hP* 55	1.895

Table 4 cont'd

Formula	Metals (M/M′)	Structure type[a]	Pearson code	(M + M′)/P
$MM'_{10}P_6$	Ba/Ni	$BaNi_{10}P_6$	*oC* 68	1.833
	Sr/Ni, Eu/Ni	‘$BaNi_{10}P_6$’	*oP* 68	
$M_{11}M'_{25}P_{20}$	U/Ni, Th/Ni	$Th_{11}Ni_{25}P_{20}$	*oP* 112	1.800
$M_4M'_3M''_2P_5$	Ca/Cu/Zn	$Ca_4Cu_3Zn_2P_5$	*hP* 28	1.800
$M_7M'_2P_5$	Ni/Si	?	*oP* ?	1.800
MM'_6P_4	U/Cr (α)	α-UCr_6P_4	*hP* 11	1.750
	U/Cr (β)	β-UCr_6P_4	*oP* 22	
	Li/Co, Mg/Co, Mg/Rh	$LiCo_6P_4$	*hP* 11	
$M_{7-x}M'_xP_4$	Ti/Mo ($x = 0.5$)	Nb_7P_4	*mC* 44	1.750
$M_2M'_5P_4$	Yb/Cu	$Yb_2Cu_5P_4$	*hR* 12−1	1.750
$M_3M'_2M''_2P_4$	Ca/Cu/Zn, Eu/Cu/Zn	$Ca_3Cu_2Zn_2P_4$	*hP* 11	1.750
$M_4M'_2M''P_4$	Na/Ca/Si, Na/Sr/Si, Na/Eu/Si, Na/Eu/Ge, Na/Eu/Sn, Na/Eu/Pb, Na/Na/W, Na/Eu/Al, Na/($Na_{0.5}Sr_{0.5}$)/Nb, Na/($Na_{0.5}Sr_{0.5}$)/Ta,	Na_6ZnO_4	*hP* 22	1.750
$M_{12-x}M'_xP_7$	Ti/Mo ($x = 4.2{-}6.8$)	$Cr_{12}P_7$	*hP* 26	1.714
$M_2M'_{30}P_{19}$	U/Cr, Zr/Cr	$Zr_2Cr_{30}P_{19}$	*hP* 51	1.684
$M_2M'M''_2P_3$	Ca/Cu/Zn, Eu/Cu/Zn	$Ca_2CuZn_2P_3$	*hP* 16	1.667
$M_6M'_{74}P_{49}$	U/Mo	$U_6Mo_{74}P_{49}$	*hP* 129	1.633
$M_2M'_{6-x}P_{5-y}$	Ho/Cu ($x = 0.41$; $y = 0.50$)	$Ho_2Cu_{5.59}P_{4.50}$	*hR* 39−2.73	1.600
$M_{15}M'_{18}P_{21}$	Sm/Ni, Tb/Ni	$Tb_{15}Ni_{18}P_{21}$	*hP* 128	1.571
$MM'_{13}P_9$	U/Mo	$UMo_{13}P_9$	*hP* 23	1.556
MM'_2P_2	Mg/Be, Ca/Be, Ca/Mn, Mg/(Mg_xZn_{1-x}) ($x = 0.375$), Ca/Zn, Ca/Cd, Sr/Mn, Sr/Zn, Sr/Cd, Ba/Mg, Ba/Cd, Zr/Cu, Eu/Mn, Eu/Zn, U/Cu, U/Ni, Eu/Cd Ag/(Zn,La), Ag(Zn,Sm), Cu/(Zn,Sm), Y/(Zn,Cu), La/(Zn,Cu), Ce/(Zn,Cu), Yb/(Mn,Cu), Th/Cu, Yb/Zn, Yb/(Zn,Cu), Yb/Cu	$CaAl_2Si_2$	*hP* 5	1.500
	Th/Ni (α)	$BaCu_2S_2$	*oP* 20	
	Ba/Ge, Ba/Pd	$BaGe_2As_2$	*tP* 20	
	Th/Co, U/Co, Th/Ni (β), U/Os, La/Rh, Ce/Rh	$CaBe_2Ge_2$	*tP* 10	
	Ca/Ir, Sr/Ir, Eu/Ir	$EuIr_2P_2$	*hP* 15	
MM'_2P_{2-x}	Eu/Pt ($x = 0.38$), Ca/Pt ($x = 0.57$)	$BaAl_4$, def.	*tI* $20 - 2x$	1.500
MM'_2P_2	Ce/Ru, Ca/Ru, Sr/Ru, Ba/Ru, Eu/Ru, Eu/Co, Sm/Co, Sr/Co, Dy/Ni, Dy/Pd, Dy/Ru, Er/Pd, Er/Ru, Eu/Fe, Sr/Fe, Sr/$Cu_{0.875}$ Ba/Zn, Ba/Ir, Cs/Mn	$BaAl_4$, $ThCr_2Si_2$	*tI* 10	1.500
$M_2M'P_2$	K/Si, Cs/Si	K_2SiP_2	*oI* 20	1.500
	Li/Ce, Li/Pr	$CaAl_2Si_2$	*hP* 5	
	Ba/Ge	Ba_2GeP_2	*mP* 20	
$M_{11}M'P_8$	$Ti_{11.34}$/$Cu_{0.66}$	$Ti_{11}CuP_8$	*oP* 40	1.500
$M_{10}M'_{12}P_{16}$	Ca_{10-x}/Si_{12-2x}	?	*mP* ?	1.375
$M_2M'_2P_3$	Nb/Ni	$Nb_6Ni_6P_9$	*hP* 21	1.333
$M_{4-x}M'_xP_3$	Mo/Ti ($x = 0.2$)	Mo_4P_3	*oP* 56	1.333
$M_3M'P_3$	Ca/In, Sr/In	Ca_3AlAs_3	*oP* 28	1.333
$M_6M'_2P_6$	Ba/Sn	$K_6Sn_2Te_6$	*mP* 28	1.333
$M_6M'_{10}P_{12}$	Ag/Ge	$Ag_6Ge_{10}P_{12}$	*cI* 56	1.333
MM'_3P_3	Ln/Zn (Ln = Y, La–Er), Pr/Cd	$ScAl_3C_3$	*hP* 14	1.333
$M_6M'_4M''_6P_{12}$	Ag/Sn/Si, Ag/Sn/Ge	$Ag_6Ge_{10}P_{12}$	*cI* 56	1.333
$M_3M'_2P_4$	Ca/Ge, Sr/Ge	$Ca_3Ge_2P_4$	*mP* 36	1.250
	Sr/In, Eu/In	$Sr_3In_2P_4$	*oP* 18	
	Ba/Sn	$Ba_3Sn_2P_4$	*mP* 36	
$M_4M'P_4$	Sr/Ge, Ba/Si, Ba/Ge, Ca/Si, Sr/Si	Ba_4SiAs_4	*cP* 72	1.250

(cont'd overleaf)

Table 4 cont'd

Formula	Metals (M/M′)	Structure type[a]	Pearson code	(M + M′)/P
$M_3M'_4P_6$	U/Ni	$U_3Ni_4P_6$	*tP* 13	1.167
	Ba/Si	$Ba_3Si_4P_6$	*mP* 26	
$M_5M'_2P_6$	Sr/Sn	$Ca_5Sn_2As_6$	*oP* 26	1.167
$MM'P_2$	Cd/Si, Mg/Si, Zn/Ge, Cd/Ge, Zn/Si, Zn/Sn, Cd/Sn	$CuFeS_2$	*tI* 16	1.000
	Mo/Ni, Co/W, Ni/W, Co/Mo	$MoNiP_2$	*hP* 8	
	Ni/Nb	$NbNiP_2$	*oP* 16	
	Ti/Mo	NiAs	*hP* 4	
	U/Cu	$UCuP_2$	*tI* 16	
	U/Pd, Sm/Cu	$ZrAl_3/SrZnBi_2$	*tI* 16	
	Mg/Ge, Al/Ga, Ga/In	ZnS	*cF* 8	
	U/Co	$UCuAs_2$	*tP* 8	
	Nd/Cu, Ho/Cu, Ce/Ag	$TbCu_{1+x}P_{2-x}$	*tP* 16	
MM'_2P_3	Ni/Mo	$NiMo_2As_3$	*mC* 24	1.000
	Cu/Ge, Cu/Si	ZnS	*cF* 8	
MM'_3P_4	Ni/Si	Cu_3AsS_4	*tI* 16	1.000
$M_{1-x}M'_xP$	Ti/Mo ($x = 0.1$)	WC	*hP* 2	1.000
$M_{1-x}M'_xP$	Ti/Mo ($x = 0.1$)	$PbCl_2$	*oP* 12	1.000
$M_{1-x}M'_xP$	Ti/Mo ($x = 0.05$)	TiAs	*hP* 8	1.000
$M_2M'P_3$	$Ni_{0.84}Si_{0.16}/Si_{0.56}$	$Ni_{3.36}Si_{1.76}P_6$	*oI* 12−0.88	1.000
	Ba/Pd	Ba_2PdP_3	*mP* 24	

[a] dist. = distorted type; def. = defect type; fill. = filled up type; stack. var. = stacking variant.

Table 5 Ternary polyphosphides (ordered according to a descending ratio (M + M')/P)

Formula	Metals (M/M′)	Structure type[a]	Pearson code	Polyanionic structure[b]	(M + M′)/P
$M_5M'_2P_3$	Ni/Si	$Ni_5Si_2P_3$	*oP* 80	(P^{3-}) and ($P_2{}^{n-}$) dumbbells	2.333
$MM'P$	Sr/(Pt_xP_{2-x}) ($x = 0.75$), Eu/(Pt_xP_{2-x}) ($x = 0.65$)	AlB_2	*hP* 3	Partially P–P network	2.000
$M_5M'_6P_6$	Ca/Pd	$Ca_5Pd_6P_6$	*oP* 34	Partially P–P dumbbells	1.833
MM'_8P_5	La/Co, Eu/Co, Pr/Cr	$LaCo_8P_5$	*oP* 28	(P^{3-}) and ($P_2{}^{n-}$) dumbbells	1.800
$M_4M'_5P_5$	Sr/Pd, Ca/Pd	$Sr_4Pd_5P_5$	*oC* 56	(P^{3-}) and ($P_2{}^{n-}$) dumbbells	1.800
$M_4M'_3P_4$	Li/Eu	$Li_4Sr_3Sb_4$	*oI* 22	(P^{3-}) and ($P_2{}^{4-}$) dumbbells	1.750
$M_2M'_3P_3$	Sr/Pd	$Sr_2Pd_3P_3$	*oP* 32	(P^{3-}) and ($P_2{}^{4-}$) dumbbells	1.667
$M_2M'_6P_5$	Ca/Cu	Ce_2NiGa_{10}	*tI* 26	(P^{3-}) and ($P_2{}^{4-}$) dumbbells	1.600
$M_2M'_7P_6$	Sr/Rh	$Sr_2Rh_7P_6$	*tP* 30	(P^{3-}) and ($P_2{}^{4-}$) dumbbells	1.500
MM'_2P_2	Ln/Co (Ln = La → Nd, Sm, Eu), Li/Cu, Cs/Co, Ca/$Cu_{1.75}$, Ca/Ni, Ca/Co, Ca/Fe, Ba/Ni Sr/Co, Sr/$Cu_{1.75}$, Sr/Ni (β), Eu/$Cu_{1.75}$, Sr/Fe, La/Fe, Ce/Fe, U/Fe, Eu/Fe, Cs/Fe, Pr/Fe Ln/Ni (Ln = La → Nd, Sm, Eu, Tb → Yb), Y/Ni, U/Ni, Li/Ni, Ln/Pd (Ln = La → Nd, Sm → Er, Yb), Ca/Pd, Sr/Pd, Y/Pd, Ca → Ba/Ru, Y/Ru, Ln/Ru (Ln = La → Nd, Eu, Sm → Yb), Sr → Ba/Rh, Eu/Rh,	$ThCr_2Si_2$[c]	*tI* 10	($P_2{}^{n-}$) dumbbells	1.500

Table 5 cont'd

Formula	Metals (M/M′)	Structure type^a	Pearson code	Polyanionic structure^b	(M + M′)/P
	Sr → Ba/Os, Eu/Os, Cs/Ru, Th/Ru, U/Ru, U/Ni$_{1.5}$, Cs/Mn, Cs/Rh, Cs/Ir				
	Ba/Pd	$CeMg_2Si_2$^{c}	*tP* 5	$(P_2{}^{n-})$ dumbbells	
	Th/Ni, Th/Ru, U/Ru, U/Ru(P$_{1.9}$)	$ThRu_2P_2$	*oP* 20	${}^{1}_{\infty}(P^{n-})$ chains	
	Sr/Ni (α)	$SrNi_2P_2$	*oI* 30	$(P_2{}^{n-})$ dumbbells	
$M_2M'P_2$	K/Pd, K/Ni, Cs/Ni, Cs/Pd, Cs/Pt	K_2PdAs_2	*oC* 20	$(P_2{}^{4-})$ dumbbells	1.500
	K/Ga	K_2GaSb_2	*mP* 40	(P^{3-}) and $(P_2{}^{4-})$ dumbbells	
	Au/Pb, Au/Tl, Au/Hg	Au_2PbP_2	*oC* 20	${}^{1}_{\infty}(P^{-})$ chains	
$M_5M'_4P_6$	Li/Cu	$Li_5Cu_4P_6$	*oI* 30	$(P_2{}^{4-})$ dumbbells	1.500
$M_7M'_5P_8$	Li/Cu	$Li_7Cu_5P_8$	*oI* 29.5	$(P_2{}^{4-})$ dumbbells	1.500
$M_3M'_8P_8$	Ln/Cu (Ln = Y, Gd–Tm)	$Y_3Cu_{7.65}P_8$	*hR* 57−1.05	$(P_2{}^{n-})$ dumbbells	1.375
$M_{14}M'P_{11}$	Ca/Mn, Ca/Al, Eu/Mn	$Ca_{14}AlSb_{11}$	*tI* 208	linear $(P_3{}^{7-})$ chains	1.364
$M_2M'_3P_4$	Ba/Cu	$Ba_2Cu_3P_4$	*oI* 36	$(P_2{}^{5-})$ dumbbells	1.250
	Na/Sr, Na/Eu	Gd_5Si_4	*oP* 36	$(P_2{}^{4-})$ dumbbells	
$M_2M'P_3$	Ba/Pd	Ba_2PdP_3	*oP* 24	$(P_3{}^{n-})$ chains	1.000
$M_2M'P_3$	Ln/Au (Ln = La, Ce, Pr)	Ce_2AuP_3	*oP* 24	(P^{3-}) and $(P_2{}^{4-})$ dumbbells	1.000
	Nd/Au	Nd_2AuP_3	*mP* 24	(P^{3-}) and $(P_2{}^{4-})$ dumbbells	
MM'_2P_3	Ba/Pt	FeS_2, dist.	*mP* 24	$(P_2{}^{4-})$ dumbbells	1.000
MM'_4P_5	K/Ba	KBa_4P_5	*tP40*	(P^{2-}) dumbbells and $(P_3{}^{5-})$ trimers	1.000
$M_5M'_9P_{16}$	Sn$_{0.84}$/Si	$Sn_{4.2}Si_9P_{16}$	*hR* 32−2.8	$(P_3{}^{n-})$ chain	0.875
MM'_4P_6	Sr/Pt	FeS_2, dist.	*mC* 44	$(P_2{}^{4-})$ dumbbells	0.833
$M_8M'_{16}P_{30}$	Ba/Cu	$Ba_8Cu_{16}P_{30}$	*oP* 216	$(P_{18}{}^{20-})$ finite chain polyanion; $(P_{12}{}^{14-})$ finite branched polyanion	0.800
MM'_2P_4	Ba/Ni, Ba/Pd	$BaPd_2P_4$	*tI* 14	$(P_4{}^{4-})$ *cyclo*-P_4	0.750
	Ba/Cu	$BaCu_2P_4$	*oF* 56	${}^{1}_{\infty}(P^{-})$ chains	
$M_6M'_6P_{17}$	La/Ni, Ce/Ni, Pr/Ni, La/Pd, Ce/Pd	$La_6Ni_6P_{17}$	*cI* 58	(P^{3-}) and $(P_4{}^{6-})$ pyramidal	0.706
$MM'P_3$	Al/Si	$AlSiP_3$	*oP* 20	(P^{3-}) and $(P_2{}^{4-})$ dumbbells	0.667
	Ce/Si	$CeSiP_3$	*oP* 40	(P^{3-}) and ${}^{1}_{\infty}(P^{-})$ chains	
$M_2M'P_5$	Ti/Ni	Ti_2NiP_5	*oP* 32	(P^{3-}) and ${}^{1}_{\infty}(P_2{}^{2-})$ branched anion and ${}^{1}_{\infty}(P_2{}^{3-})$ branched anion with half bonds	0.600
$M_2M'_5P_{12}$	Co/Re	$Ni_2Re_5As_2$	*oP* 38	(P^{3-}) and $(P_2{}^{4-})$ dumbbells	0.583
$MM'P_4$	Mn/Co	FeS_2	*oP* 6	$(P_2{}^{4-})$ dumbbells	0.500
	Cd/Cu	?	*oF* 60	?	
$M_4M'P_{10}$	Cu/Sn	Cu_4SnP_{10}	*cF* 60	$(P_{10}{}^{6-})$ adamantane	0.500
$M_{1-x}M'_xP_4$	Cr/Mn ($x = 0.3-0.7$)	$Cr_{1-x}Mn_xP_4$	*aP* 20	${}^{2}_{\infty}(P_4{}^{2-})$ cond. *cyclo*-P_{10}	0.500
MM'_4P_{12}	Ln/Fe, Th/Fe, Ln/Ru, Ln/Os, Ln/Co, U/Fe, Th/Fe	$CoAs_3$, fill.	*cI* 34	$(P_4{}^{4-})$ planar *cyclo*-P_4	0.417
MM'_4P_{16}	V/Ni, Nb/Ni, W/Ni	VNi_4P_{16}	*mC* 84	$(P_8{}^{8-})$ *cyclo*-P_6 in boat form with a P_2 branch	0.313
$MM'P_8$	Mo/Ni, W/Ni	$MoNiP_8$	*hP* 20	$(P_8{}^{6-})$ *bicyclo*-P_8	0.250
MM'_2P_{12}	Mo/Fe, W/Fe, V/Fe	$MoFe_2P_{12}$	*oP* 60	${}^{1}_{\infty}(P_6{}^{4-})$ chain of *cyclo*-P_6 (1,2-boat)	0.250
	Ti/Mn, Nb/Mn, Mo/Mn, W/Mn, Nb/Mn, Nb/Fe	$TiMn_2P_{12}$	*mC* 60	${}^{3}_{\infty}(P_{12}{}^{8-})$ cond. *cyclo*-P_{18}	
$MM'P_{14}$	Hg/Pb, Cd/Pb, Zn/Pb,	$HgPbP_{14}$	*oP* 64	${}^{1}_{\infty}(P_{14}{}^{4-})$ tube with M in the frame	0.143
	Hg/Sn, Cd/Sn, Zn/Sn, Cu/Sn, Cu/Pb, Ag/Sn, Ag/Pb, Au/Sn, Au/Pb, Au$_{1-x}$Sn$_{1+x}$				

[a] dist. = distorted type; def. = defect type; deriv. = derivative; fill. = filled up. [b] cond. = condensed. [c] These compounds have a $(P_2{}^{n-})$ dumbbell, where n and hence the P–P bond length varies with composition.

3 SYNTHESIS[1–15]

3.1 Practical Precautions

All operations with phosphorus and reactive phosphides should be done in a hood or dry box and equipment should be on hand to deal with the possibility of a phosphorus fire. Phosphides may ignite if milled mechanically under ambient conditions and even highly purified red phosphorus may contain small inclusions of white phosphorus. Therefore, all grinding should be done under an inert atmosphere. On contact with wet air or wet inert gas, phosphides may produce phosphines (odor, self ignitability). Phosphines have also been shown to be physiologically active.[3,22]

Small amounts of reactive phosphides may be transferred into a $CuSO_4$ solution in small portions under stirring, for chemical disposal. Alternatively, the material can be oxidized with a Br_2/alcohol solution. An odor-free method of oxidation with HNO_3 is the use of an autoclave.[23]

3.2 Solid-State Reactions

The most general method for the preparation of solid phosphides is from the elements; however, there are several problems to overcome in that highly electropositive metals are often air- and moisture-sensitive, so that the educts and often the products must be handled under inert conditions (glove box or Schlenk technique). A well described example for the synthesis of the air- and moisture-sensitive phosphides Na_3P_7 and Na_3P_{11} has been described.[24]

In the case of impure starting compounds (hydroxide and oxide layers are frequent impurities), corrosion problems appear leading, for example, to the formation of phosphide oxides. Such corrosion problems may be prevented by the use of inner containers made from Mo, Nb, or Ta. Silica as a crucible material is also problematic, since silicon might replace some of the phosphorus atoms, and this is hardly detectable by X rays.

The high phosphorus vapor pressure, especially in the case of the preparation of polyphosphides, makes thick-walled containers and low reaction temperatures necessary. Kinetic hindrance which occurs during the vaporization of phosphorus is reduced by adding traces of halogen or sulfur.[25] The disadvantage is the formation of by-products, such as phosphide halides or phosphide sulfides. In cases where reaction layers form on unreacted material, preventing diffusion, repeated grinding, pressing, and heating is necessary. Another method is to dissolve oxide layers by the use of fluxes.[26,27] The flux can be a metal, a halide (low-melting eutectic), or an oxide (e.g. B_2O_3). The most effective metal flux for phosphides is liquid tin. Most of the binary and ternary phosphides are stable in 2N HCl and the remaining flux can easily be removed. Nevertheless, one has to keep in mind that tin inclusion in the phosphide crystals might occur. Also, the higher homologue lead can be used as a flux agent. Since $PbCl_2$ is insoluble in cold water, the lead matrix needs to be dissolved in an oxidizing mixture of H_2O_2 and acetic acid. Crystals of metal-rich phosphides like $Ca_5Rh_{19}P_{12}$, $Yb_6Co_{30}P_{19}$, or $Eu_6Rh_{30}P_{19}$ have been grown with this technique.[28] Halide fluxes are also useful when one of the metal components has a high vapour pressure, for example, for the preparation of the series $REZn_3P_3$ or $RECd_3P_3$.[29]

To prevent strong exothermic reactions, slow heating in the temperature region of the vaporization of P (850 K $\leq T \leq$ 900 K) is recommended. The phosphorus pressure may also be reduced during synthesis via the formation of an intermediate phosphide. This phosphide then acts as a phosphorus source in the course of the reaction. For the synthesis of high-melting metal-rich phosphides, a prereaction in an arc furnace, followed by annealing with additional phosphorus in silica tubes, is possible. In some cases, metal-rich phosphides of the early transition metals can directly be prepared via arc-melting.[30] The preparation of ternary phosphides is simplified via binary compounds to reduce the reaction temperatures, the content of impurities, and the sensitivity of the educts. To prevent decomposition, high-pressure techniques are sometimes useful. This was especially useful for the preparation of the skutterudites $REFe_4P_{12}$ with the heavier rare earth elements.[31]

3.3 Thermal Decomposition, Gas-phase Reactions

Further methods of preparation are the decomposition of higher phosphides under controlled temperature and pressure, yielding compounds with lower P content. Only with highly volatile metals one also observes the gaseous metal, M(g). Under low pressure and low temperature a complete series of $[K(K_3P_7)_m(K_2P_4)_n]^+$ moieties can be formed from K(g) and P_4(g) under He gas; this method is yet to be fully exploited.[32] Chemical vapor transport reactions are suitable for the preparation and purification of phosphides, if the metals form gaseous compounds, for example, halides or oxides.[33] Even large single crystals for neutron diffraction can be obtained.[34]

Whisker growth of hexagonal β-HfP, cubic α-ZrP, and hexagonal β-TiP is possible via a mixed-metal, impurity-activated chemical vapor deposition (CVD) process from $HfCl_4/ZrCl_4/TiCl_4 + PCl_3 + H_2 + Ar$ gas mixtures at 1050 °C. Si + Pd and Si + Pt were used as mixed-metal impurity components. Such whiskers are stable in concentrated HCl.[35]

3.4 Synthesis in Solvents

Because of the solubility of alkali metals in NH_3(l), some alkali metal phosphides have been prepared from NH_3(l). Reactions in solvents, either by using compounds containing polyanions or, in the course of suitable syntheses, from compounds starting with isolated phosphorus anions or from

P_4, yield a variety of new compounds. Once in solution, higher condensed units such as $P_{19}{}^{3-}$, $P_{21}{}^{3-}$, or $P_{26}{}^{4-}$ are accessible through metal–organic reactions, and they crystallize as solvates (for low coordinated phosphides stabilized in the coordination sphere of transition metals, see Scherer[36]).[37,38] The species present in solvent-free and solvated phases usually differ. An example of the conversion of polyanions into alkylated polyphosphanes is $P_7{}^{3-}$ and P_7R_3.[6,39] The latter can also be prepared from Na/K alloy and P_{white} in monoglyme with $ClSiMe_3$. Conversely, P_7R_3 is converted into solvated Li_3P_7 via metalation. Besides $NH_3(l)$, ethylenediamine, *en*, can be used for binding the alkali metal ions.

A variety of ammonia solvated alkali metal phosphides has recently been prepared in the Korber group. Examples of these peculiar compounds are $Cs_2P_4{\cdot}3NH_3$ with the 6π aromatic $P_4{}^{2-}$ anion[40] and $Cs_3P_{11}{\cdot}3NH_3$.[41]

3.5 Nanoparticles

Nanocrystalline Co_2P, Ni_2P, and Cu_3P can be prepared in a mild one-step route via simple solvothermal direct reaction of the metal halides with yellow phosphorus between 350 and 410 K using ethylenediamine as solvent.[42] Using the precursors Na_3P and $CoCl_2$ with benzene as solvent, mixtures of sphere-shaped Co_2P and spindle-shaped CoP nanocrystals can be obtained in yields of about 90%.[43] Silica supported phosphide samples can be prepared by pore volume impregnation of nickel nitrate and diammonium hydrogen phosphate, followed by H_2/N_2 reduction of the dried and calcined samples.[44] Nanoscale particles of catalytically active SiO_2/Ni_2P can be obtained by reduction of nanoparticulate phosphate precursors.[45] Crystalline nanoclusters of Fe_2P, RuP, Co_2P, Rh_2P, Ni_2P, Pd_5P_2, or PtP_2 can be obtained in a silica xerogel matrix from single-source molecular precursors.[46] An overview on the nanoscale phosphide particles was given by Lukehart *et al.*[47]

3.6 Other Methods

The reduction of phosphates by carbon is a classical method, but the purity of phosphides obtained this way can be suspect. This also holds for replacement reactions, in which a redox process between a transition metal and a metal phosphide is used for the preparation of phosphides with high thermal stability. Binary main-group element and transition metal phosphides like AlP, CrP, NbP, MoP, or WP can be prepared by the reaction of the powdered metals with a melt of lithium metaphosphate $LiPO_3$.[48] Bulk samples of transition metal phosphides like Co_2P or NiMoP can be obtained via reduction of metal oxide/phosphate mixtures in a mixture of 5% H_2 in N_2. MoP, WP, Fe_2P, Ni_2P, FeP, and RuP can be synthesized by direct reduction of the transition metal phosphates in hydrogen atmosphere between 670 and 1320 K.[49]

Molecular beam methods are now widely used for the preparation of common semiconductors such as GaP and their intergrowth with other compounds. Thin films of iron phosphides of 0.5 to 25 μm thickness can be electrodeposited from sulfate solutions. Depending on the deposition conditions (time, pH, temperature), the phosphides FeP, Fe_2P, and/or Fe_3P occur.[50] The preparation of higher polyphosphides, for example, KP_{15}, as thin films demonstrates the range of still yet unexplored preparative methods.[51] This is also valid for the electrolysis of phosphates.[52] The latter techniques is mostly suited for metal-rich phosphides.[53]

4 BOND LENGTHS, BOND ANGLES, COORDINATION, VOLUMES

4.1 General Remarks

The coordination of the metal atoms and the phosphorus atoms depends strongly on the stoichiometric P/M ratio. For a compound MP_x the mean coordination number $\overline{CN}$ is a rough measure, taking into account only heteroatomic bonds: $x = \overline{CN}(M)\overline{CN}(P)$. Additional M–M and P–P bonds lead to much more complicated coordinations, often very difficult to identify. One way to analyze the coordination is to use classical polyhedra, and compare interatomic distances with tabled covalent, ionic, and metallic radii. Appropriate values for phosphorus are: $R_{cov} = 111$ pm (single bond); $R_{met} = 118$ pm ($CN = 12$); $R(P^{3-}) = 194$ pm ($CN = 6$); $R_{vdW} = 190$ pm. Weaker P–P interactions occur at larger d(P–P) distances, which can be analyzed in terms of Pauling bond order (PBO) or related procedures, for example, $d(P–P) = 239$ pm in cubic high-pressure phosphorus corresponds to PBO ∼0.5.

4.2 P–P Bonds

The P–P bond lengths in polyphosphides may be compared with that of a single bond $d_1(P^{\pm 0}) = 222.8$ pm derived from black phosphorus.[54] The range 215–230 pm is observed, depending on the structural function and the relative charges of the P atoms (Figure 1). With strong electropositive cations the P–P distance of $P_2{}^{4-}$ dumbbells $\bar{d} = 229(3)$ pm is considerably larger than $\bar{d} = 221(2)$ pm with neutral molecules. Transition metal diphosphides M^{IV} show a value $\bar{d} \sim 233(6)$ pm, but the bond lengths are tunable by the valence electron concentration (VEC). This corresponds to different tendencies for metal oxidation and reduction by charge transfer. The *cyclo*-$P_n{}^{n-}$ and corresponding neutral molecules are characterized by $\bar{d} = 222(2)$ pm. The bond lengths in skutterudites (e.g. CoP_3) are much larger with $\bar{d} = 228(5)$ pm in the $P_4{}^{4-}$ rings, possibly also generated by redox charge transfer. In the helical $^1_\infty(P^-)$ units $\bar{d} = 221(2)$ pm, but with significant alterations by the cation

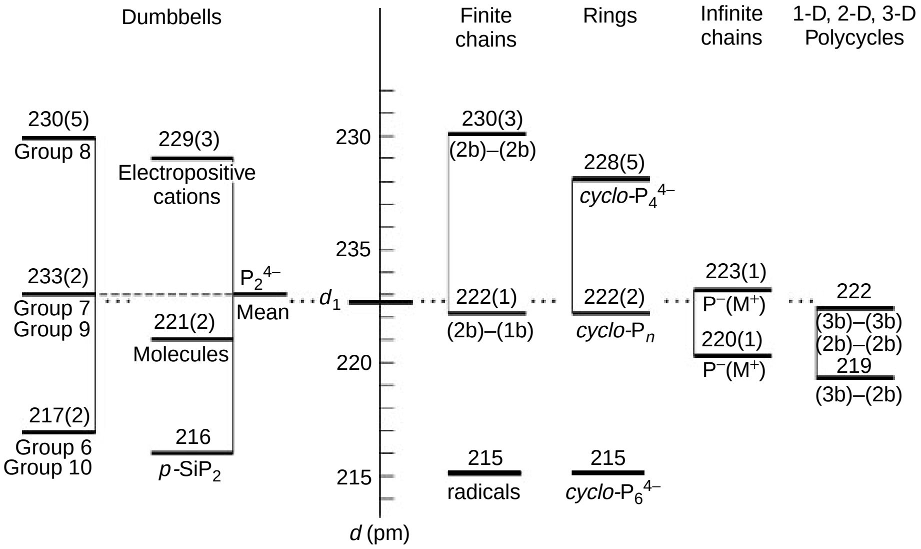

Figure 1 Bond lengths of dumbbells, finite chains, rings, infinite chains, and 1-D, 2-D, and 3-D polycycles in polyphosphides. The level of $d_1(\text{P–P}) = 222.8\,\text{pm}$ is dotted

charge: $\bar{d}(\text{M}^+) = 223(1)\,\text{pm}$ and $\bar{d}(\text{M}^{2+}) = 220(1)\,\text{pm}$. The range is the same as for *cyclo*-$\text{P}_n{}^{n-}$. The structures of finite chains $\text{P}_n{}^{(n+2)-}$ show the differences between central and terminal bonds: (2b)–(2b) = 230(3) pm, but (2b)–(1b) = 222(1) pm. In the polycyclic 1-D, 2-D, and 3-D structures the bond lengths are strongly influenced by the P/M ratio and the different strain in the individual arrangements, for example, the (2b)–(2b) distances are most affected by the ring sizes. Furthermore, there are differences between main-group compounds and transition metal compounds. Therefore the individual values cover large ranges: $230 \geq$ (3b)–(3b) $\geq$ 217 pm; $224 \geq$ (3b)–(2b) $\geq$ 214 pm; and $226 \geq$ (2b)–(2b) $\geq$ 219 pm. In general, $d(\text{3b–3b}) \sim d(\text{2b–2b}) > d(\text{3b–2b})$, with mean values of about 222, 222, and 219 pm, respectively. Again, the shortening of (3b)–(2b) distances reflects bond polarity. In flexible structures such as the $^2_\infty(\text{P}_5{}^{3-})$ network of the rare earth pentaphosphides, (3b)–(3b) = 219 pm is shorter than (2b)–(2b) = 221 pm, as expected. However, in other structures, for example, in the ladder-like spines of the tubular type, the internal strain in the (3b)–(3b) bond results in remarkable stretching of those bonds. Temperature- and pressure-dependent structure determinations reveal very small changes of the P–P bonds.

4.3 P–P–P Bond Angles

The mean bond angles in P(black) and P(violet)[55] are 100.2° and 101.2°, respectively, and correspond to those in polyphosphide networks. In unstrained parts of these networks, the bond angles cover the narrow range 98–104°. Large deviations exist with *cyclo*-P_3 and *cyclo*-P_4 (bent bonds), as well as in transition metal phosphides which are forced by the metal coordination (60–120°).

4.4 M–P Bonds, Coordination

Coordination to metals follows the usual trends. The transition metals try to achieve octahedral coordination (with a few exceptions), but the cations of the electropositive group 1–3 elements exhibit a rich variety. The coordination polyhedra are determined by radius ratios more than by topological preferences. For polyphosphides in general, all P atoms are involved in M–P interactions according to the number of lone pairs present. The anionic $(1\text{b})\text{P}^{2-}$ and $(2\text{b})\text{P}^{-}$ as well as the neutral $(3\text{b})\text{P}^{0}$ species adopt quasi-tetrahedral coordination, especially if main-group cations are involved. Only a few exceptions are known, for example Li_3P_7. With more covalent M–P bonds, the number $(m+n)$ of available lone pairs of a polyanion $\text{P}_m{}^{n-}$ is strongly related to the metal coordination number; that is, $\text{CN(M)} \leq (m+n)$. If $\text{CN(M)} > (m+n)$, ion–ion and ion–dipole interactions dominate. The relation $d[\text{M–(2b)P}] > d[\text{M–(3b)P}]$ is true in most cases.

Table 6 gives a survey on the range of M–P distances. The upper limits are uncertain[9] because the selected distances are only compared with atomic radii and take not into account the topology (convex polyhedra procedure). The M–P coordination in solid phosphides demonstrates both coordination and donor functions in isolated complex compounds (cf. the $(\text{E}15)_n$ complexes, stabilized in the coordination sphere of transition metals).[36] This is especially true with the polyphosphides. An extreme is $\text{Cu}_2\text{P}_3\text{I}_2$ (see Section 6.5.7), which is an adduct of CuI and elemental phosphorus (charge transfer complex). Chains of polycyclic

Table 6 Physical parameters of selected binary phosphides MP_x

Compound	CN (M)	d(M–P) (pm)	d(M–M) (pm)
Li_3P	3,4	246–277	254–354
LiP	6	257–279	279–374
Li_3P_7	12,6,5	250–473	292–311
LiP_5	7	240–342	>400
LiP_7	6	267–288	>489
Na_3P	3,4	287–323	294–324
NaP	8	288–367	329–392
Na_3P_7	4–6	286–340	349–412
Na_3P_{11}	11	291–383	431–439
NaP_7	6	294–304	>535
K_3P	3,4	328–369	335–469
K_4P_3	4,7,6	332–356	370–433
KP	8	308–413	345–448
K_4P_6 (α)	10,8	335–347	417–469
K_4P_6 (β)	10,8	332–348	416–468
KP_{15}	6	324–348	413, >500
Rb_4P_6	10,6	347–362	>420
Cs_4P_6	10,8	358–379	>423
Cs_3P_7	9,8,7	350–388	>449
Be_3P_2	4	215–223	266–271
BeP_2	4	215–218	≥ 215
Mg_3P_2	4	256–261	320–374
MgP_4	6	260–286	>454
CaP	6	289–290	301–461
CaP_3	11	292–375	370–410
Sr_5P_4	6	303–348	353–420
SrP	6	305–317	405–507
Sr_3P_4	8	304–328	408–414
SrP_2	6,9	302–336	402–418
SrP_3	11,9	305–358	391–476
Sr_3P_{14}	8,9	315–371	462–492
Ba_3P_2	6	321–357	>421
Ba_4P_3	6,7	309–456	351
Ba_3P_4	8	315–348	421–438
BaP_3	10	321–362	399–501
Ba_3P_{14}	8,9	327–368	446–507
BaP_{10}	12	333–374	>645
ScP	6	266	376
LaP	6	301	426
LaP_2	9	292–315	385–449
LaP_5	8	299–312	>380
LaP_7	10	306–323	>507
Ti_7P_4	4,5	241–277	280–343
Ti_5P_3	5	248–274	312–315
$Ti_5P_{3.16}$	6,7	218–277	255–310
TiP	6	244–255	311–350
TiP_2	9	251–274	334–346
Zr_3P	2–4	267–286	297–368
$Zr_{14}P_9$	4,5	254–314	300–367
ZrP	6	263	373
ZrP_2	9	266–279	351–362
Hf_3P	2–4	265–287	293–362
Hf_2P	3–5	258–307	304–359
Hf_3P_2	5	259–309	306–368
HfP	6	255–268	332–365
V_3P	2–4	236–264	238–320
V_2P	4,5	234–267	255–304
VP	6	241	311–318
$VP_{1.74}$	11,12	234–263	309–323
VP_2	8	243–249	279–311
VP_4	6	236–244	325
Nb_2P	2–5	243–296	283–352
Nb_5P_3	4,5	243–296	285–364
Nb_7P_4	4,5	245–301	286–353
Nb_8P_5	4,5	246–296	>254
NbP	8	235–330	330–333
Nb_2P_5	8	250–268	299–335
Ta_3P	2,4	250–343	265–329
Ta_2P	3–5	247–301	287–361
Ta_5P_3	5	217–319	281–365
TaP	8	236–330	330–333
Cr_3P	2–4	225–252	244–294
$Cr_{12}P_7$	4,5	224–266	266–299
CrP	6	232–244	265–312
CrP_2	8	235–249	278–303
CrP_4	6	229–239	318
Mo_3P	2,4	245–266	263–313
Mo_8P_5	4,5	233–314	290–380
Mo_4P_3	5,6	235–301	284–327
MoP_2	7	245–252	315–325
MoP_4	6	236–242	323
WP	6	247–254	286–325
$WP_2{}^c$	8	246–264	293–317
$WP_2{}^d$	7	248–249	317–324
Mn_3P	2–4	230–244	246–304
$Mn_2P^{a,b}$	4,5	227–285	270–275
$Mn_{1.88}P^a$	4,5	230–252	266–276
MnP^e	6	223–247	269–317
MnP^f	6	230–239	269–388
MnP_4 (8)	6	222–241	294–374
MnP_4 (6)	6	222–237	392–296
MnP_4 (2)	6	222–237	321–371
Tc_3P	2–4	239–266	262–323
TcP_3	6	235–245	309
TcP_4	6	233–253	300
Re_2P	3,4	234–271	275–294
Re_3P_4	6	238–256	279–302
Re_6P_{13}	6	229–270	278–294
Re_2P_5	6	228–259	285–296
ReP_4	6	235–252	301
Fe_3P	2–4	226–241	241–299
Fe_2P	4,5	222–248	261–271
FeP	6	224–235	266–279
FeP_2	6	225–226	273
FeP_4 (α)	6	219–233	>350
FeP_4 (β)	6	217–231	>404
FeP_4 (γ)	6	219–233	>352
Ru_2P	4,5	226–282	275–295
RuP_2	6	235–237	287
RuP_3	6	228–241	280–287
RuP_4	6	228–244	>358
OsP_2	6	235–238	292
OsP_4 (β)	6	∼232–241	>364
CoP	6	222–236	260–328
CoP_2	6	221–229	267
Co_2P	4,5	214–267	254–283
CoP_3	6	222	385
Rh_2P	4	238	276
Rh_3P_2	4,5	228–232	282–285
Rh_4P_3	5	227–261	280–294

(cont’d overleaf)

Table 6 cont'd

Compound	CN (M)	d(M–P) (pm)	d(M–M) (pm)
RhP_3	6	233	>400
Ni_3P	2–4	221–234	244–298
Ni_8P_3	3,4	218–290	239–297
$Ni_{12}P_5$	4	223–260	253–270
Ni_2P	4,5	221–227	261–268
NiP	6	223–295	253–276
NiP_2	4	220–221	304
NiP_3	6	228	391
$Pd_{15}P_2$	2	226–299	264–322
Pd_6P	2	221–299	269–308
$Pd_3P_{0.8}$	3	222–314	282–320
Pd_7P_3	3,4	219–278	269–322
PdP_2	4	234–239	310
Pt_5P_2	2,3	231–261	276–286
PtP_2	6	239	403
Cu_3P	3,4	235–299	254–294
CuP_2	4	228–250	248–385
Cu_2P_7	4	227–240	>374
AgP_2	4	250–270	282–338
Ag_3P_{11}	4	247–261	371
Au_2P_3	2,4	233–301	293–314
Zn_3P_2	4	228–277	>310
ZnP_2 (red)	4	236–243	>390
ZnP_2 (black)	4	234–243	>378
Cd_3P_2	4	259–305	>432
Cd_7P_{10}	4	249–286	317–373
CdP_2 (α)	4	250–263	413–421
CdP_2 (β)	4	253–259	402–436
CdP_4	4	265–274	>462
$B_{13}P_2$	2	185–266	176–216
B_6P	1	191	174–188
BP	4	197	321–322
AlP	4	235	384
InP	4	254	415
InP_3	6	264–290	444–445
TlP_5	2,3	299–325	410
SiP	3	226–230	234
SiP	4	227	>316
SiP_2	6	240	>316
SiP_2	4	227	>316
GeP	6	238–320	354–375
GeP_3	6	250–285	427
Sn_4P_3	3,6	266–295	325
SnP	6	255–341	383
SnP_3	6	266–292	455–467
NdP	6	291	412
NdP_5	8	299–305	>494
Eu_3P_2	6	295–331	354–425
Eu_4P_3	6	292–336	350–392
Eu_5P_4	7	299–339	347
EuP	6	289	409
Eu_3P_4	8	300–321	404–408
EuP_2	6,9	300–334	398–415
EuP_3 (α)	8	274–384	387–427
EuP_3 (β)	9	311–390	385–441
EuP_7	9	306–326	>533
GdP	6	286	405
GdP_5	8	295–302	493
YbP_5 (α)	8	287–299	487–593
YbP_5 (β)	8	280–297	438–525
ThP	6	291	412
Th_3P_4	8	297–298	402
Th_2P_{11}	6–9	290–307	>310
ThP_7	12	296–319	>372
UP	6	279	>395
UP_2[g]	9	276–289	380
U_3P_4	8	284	383

[a]Fe_2P type. [b]Ni_2P type. [c]$OsGe_2$ type. [d]MoP_2 type. [e]MnP type. [f]NiAs (orthorhombic) type. [g]UAs_2 type.

P_{12} units, formed by (3b)P^0, cross the CuI substructure and complete the Cu coordination by one third of the available lone pairs. Hexagonal bipyramidal units $M_2P_6{}^{2-}$ of the M_4P_6 phases (M = K, Rb, Cs) are $M_2[\mu\text{-}(\eta^6\text{-}P_6)]$ complexes stabilizing the unusual 2π system $P_6{}^{4-}$ with short P–P bonds. In Th_2P_{11} a *cyclo*-$P_6{}^{6-}$ chair acts as a twofold η^3 ligand bridging two Th atoms, forming a hexagonal scalenohedron. In the same structure, condensed skew-boat P_6 and *endo*-$P_8(C_{2v})$ rings coordinate Th atoms. The Th coordination of ThP_7 is built from a corrugated 3-D net of condensed P_6 and P_{12} rings. Trivalent rare earth metals in LnP_5 are enveloped, sandwich-like, by two *cyclo*-P_{12} with tetragonal antiprismatic eight-fold coordination. Various modifications of M–P coordination are also known with M^{2+} and M^{3+} bonded to chains and rings with multiple configurations and conformations. The donor qualities of polyphosphides can clearly be shown by comparison of the crystal structures of solvent-free and solvated compounds, showing that complete separation of cation and polyanion is only possible with the help of crown ether cryptates, or large cations, for example $(NPh_4)^+$. Examples of these structures are given in Figures 2 and 3.

4.5 Solid-State Volumes

The molecular volumes of solid phosphides can be approximated by individual increments ($V_m = \sum V_i$).**56** Knowledge of the structures is not necessary. Saltlike and semimetallic compounds behave differently, but there is no difference between compounds of main-group metals or transition metals. The observed relationships allow for valuable analysis with respect to structure and properties, and give very good estimates of the unit cell content (Figure 4). With saltlike phosphides the phosphorus increment, V_P, increases with increasing negative charge q(P) and decreases with increasing cation charge q(M). A suitable empirical relation is given by equation (1):

$$V_p(q(\mathrm{P}), q(\mathrm{M})) = \exp(\alpha q(\mathrm{P}) q(\mathrm{M}) + \beta q(\mathrm{P}) + \gamma q(\mathrm{M}) + \delta) \quad \text{in cm}^3\,\text{mol}^{-1} \tag{1}$$

with $\alpha = 0.046$, $\beta = -0.368$, $\gamma = -0.066$, and $\delta = 2.630$. In semimetallic phosphides, V_P(sm) is generally smaller and

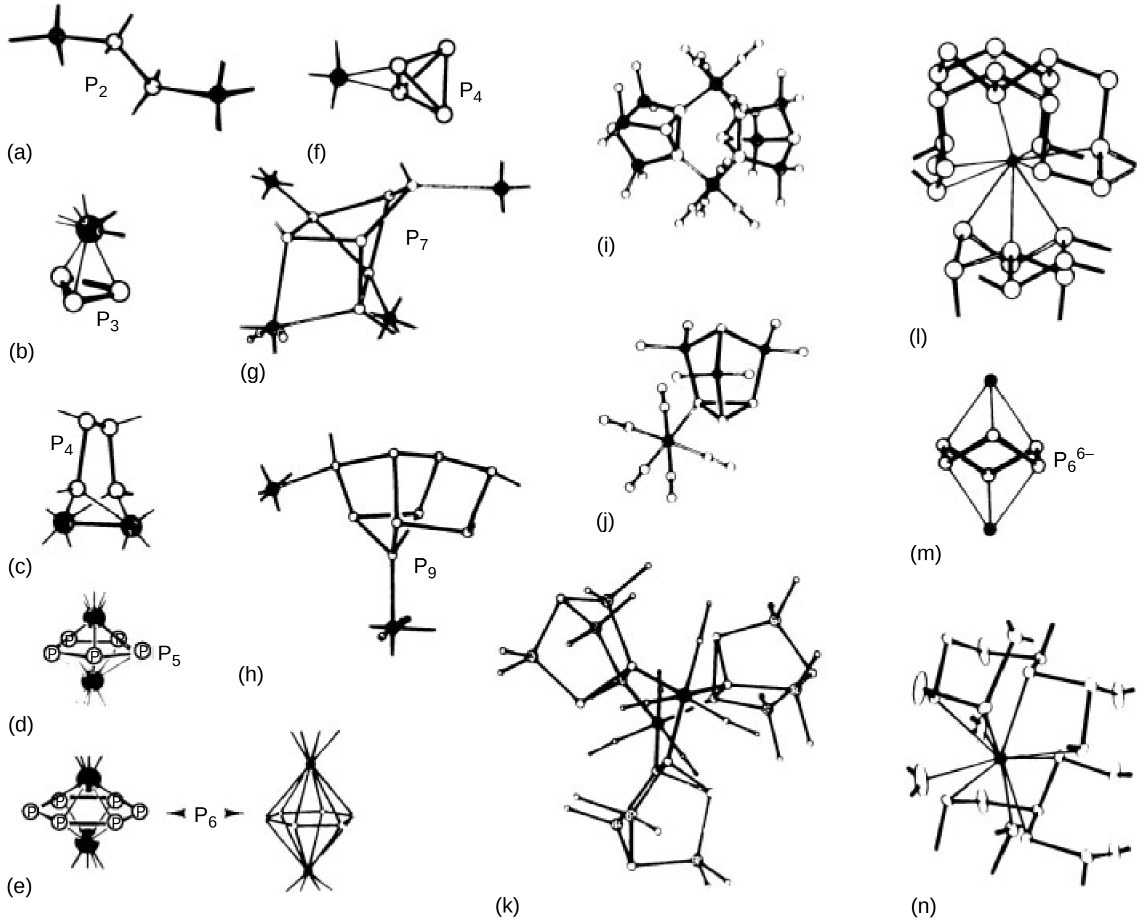
P2
(a)
P4
(f)
(i)
(l)
P3
(b)
P7
(g)
(j)
P4
(c)
P9
(h)
P6 6–
(m)
P P P P P P5
(d)
P P P P P P P6
(e)
(k)
(n)

Figure 2 Donor properties of polyphosphides and phosphanes: metal atoms, filled circles; phosphorus atoms, open circles; substituents R indicated by lines. (a) μ, η^1,η^1-P_2R_4; (b) η^3-P_3; (c) μ, η^2,η^2-P_4R_4; (d) μ,η^5,η^5-P_5; (e) μ,η^6,η^6-P_6; (f) η^2-P_4; (g) η^1,η^1,η^1,μ-P_7R_3; (h) η^1,η^1-P_9R_3; (i) μ,η^1,η^1-$P_4Si_3Me_6$; (j) η^1-$P_4Si_3Me_3$; (k) μ,η^1,η^1-$P_4Si_3Me_3$; (l) Eu coordination in EuP_7; (m) μ,η^3,η^3-P_6^{6-} in Th_2P_{11}; (n) Th coordination in ThP_7

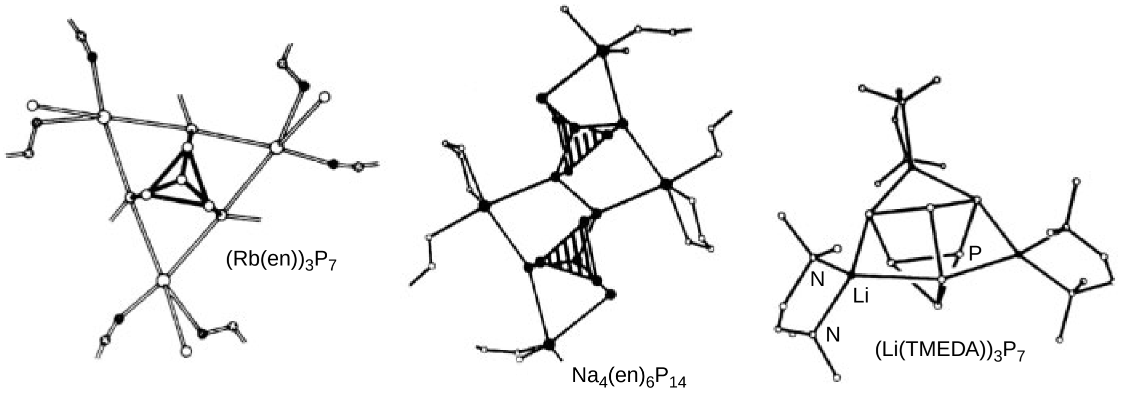
(Rb(en))3P7
Na4(en)6P14
P
N
Li
N
(Li(TMEDA))3P7

Figure 3 Some solvated polyphosphides (cf. Table 7). Note the specific positions of the alkali metal atoms with respect to the (2b)P^- atoms of the cages

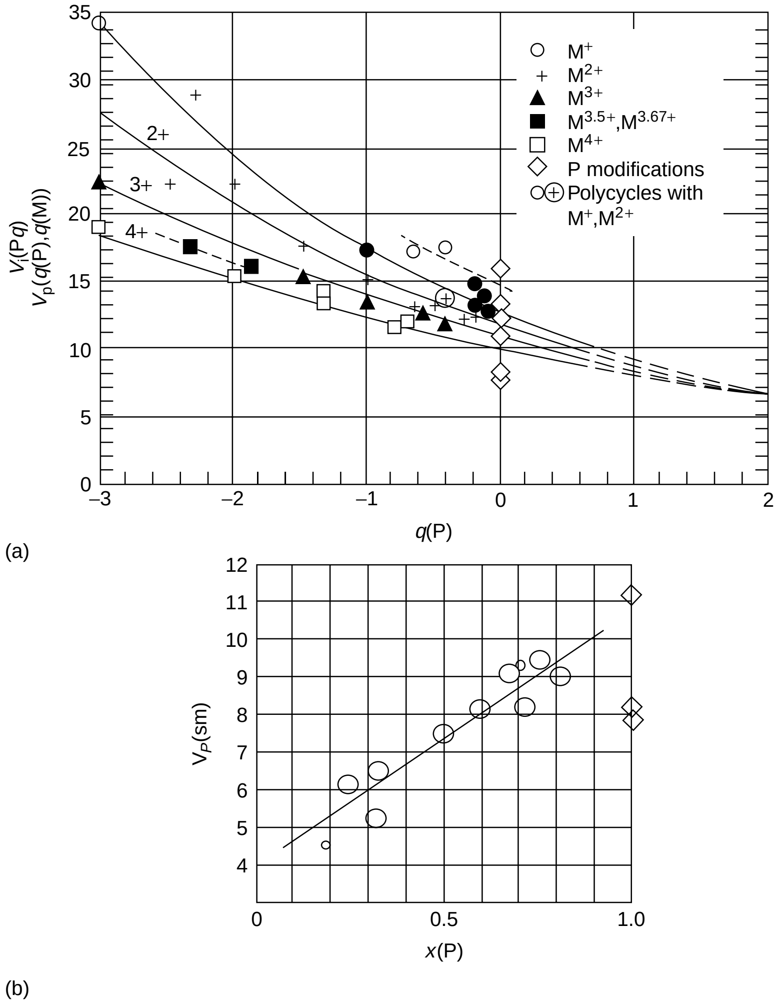

Figure 4 (a) Volume increments of phosphorus atoms (in $cm^3\ mol^{-1}$) with formal charges $q(P)$ and $q(M)$. The solid lines represent the functions $V_P(q(P), q(M))$ corresponding to equation (1). The broken lines connect volumes for cations with mixed valencies and extreme volumes, respectively. (b) Volume increment of P (in $cm^3\ mol^{-1}$) with molar ratio in semimetallic compounds. Mean values of sequences of compounds are given by large dots, the compounds 'Fe_4P' and Re_6P_{13} are marked by small dots. The volumes of the various P modifications are given by open squares

depends on the mole fraction $x(P)$: $V_P(sm) = 7.0 \times x(P) + 4.0$ [$cm^3\ mol^{-1}$]. With electropositive metals, the observed volume V_m° is much smaller than the sum of the volumes of the elements, but the difference decreases with increasing $x(P)$. The sum of the increments $\sum V_i$(saltlike) and $\sum V_i$(sm) span the region of V_m°, and the better fit corresponds with the physical properties. Larger deviations indicate peculiarities, for example, cluster anion formation or metals. Structural changes in homologous compounds can be analyzed and predicted according to the theorem of optimal volumes.[56]

5 CHEMICAL REACTIONS OF PHOSPHIDES

There is a broad range of chemical reactivity, for example, K_3P hydrolyzes very easily, whereas KP_{15} can only be digested by nitric acid and bromine. In general, the compounds $(E1)_3P$, $(E2)_3P_2$, and (E13)P are attacked by water, but E3P are stable (where E1 represents a group 1 metal, E2 a group 2 metal, etc.). The same is true with the transition metal phosphides in general. Only a few systematic studies exist.

The polyanions may become molecules and other derivatives as a result of chemical reaction. Suitable synthons are, for example, the solid M_3P_7 compounds which can be used in both heterogeneous and homogeneous reactions as well (Scheme 1).

A typical heterogeneous reaction transfers crystalline M_3P_7(s) into solvated molecules R_3P_7(solv). Via R–R* exchange, new compounds such as $P_7(MMe_3)_3$, $P_{11}(MMe_3)_3$, and $P_7(MPh_3)_3$ with M = Si, Ge, Sn, and Pb, and the pure P_7H_3 can be obtained (Scheme 1 path A).[57]

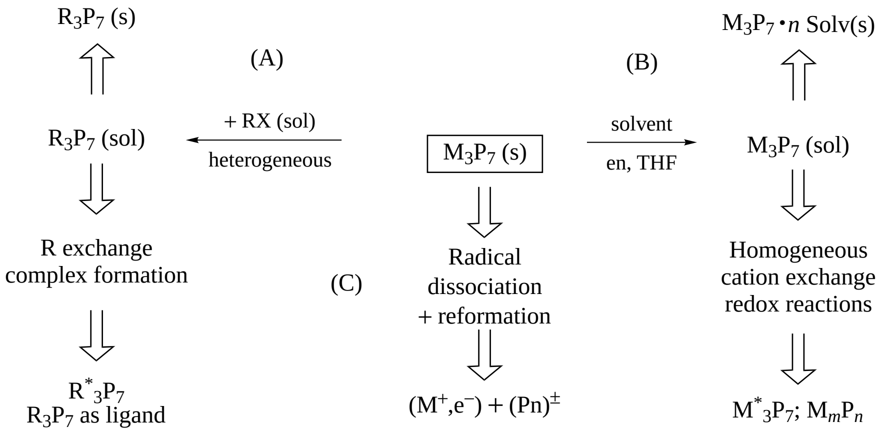

Scheme 1

Solutions of binary metal phosphides are accessible with polar solvents. The completely colorless solutions, obtained only with pure compounds and dry solvents, turn into deep red solutions on oxidation.[39] The state of the metal phosphides in solution is uncertain, but there is some evidence for solvated ion complexes (path B). The hydrogen phosphides $Li_2HP_7(solv)_x$ and $LiH_2P_7(solv)_x$ are formed by $[Li_3P_7(solv)_x + P_2H_4; Li_3P_7(solv)_x + P_7H_3]$. Na_3P_{21} is formed from P_4 and Na in solution, crystallizes as $Na_3P_{21}(THF)_{15}$, and can be transformed into $NaP_{21}R_2(solv)_x$ and then into $HP_{21}R_2$. The latter reaction steps demonstrate directly the difference in nucleophilicity of the three P^- atoms. Oxidation with P_4 in ethylenediamine leads from Na_3P_7 to $Na_4(en)_6P_{14}$ and from Cs_4P_6 to $Cs_3(en)_3P_{11}$. The latter reaction corresponds to the solid-state reaction $Na_3P_7(s) + P_4(g) \rightarrow Na_3P_{11}(s)$.

The radical decomposition (path C) of phosphides in solution with Ph_2CO yields in the case of Na_3P_7 the deep blue Ph_2CO^- and light red amorphous residues of a new, but as yet uncharacterized, form of elementary phosphorus. K_4P_6 reacts with Ph_2CO in solution under easy abstraction of only one part of potassium $(K + Ph_2CO \rightarrow K^+ + Ph_2CO^-)$, yielding K_3P_7. This homolytic cleavage is completely equivalent to the thermal reaction of K_4P_6 with SiO_2 (quartz wall) at temperatures around 470 K, forming K_3P_7 and $(K_2O + Si)$ from K(g) and SiO_2(s).[58]

From reaction in solutions, a variety of polyphosphides is obtained that are not known as solvent-free binary compounds (Table 7). Several have been characterized by ^{31}P NMR spectroscopy in solution,[38] for example, $P_{19}{}^{3-}$ and $P_{26}{}^{4-}$, which have no counterparts in binary systems. LiP_5 forms a $^3_\infty(P_5{}^-)$ polyanion in the solid state, but the corresponding anion in solution is monomeric $P_5{}^-$, an analogue of the cyclopentadienyl anion. The helical polyanions $^1_\infty(P_7{}^-)$ of LiP_7 and NaP_7 have no monomeric counterpart in the solution; here the anion is present as $R_2P_7{}^-$. Adding simply a salt (KI), trimeric $P_{21}{}^{3-}$ is formed as a finite anion in solution and it can be isolated as a solvated salt.

Table 7 Occurrence of heptaphosphides, $P_7{}^{n-}$

Unit	Linkage	Examples	Figure
$P_7{}^-$	Oligomeric	$(Li\text{-}crown_2)_3P_{21}(THF)_2$	6c
$[(3b)_6(2b)_1P_7]$	Polymeric	CsP_7, type 5	6e
		NaP_7, type 4	6d
		$K_4P_{21}I$, types 6 and 9	6b
$P_7{}^{2-}$	Oligomeric	$Na_4(en)_6P_{14}$	6g
$[(3b)_5(2b)_2P_7]$	Polymeric	EuP_7, Cu_2P_7	6h, 6j
$P_7{}^{3-}$	Oligomeric	Li_3P_7 to Cs_3P_7	6a
$[(3b)_4(2b)_3P_7]$		Ba_3P_{14}, Ba_2P_7Cl	type 1
	Polymeric	LaP_7	6i
$P_7{}^{4-}$	Oligomeric	?	
$[(3b)_3(2b)_4P_7]$	Polymeric	ThP_7	2n

The effect of the solvent is demonstrated by solvent-free Li_3P_7 and solvated $(Li(TMEDA))_3P_7$; the first forms a 3-D network with ion–ion and ion–dipole Li–P interactions,[59] whereas the latter is an isolated solvated ion pair.

The reaction of white or red phosphorus or of alkali and alkaline-earth metal phosphides in liquid ammonia was extensively investigated by Korber and coworkers.[40,60–71] The simplest experiment is just the recrystallization of binary phosphides from liquid ammonia, as is realized for the ammoniates $Cs_3P_{11}{\cdot}3NH_3$[66] and $Cs_3P_7{\cdot}3NH_3$.[68] The reduction of red phosphorus with Ba in liquid ammonia leads to $Ba_3P_{14}{\cdot}18NH_3$.[61] Here, $P_7{}^{3-}$ units are joined via P–Ba contacts to $^1_\infty[Ba_2(P_7)_2]^{2-}$ chains that are separated by $Ba(NH_3)_8{}^{2+}$ cations. The highly interesting 6π aromatic polyphosphide $P_4{}^{2-}$ is obtained via reaction of diphosphine with cesium in liquid ammonia.[40] Mixed cations like in $Ba_3P_{14}{\cdot}18NH_3$[60] can be introduced through a reaction of Cs_3P_{11} with a cation exchange resin loaded with Ba^{2+}. Through a complete ion exchange, $[Li(NH_3)_4]_3P_{11}{\cdot}5NH_3$ can be obtained from Cs_3P_{11}.[69]

Interesting new compounds occur if some of the alkali metal ions are exchanged by much larger substituted ammonium cations. Recently reported examples are $(NEtMe_3)Cs_2P_7{\cdot}2NH_3$,[62] $(Me_4N)_2RbP_7(NH_3)$ and

$(Et_4N)Cs_2P_{11}$,**64** $(NEt_3Me)Cs_2P_7{\cdot}NH_3$ and $(NEt_4)Cs_2P_7{\cdot}4\,NH_3$,**70** or $(NEt_3Me)_2CsP_{11}{\cdot}5NH_3$.**71** Through proton-charged exchange resins or via in situ formation of $NaNH_2$, also some phosphorus–hydrogen species like $HP_{11}{}^{2-}$,**63** $HP_7{}^{2-}$,**65** or $[Na(NH_3)_3(P_3H_3)]^{-}$**67** are accessible as ammoniates.

Finally, it is worthwhile to note that most of these ammoniates are only stable at low temperatures (typically at liquid NH_3 temperature). If the compounds lose ammonia through heating or in a vacuum, decomposition sets in.

6 STRUCTURE AND BONDING[16,17]

6.1 General Remarks

Phosphide structures cover a great range of complexity, depending on composition and bonding. The polyphosphides are characteristic of the element phosphorus and offer cluster anions or polymeric networks of homoatomic-bonded P atoms as the primary structural fragments, whereas coordination by metal atoms is best described in terms of additional donor–acceptor interaction through the phosphorus electron pairs. The structures of the electron-rich phosphides with larger M/P ratios are usually described in terms of metal-atom polyhedra, centered by P atoms; these structures are not specific for phosphorus but occur also with borides, carbides, silicides, and so on. A peculiarity are phosphorus compounds with B_{12} units, similar to $B_{12}BP_2$, in which the BP_2 part of these structures is replaced by other atoms. Isomorphism is common with arsenides and sometimes occurs with antimonides.

In the following sections, only selected structures are discussed. A more complete account is given by the available textbooks and review articles.**1–15**

6.2 Monophosphides

The diversity in structure and bonding possible for phosphides is effectively demonstrated by the monophosphides. Monophosphides MP of the group 1 and 2 elements (E1, E2) are polyphosphides with $^{1}_{\infty}(P^{-})$ chains and $P_2{}^{4-}$ dumbbells, respectively. E11 and E12 monophosphides are not known. The E3 and E13 monophosphides are the so-called ‘normal’ compounds with $3x = q(M)$ (see Section 2). With E13, they form the zinc blende structure with tetrahedral heteroatomic bonds. Ternary derivatives such as $MgGeP_2$ and $CuSi_2P_3$ have a random distribution of the M atoms, whereas $CdGeP_2$, crystallizes in the ordered chalcopyrite type with a $^{3}_{\infty}[GeP_{4/2}]^{2-}$ tetrahedral net (see Section 6.4). The E3 monophosphides form the NaCl structure. CeP is remarkable because of its physical properties (metal–semiconductor transition; heavy-fermion behavior). The E14 monophosphides show the ‘break’ usually observed when passing the Zintl border. Binary lead phosphides are not known; SiP and GeP are compounds with formally M^{III}, whereas SnP is an Sn^{II} compound. The nine-electron (9e) systems SiP (GeP) and SnP form topologically identical structures but with opposite atom and electron distributions.**72,73** The bonding of the four-atomic layer structure (GaS type) corresponds in the case of SiP to a molecule**72** $|P{\equiv}Si{-}Si{\equiv}P|$ with Si^{3+} and P^{3-}, whereas the SnP structure is equivalent to $|Sn{\equiv}P{-}P{\equiv}Sn|$ with Sn^{2+} and P^{2-}.**73** Conversely, in SnP_3, tin is oxidized to Sn^{3+} (see Section 6.4).

It is important to note that M^{IV} is the maximum oxidation state in binary phosphides (cf. Th_3P_4, Th_2P_{11}, ThP_7) and higher oxidation states are stabilized only by the formation of complexes (see Section 6.2). An exception may be UP_2 with the $PbCl_2$-type structure, but the P–P distances (269 pm) indicate an oxidation state $q(U) < 6$. Phosphorus compounds of group 15–17 elements are not covered here: PSb, PBi, and PTe do not exist, while other compounds such as PAs (Section 7) are not termed phosphides.

The group 4–10 monophosphides form similar, but clearly differentiated structure types, owing to their electron numbers. In all structures, the P atoms are trigonal prismatically coordinated by M atoms, whereas the M atoms have octahedral and/or trigonal prismatic coordination. VP (NiAs type), CrP, WP, MnP, FeP, RuP, CoP (MnP type), and NiP (NiP type) are characterized by 1-D chains of face-condensed MP_6 octahedra. This leads in the NiAs type to linear M_{∞} chains, whereas in the latter two types, zig-zag chains are present, indicating gradually changing M–M interactions. In the MnP and NiP types, increasing P_2 formation occurs (P–P = 240–250 pm). TiP, ZrP, and HfP exhibit the TiAs type with pairs of face-sharing MP_6 octahedra. The M–M distances indicate M_2 pairing, corresponding to M^{III} with a d^1 configuration. NbP, TaP (NbAs type), and MoP (WC type) possess trigonal prismatic MP_6 coordination. The two structures differ in the relative orientation of the trigonal prisms but, in both, the M atom is trigonally planar surrounded by three empty centers of P_6 prisms. This facilitates the formation of three, three-center bonding states, sufficient for d^2 configurations (only NbP, HfS, and isoelectronic compounds have the NbAs structure; cf. also MoS_2 and $NaNbO_2$). Note that MoP is the only E6 monophosphide with the WC structure.

6.3 Heteroatomic Bonded Phosphides

This group consists mainly of the classical metal phosphides MP_x with $3x = q(M)$. Li_3P, Na_3P, and K_3P have the hexagonal Na_3As structure; Rb_3P and Cs_3P are not known. $K_{3-x}P$ has the cubic Li_3Bi structure**74** with a strong tendency for a lower K content down to K_2P, forming partially $P_2{}^{4-}$ dumbbells in the same structural frame. This seems to indicate that polyphosphide formation becomes more pronounced with increasing radii of the alkali metal cations. Cu_3P, however, possesses a phase with $Cu_{3-x}P$ ($0.09 \le x \le 0.26$). The structure is similar but not identical to the LaF_3 type of structure.**75** Phosphides M_3P_2 of the divalent E2 and E12 metals have the structure of Mn_2O_3 and Zn_3As_2, respectively, or form the deficient Th_3P_4 type ($Ba_4P_{2.67}\square_{0.33}$). Ternary compounds like LiZnP, LiCdP, Li_3AlP_2, Li_5SiP_3, Li_7VP_4, and Li_9TiP_4 have CaF_2 or Li_3Bi structures with varying statistical distributions of the M atoms. Ordering is observed in some compounds, which is characteristic of the larger alkali metals. Unexpected structures are seen for RbZnP and SrAgP (and others), which are related to the AlB_2 and Ni_2In types with heterographite-like $^{1}_{\infty}[ZnP]^{-}$ and $^{1}_{\infty}[AgP]^{2-}$ nets in a frame of trigonal prisms, formed by Rb and Sr, respectively. Quasibinary compounds of general formula $E1(E'1)_2P$ and E1E2P are not yet known, contrary to the corresponding arsenides and antimonides. The NaCl and ZnS-type structures of E3 and E13 metals are discussed in Section 6.2.

The unique cubic Th_3P_4 structure (U_3P_4, Np_3P_4) is built from condensed ThP_8 dodecahedra (bisdisphenoids). Eu_3P_2 has the deficient Th_3P_4 structure ($Eu_4P_{2.67}\square_{0.33}$), whereas the mixed-valence compound Eu_4P_3 forms a slightly rhombohedrically distorted structure of this type.**[76]** The mixed valent Sn_4P_3 forms a layer structure similar to Bi_4Se_3.**[77,78]**

6.4 Phosphidometallates

Ternary phosphides may be also discussed as products of Lewis acid–base reactions of binary components. This is of value especially if the more acidic component is distinguished by pronounced coordination. The low coordination number (CN) of two is shown by the isolated linear $[BP_2]^{3-}$, $[BeP_2]^{4-}$, and $[HgP_2]^{4-}$ anions of Na_3BP_2, K_4BeP_2, and K_4HgP_2, respectively (Figure 5).**[79–81]** They are isosteric analogs of CO_2 and $[HgO_2]^{2-}$. The corresponding polymeric chain $^{1}_{\infty}[AuP]^{2-}$ with CN $= 2$ is present in K_2AuP.**[82]** Similar chains occur in the $^{1}_{\infty}[NiP_2]^{2-}$ anion of Cs_2NiP_2**[83]** and K_2NiP_2,**[84]** but with side-on bonded P_2 pairs instead of simple P bridges, and the Ni atoms have a planar rectangular NiP_4 coordination. Analogs of $CO_3{}^{2-}$ with CN $= 3$ are the $[SiP_3]^{5-}$ and $[InP_3]^{6-}$ anions of Cs_5SiP_3**[85]** and K_6InP_3.**[86]** In these structures, the large cations form quartets of trigonal prisms (isolated and linked to chains, respectively), the metal-rich transition metal phosphides (Figure 5). The $[Al_2P_4]^{6-}$ and $[In_2P_4]^{6-}$ anions of $Cs_6Al_2P_4$**[87]** and $Cs_6In_2P_4$**[88]** are directly comparable with $BeCl_2$ and the nonexistent $(SiO_2)_2$ dimer.

Complex anions with CN $= 4$ occur frequently with E13, E4, E14, E5, and E6 as central atoms. Isolated tetrahedral tetraphosphametallate anions are $[AlP_4]^{9-}$ in $Na_3Eu_3AlP_4$,**[89]** $[TiP_4]^{8-}$ in Sr_4TiP_4,**[90]** $[SiP_4]^{8-}$ in $Na_4Sr_2SiP_4$, $[PbP_4]^{8-}$ in $Na_2Eu_2PbP_4$,**[91]** $[NbP_4]^{7-}$ in Na_5SrNbP_4, and $[WP_4]^{6-}$ in Na_6WP_4.**[92]** Tetrahedral dimers $[Sn_2P_6]^{10-}$ are present in $Na_{10}Sn_2P_6$,**[93]** isosteric with Al_2Cl_6, and the 1-D polymers of the SiS_2 type are realized as $^{1}_{\infty}[E13P_2]^{3-}$ and $^{1}_{\infty}[E14P_2]^{2-}$, for example, in K_2NaGaP_2**[94]** and K_2SiP_2 (Figure 5).**[95]** A 3-D tetrahedral net is realized in Na_3InP_2,**[96]** Ag_2SiP_2,**[97]** and the complex structures of $Ln$$Si_2P_6$ (Ln = La, Ce, Pr, Nd).**[98]**

An interesting compound is AuSiP**[97]** (Figure 5) in which the silicon and phosphorus atoms form two-dimensionally infinite puckered Si_3P_3 nets that are separated by the gold atoms, a structure similar to the Zintl phase $CaSi_2$. The monoclinic transition metal compounds TSi_3P_3 (T = Co, Rh, Ir) and TSi_4P_4 (T = Fe, Ru, Os) adopt very complicated structures.**[99–101]** Note that it is difficult to distinguish silicon and phosphorus on the basis of X-ray data, since these elements have similar scattering factors.

Pecularities occur with K_2GaP_2 and Ca_5P_8 in that the 1-D chain of $[GaP_2]^{2-}$ exhibits connected five-membered rings with P_2 pairs (isosteric with BS_2), and $P_8{}^{10-}$ in Ca_5P_8 is a $[S_2O_6]^{2-}$ analogue**[102]** (see Section 6.5.3). The unit $Ge_2P_4{}^{8-}$ in Ba_2GeP_2**[103]** is not fully understood; the anion looks like the 38e systems $[S_2O_4]^{2-}$ and $[N_2(CF_3)_4]$ with a single Ge–Ge bond, but is in fact a 36e system like $Cl_2C{=}CCl_2$, suggesting the possibility of a diradical.

6.5 Polyphosphides

According to their structures and physical properties, the polyphosphides are valence compounds in the classical sense. All valence electrons are in localized states and, therefore, these compounds are (or should be) insulators or semiconductors. Nevertheless, some compounds are semimetals or even metals if conduction bands are formed by sufficient overlap, but their structures often remain in accord with the picture of localized states.

To describe the polymeric and polycyclic structures, selected fragments that are related to well-known molecules or clusters are chosen. This fragmentation is arbitrary to some extent and, therefore, it is of value to look for alternative ways, which may be relevant in relating their structures to their synthesis and reactions. The helical $^{1}_{\infty}(P_7{}^{-})$ chain of LiP_7 can be fractionated into, for example, sequences of polymerized $P_7{}^{-}$ units or may be discussed in terms of condensed $P_9{}^{-} = [P_{2/2}P_5 - P_{2/2}]$ units in order to demonstrate the twofold symmetry elements perpendicular to the helical axis. The $P_{16}{}^{2-}$ unit is either a polymer of $P_9 + P_7$ or a condensate of two P_9 units. In the case of polycycles with different ring sizes, the arbitrariness is reduced to the question of which ring type is seen to be the more general one, with respect to systematics or to generating the systems. The remarkable stoichiometrical variations can be rationalized by only a few simple structural subunits, which are parts of the known or hypothetical modifications of phosphorus. There exist many possibilities for polyanionic structures, such as the formation of isolated polycycles and of 1-D, 2-D, and 3-D polymers including their numerous conformational variations.

6.5.1 *Heptaphosphides*

The heptaphosphides of the cations M^{n+} ($n = 1{-}4$) are excellent examples to support a general discussion of the structural possibilities (Table 7, Figure 6).

The first family generates 1-D and 2-D polyanionic structures. $K_4P_{21}I({=}\,KI{\cdot}3KP_7)$ shows a structure with the

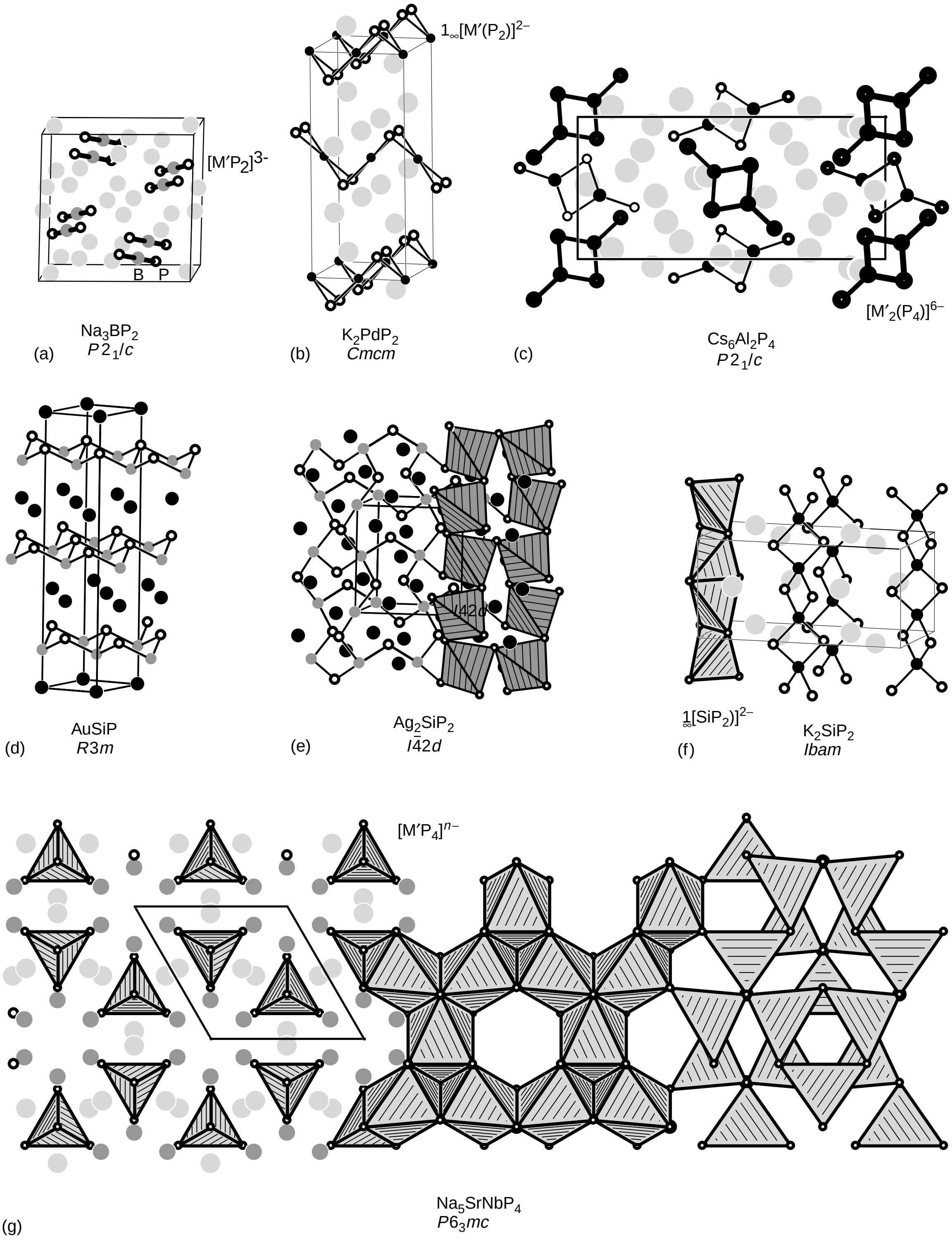

[M′P2]3-
B P
Na3BP2
(a) P21/c
1∞[M′(P2)]2–
K2PdP2
(b) Cmcm
[M′2(P4)]6–
Cs6Al2P4
(c) P21/c
AuSiP
(d) R3m
I42d
Ag2SiP2
(e) I4̄2d
1∞[SiP2)]2–
K2SiP2
(f) Ibam
[M′P4]n–
Na5SrNbP4
(g) P63mc

Figure 5 Examples of ternary phosphides with different coordination numbers of heteroatomic bonded metal atoms. (a) Linear unit $[\mathrm{BP_2}]^{3-}$ ($\mathrm{M_3M'P_2}$, $\mathrm{Na_3BP_2}$ type), isosteric with $\mathrm{CO_2}$; (b) $^{1}_{\infty}$ $[\mathrm{M'(P_2)}]$ zig-zag chain with $\mathrm{P_2}^{4-}$ dumbbells ($\mathrm{M_2M'P_2}$, $\mathrm{K_2PdAs_2}$ type) (P atoms, open circles; M atoms, grey circles; M′ atoms, small filled circles); (c) planar $[\mathrm{M'_2P_4}]^{6-}$ units ($\mathrm{M_6M'_2P_4}$, $\mathrm{Cs_6Al_2P_4}$ type), corresponding to the unknown $(\mathrm{SiO_2})_2$ dimer; (d) MM′P (AuSiP type), emphasizing the two-dimensional [SiP] network; (e) $\mathrm{M_2M'P_2}$ ($\mathrm{Ag_2SiP_2}$ type), emphasizing the three-dimensional network of condensed $\mathrm{SiP_4}$ tetrahedra; (f) $^{1}_{\infty}$ $[\mathrm{SiP_2}]^{2-}$ ($\mathrm{M_2M'P_2}$, $\mathrm{K_2SiP_2}$ type), isosteric with $\mathrm{SiS_2}$. The edge linked tetrahedra are shown in the left part (M atoms, grey circles; Si, black circles, and P, open circles). (g) $\mathrm{M_5M'M''P_4}$ ($\mathrm{Na_6ZnO_4}$ type) emphasizing the $[\mathrm{M''P_4}]^{n-}$ tetrahedra (left), the octahedra around $\mathrm{M^{II}}$ as in the corresponding Sr and Eu compounds (center), as well as the tetrahedra around Na (right)

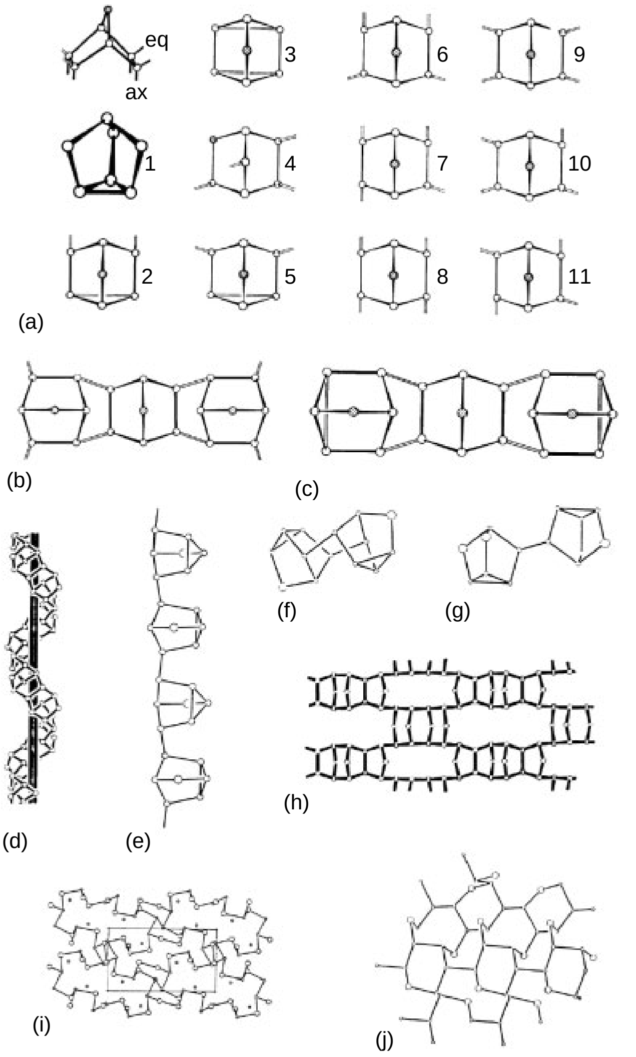

Figure 6 (a) Representatives of the heptaphosphanorbornane (top left) with axial (ax) and equatorial (eq) connectivities; (i) indicates intramolecular saturation of bonds in the descriptions below. (1) (P_7^{3-}); (2) (ax_2i_2)P_7^- (end-on type of oligomeric P_{21}^{3-}); (3) (i_4)P_7^- (possible monomeric structure of P_7H); (4) LiP_7 type; (5) (eq_2i_2)P_7^- (CsP_7 type); (6) (ax_2eq_2)P_7^- (end-on type of polymeric P_{21}^{3-}); (7) (ax_3eq)P_7^- (unknown); (8) (ax_4)P_7^- (unknown); (9) (eq_4)P_7^- (central part of oligomeric and polymeric P_{21}^{3-} as well as of P(Hittorf)); (10) (ax_3eq_3)P_7^- (unknown); (11) (ax_2eq_2)P_7^- (unknown). (b) ${}^{2}_{\infty}(P_{21}^{3-})$, as built from type $(6)_2$ and type (9). (c) (P_{21}^{3-}), as built from type $(2)_2$ and type (9). (d) Helical unit ${}^{1}_{\infty}(P_7^-)$ wound around the central axis as in LiP_7 and NaP_7, built from type (4). (e) CsP_7 as ${}^{1}_{\infty}(P_7^-)$ chain of cages of type (5). (f) (P_{14}^{2-}), hypothetical dimer of type (2). (g) P_{14}^{4-} as found in $Na_4(en)_6P_{14}$. (h) ${}^{2}_{\infty}(P_7^{2-})$ network of tubular fragments in Cu_2P_7. (i) ${}^{3}_{\infty}(P_7^{3-})$ in LaP_7. (j) ${}^{2}_{\infty}(P_7^{2-})$ in EuP_7

fourfold equatorial-bonded type 9, as well as with the partially axial-bonded type 6. The formation of oligomeric P_{14}^{2-} and P_{21}^{3-}, however, can be realized in a simple way by combining type 2 with type 9. The formation of the type 5 cage leads to the CsP_7 structure type and only a small further step forms an isolated P_7^{3-} group with the structure of the well-known P_4S_3 molecule. On the other hand, type 4 units as members of the second family wind into a helical structure. LiP_7 and NaP_7 crystallize with this structure of helical tubes, whereas RbP_7 and CsP_7 have a more linear structure with connected P_7 cage units. The cavities for the cations are too small for K^+ in the helical structure but are too large in the other, and indeed the reaction of potassium and phosphorus (P:K ratio = 7:1, without iodine) leads only to mixtures of lower and higher phosphides; in the presence of iodine, $K_4P_{21}I$ is formed. From the unit cell volumes, space filling in this compound is evidently better than in both MP_7 structures. Only rubidium forms both compounds with nearly the same space filling.

A monomeric P_7^{2-} is not possible, but the dimeric P_{14}^{4-} is known from the solvated $Na_4(en)_6P_{14}$.**[39]** EuP_7 is a Eu^{II} compound with a polymeric P_7^{2-} structure of two-dimensional puckered layers resulting from a network of six-membered rings (chair conformation; axial and equatorial linkage).**[104]** For a description of P_7^{2-} in Cu_2P_7, see Section 6.5.6.

The structure of the heptaphosphides of the rare earth metals La, Ce, and Pr contains a polymeric polyanionic network ${}^{3}_{\infty}(P_7^{3-})$ with seven-membered and large 20-membered rings, which, nevertheless, can be related in a simple way to the P_7^{3-} cage (see Section 6.5.2).

ThP_7 is the only known compound with a P_7^{4-} substructure.**[105]** The 3-D network is formed by a condensed system of six-membered and 12-membered rings yielding characteristic crown-shaped cavities occupied by Th atoms.

6.5.2 Cyclic and Polycyclic Systems

The quasimolecular P_7^{3-} cage is the essential building unit of the bright yellow alkali metal phosphides M_3P_7 (formerly described erroneously as M_2P_5) and of the red alkaline earth metal phosphides Sr_3P_{14} and Ba_3P_{14}, as well as of the chloride phosphide Ba_2P_7Cl.**[106]** These compounds are extremely reactive, and the compounds M_3P_7 are unique in their behavior, for example, they transform to plastically crystalline modifications and they are volatile in vacuo.

The heptaheteronortricyclanes P_7^{3-} and P_7R_3 (and the related P_4S_3, As_7^{3-}, Sb_7^{3-}, etc.) differ in their topology. The bond lengths and bond angles, as well as the height of the cage, depend on their function and charges. Neutral cages are more elongated than charged ones, and the significant variations within the charged units result from progressive electron transfer in going from Li to Cs. The P_{11} cages behave similarly.

The ternary Cu_4SnP_{10} with an unusual $Sn^{II}Cu_3$ unit is the only compound with the adamantane-like P_{10}^{6-} cage.**[107]** This is remarkable, because in that region of composition some compounds exist. Obviously, the units P_7^{3-} and P_6^{4-} are more stable. A polymeric tubular 2-D isomer was found in $Au_7P_{10}I$.**[108]**

Just as the cages P_7^{3-} and P_{10}^{6-} are derivatives of the tetrahedral P_4 molecule, the P_{11}^{3-} cage, characteristic for the M_3P_{11} alkali metal phosphides,**[109]** is a derivative of the

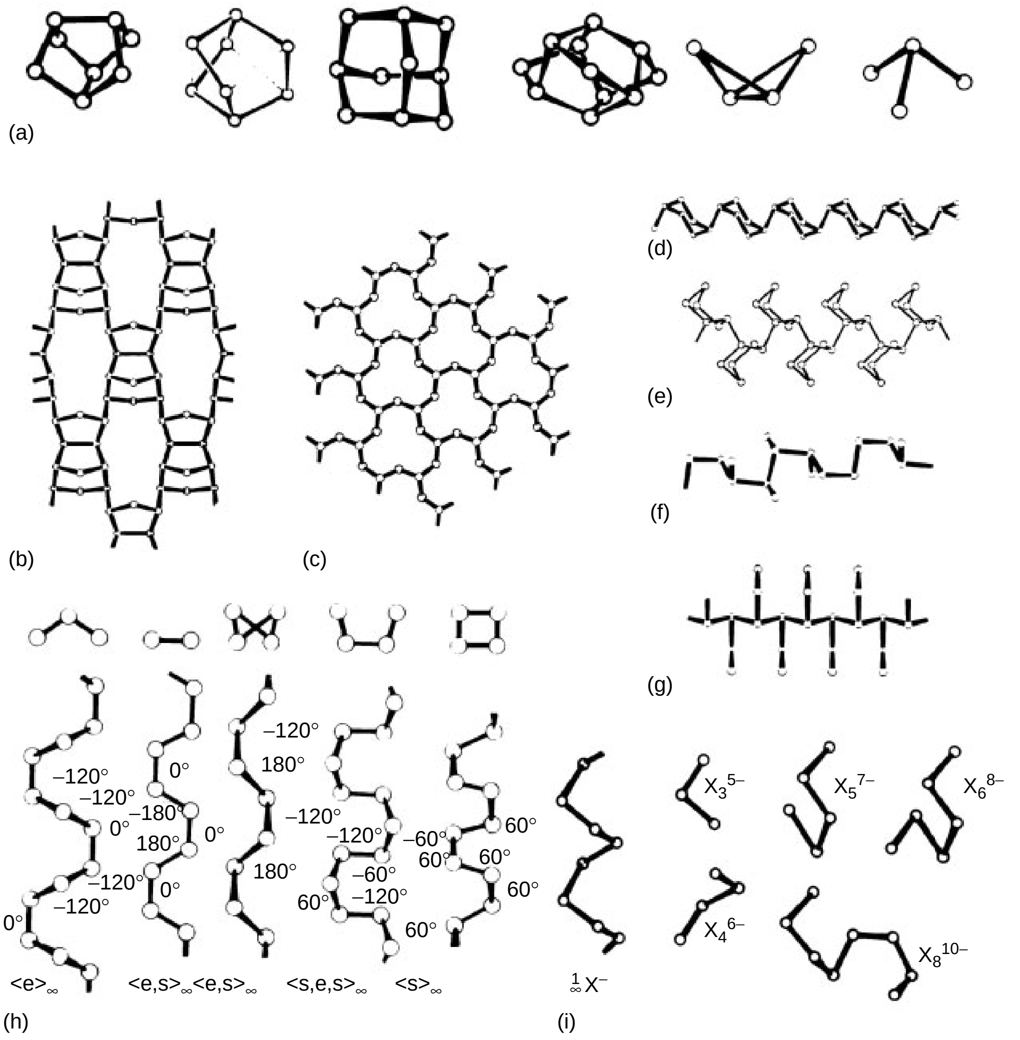

Figure 7 (a) Molecular units (left to right) P_8^{4-}, P_8^{6-}, P_{10}^{6-}, P_{11}^{3-}, P_4^{2-}, and P_4^{6-}. (b) $^2_\infty(P_{11}^{3-})$ of Ag_3P_{11}. (c) $^2_\infty(P_{10}^{6-})$ of $Au_7P_{10}I$. (d) Chain of six-membered rings (chair conformation) as found in BaP_3 and Au_2P_3. (e) Chain of six-membered rings (boat conformation, 1,2 connection) from $MoFe_2P_{12}$. (f) Branched $^1_\infty(P^-)$ from RuP_3. (g) Branched $^1_\infty(P^-)$ from ReP_3. (h) Different conformations of $^1_\infty(X^-)$ chains with their torsion angles and their projections along the helix axes. (i) Infinite and finite chains $X_n^{(n+2)-}$ with $n = 3, 4, 5, 6$, and 8

as yet unknown phosphacubane. This magnificently shaped chiral group is a system of six five-membered rings with D_3 symmetry. Both enantiomers are present in the crystal. On the other hand, the Ag_3P_{11} structure is built of $^1_\infty(P_{11}^{3-})$ tubular polymers.**[110]** In $MoNiP_8$ the chiral P_8^{6-} polyanion is present,**[111]** which is a phosphacubane with three opened edges, whose bridging directly leads to P_{11}^{3-}. Some of these structures are illustrated in Figure 7. At this point, it is worthwhile to note that the neutral fragment P_8Se_3, which is isoelectronic to P_{11}^{3-} (ufosane) occurs in the structure of $(CuI)_2P_8Se_3$.**[112,113]**

The M_3P_{11} phases transform into plastically crystalline modifications like the M_3P_7 phases.**[4,114]** In the high-temperature form (β), the phosphides match the structure of the intermetallic Li_3Bi. The Bi positions are surrounded by the cages of P_7^{3-} and P_{11}^{3-} with orientational disorder.

The compounds M_4P_6 of the alkali metals K, Rb, and Cs have a unique structure with planar and isometric P_6 rings.**[58]** The structure is a defect variant of the trigonal prismatic AlB_2 type**[115]** and the unusually short P–P bond distances of about 215 pm are not affected by the metal substructure. These compounds were the first examples of an unsaturated P–P bond system, although it was not possible to decide between a disordered double bond and a quasiaromatic 2π system (PBO $= 1.167$ from the P–P distance). An aromatic 6π polyphosphide in the form of a four-membered ring (P_4^{2-}) has been isolated in the solvated compound $Cs_2P_4{\cdot}2NH_3$ as well as in liquid ammonia.**[40]** The presence of the missing link in the sequence of the E_4 members has been excellently proven by X-ray (d(P–P) $= 214.7$ pm) diffraction, ^{31}P NMR as well as quantum-chemical calculations. The synthesis shows the application of a new preparative route, using

P_2H_4 as well as ammonia (*cf. 6.7.3*).[38] Polymers of P_6^{4-} were found in BaP_3, Au_2P_3, and the $MoFe_2P_{12}$ phases as well.[108,115–117]

Cyclo-P_6^{6-} has the usual chair conformation and is observed as part of the Th_2P_{11} structure.[118] The six-membered rings are inserted in a complicated 2-D phosphorus substructure and act as doubly tridentate ligands for Th. *Cyclo*-P_6^{6-} is also present in the arsenic-like structures of SnP_3, GeP_3, and InP_3,[119–121] indicating a metal oxidation state $q(\mathrm{M}) = +3$. The skutterudite structure type ($CoAs_3$ and derivatives, cf. Sections 8.2 and 8.7) is formed by some transition metal triphosphides (M^{3+}) and is characterized by planar *cyclo*-P_4^{4-}.[122,123]

6.5.3 Polyanionic Chains

In principle, all catenations of type $(2b)P_n^{-}$ $(1b)P_2^{2-}$-:2 ($0 \le n \le \infty$) belong to the large family of chain structures with $(n+2)$ atoms. Branched chains with m nodes are characterized by $(3b)P_m^0$ $(2b)P_{n-2m}^{-}$ $(1b)P_{2+m}^{2-}$. The 1-D polyanion ${}^1_\infty(P^-)$ is characteristic of the monophosphides of the alkali metals and the diphosphides of divalent metals, but is also present in $M^{IV}P_2$ compounds: SiP_2 ($GeAs_2$ type),[124] TiP_2, ZrP_2, and HfP_2 (Co_2P type) as well as $CeSiP_3$ and GdPS contain chains and isolated P^{3-} and S^{2-}, respectively.[125,126] The M-atom coordination varies from CN 4 (e.g. Zn^{2+} tetrahedral and Pd^{2+} square planar to four $(2b)P^-$) up to CN 9 (e.g. EuP_2), corresponding to the polyanionic arrangement. There is a series of structures that provides impressive examples of configurational and conformational variability, obviously forced by external conditions such as size and coordination of the cations. Figure 7(h) demonstrates how the sequence of torsional angles labels the chains, including fourfold helices as well as chains with changing rotational direction. The cation coordination may even change the configuration of a $(P^-)_\infty$ polyanion, for example, in the RuP_3 structure, where a branched isomer ${}^1_\infty(P_3^{3-}) = {}^1_\infty[(3b)P^0(2b)P^-(1b)P^{2-}]$ is present[127] with three different states of charge according to an internal bond disproportionation. ReP_3 and Re_2P_5 behave similarly.[128,129]

With increasing charge transfer, finite $P_n^{(n+2)-}$ chains ($2 \le n \le 8$) occur. These polyanions are present in compounds of M^{II}–M^{IV}. Three peculiarities should be mentioned here: (i) the coexistence of P_4^{6-} and P_8^{10-} in some structures and P_3^{5-} and P_5^{7-} in others; (ii) the existence of the pyramidal isomer P_4^{6-} in Ni_5P_4 and in $La_6Ni_6P_{17}$;[130,131] (iii) the remarkable isomer P_8^{10-} with the structure of a hexaphosphadiphosphate(IV) anion, present in Ca_5P_8.[102]

Important representatives of P_2^{4-} dumbbells are the pyrites (e.g. p-PtP_2) and the marcasites (e.g. m-FeP_2) with and without M–M bonds, for example CoP_2. Dumbbells P_2^{4-} and M–M chains characterize the structures of MoP_2 and WP_2 (see Figure (16)).[132] CoPS is given as a representative of a phosphide sulfide with either $(PS)^{3-}$ dumbbells or mixtures of P_2^{4-} and S_2^{2-}.[133] In CuPS, a 1-D chain of twofold-connected P atoms with exo-bonded sulfur atoms occurs.[134] The polymeric $(PS)^-$ anion is isosteric with the as yet unknown phosphorus monochloride.

In the p-SiP_2 structure[135] the short P–P distance (215 pm) demonstrates a considerable amount of P → Si back-bonding according to the formulation Si^{2+} and $(P{=}P)^{2-}$. Examples are the tunable (P–P) bond lengths in the pyrite structure, as well as in the phosphides of the MM'_2P_2 type ($BaAl_4/ThCr_2Si_2$), containing a formal P_2^{n-} dumbbell.[136] MnP and ThP_7 contain unusually large P–P bond lengths in ${}^1_\infty(P^{n-})$ polyanions ($2 \le n \le 3$) with $d(\mathrm{P{-}P}) = 240\,\mathrm{pm}$ and bond orders PBO ~ 0.5.[105,137] $LaCo_8P_5$ and Ti_2NiP_5 should be regarded similarly.[138,139]

Many structures with $P_n^{(n+2)-}$ fragments belong to the large family of structures built of trigonal prisms in different orientations and sometimes combined with cubes. The frame is formed by the M atoms, with P atoms and defects centering the polyhedra. Ba_3P_4 is one example of a complete trigonal prismatic defect structure $Ba_3P_4\square_2$, resulting in a P_4^{6-} chain fragment. The frame of $Na_2Sr_3P_4$ is built by trigonal prisms and cubes of Sr.[140] The prisms are centered by P atoms and defects, resulting in P_2^{4-} and the cubes are centered by Na atoms. A shear variant is Sr_5P_4, where half of the dumbbells are fragmented into P^{3-}. A fascinating structure is shown by Ba_4P_3, where Ba forms intersecting rings of P-centered trigonal prisms, empty tetrahedra, and empty tetragonal pyramids. The P_2 pairs fill the resulting channels formed by pairs of Ba_6 prisms with different orientation: $Ba_8(P^{3-})_4(P_2^{4-})$ (Figure 8).[141]

6.5.4 Radical Anions

Completely unexpected was the discovery of the radical anions P_3^{4-} (19e) and P_4^{5-} (25e) in K_4P_3 and K_5P_4 (Figure 9).[142] Both compounds are extremely sensitive to thermal and mechanical treatment. P_3^{4-}, isosteric to O_3^-, is paramagnetic with $\mu_{\mathrm{eff}} = 1.6\mu_{\mathrm{B}}$ at 300 K.

A similar polyanion radical with 19e has been found in $Ba_3P_3I_2$,[143] which can be formulated as $(BaI_2)\cdot(Ba_2P_3)$. The P–P bond distances between K_5P_4 and $Ba_3P_3I_2$ differ by 11 pm, which indicates a much more localized double bond in the Ba compound. A more symmetric P_3^{4-} radical anion occurs in $Ba_5P_5I_3$. Here the radical anion exists beside a classical P_4^{6-} chain with 26e. The two radicals presented here seem to show magnetic coupling, since diamagnetism is observed in the investigated temperature range. It should be pointed out that similar radical polyanions E_4^{5-} exist with E = As and Sb.

The structures of K_4P_3 and K_5P_4 also contain filled prisms of M atoms. These polyphosphides are the binary aristotypes of a series of ternary compounds with the general formula $M_{m+2n}X_{m+n}$ where m,n give the number of slabs of CrB (m) and Ni_2In (n), respectively. For K_4P_3, $m = 2$, $n = 1$, and for K_5P_4, $m = 3$, $n = 1$.

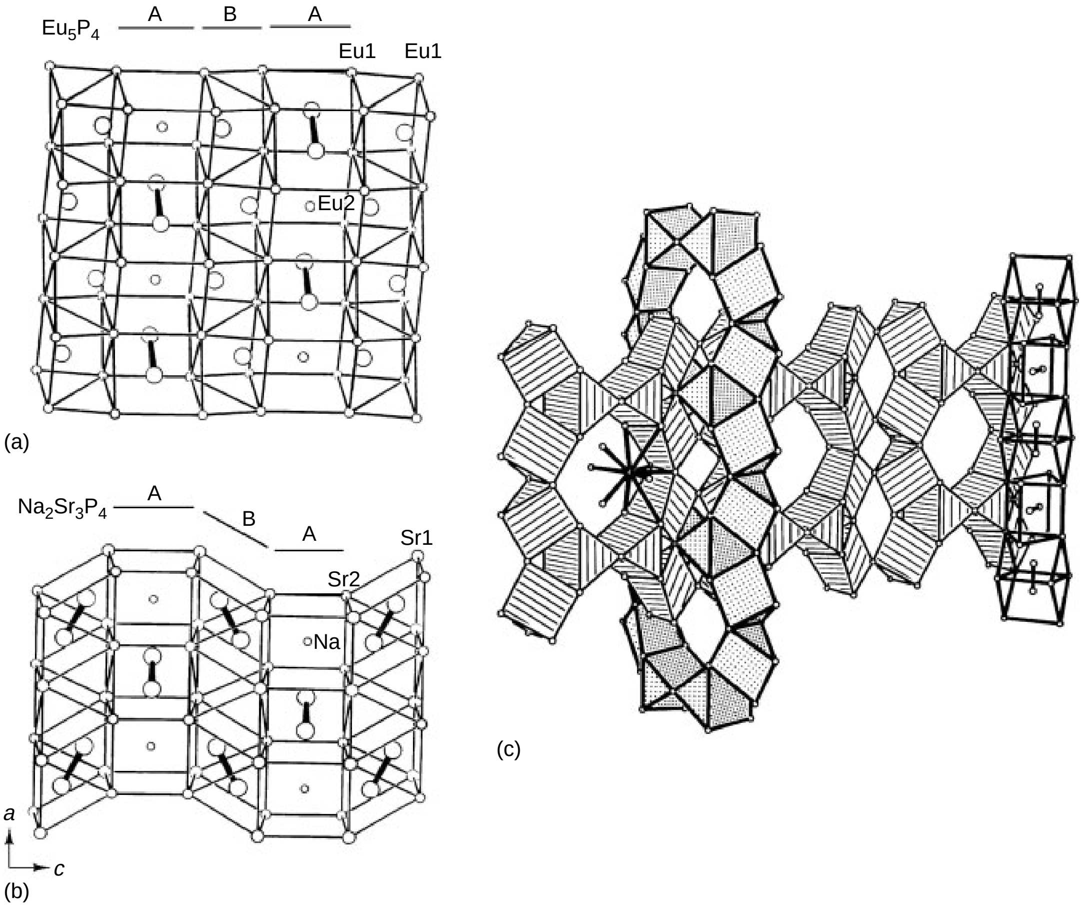

Figure 8 Examples of structures with trigonal M_6 prisms. (a) Eu_5P_4 with trigonal Eu_6 prisms centered by P atoms and defects resulting either in isolated atoms P^{3-} or dumbbells $P_2{}^{4-}$. (b) The shear variant $Na_2Sr_3P_4$ with trigonal prisms and only dumbbells. Small circles are metal atoms, large circles P atoms. (c) Ba_4P_3 types: intersecting rings of P-centered trigonal prisms, empty tetrahedra, and empty tetragonal pyramids. The two kinds of rings are striped and dotted. In the center of one ring a tenfold coordinated (bisdisphenoid) P atom is shown. The resulting channels, formed by pairs of Ba_6 prisms with different orientation, and filled with P_2 pairs, are emphasized at the right

6.5.5 2-D and 3-D Nets

Corrugated 2-D and 3-D polyanionic nets occur if the mean charge $q(\mathrm{P})$ is in the range $0.20 \leq q \leq 0.73$. The nets are formed by condensed and connected P_n rings of different sizes and conformations ($n = 5$, 6, 7, 8, 10, 12, 14, 18, 20, 22; Figure 10). Derivatives of black phosphorus are the triphosphides MP_3 of divalent Ca, Sr, Ba, and Eu.**[144,145]** By removing 1/4 of the atoms in different ways, 2/3 of the phosphorus atoms remain as $(2b)P^-$. Removing only neighboring atoms the 1-D BaP_3 structure is formed, containing infinite connected six-membered rings with chair conformations and axial linkages. This polyanionic structure is comparable with that of Au_2P_3 and can be regarded as the polymeric analogue of the planar hexagonal *cyclo*-$P_6{}^{4-}$. In SrP_3, half of the P_6 rings remain complete but in CaP_3 all of them are opened and yield P_{14} rings. α-EuP_3 follows CaP_3 and not SrP_3. The ${}^3_\infty(P_5{}^-)$ net of LiP_5**[146]** is related to the pattern of black phosphorus as well as that of gray arsenic.**[147]** One-dimensional bands of condensed six-membered rings are connected by twofold-linked $(2b)P^-$, with these atoms occupying axial as well as equatorial positions (Figure 10).

The pentaphosphides LnP_5 of the trivalent rare earth metals form three very similar structures, with mainly identical ${}^2_\infty(P_5{}^{3-})$ networks. They can be derived from a structure similar to that of gray arsenic but with the six-membered rings in a boat conformation. The charge transfer disintegrates this net by removing 1/6 of the atoms and yields a 2-D net of condensed 12-membered rings. In that case, 3/5 of the remaining atoms are $(2b)P^-$. The 2-D polyanionic net is adapted, stepwise, to the decreasing size of the Ln^{3+} cations, which takes place mainly by changing the dihedral P–P angles. The structures can be interpreted as stages of a reaction path brought about by application of pressure.**[1]**

The unique 2-D substructure $P_{11}{}^{8-}$ formed by Th_2P_{11} is more precisely described as $(P_{16}{}^{10-} + P_6{}^{6-})$.**[118]** Puckered P layers consist of ${}^1_\infty(P_{16})$ bands with isolated P_6 rings inserted.

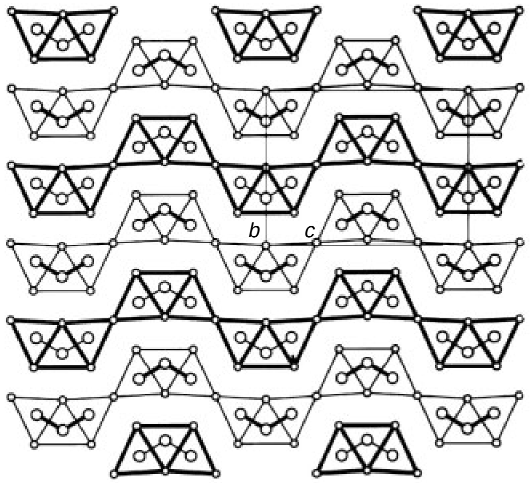

K_4P_3 {$(W_3Co)B_3$} type

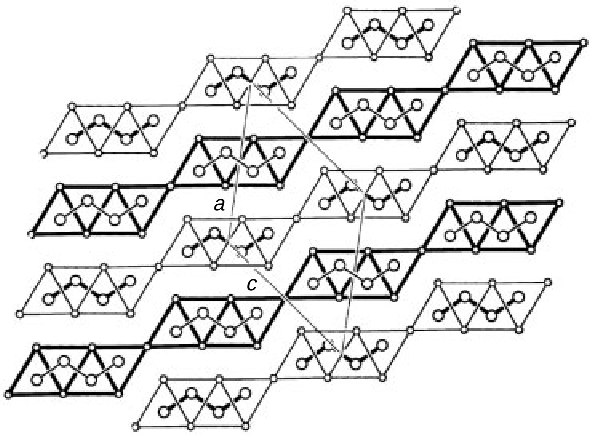

K_5P_4 {$(Y_4Ga)Co_4$} type

Figure 9 The known polyphosphides with radical polyanions $P_3{}^{4-}$ and $P_4{}^{5-}$. Atoms connected by thin and thick lines are separated from each other by half a translation period of the projection direction. Small circles are K atoms, large circles P atoms. The unit cells are indicated by thin lines together with the labelled axes

The P_{16} bands are formed by condensed skew-boat P_6 rings and *endo*-P_8 rings. The inserted P_6 chairs are partially opened to P_3 fragments bonded to the bands and, therefore, give rise to a periodic structural modulation caused by valency and generated by a rearrangement of a single P–P bond. The Th_2P_{11} structure is an example of a frozen-in ring-opening reaction.

The tetraphosphides of divalent M^{2+} (Mg, Cd, transition metals) and the diphosphides of monovalent Cu^+ and Ag^+ form $^{2}_{\infty}(P_4{}^{2-})$ nets. They have condensed P_{10} rings in common, but with a rich variation in their linkages.[17,148,149] The structure of Cu_4SiP_8[150] is related to these structure types.

6.5.6 *Tubular Structures*

Rolling up into tubes is the special contribution of phosphorus to curved 2-D surface structures. The tubular character of the Hittorf phosphorus structure is preserved in the polyanionic linkage of the compounds with the smallest (P^-):(P^0) ratio. In $Cu_2P_3I_2$ this ratio is zero,[151] that is, this structure is formed by insertion of elemental phosphorus in CuI! The peculiar crystal chemistry of such compounds is summarized in Section 6.5.7. The tubular $^{1}_{\infty}(P_{12}{}^{0})$ substructure consists of connected P_8 cages of regular type and planar P_4 rings. Needle-shaped crystals are typical of the alkali metal compounds MP_{15}, MP_{11}, and $MP_{10.3}$.[152–154] The fivefold $^{1}_{\infty}(P_{15}{}^{-})$ tubes represent the polymerization of alternating $P_7{}^-$ and $P_8{}^{\pm 0}$ units, the former a norbornane derivative of the latter, and comparable with the As_4S_4 molecule. In principle, the sequence of $P_7{}^-$ and P_8 may be variable, but the 1:1 structure seems to be the optimized modulation in crystalline compounds. In $KP_{10.3}$ and $RbP_{10.3}$, units such as $P_{35}{}^-$ were identified in a preliminary study (an extremely complicated twofold, noncommensurate superstructure). On the other hand, the structures of the very closely related RbP_{11} and CsP_{11} are characterized by $^{1}_{\infty}(P_{15}{}^{-})$ tubes and $^{1}_{\infty}(P_7{}^{-})$ chains of type 5. The repetition lengths of $P_{15}{}^-$ and $P_7{}^-$ chains correspond as $\tau(P_{15}{}^-) = 2\tau(P_7{}^-)$. Therefore, a whole series of compounds with twin-slab structures may exist in a very narrow compositional range, differing slightly in energy but, of course, having very different kinetics. Linear fivefold tubes are also characteristic for ternary phases like $HgPbP_{14}$ and for the chalcogenides $P_{14}S$ and $P_{14}Se$, respectively.[155–158] Lead and sulfur act as heteroatoms in the frame. The above mentioned alternation of $P_7{}^-$ and $P_8{}^{\pm 0}$ subunits is a necessary condition to form strain-reduced tubular structures. Thus no $^{1}_{\infty}(P_5{}^{-})$ structures exist in crystalline compounds. In LiP_5,[146] a strain-free 3-D structure with P_6 chairs is formed. Another possibility is realized with TlP_5 and BaP_{10},[159,160] where the curvature of $^{1}_{\infty}(P_5{}^{-})$ tubes is compensated for by the formation of an upside down polymerization of those tubes and results in a corrugated complex 2-D structure of alternating parallel and antiparallel oriented fivefold tubes that are partially opened at the roofs (Figure 11; Table 8).

The winding of these tubes into spirals results in the structures of LiP_7 and NaP_7.[161] The fourfold $^{1}_{\infty}(P_7{}^{-})$ helix is a very rigid building unit and not suited for the larger alkali metals. This unit is especially interesting with respect to its dimensionality. It represents, on one hand, a more complicated 1-D chain, where the chain links are connected via two bonds in both directions, typical for the tubelike chains. On the other hand, by looking at the tubes as rolled-up surfaces, the phosphorus substructure of LiP_7 is a rolled-up 2-D structure that results in different curvature and strain in the central and peripheral regions. The structures of $K_4P_{21}I$, Ag_3P_{11}, and Cu_2P_7 (with polymers of $P_7{}^-$, $P_{11}{}^{3-}$ and $P_7{}^{2-}$) are characterized by 2-D arrangements of connected short tubelike parts, whose connection result in larger P_n rings, appropriate as cavities for the other atoms.[110,149,162]

There is one very impressive feature in all tubular chains and in structures with shorter or longer parts of these, that is, the wavelike development along the chain direction.

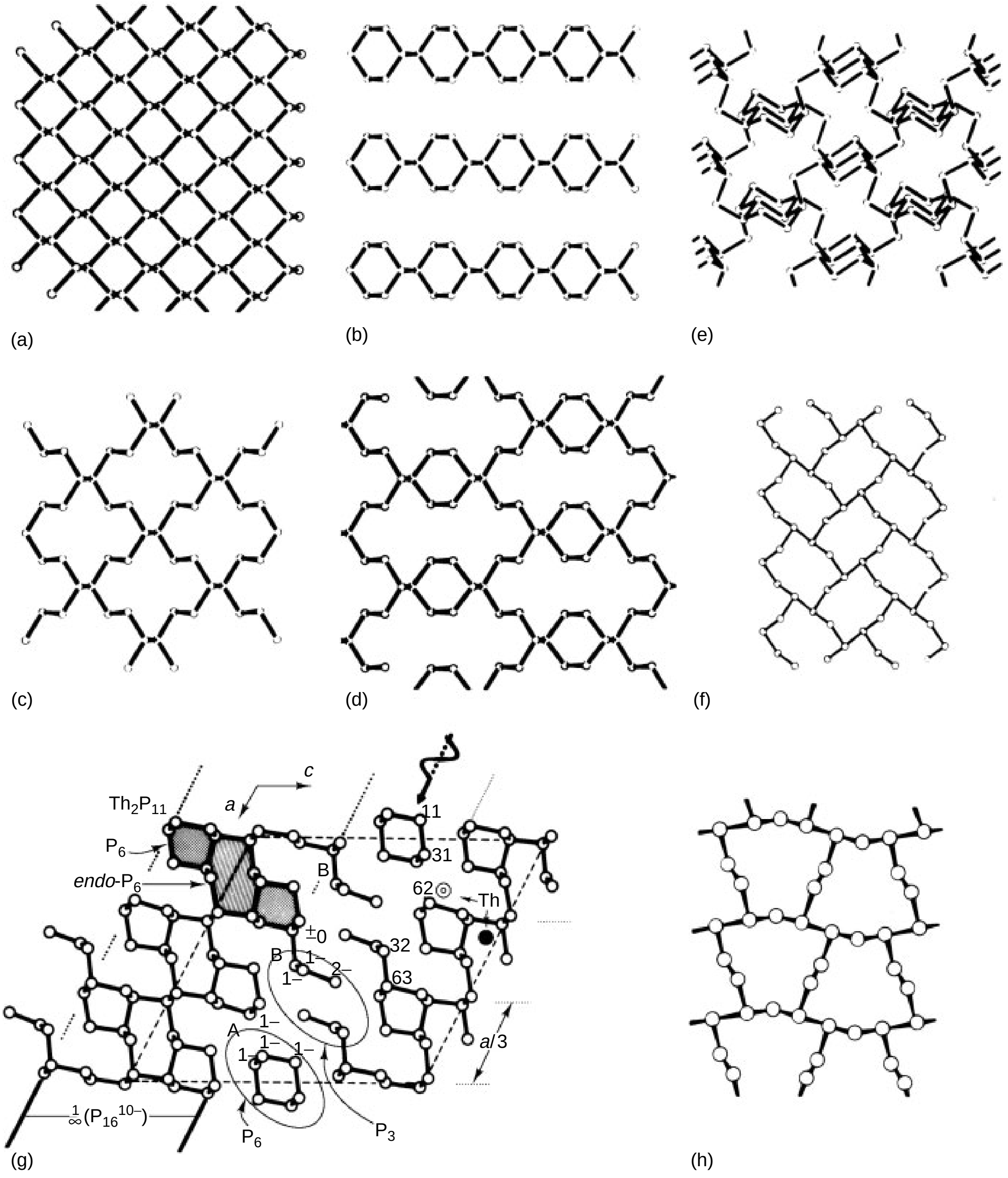

Figure 10 (a) Black phosphorus; its derivatives (b) BaP_3; (c) CaP_3 and α-EuP_3; (d) β-SrP_3 and β-EuP_3. (e) Shows the $^{3}_{\infty}(P_5^{-})$ network of LiP_5 and (f) the condensed P_{10} rings of MgP_4 (similar network exists in CuP_2). (g) Shows the substructure $^{1}_{\infty}(P_{16}^{10-})$ of Th_2P_{11} with inserted P_6^{6-} rings. The arrow gives the direction of modulation while A and B (each circled) denote the two stages of modulation. (h) The $^{2}_{\infty}(P_5^{3-})$ unit of LnP_5

6.5.7 Phosphorus Frameworks in Matrices

Although some of these compounds belong indeed to the phosphide halides (see Section 6.7.2), they are discussed separately here, owing to their interesting structural features. The monovalent copper halides CuBr and CuI act as solvents for a large variety of polymeric and oligomeric main-group molecules. The first compound of this structural family was $Cu_2P_3I_2$, that is, $(CuI)_8P_{12}$.[151] Also, the compounds $(CuI)_3P_{12}$ and $(CuI)_2P_{14}$ with phosphorus strands similar to Hittorf's phosphorus have been reported.[163] All of these structures can be considered as neutral phosphorus substructures that are embedded in a copper halide matrix. Some of the neutral phosphorus fragments are presented in Figure 12. As an example for the packing of the 1-D phosphorus units in the copper halide matrix, the structure of $(CuI)_2P_{14}$[164] is

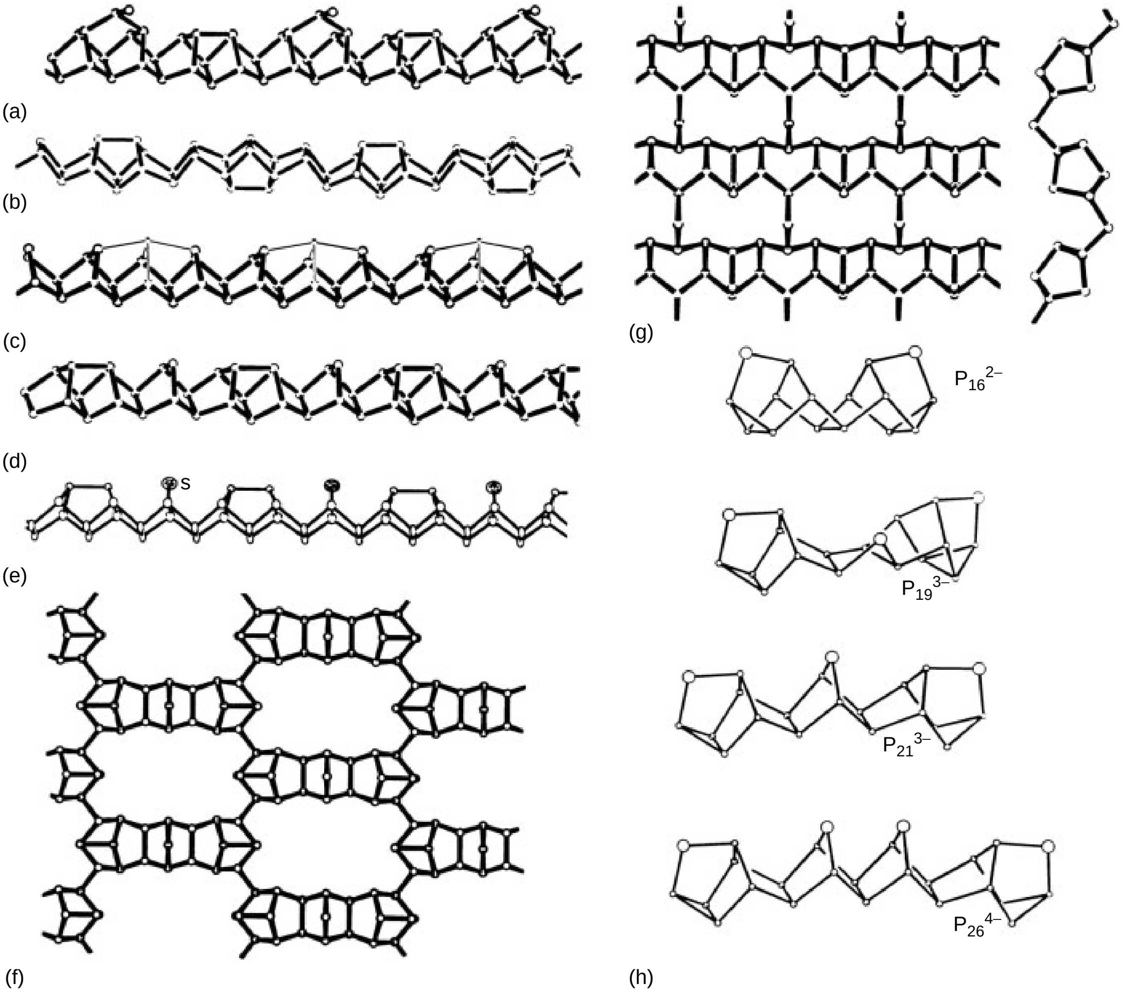

Figure 11 (a) Tubular unit in P (Hittorf); (b) $Cu_2P_3I_2$: $^1_\infty(P_{12}{}^{\pm 0})$ polymer generated by glide plane operation from P_{12} units; note the fragments P_8 (cf. Figure 7a) and P_4 rings; (c) framework $^1_\infty(P_{14}M^{II})$ as in the structure of $HgPbP_{14}$ type (M^{II} indicated by small spheres); (d) $^1_\infty(P_{15}{}^{-})$ from MP_{15}; (e) $^1_\infty(P_{14}S)$ (isoelectronic with $P_{15}{}^{-}$); (f) $^2_\infty(P_{21}{}^{3-})$ framework from $K_4P_{21}I$; (g) 2-D arrangement of linked pentagonal tubes as found in BaP_{10} and TlP_5 (seen perpendicular and parallel to the puckered layer); (h) structures of polyanions from solutions (cf. Table 8)

Table 8 Selected polyphosphide solvates and salts

Compound	Methods	Anionic partial structure
$MP_5(solv)_x$ (M = Li, Na, K)	^{31}P NMR	($P_5{}^{-}$) planar *cyclo*-P_5
$M_4P_6(solv)_x$ (M = K, Rb, Cs)	^{31}P NMR	($P_6{}^{4-}$) planar *cyclo*-P_6
$Cs_2P_4\cdot 2NH_3$	X ray; ^{31}P NMR	($P_4{}^{2-}$) aromatic planar anion
$[(Li)(TMEDA)]_3P_7$	X ray	($P_7{}^{3-}$) nortricyclane
$Li_3(en)_5P_7$	X ray	($P_7{}^{3-}$) nortricyclane
$Li_3P_7(solv)_3$, amorphous	^{31}P NMR	($P_7{}^{3-}$) nortricyclane
$[Rb(en)]_3P_7$	X ray	($P_7{}^{3-}$) nortricyclane
$Cs_3(en)_3P_{11}$	X ray	($P_{11}{}^{3-}$) 'ufosane'
$Na_4(en)_6P_{14}$	X ray	($P_{14}{}^{4-}$) from two $P_7{}^{2-}$
$Li_2P_{16}(THF)_8$	^{31}P NMR	($P_{16}{}^{2-}$) from ($P_9{}^{-}$) and ($P_7{}^{-}$)
$Na_2P_{16}(crown)_3(THF)_2$	^{31}P NMR	($P_{16}{}^{2-}$) from ($P_9{}^{-}$) and ($P_7{}^{-}$)
$[P(Ph)_4]_2P_{16}$	X ray	($P_{16}{}^{2-}$) from ($P_9{}^{-}$) and ($P_7{}^{-}$)
$M_3P_{19}(solv)_x$ (M = Li, Na, K)	^{31}P NMR	($P_{19}{}^{3-}$) from ($P_9{}^{-}$) and $(P_5{}^{-})_2$
$M_3P_{21}(THF)_{15}$ (M = Li, Na)	^{31}P NMR	($P_{21}{}^{3-}$) trimer of ($P_7{}^{-}$)
$[Li(crown)_2]_3P_{21}(THF)_2$	X ray	($P_{21}{}^{3-}$) trimer of ($P_7{}^{-}$)
$M_4P_{26}(solv)_{16}$ (M = Li, Na)	^{31}P NMR, X ray	($P_{26}{}^{4-}$) from $(P_9{}^{-})_2$ and ($P_8{}^{2-}$)

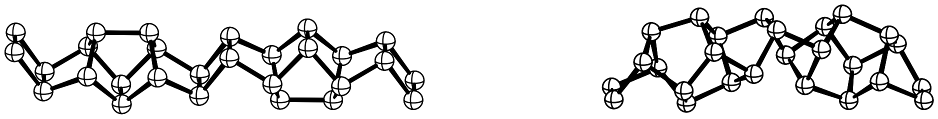

${}^{1}_{\infty}[P_{12}]$ in $(CuI)_8P_{12}$ ${}^{1}_{\infty}[P_{12}]$ in $(CuI)_3P_{12}$

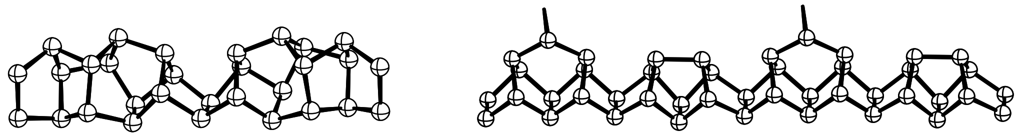

${}^{1}_{\infty}[P_{14}]$ in $(CuI)_2P_{14}$ Hittorf's phosphorus

Figure 12 Phosphorus units in the structures of $(CuI)_8P_{12}$, $(CuI)_3P_{12}$, and $(CuI)_2P_{14}$ as compared to Hittorf's phosphorus

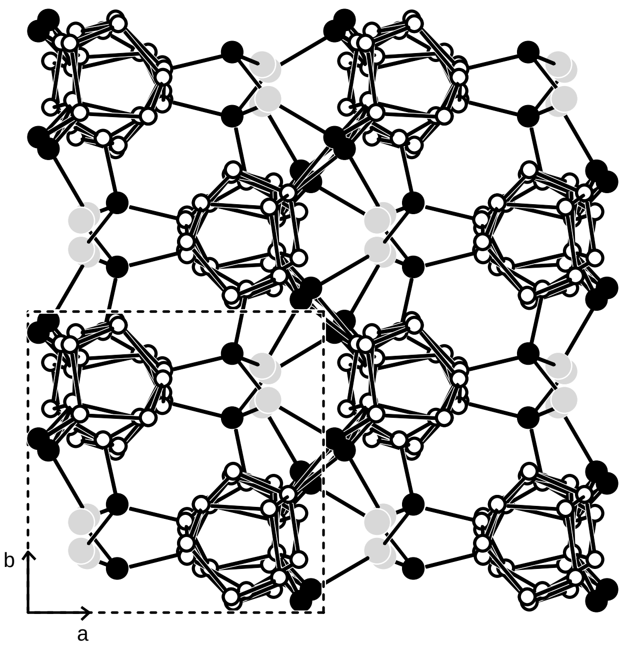

Figure 13 View of the $(CuI)_2P_{14}$ unit cell along the [001] direction. Copper, iodine, and phosphorus atoms are drawn as black filled, grey, and small open circles, respectively. The phosphorus substructure and some relevant Cu–I and Cu–P bonds are emphasized

shown in Figure 13. Besides the neutral substructures, also some fragments with 1-D phosphorus anionic units exist, like ${}^{1}_{\infty}[P_{15}{}^{1-}]$ in $(CuI)_2CuP_{15}$[165] or ${}^{1}_{\infty}[P_{20}{}^{2-}]$ in $(CuBr)_{10}Cu_2P_{20}$.[166] All tubular phosphorus modifications (see Section 6.5.6) can be considered as to be constituted from five and six-membered rings, however, one can easily recognize well-known building units, for example, the P_8 realgar analogue, the norbornane analogue as well as four-membered rings. It is thus not astonishing that these compounds form. We note, that some of these tubular units observed in the copper phosphide halides have been theoretically predicted by Häser to be more stable than other isomeric forms.[167] This structural concept has also been extended to molecules like P_4Se_4 in $(CuI)P_4Se_4$[168] or $(CuI)_3P_4Se_4$.[169]

The CuI containing compounds have been investigated with respect to a potential copper ionic conductivity.[170,171] First hints for a copper mobility were obtained by Möller and Jeitschko through the ion exchange reaction in aqueous $AgNO_3$ solution: $Cu_2P_3I_2 + 4Ag^+ \rightarrow Ag_2P_3I_2 + 2Ag\downarrow + 2Cu^{2+}$.[151] During the reaction, elemental silver is deposited and the reaction solution becomes blue owing to solvated Cu^{2+}. Conductivity data (impedance spectroscopy) show predominantly ionic conductivity for $(CuI)_8P_{12}$ and $(CuI)_3P_{12}$ with activation energies of 0.45 and 0.59 eV. In contrast, $Cu_3P_{15}I_2$ has a predominantly electronic conductivity with a higher activation energy of about 0.72 eV.[171] A remarkable feature in $Cu_6P_{10}Br_5$ as well as in $Cu_3P_{15}I_2$ is the occurence of neighbouring copper cations (3x and 2x) along the spine of the tubular units, leading to some hints of enhanced ion mobility along the needle axis (tube axis).

The only compounds in the system carbon–phosphorus which have been considered up to a distinct level are compounds with a substitutional replacement in C_{60} like $C_{59}P$ or $C_{69}P$,[172] endohedral $P@C_{60}$,[173] and a crystallization product between neutral C_{60} and neutral P_4, that is, $(P_4)_2C_{60}$.[174]

6.5.8 *Isomerism*

In solid-state structures of polyphosphides, one observes all limiting cases of formal charge distribution within different isomeric polyanionic networks, for example,

$$(P_3)^{3-} : CoP_3\{[(2b)P^-]_3\} \hat{=} {}^{1}_{\infty}\{[(3b)P^0][(2b)P^-][(1b)P^{2-}]\}RuP_3 \qquad (2)$$

$$(P_4)^{6-} : Sr_3P_4\{[(2b)P^-]_2[(1b)P^{2-}]_2\} \hat{=} \{[(3b)P^0][(1b)P^{2-}]_3\}Ni_5P_4 \qquad (3)$$

Here, both 'isomers' are homogeneous with respect to their partial structures. Heterogeneous mixtures are

$$P_3{}^{7-} : CeSiP_3\{[2(0b)P^{3-}] + {}^{1}_{\infty}[P^-]\} \hat{=} \{[(0b)P^{3-} + P_2{}^{4-}]\}AlSiP_3 \qquad (4)$$

$$P_4{}^{6-} : \alpha\text{-}CeP_2\{[2P_4{}^{6-}]\} \hat{=} \{[P_3{}^{5-} + P_5{}^{7-}]\}\beta\text{-}CeP_2 \qquad (5)$$

Further examples are the two SiP_2 modifications with $P_2{}^{4-}$ dumbbells on one side and $\{{}^1_\infty(P^-) + P^{3-}\}$ on the other. The pair MoP_2/TiP_2 with $q(M) = 4$ behaves analogously, but with additional Mo–Mo interactions in MoP_2.

The phosphide sulfides GdPS, CoPS, and NbPS ($q(M) = 3$) contain $\{{}^1_\infty(P^-) + S^{2-}\}$, $\{(P_2{}^{4-} + S_2{}^{2-})$ or $(PS^{3-})\}$, and $\{(P_2{}^{4-} + S_2{}^{2-}) + Nb_2$ pairs$\}$.

6.6 Metal-rich Transition Metal Phosphides

The metal-rich varieties of the transition metal phosphides have many structures and properties in common with the so-called refractory hard metals. In these compounds, MP_x, the M–M interactions become increasingly important with decreasing x. This is indicated by the M–M distances which are in the region of metallic and also of covalent diameters ($2R_{met}$ and $2R_{cov}$, respectively). The difference with closed-shell cations is clearly demonstrated by comparison of the isotypic pair Na_2O/Rh_2P with the ratio $d(M–M)/d(M–X) = 1.155$. The transparent insulator Na_2O has $d(Na–Na) = 278\,\mathrm{pm} < 2R_{cov} = 314\,\mathrm{ppm}$ $\langle 372\,\mathrm{pm} = 2R_{met}$; the closed-shell cations Na^+ have no electrons for Na–Na bonds and, therefore, the close M–M approach has no effect. On the other hand, the opaque 'hard' metal Rh_2P has $d(Rh–Rh) = 275\,\mathrm{pm} \sim 2R_{met} = 270\,\mathrm{pm} > 2R_{cov} = 250\,\mathrm{pm}$; obviously, the Rh–Rh approach at d(Rh–Rh) is sufficient for M–M interactions because of the open-shell configuration of the Rh cations. Sometimes it may be difficult to state that M–M bonding exists without knowledge of the electronic band structure, however, excellent proof is provided by the occurrence of distinct clusters (M_2 pair, M_3 triangle, empty M_6 cluster).

The structures of the metal-rich transition metal phosphides are primarily governed by the M-atom arrangement, whose octahedral and trigonal prismatic holes are partially centered by isolated P atoms. Trigonal prismatic (tp) sixfold coordination dominates, and is frequently extended up to ninefold coordination by additional atoms above the rectangular prism faces (mono-, di-, tricapped). Depending on how it is described a structure can emphasize quite different patterns of repeating units; this is demonstrated for $Zr_2Fe_{12}P_7$ in Figure 14.[175]

1. Metallurgists act like egalitarians in describing structures as stackings of nets where all atoms become simple nodes, classified with Schläfli symbols. Owing to this, all differentiation between the atoms is lost. The $Zr_2Fe_{12}P_7$ structure is formed by two different nets at two different heights, that is, the net $\{5^3 + (456)_3 + (4356)_3 + (343434) + (345^2)_3\} \hat{=} ZrFe_6P_4$ (drawn bold in Figure 14(a)) and the net $\{(343434) + (3464)_3 + (4^26)_3 + (3434^2)_3 \hat{=} ZrFe_6P_3$ (drawn thin in Figure 14a).
2. Dividing structures into suitable units can serve to rationalize a series of structures by one formula. The resulting vacant sites may be filled by additional atoms

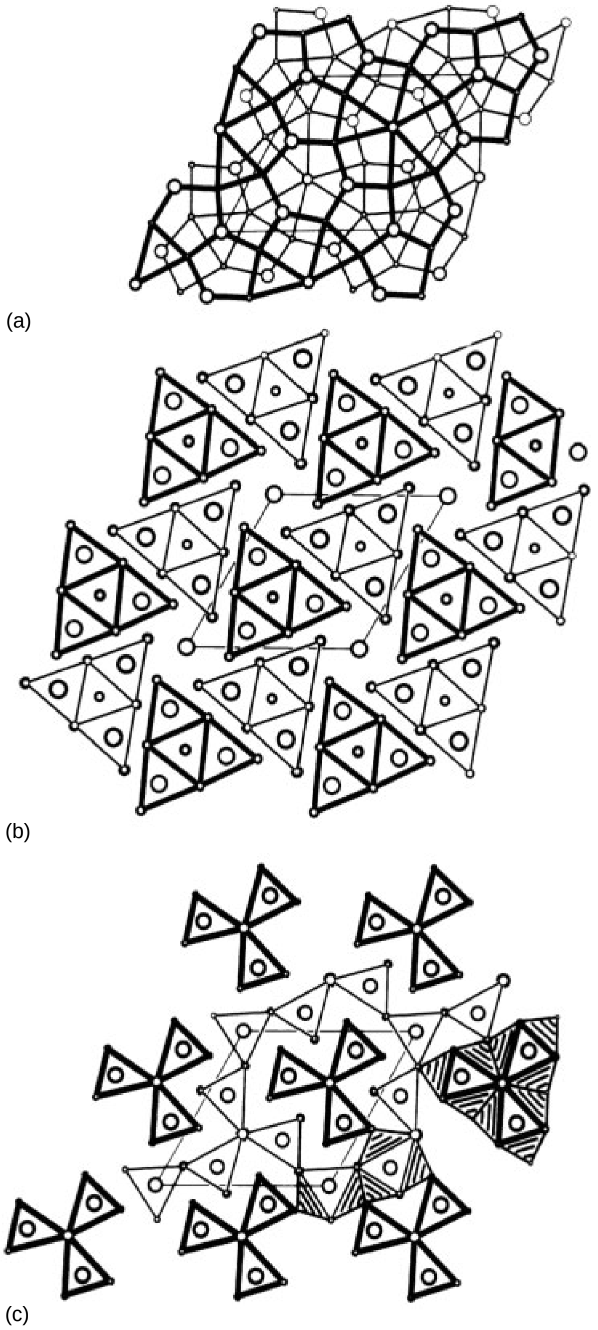

Figure 14 Three different representations of the $Zr_2Fe_{12}P_7$ structure type projected along the c axis. Atoms connected by thin and thick lines are separated from each other by half a translation period. Smallest circles are Fe atoms, medium circles Zr atoms, large circles P atoms. (a) Two different nets in two different heights. For the Schläfli symbols, see text. (b) Large trigonal prismatic building blocks AB_6C_3 from four trigonal B_6 prisms (with overemphasized schematic separation of blocks in different heights). Note that the three outer B_6 prisms of the blocks are base centered. The vacant sites between the blocks are filled with the P atoms. (c) Trigonal prism strands ${}^1_\infty[ZrFe_6P_3]$ and an open network of trigonal prisms ${}^3_\infty[ZrFe_6P_4]$. The threefold capping of the trigonal prisms is emphasized at the upper right. This leads to a complete 3-D structure with CN 9 for the P atoms

(Figure 14b). Here $Zr_2Fe_{12}P_7$ is a member of the family with the generalized formula $A_nB_{(n+1)(n+2)}C_{n(n+m)+1}$ with $n,\ m = 1$. Hereby blocks of prisms of composition $AB_6C_3 \hat{=} ZrFe_6P_3$ are evident. The vacant site is filled by a P atom: $2\ ZrFe_6P_3 + P \hat{=} Zr_2Fe_{12}P_7$. This purely geometrical description is extremely helpful in differentiating the huge family of metal-rich phosphides.

3. The more individual the chemical description, the better the structure is identified in terms of different bonding or interaction. The appropriate fundamental units in the present structures are, therefore, the P-centered trigonal prisms, sometimes extended by their trigonal prismatic caps. In this way, the $Zr_2Fe_{12}P_7$ structure is separated into two interpenetrating patterns of trigonal prisms, that is, a tristar $^1_\infty[(PFe_{4/2}Zr_{2/6})] \hat{=} P_3Fe_6Zr$ and an infinite net with $^1_\infty[PFe_{6/4}(PZr_{2/6}Fe_{2/2}Fe_{2/4})_3] \hat{=} P_4Fe_6Zr$. The interaction of these subunits to a complete 3-D structure is performed by threefold capping of the trigonal prisms (Figure 14c).

6.6.1 M_3P and Related Structures

The Fe_3P type, Ti_3P type, and α-V_3S type are a group of similar structures, characterized by a frame of M atoms whose patterns are related to the stella quadrangula pattern as derived from the tetraederstern motif; this is very common in intermetallic phases.[13,121] The M-atom frame may also be seen as intersecting thin slabs of a face-centered cubic metal. The channels are filled by 1-D columns of slightly distorted M_4P_4 heterocubane units, showing a clear separation of M_2 regions and MP regions, respectively. The P atoms have CN 9 and CN 8. The $Ni_{12}P_5$ structure is related to the above cited types, but with a different pattern of the M-atom frame. This now corresponds to a simple cubic arrangement whose cubic holes are alternating, centered by P atoms (CsCl type), as in the Ni_8P unit. Again the channels are filled by Ni_4P_4 columns, resulting in $Ni_{12}P_5$. The latter P atoms are 10-fold coordinate (Figure 15).

A second group of M_3P phases has the cementite Fe_3C structure (Table 3) built from distorted trigonal prisms and octahedra of M atoms, the former centered by P as well as M. The complete structure can be derived from a hexagonal close-packed M structure by twinning. The $Pd_{4.8}P$ structure is a modified Fe_3C type.

6.6.2 M_2P and Related Structures

The M_2P phases form mainly four structure types: Co_2P, Fe_2P, Ta_2P, and Rh_2P. The Co_2P type is a branch[176] of the widely occurring $PbCl_2$ structure with chains of twofold-linked tricapped trigonal prisms centered by P atoms (Figure 16). Ternary representatives are ZrFeP, TiFeP, and so on. Some modifications may occur in the direction of the related Co_2Si type with dicapped trigonal prisms.

The Fe_2P type demonstrates another variety of tricapped prism linkage, that is, a disproportionation into isolated and threefold linked units. Completely different is the Ta_2P structure[177] (Figure 16), where condensed M_6X_8 clusters and strings of condensed M_4 tetrahedra can be recognized: $^1_\infty[Ta_6Ta_{4/2}P_{12/2}] + {^1_\infty}[Ta_4] = Ta_{12}P_6$. Again the P atoms are trigonal prismatically coordinated. Nb_7P_4 is closely related, forming simple 1-D cluster chains with single Nb atoms completing the P coordination to trigonal prisms: $^1_\infty[Nb_4Nb_{2/2}P_{8/2}] + 2Nb = Nb_7P_4$. Another related arrangement is adopted by Nb_8P_5.[178]

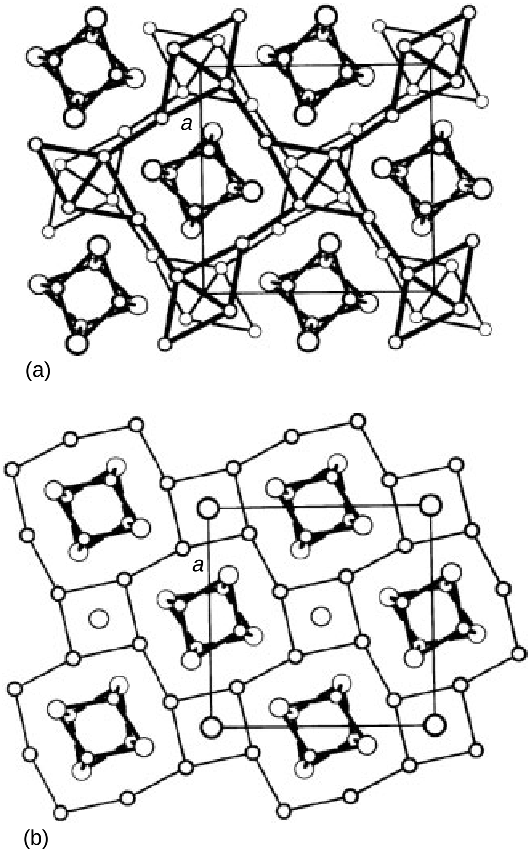

Figure 15 (a) Ni_3P type with emphasized 1-D heterocubanes Ni_4P_4 and tetraederstern network. (b) $Ni_{12}P_5$ type with heterocubanes Ni_4P_4 and connected PNi_8 cubes. Small circles are Ni atoms, large circles P atoms

A huge series of ternary phosphides $M_mM_nP_x$ exists with $m + n \sim 2x$ having structures with (mainly) tricapped trigonal prisms around phosphorus, for example, Co_2P and Fe_2P. Depending upon the M/M′ ratio in the range $1 > M/M' > 0.125$ (ZrRuP–$LaCo_8P_5$), patterns of fascinating shapes occur, which can be regarded as higher homologues of the Co_2P chains and Fe_2P stars.

The field of transition metal-rich phosphides in the ternary systems R–T–P (R = Zr, Hf, rare earth metal, actinoid metal) has intensively been investigated in the last 10 years by the groups of Franzen and Kleinke, Guérin, Jeitschko, Kuz'ma, and Mewis. From a geometrical point of view, the main building motifs of these structures are mono-, di-, or tricapped

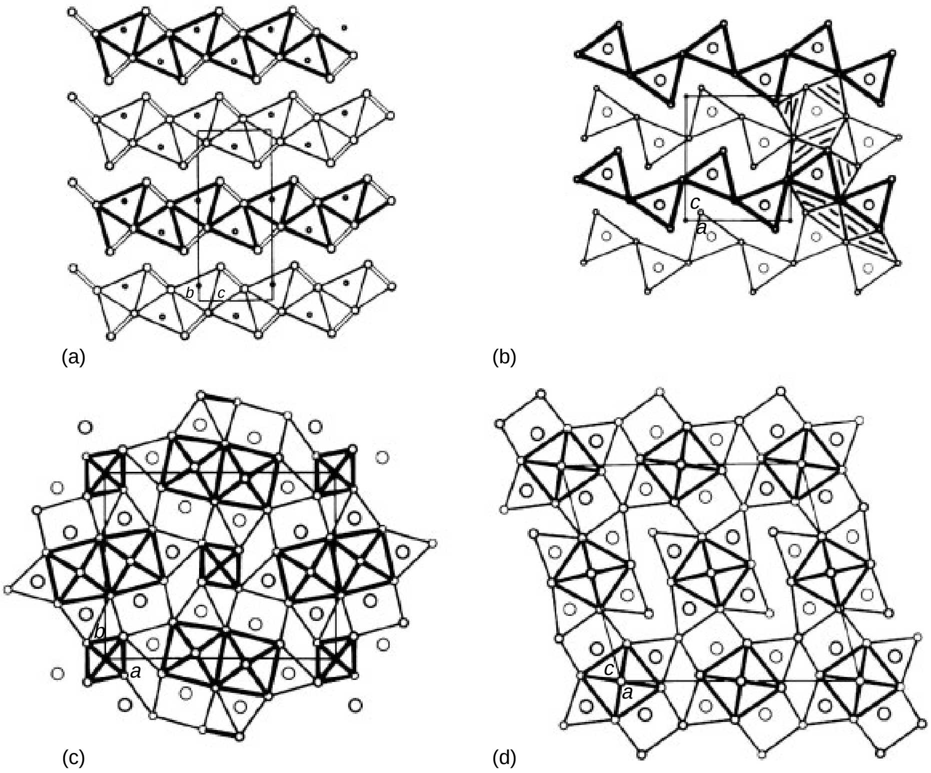

Figure 16 Top: AB$_2$ structure types with emphasized trigonal prisms. Thin and thick lines connect atoms that are separated from each other by half a translation period of the projection direction. Small circles are metal atoms, large circles phosphorus atoms: (a) MoP$_2$, the P$_2{}^{4-}$ dumbbell is indicated by an open thick bond; (b) Co$_2$P (PbCl$_2$) with layers of trigonal prisms. Some empty half octahedra have been indicated in the right. Below: phosphides with condensed and isolated metal octahedra: (c) Ta$_2$P with condensed M$_6$ octahedra, in which note the 1-D chain of Ta$_{4/2}$ between the octahedra: (d) Nb$_7$P$_4$ with emphasized octahedra; small circles are metal atoms, large circles P atoms. Note that in (c) and (d) the P atoms are in positions corresponding to X in M$_6$X$_8$ clusters

trigonal prisms around the phosphorus atoms. This crystal chemistry is to some extent similar to silicide chemistry.[179] The different patterns of the connectedness of the trigonal prisms was summarized in a recent review by Kuz'ma and Chykhrij.[14] A survey on the phase diagrams and the typical coordination polyhedra was given by Chykhrij.[15] Many of these metal-rich phosphides belong to structural families with distinct building rules.[179–181]

M′–M′ bonding plays an important role in most of these compounds, owing to the large transition metal content. Thus, one observes a large variety of M′–M′ bonds in the various structure types of transition metal-rich phosphides. As examples, we present the cobalt and iron substructures of the Yb$_6$Co$_{30}$P$_{19}$[182] and La$_2$Fe$_{25}$P$_{12}$[183] structures (Figure 17). The pronounced M′ networks leave larger channels where the rare earth or actinoid metal atoms are located. Overviews on other M′ substructures have been reported.[184–186] In these drawings, only M′–M′ distances shorter than 280 pm are shown.

6.6.3 Phosphide Structures with $x > 0.5$

Ti$_5$P$_3$ (Mn$_5$Si$_3$ type)[187] is a member of the face-condensed octahedral M$_6$X$_8$ clusters: ${}^1_\infty$(Ti$_{6/2}$P$_{6/2}$). The packing of the cluster columns forms large channels which are filled by 1-D linear Ti chains with short Ti–Ti distances (254 pm). The structure ${}^1_\infty$[Ti$_2$(Ti$_3$P$_3$)] is directly comparable with that of (□K)(Mo$_3$Se$_3$). The empty M$_6$ octahedra may be filled for electronic reasons by C and N (a well-known feature of cluster compounds), yielding the Nowotny phases (e.g. V$_5$P$_3$N).

Other real cluster compounds are Ag$_6$Ge$_{10}$P$_{12}$ and Ag$_6$Sn$_4$Ge$_6$P$_{12}$ with the units {[Ag$_6$Ge$_4^{\mathrm{II}}$]P$_{12}$} and {[Ag$_6$Sn$_4^{\mathrm{II}}$] P$_{12}$} connected by Ge$^{\mathrm{IV}}$ to a 3-D structure.[188] The cluster units are Rh$_6$(μ_3-CO)$_4$(CO)$_{12}$ analogs with Ag$_6{}^{4+}$ octahedra which are fourfold μ_3-capped by Ge$^{\mathrm{II}}$ and Sn$^{\mathrm{II}}$, and bonded to 12 P atoms as exo ligands. These systems act as thermally activated threefold two-level systems (Figure 18).[189]

Transition metal clusters can also occur in compounds with a much higher phosphorus content. A recent example is the structure of Ag$_3$SnP$_7$,[190] which contains isolated tetrahedral Ag$_3$Sn clusters and ${}^1_\infty$[P$_7$] chains (Figure 12). Similar distorted tetrahedral Cu$_3$Sn clusters occur also in the Cu$_4$SnP$_{10}$ structure described in Section 6.5.2.[107]

Hf$_3$P$_2$ has the Sb$_2$S$_3$ structure with a 3-D net of connected groups of six condensed Hf$_6$ *tp*'s, four of which are P centered and monocapped.[191] Rh$_4$P$_3$ forms parallel zig-zag slabs of *tp*'s with different orientation, alternately centered by the P

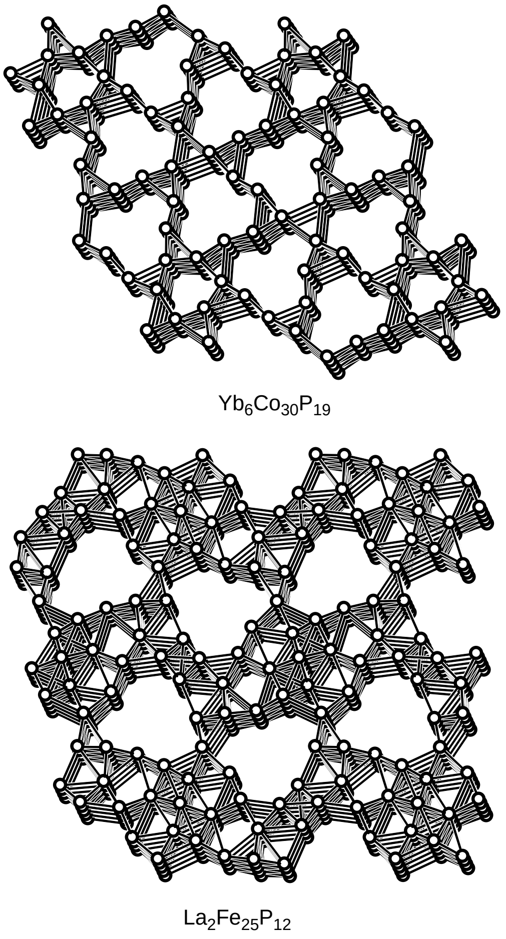

Figure 17 Transition metal substructures in $Yb_6Co_{30}P_{19}$ and $La_2Fe_{25}P_{12}$. All Co–Co and Fe–Fe distances equal or smaller than 280 pm are drawn

atoms.[192] Mo_4P_3 is related but with larger NiAs-type segments. In both structures, phosphorus has CN 7 and 6. The Re_3P_4 structure is a deficient variant of NiAs ($\square Re_3As_4$) and is also related to cluster compounds.[193] Triplets of face-condensed P_6 octahedra are centered by Re atoms forming linear Re_3 groups. The octahedra are further connected via common edges.

Many more complex structures of metal-rich phosphides can be formally cut into 2-D slabs of different size and can thus be considered as intergrowth structures.[194,195] These slabs are parts of quite different arrangements but have common areas which fit together. The structures of the small slabs derive from simple binary or ternary types like AlB_2, Cu_3Au, $CeMg_2Si_2$, SrPtSb, $CaAl_2Si_2$, $ThCr_2Si_2$, or $CaBe_2Ge_2$. As examples, the structures of $Ca_5Pd_6P_6$, $Ca_4Pd_5P_5$,[196] $Ca_3Cu_2Zn_2P_4$, $Ca_4Cu_3Zn_2P_5$,[197] $Sr_2Pd_3P_3$,[198] and $Eu_2Pt_7AlP_3$[199] are presented in Figure 19. Such intergrowth structures are also formed in the families of pnictide oxides and arsenides.[200] Even more complex intergrowth structures of Cu_3P, $LaLi_3P_2$, and $PrLi_2P_2$ related

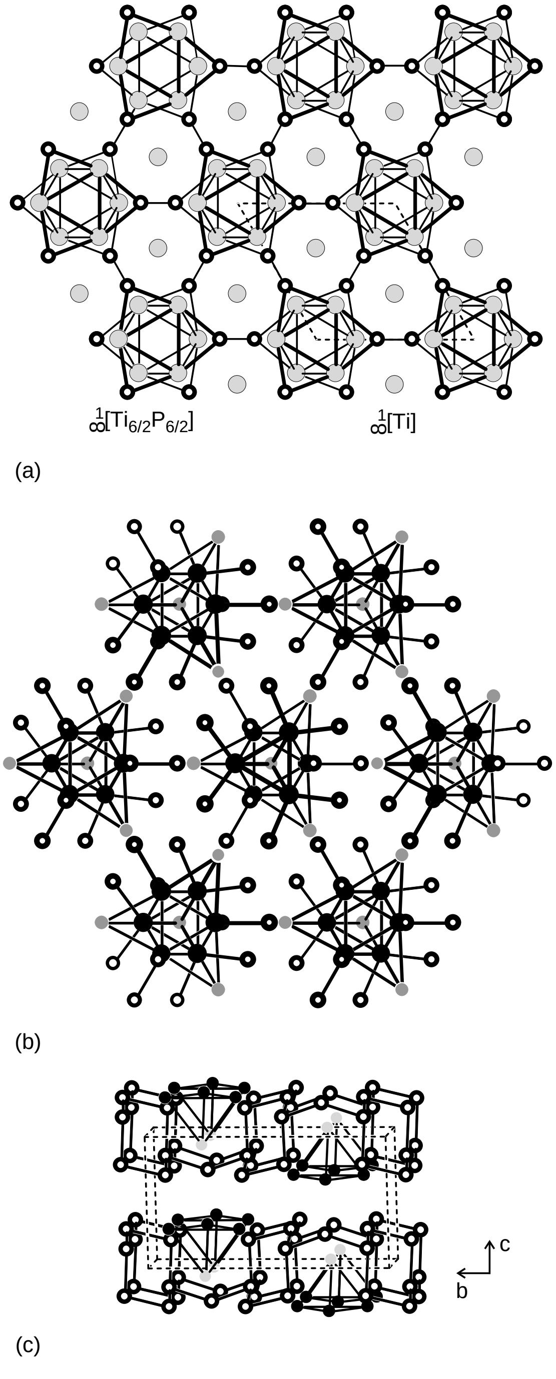

Figure 18 (a) M_5P_3 (Mn_5Si_3 type) structure of Ti_5P_3 with emphasized $^1_\infty[Ti_{6/2}P_{6/2}]$ octahedral chain and $^1_\infty[Ti]$ metal-atom piles. The chain $Ti_{6/2}P_{2/2}$ corresponds to face-condensed M_6X_8 clusters (2X are omitted). Small circles are Ti atoms, large circles P atoms. (b) $M_6M'_4M''_6P_2$ structure showing $[Ag_6M^{II}_4]P_{12}$ cluster in $Ag_6Ge_{10}P_{12}$, view along the cubic [111] direction. Small circles are Ge^{II} atoms, medium circles Ag atoms, large circles P atoms. The Ge^{IV} atoms as well as the unit cell edges have been omitted for clarity. The Ge^{IV} atoms are in tetrahedral holes formed by the P atoms of neighboring clusters; (c) view of the Ag_3SnP_7 structure approximately along the [100] direction (Ag, black filled circles, Sn, grey circles, P, open circles). The tetrahedral Ag_3Sn cluster and the $[P_7]$ network are emphasized

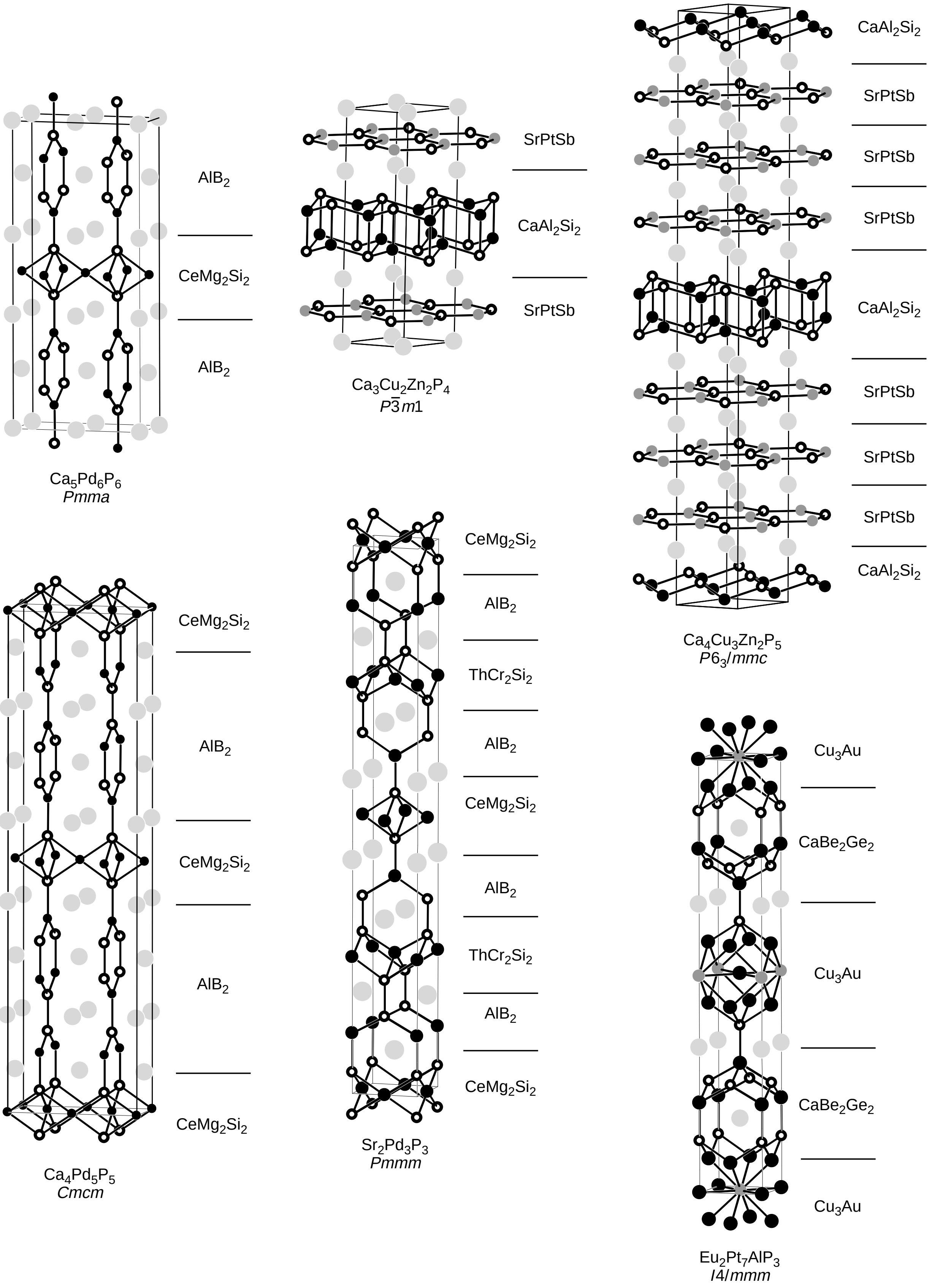
AlB_2
$CeMg_2Si_2$
AlB_2
SrPtSb
$CaAl_2Si_2$
SrPtSb
$CaAl_2Si_2$
SrPtSb
SrPtSb
SrPtSb
$CaAl_2Si_2$
SrPtSb
SrPtSb
SrPtSb
$CaAl_2Si_2$
$CeMg_2Si_2$
AlB_2
$CeMg_2Si_2$
AlB_2
$CeMg_2Si_2$
$CeMg_2Si_2$
AlB_2
$ThCr_2Si_2$
AlB_2
$CeMg_2Si_2$
AlB_2
$ThCr_2Si_2$
AlB_2
$CeMg_2Si_2$
Cu_3Au
$CaBe_2Ge_2$
Cu_3Au
$CaBe_2Ge_2$
Cu_3Au

$Ca_5Pd_6P_6$
Pmma

$Ca_3Cu_2Zn_2P_4$
$P\bar{3}m1$

$Ca_4Cu_3Zn_2P_5$
$P6_3/mmc$

$Ca_4Pd_5P_5$
Cmcm

$Sr_2Pd_3P_3$
Pmmm

$Eu_2Pt_7AlP_3$
$I4/mmm$

Figure 19 Some examples of slab structures (longest crystallographic axes in upright position)

slabs occur for the rhombohedral structures of $Yb_3Cu_{8-x}P_6$ and $Y_3Cu_{8-x}P_8$[201,202] with values of up to 60 Å for the c axis. Also, the $Ho_2Cu_{6-x}P_{5-y}$ structure belongs to this family.

In this context, it should be emphasized that the phosphides of the $BaAl_4$/$ThCr_2Si_2$ type show various P–P distances which change their length with size and electron configuration of the M atoms. Compounds like $CaCu_{1.75}P_2$ (225 pm P–P distance) or $CaNi_2P_2$ (230 pm) have P_2 pairs with a P–P single bond, while the bond order (see Sections 4.1 and 4.2) in $CaCo_2P_2$ (245 pm) is around 0.5.[203] Other phosphides have much longer P–P distances (up to 384 pm in $BaFe_2P_2$[203]) and consequently have no P–P bonds. The influence of the electron count on M–P and P–P bonding in such phosphides has theoretically been investigated by Hoffmann and Zheng.[204–206] So far, more than 600 compounds crystallize with the $BaAl_4$/$ThCr_2Si_2$ type. Just and Paufler have listed the c/a ratios of all of these compounds and they analyzed the dependence of the z parameter of the X atoms from the c/a ratio.[207] In a recent work, it was clearly demonstrated that there are definitely two branches for this family of compounds: the $BaZn_2P_2$ branch with isolated phosphorus atoms and the $BaAl_4$/$ThCr_2Si_2$ branch where Al–Al and Si–Si bonds (or X–X bonds in general) occur.[208,209] The simple formula $d_{X-X} = (0.16 + 0.04(c/a))\cdot c$ allows a fast estimation of the X–X distance. Changes of the P–P distance under high pressure also influence the oxidation state of the transition metal (see Section 8.6).

6.7 Phosphide Oxides, Halides, and Hydrogenphosphides

The first proof for an oxygen incorporation in pnictides was found with Eu, not for a phosphide, but for an antimonide.[5,210] Later on, more systematic studies of the quasibinary systems M_3Pn_2–MX_2 and M_3Pn_2–MO (M = Ca, Sr, Ba, Eu; X = O, Cl, Br, I; Pn = P, As, Sb) by Hadenfeldt and coworkers[211–213] led to a series of new compounds. Further on, phosphide oxides have been obtained during phase investigations of the binary alkaline-earth metal–phosphorus systems.[214] Most likely oxygen was gettered in the samples through oxydic or hydroxidic surface impurities of the alkaline-earth metals. In recent years, also a huge number of quaternary phosphide oxides with ZrCuSiAs and related structures[215] and a variety of phosphide halides with peculiar crystal structures have been reported.[216,217] The main difference of these solid-state compounds to phosphorus halides and phosphates is the absence of P–O and P–X bonds.

6.7.1 Phosphide Oxides

The first hints for phosphide oxides have been observed by Maass in 1970.[218,219] He obtained products assumed to be the phosphides Sr_2P and Ba_2P during phase analytical investigations in the systems Sr–P and Ba–P, but he already suspected that these phases might indeed be phosphide oxides. Detailed X-ray investigations by Hadenfeldt and coworkers revealed the correct compositions AE_4P_2O (AE = Ca, Sr, Ba).[211,213] These phosphide oxides crystallize with a tetragonal K_2NiF_4 or orthorhombic La_2CuO_4 type structure (Figure 20) with an octahedral OM_6 coordination of the oxygen atoms. According to the Zintl-Klemm electron transfer, the cations M^{2+} and the anions P^{3-} and O^{2-} are present, and thus these phosphide oxides are expected to be insulators or semiconductors that correspond, for example, with the greenish yellow color of Ca_4P_2O.

Besides the ternary phosphide oxides, a huge number of quaternary transition metal-containing phases has been reported. The $Ba_2Mn_3P_2O_2$ structure[220] (Figure 20) has octahedrally coordinated oxygen atoms (4Ba + 2Mn). The Mn2 and phosphorus atoms form a tetrahedral network that resembles the RET_2P_2 phosphides with $BaZn_2P_2$ structure (see Section 6.6.3). The manganese atoms in these pnictide oxides show magnetic ordering at comparatively high Néel temperatures.[214] Octahedral oxygen coordination also occurs in the phosphide oxides $Na_3Sr_7(P_3)_3O$, $Na_3Eu_7(P_3)_3O$,[221] $Th_4Fe_{17}P_{10}O_{1-x}$,[222] and $Ba_{11}KP_7O_2$.[223] The $Na_3Sr_7(P_3)_3O$ structure contains bent $P_3{}^{5-}$ units while isolated P^{3-} and dimeric $P_2{}^{4-}$ anions occur in $Ba_{11}KP_7O_2$. All phosphorus atoms in $Th_4Fe_{17}P_{10}O_{1-x}$ are isolated with trigonal prismatic coordination.

All of the remaining transition metal-containing phosphide oxides have oxygen atoms in a tetrahedral coordination of rare earth or actinoid atoms. So far 35 isotypic phosphide oxides with ZrCuSiAs type structure (Figure 20) have been reported, that are ThCuPO,[224] UCuPO,[225] and the rare earth series REMnPO,[226] REFePO, RECoPO,[227] REZnPO,[228] and RERuPO[227] with the early rare earth metals. According to the isolated phosphorus atoms we can formulate, for example, $RE^{3+}Fe^{2+}P^{3-}O^{2-}$. Several crystals of these phosphide oxides have a golden tint while powders are dark grey. Certainly, chemical bonding in RETPO is not purely heteroatomic and one can at least assume some weak T–T bonding.[226,227] Besides the simple ZrCuSiAs type, the tetragonal structures $U_2Cu_2P_3O$,[229] $Th_2Ni_{3-x}P_3O$,[224] and $La_3Cu_4P_4O_2$[215,230] have been reported. These structures have a much longer tetragonal axis and they may be considered as intergrowth structures of simple slabs that derive from the $HfCuSi_2$, $CaBe_2Ge_2$, and $BaZn_2P_2$ type structures (for details see Ref. 224 and 230). Only the phosphorus atoms in $Th_2Ni_{3-x}P_3O$ and $La_3Cu_4P_4O_2$ form pairs. The only exception in the series of phosphide oxide structures (all other structures presented in Figure 20 are tetragonal) is the rhombohedral NdZnPO type.[228] Also, this structure is built up from NdO layers with tetrahedrally coordinated oxygen and from ZnP layers (Figure 20). According to the transparent crystals and the formal oxidation states $Nd^{3+}Zn^{2+}P^{3-}O^{2-}$, one expects semiconducting behavior.

6.7.2 Phosphide Halides

The occurrence of ternary compounds containing phosphorus besides halogen is a small but still increasing field of

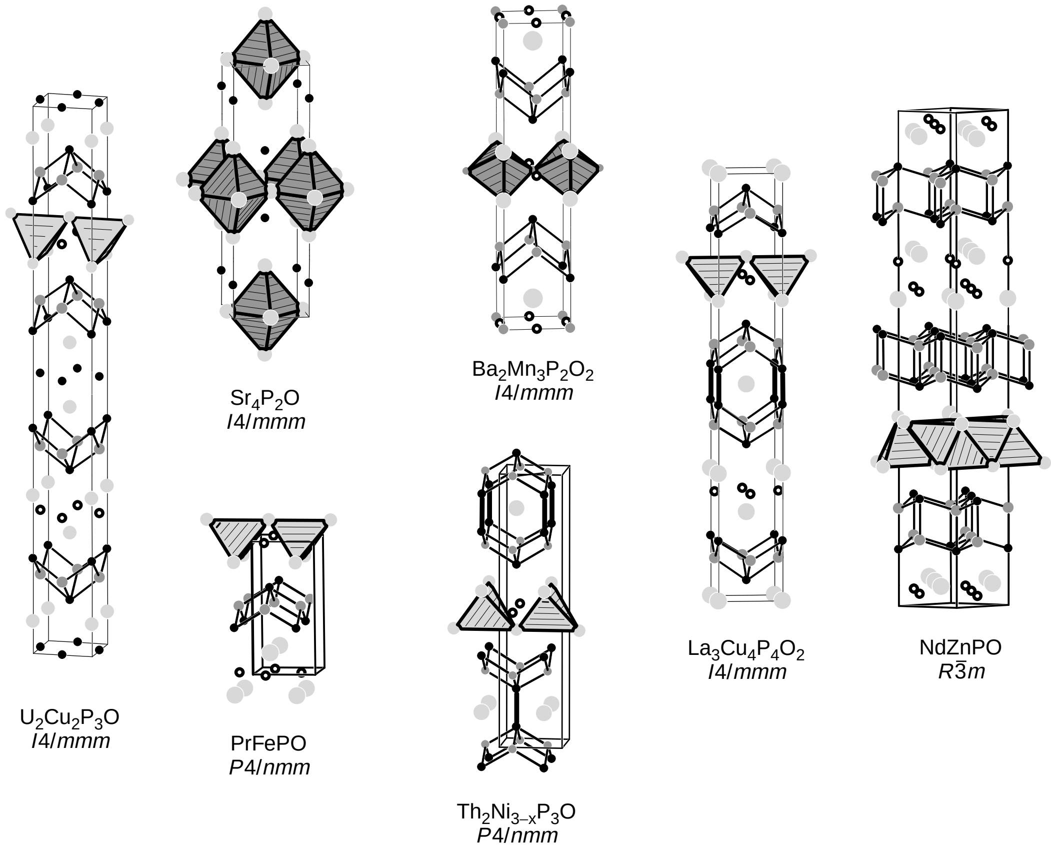

Figure 20 Crystal structures of various ternary and quaternary phosphide oxides of the alkaline earth, rare earth, and actinoid metals. Alkaline earth (rare earth, actinoid), transition metal, phosphorus, and oxygen atoms are drawn as large light grey, medium grey, filled, and open circles, respectively. Some relevant coordination polyhedra around the oxygen atoms and the transition metal–phosphorus bonds are emphasized

interest (see Table 9). In all compounds, one observes a clear charge separation, that is, the phosphide halides are pure salts. Some of the copper halides, containing phosphorus frameworks, have already been discussed (cf. Section 6.5.7). Those with radicalic polyanions are summarized in Section 6.5.4. The first phosphide halides have been detected when halogen was added to the reaction mixtures in order to overcome the kinetic hindrance of phosphorus to go into the gas phase.

The crystal chemistry of the phosphide oxides discussed above is closely related to the structural slabs of the well-known $BaZn_2P_2$ type (isolated P^{3-}) /$BaAl_4$ type (P_2 pairs) and related compounds. This is different for the phosphide halide structures. Some relevant structures of the phosphide halides are presented in Figure 21 and a list is given in Table 9. These structures contain isolated phosphorus atoms, P_2 pairs, or one-dimensional spirals like in the structure of elemental selenium.

The Eu_2PBr and Eu_2PI structures[231] belong to the $NaFeO_2$ type space group $R\bar{3}m$, as do Ca_2PBr, Sr_2PBr, and Ba_2PBr.[232] Both phosphorus and halogen atoms have a distorted octahedral europium coordination, and these octahedra are condensed via common edges. These phosphide halides are simple salts according to $(2\,Eu^{2+})\,P^{3-}Br^{-}$. Antiferromagnetic ordering of the europium magnetic moments has been observed for Eu_2PBr and Eu_2PI.[233] The phosphorus atoms are isolated in the structures of Cd_3PCl_3[234] and $(Hg_2P)_2HgBr_4$.[235] Each phosphorus atom is tetrahedrally coordinated by cadmium forming linear chains of edge-sharing tetrahedra in $Cd_3PCl_3 \equiv (3Cd^{2+})\,P^{3-}\,(3Cl^{-})$. These chains are embedded in the packing of the chlorine atoms. The most remarkable structure occurs for $(Hg_2P)_2HgBr_4$ which is the phosphorus analogue of the Millon's base salts. The $[Hg_2P]^{+}$ cation has the same topology as the $[Hg_2N]^{+}$ cation.

P_2 pairs occur in the structures of Cd_2PCl_2[236] and $Hg_7P_4Br_6$.[237] The monoclinic structure of Cd_2PCl_2 has some similarities to the well-known K_2NiF_4 type. The P_2 pairs (P–P 218 pm) are located in slightly elongated, distorted octahedra of cadmium atoms. These octahedra have the same topology as the NiF_6 octahedra in K_2NiF_4. The layers of the corner-sharing P_2Cd_6 octahedra are separated by the chloride anions. According to the P–P single bond distance of 218 pm, an adequate formula is $(4Cd^{2+})\,P_2{}^{4-}\,(4Cl^{-})$. The structural characteristics of $Hg_7P_4Br_6$ are similar, but the condensation of the distorted P_2Hg_6 octahedra is different. Assuming a P–P single bond (220 pm), the formula is $(7Hg^{2+})\,(2P_2{}^{4-})\,(6Br^{-})$.

Table 9 Ternary phosphide halides

Compound	Crystal chemical formulation	Anionic partial structure
$M_4P_{21}I$ (M = K, Rb)	$(MI)\cdot(MP_7)_3$	$^{2}_{\infty}(P_{21}{}^{3-})$ framework (Figure 11f)
2 $\lvert Ba_2P_7Cl\rvert$	$(BaCl_2)\cdot(Ba_3P_{14})$	$P_7{}^{3-}$ nortricyclane
$Ba_3P_3I_2$	$(BaI_2)\cdot(Ba_2P_3)$	$P_3{}^{4-}$ radical anion (19e)
2 $\lvert Ba_5P_5I_3\rvert$	3 $(BaI_2)\cdot 2\ (Ba_2P_3)\cdot(Ba_3P_4)$	2× $P_3{}^{4-}$ radical anion (19e) $P_4{}^{6-}$ chain (26e)
4 $\lvert Cu_2P_3I_2\rvert$	8 $(CuI)\cdot P_{12}$	$^{1}_{\infty}(P_{12}{}^{\pm 0})$ polymer from P_8 (realgar type) and P_4 rings (Figure 7a, 12)
3 $\lvert CuP_4I\rvert$	$3(CuI)\cdot P_{12}$	$^{1}_{\infty}(P_{12}{}^{\pm 0})$ polymer condensed from distorted units (Figure 12)
3 $\lvert CuP_7I\rvert$	$2(CuI)\cdot P_{14}$	$^{1}_{\infty}(P_{14}{}^{\pm 0})$ polymer condensed P_7 (norbornane) and P8 (realgar)(Figure 12)
$Cu_3P_{15}I_2$	$2(CuI)\ \cdot CuP_{15}$	$^{1}_{\infty}(CuP_{15}{}^{\pm 0})$ polymer from P_8 (realgar type) and (CuP_8) (cf. Figure 7)
2 $\lvert Cu_6P_{10}Br_5\rvert$	$10(CuBr)\cdot Cu_2P_{20}$	$^{1}_{\infty}(P_{20}{}^{2-})$ polymer from P_8 (realgar type) and (CuP_8) (cf. Figure 7)
M_2PX (M = Ca, Sr, Ba; Eu; X = Br, I)	$2\ (M^{2+})\ P^{3-}X^-$	isolated P^{3-}
Hg_2P_3X (X = Cl, Br)	$2(Hg^{2+})\ (P^-)_3\ (X^-)$	$^{1}_{\infty}(P^-)$ polyanion
Cd_2P_3X (X = Cl, Br)	$2(Cd^{2+})\ (P^-)_3\ (X^-)$	$^{1}_{\infty}(P^-)$ polyanion
2 $\lvert Cd_2PCl_2\rvert$	$4(Cd^{2+})\ (P_2{}^{4-})\ 4(Cl^-)$	$(P_2{}^{4-})$ dumbbells
M_3PCl_3 (M = Zn, Cd)	3 $(MCl_2)\cdot M_3P_2$	isolated P^{3-}
$M_5P_2Br_4$ (M = Cd, Hg)	$5\ (M^{2+})\ 2(P^{3-})\ 4(Br^-)$	$[M_2P]^+$ isoelectronic with $[M_2N]^+$
$M_7P_4X_6$ (M = Cd, Hg; X = Cl, Br)	$7\ (M^{2+})\ 2\ (P_2{}^{4-})\ 6\ (X^-)$	$(P_2{}^{4-})$ dumbbells
2 $\lvert M_4P_2X_3\rvert$ (M = Cd, Hg; X = Cl, Br, I)	$8\ (M^{2+})\ (P_2{}^{4-})\ 2\ (P^{3-})\ 6\ (Cl^-)$	$(P_2{}^{4-})$ dumbbells and isolated P^{3-}
$Ge_{38}P_8X_8$ (X = Cl, Br, I)	$[Ge_{38}P_8]^{8+}8X^-$	*Clathrate-I* type
$[Sn_{24}P_{19.3}\square_{2.7}]\ I_8$	$[Sn_{24}P_{19.3}\square_{2.7}]\ ^{8+}\ 8\ I^-$	*Clathrate-I* type
$[Sn_{24}P_{19.6}\square_{2.4}]\ Br_8$	$[Sn_{24}P_{19.6}\square_{2.4}]\ ^{8+}\ 8Br^-$	*Clathrate-I* type
$[Sn_{24}P_{19.3}\square_{2.7}]\ Br_xI_{8-x} (x = 0-8)$	$[Sn_{24}P_{19.3}\square_{2.7}]\ ^{8+}\ 8\ (Br_xI_{8-x})^-$	*Clathrate-I* type
$[Sn_{14}In_{10}P_{21.2}\square_{0.8}]\ I_8$	$[Sn_{14}In_{10}P_{21.2}\square_{0.8}]^{8+}\ 8\ I^-$	*Clathrate-I* type
$[Sn_{10}In_{14}P_{22}]\ I_8$	$[Sn_{10}In_{14}P_{22}]^{8+}\ 8\ I^-$	*Clathrate-I* type
$[Sn_{17}Zn_7P_{22}]\ I_8$	$[Sn_{17}Zn_7P_{22}]^{8+}\ 8\ I^-$	*Clathrate-I* type
$[Sn_{19.3}Cu_{4.7}P_{22}]\ I_8$	$[Sn_{19.3}Cu_{4.7}P_{22}]^{8+}\ 8\ I^-$	*Clathrate-I* type
$Ba_8\ [Cu_{16}P_{30}]$	$8\ Ba^{2+}\ [Cu_{16}P_{30}]^{16-}$	*Clathrate-I* type, dist.; 184e?; $(P_{18}{}^{20-})$ finite chain polyanion; $(P_{12}{}^{14-})$ finite branched polyanion

Hg_2P_3Cl and Hg_2P_3Br**[238]** contain one-dimensional infinite chains of phosphorus atoms at P–P distances of 219 and 220 pm, in agreement with P–P single bonds, leading to the formula $(2Hg^{2+})\ (3P^-)\ Br^-$. The related cadmium compounds Cd_2P_3X (X = Cl, Br, I)**[239]** have been studied with respect to their semiconducting behavior with band gaps of 0.6, 0.7, and 0.2 eV for Cl, Br, and I, respectively. The most phosphorus-rich phosphide halides are Ba_2P_7Cl and $M_4P_{21}I$ (M = K, Rb) with isolated $P_7{}^{3-}$ anions and 2-D layers of condensed fragments of Hittorf's phosphorus (Figures 6 and 11). For details, see Section 6.5.

Also, some phosphide halides with the clathrate-I structure have been reported (see Table 9).**[240–249]** Clathrates are a fascinating group of compounds, because they exist not only as noble gas hydrates $(E18)_8(H_2O)_{46}$, but also with M^{13}, M^{14}, and M^{15} as framework elements. All clathrates with M, M′, P and X (X = Cl, Br, I) belong to the *clathrate*-I type. The framework consists of Y_{20} dodecahedral and Y_{24} tetrakaidodecahedral cages (Y = skeleton atoms M, M′, P). The anions are located in these cages according to size and charge. The cationic Y_{46} skeleton requires $46 \times 4e = 184$ *electrons* and all Y atoms are $(4b)Y$. In Table 9 (lower part), the compounds with P as a part of the skeleton are given. If 184 electrons are available from less than 46 atoms, some defects (□) are present. The clathrates containing (In, Zn, Sn, P, Cu, □) have the skeleton (184e) and in total an ionic charge of 8+. They also belong to the *clathrate*-I type. The phosphide $Ba_8[Cu_{16}P_{30}]$,**[249]** has been included here, even though there is no halogen present (cf. Table 5), but is a *clathrate*-I type, too. It forms a fourfold superstructure of the cubic subcell and consists of an anionic framework with a charge of 16− under the assumption that 8 Ba^{2+} atoms are present. All copper atoms are exclusively coordinated by phosphorus atoms. However, from the 30 P atoms, 150e are delivered for the skeleton bonding. Therefore, the copper atoms should provide $184e - 150e - 16e = 18e$ with 16 Cu atoms. With a skeleton requiring (184e), 2 Cu atoms should have the charge 2+. As this compound was proven to be a semiconductor with a band gap of 0.7 eV, a valence compound is very likely. This could be reached, for example, by the substitution of Cu by P, leading to $Ba_8[(Cu_{15.5}P_{0.5})P_{30}]$. Besides this open question, the structure consists of a finite polyanionic chain $(P_{18}{}^{20-})$ and a finite branched polyanion $(P_{12}{}^{14-})$ (dodecaphospha-4,5-diethyloctane). Considering a weak P–P bond in this polyanion

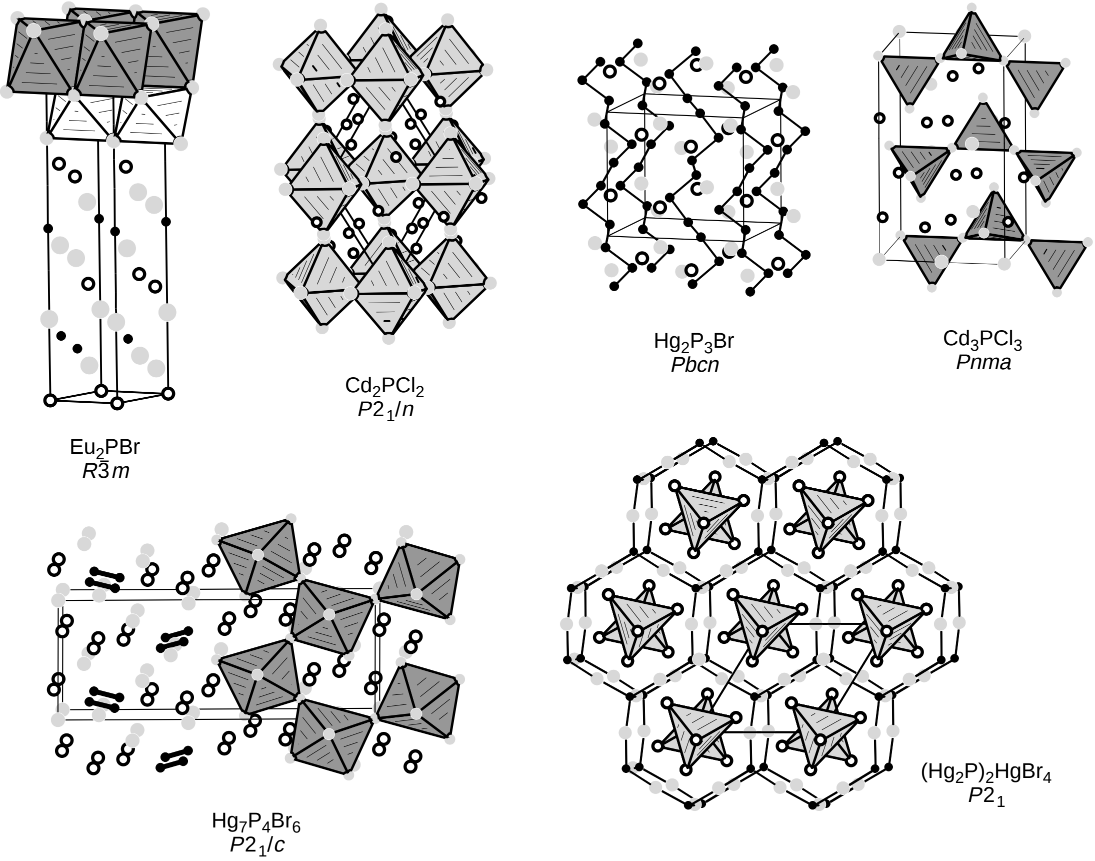

Figure 21 Crystal structures of various ternary phosphide halides. Europium (cadmium, mercury), phosphorus, and halogen atoms are drawn as large light grey, filled, and open circles, respectively. Some relevant coordination polyhedra around the phosphorus atoms and the P–P bonds are shown. The HgBr$_4$ tetrahedra in the (Hg$_2$P)$_2$HgBr$_4$ structure fill the channels of the three-dimensional [Hg$_2$P] network

with a $PBO = 0.5$, the charge is augmented even to $P_{12}{}^{15-}$. However, the discrepancies between composition, properties, and structure still need to be clarified.

6.7.3 *Hydrogenphosphides*

There are only few well defined examples of compounds being composed from a metal, phosphorus, and hydrogen. However, with the occurrence of new compounds it often was stated, that undiscovered hydrogen takes part in the formation of a compound. We will here not refer to the compounds, for example, monophosphane(3), diphosphane(4) and the higher phosphanes, as this has been reviewed by Baudler in a very comprehensive paper.[38] Despite the fact that the phosphines form numerous compounds, the compound LiP$_5$H$_4$ should be mentioned because the metalation of P$_2$H$_4$, especially with Li, gives access to a lot of other phosphanes.[250] The reaction of P$_2$H$_4$ in liq. NH$_3$ is a new route to polyphosphides and hydrogen phosphides.[251]

The alkali metals form the complete series of APH$_2$ compounds (A = Li → Cs) via preparation in liquid ammonia. These compounds can be described as derivatives from phosphine named as alkali metal phosphanide(2), or as alkali metal dihydrogen phosphide.[252,253] They show interesting phase transitions caused by rotation of the PH$_2$ moiety. However, owing to their extreme sensitivity against moisture and oxygen, these compounds have not been investigated further.

With A = Rb[254] and Cs,[255] compounds of the type A_2[PH] can be prepared containing an isolated hydrogenphosphide anion [PH]$^{2-}$, which could also be named for example, as dicesiumphosphanide(1), when starting from phosphane(3). The orientation of the PH unit could not be determined by X-ray analysis, but its existence has been proven by solid-state ^{1}H-NMR. The metal phosphide Ti$_3$P forms hydrides or deuterides up to a maximum content of 2.6 H (D). The exact crystal structure depends on the H (D) content and the temperature.[256] We note, that exact reliable studies of compounds M/P/H are very rare.

7 PHOSPHORUS–ARSENIC SUBSTITUTION

The only binary P/As compounds are the $(P_{1-x}As_x)_4$ molecules,[257] the limited mixed crystal series $P_{1-x}As_x$

of black phosphorus and gray arsenic,[258] and $P_{20}As$, a derivative of $P_{Hittorf}$, where As occupies special positions.[259] Arsenic can substitute phosphorus positions also in the neutral one-dimensional phosphorus chains of $Cu_2P_3I_2$ with a maximum substitution $Cu_2P_{1.8}As_{1.2}I_2$.[260] The mixed pnictogen modifications demonstrates an increased stability relative to $Cu_2P_3I_2$.

In metal phosphides, the substitution of P with As is much more common. A series of pyrite representatives $M^{IV}PAs$ are known (not given in the tables) with either statistically distributed $P_2{}^{4-}$ and $As_2{}^{4-}$ units, or statistically orientated $(PAs)^{4-}$ dumbbells. The molecule-like $P_7{}^{3-}$ anion, as well as the defect variants of the black phosphorus structure (EuP_3 etc.), shows complete miscibility. The whole series of valence tautomeric systems $(P_{1-x}As_x)_7{}^{3-}$ was proven to exist in ethylenediamine solutions of $Rb_3(P_{1-x}As_x)_7$ mixed crystals.[261] Mixed crystals in the whole range also exist with EuP_3, EuP_2, and EuP. A statistical distribution of P and As is found in the three different polyanionic substructures ${}^{2}_{\infty}(P_{1-x}As_x)_3{}^{2-}$, ${}^{1}_{\infty}(P_{1-x}As_x)_2$, and $(P_{1-x}As_x)_2{}^{2-}$. In $Eu(P_{1-x}As_x)_3$, a weak preference of As for the $(2b)P^-$ positions occurs, which form the most flexible part of the polymeric structure. During thermal decomposition the P:As ratio is changed systematically and in accordance with an enrichment of As in the solid with a smaller P:Eu ratio. With $Eu(P_{1-x}As_x)_2$, a structural phase transition takes place from the EuP_2 to the $EuAs_2$ type, which mainly differs in the conformation of the chains ${}^{1}_{\infty}(P^-)$.[262]

EuP belongs to the NaCl structure with Eu^{3+} and P^{3-}, but EuAs forms the Na_2O_2 structure with Eu^{2+} and $As_2{}^{4-}$. The polyanionic EuAs structure is stable in $EuP_{1-x}As_x$ mixed crystals within $0.05 \leq x \leq 1.00$.[263] The relationships are quite different in the strained helical polyanionic structures of LiP_7 and NaP_7, where the As atoms demonstrate a pronounced preference for the peripheral atomic positions of the ${}^{1}_{\infty}(P_{1-x}As_x)_7{}^{3-}$ helix. This distribution seems to be affected by structural strain more than by differences in polarity.[264]

Phosphorus–arsenic substitution can help to stabilize peculiar compounds that do not exist as binary phases. So far, a binary arsenide W_5As_4 has not been reported. Nevertheless, $W_5As_{2.5}P_{1.5}$[265] can be synthesized. It adopts the tetragonal Ti_5Te_4 type, as Mo_5As_4 does. Most likely radii criteria are responsible for the stability range of this pnictide which contains one-dimensional chains of vertex-shared W_6 clusters.

The $BaAl_4$ related phosphide $SrNi_2P_2$ has been investigated with respect to P/As substitution $SrNi_2P_{2-x}As_x$ up to $x = 1.25$.[266] The arsenic substitution has a drastic effect on the first-order phase transition of the $I4/mmm$ HT modification (at room temperature) to the $Immm$ LT modification (around 100 K), where the unit cell is tripled. The LT modification displays a modulation of shorter (246 pm) and longer (326 pm) P/As–P/As distances.

8 PHYSICAL PROPERTIES AND APPLICATIONS

For the determination of reliable physical data, the use of well defined and sufficiently sized single crystals is a necessary prerequisite (see Section 3). Even small amounts of impurity phases can irreversibly affect the property measurements.

8.1 Colors and Band Gaps

Metal phosphides cover the full range of colors from colorless to black, sometimes with metallic luster. The corresponding band gaps E_g are given for some compounds in Figure 22. General trends can be seen: (a) the band gap E_g is dependent on the polyanionic partial structure and increases with increasing P/M for comparable connectivities of P substructures; (b) E_g decreases with increasing charge $q(M)$ in comparable anionic structures; (c) within the same group, E_g decreases with the heavier cation; (d) transition metals seem to lower E_g; (e) with decreasing mean charge $q(P)$ (cf. family 4), one obtains a ‘diluted’ structure, and therefore larger E_g; (f) the interconnection of building units leads to a decrease of the gap; (g) tubular and infinite chain structures are related to the Hittorf violet P value (families 2 and 3); (h) the large spread of E_g values with isolated P^{3-} ions demonstrates the influence of cation charge P/M ratios, and electronegativity differences of P and M. It is not possible to derive the optical and electrical properties from the M/P ratio alone (metal rich, nonmetal rich); a detailed knowledge of the structures is necessary. Although semiconducting and even semimetallic behavior can be expected with compounds having distinct M–P, P–P, and M–M bonds, which can be derived from their structure and band structure calculations, these properties are not well understood (this is especially true for metallic compounds).

8.2 Superconductivity

Some phosphides are also superconducting (Table 10). Two interesting examples are the filled skutterudite $LaFe_4P_{12}$ as well as the ternary Fe_2P analogue ZrRuP with $T_c = 13\,K$. The ternary transition metal phosphides MoNiP (ZrNiAl type) and MoRuP (TiNiSi type) were prepared under high-pressure (4 GPa) high-temperature (1870 °C) conditions. Both phosphides show a transition to the superconducting state around 15.5 K. These are the so far highest T_c’s for metal phosphides.[267] The superconducting properties seem to arise from the Mo 4d electrons,[268] as the variety of Mo containing compounds indicates (Table 10). The $ZrFe_4Si_2$ type phosphides $ZrNi_4P_2$, $ZrRu_4P_2$, and $HfRu_4P_2$ have been prepared under high-temperature, high-pressure conditions. While no superconductivity could be detected for the nickel compounds down to 2 K, superconducting transitions are found at 11 K and 9.5 K for $ZrRu_4P_2$, and $HfRu_4P_2$, respectively. The upper critical field H_{c2} for $ZrRu_4P_2$ of 12.2 T at 0 K is remarkable.[269] The two superconducting modifications of ZrRuP have been

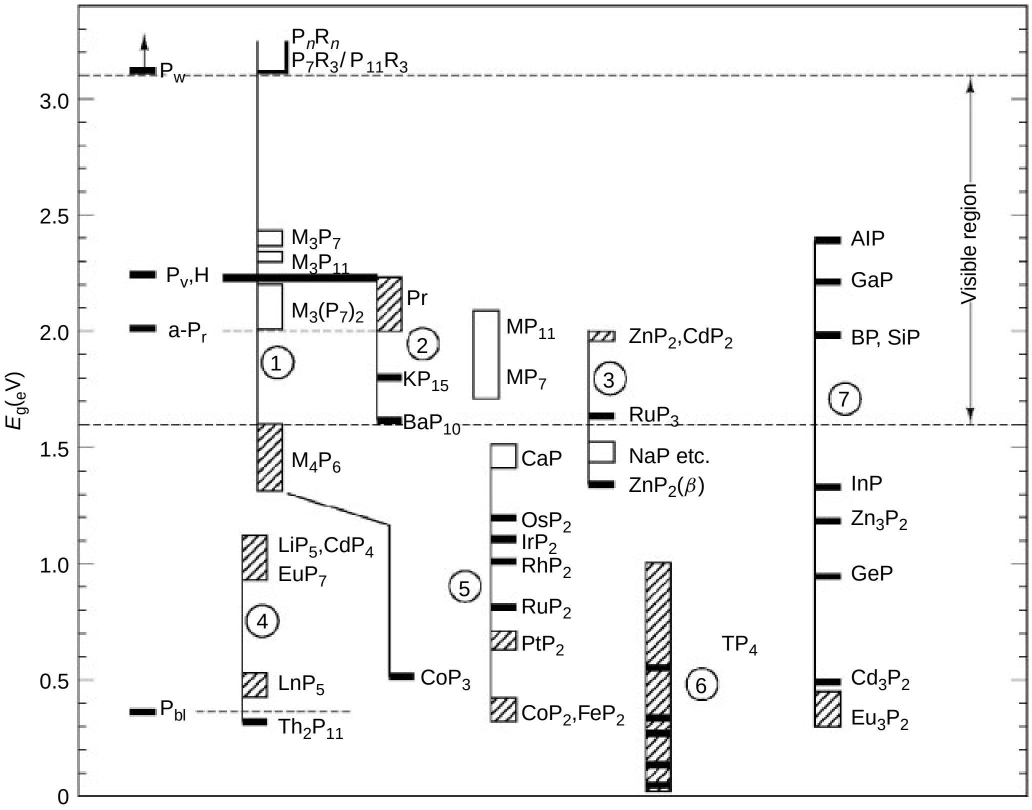

Figure 22 Ordering of E_g values according to structural relationships. Values estimated only from structure and color are represented by open rectangles. The structural correlations are (1) cycles and polycycles, (2) tubular and related structures, (3) infinite chain, (4) nets related to black phosphorus, (5) dumbbells, (6) nets with transition metals, and (7) isolated P^{3-}. Metallic phosphides are not given

Table 10 Superconducting materials

Phase	T_c (K)	Phase	T_c (K)
P_{met}	5.8[271]	Pd_7P_3[b]	0.70[272]
$(P_{1-x}As_x)_{met}$	≤10[273]	TiRuP	1.2[274]
$(GaP)_{met}$	9.3[275]	$ZrRuP_{ortho}$	3.76[270,276,277]
SnP	2.8–4.0[278]	$ZrRuP_{hex}$	13.0[270,276,277]
$ZrP_{0.95}$	≈4.6[279]	$ZrRu_4P_2$	11.0[269]
ZrP_2	(4.5)[274]	HfRuP	10.8[274]
TaP_2	0.4[269,280]	$HfRu_4P_2$	9.5[269]
$V_3(Si_{1-x}P_x)$	14.8–16.6[281]	TaRhP	4.7[277]
Mo_3P	∼7[282]	MoNiP	15.5[267,268]
Mo_4P_3	2.5[283]	MoRuP	15.5[267,268]
Mo_5P_8	5.8[282]	WNiP	∼5[267]
Mo_4P_3	3.0[282]	WRuP	∼5[267]
W_3P	2.76[282,284]	$LaFe_4P_{12}$	4.08[285]
Rh_2P	1.3[272]	$LaRu_4P_{12}$	7.20[285]
Rh_4P_3	1.22[283]	$LaRu_2P_2$	4.1[136]
Pd_7P_3[a]	1.00[272]		

[a] High-temperature form. [b] Low-temperature form.

reinvestigated by synchrotron X-ray diffraction. The hexagonal ZrNiAl modification becomes superconducting at 13 K while orthorhombic TiNiSi type *o*-ZrRuP has a T_c of approximately 4 K.[270] Details of the pressure-induced phase transitions have been reported. The superconductivity of GaP under pressure, as well as that of SnP, is also noteworthy (Sn ?). A famous example is the cubic high-pressure modification P_{cub} ($T_c = 5.8\,K$). T_c increases up to 10 K upon substitution with As.

8.3 Thermochemistry

Real information about the thermodynamic stability of solid phosphides is very rare.

The bright yellow higher alkali metal compounds M_3P_7 sublime congruently and dissociatively into their elements, $M_3P_7(s) = 3M(g) + \frac{7}{4}P_4(g)$ (cf. NH_4Cl), whereas Li_3P_7 decomposes to lower phosphides under similar conditions.[286] The large entropy contribution to the stability of these compounds makes them unique among alkali metal phosphides. The M_3P_7(s) compounds are stable with respect to both phosphorus-rich and metal-rich compounds in the corresponding system. The metal-richest alkali metal phosphides decompose stepwise by evaporation of metal up to the M_3P_7 formation. The phosphorus-richest alkali metal polyphosphides, MP_{15}(s), decompose under vacuum conditions in one step directly to the corresponding M_3P_7(s) phases. This is surprising, since there are many phases known between MP_{15} and M_3P_7. However, some experimental details indicate the intermediate formation of the other phases. The relative stability of the intermediate phases is strongly influenced by the unique behavior of the M_3P_7 phases, whose stability changes rapidly with pressure and temperatures. With respect to red phosphorus, the evaporation of P_4 from MP_{15} is strongly activated.

The heptaphosphides LnP_7 (La to Pr) decompose at about 600 K, forming the corresponding pentaphosphides.**[287]** At about 750 K, further decomposition starts, yielding the diphosphides. All other pentaphosphides LnP_5 (Nd to Lu) decompose directly to the monophosphides. The mean enthalpy for vaporizing one P_4(g) is about 150 kJ mol^{-1} for LnP_7, about 200 kJ mol^{-1} for LnP_5, and 170 kJ mol^{-1} for YbP_5 (α, β). Although, in general, the P_4(g) equilibrium pressure at a given temperature increases with decreasing cation radius, some irregularities obviously are affected by the electron configuration of Ln^{3+} as well as by the different stabilities of the decomposition products.

The binary system Eu/P is an example of phases with a negligible metal partial pressure.**[145]** The polyphosphides vaporize incongruently according to the reaction $a\mathrm{EuP}_m(\mathrm{s}) \rightarrow a\mathrm{EuP}_n(\mathrm{s}) + \mathrm{P}_4(\mathrm{g})$, where $a(m-n) = 4$. The stability regions of the europium polyphosphides are known from vapor pressure measurements demonstrating the large stability of β-EuP_3 and low stability of EuP_2. EuP_2 is only stable above 750 K and below that temperature β-EuP_3 decomposes directly to Eu_3P_4. From the stability regions one can derive appropriate methods of synthesis. It is interesting that the phosphorus-richest phases possess the largest atomic excess enthalpy. The entropy of formation per mole of P_4(g) during the vaporization reaction, ΔS (600 K), increases slowly from Eu_3P_4 to EuP_2, α-EuP_3, and violet Hittorf's phosphorus (131, 144, 162, and 175 J K^{-1} mol^{-1}), but is much larger for β-EuP_3 and EuP_7 (212 and 215 J K^{-1} mol^{-1}). This effect seems to be related to the phosphorus partial structures: there are, on one hand, short $P_4{}^{6-}$ chains, 1-D chains ${}^1_\infty(P^-)$, twistable 2-D nets ${}^2_\infty(P_3{}^{2-})$, and a strained network of connected tubes, but, on the other hand, 2-D polyanions with strain-free P_6 and P_8 rings.

From the heat capacities of LiP_{15} and KP_{15}, it was derived that the soft vibrational modes at low temperature are only affected by interaction between the metal cation and the six nearest neighbors.**[288]** Therefore, the covalently bonded $P_{15}{}^-$ tubes and the ionic interaction between the cation and the polyanion produce two distinctly separate sets of vibrational excitations (see below). At low temperatures, interchain vibrations occur, partially transmitted through the cations. At higher temperatures, intrachain vibrations, propagated through the covalently bonded tubes, are the dominant vibrational modes.

The thermal properties of the huge number of ternary or even quaternary phosphides have only scarcely been investigated. However, these data are important for planning the syntheses of new compounds. For example, the ternary skutterudite type phosphides do not melt congruently.

8.4 Magnetic Properties

The magnetic properties and Mössbauer spectra allow the characterization of the electronic state of transition metal and rare earth cations, which is necessary to prove the above mentioned electron transfer.**[8,289]** The polyphosphides allow the consecutive separation of magnetic cations to study electronic interactions and magnetic ordering phenomena. Magnetic phase transitions have been studied with rare earth monophosphides and others. All europium polyphosphides are Eu^{II} compounds, but in EuPtP the valence increases with decreasing temperature.**[290]** The pentaphosphides LnP_5 are Ln^{III} compounds. Deviations from the Curie–Weiss law are caused by: (i) transitions to magnetically ordered phases at low temperature (Sm, Gd, Dy, and Tb); (ii) crystal field splitting of the degenerate ground states (Ce, Nd, and Tm); and (iii) contributions of van Vleck's TIP (Sm and Pr). TbP_5 and DyP_5 order ferromagnetically within cation layers and antiferromagnetically, coupled via P atoms, between adjacent layers. The crystal field splitting, as well as the susceptibilities, can be simulated by assuming only two different interaction parameters, corresponding to (2b)P^- and (3b)P^0, respectively. With the mixed crystals $M(P_{1-x}As_x)_3$ ($M = $ Ca, Sr, Ba, Eu; $0 \leq x \leq 1$), the longitudinal Hall effect has been observed for the first time. The unexpected large anomalies in magnetoresistance are caused by the coexistence of the galvanomagnetic properties of group 15 elements and the magnetic properties of europium cations. Multiple magnetic phase transitions occur in the (T,B) phase diagrams, which are changed by pressure and x(As), and exhibit a rich variety of phenomena (paramagnetic, incommensurate ordered antiferromagnetic, spin-flop phases).**[145]**

The ternary phosphides show an extremely large variety of magnetic phenomena. With the diamagnetic rare earth elements scandium, yttrium, lanthanum, and lutetium, the rare earth–transition metal–phosphides are mostly Pauli paramagnets. The small susceptibility contribution arises from the conduction electrons of these metallic compounds. This is also the case for related phosphides with titanium, zirconium, or hafnium as the electropositive component. In some peculiar cases, the transition metal atoms carry the magnetic moments. Interesting examples are the 125 K ferromagnet $LaCo_2P_2$**[291]** or the 113 K antiferromagnet $CaCo_2P_2$.**[292]** In the calcium compound, the cobalt magnetic moments order ferromagnetically in the basal plane, but these planes order antiferromagnetically along the c axis, corresponding to a propagation vector $\mathbf{k} = (0, 0, 1)$. Also, some of the $RE_2Co_{12}P_7$ phosphides show magnetic moments on the cobalt atoms.**[293]** A highly interesting phosphide in this context is $EuCo_2P_2$, where a transition from the 4f Eu local moment to 3d Co itinerant magnetism occurs under an applied pressure of 3.1 GPa.**[294]**

The families of equiatomic phosphides CeTP, EuTP, and YbTP have thoroughly been investigated with respect to valence changes or mixed-valency. All these data are reviewed in recent articles.[14,295–297] Also, the families of RET_2P_2 and $RE_2T_{12}P_7$ phosphides have intensively been studied with respect to their magnetic properties by Jeitschko and coworkers. Most data are summarized in the review by Kuz'ma.[14] Crystal growth of the RET_2P_2 and $RE_2T_{12}P_7$ phosphides from a tin flux offers the possibility to measure the susceptibilities || and ⊥ to the crystallographic *c* axis. Numerous magnetic structures of the RET_2P_2 and $RE_2T_{12}P_7$ phosphides have been determined from neutron diffraction data. Figure 23 gives an overview of the different magnetic cobalt substructures in MCo_2P_2 (M = Ca, Sr, Ce, Pr, Eu).[292]

Various cerium and uranium-based phosphides have been studied with respect to the magnetic ordering phenomena. A remarkable compound is Ce_2AuP_3 that orders ferromagnetically with a relatively high Curie temperature of 31 K. Some of the uranium phosphides have comparatively high magnetic ordering temperatures that approximately scale with the structure type and the uranium content (Figure 24).[298]

8.5 Vibrational Spectra and Optical Applications

Raman and IR spectra of polyphosphides clearly show the separation of internal and external modes (Figure 25). The external modes are strongly pressure and temperature dependent, whereas the internal cluster modes are nearly unaffected. In the plastically crystalline phases of M_3P_7 and M_3P_{11} the external modes disappear completely.[299] The internal modes are still present in the melt, demonstrating molecule-like behavior as well as the high thermal stability of those polycyclic anions. With solid Rb_4P_6 and Cs_4P_6, the vibrational behavior of P_6^{4-} is like that of benzene! The vibrations of the 1-D tubular polymers P_{15}^- in KP_{15}, and the corresponding ones in Hittorf's phosphorus, are separated in a very similar way.[300] They can be assigned to the structural fragments P_7, P_8, and P_9. Vibrational spectra of amorphous red phosphorus prove the presence of similar tubes with P_8 and P_9, as well as of P_7 cages of the nortricyclane type.

In 2-D corrugated polyanionic nets (α-EuP_3), the separation of vibrations is still present. The high-frequency modes are mainly associated with vibrations within the layer, whereas the low-frequency modes are dominated by M–P vibrations.

High-quality single crystals of $ZnGeP_2$ can be synthesized from the binary zinc and germanium phosphides. $ZnGeP_2$ is used for infrared laser radiation frequency conversion.[301] Binary indium phosphide InP is an important material for optoelectronic and electronic devices as well.[302] In this context, the interactions of various transition metals with InP have thoroughly been investigated in order to check for potential high-temperature contacts to InP.

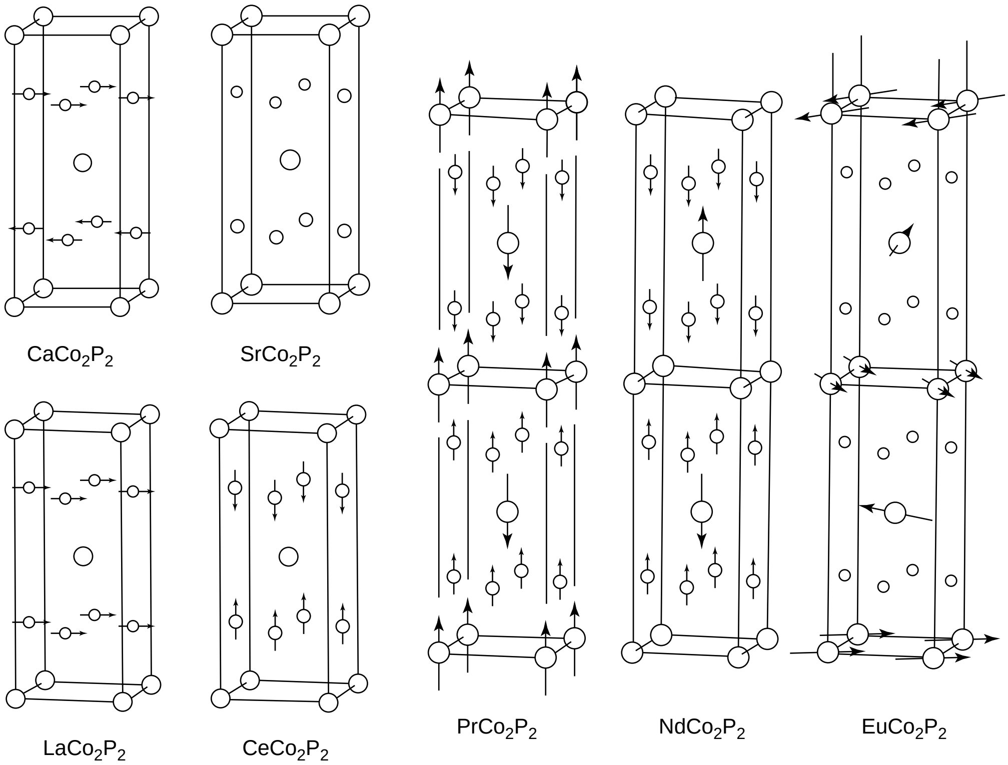

Figure 23 Magnetic structures of the phosphides ACo_2P_2 (A = Ca, Sr, La, Ce, Pr, Nd, Eu). The cobalt atoms (small circles) with their ordered magnetic moments are shown together with the A atoms (large circles), which are in the positions (0 0 0) and (1/2 1/2 1/2) of the body-centered nuclear cell (from Reehuis *et al.*[292])

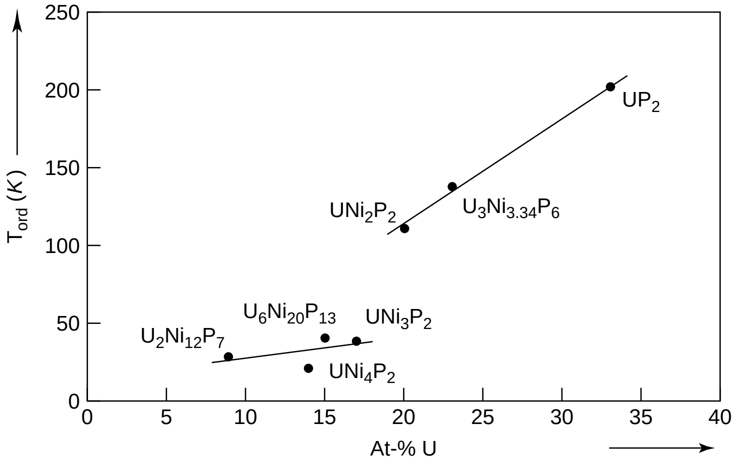

Figure 24 Magnetic ordering temperatures of uranium nickel phosphides with crystal structures belonging to two different structural families (from Ebel *et al.*[298])

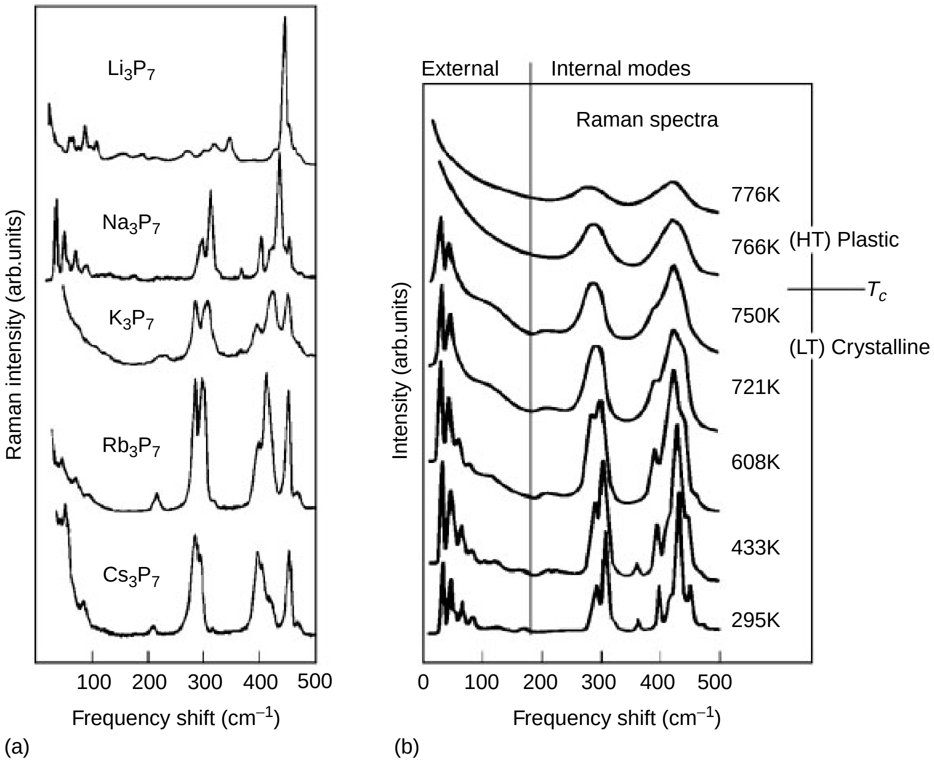

Figure 25 (a) Raman spectra of solid M_3P_7 (M = Li, Na, K, Rb, Cs) and (b) temperature-dependent Raman spectra of Na_3P_7, indicating the first-order phase transition at T_c from the low-temperature (LT) crystalline α-phase to the high-temperature (HT) plastically crystalline β-phase. Note the disappearing of the sharp external lattice modes just above T_c

8.6 Phase Transitions with Temperature and Pressure

Phase transitions with temperature and pressure have mostly been studied with simple (binary) compounds.[303,304] There is a complete lack of systematic studies. Some phase transitions with temperature have been discussed.[114,145,299,305] Pressure-induced phase transitions, for example, of SiP, GeP, ZnP_2, and europium phosphides, have been reported.[124,306] Eu_4P_3 undergoes a phase transition from the rhombohedral phase ($Eu_4P_3 \equiv Eu^{II}_3Eu^{III}P_3$) into Eu_4P_3 with Th_3P_4 type structure at 8(1) GPa, where the average oxidation state of Eu is still noninteger.[307] α-Co_2P (*oP*12, Co_2Si type) undergoes a reconstructive phase transformation at 1428 K into β-Co_2P (*hP*9, Fe_2P type) before it melts at 1659 K. Among this big class of compounds, β-Co_2P is the only known high-temperature phase. Furthermore, it shows the highest axial ratio c/a and the smallest distortion of the *hcp* structure.[308]

The monophosphides REP (RE = La, Ce, Pr, Nd, Sm, Gd, Tb, Tm, Yb) crystallize in the NaCl-type structure at ambient pressure. All of them undergo phase transitions, some into a tetragonally distorted CsCl related structure (La, Pr, Nd) and the others into a more complicated unknown high-pressure phase (Sm, Gd, Tb, Tm, Yb) at pressures from 35 to 51 GPa, respectively.[309] It might be that a disproportionation occurs, similar to that in Eu_2As_2.[310]

The Mo phosphides have not only been investigated because of their interesting superconducting properties (see Section 8.2) but also because of their potential catalytic activity for hydroprocessing of crude oil (see Section 8.8). The high-temperature powder diffraction of MoP_2 indicates decomposition into unknown products above 839 K. The high-pressure experiment indicates that no phase transition occurs up to 6.8 GPa. Even the pressure dependance of the bulk modulus shows no anomaly for this compound, indicating that MoP_2 cannot be regarded as a layered compound.[311]

Some of the tetragonal RET_2P_2 phosphides have been investigated under high-pressure conditions. To give an example, $SrRh_2P_2$ shows an extremely anisotropic compressibility, with a much stronger decrease of the c lattice parameter.[312] This leads to a decrease of the P–P distance from 328 pm at ambient pressure to 231 pm at 6.8 GPa, thus strongly influencing the chemical bonding from isolated P^{3-} ions to ${P_2}^{4-}$ pairs.[313] It is fundamental to note that upon oxidation of phosphorus ($P^{3-} \rightarrow P^{2-} + e^-$), the rhodium atoms are reduced. Other RET_2P_2 phosphides show continuous decrease of the lattice parameters.

The cluster compounds $[Ag_6M^{II}_4P_{12}]Ge_6$ with M^{II} = Ge, Sn show at low temperatures a valence fluctuation of the inner core ${Ag_6}^{4+}$, which can be seen in the elastic behavior[314] and vibrational anharmonicity[315] as well as in the measurements of the specific heat.[316] The valence fluctuations generate a pronounced Schottky anomaly, which can be emphasized more clearly by the comparison and therefore possible normalisation of cluster compounds.

8.7 Thermoelectrics – Skutterudites

Although the first filled skutterudites were already synthesized in the late 1970s by Jeitschko and coworkers,[317] this class of phosphides has found renewed interest in recent years with respect to the outstanding thermoelectric properties. However, the thermoelectric properties of the filled skutterudites with the higher homologues arsenic and antimony are superior to the phosphides. Most of the research on filled lanthanide skutterudites has recently been reviewed by Uher,[318] Nolas *et al.*[319] and Sales.[320] Besides the thermoelectric properties, filled skutterudites have attracted considerable interest because of their rich variety of electronic and magnetic ground states, such as heavy-fermion mediated superconductivity, ferro- or antiferromagnetism, hybridization gaps (Kondo insulator behavior), non-Fermi-liquid behavior and quantum critical points, quadrupolar ordering, and field-induced heavy-fermion states.[321] The binary cobalt skutterudite CoP_3 can take up lithium with a reversible capacity of 400 mAh/g at an average potential of 0.9 V versus Li/Li^+.[322]

8.8 Catalysis

Various catalytically active transition metal phosphides, for example, Co_2P, Ni_2P, MoP, WP, CoMoP, or NiMoP, can be prepared from metal oxide/phosphate or nitrate/ammonium metatungstate precursors by reduction in a hydrogen flow.[323,324] The product selectivities of these phosphides resemble those of classical sulfidic catalysts. Typical application areas are reactions such as the hydrodenitrogenation of *o*−propylaniline at 3 MPa and 643 K. The cobalt phosphide Co_2P has been tested as a hydrodesulfurization (HDS) catalyst[325] for fuel purification. The phosphide is prepared on a silica matrix. In technical HDS catalysts, it is assumed that transition metal phosphides form as reactive species on the catalysts surface. Amorphous Ni_2P can be used in heterogeneous catalysis.[326] Fine powders can be obtained by reaction of aqueous nickel chloride with sodium hypophosphite using highly diluted sodium borohydride to initiate the reduction.

The semiconducting polyphosphide RuP_3 has shown to possess a photoelectric reactivity, which is traced back to the presence of Ru pairs with metal−metal bonds. This working hypothesis of the presence of two adjacent metal centers as a prerequisite for catalytic properties has shown to be very powerful.[327]

8.9 Precipitation hardening

The ternary phosphide FeTiP (mineral name florenskyite), recently discovered in the Kaidun meterorite,[328] is responsible for precipitation hardening in certain interstitial-free ferritic steels.[329] FeTiP (Fe_2P type structure) is a very stable compound. Chemical bonding is governed by strong metal−phosphorus interactions. Similar ternary phosphides occur also as precipitations in Pd–Ni–Cu–P glassy alloys modified by addition of Cr, Mo, Fe, or Ta.[330] The phosphides NiCrP, MoNiP, FeNiP, and (Pd, Ta)NiP with Fe_2P type structure strongly influence the microstructure and the mechanical properties of the glassy alloys. Binary iron phosphides are also the source for PH_3 generation on wet commercial ferrosilicon alloys.[331]

9 RELATED ARTICLES

Arsenic: Inorganic Chemistry; Borides: Solid-state Chemistry; Carbides: Transition Metal Solid-state Chemistry; Chalcogenides: Solid-state Chemistry; Electronic Structure of Solids; Mixed Valence Compounds; Phosphorus: Inorganic Chemistry; Thin Film Synthesis of Solids; Zintl Compounds.

10 REFERENCES

1. B. Aronsson, T. Lundström, and S. Rundquist, 'Borides, Silicides and Phosphides', Methuen, London, 1965.
2. D. E. C. Corbridge, 'The Structural Chemistry of Phosphorus', Elsevier, Amsterdam, NY, 1974.
3. D. E. C. Corbridge, 'Phosphorus', Elsevier, Amsterdam, NY, 1978; 'Phosphorus: An Outline of its Chemistry, Biochemistry and Technology', 4th edn., Elsevier, Amsterdam, NY, 1990.
4. H. G. von Schnering, in 'Homoatomic Rings, Chains and Macromolecules of Main Group Elements', ed. A. L. Rheingold, Elsevier, Amsterdam, NY, 1977, Chap. 14.
5. H. G. von Schnering, *Angew. Chem.*, 1981, **93**, 44; *Angew. Chem., Int. Ed. Engl.*, 1981, **20**, 33.
6. H. G. von Schnering, *Nova Acta Leopold. N. F.*, 1985, **59**, 165; *ACS Symp. Ser.*, 1983, **232**, 69.
7. W. Jeitschko, *Int. Rev. Sci., Inorg. Chem., Ser. Two*, 1974, **5**, 219.
8. F. Hulliger, *Struct. Bonding*, 1968, **4**, 83; K. A. Gschneidner Jr and L. Eyring eds, 'Handbook on the Physics and Chemistry of Rare Earths', North-Holland, Amsterdam, NY, 1979, Chap. 33; F. Hulliger, in 'Structural Chemistry of Layer-type Phases', ed. F. Levy, Reidel, Dordrecht, 1976; F. Hulliger, in 'Structure and Bonding in Crystals', eds. M. O'Keeffe and A. Navrotsky, Academic Press, New York, 1981, Vol. II, Chap. 26; V. I. Kosyakov and I. G. Vasil'eva, *Russ. Chem. Rev. (Engl. Transl.)*, 1979, **48**, 153.
9. 'Inorganic Crystal Structure Database', FIZ Karlsruhe; F. H. Allen, G. Bergerhoff, and R. Sievers, 'Crystallographic Databases', International Union of Crystallography, Chester, 1987.
10. P. Villars and L. D. Calvert, 'Pearson's Handbook of Crystallographic Data for Intermetallic Phases', 2nd edn., American Society for Metals, Metals Park, Ohio, 1991, and desk edition, 1997.
11. W. B. Pearson, 'The Crystal Chemistry and Physics of Metals and Alloys', Wiley, New York, 1972.
12. B. G. Hyde and S. Andersson, 'Inorganic Crystal Structures', Wiley, New York, 1989.
13. K. Schubert, 'Kristallstrukturen Zweikomponentiger Phasen', Springer, Berlin, 1964.
14. Yu. Kuz'ma and S. Chykhrij, Phosphides, in 'Handbook on the Physics and Chemistry of Rare Earths', eds, K. A. Gschneidner Jr and L. Eyring, Elsevier, Amsterdam, NY, 1996, Vol. 23, Chap. 156.
15. S. Chykhrij, *Pol. J. Chem.*, 1999, **73**, 1595.
16. H. G. von Schnering and W. Hönle, *Chem. Rev.*, 1988, **88**, 243.
17. W. Jeitschko, U. Flörke, M. H. Möller, and R. Rühl, *Ann. Chim. Fr.*, 1982, **7**, 413.
18. SciFinder Scholar version 2004, http://www.cas.org/SCIFINDER/SCHOLAR/.
19. E. Zintl, *Angew. Chem.*, 1939, **52**, 1; S. Chykhrij, *Pol. J. Chem.*, 1999, **73**, 1595; G. Brauer and E. Zintl, *Z. Phys. Chem., Abt. B*, 1937, **37**, 323; W. Klemm, *Proc. Chem. Soc., London*, 1958, 329; W. Klemm, *Trab. Reun. Int. React. Sólidos*, 1956, **1**, 447.
20. S. M. Kauzlarich ed., 'Chemistry, Structure, and Bonding of Zintl Phases and Ions', VCH, New York, 1996.
21. E. Mooser and W. B. Pearson, *Phys. Rev.*, 1956, **101**, 1608.
22. G. Gassmann and D. Glindemann, *Angew. Chem.*, 1993, **105**, 749; *Angew. Chem., Int. Ed. Engl.*, 1993, **32**, 761.
23. O. Buresch, W. Hönle, and H. G. von Schnering, *Fres. Z. Anal. Chem.*, 1986, **325**, 607.
24. W. Hönle and H. G. von Schnering, *Inorg. Synth.*, 1995, **30**, 56.
25. H. Schäfer and M. Trenkel, *Z. Anorg. Allg. Chem.*, 1972, **391**, 11.
26. P. Jolibois, *C.R. Seances Acad. Sci.*, 1910, **150**, 106; Yu. Kuz'ma and S. Chykhrij, Phosphides, in 'Handbook on the Physics and Chemistry of Rare Earths', eds, K. A. Gschneidner Jr and L. Eyring, Elsevier, Amsterdam, NY, 1996, Vol. 23, Chap. 156. and references cited therein; R. Kaner, C. A. Castro, R. P. Gruska, and A. Wold, *Mater. Res. Bull.*, 1977, **12**, 1143.
27. M. G. Kanatzidis, R. Pöttgen, and W. Jeitschko, *Angew. Chem.*, in press.
28. A. Wurth, A. Lohken, and A. Mewis, *Z. Anorg. Allg. Chem.*, 2002, **628**, 661.
29. A. T. Nientiedt and W. Jeitschko, *J. Solid State Chem.*, 1999, **146**, 478.
30. (a) H. Kleinke and H. F. Franzen, *J. Solid State Chem.*, 1997, **131**, 379; (b) H. Kleinke and H. F. Franzen, *J. Solid State Chem.*, 1998, **136**, 221; (c) H. Kleinke and H. F. Franzen, *J. Alloys Compd.*, 1997, **255**, 110.
31. I. Shirotani, Y. Shimaya, K. Kihou, Ch. Sekine, and T. Yagi, *J. Solid State Chem.*, 2003, **174**, 32.
32. T. P. Martin, *Angew. Chem.*, 1986, **98**, 197; *Angew. Chem., Int. Ed. Engl.*, 1986, **25**, 197.
33. Y. A. Ugai, O. Y. Gukov, and A. A. Illarionov, *Izv. Akad. Nauk SSSR, Neorg. Mater.*, 1978, **14**, 1012; R. Glaum and R. Gruehn, *Z. Kristallogr.*, 1987, **178**, 72; U. Flörke, *Z. Anorg. Allg. Chem.*, 1983, **502**, 218; M. W. Richardson and B. Noläng, *J. Cryst. Growth*, 1977, **42**, 90; K.-Th. Wilke, J. Bohm, 'Kristallzüchtung', Verlag Harri Deutsch, Thun, Frankfurt/Main, 1988.

34. R. Gruehn and R. Glaum, *Angew. Chem. Int. Ed. Engl.*, 2000, **39**, 692.

35. M. Fujii, H. Iwanaga, and S. Motojima, *J. Cryst. Growth*, 1996, **166**, 99.

36. O. J. Scherer, *Angew. Chem.*, 1985, **97**, 905; 1990, **102**, 1137.

37. C. Hugot, *C. R. Seances Acad. Sci.*, 1895, **121**, 207; E. C. Evers, *J. Am. Chem. Soc.*, 1951, **73**, 2038; P. Royen and H. Zschaage, *Z. Naturforsch.*, 1953, **8B**, 777; G. Fritz and W. Hölderich, *Naturwissenschaften*, 1975, **62**, 573.

38. M. Baudler, *Angew. Chem.*, 1987, **99**, 429; *Angew. Chem., Int. Ed. Engl.*, 1987, **26**, 419; M. Baudler, *Angew. Chem.*, 1982, **94**, 520; *Angew. Chem., Int. Ed. Engl.*, 1982, **21**, 492; M. Baudler, *Pure Appl. Chem.*, 1980, **52**, 755; *ACS Symp. Ser.*, 1981, **171**, 261; *Z. Chem.*, 1984, **24**, 352; M. Baudler and K. Glinka, *Chem. Rev.*, 1993, **93**, 1623.

39. W. Hönle, V. Manriquez, C. Mujica, D. Weber, and H. G. von Schnering, 29th IUPAC Congress, Köln, 1983, Abstr., 36.

40. F. Kraus, J. C. Aschenbrenner, and N. Korber, *Angew. Chem., Int. Ed. Engl.*, 2003, **42**, 4029.

41. D. Knettel, M. Reil, and N. Korber, *Z. Naturforsch.*, 2001, **56b**, 965.

42. Y. Xie, H. L. Su, X. F. Xian, X. M. Liu, and Y. T. Qian, *J. Solid State Chem.*, 2000, **149**, 88.

43. X. F. Quian, Y. Xie, Y. T. Quian, X. M. Zhang, W. Z. Wang, and L. Yang, *Mater. Sci. Eng., B*, 1997, **49**, 135.

44. V. Zuzaniuk, C. Stinner, R. Prins, and Th. Weber, *Stud. Surf. Sci. Catal.*, 2002, **143**, 247.

45. K. L. Stamm and S. L. Brock, 225th ACS National Meeting, New Orleans, March 2003, Abstract INOR−242.

46. C. M. Lukehart, S. B. Milne, and S. R. Stock, *Chem. Mater.*, 1998, **10**, 903.

47. C. M. Lukehart, S. B. Milne, S. R. Stock, and J. E. Wittig, *Trends Inorg. Chem.*, 1996, **4**, 9.

48. V. V. Lesnyak, D. A. Straiichuk, V. S. Sudavtsova, and M. S. Slobodyanik, *Russ. J. Appl. Chem.*, 2001, **74**, 1274.

49. J. Gopalakrishnan, S. Pandey, and K. K. Rangan, *Chem. Mater.*, 1997, **9**, 2113.

50. S. K. Zecevic, J. B. Zotovic, S. Lj. Gojkovic, and V. Radmilovic, *J. Electrochem. Chem.*, 1998, **448**, 245.

51. D. J. Olego, J. Baumann, R. Schachter, C. Michel, M. Kuck, S. Gersten, and L. G. Polgar, *Phys. Rev. B*, 1985, **31**, 2240.

52. D. Bellavance, M. Vlasse, B. Morris, and A. Wold, *J. Solid State Chem.*, 1969, **1**, 275; H. Hartmann and J. Orban, *Z. Anorg. Allg. Chem.*, 1936, **226**, 257.

53. J. H. Albering, *Z. Kristallogr.*, 1998, **Suppl. 15**, 23.

54. A. Brown and S. Rundquist, *Acta Crystallogr.*, 1965, **19**, 684; A. Morita, *Appl. Phys.*, 1986, **A39**, 227 and references cited therein.

55. H. Thurn and H. Krebs, *Acta Crystallogr.*, 1969, **B25**, 125.

56. W. Klemm and H. G. von Schnering, *Z. Anorg. Allg. Chem.*, 1982, **491**, 9; W. Biltz and W. Klemm, in 'Raumchemie der festen Stoffe', ed. W. Biltz, Leopold-Voss-Verlag, Leipzig, 1934.

57. G. Fritz, K. D. Hoppe, W. Hönle, D. Weber, C. Mujica, V. Manriquez, and H. G. von Schnering, *J. Organomet. Chem.*, 1983, **249**, 63; C. Mujica, D. Weber, and H. G. von Schnering, *Z. Naturforsch.*, 1986, **41B**, 991.

58. W. Schmettow, A. Lipka, and H. G. von Schnering, *Angew. Chem.*, 1974, **86**, 10; *Angew. Chem., Int. Ed. Engl.*, 1974, **13**, 5; H.-P. Abicht, W. Hönle, and H. G. von Schnering, *Z. Anorg. Allg. Chem.*, 1984, **519**, 7; H. G. von Schnering, T. Meyer, W. Hönle, W. Schmettow, W. Hinze, W. Bauhofer, and G. Kliche, *Z. Anorg. Allg. Chem.*, 1987, **553**, 261.

59. W. Hönle, H. G. von Schnering, A. Schmidtpeter, and G. Burget, *Angew. Chem.*, 1984, **96**, 796; *Angew. Chem., Int. Ed. Engl.*, 1984, **23**, 817.

60. N. Korber and J. Daniels, *Z. Anorg. Allg. Chem.*, 1996, **622**, 1833.

61. N. Korber and J. Daniels, *Z. Anorg. Allg. Chem.*, 1999, **625**, 189.

62. N. Korber and J. Daniels, *Acta Crystallogr. C*, 1996, **52**, 2454.

63. N. Korber, J. Daniels, and H. G. von Schnering, *Angew. Chem.*, 1996, **108**, 1188.

64. N. Korber and H. G. von Schnering, *Chem. Ber.*, 1996, **129**, 155.

65. J. C. Aschenbrenner and N. Korber, *Z. Anorg. Allg. Chem.*, 2004, **630**, 31.

66. D. Knettel, M. Reil, and N. Korber, *Z. Naturforsch., B*, 2001, **56**, 965.

67. N. Korber and J. Aschenbrenner, *J. Chem. Soc., Dalton Trans.*, 2001, 1665.

68. N. Korber and J. Daniels, *Helv. Chim. Acta*, 1996, **79**, 2083.

69. N. Korber and F. Richter, *Chem. Commun.*, 1996, 2023.

70. N. Korber and J. Daniels, *J. Chem. Soc., Dalton Trans.*, 1996, 1653.

71. N. Korber and J. Daniels, *Polyhedron*, 1996, **16**, 2681.

72. T. Wadsten, *Chem. Scr.*, 1975, **8**, 63.

73. J. Gullman, *J. Solid State Chem.*, 1990, **87**, 202.

74. M. Hartweg, U. Hartweg, and H. G. von Schnering, unpublished results.

75. R. Cardoso-Gil, Darstellung, Struktur und Eigenschaften der Pnictide M_3X (M = Cu, Li, Na, K; X = P, As, Sb, Bi), von Sr_5P_4, KLiAs, $Rb_7[NbAs_4]$, sowie $Na_{16}Rb_6MSb_7$ mit dem Anion M^- (M = Rb, I, Na, Au), Universität Stuttgart, 1994.

76. H. G. von Schnering and M. Wittmann, unpublished results.

77. O. Olofsson, *Acta Chem. Scand.*, 1970, **24**, 1153.

78. P. Eckerlin and W. Kischio, *Z. Anorg. Allg. Chem.*, 1968, **363**, 1.

79. M. Somer, T. Popp, K. Peters, and H. G. von Schnering, *Z. Kristallogr.*, 1991, **193**, 281.

80. M. Somer, M. Hartweg, K. Peters, and H. G. von Schnering, *Z. Kristallogr.*, 1990, **192**, 263; M. Somer, M. Hartweg,

K. Peters, and H. G. von Schnering, *Z. Anorg. Allg. Chem.*, 1991, **595**, 217.

81. B. Eisenmann and M. Somer, *Z. Kristallogr.*, 1990, **193**, 217; B. Eisenmann and M. Somer, *Z. Naturforsch.*, 1989, **B44**, 1228.
82. B. Eisenmann, J. Klein, and M. Somer, *Z. Kristallogr.*, 1991, **197**, 277.
83. A. Czybulka, M. Noack, and H.-U. Schuster, *Z. Anorg. Allg. Chem.*, 1992, **609**, 122.
84. M. Somer, M. Hartweg, K. Peters, and H. G. von Schnering, *Z. Kristallogr.*, 1990, **193**, 291.
85. B. Eisenmann, J. Klein, and M. Somer, *Angew. Chem.*, 1990, **102**, 92.
86. W. Blase, G. Cordier, and M. Somer, *Z. Kristallogr.*, 1991, **195**, 121.
87. M. Somer, L. Walz, D. Thiery, and H. G. von Schnering, *Z. Kristallogr.*, 1990, **193**, 303.
88. W. Blase, G. Cordier, and M. Somer, *Z. Kristallogr.*, 1991, **195**, 123.
89. J. Armand, Doktorabeit, Darstellung, Struktur und Eigenschaften von $Eu_5In_2As_6$; Eu_3InAs_3; $Eu_3In_2P_4$; $Na_3Eu_3AlP_4$ und Li_4EuP_2, Fachhochschule Burgsteinfurt, 1989.
90. J. Nuβ, W. Hönle, and H. G. von Schnering, unpublished results.
91. H. G. von Schnering, M. Hartweg, H. Kalpen, J. Nuβ, and W. Hönle, *Z. Kristallogr.*, 1988, **182**, 238.
92. J. Lin, W. Hönle, and H. G. von Schnering, *J. Alloys Compd.*, 1992, **183**, 403.
93. B. Eisenmann, J. Klein, and M. Somer, *Z. Kristallogr.*, 1991, **197**, 269.
94. M. Somer, K. Peters, and H. G. von Schnering, *Z. Anorg. Allg. Chem.*, 1992, **613**, 19.
95. B. Eisenmann and J. Klein, *J. Less-Common Met.*, 1991, **175**, 109.
96. W. Blase, G. Cordier, and M. Somer, *Z. Kristallogr.*, 1991, **195**, 119.
97. P. Kaiser and W. Jeitschko, *Z. Naturforsch. B*, 1997, **52**, 462.
98. P. Kaiser and W. Jeitschko, *J. Solid State Chem.*, 1996, **124**, 346.
99. Ch. Perrier, H. Vincent, P. Chaudouët, B. Chenevier, and R. Madar, *Mater. Res. Bull.*, 1995, **30**, 357.
100. M. Kirschen, H. Vincent, Ch. Perrier, P. Chaudouët, B. Chenevier, and R. Madar, *Mater. Res. Bull.*, 1995, **30**, 507.
101. P. Kaiser and W. Jeitschko, *Z. Kristallogr.*, 1996, **Suppl. 11**, 100.
102. C. Hadenfeldt and F. Bartels, unpublished results.
103. B. Eisenmann, H. Jordan, and H. Schäfer, *Z. Naturforsch.*, 1982, **B37**, 1221.
104. H. G. von Schnering and M. Wittmann, *Z. Naturforsch.*, 1980, **356**, 824.
105. S. Rundquist, *Acta Chem. Scand.*, 1962, **16**, 287; R. Guérin, M. Sergent, and J. Prigent, *J. Mater. Res. Bull.*, 1975, **10**, 975.
106. H. G. von Schnering and G. Menge, *Z. Anorg. Allg. Chem.*, 1981, **481**, 33.
107. W. Hönle and H. G. von Schnering, *Z. Kristallogr.*, 1980, **153**, 339.
108. W. Jeitschko and M. H. Möller, *Acta Crystallogr.*, 1979, **B35**, 573.
109. W. Wichelhaus and H. G. von Schnering, *Naturwissenschaften*, 1973, **60**, 104; H. G. von Schnering, M. Somer, G. Kliche, W. Hönle, T. Meyer, J. Wolf, L. Ohse, and P. B. Kempa, *Z. Anorg. Allg. Chem.*, 1991, **601**, 13.
110. M. H. Möller and W. Jeitschko, *Inorg. Chem.*, 1981, **20**, 828.
111. M. V. Dewalsky and W. Jeitschko, *Acta Chem. Scand.*, 1991, **45**, 828.
112. A. Pfitzner, S. Reiser, and T. Nilges, *Angew. Chem.*, 2000, **112**, 4328.
113. S. Nilges, T. Nilges, H. Haeuseler, and A. Pfitzner, *J. Mol. Struct.*, 2004, **706**, 89.
114. H. G. von Schnering, Int. Conf. Phosph. Chem., Collect. Abstr., Halle/Saale, Pergamon Press, 1979, 199; H. G. von Schnering, W. Hönle, V. Manriquez, T. Meyer, Ch. Mensing, and W. Giering, 2nd. Int. Conf. Solid State Chem., Collect. Abstr. FV 54, Eindhoven, 1982; W. Hönle, V. Manriquez, and H. G. von Schnering, *Z. Kristallogr.*, 1983, **162**, 104; W. Hönle, T. Meyer, Ch. Mensing, and H. G. von Schnering, *Z. Kristallogr.*, 1985, **170**, 78; T. K. Chattopadhyay, W. May, H. G. von Schnering, and G. S. Pawley, *Z. Kristallogr.*, 1983, **165**, 47.
115. R.-D. Hoffmann and R. Pöttgen. *Z. Kristallogr.*, 2001, **216**, 127; R. Nesper, H. G. von Schnering, *Tschermaks Mineral. Petrogr. Mitteilungen*, 1983, **32**, 195.
116. H. G. von Schnering and W. Dahlmann, *Naturwissenschaften*, 1971, **58**, 623.
117. U. Flörke and W. Jeitschko, *Inorg. Chem.*, 1983, **22**, 1736.
118. H. G. von Schnering, M. Wittmann, and R. Nesper, *J. Less-Common Met.*, 1980, **76**, 213.
119. J. Gullman and O. Olofsson, *J. Solid State Chem.*, 1972, **5**, 441.
120. P. C. Donohue and H. S. Young, *J. Solid State Chem.*, 1970, **1**, 143.
121. N. Kinomura, K. Terao, S. Kikkawa, H. Horiuchi, and M. Koizumi, *Mater. Res. Bull.*, 1983, **18**, 53.
122. S. Rundquist and N. O. Ersson, *Ark. Kemi*, 1969, **30**, 103.
123. S. Rundquist, *Ark. Kemi*, 1962, **20**, 67.
124. J. Osugi, R. Namikawa, and Y. Tanaka, *Rev. Phys. Chem. Jpn.*, 1966, **36**, 35; T. Wadsten, *Acta Chem. Scand.*, 1967, **21**, 593.
125. H. Hayakawa, S. Ono, A. Kobayashi, and Y. Sasaki, *Nippon Kagaku Kaishi*, 1978, **9**, 1214.
126. F. Hulliger, R. Schmelczer, and D. Schwarzenbach, *J. Solid State Chem.*, 1977, **21**, 371.

127. W. Hönle and H. G. von Schnering, *Z. Kristallogr.*, 1987, **179 & 180**, 443.

128. R. Rühl and W. Jeitschko, *Acta Crystallogr.*, 1982, **B38**, 2784.

129. R. Rühl and W. Jeitschko, *Inorg. Chem.*, 1982, **21**, 1886.

130. M. Elfström, *Acta Chem. Scand.*, 1965, **19**, 1694.

131. D. J. Braun and W. Jeitschko, *Acta Crystallogr.*, 1978, **B34**, 2069; W. Jeitschko and W. K. Hofmann, *J. Less-Common Met.*, 1983, **95**, 317.

132. R. Rühl and W. Jeitschko, *Monatsh. Chem.*, 1983, **144**, 817.

133. F. Hulliger, *Nature*, 1963, **198**, 382.

134. J. K. Kom, J. Flahaut, and L. Domange, *Compt. Rend.*, 1962, **255**, 701.

135. T. Wadsten, *Acta Chem. Scand.*, 1967, **21**, 1374; P. C. Donohue, W. J. Siemons, and J. L. Gillson, *J. Phys. Chem. Solids*, 1968, **29**, 817; T. K. Chattopadhyay and H. G. von Schnering, *Z. Kristallogr.*, 1984, **167**, 1.

136. W. Jeitschko, U. Meisen, M. H. Möller, and M. Reehuis, *Z. Anorg. Allg. Chem.*, 1985, **527**, 73; W. K. Hofmann and W. Jeitschko, *J. Solid State Chem.*, 1984, **51**, 152; W. Jeitschko and B. Jaberg, *J. Solid State Chem.*, 1980, **35**, 312; W. Jeitschko and W. K. Hofmann, *J. Less-Common Met.*, 1983, **95**, 317; A. Mewis, *Z. Naturforsch.*, 1984, **B39**, 713; A. Mewis, *Z. Naturforsch.*, 1980, **B35**, 141; G. Wenski and A. Mewis, *Z. Naturforsch.*, 1986, **B41**, 38; W. Jeitschko, R. Glaum, and L. Boonk, *J. Solid State Chem.*, 1987, **69**, 93.

137. H. G. von Schnering and D. Vu, *J. Less-Common Met.*, 1986, **116**, 259.

138. U. Meisen and W. Jeitschko, *Z. Kristallogr.*, 1984, **167**, 135.

139. M. V. Dewalsky, W. Jeitschko, and U. Wortmann, *Chem. Mater.*, 1991, **3**, 316.

140. W. Hönle, J. Lin, M. Hartweg, and H. G. von Schnering, *J. Solid State Chem.*, 1992, **97**, 1.

141. C. Hadenfeldt, H. U. Terschüren, W. Hönle, L. Schröder, and H. G. von Schnering, *Z. Anorg. Allg. Chem.*, 1993, **619**, 843.

142. H. G. von Schnering, M. Hartweg, U. Hartweg, and W. Hönle, *Angew. Chem.*, 1989, **101**, 98; W. Hönle, M. Hartweg, U. Hartweg, and H. G. von Schnering, *Z. Kristallogr.*, 1989, **186**, 131.

143. J. Nuss and M. Jansen, *Z. Anorg. Allg. Chem.*, 2003, **629**, 387.

144. W. Dahlmann and H. G. von Schnering, *Naturwissenschaften*, 1973, **60**, 518; W. Dahlmann and H. G. von Schnering, *Naturwissenschaften*, 1973, **60**, 429; H. G. von Schnering and W. Dahlmann, *Naturwissenschaften*, 1971, **58**, 623.

145. M. Wittmann and H. G. von Schnering, 5th Eur. Cryst. Meet., Collect. Abstr., Copenhagen, 1979, 80-P1-5a; W. Schmettow, Ch. Mensing, and H. G. von Schnering, *Z. Anorg. Allg. Chem.*, 1984, **510**, 51; W. Bauhofer, E. Gmelin, M. Möllendorf, R. Nesper, and H. G. von Schnering, *J. Phys. C: Solid State Phys.*, 1985, **18**, 3017.

146. J. Schmedt auf der Günne, S. Kaczmarek, L. van Wüllen, H. Eckert, D. Paschke, A. J. Foecker, and W. Jeitschko, *J. Solid State Chem.*, 1999, **147**, 341.

147. H. G. von Schnering and W. Wichelhaus, *Naturwissenschaften*, 1972, **59**, 78.

148. O. Olofsson, *Acta Chem. Scand.*, 1965, **19**, 229.

149. M. H. Möller and W. Jeitschko, *Z. Anorg. Allg. Chem.*, 1982, **491**, 225.

150. P. Kaiser and W. Jeitschko, *Z. Anorg. Allg. Chem.*, 1996, **622**, 53.

151. M. H. Möller and W. Jeitschko, *J. Solid State Chem.*, 1986, **65**, 178.

152. W. Wichelhaus, Chemie und Strukturchemie von Polyphosphiden der Lithiums und Natriums, Universität Münster, 1973; H. G. von Schnering and H. Schmidt, *Angew. Chem.*, 1967, **79**, 323; R. P. Santandrea, Ch. Mensing, and H. G. von Schnering, *Thermochim. Acta*, 1987, **117**, 261.

153. H. G. von Schnering, H. Schmidt, and D. Makus, unpublished results.

154. W. Schmettow, Über die Phosphide der Rubidiums, Universität Münster, 1975.

155. H. Krebs, I. Pakulla, and G. Zürn, *Z. Anorg. Allg. Chem.*, 1955, **278**, 274; H. Krebs and Th. Ludwig, *Z. Anorg. Allg. Chem.*, 1958, **294**, 275.

156. W. Ott, Über Synthesen und Strukturen von Polyphosphiden, Universität Stuttgart, 1977; U. D. Scholz and W. Jeitschko, *J. Solid State Chem.*, 1987, **67**, 271.

157. H. G. von Schnering, W. Hönle, and A. Schwarz, unpublished results.

158. M. Eschen, J. Wallinda, and W. Jeitschko, *Z. Anorg. Allg. Chem.*, 2002, **628**, 2764.

159. O. Olofsson and J. Gullman, *Acta Chem. Scand.*, 1971, **25**, 1327.

160. H. G. von Schnering and G. Menge, *Z. Anorg. Allg. Chem.*, 1982, **491**, 286.

161. H. G. von Schnering and W. Wichelhaus, *Naturwissenschaften*, 1972, **59**, 78; N. Korber and J. Aschenbrenner, *J. Chem. Soc., Dalton Trans.*, 2001, 1665.

162. W. Hönle, Über niedere Phosphide, Arsenide und Antimonide der Alkalimetalle, Universität Münster, 1975.

163. A. Pfitzner, *Chem. – Eur. J.*, 2000, **6**, 1891.

164. A. Pfitzner and E. Freudenthaler, *Z. Naturforsch. B*, 1997, **52**, 199.

165. A. Pfitzner and E. Freudenthaler, *Z. Kristallogr.*, 1995, **210**, 59.

166. E. Freudenthaler and A. Pfitzner, *Z. Kristallogr.*, 1997, **212**, 103.

167. M. Häser, ‘Systematik der Phosphorgerüste, eine theoretische Untersuchung’. Habilitationsschrift, Karlsruhe 1996; St. Böcker and M. Häser, *Z. Anorg. Allg. Chem.*, 1995, **621**, 358.

168. A. Pfitzner, S. Reiser, and H.-J. Deiseroth, *Z. Anorg. Allg. Chem.*, 1999, **625**, 2196.

169. A. Pfitzner and S. Reiser, *Inorg. Chem.*, 1999, **38**, 2451.

170. E. Freudenthaler, A. Pfitzner, and D. C. Sinclair, *Mater. Res. Bull.*, 1996, **31**, 171.
171. E. Freudenthaler and A. Pfitzner, *Solid State Ionics*, 1997, **101 – 103**, 1053.
172. C. Möschel and M. Jansen, *Z. Anorg. Allg. Chem.*, 1999, **625**, 175.
173. B. Pietzak, A. Weidinger, K.-P. Dinse, and A. Hirsch, *Dev. Fullerene Sci.*, 2002, **3**, 13.
174. I. Wyn Locke, A. D. Darwish, H. W. Kroto, K. Prassides, R. Taylor, and D. R. M. Walton, *Chem. Phys. Lett.*, 1994, **225**, 186.
175. E. Ganglberger, *Monatsh. Chem.*, 1968, **99**, 557.
176. W. Jeitschko and R. O. Altmeyer, *Z. Naturforsch. B*, 1990, **45**, 947.
177. A. Nylund, *Acta Chem. Scand.*, 1966, **20**, 2393.
178. S. Anugul, C. Pentchour, and S. Rundqvist, *Acta Chem. Scand.*, 1973, **27**, 26.
179. Yu. Prots' and W. Jeitschko, *Inorg. Chem.*, 1998, **37**, 5431.
180. J. Y. Pivan and R. Guérin, *J. Solid State Chem.*, 1998, **135**, 218; C. Le Sénéchal, V. Babizhets'ky, S. Députier, J. Y. Pivan and R. Guérin, *J. Solid State Chem.*, 1999, **144**, 277.
181. C. Le Sénéchal, V. Babizhets'ky, S. Députier, J.-Y. Pivan, and R. Guérin, *Z. Anorg. Allg. Chem.*, 2001, **627**, 1325.
182. W. Jeitschko and U. Jakubowski-Ripke, *Z. Kristallogr.*, 1993, **207**, 69.
183. B. I. Zimmer and W. Jeitschko, *Z. Kristallogr.*, 1994, **209**, 950.
184. J. H. Albering and W. Jeitschko, *J. Solid State Chem.*, 1995, **117**, 80.
185. J. H. Albering and W. Jeitschko, *Z. Naturforsch. B*, 1992, **47**, 1521.
186. J. H. Albering and W. Jeitschko, *J. Alloys Compd.*, 1996, **241**, 44.
187. G. Brauer, K. Gingerich, and M. Knausenberger, *Angew. Chem.*, 1964, **76**, 187; H. Bärnighausen, M. Knausenberger, and G. Brauer, *Acta Crystallogr.*, 1965, **19**, 1.
188. H. G. von Schnering and K. G. Häusler, *Rev. Chim. Miner.*, 1976, **13**, 71; W. Hönle and H. G. von Schnering, *Z. Kristallogr.*, 1979, **149**, 125.
189. E. Gmelin, W. Hönle, Ch. Mensing, H. G. von Schnering, and K. Tentschev, *J. Therm. Anal.*, 1989, **35**, 2509.
190. M. M. Shatruk, K. A. Kovnir, A. V. Shevelkov, and B. A. Popovkin, *Angew. Chem.*, 2000, **112**, 2561.
191. T. Lundström, *Acta Chem. Scand.*, 1968, **22**, 2191.
192. S. Rundqvist, *Acta Chem. Scand.*, 1960, **14**, 893.
193. R. Rühl, U. Flörke, and W. Jeitschko, *J. Solid State Chem.*, 1984, **53**, 55.
194. E. Parthé, B. Chabot, and K. Cenzual, *Chimia*, 1985, **39**, 164.
195. S. Andersson, *Angew. Chem.*, 1983, **95**, 67.
196. D. Johrendt and A. Mewis, *Z. Anorg. Allg. Chem.*, 1995, **621**, 57.
197. L. Frik and A. Mewis, *Z. Anorg. Allg. Chem.*, 1999, **625**, 126.
198. D. Johrendt and A. Mewis, *Z. Anorg. Allg. Chem.*, 1992, **607**, 169.
199. C. Lux, G. Wenski, and A. Mewis, *Z. Naturforsch. B*, 1991, **46**, 1035.
200. J. H. Albering and W. Jeitschko, *Z. Naturforsch. B*, 1996, **51**, 257.
201. Yu. B. Kuz'ma, S. I. Chykhrij, Yu. A. Mozharivskyj, W. Tremel, and R. O. Demchyna, *J. Alloys Compd.*, 1998, **278**, 169.
202. Yu. Mozharivskyj and Yu. B. Kuz'ma, *J. Solid State Chem.*, 2000, **151**, 150.
203. A. Mewis, *Z. Naturforsch.*, 1980, **35b**, 141.
204. Ch. Zheng and R. Hoffmann, *Z. Naturforsch.*, 1986, **41b**, 292.
205. Ch. Zheng, *J. Am. Chem. Soc.*, 1993, **115**, 1047.
206. R. Hoffmann, 'Solids and Surfaces: A Chemist's View of Bonding in Extended Structures', VCH, New York, 1988.
207. G. Just and P. Paufler, *J. Alloys Compd.*, 1996, **232**, 1.
208. D. Schmitz and W. Bronger, *Z. Anorg. Allg. Chem.*, 1987, **553**, 248.
209. H. G. von Schnering, R. Türck, W. Hönle, K. Peters, E.-M. Peters, R. Kremer, and J.-H. Chang, *Z. Anorg. Allg. Chem.*, 2002, **628**, 2772.
210. Y. Wang, L. D. Calvert, and J. B. Taylor, *Acta Crystallogr. B*, 1980, **36**, 220.
211. C. Hadenfeld and H. O. Vollert, *J. Less-Common Met.*, 1988, **144**, 143.
212. C. Hadenfeld and H. Herdejürgen, *Z. Anorg. Allg. Chem.*, 1988, **558**, 35.
213. C. Hadenfeld and H.-U. Terschüren, *Z. Anorg. Allg. Chem.*, 1991, **597**, 69.
214. S. L. Brock and S. M. Kauzlarich, *Comments Inorg. Chem.*, 1995, **17**, 213.
215. J. W. Kaiser and W. Jeitschko, *Z. Naturforsch.*, 2002, **57b**, 165.
216. A. V. Shevelkov, M. Yu. Mustyakimov, E. V. Dikarev, and B. A. Popovkin, *J. Chem. Soc., Dalton Trans.*, 1996, 147.
217. A. V. Olenev, O. S. Oleneva, A. V. Shevelkov, and B. A. Popovkin, *Russ. Chem. Bull. Int. Ed.*, 2003, **52**, 147.
218. K. E. Maass, *Z. Anorg. Allg. Chem.*, 1970, **374**, 1.
219. K. E. Maass, *Z. Anorg. Allg. Chem.*, 1970, **374**, 19.
220. N. T. Stetson and S. M. Kauzlarich, *Inorg. Chem.*, 1991, **30**, 3969.
221. J. Lin, W. Hönle, and H.-G. von Schnering, *J. Alloys Compd.*, 1992, **178**, 455.
222. J. H. Albering and W. Jeitschko, *J. Solid State Chem.*, 1995, **117**, 80.
223. M. Lulei, *Z. Anorg. Allg. Chem.*, 1997, **623**, 1796.

224. J. H. Albering and W. Jeitschko, *Z. Naturforsch.*, 1996, **51b**, 257.

225. D. Kaczorowski, J. H. Albering, H. Noël, and W. Jeitschko, *J. Alloys Compd.*, 1994, **216**, 117.

226. A. T. Nientiedt, W. Jeitschko, P. G. Pollmeier, and M. Brylak, *Z. Naturforsch.*, 1997, **52b**, 560.

227. B. I. Zimmer, W. Jeitschko, J. H. Albering, R. Glaum, and M. Reehuis, *J. Alloys Compd.*, 1995, **229**, 238.

228. A. T. Nientiedt and W. Jeitschko, *Inorg. Chem.*, 1998, **37**, 386.

229. D. Kaczorowski, M. Potel, and H. Noël, *J. Solid State Chem.*, 1994, **112**, 228.

230. R. J. Cava, H. W. Zandbergen, J. J. Krajewski, T. Siegrist, H. Y. Hwang, and B. Batlogg, *J. Solid State Chem.*, 1997, **129**, 250.

231. C. Hadenfeldt and W. Held, *J. Less-Common Met.*, 1986, **123**, 25.

232. C. Hadenfeldt and W. Kosiol, *Z. Naturforsch.*, 1975, **30b**, 378.

233. H. Raffius, B. D. Mosel, W. Müller-Warmuth, U. Pegelow, C. Hadenfeldt, W. Jeitschko, and T. Vomhof, *J. Phys. Chem. Solids*, 1994, **55**, 219.

234. A. V. Shevelkov, E. V. Dikarev, and B. A. Popovkin, *Russ. J. Inorg. Chem.*, 1997, **42**, 1121.

235. A. V. Shevelkov, M. Yu. Mustyakimov, E. V. Dikarev, and B. A. Popovkin, *J. Chem. Soc., Dalton Trans.*, 1996, 147.

236. A. V. Olenev, O. S. Oleneva, A. V. Shevelkov, and B. A. Popovkin, *Russ. Chem. Bull.*, 2003, **52**, 570.

237. A. V. Shevelkov, E. V. Dikarev, and B. A. Popovkin, *J. Solid State Chem.*, 1993, **104**, 177.

238. A. V. Shevelkov, E. V. Dikarev, and B. A. Popovkin, *Z. Kristallogr.*, 1994, **209**, 583.

239. P. C. Donohue, *J. Solid State Chem.*, 1972, **5**, 71.

240. H. G. von Schnering and H. Menke, *Angew. Chem.*, 1972, **84**, 30.

241. H. Menke and H. G. von Schnering, *Naturwissenschaften*, 1972, **59**, 420.

242. H. Menke and H. G. von Schnering, *Z. Anorg. Allg. Chem.*, 1973, **395**, 223.

243. M. M. Shatruk, K. A. Kovnir, A. V. Shevelkov, I. A. Presnyakov, and B. A. Popovkin, *Inorg. Chem.*, 1999, **38**, 3455.

244. M. M. Shatruk, K. A. Kovnir, and A. V. Shevelkov, VIIth European Conference On Solid State Chemistry. Book of Abstracts. Madrid, 1999, O11.

245. M. M. Shatruk, K. A. Kovnir, A. V. Shevelkov, and B. A. Popovkin, *Russ. J. Inorg. Chem. (Zh. Neorg. Chem.)*, 2000, **45**, 203.

246. M. M. Shatruk, K. A. Kovnir, M. Lindsjoe, I. A. Presniakov, L. A. Kloo, and A. V. Shevelkov, *J. Solid State Chem.*, 2001, **161**, 233.

247. L. N. Reshetova, J. V. Zaikina, A. V. Shevelkov, K. A. Kovnir, M. Lindsjo, and L. Kloo, *Z. Anorg. Allg. Chem.*, 2002, **628**, 2145.

248. K. A. Kovnir, J. V. Zaikina, A. V. Olenev, L. N. Reshetova, A. V. Shevelkov, E. V. Dikarev, N. Senthikumaran, F. Haarmann, and M. Baenitz, IXth European Conference On Solid State Chemistry. Book of Abstracts, Stuttgart, 2003, P115.

249. J. Dünner and A. Mewis, *Z. Anorg. Allg. Chem.*, 1995, **621**, 191.

250. M. Baudler, R. Heumüller, and W. Faber, *Z. Naturforsch.*, 1995, **50b**, 786.

251. M. Baudler and P. Winzek, *Z. Anorg. Allg. Chem.*, 1999, **625**, 417.

252. H. Jacobs and K. M. Hassiepen, *Z. Anorg. Allg. Chem.*, 1985, **531**, 108.

253. G. Bergerhoff and E. Schultze-Rhonhof, *Acta Crystallogr.*, 1962, **15**, 420.

254. M. Somer, W. Carillo Cabrera, E.-M. Peters, K. Peters, and H. G. von Schnering, *Z. Kristallogr. – NCS*, 1997, **212**, 299.

255. H. G. von Schnering, M. Somer, K. Peters, W. Carillo Cabrera, and Y. Grin, *Z. Kristallogr. – NCS*, 2001, **216**, 42.

256. T. Larsson, P.-J. Ahlzen, Y. Andersson, S. Rundqvist, and R. Tellgren, *J. Alloys Compd.*, 1996, **236**, 26.

257. G. A. Ozin, *J. Chem. Soc. A*, 1970, 2307.

258. W. Klemm and I. V. Falkowski, *Z. Anorg. Allg. Chem.*, 1948, **256**, 343.

259. W. Hönle and H. G. von Schnering, unpublished results.

260. B. Jayasekera, J. A. Aitken, M. J. Heeg, and S. L. Brock, *Inorg. Chem.*, 2003, **42**, 658.

261. W. Hönle and H. G. von Schnering, *Angew. Chem.*, 1986, **98**, 370; *Angew. Chem., Int. Ed. Engl.*, 1986, **25**, 352.

262. W. Schmettow, D. Sommer, Ch. Mensing, and H. G. von Schnering, 2. Vortragstagung der Fachgruppe Festkörperchemie der GDCh, Stuttgart, 1980.

263. A. Werner, H. D. Hochheimer, M. Wittmann, H. G. von Schnering, and E. Hinze, *J. Less-Common Met.*, 1982, **87**, 327.

264. W. Hönle and H. G. von Schnering, IVth Eur. Crystallogr. Meet. Oxford, Collect. Abstr. B, University of Oxford, 1977, 552.

265. F. Charki, S. Députier, P. Bénard-Rocherulle, R. Guérin, and E. H. El Ghadraoui, *J. Solid State Chem.*, 1997, **131**, 310; P. Bénard-Rocherulle, S. Députier, F. Charki, and R. Guérin, *Powder Diffraction*, 1999, **14**, 126.

266. V. Keimes, A. Hellmann, D. Johrendt, A. Mewis, and Th. Woike, *Z. Anorg. Allg. Chem.*, 1998, **624**, 830.

267. I. Shirotani, M. Takaya, I. Kaneko, Ch. Sekine, and T. Yagi, *Solid State Commun.*, 2000, **116**, 683.

268. I. Shirotani, M. Takaya, I. Kaneko, Ch. Sekine, and T. Yagi, *Physica C*, 2001, **357–360**,(Part 1), 329.

269. I. Shirotani, G. Iwasaki, I. Kaneko, Ch. Sekine, S. Todo, and T. Yagi, *Solid State Commun.*, 1997, **104**, 217.

270. I. Shirotani, K. Tachi, N. Ichihashi, T. Adachi, T. Kikegawa, and O. Shimomura, *Phys. Lett. A*, 1995, **205**, 77.

271. I. V. Berman and N. B. Brandt, *Zh. ETF Pis. Red.*, 1968, **7**, 412; *Sov. Phys. JETP Lett.*, 1968, **7**, 323; J. Wittig and B. T. Matthias, *Science*, 1968, **160**, 994.

272. Ch. J. Raub, W. H. Zachariasen, T. H. Geballe, and B. T. Matthias, *J. Phys. Chem. Solids*, 1963, **24**, 1093.

273. I. Shiritani, K. Tsuburaya, K. Itakura, C. W. Lee, S. Shiba, H. Kawamura, and T. Yagi, *Synth. Met.*, 1989, **29**, 635.

274. G. R. Stewart, G. P. Meisner, and H. C. Ku, 'Proceedings Superconductivity in d- and f-Band Metals', eds. W. Weber and W. Buckel, Kernforschungszentrum, Karlsruhe, 1982, p. 331.

275. Yu. A. Timofeev, B. V. Vinogradov, and E. N. Yakovlev, *Sov. J. Low Temp. Phys.*, 1981, **7**, 717.

276. G. P. Meisner and H. C. Ku, *Appl. Phys. A*, 1983, **31**, 201.

277. R. Mueller, R. N. Shelton, J. W. Richardson Jr, and R. A. Jacobson, *J. Less-Common Met.*, 1983, **92**, 177.

278. P. C. Donohue, *Inorg. Chem.*, 1970, **9**, 335.

279. A. R. Moodenbaugh, D. C. Johnston, and R. Viswanathan, *Mater. Res. Bull.*, 1974, **9**, 1671.

280. K. Andres, G. W. Hull, and F. Hulliger, *Mater. Sci.*, 1972, **7**, 344.

281. J. Hallais, *Ann. Chim.*, 1971, **7**, 309.

282. I. Shirotani, I. Kaneko, M. Takaya, C. Sekine, T. Yagi, *Physica B*, 2000, **281&282**, 1024; R. D. Blaugher, J. K. Hulm, and P. N. Yocom, *J. Phys. Chem. Solids*, 1965, **26**, 2037.

283. Z. Fisk, unpublished results.

284. R. D. Blaugher and J. K. Hulm, unpublished results.

285. G. P. Meisner, *Physica B + C*, 1981, **108**, 763.

286. R. P. Santandrea, Ch. Mensing, and H. G. von Schnering, *Thermochim. Acta*, 1986, **98**, 301.

287. H. G. von Schnering and Ch. Mensing, unpublished results.

288. R. P. Santandrea, E. Gmelin, C. Santandrea, and H. G. von Schnering, *Thermochim. Acta*, 1983, **67**, 263.

289. J. Rossat-Mignod, P. Burlet, S. Quezel, and J. M. Effantin, *Ann. Chim. Fr.*, 1982, **7**, 471.

290. C. Lux, A. Mewis, N. Lossau, G. Michels, and W. Schlabitz, *Z. Anorg. Allg. Chem.*, 1991, **593**, 169.

291. M. Reehuis, C. Ritter, R. Ballou, and W. Jeitschko, *J. Magn. Magn. Mater.*, 1994, **138**, 85.

292. M. Reehuis, W. Jeitschko, G. Kotzyba, B. Zimmer, and X. Hu, *J. Alloys Compd.*, 1998, **266**, 54.

293. M. Reehuis, B. Ouladdiaf, W. Jeitschko, T. Vomhof, B. Zimmer, and E. Ressouche, *J. Alloys Compd.*, 1997, **261**, 1; M. Reehuis, N. Stüßer, A. Nientiedt, T. Ebel, W. Jeitschko, and B. Ouladdiaf, *J. Magn. Magn. Mater.*, 1998, **177 – 181**, 805.

294. M. Chefki, M. M. Abd-Elmeguid, H. Micklitz, C. Huhnt, W. Schlabitz, M. Reehuis, and W. Jeitschko, *Phys. Rev. Lett.*, 1998, **80**, 802.

295. R. Pöttgen and D. Johrendt, *Chem. Mater.*, 2000, **12**, 875.

296. R. Pöttgen, D. Johrendt, and D. Kussmann, 'Handbook on the Physics and Chemistry of Rare Earths', eds. K. A. Gschneider, Jr, L. Eyring, and G. H. Lander, Elsevier Science, Amsterdam, NY, 2001, Chap. 207.

297. T. Iwasaki, A. Sekiyama, A. Yamasaki, M. Okazaki, K. Kadono, H. Ztsunomiya, S. Imada, Y. Saitoh, T. Matsushita, H. Harima, S. Yoshii, M. Kasaya, A. Ochiai, T. Oguchi, K. Katoh, Y. Niide, K. Takegahara, and S. Suga, *Phys. Rev. B*, 2002, **65**, 195109.

298. T. Ebel, J. H. Albering, and W. Jeitschko, *J. Alloys Compd.*, 1998, **266**, 71.

299. W. Henkel, K. Strössner, H. D. Hochheimer, W. Hönle, and H. G. von Schnering, 'Proceeding of the 8th Internatioanl Conference Raman Spectrum., Bordeaux 1982', Wiley, New York, 1982; F. Bolduan, W. Hönle, H. D. Hochheimer, and W. Henkel, *Phys. Status Solidi*, 1985, **B132**, 41.

300. G. Fasol, M. Cardona, W. Hönle, and H. G. von Schnering, *Solid State Commun.*, 1984, **52**, 307.

301. Yu. M. Andreev, G. A. Veruzubova, A. I. Gribenyukov, and V. V. Korotkova, *J. Korean. Phys. Soc.*, 1998, **33**, 356.

302. S. E. Mohney, *J. Electron. Mater.*, 1998, **27**, 24.

303. L. Merrill, *J. Phys. Chem. Ref. Data*, 1977, **6**, 1205.

304. L. Gerward, J. Staun Olsen, U. Benedict, S. Dabos-Seignon, and H. Luo, *High Temp.-High Press.*, 1990, **22**, 523; Y. Okayama, H. Takahashi, N. Mori, Y. S. Kwon, Y. Haga, and T. Suzuki, *J. Magn. Magn. Mater.*, 1992, **108**, 113; J. Staun Olsen, L. Gerward, U. Benedict, H. Luo, and O. Vogt, *J. Appl. Crystallogr.*, 1989, **22**, 61; V. A. Rubtsov, E. M. Smolyarenko, V. M. Trukhan, V. N. Yakimovich, and L. K. Orlik, *Cryst. Res. Technol.*, 1989, **24**, 55.

305. C. Lux, A. Mewis, N. Lossau, G. Michels, and W. Schlabitz, *Z. Anorg. Allg. Chem.*, 1991, **593**, 169.

306. T. Chattopadhyay, J. Voiron, and H. Bartholin, *J. Magn. Magn. Mater.*, 1988, **72**, 35; A. Jayaraman, R. G. Maines, and T. Chattopadhyay, *Pramana*, 1986, **27**, 291.

307. R. Cardoso-Gil, R. Niewa, M. Schmidt, M. Armbrüster, M. Hanfland, K. Klementiev, and U. Schwarz, *Z. Anorg. Allg. Chem.*, 2003, **629**, 454.

308. M. Ellner and E. J. Mittemeijer, *Z. Anorg. Allg. Chem.*, 2001, **627**, 2257.

309. T. Adachi, I. Shirotani, and O. Shimomura, *Japan. Nippon Kessho Gakkaishi*, 1999, **41**, 146.

310. A. Werner, H. D. Hochheimer, M. Wittmann, H. G. von Schnering, and E. Hinze, *J. Less-Common Met.*, 1982, **87**, 327.

311. V. Soto, K. Knorr, L. Ehm, C. Baehtz, B. Winkler, and M. Avalos-Borja, *Z. Kristallogr.*, 2004, **219**, 309.

312. A. Wurth, D. Johrendt, A. Mewis, C. Huhnt, G. Michels, M. Röpke, and W. Schlabitz, *Z. Anorg. Allg. Chem.*, 1997, **623**, 1418; C. Huhnt, G. Michels, M. Röpke, W. Schlabitz, A. Wurth, D. Johrendt, and A. Mewis, *Phys. Rev. B: Condens. Matter*, 1997, **240**, 26.

313. I. B. Shameem Banu, M. Rajagopalan, and G. Vaintheeswaran, *Solid State Commun.*, 2000, **116**, 451.

314. J. E. Macdonald, G. A. Saunders, Y. K. Yogurtcu, and W. Hönle, *J. Phys. Chem. Solids*, 1985, **46**, 951.

315. J. D. Comins, C. Heremans, M. D. Salleh, G. A. Saunders, and W. Hönle, *J. Mater. Sci. Lett.*, 1986, **5**, 1195.

316. E. Gmelin, W. Hönle, H. G. von Schnering, and K. Tentschev, *J. Therm. Anal.*, 1989, **35**, 2509.

317. W. Jeitschko and D. Braun, *Acta Crystallogr. B*, 1977, **33**, 3401; D. Braun and W. Jeitschko, *J. Less-Common Met.*, 1980, **72**, 147; D. Braun and W. Jeitschko, *J. Solid State Chem.*, 1980, **32**, 357; D. Braun and W. Jeitschko, *J. Less-Common Met.*, 1980, **76**, 33.

318. C. Uher, ‘Semiconductors and Semimetals’, Academic Press, San Diego, 2001, p. 139. Vol. 69, Chap. 5.

319. G. S. Nolas, D. T. Morelli, and T. M. Tritt, *Annu. Rev. Mater. Sci.*, 1999, **29**, 89.

320. B. C. Sales, *MRS Bulletin*, 1998, **23**, 15.

321. B. C. Sales, ‘Handbook on the Physics and Chemistry of Rare Earths’, eds. K. A. Gschneider, Jr, J.-C. G. Bünzli, and V. K. Pecharsky, Elsevier Science, Amsterdam, NY, 2001, Chap. 211.

322. V. Pralong, D. C. S. Souza, K. T. Leung, and L. F. Nazar, *Electrochem. Commun.*, 2002, **4**, 516.

323. C. Stinner, R. Prins, and Th. Weber, *J. Catal.*, 2001, **202**, 187.

324. R. Prins, G. Pirngruber, and Th. Weber, *Chimia*, 2001, **55**, 791.

325. D. H. Bale and M. E. Bussell, 223rd ACS National Meeting Orlando, April 2002, Abstract COLL – 309.

326. J. King, M. E. Bussell, 223rd ACS National Meeting Orlando, April 2002, Abstract COLL – 311.

327. H. Tributsch and W. Hönle, *J. Electroanal. Chem. Interfacial Electrochem.*, 1986, **198**, 269.

328. A. V. Ivanov, M. E. Zolensky, A. Saito, K. Ohsumi, S. V. Yang, N. N. Kononkova, and T. Mikouchi, *Am. Mineral.*, 2000, **85**, 1082.

329. R. P. Gupta, G. Martin, S. Lanteri, P. Maugis, and M. Guttmann, *Philos. Mag. A*, 2000, **80**, 2393.

330. Ch. Ma and A. Inoue, *Mater. Trans.*, 2003, **44**, 188.

331. Q. C. Horn, R. W. Heckel, and C. L. Nassaralla, *Metall. Mater. Trans. B*, 1998, **29**, 325.

Phosphorus: Inorganic Chemistry

Paul F. Kelly
Loughborough University, Loughborough, UK

Based in part on the article Phosphorus: Inorganic Chemistry by Josef Novosad which appeared in the Encyclopedia of Inorganic Chemistry, First Edition.

1	Introduction	1
2	Utilization of Phosphorus	2
3	Allotropes of Phosphorus and their Production	4
4	Chemical Properties of Phosphorus – Introduction	9
5	Phosphorus Anions, Cations, and Hydrides	9
6	Compounds with Group 13, 14, and 15 Elements	10
7	Compounds with Group 16 Elements	12
8	Phosphorus Halides	16
9	Transition Metal Chemistry	18
10	Summary – and the Future	19
11	Related Articles	20
12	References	20

1 INTRODUCTION

1.1 Discovery and Development

Phosphorus, atomic number 15, was first isolated by the alchemist Henning Brandt in 1669, during the course of attempts to discover the ubiquitous philosopher's stone. Brandt's method involved the putrefaction of urine followed by concentration and distillation of a red oil, which was then recombined with part of the residue. Subsequent redistillation yielded phosphorus, which was collected in water. That he had succeeded in generating something out of the ordinary was evidenced not only by the fact that the new material glowed in the dark but that it also burned when exposed to air. The rather poignant fact that during WWII bombing raids, the latter property resulted in the destruction of the very place, Hamburg, where Brandt discovered the element, has not been lost on commentators. Brandt's method yielded only 1% of the available phosphorus. Improvements soon followed, however, from the work of a range of chemists – some famous (e.g. Robert Boyle, whose process was revealed posthumously to the Royal Society in 1694) and some largely forgotten (e.g. Boyle's assistant Ambrose Godfrey who, by the time of his death in 1741, had amassed considerable wealth from production of the element). Boyle also demonstrated that small amounts of air have to be present in order to see the element glow (now known to result from transient oxides[1]) and named the element as 'aerial noctiluca'; in due course the name phosphorus (from Greek, meaning lightbearer) was generally accepted.

Around 30 years after Godfrey's death, Gahn and Scheele deduced the presence of phosphate in bone and showed that treatment of bone ash with sulfuric acid, followed by heating of the resulting phosphoric acid with charcoal resulted in elemental phosphorus. The process was refined in France by Pelletier and then Coignet, ensuring that French exports of the element to Britain rose to 4.5 tons per annum in the 1840s. Within a few decades, however, the British firm Albright & Wilson had an annual production about 100 times greater than this and by the turn of the century had taken things a stage further with the introduction of an electric furnace process that allowed direct conversion of naturally occurring phosphate to phosphorus via heating with sand and carbon. This is effectively the technique used today, and the demand for phosphoric acid (and to a lesser extent other materials such as PCl_3) lead to worldwide production greater than 1 million tons in the mid-1970s, though a decrease in demand for phosphate from the detergent industry and the development of methods for direct conversion of mineral phosphate to high purity phosphoric acid has meant that annual production of the element now runs at about half a million tons. For details of the history of phosphorus and the development of its industrial chemistry, the interested reader is directed to recent, highly readable 'biography' of the element.[2] Many other works provide very fine introductions to the chemistry of the element.[3–5]

Since its production became routine, the chemistry of phosphorus has grown more and more, with a 'cutting edge' that has brought together both the apparently complex (for example the structure of allotropes, such as Hittorf's violet) and the ostensibly simple (such as a double-bonded bismuthene of the type $RP{=}BiR'$). That the former was first prepared in 1865, whereas the latter is a breakthrough only recently achieved,[6] serves to highlight the complex nature of the element and its compounds. If the three prime motives behind the work on phosphorus in the last century were to be brought together, they would seem to make strange bedfellows. The incentives driving the production of toxic pesticides and nerve gases, of polyphosphate sequestering agents for detergents, and finally of substituted phosphane ligands for industrially pertinent catalytic systems, would seem to share little apart from mere cupidity. But for all that, there is a subtle and important chemistry that links all of these and there have been innumerable academic and technological advances that have stemmed from them.

1.2 Atomic Properties of Phosphorus

As noted below, phosphorus exists in a number of allotropic forms but all, of course, share atomic properties. Phosphorus exists as only one stable isotope, ^{31}P, which has a mass of 30.97376. In addition, about 16 radioactive isotopes are known,**[7]** of which ^{32}P is by far most important. The fact that it is a pure β-emitter of a half-life of 14.28 days ($E_{\max} = 1.710\,\text{MeV}$) and that phosphorus is so important within biological systems (thus allowing ^{32}P labelled materials to be used in tracer studies) has ensured demand for this isotope. Fortunately, this demand can be readily met via the large scale generation of the material through the neutron irradiation of ^{32}S(n,p) or ^{31}P(n,γ) targets.

The fact that ^{31}P is 100% abundant in nature and that it is a spin 1/2 system makes it potentially ideal for nmr work, and with the advent – and ready availability – of modern FT spectrometers, ^{31}P nmr spectroscopy has become very much 'routine'. While its inherent sensitivity to the NMR effect is lessened by a magnetogyric ratio of $10.84 \times 10^{7}\,\text{rad}\,\text{s}^{-1}\,\text{T}^{-1}$ (thus making it less sensitive than ^{1}H and ^{19}F for example), the technique is still readily applicable to small-scale work.

In the ground state, phosphorus has the electronic configuration $[\text{Ne}]3\text{s}^2 3\text{p}_x 3\text{p}_y 3\text{p}_z$ with three unpaired electrons; this, together with the availability of low-lying vacant 3d orbitals accounts for the predominance of the oxidation states III and V in phosphorus chemistry.

2 UTILIZATION OF PHOSPHORUS

There are two quite different aspects to be taken into account when assessing the utilization of the element. One is to think of the many ways in which nature cycles phosphorus through the environment – broadly speaking this is out of our control, though as will be noted, there is ample opportunity for pollution concerns involving this element. The other is to think of ways in which we can utilize the element industrially or in the laboratory. This section will provide a brief introduction to both areas.

2.1 Natural Phosphorus Distribution and Cycles

Phosphorus is the 11th most abundant element in the Earth's crust (occurring to the extent of about 1120 ppm), though it is important to realize that, unlike its close neighbor in the periodic table, sulfur, it is never found in an elemental form. The predominant mineral form in which phosphorus is found is the orthophosphate family, and of the many hundred examples known, the apatites ($3\text{Ca}_3(\text{PO}_4)_2{\cdot}\text{CaX}_2[\text{Ca}_{10}(\text{PO}_4)_6\text{X}_2]$) are most common and most significant industrially.**[8]** The total mass of such material to which we have access is estimated to be equivalent to somewhere in the region of 9×10^{9} tons of phosphorus. Utilization of this has increased sequentially over the last 100 years; thus in 1900 about 3 million tons were mined. By 1928, this had risen to >10 million tons per annum for the first time; the 100 million tons per annum barrier was broken in 1972 and world production peaked at 166 million tons in 1988. The figure for 2000 was 133 million tons, equivalent to about 18 million tons of elemental phosphorus, though only a fraction of the material mined is now actually converted to the element.**[9]**

In considering how phosphorus cycles through the environment, we have to bear in mind one important point – unlike many other Main Group elements that play a major role in environmental (and hence biological) processes, phosphorus will not naturally form significant amounts of any volatile compound. Thus, phosphate cycles very slowly; the primary inorganic phosphate cycle (Figure 1), which consists of three steps, starts with the leaching of phosphate from the land by weathering. This material will be carried by rivers down to the oceans, after which the precipitation of apatite phosphate into the sea occurs. In the final step, the marine deposits are subjected to a geological process that ultimately brings the phosphate material back to dry land. Of course, this kind of geological process requires a passage of immense time to progress – many millions of years – and the presence of life on earth augments this cycle with its own organic perambulations.

Oceanic plants and algae take up phosphate and they either die or are consumed. The phosphate is then released again into the environment by decay or excretion. Of course, this cycle links to the inorganic cycle through the replenishment of phosphate (food) in the seas via river leaching; the precipitation mentioned earlier is augmented by the organic debris that generates sediments. Although the net transfer of phosphorus is in the direction of the primary cycle, there are movements in the opposite direction: from water to land by fish-eating creatures such as seabirds and humans, and from sediment to solution by decay and hydrolysis processes.

As alluded to earlier, phosphorus has a major role play in life. There are two fundamentally important aspects to this role. First, phosphorus (in the form of inorganic, primarily calcium, phosphates) is the major structural material in vertebrate bone. Second, phosphate esters provide linkages in biologically important systems. The major energy storage and transfer mechanisms in all living systems involve the synthesis and breakdown of phosphate ester linkages such as those present in adenosine diphosphate (ADP) and adenosine triphosphate (ATP); whereas the storage and transfer of coded genetic information involve Nucleic Acids (DNA, RNA) that are diesters of phosphoric acid.

2.2 Utilization of Phosphorus in the Laboratory/Industry

As we will see, worldwide production of elemental phosphorus continues on a massive scale. This reflects the fact that many processes rely on its conversion to industrially relevant materials. One of the most significant of these processes is the conversion to phosphoric acid, which then finds use in a wide range of applications. This technique of

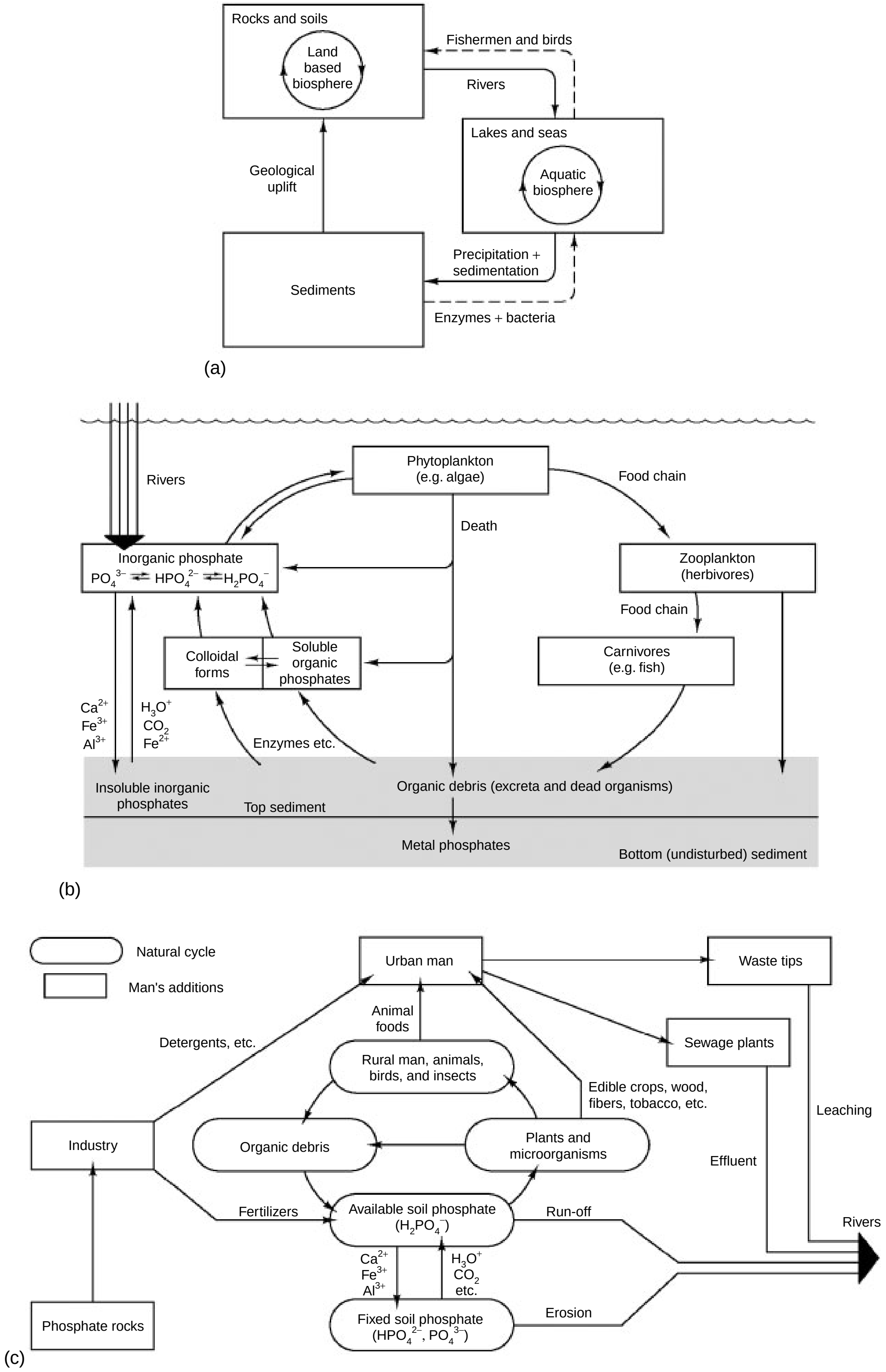
Rocks and soils
Land based biosphere
Fishermen and birds
Rivers
Lakes and seas
Aquatic biosphere
Geological uplift
Precipitation + sedimentation
Sediments
Enzymes + bacteria
(a)
Rivers
Phytoplankton (e.g. algae)
Food chain
Death
Inorganic phosphate
$PO_4^{3-} \rightleftharpoons HPO_4^{2-} \rightleftharpoons H_2PO_4^-$
Zooplankton (herbivores)
Food chain
Colloidal forms
Soluble organic phosphates
Carnivores (e.g. fish)
Ca^{2+} Fe^{3+} Al^{3+}
H_3O^+ CO_2 Fe^{2+}
Enzymes etc.
Insoluble inorganic phosphates
Top sediment
Organic debris (excreta and dead organisms)
Metal phosphates
Bottom (undisturbed) sediment
(b)
Natural cycle
Man's additions
Urban man
Waste tips
Animal foods
Detergents, etc.
Sewage plants
Rural man, animals, birds, and insects
Edible crops, wood, fibers, tobacco, etc.
Leaching
Industry
Organic debris
Plants and microorganisms
Effluent
Fertilizers
Available soil phosphate ($H_2PO_4^-$)
Run-off
Rivers
Ca^{2+} Fe^{3+} Al^{3+}
H_3O^+ CO_2 etc.
Erosion
Phosphate rocks
Fixed soil phosphate (HPO_4^{2-}, PO_4^{3-})
(c)

Figure 1 (a) The primary and secondary cycles; (b) the water-based phosphate cycle; (c) the land-based phosphate cycle.[8] (Reproduced by permission of The Royal Society of Chemistry) production of the acid is known as the ‘thermal’ process, and involves burning of the phosphorus to produce phosphorous pentoxide (P_4O_{10}), which is then hydrated. In reality, however, >90% of the phosphoric acid production comes in the form of high volume, low cost, low purity material that results from the ‘wet’ process (see Section 7.2). Large amounts of the element are also converted to P_4S_{10}, PCl_3, and $POCl_3$ – again, further details of such processes and the uses of the products are presented later in the relevant sections. The standard process of conversion of naturally occurring phosphates to phosphorus generates the ‘white’ allotrope; this in turn can be converted to the ‘red’ form, which has a different reactivity pattern and finds much use – again, details of this are provided later.

In terms of research work in laboratories investigating phosphorus chemistry, the element itself is often the starting material of choice. Here again the different reactivities of the white and red allotropes come into play – in such circumstances the ease of handling of the less reactive, far less toxic red form may be a consideration, though many of the reactions we will see below utilize the white form via appropriate use of anaerobic handling techniques. Many phosphorus compounds that act as important starting materials for further work are readily available. The kinds of reactions that may allow one to convert some of these materials to further compounds hinge upon the reactivity of the bonds between phosphorus and other elements. Examples of reactivity of such bonds will be seen in later sections. Perhaps the most common involves a nucleophilic attack upon the P–Cl bond and concomitant substitution – in this way many examples of substituted phosphanes can be generated. There are of course plenty of other examples of reactive bonds, ranging from P–H to the P=S double bond in some phosphorus sulfides (which are readily desulfurized with sulfur scavengers such as PPh_3).

By way of assessment of the relative bond strengths, the following correlations have been drawn up[**3**] (see also Table 1).

- P–H bonds are weaker than N–H or C–H and are comparable in strength with Si–H or S–H.
- P–halogen bonds are roughly as strong as C–halogen and stronger than N–halogen.
- P–O bonds are stronger than N–O or C–O.
- P–C bonds are at least as strong as C–C, but may be a little weaker than N–C.
- P–P bonds are somewhat weaker than C–C, but stronger than N–N or As–As, and comparable with Si–Si or S–S.
- P–N bonds are fairly strong and comparable with P–P; they are stronger than N–N but a little weaker than P–C.
- P=O bonds are stronger than P=S and much stronger than P–O, but somewhat weaker than C–O or N–O.
- P=P bonds are considerably weaker than N=N or C=C.
- P≡P bonds are weaker than N≡N, P≡N, or C≡C, but stronger than As≡As.
- P≡N is probably the strongest bond formed by phosphorus.

Table 1 Some examples of bond distances and strengths in phosphorus compounds

P–X	Single-bond lengths (pm)	P–X bond enthalpies (kJ mol^{-1})
P–H	142	328 (PH_3)
P–F	153	490 (PF_3)
P–Cl	200	319 (PCl_3)
P–Br	214	264 (PBr_3)
P–I	247	184 (PI_3)
P–B	197	–
P–C	184	264 (PMe_3)
P–N	177	ca. 290
P–P	222	209 (P_4)
P–O	162	407 (P_4O_6)
P–S	209	–

Upon undertaking chemistry of phosphorus systems, the question of characterization of reaction products comes to the fore. In addition to X-ray crystallography, which has been absolutely invaluable in many situations, ^{31}P nmr and infrared spectroscopy are routinely applied to phosphorus systems. Figure 2 and Figure 3 provide some indicative chemical shifts (on the basis of the standard phosphorus reference, namely 85% aqueous phosphoric acid) and stretching frequencies that result from these techniques.

3 ALLOTROPES OF PHOSPHORUS AND THEIR PRODUCTION

Phosphorus exists in many allotropic modifications of various complexity (see Figure 4); a 2002 review perhaps sums up the situation best by referring to phosphorus as being available in a ‘bewildering variety of physical states’.[**10**] In terms of materials that may be used in standard laboratory conditions, these may be assigned to three different ‘families’ – ‘white’, ‘red’ (or ‘violet’), and ‘black’ phosphorus, and we will look at their structures in due course. Before doing so, it is worth noting that the simplest possible scenario, monatomic P, is known to exist but only becomes the predominant species in phosphorus vapor at temperatures in the order of 3000 K (at atmospheric pressure). Below such temperatures, diatomic P_2 (P–P distance 187 pm) predominates and is, of course, analogous to the simplest form of phosphorus’ lighter congener N_2. The fact that P_2 is not stable at RT provides a good example of the changes in relative bond strengths upon descending a group from the first main row to the second. Put simply, while the N≡N triple bond is *more* than three times the strength of an N–N single, the P≡P bond strength is *less* than thrice that of the single bond. P_2 is in fact in equilibrium with P_4; thus dissociation of P_4 into $2P_2$ reaches 50% at ≈2100 K and dissociation of P_2 into 2P reaches 50% at ≈2800 °C. There is

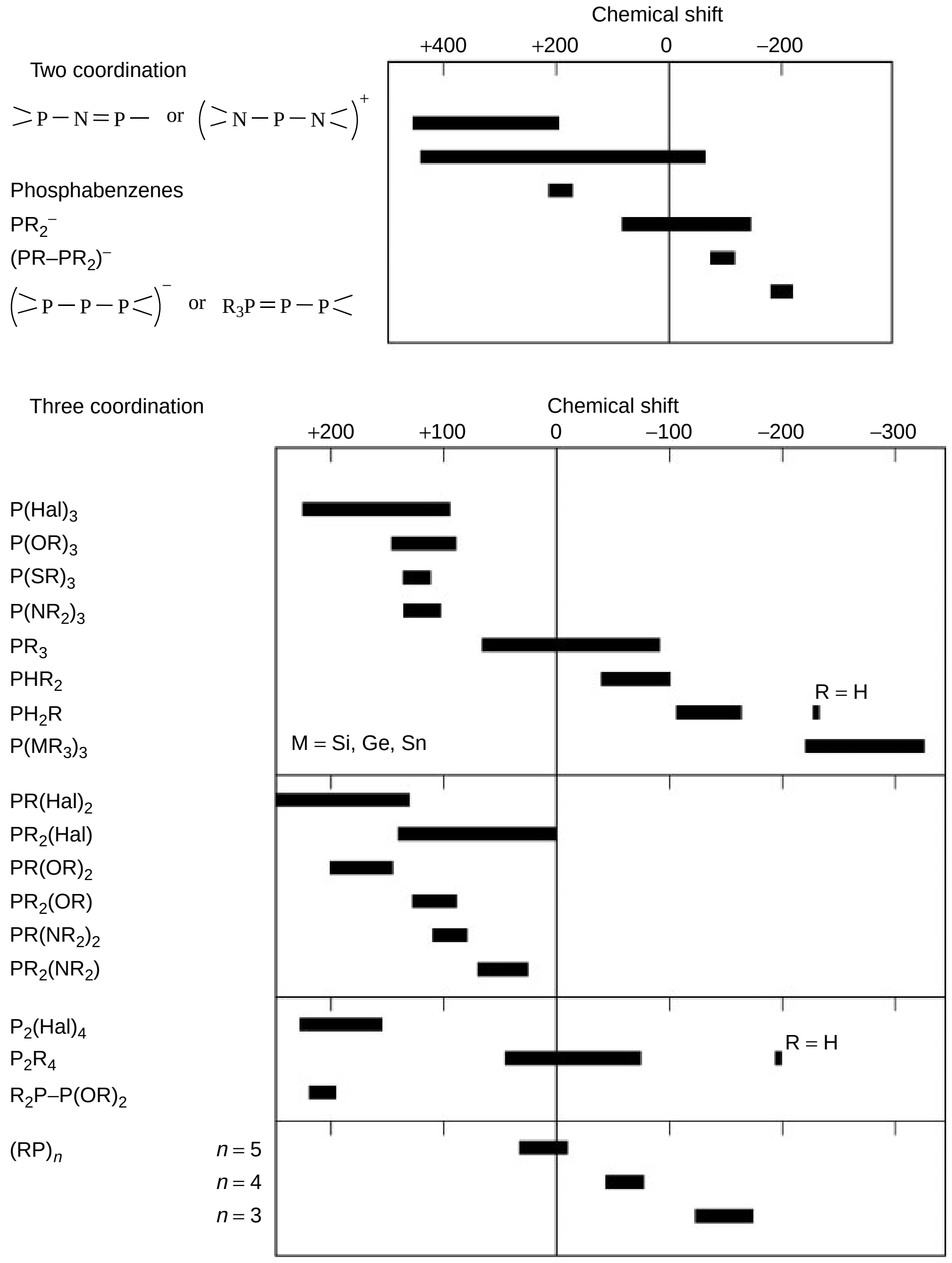

Figure 2 The chemical shift ranges for phosphorus in various coordination numbers

evidence of the formation of other species such as P_3, P_6, P_8, as well.

3.1 White Phosphorus

As noted earlier, for many years after its discovery the only source of phosphorus was urine and all the original work on production of the element involved production of the allotrope known as white phosphorus (after its white – or yellowish – waxy appearance) (Table 2). The efficient preparation of this allotrope by heating phosphate rock with sand and coke was first patented by A. Muller in 1861 and two rival groups – J. B. Readman and T. Parker/A. E. Robinson – both filed patents for the use of electric furnaces to accomplish this task in 1888.[2] This remains effectively the current method for phosphorus production well over a century later. Thus a typical modern phosphorus furnace produces about 4 tons of white phosphorus per hour via the action of massive carbon electrodes upon multitonne mixtures of phosphate rock, silica, and coke, at a reaction temperature in the region of 1400 to 1500 °C. The phosphorus vapor is driven off and then condensed by water, producing an approximately

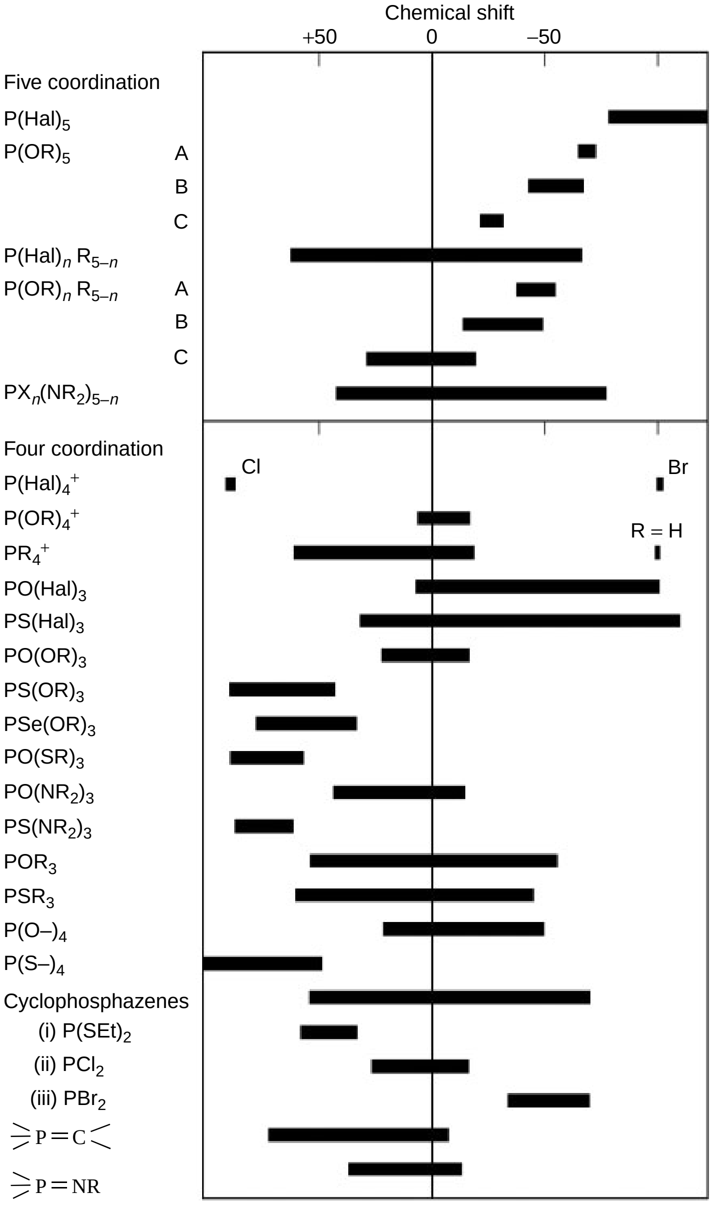

Figure 2 cont'd

90% yield of elemental phosphorus based on the phosphorus content in the raw material.

The white phosphorus produced in the above manner is the most common form of the element. It forms a waxy solid that is insoluble in water – in fact, storage under water proves one of the safest means of containing the material as it ignites in air with a self-ignition temperature of 34 °C (an aqueous copper sulfate solution is commonly used to deactivate spillage of the solid material). It is soluble, to varying degrees, in a range of solvents; in CS_2 for example, dissolution of about 880 g phosphorus per 100 g CS_2 can be achieved. It is worth noting that the element in its white form is extremely toxic. Upon ingestion, doses as low as 100 mg can prove fatal via liver failure, while prolonged intake of smaller amounts of the material can also have dire consequences. Thus, the rather comical sounding phrase 'phossy jaw' belies the agonies endured by sufferers of this industrial disease, prevalent among match workers in the late 1800s and early 1900s. The grotesquely awful accounts of the symptoms of the malady, and of the surgical procedures required to halt its progress, are not easily forgotten.[2,11,12]

Two solid forms of white phosphorus are known, with the cubic α-form converting to the β-form at 197 K. The basic molecular structure of both consists of the P_4 tetrahedron (**1**). Recent work has raised the intriguing suggestion that liquid phosphorus, consisting of the P_4 molecules, undergoes a high-pressure transformation to a polymeric form. Indications are

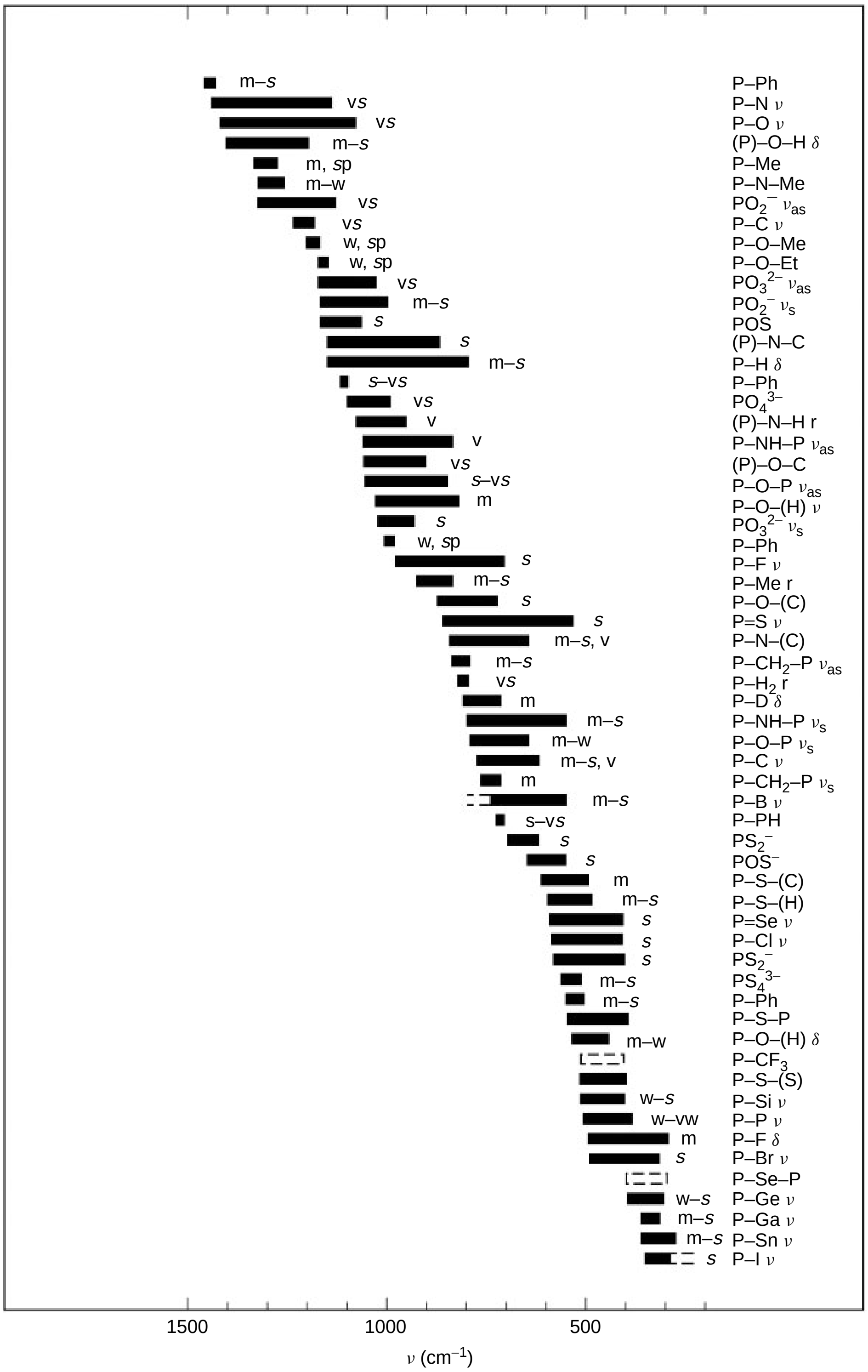

Figure 3 Infrared correlation chart for phosphorus compounds[3]

that this is a rare example of a first-order liquid–liquid phase transition.[13]

Though white phosphorus is the most commonly used form of the element, it is thermodynamically less stable than the other allotropes.

3.2 Red Phosphorus

Amorphous red phosphorus was first obtained by Anton von Schrötter in 1845 through heating white phosphorus with exclusion of air for several days, and is now made on a

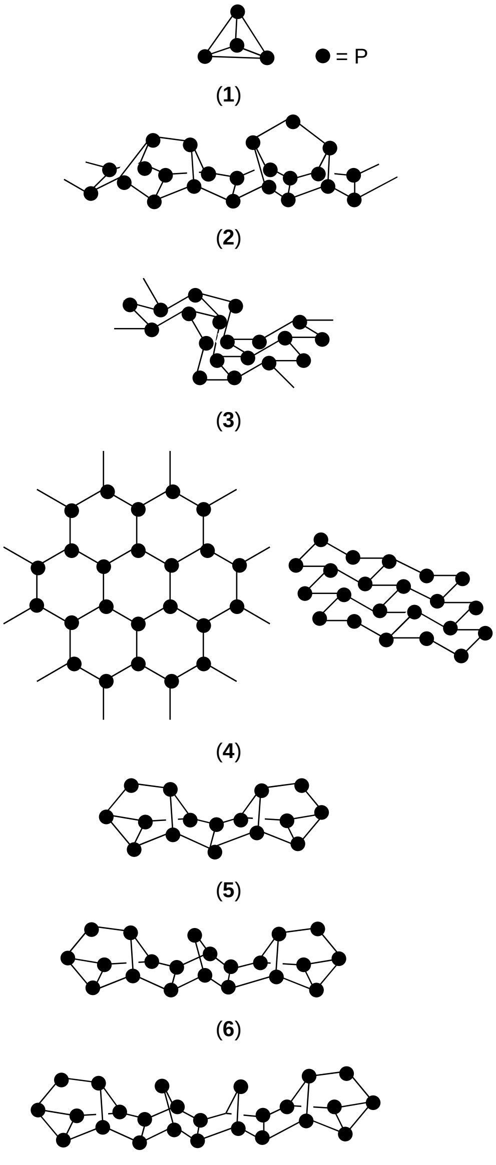

Figure 4 The structures of P_4, white phosphorus (**1**); Hittorf's violet allotrope (**2**); Orthorhombic black allotrope (**3**); Rhombohedral black allotrope (**4**) showing the hexagonal arrangement and the distortion from planar; the phosphides $[P_{16}]^{2-}$ (**5**), $[P_{21}]^{3-}$ (**6**) and $[P_{26}]^{4-}$ (**7**)

Table 2 Physical properties of phosphorus (α-white form)

Atomic number	15
Atomic mass	30.973762
Crystal system	cubic
Unit cell	$a = 185.1$ pm; 58 P_4 per cell
Density (solid)	1.83 g cm^{-3}
Density (liquid)	1.74 g cm^{-3}
Melting point	44.1 °C
Boiling point	280.5 °C
Heat of fusion	2.51 kJ mol^{-1}
Heat of vaporization	51.9 kJ mol^{-1}
Heat of sublimation	56.3 kJ mol^{-1} (P_4)
Critical temperature	675 °C
Critical pressure	8 Mpa
Coefficient of thermal expansion, 0–44 °C, per °C	125×10^{-6}
Hardness (Moh's scale)	0.5
Thermal conductivity	0.235 W m^{-1} K^{-1}

commercial scale by a similar route. In the modern process, the conversion is carried out in massive, high-temperature ball mills in which multitonne quantities of iron shot act as the milling agents. The white phosphorus is fed into the ball mill at such a speed as to maintain the reaction temperature through the heat of reaction. After cooling, the reactor is filled with water, the product milled to a fine powder and then pumped into vessels to be washed with sodium hydroxide (to remove traces of white phosphorus), filtered and dried under inert gas. Of worldwide production in 1999, the distribution of products utilizing red phosphorus has been estimated as: matches (44%), aluminium phosphide (24%), flame retardants (18%), and pyrotechnics (6%), with the remaining 8% used for a variety of other products. The utilization in safety matches comes in the formulation of the striking surface on the matchbox; in contrast, when mixed with plastics (usually to the extent of 5–10% by weight), red phosphorus imparts flame retardant properties and such materials find widespread use in the electronics industry. Aluminium phosphide finds use as a fumigant in grain silos (thanks to its tendency to release phosphine, PH_3, as it breaks down), while in pyrotechnics, red phosphorus is used to generate smoke.

This allotrope is denser than white P_4 (≈2.16 g cm^{-3}), has a much higher melting point (≈600 °C), and is much less reactive; it is therefore safer and easier to handle and is essentially nontoxic. The amorphous material can be transformed into various crystalline red modifications by suitable heat treatment. At 723 K, two distinct crystalline forms can be generated, while a third forms upon taking the temperature up to 800 K. While there is still apparent uncertainty about the structure of these modifications (with work of the structure of the amorphous material, e.g. continuing apace),[14] another form – generated at still higher temperatures (or – as originally performed in 1865 – by crystallization from molten lead) has been fully elucidated. This product is often referred to as Hittorf's violet allotrope (**2**) and its monoclinic structure consists of alternating P_8 and P_9 subunits linked by P_2 groups to generate tubular like chain arrangements with P_{21} as the effective repeat unit. These chains then interact with other chains, generating a complicated overall arrangement.

3.3 Black Phosphorus

Black phosphorus is actually thermodynamically the most stable form of the element and may be prepared in both amorphous and orthorhombic (**3**) forms by the action of temperatures and pressure upon white phosphorus. Increasing the pressure results in rhombohedral (**4**) and cubic forms. All are even more highly polymeric than the red form and have correspondingly higher densities (orthorhombic $d = 2.69\,\mathrm{g\,cm^{-3}}$; rhombohedral $d = 3.56\,\mathrm{g\,cm^{-3}}$; cubic $d = 3.88\,\mathrm{g\,cm^{-3}}$). The structure of this allotrope has recently led to theoretical predictions that black phosphorus analogues of carbon nanotubes may be feasible.[15]

4 CHEMICAL PROPERTIES OF PHOSPHORUS – INTRODUCTION

4.1 Coordination Number and Geometry

In one way or another, the whole of the periodic table barring the Noble Gases can become involved in the chemistry of phosphorus. In the resulting compounds, the phosphorus atoms may adopt a whole range of coordination numbers (CN) and geometries, although as one might imagine some are substantially more common than others. For example, a CN of 3 is one of the most common coordination numbers for phosphorus, with a massive range of examples corresponding to a general formula P(X)(Y)(Z). In such cases, X, Y, and Z may be H, halogen, organic substituents, OR, NR_2, PR_2, SR, or SiR_3 groups, and so on. This tendency towards a CN of 3 is also exhibited by phosphorus within molecules containing more than one phosphorus atom, such as the P_4 allotrope or P_4S_3. In most cases, the geometry at the phosphorus for CN species will be pyramidal, with a lone pair on the P.

The ubiquity of compounds of the type P(X)(Y)(Z), together with the lone pair on the phosphorus leads invariably to a vast array of concomitant compounds of the type (A)P(X)(Y)(Z), wherein the phosphorus exhibits CN of 4. Thus the enormous range of phosphanes of the type PR_3, coupled with their ability to coordinate with metal centers and the many catalytic properties of the resulting complexes, ensures that 4-coordinate phosphorus is of utmost chemical and industrial importance. Away from metal chemistry, $POCl_3$ and P_4S_{10} also exhibit 4-coordinate phosphorus atoms and, as we will see, they both have enormous technological relevance. The basic geometry for phosphorus of CN 4 will be tetrahedral.

Higher CN values are also possible and, indeed, important for phosphorus. Thus, PF_5 exhibits a trigonal bipyramidal structure while addition of fluoride generates the octahedral, 6-coordinate $[PF_6]^-$ anion. Care needs to be taken when assessing formulations though; as we will see, the structural chemistry of PCl_5 varies between its vapor state and when it is in solution. Still higher CN values are rarer as are CN values of <3. Both extremes are possible, however, as in the high coordinate structure of transition metal phosphides or the doubly coordinate phosphorus present in the first stable phosphabismuthene (Section 6.3). An even lower CN is found in compounds such as MeCP and indeed, as already noted, the ultimate example of low-coordination number phosphorus – the naked P atom – is attainable, but only at high temperatures.

4.2 Phosphorus Compounds – Overview

The following review (over the subsequent five chapters) does not profess to be an all-encompassing listing of every type of phosphorus compound. That would clearly take up far too much space and would duplicate the efforts of more comprehensive works and, indeed, of other entries to this encyclopedia. Rather, after looking at the formation of phosphorus anions and cations, the entries are listed in order of the Main Group of the periodic table and in each case give a flavor of the phosphorus chemistry associated with that Group. That said, there is no specific entry for groups 1 and 2 as they are involved in the formation of the aforementioned phosphide anions, nor have examples of compounds with Noble Gas – P bonds been reported yet for group 18.

The main impetus behind inclusion of systems is to highlight the following:

1. industrially important compounds;
2. systems that are the subject of great current interest;
3. systems that result in unusual bonding arrangements, thereby highlighting the ability of phosphorus to exhibit great structural diversity in all areas of its chemistry and to assist in the stabilization of unusual arrangements of *other* elements.

5 PHOSPHORUS ANIONS, CATIONS, AND HYDRIDES

5.1 Phosphorus Anions and Cations

Reduction of elemental phosphorus gives rise to a range of phosphide species. As might be expected, this is the chemistry that dominates group 1 elements' reactivity towards phosphorus, and all form phosphides of the stoichiometry M_3P_7 and MP_{15}. Likewise, all of the group 2 metals form phosphides of formula M_3P_2. The ability to react directly with phosphorus is not limited to these elements though – in fact, a majority of the rest of the periodic table can react likewise. Overall, the variety of stoichiometries known for metal phosphides is enormous, ranging from metal-rich systems (such as $M_{12}P_5$) to 1:1 arrangements and right through to very phosphorus rich systems such as M_4P_{26}. In general, these materials can be generated by direct reaction of the elements, though many other synthetic techniques can be employed. The structural aspects of phosphides are discussed in great detail elsewhere in this encyclopedia (*see* ***Phosphides: Solid-state Chemistry***). Suffice to say here that one of the most important

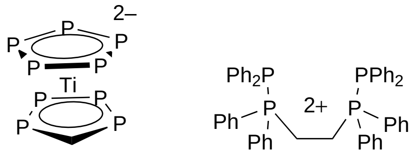
(8) (9)

Figure 5 The structures of $[Ti(P_5)_2]^{2-}$ and 1,2-$[Ph_2(PPPh_2)_2(CH_2)_2]^{2+}$

aspects of this area stems from the ability of phosphorus to form extended catenated arrangements. This is apparent in the structure of the elemental forms and provides the basis for the buildup of large anionic structures such as $[P_{16}]^{2-}$ (**5**), $[P_{21}]^{3-}$ (**6**) and $[P_{26}]^{4-}$ (**7**).

Smaller structures can also provoke extreme interest and a good example comes in the form of the cyclic $[P_5]^-$ ion that has been shown to bind to metals in a manner analogous to the cylcopentadienyl anion as exemplified by the $[Ti(P_5)_2]^{2-}$ anion (**8**) (see Figure 5).[16]

In some cases, the phosphide anions produced in reactions also contain hydrogen atoms bound to the structure. Thus, a recent example has shown that direct reduction of white phosphorus with sodium in liquid ammonia generates the catena-trihydrogen triphosphide $[P_3H_3]^{2-}$.[17]

Surprisingly, oxidation to ‘naked’ cations is yet to be unambiguously achieved, at least in terms of material that may be isolated (many examples of cations have been witnessed in mass spectrometric measurements on vaporized samples of the element);[18] the $[P_5]^+$ cation has, however, been postulated as an intermediate in the reactions that generate $[P_5I_2]^+$ and $[P_3I_6]^+$.[19] Introducing organic groups does allow cationic systems containing P–P bonds to be prepared; the $[dppe(PPh_2)]^{2+}$ dication (**9**) is a good example.[20]

5.2 Hydrides of Phosphorus

Although the simple hydride phosphane, PH_3, is by far the most important of these compounds, many other examples of compounds containing only P and H are known; this range is made even larger if one also includes species detected by mass spectrometry or ^{31}P nmr, but not isolated in pure form (Ref. 21 lists 85 such species for example, ranging from hydrogen rich PH_3 to phosphorus rich $P_{22}H_4$ via 1:1 ratio examples such as $P_{10}H_{10}$).[21] Hydrides of the type P_nH_{n+2} are open chains; P_nH_n are simple rings, whilst the more phosphorus rich compounds are cages. Most of the phosphanes are obtained from thermolysis reactions of diphosphane, although methanolysis of silyl derivatives provides a good route to P_5H_5 and P_7H_3.

Diphosphane P_2H_4 can be generated by passing a high voltage electric discharge through PH_3; it can be isolated as a colorless, volatile liquid (mp −99 °C, bp 56 °C). It is relatively unstable and decomposes to give PH_3 among other hydrides; with liquid ammonia, it generates a range of ammonium polyphosphides, including $[NH_4]_3[P_{19}]$ and $[NH_4]_3[P_{21}]$, as well as the anionic hydride $[H_2P_{14}]^{2-}$.[22] The triphosphane P_3H_5 is isolated as a white solid, also by the decomposition of diphosphane.

The most stable hydride of phosphorus is phosphane (PH_3). It is an extremely poisonous, highly reactive, colorless gas that has a faint garlic odor at concentrations about 2 ppm by volume. It can be generated in a number of ways, including the alkaline hydrolysis of white phosphorus, which is the industrial process. It also forms in the pyrolysis of P_4O_6 and by hydrolysis of some phosphides such as AlP (which forms the basis of the use of the latter phosphide as fumigant). As would be expected for a PX_3 molecule, phosphane has a pyramidal structure with P–H distance of 142 pm and an angle of 93.6°; it melts at −133.5 °C and boils at −87.7 °C. Phosphane undergoes gradual decomposition in water; products include phosphorus and hydrogen. In liquid ammonia, however, phosphane dissolves to give NH_4^+ PH_2^-, and with potassium gives KPH_2 in the same solvent.

Phosphane burns readily in air; the pure gas ignites in air at about 150 °C but when contaminated with traces of P_2H_4 it is spontaneously flammable. It also photodissociates, under flash photolysis at above 195 nm, generating PH and PH_2 radicals. PH_3 is also a strong reducing agent; many metal salts are reduced to the metal. When heated with sulfur, PH_3 yields H_2S and a mixture of phosphorus sulfides. Probably the most important reaction industrially is the hydrophosphorylation of formic acid in aqueous hydrochloric acid; the tetrakis (hydroxymethyl) phosphonium chloride so formed is the major ingredient with urea – formaldehyde or melamine – formaldehyde resins for the permanent flameproofing of cotton cloth.

6 COMPOUNDS WITH GROUP 13, 14, AND 15 ELEMENTS

6.1 Group 13 Elements

As with all group 13 elements (Figure 6), boron forms a 1:1 phosphide, that is, BP; in addition, unlike its congeners it also forms a lower phosphide, namely $B_{13}P_2$. Given the Lewis acidity of alkyl boron species, it is not surprising that phosphane adducts are known; one interesting example comes in the form of $(C_6F_5)_3BPH_3$ that has been shown to release the phosphane above room temperature, providing a potential safe storage form for the latter gas.[23] While it has long been known that thermolysis of adducts of the type $R_2PH{\cdot}BH_3$ generates cyclic phosphinoboranes, usually trimers of the type $(R_2P\text{-}BH_2)_3$, it is only recently that conversion to high molecular weight poly(phosphinoboranes) (**10**) has been achieved via a rhodium catalyzed reaction.[24] Thus, by way of example,

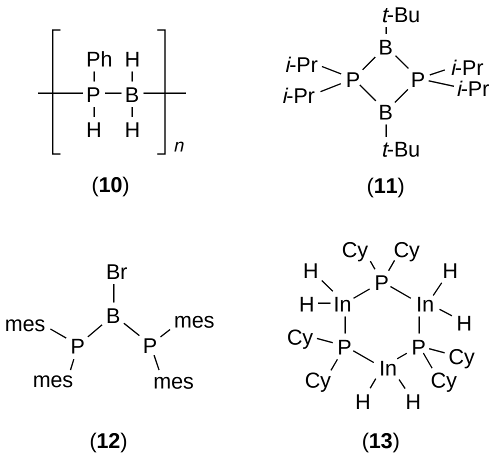

(**10**) (**11**)

(**12**) (**13**)

Figure 6 The structure of some P-Group 13 species

refluxing $\mathrm{PhPH_2.BH_3}$ with the rhodium catalyst in toluene for 14 hours generates an air and water stable polymer with average molecular weight of 5600 (i.e. 46 repeat units). Heating in the absence of toluene generates a higher molecular weight material. Such observations add a new class of compounds to the already significant number area of main group, phosphorus-based polymers, the subject of a 2002 review.[25]

The four-membered cyclic compound $({}^i\mathrm{Pr_2P})_2(\mathrm{B}{}^t\mathrm{Bu})_2$ (**11**) has elicited much interest, thanks to it being a rare example of a singlet diradical, which is indefinitely stable at ambient temperatures.[26] As noted above, phosphinoboranes tend to be oligomeric rings; monomeric species may be isolated though if large substituent groups are employed. Thus, $(\mathrm{mes_2P})_2\mathrm{BBr}$ is an orange solid with the structure shown (**12**).[27] The introduction of phosphorus into borane (and carborane) structures has yielded a wealth of chemistry.[28,29] This can be done either by building from small B and P constituents (thus pyrolysis of $\mathrm{B_2Cl_4/PCl_3}$ mixtures leads to [*closo*-1,2-$\mathrm{P_2B_4Cl_4}$])[30] or by reaction of large boranes with, for example, $\mathrm{PCl_3}$.[31] For the heavier members of the group, similar acid-base chemistry is possible – by way of example, the trimeric phosphido-indium hydride complex $[\{\mathrm{InH_2(Pcy_2)}\}_3]$ (**13**) has been reported.[32]

The most important aspect of the phosphorus chemistry of Al, Ga, and In stems from the fact that their phosphides exhibit unusual (and desirable!) electrical properties. All act as semiconductors, with band gap energies that drop as the group is descended (236, 218 and 130 $\mathrm{kJ\,mol^{-1}}$ for AlP, GaP and InP respectively). They have found extensive use in LED technology and are inextricably linked to the history of LED development. Indeed, the first red LEDs utilized gallium arsenide phosphide (GaAsP); subsequent switching to gallium phosphide (GaP) paved the way for the introduction of new colors. Introduction of gallium aluminium arsenide phosphide (GaAlAsP) LEDs in the 1980s led to brighter colors, a process that continued in the next decade thanks to the introduction of indium gallium aluminium phosphide (InGaAlP) systems.

As already mentioned, aluminium phosphide finds use as a fumigant thanks to its ability to slowly release $\mathrm{PH_3}$. Its effectiveness comes at a price; for example, it has been estimated that 10 000 deaths by deliberate ingestion occur per annum in India alone.[33]

6.2 Compounds with Group 14 Elements

The organic chemistry of phosphorus is dealt with elsewhere in this encyclopedia. In the case of phosphanes $\mathrm{PR_3}$ and their coordination chemistry, their importance cannot be overstated.[34] In fact, it is fair to say that development of transition metal phosphane complexes as catalysts for a range of transformations has had a profound effect upon the way the interface between organic and inorganic chemistry is viewed. After all, here we have organic ligands generating inorganic complexes which then catalyze organic transformations. As such, they have been one of the driving forces in the breaking down of traditional barriers between the disciplines, resulting in the growing tendency to unite inorganic and organic work together under the banner of 'synthetic chemistry'.

It is worth just considering some materials that are undoubtedly organic in nature but whose properties tell us something fundamental about the behavior of phosphorus.[35] These are very much at the forefront, not only of the chemistry of the element but also in bonding models in general (Figure 7). An excellent example comes in the form of 4-membered phosphorus ring within $({}^i\mathrm{PrNCP_2})_2$ (**14**); as indicated, the structure consists of a dimer held together by two 1-electron P–P bonds (the difference in bond order within the system is easily confirmed by the bond lengths).[36]

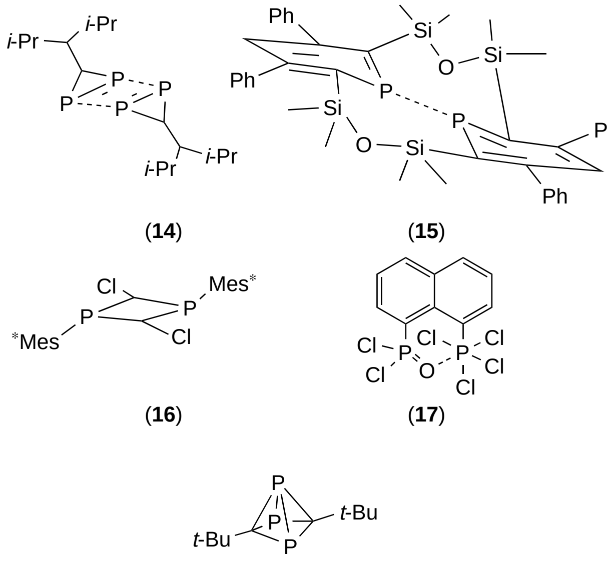

(**14**) (**15**)

(**16**) (**17**)

(**18**)

Figure 7 The structure of some P–C species with unusual bonding arrangements

Compound (**15**) also exhibits a 2-centre, 1e bond between P atoms and again the bond is long (about 2.76 Å),[37] while the unusual biradicaloid (**16**) is thermally stable up to 150 °C.[38] The constraints placed upon the phosphorus atoms in compound (**17**) result in hypercoordination of the phosphorus adjacent to the oxygen,[39] while (**18**) constitutes the first cationic phosphorus-carbon cluster, namely *nido*-[3,5-^{t}Bu$_2$-1,2,4-C_2P_3]$^+$.[40] All such observations show great promise for future development.

The first example of a silylphosphane, H_2PSiH_3, was reported in 1953[41] and a vast amount of work has gone into the preparation of Si–P systems since then, resulting in a wide range of synthetic strategies and structural motifs (Figure 8).[42] Examples of the general formula $RR'PSiR'R''R'''$ are now known for all manner of combinations of substituent. Silyl species may also take the place of the R and R′ groups on the phosphorus atoms in the aforementioned formulation; thus $P(SiMe_3)_3$, for example, is an important ligand. Many intriguing structures have resulted from work in this area, such as the four-membered ring within (**19**).[43] Reaction of Me_2SiCl_2 with LiPH^{t}Bu results in $(Me_2Si)_3P_2(P^tBu)_2$[44] (**20**), while $P_2(PSi^tBu_3)_2$ (**21**) and $P_7(Si^tBu_3)_3$ (**22**) form in the reaction of white phosphorus with $(Si^tBu_3)_2$.[45] An even higher phosphorus content is found in $P_{11}(SiMe_3)_3$ (**23**), which results from the reaction of Na_3P_{11} with Me_3SiCl.[46]

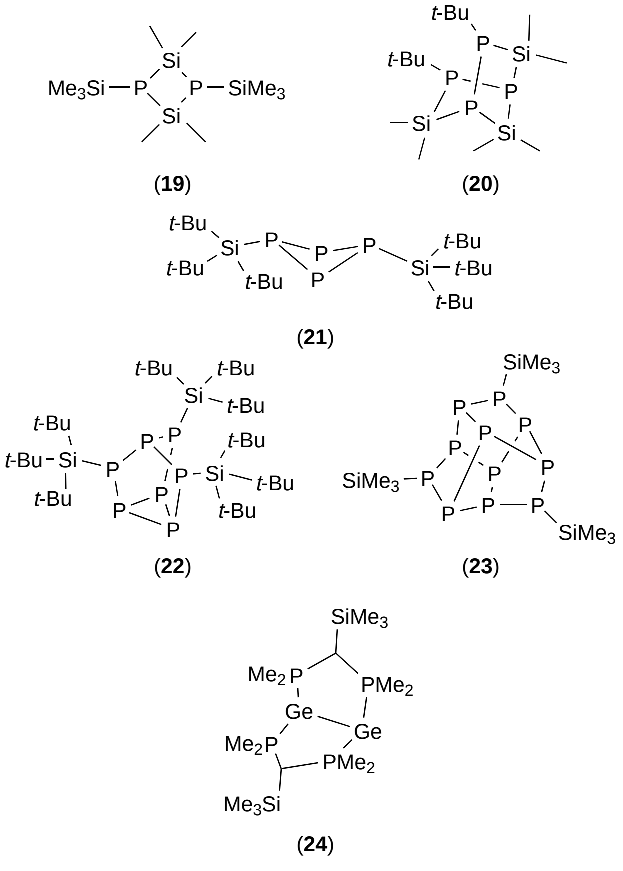

(**19**) (**20**)

(**21**)

(**22**) (**23**)

(**24**)

Figure 8 The structure of some P–Si and P–Ge species

Phosphasilenes $RR'Si{=}PR''$, wherein the substituents are bulky stabilizing groups, are also known. Addition across the Si–P double bond – with concomitant cycle formation – can be achieved by many species including nitriles, sulfur, and phosphorus itself.

Systems based on single bonds between the heavier group 14 elements and phosphorus are well documented – (**24**) is a nice example of the stabilization of a Ge(I) species this way.[47] It is even possible to obtain multiple bonds to the heavier elements; thus the chemistry of double-bonded germaphosphines and stannaphosphines – bearing Ge=P and Sn=P bonds – has been developed thanks again to the use of bulky, stabilizing substituents.[48] There has even been recent speculation to the possibility of stabilizing the analogous triple bond.[49]

6.3 Compounds with Group 15 Elements

Extensive chemistry of P–N systems is known and many such compounds – for example, the polyphosphazenes – are of intense industrial importance. The chemistry of all such systems is covered elsewhere (*see* ***Phosphorus–Nitrogen Compounds***).

As with group 14 elements, it is possible to form double bonds between the heavier group 15 atoms and phosphorus. While the first examples of phosphaarsenes and phosphastilbenes were prepared as early as 1983,[50] it was only in 2002 that the first phosphabismuthene of the type RP=BiR′ was reported.[4] The key to the stability of the product in this case is the use of bulky groups: $R = 2{,}4{,}6\text{-}(^tBu)_3C_6H_2$ and $R' = 2{,}6\text{-}\{(Me_3Si)_2CH\}\text{-}4-\{(Me_3Si)_3C\}C_6H_2$. The P–Bi distance in this case is 2.454 Å.

7 COMPOUNDS WITH GROUP 16 ELEMENTS

7.1 Phosphorus Oxides

P_4O_{10}, commonly referred to as phosphorus pentoxide (Figure 9), is the most important oxide of phosphorus. It is generated by the burning of white phosphorus in aerated towers; if condensed rapidly from the vapor phase, it is obtained in the hexagonal form, which in turn may be transformed into other modifications by suitable thermal and high-pressure treatment. The molecular structure of P_4O_{10} (**25**) is based upon the tetrahedron within P_4, but with O inserted into all P–P bonds and a terminal oxygen added to all phosphorus atoms, though its most stable, orthorhombic form has a sheet polymeric structure.

In the laboratory, P_4O_{10} often finds use as a powerful dehydrating agent – so powerful in fact that it can convert ethanol to ethylene, H_2SO_4 to SO_3, HNO_3 to N_2O_5, and

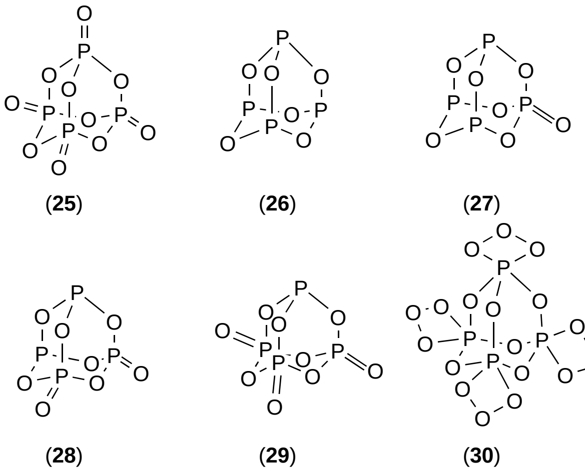

Figure 9 The structure of phosphorus oxides

amides ($RCONH_2$) to nitriles (RCN). It is this desire for water, which fuels its main industrial use – the conversion to phosphoric acid. The acid produced in this manner (i.e. ultimately from phosphate rocks via the 'thermal route') is very pure, with only the removal of arsenic being required before it is available for a variety of technical, food, and pharmaceutical applications.

Other industrially important uses of P_4O_{10} include the reactions with ethers, an example of which is the formation of triethyl phosphate via reaction with diethyl ether followed by pyrolysis. The product (which has a worldwide production of many thousands of tons per annum) finds use as ketene synthesis, a flame retardant, and a plasticizer within the plastics industry; a less 'conventional' use is as a simulant for the sarin when modeling situations involving the latter nerve agent.

The second most commonly studied oxide is P_4O_6 (**26**), which is obtained by controlled oxidation of phosphorus in an atmosphere of 75% O_2 and 25% N_2 at low pressure. Heating P_4O_6 under vacuum in a sealed tube gives a mixture of red phosphorus and the oxides P_4O_7 (**27**), P_4O_8 (**28**), and P_4O_9 (**29**). These oxides have structures in between those of P_4O_6 and P_4O_{10}, in that they have one, two, or three apical oxygen atoms attached to phosphorus atoms (cf the higher sulfides). In terms of specific preparations, P_4O_7 is best prepared from P_4O_6 dissolved in THF, using Ph_3PO as a catalyst at room temperature, while P_4O_8 has been made in pure form via the high-temperature reaction of P_4O_9 with red phosphorus.[51] Recently, a new oxide of formulation P_4O_{18} has been prepared (**30**) – this remarkable compound is actually an ozonide of P_4O_6.[52]

7.2 Oxoacids and Anions of Phosphorus

A diverse range of oxoacids of phosphorus is known. The presence of hydrogen in such systems is either in the form of POH groups (in which the hydrogen atom is ionizable) or P–H groups (from which a proton cannot be ionized). Overall, the acids can be divided into two series of oxoacid, namely, the phosphoric and phosphorous acids, in which the oxidation state of phosphorus is (V) and (III) respectively. In all of these, phosphorus is four-coordinate and tetrahedrally surrounded wherever possible. Deprotonation of the acids leads to families of anions.

Phosphoric acid, H_3PO_4, is by far the most important of these acids. Indeed, of all the inorganic acids, it is second only to sulfuric acid in terms of volume of production (and in fact in terms of net value of production it probably exceeds the latter). We have already seen how it can be produced via phosphorus abstraction and then burning/hydration, that is, the so-called 'thermal' route, and that this generates high purity material. The other main – and now most important in terms of volume – route is via the 'wet' process. Here phosphate rock is mixed with sulfuric acid and some recycled phosphoric acid; this slurry is then filtered (removing the calcium sulfate) leaving the impure phosphoric acid. The heavy-metal content of the acid at this stage means that it can only be used within fertilizers; further purification is needed to take the material to food grade, for example, and this is performed via solvent extraction techniques.

As might be expected from its structure, phosphoric acid is tribasic; the dissociation constants at 25 °C are: $pK_1 = 2.15$, $pK_2 = 7.20$, $pK_3 = 12.37$. As a result of this, the acid gives three series of salts, for example, NaH_2PO_4, Na_2HPO_4, Na_3PO_4. While its greatest use is undoubtedly in the manufacture of phosphates for use as fertilizers (accounting for 85% of the total usage of material made by the 'wet' route) and animal feed, its phosphate derivatives are also utilized in water treatment, detergents, toothpastes, fire control chemicals, and many more. In addition, the acid itself is added to colas and soft drinks in general (giving a sharp, sour taste) and is used (in the presence of metal ions such as zinc) to impart corrosion resistance to metal surfaces and to polish aluminium bodies.

Phosphorous acid, H_3PO_3, is generated by hydrolysis of PCl_3 – industrially this is carried out by spraying the chloride into steam at 190 °C. Esters of the acid, both the trialkyl esters [$P(OR)_3$] and the dialkyl esters [$(RO)_2P(O)H$], can be produced directly by substituting the appropriate acid for the water. The esters find much use; thus, triphenyl phosphite is most widely used in the manufacture of polyvinyl chloride, while trinonylphenyl phosphite is an excellent stabilizer for the same polymer.

Hypophosphoric acid ($H_4P_2O_6$) can be generated by removal of water from its 'dihydrate' (which is actually a hydroxonium salt), which in turn is formed by reacting red phosphorus with sodium chlorite followed by ion exchange on an acid column. In the absence of moisture, the acid is stable at low temperatures but at room temperature it undergoes rearrangement and disproportionation to give a mixture of pyrophosphorous acid [$(HO)_2POP(OH)_2$], pyrophosphoric acid ($H_4P_2O_7$), and isohypophosphoric acid $[H(HO)(O)POP(O)(OH)_2]$.[53]

Hypophosphorous acid is generated by acidification of the calcium salt $Ca[H_2PO_2]$, itself prepared by the action of calcium hydroxide on phosphorus. Its sodium salt ($NaH_2PO_2{\cdot}H_2O$) finds use as a reducing agent for the electrodeless nickel plating on metallic parts such as steel or aluminum.[54] The possibility of P–H and P–P bonds in phosphorus oxoacids, coupled with the ease of polymerization via P–O linkages, enables a large range of acids to be synthesized. Deprotonation of such acids will allow the formation of phospho-anions. Isolation of simple monophosphates is possible, though even in such simple systems the degree of protonation of the anions is variable, as the recent isolation of $[\,Ga_4(C_{10}H_9N_2)_2(PO_4)(H_{0.5}PO_4)_2(HPO_4)_2(H_2PO_4)_2(H_2O)_2\,]$, in which four types of monophosphates are present in the same compound, attests.[55] The number of acids allied to their polybasicity and the multiple possible ways such anionic units can link together (via P–O–P bonds) results in a vast range of structural types. As these are covered in another section (*see* ***Phosphates: Solid-state Chemistry***), we will not go into any great detail here – suffice to say that the classification of inorganic phosphates is based upon the geometrical configuration of their anions. In the area corresponding to the classical condensed phosphates, anions can be represented by the formula $[P_nO_{3n+1}]^{(n+2)-}$. They are usually called *linear polyphosphates*. When n becomes very large, the ratio is P:O → 1:3. For this limiting value, two geometrical configurations are possible:

1. a long-chain polyphosphate
2. a cyclic configuration with anions corresponding to the formula $[P_nO_{3n}]^{n-}$ describing all *cyclo*-metaphosphates.

Cations containing P–O units can also be generated – an unusual example being the $[P(OH)_4]^+$ ion, recently isolated and characterized by X-ray crystallography for the first time.[56]

One of the most important aspects of phosphate chemistry is the use of sodium tripolyphosphate (STPP), $Na_5P_3O_{10}$, in the detergent market. It acts, for example, as a water softener by sequestering Mg^{2+} and Ca^{2+} (e.g. it will bind the equivalent of 158 mg CaO/g).[57] Ecological concerns relating to eutrophication of lakes induced by phosphate waste has meant that restrictions imposed on its use over the last few decades has resulted in a dramatic decline of its use. Thus in the space of a decade, the use of STPP in detergents dropped by 50% within the United States, Europe, and Japan; now, 95% of all detergents sold in Japan are STPP free and contain zeolite instead.[57] Studies have suggested, however, that the effect of phosphates may not be as dramatic as was first feared and that the algal blooms in eutrophicated lakes may have actually stemmed from a lack of zooplankton brought about by other means of industrial poisoning.[2]

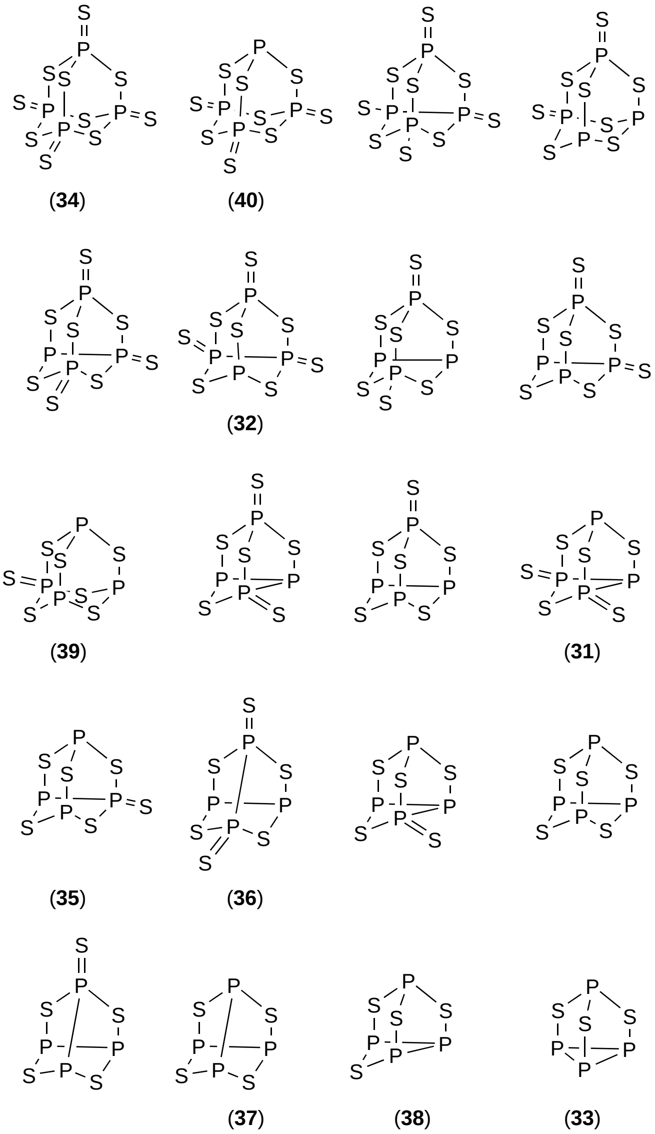

Figure 10 The structure of all currently known phosphorus sulfides

7.3 Phosphorus Sulfides and Selenides

Many areas of main group chemistry continue to provide contemporary challenges and novel chemistry despite a having a significantly long history of investigation. A perfect example of such a system comes with the binary phosphorus sulfides. Though work in this area stretches back into the nineteenth century, new examples continue to come to light (thanks in no small part to the facile and now routine use of ^{31}P nmr to monitor reaction systems). By way of example, the ostensibly straightforward reaction brought about by photolyzing a mixture of the elements at 0 °C has been the subject of a recent study, which revealed no fewer than 12 phosphorus sulfides in the reaction mixtures, two of which (**31** and **32**) were novel.[58] All values of n (from 3–10) within the general formula P_4S_n are now known (Figure 10), though only those at

Table 3 Physical properties of some phosphorus sulfides

Property	P_4S_3	α-P_4S_4	P_4S_5	P_4S_7	P_4S_{10}
Color	Yellow	Pale yellow	Bright yellow	V. pale yellow	Yellow
Mp (°C)	174	230 (d)	170–220 (d)	308	288
Bp (°C)	408	–	–	523	514
Density (g cm^{-3})	2.03	2.22	2.17	2.19	2.09
Solubility in CS_2 (g per 100 g CS_2)	100	sol.	0.5	0.029	0.222

the extreme n values – that is, P_4S_3 (**33**) and P_4S_{10} (**34**) – have industrial significance, and of these P_4S_{10} is by far the most important. Physical properties of some of these compounds are listed in Table 3.

The structures of the known phosphorus sulfides are provided in Figure 10. Interconversion between them can be carried out in a number of ways. One conceptually obvious way is to add sulfur to a low sulfur content example, and this has been achieved in some cases by simply adding more elemental sulfur with heating. A more subtle technique has been developed recently wherein Ph_3SbS acts as sulfur source; in this way two new polymorphs (δ (**35**) and ε (**36**) forms) of P_4S_6 were generated from α-P_4S_4 in CS_2.[59] The multistep formation of two forms of P_4S_4 (**37**, **38**) from P_4S_3 via two forms of $P_4S_3I_2$, and the sulfur source $[Me_3Sn]_2S$ has been known for some time.

A logical reversal of the above process would involve removal of sulfur from a higher sulfide and indeed this can be done. Triphenylphosphine is an effective scavenger of sulfur – via concomitant formation of Ph_3PS – and this technique was recently used to generate (**39**) for the first time.[60] This process can also be achieved by direct reaction of a lower sulfide with a higher sulfur content example; thus, P_4S_9 (**40**) is formed reversibly by heating a 2:1 mixture of P_4S_7 and $2P_4S_{10}$, for example. Likewise, high-temperature reaction of phosphorus with a high-sulfur content phosphorus sulfide acts as a source of lower sulfides.

Industrially, P_4S_{10} (often referred to as phosphorus pentasulfide, P_2S_5) is generated by direct combination of the elements. Both are introduced in liquid form into a cast-iron reactor under a nitrogen atmosphere. Here initial temperatures may be in the region of 200 °C but this rises due to the exothermic nature of the reaction. Finally, the product is flushed from the system and vacuum distilled from residues. Though worldwide production is undoubtedly still high, concerns over the two main products – zinc dialkyldithiophosphates (ZDDP) engine oil additives, and organophosphorus pesticides – have reduced demand. By way of illustration, pesticide production in the United States consumed about 43 600 tons of P_4S_{10} in 1979; by the turn of the millennium this was down by about 30 000 tons per annum.[61]

Although the aforementioned products – engine oil additives and pesticides – could not be more different in terms of the nature of their utilization, their preparation stems from the same reaction, namely the alcoholysis of P_4S_{10}. The resulting dialkyldithiophosphoric acids, $SS(H)P(OR)_2$, can react with zinc salts to generate ZDDP. These have structures based on the ability of the $[S_2P(OR)_2]^-$ anion to act as bidentate ligand towards zinc, and when added to engine oils they act as both antiwear and, to a less important degree, antioxidizing agents. Their antiwear capability stems from the fact that degradation of the ZDDPs within the extreme environment of the engine results in the formation of a protective layer over engine parts. Varying the precise group on the original alcohol allows the properties of the ZDDPs to be adjusted; secondary alcohol–based ZDDPs account for about 85% of the market.

Organophosphorus pesticides are formed via further derivatization of the dialkyldithiophosphoric acids, resulting in compounds such as $(EtO)_2P(S)OC_6H_4NO_2$ (parathion) and $(MeO)_2P(S)SC(CH_2CO_2Et)HCO_2Et$ (malathion). As with ZDDPs, their effectiveness is tempered by environmental concerns. In the case of the pesticides, the long-term health risks associated with their use are still a matter of debate; certainly they require careful handling and it would appear that sensitivity towards them can vary from person to person. Concerns over ZDDPs stem from the fact that they have a detrimental effect on catalytic converters fitted to exhausts, with phosphorus deposits interfering with the active metal surfaces. Even so, ZDDPs are still used in great quantities, with the North American market alone amounting to about \$180 million worth of the material.

Fewer examples are known of molecular phosphorus selenides than sulfides. P_4Se_3[62] (**41**) and P_4Se_5[63] (**42**) have both been prepared as have P_2Se_5[64] and a range of polymeric species. This tendency towards polymerization is actually quite marked for PSe systems – thus, *catena*-P_4Se_4 is known in which terminal selenium atoms link to the next unit (**43**).[65] The range of molecular units is increased if one also considers PSe units stabilized within CuI matrices, an example of which is the β-P_4Se_4 cage (**44**) within $(CuI)_3P_4Se_4$, which is prepared by the high-temperature reaction of CuI with phosphorus and selenium in silica ampules.[66] The ability of such techniques to result in formation of unusual products is further exemplified by the isolation of $(CuI)_2P_8Se_3$ (**45**) from a similar reaction.[67] Using polyselenophosphates as flux for high-temperature reactions involving metals also allows the isolation of unusual species such as the mercury anion (**46**) in Figure 11.[68]

In addition, mixed sulfide selenide systems such as P_4S_2Se are also known, while P–Te bonds are found in BaP_4Te_2. This new material is generated by direct reaction of the elements at 475 °C and consists of P_4Te_2 chains made up of six-membered phosphorus rings linked to tellurium atoms (**47**). The P–Te

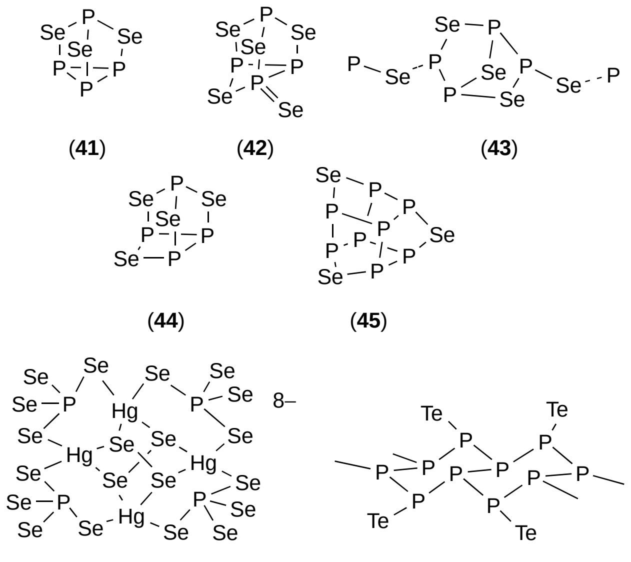

(41) (42) (43) (44) (45) (46) (47)

Figure 11 The structure of a range of P–Se and P–Te species

bond length is 2.54 Å.[69] No simple, direct molecular analogues of the phosphorus sulfides or selenides are yet known.

8 PHOSPHORUS HALIDES

Phosphorus combines with halogens in various ratios to form phosphorus halides – three key stoichiometries are known, P_2X_4, PX_3, and PX_5, together with a small number of subhalides such as P_7Br_3. In addition, compounds in which other atoms (such as sulfur or oxygen) have replaced one or more of the halogens in the above formulations are well known and often of great importance. Transient PX monohalides can be generated and work on the spectroscopic properties of PI, for example, is still ongoing.[70]

8.1 Diphosphorus Tetrahalides, P_2X_4 and Subhalides

The most stable of these compounds is the iodide and it is the only one that may be readily prepared by direct reaction of the elements (using red phosphorus at high temperature or white phosphorus in CS_2), though P_2Br_4 is one of the products of the reaction of phosphorus and bromine in CS_2.[71] Formation of the fluoride is via mercury-induced coupling of the PF_2 units in PF_2I, while the chloride forms after the microwave discharge through PCl_3 vapor. All are sensitive to hydrolysis, though the products of such reactions vary (with the fluoride, e.g. giving F_2POPF_2). The chloride slowly decomposes at room temperature to products including PCl_3.

As already noted, the reaction of iodine with phosphorus can generate P_2I_4; P_3I_5 has also been identified as an additional product of the reaction,[72] while if performed in the presence of $[Ag(CH_2Cl_2)][Al(OC(CF_3)_3)_4]$ the low-temperature reaction has been shown to generate the transient $[P_2I_5]^+$ cation, which in turn leads to $[P_3I_6]^+$ (**48**) (Figure 12).[73,74] The structure of the latter consists of two terminal PI_2 units bridged by a further PI_2. The same work also led to the isolation of salts of the $[P_5I_2]^+$ cation (**49**) via reactions of $[Ag(P_4)_2][Al(OC(CF_3)_3)_4]$ with iodine; analogous $[P_5Br_2]^+$ also forms in this way, in this case via a $[PBr_2]^+$ intermediate. $[P_2Br_5]^+$, P_4Br_2 (**50**), and P_7Br_3 (**51**) are also known, the latter two having been identified in solution.

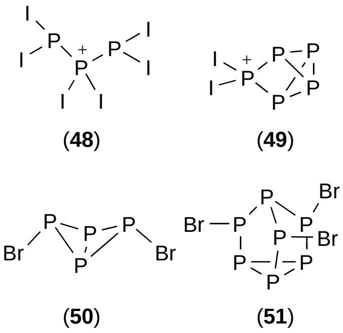

(48) (49) (50) (51)

Figure 12 The structure of some phosphorus–halogen species containing P–P bonds

8.2 Phosphorus Trihalides

Trihalides of formula PX_3 are known for all the halogens and their physical properties are shown in Table 4. Apart from the fluoride, they are all generated by direct reaction of the elements; PF_3 is made by fluorination of PCl_3. PF_3 is harder to handle than the others thanks to both its gaseous nature at normal temperature and pressure and also to its high toxicity (via interaction with blood hemoglobin). Though it fumes in air (and has appreciable toxicity), PCl_3 is more readily handled and finds massive use industrially; indeed, in 2001 the demand in the United States alone amounted to 305 000 tons.[75] Pesticide production accounted for 70% of this; other uses included the manufacture of $POCl_3$ (12%); surfactants and sequestrations agents for water treatment chemicals (11%); plastics additives, including flame retardants, plasticizers, and phosphite antioxidants and stabilizers (5%). It is generated by direct chlorination of elemental phosphorus suspended in preprepared phosphorus trichloride – as the system refluxes, the resulting PCl_3 is continuously removed. Its usefulness in the laboratory and in the industry stems from the ready substitution and/or oxidation reactions that can be applied to it. Typically, salt elimination or the production of HCl acts as driving force to the substitution reactions; thus PCl_3 is a prime starting material for the preparation of phosphanes via reaction with Grignard reagents. Its ready oxidation to important compounds such as H_3PO_3 and $POCl_3$ is also of great importance; thus a total of about 36 000 tons of PCl_3

Table 4 Some physical properties and ^{31}P NMR chemical shifts of the phosphorus trihalides and pentahalides

Compound	Physical state at 25 °C	Mp (°C)	Bp (°C)	P–X (pm)	δ (ppm)
PF_3	Colorless gas	−151.5	−101.8	156	−97
PCl_3	Colorless liquid	−93.6	76.1	204	−219
PBr_3	Colorless liquid	−41.5	173.2	222	−227
PI_3	Red solid	61.2	decomp. >200	243	−178
PF_5	Colorless gas	−93.7	−84.5	153 (eq) 158 (ax)	35
PCl_5	Off-white solid	167	160 (subl.)	202 (eq) 214 (ax)	80
PBr_5	Red–yellow solid	<100 (d.)	106 (d.)		101
PI_5	Brown–black solid	41			

was converted to $POCl_3$ in the United States in 2001, for example. Examples of further reactions of PCl_3 are given in Scheme 1.

The chemical properties of PBr_3 are similar to those of PCl_3, although there is a difference in reactivity due to the difference in the degree of polarity of the phosphorus–halogen bonds. PI_3 is a powerful and versatile deoxygenating agent, effecting the conversion of selenoxides (R,R′SeO) into selenides, for example.[76]

It is also worth noting that mixed trihalides are known. One example comes in the form of PF_2Cl, which is best made (93% yield) by the reaction of Et_2NPF_2 with PCl_3.[77] The greater reactivity of the P–Cl bond means that it can be used as a source of the PF_2 fragment. The mixed species PCl_2Br, $PClBr_2$, PCl_2I, $PClI_2$, PBr_2I, $PBrI_2$, and PClBrI are formed by the rearrangement of a mixture of the pure trihalides.

8.3 Phosphorus Pentahalides, PX_5

Pentahalides of formula PX_5 are known for all the halogens. PF_5 can be made either by fluorinating PCl_5 with AsF_3 (or CaF_2), or by thermal decomposition of $NaPF_6$ or $Ba(PF_6)_2$, while the industrial demands for PCl_5 are met by reaction involving the action of chlorine upon phosphorus trichloride. PBr_5 is prepared by the reaction of equimolar amounts of PBr_3 and bromine in an appropriate solvent, while PI_5 forms by the action of HI, LiI, NaI, or KI on PCl_5 dissolved in MeI.

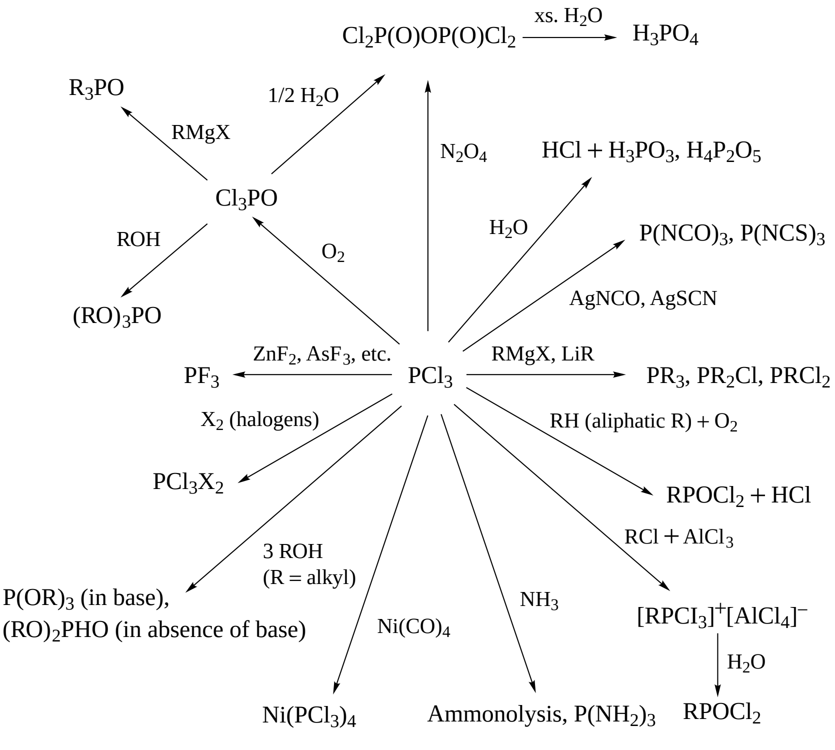

Cl2P(O)OP(O)Cl2
xs. H2O
H3PO4
R3PO
1/2 H2O
RMgX
N2O4
HCl + H3PO3, H4P2O5
Cl3PO
H2O
P(NCO)3, P(NCS)3
ROH
O2
AgNCO, AgSCN
(RO)3PO
ZnF2, AsF3, etc.
RMgX, LiR
PF3
PCl3
PR3, PR2Cl, PRCl2
X2 (halogens)
RH (aliphatic R) + O2
PCl3X2
RPOCl2 + HCl
RCl + AlCl3
3 ROH
(R = alkyl)
P(OR)3 (in base),
(RO)2PHO (in absence of base)
NH3
[RPCl3]+[AlCl4]−
Ni(CO)4
H2O
Ni(PCl3)4
Ammonolysis, P(NH2)3
RPOCl2

Scheme 1 Reactions of PCl_3

The simple formulation 'PX_5' belies the complex structural features these compounds exhibit. Electron diffraction data for PF_5 indicates a trigonal bipyramidal structure; however, the ^{19}F NMR spectrum shows only a single fluorine resonance peak (with concomitant ^{31}P coupling) indicative of a fast exchange by Berry Pseudorotation.[78] When dissolved in nonpolar solvents, PCl_5 is monomeric and molecular, whereas in ionizing solvents such as CH_3NO_2 there are two competing ionizing equilibria generating $[PCl_4][PCl_6]$ and $[PCl_4]Cl$. Solid PBr_5 exists as $[PBr_4]^+Br^-$ which then dissociates completely to PBr_3 and Br_2 in the vapor phase. PI_5 appears to exist as $[PI_4]^+I^-$ in solution.

In terms of physical properties, PF_5 is a thermally stable and chemically reactive colorless gas that fumes on contact with moist air and immediately hydrolyzes with water. PCl_5 reacts violently with water to give HCl and H_3PO_4, but in equimolar amounts the reaction can be moderated to give $POCl_3$. PCl_5 chlorinates alcohols to alkyl halides, and carboxylic acids to the corresponding RCOCl, and examples of further reactivity are given in Scheme 2; PBr_5 is an effective bromination agent, as expected from the weakness of the axial P–Br bond.

In terms of mixed species, all the molecular chlorofluorides, PCl_xF_{5-x}, are known, as is PBr_2F_3. The latter forms both as an unstable liquid (decomp. 15 °C) and as a white crystalline powder $[PBr_4]^+[PF_6]^-$ (subl. 135 °C with decomposition).

In addition to the aforementioned sulfides and oxides of phosphorus, all the oxohalides POX_3 and thiohalides SPX_3 have been made and fully characterized, with phosphoryl oxide $POCl_3$ being by far the most important. It is made in large quantities (about 47 000 tons in 2001 in the USA alone) by the action of oxygen upon PCl_3, and finds use in the manufacture of phosphate esters for plasticizers, flame retardants, hydraulic fluids, and other applications. POF_3 may be prepared by the fluorination of $POCl_3$ with metallic fluorides, $POBr_3$ by the action of PBr_5 on P_4O_{10}, and POI_3 by iodinating $POCl_3$ with LiI. In the appropriate conditions, sulfur reacts with PX_3 to produce PSX_3. Most of the phosphoryl and thiophosphoryl halides produced are colorless gases or volatile liquids, though POI_3 (violet) $PSBr_3$ (yellow) and PSI_3 (red) (mp 48 °C) form as colored solids. All these compounds (Table 5) hydrolyze readily on contact with water.

9 TRANSITION METAL CHEMISTRY

In terms of the total number of species known, the transition metals chemistry of phosphorus is dominated by the metal phosphides and by complexes of organo-substituted phosphanes. Both are dealt with in some detail in other sections; suffice to say here that transition metal phosphane complexes are of paramount importance in terms of catalytic behavior in all manner of industrial and academic-related scenarios – and as such have been extensively reviewed.[34]

Molecular complexes of 'naked' phosphorus ligands can be generated and the area has been well reviewed.[79] Figure 13 provides examples containing progressively larger phosphorus units; thus we see examples of ligands bearing the following number of P atoms: 1,[80] 2,[81] 3,[82] 4,[83,84] 5,[85] 6,[86] 7,[87] 8,[88] 10,[89] 12 and 14.[90] This list is only a fraction of the total number of examples known – bearing in mind that for many of the units there are numerous coordination modes known.

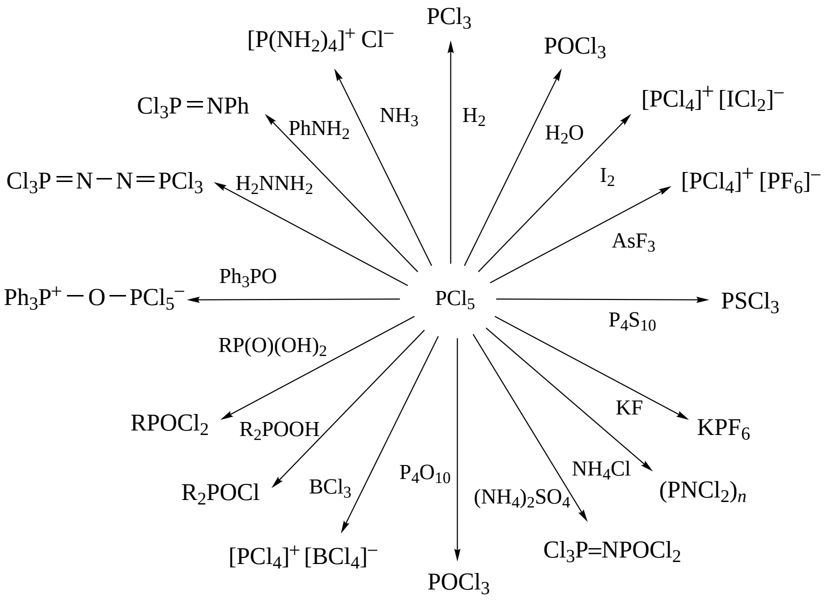

Scheme 2 Reactions of PCl_5

Table 5 Some physical properties and ^{31}P NMR chemical shifts δ of phosphoric and thiophosphoric trihalides and mixed halides

Compound	Physical state at 25 °C	Mp (°C)	Bp (°C)	Density (g cm^{-3})	δ (ppm)
POF_3	Colorless gas	−39.1	−39.7	–	−35.5
$POCl_3$	Colorless liquid	1.25	105.1	1.645	−2.2
$POBr_3$	Solid	55	191.7	–	−102.9
POI_3	Dark violet cryst.	53	–	–	–
$POFCl_2$	Colorless liquid	−80.1	52.2	1.5931	0
POF_2Cl	Colorless gas	−96.4	3.1	1.6555	−15
POF_2Br	Liquid	−84.0	30.5	2.099	–
PSF_3	Colorless gas	−148.8	−52.2	–	−32.4
$PSCl_3$	Colorless liquid	−35	125	1.6271	28.8
$PSBr_3$	Yellow crystals	37.8	212 (decomp.)	2.85	111.8
PSI_3	Dark violet cryst.	53	decomp.	–	–
PSF_2Cl	Colorless gas	−155.2	6.3	1.484	−50.0
$PSFCl_2$	Colorless liquid	−96	64.7	1.590	–
PSF_2Br	–	−136.9	35.5	1.94	−28.6
$PSFBr_2$	–	−75.2	125.3	2.390	–

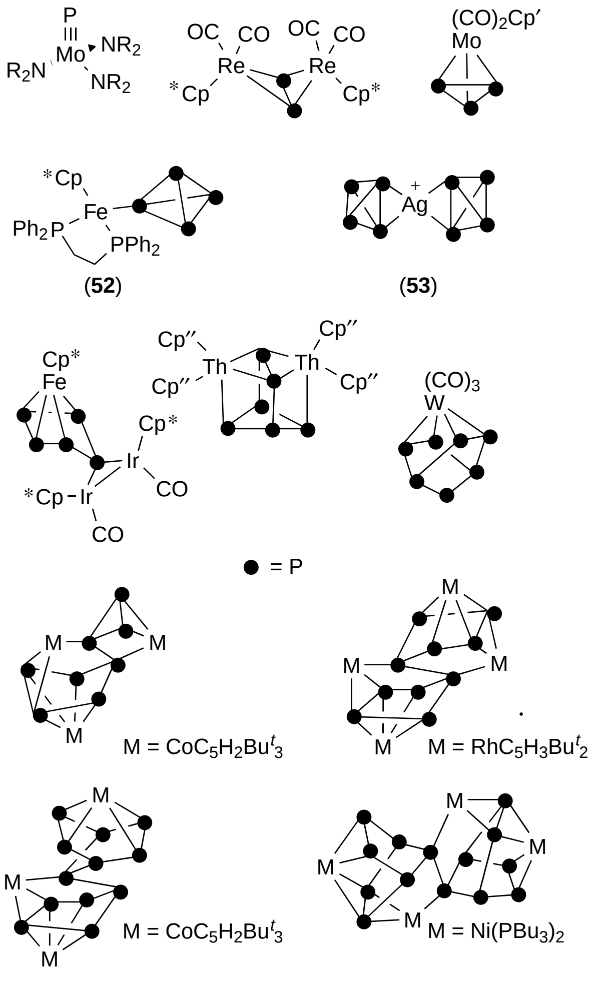

(**52**) (**53**)

Figure 13 The structure of a range of metal-phosphide complexes

To highlight but two of them (both recent): first, the isolation of the iron complex (**52**) provided the first example of a perfectly air stable complex within which P_4 binds through just one atom.[83] This well illustrates the effect that coordination can have on the properties of compounds (consider the air-sensitivity of the free P_4 unit found in white phosphorus). The second is a similar complex of silver in which the P_4 unit now binds side as shown (**53**); this is the first example of such a binding mode and has elicited much interest.[84]

10 SUMMARY – AND THE FUTURE

Even from such a brief overview of its chemistry, it should be clear that phosphorus is an element still at the forefront of all areas of practical chemistry – from purely academic right to decidedly industrial. Though many of the latter uses are declining because of environmental concerns – witness the decrease in the use of phosphate detergents, ZDDP oil additives and organophosphorus pesticides – the fact remains that demand for the element is still enormous. Eventually, as the twenty-first century progresses, this demand will impact upon resources, and economics will dictate that phosphate recovery, – for example, from sewage – becomes vital. Much work to this end is already underway.[91]

In the laboratory, use of the phosphorus and its compounds continues apace, either in the form of well-known ligands (such as phosphanes) imparting unusual and often desirable properties upon their complexes, or more fundamental reactions, often of the element itself. As some of the structures shown in this report attest, it may be 335 years since Brandt's first forays into elemental phosphorus chemistry but the material continues to intrigue, perplex, and surprise in equal measure – and it shows no sign of abating on that front.

11 RELATED ARTICLES

Phosphates: Solid-state Chemistry; Phosphides: Solid-state Chemistry; Phosphorus–Nitrogen Compounds; Phosphorus: Organophosphorus Chemistry.

12 REFERENCES

1. R. J. van Zee and A. U. Khan, *J. Am. Chem. Soc.*, 1974, **96**, 6805.
2. J. Emsley, ‘The Shocking History of Phosphorus’, Pan, London, 2001.
3. D. E. C. Corbridge, ‘Phosphorus: An Outline of its Chemistry, Biochemistry and Technology’, Elsevier, Amsterdam, 1985.
4. J. R. van Wazer, ‘Phosphorus and Its Compounds’, Interscience Publishers, New York, 1961, Vol. 2.
5. J. Emsley and D. Hall, ‘The Chemistry of Phosphorus’, Harper & Row, London, 1976.
6. T. Sasamori, N. Takeda, M. Fujio, M. Kimura, S. Nagase, and N. Tokitoh, *Angew. Chem., Int. Ed. Engl.*, 2002, **41**, 139.
7. D. R. Lide, ed., ‘CRC Handbook of Chemistry and Physics’, CRC Press, Boca Raton, FL, 1990–1991, Sect. 11, p. 37.
8. J. Emsley, *Chem. Ber.*, 1977, **13**, 459.
9. D. A. Buckingham and S. Jasinski, *Phosphate Rock Statistics*, USGS, 2002, available at http://minerals.usgs.gov/minerals/pubs/of01-006/phosphate.pdf.
10. M. E. Schlesinger, *Chem. Rev.*, 2002, **102**, 4267.
11. P. A. B. Raffle., ed., ‘Hunter’s Diseases of Occupations’, Edward Arnold, London, 1994.
12. A. Hamilton, ‘Exploring the Dangerous Trades: The Autobiography of Alice Hamilton, M.D.’, Little, Brown and Company, Boston, MA, 1943, p. 114; Excerpted at http://historymatters.gmu.edu/d/105/
13. Y. Katayama, T. Mizutani, W. Utsumi, O. Shimomura, M. Yamakata, and K. Funakoshi, *Nature*, 2000, **403**, 170.
14. P. Jovari and L. Pusztai, *Appl. Phys. A*, 2002, **74**(Suppl. S), S1092.
15. G. Seifert and E. Hernandez, *Phys. Chem. Lett.*, 2000, **318**, 355.
16. E. Urnezius, W. W. Brennessal, C. J. Cramer, J. E. Ellis, and P. R. Schleyer, *Science*, 2002, **295**, 832.
17. N. Koerber and J. Aschenbrenner, *J. Chem. Soc., Dalton Trans.*, 2001, 1165.
18. Z. Y. Liu, R. B. Huang, and L. S. Zheng, *Z. Phys. D: At. Mol. Clusters*, 1996, **38**, 171.
19. I. Krossing, *J. Chem. Soc., Dalton Trans.*, 2002, 501.
20. N. Burford, P. J. Rogogna, R. McDonald, and M. Ferguson, *Chem. Commun.*, 2003, 2066.
21. M. Baudler, *Angew. Chem., Int. Ed. Engl.*, 1987, **26**, 419.
22. M. Baudler and P. Winzek, *Z. Anorg. Allg. Chem.*, 1999, **625**, 417.
23. D. C. Bradley, M. B. Hursthouse, M. Motevalli, and Z. Dao-Hong, *J. Chem. Soc., Chem. Commun.*, 1991, 7.
24. H. Dorn, R. A. Singh, J. A. Massey, A. J. Lough, and I. Manners, *Angew. Chem., Int. Ed. Engl.*, 1999, **38**, 3321.
25. A. R. McWilliams, H. Dorn, and I. Manners, *Top. Curr. Chem.*, 2002, **220**, 141.
26. D. Scheschkewitz, H. Amii, H. Gornitzka, W. W. Schoeller, D. Bourissou, and G. Bertrand, *Science*, 2002, **295**, 1880.
27. H. H. Karsch, G. Hanika, B. Huber, K. Meindl, S. Konig, K. Kruger, and G. Muller, *J. Chem. Soc., Chem. Commun.*, 1989, 373.
28. A. K. Saxena, J. A. Maguire, and N. S. Hosmane, *Chem. Rev.*, 1997, **97**, 2421.
29. B. Stibr, *Collect. Czech. Chem. Commun.*, 2002, **67**, 843.
30. W. Haubold, W. Keller, and G. Sawitzki, *Angew. Chem., Int. Ed. Engl.*, 1988, **27**, 925.
31. B. Gruner, D. Hnyk, I. Cisarova, Z. Plzak, and B. Stibr, *J. Chem. Soc., Dalton Trans.*, 2002, 2954.
32. M. L. Cole, D. E. Hibbs, C. Jones, and N. A. Smithies, *J. Chem. Soc., Dalton Trans.*, 2000, 545.
33. A. J. Christophers, S. Singh, and D. G. Goddard, *Med. J. Aust.*, 2002, **176**, 403.
34. J. H. Downing and M. B. Smith, Phosphorus ligands, in ‘Comprehensive Coordination Chemistry II’, ed. A. B. P. Lever, Elsevier, Oxford, 2003, Vol.1, p. 253.
35. F. Mathey, *Angew. Chem., Int. Ed. Engl.*, 2003, **42**, 1578.
36. Y. Canac, D. Bourissou, A. Baceiredo, H. Gornitzka, W. W. Schoeller, and G. Bertrand, *Science*, 1998, **279**, 2080.
37. L. Cataldo, S. Choua, T. Berclaz, M. Geoffroy, N. Mezailles, L. Ricard, F. Mathey, and P. Le Floch, *J. Am. Chem. Soc.*, 2001, **123**, 6654.
38. E. Niecke, A. Fuchs, F. Baumeister, M. Neiger, and M. Schoeller, *Angew. Chem., Int. Ed. Engl.*, 1995, **34**, 555.
39. P. Killian, A. M. Z. Slawin, and J. D. Woollins, *Chem. Commun.*, 2003, 1174.
40. J. M. Lynam, M. C. Copsey, M. Green, J. C. Jeffery, J. E. McGrady, C. A. Russell, J. M. Slattery, and A. C. Swain, *Angew. Chem., Int. Ed. Engl.*, 2003, **342**, 2778.
41. G. Fritz, *Z. Naturforsch.*, 1953, **8b**, 776.
42. G. Fritz and P. Scheer, *Chem. Rev.*, 2000, **100**, 3341.
43. M. Baudler, G. Scholz, K. Tebbe, and M. Feher, *Angew. Chem., Int. Ed. Engl.*, 1988, **28**, 339.
44. I. Kovacs, G. Baum, G. Fritz, D. Fenske, N. Wiburg, H. Schuster, and K. Karaghiosoff, *Z. Anorg. Allg. Chem.*, 1993, **619**, 453.
45. G. Fritz and J. Harer, *Z. Anorg. Allg. Chem.*, 1983, **504**, 23.
46. H. G. vonSchnering, D. Fenske, W. Honle, M. Binneweis, and K. Peters, *Angew. Chem., Int. Ed. Engl.*, 1979, **18**, 679.

47. H. H. Karsch, B. Deubelly, J. Reide, and G. Muller, *Angew. Chem., Int. Ed. Engl.*, 1987, **26**, 673.
48. A. Kandri-Rodi, J.-P. Declercq, A. Dubourg, H. Ranaivonjatovo, and J. Escudie, *Organometallics*, 1995, **14**, 1954.
49. C. H. Lai, M. D. Su, and S. Y. Chu, *J. Phys. Chem. A*, 2002, **106**, 575.
50. A. H. Cowley, J. E. Kilduff, J. G. Lasch, S. K. Mehrotra, N. C. Norman, M. Pakulski, B. R. Whittlesey, J. L. Atwood, and W. E. Hunter, *Inorg. Chem.*, 1984, **23**, 2582.
51. S. Strojek and M. Jansen, *Z. Naturforsch.*, 1997, **B52**, 906.
52. T. M. Klapotke, *Angew. Chem., Int. Ed. Engl.*, 2003, **42**, 3461.
53. H. Remy and H. Falius, *Chem. Ber.*, 1959, **92**, 2199.
54. H. Niederprum, *Angew. Chem., Int. Ed. Engl.*, 1975, **14**, 614.
55. C.-Y. Chen, F.-R. Lo, H.-M. Kao, and K.-H. Lii, *Chem. Commun.*, 2000, 1061.
56. R. Minkwitz and S. Schneider, *Angew. Chem., Int. Ed. Engl.*, 1999, **38**, 210.
57. E. Smulders, ‘Laundry Detergents’, Wiley-VCH, Weinheim, 2002.
58. M. E. Jason, T. Ngo, and S. Rahman, *Inorg. Chem.*, 1997, **36**, 2633.
59. H. Nowottnick and R. Blachnik, *Z. Anorg. Allg. Chem.*, 1999, **625**, 1966.
60. H. Nowottnick and R. Blachnik, *Z. Anorg. Allg. Chem.*, 2000, **626**, 611.
61. The Innovation Group, *Chemical Profiles*, 2002, http://www.the-innovation-group.com/ChemProfiles/Phosphorus%20Pentasulfide.htm.
62. J. R. Rollo, G. R. Burns, W. T. Robinson, R. J. H. Clark, H. M. Dawes, and M. B. Hursthouse, *Inorg. Chem.*, 1990, **29**, 2889.
63. G. J. Penney and G. M. Sheldrick, *J. Chem. Soc.*, 1971, 245.
64. R. Blachnik, P. Lonnecke, K. Boldt, and B. Engelen, *Acta Crystallogr., Sect. C*, 1994, **50**, 659.
65. M. Ruck, *Z. Anorg. Allg. Chem.*, 1994, **620**, 1832.
66. A. Pfitzner and S. Reiser, *Inorg. Chem.*, 1999, **38**, 2451.
67. A. Pfitzner, S. Reiser, and T. Nilges, *Angew. Chem., Int. Ed. Engl.*, 2000, **39**, 4160.
68. K. Chondroudis and M. G. Kanatzidis, *Chem. Commun.*, 1997, 401.
69. S. Jorgens, D. Johrendt, and A. Mewis, *Chem. Eur. J.*, 2003, **9**, 2405.
70. K. D. Setzer, M. Beutel, and E. H. Fink, *J. Mol. Struct.*, 2003, **221**, 19.
71. B. W. Tattershall and N. L. Kendall, *Polyhedron*, 1994, **13**, 1517.
72. K. B. Dillon and B. Y. Xue, *Inorg. Chim. Acta*, 2001, **320**, 172.
73. I. Krossing and I. Raabe, *Angew. Chem., Int. Ed. Engl.*, 2001, **40**, 4406.
74. M. Gonsior, I. Krossing, L. Muller, I. Raabe, M. Jansen, and L. vanWullen, *Chem. – Eur. J.*, 2002, **8**, 4475.
75. The Innovation Group, *75 Chemical Profiles*, 2002, http://www.the-innovation-group.com/ChemProfiles/Phosphorus%20Trichloride.htm.
76. J. N. Denis and A. Krief, *J. Chem. Soc., Chem. Commun.*, 1980, 544.
77. W. Albers, W. Kruger, W. Storzer, and R. Schmutzler, *Synth. React. Inorg. Met.-Org. Chem.*, 1985, **15**, 187.
78. R. S. Berry, *J. Chem. Phys.*, 1960, **32**, 933.
79. O. J. Scherer, *Acc. Chem. Res.*, 1999, **32**, 751.
80. C. C. Cummins, *Chem. Commun.*, 1998, 1777.
81. O. J. Scherer, M. Ehses, and G. Wolmershauser, *J. Organomet. Chem.*, 1997, **531**, 217.
82. M. Scheer, K. Schuster, A. Krug, and H. Hartung, *Chem. Ber.*, 1997, **130**, 1299.
83. I. de los Rios, J.-R. Hamon, P. Hamon, C. Lapinte, L. Toupet, A. Romerosa, and M. Peruzzini, *Angew. Chem., Int. Ed. Engl.*, 2001, **40**, 3910.
84. I. Krossing and L. vanWullen, *Chem. – Eur. J.*, 2002, **8**, 700.
85. M. Detzel, T. Mohr, O. J. Scherer, and G. Wolmershauser, *Angew. Chem., Int. Ed. Engl.*, 1994, **33**, 1110.
86. O. J. Scherer, B. Werner, G. Heckmann, and G. Wolmershauser, *Angew. Chem., Int. Ed. Engl.*, 1991, **30**, 553.
87. S. Charles, J. A. Danis, J. C. Fettinger, and B. W. Eichhorn, *Inorg. Chem.*, 1997, **36**, 3772.
88. O. J. Scherer, G. Berg, and G. Wolmershauser, *Chem. Ber.*, 1996, **129**, 53.
89. O. J. Scherer, B. Hobel, and G. Wolmershauser, *Angew. Chem., Int. Ed. Engl.*, 1992, **31**, 1027.
90. R. Ahlrichs, D. Fenske, K. Fromm, H. Krautscheid, U. Krautscheid, and O. Treutler, *Chem. – Eur. J.*, 1996, **2**, 238.
91. For an overview and bibliography covering many aspects of this area see the Natural History Museum’s site at http://www.nhm.ac.uk/mineralogy/phos/

Phosphorus–Nitrogen Compounds

Ionel Haiduc
Universitatea ‘Babes-Bolyai’, Cluj-Napoca, Romania

Based in part on the article Phosphorus–Nitrogen Compounds by Robert H. Neilson which appeared in the Encyclopedia of Inorganic Chemistry, First Edition.

1	Introduction	1
2	Monophosphorus–Nitrogen Compounds	1
3	Acyclic Diphosphorus–Nitrogen Compounds	10
4	Oligomeric Linear and Branched P–N Chains; Dendrimers	14
5	Cyclic Phosphorus–Nitrogen Compounds	14
6	High Molecular Polymeric P=N Compounds	19
7	Applications	19
8	References	20

1 INTRODUCTION

Phosphorus–nitrogen chemistry is a very fertile area of chemistry. There is a great variety of compounds with phosphorus–nitrogen molecular skeletons, with both inorganic and organic substituents at either or each of the two sites. The progress in phosphorus–nitrogen chemistry is continuous and novel and interesting compounds are frequently reported. The routine use of single crystal X-ray structure determinations in the last decade contributed greatly to a new surge in phosphorus–nitrogen chemistry. This article cannot cover exhaustively the field and emphasis will be placed upon new results. Classical phosphorus–nitrogen chemistry will not, however, be ignored. Whenever possible, references to review literature will be cited, to open the gate to more detailed information for the interested reader.

Purely inorganic phosphorus–nitrogen compounds are relatively few and little studied. These include the phosphorus nitrides $(PN)_x$, $(P_3N_5)_x$, and the so-called ‘phospham’ $[PN_2H]_x$, all of which are ill-defined amorphous polymeric materials.[1,2] Recently, such materials have been receiving increased attention.[3] Thus, a reaction product of P_3N_5 with $RbNH_2$ at 400 °C, namely, $Rb_8[P_4N_6(NH)_4](NH_2)_2$, was found to contain an adamantane-like anion $[P_4N_6(NH)_4]^{6-}$ isostructural with P_4O_{10}.[4] A series of lithium phosphazo ceramic materials, Li_7PN_4, $Li_{12}P_3N_9$, $Li_{10}P_4N_{10}$, and $LiPN_2$, have been obtained and characterized. The latter contains an anionic network isostructural with SiO_2 (β-cristobalite), whereas $Zn_7[P_{12}N_{24}]Cl_2$ has a zeolite-type tridimensional crystal structure.[5]

Well characterized purely inorganic P–N compounds are the cyclic and polymeric halocyclophosphazenes $(X_2PN)_n$ ($X = F$, Cl, Br, $n = 3, 4, 5, 6\ldots$, characterized as discrete compounds up to $n = 19$ in the case of $X = F$ and up to $n = 8$ in the case of $X = Cl$), the amides $[(NH_2)_2PN]_n$ ($n = 3$, 4),[6] the metaphosphimic acids and their salts $[(HO)(O)PN]_n$ ($n = 3, 4\ldots$).

The introduction of organic substituents at phosphorus or/and nitrogen gave rise to a very extensive field, displaying a broad diversity of compounds, based on variation of oxidation states (mainly +III and +V, but also +II, +IV, and so on, in compounds with P–P bonds) and coordination numbers, from the rare coordination numbers 1 and 2, to common coordination numbers 3, 4, 5, and 6. The ability of phosphorus to form single P–N, double P=N, and sometimes even triple P≡N bonds is an additional feature contributing to the great diversity of phosphorus–nitrogen compounds.

A few chemical reactions leading to P–N compounds are rather general and versatile, and can be performed with compounds in any of the oxydation states and coordination numbers. These include: (a) elimination of halogen or metal halides between a phosphorus–halogen bond and an amine or metalated amine; (b) elimination of an organosilicon halide (usually Me_3SiCl) between a P–X ($X = F$, Cl, Br) and a Si–N compound; (c) elimination of dinitrogen between a phosphorus(III) compound and an organic or element–organic azide (oxidative addition) with formation of a P(V) compound (Scheme 1). Intelligent use of these reactions affords the synthesis of an immense number of P–N compounds.

The chemistry of phosphorus–nitrogen compounds is well covered in a series of specialized monographs (some concentrating on phosphazenes), the Royal Chemical Society’s Specialist Periodical Reports (annual surveys), and numerous review articles (to be cited in the appropriate place of this chapter).

2 MONOPHOSPHORUS–NITROGEN COMPOUNDS

2.1 Mono-coordinate Phosphorus(III)

Iminophosphenium cations, $[{:}P{\equiv}N\text{–}Mes^*]^+$, can be generated from $ClP{=}NMes^*$ with anhydrous $AlCl_3$ or

$$\begin{array}{llcll}
\text{P–X} & + \text{ H–N} & \longrightarrow & \text{P–N} & + \text{ HX} \\
\text{P–X} & + \text{ Li–N} & \longrightarrow & \text{P–N} & + \text{ LiX} \\
\text{P}^{\text{III}} & + \text{ RN}_3 & \longrightarrow & \text{P}^{\text{V}}\text{–NR} & + \text{ N}_2 \\
\text{P–X} & + \text{ Si–N} & \longrightarrow & \text{P–N} & + \text{ Si–X}
\end{array}$$

Scheme 1

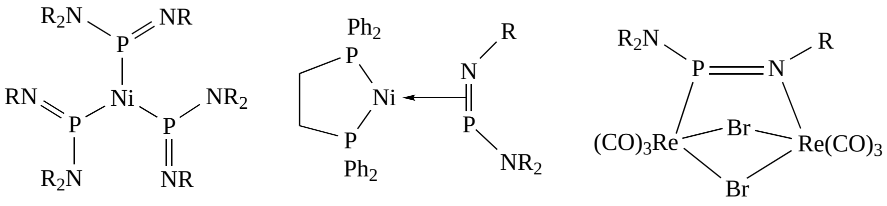

Scheme 2

$GaCl_3$. The presence of the triple bond is supported by the very short phosphorus–nitrogen interatomic distance of 1.475(8) Å measured by x-ray diffraction in the solid.[7] A trifloromethanesulfonate salt $[P{\equiv}N–Mes^*]^+\ [OSO_2CF_3]^-$ (**1**) is also known and can be stabilized by further coordination with 2,2′-bipyridyl and other donors, which make the phosphorus atom three-coordinate.[8]

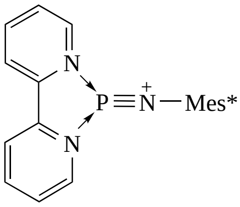

(**1**)

2.2 Two-coordinate Phosphorus(III)

2.2.1 *Phosphinimines (iminophosphines) RP=NR′*

Phosphinimines, RP=NR′, are expected as products of reaction between dihalogenophosphines and primary amines, but they can be obtained as monomers only with very bulky R groups (R = Mes*, Dipp) and cyclic phosph(III)azanes are isolated in most cases depending upon reaction conditions.[9,10] For a review including their interesting chemistry, see Reference[11] They can act as ligands, with formation of unusual metal complexes, including some in which the P=N bond is coordinated as dihapto, or as M–P=N–M bridging through both phosphorus and nitrogen (Scheme 2).[12]

Silylated aminophosphinimines, $R_2N–P{=}NR$ ($R = SiMe_3$) are obtained from $LiNR_2$ with PX_3 (X = F, Cl, Br)[13] or $R_2N–PF_2$, or in reactions involving elimination of chlorotrimethylsilane.[14] They dimerize slowly to cyclic phosphazanes.[15]

A phosphorus analog of benzimidazole (**2**), containing dicoordinate phosphorus, is mentioned as the reaction product between triethylphosphite, $P(OEt)_3$, and *ortho*-phenylenediamine.[16]

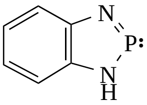

(**2**)

2.2.2 *Phosphinedi(imino) Anions [RN–P–NR]⁻*

Dicoordinate phosphorus is present in the anion $[RN–P–NR]^-$, which can be formulated with the aid of two resonance structures; the anion can be also isolated in dimeric form, containing a P_2N_2 ring (Scheme 3):

The reaction of phosphorus trichloride with *tert*-butylamine was reported to give a dicoordinate phosph(III)azene $Bu^tN{=}P–NHBu^t$, which can be deprotonated to the $[Bu^tNPNBu^t]$ anion.[17] The crystal structure of $K[Bu^tNPNBu^t]$ has been determined.[18] The anion has also been found in a gallium[19] and a lithium[20] complex. In monomeric form, the $[RN–P–NMes]^-$ anion can be obtained when R = mesityl ($Mes = 2,4,6\text{-}Me_3C_6H_2$), *tert*-butyl and 1-adamantanyl, as dimeric lithium ring compounds (**3**)[21]

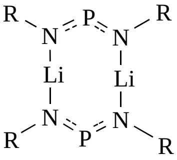

(**3**)

2.2.3 *Aminophosphenium Cations $[R–P–NR'_2]^+$*

A variety of aminophosphenium cations and their coordination chemistry have been reported.[22] Examples are

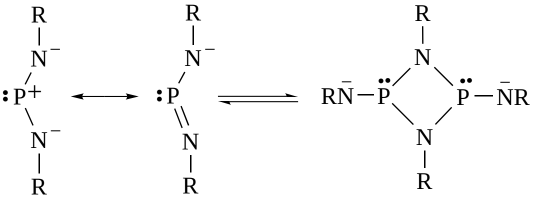

Scheme 3

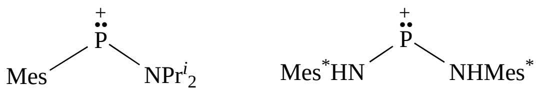

Scheme 4

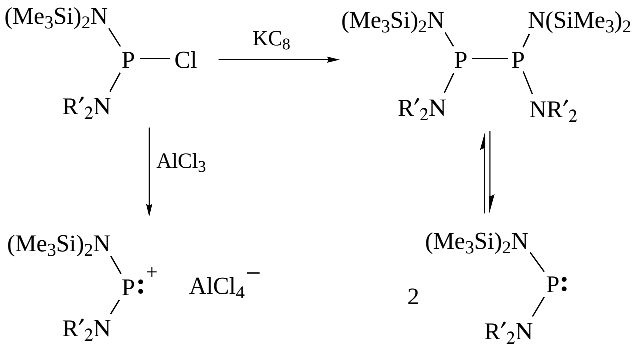

Scheme 5

$[\mathrm{Mes{-}P{-}NPr^{\mathit{i}}_2}]^+$, and $[\mathrm{Mes^*NH{-}P{-}NR_2}]^+$ among others.[23] The cations $[\mathrm{Mes^*Q{-}P{-}NHMes^*}]^+$ (Q = O, NH) are formed by addition of Mes*QH to the triple bond of Mes*N≡P molecule (Scheme 4).[24]

Radicalic and cationic $[(\mathrm{Pr^{\mathit{i}}_2N}){-}\mathrm{P}{-}\mathrm{N(SiMe_3)_2}]^{n+}$ ($n = 0$ and 1) have been obtained by treating the corresponding chloride with potassium graphite and aluminum chloride, respectively (Scheme 5).[25]

2.3 Three-coordinate Phosphorus(III)

2.3.1 *Aminophosphines $R_2P{-}NR'_2$, Diaminophosphines $RP({-}NR')_2$ and Triaminophosphines $P({-}NR'_2)_3$*

The prototype of this class, aminophosphine, $H_2P{-}NH_2$, cannot be isolated because of the tendency of condensation with formation of P–NH–P compounds The primary product of the reaction between PCl_3 and ammonia is $P(NH_2)_3$, but it readily undergoes elimination of ammonia and condensation to a series of PNP compounds, ending up with a polymeric material of composition $P_2(NH)_3$. Derivatives substituted either at phosphorus or nitrogen have been reported, for example, $R_2P{-}NH_2$ with R = F, CF_3 and $RP(NH_2)_2$ where R = MeO, EtO, PhO, Et_2N and MePhN, as ammonolysis products of the corresponding substituted phosphorus chlorides.[26]

Phosphorus trichloride reacts with primary amines in various modes, depending on the nature and bulkiness of the organic groups and reaction condition (solvent, temperature, duration) and amino derivatives Cl_2PNHR, $ClP(NHR)_2$ or $P(NHR)_3$ can be isolated only in particular cases. An added difficulty is the condensation tendency of the P–NHR groups, with elimination of amine and formation of bis(phosphino)amine derivatives or cyclic compounds. Alkylaminodichlorophosphines, $Cl_2P{-}NHR$ (R = Et, *n*-Pr, *iso*-Pr, *iso*-Bu, Am), and tris(aminophosphines), $P(NHR)_3$ (R = *iso*-Bu, CH_2Ph), can be isolated (Scheme 6).[27]

Aminofluorides, $F_2P{-}NR_2$ (R = Me, Et, C_5H_{10}), can be obtained from the corresponding chlorides with SbF_3 or NaF in tetramethylsulfone.[28]

Derivatives of secondary amines are more readily available and can be prepared by using substitution[29,30,31,32] or redistribution[33,34] reactions in a solvent, preferably in the presence of an acid scavenger, which can be excess amine (Scheme 7).

Fully substituted derivatives, such as $R_2P{-}NR_2$ (R = Me),[35] can be prepared from $Cl_2P{-}NR_2$ by using organometallic alkylating agents or from organodihalides, RPX_2 (X = F, Cl, Br, I) with secondary amines.[36] A convenient method is based on the reaction of organophosphine dichlorides, $RPCl_2$, with diorganoaminosilanes, $Me_3SiNR'_2$, with elimination of trimethylchlorosilane (Scheme 8).[37]

Alkylamino derivatives of trivalent phosphorus exist in a prototropic equilibrium with P–H iminophosphoranes. The

$$\mathrm{PCl_3 + 2RNH_2 \longrightarrow Cl_2P{-}NHR + RNH_2{\cdot}HCl}$$
$$\mathrm{PCl_3 + 6RNH_2 \longrightarrow P(NHR)_3 + 3RNH_2{\cdot}HCl}$$

Scheme 6

$$\mathrm{PCl_3 + R_2NH.HCl \longrightarrow Cl_2P{-}NR_2 + 2HCl}$$
$$\mathrm{PCl_3} + 2n\mathrm{HNR_2} \longrightarrow \mathrm{P(NR_2)}n\mathrm{Cl}_{3-n} + n\mathrm{R_2NH{\cdot}HCl}$$
$$\mathrm{P(NR_2)_2 + PCl_3 \longrightarrow Cl_2P{-}NR_2 + ClP(NR_2)_2}$$
$$\mathrm{ClP(NR_2)_2 + PCl_3 \longrightarrow 2Cl_2P{-}NR_2}$$

Scheme 7

$$\mathrm{Cl_2P{-}NMe_2 + 2MeMgBr \longrightarrow Me_2P{-}NMe_2 + MgBr_2 + MgCl_2}$$
$$\mathrm{RPX_2 + 4HNR'2 \longrightarrow RP(NR'_2)_2 + 2HX{\cdot}HNR'_2}$$
$$\mathrm{RPCl_2 + 2Me_3SiNR'_2 \longrightarrow RP(NR'_2)_2 + 2Me_3SiCl}$$

Scheme 8

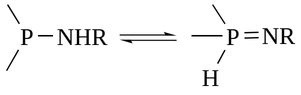

Scheme 9

position of the equilibrium depends on the nature of solvents and substituents at phosphorus and nitrogen sites and is shifted towards the tautomeric form with the least mobile proton (Scheme 9).[38]

Triamino derivatives $(R_2N)_2PNH_2$ can be deprotonated with LiBu and the salts can further react with organometallic chlorides (Scheme 10).[39]

Silylated aminophosphines, for example, $R_2P–N(SiMe_3)_2$ and $R_2P–NR'(SiMe_3)$, are cleanly prepared from lithiated disilazane and aminosilanes, $LiN(SiMe_3)_2$ and $LiNR'(SiMe_3)$, ($R = Me$, Ph, Cl, F; $R' =$ alkyl, Ph) and R_2PCl,[40] respectively. A series of sterically hindered silylaminophosphines, $Bu^tR_2Si(Me_3Si)NPMeR$ ($R =$ Me, Ph), displaying interesting chemistry, have been recently reported.[41]

2.4 Three-coordinate Phosphorus(V)

2.4.1 *Monomeric (amino)Phosphonitriles, $N{\equiv}P(–NR_2)_2$*

Compounds containing a phosphorus–nitrogen triple bond are rare, but an unstable species $N{\equiv}P(NPr^i{}_2)_2$ can be generated at −40 °C by photolysis of $(Pr^i{}_2N)_2PN_3$. Its existence was demonstrated by trapping reactions (e.g. insertion into the Si–Cl bond of Me_3SiCl with formation of $Cl(Pr^i{}_2N)_2P{=}NSiMe_3$). In the absence of a trapping agent, it dimerizes to form a unique dimeric cyclodiphosphazene (Scheme 11, R = *iso*-Pr).[42] Other monomeric phosphonitriles are unknown so far, but their cyclic oligomers (cyclophosphazenes) and high polymers (polyphosphazenes) are extremely well known.

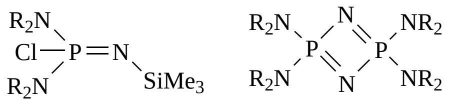

Scheme 11

2.4.2 *Bis(imino)Phosphoranes $RP({=}NR')_2$, Phosphonic Acid Imides $RP(O)({=}NR')$ and Chalcogeno Analogs*

Bis(imino)phosphoranes, $R\text{-}P({=}NR')_2$ of various types, methylene-iminophosphoranes, $R\text{-}P({=}CR_2)({=}NR')$ as well as numerous iminooxo, iminothio, and iminoseleno derivatives, $RP(Q)({=}NR')$ ($Q =$ O, S, Se), are known and have been reviewed.[43,44]

The bis(imino)phosphoranes are prepared by a reaction sequence involving iminophosphine and cyclophosphatetrazenes, but readily dimerize to cyclic four-coordinate compounds (diiminocyclodiphosphazanes) even with bulky organic substituents at nitrogen *R* = *tert*-Bu, CEt_3, 1-Ad (Scheme 12).[45]

Silylated bis(imino)phosphoranes, $(Me_3Si)_2N–P({=}NSiMe_3)_2$, can be prepared by a Staudinger reaction, from $(Me_3Si)_2N–P{=}NSiMe_3$ with Me_3SiN_3.[46]

2.5 Four-coordinate phosphorus(V)

The four-coordinate phosphorus(V)–nitrogen compounds are extremely numerous and detailed data about phosphonic[47] and phosphinic[48] acid derivatives and others[49] can be found in the handbook literature.

The formal replacement of oxygen in phosphorus(V) oxoacids results in a family of imino derivatives, including iminophosphoranes, $R_3P{=}NR'$, diiminophosphinates, $[R_2P(NR')_2]^-$, triiminophosphonates, $[RP(NR')_3]^{-2}$,

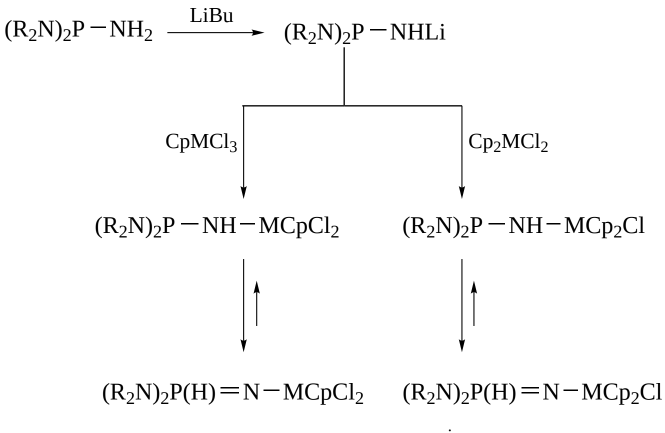

M = Ti, Zr, Hf; R = Pr^i, Cy

Scheme 10

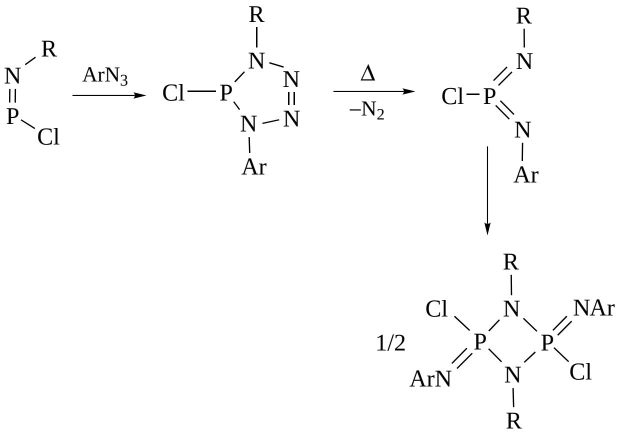

Scheme 12

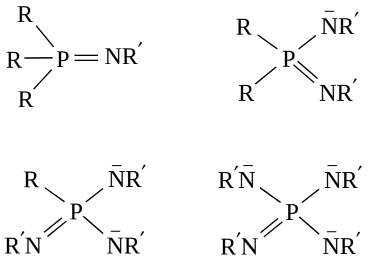

Scheme 13

and tetraiminophosphates $[P(NR')_4]^{-3}$, which have been reviewed (Scheme 13).[50,51]

2.5.1 *Phosphoraneimines (iminophosphoranes) $R_3P{=}NR'$*

Numerous phosphoraneimines (iminophosphoranes), $R_3P{=}NR'$, are known.[52]

Triphenylphosphoraneimine, $Ph_3P{=}NH$, is obtained in the reaction of triphenylphosphine with chloramine, through a phosphonium intermediate (Scheme 14).[53]

Trichlorophosphoraneimines, $Cl_3P{=}NR$, are the most accessible compounds of this class. They can be prepared by reacting phosphorus pentachloride with primary amines or their hydrochlorides, usually in carbon tetrachloride as solvent. The intermediate aminotetrachlorophosphorane $Cl_4P{-}NHR$ is seldom isolated. With aromatic amines the products are monomeric only when the aromatic amine is weakly basic, otherwise the phosphoraneimine will dimerize to cyclic dimers $[Cl_3PNR]_2$ (see Section 5.4).[54]

$$PPh_3 + NH_2Cl \longrightarrow [Ph_3P{-}NH_2]^+Cl^- \xrightarrow{\text{base}} Ph_3P{=}NH$$

Scheme 14

$$PCl_5 + RNH_2 \xrightarrow[-HCl]{} Cl_4P{-}NHR \xrightarrow[-HCl]{} Cl_3P{=}NR$$

Scheme 15

N-Alkyl derivatives, $Cl_3P{=}Nalk$, can be similarly prepared (Scheme 15).[55]

Halogenoiminophosphoranes, $ClPh_2P{=}NAr'$, can be prepared by heating Ph_2PCl_3 with arylamine hydrochlorides, to form phosphonium salts, $[ClPh_2P(NHAr)]^+Cl^-$, which can be further dehydrochlorinated with pyridine to give the desired products.[56] This reaction, known as Kirsanov reaction, is very general and can also be used with trialkoxy(aroxy)dichlorophosphoranes, $(RO)_3PCl_2$,[57] carboxylic acid amides, $ArCONH_2$,[58] sulfonamides, RSO_2NH_2,[59] and many other compounds containing primary amino groups, to form the corresponding derivatives bearing trichlorophosphazo moieties. A very large number of such compounds is listed in Reference[60] The reaction also works with phosphorus compounds bearing NH_2 groups; thus, for example, $(ArO)_2P(Q)NH_2$ ($Q = O$, S) react with PCl_5 to form $(ArO)_2P(Q){-}N{=}PCl_3$ derivatives.[61]

Thionyliminophosphoranes, $(RO)R'_2P{=}N{-}SR(O){=}N{-}R''$ ($R'' = H$, $SiMe_3$) (and polymers derived from them) have been prepared by elimination of Me_3SiOR from $(RO)R'_2P{=}N{-}SiMe_3$ and $RO{-}SR(O){=}N{-}SiMe_3$.[62]

P, N-Organosubstituted iminophosphoranes are important synthetic reagents in organic chemistry. A good method for their synthesis is the reaction of tertiary phosphines with organic azides (known as Staudinger reaction, equation 1).[63] The reaction is much used for the formation of P=N bonds.[64]

$$PR_3 + R'N_3 \longrightarrow R_3P{=}NR' + N_2 \qquad (1)$$

Dibromotriphenylphosphorane reacts with arylamines in the presence of triethylamine (in benzene) to form N-aryliminophosphoranes (equation 2).[65]

$$Ph_3PBr_2 + ArNH_2 + NEt_3 \longrightarrow Ph_3P{=}NAr + [Et_3NH]^+Br^- \qquad (2)$$

With alkylamines, the primary reaction products are aminophosphonium salts, $[Ph_3PNHR]^+Br^-$, which need to be dehydrobrominated with ammonia or sodium amide.[66] In a similar manner, dichlorotriphenylphosphorane reacts with hydrazine dihydrochloride, at 180–220 °C, to form a bis(phosphorane)diimine after treatment with a strong base (liquid ammonia or potassium *tert*-butoxide), equation (3).[67]

$$Ph_3PCl_2 + H_2N{-}NH_2{\cdot}2HCl \longrightarrow [Ph_3P{-}NHNH{-}PPh_3]^{+2}2Cl^- \longrightarrow Ph_3P{=}N{-}N{=}PPh_3 \qquad (3)$$

Dichlorotriphenylphosphorane also reacts with sulfonylamides, on heating, to form $Ph_3P{=}N{-}SO_2Ar$.**68** A N-trimethylsilyl derivative, $Ph_3P{=}N{-}SiMe_3$, can be obtained from Ph_3PBr_2 and hexamethyldisilazane (Scheme 16)**69** and a series of other N-silylated iminophosphoranes, $R_3P{=}N{-}SiMe_3$ (R = alkyl, aryl, OR', NR'_2) has been obtained by the Staudinger reaction, from PR_3 with Me_3SiN_3.**70**

Arylaminophosphoranes are formed in very good yields from aromatic amines, $ArNH_2$ ($Ar = Ph$, $p\text{-}MeC_6H_4$, $p\text{-}BrC_6H_4$, $p\text{-}O_2NMeC_6H_4$, $p\text{-}MeCOC_6H_4$, $1\text{-}C_{10}H_7$, 2-pyridyl) with triphenylphosphine and acetylenedicarboxylate in 1:1:1 ratio, in boiling toluene or *p*-xylene.**71**

The deprotonation of phosphoraneimines, $R_3P{=}NH$, generates an anionic ligand $[R_3P{=}N]^-$ (not known as discrete species) capable of fascinating coordination chemistry, owing to its bonding versatility; it can coordinate as monodentate terminal group (with both linear $M{\equiv}N{-}PR_3$ and bent $M{-}N{-}PR_3$ structures), symmetrical and unsymmetrical bridging (to form four-membered M_2N_2 rings with $\text{-}PR_3$ exocyclic groups) and μ_3-bridging leading to formation of cubane structures (Scheme 17).**72** Interesting compounds are formed with $-N{=}PR_3$ moieties as substituents in main group chemistry.**73** Polymetallic clusters with R_3PN ligands are also known.**74**

Iminophosphoranes can also coordinate in protonated form, for example, in $[Cl_2Be(\mu\text{-}HNPEt_3)]_2$ (**4**).**75**

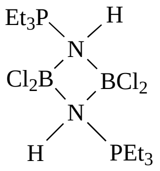
Et3P
H
N
Cl2B
BCl2
N
H
PEt3

(**4**)

N-Substituted iminophosphoranes, $R_3P{=}NR'$, also coordinate through nitrogen to magnesium,**76** group 13 metals (M = Al, Ga, In),**77** copper(I)**78** and other metals (Scheme 18).

Alkyliminophosphoranes can be deprotonated at α-carbon position with LiR reagents and the resulting anions can act as chelating or bridging ligands, to form a variety of unusual compounds (Scheme 19).

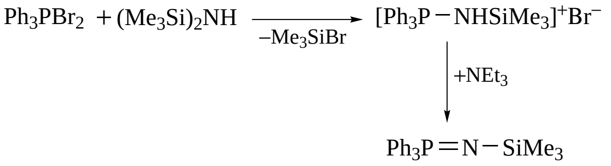
Ph3PBr2 + (Me3Si)2NH
–Me3SiBr
[Ph3P−NHSiMe3]+Br−
+NEt3
Ph3P=N−SiMe3

Scheme 16

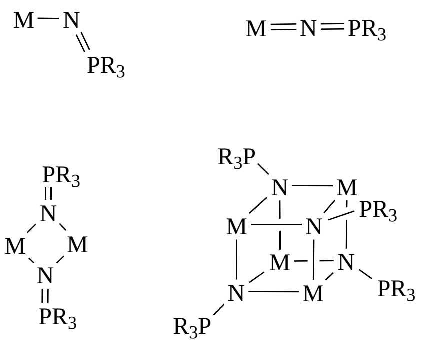
M−N
PR3
M=N=PR3
PR3
N
M
M
N
PR3
R3P
N
M
M
N
PR3
M
N
N
M
PR3
R3P

Scheme 17

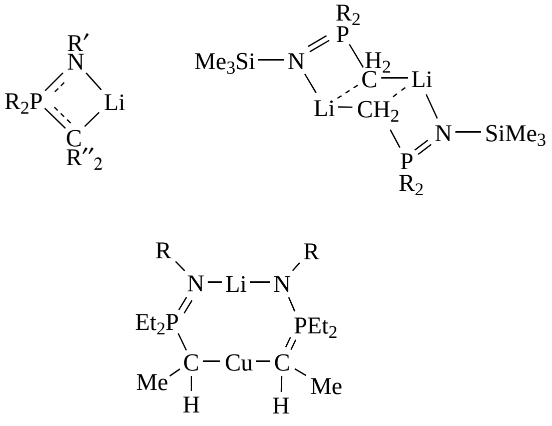
R′
N
R2P
Li
C
R″2
R2
P
Me3Si−N
H2
C
Li
Li−CH2
N−SiMe3
P
R2
R
R
N−Li−N
Et2P
PEt2
C−Cu−C
Me
Me
H
H

Scheme 19

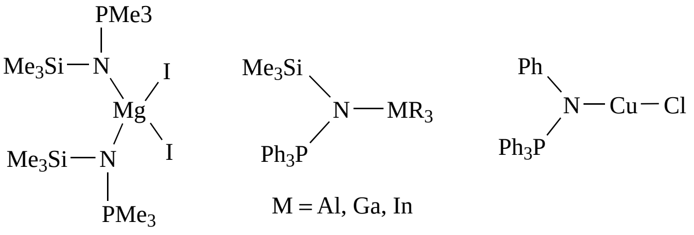
PMe3
Me3Si−N
I
Mg
I
Me3Si−N
PMe3
Me3Si
N−MR3
Ph3P
M = Al, Ga, In
Ph
N−Cu−Cl
Ph3P

Scheme 18

2.5.2 *Phosphinimidoamines $R_2P(=NR')(NR'_2)$ and Diimidophosphinic Anions $[R_2P(NR')_2]^-$*

Phosphinimidoamides, $R_2P(=NR')(NR'_2)$, and their chlorides, are prepared by reactions of azides with various secondary phosphines derivatives (Scheme 20).[79]

A similar reaction with arylsulfonyl azides yields $R_2P(=N–SO_2Ar)X$ ($X = Cl$, OR, NH_2, $NHNH_2$, etc.).[80] Secondary phosphines also react with silylazides, to form N-silylated imidoamino derivatives (Scheme 21).[81]

Other useful reactions for the synthesis of $Ph_2P(NSiMe_3)(NHSiMe_3)$ involve diphenyldiaminophosphonium intermediates (Scheme 22).[82]

Deprotonation of $R_2P(=NR')(NHR')$ produces $[R_2P(NR)_2]^-$ anions, which can be interesting ligands and numerous metal complexes of methylated diiminophosphinato anions, have been characterized structurally.[83] Thus, the diiminophosphinic anion, $[Me_2P(NMe)_2]^-$ forms a platinum chelate in a reaction with Zeise's salt.[84] A useful ligand of this class is the anion $[\mathrm{Bu}^t_2\mathrm{P(NSiMe_3)_2}]^-$, which is highly basic and forms very stable metal complexes.[85] Cyclic compound (**5**) ($R = SiMe_3$) with bridging diimidodiphosphinato ligands is formed with copper(I).[86]

$$R_2P–H + 2R'N_3 \longrightarrow R_2P(=NR')(NHR') + 2N_2$$

$$R_2P–Cl + R''N_3 \longrightarrow R_2P(=NR')Cl + N_2$$

$$R_2P–NHR' + R''N_3 \longrightarrow R_2P(=NR'')(NHR') + N_2$$

$$R_2P–NR'_2 + R''N_3 \longrightarrow R_2P(=NR'')(NR'_2) + N_2$$

Scheme 20

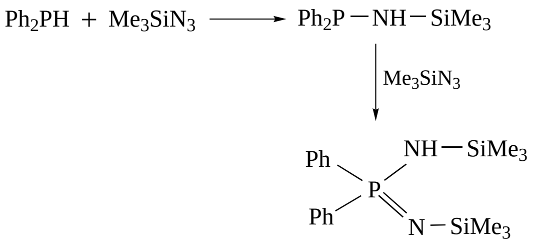

Scheme 21

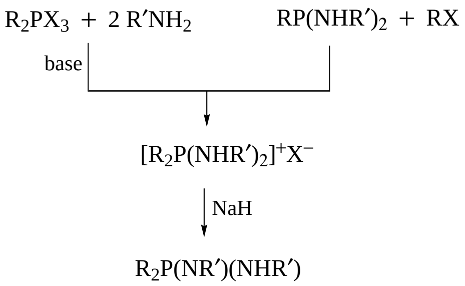

Scheme 22

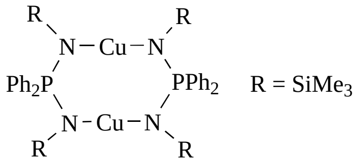

(**5**)

2.5.3 *Phosphonimidodiamines $RP(=NR')(–NR'_2)_2$ and Triimidophosphonic Anions $[RP(NR')_2]^{2-}$*

A representative of this class, $PhP(=NPh)(NHPh)_2$, has been prepared by the reaction of phenylphosphine with phenylazide (equation 4). Deprotonation affords triimidophosphonic anions $[RP(NR')_2]^-$.[87]

$$PhPH_2 + 3PhN_3 \longrightarrow Ph–P(=NPh)(NHPh)_2 + 3N_2 \tag{4}$$

The $[HP(NR)_3]^{-2}$ anion (R = 2-methoxyphenyl) can be regarded as an imido analog of phosphite $[HPO_3]^{-2}$ and is obtained by lithiation of the reaction product between phosphorus trichloride and 2-methoxyaniline. The lithium 'salt' is in fact a polycyclic cage compound.[88]

2.5.4 *Amidophosphoric Triamines $P(=NR')(–NR'_2)_3$ and Tetraimidophosphato Anions $[P(NR')_4]^{-3}$*

Compounds of this class can be prepared with the aid of Staudinger reaction, for example, $P(=NPh)(NMe_2)_3$.[89] The derived anions $[P(NHR)_4]^{-3}$ are imido analogs of phosphate. The anion with R = Ph is formed by deprotonation of tetraaminophosphonium halides $[P(NHPh)_4]^+X^-$ with butyllithium.

2.5.5 *Phosphinic Acid Amides $R_2P(=O)(–NR'_2)$ and Thio Analogs*

Phosphinic acid chlorides react with concentrated. aqueous ammonia to form amides, $R_2P(O)NH_2$,[90] and with primary and secondary amines, in the presence of HCl scavengers (pyridine, triethylamine, etc.) to form $R_2P(Q)(NR'_2)$ (Q = O or S), for example, R = Ph, Q = O, R′Et, Pr, *iso*-Pr, Bu, *tert*-Bu, $PhCH_2$.[91] Oxidation and addition of sulfur to $R_2P–NR'_2$ also yield phosphinic acid amides, $R_2P(Q)(NR'_2)$ (Q = O or S).[92] Related compounds are the hydrazides, $R_2P(Q)NHNHR'$ (Q = O, S; R′ = H, alkyl).[93]

2.5.6 *Phosphonic Acid Diamides $RP(=O)(NR'_2)_2$ and Thio Analogs*

Phosphonic acid diamides, $\mathrm{RP(=O)(NR'_2)_2}$ are obtained by reacting the dichlorides, $\mathrm{RP(=O)Cl_2}$ with ammonia, primary or secondary amines.[94] The number of known compounds of this class is legion[95] and typical examples can be cited, for example, $\mathrm{MeP(O)(NH_2)_2}$,[96] $\mathrm{PhP(O)(NH_2)_2}$,[97] $\mathrm{MeP(O)(NHR')_2}$, with R′ = Me, Ph, *p*-$\mathrm{MeC_6H_4}$, *p*-$\mathrm{ClC_6H_4}$,[98,99] $\mathrm{EtP(O)(NR_2)_2}$ (R = Me, Et, Pr),[100] $\mathrm{PhP(O)(NHR)_2}$ (R = Et, Bu, But, C5H11, Ph, other aryls)[101] and many others. Numerous mixed amide-halides, $\mathrm{RP(O)(X)(NR'_2)}$ and amide-esters, $\mathrm{RP(O)(NR')(OR'')}$ are also known.[95] Related compounds are the hydrazides, for example, $\mathrm{PhP(O)(NHNH_2)_2}$,[102] and $\mathrm{PhP(O)(NHNHPh)_2}$.[103]

Alkoxyaminophosphines react with alkyl halides in an Arbuzov–Michaelis type reaction to form phosphonic acid diamides via thermally unstable phosphonium intermediates (equation 5).[104]

$$\mathrm{P(OR)(NR'_2)_2 + RX \longrightarrow [RP(OR)(NR'_2)_2]^+X^- \longrightarrow RP(O)(NR'_2)_2 + RX} \tag{5}$$

Thio analogs of these compounds, for example, $\mathrm{PhP(S)(NHR)_2}$ can also be prepared similarly, from the corresponding thiophosphonic halides and amines[105] or by oxidative addition of sulfur to diaminophosphines, $\mathrm{RP(NR'_2)_2}$.[106]

Phenylphosphonic acid diamides, $\mathrm{PhP(Q)(NHBu^t)_2}$ (Q = S, Se) were prepared from $\mathrm{PhP(NHBu^t)_2}$ by oxidative addition of sulfur or selenium and the oxo derivative $\mathrm{PhP(O)(NHBu^t)_2}$ by oxidation with *tert*-butyl peroxide. Their lithiation produces unusual cyclic or polycyclic dilithium salts of the phosphonate dianions $\mathrm{[PhP(Q)(NBu^t)_2]^{-2}}$ (Q = O, S, Se). The dimethylaluminum derivatives $\mathrm{PhP(Q)(NBu^t)_2AlMe_2}$ (Q = S, Se) obtained from $\mathrm{PhP(Q)(NHBu^t)_2}$ with $\mathrm{AlMe_3}$ are four-membered chelate rings.[107]

2.5.7 *Phosphoric Acid Triamides $O{=}P(NR'_2)_3$ and Thio Analogs*

The prototype of this class, $\mathrm{OP(NH_2)_3}$, is formed in the reaction of $\mathrm{OPCl_3}$ with liquid ammonia[108] or with gaseous $\mathrm{NH_3}$ in trichloromethane solution at low temperature.[109] Substituted phosphoric acid triamides $\mathrm{O{=}P(NR_2)_3}$ are prepared in the reaction of phosphorus oxotrichloride with secondary amines, under heating or in the presence of acid scavengers; under milder conditions the mono- and diamido chlorides can be easily obtained (equation 6).[110] Hexamethylphosphoric acid triamide, $\mathrm{OP(NMe_2)_3}$, an excellent aprotic organic solvent prepared from $\mathrm{OPCl_3}$ and dimethylamine, deserves to be mentioned here.[111]

$$\mathrm{OPCl_3 + HNR_2 \longrightarrow Cl_2P(O){-}NR_2 \longrightarrow ClP(O)(NR_2)_2 \longrightarrow P(O)(NR_2)_3} \tag{6}$$

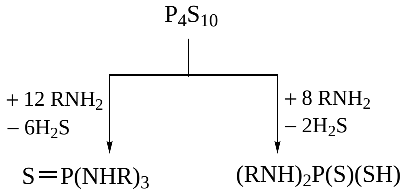

Scheme 23

Phosphorus oxotrifluoride, $\mathrm{OPF_3}$, reacts under milder conditions (at room temperature) to form $\mathrm{F_2(O)P{=}NR_2}$ and $\mathrm{F_2(O)P{-}NHR}$. Similar reactions of $\mathrm{SPCl_3}$ (on prolonged heating) or $\mathrm{SPF_3}$ (under milder conditions) with secondary amines give $\mathrm{SP(NR_2)_3}$.[112,113,114] Hydrazides, for example, $\mathrm{OP(NHNHAr)_3}$ can be similarly prepared. With primary amines (e.g. arylamines), the final products can be dimeric cyclic compounds $\mathrm{[(ArNH)(Q)PNAr]_2}$ (Q = O, S) especially after prolonged heating.[115]

Alternative preparations for phosphoric acid triamides, $\mathrm{QP(NR_2)_3}$, Q = O, S, include oxidative additions of tris(amino)phosphines, $\mathrm{P(NR_2)_3}$, with oxygen and sulfur.[116]

In the solid state, tris(alkylamido) derivatives $\mathrm{OP(NHMe)_3}$ and $\mathrm{OP(NHBu^t)_3}$ form supramolecular architectures through hydrogen bond self-assembly. Lithiation of $\mathrm{OP(NHR)_3}$ and $\mathrm{SP(NHR)_3}$ also yields self-assembled structures, formed through Li–O and Li–S interactions.[117]

The reaction of tetraphosphorus decasulfide with primary amines (1:12 M ratio) gives thiophosphoryltriamides, $\mathrm{SP(NHR_2)_3}$; with a 1:8 ratio, the product is a dithiophosphoric acid diamide $\mathrm{(RNH)_2P(S)(SH)}$ (Scheme 23).[118] The dithioacid diamides form metal complexes, for example, $\mathrm{Ni[S_2P(NHPh)_2]_2}$.[119]

Numerous phosphoric acid ester amides and thio analogs, $\mathrm{(RO)P(Q)(NR'_2)_2}$ and $\mathrm{(RO)_2P(Q)(NR'_2)}$ are also known. Among these, $\mathrm{(ArO)P(S)(NH_2)_2}$ are cited; they can be prepared from the dichloride in liquid ammonia.[120]

2.5.8 *Aminophosphonium Salts $[R_{4-n}P(NR'_2)_n]^+X^-$ $(n = 1-3)$*

Triphenyl(amino)phosphonium chloride, $\mathrm{[Ph_3PNH_2]^+Cl^-}$, is formed in a Staudinger reaction of $\mathrm{PPh_3}$ with $\mathrm{Me_3SiNH_2}$ in the presence of water, obviously through hydrolysis of the normal product $\mathrm{Ph_3P{=}NSiMe_3}$ obtained under anhydrous conditions.[121]

Diaminophosphonium salts, $\mathrm{[R_2P(NR'_2)_2]^+X^-}$, can be prepared by reactions of bis(dialkylamino)phosphines, $\mathrm{RP(NR'_2)_2}$, with alkyl halides.[122] Diphosphines are cleaved by chloramine to form diaminophosphonium salts (equation 7).[123]

$$\mathrm{R_2P - PR_2 + 4NH_2Cl \longrightarrow 2[R_2P(NH_2)_2]^+Cl^- + 2Cl^-} \tag{7}$$

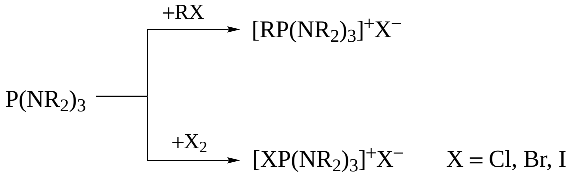

Scheme 24

Dihalogenodiaminophosphonium salts, $[PX_2(NR_2)_2]^+X^-$, are formed by oxidative addition of halogens to $[P(NR_2)_2]^+X^-$ (equation 8).[124]

$$[P(NR_2)_2]^+X^- + X_2 \longrightarrow [PX_2(NR_2)_2]^+X^- \qquad (8)$$

Tris(amino)phosphines, $P(NR_2)_3$, react with alkyl halides and with halogens to form triaminophosphonium salts (Scheme 24).[125,126]

Bis(dialkylaminophosphines, $RP(NR'_2)_2$, with chloramine, NH_2Cl, also form tris(amino)phosphonium salts $[RP(NR'_2)_2(NH_2)]^+Cl^-$.[127]

The inorganic cation $[P(NH_2)_4]^+$ is known[128] but substituted derivatives at either phosphorus or nitrogen sites are more common. Some interesting chemistry of tetra(anilino)phosphonium cation, $[P(NHPh)_4]^+$, which can be deprotonated stepwise to end up with the trianionic $[P(NPh)_4]^{3-}$ species, has been described.[129]

Triamino-halogenophosphonium halides, $[(R_2N)_3PX]^+ X^-$, on heating eliminate alkyl halides with formation of phosphinoamioimines, which in turn dimerize to cyclic derivatives containing the tetraazaphosphonium moiety $[PN_4]^+$ moiety (R = Et, X = Br) (Scheme 25).[130]

2.6 Five-coordinate Phosphorus(V)

2.6.1 Aminophosphoranes $R_4P–NR'_2$ and Diaminophosphoranes $R_3P(NR'_2)_2$

Aminotetrafluorophosphoranes, $F_4P\text{-}NR_2$ can be prepared from phosphorus pentafluoride and secondary amines,[131] aminosilanes[132] or disilazanes,[133] and by redistribution between PF_5 and $P(NMe_2)_3$.[134] Thus, phosphorus pentafluoride reacts with $Me_3Si–NEt_2$ at −78 °C with Me_3SiF elimination to form $F_4P–NEt_2$, which further eliminates Me_3SiF at 150–170 °C to form $F_3P(NEt_2)_2$ (Scheme 26).[135] In the gas phase, phosphorus pentafluoride reacts with ammonia to form *cis*-$F_3P(NH_2)_2$.[136]

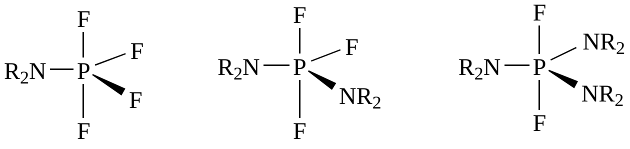

Scheme 26

With primary amines, aminotetrafluorophosphoranes are formed only if R is a bulky organic group or an aromatic group in the presence of a tertiary amine. Otherwise, cyclic dimers $[F_3PNR]_2$ are formed.[137] Fluorination of $P(NMe_2)_3$ with sulfur tetrafluoride yields triaminodifluorophosphorane, $F_2P(NMe_2)_3$.[138]

2.6.2 Phosphatranes

Phosphatranes are tricyclic compounds, with phosphorus and nitrogen as bridgeheads, which can be prepared by reaction of $P(NMe_2)_3$ with triethanolamine $(CH_2CH_2OH)_3$. The phosphatranes contain a transannular P–N bond, but a weaker interaction leads to quasiphosphatranes (Scheme 27, R = Me, R′ = Cl, Br, I, CH_2Br, CH_2I). Their nonconventional chemistry of phosphatranes and quasiphosphatranes has been reviewed.[139] Some of these compounds are highly basic (‘superbases’).[140]

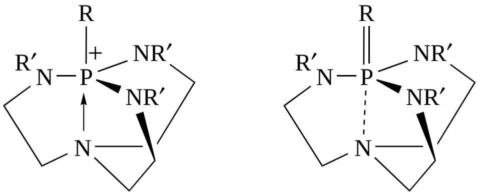

Q = O, S, NR

Scheme 27

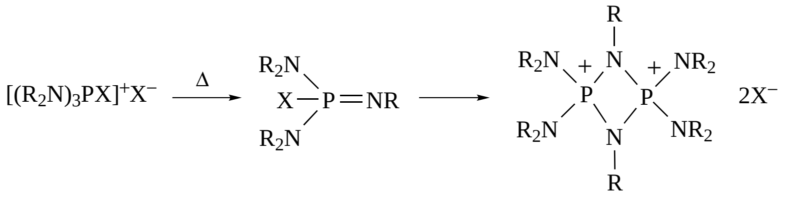

Scheme 25

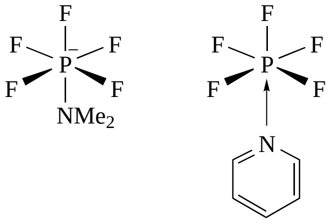

Scheme 28

2.7 Six-coordinate Phosphorus(V)

2.7.1 *Aminophosphates $[R_5P–NR'_2]^-$ and Phosphorus(V) Halide Amine Adducts $R'_3N.PX_5$*

Addition of fluoride anion to five-coordinate tetrafluoroaminophosphines $Me_2N–PF_4$ leads to anionic dialkylaminopentafluorophosphates $[Me_2N–PF_5]^-$. Organophosphorus tetrafluorides form tertiary amine adducts $R_3N{\cdot}R'PF_4$ (R = F, Ph, CF_3) and phosphorus pentafluoride forms a six-coordinate pyridine adduct, $PF_5{\cdot}NC_5H_5$ (Scheme 28).[141]

3 ACYCLIC DIPHOSPHORUS–NITROGEN COMPOUNDS

3.1 Three-coordinate Phosphorus(III)

3.1.1 *Bis(Phosphino)amines $R_2P–NR'–PR_2$*

The bis(phosphino)amines or diphosph(III)azanes, $R_2P–NH–PR_2$, can be readily prepared by ammonolysis of R_2PCl (R = Ph)[142] or by reactions between R_2PCl and silazanes. The usual product of the reaction between Ph_2PCl with $(Me_3Si)_2NH$ is $Ph_2PNHPPh_2$, but this may further react with excess Ph_2PCl to form P–P bond compounds, $[Ph_2P–PPh_2–NHPPh_2]^+Cl^-$ and $[Ph_2P–PPh_2{=}N–PPh_2–PPh_2]^+Cl^-$ (Scheme 29).[143]

The bis(phosphino)amines are versatile ligands and an extensive coordination chemistry, based on variable coordination patterns (Scheme 30), has been developed on this basis.[144–157]

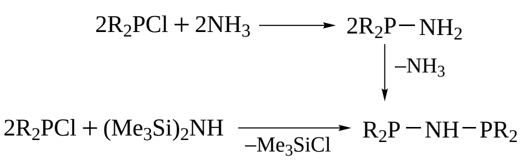
$2R_2PCl + 2NH_3 \longrightarrow 2R_2P-NH_2$
$-NH_3$
$2R_2PCl + (Me_3Si)_2NH \xrightarrow[-Me_3SiCl]{} R_2P-NH-PR_2$

Scheme 29

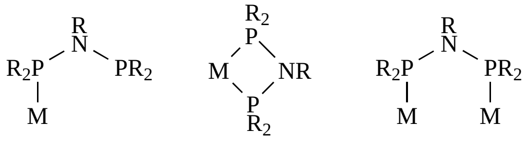

Scheme 30

$$(Ph_2P)_2NH + RLi \longrightarrow (Ph_2P)_2NLi + RH$$
$$(Ph_2P)_2NH + NaH \longrightarrow (Ph_2P)_2NNa + H_2$$

Scheme 31

Bis(phosphino)amines (R = H) can be easily deprotonated with lithium alkyls or sodium hydride in THF or other basic solvents (Scheme 31), and the N-lithiated derivatives react with metal and organometallic halides to give a broad variety of metal compounds.

An unusual reaction of $LiN(PPh_2)_2$ with $PbCl_2$ gives an unique dilead bicyclic complex, in addition to a linear tetraphosphadiazene (Scheme 32).[158]

Polynuclear clusters with Ph_2PNHPh_2 external ligands, for example, $[Cu_6(Ph_2PNHPPh_2)_4(\mu_3\text{-}SePh)_4][BF_4]_2$ have been structurally characterized.[159]

A rare coordination pattern of the $[Ph_2PNPPh_2]^-$ ligand is observed in the lanthanide complexes (Scheme 33).[160]

Lithium, potassium, and sodium $[Ph_2PNPPh_2]^-$ salts have been characterized structurally and display different molecular architectures.[161]

In some cases, the reactions of $LiN(PPh_2)_2$ with metal salts are not straightforward. Thus, this reagents reacts with anhydrous MCl_2 (M = Co, Ni, Pd) in boiling toluene, to form bis(chelate) complexes of a new ligand $[Ph_2PNPPh_2NPPh_2]^-$, in addition to $N(PPh_2)_3$, as a result of complex redistribution of the building units.[162] The reactions of $LiN(PPh_2)_2$ with AsI_3, $BiBr_3$ and SbI_3 result in the serendipitous formation of a P–P bond compound $Ph_2P–NPh_2P–PPh_2N–PPh_2$, in addition to elemental As, Sb or Bi; under different reaction conditions, AsI_3 may also produce eight-membered ring $Ph_8P_4N_2As_2$ or seven-membered ring $Ph_8P_4N_2As$ derivatives (Scheme 34).[163]

N-Organosubstituted derivatives are also known. Heating aniline hydrochloride with excess PCl_3 gives crystalline $Cl_2P–NPh–PCl_2$[164] and N-alkyl derivatives (R = Me, Et) can be similarly prepared and further converted into tetrafluoro derivatives (Scheme 35).[165] Of these, N-methylbis(difluorophosphino)amine, $MeN(PF_2)_2$, has been extensively used as a chelating and bridging ligand.[166]

Depending upon conditions (steric and electronic properties of the substituents, stoichiometry, solvent, and basic acid scavenger used) the reactions of substituted anilines with Ph_2PCl can afford in good yields either aminophosphines $Ph_2P–NHAr$, diphosphinoamines $(Ph_2P)_2N$ and even iminobiphosphines (containing P–P bonds) $RN{=}PPh_2–PPh_2$.[167]

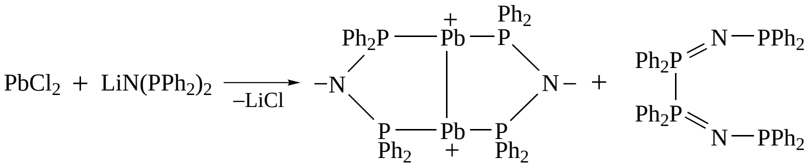

Scheme 32

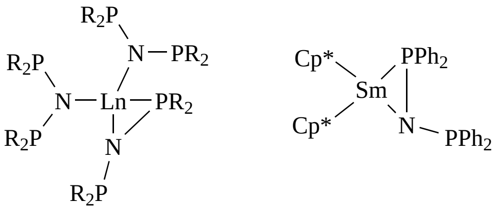

Ln = La, Nd, Er

Scheme 33

A complex of $(PhNH)_2P–NPh–(NHPh)_2$ (unknown in free state) is formed in the reaction of *cis*-$[Mo(CO)_4(Cl_2PNPhPCl_2)]$ or *cis*-$[Mo(CO)_4(PCl_3)_2]$ with aniline, and from $[Mo(CO)_4(NBD)]$ (NBD = norbornadiene) with $P(NHPh)_3$.[168]

3.1.2 Aminoderivatives of Diphosphines, $(R_2N)_2P–P(NR_2)_2$

Diaminochlorophospines, $(R_2N)_2PCl$, can be coupled with the aid of sodium metal to form tetrakis(dialylamino)diphosphines, $(R_2N)_2P–P(NR_2)_2$, albeit in moderate yield. These are readily oxidized to four-coordinate oxo and thio derivatives, $(R_2N)_2(Q)P–P(Q)(NR_2)_2$ ($R = Me$; $Q = O$ or S) in controlled reactions with oxygen and sulfur, respectively.[169]

3.1.3 Other Related Compounds

Interesting compounds containing $N–PR_2$ donor moieties, very useful as inorganic chelate ring forming ligands, include bis(phosphinamino)phosphines, $RP(NR'PR_2)_2$ (which can be deprotonated when $R' = H$ to form the corresponding dianions), bis(phosphinamino)silanes, $R_2Si(NR'PR_2)_2$, bis(phosphino)thioimides, $S(=NPR_2)_2$ and others. Their coordination chemistry has been reviewed.[170]

3.2 Four-coordinate Phosphorus(V)

3.2.1 Bis(phosphorane)immonium Cations $[R_3P=N=PR_3]^+$

The hexachloro cation $[Cl_3P=N=PCl_3]^+$ can be prepared in several ways. Thus, the reaction of PCl_5 with NH_4Cl under strictly controlled conditions (to avoid formation of cyclophosphazenes) yields $[Cl_3PNPCl_3]^+ [PCl_6]^-$.[171] The later salt can be conveniently converted to the chloride $[Cl_3PNPCl_3]^+Cl^-$ by reacting it with 4-(dimethylamino)pyridine, and the phosphazenium chain can be grown to $[Cl_3P=N(Cl_2P=N)_n = PCl_3]$ ($n = 1$, 2 and 3) by further reactions with $Cl_3P=NSiMe_3$.[172] The salt $[Cl_3PNPCl_3]^+Cl^-$ is also formed in the chlorination of $Cl_3P=N–P(S)Cl_2$ with gaseous chlorine,[173] and a hexachloroantimonate, $[Cl_3PNPCl_3]^+ [SbCl_6]^-$ is obtained in the reaction of $[NH_4]^+ [SbCl_6]^-$ with PCl_5.[174]

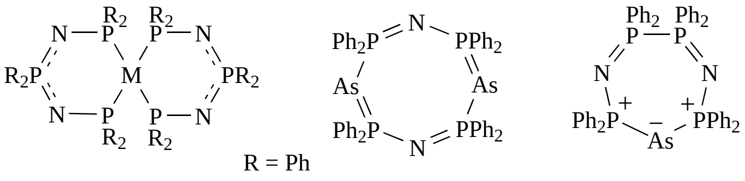

Scheme 34

$$3RNH_2{\cdot}HCl + 2PCl_3 \longrightarrow Cl_2P{-}NH{-}PCl_2 + 3RNH_2{\cdot}HCl$$

$$3Cl_2P{-}NR{-}PCl_2 + 4SbF_3 \longrightarrow 3F_2P{-}NR{-}PF_2 + 4SbCl_3$$

Scheme 35

The pyrolysis of tetraaminophosphonium halides, $[P(NH_2)_4]^+X^-$, yields a hexaaminodiphosphazenium cation $[(H_2N)_3PNP(NH_2)_3]^+X^-$ (X = Cl, I).[175]

Phenylsubstituted cations (as chloride salts)), $[PhCl_2PNPCl_2Ph]^+Cl^-$ and $[Ph_2ClPNPClPh_2]^+Cl^-$, are prepared from $PhPCl_4$ and Ph_2PCl_3, respectively, on heating with ammonium chloride in refluxing tetrachloroethane.[176] The hexaphenyl cation, $[Ph_3PNPPh_3]^+$ (known as PPN), is remarkable owing to its ability to facilitate crystallization of its salts.[177]

3.2.2 *Phosphoryl–phosphoranimines, $XR_2P{=}N{-}P({=}Q)R_2$*

A broad variety of compounds of general composition $XR_2P{=}N{-}P({=}Q)R_2$, for example, with R = alkyl, Ph; X = Oalkyl, Q = O and R = Ph, X = Cl, OMe, SMe, Q = O or S are known.[178] Several phosphorylphosphoraneimines have been prepared by Si–N bond cleavage (Scheme 36).[179]

Related compounds of the type $(Me_2N)_2P(Q){-}N{=}P(NMe_2)_3$ have been obtained from $P(NMe_2)_3$ with $(Me_2N)_2P(X)N_3$ in a Staudinger type reaction.[180]

Chloro-substituted phosphorylphosphoranimines, $Cl_3P{=}N{-}P(Q)Cl_2$ (Q = O, S) are readily obtained from $[Cl_3PNPCl_3]^+Cl^-$ with sulfur dioxide and hydrogen sulfide, respectively (Scheme 37).[181] These compounds are useful starting materials for a series of PNP derivatives.[182]

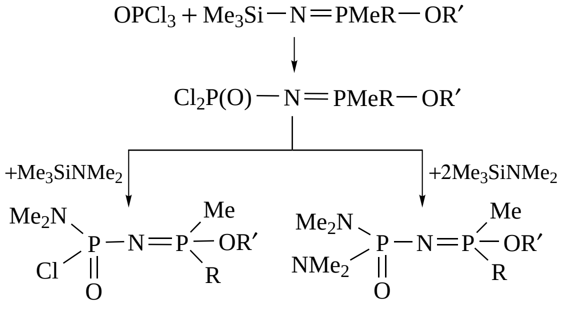
$OPCl_3 + Me_3Si{-}N{=}PMeR{-}OR'$
$Cl_2P(O){-}N{=}PMeR{-}OR'$
$+Me_3SiNMe_2$
$+2Me_3SiNMe_2$
Me_2N
Cl
O
Me
R
OR'
NMe_2

Scheme 36

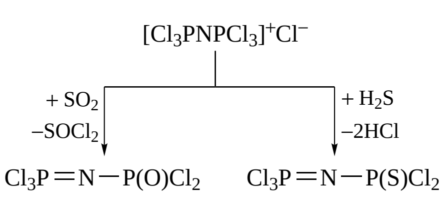

Scheme 37

3.2.3 *Phosphonium-phosphoranimines $[XR_2P{=}N{-}PR_2X]^+Y^-$*

Compounds of the type $[XR_2P{=}N{-}PR_2X]^+Y^-$ with R = Me, Ph; X = Cl, Br, NH_2, OMe, SMe (in various combinations) have been prepared by reactions similar to those described above.[183]

3.2.4 *Di(imino)imidodiphosphinates $R_2(R'N{=})P{-}NH{-}P({=}NR')R_2$*

Di(imino)diphosphazenates can be deprotonated and the resulting anions can serve as versatile ligands.[184] Sodium, potassium, calcium complex salts of $[N\{P(NMe_2)_2{=}NSiMe_3\}_2]^{2-}$ anion[185] and metal complexes (e.g. zinc)[186] have been prepared and investigated structurally.

3.2.5 *Di(chalcogeno)imidodiphosphinates $R_2P({=}Q){-}NR'{-}P({=}Q)R_2$, (Q = O, S, Se, Te) and Related Compounds*

Dichalcogenoimidodiphosphinates and -phosphates, $R_2(Q)P{-}NH{-}P(Q)R_2$ (R = alkyl, aryl, alkoxy; Q = O, S, Se) became very popular as excellent ligands and display an extensive coordination chemistry based on a broad diversity of coordination patterns (Scheme 38).[187]

N-Substituted di(chalcogeno)diphosphates $(RO)_2(Q)P{-}NR'{-}P(Q)(OR)_2$ (Q = O, S) and amides $(R_2N)_2(O)P{-}NR'{-}P(O)(NR_2)_2$ are best prepared by alkali metal halide elimination between $(RO)_2P(Q)Cl$ and $MNR'P(Q)(OR)_2$ (M = Na, Li).[188] Coupling of chlorides, $X_2(Q)PCl$, with amides, $X'_2(Q)PNHR'$ can also be used for the synthesis of a variety of dichalcogenodiphosphazanes, $X_2(Q)P{=}NR'{-}P(Q)X'_2$ (X, X′ = OR, NR_2, in various combinations).[189]

Diphosphazane dioxides, $R_2P(O)R_2{-}NR'{-}P(O)R_2$ are excellent ligands for actinides (Th, U).[190]

3.2.6 *Bis(iminophosphoryl)methanes, $R'N{=}PR_2CH_2PR_2{=}NR'$ and Bis(iminophosphoryl)ethanes, $R'N{=}PR_2CH_2CH_2PR_2{=}NR'$*

The compounds of this class, mostly silyl derivatives ($R' = SiMe_3$), prepared by Staudinger reactions from the corresponding diphosphines and silyl azides (Scheme 39), received recent attention owing to their versatility as nitrogen-donor ligands.[191]

A peculiar property of the bis(iminophosphoryl)methanes is the facile mono and deprotonation of the methyene bridge with organolithium reagents.[192] Thus, with $H_2C(NPPh_2NSiMe_3)_2$ unusual dimeric lithium complexes were obtained (Scheme 40)[193] and Ti, Zr, Hf carbene complexes were formed with the same doubly deprotonated ligands.[194]

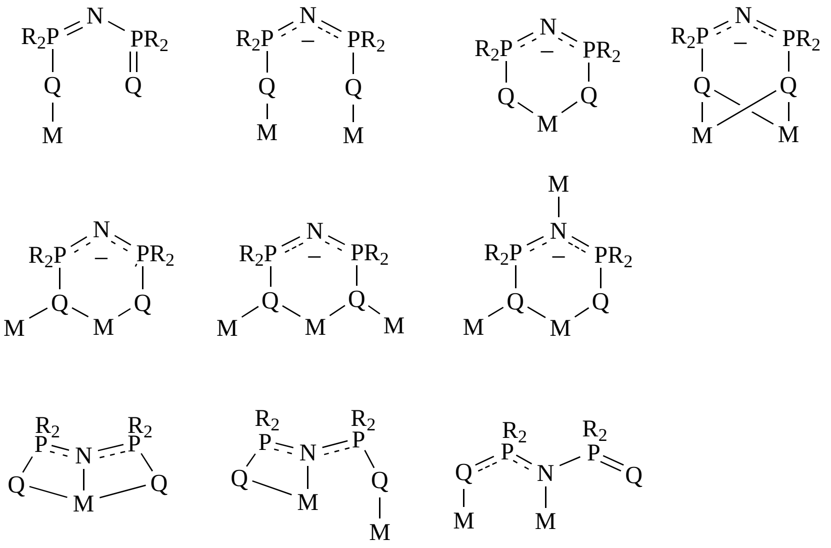

Scheme 38

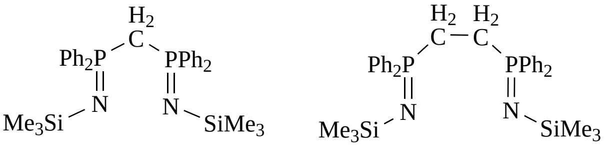

Scheme 39

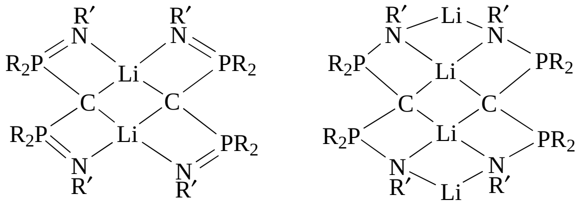

Scheme 40

Related complexes of titanium and zirconium, derived from bis(iminophosphoryl)ethanes, $R'N{=}PR_2CH_2CH_2PR_2{=}NR'$ ($R = Ph$, $R' = SiMe_3$) have been reported.[195]

3.3 Mixed Phosphorus(III)-Phosphorus(V) Compounds

3.3.1 *Chalcogenophosphinylaminophosphines* *$R_2(Q)P$–NR–PR_2 ($Q = O, S$)*

Hybrid compounds, containing both P(III) and P(V) groups, R_2P–NR'–$P(Q)R_2$ ($Q = O, S, Se'$; $R'{=}H$ or alkyl, aryl), are also versatile ligands and can act as chelating to form five-membered rings or as bridging, to form eight-membered rings (Scheme 41).[196]

Chiral N-phosphine substituted iminophosphoranes, R_2P–$N{=}PR_3$, are unexpectedly formed on attempted metallation of cyclopropyl(triphenyl)phosphonium bromide with sodium amide.[197]

3.3.2 *Iminophosphorano(amino)phosphines,* *$R'N{=}PR_2$–NR''–PR_2*

This class is illustrated by some silylated derivatives, $Me_3SiN{=}PPh_2$–NR'–PPh_2 with $R' = Et$, n-Pr, n-Bu, prepared from $Ph_2PNR'PPh_2$ with trimethylsilylazide (Scheme 42). Theses compounds can be readily undergo oxidative addition of sulfur and selenium to the P(III) site and react with

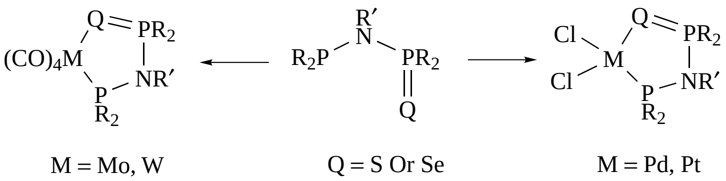

Scheme 41

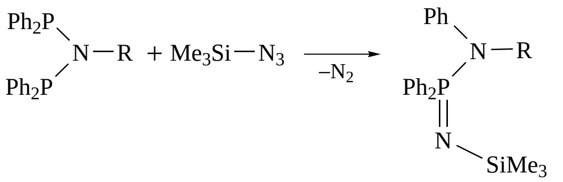

Scheme 42

phosphoryl azide to form $Me_3Si–N{=}PPh_2–NR–P(Q)Ph_2$ with Q = S, Se and =N–P(O)(OPh)$_2$, respectively.[198]

4 OLIGOMERIC LINEAR AND BRANCHED P–N CHAINS; DENDRIMERS

Short phosphorus–nitrogen chains containing P=N bonds can be synthesized by several routes. A triphosphadiazenium cation, as chloride salt, $[Cl_3P{=}N–PCl_2{=}N–PCl_3]^+Cl^-$, is formed on heating $[Cl_3PNPCl_3]^+$ $[PCl_6]^-$ with ammonium chloride.[199] Surprisingly, the treatment of the silylated phosphaneimine $Me_3SiNPEt_3$ with xenon difluoride yields an octaethyltriphosphadiazenium trifluorodimethylsilicate $[Et_3PNPEt_2NPEt_3]^+$ $[Me_2SiF_3]^-$.[200] Related cationic chains containing four and five phosphorus atoms, $[Cl(Cl_2P{=}N)_nPCl_3]^+$ are formed in thermal reactions of cyclophosphazenes $(Cl_2PN)_n$ ($n = 3$ and 4) with phosphorus pentachloride.[201]

The tetraphosphadiazene compound $Ph_2P–N{=}PPh_2PPh_2$ N–PPh$_2$ forms both linear dinuclear complexes and rare seven-membered chelate ring complexes with various metals. It can be oxidized by sulfur and selenium, to form $Ph_2(Q)P–N{=}PPh_2PPh_2{=}NP(Q)Ph_2$ (Q = S, Se), which are also interesting ligands.[202]

The diselenium derivative reacts with $Ru_3(CO)_{12}$ to produce a complex of the $[Ph_2P–N{=}PPh_2–N{=}PPh_2]^-$ ligand.[203]

A dinuclear compound, $(Me_2N)_3P{=}N–P({=}NH)(NMe_2)_2$, with a high nitrogen:phosphorus ratio[204] is the first member of a series of strongly basic, branched polyamino-imino phosphazenes (Scheme 43).[205]

Step-by-step growth of phosphazene chains can be achieved and the five-phosphorus chain can be converted into a dendrimeric structure.[206] The fascinating chemistry of dendrimeric phosphors–nitrogen molecular architecture has been reviewed.[207]

5 CYCLIC PHOSPHORUS–NITROGEN COMPOUNDS

5.1 Two-coordinate Phosphorus

Some cyclic four- and five-membered inorganic rings may contain two-coordinate phosphorus. Their synthesis is based on cycloaddition reactions of amino-iminophosphines or alkyl azides to iminophosphenium cations (Scheme 44).[208]

The silylated aminoiminophosphine $(Me_3Si)_2N–P{=}N–SiMe_3$ reacts with anhydrous aluminum chloride at 40 °C with elimination of Me_3SiCl to form a dicoordinate phosphorus–nitrogen ligand, in a four-membered chelate ring complex.[209] Anhydrous aluminum chloride extracts a chlorine ion from $[ClPNR]_2$ to form a cyclic cation with a dicoordinated

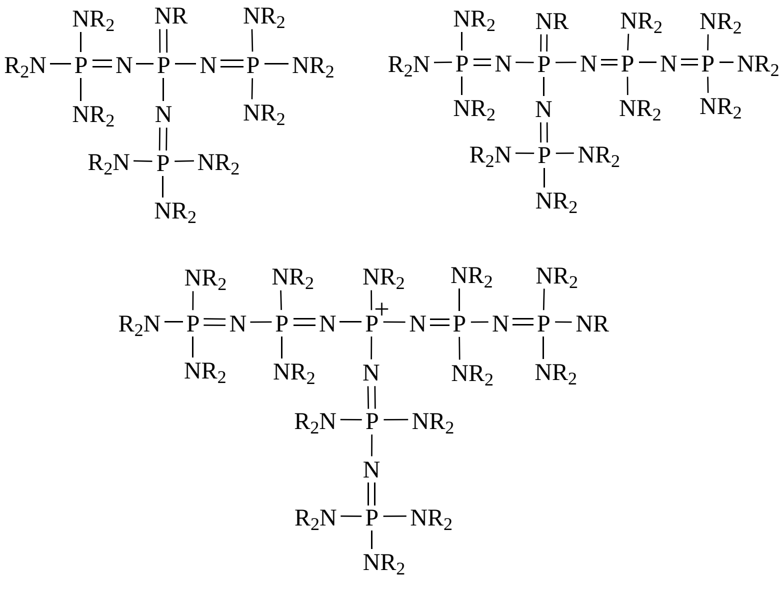

Scheme 43

phosphorus,[210] which displays interesting derivative chemistry (Scheme 45).[211]

Two-coordinate phosphorus is also present in some three-membered P–N–C heterocycles, azaphosphirenes (Scheme 46), which have been reviewed.[212]

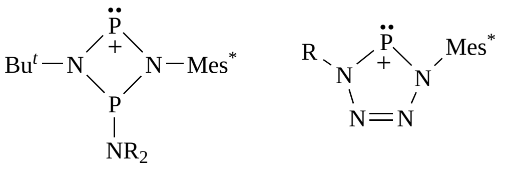

Scheme 44

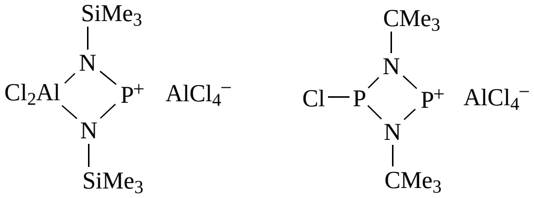

Scheme 45

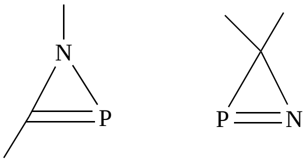

Scheme 46

5.2 Three-coordinate Phosphorus(III)

There are several (sometimes interconvertible) cyclophosph(III)azanes, illustrated in Scheme 47. Bicyclic, tricyclic, adamantane cage, and more complex structures can be obtained by minor variations of the reaction conditions, also depending on the nature of the substituents at phosphorus and nitrogen sites.[213] For reviews see Reference 214.

Generally, the phosphorus(III)–nitrogen rings are formed in reactions of primary amines with phosphorus(III) compounds containing at least two halogen atoms. Primary amines or lithiated silyamines such as $LiNRSiMe_3$ react with PCl_3 to yield dimeric $[ClPNR]_2$ (e.g. R = *tert*-Bu).[215]

The reaction of phenyldichlorophosphine, $PhPCl_2$, with aniline is complex and the products depend on several factors. In the presence of triethylamine as acid scavenger a cyclic trimer $(PhPNPh)_3$ is formed.[216] Six-and eight-membered cyclophosph(III)azanes $(ClPNR)_n$ (R = Et, $n = 3$ and 4) were reported as products of reactions between N-ethylhexamethyldisilazane with phosphorus trichloride.[217] The reaction of PCl_3 with primary amines in excess yields dimeric $[(RHN)PNR]_2$,[218] but methylamine forms a cage compound with adamantane structure.[219] A bicyclic compound is obtained in the reaction of $MeN(PCl_2)_2$ with methylamine, whereas ethylamine forms the trimer $(ClPNEt)_3$.[220]

Monomeric iminophosphines, which can be prepared with bulky R groups (R = Mes* or Dipp; X = Cl or $CF_3SO_3^-$), are in equilibrium with their cyclic dimers, and both can be converted to the corresponding cyclic phosphazane trimers (Scheme 48).[221,222]

Cyclodiphosph(III)azanes are versatile ligands[223–225] and their coordination chemistry has been reviewed.[226] Imidoderivatives in particular, in deprotonated form, produce interesting cage compounds with a series of metals[227] and toroidal macrocycles formed from P_2N_2 rings have been described.[228] Some macrocyclic tetramers made of four P_2N_2

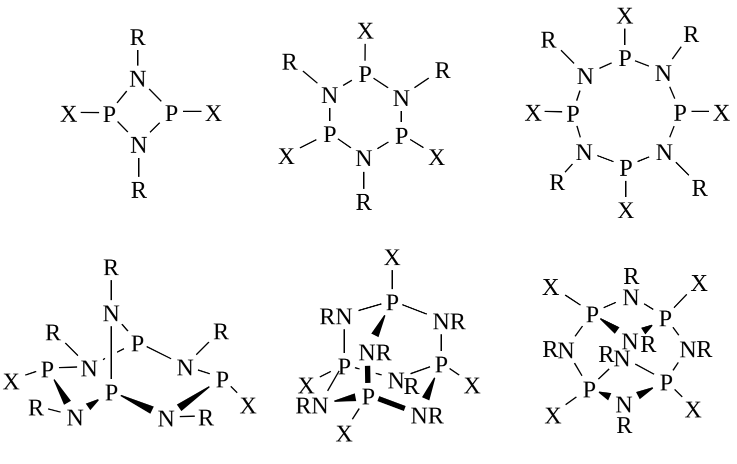

Scheme 47

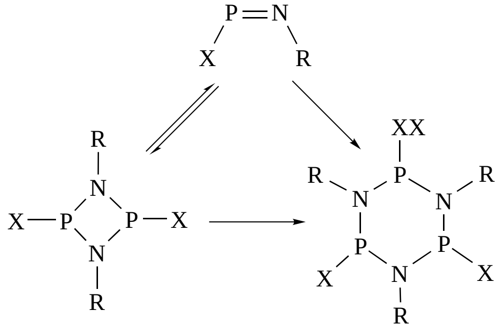

Scheme 48

rings connected through nitrogen and oxygen are versatile ligands forming unusual complexes.[229]

Molybdenum carbonyl complexes of cyclotriphosph(III)azanes, $[(RO)PNEt]_3$ ($R = CH_2CF_3$ or $C_6H_3Me_2$-2,6)[230] and metal complexes of $[ArOPNEt]_3$ ($Ar = 2,6\text{-}Pr^i_2C_6H_3$)[231] have been described.

The tetraphosphorus(III)hexaazaadamantane derivative, $P_4(NMe)_6$, is obtained from phosphorus trichloride and methylamine,[232] and a tricyclic compound of composition $P_4(NPr^i)_6$ is formed from $ClP(NPr^i)_2PNPr^iSiMe_3$ by elimination of Me_3SiCl. It isomerizes on heating into the adamantane structure.[233] Another tricyclic compound, $P_4(NBu^t)_6$ with nonadamantane structure is formed by reacting $[ClPNBu^t]_2$ with $[(LiNBu^t)PNBu^t]_2$.[234]

There are interesting interconversion reactions between monocyclic four-membered Cyclodiphosph(III)azanes, bicyclic, tricyclic, and adamantoid polycyclics.[235]

5.3 Four-coordinate Phosphorus

5.3.1 Cyclophosph(V)azanes

These are cyclic compounds consisting of 'saturated' $[PN]_n$ ($n = 2, 3, 4\ldots$) alternant rings, with exocyclic double bonds at phosphorus.[236]

Cyclic dioxodiphosphazanes, $[R(O)PNR']_2$, are obtained from phosphonic acid dichlorides and primary amines,[237] and by thermal condensation of phosphonic acid diamides (Scheme 49).[238]

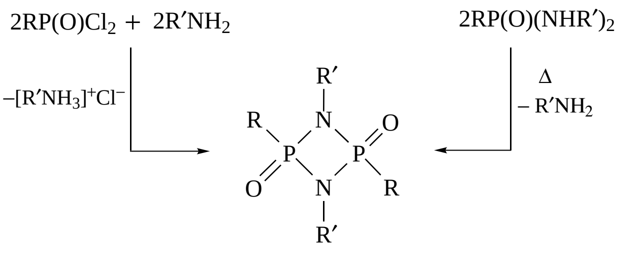

Scheme 49

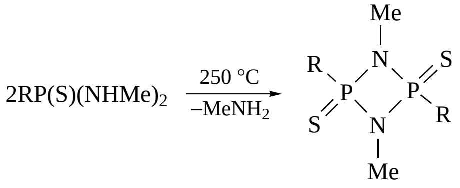

Scheme 50

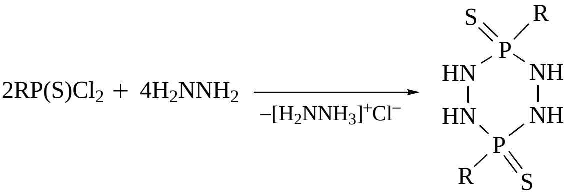

Scheme 51

Oxidative addition of chalcogens to cyclodiphosph(III)azanes, $[RPNR']_2$, leads to dichalcogeno cyclodiphosph(V)azanes, $[R(Q)PNR']_2$ ($Q = O$, S, Se) with preservation of the four-membered P_2N_2 ring.[239] Similar compounds are obtained by substitution of chlorine in reactions of five-coordinate cyclodiphosph(V)azanes, $[Cl_3PNR]_2$ with sulfur dioxide[240] and hydrogen sulfide,[241] respectively. Staudinger reactions with organic azides afford bis(imino)Cyclodiphosph(V)azanes $[R(R''N)PNR']_2$.[242]

Thermal condensation of thiophosphonic acid amides upon heating produces a mixture of cis and trans isomers of cyclodiphosph(V)azane derivatives (Scheme 50).[243]

Thiophosphonic acid dichlorides react with hydrazine to form six-membered ring compounds (Scheme 51).[244]

The anionic derivatives of cyclodiphosph(V)azanes, obtained by deprotonation of $[RNH(Q)PNR]_2$ ($Q = O$, S, Se) with organolithium reagents are versatile ligands, forming unusual metal complexes. These cyclic dimers also react with $AlMe_3$ to form dimethylaluminum derivatives.[245,246]

5.3.2 Cyclophosph(V)azenes

Cyclophosph(V)azenes are a family of rings formed by alternation of four-coordinate phosphorus and dicoordinate nitrogen atoms, also involving a formal alternation of single and double bonds in the ring (*see* ***Inorganic Ring Systems***). Whether this alternation results in an aromatic delocalization is a subject of much debate, but it seems that a view based on p_π-d_π bonds conjugations is now widely accepted. The best studied are the six-membered and eight-membered ring derivatives, that is, the trimers and tetramers of the X_2PN building units. Chloro derivatives $[Cl_2PN]_n$, with n from 3 to 8, have been isolated and characterized,[247] and fluoro derivatives $[F_2PN]_n$, with n from 3 to19, were isolated by fractional distillation and vapor phase chromatography.[248] Historically, the cyclophosphazenes were among the first phosphorus–nitrogen compounds discovered and characterized. They were first obtained as early as 1834[249] and first characterized as cyclic compounds, remarkably, in 1895.[250] The subject is extensively covered in several books and numerous reviews[251] and only the basics and a few recent highlights can be mentioned here.

The chloro derivatives $[Cl_2PN]_n$ (especially the trimer and tetramer) are readily available from the reaction of phosphorus pentachloride with ammonium chloride (in a chlorinated solvent, at 140–150 °C) (equation 9).[252]

$$PCl_5 + NH_4Cl \longrightarrow \frac{1}{n}[Cl_2PN]n + 4HCl \qquad (9)$$

Reactions based on Si–N bond cleavage can be also very useful, especially for the synthesis of organosubstituted derivatives (Scheme 52).[253]

The synthesis of the trimer $[Cl_2PN]_3$ from PCl_5 and $N(SiMe_3)_3$ (in 76% yield) is described as an improved route to this cyclic compound, although under different condition the same reaction can give $Cl_3P{=}NSiMe_3$, which in turn is a useful precursor for chain-like polyphosphazenes.[254]

A surprising reaction leading to organosubstituted cyclotriphosphazenes, $[RMePN]_3$, involves Me_3SiOPh and PhOH elimination between $Me_3SiN{=}PMeR(OR')$ and R′OH (R = Me or Ph, R′ = Ph or CF_3CH_2O).[255] Interestingly, heating the pure cis or trans trimer $[MePhPN]_3$ results in a rearrangement with formation of a mixture of cis and trans trimer and all four geometric isomers of the tetramer $[MePhPN]_4$.[256]

An extensive chemistry based on nucleophilic substitution of chlorine with amino, alkoxo, thiolato, and organic groups has been developed. It cannot be covered here and the reader is directed to the review literature cited, which covers the subject in detail. Owing to the peculiar structure of the cyclophosphazene rings, several isomers, that is, geminal and nongeminal, cis and trans, can be formed in substitution reactions. The hexakis(amino)cyclophosphazenes derived from primary amines, $[(RNH)_2PN]_3$ display interesting supramolecular self-assembly in solid state through NH···N hydrogen bonds.[257]

A peculiar reaction is the hydrolysis of $(Cl_2PN)_n$, which yields no hydroxo derivatives, $[(HO)_2PN]_n$, as might be expected, but rather their tautomeric forms, $[HO(O)PNH]_n$ ($n = 3$–8), that is, the ‘metaphosphimic acids’.[258] Interestingly, the fully alkoxo substituted derivatives $[(RO)_2PN]_3$ can be converted to esters of metaphosphimic acids in a thermal Arbusov–Michaelis type rearrangement (Scheme 53).[259]

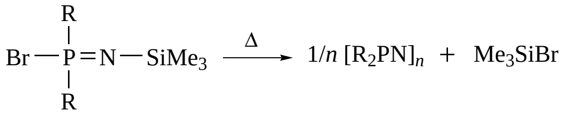

$$Br{-}\underset{R}{\overset{R}{P}}{=}N{-}SiMe_3 \xrightarrow{\Delta} 1/n\,[R_2PN]_n + Me_3SiBr$$

Scheme 52

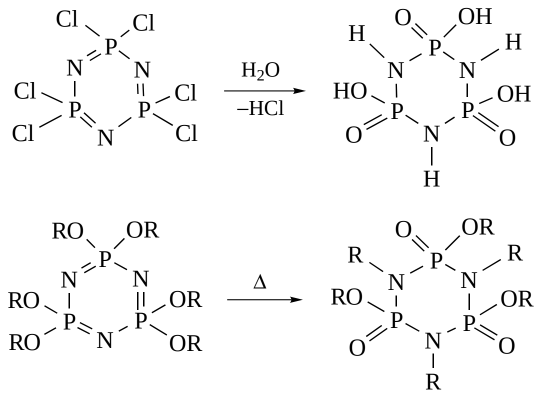

Scheme 53

In addition to classical substituents such as NH_2, NHR, NR_2, OR, SR in various combinations, in recent years some more exotic groups have been attached to phosphazene rings. Among the novel cyclic phosphazenes the carborane substituted derivatives are worth mentioning.[260] Other unusual derivatives include chiral cyclophosphazenes,[261] cyano-,[262] ferrocenylphenoxy-,[263] and ferrocenylhydrazone-cyclophosphazenes.[264] Another interesting development is the synthesis of crown ethers with chlorocyclophosphazene subunits (Scheme 54).[265]

Polyfluororoalkoxy-cyclophosphazenes display high thermal and hydrolytic stability and do not rearrange to oxophosphazanes on heating.[266] They are promising high temperature lubricants.

Some unusual compounds are the cyclophosphazenes with phosphazene side chains for example, neutral $F_5P_3N_3{-}N{=}PF_2{-}N{=}PCl_2{-}N{=}PCl_3$,[267] and the anionic -$[F_5P_3N_3{-}N{=}PF_2{-}N{=}PF_2{-}N{=}PF_5]^{2-}$ species, the latter obtained from $(F_2PN)_3$ and $[(Me_2N)_3S]^+$ $[Me_3SiF_2]^{2-}$ salt.[268]

An important recent achievement is the use of cyclophosphazenes as ligands, to form a variety of metal complexes.[269] Thus, the amino-substituted cyclophosphazenes,[270] the cyclophosphazenes bearing pyrazolyl substituents,[271] pyridyloxy-susbtituted cyclophosphazenes,[272] and those with phosphine side groups are versatile ligands.[273] Cyclophosphazenes containing ethynyl side groups form organometallic cobalt carbonyl complexes using the carbon–carbon triple bond.[274]

Cyclic iminophosphazenate anions (Scheme 55) are among the most interesting ligands and they display a broad diversity of coordination patterns.[275] Some are shown in Scheme 56. A hexakis(anisidyl) cyclotriphosphazenate anion, $[(2\text{-}MeOC_6H_4N)_6P_3N_3]^{6-}$, is unique in that it can chelate 12 lithium ions by a single ligand.[276]

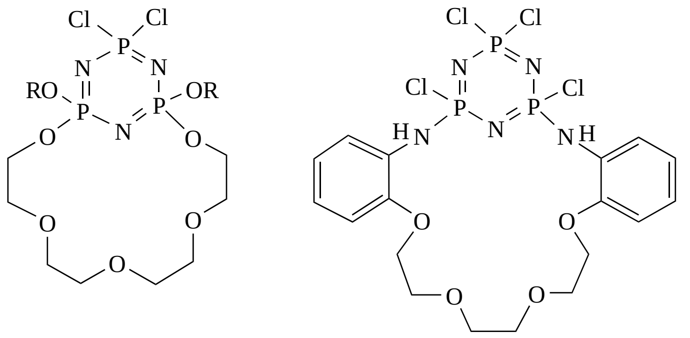

Scheme 54

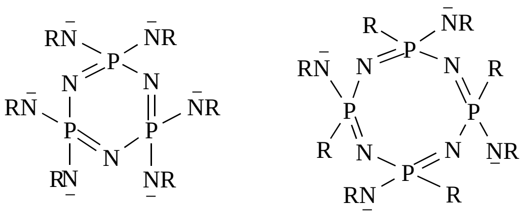

Scheme 55

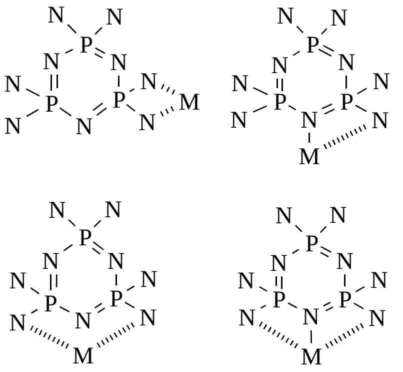

Scheme 56

5.4 Five-coordinate Phosphorus

Cyclophosph(V)azanes with five-coordinate phosphorus are mostly dimeric, four-membered ring derivatives, $[X_3PNR]_2$ (**6**). Several reviews cover the subject.[277] A simple preparation of these compounds involves the reaction of PCl_5 with primary amines (or their hydrochlorides), the so-called Kirsanov reaction. Weakly basic amines form monomeric $Cl_3P{=}NR$, but with more basic amines (e.g. with R = alkyl), the products are the cyclic dimers. Various anilines give either a monomer or a cyclic dimer, depending upon their basicity.[278]

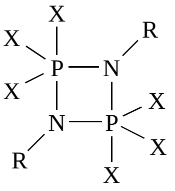

(**6**)

Cyclophosph(V)azanes containing six-coordinate phosphorus are rare.[279] Some can be obtained by treating $[F_3PNBu^t]_2$ with $LiBu^t$, resulting in zwitterionic compounds.[280] Addition of fluoride anions (from hydrogen, alkali metal or ammonium fluorides) to the dimer $[F_3PNMe]_2$ results in the formation of six-coordinate derivatives (Scheme 57).[281]

5.5 Heterocyclophosph(III)azanes

A series of four-membered rings containing phosphorus(III), two nitrogen atoms, and a heteroelement (boron, aluminum, silicon, arsenic) has been obtained by reactions of

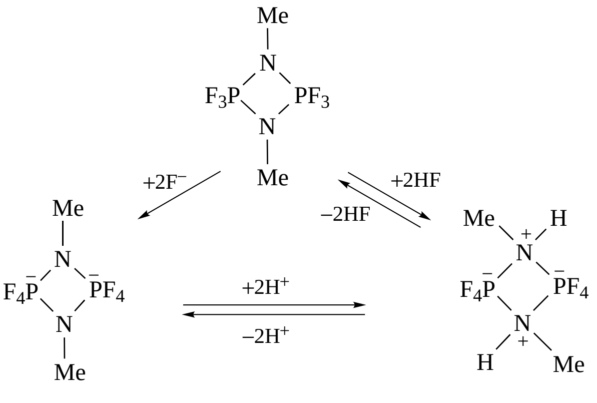

Scheme 57

$R_2N–P{=}NR$ ($R = SiMe_3$ or *tert*-Bu) with the corresponding element halides (Scheme 58).[282]

Four- and eight-membered heterocycles containing phosphorus(III), nitrogen and sulfur(VI) have been obtained by reacting phosphorus halides with dialkylsulfamide $O_2S(NHR')_2$ (Scheme 59).[283]

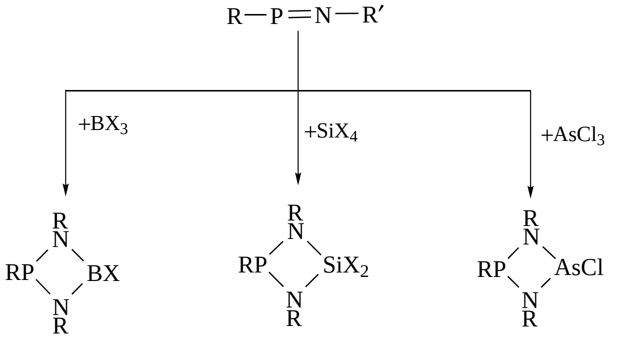

Scheme 58

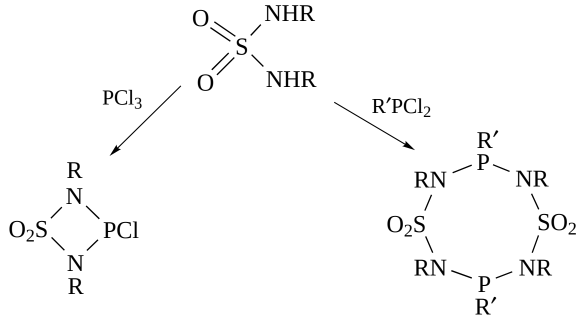

Scheme 59

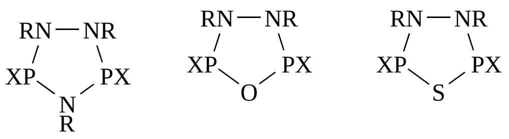

Scheme 60

Several five-membered heterocycles are derived from bis(dihalogenophosphinyl) hydrazines, $X_2PNMeNMePX_2$ (Scheme 60).[284]

5.6 Heterocyclophosph(V)azenes

Phosphorus can be partially replaced in cyclophosphazene rings by some heteroelements, for example, boron, silicon, arsenic, antimony, sulfur and the broad variety of such heterocycles cannot be discussed here in any detail, but their chemistry is well covered in several reviews.[285] Examples include boracyclophosphazenes,[286] numerous metal-containing heterocyclophosphazenes,[287] and sulfur-containing heterocyclophosphazenes,[288] to name only a few (Scheme 61).

6 HIGH MOLECULAR POLYMERIC P=N COMPOUNDS

The polymeric phosphazenes are treated in chapter (*see* ***Polyphosphazenes***) A recent monograph covers the chemistry of polyphosphazenes (nomenclature, synthesis of cyclic 'monomers', ring opening polymerization, condensation polymerization, substitution, polymer properties, and applications;[289] more than 1000 literature citations).[290] Other reviews have also been published recently.[291] Sulfur-containing polyphosphazenes have also been described.[292]

7 APPLICATIONS

Phosphorus–nitrogen compounds have numerous interesting applications, which cannot be covered here. Only a few are mentioned. Thus, the lithiated phosphorane imine $Ph_3P{=}NLi$ is a useful synthetic reagent in organic chemistry for the preparation of various nitriles.[293]

Applications of polyphosphazenes as flame retardants, electrolytes for special batteries, and biomaterials have been described.[294–295] Some cyclophosphazene derivatives can serve as hosts for small molecule Clathration.[296]

Polythionylphosphazenes can be applied as phosphorescent oxygen sensors.[297]

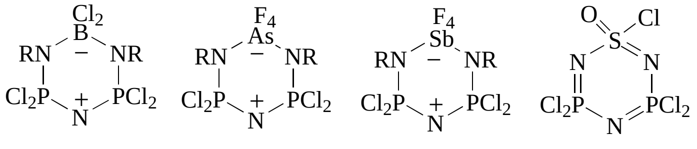

Scheme 61

8 REFERENCES

1. H. G. Heal, ‘The Inorganic Heterocyclic Chemistry of Sulfur, Nitrogen and Phosphorus’, Academic Press, London, 1980, Chap. 13, p. 250.
2. E. V. Borisov and E. E. Nifantiev, *Russ. Chem. Rev.*, 1977, **46**, 482.
3. A. Steiner, S. Zacchini, and P. I. Richards, *Coord. Chem. Rev.*, 2002, **227**, 212.
4. F. Golinski and H. Jacobs, *Z. Anorg. Allg. Chem.*, 1995, **621**, 29.
5. a) W. Schnick, *Angew. Chem., Int. Ed. Engl.*, 1993, **32**, 806; b) W. Schnick and J. Lücke, *Z. Anorg. Allg. Chem.*, 1990, **588**, 19; c) W. Schnick and J. Lücke, *Angew. Chem., Int. Ed. Engl.*, 1992, **31**, 213.
6. a) M. C. Miller and R. A. Shaw, *J. Chem. Soc.*, 1963, 3233; b) D. B. Sowerby and L. F. Audrieth, *Chem. Ber.*, 1961, **94**, 2670.
7. a) E. Niecke, M. Nieger, and F. Reichert, *Angew. Chem., Int. Ed. Engl.*, 1988, **27**, 1715; b) N. Burford, J. A. C. Clyburne, P. L. Bakshi and T. S. Cameron, *Organometallics* 1995, **14**, 1578.
8. N. Burford, T. S. Cameron, K. N. Robertson, A. D. Phillips, and H. A. Jenkins, *Chem. Commun.*, 2000, 2087.
9. F. Garcia, G. T. Lawson, D. J. Linton, D. Moncrieff, M. McPartlin, A. D. Woods, and D. S. Wright, *Chem. – Eur. J.*, 2002, **8**, 5723.
10. N. Burford, T. S. Cameron, K. D. Conroy, B. Ellis, M. Lumsden, C. L. B. MacDonald, R. McDonald, A. D. Phillips, P. J. Ragogna, R. W. Schurko, D. Walsh, and R. E. Wasylishen, *J. Am. Chem. Soc.*, 2002, **124**, 14012.
11. E. Niecke and D. Gudat, *Angew. Chem., Int. Ed. Engl.*, 1991, **30**, 217.
12. a) O. J. Scherer, R. Konrad, C. Kruger, and Y. H. Tsay, *Chem. Ber.*, 1982, **115**, 414; b) O. J. Scherer, R. Konrad, E. Guggolz, and M. L. Ziegler, *Angew. Chem., Int. Ed. Engl.*, 1982, **21**, 297; c) O. J. Scherer, J. Kerth, R. Anselmann, and W. S. Sheldrick, *Angew. Chem., Int. Ed. Engl.*, 1983, **22**, 984; d) O. J. Scherer, R. Walter, and W. S. Sheldrick, *Angew. Chem., Int. Ed. Engl.*, 1985, **24**, 525.
13. E. Niecke and W. Flick, *Angew. Chem., Int. Ed. Engl.*, 1973, **12**, 585.
14. a) S. Pohl, *Chem. Ber.*, 1979, **112**, 3159; b) E. Niecke, W. Flick, and S. Pohl, *Angew. Chem., Int. Ed. Engl.*, 1976, **15**, 309; c) O. J. Scherer and N. Kuhn, *Chem. Ber.*, 1974, **107**, 2123.
15. O. J. Scherer and W. Glassel, *Chem. Ber.*, 1977, **110**, 3874.
16. K. Pilgram and F. Korte, *Tetrahedron*, 1963, **19**, 37.
17. R. R. Holmes and J. A. Forstner, *Inorg. Chem.*, 1963, **2**, 380.
18. A. D. Bond, E. L. Doyle, F. GarcÌa, R. A. Kowenicki, D. Moncrieff, M. McPartlin, L. Riera, A. D. Woods, and D. S. Wright, *Chem. – Eur. J.*, 2004, **10**, 2271.
19. I. Schranz, D. F. Moser, L. Stahl, and R. J. Staples, *Inorg. Chem.*, 1999, **38**, 5814.
20. A. D. Bond, E. L. Doyle, S. J. Kidd, A. D. Woods, and D. S. Wright, *Chem. Commun.*, 2001, **777**.
21. R. Deutsch, E. Niecke, M. Nieger, and W. W. Schoeller, *Chem. Ber.*, 1992, **125**, 1119.
22. a) M. Witt and H. W. Roesky, *Chem. Rev.*, 1994, **94**, 1163; b) D. Gudat, *Coord. Chem. Rev.*, 1997, **163**, 71.
23. a) R. W. Reed, Z. Xie, and C. A. Reed, *Organometallics*, 1995, **14**, 5002; b) A. B. Drapailo, A. N. Chernega, V. D. Romanenko, R. Madhoumi, J. M. Sotiropoulos, L. Lamande, and M. Sanchez, *J. Chem. Soc., Dalton Trans.*, 1994, 2925.
24. N. Burford, T. S. Cameron, J. A. C. Clyburne, K. Eichele, K. N. Robertson, S. Sereda, R. E. Wasylishen, and W. A. Whitla, *Inorg. Chem.*, 1996, **35**, 5460.
25. J. P. Bezombes, K. B. Borisenko, P. B. Hitchcock, M. F. Lappert, J. E. Nycz, D. W. H. Rankin, and H. E. Robertson, *J. Chem. Soc., Dalton Trans.*, 2004, 1980.
26. M. Becke-Goehring and J. Schulze, *Chem. Ber.*, 1958, **91**, 1188.
27. A. Michaelis, *Liebigs Ann. Chem.*, 1903, **326**, 129.
28. a) H. Nöth and H. J. Vetter, *Chem. Ber.*, 1963, **96**, 1109; b) R. Schmutzler, *Inorg. Chem.*, 1964, **3**, 415.
29. Yu. L. Kruglyak, S. I. Malekin, and I. V. Martynov, *Zh. Obshch. Khim.*, 1969, **39**, 466.
30. V. Mark, *Org. Synth.*, 1966, **46**, 42.
31. C. Stuebe and H. P. Lankelma, *J. Am. Chem. Soc.*, 1956, **78**, 976.
32. R. R. Holmes and R. P. Wagner, *J. Am. Chem. Soc.*, 1962, **84**, 357.
33. J. R. Van Wazer and L. Maier, *J. Am. Chem. Soc.*, 1964, **86**, 811.
34. H. Nöth and H. J. Vetter, *Chem. Ber.*, 1961, **94**, 1505.
35. A. B. Burg and P. J. Slota, *J. Am. Chem. Soc.*, 1960, **82**, 2148.
36. a) A. Michaelis, *Chem. Ber.*, 1898, **31**, 1037; b) T. Weil, B. Prijs, and H. Erlenmeyer, *Helv. Chim. Acta.*, 1952, **35**, 1412; c) B. A. Arbuzov, N. I. Rizpolozhenskii, and M. A. Zvereva, *Izv. Akad. Nauk, SSSR, Ser. Khim.*, 1955, 1021; d) H. Hoffmann, R. Grünewald, and L. Horner, *Chem. Ber.*, 1960, **93**, 861; e) G. Ewart, D. S. Payne, A. L. Porte, and A. P. Lane, *J. Chem. Soc.*, 1962, 3984.
37. a) W. Abel, D. A. Armitage, and G. R. Wiley, *J. Chem. Soc.*, 1965, **57**,; b) M. G. Barlow, M. Green, R. N. Haszeldine, and H. G. Higson, *J. Chem. Soc. C* 1966, 1592.
38. O. I. Kolodyazhnyi and N. Prynada, *Tetrahedron Lett.*, 2000, **41**, 7997.
39. M. Raab, G. Tirreé, M. Nieger, and E. Niecke, *Z. Anorg. Allg. Chem.*, 2003, **629**, 769.
40. a) R. H. Neilson and P. Wisian-Neilson, *Inorg. Chem.*, 1982, **21**, 3568; b) P. Wisian-Neilson and R. H. Neilson, *Inorg. Synth.*, 1989, **25**, 69.

41. R. C. Samuel, R. P. Kashyap, M. Krawiec, W. H. Watson, and R. H. Neilson, *Inorg. Chem.*, 2002, **41**, 7113.

42. A. Baceiredo, G. Bertrand, J. P. Majoral, G. Sicard, J. Jaud, and J. Galy, *J. Am. Chem. Soc.*, 1984, **106**, 6088.

43. b) M. Regitz and O. J. Scherer, eds, 'Multiple Bonds and Low coordination in Phosphorus Chemistry', G. Thieme Verlag, Stuttgart.

44. V. D. Romanenko and M. Sanchez, *Coord. Chem. Rev.*, 1997, **158**, 275.

45. E. Niecke, V. von der Gonna, and M. Nieger, *Chem. Ber.*, 1990, **123**, 2329.

46. a) E. Niecke and W. Flick, *Angew. Chem., Int. Ed. Engl.*, 1974, **13**, 134; b) O. J. Scherer and N. Kuhn, *Chem. Ber.*, 1974, **107**, 2123.

47. K. H. Worms and M. Schmidt-Dunker, in 'Organic Phosphorus Compounds', eds. G. M. Kosolapoff and L. Maier, Wiley-Interscience, New York, 1973, Vol. 7, p. 1.

48. P. C. Crofts, in 'Organic Phosphorus Compounds', eds. G. M. Kosolapoff and L. Maier, Wiley-Interscience, New York, 1973, Vol. 6, p. 1.

49. E. Fluck and W. Haubold, in 'Organic Phosphorus Compounds', eds. G. M. Kosolapoff, and L. Maier, Wiley-Interscience, New York, 1973, Vol. 6, p. 579.

50. A. Steiner, S. Zacchini, and P. I. Richards, *Coord. Chem. Rev.*, 2002, **227**, 193.

51. G. M. Aspinall, M. C. Copsey, A. P. Leedham, and C. A. Russell, *Coord. Chem. Rev.*, 2002, **227**, 217.

52. A. W. Johnson, 'Ylides and Imines of Phosphorus', Wiley, New York, 1993.

53. a) H. H. Sisler, H. S. Ahuja, and N. L. Smith, *J. Org. Chem.*, 1961, **26**, 1819; b) R. Appel, G. Kohnlein, and R. Schöllhorn, *Chem. Ber.*, 1965, **98**, 1355.

54. I. N. Zhmurova and A. V. Kirsanov, *Zh. Obshch. Khim.*, 1962, **32**, 2576.

55. A. C. Chapman, W. S. Holmes, N. L. Paddock, and H. T. Searle, *J. Chem. Soc.*, 1961, 1825.

56. I. N. Zhmurova and A. V. Kirsanov, *Zh. Obshch. Khim.*, 1963, **33**, 1015.

57. I. N. Zhmurova and A. V. Kirsanov, *Zh. Obshch. Khim.*, 1959, **29**, 1687.

58. a) A. V. Kirsanov and G. I. Derkach, *Zh. Obshch. Khim.*, 1956, **26**, 2009; b) A. V. Kirsanov and R. G. Makitra, *Zh. Obshch. Khim.*, 1956, **26**, 905.

59. a) A. V. Kirsanov and N. L. Egorova, *Zh. Obshch. Khim.*, 1955, **25**, 187; b) E. S. Levchenko and A. V. Kirsanov, *Zh. Obshch. Khim.*, 1957, **27**, 3078.

60. E. Fluck and W. Haubold, in 'Organic Phosphorus Compounds', eds. G. M. Kosolapoff and L. Maier, Wiley-Interscience, New York, 1973, Vol. 6, p. 776.

61. A. V. Kirsanov and I. N. Zhmurova, *Zh. Obshch. Khim.*, 1958, **28**, 2478.

62. V. Chunechom, T. E. Vidal, H. Adams, and M. L. Turner, *Angew. Chem., Int. Ed. Engl.*, 1998, **37**, 1930.

63. H. Staudinger and J. Meyer, *Helv. Chim. Acta*, 1919, **2**, 635.

64. G. Singh and H. Zimmer, *Organomet. Chem. Rev.*, 1967, **2**, 279.

65. L. Horner and H. Oedinger, *Liebigs Ann. Chem.*, 1959, **627**, 142.

66. a) H. Zimmer and G. Singh, *J. Org. Chem.*, 1964, **29**, 1579; b) H. J. Bestmann and O. Klein, *Tetrahedron Lett.*, 1966, 6181.

67. R. Appel and G. Schölhorn, *Angew. Chem., Int. Ed. Engl.*, 1964, **3**, 805.

68. V. I. Shevchenko, V. T. Stratienko, and A. M. Pinchuk, *Zh. Obshch. Khim.*, 1954, **34**, 3954.

69. H. Nöth, L. Meinel, and H. Medersteig, *Angew. Chem., Int. Ed. Engl.*, 1965, **4**, 709.

70. a) J. C. Wilburn, R. H. Neilson, and P. Wisian-Neilson, *Inorg. Chem.*, 1979, **18**, 1429; b) Yu. G. Golobov, I. N. Zhmurova, and L. F. Kasukhin, *Tetrahedron*, 1981, **37**, 437.

71. I. Yavari, M. Adib, and L. Hojabri, *Tetrahedron*, 2002, **58**, 7213.

72. a) K. Dehnicke, M. Krieger, and W. Massa, *Coord. Chem. Rev.*, 1999, **182**, 19; b) A. Steiner, S. Zacchini, and P. I. Richards, *Coord. Chem. Rev.*, 2002, **227**, 193.

73. K. Dehnicke and F. Weller, *Coord. Chem. Rev.*, 1997, **158**, 103.

74. H. Link, P. Reiss, S. Chitsaz, H. Pfistner, and D. Fenske, *Z. Anorg. Allg. Chem.*, 2003, **629**, 755.

75. B. Neumüller and K. Dehnicke, *Z. Anorg. Allg. Chem.*, 2004, **630**, 799.

76. A. Müller, M. Krieger, B. Neumüller, K. Dehnicke, and J. Magull, *Z. Anorg. Allg. Chem.*, 1997, **623**, 1081.

77. A. Maurer, D. Fenske, J. Beck, W. Hiller, J. Strähle, E. Böhm, and K. Dehnicke, *Z. Naturforsch*, 1988, **43b**, 5.

78. H. Schmidbaur and W. Wolfsberger, *Chem. Ber.*, 1967, **100**, 1000.

79. a) K. L. Paciorek and R. H. Kratzer, *J. Org. Chem.*, 1966, **31**, 2425; b) V. A. Gilyarov and M. I. Kabachnik, *Zh. Obshch. Khim.*, 1966, **36**, 282; c) V. A. Gilyarov, A. M. Maksutov, and M. I. Kabachnik, *Zh. Obshch. Khim.*, 1967, **37**, 2501; d) W. Wiegrabe and H. Bock, *Chem. Ber.*, 1968, **101**, 1414; e) V. A. Gilyarov, A. M. Maksutov, and M. I. Kabachnik, *Zh. Obshch. Khim.*, 1967, **37**, 2501; f) W. Wiegrabe and H. Bock, *Chem. Ber.*, 1968, **101**, 1414; g) N. Zhmurova and A. V. Kirsanov, *Zh. Obshch. Khim.*, 1963, **33**, 1015; h) O. J. Scherer and G. J. Schieder, *J. Organomet. Chem.*, 1969, **19**, 315.

80. a) V. I. Shevchenko and V. T. Stratienko, *Zh. Obshch. Khim.*, 1960, **30**, 1958; b) V. I. Shevchenko, V. T. Stratienko, and A. M. Pinchuk, *Zh. Obshch. Khim.*, 1960, **30**, 1566.

81. K. L. Paciorek and R. H. Kratzer, *J. Org. Chem.*, 1966, **31**, 2426.

82. a) H. J. Cristau, C. Garcia, J. Kadoura, and E. Torreilles, *Phosphorus, Sulfur & Silicon*, 1990, **49/50**, 151; b)

O. J. Scherer, G. Schanbl, and T. Lenhard, *Z. Anorg. Allg. Chem.*, 1979, **449**, 167.

83. M. Witt and H. W. Roesky, *Chem. Rev.*, 1994, **94**, 1163.
84. O. J. Scherrer and A. Nahrstedt, *Angew. Chem.*, 1979, **91**, 238.
85. a) B. F. Straub, F. Eisenträger, and P. Hofmann, *Chem. Commun.*, 1999, 2507; b) B. F. Straub, F. Rominger, and P. Hofmann, *Chem. Commun.*, 2000, 1611; c) B. F. Straub, F. Rominger, and P. Hofmann, *Organometallics* 2000, **19**, 4305.
86. H. Ackermann, O. Bock, U. Müller, and K. Dehnicke, *Z. Anorg. Allg. Chem.*, 2000, **626**, 1854.
87. A. Michaelis, *Liebigs Ann. Chem.*, 1903, **326**, 129.
88. L. T. Burke, E. Hevia-Freire, R. Holland, J. C. Jeffery, A. P. Leedham, C. A. Russell, A. Steiner, and A. Zagorski, *Chem. Commun.*, 2000, 1769.
89. H. J. Vetter and H. Nöth, *Chem. Ber.*, 1963, **96**, 1308.
90. a) K. Issleib and H. Oehme, *Z. Anorg. Allg. Chem.*, 1966, **343**, 268; b) I. N. Zhmurova, I. Yu. Voitsekhovskaya, and A. V. Kirsanov, *Zh. Obshch. Khim.*, 1959, **29**, 2083.
91. a) V. Gutmann, G. Mörtl, and K. Utvary, *Monatsh. Chem.*, 1962, **93**, 1114; b) G. K. Fedorova, Ya. P. Shaturskii, and A. V. Kirsanov, *Zh. Obshch. Khim.*, 1965, **35**, 1984; c) I. A., Nuretdinov, R. R. Shagidulin, Yu. Ya. Shamonin, and N. P. Grechkin, *Izv. Akad. Nauk SSSR, Ser. Khim.*, 1966, **839**,; d) G. Tomachewski and W. Kuhn, *J. Prakt. Chem.*, 1968, **38**, 222.
92. a) N. L. Smith and H. H. Sisler, *J. Org. Chem.*, 1961, **26**, 5145; b) A. E. Miskin and V. P. Evdakov, *Zh. Obshch. Khim.*, 1968, **38**, 1776.
93. a) E. Steininger, *Monatsh. Chem.*, 1966, **97**, 383; b) H. Bock and G. Rudolph, *Chem. Ber.*, 1965, **98**, 2273; c) R. P. Neilson and H. H. Sisler, *Inorg. Chem.*, 1963, **2**, 753.
94. a) G. Doak and L. Freedman, *J. Am. Chem. Soc.*, 1954, **76**, 1621; b) K. Kennard and C. Hamilton, *J. Am. Chem. Soc.*, 1955, **77**, 1156; c) G. Kosolapoff and L. Payne, *J. Org. Chem.*, 1956, **21**, 413.
95. K. H. Worms and M. Schmidt-Dunker, in ‘Organic Phosphorus Compounds’, eds. G. M. Kosolapoff and L. Maier, J. Wiley & Sons, New York, 1976, Vol. 7, p. 322.
96. R. Rätz, *J. Am. Chem. Soc.*, 1955, **77**, 4170.
97. W. C. Smith and L. F. Audrieth, *J. Org. Chem.*, 1957, **22**, 265.
98. B. Helferich and L. Schröder, *Liebigs Ann. Chem.*, 1963, **670**, 48.
99. N. N. Melnikov, A. F. Grapov, L. V. Razvodovskya, and S. L. Portnova, *Zh. Obshch. Khim.*, 1965, **35**, 1771.
100. G. M. Kosolapoff and L. B. Payne, *J. Org. Chem.*, 1956, **21**, 413.
101. V. Gutmann, G. Mortl, and K. Utvary, *Monatsh. Chem.*, 1961, **92**, 1258.
102. W. C. Smith, R. Gher, and L. F. Audrieth, *J. Org. Chem.*, 1957, **22**, 265.
103. A. Michaelis, *Liebigs Ann. Chem.*, 1896, **293**, 193.
104. A. Schönberg, *Chem. Ber.*, 1955, **68**, 163.
105. E. J. Reist, I. G. Jung, and B. R. Baker, *J. Org. Chem.*, 1960, **25**, 666.
106. A. Michaelis and G. Schluter, *Chem. Ber.*, 1898, **31**, 1037.
107. G. G. Briand, T. Chivers, M. Krahn, and M. Parvez, *Inorg. Chem.*, 2002, **41**, 6808.
108. M. Goehring and K. Niedenzu, *Chem. Ber.*, 1956, **89**, 1774.
109. R. Klement, *Inorg. Synth.*, 1960, **6**, 108.
110. A. Michaelis, *Liebigs Ann. Chem.*, 1903, **326**, 223.
111. H. Normant, *Angew. Chem.*, 1967, **79**, 1029.
112. L. F. Audrieth and A. D. F. Toy, *J. Am. Chem. Soc.*, 1942, **64**, 1553.
113. a) G. A. Olah and A. A. Oswald, *J. Org. Chem.*, 1959, **24**, 1443; b) G. A. Olah and A. A. Oswald, *J. Org. Chem.*, 1959, **24**, 1443.
114. C. Stölzer and A. Simon, *Chem. Ber.*, 1960, **93**, 1323.
115. a) P. Otto, *Chem. Ber.*, 1895, **28**, 613; b) A. Michaelis, *Chem. Ber.*, 1895, **28**, 1237.
116. a) C. Steube and H. P. Lankelma, *J. Am. Chem. Soc.*, 1956, **78**, 976; b) H. J. Vetter and H. Nöth, *Chem. Ber.*, 1963, **96**, 1308.
117. T. Chivers, M. Krahn, G. Schatte, and M. Parvez, *Inorg. Chem.*, 2003, **42**, 3994.
118. a) A. C. Buck, J. D. Bartleson, and H. P. Lankelma, *J. Am. Chem. Soc.*, 1948, **70**, 744; b) G. Wise and H. P. Lankelma, *J. Am. Chem. Soc.*, 1952, **74**, 529.
119. R. Micu-Semeniuc, L. Silaghi-Dumitrescu, and I. Haiduc, *Inorg. Chim. Acta*, 1979, **33**, 281.
120. M. Goehring and K. Niedenzu, *Chem. Ber.*, 1956, **89**, 1768.
121. H. Vogt, A. Fischer, and P. G. Jones, *Z. Naturforsch*, 1996, **51b**, 865.
122. a) N. L. Smith, *J. Org. Chem.*, 1963, **28**, 863; b) A. P. Lane, D. A. Morton-Blake, and D. S. Payne, *J. Chem. Soc. A*, 1967, 1492.
123. S. E. Frazier and H. H. Sisler, *Inorg. Chem.*, 1966, **5**, 925.
124. M. Becke-Goehring and P. Hormuth, *Z. Anorg. Allg. Chem.*, 1969, **369**, 105.
125. R. Hudson, P. Chopard, and G. Salvadori, *Helv. Chim. Acta*, 1964, **47**, 632.
126. H. Nöth and H. J. Vetter, *Chem. Ber.*, 1965, **98**, 1981.
127. W. A. Hart and H. H. Sisler, *Inorg. Chem.*, 1964, **3**, 617.
128. A. Schmidpeter, *Actes Congr. Int. Composes Phosphore*, 1978, **2**, 77.
129. J. F. Bickley, M. C. Copsey, J. C. Jeffery, A. P. Leedham, C. A. Russell, D. Stalke, A. Steiner, T. Stey, and S. Zacchini, *J. Chem. Soc., Dalton Trans.*, 2004, 989.
130. H. Thönnessen, P. G. Jones, and R. Schmutzler, *Z. Anorg. Allg. Chem.*, 2003, **629**, 1265.
131. D. R. Brown, G. W. Fraser, and D. W. A. Sharp, *J. Chem. Soc. A*, 1966, 171.

132. a) R. Schmutzler, *J. Chem. Soc., Dalton Trans.*, 1973, 2687; b) R. H. Neilson and W. A. Kusterbeck, *J. Organomet. Chem.*, 1979, **166**, 309.

133. a) R. Schmutzler, *Angew. Chem., Int. Ed. Engl.*, 1964, **3**, 753; b) D. B. Denney, D. Z. Denney, B. C. Chang, and K. L. Marsi, *J. Am. Chem. Soc.*, 1969, **91**, 5243.

134. D. R. Brown, K. D. Crosbie, G. W. Fraser, and D. W. A. Sharp, *J. Chem. Soc. A*, 1969, 551.

135. R. Schmutzler, *Angew. Chem., Int. Ed. Engl.*, 1964, **3**, 753.

136. M. Lustig and G. W. Roesley, *Inorg. Chem.*, 1970, **9**, 1289.

137. J. J. Harris and B. Rudner, *J. Org. Chem.*, 1968, **33**, 1392.

138. D. H. Brown, K. D. Crosbie, J. I. Darragh, D. S. Ross, and D. W. A. Sharp, *J. Chem. Soc. A*, 1970, 914.

139. a) J. G. Verkade, *Pure Appl. Chem.*, 1980, **52**, 1131; b) J. G. Verkade, *Coord. Chem. Rev.*, 1994, **137**, 233.

140. B. Kovacevic, D. Baric, and Z. B. Maksic, *New J. Chem.*, 2004, **28**, 284.

141. W. S. Sheldrick, *J. Chem. Soc., Dalton Trans.*, 1974, 1402.

142. M. Necas, J. Marek, and J. Novosad, *Phosphorus Res. Bull*, 2001, 73.

143. H. Nöth and L. Meinel, *Z. Anorg. Allg. Chem.*, 1967, **349**, 225.

144. M. Witt and H. W. Roesky, *Chem. Rev.*, 1994, **94**, 1163.

145. a) P. Bhattacharyya and J. D. Woolins, *Polyhedron*, 1995, **14**, 3367; b) T. Q. Ly and J. D. Woollins, *Coord. Chem. Rev.*, 1998, **176**, 451.

146. T. Appleby and J. D. Woollins, *Coord. Chem. Rev.*, 2002, **235**, 121.

147. M. S. Balakrishna, V. S. Reddy, S. S. Krishnamurthy, J. F. Nixon, and J. C. T. R. Burkett St. Laurent, *Coord. Chem. Rev.*, 1994, **129**, 1.

148. J. Ellermann, J. Sutter, F. A. Knoch, and M. Moll, *Angew. Chem., Int. Ed. Engl.*, 1993, **32**, 700.

149. S. Jamali, M. Rashidi, M. C. Jennings, and R. J. Puddephatt, *J. Chem. Soc., Dalton Trans.*, 2003, 2313.

150. L. Han, L. X. Shi, L. Y. Zhang, Z. N. Chen, and M. C. Hong, *Inorg. Chem. Commun.*, 2003, **6**, 281.

151. H. Liu, M. J. Calhorda, M. G. B. Drew, V. Felix, J. Novosad, L. F. Veiros, F. F. de Biani, and P. Zanello, *J. Chem. Soc., Dalton Trans.*, 2002, 4365.

152. W. Y. Wong, F. L. Ting, and W. L. Lam, *Eur. J. Inorg. Chem.*, 2002, 2103.

153. E. J. Sekabunga, M. L. Smith, T. R. Webb, and W. E. Hill, *Inorg. Chem.*, 2002, **41**, 1205.

154. J. Ellermann, M. Schütz, F. W. Heinemann, and M. Moll, *Z. Anorg. Allg. Chem.*, 1998, **624**, 257.

155. M. T. Gamer, G. Canseco-Melchor, and P. W. Roesky, *Z. Anorg. Allg. Chem.*, 2003, **629**, 2113.

156. V. V. Sushev, A. N. Kornev, Y. V. Fedotova, Yu. A. Kursky, T. G. Mushtina, G. A. Abakumov, L. N. Zakharov, and A. L. Rheingold, *J. Organomet. Chem.*, 2003, **676**, 89.

157. E. Simón-Manso, P. Gantzel, and C. P. Kubiak, *Polyhedron*, 2003, **22**, 1641.

158. A. Winkler, W. Bauer, F. W. Heinemann, V. Garcia-Montalvo, M. Moll, and J. Ellermann, *Eur. J. Inorg. Chem.*, 1998, 437.

159. V. W. W. Yam, C. H. Lam, W. K. M. Fung, and K. K. Cheung, *Inorg. Chem.*, 2001, **40**, 3435.

160. a) P. W. Roesky, M. T. Gamer, and M. Puchner, *Chem. – Eur. J.*, 2002, **8**, 5265; b) M. T. Gamer, G. Canseco-Melchor, and P. W. Roesky, *Z. Anorg. Allg. Chem.*, 2003, **629**, 2113; c) M. T. Gamer and P. W. Roesky, *Inorg. Chem.*, 2004, **43**, 4903.

161. J. Ellermann, M. Schutz, F. W. Heinemann, and M. Moll, *Z. Anorg. Allg. Chem.*, 2003, **629**, 139.

162. a) J. Ellermann, J. Sutter, C. Schelle, F. A. Knoch, and M. Moll, *Z. Anorg. Allg. Chem.*, 1993, **619**, 2006; b) J. Ellermann, J. Sutter, F. A. Knoch, and M. Moll, *Angew. Chem., Int. Ed. Engl.*, 1993, **32**, 700.

163. M. Dotzler, A. Schmidt, J. Ellermann, F. A. Knoch, and M. Moll, *Polyhedron*, 1996, **15**, 4425.

164. S. Goldschmidt and H. L. Krauss, *Liebigs Ann. Chem.*, 1955, **595**, 193.

165. a) J. F. Nixon, *J. Chem. Soc. A*, 1968, 2689; b) R. Jefferson, J. F. Nixon, T. M. Painter, R. Keat, and L. Stobbs, *J. Chem. Soc., Dalton Trans.*, 1973, 1414.

166. a) R. B. King, *Acc. Chem. Res.*, 1980, **13**, 243; b) I. Haiduc and I. Silaghi-Dumitrescu, *Coord. Chem. Rev.*, 1986, **74**, 155.

167. Z. Fei, R. Scopelliti, and P. J. Dyson, *J. Chem. Soc., Dalton Trans.*, 2003, 2772.

168. H. J. Chen, A. Tarassoli, R. C. Haltiwanger, V. S. Allured, and A. D. Norman, *Inorg. Chim. Acta*, 1982, **65**, L 69.

169. H. Nöth and H. J. Vetter, *Chem. Ber.*, 1961, **94**, 1505.

170. M. S. Balakrishna, P. Chandrasekaran, and P. P. George, *Coord. Chem. Rev.*, 2003, **241**, 87.

171. M. Becke-Goehring and E. Fluck, *Inorg. Synth.*, 1966, **8**, 94.

172. E. Rivard, A. J. Lough, and I. Manners, *Inorg. Chem.*, 2004, **43**, 2765.

173. M. Becke-Goehring and W. Lehr, *Z. Anorg. Allg. Chem.*, 1963, **325**, 287.

174. A. Schmidpeter and K. Düll, *Chem. Ber.*, 1967, **100**, 1116.

175. A. Schmidpeter and C. Wigand, *Angew. Chem., Int.Ed. Engl.*, 1968, **7**, 210; 1969, **8**, 615.

176. a) E. Fluck and R. M. Reinisch, *Chem. Ber.*, 1963, **96**, 3085; b) E. Fluck and F. L. Goldmann, *Chem. Ber.*, 163, **96**, 3091.

177. a) R. Appel, A. Hauss, and G. Buchler, *Z. Naturforsch*, 1961, **16 B**, 405; b) J. K. Ruff and W. Schlienz, *Inorg. Synth.*, 1974, **15**, 84; c) G. R. Lewis and I. Dance, *J. Chem. Soc., Dalton Trans.*, 2000, 299.

178. a) A. Schmidpeter, H. Brecht, and H. Groeger, *Chem. Ber.*, 1967, **100**, 3063; b) A. Schmidpeter and H. Groeger, *Chem. Ber.*, 1967, **100**, 3979.

179. J. J. Longlet, S. G. Bodige, W. H. Watson, and R. H. Neilson, *Inorg. Chem.*, 2002, **41**, 6507.

180. H. J. Vetter, *Z. Naturforsch*, 1964, **9b**, 167.

181. a) M. Becke-Goehring, E. Fluck, and W. Lehr, *Z. Naturforsch*, 1962, **17b**, 126.

182. A. Kiliç, S. Begeç, Z. Kiliç, and T. Hökelek, *J. Mol. Struct.*, 2000, **516**, 255.

183. a) H. Schmidpeter and J. Ebeling, *Chem. Ber.*, 1968, **101**, 815; b) A. Schmidpeter and H. Groeger, *Z. Anorg. Allg. Chem.*, 1966, **345**, 106; c) A. Schmidpeter and H. Groeger, *Chem. Ber.*, 1967, **100**, 3979; d) I. T. Gilson and H. H. Sisler, *Inorg. Chem.*, 1965, **4**, 273; e) H. H. Sisler, H. S. Ahuja and N. L. Smith, *Inorg. Chem.*, 1962, **1**, 84.

184. P. Yash and S. K. Pandey, *Phosphorus, Sulfur & Silicon*, 2003, **178**, 159.

185. R. Hasselbring, S. K. Pandey, H. W. Roesky, D. Stalke, and A. Steiner, *J. Chem. Soc., Dalton Trans.*, 1993, 3447.

186. S. K. Pandey, A. Steiner, H. W. Roesky, and D. Stalke, *Inorg. Chem.*, 1993, **32**, 5444.

187. a) I. Haiduc, in 'Comprehensive Coordination Chemistry-II, Volume 1, Fundamentals: Ligands, Complexes, Synthesis, Purification and Structure', ed. vol. A. B. P. Lever, Elsevier-Pergamon, Amsterdam, Oxford, 2004, p. 323; b) I. Haiduc, *J. Organomet. Chem.*, 2001, **623**, 29; c) C. Silvestru and J. E. Drake, *Coord. Chem. Rev.*, 2001, **223**, 117; d) T. Q. Ly and J. D. Woollins, *Coord. Chem. Rev.*, 1998, **176**, 451; e) J. D. Woollins, *J. Chem. Soc., Dalton Trans.*, 1996, 2893.

188. B. A. Arbuzov, P. I. Alimov, and M. A. Zvereva, *Izvest. Akad. Nauk SSSR, Ser. Khim*, 1954, **1042**, 1047.

189. P. I. Alimov, M. A. Zvereva and O. N. Fedorova, *Khim. Prom*, 1955, **164**,; *Chem. Abstr.*,1958, **52**, 244a.

190. K. Aparna, S. S. Krishnamurthy, and M. Nethaji, *J. Chem. Soc., Dalton Trans.*, 1995, 2991.

191. a) R. P. Kamalesh Babu, R. McDonald, S. A. Decker, M. Klobukowski, and R. G. Cavell, *Organometallics*, 1999, **18**, 4226; b) R. P. Kamalesh Babu, R. McDonald, and R. G. Cavell, *Organometallics*, 2000, **19**, 3462; c) K. Aparna, M. Fergusson, and R. G. Cavell, *J. Am. Chem. Soc.*, 2000, **122**, 726; d) R. P. Kamalesh Babu, R. McDonald, and R. G. Cavell, *J. Chem. Soc., Dalton Trans.*, 2001, 2210.

192. R. P. Kamalesh Babu, K. Aparna, R. McDonald, and R. G. Cavell, *Inorg. Chem.*, 2000, **39**, 4981.

193. C. M. Ong and D. W. Stephan, *J. Am. Chem. Soc.*, 1999, **121**, 2939.

194. R. G. Cavell, R. P. Kamalesh Babu, and K. Aparna, *J. Organomet. Chem.*, 2001, **617**, 158.

195. M. J. Sarfield, M. Said, M. Thornton-Pett, L. A. Gerrard, and M. Bochmann, *J. Chem. Soc., Dalton Trans.*, 2001, 822.

196. M. S. Balakrishna, R. Klein, S. Uhlenbrock, A. A. Pinkerton, and R. G. Cavell, *Inorg. Chem.*, 1993, **32**, 5676.

197. A. S. Batsanov, M. G. Davidson, I. Fernandez, J. A. K. Howard, F. López-Ortiz, and R. D. Price, *J. Chem. Soc., Perkin Trans.*, 2000, 4237.

198. M. S. Balakrishna, S. Teipel, A. A. Pinkerton, and R. G. Cavell, *Inorg. Chem.*, 2001, **40**, 1802.

199. M. Becke-Goehring and W. Lehr, *Z. Anorg. Allg. Chem.*, 1963, **325**, 287.

200. H. Ackermann, R. Leo, W. Massa, and K. Dehnicke, *Z. Anorg. Allg. Chem.*, 2004, **630**, 1205.

201. E. F. Moran, *J. Inorg. Nucl. Chem.*, 1968, **30**, 1405.

202. A. M. Z. Slawin, M. B. Smith, and J. D. Woollins, *J. Chem. Soc., Dalton Trans.*, 1997, 3397.

203. A. M. Z. Slawin, M. B. Smith, and J. D. Woollins, *Chem. Commun.*, 1996, 2095.

204. F. Hartmann, D. Mootz, C. Hasenfratz, and R. Schwesinger, *Z. Naturforsch*, 1996, **51b**, 1375.

205. R. Schwesinger, C. Hasenfratz, H. Schlemper, L. Walz, E. M. Peters, K. Peters, and H. G. von Schnering, *Angew. Chem., Int. Ed. Engl.*, 1993, **32**, 1361.

206. G. Magro, B. Donnadieu, A. M. Caminade, and J. P. Majoral, *Chem. – Eur. J*, 2003, **9**, 2151.

207. a) J. P. Majoral, A. M. Caminade, and V. Maraval, *Chem. Commun.*, 2002, 2929; b) J. P. Majoral, C. Larre, R. Laurent, and A. M. Caminade, *Coord. Chem. Rev.*, 1999, **190/192**, 3; c) J. P. Majoral and A. M. Caminade, *Chem. Rev.*, 1999, **99**, 845.

208. G. David, E. Niecke, M. Nieger, V. von der Gönna, and W. W. Schoeller, *Chem. Ber.*, 1993, **126**, 1513.

209. E. Niecke and R. Kroher, *Angew. Chem.*, 1976, **88**, 758.

210. a) E. Niecke and R. Kroher, *Angew. Chem., Int. Ed. Engl.*, 1976, **15**, 692; b) P. B. Hitchcock, H. A. Jasim, M. F. Lappert, and H. D. Williams, *J. Chem. Soc., Chem. Commun.*, 1986, 1634; c) S. Pohl, *Chem. Ber.*, 1979, **112**, 3159.

211. N. Burford and D. J. LeBlanc, *Inorg. Chem.*, 1999, **38**, 2248.

212. R. Streubel, *Coord. Chem. Rev.*, 2002, **227**, 175.

213. F. Garcia, G. T. Lawson, D. J. Linton, D. Moncrieff, M. McPartlin, A. D. Woods, and D. S. Wright, *Chem. – Eur. J*, 2002, **8**, 5723.

214. a) R. Keat, in 'The Chemistry of Inorganic Homo- and Heterocycles', eds. I. Haiduc and D. B. Sowerby, Academic Press, London, 1987, Chap. 19, p. 467; b) H. G. Heal, 'The Inorganic Heterocyclic Chemistry of Sulfur, Nitrogen and Phosphorus', Academic Press, London, 1980, Chap. 11, p. 187; c) I. Haiduc, 'The Chemistry of Inorganic Ring Systems', Wiley-Interscience, London, 1970, Vol. 2, p. 804.

215. a) O. J. Scherer and P. Klusmann, *Angew. Chem., Int. Ed. Engl.*, 1969, **8**, 752; b) K. W. Muir and J. F. Nixon, *Nachr. Chem. Techn.*, 175, **23**, 395.

216. a) G. Bulloch, R. Keat, and D. G. Thompson, *J. Chem. Soc., Dalton Trans.*, 1977, 99; b) M. L. Thompson, A. Tarassoli, R. C. Haltiwanger, and A. D. Norman, *J. Am. Chem. Soc.*, 1981, **103**, 6770.

217. E. W. Abel, D. A. Armitage, and G. R. Wiley, *J. Chem. Soc.*, 1965, 57.

218. R. R. Holmes and J. A. Forstner, *Inorg. Chem.*, 1963, **2**, 380.

219. a) R. R. Holmes, *J. Am. Chem. Soc.*, 1961, **83**, 1334; b) A. Wolf and J. G. Riess, *Bull. Soc. Chim. Fr.*, 1973, 1587;

c) M. Bermann and J. R. van Wazer, *Inorg. Chem.*, 1973, **12**, 2186.

220. G. Bulloch and R. Keat, *J. Chem. Soc., Dalton Trans.*, 1974, 2010.

221. O. J. Scherer and W. Glassel, *Chem. Ber.*, 1977, **110**, 3874.

222. N. Burford, T. S. Cameron, K. D. Conroy, B. Ellis, M. Lumsden, C. L. B. MacDonald, R. McDonald, A. D. Phillips, P. J. Ragogna, R. W. Schurko, D. Walsh, and R. E. Wasylishen, *J. Am. Chem. Soc.*, 2002, **124**, 14012.

223. D. F. Moser, L. Grocholl, L. Stahl, and R. J. Staples, *J. Chem. Soc., Dalton Trans.*, 2003, 1402.

224. A. D. Woods and M. McPartlin, *J. Chem. Soc., Dalton Trans.*, 2004, 90.

225. V. S. Reddy, S. S. Krishnamurthy, and M. Nethaji, *J. Chem. Soc., Dalton Trans.*, 1995, 1933.

226. a) L. Stahl, *Coord. Chem. Rev.*, 2000, **210**, 203; b) G. G. Briand, T. Chivers and M. Krahn, *Coord. Chem. Rev.*, 2002, **233**, 237; c) M. S. Balakrishna, V. S. Reddy, S. S. Krishnamurthy, J. F. Nixon, and J. C. T. R. Burkett St. Laurent, *Coord. Chem. Rev.*, 1994, **129**, 1.

227. a) D. F. Moser, L. Grocholl, L. Stahl, and R. J. Staples, *J. Chem. Soc., Dalton Trans.*, 2003, 1402; b) A. D. Bond, E. L. Doyle, F. Garcia, R. A. Kowenicki, D. Moncrieff, M. McPartlin, L. Riera, A. D. Woods, and D. S. Wright, *Chem. – Eur. J*, 2004, **10**, 2271; c) I. Schranz, L. P. Grocholl, L. Stahl, R. J. Staples, and A. Johnson, *Inorg. Chem.*, 2000, **39**, 3037; d) G. G. Briand, T. Chivers, M. Parvez, and G. Schatte, *Inorg. Chem.*, 2003, **42**, 525.

228. E. L. Doyle, L. Riera, and D. S. Wright, *Eur. J. Inorg. Chem.*, 2003, 3279.

229. a) E. L. Doyle, C. Tubb, S. J. Kidd, M. McPartlin, A. D. Woods, and D. S. Wright, *Chem. Commun.*, 2001, 2542; b) A. Bashall, A. D. Bond, E. L. Doyle, F. Garcia, S. J. Kidd, G. T. Lawson, M. C. Parry, M. McPartlin, A. D. Woods, and D. S. Wright, *Chem. – Eur. J.*, 2002, **8**, 3377; c) A. D. Bond, E. L. Doyle, F. Garcia, R. A. Kowenicki, M. McPartlin, L. Tiera, and D. S. Wright, *Chem. Commun.*, 2003, 2990; d) E. L. Doyle, F. Garcia, S. M. Humphrey, R. A. Kowenicki, L. Riera, A. D. Woods, and D. S. Wright, *J. Chem. Soc., Dalton Trans.*, 2004, 807.

230. R. Murugavel, S. S. Krishnamurthy, and M. Nethaji, *J. Chem. Soc., Dalton Trans.*, 1993, 3635.

231. R. Murugavel, G. Prabusankar, V. S. Shete, and K. Baheti, *Phosphorus, Sulfur & Silicon*, 2001, **168/169**, 263.

232. R. R. Holmes, *J. Am. Chem. Soc.*, 1961, **83**, 1334.

233. O. J. Scherer, K. Andres, C. Krüger, Y. H. Tsai, and G. Wolmerhäuser, *Angew. Chem., Int. Ed. Engl.*, 1980, **19**, 571.

234. J. K. Brash, T. Chivers, M. L. Krahn, and M. Parvez, *Inorg. Chem.*, 1999, **38**, 290.

235. a) A. Bashall, E. L. Doyle, F. Garcia, G. T. Lawson, D. J. Linton, D. Moncrieff, M. McPartlin, A. D. Woods, and D. S. Wright, *Chem. – Eur. J*, 2002, **8**, 5723; b) A. D. Norman and R. M. Hands, *Main Group Chem. News* 1996, **4**, 25.

236. I. Haiduc, 'The Chemistry of Inorganic Ring Systems', Wiley-Interscience, London, 1970, Vol. 2, p. 761.

237. B. Helferich and L. Schröder, *Liebigs Ann. Chem.*, 1963, **670**, 48.

238. a) A. Michaelis, *Liebigs Ann. Chem.*, 1896, **293**, 207; b) P. M. Zavlin, V. A. Zamora, and A. S. Fedoseeva, *Zh. Obshch. Khim.*, 1971, **41**, 481.

239. a) R. Keat, D. S. Rycroft, and D. G. Thompson, *J. Chem. Soc., Dalton Trans.*, 1979, 1224; b) R. Keat and D. G. Thompson, *J. Chem. Soc., Dalton Trans.*, 1980, 928.

240. a) M. Green, R. N. Haszeldine, and G. S. A. Hopkins, *J. Chem. Soc. A*, 1966, 1766; b) V. P. Kukhar, *Zh. Obshch. Khim.*, 1970, **40**, 785.

241. M. Becke-Goehring, L. Leichner, and B. Scharf, *Z. Anorg. Allg. Chem.*, 1966, **343**, 154.

242. W. Zeiss, C. Feldt, J. Weiss, and G. Dunkel, *Chem. Ber.*, 1978, **111**, 1180.

243. C. D. Flint, E. H. M. Ibrahim, R. A. Shaw, B. C. Smith, and C. P. Thakur, *J. Chem. Soc. A*, 1971, 3513.

244. H. Tolkmith and E. C. Britton, *J. Org. Chem.*, 1959, **24**, 705.

245. a) T. Chivers, C. Fedorchuk, M. Krahn, M. Parvez, and G. Schatte, *Inorg. Chem.*, 2001, **40**, 1936; b) T. Chivers, M. Krahn, M. Parvez, and G. Schatte, *Inorg. Chem.*, 2001, **40**, 2547.

246. G. R. Lief, C. J. Carrow, L. Stahl, and R. J. Staples, *Organometallics*, 2001, **20**, 1629.

247. L. G. Lund, N. L. Paddock, S. E. Proctor, and H. T. Searle, *J. Chem. Soc.*, 1960, 2542.

248. A. C. Chapman, N. L. Paddock, D. H. Paine, H. T. Searle, and D. R. Smith, *J. Chem. Soc.*, 1960, 3608.

249. a) J. Liebig and H. Wöhler, *Ann. Chem.*, 1834, **11**, 139; b) H. Rose, *Ann. Chem.*, 1834, **11**, 131.

250. a) H. N. Stockes, *Am. Chem. J*, 1895, **17**, 275; b) H. N. Stockes, *Am. Chem. J*, 1896, **18**, 629; 780; c) H. N. Stockes, *Am. Chem. J*, 1897, **19**, 782.

251. a) I. Haiduc, 'The Chemistry of Inorganic Ring Systems', Wiley-Interscience, London, 1970, vol. 2, p. 624; b) H. R. Allcock, 'Phosphorus-Nitrogen Compounds', Academic Press, New York, 1972; c) R. A. Shaw, *Pure Appl. Chem.*, 1974, **44**, 317; d) R. A. Shaw, *Pure Appl. Chem.*, 1980, **52**, 1063; e) H. G. Heal, 'The Inorganic Heterocyclic Chemistry of Sulfur, Nitrogen and Phosphorus', Academic Press, London, 1980, Chap 12, p. 214; f) C. W. Allen, in 'The Chemistry of Inorganic Homo- and Heterocycles', eds. I. Haiduc and D. B. Sowerby, Academic Press, London, 1987, vol. 2, Chap 20, p. 501; g) C. W. Allen, *Coord. Chem. Rev.*, 1994, **130**, 137; h) C. W. Allen, *Chem. Rev.*, 1991, **91**, 119; i) H. R. Allcock, 'Chemistry and Applications of Polyphosphazenes', Wiley-Interscience, New York, 2003; j) R. De Jaeger ed., 'Phosphazenes: A Worldwide Insight', Nova Science Pub, New York, 2004.

252. a) R. Schenk and G. Römer, *Chem. Ber.*, 1924, **57**, 1343; b) M. L. Nielsen and G. Crawford, *Inorg. Synth.*, 1960, **6**, 94.

253. P. Wisian-Neilson and R. H. Neilson, *Inorg. Chem.*, 1980, **19**, 1975.

254. H. R. Allcock, C. A. Crane, C. T. Morrissey, and M. A. Olshavsky, *Inorg. Chem.*, 1999, **38**, 280.

255. P. Wisian-Neilson, R. S. Johnson, H. Zhang, J. H. Jung, R. H. Neilson, J. Ji, W. H. Watson, and M. Krawiec, *Inorg. Chem.*, 2002, **41**, 4775.

256. J. H. Jung, J. C. Pomeroy, H. Zhang, and P. Wisian-Neilson, *J. Am. Chem. Soc.*, 2003, **125**, 15537.

257. J. F. Bickley, R. Bonar-Law, G. T. Lawson, P. I. Richards, F. Rivals, A. Steiner, and S. Zacchini, *J. Chem. Soc., Dalton Trans.*, 2003, 1235.

258. a) M. L. Nielsen, *Inorg. Synth.*, 1960, **6**, 79; b) F. M. Pollard, G. Nickless, and R. W. Warender, *J. Chromatogr.*, 1962, **10**, 485; c) F. M. Pollard, G. Nickless and A. M. Bigwood, *J. Chromatogr.*, 1963, **11**, 527.

259. B. W. Fitzsimmons, C. Hewlett, and R. A. Shaw, *J. Chem. Soc.*, 1965, 7432.

260. D. Abizanda, O. Crespo, M. C. Gimeno, J. Jiménez, and A. Laguna, *Chem. – Eur. J*, 2003, **9**, 3310.

261. a) I. Dez, J. Levalois-Mitjaville, H. Grützmacher, V. Gramlich, and R. de Jaeger, *Eur. J. Inorg. Chem.*, 1999, 1673; b) D. B. Davies, T. A. Clayton, R. J. Eaton, R. A. Shaw, A. Egan, M. B. Hursthouse, G. Sykara, I. Porwolik-Czomperlik, M. Siwy, and K. Brandt, *J. Am. Chem. Soc.*, 2000, **12**, 12447.

262. H. R. Allcock, J. S. Rutt, M. F. Weller, and M. Parvez, *Inorg. Chem.*, 1993, **32**, 2315.

263. S. Sengupta, *Polyhedron*, 2003, **22**, 1237.

264. V. Chandrasekhar, G. T. S. Andavan, S. Nagendran, V. Krishnan, R. Azhakar, and R. Butcher, *Organometallics*, 2003, **22**, 976.

265. a) A. Maia, D. Landini, M. Penso, K. Brandt, M. Siwy, G. Schroeder, and B. Grierczyk, *New. J. Chem.*, 2001, 1078; b) I. Porwolik-Czomperlik, K. Brandt, T. A. Clayton, D. B. Davies, R. J. Eaton, and R. A. Shaw, *Inorg. Chem.*, 2002, **41**, 4944.

266. A. J. Elias, R. L. Kirchmeier, and J. M. Shreeve, *Inorg. Chem.*, 1994, **33**, 2727.

267. H. W. Roesky, W. G. Böwing, and E. Niecke, *Chem. Ber.*, 1971, **104**, 653.

268. E. Lork, P. G. Watson, and R. Mews, *Chem. Commun.*, 1995, 1717.

269. a) V. Chandrasekar and S. Nagendran, *Chem. Soc. Rev.*, 2001, **30**, 193; b) H. R. Allcock, J. L. Desorcie, and G. H. Riding, *Polyhedron*, 1987, **2**, 119.

270. A. Chandrasekaran, S. S. Krishnamurthy, and M. Nethaji, *Inorg. Chem.*, 1994, **33**, 3085.

271. a) K. R. J. Thomas, V. Chandrasekar, P. Pal, S. R. Scott, R. Hallford, and A. W. Cordes, *Inorg. Chem.*, 1993, **32**, 606; b) K. R. J. Thomas, V. Chandrasekar, P. Pal, S. R. Scott, R. Hallford, and A. W. Cordes, *J. Chem. Soc., Dalton Trans.*, 1993, 2589; c) K. R. J. Thomas, P. Tharmaraj, V. Chandrasekar, C. D. Bryan, and A. W. Cordes, *Inorg. Chem.*, 1994, **33**, 5382; d) K. R. J. Thomas, P. Tharmaraj, V. Chandrasekhar, and E. R. T. Tiekink, *J. Chem. Soc., Dalton Trans.*, 1994, 1301; e) K. R. J. Thomas, P. Tharmaraj, and V. Chandrasekar, *Polyhedron*, 1995, **14**, 977, 1607; f) Y. Byun, D. Min, J. Do, H. Yun and Y. Do, *Inorg. Chem.*, 1996, **35**, 3981.

272. a) E. W. Ainscough, A. M. Brodie, and C. V. Depree, *J. Chem. Soc., Dalton Trans.*, 1999, 4123; b) B. H. Koo, Y. Byun, E. Hong, Y. Kim, and Y. Do, *Chem. Commun.*, 1998, 1227.

273. G. A. Carriedo, F. J. G. Alonso, P. A. González, C. D. Valenzuela, and N. Y. Saéz, *Polyhedron*, 2002, **21**, 2579.

274. M. Bahadur, C. W. Allen, W. E. Geiger, and A. Bridges, *Can. J. Chem.*, 2002, **80**, 1387.

275. a) G. T. Lawson, C. Jacob, and A. Steiner, *Eur. J. Inorg. Chem.*, 1999, 1881; b) G. T. Lawson, f. Rivals, M. Tascher, C. Jacob, J. M. Bickley, and A. Steiner, *Chem. Commun.*, 2000, 341; c) F. Rivals and A. Steiner, *Chem. Commun.*, 2001, 1426; d) F. Rivals and A. Steiner, *Z. Anorg. Allg. Chem.*, 2003, **629**, 139.

276. F. Rivals and A. Steiner, *Chem. Commun.*, 2001, 1426.

277. a) A. Schmidpeter, in 'The Chemistry of Inorganic Homo- and Heterocycles', eds. I. Haiduc and D. B. Sowerby, Academic Press, London, 1987, Vol. 2, p. 616; b) H. G. Heal, 'The Inorganic Heterocyclic Chemistry of Sulfur, Nitrogen and Phosphorus', Academic Press, London, 1980, Chap. 11, p. 197; c) I. Haiduc, 'The Chemistry of Inorganic Ring Systems', Wiley-Interscience, London, 1970, vol. 2, p. 787; d) M. Bermann, *Adv. Inorg. Chem. Radiochem*, 1972, **14**, 1; e) A. F. Grapov, I. V. Razvodovskaya and N. N. Melnikov, *Russ. Chem. Rev.*, 1981, **50**, 334.

278. H. A. Klein and H. P. Latscha, *Z. Anorg. Allg. Chem.*, 1974, **406**, 214.

279. A. Schmidpeter, in 'The Chemistry of Inorganic Homo- and Heterocycles', eds. I. Haiduc and D. B. Sowerby, Academic Press, London, 1987, Vol. 2, Chap. 21, p. 617.

280. O. Schlak, R. Schmutzler, H. M. Schiebel, M. I. M. Wazeer, and R. K. Harris, *J. Chem. Soc., Dalton Trans.*, 1974, 2153.

281. a) H. Hahn, K. Utvary, and W. Meindl, *Monatsh. Chem.*, 1983, **114**, 1167; b) K. Utvary and K. Kubjacek, *Monath. Chem.*, 1986, **117**, 387.

282. a) E. Niecke and W. Bitter, *Chem. Ber.*, 1976, **109**, 415; b) E. Niecke and R. Kröher, *Z. Naturforsch*, 1979, **34b**, 837; c) O. J. Scherer and G. Schnabl, *Z. Naturforsch*, 1976, **31b**, 142.

283. a) H. W. Roesky, S. K. Mehrotra, C. Platte, D. Amirzadeh-Asl, and B. Roth, *Z. Naturforsch*, 1980, **35b**, 1130; b) A. H. Cowley, S. K. Mehrotra, and H. W. Roesky, *Inorg. Chem.*, 1981, **20**, 712.

284. H. Nöth and R. Ullmann, *Chem. Ber.*, 1976, **109**, 1942.

285. a) I. Haiduc, 'The Chemistry of Inorganic Ring Systems', Wiley-Interscience, London, 1970, vol. 2, p. 813; b) C. W. Allen, in 'The Chemistry of Inorganic Homo- and Heterocycles', I. Haiduc and D. B. Sowerby, Academic Press,

London, 1987, Vol. 2, Chap. 20, p. 577; c) D. P. Gates and I. Manners, *J. Chem. Soc., Dalton Trans.*, 1997, 2525.

286. D. P. Gates, A. R. McWilliams, R. Ziembinski, L. M. Liable-Sands, I. A. Guzei, G. P. A. Yap, A. L. Rheingold, and I. Manners, *Chem. – Eur. J*, 1998, **4**, 1489.

287. a) M. Witt and H. W. Roesky, *Chem. Rev.*, 1994, **94**, 1163; b) M. Witt, H. W. Roesky and M. Noltemeyer, *Inorg. Chem.*, 1997, **36**, 3476.

288. a) J. Elias, B. Twamley, and J. M. Shreeve, *Inorg. Chem.*, 2001, **40**, 2287; b) Van de Grampel and J. C. *Coord. Chem. Rev.*, 1992, **112**, 247.

289. C. W. Allen, *Coord. Chem. Rev.*, 1994, **130**, 137.

290. H. R. Allcock, ‘Chemistry and Applications of Polyphosphazenes’, Wiley-Interscience, New York, 2003.

291. R. H. Neilson and P. Wisian-Neilson, *Chem. Rev.*, 1988, **88**, 541.

292. a) I. Manners, *Coord. Chem. Rev.*, 1994, **137**, 109; b) J. C. van de Grampel, *Coord. Chem. Rev.*, 1992, **112**, 247; c) A. R. McWilliams, D. P. Gates, M. Edwards, L. M. Liable-Sands, I. Guzei, A. L. Rheingold, and I. Manners, *J. Am. Chem. Soc.*, 2000, **122**, 8848; d) D. P. Gates, M. Edwards, L. M. Liable-Sands, A. L. Rheingold, and I. Manners, *J. Am. Chem.*, 1998, **120**, 3249; e) Y. Ni, A. J. Lough, A. L. Rheingold, and I. Manners, *Angew. Chem., Int. Ed. Engl.*, 1995, **34**, 998; f) J. A. Dodge, I. Manners, H. R. Allcock, G. Renner, and O. Nuyken, *J. Am. Chem. Soc.*, 1990, **112**, 1268; g) Y. Ni, P. Park, M. Liang, J. Massey, C. Waddling, and I. Manners, *Macromolecules*, 1996, **29**, 3401.

293. M. Taillefer, N. Rahier, E. Minta, and H. J. Cristau, *Phosphorus, Sulfur & Silicon*, 2002, **177**, 1847.

294. J. E. Mark, H. R. Allcock, and R. West, ‘Inorganic Polymers’, Prentice Hall, Englewood Cliffs, NJ, 1992.

295. H. Nakamura, T. Masuko, M. Kojima, and J. H. Magill, *Macromol. Chem. Phys.*, 1999, **200**, 2519.

296. H. R. Allcock, N. J. Sunderland, A. P. Primrose, A. L. Rheingold, I. A. Guzei, and M. Parvez, *Chem. Mater.*, 1999, **11**, 2478.

297. a) Z. Pang, X. Gu, A. Yekta, Z. Masoumi, J. B. Coll, M. A. Winnik, and I. Manners, *Adv. Mater.*, 1996, **8**, 768; b) D. P. Gates and I. Manners, *J. Chem. Soc., Dalton Trans.*, 1997, 2525.

Phosphorus: Organophosphorus Chemistry

Robert Engel[1] **& JaimeLee Iolani Cohen**[2]
[1] *Queens College, City University of New York, Flushing, NY, USA*
[2] *Pace University, New York, NY, USA*

1	Introduction	1
2	Phosphinidine	1
3	Trivalent Organophosphorus Compounds	2
4	Tetravalent Organophosphorus Compounds	6
5	Pentavalent Organophosphorus Compounds	9
6	Hexavalent Organophosphorus Compounds	15
7	Organophosphorus Nomenclature	15
8	Related Articles	15
9	References	15

Glossary

Addition–elimination: an overall substitution reaction that takes place in two steps, the first being addition across an unsaturated linkage and the second an elimination involving one of the components added in the first step and one originally present
Cheleotropic fragmentation: a fragmentation reaction in which two σ bonds to a single atom are broken
Dehydrohalogenation: an elimination reaction in which the elements of a hydrogen halide molecule are eliminated from adjacent atoms leaving a π bond
Diastereoisomers: stereoisomers that are not enantiomers
Electrophilic reaction: a reaction in which an electron-rich species is attacked by an electron deficient site of another reagent to form a new covalent bond
Enantiomers: molecules whose structures are nonsuperimposable mirror images of each other
Exocyclic bond: a bond that is connected to and external to a ring structure
Nucleophile: an electron-rich species, generally with an unshared electron pair, that forms a new bond by attack of an electron deficient site other than a hydrogen
Pseudorotation: an internal motion of ligands about a central atom that exchanges several types of ligand positions and produces a permuted form of the original molecule without breaking and reforming bonds
Sigmatropic rearrangement: a rearrangement that occurs involving the concerted shift of electrons and the breaking and making of σ bonds
Stereogenic: a site within a molecule that imparts chirality to the molecule
Stereospecificity: a characteristic of a reaction in which one stereoisomer is formed or decomposed to the exclusion of other stereoisomers
Umpolung: a characteristic of a reaction system in which the polarity of a reactive functional group is inverted by a simple chemical transformation
Ylide: a zwitterion in which opposite charges are located on adjacent atoms and are not fully neutralized by bond formation

1 INTRODUCTION

The use of the term ‘organophosphorus compound’ has generally been limited to those materials that contain a direct carbon–phosphorus covalent bond. We continue this restriction in the present discussion. As a result, we will omit from this discussion the chemistry and nature of materials, while containing both carbon and phosphorus, that lack the direct covalent connection of the two elements. Other sources provide significant information on such materials as simple esters of phosphoric and phosphorous acid.[1,2]

The present consideration will be particularly concerned with the generation of those compounds containing at least one direct carbon–phosphorus covalent bond, with special emphasis given to the formation (and cleavage) of that type of bond. The organization of this treatment is based on the number of bonds present involving the phosphorus atom. Thus, phosphinidine (neutral, one carbon–phosphorus covalent bond) is considered first and working through hexacoordinate phosphorus. Included in the present consideration are reactions of elemental phosphorus that can lead to compounds with varying numbers of carbon–phosphorus covalent bonds depending on the reaction conditions.

2 PHOSPHINIDINE

For sometime, phosphinidines, monovalent organophosphorus species with the general formulation (R–P), have been postulated as reactive intermediates in the thermal and photochemical decomposition of several types of stable organophosphorus compounds. While not isolated as stable molecules, these monovalent species can be inferred on the basis of the isolation of products whose structures can be derived rationally from the postulation of such species, as well as on the mass spectra of the transient species themselves. We may view phosphinidines as the phosphorus analogues of nitrenes (R–N), highly reactive monovalent nitrogen species formed as transient intermediates in the thermal decomposition of azides and in the α-elimination reaction of N-tosylates.

Although there is a structural analogy of the two species, there are chemical and electronic differences between nitrenes and phosphinidines.

The production of a short series of organic phosphinidines by the thermolysis or photolysis of cyclophosphines $[R–P]_{4-6}$ (see Section 3.6) and by the reaction of organic phosphonous dichlorides ($RPCl_2$) (see Section 3.5) with electropositive metals has been reviewed by Schmidt.[3] While the noted reactions of phosphinidines lead to certain products attributable to phosphinidine intermediates, particular reactions are noteworthy by their failure to lead to products anticipated by analogy with nitrene and carbene chemistry. Although reactions involving the insertion of the phosphinidine into sulfur−sulfur bonds and the addition to the termini of conjugated dienes are observed, an anticipated addition to alkenes to form a three-membered ring fails to occur.[4] A phosphinidine intermediate has been postulated to be formed in the photolysis of a diphosphene (Ar–P=P–Ar) in which adjacent 1,1-dimethylethyl groups provide steric interaction, presumably preventing the monovalent phosphorus from undergoing intermolecular reaction. Rather, intramolecular insertion into a carbon−hydrogen bond occurs.[5] This type of reaction is common with nitrene and carbenoid intermediates. Matrix-isolation investigations should be useful for the investigation of the electronic nature of phosphinidines.

3 TRIVALENT ORGANOPHOSPHORUS COMPOUNDS

3.1 Overview

Several categories of organic phosphorus(III) compounds are of particular interest and will be considered here. In addition to differences in the nature of the bonding at phosphorus, these categories of compounds exhibit variations in chemical and physical properties owing simply to the nature of the ligands attached to phosphorus. For example, although they share some similarity in the mode of generation of the carbon−phosphorus bond, derivatives of the phosphonous acids $[R–P(OH)_2]$, such as the dihalide $[R–PCl_2]$, exhibit behavior quite different from that of phosphines $[R_3P]$ although the degree of substitution about phosphorus is the same.

3.2 Phosphines

In general, phosphines are tricoordinated phosphorus compounds that bear only hydrogen or carbon (alkyl, aryl, alkenyl) substituents at phosphorus. Subcategorization of phosphines is based on the degree of carbon substitution about phosphorus. Primary phosphines $[RPH_2]$ are those compounds that bear only a single carbon functionality attached to phosphorus. These compounds can be prepared by numerous methods, a common approach using the nucleophilic character of unsubstituted phosphine $[PH_3]$ or the phosphide anion $[PH_2{}^-]$. For example, methyl phosphine is prepared from sodium phosphide (itself derived from tetrasodium diphosphide or elemental phosphorus (*vide infra*)) and iodomethane in 62% yield by a nucleophilic substitution reaction. The reaction itself is presumed to occur quantitatively, but difficulties in isolation of the pure compound result in the observed decreased yield.[6]

The generation of phosphine (and the phosphide anion) from elemental phosphorus for use in this type of reaction is common. While unreactive with neutral water (although undergoing rapid oxidation with oxygen at 34 °C), elemental phosphorus (white, P_4) generates phosphine readily in basic medium.[7] On heating above 400 °C, white phosphorus $[P_4]$ generates a different allotropic form known as red phosphorus in which a P–P bond within the fundamental P_4 tetrahedron is broken and individual tetrahedra are linked in a polymeric chain. This form of elemental phosphorus is less reactive that white phosphorus, but still is quite useful for synthetic purposes.

The direct reaction of organometallics such as organolithium or Grignard reagents with elemental phosphorus (white or red) can be used to generate the primary phosphines. The phosphide $[RPM_2]$ that is immediately formed reacts with water to generate the primary phosphine, or the addition of an alcohol to the reaction workup produces esters of phosphonous acids (see Section 3.5). Once the original organometallic has been used to generate the phosphide $[RPM_2]$, more highly substituted phosphines may be prepared by the addition of haloalkanes, or by reaction with appropriate carbonyl or epoxide reagents.[8–10]

Other approaches to the preparation of primary phosphines include the addition of phosphine itself to the carbonyl carbon of aldehydes or ketones (producing α-hydroxyalkylphosphonates),[11] or by conjugate addition reactions of phosphine to α, β-unsaturated reagents such as acrylonitrile or ethyl acrylate (equation 1).[12] Silylphosphines $[R_2PSiR'_3]$ also undergo conjugate addition reactions with acrylonitrile, replacing the phosphorus−silicon bond with a phosphorus−carbon bond.[13] Other organometallics, such as complex zirconium phosphides, undergo reaction with alkenes leading to preferential formation of primary phosphines by addition across the alkene linkage.[14] More highly substituted phosphines are formed as relatively minor side-products.

$$H_3P + H_2C{=}CHCN \xrightarrow{KOH} \underset{52\%}{H_2PCH_2CH_2CN} \qquad (1)$$

Secondary phosphines $[R_2PH]$ similarly can be derived from primary phosphines (and tertiary phosphines $[R_3P]$ from secondary phosphines) by way of nucleophilic attack by the electron-rich phosphorus of the phosphine on suitable substrates such as haloalkanes or epoxides (equation 2).[15] Tertiary phosphines themselves remain quite nucleophilic, leading to the formation of quaternary phosphonium salts, the formation and reaction of which are discussed later (see Section 4.2).

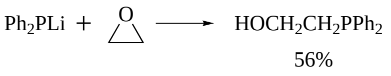

(2)

An alternative approach to the synthesis of tertiary phosphines starting with phosphorus(III) reagents as the source of phosphorus involves the attack of organometallic species on phosphorus halides. Starting with phosphorus trichloride, symmetrical tertiary phosphines can be prepared through the use of an excess of the appropriate Grignard reagent, as in the preparation of triphenylphosphine (equation 3).[16] Esters or mixed ester acid halide derivatives of phosphorous acid [$P(OH)_3$] may also be used in this type of reaction. A degree of selectivity is noted for the attack of organometallic species on these types of phosphorus reagents;[17] in general, the acid halide linkages are more reactive than are the ester linkages.

$$PhMgBr + PCl_2 \longrightarrow \underset{76\%}{PPh_3} \qquad (3)$$

Unsymmetrical tertiary phosphines [RR'_2P] may similarly be prepared by reaction of the organometallic with $RPCl_2$ or R_2PCl. The generation of these latter materials use the reactive derivatives of phosphonous acids [$RP(OH)_2$] or phosphinous acids [R_2POH]. Early efforts for the generation of these acid halides generally involved the appropriate organomercury or organolead reagents in reaction with phosphorus trichloride, providing monoalkylation. However, more efficacious approaches are available through the use of organocadmium or organotin reagents.

Particularly high-yield preparations of both alkyl- and aryldichlorophosphines are obtained through the use of aluminum chloride. The aluminum chloride mediated reaction of phosphorus trichloride with haloalkanes generates an intermediate that can be reduced to the corresponding alkyldichlorophosphine (equation 4). For the preparation of aryldichlorophosphines, aluminum chloride serves a Friedel–Crafts catalyst for electrophilic aromatic substitution by phosphorus on the aromatic ring (equation 5). These synthetic approaches to dihalophosphines have been reviewed.[17]

$$CH_3I + PCl_3 + AlCl_3 \xrightarrow[Fe]{KCl} \underset{80\%}{H_3CPCl_2} \qquad (4)$$

$$C_6H_6 + PCl_3 \xrightarrow{AlCl_3} \underset{70\%}{PhPCl_2} \qquad (5)$$

Primary and secondary phosphines are also capable of undergoing addition reactions across alkene linkages under the influence of radical initiators. In this way, more complex highly substituted phosphines can be generated. An illustration of this type of reaction is seen in the preparation of an unsymmetrically substituted tertiary phosphine, 1-phosphabicyclo[3.3.1]nonane, *via* two intramolecular addition reactions using a primary phosphine (equation 6).[18]

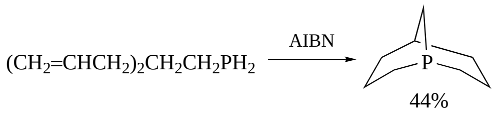

(6)

An additional approach toward the preparation of tertiary phosphines is by the reduction of more highly coordinated phosphorus species, particularly phosphine oxides [$O{=}PR_3$] and phosphine sulfides [$S{=}PR_3$] (see Section 5.2), but also phosphonium salts [$R_4P^+X^-$] and quasiphosphonium salts [$R_3P\text{-}YR'^+X^-$] (see Sections 4.2 and 4.4). Numerous reducing agents have been used to accomplish these conversions, including hexachlorodisilane [$Cl_3Si{-}SiCl_3$], trichlorosilane [$HSiCl_3$], phenylsilane [$PhSiH_3$], and lithium aluminum hydride [$LiAlH_4$].

When a phosphine oxide or sulfide bearing a stereogenic phosphorus atom is used, reduction of each of these reagents, except for lithium aluminum hydride, generally occurs with nearly complete stereospecificity. The nature of the stereospecificity (retention or inversion of the reaction) depends on the particular reaction conditions used. Alternatively, use of lithium aluminum hydride generally leads to racemization about phosphorus. The use of lithium aluminum hydride for stereospecific reduction of a tertiary phosphine oxide to the corresponding phosphine with retention of configuration has been accomplished with methyl triflate as an adjunct reactant. Up to 99% enantiomeric excess in the product has been obtained.[19] An example of the stereospecific reduction of a chiral tertiary phosphine oxide using phenylsilane is illustrated (equation 7). The nature of these reductions and their stereochemical outcomes has been reviewed.[20,21]

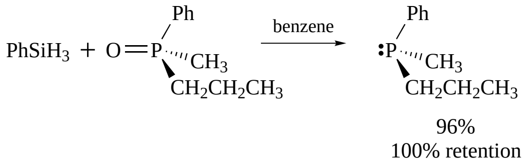

(7)

The stereochemical integrity of tertiary phosphines (their resistance to inversion of configuration) is significantly greater than that associated with tertiary amines of corresponding structure. For tertiary phosphines, the energy barrier for inversion is calculated to be somewhat higher than the 25 kcal mol^{-1} noted to be required for the spontaneous process to occur at room temperature. The 25 kcal mol^{-1} is significantly more than the value for tertiary amines. Such calculations appear to be validated by the experimental observations that simple (acyclic) unsymmetrical tertiary amines are not capable of maintaining stereochemical integrity about nitrogen at room temperature, whereas maintenance of configuration about stereogenic phosphorus of tertiary phosphines is commonly found. The nature of stereogenic phosphorus in phosphines and other phosphorus species has been reviewed.[21]

In some instances, relatively mild nucleophilic agents are capable of generating tertiary phosphines from phosphonium or quasiphosphonium salts (see Section 4.4). Reagents such as KCN, alkoxide salts, or even tertiary amines are capable of attacking certain substituents to remove them from phosphorus leaving the tertiary phosphine with retention of configuration at phosphorus.[18]

One mode of reactivity of phosphines that can be troublesome is their tendency to undergo oxidation readily, even by simple exposure to air, to generate phosphine oxides. The tendency to undergo this reaction is, of course, dependent on the structure of the substituents on phosphorus. One approach to stabilization of phosphines for storage, as well as during certain reactions, is their conversion to (and reversion from) phosphine-boranes. Tertiary phosphines, chiral or achiral at phosphorus, may readily be converted to the corresponding phosphine-borane (with retention of configuration if chiral) by reaction with borane and reverted to the original phosphine (again, with retention of configuration if chiral) by treatment with a tertiary amine (equation 8).[22,23]

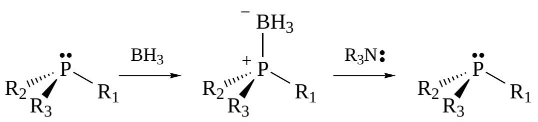

(8)

3.3 Methylenephosphines

Although species of the general formulation $R{-}P{=}CR'_2$ wherein trivalent phosphorus is bound to only two (carbon) atoms have been proposed for many years as intermediates in a variety of chemical reactions, it was not until 1978 that a stable compound of this class was isolated.[24] This effort involved the generation of a sterically hindered system with three bulky aromatic rings bound around the P=C site (equation 9) that could reversibly add hydrogen chloride. The ^{31}P NMR spectrum exhibited a signal at relatively low field in accord with the postulation of such trivalent doubly coordinated phosphorus. Approaches toward this type of species have been reviewed.[25]

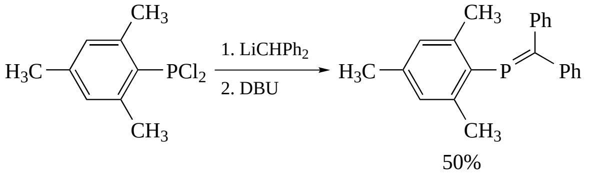

(9)

While such stable mono-phosphorus species have been prepared, emphasis continues to be given to transient systems[26] and those bearing metal complexation at phosphorus.[27,28] An intriguing cumulene analogue bearing the P=C=P linkage has been prepared,[29] as well as diphosphinidenecyclobutene species.[30] The preparation and properties of such species has recently been reviewed.[31]

3.4 Phosphabenzenes and Other Potential Aromatic Species

Phosphabenzene, the phosphorus analogue of pyridine, is a species that, as with the methylenephosphines, formally contains a doubly coordinated phosphorus singly bound to one carbon and doubly bound to another. The first isolation of a phosphabenzene derivative was reported in 1966 using the reaction as shown below (equation 10).[32] The parent phosphabenzene molecule was first isolated by the reaction (equation 11) of phosphorus tribromide with a stannane derivative, albeit in low yield.[33] Further spectroscopic investigation of this parent molecule indicated it to be planar with indications of multiple bond character between phosphorus and carbon and aromatic delocalization.[34]

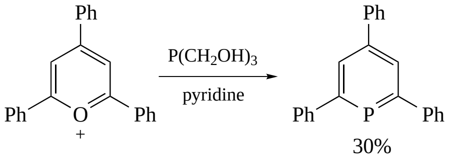

(10)

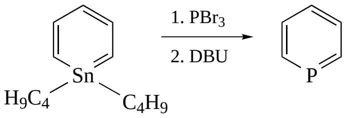

(11)

Although the phosphabenzene species exhibit ^{31}P and ^{1}H NMR spectra in accord with the postulation of aromatic character analogous to that of pyridine (the ^{31}P signal occurs at significantly low field), these materials lack the nucleophilic character at phosphorus commonly associated with the analogous nitrogen systems (pyridine). However, the substituted phosphabenzene system appears to act as a good electrophile in that it readily undergoes electrophilic aromatic substitution reactions, in accord with the postulation of aromatic character for the ring.

Recent efforts in regard to phosphabenzene derivatives have particularly been concerned with metal complexes[35] and theoretical considerations.[36] These areas have been reviewed recently.[31]

The preparation of phosphorus analogues of aromatic nitrogen-containing heterocycles has been extended as well to other systems than pyridine. Of particular interest are those compounds generally referred to as phospholes. These are five-membered ring systems bearing a phosphorus atom within the ring structure. The parent $\sigma^3\lambda^3$-phosphole in which a trigonal phosphorus atom is present is shown as (**1**). Such systems are formally analogues of pyrrole, although the geometry of the phosphorus is clearly different from that of the actual nitrogen-containing pyrrole. Further, calculations and experimental data concerning aromaticity of the phosphole ring system are ambiguous regarding the aromatic character of phosphole, whereas pyrrole is clearly aromatic. In keeping with the ambiguous character of the $\sigma^3\lambda^3$-phospholes, they are found to undergo Diels–Alder reactions occurring within the coordination sphere of a metal, evidence of a decreased, but not necessarily absent, aromatic character of a conjugated system. Isomeric structures describable as $\sigma^2\lambda^3$-phospholes (**2**) may be generated from the $\sigma^3\lambda^3$-phospholes by [1,5] sigmatropic rearrangement, although, with few exceptions, these species exist only as transient intermediates. Of course, structures further substituted with heteroatoms (particularly nitrogen), such as that of the 1,2,3-σ^2-diazaphosphole type (**3**), are quite stable and exhibit typical aromatic ring chemistry such as undergoing electrophilic aromatic substitution reactions.[37] The preparations, structures, and reactions of phospholes have been reviewed.[38]

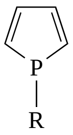

(**1**)

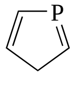

(**2**)

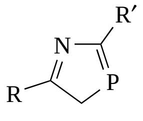

(**3**)

3.5 Phosphinous and Phosphonous Acids and Their Derivatives

Acid chloride derivatives of phosphinous acids [R_2POH] and phosphonous acids [$RP(OH)_2$] have been mentioned previously (see Section 3.2) as precursors in the preparation of phosphines. In addition to the common routes of preparation for these trivalent phosphorus acids, particularly through the use of organometallic reagents and Friedel–Crafts reactions as noted, several other routes have been developed for their syntheses that are worthy of note.

For example, two reports of preparation of such species from elemental (red) phosphorus have been noted. The direct preparation of 1-hydroxyphosphonous acids, albeit in moderate yield, is accomplished by the treatment of elemental phosphorus with aldehydes in aqueous basic medium (equation 12).[39] Using polar aprotic solvents, the double direct addition of elemental phosphorus to arylalkenes proceeds to form phosphinous acids in better yields.[40] Further, acid chloride derivatives are available also by the controlled reaction of elemental phosphorus with chloroalkanes.[8]

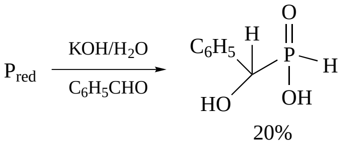

(12)

Unsaturated phosphonous dichlorides have been prepared by the photochemically induced addition of PCl_3 across conjugated dienes.[41] These adducts are quite susceptible to dehydrohalogenation to reform conjugated dienes with a phosphorus(III) site attached (equation 13). Several reports have also been made concerning the addition of phosphorus halides across the moderately strained cyclopropane ring contained in 1,3-dehydroadamantane, as shown (equation 14).[42] This result holds promise for the preparation of additional phosphinous and phosphonous halides using equally or more strained cyclopropane ring systems.

$$\underset{}{Cl_3P + H_2C{=}CH\text{-}CH{=}CH_2} \xrightarrow{h\nu} \underset{45\%}{Cl_2PCH_2CH{=}CHCH_2Cl} \xrightarrow{(C_2H_5)_3N} \underset{50\%}{Cl_2PCH{=}CH\text{-}CH{=}CH_2} \quad (13)$$

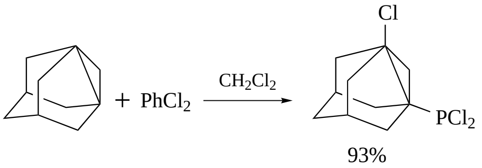

(14)

A different approach toward preparation of phosphinous and phosphonous iodides uses the reaction of iodoalkanes with either PI_3 or PI_5.[43] This reaction is specific for iodoalkanes and phosphorus iodides and is not applicable to other halides. From the resultant highly reactive phosphinous and phosphonous iodides, the full range of the parent acid derivatives may be prepared (esters, other acid halides, anhydrides, amides). We will not be concerned here with these preparations of derivatives of the parent acids, topics that are considered in other reports.[1,2]

Esters of the phosphinous [$R_2P(OR')$] and phosphonous [$RP(OR')_2$] acids, as with phosphines, are capable of serving as nucleophiles. These compounds act as nucleophiles toward the normal range of electrophilic substrates including haloalkanes, tosylate esters, and carbonyl compounds, among others, to generate quasiphosphonium ion intermediate species (see Section 4.4). (In those instances where tertiary phosphines are acting as nucleophiles with one of the aforementioned substrates, the resultant phosphonium ion constitutes the product of the reaction.) However, the quasiphosphonium ions that result from reaction of alkyl or silyl esters of phosphinous and phosphonous acids are capable of continuing reaction by a further nucleophilic displacement reaction. This reaction involves cleavage of the ester linkage with concomitant formation of a tetracoordinated quinquevalent phosphorus site. The overall reaction, generally referred to as the Michaelis–Arbuzov reaction, is illustrated below (equation 15). The product in the reaction shown, starting with the diester of a phosphonous acid, is an ester of a phosphinic acid [$R_2P(O)OH$]. The corresponding product starting with the ester of a phosphinous acid would be a tertiary phosphine oxide [R_3PO]. Of course, the Michaelis–Arbuzov reaction may be used to produce a new carbon–phosphorus bond in phosphonates [$(RO)_2P(O)R'$] starting with esters of phosphorous acid [$(RO)_3P$], the latter of which are not truly organophosphorus species.

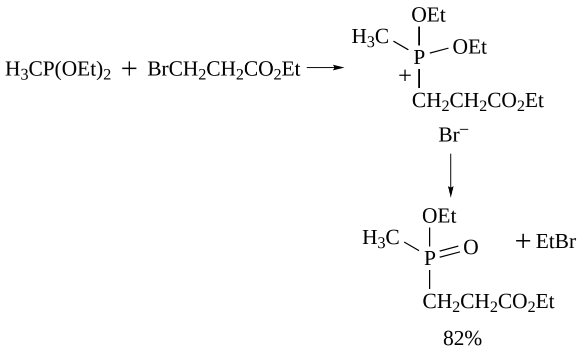

(15)

If a nucleophilic addition at a carbonyl or imine carbon occurs, the product is still a phosphinate (from a phosphonous ester) or a phosphine oxide (from a phosphinous ester), but the reaction is commonly referred to as an Abramov or Pudovik reaction. An example of the Pudovik reaction is shown below (equation 16). Addition of the phosphorus nucleophile to the β-carbon atom of an α, β-unsaturated substrate (Michael addition) is commonly referred to as a hydrophosphinylation reaction.[44]

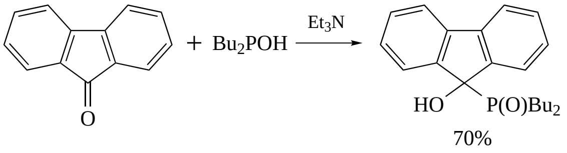

(16)

A related reaction that yields the same types of products as does the Michaelis–Arbuzov reaction begins with either a phosphinous acid or a monoester of a phosphonous acid. (The corresponding reaction may also be performed with a diester of phosphorous acid.) By treatment with an appropriate base, the conjugate base of the phosphorus-containing acid is generated that serves as the nucleophilic reagent for direct formation of the phosphonate or phosphine oxide product (or phosphonate product from a phosphorous acid diester). This procedure is commonly referred to as the Michaelis–Becker reaction.[44]

The several series of reactions noted here have recently been reviewed.[44,45] More will be noted concerning these reactions later in the present consideration (see Section 5.2).

3.6 Biphosphines and Cyclophosphines

Biphosphines are tricoordinated phosphorus(III) compounds that bear a single phosphorus–phosphorus bond, as in the general structure (**4**). Cyclophosphines may be considered to be expanded biphosphines in which a series of tricoordinated phosphorus(III) sites are connected to each other to complete a ring structure, as in structure (**5**). Additional substituents are present on each phosphorus atom to provide the tricoordinated status. Generally *not* included among these materials are polyphosphine compounds containing two or more tricoordinated phosphorus(III) sites *without* the phosphorus–phosphorus bond, or ring systems simply containing one or more phosphorus(III) sites without a phosphorus–phosphorus bond.

$R_2P\text{-}PR_2$

(**4**)

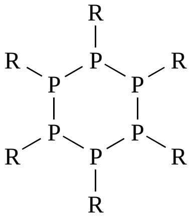

(**5**)

Biphosphines may be formed by several methods involving the treatment of phosphinous halides with either electropositive metals or organomercury compounds. An additional intriguing approach involves the reaction of metal organophosphides (see Section 3.2) with 1,2-dibromoethane to form the phosphorus–phosphorus bond and extrude ethylene (equation 17).

$$Et_2PLi + BrCH_2CH_2Br \longrightarrow \underset{84\%}{Et_2P\text{-}PEt_2} + H_2C{=}CH_2 \qquad (17)$$

The preparation of cyclophosphines has been accomplished starting with the corresponding primary phosphines and phosphonous dichlorides under a variety of conditions. Varying sizes of rings are generated depending on the reaction conditions.[46] The syntheses and characteristics of biphosphines and cyclophosphines have been reviewed.[2]

4 TETRAVALENT ORGANOPHOSPHORUS COMPOUNDS

4.1 Overview

Phosphorus(IV) compounds incorporate a positive charge formally located at the phosphorus site. In some instances, this is clearly a localized positive charge, as is found in simple tetraalkylphosphonium salts, with an associated gegenion. In other instances, the nature of the charge and its location are open to more complex considerations. For example, ylides, that may be generated from classical phosphonium salts, are not only zwitterions (as opposed to a more classical two component salt) but also may be described with formal positive and negative charges on adjacent atoms. Generally, the negative site is at a carbon atom directly bound to a phosphorus, which is the positive site. Such species are understood to have a significant π-covalent character to the carbon–phosphorus linkage with a corresponding diminution of the charge separation. In this section, we will consider not only the simple phosphonium salts, but also quasiphosphonium species in which at least one of the ligands bound directly to the positively charged phosphorus center through an atom other than carbon, as well as derived ylides.

4.2 Phosphonium Ions

Quaternary phosphonium salts, having the general formulation $[R_4P^+X^-]$, are formal analogues of quaternary ammonium salts. While there are structural similarities in structure (general tetrahedral) and modes of formation, there are also fundamental differences in the natures of the two types of compounds.

A fundamental route for the preparation of simple tetraalkylphosphonium salts is the reaction of a tertiary phosphine with a haloalkane or other substrate upon which a simple nucleophilic substitution reaction can occur. (In comparing phosphorus nucleophiles with the corresponding nitrogen-centered nucleophiles, it must be remembered that the phosphorus is significantly more nucleophilic than is the nitrogen. For example, while triphenylamine is devoid of nucleophilic character in reaction with ordinary haloalkanes, triphenylphosphine exhibits high reactivity.) Reactivity of the phosphorus in such nucleophilic substitution reactions, as with other types of nucleophiles, decreases with increasing substitution about the electrophilic site of the substrate.

The reaction of aromatic halides with tertiary phosphines requires special reaction conditions, as they are not susceptible to the simple nucleophilic substitution reaction. Strong heating, generally in a closed pressure tube, with the tertiary phosphine in the presence of a nickel(II) halide salt allows substitution of the halogen by phosphorus, probably by way of an addition–elimination reaction.[47–51] In this manner, tetraarylphosphonium halides, such as tetraphenylphosphonium chloride (**6**), may be produced in good yield. This approach has been used for the construction of an intriguing series of polyphosphonium ion dendrimer species.[52]

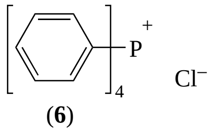

(**6**)

While tetraalkylphosphonium salts may be generated by the reaction of elemental phosphorus (white or red; see Section 3.2) with haloalkanes, the reaction is complicated by the concomitant formation of trialkylphosphine dihalides. The resultant mixture is generally converted to the corresponding trialkylphosphine oxide by treatment with ethanol under heating. This process consumes both phosphorus components of the mixture.

Recently, the major driving force for the investigation of methods for preparation of quaternary phosphonium salts has been their ability to serve as precursors for ylides in Wittig and related olefination reactions for organic syntheses. These materials will be surveyed in the following section.

4.3 Phosphonium Ylides and Related Species

The fundamental work of Wittig and his students from the early 1950s has provided organic chemists with a fundamental approach toward the facilitation of the syntheses of a wide range of chemical structures.[53] The reaction, as originally developed by Wittig and his students, and further modified by numerous researchers, involves the conversion of a carbonyl group of an aldehyde or a ketone to a substituted alkene linkage. This olefination reaction provides a direct method for what previously required a usually complex and highly inefficient series of reactions. This organic synthetic approach depends on the facile generation of quaternary phosphonium salts and their subsequent use in the formation of phosphorus ylides, as well as in the construction of structurally complex organophosphorus compounds for which stereochemical outcomes are predictable.[54]

Particularly notable modifications of the fundamental Wittig reaction are those described as a 'phospha-Wittig' process (as illustrated in equation 18)[55] and the 'aza-Wittig' process (as illustrated in equation 19) and useful for the preparation of secondary amines.[56]

$$\mathrm{ArP{=}P(CH_3)_3 + RCHO \longrightarrow RCH{=}PAr} \qquad (18)$$

$$\mathrm{RN{=}P(OR')_3 + R''CHO \longrightarrow RN{=}CHR''} \qquad (19)$$

The Wittig olefination reaction, the modifications, and the nature of the organophosphorus intermediates has been reviewed.[57]

Stabilized species in the phosphorus ylide category are normally generated in a two-step sequence beginning with the formation of the quaternary phosphonium salt. This is usually accomplished with ease by the reaction of triphenylphosphine with the appropriate haloalkane. Salt formation is followed by deprotonation at the carbon adjacent to phosphorus using an appropriate base to generate a zwitterionic species stabilized by the adjacent functionality (illustrated in equation 20). The resultant phosphorus species reacts with an introduced carbonyl compound to generate an intermediate oxaphosphatane that undergoes decomposition to produce alkene and phosphine oxide at relatively low temperatures (equation 21).

$$\mathrm{Ph_3P + XCH_2C(O)R' \longrightarrow Ph_3\overset{+}{P}\text{-}CH_2C(O)R'} \\ \xrightarrow{\text{base}} \mathrm{Ph_3P{=}CHC(O)R'} \qquad (20)$$

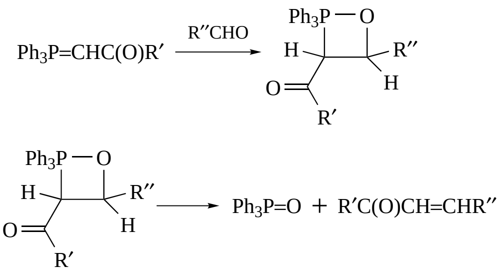

(21)

The stability of ylides such as shown in equations (20) and (21) can be significantly greater than those with simple alkyl groups attached. This stability depends on the degree to which the negative charge is delocalized by the substituent. Those species having a greater degree of stabilization by charge delocalization usually require only weaker basic reagents for their formation from the phosphonium salts than the unstabilized ylides require.[58]

4.4 Quasiphosphonium Ions

Quasiphosphonium ions are tetracoordinated phosphorus sites bearing a positive charge within which at least one of the substituents about phosphorus is a heteroatom. Such species may be generated in a variety of ways and have intriguing chemistry associated with them depending on the particular substituents.

In certain notable instances, attack by a phosphine on a halogenated organic compound occurs at the halogen atom rather than at carbon. Of particular significance here is the reaction of tertiary phosphines, commonly triphenylphosphine, with tetrahalomethanes that proceeds to form a quasiphosphonium ion intermediate. In the presence of an alcohol, such an intermediate continues to react with the alcohol to generate a new oxygen-containing quasiphosphonium species that subsequently undergoes decomposition to form the haloalkane and triphenylphosphine oxide (equation 22).[59] Overall, presupposing the judicious choice of solvent, this approach provides a clean and efficient method for the stereospecific conversion of alcohols to the corresponding haloalkanes without skeletal rearrangement or the involvement of acidic reagents.

$$\mathrm{Ph_3P + CCl_4 \longrightarrow [Ph_3P\text{-}Cl]^{+-}CCl_3 \xrightarrow{ROH} Ph_3P{=}O + RCl} \qquad (22)$$

Quasiphosphonium ions involving oxygen directly bound to the positive phosphorus site are generated as intermediates in numerous other reactions. For example, the Michaelis–Arbuzov reaction (see Section 3.5) produces a quasiphosphonium ion as an intermediate that undergoes attack by the associated anion at the carbon end of the C–O–P linkage.[7] The reaction follows a different course when aryl ester linkages are present on the starting trivalent phosphorus acid derivative. In such instances, a quasiphosphonium ion is generated that is capable of taking part in several competing processes, but generally not a simple displacement process as is found with alkyl esters.[59,60] With intense heating, the intermediate salt can decompose to give products formally analogous to those of the normal Michaelis–Arbuzov reaction (equation 23). However, complex equilibria are established that lead to several other types of products, including those of disproportionation.

$$\mathrm{(ArO)_3P + RX \longrightarrow (ArO)_3\overset{+}{P}R + X^- \xrightarrow{heat} ArX + (ArO)_2P(O)R} \qquad (23)$$

The formation of the diaryl ester of the phosphonic acid as shown in equation (23) requires stronger heating than for other Michaelis–Arbuzov reactions using alkyl esters. This is the result of difficulty in accomplishing the nucleophilic displacement reaction on the aromatic ring. More will be noted later (see Section 5.2) concerning the Michaelis–Arbuzov reaction of aryl esters of phosphorous acid.

A particularly interesting category of such oxygen-bound quasiphosphonium ion is that related to the stabilized ylides previously noted (see Section 4.3). If a Michaelis–Arbuzov reaction is performed involving a trialkyl phosphite and a haloalkane with α, β-unsaturation (generally a C=O linkage of a carbonyl or ester linkage), the quasiphosphonium salt generated has the ability to be converted readily to a stabilized anionic species. The preparations and uses of these reagents have been thoroughly reviewed.[57,58]

Several types of phosphoryl-containing stabilizing groups have been developed as reagents for the olefination process, as shown below. These include phosphonate-stabilized carbanions (**7**) and phosphine oxide-stabilized carbanions (**8**). Species containing two phosphorus centers, as with (**9**) and (**10**), are of great utility for the introduction of phosphorus-substituted olefinic linkages in place of a carbonyl oxygen.

$\mathrm{(RO)_2P(O)\overset{-}{C}HCO_2R'}$

(**7**)

$\mathrm{Ph_2P(O)\overset{-}{C}HCO_2R}$

(**8**)

$\mathrm{Ph_3P{=}CHP(O)(OR)_2}$

(**9**)

$\mathrm{(RO)_2P(O)\overset{-}{C}HP(O)(OR')_2}$

(**10**)

Species of the type (**9**) have been used for the construction of phosphonic acid analogues of natural nucleotides, such as (**11**).[61]

Quasiphosphonium intermediate species are found to be involved in the transition metal–catalyzed reaction of haloaromatics[62–67] and vinylic halides[68,69] with trivalent phosphorus-containing esters. These reactions, while giving products that appear to be from a Michaelis–Arbuzov type reaction, actually involve addition–elimination reactions.

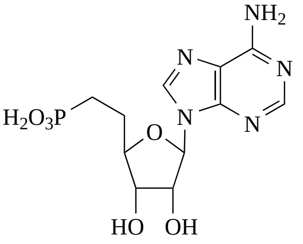

(**11**)

A further synthetically useful reaction is worthy of note here as it involves a pair of quasiphosphonium ion intermediates. Commonly referred to as the Mitsunobu reaction,[70] a variety of phosphorus reagents, including trialkyl or triaryl esters of phosphorous acid, may be used in this reaction to replace the hydroxyl of an alcohol with a halide and inversion of configuration about the carbinol carbon site. Triphenylphosphine is the most commonly used trivalent phosphorus reagent for this conversion, reacting with the diester of an azodicarboxylic acid in the presence of an acid to form the quasiphosphonium ion bearing a nitrogen atom bound to the positive phosphorus site. This intermediate then undergoes reaction with the selected alcohol generating a new quasiphosphonium species bearing a phosphorus–oxygen bond. Finally, as with the Michaelis–Arbuzov reaction and the tetrahalomethane reactions noted previously, the associated anion performs a nucleophilic substitution reaction at the original carbinol carbon site yielding the product with inversion of configuration about the carbinol carbon (equation 24).

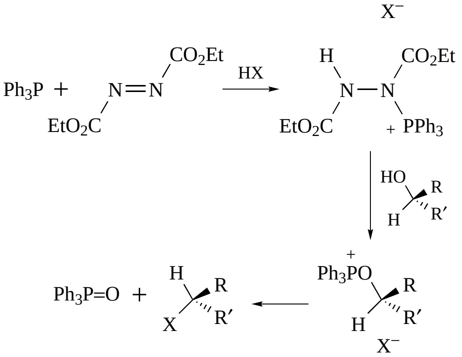

(24)

Using ^{31}P NMR, the intermediacy of the quasiphosphonium ion bearing the phosphorus–oxygen linkage has been demonstrated experimentally. In the absence of added acid, the same product formation occurs, but the intermediate quasiphosphonium species has not been detected experimentally. However, evidence of an intermediate oxyphosphorane (see Section 5.3) has been demonstrated under these conditions, as it has under acidic conditions, and such an intermediate has independently been shown to provide the usual products of the reaction. Evidence is available in other systems for the equilibrium of oxyphosphoranes with oxygen-containing quasiphosphonium salts.

5 PENTAVALENT ORGANOPHOSPHORUS COMPOUNDS

5.1 Overview

Numerous categories of pentavalent organophosphorus compounds are known that differ quite significantly in their structures and reactivities. We will consider a number of these general categories here, starting with species that, while pentavalent, are tetracoordinated at phosphorus. These include the oxidized forms of phosphines (phosphine oxides, phosphine sulfides, and related materials) as well as phosphonic and phosphinic acids and their derivatives. Pentacoordinated pentavalent organophosphorus compounds that are considered here include the phosphoranes, the oxyphosphoranes, and polyhalogen phosphorus compounds.

5.2 Phosphine Oxides, Sulfides, and Related Compounds

Tertiary phosphines readily undergo oxidative addition reactions to form phosphine oxides (**12**) when challenged with a variety of oxidizing agents, including nitric acid, manganese dioxide, permanganate ion, dichromate ion, hydrogen peroxide, and even molecular oxygen as present in air. Similarly, sulfur or selenium may be added readily to generate the corresponding phosphine sulfides (**13**) or phosphine selenides (**14**).

$R_3P{=}O$ (**12**) $R_3P{=}S$ (**13**) $R_3P{=}Se$ (**14**)

Tertiary phosphine oxides are also produced as significant by-products in several of the reactions of phosphines that have been noted previously, including the Wittig olefination and the conversions of alcohols to haloalkanes with triphenylphosphine as an adjunct reagent. The tertiary phosphine oxides produced in such reactions present a problem in chemical economics, as they themselves possess little chemical utility. The phosphine may be regenerated, but several steps are required, as previously noted with preparations of phosphines by reduction (see Section 3.2).

Tertiary phosphine oxides and sulfides are also produced by way of the Michaelis–Arbuzov reaction beginning with phosphonous esters [R_2POR'] and thiophosphonous esters [R_2PSR'], when used in reaction with haloalkanes (see Section 3.5). Similarly, phosphine oxides are formed from trivalent phosphorus reagents in the Michaelis–Becker reaction as well as the conjugate addition reactions of phosphinous acid derivatives with α, β-unsaturated compounds (see Section 3.5).

A direct approach for the preparation of phosphine oxides in reasonable yield involves the treatment of elemental phosphorus (either white or red) with primary haloalkanes in a basic (KOH) medium of water/dioxane with the presence of a phase-transfer catalyst.[9,10]

The structurally related phosphinamines (aza-Wittig reagents; see Section 4.3) are formally in this category as phosphorus is singly bound to each of three alkyl (or aryl) groups and doubly bound to an electronegative atom (nitrogen). A most interesting mode of preparation of such materials is by the reaction of a tertiary phosphine with an alkyl azide (equation 25).

$$R_3P + N_3R' \longrightarrow N_2 + R_3P{=}NR' \qquad (25)$$

As may be noted, major advances in the development of preparative routes for tetracoordinated quinquevalent organophosphorus compounds occurred in the late nineteenth and early twentieth centuries. In more recent times, owing to increased applications and potential applications for derivatives of phosphonic and phosphinic acids, including biomedical regulation, pest control, flame retardation, and biochemical mechanistic exploration, among others, increased attention has been given to approaches for the preparation of such materials.

As previously discussed, the Michaelis–Arbuzov reaction is the best-known method for the preparation of phosphonic and phosphinic acids and their derivatives. However, the original approach has numerous drawbacks, not the least of which are the reaction yields, which usually are only moderate, and the stringent heating conditions usually required. A significant development for the fundamental reaction in relatively recent years has been the use of silyl esters of the trivalent phosphorus-containing acid rather than alkyl or aryl esters.[71] The advantage of using silyl esters is twofold: first, less stringent conditions are generally required to cleave the ester linkages and generate the free phosphorus-containing acid target (equation 26), and, second, there is great selectivity observed in the displacement step of the overall process with the silyl ester being displaced preferentially to ordinary alkyl ester linkages (equation 27).

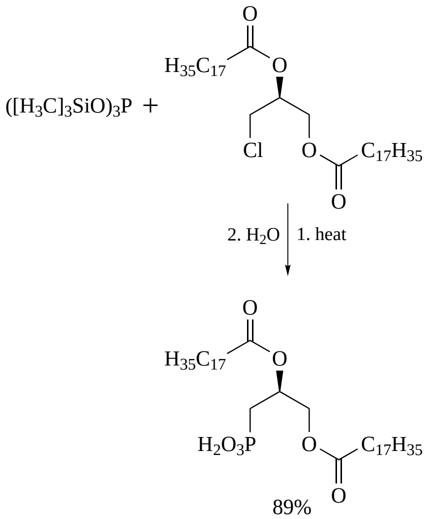

(26)

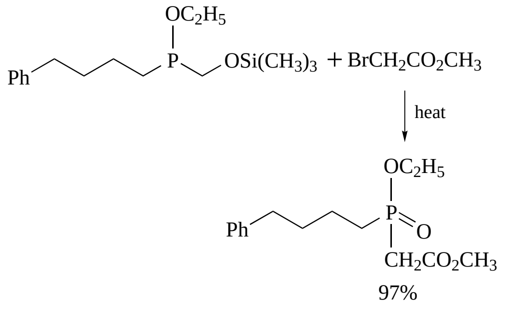

(27)

The reaction is also facile (no external heating) and proceeds in high yield when the substrate is an acyl halide or related material. Such reactions, producing acylphosphonate derivatives (equation 28), are of use for the preparation of compounds for a variety of practical applications.[72]

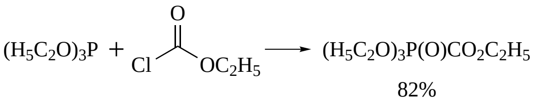

(28)

The closely related Michaelis–Becker reaction also is attendant with difficulties. There are particular problems with solubility of the reagents that hinder facile reaction. Some advance in overcoming this type of problem is accomplished in some instances using amines as the base, and even Mannich-type bases for which the base serves not only as the deprotonating agent, but also as a masked substrate for reaction.

The cleavage of carbon–phosphorus bonds in phosphoryl compounds is another matter for consideration. Once a carbon–phosphorus bond is generated, usually it is extremely difficult to cleave it without major damage to the remainder of the molecule. However, phosphonate and phosphinate esters, as well as phosphine oxides, in which a hydroxyl or carbonyl group is present at the carbon directly attached to phosphorus are subject to facile cleavage of the carbon–phosphorus bond.

For example, acylphosphonate esters (as produced in equation 28 above) easily undergo cleavage of the carbon–phosphorus bond in aqueous and other basic media. (With the free acid, conversion to the conjugate base of the parent acid renders the carbon–phosphorus bond resistant to cleavage.)[73] Synthetic targets here involve not only organophosphorus compounds, but others derived from the parent organophosphorus compound such as amides (equation 29). In addition to such carbonyl linkages, a hydroxyl substituent located off the carbon directly bound to phosphorus in such systems also renders the carbon–phosphorus bond labile under basic conditions, as long as a free phosphorus acid site is not present.[74] With this in mind, the use of α-hydroxyphosphoryl compounds holds significant promise as *umpolung* reagents for organic syntheses.[75] The susceptibility of such carbon–phosphorus bonds to selective cleavage holds great potential for synthetic utility that has only begun to be exploited.[76]

$$PhC(O)P(O)(OC_2H_5)_2 + PhCH_2CH_2NH_2 \longrightarrow \underset{82\%}{PhC(O)NHCH_2CH_2Ph} \qquad (29)$$

Approaches are being developed that will introduce oxygen substituents to otherwise unsubstituted carbon directly attached to phosphorus and thus allow facile cleavage of the carbon–phosphorus bond.[77]

The preparation of species such as α-hydroxyphosphonates has been alluded to only briefly here (see Section 3.5). We would note two direct approaches that are available for the preparation of these materials, both involving nucleophilic addition to carbonyl carbon.[7] One of these is referred to as the Abramov reaction that involves the addition of a fully esterified trivalent phosphorus acid to a carbonyl carbon followed by a dealkylation of the phosphorus ester site. This preparation is quite inefficient when ordinary ester linkages are used, but the use of silyl esters overcomes most of these difficulties and allows facile isolation of the target compounds (equation 30). Note that reaction occurs preferentially at the carbonyl carbon and not by displacement of halogen at carbon. Addition occurs preferentially at carbonyl carbon compared to displacement at a carbon–halogen linkage, and provides product *if removal of the ester linkage is facile*.

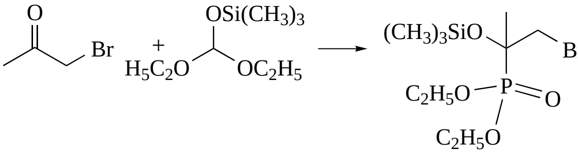

(30)

89%

An alternative approach that avoids many of the difficulties of the Abramov reaction uses a trivalent phosphorus component with at least one acidic site on phosphorus. The Pudovik reaction uses a base for the removal of the acidic proton and facilitates attack by the electron-rich phosphorus anionic site on the carbonyl carbon. A variety of bases have been used for this purpose, as have phosphorus reagents with differing numbers of acidic sites on the phosphorus component. High yields of adducts are possible under very mild conditions using this approach (equation 31). The facile cleavage of α-hydroxyphosphonate esters and related compounds is not surprising in light of their preparation by this reaction as it is fundamentally an ‘aldol’ type process that is truly reversible under basic conditions.

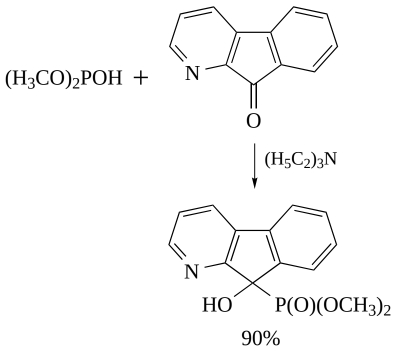

(31)

90%

The corresponding reactions using imines as substrates have advanced recently as the demand for analogues of amino acids has grown. As with the reactions involving the simple carbonyl compounds, addition of trivalent phosphorus reagents at imino carbon occurs in a facile manner under a wide range of conditions.[7] This procedure (for example, equation 32) has allowed the investigation of numerous biological processes using the carbon–phosphorus analogues of the natural materials.

$$PhCH_2CH{=}NH + (H_5C_2O)_2POH \xrightarrow[\substack{H_3O^+ \\ \text{work-up}}]{} \underset{71\%}{PhCH_2CH(NH_2)PO_3H_2} \qquad (32)$$

Phosphoryl compounds may also be generated by the addition of trivalent phosphorus reagents in a conjugate addition mode to a variety of α,β-unsaturated substrates. This constitutes another approach for the generation of new carbon–phosphorus bonds. Most often these reactions have been used for the preparation of esters of phosphonic acids, although other types of phosphoryl compound may easily be generated by this method. The reaction conditions used vary greatly, generally being divided into categories roughly analogous to those used for the Abramov and Pudovik reactions respectively (*vide supra*). Examples of both approaches are shown (equations 33 and 34). In general, higher product yields are obtained using the neutral (nonbasic) conditions with silyl ester reagents.

$$(H_5C_2O)_2POSi(CH_3)_3 + H_2C{=}CHCO_2C_4H_9 \longrightarrow \underset{82\%}{(H_5C_2O)_2P(O)CH_2CH_2CO_2C_4H_9} \qquad (33)$$

$$(H_5C_2O)_2POH + PhCH{=}CHCONH_2 \xrightarrow{NaOC_2H_5} \underset{74\%}{(H_5C_2O)_2P(O)CH(Ph)CH_2CONH_2} \qquad (34)$$

In complete analogy with procedures noted for the preparation of phosphines (see Section 3.2), carbon–phosphorus bonds may be generated directly from P(V) halide species using organometallic reagents (equation 35).

$$HC{\equiv}CMgCl + H_3CP(O)(Cl)OCH_3 \longrightarrow \underset{50\%}{HC{\equiv}CP(O)(CH_3)OCH_3} \qquad (35)$$

For the generation of phosphoryl compounds with an *aromatic* group attached directly to phosphorus, numerous reaction systems have been devised using catalytic agents (equation 36).[78–82] Overall, these reactions appear to be similar to the Michaelis–Arbuzov and Michaelis–Becker reactions discussed previously. However, the mode of formation of the carbon–phosphorus bond is actually rather different, involving addition–elimination processes. In similar manner are formed phosphoryl compounds with a vinylic carbon–phosphorus bond (see Section 4.4).

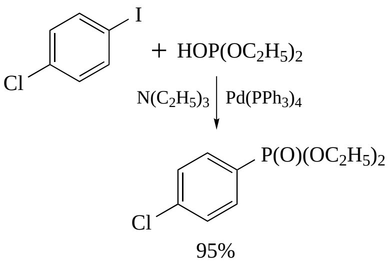

(36)

An intriguing approach to phosphonates (and potentially phosphinates and phosphine oxides) substituted at the 2-position relative to phosphorus has been reported.[83] This approach involves the conjugate addition reaction of a trivalent phosphorus reagent (*vide supra* - see equation 34) with an α,β-unsaturated carbonyl-type substrate. However, under the reaction conditions used, an intermediate pentacoordinated species (an oxyphosphorane; see Section 5.3) is isolated that can be treated with a variety of electrophilic reagents to produce the phosphonate with the electrophilic reagent substituted at the 2-position. An example is shown in equation (37).

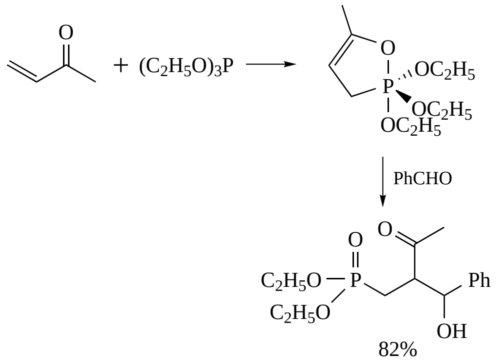

(37)

As was noted in Section 3.2, phosphine oxides and phosphine sulfides can be reduced by a range of reagents to produce the trivalent phosphorus species related to them. In some instances, more than simple reduction occurs. For example, lithium aluminum hydride often effects the reduction of the full range of pentavalent and tetracoordinated phosphorus to the parent phosphines, removing all groups attached to phosphorus other than carbon, and replacing them with hydrogen. In certain instances (using THF as reaction medium and with careful control of the temperature), the degree of reduction can be limited. Heterogeneous reactions using sodium borohydride in ether solvents have been found to permit isolation of phosphorus products in higher oxidation states than the phosphine. Similarly, halosilane reducing agents can be used to allow isolation of such trivalent phosphorus compounds in oxidation states higher than the phosphine, starting with halogen derivatives of phosphonous and phosphinous acids.[20] An example of such a reduction is shown in equation (38).

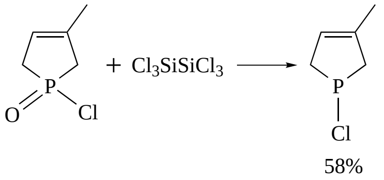

(38)

5.3 Phosphoranes and Related Compounds

The term phosphorane refers to compounds bearing a pentavalent pentadirectional phosphorus site. Our discussion here will give particular attention to organophosphoranes, compounds that have at least one of the five bonds from phosphorus to carbon, and will include classical phosphoranes in which all five bonds to phosphorus are directly from carbon atoms, as well as the oxyphosphoranes wherein one or more of the five bonds is to oxygen.

Before considering the chemical reactions involving such species, it is important to review the stereochemical aspects associated with a pentacoordinated phosphorus site. Coordination of five ligands about a single atomic center (phosphorus) could be imagined to assume either a trigonal-bipyramidal (tbp) or a square-planar (sp) configuration. If fact, the tbp structure is that which is commonly found in phosphoranes.[84]

A tbp configuration has intriguing consequences for stereochemical considerations.[85–88] Consider a phosphorane of the general structure PX$_5$, one with five identical ligands associated with the central phosphorus site. In the tbp array, two distinct types of positions exist for the ligands relative to the central phosphorus, as illustrated with (**15**). Herein, three of the ligands lie in a planar trigonal array about the central atom (equatorial positions) and two lie directly above and below that plane (apical positions). In general, the bond distances for the two types of ligands are not identical, but, even if equal in length, equatorial and apical ligands are in distinct positions owing to their different relationships with the remaining ligands.

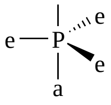

(**15**)

Given this array having two distinct types of positions about phosphorus, it might be anticipated that nominally identical ligands X would be distinguishable in apical and equatorial positions under all conditions where dissociation is not occurring. In fact, it is a simple matter to prepare materials having five nominally identical ligands about phosphorus for which, without dissociation, the five are indistinguishable. That is, there is an exchange process for ligands about such a phosphorus center even in the absence of dissociation. This exchange of ligand sites occurs by a process referred to as *pseudorotation*,[89] as illustrated in Scheme 1. This process may be described as involving one of the equatorial ligands being retained 'static' (for the period of the particular pseudorotation cycle) in the equatorial position while the remaining four ligands undergo an 'umbrella-type' inversion process, exchanging equatorial and apical positions. In a subsequent pseudorotation cycle, some other equatorial ligand is retained in the equatorial position while the remaining four ligands exchange sites. Through the use of graphical methods,[85,89] it may be determined quickly that all ligands will occupy each type of position for equivalent periods of time when pseudorotation occurs rapidly (Figure 1).

The rapid exchange of sites by way of pseudorotation at ordinary temperatures renders indistinguishable those nominally identical ligands about phosphorus that would be distinguishable in the absence of site exchange. The process of pseudorotation also has significant consequences for phosphoranes bearing five nonidentical ligands. Consider the generalized structures Pabxyz wherein each of the ligands is unique. In the absence of pseudorotation (or dissociation and recombination), 10 diastereoisomeric racemic forms of such a formulation with a tbp array could possibly exist. A sequence of no more than five pseudorotation cycles, however, is all that is required for the interconversion of enantiomers and each pseudorotation cycle converts a given structure into one of its diastereoisomers.

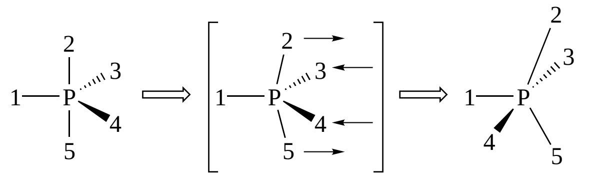

tbp 2 and 5 apical

tbp 3 and 4 apical

Scheme 1

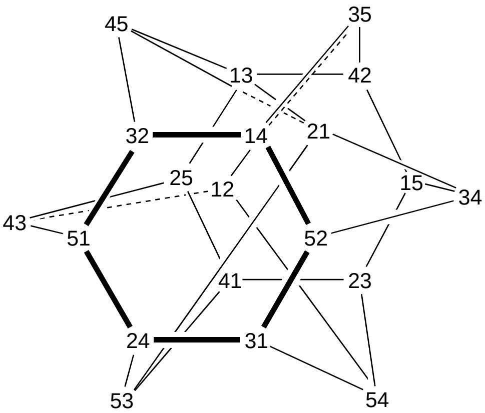

Figure 1 Each juncture of lines represents a configuration for which the pair of numbers indicates the ligands that are in the apical positions. Lines interconnecting number pairs represent cycles of pseudorotation; that ligand of the five not indicated by a number at either end of a given line is the 'static' equatorial ligand for that particular pseudorotation cycle. The interchange of numbers (as '15' '51') indicates a pair of enantiomers for the system Pabxyz

In contrast with a tetrahedral center substituted as Cabxy for which the interchange of any two ligands generates the enantiomeric form, with a tbp structure of Pabxyz interchange of any two equatorial, or the two apical ligand sites generates the enantiomeric form and interchange of any apical with any equatorial site generates a diastereoisomeric form.

In some instances, particular pathways of pseudorotation are precluded by the presence several suitably substituted ring systems or other restrictive structural elements. In these instances, optically active phosphoranes should be capable of existence. This has, in fact, been accomplished with the preparation of the pentaarylphosphorane biphenylylene(4-methylbiphenylylene)biphenyl-2-ylphosphorane in the degradation of an optically active hexacoordinated phosphorus species (see Section 6).[90]

In most instances of organophosphorus compounds, the stereochemistry is significantly less complex than for the general Pabxyz situation. Particularly, the presence of ring structures joining two of the positions of the tbp structure eliminates the possibility of certain pseudorotation process occurring.

In addition to considering tbp structures centered about phosphorus for isolable molecules, transient, intermediates bearing pentavalent pentadirectional phosphorus occur in numerous organophosphorus reactions. The formation of a tbp array by the introduction of an additional ligand to a tetrahedral array about phosphorus is generally considered to occur by the addition of the incoming ligand to a tetrahedral face to generate a new apical ligand site. Further, loss of a ligand to regenerate a tetrahedral array occurs from an apical/tetrahedral face position. Within the tbp structure, the more electronegative ligands tend to occupy preferentially the apical positions. These factors, along with the process of pseudorotation (and the limitations placed on the pseudorotation process by the presence of rings), make certain reactions facile while it hinders others.

Organophosphoranes with only a single carbon–phosphorus linkage may be prepared in several ways. One important method, as illustrated in Scheme 2,[91] has been developed for the preparation of a wide range of other organophosphorus compounds.[92–96]

The formation of this oxyphosphorane occurs by initial attack of the electron-rich phosphorus at the β-position of the substrate forming a transient quasiphosphonium ion,

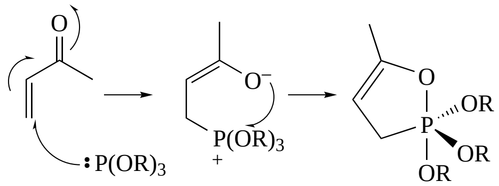

Scheme 2

followed by intramolecular addition of the electron-rich oxygen to a face of the quasiphosphonium ion tetrahedral structure placing the last-added oxygen in an apical position of the oxyphosphorane. Subsequently, the reaction of the oxyphosphorane with an electrophilic substrate involves the original α-carbon of the parent α, β-unsaturated species and cleavage of the phosphorus–oxygen linkage from an apical position. Only limited pseudorotation processes are possible with the oxyphosphorane intermediate species as shown in Scheme 2. An example of the use of this approach in a synthesis of a structurally more complex organophosphorus target molecule is exhibited in equation (39).[92]

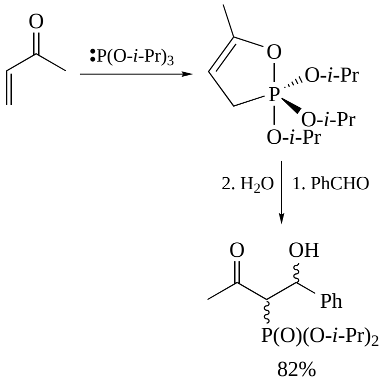

(39)

A category of phosphorane bearing a single carbon–phosphorus bond is produced from the phosphonous dihalides (see Section 3.5). Phosphonous dihalides, as do other trivalent phosphorus compounds, add halogen molecules to generate phosphoranes of the general type RPX_4, as shown in equation (40). Similar halogen adducts are formed with organophosphorus parents such as R_2PX and R_3P.

$$\mathrm{CF_3PF_2 + Cl_2 \longrightarrow \underset{79\%}{CF_3\,PF_2Cl_2}} \qquad (40)$$

Phosphoranes bearing four carbon–phosphorus bonds and one to an oxygen atom can be generated by the addition of alcohols to ylides (see Section 4.3). In this reaction, the hydroxyl of the alcohol formally adds across the ylidic carbon–phosphorus linkage, as shown in equation (41).

$$\mathrm{PH_3P{=}CH_2 + H_3COH \longrightarrow \underset{60\%}{Ph_3P(CH_3)OCH_3}} \qquad (41)$$

The general approach for the preparation of ylides bearing five carbon–phosphorus bonds was developed by Wittig.[97] Phosphonium salts bearing no hydrogens on carbon directly attached to phosphorus undergo addition reactions with organolithium reagents to generate the corresponding phosphorane. (If hydrogen is attached to even one of the carbons bound to phosphorus, ylide formation occurs rather than does addition.) Such addition reactions are thereby fundamentally limited to tetraarylphosphonium salts, as illustrated in equation (42). A notable exception occurs with the highly strained phosphonium salt, homocubyldiphenylphosphonium bromide, wherein two hydrogens are attached to carbon bound to phosphorus (equation 43). The facile formation of the phosphorane (as opposed to deprotonation) in this instance is attributed to the increased strain that would be involved with the formation of the ylide. Addition of the phenyl group (with phenyllithium, or a methyl group using methyllithium adding to homocubyldimethylphosphonium bromide) to phosphorus allows a C–P–C linkage to exist with an angle close to 90° (spanning an apical and an equatorial position of phosphorus) without adding strain to the system. The ^1H NMR spectra of these phosphoranes indicate that they undergo rapid pseudorotation at room temperature. In this process, the equatorial position bound within the ring system can never be the static position.

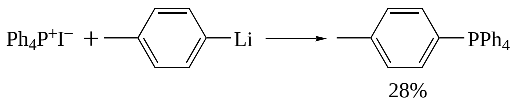

(42)

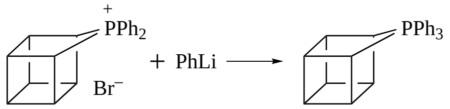

(43)

Phosphoranes bearing five phosphorus–carbon bonds are unreactive in many of the processes seen for oxyphosphoranes (such as completion of the Michaelis–Arbuzov reaction or the addition reactions as shown in equation 39). However, they are capable of undergoing thermal or photochemical cleavage of a carbon–phosphorus bond under particular circumstances. For example, the homocubyltriphenylphosphorane (equation 43) undergoes a cheleotropic fragmentation to generate triphenylphosphine and the tricyclic octadiene fragment as shown in equation (44). Other fragmentation reactions of phosphoranes under thermal or photochemical conditions have been observed that lead to triarylphosphines and hydrocarbons as fragments (equation 45).

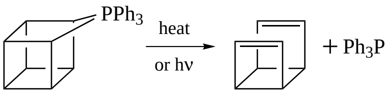

(44)

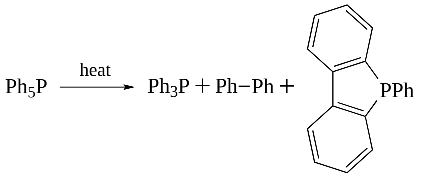

(45)

Pentaarylphosphoranes also undergo cleavage of carbon–phosphorus bonds in aqueous acid or base, as well as halogenolysis. In the latter instance, a quaternary phosphonium salt is generated along with the haloaromatic product (equation 46).[98]

$$Ph_5P + Br_2 \longrightarrow Ph_4P^+Br^- + PhBr \qquad (46)$$

6 HEXAVALENT ORGANOPHOSPHORUS COMPOUNDS

Compounds in which six ligands are attached to a single phosphorus center generally bear a formal negative charge at that phosphorus. Several approaches to such compounds are available, depending on the degree of carbon substitution about the phosphorus center. For example, halophosphoranes add an anion to generate the hexacoordinated phosphorus site as illustrated in equation (47).

$$Ph_2PF_3 + CsF \longrightarrow Ph_2\overset{-}{P}F_4\ Cs^+ \qquad (47)$$

Fully carbon-substituted hexacoordinated phosphorus can be produced by reaction of a quaternary phosphonium salt with suitable organolithium reagents.[99] Since such a site has an octahedral array of ligands, chiral hexacoordinated phosphorus should be possible with appropriate ligands. Optically active hexacoordinated phosphorus compounds of this type bearing bidentate organic ligands have been isolated. The racemic materials bearing the 2,2′-biphenylylene ligands have been constructed (equation 48) and resolved by classical means using brucine derivatives.

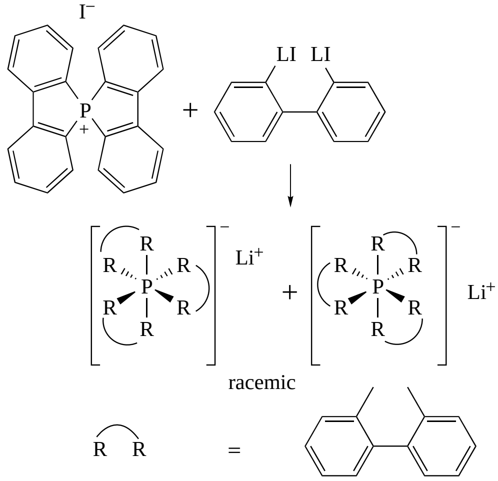

(48)

Hexacoordinated phosphorus species bearing a formal *positive* charge have been generated, albeit without a carbon–phosphorus bond. Rather, compounds of the type for which an example is shown as (**16**) have been prepared with four oxygen and two nitrogen ligands with an overall positive charge.[100]

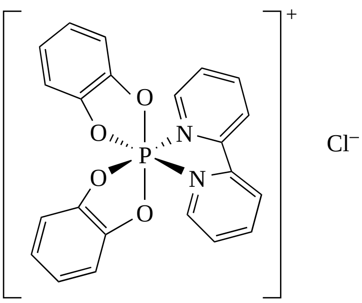

(**16**)

7 ORGANOPHOSPHORUS NOMENCLATURE

There has been established a systematic nomenclature for organophosphorus compounds. In Table 1 is provided a summary of the standard English and German nomenclature for the variety of compounds noted in this article.

8 RELATED ARTICLES

Cluster Compounds: Inorganometallic Compounds Containing Transition Metal & Main Group Elements; Electronic Structure of Main-group Compounds; Molecular Orbital Theory; Phosphorus: Inorganic Chemistry.

9 REFERENCES

1. R. Engel, ed., ‘Handbook of Organophosphorus Chemistry’, Dekker, New York, 1992.
2. M. Regitz, ed., ‘Methoden der Organischen Chemie (Houben-Weyl)’, Thieme, Stuttgart, 1982, Band E1, E2.
3. U. Schmidt, *Angew. Chem., Int. Ed. Engl.*, 1975, **14**, 523.
4. W. A. Henderson Jr, M. Epstein, and F. S. Seichter, *J. Am. Chem. Soc.*, 1963, **85**, 2462.
5. M. Yoshifuji, T. Sato, and N. Inamoto, *Chem. Lett.*, 1988, 1735.
6. E. C. Evers, E. H. Street Jr, and S. L. Jung, *J. Am. Chem. Soc.*, 1951, **73**, 5088.
7. R. Engel and J. I. Cohen, ‘Synthesis of Carbon-Phosphorus Bonds’, 2nd edn., CRC Press, Boca Raton, FL, 2004, Chap. 2.

Table 1 Organophosphorus nomenclature

Compound	English	German
$\mathrm{R{-}P}$	Phosphinidine (alkylphosphinidine)	Phosphinidine
$\mathrm{R{-}P{=}CH_2}$	Methylenephosphine (alkyl(alkylidene)phosphine)	Methylenephosphane
$\mathrm{R_3P}$	Phosphine (trialkylphosphine)	Phosphan
$\mathrm{R_2POH\ [R_2P(O)H]}$	Phosphinous acid (alkylphosphinous acid; esters: alkyl dialkylphosphinite)	phosphinige Saüre
$\mathrm{R{-}P(OH)_2[R{-}P(O)(H)OH]}$	Phosphonous acid (alkylphosphonous acid; esters: dialkyl alkylphosphonite)	phosphonige Saüre
$\mathrm{P(OH)_3[HP(O)(OH)_2]}$	Phosphorous acid (esters: trialkyl phosphite)	phosphorige Saüre
$\mathrm{X^{-}\,{}^{+}PR_4}$	Phosphonium salt (tetraalkylphosphonium halide)	Phosphoniumsalze
$\mathrm{R_3P{=}CR_2}$	Methylenephosphorane (alkylidenetrialkylphosphorane)	Methylenphosphorane
$\mathrm{R_3P{=}O}$	Phosphine oxide (trialkylphosphine oxide)	Phosphan Oxid
$\mathrm{R_2P(O)OH}$	Phosphinic acid (dialkylphosphinic acid; esters: alkyl dialkylphosphinate)	Phosphinsaüre
$\mathrm{RP(O)(OH)_2}$	Phosphonic acid (alkylphosphonic acid; esters: dialkyl alkylphosphonate)	Phosphonsaüre
$\mathrm{O{=}P(OH)_3}$	Phosphoric acid (phosphate; esters: trialkyl phosphate)	Phosphorsaüre
$\mathrm{R_5P}$	Phosphorane (pentaarylphosphorane)	Pentaorganophosphor Verbindungen
$\mathrm{M^{+}\,{}^{-}PR_6}$	Phosphate (metal (hexaaryl)phosphate)	Hexaorganophposphor Verbindungen

8. M. M. Rauhut, in ‘Topics in Phosphorus Chemistry’, eds. M. Grayson and E. J. Griffith, Interscience, New York, 1964, Vol. 1, p. 1.
9. B. A. Trifamov, N. K. Gusarova, and L. Brandsma, *Phosphorus Sulfur*, 1996, **109–110**, 610.
10. N. K. Gusarova, S. I. Shaikhudinova, A. M. Reutskaya, A. A. Tartarinova, and B. A. Trofimov, *Russ. Chem. Bull.*, 2000, **49**, 1320.
11. M. Epstein and S. A. Buckler, *J. Am. Chem. Soc.*, 1961, **83**, 3279.
12. M. M. Rauhut, I. Hechenbleikner, H. A. Currier, F. C. Schaefer, and V. P. Wystrach, *J. Am. Chem. Soc.*, 1959, **81**, 1103.
13. W. Wolfsberger, *Chem. Ztg.*, 1991, **115**, 289 (*Chem. Abstr.*, 1992, **116**, 59,500e).
14. S. Nielsen-Marsh, R. J. Crowte, and P. G. Edwards, *J. Chem. Soc., Chem. Commun.*, 1992, 699.
15. K. Issleib and H. M. Möbius, *Chem. Ber.*, 1961, **94**, 102.
16. J. Dodonow and H. Medox, *Chem. Ber.*, 1928, **61**, 907.
17. R. Engel, ‘Synthesis of Carbon-Phosphorus Bonds’, CRC Press, Boca Raton, FL, 1988.
18. T. Imamoto, in ‘Handbook of Organophosphorus Chemistry’, ed. R. Engel, Dekker, New York, 1992, Chap. 1, p. 1.
19. T. Imamoto, S.-i. Kikuchi, T. Miura, and Y. Wada, *Org. Lett.*, 2001, **3**, 87.
20. R. Engel, in ‘Handbook of Organophosphorus Chemistry’, ed. R. Engel, Dekker, New York, 1992, Chap. 5, p. 193.
21. W. E. McEwen, in ‘Topics in Phosphorus Chemistry’, eds. M. Grayson and E. J. Griffith, Interscience, New York, 1965, Vol. 2, p. 1.
22. T. Imamoto, T. Kusumoto, N. Suzuki, and K. Sato, *J. Am. Chem. Soc.*, 1985, **107**, 5301.
23. T. Imamoto, T. Oshiki, T. Onozawa, T. Kusumoto, and K. Sato, *J. Am. Chem. Soc.*, 1990, **112**, 5244.
24. T. C. Klebach, R. Lourens, and F. Bickelhaupt, *J. Am. Chem. Soc.*, 1978, **100**, 4886.
25. E. Fluck, in ‘Topics in Phosphorus Chemistry’, eds. M. Grayson and E. J. Griffith, Interscience, New York, 1980, Vol. 10, p. 193.
26. J.-F. Pilard, A.-C. Gaumont, C. Friot, and J.-M. Denis, *Chem. Commun.*, 1998, 457.
27. B. Breit, R. Winde, and K. Harms, *J. Chem. Soc, Perkin Trans. 1*, 1997, 2681.
28. L. Weber, B. Quasdorff, H. G. Stammler, and B. Neumann, *Chem. Eur. J.*, 1998, 469.
29. C. A. Akpan, P. B. Hitchcock, J. F. Nixon, M. Yoshifuji, T. Niitsu, and N. Inamoto, *J. Organomet. Chem.*, 1988, **338**, C35.
30. M. Yoshifuji, Y. Ichikawa, K. Toyota, E. Kasajima, and Y. Okamoto, *Chem. Lett.*, 1997, 87.
31. M. Yoshifuji, *Pure Appl. Chem.*, 1999, **71**, 503.
32. G. Märkl, *Angew. Chem., Int. Ed. Engl.*, 1966, **5**, 846.
33. A. Ashe, *J. Am. Chem. Soc.*, 1971, **93**, 3293.
34. R. J. Kuczkowski and A. Ashe, *J. Mol. Spect.*, 1972, **42**, 457.
35. M. Regitz and O. J. Scherer, ‘Multiple Bonds and Low Coordination in Phosphorus Chemistry’, Georg Theime Verlag, Stuttgart, 1990.
36. S. M. Bachrach and P. Magdalinos, *J. Mol. Struct. (Theochem)*, 1996, **368**, 1.

37. J. Luber and A. Schmidpeter, *J. Chem. Soc., Chem. Commun.*, 1976, 887.
38. A. Hughes, in 'Handbook of Organophosphorus Chemistry', ed. R. Engel, Dekker, New York, 1992, Chap. 10, p. 483.
39. D. Semenzin, G. Etemad-Moghadam, D. Albouy, and M. Koenig, *Tetrahedron Lett.*, 1994, **35**, 3297.
40. N. K. Gusarova, B. A. Trofimov, T. N. Rakhmatulina, S. F. Malysheva, S. N. Arbuzova, S. I. Shaikhudinova, and A. I. Albanov, *Izv. Akad. Nauk, Ser. Khim.*, 1994, 1680.
41. M. N. Krivchun, M. V. Sendyurev, B. I. Ionin, and A. A. Petrov, *Zhur. Obshch. Khim.*, 1990, **60**, 2395 (*Chem. Abstr.*, 1991 **115**, 136,184p).
42. B. I. No, Y. L. Zotov, and R. M. Petruneva, *Zhur. Obshch. Khim.*, 1991, **61**, 1906; (*Chem. Abstr.*, 1992, **116**, 194,441b).
43. N. G. Feshchenko and Z. K. Gorbatenko, *Zhur. Obshch. Khim.*, 1992, **62**, 81; (*Chem. Abstr.*, 1993, **118**, 147,591g).
44. R. Engel and J. I. Cohen, 'Synthesis of Carbon-Phosphorus Bonds', 2nd edn., CRC Press, Boca Raton, FL, 2004, Chap. 3.
45. R. Engel, *Org. React.*, 1988, **36**, 175.
46. M. Baudler, J. Hahn, and E. Clef, *Zeit. für Naturforsch. B*, 1984, **39B**, 438.
47. H.-D. Block (1983), *U.S. Patent* 4,391,761.
48. K. Issleib, K. Balszuweit, S. Richter, and J. Koetz, 1985, *East German Patent* 219,776.
49. J. A. Connor and A. C. Jones, *J. Chem. Soc., Chem. Commun.*, 1980, 137.
50. N. Hall and R. Proce, *J. Chem. Soc., Perkin Trans. 1*, 1979, 2634.
51. V. P. Kukhar and E. I. Sagina, *J. Gen. Chem. U.S.S.R.*, 1977, **47**, 1523.
52. K. Rengan and R. Engel, *J. Chem. Soc., Perkin Trans 1*, 1991, 987.
53. G. Wittig and G. Geissler, *Justig Liebig's Ann. Chem.*, 1953, **580**, 44.
54. E. C. Dunne, E. J. Coyne, P. B. Crowley, and D. G. Gilheany, *Tetrahedron Lett.*, 2002, **43**, 2449.
55. J. D. Protasiewicz, *Coord. Chem. Rev.*, 2000, **210**, 181.
56. T. Gajda, A. Koziara, K. Osowska-Pacewicka, S. Zawzdski, and A. Zwierzak, *Synth. Commun.*, 1992, **22**, 1929.
57. B. E. Maryanoff and A. B. Reitz, *Chem. Rev.*, 1989, **89**, 863.
58. W. S. Wadsworth Jr, *Org. React.*, 1977, **25**, 73.
59. H. R. Hudson, in 'Topics in Phosphorus Chemistry', eds. M. Grayson and E. J. Griffith, Interscience, New York, 1983, Vol. 11, p. 339.
60. K. Henrick, H. R. Hudson, R. W. Matthews, E. M. McPartlin, L. Powrozuyk, and O. O. Shode, *Phosphorus, Sulfur, Rel. Elem.*, 1987, **30**, 157.
61. R. W. McClard and J. F. Witte, in 'Handbook of Organophosphorus Chemistry', ed. R. Engel, Dekker, New York, 1992, Chap. 13, p. 655.
62. D. A. Sweigart, *J. Chem. Soc., Chem. Commun.*, 1980, 1159.
63. G. R. John and A. P. Kane-Maguire, *J. Chem. Soc., Dalton*, 1979, 873.
64. G. R. John and A. P. Kane-Maguire, *J. Organomet. Chem.*, 1976, **120**, C45.
65. N. A. Bailey, E. H. Blunt, G. Fairhurst, and C. White, *J. Chem. Soc., Dalton*, 1980, 829.
66. P. Tavs, *Chem. Ber.*, 1970, **103**, 2428.
67. T. M. Balthazor and R. C. Grabiak, *J. Org. Chem.*, 1980, **45**, 5425.
68. G. Axelrad, S. Laosooksathit, and R. Engel, *Synthetic Commun.*, 1980, **10**, 933.
69. F. Hammerschmidt and E. Zbiral, *Liebig's Ann. Chem.*, 1979, 492.
70. D. L. Hughes, *Org. React.*, 1992, **42**, 335.
71. T. Hata and M. Sekine, in 'Phosphorus Chemistry Directed Toward Biology', ed. W. J. Stec, Pergamon, New York, 1980, p. 197.
72. S. Asano, T. Kitihara, T. Ogawa, and M. Matsui, *Agr. Biol. Chem.*, 1973, **37**, 1193.
73. R. Karaman, A. Goldblum, E. Breuer, and H. Leader, *J. Chem. Soc., Perkin Trans. 1*, 1989, 765.
74. G. Sturtz, B. Corbel, and J.-P. Paugam, *Tetrahedron Lett.*, 1976, 47.
75. D. Seebach, *Angew. Chem., Int. Ed. Engl.*, 1979, **18**, 239.
76. M. Sekine, M. Satoh, H. Yamagata, and T. Hata, *J. Org. Chem.*, 1980, **45**, 4162.
77. S. Kim and Y. G. Kim, *Bull. Korean Chem. Soc.*, 1991, **12**, 106; (*Chem. Abstr.*, 1991, **114**, 247,386e).
78. T. Hirao, T. Masunaga, Y. Oshiro, and T. Agawa, *Bull. Chem. Soc. Jpn.*, 1982, **55**, 909.
79. Y. Xu, Z. Li, J. Xia, H. Guo, and Y. Huang, *Synthesis*, 1983, 377.
80. Y. Xu and J. Zhang, *Synthesis*, 1984, 778.
81. Y. Xu, Z. Li, H. Guo, and Y. Huang, *Synthesis*, 1984, 781.
82. S. E. Tunney and J. K. Stille, *J. Org. Chem.*, 1987, **52**, 748.
83. C. K. McClure and K.-Y. Jung, *J. Org. Chem.*, 1991, **56**, 867.
84. L. S. Bartell and K. W. Hansen, *Inorg. Chem.*, 1965, **4**, 1777.
85. P. C. Lauterbur and F. Ramirez, *J. Am. Chem. Soc.*, 1968, **90**, 6722.
86. M. J. Gallagher and J. D. Jenkins, in 'Topics in Phosphorus Chemistry', eds. M. Grayson, and E. J. Griffith, Interscience, New York, 1968, Vol. 3, p. 3.
87. F. Ramirez, *Acc. Chem. Res.*, 1968, **1**, 168.
88. K. Mislow, *Acc. Chem. Res.*, 1970, **3**, 321.
89. R. S. Berry, *J. Chem. Phys.*, 1960, **32**, 933.
90. D. Hellwinkel, *Chem. Ber.*, 1966, **99**, 3642.
91. F. Ramirez, *Synthesis*, 1974, 90.
92. C. K. McClure, K.-Y. Jung, and C. W. Grote, *Phosphorus Sulfur*, 1990, **51/52**, 418.

93. C. K. McClure and C. W. Grote, *Tetrahedron Lett.*, 1991, **32**, 5313.

94. C. K. McClure and P. K. Mishra, *Phosphorus Sulfur*, 1996, **111**, 709.

95. C. K. McClure, P. K. Mishra, and C. W. Grote, *J. Org. Chem.*, 1997, **62**, 2437.

96. C. K. McClure, C. W. Grote, and A. L. Rheingold, *Tetrahedron Lett.*, 1993, **34**, 983.

97. G. Wittig and M. Rieber, *Justis Liebig's Ann. Chem.*, 1949, **562**, 187.

98. G. Wittig and G. Geissler, *Justis Liebig's Ann. Chem.*, 1953, **580**, 44.

99. D. Hellwinkel, *Chem. Ber.*, 1966, **99**, 3628.

100. A. Schmidpeter, T. Criegern, and K. Blanck, *Z. Naturforsch.*, 1976, **31B**, 1058.

Photochemistry of Transition Metal Complexes

Tom Bitterwolf
University of Idaho, Moscow, ID, USA

Based in part on the article Photochemistry of Transition Metal Complexes by Lisa McElwee-White which appeared in the Encyclopedia of Inorganic Chemistry, First Edition.

1 Introduction 1
2 Reviews and Books on Inorganic Photochemistry 1
3 Synthetic and Mechanistic Photochemistry 2
4 $Fe(DMPM)_2H_2$ and Related Compounds 13
5 Ligand Exchange, Bond Homolysis, and Heterolysis 14
6 Bimetallic Carbonyl and Cyclopentadienyl Carbonyl Compounds 14
7 Reactions of Photochemically Generated Radicals 19
8 Metal to Ligand Charge Transfer Properties 19
9 Applications of Charge Transfer Excitation 22
10 Ligand Reactions and Rearrangements 25
11 Photocrystallography 29
12 Linkage Isomerism and Ligand Conformational Changes 31
13 Applications of Photochemical Reactions 31
14 Photopharmaceutical Applications 33
15 References 33

1 INTRODUCTION

The 10 years since the last edition of the Encyclopedia of Inorganic Chemistry have seen dramatic growth in inorganic and organometallic photochemistry. The routine use of photochemistry to effect molecular transformations continues unabated, and the application of new spectroscopic techniques has allowed the analysis of photochemical processes in exquisite detail. The very definition of what it means to carry out high speed studies has evolved from nanoseconds to femtoseconds in this period. For example, the photochemical C–H activation processes have been probed at increasingly high speeds permitting events from the moment of excitation, through carbonyl-loss, to oxidative addition to be examined. The use of nontraditional solvents ranging from noble gases to supercritical fluids has emerged and species with noble gases or alkanes within the solvation sphere are no longer regarded as unusual. Old and familiar compounds such as the family of metal bipyridinyl, or more generally diimine, derivatives have made the leap to bioinorganic chemistry as probes for electron transmission in proteins and DNA while others such as the venerable Roussin's salts and esters are attractive reagents for the delivery of nitrogen oxide in photopharmaceutical applications. Well understood reactions such as the photochemical cleavage of the Mo–Mo bond in $[Cp(CO)_3Mo]_2$ derivatives have allowed the phenomenon of radical cage recombination to be examined in great detail.

The challenge for this reviewer has thus not been one of finding enough to write about but dealing with hyperabundance and the necessity to compress and exclude. Early on in the process it was recognized that exciting topics such as solid-state photochemistry and nanomaterials with unique optical properties had to be left for another review. Some topics such as the photochemistry of $[Cp(CO)_2Fe]_2$ and the use of chromium carbene complexes in organic synthesis that have been recently reviewed are discussed only in broad outline with the reader urged to refer to the secondary literature. The literature has been reviewed through 2003. This reviewer regrets the omission of much good work and hopes that what remains is of some lasting use to the community.

2 REVIEWS AND BOOKS ON INORGANIC PHOTOCHEMISTRY

Photochemistry and Photophysics of Metal Complexes by Roundhill provides a comprehensive review of the literature of inorganic and organometallic photochemistry through 1993.[1] Of particular note are the chapters on the photochemistry, photophysics, and photoredox behavior of $Ru(bipy)_3^{2+}$ and the photochemistry of classical transition metal complexes. Additional reviews on the photochemistry of Fe(III)[2] and Cr(III)[3] species have appeared. Professor Arthur Adamson has provided a retrospective on inorganic photochemistry and his seminal contributions to this field.[4] Reviews of the photochemistry of chromium, manganese, and iron porphyrins,[5] the excited state properties of metal phosphine complexes,[6] and chemistry induced by MLCT excitations[7] have appeared. The photochemistry of several coordination compounds, notably $Fe(CN)_5L^{3-}$, with relevance to energy conversion,[8] and the thermal and light induced electron transfers from main group hydrides and organometallic complexes[9] have been reviewed.

As will be seen below, much of the progress in understanding the intimate details of photochemical processes have come about because of ultrahigh speed methods that have pushed photochemistry into the femtosecond time scale.[10] The award of the Nobel Prize to Professor Ahmed H. Zewail for his contributions to these studies is tribute to the importance of this field.[11] With the introduction of femtosecond spectroscopic techniques it is now possible to directly observe the excited state species itself. In ultrafast time-resolved IR spectroscopy, this means that vibrationally hot species may be followed as they undergo dissociation, triplet formation, or relaxation to ground state.[12]

Several reviews have appeared describing the application of spectroscopic techniques to the study of photochemical reaction intermediates. Omberg *et al.*[13] and Ford[14] have described the use of time-resolved IR while several authors have described frozen matrix techniques and applications.[15] Tyler has reviewed the basic principles of organometallic photochemistry for chemical educators.[16]

High level ab initio and dft quantum mechanical calculations of both ground and excited states have emerged as strong supplements to photochemical studies, particularly those conducted at the femtosecond time scale. Some of these applications have been reviewed.[17]

Other reviews will be noted within the text as relevant.

3 SYNTHETIC AND MECHANISTIC PHOTOCHEMISTRY

3.1 Mononuclear Transition Metal Carbonyl Compounds

The photochemistry of simple metal carbonyl, cyclopentadienyl metal carbonyl, and arene metal carbonyl compounds continues to be examined for synthetic applications as well as insight into the fundamental photophysics of excited state processes. At the outset it is probably useful to recall that the energy necessary to break a typical metal carbonyl bond is ca. $190-210\,\mathrm{kJ\,mol^{-1}}$,[18] while the energy of a 325-nm laser is $370\,\mathrm{kJ\,mol^{-1}}$. At least in principle, 570 nm light should be capable of initiating decarbonylation reactions. In practice, the extra energy in an excitation event in condensed phases is dissipated through intramolecular vibrations or through local solvent heating. In the gas phase, these processes are not available thus multiple carbonyl-loss is observed.[19]

Iron, nickel, and cobalt carbonyls were reported by Mond[20] in the early 1900s with the group VI carbonyls being reported by Job and Cassal in mid-1920s.[21] The photolysis of $Fe(CO)_5$ to yield $Fe_2(CO)_9$ was reported by Dewar almost coincident with the initial syntheses of the pentacarbonyl itself.[22] Photochemical exchange of carbonyl groups for a variety of ligands is well known having been first reported by Strohmeier in 1960.[23]

Gas matrices provided a medium for the first direct observation of the photochemical carbonyl-loss intermediates of the metal carbonyls. Beginning with the 1969 report by Rest and Turner of the formation of $Ni(CO)_3$ in Ar, Kr, and Xe matrices,[24] observation of the carbonyl-loss species of $Fe(CO)_5$,[25] $Ta(CO)_6$,[26] and the group VI metal carbonyls[27] followed shortly thereafter. Cyclopentadienyl and arene metal carbonyl compounds have also been examined in a variety of noble gas and alkane matrices. Thus the carbonyl-loss species of $CpV(CO)_4$,[28] $CpNb(CO)_4$,[29] $CpTa(CO)_4$,[29] $(C_6H_6)Cr(CO)_3$,[30] $CpMn(CO)_3$,[30,31] $CpRe(CO)_3$,[30b,32] $Ru(CO)_2(dppe)$,[33] $CpCo(CO)_2$,[34] $CpRh(CO)_2$,[34] and $CpIr(CO)_2$[34] have all been observed. For example, a difference IR spectrum for $CpNb(CO)_4$ in Nujol after photolysis is presented in Figure 1. Poliakoff and Turner reviewed the photochemistry, reaction chemistry, and spectroscopy of $Fe(CO)_4$ in both 1987[35] and 2001[36] and the photochemistry of $Fe(CO)_5$ itself has been reviewed through 1999.[37]

Gas-phase photochemistry of $Fe(CO)_5$ has been carried out at three wavelengths, 351, 248, and 193 nm. At 351 nm $Fe(CO)_4$ and $Fe(CO)_3$ are produced while at 248 nm $Fe(CO)_2$ is also observed. The gas-phase structures of these materials were determined by comparison of their IR spectra with those in condensed phases. At 193 nm, a new species believed

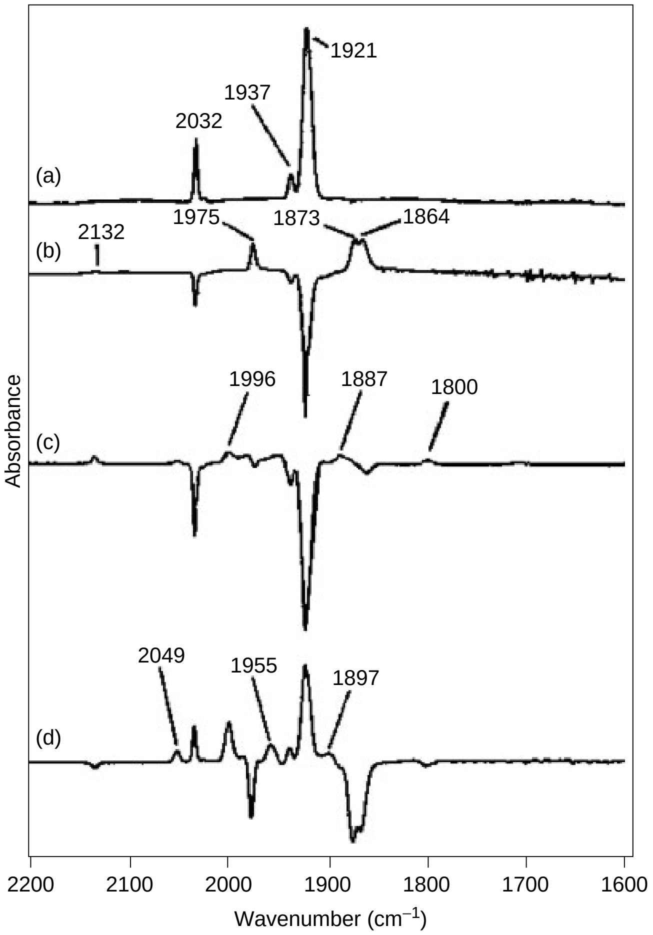

Figure 1 IR spectra with $(\eta^5\text{-}C_9H_7)Ta(CO)_4$ isolated in a Nujol matrix: (a) starting material, (b) subtraction spectrum, 60 min irradiation at $340 < \lambda < 620$ nm (100 min total at $\lambda > 340$ nm) minus starting material, (c) subtraction spectrum, 20 min irradiation at $\lambda < 285$ nm minus 100 min irradiation at $\lambda > 340$, (d) subtraction spectrum, anneal to 173 K minus 125 min total photolysis at $\lambda > 225$ nm. (Reprinted from Ref. 29. © 1998, with permission from Elsevier)

to be an excited state of $Fe(CO)_3$ was observed.[38] The photochemistry of $CpMn(CO)_3$ has been studied by time-resolved IR in the gas phase. Photolysis at 355 nm results in formation of $CpMn(CO)_2$ and CpMn(CO), while the latter predominates upon 266 nm photolysis. In contrast to the iron studies described above, the positions of the observed vibrational bands were not consistent with those observed in condensed phases.[39] Ultrafast gas-phase studies of $CpMn(CO)_3$ have established that loss of the first CO occurs in 66 fs.[40] Theoretical studies of the excited states of $CpMn(CO)_3$ predict two excited states, a weakly bonding state and a dissociative state that is responsible for the observed rapid loss of CO.[41] $(C_6H_6)Cr(CO)_2$ and $(C_6H_6)Cr(CO)$ been generated photochemically in the gas phase.[42] Gas-phase and solution studies of the photolysis of $CpCo(CO)_2$ have identified CpCo(CO) as the intermediate in reactions with ligands.[43]

Gas-phase photochemistry of $W(CO)_6$ at 355 nm yields $W(CO)_5$. The reactions of this species with NH_3, C_2H_6, CF_4, SF_6, and Xe were examined. NH_3 and C_2H_6 form stable species under these conditions while Xe formed an unstable species. Neither CF_4 nor SF_6 formed complexes.[44]

Femtosecond photochemistry (267 nm) of gas-phase $M(CO)_6$, $M = Cr$, Mo, W,[45] $Fe(CO)_5$,[46] and $Ni(CO)_4$,[47] has established multiple processes in the first 1000 fs after excitation. For example, $Fe(CO)_5$ undergoes five consecutive processes. The first four of which occur within 3300 fs and represent a continuous pathway from the Frank-Condon region down to the lowest singlet state of $Fe(CO)_4$. The fifth stage corresponds to loss of a second carbonyl group. A review of this work appeared in 2001.[48] In the case of $Fe(CO)_5$, CASSCF/MR-CCI calculations have been carried out on the excited states.[49]

Important theoretical insights are forcing revisions of long held views on the fundamental nature of photoprocesses in metal complexes. The dominant paradigm has been built upon an assumption that photodissociation of ligands arises from LF transitions.[50] For the case of the group VI metals this assignment was built upon the work of Gray and Beach[51] who assigned low-energy shoulders in the electronic spectra of these compounds to LF transitions. It should be noted that these authors expressed some hesitation with these assignments in that it required the ligand field splittings of all of the group VI metals to be the same. A typical qualitative MO level diagram of $Cr(CO)_6$ is presented in Figure 2.

Recent theoretical studies by several groups have determined that the LF transitions are at much higher energy than previously appreciated, and have determined that the observed low-energy shoulders are due to symmetry-forbidden MLCT excitations.[52] The observed dissociations arise from strongly avoided crossings of the CT and LF states as the M–CO bond elongates. The potential energy diagram for $Cr(CO)_6$ illustrating the effect of distance along the $(CO)_5Cr$–CO bond coordinate for singlet excited states is presented in Figure 3. State a^1T_{1u} in this diagram corresponds to the LF transition, while a^1T_{2u}, a^1E_u, and a^1A_{2u} are CT transitions. States a^1T_{2u} and a^1E_u give rise to $^1B_2$ and

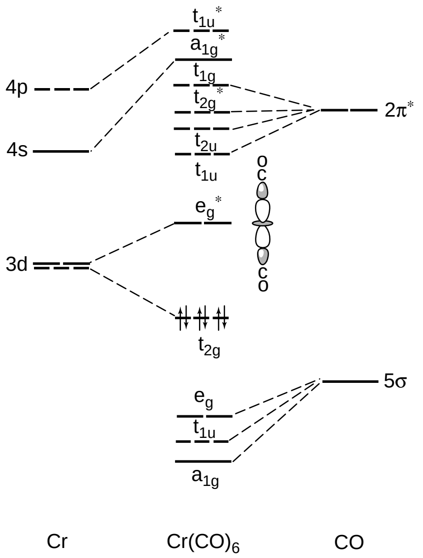

Figure 2 Typical qualitative MO diagram for a d^6 metal carbonyl complex. (Reprinted with permission from Ref. 52b. © 1997 American Chemical Society)

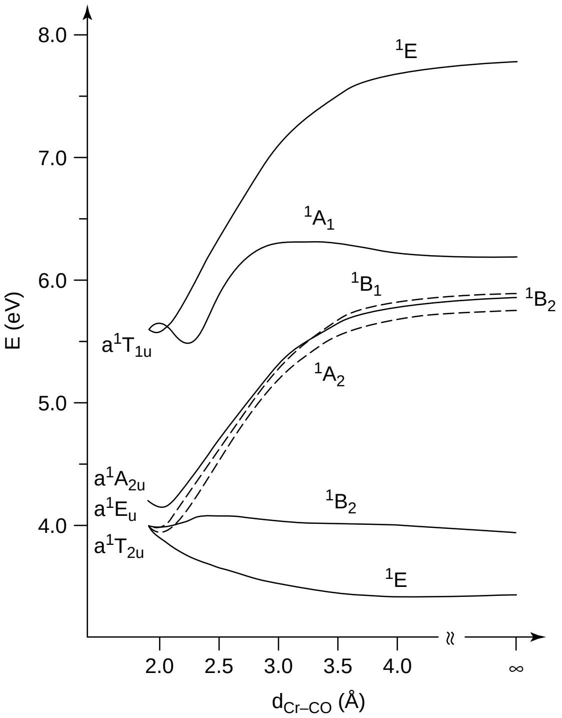

Figure 3 Potential energy curve along the Cr–CO dissociation coordinate for singlet states (in C_{4v} symmetry) arising from the lowest excited configuration. (Reprinted with permission from Ref. 52b. © 1997 American Chemical Society)

^1E in the C_{4v} point group. Combined with studies on the photoprocesses of $Mn(CO)_5Cl$, and $Mn_2(CO)_{10}$,[53] as well as diimine compounds to be discussed below, these new interpretations have far reaching impact. It should be noted that in this article we shall retain the spectral assignment notation of the original authors although it is assumed that these may be subject to reexamination.

Photolyses in frozen N_2 matrices result in the substitution of N_2 for CO yielding $M(CO)_{n-x}(N_2)_x$,[54] $CpM(CO)_{n-x}(N_2)_x$,[19,21,23,55] or $(C_6H_6)Cr(CO)_{n-x}(N_2)_x$[21] photoproducts. N_2 species can also be observed by photolysis of metal carbonyls impregnated in polyethylene films followed by exposure of the films to N_2.[56] Similar routes to H_2 species will be described below. $Fe(CO)_4(N_2)$, $CpMn(CO)_2(N_2)$ and $(C_6H_6)Cr(CO)_2(N_2)$ have been observed by time-resolved IR spectroscopy in the gas phase.[57]

Observations by Perutz and Turner that the electronic absorptions and IR stretching frequencies of $Cr(CO)_5$ in frozen gas matrices were sensitive to the nature of the matrix prompted the suggestion that the organometallic species are best regarded as '$Cr(CO)_5S$' in which the matrix molecules serve as weak ligands.[58] Subsequent studies on a range of organometallic photointermediates confirmed this hypothesis. Noble gas complexes have been observed in liquid noble gases,[59] as well as in the gas phase[60] and supercritical phases.[61] Time-resolved IR spectra of $W(CO)_6$ in Ar, Kr, and Xe are presented in Figure 4. Curiously, although CpRh(CO) forms solvated species with both Kr and Xe, CpCo(CO) and Cp*Co(CO) do not appear to interact with either solvent.[62] As will be discussed below, these differences have been associated with the spin state of the photointermediates. Quantum mechanical ab initio calculations at the MP2 and CCSD(T) level of theory have been carried out for the group VI metal derivatives, $M(CO)_5$ Ng, where Ng = Ar, Kr, Xe.[63] Transition metal-noble gas compounds have been reviewed to 2001[64] and more generally, organometallic photochemistry in liquefied and supercritical noble gases has been reviewed through 1995.[65]

Supercritical carbon dioxide is increasingly important as a solvent for Green chemical applications, including organometallic photochemistry, yet few studies have been conducted to directly observe CO_2 bound species. Time-resolved IR studies of the photolysis of the group VI carbonyls in supercritical noble gases or CO_2 resulted in direct observation of a series of complexes including $W(CO)_5Ar$, $M(CO)_5Kr$, $M(CO)_5Xe$, and $M(CO)_5(CO_2)$, where M = Cr, Mo, and W.[66] $W(CO)_5(CO_2)$ has also been observed by time-resolved IR of the flash photolysis of $W(CO)_6$ and CO_2 in the gas phase.[67] It was observed that Xe and CO_2 have similar strengths of interaction (ca. $33\,kJ\,mol^{-1}$) with the electron-deficient metal species.

The relative rates of exchange of noble gas solvated species, $M(CO)_5S$ and $CpRe(CO)_2S$, with CO was shown to be Xe < Kr < Ar, and Re ≪ W < Mo ≈ Cr.[61b] Comparison of the rates of reaction of CpM(CO)2S, where M = Mn or Re and S = Kr, Xe, *n*-heptane, with CO under pseudo first-order conditions established the relative order Xe ≈ *n*-heptane < Kr, and Re ≪ Mn.[68]

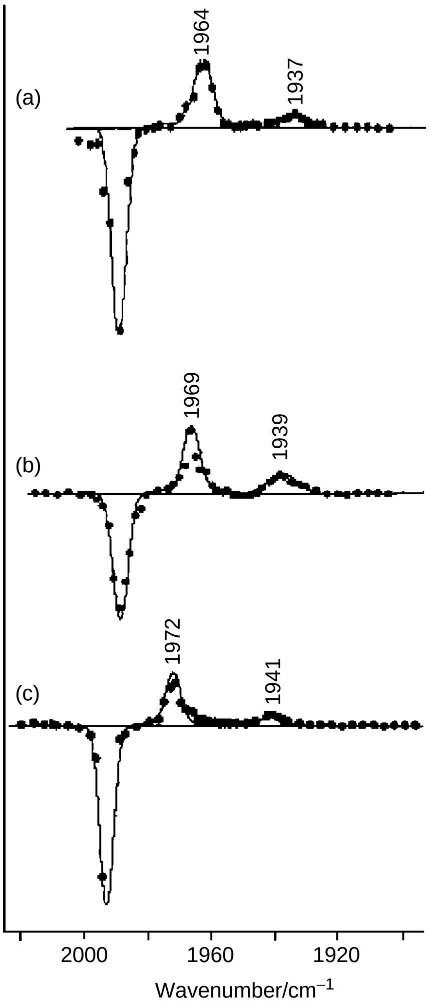

Figure 4 FTIR difference spectra of $W(CO)_6$100 ns after photolysis (355 nm) in (a) sc Xe, (b) sc Kr, and (c) sc Ar. (Reprinted with permission from Ref. 61a. © 1996 American Chemical Society. Composite of Figures 1a, 4a and 6a, *JACS*, 1996, **118**, 10525)

The reactivity of a number of alkane complexes has been examined and this field has been reviewed through 1996 by Hall and Perutz.[69] Flash photolysis of $Cr(CO)_6$ in cyclohexane showed that solvation occurs within the first picosecond after photolysis, a fact that appears to rule out spin crossing as an important component in the dissociation of CO from $Cr(CO)_6$.[70] The stability of $CpRe(CO)_2$(alkane) is particularly striking. Comparison of the rate constants for heptane solvated metal complexes with CO, Table 1, reveals that the rate constant for $CpRe(CO)_2$(heptane) is five orders of magnitude slower than that of $CpV(CO)_3$(heptane). In fact, the stability of the $CpRe(CO)_2$(alkane) complexes is so high that it has been possible to carry out low-temperature NMR on the cyclopentane complex generated by continuous photolysis of the sample in the NMR probe.[71] The 500 MHz 1D 1H NMR spectra of $CpRe(CO)_3$ in cyclopentane and its isotopomers is presented in Figure 5.

Rates of reaction of CO with $(arene)Mo(CO)_2(alkane)$ and $M(CO)_5(alkane)$, where M = Cr, Mo, W, have demonstrated that the reaction with $Cr(CO)_5(alkane)$ involves an interchange mechanism while for Mo and W the mechanism is more associative.[72] These results are consistent with the known ability of the higher homologs to expand beyond a coordination number of 6. Flash photolysis and ultra high speed detection (0.4 ps, $4\,cm^{-1}$ resolution) have allowed direct observation (Figure 6) of the vibrational cooling of $CpCo(CO)(n\text{-hexane})$, $CpCo(CO)(n\text{-hexene})$,[73] and the group VI carbonyls.[74]

Table 1 Second order rate constants, k_2 ($mol^{-1}dm^3s^{-1}$), for reaction of metal heptane complexes with CO in solution at 298 K (S = heptane)

$CpV(CO)_3S$	$(C_6H_6)Cr(CO)_2S$	$CpMn(CO)_2S$
1×10^8	2×10^6	8×10^5
$CpNb(CO)_3S$		
7×10^6		
$CpTa(CO)_3S$		$CpRe(CO)_2S$
5×10^6		2×10^3

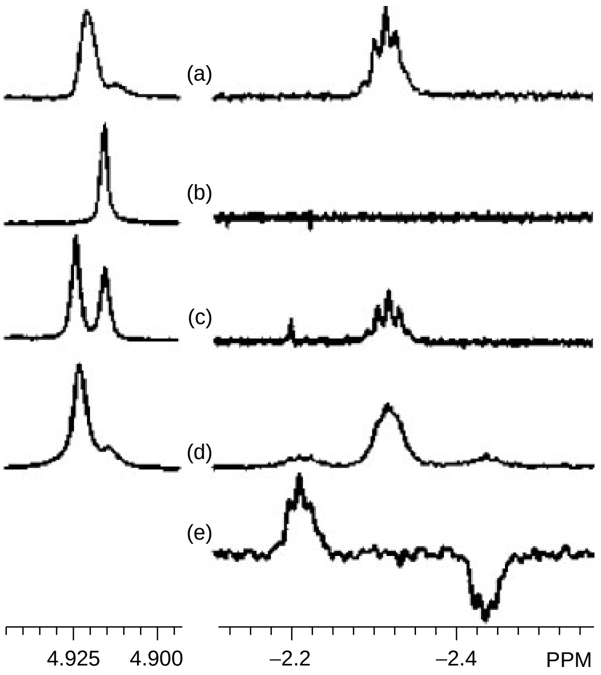

Figure 5 500 MHz 1D ^1H NMR spectra at 180 K of $CpRe(CO)_3$ photolysis products during continuous irradiation in (a) 95:5 C_5H_{10}:C_5D_{10}, (b) C_5D_{10}, (c) 50:50 C_5H_{10}:C_5D_{10}, (d) ^{13}C labeled sample, 85:15 C_5H_{10}:C_5D_{10}, (e) ^{13}C edited experiment showing $^1J_{CH}$. Resonances ca. 4.9 ppm correspond to $CpRe(CO)_2(C_5H_{10})$ and $CpRe(CO)_2(C_5D_{10})$, while the multiplet at ca. −2.3 ppm is an agostic Re–CH interaction. (Reprinted with permission from Ref. 71. © 1998 American Chemical Society)

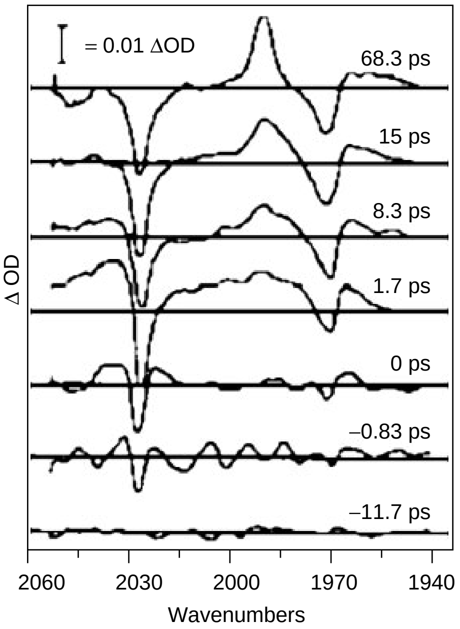

Figure 6 Transient IR spectra of $CpCo(CO)_2$ in n-hexane showing evolution of vibrationally hot CpCo(CO)(hexane). (Reprinted with permission from Ref. 73. © 1994 American Chemical Society)

Photoacoustic calorimetry has been used to establish the enthalpies of M–CO bond dissociation from the group VI carbonyls in a series of hydrocarbons. From these studies, the bond strength of Cr, Mo, and W to heptane were calculated to be 42, 38, and $54\,kJ\,mol^{-1}$, respectively.[75] The enthalpies and volumes of reaction for the substitution of CO in $Mo(CO)_6$ by alkane and the subsequent displacement of the alkane by THF have been determined by photoacoustic calorimetry. Enthalpies of substitution for CO by alkane and alkane by THF were found to be 520 and $-250\,kJ\,mol^{-1}$, respectively. The volumes of reaction were determined to be 18 and $-1\,mL\,mol^{-1}$. Utilizing known Mo–CO bond energies, Mo–alkane and Mo–THF bond energies were calculated to be 190 and $440\,kJ\,mol^{-1}$, respectively.[76] Similar studies involving reaction of piperidine with $Mo(CO)_6$ in heptane yielded Mo–heptane and Mo–piperidine bond dissociation energies of 300 and $590\,kJ\,mol^{-1}$, respectively.[77] In contrast to earlier studies, the quantum yield for substitution of CO by alkane was found to be independent of the length of the alkane chain suggesting that the product determining step does not involve coordination of solvent. Recently, laser-induced optoacoustic spectroscopy was used to determine the enthalpies and volumes of reaction of tetrahydrothiophene, THT, with $Mo(CO)_6$ in alkanes. The resulting bond energies for Mo–alkane and Mo–THT were found to be 55 and $155\,kJ\,mol^{-1}$, respectively.[78]

Photochemical reactions continue to be utilized for the introduction of ligands to metal carbonyl compounds. The following examples are drawn from a very large number of reactions in the literature. In contrast to the thermal exchange of carbonyl for phosphines observed for $CpTa(CO)_4$,[79] $Cp^*Ta(CO)_4$ ligand exchange requires photochemical conditions.[80] Photolysis of $CpNb(CO)_4$ in supercritical ethene yields $CpNb(CO)_3(C_2H_4)$ and the thermal reverse of this reaction follows clean second order kinetics.[81] The photolysis of $Cp'Tc(CO)_3$, where $Cp' = Cp$ or Cp*, and $Tp^*Tc(CO)_3$ with PPh_3 yields the expected monophosphine products.[82] Photolysis of $(C_6H_6)Cr(CO)_3$ and $(C_5H_{5-n}Me)Mn(CO)_3$, where $n = 0, 1$, with nitrogen ligands such as pyridine and pyrazine yielded seemingly conventional mono and binuclear derivatives, respectively. However, upon examination these derivatives proved to be paramagnetic and photolabile. The magnetic moments of the complexes were found to decrease with decreasing temperature suggesting that the paramagnetism arises from low lying ligand field states that may be populated thermally or photochemically at room temperature.[83]

In condensed phases, it is generally observed that one carbonyl group is lost following single photon excitation since excess energy in the molecule is quickly dissipated to solvent. For $Fe(CO)_5$, however, disubstitution has been observed with PPh_3,[84] $AsPh_3$, and $P(OMe)_3$.[85] Of particular importance was the observation based on flash photolysis studies that both $Fe(CO)_4(PPh_3)$ and $Fe(CO)_3(PPh_3)_2$ were primary photolysis products.[86] Subsequent studies have established that $Fe(CO)_4$ exists as a triplet and that reaction of $^3Fe(CO)_4$ with ligands can proceed by two routes, one involving immediate spin crossover to $Fe(CO)_4L$, while the second involves spin conservation and displacement of a CO to give $^3Fe(CO)_3L$, which subsequently reacts with a second ligand to yield $Fe(CO)_3L_2$.[87] Similar reactions of 17 electron intermediates are commonly used to explain the rapid ligand exchange of organometallic radicals.[88]

The triplet nature of $Fe(CO)_4$ has consequences on the rate of reactions of simple ligands such as CO,[89] N_2,[90] and H_2. In these cases, the rates of reaction of $^3Fe(CO)_4$ in the gas phase are substantially lower (three orders of magnitude in the case of H_2) than its homologs, $Ru(CO)_4$[91] and $Os(CO)_4$,[92] supporting the proposal that ligand addition requires a crossing from a triplet to a singlet potential energy surface during the course of the reaction.[93]

Oxidative addition of H_2, alkanes, and silanes to electron-deficient metal species has attracted considerable attention. A continuum exists between nonclassical, or σ, complexes such as η^2-H_2 or the solvated alkane complexes described above and the classical, or fully oxidatively added, species such as dihydrides. Photochemistry represents a major, and in many cases only, source of the reactive intermediates central to this chemistry. As such, detailed studies have been conducted of the reactions of photointermediates with these reagents in a variety of media and phases. The chemistry of dihydrogen and σ bonded complexes has been extensively reviewed by Heinekey and Oldham,[94] Sweany,[95] and Kubas.[96]

In the early 1980s, Sweany carried out studies of $Fe(CO)_5$ and $HCo(CO)_4$ in H_2 doped Ar matrices and established the ability of H_2 to oxidatively add to photochemically generated electron-deficient metal species to form $H_2Fe(CO)_4$ and $H_3Co(CO)_4$ under these conditions. At about the same time careful examination of the products formed when group VI carbonyls were photolyzed in H_2 doped Ar matrices suggested that the species were not the oxidative addition product, $H_2Cr(CO)_5$, but rather a complex of molecular hydrogen, $Cr(CO)_5(H_2)$.[97] The significant feature in the analysis was the decrease in carbonyl stretching frequency of the reaction product, opposite to the effect observed for oxidative addition. After the publication by Kubas[98] of the synthesis, neutron diffraction, and X-ray structure of $W(CO)_3(PCy_3)(H_2)$ clearly containing an intact H_2 ligand, Sweany published a detailed report of his matrix studies for $Cr(CO)_6$.[99]

The spectrum of $Cr(CO)_6$ in H_2 doped Ar as reported by Sweany is presented in Figure 7 for both its historical significance and to illustrate a frequently observed feature of frozen matrix photochemistry. Photolysis of $Cr(CO)_6$ results in CO-loss and formation of $Cr(CO)_5$ and perhaps some $Cr(CO)_4$. As we have already noted, these are best described as solvated species, $Cr(CO)_5Ar$, and $Cr(CO)_4Ar_2$. In the H_2 doped matrix, these species react to form small amounts of $Cr(CO)_5(H_2)$, $Cr(CO)_4(H_2)_2$, and $Cr(CO)_4(H_2)$. Long wavelength photolysis is frequently observed to result in reversal of high energy photolyses owing to photodissociation of the weakly bound solvent species.[100] In these H_2 doped matrices, the H_2 is more mobile than CO, thus the coordinatively unsaturated species formed on long wavelength photolysis are captured by H_2 as illustrated by the dramatic growth of the band for $Cr(CO)_5(H_2)$.

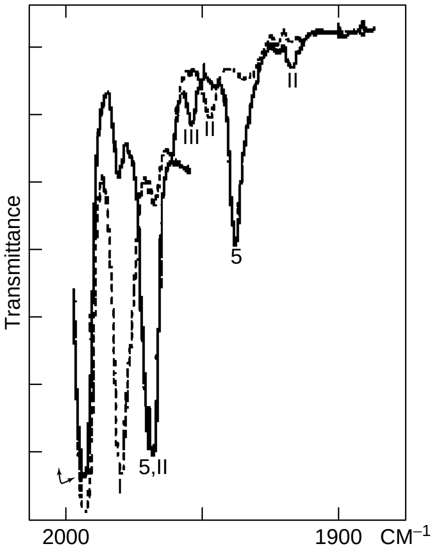

Figure 7 Ar matrix of $Cr(CO)_6$ doped with H_2. Solid lines represent spectrum after broad band irradiation followed by irradiation through cobalt glass. Dashed lines represent the spectrum of the same matrix after 90 min irradiation with the visible light from a Nernst glower. Band assignments: I, $Cr(CO)_5(H_2)$; II, $Cr(CO)_4(H_2)_2$; III, $Cr(CO)_4(H_2)$; 6, $Cr(CO)_6$; 5, $Cr(CO)_5$. (Reprinted with permission from Ref. 99. © 1985 American Chemical Society)

Liquid and supercritical noble gases are ideal media for studying H_2 species since H_2 is completely miscible under these conditions. The group VI metal carbonyl hydrides, $M(CO)_5(H_2)$, and cis-$Cr(CO)_4(H_2)_2$ were formed photochemically in liquid Xe/H_2 mixtures.[101] H_2 and N_2 complexes of a number of half-sandwich compounds were formed in supercritical Xe. These included $(C_nR_n)M(CO)_2Y$, where $R = H$, Me, $M = Mn$, Re ($n = 5$), Cr ($n = 6$), and $(C_4H_4)Fe(CO)_2Y$, where $Y = H_2$ or N_2. In all cases except Re, nonclassical H_2 complexes were formed.[102]

Room temperature, time-resolved IR studies of $LM(CO)_4$, where $L = Cp$ or Ind, $M = Nb$ or Ta, in heptane saturated with H_2 have been carried out. $CpNb(CO)_4$ gives rise to both classical, $CpNb(CO)_3(H)_2$, and nonclassical, $CpNb(CO)_3(\eta^2\text{-}H_2)$ species. In contrast, $CpTa(CO)_4$ yields the classical product, $CpTa(CO)_3(H)_2$ while $IndTa(CO)_4$ gives rise to the nonclassical, $IndTa(CO)_3(\eta^2\text{-}H_2)$ product indicating a delicate electronic and possibly steric balance between the two forms.[103]

Photoacoustic calorimetry and time-resolved IR have been used to study the photochemical reaction of $CpV(CO)_4$ with H_2 and N_2. By combining the data from these techniques, bond dissociation energies of V-H_2 and V-N_2 could be calculated to be $91 \pm 20\,\mathrm{kJ\,mol^{-1}}$, and $120 \pm 9\,\mathrm{kJ\,mol^{-1}}$, respectively.[104] Similar studies on $(C_6H_6)Cr(CO)_3$ permitted the Cr–H_2 and Cr–N_2 bond dissociation energies to be determined as $60 \pm 4\,\mathrm{kJ\,mol^{-1}}$ and $66 \pm 4\,\mathrm{kJ\,mol^{-1}}$, respectively.[105] The gas-phase photochemistry of $CpMn(CO)_3$ and $(C_6H_6)Cr(CO)_3$ with H_2 and N_2 have been examined. The products $CpMn(CO)_2Y$ and $(C_6H_6)Cr(CO)_2Y$, where $Y = H_2, N_2$, were observed directly, but the addition products of $CpMn(CO)$ and $(C_6H_6)Cr(CO)$ were thought to be obscured by overlap with other absorptions.[106]

A photochemical flow reactor (Figure 8) utilizing supercritical fluids or hydrogen saturated solvents has been developed for the preparation of gram scale quantities of labile dihydrogen and alkene complexes. Thus, $Cr(CO)_5$(alkene),[107,108] $CpMn(CO)_2$(propene),[42] and $CpMn(CO)_2(H_2)$[109] have been prepared in good yield. A series of phosphine substituted manganese compounds, $(C_5H_4CH_3)Mn(CO)_2L$, where $L = PMe_{3-n}Ph_n$, have been photolyzed with N_2 in supercritical Xe and CO_2. Little difference was found in the effectiveness of the two solvents.[110] The use of supercritical fluids as Green solvents in thermal and photochemical applications has been reviewed.[111]

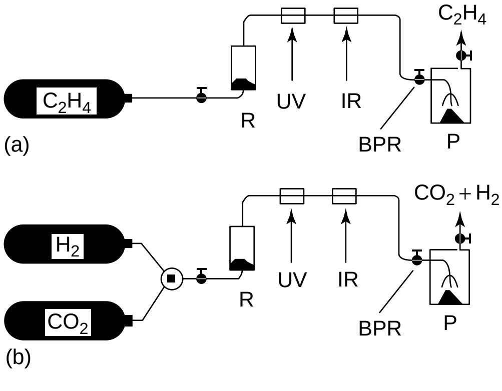

Figure 8 Schematic diagram of flow reactor for photochemical synthesis in supercritical fluids. (Reproduced by permission of Ref. 108)

Photochemical reductive elimination of H_2 from dihydrides serves as a route to generating reactive intermediates. Photolysis of $Ru(PPh_3)_3(CO)H_2$ in benzene yields $Ru(PPh_3)_3CO$. Ultrafast measurements found that hydride loss and $Ru(PPh_3)_3CO$ formation is complete in 6 ps.[112] Photolysis of both $Ru(CO)_2(PPh_2)_2H_2$ and $Ru(CO)_3(PPh_3)_2$ in gas matrices resulted in the formation of the same $Ru(CO)_2(PPh_3)_2$ intermediate.[113]

New high-yield routes to *trans*-$Cp^*Re(CO)_2H_2$ have permitted a detailed examination of the photochemistry of this species (Scheme 1). Noble gas matrix and solution photolyses in cyclohexane and Xe establish the primary photoprocess of *trans*-$Cp^*Re(CO)_2H_2$ to be unimolecular, nondissociative isomerization to the cis isomer. In solution, slow cis to trans isomerization is observed. Reductive elimination of H_2 is only observed from the cis isomer.[114]

The field of photochemical dihydride reductive elimination has been reviewed by Perutz[115] and Bergamini *et al.*[116]

Dihydride photochemistry is not limited to reductive elimination. $CpRe(PPh_3)_2H_2$ is known to photochemically catalyze H/D exchange between C_6D_6 and other arenes or alkanes.[117] Photochemical studies of the mechanism of this process have ruled out loss of phosphines and instead postulate photochemical transfer of one or both hydrides to the cyclopentadienyl ligand yielding a 14-e intermediate, $(\eta^3\text{-}C_5H_7)Re(PPh_3)_2$, as a likely intermediate.[118]

Sigma complexes of Si–H bonds were first reported by Graham[119] in 1969 although the nonclassical nature of the bonding was not recognized until after the first reports on H_2 complexes. The early history of this field has been reviewed by Graham[120] and Schubert,[121] and the literature through 2001 has been reviewed by Kubas.[96]

The rates of oxidative addition of Et_3SiH, Et_2MeSiH, $EtMe_2SiH$, and Et_2SiH_2 to photochemically generated $Cp'Mn(CO)_2$, where $Cp' = Cp$, CpMe, and Cp*, have been determined in both neat silane and a 50/50 mixture of silane and methylcyclohexane.[122]

Examination of the reactions of several organometallic species with silanes has established that the spin state of the photointermediate is important in rates of reaction. In general, triplet intermediates do not form strong agostic bonds to alkanes or alkyl groups, thus tend to go directly to Si–H oxidative addition. In contrast, singlet photointermediates may form relatively stable adducts that must undergo rearrangement prior to Si–H oxidative addition. Femtosecond UV pump/IR probe experiments have established that species known to have triplet states such as $CpV(CO)_3$, $CpCo(CO)$, and $Fe(CO)_4$ are stable, unsolvated species in

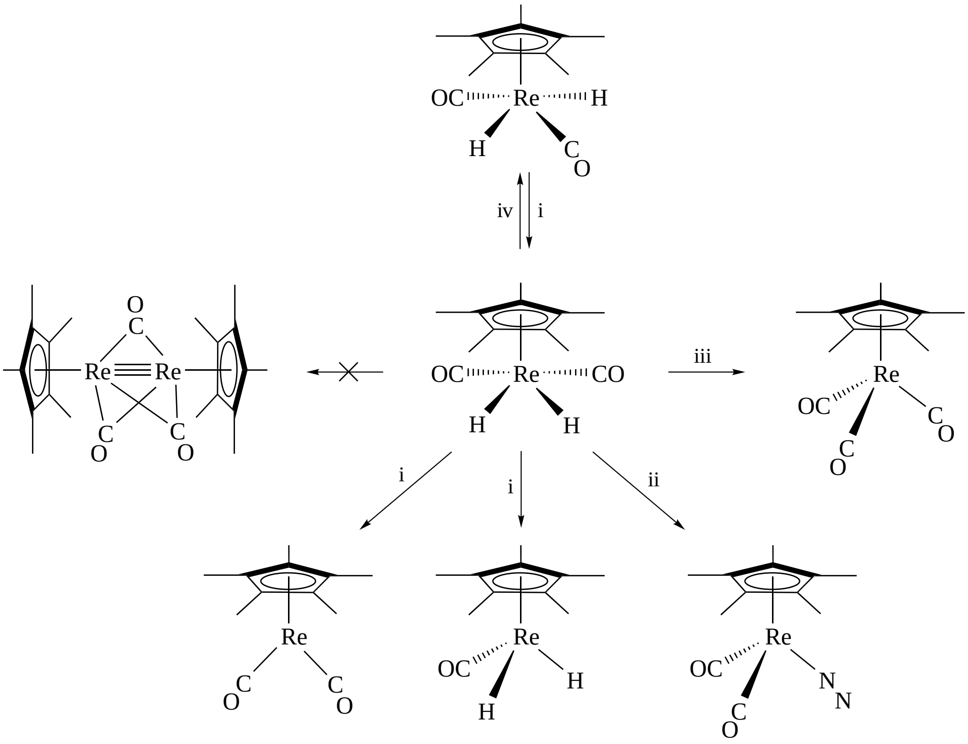

Scheme 1 Photochemistry of $CpRe(CO)_2(H)_2$ in Nujol. (i) Photolysis processes in Nujol, 12 K; (ii) secondary process in N_2 matrix; (iii) secondary process in CO matrix, (iv) thermal reversal in Nujol, 298 K. Ref. 114

alkanes while triplet $CpMn(CO)_2$ rapidly relaxed to its solvated singlet in ca.120 ps.[123,124] In contrast to their long-term stability in alkanes, the triplet species, $CpV(CO)_3$, CpCo(CO), and $Fe(CO)_4$, undergo fast spin crossover and Si–H oxidative addition. Singlet intermediates such as CpRh(CO) or $CpRe(CO)_2$ react rapidly to form either Si–H oxidative addition products or solvated species. In the case of rhodium, the $CpRh(CO){\cdot}Et_3SiH$ species requires almost 370 µs to transform to $CpRh(CO)(H)(Et_3Si)$ while in the case of $CpRe(CO)_2{\cdot}Et_3SiH$ about 6.8 µs are required for rearrangement to the oxidative addition product.[125] The proposed mechanism for $CpRe(CO)_3$ is presented in Figure 9. The more complicated mechanism of $CpMn(CO)_3$ in which both singlet and triplet species are observed is shown in Figure 10. The rearrangement of $CpMn(CO)_2(Et_3SiH)$ to $CpMn(CO)_2(HSiEt_3)$ has been observed using photoacoustic calorimetry.[126] Harris has reviewed these results as well as parallel results (discussed below) relating to C–H activation.[127]

C–H activation has been extensively examined since the virtually simultaneous discovery by Graham[128] and Bergman[129] that photochemically generated, electron-deficient organometallic species could insert into the C–H bond of an alkane. Numerous recent reviews and books have appeared describing both photochemical and thermal strategies for generating the critical electron-deficient intermediates. Because of the sheer magnitude of this field, we shall focus here on studies directed toward understanding the mechanism of these reactions based on the photochemical generation of active species.

An excellent short review of C–H bond activation including both thermal and photochemical mechanisms has been provided by Labinger and Bercaw.[130] Lees has reviewed the photochemical and photophysical features of these reactions.[131] Bergman has described the contributions of his group toward the understanding of the mechanisms of C–H activation up to 1992,[132] and within the context of physical organic chemical methods.[133] Schneider has examined the similarities between Si–H and C–H activation.[134] Shilov and Shul'pin have provided extensive reviews of C–H activation.[135] As with Si–H oxidative addition, the spin state of the photochemical intermediate plays a major role in the probability of insertion. This has been reviewed for the specific case of methane activation.[136]

Photolysis of $Cp^*M(CO)_2$, M = Rh or Ir, and $CpIr(CO)_2$ in methane matrices afforded the first direct observation of C–H activation from a photointermediate.[137] Similarly, photolysis of $Cp^*Ir(CO)(H)_2$ in methane matrices yielded $Cp^*Ir(CO)(H)(CH_3)$.[138] The rate of oxidative addition of alkanes to a CpRh(CO) photointermediate in the gas phase has been measured.[139]

A detailed stepwise mechanism for C–H activation emerged from the flash photolysis of $Cp^*Rh(CO)_2$ and neopentane in liquid Kr. Cp*Rh(CO)Kr was shown to be in equilibrium

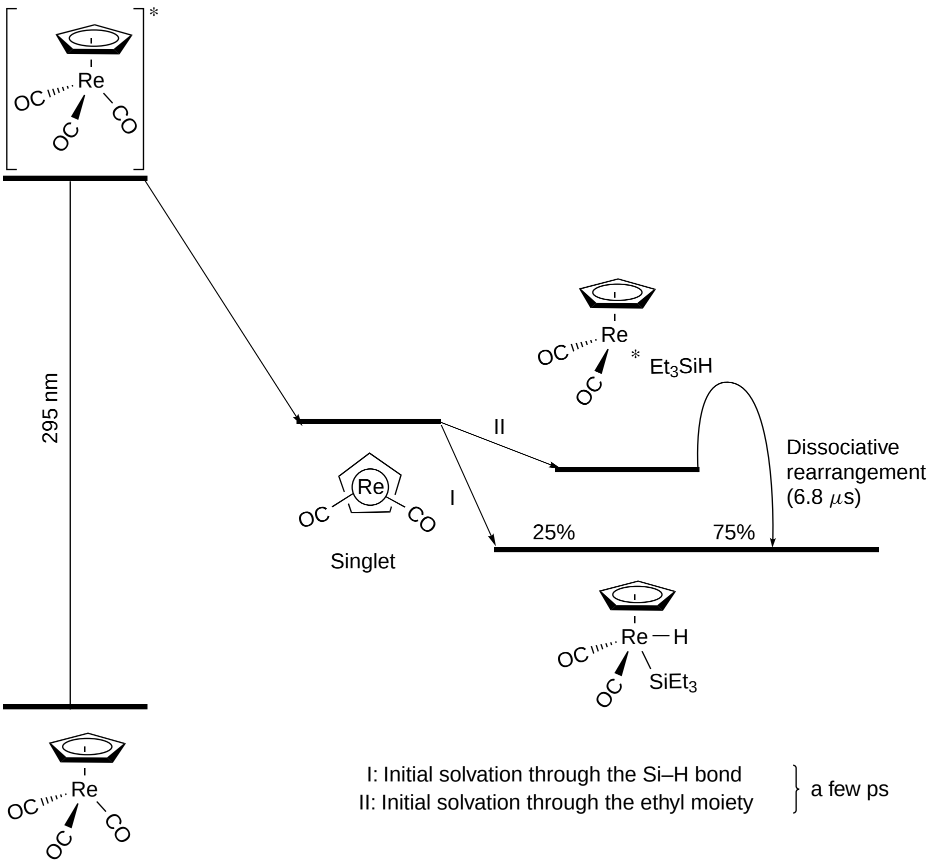

Figure 9 Proposed reaction mechanism of Si–H bond activation by CpRe(CO)$_3$. (Reprinted with permission from Ref. 127. © 1999 American Chemical Society)

with Cp*Rh(CO)(σ-C_5H_{12}). The latter thermally converts to Cp*Rh(CO)(H)(C_5H_{11})with a rate of 4.08×10^4 sec^{-1}. The use of d^{12}-neopentane made it possible to observe both the Kr and neopentane species.[140] Similar experiments had been performed earlier with cyclohexane in Kr, but it had not been possible to directly observe the σ-cyclohexane complex.[141] More recent studies of Cp*Rh(CO)$_2$ in Kr with a series of alkanes has established an alkane structural effect on the rate of C–H oxidative addition. It was found that the equilibrium between the Kr and σ-alkane complexes shifts toward the alkane complex as alkane size increases. This is attributed to the relative polarizabilities of the alkane ligands. The rate of conversion from σ-alkane to oxidative addition product follows a reverse trend. It is proposed that the transition states for oxidative addition of the various alkanes lie closer together in energy than do the energies of the σ-alkane precursors. Thus differences in activation energy, and hence rate of oxidative addition, directly reflect the stability of the σ-alkane complex.[142] Deuterium isotope effects for this reaction have been examined. A large normal isotope effect ($k_H/k_D = 10$) was observed for the C–H activation step, while a negative isotope effect ($k_H/k_D = 0.1$) was observed for the preequilibrium. The authors attribute this negative isotope effect to greater stabilization of the σ-deutero alkane complex.[143]

Picosecond transient absorption spectroscopy of Cp*M(CO)$_2$, where M = Rh and Ir, establish a biexponential decay of the excited state species that have been assigned to a fast nondissociative relaxation from the excited state and a slow dissociative step. The low quantum yields observed upon preparative photolysis are attributed to the fast nondissociative decay.[144] Building upon wavelength dependence and quantum yield studies by Lees,[145] a theoretical model of the excited states of CpM(CO)$_2$, where M = Rh and Ir, suggests that two excited states are strongly mixed. These excited states correspond to a MLCT state that is responsible for the observed photochemistry and a ligand Cp to metal and CO charge transfer excitation that quickly relaxes without initiating photochemistry.[146] Subpicosecond IR studies of the photolysis of CpRh(CO)$_2$ in cyclohexane have observed a species consistent with (η^5-C_5H_5)Rh(CO)(C_6H_{12}) ruling out a haptotropic (η^3-C_5H_5)Rh(CO)(C_6H_{12}) species in the reaction.[147] Somewhat unexpectedly, the photochemical ligand exchange of Cp′Rh(CO)$_2$, where Cp′ = Cp and Cp*, with PPh$_3$ appears to proceed through an associative mechanism involving an η^3-Cp′ ring.[148]

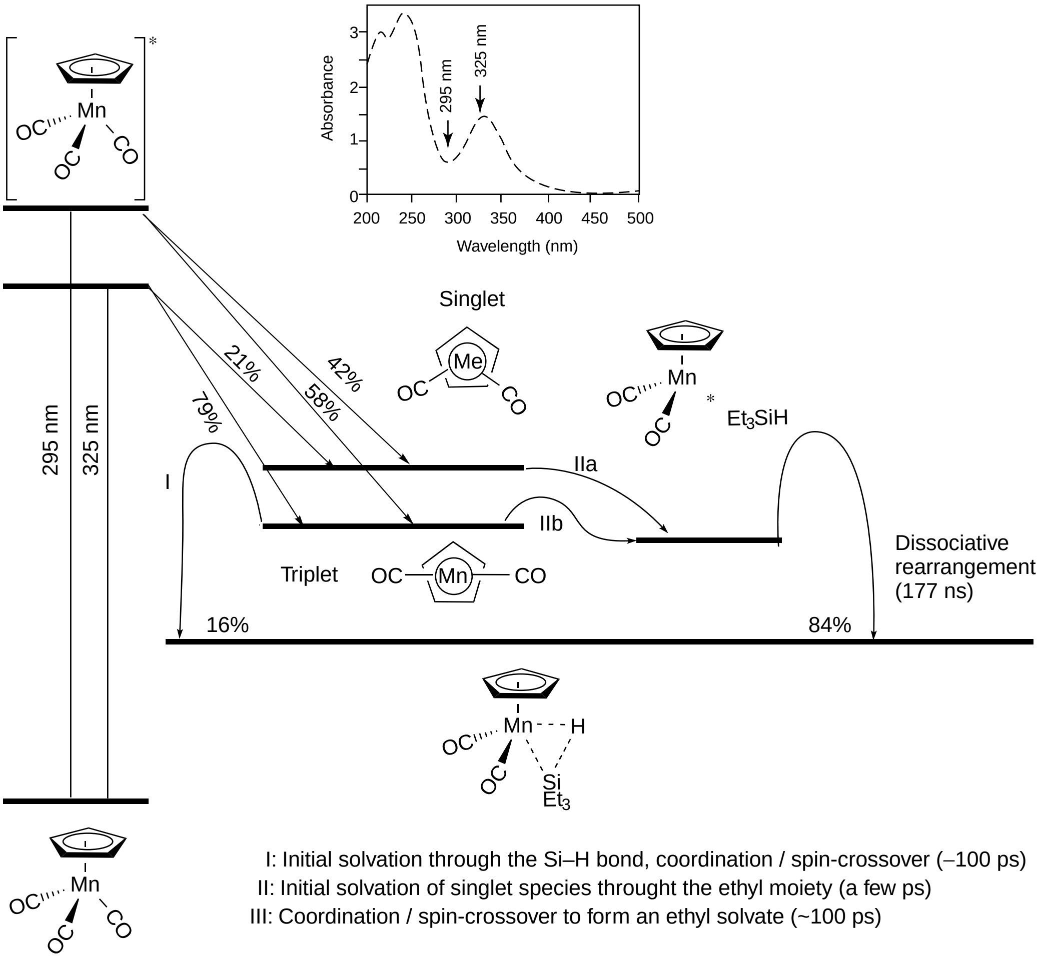
Absorbance
3
2
1
0
295 nm
325 nm
200 250 300 350 400 450 500
Wavelength (nm)
Mn
OC
CO
OC
*
295 nm
325 nm
21%
42%
79%
58%
Singlet
Me
OC
CO
Mn
OC
OC
*
Et3SiH
IIa
IIb
I
Triplet
OC
Mn
CO
Dissociative
rearrangement
(177 ns)
16%
84%
Mn
H
OC
OC
Si
Et3
Mn
OC
CO
OC
I: Initial solvation through the Si–H bond, coordination / spin-crossover (–100 ps)
II: Initial solvation of singlet species throught the ethyl moiety (a few ps)
III: Coordination / spin-crossover to form an ethyl solvate (~100 ps)

Figure 10 Proposed mechanism of Si–H activation by $CpMn(CO)_3$. Inset: UV–vis spectrum of $CpMn(CO)_3$ in neat Et_3SiH under experimental conditions. (Reprinted with permission from Ref. 127. © 1999 American Chemical Society)

The photochemical transformation of $CpIr(CO)(\eta^2\text{-}C_2H_4)$ to $CpIr(CO)(H)(C_2H_3)$ in an Ar matrix is presented in Figure 11(a). The oxidative addition is reflected in the increase of the carbonyl stretching frequency reflecting the formal transformation from Ir(I) to Ir(III). In a methane matrix (Figure 11(b)), a second species is observed corresponding to $CpIr(CO)(H)(CH_3)$ arising from the dissociation of ethane. Interestingly, a pronounced wavelength dependence was observed for the photolyses in methane matrices. Upon low-energy irradiation ($\lambda > 365$ nm) $CpIr(CO)(H)(C_2H_3)$ was formed exclusively, but with increasing energy of the incident radiation methane activation was found to compete with ethane activation.[149] It seems likely that higher energies introduce a dissociative component to the reactions not present at lower energies.

Reaction of CH_4, C_2H_4, and C_2H_6 with $Cp^{*}Ir(CO)_2$ in supercritical CO_2, Xe, and CHF_3 has been examined. H_2 addition is unaffected in sc CHF_3, but oxidative addition of ethane is almost completely suppressed, perhaps owing to hydrogen bonding by the solvent. ‘Solvent free’ photolysis has also been carried out in supercritical methane, ethane, and ethene.[150]

Density functional theory modeling of the group IX CpM(CO) intermediates correlates the activation barrier to oxidative addition of a C–H bond to the singlet-triplet splitting, ΔE_{st}, of the 16 electron intermediate. Smaller values of ΔE_{st} are observed with the lower transition metals in agreement with the ease of oxidative addition.[151]

While examining analogs for $CpRh(CO)_2$, Ghosh and Graham prepared $Tp^{*}Rh(CO)_2$ and found that this species activated aromatic and alkane C–H bonds with great efficiency under daylight or tungsten illumination.[152] Gas matrix studies established that both CO dissociation and Tp* ligand dechelation occurred upon photolysis.[153] Extensive studies by Lees[154] and Bergman[155] have established a detailed mechanism for these reactions (Scheme 2). Consistent with the matrix studies, photolysis may lead to dechelation of the κ^3-Tp* ligand or CO-loss with dechelation dominating at longer wavelengths while CO-loss is more significant at shorter wavelengths. Dechelation is inconsequential with

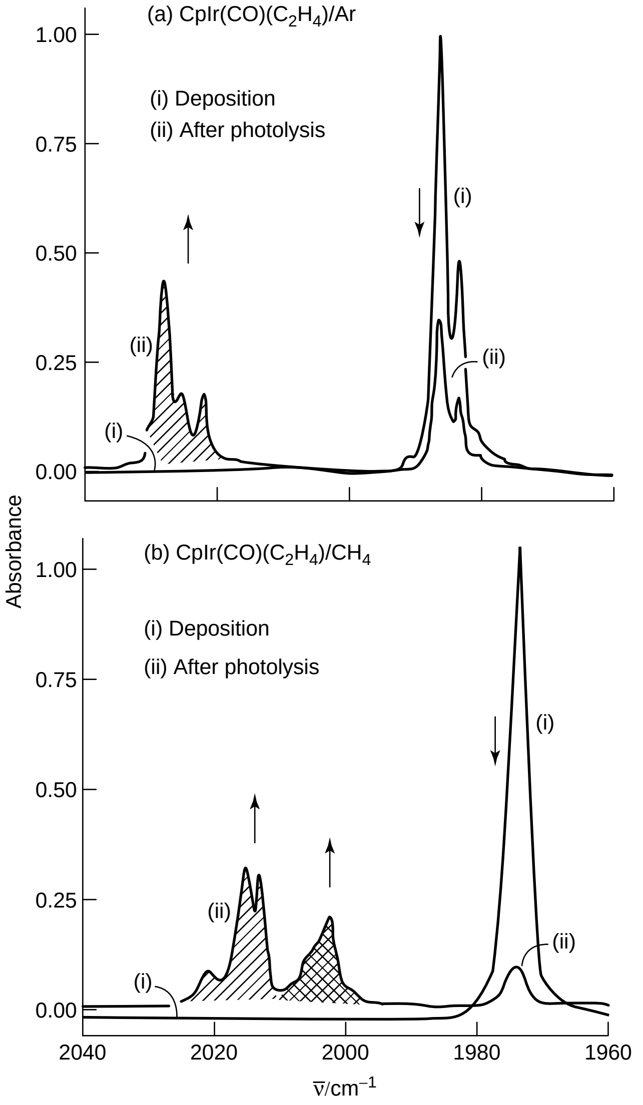

Figure 11 IR spectrum of $CpIr(CO)(\eta^2\text{-}C_2H_4)$ in (a) Ar showing $CpIr(CO)(H)(C_2H_3)$ and (b) CH_4 matrices showing both $CpIr(CO)(H)(C_2H_3)$ and $CpIr(CO)(H)(CH_3)$. Spectra (i) are as deposited, while (ii) are photolyzed samples. (Reprinted with permission from Ref. 149. © 1993 American Chemical Society)

respect to C–H activations since the dangling pyrazolyl ligand rapidly recombines with the metal. Solvation of the CO-loss species occurs within a few ps and is followed by dechelation of the κ^3-Tp* ligand giving rise to κ^2-Tp*Rh(CO)(RH). This species undergoes C–H bond activation to give κ^2-Tp*Rh(CO)(H)(R) followed by reattachment of the pyrazolyl ligand to yield the product, κ^3-Tp*Rh(CO)(H)(R).

One of the significant challenges in synthetic chemistry is to follow a C–H activation step with further bond making or breaking transformations. In the processes described above, the C–H oxidative addition product is the thermodynamic sink of the reaction. Three processes that have transcended this difficulty are carbonylation, dehydration, and borylation.

In the course of examining the photochemistry of benzene solutions of $H_3Ir(CO)(dppe)$ under CO, Fischer and Eisenberg observed formation of benzaldehyde. The actual catalytic species was determined to be HIr(CO)(dppe).[156] Examination of related metal complexes, notably $Rh(CO)L_2Cl$, where L = PPh_3 or PMe_3, established that both aromatic and saturated hydrocarbons could serve as substrates for photochemical carbonylation.[157] The significance of this reaction is perhaps reflected in issuance of several patents.[158] An examination of a range of phosphorus ligands established that the order of reactivity was $PMe_3 \approx$ 1,3,4-trimethylphospholane $\approx$ 1,3,4-trimethylphospholene $> P(CH_2O)_3CMe > PEt_3 > P(CHMe_2)_3 \approx PPh_3 \approx P(OMe)_3 >$ dppe.[159] A catalytic mixture consisting of $Rh_2(CO)_4Cl_2$ and PMe_3 was found to catalyze pentane carbonylation at a rate ca. 20 times that of $Rh(CO)(PMe_3)_2Cl$.[160] The effect of CO pressure on the dehydration and carbonylation of pentane established that increasing CO pressure suppresses dehydration, while increasing CO pressure to 600 mm reportedly displaced a phosphine from rhodium creating a more active catalyst.[161] A wavelength dependence on the regioselectivity of the reaction has been reported.[162] Photodehydrogenation,[163] C-Si[164] and C–C bond forming reactions[165] have been observed in the absence of CO. Evidence for the intermediacy of the CO-loss species, $Rh(PMe_3)_2Cl$, in dehydrogenation reactions has been reported.[166] The carbonylation of propane in liquid propane,[167] ethane in both supercritical ethane and supercritical CO_2,[168] and methane in supercritical CO_2 have been reported.[169] Several reviews of these reactions have been published.[170]

The mechanism of the $Rh(CO)(PMe_3)_2Cl$ catalyzed carbonylation has come under scrutiny. In the absence of CO, benzene is found to react photochemically with the catalyst to form two isomers of $Rh(CO)(PMe_3)_2(H)(Ph)Cl$ and $Rh(CO)(PMe_3)_2Ph$ arising from HCl loss from the Rh(III) species.[171] Closely related to this is the oxidative addition of benzene to $Rh(PMe_3)_3Cl$ to give $Rh(PMe_3)_3(H)(Ph)Cl$. This species could be isolated and a molecular structure was obtained confirming the cis orientation of the phenyl and hydride ligands.[172] $Rh(CO)(PMe_3)_2(H)(Ph)Cl$ undergoes secondary photolysis resulting in reductive elimination of benzaldehyde. Although benzene does oxidatively add to the CO-loss species, $Rh(PMe_3)_2Cl$, this did not appear to be the primary route to carbonylation. Instead, oxidative addition to an intact, excited state catalyst appears to be the precursor to the Rh(III) species.[173] Time-resolved optical and IR studies of the photolysis of $Rh(CO)L_2Cl$, L = PMe_3, PPh_3, P(*p*-toluyl)$_3$, in a variety of solvents has established that an initial excited state species is formed (<30 ps) and that this species decays to $RhL_2(sol)Cl$ over 40 to 560 ps depending upon L and solvent. The solvated species undergo oxidative addition to form Rh(III) species. CO suppresses the formation of the solvated species. It was confirmed that some fraction of the excited state species react directly with solvent without CO-loss to form Rh(III) species.[174] Nujol matrix photolysis of $Rh(CO)L_2Cl$, where L = PMe_3 and PBu_3, resulted in the formation of a new

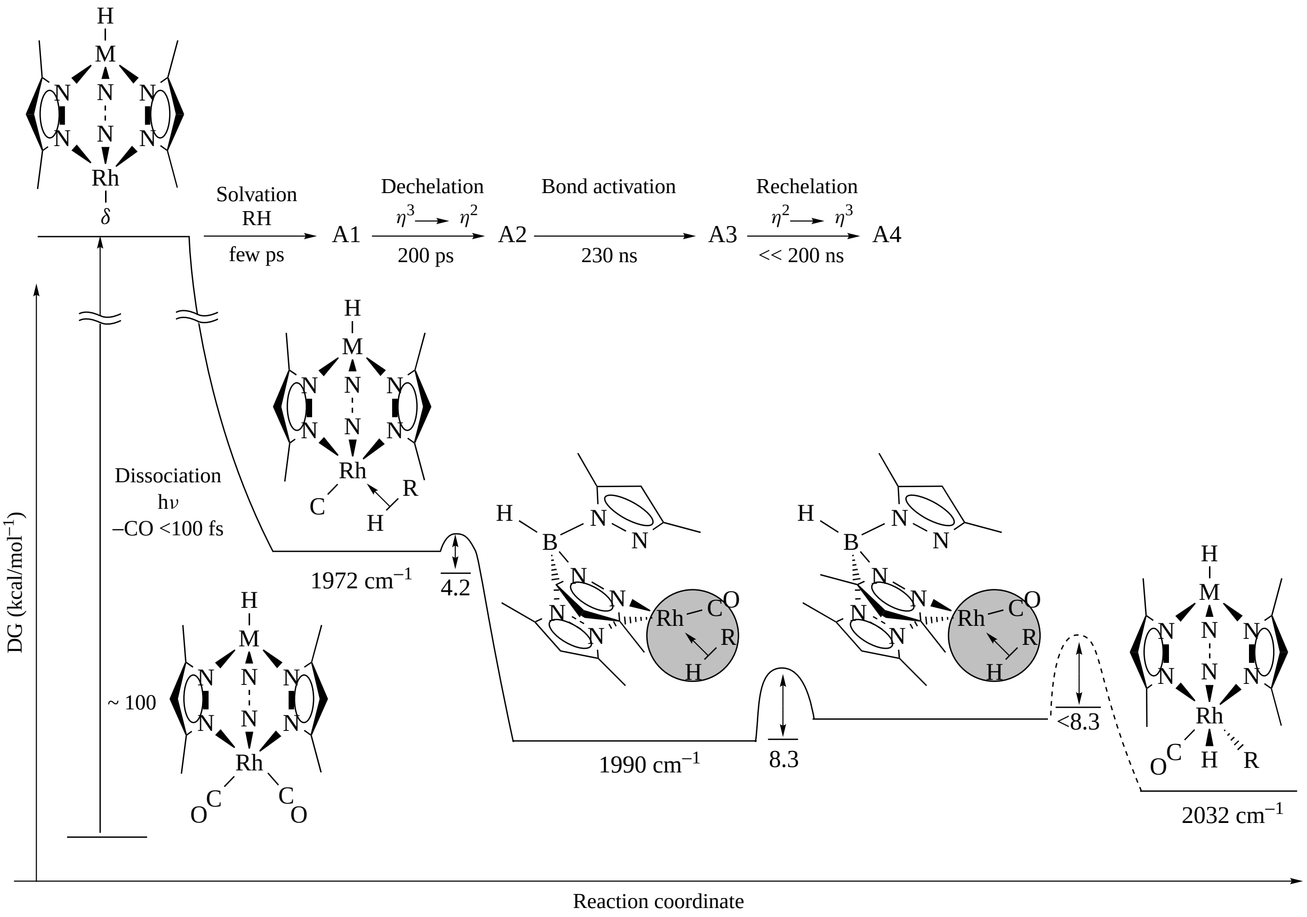
Solvation
RH
few ps
A1
Dechelation
$\eta^3 \rightarrow \eta^2$
200 ps
A2
Bond activation
230 ns
A3
Rechelation
$\eta^2 \rightarrow \eta^3$
<< 200 ns
A4
Dissociation
hν
–CO <100 fs
~ 100
DG (kcal/mol^{-1})
1972 cm^{-1}
4.2
1990 cm^{-1}
8.3
<8.3
2032 cm^{-1}
Reaction coordinate

Scheme 2 Reaction mechanism for photochemical C–H activation by Tp*Rh(CO)$_2$. Ref. 155d

carbonyl-containing species (Figure 12), believed on the basis of dft calculations to be a nonplanar triplet.[175] A very recent flash photolysis study of Ir(CO)(PPh$_3$)$_2$Cl has been interpreted in terms of the formation of a long-lived electronically excited state of the iridium complex having an IR carbonyl stretch very close to that of the ground-state molecule.[176] Whether this is related to the species observed upon Nujol matrix photolysis is not yet known.

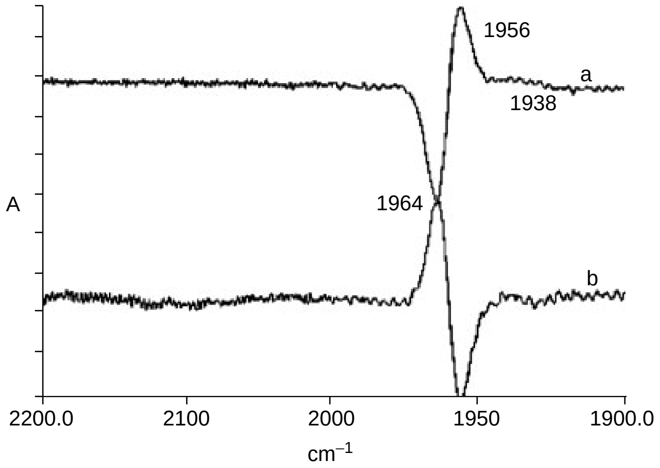

Figure 12 Photolysis of Rh(CO)(PMe$_3$)$_2$Cl in Nujol matrix at ca. 90 K. (a) 4 h photolysis ($\lambda > 400$ nm). (b) Sample annealed to 153 K. (Reprinted from Ref. 175. © 2002, with permission from Elsevier)

Thermal and photochemical borylation of alkanes and arenes via C–H activation provide a strategy for functionalizing hydrocarbon feedstocks.[177] Photolysis of a series of transition metal boryl compounds, Cp*M(CO)$_n$B(OR)$_2$, where M = Fe($n = 2$), Ru ($n = 2$), or W ($n = 3$), R = B-1, 3, O$_2$C$_6$H$_2$-3, 5-Me$_2$, in the presence of benzene, alkanes, or alkenes results in the formation of alkyl boronate esters and the corresponding transition metal hydride.[178] M(CO)$_5$B(OR)$_2$, where M = Mn and Re, reacted with benzene to yield phenyl boronate ester and the corresponding metal hydride (Scheme 3).[179] Yields were as high as 85% with the tungsten compound. A strong preference was found for substitution at primary carbons of the alkanes. Photolyses in the presence of PMe$_3$ provided strong evidence of photochemical CO-loss as the initiating step in these reactions and, indeed, the CO-loss species of Cp*W(CO)$_3$B(catechol) has been observed

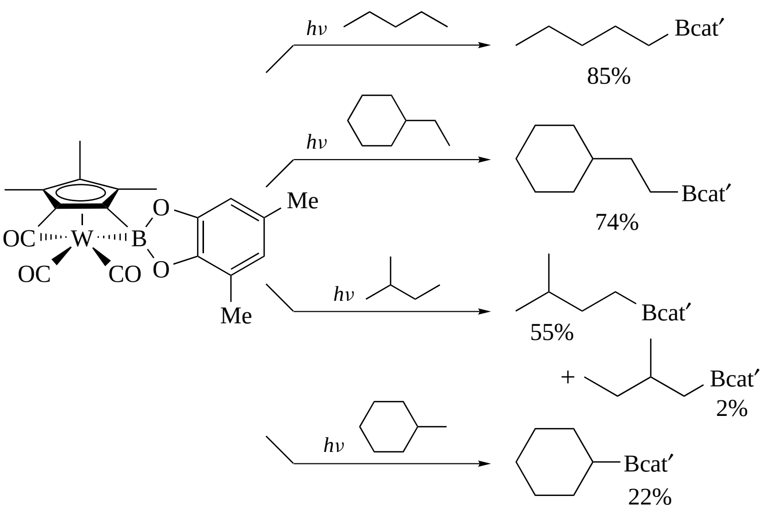

Scheme 3 Photolysis reactions of $CpW(CO)_3Bcat'$ with yields of products. Ref. 178b

directly in frozen Nujol matrices.[180] The iron complex shows a strong preference for arene functionalization over alkane while the tungsten complex is equally effective at both. Dft modeling finds that reactions of $CpFe(CO)BO_2C_2H_4$ favor a one step, σ-bond metathesis involving a four-center transition state, while $CpW(CO)_2BO_2C_2H_4$ favors a two step process in which oxidative addition proceeds reductive elimination of $RBO_2C_2H_4$. arene addition to the iron intermediate is stabilized by interaction between the 'empty' boron p orbital and the π orbitals of the benzene.[181]

Photolysis of $Cp'M(CO)_3$, where M = Mn or Re, Cp′ = Cp or Cp*, in the presence of pentane and 4, 4, 4′, 4′, 5, 5, 5′, 5′-octamethyl-2, 2′ = bi-1, 3, 2-dioxaborolane (B_2Pin_2) resulted in formation of primary pentylboronate ester in yields as high as 95% for the Cp* derivatives. Photolysis of *trans*-$Cp^*Re(CO)_2(Bpin)_2$ in pentane produced pentylboronate ester in 100% yields suggesting that $Cp'M(CO)_2(Bpin)_2$ species are likely intermediates in these syntheses.[182] The analogous oxidative addition of a B–B bond has been observed upon photolysis of Cp_2WH_2 and CatBBCat (Cat = 4-tert-butylcatechol) in benzene yielding $Cp_2W(Bcat)_2$.[183]

In an interesting footnote to these alkane and aromatic borylation reactions, photolysis of $Cp^*M(CO)_3Me$, M = Mo or W, and H_3BPMe_3 resulted in the formation of methane and $Cp^*M(CO)_3BH_2PMe_3$.[184]

4 Fe(DMPM)$_2$H$_2$ AND RELATED COMPOUNDS

In the late 1970s, DuPont workers demonstrated that $Fe(dmpe)_2(H)(Napthyl)$ undergoes reactions with a variety of R–H groups to give oxidative addition products, $Fe(dmpe)_2(H)(R)$ with the assumption that a 16-electron intermediate, $Fe(dmpe)_2$, was responsible for the chemistry.[185] Subsequent work in Australia[186] and Italy[187] demonstrated that $M(dmpe)_2H_2$, where M = Fe, Ru, Os, could undergo photochemical loss of H_2 to generate the same reactive intermediate. Oxidative addition of alkanes (including methane in supercritical Xe[188]), alkene, arene, and acetylenic C–H bonds to these intermediates has been studied.[189] A patent has been issued for the use of $Fe(dmpe)_2H_2$ for photochemical dehydrogenation of alkanes.[190] Thiophenes react with $Fe(dmpe)_2$ to insert both C–H and C–S bonds.[191] Photolysis of $Fe(dmpe)_2H_2$ in Ar matrices permitted direct UV detection of $Fe(dmpe)_2$. In solution, time-resolved spectra established that H_2 loss occurs within 30 ns. Rates of reaction between $Fe(dmpe)_2$ and a variety of substrates were measured. The order of decreasing rate was found to be: $CO \gg H_2 > C_2H_4 > N_2 >$ cyclopentene $> Et_3SiH$.[192] A dft analysis has been carried out on $M(PH_3)_4$, where M = Fe, Ru, as models of the dmpe complexes. Singlet $Ru(PH_3)_4$ was calculated to have a D_{2d} geometry while the corresponding singlet iron species was found to have a C_{2v} geometry. Triplet $M(PH_3)_4$ for both Fe and Ru were found to have C_{2v} geometries. Interestingly, the singlet ruthenium species was calculated to be 11.7 kcal $^{-1}$ mol more stable than the triplet, while the singlet iron species was found to be 8.0 kcal mol^{-1} less stable than its triplet.[193]

Matrix photolysis of the series $Ru(P2)_2H_2$, where P_2 = depe, $Et_2PC_2H_4Pet_2$, dppe, $Ph_2PC_2H_4PPh_2$, dfepe, $(C_2F_5)_2PC_2H_4P(C_2F_5)_2$ established that in all cases H_2 loss yields $Ru(P_2)_2$. The rates of reaction of the various photointermediates with H_2 and CO established a rate order of $Ru(dfepe)_2 < Ru(dppe)_2 < Ru(depe)_2$.[194]

$PtLH_2$, where L = $(t\text{-}Bu_2P)_2C_2H_4$,[195] undergoes photolysis to yield PtL that has been found to effect arene C–H activation but not alkane.[196] The concerted elimination of H_2 has been confirmed in that an equimolar solution of $PtLH_2$ and $PtLD_2$ gave only H_2 and D_2 as products. A qualitative bonding model assigns the HOMO to a $\sigma(x^2\text{-}y^2)$ and the LUMO to the corresponding $\sigma^*(x^2 - y^2)$. Excitation is expected to result in loss of H_2. This is consistent with parahydrogen studies in which H_2 adds in a concerted, pairwise manner to $Pt(Ph_2PCH_2CHMeOPPh_2)$.[197]

5 LIGAND EXCHANGE, BOND HOMOLYSIS, AND HETEROLYSIS

Photochemical homolysis of metal–ligand bonds has been observed with a number of simple organometallic derivatives. For example, photolysis of $CpFe(CO)_2R$, where R = Bz,[198] $C(Ph)(H)(OSiMe_3)$,[199] in the presence of excellent ligands such as CO or phosphines result in homolysis of the Fe–C bonds. Subsequent recapture of the carbon radical by exocyclic attack on the Cp ring of the intermediate $CpFe(CO)_2L$, yields *exo*-$C_5H_5RFe(CO)_2L$.

The photochemical generation of methyl radicals has been applied to studies of DNA cleavage. The photochemical generation of methyl radicals from $Co(cyclam)Me(H_2O)(ClO_4)_2$ has been known for some time.[200] Photolysis of $Co(cyclam)Me(H_2O)(ClO_4)_2$ in the presence of plasmid DNA results in the conversion of supercoiled DNA to the nicked circular form. The likely mode of DNA damage is hydrogen atom abstraction by pathways very similar to those of hydroxyl radicals.[201] group VI $CpM(CO)_3R$, $CpFe(CO)_2R$, where R = Me, Ph, and $[CpFe(CO)_2]_2C_6H_4$ compounds have also been used in studies of DNA double strand scission.[202] Of particular interest were cyclopentadienyl complexes bearing DNA recognition elements on their rings. These species form bioconjugate complexes with DNA placing the photoactive species immediately adjacent to the DNA strand.[203]

Photochemical bond heterolysis is a much less common, or at least much less studied, phenomenon than ligand dissociation or bond heterolysis. $CpFe(CO)_2X$, where X = halide, are well known to undergo CO-loss upon photolysis,[204] and the $CpFe(CO)Cl$ species has been observed in gas matrices.[205] In the presence of nitrogen bases such as pyrrole,[206] cyclic imides,[207] nucleobases,[208] and nucleosides, LH, $CpFe(CO)_2I$ undergoes photolysis to form $CpFe(CO)_2L$. Quantum yields of the heterolysis reaction have been recorded in the range of 488–647 nm. The most effective photoconversions were found to occur at long wavelength ($\phi = 0.38 \pm 0.02$, $\lambda = 647$ nm) and have been attributed to a LF transition.[209]

6 BIMETALLIC CARBONYL AND CYCLOPENTADIENYL CARBONYL COMPOUNDS

The photochemistry of bimetallic carbonyl and cyclopentadienyl carbonyl compounds is characterized by both carbonyl-loss and metal–metal bond homolysis.[210] Like the mononuclear carbonyls, carbonyl-loss species may react with a variety of ligands, or may undergo internal reorganization such as the formation of semibridging, bridging, or 4-electron bridging carbonyl groups to maximize bonding. Metal–metal bond homolysis produces radical species that may react with ligands to substitute carbonyl groups or may initiate hydride or halide abstraction reactions.

The photolysis of $Mn_2(CO)_{10}$ is representative of the behavior of many bimetallic carbonyl compounds. In solution[211] and in the gas phase[212] strongly wavelength dependent photochemistry has been observed. At low energy, Mn–Mn bond homolysis predominates while at high energy CO-loss is observed.

Photolysis of $Mn_2(CO)_{10}$ in 3-methylpentane glass or Ar matrix resulted in loss of a carbonyl ligand and formation of a species with a bridging carbonyl.[213] The low IR stretching frequency of the bridging carbonyl, ca. 1760 cm^{-1}, requires that it be assigned as a 4-electron bridging carbonyl, μ-η^1:η^2-CO. The difference spectrum illustrating the formation of the CO-loss species in 3MP is shown in Figure 13. Under these matrix conditions $Mn(CO)_5$ radicals are not observed owing to rapid recombination within the solvent cage. UV flash photolysis with UV[214] and IR[215] detection of $Mn_2(CO)_{10}$ in cyclohexane solution directly observed the radical (Figure 14) and CO-loss (Figure 15) channels. The excited state species dissociates with an upper limit of 2–3 ps. The vibrationally hot $Mn_2(CO)_9$ species cools through two distinct channels in 15 and 170 ps, respectively. Although these channels were initially associated with formation of the bridging carbonyl intermediate, later work in 3-methylpentane glass provided strong evidence for formation of a solvated species, $Mn_2(CO)_9(sol)$ that then decays to the bridged form.[216] Photolysis at 400 nm rather than in the UV permitted the $Mn(CO)_5$ radical formation and cooling to be observed without interference by the CO-loss product.[217] The EPR spectrum of $Mn(CO)_5$ radicals was recorded by trapping the gas

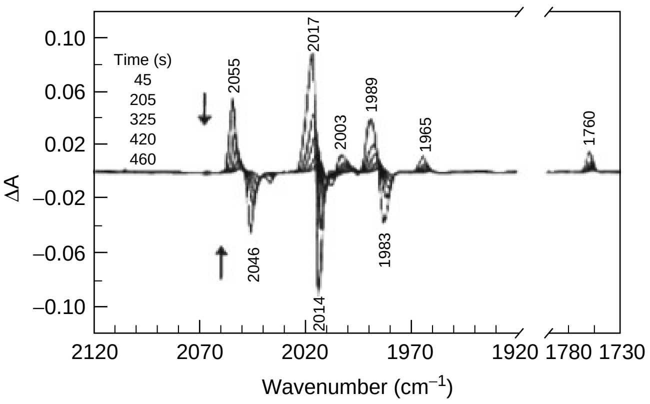

Figure 13 Difference FTIR spectrum of $Mn_2(CO)_8(\mu$-η^1, η^2-CO) at 155 K in 3MP as a function of time. (Reprinted with permission from Ref. 219. © 1995 American Chemical Society)

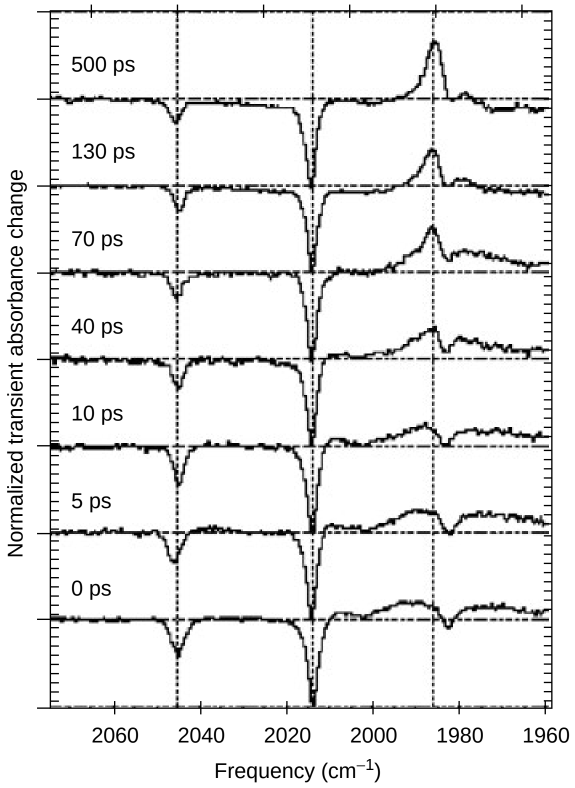

Figure 14 Normalized time-resolved IR spectra of 400 nm photodissociation of $Mn_2(CO)_{10}$ in cyclohexane for several pump probe delay times. Vibrational cooling of the $Mn(CO)_5$ radical can be observed to be complete by 70 ps. (Reprinted from Ref. 217. © 2002, with permission from Elsevier)

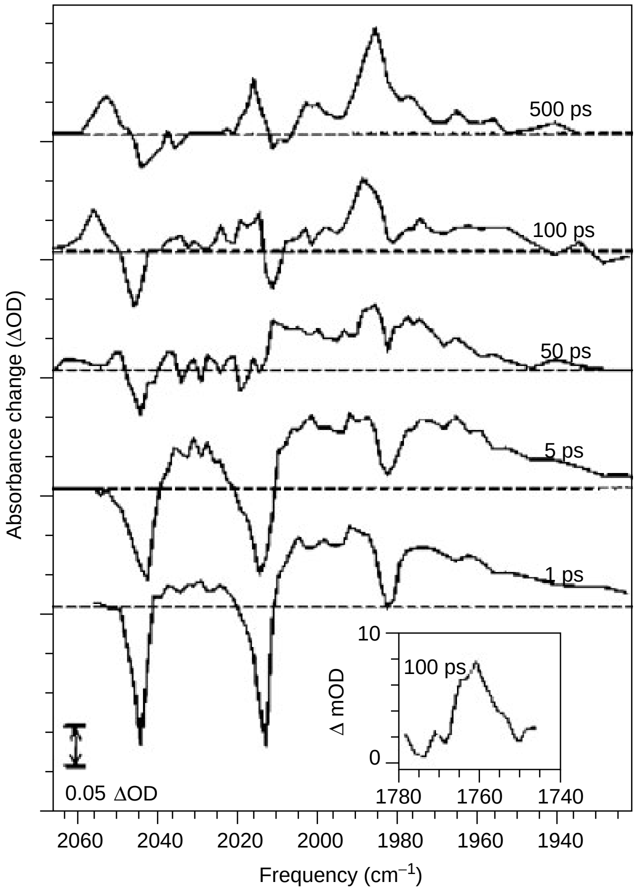

Figure 15 Transient IR spectra of 310 nm photodissociation of $Mn_2(CO)_{10}$ in cyclohexane at several time delays. Insert is bridging carbonyl region at 100-ps delay. Both $Mn(CO)_5$ radical and $Mn_2(CO)_8(\mu\text{-}\eta^1, \eta^2\text{-CO})$ are observed. (Reprinted with permission from Ref. 215. © 1996 American Chemical Society)

phase photochemically generated radicals in an adamantane matrix.[218]

Several theoretical studies of the ground and excited states of $Mn_2(CO)_{10}$ have been reported.[220]

Extended photolysis of $Mn_2(CO)_{10}$ in 3-methylpentane glass gives rise to $Mn_2(CO)_8$ resulting from double CO-loss and an isomer of $Mn_2(CO)_9$ with a semibridging carbonyl.[221] Dft calculations have been used to probe possible structures of the $Mn_2(CO)_8$ species.[222]

Examination of the photochemical products of the series $Mn_2(CO)_{10}$, $MnRe(CO)_{10}$, $Re_2(CO)_{10}$ allows a comparison of the tendency of the various species to form solvated or bridging carbonyl complexes upon CO-loss. As noted above, $Mn_2(CO)_9$ forms a solvated species that readily converts to a bridged carbonyl intermediate. In contrast, $MnRe(CO)_9$ forms a stable solvated species that requires visible light to transform it into an analogous bridging carbonyl species. $Re_2(CO)_9$, consistent with the reluctance of third row transition metals to form carbonyl bridges, forms only a solvated species.[219]

When $Mn_2(CO)_{10}$ and PR_3 are photolyzed in 3-methylpentane at 90 K only CO-loss is observed. Warming solutions containing $Mn_2(CO)_8(\mu\text{-}\eta^1\text{:}\eta^2\text{-CO})$ and PBu_3 results in formation of equatorial $Mn_2(CO)_9(PBu_3)$ that rearranges to its axial isomer. When photolyses are carried out at 213 K the solvent is fluid, thus both CO-loss and radical channels are accessible. It is believed that the rate of reaction between $Mn(CO)_5$ radicals and PBu_3 are high leading to effective formation of $Mn(CO)_4(PBu_3)$ radicals that recombine to initially give axial, equatorial, and, equatorial isomers of $Mn_2(CO)_8(PBu_3)_2$. These isomers transform over time to the more stable axial, axial isomer.[223]

Substantial progress has been made in understanding the photochemistry of the group VI and group VIII cyclopentadienyl metal carbonyl compounds, $Cp_2M_2(CO)_6$, where M = Cr, Mo, W, and $Cp_2M_2(CO)_4$, where M = Fe, Ru, Os. The photochemistry of these compounds has been recently reviewed[224] thus only the highlights of these studies will be described here. As described for $Mn_2(CO)_{10}$, these metal–metal bonded compounds possess two, wavelength dependent, photochemical reaction channels, M–M bond homolysis and CO-loss. In rigid media such as low-temperature matrices only the first of these processes is observed, while in solution both pathways are available.

Photolysis of $Cp_2M_2(CO)_6$, where M = Mo and W, in frozen matrices yields a pentacarbonyl species with both semibridging and 4-electron bridging carbonyl groups.[225] For Mo, this species is stable in solution when formed ($\lambda_{irr} =$ 308 nm) at 200 K, but decays at 240 K to $Cp_2Mo_2(CO)_6$ and $Cp_2Mo_2(CO)_4$. Photolysis of $Cp_2Mo_2(CO)_6$ at visible wavelengths results in radical formation. The recombination of these $CpMo(CO)_3$ radicals gives both gauche and trans forms. The rapid isomerization of the gauche to the more stable trans form has been followed by time-resolved IR.[226] Photolysis of $Cp^*{}_2Cr_2(CO)_4$ in solution results in the formation of $Cp^*{}_2Cr_2(\mu\text{-}CO)_3$. This species reacts with CO about 1000 times faster than $Cp_2Fe_2(\mu\text{-}CO)_3$.[227]

Photolysis of $Cp_2M_2(CO)_4$, where M = Fe, Ru, Os, in frozen matrices gives rise to CO-loss and formation of species characterized by a M=M double bond and three bridging carbonyl groups.[228] CO-loss has also been observed for $Cp^*{}_2Ru_2(CO)_4$ in 3-MP with formation of $Cp^*{}_2Ru_2(\mu\text{-}CO)_3$. Extended photolysis ejects a second CO with formation of $Cp^*{}_2Ru_2(\mu\text{-}CO)_2$.[229] For $Cp^*{}_2Fe_2(\mu\text{-}CO)_3$, a molecular structure has confirmed the core geometry.[230] In solution, both CO-loss and M–M bond homolysis are observed.

For $Cp_2Fe_2(CO)_4$, the seemingly simple CO-loss photochemistry becomes quite complex when examined using high speed methods. As summarized in Reference 224b (Fe review), excitation of the doubly bridged isomer, $Cp_2Fe_2(CO)_2(\mu\text{-}CO)_2$, gives an excited state species that decays with CO-loss in ca. 1.6 ps to singlet $Cp_2Fe_2(CO)(\mu\text{-}CO)_2$, or more likely, $Cp_2Fe_2(CO)_2(\mu\text{-}CO)(sol)$.[231] Spin crossover gives rise to the triply bridged, triplet, $Cp_2Fe_2(\mu\text{-}CO)_3$,[232] while a second channel gives a short-lived (>70 ps) singlet species corresponding to either $Cp_2Fe_2(CO)_2(\mu\text{-}CO)$ or $Cp_2Fe_2(CO)_2(\mu\text{-}\eta^1{:}\eta^2\text{-}CO)$ that relaxes to a very long-lived species $Cp_2Fe_2(\mu\text{-}CO)_2(\mu\text{-}\eta^1{:}\eta^2\text{-}CO)$. These processes are summarized in Scheme 4.

At long photolysis times (Scheme 5), the triplet $Cp_2Fe_2(\mu\text{-}CO)_3$ loses a CO to give the triplet $Cp_2Fe_2(CO)_2$. Further photolysis converts this triplet to a doubly bridged singlet, $Cp_2Fe_2(\mu\text{-}CO)_2$. These dicarbonyl species are characterized by iron–iron triple bonds.[233]

Introduction of a bridging alkylidene group suppresses radical formation and favors formation of species with bridging carbonyl groups. For example, detailed studies of the photochemistry of $Cp_2Fe_2(\mu\text{-}CO)_3(\mu\text{-}CHCH_3)$ ruled out metal–metal homolysis as a reaction pathway.[234] Photolysis of $Cp^*{}_2Fe_2(CO)_2(\mu\text{-}CO)(\mu\text{-}CH_2)$ in 3-MP matrices results in loss of CO to give $Cp^*{}_2Fe_2(\mu\text{-}CO)_2(\mu\text{-}CH_2)$. Extended photolysis results in the loss of a second CO to give $Cp^*{}_2Fe_2(\mu,\eta^{1:2}\text{-}CO)(\mu CH_2)$.[235] These processes are summarized in Scheme 6. Similarly, photolysis of $Cp_2Co_2(CO)_2(\mu\text{-}CH_2)$ in 3-MP matrices results in loss of CO to give $Cp_2Co_2(\mu\text{-}CO)(\mu\text{-}CH_2)$, while extended photolysis results in loss of the remaining CO to give an unseen species believed to be $Cp_2Co_2(\mu\text{-}CH_2)$ with a formal bond order of 3 between the cobalt atoms.[236]

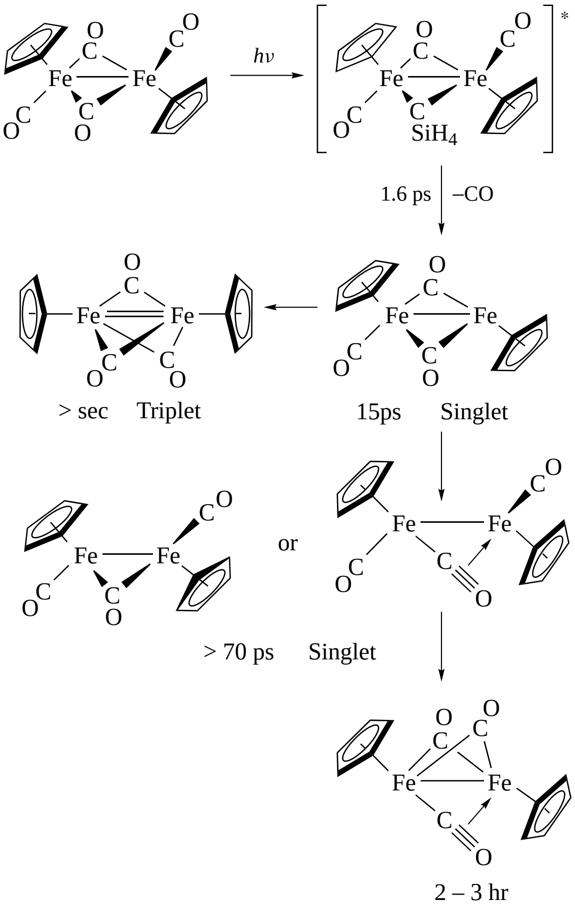

Scheme 4 Proposed overall mechanism for CO-loss process of $Cp_2Fe_2(CO)_4$. Ref. 224b

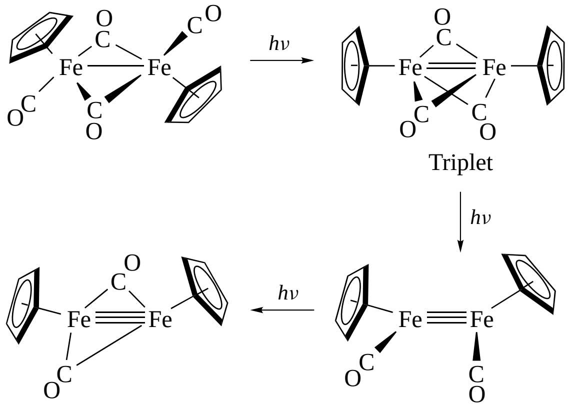

Scheme 5 Photoproducts from extended photolysis of $Cp_2Fe_2(CO)_4$. Ref. 233

Coupling of rings, for example, $(\mu\text{-}Cp\text{-}Q\text{-}Cp)M_2(CO)_n$, where Q = CH_2, CMe_2, C_2H_4, $SiMe_2$, M = Mo, W ($n = 6$),

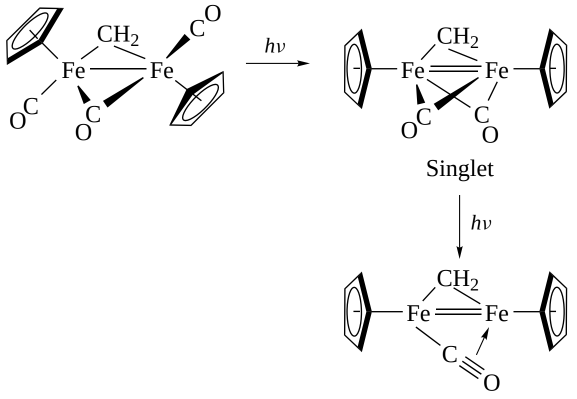

Scheme 6 Photoproducts from the extended photolysis of $Cp_2Fe_2(CO)_2(\mu\text{-}CO)(\mu\text{-}CH_2)$. Ref. 235

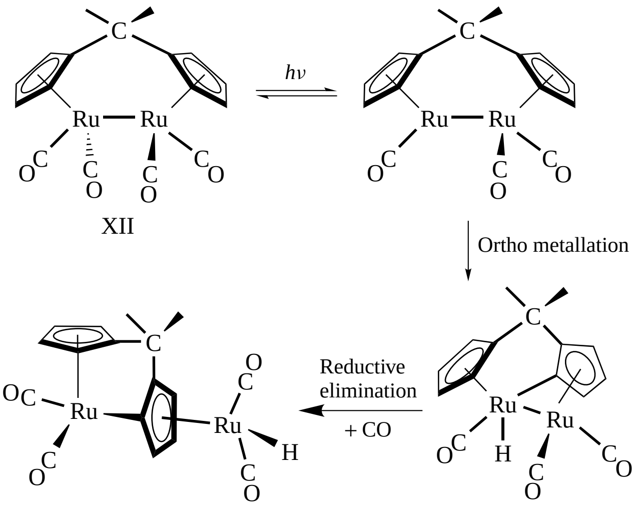

Scheme 7 Proposed mechanism of ‘twist’ reaction of (μ-η^5, η^5-Cp-CR_2-Cp)$Ru_2(CO)_4$. Ref. 237b

Fe, Ru ($n = 4$), also suppresses radical formation upon photolysis and leads to CO-loss species with a mixture of bridging and semibridging carbonyl groups.[237] Since the coupled bridges also preclude formation of linear species stabilized by multiple bridging COs, these compounds tend to undergo simple ligand exchange reactions.[238] In the absence of potential ligands, Mo, W, and Ru compounds undergo an internal C–H activation, twist reaction, with formation of a metal-to-ring sigma bond and transfer of the ring hydrogen to the second metal atom to form a hydride (Scheme 7). In the presence of chlorine-containing solvents, the corresponding chloride compounds can be isolated. The kinetics of the back reaction from the twist hydride, (μ, η^5:$\eta^{5:1}$-C_5H_4-CMe_2-C_5H_3)[$Ru(CO)_2$][$Ru(CO)_2$)H] are cleanly first order, but the kinetics of the formation of the twist hydride itself are more complex.[239] A very similar photochemistry has been observed with the heterobimetallic compounds (μ-Cp-CR_2-Cp)$RuM(CO)_5$, where R = H, Me, M = Mo, W.[240]

Photolysis of Cp_2 $W_2(CO)_4$(μ-dppm) in which the metals are tethered with a bidentate dppm ligand leads to C–H oxidative addition reactions analogous to the twist reactions described above (Scheme 8). The product in this case, (μ-$\eta^{5:1}$-C_5H_4)(η^5-C_5H_5)$W_2(CO)_3$(μ-H)(μ-dppm), undergoes additional decarbonylation to yield (η^5-C_5H_5)$_2$(μ-CO)$_2$(μ-dppm) in which the oxidative addition is reversed.[241] The mixed W, Mo analog undergoes CO-loss to give (μ-$\eta^{5:1}$-C_5H_4)(η^5-C_5H_5)$MoW(CO)_3$(μ-H)(μ-dppm) in which C_5H_4 is η^5 bonded to the tungsten and η^1 bonded to molybdenum.[242]

Photolysis of Re–Re bonded $Cp^*{}_2Re_2(CO)_4$(μ-η^1, η^1-$MeO_2CC_2CO_2Me$) with fluorescent light results in the clean rearrangement to $Cp^*{}_2Re_2(CO)_4$(μ-η^2, η^2-$MeO_2CC_2CO_2Me$). Further photolysis with UV light yields $Cp^*{}_2Re_2(CO)_2$(μ-CO)(μ-η^2, η^2-$MeO_2CC_2CO_2Me$).[243] Time-resolved IR studies indicate that an intermediate is formed within <150 ns of irradiation. This intermediate transforms cleanly to $Cp^*{}_2Re_2(CO)_4$(μ-η^2, η^2-$MeO_2CC_2CO_2Me$) over a period of several ps. It is proposed that photolysis results in Re–Re bond homolysis and that the resulting acetylene bridged diradical rearranges to a bis(metallacarbene), or 1, 4-dimetallabutadiene (Scheme 9).[244]

Photolysis of [μ-η^5,η^5-$(C_5R_4)_2SiMe_2$]$Ru_2(CO)_4$, R = H, Me, results in a dramatic molecular rearrangement with formation of (μ-$\eta^{5:1}$-C_5R_4)(μ-η^5-$C_5R_4SiMe_2$)[$Ru(CO)_2$]$_2$ in which the Ru–Ru bond and one Cp–Si bond are broken (Scheme 10).[237b,245] Similarly, photolysis of (μ-η^5, η^5-$C_5H_4C_5H_4$)$Ru_2(CO)_4$ breaks both the Ru–Ru and Cp–Cp bonds resulting in the thermally reversible formation of (μ-η^5-C_5H_4)$_2$[$Ru(CO)_2$]$_2$ (Scheme 11).[246] In both cases, these appear to be internal transformations.

Photolysis of $Cp_2M_2(CO)_6$, M = Mo and W, or $Cp_2Fe_2(CO)_4$ under H_2 pressure gives rise to the corresponding metal hydrides, $CpM(CO)_nH$, by a mechanism that involves oxidative addition to the CO-loss species followed by reductive elimination to give $CpM(CO)_nH$ and $CpM(CO)_{n-1}H$

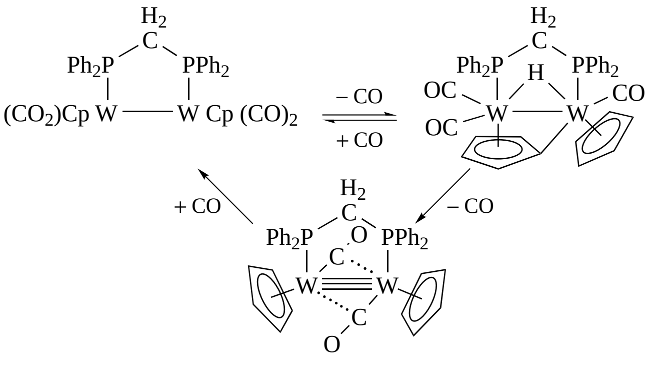

Scheme 8 Cp-H oxidative addition upon photolysis of $Cp_2Mo_2(CO)_4$(μ-dppm). Ref. 241a

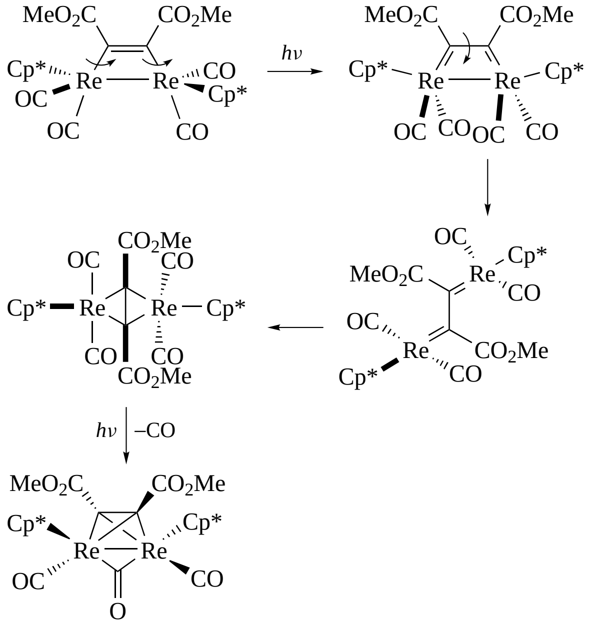

Scheme 9 Photochemical rearrangement of $Cp^*_2Re_2(CO)_4(\mu\text{-}MeO_2CC_2CO_2Me)$ via dimetallabutadiene intermediate. Ref. 244

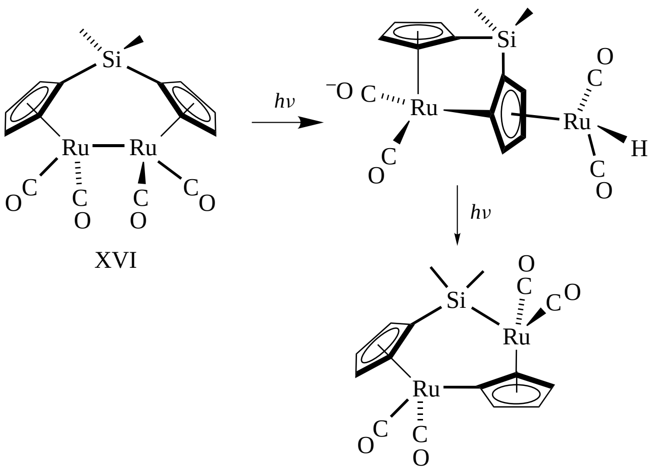

Scheme 10 Sequential photolysis mechanism of $(\mu\text{-}\eta^5, \eta^5\text{-}Cp\text{-}SiMe_2\text{-}Cp)Ru_2(CO)_4$ resulting in Si–Cp bond breaking (Ref. 237b)

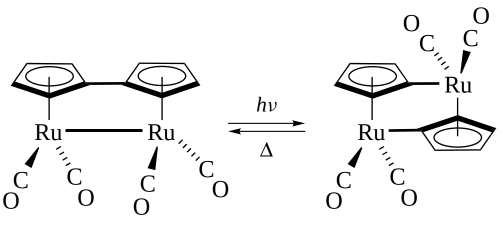

Scheme 11 Ru–Ru and Cp–Cp bond breaking upon photolysis of $(\mu\text{-}\eta^5, \eta^5\text{-}Cp\text{-}Cp)Ru_2(CO)_4$ (Ref. 246)

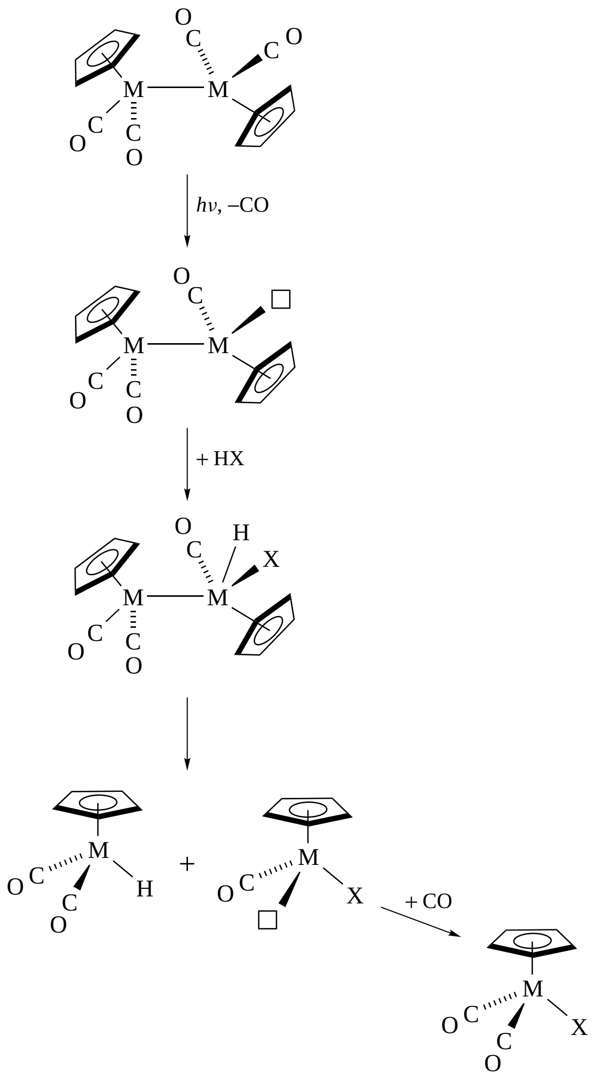

Scheme 12 Mechanism of oxidative addition of H_2 or $HSnBu_3$ to $Cp_2M_2(CO)_4$ or $Cp_2M_2(CO)_6$ CO-loss products (Ref. 247)

(Scheme 12). Subsequent CO capture by this latter species gives a second mole of product.[247] It has been independently shown that $CpM(CO)_nH$, where M = Ru, Os, species lose CO upon photolysis in frozen matrices[228d] (see my Ru, Os paper).

Flash photolysis of the heterobinuclear compound, $Cp(CO)_3Mo\text{-}Co(CO)_4$, in 3MP glass results in loss of CO to form a solvated species with all terminal carbonyl groups. This species rearranges to give a product with a bridging carbonyl group. Comparison of the carbonyl bands of the solvated species with a number of derivatives of $CpMo(CO)_3$ and $Co(CO)_4$ led to the proposal that the initial CO-loss occurs only from the Mo. Photolysis of $Cp(CO)_3Mo\text{-}Co(CO)_3L$ and $Cp(CO)_2LMo\text{-}Co(CO)_3L$, where L = PBu_3, generates a complex set of CO-loss intermediates.[248] In solution, photolysis homolysis of the Mo–Co bond gives rise to radicals.[249]

7 REACTIONS OF PHOTOCHEMICALLY GENERATED RADICALS

The well known formation of radicals by M–M bonded bimetallic compounds has been exploited by Tyler and his group in the study of radical cage effects in a variety of media. Initial studies by this group on photodegradable polymers containing $Cp_2Mo_2(CO)_6$ or $Cp_2Fe_2(CO)_4$ units in the polymer backbone[250] led to a recognition that various ring substituted $Cp'_2Mo_2(CO)_6$ compounds could serve as probes of cage effects in solvents. A photochemical cage-efficiency factor, F_{cP}, defined as kcP/(kcP + kdP), where kcP is the rate constant for cage recombination of a photochemically generated radical cage pair and kdP is the rate constant for cage escape, is measured by determining the quantum yield of $Cp'Mo(CO)_3Cl$ formation as a function of viscosity in a solution consisting of two solvents of different viscosity and CCl_4 as a radical trap.[251] It is assumed that at sufficiently high concentrations of CCl_4, all radicals that escape the solvent cage will be trapped, thus it would be expected that formation of $Cp'Mo(CO)_3Cl$ should increase as solvent viscosity decreases as is observed. Alternatively, as the mass of the $Cp'Mo(CO)_3$ radical increases with the introduction of ring substituents the F_{cP} should increase.

A femtosecond photolysis study of $Re_2(CO)_{10}$ in CCl_4 and hexane has been interpreted in terms of the solvent acting as a viscous medium for $Re(CO)_5$ radicals.[252] Those $Re(CO)_5$ radicals that do diffuse out of the solvent cage may react with the chlorinated solvent to form $Re(CO)_5Cl$. The absence of IR bands for intermediates other than the $Re(CO)_5$ radical rule out the possibility of a 19-e intermediate, and support a mechanism in which involves only C–Cl bond activation.[253]

Photochemically generated radicals may also abstract halide ligands from other metal complexes. The reaction between $CpW(CO)_3$ radicals and $ClRh(dmgH)_2PPh_3$ yields $CpW(CO)_3Cl$ and $[Rh(dmgH)_2PPh_3]_2$. Kinetic studies confirm that the reaction proceeds by simple halide abstraction followed by dimerization of the $[Rh(dmgH)_2PPh_3]$ radical.[254]

8 METAL TO LIGAND CHARGE TRANSFER PROPERTIES

A substantial literature exists describing the photochemistry and photophysics of $Ru(bipy)_3{}^{2+}$ and related compounds, and progress on the study of these and related compounds has continued unabated since the first edition of the Encyclopedia of Inorganic Chemistry. Some properties of these compounds, such as their ability to transfer electrons, have been exploited by Gray, Barton, and others to explore the electron transmission through proteins and DNA, while a second thrust of research has been directed toward injecting electrons into the conduction band of wide band gap semiconductors such as TiO_2. These applications will be discussed below. As we have seen above, the availability of new ultrafast spectroscopic detection methods have pushed the examination of charge transfer processes into the femtosecond range. Driven partially by the availability of time-resolved IR and resonance Raman methods mixed carbonyl/diimine compounds have been extensively examined.

$Ru(bipy)_3{}^{2+}$ is the prototype of a very large family of MLCT species. In the standard model of the photoprocesses of this compound, a photon excites the molecule to an initial Frank-Condon singlet state, ^{1}MLCT, that rapidly transforms to a triplet, ^{3}MLCT, with a quantum yield of near unity.[255] Femtosecond pump probe experiments have established a half-life of about 100 fs for the formation of the triplet state.[256] Recent studies utilizing femtosecond time-resolved fluorescence emission spectroscopy has observed fluorescence emission from the Frank-Condon state itself and the lifetime of this state has been estimated to be 40 ± 15 fs.[257]

A long standing question concerning the degree of charge delocalization in the initially formed ^{3}MLCT state has been resolved. It has been known for some time that the long-lived ^{3}MLCT state of $Ru(bipy)_3{}^{2+}$ has a dipole of ca. 14 D,[258] requiring that the charge be localized on one of the bipyridinyl ligands. Time-resolved IR studies have unambiguously established the charge localization nature of the excited state species on the 100-ns time scale.[259] Absorption,[260] transient circular dichroism,[261] Raman[262] and electroabsorption (Stark effect)[263] experiments suggested the direct formation of a localized excited state, while emission spectral studies[264] lent support for an initially formed delocalized state that rapidly evolves to a localized state. Very recent ultrafast absorption anisotropy measurements provide strong evidence for a delocalized intermediate that decays to a localized intermediate in 50−173 fs depending upon the solvent. It was suggested that the charge localization is coupled to or controlled by the inertial solvent dynamics occurring in response to the photo-induced charge transfer.[265] Variable-temperature emission studies have been used to probe the coupling between solvent dynamics and solute structure.[266]

A large number of studies have been directed toward understanding the excited state behavior of metal complexes containing both carbonyl and diimine ligands. The presence of the carbonyl chromophore serves as a reporter ligand for electronic changes taking place within the molecule. In general, MLCT transitions increase the positive charge at the metal thus reducing the extent of back bonding and causing metal carbonyl vibrations to shift to higher frequencies. Interligand transitions such as IL$\pi\pi^*$ states often result in a modest increase in electron density at the metal and hence a shift of the carbonyl frequencies to lower values. Ligand field transitions that were once believed to play a significant role in the photophysics of these species have been shown by calculation to be far too large to meaningfully participate. Instead, M → CO MLCT transitions appear to be more energetically favorable than previously believed. We noted above in the context of metal carbonyl complexes the radical transformation this necessitates in our understanding of events such as photochemical carbonyl-loss. The dominant ligands examined in these studies have been bipyridinyl, phenanthroline, and their many derivatives, and bulky alkyl derivatives of 1, 4-diazabutadiene (DAB). Some representative examples of compounds studied include: $M(CO)_4$(diimine), where M = Cr, Mo, W, $M(CO)_3X$(diimine), M = Mn, Re, X = H, halide, alkyl, and $Ru(CO)_2(X)(R)$(diimine), where X = halide.

The group VI compounds $M(CO)_4$(DAB) were first prepared by Tom Dieck and his coworkers in the 1960s[267] and their strong solvatochromism arising from the antiparallel dipole of the excited state was reported shortly thereafter.[268] Resonance Raman studies established the relationship between the MLCT absorption and several molecular vibrations, most notably the carbonyl stretching frequencies.[269] The resonance Raman spectra of this class of compounds has been reviewed.[270] Vlček has published a detailed review of the photophysics and photochemistry of the group VI diimine compounds.[271]

As noted above, strong bands in the visible spectra of $M(CO)_4$(diimine) complexes are associated with a MLCT transition that is sensitive to the character of the ligand as well as the solvent environment. In the light of high level TD-DFT[272] and CASSCF/CASPT2[273] calculations, a weaker band or shoulder in the 400–370 nm region that had been associated with ligand field transitions[274] has now been reassigned to an M → CO MLCT transition. The high molar absorptivity of the bands at ca. 400 nm in $M(CO)_4$(diimine) and $M(CO)_4$(en) (for which there are no accessible ethylenediamine π^* states for MLCT) lend further support to this reassignment.

The photochemical loss of CO from $M(CO)_4$(diimine) complexes continues to be exploited for synthetic purposes,[275] and as a probe for the photophysics of the excited states. Photosubstitution quantum yields depend upon the wavelength of irradiation, nature of the diimine ligand, the metal, and the incoming ligand. Dissociative ligand field excitations have been observed while the mechanism of substitution upon MLCT excitation depends upon the nature of the metal and incoming ligand.[276] A long standing belief that ligand field dissociations were attributable to ^{3}LF states have been challenged with observations on $W(CO)_4$(en),[277] $Cr(CO)_4$(bipy)[278] and $W(CO)_5L$, L = 4-cyanopyridine, 4-formylpyridine[279] that suggest that photodissociation occurs directly from the singlet state prior to intersystem crossing to form the triplet. In light of the discussion above concerning the reassignment of LF transitions to M → CO MLCT transitions, it is likely that the M → CO MLCT singlet may be the actual reactive state.

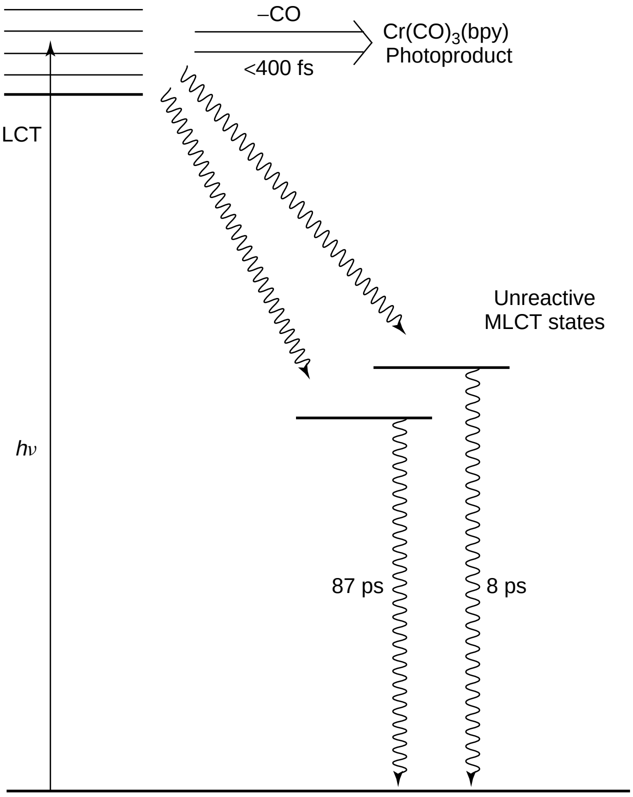

Figure 16 Excited state dynamics of $Cr(CO)_4$(bipy). (Reprinted with permission from Ref. 280b. © 1999 American Chemical Society)

The role of singlet and triplet MLCT states has also been brought into question. In the case of $Cr(CO)_4$(bipy) excitation into the MLCT band gives rise to an excited singlet Frank-Condon species that decays in less than 400 fs either through a prompt loss of an axial CO, or relaxation to two triplet states that decay independently (8 and 87 ps, respectively) to the ground state.[280] The excited state dynamics of $Cr(CO)_4$(bipy) is illustrated in Figure 16.

The group VII diimine compounds, $M(CO)_3X$(diimine), where X = halide, H, Me, Et, Bz, or metal fragments such as $Mn(CO)_5$, or $M(CO)_4L$(diimine), where L = nitrogen base, have been extensively studied. Notably, excited states of the rhenium compounds are better reducing and oxidizing agents than the ground-state species,[281] lending themselves to processes such as CO_2 reduction.[282] $\{Re(CO)_3[P(OEt)_3]bipy\}^{1+}$ has been shown to be a particularly efficient catalyst for the reduction of CO_2.[283]

Examination of the emission behavior of $Re(CO)_3X$(diimine), X = Cl, Br, I, diimine = bipy, *i*Pr-DAB, established that variation in halogen alters both the energy of the emission and the character of the lowest emitting state itself. For chloride, the lowest energy excited state is MLCT, while for iodide the excited state gains more halide character and is better described as an X → π^*(diimine) XLCT excitation.[284]

A qualitative MO scheme comparing the chloride and iodide complexes is presented in Figure 17. The XLCT states are characterized by longer lifetimes and are better luminophores because of higher emission quantum yields.[285] MO calculations on the manganese analogs show a mixing of metal and halide contributions to the excited states.[286] The photodissociation and electronic spectroscopy of the hypothetical $Mn(CO)_3H(H\text{-}DAB)$ has been modeled using wave packet propagations on CASSCF/MR-CCI potentials. Relevant to the nature of the excited states, a low lying, visible absorption band was found to correspond to a $3d_{xz} \rightarrow \pi^*$(DAB) MLCT excitation, while a UV band had components of both $3d_{yz} \rightarrow 3d_{xy}$ and $\sigma_{\text{Mn-H}} \rightarrow \pi^*$(DAB) excitations.[287]

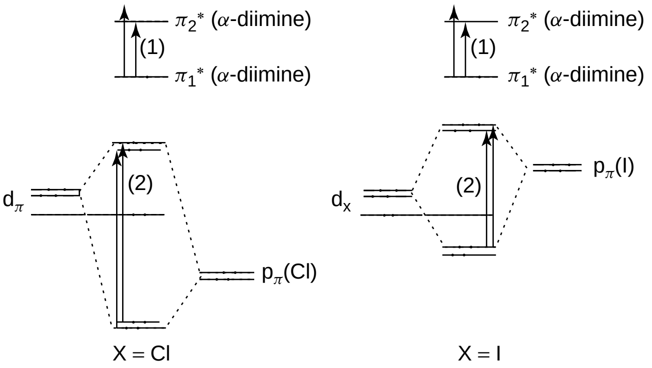

Figure 17 Qualitative MO scheme for $Re(CO)_3Cl$(diimine) and $Re(CO)_3I$(diimine). (Reprinted with permission from Ref. 285b. © 1996 American Chemical Society)

The shifts in excited state character described above arises from the relative energies of the d orbitals and either the sigma bond to X or the p(π) electrons on X. This effect is clearly seen with the alkyl series: Me, Et, and Bz. Photolysis of $Re(CO)_3R(i\text{-Pr-DAB})$ results in efficient homolysis for Et and Bz, but not for Me. These observations were rationalized by comparing the relative energies of the MLCT and σ_b(Re–R)π^* states.[288] Photoelectron spectra of the methyl derivative demonstrated that the ionization energy of the σ_b (Re–Me) orbital is higher than that of the d_π(Re) orbitals. While the photoelectron spectrum of the ethyl complex could not be recorded, photoelectron spectra of analogous $(CO)_5MM(CO)_3(i\text{-Pr-DAB})$, where M and M′ = Mn or Re, were recorded. In the metal–metal bonded compounds the σ_b orbitals were found to have ionization energies below those of the d_π(Re) orbitals.[289] These metal–metal bonded species are known to undergo homolysis upon photolysis.[290] The excited state of $Re(CO)_3Bz(i\text{-Pr-DAB})$ has been directly observed by time-resolved electronic and IR spectroscopies. The relatively long lifetime of the excited state species (ca 250 ns) and the relatively small positive shift of the carbonyl frequencies both are indicative of a $\sigma\pi^*$ MLCT excited state rather than a Re → DAB MLCT state.[291] Both the methyl and benzyl derivatives of $Re(CO)_3R(bipy)$ undergo homolysis upon UV photolysis.[292]

Very recent ultrafast dynamics studies have demonstrated that the Frank-Condon ^{1}MLCT state of $Re(CO)_3R(dmb)$, dmb = 4,4′-dimethyl-2,2′-bipyridine, undergoes rapid (≤400 fs for Me, ca. 800 fs for Et) branching into two channels, a homolysis channel via a ^{3}SBLCT (triplet σ-bond to ligand charge transfer) or to a ^{3}MLCT state. For the methyl derivative, the ^{3}MLCT state is lower in energy than the ^{3}SBLCT state. The ^{3}MLCT state decays with a 35 ns lifetime to the ground state. Methyl homolysis occurs with a quantum efficiency of 0.4 (293 K). In contrast, the ^{3}MLCT state of the ethyl derivative lies above that of the ^{3}SBLCT state and can decay into it with a lifetime of 213 ps (in CH_2Cl_2). The homolysis quantum yield of the ethyl derivative is unity with both prompt and delayed channels to homolysis.[293] These pathways are illustrated in Figure 18. Chemically induced dynamic electron polarization pattern (CIDNEP) studies of the photochemically generated alkyl radicals support a triplet assignment to the dissociative state.[294] CASSCF/MR-CCI calculations on $M(CO)_3(H)(H\text{-}DAB)$, where M = Mn, Re, complexes underscore the significance of the relative energies of the MLCT and SBLCT states in directing the progress of these homolysis reactions.[295]

The photochemical behavior of the $Mn(CO)_3X$(diimine) compounds differs from that of the rhenium compounds in that CO-loss becomes a significant competitive process. For example, $Mn(CO)_3X(bipy)$, where X = Cl, Br, I, and $Mn(CO)_3X(i\text{-Pr-DAB})$, where X = Cl, Br, and Me, have all been shown to lose CO as a primary photochemical step.[296] The differences in photochemistry between the rhenium and manganese compounds have been attributed to the differing M–CO bond strengths.[297] For $Mn(CO)_3Bz(i\text{-Pr-DAB})$ and the metal–metal bonded derivatives,[298] $(CO)_5Mn\text{-}Mn(CO)_3$(diimine), where diimine = bipy, *p*-tol-DAB, radical formation is observed. Perhaps the most interesting case (Scheme 13) is that of *fac*-$Mn(CO)_3X(bipy)$ for which initial photolysis results in loss of CO from an equatorial position followed by a rapid shift of the halide to the open position creating an axial vacancy.[299] Recapture of CO yields *mer*-$Mn(CO)_3X(bipy)$. Surprisingly, the *mer* isomer undergoes photolysis with homolysis of the Mn–X bond.[300] A DFT analysis has provided an explanation of both the initial equatorial CO-loss and halide shift events.[301]

Charge-transfer-to-solvent reactions are a special class of MLCT processes. Commonly a halogenated solvent serves as the acceptor with formation of a halide ion and a radical. Subsequent reaction chemistry between the oxidized metal species and either the halide ion or radical may take place.[302] For example, photolysis of $Fe(et_2dtc)_2(CO)_2$ in $CHCl_3$ results in formation of $Fe(et_2dtc)_2Cl$ via electron transfer to solvent from a MLCT excited state.[303] Similarly, photolysis of $(Cp\text{-}CH_2\text{-}Cp)Fe_2(\mu\text{-}CO)_2(\mu\text{-dppm})$ in $CHCl_3$

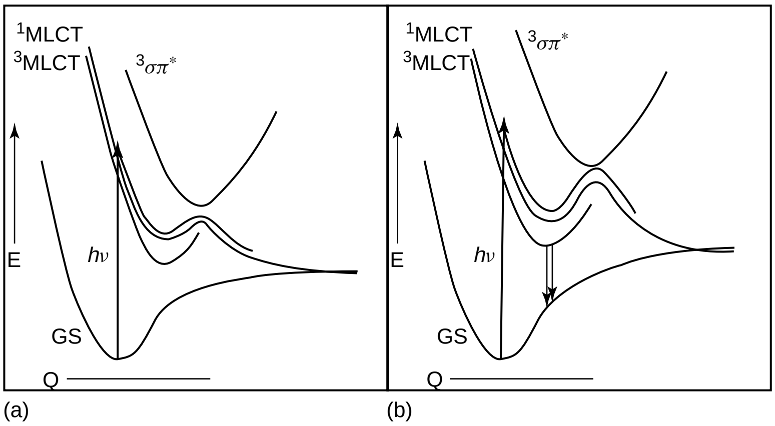

Figure 18 Schematic representation of the potential energy curves of the ground, ^{3}MLCT, ^{1}MLCT, and $^3\sigma\pi^*$ states of $Re(CO)_3R(dmb)$ with R = Et, Bz, and *i*-Pr (a) and R = CH_3 and CD_3 (b). Note that the barrier to dissociation for CH_3/CD_3 is substantially larger than that of Et, Bz, and *i*-Pr accounting for the differences in radical quantum yield. (Ref. 293a. Reproduced by permission of Wiley-VCH)

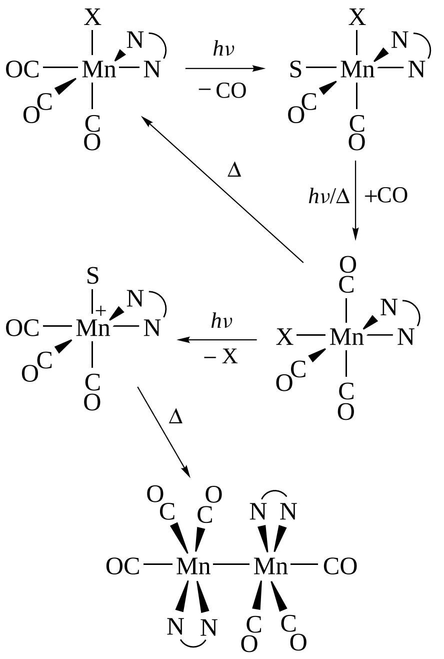

Scheme 13 Mechanism of *fac*-$Mn(CO)_3X$(diimine) to *mer*-$Mn(CO)_3X$(diimine) and subsequent loss of X radical. Ref. 300a

results, after workup, in the isolation of $(CHOCp\text{-}CH_2\text{-}Cp)Fe_2(\mu\text{-}CO)_2(\mu\text{-}dppm)$ arising from the reaction of a $CHCl_2$ radical with the radical cation of $(Cp\text{-}CH_2\text{-}Cp)Fe_2(\mu\text{-}CO)_2(\mu\text{-}dppm)$ followed by transformation to the aldehyde.[304] Photolysis of $CpL_2M{\equiv}CR$, where M = Mo, W, L = CO, $P(OMe)_3$, R = Ph, Me, cyclopropyl in halogenated solvents results in oxidation of the complex. Electron transfer from the MLCT excited state of the carbene to solvent is the likely cause of oxidation.[305]

9 APPLICATIONS OF CHARGE TRANSFER EXCITATION

As noted above, photochemical MLCT excited state species can be better electron acceptors and donors than their ground-state species. The photochemical reduction of CO_2 was noted in which the excited state of photostable $Re(CO)_3X$(diimine) complexes interact with a sacrificial electron donor to give $[Re(CO)_3X(diimine)]^{1-}$.

Direct transfer of an electron from the excited state to the conduction band of semiconductors has been extensively explored.[306] Of particular interest is the development of low cost alternatives to silicon based photovoltaic devices.[307] Efficient electron transfer is achieved when an excited state of sensitizer species is matched to the conduction band energies of a semiconductor. For example, the Frank-Condon states of $Ru(bipy)_2X_2$, where X = SCN, CN, or $Ru(CO)_3Cl(bipy)$ and related species are compatible with the conduction bands of TiO_2, ZnO, and SnO_2 (Figure 19). Direct measurement of the rate of electron injection has been achieved by nano- or femtosecond mid-IR measurements[308] of a broad feature (1600–1800 cm^{-1}) assigned to electrons in the conduction band of TiO_2.[309] The rates of injection have been found to be dependent upon the nature of the sensitizer, the semiconductor, and the nature of their interaction. For $Ru(bipy)_2(SCN)_2$ type sensitizers, the rate of electron injection into TiO_2, SnO_2, and ZnO were found to be ~50 fs, ~4 ps, and ~100 ps, respectively. The differences were attributed to a d orbital based conduction band in TiO_2 and s orbital based conduction band in SnO_2 and ZnO. Alternately this can be described as a difference in the density of states in the conduction band. A detailed study of the electron transfer revealed two channels. A fast (fs) injection is attributed to electron transfer from the singlet Frank-Condon excited state,[310] while slower (ps) transfer arises from a long-lived triplet MLCT state.[311] The sensitivity of the electron injection rates to wavelength and to

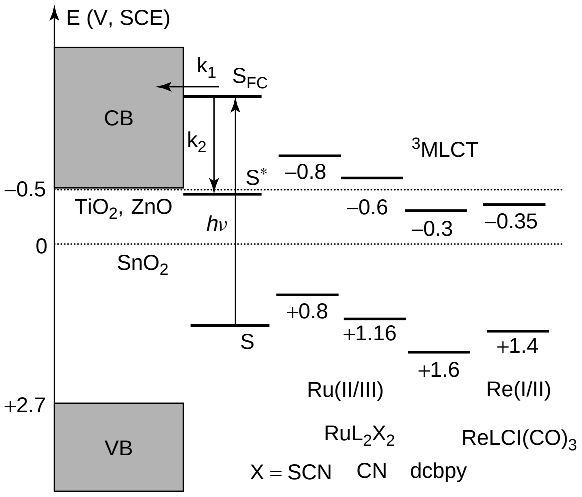

Figure 19 Schematic diagram of electron injection and energetics of sensitizers and semiconductors. (Reprinted with permission from Ref. 313. © 2001 American Chemical Society)

the redox potential of the sensitizer species provides further support for this model.[312] It is suggested that the interligand electron transfer processes may play a role in determining the rates from the triplet state. Lian and his coworkers have presented a comprehensive review of these studies.[313]

The length of the spacer connecting a sensitizer to the surface has also been shown to be significant with the rate of electron transfer decreasing with increasing spacer length.[314] For carboxylate functionalized sensitizer molecules, the number of carboxylate groups, that is, the number of possible points of attachment with the metal oxide surface, determines the efficiency of electron transfer.[315] Comparisons of electron injection kinetics for TiO_2 sensitized with Ru(4,4′-dicarboxy-2,2′-bipyridyl)$_2$(SCN)$_2$, and its tetrabutyl ammonium salt provide evidence for a role for coadsorbed protons in the electron injection process.[316]

As noted above, MLCT excited states of diimine metal complexes are both better reductants and oxidants than the ground-state species. This property has been exploited by Gray, Barton, and others for the study of proteins, DNA, and other biological molecules. Flash/quench experiments were first developed to provide a high driving force method to measure rates of electron transfer in proteins.[317] In these experiments an excited diimine complex, typically a member of the $Ru(bipy)_2(diimine)^{2+}$ family of complexes, is oxidatively quenched with $Ru(NH_3)_6{}^{3+}$, $Co(NH_3)_5Cl^{2+}$, or methyl viologen, or reductively quenched with *p*-methoxy-*N*,*N*-dimethylaniline to yield a highly active redox species.

Barton has carried out extensive studies into the transport of charge through DNA utilizing the flash/quench method to inject charge.[318] In the absence of imperfections to the DNA stack, electron transport to sites 200 Å away from the point of charge injection have been observed.[319] These studies, which have been extensively reviewed,[320] forced a significant paradigm shift[321] in understanding of the mechanism of charge transport through the overlapping π-stack of the base pairs in DNA. Indeed, disruption of charge transport is diagnostic of base bulges,[322] mismatches,[323] or the presence of nonaromatic residues[324] in the DNA π-stack. The importance of intercalation of the metal sensitizer has been established through comparisons of intercalating and nonintercalating species covalently bound to the terminus of an oligonucleotide sequence.[325] In these studies, the 5′-G of a 5′-GG-3′ guanine doublet served as a measure of charge transport as this doublet has been shown to be particularly sensitive to oxidative damage.[326]

Studies of the rate of electron transport through the DNA using acceptors and donors that were intercalated but not covalently bound to the DNA established very high rates of ground-state recombination on the order of 10^{10} sec^{-1}, but ambiguities as to the relative spacing of the intercalated species complicated the interpretation.[327] To fully clarify the ability of the DNA stack to transport charge, a series of metal modified DNA duplex assemblies were prepared in which donor and acceptor species were covalently bound to the ends of the assembly (Figure 20). Using 15 base pair assemblies donor/acceptor distances on the order of 41 Å could be achieved and a lower limit of 3×10^9 sec^{-1} was measured.[328]

The broad field of photoreactions between Ru and Os complexes and DNA has been reviewed with an emphasis on tuning the excited state properties of the organic ligands so as to optimize electron transfer as opposed to ligand substitution.[329]

Gray and his coworkers have examined electron transport through proteins utilizing flash/quench techniques.[330] Recent studies have employed $Ru(bipy)_3{}^{2+}$ bound to an alkyl or aryl chain terminated with imidazole, adamantly or ethylbenzene functions. The chains thread themselves down channels in proteins placing the functionality within the pocket of a metalloenzyme active site where they effectively transfer charge from the ruthenium complex to the interior of the protein.[331] The P450 conjugate with ethylbenzene terminated $Ru(bipy)_3{}^{2+}$ is illustrated in Figure 21. Very high speed charge transfer using these materials permits the creation of reaction intermediates that do not accumulate in significant quantities using natural reductants.

Electron transport between cubane [Fe_4S_4] clusters,[332] cytochrome *c*,[333] or Cu^{1+} centers in blue copper proteins[334] and the periphery of the proteins has been examined by complexing ruthenium species to surface histidines. In the case of the iron sulfur cubane in *Chromatium vinosum,* four surface histidines served as points of ruthenium attachment. The rates of electron transport from the Fe_4S_4 core to ruthenium varied over two orders of magnitude and were used to diagnose the preferred channel for electron transport. Cysteine and lysine residues have also been used as binding sites in studies of cytochrome *c*[335,336] and cytochrome P450 cam[337] proteins.

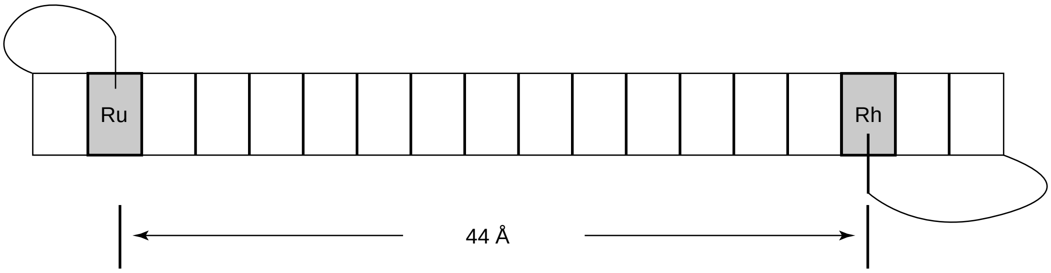

Figure 20 Schematic of the doubly modified duplex showing the most probable (50%) separation of the intercalated metal complexes. (Reproduced by permission of Ref. 327)

Ru-Im

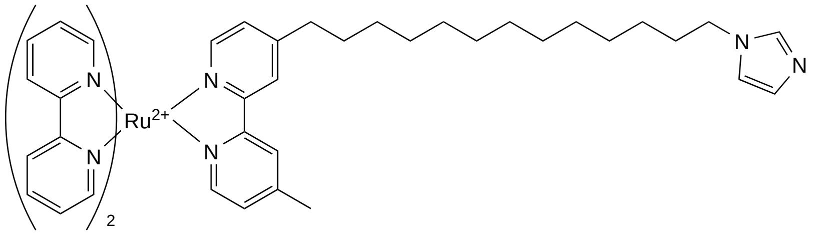
N
N
Ru2+
N
N
N
N
2

Ru-Ad

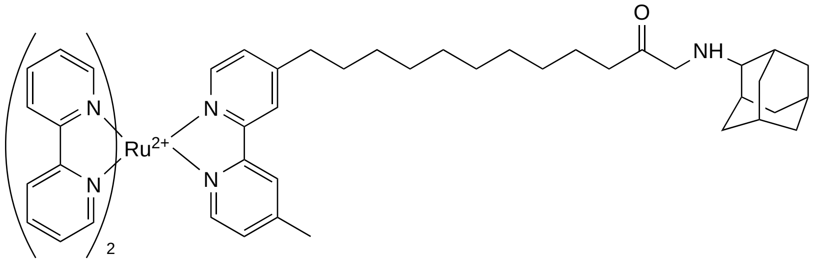
O
NH
N
N
Ru2+
N
N
2

Ru-EB

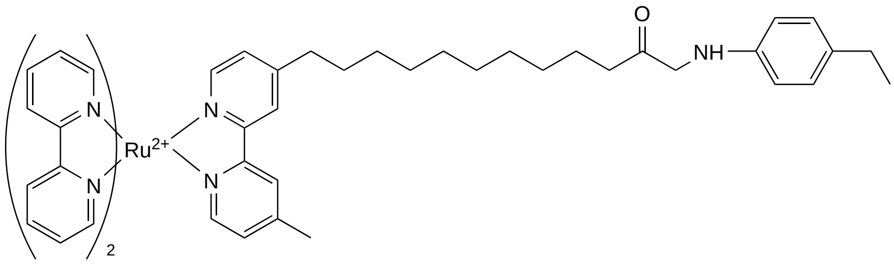
O
NH
N
N
Ru2+
N
N
2

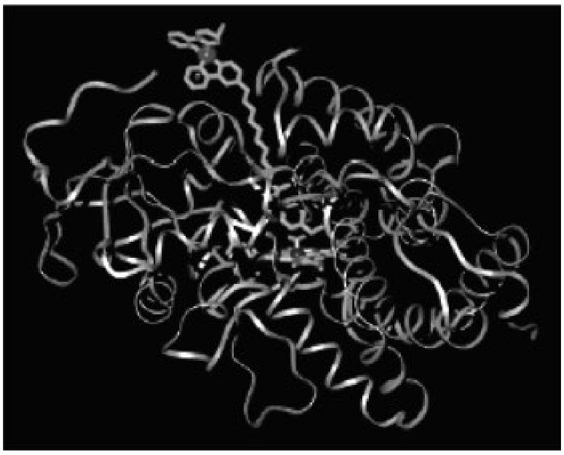

Figure 21 View of the Ru-EB/P450 complex. (Ref. 331b. Reproduced by permission of Wiley-VCH)

The photochemical electron transfer triggering of folding of proteins such as cytochrome *c* has been examined.[338]

10 LIGAND REACTIONS AND REARRANGEMENTS

Time-resolved optical and time-resolved IR methods have been employed by Ford and his coworkers to probe the intermediates involved in the migratory insertion of methyl groups to carbonyl groups utilizing the principle of microscopic reversibility. Photolysis of metal-acyl derivatives, $M(CO)_nC(O)Me$ typically results in loss of CO. For $Mn(CO)_5C(O)Me$, a long-lived, transient species was observed whose spectrum showed only modest sensitivity to solvent.[339] These results were interpreted in terms of an η^2-acyl intermediate similar to that observed for $Co(CO)_3C(O)Me$ in argon matrices.[340] In contrast, room temperature, time-resolved IR studies of $CpFe(CO)_2C(O)Me$ and $IndFe(CO)_2C(O)Me$ suggest that a solvento species is the more likely intermediate in all solvents studied.[341] Figure 22 presents a 3-D stack plot of the absorbance changes in the carbonyl region for $CpFe(CO)_2(C(O)CD_3)$. In low-temperature (195 K) MCH, an unusually large frequency shift of the intermediate compared to the unphotolyzed species was taken as evidence of an η^2-acyl intermediate. It was suggested that there may be a strong temperature dependence of the solvated and η^2-acyl forms in weakly coordinating solvents. These studies have been reviewed.[342]

Aqueous solutions of $MeReO_3$ have been found to be very light sensitive. Analysis of the reaction products established methane and ReO_3 as products. In chlorinated solvents, CH_3Cl formed pointing to C–Re bond homolysis as a likely mechanism. Molecular orbital diagrams of $MeReO_3$ suggest that the HOMO is the Re-CH_3 bond with an e* LUMO that is antibonding toward the Re=O bonds. LMCT transitions would be expected to result in the observed bond homolysis (Figure 23).[343] In Ar matrices, photolysis of $MeReO_3$ gives rise to $CH_2{=}ReO_2OH$. It is proposed (Scheme 14) that the primary photochemical event is Re–C bond homolysis, and

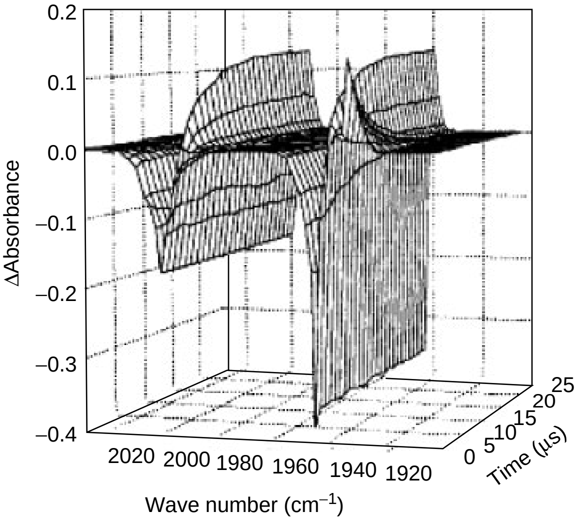

Figure 22 3-D stack plot of TRIR spectra following 308 nm flash photolysis of $CpFe(CO)_2(C(O)CD_3)$ in cyclohexane. (Reprinted with permission from Ref. 341a. © 1998 American Chemical Society)

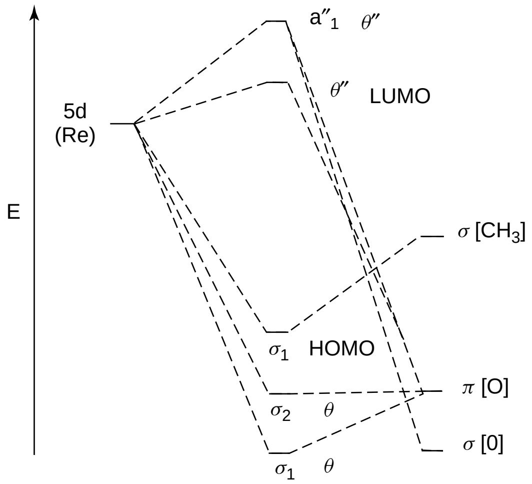

Figure 23 Qualitative MO diagram of CH_3ReO_3. (Reprinted with permission from Ref. 343. © 1991 American Chemical Society)

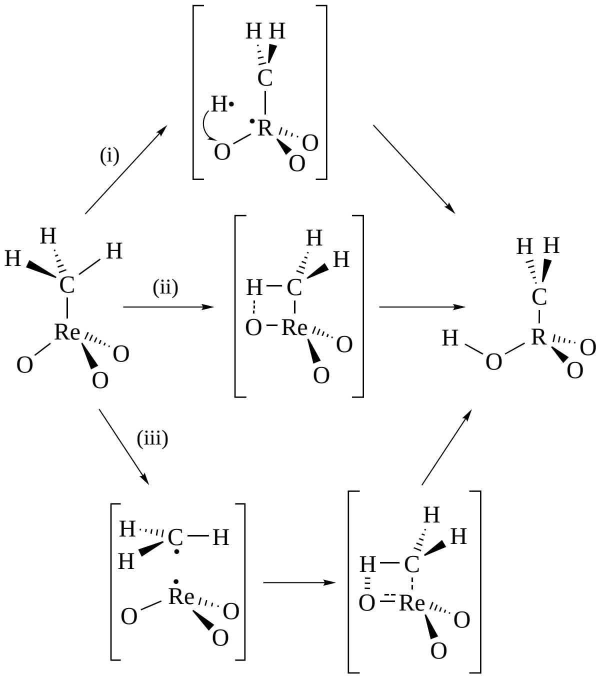

Scheme 14 Possible mechanism for photoconversion of $Re(CH_3)O_3$ to $Re(CH_2)(OH)O_2$ in an Ar matrix at ca. 14 K. Ref. 344a

that the resulting methyl and rhenium radicals recombine with cleavage of a C–H bond.[344] The similarity of $CH_2{=}ReO_2OH$ to species that have been proposed as intermediates in olefin metathesis and isomerization reactions was noted.[345] Continued photolysis of $CH_2{=}ReO_2OH$ yields a species with a single CO group. By analogy to the photochemical rearrangement of siloxiranylidene to H2SiCO upon photolysis in Ar matrices[346] the rhenium product is tentatively assigned as $H_2Re(CO)(O)OH$.

Me_3ReO_2[347] and Me_4ReO[348] have been examined in Ar matrices and found to undergo photolysis with loss of methane and formation of $CH_2{=}Re$ intermediates. Secondary photolysis of $CH_2{=}Re(CH_3)O_2$ results in formation of $(CH_2{=})_2Re(O)OH$. Me_3ReO_2 has recently been shown by gas electron diffraction to have a highly distorted trigonal bipyramidal geometry in which the two oxygen ligands occupy pseudoequatorial positions and the axial Me-Re-Me bond angle is 146°.[349]

Reactions of organic ligands within the coordination sphere of a metal result in carbon–carbon bond formation and has been recently exploited as a high-yield route to cycloaddition reactions. Photolysis of $Cp'_2M_2(CO)_4(\mu\text{-}\eta^{2:2}\text{-}C_2H_2)$, where $Cp' = C_5H_4C_4H_9$, has been shown by Nujol matrix photochemistry to eject a CO with formation of a species with a bridging or 4-electron bridging carbonyl.[350] This electron-deficient intermediate may react with any number of alkene or alkyne compounds to give a simple η^2-alkene or alkyne species that undergoes subsequent C–C bond formation joining the organic fragments (Scheme 15).[351] For example, reaction of $Cp_2Mo_2(CO)_4(\mu\text{-}\eta^{2:2}\text{-}C_2H_2)$ with ethene yields $Cp_2Mo_2(CO)_3(\mu\text{-}\eta^{1:4}\text{-}1,$ 3-butadien-1-yl) and $Cp_2Mo_2(CO)_3(\eta^4\text{-butadiene})$ with the latter being the thermodynamically stable species.[352] Clearly significant reorganization of the ethyne, ethene complex must accompany formation of the butadiene species and possible mechanisms for these rearrangements are discussed by Kreiter.[353] Prior to Kreiter's photochemical studies, Knox *et al.* carried out thermal reactions of $Cp_2M_2(CO)_4(\mu\text{-}\eta^{2:2}\text{-alkyne})$ derivatives with alkynes and isolated analogous polyene 'fly-over' derivatives.[354]

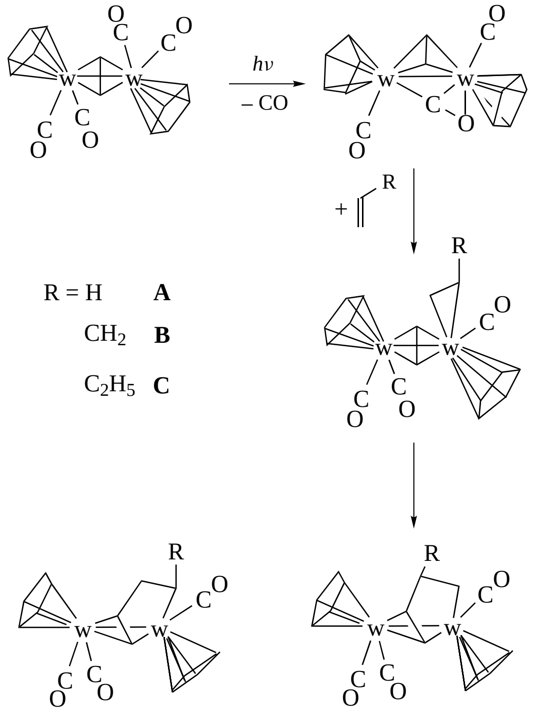

Scheme 15 Reaction mechanism for alkene addition to $Cp_2W_2(CO)_4(\mu\text{-}\eta^{2:2}\text{-alkyne})$. Ref. 353

Photolysis of the fulvalene derivative, $(\mu\text{-}\eta^5\text{-}\eta^5\text{-}C_5H_4C_5H_4)Ru_2(CO)_4$, with trans-2-butene yields mono and disubstituted species, $(\mu\text{-}\eta^5\text{-}\eta^5\text{-}C_5H_4C_5H_4)Ru_2(CO)_3L$ and $(\mu\text{-}\eta^5\text{-}\eta^5\text{-}C_5H_4C_5H_4)Ru_2(CO)_2L_2$, where L = 2-butene. Some rearrangement of the trans-2-butene to cis-2-butene was observed. In contrast, photolysis of $(\mu\text{-}\eta^5\text{-}\eta^5\text{-}C_5H_4C_5H_4)Ru_2(CO)_4$ with $MeO_2CC_2CO_2Me$ gives $(\mu\text{-}\eta^5\text{-}\eta^5\text{-}C_5H_4C_5H_4)Ru_2(CO)_2(\mu\text{-}\eta^1,\ \eta^1\text{-}MeO_2CC_2CO_2Me)$ in which

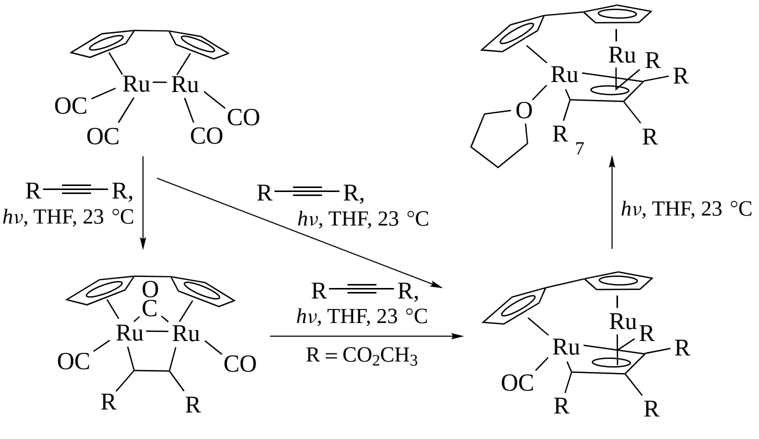

Scheme 16 Reaction products upon photolysis of $(\mu\text{-}\eta^5,\ \eta^5\text{-Cp-Cp})Ru_2(CO)_4$ and $MeO_2CC_2CO_2Me$ in THF. Ref. 355

the acetylene ligand bridges parallel to the Ru–Ru bond. Continued photolysis of this species in the presence of alkyne gives the metallacyclopentadienyl derivative, (μ-η^5-η^5-$C_5H_4C_5H_4$)$Ru_2(CO)$[μ-η^2, η^4-$C_4(CO_2Me)_4$] (Scheme 16).[355]

Metal-mediated cycloaddition reactions serve to bring together organic fragments in pericyclic reactions beyond the range typically observed in classical organic chemistry. For example, the Diels-Alder reaction of a diene with a dienophile is described as a [4 + 2] cycloaddition. So-called higher order metal promoted cycloaddition reactions include [4 + 4], Ni(O),[356] [5 + 4], Rh(I),[357] and [5 + 2], Rh(I),[358] cycloadditions. These reactions have recently been reviewed.[359] Photolysis of chromium complexes containing η^6 ligands and manganese complexes containing η^5 ligands have expanded the range of cycloaddition reactions to include [6 + 2], [6 + 4], [5 + 2], and [5 + 4] cycloadditions. Photolysis of (η^6-C_7H_8)$Cr(CO)_3$,[360] (η^6-C_8H_8)$Cr(CO)_3$,[361] (η^5-2, 4-$Me_2C_5H_5$)$Mn(CO)_3$,[362] or (η^5-C_6H_7)$Mn(CO)_3$[363] results in loss of CO to yield an electron-deficient species that may react with alkynes or alkenes to give bicyclo derivatives. Additions to (η^6-C_8H_8)$Cr(CO)_3$ are also known.[364] In those cases where a diene or alkyne is used with (η^6-C_7H_8)$Cr(CO)_3$ isolable ($\eta^{4:2}$-bicyclo[4.4.1]undeca-2,4,8-triene)$Cr(CO)_3$ or ($\eta^{4:2}$-bicyclo[4.2.1]nona-2,4,7-triene)$Cr(CO)_3$,[365] derivatives are formed. Reactions of alkynes with (η^5-C_6H_7)$Mn(CO)_3$ give ($\eta^{3:2}$-bicyclo[3.2.1]nona-2,6-dien-4-yl)$Mn(CO)_3$.[366] Where a substituted alkene is employed as a reactant, the resulting (η^4-bicyclo[4.2.1]nona-2,4-diene)$Cr(CO)_3$ is unstable to ligand loss. In the presence of excess cycloheptatriene these reactions can be catalytic. Heteroatom groups in the cycloheptatriene ring, C_6H_6X, have also been utilized,[367] as have cycloheptatriene ligands with pendant alkene and butadiene groups.[368] Isocyanates and ketenes add in a manner analogous to alkenes.[369] Chiral resolution of substituted cycloheptatriene chromium complexes permits the stereoselective addition of alkenes and alkynes yielding chiral bicyclic products.[370] A vast literature exists exploiting metal catalyzed higher order cycloaddition reactions for the synthesis of bi and tricyclo organic species and several reviews have been published.[371]

Mechanistic studies of the metal catalyzed cycloaddition reactions establish the intermediacy of a species bearing cyclopolyenyl or cyclopolyene ligand and a π -bound alkene or alkyne. Low-temperature solution studies established that coupling takes place in two steps, often with rearrangement of the alkene or alkyne fragments. This process is illustrated for alkyne addition to a cycloheptatriene ligand in Scheme 17.

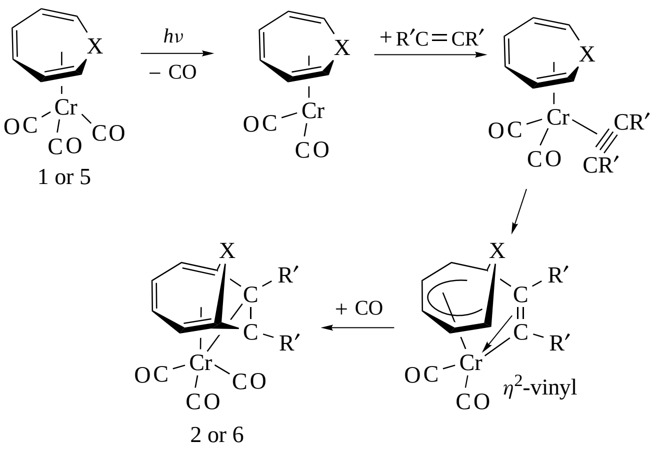

Scheme 17 Proposed mechanism for [6 + 2] cycloaddition. Ref. 366

The Pauson–Khand reaction typically involves the thermal reaction of a $Co_2(CO)_6$(μ-$\eta^{2:2}$-alkyne) with alkene to form a substituted cyclopentenone. A photochemical version of this reaction has been reported.[372] Matrix studies of $Co_2(CO)_6$(μ-$\eta^{2:2}$-alkyne) have established that CO-loss occurs from a single position, but that photochemical rearrangement of the $Co_2(CO)_5$(μ-$\eta^{2:2}$-alkyne) photointermediate readily takes place.[373] Reaction of this intermediate with alkene is followed by coupling to form the cyclopentenone product.

The discovery of the synthesis of β-lactams by photolysis of chromium carbene complexes with imines[374] has led to an extensive application of group VI Fischer carbene photochemistry to organic synthesis. By analogy, intramolecular reactions of aldehydes give β-lactones.[375] In the presence of olefins, these reactions give rise to cyclobutanones,[376] while reactions with alcohols or amines yield carboxylic acid derivatives.[377] Examination of a series of derivatives, $(CO)_4LCrC(OEt)Me$, where L = CO, PPh_3, PBu_3, and $(CO)_3(dppe)CrC(OEt)Me$ established that increasing the σ-donor (or conversely decreasing the π-acceptor) ability of ligands suppresses the β-lactone formation in reactions with imines.[378] The ability of chromium carbenes to accommodate a range of heteroatom functions, $(CO)_5Cr{=}C(R)X$, where X = OR, NH_2, NHR, NR_2, SR, and PR_2, and their relative simplicity of preparation presents with organic chemist with a wide palette of choices in synthesis. The organic chemistry of the photochemical reactions has been extensively reviewed.[379]

The reactions described above appear to parallel known reactions of ketenes, thus most of the mechanistic interpretations have presumed an intermediate in which a ketene is stabilized by the metal center.[380] A good many studies have been directed toward understanding the photochemistry of Fischer carbenes, and observing the putative ketene intermediate. UV/visible spectroscopy of tungsten carbenes typically consist of three bands, a very weak band above 500 nm assigned to a spin-forbidden MLCT, a moderately intense band ca. 400 nm assigned as a spin-allowed MLCT, and a second moderately intense band ca. 350 nm assigned to a LF transition.[381] There is some evidence for an additional LF band masked by the MLCT band.[382] For the corresponding chromium species these band maxima are often shifted to higher energy. The MLCT bands are photochemically insensitive, while the LF bands are

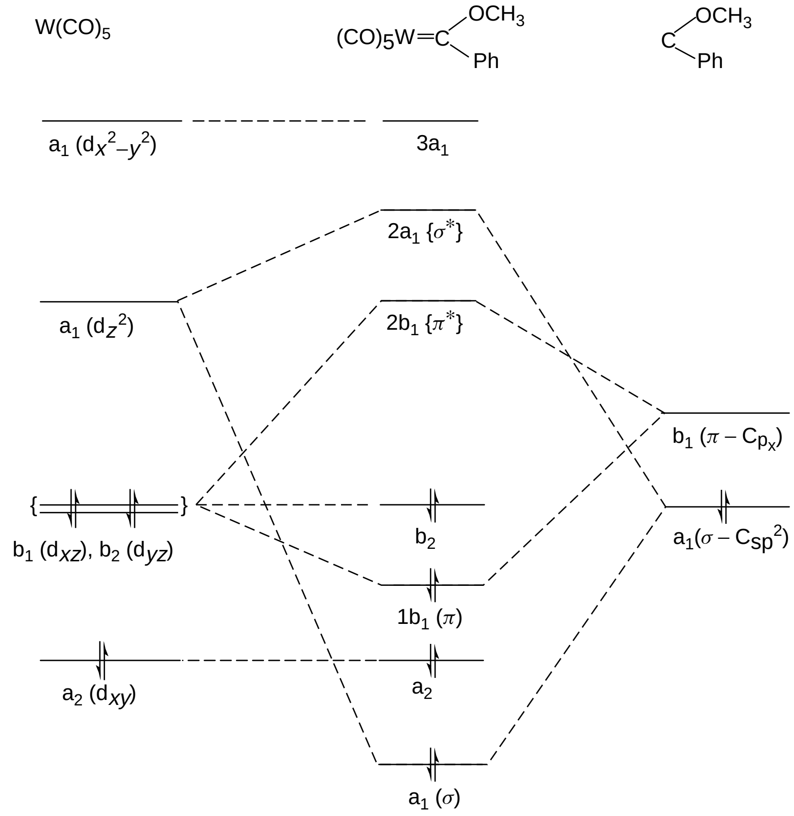

Figure 24 Simplified 1-electron energy level diagram for $(CO)_5WC(OMe)Ph$. (Reprinted with permission from Ref. 381. © 1983 American Chemical Society)

found to be responsible for the observed photoreactivity. It should perhaps be noted that almost all interpretations of the spectroscopy of these compounds have been based on an MO diagram (Figure 24) originally reported by Block, Fenske, and Casey[383] and subsequently modified by Geoffroy.[384] Recent MO studies based on dft methods offer new insight into the bonding of the Fischer carbenes and develop an orbital correlation diagram that is importantly nuanced from the more traditional view, Figure 25.[385] In particular, the recognition that the Cr-C-X π-interaction is a three-center, 4-electron bond reverses the order of the σ and π bonds between the metal and carbene fragments and redefines the HOMO to be one component of this bonding interaction. Significantly, these new results are in excellent agreement with PES studies of these carbene compounds.[386]

Ligand exchange studies on Fischer carbenes demonstrate that photolysis results in exclusive *cis* substitution.[387] Resonance Raman[388] and matrix studies[389] demonstrate that photolysis into the MLCT band of $(CO)_5MC(OMe)Ph$, where $M = Cr$, W, initiates an anti $\rightleftarrows$ syn isomerization of the methoxy group. Time-resolved Raman studies have established that this transformation occurs in <10 ns.[390] Photolysis into the LF band causes both carbene isomerization and CO-loss.[391] Time-resolved resonance Raman studies demonstrated that photolysis of $(CO)_5WC(OMe)Ph$ in acetonitrile into the LF band results in CO-loss and formation of a solvated intermediate as well as a second intermediate in which the vacant site appears to be blocked by an agostic interaction between the methoxy methyl and the tungsten.[392] Very careful matrix studies have now effectively ruled out the formation of a metal-ketene species.[384] An interesting set of studies comparing a set of chromium carbene compounds known to undergo reaction with imines to form β-lactams with a second set that have low photochemical reactivity established that the former compounds underwent reaction with N_2 or ethene dopants while the second group did not. Solution flash studies showed that the rate of reaction between the CO-loss species and CO was solvent dependent while the latter group was not.[393] As of this writing, the identity, or even existence, of an intermediate that mimics metal-ketene behavior is still quite unsettled. It is likely that application of ultrarapid time-resolved IR methods will be necessary to resolve the current conundrum.

Interestingly, thermal reactions of olefins with Fischer carbenes give rise to cyclopropanation products.[394] Although relatively rare, photochemical cyclopropanations have been reported.[395]

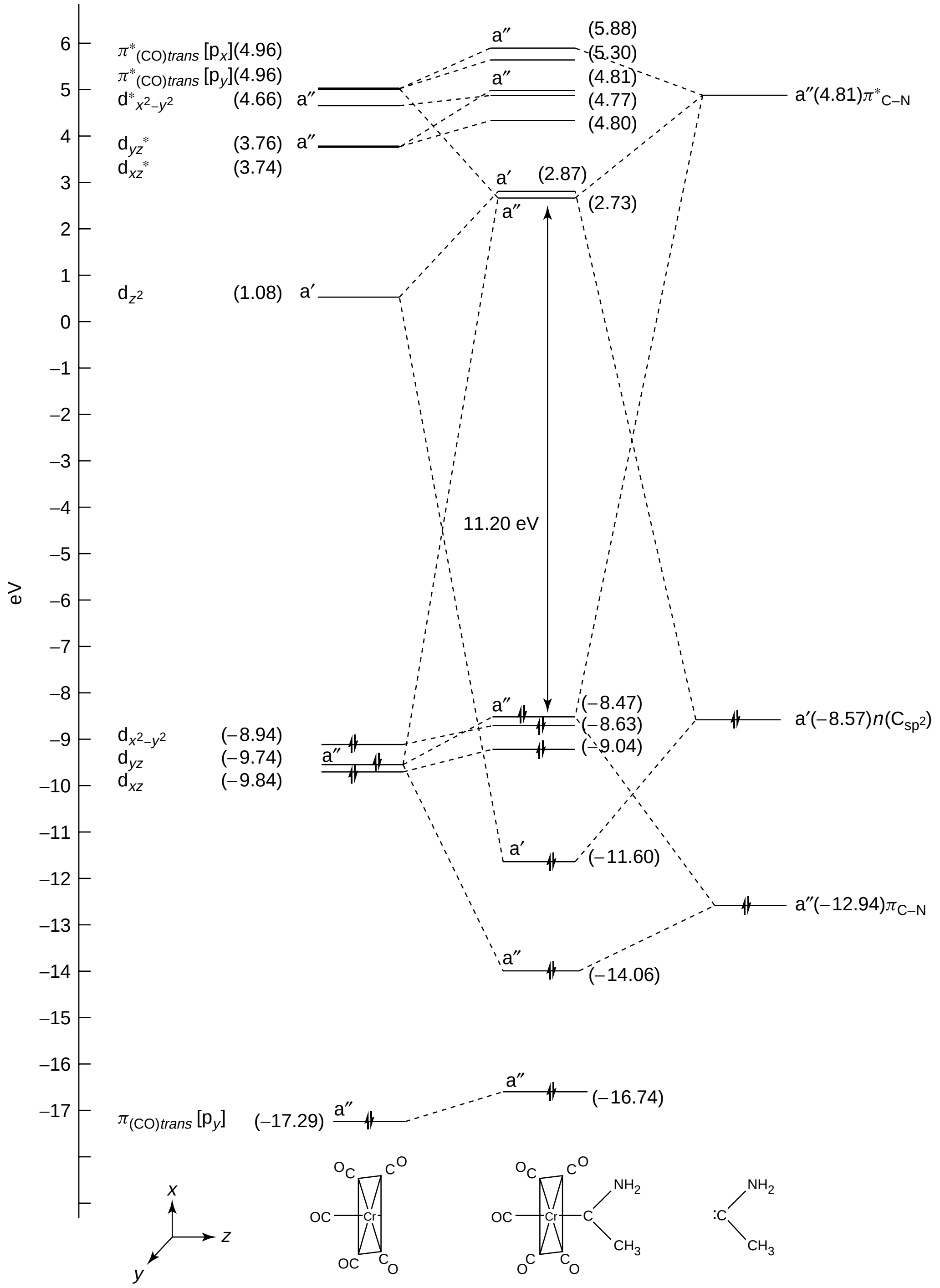
eV
6
5
4
3
2
1
0
−1
−2
−3
−4
−5
−6
−7
−8
−9
−10
−11
−12
−13
−14
−15
−16
−17
π*(CO)trans [px](4.96)
π*(CO)trans [py](4.96)
d*x2−y2 (4.66) a″
dyz* (3.76) a″
dxz* (3.74)
dz2 (1.08) a′
dx2−y2 (−8.94)
dyz (−9.74) a″
dxz (−9.84)
π(CO)trans [py] (−17.29) a″
a″ (5.88)
(5.30)
a″ (4.81)
(4.77)
(4.80)
a′ (2.87)
a″ (2.73)
11.20 eV
a″ (−8.47)
(−8.63)
(−9.04)
a′ (−11.60)
a″ (−14.06)
a″ (−16.74)
a″(4.81)π*C–N
a′(−8.57)n(Csp2)
a″(−12.94)πC–N
x
z
y
OC
CO
OC
Cr
OC
CO
NH2
C
CH3
:C
NH2
CH3

Figure 25 Orbital correlation diagram for $(CO)_5CrC(NH_2)CH_3$. (Reprinted with permission from Ref. 385b. © 1997 American Chemical Society)

11 PHOTOCRYSTALLOGRAPHY

Linkage isomerism is a well known phenomenon in inorganic chemistry[396] with the recognition that ligands such as nitrite might exist in both oxygen (nitrite) and nitrogen (nitro) bound forms dating back to the dawn of modern inorganic chemistry.[397] The recognition that linkage isomerism could be initiated by light is much more recent having been first reported for $Co(NH_3)_5(NO_2)^{2+}$ by Adell.[398] A group of significant new studies build upon photocrystallography, an important new technique pioneered by Coppens and his coworkers. The methodology for photocrystallography has been reviewed.[399] In essence, photocrystallography is a low-temperature matrix method in which crystallographic data sets are compared before and after photolysis to produce a photodifference map from which the electron density and atomic positions of a metastable species may be calculated.

The first application of photocrystallography was directed toward resolving a long standing puzzle involving low temperature, photochemically generated, metastable states of nitroprusside that had first been observed in 1977.[400] Coppens' studies established the two metastable states to be the oxygen bound, isonitrosyl, and the side-on, η^2-NO, linkage isomers of the nitrosyl ligand (Figure 26).[401] This assignment has recently been confirmed by neutron scattering studies.[402] Matrix studies of the photochemistry of CpNi(NO) by Rest had demonstrated a photoproduct with an exceptionally low NO stretch the identity of which was left unresolved.[403] It has now been demonstrated by photocrystallography that the species is the η^2-NO linkage isomer, Figure 27.[404] Several additional examples of nitrosyl linkage isomerism have been identified.[405] Sulfur dioxide linkage isomerism has been observed in $[Ru(NH_3)_4(H_2O)(SO_2)]^{+2}$ has been observed[406] as has N_2 linkage isomerism in $[Os(NH_3)_5N_2]^{2+}$.[407]

In a remarkable extension of photocrystallography, the high intensity beam line at the National Synchrotron Light Source at the Brookhaven National Laboratory has been used in a stroboscopic diffraction experiment to determine the molecular structure (Figure 28) of the 50 µs lifetime, triplet excited state of $[Pt_2(pop)_4]^{4-}$.[408] In these studies, high intensity laser flashes are followed immediately by 33 µs X-ray pulses, Figure 29. The photochemistry of $[Pt_2(pop)_4]^{4-}$ has been extensively studied[409] and the ability of the excited state to abstract hydrogen atoms has been employed in the cleavage of duplex DNA by abstraction of both the 4′ and 5′-hydrogens from the 2′-deoxyribose groups.[410] Polarized electronic absorption measurements had predicted a Pt–Pt bond contraction upon excitation owing to a $5d\sigma^* \rightarrow 6p\sigma$ excitation.[411] These predictions have been confirmed by the

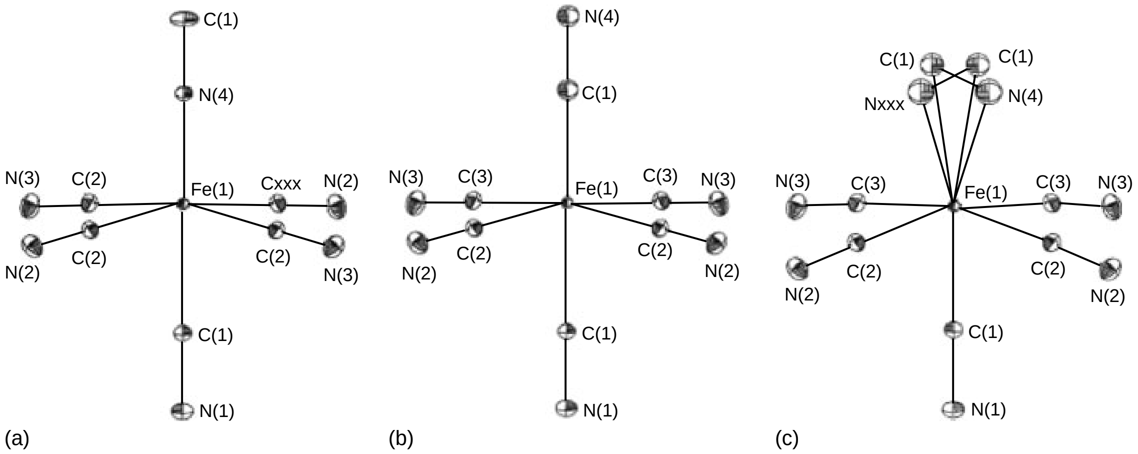

Figure 26 Ortep diagrams of the nitroprusside anion (a), and its isonitrosyl (b), and side-on, η^2-NO, (c) linkage isomers[401]

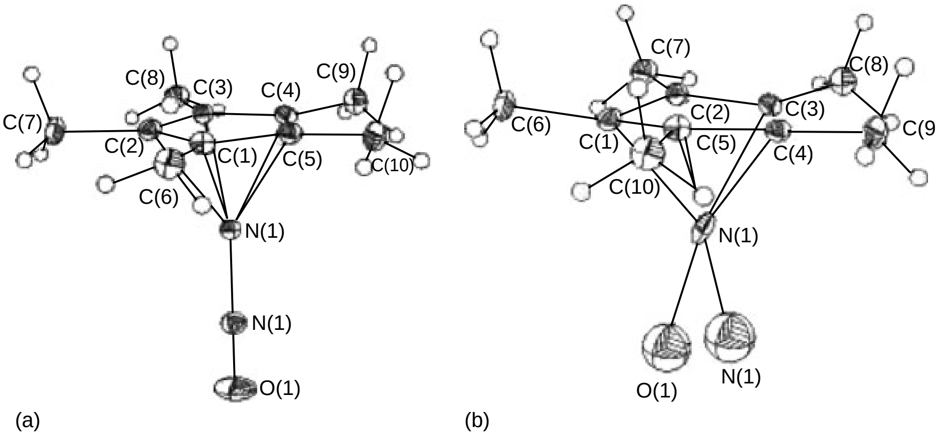

Figure 27 Ortep diagrams of CpNi(NO) (a), and its side-on, η^2-NO, (b) linkage isomer[404]

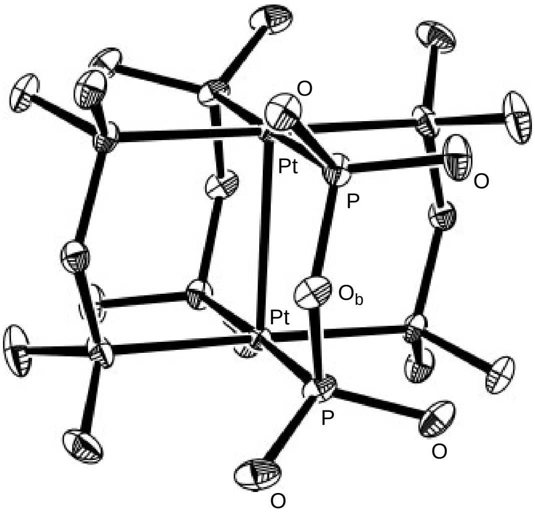

Figure 28 Ortep diagram of the $\{Pt_2(pop)_4\}^{4-}$ ion[408a]

photocrystallographic studies that demonstrate a contraction of the 2.9126(2) Å ground-state bond length by 0.28(9) Å in the excited state. These results are consistent with an estimate of a 0.225 Å change based on shifts in the Raman Pt–Pt stretching frequency,[412] and have been independently confirmed by a second time-resolved diffraction study.[413] Photocrystallographic methods for the investigation of molecular excited states have been reviewed.[414]

12 LINKAGE ISOMERISM AND LIGAND CONFORMATIONAL CHANGES

As noted above, photocrystallography has been used to identify nitrosyl linkage isomers in a variety of molecules. The unambiguous identification of these linkage isomers has permitted firm identification to be made in other cases where matrix studies indicated photochemical changes in nitrosyl environments. For example, rhenacarborane nitrosyl compounds, [1, $2\text{-}R_2\text{-}3$, $3\text{-}(CO)_2\text{-}3\text{-}NO$-*closo*-3, 1, $2\text{-}ReC_2B_9H_9$], where R = H and Me, undergo photolysis to give both isonitrosyl and η^2-NO isomers depending upon the energy of the incident radiation.[415] $[CpM(CO)_2NO]^{1+}$, where M = Mn, Re, were studied in inert ionic matrices, NEt_3OctPF_6, and were found to undergo linkage isomerism upon photolysis.[416] In fact, continuing studies suggest that photochemical linkage isomerism may be the rule rather than the exception for this class of compounds.

The allyl ligand in $CpM(CO)_2(\eta^3\text{-}C_3H_7)$, where M = Mo, W, is known to assume both endo and exo orientations relative to the cyclopentadienyl ring.[417] Nujol and frozen gas matrix studies of the molybdenum compound have demonstrated that low-energy photolysis results in selective transformation of the endo form to the exo form.[418] The transformation is attributed to an excitation that populates the σ^* orbital of the bond responsible for fixing the geometry of the allyl ligand. Earlier observations on the tungsten compound were reinterpreted in light of these observations.[419]

13 APPLICATIONS OF PHOTOCHEMICAL REACTIONS

13.1 Catalysis

A number of strategies for the photochemical initiation of anion or cation catalyzed polymerization have been explored. For example, visible photolysis of the Reineckate anion, $[Cr(NH_3)_2(NCS)_4]^{1-}$, has long been known to release a thiocyanate ion.[420] Photolysis of the Reineckate anion in the presence of ethyl cyanoacrylate initiates polymerization.[421] The release of acac anions, and benzoylcyclopentadienyl

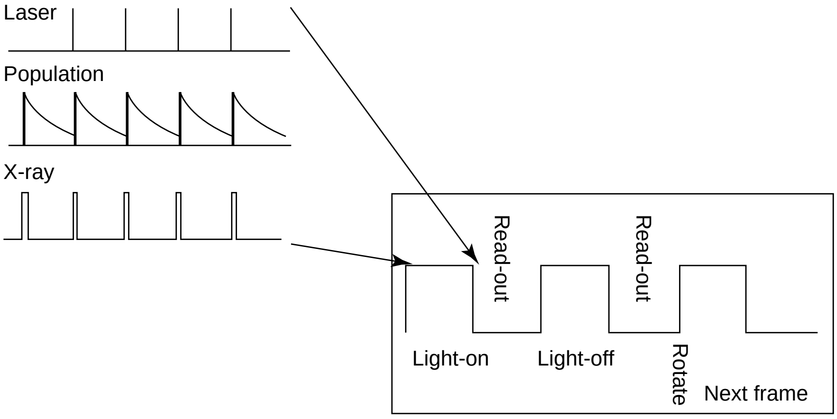

Figure 29 Time-structure and data collection sequence for stroboscopic diffraction experiments indicating the relationship between laser flash, photointermediate production, and X-ray data collection. (Ref. 414b. Reproduced by permission of Royal Society of Chemistry)

anions from Pt(acac)$_2$,[422] and 1,1′-dibenzoylferrocene,[423] respectively, have also been used as polymerization initiators. In the latter case resonance Raman studies have shown that the transition responsible for anion release has MLCT character.[424]

Photolysis of (arene)$_2$M^{2+}, where M = Fe, Ru, initiate arene loss by reduction of hapticity of the arene ligand followed by sequential introduction of solvent as the arene is fully displaced. In the case of (arene)$_2$Ru^{2+} the relative wavelength insensitivity of quantum yields for arene loss, and the ability to initiate ligand loss by spin exchange from acetophenone argue for a triplet photoactive state.[425] In the case of the (mes)$_2$Fe^{2+} complex, deligation occurs from both the MLCT and LF transitions.[426]

The photochemistry of Cp(arene)Fe^{1+} complexes has been extensively examined since the discovery of photochemical arene loss by Nesmeyanov,[427] and this class of compounds has received considerable attention as a cationic photocatalyst for the polymerization of epoxides,[428] dicyanate esters,[429] and styrene[430] among others. As in the case of the bis(arene)metal complexes described above, photolysis is believed to initiate an $\eta^6 \rightarrow \eta^4$ transformation whereupon solvent enters the open site and thermally displaces the arene ligand. Consistent with this the quantum yields indicate a significant associative component in the ligand displacement.[431] Time-resolved studies indicate that the initial photochemical event occurs on the fs or ps scale.[432] There has been substantial confusion concerning the role of singlet and triplet excited states in the observed photochemistry. Sensitization studies established a reactive role for the triplet manifold, but did not exclude a role for the excited singlet states.[433] Recent detailed quantum yield studies at several wavelengths have established that arene loss occurs from both singlet and triplet excited states. It has been noted elsewhere in this review that singlet and triplet excited states differ considerably in their reactivity toward ligands, and it is proposed that these reactivity differences account for the quantum efficiency differences in the Cp(arene)Fe^{1+} series.[434] A summary of the proposed excited states is presented in Figure 30.

The identity of the actual catalytic species in polymerization reactions has been obscured by the fact that the CpFeS$_3$$^{1+}$ species itself can undergo further decomposition to FeS$_6$$^{2+}$ and Cp$_2$Fe. In an elegant series of experiments, Kutal has utilized electrospray mass spectrometry to directly observe species generated within ms of photolysis. In these experiments, a solution containing catalyst in acetonitrile, ACN, or 1, 2-dichloroethane containing cyclohexene oxide, CHO, were photolyzed in the electrospray tip using an optical fiber coupled to a laser. By varying the distance of the fiber from the end of the spray tip the time delay from photolysis to observation of products could be changed. The arrangement of this apparatus is illustrated in Figure 31.These experiments confirmed the presence of CpFe(ACN)$_2$$^{1+}$, and CpFe(ACN)$_3$$^{1+}$ in the reaction mixture after photolysis. When CHO was present in solution, a suite of species, CpFe(H$_2$O)(CHO)$_n$$^{1+}$, where n = 1–5, were observed. It is speculated that some of the higher n species contain oligomers of CHO.[435]

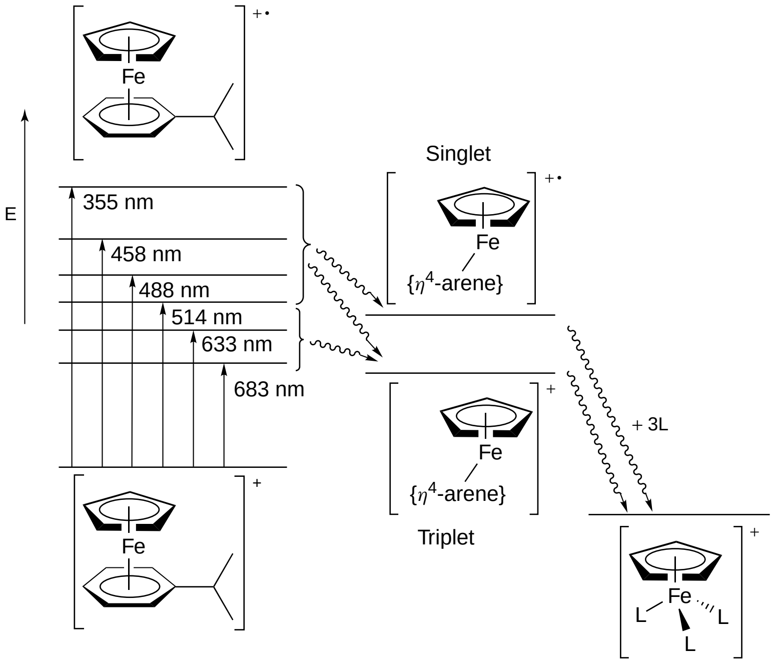

Figure 30 Reaction mechanism for arene dissociation from CpRu(i-PrPh)$^{1+}$ indicating photon energies giving rise to singlet and triplet intermediates. (Reprinted with permission from Ref. 434a. © 2000 American Chemical Society)

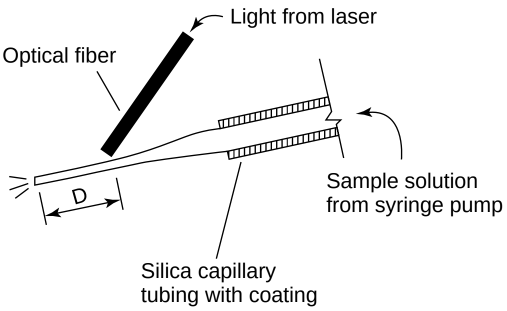
Light from laser
Optical fiber
D
Sample solution from syringe pump
Silica capillary tubing with coating

Figure 31 Schematic diagram of the nanospray tip for the electrospray source. (Reprinted with permission from Ref. 435a. © 2003 American Chemical Society)

Several reviews describing the use of metal complexes as photochemical polymerization initiators have appeared.[436]

14 PHOTOPHARMACEUTICAL APPLICATIONS

Nitrogen oxide is now known to play a broad role in biological processes including vasodilation, infection defense, and intercellular signaling. Considerable effort has been devoted to the design of compounds capable of delivering NO to a targeted site with one strategy being the photoliberation of NO.

Vasodilation studies of isolated rat tail arteries have demonstrated that $Fe_4(NO)_4(\mu_3\text{-}S)_4$ and $Fe_4(NO)_7(\mu_3\text{-}S)_3$, Roussin's black monoanion, thermally release NO in solution[437] and that this release is enhanced by visible light.[438] Roussin's black anion and red dianion, $Fe_2(NO)_4(\mu\text{-}S)_2$, are photoactive toward NO release, however, cell culture experiments have shown Roussin's black anion to be toxic making it an unlikely candidate for biological applications.[439] Chinese hamster cell cultures incubated with Roussin's red dianion showed a marked sensitization to γ-radiation cell death when simultaneously irradiated with visible light. Nitric oxide release by Roussin's black anion requires oxygen and results in formation of ferrous ions and ferric precipitates.[440] The red dianion produces the black anion upon photolysis. The so-called Roussin's esters, $Fe_2(NO)_4(\mu\text{-}SR)_2$ are attractive bases for pharmaceutical NO delivery systems in that the R groups can be modified to enhance specificity. Photolysis of water-soluble derivatives in aerated solutions results in release of all four NO groups. Flash photochemical studies suggest that the loss of NO is reversible in deaerated solutions, but that in the presence of oxygen the $Fe_2(NO)_3(\mu\text{-}SR)_2$ species irreversibly reacts with oxygen leading to complete decomposition.[441] Ru(salen)(ONO)(NO), salen $=$ N,N'-ethylenebis(salicylideneiminato) dianion, and related Ru salen derivatives[442] and *trans*-Cr(cyclam)(ONO)$^{2+}$, cyclam $= 1, 4, 8, 11$ tetraazacyclotetradecane,[443] have been shown to release NO upon photolysis and are attractive targets for biological NO delivery. The studies by the Ford group have been reviewed.[444]

15 REFERENCES

1. M. D. Roundhill, 'Photochemistry and Photophysics of Metal Complexes', Plenum Press, New York, 1993.
2. A. D. Kirk, *Chem. Rev.*, 1999, **99**, 1607.
3. J. Sima and J. Makanova, *Coord. Chem. Rev.*, 1997, **160**, 161.
4. A. W. Adamson, *Coord. Chem. Rev.*, 1993, **125**, 1.
5. K. S. Suslick and R. A. Watson, *New J. Chem.*, 1992, **16**, 633.
6. A. Vogler and H. Kunkely, *Coord. Chem. Rev.*, 2002, **230**, 243.
7. A. Vogler and H. Kunkely, *Coord. Chem. Rev.*, 2000, **208**, 321.
8. C. G. Garcia, J. F. De Lima, and N. Y. M. Iha, *Coord. Chem. Rev.*, 2000, **196**, 219.
9. W. Kaim, *Top. Curr. Chem.*, 1994, **169**, 231.
10. H. Yang and C. B. Harris, *Pract. Spect.*, 2001, **26**, 81.
11. (a) A. H. Zewail, *J. Phys. Chem.*, 2000, **104**, 5660; (b) A. H. Zewail, in 'Nobel Lectures', World Scientific Publishing. Company, Singapore, 1996 – 2000, p. 274.
12. (a) I. P. Clark, M. W. George, and J. J. Turner, *J. Phys. Chem.*, 1997, **101**, 8367; (b) A. Vlcek Jr, I. R. Farrell, D. J. Liard, P. Matousek, M. Towrie, A. W. Parker, D. C. Grills, and M. W. George, *J. Chem. Soc., Dalton Trans.*, 2002, 701.
13. K. M. Omberg, T. J. Meyer, and J. R. Schoonover, *Rec. Res. Dev. Inorg. Chem.*, 2000, **2**, 69.
14. (a) P. C. Ford, J. S. Bridgewater, S. Massick, and J. Marhenke, *Catal. Today*, 1999, **49**, 419; (b) K. L. McFarlane, B. Lee, J. Bridgewater, and P. C. Ford, *J. Organomet. Chem.*, 1998, **554**, 49.
15. (a) A. J. Downs and T. M. Greene, *Adv. Inorg. Chem.*, 1998, **46**, 101; (b) R. N. Perutz, *NATO ASI Ser. C.*, 1996, **483**, 95; (c) T. E. Bitterwolf, in 'Handbook of Vibrational Spectroscopy', eds. J. M. Chalmers and P. R. Griffiths, Wiley, West Sussex, 2002, Vol 4, p. 3137.
16. D. R. Tyler, *J. Chem. Educ.*, 1997, **74**, 668.
17. (a) C. Daniel, *Coord. Chem. Rev.*, 2003, **238–239**, 143; (b) M. C. Heitz, K. Finger, and C. Daniel, *Coord. Chem. Rev.*, 1997, **159**, 171.
18. J. K. Klassen, M. Selke, A. A. Sorensen, and G. K. Yang, *J. Am. Chem. Soc.*, 1990, **112**, 1267.
19. (a) G. Nathanson, B. Gitlin, A. M. Rosen, and J. T. Yardley, *J. Chem. Phys.*, 1981, **74**, 361; (b) J. T. Yardley, B. Gitlin, G. Nathanson, and A. M. Rosan, *J. Chem. Phys.*, 1981, **74**, 370; (c) W. Tumas, B. Gitlin, A. M. Rosan, and J. T. Yardley, *J. Am. Chem. Soc.*, 1982, **104**, 55.

20. L. Mond, H. Hirtz, and M. D. Cowap, *Proc. Chem. Soc.*, 1910, 26 67. CA: 4, 11774.
21. (a) A. Job and A. Cassal, *Compt. Rend.*, 1926, **183**, 392; (b) A. Job and J. Rouvillois, *Compt. Rend.*, 1928, **187**, 564.
22. J. Dewar and H. O. Jones, *Chem. News J. Ind. Sci.*, 1907, **95**, 109.
23. W. Strohmeier and K. Gerlach, *Chem. Ber.*, 1960, **93**, 2087.
24. A. J. Rest and J. J. Turner, *J. Chem. Soc., Chem. Commun.*, 1969, 1026.
25. M. Poliakoff, B. Davies, A. McNeish, and J. J. Turner, *J. Photochem.*, 1978, **9**, 189.
26. R. L. DeKock, *Inorg. Chem.*, 1971, **10**, 1205.
27. M. A. Graham, M. Poliakoff, and J. J. Turner, *J. Chem. Soc. A*, 1971, 2939.
28. R. B. Hitam and A. J. Rest, *Organometallics*, 1989, **8**, 1598.
29. T. E. Bitterwolf, S. Gallagher, J. T. Bays, W. B. Scallorn, A. L. Rheingold, I. A. Guzei, L. Liable-Sands, and J. C. Linehan, *J. Organomet. Chem.*, 1998, **557**, 77.
30. (a) A. J. Rest, J. R. Sodeau, and D. J. Taylor, *J. Chem. Soc., Dalton Trans.*, 1978, 651; (b) T. E. Bitterwolf, K. A. Lott, A. J. Rest, and J. Mascetti, *J. Organomet. Chem.*, 1991, **419**, 113.
31. (a) P. S. Braterman and J. D. Black, *J. Organomet. Chem.*, 1972, **39**, C3; (b) J. D. Black, M. J. Boylan, and P. S. Braterman, *J. Chem. Soc., Dalton Trans.*, 1981, 673.
32. J. Chetwynd-Talbot, P. Grebenik, R. Perutz, and M. H. A. Powell, *Inorg. Chem.*, 1983, **22**, 1675.
33. M. K. Whittlesey, R. N. Perutz, I. G. Virrels, and M. W. George, *Organometallics*, 1997, **16**, 268.
34. A. J. Rest, I. Whitwell, W. A. G. Graham, J. K. Hoyano, and A. D. McMaster, *J. Chem. Soc., Dalton Trans.*, 1987, 1181.
35. M. Poliakoff and E. Weitz, *Acc. Chem. Res.*, 1987, **20**, 408.
36. M. Poliakoff and J. J. Turner, *Angew. Chem, Int. Ed. Engl.*, 2001, **40**, 2809.
37. N. Leadbeater, *Coord. Chem. Rev.*, 1999, **188**, 35.
38. T. A. Seder, A. J. Ouderkirk, and E. Weitz, *J. Chem. Phys.*, 1986, **85**, 1977.
39. Y. Zheng, W. Wang, J. Lin, Y. She, and K. Fu, *J. Phys. Chem.*, 1992, **96**, 7650.
40. C. Daniel, J. Full, L. Gonzalez, C. Kaposta, M. Krenz, C. Lupulescu, J. Manz, S. Minemoto, M. Oppel, P. Rosendo-Francisco, S. Vajda, and L. Woste, *Chem. Phys.*, 2001, **267**, 247.
41. (a) D. Ambrosek, M. Oppel, L. González, and V. May, *Chem. Phys. Lett.*, 2003, **380**, 536; (b) J. Full, C. Daniel, and L. González, *Phys. Chem. Chem. Phys.*, 2003, **5**, 87; (c) J. Full, L. González, and C. Daniel, *J. Phys. Chem.*, 2001, **105**, 184.
42. W. Wang, J. Wenhua, P. Jin, Y. Liu, S. Yanwei, Y. She, and K. Fu, *Chin. Phys. Lett.*, 1991, **8**, 491.
43. E. P. Wasserman, R. G. Bergman, and C. B. Moore, *J. Am. Chem. Soc.*, 1988, **110**, 6076.
44. M. Jyoo, H. Takeda, K. Omiya, Y. Ishikawa, and S. Arai, *Bull. Chem. Soc. Jpn.*, 1993, **66**, 3618.
45. (a) S. A. Trushin, W. Fuss, and W. E. Schmidt, *Chem. Phys.*, 2000, **259**, 313; (b) S. A. Trushin, W. Fuss, and W. E. Schmidt, *J. Phys. Chem.*, 1998, **102**, 4129.
46. S. A. Trushin, W. Fuss, K. L. Kompa, and W. E. Schmidt, *J. Phys. Chem.*, 2000, **104**, 1997.
47. W. Fuss, W. E. Schmidt, and S. A. Trushin, *J. Phys. Chem.*, 2001, **105**, 333.
48. W. Fuss, S. A. Trushin, and W. E. Schmidt, *Res. Chem. Intermed.*, 2001, **27**, 447.
49. (a) O. Rubner, T. Baumert, M. Bergt, B. Kiefer, G. Gerber, and V. Engle, *Chem. Phys. Lett.*, 2000, **316**, 585; (b) O. Rubner, V. Engle, M. R. Hachey, and C. Daniel, *Chem. Phys. Lett.*, 1999, **302**, 489.
50. (a) G. L. Geoffroy and M. S. Wrighton, ‘Organometallic Photochemistry’, Academic, New York, 1979; (b) G. J. Ferraudi, ‘Elements of Inorganic Photochemistry’, John Wiley & Sons, New York, 1988.
51. (a) N. A. Beach and H. B. Gray, *J. Am. Chem. Soc.*, 1968, **90**, 5713; (b) H. B. Gray and N. A. Beach, *J. Am. Chem. Soc.*, 1963, **85**, 2922.
52. (a) A. Rosa, E. J. Baerends, S. J. A. van Gisbergen, E. van Lenthe, J. A. Grownsveld, and J. G. Snijders, *J. Am. Chem. Soc.*, 1999, **121**, 10356; (b) C. Pollak, A. Rosa, and E. J. Baerends, *J. Am. Chem. Soc.*, 1997, **119**, 7324; (c) K. Pierloot. E. Tsokos, and L. G. Vanquickenborne, *J. Phys. Chem.*, 1996, **100**, 16545.
53. (a) E. J. Baerends and A. Rosa, *Coord. Chem. Rev.*, 1998, **177**, 97; (b) M. P. Wilms, E. J. Baerends, A. Rosa, and D. J. Stufkens, *Inorg. Chem.*, 1997, **36**, 1541.
54. (a) A. J. Rest, *J. Organomet. Chem.*, 1972, **40**, C76; (b) M. Poliakoff and J. J. Turner, *J. Chem. Soc., Dalton Trans.*, 1974, 2276; (c) J. Burdett, A. J. Downs, G. P. Gaskill, M. A. Graham, J. J. Turner, and R. F. Turner, *Inorg. Chem.*, 1978, **17**, 523.
55. O. Crichton, A. J. Rest, and D. J. Taylor, *J. Chem. Soc., Dalton Trans.*, 1980, 167.
56. (a) A. I. Cooper and M. Poliakoff, *Chem. Phys. Lett.*, 1993, **212**, 611; (b) S. E. J. Goff, T. F. Nolan, M. W. George, and M. Poliakoff, *Organometallics*, 1998, **17**, 2730; (c) G. I. Childs, S. Gallagher, T. E. Bitterwolf, and M. W. George, *J. Chem. Soc., Dalton Trans.*, 2000, 4534.
57. (a) Y. Zheng, W. Wang, J. Lin, Y. She, and K. Fu, *J. Chem. Phys.*, 1992, **96**, 9821; (b) J. Wang, G. T. Long, and E. Weitz, *J. Chem. Phys. A*, 2001, **105**, 3765.
58. R. N. Perutz and J. J. Turner, *J. Am. Chem. Soc.*, 1975, **97**, 4791.
59. (a) M. B. Simpson, M. Poliakoff, J. J. Turner, W. B. Maier II, and J. G. McLaughlin, *J. Chem. Soc., Chem. Commun.*, 1983, 1355; (b) B. H. Weiller, *J. Am. Chem. Soc.*, 1992, **114**, 10910; (c) B. H. Weiller, E. P. Wasserman, C. B. Moore, and R. G. Bergman, *J. Am. Chem. Soc.*, 1993, **115**, 4326.
60. J. R. Wells and E. Weitz, *J. Am. Chem. Soc.*, 1995, **114**, 2783.

61. (a) X. Z. Sun, M. W. George, S. G. Kazarian, S. M. Nikiforov, and M. Poliakoff, *J. Am. Chem. Soc.*, 1996, **118**, 10525; (b) X. Z. Sun, D. C. Grills, S. M. Nikiforov, M. Poliakoff, and M. W. George, *J. Am. Chem. Soc.*, 1997, **119**, 7521; (c) M. K. Kuimova, W. Z. Alsindi, J. Dyer, D. C. Grills, O. S. Omar, P. Matousek, A. W. Parker, P. Portius, X. Sun, Z. Xue, M. Towrie, C. Wilson, J. Yang, and M. W. George, *J. Chem. Soc., Dalton Trans.*, 2003, 3996.
62. A. A. Bengali, R. G. Bergman, and C. B. Moore, *J. Am. Chem. Soc.*, 1995, **117**, 3879.
63. A. W. Ehlers, G. Frenking, and E. J. Baerends, *Organometallics*, 1997, **16**, 4896.
64. D. C. Grills and M. W. George, *Adv. Inorg. Chem.*, 2001, **5**, 113.
65. M. Poliakoff and J. J. Turner, *Adv. Spectrosc.*, 1996, **23**, 275.
66. X.-Z. Sun, M. W. George, S. G. Kazarian, S. N. Nikiforov, and M. Poliakoff, *J. Am. Chem. Soc.*, 1996, **118**, 10525.
67. Y. Sheng, W. Wang, J. Lin, and K. J. Fu, *Chem. Phys. Lett.*, 1993, **202**, 148.
68. D. C. Grills, X. Z. Sun, G. I. Childs, and M. W. George, *J. Phys. Chem.*, 2000, **104**, 4300.
69. C. Hall and R. N. Perutz, *Chem. Rev.*, 1996, **96**, 3125.
70. (a) T. P. Dougherty and E. J. Heilweil, *Chem. Phys. Lett.*, 1994, **227**, 19; (b) J. M. Kelly, H. Herrmann, and E. Koerner von Gustorf, *J. Chem. Soc., Chem. Commun.*, 1973, 105; (c) X. L. Xie and J. D. Simon, *J. Am. Chem. Soc.*, 1990, **112**, 1130; (d) J. D. Simon and X. L. Xie, *J. Phys. Chem.*, 1986, **90**, 6751.
71. S. Geftakis and G. E. Ball, *J. Am. Chem. Soc.*, 1998, **120**, 9953.
72. C. Breheny, J. M. Kelly, C. Long, S. O'Keeffe, M. T. Pryce, G. Russell, and M. M. Walsh, *Organometallics*, 1998, **17**, 3690.
73. T. P. Dougherty and E. J. Heilweil, *J. Chem. Phys.*, 1994, **100**, 4006.
74. T. P. Dougherty and E. J. Heilweil, *Chem. Phys. Lett.*, 1994, **227**, 19.
75. J. M. Morse, G. H. Parker, and T. J. Burkey Jr, *Organometallics*, 1989, **8**, 2471.
76. T. Jiao, G.-L. Leu, G. J. Farrell, and T. J. Burkey, *J. Am. Chem. Soc.*, 2001, **123**, 4960.
77. G.-L. Leu and T. J. Burkey, *J. Coord. Chem.*, 1995, **34**, 87.
78. S. Gittermann, T. Jiao, and T. J. Burkey, *Photochem. Photobiol. Sci.*, 2003, **2**, 817.
79. T. E. Bitterwolf, D. Lukmanova, S. Gallagher, A. L. Rheingold, I. A. Gusei, and L. Liable-Sands, *J. Organomet. Chem.*, 2000, **605**, 168.
80. M. Herberhold, G. Frohmader, J. Peukert, and W. Milius, *Z. Naturforsch*, 2000, **55**, 1188.
81. J. C. Linehan, C. R. Yonker, J. T. Bays, S. T. Autrey, T. E. Bitterwolf, and S. Gallagher, *J. Am. Chem. Soc.*, 1998, **120**, 5826.
82. J. E. Joachim, C. Apostolidis, B. Kanellakopulos, D. Meyer, B. Nuber, K. Raptis, J. Rebizant, and M. L. Ziegler, *J. Organomet. Chem.*, 1995, **492**, 199.
83. W. Kaim, T. Roth, B. Olbrich-Deussner, R. Gross-Lannert, J. Jordanov, E. Roth, and K. H. Eberhard, *J. Am. Chem. Soc.*, 1992, **114**, 5693.
84. J. Lewis, R. S. Nyholm, S. S. Candhu, and M. H. B. Stiddard, *J. Chem. Soc.*, 1964, 2825.
85. H. Angermund, A. K. Bandyopadhay, F. W. Grevels, F. Mark, and K. Schappert, 8th International. Symposia. Photochem. Photophys. Coord. Compds., Santa Barbara, CA, August, 1989.
86. M. A. Schroder and M. S. Wrighton, *J. Am. Chem. Soc.*, 1976, **98**, 551.
87. (a) P. T. Snee, C. K. Payne, S. D. Mebane, K. T. Kotz, and C. B. Harris, *J. Am. Chem. Soc.*, 2001, **123**, 6909; (b) S. K. Mayak, G. J. Farrell, and T. J. Burkey, *Inorg. Chem.*, 1994, **33**, 2236; (c) S. K. Nayak and T. J. Burkey, *J. Am. Chem. Soc.*, 1993, **115**, 6391; (d) S. K. Nayak and T. J. Burkey, *Inorg. Chem.*, 1992, **31**, 1125.
88. S. Sun and D. A. Sweigart, *Adv. Organomet. Chem.*, 1996, **40**, 171.
89. R. J. Ryther and E. Weitz, *J. Phys. Chem.*, 1991, **95**, 9842.
90. J. Wang, G. T. Long, and E. Weitz, *J. Phys. Chem.*, 2001, **105**, 3765.
91. P. L. Bogdan and E. Weitz, *J. Am. Chem. Soc.*, 1989, **111**, 3163.
92. P. L. Bogdan and E. Weitz, *J. Am. Chem. Soc.*, 1990, **112**, 639.
93. W. Wang, A. A. Narducci, P. G. House, and E. Weitz, *J. Am. Chem. Soc.*, 1996, **118**, 8654.
94. D. M. Heinekey and W. Oldham, *Chem. Rev.*, 1993, **93**, 913.
95. R. L. Sweany, in 'Transition Metal Hydrides', ed. A. Dedieu, VCH, New York, NY, 1992, p. 65.
96. G. J. Kubas, 'Metal Dihydrogen and σ-bond Complexes', Kluwer Academic/Plenum Publishers, New York, 2001.
97. R. L. Sweany, Evidence for a Complex of Molecular Hydrogen. The reaction of Matrix-Isolated Pentacarbonyl Chromium and Its Congers with Dihydrogen, Paper given at the Inorganic Chemistry Symposium, Bloomington, IN, May, 1982.
98. G. J. Kubas, R. R. Ryan, B. I. Swanson, P. J. Vergamini, and H. J. Wasserman, *J. Am. Chem. Soc.*, 1984, **106**, 451.
99. R. L. Sweany, *J. Am. Chem. Soc.*, 1985, **107**, 2374.
100. (a) W. Gerhartz, F.-W. Grevels, W. E. Klotzbücher, E. A. Koerner von Gustorf, and R. N. Perutz, *Z. Naturforsch. B.*, 1985, **40**, 518; (b) R. B. Hitam, K. A. Mahmoud, and A. J. Rest, *Coord. Chem. Rev.*, 1984, **55**, 1.
101. R. K. Upmacis, M. Poliakoff, and J. J. Turner, *J. Am. Chem. Soc.*, 1986, **108**, 3645.
102. S. M. Howdle, M. A. Healey, and M. Poliakoff, *J. Am. Chem. Soc.*, 1990, **112**, 4804.

103. G. I. Childs, D. C. Grills, S. Gallagher, T. E. Bitterwolf, and M. W. George, *J. Chem. Soc., Dalton Trans*, 2001, 1711.

104. F. P. A. Johnson, V. K. Popov, M. W. George, V. N. Bagratashvili, M. Poliakoff, and J. J. Turner, *Mendeleev Commun.*, 1991, 145.

105. E. F. Walsh, M. W. George, S. Goff, S. M. Nikiforov, V. K. Popov, X.-Z. Sun, and M. Poliakoff, *J. Phys. Chem.*, 1996, **100**, 19425.

106. U. Zheng, W. Wang, J. Lin, Y. She, and K. Fu, *J. Phys. Chem.*, 1992, **96**, 9821.

107. J. L. King, K. Molvinger, and M. Poliakoff, *Organometallics*, 2000, **19**, 5077.

108. J. A. Banister, P. D. Lee, and M. Poliakoff, *Organometallics*, 1995, **14**, 3876.

109. P. D. Lee, J. L. King, S. Seebald, and M. Poliakoff, *Organometallics*, 1998, **17**, 524.

110. J. A. Banister, M. W. George, S. Grubert, S. M. Howdle, M. Jobling, F. P. A. Johnson, S. L. Morrison, M. Poliakoff, and U. Schubert, *J. Organomet. Chem.*, 1994, **484**, 129.

111. M. Poliakoff, S. M. Howdle, and M. W. George, *Proc. Tech. Proc.*, 1996, **12**(High Press. Chem. Eng.), 67.

112. M. Colombo, M. W. George, J. N. Moore, D. I. Pattison, R. N. Perutz, I. G. Virrels, and T.-Q. Ye, *J. Chem. Soc., Dalton Trans.*, 1997, 2857.

113. R. J. Mawby, R. N. Perutz, and K. Whittlesey, *Organometallics*, 1995, **14**, 3268.

114. R. G. Ball, A. K. Campen, W. A. G. Graham, P. A. Hamley, S. G. Kazarian, M. O. Ollino, M. Poliakoff, A. J. Rest, L. Sturgeoff, and I. Whitwell, *Inorg. Chim. Acta*, 1997, **259**, 137.

115. R. N. Perutz, *Pure Appl. Chem.*, 1998, **70**, 2211.

116. P. Bergamini, E. Costa, S. Sostero, and O. Traverso, *Coord. Chem. Rev.*, 1993, **125**, 53.

117. W. D. Jones and J. A. Macguire, *Organometallics*, 1986, **5**, 590.

118. (a) W. D. Jones, G. P. Rosini, and J. A. Maguire, *Organometallics*, 1999, **18**, 1754; (b) W. D. Jones, J. A. Maguire, and G. P. Rosini, *Inorg. Chim. Acta*, 1998, **270**, 77.

119. A. J. Hart-Davis and W. A. G. Graham, *J. Am. Chem. Soc.*, 1969, **91**, 3375.

120. W. A. G. Graham, *J. Organomet. Chem.*, 1986, **300**, 81.

121. U. Schubert, *Adv. Organomet. Chem.*, 1990, **30**, 151.

122. B. J. Palmer and R. H. Hill, *Can. J. Chem.*, 1996, **74**, 1959.

123. P. T. Snee, C. K. Payne, K. T. Kotz, H. Yang, and C. B. Harris, *J. Am. Chem. Soc.*, 2001, **123**, 2255.

124. P. T. Snee, H. Yang, K. T. Kotz, C. K. Payne, and C. B. Harris, *J. Phys. Chem.*, 1999, **103**, 10426.

125. H. Tanachat, M. C. Asplund, K. T. Kotz, M. J. Wilkens, H. Frei, and C. B. Harris, *J. Am. Chem. Soc.*, 1998, **120**, 10154.

126. S. Hu, G. J. Farrell, C. Cook, R. Johnston, and T. J. Burkey, *Organometallics*, 1994, **13**, 4127.

127. H. Yang, K. T. Kotz, M. C. Asplund, M. J. Wilkens, and C. B. Harris, *Acc. Chem. Res.*, 1999, **32**, 551.

128. J. K. Hoyano and W. A. G. Graham, *J. Am. Chem. Soc.*, 1982, **104**, 3723.

129. A. H. Janowicz and R. G. Bergman, *J. Am. Chem. Soc.*, 1982, **104**, 352.

130. J. A. Labinger and J. E. Bercaw, *Nature*, 2002, **417**, 507.

131. (a) A. J. Lees, *J. Organomet. Chem.*, 1998, **554**, 1; (b) A. J. Lees and A. A. Purwoko, *Coord. Chem. Rev.*, 1994, **132**, 155.

132. R. G. Bergman, *Adv. Chem. Ser.*, 1992, **230**, 211.

133. S. A. Blum, K. L. Tan, and R. G. Bergman, *J. Org. Chem.*, 2003, **68**, 4127.

134. J. J. Schneider, *Angew. Chem, Int. Ed. Engl.*, 1996, **35**, 1068.

135. (a) A. E. Shilov and G. B. Shul'pin, *Chem. Rev.*, 1997, **97**, 2879; (b) A. E. Shilov and G. B. Shul'pin, 'Activation and Catalytic Reactions of Saturated Hydrocarbons in the Presence of Metal Complexes', Kluwer, Dordrecht, Boston, 2000.

136. B. F. Minaev, *Bull. Pol. Acad. Sci.*, 2000, **48**, 131.

137. A. J. Rest, I. Whitwell, W. A. G. Graham, J. K. Hoyano, and A. D. McMaster, *J. Chem. Soc., Chem. Commun.*, 1984, 624.

138. (a) P. E. Bloyce, A. J. Rest, I. Whitwell, W. A. G. Graham, and R. Holmes-Smith, *J. Chem. Soc., Chem. Commun.*, 1988, 846; (b) P. E. Bloyce, A. J. Rest, and I. Whitwell, *J. Chem. Soc., Dalton Trans.*, 1990, 813.

139. E. P. Wasserman, C. B. Moore, and R. G. Bergman, *Science*, 1992, **255**, 315.

140. A. A. Bengali, R. H. Schultz, C. B. Moore, and R. G. Bergman, *J. Am. Chem. Soc.*, 1994, **116**, 9585.

141. B. H. Weiller, E. P. Wasserman, R. G. Bergman, C. B. Moore, and G. C. Pimentel, *J. Am. Chem. Soc.*, 1989, **111**, 8288.

142. B. K. McNamara, J. S. Yeston, R. G. Bergman, and C. B. Moore, *J. Am. Chem. Soc.*, 1999, **121**, 6437.

143. R. H. Schultz, A. A. Bengali, M. J. Tauber, B. H. Weiller, E. P. Wasserman, K. R. Kyle, C. B. Bradley, and R. G. Bergman, *J. Am. Chem. Soc.*, 1994, **116**, 7369.

144. (a) S. E. Bromberg, T. Lian, R. G. Bergman, and C. B. Harris, *J. Am. Chem. Soc.*, 1996, **118**, 2069; (b) J. B. Asbury, K. Hang, J. S. Yeston, J. G. Cordaro, R. G. Bergman, and T. Lian, *J. Am. Chem. Soc.*, 2000, **122**, 12870.

145. (a) D. E. Marx and A. J. Lees, *Inorg. Chem.*, 1988, **27**, 1121; (b) D. P. Crolet and A. J. Lees, *J. Am. Chem. Soc.*, 1992, **114**, 4186; (c) A. A. Purwoko and A. J. Lees, *J. Organomet. Chem.*, 1995, **504**, 107; (d) N. Dunwoody and A. J. Lees, *Organometallics*, 1997, **16**, 5770.

146. Z. Hu, R. J. Boyd, and H. Nakatsuji, *J. Am. Chem. Soc.*, 2002, **124**, 2664.

147. J. B. Asbury, H. N. Ghosh, J. S. Yeston, R. G. Bergman, and T. Lian, *Organometallics*, 1998, **17**, 3417.

148. D. Drolet and A. J. Lees, *J. Am. Chem. Soc.*, 1990, **112**, 5878.

149. T. W. Bell, S.-A. Brough, M. G. Partridge, R. N. Perutz, and A. D. Rooney, *Organometallics*, 1993, **12**, 2933.

150. J. A. Banister, A. I. Cooper, S. M. Howdle, M. Jobling, and M. Poliakoff, *Organometallics*, 1996, **15**, 1804.
151. M.-D. Su and S.-Y. Chu, *Int. J. Quant. Chem.*, 1998, **70**, 961.
152. C. K. Ghosh and W. A. G. Graham, *J. Am. Chem. Soc.*, 1987, **109**, 4726.
153. P. E. Bloyce, J. Mascetti, and A. J. Rest, *J. Organomet. Chem.*, 1993, **444**, 223.
154. (a) A. A. Purwoko and A. J. Lees, *Inorg. Chem.*, 1995, **34**, 424; (b) A. A. Purwoko and A. J. Lees, *Inorg. Chem.*, 1996, **35**, 675; (c) A. A. Purwoko, S. D. Tibensky, and A. J. Lees, *Inorg. Chem.*, 1996, **35**, 7049.
155. (a) T. Lian, S. E. Bromberg, H. Yang, R. G. Bergman, and C. B. Harris, *J. Am. Chem. Soc.*, 1996, **118**, 3769; (b) S. E. Bromberg, H. Yang, M. C. Asplund, T. Lian, B. K. McNamara, K. T. Kotz, J. S. Yeston, M. Wilkens, H. Frei, R. G. Bergman, and C. B. Harris, *Science*, 1997, **278**, 260; (c) J. Yeston, B. McNamara, R. G. Bergman, and C. B. Moore, *Organometallics*, 2000, **19**, 3442; (d) M. C. Asplund, P. T. Snee, J. S. Yeston, M. K. Wilkens, C. K. Payne, H. Yang, K. T. Kotz, H. Frei, R. G. Bergman, and C. B. Harris, *J. Am. Chem. Soc.*, 2002, **124**, 10695.
156. B. J. Fisher and R. Eisenberg, *Organometallics*, 1983, **2**, 764.
157. (a) L. Zhang, *Nan. Hua. Daxue. Xue*, 1997, **19**, 25; (b) E. M. Gordon and R. Eisenberg, *J. Mol. Catal.*, 1988, **45**, 57; (c) A. J. Kinin and R. Eisenberg, *Organometallics*, 1988, **7**, 2124; (d) T. Sakakura, and M. Tanaka, *Chem. Lett.*, 1987, 249; (e) T. Sakakura and M. Tanaka, *J. Chem. Soc., Chem. Commun.*, 1987, 758; (f) E. M. Gordon and R. Eisenberg, *J. Organomet. Chem.*, 1986, **306**, C53; (g) A. Kunin and R. Eisenberg, *J. Am. Chem. Soc.*, 1986, **108**, 535.
158. (a) M. Tanaka, T. Sakakura, H. Wada, and Y. Sasaki, Manufacture of aromatic aldehydes Jpn. Kokai Tokkyo Koho, 1991, Application: JP 90–64813 19900315. CAN 116:173771; (b) T. Sakakura and T. Sako, Preparation of aromatic aldehydes or aromatic alcohols, Jpn. Kokai Tokkyo Koho, 1999, Application: JP 97–159343 19970617. CAN 130:110052.
159. T. Sakakura, T. Sodeyama, K. Sasaki, K. Wada, and M. Tanaka, *J. Am. Chem. Soc.*, 1990, **112**, 7221.
160. N. K. Khannanov, G. N. Menchikova, and E. A. Grigoryan, *Izv. Akad. Nauk., Ser. Khim.*, 1994, 1013.
161. N. K. Khannanov, G. N. Menchikova, and E. A. Grigorjan, *Kinet. Katal.*, 1993, **34**, 63.
162. (a) T. Sakakura, K. Sasaki, Y. Tokunaga, K. Wada, and M. Tanaka, *Chem. Lett.*, 1988, 155; (b) T. Sakakura, M. Tanaka, *Chem. Lett.*, 1987, 1113.
163. (a) T. Sakakura, F. Abe, and M. Tanaka, *Chem. Lett.*, 1991, 297; (b) M. Tanaka, T. Sakakura, and K. Ishida, Catalytic photochemical dehydrogenation of hydrocarbons in the presence of rhodium-organophosphorus complex, Katsuaki. Jpn. Kokai Tokkyo Koho, 1991, Application: JP 89–333048 19891222. CAN 116:6134; (c) J. A. Maguire, W. T. Boese, and A. S. Goldman, *J. Am. Chem. Soc.*, 1989, **111**, 7088; (d) J. A. Maguire, W. T. Boese, and A. S. Goldman, *J. Am. Chem. Soc.*, 1990, **112**, 7835; (e) K. C. Shih and A. S. Goldman, *Organometallics*, 1993, **12**, 3390; (f) T. Sakakura, T. Hayashi, and M. Tanaka, *Chem. Lett.*, 1987, 859.
164. T. Sakakura, Y. Tokunaga, T. Sodeyama, and M. Tanaka, *Chem. Lett.*, 1987, 2375.
165. (a) K. Sasaki, T. Sakakura, Y. Tokunaga, K. Wada, and M. Tanaka, *Chem. Lett.*, 1988, 685; (b) K. Sasaki, T. Sakakura, Y. Tokunaga, K. Wada, and M. Tanaka, *Chem. Lett.*, 1988, 685; (c) T. Sakakura, T. Sodeyama, Y. Tokunaga, and M. Tanaka, *Chem. Lett.*, 1987, 2211.
166. G. P. Rosini, S. Soubra, M. Vixamar, S. Wang, and A. S. Goldman, *J. Organomet. Chem.*, 1998, **554**, 41.
167. T. Sakakura, K. Ishiguro, M. Okano, and T. Sako, *Chem. Lett.*, 1997, 1089.
168. T. Bitterwolf, D. L. Kline, J. Linehan, C. R. Yonker, and R. S. Addleman, *Angew. Chem., Int. Ed. Engl.*, 2001, **40**, 2692.
169. J.-C. Choi, Y. Kobayashi, and T. Sakakura, *J. Org. Chem.*, 2001, **66**, 5262.
170. (a) M. Tanaka and T. Sakakura, *Adv. Chem. Ser., Homogeneous Transi. Met. Catal. React.*, 1992, **230**, 181; (b) M. Tanaka and T. Sakakura, *Sol. Energy Mater*, 1991, **24**, 406.
171. S. E. Boyd, L. D. Field, and M. G. Partridge, *J. Am. Chem. Soc.*, 1994, **116**, 9492.
172. J.-C. Choi and T. Sakakura, *J. Am. Chem. Soc.*, 2003, **125**, 7762.
173. G. P. Rosini, W. T. Boese, and A. S. Goldman, *J. Am. Chem. Soc.*, 1994, **116**, 9498.
174. (a) J. S. Bridgewater, T. L. Netzel, J. R. Schoonover, S. M. Massik, and P. C. Ford, *Inorg. Chem.*, 2001, **40**, 1466; (b) J. S. Bridgewater, B. Lee, S. Bernhard, J. R. Schoonover, and P. C. Ford, *Organometallics*, 1997, **16**, 5592.
175. T. E. Bitterwolf, W. B. Scallorn, J. T. Bays, C. A. Weiss, J. C. Linehan, J. Franz, and R. Poli, *J. Organomet. Chem.*, 2002, **652**, 95.
176. R. H. Schultz, *J. Organomet. Chem.*, 2003, **688**, 1.
177. T. Ishiyama and N. Miyaura, *J. Organomet. Chem.*, 2003, **680**, 3.
178. (a) K. M. Waltz and J. F. Hartwig, *J. Am. Chem. Soc.*, 2000, **122**, 11358; (b) K. M. Waltz and J. F. Hartwig, *Science*, 1997, **277**, 211.
179. (a) K. M. Waltz, C. N. Muhoro, and J. F. Hartwig, *Organometallics*, 1999, **18**, 3383; (b) K. M. Waltz, X. He, C. Muhoro, and J. F. Hartwig, *J. Am. Chem. Soc.*, 1995, **117**, 11357.
180. T. E. Bitterwolf, C. M. Waltz, and J. F. Hartwig, Manuscript in Preparation, 2003.
181. W. H. Lam and Z. Lin, *Organometallics*, 2003, **22**, 473.
182. H. Chen and J. F. Hartwig, *Angew. Chem., Int Ed. Engl.*, 1999, **38**, 2291.
183. J. F. Hartwig and X. He, *Angew. Chem., Int Ed. Engl.*, 1996, **35**, 315.

184. Y. Kawano, T. Yasue, and M. Shimoi, *J. Am. Chem. Soc.*, 1999, **121**, 11744.

185. (a) C. A. Tolman, S. D. Ittle, A. D. English, and J. P. Jesson, *J. Am. Chem. Soc.*, 1979, **101**, 1742; (b) C. A. Tolman, S. D. Ittle, A. D. English, and J. P. Jesson, *J. Am. Chem. Soc.*, 1978, **100**, 7577; (c) C. A. Tolman, S. D. Ittle, A. D. English, and J. P. Jesson, *J. Am. Chem. Soc.*, 1978, **100**, 4080.

186. M. V. Baker and L. D. Field, *J. Am. Chem. Soc.*, 1986, **108**, 7433.

187. P. Bergamini, S. Sostero, and O. Traverso, *J. Organomet. Chem.*, 1986, **299**, C11.

188. (a) L. D. Field, A. V. George, and B. A. Messerle, *J. Chem. Soc., Chem. Commun.*, 1991, 1339; (b) R. L. Burwell Jr, *Chemtracts: Ing. Chem.*, 1991, **3**, 352.

189. (a) M. V. Baker and L. D. Field, *J. Am. Chem. Soc.*, 1987, **109**, 2825; (b) M. V. Baker and L. D. Field, *J. Am. Chem. Soc.*, 1987, **109**, 2825.

190. L. D. Field, Catalytic conversion of alkanes to alkenes, PCT Int. Appl. (1988), Application: WO 87-AU377 19871110. Priority: AU 86–8903 19861111. CAN 110:193122.

191. I. E. Buys, L. D. Field, T. W. Hambley, and A. E. D. McQueen, *J. Chem. Soc., Chem. Commun.*, 1994, 557.

192. M. K. Whittlesey, R. J. Mawby, R. Osman, R. N. Perutz, L. D. Field, M. P. Wilkinson, and M. W. George, *J. Am. Chem. Soc.*, 1993, **115**, 8627.

193. S. A. Macgregor, O. Eisenstein, M. K. Whittlesey, and R. N. Perutz, *J. Chem. Soc., Dalton Trans.*, 1998, 291.

194. L. Cronin, M. C. Nicasio, R. N. Perutz, R. G. Peters, D. M. Roddick, and M. K. Whittlesey, *J. Am. Chem. Soc.*, 1995, **117**, 10047.

195. T. Yoshida, T. Yamagata, T. H. Tulip, J. A. Ibers, and S. Otsuka, *J. Am. Chem. Soc.*, 1978, **100**, 2063.

196. R. Boaretto, S. Sostero, and O. Traverso, *Inorg. Chim. Acta*, 2002, **330**, 59.

197. M. Jang, S. B. Duckett, and R. Eisenberg, *Organometallics*, 1996, **15**, 2863.

198. J. P. Blaha and M. S. Wrighton, *J. Am. Chem. Soc.*, 1985, **107**, 2694.

199. N. E. Carpenter, M. A. Khan, and K. M. Nicholas, *Organometallics*, 1999, **18**, 1569.

200. (a) A. Bakac, and J. H. Espenson, *Inorg. Chem.*, 1989, **28**, 3901; (b) A. Bakac and J. H. Espenson, *Inorg. Chem.*, 1987, **26**, 4353.

201. C. G. Riordan and P. Wei, *J. Am. Chem. Soc.*, 1994, **116**, 2189.

202. (a) D. L. Mohler, J. Gray Coonce, and D. Predecki, *Bioorg. Med. Chem. Lett.*, 2003, **13**, 1377; (b) D. L. Mohler, E. K. Barnhardt, and A. L. Hurley, *J. Org. Chem.*, 2002, **67**, 4982; (c) D. L. Mohler, D. R. Dain, A. D. Kerekes, W. R. Nadler, and T. L. Scott, *Bioorg. Med. Chem. Lett.*, 1998, **8**, 871.

203. (a) A. L. Hurley, M. P. Maddox III, T. L. Scott, M. R. Flood, and D. L. Mohler, *Org. Lett.*, 2001, **3**, 2761; (b) A. L. Hurley and D. L. Mohler, *Org. Lett.*, 2000, **2**, 2745.

204. (a) D. G. Always and K. W. Barnett, *J. Organomet. Chem.*, 1975, **99**, C52; (b) D. G. Always and K. W. Barnett, *Inorg. Chem.*, 1978, **17**, 2826; (c) D. G. Always and K. W. Barnett, *Adv. Chem. Ser.*, 1978, **168**, 115.

205. R. H. Hooker, K. A. Mahmoud, and A. J. Rest, *J. Chem. Soc., Dalton Trans.*, 1990, 1231.

206. (a) J. Zakrzewski, *J. Organomet. Chem.*, 1991, **412**, C23; (b) J. Zakrzewski and C. Giannotti, *J. Organomet. Chem.*, 1990, **388**, 175; (c) J. Zakrzewski, *J. Organomet. Chem.*, 1987, **327**, C41.

207. J. Zakrzewski, *J. Organomet. Chem.*, 1989, **359**, 215; (b) M. Bukowska-Strzyzewska, A. Tosik, D. Wodka, and J. Zakrzewski, *Polyhedron*, 1994, **13**, 1689.

208. J. Zakrzewski, A. Tosik, and M. Bukowska-Strzyzewska, *J. Organomet. Chem.*, 1995, **495**, 83; (b) K. Kowalski, and J. Zakrzewski, *J. Organomet. Chem.*, 2003, **668**, 91.

209. C. E. Borja, V. Jakúbek, and A. J. Lees, *Inorg. Chem.*, 1998, **37**, 2281.

210. J. J. Turner, M. Poliakoff, and M. A. Healy, *Pure Appl. Chem.*, 1989, **61**, 787.

211. T. Kobayashi, H. Ohtani, H. Noda, S. Teratani, H. Yamazaki, and K. Yasufuku, *Organometallics*, 1986, **5**, 110.

212. (a) S. K. Kim, S. Pedersen, and A. H. Zewail, *Chem. Phys. Lett.*, 1995, **233**, 500; (b) D. A. Prinslow and V. Vaida, *J. Am. Chem. Soc.*, 1987, **109**, 5097.

213. (a) 3-MP glass: A. S. Hepp and M. S. Wrighton, *J. Am. Chem. Soc.*, 1983, **105**, 5934; (b) Ar matrix: I. A. Dunkin, P. Härter, and C. J. Shields, *J. Am. Chem. Soc.*, 1984, **106**, 7248.

214. J. Z. Zhang and C. B. Harris, *J. Chem. Phys.*, 1991, **95**, 4024.

215. J. C. Owrutsky and A. P. Baronavski, *J. Chem. Phys.*, 1996, **105**, 9864.

216. S. Zhang, H. T. Zhang, and T. L. Brown, *Organometallics*, 1992, **11**, 3929.

217. D. A. Steinhurst, A. P. Baronavski, and J. C. Owrutsky, *Chem. Phys. Lett.*, 2002, **361**, 513.

218. K. Mach, J. Novakova, and J. B. Raynor, *J. Organomet. Chem.*, 1992, **439**, 341.

219. T. L. Brown and S. Zhang, *Inorg. Chem.*, 1995, **34**, 1164.

220. (a) O. Kühn, M. R. D. Hachey, M. M. Rohmer, and C. Daniel, *Chem. Phys. Lett.*, 2000, **322**, 199; (b) A. Rosa, G. Ricciardi, E. J. Baerends, and D. J. Stufkens, *Inorg. Chem.*, 1996, **35**, 2886; (c) A. Rosa, G. Ricciardi, E. J. Baerends, and D. J. Stufkens, *Inorg. Chem.*, 1995, **34**, 3425.

221. F. A. Kvietok and B. E. Bursten, *Organometallics*, 1995, **14**, 2395.

222. (a) T. A. Barckholtz and B. E. Bursten, *J. Organomet. Chem.*, 2000, **596**, 212; (b) T. A. Barckholtz and B. E. Bursten, *J. Am. Chem. Soc.*, 1998, **120**, 926.

223. H. T. Zhang and T. L. Brown, *J. Am. Chem. Soc.*, 1993, **115**, 107.

224. (a) T. E. Bitterwolf, *Coord. Chem. Rev.*, 2001, **211**, 235; (b) T. E. Bitterwolf, *Coord. Chem. Rev.*, 2000, **206 – 207**, 419.

225. (a) R. H. Hooker and A. J. Rest, *J. Chem. Soc., Dalton Trans.*, 1990, 1221; (b) R. H. Hooker, K. A. Mahmoud, and A. J. Rest, *J. Organomet. Chem.*, 1983, **254**, C25; (c) M. L. Baker, P. E. Bloyce, A. W. Campen, A. J. Rest, and T. E. Bitterwolf, *J. Chem. Soc., Dalton Trans.*, 1990, 2825.

226. (a) J. C. Linehan, C. R. Yonker, R. S. Addleman, S. T. Autrey, J. T. Bays, T. B. Bitterwolf, and J. L. Daschbach, *Organometallics*, 2001, **20**, 401; (b) J. Peters, M. W. George, and J. J. Turner, *Organometallics*, 1995, **14**, 1503.

227. I. G. Virrels, T. F. Nolan, M. W. George, and J. J. Turner, *Organometallics*, 1997, **16**, 5879.

228. (a) R. H. Hooker, K. A. Mamoud, and A. J. Rest, *J. Chem. Soc., Chem. Commun.*, 1983, 1022; (b) Fe: A. F. Hepp, J. P. Blaha, C. Lewis, and M. S. Wrighton, *Organometallics*, 1984, **3**, 174; (c) P. E. Bloyce, A. K. Campen, R. H. Hooker, A. J. Rest, N. R. Thomas, T. E. Bitterwolf, and J. E. Shade, *J. Chem. Soc., Dalton Trans.*, 1990, 2833; (d) T. E. Bitterwolf, J. C. Linehan, and J. E. Shade, *Organometallics*, 2001, **20**, 775.

229. S. N. Collins, C. M. Brett, B. C. Bursten, *J. Cluster. Sci.*, 2004, **15**, 469.

230. J. P. Blaha, B. E. Bursten, J. C. Dewar, R. B. Frankel, C. L. Randolph, B. A. Wilson, and M. S. Wrighton, *J. Am. Chem. Soc.*, 1985, **107**, 4561.

231. M. W. George, T. P. Dougherty, and E. J. Heilweil, *J. Phys. Chem.*, 1996, **100**, 201.

232. C. J. Arnold, T.-Q. Ye, R. N. Perutz, R. E. Hester, and J. N. Moore, *Chem. Phys. Lett.*, 1996, **248**, 464.

233. (a) F. A. Kvietok and B. E. Bursten, *J. Am. Chem. Soc.*, 1994, **116**, 9807; (b) M. Vitale, M. E. Archer, and B. E. Bursten, *J. Chem. Soc., Chem. Commun.*, 1998, 179.

234. S. D. McKee and B. E. Bursten, *J. Am. Chem. Soc.*, 1991, **113**, 1210.

235. Y. H. Spooner, E. M. Mitchell, and B. E. Bursten, *Organometallics*, 1995, **14**, 5251.

236. (a) T. E. Bitterwolf, A. Saygh, J. E. Shade, A. L. Rheingold, G. P. A. Yap, and L. Liable-Sands, *J. Organomet. Chem.*, 1998, **562**, 89; (b) E. M. Mitchell and T. A. Barckholtz, B. E. Bursten, *Inorg. Chim. Acta*, 1996, **252**, 405.

237. (a) T. E. Bitterwolf, A. Saygh, J. L. Haener, R. Fierro, J. E. Shade, A. L. Rheingold, L. Liable-Sands, and H. G. Alt, *Inorg. Chim. Acta*, 2002, **334**, 54; (b) T. E. Bitterwolf, J. E. Shade, and J. A. Hansen, *J. Organomet. Chem.*, 1996, **514**, 13.

238. (a) T. E. Bitterwolf, J. L. Haener, J. E. Shade, A. L. Rheingold, and G. P. A. Yap, *J. Organomet. Chem.*, 1997, **547**, 23; (b) S. D. McKee, J. A. Krause, D. M. Lunder, and B. E. Bursten, *J. Coord. Chem.*, 1994, **32**, 249.

239. P. Burger, *Angew. Chem., Int Ed. Engl.*, 2001, **40**, 1917.

240. T. E. Bitterwolf, A. Saygh, J. E. Shade, A. L. Rheingold, G. P. A. Yap, and L. Lable-Sands, *Inorg. Chim. Acta*, 2000, **300–302**, 800.

241. (a) M. A. Alverez, M. E. Garcia, V. Riera, M. A. Ruiz, C. Bois, and Y. Jeannin, *J. Am. Chem. Soc.*, 1995, **117**, 1324; (b) M. A. Alverez, M. E. Garcia, V. Riera, and M. A. Ruiz, *J. Am. Chem. Soc.*, 1993, **115**, 3786.

242. C. Alvarez, M. E. Garcia, V. Riera, and M. A. Ruiz, *Organometallics*, 1997, **16**, 1378.

243. C. P. Casey, R. S. Cariño, R. K. Hayashi, and K. D. Schladetzky, *J. Am. Chem. Soc.*, 1996, **118**, 1617.

244. C. P. Casey, W. T. Boese, R. S. Cariño, and P. C. Ford, *Organometallics*, 1996, **15**, 2189.

245. T. Fox and P. Burger, *Eur. J. Inorg. Chem.*, 2001, 795.

246. R. Boese, J. K. Cammack, A. J. Matzger, K. Pflug, W. B. Tolman, K. P. C. Vollhardt, and T. W. Weidman, *J. Am. Chem. Soc.*, 1997, **119**, 6757.

247. T. E. Bitterwolf, J. C. Linehan, and J. E. Shade, *Organometallics*, 2000, **19**, 4915.

248. X. Song and T. L. Brown, *Inorg. Chem.*, 1995, **34**, 3220.

249. X. Song and T. L. Brown, *Organometallics*, 1995, **14**, 1478.

250. (a) S. C. Tenhaeff and D. R. Tyler, *Organometallics*, 1992, **11**, 1466; (b) S. C. Tenhaeff and D. R. Tyler, *Organometallics*, 1992, **10**, 1116.

251. (a) E. Schutte, T. J. R. Weakley, and D. R. Tyler, *J. Am. Chem. Soc.*, 2003, **125**, 10319; (b) J. L. Male, M. Yoon, A. G. Glenn, T. J. R. Weakley, and D. R. Tyler, *Macromolecules*, 1999, **32**, 3898; (c) J. L. Male, B. E. Lindfors, K. J. Covert, and D. R. Tyler, *J. Am. Chem. Soc.*, 1998, **120**, 13176; (d) B. E. Lindfors, J. L. Male, K. J. Covert, and D. R. Tyler, *J. Chem. Soc., Chem. Commun.*, 1997, 1687; (e) J. L. Male, B. E. Lindfors, K. J. Covert, and D. R. Tyler, *Macromolecules*, 1997, **30**, 6404; (f) K. J. Covert, E. F. Askew, J. Grunkemeier, and T. Koenig, *J. Am. Chem. Soc.*, 1992, **114**, 10446.

252. H. Yang, P. T. Snee, K. T. Kotz, C. K. Payne, and C. B. Harris, *J. Am. Chem. Soc.*, 2001, **123**, 4204.

253. H. Yang, P. T. Snee, K. T. Kotz, C. K. Payne, H. Frei, and C. B. Harris, *J. Am. Chem. Soc.*, 1999, **121**, 9227.

254. S. L. Scott, J. H. Espenson, and A. Bakac, *Organometallics*, 1993, **12**, 1044.

255. J. N. Demas and A. W. Adamson, *J. Am. Chem. Soc.*, 1971, **93**, 1800.

256. (a) N. H. Damrauer, G. Cerullo, A. Yeh, T. R. Boussie, C. V. Shank, and J. K. McCusker, *Science*, 1997, **275**, 54; (b) A. Vlcek Jr, *Chemtracts*, 1998, **11**, 621.

257. A. C. Bhasikuttan, M. Suzuki, S. Nakashima, and T. Okada, *J. Am. Chem. Soc.*, 2002, **124**, 8398.

258. E. M. Kober, B. P. Sullivan, and T. J. Meyer, *Inorg. Chem.*, 1984, **23**, 2098.

259. K. M. Omberg, J. R. Schoonover, J. A. Treadway, R. M. Leasure, R. B. Dyer, and T. J. Meyer, *J. Am. Chem. Soc.*, 1997, **119**, 7013.

260. H. Riesen, L. Wallace, and E. Krausz, *Inorg. Chem.*, 1996, **35**, 6908.

261. J. S. Gold, S. J. Milder, and J. W. Lewis, *Inorg. Chem.*, 1985, **23**, 8285.

262. (a) P. J. Carol and L. E. Brus, *J. Am. Chem. Soc.*, 1987, **109**, 7613; (b) P. G. Bradley, N. Kress, B. A. Hornberger, R. F. Sallinger, and W. H. Woodruff, *J. Am. Chem. Soc.*, 1981, **103**, 7441; (c) M. Forster and R. E. Hester, *Chem. Phys. Lett.*, 1981, **81**, 42.

263. D. H. Oh, M. Sano, and S. G. Boxer, *J. Am. Chem. Soc.*, 1991, **113**, 6880.

264. (a) H. Yersin, W. Humbs, and J. Strasser, *Coord. Chem. Rev.*, 1997, **159**, 325; (b) D. Braun, P. Huber, J. Wudy, J. Schmidt, and H. Yersin, *J. Phys. Chem.*, 1994, **98**, 8044; (c) D. Braun, E. Gallhuber, and H. Yersin, *Chem. Phys. Lett.*, 1990, **171**, 122.

265. A. T. Yeh, C. V. Shank, and J. K. McKusker, *Science*, 2000, **289**, 935.

266. N. H. Damrauer and J. K. McCusker, *Inorg. Chem.*, 1999, **38**, 4268.

267. (a) H. Bock and H. tom Dieck, *Angew. Chem., Int. Ed. Engl.*, 1966, **5**, 520; (b) H. Bock and H. tom Dieck, *Chem. Ber.*, 1967, **100**, 228; (c) H. tom Dieck and I. W. Renk, *Chem. Ber.*, 1971, **104**, 110.

268. H. tom Dieck and I. W. Renk, *Angew. Chem., Int. Ed. Engl.*, 1970, **9**, 793.

269. L. H. Staal, D. J. Stufkens, and A. Oskam, *Inorg. Chim. Acta*, 1978, **26**, 255.

270. J. van Slageren, A. Klein, S. Záliš, and D. J. Stufkens, *Coord. Chem. Rev.*, 2001, **219 – 221**, 937.

271. A. Vlček Jr *Coord. Chem. Rev.*, 2002, **230**, 225.

272. (a) S. Záliš, I. R. Farrell, and A. Vlček Jr, *J. Am. Chem. Soc.*, 2003, **125**, 4580; (b) I. R. Farrell, F. Hartl, S. Záliš, and A. Vlček Jr, *J. Chem. Soc., Dalton Trans.*, 2000, 4323; (c) I. R. Farrell, J. van Slageren, S. Záliš, and A. Vlček Jr, *Inorg. Chim. Acta*, 2001, **315**, 44.

273. (a) D. Guillaumont, C. Daniel, and A. Vlček Jr, *Inorg. Chem.*, 1997, **36**, 1684; (b) D. Guillaumont, C. Daniel, and A. Vlček Jr, *J. Phys. Chem.*, 2001, **105**, 1107.

274. K. A. Rawlins and A. J. Lees, *Inorg. Chem.*, 1989, **28**, 2154.

275. F.-W. Grevels, K. Kerpen, W. E. Klotzbücher, K. Schaffner, R. Goddard, B. Weimann, C. Kayran, and S. Özkar, *Organometallics*, 2001, **20**, 4775.

276. (a) W.-F. Fu and R. van Eldik, *Inorg. Chem.*, 1998, **37**, 1044; (b) W.-F. Fu and R. van Eldik, *Organometallics*, 1997, **16**, 572.

277. R. S. Panesar, N. Dunwoody, and A. J. Lees, *Inorg. Chem.*, 1998, **37**, 1648.

278. I. G. Virrels, M. W. George, J. J. Turner, J. Peters, and A. Vlček Jr, *Organometallics*, 1996, **15**, 4089; (b) J. Víchová, F. Hartl, and A. Vlček Jr, *J. Am. Chem. Soc.*, 1992, **114**, 10903.

279. E. Lindsay, A. Vlček, and C. H. Langford Jr *Inorg. Chem.*, 1993, **32**, 3822.

280. A. Vlček Jr, I. R. Farrell, D. J. Liard, P. Matousek, M. Towrie, A. W. Parker, D. C. Grills, and M. W. George, *J. Chem. Soc., Dalton Trans.*, 2002, 701; (b) I. R. Farrell, P. Matousek, and A. Vlček Jr, *J. Am. Chem. Soc.*, 1999, **121**, 5296; (c) I. G. Virrels, M. W. George, J. J. Turner, J. Peters, and A. Vlček Jr, *Organometallics*, 1996, **15**, 4089.

281. (a) P. A. Mabrouk and M. S. Wrighton, *Chem. Phys. Lett.*, 1984, **103**, 332; (b) J. C. Luong, L. Nadjo, and M. S. Wrighton, *J. Am. Chem. Soc.*, 1978, **100**, 5790.

282. (a) N. Sutin, C. Creutz, and E. Fujita, *Comm. Inorg. Chem.*, 1997, **19**, 67; (b) O. Ishitani, M. W. George, T. Ibusuki, F. P. A. Johnson, K. Koike, K. Nozaki, C. Pac, J. J. Turner, and J. R. Westwell, *Inorg. Chem.*, 1994, **33**, 4712; (c) J. Hawecker and J.-M. Lehn, *Helv. Chim. Acta*, 1986, **69**, 1990; (d) J. Hawecker, J.-M. Lehn, and R. J. Ziessel, *J. Chem. Soc., Chem. Commun.*, 1983, 536.

283. (a) H. Hori, F. P. A. Johnson, K. Koike, O. Ishitani, and T. Ibusuki, *J. Photochem. Photobiol., A*, 1996, **96**, 171; (b) H. Hori, O. Ishitani, K. Koike, F. P. A. Johnson, and T. Ibusuki, *Energy Conv. Manag.*, 1995, **36**, 621.

284. (a) D. R. Striplin and G. A. Crosby, *Coord. Chem. Rev.*, 2001, **211**, 163; (b) D. R. Striplin and G. A. Crosby, *Chem. Phys. Lett.*, 1994, **221**, 426; (c) K. S. Schanze, D. B. MacQueen, T. A. Perkins, and L. A. Cabana, Leonardo, *Coord. Chem. Rev.*, 1993, **122**, 63.

285. (a) B. D. Rossenaar, D. J. Stufkens, and A. Vlček Jr, *Inorg. Chem.*, 1996, **35**, 2902; (b) B. D. Rossenaar, D. J. Stufkens, and A. Vlček Jr, *Inorg. Chim. Acta*, 1996, **247**, 247.

286. G. J. Stor, D. J. Stufkens, P. Vernooijs, E. J. Baerends, J. Fraanje, and K. Goubitz, *Inorg. Chem.*, 1995, **34**, 1588.

287. (a) D. Guillaumont and C. Daniel, *J. Am. Chem. Soc.*, 1999, **121**, 11733; (b) D. Guillaumont and C. Daniel, *Coord. Chem. Rev.*, 1998, **177**, 181; (c) K. Finger, C. Daniel, P. Saalfrank, B. Schmidt, and *J. Phys. Chem.*, 1996, **100**, 3368.

288. B. D. Rossenaar, C. J. Kleverlaan, D. J. Stufkens, and A. Oskam, *J. Chem. Soc., Chem. Commun.*, 1994, 63.

289. (a) B. D. Rossenaar, C. J. Kleverlaan, M. C. E. van de Ven, D. J. Stufkens, A. Oskam, J. Fraanje, and K. Goubitz, *J. Organomet. Chem.*, 1995, **493**, 153; (b) B. D. Rossenaar, C. J. Kleverlaan, M. C. E. van de Ven, D. J. Stufkens, and A. Vlček Jr. *Chem. Eur. J.*, 1996, **2**, 228.

290. (a) R. R. Andréa, D. J. Stufkens, and A. Oskam, *J. Organomet. Chem.*, 1985, **290**, 63; (b) D. J. Stufkens, M. P. Aarnts, J. Nijhoff, B. D. Rossenaar, and A. Vlcek Jr, *Coord. Chem. Rev.*, 1998, **171**, 93; (c) M. P. Aarnts, D. J. Stufkens, and A. Vlcek Jr. *Inorg. Chim. Acta*, 1997, **266**, 37; (d) B. D. Rossenaar, E. Lindsay, D. J. Stufkens, and A. Vlcek Jr, *Inorg. Chim. Acta*, 1996, **250**, 5.

291. B. D. Rossenaar, M. W. George, F. P. A. Johnson, D. J. Stufkens, J. J. Turner, and A. Vlček Jr *J. Am. Chem. Soc.*, 1995, **117**, 11582.

292. L. A. Lucia, R. D. Burton, and K. S. Schanze, *Inorg. Chim. Acta*, 1993, **208**, 103.

293. (a) I. R. Farrell, P. Matousek, C. J. Kleverlaan, and A. Vlček Jr, *Chem. Eur. J.*, 2000, **6**, 1386; (b) C. J. Kleverlaan and D. J. Stufkens, *Inorg. Chim. Acta*, 1999, **284**, 61; (c) C. J. Kleverlaan, D. J. Stufkens, I. P. Clark, M. W. George,

J. J. Turner, D. M. Martino, H. van Willigen, and A. Vlček Jr, *J. Am. Chem. Soc.*, 1998, **120**, 10871.

294. (a) C. J. Kleverlaan, D. M. Martino, J. Van Slageren, H. Van Willigen, D. J. Stufkens, and A. Oskam, *Appl. Magn. Reson.*, 1998, **15**, 203; (b) C. J. Kleverlaan, D. M. Martino, H. van Willigen, D. K. Stufkens, and A. Oskam, *J. Phys. Chem.*, 1996, **100**, 18607.

295. D. Guillaumont, M. P. Wilms, C. Daniel, and D. J. Stufkens, *Inorg. Chem.*, 1998, **37**, 5816.

296. (a) B. D. Rossenaar, F. Hartl, D. J. Stufkens, C. Amatore, E. Maisonhaute, and J.-N. Verpeaux, *Organometallics*, 1997, **16**, 4675; (b) B. D. Rossenaar, D. J. Stufkens, A. Oskam, J. Fraanje, and K. Goubitz, *Inorg. Chim. Acta*, 1996, **247**, 215.

297. R. R. Andréa, W. D. J. de Lange, and D. J. Stufkens, Al. Oskam, *Inorg. Chem.*, 1989, **28**, 318.

298. (a) B. D. Rossenaar, T. van der Gaaf, R. van Eldik, C. H. Langford, D. J. Stufkens, and A. Vlček Jr, *Inorg. Chem.*, 1994, **33**, 2865; (b) D. J. Stufkens, J. W. M. van Outersterp, A. Oskam, B. D. Rossenaar, and G. J. Stor, *Coord. Chem. Rev.*, 1994, **132**, 147; (c) T. van der Gaaf, D. J. Stufkens, A. Oskam, and G. Goubitz, *Inorg. Chem.*, 1991, **30**, 599; (d) T. van der Gaaf, R. M. J. Hofstra, P. G. M. Schilder, M. Rijkhoff, D. J. Stufkens, and J. G. M. van der Linden, *Organometallics*, 1991, **10**, 3668.

299. C. J. Kleverlaan, F. Hartl, and D. J. Stufkens, *J. Photochem. Photobiol., A*, 1997, **103**, 231.

300. (a) G. J. Stor, S. L. Morrison, D. J. Stufkens, and A. Oskam, *Organometallics*, 1994, **13**, 2641; (b) D. J. Stufkens, J. W. M. van Outersterp, A. Oskam, B. D. Rossenaar, and G. J. Stor, *Coord. Chem. Rev.*, 1994, **132**, 147.

301. A. Rosa, G. Ricciardi, E. J. Baerends, and D. J. Stufkens, *J. Phys. Chem.*, 1996, **100**, 15346.

302. (a) A. Vogler and H. Kunkely, *Coord. Chem. Rev.*, 1998, **177**, 81; (b) P. E. Hoggard, *Coord. Chem. Rev.*, 1997, **159**, 235.

303. H. Kunkely and A. Vogler, *J. Photochem. Photobiol., A*, 2003, **154**, 289.

304. J. E. Shade, W. H. Pearson, J. E. Brown, and T. E. Bitterwolf, *Organometallics*, 1995, **14**, 157.

305. J. D. Carter, K. B. Kingsbury, A. Wilde, T. K. Schoch, C. J. Leep, E. K. Pham, and L. McElwee-White, *J. Am. Chem. Soc.*, 1991, **113**, 2947.

306. (a) S. K. Deb, R. Ellingson, S. Ferrere, A. J. Frank, B. A. Gregg, A. J. Nozik, N. Park, and G. Schlichthorl, European Commission Report, EUR 18656, 2nd World Conference on Photovoltaic Solar Energy Conversion, 1998, Vol. I, 238; (b) A. J. Nozik and R. Memming, *J. Phys. Chem.*, 1994, **100**, 13061; (c) A. Hagfeldt and M. Grätzel, *Chem. Rev.*, 1995, **95**, 49; (d) P. V. Kamat, *Prog. React. Kinet.*, 1994, **19**, 277.

307. (a) M. Grätzel, *Nature*, 2001, **414**, 338; (b) B. Oregan and M. Grätzel, *Nature*, 1991, **353**, 737; (c) K. Kalyanasundaram and M. Gratzel, *Coord. Chem. Rev.*, 1998, **177**, 347.

308. (a) Y. Wang, J. B. Asbury, and T. Lian, *J. Phys. Chem.*, 2000, **104**, 4291; (b) J. B. Asbury, R. J. Ellingson, H. N. Ghosh, S. Ferrere, A. J. Nozik, and T. Lian, *J. Phys. Chem. B*, 1999, **103**, 3110; (c) R. Ellingson, J. B. Asbury, S. Ferrere, H. N. Ghosh, J. R. Sprague, T. Lian, and A. J. Nozik, *Zeit. Phys. Chem.*, 1999, **212**, 77; (d) R. J. Ellingson, J. B. Asbury, S. Ferrere, H. N. Ghosh, J. R. Sprague, T. Lian, and A. J. Nozik, *J. Phys. Chem. B*, 1998, **102**, 6455; (e) T. A. Heimer and E. J. Heilweil, *J. Phys. Chem.*, 1997, **101**, 100990.

309. F. Cao, G. Oskam, P. C. Searson, J. M. Stipkala, T. A. Heimer, F. Farzad, and G. J. Meyer, *J. Phys. Chem.*, 1995, **99**, 11974.

310. G. Benkö, J. Kallioninen, J. E. I. Korppi-Tommola, A. P. Yartsev, and V. Sundström, *J. Am. Chem. Soc.*, 2002, **124**, 489.

311. G. Benkö, P. Myllyperkiö, J. Pan, A. Pl Yartsev, and V. Sundström, *J. Am. Chem. Soc.*, 2003, **125**, 1118.

312. (a) J. B. Asbury, N. A. Anderson, E. Hao, X. Ai, and T. Lian, *J. Phys. Chem.*, 2003, **107**, 7376; (b) J. B. Asbury, Y.-Q. Wang, E. Hao, H. N. Ghosh, and T. Lian, *Res. Chem. Intermed.*, 2001, **27**, 393.

313. J. B. Asbury, E. Hao, Y. Wang, H. N. Ghosh, and T. Lian, *J. Phys. Chem.*, 2001, **105**, 4545.

314. (a) N. A. Anderson, X. Ai, D. Chen, D. Mohler, and T. Lian, *J. Phys. Chem.*, 2003, **107**, 14231; (b) J. B. Asbury, E. Hao, Y. Wang, and T. Lian, *J. Phys. Chem.*, 2000, **104**, 11957.

315. K. Hara, H. Horiuchi, R. Katoh, L. P. Singh, Lok. H. Sugihara, K. Sayama, S. Murata, M. Tachiya, and H. Arakawa, *J. Phys. Chem.*, 2002, **106**, 374.

316. Y. Tachibana, Md. K. Nazeeruddin, M. Gratzel, D. R. Klug, and J. R. Durrant, *Chem. Phys.*, 2002, **285**, 127.

317. I.-J. Chang, H. B. Gray, and J. R. Winkler, *J. Am. Chem. Soc.*, 1991, **113**, 7056.

318. (a) M. E. Nunez and J. K. Barton, *Curr. Op. Chem. Biol.*, 2000, **4**, 199; (b) K. E. Erkkila, D. T. Odom, and J. K. Barton, *Chem. Rev.*, 1999, **99**, 2777; (c) N. J. Turro, J. K. Barton, and D. A. Tomalia, *Acc. Chem. Res.*, 1991, **24**, 332.

319. M. E. Nunez, D. B. Hall, and J. K. Barton, *Chem. Biol.*, 1999, **6**, 85.

320. (a) T. T. Williams and J. K. Barton, *Small Molecule DNA and RNA Binders*, eds. M. Demeunynck, C. Bailly, and W. D. Wilson, 2003, **1**, 146; (b) S. Delaney and J. K. Barton, *J. Org. Chem.*, 2003, **68**, 6475; (c) R. Treadway, M. G. Hill, and J. K. Barton, *Chem. Phys.*, 2002, **281**, 409; (d) M. Boon and J. K. Barton, *Curr. Opin. Struct. Biol.*, 2002, **12**, 320; (e) J. K. Barton, *Pure Appl. Chem.*, 1998, **70**, 873; (f) R. E. Molmlin, P. J. Dandliker, and J. K. Barton, *Angew. Chem., Int. Ed. Engl.*, 1998, **36**, 2715.

321. N. J. Turro and J. K. Barton, *J. Biol. Inorg. Chem.*, 1998, **3**, 201.

322. D. B. Hall and J. K. Barton, *J. Am. Chem. Soc.*, 1997, **119**, 5045.

323. (a) E. M. Boon, J. L. Kisko, and J. K. Barton, *Meth. Enzymol.*, 2002, **353**, 506; (b) P. K. Bhattacharya, and J. K. Barton, *J. Am. Chem. Soc.*, 2001, **123**, 8649; (c) E. M. Boon, D. M. Ceres, T. G. Drummond, M. G. Hill, and J. K. Barton, *Nat. Biotechnol.*, 2001, **40**, 1096.

324. (a) H. A. Wagenknecht, S. R. Rajski, M. Pascaly, E. D. A. Stemp, and J. K. Barton, *J. Am. Chem. Soc.*, 2001, **123**, 4400; (b) S. R. Rajski and J. K. Barton, *Biochemistry*, 2001, **40**, 5556; (c) S. R. Rajski, S. Kumar, R. J. Roberts, J. K. Barton, *J. Am. Chem. Soc.*, 1999, **121**, 5615.

325. S. Delaney, M. Pascaly, P. K. Bhattacharya, and J. K. Barton, *Inorg. Chem.*, 2002, **41**, 1966.

326. (a) E. D. A. Stwmp, M. R. Arkin, and J. K. Barton, *J. Am. Chem. Soc.*, 1997, **119**, 2921; (b) M. R. Arkin, E. D. A. Stemp, S. C. Pulver, and J. K. Barton, *Chem. Biol.*, 1997, **4**, 389.

327. M. R. Arkin, E. D. A. Stemp, R. E. Holmlin, J. K. Barton, A. Hörmann, E. J. C. Olson, and P. F. Barbara, *Science*, 1996, **273**, 475.

328. C. J. Murphey, M. R. Arkin, Y. Jenkins, N. D. Ghatlia, S. H. Bossmann, N. J. Turro, and J. K. Barton, *Science*, 1993, **262**, 1025.

329. C. Moucheron, A. Kirsch-De Mesmaeker, and J. M. Kelly, *J. Photochem. Photobiol., B*, 1997, **40**, 91.

330. D. S. Wuttke, M. J. Bjerrum, I.-J. Chang, J. R. Winkler, and H. B. Gray, *Biochim. Biophys. Acta*, 1992, **1101**, 168.

331. (a) A. R. Dunn, I. J. Dmochowski, J. R. Winkler, and H. B. Gray, *J. Am. Chem. Soc.*, 2003, **125**, 12450; (b) J. J. Wilker, I. J. Dmochowski, J. H. Dawson, J. R. Winkler, and H. B. Gray, *Angew. Chem., Int. Ed. Engl.*, 1999, **38**, 90; (c) I. J. Dmochowski, B. R. Crane, J. J. Wilker, J. R. Winkler, and H. B. Gray, *Proc. Nat. Acad. Sci.*, 1999, **96**, 12987.

332. E. Babini, I. Pertini, M. Borsari, F. Capozzi, C. Luchinat, X. Zhang, G. L. C. Moura, I. V. Kurnikov, D. N. Beratan, A. Ponce, A. J. Di Bilio, J. R. Winkler, and H. B. Gray, *J. Am. Chem. Soc.*, 2000, **122**, 4532.

333. (a) G. A. Mines, M. J. Bjerrum, M. G. Hill, D. R. Casimiro, I.-J. J. R. Winkler, and H. B. Gray, *J. Am. Chem. Soc.*, 1996, **118**, 1961; (b) M. J. Bjerrum, D. R. Casimiro, I.-J. Chang, A. J. Di Bilio, H. B. Gray, M. G. Hill, R. Langen, G. A. Mines, and L. K. Skov J. R. Winkler, D. S. Wuttke, *J. Bioenerg. Biomember.*, 1995, **27**, 295; (c) D. R. Casimiro, D. N. Beratan, J. N. Onuchic, H. B. Gray, and J. R. Winkler, *Poly. Mat. Sci. Eng.*, 1994, **71**, 660.

334. (a) A. J. Di Bilio, C. Dennison, H. B. Gray, B. E. Ramirez, A. G. Sykes, and J. R. Winkler, *J. Am. Chem. Soc.*, 1998, **120**, 7551; (b) A. J. Di Bilio, C. Dennison, H. B. Gray, B. E. Ramirez, A. G. Sykes, and J. R. Winkler, *J. Am. Chem. Soc.*, 1998, **120**, 7551; (c) R. Langen, I.-J. Chang, J. P. Germanas, J. H. Richards, J. R. Winkler, and H. B. Gray, *Science*, 1995, **268**, 1733.

335. G. Engstrom, R. Rajagukguk, A. J. Saunders, C. N. Patel, S. Rajagukguk, T. Merbitz-Zahradnik, K. Xiao, G. J. Pielak, B. Trumpower, C.-A. Yu, L. Yu, B. Durham, and F. Millett, *Biochemistry*, 2003, **42**, 2816.

336. L. P. Pan, M. Frame, B. Durham, D. Davis, and F. Millett, *Biochemistry*, 1990, **29**, 3231.

337. J. Contzen, S. Kostka, R. Kraft, and C. Jung, *J. Inorg. Biochem.*, 2002, **91**, 607.

338. J. R. Telford, P. Wittung-Stafshede, H. B. Gray, and J. R. Winkler, *Acc. Chem. Res.*, 1998, **31**, 755.

339. W. T. Boese and P. C. Ford, *J. Am. Chem. Soc.*, 1995, **117**, 8381; (b) W. D. Boese, and P. C. Ford, *Organometallics*, 1994, **13**, 3525; (c) W. T. Boese, B. Lee, D. W. Ryba, S. T. Belt, and P. C. Ford, *Organometallics*, 1993, **12**, 4739.

340. R. L. Sweany, *Organometallics*, 1989, **8**, 175.

341. (a) K. L. McFarlane, B. Lee, W. Fu, R. van Eldik, and P. C. Ford, *Organometallics*, 1998, **17**, 1826; (b) K. L. McFarlane and P. C. Ford, *Organometallics*, 1998, **17**, 1166; (c) D. W. Ryba, R. van Eldik, and P. C. Ford, *Organometallics*, 1993, **12**, 104; (d) S. T. Belt, D. W. Ryba, and P. C. Ford, *J. Am. Chem. Soc.*, 1991, **113**, 9524.

342. W. T. Boese, K. L. McFarlane, B. Lee, J. G. Rabor, and P. C. Ford, *Coord. Chem. Rev.*, 1997, **159**, 135.

343. H. Kunkely, T. Türk, C. Teixeira, C. dr Merlć de Bellefon, W. A. Herrmann, and A. Vogler, *Organometallics*, 1991, **10**, 2090.

344. (a) L. J. Morris, A. J. Downs, T. M. Greene, G. S. McGrady, W. A. Herrmann, P. Sirsch, W. Scherer, and O. Gropen, *Organometallics*, 2001, **20**, 2344; (b) L. J. Morris, A. J. Downs, T. M. Greene, G. S. McGrady, W. A. Herrmann, P. Sirsch, O. Gropen, and W. Scherer, *J. Chem. Soc., Chem. Commun.*, 2000, **67**,.

345. (a) W. A. Herrmann, *J. Organomet. Chem.*, 1995, **500**, 149; (b) D. M. Hoffman, in ‘Comprehensive Organometallic Chemistry, II’, ed. C. P. Casey, Pergamon, Oxford, U.K., 1995, Vol. 6, p. 231.

346. G. Maier, H. P. Reisenauer, and H. Egenolf, *Organometallics*, 1999, **18**, 2155.

347. A. J. Downs, G. Dierker, J. C. Green, T. M. Greene, G. S. McGrady, L. J. Morris, W. Scherer, and P. Sirsch, *J. Chem. Soc., Dalton Trans.*, 2002, 3349.

348. L. J. Morris, A. J. Downs, J. C. Green, T. M. Greene, S. J. Teat, and S. Parsons, *J. Chem. Soc., Dalton Trans.*, 2002, 3142.

349. A. Haaland, W. Scherer, H. V. Volden, H. P. Verne, O. Gropen, G. S. McGrady, A. J. Downs, G. Dierker, W. A. Herrmann, P. W. Roesky, and M. R. Geisberger, *Organometallics*, 2000, **19**, 22.

350. T. E. Bitterwolf and J. T. Bays, *J. Organomet. Chem.*, 1998, **561**, 49.

351. C. G. Kreiter, A. Würtz, and P. Bell, *Chem. Ber.*, 1992, **125**, 377.

352. C. G. Kreiter and U. Kern, *J. Organomet. Chem.*, 1993, **459**, 199.

353. C. G. Kreiter, U. Kern, G. Wolmershäuser, and G. Heckmann, *Eur. J. Inorg. Chem.*, 1998, 127.

354. (a) S. A. R. Knox, R. F. D. Stansfield, F. G. A. Stone, M. J. Winter, and P. Woodward, *J. Chem. Soc., Dalton Trans.*, 1982, 173; (b) S. A. R. Knox, R. F. D. Stansfield, F. G. A. Stone, M. J. Winter, and P. Woodward, *J. Chem. Soc., Chem. Commun.*, 1978, 221.

355. M.-C. Chen, M. J. Eichberg, K. P. C. Vollhardt, R. Sercheli, I. M. Wasser, and G. D. Whitener, *Organometallics*, 2002, **21**, 749.

356. (a) P. A. Wender, N. C. Ihle, and C. R. D. Correia, *J. Am. Chem. Soc.*, 1998, **110**, 5904; (b) P. A. Wender, J. Nuss, D. B. Smith, A. Suarez-Sobrino, J. Vgberg, D. Decosta, and J. Bordner, *J. Org. Chem.*, 1997, **62**, 4908.

357. M. Lauthens, W. Tam, J. C. Lauthens, L. G. Edwards, C. M. Crudden, and A. C. Smith, *J. Am. Chem. Soc.*, 1995, **117**, 6863.

358. P. A. Wender and J. A. Love, *Adv. Cycloadd.*, 1999, **5**, 1.

359. M. Lautens, W. Klaute, and W. Tam, *Chem. Rev.*, 1996, **96**, 49.

360. (a) C. G. Kreiter, R. Eckert, W. Frank, and G. J. Reiss, *Inorg. Chim. Acta*, 1996, **251**, 95; (b) J. A. Rigby, H. S. Ateeq, N. R. Charles, J. A. Henshilwood, K. M. Short, and P. M. Sugathapala, *Tetrahedron*, 1993, **49**, 5495; (c) T. van Houwelingen, D. J. Stufkens, and A. Oskam, *Organometallics*, 1992, **11**, 1146.

361. J. H. Rigby, S. Scribner, and M. J. Heeg, *Tetrahedron Lett.*, 1995, **36**, 8569.

362. (a) C. G. Kreiter, E.-C. Koch, W. Frank, and G. J. Reiss, *Zeit. Naturfur., B*, 1996, **51**, 1473; (b) C. G. Kreiter, E.-C. Koch, W. Frank, and G. J. Reiss, *J. Organomet. Chem.*, 1995, **490**, 125; (c) C. G. Kreiter, E.-C. Koch, W. Frank, and G. J. Reiss, *Inorg. Chim. Acta*, 1994, **220**, 77.

363. (a) C. G. Kreiter, N. K. Wachter, and G. J. Reiss, *Eur. J. Inorg. Chem.*, 1999, 655; (b) C. G. Kreiter, C. Fiedler, W. Frank, and G. J. Reiss, *J. Organomet. Chem.*, 1995, **490**, 133.

364. C. G. Kreiter and R. Eckert, *Chem. Ber./Recl.*, 1997, **130**, 9.

365. I. Fischler, F. W. Grevels, J. Leitich, and S. Ozkar, *Chem. Ber.*, 1991, **124**, 2857.

366. (a) H.-J. Chung, J. B. Sheridan, M. L. Cote, and R. A. Lalancette, *Organometallics*, 1996, **15**, 4575; (b) C. G. Kreiter, C. Fiedler, W. Frank, and G. J. Reiss, *J. Organomet. Chem.*, 1995, **490**, 133; (c) K. Chafee, P. Huo, J. B. Sheridan, A. Barbieri, A. Aistars. R. A. Lalancette, R. L. Ostrander, and A. L. Rheingold, *J. Am. Chem. Soc.*, 1995, **117**, 1900; (d) C. Wang, J. B. Sheridan, H.-J. Chung, M. L. Cote, R. A. Lalancette, and A. L. Rheingold, *J. Am. Chem. Soc.*, 1994, **116**, 8966.

367. (a) J. H. Rigby and F. C. Pigge, *Tetrahedron Lett.*, 1996, **37**, 2201; (b) J. H. Rigby and F. C. Pigge, *J. Org. Chem.*, 1995, **60**, 7392; (c) J. H. Rigby, K. M. Short, H. S. Ateeq, and J. A. Henshilwood, *J. Org. Chem.*, 1992, **57**, 5290; (a) J. H. Rigby, N. C. Warshakoon, and A. J. Payen, *J. Am. Chem. Soc.*, 1999, **121**, 8237; (b) J. H. Rigby and N. C. Warshakoon, *Tetrahedron Lett.*, 1997, **38**, 2049; (c) J. H. Rigby and N. C. Warshakoon, *J. Org. Chem.*, 1996, **61**, 7644; (d) J. A. Rigby, H. S. Ateeq, and A. C. Krueger, *Tetrahedron Lett.*, 1992, **33**, 5873; (a) J. H. Rigby, S. D. Rege, V. P. Sandanayaka, and M. Kirova, *J. Org. Chem.*, 1996, **61**, 842; (b) J. H. Rigby, H. S. Ateeq, N. R. Charles, S. V. Cuisiat, M. D. Ferguson, J. A. Henshilwood, A. C. Krueger, C. O. Ogbu, K. M. Short, and M. J. Heeg, *J. Am. Chem. Soc.*, 1993, **115**, 1382.

368. (a) J. H. Rigby, M. Kirova, N. Niyaz, and F. Mohammadi, *Synlett*, 1997, 805; (b) J. H. Rigby and V. P. Sandanayaka, *Tetrahedron Lett.*, 1993, **34**, 935.

369. (a) J. H. Rigby and F. C. Pigge, *Synlett*, 1996, 631; (b) J. H. Rigby, G. Ahmed, and M. D. Ferguson, *Tetrahedron Lett.*, 1993, **34**, 5397.

370. J. H. Rigby and P. Sugathapala, *Tetrahedron Lett.*, 1996, **37**, 5293.

371. (a) J. H. Rigby, *Tetrahedron*, 1999, **55**, 4521; (b) J. H. Rigby, *Adv. Cycloadd.*, 1999, **6**, 97; (c) J. H. Rigby, *Org. React.*, 1997, **49**, 331; (d) J. H. Rigby, *Adv. Met.-Org. Chem.*, 1995, **4**, 89; (e) J. H. Rigby and A. C. Krueger, *Adv. Detailed React. Mech.*, 1995, **4**, 1.

372. B. L. Pagenkopf and T. Livinghouse, *J. Am. Chem. Soc.*, 1996, **118**, 2285.

373. (a) T. E. Bitterwolf, W. B. Scallorn, and C. A. Weiss, *J. Organomet. Chem.*, 2000, **605**, 7; (b) C. M. Gordon, M. Kiszka, I. R. Dunkin, W. J. Kerr, J. S. Scott, and J. Gebicki, *J. Organomet. Chem.* 1997, **554**, 147.

374. M. A. McGuire and L. S. Hegedus, *J. Am. Chem. Soc.*, 1982, **104**, 5538.

375. P.-J. Colson and L. S. Hegedus, *J. Org. Chem.*, 1994, **59**, 4972.

376. (a) B. Brown and L. S. Hegedus, *J. Org. Chem.*, 1998, **63**, 8012; (b) A. G. Riches, L. A. Wernersbach, and L. S. Hegedus, *J. Org. Chem.*, 1998, **63**, 4691; (c) S. Koebbing, J. Mattay, and G. Raabe, *Chem. Ber.*, 1993, **126**, 1849; (d) S. Koebbing and J. Mattay, *Tetrahedron Lett.*, 1992, **33**, 927.

377. (a) J. Zhu, C. Deur, and L. S. Hegedus, *J. Org. Chem.*, 1997, **62**, 7704; (b) L. S. Hegedus, *Acc. Chem. Res.*, 1995, **28**, 299.

378. A. Arrieta, F. P. Cossio, I. Fernández, M. Gómez-Gallego, B. Lecea, M. J. Mancheño, and M. A. Sierra, *J. Am. Chem. Soc.*, 2999, **122**, 11509.

379. (a) L. S. Hegedus, *Tetrahedron*, 1997, **53**, 4105; (b) H. G. Schmalz, *Nachricht. Chem., Tech. Labor.*, 1994, **42**, 608; (c) L. S. Hegedus, in ‘Comprehensive Organometallic Chemistry II’, eds. E. W. Abel, F. G. A. Stone, and G. Wilkinson, Pergamon, Oxford, UK, 1991, Vol 12, p. 549.

380. L. S. Hegedus, G. de Weck, and S. D’Andrea, *J. Am. Chem. Soc.*, 1988, **110**, 2122.

381. H. C. Foley, L. M. Strubinger, T. S. Targos, and G. L. Geoffroy, *J. Am. Chem. Soc.*, 1983, **105**, 3064.

382. L. K. Fong and N. J. Cooper, *J. Am. Chem. Soc.*, 1984, **106**, 2595.

383. T. F. Block, R. F. Fenske, and C. P. Casey, *J. Am. Chem. Soc.*, 1976, **98**, 441.

384. M. L. Gallagher, J. B. Greene, and A. D. Rooney, *Organometallics*, 1997, **16**, 5260.

385. (a) M. Cases, G. Frenking, M. Duran, and M. Solà, *Organometallics*, 2002, **21**, 4182; (b) C.-C. Wang, Y. Wang,

H.-J. Liu, K.-J. Lin, L.-K. Chou, and K.-S. Chan, *J. Phys. Chem. A*, 1997, **101**, 8887.

386. T. F. Block and R. F. Fenske, *J. Am. Chem. Soc.*, 1977, **99**, 4321.
387. E. O. Fischer and H. Fischer, *Chem. Ber.*, 1974, **107**, 657.
388. A. D. Rooney, J. J. McGarvey, K. C. Gordon, R.-A. McNicholl, U. Schubert, and W. Hepp, *Organometallics*, 1993, **12**, 1277.
389. P. C. Servaas, D. J. Stufkens, and A. Oskam, *J. Organomet. Chem.*, 1990, **390**, 61.
390. A. D. Rooney, J. J. McGarvey, and K. C. Gordon, *Organometallics*, 1995, **14**, 107.
391. J. R. Knorr and T. L. Brown, *Organometallics*, 1994, **13**, 2178.
392. S. E. J. Bell, K. C. Gordon, and J. J. McGarvey, *J. Am. Chem. Soc.*, 1988, **110**, 3107.
393. K. O. Doyle, M. L. Gallagher, M. T. Price, and A. D. Rooney, *J. Organomet. Chem.*, 2001, **617 – 618**, 269.
394. (a) J. Barluenga, M. A. Fernández-Rodriguez, F. Andina, and E. Aguilar, *J. Am. Chem. Soc.*, 2002, **124**, 10978; (b) J. Barluenga, S. López, A. A. Trabanco, A. Fernández-Rodriguez, and J. Flórez, *J. Am. Chem. Soc.*, 2000, **122**, 8145; (c) D. F. Harvey and K. P. Lund, *J. Am. Chem. Soc.*, 1991, **113**, 8916.
395. (a) P. J. Campos, D. Sampedro, and M. A. Rodriguez, *J. Org. Chem.*, 2003, **68**, 4674; (b) M. A. Sierra, J. C. del Amo, M. J. Mancheño, and M. Gómez-Gallego, *Tetrahedron Lett.*, 2001, **42**, 5435.
396. F. A. Cotton and G. Wilkinson, ‘Advanced Inorganic Chemistry’, 5th edn., J. Wiley, New York, 1988, p. 38.
397. S. M. Jørgensen, *Anorg. Chem.*, 1894, **5**, 168; J. E. Huheey, E. A. Keiter, and R. L. Keiter, ‘Inorganic Chemistry’, Harper Collins, New York, 4th ed., p. 513.
398. B. Adell, *Z. Anorg. Allg. Chem.*, 1955, **279**, 219.
399. (a) P. Coppens, I. Novozhilova, and A. Kovalevsky, *Chem. Rev.*, 2002, **102**, 861; (b) D. V. Fomitchev, I. Novozhilova, and P. Coppens, *Tetrahedron*, 2000, **56**, 6813; (c) P. Coppens, D. V. Fomitchev, M. D. Carducci, and K. Culp, *J. Chem. Soc., Dalton Trans.*, 1998, 865.
400. (a) T. Woike, W. Krasser, and P. S. Berchthold, *Phys. Rev. Lett.*, 1984, **53**, 1767; (b) U. Hauser, V. Oestreich, and H. D. Rohrweck, *Z. Phys. A*, 1977, **280**, 17; (c) U. Hauser, V. Oestreich, and H. D. Rohrweck, *Z. Phys. A*, 1977, **280**, 125.
401. M. D. Carducci, M. R. Pressprich, and P. Coppens, *J. Am. Chem. Soc.*, 1997, **119**, 2669.
402. J. Paulsen, V. Rusanov, R. Benda, C. Herta, C. Schünemann, C. Janiak, T. Dorn, A. I. Chumakov, H. Winkler, and A. X. Trautwein, *J. Am. Chem. Soc.*, 2002, **124**, 3007.
403. (a) O. Crichton and A. J. Rest, *J. Chem. Soc., Chem. Commun.*, 1973, 407; (b) O. Crichton and A. J. Rest, *J. Chem. Soc., Dalton Trans.*, 1977, 986.
404. D. V. Fomitchev, T. R. Furlani, and P. Coppens, *Inorg. Chem.*, 1998, **37**, 1519.
405. (a) L. Cheng, I. Novozhilova, C. Kim, A. Kovalevsky, K. A. Bagley, P. Coppens, and G. B. Richter-Addo, *J. Am. Chem. Soc.*, 2000, **122**, 7142; (b) C. Kim, I. Novozhilova, M. S. Goodman, K. A. Bagley, and P. Coppens, *Inorg. Chem.*, 2000, **39**, 5791; (c) D. V. Fomitchev, P. Coppens, T. Li, K. A. Bagley, L. Chen, and G. B. Richter-Addo, *J. Chem. Soc., Chem. Commun.*, 1999, 2013; (d) D. V. Fomitchev and P. Coppens, *Inorg. Chem.*, 1996, **35**, 7021.
406. (a) A. Y. Kovalevsky, K. A. Bagley, J. M. Cole, and P. Coppens, *Inorg. Chem.*, 2003, **42**, 140; (b) A. Y. Kovalevsky, K. A. Bagley, and P. Coppens, *J. Am. Chem. Soc.*, 2002, **124**, 9241.
407. D. V. Fomitchev, K. A. Bagley, and P. Coppens, *J. Am. Chem. Soc.*, 2000, **122**, 532.
408. (a) I. V. Novozhilova, A. V. Volkov, and P. Coppens, *J. Am. Chem. Soc.*, 2003, **125**, 1079; (b) C. D. Kim, S. Pillet, G. Wu, W. K. Fullagar, and P. Coppens, *Acta Crystallogr. A*, 2003, **58**, 133.
409. D. M. Roundhill, H. B. Gray, and C.-M. Che, *Acc. Chem. Res.*, 1989, **22**, 55.
410. (a) S. A. Ciftan and H. H. Thorpe, *J. Am. Chem. Soc.*, 1989, **120**, 9995; (b) C. A. Kalsbeck, D. M. Gingell, J. E. Malinsky, and H. H. Thorpe, *Inorg. Chem.*, 1994, **33**, 3313.
411. A. E. Steigman, S. F. Rice, H. B. Gray, and V. M. Miskowski, *Inorg. Chem.*, 1987, **26**, 1112.
412. K. H. Leung, D. L. Phillips, C.-M. Che, and V. M. Miskowski, *J. Raman. Spectrosc.*, 1999, **30**, 987.
413. Y. Ozawa, M. Terashima, M. Mitsumi, K. Toriumi, N. Yasuda, H. Uekusa, and Y. Ohashi, *Chem. Lett.*, 2003, **32**, 62.
414. (a) P. Coppens and I. V. Novozhilova, *Faraday Discuss.*, 2003, **122**, 1; (b) P. Coppens, *J. Chem. Soc., Chem. Commun.* 2003, 1317.
415. T. E. Bitterwolf, C. A. Weiss, W. P. Scallorn, and P. A. Jellis, *Organometallics*, 2002, **21**, 1856.
416. T. E. Bitterwolf, *J. Photochem. Photobiol. A*, 2004, **163**, 209.
417. (a) J. W. Faller, D. F. Chodosh, and D. J. Katahira, *J. Organomet. Chem.*, 1980, **187**, 227; (b) A. Davidson and W. C. Rode, *Inorg. Chem.*, 1967, **7**, 2124; (c) R. B. King, *Inorg. Chem.*, 1966, **5**, 2242.
418. (a) C. Limberg, A. J. Downs, T. M. Greene, and T. Wistuba, *Eur. J. Inorg. Chem.*, 2001, 2613; (b) T. E. Bitterwolf, J. T. Bays, B. Scallorn, C. A. Weiss, M. W. George, I. G. Virrels, J. C. Linehan, and C. R. Yonker, *Eur. J. Inorg. Chem.*, 2001, 2619.
419. R. B. Hitam, K. A. Mahmoud, and A. J. Rest, *J. Organomet. Chem.*, 1985, **291**, 321.
420. M. Cusumano and C. H. Langford, *Inorg. Chem.*, 1978, **17**, 2222.
421. C. Kutal, P. A. Grutsch, and D. B. Yang, *Macromolecules*, 1991, **24**, 6872.

422. (a) R. J. Lavallee, B. J. Palmer, R. Billing, H. Hennig, G. Ferraudi, and C. Kutal, *Inorg. Chem.*, 1997, **36**, 5552; (b) B. J. Palmer, C. Kutal, R. Billing, and H. Hennig, *Macromolecules*, 1995, **28**, 1328.

423. Y. Yamaguchi and C. Kutal, *Macromolecules*, 2000, **33**, 1152; (b) Y. Yamaguchi and C. Kutal, *Inorg. Chem.*, 1999, **38**, 4861.

424. W. Ding, C. T. Sanderson, R. C. Conover, M. K. Johnson, I. J. Amster, and C. Kutal, *Inorg. Chem.*, 2003, **42**, 1532.

425. R. J. Lavallee and C. Kutal, *J. Organomet. Chem.*, 1998, **562**, 97; (b) R. J. Lavallee and C. Kutal, *J. Photochem. Photobiol. A*, 1997, **103**, 213.

426. G. Gamble, P. A. Grutsch, G. Ferraudi, and C. Kutal, *Inorg. Chim. Acta*, 1996, **247**, 5.

427. A. N. Nesmeyanov, N. A. Volkenau, and L. S. Shilovtseva, *Dokl. Akad. Nauk SSSR*, 1970, **190**, 857.

428. (a) A. Roloff, K. Meier, and M. Reideker, *Pure Appl. Chem.*, 1986, **58**, 1267; (b) K. M. Park and G. B. Schuster, *J. Organomet. Chem.*, 1991, **402**, 355.

429. (a) T. G. Kotch, A. J. Lees, S. J. Fuerniss, and K. I. Papathomas, *Chem. Mater.*, 1995, **7**, 801; (b) T. G. Kotch, A. J. Lees, S. J. Fuerniss, K. I. Papathomas, and R. Snyder, *Polym. Mater. Sci. Eng.*, 1992, **66**, 462.

430. P. Wang, Y. Shen, S. Wu, E. Adamczak, L. Linden, and J. F. Rabek, *J. Macromol. Sci. Pure Appl. Chem.*, 1995, **A32**, 1973.

431. K. R. Mann, A. M. Blough, J. L. Schrenk, R. S. Koefod, D. A. Freedman, and J. R. Matachek, *Pure Appl. Chem.*, 1995, **67**, 95.

432. D. R. Chrisope, K. M. Park, and G. B. Schuster, *J. Am. Chem. Soc.*, 1989, **111**, 6195.

433. T. Karatsu, Y. Shibuki, N. Miyagawa, S. Takahara, A. Kitamura, and T. Yamaoka, *J. Photochem. Photobiol., A*, 1997, **107**, 83.

434. (a) V. Jakúbek and A. J. Lees, *Inorg. Chem.*, 2000, **39**, 5779; (b) V. Jakúbek and A. J. Lees, *J. Chem. Soc., Chem. Commun.*, 1999, 1631.

435. (a) W. Ding, K. A. Johnson, C. Kutal, and I. J. Amster, *Anal. Chem.*, 2003, **75**, 4624; (b) W. Ding, I. J. Amster, and C. Kutal, *Prog. Coord. Bioinorg. Chem.*, 2003, 233; (c) W. Ding, K. A. Johnson, I. J. Amster, and C. Kutal, *Inorg. Chem.*, 2001, **40**, 6865.

436. (a) C. A. Turner, W. Ding, I. J. Amster, and C. Kutal, *Coord. Chem. Rev.*, 2002, **229**, 9; (b) C. Kutal, Y. Yamaguchi, W. Ding, C. T. Sanderson, X. Li, G. Gamble, and I. J. Amster, *ACS Symp. Ser.*, 2003, **847**,(Photoinitiated Polymerization), 332; C. Kutal, *Photosci. Photoeng.*, 1997, **2**, 135; D. B. Yang and C. Kutal, in ‘Radiat. Curing’, ed. S. P. Pappas, Plenum, New York, 1992, p. 21.

437. F. W. Flitney, I. L. Megson, D. Flitney, and A. R. Butler, *Br. J. Pharmacol.*, 1992, **107**, 842.

438. F. W. Flitney, I. L. Megson, J. L. M. Thomson, and G. D. Kennovin, *Br. J. Pharmacol.*, 1996, **117**, 1549.

439. J. Bourassa, W. DeGraff, S. Kudo, D. A. Wink, J. B. Mitchell, and P. C. Ford, *J. Am. Chem. Soc.*, 1997, **119**, 2853.

440. J. Bourassa, B. Lee, S. Bernard, J. Schoonover, and P. C. Ford, *Inorg. Chem.*, 1999, **38**, 2947.

441. C. L. Conrado, J. L. Bourassa, C. Egler, S. Wecksler, and P. C. Ford, *Inorg. Chem.*, 2003, **42**, 2288.

442. (a) C. F. Works, C. J. Jocher, G. D. Bart, X. Bu, and P. C. Ford, *Inorg. Chem.*, 2002, **41**, 3728; (b) C. F. Works and P. C. Ford, *J. Am. Chem. Soc.*, 2000, **122**, 7592.

443. (a) M. A. DeLeo and P. C. Ford, *Coord. Chem. Rev.*, 2000, **208**, 47; (b) M. De Leo and P. C. Ford, *J. Am. Chem. Soc.*, 1999, **121**, 1980.

444. P. C. Ford, *Int. J. Photoeng.*, 2001, **3**, 161.

Photochemistry of Transition Metal Complexes: Theory

Chantal Daniel
Université Louis Pasteur, Strasbourg, France

Based in part on the article Photochemistry of Transition Metal Complexes: Theory by Jeffrey I. Zink which appeared in the Encyclopedia of Inorganic Chemistry, First Edition.

1 Introduction 1
2 State Correlation Diagrams 2
3 Quantum Chemical Methods 2
4 Potential Energy Surfaces 7
5 Wave Packet Dynamics 7
6 Electronic Spectroscopy 8
7 Photoreactivity 10
8 Related Articles 13
9 Further Reading 14
10 References 14

Abbreviations

SCF = self-consistent field; RHF = restricted Hartree Fock; MC-SCF = multiconfiguration self-consistent field; CI = configuration interaction; MP2 = Moller Plesset second order; MR-CI = multireference configuration interaction; CCSD = coupled cluster single double; CCSD (T) = CCSD (triple); EOM-CCSD = equation-of-motion–coupled cluster single double; CASSCF = complete active space self-consistent field; RASSCF = restricted active space self-consistent field; CASPT2 = complete active space perturbation theory second order; SS-CASPT2 = single-state complete active space perturbation theory second order; MS-CASPT2 = multistates complete active space perturbation theory second order; DFT = density functional theory; TD-DFT = time-dependent density functional theory; Δ-SCF = delta self-consistent field; SAC-CI = symmetry adapted cluster configuration interaction; B3LYP = Becke's three parameters Lee, Yang, Parr functional.

1 INTRODUCTION

The visible–UV absorption spectrum of transition metal complexes is characterized by a high density of various electronic excited states (metal-centered, metal-to-ligand-charge-transfer, ligand-to-ligand-charge-transfer, sigma-bond-to-ligand-charge-transfer, intra-ligand, ligand-to-metal-charge-transfer). The presence of electronic states of different character, structure, reactivity, and dynamics in a limited domain of energy gives to this class of molecules exceptional photophysical and photochemical properties. The richness of their photochemistry[1,2] is mainly governed by their electronic flexibility (*see* ***Photochemistry of Transition Metal Complexes***). Two contrasting behaviors following irradiation can be considered: (1) the molecular system is trapped in long-lived excited states of a well-defined structure, leading to the beautifully resolved absorption/emission spectroscopy or electron/energy transfer; (2) the molecule lands on repulsive potential energy surfaces inducing extremely fast ligand dissociation in a femtosecond timescale. The bipyridine-substituted complexes intensively studied over the last 30 years are representative of the first category,[3] whereas transition metal carbonyls illustrate the second behavior.[4] Most of the time, bound and repulsive electronic excited states coexist in a limited domain of energy and may interfere in the Franck–Condon region, generating structureless absorption spectra. The interaction between various electronic states in different regions of the potential energy surfaces leads to critical geometrical structures such as saddle points, conical intersections, or local minima. Consequently, the observed response to the light of the molecular system is entirely governed by the sequence of many concurrent elementary processes. The development of short time-resolved spectroscopy[5] (picoseconds–femtoseconds timescale) in different domains (resonance Raman, FT-infra-red, FT-electron paramagnetic resonance, emission, absorption UV/visible) has contributed to a better understanding of excited-state structures as well as of fast processes. However, several fundamental questions still remain unresolved. One important aspect is the differentiation between (1) chemically active electronic states leading to the formation or breaking of bonds, isomerization, and production of radicals and (2) long-lived excited states involved in the photophysics or subsequent secondary processes such as electron/energy transfer. The complicated mechanisms, which underlie the photoreactivity, involve different electronic states, various reaction paths, and elementary processes such as direct/indirect dissociation, internal conversion, or intersystem crossing. The simulation of the dynamics following the photon absorption should describe two different situations: (1) ultrafast direct dissociation from the absorbing state itself (adiabatic process) and (2) indirect dissociation via internal conversion or intersystem crossing (nonadiabatic process).

The determination of the timescales and of the several channels of deactivation of the excited molecule is essential. For this reason, a strong interplay between experiments and theory is mandatory. The first role of the theoretical study is to elucidate the electronic structure of the molecules, to determine the low-lying electronic transitions, and to assign the observed bands. This is probably the easiest task and several computational methods started to emerge in the 1990 s able to describe with reasonable accuracy electronic spectroscopy in transition metal complexes. The second aspect associated with the calculation of accurate multidimensional potential energy surfaces describing the reactivity of electronic excited states is the bottleneck of the theoretical study. The main difficulty is related to the dimensionality of the problem, which cannot be solved exactly because of the large number of nuclear coordinates and electronic states. This implies a selective choice of a few degrees of freedom in the treatment of the dynamics that has to include several coupled electronic excited states, either nonadiabatically or by spin-orbit.

2 STATE CORRELATION DIAGRAMS

Until the beginning of the 1980s, the understanding of transition metal photochemistry was based on molecular orbital diagrams coupled with an analysis in terms of bonding and antibonding character.**[6]** It was generally assumed that photodissociation was a consequence of exciting an electron from a bonding to an antibonding orbital. However, this conceptually appealing chemical analysis has a number of drawbacks: (1) how is the observation of concurrent photochemical reactions at a given wavelength explained; (2) why visible irradiation into the metal-to-ligand-charge-transfer band leads to the loss of a carbonyl in manganese α-diimine complexes [M(R)(CO)$_3$(α-diimine)], whereas the result of this irradiation on rhenium analogs gives rise to the homolytic cleavage of the Re–R bond; (3) how is the occurrence of a given photochemical reaction upon excitation at different wavelengths with quantum yields relatively insensitive to this factor analyzed? A more spectroscopic approach based on the ligand field excited-state theory was developed simultaneously in order to analyze and predict the changes of bonding properties when going from the electronic ground state to the excited state and to explain the stereo selectivity in photosubstitution reactions.**[7]** The photostereochemistry and electronic selection rules in strong field d^3 and d^6 transition metal complexes have been described by means of the properties of the relevant wave functions and orbital/state correlation diagrams.**[8]**

On the basis of the state correlation diagram depicted in Figure 1, which connects the different stereoisomers of the pentacoordinate fragment [Rh(NH$_3$)$_4$Cl]$^{2+}$, Vanquickenborne *et al.* infer the main characteristics of the complicated photochemical mechanism in [Rh(NH$_3$)$_4$Cl$_2$]$^+$ and related complexes. This work gave the first evidence that the formulation of electronic selection rules was underlying the photosubstitution mechanism in d^3 and d^6 complexes. In principle, this idea was applicable to any complex with any coordination number. However, at this stage the greatest experimental detail and the most advanced theoretical development limited the theoretical study to the ligand field (d to d excitation or metal-centered) excited states of six-coordinate complexes of metals of d^3 or d^6 configurations. The development of new quantum chemical methods including electronic correlation effects and the accessibility to powerful computers has enabled the computation of states energy levels with a better accuracy (see Section 3). Nowadays, it is possible to describe semiquantitatively the electronic ground state and low-lying excited states of the reactant and primary photoproducts, and to build more reliable state correlation diagrams based on spin and symmetry properties.

State correlation diagrams have helped identify the active excited states of a number of photochemical reactions**[6]** on the basis of spin and symmetry rules, leading to a clearer picture of the mechanism of photodissociation. The state correlation diagram in Figure 2 that connects the electronic ground state (a^{1}A$'$) and the low-lying singlet and triplet MLCT and SBLCT states of the reactant to those of the primary products describes the observed homolytic cleavage of the metal$-$R bond in [M(R)(CO)$_3$(α-diimine)] complexes. The qualitative mechanism underlying this photochemical reaction involves nonadiabatic transitions (intersystem crossing, internal conversion) occurring after the absorption to the low-lying ^{1}MLCT states, which lead to the biradicals primary products R$^{\bullet}$ + M(CO)$_3$(α-diimine) originating from the ^{3}SBLCT dissociative state. If the state correlation diagrams are a useful mere approximation of the one-dimensional potential energy curves (PEC) and constitute a good starting point of a more realistic theoretical study, they are subject to several limitations. In particular, they give no information about the role of intersystem crossing and ignore the energy barriers that do not result from avoided crossings.

3 QUANTUM CHEMICAL METHODS

The first goal is to obtain accurate transition energies (within 0.10$-$0.15 eV) and reliable dipole transition moments in order to assign bands located in the UV-visible spectral domain of energy in various transition metal complexes. The second aspect relates to the calculation of PES or cuts along specific nuclear coordinates describing the reactivity of electronic excited states. When handling transition metal complexes, the quantum chemical calculations giving access to the potential energy and to the properties involved in electronic spectroscopy and photochemical reactivity (transition dipole moments, spin-orbit coupling, nonadiabatic coupling) cannot be routinely performed.**[9]** However, efficient theories and algorithms combined with the availability of very fast computers has enabled such challenging computations, which have to be carried out with care. This section aims at describing the theoretical procedures and the most significant developments in the field.

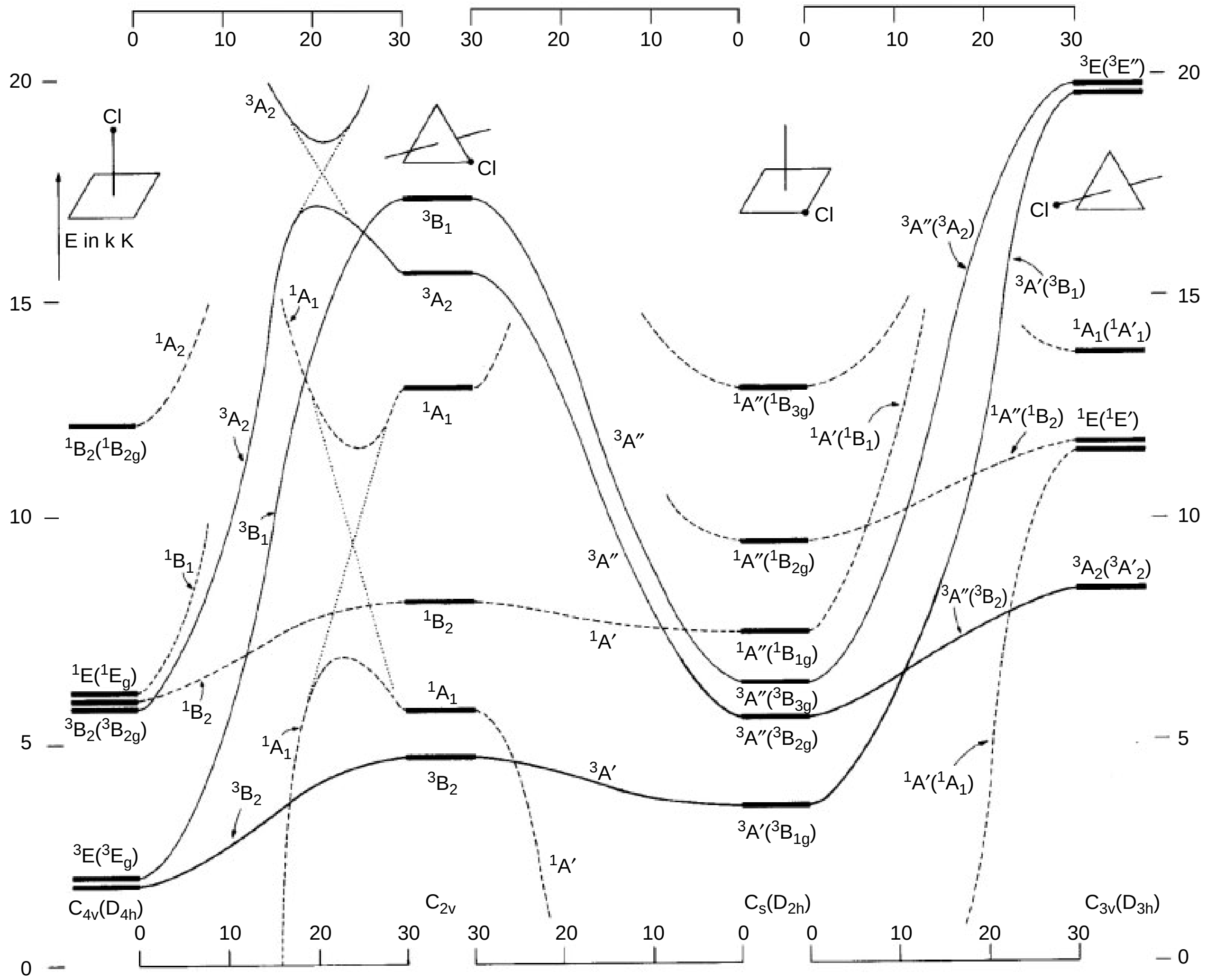

Figure 1 State energy correlation diagram connecting the four $[Rh(NH_3)_4Cl]^{2+}$ species (square pyramid (Cl axial), trigonal bipyramid (Cl equatorial), square pyramid (Cl equatorial), trigonal bipyramid (Cl axial)). Triplets are shown in full lines and singlets in dotted lines.[8] (Reprinted with permission from Ref. 8. © 1978 American Chemical Society)

The size of the molecular system, its symmetry, and the density of states as well as the saturation of the metal center d shells or the metal–ligand interactions will generate particular difficulties. The choice of the method will be a compromise taking into account the following factors: (1) the feasibility and computational cost; (2) the validity of some approximations; (3) the wanted level of accuracy; and (4) the control that can be performed on the analysis of the results. Four types of methods based on different mathematical formalisms are available for treating electronic spectroscopy in transition metal complexes:[9] (1) the density functional theory (DFT) like the delta self-consistent field (Δ-SCF) and the time-dependent density functional theory (TD-DFT); (2) the variational approaches such as the self-consistent field (SCF), configuration interaction (CI), multiconfiguration self-consistent field (MC-SCF), multireference configuration interaction (MR-CI); (3) the cluster expansion methods such as the equation-of-motion–coupled cluster single double (EOM-CCSD), the symmetry adapted cluster configuration interaction (SAC-CI); (4) the single state (SS) or multistate (MS) second-order perturbational approaches applied to zeroth-order variational wave functions and so-called single state complete active space perturbation theory second order (SS-CASPT2) and MS-CASPT2 (Scheme 1).

3.1 Variational Methods

The few attempts at describing excited states in transition metal complexes within the restricted Hartree Fock (RHF) formalism were rapidly abandoned because of computational difficulties (convergence of the low-lying states in the open-shell formalism) and theoretical deficiencies (inherent lack

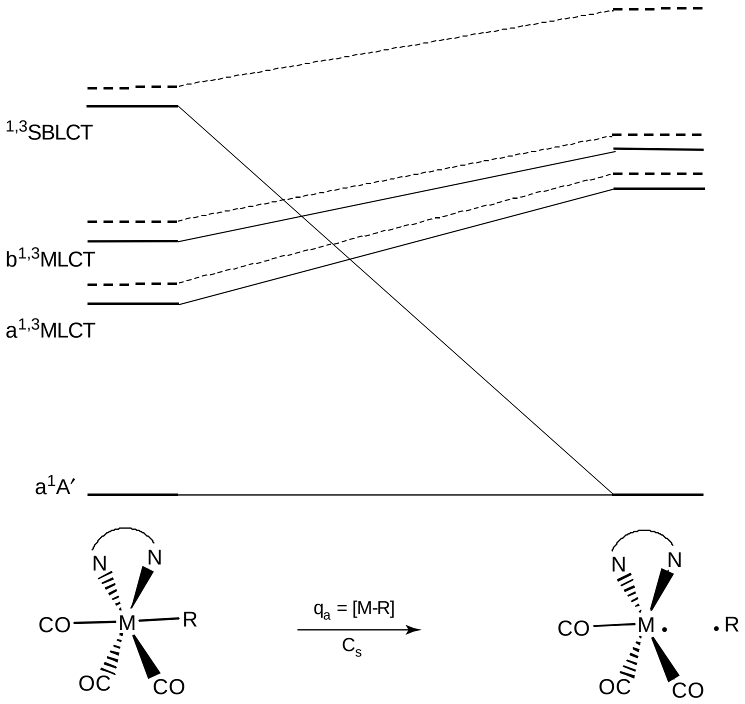
1,3SBLCT
b1,3MLCT
a1,3MLCT
a1A′
N
N
CO
M
R
OC
CO
qa = [M-R]
Cs
N
N
CO
M
R
OC
CO

Figure 2 State energy correlation diagrams connecting the low-lying singlet and triplet metal-to-ligand-charge-transfer (MLCT) states and sigma-bond-to-ligand-charge-transfer (SBLCT) states of (R)M(CO)$_3$(α-diimine) to the corresponding states of the M–R bond homolysis primary products R$^\bullet$ + $^\bullet$M(CO)$_3$(α-diimine)

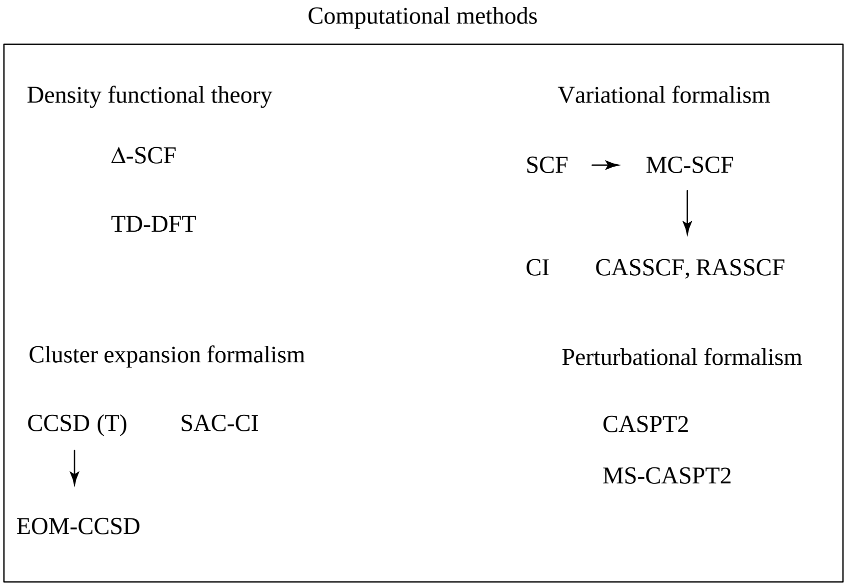
Computational methods
Density functional theory
Δ-SCF
TD-DFT
Variational formalism
SCF
MC-SCF
CI
CASSCF, RASSCF
Cluster expansion formalism
CCSD (T)
SAC-CI
EOM-CCSD
Perturbational formalism
CASPT2
MS-CASPT2

Scheme 1

of electronic correlation, inconsistent treatment of states of different multiplicities, and d shell occupations). The simplest and most straightforward method to deal with correlation energy errors is the CI approach where the single determinant HF wave function is extended to a wave function composed of a linear combination of many determinants Φ_i in which the coefficients C$_i$ are variationally optimized.

$$\psi_{\mathrm{CI}} = \sum_i C_i \Phi_i \tag{1}$$

Within the CI formalism, the configuration mixing is introduced (multideterminantal approach) but the predetermined reference set of molecular orbitals is not reoptimized for the different electronic states. However, most of the time and especially in transition metal complexes, strong correlation effects affect the electron density. Therefore, it is necessary to optimize the molecular orbitals according to a multiconfigurational scheme including static electronic correlation effects, which describe the interaction between two electrons in a pair at large separation space. The so-called MC-SCF method and its extension CASSCF (complete active space self-consistent field)**[10]** or RASSCF (restricted active space self-consistent field)**[11]** methods have their origin in this fundamental problem. In the MC-SCF method, the energy is minimized with respect to the molecular orbitals relaxation (term κ) and the CI expansion, and the wave function is given by the following expression,

$$\psi_{\text{MC-SCF}} = \exp(-\hat{\kappa}) \sum_i C_i \Phi_i \qquad (2)$$

These methods provide zero-order wave functions used as references in subsequent CI, MR-CI, or multistates complete active space perturbation theory second order (MS-CASPT2) calculations, which take into account the dynamical correlation effects describing the interaction between two electrons at a short interelectronic distance (so-called cusp region). The MC-SCF approach is even more crucial in excited-states calculations where the mixing of electronic states and the dramatic changes of electron density during the excitation process have to be taken into account. The large variation in the number of d electrons pairs among the various electronic states is a major difficulty when correlated methods are applied to transition metal complexes. The most widely used MC-SCF method is the CASSCF based on a partitioning of the occupied molecular orbitals into subsets corresponding to how they are used to build the wave function. The problem is reduced to the partition into sets of active and inactive orbitals and to a selection of correlated electrons. This discriminating strategy based on the physics and chemistry of the study includes all configuration state functions (CSFs), which are generated by distributing the active electrons among the active orbitals in all possible ways consistent with the spin and the symmetry of the wave function. In practical applications, where the number of configurations may exceed 10^6, such a partitioning is not straightforward. The validity of the subsequent MR-CI or MS-CASPT2 treatments depends entirely on the quality of the CASSCF wave function. This strategy, which is not easily automated, cannot be used as a black box. Most of the time, the orbitals are optimized for the average energy of a number of excited states large enough to include the electronic spectrum of interest. This procedure avoids root inversions as well as convergence problems, and leads to a set of orthogonal wave functions of given spin and symmetry and to transition densities of reasonable accuracy used in property calculation (dipole transition moments). The transition energies accuracy is obtained by the addition of the remaining correlation effects by means of MR-CI or MS-CASPT2 calculations. If the active space chosen is large enough according to the physicochemical aspect of the problem, results of high accuracy will be produced by the CASSCF/CI procedure, where the configuration selection scheme on the top of the CASSCF wave function is performed by single and double replacement out of either a single reference (CI) or multireference space (MR-CI). The slow convergence of the method, the size of which increases dramatically with the number of references, and the default of size-extensivity leading to incorrect scaling of the energy with the number of correlated electrons are very limiting for a general use of the MR-CI formalism in nontrivial applications. However, the CASSCF/MR-CI approach is actually the only ab initio method leading to reliable PES describing electronic excited-state reactivity in transition metal complexes.

3.2 Second-order Perturbational Approach

An alternative to the fully variational approach depicted above is a mixed procedure where a multiconfigurational variational method is used to build a zero-order wave function supplemented by a second-order perturbational treatment of the dynamical correlation effects. The so-called complete active space perturbation theory second order (CASPT2) and its multistate extension MS-CASPT2 methods**[11]** are size-extensive and give very accurate transition energies as soon as the zero-order variational wave function includes the correct spectroscopy of the system under study. Otherwise the perturbational treatment is no longer valid because of the presence of intruder states interacting with the reference space, and the treatment is not included at the zero-order level. This leads to an erratic behavior of the perturbation and out of range transition energies of more than 2.0 eV. In these nontrivial cases, either a level-shift technique has to be applied with care (weak intruder states) or the CASSCF active space has to be increased (strong intruder states) as illustrated by the theoretical study of the spectroscopy of $Mn_2(CO)_{10}$ or $HRe(CO)_5$.**[12,13]** If this method is the method of choice for the determination of accurate transition energies in transition metal complexes (see Section 6), it seems less adapted to the calculation of PEC or PES due to the inconsistent behavior of intruder states along the reaction pathways.

3.3 Cluster Expansion Methods

The cluster expansion methods are based on an excitation operator, which transforms an approximate wave function into the exact one according to the exponential ansatz

$$\Psi = \exp(T)|0\rangle \qquad (3)$$

where T is a sum of single- to N-particle excitation operators (coupled-cluster theory)[14] or of the symmetry adapted single- to N-particles excitation operators (symmetry adapted cluster theory).[15] The simplest truncation of T is to the second-order where the single and double excitations are included in the cluster expansion (coupled cluster single double, CCSD[16] or SAC) based on the HF single determinant$|0\rangle$. When electron correlation effects are dominated by pair effects, these methods recover 90–95% of the exact correlation energy if the wave function is described by a dominant closed-shell determinant. The remaining correlation effects due to higher excitations are estimated by approximate methods like in the CCSD(T) approach where the triple excitations are included perturbationally. These methods are size-extensive by definition and independent on the choice of reference orbitals. However, these methods, which converge efficiently, are hardly generalized to multireference starting wave functions. As far as the excited states and associated properties are concerned, two cluster–expansion-based methods developed originally for open-shell situations have been proposed. The first, the so-called SAC-CI method, supposes that the major part of electron correlation in the closed-shell ground state is transferable to the excited states since the excitation of interest involves only one and/or two electrons. The mechanism of photofragmentation of $Ni(CO)_4$ by a XeCl laser at 308 nm has been studied on the basis of SAC-CI PEC.[17] More recently a detailed investigation of the excited-state structures and reactivity of $CpM(CO)_2$ ($Cp = \eta^5$-C_5H_5; M = Rh, Ir) has provided theoretical insights into the photochemistry of these molecules.[18] The origin of the low-quantum efficiencies for the C–H/S–H bond activations of $CpM(CO)_2$ has been attributed to the smaller proportion of the MLCT character in the high-energy states. In the CC-based methods, the so-called equation-of-motion–coupled cluster single double (EOM-CCSD)[19] ionization potentials, electron affinities, and excitation energies are obtained directly from the equation of motion operating on the ground-state wave function. This approach is characterized by an unambiguous treatment of excited states where the only choices are the atomic basis sets, and the excitation level of the operators is very demanding computationally and it has been applied to only one transition metal complex, namely, $FeCl_4^-$ leading to promising results for charge transfer transitions from the $^6A_1$ ground state.[20] A recent workable extension, the so-called extended similarity transformed EOM-CCSD (extended-STEOM-CC), has been applied with more or less success to a few transition metal compounds.[21]

3.4 Density Functional Based Methods

The optical spectra of transition metal complexes have long been interpreted by means of DFT methods. However, the Kohn–Sham orbitals calculated within the DFT formalism describe the electronic ground state in a single determinant scheme. While this method was well established for the ground state and the lowest states within a symmetry class from its early days, its extension to excited-state description is still in development. The first option proposed in 1977 by Ziegler and Baerends,[22] within the framework of the time-independent formalism, and generalized in 1994 by Daul[23] (so-called Δ-SCF method) is based on symmetry-dictated combinations of determinants able to evaluate in a nonambiguous way the space and spin multiplets. It has been applied with success to a variety of highly symmetric molecules.[23] However, several limitations make this approach only accessible to experts in the subject.

An alternative to the time-independent DFT method is the so-called time-dependent DFT This method based on the linear response theory is the subject of recent and promising theoretical developments.[24,25] The treatment of molecular properties by means of the linear response of the charge density to an applied field is based on a well-founded formalism that allows direct computation of polarizabilities, excitation energies, and oscillator strengths within the framework of the DFT. Only excitations corresponding to linear combinations of singly excited determinants are included like in single excitations CIs, but taking into account additional electronic correlation effects. The accuracy of the response calculation is very sensitive to the approximation made for the exchange-correlation potential v_{xc} as well as to its repercussion on its derivative $\partial v_{xc}/\partial\rho$ (derivative discontinuity in the bulk region). Owing to an underestimation of the attractive character of the exchange-correlation potential, the charge density will be too diffusible. Consequently, the ionization threshold will be systematically too low with a dramatic effect on high excitation energies and polarizabilities, which will be overestimated. Moreover, excitations involving a substantial change in the charge density like charge transfer states will be described with difficulty by conventional functionals. In spite of these drawbacks, the TD-DFT approach remains a computationally simple and efficient method able to treat practical problems in a reasonable timescale at a low cost as compared to highly correlated ab initio methods.[9,26] From an overview over recent TD-DFT calculations on transition metal complexes spectroscopy, the most important points to be considered are (1) the applied functional and (2) the level of geometry optimization of the molecule. For medium size molecules or transition metal complexes, TD-DFT results have been shown to be competitive with the highest level ab initio approaches, but cases where current exchange-correlation functionals dramatically fail are known to exist.[27,28] In a recent paper, the photochemistry of the phosphine-substituted transition metal–carbonyl complexes $Cr(CO)_5PH_3$ and *ax*-$Fe(CO)_4PH_3$ has been investigated by means of TD-DFT PEC and wave packet dynamics.[29]

4 POTENTIAL ENERGY SURFACES

The PES plays a central role in the understanding of chemical/photochemical reaction mechanisms, the quantum description of the nuclear motion being determined by the shape of the PES. In principle, photochemical mechanisms are described by reaction paths on ground and excited states PES, which can be determined according to the procedures developed for chemical reactivity. The new problem in photoinduced mechanisms is the complicated landscape of the PES characterized by the presence of a variety of critical geometries such as minima, transition states, high-order saddle points, avoided crossings, conical intersections resulting from nonadiabatic interactions between N-dimensional PES. For a given atomic basis set, the computational method used to solve the electronic problem has to be flexible enough to characterize correctly different regions of the molecular PES at the same level of accuracy. An inadequate wave function would result in a biased description of the different regions and such computed PES would not reproduce the exact Born–Oppenheimer potentials.

One of the most significant advances made in applied quantum chemistry in the past 20 years is the development of computationally workable schemes based on the analytical energy derivatives able to determine stationary points, transition states, high-order saddle points, and conical intersections on multidimensional PES.[30] The determination of equilibrium geometries, transition states, and reaction paths on ground-state potentials has become almost a routine at many levels of calculation (SCF, MP2, DFT, MC-SCF, CCSD, CI) for molecular systems of chemical interest.[31,32] The availability of reliable and efficient analytic energy gradient procedures (first and second derivative) for the search of various critical points on several interacting complex surfaces at a high correlated level (CASSCF, MR-CI, CASPT2, CCSD(T) and its extension EOM-CCSD) will have a significant impact on the theoretical study of transition metal photoreactivity. Indeed, although reaction paths are uniquely defined in any coordinate system, they cannot be determined unambiguously without the knowledge of reference points on the PES from which the analytical energy derivation procedure may start. Unfortunately, the derivative formulation for highly correlated wave functions is very complex and if analytical first derivatives are available for the standard methods, second derivatives calculations are even more complicated.

Density functional methods are competitive with the above traditional wave function methods for numerous applications such as the computation of ground-state PES. A few applications of transition metal photochemistry have been proposed on the basis of the Δ-SCF approach implying several approximations on the excited-state reaction-path definition by symmetry constraints not always appropriate in a ‘coordinate driving’ scheme.[33] Excited-state gradients have been recently implemented in DFT for various functionals, the feasibility of the approach having been tested for small molecules only.[34] The mathematical and computational machinery for structure optimization is based on several various algorithms, the complexity of which depends on the wanted accuracy at the electronic level. The application of these methods to transition metal photochemistry raises serious practical difficulties as illustrated above. For simple mechanisms involving the electronic ground-state interaction with one excited state, the global structure of the low-energy part of the PES can be visualized within a 3-D cross-section plotting of the energy on a grid while the critical points (minima, transition states, conical intersections) are fully optimized using rigorous ab initio correlated methods (MC-SCF).[35,36] This procedure has been extended recently to the study of the photodissociation of $Cr(CO)_6$ giving mechanistic details of the geometrical relaxation of the $Cr(CO)_5$ photoproduct.[37]

More generally, the high density of electronic states that characterizes the absorption spectrum of transition metal complexes generates a very complicated PES involving several different multiplets in the UV/visible domain of energy. As the systematic investigation of the full PES is practically intractable, the study of photochemical processes in transition metal complexes is generally based on several approximations: (1) the nuclear dimensionality is reduced to $N \leq 2$; (2) the reaction path is approximated by metal–ligand bond elongation coordinates; (3) the highest symmetry is retained along the reaction path; (4) a limited evaluation of geometrical relaxation effects in excited states is performed. These approximations are based on the following criteria: (1) the observed or calculated structural deformations on moving from the electronic ground state to the excited state; (2) the observed or calculated structural deformations on moving from the reactant to the products; (3) the temporal hierarchy of the various elementary processes participating in the photochemical behavior. The validity of these approximations is checked on the basis of the observables directly comparable with the experimental data such as the bond dissociation energies, the main spectral features, or the timescales of primary reactions. In contrast, the electronic problem is treated by means of the most accurate quantum chemical methods in order to get a semiquantitative characterization of electronic spectroscopy in the Franck–Condon region and a correct description of the dissociative processes. The analysis of the main topological characteristics of the PES represented by contour maps (2-D) or profiles (1-D) of the potentials $V(q_i)$ is the first step toward a qualitative understanding of the photochemical mechanisms.

5 WAVE PACKET DYNAMICS

The motion of the molecular system under the influence of the potential is determined by the equations of dynamics. Consequently the shape of the computed PES governs entirely this motion. As explained in the previous section, since several approximations have to be made at the level of the dimensionality of the PES, it is very important to define clearly the initial conditions of the simulation and to estimate the hierarchy in time of the various elementary processes involved in the photochemical reactivity. In conventional photochemical experiments with long pulse duration and narrow frequency resolution, only a few near-degenerate electronic states are directly populated. The energy is not large in excess, and in a first approximation the reaction paths can be defined by the metal–ligand bond elongation coordinates corresponding to the observed photochemical reactions. In the case of very fast dissociative processes (10 fs to 1 ps), the system should not deviate significantly from this 'pseudominimum energy path', and many of the other vibrational degrees of freedom can be frozen. Typically, one or two coordinates corresponding to the bond elongations describing the observed photochemical reactions (CO loss or metal–R, R = H, alkyl, metal, X) are selected for building 1-D or 2-D PES, the other degrees of freedom being frozen to the Franck–Condon geometry.[38]

The quantum dynamics of photodissociation processes can be performed within the time-independent or time-dependent framework.[37] In the time-dependent picture used in the applications presented in the next section, the time-dependent Schrödinger equation is solved

$$i\hbar\frac{\partial}{\partial t}\varphi_e(t) = \hat{H}_e\varphi_e(t) \tag{4}$$

where $\varphi_e(t)$ is a wave packet (coherent superposition of all stationary eigenstates in the electronic excited state) evolving on the excited electronic state e potential. In order to describe the initial absorption followed by direct dissociation, it is assumed that the initial vibrational state ϕ_{g_i} in the electronic ground sate multiplied by the transition dipole function μ_{eg} is instantaneously promoted by the photon to the upper electronic state (Scheme 2).

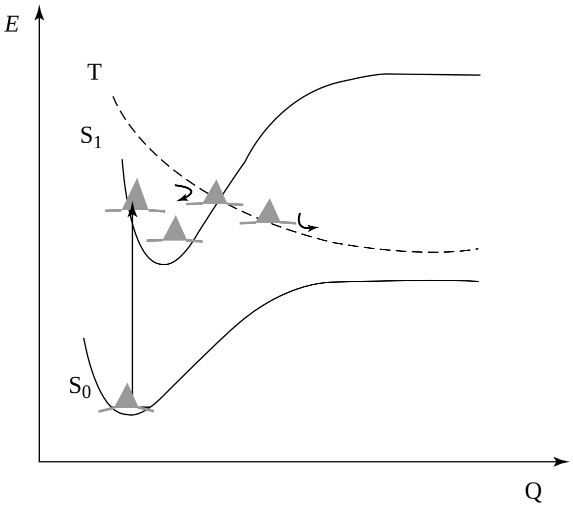

Scheme 2

This initial wave packet that is not eigenstate of $\hat{H}_e$, starts to move under its action. The advantage of this approach is that the motion of the wave packet, the center of which remains close to a classical trajectory, can be followed in real time. The motion of the wave packet from the Franck–Condon region to the exit channel is described by the autocorrelation function

$$\mathrm{S}(t) = \langle\varphi_e(0)(0)|\varphi_e(t)\rangle \tag{5}$$

given by the overlap of the evolving wave packet with the initial wave packet at $t = 0$. The absorption spectrum is calculated as the Fourier transform of the autocorrelation function

$$\sigma_{\mathrm{tot}}(\omega)\alpha\omega \int_{-\infty}^{+\infty} \mathrm{d}t\,\mathrm{S}(t)e^{iEt/\hbar} \tag{6}$$

where $E = E_i + \hbar\omega$.[39] Wave packet calculations lead to the timescale and probabilities of dissociation and to the branching ratio between concurrent primary processes occurring from a single electronic excited state. In the cases of indirect dissociative processes involving nonadiabatic transitions (jumps between different PES), a set of coupled time-dependent Schrödinger equations has to be solved

$$\left.\begin{aligned} i\hbar\frac{\partial}{\partial t}\varphi_e(t) &= \hat{H}_e\varphi_e(t) + V_{ee'}\varphi_{e'}(t) \\ i\hbar\frac{\partial}{\partial t}\varphi_{e'}(t) &= \hat{H}_{e'}\varphi_{e'}(t) + V_{e'e}\varphi_e(t) \end{aligned}\right\} \tag{7}$$

with the same initial conditions as above but in a different basis, the so-called diabatic,[40] where the original adiabatic PES have been transformed in order to minimize the kinetic coupling between them and to introduce potential coupling terms $V_{ee'}$. This strategy is very efficient in describing simultaneously intersystem crossings and internal conversions, which are important processes in photoinduced reactivity in transition metal complexes. The wave packet approach yields important quantities such as the time evolution of electronic states population, the dissociation probabilities, or the branching ratio between concurrent processes.

6 ELECTRONIC SPECTROSCOPY

6.1 The Blue Copper Protein

In a beautiful recent work, the groups of K. Pierloot and B. O. Roos[41,42] have proposed a fairly complete understanding of the relation between the electronic spectra and the structure of the mononuclear copper-cysteinate proteins. This theoretical work is based on DFT geometry optimizations of several blue copper protein models from $[\mathrm{Cu(NH_3)_2(SH)(SH_2)}^+]$ to

[Cu(imidazole)$_2$(SCH$_3$)(S(CH$_3$)$_2$)$^+$], the structures of which are compared to the crystal structures of plastocyanin and nitrite reductase. The effect of the protein surrounding on the spectra has been simulated by a single point-charge model. The CASSCF/CASPT2 calculated electronic spectra of the [Cu(imidazole)(SH)(SH$_2$)$^+$] model at the crystal structure, but with CASPT2 optimized Cu–S$_{\text{Cystein}}$ and Cu–S$_{\text{Methionin}}$ bond distances, reproduce the experimental absorption spectra of the blue copper protein plastocyanin and nitrite reductase with an error of less than 0.22 eV (Table 1).

The key point in this type of study is the choice of the model systems, the structure of which should be very close to the real systems. Indeed, the change in geometry has a dramatic effect on the electronic structure itself and on the electronic spectroscopy as illustrated by the assignment of the experimental bands in these systems in Table 1. It has been shown that both trigonal and tetragonal structures of models of the blue copper proteins are rather similar (nearly tetrahedral). Therefore, some proteins stabilize the trigonal structure (e.g. plastocyanin) whereas others stabilize the tetragonal structure (e.g. nitrite reductase). The electronic spectra of blue copper proteins are well characterized and have been recorded by several spectroscopic techniques. The spectra show a prominent peak centered at 2.08 eV in plastocyanin and 2.19 eV in nitrite reductase responsible for the blue color and a weak band around 1.5 eV. All the transitions reported in Table 1 correspond to excitations either to the π^*(Cu–S$_{\text{Cys}}$) (plastocyanin) or to the σ^*(Cu–S$_{\text{Cys}}$) (nitrite reductase) orbitals strongly delocalized onto S$_{\text{Cys}}$. The lowest part of the spectra is attributed to ligand field (LF) states by the authors, the upper part being characterized by the presence of high-lying charge transfer states from the π(Cu–S$_{\text{Cys}}$) or the σ(Cu–S$_{\text{Cys}}$) orbitals.

Table 1 Comparison between the calculated and experimental spectra of plastocyanin and nitrite reductase. The transition energies are given in eV

	Calculated^a	Experimental^b
Plastocyanin		
σ^* (Cu–S) $\rightarrow \pi^*$(Cu–S)	0.55	0.63
3d$_{z^2}$(Cu) $\rightarrow \pi^*$(Cu–S)	1.46	1.35
3d$_{yz}$ (Cu) $\rightarrow \pi^*$(Cu–S)	1.62	1.60
3d$_{xz}$ (Cu) $\rightarrow \pi^*$(Cu–S)	1.58	1.74
π(Cu–S) $\rightarrow \pi^*$(Cu–S)	1.96	2.09
σ (Cu–S) $\rightarrow \pi^*$(Cu–S)	2.75	2.67
Nitrite reductase		
π^* (Cu–S) $\rightarrow \sigma^*$(Cu–S)	0.55	0.7
3d$_z^2$(Cu) $\rightarrow \sigma^*$(Cu–S)	1.54	1.49
3d$_{yz}$ (Cu) $\rightarrow \sigma^*$(Cu–S)	1.61	1.69
3d$_{xz}$ (Cu) $\rightarrow \sigma^*$(Cu–S)	1.73	1.86
π(Cu–S) $\rightarrow \sigma^*$(Cu–S)	1.97	2.19
σ(Cu–S) $\rightarrow \sigma^*$(Cu–S)	2.81	2.74

[a] Calculated spectra for plastocyanin and nitrite reductase[41,42]
[b] Experimental spectra for plastocyanin and nitrite reductase.[43]

6.2 Ru-halide Charge Transfer Complexes

Transition metal–carbonyl-diimine complexes [Ru(E)(E$'$)(CO)$_2$(α-diimine)] (E, E$'$ = halide, alkyl, benzyl, metal fragment; α-diimine = 1,4-diazabutadiene or 2,2$'$-bipyridine) are widely studied for their unconventional photochemical, photophysical, and electrochemical properties. These molecules have a great potential as luminophores, photosensitizers, and photoinitiators of radical reactions and represent a challenge to the understanding of excited-state dynamics.[28,44] The near-UV/visible electronic spectroscopy of [Ru(X)(Me)(CO)$_2$(iPr-DAB)] (X = Cl or I; iPr-DAB = N,N'-di-isopropyl-1,4-diaza-1,3-butadiene) has been investigated through CASSCF/CASPT2 and TD-DFT calculations on the model complexes [Ru(X)(Me)(CO)$_2$(Me-DAB)] (X = Cl or I) (Table 2).

Table 2 Lowest part of the absorption spectra of [Ru(Cl)(Me)(CO)$_2$(Me-DAB)] and [Ru(I)(Me)(CO)$_2$(Me-DAB)]. Transition energies are in cm^{-1} (oscillator strengths are given in parenthesis)

	Experiment	Transition	CASPT2	Transition	TD-DFT (PBE Hybrid)
X = Cl	21 790 (22 990) 459 nm (435 nm)	**MLCT**/XLCT a^{1}A$'$ $\rightarrow$ b^{1}A$'$	22 230 (0.09)	**XLCT**/MLCT a^{1}A$'$ $\rightarrow$ b^{1}A$'$	17 640 (0.013)
	28 090 (356 nm)	SBLCT a^{1}A$'$ $\rightarrow$ c^{1}A$'$	29 410 (0.09)	SBLCT a^{1}A$'$ $\rightarrow$ c^{1}A$'$	24 780 (0.018)
		MLCT a^{1}A$'$ $\rightarrow$ d^{1}A$'$	34 030 (0.0)	MLCT a^{1}A$'$ $\rightarrow$ d^{1}A$'$	28 410 (0.0)
	30 300 (330 nm)	**XLCT**/MLCT A^{1}A$'$ $\rightarrow$ e^{1}A$'$	33 500 (0.09)	**MLCT**/XLCT a^{1}A$'$ $\rightarrow$ e^{1}A$'$	28 840 (0.057)
X = I	18 180–21 600 (550–463 nm)	XLCT a^{1}A$'$ $\rightarrow$ b^{1}A$'$	16 430 (0.03)	XLCT a^{1}A$'$ $\rightarrow$ b^{1}A$'$	15 070 (0.004)
	26 737 (374 nm)	SBLCT a^{1}A$'$ $\rightarrow$ c^{1}A$'$	22 7800 (0.22)	SBLCT a^{1}A$'$ $\rightarrow$ c^{1}A$'$	23 450 (0.052)
	$>$ 30 770 (324 nm)	MLCT a^{1}A$'$ $\rightarrow$ e^{1}A$'$	25 820 (0.16)	MLCT a^{1}A$'$ $\rightarrow$ e^{1}A$'$	27 510 (0.055)

Table 3 Calculated TD-DFT transition energies (in cm^{-1}) to the low-lying singlet excited states of $[Ru(R)(Me)(CO)_2(Me\text{-}DAB)]$ ($R = Cl, SnH_3$) calculated as a function of various functionals and associated oscillator strengths (in parenthesis)

	Transition	BP	B3LYP	hybrid PBE	Hand HLYP
$X = Cl$	XLCT/MLCT $A^1A' \rightarrow b^1A'$	12 090 (0.006)	16 210 (0.011)	17 640 (0.013)	24 440 (0.021)
	SBLCT $a^1A' \rightarrow c^1A'$	20 240 (0.006)	23 310 (0.015)	24 780 (0.018)	29 840 (0.028)
	MLCT XLCT $a^1A' \rightarrow e^1A'$	24 560 (0.067)	27 500 (0.060)	28 840 (0.057)	35 890 (0.032)
$X = SnH_3$	SBLCT $a^1A' \rightarrow b^1A'$	19 870 (0.034)	22 020 (0.063)	22 260 (0.069)	23 560 (0.106)
	MLCT $a^1A' \rightarrow e^1A'$	25 790 (0.072)	29 760 (0.042)	28 080 (0.058)	31 440 (0.039)

The convergence on the calculated transition energies to the low-lying metal-to-ligand-charge-transfer (MLCT), X-to-ligand-charge-transfer (XLCT, X being an halide ligand), or sigma-bond-to-ligand-charge-transfer (SBLCT) has been analyzed for both methods with respect to various methodological aspects: basis set effects and functional influence on the TD-DFT results versus the influence of the size and quality of the CASSCF active space and of the level of the perturbational treatment (single state or multistate) on the CASSCF/CASPT2 transition energies. Both methods reproduce the red shift of the absorption bands well when moving from the chloride to the iodide complex as well as the displacement of the strongly MLCT absorbing state from the visible to the UV domain of energy.

On the basis of these accurate calculations, it is shown that whereas the lowest singlet state can be assigned to a pure XLCT state in $[Ru(I)(Me)(CO)_2(Me\text{-}DAB)]$, its character is mainly MLCT in $[Ru(Cl)(Me)(CO)_2(Me\text{-}DAB)]$ in agreement with the time-resolved absorption/emission, IR, and resonance Raman experiments.[45] This remarkable difference has profound consequences not only on the spectroscopy but also on the photoreactivity of this class of molecules used as sensitizers and/or catalysts in photochemical reductions.

As illustrated by the results reported in Table 3, the TD-DFT transitions energies are dramatically affected by the nature of the functional, especially in the case of the halide compound. The influence of the functional is less dramatic for the nonhalide complex $[Ru(SnH_3)(Me)(CO)_2(Me\text{-}DAB)]$.

7 PHOTOREACTIVITY

7.1 Photodissociation of the CO-Ligated Heme Group

The initial step (ultrafast CO loss within 50 fs) of the photodissociation process of CO-ligated iron porphyrin imidazole (Scheme 3), the model system for the CO-Ligated hemoglobin and myoglobin, has been investigated by means of TD-DFT.[46] On the basis of the one-dimensional PEC calculated as a function of the Fe–CO bond elongation (Figure 3) without relaxation of the other nuclear degrees of freedom, a qualitative mechanism has been proposed.

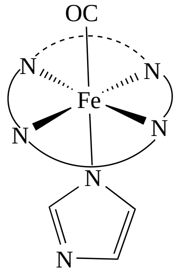

Scheme 3 After irradiation into the lowest Q bands calculated at 2.40 (1A′) and 2.42 eV (1A″) (vs. experimental values of 2.8 eV (Q_x band) and 2.30 eV (Q_y band)) and corresponding to $\pi \rightarrow \pi^*$ excitations localized on the porphyn cycle, the system will evolve on the bound part of the associated potentials (Figure 3).

Around 1.98 Å, it will overcome small energy barriers generated by avoided crossing between the bound 1A′ and 1A″ states and the repulsive 3A′ and 5A″ upper states calculated at 2.88 and 2.87 eV, respectively and corresponding to MLCT ($d_{Fe} \rightarrow \pi^*_{CO}$) transitions. A refined treatment of the potentials leading to a more realistic relative position of the electronic ground state and Q-band 1A′, 1A″ potential wells should confirm this mechanism and explain the observed timescale of dissociation (50 fs) characteristic of a direct ultrafast process.[47]

7.2 Photodissociation Dynamics of Metal-to-ligand-charge-transfer States in *α*-diimine complexes

7.2.1 Dissociative versus Nondissociative Metal-to-Ligand-Charge-Transfer (MLCT) States in M(H)(CO)₃(α-diimine) Complexes (M = Mn, Re)

The photodissociation dynamics of $M(H)(CO)_3(H\text{-}DAB)$ ($M = Mn, Re$), model systems for $M(R)(CO)_3(\alpha\text{-diimine})$

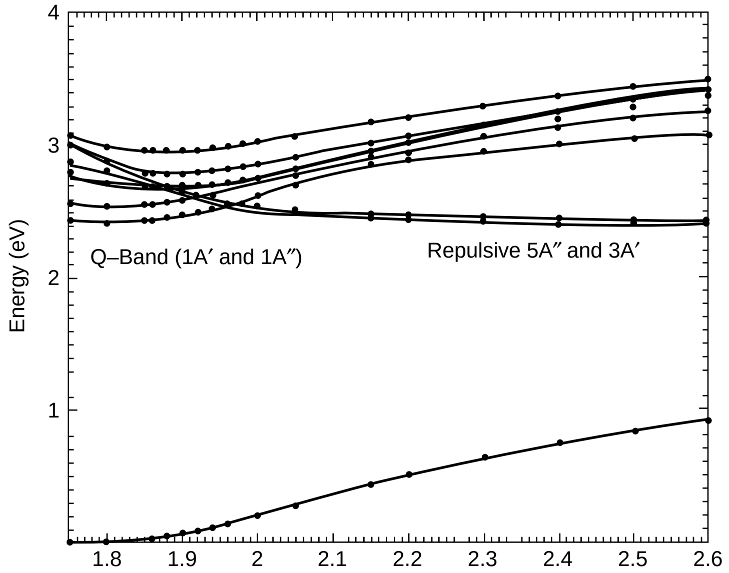

Figure 3 TD-DFT potential energy curves of the electronic ground state and low-lying singlet excited states as a function of the Fe–CO bond elongation.[46] (Reprinted with permission from Ref. 46. © 1978 American Chemical Society)

complexes (with M = Mn, Re, R representing a metal fragment or alkyl or halide groups bound to the metal by high-lying σ_{M-R} orbitals) have been investigated in two recent studies.[48,49] The main purpose was to understand the change of photochemical behavior upon visible irradiation, that is, from the CO loss and/or Mn–R bond homolysis to the Re–R bond homolysis and/or emission when going from the first-row to the third-row transition metal complexes.[44] Despite the presence of many potentially photoactive low-lying singlet and triplet excited states (nine for the manganese complex and seven for the rhenium one), it has been shown that only two states, the ^{1}MLCT ($d_M \rightarrow \pi^*_{\mathrm{DAB}}$) absorbing state and the ^{3}SBLCT ($\sigma_{\mathrm{M-R}} \rightarrow \pi^*_{\mathrm{DAB}}$) state will control the photochemistry of this class of molecules. As illustrated by the contour plot of the 2-D PES calculated as a function of the q_a = [M–H] and q_b = [M–CO$_{ax}$], the ^{1}MLCT absorbing state itself is dissociative for the CO loss in Mn(H)(CO)$_3$(H-DAB) (Figure 4) and is bound in Re(H)(CO)$_3$(H-DAB) (Figure 5).

The dissociative character of the MLCT state in the first-row transition metal complexes is due to the weakening of the Mn–CO$_{\mathrm{axial}}$ bond when exciting an electron from the d_{Mn} orbital, which is responsible for the $d\pi p\pi$ Mn–CO$_{ax}$ back bonding interaction, to the π^*_{DAB} localized on the acceptor group. This effect is less important in the third-row transition metal complexes where the metal–CO$_{\mathrm{axial}}$ interaction occurs mainly through the interaction with the diffused p of the metal. Moreover, the ^{3}SBLCT state presents a valley of dissociation for the metal–hydrogen bond breaking in both molecules. However, after absorption to the ^{1}MLCT in the visible energy domain, Mn(H)(CO)$_3$(H-DAB) will completely dissociate within 450 fs according to an ultrafast direct dissociative process (Figure 4) leading exclusively to the departure of the axial CO ligand. This theoretical study was the first evidence of the MLCT reactivity in transition metal α-diimine complexes currently observed experimentally.

7.2.2 *Role of the Triplet Sigma-Bond-to-Ligand-Charge-Transfer (SBLCT) State in the Photoreactivity of Re(R)(CO)$_3$(α-diimine) (R = H, Alkyl)*

As illustrated by the contour plot of the 2-D PES depicted in Figure 5 and in contrast to the manganese analogue, the ^{1}MLCT absorbing state is bound along both channels (axial CO loss and Re–H bond homolysis) in Re(H)(CO)$_3$(H-DAB). Within the 2-D approximation (q_a = Re–H, q_b = Re–CO$_{ax}$), one possibility of deactivation of [Re(H)(CO)$_3$(H-DAB)]* is via intersystem crossing to the ^{3}SBLCT state, this potential being repulsive for the homolytic cleavage, which is observed in a series of analogues like Re(R)(CO)$_3$(*i*Pr-DAB) (R = methyl, ethyl, metal fragment) with various quantum yields ($\phi = 10^{-2}$ for R = methyl, $\phi \approx 1.0$ for R = ethyl or benzyl).[44] After initial excitation under visible irradiation, the system gets trapped in the potential well of the MLCT state (Figure 5a). Within a very short timescale (50 fs), the ^{3}SBLCT state is populated via ^{1}MLCT $\rightarrow$ ^{3}SBLCT intersystem crossing (Figure 5b).

As soon as the wave packet reaches the ^{3}SBLCT potential, it evolves along the dissociation channel toward the formation of the diradicals H$^\bullet$ + $^\bullet$[Re(CO)$_3$(H-DAB)]. The reaction is rather slow and inefficient in this model complex with a probability of dissociation less than 2% within 2 ps.

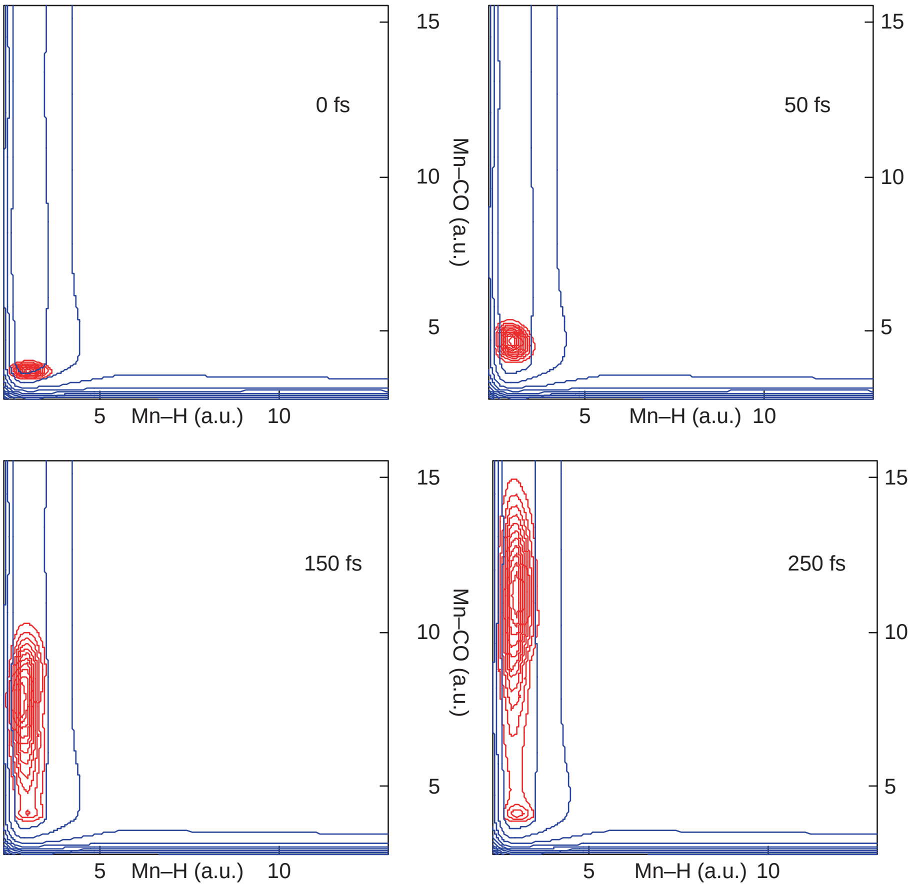

Figure 4 Time evolution of the wave packet $\Psi_{1_{MLCT}}(t)$(red solid lines) on the ab initio $V_{1_{MLCT}}$ (q_a, q_b) potential of the ^{1}MLCT absorbing state (contour plot in blue solid lines) of (H)Mn(CO)$_3$(H-DAB), model system for (R)Mn(CO)$_3$(α-diimine) complexes. (q_a = [Mn–H]; q_b = [Mn–CO$_{ax}$])

This example illustrates the complexity of the excited-state dynamics in this class of molecules. The early-stage dynamical behavior (in the first ps) may be tailored by the metal center, the α-diimine group, or the surrounding ligands. These chemical factors govern the character and electronic localization of the excited states, their relative position, and the presence of critical geometries. Moreover, the shape and relative positions of the PES may be also modified by the other experimental conditions like solvent effects.

7.3 Analysis and Control of Excited-states Dynamics in CpMn(CO)$_3$

Polyatomic molecules are characterized by complex internal motions leading to several possible rearrangements. With the advent of ultrafast lasers, much hope arose for achieving mode selectivity in chemical reactions based on the interaction between the laser pulses and the dynamics of the molecule. In the quest to steer complex systems, an especially attractive control scheme is the adaptive optimal laser pulse control. An algorithm ‘teaches’ a light field to prepare specific products on the basis of fitness information, such as product yields. This genetic algorithm iteratively creates an optimal laser pulse that prepares the desired target, solving the Schrödinger equation exactly in real time.[50] These experiments have been recently extended to transition metal carbonyls.[51] It has also been shown that feedback control can optimize individual fragmentation and ionization paths in CpMn(CO)$_3$ (Cp = η^5-C$_5$H$_5$). For such complex reactive systems, the question remains whether the optimal laser field contains a set of rational rules that govern the dynamics. A recent work combining femtosecond high-resolution pump-probe experiments and ab initio quantum calculations of the relevant PEC and wave packet simulations has enabled the deciphering of the dynamics of two competing processes in CpMn(CO)$_3$ induced by an optimal femtosecond pulse, which was generated from adaptive learning algorithms,[52]

$$\mathrm{CpMn(CO)_3} + \mathit{LaserFiled} \longrightarrow \mathrm{CpMn(CO)_3}^{+} + \bar{e} \qquad (8)$$

$$\longrightarrow \mathrm{CpMn(CO)_2}^{+} + \mathrm{CO} + \bar{e} \qquad (9)$$

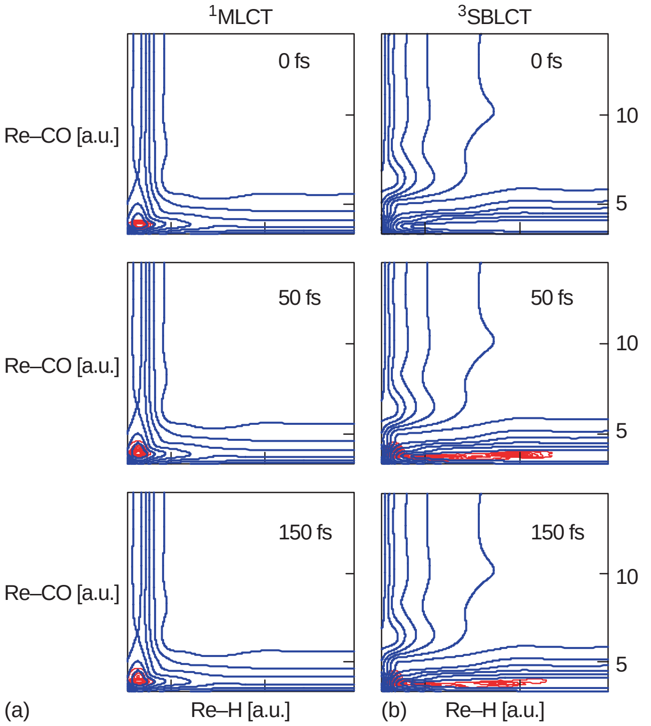

Figure 5 Time evolution of the wave packet $\Psi_{1_{\mathrm{MLCT}}}(t)$(red solid lines) on the ab initio $V_{1_{\mathrm{MLCT}}}$ (q_a, q_b) and $V_{3_{\mathrm{SBLCT}}}$ (q_a, q_b) potentials of the ^{1}MLCT absorbing state (contour plot in blue solid lines, (a)) and ^{3}SBLCT state (contour plot in blue solid lines, (b)) coupled by spin-orbit of (H)Re(CO)$_3$(H-DAB), model system for (R)Re(CO)$_3$(α-diimine) complexes. (q_a = [M–H]; q_b = [M–CO$_{ax}$])

When a nonoptimal laser pulse is used in the coherent pump/probe experiment, the two fragments CpMn(CO)$_3^+$ and CpMn(CO)$_2^+$ are detected, the last one within 66 fs. The dynamics of this process is depicted in Figure 6(a), which shows the evolution of the initial wave packet prepared on the a^{1}A$'$ ground state (t = 0 fs) at 50 and 135 fs. Under the pump pulse (3.43 eV frequency and 100 fs duration), the system evolves to the neutral states b^{1}A$''$ and c^{1}A$'$, whereas the ionic states b^{2}A$'$ and a^{2}A$''$ are obtained by the second pulse (probe pulse of 4.852 eV and 85 fs duration). One part of the wave packet starts an oscillatory motion into the potential well of the b^{1}A$''$ state with a period of 80 fs, while a small percentage is transferred to the a^{1}A$''$ through nonadiabatic transitions, leading to the neutral species CpMn(CO)$_2$. The probe pulse will put in evidence two fragments as illustrated in Figure 6(a).

A control mechanism has been proposed on the basis of the joint analysis of the experimental and theoretical information. The control scheme leading selectively to the formation of CpMn(CO)$_3^+$ is represented in Figure 6(b). The experiment realized with an optimal laser field is simulated by one pump pulse (at 3.49 eV) followed by a probe pulse (at 4.716 eV) designed with the adequate properties of phase, frequency, and duration. Within these specific conditions, the quasi-bound state c^{1}A$'$ is populated selectively and the CO dissociation is quenched as illustrated in Figure 6(b). The bottleneck of this type of theoretical study is the construction of accurate multidimensional PES, taking into account other degrees of freedom important in the dynamics. Within the limit of the theoretical model, it is mandatory to perform such simulations in close collaboration with experimentalists. The confrontation between the phenomena observed in the femtosecond laser pulse experiments and the results of quantum dynamics is primordial.

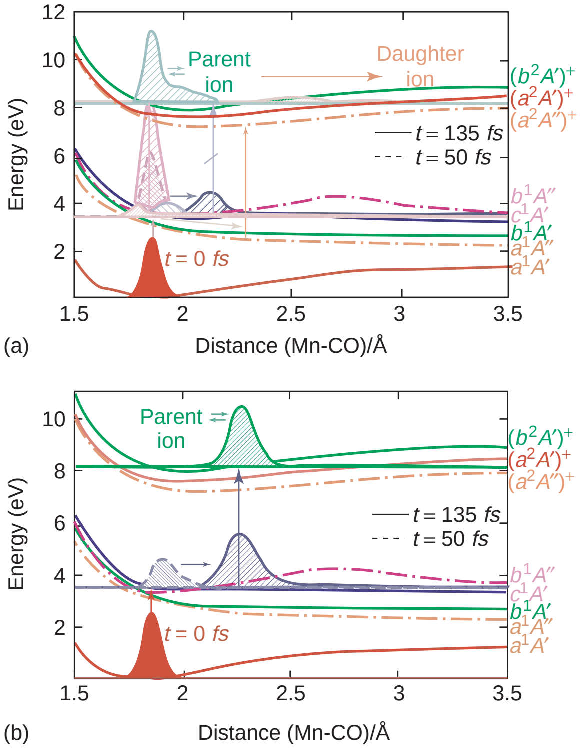

Figure 6 Adiabatic ab initio potentials with snapshots of the time evolution of the laser-induced wave packets (at $t = 0$ fs, original ground state; $t = 50$ fs, dashed envelope; $t = 135$ fs, solid envelope). (a) Simulation of the pump/probe experiment with competing pathways leading to CpMn(CO)$_3^+$ and CpMn(CO)$_2^+$ (R1 and R2 primary processes); (b) simulation of the control pathway leading exclusively to the CpMn(CO)$_3^+$ ions by quenching the internal conversion from the c^{1}A$'$ and b^{1}A$''$ absorbing states to the low-lying dissociative states b^{1}A$'$ and a^{1}A$''$

8 RELATED ARTICLES

Carbonyl Complexes of the Transition Metals; Electronic Structure of Organometallic Compounds; Hydride Complexes of the Transition Metals; Ligand Field Theory & Spectra; Manganese: Organometallic Chemistry; Photochemistry of Transition Metal Complexes; Rhenium: Organometallic Chemistry; Ruthenium: Organometallic Chemistry.

9 FURTHER READING

R. Schinke, ‘Photodissociation Dynamics’, Cambridge University Press, Cambridge, 1993.

10 REFERENCES

1. S. Campagna, S. Serroni, and F. Barigelletti, Guest Editors *Coord. Chem. Rev.*, 2000, **208**, 1, Special Issue 13th International Symposium on Photochemistry and Photophysics of Coordination Compounds (Lipari, Italy 1999).
2. *Coord. Chem. Rev.* 2002, **230**, 282, Dick Stufkens Special Issue (Amsterdam, 2001).
3. T. J. Meyer, *Pure Appl. Chem.*, 1986, **58**, 1193.
4. G. L. Geoffroy and M. S. Wrighton, ‘Organometallic Photochemistry’, Academic Press, New York, 1979.
5. L. C. Abbott, C. J. Arnold, K. C. Gordon, R. E. Hester, J. N. Moore, R. N. Perutz, and T. Q. Ye, *Laser Chem.*, 1999, **19**, 279; S. E. J. Bell, J. H. Rice, J. J. Mc Garvey, R. E. Hester, J. N. Moore, R. N. Perutz, T. Q. Ye, Y. Mizutani and T. Kitawaga, *Laser Chem.*, 1999, **19**, 271.
6. A. Veillard, in ‘Photoprocesses in Transition Metal Complexes, Biosystems and other Molecules. Experiment and Theory’, ed. E. Kochanski, NATO ASI Series C Vol. 376, Kluwer Academic Dordrecht, Boston, London, 1992, p. 173.
7. J. I. Zink, Photochemistry of Transition Metal Complexes: Theory, ‘Encyclopedia of Inorganic Chemistry’, 1st edn., Wiley, Chichaster, 1994, p. 3243.
8. L. G. Vanquickenborne and A. Ceulemans, *Inorg. Chem.*, 1978, **10**, 2730.
9. C. Daniel, *Coord. Chem. Rev.*, 2003, **238–239**, 143.
10. B. O. Roos, Advances in Chemical Physics: ab Initio, in ‘Methods in Quantum Chemistry’, ed. L. K. Lauley, John Wiley & Sons Ltd., Chichester, 1987, p. 399.
11. K. Andersson, P. Malmqvist, and B. O. Roos, *J. Chem. Phys.*, 1992, **96**, 1218.
12. O. Kühn, M. R. D. Hachey, M. M. Rohmer, and C. Daniel, *Chem. Phys. Lett.*, 2000, **322**, 199.
13. J. Bossert, N. Ben Amor, A. Strich, and C. Daniel, *Chem. Phys. Lett.*, 2001, **342**, 617.
14. J. Paldus, J. Cizek, and I. Shavitt, *Phys. Rev. A*, 1972, **5**, 50.
15. H. Nakatsuji and K. Hirao, *J. Chem. Phys.*, 1978, **68**, 2035.
16. R. J. Bartlett, *Ann. Rev. Phys. Chem.*, 1981, **32**, 359.
17. M. Hada, Y. Imai, M. Hidaka, and H. Nakatsuji, *J. Chem. Phys.*, 1995, **103**, 6993.
18. Z. Hu, R. J. Boyd, and H. Nakatsuji, *J. Am. Chem. Soc.*, 2002, **11**, 2664.
19. J. F. Stanton and R. J. Bartlett, *J. Chem. Phys.*, 1993, **98**, 7029, 9335.
20. N. Oliphant and R. J. Bartlett, *J. Am. Chem. Soc.*, 1994, **116**, 4091.
21. M. Nooijen and V. Lotrich, *J. Chem. Phys.*, 2000, **113**, 494.
22. T. Ziegler, A. Rauk, and E. J. Baerends, *Theor. Chim. Acta*, 1977, **43**, 261.
23. C. Daul, *Int. J. Quant. Chem. Symp.*, 1994, **52**, 867.
24. M. E. Casida, ‘Recent Advances in Density Functional Methods’, World Scientific, Singapore, 1996.
25. M. E. Casida, in ‘Recent Developments and Applications of Modern DFT’, ed. J. M. Seminario, Elsevier Science, Amsterdam, 1996, p. 391.
26. A. Rosa, G. Ricciardi, and E. J. Baerends, *J. Phys. Chem. A*, 2001, **105**, 3311.
27. A. Dreuw, J. L. Weisman, and M. Head-Gordon, *J. Chem. Phys.*, 2003, **119**, 2943.
28. M. Turki, C. Daniel, S. Záliš, A. Vlček Jr, J. van Slageren, and D. J. Stufkens, *J. Am. Chem. Soc.*, 2001, **123**, 11431.
29. T. P. M. Goutmans, A. W. Ehlers, M. C. van Hermert, A. Rosa, E. J. Baerends, and K. Lammertsma, *J. Am. Chem. Soc.*, 2003, **125**, 3558.
30. H. B. Schlegel, in ‘Modern Electronic Structure Theory’, ed. D. R. Yarkony, World Scientific, Singapore, 1995, p. 459.
31. P. Pulay, in ‘Modern Electronic Structure Theory’, ed. D. R. Yarkony, World Scientific, Singapore, 1995, p. 1191.
32. R. Shepard, in ‘Modern Electronic Structure Theory’, ed. D. R. Yarkony, World Scientific, Singapore, 1995, p. 345.
33. E. J. Baerends and A. Rosa, *Coord. Chem. Rev.*, 1998, **177**, 97.
34. C. V. Caille and R. D. Amos, *Chem. Phys. Lett.*, 2000, **317**, 159.
35. A. L. Sobolewski and W. Domcke, *Chem. Phys.*, 2000, **259**, 181.
36. S. Matsika and D. R. Yarkony, *J. Phys. Chem. A*, 2002, **106**, 2580.
37. M. J. Paterson, P. A. Hunt, M. Robb, and O. Takahashi, *J. Phys. Chem. A*, 2002, **106**, 10494.
38. M. C. Heitz and C. Daniel, *J. Am. Chem. Soc.*, 1997, **119**, 8269.
39. E. J. Heller, *Acc. Chem. Res.*, 1981, **14**, 368.
40. C. Daniel, Transition Metal and Rare Earth Compounds, Excited States, Transitions and Interactions, in ‘Topics in Current Chemistry’, ed. H. Yersin, Springer Verlag, Berlin, 2004, Vol. 241, p. 119.
41. K. Pierloot, J. O. A. D. Kerpel, U. Ryde, and B. O. Roos, *J. Am. Chem. Soc.*, 1997, **119**, 218.
42. K. Pierloot, J. O. A. D. Kerpel, U. Ryde, M. H. M. Olsson, and B. O. Roos, *J. Am. Chem. Soc.*, 1998, **120**, 13156.
43. L. B. LaCroix, S. E. Shadle, Y. Wang, B. A. Averill, B. Hedman, K. O. Hodgson, and E. I. Solomon, *J. Am. Chem. Soc.*, 1996, **118**, 7755.
44. D. J. Stufkens and A. Vlček Jr, *Coord. Chem. Rev.*, 1998, **177**, 127.

45. H. A. Nieuwenhuis, D. J. Stufkens, R. A. McNicholl, A. H. R. Al-Obaidi, C. G. Coates, S. E. J. Bell, J. J. McGarvey, J. Westwell, M. W. George, and J. J. Turner, *J. Am. Chem. Soc.*, 1995, **117**, 5579.

46. A. Dreuw, B. D. Dunietz, and M. Head-Gordon, *J. Am. Chem. Soc.*, 2002, **124**, 12070; B. D. Dunietz, A. Dreuw, and M. Head-Gordon, *J. Phys. Chem. B*, 2003, **107**, 5623.

47. M. C. Heitz, D. Guillaumont, I. Cote-Bruand, and C. Daniel, *J. Organomet. Chem.*, 2000, **609**, 66.

48. D. Guillaumont and C. Daniel, *J. Am. Chem. Soc.*, 1999, **121**, 11733.

49. I. Bruand-Cote and C. Daniel, *Chem. A Eur. J.*, 2002, **8**, 1361.

50. R. S. Judson and H. Rabitz, *Phys. Rev. Lett.*, 1992, **68**, 1500.

51. T. Brixner, N. H. Damrauer, P. Niklaus, and G. Gerber, *Nature*, 2001, **414**, 57.

52. C. Daniel, J. Full, L. González, C. Lupulescu, J. Manz, A. Merli, S. Vajda, and L. Wöste, *Science*, 2003, **299**, 536.

Photoelectron Spectroscopy of Transition Metal Systems

Jennifer C. Green
University of Oxford, Oxford, UK

1	Introduction	1
2	Experimental Considerations	2
3	The Orbital Picture of Photoionization	4
4	Intensities of PE Bands	5
5	Spectral Features of Transition Metal Molecules	13
6	Calculation of Ionization Energies	19
7	Case Studies	21
8	Conclusion	26
9	Related Articles	27
10	References	27

Abbreviations

IE = ionization energy; KE = kinetic energy; PES = photoelectron spectroscopy; SCK = super-Coster−Kronig; UPS = ultraviolet photoelectron spectroscopy; XPS = X-ray photoelectron spectroscopy.

1 INTRODUCTION

Photoelectron spectroscopy (PES) is the study of the electrons emitted when high-energy electromagnetic radiation interacts with matter. In a photoelectron experiment, photons of fixed energy, $h\nu$, are used, and the kinetic energy distribution of the photoelectrons is determined. In such a way, binding energies of the various electrons in atoms, molecules, and solids may be measured. PES provides the most direct experimental method of probing the allowed energy levels of electrons in substances, and characterizing their electronic structure.

Such investigations of valence electrons of transition metal molecules has led to the development and refinement of bonding models. Not only has calculation of ionization energies provided a stimulating challenge to the quantum chemist, but also such direct access to bonding information has influenced the direction of synthetic research. Ionization energies are key thermodynamic parameters in the understanding of oxidation and proton affinity, both important reactions for transition metal compounds. Binding energies also serve as a good measure of substituent effects, and can assist in monitoring the effect of chemical variation on a molecule.

In a similar fashion, studies on valence electrons in solids have proved critical in the understanding of valence bands and their relation to structure and bulk properties of transition metal materials.

High-energy photons, such as are provided by X-rays, are able to ionize core electrons of elements. The core ionization of a particular shell of a particular element occurs over a narrow energy range and is characteristic of that element. Study of core ionization thus forms the basis of a very useful analytical technique named *Electron Spectroscopy for Chemical Analysis*, or ESCA. Electrons with energies of around 1.5 keV can only escape from depths of typically 15 Å so, when applied to the solid state, ESCA is essentially a surface technique, and as such has proved very useful in the study of heterogeneous catalysis and corrosion. As the core ionization energy is to a certain extent sensitive to the chemical environment of the element, there exists the potential for distinguishing between different chemical environments, and obtaining a measure of the ‘charge’ on an atom.

This chapter is concerned primarily, though not exclusively, with the study of valence levels in transition metal molecules. There are a number of recent reviews that address various aspects of this topic.[1–7]

1.1 Photoionization

Photoionization, also known as photoemission, is normally a simple one-photon, one-electron process. The Einstein equation[8] (equation 1) defines the energetic relationship between the frequency of the monochromatic radiation, ν, and the kinetic energy of an ejected electron, E_k:

$$h\nu = I_k + E_k \tag{1}$$

I_k is the ionization energy, or binding energy, of the kth electron in the molecule. Ionization energies (IEs) are characteristic of the molecule, and are invariant to the photon energy used. The lowest photon energy at which ionization is possible corresponds to the first ionization energy of a molecule. If the photon energy is sufficient, a whole range of different species of electrons, with different ionization energies, may be emitted in separate photoionization events. As the energies of electrons in molecules are quantized, the kinetic energy distribution of the photoelectrons consists of a series of discrete bands. A photoelectron (PE) spectrum consists of a plot of the energy distribution, $n(E)$, that is the number of photoelectrons with a particular energy, E, against the ionization energy, I_k, or alternatively the kinetic energy (KE), E_k.[9]

1.2 Interpretation of a PE Spectrum

Photoionization can be represented by equation (2):

$$M + h\nu \longrightarrow M^+ + e^- \qquad (2)$$

where M represents the neutral species, which is in its ground electronic state, of energy $E(1)$, and M^+ the ionized system that may be formed either in its ground electronic state, of energy $E^+(1)$, or a variety of excited states of energies $E^+(j)$. It is the quantization of the energy states of M^+ that leads to the discrete band structure of a photoelectron spectrum. The jth ionization energy, I_j, is given by the difference in energy between the excited ion state, $E^+(j)$, and the molecular ground state, $E(1)$ (equation 3):

$$I_j = E^+(j) - E(1) \qquad (3)$$

Thus, a photoelectron spectrum gives directly the energy of the accessible ion states with respect to the ground state and, consequently, with respect to each other.

Photoionization can result either from the direct interaction of a photon with the ionizing electron or by an indirect process. An example of the latter is autoionization where a photon is absorbed to produce an excited state of the molecule, M*, by a resonance transition. The excited state then subsequently decays to the molecular ion and a photoelectron (equation 4):

$$M + h\nu \longrightarrow M^* \longrightarrow M^+ + e^- \qquad (4)$$

The energy of the photoelectron is the same as for direct photoionization.

Within an orbital picture of molecular electronic structure, formation of ion states can be described by removal of electrons from occupied orbitals in a molecule (Figure 1). Koopmans**[10]** put this model on a quantitative footing by relating the ionization energy of a molecule to the negative of the self-consistent field (SCF) orbital energy, $-\varepsilon_j$ (equation 5):

$$I_j = -\varepsilon_j \qquad (5)$$

Various approximations are involved in the derivation of *Koopmans' Theorem*, so quantitative predictions of IE are not accurate, but it is of considerable use in predicting the number and type of primary bands in the PE spectrum of a molecule, though not necessarily their energy ordering.

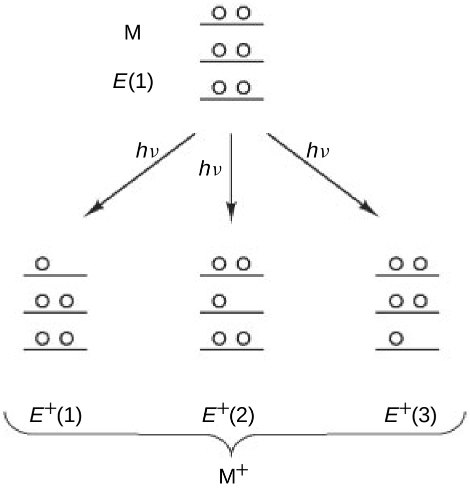

Figure 1 Schematic representation of the formation of three ion states of energies $E^+(1)$, $E^+(2)$, and $E^+(3)$, by the removal of bound electrons from three molecular orbitals of a molecule, M, with energy $E(1)$

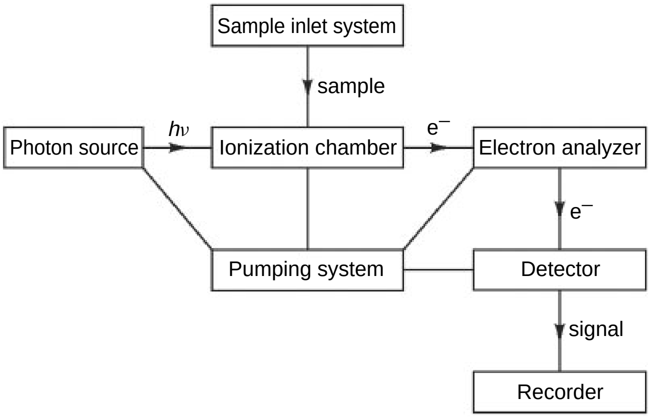

Figure 2 Block diagram showing the essential components of a photoelectron spectrometer

2 EXPERIMENTAL CONSIDERATIONS

The essential components of a photoelectron spectrometer are shown in Figure 2. They consist of a source of monochromatic radiation, an ionization chamber in which molecules or a solid can be ionized, an electron energy analyzer, an electron detector, and a recorder. A pumping system is also required to maintain a good vacuum. Gas-phase work needs a rapid pumping system, but for the electrons to avoid capture during their analysis the base pressure need be no better than 10^{-5} Torr. In studying solids, clean sample surfaces must be maintained and ultrahigh vacuum (UHV) conditions are necessary with pressures less than 4×10^{-11} Torr.

Cleanliness of all surfaces is essential to maintain the equipotentials needed for accurate electron energy analysis.

Table 1 Photon energies of characteristic lines from low energy resonance sources and X-ray sources

Line	Energy (eV)[a]	X-ray	Energy (eV)[a]
He I	21.22	Y Mζ	132.3
He II	40.81	Zr Mζ	151.4
Ne I	16.67, 16.85	Na Kα	1041.0
Ne II	26.81, 26.91	Mg Kα	1253.6
Ar I	11.62, 11.83	Al Kα	1486.6
Ar II	13.30, 13.48	Ti Kα	4510.9
H Lyman α	10.20	Cr Kα	5414.7
H Lyman β	12.09	Cu Kα	8047.8

[a] $1\ \text{eV} = 1.602 \times 10^{-19}$ J.

2.1 Light Sources

The ideal properties of a light source for photoelectron spectroscopy are a very narrow line, absence of any other lines, and a high intensity. Commonly used laboratory sources are summarized in Table 1. In ultraviolet photoelectron spectroscopy, the most useful and widely used light source is a helium discharge lamp. The He I resonance line (21.2 eV) is generated by the transition from an excited state of He ^{1}P (1s2p) to the ground state, ^{1}S (1s^2). Discharges in helium gas can also generate lines from ionized He. The equivalent transition in He$^+$ gives the He II line (40.8 eV), with a more energetic photon, enabling more tightly bound electrons to be ionized, and also band intensity variations to be studied. Higher lines of the $^1\text{P} \rightarrow {}^1\text{S}$ series are also present in the discharge, but they are of lower intensity and the associated satellite band structure is weak.

X-ray photoelectron spectroscopy (XPS) uses X-rays generated by allowing an intense beam of electrons to strike an appropriate target material. The inherent width of X-ray lines is greater than the line sources of ultraviolet photoelectron spectroscopy (UPS), but diffraction from a spherically bent crystal can reduce the line width to around 0.25 eV.

Table 1 gives the photon energies of common laboratory line sources.

Synchrotron radiation is continuum radiation from the infrared to the soft X-ray region produced by accelerating free electrons in a magnetic field. The construction of many synchrotron facilities throughout the world has revolutionized photoelectron spectroscopy. They provide intense, tunable photon sources over a wide range of energies. The radiation is polarized. Availability of continuously varying photon energy allows the measurement of photoionization cross sections and their variation with photon energy. Such studies greatly increase the power of a PE investigation.

2.2 Energy Analyzers

The crucial part of a PE experiment is to separate the photoelectrons according to their energy. Ideally both the spectral resolution and the sensitivity should be high, though the one requirement tends to conflict with the other. Analyzers are of two main types. Some retard the electrons and result in difference in transmission of electrons with a varying retardation potential; these produce integrated spectra. More commonly dispersive analyzers are used, in which deflecting fields separate electrons of different energies spatially and give differential spectra.

Much ingenuity has gone into the design of analyzers, resulting in a variety of systems.[11,12] A hemispherical analyzer consists of two concentric metal spheres with an entrance slit and retarding grid or lens at one end and an exit slit at the other. The voltage difference between the two spheres selects the kinetic energy of the electrons that are focused on the exit slit, the pass energy, PE. The analyzer can be operated either holding it at a constant pass energy and varying the retarding potential, R, or by keeping a constant retard ratio, (PE + R)/PE and scanning the pass energy. Constant pass energy maintains constant resolution throughout the scan. A cylindrical mirror analyzer has two coaxially arranged cylinders. The inner cylinder is grounded and the outer one has a negative voltage. Cylindrical mirror analyzers may also be operated in the two modes described above.

2.3 Detectors and Recorders

With the level of electron currents normally generated in a PES experiment, it is common to detect electrons singly using an electron multiplier, commonly called a channeltron. A channeltron is a horn shaped tube that has its inner surface coated with an emissive material. Such a device has the capacity to convert a single electron into a small pulse. A high voltage is applied between the mouth and the end of the tube; an electron entering the mouth is accelerated by the potential, strikes the wall and emits a bunch of secondary electrons. This process is repeated along the curved path of the horn until the ensuing pulse is collected at the end. The pulses are amplified and counted. Multichannel position sensitive detectors take advantage of the spatial resolution of deflection analyzers, and enable electrons over a range of kinetic energies to be counted simultaneously, thus cutting down on the time taken to achieve a good signal to noise ratio.

The advent of microprocessors has led to computer control of analyzer voltages and recording of count rates. This enables multiple scanning of spectra, with the advantage that relative band intensities are not affected by slow changes in sensitivity.

2.4 Samples

To measure a gas-phase spectrum of a transition metal molecule, the compound must possess sufficient volatility to generate a pressure of $10^{-2} - 10^{-1}$ Torr at a temperature below its decomposition point. Such conditions clearly restrict the number of compounds that can be measured in this state. Many of the more covalent transition metal compounds will survive such treatment, and gas-phase PES has been particularly beneficial in the development of the theory of bonding in organometallic compounds.[1]

For ionic and involatile compounds, data must be obtained in the solid state. This has disadvantages in that bands tend to be broader, calibration of samples presents difficulties, and only surface layers of the sample are probed. These may well not be characteristic of the bulk. Also surfaces are very sensitive to contamination, and effective sample cleaning is needed; rigorous vacuum conditions must prevail during the experiment to prevent recontamination.

2.5 Spectral Calibration

Calibration of binding energies for gaseous samples is straightforward. Reference gases with narrow PE bands, whose IEs are known (such as He, Ne, Ar, Xe, and N_2), are run concurrently with the sample, providing an energy scale.

Calibration of analyzers to determine their transmission factors as a function of electron energy is normally achieved by the use of rare gases with known ionization cross sections.

3 THE ORBITAL PICTURE OF PHOTOIONIZATION

For a closed-shell molecule, Koopmans' approximation identifies an IE with the negative of the SCF orbital energy (equation 5); if this were the case, a PE spectrum would provide an exact mapping of the occupied orbitals of a molecule (Figure 3).

When an electron is ionized from a molecule, the electron–electron repulsion decreases. A consequence of this is that the remaining electrons become more tightly bound, and their orbitals contract. Koopmans' approximation (equation 5) assumes identical orbitals for ion and molecule and neglects this relaxation. Also, Koopmans' approximation is based on an SCF model for molecular electronic structure; this is flawed in the sense that it assumes that electrons move in an averaged potential created by the core and the other electrons. In fact, electrons correlate their motion in order to avoid each other and decrease electron–electron repulsion; thus the true molecular energy is less than that estimated by an SCF method. As there are more electrons in a molecule than in its ion, the correlation correction is larger in the former. The effect of these changes on the Koopmans' estimate for ionization energy is illustrated in Figure 4.

It can be seen that the relaxation correction decreases the Koopmans' estimate, whereas the difference in the two correlation corrections increases the estimate. The errors are thus, to a certain extent, self-compensating. Transition metal d orbitals are often associated with much greater relaxation corrections than ligand orbitals, and this can lead to an inversion of ordering between an orbital energy calculation and the associated PE bands. Thus, it is not uncommon to find from a calculation a filled metal orbital to be more stable than a ligand orbital but to give rise to the first IE of a molecule.

SCF calculations also frequently neglect relativistic effects, which may well be important, especially for third row transition metal and actinide compounds.

The most significant deduction from the orbital model is that there is a one-to-one correspondence between the primary features of a PE spectrum and the occupied orbitals of a

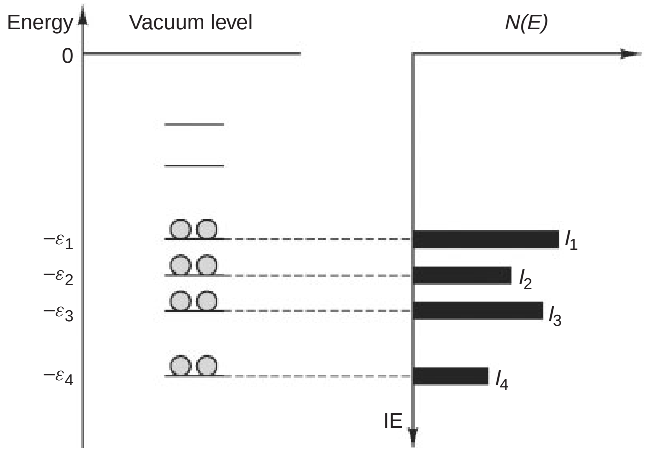

Figure 3 Representation of the relationship, according to Koopmans' theorem, between the orbital energies, $-\varepsilon_j$, of a closed-shell molecule and its ionization energies, I_j, displayed in a photoelectron spectrum

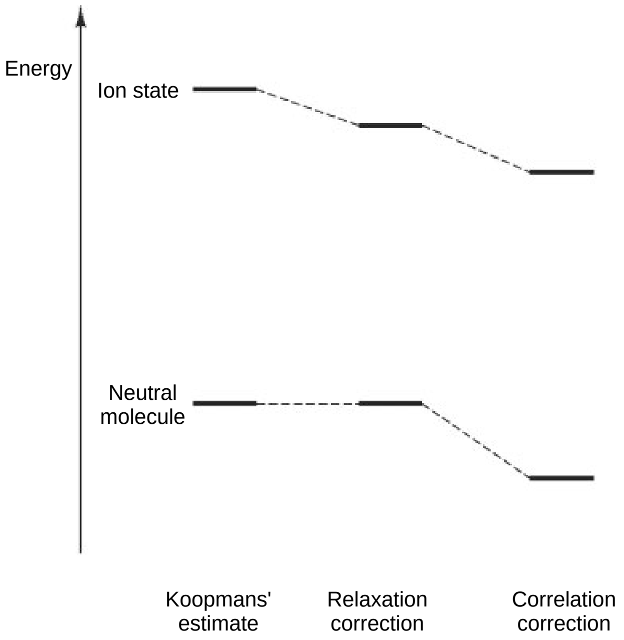

Figure 4 Diagrammatic representation of the relaxation and correlation energy corrections needed in deriving accurate IE from Koopmans' estimates

closed-shell molecule. Such is the power of this model that it is the starting point of most PE spectral interpretations. In fact, many PE bands show structure, and observations of additional bands are not uncommon. Most chemists prefer an interpretative approach, which is as simple as possible, but are ready to increase the sophistication of their models as the experimental facts demand. Consequently, an orbital approach to spectral assignment is the basis of the ensuing section.

Core binding energies also differ from the Koopmans estimate, the negative of the core orbital energy. When an inner electron leaves an atom of a molecule, the outer orbitals readjust because the nuclear charge is less effectively screened. The change due to outer shell readjustment is known as intra-atomic (or intramolecular) relaxation energy.

To the outer electrons, after ionization, the core looks like that of the atom with the next highest atomic number. This assumption, known as the equivalent core approximation, has been used in relating thermodynamic parameters to core binding energies.[13]

Though the binding energy of a particular type of core electron is characteristic of a given atom, the binding energies do vary over a narrow range depending on the chemical environment of the atom. For the initial state, the energy of a core electron is affected by the distribution of the valence electrons, as they generate a Coulombic potential that the core electron experiences. For the final state, the relaxation of the valence electrons towards the core hole will vary with the surrounding ligands. Both effects combine to give the experimental chemical shift for a molecule.

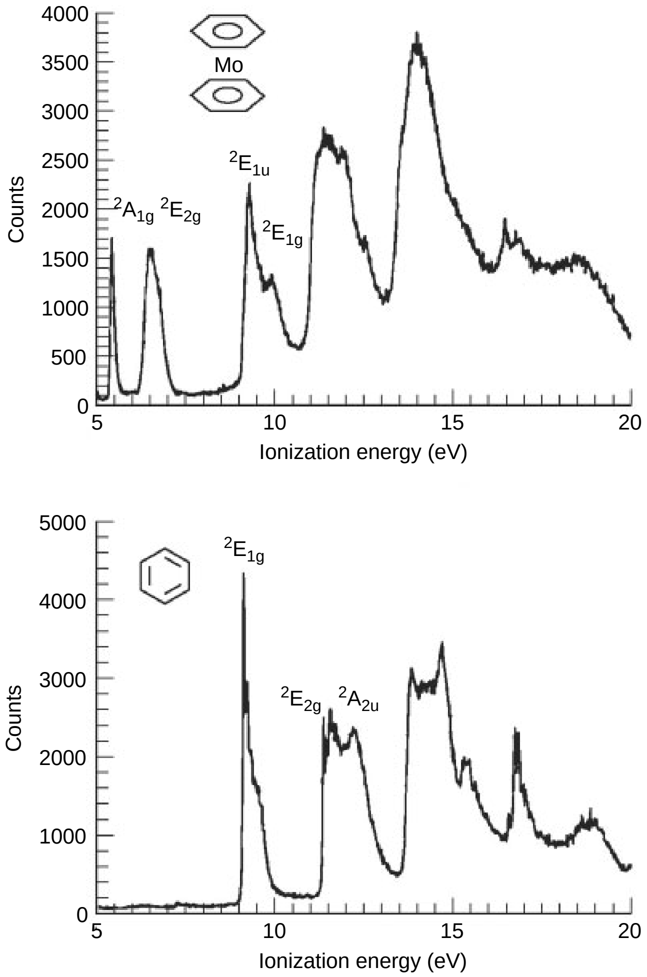

Figure 5 He I spectra of $Mo(\eta\text{-}C_6H_6)_2$ and C_6H_6. Bands are labeled according to the symmetry of the ion states formed

3.1 PE Spectrum and Orbital Structure of $Mo(\eta\text{-}C_6H_6)_2$

The PE study of the sandwich molecule $Mo(\eta\text{-}C_6H_6)_2$ (*see Hydrogenation*) illustrates the close relation between a PE spectrum of a molecule and its orbital structure.[14] Figure 5 shows the gas-phase He I PE spectrum of the complex, together with that of the free ligand benzene. It is immediately apparent that the majority of the ionization bands of benzene appear in the spectrum of the complex unshifted in energy and largely unchanged in shape. The fine structure of the bands, which is associated with vibrations of the molecular ion (see Section 5.1), is less well resolved and modified in the heavier molecule. The first ionization band of benzene, which is associated with ionization from the top e_{1g} π orbital, is perturbed on complexing and is split into two. In addition, the spectrum of $Mo(\eta\text{-}C_6H_6)_2$ contains two additional low IE bands, one considerably more intense than the other, which have no counterpart in the benzene spectrum. These are associated with ionization of the six metal d electrons of Mo(0).

The relation to the orbital structure of a sandwich molecule becomes clear on inspection of Figure 6. Bonding in the molecule is primarily produced by donation from the top π orbitals of benzene into the d_{xz} and d_{yz} orbitals of Mo, resulting in the e_{1g} MO, and back donation from the filled $d_{x^2-y^2}$ and d_{xy} orbitals of Mo into the empty $e_{2u}\pi$ orbitals of benzene, resulting in the e_{2g} MO. The consequent stabilization of the e_{2g} orbitals with respect to the a_{1g} orbital, which is largely d_{z^2} in character and nonbonding, results in the e_{2g} electrons having a higher IE than the a_{1g} electrons. In a similar fashion, the metal–ligand-bonding character of the e_{1g} orbital is reflected in the higher IE for the e_{1g} electrons compared with that of the e_{1u}. Only Mo p orbitals can contribute to the e_{1u} interaction and they are less effective at bonding than the Mo d orbitals. The band assignment has been confirmed[15] by studying the intensity variation of the bands with photon energy (see Section 4.2).

4 INTENSITIES OF PE BANDS

In addition to the energy information in a PE spectrum, there is also intensity information. Whereas the derived IEs of

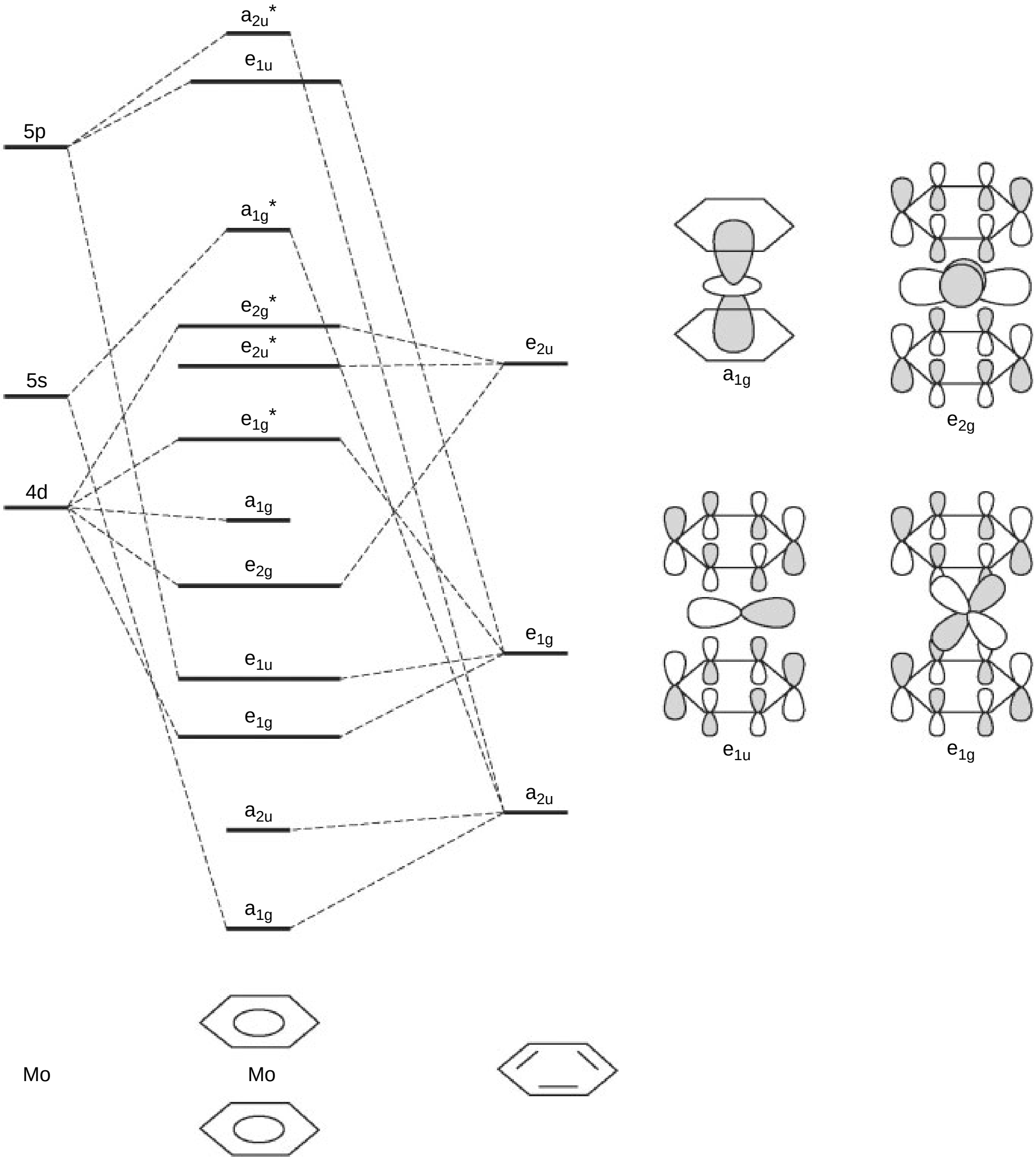

Figure 6 MO scheme for Mo(η-C_6H_6)$_2$; the 18 valence electrons occupy the orbitals up to the a_{1g} level

the photoelectrons are characteristic only of the sample being studied, the band intensities depend, in addition, on the angle of observation of the photoelectron with respect to the photon beam, the polarization of the photons, and also the photon energy. Interpretation of the variations in intensity can give further information on electronic structure.

The probability of photoionization to an ion state is termed a photoionization or photoelectron *cross section*, commonly denoted σ (ω). Photoionization is a dipole transition between the initial and final states. The only difference from discrete electronic excitations is that the final state lies in the continuum. This means that for each energy $E > 0$ there is a solution of the Schrödinger equation. This solution does not decay at infinity, but oscillates periodically and corresponds physically to an electron asymptotically free. Moreover, each energy is infinitely degenerate, corresponding to the infinite choices for the direction of the photoelectron momentum, or equivalently for each value of the photoelectron angular momentum. For example, in the hydrogen atom, for each energy $E > 0$ there is a ψ_{Elmms} final orbital, that is an s wave, a p wave, and so on. Transition probability is controlled by the dipole transition moment

$$\mathbf{M}_{\mathrm{fi}} = < \Psi_{\mathrm{f}} | \mathbf{r} | \Psi_{\mathrm{i}} > \qquad (6)$$

and the cross section is the sum of the squares

$$\sigma = \sum_{\mathrm{f}} |\mathbf{M}_{\mathrm{fi}}|^2 \tag{7}$$

over all final states available.[16,17] In an orbital approximation, this reduces to the interaction between the vacated orbital ϕ_i and the photoelectron wave ε_f.

4.1 Angular Variation

As angular momentum is conserved in photoionization, the wavefunction of the ejected electron is constrained by the dipole selection rule, and in the Russell–Saunders coupling limit the quantum number l must change by ± 1. For example, ejection from an s orbital gives rise to a p electron wave, whereas ejection of a d electron can give photoelectrons with p or f character. The angular distribution of photoelectrons depends on the angular momentum mix of these outgoing spherical waves. Generally the $1 \rightarrow l+1$ transition is the dominant contribution.

If the electrons are observed at an angle θ to the direction of the electric vector of a plane polarized light beam, the intensity $I(\theta)$ is given by equation (8):[18]

$$I(\theta) = \frac{\sigma}{4\pi}\left[1 + \frac{\beta}{2}(3cos^2\theta - 1)\right] \tag{8}$$

where σ is the total cross section integrated over all angles, and β, known as the anisotropy parameter, is the only parameter needed to describe the angular distribution of the photoelectrons. For a pure p wave resulting from ionization of an s orbital, β has a value of 2, so the angular distribution has a $\cos^2\theta$ distribution and the most probable direction of ejection of the s electron is at right angles to the electric vector. Equation (8) must be modified for the cases of unpolarized or partially polarized light.[12] The range of allowed values for the asymmetry parameter, β, is from -1 to 2. In molecules, because of the loss of spherical symmetry, much more extensive mixing is possible, and interpretation is correspondingly more complicated.[19] For most ionizations from atoms and molecules, β will vary with photon energy.

So far there have been few β measurements on molecules containing transition metals. A study on various organometallics, including *Ferrocene* and the group 6 hexacarbonyls, showed that the variation of β with photon energy differed according to the orbital being ionized, and was used on an empirical level to confirm some assignments.[20]

4.2 Variation with Photon Energy

As all one-electron photoionizations are allowed, photoionization cross sections, σ, for particular ion states are all of the same order of magnitude. They vary with the photon energy used, and the variation is characteristic of the nature of the vacated orbital. Studying PE cross sections is thus a very useful way of obtaining more information on electronic structure and assigning PE bands.

4.2.1 Atomic Cross Sections

Cross section variations are best understood for atoms, and a useful compilation of calculated atomic cross sections for direct photoionization exists.[21] Most qualitative features can be understood in terms of the interaction between the vacated orbital and the outgoing electron wave (equation 6). A cross section is usually highest near the threshold and after that decreases with increasing photon energy. This is a consequence of the photoelectron having a greater KE, and hence a shorter wavelength. As the electron wave becomes more oscillatory the positive and negative parts of the dipole matrix element with the vacated orbital tend to cancel one another (Figure 7(a)) and the cross section suffers rapid decay as exemplified by the 2p cross sections of the elements B to Ne (Figure 7(b), 7(c)). At very high photon energies, the cross section should vary as ν^{-3}.

For orbitals with a radial node, there is a minimum in the cross section, known as a Cooper minimum.[22,23] At some photon energy, the contributions from the inner and outer parts of the orbital will tend to cancel one another (Figure 7(d)). Figure 7(e) illustrates the occurrence of such a minimum in the cross section of the 3p electrons of the elements Si to Cl. Figure 7(f) shows the cross section of the t_1 band of $TiCl_4$, which shows a Cooper minimum at 40 eV;[24] by symmetry, this is pure Cl 3p in character (see also Section 4.2.4). If an orbital has more than one radial node, there may be a corresponding number of Cooper minima in the cross section. The minima may occur just above threshold, as is the case for the 3s orbital of Na, or several hundred eV, as is found for 4d and 5f electrons of transition elements. Rules for Cooper minima, which have been arrived at by experimental and theoretical investigations, are as follows:

1. Cooper minima only appear in $l \rightarrow l+1$ transitions.
2. They occur only for outer and near outer subshells, and only for those orbitals with radial nodes.
3. They are generally not zero minima because even though the $l \rightarrow l+1$ dipole matrix element vanishes, the $l \rightarrow l-1$ one does not.

With such minima, the photon energy may be tuned to minimize the contribution from certain types of orbitals to a PE spectrum. The angular parameter, β, can vary substantially in the region of a Cooper minimum as the contribution from the $l \rightarrow l+1$ wave is small, leading to domination of β by the $l-1$ wave.

Orbitals with high angular momentum (i.e. d or f orbitals) often have maxima in their ionization cross sections some way above threshold. This is in contrast to s and p orbitals

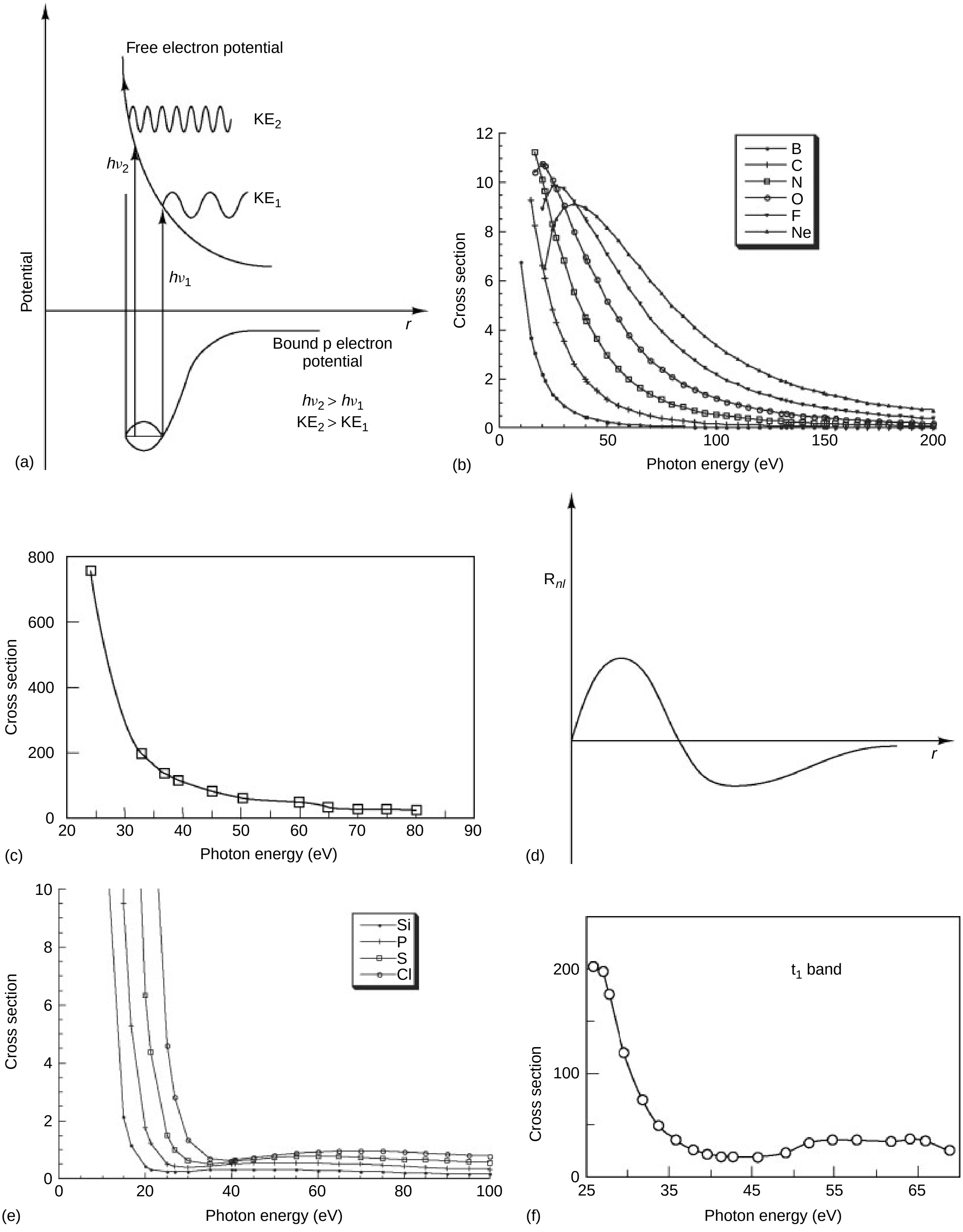

Figure 7 (a) Representation of the interaction of a bound 2p electron and electron waves of low and high kinetic energy; (b) calculated 2p cross sections for B-Ne (c) experimental cross section for a C 2p electron (d) potential and radial wavefunction for a 3p electron; (e) calculated 3p cross sections for Si-Cl (f) cross section for t_1 band of $TiCl_4$, which has Cl3p character

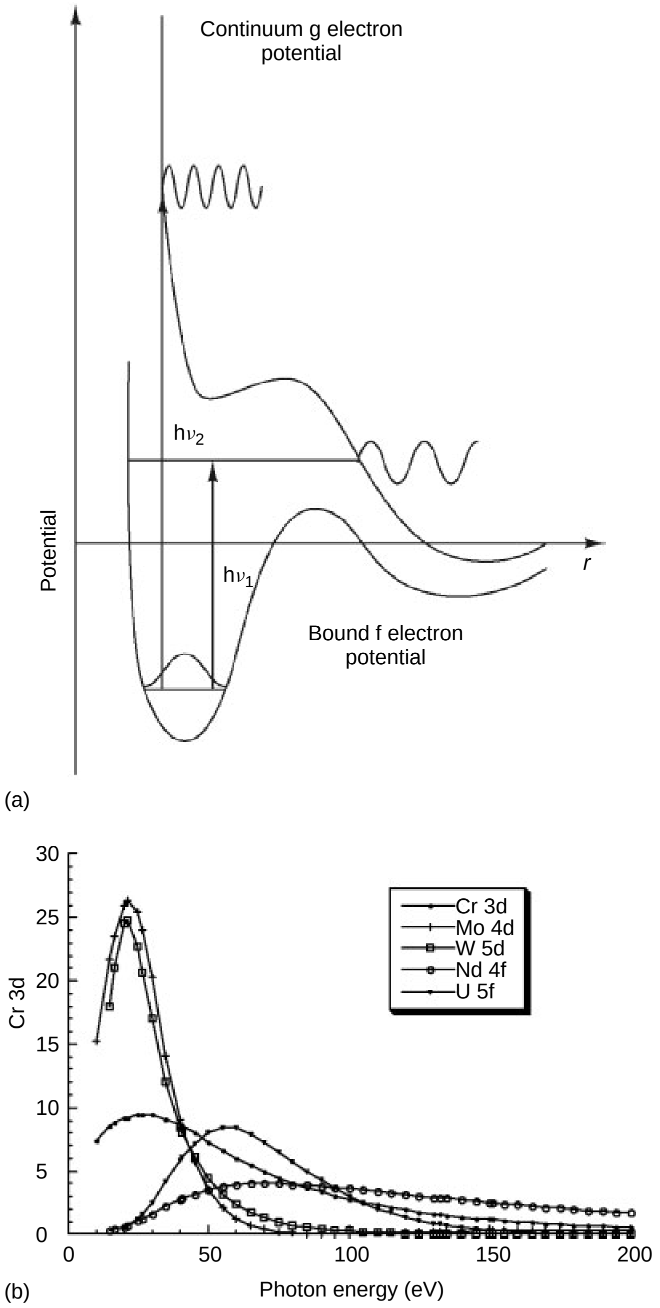

Figure 8 (a) Schematic representation of the radial potential and wavefunctions for a bound f electron and a continuum g electron, illustrating the origin of the delayed maximum; (b) calculated ionization cross section of d electrons for Cr, Mo, and W and f electrons for Nd and U

where maxima, if they exist, tend to be very close to threshold. The effective potential experienced by an electron in an atom is given by the central field potential[25] and the radial wave equation is given by equation (9):

$$\left[\frac{\mathrm{d}^2}{\mathrm{d}r^2} + \frac{l(l+1)}{r^2} + V(r)\right]\Psi_{nl}(r) = E\Psi_{nl}(r) \qquad (9)$$

$V(r)$ is the Coulombic potential, which is attractive, and $[(l(l+1)/r^2)]$ is termed the centrifugal repulsion term and results from the solution of the angular part of the Schrödinger equation. For high values of l, the effect of the centrifugal term is to create a double well potential, which has an intermediate range maximum that may be positive. Figure 8(a) illustrates the case for a bound f electron that exists in the inner well, escaping as a g electron wave. At low photon energies, the ensuing wave has insufficient energy to penetrate the centrifugal barrier, so the interaction between the f electron and the g wave is small. At higher photon energies, the interaction improves and the cross section will pass through a maximum before decaying owing to the normal oscillatory effects.

Figure 8(b) shows the calculated cross sections for Cr 3d, Mo 4d, W 5d, Nd 4f, and U 5f orbitals. The delayed maxima for the f electrons occur at a higher photon energy than those of the d electrons as the centrifugal barrier is higher in the former case. This results in f electrons having very low cross sections at He I energies. The ionization cross section of the f electrons of $\mathrm{U}(\eta\text{-}\mathrm{C}_8\mathrm{H}_8)_2$ (see Section 4.2.5) shows a delayed maximum at 39 eV.[26] The maximum cross section for Cr is lower than for Mo and W, and this is generally the case for first-row transition metal compounds. However, as 3d orbitals have no radial nodes, their cross sections decay much less rapidly with photon energy than those of 4d and 5d metals. Similar features are apparent when comparing 4f and 5f cross sections.

In the critical energy region between 20 and 40, d and f electron cross sections tend to increase, or decay rather more slowly than those of s and p electrons. As a consequence, changes in relative band intensity between He I and He II spectra can often be used to distinguish between metal and ligand bands. This is illustrated in the He I and He II PE spectra of $\mathrm{Re}_3\mathrm{Cl}_9$ and $\mathrm{Re}_3\mathrm{Br}_9$[27] (Figure 9).

A Cooper minimum occurs around 39 eV for Cl 3p ionizations, which makes their He II cross sections very low. Br 4p cross sections are calculated to drop by a factor of 16 between He I and He II photon energies. The peaks associated with Re character tend to gain in intensity relative to the halide ones as the photon energy is increased. For the chloride, the lowest IE bands are associated with metal–metal-bonding orbitals of the Re_3 cluster, whereas for the bromide the lowest IE bands are bromine 4p in character. For both compounds, the covalent nature of the metal–halide σ bonds results in metal-like cross section behavior in the highest IE ionizations of the spectra shown.

4.2.2 Autoionization and Giant Resonances

All the cross section variations discussed above are the result of direct ionization. If autoionization (Section 1.2) occurs, it can have a substantial effect on PE band intensities at photon energies close to an autoionizing resonance frequency.

Resonant excitation of inner electrons can also have considerable effects on the photoionization cross sections of d

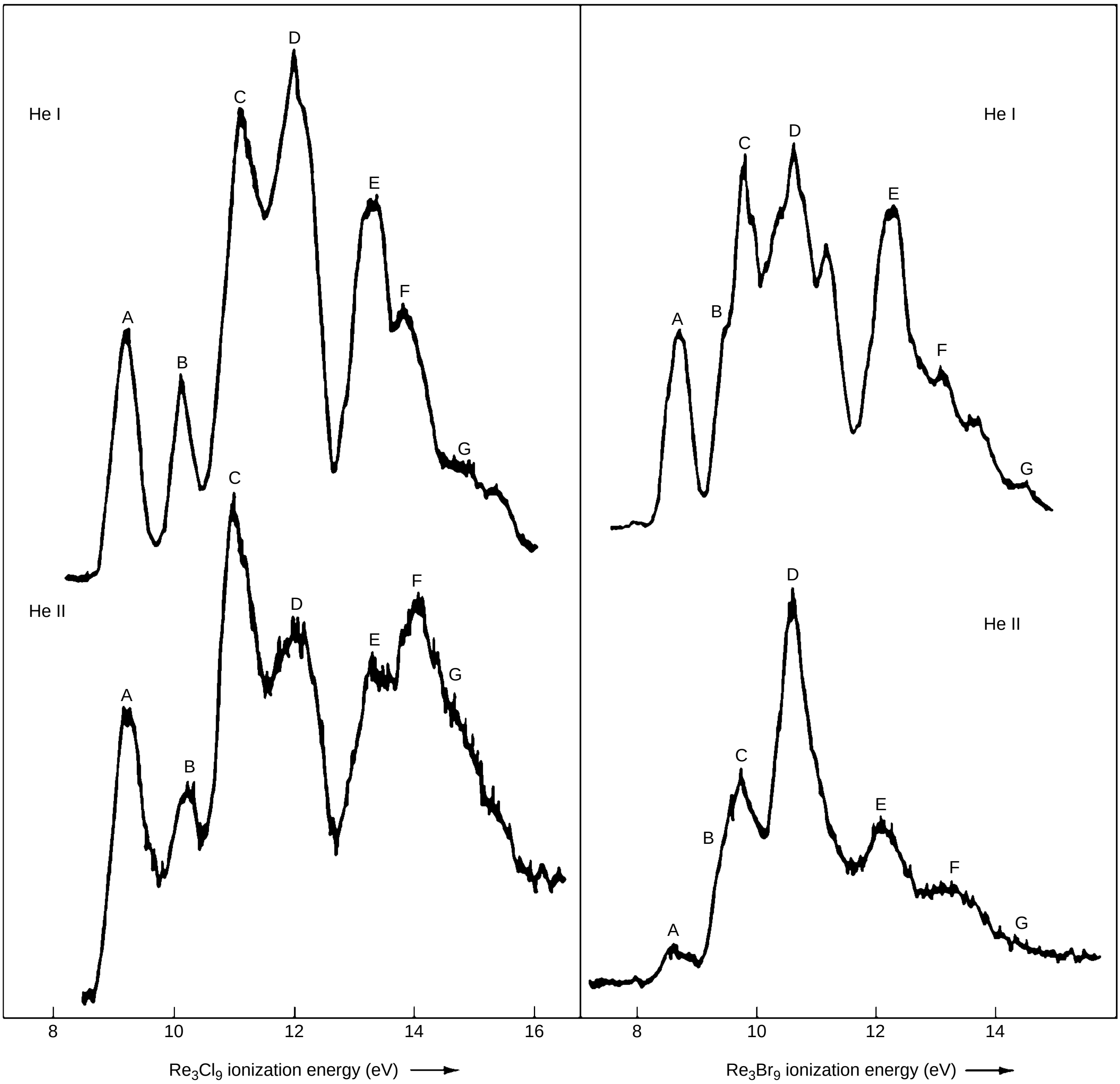

Figure 9 He I and He II PE spectra of Re_3Cl_9 and Re_3Br_9

and f electrons. Let us take the principal quantum number of the ionizing d and f electrons as n. If the photon energy is sufficient, an electron can be promoted from an inner np or nd shell to an empty nd or nf orbital. When d and f electrons are bound, the wavefunctions have nearly all of their amplitude in the inner well of their potential, which results in very large probabilities for transitions from inner p to valence d (or inner d to valence f) orbitals of the same principal quantum number. The spatial proximity results in strong interactions between the np or nd hole and the $n\mathrm{d}^{x+1}$ or $n\mathrm{f}^{x+1}$ states, and the energies of the configurations are spread over many eV, many of which lie above the np or nd ionization threshold. One possible fate of such excited states is termed super Coster–Kronig (SCK) decay, whereby the d or f electron falls back into the hole and another d or f electron is ionized. As far as its KE is concerned, the ionized electron is indistinguishable from one resulting from direct photoionization resulting in the same ion state (Figure 10).

In an independent particle picture, one has a discrete state, like $3\mathrm{p}^{-1}3\mathrm{d}^{x+1}$, interacting with the continuum $3\mathrm{d}^{x-1}\varepsilon\mathrm{f}$, $\varepsilon\mathrm{p}$. Configuration interaction mixes the discrete state, which loses its separate existence, in the continuum. The transition moment

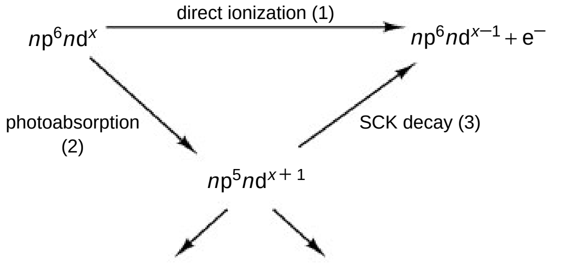

$n\mathrm{p}^6 n\mathrm{d}^x$
direct ionization (1)
$n\mathrm{p}^6 n\mathrm{d}^{x-1} + \mathrm{e}^-$
photoabsorption (2)
SCK decay (3)
$n\mathrm{p}^5 n\mathrm{d}^{x+1}$

Figure 10 Illustration of two channels for ionization of a d electron, direct photoionization, and photoabsorption followed by SCK decay

associated with the excitation into the discrete configuration, which can be very large if initial and final orbitals are strongly localized in the same region of space, for example, 3p → 3d, interferes with that due to the original continuum, giving rise to sharp features in the cross section, with the characteristic 'Fano profile'[28,29]

The strength of the resonance, and the shape of the profile, is governed both by transition moments, for example, $<3\mathrm{p}|\mu|3\mathrm{d}>$, and the interaction between the discrete and continuum state, for example, $<3\mathrm{p}^{-1}3\mathrm{d}^{x+1}|1/\mathrm{r}_{12}|3\mathrm{d}^{x-1}\varepsilon\mathrm{f}>$. The increases are preceded by a dip in the cross section; somewhat counterintuitively, opening another channel for photoionization can lead to a decreased ionization probability. As well as possessing momentum, the photoelectrons possess phase. Interference between the two channels, the direct and indirect processes, lead to the resonance shape. This phenomenon is generally called autoionization, and, in particular for core excitation and decay all involving orbitals of the same principal quantum number, SCK decay. As a consequence, d and f cross sections are strongly modified in the resonance region. The process is only effective for high angular momentum electrons because the centrifugal barrier associated with their effective potential is necessary to retain the excited electron. The lifetime of the excited state is very short, and uncertainty-broadening leads to the effect on PE cross sections being spread over many electron volts.

Figure 11 shows the d band cross sections for the group 6 hexacarbonyls $\mathrm{M(CO)_6}$, where M = Cr, Mo, or W;[30] the effect of the resonance absorption on the cross sections is clearly evident at energies around that needed for inner np shell ionization, which is indicated on the energy scale. Two resonances are seen for W 5d ionization as the spin–orbit splitting of the 5p core hole is of the order of 10 eV and is sufficiently large to be resolved.

Giant resonances are also evident in the $\mathrm{U}(\eta\text{-}\mathrm{C_8H_8})_2$ f band cross section at 97.5 and 107.5 eV (Section 4.2.5); the 5d core electrons of the uranium atom ionize at 101 and 110 eV.[26]

4.2.3 *Molecular Cross Sections; the Gelius Model*

Cross sections of molecules show many of the features of the atoms that constitute them; the characteristic patterns

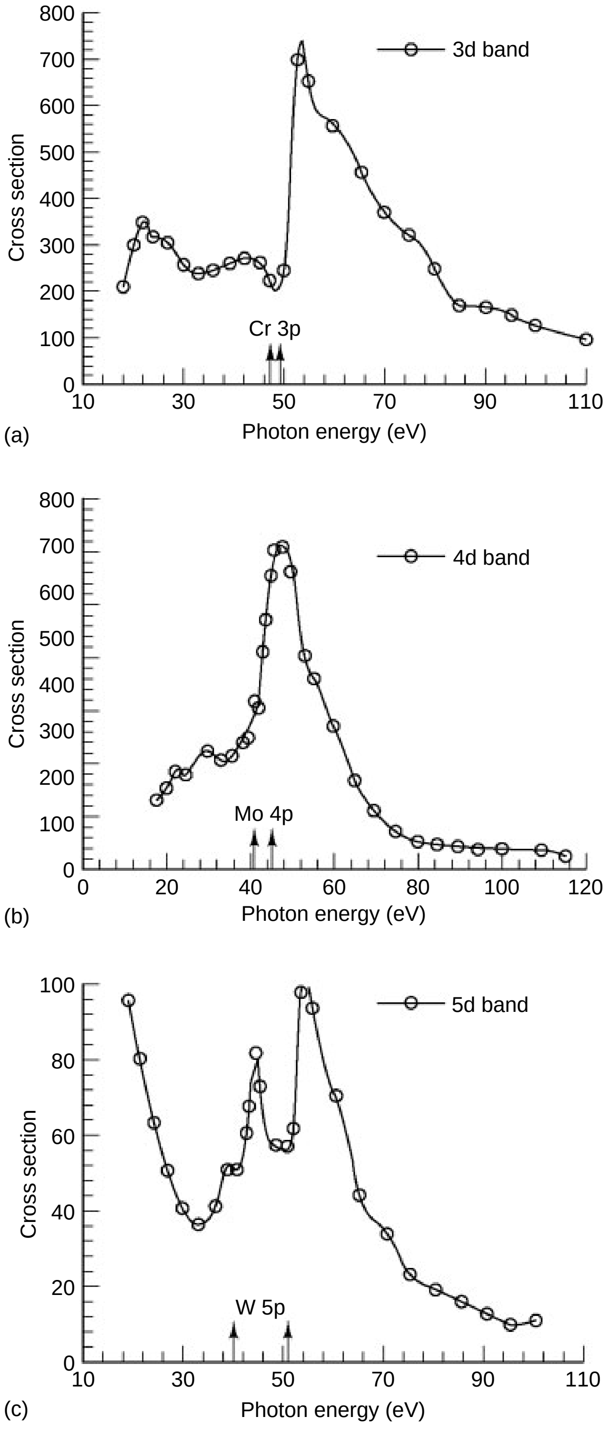

Figure 11 Photoionization cross sections of the d ($\mathrm{t_{2g}}$) electrons of (a) $\mathrm{Cr(CO)_6}$, (b) $\mathrm{Mo(CO)_6}$, and (c) $\mathrm{W(CO)_6}$, as a function of photon energy. The cross sections are given in arbitrary units. The vertical arrows mark the ionization energies of the 3p, 4p, and 5p electrons of Cr, Mo, and W, respectively

of ionization from atomic orbitals are carried over to the molecular orbitals to which they contribute. The most commonly used model for interpreting molecular photoionization cross sections is the Gelius model,[22,23] in which the one-electron cross section, σ_j, for the jth MO is given by equation (10). The summation is carried out over all the AOs, $\chi_i{}^{\mathrm{A}}$, on the different atoms, A, which contribute to the MO, ϕ_j:

$$\sigma_j = \sum_{\mathrm{A},i} P_{j,i,A}\sigma_i^A \tag{10}$$

The $\sigma_i{}^A$ are one-electron atomic cross sections and the $P_{j,i,\mathrm{A}}$ are factors describing the weight of the contribution of the AOs to the MO. In a LCAO MO treatment they are given by the squares of the coefficients $c_{j,i,\mathrm{A}}$ of the AO χ_i in the MO ϕ_j (equation 11):

$$P_{j,i,A} = (c_{j,i,A})^2 \tag{11}$$

The model is valid when the contribution of the overlap electron density to the cross section is negligible and the effects of the anisotropy of the molecular ion potential on the outgoing electron wavefunction are small. Both of these conditions are most likely to hold when the photoelectron KE is high. At low photon energies, molecular effects on ionization cross sections are well documented, but even in these regions atomic effects are evident and the Gelius model provides a good basis for molecular cross section interpretation.

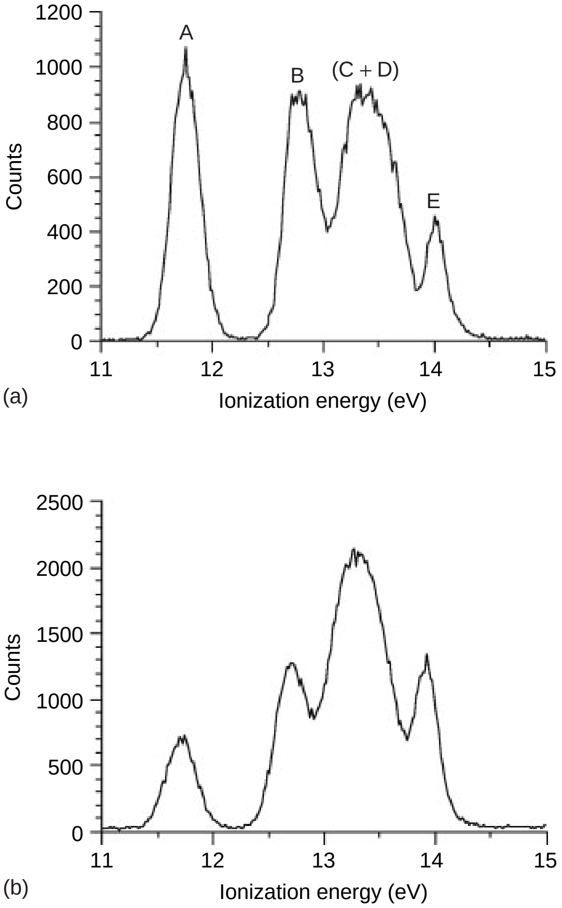

Figure 12 The PE spectrum of $TiCl_4$, acquired at (a) 24 and (b) 40 eV. Bands A and E are the t_1 and a_1 ionizations respectively and have predominantly Cl character. While A shows a Cooper minimum at 40 eV, E is relatively intense owing to a shape resonance

4.2.4 *Molecular Effects and Shape Resonances*

Though many of the features of molecular PE cross sections can be attributed to atomic effects, some features, such as shape resonances, are critically dependent on the form of the molecular potential.[25,31] This itself is determined in part by the physical shape of the molecule, from which the name of the effect derives. Shape resonances manifest themselves as increases in cross section, which are frequently sharp and generally at relatively low PE kinetic energies. They are generally viewed as attributable to momentary trapping of the electron in a quasi-bound continuum orbital created by an effective potential of the molecular ion, or, excitation into antibonding orbitals located in the continuum.[32]

An alternative, though not incompatible, view of shape resonances, is to regard them rather like Extended X-ray Absorption Fine Structure (EXAFS), where an ionizing electron is scattered from neighboring atoms, and so has maxima and minima in its amplitude as a function of its energy, as a result of the scattered waves reinforcing or interfering with the outgoing wave. In this model also, it is apparent that the resonances are a function of the shape and size of the molecule.[30,33]

It has been observed empirically that the a_1 bands of tetrahedral molecules show shape resonances. OsO_4 provides an example.[34] The $^2A_1$ band shows a sharp rise in intensity around 52.5 eV (Section 7.1). The related $^2A_1$ band of $TiCl_4$ shows a shape resonance at a lower photon energy of 40 eV (Figure 12).[24]

Maxima in the PE ionization cross sections of metallocenes and related sandwich molecules have been identified and assigned to shape resonances.[35–37] The molecular potential for this series of molecules is expected be very similar throughout the series and largely independent of the nature of the metal. For bis-cyclopentadienyl metal compounds, a shape resonance occurs in a region between 36 and 40 eV, whereas the $p \rightarrow d$ resonances occur over a range of 43 to 75 eV depending on the metal. Bis-arene and cycloheptatrienyl-cyclopentadienyl compounds show similar features.[37,38] In the most part, the shape resonances are most apparent in the metal-based orbitals, the strength of the resonance increasing with the metal character. An exception to this is the ionization cross section from the e_1'' HOMOs (highest occupied molecular orbitals) of cobaltocene and nickelocene.[36] These antibonding d orbitals show smaller $p \rightarrow d$ resonances than the more metal localized a_1' and e_2' orbitals, in accord with the expectation of their respective metal characters, but significantly stronger shape resonances.

These and other instances of the presence of shape resonances in the region of 40 eV photon energy provides a cautionary note for the interpretation of relative increases in band intensity in He II spectra, compared to He I spectra as attributable to metal d character.

4.2.5 Evidence for Covalency from Cross Section Variation

Though cross section variation can be studied to a very limited extent using line sources, synchrotron radiation is far superior for investigations of this type. Synchrotron studies are used extensively on transition metal solids for deconvoluting valence bands into partial densities of states from the contributing AO. Studies on transition metal molecules have demonstrated the power of the technique for band assignment and the investigation of covalency.

Uranocene, U(η^8-C_8H_8) provides an excellent example.**[26]** The f ionization band, the first of the spectrum, shows two characteristic features, a delayed maximum and a giant resonance. Figure 13(a) shows the cross section of this band. The next two bands are primarily ring C 2pπ bands of e_2 symmetry. They show the characteristic decay associated with nodeless 2p orbitals (Figure 13(b)). The second band, however, has, superimposed on this decay, a maximum around 40 eV and a double resonance between 95 and 125 eV. This indicates partial 5f character and assigns the orbital to the e_{2u} orbital. The third band is consequently associated with the e_{2g} orbital and its higher IE is indicative of the fact that the U 6d orbitals form more effective bonds that the 5f in this instance.

The group 8 *Metallocene Complexes*, ferrocene, ruthenocene, and osmocene, have been studied using synchrotron radiation over the photon energy range 16–115 eV.**[35]** They have an orbital structure very similar to that of Mo(η-C_6H_6)$_2$ (Figure 6). The d ionization bands have the cross section variations shown in Figure 13. They all show cross section features attributable to nd resonant photoemission in the region of np $\rightarrow$ nd resonant absorption, that of Ru being particularly strong. Ferrocene shows a Fano dip in its cross section profile at 55 eV and no maximum. For Ru and Os, the cross sections are very low (around 100 eV) as they approach the Cooper minima in the d cross sections. For the Fe 3d orbital, which has no radial node and hence no Cooper minimum, the cross section stays relatively high. For the metallocenes, the e_1 ring π orbitals form two sets of MOs: one of e_1' symmetry, which has a possible contribution from metal p orbitals, and one of e_1'' symmetry, to which metal d orbitals can contribute. The relative intensities, or branching ratios, of the two bands lying above the d bands in IE are plotted in Figure 14. These two bands, which differ in their cross section behavior, are assigned to the e_1' and e_1'' MOs. In all cases, the higher IE band shows features characteristic of d cross section behavior:

1. At low photon energies, they are less intense in the region where the d cross section is less than that of C 2p orbitals.
2. They show minima and maxima over the resonance region at energies corresponding to those found in the d band.
3. For Ru and Os, they become less intense at high photon energies in the region of the Cooper minima. For Fe, at high photon energies the branching ratio of the higher energy band continues to increase.

This behavior confirms that the higher IE bands are associated with the e_1' ionizations and that the e_1'' orbitals have d character.

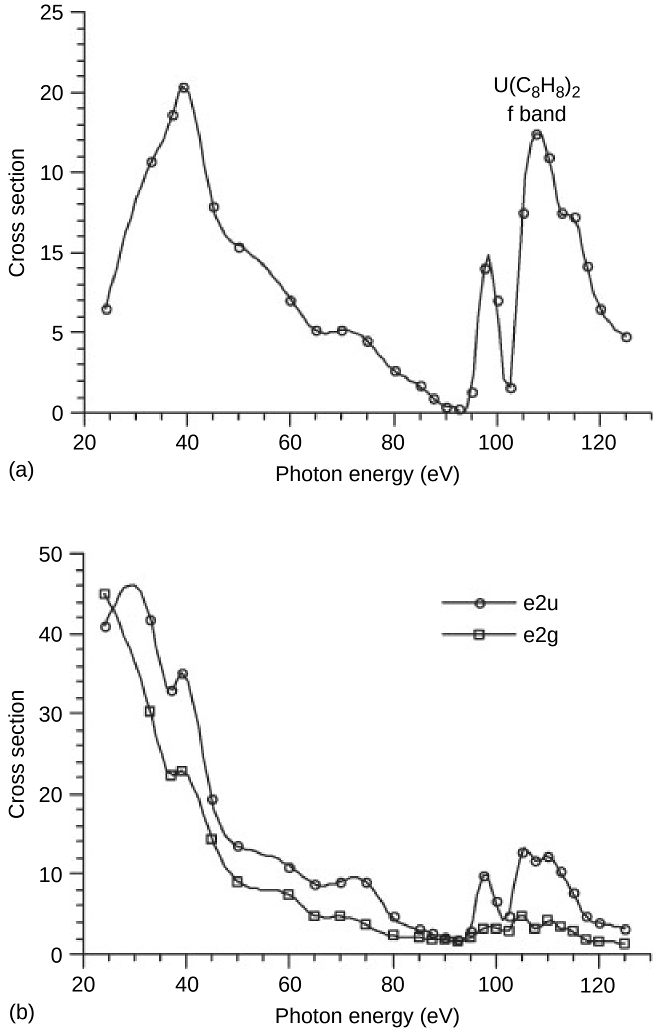

Figure 13 PE cross sections of uranocene (a) f band showing a delayed maximum and a giant resonance (b) e_{2u} and e_{2g} bands, the e_{2u} band shows features characteristic of f character

5 SPECTRAL FEATURES OF TRANSITION METAL MOLECULES

PE bands frequently exhibit structure as a result of a variety of vibrational and electronic states accessible to a molecular

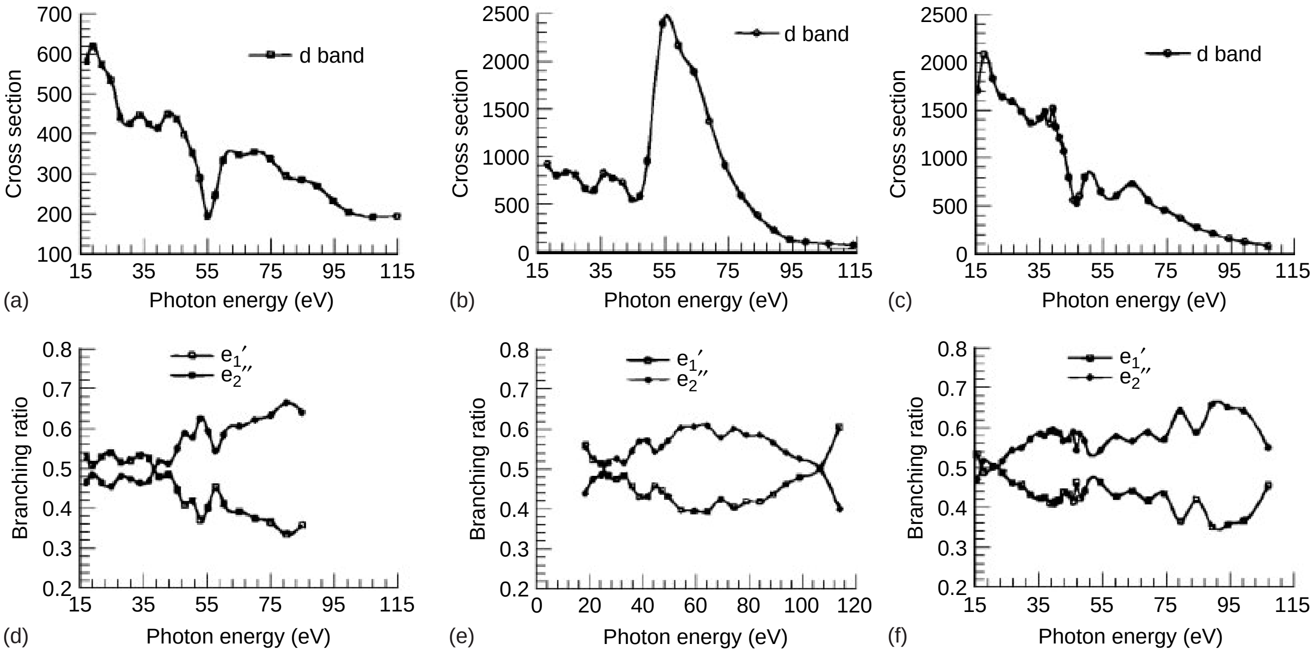

Figure 14 Photoionization cross sections (arbitrary units) of the d bands of (a) Fe(η-C_5H_5)$_2$, (b) Ru(η-C_5H_5)$_2$, and (c) Os(η-C_5H_5)$_2$. Branching ratios of the e$'_1$ and e$''_1$ orbitals of (d) Fe(η-C_5H_5)$_2$, (e) Ru(η-C_5H_5)$_2$, and (f) Os(η-C_5H_5)$_2$

ion formed by removal of an electron from a single molecular energy level. Even if such structure is unresolved, it can affect the band shape. Such structure is not only of intrinsic interest, but can be of considerable help in assigning PE bands and providing detailed information on the molecular electronic structure.

5.1 Vibrational Structure and Band Profiles

Photoionization may give rise to molecular ions either in their ground vibrational state or in one of a number of vibrationally excited states. It takes around 10^{-15} s for an electron to leave a molecule, so that during this time the motions of the atomic nuclei that make up the vibrations are effectively frozen. The vibrational timescale is of the order of 10^{-13} s. The transitions are governed by the Franck–Condon principle and can be represented by vertical lines on a potential energy diagram (Figure 15). In a PES experiment, the neutral molecules are almost invariably in their ground vibrational level. If there is little difference between the potential energy surfaces of the neutral molecule and the molecular ion state, the most probable transition is to the lowest vibrational level of the ion state, and the peak corresponding to the $\nu'' = 0 \rightarrow \nu' = 0$ transition dominates; the associated IE is known as the adiabatic IE. Significant changes in the potential energy surface result in transition to higher vibrational levels being more probable, and can result in an extensive vibrational progression being visible in a PE band. The IE associated with excitation to the most probable vibrational state is called the vertical IE.

The most likely cause of a significant difference between the molecular and ion state potential energy curves is that the electron removed is strongly bonding or antibonding. Vibrational progressions are therefore often associated with ionization from bonding or antibonding MOs. The separation of the vibrational levels observed in a PE band is characteristic of the ion state. Comparison of the measured vibrational frequency with that of the comparable vibration in the molecule can indicate which is the case. If the vibrational structure is unresolved, as is often the case in transition metal molecules with their many low-frequency vibrations, the band shape can still give some indication of the bonding nature of the vacated orbital; narrow bands are associated with nonbonding orbitals and broad bands with bonding (or antibonding) orbitals. Selection rules require that on ionization from nondegenerate orbitals only totally symmetric vibrations are excited.

Detection of vibrational structure in PE bands of transition metal molecules requires good resolution and careful control of surface potentials. Repetitive rapid scanning of spectra and addition using a calibrant line have been used effectively to correct for potential drift.[39] For the group 6 hexacarbonyls, $M(CO)_6$ where M = Cr, Mo, or W, not only ν(CO) but also ν(M–C) have been detected in the metal bands. Figure 16 shows the first PE band of the He I spectrum of $Mo_2(O_2CMe)_4$, a molecule with a quadruple metal–metal bond.[40,41] It is assigned to the $^2B_{2g}$ ion state corresponding to ionization from the δ symmetry metal–metal-bonding orbital.[42] A vibrational

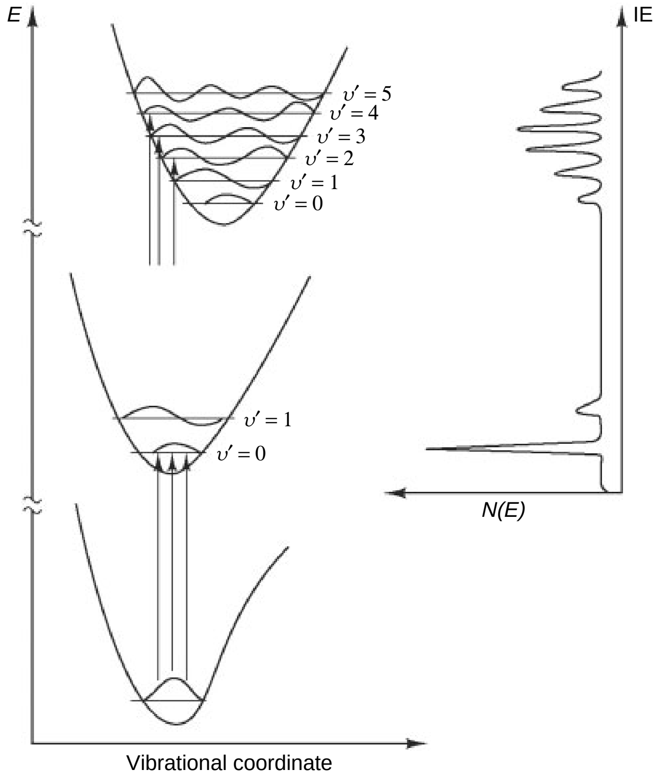

Figure 15 Potential energy curves showing the form of vibrational wavefunctions of a molecule and states of a molecular ion to illustrate the origin of vibrational excitation in ionizing transitions. The resultant PE bands are represented on the right

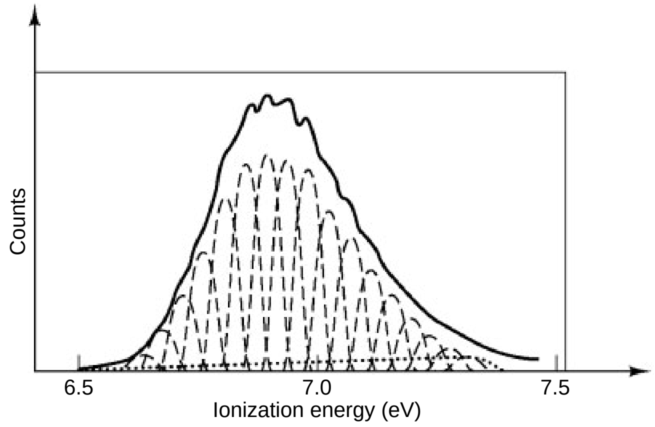

Figure 16 He I PE spectrum of the first IE band of $Mo_2(O_2CMe)_4$ and simulated analysis of the vibrational structure

progression is clearly visible over the top of the band, and the whole band shape has been fitted with 18 vibrational components. The vibrational spacing is calculated to lie between 355 and 365 cm^{-1}, and corresponds to the a_{1g} Mo–Mo stretching vibration in the $^2B_{2g}$ ion state. Comparison with a value of 406 cm^{-1} for the equivalent stretch in the molecular ground state suggests that the metal–metal-bonding is reduced in the ion, and a Franck–Condon analysis gives an increase of around 0.1 Å in the Mo–Mo distance between the molecule and the ion. Though this bond weakening may in part be attributed to removal of a bonding electron, the effect of the positive charge in the ion on the overall bond strength must also be considered.

The first band of the PE spectrum of $Ni(\eta^5\text{-}C_5H_5)(NO)$ shows a vibrational progression (Figure 17). In the initial assignment, band A_1 was assigned to a ligand band and band A_2 to a metal ionization.**[43]** However, cross section studies**[44]** showed them to have an identical ligand origin and that they were vibrational components of a single primary ligand band with a separation of $1850 \pm 81\,cm^{-1}$ corresponding to excitation of the NO stretch in the molecular ion.

5.2 Jahn–Teller Splitting

Ionization from a filled degenerate set of orbitals leads to a degenerate ion state that, for a nonlinear molecule, will be susceptible to Jahn–Teller distortion (see *Jahn–Teller Effect*). This distortion is brought about by excitation of one of the Jahn–Teller active degenerate vibrational modes of the undistorted molecule. When the distortion is small, and the vibrational intervals sufficiently large, a single band profile showing a Jahn–Teller vibrational progression is observed. Such is the case for ionization of the t_1 band of OsO_4 (Section 6.1).**[45]** When the distortion is large and the individual vibrational levels are unresolved, the band profile may show two or more separate maxima, each corresponding to a distinct electronic state of the molecular ion (Figure 18).

Such is the case with the first ionization band of [Ti{(*t*-Bu)NCH=CHN(*t*-Bu)}$_2$] (**1**), which is shown in Figure 19. The compound has D_{2d} symmetry and a closed-shell ground state. The HOMOs are a degenerate pair of e symmetry and fully occupied with four electrons. The compound is best regarded as a Ti(IV) derivative with the diazabutadiene ligands each doubly reduced. The highest lying occupied orbitals of the complex are principally composed of the neutral ligand π symmetry lowest unoccupied molecular orbitals, LUMOs. These ligand π_3 orbitals are doubly occupied in the complex and are C–C π bonding and C–N π antibonding. On

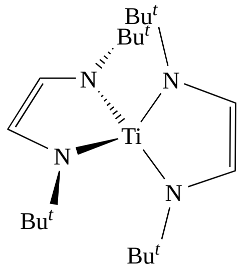

(**1**)

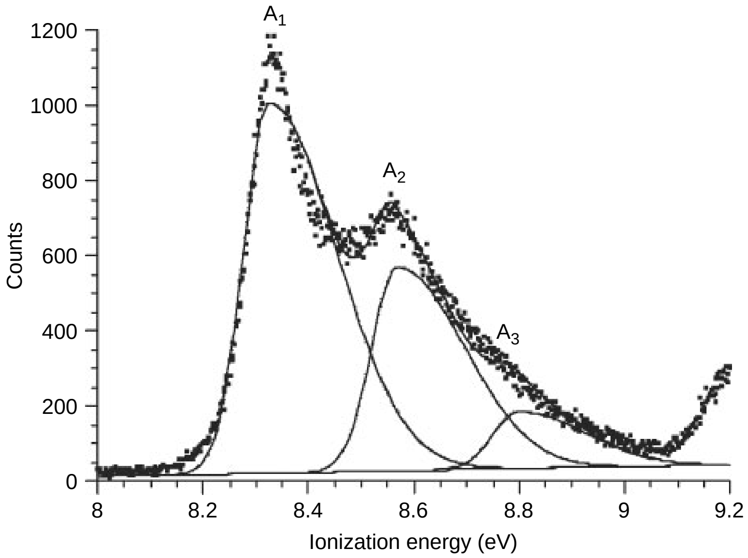

Figure 17 The first band of the PE spectrum of Ni(η^5-C_5H_5)(NO) showing three vibrational components corresponding to an NO stretch

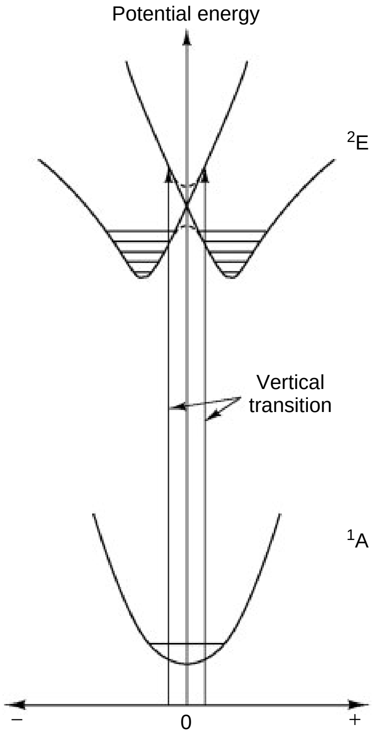

Figure 18 Representation of the potential energy surfaces involved in photoionization from a nondegenerate ground state of a molecule to a ^{2}E Jahn–Teller active state of a molecular ion. The distortion coordinate is the Jahn–Teller active vibration. The vertical arrows represent the most probable transitions

ionization from the e^4 configuration, a Jahn–Teller unstable ^{2}E state is produced. The compound distorts by deformation of a chelate ring, the C–C bond lengthens, and the C–N bonds shorten as is found for a singly reduced diazabutadiene ligand. This effectively traps two electrons on one ligand and one on the other. Such a ground state structure is found for Ga[(*t*-Bu)NCH=CHN(*t*-Bu)]$_2$,**46** which is isovalent with [Ti{(*t*-Bu)NCH=CHN(*t*-Bu)}$_2$]$^+$. The first ionization band shows two well-separated maxima, the first corresponding to the ground state with inequivalent rings, the higher energy one to states where the remaining electrons are trapped in rings of inappropriate dimensions.

5.3 Spin–Orbit Splitting

The ion states formed by removal of an electron from a fully occupied degenerate level may also be split by spin–orbit

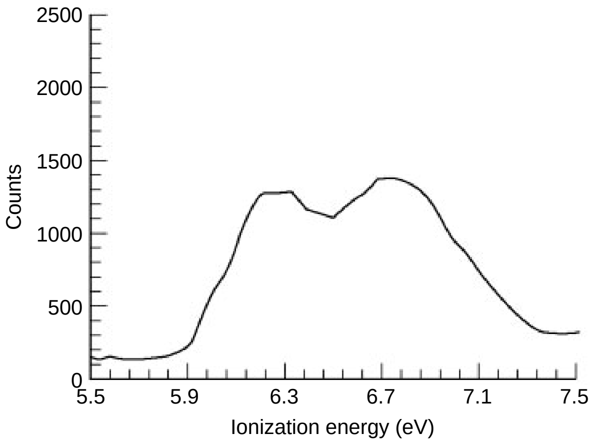

Figure 19 First IE band of the He I PE spectrum of [Ti{(*t*-Bu)NCH=CHN(*t*-Bu)}$_2$], showing a double maximum owing to dynamic Jahn–Teller distortion of the ^{2}E ion state

coupling. If the degenerate level occupied by the resultant unpaired spin has orbital angular momentum, the spin and orbital angular momentum can either reinforce or oppose each other, giving two allowed states. The magnitude of spin–orbit coupling is a function of the atoms present in a molecule; as it is primarily a relativistic effect, it increases with the atomic number of an atom, and decreases with the angular momentum of the orbital involved, that is, for orbitals of the same principal quantum number it is greater for p than d orbitals, and for d than f orbitals. If the splitting is sufficient in comparison to the inherent bandwidth, PES can resolve spin–orbit split ion states, so ionization from a filled degenerate level may give rise to more than one band.

In valence shell spectra, such resolution is commonly observed in third row transition metal compounds for 5d based electrons, where the atomic spin–orbit-coupling parameters, ζ_{5d}, are of the order of 0.3–1.0 eV. It has yet to be observed, however, for first and second row transition metal compounds for 3d and 4d valence electrons, as ζ_{3d} lies in the range 0.01 to 0.1 eV and ζ_{4d} in the range 0.02 to 0.2 eV. For example, in $[Os(\eta\text{-}C_5H_5)_2]^+$ the $e_2{}^3$ configuration leads to well-separated ion states, $^2E_{5/2}$ and $^2E_{3/2}$, with the associated PE bands being of equal intensity and separated by 0.35 eV.[35] Spin–orbit splitting in a transition metal compound can also arise from the presence of heavy ligand atoms, and is frequently resolved for bromide and iodide compounds but not for chlorides (for Cl $\zeta_{3p} = 0.073$ eV, for Br $\zeta_{4p} = 0.305$ eV, for I $\zeta_{5p} = 0.628$ eV). When both a third row metal and a halide are present, second order effects can determine the splitting and the intensity distribution of the ion states.[47]

When orbitals are contracted in the core, spin–orbit effects are much greater and many p, d, and f core ionization spectra show multiplet structure.

Spin–orbit and Jahn–Teller effects compete to lift the degeneracy of a degenerate ion state. Whether this results in distorted states, as a consequence of Jahn–Teller distortion, or undistorted states, with defined angular momentum, depends on the relative magnitudes of the two effects. If both are of the same order, anomalous intensity distributions may be evident. The PE spectrum of $W(\eta^7\text{-}C_7H_7)(\eta^5\text{-}C_5H_5)$, which is isoelectronic with $[Os(\eta\text{-}C_5H_5)_2]$, has $^2E_{5/2}$ and $^2E_{3/2}$ bands of unequal intensity (Figure 20).[46] In this case, the mixing between the d orbitals and the ring $e_2\pi$ orbitals is extensive. The d orbitals give rise to spin–orbit splitting, whereas the ring lifts the degeneracy by Jahn–Teller distortion. The net result is a complex vibronic structure with two bands separated by spin–orbit coupling but having unequal intensities.

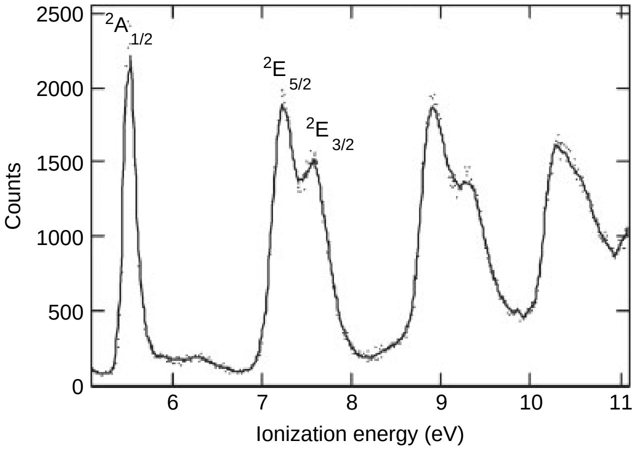

Figure 20 PE spectrum of $W(\eta^7\text{-}C_7H_7)(\eta^5\text{-}C_5H_5)$ showing two spin–orbit components for the ^2E band with unequal intensity owing to the Ham effect

5.4 Exchange Splitting

When ionizing from closed-shell molecules, removal of one electron leads to a doublet ion state. For an open shell molecule, which has one or more incompletely filled subshells, ionization by a simple one-electron process may lead to more than one spin state of the molecular ion. For example, $Nb(\eta\text{-}C_6H_5Me)_2$ is a 17-electron compound (see *Subunit*) contrasting with an electron count of 18 for $Mo(\eta\text{-}C_6H_6)_2$, but it has a similar orbital structure. There is one less electron to occupy the orbital scheme (Figure 6), and the outer configuration is $e_{2g}{}^4a_{1g}{}^1$, giving a $^2A_{1g}$ molecular ground state. Three ion states are accessible by ionizing electrons from the two orbitals. Ionization of the a_{1g} electron gives a $^1A_{1g}$ ion state, but ionization of an e_{2g} electron may give either a triplet or a singlet ion state of symmetry $^3E_{2g}$ or $^1E_{2g}$, respectively. Figure 21 shows that the three accessible states are spectroscopically resolved.[48] If the ionization cross sections of the a_{1g} and e_{2g} orbitals were equal, the intensity ratios of the bands would be 1:3:1.

In these cases, there no longer exists a relationship between the number of PE bands and the number of occupied orbitals, and photoionization can generate a large number of ionic states. The rules for predicting the ion states formed and the relative intensities of the PE bands have been derived by a fractional parentage method and can be summarized as follows:[49]

1. If a closed shell is ionized, all states arising from the coupling of the positive hole with the open shell will be realized, the relative cross sections for the production of these states being proportional to the total (i.e. spin–orbit) degeneracies.
2. If the orbitals belonging to different subshells are assumed to have the same one-electron cross sections, the integrated ionization cross section of a particular subshell is proportional to the occupancy of that orbital in the subshell of the molecule.
3. If an open shell is ionized, the relative probabilities of producing different ionic states will reflect the fractional parentage coefficients, which may be proportional to spin–orbit degeneracies (if the ground-state configuration generates only one term), but in general will not.

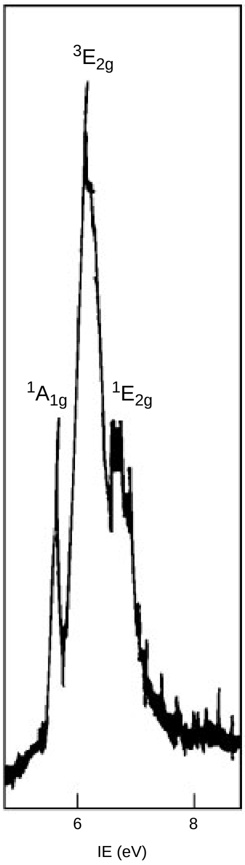

Figure 21 He I PE spectrum of Nb(η-$C_6H_5Me)_2$ showing three bands corresponding to $^1A_{1g}$, $^3E_{2g}$, and $^1E_{2g}$ ion states

4. If a molecule contains two or more open shells, the coupling that already exists between the different open shells in the molecule must be considered. The probability of ionization is usually expressed in terms of Racah coefficients and fractional parentage coefficients.

For exchange splittings to be spectroscopically resolved, the exchange integrals between the electrons involved must be relatively great. This is the case with the open f shells of the lanthanides, and the ionization patterns of the lanthanides are very characteristic of the number of f electrons being ionized.

Exchange splittings can also be detected for ionization of closed-shell cores in open shell molecules and ions, though care must be taken to distinguish band structure resulting from exchange splitting from spin–orbit (Section 5.3) and shake-up structure (Section 5.5). The structure is most likely to be resolvable when the core and the open valence shell have the same principal quantum number, as the exchange integrals are greatest when the electrons concerned occupy the same spatial region. The simplest cases are found in the core s electron spectra of S state ions like Mn^{2+}, which has a ^6S state from the d^5 configuration. Ionization of an s core orbital produces no orbital angular momentum so only two states are produced, ^5S and ^7S, resulting from coupling of the spin of the core hole to the five unpaired valence electrons. Figure 22 shows the multiplet splitting in Mn(η-$C_5H_5)_2$, which is 5.2 eV.

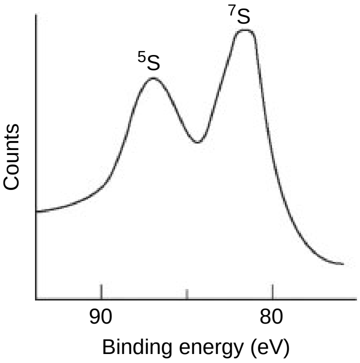

Figure 22 Multiplet splitting in the Mn 3s core ionization of Mn(η-$C_5H_5)_2$

5.5 Many-electron Processes

PE spectra can show bands corresponding to ion states that cannot be accessed from the ground-state molecular configuration by the removal of one electron. Such signals can normally be represented by removal of one electron synchronized with excitation of another; they are hence referred to as many-electron processes, and the additional satellite structure accompanying the primary band as shake-up structure. A classic example of a two-electron transition is the very weak band found in the spectrum of atomic mercury for the process shown in equation (12):**50**

$$Hg(5d^{10}6s^2 : {}^1S) + h\nu \longrightarrow Hg(5d^{10}6p^1 : {}^2P) + e \qquad (12)$$

In a one-electron description, this corresponds to the ionization of one s electron and the excitation of the other to a p orbital. Two-electron transitions occur because the motions of the electrons are not completely independent but are correlated. One technique that MO theory uses to introduce some measure of electron correlation is called configuration interaction. The ground state for Hg can be improved over the single $5d^{10}6s^2$ (^1S) configuration wavefunction by mixing it with a state of identical symmetry from a different (but higher energy) configuration $5d^{10}6p^2$ (^1S); the result is a lower energy wavefunction (equation 13):

$$\Psi(^1S) = \Psi(s^2) + \mu\Psi(p^2) \qquad (13)$$

The magnitude of μ, the mixing coefficient, determines the relative strength of the satellite peak.

Shake-up structure can be very intense in core spectra. Study, in the solid state, of the redox pairs $[FeCl_4]^{2-/1-}$ and $[CuCl_4]^{3-/2-}$ show strong 3p satellites in the metal core spectra for the Cu(II) and Fe(II) complexes.[5] This indicates considerable electronic reorganization on oxidation. Creation of the metal core hole increases the effective nuclear charge on the metal. The filled metal–ligand-bonding orbitals become more metal in character and the half-filled antibonding orbitals more ligand like. This electronic reorganization is reflected in the appearance of satellite bands. For these compounds satellite peaks also appear in the valence spectra.

Very intense shake-up structure is also commonly associated with the C and O 1s core spectra of metal carbonyls and with CO bound to metal surfaces.[48] For example, the C and O 1s core spectra of $Cr(CO)_6$ are shown in Figure 23(a). In these cases, Metal to Ligand Charge Transfer (MLCT) is implicated. If the CO unit has a core hole, the state where an electron occupies the 2π orbital and the metal has a hole in the d shell is of lower energy than that where the CO is ionized and the d shell remains intact. (Using a core equivalent picture, it is as though, when the hole is on the C atom, the CO group has been transformed into NO.) The 2π orbital is now lower in energy than the metal d orbital. As the metal d orbitals commonly overlap with the 2π orbital, it is the mix of these that will differ in the ground-state wavefunctions for the neutral species and the core ionized species. When the two wavefunctions differ substantially, there is a high probability of accessing valence excited states on core ionization as well as the ground state, and strong shake-up bands result. This is illustrated diagrammatically in Figure 23(b).

For small molecules weak shake-up bands in valence PE spectra have been detected by careful study, but for transition metal molecules the multiplicity and breadth of the valence PE bands make detection of weak shake-up structure difficult.

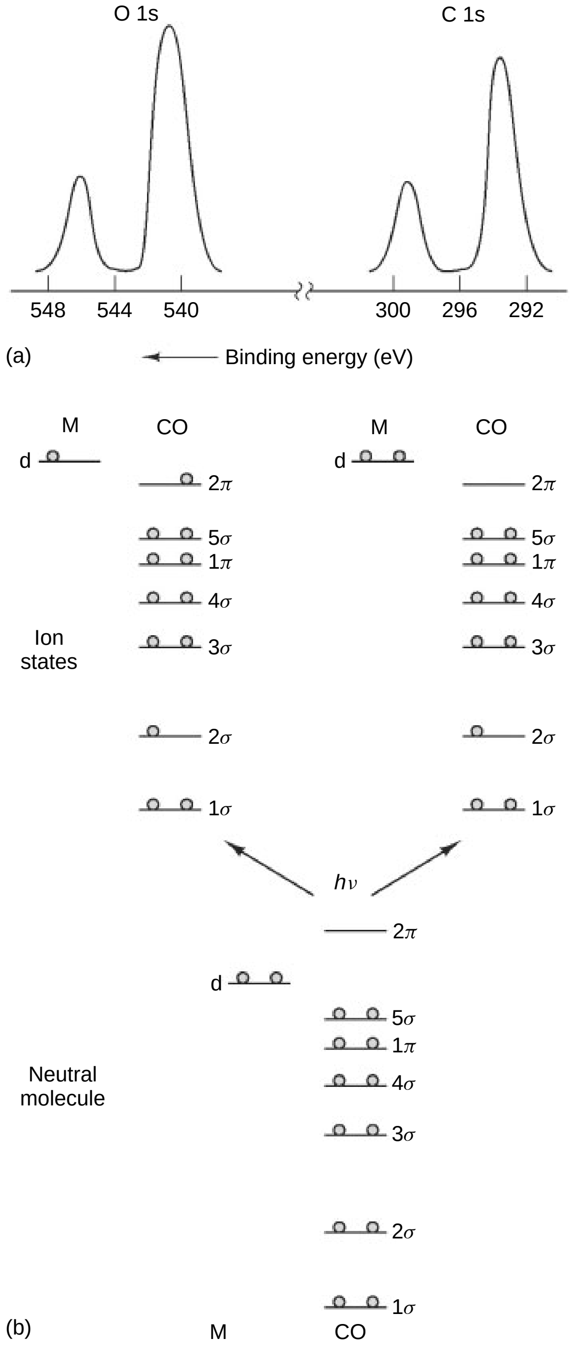

Figure 23 (a) C 1s and O 1s spectra of $Cr(CO)_6$ (b) Schematic energy level diagram for a neutral metal CO system and two ionic states with a 2σ (C 1s) core hole

6 CALCULATION OF IONIZATION ENERGIES

The availability of accurate energy data on electronic states from PE spectroscopy has provided important benchmarks for electronic structure calculations. Such calculations, in their turn have been very valuable in establishing correct assignments of PE spectra. Though this article is primarily concerned with the experimental phenomena, it is useful to illustrate the accuracy of various methods for calculating ionization energies.

6.1 Ionization Energies in ab initio and Density Functional Theory

Ab initio theory provides two basic approaches to calculating ionization energies.[6] One uses Koopmans' Theorem (KT), which has been discussed in Section 1.2, and only requires a single SCF calculation of the ground state. The ΔSCF approximation, where the IE is equated with the difference of the molecular ground-state energy and the energy of the ion in the appropriate electronic state, requires a separate SCF calculation for each ionic state. The difference is termed relaxation energy, which always lowers the KT value. These methods may be refined by separate correlation of the ground and ionic wavefunctions, thus obtaining correlated values of the IEs (see Section 3, Figure 4). Both relaxation

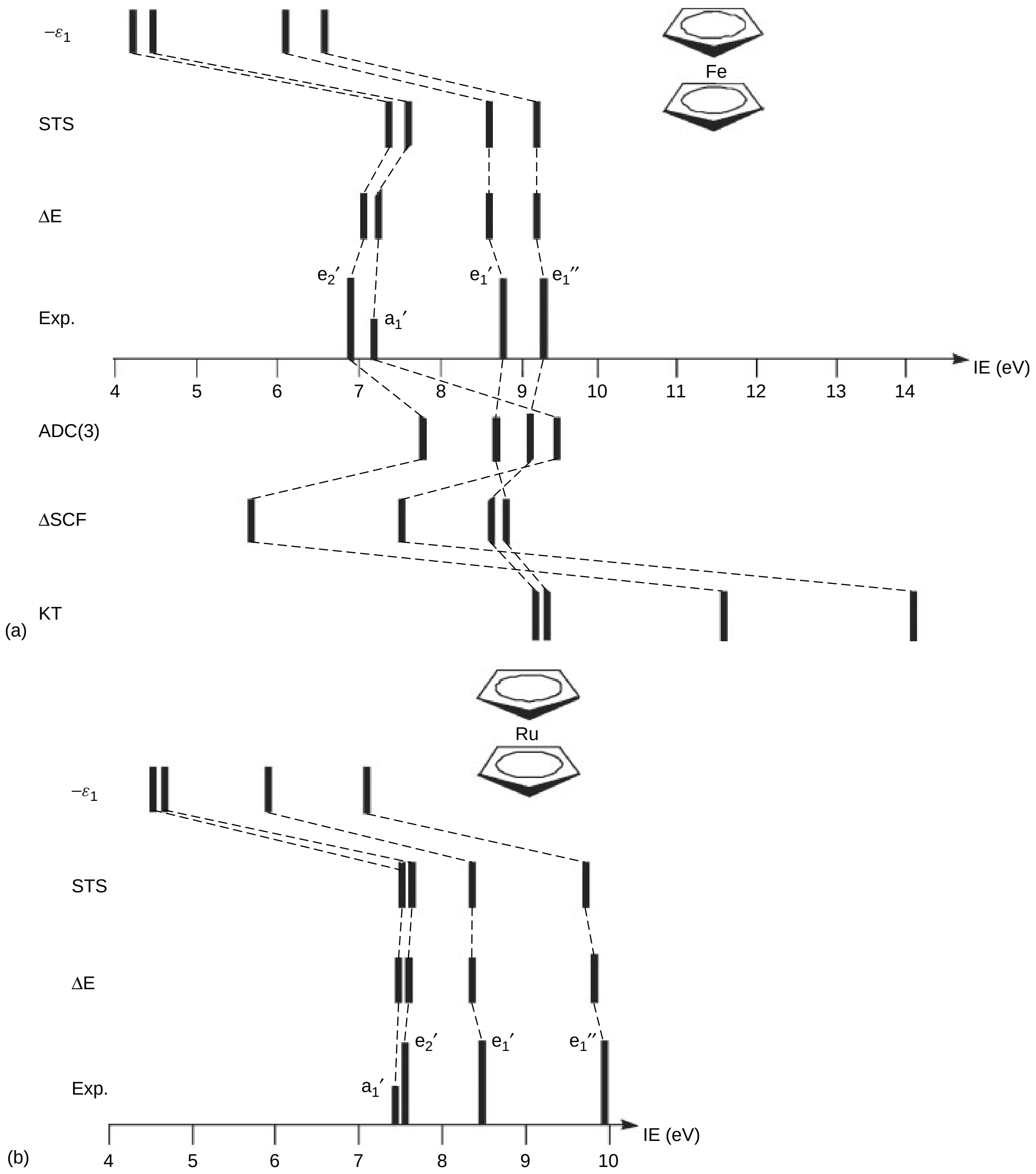

Figure 24 Comparison of experimental and calculated IE for 9a0 ferrocene (b) ruthenocene. Orbital energies ($-\varepsilon_{\mathrm{I}}$) Slater transition state method (STS) ion state calculation (ΔE) Experimental values (Exp.) Correlation corrections (ADC(3)) ab initio ion state calculations (ΔSCF) Koopmans theorem (KT)

and correlation effects in transition metal compounds can be very substantial in an ab initio framework.

A popular alternative is to employ density functional theory (DFT) methods. Kohn-Sham (KS) orbital energies in the ground state are a more reliable predictor of the ion state ordering than Koopmans' theorem. There are good theoretical reasons for interpreting them as approximate vertical IE.[49] For transition metal compounds ΔE methods, the DFT equivalent of ΔSCF, give good numerical results. Problems are associated with the DFT treatment of states of multideterminantal nature, like in the case of open shell ground-state systems.

6.2 IE of Simple Metallocenes

The metallocenes form useful benchmarks to test the quality of IE calculations and to illustrate the success of modern DF calculations to replicate vertical IE.[6] Their PE spectra are reliably assigned and they provide a testing ground for the calculation of exchange splitting and spin–orbit coupling. Figure 24 provides a visual comparison of DFT methods and ab initio methods for ferrocene. Kohn-Sham one-electron energies ($-\varepsilon_I$), IE calculated by the Slater transition state method (STS) and the ΔE method (direct calculation of the molecular ions in their ground and excited states) comprise the DFT methods and KT, ΔSCF, and Algebraic Diagrammatic Construction (ADC)(3) the ab initio ones. The experimental vertical ionization energies for $Fe(\eta\text{-}C_5H_5)_2$ are also shown. For $Ru(\eta\text{-}C_5H_5)_2$, only experimental and DFT values are given.

Both the Slater transition state values and the ΔE values for the IE are in excellent agreement with experiment. What is also impressive is that the negative of the Kohn-Sham orbital energies, although about 3 eV less than the IE, have the same ordering and energy separations as do the ion states. Values from the ab initio methods are erratic in their ion state ordering, and the values for the ligand based bands are significantly more accurate than those for the metal bands. The advantage of DFT methods in ion state assignment is evident throughout, and the numerical precision of the DFT ΔE method is impressive.

Figure 25 shows comparisons between theory and experiment for $Os(\eta\text{-}C_5H_5)_2$ and $Mn(\eta\text{-}C_5H_5)_2$. In the case of $Os(\eta\text{-}C_5H_5)_2$ (Figure 25(a)), the ${}^2E_2'$ ion state is split by spin-orbit coupling to form $J = 5/2$ and $J = 3/2$ ion states (see Section 5.3). DFT calculation on the ion states including spin – orbit-coupling models the splitting well. The splitting of the ${}^2E_2'$ and ${}^2E_1''$ states is a consequence of their Os 5d orbital character, that of the ${}^2E_1'$ state is Os p orbital based, a d orbital contribution here being disallowed on symmetry grounds.

Calculation of exchange splittings is illustrated by the PE spectrum of $Mn(\eta\text{-}C_5H_5)_2$. Manganocene exists in the gas phase in a predominantly high spin form with $S = 5/2$. Ionization of the half-occupied d orbitals only gives quintet states, but ionization from the doubly occupied ligand orbitals gives rise to both quintet and septet states. The experimental and calculated values are represented in Figure 25(b). Agreement is not as close here as in the closed-shell molecules.

The calculation suggests that the principal ligand band centered at 8.8 eV should be assigned to three of the ligand ion states, not four as previously thought. The ${}^5E_1''$ ion state arising from ionization of the e_1'' ligand orbitals is found at considerably higher IE than the other ligand bands. It has the same symmetry as the lowest accessible ion state from high-spin manganocene, which originates from a largely metal-based ionization. Presumably strong interaction between these two ion states is responsible for the energy shift. At the temperature of the experiment, some manganocene also exists in a $S = 1/2$ ground state. The triplet ground state of the associated ion, ${}^3E_2'$, can also be detected in the PE spectrum. The calculation gets good numerical agreement with the experimental value for this state but underestimates the separation from the ${}^5E_1''$ state of the predominant ion species.

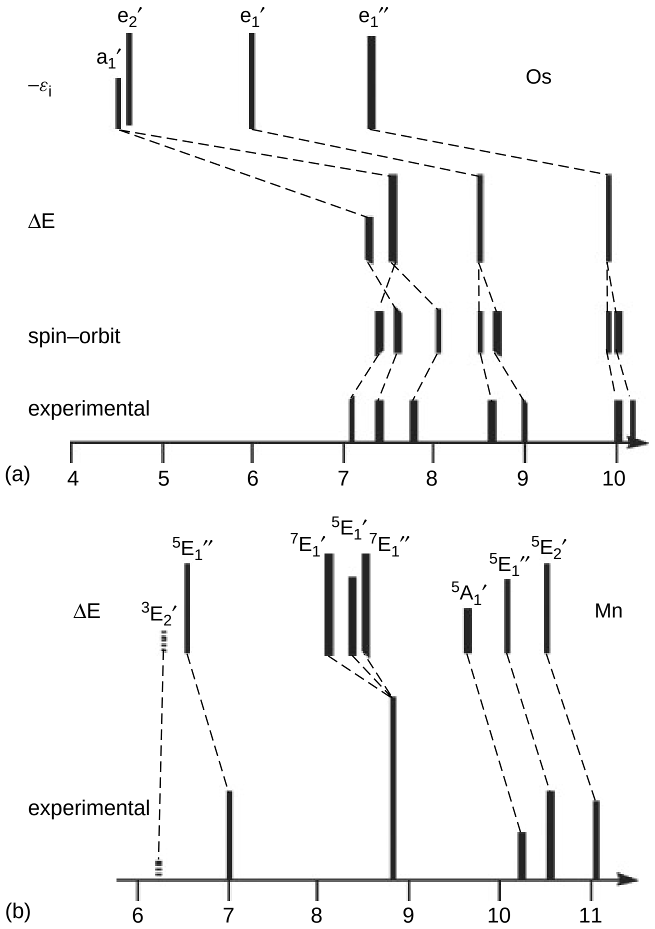

Figure 25 Comparison of calculated and experimental IE for (a) osmocene (b) manganocene

7 CASE STUDIES

This section illustrates some of the problems in transition metal chemistry that PES has clarified.

7.1 Osmium Tetroxide: an Example of a Tetrahedral Molecule

The valence electronic structures of d^0 tetrahedral transition metal molecules are of the form

$$(1a_1)^2(1t_2)^6(2t_2)^6(1e)^4(2a_1)^2(3t_2)^6(1t_1)^6$$

Table 2 Symmetries of Os and O atomic orbitals in the T_d symmetry of OsO_4

Symmetry	Os	O[a]
a_1	6s	2s, 2p (σ)
E	5d	2p (π)
t_2	5d, 6p	2s, 2p (σ), 2p (π)
t_1	–	2p (π)

[a] The O 2p orbitals are classified σ and π with respect to the Os–O direction.

where the numbering scheme ignores orbitals correlating with the core orbitals of the constituent atoms. Symmetry analysis of the possible contributing AOs is given in Table 2. The e and the a_1 orbitals are rigorously π and σ respectively with respect to the metal–oxygen interaction, whereas the t_2 orbitals may have both π and σ contributions. The t_1 orbital is nonbonding for a metal with no valence shell f orbitals. The $1a_1$ and $1t_2$ orbitals are essentially O 2s core-like orbitals and are not probed in the He I spectra, so we expect bands corresponding to five primary ion states: $^2A_1$, ^2E, $^2T_1$, and two $^2T_2$. The He I spectrum shows five separated bands, 1–5 (Figure 26(a)).

Assignment of the spectra has been surprisingly controversial for such a small molecule,[34] but illustrates well how detailed analysis of band structure along the lines of Section 5 can illuminate such a problem.

Vibrational structure is resolved on the first four bands. Band 5 is broad, doubtless containing unresolved vibrational structure, but it shows two maxima. In bands 2, 3, and 4, only the totally symmetric a_1 stretching vibration is excited. Band 1 shows, as well as a symmetric progression, an e progression, which indicates that the ion state is not tetrahedral. This is consistent with the band being assigned to a Jahn–Teller distorted ^2T state.

The five bands show considerable relative intensity changes with photon energy (Figure 26(a)). Measurement of their photoionization cross sections shows that only band 5 has any significant Os 5d character; the cross section shows a double maximum in the region of the Os 5p → 5d giant resonance (Figure 26(b)). Os 5d character is expected in at least two of the bonding levels, of e and t_2 symmetry, because of the presumed strong multiply bonded character of OsO_4.

This poses a conundrum. If band 5 is assigned to just one primary ion state, leaving bands 2–4 to be assigned to the other three, we must conclude that none of the orbitals associated with bands 2–4 has any significant metal 5d–oxygen bonding character. The classic picture of multiple bonding in OsO_4 would have to be abandoned. If, on the other hand, two primary ion states are associated with band 5, bands 2–4 must arise from just two primary ion states. The most likely pair of bands to arise from the same primary state is bands 2 and 3. They have very similar cross section characteristics, whereas those of band 4 are very different, and they have

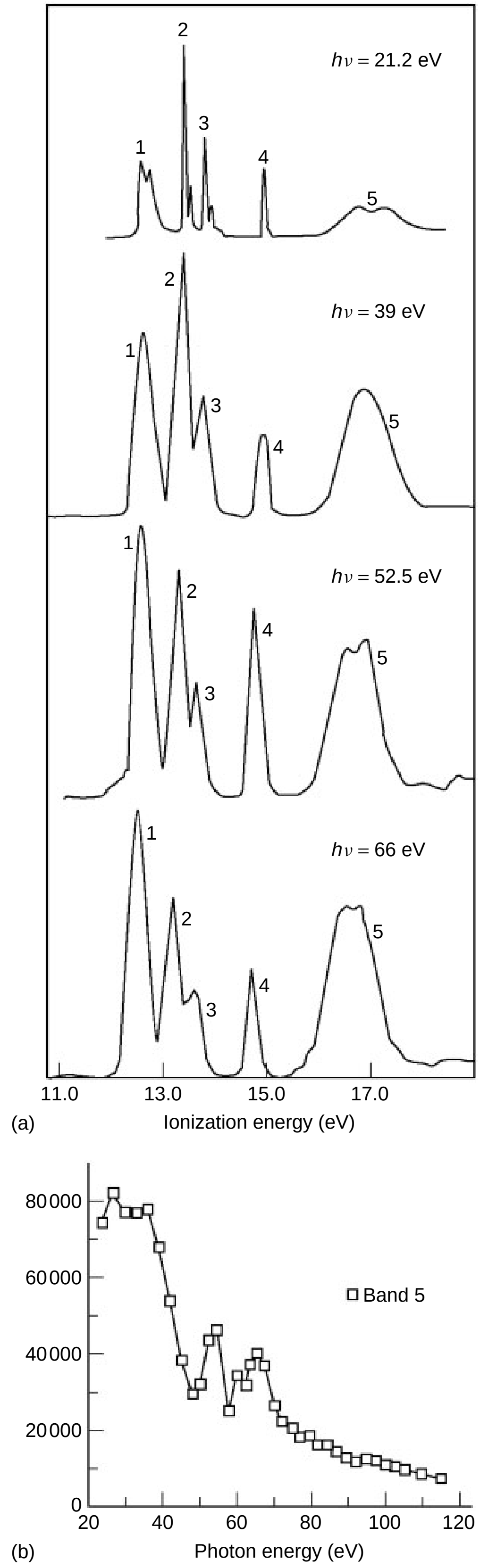

Figure 26 (a) PE spectra of OsO_4 at various photon energies; (b) cross section of band 5

similar vibrational structure. The relative intensity of bands 2 and 3 is 2:1 over a wide photon energy range, the lower energy ion state being the more intense. The splitting pattern is not that expected of Jahn–Teller distortion of a ^{2}T ion state (Section 5.3), but is rather like that found for spin–orbit splitting. The presence of only a totally symmetric stretching frequency supports the assignment to spin–orbit components. Two facts rule out the origin of the spin–orbit splitting being an Os 5d contribution. Firstly, the cross section variation shows minimal 5d contribution to the associated orbital; secondly, splitting of a ^{2}T state where the orbital origin is d gives an energy ordering $E'' < U'$, namely, the doubly degenerate spin–orbit state is of lower energy than the fourfold degenerate one. This is the reverse order from that found experimentally. To obtain the energy ordering $U' < E''$, the orbital origin of the splitting must be p. Such a splitting may arise from interaction with either the valence 6p orbitals or the underlying core 5p orbitals or a combination of both. The primary ion state must therefore be $^2T_2$, leading to the assignment of band 1 to $^2T_1$.

The MO scheme shown in Figure 27 is based on this assignment. The energy levels are seen to be determined by the metal contribution with the orbitals with Os 5d character lying lowest, followed by the a_1 with Os s character, then the Os p-type orbitals, and lastly the nonbonding orbitals with no Os character. This is in contrast to the classical view of a tetrahedral molecule, in which the σ bonding orbitals are generally considered to be more tightly bound than the π bonding orbitals.

7.2 Carbene Complexes of Pd and Pt

Isolation of stable carbenes by the deprotonation of imadazolium salts has opened up new routes to the synthesis of transition metal carbenes. The bis(carbenes) of the group 10 metals are particularly striking being stable two-coordinate complexes (**2**).

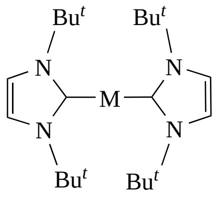

(**2**)

Figure 28 shows their PE spectra[51] and that of the free carbene.[52] The HOMO of the carbene is a σ symmetry orbital on the two-coordinate carbon, the carbon 'lone pair'. In the low IE region, the spectrum also shows ionization from the two highest π levels; above 10 eV (not shown), the spectrum is dominated by ionizations from the Bu^t group. In the spectra of the complexes, the two π bands are relatively unperturbed.

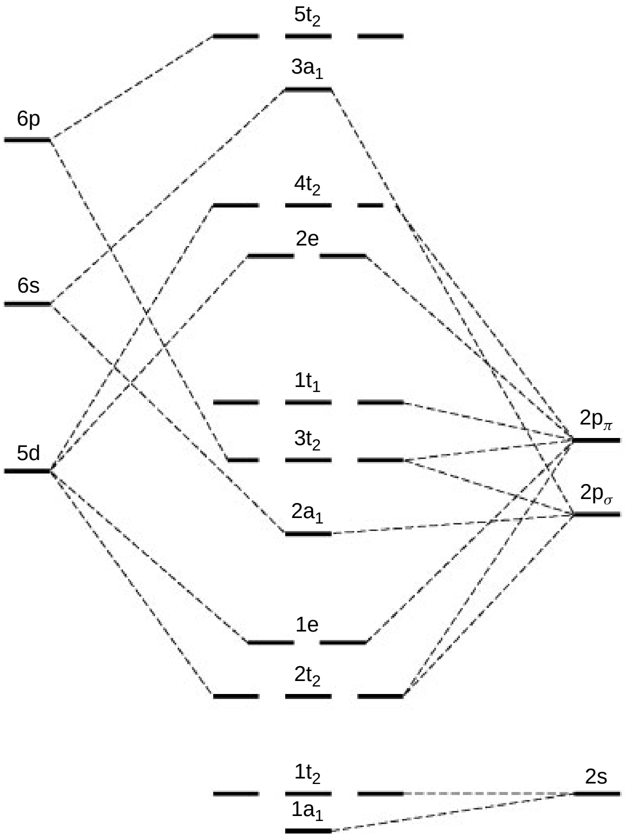

Figure 27 MO scheme for OsO_4 based in the interpretation of its PE spectrum. The MOs are filled with 32 electrons up to the $1t_1$ level

For the Pd carbene complex, the ligand lone pair band appears to be halved in intensity. The two carbene σ orbitals form σ_u and σ_g combinations; the former can overlap with the metal p valence orbitals and the latter with a s + d(z^2) hybrid. The lower lying PE band corresponds to the less strongly bonding σ_u orbital. Ionization from the strongly bonding σ_g orbital lies under the main band of the spectrum and is not identifiable. For the Pt complex, the σ_u orbital is more tightly bound and its PE band overlaps with those of the ligand π orbitals. The spectra of the Pd and Pt complexes show additional bands at lower IE attributable to the metal ionizations; they all show an increase in relative intensity in the He II spectrum.[51] They are most conveniently classified as σ, π, and δ with respect to the C-M-C axis. For Pd, the σ band lies under the He self ionization; it is fully visible in the He II spectrum. For Pt, it lies at higher energy. Calculations suggest that this is a nonbonding orbital of s-d(z^2) character so the stabilization relative to Pd is probably due to the relativistic stabilization of the Pt 6s orbital. The Pt π and δ bands are split by spin–orbit coupling but lie at similar average energies to the unsplit Pd ones. Overall the spectra demonstrate strong σ interactions between the carbene and the metal and negligible π bonding. Pt binds the carbene more strongly than Pd.

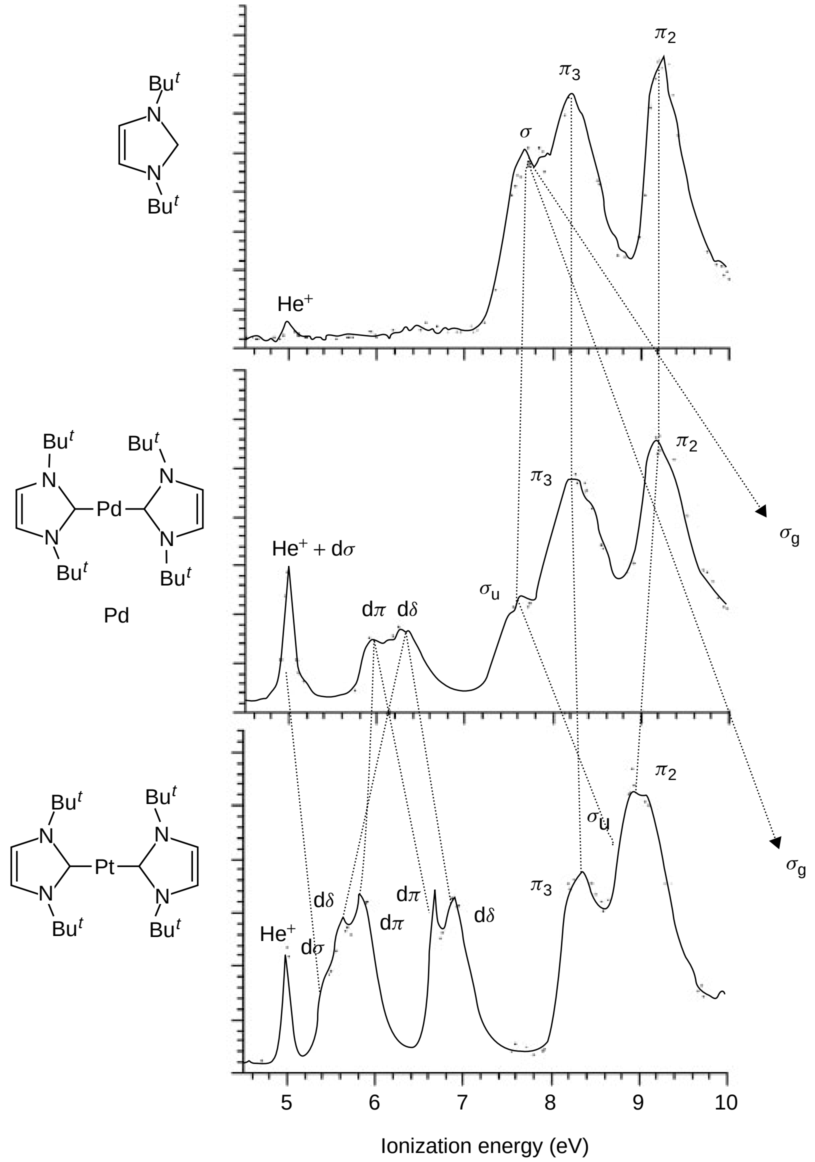

Figure 28 PE spectra of $C_3H_2N_2Bu^t_2$ and its complexes with Pd and Pt

7.3 $Os_3(CO)_{12}$ and $Re_3H_3(CO)_{12}$: an Investigation of Two Carbonyl Clusters

The electronic structure of transition metal clusters is difficult to probe by electronic absorption spectroscopy, which has proved so fruitful in revealing the d orbital orderings of classical complexes, because of the multiplicity of overlapping absorption bands. The one-to-one correlation between occupied orbitals and PE bands means that PES can give valuable information on the smaller clusters. The information obtained has given support to the semiempirical theoretical treatments of this class of molecules.

$Os_3(CO)_{12}$ (**3**) and $Re_3H_3(CO)_{12}$ (**4**) are isoelectronic. They both have D_{3h} symmetry with four terminally bonded carbonyl groups attached to each metal atom (these are indicated by lines in (**3**) and (**4**)). In the Os compound, the Os atoms are directly bonded in an equilateral triangle, whereas in the Re compound, the metal–metal interactions are symmetrically bridged by the three hydrogens.

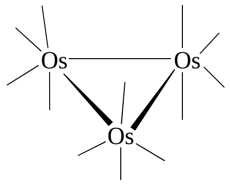

(**3**)

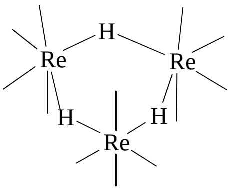

(**4**)

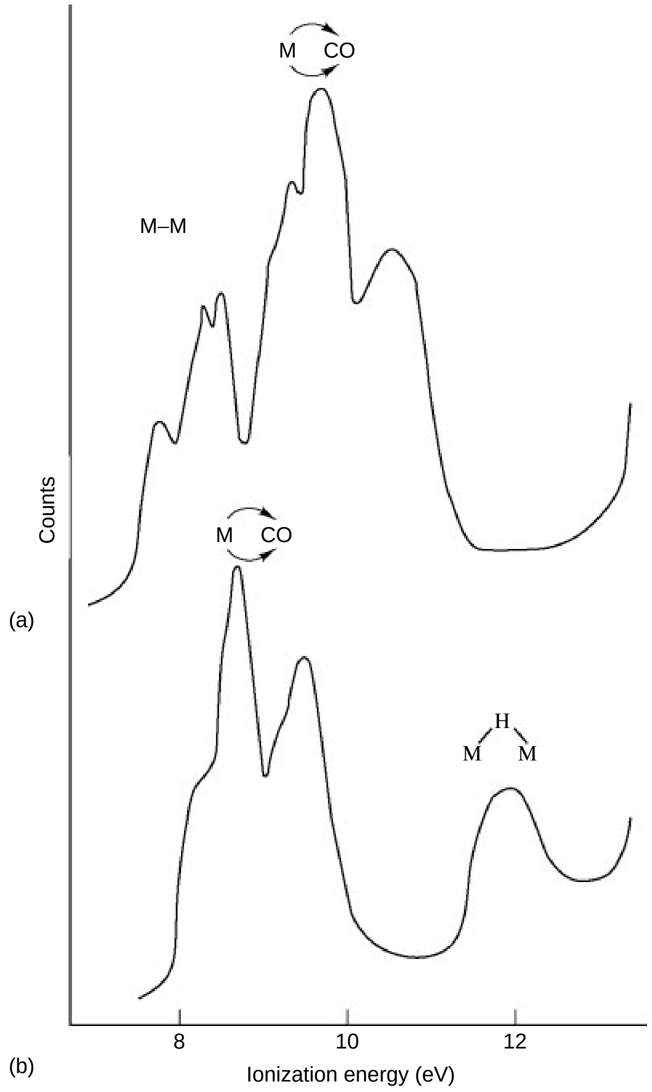

Figure 29 He I PE spectra of (a) $\mathrm{Os_3(CO)_{12}}$ and (b) $\mathrm{Re_3H_3(CO)_{12}}$

Six of the d electrons of each metal are involved in back bonding to the four associated CO groups and the rest are available for binding the triangular cluster. In the case of $\mathrm{Os_3(CO)_{12}}$, each metal has two electrons for cluster binding and the metal triangle may be regarded as being held together by three single bonds. In the D_{3h} symmetry of the molecule, they are constituted by occupied orbitals of a_1' and e' symmetry. The PE spectrum of $\mathrm{Os_3(CO)_{12}}$[53] (Figure 29(a)) shows as its first band ionization from the Os–Os bonding a_1' orbital, followed by a spin–orbit split e' band. The remainder of the d band structure is assigned to metal–carbonyl back bonding orbitals. It is generally found to be the case that metal–metal bonds have lower IE than metal–carbonyl back bonding electrons.

In the PE spectrum of $\mathrm{Re_3H_3(CO)_{12}}$[53] (Figure 29(b)), the metal–metal-bonding bands have disappeared, to be replaced by a broad band lying between the d band and the main carbonyl ionizations. Also, the metal–carbonyl back bonding ionizations have shifted to lower IE. An MO scheme for $\mathrm{Re_3H_3(CO)_{12}}$ is readily derived from that of $\mathrm{Os_3(CO)_{12}}$ by considering the effect of moving a proton from each of the Os nuclei to the edge-bridging positions (Figure 30). The back bonding orbitals are raised in energy as the metal nuclear charge is now less, but the a_1' and e' cluster orbitals are considerably stabilized by the protonation.

Comparison of the He II band intensities with those from the He I spectrum confirm that the band at ca. 12 eV in the spectrum of $\mathrm{Re_3H_3(CO)_{12}}$ comes from an orbital with a high degree of H 1s character. The role of the bridging hydrogens in the cluster is not just to provide the necessary electrons for the cluster-electron count, but also to stabilize the cluster-bonding orbitals.

7.4 Phosphametallocenes

An extensive chemistry has been developed of organometallic compounds where P replaces C-H in aromatic carbocyclic rings coordinated to transition metals. In many cases the phosphametallocenes resemble closely the all carbon parent. In other cases, the structures and chemistry differ. PE spectroscopy has helped identify the causes of these similarities and differences. The spectra of the phosphametallocenes are more complex than the carbocyclic analogs as ionization bands from the P lone pairs occur in the low-energy region and frequently overlap with the ring π and even the d bands. Comparison of the spectra of $\mathrm{Mo(\eta^6\text{-}P_3C_3Bu^t_3)(CO)_3}$ with $\mathrm{Mo(\eta^6\text{-}C_6H_3Bu^t_3)(CO)_3}$ showed that the P substituted compound had the higher d ionization energy.[54] Substituting P into the ring decreases the HOMO–LUMO gap; this makes the rings better acceptors of electron density from the metal and increases the strength of δ back bonding.

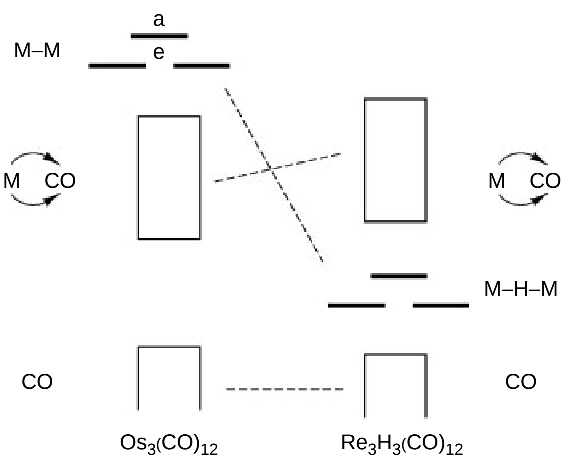

Figure 30 MO schemes for the isoelectronic molecules $\mathrm{Os_3(CO)_{12}}$ and $\mathrm{Re_3H_3(CO)_{12}}$, showing the energy relation between their MOs as three protons are removed from the Os nuclei and placed in bridging positions between the metal atoms

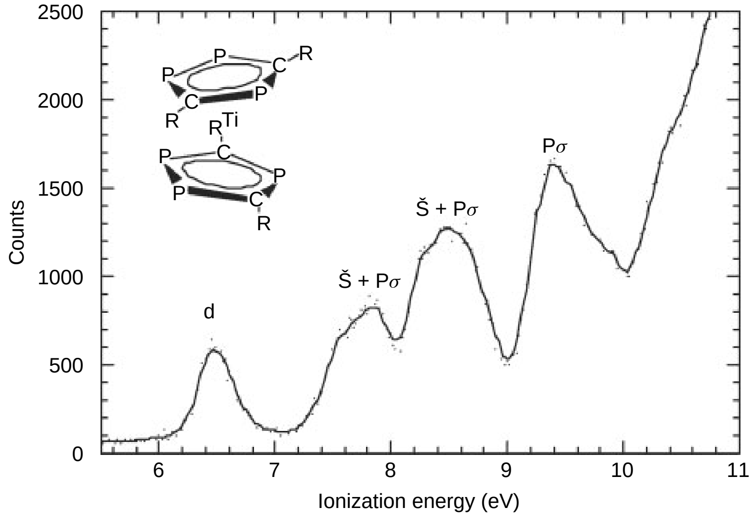

Figure 31 PE spectrum of Ti(η^5-$P_3C_2Bu^t_2$)$_2$

The capacity to form δ bonds makes P containing carbocyclic rings particularly good at stabilizing low oxidation states in early transition metals. A striking example is the hexaphosphatitanocene, Ti(η^5-$P_3C_2Bu^t_2$)$_2$, the parent titanocene, Ti(η^5-C_5H_5)$_2$ being unknown. Also, the degeneracy of the ring π orbitals is lifted and one combination is preferred for δ bond formation by the metal resulting in a diamagnetic compound for this Ti(II) species. The PE spectrum (Figure 31) shows the d band to have an ionization energy of 6.5 eV.**[55]**

Phosphorus substitution has also increased the number of four-membered ring compounds. P has a natural bond angle around 90° so less strain is present in P_2C_2 rings than C_4 rings. The series of compounds M(η^4-$P_2C_2Bu^t_2$), M=Ge, Sn, and Pb, have both lone pairs on the P atoms and also on the group 14 metal. PE studies (Figure 32) have shown that the metal lone pair is significantly more stable than the P ones, which explains why the molecules coordinate Lewis acids at the P atoms.

8 CONCLUSION

Photoelectron spectroscopy is the most direct method of investigating electronic structure. The orbital structure of a molecule is reflected in the band structure of a PE spectrum. Detailed assignment of a spectrum is facilitated by varying the photon energy used for spectral acquisition. Effects of chemical substitution on molecular energetics can be probed

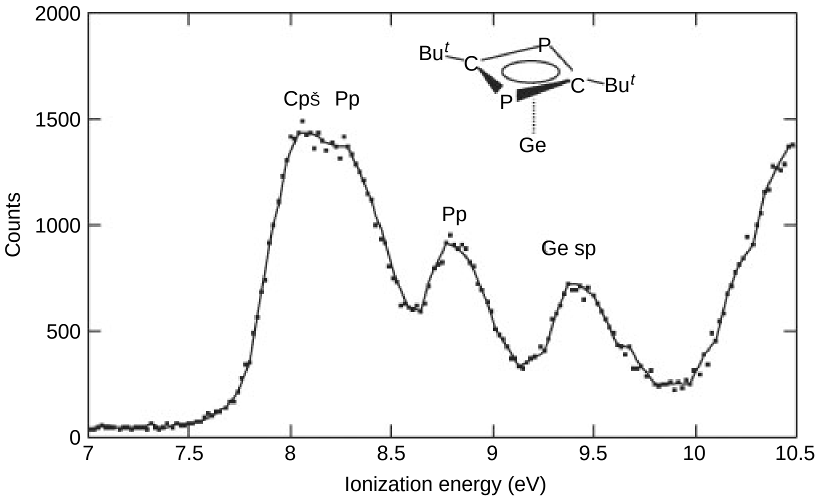

Figure 32 PE spectrum of Ge(η^4-$P_2C_2Bu^t_2$)$_2$

directly. PES enables the determination of ionization energies, which are important thermodynamic parameters, and also are invaluable benchmarks in the testing of electronic structure calculations.

9 RELATED ARTICLES

Coordination & Organometallic Chemistry: Principles; Electronic Structure of Main-group Compounds; Electronic Structure of Organometallic Compounds; Electronic Structure of Clusters; Ligand Field Theory & Spectra; Molecular Orbital Theory; Symmetry Point Groups.

10 REFERENCES

1. J. C. Green, *Struct. Bonding*, 1981, **43**, 37.
2. J. C. Green, *Acc. Chem. Res.*, 1994, **27**, 131.
3. N. E. Gruhn and D. L. Lichtenberger, ‘Inorganic Electronic Structure and Spectroscopy’, John Wiley & Sons, 1999, Vol. 2.
4. G. M. Bancroft and Y. F. Hu, ‘Inorganic Electronic Structure and Spectroscopy’, Wiley-Interscience, 1999, Vol. 1.
5. E. I. Solomon, L. Basumallick, P. Chen, and P. Kennepohl, *Coord. Chem. Rev.*, 2005, **249**, 229.
6. J. C. Green and P. Decleva, *Coord. Chem. Rev.*, 2005, **249**, 209.
7. X. Li, G. M. Bancroft, and R. J. Puddephatt, *Acc. Chem. Res.*, 1997, **1997**, 213.
8. A. Einstein, *Ann. Physik*, 1905, **17**, 132.
9. D. W. Turner, C. Baker, A. D. Baker, and C. R. Brundle, ‘Molecular Photoelectron Spectroscopy’, Wiley, London, 1970.
10. T. Koopmans, *Physica*, 1934, **1**, 104.
11. J. H. D. Eland, ‘Photoelectron Spectroscopy’, 2nd edn., Butterworths, London, 1984.
12. P. K. Ghosh, ‘Introduction to Photoelectron Spectroscopy’, Wiley, New York, 1983.
13. W. L. Jolly, in ‘Electron Spectroscopy: Theory, Technique and Applications’, ed. A. D. Baker, Academic press, London, 1977, Vol. 1.
14. S. Evans, J. C. Green, S. E. Jackson, and B. Higginson, *J. Chem. Soc., Dalton Trans.*, 1974, 304.
15. J. Brennan, G. Cooper, J. C. Green, M. P. Payne, and C. M. Redfern, *J. Electron Spectrosc. Relat. Phenom.*, 1987, **43**, 297.
16. S. T. Manson, *Adv. Electron. Electr. Phys.*, 1976, **41**, 73.
17. D. R. Bates, *Mon. Not. R. Astron. Soc.*, 1946, **106**, 432.
18. V. Schmidt, *Phys. Lett. A*, 1973, **45**, 63.
19. J. Berkowitz, ‘Photoabsorption, Photoionization and Photoelectron Spectroscopy’, Academic press, New York, 1979.
20. G. A. Von Wald and J. W. Taylor, *J. Electron Spectrosc. Relat. Phenom.*, 1988, **47**, 315.
21. J. J. Yeh and I. Lindau, *At. Data Nucl. Data Tables*, 1985, **32**, 1.
22. U. Gelius, ‘Electron Spectroscopy’ ed. D. A. Shirley, North-Holland, Amsterdam, 1972.
23. U. Gelius and K. Siegbahn, *Faraday Discuss. Chem. Soc.*, 1972, **54**, 257.
24. B. E. Bursten, J. C. Green, N. Kaltsoyannis, M. A. MacDonald, K. H. Sze, and J. S. Tse, *Inorg. Chem.*, 1994, **33**, 5086.
25. J. L. Dehmer, *J. Chem. Phys.*, 1972, **56**, 4496.
26. J. G. Brennan, J. C. Green, and C. M. Redfern, *J. Am. Chem. Soc.*, 1989, **111**, 2373.
27. B. E. Bursten, F. A. Cotton, J. C. Green, E. A. Seddon, and E. A. Stanley, *J. Am. Chem. Soc.*, 1980, **102**, 955.
28. U. Fano, *Phys. Rev.*, 1961, **124**, 1866.
29. U. Fano and J. W. Cooper, *Phys. Rev., A*, 1965, **137**, 1364.
30. J. Tse, *J. Chem. Phys.*, 1988, **89**, 920.
31. J. L. Dehmer, in ‘Resonances in Electron-Molecule Scattering, Van der Waals Complexes, and Reactive Chemical Dynamics’, ed. D. G. Truhlar, American Chemical Society, Washington, DC, 1984.
32. P. W. Langhoff, ed., ‘Resonances in Electron-Molecule Scattering, Van der Waals Complexes and Reactive Chemical Dynamics’, American Chemical Society, 1984, Vol. 263.
33. J. D. Bozek, G. M. Bancroft, J. N. Cutler, K. H. Tan, B. W. Yates, and J. S. Tse, *Chem. Phys.*, 1989, **132**, 257.
34. J. C. Green, M. F. Guest, I. H. Hillier, S. A. Jarrett-Sprague, N. Kaltsoyannis, M. A. MacDonald, and K. H. Sze, *Inorg. Chem.*, 1992, **31**, 1588.
35. G. Cooper, J. C. Green, and M. P. Payne, *Mol. Phys.*, 1988, **63**, 1031.
36. J. Brennan, G. Cooper, J. C. Green, M. P. Payne, and C. M. Redfern, *J. Electron Spectrosc. Relat. Phenom.*, 1993, **66**, 101.
37. J. C. Green, N. Kaltsoyannis, K. H. Sze, and M. MacDonald, *J. Am. Chem. Soc.*, 1994, **116**, 1994.
38. J. G. Brennan, G. Cooper, J. C. Green, N. Kaltsoyannis, M. P. Payne, C. M. Redfern, K. H. Sze, and M. A. MacDonald, *Chem. Phys.*, 1992, **164**, 271.
39. J. L. Hubbard and D. L. Lichtenberger, *J. Am. Chem. Soc.*, 1982, **104**, 2132.
40. D. L. Lichtenberger and C. H. Blevins II, *J. Am. Chem. Soc.*, 1984, **106**, 1636.
41. D. L. Lichtenberger, C. D. Ray, F. Stepniak, Y. Chen, and J. H. Weaver, *J. Am. Chem. Soc.*, 1992, **114**, 10492.
42. J. C. Green and A. J. Hayes, *Chem. Phys. Lett.*, 1975, **31**, 306.
43. S. Evans, M. F. Guest, I. H. Hillier, and A. F. Orchard, *J. Chem. Soc., Faraday Trans. II*, 1974, 417.
44. C. N. Field, J. C. Green, M. Mayer, V. A. Nasluzov, N. Rösch, and M. R. F. Siggel, *Inorg. Chem.*, 1996, **35**, 2504.

45. R. McDowell and M. Goldblatt, *Inorg. Chem.*, 1971, **10**, 625.
46. J. C. Green, M. L. H. Green, C. N. Field, D. K. P. Ng, and S. Y. Ketkov, *J. Organomet. Chem.*, 1995, **501**, 107.
47. M. B. Hall, *J. Am. Chem. Soc.*, 1975, **97**, 2057.
48. E. W. Plummer, W. R. Salaneck, and J. S. Miller, *Phys. Rev., B*, 1978, **18**, 1673.
49. D. P. Chong, O. V. Gritsenko, and E. J. Baerends, *J. Chem. Phys.*, 2002, **116**, 1760.
50. D. C. Frost, C. A. McDowell, and A. Ishitani, *Mol. Phys.*, 1972, **24**, 861.
51. J. C. Green, R. G. Scurr, P. L. Arnold, and F. G. N. Cloke, *J. Chem. Soc. Chem. Commun.*, 1997, 1963.
52. A. J. I. Arduengo, H. Bock, H. Chen, M. Denk, D. A. Dixon, J. C. Green, W. A. Herrmann, N. Jones, M. Wagner, and R. West, *J. Am. Chem. Soc.*, 1994, **116**, 6641.
53. J. C. Green, D. P. M. Mingos, and E. A. Seddon, *Inorg. Chem.*, 1981, **20**, 2595.
54. S. B. Clendenning, J. C. Green, and J. F. Nixon, *J. Chem. Soc., Dalton Trans.*, 2000, 1507.
55. F. G. N. Cloke, J. C. Green, J. R. Hanks, J. F. Nixon, and J. L. Suter, *J. Chem. Soc., Dalton Trans.*, 2000, 3534.

Photosynthesis

Christopher R. Staples & Robert E. Blankenship
Arizona State University, Tempe, AZ, USA

1	Introduction	1
2	Photosynthetic Pigments	4
3	Energetics and Efficiencies of Photosynthesis	7
4	Antenna Structure and Function	8
5	Structure and Mechanism of the Type II RC from Purple Bacteria	14
6	Photosystem I and Photosystem II from Oxygen-evolving Organisms	18
7	Cytochrome *bc* and *bf* Complexes	23
8	Related Articles	25
9	References	25

Glossary

Antenna: photosynthetic pigment complex that absorbs energy and transfers it to a reaction center
Photosystem I: reaction center from oxygen-evolving photosynthetic organisms that oxidizes plastocyanin and reduces $NADP^+$
Photosystem II: reaction center from oxygen-evolving photosynthetic organisms that oxidizes water and reduces plastoquinone
Reaction Center: pigment-protein complex that carries out photosynthetic energy storage

Abbreviations

BChl = Bacteriochlorophyll; BPh = Bacteriopheophytin; Q = Quinone; Chl = Chlorophyll; P = Pigment; cyt = Cytochrome; RC = Reaction Center.

1 INTRODUCTION

1.1 General Introduction[1–4]

Photosynthesis is a biological process carried out by plants, algae and certain bacteria, whereby light energy is converted into chemical energy. The stored energy is then used to sustain life processes. The vast majority of photosynthesis is carried out by organisms that contain *Chlorophylls* or related compounds as principal *pigments*, and this article is limited to discussion of these organisms. The emphasis in this article will be on those aspects of photosynthesis that draw most heavily on the concepts and methodologies of inorganic chemistry. This includes properties of *Excited States* and photochemical reactions, structures of pigments and *proteins* involved in energy transduction, and in particular the role of metal ions in many of these structures and processes. In most cases, literature references are to recent comprehensive reviews and not to the original publications.

While this article attempts to be a brief but comprehensive introduction to the field of photosynthesis, certain important aspects of the subject are covered in other articles of this encyclopedia and are therefore omitted. Chief among these is the manganese-containing oxygen-evolving complex of Photosystem II, treated in ***Manganese: The Oxygen-evolving Complex & Models***. Additional information can also be found in articles on ***Iron: Heme Proteins & Electron Transport***; ***Electron Transfer Reactions: Theory***; ***Long-range Electron Transfer in Biology***; ***Iron–Sulfur Proteins***; and ***Copper Proteins with Type 1 Sites***.

1.2 Temporal Stages of Photosynthesis

Photosynthesis is an extremely complex series of chemical and physical events ranging in time scale from the essentially instantaneous process of photon absorption to the much slower processes of plant growth, which may take years. The overall process is conveniently although somewhat arbitrarily divided into four temporal stages: (1) Photon absorption and *excitation transfer*, (2) Primary *Photochemistry*, (3) Stabilization of high energy intermediates and (4) CO_2 reduction and long-term energy storage. The chemical transformations of photosynthesis have often been divided into the *light reactions* and the *dark reactions*, with stages 1–3 included in the light reactions and stage 4 in the dark reactions. The term light reactions is something of a misnomer, as the vast majority of the processes are thermal reactions, with only one or two (depending on the class of organism) as true photochemical reactions. The dark reactions are those processes by which carbon dioxide is incorporated into organic compounds, which are then further metabolized into other molecules the organisms can use for cellular processes.

1.3 The Photosynthetic Unit

The vast majority of the pigments in a photosynthetic organism are not chemically active, but function primarily as an *antenna*. They absorb photons and transfer energy to a highly organized integral *membrane* protein called a *reaction center*. The antenna system, its associated reaction center and ancillary electron transfer carriers are collectively known as a *photosynthetic unit*.

The energy transfer process in the antenna system is generally considered to take place according to a resonance transfer mechanism first proposed by Förster (see below). The antenna system increases the effective cross-section of photon absorption by increasing the number of pigments associated with each photochemical complex. The intensity of sunlight is sufficiently dilute so that any given chlorophyll molecule only absorbs at most a few photons per second. If each chlorophyll had an entire electron transfer system associated with it, the system would be idle the vast majority of the time. By incorporating many pigments into a single chemical unit, the biosynthetically expensive reaction center and electron transport chain can be used to maximum efficiency.

The essence of photosynthetic energy storage is light-induced *redox* chemistry that takes place in the reaction center. X-ray crystallographic structures of several reaction center complexes are now available, and they have contributed immensely to the molecular level understanding of the mechanism of the electron transfer processes that take place in the reaction center. These structures along with the pathways and kinetics of electron transfer that take place within them are discussed in more detail below (*see* ***Long-range Electron Transfer in Biology***).

1.4 Types of Photosynthetic Organisms and Evolutionary Origins[1,5]

A remarkable variety of organisms carry out photosynthesis. These range from very primitive *bacteria* to higher plants, inhabiting almost every ecosystem on the planet. The living world is often divided into three main groups: *eubacteria, archaea*[6] (together known as *prokaryotes*) and *eukaryotes*. Photosynthesis is very widely distributed among the eubacteria, sometimes called the true bacteria, as well as the more advanced eukaryotic cells.

Chlorophyll-based photosynthesis has never been described in any members of the archaea. Some halophilic archaea carry out an energy storage process that is sometimes literally described as photosynthesis, using a membrane protein called *bacteriorhodopsin*. Bacteriorhodopsin utilizes a purple pigment called retinal. This process works by light-induced ion translocation rather than by light-induced electron transport as is found in all chlorophyll-based photosynthetic organisms.[7] Halobacteria, which grow in extremely salty water, are facultative aerobes; they can grow when oxygen is absent. Purple pigments, known as retinal (a pigment also found in the human eye), act similar to chlorophyll. The complex of retinal and membrane proteins is known as bacteriorhodopsin, which generates a proton gradient that powers an ADP-ATP pump, generating ATP from sunlight without chlorophyll. The structural and mechanistic aspects of bacteriorhodopsin-based energy storage are fundamentally different from those of chlorophyll-based photosynthesis, and these are almost certainly independent evolutionary developments.

Eukaryotic photosynthetic organisms include various types of algae, mosses, ferns and higher plants. In all these organisms, photosynthesis is confined to a subcellular organelle known as the *Chloroplast*. In many ways, the chloroplast is similar to certain types of photosynthetic bacteria, and can be regarded as a semiautonomous miniature cell within the larger eukaryotic cell. All pigments associated with photosynthesis are made and localized in the chloroplast, as well as numerous *proteins* that carry out the chemical processes associated with photosynthesis. The chloroplast also contains its own DNA, which codes for many chloroplast proteins, and contains its own protein synthesis machinery. However, many chloroplast proteins are coded for by nuclear DNA and imported from the cytoplasm, so the chloroplast is not completely functional on its own. It is now generally accepted that chloroplasts arose by a process called endosymbiosis.[1] In this process, a primitive photosynthetic bacterium was symbiotic with a primitive eukaryotic cell. The bacterium gradually lost autonomy, eventually becoming what are now known as chloroplasts. This process occurred several times in the past.[8] Primary endosymbiosis resulted in green algae, red algae, and glaucocystophytes. All other groups of algae are the result of secondary endosymbiosis of a eukaryotic algae. In fact, Chlorarachniophytes and Cryptophytes still maintain the vestigial nucleus of the endosymbiont, called a nucleomorph.[9,10]

The evolutionary history of the proteins involved in photosynthesis is only now becoming clearer. Recently, the entire genomes of many photosynthetic and nonphotosynthetic organisms have become available. This has allowed for large-scale phylogenetic analyses to be performed on genes involved in photosynthesis.[11] A search was undertaken for photosynthesis specific genes by finding all genes shared within all the photosynthetic organisms, and subtracting from this set all homologous genes also found in nonphotosynthetic organisms. Remarkably, only a very small set of genes were specific for photosynthesis. This finding supports the hypothesis that most of the genes involved in photosynthesis were recruited from other pathways. It was also found that extensive horizontal gene transfer has taken place among photosynthetic bacteria and indeed all classes of bacteria, as analyses of individual genes pointed to differing phylogenetic relationships among organisms, and supported different tree topologies.[11] Thus, the evolution of photosynthesis has been as much horizontal as vertical.

1.5 Organization of the Photosynthetic Membrane[1]

In eukaryotic photosynthetic organisms, the first three temporal stages of the photosynthetic energy storage process take place almost exclusively within or on membranes inside the chloroplast, called *thylakoid membranes*. In most chloroplasts, many of the thylakoid membranes are stacked together into what are called *grana membranes*. The unstacked membranes are called *stromal membranes*. The stacking of membranes into separated granal and stromal membrane regions is thought to facilitate the distribution of excitations between the two photochemical systems in oxygenic photosynthesis (see below).

The final stage of carbon fixation largely occurs in the soluble portion of the chloroplast, called the *stroma*. In *prokaryotic*

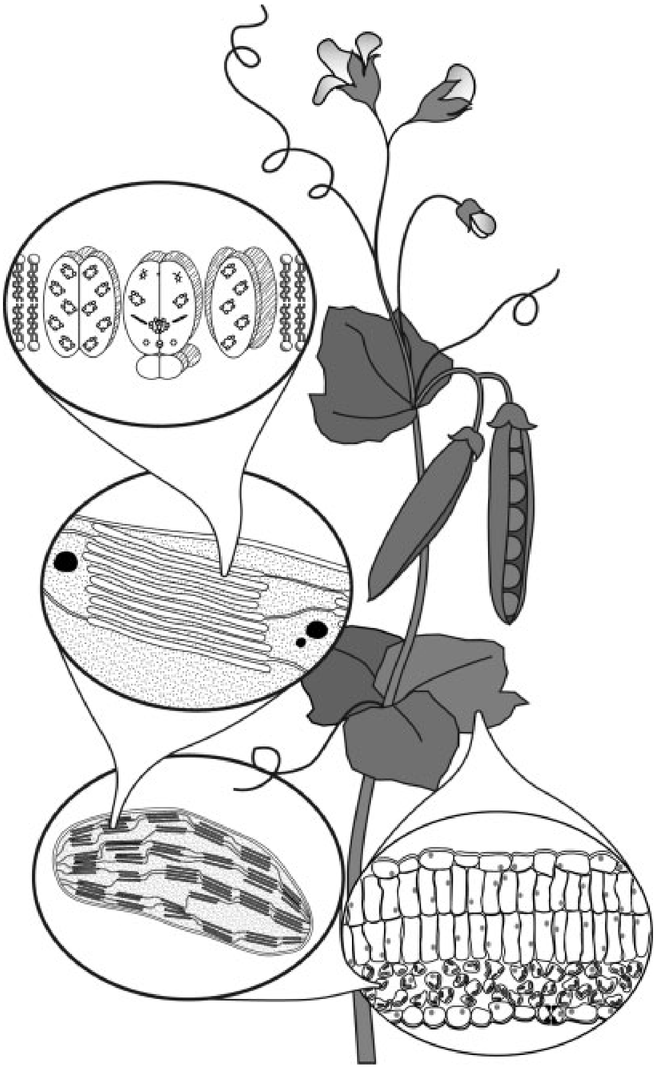

Figure 1 Exploding diagram of the photosynthetic apparatus of a typical higher plant. The first expansion bubble shows a cross-section of a leaf, with the different types of cells; the dark spots are the chloroplasts. The second bubble is a chloroplast; the thylakoid membranes are the dark lines, the stroma is the stippled area. The third bubble shows a grana stack of thylakoids. The fourth bubble shows a schematic picture of the molecular structure of the thylakoid membrane, with a reaction center flanked by antenna complexes. (Ref. 1. Reproduced by permission of Blackwell)

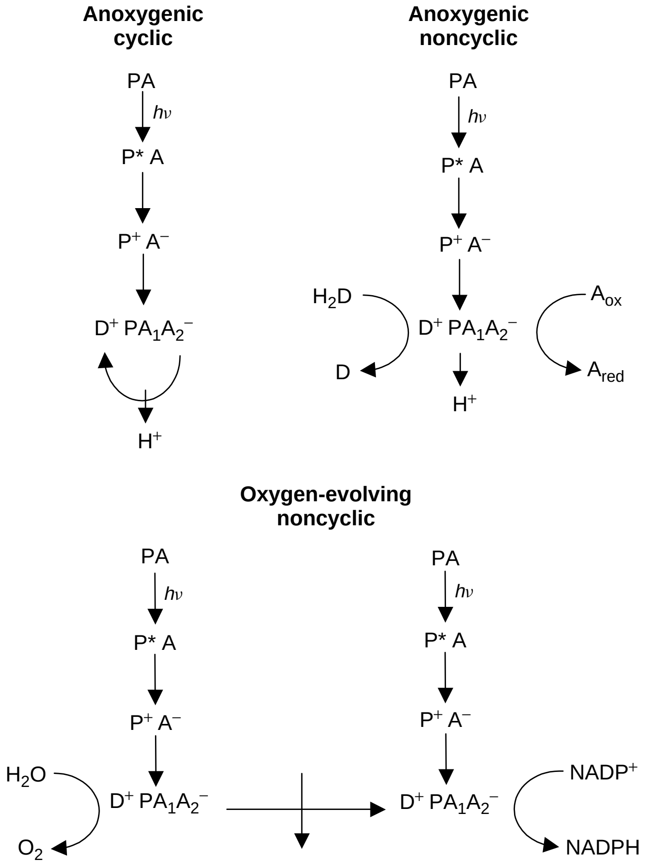

Figure 2 Cyclic and noncyclic patterns of electron flow in photosynthetic organisms. The anoxygenic cyclic pathway is found in purple bacteria and in the filamentous green bacteria. The anoxygenic noncyclic pathway is found in the green sulfur bacteria. These organisms can also carry out cyclic electron flow, which is not shown. The oxygen-evolving noncyclic pathway is found in cyanobacteria, prochlorophytes, and all eukaryotic chloroplasts. Cyclic electron flow around Photosystem I can also take place in these organisms. Abbreviations: P, reaction center photoactive pigment, eg P700; D, electron donor; A, electron acceptor; H^+, hydrogen ions that are moved across a membrane, coupled to electron flow; $h\nu$, light absorption. (Ref. 5, by kind permission of Springer Science & Business Media)

photosynthetic organisms, the first three stages take place within a specialized region of the inner cell membrane, while the carbon fixation reactions take place in the cytoplasm. Figure 1 shows a schematic diagram of the chloroplast.

1.6 Patterns of Photosynthetic Electron Transport

The photochemical electron transfer step and the initial secondary reactions that stabilize the photochemical products all take place within the reaction center complex. For subsequent turnovers of the reaction center to take place, there must be a way to remove electrons from the reduced acceptor and replace them to the oxidized donor. Figure 2 illustrates some of the different patterns of electron transport found in various photosynthetic organisms.

In many organisms, a cyclic process takes place, in which the reduced electron acceptor transfers its electron through a series of carriers back to the oxidized donor. Energy conservation is achieved by coupling proton translocation across a membrane to the electron flow. This type of cyclic electron flow occurs in eukaryotes under some conditions and in many anoxygenic photosynthetic bacteria. No NADPH is produced, only ATP. This process occurs when cells may require additional ATP, or when there is no $NADP^+$ to reduce to NADPH. In other organisms, noncyclic electron flow takes place, in which one freely available *substrate* is oxidized and another is reduced. Perhaps the most important pattern is the noncyclic electron flow found in oxygen-evolving organisms, in which H_2O serves as the oxidizable substrate and CO_2 is the ultimate electron acceptor, although the pyridine nucleotide $NADP^+$ serves as an intermediate acceptor. In this case, it is necessary for two photochemical steps to cooperate. This is described in more detail below. All these modes of electron flow can lead to proton pumping and electrical potentials across the membrane, and the energy stored in these gradients (called the *protonmotive force*) can be used to make ATP.

In addition to the ATP formed by both cyclic and noncyclic flow, reduced and oxidized substrates are accumulated during noncyclic electron flow. The oxidized substrates are waste products and are excreted by the cell. The reduced compounds provide much of the energy necessary for carbon reduction. In those organisms that primarily carry out cyclic electron flow, the highly reducing compounds required for carbon reduction are not generated as direct products of light-driven electron transport. Instead, energy-dependent reverse electron flow from a weak reductant takes place.

2 PHOTOSYNTHETIC PIGMENTS[3]

2.1 Structure and Distribution of Photosynthetic Pigments

Hundreds of distinct pigments are found in various photosynthetic organisms. They can be grouped into three main classes: chlorophylls (including bacteriochlorophylls), carotenoids, and bilins. The chlorophylls are cyclic tetrapyrroles with a central Mg. They are found in both antenna and reaction center complexes of all types of photosynthetic systems, and their presence can be regarded as the unique signature of a photosynthetic organism. Figure 3 shows structures of some of the various chlorophylls and other photosynthetic pigments, and Table 1 indicates the distribution in different classes of photosynthetic organisms.

The photophysical and photochemical properties of chlorophylls are ideally suited for their roles in photosynthetic energy storage. They are unquestionably the product of an extensive chemical and biological evolutionary process, and many organisms have developed specialized chlorophylls that enable them to inhabit particular environments that are enriched in certain wavelengths of light. Other organisms have large antenna complexes that contain up to thousands of pigments. This enables them to survive in extremely dim light. For example, a green sulfur bacterium has been found growing photosynthetically 100 meters deep in the Black Sea, where a single molecule of bacteriochlorophyll receives a single photon once every eight hours.[12] Other organisms grow inside rocks, in harsh environments such as deserts, where they receive only very minimal light.

Carotenoids are found in all native photosynthetic organisms. They serve a dual function, as both accessory antenna pigment and also are essential in photoprotection of photosynthetic systems from the effects of excess light, especially in the presence of oxygen. Bilins are open-chain tetrapyrroles that are present in antenna complexes called phycobilisomes. These complexes are found in cyanobacteria and red algae. Structures of representative carotenoid pigments are shown in Figure 3.

2.2 Spectroscopy of Chlorophylls[3]

Chlorophylls and bacteriochlorophylls typically exhibit three intense electronic absorption bands in the visible and

Table 1 Distribution of photosynthetic pigments

	Chlorophyll				Bacteriochlorophyll							
Type of Organism	*a*	*b*	*c*	*d*	*a*	*b*	*c*	*d*	*e*	*g*	Carotenoid	Bilin
Eukaryotes												
Higher plants, mosses, ferns	+	+									+	
Green algae	+	+									+	
Euglenoids	+	+									+	
Diatoms	+		+								+	
Dinoflagellates	+		+								+	
Brown algae	+		+								+	
Red algae	+										+	+
Prokaryotes											+	
Cyanobacteria	$+^{a}$	$+^{a}$		$+^{a}$							+	+
Purple bacteria					$+^{b}$	$+^{b}$					+	
Green sulfur bacteria					+		+	+	+		+	
Green filamentous bacteria					+		+				+	
Heliobacteria										+	+	

[a]All cyanobacteria contain Chl *a*, and some types contain in addition Chl *b* or Chl *d*. [b]Purple bacteria contain either Bchl *a* or *b*, but not both in the same species.

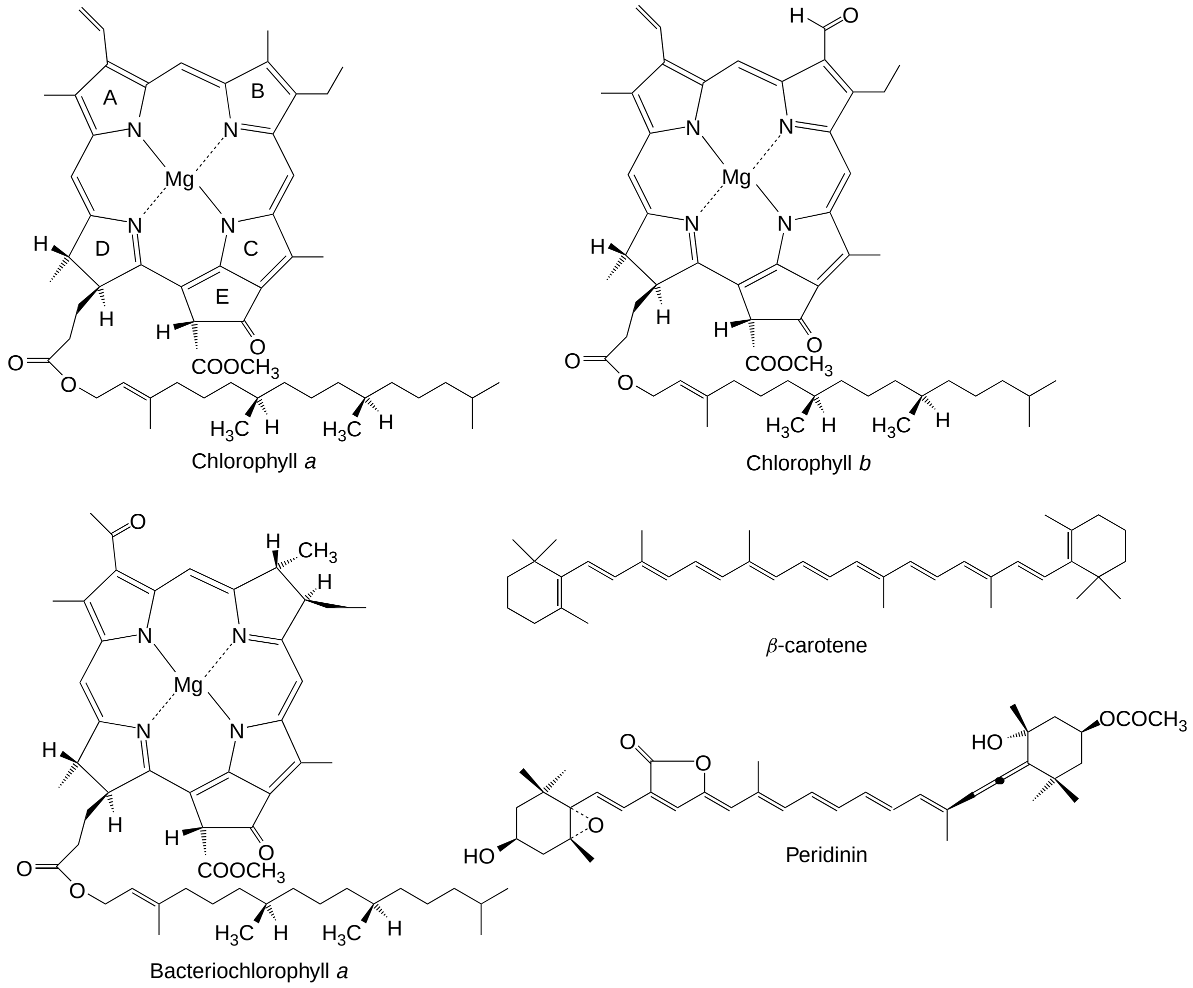

Figure 3 Structures of chlorophylls and other photosynthetic pigments

near IR regions of the spectrum. These are designated the Soret (sometimes called the B band), the Q_x and Q_y bands, from shortest to longest wavelength. Figure 4 shows the absorption and fluorescence spectra for chlorophyll *a* and bacteriochlorophyll *a*. Table 2 lists the wavelengths and extinction coefficients for a number of chlorophylls and bacteriochlorophylls in vitro. The same pigments in vivo invariably exhibit red-shifted absorption bands, sometimes by over 100 nm. The transitions are $\pi \rightarrow \pi^*$ in nature, and involve electron redistribution over the entire conjugated part of the macrocycle. The Quinone (Q) bands are nondegenerate transitions owing to the low symmetry of the molecule. The x and y subscripts refer to the direction of the transition dipole moment with reference to the molecular axes. The lowest energy Q_y band is invariably polarized along the axis bisecting rings A and C (see Figure 3), while in most cases the Q_x band is polarized along the axis bisecting rings B and D. The four orbital model of Gouterman for the electronic states of porphyrins (*see* ***Iron Porphyrin Chemistry***), while admittedly somewhat oversimplified, is adequate for many purposes.[13] More accurate calculations of the electronic properties of many chlorophylls and bacteriochlorophylls are now available.[14,15]

The conjugated chlorophyll macrocycle has intense visible and near-infrared absorption, with an extinction coefficient in the longest wavelength Q_y band of approximately $100\,\mathrm{mM}^{-1}\,\mathrm{cm}^{-1}$ (Figure 4 and Table 2).[1,16] The chlorophylls therefore absorb well in the region of the spectrum in which the solar spectrum has its most intense output, as shown in Figure 5.[1] The presence of the closed-shell Mg^{2+} ion ensures a long excited-state lifetime in the nanosecond range, in contrast to transition metal-containing porphyrins, which decay in picoseconds owing to internal charge transfer processes. This long excited-state lifetime facilitates a high quantum yield of photochemistry, in that extremely rapid competing pathways for excited-state decay are not present. The metallated pigments are generally much more abundant than are the free base porphyrins, although metal-free chlorophylls, known as *pheophytins*, are present in small quantities in many photosynthetic systems and function as essential redox carriers in reaction centers (see below).

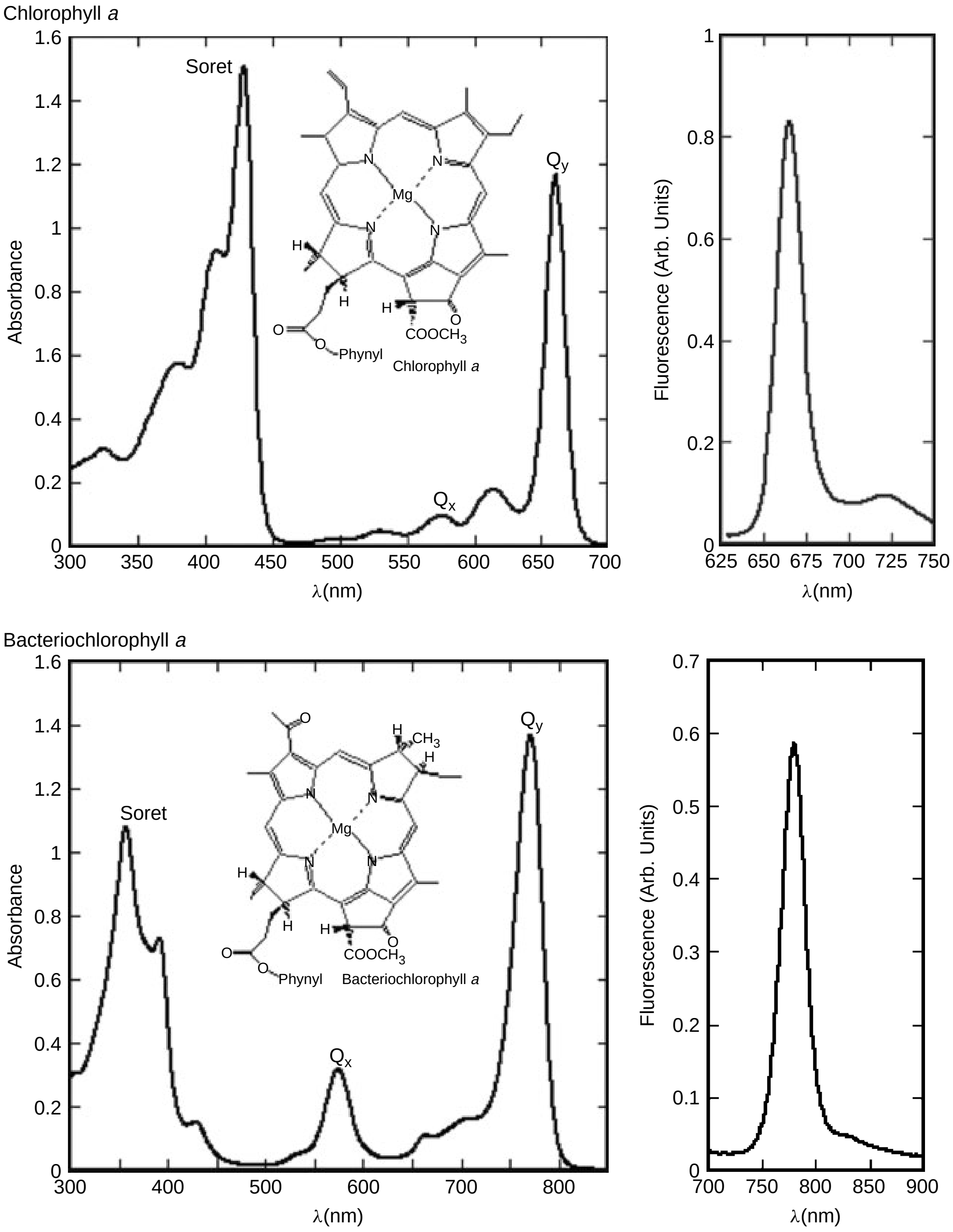

Figure 4 Absorption spectra of chlorophyll *a* and bacteriochlorophyll *a* in diethyl ether. (Ref. 1. Reproduced by permission of Blackwell)

The fluorescence emission of chlorophylls and bacteriochlorophylls is invariably emitted from the lowest energy excited sate, with typical Stokes shifts of 10–15 nm from the Q_y absorbance maximum. Fluorescence lifetimes of 2–5 ns are usually observed for monomeric pigments in organic solvents. Fluorescence of chlorophyll and bacteriochlorophyll in vivo is very strongly quenched; excited-state lifetimes are typically a few tens of picoseconds and fluorescence quantum yields are at most a few percent. The dominant excited-state decay pathways in vivo are excitation transfer, in which the excited state is transferred from one antenna pigment to another and ultimately photochemistry to form charge-separated states. The rate of photochemistry in the photosynthetic reaction center is fast enough compared to fluorescence and other nonradiative decay pathways so that the quantum yield of photochemistry is nearly unity.

The quantum yield Φ_i for any process that deactivates the excited state is given by the rate constant for that process

Table 2 Absorption properties of chlorophylls and bacteriochlorophylls in vitro[a]

Compound	Solvent	Absorption Maxima (nm) Soret	Q_x	Q_y
Chlorophyll *a*	Diethyl ether	430	578	662 (90)
Chlorophyll *b*	Diethyl ether	455	549	644 (56.2)
Chlorophyll *c*	Diethyl ether	444	578	628
Chlorophyll *d*	Diethyl ether	447		688
Bacteriochlorophyll *a*	Diethyl ether	358	577	773 (90.0)
Bacteriochlorophyll *b*	Diethyl ether	368	578	794 (106)
Bacteriochlorophyll *c*	Diethyl ether	429		659
Bacteriochlorophyll *d*	Diethyl ether	423		651
Bacteriochlorophyll *e*	Acetone	458		647
Bacteriochlorophyll *g*	Diethyl ether	364, 404	565	767

[a] Values taken from Ref. 13, which contains original references. Numbers in parentheses in Q_y column are millimolar extinction coefficients ($mM^{-1}\,cm^{-1}$).

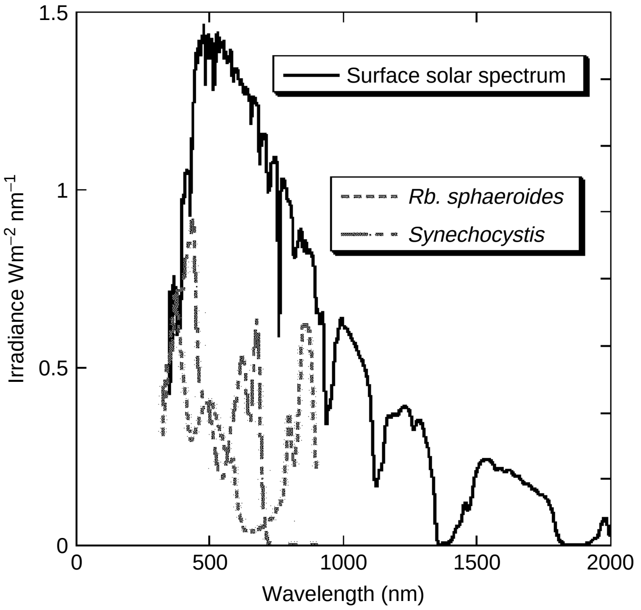

Figure 5 Solar spectrum superimposed on absorption spectrum of chlorophyll. (Ref. 1. Reproduced by permission of Blackwell)

(k_i) divided by the sum of rate constants for all possible excited-state decay processes (k_t) for further details.

$$\Phi_i = \frac{k_i}{k_t} \tag{1}$$

where

$$k_t = \sum_i k_i = k_f + k_p + k_{nr} \tag{2}$$

and k_f is the rate constant for fluorescence, k_p is the rate constant for photochemistry and k_{nr} is the rate constant for all other nonradiative processes, such as internal conversion and *Intersystem Crossing*. The excited-state decays by a set of parallel first-order pathways with an observed rate constant k_t equal to the sum of the rate constants for all pathways.[17] Because the photosynthetic system is basically a solid-state system without free diffusion in solution, the observed rate constants are usually first order. Multiexponential excited-state decays are often observed, however, reflecting both the complexities of the energy transfer network and also heterogeneity in the samples.

3 ENERGETICS AND EFFICIENCIES OF PHOTOSYNTHESIS

3.1 Redox Properties of Excited States[18,19]

The essence of photosynthetic energy storage is the photoinduced electron transfer process that takes place in the reaction center complex. This is most easily understood by considering the redox properties of the excited states of the reaction center pigments. Excited states typically have chemical properties that are dramatically different from those of the *Ground State* molecules. In particular, the redox potentials of the molecule are greatly modified by electronic excitation. A great deal of evidence from both organic and inorganic photochemistry indicates that the excited state can be both a stronger oxidant and a stronger reductant than is the ground state. Qualitatively, this can be understood as the electron occupying the excited orbital serving as a strong reductant, while the remaining hole can act as a strong oxidant.

It is not possible to measure excited-state redox potentials directly with a conventional redox titration, owing to their transient nature. However, redox potentials of the excited state can be estimated, using the ground-state potentials and the excitation energy.[18,19] If the entropy change upon excitation is small, which appears to be the case for many systems, the midpoint redox potential for the excited state of the pigment (P) acting as a reductant is given in equation (3):

$$E_m\left(\frac{P^+}{P^*}\right) = E\left(\frac{P}{P^*}\right) - E_m\left(\frac{P^+}{P}\right) \tag{3}$$

where $E_m(P^+/P^*)$ is the midpoint redox potential for the excited-state half reaction:

$$P^+ + e^- \longrightarrow P^* \tag{4}$$

The excitation energy $E(P/P^*)$ is the 0–0 energy for the lowest excited singlet state, usually approximated as the average of the absorbance and fluorescence energies:

$$P + h\nu \longrightarrow P^* \tag{5}$$

Table 3 Ground and excited singlet state redox potentials of photosynthetic pigments in vitro and in vivo[a]

	E (P/P^*)	E_m (P^+/P)	E_m (P^*/P^+)	E_m (P/P^-)	E_m (P^*/P^-)
Chlorophyll *a*	1.85	+0.78	−1.07	−0.87	+0.98
Bacteriochlorophyll *a*	1.58	+0.64	−0.94	−0.84	+0.74
P700	1.75	+0.49	−1.26		
P680	1.80	~1.1	~−0.7		
P870	1.39	+0.45	−0.94		
P840	1.46	+0.25	−1.21		
P800	1.54	+0.25	−1.29		

[a] Most values taken from Reference 16, which contains original references. $E(P/P^*) = 0\text{–}0$ excitation energies (eV); all other values are midpoint redox potentials of ground and excited states (V), versus NHE, calculated as described in text.

Finally, the midpoint redox potential for the oxidation of the ground state is given by equation (6):

$$P^+ + e^- \longrightarrow P \qquad (6)$$

This quantity is easily measured by a standard redox titration. Values for the excited-state redox potentials of chlorophyll *a* and bacteriochlorophyll *a* in vitro, as well as in a number of photosynthetic reaction centers are given in Table 3. The large negative values testify to the fact that the excited states are extremely strong reductants. Also shown are the potentials for the excited state acting as an oxidant $E_m(P^*/P^-)$ for the two isolated pigments, calculated analogously from the redox potential of the pigment anion $E_m(P/P^-)$. However, current evidence strongly suggests that the reaction center pigment excited state acts as a reductant in all reaction centers, as well as in most chlorophyll photoreactions in vitro.

3.2 Electron Transfer Schemes for Reaction Centers

The electron transfer patterns shown in Figure 2 can be combined with information on ground-state redox potentials of known electron carriers and the excited-state redox potentials given in Table 3 to construct detailed electron transfer schemes for photosynthetic systems. Schemes for the major classes of photosynthetic reaction centers are shown in Figure 6. A more in-depth discussion of some of these complexes is given below. In Figure 6, the electron carriers are placed at their midpoint redox potentials and the vertical arrow denotes energy input by a photon, thereby changing the redox potential of the reaction center photoactive pigment from that of the ground state to that of the excited state.

3.3 The Efficiency of Photosynthetic Energy Storage

It is not possible to give a single value for the energy storage efficiency of photosynthesis. Almost any value from 0 to 100% can be cited, depending on exactly how the question is formulated and where in the process the calculation is made. For example, the free energy stored in the initial radical pair products in isolated purple bacterial reaction centers is at least 90% of the photon energy. However, at each stage of the stabilization process a significant amount of energy is lost. This energy loss makes the process irreversible, and allows the energy to be stored in a form that can be utilized for cellular processes.

The overall thermodynamics of the photochemical energy storage also depend on the concentrations of the various forms of the redox carriers, and can be somewhat different from the midpoint potentials illustrated in Figure 6, which assume equimolar concentrations of oxidized and reduced forms. This point has been considered in detail by several authors with reference to viewing the photosynthetic system as a power converter.**[20–23]**

Using the midpoint redox potentials for the reductant H_2O (+0.82 V) and oxidant $NADP^+$ (−0.32 V) substrates in oxygen-evolving photosynthesis, the in situ measured maximum quantum yields for each photoreaction of essentially unity, and the excitation energies given in Table 3, the overall energy storage by the oxygenic photosynthetic system can be easily calculated to be approximately 41% of the energy in the photons. (Four turnovers of each photosystem are required to produce one molecule of O_2 and two molecules of NADPH.)

If the calculation is made instead using the ultimate electron acceptor CO_2, and measured whole plant quantum yields in dim monochromatic light, then the energy storage drops to about 27%. Further losses are incurred if white light is utilized as an energy source, as photochemistry takes place only from the lowest excited singlet state, and the energy difference between a blue and a red photon is lost as heat. A value of 5% has been estimated for an average energy conversion efficiency for sunlight falling on a leaf.**[23]** This number also includes losses due to growth and wasteful processes such as photorespiration.

If one takes the global view of the energy stored in biomass compared to the total solar energy incident on the Earth, then the estimated overall efficiency is about 0.05%.**[24]** This includes losses due to reflection, absorption by nonphotosynthetic pigments, the fact that much of the solar output is in the near-infrared region, which is not efficiently used by abundant organisms, and various cellular processes.

4 ANTENNA STRUCTURE AND FUNCTION

4.1 Mechanism of Excitation Transfer[25,26]

The photosynthetic antenna system is organized to collect and deliver excited-state energy to the reaction center complexes. The delivery of energy is by means of excitation transfer. Excitation transfer in photosynthetic systems is

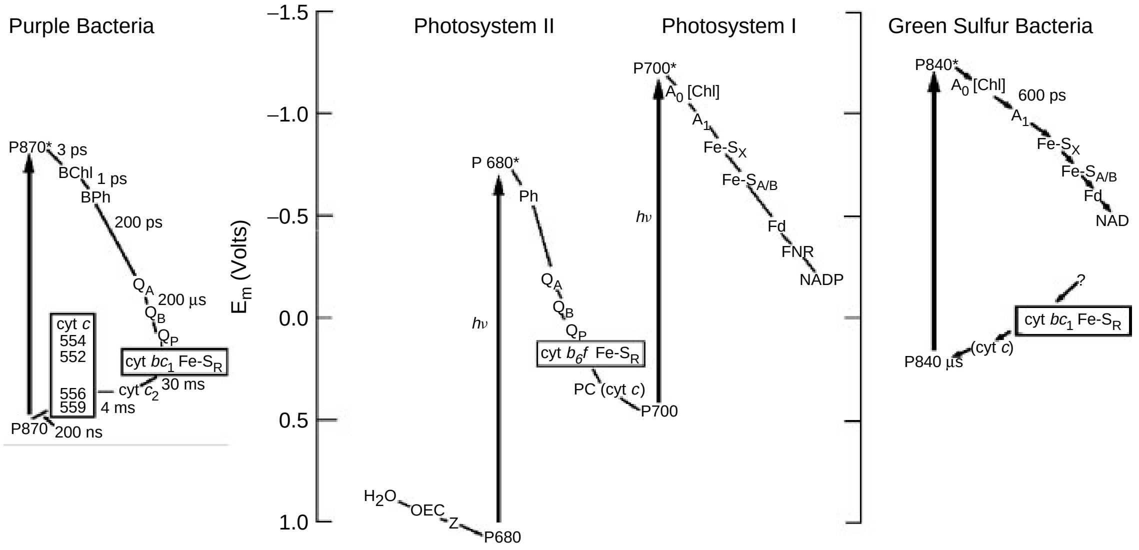

Figure 6 Electron transfer schemes for photosynthetic reaction centers. Heavy vertical arrows indicate energy input by photon absorption, thinner arrows indicate preferred electron transfer pathways. Carriers in parentheses indicate alternate species in some organisms. Question marks indicate carriers or electron transfer steps that are likely but have not been unambiguously established. The cytochrome bc_1 and b_6f complexes are boxed, and the details of the electron flow in these complexes are omitted. All redox potentials are referenced to the normal hydrogen electrode. Abbreviations: AC auracyanin; BChl, bacteriochlorophyll; BPh, bacteriopheophytin; Chl, chlorophyll; cyt, cytochrome; Fd, soluble ferredoxin; Fe-$S_{A/B}$, iron-sulfur centers contained on a low-molecular-weight peptide peripheral to the reaction center core; Fe-S_R, Rieske iron-sulfur center; Fe-S_X, iron-sulfur center contained in the reaction center core; FNR, ferredoxin-NADP reductase; $h\nu$, photon; NAD(P), nicotinamide adenine dinucleotide (phosphate); OEC, oxygen-evolving center; P870, P680, P700, P840, P800, reaction center photoactive pigment with absorption maximum in nanometers at the indicated wavelength; PC, plastocyanin; Ph, pheophytin; Q, quinone (subscript indicates a specific quinone); Z, tyrosine radical donor to Photosystem II

generally considered to take place by means of the Förster resonance transfer mechanism. If two pigments are separated by more than several Angstroms and the transitions are allowed, the transfer between energy donor and energy acceptor occurs primarily via a Coulomb (dipole-dipole) mechanism, with rate constant given by equation (7):

$$k_e = k_f\left(\frac{R_o}{R}\right)^6 \tag{7}$$

where k_f is the rate constant for fluorescence, R is the distance between energy donor and acceptor and R_o is the ‘‘critical distance’’ at which energy transfer is 50% efficient. R_o is given by equation (8) (in units of nm^6):

$$R_o^6 = \left(\frac{8.785\times10^{17}\kappa^2}{n^4}\right)\int\frac{F(\nu)\varepsilon(\nu)\,d\nu}{\nu^4} \tag{8}$$

where $\varepsilon(n)$ is the molar extinction coefficient on a wavenumber scale, $F(n)$ is the normalized emission spectrum of the energy donor, n is the refractive index and κ^2 is an orientation factor, given by equation (9):

$$\kappa^2 = (\cos\alpha - 3\cos\beta_1\cos\beta_2)^2 \tag{9}$$

where α is the angle between the two transition dipoles and the β’s are the angles between each dipole and the line joining them. The values of κ^2 can range from 0 to 4. For a random orientation of the transition dipoles, the average value of κ^2 is 2/3.

Typical values of R_o between chlorophylls and bacteriochlorophylls are 60–100 Å (assuming $\kappa^2 = 1$). Excitation transfer is therefore a longer range process than is electron transfer (see below). In fact, the structures of antenna complexes have undoubtedly been fine tuned by evolution to minimize excited-state electron transfer processes, while at the same time efficiently delivering energy to the reaction center.

If the pigments are very close to each other, then the simple picture described above breaks down. Electron exchange terms can contribute to the energy transfer process. This is thought to be the case particularly for carotenoid to chlorophyll energy transfer, where forbidden transitions are involved, so that the Coulomb terms are zero. In the case of strongly interacting pigments, exciton coupling results, in which it is most useful to view the system as a supermolecule rather than as individual chromophores. Currently a large amount of structural data is available for photosynthetic antenna complexes. The structures of many of them will be discussed below. It is clear from a variety of evidence that in certain cases the very weak coupling case described by equation (7) is probably adequate, while in others the exchange mechanism may be important. Excitonic effects are clearly apparent in many photosynthetic complexes.[25]

4.2 Structure of Photosynthetic Antenna Complexes[4]

A remarkable variety of antenna complexes have been identified from various classes of photosynthetic organisms. There seems to be little doubt that there have been multiple evolutionary origins of antenna complexes, as there is no common structural theme evident. Figure 7 shows a rogue's gallery of various types of photosynthetic antenna complexes. These include the cyanobacterial phycobilisome type antennas that act as light guides, large multimeric circular complexes integral to the membrane found in proteobacteria, enormous chlorosome structures in green sulfur bacteria containing rods of self-assembled bacteriochlorophyll with relatively little protein. Many antenna complexes, like the chlorophyll a/b Light-harvesting complexes, are integral membrane complexes in which pigments (chlorophylls and carotenoids) are associated with proteins to form well-defined pigment-protein complexes that span the photosynthetic membrane and probably interact directly with the reaction centers, which are also integral membrane proteins. Others are only peripherally attached to the membrane and are easily removed by gentle treatments. The phycobilisome and the chlorosome complexes are examples of *peripheral* antenna complexes. The phycobilisomes are large complexes containing bilins, which are open-chain tetrapyrroles, as pigments that are covalently attached to proteins.[27,28] Chlorosomes contain specialized bacteriochlorophyll pigments (bacteriochlorophylls c, d, or e), which form large pigment aggregates with relatively little involvement of protein.[29–31]

Phycobilisomes are large supramolecular aggregates attached to the stromal side of the thylakoid membrane in cyanobacteria, red algae, and cryptomonads.[32] The size of phycobilisomes varies amongst species and growth conditions and can easily reach sizes of 2 MDa. All pigment binding protein species show a first level quaternary arrangement of α and β subunits forming an $\alpha\beta$-dimer. This further arranges into second level round disklike structures of $(\alpha\beta)_3$ or $(\alpha\beta)_6$ units. On this core are arranged six additional rodlike structures made up of phycocyanin. Also associated with the phycobilisome are colorless linker proteins. High-resolution X-ray structures are available for several of the bilin-containing proteins of the phycobilisomes.

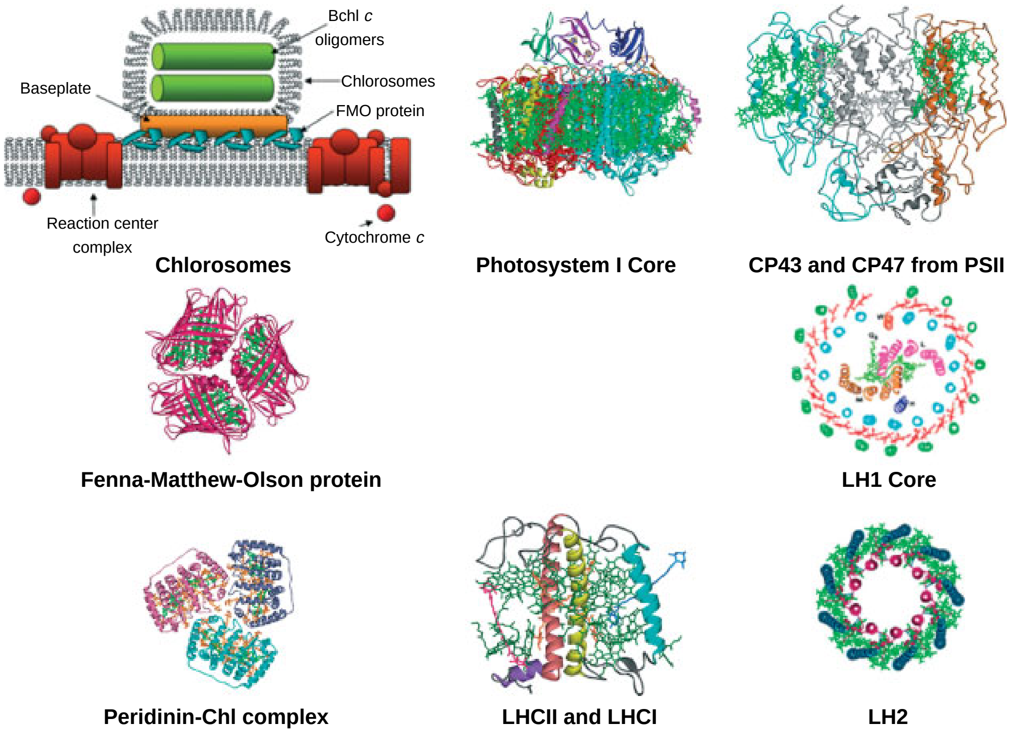

Chlorosomes **Photosystem I Core** **CP43 and CP47 from PSII**

Fenna-Matthew-Olson protein **LH1 Core**

Peridinin-Chl complex **LHCII and LHCI** **LH2**

Figure 7 Rogue's gallery of structures of peripheral antenna complexes. As labelled these include Chlorosomes from green sulfur bacteria, fused antenna domains of the Photosystem I core, the CP43 and CP47 proteins of Photosystem II, the Fenna-Matthew-Olson (FMO) protein associated with chlorosomes, LHI proteins surrounding a purple bacterial photosynthetic core, the peridinin-chlorophyll a protein of dinoflagellate algae, the LHCI and LHCII proteins found in plants and many algae, and the LHII protein complex that is associated with LHI in purple bacteria

These include structures of phycoerythrin, C-phycocyanin and allophycocyanin. From the known high-resolution structures of the component proteins, in conjunction with biochemical, spectroscopic, and electron microscopic measurements, structures for the phycobilisome have been proposed. Figure 8(a) shows a recent proposed structure for the arrangement of the proteins in a phycobilisome from *Thermosynechococcus vulcanus*.[32] A tricylindrical allophycocyanin core is surrounded by three pairs of phycocyanin rods (R1, R2, R3). It is proposed that the bilin-containing core and the rods are connected by protein connecters in the phycobilisome-like phycocyanin 622. Other structures include structure of allophycocyanin a and allophycocyanin b,[33] C-phycocyanin from the red algae *Porphyra yezoenis*,[34–38] and the structures of phycoerythrin,[39–41] R-phycocyanin.[42] Figure 8(b) shows the energy pathway within the phycobilisome. It can be seen that some of the pigments are very close together, while others are separated by much longer distances. Thus, for some energy transfer processes the simple Förster dipole-dipole mechanism described in the previous section is probably inadequate. Figure 8(c) and 8(d) show the ribbon representation of the allophycocyanin α-subunit and β-subunits, respectively. Three $\alpha\beta$ monomers are arranged around a 3-fold axis to form a hexameric disc shaped $(\alpha\beta)_3$ trimer, shown in Figure 8(e). Hexamers like these are stacked to form the rods of the phycobilisome (Figure 8(a) and 8(b)).

Another antenna complex where high-resolution structural information is available is the bacteriochlorophyll *a* binding protein (also known as the Fenna-Matthews-Olson or FMO protein) from green sulfur bacteria.[43] This complex serves as the bridge between the peripheral chlorosome complex and the membrane-bound reaction center complexes. In this

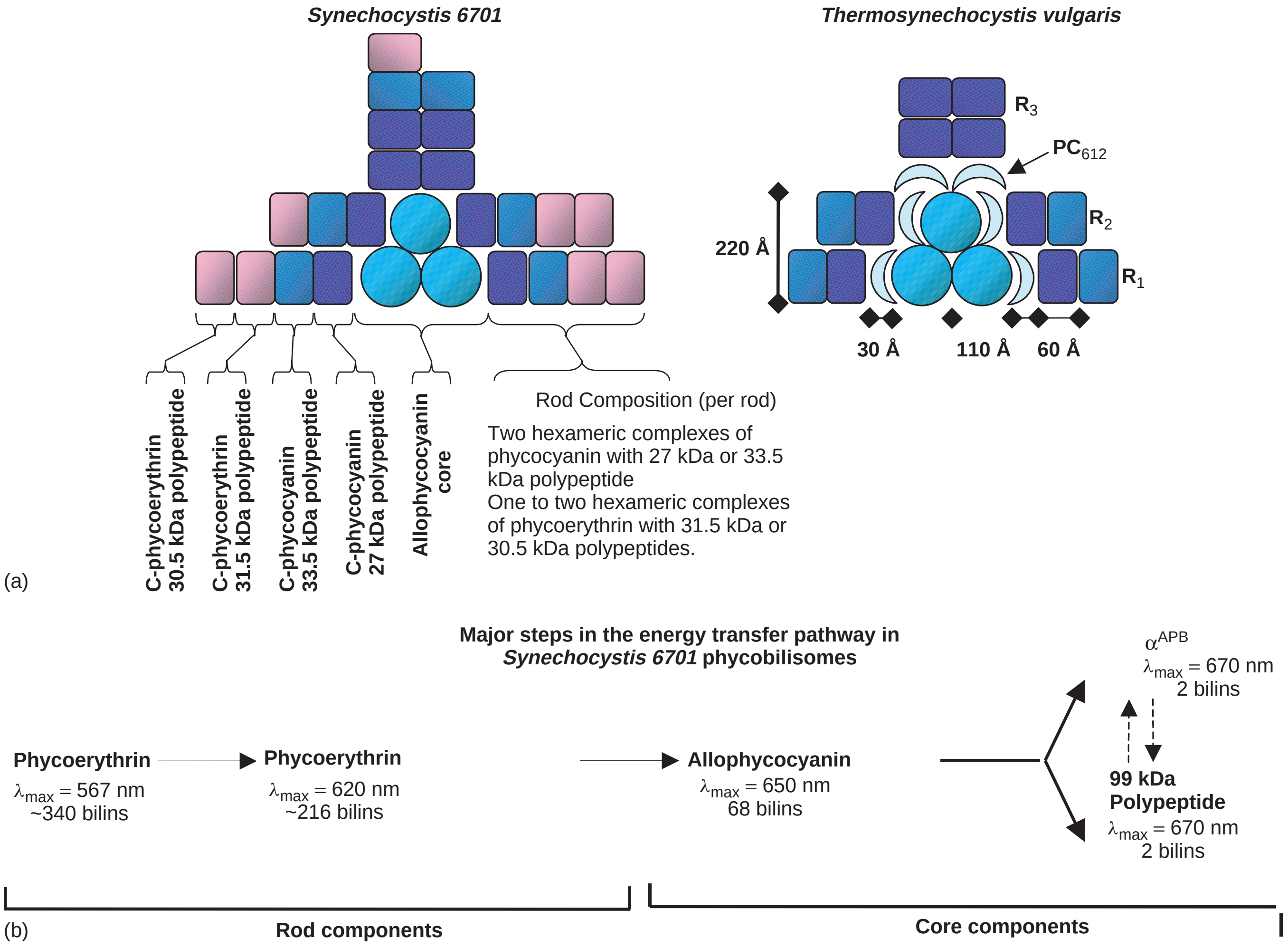
Synechocystis 6701
Thermosynechocystis vulgaris
R3
PC612
R2
R1
220 Å
30 Å
110 Å
60 Å
C-phycoerythrin 30.5 kDa polypeptide
C-phycoerythrin 31.5 kDa polypeptide
C-phycocyanin 33.5 kDa polypeptide
C-phycocyanin 27 kDa polypeptide
Allophycocyanin core
Rod Composition (per rod)
Two hexameric complexes of phycocyanin with 27 kDa or 33.5 kDa polypeptide
One to two hexameric complexes of phycoerythrin with 31.5 kDa or 30.5 kDa polypeptides.
(a)
Major steps in the energy transfer pathway in Synechocystis 6701 phycobilisomes
Phycoerythrin
λmax = 567 nm
~340 bilins
Phycoerythrin
λmax = 620 nm
~216 bilins
Allophycocyanin
λmax = 650 nm
68 bilins
αAPB
λmax = 670 nm
2 bilins
99 kDa Polypeptide
λmax = 670 nm
2 bilins
(b)
Rod components
Core components

Figure 8 (a) Structure of the phycocyanin antenna complex from the cyanobacterium *Synechocystis* 6701 and proposed structure of the complex from *Thermosynechocystis vulgaris*, (Ref. 32. Reproduced by permission of American Society for Biochemistry & Molecular Biology). (b) Energy transfer route in the phycobilisomes. (c) Crystal structure of the allophycocyanin α-subunit. (d) Crystal structure of the allophycocyanin β-subunit. (e) Hexameric arrangement of three $\alpha\beta$ units to make the disc-like $(\alpha\beta)_3$ hexamer

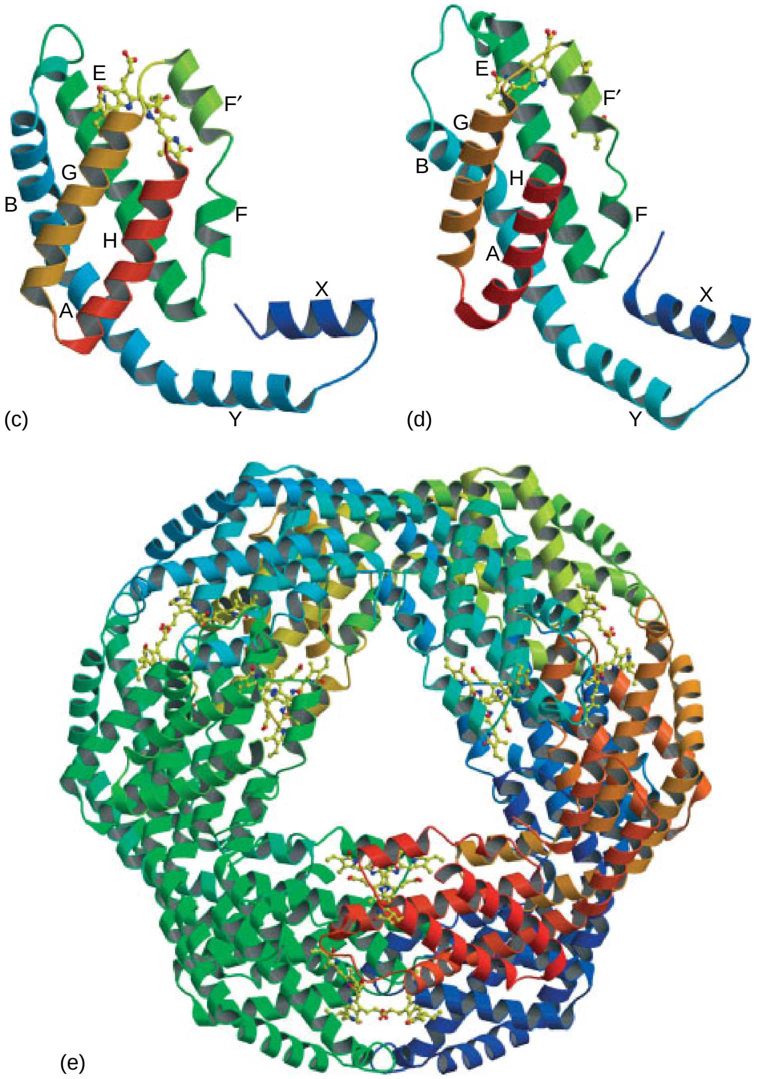

Figure 8 cont'd

case, the pigments interact moderately strongly, at distances of approximately 10 Å. Because this was the first chlorophyll protein complex to have its detailed structure determined, it has been the subject of intense spectroscopic and theoretical analysis.[44]

4.3 Supercomplexes

4.3.1 The Structure of the Light-harvesting LH1 and LH2 Complexes of Purple Photosynthetic Bacteria[45]

The basic structure of all the component proteins making up the Light-harvesting (LH) complexes of purple photosynthetic bacteria is similar.[46,47] It consists of two polypeptides (α- and β-subunits) that fold into transmembrane α-helices and form a heterodimer that noncovalently binds bacteriochlorophyll and carotenoids. Several of these heterodimeric units group together to form ring structures. The size of these ring structures differs between LH1 and LH2, with LH1 being much larger (about 120 Å in diameter) and encircling the reaction center complex. The smaller LH2 rings (60–70 Å diameter) group around the LH1-reaction center complex, but their exact arrangement is unclear (Figure 9).

Electron and atomic force microscopy has shown that the LH2 complexes from *Rhodopseudomonas acidophila*, *Rhodovulum sulfidophilum*, and *Rhodobacter sphaeroides* are all monomers of the basic $\alpha\beta$-subunits. Crystal structures of the LH2 complexes from *Rps. acidophila* and *Rs. molischianum* have also been reported. Each $\alpha\beta$-unit binds 3 bacteriochlorophyll and two carotenoid molecules, although in the crystal structure only one carotenoid electron density was clearly defined. The arrangement of the $\alpha\beta$-subunits is

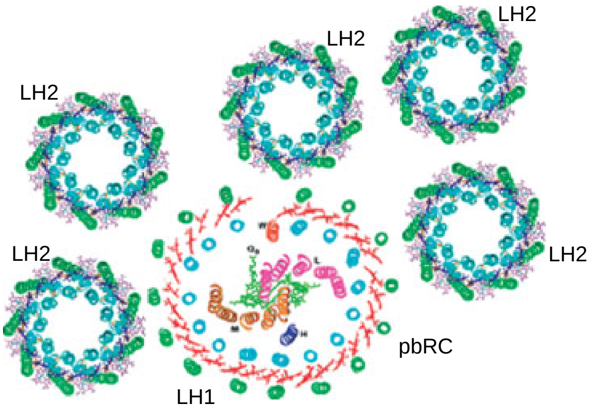

Figure 9 The bacterial supercomplexes found in purple bacteria (*Rhodopseudomonas palustris*). A single reaction center complex is surrounded by a nearly circular ring of LHI. In close proximity are additional smaller rings of LHII. A gap exists in the LHI ring in some but not necessarily all cases, presumably for the entry of PufX or some other protein

that of a double row of α-helices, with the α-protein inside and the β-protein outside. Once again the bacteriochlorophylls are stacked in two layers, one near the cytoplasmic side of the inner membrane and the other to the periplasmic side. The bacteriochlorophyll rings of the top portion of LH2 are nearly parallel to each other, with a Mg-Mg distance of around 9 Å. The ring of nearly parallel bacteriochlorophylls is nearly perpendicular to the plane of the bacteriochlorophylls in the other ring when overlapping (as they do at B850$\alpha\beta$ and B800) facilitating faster electron transfer.

While the structure of LH2 is well resolved, the structure of LH1 remains less well understood. Because of the sequence similarity of LHI $\alpha\beta$-subunits of *Rhodobacter sphaeroides* to the LH2 $\alpha\beta$-subunits of *Rhodospirillum molischianum*, the structure of the LH1 subunits was modeled versus the crystal structure of *Rs molischianum* LHII.[48,49] The crystal structure of *Rhodobacter sphaeroides* Rb RC was then modeled into the center of a ring of LHI $\alpha\beta$-subunits. Using this method, the resultant modeled ring contained 16$\alpha\beta$-subunits, binding 32 bacteriochlorophyll molecules. The general size and helix positions generally agreed with an 8.5 Å electron microscopy projection map of *R. rubrum* LH1 (which was done without *R. rubrum* RC present). However, it is now clear that in many (but not necessarily all) cases in vivo there is a break in the ring, so that it is not a perfect circle, but has an opening. In some cases this has been proposed to be the site where a photosynthetic regulatory protein PufX resides. PufX has been shown to copurify with the LH1-RC complex from *Rhodobacter sphaeroides*. A structure of the RC-LH1 complex from *Rhodopseudomonas palustrus* is shown in Figure 9.[50] In this case, PufX is not present and an as yet unidentified protein interrupts the ring.

4.3.2 *Superstructures of PSI or PSII in some Organisms in cases of Iron Stress or Low Light*[51–53]

In cyanobacteria under conditions of iron limitation leading to iron stress, the phycobilosomes are deconstructed, and a macromolecular supercomplex is synthesized. Iron stress induces the expression of a protein that is very similar in structure to CP43, only lacking the large hydrophilic loop that joins the ends of transmembrane helices 5 and 5′, and is called C43′.[54] CP43′ is encoded by the *isiA* gene. Another gene, *isiB*, encodes a flavodoxin, which replaces the iron-containing ferredoxin as the electron acceptor for PSI during iron stress.[53,55–57] Electron microscopy of the PSI/CP43′ supermacromolecular complex shows that in *Synechocystis* PC 6803 under iron stress 18 subunits of CP43′ form a well-structured ring around the cloverleaf of PSI, thereby increasing the light-harvesting capacity of PSI by 70% (Figure 10(a)). Each CP43′ subunit binds between 12 and 13 chlorophyll a molecules, based upon modeling calculations and comparisons to the CP43 subunit of PSII.

Prochlorophytes are cyanobacteria that do not contain phycobiliproteins, but rather contain chlorophyll a/b binding Pcb proteins. Pcb sequences are homologous to the sequences of IsiA and CP43. It was shown that in low-light adapted strains of the prochlorophyte *Prochlorococcus marinus* SS120, similar to the case with CP43′ of *Synechocystis* PC 6803, Pcb forms an 18-subunit ring around the trimeric PSI, even under conditions of Fe sufficiency. Another prochlorophyte,

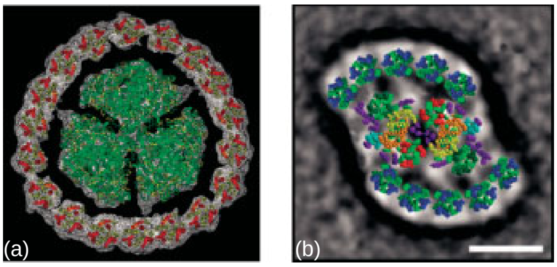

Figure 10 Bacterial supercomplexes found under conditions of light starvation or iron stress. (a) Modeling of the Cα backbone and chlorophylls (yellow) of the PSI trimer (green) and CP43″ helices (red) using data from X-ray diffraction studies of the PSI complex of *Synechocystis* PCc 6803 induced during iron stress (deficiency). (Reprinted with permission from Ref. 54. © 2003 American Chemical Society) (b) Structure of the Pcb-PSII supercomplex isolated from *prochloron didemni*, incorporating the X-ray structures of the PSII core dimer and the Pcb homolog CP43 from *synechocystis elongatus*. CP43 was used to model Pcb. The CP43 transmembrane helices are shown in blue, with the chlorophyll a molecules in green. Other colors are for the transmembrane helices of the PSII core, with D1 = yellow, D2 = orange, CP47 = red, CP43 = dark green, cytochrome b_{559} = cyan, and the low-molecular-weight subunits = purple. (Reproduced from T.S. Bibby, J. Nield, M. Chen, A. W. Larkum, and J. Barber, 'Structure of a photosystem II supercomplex isolated from Prochloron didemni retaining its chlorophyll a/b light-harvesting system' *Proc Natl Acad Sci U.S.A.*, 2003, **100**, 9050. © 2003 National Academy of Sciences, USA)

Prochloron didemni, is a symbiont that lives in a layer under the body of a marine ascidian. An 18-subunit ring structure is not formed around PSI, but rather a separate macromolecular complex of ten Pcb subunits and two PSII complexes form a supercomplex.[51,58,59] As shown in Figure 10(b), two complexes of PSII make up the core of the supercomplex. Five Pcb subunits line in a row on either side of the core. It is assumed, based upon sequence and structural homology to CP43, that thirteen chlorophylls bind to each Pcb subunit.

The integral membrane chlorophyll a/b antenna complex from higher plants forms two-dimensional crystals, which have been analyzed using electron diffraction and electron microscopy, and also by three dimensional crystals by X-ray crystallography.[46,50,53,57]

4.4 Kinetics and Energetics of Excitation Transfer

Excitation transfer must be fast enough to deliver excitations to the photochemical reaction center and have them trapped in a time short compared to the excited-state lifetime in the absence of trapping. Excited-state lifetimes of isolated antenna complexes, where the reaction centers have been removed, are typically in the 1–5 ns range. Observed excited-state lifetimes of systems where antennas are connected to reaction centers are generally on the order of a few tens of picoseconds, which is sufficiently fast to ensure that under physiological conditions that almost all the energy is trapped by photochemistry.

In many antenna complexes, an energy gradient or funnel is present, in which a series of pigments is found with progressively more red-shifted Q_y absorption maxima (and consequently progressively lower excited-state energies). In most known cases, the lowest energy antenna pigments are physically closest to the reaction center, and the higher energy pigments are the farthest. This gradient provides a funneling effect for the excitations, and imparts a directionality and irreversibility to the energy transfer process, although at the cost of the difference in energy levels of the pigments. This funneling effect is particularly apparent in large peripheral antenna complexes such as phycobilisomes and chlorosomes, where there may be up to several thousand antenna pigments per reaction center. In this case, it is clear from the structural data shown in Figure 8 that the shorter wavelength absorbing pigments are located toward the ends of the rods and the longer wavelength absorbing one are toward the core, which is in turn attached to the membrane where the reaction center is located. The energy flow is therefore downhill energetically while at the same time moving the excited state physically closer to the reaction center where photochemistry will eventually take place.

5 STRUCTURE AND MECHANISM OF THE TYPE II RC FROM PURPLE BACTERIA[45,60]

The structure of the purple bacterial Type II RCs (PbRCs) have been known for nearly 20 years, and as such are very well characterized spectroscopically, biochemically, and structurally.[61–64] These were the first reaction center complexes to be purified, and the first to be studied by picosecond kinetic methods. The chemical composition of the reaction centers from selected purple bacteria and the functionally related reaction center from the green bacterium *Chloroflexus aurantiacus* is summarized in Table 4. The RC from *Rb. sphaeroides* contains three protein subunits, known as L (light), M (medium), and H (heavy). PbRC is a stripped down version of PSII, with its subunits L and M similar structurally to D1 and D2 and representing an ancient duplication. H is a cytoplasmic subunit, and in some species a periplasmic cytochrome subunit C is present. The PbRC has no internal antenna and thus must harvest light using external antennas. The internal electron transfer chain is almost identical in layout to PSII. There are some important differences, however, the most glaring of which is that PbRC utilizes bacteriochlorophyll rather than chlorophyll. The structure of the reaction centers from two organisms are known, *Rhodobacter sphaeroides* and *Rhodopseudomonas viridis*. All of the reported crystal structures of RCs and LHs (circular antenna complexes discussed earlier) except that of *Rv* are from bacteriochlorophyll a-containing species. The RC from *Rv* contains bacteriochlorophyll b. The structure of the *Rhodopseudomonas viridis* PbRC is shown in Figure 11. The reaction center protein forms a scaffolding upon which the cofactors are arranged. The part of the protein that crosses the lipid bilayer is almost purely alpha helical in

Table 4 Chemical composition of bacterial reaction centers

Organism	BChl *a*	BChl *b*	BPheo *a*	BPheo *b*	Protein Subunits[a]	Ubiquinone	Menaquinone	Metal	Carotenoid
Rhodopseudomonas viridis	–	4	–	2	LMHC	1	1	Fe	1
Rhodobacter sphaeroides	4	–	2	–	LMH	2	0	Fe[b]	1
Chromatium vinosum	4	–	2	–	LMHC	1	1	Fe	1
Chloroflexus aurantiacus	3	–	3	–	LM(C)[c]	0	2	Mn	0

[a] Molecular masses (from gene sequences) of the subunits are approximately L-31, M-34, H-28, C-41 kDa. [b] Certain strains of this organism contain Mn. [c] This organism contains a cytochrome subunit, although it is lost during preparation.

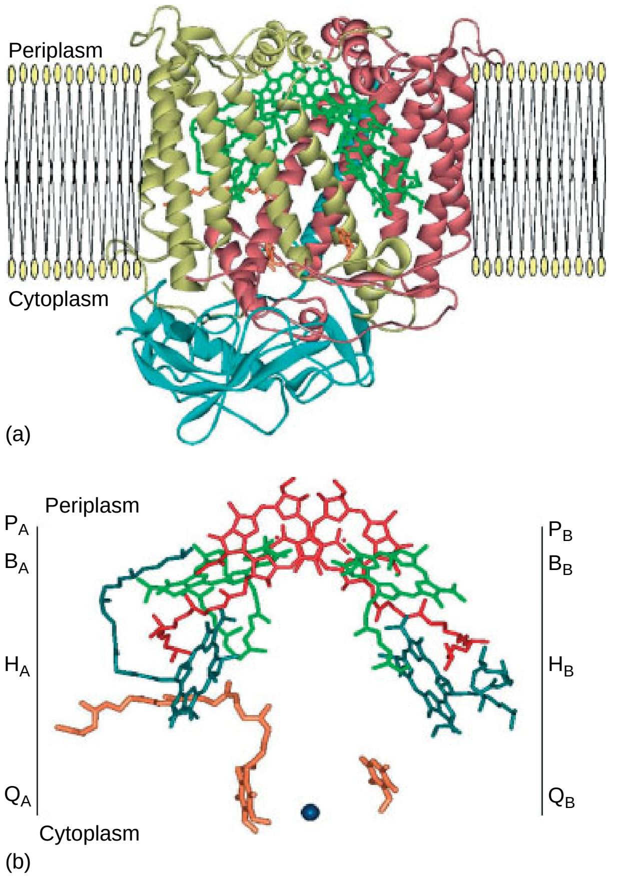

Figure 11 (a) Crystal structure of the *Rhodopseudomonas viridis* reaction center. Coordinates taken from the Protein Data Bank and visualized using Accelrys DSViewer Pro. (b) Arrangement of the chromophores in the *Rhodobacter sphaeroides* reaction center. The red pigments at the top labeled D_A and D_B are the bacteriochlorophyll *a* special pair, known as P870. The light green pigments labeled B_A and B_B are the accessory bacteriochlorophyll *a* molecules and the azure pigments labeled H_A and H_B are bacteriopheophytin *a* molecules. The orange molecules labeled Q_A and Q_B are the ubiquinone acceptors. The blue ball is an Fe atom

secondary structure, and contains predominantly nonpolar amino acids, with almost no charged amino acids. There are 11 transmembrane helices, with 5 each from L and M, and one from the H subunit. The L and M proteins have a pseudo-2 fold axis of symmetry, running approximately perpendicular to the plane of the membrane. The symmetry is broken by the H subunit, which has no symmetry-related counterpart, and also by the fact that the L and M subunits have only about 60% sequence identity. In addition to the protein complement, these reaction centers contain several additional *cofactors*, most of which are not covalently attached to the protein. These include bacteriochlorophyll *a* (in some cases *b*), the corresponding metal-free bacteriopheophytins, two quinones (either ubiquinone or menaquinone), a nonheme Fe, (replaced by Mn in some species) and in most cases a molecule of carotenoid. The cytochrome subunit contains four heme *c* groups, covalently bound to cysteine residues. As in the other RCs, the electron transfer chain is comprised of two branches: two accessory BChls in close proximity to the special pair (B_A, B_B), two bacteriopheophytins (H_A, H_B), and a pair of quinones (Q_A, Q_B) (Figure 11(b)). The primary electron donor in the PbRC is called a ''special pair'' because of strong excitonic coupling. This is primarily due to perfect stacking of the chlorin rings of the two bacteriochlorophyll *a*'s (P_A and P_B) of the special pair. The Mg–Mg distance is 7.6 Å, but there are strong $\pi-\pi$ interactions between the two chlorin rings. The special pair is called P870, after the wavelength maximum of their Q_y absorbance band. This pair of pigments together form the photoactive pigment whose excited state loses an electron to form the primary ion pair state. The EPR and ENDOR spectra of the oxidized special pair and acceptor complex have been studied extensively.[65,66] The unpaired electron in the primary donor is approximately equally shared between the two pigments, resulting in a reduction of the hyperfine coupling constants by a factor of two, compared to the cation radical of the monomeric pigment in solution. A variety of evidence indicates that electron transfer proceeds only down the pigments on the A branch, and then crosses over from the A to the B branch at the quinones. The function of the pigments in the B branch is not yet clear, and may be primarily structural.

It has been established that the electron flow in Pb is cyclic (see Figure 2). Upon absorption of a photon by the special pair (P_A/P_B), an electron is promoted to an excited state, whereupon it is transfered through B_A to H_A in 2–3 picoseconds. The reduced bacteriopheophytin (H_A^{-}) donates an electron to Q_A in 200 ps. Within 200 µs, the electron is transfered to Q_B, forming Q_B semiquinone. After a second round of excitation, transfers, and reduction of Q_B semiquinone, QH_2 is released after taking up two protons from the cytoplasmic side of the inner membrane. This is quite similar to the case with PSII of cyanobacteria and the chloroplasts of higher plants. In Pb, the QH_2 is used to reduce cytochrome bc_1 oxidoreductase (to be discussed later), which in turn reduces cytochrome c_2. Cytochrome bc_1 pumps two protons across the inner membrane into the periplasm, resulting in a proton gradient that is used by ATP synthase to make ATP. Cytochrome c_2 completes the cyclic electron flow by rereducing the RC special pair. As opposed to anoxygenic photosynthetic bacteria, cyanobacteria and chloroplasts utilize a cytochrome b_6f in place of cytochrome bc_1.

5.1 Kinetics and Pathways of Electron Transfer within Reaction Centers[66,67]

A tremendous number of different techniques have been brought to bear on the bacterial reaction center system, including almost every imaginable kind of spectroscopy, as well as a wide range of biochemical and genetic manipulations. Here it is only possible to give a brief summary of some of the results. The focus will be on the first few reactions following excitation of the special pair, either directly by photon absorption or indirectly by excitation transfer from antenna or other reaction center pigments. The technique of picosecond absorbance transient difference spectroscopy has been especially informative with respect to elucidating the pathway of electron flow in these complexes, and will therefore be emphasized. Figure 12 summarizes the photochemical and early secondary reactions that take place in isolated reaction centers. A variety of evidence indicates that the electron transfer pathway and kinetics in isolated reaction centers are not significantly altered from their behavior in vivo.

Following excitation of the special pair, the excited state of P870 (P960 in organisms that contain bacteriochlorophyll *b*, such as *Rps. viridis*) has a lifetime of about 3 ps at room temperature, decreasing to about 1 ps at cryogenic temperatures. This excited state (P870*) is conveniently monitored by measuring stimulated emission in the 900 nm region. As P870* decays, absorbance bands bleach at 535 nm and 760 nm, assigned to Q_x and Q_y transitions of the bacteriopheophytin on the A branch, while at the same time a broad new band appears in the 650 nm region. The new state formed is the radical ion pair state $P870^+$ $BPh_A{}^-$, in which an electron has been transferred from the excited special pair to the bacteriopheophytin on the A branch. The A branch bacteriopheophytin is implicated largely by the spectra in the Q_x region. The two bacteriopheophytin molecules have slightly different spectral signatures, owing to differences in the amino acid polarities in their immediate environments.

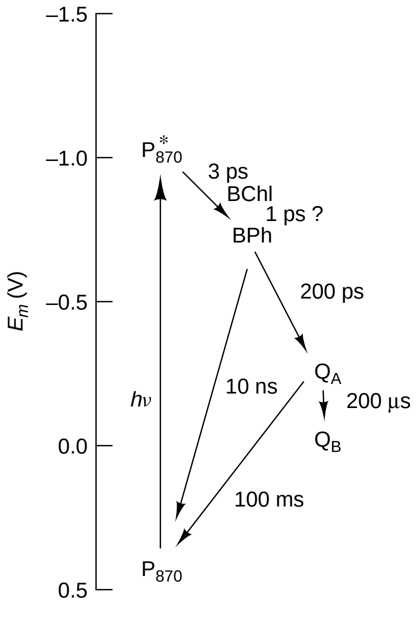

Figure 12 Energy-kinetic diagram for electron transfer in purple bacterial reaction centers at room temperature. Numbers given are typical for several species of purple bacteria

The $P870^+$ $BPh_A{}^-$ ion pair state decays in 200–300 ps to form the $P870^+$ $Q_A{}^-$ state. The electron is then transferred to Q_B in 100–200 µs finally to form the state $P870^+$ $Q_B{}^-$. The $Q_A{}^- \rightarrow Q_B{}^-$ reaction is thermally activated, while all the others are nearly independent of temperature, actually speeding up slightly at cryogenic temperatures. The implications of this are discussed in the next section.

The arrangement of cofactors shown in Figure 11 suggests that an earlier charge-separated state may precede the $P870^+$ $Bph_A{}^-$ state, namely $P870^+$ $BChl_A{}^-$, where $BChl_A$ is the accessory bacteriochlorophyll labeled B_A. This state is generally considered to be involved in the primary electron transfer process, although the nature of its involvement has been a matter of intense debate.[67–69] The data clearly indicate that the rate constant for its decay is faster than that of its formation, thereby precluding buildup of substantial amounts of the state. The energy of the $P870^+$ $BChl_A{}^-$ state is close to that of P870*. The distances and calculated electronic couplings between the special pair and BPh_A are sufficiently long and weak, respectively, that it is extremely unlikely for the electron transfer process to take place directly from P870* to BPh_A. Electrochromic effects of the newly created charges on the electronic properties of the nearby pigments further complicate the picture.

Perhaps the most striking aspect of the comparison of the structural and kinetic data on reaction centers is the apparent two-fold symmetry of the structure, contrasted with the clear evidence for asymmetry in the electron transfer pathway. Estimates of the branch ratio for electron transfer down the A branch in Figure 11, compared to the B branch are as high as 200:1.[70] A considerable effort, including analysis of many site-directed mutants, has gone into trying to understand the factors that facilitate electron transfer down the A branch instead of the B branch. Surprisingly, excitation with blue light causes a significant fraction of B side electron transfer.

Another interesting feature of the electron transfer times shown in Figure 12 is that the rates of recombination processes, in which the electron simply returns from one of the acceptors directly to the oxidized special pair, are invariably a factor of fifty or more slower than are the rate constants for the forward reaction. It is because of this kinetic control of the rates of wasteful processes that the quantum yield for photochemistry is so high. One of the major factors thought to be involved in the slow recombination rates is the large energy gap involved. This is best understood by considering some theoretical aspects of biological electron transfer reactions.

5.2 Theoretical Analysis of Electron Transfer Reactions (*see Long-range Electron Transfer in Biology*)[71–73]

Biological electron transfer reactions have been the subject of a great deal of both experimental and theoretical analysis in a wide range of systems. Of these systems, the bacterial photosynthetic reaction center is attractive, because it exhibits in a single complex a number of unusual features, including the ability to follow the reactions from liquid helium temperatures to above room temperature, and the ability to modify the free energy of the process by chemical, genetic and electrical methods. The structure of the complex is known at high resolution, diffusion processes are not involved, and a wealth of kinetic and other spectroscopic data are available. No other biological system possesses all these features.

The theoretical description of biological electron transfer has grown out of the pioneering work of Marcus on inorganic reactions in solution. The electron transfer process can be viewed as a nonradiative relaxation process from an initial state with the electron donor (D) reduced and the acceptor (A) oxidized to a final state with the donor oxidized and the acceptor reduced, according to equation (10).

$$D_{\mathrm{red}} + A_{\mathrm{ox}} \longrightarrow D_{\mathrm{ox}} + A_{\mathrm{red}} \qquad (10)$$

The Fermi Golden rule describes the first-order rate constant for the electron transfer process, according to equation (11), where the summation is over all the vibrational substates of the initial state i, weighted according to their probability P_i, times the square of the electron transfer matrix element in brackets. The delta function ensures conservation of energy, in that only initial and final states of the same energy contribute to the observed rate. This treatment assumes a weak coupling between D and A, also known as the nonadiabatic limit.

$$k_{\mathrm{et}} = \frac{2\pi}{\eta}\sum_i P_i|\rangle\Psi_f|\tilde{V}|\Psi_i\langle|^2\delta(E_f - E_i) \qquad (11)$$

Note that the wave functions for the initial and final states (Ψ_i and Ψ_f include both donor and acceptor. This equation is usually simplified by making the Born-Oppenheimer approximation for the separation of nuclear and electron wave functions, resulting in equation (12), in which $\tilde{V}$ is the electronic matrix element describing the coupling between the electronic state of the reactants with those of the product, and FC is the Franck–Condon factor.

$$k_{\mathrm{et}} = \frac{2\pi}{\eta}\tilde{V}^2 FC \qquad (12)$$

The electronic coupling matrix element experimentally depends primarily on the distance and orientation of the reacting species. A variety of evidence indicates that this parameter depends exponentially on the distance between the reacting groups. The Franck–Condon factor depends on the overlap of the nuclear wave functions of the initial and final states, suitably weighted by the Boltzmann factor. This term includes effects of temperature and the free energy change of the reaction. Another parameter important to describe the electron transfer process is the reorganization energy λ, which can be considered to be the amount of energy required to distort the geometry of the reactants into that of the products without the electron transfer actually taking place. Three general regimes can be considered for the free energy dependence of the electron transfer rate constant, diagrammed schematically in Figure 13.[72]

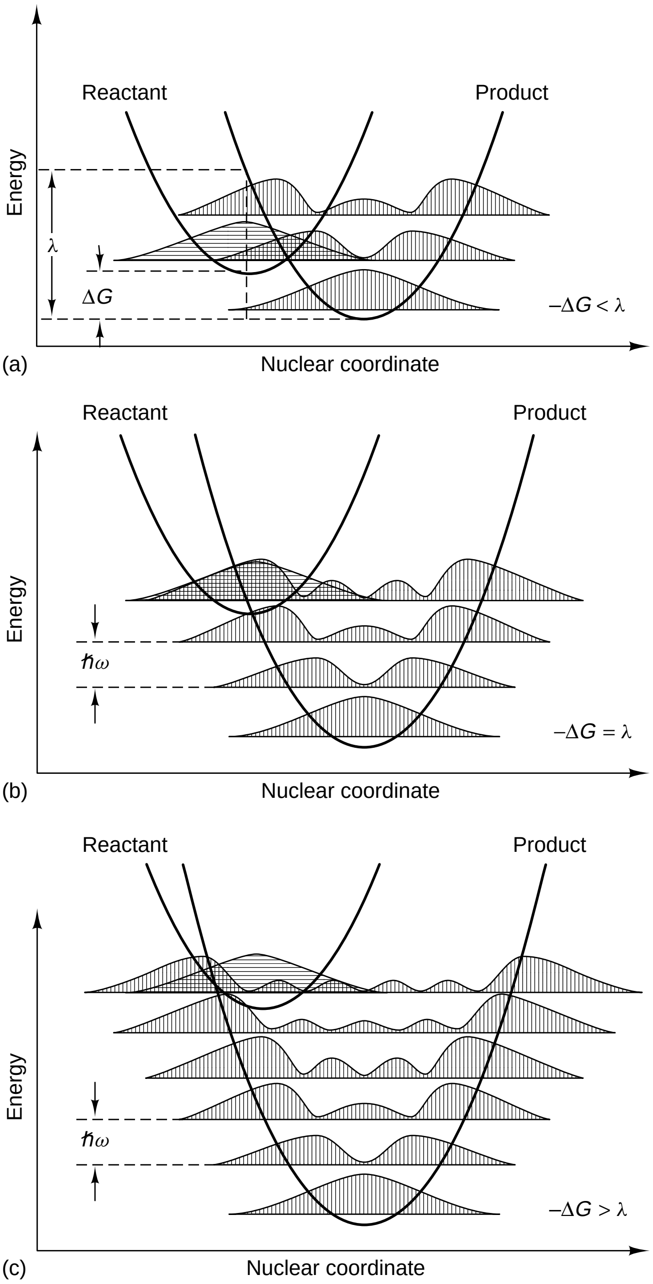

Figure 13 Potential energy surfaces for electron transfer reactions. Harmonic oscillator potential energy functions for reactants and product are shown, including the nuclear wave functions, which are shaded. The dark shaded region indicates the magnitude of overlap of the nuclear wave functions, which is the Franck–Condon factor. (a) is the ‘‘normal’’ region, (b) is the ‘‘activationless’’ region and (c) is the ‘‘inverted’’ region as defined in the text. (Ref. 72. Reproduced by permission of Nature Publishing Group. www.nature.com)

If $-\Delta G^{o} < \lambda$, the process exhibits normal activated behavior, illustrated by Figure 13(a). This is the case for endergonic to slightly exergonic reactions. If the reaction is significantly exergonic, so that $-\Delta G^{o} = \lambda$ then the potential energy curves for the reactants and products intersect near the bottom of the reactant potential well, and the reaction is in the ''activationless'' regime (Figure 13b). The Franck–Condon factor is at a maximum and the reaction is extremely fast with a very weak temperature dependence. Finally, for extremely exergonic reactions with $-\Delta G^{o} > \lambda$, the system is in the ''inverted'' regime, and the Franck–Condon factor and therefore the rate decreases again (Figure 13c).

The Marcus inverted region has been invoked as a major reason that the recombination reactions from the early charge-separated states in photosynthetic reaction centers are so slow compared to the forward reaction at the same point (Figure 11). This may indeed be the case, although many other factors are involved that have not been considered in this brief and oversimplified discussion. Readers should consult specialist reviews for more in-depth consideration of these issues.

5.3 Role of the Fe and Pathways of Proton Uptake

The nonheme Fe in the reaction center is centrally positioned between the two quinone molecules. It has a distorted octahedral geometry with four histidine nitrogen ligands and two oxygen ligands from a glutamic acid (Figure 14).**[1]** The Fe is low-spin Fe^{2+}, and exhibits no EPR spectrum unless one of the quinones is in the semiquinone state. Under these conditions, the Fe^{2+} and Q^{-} antiferromagnetically couple to give rise to a very broad EPR signal centered at $g = 1.8$. The magnetic and electronic properties of this Fe–quinone complex have been analyzed in detail by Feher and coworkers.**[74]**

The position of the Fe^{2+} between the two quinones has prompted suggestions that it may be directly involved in the electron transfer between the two quinones, or that the unpaired spins may somehow affect the electron transfer process. However, neither of these appear to be the case. Complexes in which the diamagnetic ion Zn^{2+} has been substituted for Fe^{2+} are essentially indistinguishable from the native complex in terms of electron transfer properties.**[75]** In addition, metal-free complexes still carry out the $Q_A{}^{-} \rightarrow Q_B$ reaction at nearly normal rates. In these latter complexes, the quantum yield of the formation of the $Q_A{}^{-}$ state is reduced by approximately half, however.**[76]** It may be that the Fe^{2+} serves mainly a structural role to hold the two halves of the complex, as it is one of the few groups to be coordinated to both the L and M subunits.

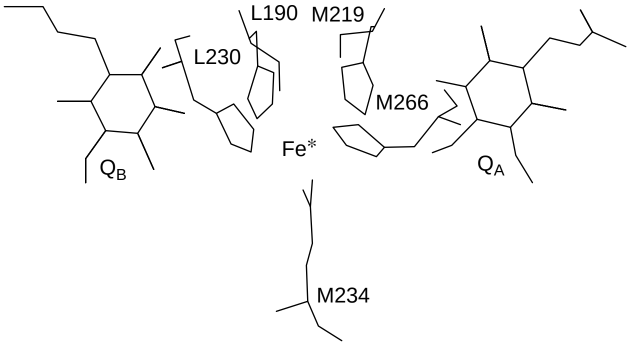

Figure 14 Structure of the photosynthetic reaction center from *Rhodobacter sphaeroides* in the region of the Fe^{2+} and quinones. The residue numbers refer to the L and M subunits of the reaction center

The photochemistry of the reaction center takes place one electron at a time. However, one of the products of the electron transfer process is a reduced ubiquinone, which has taken up two electrons as well as two protons. To form this species, the reaction center must turn over twice, with electrons entering the complex by donation of cytochrome c_2 with the oxidized special pair. The electrons accumulate in the quinone acceptors and protons are taken up from the surrounding medium. Finally, a fully reduced ubiquinol is formed, which is released from the complex into the hydrocarbon portion of the membrane. The quinol is subsequently reoxidized at the cytochrome bc_1 complex (described below).

A pathway of protonatable residues connects the Q_B binding site with the aqueous cytoplasmic compartment. The particular residues involved in the proton transport pathway have been identified in large part using site-directed mutants. Figure 15 shows the proposed pathway of H^{+} transfer in *Rhodobacter sphaeroides*.**[77]**

6 PHOTOSYSTEM I AND PHOTOSYSTEM II FROM OXYGEN-EVOLVING ORGANISMS

Only the cyanobacteria and prochlorophytes are capable of oxygenic photosynthesis. All other photosynthetic bacteria are anoxygenic. The oxygenic photosynthesis performed by algae and higher plants is essentially done by a endosymbiotic cyanobacteria. The membrane-bound proteins that perform photosynthesis are termed photosynthetic systems (or photosystems, (PS)). These photosystems are divided into groups depending upon their terminal electron acceptors. Type I reaction center (RC) complexes have high-potential Fe_4S_4– clusters as their terminal electron acceptors. This type includes PSs from anoxygenic heliobacter and green sulfur bacteria, as well as the PSI component of the oxygenic PS. Type II RCs have a quinone-type terminal electron acceptor. This type includes the RCs of green filamentous bacteria, purple bacteria, and the PSII component of oxygenic PS. All anoxygenic bacteria possess only one of either of these two types of RC, but oxygenic organisms use both PSI and PSII in concert and interdependently.

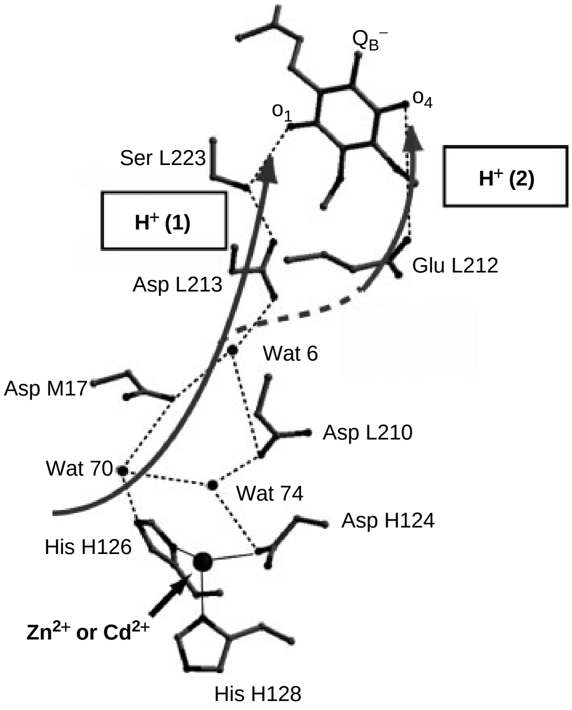

Figure 15 Pathway of H^+ uptake in *Rhodobacter sphaeroides*. The solid line is the pathway for the first H^+ to bind Q_B; the dashed line is the pathway to protonate the other oxygen by the second H^+. Binding of metal ions at the site indicated blocks proton transfer. (Reprinted from Okamura *et al*., *Biochim. et Biophys. Acta*, 2000, **1458**, 148. © 2000, with permission from Elsevier)

Type I and Type II RCs are related in sequence and structure, and they both possess a core (or internal) antenna system. One major difference between Type I and II RCs is that in Type II RCs the antenna proteins are separate peptide sequences, whereas in the Type I RCs the antenna peptide is fused to the core protein

All photosynthetic organisms that produce O_2 contain two photosystems connected in series, as shown in Figure 16. Four main protein complexes are embedded in the membrane, Photosystems I and II, the cytochrome b_6f complex and the ATP synthase or coupling factor. The two photosystems are entirely distinct entities, with different pigment and protein compositions and different genes coding for the proteins. All four of these complexes have been purified, extensively studied, and crystallized (see more below).

6.1 Structure and Mechanism of PSI[78,79]

In contrast to Photosystem II, which operates in a highly oxidizing regime, Photosystem I is much more reducing. The redox potentials of the early electron acceptors in Photosystem I are approximately −1 V, with the excited state of the photoactive chlorophyll P700, estimated to be −1.26 V (Table 3).

The crystal structure of photosystem I from the thermophilic cyanobacterium *Synechococcus elongatus* was published in June of 2001.[79] A cartoon diagram of PSI is shown in Figure 17(a). It was shown to be comprised of 12 protein subunits containing 127 cofactors comprising 96 chlorophylls, 2 phylloquinones, 3 Fe_4S_4 clusters, 22 carotenoids, 4 lipids, a putative Ca^{2+} ion and 201 water molecules. The crystal structure revealed PSI to be a trimer of multimers arranged in a cloverleaf pattern with a C3 axis of symmetry perpendicular to the membrane plane. PSI is comprised of nine protein subunits with transmembrane α-helices (PsaA, PsaB, PsaF, PsaI, PsaJ, PsaK, PsaL, PsaM and PsaX). On the stromal side are three subunits (PsaC, PsaD, PsaE). The core proteins PsaA and PsaB share sequence similarity to each other and to D1 and D2 proteins of PSII. The lumenal side of the PS is comprised largely of loops connecting the transmembrane helices, however there is a hollow near the center of the complex on the lumenal side that is believed to be the docking site for the electron carriers cytochrome c_6 and plastocyanin.

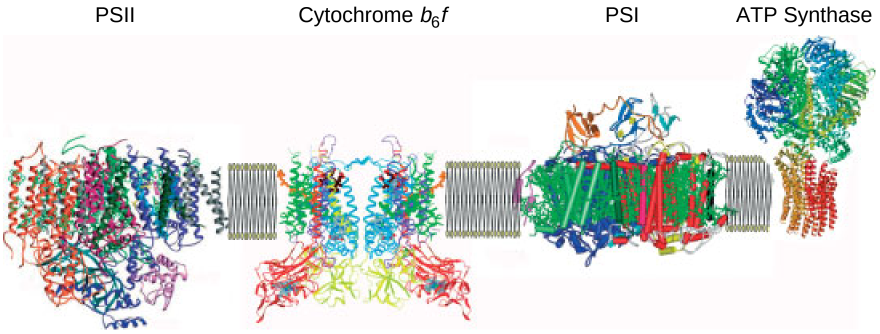

Figure 16 Membrane organization in oxygen-evolving photosynthetic systems. The four main complexes present in the membrane are (from left to right) Photosystem II, the Cytochrome b_6f complex, Photosystem I, and ATP synthase. All complexes now have published crystal structures, ribbon diagrams of which are shown in the Figure. Coordinates taken from the Protein Data Bank and visualized using Accelrys DSViewer Pro, or 2-D pictures were taken from the PDB website and modified

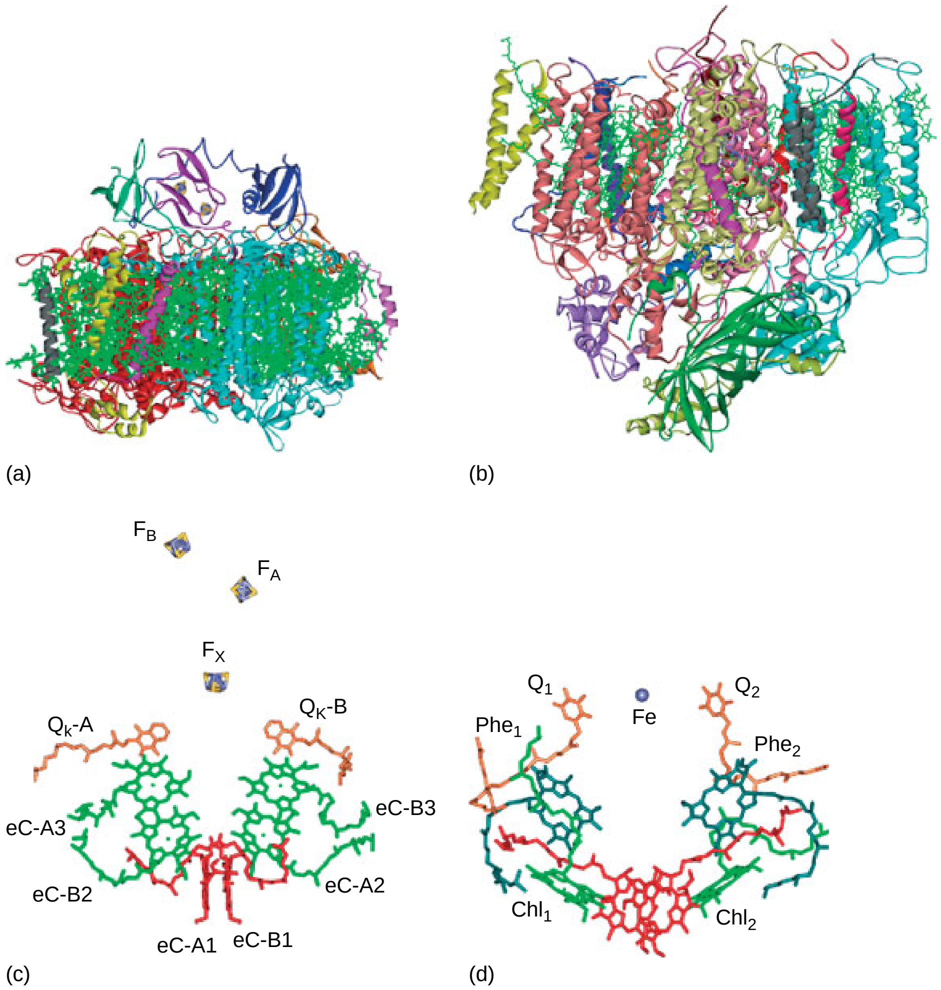

Figure 17 Crystal structures for (a) Photosystem I and (b) Photosystem II (code 1JB0 for PSI from the cyanobacterium *Thermosynechococcus elongatus*, and code 1S5L for PSII from *T. elongates*, respectively). Upper panel: Side views of the pigment-protein complexes in the reaction centers. Lower panel: cofactors of electron transfer in the reaction centers. Both models are shown at the same scale. A. For Photosystem I, PsaE is shown in green, PsaC in dark purple, PsaD in dark blue, PsaA in teal, PsaB in red. Other colored helices are from PsaK, M, F, J, L, and I. B. For Photosystem II, D1 and D2 are the core proteins of the Photosystem II reaction center. CP43 and CP47 are membrane-bound antenna complexes, MSP (dark green) is the ''Manganese Stabilizing Protein.'' C and D. Redox cofactors of electron transfer in two types of the photosynthetic reaction centers (c) The iron-sulfur (type I) RC. Two branches of potential electron carriers in the PSI include eC-A1-eC-B1, primary donor P700 (red); eC-A2 (eC-B2), accessory Chls; eC-A3 (eC-B3), primary acceptor A_0 and its symmetric counterpart; Q_K-A (Q_K-B), phylloquinones (secondary acceptors); F_x, F_A, F_B, iron-sulfur clusters (d) The two branches of the potential electron carriers in PSII. The branches include the primary donor P680 (red), accessory chlorophylls Chl_1 and Chl_2 (green), secondary acceptors pheophytin Phe_1 and Phe_2, and the quinones Q_1 and Q_2. The manganese cluster of the water-splitting protein is not shown. The coordinates were obtained from the Protein Data Bank and visualized using Accelrys DSViewer Pro

On the lumenal side, PsaC is shown to contain the two iron-sulfur clusters F_A and F_B. It also contains a putative binding site loop for interactions with ferredoxin or flavodoxin (the terminal electron acceptors). PsaD is primarily used for the proper positioning of the iron-sulfur clusters of PsaC with respect to F_x, as electrons must pass through F_x to F_A and then to F_B.

The electron transfer chain of PSI is shown in Figure 17(c). The primary electron transfer chain of PSI is split into two branches, as it is in PSII. The A branch contains the chlorophylls eC-A1, eC-B2, eC-A3 and phylloquinone QK-A, and the B branch contains chlorophylls eC-B1, eC-A2, eC-B3 and phylloquinone QK-B. There is a pair of chlorophylls (eC-A1 and eC-B1) that are parallel at a 3.6 Å interplanar distance and with a partial overlap of the chlorin rings. The Mg1-Mg2 distance is 6.3 Å. These two chlorophylls make up P700, the primary electron donor. Unlike the PbRCs, the pair of chlorophylls is not homodimeric. In RCI, eC-B2 is a chlorophyll *a*, but eC-A1 is a chlorophyll *a*', the $C13^2$ epimer of chlorophyll *a*. The asymmetry in P700 extends to the immediate binding pocket of the two chlorophylls, with eC-A1 being hydrogen bonded through water molecules to transmembrane helices while eC-B1 has no hydrogen bonds. Hydrogen bonds generally increase the redox potential of the redox-active species the hydrogen bond contacts, therefore the $P700^+$ should be largely localized on the nonhydrogen bonded eC-B1. This has been confirmed to be true by ENDOR experiments.[80]

Before discussing the subject of which pathway the ejected electron from $P700^+$ follows, the general arrangement of the components of the pathway will be further discussed. The next pair of chlorophyll molecules in the pathway are labelled eC-A2 and eC-B2, although eC-B2 is closer to eC-A1, and eC-A2 is closer to eC-B1. Following these chlorophylls, are eC-A3 and Q_K-A in the eC-A1 pathway, and eC-B3 and Q_K-B in the eC-B1 pathway. One or both of the chlorophylls eC-A3 or eC-B3 may be the electron acceptor termed A_0 determined from picosecond transient absorption and ESR measurements. One or both of the phylloquinones (Q_K-A and Q_K-B) may represent the electron acceptor A_1 determined from nanosecond transient absorption spectroscopy. Following the phylloquinones, any electron travelling in either pathway must pass through the single Fe_4S_4 cluster F_x. From there, the electron passes through F_A to F_B and out of the RC to ferredoxin or flavodoxin.

At one time it was controversial as to whether both pathways of PSI were active. Subsequently, kinetic investigations have shown that the two sides of the pathway are active, but it was demonstrated that the rate of electron transfer from each pylloquinone to F_x was different ($35 \times 10^6 s^{-1}$ and $4.4 \times 10^6 s^{-1}$), but substantial. Mutational studies have shown the A branch is the slower one.[81–84] The asymmetry between the two pathways appears to be larger in cyanobacteria than in higher plant PSI.

PSI collects its energy through internal-antenna proteins, but ones that are fused with the core proteins, unlike those found in PSII. The N-terminal halves of PsaA and PsaB are similar to the PSII internal-antenna proteins CP43 and CP47. However, unlike in PSII there are a huge number of chlorophyll residues present in PSI. 90 Chl *a* and 22 carotenoid bind to the internal-antenna system of PSI, with 79 alone binding to PsaA and PsaB. The arrangement of the chlorophyll *a* molecules is generally like that found in PSII, in that they are stacked in two layers, one near the stromal side of the membrane and the other to the lumen side. The C-terminal domains of PsaA and PsaB cannot, unlike D1 and D2 of PSII, be considered pure RC domains, but rather RC/antenna hybrid domains.

The three Fe–S clusters have been studied extensively by EPR.[85,86] F_A has *g* values of 2.05, 1.94 and 1.86, F_B has values of 2.07, 1.92 and 1.89, and F_X2.04, 1.88 and 1.78. If both F_A and F_B are reduced at the same time, the clusters interact to give a composite spectrum with resonances at 2.05, 1.94, 1.92 and 1.89. When the electron transfer is interrupted, the recombination is from an earlier acceptor and is almost always faster than when a later acceptor is reduced.

6.2 Structure and Mechanism of Photosystem II[87–90]

Photosystem II is unique among photosynthetic reaction centers in that it has the capability to oxidize H_2O to O_2. This difficult chemistry is carried out in a Mn-containing complex, which accumulates four oxidizing equivalents from four photochemical turnovers of the photoactive pigments. The oxygen evolution system is described in detail in ***Manganese: The Oxygen-evolving Complex & Models***, so is not considered here. The redox potential of the oxidized reaction center photoactive pigment, $P680^+$, is not known precisely, but has been estimated to be approximately +1.1 V (Figure 6 and Table 3). These reaction centers are considerably more complicated than those found in purple bacteria, and include nearly two dozen distinct proteins, some of which are integral to the membrane, while others are associated on one side or the other of the membrane.

The 3.8 Å resolution X-ray crystal structure of Photosystem II from the thermophilic cyanobacterium *Thermosynechococcus elongatus* (formerly *Synechococcus elongatus*) was published in February 2001,[87] additional structures at higher resolution and with better crystallographic parameters were later published.[90] The most recent PSII structure is shown in Figure 17(b).

The crystals of PSII used were able to perform water oxidation, so it is assumed that the PSII was in the active and correct form. PSII from *Se* is comprised of 36 transmembrane helices, with 22 of them assigned to the PSII proteins CP47, CP43, D1 and D2. The remaining come from the low-molecular-mass subunits, which include the α and β subunits of cytochrome *b*-559. Extrinsic proteins evident in the crystal structure but not well defined were the 33 kDa protein and cytochrome *c*-550. The arrangement of the α helices D1 and D2 in PSII from *Se* resembles that of subunits L and M in the published structure of the purple bacterial reaction center and the five carboxy-terminal helices of PsaA and PsaB from photosystem I (PSI). CP47 and CP43 consist of six transmembrane α-helices arranged in trimers of dimers. They are structurally similar to the six amino-terminal transmembrane portions of PsaA an PsaB. D1 and D2 form a dimer at the reaction center core. The oxygen-evolving complex is bound to D1. CP43 and CP47 are related by pseudo-C2 symmetry and are present on opposite sides of the D1/D2 core. Other subunits present in the structure are largely present for their stabilizing effects and include the transmembrane α-helical proteins PsbI, PsbX, PsbH, PsbK, PsbL.

The internal-antenna proteins CP43 and CP47 contain 12 and 14 chlorophyll *a*, respectively, which are largely found in two layers near the stromal and lumenal ends of the transmembrane α-helices. Figure 17(d) shows the doubly branching electron transfer pathway of PSII. At the center of the D1/D2 dimeric interface lie two chlorophyll *a* molecules (PD1 and PD2) with Mg-Mg distance of 10 Å, the planes of which are aligned in parallel, with an interplanar distance of 5 Å. These probably represent P680. Since they are relatively far apart, in comparison to PSI or the purple bacteria reaction center, they would not be called a special pair *per se*, and do not have the strongest of excitonic coupling. On either side of this pair and located at distances of 9.8 Å and 10 Å, respectively, from P_{D1} and P_{D2}, are two chlorophyll molecules (Chl_{D1} and Chl_{D2}) that form the first link in the bifurcating electron transfer chain. These are followed by two pheophytin molecules, and then bound quinone molecules (Q_A and Q_B, although in the crystal structure the mobile Q_B site was unoccupied). The Q_A site is occupied by a tightly bound plastoquinone molecule. The role of the nonheme iron molecule present in the structure is probably for stabilization. The nonheme iron perturbs the EPR spectra of $Q_A{}^-$ and $Q_B{}^-$ in a manner very similar to that observed in the bacterial system.

The mechanism of transfer of electrons out of PSII is as follows: ejection of an electron from the excited primary donor P680 produces a cationic radical $P680^+$. The ejected electron passes probably through Chl_{D1}, through pheophytin to the electron acceptor Q_A that is tightly bound at the stromal side of subunit D2, which accumulates two electrons. Four successive light-induced charge separating steps occur on P680, and after each charge separation event, $P680^+$ abstracts an electron from the nearby manganese cluster (described in greater detail in *see* ***Manganese: The Oxygen-evolving Complex & Models***) through the redox-active tyrosine residue labelled TyrZ (Tyr 161 of D1). After two charge separations, the now doubly reduced Q_A doubly reduces the dissociable Q_B bound in its binding site on D1. Q_BH_2 dissociates and drifts off into the membrane plastoquinone pool, to be replaced a new oxidized Q_B.[87,90] The four positive charges accumulated on the manganese cluster are used to oxidize two water molecules, producing O_2 and four H^+.

The similarity between Photosystem II and the purple bacterial reaction center breaks down on the oxidizing or donor side, as the bacterial complex does not evolve oxygen. Another aspect of Photosystem II that is unique among all photosynthetic reaction centers is the involvement of redox-active amino acids in the main path of electron transfer.[91] A tyrosine residue (almost certainly a tyrosinate ion) is the immediate electron donor to $P680^+$, the oxidized photoactive pigment in Photosystem II, donating an electron in tens to hundreds of nanoseconds. The neutral tyrosine radical formed by electron donation to $P680^+$ then extracts an electron from the Mn-containing complex in hundreds of microseconds to milliseconds, depending on how many oxidizing equivalents have previously been accumulated in the Mn complex. This radical species is therefore only observed transiently. A second tyrosine radical is also found in the Photosystem II complex. This radical is stable and is clearly not involved in mainstream electron transfer from H_2O to P680, and its function is not well understood. The tyrosine that gives rise to this radical is in a symmetry-related position to the tyrosine that is active in the normal pathway of electron flow, based on the proposed structures of Photosystem II.

Even though the two photosystems are functionally connected, they are not physically associated, and a variety of evidence indicates that they are predominantly found in different regions of the membrane. Photosystem II is located primarily in the stacked grana regions of the thylakoid membranes (Figure 1), while Photosystem I is found in the unstacked stroma membrane regions and at the edges or margins of the stacks. This places the two photosystems up to several hundred angstroms apart and requires that diffusible electron transfer intermediates couple them together. A large freely diffusible pool of plastoquinone is present within the membrane. Plastoquinone is reduced by Photosystem II and oxidized by the cytochrome b_6f complex, and is clearly involved in the coupling of the two photosystems, although it is probably not the only species involved. Another diffusible species is the blue copper protein plastocyanin,[92–95] which is located in the aqueous space inside the thylakoid membrane. There is evidence that plastocyanin also has substantial lateral mobility, connecting complexes that are physically quite distant. The fact that the two photosystems are spatially separated and that freely diffusible intermediates connect them suggests that there is not a one-to-one coupling of photosystems, in which a particular Photosystem II always reacts with a particular Photosystem I. Instead, reducing equivalents are deposited into a common pool by Photosystem II and withdrawn from the pool by Photosystem I. This arrangement does not require that the stoichiometries of the two photosystems be the same, and indeed the ratio of the abundance of photosystems is somewhat variable, depending on light intensity and light quality, or the spectral distribution of light.

A number of other electron carriers are present in various photosynthetic systems. These include soluble carriers such as the blue copper protein plastocyanin and auracyanin[96–99] (*see* ***Copper Proteins with Type 1 Sites***) and soluble cytochromes and ferredoxins (*see* ***Iron–Sulfur Proteins***), as well as additional membrane-bound complexes. The membrane-bound multisubunit cytochrome b_6f complex is discussed is Section 7.

6.3 Photosystems from Other Organisms

The photosystems found in some types of non-oxygen-evolving bacteria are structurally and functionally analogous to Photosystem I in the same way that the reaction centers from purple bacteria are analogous to Photosystem II.[1,5,67,100–103] These bacterial species include the green sulfur bacteria and the heliobacteria. Study of these systems may help to understand certain aspects of the structure and function of Photosystem I, as well as the evolution of photosynthetic reaction centers. Interestingly, in these systems the reaction center core appears to consist of a homodimeric complex instead of the heterodimeric protein complexes found in all other photosystems.[101,103] This might possibly represent a more primitive arrangement.

7 CYTOCHROME *bc* AND *bf* COMPLEXES

7.1 Structure and Mechanism of the Cytochrome *bc*$_1$ Complex[104–108]

As part of the cyclic electron flow of the photosystems of anoxygenic purple bacteria, cytochrome bc_1 is used. It is also a component of the eukaryotic (mitochondrial), and bacterial respiratory chain. In cyanobacteria and higher plants (chloroplasts), cytochrome bc_1 is replaced in the photosynthetic electron transfer chain with the analogous protein complex, cytochrome b_6f (see later). The cytochrome bc_1 complex is comprised of, minimally, three protein subunits: cytochrome *b*, cytochrome c_1, and a ''Rieske'' iron-sulfur protein (*see* ***Iron–Sulfur Proteins***). Additional subunits are found in some organisms, and in some cases the function of these subunits are not known. A schematic diagram of the catalytic core of the cytochrome bc_1 from bovine heart mitochondria is shown in Figure 18.[1] The structure of the complex from purple bacteria has a similar core structure. The cytochrome b portion of the complex was shown to be an integral membrane protein with 8 transmembrane helices. Cytochrome b binds two heme b cofactors, one near the periplasmic side of the inner membrane and the other near the cytoplasmic side. The heme near the periplasmic side has a relatively low redox potential of $-100\,\text{mV}$ and is thus termed ''b_L'', whereas the other has a potential of $+50\,\text{mV}$ and is termed ''b_H.'' The main function of cytochrome bc_1 in the cell is to participate in the so-called ''Q-cycle'' (to be described later). Within cytochrome *b* are two binding sites for ubiquinone/ubiquinol. The site of quinol oxidation is near b_L and is labelled Q_o, while the other binding site is that of quinone reduction, and is near b_H. It is labelled the Q_i site (for ''internal''). On the periplasmic side of the membrane, and anchored by a single N-terminal transmembrane α-helix, is the Rieske Iron-Sulfur Protein (ISP). A flexible loop connects the transmembrane helix of ISP to the periplasmic domain. Within the periplasmic domain is a single uniquely liganded Fe_2S_2 cluster. The cluster is unusual in that one iron is liganded by histidine residues, while the other is liganded by cysteine residues. Typically Fe_2S_2 clusters are liganded by four cysteine residues. This arrangement makes the histidine-liganded iron much more easily reduced, and localizes the reducing equivalents on that iron when reduced. The result is the raising of the cluster redox potential to $+280\,\text{mV}$, a much higher value than cysteine-only liganded clusters.

Cytochrome bc_1 makes use of a modified Q-cycle, as shown overlaying the schematic in Figure 18. In this scheme, two molecules of ubiquinone are oxidized per one reduced. The net effect is the production of a proton gradient across the inner membrane. The reaction mechanism of this is described as follows:

(1) One ubiquinol molecule binds to the Q_o site and an electron is transferred to the nearby Rieske ISP, while a proton is released to the periplasm.

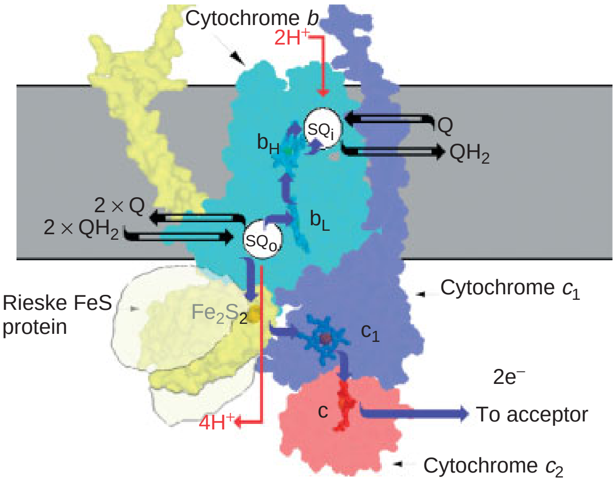

Figure 18 Schematic structure of the cytochrome bc_1 complex from mitochondria. The structure of the complex from purple photosynthetic bacteria is thought to be similar. The pathway of electron and proton transfer (modified Q-cycle) is overlaid on the schematic structure. Movement of the Rieske FeS protein is shown by the semitransparent yellow areas[1]

(2) The electron from the resultant ubisemiquinone is released to b_L, with the concurrent release of another proton to the periplasm. The electron is then transferred to b_H.

(3) There is a large movement of the Rieske ISP towards the cytochrome c_1, such that the Fe_2S_2 cluster is moved 20 Å closer to the heme cofactor.

(4) A ubiquinone molecule binds to site Q_i and is reduced to the semiubiquinone state by the now reduced b_H.

(5) The now oxidized ubiquinone at the Q_o site is released to the intermembrane space.

(6) The movement of the Rieske protein allows for the transfer of one electron to heme c_1, and subsequently to the soluble electron carrier cytochrome c_2, which is docked on the cytochrome c_1.

(7) A new ubiquinol molecule binds to the Q_o site and follows the same oxidation as the first molecule. This also results in two more protons being released to the periplasmic space.

(8) The now reduced b_H reduces the ubisemiquinone at the Q_i site, and two protons are taken up to produce a ubiquinol on the cytoplasmic side. There is thus a net uptake of two protons from the cytoplasm, and a net release of four protons to the periplasm, resulting in an overall net pumping of two protons from the cytoplasm to the periplasm. This results in a proton gradient, a protonmotive force, across the inner membrane, which is utilized by ATPase to synthesize ATP from ADP.

The hinge action of the Rieske ISP serves as a gating mechanism, preventing the double transfer of electrons through cytochrome c_1 to cytochrome c_2, which would short circuit the whole process described above (resulting in no net protonmotive force being established).[1]

7.2 Structure and Mechanism of Cytochrome b_6f [109–112]

Cytochrome b_6f is used in place of cytochrome bc_1 in cyanobacteria and chloroplasts. Light energy utilized by PSII results in plastoquinol production from plastoquinone. Reducing equivalents carried by the plastoquinol are then transferred across b_6f, through cytochromes bound to b_6f, to plastocyanin or cytochrome c_6. Reduced plastocyanin or cytochrome c_6 is then used to rereduce PSI. The crystal structure of cytochrome b_6f at 3.0 Å resolution is shown in Figure 19. Cytochrome b_6f is a dimer of multimers. Cytochrome b_6f contains four large subunits. Cytochrome b_6 is a transmembrane helical protein that binds two cytochrome b hemes. It is homologous to the N-terminal domain of cytochrome b of the cytochrome bc_1 complex. The Rieske Iron-Sulfur Protein is similar to that found in cytochrome bc_1, with a helical tether connected through a flexible loop to a lumen domain. The helical tether of one multimer extends into the other multimer, serving to unify the complex. It contains a Fe_2S_2 cluster that is liganded with two cysteines and two histidines. Subunit IV is also a transmembrane helical protein, and is homologous to the C-terminal domain of cytochrome b of the cytochrome bc_1 complex. Cytochrome f is analogous to cytochrome c_1 of cytochrome bc_1, but is unrelated by

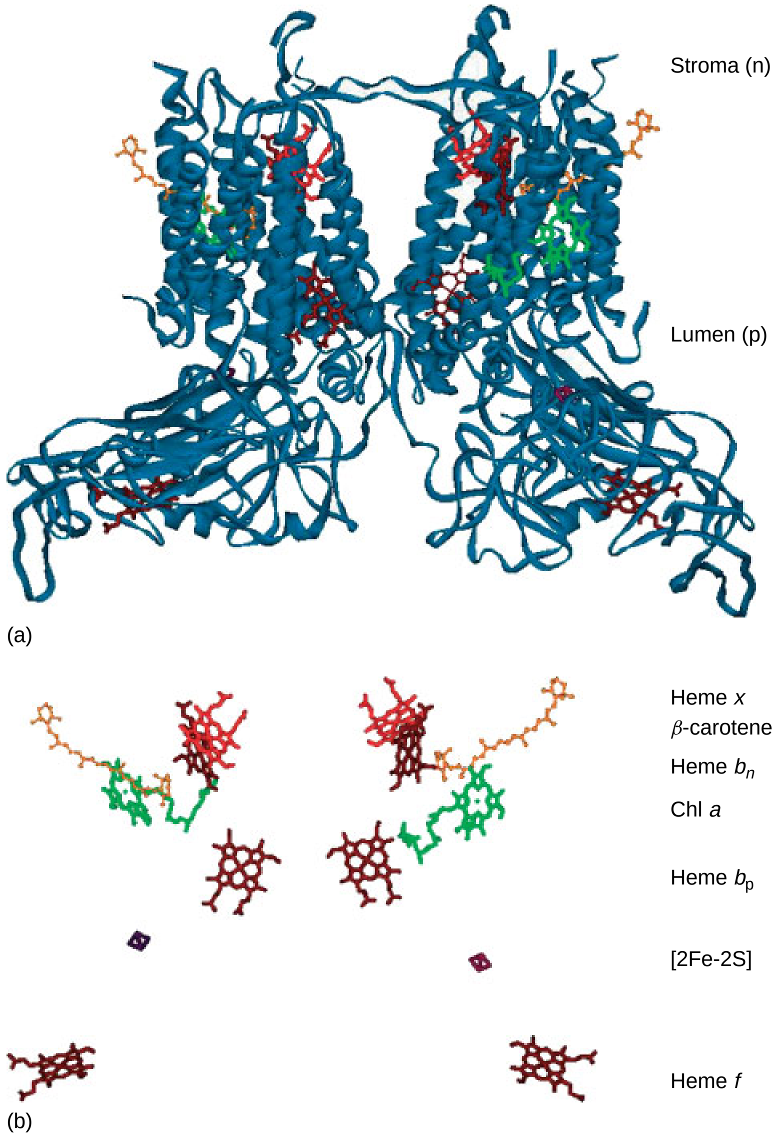

Figure 19 (a) Crystal structure of the cytochrome b_6f complex from *Mastigocladus laminosus* at 3.0 Å resolution. The coordinates were obtained from the Protein Data Bank and visualized using accelrys DSViewer Pro. (b) The electron and proton transfer chain of cytochrome b_6f with the protein stripped away

homology or structure. The heme of cytochrome f maps to 12 Å different position versus the heme of cytochrome c_1, both relative to the heme b position. Cytochrome f has two extrinsic domains. A large domain has a position analogous to the bc_1 extrinsic cytochrome c_1 domain. The small domain of cytochrome f maps to a position occupied by subunit 8 in bc_1. Cytochrome f also does not have the intermonomer contacts that cytochrome c_1 has. There are also four small transmembrane helical subunits (PetG, PetL, PetM, and PetN), which serve to stabilize the complex and generally form a ring around the inner subunits.[109]

Some of the structural elements of the cofactors are described below. A chlorophyll a molecule is bound between helices F and G of subunit IV with no direct protein-Mg bonds. The function of this chlorophyll is not known. The 9-cis-β-carotene is inserted near the center of transmembrane region between PetL and PetM. It is 14 Å from chlorophyll a, and thus cannot be there to quench the chlorophyll excited triplet state. The roles of these two elements are uncertain. As shown in Figure 19(b), two hemes (b_n and b_p, near the stromal and lumen sides of the membrane, respectively) are bound in cytochrome b_6. These are both bis-histidine liganded and are in analogous positions to heme b_L and b_H of the cytochrome bc_1 complex. One major surprise in the crystal structure is the presence of a hitherto unknown and unreported heme. This heme is not, based upon density maps, a member of any known heme family, and it is thus termed ‘‘heme x.’’ The heme is covalently linked through a thioether bond to cysteine 35, but there are no protein ligands to the iron. Rather, the iron is liganded to a water molecule that is hydrogen bonded to the propionate side chain of heme b_n and to the backbone amide of invarient Gly38 of cytochrome b_6. It is thought that heme x is a universal feature of cytochrome b_6f from other organisms because many residues in the binding pocket (both from subunit IV and cytochrome b_6) are invariant amongst different organisms based upon sequence comparisons. That the heme x and heme b_n are perpendicular to each other and in contact implies that electron flow through heme x is important. Heme x is located at the same position as the n-side ubiquinone and antimycin A binding site in the bc_1 complex. This is then why no inhibitors of n-side electron transfer in the cytochrome b_6f complex have been identified that are similar to antimycin. However, the exact role of heme x is unclear.[109]

In the crystal structure, an endogenous plastoquinone is found bound at the n side of each central cavity adjacent to heme x, clearly identifying it as the Q_n site. The Q_p site is inferred from structural elements and because in some crystals a quinone mimick is bound at the roof of the central cavity at the putative Q_p site. The mechanism of quinone oxidation and reduction is generally similar to that of cytochrome bc_1 (see above). As in cytochrome bc_1, it is probably necessary for the Rieske ISP lumen domain to rotate back and forth during turnover to gate electron flow.

As for the mechanism of the Q-cycle, the overall stoichiometry of protons translocated across the membrane to electrons is 2:1, rather than the 1:1 that would be predicted by a simple mechanism in which the quinone was reduced on one side of the membrane, picking up protons from the aqueous environment and then oxidized near the other side of the membrane, liberating the protons to the aqueous phase on the other side. A variety of evidence indicates that the two electrons that come from oxidation of a quinol do not follow the same pathway. One reduces the Rieske protein and then is transferred to cytochrome c_1, next to cytochrome c_2, and eventually rereduces the oxidized reaction center special pair. The other electron reduces the lower potential heme b, then the higher potential heme b. After two quinol oxidations, the electrons that went through the hemes b reduce an oxidized quinone at the quinone reducing site, in the process picking up two additional protons on the cytoplasmic side of the membrane. The net reaction is that for every two electrons that go through the Rieske protein branch, two quinols are oxidized and one is reduced. In the process, four protons are liberated to the periplasmic side of the membrane. The energy generated by the proton gradient, as well as an electrical potential gradient created by the electrogenic electron flow across the membrane through the b hemes, is then utilized to make ATP. This is thought to take place by a chemiosmotic mechanism, first proposed by Mitchell.

8 RELATED ARTICLES

Copper Proteins with Type 1 Sites; Iron: Heme Proteins & Electron Transport; Long-range Electron Transfer in Biology; Manganese: The Oxygen-evolving Complex & Models.

9 REFERENCES

1. R. E. Blankenship, ‘Molecular mechanisms of photosynthesis’, Blackwell Science, Oxford, 2002.
2. B. Ke, ‘Photosynthesis Photobiochemistry and Photobiophysics’, Kluwer Academic Publishers, Dordrecht, 2001.
3. H. Scheer ed., ‘Chlorophylls’, CRC Press, Boca Raton, FL, 1991.
4. ‘Light-Harvesting Antennas in Photosynthesis’, Klewer Academic Publishers, Dordrecht, 2003.
5. R. E. Blankenship, *Photosynth. Res.*, 1992, **33**, 91.
6. C. R. Woese, *Microbiol. Rev.*, 1987, **51**, 221.
7. B. W. Edmonds and H. Luecke, *Frontiers Biosci.*, 2004, **9**, 1556.
8. J. D. Palmer and C. F. Delwiche, *Proc. Natl. Acad. Sci. U.S.A.*, 1996, **93**, 7432.

9. S. Douglas, S. Zauner, M. Fraunholz, M. Beaton, S. Penny, L. T. Deng, X. Wu, M. Reith, T. Cavalier-Smith, and U. G. Maier, *Nature*, 2001, **410**, 1091.
10. S. E. Douglas, C. A. Murphy, D. F. Spencer, and M. W. Gray, *Nature*, 1991, **350**, 148.
11. J. Raymond, O. Zhaxybayeva, J. P. Gogarten, S. Y. Gerdes, and R. E. Blankenship, *Science*, 2002, **298**, 1616.
12. S. Hart, Photosynthesis in the Abyss in 2003.
13. M. Gouterman, in 'The Porphyrins', ed. D. Dolphin, Academic Press, New York, 1978, p. 1.
14. J. Linnanto and J. Korppi-Tommola, *Phys. Chem. Chem. Phys.*, 2000, **2**, 4962.
15. J. Crystal and R. A. Friesner, *J. Phys. Chem. A.*, 2000, **104**, 2362.
16. A. J. Hoff and J. Amesz, in 'Chlorophylls', ed. H. Scheer, CRC Press, Boca Raton, FL, 1991, p. 723.
17. J. H. Espensen, 'Chemical Kinetics and Reaction Mechanisms', McGraw-Hill, New York, 1981.
18. R. E. Blankenship and R. C. Prince, *Trends Biochem. Sci.*, 1985, **10**, 382.
19. G. R. Seely, *Photochem. Photobiol.*, 1978, **27**, 639.
20. J. R. Bolton, *Science*, 1978, **202**, 705.
21. W. W. Parson, *Photochem. Photobiol.*, 1978, **28**, 389.
22. L. N. Bell and N. D. Gudkov, 'The Photosystems: Structure, Function and Molecular Biology', Elsevier, Amsterdam, 1992.
23. J. R. Bolton, *Annu. Rev. Energ.*, 1979, **4**, 353.
24. D. O. Hall and K. K. Rao, 'Photosynthesis', Cambridge University Press, Cambridge, MA, 1999.
25. H. van Amerongen, L. Valkunas, and R. van Grondelle, 'Photosynthetic Excitons', World Scientific, Singapore, 2000.
26. R. van Grondelle, *Biochim. Biophys. Acta*, 1985, **811**, 147.
27. A. R. Grossman, M. R. Schaefer, G. G. Chiang, and J. L. Collier, *Microbiol. Rev.*, 1993, **57**, 725.
28. W. A. Samsonoff and R. MacColl, *Arch. Microbiol.*, 2001, **176**, 400.
29. A. Ben-Shem, F. Frolow, and N. Nelson, *FEBS Lett.*, 2004, **564**, 274.
30. G. Hauska, T. Schoedl, H. Remigy, and G. Tsiotis, *Biochim. Biophys. Acta*, 2001, **1507**, 260.
31. R. E. Blankenship and K. Matsuura, in 'Light-Harvesting Antennas', eds. B. R. Green, and W. W. Parson, Klewer Academic Publishers, Dordrecht, 2003, p. 195.
32. N. Adir and N. Lerner, *J. Biol. Chem.*, 2003, **278**, 25926.
33. J. Y., Liu, T. Jiang, J. P. Zhang, and D. C. Liang, *J Biol Chem.*, 1999, **274**, 16945.
34. A. K. Padyana, V. B. Bhat, K. M. Madyastha, K. R. Rajashankar, and S. Ramakumar, *Biochem. Biophys. Res. Commun.*, 2001, **282**, 893.
35. N. Adir, R. Vainer, and N. Lerner, *Biochim. Biophys. Acta*, 2002, **1556**, 168.
36. N. Adir, Y. Dobrovetsky, and N. Lerner, *J. Mol. Biol.*, 2001, **313**, 71.
37. B. Stec, R. F. Troxler, and M. M. Teeter, *Biophys. J.*, 1999, **76**, 2912.
38. T. Schirmer, W. Bode, and R. Huber, *J. Mol. Biol.*, 1987, **196**, 677.
39. C. Contreras-Martel, J. Martinez-Oyanedel, M. Bunster, P. Legrand, C. Piras, X. Vernede, and J. C. Fontecilla-Camps, *Acta Crystallogr. D Biol. Crystallogr.*, 2001, **57**, 52.
40. R. Ficner, K. Lobeck, G. Schmidt, and R. Huber, *J. Mol. Biol.*, 1992, **228**, 935.
41. R. Ficner, and R. Huber, *Eur. J. Biochem.*, 1993, **218**, 103.
42. T. Jiang, J. P. Zhang, W. R. Chang, and D. C. Liang, *Biophys. J.*, 2001, **81**, 1171.
43. D. E. Tronrud, M. F. Schmid, and B. W. Matthews, *J. Mol. Biol.*, 1986, **188**, 443.
44. S. Savikhin, D. R. Buck, and W. S. Struve, *J. Phys. Chem. B*, 1998, **102**, 5556.
45. X. Hu, T. Ritz, A. Damjanovic, F. Autenrieth, and K. Schulten, *Q. Rev. Biophys.*, 2002, **35**, 1.
46. R. J. Cogdell, H. W. Isaaks, T. D. Howard, K. McLaskey, N. J. Fraser, and S. M. Prince, *J. Bacteriol.*, 1999, **181**, 3869.
47. R. J. Cogdell, N. W. Isaacs, A. A. Freer, T. D. Howard, A. T. Gardiner, S. M. Prince, and M. Z. Papiz, *FEBS Lett.*, 2003, **555**, 35.
48. J. Koepke, X. Hu, C. Muenke, K. Schulten, and H. Michel, *Structure*, 1996, **4**, 581.
49. D. Leupold, B. Voigt, W. Beenken, and H. Stiel, *FEBS Lett.*, 2000, **480**, 73.
50. A. W. Roszak, T. D. Howard, J. Southall, A. T. Gardiner, C. J. Law, N. W. Isaacs, and R. J. Cogdell, *Science*, 2003, **302**, 1969.
51. T. S. Bibby, J. Nield, M. Chen, A. W. Larkum, and J. Barber, *Proc. Natl. Acad. Sci. U.S.A.*, 2003, **100**, 9050.
52. T. S. Bibby, J. Nield, F. Partensky, and J. Barber, *Nature*, 2001, **413**, 590.
53. E. J. Boekema, A. Hifney, A. E. Yakushevska, M. Piotrowski, W. Keegstra, S. Berry, K. P. Michel, E. K. Pistorius, and J. Kruip, *Nature*, 2001, **412**, 745.
54. J. Nield, E. P. Morris, T. S. Bibby, and J. Barber, *Biochemistry*, 2003, **42**, 3180.
55. E. G. Andrizhiyevskaya, D. Frolov, R. Van Grondelle, and J. P. Dekker, *Biochim. Biophys. Acta*, 2004, **1656**, 104.
56. E. G. Andrizhiyevskaya, T. M. Schwabe, M. Germano, S. D'Haene, J. Kruip, R. van Grondelle, and J. P. Dekker, *Biochim. Biophys. Acta*, 2002, **1556**, 265.
57. T. S. Bibby, J. Nield, and J. Barber, *J. Biol. Chem.*, 2001, **276**, 43246.
58. J. Nield, C. Funk, and J. Barber, *Philos. Trans. R. Soc. London B. Biol. Sci.*, 2000, **355**, 1337.
59. O. Kruse, *Naturwissenschaften*, 2001, **88**, 284.

60. R. J. Cogdell and A. T. Gardiner, *Microbiol. Today*, 2001, **28**, 120.
61. J. Deisenhofer and H. Michel, *Science*, 1989, **245**, 1463.
62. J. Deisenhofer and H. Michel, *Biosci. Rep.*, 1989, **9**, 383.
63. J. Deisenhofer and H. Michel, *Embo J.*, 1989, **8**, 2149.
64. G. Feher, J. P. Allen, M. Y. Okamura, and D. C. Rees, *Nature*, 1989, **339**, 111.
65. G. Feher, *J. Chem. Soc. Perkin Trans.*, 1992, **2**, 1861.
66. W. Lubitz and G. Feher, *Appl. Magn. Reson.*, 1999, **17**, 1.
67. W. W. Parson, in ‘Chlorophylls’, ed. H. Scheer, CRC Press, Boca Raton, FL, 1991, p. 1153.
68. W. Holzappel, U. Finkele, W. Kaiser, D. Osterhelt, H. Scheer, H. U. Stilz, and W. Zinth, *Proc. Natl. Acad. Sci. U.S.A.*, 1990, **87**, 5168.
69. C. Kirmaier and D. Holten, *Proc. Natl. Acad. Sci. U.S.A.*, 1990, **87**, 3552.
70. E. C. Kellogg, S. Kolaczkowski, M. R. Wasielewski, and D. M. Tiede, *Photosynth. Res.*, 1989, **22**, 47.
71. R. A. Marcus and N. Sutin, *Biochim. Biophys. Acta*, 1985, **811**, 265.
72. C. C. Moser, J. M. Keske, K. Warncke, R. S. Farid, and P. L. Dutton, *Nature*, 1992, **355**, 796.
73. C. C., Moser, C. C. Page, R. J. Cogdell, J. Barber, C. A. Wraight, and P. L. Dutton, *Adv. Protein Chem.*, 2003, **63**, 71.
74. W. E. Butler, R. Calvo, D. R. Fredkin, R. A. Isaacson, M. Y. Okamura, and G. Feher, *Biophys. J.*, 1984, **45**, 947.
75. R. J. Debus, G. Feher, and M. Y. Okamura, *Biochemistry*, 1986, **25**, 2276.
76. C. Kirmaier, D. Holten, R. J. Debus, G. Feher, and M. Y. Okamura, *Proc. Natl. Acad. Sci. U.S.A.*, 1986, **83**, 6407.
77. M. Y. Okamura, and G. Feher, *Annu. Rev. Biochem.*, 1992, **61**, 861.
78. J. M. Anderson, *Photosynth. Res.*, 1992, **34**, 341.
79. P. Jordan, P. Fromme, H. T. Witt, O. Klukas, W. Saenger, and N. Krauss, *Nature*, 2001, **411**, 909.
80. H. Käss, P. Fromme, H. Witt, and W. Lubitz, *J. Phys. Chem. B*, 2001, **105**, 1225.
81. H. Witt, E. Bordignon, D. Carbonera, J. P. Dekker, N. Karapetyan, C. Teutloff, A. Webber, W. Lubitz, and E. Schlodder, *J. Biol. Chem.*, 2003, **278**, 46760.
82. L. Cui, S. E. Bingham, M. Kuhn, H. Kass, W. Lubitz, and A. N. Webber, *Biochemistry*, 1995, **34**, 1549.
83. A. N. Webber, H. Su, S. E. Bingham, H. Kass, L. Krabben, M. Kuhn, R. Jordan, E. Schlodder, and W. Lubitz, *Biochemistry*, 1996, **35**, 12857.
84. H. Ishikita and E. W. Knapp, *J. Biol. Chem.*, 2003.
85. T. Mehari, K. G. Parrett, P. V. Warren, and J. H. Golbeck, *Biochim. Biophys. Acta Bio-Energetics.*, 1991, **1056**, 139.
86. J. H. Golbeck and D. A. Bryant, *Curr. Topics Bioenerget.*, 1991, **16**, 83.
87. A. Zouni, H. T. Witt, J. Kern, P. Fromme, N. Krauss, W. Saenger, and P. Orth, *Nature*, 2001, **409**, 739.
88. A. Zouni, R. Jordan, E. Schlodder, P. Fromme, and H. T. Witt, *Biochim. Biophys. Acta*, 2000, **1457**, 103.
89. K. Ifuku, T. Nakatsu, H. Kato, and F. Sato, *Acta Crystallogr. D. Biol. Crystallogr.*, 2003, **59**, 1462.
90. N. Kamiya and J. R. Shen, *Proc. Natl. Acad. Sci. U.S.A.*, 2003, **100**, 98.
91. G. T. Babcock, B. A. Barry, R. J. Debus, C. W. Hoganson, M. Atamian, L. McIntosh, I. Sithole, and C. F. Yocum, *Biochemistry*, 1989, **28**, 9557.
92. M. R. Redinbo, D. Cascio, M. K. Choukair, D. Rice, S. Merchant, and T. O. Yeates, *Biochemistry*, 1993, **32**, 10560.
93. E. Danielsen, H. V. Scheller, R. Bauer, L. Hemmingsen, M. J. Bjerrum, and O. Hansson, *Biochemistry*, 1999, **38**, 11531.
94. A. Haldrup, H. Naver, and H. V. Scheller, *Plant J.*, 1999, **17**, 689.
95. P. Joliot and A. Joliot, *Proc. Natl. Acad. Sci. U.S.A.*, 2002, **99**, 10209.
96. C. S. Bond, R. E. Blankenship, H. C. Freeman, J. M. Guss, M. J. Maher, F. M. Selvaraj, M. C. Wilce, and K. M. Willingham, *J. Mol. Biol.*, 2001, **306**, 47.
97. M. Lee, M. J. Maher, H. C. Freeman, and J. M. Guss, *Acta Crystallogr. D Biol. Crystallogr.*, 2003, **59**, 1545.
98. J. D. McManus, D. C. Brune, J. Han, J. Sanders-Loehr, T. E. Meyer, M. A. Cusanovich, G. Tollin, and R. E. Blankenship, *J. Biol. Chem.*, 1992, **267**, 6531.
99. G. Van Driessche, W. Hu, G. Van de Werken, F. Selvaraj, J. D. McManus, R. E. Blankenship, and J. J. Van Beeumen, *Protein Sci.*, **8**, 947.
100. R. E. Blankenship, and H. Hartman, *Trends Biochem. Sci.*, 1998, **23**, 94.
101. M. Büttner, D.-L. Xie, H. Nelson, W. Pinther, G. Hauska, and N. Nelson, *Proc. Natl. Acad. Sci. U.S.A.*, 1992, **89**, 8135.
102. W. Nitschke, U. Feiler, and A. W. Rutherford, *Biochemistry.*, 1990, **29**, 3834.
103. U. Liebl, M. Mockensturm-Wilson, J. T. Trost, D. C. Brune, R. E. Blankenship, and W. Vermaas, *Proc. Natl. Acad. Sci. U.S.A.*, 1993, **90**, 7124.
104. E. A. Berry, L. S. Huang, Z. Zhang, and S. H. Kim, *J. Bioenerg. Biomembr.*, 1999, **31**, 177.
105. E. A. Berry, M. Guergova-Kuras, L. S. Huang, and A. R. Crofts, *Annu. Rev. Biochem.*, 2000, **69**, 1005.
106. W. A. Cramer, G. M. Soriano, M. Ponomarev, D. Huang, H. Zhang, S. E. Martinez, and J. L. Smith, *Annu. Rev. Plant Physiol. Plant Mol. Biol.*, 1996, **47**, 477.
107. D. Xia, C. A. Yu, H. Kim, J. Z. Xia, A. M., Kachurin, L. Zhang, L. Yu, and J. Deisenhofer, *Science*, 1997, **277**, 60.
108. Z. Zhang, E. A. Berry, L. S. Huang, and S. H. Kim, *Subcell Biochem.*, 2000, **35**, 541.

109. G. Kurisu, H. Zhang, J. L. Smith, and W. A. Cramer, *Science*, 2003, **302**, 1009.
110. D. Stroebel, Y. Choquet, J. L. Popot, and D. Picot, *Nature*, 2003, **426**, 413.
111. J. Yan and W. A. Cramer, *J. Biol. Chem.*, 2003, **278**, 20925.
112. H. Zhang, and W. A. Cramer, *Methods Mol. Biol.*, 2004, **274**, 67.
113. M. Y. Okamura, M. L. Paddock, M. S. Graige, and G. Feher, *Biochim. Biophys. Acta*, 2000, **1458**, 148.

Acknowledgment

Christopher R. Staples is supported by a grant MCB-0415283 from the US National Science Foundation.

Platinum-based Anticancer Drugs

Marc S. Robillard & Jan Reedijk
Leiden University, Leiden, The Netherlands

Based in part on the article Platinum-based Anticancer Drugs by Steven J. Brown, Christine S. Chow & Stephen J. Lippard which appeared in the Encyclopedia of Inorganic Chemistry, First Edition.

1 Introducing Cisplatin 1
2 Mechanism of Action of Cisplatin 1
3 Problems with Cisplatin 4
4 Cisplatin Derivatives and New Approaches 4
5 Summary and Outlook 10
6 Related Articles 10
7 References 10

1 INTRODUCING CISPLATIN[1]

Cancer is one of the major causes of death in the western world. It refers to approximately 150 diseases that exhibit some common characteristics: an uncontrolled growth of cells and the ability to invade and damage normal tissues either locally, or at distant sites in the body. Nowadays, three classical approaches exist to treat cancer: surgical excision, irradiation, and chemotherapy. The role of each depends on the type of cancer and its development stage.

cis-Diamminedichloroplatinum(II) (**1**, Figure 1), generally referred to as cisplatin, is widely used as a chemotherapeutic agent. Its anticancer properties remained unnoticed until 1964, when Barnett Rosenberg investigated the effects of electric fields on the growth of *Escherichia coli* bacteria. He observed a strong filamentous growth, but an arrest of cell division. Rosenberg and coworkers subsequently found that the electric field was not responsible for the cell division arrest, but that this effect had to be attributed to traces of platinum compounds such as *cis*-$Pt(NH_3)_2Cl_2$ and *cis*-$Pt(NH_3)_2Cl_4$. These compounds were formed by the slow reaction of the platinum electrodes with the electrolyte NH_4Cl solution. Soon a number of compounds were tested, and only the ones having cis geometry were found to block cell growth. The most active complex, cisplatin, was found to have antitumor activity, while its trans isomer (transplatin, **2**) did not show antitumor activity.

After this serendipitous discovery, clinical trials were performed to investigate the efficacy of cisplatin against a variety of solid tumors. Cisplatin entered Phase I clinical trials in 1971, was approved by the U.S. FDA in 1978, and was developed into one of the most widely used drugs in cancer chemotherapy. Cisplatin is especially effective against solid tumor types, such as testicular, ovarian, head and neck, and small-cell lung cancer.[2] For testicular cancer, when recognized in an early stage, curing rates exceed 90%.

2 MECHANISM OF ACTION OF CISPLATIN

2.1 Introduction

The activity of cisplatin is generally accepted to originate from its binding to DNA.[3] Most conclusive evidence for this is the observation that cells deficient in DNA-repair ability are hypersensitive to cisplatin. Cisplatin and other platinum drugs are thus categorized as DNA-binding drugs. A molecule bound to DNA may interfere with transcription and/or DNA replication mechanisms, triggering processes, such as apoptosis, that lead to cell death.

2.2 Cellular Uptake of Cisplatin

Cisplatin is administered by intravenous injection. In blood and extracellular body fluids, the physiological chloride concentration is about 100 mM, which strongly suppresses cisplatin hydrolysis. Thus, cisplatin reaches the outer surface of cancer cells mainly as a neutral molecule. The precise mechanism of cellular uptake of cisplatin remains unclear. However, it is generally believed that passive diffusion is the main mechanism, although some evidence supports the involvement of active transport mechanisms.[4] After entering the cell, the chloride concentration drops to 4 mM and hydrolysis of cisplatin takes place. Although various hydrolysis products may form, the predominant species is the $[PtCl(H_2O)(NH_3)_2]^+$ cation,[5] which is in equilibrium with its deprotonated form $[PtCl(OH)(NH_3)_2]$. Since water is a far better leaving group than hydroxide or chloride, the cationic aqua form is the species that is most likely to react with DNA and other molecules in the cell. Inside the cell, many competitors for DNA binding are present.[6] Alternative targets include phospholipids and phosphatidylserine in the membrane, and RNA and sulfur-containing proteins in the cytosol.

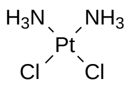

(**1**)

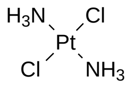

(**2**)

Figure 1 Structural formulae of cisplatin (**1**) and transplatin (**2**)

2.3 Formation of Cisplatin-DNA Adducts

A schematic structure of a single-stranded DNA fragment with the four common nucleobases is depicted in Figure 2. Platinum is a soft metal and therefore coordinates preferentially to the N atoms in DNA. At physiological pH, the N3 atoms of thymine are protonated, the N3 of purines are sterically hindered, and aromatic sites without a σ-lone pair are also excluded from platinum coordination. Four binding sites are left for platination: the N7 atoms of guanine and adenine, the N1 of adenine, and the N3 of cytosine. All four can be platinated, but the first binding step shows a strong preference for the N7 atom of guanine.[7] This preference can be explained by its strong basicity, and by the possibility of hydrogen bonding between ammine protons of cisplatin with the O6 atom of guanine (during the approach and also after binding).

Following activation via intracellular aquation reactions, cisplatin forms a variety of stable bifunctional adducts with DNA, as depicted in Figure 3. Cisplatin mainly forms 1,2-intrastrand cross-links on adjacent purine bases. It has been found that 60–65% of the platinum bound to DNA is in the form of 1,2-d(GG) intrastrand cross-links and 20–25% in intrastrand 1,2-d(AG) cross-links.[8,9] Other adducts formed are the 1,3-d(GXG) and 1,4-d(GXXG) cross-links, accounting for at most 6%. Only a small percentage of cisplatin (1.5%) was found to be involved in interstrand adducts. It remains

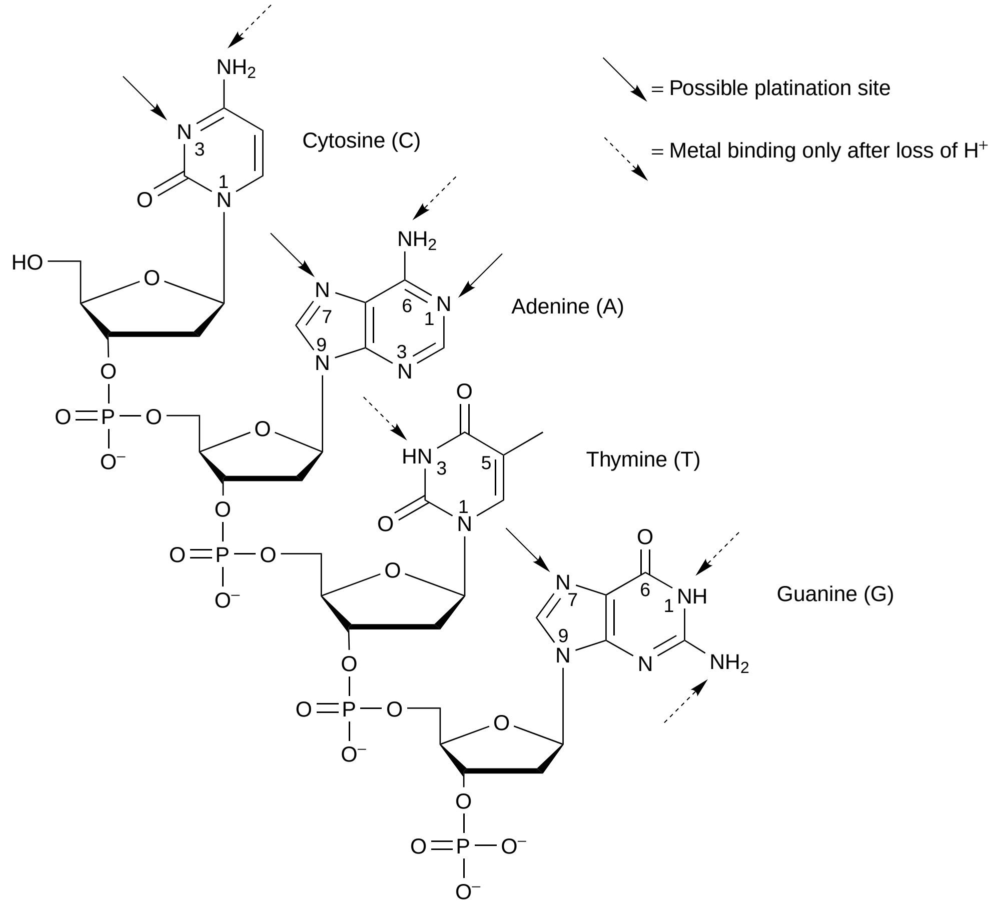

Figure 2 Possible platinum binding sites on DNA bases

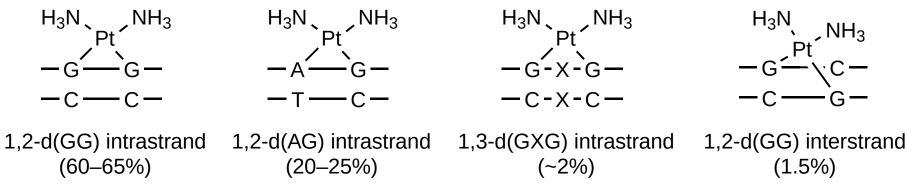

1,2-d(GG) intrastrand (60–65%)
1,2-d(AG) intrastrand (20–25%)
1,3-d(GXG) intrastrand (~2%)
1,2-d(GG) interstrand (1.5%)

Figure 3 Various types of cisplatin-DNA adducts and their frequency

unclear which of the above described platinum-DNA adducts are responsible for the cytotoxic effect. Because of the high prevalence of the 1,2-intrastrand adduct and the inability of the inactive transplatin to form this cross-link, a pivotal role has been suggested for the 1,2-d(GG) adduct. This assumption is supported by the finding that nucleotide excision repair (NER), an important DNA-repair system, repairs 1,3-intrastrand adducts more efficiently than 1,2-intrastrand adducts, while the 1,2-d(GG) adducts are repaired the least effectively. However, the minor adducts have been suggested to play an important role as well.[8]

2.4 3-D Structure of the Major Cisplatin-DNA Adduct

The binding of cisplatin to DNA induces structural distortions in the double helix. The structural features of DNA oligomers containing the 1,2-d(GG)-cisplatin adduct have been studied using X-ray crystallography and NMR spectroscopy.[3,4] In a recent theoretical study, many similarities in the structures of various 1,2-intrastrand adducts have been discussed.[10] Common distortions that are found are the kinking of the helical axis toward the major groove (55–79°) and the partial unwinding (~20°) of the double helix. An example of an NMR solution structure is given in Figure 4.

2.5 Protein Recognition of Cisplatin-DNA Adducts[3,9]

The altered structure of the DNA duplex attracts proteins involved in DNA damage recognition and high-mobility group domain (HMG) proteins, which have been postulated to mediate the antitumor activity of cisplatin.

Cells deficient in DNA repair are hypersensitive to cisplatin and some cisplatin-resistant cell lines show increased DNA repair and increased expression of the DNA. Platinum-induced DNA lesions are primarily repaired by the NER system. This system involves more than 20 proteins responsible for damage recognition, incision of the DNA strand on both sides of the lesion, removal of the damaged bases, and finally ligation by a DNA ligase.

A different class of proteins that specifically recognize cisplatin-damaged DNA is the so-called HMG proteins. The HMG domain is a DNA-binding motif that comprises about 80 amino acids. This domain is found in a variety of chromosomal proteins and transcription factors. Binding to DNA is associated with recognition of structural distortion of the DNA helix. Several HMG domain proteins have been shown to selectively bind to 1,2-d(GG) and 1,2-d(AG), but not to the less kinked 1,3-d(GXG) adducts. A crystal structure of a cisplatin-1,2-d(GG) adduct in an oligonucleotide complexed with a HMG domain has been reported and is schematically depicted in Figure 5.[12] Binding of HMG proteins to damaged DNA has been suggested to shield the platinum-DNA complex from repair enzymes, thus enhancing the cytotoxicity of cisplatin. Another hypothesis for the role of HMG proteins in the mechanism of cisplatin is that Pt-DNA adducts highjack proteins away from their normal binding sites, thus disturbing normal DNA transcription. These two mechanisms are not mutually exclusive and might mediate cisplatin's activity altogether.

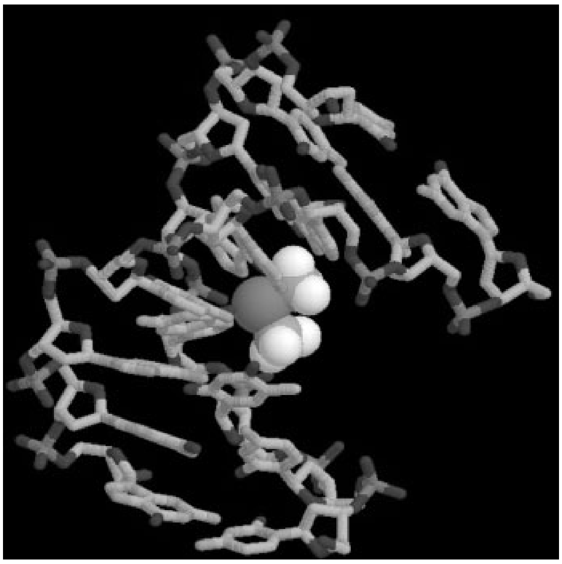

Figure 4 NMR solution structure of d(CCTG*G*TCC)·d(GGACCAGG) with the cisplatin 1,2-(GG) intrastrand cross-link showing bending of the double helix toward the major groove.[11]

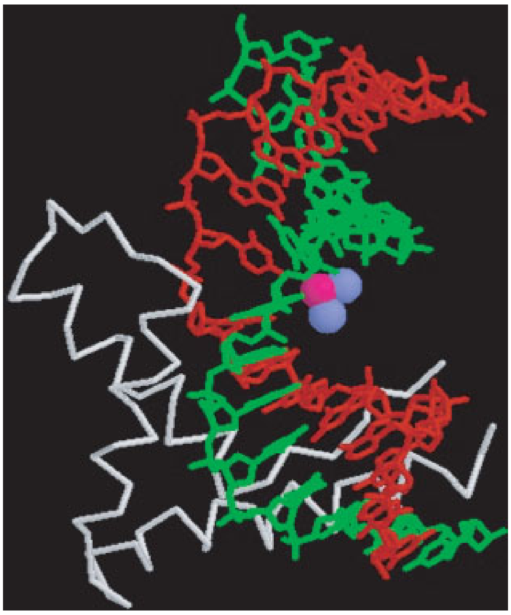

Figure 5 Schematic X-ray structure of the complex of HMG1 domain A with a 1,2-d(GG) intrastrand adduct of cisplatin with d(CCTCTCTG*G*ACCTTCC)·d(GGAAGGTCCAGAGAGG)[12]

3 PROBLEMS WITH CISPLATIN

There are some serious drawbacks to the use of cisplatin in anticancer therapy. Severe toxicity problems occur, such as failure of the kidneys and bone marrow (nephrotoxicity and hematoxicity), nausea, intractable vomiting (emesis), peripheral neuropathy, deafness (ototoxicity), and seizures.[13] These toxic side effects of cisplatin limit the dose that can be administered to patients; typical doses are 100 mg day^{-1} for up to five consecutive days.[14] The nephrotoxicity can be reduced by hydration and diuresis. 5-HT3-receptor blockers control nausea and emesis. Much effort has been devoted to the development of chemoprotective agents, which alleviate the side effects on normal tissues without compromising antitumor activity – mainly sulfur-containing agents such as sodium dithiocarbamate (Naddtc), 2-mercaptoethanesulphonate (mesna), and amifostine (WR-2721). Amifostine has recently been approved for coadministration with cisplatin, which reduces nephro- and neurotoxicity.[13]

The major clinical problem encountered is the resistance against cisplatin. Some types of cancer are intrinsically insensitive to cisplatin treatment, whereas other cancers develop resistance during chemotherapy. This phenomenon limits the applicability of cisplatin to a relatively narrow range of tumors. The cisplatin-resistance mechanism seems to be multifactorial. Several main factors have been identified as potential modulators of cellular resistance, and are discussed below.

Decreased uptake leads to lower intracellular drug concentrations. In many cisplatin-resistant cell lines, reduced accumulation was observed.[4,8] The cisplatin membrane transport system is poorly understood, but studies on cisplatin-resistant cells with decreased drug accumulation have identified two membrane proteins that may be involved in uptake and efflux respectively: a 48-kDa protein with decreased expression and a 200-kDa glycoprotein with increased expression.

Another mechanism is increased intracellular detoxification. Cisplatin is scavenged by intracellular thiol-containing molecules, especially glutathione (GSH), which is present in cells at high concentrations (0.5–10 mM).[15] Glutathione reacts with platinum drugs to form deactivated conjugates, which are readily excreted by a glutathione S-conjugate export pump.[8] Raised intracellular concentrations of GSH often correlate with cisplatin resistance. Another intracellular thiol that could play a role is metallothionein. This protein consists of 62 aminoacids, 20 of which are cysteine, and is presumed to take part in the detoxification of heavy metal ions in cells. Thiol-containing biomolecules have primarily been associated with resistance and toxicity, however, it has been suggested that cisplatin binding to GSH may serve as a drug reservoir modulating the kinetics of DNA platination.[15]

Increased DNA repair was observed in some cisplatin-resistant cell lines.[8] For the 1,2-intrastrand adducts of cisplatin, the NER system is of particular importance. It has been shown that several DNA-repair proteins such as the Xeroderma Pigmentosum Group A (XPA) protein, which is involved in damage recognition in NER, can be overexpressed in resistant cell lines, resulting in efficient repair and therefore reduced toxicity.

Enhanced tolerance to DNA adducts has been found in some cisplatin-resistant cells.[13] Mechanisms that are involved are enhanced postreplicative bypass – the ability of the replication complex to synthesize DNA downstream a cisplatin-induced lesion – and defects in the repair process named mismatch repair (MMR).

Another mechanism of resistance that has recently been suggested is the failure of apoptotic pathways.[8]

4 CISPLATIN DERIVATIVES AND NEW APPROACHES

4.1 Cisplatin Analogs Used in the Clinic

The clinical drawbacks associated with cisplatin therapy stimulated the search for other antitumor-active platinum complexes with improved pharmacological properties. Over 3000 platinum compounds have been synthesized and tested in vitro in the past 30 years.[1,3] However, less than 1% of these have entered clinical trials and very few have as yet emerged as clinically acceptable. The most successful of these second-generation platinum compounds is carboplatin (**3**, Figure 6). Since its introduction in 1986, it has largely replaced cisplatin in the treatment of patients that suffer from toxic side effects. Although less antitumor-active, carboplatin is also less toxic than cisplatin, allowing the use of higher doses in order to achieve a comparable level of clinical efficacy. The decreased toxicity is achieved by the substitution of the chloride-leaving groups by a didentate dicarboxylate,

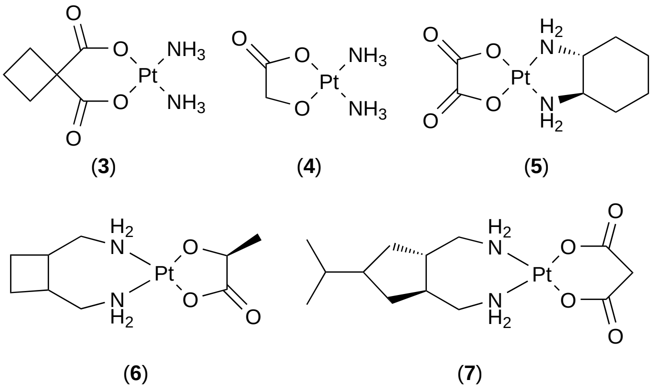
(**3**) (**4**) (**5**)

(**6**) (**7**)

Figure 6 Cisplatin analogs used in the clinic. Numbers refer to: carboplatin (**3**), nedaplatin (**4**), oxaliplatin (**5**), lobaplatin (**6**), and SKI 2053R (**7**)

lowering the rate of aquation and thereby the reactivity of the compound.[13] The kinetics of DNA damage by carboplatin, mainly the initial binding step leading to monofunctional adducts, are much slower compared to cisplatin. Interestingly, it seems possible that nucleobases attack carboplatin directly without prior aquation of the drug, leading to long-lived ring-opened species.

Nedaplatin (**4**) is a drug similar to carboplatin and has been clinically used in Japan since 1995. Unfortunately, both drugs are cross-resistant with cisplatin, which implies that they are affected by the same resistance mechanisms. This may be related to the fact that the drugs cause the same type of DNA damage as cisplatin.

Oxaliplatin (**5**) (recently renamed Eloxatin) has been approved for the secondary treatment of metastatic colorectal cancers.[13] It appears to have a different spectrum of activity compared to cisplatin, and has been shown to circumvent cisplatin resistance. The MMR protein complex binds to DNA globally modified by cisplatin, but not to that by oxaliplatin. Furthermore, MMR-deficient cells are slightly more resistant to cisplatin, but not to oxaliplatin. It has been proposed that steric effects caused by the 1,2-diaminocyclohexane ring may prevent the MMR complex from recognizing the lesion.

Lobaplatin (**6**) exhibits a lower reactivity toward isolated DNA and serum proteins compared to cisplatin. Preclinical data suggested a lack of cross-resistance to cisplatin. However, as yet no clear evidence is available of clinical activity in cisplatin-resistant tumors. Lobaplatin has recently gained approval in China.[13]

SKI 2053R (**7**), containing an even bulkier amine ligand than (**6**), was shown to be active in murine leukemia with acquired resistance to cisplatin. Clinical activity in cisplatin-resistant tumors has not yet been reported. On the basis of studies in gastric cancer patients, SKI 2053R has received approval in South Korea.[13]

4.2 Structure–Activity Relationship (SAR)

The majority of the vast amount of platinum complexes synthesized fit a set of structure−activity relationships (SARs).[1] For a platinum drug to exhibit antiproliferative activity, the Pt(II) or Pt(IV) complex should have a cis geometry and the general formula of *cis*-$[PtX_2(Am)_2]$ or *cis*-$[PtX_2Y_2(Am)_2]$, where X is the leaving group and Am is an inert amine with at least one N–H functionality. Monofunctionally binding cationic complexes are inactive. The leaving group should be an anion with intermediate binding strength to platinum and should have a weak trans effect to avoid labilizing the amine. Complexes with labile leaving groups such as ClO_4^- or NO_3^- are highly toxic, probably because of the high reactivity toward intracellular biomolecules other than DNA. Complexes with rather inert leaving groups, such as I^- or SCN^- are generally inactive. In recent years, however, a large number of new compounds that do not satisfy the classical SARs have been reported to show antitumor activity. The demonstration of antitumor activity for these complexes indicates that cisplatin-like DNA lesions are not the only cause of cytotoxicity. Some examples are presented below.

In the search for a more successful drug, numerous alternative concepts in the design of new platinum drugs emerged. Requirements that have influenced the search for new complexes include: reduction in toxicity, increased spectrum of activity, circumventing resistance, and oral activity to facilitate outpatient treatment.[4] The remainder of this section will give an overview of the various approaches used, classical and novel. Platinum complexes with appended functionalities will be discussed in more detail.

4.3 Platinum(IV) Complexes[16]

One of the advantages of Pt(IV) complexes is that some of them can be administered orally, expanding chemotherapy to ‘outpatient treatment’. Furthermore, Pt(IV) complexes show a reduced toxicity as they are octahedrally coordinated, resulting in slower ligand-substitution reactions than their Pt(II) analogs. It is generally believed that platinum(IV) complexes are reduced to platinum(II) by extracellular and intracellular agents prior to reaction with DNA, and thus act as a prodrug. The stability of the complexes depends on both the axial and equatorial ligands: carboxylato or hydroxo axial ligands lead to more inert complexes than axial chloride. The reduction potential of platinum(IV) complexes has been found to correlate with DNA binding and in vitro cytotoxicity. Recently, Hall *et al.* were able to monitor the fate of Pt(IV) drugs in situ using X-ray Absorption Near Edge Spectroscopy (XANES).[17] One of the most successful Pt(IV) complexes is satraplatin (**8**, Figure 7), also known as JM216, which

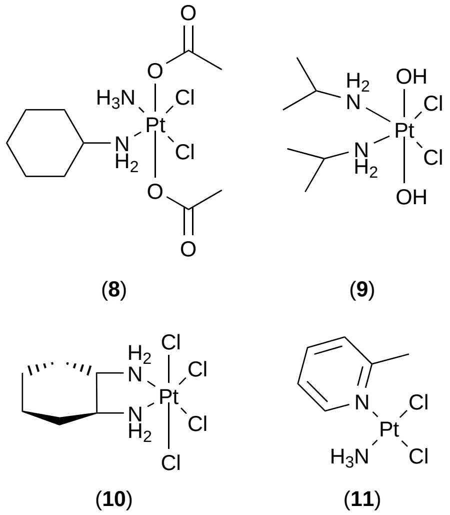

Figure 7 Pt(IV) complexes satraplatin (**8**), iproplatin (**9**), and ormaplatin (**10**) and the sterically hindered Pt(II) complex ZD0473 (**11**)

entered clinical trials in 1992. Satraplatin possesses in vivo oral antitumor activity against a variety of murine and human subcutaneous tumor models, and has a relatively mild toxicity profile with myelosuppression being dose limiting. However, Phase III trials were abandoned because of variability in drug uptake. Two other compounds, iproplatin (**9**) and ormaplatin (**10**) entered clinical trials as well, but were abandoned because of the lack of superior performance and neurotoxicity, respectively.[16]

4.4 Sterically Hindered Platinum(II) Complexes

As mentioned in Section 3, one of the main mechanisms of cisplatin-resistance is an increased intracellular thiol-mediated detoxification. ZD0473 (**11**, Figure 7), *cis*-$[\mathrm{PtCl_2(NH_3)}$(2-methylpyridine)], is currently in Phase III trials and is a highly promising lead in which the replacement of an ammine ligand by a 2-methylpyridine ligand induces a marked decline in the reactivity of the platinum toward thiourea, methionine, Guanosinemonophosphate (GMP), and pyridine compared to cisplatin and *cis*-$[\mathrm{PtCl_2(NH_3)}$(pyridine)].[13,18] The methyl group is nearly perpendicular to the platinum plane, sterically hindering an axial approach to the platinum. Preclinical evaluation shows significant activity of ZD0473 on a variety of cell lines, including several that possess acquired resistance to cisplatin and carboplatin. Across a panel of cisplatin-sensitive and resistant human ovarian carcinoma xenografts, ZD0473 shows improved or comparable activity to that observed for cisplatin. Furthermore, it is the first platinum(II) drug to demonstrate good oral availability and activity.

4.5 Trans-Platinum(II) Complexes

Although the trans isomer of cisplatin, *trans*-$\mathrm{PtCl_2(NH_3)_2}$ or transplatin, is inactive, substitution of the ammine ligands resulted in a number of antitumor-active trans complexes (Figure 8).[19] The inactivity of transplatin is thought to be the result of its inability to form 1,2-intrastrand adducts. However, deactivation by binding to proteins and other cellular components has also been suggested to play a role.[20] Sterically demanding ligands, as in ZD0473 (**11**, Figure 7), may reduce the detoxification reactions that prevent binding to DNA. The antitumor-active trans complexes can be divided into four series: (1) *trans*-Pt(II)$\mathrm{Cl_2}$ complexes with planar aromatic ligands (**12** and **13**, Figure 8); (2) *trans*-iminoether complexes (**14**); (3) *trans*-Pt(II)$\mathrm{Cl_2}$ complexes with asymmetric aliphatic amines (**15**); and (4) *trans*-Pt(IV) mixed amine complexes (**16**). The complexes with planar ligands show reduced DNA-binding kinetics compared to transplatin and enhanced interstrand cross-linking compared to cisplatin. The cytotoxicity is higher than for their cis isomers and transplatin and, presumably as result of the altered DNA-binding mode, no cross-resistance with cisplatin was observed. The iminoether complexes also exhibit reduced DNA-binding kinetics, are more cytotoxic than their cis counterparts, and lack cross-resistance with cisplatin in vitro. Compound (**14**) inhibits DNA synthesis even though it preferentially forms monofunctional adducts. Complexes with asymmetric aliphatic amines mainly form interstrand adducts and exhibit a cytotoxic activity in cisplatin-sensitive cells comparable to cisplatin. In some cases, a lack of cross-resistance was found. The Pt(IV) mixed amine complexes promote DNA interstrand cross-links and are active against cisplatin-resistant tumors. Interestingly, the corresponding *trans*-Pt(II) complexes without the axial hydroxo groups are inactive.

4.6 Polynuclear Complexes[21]

Dinuclear and trinuclear compounds represent a new class of platinum anticancer complexes and are among the most studied platinum compounds in antitumor chemistry. Many of these complexes circumvent cisplatin-resistance mechanisms.[22] In contrast to cisplatin, the polynuclear complexes predominantly form interstrand cross-links. The dinuclear complex $[\{trans\text{-}\mathrm{PtCl(NH_3)_2}\}_2\{\mu\text{-}(\mathrm{H_2N(CH_2)}_n\mathrm{NH_2})\}]^{2+}$ $(1,1/t,t)$ (**17**, Figure 9) is antitumor-active and shows no cross-resistance in cisplatin-resistant cell lines. Binding studies showed that DNA binding for this compound is different from that for cisplatin, as illustrated by the increased interstrand cross-linking. However, clinical testing was abandoned because of severe neurotoxicity.

The trinuclear platinum(II) complex, $[\{trans\text{-}\mathrm{PtCl(NH_3)_2}\}_2$ $\{\mu\text{-}trans\text{-}\mathrm{Pt(NH_3)_2(H_2N(CH_2)_6NH_2)}\}]^{4+}$ $(1,0,1/t,t,t,$ BBR-3464, **18**) was found to be very cytotoxic and effective against

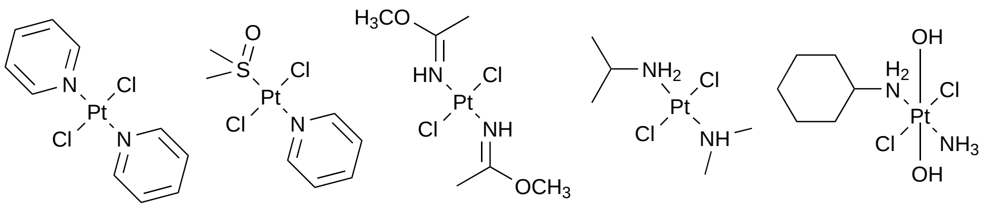

(**12**) (**13**) (**14**) (**15**) (**16**)

Figure 8 Antitumor-active trans complexes. Numbers are explained in the text

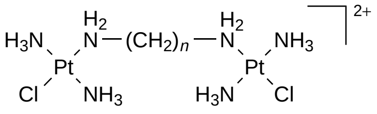

(17)

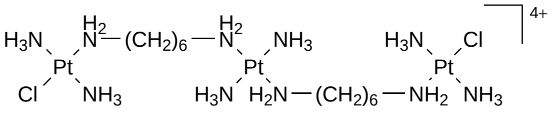

(18)

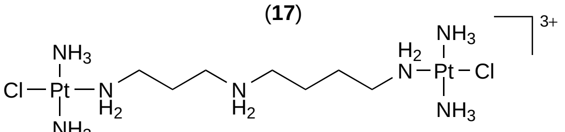

(19)

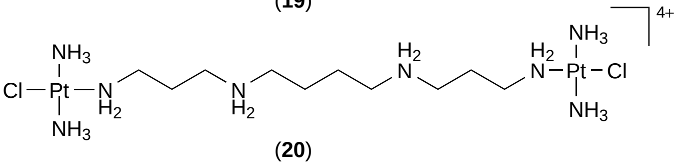

(20)

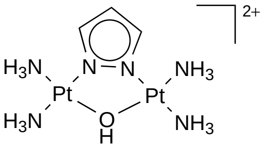

(21)

Figure 9 Selection of polynuclear platinum complexes. Numbers are explained in the text

cisplatin-resistant tumor cells. The overall +4 charge greatly enhances the affinity for DNA and the complex mainly forms long-range interstrand cross-links.

Dinuclear complexes formed with polyamines have attracted attention since polyamines are known to interact with the DNA backbone. Dinuclear cationic trans complexes that use the naturally available polyamines spermine (**19**) and spermidine (**20**) as linkers have been shown to be very active and to circumvent cisplatin resistance in L1210 murine leukemia cells in vitro. The internal charge, from an incorporated amine (**19**) and (**20**) or a platinum atom (**18**), featured in the diamine linker, seems to contribute significantly to the anticancer activity of the complexes.

Recently, a new type of dinuclear platinum(II) complex, $[\{cis\text{-Pt(NH}_3)_2\}_2(\mu\text{-OH})(\mu\text{-pyrazolate})]^{2+}$ (**21**), was developed and found to have a very high activity. The bridging ligand in this complex is the rigid pyrazole, which was designed to induce minimal distortions when chelating at two neighboring G bases of DNA. It is anticipated that in this way the adduct is not, or hardly recognized by repair mechanisms. The crystal structure of the complex with two ethylguanine model bases has been resolved and shows that the orientation of the nucleobases is similar to the normal configuration of nucleobases in DNA.[23] Furthermore, a reaction with a double-stranded oligonucleotide containing a GG sequence resulted in hardly any distortion.[5]

4.7 Platinum Drugs with Extra Functionalities

To develop platinum drugs with improved properties compared to cisplatin, a plethora of cisplatin analogs have been designed with appended additional functionalities. The rationale is that these incorporated moieties could lead to a host of favorable pharmacokinetic properties, such as: targeting to cancer cells, improved transport into the cell, and increased affinity for DNA. Furthermore, to overcome the problem of resistance, pendant DNA interacting moieties have been incorporated in platinum drugs to induce an interaction with DNA distinct from that of the parent drugs. A selection of the myriad of approaches toward platinum drugs with altered properties is given below.

Chottard[24] prepared a large series of dichloro(ethylenediamine)platinum ($Pt(en)Cl_2$) derivatives, bearing a side chain with various functional groups, with the aim to examine how charge, polarity, and steric features of the side-chain affect the antitumor activity. The expectation was that compounds bearing an electropositive side chain, such as one or more ammonium groups, would be driven to the polyanion DNA and therefore exhibit the highest activity. However, the highest activity was obtained for complexes with appended bulky hydrophobic groups.

Intercalators are planar compounds that bind reversibly to DNA by π-stacking between base pairs. DNA intercalators have been attached to platinum complexes to increase the localization of the drug in the vicinity of its target and to reduce the exposure of platinum to deactivating intracellular nucleophiles such as thiols. Denny and McFadyen prepared a series of these complexes by conjugating $Pt(en)Cl_2$ to anilinoacridine (**22**, Figure 10) and acridinecarboxamide (**23**).[1] These complexes exhibited improved activity in cisplatin-resistant cell lines compared to cisplatin, but there was no improvement relative to the carrier ligands. Murray[25] recently demonstrated a similar cytotoxicity profile for 9-aminoacridinecarboxamide appended platinum complexes (**24**). However, these complexes displayed an altered sequence specificity compared to that of cisplatin and the above-mentioned acridinecarboxamide platinum complexes (**23**). Furthermore, the presence of the intercalating group greatly increased the rate of reaction with DNA. Phenazinecarboxamide-platinum conjugates (**25**) also exhibit[26] enhanced rates of DNA platination when compared to unfunctionalized $Pt(en)Cl_2$. Furthermore, they were shown to be significantly more cytotoxic against murine P388/W than either cisplatin, $Pt(en)Cl_2$, or the metal-free ligands. Other intercalators that have been conjugated to

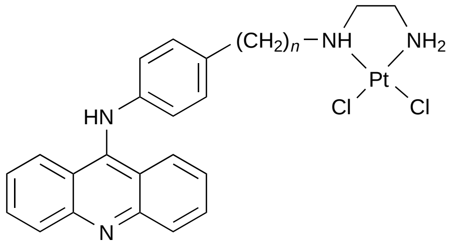

(**22**)

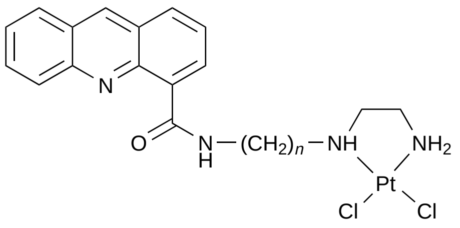

(**23**)

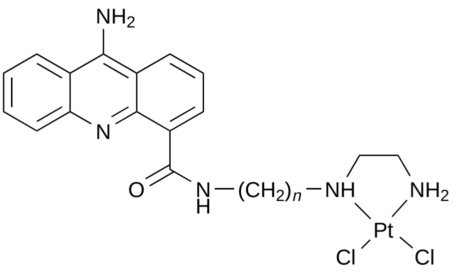

(**24**)

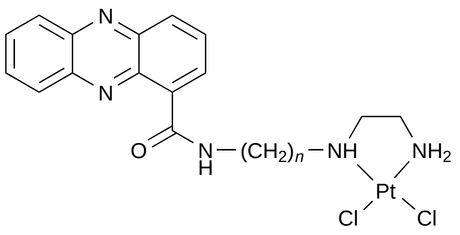

(**25**)

Figure 10 Platinum complexes conjugated to DNA intercalators. Names are given in the text

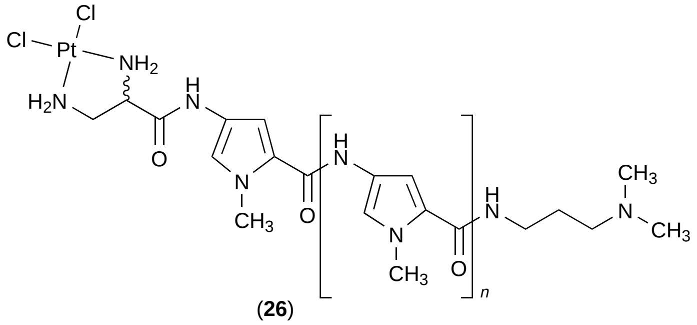

(**26**)
a: $n = 1$
b: $n = 2$

Figure 11 A cisplatin analog conjugated to netropsin (**26a**) and distamycin (**26b**)

platinum drugs include quinolones, phenanthridinium, and anthraquinones.

Cisplatin analogs have also been linked to the DNA minor groove binders netropsin (**26a**) and distamycin (**26b**) with the aim to alter the interaction of the platinum moiety with the DNA (Figure 11).[9] These two oligopeptides are potent antibacterial, antiviral, and antineoplastic agents whose pharmacological activity has been correlated with their ability to bind to DNA. These nonintercalative compounds form noncovalent complexes with double-helical DNA in the minor groove and exhibit a preference for AT-rich domains. Kelland[27] found a strong and irreversible binding to AT regions in the minor groove for the platinum-peptide conjugates. Unfortunately, the antitumor activities found were much lower than cisplatin. In contrast, Brabec[9] showed that the distamycin-platinum conjugate coordinates to DNA with similar base-sequence preferences as the untargeted platinum drug, and concluded that not distamycin, but the platinum moiety acts as a targeting agent.

A number of researchers have used carrier groups that bind targets other than DNA, such as estrogen analogs, targeting platinum to some breast and prostate cancer cells that are known to overexpress estrogen receptors (**27** and **28**, Figure 12).[13,28] The antitumor activity of these complexes has been confirmed in estrogen-positive tumors, whereas estrogen-negative tumors did not respond. Keppler used ligands containing amino phosphonic acid groups in order to produce platinum drugs with selective activity in bone tumors (**29**) and (**30**).[13] Others have used carbohydrates[29] and bile acid.[30] Okuno developed an example of a carrier

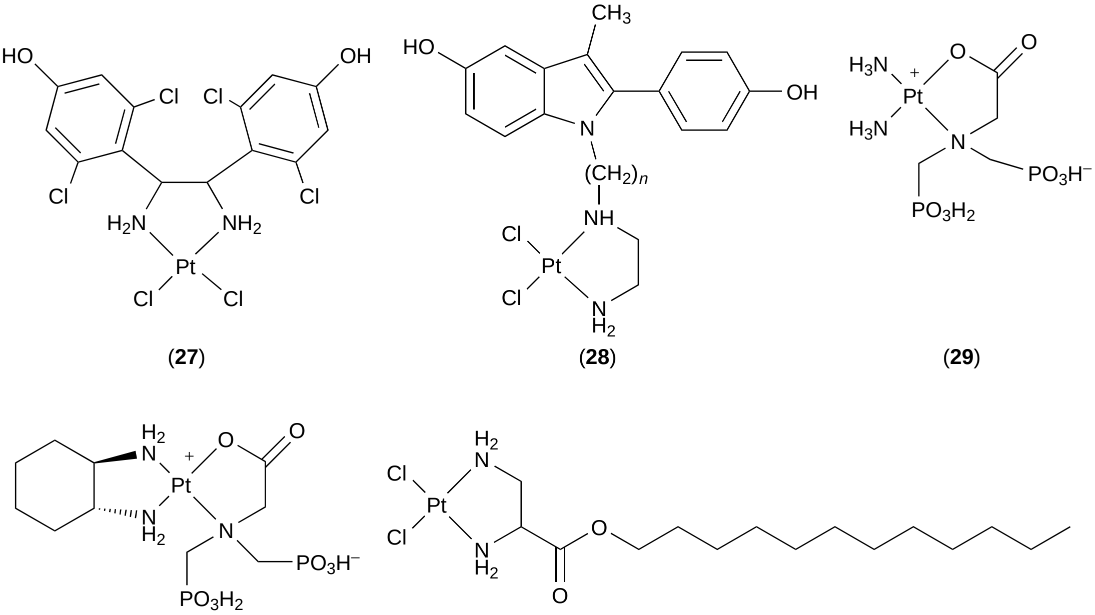

(**27**) (**28**) (**29**)

(**30**) (**31**)

Figure 12 Platinum complexes with estrogen analogs (**27**) and (**28**), and amino phosphonic acid ligands (**29** and **30**), and a cisplatin analog conjugated to a lipophilic carrier via a cleavable linker (**31**)

that is released after delivery of the platinum drug (**31**).[31] A lipophilic alkyl ester is attached to Pt(en)Cl_2, increasing platinum membrane transport, after which the ester is cleaved inside the cell by enzymatic hydrolysis.

Evidence that interactions between platinum drugs and peptides play a role in toxicity and resistance mechanisms in chemotherapy stimulated the investigation of platinum complexes with amino acids and small peptides.[32] A large variety of complexes have been described, coordinated in a mono-, di-, tri- or tetradentate fashion. The amino acids with aliphatic side chains or hydroxyl groups usually form chelated complexes through NH_2 and COO^- groups, but monodentate coordination through NH_2 is also possible. Amino acids with a carboxylate residue react in the same way, although the carboxylate can coordinate as well. In the sulfur-containing amino acids, the sulfur is the preferred coordination site. The amide N and O atoms are also coordination sites for platinum in peptide complexes. Although the majority of the numerous platinum–peptide and platinum–amino acid complexes described in the literature serve as models for cisplatin–peptide interactions in the cell, a few amino acid and dipeptide platinum complexes have been developed as potential anticancer drugs.[32–34] The idea behind this is based on the possibility for selective and increased transportation of the platinum moiety through membranes into cancerous cells, since amino acids are essential for cell growth.

Peptides and proteins have found tremendous use in tumor imaging and therapy when used as receptor-targeting moieties conjugated to radioactive metals. Likewise, a few groups have targeted platinum drugs to specific cancer cells using peptides or proteins as carriers. Wilchek[35] conjugated cisplatin to carboxyl groups of carboxymethyl dextran, which was targeted to the liver by the trinitrophenyl-functionalized streptavidin protein. Schally[36] synthesized a series of hexapeptide and heptapeptide analogs of the luteinizing hormone–releasing hormone (LH-RH) containing pendant $PtCl_2$-diaminopropionic and $PtCl_2$-diaminobutyric moieties. These analogs showed a wide range of receptor-binding affinities to cell membranes of human breast cancer and rat Dunning prostate cancer, as well as cytotoxic activity against human breast cancer and prostate cancer cell lines in vitro.

A promising concept is attaching multiple drug molecules to water-soluble polymers. These conjugates are attractive as a means of increasing drug solubility, reducing toxicity, and localizing more of the drug in the tumor via the Enhanced Permeability and Retention effect (EPR effect).[13,37] This phenomenon is due to the increased permeability of tumor vasculature that permits large macromolecules to enter the tumor tissue, where they are retained because of poor lymphatic and capillary drainage. Eventually, the polymer conjugates are taken up by the cell by endocytosis. Macromolecular agents have long plasma half-lives, because they are too large to pass through the normal vessel walls. After endocytosis, the conjugated drug is released by hydrolytic or enzymatic cleavage. The concept of polymeric anticancer agents has been established clinically in Phase I studies with HPMA copolymers conjugated to doxorubicin.[38] The macromolecules used as carriers for platinum drugs are numerous, and include the HPMA-peptide copolymer (**32**)

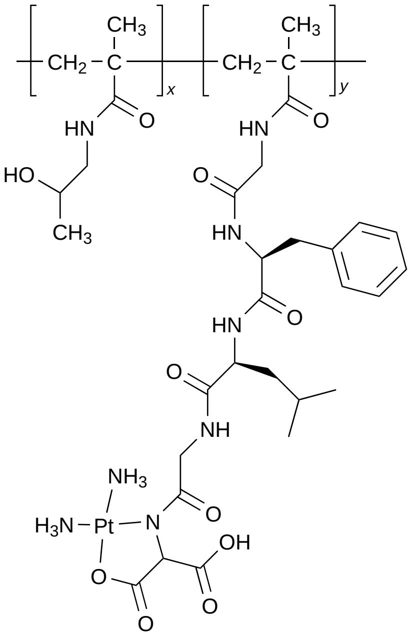

(**32**)

Figure 13 HPMA copolymer platinate AP5280 (**32**); $x = 90$ mol%, $y = 10$ mol%

(Figure 13), known as AP5280, which is a very promising potential anticancer drug now undergoing Phase I clinical trials. The amidomalonate-platinum chelate can be released inside the cell through enzymatic cleavage of the Gly-Phe-Leu-Gly peptide tether by lysozomal enzymes. In preclinical studies, (**32**) was shown to have similar or higher anticancer activity than cisplatin and carboplatin at only a fraction of its maximum tolerated dose (MTD). Moreover, increased tumor cell uptake and DNA adduct formation, and diminished toxicity compared to the parent compounds was observed.

4.8 Combinatorial and Parallel Synthesis Approaches

An alternative to traditional therapeutic drug development, the sequential synthesis and testing in a labor-intensive manner, is combinatorial chemistry. Combinatorial methods constitute tools with which large libraries of compounds can be synthesized through the combination of only a few building blocks, and subsequently screened for a desired property within a short period of time (high-throughput screening). Application of this method for inorganic compounds, with the exception of solid-state materials, has been demonstrated only in a few laboratories and has mainly dealt with (immobilized) catalyst design and enzyme mimetics. Interestingly, Lippard demonstrated that the platinum drug discovery process can be significantly accelerated by the preparation and mechanism-based screening of solution-phase platinum drug libraries.[33,39,40] In one case, roughly 3600 reactions were run and the products screened for their ability to inhibit transcription of β-lactamases in HeLa cells. The so-obtained library generated 14 hits, which were subsequently evaluated with respect to their cytotoxicity. Four compounds displayed good activity, of which three had been previously identified as potential drug candidates.

Solid-phase synthesis has been shown to be ideal for the preparation of libraries of potential drugs, and the advantages involved are likely to pertain to platinum drugs. In this respect, our group reported the solid-phase synthesis of dichloroplatinum(II) tripeptide complexes and dinuclear platinum(II) complexes.[41,42] Using this technique, a library of complexes was generated in an automated synthesizer and conveniently screened for cytotoxicity via an adapted MTT assay.[43]

5 SUMMARY AND OUTLOOK

Out of all the platinum compounds synthesized the last few decades, only a handful has emerged as clinically acceptable. Reduction of toxicity, increased spectrum of activity, and circumventing resistance are still main goals in platinum drug development. To this end, the field has moved toward the exploration of unconventional platinum compounds with often new modes of binding. The creation of functionalized platinum drugs with a higher target selectivity, or better cellular uptake in general, has received a lot of attention. Another promising strategy is the protection against inactivating reactions by using bulky nonleaving ligands. Alternatively, combinatorial methods could accelerate the search for the needle in the haystack through the rapid enrichment and evaluation of the collection of available platinum complexes known to date.

6 RELATED ARTICLES

Metal-based Drugs; Nucleic Acid–Metal Ion Interactions.

7 REFERENCES

1. E. Wong and C. M. Giandomenico, *Chem. Rev.*, 1999, **99**, 2451.
2. G. Giaccone, *Drugs*, 2000, **59**, 9.
3. E. R. Jamieson and S. J. Lippard, *Chem. Rev.*, 1999, **99**, 2467.
4. Z. Guo and P. J. Sadler, *Adv. Inorg. Chem.*, 2000, **49**, 183.
5. J. Reedijk, *Proc. Natl. Acad. Sci. U.S.A.*, 2003, **100**, 3611.
6. J. Reedijk, *Chem. Rev.*, 1999, **99**, 2499.
7. M. J. Bloemink and J. Reedijk, Cisplatin and Derived Anticancer Drugs: Mechanism and Current Status of DNA Binding, in 'Metal Ions in Biological Systems', eds. A. Sigel

and H. Sigel, Marcel Dekker Inc., New York, 1996, Vol. 32, p. 641.

8. M. A. Fuertes, C. Alonso, and J. M. Pèrez, *Chem. Rev.*, 2003, **103**, 645.
9. V. Brabec, *Prog. Nucleic Acid Res.*, 2002, **71**, 1.
10. L. G. Marzilli, J. S. Saad, Z. Kuklenyik, K. A. Keating, and Y. Xu, *J. Am. Chem. Soc.*, 2001, **123**, 2764.
11. D. Yang, S. S. G. E. van Boom, J. Reedijk, J. H. van Boom, and A. H. J. Wang, *Biochemistry*, 1995, **34**, 12912.
12. U. M. Ohndorf, M. A. Rould, Q. He, C. O. Pabo, and S. J. Lippard, *Nature*, 1999, **399**, 708.
13. M. A. Jakupec, M. Galanski, and B. K. Keppler, *Rev. Physiol. Biochem. Pharmacol.*, 2003, **146**, 1.
14. J. Reedijk, *Chem. Commun.*, 1996, 801.
15. J. Reedijk and J. M. Teuben, Platinum – Sulfur Interactions Involved in Antitumor Drugs, Rescue Agents, and Biomolecules, in ‘30 Years of Cisplatin, Chemistry and Biochemistry of a Leading Anticancer Drug’, ed. B. Lippert, Wiley VCH, Weinheim, 1999, p. 339.
16. M. D. Hall and T. W. Hambley, *Coord. Chem. Rev.*, 2002, **232**, 49.
17. M. D. Hall, G. J. Foran, M. Zhang, P. J. Beale, and T. W. Hambley, *J. Am. Chem. Soc.*, 2003, **125**, 7524.
18. L. R. Kelland, S. Y. Sharp, C. F. O’Neill, F. I. Raynaud, P. J. Beale, and I. R. Judson, *J. Inorg. Biochem.*, 1999, **77**, 111.
19. J. M. Perez, M. A. Fuertes, C. Alonso, and C. Navarro-Ranninger, *Crit. Rev. Oncol. Hematol.*, 2000, **35**, 109.
20. G. Natile and M. Coluccia, *Coord. Chem. Rev.*, 2001, **216–217**, 383.
21. N. J. Wheate and J. G. Collins, *Coord. Chem. Rev.*, 2003, **241**, 133.
22. N. Farrell, Y. Qu, U. Bierbach, M. Valsecchi, and E. Menta, Structure-activity Relationships Within Di-and Trinuclear Platinum Phase-I Clinical Anticancer Agents, in ‘30 Years of Cisplatin, Chemistry and Biochemistry of a Leading Anticancer Drug’, ed. B. Lippert, Wiley VCH, Weinheim, 1999, p. 479.
23. S. Komeda, H. Ohishi, H. Yamane, M. Harikawa, K. Sakaguchi, and M. Chikuma, *J. Chem. Soc., Dalton Trans.*, 1999, 2959.
24. P. Mailliet, E. Segal-Bendirdjian, J. Kozelka, M. Barreau, B. Baudoin, M.-C. Bissery, S. Gontier, A. Laoui, F. Lavelle, J. B. Le Pecq, and J.-C. Chottard, *Anti-Cancer Drug Des.*, 1995, **10**, 51.
25. M. D. Temple, P. Recabarren, W. D. McFadyen, R. J. Holmes, W. A. Denny, and V. Murray, *Biochim. Biophys. Acta*, 2002, **1574**, 223.
26. L. C. Perrin, P. D. Prenzler, C. Cullinane, D. R. Phillips, W. A. Denny, and W. D. McFadyen, *J. Inorg. Biochem.*, 2000, **81**, 111.
27. M. Lee, J. E. Simpson Jr, A. J. Burns, S. Kupchinsky, N. Brooks, J. A. Hartley, and L. R. Kelland, *Med. Chem. Res.*, 1996, **6**, 365.
28. F. Kratz and M. T. Schütte, *Cancer J.*, 1998, **11**, 176.
29. Y. Chen, M. J. Heeg, P. G. Braunschweiger, W. Xie, and P. G. Wang, *Angew. Chem., Int. Ed. Engl.*, 1999, **38**, 1768.
30. R. Paschke, J. Kalbitz, and C. Paetz, *Inorg. Chim. Acta*, 2000, **304**, 241.
31. Y. Kageyama, Y. Yamazaki, and H. Okuno, *J. Inorg. Biochem.*, 1998, **70**, 25.
32. A. Iakovidis and N. Hadjiliadis, *Coord. Chem. Rev.*, 1994, **135–136**, 17.
33. K. E. Sandman, P. Fuhrmann, and S. J. Lippard, *J. Biol. Inorg. Chem.*, 1998, **3**, 74.
34. M. Watabe, T. Kobayashi, T. Kawahashi, A. Hino, T. Watanabe, T. Mikami, T. Matsumoto, and M. Suzuki, *J. Inorg. Biochem.*, 1999, **73**, 1.
35. L. Chen, B. Schechter, R. Arnon, and M. Wilchek, *Drug Dev. Res.*, 2000, **50**, 258.
36. T. Janáky, A. Juhász, Z. Rékási, P. Serfözä, J. Pinski, L. Bokser, G. Srkalovic, S. Milovanovic, T. W. Redding, G. Halmos, A. Nagy, and A. V. Schally, *Proc. Natl. Acad. Sci. U.S.A.*, 1992, **89**, 10203.
37. E. Gianasi, M. Wasil, E. G. Evagorou, A. Keddle, G. Wilson, and R. Duncan, *Eur. J. Cancer*, 1999, **35**, 994.
38. P. A. Vasey, S. B. Kaye, R. Morrison, C. Twelves, P. Wilson, R. Duncan, A. H. Thomson, L. S. Murray, T. E. Hilditch, T. Murray, S. Burtles, D. Fraier, E. Frigerio, and J. Cassidy, *Clin. Cancer Res.*, 1999, **5**, 83.
39. K. E. Sandman and S. J. Lippard, Activity of Platinum Compounds in Combinatorial Libraries, in ‘30 Years of Cisplatin, Chemistry and Biochemistry of a Leading Anticancer Drug’, ed. B. Lippert, Wiley VCH, Weinheim, 1999, p. 523.
40. C. J. Ziegler, A. P. Silverman, and S. J. Lippard, *J. Biol. Inorg. Chem.*, 2000, **5**, 774.
41. M. S. Robillard, A. R. P. M. Valentijn, N. J. Meeuwenoord, G. A. van der Marel, J. H. van Boom, and J. Reedijk, *Angew. Chem., Int. Ed. Engl.*, 2000, **39**, 3096.
42. S. van Zutphen, M. S. Robillard, G. A. van der Marel, H. S. Overkleeft, H. den Dulk, J. Brouwer, and J. Reedijk, *Chem. Commun.*, 2003, 634.
43. M. S. Robillard, M. Bacac, H. van den Elst, A. Flamigni, G. A. van der Marel, J. H. van Boom, and J. Reedijk, *J. Comb. Chem.*, 2003, **5**, 821.

Platinum: Inorganic & Coordination Chemistry

Robert H. Crabtree[1] & Hugo Torrens[2]

[1]Yale University, New Haven, CT, USA
[2]National A. University of Mexico (UNAM), Cd. Universitaria, D.F., Mexico

1 Introduction 1
2 Properties and Extraction of the Element 1
3 Binary Compounds 2
4 Zerovalent Complexes 3
5 Complexes of ‘Monovalent’ Platinum 3
6 Complexes of Divalent Platinum 4
7 Complexes of ‘Trivalent’ Platinum 6
8 Complexes of Tetravalent Platinum 6
9 Related Articles 7
10 References 7

Glossary

Platinum ‘blue’: blue oligomeric mixed valent Pt complex with Pt–Pt bonds

1 INTRODUCTION

Platinum is the best known of the platinum group metals (PGMs), which are Ru, Rh, Pd, Os, Ir, and Pt. The PGMs are both rare and very useful for their catalytic activity and their resistance to chemical attack. Platinum has been found in ancient Egyptian artefacts, and the pre-Columbian indigenous peoples of the Americas were familiar with the metal.[1a] The first European description of the element comes from Ulloa, who accompanied the French expedition of 1736 to measure the length of a degree of latitude at the Equator. His report[1b] concerned an unworkable metal called platina found in the Columbian gold mines. In 1741, a South American sample was brought to Europe and investigated scientifically. Only in 1783 did Lavoisier succeed in melting platinum for the first time. By 1805, Woolaston was producing and fabricating platinum by powder metallurgy in quantity from South American sources. It was sometimes called ‘white gold’ although this term is now used for Au–Pd alloys. The metal has now been found in many countries and it is currently produced in Russia, Columbia, Australasia, the US, Borneo, Burma, and Canada.[2a] The element can be recovered from many cupronickel ores, from anode sludge in electrolytic Cu refining, and from the residues in the Mond process for Ni refining. Useful reviews of the element and its chemistry have appeared.[2]

2 PROPERTIES AND EXTRACTION OF THE ELEMENT

The main properties are listed in Table 1.[1a] The best methods of platinum refining remain trade secrets, but general descriptions have been published.[1,2] In the Ni ores from Sudbury, Ontario, the Pt metals concentrate in a metal fraction formed by controlled oxidation of a sulfide ore; this can be magnetically separated and refined to produce relatively pure PGM. An aqua regia treatment dissolves most of the Pd and Pt, and the Pt is precipitated with NH_4Cl as the salt $(NH_4)_2[PtCl_6]$. This is pyrolyzed to give the metal, followed by purification via cycles of redissolution-reprecipitation. Resins containing certain macrocyclic ligands, which can selectively bind and release a number of metals, including Pt, are becoming commercially available, and their availability may change the refining process in the future. Procedures for recovering

Table 1 Some properties[a] of elemental Pt

At. no.	78
At. wt.	195.08(3)
Density	21.45 (20 °C)
Mp	1769
Bp	4170
Electronegativity (Pauling)	2.28
Metallic radius	1.39 Å
Covalent radius	1.31 Å
Isotopes (abundance %, I, half-life)[a]	190 (0.01, 0, 7×10^{11} y) 192 (0.8, 0, ca. 10^{15} y) 194 (32.9, 0, –) 195 (33.8, 1/2, –)[b] 196 (25.3, 0, –) 198 (7.2, 0, –)
Ionization potentials (eV)	
$\mathrm{Pt^0 \rightarrow Pt^I}$	9.0
$\mathrm{Pt^I \rightarrow Pt^{II}}$	18.56
$\mathrm{Pt^{II} \rightarrow Pt^{III}}$	28.5
$\mathrm{Pt^{III} \rightarrow Pt^{IV}}$	41.1
Electron affinity (eV)	2.12
Oxidation potentials (V)	
$\mathrm{Pt \rightarrow Pt^{2+} + 2e^-}$	-1.2
$\mathrm{Pt + 4Cl^- \rightarrow PtCl_4{}^{2-} + 2e^-}$	-0.75
$\mathrm{Pt + 4I^- \rightarrow PtI_4{}^{2-} + 2e^-}$	-0.40
Sublimation energy (kcal $\mathrm{mol^{-1}}$ at 20^0C)	121.6
Common oxidation states and geometries	$\mathrm{Pt^0}$, tetrahedral[c] $\mathrm{Pt^{II}}$ square planar[d] $\mathrm{Pt^{IV}}$, octahedral

[a]There are also a number of short-lived artificially produced isotopes with at. wts from 184 to 200. The longest lived is ^{193}Pt with $t_{1/2} < 500$ y. [b]Nuclear magnetic moment (μ): 0.6. [c]Planar three coordination rare. [d]Trigonal bipyramidal five coordination rare.

Pt from laboratory wastes have been described.[3] Platinum can be successfully electroplated, at least in thin films. Many of the Pt alloys follow the Hume-Rothery[4] structural rules, in which the structure adopted can be related to the average valence electron number for the alloy. Pt–Ir alloy (80−20) is especially useful for its ductility.

The use of the element in many industrially important catalysts is a measure of its exceptional catalytic activity. The important applications are: petroleum reforming; hydrogenation of unsaturated substrates; hydrosilation of unsaturated substrates; oxidation of SO_2 to give SO_3; oxidation of NH_3 to give HNO_3; and the oxidation of hydrocarbons in fuel cells. Platinum catalysts have important environmental applications in removing pollutants from power generator, internal combustion, and gas turbine engine effluents.[5] Autocatalysts convert over 90% of hydrocarbons, carbon monoxide, and oxides of nitrogen from gasoline engines into less harmful carbon dioxide, nitrogen, and water vapour.

Apart from the massive form, the element is most often encountered as ‘platinum black’, a finely divided and highly reactive material that has some catalytic activity. It can be prepared by reducing chloroplatinic acid with any of a variety of reductants, such as alkaline formaldehyde.[6] For practical applications, the metal is often deposited in colloidal form on an oxide, graphite, or other support, so that it better retains its high surface area and therefore its catalytic activity. Supported colloidal Pt has some advantages as a catalyst in organic synthesis.[7]

Sensors based on platinum are used in temperature measurement because of the substantial change of electrical resistivity with temperature. CO detectors are common safety features in homes and industrial buildings. Oxygen sensors, known as Lambda or Exhaust Gas Oxygen (EGO) sensors, use platinum and are a central component of the engine control system in a catalyst-equipped vehicle.

Zirconia grain stabilized Pt has advantages in practical applications of platinum by giving longer useful life at high temperature;[8] ACT™ coatings are useful in thermocouples and other high-temperature components.[9] The metal has the same coefficient of thermal expansion as soda glass and so an excellent glass-metal seal can be obtained. Platinum and platinum alloys are used in the fabrication of vessels that hold, channel, and form the molten glass because platinum’s high melting point, strength, and resistance to corrosion allow it to withstand the abrasive action of molten glass.

The use of platinum in jewelry is a result of its high strength and resistance to chemical attack (tarnish). It is estimated that over 90% of all hard disks produced contained platinum in their magnetic layers.

Besides numerous biomedical metallic devices, platinum is now used clinically in several important antitumor drugs notably Cisplatin (*cis*-$[PtCl_2(NH_3)_2]$), Carboplatin (*cis*-$[Pt(1,1\text{-ciclobutanedicarboxilato})(NH_3)_2]$), and Oxaliplatin ([Pt(oxalato)(*trans*-L-diaminocyclohexane)]), which are known to bind to DNA and inhibit cell division (*see* ***Platinum-based Anticancer Drugs***).

Platinum is not attacked by any of the mineral acids, but does dissolve in aqua regia, an HCl–HNO_3 mixture. The nitric acid provides the oxidizing power and the HCl provides the chloro ligands that stabilize Pt^{IV} in solution. The metal is also attacked by fused alkalis, by fused sodium peroxide and, at red heat, by chlorine and fluorine, especially in the presence of NaCl or other halide ion sources.

Platinum is found in compounds having a smaller range of oxidation states than is the case for many of the earlier elements in the periodic table. The differences between it and Pd are somewhat more marked than for analogous pairs of earlier elements. The coordination numbers (*see* ***Coordination Numbers & Geometries***) tend to be lower than for earlier elements: a CN of six is rarely exceeded and a CN of four is common. Many important concepts in coordination chemistry, such as square-planar coordination and the *trans* effect, were first discovered in Pt complexes. The high electronegativity of the element is reflected in a poor π-basic character, which helps account for the lack of a binary carbonyl.

3 BINARY COMPOUNDS

3.1 Halides

PtF_6 can be prepared from the elements as a red vapor which condenses at 69 °C and freezes at 61.3 °C; it shows a Jahn−Teller distortion, appropriate for its d^4 configuration. It is one of the molecules with the highest experimentally determined electron affinity[10] and therefore one of the strongest oxidants known and even gives $[O_2]^+$ $[PtF_6]^-$ and Xe^+ $[PtF_6]^-$ or Xe^{2+} $[PtF_6]^{2-}$ with O_2 and Xe;[11] the latter was the first noble gas compound (*see* ***Noble Gases: Inorganic Chemistry***). Dark red PtF_5 is tetrameric with four Pt–F–Pt bridges. The diamagnetic yellow−brown PtF_4 is formed from BrF_3 and Pt. All these species are hydrolytically unstable. An oxyfluoride, $PtOF_3$ is also known. The compound, once thought to be $[PtOF_4]$, was later shown to be $[O_2]^+$ $[PtF_6]^-$.[2] The molecular structures of the platinum fluorides have been determined.[12]

The highest chloride is $PtCl_4$, which is obtained as a red−brown solid from the elements at 300 °C or from heating chloroplatinic acid. Heating the tetrachloride gives the dichloride, which comes in a monomeric α-form as well as a hexanuclear form containing discrete $[Pt_6Cl_{12}]$ clusters. Br and I also form black $[PtX_4]$ as the highest binary halides. On heating, these convert to the dihalides. Rather unstable mono- and trichlorides have also been reported; the first may well be a cluster compound and the second probably contains both Pt^{II} and Pt^{IV}.

3.2 Chalcogen Compounds and Related Derivatives

Platinum is not oxidized when heated in air. PtO, linear PtO_2 and trigonal PtO_3 have been studied in argon matrices.**13** The brown trioxide which has been obtained in impure form by anodic oxidation probably contains Pt^{VI}, but the dioxide, PtO_2, is far better known. It is obtained as a red–brown hydrous material from hot Pt^{IV} solutions and sodium carbonate, but it loses most of the associated water to give the black anhydrous dioxide on heating to 200 °C. The amphoteric yellow trihydrate dissolves in NaOH to give $Na_2[Pt(OH)_6]$ and in HCl to give $H_2[PtCl_6]$. The monohydrate is a precursor of Adam's catalyst,**14** used extensively for the hydrogenation of organic compounds, when it is activated by reduction to finely divided Pt with H_2. Fusion of ammonium chloroplatinate and sodium nitrate has been recommended**14** for the preparation of Adam's catalyst. Chloroplatinic acid and sodium borohydride also gives a useful catalyst. Platinum sulfide on carbon is also available as a hydrogenation catalyst; it is less sensitive to poisons and does not reduce haloarene groups. A black, air-unstable hydrous Pt^{II} oxide is also known.

On heating, elemental Pt can also combine with elements such as B, Si, Ge, Pb, P, As, Sb, S, and Se, especially under reducing conditions. The phase diagrams are quite complex and several solid compounds are formed.**15** PtQ and PtQ_2 are known for Q = S and Te. For Se, $Pt_{10}Se_8$ and $PtSe_2$ are known. The PtQ_2 phases have the CdI_2 structure and are relatively easily oxidized. Pt_2Si and PtSi are both known, as well as PtP_2 and $PtAs_2$. PtO and PtS have square-planar Pt and tetrahedral Q. PtTe is a superconductor below 4 K.**16**

3.3 Hydrides

Platinum is able to absorb hydrogen gas, although not to the extent found for Pd (*see* ***Palladium: Inorganic & Coordination Chemistry***).

4 ZEROVALENT COMPLEXES

Complexes of Pt^0 can be tetrahedral, planar three-coordinate, or linear two-coordinate. Soft ligands and π-acceptor ligands are required to stabilize this low oxidation state. Acetylenes ($[Pt(\eta^2\text{-PhC}{\equiv}\text{CPh})_2]$),**17** olefines (($[Pt(\eta^2\text{-PhCH}{=}\text{CH}_2)_3)]$),**17** and especially phosphines are the most common ligands found in zerovalent complexes of platinum. Compounds with mixed ligands, including p-block elements donor ligands, are also known.

4.1 Phosphine Complexes

The most important zerovalent complexes are the phosphine derivatives of which the best known is the tetrahedral tetrakis(phosphine) $[Pt(PPh_3)_4]$, formed by reducing $[PtCl_2(PPh_3)_2]$ with hydrazine or alcoholic KOH in the presence of excess phosphine. A very wide range of similar complexes with alkyl-, alkaryl-, and fluorophosphines as well as with phosphites is now known. $[Pt(PPh_3)_4]$ dissociates readily in solution by sequential loss of PPh_3 (see equation 1).

$$[Pt(PPh_3)_4] \rightleftharpoons [Pt(PPh_3)_3] \rightleftharpoons [Pt(PPh_3)_2] \rightleftharpoons [Pt(PPh_3)]_n \qquad (1)$$

The tris(phosphine) complex is planar, and the bis(phosphine) seems to be linear, by analogy with the isolable $[Pt(PCy_3)_2]$ species, for which a structure has been obtained.**18** The latter reacts with H_2 to give $[PtH_2(PCy_3)_2]$ and with X–H to give $[PtHX(PCy_3)_2]$ (X = C_6F_5, C_6F_5O, C_6F_5NH, and C_4F_4N). Water will protonate the very basic $[Pt(PEt_3)_3]$ to give $[PtH(PEt_3)_3]^+ OH^-$. The phosphite and fluorophosphine $[PtL_4]$ complexes are not dissociated in solution, as might be expected from their stronger π-acceptor power and smaller *Cone Angle*. Patterned Pt coatings can be deposited on silica via thermal decomposition of $[Pt(PF_3)_4]$.**19**

These complexes are important catalyst precursors and synthetic precursors in Pt chemistry. For example, oxidative addition of a variety of species XY to $[Pt(PPh_3)_4]$ normally gives $[PtXY(PPh_3)_2]$ (XY = Cl_2, MeI, Cl–$Cu(PPh_3)_3$, HCl, etc.).**20** In the case of HX addition, the Pt–H bond is sometimes sensitive to subsequent protonation and the final product can be $[PtX_2(PPh_3)_2]$, as is the case for X = Cl. Hydrogen does not react with $[Pt(PPh_3)_4]$, however.

The reaction with molecular oxygen gives an η^2-peroxy complex, $[Pt(\eta^2\text{-O}_2)(PPh_3)_2]$, in which the oxygen is reactive, and the complex can oxidize PPh_3, RNC, and alkenes to $OPPh_3$, RNCO, and the epoxide. SO_2, NO_2, NO, and CO_2 react to give the sulphato, dinitrato, dinitro, and carbonato complexes. The dioxygen complex is planar and seems to have substantial Pt^{II} character.**21**

Ligand exchange of $[Pt(P(OR)_3)_4]$ with free phosphite is dissociative, as expected for an 18-electron complex (*see Eighteen Electron Compounds*). $[Pt(PF_3)_4]$ is very stable and does not react with potential substrates for oxidative addition.

5 COMPLEXES OF 'MONOVALENT' PLATINUM

A number of species with Pt–Pt bonds have the +1 oxidation state. For example, the reaction of $[PtCl_4]^{2-}$ with $Ph_2PCH_2PPh_2$ under reducing conditions gives complex (**1**).**22** Treating $Pt^{IV}O_2$ with carbon monoxide in concentrated H_2SO_4 affords the homoleptic, dinuclear, cationic Pt^I carbonyl complex $[\{Pt(CO)_3\}_2]^{2+}$.**23** The apparently irregular behaviour of ${}^1J({}^{195}Pt\text{–}{}^{195}Pt)$ in this class of compounds seems to be caused by an interplay between the influence of the ligands, relativistic effects on Pt–Pt and Pt-ligand bonds as well as 'atomical orbital contributions' to the nuclear spin–spin coupling constants.**24**

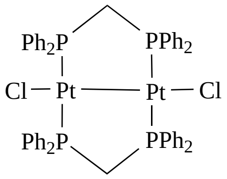

(**1**)

6 COMPLEXES OF DIVALENT PLATINUM

Pt^{II} is almost always 16-electron and square planar, as expected for a d^8 metal, although rare five-coordinate complexes are sometimes formed. This is the most stable oxidation state. Substitution reactions usually go by an associative pathway via an 18-electron five-coordinate intermediate. A high *trans* effect ligand such as thiourea (tu) favors substitution *trans* to itself by its preference for the equatorial site in the intermediate (see equation 2).

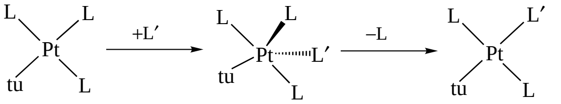

(2)

6.1 Hydride Complexes

One of the first hydride complexes, discovered by Chatt *et al.*, was *trans*-$[PtHCl(PEt_3)_2]$.[25] This and similar complexes can be formed by oxidative addition of HX to $[PtL_4]$ or by the action of a reducing agent such as hydrazine, alcoholic base, or $NaBH_4$ on $[PtCl_2L_2]$.[26] Some reductants, for example, trialkylgermanes, react with $[PtX_2(PPh_3)_2]$ to give $[PtHX(PPh_3)_2]$ by a radical chain pathway.[27] Hydrogen is also effective in the hydrogenolysis of Pt–X bonds ($X = Cl$, SiR_3, Ph, $SnCl_3$); for example, hydrogenolysis of $[PtCl(SiMe_3)(dppe)]$ at 60 °C and 1 atm produces the corresponding *cis* dihydride, rare for platinum. Another useful reagent is formic acid, which loses CO_2 and delivers hydride to a variety of $[PtHX(PPh_3)_2]$ species. Hydrolysis of the carbonyl $[PtX(CO)(PPh_3)_2]^+$ also gives $[PtHX(PPh_3)_2]$, probably via decarboxylation of a Pt–COOH intermediate.[28] Unusual dinuclear hydrides with Pt–H–Pt bridges, such as $[Pt_2H_3L_2]^+$ or $[(dppe)Pt(\mu\text{-}H)_2PtH(dppe)]^+$, which has both square planar and trigonal bipyramidal Pt,[29] are also known. Elemental sulfur (S_8) insert only one sulfur atom into the Pt hydride bonds of [PtHRL] (L = diphosphine) forming [Pt(SH)RL].[30] Proton NMR is very useful for studying Pt hydrides, where the ^{195}Pt–H coupling constants can be in the range of 700–1400 Hz. The Pt–$\underline{H}$ chemical shifts, J(Pt–H) coupling constants, and ν(Pt–H) IR stretching frequencies show a correlation with the nature of the *trans* ligand, as is also true for Ir.[31]

6.2 Pt–TM Bonds

Platinum forms an unusually large range of Pt–E bonds where E can be almost any element. A number of Pt–M species are known, where M is a transition metal; for example, $[Pt(PPh_3)_4]$ reacts with $[NiI_2(PPh_3)_2]$ to give $[I(PPh_3)_2Pt\text{–}NiI(PPh_3)_2]$. Square-planar Pt can also stack readily in the solid in such a way that weak Pt–Pt bonds are formed along the stack direction. Typical is Magnus' Green Salt, $[Pt(NH_3)_4][PtCl_4]$ (Pt–Pt = 3.23 Å); this complex and species like it show unusual colors as well as semiconducting and photoconducting properties.[32] A striking temperature dependance of the luminescence properties have been noted for several linear-chain platinum complexes[33] Some of these compounds show interesting vapochromic and vapoluminiscence properties.[34] The structure of the cluster $[Pt_3Ru_6(CO)_{21}(\mu\text{-}H)_3(\mu_3\text{-}H)]$ shows that the close-packed metals are segregated by layers in a bioctahedral arrangement ($Ru_3Pt_3Ru_3$); the complex is a hydrogenation catalyst for alkynes.[35]

6.3 Pt-Group 13 and Pt-Group 14 Bonds

Boryls are known via equation (3), which seems to occur by oxidative addition of the B–Cl bond followed by loss of HCl. The same type of complex is formed by oxidative addition of Ph_2BCl to $[Pt(PPh_3)_4]$.[36]

$$[PtHCl(PEt_3)_2] \xrightarrow{BClPh_2} [Pt(BPh_2)Cl(PEt_3)_2] \qquad (3)$$

Complexes bearing Pt–Si and Pt–Ge bonds have been invoked as potential intermediates in the formation of polysilanes ans polygermanes. The metallacycle $[(Et_3P)_2Pt(\mu\text{-}\eta^2\text{-}H_2CO)Ge(N(SiMe_3)_2)_2]$ takes part of a photochemical cycloreversion reaction with Pt hydride formation, releasing CO.[37]

Among group 14 elements, Sn is perhaps the most important. Pt^{II} solutions form intense colors in the presence of $SnCl_2$, and reaction of $SnCl_2$, with chloroplatinic acid gives a hydrogenation catalyst which is stable against colloid formation.[38] Although five coordination is rare for Pt^{II}, unusual species such as the trigonal bipyramidal $[Pt(SnCl_3)_5]^{3-}$ have been isolated from $SnCl_2$/chloroplatinic acid solutions. $SnCl_3$ groups are probably strongly π-accepting via their Sn–Cl σ^* orbitals.

6.4 Complexes with Amines and N-donors

Pt^{II} amine complexes were very important in Werner's early studies in coordination chemistry (*see* ***Coordination Chemistry: History***).[39] The *cis* and *trans* bis(amine) complexes $[PtCl_2(NH_3)_2]$ have taken on special importance with the discovery that they bind to DNA, and the *cis*-form is in clinical use as an antitumor drug that has led to sharp falls in mortality from a variety of organ cancers.[40] In accord with the expectations of the *trans* effect, the *trans* compound is formed from chloride ion attack on $[Pt(NH_3)_4]^{2+}$, while the *cis* complex is formed from NH_3 attack on $[PtCl_4]^{2-}$. The ionic isomers $[Pt(NH_3)_4]^{2+}$ $[PtCl_4]^{2-}$ are also known. In connection with the DNA problem, a large number of complexes between *cis*-$[PtCl_2(NH_3)_2]$ and the nucleic acid bases, nucleotides, and nucleic acid oligomers have been studied. In DNA, Pt probably chelates to the N(7) atoms of two guanines.[41] Halo-bridged complexes of the type $[(amine)XPt(\mu\text{-}X)_2PtX(amine)]$ are known, which undergo bridge-splitting reactions with amines and other ligands to give the *trans*-$[PtX_2L_2]$ species. The aromatic chelating ligands bipy and phen form an important series of completes of the $[PtX_2L]$ type (L = bipy or phen; X = halides, alkyls, aryls). The dimethylglyoximate complex $[Pt(dmg)_2]$ has N–O···H–O–N hydrogen bonds between the two planar ligands. Monoximes also form similar complexes.[42] Phthalocyanine and porphyrin complexes are also known.

The strong tendency toward forming planar complexes is shown by the reaction of $K(BH(pz)_3)$ (pz = pyrazolyl = $C_3H_3N_2$) with $[PtBr_2(PEt_3)_2]$, which gives the dinuclear species $[LBr_2Pt(pz)BH(pz)_2PtBrL]$ (L = PEt_3) where the normally *facial* tridentate $(BH(pz)_3)^-$ ligand is monodentate to one Pt and bidentate to the other in order to maintain planar four-coordination at both metals.[43]

Hydrazine reacts with Pt^{II} halides to give hydrides but intermediates with unusual structures have also been isolated from the solutions, for example (**2**).

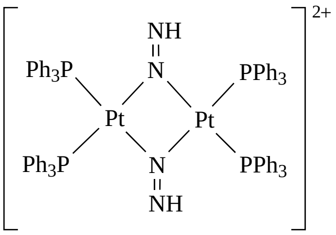

(**2**)

Azide forms the $[Pt(N_3)_4]^{2-}$ anion which reacts with PPh_3 (L) to give $[Pt(N_3)_2L_2]$, which in turn reacts with CO to form $[Pt(NCO)_2L_2]$ with loss of N_2.[44] The nitrile complexes $[PtCl_2L_2]$ (L = RCN), formed from the halide salt and the nitrile, are useful soluble precursors for synthetic chemistry. An unusual five-coordinate adduct, $[PtI(MeCN)_2(PPh_3)_2]I$, is formed from $[PtI_2(PPh_3)_2]$ and MeCN; reflux in benzene leads to loss of the methyl group to give $[Pt(MeCN)(CN)(PPh_3)_2]I$. Several NO derivatives are known, such as $K[Pt(NO)Cl_3]$ from $K_2[PtCl_4]$ and NO. Polymers with side-chain cyanobiphenyl groups give nematic phase liquid crystalline Pt complexes.[45]

6.5 Complexes with P-Donors and Related Ligands

The two most important classes of compounds are $[PtX_2L_2]$, from $[PtX_4]^{2-}$ and 2L, and $[LXPt(\mu\text{-}X)_2PtXL]$, made from $[PtX_2L_2]$ and PtX_2 (X = halide; L = phosphines, arsines, and stibines). Both *cis* and *trans* forms of the mononuclear species can usually be isolated. The dinuclear species easily undergoes bridge-splitting reactions with a variety of ligands to give substituted mononuclear derivatives. They are usually air stable and soluble in organic solvents. A detailed account of the syntheses of this class of compound has been given.[1a] The solvent-free mechanochemical synthesis of *cis*-$[PtCl_2(PPh_3)_2]$ and *cis*-$[PtCl_2(CO_3)]$ have been described.[46] The ^{31}P NMR spectra of the phosphine and phosphite complexes commonly show ^{31}P–^{195}Pt coupling constants of 3000–6000 Hz.

Five coordination is rare but sometimes seen with polydentate ligands such as (**3**), which gives a trigonal bipyramidal derivative [PtClL], where the Cl is axial.

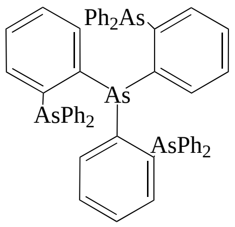

(**3**)

$[Pt(diars)_2]^{2+}$ gives five-coordinate adducts in solution with a variety of ligands X^-, such as X = N_3, Cl, SCN, Br, and I (equation 4); in the solid state the I compound has two equivalent long bonds to I (3.52 Å), however.

$$[Pt(diars)_2]^{2+} + X^- \longrightarrow [PtX(diars)_2]^+ \qquad (4)$$

Cyclometalation is a common reaction of Pt^{II} complexes of suitable N- and P-donor ligands; this gives organometallic derivatives with a Pt–C bond. For example, the product from azobenzene and $[PtCl_4]^{2-}$ is the chloro-bridged dinuclear species (**4**).

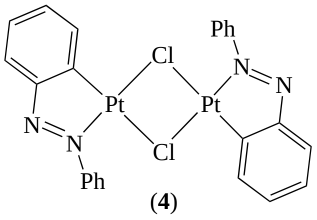

(**4**)

Tridentate 'pincer' ligands,[47] $(2,6\text{-}(CH_2ER_n)_2C_6H_3)^-$E = N (NCN), P (PCP), $n = 2$ or E = S (SCS), $n = 1$, form relatively stable complexes with Pt. Protonation of [PtH(PCP)]

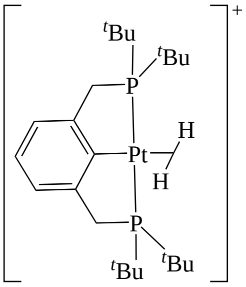

(**5**)

(R = *t*Bu) gives the Pt^{II} dihydrogen complex $[Pt(PCP)(H_2)]^+$ (**5**).[48]

6.6 Complexes with O-, S-, and Related Donors

Aqua ions are known but not very stable. Substitution of Pt^{II} in aqueous solution is sometimes zero-order in the added ligand, L, or can have both L-dependent and L-independent contributions to the rate, probably because intermediate formation of an unstable aqua complex is the rate-determining step for the L-independent pathway. A large number of O-donors, particularly anionic ones, give stable complexes, for example, carbonato, acetate, oxalate, acetylacetonate, and alkoxide. Tetrameric platinum(II) acetate is formed by formic acid reduction of Pt^{IV} solutions in acetic acid. It does not appear to be a very useful synthetic precursor for Pt^{II} chemistry. The acetylacetonate $[Pt(acac)_2]$ is monomeric and square planar.

Thiolates form stable complexes, almost always bridged, as in $[LClPt(\mu\text{-}SR)_2PtClL]$, obtained from $[LClPt(\mu\text{-}Cl)_2PtClL]$ and thiolate. Rare monomeric forms can be made by adding RSH to [PtL4] to give *trans*-$[Pt(H)(SR)L_2]$.[49] Thioether complexes such as $[(R_2S)ClPt(\mu\text{-}Cl)_2PtCl(SR_2)]$ are synthetically useful because the thioether can casily be displaced by other ligands. Monomeric *trans*-$[PtX_2L_2]$ (X = halide; L = thioether) are also known.[50] Thiourea (tu), which binds via S, has a very high *trans* effect, leading to rapid substitution in the position *trans* to S. The Krnakov test for distinguishing *cis*- from *trans*-$[PtX_2L_2]$ derivatives relies on this property of tu.[51] in its reaction with *cis*-$[PtX_2L_2]$ derivatives, tu labilizes the Pt–Cl bonds and ionic $[Pt(tu)_4]^{2+}$ is formed. In *trans*-$[PtX_2L_2]$ derivatives, on the other hand, tu substitutes for L only, and *trans*-$[PtX_2(tu)_2]$ is formed. A series of dithiolene complexes $[Pt(S_2C_2R_2)_2]$ is known; the one-electron redox activity of these species is thought to be ligand centered. Thiocyanate and selenocyanate form a large series of compounds, some of which are S- (Se-) and others N-bound.[1a] $[Me_2Et_2N][Pt(dmit)_2]$ (dmit = 4,5-dimercapto-1,3-dithiole-2-thione) is a superconductor with $T_c = 4\,K$ at 2.4 kbar.[52]

6.7 Complexes with Halides

The yellow $K_2[PtF_4]$ is known but the ion is hydrolyzed in aqueous solution and F complexes in general are very rare for Pt^{II}. The red crystalline $K_2[PtCl_4]$, formed from dissolving $PtCl_2$, in HCl and adding KCl, is one of the most important Pt^{II} complexes and an important starting material in much Pt^{II} chemistry. Slow solvolysis occurs in water to give $[PtCl_{4-n}(OH_2)_n]^{(2-n)+}$. The brown $K_2[PtBr_4]$ is also well known, but black $K_2[PtI_4]$ is rather unstable. $[X_2Pt(\mu\text{-}X)_2PtX_2]^{2-}$ salts are also known for Cl, Br, and I. Many of the complexes described in this article have halides as coligands. Bridged halo species of the type $[LXPt(\mu\text{-}X)_2PtLX]$ are particularly common. $[PtI_2(PMe_3)_3]$ is a rare example of a five-coordinate halo complex.

7 COMPLEXES OF ‘TRIVALENT’ PLATINUM

Pt^{III} complexes have been reviewed.[53] These are often mixed Pt^{II}/Pt^{IV} complexes; many have a chain structure[54] with M···M interactions or even M–M bonds. Others have $Pt^{II}-Hal-Pt^{IV}-Hal-Pt^{II}$ chains. An example of the latter has $\{Pt^{IV}L_4Cl_2\}^{2+}$ units alternating with $\{Pt^{II}L_2Cl_2\}$ units. Many analogs are now known.[55] The related platinum blues are oligomeric mixed valence compounds with Pt···Pt interactions and formed from $[PtCl_2(NH_3)_2]$ and pyrimidines, of which examples have now been crystallized.[56]

Few mononuclear complexes of the Pt^{III} oxidation level are known, and it is always hard to tell if a $Pt^{II}(L^{+}\bullet)$ description is more appropriate. The paramagnetic blue $[Pt(C_6F_5)_3]^-$ is known, formed from $[Pt(C_6F_5)_4]^{2-}$ and Cl_2.[57] Thiamacrocycles, such as 1,4,7-trithiacyclononane (= L), can stabilize Pt^{III} in $[PtL_2]^{3+}$, a square pyramid in which one S of the ligand remains unbound.[58]

The bridging ligand POP $\{= (HO)(O^-)POP(O^-)(OH)\}$ forms dinuclear Pt complexes $[Pt_2(POP)_4]^{4-}$ that can be oxidized to the (III, III) ($[X_2Pt_2(POP)_4]^{4-}$) level with halogens. The most interesting property of these systems is the ability of $[Pt_2(POP)_4]^{4-}$ on irradiation to promote homolytic C–H bond scission of organic compounds, which can either result in dehydrogenation or dehydrodimerization of the organic compound.[59] The primary process is abstraction of an H atom by the excited state triplet, which has Pt–Pt σ^* radical character, to give a Pt hydride intermediate.

The structure of the dimeric Pt^{III}–Pt^{III} complex $[Pt_2(CN)_{10}]^{4-}$ has been studied in aqueous solution by EXAFS. A nonsupported Pt–Pt bond (2.73(1) Å) connects two $Pt(CN)_5$ entities in the dimer.[60]

8 COMPLEXES OF TETRAVALENT PLATINUM

Unlike Pd, which only reluctantly forms M^{IV} complexes, the tetravalent state is common for Pt. The lower ionization energy and higher M–L bond strengths for Pt are probably responsible for the difference. As a d^6 ion, octahedral coordination is the rule and complexes are diamagnetic and low spin. Substitution reactions in these 18-electron species usually go by a dissociative pathway via a 16-electron five-coordinate intermediate. They can be catalyzed by Pt^{II}, in which case electron transfer becomes important.**[61]**

8.1 Hydride Complexes

Platinum(IV) hydride chemistry has been reviewed recently.**[62]** These are usually formed by oxidative addition to a Pt^{II} species and are rather unstable. The reaction shown in equation (5), for example, is readily reversible, because the product easily loses HCl. Hydrido complexes are often involved as intermediates in reactions in which the first step is oxidative addition of an H–X species to Pt^{II}.

$$\textit{trans}\text{-}[PtHCl(PEt_3)_2] + HCl \longrightarrow [PtH_2Cl_2(PEt_3)_2] \qquad (5)$$

8.2 Complexes with Pt–TM Bonds

Mixed Pt^{IV}–Pt^{II} species having a metallic luster are known in which the metals are stacked with close Pt–Pt distances. For example, $K_{1.6}[Pt(C_2O_4)_2]$ $2.5H_2O$ has a distance of only 2.75 Å, and the system seems to be fully delocalized. ‘Trivalent’ $K_2[Pt(CN)_5]$ $3H_2O$ is of the same type.

8.3 Complexes with Group 14 Donors

These can be isolated from R_3E–H (E = Si, Ge, Sn) additions to Pt^{II} complexes. They are usually rather unstable, and lose the group 14 ligand and the group that lies *trans* to the highest *trans* effect group (see equation 6).**[1a]**

$$\textit{trans}\text{-}[PtI_2(PEt_3)_2] + H\text{–}SiH_2Cl \longrightarrow [PtHI_2(SiH_2Cl)(PEt_3)_2] \qquad (6)$$

8.4 Complexes with Group 15 Donors

These constitute a very large group of compounds. For example, all the $[Pt(NH_3)_nCl_{6-n}]^{(n-2)+}$ complexes are known except that in which n is one. They are usually made either by substitution of a Pt^{IV} species or by oxidation of a Pt^{II} precursor (see equations 7 and 8).

$$[PtCl_6]^{2-} + 6NH_3 \longrightarrow [Pt(NH_3)_6]Cl_4 + Cl_2^{-} \qquad (7)$$

$$[PtBr_2(NH_3)_2] + Br_2 \longrightarrow [PtBr_4(NH_3)_2] \qquad (8)$$

$[Pt(NH_3)_6]^{4+}$ reacts with acacH to give (**6**) in which a diimine complex has been formed by loss of water.**[63]** The Pt^{IV} amido complex $K_2[Pt(NH_2)_6]$ is also known.**[64]**

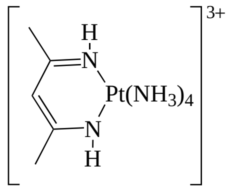

(**6**)

An azide $K_2[Pt(N_3)_6]$ is known, and $[PtCl_2(NCMe)_2]$ reacts with Cl_2 to give $[PtCl_4(NCMe)_2]$. Many phosphine and arsine complexes undergo oxidative addition to give Pt^{IV} derivatives, as was shown in equation (5), but phosphines and other reductants can also reduce Pt^{IV} to Pt^{II}, so some of the products can be unstable. Attempts to substitute Cl for I in $[PtCl_4(PR_3)_2]$, for example, led to formation of $[PtI_2(PR_3)_2]$ and free I_2.

8.5 Complexes with Group 16 Donors

$[PtCl_2(NH_3)_2]$ reacts with H_2O_2 to give the Pt^{IV} bis(hydroxy) species $[PtCl_2(OH)_2(NH_3)_2]$.**[65]** An interesting S-donor example is $(NR_4)_2[Pt(S_5)_3]$, in which three chelating dianionic $S_5{}^{2-}$ ligands are present. The compound has been resolved into its optical isomers, one of the very few purely inorganic species for which this has been accomplished.**[66]** A related species, $[Pt(Se_4)_3]^{2-}$, has also been isolated from a Pt^{II} salt and the $Se_5{}^{2-}$ ion; since the product is Pt^{IV} this involves redox steps.**[67]** The thioether complexes $[PtBr_4(SR_2)_2]$, formed via oxidation of the Pt^{II} species, are also known.

8.6 Complexes with Group 17 Donors

The very soluble hexachloroplatinic acid, $H_2[PtCl_6]{\cdot}nH_2O$, is the most useful precursor for synthetic and catalytic work. For the hydrosilation of unsaturated substrates, the catalyst of choice is chloroplatinic acid, because of its very high activity. There is currently some doubt as to whether the true catalyst is homogeneous or colloidal metal and therefore heterogeneous (*see* ***Hydrosilation Catalysis***). Nearly all halides and pseudohalides (= X) form salts of the $[PtX_6]^{2-}$ ion and of the $[PtX_4(NH_3)_2]$ type.

9 RELATED ARTICLES

Hydrosilation Catalysis; Palladium: Inorganic & Coordination Chemistry; Platinum: Organometallic Chemistry.

10 REFERENCES

1. (a) D. McDonald, ‘A History of Platinum’, Johnson Matthey, London, 1982; (b) A. Ulloa and J. Juan, ‘Relación Histórica del

Viaje a la América Meridional', A. Marin, (printer) Madrid, 1748.

2. (a) D. M. Roundhill, in 'Comprehensive Coordination Chemistry', ed. G. Wilkinson, Pergamon, Oxford, 1987, Chap. 52; (b) S. E. Livingstone, in 'Comprehensive Inorganic Chemistry', ed. J. C. Bailar, Pergamon, Oxford, 1973, Chap. 43; (c) F. R. Hartley, 'The Chemistry of Pd and Pt', Wiley, Chichester, 1973; (d) N. N. Greenwood and A. Earnshaw, 'Chemistry of the Elements', 2nd edn., Butterworth Heinemann, 1997; (e) F. E. Beamish, A. E. McBryde, and R. R. Barefoot, in 'Rare Metals Handbook', ed. C. A. Hampel, Krieger Publishing, 1971.
3. H. L. Grube, in 'Handbook of Preparative Inorganic Chemistry', ed. G. Brauer, Academic Press, New York, 1965, Vol. 2, p. 1561.
4. W. Hume-Rothery, *Platinum Met. Rev.*, 1966, **10**, 94.
5. A. Obuchi and A. Ohi, *Appl. Catal. B: Environ.*, 1993, **2**, 71.
6. R. Feulgen, *Ber. Dtsch. Chem. Ges.*, 1921, **54**, 360.
7. A. Fürstner, *Angew. Chem., Int. Ed. Engl.*, 1993, **32**, 164.
8. R. B. McGrath and G. C. Badcock, *Platinum Met. Rev.*, 1987, **31**, 8.
9. D. R. Coupland, *Platinum Met. Rev.*, 1993, **37**, 62.
10. G. L. Gutsev and A. I. Boldyrev, *Adv. Chem. Phys.*, 1985, **61**, 169.
11. (a) N. Bartlett, *Proc. Chem. Soc., London*, 1962, 218; (b) L. Graham, O. Graudejus, N. K. Jha, and N. Bartlett, *Coord. Chem. Rev.*, 2000, **197**, 321.
12. (a) R. Wesendrup and P. Schwerdtfeger, *Inorg. Chem.*, 2001, **40**, 3351; (b) A. D. Richardson, K. Hedberg, and G. M. Lucier, *Inorg. Chem.*, 2000, **39**, 2787; (c) O. Graudejus, A. P. Wilkinson, L. C. Chacon, and N. Bartlet, *Inorg. Chem.*, 2000, **39**, 2794.
13. W. D. Bare, A. Citra, G. V. Chertihin, and L. Andrews, *J. Phys. Chem.*, 1999, **103**, 5456.
14. L. F. Fieser and M. Fieser, 'Reagents for Organic Synthesis', Wiley, New York, 1990, Vol. 1, p. 890.
15. 'Gmelin's Handbook of Inorganic Chemistry', Verlag Chemie, Berlin, 1940, Vol. 68C.
16. C. J. Raub, V. B. Compton, T. H. Geballe, B. T. Matthias, J. P. Maita, and G. W. Hull, *Phys. Chem. Solids*, 1965, **26**, 205.
17. C. Huber, A. Kokil, W. R. Caseri, and C. Weder, *Organometallics*, 2002, **21**, 3817.
18. R. van der Linde and R. O. de Jongh, *Chem. Commun.*, 1971, 563.
19. D. S. Y. Hsu, N. H. Tumer, K. W. Pierson, and V. A. Shamamian, *J. Vac. Sci. Technol., B*, 1992, **10**, 2251.
20. D. M. Roundhill, *Inorg. Chem.*, 1970, **9**, 254.
21. C. D. Cook, R. T. Cheng, and S. C. Nyburg, *J. Am. Chem. Soc.*, 1969, **91**, 2123.
22. R. G. Holloway, B. R. Penfold, R. Colton and M. J. McCormick, *J. Chem. Soc., Chem. Commun.*, 1976, 485.
23. Q. Xu, Y. Souma, B. T. Heaton, C. Jacob, and K. Kanamori, *Angew. Chem., Int. Ed. Engl.*, 2000, **39**, 208.
24. J. Autschbach, C. D. Igna, and T. Ziegler, *J. Am. Chem. Soc.*, 2003, **125**, 1028.
25. J. Chatt, A. Duncanson, and B. L. Shaw, *Proc. Chem. Soc., London*, 1957, 343.
26. W. R. Meyer and L. M. Venanzi, *Angew. Chem. Int. Ed. Engl.*, 1984, **23**, 529.
27. E. H. Brooks and F. Glocklin, *J. Chem. Soc. A*, 1967, 1030.
28. H. C. Clark and W. J. Jacobs, *Inorg. Chem.*, 1970, **9**, 1229.
29. G. Minghetti, A. L. Bandini, G. Banditelli, F. Bonati, R. Szostak, C. E. Strouse, C. B. Knobler and H. D. Kaesz, *Inorg. Chem.*, 1983, **22**, 2332.
30. M. S. Morton, R. J. Lachicotte, D. A. Vicic, and W. D. Jones, *Organometallics*, 1999, **18**, 227.
31. D. R. Arnold and M. A. Bennett, *Inorg. Chem.*, 1984, **23**, 2110.
32. L. Atkinson, P. Day, and R. J. P. Williams, *Nature*, 1968, **218**, 668.
33. M. Kato, C. Kosuge, K. Morii, J. S. Ahn, H. Kitagawa, T. Mitani, M. Matsushita, T. Kato, S. Yano, and M. Kimura, *Inorg. Chem.*, 1999, **38**, 1638.
34. V. W.-W. Yah, K. M.-C. Wong, and N. Zhu, *J. Am. Chem. Soc.*, 2002, **124**, 6506.
35. R. D. Adams, Z. Li, R. Swepson, W. Wu, and J. Yamamoto, *J. Am. Chem. Soc.*, 1992, **114**, 10657.
36. R. J. Cross and E. Glockling, *J. Organomet. Chem.*, 1965, **3**, 253; G. Schmid and H. Nöth, *Z. Naturforsch., Teil B*, 1965, **20**, 1008.
37. K. E. Litz, J. E. Bende, R. D. Sweeder, M. M. Banaszak Holl, and J. W. Kampf, *Organometallics*, 2000, **19**, 1186.
38. R. D. Cramer, E. L. Jenner, R. Y. Lindsay, and U. G. Stolberg, *J. Am. Chem. Soc.*, 1963, **85**, 1691.
39. G. B. Kauffman, 'Classics in Coordination Chemistry', Dover, New York, 1968.
40. (a) A. Pasini and F. Zunino, *Angew. Chem., Int. Ed. Engl.*, 1987, **26**, 615; (b) W. I. Sundquist and S. J. Lippard, *Coord. Chem. Rev.*, 1990, **100**, 293.
41. L. D. Pettit and M. Bezar, *Coord. Chem. Rev.*, 1985, **61**, 97.
42. M. Taminmura, T. Mizushima, and Y. Kinoshita, *Bull. Chem. Soc. Jpn.*, 1967, **40**, 2777.
43. D. L. Reger, J. C. Baxter, and L. Lebioda, *Inorg. Chim. Acta*, 1989, **165**, 201.
44. W. Beck and W. R. Fehlhammer, *Angew. Chem., Int. Ed. Engl.*, 1967, **6**, 169.
45. S. A. Hudson and P. M. Maitlis, *Chem. Rev.*, 1993, **93**, 861.
46. V. P. Balema, J. W. Wiench, M. Pruski, and V. K. Pecharsky, *Chem. Commun.*, 2002, 1606.
47. (a) M. A. Stark, G. Jones, and C. J. Richards, *Organometallics*, 2000, **19**, 1282; (b) M. Albrecht and G. van Koten, *Angew. Chem. Int. Ed. Engl.*, 2001, **40**, 3750.

48. B. F. M. Kimmich and R. M. M. Bullock, *Organometallics*, 2002, **21**, 1504.

49. R. Ugo, G. La Monica, S. Cenini, R. Segre, and F. Conti, *J. Chem. Soc. A*, 1971, 522.

50. J. Chat and L. M. Venanzi, *J. Chem. Soc.*, 1955, 2787; 1957, 2351.

51. N. S. Kurnakov, *J. Prakt. Chem.*, 1894, **50**, 483.

52. H. Kobayashi, K. Bun, T. Naito, R. Kato, and A. Kobayashi, *Chem. Lett.*, 1992, **10**, 1909.

53. (a) D. J. Woolins and R. T. Kelly, *Coord. Chem. Rev.*, 1985, **65**, 115; (b) K. Matsumoto and M. Ochiai, *Coord. Chem. Rev.*, 2002, **231**, 229.

54. J. S. Miller and A. J. Epstein, *Prog. Inorg. Chem.*, 1976, **20**, 1.

55. R. J. H. Clark, *J. Chem. Soc., Dalton Trans.*, 1983, 141.

56. P. Arrizabalaga, P. Castan, M. Geoffroy, and J. P. Laurent, *Inorg. Chem.*, 1985, **24**, 3656.

57. R. Uson, J. Fornies, M. Tomas, and B. Menjon, *Organometallics*, 1985, **4**, 1912.

58. M. Schröder, *J. Chem. Soc., Chem. Commun.*, 1987, 118.

59. D. C. Smith and H. B. Gray, *Coord. Chem. Rev.*, 1990, **100**, 169.

60. F. Jalilehvand, M. aliarik, J. Mink, M. Sandström, A. Ilyukhin, and J. Glaser, *J. Phys. Chem. A*, 2002, **106**, 3501.

61. M. Juillard and M. Chanon, *Chem. Rev.*, 1983, **83**, 425.

62. R. J. Puddephatt, *Coord. Chem. Rev.*, 2002, **219–221**, 157.

63. I. P. Evans, G. W. Everett, and A. M. Sargeson, *J. Am. Chem. Soc.*, 1976, **98**, 8041.

64. M. Kretschmer and L. Heck, *Z. Anorg. Allg. Chem.*, 1982, **490**, 205.

65. R. Kuroda, S. Neidle, I. M. Ismail, and R. J. Sadler, *Inorg. Chem.*, 1983, **22**, 3620.

66. R. D. Gillard, *Nouv. J. Chim.*, 1986, **10**, 783.

67. L. C. Roof and J. W. Kolis, *Chem. Rev.*, 1993, **93**, 1037.

Platinum: Organometallic Chemistry

Jwu-Ting Chen
National Taiwan University, Taipei, Taiwan

Based in part on the article Platinum: Organometallic Chemistry by Charles M. Lukehart which appeared in the Encyclopedia of Inorganic Chemistry, First Edition.

1 Introduction 1
2 Organoplatinum Complexes Containing Conventional Bonding 2
3 Organoplatinum Complexes with New Organic Motifs 4
4 Clusters and Molecular Architectures 17
5 Complexes Containing Pt–Si and Pt–H Bonds 20
6 Organoplatinum(IV) Complexes 22
7 Chemical Transformations of Organoplatinum Complexes 25
8 Related Articles 33
9 References 33

Abbreviations

TCNE = Tetracyanoethylene; Dipdba = 4,4′-diisopropyl(dibenzylideneacetone); TMM = Trimethylenemethane; dppm = (Diphenylphosphino)methane; MMLCT = Metal–metal bond to ligand charge-transfer; Tp = Hydrido(trispyrazolyl)borate Tp′ = Hydridotris(3,5-dimethyl-pyrazolyl)borate; BAr'_4 = (3,5-trifluoromethylphenyl)borate; ttab = 1,2,4,5-tetrakis(1-*N*-7-azaindolyl)benzene; tmeda = Tetramethylethylenediamine; bpma = Bis(pyridylmethyl)amine; TFE = Trifluoroethanol; dtbpm = Bis(di-*tert*-butylphosphino)methane; dmpe = Bis(dimethylphosphino)ethane; dcpe = Bis(dicyclohexylphosphino)ethane; triphos = Bis(2-diphenylphosphinoethyl)phenylphosphine; COD = 1,5-cyclooctadiene; dppbts = (Diphenylphosphinobutane)tosylate sodium; PPE = Poly(*p*-phenylene ethylene).

1 INTRODUCTION

As with diverse progress in other chemical frontiers, organometallic chemistry in the last decade exhibits tremendous change from the traditional appearance. Similar to the trend in coordination and organometallic chemistry of other metals, the quest for new ligands not only extends the territory for conventional organoplatinum chemistry, but also opens up new areas for this field.

Ligand evolution has been substantially advanced in two aspects, the broadened motif as well as the growing synthetic power. Delicate design and syntheses for ancillary ligands (*see Ancillary Ligand*) are often exhausting but can be rewarding for the invention of new organometallic functionality and reactivity. The bidentate (*see Bidentate Ligand*) and tridentate (*see Tridentate Ligand*) ligands can exert a more powerful influence on the complexes of group 10, which prefer four-coordinate square-planar geometry for the most common 2+ valence, than on the metals of other groups. From the viewpoint of the ligand usage in organometallic chemistry, phosphines and the cyclopentadienyl ligands (*see Cyclopentadienyl*) represent the periods of the 1970s and 1980s respectively. Then, the nitrogen-donating ligands experienced a renaissance in the 1990s and the carbon-donating ligands caught the succeeding tide at the end of the twentieth century. Among them, cyclometallated (*see Cyclometalation*) polydentates, aminocarbenes, and diimines are the most successful examples. The modern ligands are required to fine-tune electronic and steric influence on the metal center by varying the substituents, in addition to their intrinsic character. Fortunately, rapidly developing synthetic knowledge enables acquisition of the ligand variety and optimizes the desired properties for the complexes.

One of the major landmarks in organometallic chemistry has to be the discovery of the unprecedented organometallic bonding modes or functionalities. On the other hand, the chemistry of many conventional organometallic species has been advanced substantially. In addition to simply seeking new compounds and structures, the quest for new substances that possess specific properties and applications has become an essential issue in research. For instance, the organic π-conjugates bring abundant photophysical properties to organoplatinum. The rigid linear alkynyl units are the most favored building blocks for molecular architecture (*see* ***Self-assembled Inorganic Architectures***) of large skeletons.

Proceeding with nano technology, nano sciences created immense waves in the late twentieth century. The concept of supermolecules was created for chemical composition beyond the covalent association of atoms.**[1]** The synthesis by means of assembling large building blocks through weak interactions entered the chemical arena. Because the coordination compounds intrinsically combine the geometry and molecular assembly through metal, they are naturally employed as cornerstones for preparing supermolecules and nano-materials.

Although the compounds containing the Pt–C bonds are legitimate organoplatinum members, the species with the Pt–Si and Pt–H bonds that show comparable reactivity are often adopted into organoplatinum chemistry. Studies in platinum(IV) chemistry have opened new windows for learning the C–H activation, the long-term Holy Grail in organometallic chemistry. Apparently, the electron-rich nitrogen-donor ligands can stabilize the highly valent Pt(IV) state. Some new chemical transformations developed along with the discovery of the new platinum-alkyl and aryl compounds, affording insights into mechanistic and catalytic paradigms. Other new chemical transformations and mechanistic studies of the organoplatinum complexes concerning carbon–carbon as well as carbon–main group elements coupling reactions are discussed.

This review is selective and is prepared to provide the representative features and prevailing developments of organoplatinum chemistry, particularly in the last decade. The subjects that are closely related to coordination chemistry, luminescence behavior, catalysis, organic synthesis using transition metal complexes, and organometallic clusters, and so on, which are covered in articles in this volume, are not discussed in detail.

2 ORGANOPLATINUM COMPLEXES CONTAINING CONVENTIONAL BONDING

2.1 Ligands with Carbon Donor

Cyclometallation, which provides multidentate ligands containing carbon donors, has been known as a useful synthetic method for preparing organometallic complexes.[2] A noticeable extension in such a category, which substantially facilitates the recent development of organoplatinum chemistry, is the pincer-type ligands, which allow tridentate meridional chelation with various donor combinations to the metal.[3]

There are three typical synthetic routes for these complexes. The first way is with use of conventional oxidative addition (*see Oxidation Number*) of aryl halides to a Pt(0) precursor (Scheme 1). The second is via transmetallation (*see Transmetalation*) using anionic aryl salts (Scheme 2).[4] The third and perhaps the most convenient method for the preparation of the cyclometallated ligands is through aryl C–H activation (Scheme 3).[5] It appears that the C–H activation may be facilitated by a pre-coordination that assists the orthometallation (*see Orthometalation*) in proximity.

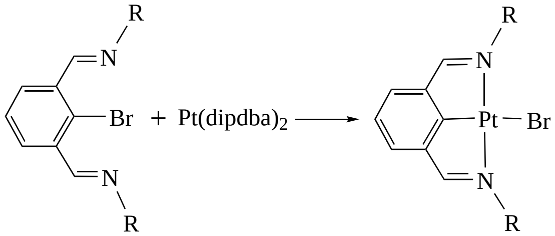

Scheme 1

Such pincer ligands have been expanded with all kinds of imaginable combinations and variations. They not only may serve as ancillary groups or be involved in the reactions, but also can result in novel reactivity or confer specific physical properties on the complexes. For instance, complexes with bifunctional ligands are used as building blocks for polymeric materials (Scheme 4).[6] The crystals of a pincer complex are found to show controlled and fully reversible crystalline-state change based on incorporation of SO_2 into the crystal lattice (Scheme 5).[7] Such transformation along with distinct color change is thought to afford gas-storage devices as opto-electronic switches. A complex (**1**) resulting from water-induced double cyclometallation with 2,6-diphenylpyridine shows [C-N-C] ligation.[8] Suitable arrangements such as [C-N-N] in (**2**) and (**3**) show photoluminescence.[9] The extension to macrocyclic derivatives leads to the synthesis of *N*-confused porphyrin complexes (Scheme 6).[10]

The amino carbene ligands open a new era of ancillary ligands in organometallic chemistry. One of the pioneering studies is the synthesis of 2-coordinate homoleptic (*see Homoleptic Compound*) complexes of low-valent noble

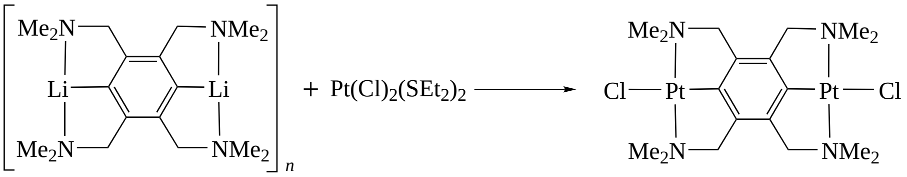

Scheme 2

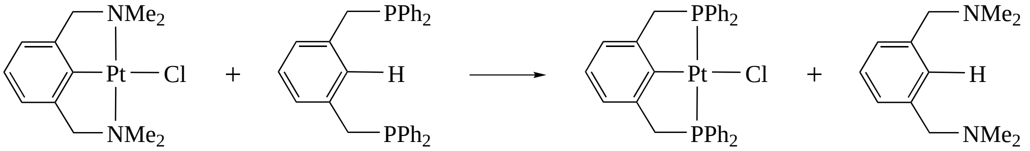

Scheme 3

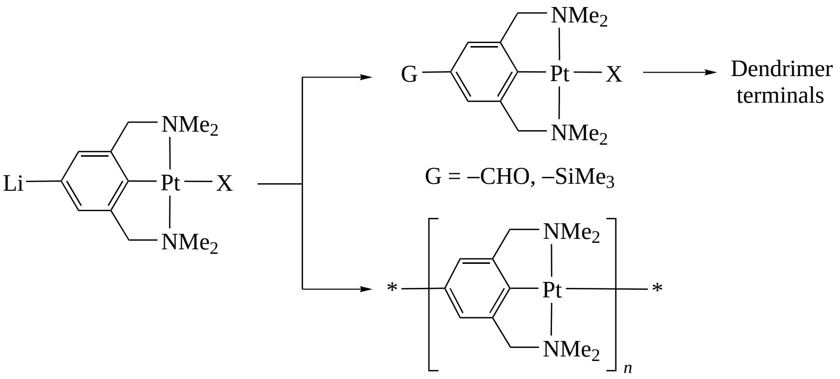
NMe2
Li
Pt
X
NMe2
G
Pt
X
Dendrimer terminals
G = –CHO, –SiMe3
*
Pt
*
n

Scheme 4

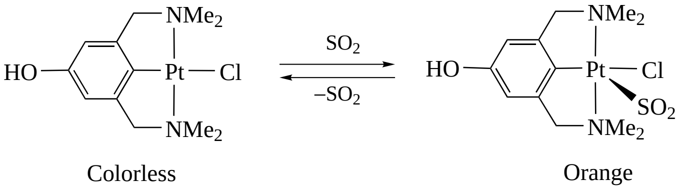
HO
NMe2
Pt
Cl
NMe2
SO2
–SO2
SO2
Colorless
Orange

Scheme 5

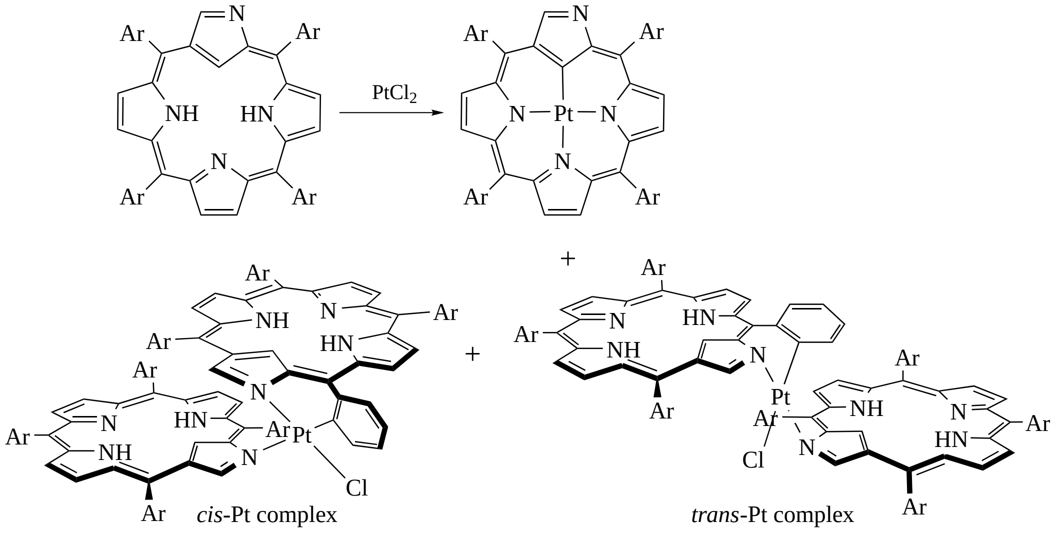
Ar
N
NH
HN
PtCl2
Pt
+
Cl
cis-Pt complex
trans-Pt complex

Scheme 6

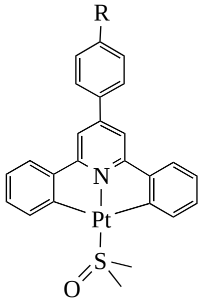

(**1**)

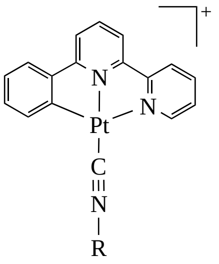

(**2**)

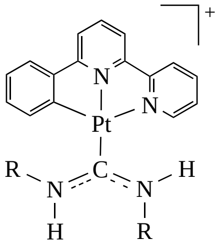
+
N
Pt
N
C
R
N
H
H
N
R

(**3**)

metals including platinum by ligand replacement, as shown in Scheme 7.[11] The NMR and X-ray crystallographic characterizations evidence the dπ-pπ back-donation (*see Back Bonding*) in the M–C bonds in the biscarbene platinum complex, which holds a linear geometry with the imidazole rings twisted 51°. The N,N'-di-*tert*-butyl biscarbene platinum derivative $Pt[C\{N(^tBu)CH\}_2]_2$ could result from cocondensation of metal vapor with an excess of ligand. The geometry of the complex is still linear, but with a 90° twisting imidazole angle.[12] The ligand variation extends to the bidentates (**4**);[13] and a tridentate ligand

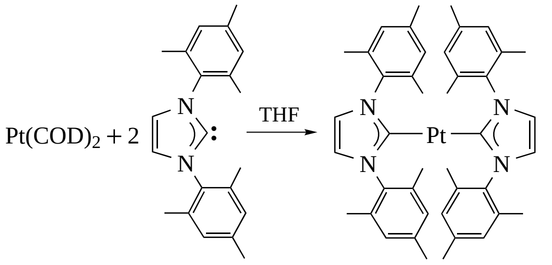

Scheme 7

of bis(pyridine) carbene provides the Pt(IV) species (**5**).**[14]** Recently, an anionic bis(phosphinidene) carbene gives a tris(carbene) pincer complex under CO atmosphere (**6**).**[15]**

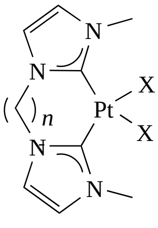

n = 1, 2

(**4**)

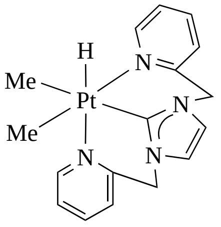

(**5**)

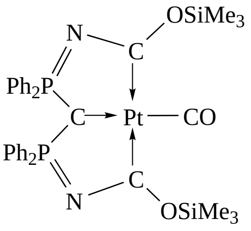

(**6**)

2.2 Ligands with Nitrogen Donors

Phosphines had been employed more in organometallic chemistry of soft late transition metals than had the ligands with nitrogen donors. An important development of exploiting new ligands in the latest decade has to be the usage of bidentate diimines. One reason for the renaissance of these long-time known species is the introduction of deliberate steric control in the proximity of metal. In a square-planar environment, the *ortho*-substituted aryls at the imino nitrogen likely dispose perpendicularly to the molecular plane as shown in (**7**). Such a configuration will have the aryl substituents at the *ortho*-carbons point to the axial coordinating sites. Bulky R group such as isopropyl thus can efficiently influence the reactivity that requires the axial vicinity.**[16,17]**

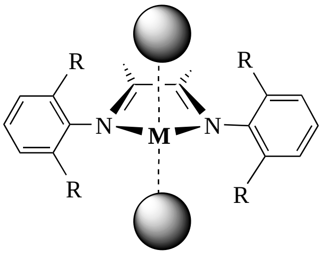

(**7**)

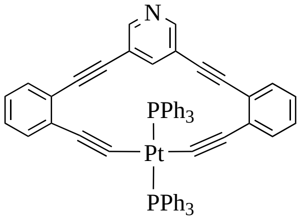

(**8**)

The diimine ligands with aryls containing different ortho substituents can generate the syn- and anti- isomers that differ in orientation of the substituents with respect to the coordination plane as shown in Scheme 8.**[18]** Such a coordination arrangement confers further chemical selectivity on the complexes (Scheme 9).**[19]** The methyl groups on C_α atoms make the reduction of the metal center more difficult than the C_α-unsubstituted complexes. On the other hand, a change of the substituent at the aromatic ring has virtually no effect. The square-planar Pt(II) dialkyl complexes appear to undergo Pt–R homolysis upon oxidation. Oxidation by a one-electron process results in subsequent disproportionation (*see Disproportionation*) to (N-N)Pt^{II}(L)Me and (N-N)Pt^{IV}(L)Me_3 cations. The former species is an analog of the active species in C–H activation and alkene polymerization reactions (*see Alkene Polymerization*).**[20]**

Shilov and coworkers discovered the oxidation of methane to methanol by mixtures of Pt^{II} and Pt^{IV}, and aroused the Holy Grail-pursuing for electrophilic C–H activation and subsequent alkane oxidation. The diimine complexes of Pt(II) methyl are indeed found to facilitate smooth benzene activation, resulting in formation of methane via Pt^{IV}(Me)(Ph)(H) intermediates (Scheme 10).**[21]** Such Pt(II)/Pt(IV) involved C–H activation reactions have been widely extended to a variety of nitrogen-donor ligands, whose electronic and steric effects shed light on the reaction mechanisms (see Section 7.1).

Chirality has been introduced into the diimine complexes to give rise to the reactivity control. For example, high stereoselective α-olefin coordination has been observed in a special di-exo-iminocyclohexane complex (Scheme 11).**[22]**

3 ORGANOPLATINUM COMPLEXES WITH NEW ORGANIC MOTIFS

3.1 σ-Donor Complexes

Metal carbonyls (*see* ***Carbonyl Complexes of the Transition Metals***) are extended to superelectrophilic cations, including square-planar $[Pt(CO)_4]^{2+}$ by reductive carbonylation of $Pt(SO_3F)_4$ or PtF_6 in super acid environment (Scheme 12).**[23]** Using a comparable approach, $[Pt(CO)_3]^{2+}$ in

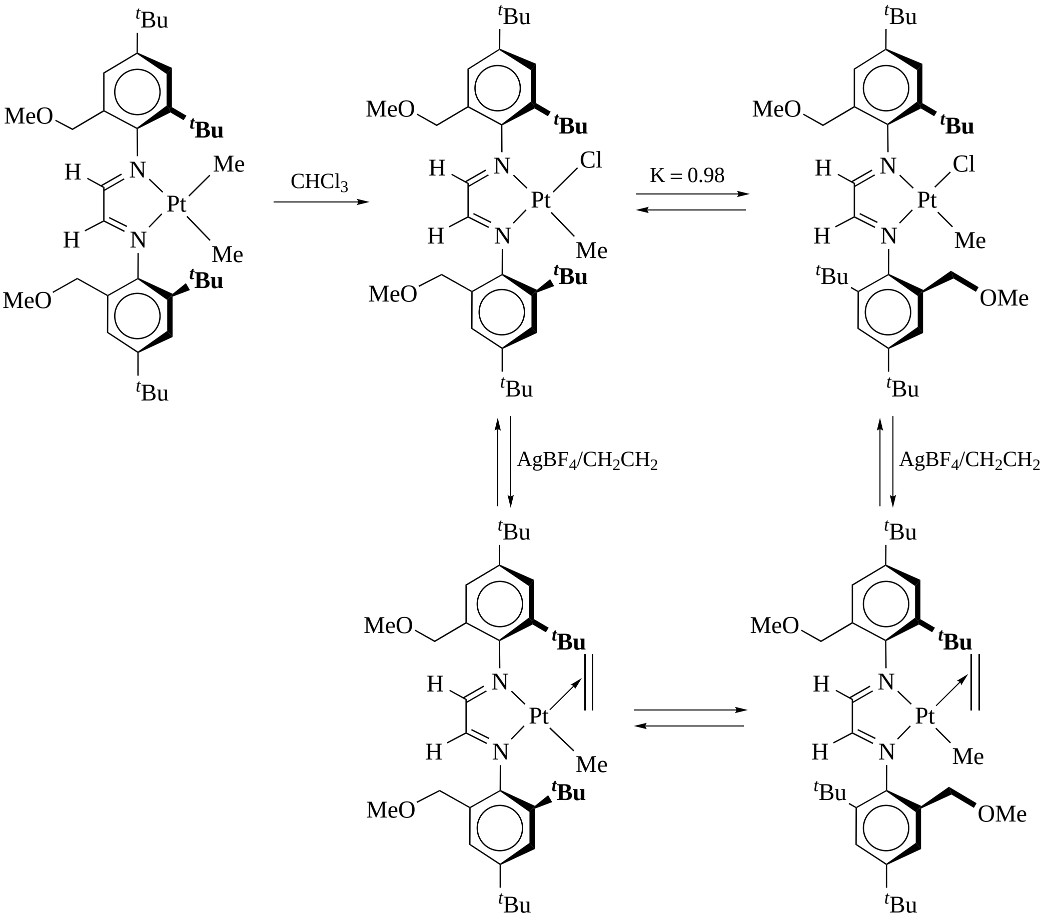

Scheme 8

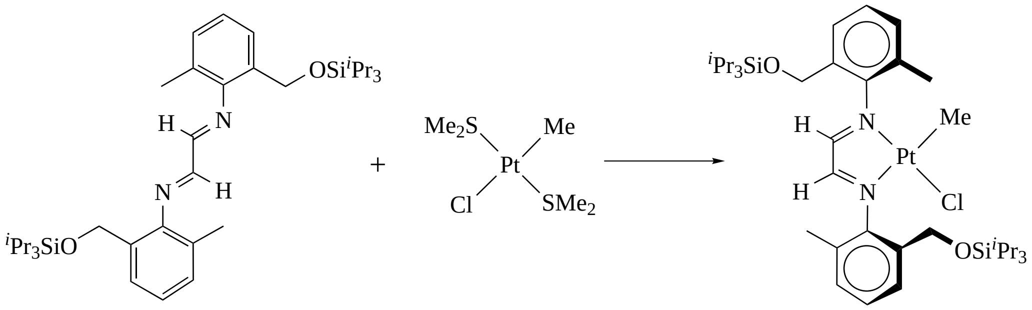

Scheme 9

S_4 symmetry of which two planar T-shape $Pt(CO)_3$ fragments are associated in perpendicular configuration through the Pt–Pt bond is obtained by the dissolution of PtO_2 in concentrated sulfuric acid (Scheme 13).**[24]** The vibrational stretching frequencies of carbonyl are over 2200 cm^{-1}, and the ^{13}C MAS NMR measurements are found below $\delta 140$.

The dialkyl complexes of platinum(II) with coordinating dimethyl sulfide typically like $Pt(SMe_2)_2Me_2$ and $Pt_2Me_4(\mu\text{-}SMe_2)_2$ have been known for certain period, and now are widely used as starting materials for the synthesis of new organoplatinum complexes with nitrogen donors.**[25]** Ligands with hybrid donors or special donating functionalities sometimes may assist the synthesis of new species. A platinum methylene complex was generated by treating lithium salt in CH_2I_2 (Scheme 14).**[26]** Thermolysis of a (perfluoroalkylphosphine)ethyl complex at 120 °C in CF_3CO_2H results in the formation of a μ-alkylidene (*see Alkylidene*) complex (Scheme 15).**[27]**

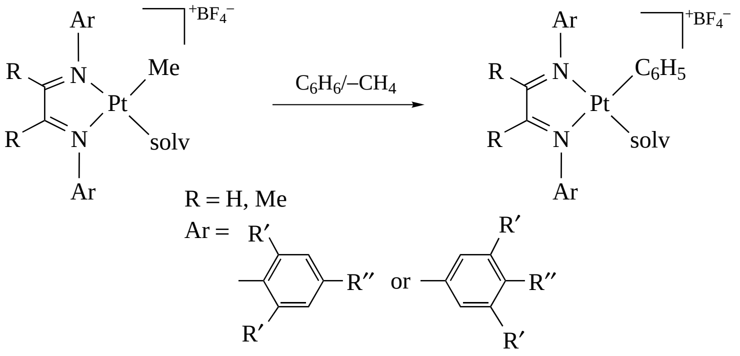
Ar
+BF4−
R
N
Me
Pt
R
N
solv
Ar
C6H6/−CH4
Ar
+BF4−
R
N
C6H5
Pt
R
N
solv
Ar
R = H, Me
Ar =
R′
R″
or
R′
R″
R′
R′

Scheme 10

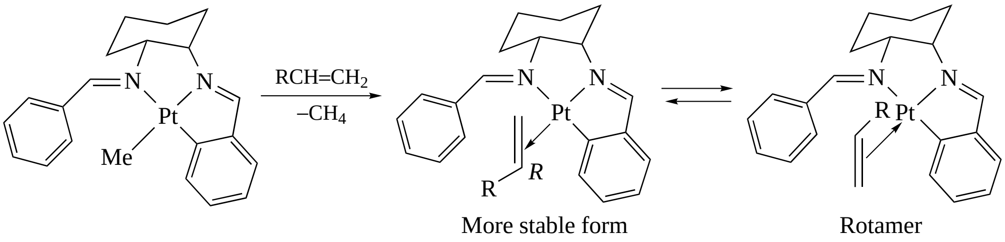
N
N
Pt
Me
RCH=CH2
−CH4
N
N
Pt
R
R
More stable form
N
N
R Pt
Rotamer

Scheme 11

$$\mathrm{PtF_6} + 6\mathrm{CO}\ (1\ \mathrm{atm}) + 4\mathrm{SbF}_{5(l)} \longrightarrow [\mathrm{Pt(CO)_4}][\mathrm{Sb_2F_{11}}] + 2\mathrm{COF_2}$$

Scheme 12

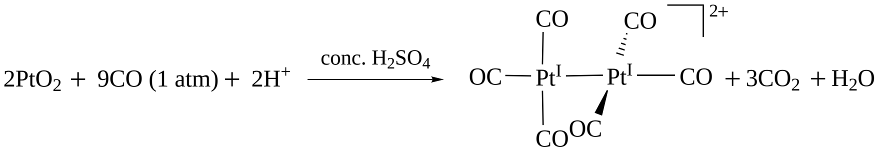
2PtO2 + 9CO (1 atm) + 2H+
conc. H2SO4
CO
CO
2+
OC
PtI
PtI
CO
+ 3CO2 + H2O
CO
OC

Scheme 13

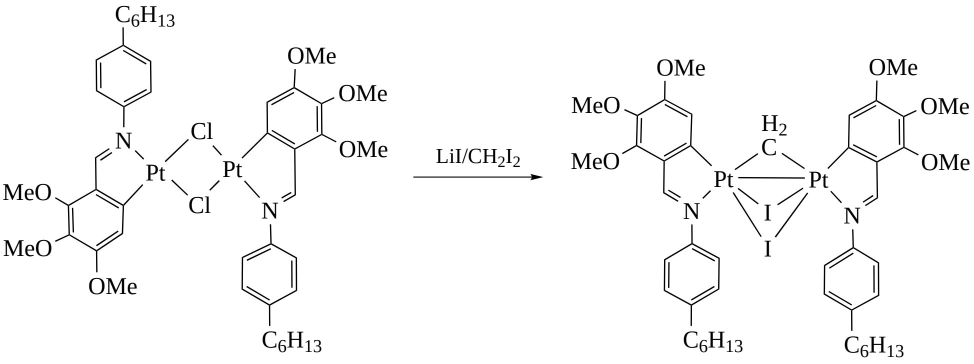
C6H13
OMe
OMe
N
Cl
OMe
Pt
Pt
MeO
Cl
N
MeO
OMe
C6H13
LiI/CH2I2
OMe
OMe
MeO
OMe
H2
C
MeO
OMe
Pt
Pt
N
I
N
I
C6H13
C6H13

Scheme 14

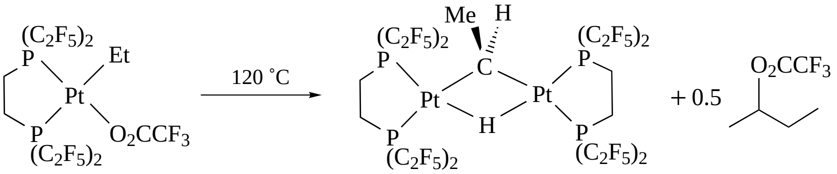

Scheme 15

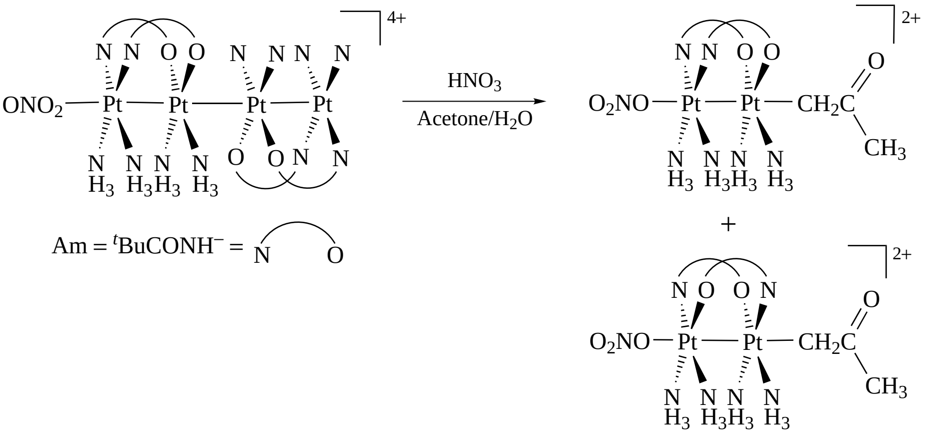

Scheme 16

The pivalamidate-bridged diplatinum^{III} ketonyl complexes may be prepared from the reaction of platinum blue complex and nitric acid in acetone.[28] Two isomers with the amidate configuration in head-to-head and head-to-tail modes and the ketonyl ligand at one axial end are characterized (Scheme 16). An alternative route is from catalyzed oxidation of olefins.[29]

Transformation between platina-β-diketones, the metallo analogues of enol tautomers of 1,3-diketones, and platina-β-diketonates was previously studied in the 1980s.[30] Recent studies indicate the reaction of platina-β-diketone with bipyridines via oxidative addition yields the diacyl hydrido Pt(IV) complex. Further ligand abstraction may result in H–bond bridged dimer and a double-deck dimer through Pt–Pt interaction (Scheme 17).[31] On the other hand, the prototype of unsupported *cis*- diacyl platinum(II) species was obtained either via nucleophilic addition to cationic acyl carbonyl complexes or CO insertion into a trans acyl alkyl complex (Scheme 18). In the latter process for propionyl methyl or acetyl ethyl complex,

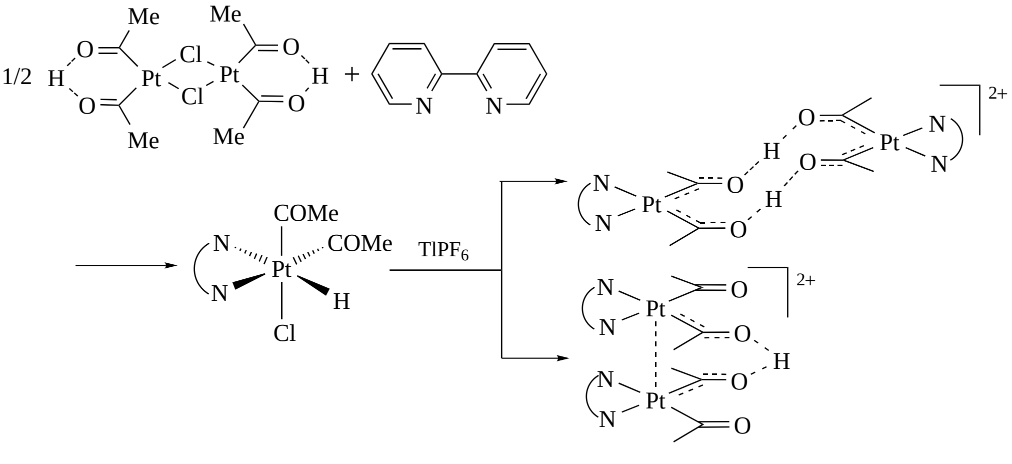

Scheme 17

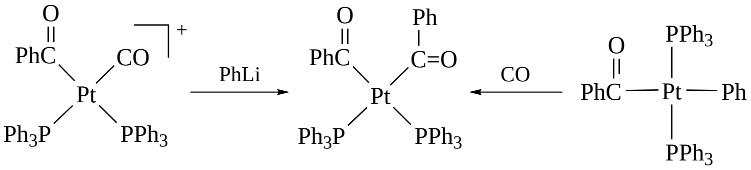

Scheme 18

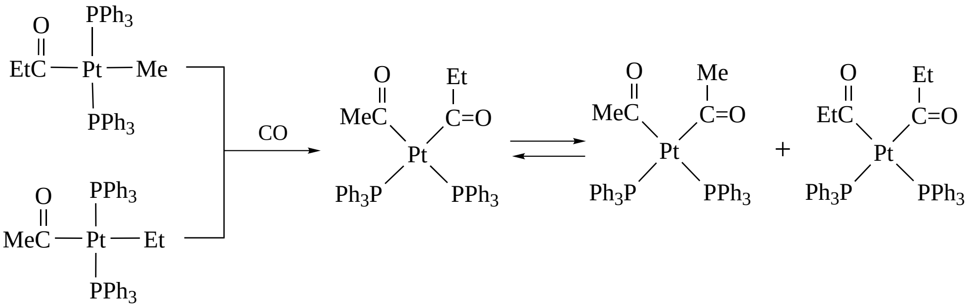

Scheme 19

the insertion may result in acyl scrambling (Scheme 19). Trans-diacyl complex was obtained from a facile decarbonylative isomerization of an α-ketoacyl alkyl complex (Scheme 20). Such diacyl species are the legitimate models for Pd-catalyzed double carbonylation reactions (*see Carbonylation*).[32]

Metallacycles (*see Metallacycle*) are readily prepared via C–C bond activation, particularly in a strained ring. Insertion of Pt(0) into biphenylene leads to the formation of biphenyl complex. Following this strategy, the reaction of semibuckminsterfullerene ($C_{30}H_{12}$) with Pt(0) yields a buckybowl complex (Scheme 21).[33] Similar ring expansion via carbon–sulfur bond cleavage is also observed. Thiaplatinacycles derived from thiophenes and Pt(0) has been achieved (Scheme 22).[34] Such reactions may serve as good models for the homogeneous hydrodesulfurization processes. In one case, a platinum hydride complex (*see* ***Hydride Complexes of the Transition Metals***) was capable of generating the biphenyl product by sulfur extrusion (Scheme 23).[35]

Alkynyl complexes, also known as metal acetylides, possess both rigid linear skeleton and π-conjugation. In the structural aspect, alkynyls make excellent linear bridging units. By means of the reactions of transmetallation (*see Transmetalation*), poly-Pt-acetylides are readily synthesized (Scheme 24).[36] Copper(I)-mediated oxidative coupling

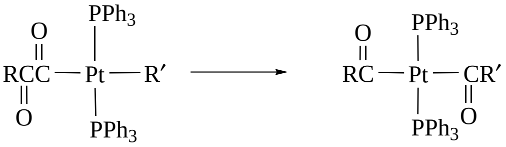

Scheme 20

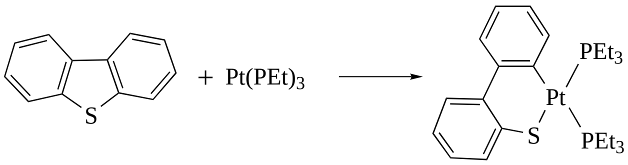

Scheme 22

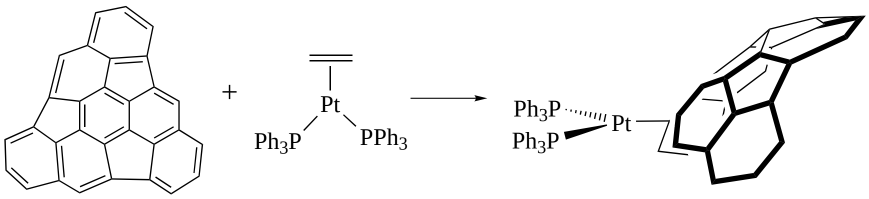

Scheme 21

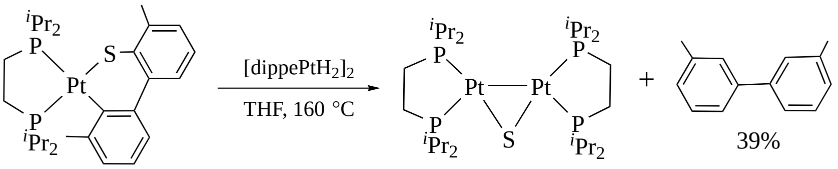

Scheme 23

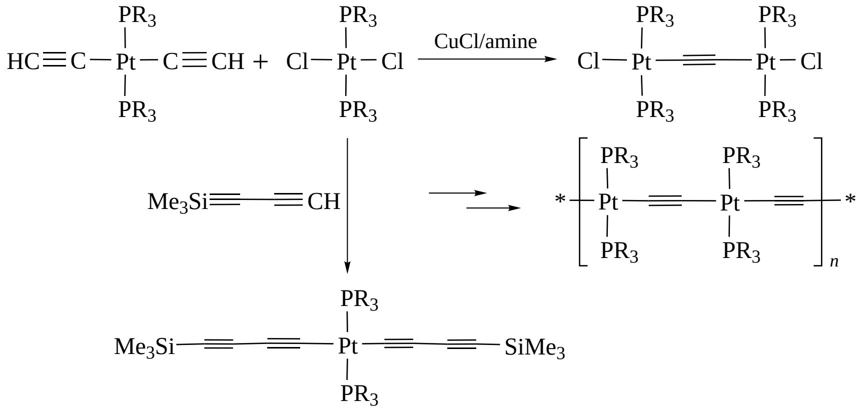

Scheme 24

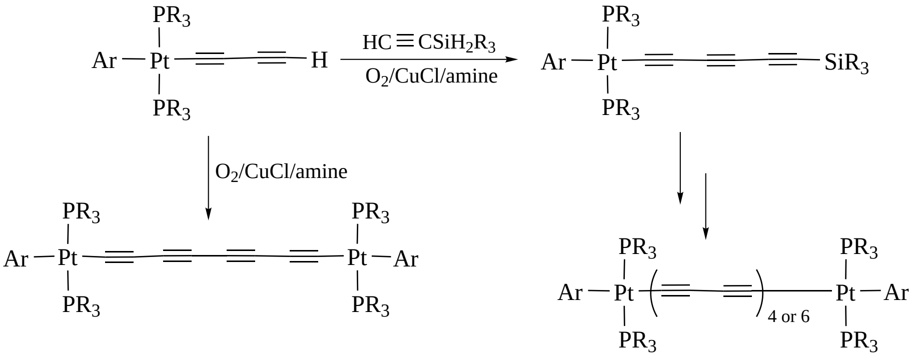

Scheme 25

achieves the extension of the poly-yne units. With use of both reactions, dinuclear complexes with the carbon-rich chain of C_8 or C_{12} are formed (Scheme 25).[37] By coupling of dialkyne, a platinocycle (**8**) is obtained.[38] Similar ideas are also used to build large size molecules (see Section 4.2). The yne-bridged unit undergoes coupling with Tetracyanoethylene (TCNE) to give μ-cyclobutene and s-cis/s-trans butadiene complexes (Scheme 26).[39]

In the photophysical aspect, many platinum acetylides exhibit a luminescent property. The photo- and electrochemical research for such species combines with the structural chemistry to pave a path toward the exploration of molecular opto-electronic devices, and is described in Section 3.3.

3.2 π-Donor Complexes

One of the most famous compounds of the 1990s has to be the fullerene (*see* ***Carbon: Fullerenes***) C_{60} (*see Buckminsterfullerene*). The first synthesized complexes of C_{60} were the mononuclear and the hexaplatinum complexes via π-coordination. The reaction of $(PPh_3)_2Pt(C_2H_4)$ and C_{60} in toluene produced a dark emerald compound, which was found to be $(PPh_3)_2Pt(\eta^2\text{-}C_{60})$ (see Figure 1). Even more interestingly, in a comparable reaction of $Pt(PEt_3)_4$ and C_{60}, a product of multiple addition $[(PEt_3)_2Pt]_6(\eta^2\text{-}C_{60})$ was recovered (see Figure 2). Both complexes were structurally characterized by X-ray crystallography.[40]

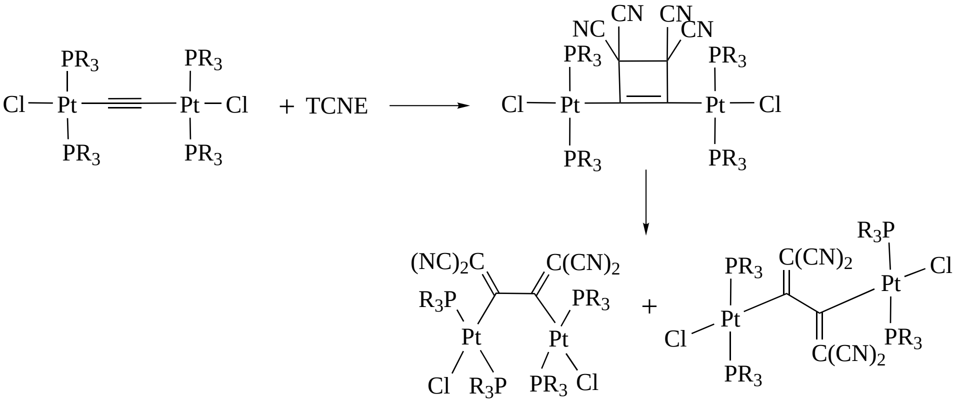

Scheme 26

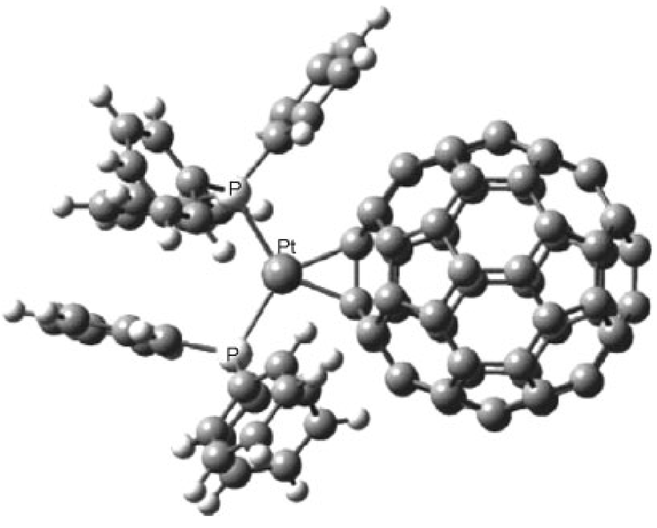

Figure 1 Structure of $[(C_6H_5)_3P]_2Pt(\eta^2\text{-}C_{60})$

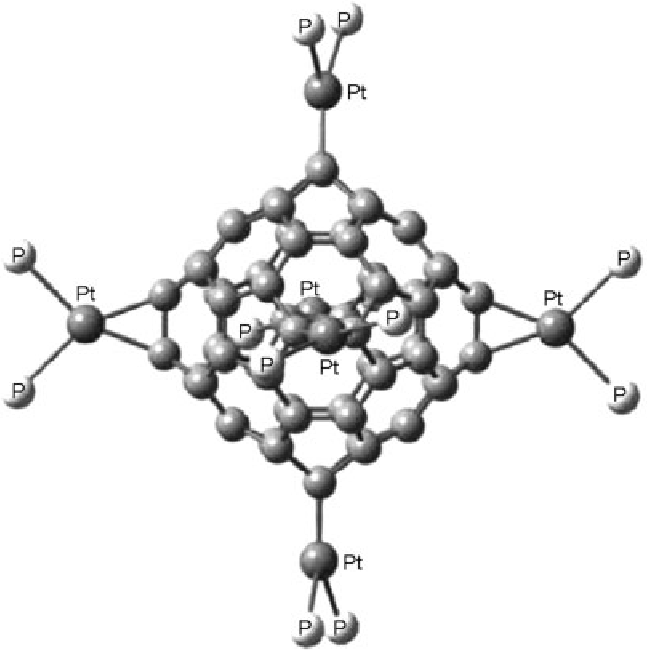

Figure 2 Structure of $[(Et_3P)_2Pt]_6C_{60}$ (The ethyl groups are omitted for clearness)

π-Olefin platinum(0) complexes are important starting materials for oxidative addition (*see Oxidative Addition*) or catalysts. Karstedt's catalysts, which are the most active ones for hydrosilylation, have been structurally characterized and found to show the structure of $Pt_2(M^{vinyl}M^{vinyl})_3$ (**9**), wherein M^{vinyl} = divinyltetramethyldisiloxane.**41** A styrene analogue $Pt^0(styrene)_3$ provides a convenient route to get an π-alkyne platinum complex by displacement (Scheme 27).**42** DFT calculations indicate that alkyne in the complexes that have the form of $L_2Pt–C_2H_2$ should be two-electron donor rather than four-electron. The bidentate

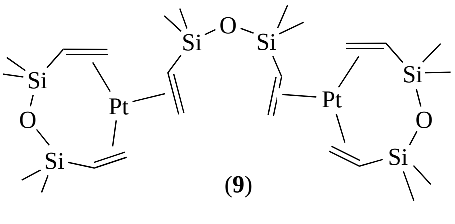

(**9**)

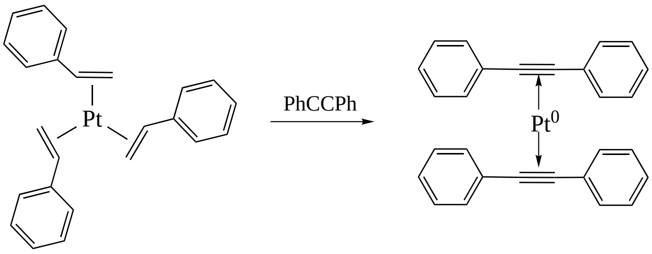

Scheme 27

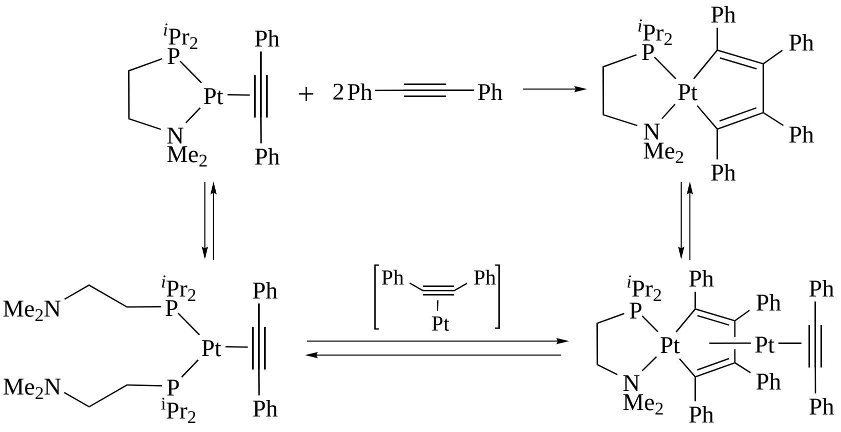

Scheme 28

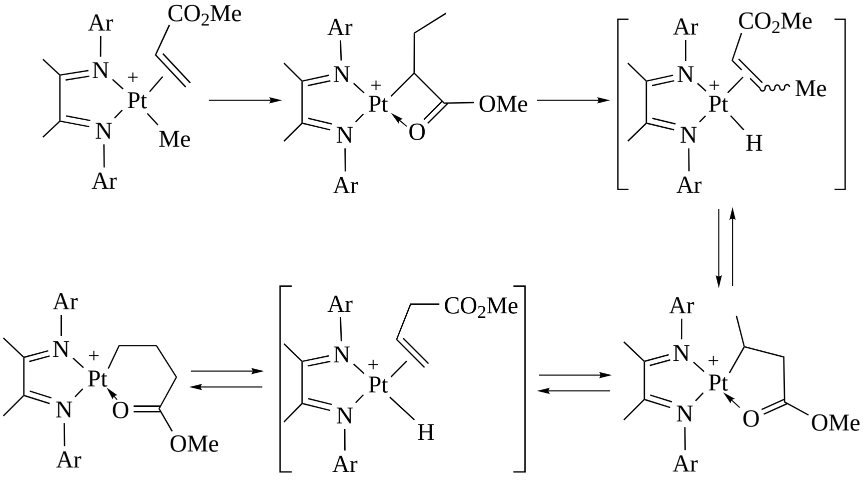

Scheme 29

phosphines can stabilize the coordinated alkene and alkyne better than do the monodentate phosphines.[43] A bidentate aminophosphine ligand is found to promote the alkyne-coupling that may lead to catalytic formation of a benzene derivative (Scheme 28).[44]

Olefin complexes (*see Alkene Complexes*) of platinum(II) are key intermediates in many very important organometallic reactions. However, direct research of well-characterized examples of metal-olefin is relatively rare, because such species are generally unstable. The diimine ligands with bulky substituents at nitrogen can kinetically stabilize the olefin ligands with electron-withdrawing substituents. In a methyl acrylate complex, migratory insertion and β-elimination leading to the formation of cyclometallated isomeric products was monitored by NMR (Scheme 29).[45] This reaction makes a good model for α-olefin polymerization. A similar (N-N)Pt-olefin compound allows the addition-elimination of the Se–Se bond and the measurement for the tunable equilibria, providing valuable reference to catalyzed addition of the main group substrates to unsaturated hydrocarbon (Scheme 30).[46] The Pt(IV)-olefin chemistry for mechanistic (*see* ***Mechanisms of Reaction of Organometallic Complexes***) concerns for alkane activation reactions are included in Section 7.1.

η^2-Alkyne complexes (*see Alkyne Complexes*) of platinum(II) are much more stable than the η^2-olefin complexes. They may be readily transformed to η^1-alkynyl and vinylidene complexes. The coupling of two η^1-alkynyl ligands results in platinacyclopentadiene species.[47] A platinum(II) disilyl(η^2-alkyne) undergoes insertion (*see Insertion*) and reductive elimination (*see Reductive Elimination*) to disilacyclohexene (Scheme 31).[48] Metal-dialkynyls can also play π-donors to form the coordination complexes of various configurations, as shown in (**10–13**) and so on.[49] Such σ,π-bridging modes may have interconversion. Multi- alkynyl complexes can even constitute clusters or higher-order structures.[50]

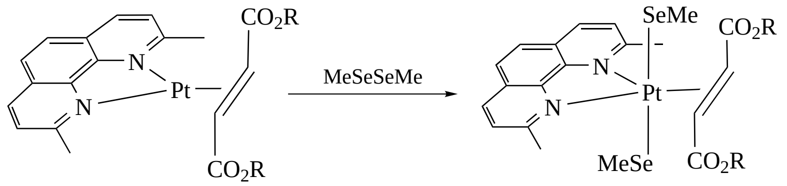

Scheme 30

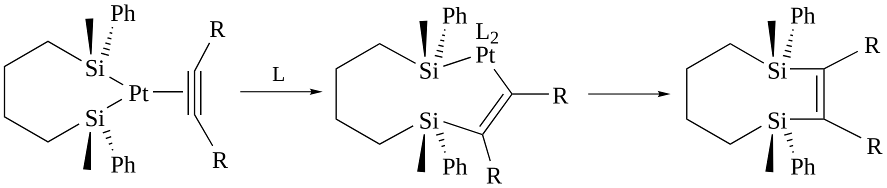

Scheme 31

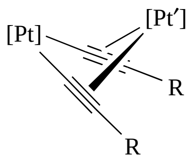

(**10**)

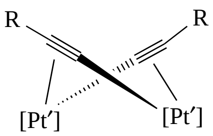

(**11**)

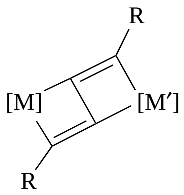

(**12**)

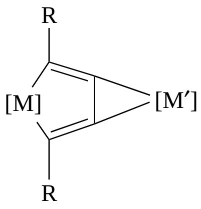

(**13**)

3.3 Organoplatinum with Photophysical Properties

By the end of last century, one characteristic development in chemical research was that chemists were able more efficiently than ever to exploit the synthetic power to assemble molecular devices that exhibited pragmatic properties. Intensive research has been focused on photophysical studies of luminescent materials (*see* ***Luminescence Behavior & Photochemistry of Organotransition Metal Compounds***). Alkynyl complexes are one of the most studied systems. For mononuclear dialkynyl complexes in the form of (**14**), the low-energy band ($3.43 \sim 3.51$ eV) corresponding to a $\pi \rightarrow \pi^*$(CCR) transition increases with the ligand σ-donor strength (L = $PCy_3 > PBu_3 > PPh_3 > P(OEt)_3 > P(OPh)_3$) (*see* ***Coordination & Organometallic Chemistry: Principles***). These transitions possess charge-transfer character as a result of overlap between π^*(CCR) and metal *p* orbitals.**[51]** One such compound is successfully fixed between two gold electrodes as a single-molecule electronic junction in a gold-[Pt]-gold setup and shows insulating behavior up to a bias voltage of 5 V.**[52]**

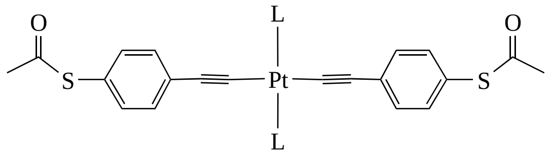

(**14**)

An A-frame dinuclear platinum complex in the form of $[Pt_2(\mu\text{-dppm})_2(\mu\text{-CCR})(CCR)_2]^+$ (**15a**) displays more red-shift lower energy bands than the mononuclear complexes. Such a change is attributed to a metal–metal bond to ligand charge-transfer (MMLCT) [$d\sigma^* \rightarrow p\sigma/\pi^*$(**15b**)] transition ($400 \sim 450$ nm) in the A-frame structure of C_{2v} symmetry, as shown in Scheme 32. The face-to-face complex (**16**) also exhibits intense low-energy bands that involve the MMLCT transition. The coordination of Cu^I or Ag^I with the alkynyl ligands (**17**) would give rise to an increase in the $d\sigma^*$ (Pt) orbital energy, as well as a decrease of the π^* (CCPh) orbital energy, thus leading to further red-shift.**[53]**

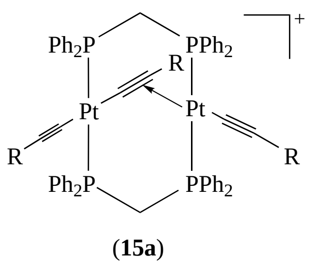

(**15a**)

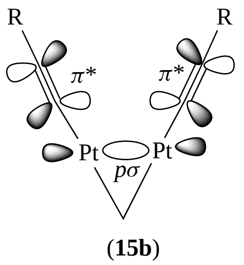

(**15b**)

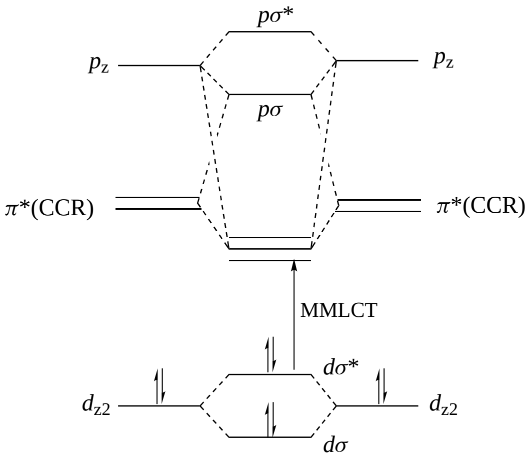

Scheme 32

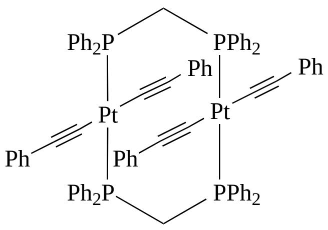

(**16**)

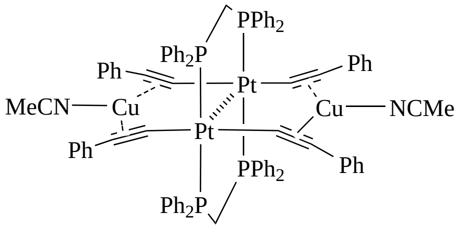

(**17**)

In the same regard, platinum(II) terpyridyl complexes (**18**) earn attention too. For the derivatives with $\mathrm{X = Ph}$, the low-energy bands (460–600 nm) are assigned to formal ^{3}LLCT states that receive substantial contribution from closely lying ^{3}MLCT levels. When $\mathrm{X = Me}$ or Cl, luminescence of much red-shift (680–800 nm) is from ^{3}MMLCT owing to metal–metal interactions occurring in head-to-tail dimers or polymers.[54] In a recent study, large solvatochromism of the diynyl complexes ($\mathrm{X = C\ C{\equiv}C{-}C{\equiv}CH}$), presumably due to metal–metal and π-stacked interactions, has been observed.[55] The cyclometallated phenyl bipyridine complexes (**19**) also show tunable excited-state properties, and the dinuclear species can reflect the metal–metal interactions in the $[d\sigma^* \rightarrow \pi^*]$ transitions.[56] The electrochemical and spectroscopic properties of the ferrocene-attached (*see Ferrocene*) dipyridyl derivatives (**20**) are found to be strongly influenced upon complexation, indicating the substantial communication of π-conjugation between the ligand and metal.[57] In the bisalkynyl diimine platinum(II) complexes or the related (phen)Pt$^{\mathrm{II}}$ derivatives, the $\mathrm{Pt} \rightarrow \pi^*$(N-N) MLCT bands dominate the photophysical behavior.[58] The wide tunable luminescent behavior of such complexes has been studied for molecular photochemical devices.[59] The luminescent behavior of organometallic compounds is the theme of the article ***Luminescence Behavior & Photochemistry of Organotransition Metal Compounds*** of this volume.

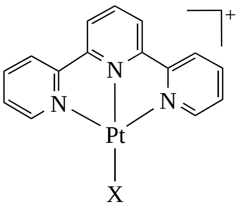

(**18**)

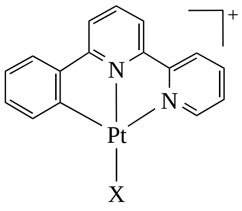

(**19**)

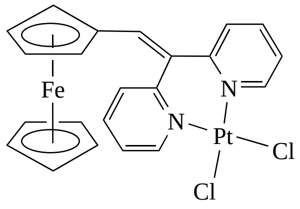

(**20**)

3.4 Complexes with Nonorthodox Bonding

In the polynuclear framework (*see* ***Polynuclear Organometallic Cluster Complexes***), allenyl and propargyl ligands are often bound to the metals with various crossing interactions, which serve to bring the metal atoms into close proximity and stabilize the hydrogen-deficient organic moiety.[60] In the

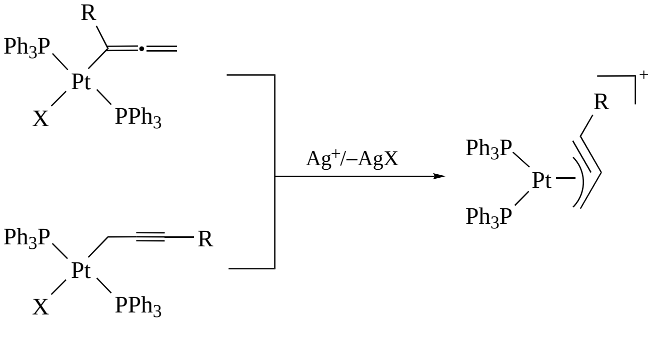

Scheme 33

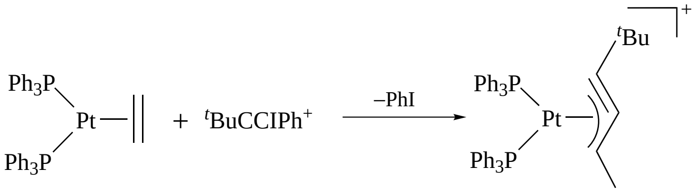

Scheme 34

mononuclear complexes, the allenyl and propargyl groups are found to associate to platinum in a resonance structure of η^3-allenyl/propargyl bonding mode (**21**). Halide abstraction either from the η^1-allenyl or from the η^1-propargyl platinum complexes in the form of $Pt(PPh_3)_2(C_3H_2R)(X)$ leads to the formation of cationic η^3-allenyl/propargyl species, as shown in Scheme 33.[61,62] Other synthetic strategies, including insertion of alkynylium (from alkynyl(phenyl)iodonium salts) into Pt-ethylene (Scheme 34)[63] or alkoxy abstraction by Lewis acid from Pt-(propargyl ether) (Scheme 35), provide the same class of products.[64] In the skeleton of PtC_3, the metal is bonded to all three carbon atoms in the same plane. Such a binding form severely distorted the organic moiety to a 145 ∼155° bent shape.

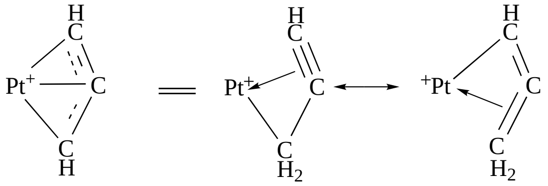

η^3-allenyl/propargyl σ,π-propargyl σ,π-allenyl

(**21**)

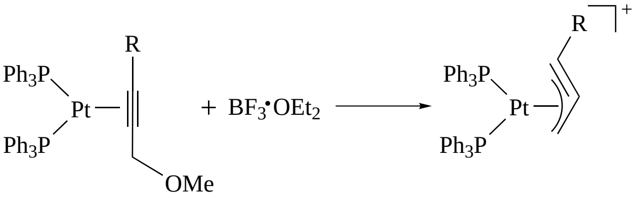

Scheme 35

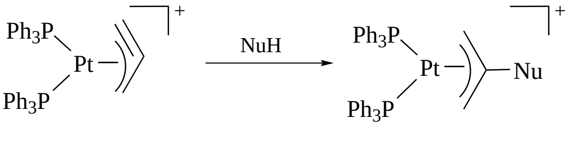

Nu = OR, SR, SeR

Scheme 36

The η^3-allenyl/propargyl platinum cations generally exhibit electrophilicity at the central carbon. The unsubstituted η^3-allenyl/propargyl species is particularly reactive and is subject to addition to a wide variety of nucleophiles (*see Nucleophile*). The reactions of the η^3-allenyl/propargyl species with alcohol, thiol, and selenol result in the formation of central-carbon substituted allyl platinum complexes (Scheme 36). Water that has two active hydrogen atoms undergoes single addition to form a 2-hydroxyallyl and double addition to form a bis(allylplatinum) ether (Scheme 37). Analogous reactions with Group 5 nucleophiles such as primary and secondary amines or with the hydroxide ion yield η^3-aza- or η^3-oxa-trimethylenemethane derivatives, respectively (Scheme 38). The central carbon of the Trimethylenemethane (TMM) derivatives spares its bonding interaction with metal to the

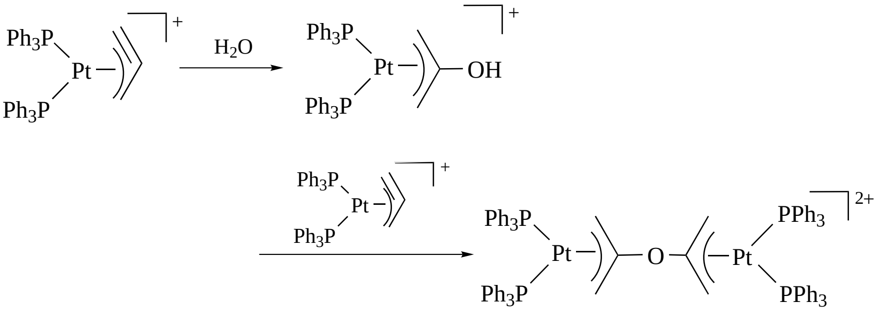

Scheme 37

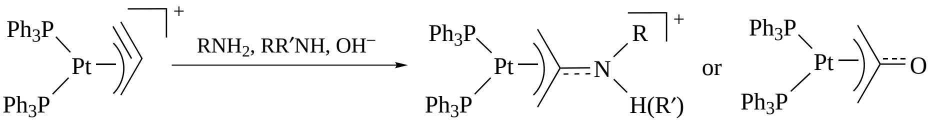

Scheme 38

adjacent heteroatom. This is also evidenced by the structural characterization of allyl (**22**), 2-hydroxyallyl (**23**), oxa-TMM (**24**), and platinacyclobutane (**25**). The dihedral angle between the planes of $C_1{-}C_2{-}C_3$ and $C_1{-}Pt{-}C_3$ decreases and the bond distance of Pt–C_2 increases with the order (**22–25**).

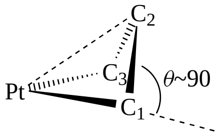

Pt-allyl (**22**)

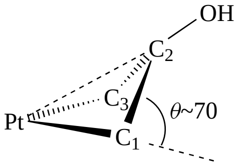

Pt-2-hydroxyallyl (**23**)

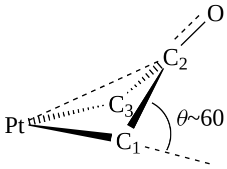

Pt-oxa-TMM (**24**)

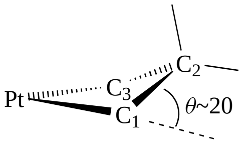

Pt-cyclobutane (**25**)

The reactions with tertiary amines or phosphines that have no active hydrogen atoms result in platinacyclobutene cations, a rare species for late transition metal (Scheme 39). Substituted carbanions are added to the η^3-allenyl/propargyl platinum complex to yield the neutral substituted-η^3-TMM derivatives that undergo further $[3 + 2]$ cycloaddition with good π-acids as TCNE or maleic anhydride to produce highly substituted cyclopentanoids (Schemes 40, 41).

The unsubstituted η^3-allenyl/propargyl platinum complex is such a potent organometallic carbon electrophile that it even reacts with phenol and carboxylic acids, or activates the C–H cleavage in the substituted methanes, alkynes, silanes, enamine, and electron-rich aromatics to form the central-carbon substituted allyl complexes (Scheme 42).[65] Such facile nucleophilic addition (*see Nucleophilic Addition: Rules for Predicting Direction*) could be charge-controlled (*see Charge Controlled Reactions*), and assisted by the presentation of a low lying acceptor orbital on the central atom along the reaction path.[66] A η^3-1-hydroxyallyl complex has been synthesized from an enone complex by treatment with CF_3SO_3H (Scheme 43). The tautomerization of 1-hydroxyallyl proceeds, presumably promoted by triflate anion, to form a keto-coordinating complex.[67]

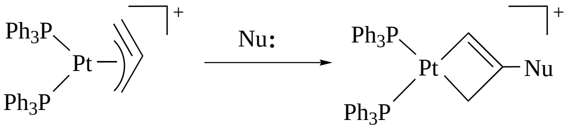

Nu = NR_3, PR_3

Scheme 39

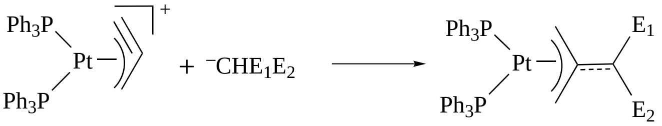

Scheme 40

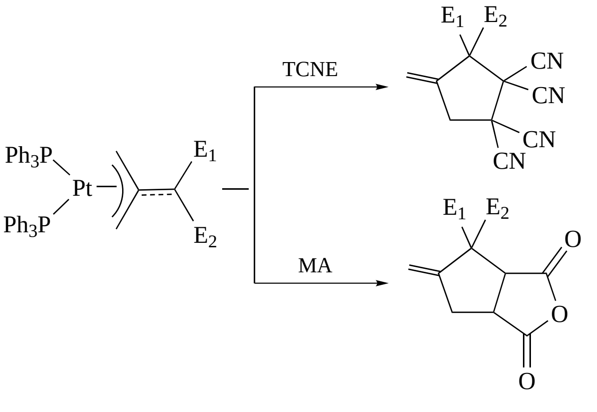

Scheme 41

Dinuclear complexes bridged with dianionic biaryl ligands that exhibit a rare μ-η^3:η^3- bonding mode and can be removed from the complex with stoichiometric oxidants to generate the free biaryls are synthesized via C–H activation and C–C coupling (Scheme 44).[68] Platinabenzenes and its η^3-cyclopentadienyl valence isomer may be prepared from the 2-(cycloprop-2-enyl)vinyl complexes by eliminating the *cis* ligand (Scheme 45).[69] A (cyclopentadienyl)platinabenzene has been obtained in the reaction of $[Pt(\eta^4\text{-cod})Cl_2]$ (Scheme 46).[70]

Diplatinum complexes with Pt(III)-Pt(III) bonds and quinone-like bridging ligands are prepared from the complex with μ-C_6F_5 group in basic solutions (Scheme 47).[71]

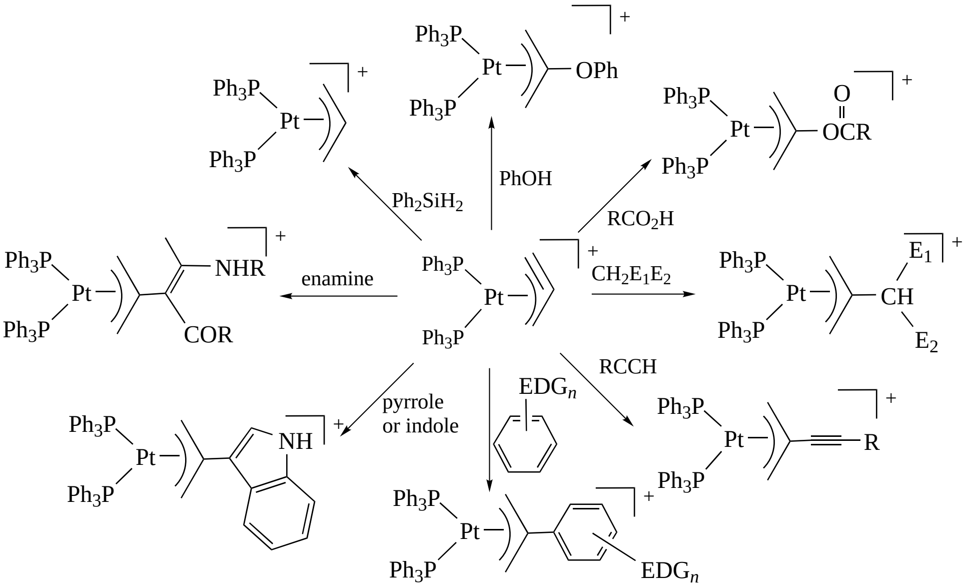
Ph2SiH2
PhOH
RCO2H
enamine
CH2E1E2
pyrrole or indole
EDGn
RCCH

Scheme 42

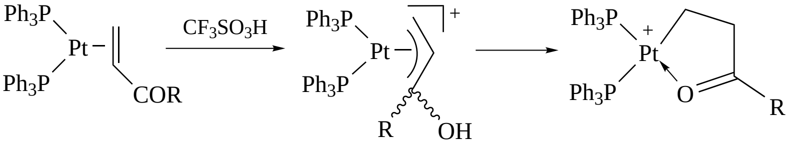

Scheme 43

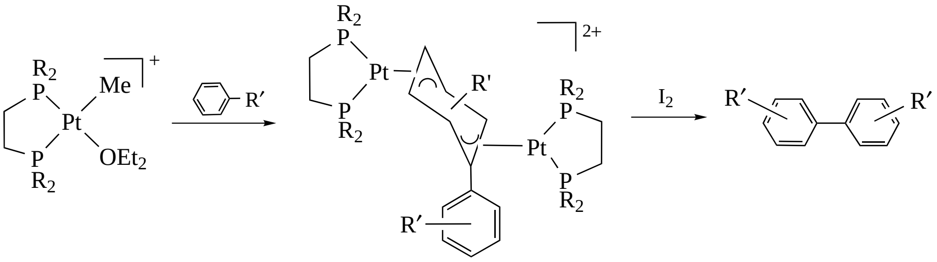

Scheme 44

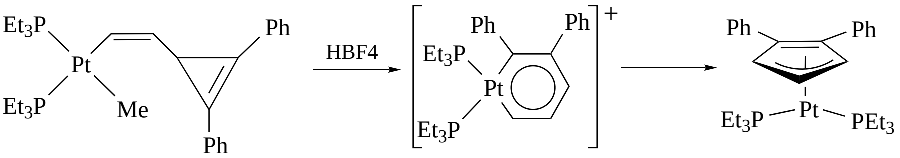

Scheme 45

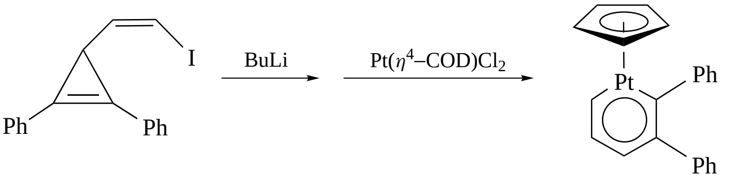

I
Ph
Ph
BuLi
Pt(η⁴–COD)Cl₂
Pt
Ph
Ph

Scheme 46

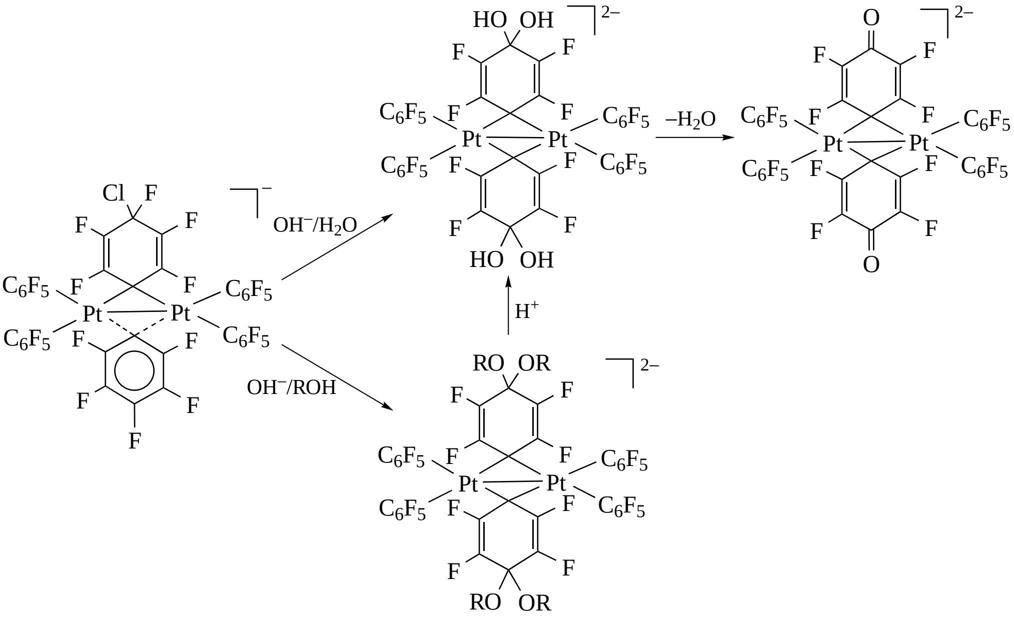

Cl F
F
F
C₆F₅
F
F
C₆F₅
Pt
Pt
C₆F₅
F
F
C₆F₅
F
F
F
−
OH⁻/H₂O
OH⁻/ROH
HO OH
2−
F
F
C₆F₅
F
F
C₆F₅
Pt
Pt
C₆F₅
F
F
C₆F₅
F
F
HO OH
−H₂O
O
2−
F
F
C₆F₅
F
F
C₆F₅
Pt
Pt
C₆F₅
F
F
C₆F₅
F
F
O
H⁺
RO OR
2−
F
F
C₆F₅
F
F
C₆F₅
Pt
Pt
C₆F₅
F
F
C₆F₅
F
F
RO OR

Scheme 47

4 CLUSTERS AND MOLECULAR ARCHITECTURES

4.1 From Organometallic Clusters to Supermolecules

The previous knowledge in the structural chemistry of organoplatinum plays a crucial role to develop new compounds with a large framework. Conventional bridging ligands such as H, CO, phosphides, and bisphosphines are still used to construct new homo- and heteronuclear metal clusters. With the new synthetic concept, anionic $[Pt_{9\sim15}(CO)_{18\sim30}]^{2-}$ encapsulated in a hexagonal channel could be assembled by ship-in-bottle catalysis of water-gas shift reactions (*see Water Gas Reaction*; *Shift Reaction*).[72] Among the heteronuclear category, platinum mixed with main group metals, such as Hg, Sn,[73] and Ga,[74] are synthesized. $Pt(GaC_5Me_5)_4$ is tetrahedral, and zero-valence is assigned to the central platinum. Beyond metal–metal interactions, ligand design brings versatile linking capability to the architecture of large frameworks. Using such skills, the clusters may be even used as building blocks.

Rational design using coordination as the motif for the construction of supramolecular polygons, polyhedra, and cages has proceeded at a rapid pace.[75,76] Square-planar complexes and linear bifunctional linkages such as alkynyl groups readily serve the building blocks for the molecular squares. Ligand variation affords both the cationic (**26**) and neutral species (**27**),[77] or even chiral assembly (**28**).[78] Such self-assembling processes generally undergo substitution reactions through the designed ligands and coordination.

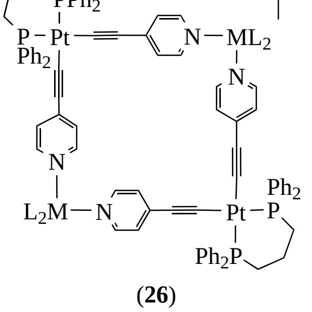

PPh₂
P
Pt
Ph₂
N
ML₂
N
N
L₂M
N
Pt
P
Ph₂
Ph₂P
4+

(**26**)

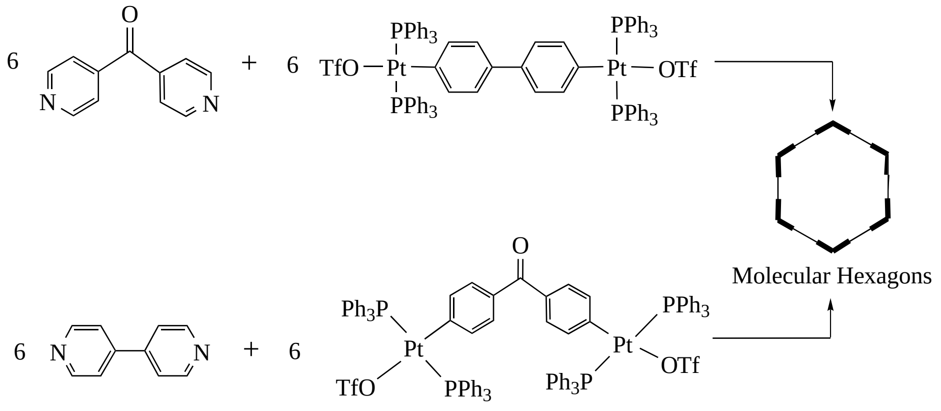

Scheme 48

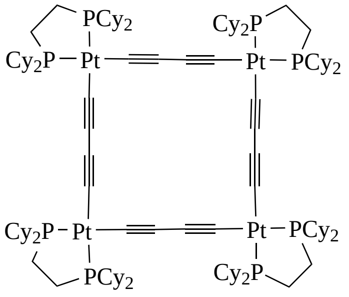

(**27**)

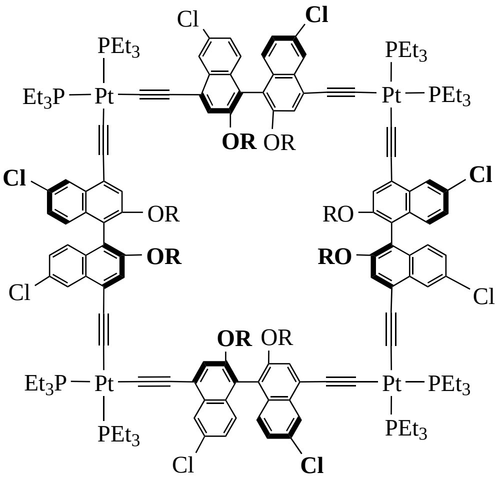

(**28**)

Ketones in 120° sp^2 configuration can give molecular hexagons (Scheme 48). Less symmetric molecular rectangles can be achieved by the reaction of a designed diplatinum clip and linear bridging ligands (Scheme 49). Similar

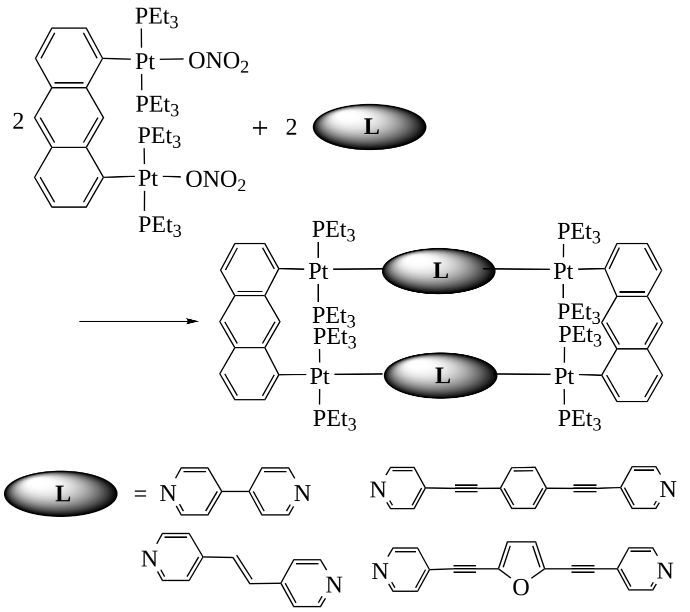

Scheme 49

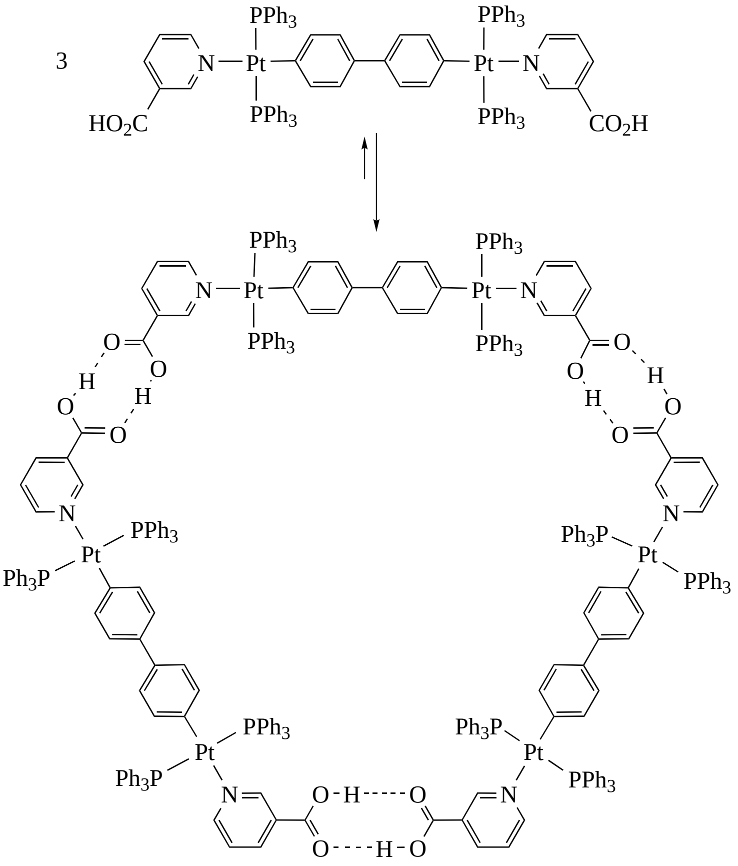

Scheme 50

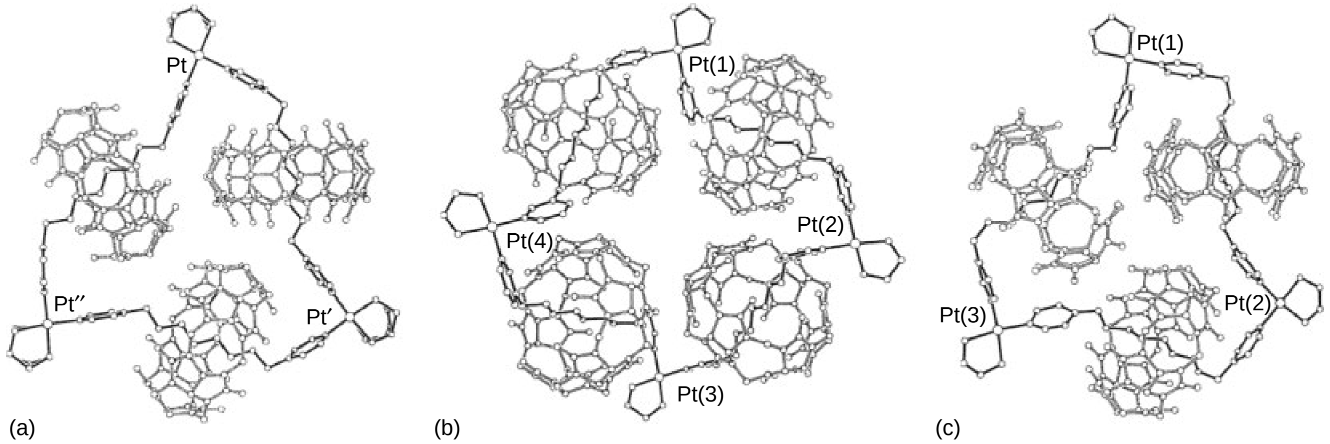

Figure 3 Ball and stick representations for the X-ray crystal structures of molecular necklaces[80]

methodology also leads to molecular rings. In addition to metal coordination, hydrogen-bonding also can serve for locking, as shown in Scheme 50.[79] With the idea of rotaxane and the synthetic strategies for the interlocked catenanes, the synthesis for 'molecular necklaces', as shown in Figure 3, was accomplished by using the strings of diaminoalkanes and the beads of cucurbituril.[80] The building block of C_3 symmetry affords the starburst structures and dendrimers.[81] Using platinum clusters as building blocks, a Pt_{18} dendrimer is assembled with alkynyl spacers.[82] Pincer complexes of platinum have been successfully tailored into dendrimers too.[83]

4.2 Polymers Containing Organoplatinum Complexes

Suitable aggregation of molecular organoplatinum may extend to construct oligomeric and polymeric species (*see* ***Oligomerization & Polymerization by Homogeneous Catalysis***). A structurally characterized helical chain, as shown in Figure 4, that consists of square-planar cyclometallated complexes (**29a,b**), is connected through a Pt → Ag bond.[84] Conjugated polymers PPE and bifunctional complex [Pt(μ-Cl)Cl(styrene)]$_2$ interact through π-coordination to constitute a three-dimensionally cross-linked network. The photoluminescence of the polymers is efficiently quenched by the Pt(II) coordination.[85] The Pt(0) complexation to PPE shows high charge carrier mobility.[86] Platinum-acetylide oligomers, Ph[CCPt(PBu$_3$)$_2$CCC$_6$H$_4$]$_n$H ($n = 1 \sim 5, 6$), show $^1\pi,\pi^*$ and $^3\pi,\pi^*$ manifolds, indicating the delocalization in both states.[87]

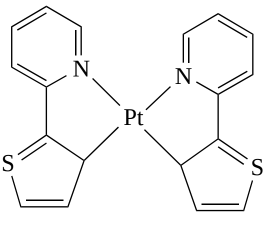

(**29a**)

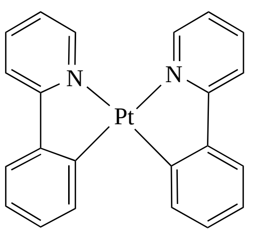

(**29b**)

5 COMPLEXES CONTAINING Pt–Si AND Pt–H BONDS

(Phosphinoalkyl)silanes undergo addition to Pt(0) or Pt(II) via Si–C or Si–H cleavage. Such reactions, giving phosphinosilyl metallacycle, are comparable to the cyclometallation (*see Cyclometalation*) in formality.[88,89] Diplatinum μ-silylenes in the form of (**30**) are prepared by the reactions of (R$_3$P)$_2$PtMe$_2$ and (IMP)SiH$_3$ [IMP = 2-^{i}Pr-6-Me(C$_6$H$_3$)].[90] Using steric bulky derivatives such as 2,6-Mes$_2$(C$_6$H$_3$)SiH$_3$, its reaction with Pt^0(PPr$_3$)$_3$ yields (Pr$_3$P)$_2$Pt(H)[SiH$_2$(2,6-Mes$_2$(C$_6$H$_3$))] instead of the dinuclear silylene.[91] Platinum η^2-disilenes in the form of (**31**) has been produced by the reactions of (R$_3$P)$_2$PtCl$_2$ and lithiodisilane, [(^{t}BuMe$_2$Si)$_2$SiLi]$_2$.[92]

Platinum-silylenes are important to numerous transformations involving organosilicon compounds. Base-stabilized Fisher-type cationic silylene complex of platinum(II) may be prepared by anion abstraction from a silyl group, as shown in Scheme 51. The counter anion is crucial

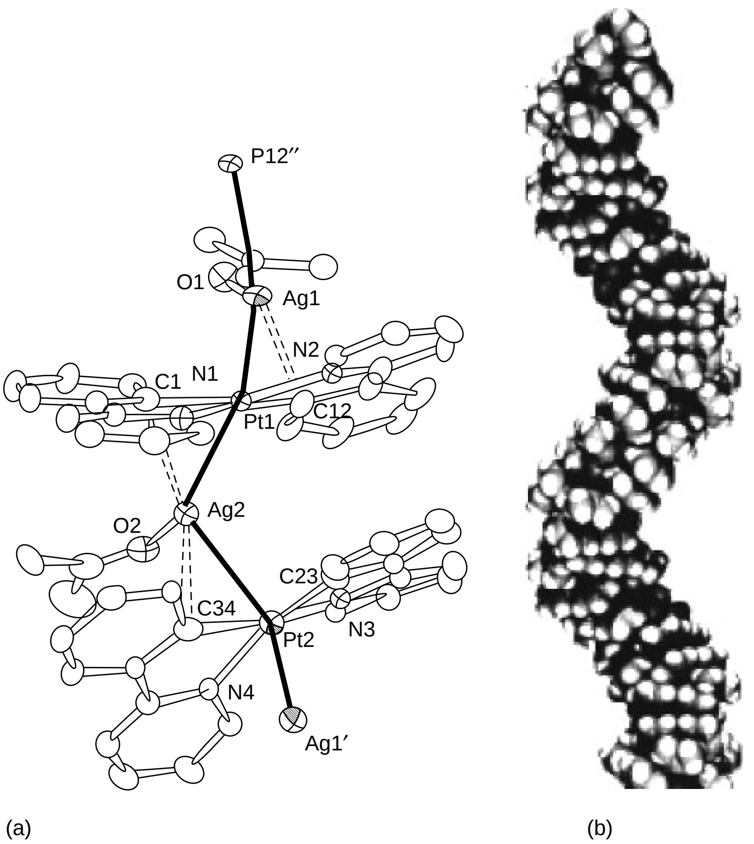

(a)

(b)

Figure 4 Structure of $[\{Pt(Phpy)_2\}_2\{Ag(acetone)\}_2]_n^{2n+}$[84]

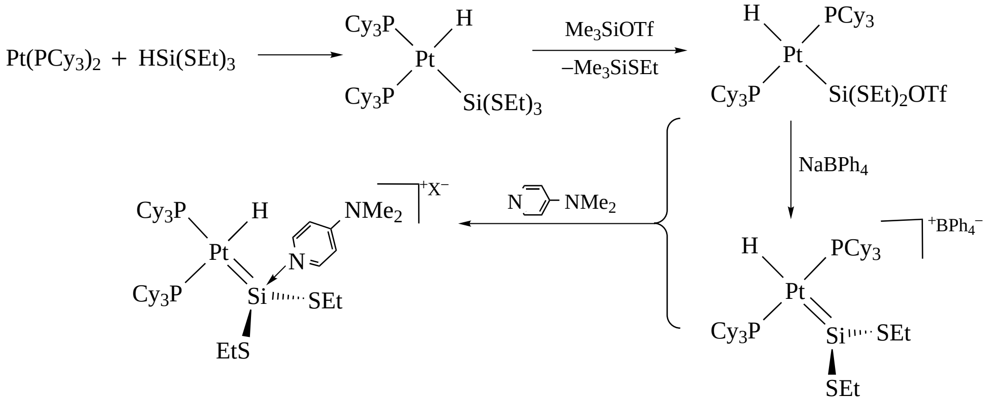
Pt(PCy3)2 + HSi(SEt)3
Cy3P
H
Pt
Cy3P
Si(SEt)3
Me3SiOTf
−Me3SiSEt
H
PCy3
Pt
Cy3P
Si(SEt)2OTf
NaBPh4
+BPh4−
H
PCy3
Pt
Cy3P
Si
SEt
SEt
N
NMe2
+X−
Cy3P
H
NMe2
Pt
N
Cy3P
Si
SEt
EtS

Scheme 51

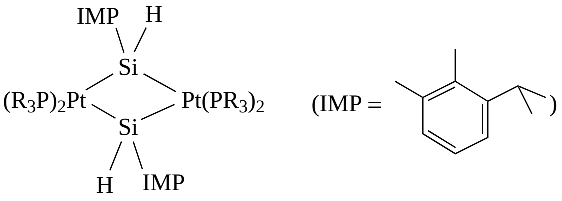
IMP
H
Si
(R3P)2Pt
Pt(PR3)2
Si
H
IMP
(IMP =
)

(**30**)

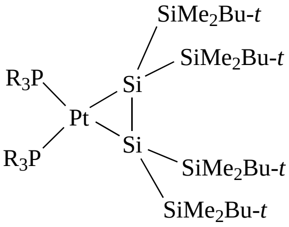
SiMe2Bu-t
SiMe2Bu-t
R3P
Si
Pt
Si
R3P
SiMe2Bu-t
SiMe2Bu-t

(**31**)

to the intramolecular H-migration from platinum to silicon. In the presence of BPh_4^-, the migration is rapid and irreversible. However, with a triflate counteranion, the migration is slow and reversible.[93] Neutral platinum silylene is generated via photolysis of a mixture of bulky silane $Mes_2Si(SiMe_3)_2$ and $Pt(PCy_3)_2$ (Scheme 52).[94] A series of dinuclear complexes in the general form of $(\mu\text{-}P^\wedge P)(CO)_3(RO_3Si)Fe\text{–}PtL_n$ has been investigated. In a reaction of $[(dppm)Fe(CO)_3(MeO_3Si)]^-$ with $[(dppm)PtCl_2]$, the product $(\mu\text{-dppm})_2(CO)_3FePtCl[Si(OMe_3)]$ indicates an unusual siloxyl migration from iron to platinum.[95]

Recent progress in chemistry involving Pt–H bonds is mainly in the Pt(IV) species, which will be described in next Section. Protonation of Pt^{II}-(R or Ar) may achieve a Pt^{IV}-(H)(R or Ar) species that can be interconverted with an alkane (or arene) complex, as shown in Scheme 53, which accounts for why these species are crucial in Pt^{II}/Pt^{IV}-involved C–H activation reactions.[96] A prior study disclosed that protonation of hydridoplatinum(II) of the type *trans*-$(PCy_3)_2Pt(H)X$ [$X = SiH_3$, H, CH_3, Ph, Cl, Br, I, CN, CF_3SO_3] and [*trans*-$(PCy_3)_2Pt(H)L](BAr'_4)$ [L = CO, 4-picoline] can take place at three possible sites, that is, H, Pt, or the trans-ligand. The electrophilic attack appears to depend on the Pt-σ adduct strength and the ancillary ligands, as illustrated in Scheme 54.[97] Shilov processes for alkane activation prefer the hard ligands that can stabilize Pt(IV), such as chloride. Thus the success of the Shilov system may be, in part, ascribed to appropriate ligands to access the kinetically more acidic Pt^{IV}-(H)(alkyl) intermediate. Meanwhile, the pathway involving alkane σ-adduct is also possible. As evidence, protonation of a pincer complex $(P^\wedge C^\wedge P)PtH$ gives a dihydrogen complex (Scheme 55).[98] In contrast, protonation of $Tp'Pt^{IV}(Me)H_2$ in dichloromethane, leading to the formation of a dimeric complex in the form of $[\kappa^2\text{-}((Hpz^*)BHpz^*_2)Pt(\mu\text{-}H)]_2[BAr'_4]_2$, provides a recent example of bridging platinum(II)-hydride. The 3-center-2-electron bond of Pt–H–Pt is analyzed by DFT calculations,

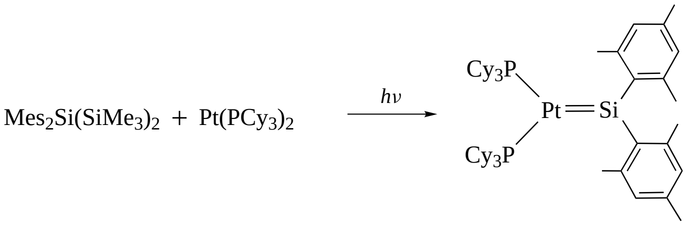
Mes2Si(SiMe3)2 + Pt(PCy3)2
hν
Cy3P
Pt
Si
Cy3P

Scheme 52

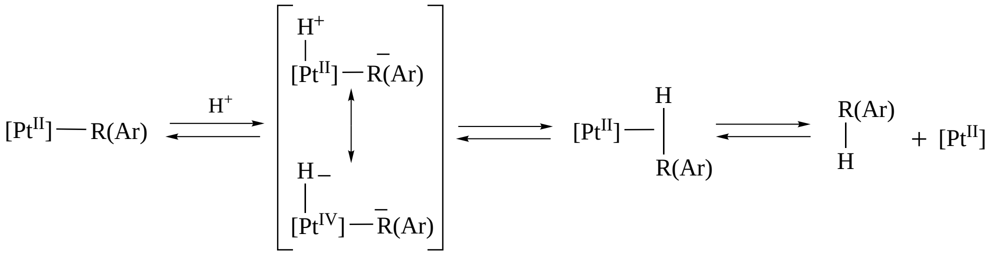

Scheme 53

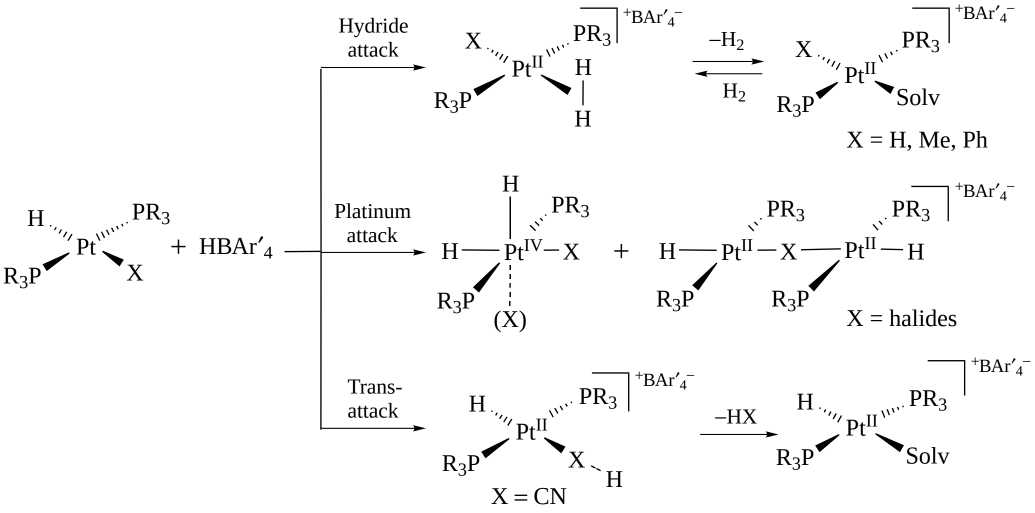

Scheme 54

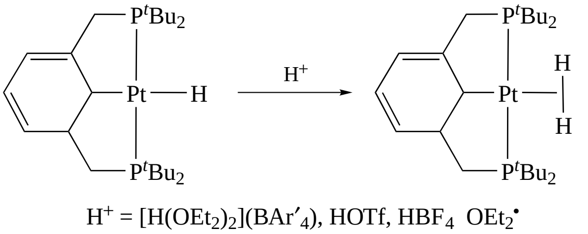

Scheme 55

and is compared with the prior analogs.**99** In a system of Pt^0/Pt^{II}, interconversion between $Pt[P(m\text{-}C_6H_4SO_3Na)_3]_3$ and $(H)Pt[P(m\text{-}C_6H_4SO_3Na)_3]_3^+$ may be simply controlled through variation of the pH of an aqueous solution.**100**

6 ORGANOPLATINUM(IV) COMPLEXES

Platinum(II) species are often known as good electrophiles. However, proper ancillary ligands of nitrogen donors, typically such as phenanthroline (phen) and bipyridine (bipy) derivatives, diimines, and so on, can make the Pt(II) center substantially electron-rich, so that the metal can feasibly undergo further oxidation to the hard electrophiles of Pt^{IV}. On another hand, square-planar 16-electron $platinum^{II}$ complexes make excellent coordination-unsaturated precursors for addition reactions. The +4 oxidation state can be much more stabilized in Pt than in Pd and Ni of the same group. $Platinum^{IV}$ hydrides are of interests as potential intermediates in C–H activation reactions (see Section 7.1) and hydrosilylation (*see Hydrosilation*) reactions as well. These complexes have been known either as stable compounds or considered as short-lived reaction intermediates. The synthetic routes for the formation of such compounds encompass (1) by protonation of organoplatinum(II),**101** (2) by transmetallation (*see Transmetalation*) reactions of organoplatinum with metal hydrides such as Me_3SnH, (3) by the reactions of organoplatinum with water, and (4) by activation of alkane or arene.**102**

Besides bidentate ligands, tripyrazolylborates (Tp) (*see Tris(pyrazolyl)borates*) derivatives, which are of anionic tridentate in facial configuration, also afford octahedral

Pt(IV) models. Tp′PtMe$_2$H, resulting from the reaction of K[Tp′PtMe$_2$] with anhydrous HCl, is thermally stable.[103] The reaction of Tp′PtR$_2$H and Et$_3$SiH first yields Tp′Pt(H)Me(SiEt$_3$), which transforms to stable Tp′PtH$_3$ in methanol.[104] Treating the six-coordinate Tp′Pt(H)Me(SiEt$_3$) with [H(OEt$_2$)$_2$](BAr′$_4$) leads to the dissociation of one pyrazolyl group to give a stable five-coordinate dihydrido(silyl) complex (Scheme 56).[105] The X-ray crystallography evidences a square-pyramidal geometry. Air-stable TpPtMeH$_2$ is formed by the reaction of TpPt(CO)Me with water (Scheme 57).[106] The reactions of TpPt(CO)Me with organolithium produce acyl or formyl complexes.

The trialkyl complexes (*see Alkyl Complexes*) of (N-N)Pt^{IV} are typically prepared by oxidative addition (*see Oxidative Addition*), as shown in Scheme 58.[107] The complex (N-N)Pt^{II}Me$_2$ with an imino-cyclohexane ligand, as shown in Scheme 11, undertakes protonation from different acids to give rise to *N*,*N*,*C*-tridentate and *N*,*N*,*C*,*N*-tetradentate chiral aminoalkyl species, respectively (Scheme 59). The chiral selectivity at the aminoalkyl carbon is opposite in

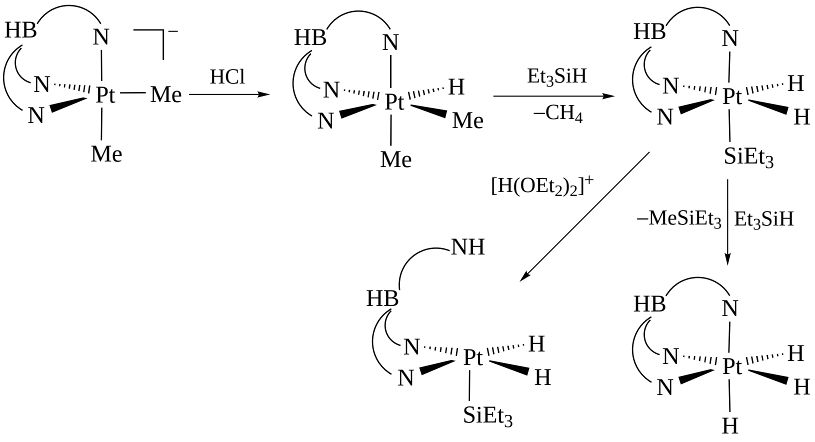

Scheme 56

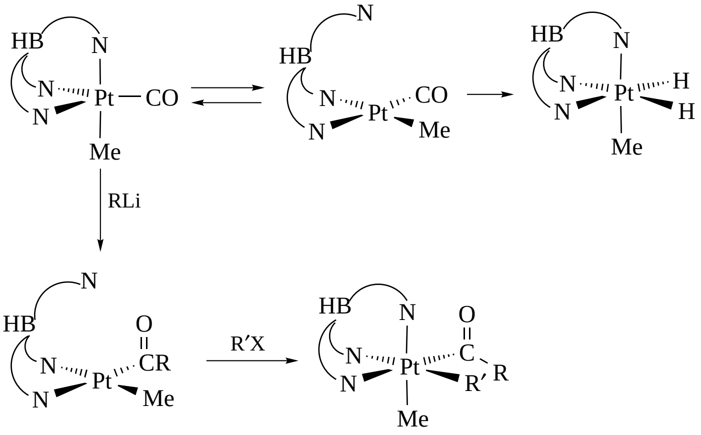

Scheme 57

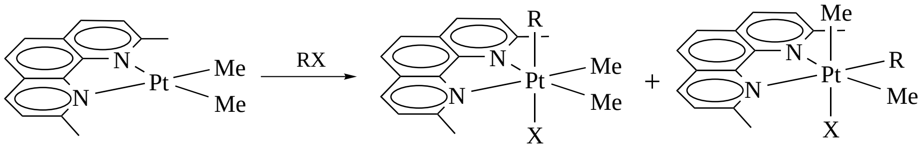

Scheme 58

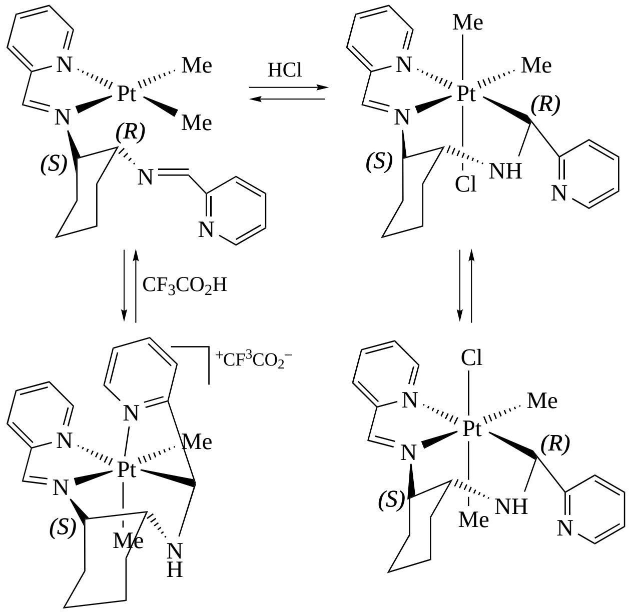

Scheme 59

these two kinds of products, indicating the stereo-control resulting from the ancillary ligand in Pt(IV) may be crucial.**108** In the complexes of (bipy)PtRMe$_2$(Cl), a Pt–Sn bond in platinum^{IV} can be established via insertion of SnCl$_2$ into a Pt–Cl bond.**109** Platinum(IV) complexes with other organic ligands are relatively less studied. TpPtMe$_2$(η^1-C$_3$H$_3$) is prepared by oxidative addition of propargyl bromide to [TpPt^{II}Me$_2$]$^-$ anion. The allenyl-propargyl tautomerization in Pt^{IV} is observed.**110** A complex of Pt^{IV} containing alkyl, alkenyl, and alkynyl ligands attaching to the same metal is obtained by the reaction of a Pt–Sn–Se species with alkyne (Scheme 60).**111** An unusual bis(carbene) platinum is synthesized by the consecutive reaction of bis(arylisocyanide) platinum^{II} with primary amine, followed by cyclometallation (Scheme 61).**112** In a designed tetrakis(azaindolyl)benzene (ttab) diplatinum complex (*see Dinuclear*), the platinum^{II} centers are within van der Waal's distances with the central benzene ring of the ligand. Transformation into a dianionic cyclohexadienyl diplatinum^{IV} complex is observed (Scheme 62).**113**

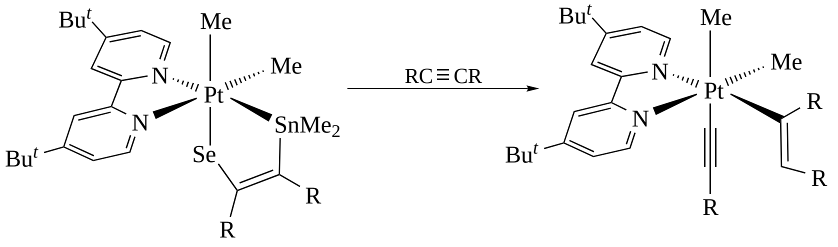

Scheme 60

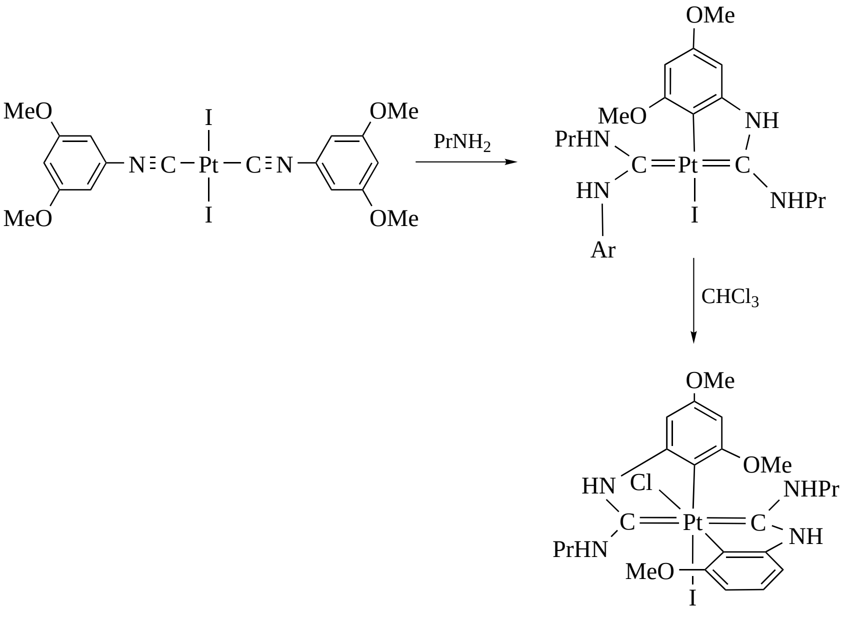

Scheme 61

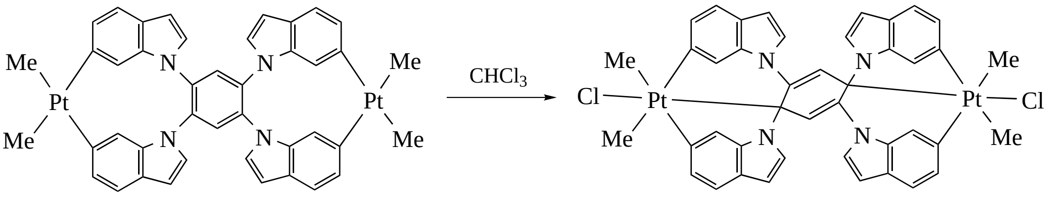

Scheme 62

7 CHEMICAL TRANSFORMATIONS OF ORGANOPLATINUM COMPLEXES

7.1 C–H and C–C Activation

Shilov's catalytic process using a mixture of Pt(II) and Pt(IV) salts for the conversion of methane into methanol and methyl chloride in aqueous solution makes a chemical paradigm for alkane functionalization. One of the new approaches finds oxidative functionalization of methane is catalyzed by a (bipyrimidine)platinum(II) complex in concentrated sulfuric acid at 100 °C.**[114]** In the reactions of selective functionalization of amino acid, using $K_2PtCl_4/CuCl_2$ catalysts, the formation of amino lactones appears to undergo the C–H activation through Pt(IV) species.**[115]** Recent extensive research in such a subject concludes the plausible mechanism may comprise the intermediates such as Pt^{II}-alkyl, Pt^{IV}-alkyl, Pt^{IV}-alkyl(hydrido)(oxidative addition adduct) (*see Oxidative Addition*), and σ-alkane adduct, and so on. Of particular interest is that the transformations among such species are expected to enlighten the reaction mechanism for the electrophilic C–H activation.

The alkane activation reactions have been observed in several Pt^{II} systems. With a labile coordinating solvent that is not subject to activation itself, such as pentafluoropyridine, $[(tmeda)Pt(Me)(NC_5F_5)]^+$ under 30 atm $^{13}CH_4$ is converted to $[(tmeda)Pt(^{13}CH_3)(NC_5F_5)]^+$ and CH_4, monitored by ^{13}C NMR.**[116]** Similar methyl exchange in a complex of the type $[(diimine)Pt(Me)(L)]^+$ (L = H_2O, CF_3CH_2OH, MeCN, etc.) is also observed.**[117]** In both cases, the use of CD_4 resulted in multiple deuterium incorporation into the methane produced, implying the formation of Pt-methane σ-complex intermediate.

By means of studying the protonolysis of various alkylplatinum^{II} complexes (Scheme 63), the microscopic reverse of C–H activation, the different kinetic processes with respect to the variation of the complex and solvent indicate that both the ionic and neutral hydrido(alkyl) platinum^{IV} species are involved, and the alkane σ-complexes account for the results of deuterium scrambling. The deprotonation may undergo these two kinds of intermediates too. The roles of solvent and ancillary ligand are both crucial. Theoretical calculations indicate that the destabilization of ionic species in nonpolar solvent translates to a higher barrier for C–H activation.**[118]** The kinetic site of protonation is likely at the metal rather than the methyl group, and the reverse deprotonation occurs from Pt^{IV} hydrido(alkyl) according to a comparable study with $(diimine)Pt(Me)_2$ in acetonitrile.**[119]**

By kinetic investigation in the reactions of reductive elimination (*see Reductive Elimination*) in $[(bpma)Pt(H)(Me)_2]^+$ under high pressure, the measurements of low activation volume for the loss of methane that involves

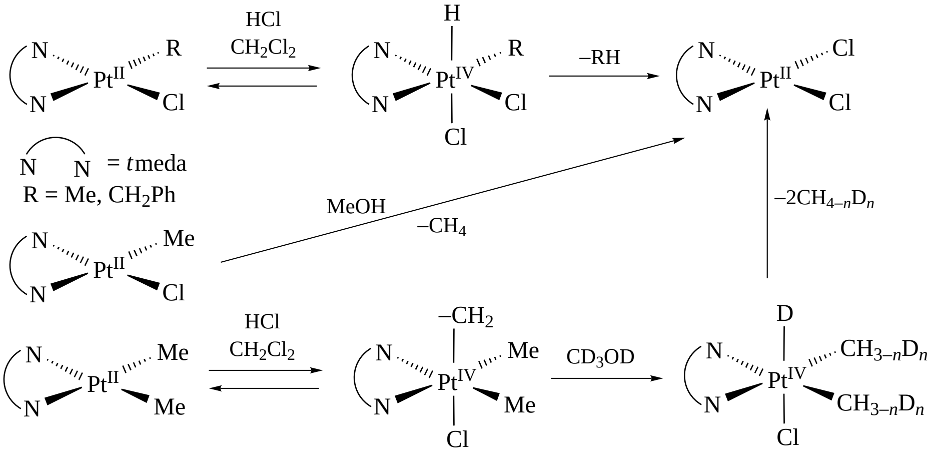

Scheme 63

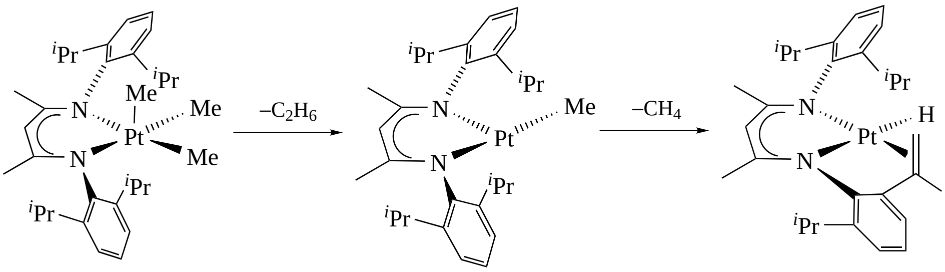

Scheme 64

the methyl cis to amine, together with the stereochemistry of deuterium incorporation into the methyl trans to amine, provide the basis for invoking a five-coordinate intermediate via pyridyl dissociation and the Pt-methane σ-complex intermediate.[120] A computational study finds that a preceding ligand loss from the six-coordinate Pt^{IV} complex may facilitate the reductive elimination of alkane.[121] Successful synthesis of a stable five-coordinate Pt^{IV}-trialkyl complex and its conversion into hydrido(olefin) complex via alkane activation indeed echoes the aforementioned mechanism (Scheme 64).[122]

Arene activation reactions are also observed. The better Pt-arene interaction than $Pt–CH_4$ might be expected to provide additional mechanistic information. The solvent-coordinated cationic complexes $[(N\text{-}N)Pt(Me)(solv)]^+$ (N-N = $[(2,6\text{-}Me_2C_6H_3)N{=}CMe]_2$, solv = H_2O, CF_3CH_2OH) react with benzene to generate $[((N\text{-}N)Pt(Ph)(solv)]^+$. Kinetic and isotope-labeling experiments establish a mechanism that comprises benzene coordination, reversible Ph–H activation, reversible formation of methane-complex, and the dissociation of methane (Scheme 65).[123] For the reactions of benzene with $(N\text{-}N)PtMe_2$, the rate-determining step is C–H bond activation. The kinetic isotope effect as well as the deuterium scrambling patterns indicate that the more sterically crowded ligand such as $[(2,6\text{-}Me_2C_6H_3)N{=}CMe]_2$ switches the rate-determining step to benzene coordination. The electron-rich ligand presumably can ease the displacement of a ligand by benzene, and thus accelerates the C–H activation.[21] Analogous reactions between arene (toluene or xylene) and $[(N\text{-}N)PtMe(OH_2)]^+$ (N-N = $[(2,6\text{-}Me_2C_6H_3)N{=}CMe]_2$) were carried out in CF_3CH_2OH with use of acetonitrile as the trapping agent. $[(N^f\text{-}N^f)PtAr_2]^+$ ($N^f\text{-}N^f$ = $[(3,5\text{-}(CF_3)_2C_6H_3)N{=}CMe]_2$) were treated with HBF_4 still using an acetonitrile trap. In both cases, different amounts of the isomeric products $[(N\text{-}N)Pt(Ar)(NCMe)]^+$ were formed. Such a study reveals the dynamic equilibrium between the isomeric $[(N\text{-}N)PtAr(CH_4)]^+$ intermediates and slow exchange between H_2O and CF_3CH_2OH. The coordination of the arene is assumed to be a rate-determining step. Isomeric selectivity is attributed to the five-coordinate transition state structure of $[(N\text{-}N)PtAr(CH_4)(TFE)^+]$ of which the stabilities may be influenced by either steric or electronic factors according to the toluene activation order meta > para > ortho.[124] For the model studies, neutral complex $(dtbpm)Pt^{II}H(neopentyl)$ reacts with electron-deficient aryl derivatives to result in reductive elimination (*see Reductive Elimination*) of neopentane as well as the formation of stable $(dtbpm)Pt^0(\eta^2\text{-arene})$ complexes that convert to (dtbpm)PtH(aryl) reversibly.[125]

The selective carbon–carbon bond activation under mild conditions is of an essential concern in both organic and

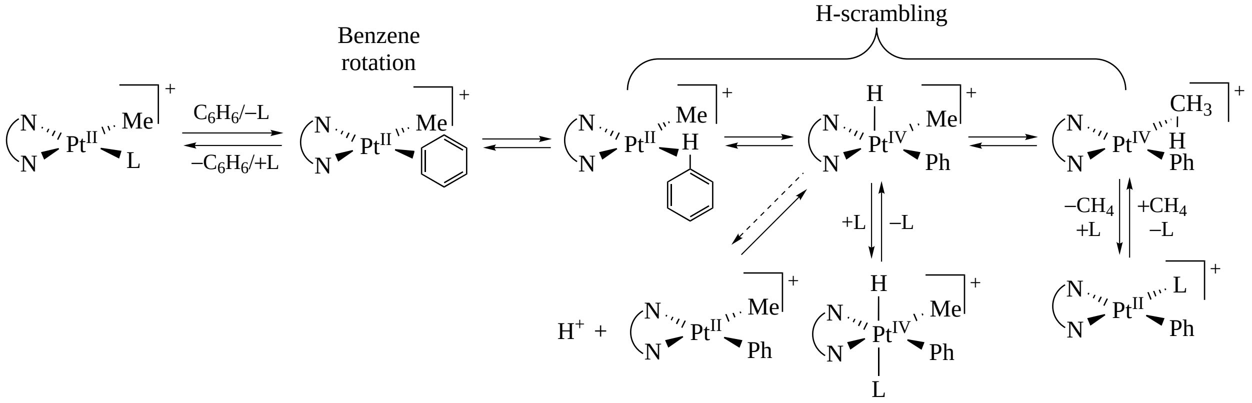

Scheme 65

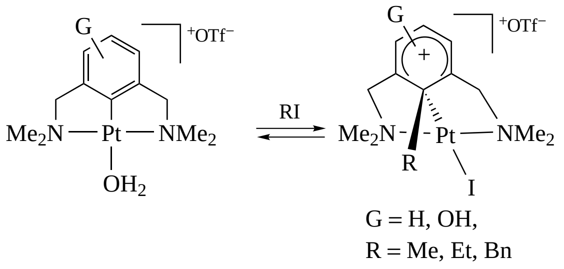

Scheme 66

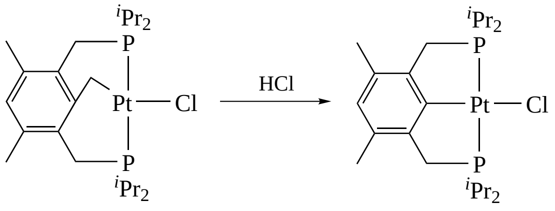

Scheme 67

organometallic chemistry. Platinum involved C–C bond activation such as the reactions of the cationic pincer complex with alkyl halides gives air-stable arenium complexes containing a new C–C bond (Scheme 66). These reactions are analogous to the organic electrophilic aromatic substitution, of which the scope may be broadened with use of the electron-releasing groups on the aromatic ring as activators.[126] A benzylic platinum complex treated with excess HCl results in the loss of MeCl, presumably via an unusual methylene transfer (Scheme 67).[127] Ring opening by relief of strain is a useful route for C–C bond cleavage. The reaction of biphenylene with a series of Pt bisphosphine precursors leads to the formation of phenylene oligomers (Scheme 68).[128]

7.2 Fundamental Reactions

In the last decade, two aspects for the study of the oxidative-addition reactions (*see Oxidative Addition*) in organoplatinum chemistry have given rise to the most progress. With regard to oxidation-state change, the reactions of organoplatinum(II) to organoplatinum(IV), particularly with nitrogen-donor ligands, earn the most attention, as described in the previous sessions.[129] Concerning bond activation, the reactions involving main group elements have caused substantial progress. Oxidative addition of imidazolium cation to Pt(0) yields *cis*-aminocarbene complexes (Scheme 69).[130] In addition to conventional C−halide, C–H, and C–C cleavage, the reaction of $Pt(PEt_3)_3$ and $PhSeP(O)(OPh)_2$ at room temperature leads to oxidative addition of P–Se bond to the metal (Scheme 70).[131] The reactions of hydrophosphinylation are established with platinum(0) and phosphinate (Scheme 71). Such reactions are employed for the synthesis of enantiomerically pure *P*-chiral alkenylphosphinates via metal-catalyzed hydrophosphinylation of alkynes.[132] Carbothiolation of alkynes by thioester using Platinum(0) is similarly achieved.[133] The hydridoplatinum-thiolate complex prepared by oxidative addition of ArSH to Pt(0) is found to induce alkyne insertion to form a *cis*-Z stereoisomer of alkenylplatinum-thiolate product (Scheme 72).[134] The substitution reactions may be pragmatic for changing bonds. Si–C bond activation of $ArMe_2SiOH$ was promoted by $[PtBr(PEt_3)_3]BF_4$ and Ag_2O, resulting in aryl transfer from silicon to platinum (Scheme 73).[135]

Reductive elimination is one of the most important fundamental bond-forming processes. Kinetic study of competitive

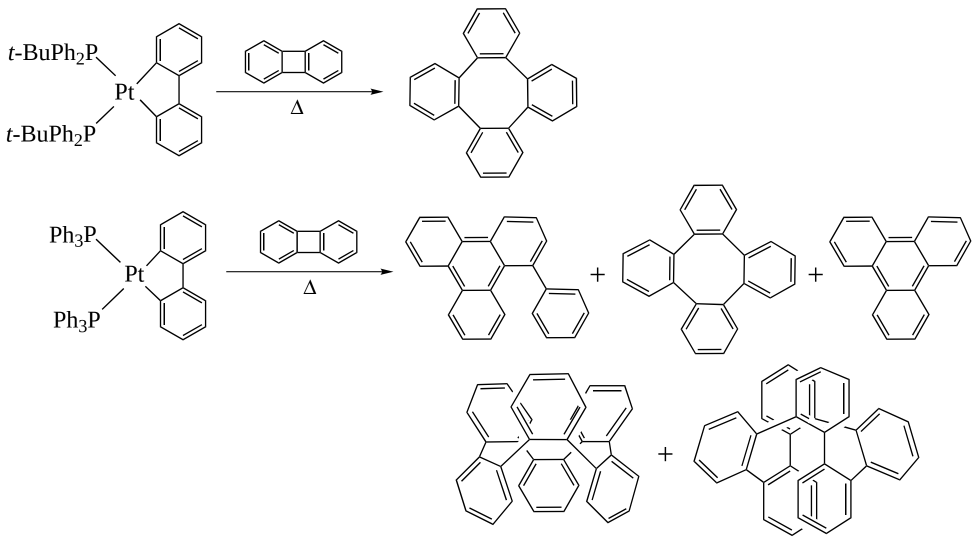

Scheme 68

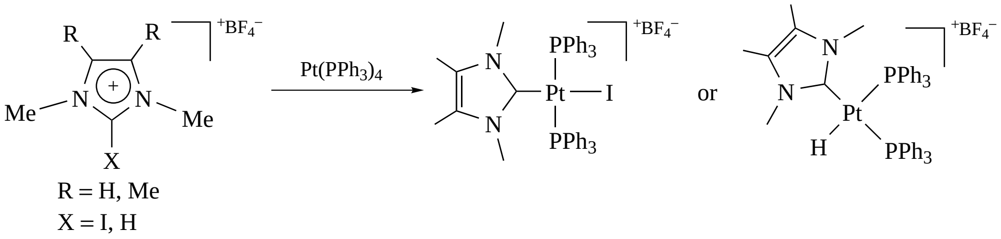

Scheme 69

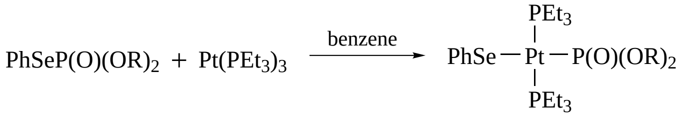

$$\mathrm{PhSeP(O)(OR)_2 + Pt(PEt_3)_3 \xrightarrow{\text{benzene}} PhSe{-}\overset{\displaystyle PEt_3}{\underset{\displaystyle PEt_3}{Pt}}{-}P(O)(OR)_2}$$

Scheme 70

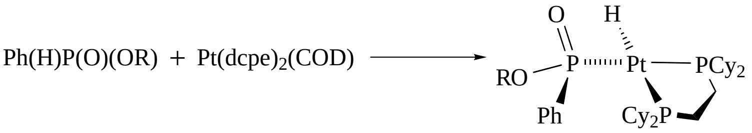

Scheme 71

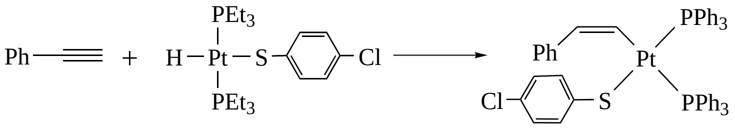

Scheme 72

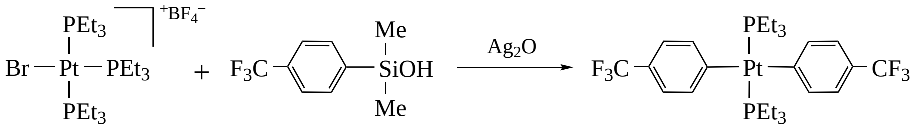

Scheme 73

formation of ethane and CH_3I from $(dppe)Pt(Me)_3I$ indicates that the C–C and C–I couplings undergo two pathways but involve a common cationic five-coordinate intermediate (Scheme 74). The mechanism is likely led by iodide dissociation. It appears that the C–C coupling is thermodynamically favored, but the C–I coupling is the kinetically favored pathway.[136] Analogous reaction of $(dppe)Pt(Me)_3(OAc)$ yields CH_3OAc via C–O coupling of the same mechanism.[137] Such reactions represent promising product-release pathways in alkane functionalization involving Pt(IV). In a system lacking a labile ligand such as $(P\text{-}P)Pt(Me)_4$, thermolysis that leads to $(P\text{-}P)Pt(Me)_2$ and ethane requires more vigorous environments. Kinetic and crossover experiments along with the variation of the bidentate phosphines suggest the five-coordinate intermediate mainly caused by predissociation of one end of the phosphine chelate is essential to reductive elimination.[138] In an electrochemical study for $(diimine)PtMe_2$, homolysis (*see Homolytic Cleavage*) of the Pt–C bond in a short-lived radical cation $[(N\text{-}N)Pt^{III}(Me)_2]^{\cdot+}$ resulting from one-electron oxidation of the starting Pt^{II} complex in acetonitrile leads to intermolecular methyl transfer, giving rise to the Pt^{II} and Pt^{IV} products of disproportionation.[20] Reductive elimination

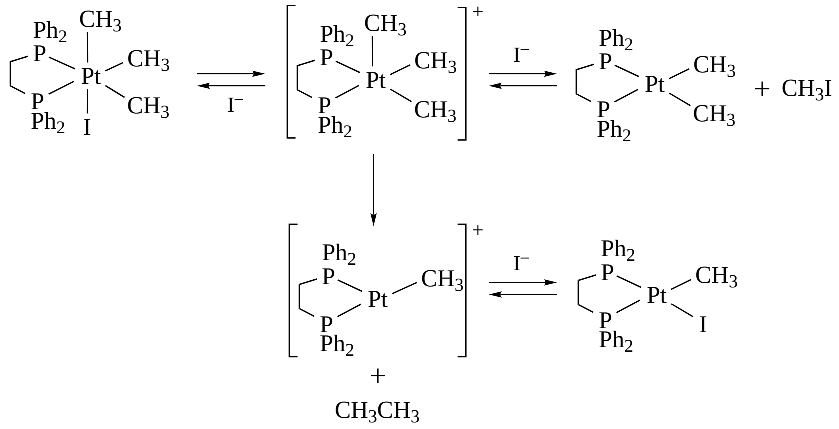

Scheme 74

of methane in $[\mathrm{Tp'Pt(Me)_2(H)}](\mathrm{BAr'_4})$ is induced by protonation at a pyrazole nitrogen atom. Addition of trapping ligand L to the kinetic products of methane loss gives $[(\mathrm{Tp'H})\mathrm{Pt(Me)L}](\mathrm{BAr'_4})$.[139] Therefore, the C–H and C–C activations in different environments need not undertake a common mechanism.

Formation of silanes via reductive elimination in four-coordinate square-planar complex *cis*-$\mathrm{PtMe(SiPh_3)(PMePh_2)_2}$ was also examined. A mechanism led by dissociation of $\mathrm{PMePh_2}$ followed by $\mathrm{CH_3}$-$\mathrm{SiPh_3}$ coupling is evidenced by the kinetic study.[140] In contrast, alkylsilane formation from *cis*-$\mathrm{PtR(SiPh_3)(PMePh_2)_2}$, wherein R = Et, or Pr, Bu bearing the β-hydrogens, is found predominantly from *cis*-$\mathrm{PtPh(SiRPh_2)(PMePh_2)_2}$, an isomer resulting from the exchange of Pt–R and Si–Ph. Apparently, β-hydrogen elimination (*see β-Hydride Elimination*) of the R group participates in the competition.[141] In *cis*-$\mathrm{Pt^{II}(C{\equiv}CAr)(SiAr'_3)(PMePh_2)_2}$, reductive coupling between the silyl and alkynyl ligands without ligand predissociation yields $\mathrm{Pt^0(ArC{\equiv}CSiAr'_3)(PMePh_2)_2}$.[142] Again, different mechanisms are undertaken in different environments.

It is generally accepted that carbonylation of metal-alkyl, leading to metal-acyl, proceeds via alkyl migrates from metal to the coordinated carbonyl. However, it is difficult to discern the path of alkyl migration (*see Alkyl Migration*) from CO insertion. This problem may be solved by using an unsymmetric ligand $\mathrm{Ph_2PCH{=}C}(t\text{-Bu})\mathrm{CH_2PCy_2}$ (P-P′). Treating $(\mathrm{P\text{-}P'})\mathrm{Pt(OTf)_2}$ with $\mathrm{BiPh_3}$ affords $(\mathrm{P\text{-}P'})\mathrm{PtPh(OTf)_2}$ in which phenyl is trans to $\mathrm{PCy_2}$. Upon warming to 40 °C, the complex isomerizes to the more stable form in which phenyl is trans to $\mathrm{PPh_2}$. Each of these two species undergoes phenyl migration respectively to form the acyl isomers as shown in Scheme 75, when they are brought into contact with CO.[143] The kinetic study for the reaction of $[\mathrm{Pt(triphos)(OC_6H_4}\text{-}p\text{-R})]^+$ with CO suggests that carbonylation proceeds via a pathway of migratory insertion rather than external nucleophilic attack at the coordinated CO by free or dissociated aryloxide (Scheme 76).[144] The interaction of the lone pair at the aryloxide oxygen with the carbonyl π^* orbital (**32**) is

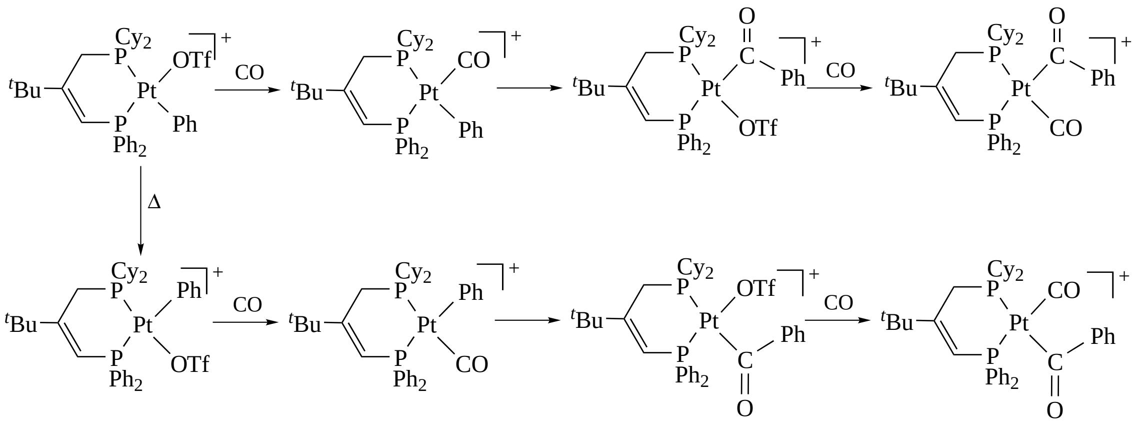

Scheme 75

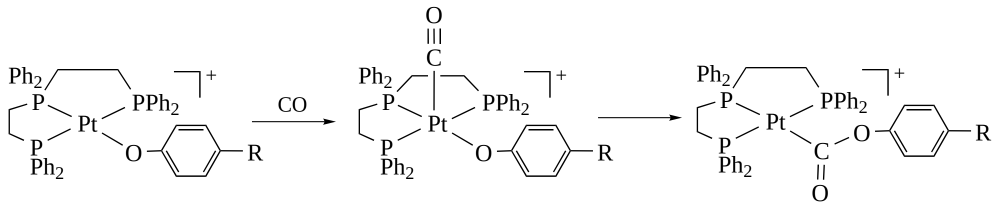

Scheme 76

attributed in the formation of the C–O bond prior to the complete cleavage of the Pt–O bond.

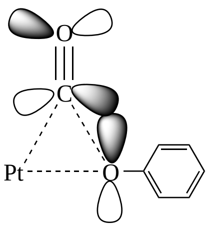

(**32**)

7.3 Ligand Transformations

Nucleophilic addition (*see Nucleophilic Addition: Rules for Predicting Direction*) of the ligands represents a major methodology for organometallic functional transformation. In order to discern how alkane functionalization takes place in aqueous Pt^{IV} systems, a water-soluble $platinum^{IV}$ alkyl, $[PtCl_5(CH_2R)]^{2-}$ ($R = H$, CH_2OH), is allowed to react with chloride and water. Both kinetics and inversion of stereochemistry support an S_N2 mechanism. Treatment of the *erythreo* isomer of platinum d_2-hydroxyethyl with chloride affords primarily *threo*-ClCHDCHDOH, which is further converted to cis isomer of 2,3-d_2-ethylene oxide, as shown in Scheme 77.[145] The oxidation of (tmeda)$Pt^{II}(CH_3)_2$ to (tmeda)$Pt^{IV}(OH)(OCH3)(CH_3)_2$ by dioxygen in methanol is found to proceed via a two-step mechanism. In the initial step, (tmeda)$Pt^{II}(CH_3)_2$ reacts with dioxygen to yield an intermediate in the form of (tmeda)$Pt^{IV}(OOH)(OCH3)(CH_3)_2$, which successively reacts with a second equivalent of (tmeda)$Pt^{II}(CH_3)_2$ to afford (tmeda)$Pt^{IV}(OH)(OCH3)(CH_3)_2$ (Scheme 78).[146] In the system of $Tp'PtH(Me)_2$, insertion of dioxygen into a Pt–H bond to form $Tp'Pt(OOH)Me_2$ in benzene has been observed. The hydroperoxo complex has been crystallographically characterized.[147] Insertion of sulfur dioxide into a Pt–C bond of (dcpe)$Pt^{II}(CH_3)_2$ affords (dcpe)$Pt^{II}(SO_2CH_3)(CH_3)$ in quantitative yields under mild conditions. The inserted species is found inert to reductive elimination (*see Reductive Elimination*).[148]

The $platinum^{II}$ complexes with water-soluble bidentate phosphine ligands catalyze the hydration of 3- or 4-pentyn-1-ol, leading to the formation of dihydrofuran derivatives. In the reaction of 2-pentyn-1-ol and (dppbts)$PtCl_2$ (dppbts = $[(m\text{-}NaSO_3C_6H_4)_2PCH_2CH_2)_2]$), a η^1-allenyl intermediate is

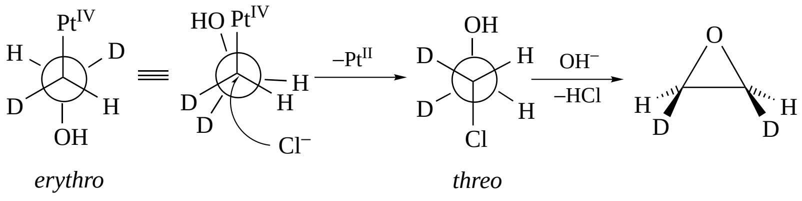

Scheme 77

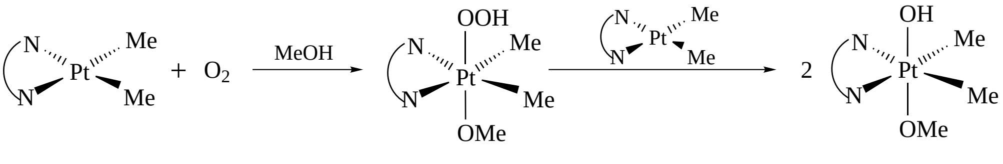

Scheme 78

characterized. Accordingly, a mechanism involving a η^3-allenyl/propargyl intermediate that undergoes intramolecular nucleophilic attack at the central carbon by the hydroxyl group similar to the reaction of Scheme 37 to achieve the heterocyclic ring closure is proposed. Further nucleophilic substitution releases the dihydrofuran product.[149] The Pt-catalyzed nucleophilic substitution reactions of 2-chloro-2-propenyl ethyl carbonate invoke a three-step mechanism that comprises (1) the formation of η^3-2-chloroallyl intermediate, (2) the formation of platinacyclobutane via nucleophilic addition at the central carbon, and (3) the formation of new η^3-allyl by the elimination of chloride.[150] The regioselective attack of hydrogen sulfide at the central carbon of η^3-2-alkoxyallyl or η^3-2-acyloxyallyl platinum complexes results in a platinathiacyclobutane (Scheme 79).[151] Such reactions are apparently distinguishable from the conventional Pd-catalyzed allyl substitution of which the nucleophilic attack likely takes place at the end carbons. The central-carbon substituted allyl complexes may also be synthesized by insertion of allene into a Pt–R bond.

Several reactions involving organic nitriles introduce nitrogen-containing ligands to platinum. For instance, nucleophilic addition of carbanions to the cationic nitrile complexes of formula $[(\text{bipy})\text{PtMe(NCR)}]^+$ yield η^1-imine enol and η^1-enamine complexes (**33**) and (**34**).[152] Addition of nitrones to coordinated organonitriles in Pt^{IV} complex results in [2 + 3] cycloaddition, which leads to the synthesis of oxadiazolines (Scheme 80).[153] Double addition of Si–H bonds in $(\text{PMe}_3)_2\text{Pt(SiHPh}_2)_2$ to the nitriles produces 3-aza-2,4-disilaplatinacyclobutanes (**35**).[154]

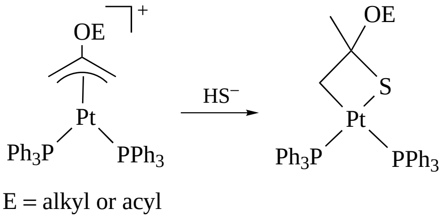

Scheme 79

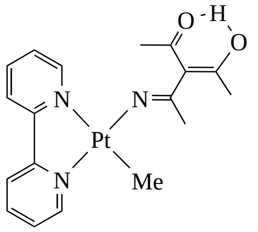

(**33**)

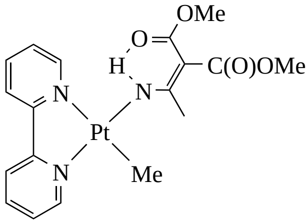

(**34**)

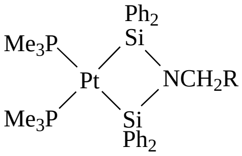

(**35**)

7.4 Organic Synthesis and Catalysis Involving Organoplatinum Complexes

Although the platinum-catalyzed reactions are not as practical as palladium used for the same purpose, several types of unique discoveries still are noteworthy. Besides electrophilic C–H activation, the platinum complexes are efficient catalysts for hydrosilation (*see* ***Hydrosilation Catalysis***) that is important to silicon polymer industry. Platinum carbene catalysts are prepared from Karstedt catalyst (**9**) and imidazolium salts. The trials of model hydrosilylation reactions show very high yields of regioselective products (<1% impurity) with remarkable TON (*see Turnover*) (<30 ppm catalyst load) (Scheme 81).[155]

Platinum(II)-catalyzed carbocyclization of α,ω-enynes has been intensively researched lately. For instance, 2-disubstituted 1-en-6-ynes react with methanol in the presence of PtCl_2 as catalyst to form carbocycles with exocyclic alkenes. The analogous reactions of 3-allyl propargyl ether or 3-allyl propargyl tosylamine in water using the same catalysts will generate cyclopropyl aldehydes besides the product of cycloisomerization (Scheme 82).[156] The coordination of the

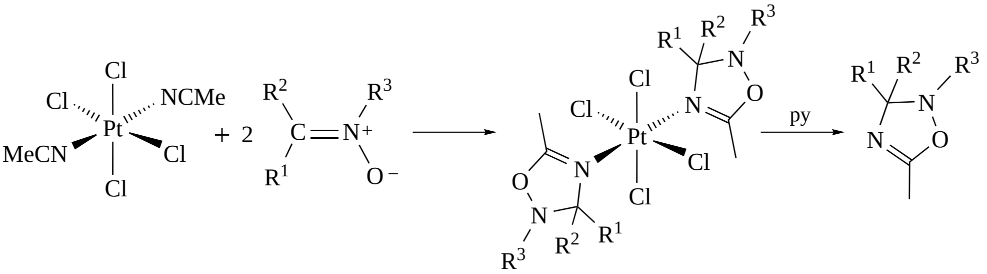

Scheme 80

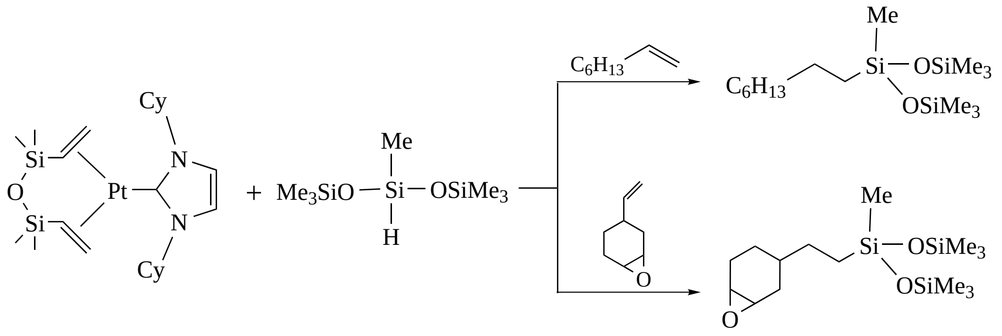
Cy
Si
O
Si
Pt
N
N
Cy
+ Me3SiO—Si—OSiMe3
Me
H
C6H13
Me
C6H13
Si—OSiMe3
OSiMe3
O
Me
Si—OSiMe3
OSiMe3
O

Scheme 81

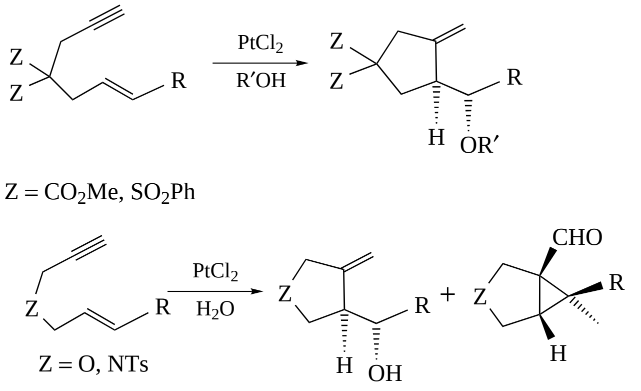
Z
Z
R
PtCl2
R′OH
Z
Z
R
H
OR′
Z = CO2Me, SO2Ph
Z
R
PtCl2
H2O
Z
R
H
OH
+
Z
CHO
R
H
Z = O, NTs

Scheme 82

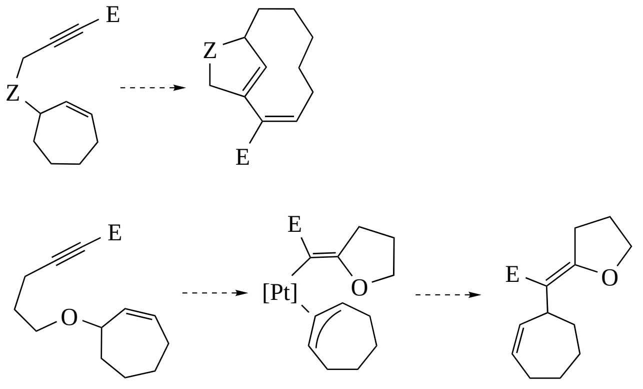
E
Z
Z
E
E
O
E
[Pt]
O
E
O

Scheme 83

Pt(II) to the alkyne of the substrate likely triggers all these events. The cycloisomerization might undergo a metallacyclic intermediate that proceeds to eliminate β-H. The formation of cyclopropanes is presumably succeeded via alkenyl platinum carbene followed by platina(IV)cyclobutane intermediates. The extension using formal metathesis of the enynes includes two transformations, the formation of 1,3-diene moieties and the stereoselective tetrasubstituted alkene derivatives via O → C allyl shift, both leading to diverse structural motifs and serving as the key step in the total synthesis of bioactive targets (Scheme 83).[157]

For activating the substrates containing main group elements, platinum catalysts are also efficient. Diboration of alkynes catalyzed by $Pt^0(PPh_3)_4$ provides access to isomerically pure cis 1,2-bisboryl alkenes.[158] Diboration to α,β-unsaturated ketones has been accomplished with $Pt^0(C_2H_4)(PPh_3)_2$ as catalyst.[159] Analogous addition to aldimines using the commercially available catalyst $Pt^{II}(COD)Cl_2$ gives rise to α-aminoboronate esters (Scheme 84).[160] Regio- and stereoselective thiosilylation reactions of alkynes using disulfides and disilanes are catalyzed by Pt(0).[161] Platinum-catalyzed silaborative coupling of 1,3-dienes to aldehydes results in regio- and stereoselective allylation with dienes (Scheme 85).[162]

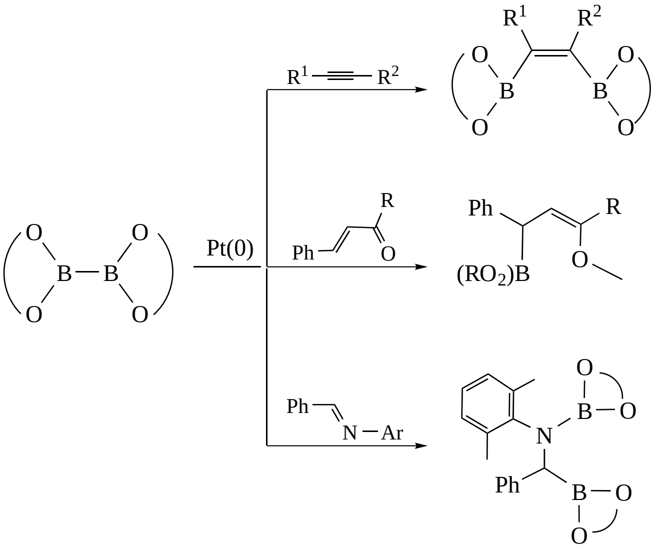
O
O
B—B
O
O
Pt(0)
R1
R2
R1
R2
O
B
O
O
B
O
Ph
R
O
Ph
R
(RO2)B
O
Ph
N—Ar
O
B—O
N
Ph
B—O
O

Scheme 84

Platinum-catalyzed double nucleophilic substitution of 2-chloroallyl acetate, yielding 2,3-substituted allyl derivatives, invokes a central-carbon substituted η^3-allyl intermediate that

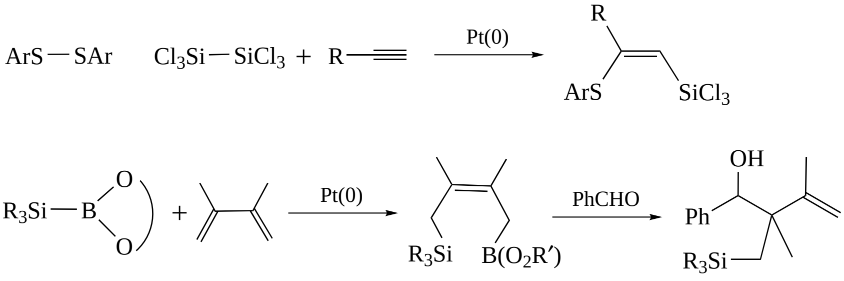

Scheme 85

is subject to the preceding nucleophilic substitution at 2-carbon.[163] Such reactions expand the scope of allyl chemistry. Zeise's (*see Zeise's Salt*) dimer $[PtCl_2(C_2H_4)]_2$ was recently applied for ring opening of 1,2-cyclopropanated sugar with O-nucleophiles, demonstrating the effort and possibility of the usage of platinum in biosynthesis.[164]

8 RELATED ARTICLES

Carbonyl Complexes of the Transition Metals; Coordination & Organometallic Chemistry: Principles; Dinuclear Organometallic Cluster Complexes; Hydride Complexes of the Transition Metals; Luminescence Behavior & Photochemistry of Organotransition Metal Compounds; Mechanisms of Reaction of Organometallic Complexes; Organic Synthesis Using Metal-mediated Coupling Reactions; Palladium: Organometallic Chemistry; Platinum: Inorganic & Coordination Chemistry; Self-assembled Inorganic Architectures.

9 REFERENCES

1. J.-M. Lehn, 'Supramolecular Chemistry, Concepts and Perspectives', VCH Verlags, Weinheim, 1995.
2. J. W. Suggs, Palladium: Organometallic Chemistry, 'Encyclopedia of Inorganic Chemistry', John Wiley & Sons, 1994, Vol. 6, p. 3023.
3. W. J. Hoogervorst, C. J. Elsevier, M. Lutz, and A. L. Spek, *Organometallics*, 2001, **20**, 4437.
4. P. Steenwinkel, H. Kooijman, W. J. J. Smeets, A. L. Spek, D. M. Grove, and G. van Koten, *Organometallics*, 1998, **17**, 5411.
5. M. Albrecht, P. Dani, M. Lutz, A. L. Spek, and G. van Koten, *J. Am. Chem. Soc.*, 2000, **122**, 11822.
6. G. Rodriguez, M. Albrecht, J. Schoenmaker, A. Ford, M. Lutz, A. L. Spek, and G. van Koten, *J. Am. Chem. Soc.*, 2002, **124**, 5127.
7. M. Albrecht, M. Lutz, A. L. Spek, and G. van Koten, *Nature*, 2000, **406**, 970.
8. G. W. V. Cave, F. P. Fanizzi, R. J. Deeth, W. Errington, and J. P. Rourke, *Organometallics*, 2000, **19**, 1355.
9. S.-W. Lai, M. C.-W. Wang, K.-K. Cheung, and C.-M. Che, *Organometallics*, 1999, **18**, 3327.
10. H. Furuta, K. Youfu, H. Maeda, and A. Osuka, *Angew. Chem., Int. Ed. Engl.*, 2003, **42**, 2186.
11. A. J. Arduengo III, S. F. Gamper, J. C. Calabrese, and F. Davidson, *J. Am. Chem. Soc.*, 1994, **116**, 4391.
12. P. L. Arnold, F. G. N. Cloke, T. Geldbach, and P. B. Hitchcock, *Organometallics*, 1999, **18**, 3228.
13. M. Muehlhofer, T. Strassner, E. Herdtweck, and W. A. Herrmann, *J. Organomet. Chem.*, 2002, **660**, 121.
14. E. M. Prokopchuk and R. J. Puddephatt, *Organometallics*, 2003, **22**, 563.
15. G. Lin, N. D. Jones, R. A. Gossage, R. McDonald, and R. G. Cavell, *Angew. Chem., Int. Ed. Engl.*, 2003, **42**, 4054.
16. L. K. Johnson, C. M. Killian, and M. Brookhart, *J. Am. Chem. Soc.*, 1995, **117**, 6414.
17. L. Deng, T. K. Woo, L. Cavallo, P. M. Margl, and T. Ziegler, *J. Am. Chem. Soc.*, 1997, **119**, 6177.
18. K. Yang, R. J. Lachicotte, and R. Eisenberg, *Organometallics*, 1998, **17**, 5102.
19. P. J. Albietz Jr, K. Yang, R. J. Lachicotte, and R. Eisenberg, *Organometallics*, 2000, **19**, 3543.
20. L. Johansson, O. B. Ryan, C. Rømming, and M. Tilset, *Organometallics*, 1998, **17**, 3957.
21. H. A. Zhong, J. A. Labinger, and J. E. Bercaw, *J. Am. Chem. Soc.*, 2002, **124**, 1378.
22. C. R. Baar, H. A. Jenkins, G. P. A. Yap, and R. J. Puddephatt, *Organometallics*, 1998, **17**, 4329.
23. H. Willner, M. Bodenbinder, R. Bröchler, G. Hwang, S. J. Rettig, J. Trotter, B. von Ahsen, U. Westphal, V. Jonas, W. Thiel, and F. Aubke, *J. Am. Chem. Soc.*, 2001, **123**, 588.

24. Q. Xu, *Coord. Chem. Rev.*, 2002, **231**, 83.
25. G. S. Hill, M. J. Irwin, C. J. Levy, L. M. Rendina, and R. J. Puddephatt, *Inorg. Synth.*, 1998, **32**, 149.
26. K. Praefcke, B. Bilgin, J. Pickardt, and M. Borowski, *J. Organomet. Chem.*, 1999, **592**, 155.
27. S. White, E. W. Kalberer, B. L. Bennett, and D. M. Roddick, *Organometallics*, 2001, **20**, 5731.
28. K. Matzumoto, J. Matsunami, K. Mizuno, and H. Uemura, *J. Am. Chem. Soc.*, 1996, **118**, 8959.
29. K. Matzumoto and M. Ochiai, *Coord. Chem. Rev.*, 2002, **231**, 229.
30. C. M. Lukehart, *Adv. Organomet. Chem.*, 1986, **25**, 45.
31. D. Steinborn, M. Gerisch, C. Bruhn, and J. A. Davies, *Inorg. Chem.*, 1999, 680.
32. J.-T. Chen, Y.-S. Yeh, C.-S. Yang, F.-Y. Tsai, G.-L. Huang, B.-C. Shu, T.-M. Huang, Y.-S. Chen, G.-L. Lee, M.-C. Cheng, C.-C. Wang, and Y. Wang, *Organometallics*, 1994, **13**, 4804.
33. R. M. Shaltout, R. Sygula, A. Sygula, F. R. Fronczek, G. G. Stanley, and P. W. Rabideau, *J. Am. Chem. Soc.*, 1998, **120**, 835.
34. A. Arévalo, S. Bernès, J. J. García, and P. M. Maitlis, *Organometallics*, 1999, **18**, 1680.
35. D. A. Vicvic and W. D. Jones, *Organometallics*, 1998, **17**, 3411.
36. K. Osakada and T. Yamamoto, *Coord. Chem. Rev.*, 2000, **198**, 379.
37. T. B. Peters, J. C. Bohling, A. M. Arif, and J. A. Gladysz, *Organometallics*, 1999, **18**, 3261.
38. E. Bosch and C. L. Barnes, *Organometallics*, 2000, **19**, 5522.
39. K. Onitsuka, N. Ose, F. Ozawa, and S. Takahashi, *J. Organomet. Chem.*, 1999, **578**, 169.
40. P. J. Fagan, J. C. Calabrese, and B. Malone, *Acc. Chem. Res.*, 1992, **25**, 134.
41. P. B. Hitchcock, M. F. Lappert, and N. J. W. Warhurst, *Angew. Chem., Int. Ed. Engl.*, 1991, **30**, 438.
42. C. Huber, A. Kokil, W. R. Caseri, and C. Weder, *Organometallics*, 2002, **21**, 3817.
43. C. Massera and G. Frenking, *Organometallics*, 2003, **22**, 2758.
44. C. Müller, R. J. Lachicotte, and W. D. Jones, *Organometallics*, 2002, **21**, 1118.
45. P. Ganis, I. Orabona, F. Ruffo, and A. Vitagliano, *Organometallics*, 1998, **17**, 2646.
46. V. G. Albano, M. Monari, I. Orabona, A. Panunzi, and F. Ruffo, *J. Am. Chem. Soc.*, 2001, **123**, 4352.
47. U. Belluco, R. Bertani, R. A. Michelin, and M. Mozzon, *J. Organomet. Chem.*, 2000, **600**, 37.
48. S.-H. Sha, K.-K. Lee, Y.-W. Kwak, H.-J. Choi, Y.-S. Park, A. Naka, and M. Ishikawa, *Organometallics*, 2001, **20**, 3718.
49. H. Lang, D. S. A. George, and G. Rheinwald, *Coord. Chem. Rev.*, 2000, **206–207**, 101.
50. J. R. Berenguer, E. Eguizábal, L. R. Falvello, J. Forniés, E. Lalinde, and A. Martín, *Organometallics*, 2000, **19**, 490.
51. T. L. Schull, J. G. Kushmerick, C. H. Patterson, C. George, M. H. Moore, S. K. Pollack, and R. Shashidhar, *J. Am. Chem. Soc.*, 2003, **125**, 3202.
52. M. Mayer, C. von Hanisch, H. B. Weber, J. Reichert, and D. Beckmann, *Angew. Chem., Int. Ed. Engl.*, 2002, **41**, 1183.
53. V. W.-W. Yam, *Acc. Chem. Res.*, 2002, **35**, 555.
54. G. Arena, G. Calogero, S. Campagna, L. M. Scolaro, V. Ricevuto, and R. Romeo, *Inorg. Chem.*, 1998, **37**, 2763.
55. V. W.-W. Yam, K. M.-C. Wong, and N. Zhu, *J. Am. Chem. Soc.*, 2002, **124**, 6506.
56. S.-W. Lai, M. C.-W. Chan, T. C. Cheung, S.-M. Peng, and C.-M. Che, *Inorg. Chem.*, 1999, **38**, 4046.
57. J. D. Carr, S. J. Coles, M. B. Hursthouse, M. E. Light, E. L. Munro, J. H. R. Tucker, and J. Westwood, *Organometallics*, 2000, **19**, 3312.
58. C. E. Whittle, J. A. Weinstein, M. W. George, and K. S. Schanze, *Inorg. Chem.*, 2001, **40**, 4053.
59. M. Hissler, J. E. McGarah, W. B. Connick, D. K. Geiger, S. D. Cummings, and R. Eisenberg, *Coord. Chem. Rev.*, 2000, **208**, 115.
60. R. R. Willis, C. E. Shuchart, and A. Wojcicki, *Organometallics*, 2000, **19**, 3179.
61. T.-M. Huang, J.-T. Chen, G.-H. Lee, and Y. Wang, *J. Am. Chem. Soc.*, 1993, **115**, 1170.
62. J.-T. Chen, *Coord. Chem. Rev.*, 1999, **190–192**, 1143.
63. P. J. Stang, C. M. Crittell, and A. M. Arif, *Organometallics*, 1993, **12**, 4799.
64. P. W. Blosser, D. G. Schimpff, J. C. Gallucci, and A. Wojcicki, *Organometallics*, 1993, **12**, 1993.
65. J.-T. Chen, R.-H. Hsu, and A.-J. Chen, *J. Am. Chem. Soc.*, 1998, **120**, 3243.
66. J. P. Graham, A. Wojcicki, and B. E. Bursten, *Organometallics*, 1999, **18**, 837.
67. S. Ogoshi, M. Morita, and H. Kurosawa, *J. Am. Chem. Soc.*, 2003, **125**, 9020.
68. W. V. Konze, B. L. Scott, and G. J. Kubas, *J. Am. Chem. Soc.*, 2002, **124**, 12550.
69. V. Jacob, T. J. R. Weakley, and M. M. Haley, *Organometallics*, 2002, **21**, 5394.
70. V. Jacob, T. J. R. Weakley, and M. M. Haley, *Angew. Chem., Int. Ed. Engl.*, 2002, **41**, 3470.
71. R. Usón, J. Forniés, L. R. Falvello, M. Tomás, J. M. Casas, A. Martin, and F. A. Cotton, *J. Am. Chem. Soc.*, 1994, **116**, 7160.
72. T. Yamamoto, T. Shido, S. Inagaki, Y. Fukushima, and M. Ishikawa, *J. Am. Chem. Soc.*, 1996, **118**, 5810.
73. G. J. Spivak, J. J. Vittal, and R. J. Puddephatt, *Organometallics*, 1999, **18**, 5474.
74. C. Gemel, T. Steinke, D. Weiss, M. Cokoja, M. Winter, and R. A. Fischer, *Organometallics*, 2003, **22**, 2705.

75. P. J. Stang and B. Olenyuk, *Acc. Chem. Res.*, 1997, **30**, 502.
76. S. R. Seidel and P. J. Stang, *Acc. Chem. Res.*, 2002, **35**, 972.
77. S. M. ALQaisi, K. J. Galat, M. Chai, D. G. Ray III, P. L. Rinaldi, C. A. Tessier, and W. J. Youngs, *J. Am. Chem. Soc.*, 1998, **120**, 12149.
78. S. J. Lee, C. R. Luman, F. N. Castellano, and W. Lin, *Chem. Commun.*, 2003, 2124.
79. N. C. Gianneschi, E. R. T. Tiekink, and L. M. Rendina, *J. Am. Chem. Soc.*, 2000, **119**, 8474.
80. K. M. Park, S. Y. Kim, J. Heo, D. Whang, S. Sakamoto, K. Yamaguchi, and K. Kim, *J. Am. Chem. Soc.*, 2002, **124**, 2140.
81. K. Onitsuka, A. Shimizu, and S. Takahashi, *Chem. Commun.*, 2003, 280.
82. A. Albinati, P. Leoni, L. Marchetti, and S. Rizzato, *Angew. Chem., Int. Ed. Engl.*, 2003, **42**, 5990.
83. R. A. Gossage, L. A. van de Kuil, and G. van Koten, *Acc. Chem. Res.*, 1998, **31**, 423.
84. T. Yamaguchi, F. Yamazaki, and T. Ito, *J. Am. Chem. Soc.*, 2001, **123**, 743.
85. C. Huber, F. Bangerter, W. R. Caseri, and C. Weder, *J. Am. Chem. Soc.*, 2001, **123**, 3857.
86. A. Kokil, I. Shiyanovskaya, K. D. Singer, and C. Weder, *J. Am. Chem. Soc.*, 2002, **124**, 9978.
87. Y. Liu, S. Jiang, K. Glusac, D. H. Powell, D. F. Anderson, and K. S. Schanze, *J. Am. Chem. Soc.*, 2002, **124**, 12412.
88. R. A. Gossage, G. D. McLennan, and S. R. Stobart, *Inorg. Chem.*, 1996, **35**, 1729.
89. H. Gilges and U. Schbert, *Organometallics*, 1998, **17**, 4760.
90. J. Braddock-Wilking, Y. Levchinsky, and N. P. Rath, *Organometallics*, 2001, **20**, 474.
91. R. S. Simons, L. M. Sanow, K. J. Galat, C. A. Tessier, and W. J. Youngs, *Organometallics*, 2000, **19**, 3994.
92. H. Hashimoto, Y. Sekiguchi, T. Iwamoto, C. Kabuto, and M. Kira, *Organometallics*, 2002, **21**, 454.
93. G. P. Mitchell and T. D. Tilley, *J. Am. Chem. Soc.*, 1998, **120**, 7635.
94. J. D. Feldman, G. P. Mitchell, J.-O. Nolte, and T. D. Tilley, *J. Am. Chem. Soc.*, 1998, **120**, 11184.
95. P. Braunstein, T. Faure, and M. Knorr, *Organometallics*, 1999, **18**, 1791.
96. A. J. Canty and G. van Koten, *Acc. Chem. Res.*, 1995, **28**, 406.
97. S. S. Stahl, J. A. Labinger, and J. E. Bercaw, *Inorg. Chem.*, 1998, **37**, 2422.
98. B. F. M. Kimmich and R. M. Bullock, *Organometallics*, 2002, **21**, 1504.
99. S. Reinartz, M. H. Baik, P. S. White, M. Brookhart, and J. L. Templeton, *Inorg. Chem.*, 2001, **40**, 4726.
100. D. S. Helfer and J. D. Atwood, *Organometallics*, 2002, **21**, 250.
101. M. D. Butts, B. L. Scott, and G. J. Kubas, *J. Am. Chem. Soc.*, 1996, **118**, 11831.
102. R. J. Puddephatt, *Coord. Chem. Rev.*, 2001, **219–221**, 157.
103. S. A. O'Reilly, P. S. White, and J. L. Templeton, *J. Am. Chem. Soc.*, 1996, **118**, 5684.
104. S. Reinartz, P. S. White, M. Brookhart, and J. L. Templeton, *Organometallics*, 2000, **19**, 3748.
105. S. Reinartz, P. S. White, M. Brookhart, and J. L. Templeton, *J. Am. Chem. Soc.*, 2001, **123**, 6425.
106. A. Haskel and E. Keinan, *Organometallics*, 1999, **18**, 4677.
107. V. De Felice, B. Giovannitti, A. De Renzi, D. Tesauro, and A. Panunzi, *J. Organomet. Chem.*, 2000, **593–594**, 445.
108. C. R. Baar, L. P. Carbray, M. C. Jennings, and R. J. Puddephatt, *J. Am. Chem. Soc.*, 2000, **122**, 176.
109. S. H. L. Thoonen, M. Lutz, A. L. Spek, B.-J. Deelman, and G. van Koten, *Organometallics*, 2003, **22**, 1156.
110. A. J. Canty, H. Jin, and J. D. Penny, *J. Organomet. Chem.*, 1999, **573**, 30.
111. M. C. Janzen, H. A. Jenkins, M. C. Jennings, L. M. Rendina, and R. J. Puddephatt, *Organometallics*, 2002, **21**, 1257.
112. S.-W. Zhang and S. Takahashi, *Organometallics*, 1998, **17**, 4757.
113. D. Song, K. Sliwowski, J. Pang, and S. Wang, *Organometallics*, 2002, **21**, 4978.
114. R. A. Periana, D. J. Taube, S. Gamble, H. Taube, T. Satoh, and H. Fujii, *Science*, 1998, **280**, 560.
115. B. D. Dangel, J. A. Johnson, and D. Sames, *J. Am. Chem. Soc.*, 2001, **123**, 8149.
116. M. W. Holtcamp, J. A. Labinger, and J. E. Bercaw, *J. Am. Chem. Soc.*, 1997, **119**, 848.
117. H. Heiberg, L. Johansson, O. Gropen, O. B. Ryan, O. Swang, and M. Tilset, *J. Am. Chem. Soc.*, 2000, **122**, 10831.
118. S. S. Stahl, J. A. Labinger, and J. E. Bercaw, *J. Am. Chem. Soc.*, 1996, **118**, 5961.
119. B. J. Wik, M. Lersch, and M. Tilset, *J. Am. Chem. Soc.*, 2002, **124**, 12116.
120. U. Fekl, A. Zahl, and R. van Eldik, *Organometallics*, 1999, **18**, 4156.
121. K. L. Bartlett, K. I. Goldberg, and W. T. Borden, *J. Am. Chem. Soc.*, 2000, **122**, 1456.
122. U. Fekl and K. I. Goldberg, *J. Am. Chem. Soc.*, 2002, **124**, 6804.
123. L. Johansson, M. Tilset, J. A. Labinger, and J. E. Bercaw, *J. Am. Chem. Soc.*, 2000, **122**, 10846.
124. L. Johansson, O. B. Ryan, C. Rømming, and M. Tilset, *J. Am. Chem. Soc.*, 2001, **123**, 6579.
125. C. N. Iverson, R. J. Lachicotte, C. Müller, and W. D. Jones, *Organometallics*, 2002, **21**, 5320.
126. M. Albrecht, A. L. Spek, and G. van Koten, *J. Am. Chem. Soc.*, 2001, **123**, 7233.

127. M. E. van der Boom, H.-B. Kraatz, L. Hassner, Y. Ben-David, and D. Milstein, *Organometallics*, 1999, **18**, 3873.
128. N. Simhai, C. N. Iverson, B. L. Edelbach, and W. D. Jones, *Organometallics*, 2001, **20**, 2759.
129. L. M. Rendina and R. J. Puddephatt, *Chem. Rev.*, 1997, **97**, 1735.
130. D. S. McGuinness, K. J. Cavell, B. F. Yates, B. W. Skelton, and A. H. White, *J. Am. Chem. Soc.*, 2001, **123**, 8317.
131. L.-B. Han, N. Choi, and M. Tanaka, *J. Am. Chem. Soc.*, 1996, **118**, 7000.
132. L.-B. Han, C.-Q. Zhao, S. Onozawa, M. Goto, N. Choi, and M. Tanaka, *J. Am. Chem. Soc.*, 2002, **124**, 3842.
133. K. Sugoh, H. Kuniyasu, T. Sugae, A. Ohtaka, Y. Takai, A. Tanaka, C. Machino, N. Kambe, and H. Kurosawa, *J. Am. Chem. Soc.*, 2001, **123**, 5108.
134. A. Ohtaka, H. Kuniyasu, M. Kinomoto, and H. Kurosawa, *J. Am. Chem. Soc.*, 2002, **124**, 14324.
135. N. Mintcheva, Y. Nishihara, M. Tanabe, K. Harabayashi, A. Mori, and K. Osakada, *Organometallics*, 2001, **20**, 1243.
136. K. I. Goldberg, J. Yang, and E. L. Winter, *J. Am. Chem. Soc.*, 1994, **116**, 1573.
137. B. S. Williams and K. I. Goldberg, *J. Am. Chem. Soc.*, 2001, **123**, 2576.
138. D. M. Crumpton-Bregel and K. I. Goldberg, *J. Am. Chem. Soc.*, 2003, **125**, 9442.
139. S. Reinartz, P. S. White, M. Brookhart, and J. L. Templeton, *Organometallics*, 2000, **19**, 3854.
140. F. Ozawa, T. Hikida, and T. Hayashi, *J. Am. Chem. Soc.*, 1994, **116**, 2844.
141. K. Hasebe, J. Kamite, T. Mori, H. Katayama, and F. Ozawa, *Organometallics*, 2000, **19**, 2022.
142. F. Ozawa and T. Mori, *Organometallics*, 2003, **22**, 3593.
143. P. W. N. M. van Leeuwen, C. F. Roobeek, and H. van der Heijden, *J. Am. Chem. Soc.*, 1994, **116**, 12117.
144. D. W. Dockter, P. E. Fanwick, and C. P. Kubiak, *J. Am. Chem. Soc.*, 1996, **118**, 4846.
145. G. A. Luinstra, J. A. Labinger, and J. E. Bercaw, *J. Am. Chem. Soc.*, 1993, **115**, 3004.
146. V. V. Rostovtsev, L. M. Henling, J. A. Labinger, and J. E. Bercaw, *Inorg. Chem.*, 2002, **41**, 3608.
147. D. D. Wick and K. I. Goldberg, *J. Am. Chem. Soc.*, 1999, **121**, 11900.
148. M. S. Morton, R. J. Lachicotte, D. A. Vicic, and W. D. Jones, *Organometallics*, 1999, **18**, 227.
149. D. W. Lucey and J. D. Atwood, *Organometallics*, 2002, **21**, 2481.
150. T. Suzuki and H. Fujimoto, *Inorg. Chem.*, 1999, **38**, 370.
151. F.-Y. Tsai, H.-W. Chen, J.-T. Chen, G.-H. Lee, and Y. Wang, *Organometallics*, 1997, **16**, 822.
152. M. E. Cucciolito, V. De Felice, F. Giordano, I. Orabona, and F. Ruffo, *Eur. J. Inorg. Chem.*, 2001, 3095.
153. G. Wagner, A. J. Pombeiro, and V. Y. Kukushkin, *J. Am. Chem. Soc.*, 2000, **122**, 3106.
154. M. Tanabe and K. Osakada, *Organometallics*, 2001, **20**, 2118.
155. I. E. Markó, S. Stérin, O. Buisine, G. Mignani, P. Branlard, B. Tinant, and J.-P. Declercq, *Science*, 2002, **298**, 204.
156. M. Méndez, M. P. Munoz, C. Nevado, D. J. Cárdenas, and A. M. Echavarren, *J. Am. Chem. Soc.*, 2001, **123**, 10511.
157. A. Fürstner, F. Stelzer, and H. Szillat, *J. Am. Chem. Soc.*, 2001, **123**, 11863.
158. T. Ishiyama, N. Matsuda, N. Miyaura, and A. Suzuki, *J. Am. Chem. Soc.*, 1993, **115**, 11018.
159. Y. G. Lawson, M. J. G. Lesley, T. B. Marder, N. C. Norman, and C. R. Rice, *Chem. Commun.*, 1997, 2051.
160. G. Mann, K. D. John, and R. T. Baker, *Org. Lett.*, 2000, **2**, 2105.
161. L.-B. Han and M. Tanaka, *J. Am. Chem. Soc.*, 1998, **120**, 8249.
162. M. Suginome, H. Nakamura, T. Matsuda, and Y. Ito, *J. Am. Chem. Soc.*, 1998, **120**, 4248.
163. J. Kadota, H. Katsuragi, Y. Fukumoto, and S. Murai, *Organometallics*, 2000, **19**, 979.
164. J. Beyer, P. R. Skaanderup, and R. Madsen, *J. Am. Chem. Soc.*, 2000, **122**, 9575.

Polonium: Inorganic Chemistry

Ralph A. Zingaro
Texas A&M University, College Station, TX, USA

1 History and Discovery 1
2 Inorganic Chemistry of the Element 1
3 Related Articles 7
4 References 7

1 HISTORY AND DISCOVERY

The discovery of this element was one of the crowning achievements during the illustrious career of Mme Marie Curie. In order to appreciate the enormity of her task, it should be recognized that the amount of polonium in pitchblende at equilibrium is of the order of 0.1 mg per tonne. During the course of her investigations with thorium and uranium ores, Mme Curie sought the cause of the unusually high levels of radioactivity, which could not be attributed to the uranium alone. Her separation of this element was based largely on the observation that a highly radioactive precipitate was formed from acid solution with H_2S. The chemical procedures she utilized forced the conclusion that the source of the greater than expected radioactivity was attributable to an element that coprecipitated with Bi_2S_3. Vacuum sublimation of the precipitate brought about a separation of the highly radioactive component. The sublimed material was probably metallic polonium. The methods used by Mme Curie yielded only traces of the new element, and the progress of the separation was followed by measuring the radioactivity. Polonium has the distinction of being the first element whose discovery was made solely on account of its radioactivity.

Most of our knowledge about the chemistry of this element was developed during the period following World War II, primarily from the nuclear energy research establishments of the USA and UK. Hence, references appearing prior to this time are historically complete but scientifically dated. Of recent reviews,[1–8] that by Bagnall[1] and the one in the Gmelin series[5] are the most up-to-date and thorough.

It was not until neutron-rich sources became available that weighable quantities of polonium became available. It can be prepared in milligram quantities by the irradiation of bismuth with neutrons. The reaction which takes place is the following:

$$^{209}_{83}\mathrm{Bi}(n, \gamma)^{210}_{83}\mathrm{Bi}(\beta, 5.0d)^{210}_{84}\mathrm{Po} \qquad (1)$$

Details on the separation procedures can be found in Gmelin.[5]

1.1 Isotopes of Polonium

Naturally occurring isotopes of polonium are formed during the radioactive decay of ^{238}U (^{218}Po, ^{214}Po,^{210}Po), ^{232}Th (^{216}Po, ^{212}Po), and ^{235}U (^{215}Po and ^{211}Po). In addition to these seven naturally occurring isotopes, at least 20 additional isotopes of this element have been prepared by the particle bombardment of various bismuth and lead isotopes. However, the isotope ^{210}Po has played the major role in adding to our knowledge about the chemistry of this element.

2 INORGANIC CHEMISTRY OF THE ELEMENT

2.1 Metallic Polonium

Polonium is a member of the oxygen group of elements and has the electronic configuration [Xe]$4f^{14}5d^{10}6s^26p^4$. In this group, there occurs the transition from the typical nonmetals (oxygen and sulphur) to the metalloids (selenium and tellurium) and the metal (polonium).

Solutions containing the metal, most commonly in nitric acid, will deposit the metal on a platinum electrode by electrodeposition. Polonium metal is deposited spontaneously from such solutions on to metals such as silver or nickel. The metal can be sublimed off such support metals at low pressures. Thermal decomposition of polonium sulfide also yields the metal. In much the same way as tellurium, the metal can be obtained from its solutions by the action of reducing agents such as hydrazine, tin(II) ion, titanium(III) ion, and dithionite. Such metal precipitates appear as gray-black powders. Thin foils, silvery in color, have been prepared by vacuum sublimation of the metal.

The metal is soft and has properties similar to those of bismuth. It melts at 254 °C and boils at 962 °C. Two allotropic crystalline forms are recognized, the low-temperature α form and the high-temperature β-form. The α form crystallizes in the 0_h^1 space group and the β-form in the $D^5{}_{3d}$ space group.

The metal has been found to diffuse easily into support metals and considerable research has been reported in this area. X-ray and optical spectra have been measured and numerous reports appear in the literature.

A Japanese patent[9] describes the treatment of metal surfaces with amorphous layers of second metals having a thickness of 0.2–2.5 µm. The metal component includes one, or more, of the following: V, Nb, Ta, N, P, As, Sb, Bi, Cr, Mo, W, S, Se, Te, and Po. The introduction of such a surface coating is claimed to improve wear and burning resistance of the metal. Also, the coating serves to increase the retention of oil films by the metal surface thus improving lubrication properties.

The deposition of polonium on metal wires gives rise to a useful α-source.**[10]** Tips of metal wires having a length 10 mm and a diameter of 0.2 mm were utilized. They were made of Al, Ni, Pd, Pt or Au. Each was immersed in 100 µl of a solution containing ^{210}Po (300 Bq ml^{-1}) for 15 h at 27°. Alpha particle emission was measured using a liquid scintillation system. There was an observed diminution in the α-pulse spectra for all of the wires except Al. This was attributed to the mutual diffusion between the wire metal and ^{210}Po. The ^{210}Po deposited on the Al wire had a tendency to be eluted with the liquid scintillator. This was attributed to physical absorption on the porous metal oxide layer on the A1 wire and ^{210}Po. The ^{210}Po deposited by the Al wire had a tendency to be eluted with the liquid scintillator. It was possible to prepare a ^{210}Po -A1 wire as a useful α-source by heating at 120° for 30 minutes.

The thermochromatography of trace amounts of a number of elements including Po, Am and Cf in their elemental states was studied.**[11]** The deposition temperatures suggest the existence of different types of intersection between the adsorbate atoms and the Ti surface. The technique is presented as having practical analytical applications.

The crystal structures of α- and β-Po metal were redetermined.**[12]** An isotopic mixture of ^{208}Po and ^{209}Po was used. The structure was determined in a helium atmosphere from x-ray powder diffraction patterns. Previous reports were considered unreliable because of the growth of Pb at a rate of 0.5 percent per day and self-heating effects. Because of the longer half lives of ^{208}Po, 2.8 years and ^{209}Po, 103 years, the growth rate of Pb and the self-heating are greatly reduced. α-Po possesses a simple cubic space group Pm3m with a equal to 3.359 ± 0.001 Å and d 9.142. β-Po possesses a rhombohedral space group R3m with a 3.868 ± 0.001 Å α 98°14.4′ and d 9.392.

Weighable amounts of ^{210}Po were produced by the irradiation of ^{209}Bi with slow neutrons.**[13]** An aqueous solution of 2×10^{-3} M Po in 0.8 M HC1 was electrolyzed and Po metal was deposited on precipitated Ag, Ni and Cu. Metallic Po was subsequently electrolytically deposited on Pt. Po metal sublimed at 400° at 1 µ and condensed in the form of a silvery mirror. Po metal dissolves readily in concentrated nitric acid to form a yellow solution. With dilute HNO_3, the metal forms an unidentified white solid. With 2N HCl, a pink solution is formed. In concentrated HNO_3, the Po dissolves as Po(IV) (yellow) which, can be reduced by SO_2, As_2O_3 or hydrazine to form a pink solution, presumably Po(II). The latter, subjected to oxidation by H_2O_2 or Cl_2 reverts to the yellow color. In air, at room temperature, the metal converts to the oxide. The oxide sublimes at 885° at atmospheric pressure, but undergoes thermal decomposition at 900° or at 500° at 1 µ to reform the metal. The oxide dissolves in dilute HCl to form a yellow solution, and in HBr to form an orange-red solution. Evaporation yields $PoCl_4$ and $PoBr_4$, respectively. In HI, the oxide forms a volatile, insoluble black solid. At room temperature the oxide has a face-centered cubic structure, a = 5.687 ± 0.005 Å. It undergoes a phase transformation at 80° to a red, tetragonal form, a = 5.626 ± 0.005 Å. The dioxide has the space group Oh5-Fm3m. The Po-O distance is 2.44 Å and Po(IV) radius is 1.04 Å when the 0 radius is taken as 1.40 Å.

Surfaces coated with Po can be freed of certain impurities such as Pb and Bi.**[14]** This is accomplished by immersion of the surface in an aqueous solution containing ammonium hydroxide and ammonium persulfate at room temperature for a period of time not exceeding 15 minutes.

2.2 Compounds with Hydrogen

By analogy with the other members of the chalcogen family, the compound H_2Po should be expected to exist. Such a compound has never been isolated in weighable quantities and only tracer-scale evidence has been furnished for its existence. Because of the increasing metallic nature of the elements as one proceeds to the heavier members of a family, such a compound would predictably be extremely unstable. Hydrogen telluride, for example, is itself unstable with respect to its component elements.

Indirect evidence for the existence of H_2Po has been found in measurements of ionization brought about by α radiation from ^{210}Po in an H_2 atmosphere. The very high increases in observed ionization which were observed (no solid window was present between the polonium source and the ionization chamber) were attributed to formation of H_2Po.

More conventional chemical approaches have been used in attempts to synthesize H_2Po. It has been reported to form by the addition of magnesium metal powder to aqueous solutions containing dissolved polonium or by the action of hydrogen generated in situ in such solutions. Claims have been made for the condensation of H_2Po at liquid air temperatures when it is generated by the action of nascent hydrogen on aqueous solutions containing polonium. It appears to be considerably less stable than BiH_3 and is thermally unstable with respect to the elements, decomposing at 34.5 °C. Other claims have been made for the existence of polonium hydride, but it has never been isolated in analytically identifiable quantities.

During the detection of ionization over the range of α-rays from polonium in a hydrogen atmosphere, abnormally rapid increases were observed when no solid window was present between the Po and the ionization chamber.**[15]** This was not explainable by the volatility of Po nor to the transfer of Po together with the recoil atoms of Ra G. This was explained by the assumption that a hydride, H_2Po is formed, which diffuses into the ionization chamber. Such a compound is rapidly destroyed by a small concentration of air or through the action of α-rays. The formation of such a hydride would explain the very high absorption power of Pt and Pd for Po.

2.3 Oxides of Polonium

The evidence for the existence of PoO and Po_2O_3 is insubstantial. When $PoSO_3$ or $PoSeO_3$, whose own existence is questionable, decompose, the product formed has been claimed to be PoO, but definitive experimental data are lacking. The synthesis of Po_2O_3 has never been claimed, but it has been speculated that it possesses a cubic structure like that of Bi_2O_3.

Only PoO_2 has been well characterized. It has been prepared by the reaction between the metal and oxygen. It has been successfully prepared using various oxygen pressures and temperatures ranging from 200–700 °C. It has been described as yellow-orange to brick red in color. The color changes from yellow-orange to brick red with increasing temperature and is described as brown-red at 780 °C. PoO_2 sublimes in an oxygen atmosphere, but thermally decomposes when heated at low pressures. The thermodynamic properties of PoO_2 have been measured.

PoO_2 at low temperature, possesses a face-centered cubic symmetry similar to fluorite, but converts into a high-temperature tetragonal form at 80 °C. The two allotropic forms coexist, even at room temperature. This is due to the heat evolved by α particle collisions with the crystal lattice.

Trioxides of sulfur, selenium, and tellurium are well recognized, but polonium trioxide has yet to be prepared in weighable quantities.

Barium oxide undergoes reaction with PoO_2 in an oxygen atmosphere at 900–950° to form $Ba_4Po_3O_{10}$ and $BaPoO_3$.[16] At PoO_2:BaO molar ratios of 0.71–0.77 and 1.04–1.25, the respective compounds are formed. At 1000°, these compounds evolve PoO_2 and Ba_2PoO_4 is formed. The PoO_2 vapor pressure was measured. Vapors of PoO_2 do not undergo reaction with CdO or ZnO at temperatures below 1050°.

Trioxides of lanthanum and gadolinium absorb PoO_2 in an oxygen atmosphere at 850–900°.[17] At a PoO_2:M_2O_3 (M=La,Gd) molar ratio equal to or less than 1.0 the formation of $La_2O_2PoO_3$ and $Gd_2Po_2O_7$ occurs. The vapor pressure of PoO_2 over $La_2O_2PoO_3$ and $Gd_2Po_2O_7$ at 820–1010° and 820–1030°, respectively, were measured. Also, the heats of formation of the two reactions were measured. $La_2O_2PoO_3$ undergoes thermal decomposition in vacuum at 440°.

2.4 Hydroxides of Polonium

The addition of alkali to an aqueous solution of Po^{II} in hydrochloric acid produces a precipitate, described as dark brown in color. This may be the hydroxide or hydrated oxide of Po^{II}. The substance has never been analyzed and very rapidly converts to Po^{IV}.

Our knowledge about the properties of polonium compounds requires that the chemistry be carried out on freshly prepared solutions since radioactive decay leads to the formation of lead isotopes upon standing. Thus, the addition of hydroxide to solutions containing Po^{IV} yields pale yellow wooly precipitates. It is well known that the acidity of hydroxides decreases as the atomic weight increases within a group. This is especially true in the case of Group 16 elements. The solubility of weighable amounts of the hydroxide of Po^{IV} has been measured as a function of the hydroxide concentration. The solubility is linear, with a slope close to two and can be described by the equation:

$$PoO(OH)_2 + 2OH^- \longrightarrow PoO_3{}^{2-} + 2H_2O \qquad (2)$$

A number of other experiments carried out at tracer level concentrations are consistent with the formation of the hydroxide of Po^{IV} and the polonite ion. Deposits of polonium on gold electrodes are soluble in boiling water and this has been attributed to formation of $Po(OH)_4$. Tracer level ^{210}Po can be precipitated from its aqueous solutions in the presence of $Bi(OH)_3$ or $Fe(OH)_3$ carriers with alkali and is presumably carried as the hydroxide. Tracer level ^{210}Po dissolves in aqueous alkali and the solubility increases with increasing concentration of hydroxide ion. Also, a neutral species, postulated to be $Po(OH)_4$ was identified by paper chromatography.

A method is described for the determination of α-radioactivity in groundwaters.[18] The α-emitters, Po, Ra, Th, and U are precipitated as the hydroxides with NH_3 using Ba (II) and Fe (II) as carriers. The overall yield for all emitters is greater than 80%. Greater sensitivity is achieved with a large sample volume.

A method very similar to that just described is utilized for the analytical determination of ^{210}Pb and ^{210}Po.[19] The two isotopes, in water samples, are concentrated by coprecipitation with iron (III) hydroxide at pH 9–10 using ammonia as the precipitant. The precipitate is redissolved using H_2O_2 and HCl. The isotopes, in samples from soils, sediment algae, or shellfish are leached out at 250° with HNO_3/HF, $HClO_4$, and HCl. An aliquot of the leaching solution is used for ^{210}Po determination, which is carried out at 85–90° for hours by suspending a silver disk in a hydrochloric acid solution at pH 1.5 and containing hydroxylamine hydrochloride and sodium citrate. No preliminary separation is required and the ^{210}Po recoveries are essentially quantitative.

A linear free energy relationship is used to predict the Gibbs free energies of formation of crystalline phases of PoO_2 and $Po(OH)_4$.[20] It is necessary to know the thermodynamic properties of the aqueous tetravalent cation, Po(IV). Details on the form of the equation used are given. The relation is used to predict the Gibbs free energies of formation of the crystalline phases as well as thermodynamically unstable phases. Use of the equation requires that the energy of formation of Po(IV) is known.

An improved method for the analytical determination of Po has been described.[21] The method involves the precipitation of $Fe(OH)_3$ on polyacrylic fibers. This matrix serves as a column upon which ^{210}Po is deposited or coprecipitated with the iron. The research presents details of the technique including ^{210}Po data for Po in coastal waters. The method is described as simple, adaptable, and reliable.

A Japanese patent[22] deals with the analytical determination of Po in the semiconductor industry. Po, in phosphoric acid solution, is first concentrated and then precipitated, presumably as the hydroxide. The precipitate is utilized as an analytical sample.

A Japanese patent**[23]** deals with additive coatings on battery cathodes. These coatings include PoO_2. The batteries use cathodes composed of a heat treated lithium compound and MnO_2 together with an additive, MO_2, where M is selected among a number of metals including Po. The mixture is heat treated at 270–380° to give a battery claimed to possess high capacity.

A Russian report**[24]** deals with the release of ^{210}Po from a Li-Pb eutectic. The eutectic was heated at 450° in a noble gas stream in various concentrations of water vapor. The release of ^{210}Po was measured. The release of ^{210}Po varied with the temperature and the state of the eutectic surface. Polonium in the gaseous phase varied from 5 to 80% of the overall concentration. Interpretation of the data invokes the formation of chemical compounds between polonium and lead as well as the formation of hydroxides of polonium.

2.5 Sulfides of Polonium

Because ^{210}Po is the daughter of ^{210}Bi, and because it has been produced by the neutron irradiation of ^{210}Bi, an established procedure for its separation has involved its precipitation from acid solution with H_2S. Measurements of the radioactivity indicated that the precipitation was essentially quantitative. Suggestions that the precipitate was Po_2S_3 did not survive the scrutiny of experiment.

Evidence for the existence of PoS is much stronger. Aqueous solutions in HCl containing Po^{II} and Po^{IV} yield a precipitate of PoS. During the course of this reaction, Po^{IV} is reduced to Po^{II} with the concurrent oxidation of sulfide to free sulfur. The same sulfide can be prepared by the reaction between polonium hydroxide and ammonium sulfide. The compound has not been successfully prepared by the direct reaction between the elements.

The biologically mediated emission of Po from a culture solution insulated with a sea sediment extract was observed.**[25]** The emitted Po compound was considered to be lipophilic because it collected in organic solvents. Microorganisms are responsible for the emission of volatile Po compounds because no volatile compounds of Po were formed in a sterile medium. There exists an argument for the existence of a biotic source for atmospheric Po in the environment, which possibly originates from abiotic sources. The emission behavior of both Po and S in the culture experiments was compared. The chemical form of the emitted Po is not known, but it was emitted with dimethyl sulfide. A volatile Po compound was formed when methylcobalamin was used in the experiments.

2.6 Chlorine Compounds of Polonium

The tetrachloride is the best known and best characterized of the binary polonium halides. It has been prepared in a number of ways. The direct action of chlorine at 200 °C on the metal, the reaction between PoO_2 and CCl_4 vapors at 200 °C, and the evaporation to dryness of solutions containing Po^{IV} in aqueous HC1 under a CCl_4 atmosphere have all been reported to yield the tetrachloride. It has been described as a bright yellow solid which when heated in a sealed tube undergoes a series of color changes. It becomes a straw-colored liquid at about 300 °C and turns scarlet at 350 °C. It can be sublimed at low pressure and at temperatures below 210 °C. Under an atmosphere of chlorine it turns purple-brown at 400 °C and then blue-green at 500 °C. Under an NH_3 atmosphere at 100 °C it converts to ammonium hexachloropolonate, $(NH_4)_2PoCl_6$.

Like $TeCl_4$, it hydrolyzes readily in the presence of moisture. It is moderately soluble in a number of alcohols and ketones. Also, in the manner of $TeCl_4$, it forms bright yellow solutions in aqueous HCl, which suggests the formation of the hexachloropolonates. The formation of $PoCl_6{}^{2-}$ in 12.2 M HCl is highly probable, but not definitive.

The action of some reducing agents, specifically SO_2 hydrazine, or arsenite, reduces solutions of Po^{IV} in HCl to pink solutions containing Po^{II}. Not all reducing agents effect this reduction.

The thermal decomposition of $PoCl_4$ at low pressures and at temperatures in the range of 200–250 °C, as well as the reduction of the tetrachloride by hydrogen at 200 °C and the direct reaction between metallic polonium and stoichiometric quantities of Cl_2, have all been reported to yield $PoCl_2$. It has been described as red, orange red, and ruby red in color. It melts above 350 °C and can be sublimed at reduced pressure at 200 °C under a nitrogen atmosphere. Evidence suggests that the addition of a mole of Br_2 forms $PoCl_2Br_2$. $PoCl_2$ is less stable than the tetrachloride and is very readily oxidized to Po^{IV}. Freshly prepared solutions in HCl are pink in color, but they are extremely unstable with respect to oxidation.

Some evidence based on electrochemical investigations has been presented for the existence of Po^{III}, but it is tenuous, at best.

The extensive use of solvent extraction methods and ion-exchange chromatography in the separation of radioactive elements has furnished good evidence for the existence of $[PoH_2OCl_5]^-$ and $[PoCl_6]^{2-}$. The coprecipitation of ^{210}Po with ammonium salts of $PbCl_6{}^{2-}$, $SnCl_6{}^{2-}$, $TeCl_6{}^{2-}$, and $PtCl_6{}^{2-}$ suggests the existence of isomorphism and the formation of $(NH_4)_2PoCl_6$. In fact, with mg quantities of ^{210}Po, a number of M_2PoCl_6 salts have been prepared where M is Cs^+, $NH_4{}^+$, K^+, Rb^+, and $NMe_4{}^+$. The reaction between $PoCl_4$ and NOCl yields a yellow solid, not unequivocally characterized, which may contain $PoCl_6{}^{2-}$ with NO^+ as the counter-ion.

It has been suggested that the white solid formed when $PoCl_4$ undergoes hydrolysis may be the oxychloride, $PoOCl_2$.

The tetrachloride of polonium is prepared by dissolving the metal in hydrochloric acid and evaporating to dryness.**[26]** $PoCl_4$, is a hydroscopic yellow solid which melts at 300° and is soluble in ethanol and acetone. The tetrachloride can be converted to dichloride, $PoCl_2$, by reduction with sulfur dioxide or hydrazine. $PoCl_2$ can also be prepared by the thermal decomposition of the tetrachloride in vacuo. Metallic polonium can be deposited electrolytically on a gold foil from a solution containing 65 Mc. of polonium in nitric acid. The electrode potential of the Po/Po (IV) couple is E°, 0.76 volts.

The absorption spectrum of Po in HCl solutions reveals the presence of at least two complexes,[27] A and B. Complex A absorbs with a maximum at 344 mμ. Complex B absorbs with a maximum at 418 mμ. The 418 mμ absorption can be used for the colorimetric determination of polonium. Although the 344 mμ absorption is stronger in weakly acidic solutions, it is difficult to utilize because of chlorine formation brought about by radiation from the polonium. The absorbance of the complex at 344 mμ was estimated by the use of a method involving the log absorbancy curves for the complex and for the chloride ion.

Weighable quantities of ^{210}Po were produced by the irradiation of ^{209}Bi with slow neutrons.[28] The free element was produced by electrochemical deposition on platinum. The Po metal dissolves readily in dilute nitric acid and yields an unknown white solid. The metal oxidizes slowly in air at room temperature, but rapidly at 250−300°. The oxide dissolves in HC1 or HBr to give, respectively, yellow and orange-red solutions. Evaporation of these solutions gives $PoCl_4$ and $PoBr_4$.

An unidentified compound, not polonium hydroxide and presumed to be $PoOCl_2$, was obtained by the evaporation of a dilute hydrochloride acid containing polonium.[29] The residue is soluble in polar organic solvents such as ethanol, ethylene glycol, dioxane, acetone, and methyl ethyl ketone. It is insoluble in benzene or chloroform.

Polonium metal was formed by the reduction of $PoCl_4$, $PoOCl_2$ as well as from the nitrate or the acetate. The solvents involved were hydrochloric acid and polar organics such as acetone, ethanol, and methyl ethyl ether. Mercury served as the reducing agent and a polonium-mercury amalgam is formed.

2.7 Bromine Compounds of Polonium

The tetrabromide of polonium has been prepared in several ways, which parallel those described for the tetrachloride. These include the direct reaction between the elements at 200 °C, dissolution of the metal in aqueous hydrobromic acid solution followed by evaporation, and by the reaction between gaseous HBr and PoO_2. Its existence has been confirmed by chemical analysis.

It has been characterized as a bright red solid, which melts in an atmosphere of bromine at about 325 °C. Exposure to the atmosphere converts it to PoO_2 and, predictably, it hydrolyzes when dissolved in water. Because of the intense α-radiation emitted by polonium, determination of its crystal structure has been difficult due to the resulting disorder.

Like the tetrachloride, it dissolves in aqueous HBr to produce an orange or red solution ($PoBr_6^{2-}$?) and it is soluble in alcohols and ketones, but not in nonpolar organic solvents.

The addition of CsBr to concentrated solutions of $PoBr_4$ in HBr causes the precipitation of Cs_2PoBr_6. This material has been studied crystallographically and shown to possess a structure like that of Cs_2TeBr_6. Crystalline $(NH_4)_2PoBr_6$ has also been isolated.

The preparation of polonium tetrabromide has been achieved in several ways.[23] These include the following:

1. The dissolution of Po or PoO_2 in HBr and evaporating to dryness
2. The heating of polonium in a stream of bromine vapor
3. The heating of PoO_2 in dry HBr

A solution of $PoBr_4$ in $2NH_4Br$, when treated with CsBr, yields a precipitate of Cs_2PoBr_6. The latter is dark red in color and decomposes at 300°. Polonium tetrabromide is soluble in aqueous HBr, ethanol, and acetone. It is highly hygroscopic and on hydrolysis yields a white solid whose composition has not been determined.[30]

Polonium dibromide is purple-brown in color and sublimes at 110° at reduced pressure with some decomposition. It is prepared by the reduction of $PoBr_4$ with H_2S or by heating $PoBr_4$ to 200° in vacuo. The dibromide is soluble in ketones as well as in dilute, aqueous HBr in which it forms a purple solution. In the latter solution, the dibromide is oxidized rapidly to Po(IV).

$PoCl_2$ undergoes reaction with bromine vapor to give a pink solid, probably $PoCl_2Br_2$. At 100°, $PoBr_4$ undergoes reaction with ammonia gas to yield $(NH_4)_2PoBr_6$. This compound explodes at 200° in a sealed tube.

$(NH_4)_2PoBr_6$ crystallizes face-centered cubic, $a = 10.82$ Å, four moles per unit cell, the density is $3.78\ g\ ml^{-1}$. $PoBr_4$ is also face-centered cubic with $a = 5.60$ Å. One Po atom is randomly distributed over a four-fold position.[31]

The Po-Br bonding in $(NH_4)_2PoBr_6$ is described as largely covalent, which is attributed to the Po-Br bond distance of 2.60 Å and a Po(IV) radius of 0.65 Å.

Cs_2PoBr_6 also crystallizes as a face-centered cubic crystal with $a = 10.99$ Å, having four molecules per unit cell and a density of $4.75\ g\ ml^{-1}$. The Po-Br distance is 2.6 Å giving a Po(IV) radius of 0.69 Å. The bonding is described as covalent.

2.8 Iodine Compounds of Polonium

The iodine chemistry of polonium differs from that of the other halogens in that evidence exists for the formation of PoI_6 in a PoI_4-I_2 system at iodine pressures of 30−70 Torr. PoI_4 has been prepared by the direct reaction between the elements, by the reaction between the dioxide and HI, and by the addition of HI to an aqueous solution of $PoCl_4$ in HCl. PoI_4 hydrolyzes in water and it is only slightly soluble in ketones and alcohols. It is soluble in HI with strong evidence for the formation of PoI_6^{2-}, which gives a red-brown solution at room temperature.

There exists no support for the synthesis of the diiodide as a crystalline solid. Its existence has been claimed in studies of the dissociation of PoI_4 in iodine vapor at temperatures in the 200–315 °C range.

When Po^{IV} ion in nitric acid is treated with HIO_3, white crystals of the iodate separate. The crystals decompose at 350–400 °C, but a satisfactory analysis has not been obtained for this material.

The vapor pressures of lead and polonium iodides have been investigated.[32] The metals were heated in an atmosphere of iodine in a closed system. The pressure of the products was determined by a statistical method. At less than 80 atomic percent iodine, PoI_4 forms in the condensed phase. At 473°K PoI_4 dissociates into PoI_2. Above 80 atomic percent iodine, the condensed phase exhibits the presence of PoI_6. The enthalpy of evaporation of PoI_6 is 116 kj $mole^{-1}$. These experiments suggest that the separation of polonium from lead can be accomplished by their volatization in iodine vapors at elevated temperatures.

The vapor pressures of iodides of polonium were measured in a closed system.[32] Metallic polonium was heated in iodine vapor and the pressures were measured. At iodine concentrations below 80 atomic percent and with increasing temperatures, polonium tetraiodide is formed in the condensed phase. The tetraiodide dissociates into PoI_2 beginning at a temperature of 473 °K. The evaporation enthalpy of PoI_2 is 94.4 kj $mole^{-1}$. At 80 atomic percent the condensed phase exhibits the presence of PoI_6.

The separation of polonium from lead is an important procedure in radiochemistry. It was proposed,[33] based upon studies of the vapor pressure of the iodides of lead and polonium, that polonium diiodide should serve for the pyrochemical separation of ^{210}Po from ^{206}Pb.

2.9 Fluorine Compounds of Polonium

The chemistry in this area is greatly limited. During the period of the Manhattan Project considerable study was devoted to the synthesis of volatile heavy metal fluorides. PoF_6 has been prepared by the reaction between ^{208}Po electroplated on platinum and elemental fluorine. Analytical data were never obtained for the hexafluoride, which is reported to be stable in the vapor phase but disproportionates to the tetrafluoride on cooling.

PoF_4 has not been definitively characterized. Both $^{210}PoCl_4$ and $^{210}PoO(OH)_2$ yield a white solid when they undergo reaction with aqueous HF. This may be PoF_4. The solubility of Po^{IV} in aqueous HF increases with increasing HF concentration and this behavior has been interpreted in terms of the formation of the $PoF_6{}^{2-}$ ion.

No report exists for the preparation of PoF_2.

Theoretical studies on the atomic number dependence of the relative effects on chemical bonding, including polonium, have been carried out,[34,35] for example PoF_6 was investigated. An analysis of bond overlap population using both nonrelativistic and relativistic DV-Xα molecular orbital calculations was performed. The results are compared with those obtained using bond energy calculations.

2.10 Polonium Compounds Containing Nitrogen

No direct evidence has been reported for the existence of a simple binary nitride. The formation of explosive Po_4N_4 has been postulated in studies of the thermal decomposition of $(NH_4)_2PoBr_6$.

Treatment of $PoCl_4$ with aqueous nitrite yields a white, crystalline solid which has been postulated to be a basic nitrite, but no definitive evidence has been presented.

The formation of a white solid formulated as $Po(NO_3)_4{\cdot}N_2O_4$ has been reported by the reaction between $PoCl_4$ or PoO_2 with liquid N_2O_4. At reduced pressure the N_2O_4 can be removed and the tetranite decomposes to $PoO_2{\cdot}3HNO_2$. A similar solvated salt, $PoO_2{\cdot}0.5HNO_3$, has been reported to form when a solution of $PoO(OH)_2$ in nitric acid is evaporated at reduced pressure. Solid $PoCl_4$, when added to aqueous nitrate, forms a basic nitrate, but the normal nitrate has not been isolated or identified from such a reaction.

Although salts containing the anion $[Po(NO_3)_x]^{x-4}$ have never been isolated, solvent extraction studies with ^{210}Po indicate that anionic nitrate complexes are formed in nitric acid solutions which contain the metal cation.

2.11 Oxo Anion Salts of Polonium

Evidence for the existence of sulfites is based primarily on analogies with the chemistry of tellurium. However, no sulfites of polonium have been isolated or characterized. Thus, the reaction of the metal with SO_3 or fuming H_2SO_4 forms a dark red products may be $PoSO_3$. The reaction of PoO_2 with gaseous SO_2 forms a white material which may be the sulfite.

Evidence for the existence of $Po(SO_4)_2$ is stronger. The reaction between $PoCl_4$ or the hydroxide of polonium with sulfuric acid (0.5–5.0 N) yields a white solid identified as the hydrated solid. The solubility of this material increases with increasing acid concentration, which suggests the formation of anionic sulfate complexes. The white solid loses its water of hydration thermally and leaves a purple solid identified as the anhydrous sulfate.

The salts $2PoO_2{\cdot}XO_3$ (X=S, Se) have been reported to form when the tetrachloride or hydroxide of polonium is treated with more dilute acid (0.02–0.25 N). The basic sulfate is yellow in color, while the selenate is white.

The existence of a carbonate is questionable. An aqueous solution saturated with CO_2, when allowed to react with $PoO(OH)_2$, forms a white solid which may be a basic carbonate. The solubility of the solid with increasing carbonate concentration suggests the formation of carbonatopolonate anions.

Although a normal acetate has not been isolated and characterized, the increase in the solubility of PoO_2 with increasing acetate concentration is taken as evidence for the formation of complex acetatopolonate anions.

The formation of an orange-yellow precipitate when Po^{IV} is added to a 1 M chromate solution is taken as evidence of the formation of $Po(CrO_4)_2$. This precipitate hydrolyzes to form a dark-brown solid whose composition approximates the stoichiometry $2PoO_2{\cdot}CrO_3$.

Both the tetrachloride and the basic oxide of Po^{IV} yield a white, gelatinous precipitate when added to phosphoric acid. Based on elemental analysis, its composition has been given as $2PoO_2{\cdot}H_3PO_4$. The formation of a normal phosphate has not been demonstrated.

No perchlorates of polonium have been isolated.

2.12 Anions Containing Polonium

By analogy with tellurium, which forms tellurides, the existence of polonides should be expected. Soluble tellurides, such as sodium telluride, are extremely sensitive to oxidation. Especially in solution, they revert rapidly to elemental tellurium. Because of its greater metallic character, polonides should oxidize even more rapidly than tellurides. Nevertheless, evidence has been presented for the existence of a number of polonides.

Among the alkali metals, only Na_2Po has been prepared. It has been prepared only at the tracer level by cocrystallization with sodium telluride. Na_2Po appears to be isomorphous with Na_2Te. The preparation was carried by reduction of an alkaline solution containing Po and Te with $Na_2S_2O_4$.

The following polonides have been prepared by the direct reaction between the elements: BaPo (cubic, NaCl structure), ZnPo (cubic, zincblende structure), CdPo (gray, zincblende structure), HgPo (black, NaCl structure), GaPo (orange, liquid at room temperature owing to α-particle stoppage), InPo (blue, low melting owing to α-particle stoppage).

A very limited body of literature exists on the chemistry of polonates. In aqueous potassium hydroxide, the formation of ${PoO_3}^{2-}$ has been postulated based on solubility studies. The fusion of weighable amounts of Po with KOH or KNO_3 is reported to yield potassium polonate. Both Sr_2PoO_4 and $Ba_4Po_3O_{10}$ have been reported to form by the reaction between SrO and BaO with PoO_2 vapor at temperatures of about 900 °C.

The treatment of radioactive waste was studied using the following methods:[36] chemical extraction, cement based stabilization, vitrification, and soil washing. Although the major constituents of interest were radium, lead, and uranium, polonium, because of its radioactivity, was also studied. Among the reagents used for the extraction of radioactive components were hydrochloric, nitric, and acetic acids, EDTA, and potassium chloride solutions. EDTA was found to be the most effective reagent for the extraction of radioactive species. The greatest decrease in radioactivity was noted by sequential extractions using combinations of mineral acids with EDTA or potassium chloride with EDTA.

The average ionic charge of polonium species in chloride solutions was measured using an anion-exchange method.[37] The method is based on measurements of the distribution ratio of polonium at a constant internal chloride ion concentration of the anion-exchanger phase. At 1.0M hydrochloric acid or sodium chloride solutions at pH of 1.0, tracer concentration of Po(IV) exist in the amionic forms $[PoCl_4(OH)]^{-1}$ and $[PoCl_4(OH)_2]^{.-2}$

3 RELATED ARTICLES

Polonium: Organometallic Chemistry; Tellurium: Inorganic Chemistry.

4 REFERENCES

1. K. W. Bagnall, *Adv. Inorg. Chem. Radiochem.*, 1962, **4**, 197.
2. H. J. Emeléus and J. S. Anderson, ‘Modern Aspects of Inorganic Chemistry’, Van Nostrand, New York, 1960, pp. 409, p. 589.
3. P. Pascal ed., ‘Nouveau Traite de Chimie Minérale’, Masson et cie., Paris, 1934, Vol. 12, p. 61.
4. J. W. Mellor, ‘A Comprehensive Treatise on Inorganic and Theoretical Chemistry’, Longmans-Green, London, 1963, Vol. IV, p. 112.
5. ‘Gmelin Handbook of Inorganic and Organometallic Chemistry’, 8th edn., Springer-Verlag, Berlin, 1990, Polonium, Suppl. Vol. 1.
6. K. W. Bagnall, ‘The Chemistry of Selenium, Tellurium and Polonium’, Elsevier, New York, 1966.
7. M. Haissinsky, ‘Le Polonium’, Hermann et cie., Paris, 1937.
8. R. C. Brasted, ‘Comprehensive Inorganic Chemistry’, Van Nostrand, New York, 1961, Vol. 8, p. 246.
9. K. Hiroshi and H. Koichi, *Japan Kokai Tokyo Koho*, 1999, 5, CODEN; JKXXAF JP 11022732 A2 19990126 Heisei.
10. T. Hashimoto, A. Habiro, M. Noguchi, and T. Kubota, *Radioisotopes*, 1990, **39**, 291.
11. S. Huebener and I. Zvara, *Radiochim. Acta*, 1980, **27**, 157.
12. R. J. DeSands and R. C. Lange, *J. Inorg. Nucl. Chem.*, 1966, **28**, 1837.
13. K. W. Bagnall and R. W. M. D’Eye, *J. Chem. Soc.*, 1954, 4295.
14. T. A. O’Neil, U. S. Patent 2476823, 1949.
15. R. W. Lawson, *Monatsh. Chem.*, 1915, **36**, 845.
16. A. S. Abakumov and A. D. Khokhlov, *Zh. Neorg. Khim. USSR*, 1982, **27**, 30.
17. A. S. Abakumov, A. D. Khokhlov, and N. F. Reznikova, *Zh. Neorg. Khim. USSR*, 1981, **26**, 2005.

18. L. Zikovsky, *J. Radioanal. Nucl. Chem.*, 2002, **251**, 329.
19. G. Jia, M. Belli, M. Blasi, A. Marchetti, S. Rosamilia, and U. Sansone, *J. Radioanal. Nucl. Chem.*, 2001, **247**, 491.
20. L. L. Barton, *J. Nucl. Mater.*, 1999, **273**, 343.
21. M. A. R. Lyengar and A. P. Thulasi, *Radiat. Prot. Environ.*, 1997, **20**, 57.
22. H. Fukuda and T. Nakanishi, Japanese Patent JP09037923, September 2, 1998.
23. M. Uehara, M. Yamasaki, A. Yanai, T. Noma, and K. Nishio, Japanese Patent Application Number 95−296818, to Sanyo Electric Company, 1997.
24. O. Schipakin, N. Borisov, and S. Churkin, *Fusion Eng. Des.*, 1995, **29**, 164.
25. N. Momoshima, L.-X. Song, S. Osaki, and Y. Maeda, *Environ. Sci. Technol.*, 2001, **35**, 2956.
26. K. W. Bagnall, R. W. M. D’Eye, and J. H. Freeman, *J. Chem. Soc.*, 1955, 2320.
27. D. J. Hunt, United States Atomic Energy Commission, MLM-979, 1954, 26.
28. K. W. Bagnall and R. W. M. D’Eye, *J. Chem. Soc.*, 1954, 4295.
29. G. Bouissieres, *Bull. Soc. Chim. Fr.*, 1952, 536.
30. C. Chamie and H. Filcakova, *J. Chim. Phys. Phys.-Chim. Biol.*, 1949, **46**, 174.
31. K. W. Bagnall, R. W. M. D’Eye, and J. H. Freeman, *J. Chem. Soc.*, 1955, 3959.
32. A. S. Abakumov and M. L. Malyshev, *Radiokhimiya*, 1980, **5**, 776.
33. A. S. Abakumova and M. L. Malyshev, *Radiokhimiya*, 1980, **22**, 547.
34. J. Onoe, *Adv. Quantum Chem.*, 2001, **37**, 311.
35. J. Onoe, *J. Phys. Soc. Jpn.*, 1997, **66**, 2328.
36. E. Stine and C. E. Morren, *Technol. Programs Radioactive Waste Manage. Environ. Restor.*, 1994, **2**, 1487.
37. H. Suganuma, *J. Radioanal. Nucl. Chem.*, 1995, **191**, 265.

Polonium: Organometallic Chemistry

Ralph A. Zingaro
Texas A&M University, College Station, TX, USA

1 Introduction 1
2 Organic Derivatives of Divalent Polonium 1
3 Related Articles 3
4 References 3

1 INTRODUCTION

The total number of publications that describes organometallic chemistry of polonium makes up one of the smallest segments of chemical literature. The element is very rare; its natural concentration in pitchblende ores is only about 0.1 mg per ton. Twenty-one isotopes are known, all of which are radioactive. Of these, ^{210}Po is most commonly used for chemical purposes because it can be synthesized in milligram amounts from $^{209}_{83}$Bi by an (n,γ) reaction. The $^{210}_{83}$Bi undergoes β-decay (5.0 days) to produce $^{210}_{84}$Po. This isotope has a half-life of about 138 days. Although the isotopes ^{208}Po and ^{209}Po have longer half-lives, 3 years and 100 years respectively, they are not available in practical chemical quantities. Another major difficulty encountered in the synthesis of organometallic compounds of polonium is the fact that the intensity of the α-emission of this isotope brings about a rapid decomposition of organic compounds. Even if polonium were available in macro quantities and its isotopes were stable, another problem would complicate the study of its organic chemistry. This is the fact that carbon–metalloid bonds become thermodynamically less stable as the metalloid becomes heavier. It is well known that organoselenium compounds have a great tendency to deposit elemental selenium upon standing. The deposition of elemental, black tellurium takes place much more readily in the case of organotellurium compounds. It is reasonable to expect that the carbon to polonium bond would be extremely weak.

Because the element is so rare, highly radioactive, and extremely expensive, classical chemical methods cannot be utilized in the study of its organometallic chemistry. Hence, one does not find any published information on the synthesis, physical properties, or spectroscopic characteristics of organopolonium compounds. It would be reasonable to make the assumption that the organic chemistry of polonium should parallel that of tellurium, the element just above it in group 16. Therefore, the identification of organopolonium compounds has relied almost exclusively on chromatographic behavior. Tellurium compounds having analogous chemical structures have been used as reference compounds. Often, ^{127}Te-labeled compounds have been utilized.

A considerable body of published information dealing with the formation of organometallic polonium compounds has evolved from studies of the β-decay products of ^{210}Bi organometallics.

Gmelin**[1]** presents the most recent and most comprehensive review of this subject. Of the 26 references cited in Gmelin, 18 are authored by Nefedov and his coworkers.**[2]** The organic chemistry of polonium is also discussed in texts authored by Bagnall.**[3,4]**

2 ORGANIC DERIVATIVES OF DIVALENT POLONIUM

2.1 Dialkyl and Diaryl Polonides

Among the organometallic derivatives of the chalcogen group, those having the structures R_2M and Ar_2M ($M = O$, S, Se, Te) are the best known. Dimethyl polonide has not been isolated and characterized. It has been thought to be produced in a number of different reports. The radioactive decay of ^{210}Pb tetramethyl as well as the reaction between sodium telluride–containing polonium and dimethyl sulfate have both been reported to yield some dimethylpolonium. When aqueous solutions containing polonium and acetic acid are electrolyzed, high losses of polonium occur during its deposition at a gold electrode. This has been explained in terms of the formation of methyl radicals, $CH_3\cdot$, which undergo reaction with the deposited polonium to produce a presumably volatile $(CH_3)_2Po$. The methyl radicals are postulated to arise from the decomposition of acetic acid by α-emission from the polonium. In spite of the use of cold vapor traps, no direct evidence for the formation of dimethylpolonium was obtained.

Ethyl radicals, $C_2H_5\cdot$, have been reported to assist in the gas-phase transport of the isotopes ^{212}Po and ^{216}Po. One interpretation of this phenomenon suggests the formation of diethyl polonide. However, an alternate explanation involves the dissociation of $(C_2H_5)_2Po$ into volatile H_2Po and ethylene.

Radiolead contains ^{210}Pb, ^{210}Bi, and ^{210}Po. Treatment of the naturally occurring isotope mixture with phenylmagnesium bromide removes most of the ^{210}Pb and ^{210}Po with concurrent formation of the phenyl–bismuth compounds. Because of the relatively short half-life of ^{210}Bi($t_{1/2} = 5.0$ days, β-emission), there occurs the formation and accumulation of organopolonium compounds, ^{210}Po ($t_{1/2} = 138$ days, α-emission). Chromatographic techniques have been utilized for the identification of the organopolonium compounds formed around the β-decay products of organo-^{210}Bi compounds.

Among the organopolonium compounds arising from the β-decay of $^{210}BiAr_3$ are the diaryl polonides, $^{210}PoAr_2$; Ar = Ph, *o*-MeC_6H_4, *m*-MeC_6H_4, *p*-MeC_6H_4*p*-ClC_6H_4, *p*-BrC_6H_4, *p*-$MeOC_6H_4$, *p*-$NH_2C_6H_4$, α-$C_{10}H_7$. The yield of (*m*-$MeC_6H_4)_2Po$ is notably higher, and this has been attributed to a greater electron density in the aromatic ring arising from a hyperconjugative effect.

It has been postulated that in the β-decay of R_3BiCl_2, the R_3Po^+ ion is formed initially. The cation then dissociates into R_2Po and R^+.

The yield of Ph_2Po from $^{210}BiPh_3$ is more than three times that formed by the β-decay of $^{210}BiPh_5$.

$PoCl_4$ can be prepared and separated because of the greater stabilities of the inorganic compounds toward α-emission. Mixtures of $PoCl_4$ and $TeCl_4$ have been allowed to undergo reaction with the Grignard reagent. Following treatment with RMgBr in Et_2O/C_6H_6, hydrolysis, reextraction into an organic solvent, drying, and removal of organic solvent, a number of $^{210}PoR_2$ compounds have been reported. Among the diaryl polonides prepared in this way are the *p*-tolyl, *p*-methoxyphenyl, and the α-naphthyl derivatives.

2.2 Triarylpolonium Halides

These compounds have the formula Ar_3PoX (X = F, Cl, Br, I). Compounds of this type have also been identified among the β-decay products of Ar_3BiX_2, formed by the reaction between the aryl Grignard reagent and halogenated radiolead. In general, the yield of Ar_3PoX from $Ar_3{}^{210}BiX_2$ increases in the sequence $Br > Cl > F$.

Triarylpolonium halides that have identified include those for X = F, Ar = 2-Me-, 3-Me-, and 4-MeC_6H_4, and the *p*-xylyl derivative. For X = Cl, in addition to the tolyl and xylyl derivatives, Ar = *p*-Cl-, *p*-Br-, *p*-MeO-, *p*-EtO-, and *p*-$H_2NSO_2C_6H_4$, and α-naphthyl. Similar compounds have been reported in which X is bromide.

When $^{210}PoCl_4$ in the presence of carrier $TeCl_4$ is treated with ArMgBr in the conventional manner, but the product is treated with KI, a number of triarylpolonium iodides have been reported. It has been claimed by Nefedov and coworkers**[1]** that black precipitates of $Ar_3(Po,Te)I$ can be recrystallized from $EtOH/Et_2O$ or $EtOH/H_2O$.

2.3 Diarylpolonium Dihalides

These compounds, whose general formula is Ar_2PoX_2, have been detected among the β-decay products of $Ar_3{}^{210}BiX_2$. For X = F, compounds which Ar is 2,5-dimethylphenyl, *p*-tolyl, *p*-anisyl, *p*-methoxyphenyl, and α-naphthyl have been claimed to be indentified by chromatographic analysis. Another method of preparation has also been reported. This involves the treatment of Ar_2Po with Ar_3BiF_2 and subsequent chromatographic purification. Similar compounds have been reported in which X is chloride or bromide.

One method of preparation of Ar_2PoCl_2 is described in which Ar_2Po is chlorinated by SO_2Cl_2 in carbon tetrachloride. The diaryl dihalide is precipitated out of the chloroform solution by the addition of petroleum ether. In this manner, the preparation of Ar_2PoCl_2 has been reported in which Ar is *p*-anisyl, mesityl, and α-naphthyl. The bis(α-naphthyl)polonium dichloride can be recrystallized from *p*-xylene.

Diaryl polonides are converted to the dibromides when they undergo reaction with Ar_2TeBr_2. Essentially, this is an oxidation reaction in which Po is oxidized from Po^{II} to Po^{IV} and tellurium is reduced from Te^{IV} to Te^{II}. Also, diaryl polonides add elemental bromine to form the dibromides. Thus, treatment of $(C_9H_{11})_2Po$ or $(\alpha\text{-}C_{10}H_7)_2Po$ in benzene with bromine yields the dibromides. They can be precipitated by the addition of petroleum ether and recrystallized from benzene/petroleum ether. In a manner parallel to that just described, *p*-tolyl and α-naphthylpolonium diiodides, Ar_2PoI_2, have been obtained by the addition of I_2 to the respective diaryl polonides.

2.4 Diarylpolonium Oxide

The conversion of $(C_9H_{11})_2Po$, dimesityl polonium, to the oxide, $(C_9H_{11})_2PoO$, by oxidation with air has been claimed. The corresponding telluride is not oxidized under these conditions.

2.5 Other Evidence for Organopolonium Compounds

Concentrations of ^{210}Po were measured in the North Atlantic troposphere.**[5]** Concentrations of ^{210}Po were measured in rain water, surface seawater, and the marine microlayer. An excess of ^{210}Po activity was measured in the aerosol relative to what was expected on the basis of ^{210}Pb and aerosol residence times. In surface seawaters, deficiencies of ^{210}Po were observed. The mechanism of ^{210}Po enrichment in the atmospheric aerosol was attributed to possible enrichments from the organic components of the marine microlayer or air−sea exchange of organic polonium species. However, no organic compounds of polonium were actually isolated or characterized.

The volatilities of 13 polonium compounds that are soluble in organic solvents was investigated.**[6]** All of the compounds were found to volatilize below 200 °C at atmospheric pressure. Polonium was found to form soluble organic compounds with the following chelating agents: 2, 3-butanediol; 4, 4, 4-trifluoro-1-(2-thiene); 8-quinoline; diethyldithiocarbamate; thiocarbanilide; 1, 5-diphenylcarbohydrazide; 1-phenyl-3-thiosemicarbazide; thiosemicarbazide; and thiourea.

3 RELATED ARTICLES

Polonium: Inorganic Chemistry; Tellurium: Organotellurium Chemistry.

4 REFERENCES

1. ‘Gmelin Handbook of Inorganic and Organometallic Chemistry’, 8th edn., Springer-Verlag, Berlin, 1990, Polonium, Suppl. Vol. 1, p. 334.
2. Original references to the publication of V.D. Nefedov and co-workers can be found in of ‘Gmelin Handbook of Inorganic and Organometallic Chemistry’, 8th edn., Springer-Verlag, Berlin, 1990, Polonium, Suppl. Vol. 1, p. 339.
3. K. W. Bagnall, ‘The Chemistry of the Rare Radioelements’, Butterworth, London, 1957, p. 3.
4. K. W. Bagnall, ‘The Chemistry of Selenium, Tellurium and Polonium’, Elsevier, New York, 1996.
5. N. Hussain, T. M. Church, A. J. Veron, and R. E. Larson, *J. Geogr. Res.*, 1998, **103**, 16059.
6. H. Mabruchi, *J. Inorg. Nucl. Chem.*, 1963, **25**, 657.

Polyhedra

R. Bruce King
University of Georgia, Athens, GA, USA

1 Introduction 1
2 Polyhedral Topology 1
3 Schlegel Diagrams 3
4 Enumeration and Classification of Polyhedra 4
5 References 4

1 INTRODUCTION

The concept of a polyhedron[1] is a useful way of describing diverse chemical structures. In this context, a polyhedron may be regarded as a set consisting of (zero-dimensional) points, that is, its *vertices*; (one-dimensional) lines connecting some of the vertices, that is, its *edges*; and (two-dimensional) surfaces formed by the edges, that is, its *faces*. The *degree* of a vertex is defined as the number of edges meeting at that vertex.

Polyhedra can appear in chemical structures as *coordination polyhedra*, in which the vertices represent ligands surrounding a central atom that is often, but not always, a metal, and *cluster* polyhedra, in which the vertices represent multivalent atoms and the edges represent bonding distances. In this connection, the five regular or Platonic polyhedra (Figure 1) are key building blocks for many molecular structures. They are characterized by the following properties: (1) all faces are equivalent regular polygons; (2) the vertices are all equivalent; (3) the edges are all equivalent. The special symmetries of regular polyhedra are described by the standard Euclidean point groups, that is, T_d, O_h, I_h, and their subgroups. Also of chemical significance are *deltahedra*, in which all faces are triangles. The most spherical deltahedra (Figure 2) are those in which the degrees are most similar. They are found in the structures of the borane anions $B_nH_n{}^{2-}$ ($6 \leq n \leq 12$). Note that the six- and twelve-vertex most spherical deltahedra (Figure 2) are also regular polyhedra, that is, the octahedron and icosahedron (Figure 1), respectively.

2 POLYHEDRAL TOPOLOGY

The topology of a polyhedron can be described by a graph, called the 1-skeleton of the polyhedron.[2] The vertices and edges of the 1-skeleton correspond to the vertices and edges, respectively, of the underlying polyhedron. Of fundamental importance are relationships between possible numbers and types of vertices (v), edges (e), and faces (f) of polyhedra. In this connection, the following elementary relationships are particularly significant:[3]

1. *Euler's relationship:*

$$v - e + f = 2 \tag{1}$$

This arises from the properties of ordinary three-dimensional space.

2. *Relationship between the edges and faces:*

$$\sum_{i=3}^{v-1} i f_i = 2e \tag{2}$$

In equation (2), f_i is the number of faces with i edges (i.e. f_3 is the number of triangular faces, f_4 is the number of quadrilateral faces, etc.). This relationship arises from the fact that each edge of the polyhedron is shared by exactly two faces. Since no face can have fewer edges than the three of a triangle, the following inequality must hold in all cases:

$$3f \leq 2e \tag{3}$$

3. *Relationship between the edges and vertices:*

$$\sum_{i=3}^{v-1} i v_i = 2e \tag{4}$$

In equation (4), v_i is the number of vertices of *degree i* (i.e. having i edges meeting at the vertex). This relationship arises from the fact that each edge of the polyhedron connects exactly two vertices. Since no vertex of a polyhedron can have a degree less than three, the following inequality must hold in all cases:

$$3v \leq 2e \tag{5}$$

4. *Totality of faces:*

$$\sum_{i=3}^{v-1} f_i = f \tag{6}$$

5. *Totality of vertices:*

$$\sum_{i=3}^{v-1} v_i = v \tag{7}$$

Equation (6) relates the f_i's to f and equation (7) relates the v_i's to v.

In generating actual polyhedra, the operations of capping and dualization are often important. *Capping* a polyhedron P_1 consists of adding a new vertex above the center of one of its

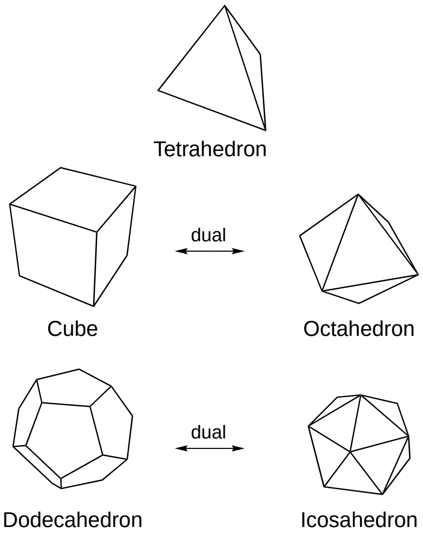
Tetrahedron
Cube
dual
Octahedron
Dodecahedron
dual
Icosahedron

Figure 1 The five regular polyhedra showing the cube/octahedron and dodecahedron/icosahedron dual pairs

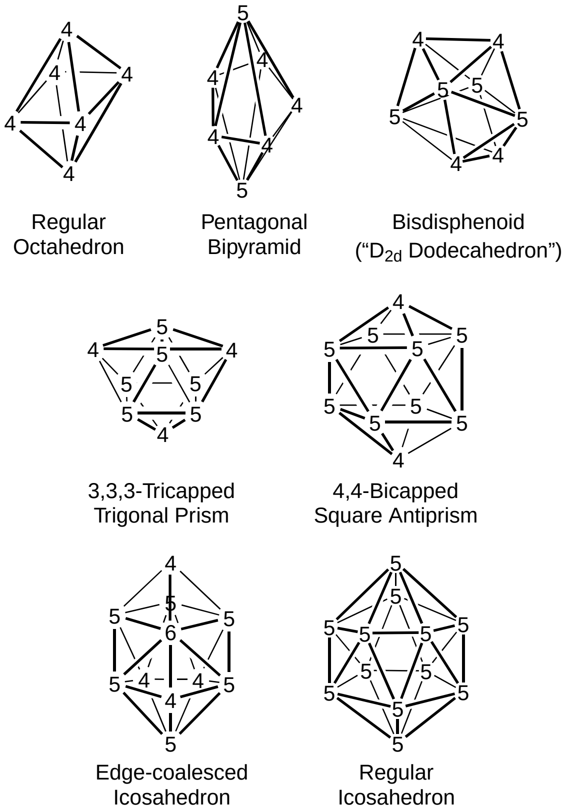
Regular Octahedron
Pentagonal Bipyramid
Bisdisphenoid ("D2d Dodecahedron")
3,3,3-Tricapped Trigonal Prism
4,4-Bicapped Square Antiprism
Edge-coalesced Icosahedron
Regular Icosahedron

Figure 2 The most spherical deltahedra, found, for example, in the structures of the boranes $B_nH_n^{2-}$ ($6 \leq n \leq 12$). The numbers on the vertices indicate the vertex degrees

faces F_1 followed by adding edges to connect the new vertex with each vertex of F_1. This capping process gives a new polyhedron P_2 having one more vertex than P_1. If a triangular face is capped, the following relationships will be satisfied where the subscripts 1 and 2 refer to P_1 and P_2, respectively: $v_2 = v_1 + 1$; $e_2 = e_1 + 3$; $f_2 = f_1 + 2$. Such a capping of a triangular face is found in the capping of a tetrahedron to form a trigonal bipyramid (Figure 3a). In general, if a face with f_k edges is capped, the following relationships will be satisfied: $v_2 = v_1 + 1$; $e_2 = e_1 + f_k$; $f_2 = f_1 + f_k - 1$. An example of such a capping process converts a pentagonal pyramid into a pentagonal bipyramid (Figure 3b).

A given polyhedron P can be converted into its dual P^* by locating the centers of the faces of P^* at the vertices of P and the vertices of P^* above the centers of the faces of P. Two vertices in the dual P^* are connected by an edge when the corresponding faces in P share an edge.

The process of dualization has the following properties:

1. The numbers of vertices and edges in a pair of dual polyhedra P and P^* satisfy the relationships $v^* = f$, $e^* = e$, $f^* = v$.
2. Dual polyhedra have the same symmetry elements and thus belong to the same symmetry point group.
3. Dualization of the dual of a polyhedron leads to the original polyhedron.
4. The degrees of the vertices of a polyhedron correspond to the number of edges in the corresponding face polygons in its dual.

The regular polyhedra (Figure 1) provide examples of dual pairs of polyhedra. Thus the octahedron ($v = 6$, $e = 12$, $f = 8$) is the dual of the cube ($v = 8$, $e = 12$, $f = 6$). The tetrahedron ($v = 4$, $e = 6$, $f = 4$) is its own dual.

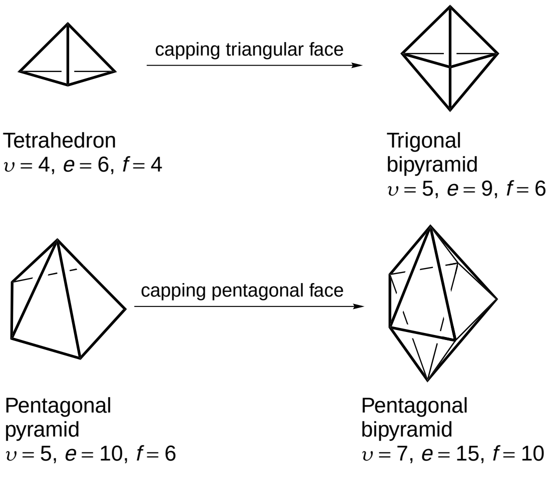
capping triangular face
Tetrahedron
v = 4, e = 6, f = 4
Trigonal bipyramid
v = 5, e = 9, f = 6
capping pentagonal face
Pentagonal pyramid
v = 5, e = 10, f = 6
Pentagonal bipyramid
v = 7, e = 15, f = 10

Figure 3 Examples of polyhedral capping: (a) capping a tetrahedron to form a trigonal bipyramid; (b) capping a pentagonal pyramid to form a pentagonal bipyramid

3 SCHLEGEL DIAGRAMS

Polyhedra are frequently depicted as two-dimensional ‘perspective’ drawings as aids to help visualize the actual three-dimensional structures. For more complicated polyhedra, these two-dimensional perspective drawings begin to have limitations since both their drawing requires skill and reconstruction of their original three-dimensional picture requires more imagination. These difficulties can be minimized by the use of Schlegel diagrams[4] rather than conventional perspective drawings to depict three-dimensional polyhedra in two dimensions. Schlegel diagrams are well known to mathematicians studying polyhedra and higher dimension polytopes but are relatively unfamiliar to chemists.

In order to obtain a Schlegel diagram of a polyhedron P, select any face of P as the *base face*, F_0. The plane containing the base face F_0 separates three-dimensional space into two half-spaces, one of which contains the entire volume of P. Select a point x_0 in the other half-space. Draw a straight line from x_0 to each of the vertices of P. Each such line will intersect the plane of F_0 at a point representing the corresponding vertex. Connect a pair of vertex projections onto the plane of F_0 with straight lines if and only if the corresponding vertices of P have an edge between them. This process leads to a projection of the three-dimensional plane of the face F_0; this projection is called the *Schlegel diagram* of the polyhedron P.

Any given polyhedron can have as many different Schlegel diagrams as it has different faces. The procedure for drawing the Schlegel diagram of the square pyramid using the square face as the base face F_0 is illustrated in Figure 4.

The following features of Schlegel diagrams are of interest:

1. The location of the point x_0 can always be chosen so that the edges in the Schlegel diagram can be drawn as *nonintersecting* straight lines. This is one of the big advantages of Schlegel diagrams over conventional perspective drawings.
2. Schlegel diagrams depict the topological but not the metric features of polyhedra. Thus, the vertex neighborhood relationships depicted by edges are preserved. However, edge lengths and angles are distorted. Since many important chemical relationships are topological rather than metric, this distortion is not necessarily serious.
3. Schlegel diagrams may not preserve all symmetry elements of the original polyhedron because of the metric distortion. The preservation of symmetry elements in Schlegel diagrams is maximized if a unique face of the polyhedron is selected as the base face.

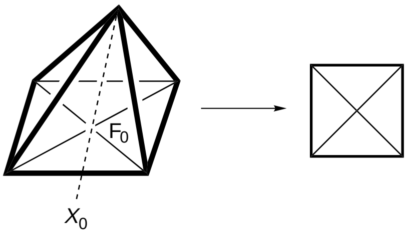

Figure 4 The Schlegel diagram of the square pyramid

The regular octahedron gives the Schlegel diagram in Figure 5. The big triangle corresponds to the base face and contains all of the other faces in the Schlegel diagram. The small triangle in the center is the projection of the face opposite to the base face. The other triangles correspond to the remaining six faces of the octahedron. This Schlegel diagram of an octahedron shows how Schlegel diagrams fail to preserve metric and symmetry properties since in a regular octahedron all of the eight triangular faces are congruent and all of the 12 edges have the same length.

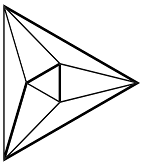

Figure 5 The Schlegel diagram of the regular octahedron

Table 1 Some properties of all polyhedra with six or fewer vertices

					Vertices			Faces		
Polyhedron name	v	e	f	Symmetry	v_3	v_4	v_5	f_3	f_4	f_5
Tetrahedron	4	6	4	T_d	4	0	0	4	0	0
Trigonal bipyramid	5	9	6	D_{3h}	2	3	0	6	0	0
Square pyramid	5	8	5	C_{4v}	4	1	0	4	1	0
Octahedron	6	12	8	O_h	0	6	0	8	0	0
Bicapped tetrahedron	6	12	8	C_{2v}	2	2	2	8	0	0
	6	11	7	C_{2v}	2	4	0	6	1	0
	6	11	7	C_s	3	2	1	6	1	0
	6	10	6	C_2	4	2	0	4	2	0
Pentagonal pyramid	6	10	6	C_{5v}	5	0	1	5	0	1
Trigonal prism	6	9	5	D_{3h}	6	0	0	2	3	0

4 ENUMERATION AND CLASSIFICATION OF POLYHEDRA

The problem of classification and enumeration of polyhedra is a complicated one. Thus there appear to be no formulas, direct or recursive, for which the number of combinatorially (topologically) distinct polyhedra having a given number of vertices, edges, faces, or any combination of these elements can be calculated.[5,6] Duijvestijn and Federico have enumerated by computer the polyhedra having up to 22 edges according to their numbers of vertices, edges, and faces and their symmetry groups and present a summary of their methods, results, and literature references to previous work.[7] Their work shows that there are 1, 2, 7, 34, 257, 2606, and 32 300 topologically distinct polyhedra having 4, 5, 6, 7, 8, 9, and 10 faces or vertices, respectively. Tabulations are available for all 301 $(= 1 + 2 + 7 + 34 + 257)$ topologically distinct polyhedra having eight or fewer faces[8] or eight or fewer vertices.[9] These two tabulations are essentially equivalent by the dualization relationship discussed above. Some of the properties of the polyhedra having six or fewer vertices are listed in Table 1.

5 REFERENCES

1. P. R. Cromwell, ‘Polyhedra’, Cambridge University Press, Cambridge, 1997.
2. B. Grünbaum, ‘Convex Polytopes’, Interscience Publishers, New York, 1967.
3. R. B. King, *J. Am. Chem. Soc.*, 1969, **91**, 7211.
4. V. Schlegel, *Nova Acta Leop. Carol.*, 1883, **44**, 343.
5. F. Harary and E. M. Palmer, ‘Graphical Enumeration’, Academic Press, New York, 1973, p. 224.
6. W. T. Tutte, *J. Combin. Theory Ser. B,* 1980, **28**, 105.
7. A. J. W. Duijvestijn and P. J. Federico, *Math. Comput.*, 1981, **37**, 523.
8. P. J. Federico, *Geometriae Dedicata*, 1975, **3**, 469.
9. D. Britton and J. D. Dunitz, *Acta Crystallogr.*, 1973, **A29**, 362.

Polynuclear Organometallic Cluster Complexes

Jerome B. Keister
State University of New York, Buffalo, NY, USA

1	Introduction	1
2	Syntheses	2
3	Chemical Reactivity	4
4	Fluxionality	6
5	Chemistry of Clusters Containing C_n ($n = 1-3$) Fragments	8
6	Other Hydrocarbyl Ligands	14
7	Organometallic Clusters as Catalysts	15
8	Organometallic Clusters as Models for Metal Surface-bound Hydrocarbyls	15
9	Related Articles	16
10	References	16

Glossary

Cluster: molecular compound containing three or more metal atoms which are joined to one another via direct and substantial metal–metal bonding
Hydrocarbyl: ligand bonded through carbon and containing hydrogen
Nuclearity: the number of metal atoms constituting the framework of a metal cluster

1 INTRODUCTION

This article concerns the transition metal clusters (*see Cluster*) of three or more metal atoms which contain a hydrocarbyl (*see Hydrocarbyl*) ligand as a part of the metal–carbon cluster core.[1] Because the chemistry of trimetallic clusters is the most well developed, these examples will be stressed. While many of the features of cluster chemistry are common with those of organometallic complexes containing a single metal atom, there are notable differences in structures and reactivities owing to the tendencies of ligands to bridge between two or more metal atoms and for ligands bound to only a single metal atom to undergo facile intramolecular migrations between metal atoms. A bridging ligand (*see Bridging Ligand*) is denoted in a chemical formula by the Greek letter μ and, if more than two metal atoms are bridged, a subscript indicates the number of metals bridged by a ligand; thus the formula $(\mu\text{-H})Os_3(\mu_3\text{-CPh})(CO)_{10}$ indicates a hydride bridging two osmium atoms and a CPh fragment bridging three metal atoms. Also *see* ***Carbonyl Complexes of the Transition Metals***; ***Hydride Complexes of the Transition Metals***; ***Dinuclear Organometallic Cluster Complexes***; ***Cluster Compounds: Inorganometallic Compounds Containing Transition Metal & Main Group Elements***.

1.1 Structure and Bonding

Organometallic complexes containing a single metal center usually obey the so-called 18-electron rule (*see Effective Atomic Number Rule*), whereas the bonding in bulk metals is best described according to band theory (*see Band Theory*).[2,3] Understandably, bonding descriptions of cluster compounds may be expected to become increasingly complex as the size of the cluster increases.

Small clusters almost invariably follow the 18-electron rule, that is, for each metal atom the sum of its valence electrons (the electrons donated by the ligands and the electrons provided via metal–metal bonds) equals 18; these clusters are said to be ‘saturated’. Common exceptions, having less than 18 electrons per metal atom, are found in clusters of the early transition metals (which contain mainly halide, oxygen, or nitrogen donor ligands) and clusters containing Pd, Pt, or, less commonly, Rh or Ir. It has been common to define saturation for a particular cluster geometry in terms of the number of electrons donated by the ligands combined with the metal valence electrons, required to give each metal atom 18 electrons in a particular cluster geometry. Since metal–metal bonds represent a shared electron pair, a closed triangular array of metals (three metal–metal bonds) requires 48 electrons to be saturated. Clusters that do not obey the 18-electron rule, called ‘unsaturated’ (*see Electron Deficient Compound*), are typically much more reactive than those that do. One of the best known examples of an unsaturated cluster is $H_2Os_3(CO)_{10}$, a 46-e cluster that has two electrons fewer than the number required by the 18-electron rule. This cluster reacts very rapidly at room temperature with Lewis bases ($L = PR_3$, CO, halides, and others) to form saturated 48-electron clusters, $H_2Os_3(CO)_{10}L$; for comparison, the saturated cluster $Os_3(CO)_{12}$ requires temperatures above 100 °C to react with most Lewis bases, the high temperature being required to generate an unsaturated intermediate by CO dissociation.

As the cluster nuclearity increases, the structures and electron counting of saturated clusters conform to the polyhedral skeletal electron pair (SEP) theory.[3] For organometallic clusters the carbon fragments of the hydrocarbyl ligands are frequently part of the cluster skeleton. Thus, $Fe_3(PhCCPh)(CO)_9$ (**1**) would be considered to be unsaturated according to the 18-electron rule, as the alkyne ligand is a four-electron donor to a $Fe_3(CO)_9$ cluster, which requires six electrons to fulfill the 18-electron rule for each metal atom. However, according to the SEP theory the cluster, the framework of which is Fe_3C_2, is saturated and is described as a *closo* structure (*see Closo Cluster*) based upon a trigonal bipyramid.

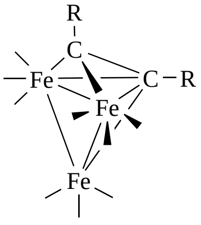

(**1**)

For still larger clusters, particularly those which consist of several fused polyhedral units, the electron counting and structural predictions are much more complex.[2]

Beyond the question of cluster core geometry, there remains the problem of explaining the arrangement of ligands around the cluster core, for example, the adoption of bridging or terminal ligand coordination.[3] No theory has adequately addressed this problem, which is particularly severe for carbonyl, hydride, and hydrocarbyl ligands. One interesting proposal that has been applied to metal carbonyl clusters concerns nonbonded interactions between ligands on the cluster surface and the match of the cavity size available in the ligand shell to the size of the cluster core.[4,5] Other theories invoke electronic arguments.[6]

1.2 Paramagnetic Clusters

While rare, a number of moderately stable clusters having an odd number of electrons have been prepared, for example, $[Fe_3(CO)_{11}]^{1-}$ and $(Cp^*Ni)_3(\mu_3\text{-}CH)(\mu\text{-}H)$. Many more which have only transient existences can be prepared by electrochemical redox processes.[7] These paramagnetic complexes are generally more reactive than the saturated analogs. Examples in which direct comparisons can be made between clusters differing only in electron count include ligand substitution (see Section 2.1) and structural isomerization. Isomerization of the clusters $[Cp^*Ir(CpCo)_2(CO)_3]^{-1/0/+1}$ occurs between isomers differing in the number of bridging versus terminal CO ligands. The relative rates of isomerization increased in the order 48 e $\ll$ 49 e $\ll$ 47 e, with the range covering 10^8.[8] Electrochemical or chemical oxidations of 48-e $H_3Ru_3(\mu_3\text{-}CX)(CO)_6(L)_3$ generate 47-e clusters $[H_3Ru_3(CX)(CO)_6L_3]^{1+}$, which exist as equilibrium mixtures of isomers differing in the orientation of one of the ligands L.[9] The rate constant for isomerization for the 47-e species is 4 orders of magnitude greater than that for the 48-e species. The 47-e clusters have lifetimes, which are correlated with the oxidation potentials of the precursors, ranging from seconds to many hours at room temperature. Decomposition occurs by disproportionation, via rate-limiting outer-sphere electron transfer, back to the 48-e precursor and very unstable 46-e species (*see* ***Paramagnetic Organometallic Complexes***; ***Electrochemistry: Applications in Inorganic Chemistry***; ***Electron Transfer in Coordination Compounds***; ***Electron Transfer Reactions: Theory***).

2 SYNTHESES

The first syntheses of organometallic clusters relied almost entirely upon serendipity, and even now designed syntheses of clusters of a desired metal composition are rarely achieved from lower nuclearity precursors. The basis for most syntheses involves ligand substitution of a hydrocarbon for a carbonyl ligand of a cluster having the desired metal composition, and then modification of the hydrocarbon unit while maintaining unchanged the metal-cluster core.[10]

2.1 Ligand Substitution on Metal Carbonyls

The first applications of ligand substitution (*see Ligand Substitution*) for the syntheses of organometallic clusters used thermal activation to remove carbonyl ligands from clusters such as $M_3(CO)_{12}$ (M = Fe, Ru, and Os). The high activation energy required for CO loss dictated that only very stable organometallic cluster products could be isolated and less stable intermediates were undetectable. For example, pyrolysis of $Os_3(CO)_{12}$ at 120 °C in the presence of ethylene gives $H_2Os_3(\mu_3\text{-}\eta^2\text{-}C{=}CH_2)(CO)_9$, but the intermediates $Os_3(CO)_{11}(CH_2{=}CH_2)$ and $HOs_3(\mu_2\text{-}\eta_2\text{-}CH{=}CH_2)(CO)_{10}$, which can be prepared by alternative, low-temperature routes, are not observed. Photolysis is sometimes more successful if the products are thermally sensitive. Some examples of these reactions are shown in equations (1–3).[9,10,56]

$$Os_3(CO)_{12} + C_6H_6 \longrightarrow H_2Os_3(\mu_3\text{-}\eta^2\text{-}C_6H_4)(CO)_9 \qquad (1)$$

$$Os_3(CO)_{12} + PPh_3 \xrightarrow[n\,=\,1-3]{} Os_3(CO)_{12-n}(PPh_3)_n \qquad (2)$$

$$Ru_3(CO)_{12} + H_2{=}CHCH{=}CH_2 \longrightarrow (\mu\text{-}H)Ru_3(\mu_3\text{-}\eta^3\text{-}HCCHCMe)(CO)_9 \qquad (3)$$

Less brutal approaches to displacement of CO ligands have provided the opportunity for designed syntheses. The most successful approaches are (1) the use of trimethylamine N-oxide to convert a bound CO ligand to CO_2, (2) the use of one-electron oxidation or reduction to generate more labile (*see Labile*) cluster radical intermediates, and (3) the use of nucleophiles (*see Nucleophile*), such as halide ions, to promote CO dissociation.

Trimethylamine N-oxide can be used to chemically remove carbonyls as CO_2; an example is shown in equation (4). While thermal substitution produces a mixture of products (equation 2), the addition of one equivalent of trimethylamine N-oxide selectively gives the monosubstituted product. Since the mechanism involves nucleophilic attack by the oxide on a carbonyl carbon, the reaction can be extremely rapid but does require the presence of an electrophilic carbonyl ligand. Consequently, the reagent is ineffective for anionic metal carbonyls and for more highly substituted clusters.

$$\mathrm{Os_3(CO)_{12} + ONMe_3 + PPh_3 \longrightarrow Os_3(CO)_{11}(PPh_3) + CO_2 + NMe_3} \tag{4}$$

Odd-electron metal clusters are frequently much more labile than are clusters which satisfy the electron counting rules. Catalytic substitution can be effected by one-electron reduction (or in some cases oxidation).**[11,12]** The sequence of reactions leading to catalytic substitution is shown in Scheme 1. This scheme for catalytic substitution depends upon the substituted product having a less favorable reduction potential than the starting cluster.

Clusters containing weakly coordinating ligands are valuable starting materials for thermally unstable complexes. Such clusters containing weakly coordinating ligands are sometimes described as being ‘lightly stabilized’. Examples of weakly coordinating ligands include acetonitrile, pyridine, ammonia, ethylene, cyclooctene, and THF. Most of these compounds are prepared via $\mathrm{ONMe_3}$-promoted substitution. In some examples, the weakly coordinating ligand bridges two or more metals and can reversibly generate a reactive site while remaining coordinated to another metal atom. Even dichloromethane has been observed as a bridging ligand with both chlorine atoms coordinating to metals. Examples of reactions using lightly stabilized clusters are shown in equations (5) and (6).

$$\mathrm{Os_3(CO)_{11}(NCMe) + H_2C{=}CH_2 \longrightarrow Os_3(CO)_{11}(H_2C{=}CH_2) + NCMe} \tag{5}$$

$$\mathrm{(\mu\text{-}H)Os_3(\mu_3\text{-}SMe)(CO)_9 + H_2C{=}CH_2 \longrightarrow (\mu\text{-}H)Os_3(\mu_2\text{-}SMe)(CO)_9(H_2C{=}CH_2)} \tag{6}$$

Nucleophilic activation by halides or other anionic reactants has been noted.**[9,13,56]** In this process, associative attack by the nucleophile on the cluster generates a labile intermediate. This attack may occur at a carbonyl ligand, forming an acyl derivative. Stable acyls can be isolated, for example, $\mathrm{[Ru_3(CO)_{11}(CO_2Me)]^-}$ from $\mathrm{Ru_3(CO)_{12}}$ and methoxide, and are indeed more labile for CO dissociation than the cluster precursor. If the nucleophilic attack is reversible, ligand substitution can be catalyzed by nucleophiles. For example, bis(triphenylphosphine)imminium chloride catalyzes $\mathrm{PPh_3}$ substitution on $\mathrm{Ru_3(CO)_{12}}$ at 25 °C. Surface-mediated activation by silica has been used to synthesize some substituted derivatives of $\mathrm{Os_3(CO)_{12}}$.**[14]**

$$\begin{aligned}
&\mathrm{Fe_3(\mu_3\text{-}PPh)_2(CO)_9 + e^- \longrightarrow [Fe_3(\mu_3\text{-}PPh)_2(CO)_9]^-}\\
&\mathrm{[Fe_3(\mu_3\text{-}PPh)_2(CO)_9]^- + PR_3 \longrightarrow [Fe_3(\mu_3\text{-}PPh)_2(CO)_8(PR_3)]^- + CO}\\
&\mathrm{[Fe_3(\mu_3\text{-}PPh)_2(CO)_8(PR_3)]^- + Fe_3(\mu_3\text{-}PPh)_2(CO)_9 \longrightarrow}\\
&\qquad\mathrm{Fe_3(\mu_3\text{-}PPh)_2(CO)_8(PR_3) + [Fe_3(\mu_3\text{-}PPh)_2(CO)_9]^-}
\end{aligned}$$

Scheme 1

2.2 Template Syntheses

Metal clusters can be assembled around main group atoms, such as S or P, which form very strong bonds to metals and which are capable of bridge bonding.**[15]** An example is given in equation (7).**[16]**

$$\mathrm{2Ru_3(CO)_9(\mu_3\text{-}PhCCH)(\mu_3\text{-}S) \longrightarrow Ru_6(CO)_{16}(\mu_3\text{-}PhCCH)_2(\mu_4\text{-}S)_2 + 2CO} \tag{7}$$

2.3 Condensation of Metal Fragments

A number of elegant syntheses of mixed-metal clusters have been accomplished through the condensation of unsaturated metal complexes with metal donors.**[17]** For example, condensation of the unsaturated cluster $\mathrm{H_2Os_3(CO)_{10}}$ with the alkylidyne (*see Alkylidyne*) complex $\mathrm{CpW(CO)_2(CR)}$ produces $\mathrm{H_2Os_3W(\mu_3\text{-}CR)(CO)_{12}}$. Metal–metal, metal–carbon, or carbon–carbon multiple bonds may serve as the sites for metal fragment condensation. Other examples are shown in equations (80 and (9).

$$\mathrm{Ru(cyclooctatriene)(cyclooctadiene) + CpW(CO)_2(CR) \longrightarrow RuW_2(\mu_3\text{-}RCCR)(CO)_7Cp_2 + RuW_3(\mu\text{-}CR)(CO)_4Cp_3} \tag{8}$$

$$\mathrm{(H)Ru_3(COMe)(CO)_{10} + CpW(CO)_3(CCPh) \longrightarrow CpWRu_3(COMe)(CO)_9(C{=}CHPh)} \tag{9}$$

2.4 Oxidative Addition Reactions

Oxidative addition (*see Oxidative Addition*) of H–C, H–Si, H–Sn, Cl–C, and other σ-bonded atom pairs have been used to add group 14 donor ligands to metal clusters. Additions of H–C, H–Si, and H–Sn bonds require an unsaturated metal center. A number of studies of the mechanism are consistent with a mechanism involving addition at a single metal atom through a three-center, synchronous process, the same as commonly occurs for monometallic complexes.**[18]** Some examples of H–Si addition to unsaturated (equation 10) and lightly stabilized (equation 11) $\mathrm{Os_3}$ clusters are shown. Oxidative additions of unactivated C–H bonds are rarer. Preferential addition of terminal C–H bonds to

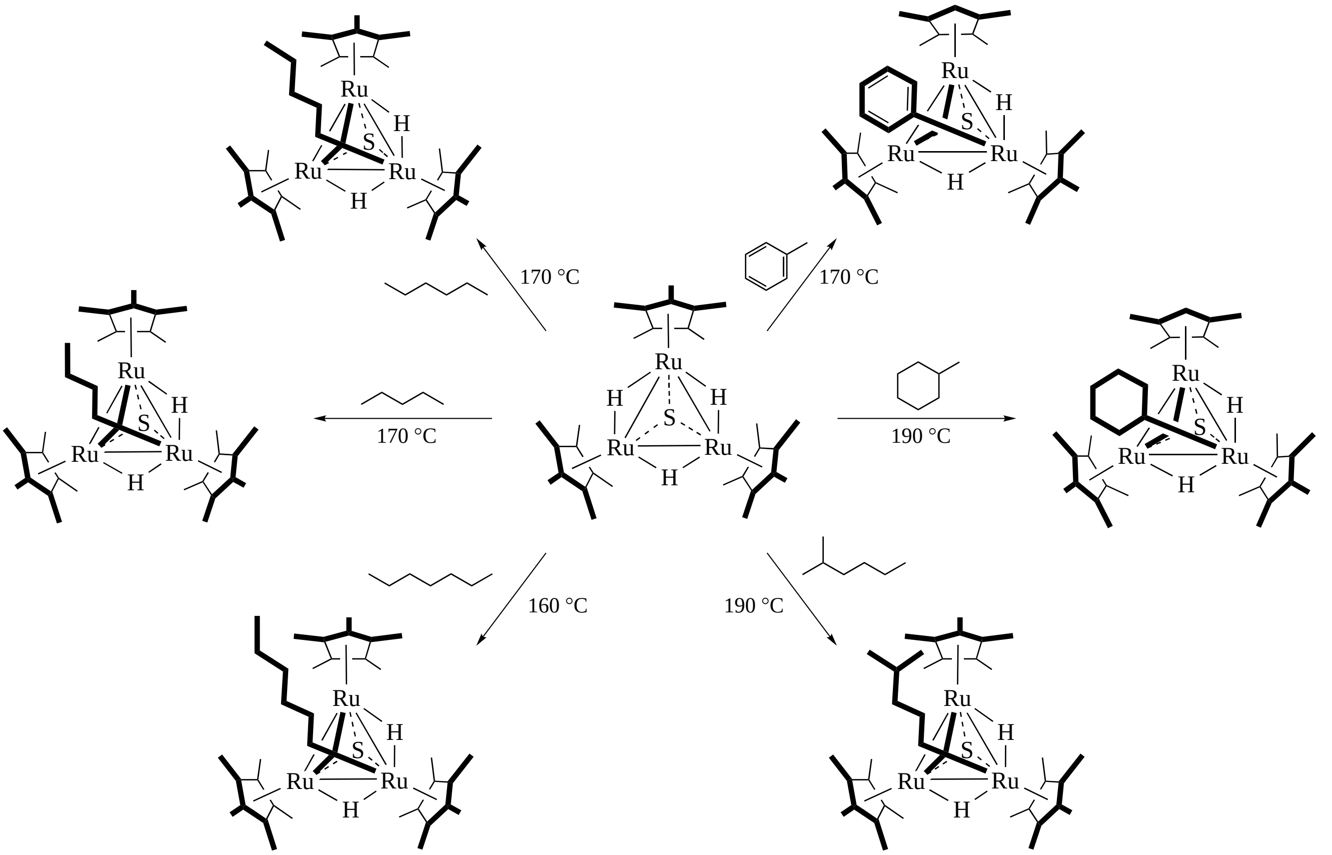

Scheme 2 (Reproduced from K. Matsubara, A. Inagaki, M. Tanaka, and H. Suzuki, *J. Am. Chem. Soc.*, 1999, **121**, 7421)

$H_3Ru_3(\mu_3\text{-}S)(Cp^*)_3$ form alkylidyne complexes $H_2Ru_3(\mu_3\text{-}S)(\mu_3\text{-}CR)(Cp^*)_3$ (Scheme 2).[19]

$$H_2Os_3(CO)_{10} + HSiEt_3 \longrightarrow H_3Os_3(CO)_{10}(SiEt_3) \qquad (10)$$

$$Os_3(CO)_{11}(NCMe) + HSi(OEt)_3 \longrightarrow HOs_3(CO)_{11}[Si(OEt)_3] + NCMe \qquad (11)$$

Additions of polar X–C bonds (e.g., X = Cl, Br, I, or OR) usually occur by nucleophilic attack by an electron-rich cluster at carbon; this reaction is less common for clusters than it is for mononuclear metal complexes. One example is addition of iodobenzene to $Ru_3(CO)_{12}$, forming $Ru_3(\mu\text{-}I)(\mu,\eta^1\text{: }\eta^6\text{-}C_6H_6)(CO)_8$.[20]

3 CHEMICAL REACTIVITY

In large part, the reactivity of a metal cluster is the same as that of the individual metal fragments. The unique features of cluster reaction chemistry involve the bridging of ligands between two or more metal atoms, ligand migration between metal atoms, and metal–metal bond cleavage and formation.

3.1 Ligand Substitution

A reaction common for all molecular metal clusters is replacement of one two-electron donor ligand by another. The mechanism is most commonly dissociative, but associative substitutions (*see Associative Substitution*) also occur.[21] A number of studies have applied quantitative analyses of the associative kinetics in terms of steric and electronic properties of the incoming ligands. Such analyses allow the identification of a ‘steric threshold’.[22] Ligand substitution on mixed-metal clusters may be faster than the rates for the corresponding homometallic clusters. However, substitution need not occur at the most labile metal atom, since intramolecular ligand migration preceding or following addition of the incoming ligand can occur to give the thermodynamically more stable product. Frequently, substitution occurs with a high degree of selectivity for one metal atom in a mixed-metal cluster. The substitutional site preference in mixed-metal trigonal bipyramidal clusters has been explained in terms of electronegativity differences.[23] Studies of substitution on $Fe_{3-n}Ru_n(CO)_{12}$ and on $(\mu\text{-}H)Fe_{3-n}Ru_n(\mu\text{-}CNMe_2)(CO)_{10}$ revealed that the relative rates are mixed Fe/Ru clusters > Fe_3 > Ru_3; however, substitution occurs exclusively on Ru. It is believed that CO dissociation occurs from an Fe atom, but that CO (or PR_3) migration generates the more stable product.

More commonly, it is to be expected that the reactivity of a mixed-metal cluster will be comparable to that of the most labile metal. For example, the rates of CO dissociation from $(\mu\text{-H})Ru_{3-n}Os_n(\mu\text{-COMe})(CO)_{10}$ fall in the series as: Ru_3 (4500) $>$ Ru_2Os (1100) $>$ $RuOs_2$(220) $\gg$ Os_3 (1). If this is the case, the relative rates for a series can provide information concerning the number of metal atoms which participate in such a transformation (*see also* ***Mechanisms of Reaction of Organometallic Complexes*** and *Ligand Substitution*).

3.2 Addition and Elimination of Molecular Hydrogen

The addition (oxidative addition, *see Oxidative Addition*) and elimination (reductive elimination, *see Reductive Elimination*) of molecular hydrogen is frequently involved in transformations of hydrocarbyl moieties attached to metal clusters. In most cases, oxidative addition of molecular hydrogen requires a vacant coordination site on a single metal atom. The rates for reductive elimination (*see Reductive Elimination*) of hydrogen from $(\mu\text{-H})_3Ru_{3-n}Os_n(\mu_3\text{-COMe})(CO)_9$ decrease in the order: $Ru_3 > Ru_2Os > RuOs_2 \gg Os_3$; this trend indicates that hydrogen elimination occurs from only one metal atom, even though each hydride bridges two metal atoms in the ground state. Bridge–terminal hydride migration has been proposed to precede reductive elimination. Several examples of H–H addition across a metal–metal bond are known. In some cases it had been proposed that the addition occurred after homolytic or heterolytic metal–metal bond cleavage, rather than ligand dissociation. Recent studies have shown that the mechanism is ligand dissociation, and then reassociation.[24]

A recent innovation has been the use of para-hydrogen to track the fate of the hydrogen atoms in addition reactions (*see* ***Mechanisms of Reaction of Organometallic Complexes*** and ***Hydride Complexes of the Transition Metals***).[25]

3.3 C–X σ Bond Activation

Oxidative addition (and the reverse process, reductive elimination, *see Reductive Elimination*) of C–H bonds is a very important process for organometallic clusters (*see* ***Mechanisms of Reaction of Organometallic Complexes***). Most commonly, oxidative addition of C–H bonds of coordinated ligands occurs at adjacent metal centers. A large variety of hydrocarbyl (*see Hydrocarbyl*) complexes are derived in this way. For example, pyridines react with $M_3(CO)_{12}$ to give both $HM_3(\mu\text{-NC}_5H_4)(CO)_{10}$ (**2**) and $H_2M_3(\mu\text{-NC}_5H_4)_2(CO)_8$ (**3**).[10] It is presumed that the pyridine initially coordinates to a single metal atom through the nitrogen, and then C–H oxidative addition occurs at an adjacent metal atom. Other C–X σ bonds, which can be cleaved in reactions on clusters include C–P, C–As, C–N, and C–S. An example of C–P cleavage is shown in equation (12). Reversible P–C cleavage has been observed for PPh_3/PPh_2 ligands on a triruthenium cluster.[26]

$$Ru_3(CO)_{11}(PPh_3) \longrightarrow \begin{array}{c} Ru_3(CO)_7(\mu\text{-PPh}_2)_2(\mu_3\text{-}\eta^2\text{-C}_6H_4) + \\ 33\% \\ Ru_4(CO)_{11}(\mu\text{-PPh})(\mu_4\text{-}\eta^4\text{-C}_6H_4) + \\ 50\% \\ Ru_5(CO)_{13}(\mu\text{-PPh})(\mu_5\text{-}\eta^6\text{-C}_6H_4) \\ 7\% \end{array} \qquad (12)$$

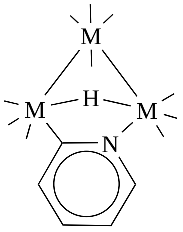

(**2**)

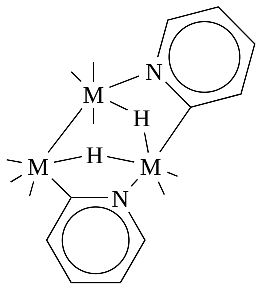

(**3**)

3.4 Protonation

Protonation, another example of oxidative addition, commonly occurs at metal–metal bonds to form a bridging hydride, although the initial site of protonation may be on a coordinated ligand. Even interstitial hydrides can be generated and removed via acid–base reactions. Protonations of neutral clusters usually require strong acids, such as CF_3CO_2H or CF_3SO_3H. Protonations of clusters may be relatively slow and, in some instances, exhibit extremely large kinetic-isotope effects.[27] Hydrogen migration onto coordinated ligands may follow.

3.5 Insertion Reactions

Insertions (*see Insertion*) of alkene, alkyne, carbonyl, carbene, and other unsaturated ligands into metal–hydride or metal–carbon bonds are well documented.[9] In these reactions, both groups must be coordinated to the metal before insertion can occur. One difference between the reactions of cluster-bound ligands and monometallic analogs is that the ligand produced by insertion frequently forms bridges between two or more metal atoms. For example, acetylene and $H_2Os_3(CO)_{10}$ produce $HOs_3(\mu\text{-}\eta^2\text{-CH=CH}_2)(CO)_{10}$. Other examples are shown in Scheme 3. Insertions into other metal–element bonds are also possible.[9] For example, alkyne insertion into the Fe–P bond of $Fe_3(\mu_3\text{-PR})(CO)_{10}$ gives $Fe_3(\mu_3\text{-}\eta^3\text{-}$

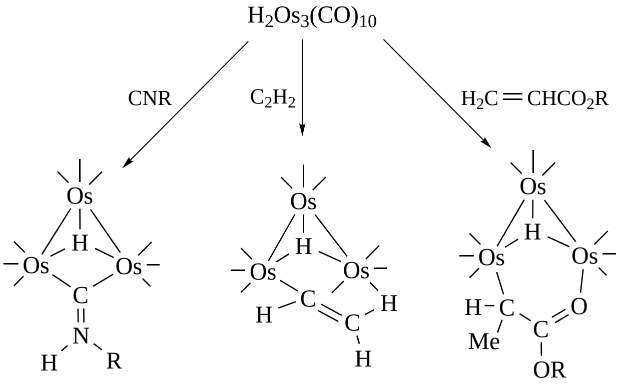

Scheme 3

RPCHCR′)(CO)$_{10}$. A second example is shown in equation (13).

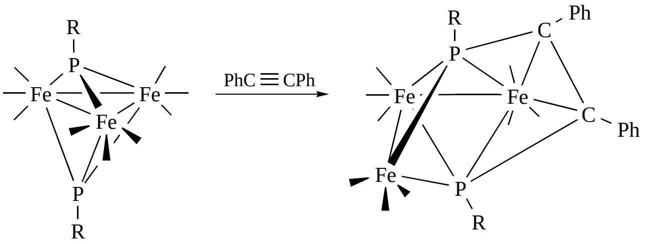

(13)

3.6 Nucleophilic Attack on Cluster-Bound Ligands

As is the case for monometallic complexes, ligands, such as CO and π-bound hydrocarbons, are activated toward nucleophilic attack. These reactions, which do not require coordination of the nucleophile to the metal, can be extremely rapid.**[9,56]**

Nucleophilic attack by hydride, alkoxide, or alkyl anions on a carbonyl ligand generates the corresponding acyl ligand. The cluster product is frequently much more labile than the neutral starting cluster, and thus the product may be derived by CO loss, for example, $Ru_3(CO)_{12}$ and methyllithium give $[Ru_3(\mu\text{-O=CMe})(CO)_{10}]^-$. Although hydride attack on coordinated CO usually generates an unstable formyl ligand, in one instance an oxymethylene ligand is formed; treatment of $[H_4Re_3(CO)_{10}]^-$ with $[BH(s\text{-Bu})_3]^-$ yields $[H_3Re_3(\mu_3\text{-}\eta^2\text{-}OCH_2)(CO)_9]^{2-}$ (equation 14).

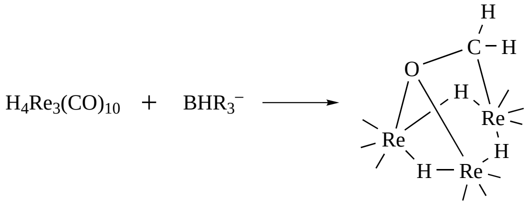

(14)

Coordinated C–C multiple bonds are also susceptible to nucleophilic attack. Reversible addition of phosphines occurs with $HOs_3(\mu\text{-}\eta^2\text{-CH=CH}_2)(CO)_{10}$, forming $HOs_3(\mu\text{-}\eta^1\text{-CHCH}_2PR_3)(CO)_{10}$ (equation 15). Additions of carbanions or hydride are irreversible. Other examples are shown in equations (16) and (17).

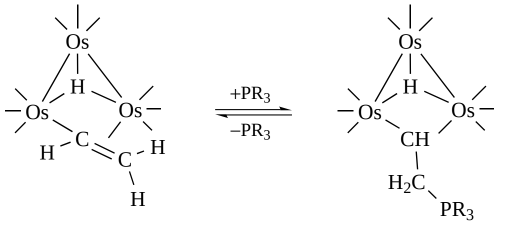

(15)

$$HRu_3(\mu_3\text{-}\eta^2\text{-CCPh})(CO)_9 + \text{CN-}t\text{-Bu} \longrightarrow HRu_3(\mu_3\text{-}\eta^2\text{-PhCCCN-}t\text{-Bu})(CO)_9 \quad (16)$$

$$HOs_3(\mu\text{-}\eta^2\text{-CHCH}_2)(CO)_{10} + CN^- \longrightarrow [HOs_3(\mu\text{-}\eta^1\text{-CHCH}_2CN)(CO)_{10}]^- \quad (17)$$

3.7 Fragmentation and Framework Rearrangement

In addition to ligand dissociation, an unsaturated metal cluster can be formed via metal–metal bond cleavage. The reactive intermediate may then undergo complete fragmentation, may achieve saturation by addition of a two-electron donor ligand, or may rearrange to another geometry. Since metal–metal bond strengths are comparable to metal–ligand bond strengths, metal–metal bond cleavage must always be considered as a factor in any reaction.**[28]**

Metal–metal bond cleavage can accompany oxidative addition reactions. An example of reversible addition of hydrogen accompanied by metal–metal bond cleavage is shown in equation (18). However, it has been shown that the mechanism actually involves CO dissociation prior to hydrogen addition, and then CO reassociation.**[24]**

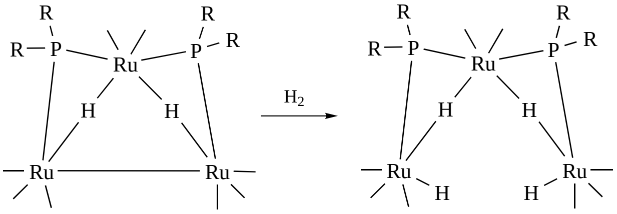

(18)

Associative attack by two-electron donors can occur under mild conditions if the addition is accompanied by metal–metal bond cleavage. An example is addition of phosphine ligands at 5 °C to $CoFeW(\mu_3\text{-PMe})(CO)_8Cp$, which forms $CoFeW(\mu_3\text{-PMe})(CO)_8(PR_3)_2$ via cleavage of the Fe–Co and W–Co bonds.

4 FLUXIONALITY

A characteristic feature of most organometallic clusters is stereochemical nonrigidity on the NMR timescale (*see*

Stereochemical Nonrigidity of Organometallic Complexes)[29] This feature has generated interest with respect to fundamental mechanisms of intramolecular migrations and the possible participation of fluxionality in transformations on clusters. However, fluxionality (*see Fluxional Molecule*) can frustrate the characterization of new compounds.

4.1 Carbonyl Ligands

Fluxionality (*see Fluxional Molecule*) of carbonyl ligands occurs both among carbonyls attached to the individual metal atoms of the cluster and as intermetallic ligand exchange. At a single metal center, carbonyls are scrambled via a three-fold rotational process. Carbonyl exchange between metal atoms occurs by migration of carbonyls between terminal and edge-bridging coordination.[4] The argument is still open concerning the mechanism.[29]

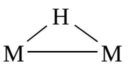

(**4**) μ-H

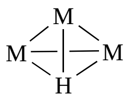

(**5**) μ_3-H

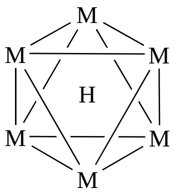

(**6**)

4.2 Hydride Ligands

Hydride ligands are the most versatile of all organometallic ligands. Hydrides can coordinate to a single metal (terminal coordination), bridge two (μ-H, **4**) or three (μ_3-H, **5**) metal atoms, or occupy an interstitial position inside a metal polyhedron (**6**). Hydrides bound to transition metal clusters most commonly bridge two metal atoms. Interconversion between bridging and terminal coordination, which has a low activation barrier, provides a facile pathway for hydride fluxionality (*see* ***Hydride Complexes of the Transition Metals***). Hydride fluxionality between metal–metal and metal–carbon bridging sites has also been observed. A classic example is $(\mu\text{-H})_3Fe_3(\mu_3\text{-CH})(CO)_9$ and its tautomers in which exchange between the methylidyne hydrogen and the hydride ligands occurs (equation 19).

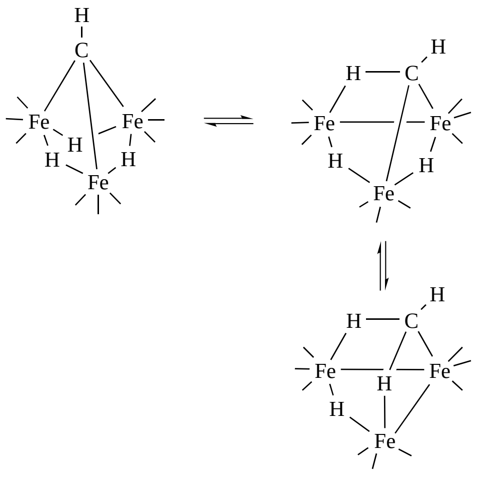

(19)

4.3 Hydrocarbyl Ligands

A variety of fluxional (*see Fluxional Molecule*) processes involving hydrocarbyl ligands attached to metal clusters have been identified.[9] Alkylidene (*see Alkylidene*) ligands can undergo fluxional processes via bridge–terminal interconversion in the same manner as carbonyl ligands. Fluxional rotation of μ_3-η^2-alkyne, -aryne, and -1,1-alkenylidene units about a triangular M_3 face is very common. Fluxionality of μ_2-η^2-alkenyl units has been documented in a number of cases. This process involves exchange of σ and π bonds between the two bridged metal atoms (equation 20).[30]

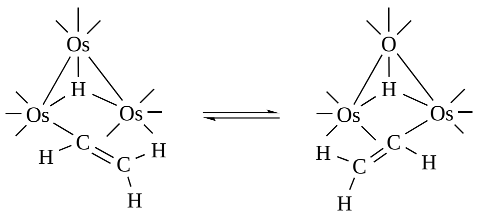

(20)

A process unique to metal clusters is rotation of a face-bonded arene ligand on a triangular metal framework. Fluxionality of carbonyl, ethylene, and benzene ligands of $Os_3(\mu_3\text{-}\eta^2\text{:}\eta^2\text{:}\eta^2\text{-}C_6H_6)(CO)_8(\eta^2\text{-}CH_2{=}CH_2)$ (**7**) has been studied by 2D NMR methods.[31] The face-capping benzene ligand undergoes a 1,2 ring-hopping motion such that the arene ring rotates relative to the Os_3 ring. The η^2-alkene rotates about the Os–alkene bond and also undergoes a trigonal twist isomerization involving the carbonyl ligands. This sort of bonding mode is also found for fullerenes (*see* ***Carbon: Fullerenes***).

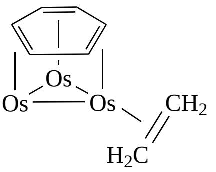

(**7**)

4.4 Others

Intermetallic fluxionality (*see Fluxional Molecule*) of phosphine ligands has been found for some triplatinum clusters.[32] Isocyanide ligands (*see Isocyanide Ligands*) display very similar fluxional behavior to CO. Fluxionality of the metal-cluster framework has been noted. For example, multinuclear NMR studies of $[Rh_9E(CO)_{21}]^{2-}$ ($E = P$ or As), $[Rh_{10}E(CO)_{22}]^{3-}$, and $[Rh_{12}Sb(CO)_{27}]^{3-}$ revealed complete fluxionality of both carbonyl and metal polyhedra at high temperatures.**33** Interconversion of open and closed structural isomers $Ru_5Pt(PBu_3)(CO)_{15}(C)$ is rapid on the NMR timescale; the process is said to resemble diffusion of metal adatoms across a metals surface.**34**

5 CHEMISTRY OF CLUSTERS CONTAINING C_n ($n = 1$–3) FRAGMENTS

While numerous clusters containing exotic hydrocarbyl ligands have been prepared and unique chemical reactivity demonstrated, the most well-established chemistry concerns hydrocarbyl fragments bound to the metal framework through one, two, or three carbon atoms. A sampling of the chemistry of these fragments will illustrate many of the unique aspects of organometallic cluster chemistry.

5.1 C_1 Units on Clusters

Interconversion of alkyl, alkylidene, alkylidyne, and carbide moieties has now been demonstrated in a variety of cluster systems. This work provides perhaps the most complete picture of the fundamental reactivity of the prototypical organometallic cluster.

Interstitial carbon atoms are a unique aspect of organometallic cluster chemistry (*see* ***Cluster Compounds: Inorganometallic Compounds Containing Transition Metal & Main Group Elements***).**35** Carbon atoms that are completely encapsulated by six or more metal atoms are inert. Even partially exposed carbides, such as $Fe_5C(CO)_{15}$ and $Fe_4C(CO)_{13}$, are relatively unreactive. However, a few examples of reactions of exposed carbides to produce alkylidyne ligands are known.**36** For example, $Fe_4(\mu_4\text{-}C)(CO)_{13}$ reacts with methanol to give $[Fe_4(\mu_4\text{-}CCO_2Me)(CO)_{12}]^-$. Protonation of $[Fe_5(\mu_5\text{-}C)(CO)_{14}]^{2-}$ yields first $[HFe_5(\mu_5\text{-}C)(CO)_{14}]^-$ and then $HFe_4(\mu_4\text{-}\eta^2\text{-}CH)(CO)_{12}$. Electrophilic attack by methyl triflate on $[Fe_4(\mu_4\text{-}C)(CO)_{12}]^{2-}$ yields $[Fe_4(\mu_3\text{-}CMe)(CO)_{12}]^-$, yet the reaction with methyl iodide produces $[Fe_4(\mu_4\text{-}CC(O)Me)(CO)_{12}]^-$, presumably via a radical intermediate. These transformations are shown in Scheme 4.**36**

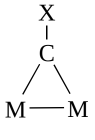

(**8**) μ-CX

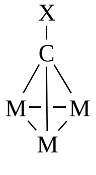

(**9**) μ_3-CX

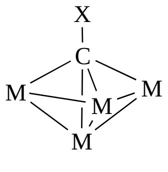

(**10**) μ_4-η^1-CX

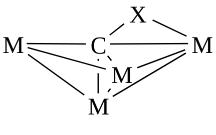

(**11**) μ_4-η^2-CX

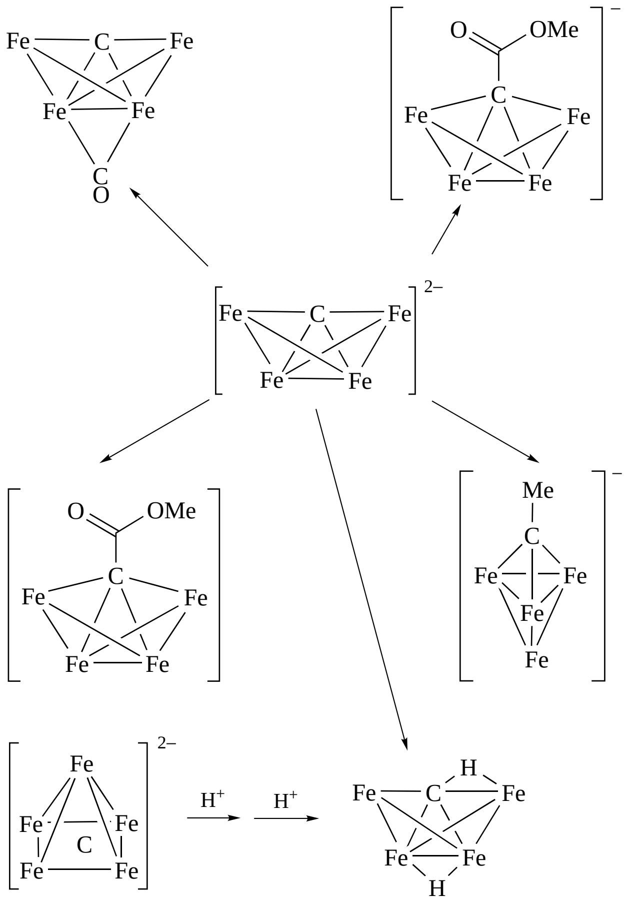

Scheme 4

Alkylidyne (*see Alkylidyne*) ligands are found as terminal CR, μ-CR (**8**), μ_3-CR (**9**), or μ_4-ligands (**10** and **11**). Of these, (**10**) and (**11**) are the least well represented, and their chemistry is for the most part unexplored. In this geometry, the CX ligand is found between the wings of butterfly metal framework, as in the clusters $HFe_4(CH)(CO)_{12}$, $HFe_4(COMe)(CO)_{12}$, or $[Fe_4(CCO_2Me)(CO)_{12}]^-$. As shown, the μ_4-CX ligand may be η^1 (**10**) or η^2 coordinated (**11**); the factors that determine the coordination mode are not thoroughly understood. This butterfly geometry may mimic the binding of an alkylidyne ligand at a step site on a metal surface, thus making studies of the chemistry of μ_4-CX ligand of general interest. However, isoelectronic (*see Isoelectronic*) species, such as $[Fe_4(\mu_3\text{-}CX)(CO)_{12}]^-$ ($X = Me$, OMe), adopt another structure which contains a μ_3-CX ligand capping a face of a metal tetrahedron. The factors that influence the adoption of each structure are presently unknown, and the differences in reactivities between the CX ligand in the two coordination modes are also unexplored. One systematic approach to the synthesis of $M_4(CX)$ clusters involves the addition of metal fragments to alkylidynetrimetal clusters. Examples of this approach are shown in equations (21) and (22).

$$\mathrm{HRu_3(\mu\text{-}CX)(CO)_{10} + Ru(CO)_5 \longrightarrow HRu_4(\mu_4\text{-}\eta^2\text{-}CX)(CO)_{12}} \qquad (21)$$

$$\mathrm{X = OMe,\ NMe_2}$$

$$\mathrm{Co_2Mo(\mu_3\text{-}CCO_2R)(CO)_3Cp_3 + Fe_2(CO)_9 \longrightarrow Co_2MoFe(CCO_2R)(CO)_5Cp_3} \qquad (22)$$

There are a few examples of coordination of an alkylidyne as a bridging ligand between two metals.**[9,36]** Most of these concern alkylidynes with π-donor substituents, such as OMe or NMe_2. The reactivity is similar to that of the μ_3-CX ligand. One unusual reaction is the rearrangement of $HRu_3(\mu\text{-}\eta^1\text{-}COMe)(CO)_{10}$ to $HRu_3(\mu\ \text{-}\eta^2\text{-}O{=}CMe)(CO)_{10}$ under photolytic conditions (equation 23).

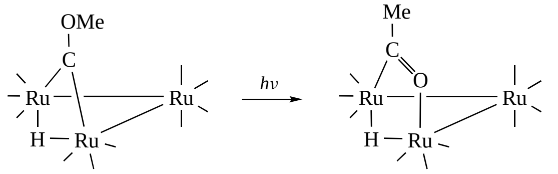

(23)

The chemistry of the μ_3-CX ligand has been much more thoroughly explored. One of the first organometallic clusters to be synthesized was $Co_3(\mu_3\text{-}CMe)(CO)_9$. Subsequently, the chemistry of the $Co_3(\mu_3\text{-}CX)(CO)_9$ derivatives was studied by Seyferth and coworkers. The bonding in clusters such as $Co_3(\mu_3\text{-}CX)(CO)_9$ is most properly described as an sp or sp^2 hybridized carbon bonded to the Co_3 framework. π interactions between available p orbitals of the methylidyne substituent and the Co_3C cluster orbitals have been identified. Cluster donation to the empty substituent orbital results in unusual stabilities for carbocations, such as $[Co_3(CCH_2)(CO)_9]^+$.**[37]** On the other hand, π donors such as NMe_2 stabilize radical cation clusters, for example, $[H_3Ru_3(CNMe_2)(CO)_6(PPh_3)_3]^+$.**[38]**

Lewis acids (*see Lewis Acids & Bases*) react with $Co_3(\mu_3\text{-}CX)(CO)_9$ (X = halogen or alkoxide) to form the moderately stable ketenylidene complex $[Co_3(CCO)(CO)_9]^+$.**[37]** Although the structure still has not been established unambiguously, the crystal structures of a number of related clusters show that the coordination of the ketenylidene is flexible (see Section 5.2).

Lewis bases (Y, *see Lewis Acids & Bases*) react with $Co_3(\mu_3\text{-}CX)(CO)_9$ (X = halide) to give either $Co_3(\mu_3\text{-}CY)(CO)_9$ or $Co_3(\mu_3\text{-}CC(O)Y)(CO)_9$. The latter may be formed by solvolysis to the ketenylidene cation. The former products are most likely formed via radical reactions. On the other hand, neutral Lewis bases L can replace the chloride from $H_3Os_3(\mu_3\text{-}CCl)(CO)_9$ to form $H_2Os_3(\mu_3\text{-}CL)(CO)_9$, where L is a nitrogen, phosphorus or sulfur donor.**[9]**

Protonation of a carbonyl ligand can give rise to a hydroxymethylidyne ligand, COH. Examples include $HM_3(\mu\text{-}COH)(CO)_{10}$ (M = Fe, Ru, and Os), $Co_3(\mu_3\text{-}COH)(CO)_9$, and $HFe_4(\mu_4\text{-}\eta^2\text{-}COH)(CO)_{12}$. Hydrogen migrations from oxygen to the metal–metal bond and the reverse reaction have been noted. Hydroxymethylidynes are likely intermediates in the coupling reactions shown in equations (24) and (25). Protonation or alkylation of isocyanides produce the analogous aminomethylidyne ligands, as shown in equations (26) and (27).

$$\mathrm{[(\mu\text{-}H)Co_3(\mu_3\text{-}CH)_2Cp_3]^+ + CO \longrightarrow [Co_3(\mu_3\text{-}\eta^2\text{-}HCCOH)Cp_3]^+} \qquad (24)$$

$$\mathrm{Os_3(CO)_{11}(NCMe) + H_2O + HCCH \longrightarrow HOs_3(\mu_3\text{-}\eta^2\text{-}HCCHCOH)(CO)_9} \qquad (25)$$

$$\mathrm{[HM_3(CO)_{10}(CNR)]^- + E^+ \longrightarrow HM_3(CO)_{10}(\mu\text{-}CNRE)} \qquad (26)$$

$$\mathrm{M = Fe,\ Ru;\ E = H,\ Me}$$

$$\mathrm{H(\mu\text{-}H)Os_3(CO)_{10}(CNR) \longrightarrow (\mu\text{-}H)Os_3(\mu\text{-}CNHR)(CO)_{10}} \qquad (27)$$

Alkylidenes have been prepared by reduction of alkylidynes, by C–H oxidative addition from alkyls, and by treatment of unsaturated metal clusters with diazoalkanes. In most instances, the alkylidene adopts a $\mu_2\text{-}\eta^1$ coordination mode. However, alkylidenes with heteroatom substituents may also be found in terminal coordination modes.**[39]** The latter are typically prepared by the Fischer-type carbene route (*see Fischer-type Carbene Complexes*) (sequential addition of nucleophilic and electrophilic alkylating agents to carbonyl or isocyanide ligands), by condensation of metal fragments with mono- or dimetallic carbene complexes, or by C–H activation of alkylamines.**[39]** These heteroatom substituted carbenes may also bind in a $\mu_3\text{-}\eta^2$ mode, as in (**12**).

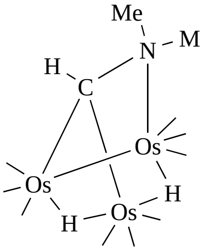

(**12**)

Few alkyls bound to clusters have been prepared. Alkyls containing β-hydrogens are usually unstable with respect to β-elimination (*see β-Elimination*). Alkyls can be stabilized by bridging via a C–H or other bond.**[9,32]** Examples include $HOs_3(\mu_2\text{-}\eta^2\text{-}H\text{–}CHMe)(CO)_{10}$, $HOs_3(\mu_2\text{-}\eta^2\text{-}H\text{–}CH_2)(CO)_{10}$, $HOs_3(\mu\text{-}\eta^2\text{-}CH_2CO_2Et)(CO)_{10}$, and $HRu_3(\mu_3\text{-}\eta^2\text{-}CH_2SEt)(CO)_9$. These complexes are formed from alkylidenes or alkylidynes by reductive elimination of a C–H bond or by alkene insertion into a metal–hydride bond.

The interconversion of alkylidyne, alkylidene, and alkyl species is amply demonstrated in the chemistry of reductive elimination (*see Reductive Elimination*) from $H_3M_3(\mu_3$-$CR)(CO)_9$ (M = Fe, Ru, and Os). The proposed mechanism for this reductive elimination is shown in Scheme 5. Reactions of $H_3Ru_3(\mu_3$-$CX)(CO)_9$ with CO produce MeX and $Ru_3(CO)_{12}/Ru(CO)_5$ when X = Ph, CO_2Me, Cl, or H. Alkylidene and alkyl intermediates can be isolated in several cases. Pyrolysis of $H_3Ru_3(\mu_3$-$CCO_2Me)(CO)_9$ in the absence of CO forms $H_2Ru_3(\mu_3$-$CHCO_2Me)(CO)_9$ (**13**). This product is formed by reductive elimination of a single C–H bond followed by coordination of the acyl to the unsaturated metal site thus created. Pyrolysis of $H_3Ru_3(\mu_3$-$CSEt)(CO)_9$ yields $HRu_3(\mu_3$-η^2-$CH_2SEt)(CO)_9$ (**14**); in this case the sulfur atom stabilizes the two vacant sites formed by reductive elimination. Under CO, complete elimination of MeX ultimately yields $Ru_3(CO)_{12}$, which is in equilibrium with $Ru(CO)_5$ under the reaction conditions. Although several pre-equilibria may be postulated to account for the kinetics, the most attractive mechanism, shown in Scheme 5, involves reversible migration of a hydrogen atom from a position bridging a Ru−Ru vector to a position bridging a Ru−C vector, generating intermediate (**15**), reversible cleavage of the agostic (*see Agostic Bonding*) Ru–H–C bond, and rate-determining addition of CO to form a saturated alkylidene cluster; subsequent reductive eliminations are faster than the first. Later studies draw a more complicated picture; pyrolysis of $H_3Ru_3(\mu_3$-$CSEt)(CO)_9$ to yield $HRu_3(\mu_3$-η^2-$CH_2SEt)(CO)_9$ involves CO dissociation before the rate-determining step and methyl acetate elimination from $H_3Ru_3(\mu_3$-$CCO_2Me)(CO)_9$ is unaffected by added CO.[40]

The 'agostic' C–H–M bond (*see Agostic Bonding*) is well established in metal-cluster chemistry. Fehlner and coworkers have shown that $H_3Fe_3(\mu_3$-$CH)(CO)_9$ exists in solution in equilibrium with $H_2Fe_3(\mu_3$-η^2-$HCH)(CO)_9$ and $HFe_3(\mu_3$-η^3-$H_2CH)(CO)_9$ (equation 19). Although the equilibrium constant is not so favorable for the agostic Ru analogs, dissolution of $H_3Ru_3(\mu_3$-$CX)(CO)_9$, where X = Et or $CHPhCH_2Ph$, in fluorosulfonic or trifluoromethanesulfonic acid forms $[H_3Ru_3(\mu_3$-η^2-$HCX)(CO)_9]^+$ (**16**) by protonation of the Ru–C bond. Protonation of the metal−carbon bond occurs because the HOMO is metal−carbon bonding in character. The NMR spectra provide evidence for fluxional (*see Fluxional Molecule*) migration of the agostic hydrogen to each of the three M−C edges. No exchange occurs between the agostic hydrogen and the hydride ligands on the NMR timescale. Agostic alkylidene-alkyl equilibria are also well known. In solution, $H_2Os_3(\mu$-$CH_2)(CO)_9L$ is in equilibrium with $HOs_3(\mu$-η^2-$HCH_2)(CO)_9L$, a slightly less stable tautomer.[41] The same tautomeric equilibrium exists for $H_2Os_3(\mu$-$CHMe)(CO)_{10}/HOs_3(\mu$-η^2-$HCHMe)(CO)_{10}$ ($K_{eq} = 0.14$); in this system, β-elimination (*see β-Elimination*) from the ethyl group is thermodynamically favored, but α-elimination is ca. 100 times faster at 19 °C (Scheme 6).

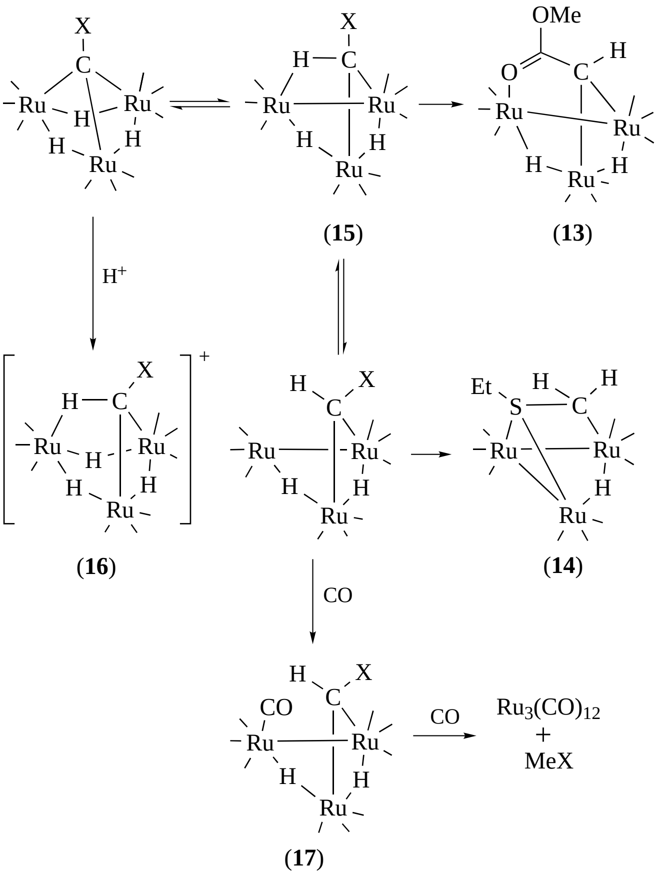

Scheme 5

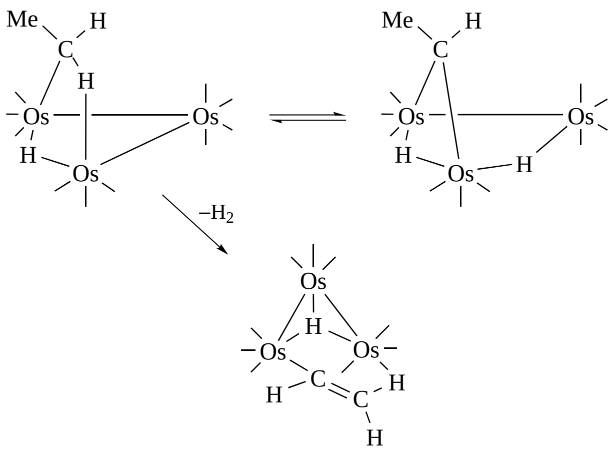

Scheme 6

The chemistry of these C_1 fragments displays all of the unique features of organometallic cluster chemistry. (1) Ligands commonly bridge two or more metal atoms in coordination modes not seen for monometallic complexes. (2) Hydrogen migrations between metal and hydrocarbyl ligands are facile. (3) Intramolecular, intermetallic ligand migrations are important.

5.2 C_2 Units on Clusters

Some of the most prolific reactants in organometallic chemistry are alkynes.[42] At some time or the other every new cluster is reacted with an alkyne. Not surprisingly, alkyne complexes dominate the C_2-containing clusters. Alkynes most commonly bridge the triangular face of the cluster, either as μ_3-η^2-∥ (**18**) or as μ_3-η^2-⊥ (**19**) ligands. In tetrametallic and larger clusters, alkynes can also bind in a μ_4-η^2 mode (*see Alkyne Complexes*) (**20**).

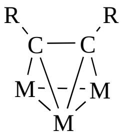

(**18**) μ_3-η^2- ∥

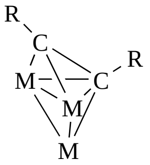

(**19**) μ_3-η^2- ⊥

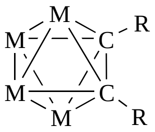

(**20**) μ_4-η^2

One of the most interesting transformations involving a coordinated alkyne is the cleavage of the carbon–carbon bond to form two alkylidyne ligands. This reaction, which is induced by loss of a two-electron donor ligand, is remarkably facile. Reversible cleavage has been demonstrated, as shown in equation (28).[36]

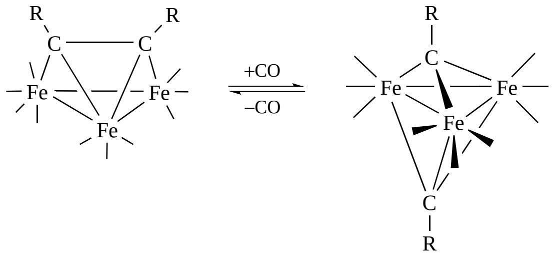

(28)

Thermolysis of metal carbonyl clusters in the presence of alkenes frequently leads to C–H addition, forming 1,1-alkenylidene or alkyne ligands.[9] Pyrolysis of $HOs_3(\mu$-η^2-$CH{=}CH_2)(CO)_{10}$ forms $H_2Os_3(\mu_3$-η^2-$C{=}CH_2)(CO)_9$. Hydrogenation of the alkenylidene yields $H_3Os_3(\mu_3$-$CMe)(CO)_9$. On the other hand, pyrolysis of propene and $Os_3(CO)_{12}$ forms both $H_2Os_3(\mu_3$-η^2-$C{=}CHMe)(CO)_9$ and $H_2Os_3(\mu_3$-η^2-$HC{=}CMe)(CO)_9$. These structures are shown in Scheme 7. Less stable alkene or alkenyl complexes can be formed using the techniques described in Section 2. Insertion of an alkyne into a metal–hydride bond produces an alkenyl ligand. Interconversions of C_2 ligands between μ-ethylidene, μ_3-ethylidyne, and μ_3-vinylidene fragments have been observed on many trimetallic clusters, including iron, cobalt,[43] ruthenium, and osmium,[9,44] and also heterometallic clusters;[45] one example is shown in Scheme 8.

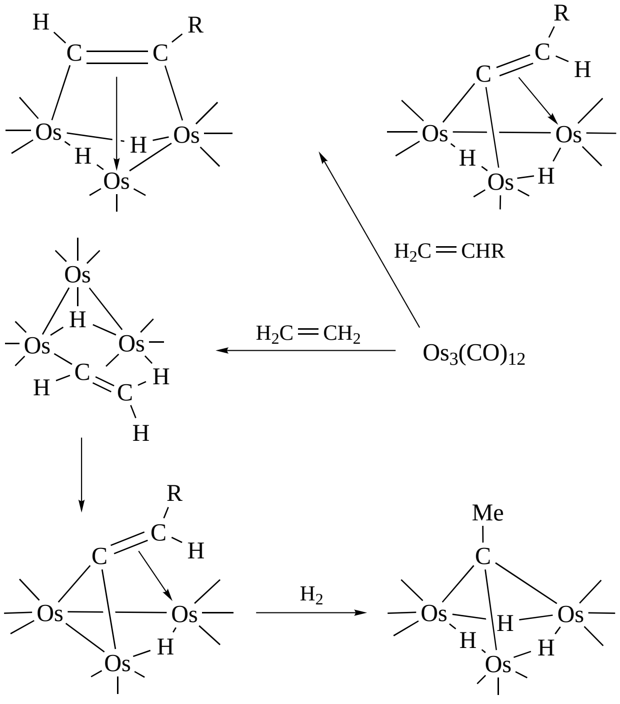

Scheme 7

Ketene and ketenylidene ligands bound to trimetallic frameworks undergo very interesting chemistry.[9,36] The transformations involving these ligands may have some relevance to the chemistry of carbon atoms on metal surfaces.

The first examples of ketene complexes were prepared by carbonyl–methylene coupling (equation 29). The ketene complex $Os_3(CH_2C(O))(CO)_{12}$ reacts with methanol, water, and hydrogen to give methyl acetate, acetic acid, and acetaldehyde, respectively. However, $[Os_3(\mu$-$I)(\mu$-$CH_2)(CO)_{10}]^-$ reacts slowly with methanol to give the enolate $[Os_3(CO)_{11}(CH_2C(O)OMe)]^-$ when the reaction is conducted under carbon monoxide. Electrophiles (E = BF_3 or methyl cation) attack at oxygen, forming $Os_3(\mu$-$I)(\mu$ -η^2-$C(OE){=}CH_2)(CO)_{10}$.[9]

$$[Os_3(\mu\text{-}I)(\mu\text{-}CH_2)(CO)_{10}]^- + CO \longrightarrow [Os_3(\mu\text{-}I)\{\mu\text{-}CH_2C(O)\}(CO)_{10}]^- \quad (29)$$

Ketenylidenes have been obtained by removal of oxygen from carbonyl ligands, which results in CO migration to the reactive carbon atom, and by methylene–carbonyl coupling and C–H oxidative addition (Scheme 9).[9,36] The ketenylidene ligand adopts two geometries as a face-capping ligand. The CCO axis of the ligand is tilted toward one metal atom in $[M_3(\mu_3$-$CCO)(CO)_9]^{2-}$ (M = Fe (33°; from the normal) and Os (26°; from the normal)) (**21**), but the CCO axis

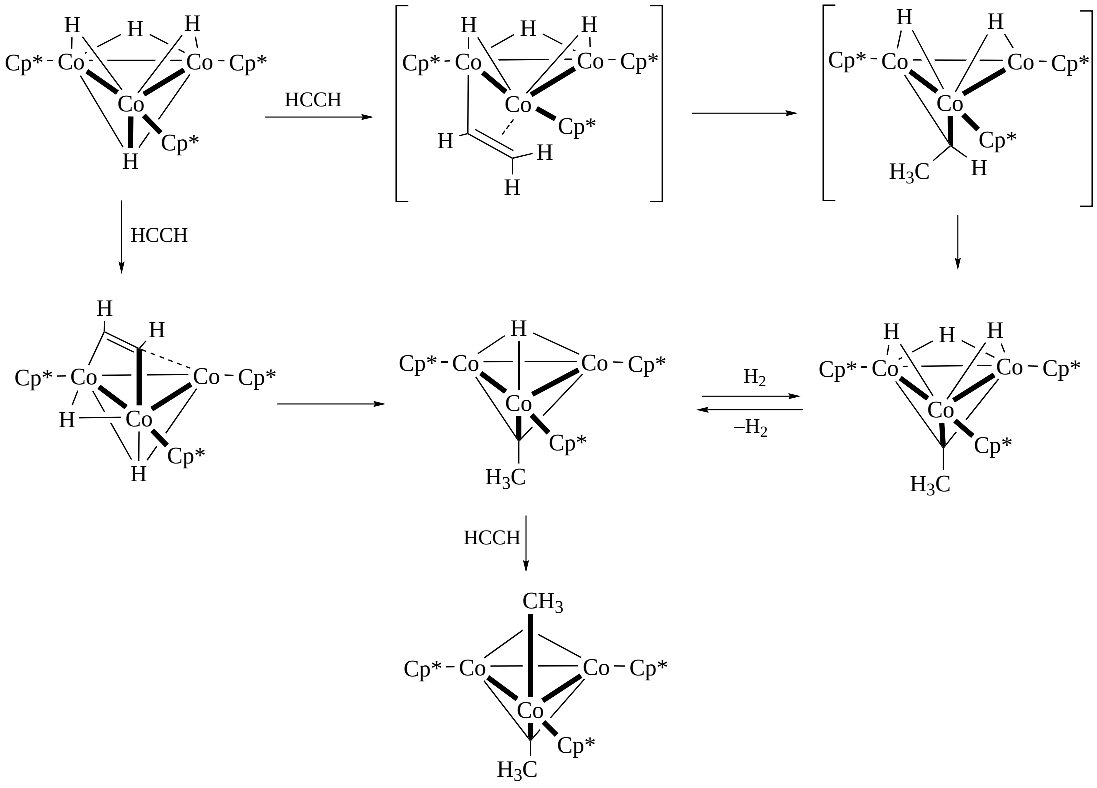

Scheme 8 (Reproduced from T. Takao, T. Takemori, M. Moriya, and H. Suzuki, *Organometallics*, 2002, **21**, 5190)

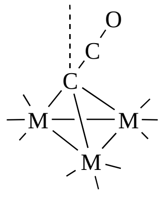

(**21**)

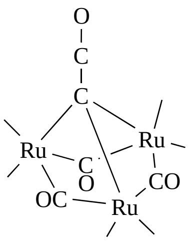

(**22**)

$[M_3(CO)_{11}]^{2-} + MeC(O)Cl \longrightarrow [M_3\{\mu_3\text{-}COC(O)Me\}(CO)_{11}]^{-}$

$[M_3\{\mu_3\text{-}COC(O)Me\}(CO)_{11}]^{-} + \text{Na/benzophenone} \longrightarrow [M_3\{\mu_3\text{-}CCO\}(CO)_9]^{2-}$

Scheme 9

is almost normal to the trimetallic plane (12°; tilt with respect to the vertical) in $[Ru_3(\mu_3\text{-}CCO)(CO)_9]^{2-}$ (**22**). The Ru_3 cluster has a different arrangement of carbonyl ligands as well, having three bridging carbonyls (*see Bridging Ligand*) (cf. only terminal carbonyls for the Os_3 and Fe_3 clusters).

The ketenylidene dianions $[M_3(CO)_9(CCO)]^{2-}$ (M = Fe, Ru, or Os) react as nucleophiles. Products derived from the reactions of ketenylidenes with electrophiles H^+ or Me^+ include methylidyne, alkylidynes, 1,1-alkenylidenes, and acetylides. Some of these reactions are shown in Scheme 10.[36] Carbon–carbon bond cleavage seems to be more facile when the CCO axis is tilted toward one of the metal atoms.

The carbonyl of the ketenylidene ligand undergoes a very interesting substitution reaction with phosphine ligands. Initial

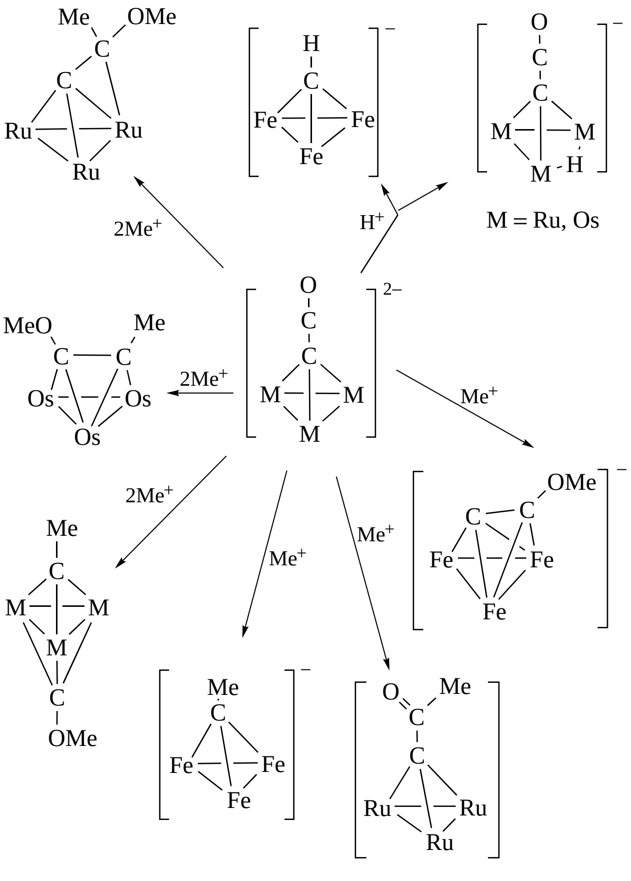

Scheme 10

substitution of [Fe$_2$Co(μ-CCO)(CO)$_9$]$^-$ by PR$_3$ occurs at a Co atom by an associative substitution mechanism (*see Associative Substitution*).[46] Subsequently, the substituted product isomerizes to [Fe$_2$Co(μ_3-CPR$_3$)(CO)$_9$]$^-$. The mechanism for isomerization is proposed to involve pairwise CO and PR$_3$ migration through metal–carbon bridging.

5.3 C$_3$ Units on Clusters

The most common C$_3$ ligands for monometallic complexes are allyl ligands, but these have not seen extensive use in cluster chemistry. More commonly, hydrogen migrations generate μ_3-η^3-allenyl and μ_3-η^3-1,3-dimetalloallyl ligands, which presumably are more favorable because of the polymetallic coordination.[9,36] Some of these clusters are shown in Scheme 11. Clusters containing allenyl ligands (**23**) have been produced in reactions of 1,3-dienes with metal carbonyl clusters. These clusters rearrange by a 1,2-hydrogen shift to more stable isomers, HRu$_3$(μ_3-η^3-RCCHCR′)(CO)$_9$ (**24**).

The M$_3$(μ_3-η^3-RCCRCR″) cluster core is a very stable one which is formed from a variety of unrelated transformations. The cluster is described as a nido form (*see Nido Cluster*) derived by removal of one vertex from a pentagonal bipyramid.

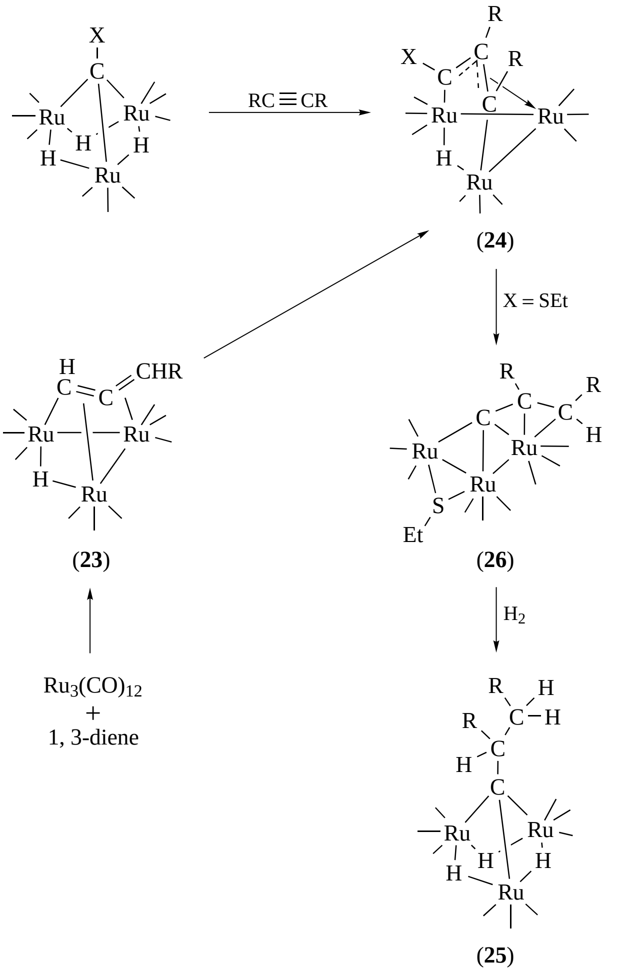

Scheme 11

The first examples were prepared in reactions of alkynes with M$_3$(CO)$_{12}$, M = Ru and Os. The C$_3$ unit can also be produced by alkylidyne–alkyne coupling.

Other than hydrogen migrations, few reactions involving the μ_3-η^3-RCCRCR″ ligand have been noted. Hydrogenation of HRu$_3$(μ_3-η^3-MeOCCRCR′)(CO)$_9$ (see **24**) produces H$_3$Ru$_3$(μ_3-CCHRCH$_2$R′)(CO)$_9$ (**25**). Isomerization of HRu$_3$(μ_3-η^3-EtSCCRCR′)(CO)$_9$ yields Ru$_3$(μ_3-η^3-CCRCHR′)(μ-SEt)(CO)$_9$ (**26**); this structure may be analogous to an intermediate in the hydrogenation reaction. Hydrogenation of Ru$_3$(μ_3-η^3-CCRCHR′)(μ-SEt)(CO)$_9$ forms H$_3$Ru$_3$(μ_3-CCHRCH$_2$R′)(CO)$_9$, in addition to HRu$_3$(μ-SEt)(CO)$_{10}$.

Rearrangement of allene on an Os$_3$ cluster also produces a M$_3$(μ_3-η^3-HCCHCH) species (Scheme 12). The reaction of the very labile Os$_3$(CO)$_{11}$(NCMe) with allene gives as the initial product Os$_3$(μ-η^3-C(CH$_2$)$_2$)(CO)$_{11}$. Photolysis of this product causes CO loss and C–H activation, forming HOs$_3$(μ_3-η^3-CH=C=CH$_2$)(CO)$_9$. Finally, thermolysis of the allenyl cluster at 125 °C produces the more stable isomer HOs$_3$(μ_3-η^3-CHCHCH)(CO)$_9$.[9]

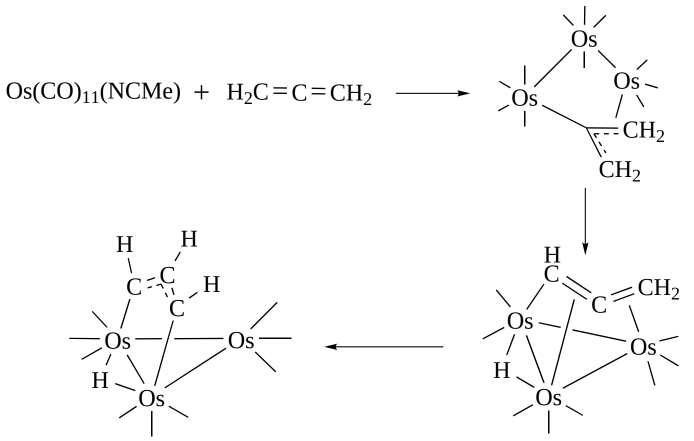

Scheme 12

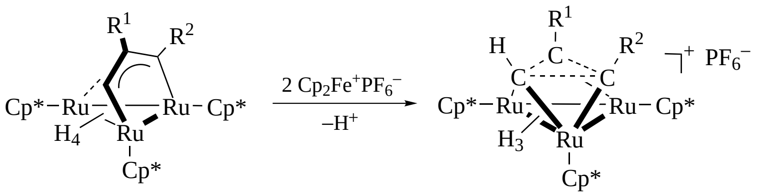

Scheme 13 (Reproduced from T. Takao, A. Inagaki, E. Murotani, T. Imamura, and H. Suzuki, *Organometallics*, 2003, **22**, 1361)

One very unusual reaction involving the μ_3-η^3-RCCRCR$''$ ligand is shown in Scheme 13. Oxidation of the $\{Cp^*Ru\}_3(H)_4(\mu_3\text{-}\eta^3\text{-HCCRCR})$ by treatment with ferricenium ion gives the cationic complex with a closed C_3 ring, which may be considered to be a η^3-cyclopropenyl. This is a rare example of a C–C reductive elimination initiated by a two-electron oxidation.**47**

6 OTHER HYDROCARBYL LIGANDS

6.1 Arenes

Arene ligands (*see Arene Complexes*) bond to monometallic complexes as η^6-, η^4-, and η^2-C_6R_6 species. Unique to trimetallic or larger clusters is the μ_3-η^2:η^2:η^2-C_6R_6 ligand.**48** This coordination mode is believed to model the geometry of benzene nondissociatively chemisorbed on the surface of a close-packed metal lattice. The prototypical cluster $Os_3(\mu_3\text{-}\eta^2{:}\eta^2{:}\eta^2\text{-}C_6H_6)(CO)_9$ (**27**) is prepared by treatment of $HOs_3(\mu_3\text{-}\eta^5\text{-cyclohexadienyl})(CO)_9$ with trityl cation and then deprotonation of $[HOs_3(\mu_3\text{-}\eta^2{:}\eta^2{:}\eta^2\text{-}C_6H_6)(CO)_9]^+$. Fluxionality of the μ_3-η^2:η^2:η^2-C_6H_6 ligand has been noted in Section 4.3.

An interesting example of the effect of electron count upon ligand bonding is the series $(Cp^*Ru)_3(H)_3(C_6H_6)^{0/1+/2+}$. The neutral, 48-e cluster and the 47-e cationic cluster contain η^2:η^2:η^2-C_6H_6 ligands, whereas the 46-e dicationic cluster contains a η^3:η^3-C_6H_6 ligand.**49**

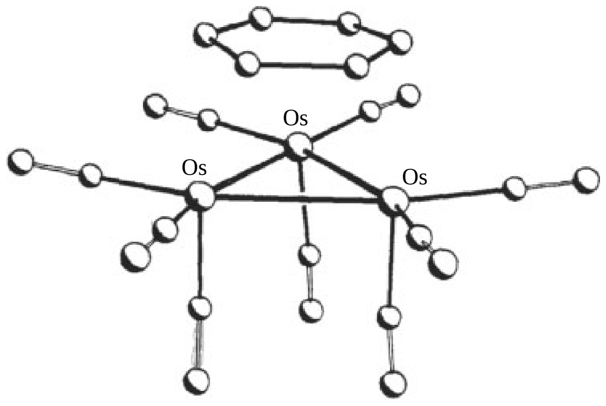

(**27**)

(Reproduced from M.A. Gallop, M.P. Gomez-Sal, C.E. Housecroft, B.F.G. Johnson, J. Lewis, S.M. Owen, P.R. Raithby, and A.H. Wright, *J. Am. Chem. Soc.*, 1992, **114**, 2502)

6.2 Fullerenes

Similar face-coordinated fullerene (*see* ***Carbon: Fullerenes***) complexes have been synthesized; also known are complexes of η^2-C_{60}, μ-η^2:η^2-C_{60}, and μ_3-η^1:η^1:η^2-C_{60}.[50] One example, $Ru_3(CO)_9(\mu_3\text{-}\eta^2{:}\eta^2{:}\eta^2\text{-}C_{60})$ (**28**), is shown below.

6.3 Dienes

Conjugated 1,3-dienes can coordinate to a single metal atom or may bridge two metals of the cluster.[9] Most commonly the diene coordinates to a single metal atom in the cis conformation, as in (**29**). The diene is found in the s-trans conformation bridging two metals in $Os_3(CO)_{10}$(1,3-butadiene) (**30**).

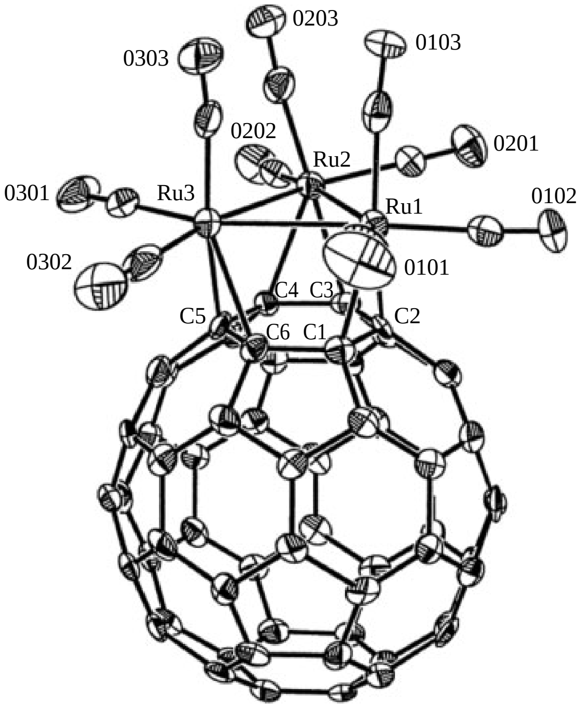

(**28**)

(Reproduced from H.F. Hsu and J.R. Shapley, *J. Am. Chem. Soc.*, 1996, **118**, 9192)

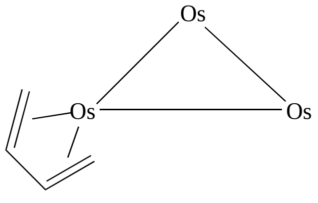

(**29**)

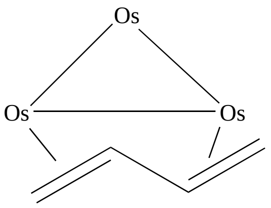

(**30**)

7 ORGANOMETALLIC CLUSTERS AS CATALYSTS

Since the discovery of the first metal clusters, researchers have followed the promise of these compounds to serve as improved catalysts for known organic transformations and as catalysts for new transformations. Many clusters have been shown to serve as precursors for both homogeneous and heterogeneous catalysts.[51–53] Unfortunately, it has proven difficult to determine unequivocally that the active catalyst retains the cluster core. Additionally, the 'unique' catalytic properties of clusters have proven elusive. In view of these difficulties and the large number of reviews which have treated various aspects of cluster catalysis, the subject will not be summarized in this article. For further information (*see* ***Carbonylation Processes by Homogeneous Catalysis***; ***Hydrogenation & Isomerization of Alkenes***; ***Organic Synthesis using Transition Metal Carbonyl Complexes***; ***Organic Synthesis using Transition Metal Complexes Containing π-Bonded Ligands***, and ***Supported Organotransition Metal Compounds***).

8 ORGANOMETALLIC CLUSTERS AS MODELS FOR METAL SURFACE-BOUND HYDROCARBYLS

Molecular transition metal clusters have long been proposed as models for some aspects of the chemistry at metal surfaces. Earl Muetterties was one of the first to promote this 'cluster-surface analogy'.[54,55]

The most successful application of the cluster-surface analogy has been the use of spectroscopic signatures of cluster-bound hydrocarbyl ligands to identify vibrational spectra of chemisorbed hydrocarbons. Hydrocarbon fragments which have been identified on metal surfaces in this way include alkylidynes, alkylidenes, vinylidenes, and carboxylates. The μ_3-CR unit has been identified on numerous metal surfaces, including the Pt(111), Ru(001), Rh(111), and Pd surfaces. Chemisorption of ethylene, acetylene, propene, and other small hydrocarbons can give rise to alkylidyne fragments through C–H cleavage and hydrogen migration, common reactions for molecular metal clusters. The methylene fragment has been identified on the Ru(001) surface by comparison of vibrational data with data from cluster models. C_2 fragments identified by comparison with cluster models include acetylene, acetylide, and vinylidene. Vibrational data for $HOs_3(\mu\text{-}O_2CH)(CO)_{10}$ are similar to bands observed for formate adsorbed on to a silver surface.

In light of the utility of spectroscopic comparisons between surface adsorbed species and cluster models, it is surprising that so few of the more unique cluster-bound hydrocarbyl ligands have been spectroscopically characterized. Given the exceptional stabilities of structures such as μ_3-η^3-RCCR′CR″ in cluster systems, it is to be expected that such fragments are also to be found on metal surfaces.

9 RELATED ARTICLES

Bonding Energetics of Organometallic Compounds; Carbonyl Complexes of the Transition Metals; Cluster Compounds: Inorganometallic Compounds Containing Transition Metal & Main Group Elements; Dinuclear Organometallic Cluster Complexes; Electronic Structure of Clusters; Hydride Complexes of the Transition Metals; Mechanisms of Reaction of Organometallic Complexes; Stereochemical Nonrigidity of Organometallic Complexes.

10 REFERENCES

1. P. Braunstein, L. A. Oro, and P. R. Raithby eds, 'Metal Clusters in Chemistry', Wiley-VCH Verlag GmbH, Wienheim, 1999, Vol. 2.
2. O. Rossell, M. Seco, and G. Segales, in 'Metal Clusters in Chemistry', eds. P. Braunstein, L. A. Oro, and P. R. Raithby, Wiley-VCH Verlag GmbH, Wienheim, 1999, Vol. 2, p. 1053.
3. D. M. P. Mingos and A. S. May, in 'The Chemistry of Metal Cluster Complexes', eds. D. F. Shriver, H. D. Kaesz, and R. D. Adams, VCH, New York, 1990, p. 11.
4. B. F. G. Johnson and A. Rodgers, in 'The Chemistry of Metal Cluster Complexes', eds. D. F. Shriver, H. D. Kaesz, and R. D. Adams, VCH, New York, 1990, Chap. 6, p. 303.
5. R. B. King, *Inorg. Chim. Acta*, 1995, **235**, 111.
6. A. Sironi, The Ligand Stereochemistry of Transition Metal Carbonyl Clusters, in 'Metal Clusters in Chemistry', eds. P. Braunstein, L. A. Oro, and P. R. Raithby, Wiley-VCH Verlag GmbH, Wienheim, 1999, Vol. 2, p. 937.
7. G. Longoni, C. Femoni, C. Iapalucci, and P. Zanello, Electron-sink Features of Homoleptic Transition-metal Clusters, in 'Metal Clusters in Chemistry', eds. P. Braunstein, L. A. Oro, and P. R. Raithby, Wiley-VCH Verlag GmbH, Wienheim, 1999, Vol. 2, p. 1137.
8. W. E. Geiger, M. J. Shaw, M. Wunsch, C. E. Barnes, and F. H. Foersterling, *J. Am. Chem. Soc.*, 1997, **119**, 2804, and references therein.
9. A. K. Smith, in 'Comprehensive Organometallic Chemistry II', eds.-in-chief E. W. Abel, F. G. A. Stone, G. Wilkinson, D. F. Shriver, and M. I. Bruce, Pergamon Press, Oxford, 1995, Vol. 7, Chap. 13, p. 747.
10. E. Sappa, in 'Comprehensive Organometallic Chemistry II', eds.-in-chief E. W. Abel, F. G. A. Stone, G. Wilkinson, D. F. Shriver, and M. I. Bruce, Pergamon Press, Oxford, 1995, Vol. 7, Chap. 14, p. 803.
11. S. R. Drake, *Polyhedron*, 1990, **9**, 455.
12. D. Astruc, 'Electron Transfer and Radical Processes in Transition-metal Chemistry', Wiley-VCH, New York, 1995.
13. G. Lavigne, in 'The Chemistry of Metal Cluster Complexes', eds. D. F. Shriver, H. D. Kaesz, and R. D. Adams, VCH, New York, 1990, Chap. 5, p. 201.
14. D. Roberto, E. Lucenti, C. Roveda, and R. Ugo, *Organometallics*, 1997, **16**, 5974.
15. G. Henkel and S. Weissgraber, in 'Metal Clusters in Chemistry', eds. P. Braunstein, L. A. Oro, and P. R. Raithby, Wiley-VCH Verlag GmbH, Wienheim, 1999, Vol. 1, p. 63.
16. R. D. Adams, in 'The Chemistry of Metal Cluster Complexes', eds. D. F. Shriver, H. D. Kaesz, and R. D. Adams, VCH, New York, 1990, Chap. 3, p. 121.
17. R. D. Adams, in 'Comprehensive Organometallic Chemistry II', eds.-in-chief E. W. Abel, F. G. A. Stone, G. Wilkinson, and R. D. Adams, Pergamon Press, Oxford, 1995, Vol. 10, Chap. 1, p. 1.
18. R. J. Hall, P. Serguievski, and J. B. Keister, *Organometallics*, 2000, **19**, 4499, and references therein.
19. K. Matsubara, A. Inagaki, M. Tanaka, and H. Suzuki, *J. Am. Chem. Soc.*, 1999, **121**, 7421.
20. A. J. Deeming and D. M. Speel, *Organometallics*, 1997, **16**, 289.
21. D. J. Darensbourg, in 'The Chemistry of Metal Cluster Complexes', eds. D. F. Shriver, H. D. Kaesz, and R. D. Adams, VCH, New York, 1990, Chap. 4, p. 171.
22. L. Chen and A. J. Poe, *Coord. Chem. Rev.*, 1995, **143**, 265.
23. P. Macchi, D. M. Proserpio, and A. Sironi, *Organometallics*, 1997, **16**, 2101.
24. F. J. Safarowic, D. J. Bierdeman, and J. B. Keister, *J. Am. Chem. Soc.*, 1996, **118**, 11805, and references therein.
25. R. Gobetto, L. Milano, F. Reineri, L. Salassa, A. Vale, and E. Rosenberg, *Organometallics*, 2002, **21**, 1919, and references therein.
26. J. A. Cabeza, I. Del Rio, V. Riera, S. Garcia-Grande, and S. B. Sanni, *Organometallics*, 1997, **16**, 1743.
27. K. R. Hash and E. Rosenberg, *Organometallics*, 1997, **16**, 3593, and references therein.
28. A. K. Hughes and K. Wade, *Coord. Chem. Rev.*, 2000, **197**, 191.
29. L. J. Farrugia and A. G. Orpen, Structure and Dynamics in Metal Carbonyl Clusters: NMR, EXAFS and Crystallographic Studies, in 'Metal Clusters in Chemistry', eds. P. Braunstein, L. A. Oro, and P. R. Raithby, Wiley-VCH Verlag GmbH, Wienheim, 1999, Vol. 2, p. 1001.
30. D. H. Hamilton and J. R. Shapley, *Organometallics*, 1998, **17**, 3087, and references therein.
31. M. A. Gallop, B. F. G. Johnson, J. Keeler, J. Lewis, S. J. Heyes, and C. M. Dobson, *J. Am. Chem. Soc.*, 1992, **114**, 2510.
32. P. Braunstein and N. M. Boag, *Angew. Chem., Int. Ed. Engl.*, 2001, **40**, 2427.
33. R. D. Adams, B. Captain, W. Fu, P. J. Pellechia, and M. D. Smith, *Ang. Chem., Int. Ed. Engl.*, 2002, **41**, 1951.
34. P. J. Dyson, Reversible Skeletal Rearrangements in Transition Metal Clusters, in 'Metal Clusters in Chemistry', eds. P. Braunstein, L. A. Oro, and P. R. Raithby, Wiley-VCH Verlag GmbH, Wienheim, 1999, Vol. 2, p. 1028.

35. S. P. Gubin, *Pure Appl. Chem.*, 1986, **58**, 567.
36. M. Akita, in ‘Comprehensive Organometallic Chemistry II’, eds.-in-chief E. W. Abel, F. G. A. Stone, G. Wilkinson, D. F. Shriver, and M. I. Bruce, Pergamon Press, Oxford, 1995, Vol. 7, Chap. 4, p. 259.
37. D. Seyferth, *Adv. Organomet. Chem.*, 1976, **14**, 97.
38. D. J. Bierdeman, J. B. Keister, and D. Jelski, *J. Organomet. Chem.*, 2001, **633**, 51, and references therein.
39. R. D. Adams, *Chem. Rev.*, 1989, **89**, 1703.
40. F. J. Safarowic and J. B. Keister, *Organometallics*, 1996, **15**, 3310, and references therein.
41. D. H. Hamilton and J. R. Shapley, *Organometallics*, 2000, **19**, 761, and references therein.
42. E. Sappa, A. Tiripicchio, and P. Braunstein, *Chem. Rev.*, 1983, **83**, 203.
43. C. E. Barnes, in ‘Comprehensive Organometallic Chemistry II’, eds.-in-chief E. W. Abel, F. G. A. Stone, G. Wilkinson, and J. Atwood, Pergamon Press, Oxford, 1995, Vol. 8, Chap. 4, p. 419.
44. T. Takao, T. Takemori, M. Moriya, and H. Suzuki, *Organometallics*, 2002, **21**, 5190.
45. M. C. Comstock and J. R. Shapley, *Coord. Chem. Rev.*, 1995, **143**, 501.
46. Y. Chi and D. Hwang, in ‘Comprehensive Organometallic Chemistry II’, eds.-in-chief E. W. Abel, F. G. A. Stone, G. Wilkinson, and R. D. Adams, Pergamon Press, Oxford, 1995, Vol. 10, Chap. 3, p. 85.
47. T. Takao, A. Inagaki, E. Murotani, T. Imamura, and H. Suzuki, *Organometallics*, 2003, **22**, 1361.
48. D. Braga, P. J. Dyson, F. Grepioni, and B. F. G. Johnson, *Chem. Rev.*, 1994, **94**, 1585.
49. H. Suzuki, *Eur. J. Inorg. Chem.*, 2002, 1009.
50. K. Lee, H. Song, and J. T. Park, *Acc. Chem. Res.*, 2003, **36**, 78.
51. B. C. Gates, *J. Mol. Catal. A: Chem.*, 2000, **163**, 55.
52. R. D. Adams and F. A. Cotton eds, ‘Catalysis by Di-and Polynuclear Metal Cluster Complexes’, Wiley-VCH, New York, 1998.
53. P. Braunstein and J. Rose, in ‘Comprehensive Organometallic Chemistry II’, eds.-in-chief E. W. Abel, F. G. A. Stone, G. Wilkinson, and R. D. Adams, Pergamon Press, Oxford, 1995, Vol. 10, Chap. 7, p. 351.
54. E. L. Muetterties, T. N. Rhodin, E. Band, C. F. Brucker, and W. R. Pretzer, *Chem. Rev.*, 1979, **79**, 91.
55. M. Moskovits, *J. Mol. Catal.*, 1993, **83**, 195.
56. A. J. Deeming, in ‘Comprehensive Organometallic Chemistry II’, eds.in-chief E. W. Abel, F. G. A. Stone, G. Wilkinson, D. F. Shriver, and M. I. Bruce, Pergamon Press, Oxford, 1995, Vol. 7, Chap. 12, p. 683.

Polyoxometalates

Michael T. Pope
Georgetown University, Washington, DC, USA

1 Introduction 1
2 Aqueous Oxoanion Hydrolysis: Isopolyanions 2
3 Heteropolyanion Structures 4
4 Lacunary Species and Their Derivatives 5
5 Redox Behavior 6
6 Polyoxoanion Derivatives and Functionalization 7
7 Giant Polyoxoanion Assemblies 8
8 Applications 10
9 Related Articles 10
10 References 10

Glossary

Addendum: predominant positive-valent element in a polyoxoanion
Heteroatom: nonaddendum positive-valent element in a heteropolyanion
Heteropolyanion: polyoxoanion with at least one kind of positive-valent element (other than hydrogen) in addition to the addenda
Heteropoly blue, heteropoly brown: mixed-valence polyoxoanion formed by partial reduction of the addenda
Isopolyanion: polyoxoanion with one kind of positive-valent element
Lacunary polyoxoanion: polyoxoanion with a surface cavity formed by removal of one or more addenda

1 INTRODUCTION

The elements, M, of groups 5 and 6 form an astonishing variety of polyoxoanions, $[(X)_xM_mO_y]^{n-}$ $(m > x)$, where X (if present) can be one or a mixture of atoms from almost all other regions of the periodic table.[1–6] By far the most, polyoxoanions are formed by Mo, W, and V, usually in their highest (d^0) oxidation states. To date, only limited numbers of polyoxoanions of Nb, Ta, and Cr are known.

The first examples of polyoxoanions are considered to have been described by Berzelius in 1826 (yellow ammonium 12-molybdophosphate and -arsenate, and their reduced 'blue' derivatives), but it was not until the last third of the nineteenth century that detailed descriptive chemistry of many polymolybdates and polytungstates began to be reported. Although lacking any structural perspective, much of the early work published between 1865 and 1930, and reviewed in the 8th edition of Gmelin,[7] has been validated by subsequent investigations.

In 1933, Keggin's determination of the structure of the tungstophosphate anion in $H_3[PW_{12}O_{40}]\cdot 6H_2O$ opened the era of structurally characterized polyoxoanions. The 'Keggin Structure' confirmed the general principles that had been earlier suggested by Pauling, although the actual structural details were different. Subsequent structural investigations of polyoxoanions appeared relatively slowly for the next 25 years (only 12 structural types were listed in a 1971 review),[8] but that situation has now completely changed with the virtually routine use of X-ray diffraction and multinuclear NMR spectroscopy for solids and solutions.

Conversion of mononuclear oxoanions into polyoxoanions requires the consumption of acid. Simple examples involving Brønsted acids (*see Acids & Acidity*) in aqueous solutions are given in equations (1–3), although alternative routes to polyoxoanions have been developed, for example, through the use of acidic oxides in aqueous and nonaqueous solvents, or by hydrothermal methods.

$$CrO_4^{2-} + 2H^+ \longrightarrow [Cr_2O_7]^{2-} + H_2O \qquad (1)$$

$$7MoO_4^{2-} + 8H^+ \longrightarrow [Mo_7O_{24}]^{6-} + 4H_2O \qquad (2)$$

$$SiO_3^{2-} + 12WO_4^{2-} + 22H^+ \longrightarrow [SiW_{12}O_{40}]^{4-} + 11H_2O \qquad (3)$$

In principle, all polyoxoanions should be, and most are, subject to decomposition by alkali, although occasionally the pH required for degradation may not be achieved in aqueous media. For example, $[Nb_6O_{19}]^{8-}$ and $[Ta_6O_{19}]^{8-}$ are the simplest oxoanions of Nb and Ta to be formed in water.

The polymerization of simple tetrahedral oxoanions involves (1) the corner linkage of tetrahedra, as with the chromates and some vanadates, and (2), much more commonly, especially with Mo and W, an expansion of coordination number to six, and the edge- and corner linkage of MO_6 octahedra. The ability of Mo^{VI}, W^{VI}, and V^V to display variable (four-, five-, six-, and occasionally seven-fold) coordination by an oxide ion is responsible in part for the large numbers of polyoxoanions formed by these elements. In contrast, hexavalent chromium is effectively limited to four coordination, and Nb^V and Ta^V to six coordination by the oxide ion.

The polyhedral (MO_n) building blocks of virtually all polyoxoanions are linked in such a way as to result in each polyhedron having either one or two (mutually *cis*) unshared vertices. The metal atoms are displaced from the centers of their coordination polyhedra toward these unshared vertices. These displacements correspond to the formation of short metal–oxygen terminal bonds resulting from oxygen p_π donation into the metal's vacant d-orbitals. Such terminal oxygens, which are very weakly basic, form part of the external surfaces of the polyoxoanions and effectively prevent further polymerization. Very rarely (about three examples

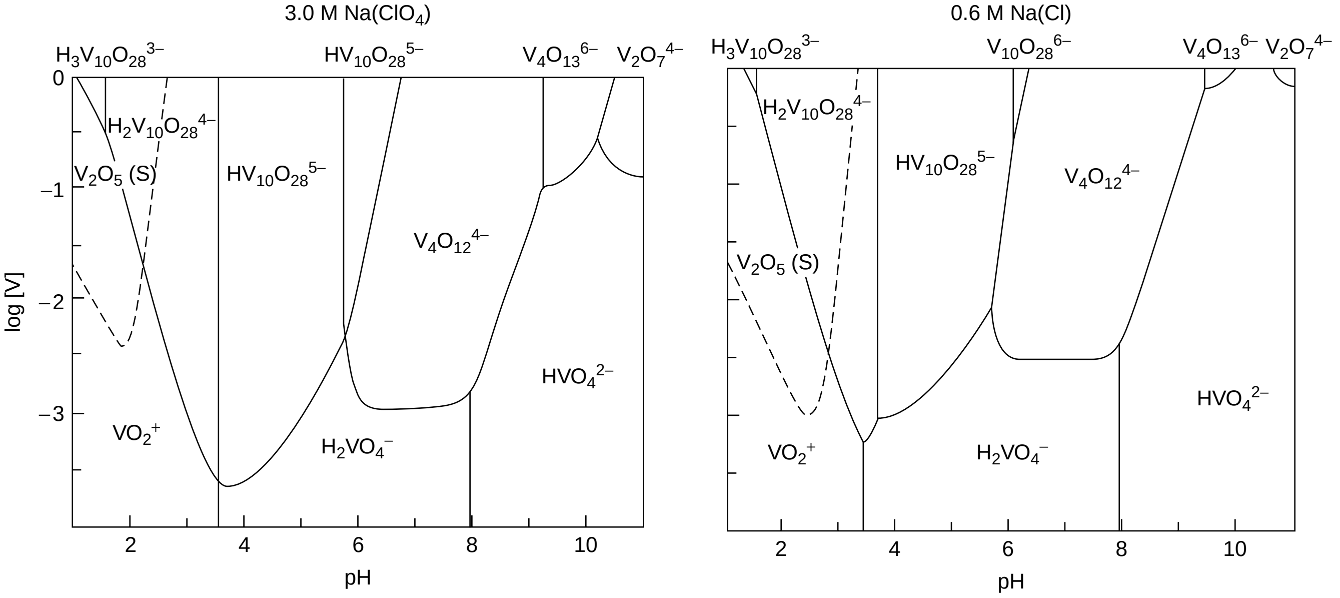

Figure 1 Predominance diagrams for aqueous polyvanadate species. (With kind permissions of Kluwer Academic Publishers)

are currently known), a polyanion may contain an MO_6 octahedron with three (*fac*) unshared vertices. As observed for mononuclear *fac*-trioxo complexes of Mo and W, the oxo oxygens are more basic and nucleophilic than those of the monooxo and *cis*-dioxo species, and polyoxoanions that contain such a structural feature tend to become protonated or undergo further condensation.

2 AQUEOUS OXOANION HYDROLYSIS: ISOPOLYANIONS

The conversion of mononuclear tetrahedral oxoanions to polyoxoanions (equation 4)

$$q\mathrm{MO_4}^{n-} + p\mathrm{H}^{+} \longrightarrow [\mathrm{M}_q\mathrm{O}_y]^{m-} + \frac{p}{2}\mathrm{H_2O} \qquad (4)$$

is governed by equilibria that are strongly dependent upon ionic strength, the nature of the countercation, temperature, and so on. Furthermore, equilibria involving some vanadates and tungstates are complicated by slow kinetics. With these caveats, we can make the following generalizations.

2.1 Isopolyanions of Group 5 Elements

Of the group 5 elements, only V^V forms a significant range of polyoxoanions. Speciation in aqueous solutions has been investigated by a combination of precise EMF measurements and ^{17}O and ^{51}V NMR spectroscopy; see Figure 1. In the ‘alkaline’ region (pH ca. 6 and above) are species based on tetrahedral coordination of V: $[V_2O_7]^{4-}$, traces of $[V_3O_{10}]^{5-}$, *cyclo*-$[V_4O_{12}]^{4-}$, and *cyclo*-$[V_5O_{15}]^{5-}$, and protonated forms of these anions. Interconversion between these species is rapid, but some kinetic data have been acquired via NMR. In the ‘acidic’ region (pH ca. 4–6), the orange decavanadates, $[H_xV_{10}O_{28}]^{(6-x)-}$ (Figure 2), with six-coordinate V, predominate. Other reported polyvanadates(V) are species that are either generated in, and isolated from, a nonaqueous solution, for example, $[V_5O_{14}]^{3-}$, the bowl-shaped $[V_{12}O_{32}]^{4-}$ (Figure 3), and $[V_{13}O_{34}]^{3-}$, or are kinetically metastable aqueous species, for example, $[H_{12}V_{13}O_{40}]^{3-}$ and $[V_{15}O_{42}]^{9-}$.

The aqueous chemistry of oxoniobates and tantalates is limited to the hexametalate anions, $[M_6O_{19}]^{8-}$ (Figure 4), although a niobium analog of decavanadate has been prepared by hydrolysis of $Nb(OEt)_5$.

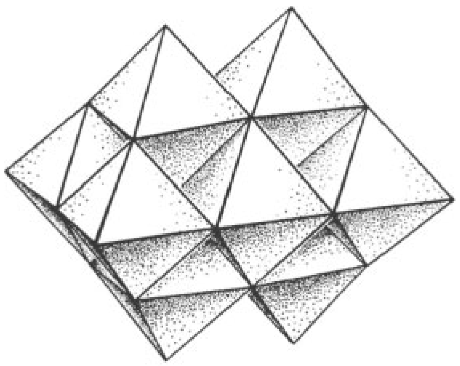

Figure 2 The D_{2h} structure of $[V_{10}O_{28}]^{6-}$ as an arrangement of VO_6 octahedra

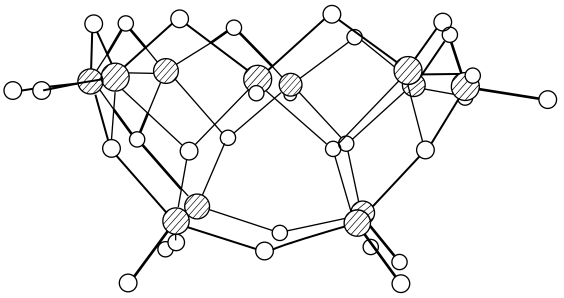

Figure 3 $[V_{12}O_{32}]^{4-}$

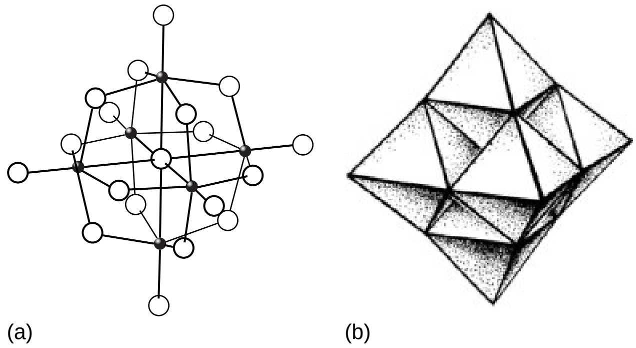

Figure 4 Bond and polyhedral representations of $[M_6O_{19}]^{n-}$ ($M = Nb^V$, Ta^V, Mo^{VI}, W^{VI})

2.2 Isopolyanions of Group 6 Elements

In group 6, Cr^{VI} polyoxoanions are based entirely on CrO_4 tetrahedra and are limited effectively to $[Cr_2O_7]^{2-}$ and $[Cr_3O_{10}]^{2-}$. Molybdenum(VI) and tungsten(VI), on the other hand, form many isopolyanions, most of which incorporate six-coordinate metal centers: $[Mo_2O_7]^{2-}$ exists only in the absence of alkali metal counter ions (*see Counter Ions*), and must be generated in nonaqueous solvents. In aqueous solution, the first stable polyanions formed (pH ca. 5) are the heptametalates, so-called 'paramolybdate' and 'paratungstate-A', $[M_7O_{24}]^{6-}$ (Figure 5). Subsequent hydrolysis differs for Mo and W: (β-)$[Mo_8O_{26}]^{4-}$ has been identified in solutions of relatively low $[Na^+]$ (see Figure 6) and an Mo_{36} species (see below) is isolated from more acidic solutions, whereas tungstates ultimately are converted to the Keggin structure 'metatungstate', (α-)$[(H_2)W_{12}O_{40}]^{6-}$ (Figure 7), although several other kinetically metastable species are known, for example, 'paratungtate-B', $[H_2W_{12}O_{42}]^{10-}$, and 'tungstate-X', (β-)$[(H_2)W_{12}O_{40}]^{6-}$. In nonaqueous solvents, other structures can be synthesized; these include $[Mo_5O_{17}H]^{3-}$, α-$[Mo_8O_{26}]^{4-}$, $[W_{10}O_{32}]^{4-}$ (Figure 8), and hexametalate species (Figure 4).

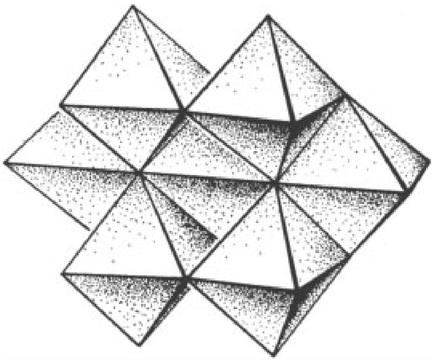

Figure 5 C_{2v} structure of $[M_7O_{24}]^{6-}$ (M = Mo, W)

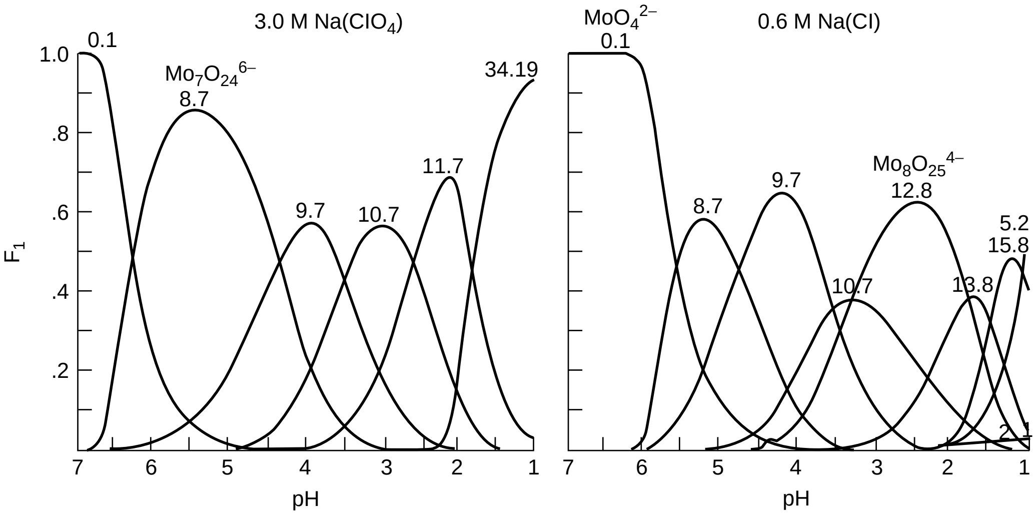

Figure 6 Distribution diagrams of polymolybdate species in two different ionic media. The curves are labeled with *p*,*q* values as defined in equation (4) (With kind permissions of Kluwer Academic Publishers)

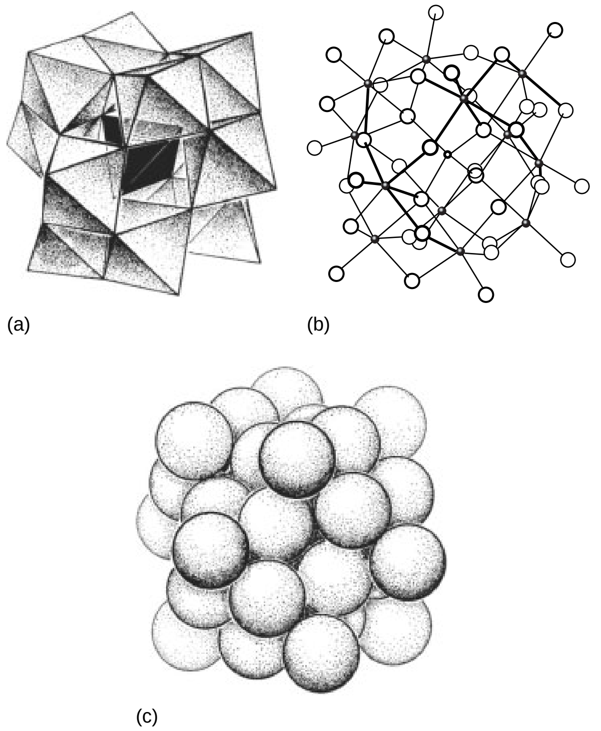

Figure 7 Polyhedral, bond, and space-filling representations of the Keggin structure, α-$[\{XO_4\}M_{12}O_{36}]^{n-}$. For the metatungstate anion X = 2H

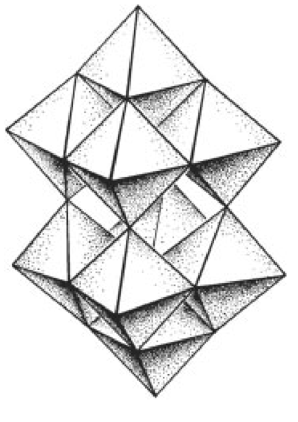

Figure 8 $[W_{10}O_{32}]^{4-}$

3 HETEROPOLYANION STRUCTURES

3.1 ‘Tetrahedral’ Heteroatoms: the Keggin- and Related Structures

The stereochemical requirements of the heteroatoms generally determine the architecture of the heteropolyanions formed. This is illustrated by the Keggin structure (Figure 7) (and its numerous derivatives), which encloses a central tetrahedral unit ranging from $\{SO_4\}^{2-}$ to ‘$\{Cu^IO_4\}^{7-}$’ (see Table 1).

Table 1 Heteroatoms, X, in Keggin heteropolyanions α-$[\{XO_4\}M_{12}O_{36}]^{n-}$

M = Mo	M = W	Net anion charge
S^{VI}		2−
P^V, As^V, Sb^V, V^V	P^V, As^V, V^V	3−
Si^{IV}, Ge^{IV}	C, Si^{IV}, Ge^{IV}, (?Mn^{IV})	4−
Ga	B, Al, Ga, Cr^{III}, Fe^{III}, Co^{III}	5−
	2H, Be, Zn, Co^{II}, Cu^{II}	6−
	H, Cu^I	7−

Structural isomers of the Keggin anion are possible, and have been confirmed in some cases. The best-known are those of C_{3v} symmetry, in which of one of the four equivalent groups of three edge-shared MO_6 octahedra of the parent anion have been rotated by $\pi/3$ radians. This structure is designated β, following α for the original Keggin anion, and has kinetic stability only. According to density functional calculations, the relative stabilities of the two isomers depends upon the oxidation state of the central heteroatom.**9** In one case, $[(AlO_4)W_{12}O_{36}]^{5-}$, an equilibrium is established between the two isomers.**10** ‘Rotation’ of two, three, and all four edge-shared groups yield γ,δ, and ε structures respectively. Whereas β isomers of $[(SiO_4)W_{12}O_{36}]^{4-}$ and the corresponding germanate are well established, and an unstable γ isomer of the silicate has been confirmed, no δ or ε isomers are known (but the ε configuration is recognizable as a part of other polyvanadate ($[H_3Mn^{IV}{}_3V_{12}O_{40}]^{5-}$) and polymolybdenum ($[(Cp^*Rh^{III})_8(Mo^V{}_{12}O_{36})(MoO_4)]^{2+}$, $[H_{14}Mo^V{}_{12}Mo^{VI}{}_4O_{52}]^{6-}$) structures, and is observed for the polycation in $[Al_{13}O_{40}H_{36}]^{5+}$). In so-called β-isomers several Keggin molybdates have been identified in solution, and although it is reasonable to presume that they have structures analogous to the β-tungstates, no unambiguous structural data are available for the fully oxidized species (but see below for a heteropoly blue structure). Possibilities for isomerism (*see Isomer*, *Types of*) increase enormously when ‘mixed-addenda’ polyoxoanions are considered, for example, $[\{PO_4\}V_2W_{10}O_{36}]^{5-}$. This example has five ‘positional’ isomers if the whole anion has an α configuration, and 13 isomers if the anion is β. That such isomers exist has been well established by NMR spectroscopy. In some cases, unique mixed-addenda anions may be synthesized and characterized; in others, mixtures of isomers are observed. Isomerization reactions generally are quite slow, but no successful method of separation of positional isomers has yet been developed.

The heteropolyanions $[\{XO_4\}_2M_{18}O_{54}]^{n-}$ (M = Mo, W; X = P, As, S) have a structure (of the so-called ‘Dawson’ type) formed by fusion of two Keggin fragments generated by the loss of three adjacent corner-shared MO_6 octahedra (see

Figure 9). The Dawson anions are formed spontaneously in molybdophosphate and -arsenate solutions of the appropriate stoichiometry and acidity, but the tungstates are formed slowly in solutions with a large excess of phosphate or arsenate. Several structural isomers (α, β, etc.) are known, especially for the tungstates. These involve 'rotation' of the edge-shared triad groups at the ends of the anion, and/or rotation of the two half-units. Further (positional) isomerism has been demonstrated for mixed-addenda species such as α-$[\{PO_4\}_2W_{12}Mo_6O_{54}]^{6-}$.

The Keggin and Dawson structures incorporate internal XO_4 tetrahedra that are attached to the oxometalate shell through each oxygen atom (μ_4 type), but structures are also known in which a tetrahedral coordination polyhedron occupies an exterior site (i.e. μ_3, one vertex is unshared). Examples are $[\{PO_4\}_2Mo_5O_{15}]^{6-}$ (Figure 10) and $[\{MoO_4\}_2Mo_6O_{18}]^{4-}$. Analogous structures are observed for polyanions in which the heteroatoms are trivalent P, As, Sb, tetravalent S, Se, and organo derivatives, $RXO_3{}^{n-}$. In the structures of $[P_6W_{18}O_{79}]^{20-}$ and $[P_5W_{18}O_{78}H_3]^{20-}$, both μ_3 and μ_4 phosphate tetrahedra are observed.

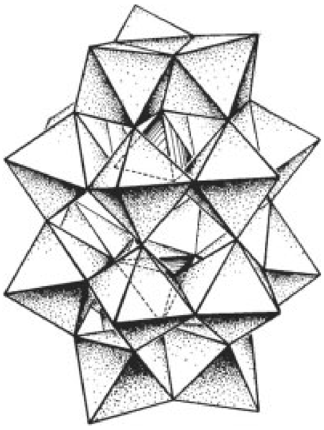

Figure 9 $[\{XO_4\}_2M_{18}O_{54}]^{n-}$, the D_{3h} 'Dawson' structure

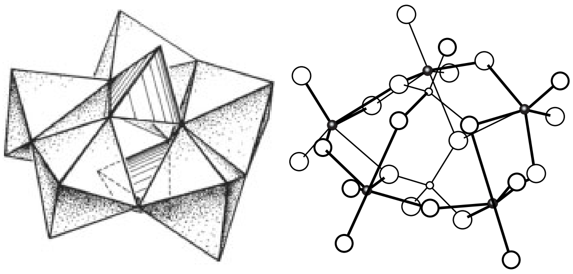

Figure 10 Polyhedral and bond representations of $[\{PO_4\}_2Mo_5O_{15}]^{6-}$

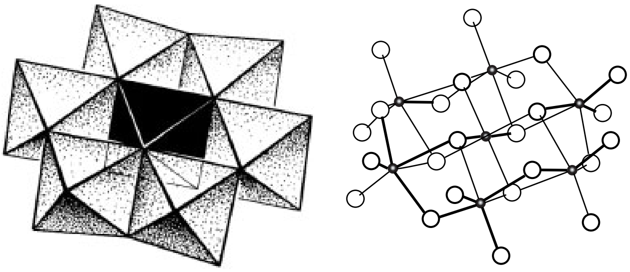

Figure 11 Polyhedral and bond representations of the 'Anderson' structure, $[\{XO_6\}M_6O_{18}]^{n-}$

3.2 Six-, Eight-, and Twelve-coordinate Heteroatoms

Several heteropolyanion structures accommodate central octahedral heteroatoms: an especially widespread type is the D_{3d} 'Anderson' structure (Figure 11 and Table 2). Note that two versions of the structure are known: with or without protonation of the central XO_6 octahedron, depending upon the oxidation state of X. Although the heptametalate anions, $[M_7O_{24}]^{6-}$ (Figure 5), can be considered to be C_{2v} isomers of the Anderson anions, few heteropolyanions have so far been shown to adopt the former structure.

Higher heteroatom coordination numbers are seen for the derivatives of lanthanide and actinide cations, which adopt the structures of $[\{CeO_8\}W_{10}O_{28}]^{8-}$ (square antiprism, *see Square Antiprism*) and $[\{UO_{12}\}Mo_{12}O_{30}]^{8-}$ (icosahedron, *see Icosahedron*), illustrated in Figures 12 and 13.

4 LACUNARY SPECIES AND THEIR DERIVATIVES

Although all polyoxoanions are ultimately decomposed to monomeric species in basic solution, control of pH leads in

Table 2 Anderson heteropolyanions: $[\{X(OH)_6\}M_6O_{18}]^{n-}$ or $[\{YO_6\}M_6O_{18}]^{n-}$

Heteroatom type	M = Mo	M = W	Net anion charge
X	Al, Ga, Cr^{III}, Fe^{III}, Co^{III}, Rh^{III}	–	3−
X	Mn^{II}, Co^{II}, Ni^{II}, Cu^{II}, Zn	Ni^{II}	4−
Y	I^{VII}	I^{VII}	5−
Y	Te^{VI}	Te^{VI}	6−
Y	Sb^{V}	Sb^{V}	7−
Y	Pt^{IV}	Mn^{IV}, Ni^{IV}, Pt^{IV}	8−

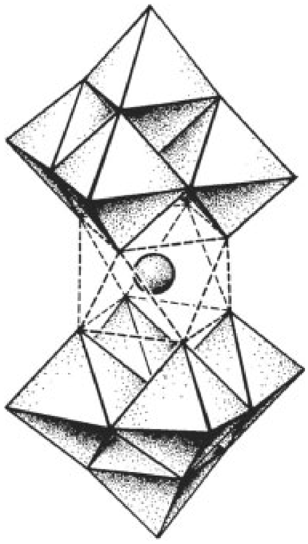

Figure 12 $[\{CeO_8\}W_{10}O_{28}]^{8-}$

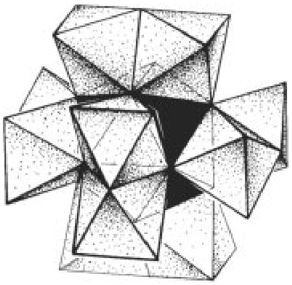

Figure 13 $[\{UO_{12}\}Mo_{12}O_{30}]^{4-}$

many cases to the formation, isolation, and characterization of ‘defect’ or ‘lacunary’ structures. These are best illustrated with the Keggin anion (Figure 7), which can form species $[XM_{11}O_{39}]^{n-}$ and $[XM_9O_{34}]^{n-}$ by the ‘removal’ of one or three (adjacent) MO_6 octahedra respectively. An intermediate structure in which two adjacent octahedra have been removed has not been observed; it would contain an MO_6 octahedron with three fac terminal oxygen atoms and is therefore expected to be quite reactive. Two kinds of XM_9 anions can be formed, both with C_{3v} symmetry: A-type, in which three corner-shared octahedra have been lost, and B-type, in which three edge-shared octahedra have been lost. Neither of these structures appears to be thermodynamically stable in solution, although both have been isolated as solid salts, and have been used to synthesize derivatives. In addition, both A- and B-type XM_9 structural units are recognizable in larger polyoxoanions. Examples are: $[P_2M_{18}O_{62}]^{6-}$, the D_{3h} Dawson structure formed by fusion of two A-PM_9 units; $[As^{III}_2W_{21}O_{69}(aq)]^{6-}$ and $[P^{V}_2W_{21}O_{71}(aq)]^{6-}$, two B- and A-type XW_9 respectively, separated by a ‘belt’ of three WO_6 octahedra; $[Co_4(H_2O)_2(PW_9O_{34})_2]^{10-}$ with two B-type PW_9; and $[(NH_4)As^{III}_4W_{40}O_{140}]^{27-}$, containing four B-type AsW_9 units. Many of these larger structures can be further converted to lacunary species, for example, X_2M_{18} (X = P, As) (‘Dawson structure’) yields X_2M_{17}, X_2M_{15}, and X_2W_{12} anions.

Derivatives of lacunary polyoxometalate structures are legion. Most investigations have been made with ‘monovacant’ XM_{11} species, which function as tetra- or pentadentate ligands. Typically, metal cations are bound into the cavity generated by the loss of MO^{4+} from the Keggin structure, with formation constants of 10^2–10^5 (for divalent first-row transition metal cations). The resulting complexes may contain an exchangeable ligand attached to the incorporated cation; examples are $[BW_{11}O_{39}Co(NO_2)]^{7-}$ and $[PW_{11}O_{39}Ru(\eta^2\text{-}MeCHCHCO_2H)]^{5-}$. In other cases, especially for higher-valent cations, covalently attached atoms or groups may be present. Table 3 summarizes some of the possibilities for these types of complexes.

Lacunary anions with more than one surface ‘vacancy’ also may be derivatized by cation complexation. The results are not always predictable. Thus, XW_9 species may yield the expected ‘plenary’ Keggin structures, for example, $[PW_9V_3O_{40}]^{6-}$ and $[SiW_9O_{37}\{Cr(H_2O)\}_3]^{7-}$, but in other cases ‘sandwich’ structures based on either XW_9 arrangement are produced, for example, $[Co_4(H_2O)_2(PW_9O_{34})_2]^{10-}$ (B-type), $[(OCe)_3(H_2O)_2(PW_9O_{34})_2]^{12-}$ and $[(H_2OCo)_3(PW_9O_{34})_2]^{12-}$ (A-type).

5 REDOX BEHAVIOR

Since polyoxometalates contain fully oxidized (d^0) metal atoms, they are resistant to oxidation, and high-valent states

Table 3 Derivatives of monovacant lacunary polyoxoanions, {P} (= e.g. $[PW_{11}O_{39}]^{7-}$)

A. Stoichiometry $[\{P\}M(L)]^{n-}$
  1. M formally six coordinate:
    L exchangeable:
      M = di- and trivalent cations of Groups 3–13, alkali, alkaline-earth cations
      L = especially H_2O, OH^-, but also numerous other ligands
    L multiply bonded or otherwise nonexchangeable:
      L = O^{2-}; M = tetra-, penta-, hexa-, and heptavalent species, e.g. $VO^{2+,3+}$, MnO^{2+}, CrO^{3+}, RuO^{3+}, TcO^{3+}, MoO^{4+}, ReO^{5+}
    Other ML^{n+} combinations: SnR^{3+}, GeR^{3+}, OsN^{3+}, $RuNO^{3+}$, $MoNO^{3+}$, $Ti(Cp)^{3+}$
  2. M formally four coordinate, L absent or weakly bonded, e.g. Cu^{2+}, Pd^{2+}, Pt^{2+}, Sn^{II}
B. Stoichiometry $[M(\{P\})_2]^{n-}$
  M formally eight coordinate (square antiprism), e.g. lanthanide(3+,4+) and many actinide(4+) cations; alkaline-earth cations (?)

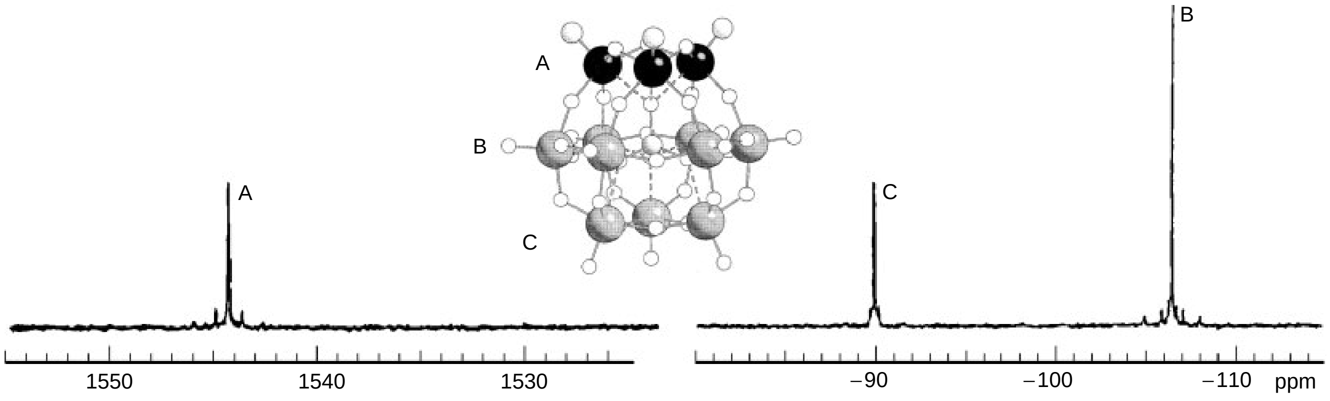

Figure 14 Tungsten-183 NMR spectrum of the heteropoly 'brown' α-$[\{SiO_4\}W^{VI}_9O_{33}(W^{IV}H_2O)_3]^{4-}$

of the heteroatoms can therefore be stabilized. Examples include tetravalent Ni, pentavalent Cr, Ru, and U, and hexa- and heptavalent Re. Such species have been used as electron transfer oxidants for organic substrates. By virtue of their structures, unusual coordination geometry–oxidation state combinations are observed, for example, tetrahedral high-spin Co^{III}, reversible $Cu^{I/II}$ couples, both in Keggin structure anions, and icosahedral f^1 species (Ce^{III}, U^V). The transition metal ion-substituted polyoxoanions (cf. Section 4) can be viewed as oxidation-resistant analogs of metalloporphyrins (*see Metalloporphyrin*) and indeed much of their reactivity, especially in nonaqueous solvents, is found to parallel that of the porphyrins, for example, as epoxidation catalysts, and the binding and activation of O_2, and so on.

Many polyoxoanions undergo facile and reversible reductions, which are conveniently studied by electrochemical methods, to yield mixed-valence heteropoly 'blues' and 'browns'.**[1]** The necessary feature for such behavior is the presence of (d^0) metal atoms with single (rather than two) terminal oxo oxygens, as found, for example, in the Keggin structure (Figure 7), but not in the Anderson structure (Figure 12). The strong axial ligand field generated by the monooxo arrangement produces a nonbonding orbital ('d_{xy}') on each metal atom. Heteropoly blues typically contain one to six Mo^V or W^V centers per anion as a result of partial occupation of these orbitals. Variable-temperature electron spin resonance (ESR) spectroscopy demonstrates for the paramagnetic one-electron reduced blues that the added electron undergoes a thermally activated 'hopping' between metal centers, that is, it is trapped on a single metal at sufficiently low temperature.**[11–13]** The blue colors of these species are the result of intensity-enhanced d–d transitions and intervalence charge transfer bands (*see Intervalence Transfer Transition*). Subsequently added 'blue' electrons couple with the first via multipath antiferromagnetic interactions (*see Antiferromagnetism*), and the delocalization of the blue electron pairs generate enhanced diamagnetism (*see Diamagnetism*) as a consequence of ring currents within the heteropolyanions.**[14]** The molybdate blues especially have long been used for colorimetric determination of trace levels of phosphate, silicate, and so on.

Heteropoly 'browns' are more highly reduced tungstates, generated by intraionic disproportionation of the blues under acidic conditions. Such species contain metal–metal bonded triangular clusters of three edge-shared $W^{IV}O_6$ octahedra (see Figure 14). The Keggin structure can therefore accommodate as many as 24 additional electrons in this fashion. Indeed, an additional eight electrons (32 in all!) can be accommodated in nonbonding molecular orbitals, two electrons per trimeric unit. Each W^{IV} bears a terminal exchangeable water ligand (thereby keeping the anion charge low), and the browns have been shown to participate in atom-transfer processes, for example, equation (5).

$$[(SiO_4)W_9O_{33}\{W^{IV}(H_2O)\}_3]^{4-} + 3Me_2SO \longrightarrow [(SiO_4)W_{12}O_{36}]^{4-} + 3Me_2S + 3H_2O \qquad (5)$$

6 POLYOXOANION DERIVATIVES AND FUNCTIONALIZATION[15]

Organic and organometallic derivatives of polyoxometalates have been synthesized by direct or indirect routes.

6.1 From Lacunary Anions

Lacunary structures such as $[PW_{11}O_{39}]^{7-}$ react straightforwardly with RMX_n ($M = Ge$, Sn, As, and so on, that is, atoms that can undergo an expansion of the coordination number from four to six) to yield $[PW_{11}O_{39}MR]^{m-}$ species. Examples of such products are $[PW_{11}O_{39}Ti(Cp)]^{4-}$, $[BW_{11}O_{39}GeC_2H_4CO_2H]^{6-}$, and $[P_2W_{15}O_{56}\{SnBu\}_3]^{9-}$. With organophosphorus and -silicon reagents, the products retain four-coordinate P and Si, for example, $[\{PhP(O)\}_2XW_{11}O_{39}]^{n-}$ and $[\{RP(O)\}_2PW_9O_{34}]^{5-}$.

An alternative route to the organostannate derivatives involves the reaction of preformed Sn^{II} polyanions, for example, $[SiW_{11}O_{39}Sn:]^{6-}$, as nucleophiles with alkyl or organometallic halides.

6.2 From ‘Complete’ Polyanions

Direct attachment of organometallic moieties to the surface oxygen atoms of ‘complete’ (plenary) polyoxoanion structures is often possible. Generally, the relative basicity of the surface oxygen atoms is increased by partial substitution of W^{VI} atoms by Nb^{V} or V^{V}. In most cases, the organometallic group is attached in a ν^3 mode employing oxygen atoms that bridge the groups of three edge-shared MO_6 octahedra of the hexametalate (Figure 5), Keggin (Figure 7), or Dawson (Figure 10) structures. Simple examples include *cis*- and *trans*-forms of $[Nb_6O_{19}\{Re(CO)_3\}_2]^{6-}$, $[1,5\text{-(cod)}IrP_2W_{15}O_{62}]^{8-}$ and $[(CpTi)SiW_9V_3O_{40}]^{4-}$, but more elaborate constructions, for example, $[\{(C_7H_8)Rh\}_5(Nb_2W_4O_{19})_2]^{3-}$, are possible. Polyoxoanions may also be derivatized at the Nb–O terminal oxygen, for example, $[Cp_3U(NbW_5O_{19})_2]^{5-}$.

6.3 Oxoalkoxo Anions

Alkoxide derivatives have mostly been prepared indirectly, although thermal treatment of $[Me_3O]_3[PMo_{12}O_{40}]$ has yielded a methyl derivative of the Keggin anion (methylation at oxygen atom bridging edge-shared MoO_6 octahedra). Through the use of polyalcohols such as pentaerythritol and $RC\{(CH_2)_2OH\}_3$, several examples of polyoxoalkoxoanions have been synthesized by solution or hydrothermal methods. Of particular note are vanadate(IV) species based on the hexametalate (Figure 4) and decavanadate (Figure 1) cores with alkoxy oxygens in surface bridging positions. Although not within the purview of this article, it should be recognized that the neutral oligomeric (*see Oligomer*) alkoxides of the early transition elements such as titanium(IV) have structures comparable, and in some instances identical ($[Ti_7O_4(OEt)_{20}]$ versus $[Mo_7O_{24}]^{6-}$, Figure 5), to those of polyoxometalates.

6.4 Functionalized Heteroatoms

Complexes in which the heteroatom bears an organic group form another class of heteropolyanion derivatives. Several analogues of the structure illustrated in Figure 10 with phosphonates, arsonates, and phosphate monoesters have been synthesized. Other examples include the zwitterionic species $[\{H_3NC_6H_4AsO_3\}_4Mo_{12}O_{34}]$, and acetal and arsinate derivatives, $[\{R_2XO_2\}Mo_4O_{12}(OH)]^{n-}$ ($X = C$, As). With some of these complexes, it has been possible to demonstrate rapid intramolecular rearrangements, pseudorotation, hydration, and group transfer.

7 GIANT POLYOXOANION ASSEMBLIES[16]

In the decade or so since the first edition of this encyclopedia, there has been a considerable growth in the synthesis and structural characterization of unusually large polyoxometalates. In most cases, these have stability in solution (NMR spectroscopy) as well as in the solid state, and can be considered as linked assemblies of polyoxoanion building blocks.

7.1 Vanadates

Most ‘large’ polyvanadates contain both V^{IV} and V^{V} centers and frequently enclose small anions as clathrate guests. Examples are $[H_4V_{18}^{IV}O_{42}\{X\}]^{9-}$ ($X = Cl$, Br, I) and $[V_{15}^{IV,V}O_{36}\{CO_3\}]^{7-}$. The largest reported polyvanadate cluster is $[V_{34}^{IV,V}O_{82}]^{10-}$, which encapsulates a $\{V_4O_8\}$ cubane template.

7.2 Niobates

Clusters of approximately D_3 symmetry containing 30 niobium centers have been reported. These consist of five $[Nb_6O_{19}]^{8-}$ anions attached in trigonal bipyramidal fashion to a central oxocluster containing two Al^{3+} and six Ln^{3+} ($Ln = Eu$, Er, Lu) cations.

7.3 Molybdates

The first examples of very large polyoxomolybdates to be structurally characterized were the Mo_{36} isopolyanion noted above (Section 2.2) and an Eu_4Mo_{29} anion. Both of these anions contain $[Mo_7O_{24}]$ groups, two in the case of Mo_{36} and four in Eu_4Mo_{29}. The latter anion probably only has an identity in the solid state. In Mo_{36}, two of the molybdenum(VI) centers in each heptamolybdate have become seven-coordinate (quasi pentagonal bipyramidal), and a structural building block $\{Mo_8\}$ consisting of the bipyramid sharing equatorial edges with five MoO_6 octahedra, and two additional corner-shared octahedra, Figure 15, can be defined.

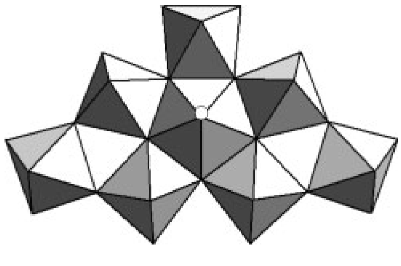

Figure 15 $\{Mo_8\}$ building block present in several large polyoxomolybdates. (Reprinted with permission from Ref. 16. © 1998 American Chemical Society)

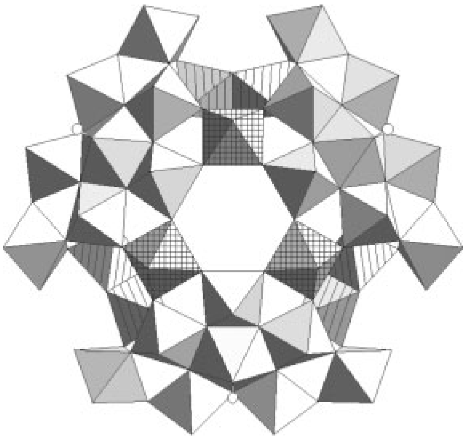

Figure 16 $[X_6\{Mo^V(\mu\text{-}H_2O)_2(\mu\text{-}OH)Mo^V\}_3\{Mo^{VI}{}_{15}(MoNO)_2\text{-}O_{58}(H_2O)_3\}]^{21-}$ ($X = V^{IV}O(H_2O)$; $Fe^{III}(H_2O)_2$). (Reprinted with permission from Ref. 16. © 1998 American Chemical Society)

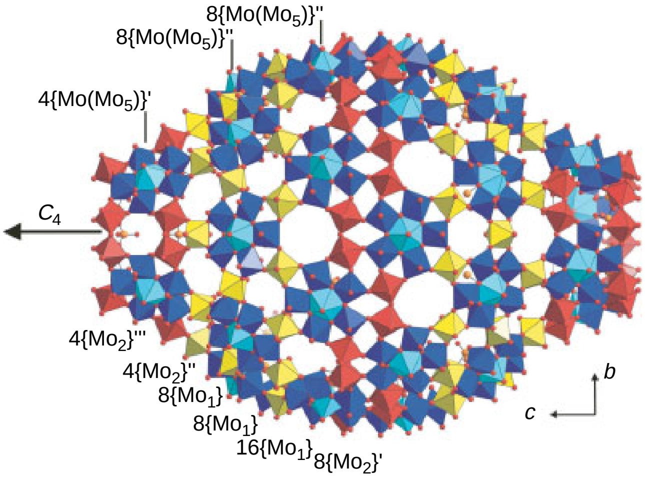

Figure 18 $[H_xMo_{368}O_{1032}(H_2O)_{240}(SO_4)_{48}]^{48-}$. (Reproduced by permission of Wiley-VCH)

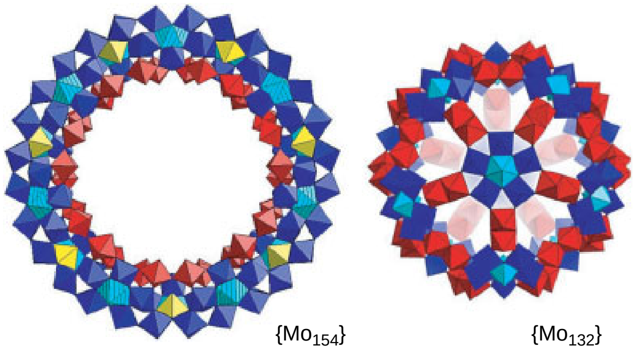

Figure 17 $[Mo_{154}O_{420}(NO)_{14}(OH)_{28}(H_2O)_{70}]^{28-}$ and $[\{Mo^V{}_2O_4\text{-}(CH_3COO)\}_{30}\{(Mo)Mo_5O_{21}(H_2O)_6\}_{12}]^{42-}$. (Reproduced by permission of Wiley-VCH)

The $\{Mo_8\}$ unit is observed in many of the spectacular polymolybdate clusters that have been reported by Müller during the last decade. These include the $\{Mo_{57}M_6\}$ anions (Figure 16), the 'giant wheels', $\{Mo_{154}\}$ (Figure 17) and $\{Mo_{176}\}$, the icosahedral 'ball' $\{Mo_{132}\}$ (Figure 17),[17] and the 'hedgehog' $\{Mo_{368}\}$ (Figure 18).[18]

7.4 Tungstates

Unlike the majority of the large polyoxomolybdates, which are mixed-valence $Mo^{V,VI}$ species, the tungstates are based on assemblies of lacunary W^{VI} units. Common building blocks are the B-type trivacant lacunary anions $[X^{III}W_9O_{33}]^{9-}$ ($X =$ As, Sb) and $[P_2W_{15}O_{56}]^{12-}$. The long-known As_4W_{40} anion contains four AsW_9 groups linked by WO_6 octahedra; more recent examples include $[As_6W_{65}O_{217}(H_2O)_7]^{26-}$ with six,[19] and $[Ln_{16}(H_2O)_{36}(WO_2)_4(W_2O_6)_8(AsW_9O_{33})_{12}(W_5O_{18})_4]^{76}$. (Figure 19) with twelve.[20] The latter anion includes lacunary W_5 groups derived from the hexatungstate anion (Figure 4), also seen in species like $[Eu_3(H_2O)_3(SbW_9O_{33})(W_5O_{18})_3]^{18-}$.

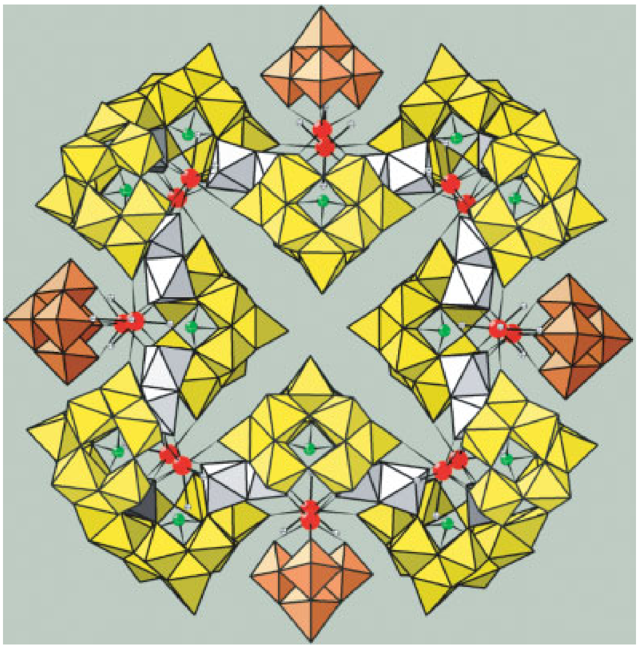

Figure 19 $[Ln_{16}(H_2O)_{36}(WO_2)_4(W_2O_6)_8(AsW_9O_{33})_{12}\text{-}(W_5O_{18})_4]^{76}$

Examples of complexes incorporating $[P_2W_{15}O_{56}]^{12-}$ are the 'tetrahedral' assemblies $[\{(TiOH)_{12}O_6\}\ (P_2W_{15}O_{56})_4]^{24-}$ and $[(UO_2)_{12}(\mu_3O)_4(\mu_2H_2O)_{12}(P_2W_{15}O_{56})_4]^{32-}$ (Figure 20).[21,22]

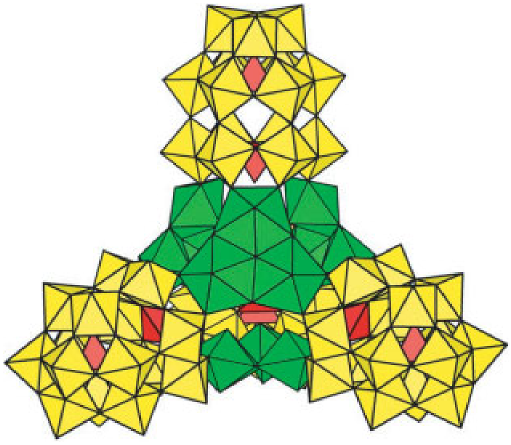

Figure 20 $[(UO_2)_{12}(\mu_3O)_4(\mu_2H_2O)_{12}(P_2W_{15}O_{56})_4]^{32}$

8 APPLICATIONS

The special properties of polyoxoanions (their large sizes, high molecular weights, solubilities in polar and nonpolar solvents, electron, and proton transfer and 'storage' capacities, high thermal stabilities, etc.) lead to numerous applications in several fields. These have been recently reviewed.[23] The earliest applications were in analytical chemistry, and it is probably true that the majority of publications involving polyoxometalates concern their analytical uses, especially for phosphate and silicate determinations via heteropoly blue formation. Another early application has been the use of tungstophosphoric acid, $H_3PW_{12}O_{40}$, as a general negative or positive stain for electron microscopy. With the development of covalently attached organic derivatives, this use is now expanded to highly selective species that target specific sites for imaging. Recently, polyoxometalates have proved to be successful phasing agents in the structural crystallography of large biomolecules such as the ribosome.[24]

Polyoxoanions have many desirable features that lead to their use as catalysts, both homogeneous and heterogeneous, and this use has expanded dramatically in recent years.[25–30] Molybdophosphates are used heterogeneously in the large-scale commercial oxidation of methacrolein to methacrylic acid, and in methane oxidation. Molybdovanadophosphates, mostly $[PMo_{10}V_2O_{40}]^{5-}$ and $[PMo_9V_3O_{40}]^{6-}$, have been developed as homogeneous reoxidants in Wacker chemistry (oxidation of alkenes, coupling of aromatics, *see Wacker Process*) and allow the process to be carried out at much lower chloride concentrations. Tungstophosphoric acids are used heterogeneously as Brønsted acid catalysts for the production of 2-propanol, 2-butanol, and *t*-butanol by alkene hydration. Numerous laboratory-scale catalytic systems have been developed. These include the use of transition metal derivatives of lacunary anions as 'metalloporphyrin analogs' for epoxidations and other oxidations; $[PMo_{10}V_2O_{40}]^{5-}/Br^-/O_2$ for brominations; polytungstates as photochemically activated oxidation catalysts.

Many polyoxometalate salts have been shown to be biologically active. Such activity includes a highly selective inhibition of enzyme function (phosphatases, dehydrogenases, isomerases), especially with the smaller vanadate and molybdate oligomers (V_4, Mo_4, Mo_5). In some cases, the selectivity seems to depend upon shape.

A large fraction of polytungstates that have been tested prove to have potent antitumoral and antiviral activity (rabies, influenza, scrapie, and the retroviruses responsible for AIDS and SAIDS).[31] Toxicity varies widely, but some species are less toxic than azidothymidine (AZT) and are effective against AZT-resistant cell lines. The polyoxoanions bind to the gp120 envelope glycoprotein of the retrovirus, and in some cases inhibit the function of the rus reverse transcriptase (cf. AZT). Reviews of Structure and Reactivity of Polyoxometalates have recently appeared.[32,33]

9 RELATED ARTICLES

Cluster Compounds: Inorganometallic Compounds Containing Transition Metal & Main Group Elements; Mixed Valence Compounds; Molybdenum: Inorganic & Coordination Chemistry; Niobium & Tantalum: Inorganic & Coordination Chemistry; Oxidation Catalysis by Transition Metal Complexes; Oxide Catalysts in Solid-state Chemistry; Oxides: Solid-state Chemistry; Polynuclear Organometallic Cluster Complexes; Tungsten: Inorganic & Coordination Chemistry; Vanadium: Inorganic & Coordination Chemistry.

10 REFERENCES

1. M. T. Pope, 'Heteropoly and Isopoly Oxometalates', Springer-Verlag, New York, 1983.
2. M. T. Pope and A. Müller, *Angew. Chem., Int. Ed. Engl.*, 1991, **30**, 34.
3. M. T. Pope and A. Müller eds, 'Polyoxometalates. From Platonic Solids to Anti-Retroviral Activity', Kluwer Academic Press, Dordrecht, 1994, p. 1.
4. C. L. Hill, *Chem. Rev.*, 1998, **98**, 1.
5. M. T. Pope and A. Müller eds, 'Polyoxometalate Chemistry: from Topology via Self-assembly to Applications', Kluwer Academic Press, Dordrecht, 2001, p. 1.
6. J. J. Borrás-Almenar, E. Coronado, A. Müller, and M. T. Pope eds, 'Polyoxometalate Molecular Science', NATO SCIENCE SERIES: II: Mathematics, Physics and Chemistry, Vol. 98, Kluwer Academic Publishers, Dordrecht 2003.

7. 'Gmelins Handbuch der Anorganischen Chemie', Verlag Chemie, Berlin; System-Nr. 53 (Molybdän), 1935, p. 312; System-Nr. 54 (Wolfram), 1933, p. 324.
8. H. T. Evans Jr *Perspect. Struct. Chem.*, 1971, **4**, 1.
9. X. Lopez, J. M. Maestre, C. Bo, and J. M. Poblet, *J. Am. Chem. Soc.*, 2001, **123**, 9571.
10. I. A. Weinstock, J. J. Cowan, E. M. G. Barbuzzi, H. Zeng, and C. L. Hill, *J. Am. Chem. Soc.*, 1999, **121**, 4608.
11. R. A. Prados and M. T. Pope, *Inorg. Chem.*, 1976, **15**, 2547.
12. M. Che, M. Fournier, and J. P. Launay, *J. Chem. Phys.*, 1979, **71**, 1954.
13. C. Sanchez, J. Livage, J. P. Launay, M. Fournier, and Y. Jeannin, *J. Am. Chem. Soc.*, 1982, **104**, 3194.
14. M. Kozik, N. Casan-Pastor, C. F. Hammer, and L. C. W. Baker, *J. Am. Chem. Soc.*, 1988, **110**, 7697.
15. P. Gouzerh and A. Proust, *Chem. Rev.*, 1998, **98**, 77.
16. A. Müller, F. Peters, M. T. Pope, and D. Gatteschi, *Chem. Rev.*, 1998, **98**, 239.
17. A. Müller, E. Krickemeyer, H. Bögge, M. Schmidtmann, and F. Peters, *Angew. Chem., Int. Ed. Engl.*, 1999, **37**, 3360.
18. A. Müller, E. Beckmann, H. Bögge, M. Schmidtmann, and A. Dress, *Angew. Chem., Int. Ed. Engl.*, 2002, **41**, 1210.
19. U. Kortz, M. G. Savelieff, B. S. Bassil, and M. H. Dickman, *Angew. Chem., Int. Ed. Engl.*, 2001, **40**, 3384.
20. K. Wassermann, M. H. Dickman, and M. T. Pope, *Angew. Chem., Int. Ed. Engl.*, 1997, **36**, 1445.
21. U. Kortz, S. S. Hamzeh, and N. A. Nasser, *Chem. Eur. J.*, 2003, **9**, 2945.
22. A. J. Gaunt, I. May, D. Collison, K. T. Holman, and M. T. Pope, *J. Mol. Struct.*, 2003, **656**, 101.
23. D. Katsoulis, *Chem. Rev.*, 1998, **98**, 359.
24. D. Janell, A. Tocilj, I. Kölln, F. Schlünzen, M. Glühmann, H. A. S. Hansen, J. Harms, A. Bashan, I. Agmon, H. Bartels, M. Kessler, S. Weinstein, F. Francheshi, and A. Yonath, in 'Polyoxometalate Chemistry: from Topology via Self-assembly to Applications', eds. M. T. Pope and A. Müller, Kluwer Academic Publishers, Dordrecht, 2001, p. 391.
25. Y. Izumi, K. Urabe, and M. Onaka, 'Zeolite, Clay, and Heteropoly Acid in Organic Reactions', VCH, Weinheim, 1992, p. 1.
26. C. L. Hill, *J. Mol. Catal.*, 1996, **114**, 1 (''Polyoxometalates in Catalysis'').
27. T. Okuhara, N. Mizuno, and M. Misono, *Adv. Catal*, 1996, **41**, 113.
28. R. Neumann, *Prog. Inorg. Chem*, 1998, **47**, 317.
29. M. Misono, *Chem. Commun.*, 2001, 1141.
30. J. B. Moffatt, 'Metal-Oxygen Clusters. The Surface and Catalytic Properties of Heteropoly Oxometalates', Kluwer Academic Publishers, Dordrecht, 2001, p. 1.
31. J. T. Rhule, C. L. Hill, and D. A. Judd, *Chem. Rev.*, 1998, **98**, 327.
32. M. T. Pope, 'Comprehensive Coordination Chemistry II', J. McCleverty, T. J. Meyer, eds. Pergamon Press, Oxford, 2004, Vol. 4, A. G. Wedd, ed., p. 635.
33. C. L. Hill, 'Comprehensive Coordination Chemistry II', J. McCleverty, T. J. Meyer, eds. Pergamon Press, Oxford, 2004, Vol. 4, A. G. Wedd, ed., p. 679.

Acknowledgment

Support from the National Science Foundation and the Donors of the Petroleum Research Fund, administered by the American Chemical Society are gratefully acknowledged. Professors Lage Pettersson and Achim Müller kindly provided copies of Figures 1, 6, 17 and 18. Figures 19 and 20 were prepared using DIAMOND version 2.1, copyright 1996–2001 Crystal Impact GbR.

Polyphosphazenes

Harry R. Allcock
The Pennsylvania Sate University, University Park, PA, USA

1 Synthesis 1
2 Structure–Property Relationships 4
3 Uses 5
4 Summary 7
5 References 7

Most synthetic polymers are totally organic macromolecules derived from petroleum. One of the exceptions is the broad class of polymers with an inorganic backbone – called polyphosphazenes.

These polymers exist with a number of different architectures, as shown in Figure 1, but they all contain a backbone or rings of alternating phosphorus and nitrogen atoms, with two organic, organometallic, or inorganic side groups linked to each phosphorous atom. Most examples have a linear or lightly branched structure (**1**) (Figure 1). However, in recent years the development of star or dendritic species (**2**) and hybrid phosphazene-organic macromolecules such as (**3–6**) has widened the scope of this field and has stimulated numerous applications in addition to those known for pure polyphosphazenes.[1]

The first stable polyphosphazenes, of type (**1**), were synthesized in the mid-1960s, and in the intervening years this field has grown into a major area of polymer science that is the largest inorganic-based system. Its chemistry is broader than that of poly(organosiloxanes) (silicones) and larger than many areas of classical organic polymer science. More than 700 different polyphosphazenes are now known, with over 250 different types of organic or organometallic side groups, extremely diverse properties, and a widening list of actual and potential applications. Major developments have occurred during the past 10 years that have enhanced interest in these materials used in fields as diverse as biomedicine, fuel cell and battery technology, advanced elastomers, and optical and optoelectronic (photonic) materials. Moreover, the fundamental chemistry has been expanded to provide valuable information about polymerization mechanisms, macromolecular substitution chemistry, and structure–property relationships. The following account emphasizes this recent work and includes selected references since 1993. For a more comprehensive overview, the reader is referred to a recent monograph[1] and to an edited volume.[2]

1 SYNTHESIS

The original synthesis pathway to poly(organophosphazenes) is shown in Scheme 1.

The starting material is hexachlorocyclotriphosphazene (**7**) prepared from phosphorus pentachloride and ammonium chloride. Thermal ring-opening polymerization of this cyclic trimer in the molten phase at 250 °C in a sealed system brings about its slow conversion to poly(dichlorophosphazene) (**8**). The same reaction can be carried out in solution in dichlorobenzene at slightly lower temperatures, provided a catalyst such as boron trichloride is used. Poly(dichlorophosphazene) is a colorless elastomeric material that is soluble in organic solvents such as benzene, toluene, tetrahydrofuran, or cyclohexane. It is also highly reactive to nucleophiles such as alkoxides, aryloxides, and primary or secondary amines, which bring about replacement of the chlorine atoms by organic groups. A few organometallic reagents behave in the same way. The most remarkable feature of this reaction is the fact that all the halogen atoms can be replaced to give polymers that are in most cases stable to air, water, and radiation. Thus, typically 30 000 chlorine atoms per polymer molecule are replaced by organic groups, often within a few hours of reaction at 25–70 °C. Two or more different types of side groups may be introduced by sequential or simultaneous substitutions and this further widens the range of properties. In general, the long chain length of the poly(dichlorophosphazene) is carried forward into the structure of the substituted macromolecules. One disadvantage of this route is that the ring-opening polymerization process does not allow control of the chain lengths or of the molecular weight distribution. Nevertheless, it is the method that has been used to produce most of the known polyphosphazenes mainly because the starting materials are readily available and standard wet-chemistry techniques are employed. This process is also used to polymerize cyclic phosphazenes that bear short, linear phosphazene side chains (so-called *phosphazophosphazenes*)[1,3] and cyclophosphazenes that have carbon or sulfur in the ring in place of one of the phosphorus atoms.[1,4] All these polymers can then be subjected to halogen-replacement reactions in the same way as poly(dichlorophosphazene). Poly(dichlorophosphazene) is also produced via an inexpensive condensation reaction of $Cl_3P{=}NP(O)Cl_2$[2], but the molecular weights tend to be lower than those generated via the ring-opening route

However, the same polymeric intermediate can now be synthesized by an alternative method, which allows considerable control over the structure of the final product.[5–9] This is a living cationic polymerization process, which takes place at room temperature in solution, and which allows excellent control of the chain lengths, gives narrow molecular weight distributions and provides access to a wide rage of block, graft, and comb copolymers with organic macromolecules or poly(organosiloxanes). The monomer for this reaction is an *N*-silylchlorophosphoranimine (**9**), which may be prepared from Me_3SiCl and PCl_5, $(Me_3Si)_3N$ and PCl_5,

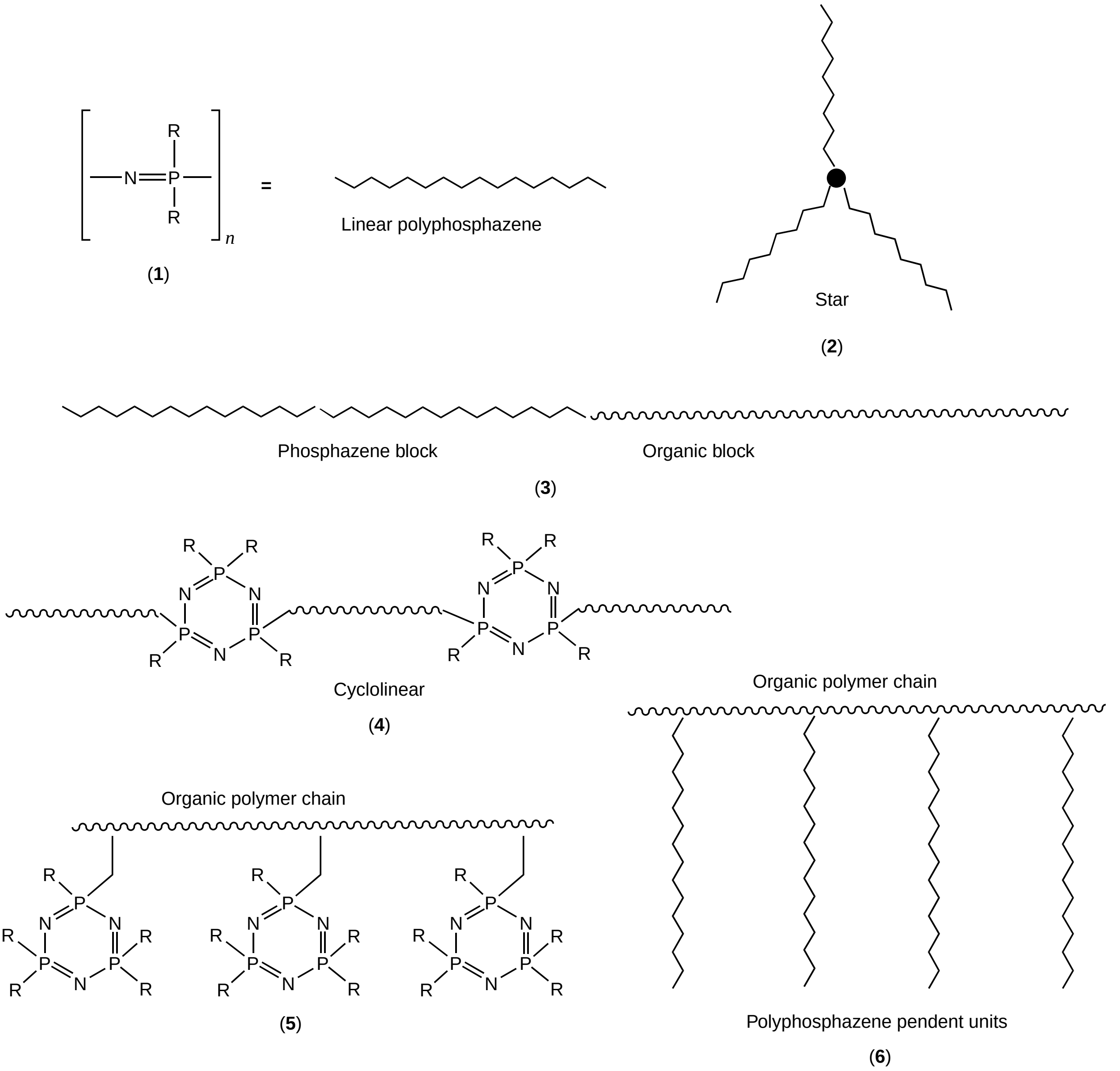
R
N
P
R
n
(1)
=
Linear polyphosphazene
Star
(2)
Phosphazene block
Organic block
(3)
Cyclolinear
(4)
Organic polymer chain
(5)
Organic polymer chain
Polyphosphazene pendent units
(6)

Figure 1 Different types of polyphosphazenes including linear classical macromolecules (**1**), star structures (**2**), block copolymers (**3**), cyclolinear polymers (**4**), and comb or graft copolymers (**5**) and (**6**). Not shown are cyclomatrix materials in which cyclic trimeric rings are connected in three dimensions[1]

or most recently from PCl_3 and $S(O)Cl_2$.[10] Polymerization of (**9**) occurs in the presence of an initiator such as phosphorus pentachloride, with trimethylchlorosilane being eliminated during the reaction. The overall sequence and a possible mechanism are shown in reactions (1)–(3).

Initiation

$$Cl_3P{=}NSiMe_3 \xrightarrow[-Me_3SiCl]{2PCl_5} Cl_3P{=}N{-}PCl_3^+\ PCl_6^- \tag{1}$$

$$Cl_3P{=}N{-}PCl_3^+\ PCl_6^- \xrightarrow[-Me_3SiCl]{2PCl_5} [Cl_3P{=}N{-}PCl_2{-}N{=}PCl_3]^+\ PCl_6^- \tag{2}$$

Propagation

$$[Cl_3P{=}N{-}PCl_2{-}N{=}PCl_3]^+\ PCl_6^- \xrightarrow[-ClSiMe_3]{Cl_3P=NSiMe_3} Cl_3P{=}(PCl_2{=}N)_n - PCl_3^+\ PCl_6^- \tag{3}$$

‘‘The living’’ polymer end unit initiates more of same monomer, a different phosphoranimine monomer, or is coupled to a phosphoranimine-terminated organic polymer.

A major advantage of the living cationic polymerization process is that, because the chain ends are still active after

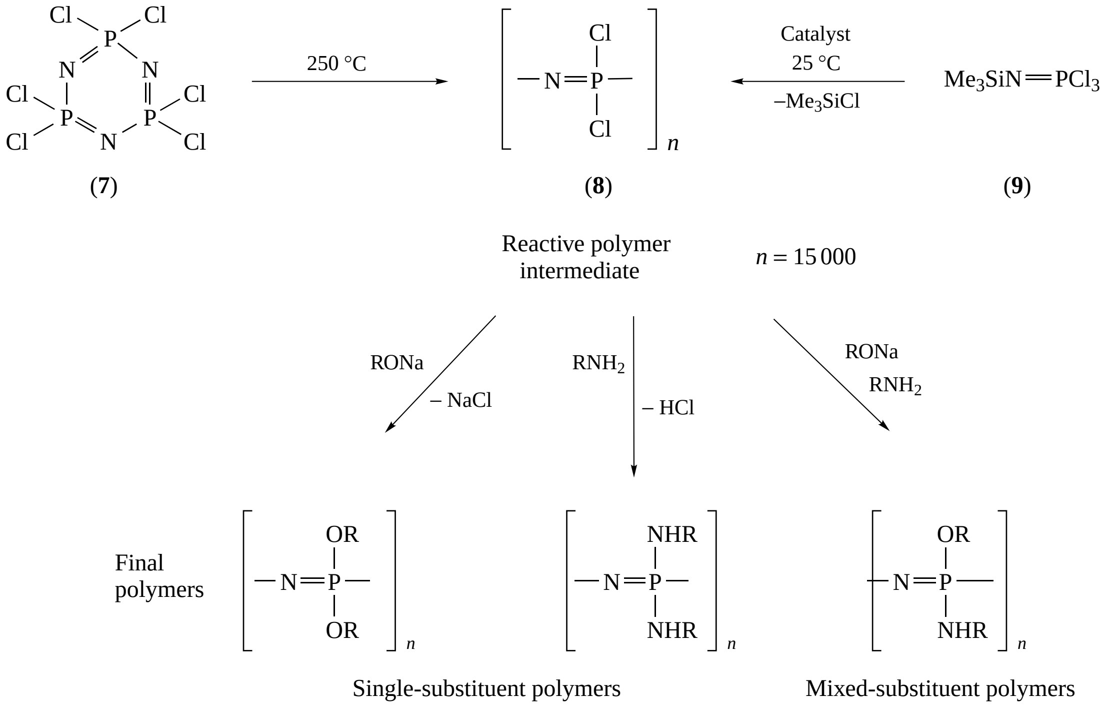
250 °C
Catalyst
25 °C
$-\mathrm{Me_3SiCl}$
$\mathrm{Me_3SiN{=}PCl_3}$
(7)
(8)
(9)
Reactive polymer intermediate
$n = 15\,000$
RONa
− NaCl
$\mathrm{RNH_2}$
− HCl
RONa
$\mathrm{RNH_2}$
Final polymers
Single-substituent polymers
Mixed-substituent polymers

Scheme 1

polymerization, they can be used to couple the polyphosphazene to other polymers to produce block copolymers with polysiloxanes or organic polymers. Moreover, the living chain ends can be quenched with species that link organic unsaturated units to the chain ends. Polymerization of these allows the preparation of comb and graft copolymers such as (**6**).

Several synthetic pathways exist for the direct preparation of poly(organophosphazenes) that are based on the polymerization of phosphoranimines that already bear organic side groups. For example, various poly(organophosphazenes) are accessible via the polymerization of $\mathrm{Me_3Si{-}N{=}PR_2(OCH_2CF_3)}$ as shown in reaction (4),[11–13] and others have been produced using anionic initiators (reaction 5).[14] Other synthesis routes involve the careful, controlled decomposition of diorganophosphorus azides (reaction 6).

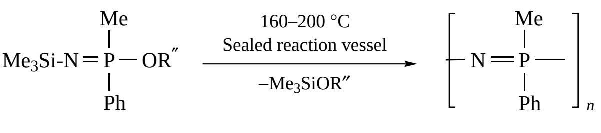

$$\mathrm{Me_3Si\text{-}N{=}P(Me)(Ph){-}OR''} \xrightarrow[-\mathrm{Me_3SiOR''}]{\text{160–200 °C, Sealed reaction vessel}} \left[\mathrm{N{=}P(Me)(Ph)}\right]_n \qquad (4)$$

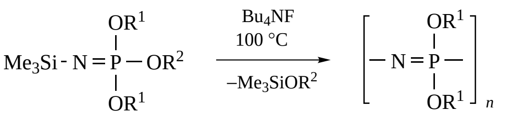

$$\mathrm{Me_3Si\text{-}N{=}P(OR^1)_2{-}OR^2} \xrightarrow[-\mathrm{Me_3SiOR^2}]{\mathrm{Bu_4NF},\ 100\ °C} \left[\mathrm{N{=}P(OR^1)_2}\right]_n \qquad (5)$$

$\mathrm{OR^1 = OCH_2CH_2OCH_3}$ or $\mathrm{OCH_2CH_2OCH_2CH_2OCH_3}$
$\mathrm{OR^2 = OCH_2CF_3}$

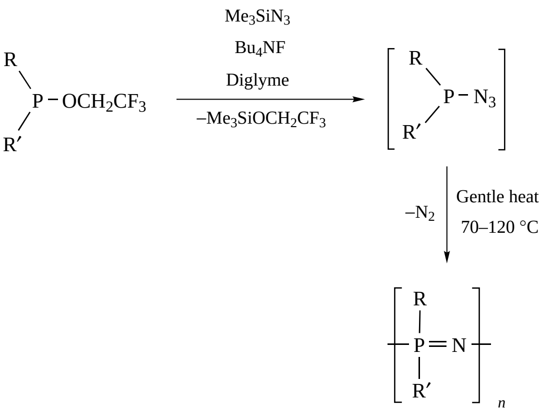
$\mathrm{Me_3SiN_3}$
$\mathrm{Bu_4NF}$
Diglyme
$-\mathrm{Me_3SiOCH_2CF_3}$
$-\mathrm{N_2}$
Gentle heat
70–120 °C

(6)

A number of recently reported synthetic methods include the formation of organic polymers with pendent cyclic or linear phosphazene side groups (reactions 7–9)[15–17] and a process for the preparation of linear polymers in which phosphazene rings are linked together by organic oligomer chains using acyclic diene metathesis (ADMET) techniques (reaction 10).[18]

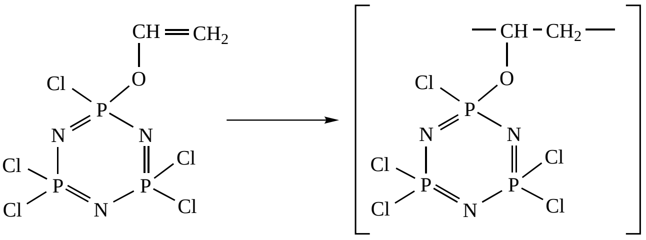

(7)

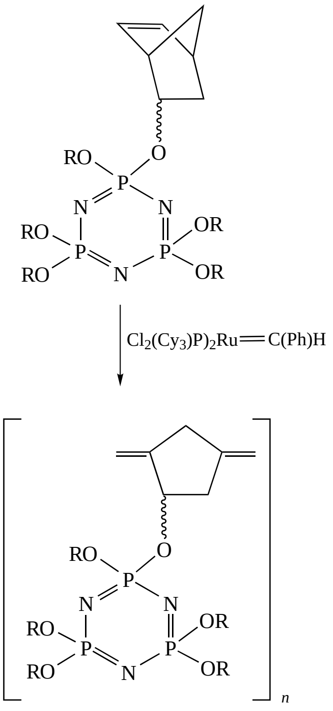

(8)

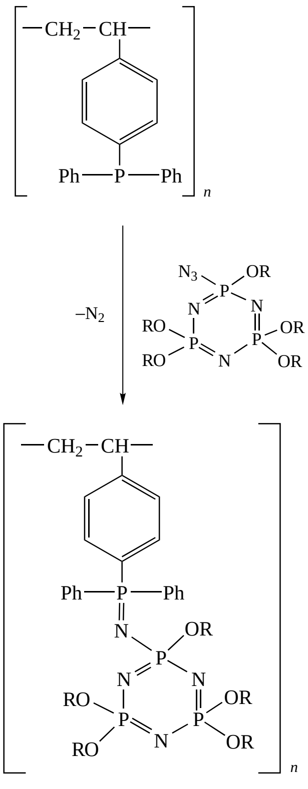

RO = CF_3CH_2O or C_6H_5O—

(9)

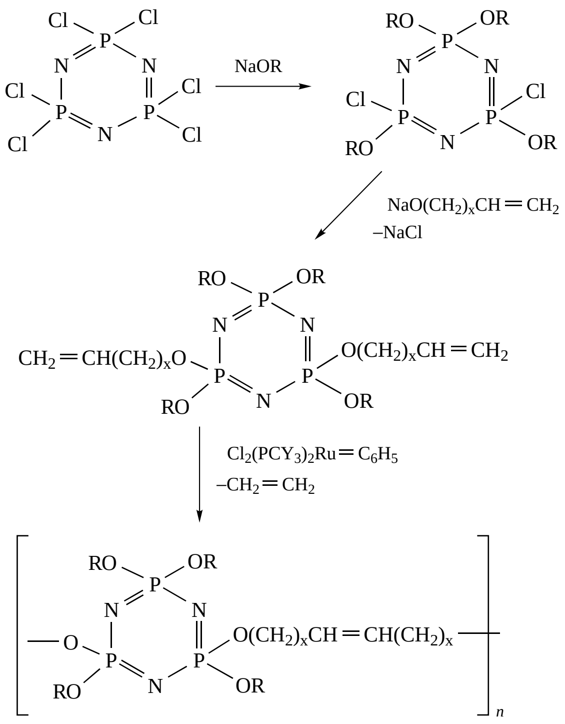

(10)

OR = OC_6H_5 or $OCH_2CH_2OCH_2CH_2OCH_3$
x = 4–9

Cy = cyclohexyl

2 STRUCTURE–PROPERTY RELATIONSHIPS

The synthesis of a large number of polyphosphazenes and an investigation of their properties has provided an almost unique opportunity to understand the relationship between the structure and properties in these systems.[1] A long-range objective is to be able to predict the properties of yet-unsynthesized polymers.

The properties of these polymers can best be understood in terms of three factors: (1) the special characteristics of the polyphosphazene backbone and its architecture, (2) the structure of the side groups linked to the skeletal phosphorus atoms, and (3) the ways in which the polymer molecules are packed together in the solid state.

1. *The Backbone.* The linear inorganic backbone imparts an unusual combination of properties. First, perhaps unexpectedly in view of the unsaturated structure, the skeletal bonds have a low barrier to torsion (perhaps as low as 0.1–0.5 Kcal/ repeating unit), which becomes translated into one of the most flexible backbones known throughout polymer chemistry. This means that some polyphosphazenes have glass-transition temperatures (T_g) as low as −100 °C. It also means that, in the absence of microcrystallinity, numerous polymers of this type are rubbery elastomers. This is a key property for

many applications. Second, the inorganic backbone is fire resistant. Small-molecule phosphorus compounds have been used for many years as fire retardants, but polyphosphazenes have this property built into their basic structure. Third, the phosphazene skeleton is transparent throughout the visible region of the spectrum and down to ∼220 mμ in the ultraviolet. This is the reason why polyphosphazenes are much more resistant to photolysis and thermolysis than most organic polymers. The backbone is also unusually resistant to cleavage by X-rays and γ-rays. It is believed that this stability is connected with the reluctance of the polar P–N bonds to split into free radicals when heated or irradiated. One other factor that depends on the backbone is the refractive index. The high-electron density in the skeleton generates a higher-base refractive index than found in most other polymers, and this is important for several optical and electro-optical applications.

2. *The Polymer Architecture.* Most of the known polyphosphazenes are linear or have lightly branched chains (**1**). However, as mentioned above, other geometries exist, including highly branched, star, or dendritic structures, comb polymers, a variety of block-copolymer structures and macromolecules that contain six-membered rings. Two polymers with approximately the same molecular weight, one linear and the other with star-geometry, both with the same side groups, will have very different properties. For example, for species with trifluoroethoxy side groups, the linear polymer has a high viscosity in solution, readily crystallizes, and gives films and fibers, but the more compact tri-star structure has a lower solution viscosity and is a noncrystalline gum.[19] Block copolymers tend to have properties that have some combination of the properties of the two component homopolymers, and this is especially true when one of the blocks is a phosphazene and the other is an organic polymer or a polysiloxane. This enables the design of polymers that combine the advantages of each while possibly minimizing the disadvantages of both. Block copolymers with, say, a hydrophilic phosphazene block and a hydrophobic organic block can form micelles in aqueous media.[20] The same is true of species that contain two different phosphazene blocks – one hydrophobic and the other hydrophilic.[21] Organic polymers with cyclophosphazene-pendent groups tend to have higher T_g's than the corresponding organic polymer and are much more resistant to combustion. Cyclolinear polymers of structure (**4**) typically have properties that are entirely different from those of the corresponding organic polymer. These too may be fire resistant.
3. *The Side Groups.* The side groups linked to phosphorus play an equally important role, as shown schematically in Figure 2. They influence not only chemical properties and solubility but solid-state properties as well.

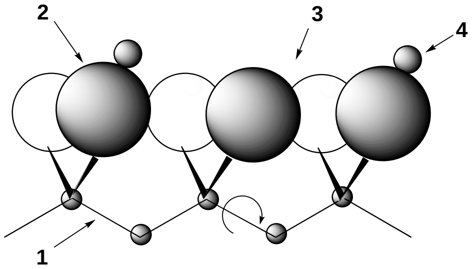

Figure 2 Properties in polyphosphazenes are determined by: (1) the backbone bonds that control the inherent flexibility of the polymer via their influence on bond torsional freedom, and also provide photo- and thermo-oxidative stability; (2) the side groups control polymer solubility, reactivity, thermal stability, crystallinity, cross-linking, and (indirectly) polymer flexibility; (3) ‘free volume’ between the side groups affects polymer motion, solvent penetration, membrane behavior, and density; (4) functional groups (usually introduced by secondary reactions) affect solubility, biological behavior, proton conduction, cross-linking, and many other properties

Small side groups, such as methoxy or ethoxy, or those that themselves are highly flexible, such as methoxyethoxyethoxy groups, do not impede the conformational reorientation of the backbone. Hence, they give rise to low glass transition temperatures and elastomeric materials. On the other hand, if the side groups are bulky (ferrocenyl, carboranyl, phenoxy, biphenyleneoxy, naphthaleneoxy, adamantyl) or capable of hydrogen bonding (phenylamino), the chain motions are restricted, the glass-transition temperatures rise, and the materials become glasses rather than elastomers. If the side group arrangement is symmetric (as for example in $[NP(OCH_2CF_3)_2]_n$), the polymer chains may crystallize and this changes what might otherwise be an elastomer to a flexible, film- or fiber-forming thermoplastic. Crystallization is inhibited if two or more different side groups (say OCH_2CF_3 and $OCH_2(CF_2)_xCF_3$) are randomly distributed along the chains because the resultant disruption of order prevents the chains from forming colinear arrays. The side groups are also the sites of secondary-reaction chemistry in which functional groups such as SO_3H, NH_2, OH, or COOH are introduced. Note that the functional units on organic side groups are responsible for properties such as hydrophobicity or hydrophilicity, color, electrical conductivity, and coordination to metal ions. For example, organic side groups that bear amino or phosphino functional units coordinate to transition metal compounds, and the oxygen atoms of alkyl ether side groups coordinate loosely to lithium ions. The side groups are also the components that participate in cross-linking reactions.

3 USES

Applications that have been or are being developed for polyphosphazenes include several diverse biomedical applications, elastomers for aerospace applications, optical materials, solid electrolytes for lithium batteries or fuel cells, gas separation membranes, and a host of applications in fire resistant technology.

1. *Biomedical Applications.* Biomedicine is a field where the tunability of materials' properties is crucial to new developments. Polyphosphazenes almost uniquely provide this versatility. Only three of the many applications will be mentioned here. First, the polymer shown as (**10**) is soluble in water as its sodium salt but is insoluble when the sodium ions are replaced by calcium. This is because the Ca^{+2} ions cross-link the chains. This phenomenon has been used to produce microspheres that encapsulate vaccine molecules for oral vaccinations.[22] Each calcium-cross-linked microsphere protects the vaccine during its passage through the stomach but releases it as the phosphazene polymer is de-cross-linked by sodium ions in the small intestine. Second, polyphosphazenes with amino acid ester side groups, such as (**11**), are hydrolytically unstable and decompose in the body to amino acid, alcohol, phosphate, and ammonia. This property is being used in the field of tissue regeneration, especially for materials that facilitate the regeneration of bone.[23] Nanofiber mats of polyphosphazenes are produced by the process of electrospinning.[24] These are then seeded with osteoblasts, which spread throughout the material and form new bone at the same rate as the polymer erodes. The ease with which the rate of polymer hydrolysis can be controlled by the type of amino acid–ester side group is crucial for the success of this approach. Third, specific polyphosphazenes with hydrophilic side groups are water-soluble but, after being cross-linked, form hydrogels. Side groups that give rise to this property are alkyl ether units such as –OCH$_2$CH$_2$OCH$_2$CH$_2$OCH$_3$ or its branched analogues, or –NHCH$_3$ and –OC$_6$H$_4$COONa. Combinations of these side groups give rise to responsive hydrogels in which the swelling or contraction of a hydrogel membrane occurs in response to changes in temperature, pH, or cation charge.[25] This is the basis of membranes that control the delivery of drugs or which turn on or off the activity of encapsulated enzymes.

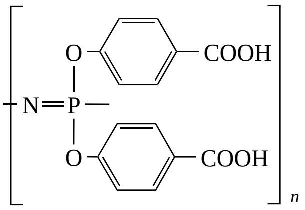

(**10**)

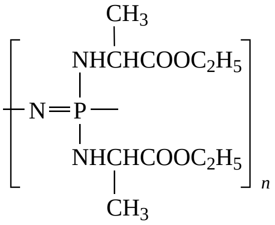

(**11**)

2. *Solid Ionic Conductors.* Membranes that provide a medium for the transport of lithium ions or protons are important components of liquid-free rechargeable lithium batteries and advanced fuel cells. Two classes of polyphosphazenes have been developed for these applications. First, polymers with oligo-ethyleneoxy side chains, such as (**12**), are good solid-state lithium ion conductors that have been examined in detail for liquid-free or gel battery applications.[26–29] Second, poly(aryloxyphosphazenes) with sulfonic, phosphonic, or sulfinimide functional groups on the aryl rings (such as **13**) show advantages for fuel cell applications, particularly for direct methanol fuel cells[30,31] for which there is an acute scarcity of suitable membrane materials.

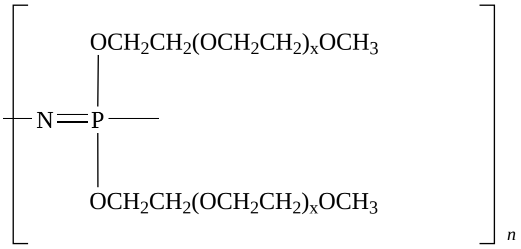

(**12**)

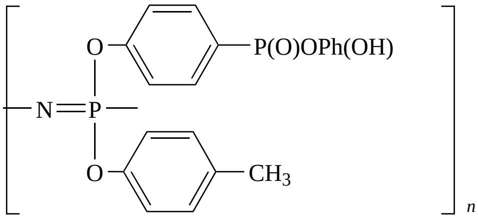

(**13**)

3. *Optical Materials.* The polyphosphazene skeleton is electron-rich, which means that it provides a refractive index increment compared to conventional saturated organic backbones. In addition, the macromolecular substitution synthesis allows highly unsaturated organic side groups to be linked to the skeleton in ways that allow the refractive index, the color, the liquid crystalline, and nonlinear optical characteristics of the polymer to be finely tuned.[32,33] Thus, the use of these polymers in opto-electronic (photonic) switches and lens systems is a subject of growing interest.
4. *Elastomers.* The most advanced applications from a commercial viewpoint are found in the use of polyphosphazenes as elastomers that remain flexible at low temperatures, are resistant to hot oil and hydraulic fluids, and resist combustion. Polymers with both trifluoroethoxy and heptafluorobutoxy side groups were originally developed for aerospace and automotive applications,[1] but other elastomers that bear both trifluoroethoxy and organosilicon side groups are now

known.[34–37] Species with two different aryloxy side groups (e.g. phenoxy and *p*-ethylphenoxy) are fire resistant elastomers that are useful as thermal and sound insulation materials.

4 SUMMARY

The impact of inorganic chemistry on technology in recent years has been confined mainly to catalysis, ceramics, and electronics. The polyphosphazenes illustrate how inorganic reaction chemistry can be used to create a new major area of polymer science and one that has the potential to bring about much needed improvements in biomedicine, membrane technology, energy generation and storage, and in aerospace engineering. The challenge for the future is to apply these or similar techniques to the development of other inorganic polymer systems with backbone elements other than phosphorus and nitrogen.

5 REFERENCES

1. H. R. Allcock, 'Chemistry and Applications of Polyphosphazenes', John Wiley, Hoboken, NJ, 2003.
2. M. Gleria, and R. De Jeager eds, 'Phosphazenes: A Worldwide Insight', Nova Science Publishers, Hauppauge, NY, 2004.
3. H. R. Allcock, S. E. Kuharcik, C. T. Morrissey, and D. C. Ngo, *Macromolecules*, 1994, **27**, 7556.
4. Y. Ni, P. Park, M. Liang, J. Massey, C. Waddling, and I. Manners, *Macromolecules*, 1996, **29**, 3401.
5. H. R. Allcock, C. A. Crane, C. T. Morrissey, J. M. Nelson, S. D. Reeves, C. H. Honeyman, and I. Manners, *Macromolecules*, 1996, **29**, 7740.
6. H. R. Allcock, S. D. Reeves, J. M. Nelson, C. A. Crane, and I. Manners, *Macromolecules*, 1997, **30**, 2213.
7. H. R. Allcock, J. M. Nelson, S. D. Reeves, C. H. Honeyman, and I. Manners, *Macromolecules*, 1997, **30**, 50.
8. H. R. Allcock, R. Prange, and T. J. Hartle, *Macromolecules*, 2001, **34**, 5463.
9. H. R. Allcock and R. Prange, *Macromolecules*, 2001, **34**, 6858.
10. B. Wang and I. Manners, *Inorg. Chem.*, 2002, **41**, 1690.
11. R. H. Neilson, D. L. Jinkerson, W. R. Kucera, J. J. Longlet, R. C. Samuel, and C. E. Wood, *Acs Symp. Ser.*, 1994, **572**, 232.
12. P. Wisian-Neilson, in 'Encyclopedia of Inorganic Chemistry (1st Ed.)', John Wiley & Sons, Chichester, 1994, Vol. 6, p. 3371.
13. M. G. Gallazzi, G. Freddi, G. Sanvito, and G. Viscardi, *J. Inorg. Organomet. Polym.*, 1996, **6**, 277.
14. K. Matyjaszewski, M. K. Moore, and M. L. White, *Macromolecules*, 1993, **26**, 6741.
15. C. W. Allen, *Coord. Chem. Rev.*, 1994, **130**, 137.
16. H. R. Allcock, W. R. Laredo, C. R. deDenus, and J. P. Taylor, *Macromolecules*, 1999, **32**, 7719.
17. H. R. Allcock, T. J. Hartle, J. P. Taylor, and N. J. Sunderland, *Macromolecules*, 2001, **34**, 3896.
18. H. R. Allcock and E. C. Kellam, *Macromolecules*, 2002, **35**, 40.
19. J. M. Nelson and H. R. Allcock, *Macromolecules*, 1997, **30**, 1854.
20. Y. Chang, J. D. Bender, M. V. B. Phelps, and H. R. Allcock, *Biomacromolecules*, 2002, **3**, 1364.
21. Y. Chang, R. Prange, H. R. Allcock, S. C. Lee, and C. Kim, *Macromolecules*, 2002, **35**, 8556.
22. A. K. Andrianov, J. R. Sargent, S. S. Sule, M. P. Le Golvan, A. L. Woods, Swarninga. Jenkins, and L. G. Payne, *J. Bioact. Compat. Pol.*, 1998, **13**, 243.
23. A. M. A. Ambrosio, H. R. Allcock, D. S. Katti, and C. T. Laurencin, *Biomaterials*, 2002, **23**, 1667.
24. S. Bhattacharyya, S. Lakshmi, J. D. Bender, Y. E. Greish, P. W. Brown, H. R. Allcock, and C. T. Laurencin, 'Proceeding of Materials Research Society Fall Meeting', Materials Research Society, Boston, MA, 2003.
25. H. R. Allcock and A. M. A. Ambrosio, *Biomaterials*, 1996, **17**, 2295.
26. H. R. Allcock, M. E. Napierala, D. L. Olmeijer, C. G. Cameron, S. E. Kuharcik, C. S. Reed, and S. J. M. O'Connor, *Electrochim. Acta*, 1998, **43**, 1145.
27. H. R. Allcock and E. C. Kellam, *Solid State Ionics*, 2003, **156**, 401.
28. L. Gao, D. D. Macdonald, M. Urquidi-Macdonald, D. L. Olmeijer, and H. R. Allcock, *Electrochim. Acta*, 2002, **47**, 3863.
29. H. R. Allcock, W. R. Laredo, and R. V. Morford, *Solid State Ionics*, 2001, **139**, 27.
30. R. Wycisk and P. N. Pintauro, *J. Membr. Sci.*, 1996, **119**, 155.
31. X. Y. Zhou, J. Weston, E. Chalkova, M. A. Hofmann, C. M. Ambler, H. R. Allcock, and S. N. Lvov, *Electrochim. Acta*, 2003, **48**, 2173.
32. H. R. Allcock, R. Ravikiran, and M. A. Olshavsky, *Macromolecules*, 1998, **31**, 5206.
33. H. R. Allcock, J. D. Bender, Y. Chang, M. McKenzie, and M. M. Fone, *Chem. Mat.*, 2003, **15**, 473.
34. H. R. Allcock, A. E. Maher, and C. M. Ambler, *Macromolecules*, 2003, **36**, 5566.
35. M. Gleria, R. Bertani, R. De Jaeger, and S. Lora, *J. Fluorine Chem.*, 2004, **125**, 329.
36. H. R. Allcock and S. E. Kuharcik, *J. Inorg. Organomet. Polym.*, 1995, **5**, 307.
37. H. R. Allcock and S. E. Kuharcik, *J. Inorg. Organomet. Polym.*, 1996, **6**, 1.

Polysiloxanes & Polysilanes

Amitabha Mitra & David A. Atwood
University of Kentucky, Lexington, KY, USA

Based in part on the article Polysiloxanes & Polysilanes by Robert West which appeared in the Encyclopedia of Inorganic Chemistry, First Edition.

1 Introduction 1
2 Polysiloxanes: Introduction 1
3 Synthesis of Polysiloxanes 3
4 Silicone Materials 5
5 Structure and Properties of Siloxanes 8
6 Polysilanes 9
7 Polysilanes: Synthesis 10
8 Polysilanes: Electronic Properties and Conformation 12
9 Technological Applications of Polysilanes 14
10 Related Articles 16
11 References 16

1 INTRODUCTION

Many kinds of polymers containing silicon atoms in the main chain have been synthesized. A few examples are shown in Figure 1. By a wide margin, the most important are the polysiloxanes, commonly called silicones, which are now the basis for a worldwide industry.[1–5] Also described in this article are the polysilane polymers, which are of interest because of their special properties reflecting extensive delocalization of the σ-electrons along the Si–Si backbone (*see σ-Bond*).[6–9]

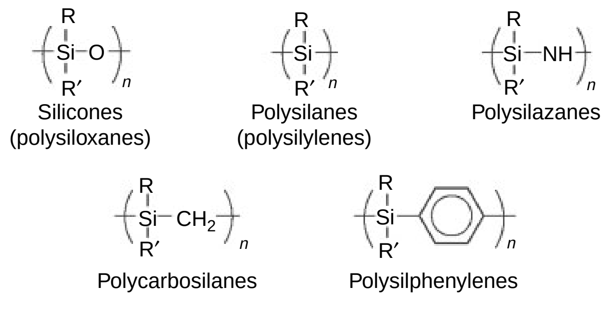

Figure 1 Some types of silicon-containing polymers

2 POLYSILOXANES: INTRODUCTION

2.1 A Brief History of Silicones

Organosilicon compounds were first synthesized in the 1860s, by the reaction of silicon tetrachloride with organozinc compounds (*see* ***Silicon: Organosilicon Chemistry***). Major advances took place only after 1900, when the more convenient *Grignard Reagents* became available. The first polysiloxanes were made by F. S. Kipping and his students in a classic series of experiments in the early part of the 20th century.[10] These workers prepared diorganodichlorosilanes, R_2SiCl_2, which, like other halosilanes, are easily hydrolyzed, initially to silanediols, $R_2Si(OH)_2$. It was anticipated that these compounds might eliminate water to give silicon analogs to ketones, $R_2Si{=}O$, hence ‘silicones’. Kipping soon realized, however, that the actual products of dehydration were cyclic or linear polymers containing Si–O–Si single bonds, rather than Si=O linkages. Nevertheless, the name silicone, applied to these polymeric materials, persists in usage even today.

The earliest commercial syntheses of silicone materials were also carried out by reactions of Grignard reagents with $SiCl_4$, followed by hydrolysis of the dichlorosilanes. This route has now been displaced by the ‘direct reaction’ between methyl chloride and silicon to give methylchlorosilanes, described more fully in Section 4.1.[11] Silicones were first introduced commercially in the late 1930s and production has increased continuously since that time.

At the beginning of this millennium, the worldwide sales of silicones were more than 10 billion dollars[12] per year. The United States is both the largest producer and consumer of silicones. Silicone manufacturers in the United States are Dow Corning, General Electric, OSi Specialties, and Wacker Companies. Basic producers in other countries include Bayer, Goldschmidt, and Wacker in Germany; Shin-Etsu, Toray, and Toshiba in Japan; Rhone-Poulenc in France; and Rhone-Poulenc and Dow-Corning in the United Kingdom. Other countries in which silicone production is known to take place are the People’s Republic of China, the Czech Republic, and the former USSR.

2.2 General Properties of Silicones

The silicone polymers can be considered inorganic–organic hybrid materials. Their structure, with a very flexible and thermally stable polymer backbone of alternating silicon and oxygen atoms, is closely related to that of silicate minerals. The alkyl or aryl side groups, however, confer hydrocarbon-like character. The polyorganosiloxane structure, unprecedented in nature, gives the silicones special properties that make them valuable in a myriad of end products. They find application in uses affecting most aspects of modern life, and nearly every branch of manufacturing.[13]

The silicones comprise a broad class of materials, including oils, elastomers, and resins. Because of backbone flexibility, silicones have the lowest viscosities in fluids and most flexibility at lowest temperatures in elastomers of any commercial materials. Silicone oils, because of their great thermal stability and inertness, are excellent heat-transfer and hydraulic fluids. The water repellency of silicones makes them invaluable for the treatment of stone and masonry. The low surface energy of polysiloxanes makes them useful in release liners, used, for example, against adhesive labels. Special formulations are used as antifoaming additives, and conversely, others make good foam stabilizers. They are extensively used in textile treating; many modern fabrics contain 0.5–1%, and some specialty fabrics up to 5%, silicone. Because silicone oils are bland and biologically inert, they are now used in most cosmetic formulations, and within the body as implants and prostheses. Silicones resist high temperatures and oxidation, and silicone resins are therefore important in finishes for smoke stacks, and so on.

The high diffusion rate of oxygen through silicone polymers makes them useful in contact lenses. Siloxanes have excellent dielectric properties, and therefore silicone oils are used to fill transformers, and silicone rubber insulation is extensively used in electronic equipment and electrical machinery. The inertness to weathering and oxidation resistance of silicones makes them excellent sealants for building construction. Because silicones have good properties at low as well as high temperatures, they are vital materials in spacecraft and high-performance aircraft. For one historic example, the boots worn by astronaut Neil Armstrong when he first stepped on to the moon were made of silicone rubber.

2.3 Polysiloxane Structures

It will be useful to consider the structure of a generalized silicone polymer, shown in Figure 2. The structure shown is that for a linear polysiloxane, such as a silicone oil or a rubber gum before cross-linking. As mentioned earlier, the backbone is constructed of alternating silicon and oxygen atoms, forming siloxane, Si–O–Si, linkages. In the terminating groups, the R substituent can be and most commonly is methyl, giving unreactive $Me_3Si–O$ terminations. Reactive terminating substituents, –OH, –OR, –H, $–CH{=}CH_2$, are introduced, especially in low-molecular weight oligomers, to permit elaboration of the structure by further reactions (*see Oligomer*).

Side chain substituent groups R′ may also be methyl, giving the pure polydimethylsiloxane polymers, the most widely used silicones. Other groups are introduced to provide special properties. The most important are phenyl groups, which lower the crystallization temperature so that the polysiloxane will maintain flexibility at extremely low temperatures. Phenyl substituents also increase heat and oxidation resistance, and so are usually introduced in polysiloxanes designed for high-temperature service. Trifluoropropyl groups, $CF_3CH_2CH_2–$, are employed to increase oil and solvent resistance, and to further lower the (already very low) surface energy of siloxanes. Experimentally, silicones are also being produced with longer fluoroalkyl substituents such as $CF_3CF_2CF_2CF_2CH_2CH_2–$. Alkyl groups such as n-C_8H_{17} are sometimes included to increase compatibility of the silicone with organic media. Finally, the reactive substituents H– or $CH_2{=}CH–$ are often introduced, usually in very small amounts, to provide the possibility for cross-linking.

Substituents R′ other than methyl are used in the minimum amount needed to confer the desired property, since all other side groups are more expensive than methyl.

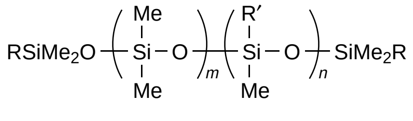

$$RSiMe_2O\left(\overset{Me}{\underset{Me}{Si}}-O\right)_m\left(\overset{R'}{\underset{Me}{Si}}-O\right)_n SiMe_2R$$

Figure 2 A typical polysiloxane

2.4 Naming and Notation

Polysiloxanes are named as derivatives of disiloxane, $H_3SiOSiH_3$. Thus $Me_3SiOSiMe_2OSiMe_3$ is octamethyltrisiloxane and $(PhMeSiO)_3$ is 1,3,5-triphenyltrimethylcyclotrisiloxane. Special notation used in the silicone industry will be important in the discussion to follow. In this shorthand system, silicon centers are designated as M, D, T, or Q. M represents a monofunctional trimethylsilyl group, with its share of the attached oxygen atom, $Me_3SiO_{0.5}$; D is a chain-extending difunctional Me_2SiO group; T is a cross-linking site, $MeSiO_{3/2}$; and Q represents a quaternary silicon atom, $SiO_{4/2}$. Some typical siloxane structures, with names and designations according to the silicone notation system, are given in Table 1.

Other substituents than methyl are sometimes designated by primes or superscripts following the letter. Thus D^H is often used for the MeSiHO unit, and D^F for the $CF_3CH_2CH_2SiHO$ unit. The useful intermediate tetramethylcyclotetrasiloxane, $(MeSiHO)_4$, can then be designated as $D^H{}_4$.

Table 1 Some typical siloxane structures

Structure	Name	Designation
$Me_3SiOSiMe_3$	Hexamethyldisiloxane	MM
$Me_3SiOSiMe_2OSiMe_2OSiMe_3$	Decamethyltetrasiloxane	MD_2M
$Me_3SiO(SiMe_2O)_nSiMe_3$	Poly(dimethylsiloxane)	MD_nM
$(Me_2SiO)_3$	Hexamethylcyclotrisiloxane	D_3
$MeSi(OSiMe_3)_3$	–	TM_3

3 SYNTHESIS OF POLYSILOXANES

3.1 The Direct Process

Silicon differs from carbon in that all of the element existing in nature is in an oxidized form, as SiO_2 or silicate minerals. The first step in the synthesis of silicones then becomes the reduction of silica to an active reduced form of silicon. The usual starting point is the electrothermal reduction of SiO_2 with carbon (equation 1). The elemental silicon can be converted to reactive $SiCl_4$ by chlorination (equation 2) or to hydrochlorosilanes by reaction with HCl (equation 3). The importance of the latter materials in silicone technology will be described later.

$$SiO_2 + C \longrightarrow Si + CO \tag{1}$$

$$Si + Cl_2 \longrightarrow SiCl_4 \tag{2}$$

$$Si + HCl \xrightarrow{Fe} HSiCl_3 + H_2SiCl_2 + SiCl_4 \tag{3}$$

A cornerstone of the modern silicone industry is the direct reaction of methyl chloride with silicon, discovered in the early 1940s by E. G. Rochow in the United States and independently by R. Müller in Germany.**[11]** The direct reaction, carried out by all basic producers of silicones, is done in a fluidized bed reactor using finely divided silicon with particle size ≈30–300 μm, at about 300 °C. In spite of decades of research in many laboratories, the exact course of the reaction is not yet known.**[14–18]**

Copper is an indispensable catalyst, usually supplied in the form of oxidized copper having a mean composition Cu_2O (but containing both Cu and CuO), in amounts of about 5%. In the reactions, it is believed that copper is converted first to CuCl, and then to the intermetallic phase Cu_3Si, which is probably the catalytically active material (equations 4–7). The Cu_3Si may react with methyl chloride to give methylchlorosilanes and copper, which diffuses into the silicon to form more Cu_3Si. Gaseous methylcopper, MeCu, has also been suggested as a transient intermediate species. As the exothermic reaction proceeds, the silicon grains become gradually smaller until they are so fine that they become swept out of the reactor in the gas stream.

$$Cu_2O + 2MeCl \longrightarrow 2CuCl + \text{by-products} \tag{4}$$

$$CuCl + Si \longrightarrow Cu + SiCl \tag{5}$$

$$3Cu + Si \longrightarrow Cu_3Si \tag{6}$$

$$Cu_3Si + 2MeCl \longrightarrow Me_2SiCl_2 + 3Cu \tag{7}$$

Besides copper, the principal catalyst, other materials are added to the direct reaction. About 0.1–1% of an electropositive element (Al, Mg, or Ca) is added to speed the reaction with methyl chloride, and to shorten the induction period before chlorosilanes begin to be produced in good yield. An element which forms a low-melting chloride (usually zinc) is also added in amounts of 0.1–1%, apparently to form a flux which helps to remove oxide coatings from the reaction mass. Finally, very small amounts (0.001–0.005%) of a group 15 element, As, Sb, or Bi, are added as ‘promoters’. The reason why the latter elements aid the direct reaction is not clear; perhaps they serve as dopants to provide reactive electron-excess sites in the silicon lattice. However, lead was found to be a poison for the catalyst.

The major, and most desired, product from the direct reaction is dimethyldichlorosilane, $(CH_3)_2SiCl_2$. Other principal products and their boiling points are shown in Table 2. Good separation of these products, which have similar volatilities, is important for further processing. It follows that large, efficient fractionating towers are an essential part of a silicone production plant.

The yields of the main products vary, as indicated in Table 2. The relative amounts depend on the purity and particle size of the silicon and the copper catalyst, the amount and nature of the additives, the temperature profile and flow velocity in the reactor, and the history of the particular contact mass. A major consideration is to maximize the selectivity for the desired Me_2SiCl_2 over $MeSiCl_3$, which is often obtained in more than useful amounts. Early in the reaction, selectivity for Me_2SiCl_2 is high; as the silicon becomes largely consumed, this selectivity decreases. The by-products Me_3SiCl and $MeSiHCl_2$ are both useful in further processing.

Minor products from the direct reaction, all normally produced in amounts less than 1%, include $SiCl_4$, $HSiCl_3$, Me_4Si, $Me(Et)SiCl_2$, disilanes, especially $Me_2Si(Cl)Si(Me)Cl_2$ and $(MeSiCl_2)_2$, disiloxanes, CH_4 and other hydrocarbons, and H_2. The reaction effluent contains all of these, plus excess MeCl, and finely divided silicon particles containing up to 20% copper as well as other metals. These solids are separated, and usually treated to recover the copper. Unreacted MeCl is separated, purified, and recycled. The monosilane fraction is distilled out and then separated into its components by careful fractional distillation. The disilane fraction can also be distilled out, and may be upgraded into useful chloromonosilanes by cleavage reactions, as shown in equation (8).

$$Me_2SiClSiMeCl_2 + HCl \xrightarrow{cat.} Me_2SiCl_2 + MeSiHCl_2 \tag{8}$$

3.2 Other Monomer-forming Reactions

The direct reaction can also be used to make phenylchlorosilanes, starting with chlorobenzene and using

Table 2 Main products from the MeCl–Si direct reaction

Product	(%)	Bp (°C)
Me_2SiCl_2	80–90	70.0
$MeSiCl_3$	5–15	65.7
$MeSiHCl_2$	3–5	40.7
Me_3SiCl	3–5	57.3

silver as catalyst (equation 9). This reaction is, however, no longer used in the United States, because traces of highly toxic polychorobiphenyls are produced as by-products. Instead, phenyl groups are introduced by the liquid phase reaction of benzene with $HSiCl_3$ or $HMeSiCl_2$, catalyzed by boron trichloride (equations 10 and 11). This reaction proceeds through the intermediate formation of B–H bonds, and then of phenylboron chlorides, which transfer phenyl groups to the silicon.

$$PhCl + Si \xrightarrow{Ag} Ph_2SiCl_2, PhSiCl_3, Ph_3SiCl, \text{etc.} \tag{9}$$

$$C_6H_6 + HSiCl_3 \xrightarrow{BCl_3} PhSiCl_3 \tag{10}$$

$$C_6H_6 + HMeSiCl_2 \xrightarrow{BCl_3} PhSiMeCl_2 \tag{11}$$

Other substituent groups are usually introduced via *Hydrosilation* reactions.[19,20] In this important reaction, Si–H bonds add across C=C or C≡C bonds in 1,2 fashion to give products. Many transition metals and their complexes will catalyze hydrosilation, but the usual catalyst is platinum (*see* ***Hydrosilation Catalysis***). Thus $CF_3CH_2CH_2Si(Me)Cl_2$ is made by hydrosilation of 3,3,3-trifluoropropene with methyldichlorosilane (equation 12). n-Alkylmethyldichlorosilanes can be made similarly, by hydrosilation of 1-alkenes. Vinylmethyldichlorosilane may be obtained in analogous fashion by hydrosilation of acetylene, as shown in equation (13). An alternate route to the same compound is hydrosilation of vinyl chloride, followed by dehydrochlorination (equations 14 and 15).

$$CF_3CH{=}CH_2 + MeSiHCl_2 \xrightarrow{Pt} CF_3CH_2CH_2SiMeCl_2 \tag{12}$$

$$HC{\equiv}CH + MeSiHCl_2 \longrightarrow H_2C{=}CHSiMeCl_2 \tag{13}$$

$$H_2C{=}CHCl + MeSiHCl_2 \longrightarrow H_2C{=}CHSiMeCl_2 \tag{14}$$

$$MeCHClSiMeCl_2 \xrightarrow[-HCl]{\Delta} H_2C{=}CHSiMeCl_2 \tag{15}$$

The platinum catalyst is effective in very small amounts, and can be introduced as H_2PtCl_6 or as elemental platinum on an inert support. A particularly active catalyst is the soluble platinum complex of divinyltetramethyldisiloxane, $CH_2{=}CHSiMe_2{-}O{-}SiMe_2CH{=}CH_2$. The hydrosilylation reaction operates through the Chalk-Harrod mechanism or one of its variants.[21,22] In these mechanisms, the first step involves the conversion of a metal alkene complex to a metal alkene silyl hydride complex. In addition to platinum, recently ruthenium, rhodium, palladium, copper, and zinc complexes are being studied as hydrosilation catalysts.[23–28]

3.3 Hydrolysis

The next step in the synthesis of silicone polymers is the hydrolysis of dimethyldichlorosilane, giving HCl and a mixture of cyclic and linear oligomeric polysiloxanes (equation 16). The rate of reaction between Me_2SiCl_2 and water is rapid, and is limited by the transfer across the aqueous–organic phase boundary.[2] Accordingly the hydrolysis is best carried out under highly turbulent conditions, often in a continuous loop reactor, with the aqueous phase being a concentrated HCl solution. A typical product mix from the hydrolysis is given in Table 3.

$$MeSiCl_2 \xrightarrow{H_2O} (Me_2SiO)_n + HO(SiMe_2O)_mH + HCl \tag{16}$$

It is interesting to note that the eight-membered ring compound D_4 is the major product in the cyclic fraction, with only small amounts of the six-ring D_3 being formed. This is because of ring strain in D_3 (discussed in Section 5). An inert organic diluent (heptane) is sometimes added to facilitate separation of the siloxane and aqueous phases; this increases the yield of cyclic products since dilution favors intramolecular cyclization. The degree of polymerization of the α,ω-dihydroxysiloxane oligomer portion is typically $\approx$18, but depends on the exact hydrolysis conditions. In practice, the hydrolysis conditions can be varied to produce a larger amount of cyclic or of linear oligomers, depending on plant requirements at the time.

If desired, the linear oligosiloxanes, and indeed any linear polydimethylsiloxane, can be converted into cyclosiloxanes by base-catalyzed pyrolysis. If this reaction is carried out under equilibrating conditions and the products are fractionally distilled with removal only of the most volatile compound, D_3, the entire mixture can be converted to this valuable intermediate. This procedure is frequently used to obtain pure D_3 and D_4, useful for polymer synthesis by ring-opening polymerization.

Sometimes, prior to aqueous hydrolysis, chlorosilanes are converted to methoxysilanes by treatment with methanol (equations 17 and 18). Hydrolysis of methoxysilanes is much slower than for chlorosilanes, but has the advantage that no HCl is formed in the reaction.

$$Me_2SiCl_2 + 2MeOH \longrightarrow Me_2Si(OMe)_2 + 2HCl \tag{17}$$

$$Me_2Si(OMe)_2 + H_2O \longrightarrow (Me_2SiO)_n + MeOH \tag{18}$$

3.4 Polymerization

The usual method for obtaining linear silicone polymers is by ring-opening polymerization[3,29–31] reactions on cyclic

Table 3 Typical products from hydrolysis of dimethyldichlorosilane

	%	Mp (°C)	Bp (°C)
D3	1	64	134
D4	42	17	175
D5	7	−38	210
D6	2	−3	245
Linear oligomers	47		

siloxanes such as D_4 or D_3, or mixed D_n oligomers. Such polymerization can be carried out under acidic or basic conditions, but base catalysis is generally preferred. Suitable catalysts are KOH or tetraalkylammonium hydroxides. Molecular weight is controlled by addition of chain-blocking substituents such as hexamethyldisiloxane, MM. Thus to make a dimethylsilicone oil of a selected average molecular weight, D_4 can be equilibrated with the calculated amount of MM, as shown in equation (19).

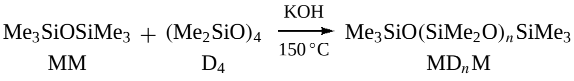

$$\underset{\text{MM}}{\text{Me}_3\text{SiOSiMe}_3} + \underset{\text{D}_4}{(\text{Me}_2\text{SiO})_4} \xrightarrow[150\,^\circ\text{C}]{\text{KOH}} \underset{\text{MD}_n\text{M}}{\text{Me}_3\text{SiO}(\text{SiMe}_2\text{O})_n\text{SiMe}_3} \quad (19)$$

In the absence of chain-terminating additives, an equilibrium mixture of cyclic and linear siloxanes is obtained, containing about 13% of rings from D_4 to D_{10}, about 3% of molecules from D_{10} to D_{1000}, the remaining 84% being high polymer with $DP > 1000$. (The ring-strained D_3 molecule is not present at equilibrium, except at very high temperatures.) This is the process used to make the gum stock for silicone elastomers. The equilibrium mixture is neutralized to destroy the catalyst and the low-molecular weight cyclic compounds are distilled out under vacuum, leaving a polymer with average molecular weight greater than one million. The kinetics and mechanism of the ring-opening reaction have been investigated in some detail.[3,29–31]

The initial step in base-catalyzed ring opening is cleavage of a cyclosiloxane ring to form a silanolate anion; attack of silanolate on cyclic molecules is then the chain-extending reaction (equation 20). Polar solvents or additives (DMSO, crown ethers, HMPA) promote the reaction by solvating the cation of the ion pair. Chain cleavage by back biting can take place, however, to give an equilibrium mixture containing both cyclic and linear polymeric siloxanes. If two different cyclosiloxanes are mixed and ring opened, the initially formed polymer is likely to be block-like, because the rates of ring opening depend on substitution at silicon. Long heating with catalyst present will ultimately produce a random copolymer.

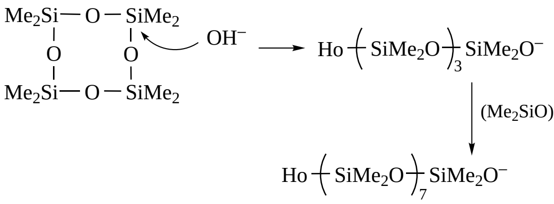

(20)

The rate of ring opening also depends on ring size. D_3, which contains strained Si–O–Si bonds, is much more reactive than D_4 or D_5 with lithium catalysts such as *n*-butyllithium. As shown in equation (21), D_3 undergoes ring-opening polymerization by successive addition of D_3 units without equilibration, to give a monodisperse 'living polymer'. This reaction provides a useful means for generating block copolymers of two different silicon monomers, by using a second cyclotrisiloxane (equation 22).

$$n\text{-BuLi} + \text{D}_3 \longrightarrow \underset{(n\text{-BuD}_3{}^-)}{n\text{-Bu}(\text{SiMe}_2\text{O})_2\text{SiMe}_2\overset{-}{\text{O}}\overset{+}{\text{Li}}} \xrightarrow{\text{D}_3}$$

$$n\text{-BuD}_6{}^- \xrightarrow{\text{D}_3} n\text{-BuD}_9{}^- \xrightarrow{\text{D}_3} n\text{-BuD}_{12}{}^- \quad (21)$$

$$n\text{-Bu}(\text{D}_3)_n{}^- + m\text{D}'_3 \longrightarrow n\text{-Bu}(\text{D}_3)_n(\text{D}'_3)_m \quad (22)$$

Silicon–hydrogen bonds react with strong bases, so cyclosiloxanes containing hydrogen attached to silicon, for example $(\text{MeSiHO})_4$, $(\text{D}^\text{H}{}_4)$, cannot be polymerized under basic conditions. The Si–H bond, however, survives under acidic conditions, and therefore acid-catalyzed ring opening is used to make siloxane polymers with hydrogen bonded to silicon.[3] Catalysts include H_2SO_4 absorbed on clay or carbon, sulfonic acids, or the acid form of sulfonated polystyrene resins. Polymerization of siloxane monomers with Lewis acid catalysts such as phosphonitrile chloride has been the subject of study recently.[31,32]

Condensation reactions of silanols provides another method for polysiloxane synthesis. Hydroxy-terminated siloxane oligomers or polymers can be further condensed to polymers of higher molecular weight by condensation with loss of water (equation 23). This reaction is catalyzed by various metal salts; tin salts have been widely used. Mixtures of two different α,ω-dihydroxysiloxane oligomers may be condensed to give block copolymers.

$$\sim\!\sim\,\text{Si—OH} + \text{HO—Si}\,\sim\!\sim \xrightarrow{-\text{H}_2\text{O}} \sim\!\sim\,\text{SiOSi}\,\sim\!\sim \quad (23)$$

A relatively new process for siloxane manufacture is aqueous phase emulsion polymerization.[33,34] Cyclosiloxanes such as D_4 when mixed with water and alkylbenzenesulfonates as a surfactant, along with some free sulfonic acid, form an emulsion. When the mixture is heated to $>60\,^\circ\text{C}$, ring opening of the cyclosiloxane takes place to give α,ω-dihydroxy oligosiloxanes, which undergo acid-catalyzed condensation to form long-chain siloxanes.

4 SILICONE MATERIALS

4.1 Siloxane Fluids

The silicone fluids are normally chain-blocked linear polymers, manufactured by ring-opening polymerization, as described in Section 3.4. The dimethylsiloxane polymers are by far the most important, but to make fluids for high-temperature use, phenylmethylsiloxane units are also included in the polymer.

4.2 Silicone Elastomers: Heat-cured[35]

The starting material is a high molecular weight polysiloxane gum made by ring-opening polymerization. To convert the gum into a useful elastomer, cross-linking is essential. This can be brought about by radicals from the decomposition of organic peroxides. Abstraction of hydrogen atoms from methyl groups takes place, and the siloxane chains become joined by Si–CH_2–CH_2–Si linkages.

In a modern variant of this vulcanization reaction, polysiloxanes containing a small amount, <1%, of methylvinylsiloxane groups are the starting materials. Aryl or alkyl peroxides are again used to initiate cross-linking, but the chemistry now involves radical addition to vinyl groups on neighboring siloxane chains, depicted in Scheme 1.

The tensile strength of cross-linked polysiloxane elastomers is low, but can be markedly improved by reinforcement with a filler. The material of choice is fumed silica with high surface area, which can increase the strength by a factor of 20. It is thought that the silica particles agglomerate to form a three-dimensional network within the siloxane, greatly reinforcing the structure.

The silica particles, however, contain reactive Si–OH groups, which can condense with Si–OH end units of the gum, forming a prematurely cross-linked elastomer during mixing. These sites can be tamed by reaction with hexamethyldisilazane, $Me_3SiNHSiMe_3$, which converts them to inactive trimethylsiloxy groups (equation 24). An even better method is pretreatment of the silica by heating it with short-chain, hydroxy-terminated siloxane oligomers. Presumably these condense with the Si–OH groups to form siloxane bonds, giving a siloxanized surface which is highly compatible with the elastomer.

$$2\ \sim\!\sim\mathrm{Si{-}OH} + \mathrm{Me_3SiNHSiMe_3} \longrightarrow 2\ \sim\!\sim\mathrm{SiOSiMe_3} + \mathrm{NH_3} \qquad (24)$$

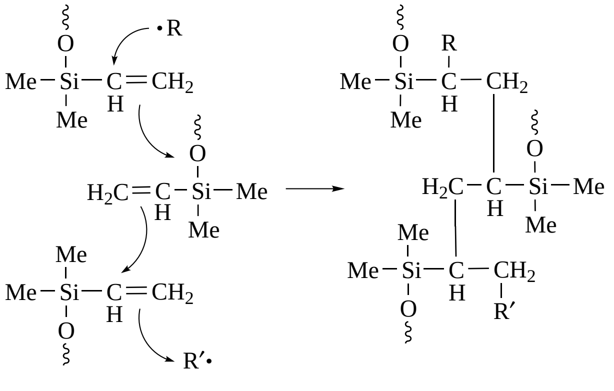

Scheme 1 Radical cross-linking of vinyl-containing polysiloxanes

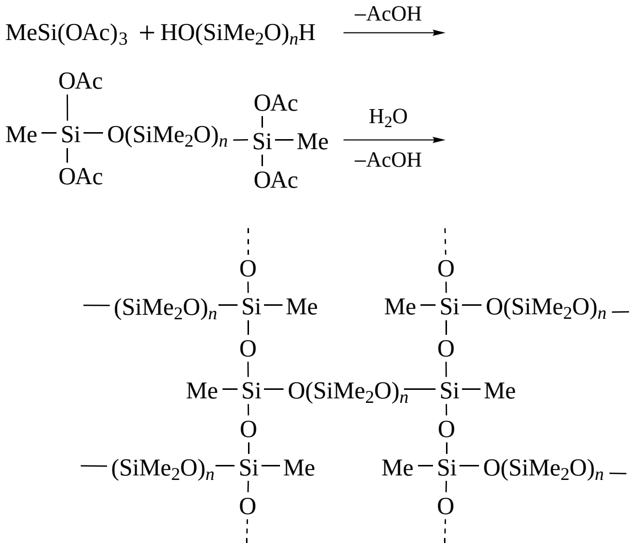

Scheme 2 Formation and cross-linking of tetraacetoxy RTV silicone

4.3 Room Temperature Vulcanizing ('RTV') Elastomers

These are silicones in liquid or paste form that can be transformed into cross-linked elastomers at or near room temperature.[36] There are two basic types, one component and two component. The one-component room temperature vulcanizing (RTV) elastomers cure upon exposure to air. A typical material of this type is synthesized from a dihydroxy-terminated siloxane oligomer and methyltriacetoxysilane (Scheme 2). The resulting tetraacetoxy compound will flow as a paste and so can be molded into shape. Hydrolysis of the acetoxy groups takes place over a period of hours. Condensation of the resulting silanols gives a highly cross-linked end product.

RTV siloxanes with alkoxy groups in place of acetoxy groups are now being used, and offer the advantage that no acid is formed during the cure. The hydrolysis of alkoxy groups is slower, but can be catalyzed with metal salts.

Two-component RTV elastomers have been developed, based on a variety of chemical reactions. Three systems will be illustrated here:

1. Hydroxy-terminated siloxane oligomers are mixed with trialkoxysilanes; catalysis by Sn^{2+} leads to condensation and cross-linking through Si–O–Si bonds, with loss of ethanol (equation 25).

$$\mathrm{HO{-}Si}\sim\!\sim\mathrm{Si{-}OH} + \mathrm{RSi(OEt)_3} \xrightarrow{\mathrm{Sn^{2+}}} \begin{array}{c}\text{cross-linked}\\ \text{polymer}\end{array} + \mathrm{ROH} \qquad (25)$$

2. Alkoxy-terminated siloxanes are treated with a trialkoxy-silane, in the presence of *t*-butyl titanate and a little water. Solvolysis followed by condensation produces the cross-linked polymer (equation 26).

$$\text{ROSi}\sim\text{Si}-\text{OR} + \text{R}'\text{Si(OR)}_3 \xrightarrow[\text{H}_2\text{O}]{(t\text{-BuO})_4\text{Ti}} \text{cross-linked polymer} + \text{ROH} \tag{26}$$

3. A vinyl-terminated siloxane polymer is mixed with a compound containing several Si–H groups, such as D_4^H, $(MeSiHO)_4$; in the presence of a platinum catalyst, hydrosilation takes place to give Si–CH_2–CH_2–Si cross-links (equation 27). A related platinum-catalyzed system employs two siloxane prepolymers, one containing some Si–H bonds and the other Si–vinyl groups. The platinum catalyst is active in extremely small amounts, so that its use is practical despite the high cost of platinum.

$$\text{H}_2\text{C}=\text{CH}-\text{Si}\sim\text{Si}-\text{CH}=\text{CH}_2 + (\text{MeSiHO})_4 \xrightarrow{\text{Pt}} \text{cross-linked polymer} \tag{27}$$

4.4 Siloxane Copolymers

Specialty polymers in which siloxanes are combined with organic polymers are a growing part of the silicone industry.[37–39] Many compositions have been described, of which only a few will be mentioned here.

Linear polysiloxanes having reactive terminal groups are often condensed with reactive organic polymers. For example, hydroxy-terminated siloxanes can be condensed with a carboxy-terminated polyester, as illustrated in equation (28). The resulting polymers behave as thermoplastic elastomers, having some of the desirable properties of both siloxanes and polyesters. Similar condensation reactions have been used to synthesize siloxane copolymers with polyamides, polyethers, polycarbonates, and so on.

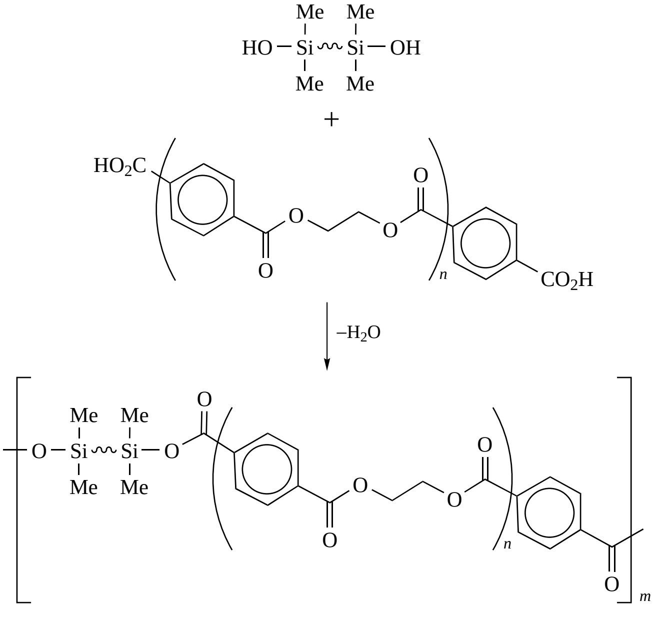

(28)

In another approach to copolymers, linear H-terminated polysiloxanes are hydrosilated to introduce reactive groups. Examples are the addition of allylamine to give reactive intermediates that can be converted to polysiloxane–polyimides or polyamides, and the hydrosilylation of allyl glycidyl ether to produce a silicone that can be copolymerized with epoxides or acrylates (equations 29 and 30).

$$\text{H}-\text{Si}\sim\text{Si}-\text{H} + \text{H}_2\text{C}=\text{CHCH}_2\text{NH}_2 \longrightarrow \text{H}_2\text{N(CH}_2)_3\text{Si}\sim\text{Si(CH}_2)_3\text{NH} \tag{29}$$

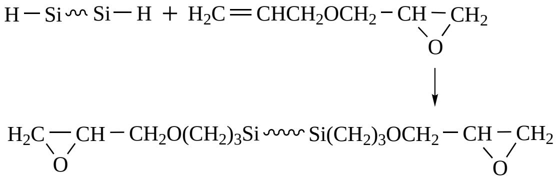
H — Si ~ Si — H + H2C = CHCH2OCH2 − CH − CH2
O
H2C — CH − CH2O(CH2)3Si ~ Si(CH2)3OCH2 − CH − CH2
O

(30)

Polysiloxanes with hydrogen atoms on the main chain are also modified by hydrosilylation with allyl glycidyl ether. The epoxy side groups may then be transformed into ionic substituents, as illustrated in Scheme 3. The resulting polysiloxanes with ionic side groups have good properties as hair and textile conditioners.

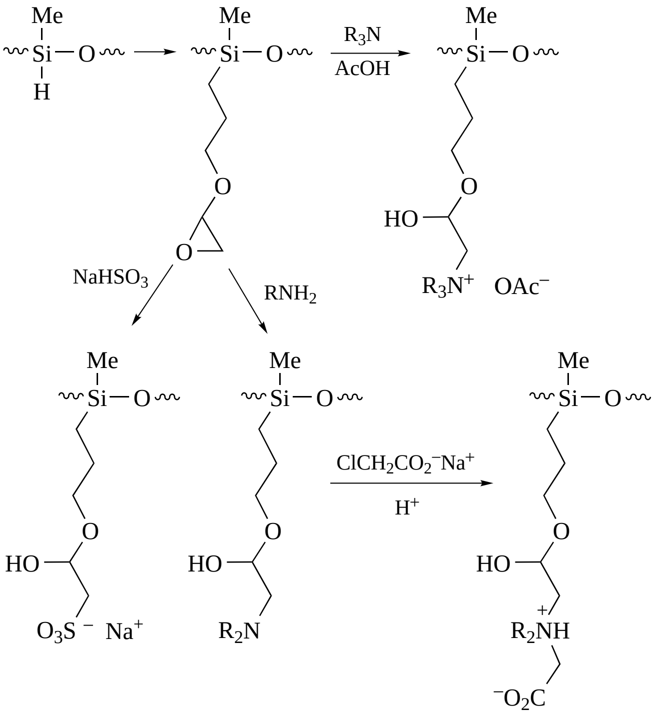

Scheme 3 Synthesis of polysiloxanes with ionic side chains

4.5 Silicone Resins

These are cross-linked compositions, containing trifunctional (T) or tetrafunctional (Q) silicon units. The simplest are produced from methyltrichlorosilane, by hydrolysis, either directly or after intermediate conversion to methyltrialkoxysilanes. Smaller amounts of dimethylsiloxane or trimethylsiloxane units may be introduced, as the corresponding chloro- or alkoxysilanes, to increase flexibility of the resin. Curing is brought about by aqueous solvolysis, usually catalyzed by metal salts, leading to highly cross-linked siloxane structures. More typical silicone resins contain mixtures of phenyl- or alkyltriethoxysilanes, mixed with $MeSi(OEt)_3$ and perhaps $Me_2Si(OEt)_2$ or Me_3SiOEt.

Depending on the composition, silicone resins may be soluble in organic solvents, or insoluble and therefore sold as aqueous emulsions. Because of their three-dimensional nature, the structures of silicone resins are complex and poorly understood. Under certain conditions cage molecules can be produced, such as the cubic structure $(RSiO)_8$ (**1**). The phenylsilicone resins, $(PhSiO)_{3/2}$, are often supposed to be ladder polymers (**2**), but the evidence for this structure is ambiguous.[40] Recent X-ray diffraction studies suggest that the resin is probably a mixture of two components: one amorphous and the other showing a regular structure in which the regular structure could be a mixture of partial cage or partial ladder structures.[41]

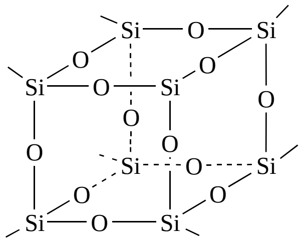
(**1**)

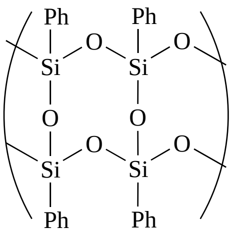
(**2**)

The single largest use of silicone resins is as water repellents for stone and masonry. The resins also find important applications in paints and finishes, especially for high-temperature use, and increasingly as additives to conventional paints. Among the numerous speciality uses which have also been developed, siloxane resins are used to coat pharmaceutical pills and as encapsulants for electronic components.

5 STRUCTURE AND PROPERTIES OF SILOXANES

The unique properties of the silicones undoubtedly reflect the structure, dynamics, and chemical bonding in these polymers, all of which are unusual. In the polydimethylsiloxane chain (Figure 3), the O–Si–O angles of 109° are nearly tetrahedral as expected, but the Si–O–Si angles have the abnormal value of 143°.[42] Large Si–O–Si bond angles of 140–145° are present in unhindered disiloxanes, so this value can be taken as the preferred unconstrained siloxane bond angle. Even larger bond angles up to 180° are found for hindered disiloxanes like $Ph_3SiOSiPh_3$. The O–Si–O and Si–O–Si angles in D_4, 109° and 143° show that this eight-membered ring is free of angle strain; larger cyclosiloxanes can also adopt strain-free conformations. In cyclotrisiloxanes, however, the O–Si–O angle is slightly decreased to 107°, and the Si–O–Si angle is strongly bent, down to 130–135°. Cyclotrisiloxanes therefore possess extra energy owing to angle strain, which accounts for their higher reactivity.

Along the random-coil polydimethylsiloxane chain, the trans arrangement is favored over *gauche*, but the rational barrier at oxygen is immeasurably low, probably less than $0.8\,\mathrm{kJ\,mol^{-1}}$. In addition, the Si–O–Si bonds probably undergo bending deformation quite easily.[43] In model compounds, the restoring force for Si–O–Si bond bending is very small. These factors probably combine to make the polysiloxane chain extremely flexible. The high degree of motion of the siloxane chains can explain the very low glass transition temperatures, high permeability, low change of viscosity with temperature, and low surface tension, all important characteristics of silicones.

Although Si–O bonds are polar (*see Photoconductivity*), the silicones are nevertheless hydrophobic (*see Hydrophobicity*) and indeed are highly useful as water-repellent materials. This paradoxical behavior must mean that the extreme flexibility and motion within the polysiloxane chain is more important than the polar character of the bonds. Presumably, the methyl groups sweep out a large volume due to the motions of the siloxane chain, so that incoming polar molecules mainly contact methyl groups rather than Si–O bonds. In addition, there is evidence that the Si–O bonds in siloxanes are actually much less polar than would be expected from the large *Electronegativity* difference between Si and O. Evidence for this is that siloxanes are very weak Lewis bases compared to ethers or alkoxysilanes.[44,45] The present theoretical explanation for the reduced basicity and polarity of siloxanes is that lone pair electrons on oxygen are delocalized into antibonding Si–C orbitals ($n-\sigma^*$ overlap).[46]

Another paradoxical property of silicones is their activity as surfactants.[47] Conventional surfactant molecules contain a hydrophilic (*see Hydrophilicity*) as well as a hydrophobic portion, but for siloxanes no hydrophilic group is necessary;

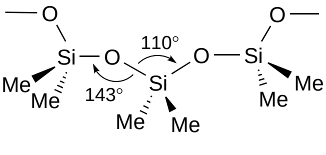

Figure 3 Segment of a dimethylpolysiloxane chain

silicones themselves can behave as surfactants. Probably the surface-active properties result because the siloxanes occupy a water–oil interface, with the more polar Si–O bonds at the aqueous surface and the organic groups in the hydrocarbon phase. The surfactant property of siloxanes makes them useful as foam stabilizers, for example, in the manufacture of polyurethane foam polymers. The molecular weight must be carefully controlled, however. If the molecular weight of the silicone is too high, it becomes insoluble, and then has the opposite effect of destroying the foam! Insoluble silicones, usually resins, are in fact employed as antifoam agents in various manufacturing processes.

Polysiloxanes with two different groups attached to silicon, such as $(PhSiMeO)_n$, contain stereogenic centers at silicon. Polymers having this type of substitution appear to be atactic or nearly so. However, stereoregular polysiloxanes have been synthesized recently by several research groups.[48–51]

6 POLYSILANES

6.1 General Introduction to Polysilane Polymers

As the name implies, polysilane polymers consist of chains made up exclusively of silicon atoms. (In the literature these polymers are named either as polysilanes or poly(silylenes); thus $(Et_2Si)_n$ can be called polydiethylsilane or poly(diethylsilylene).) Unlike the heteroatomic polysiloxanes, with alternating silicon and oxygen atoms in the polymer backbone, the polysilanes are homoatomic and therefore structurally closer to alkene polymers. However, because the atoms in the main chain are all silicon, the polysilanes show quite special properties.[6–9,52]

The cumulated silicon–silicon bonds in the polymer chain permit extensive electron delocalization to occur. The result is that the photochemical and electronic properties of polysilanes are very different from those of most other polymers, and somewhat resemble those of π-conjugated polymers such as polyacetylene, polyaniline, and polythiophene. The electron delocalization is unusual in that it involves the σ electrons of the polysilane chain, whereas in other electron-delocalized polymers the electron mobility depends on π conjugation (Figure 4). The polysilanes and related polygermanes are unique in displaying large effects owing to σ-electron conjugation. Many of the technological uses suggested for polysilanes are based on this remarkable property.

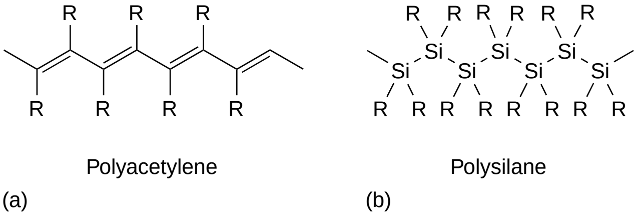

Figure 4 (a) Polyacetylene, π conjugated; (b) polysilane, σ conjugated

In linear polysilanes, silicon–silicon bonds occupy two of the four valences on each silicon atom; the other valences are taken up by bonds to substituent groups, which may be the same (**3**) or different (**4**). Exact silicon analogs to alkene polymers like polyethylene, with two hydrogen atoms on silicon, are little known because of their high reactivity. The reactivity is greatly reduced if the pendent groups are organic groups, which can include alkyl, aryl, substituted alkyl or aryl, trimethylsilyl, ferrocenyl, and so on. Copolymers are also known (**5**). An example is the copolymer (**6**), which has the popular name ‘polysilastyrene’.

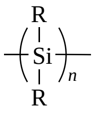
$-\!\left(\overset{R}{\underset{R}{Si}}\right)_n\!-$

(**3**)

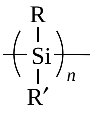
$-\!\left(\overset{R}{\underset{R'}{Si}}\right)_n\!-$

(**4**)

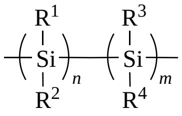
$-\!\left(\overset{R^1}{\underset{R^2}{Si}}\right)_n\!\!-\!\!\left(\overset{R^3}{\underset{R^4}{Si}}\right)_m\!-$

(**5**)

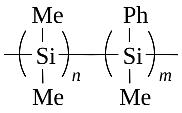
$-\!\left(\overset{Me}{\underset{Me}{Si}}\right)_n\!\!-\!\!\left(\overset{Ph}{\underset{Me}{Si}}\right)_m\!-$

(**6**)

The properties of polysilanes depend greatly on the nature of the substituent groups bonded to silicon. The range of properties varies from highly crystalline and insoluble, to partially crystalline or liquid crystalline, to glassy or rubbery amorphous materials. In general, the polysilane polymers are thermally stable to above 200 °C, and inert to water unless a hydrolyzable group such as halogen is present on the silicon. They are slowly degraded by UV light, a fact which limits their usefulness as structural materials.

The recent upsurge of interest in polysilanes stems from their uses in technology, both actual and potential. They are now being sold and used as precursors to silicon carbide ceramics.[53–57] Polysilanes are useful as photoresists[58–60] in the manufacture of microelectronic components, as shown especially by studies at IBM research laboratories.[7] These polymers are excellent charge-transport materials in an electric field[61] and so might find uses in electrophotography,[62] in novel printing technology, and in display devices. The polysilanes can serve as photoinitiators for radical reactions,[63,64] and have nonlinear optical properties, which makes them of interest for various uses in optical technology.[7,65–69] Some of these actual and potential applications will be discussed further in Section 9.

6.2 Historical Development

Oligomeric polysilanes, including the cyclic compounds $(Ph_2Si)_n, n = 4–6$, were prepared early in the 20th century, but high polymers were almost unknown until the late 1970s. Until quite recently, it was thought that silicon’s capability for chain formation was limited to a few atoms. The first description of a polysilane high polymer appeared in a 1949 paper by

Burkhard, who reported the synthesis of polydimethylsilane, $[Me_2Si]_n$, from sodium metal and dimethylchlorosilane in toluene (equation 31).[70] This polymer is a highly crystalline substance which decomposes without melting and is insoluble in all common solvents. Its intractable nature may have contributed to the relative neglect of polysilane polymers over the next three decades.

$$Me_2SiCl_2 + 2Na \xrightarrow[110\,^{\circ}C]{toluene} (Me_2Si)_n + 2NaCl \qquad (31)$$

During this time, however, cyclic and linear oligomeric polysilanes were studied, especially compounds in the permethyl series. These compounds exhibit unusual properties, reflecting electron delocalization over the silicon–silicon bonds. The linear permethylpolysilanes $Me(SiMe_2)_nMe$, have UV absorption bands which increase in wavelength and intensity as the chain length increases, behavior which resembles that of linear polyenes. Cyclic polysilanes, for example $(Me_2Si)_5$, can be reduced to anion radicals in which the unpaired electron is fully delocalized over the ring (equation 32), as shown by electron spin resonance (ESR) measurements.[71]

$$\underset{\text{Colorless}}{(Me_2Si)_5} \xrightarrow[-60\,^{\circ}C]{e^-,\ THF} \underset{\text{Blue}}{(Me_2Si)_5^{-\bullet}} \qquad (32)$$

Interest in polysilanes was reawakened in 1975, when Yajima and Hayashi found that permethylpolysilane could be transformed into silicon carbide by heating at high temperatures.[72,73] Soon afterward, papers on soluble, meltable polysilanes began to appear. The literature on polysilanes has grown rapidly since that time. The early focus on the synthesis and simple characterization of polysilanes has given way to detailed physical studies of the structure of these polymers, and of their electronic and photophysical properties.

7 POLYSILANES: SYNTHESIS

7.1 Sodium Condensation of Dichlorosilanes

The standard method for synthesis of polysilanes follows the original preparation of $(Me_2Si)_n$ by Burkhard. Diorganodichlorosilanes are treated with finely dispersed sodium metal in an inert diluent, usually above the melting point of sodium. Homopolymers are obtained from single dichlorosilanes, while cocondensation of mixtures of dichlorosilanes yields copolymers (equation 33). Toluene is the most commonly used solvent, but other aliphatic or aromatic solvents are also effective. After completion of the reaction, the mixture is quenched with alcohol and/or water to destroy any excess sodium and silyl anion, then filtered and the polymer is precipitated from hydrocarbon solution with a nonsolvent, usually 2-propanol.

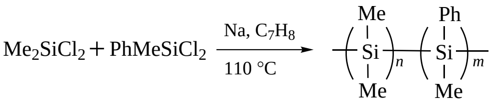

$$Me_2SiCl_2 + PhMeSiCl_2 \xrightarrow[110\,^{\circ}C]{Na,\ C_7H_8} \left(\underset{Me}{\overset{Me}{Si}}\right)_n \left(\underset{Me}{\overset{Ph}{Si}}\right)_m \qquad (33)$$

The yields of high polymer from this synthesis depend on the exact conditions and the nature of the substituent groups, but are typically low, from a few percent up to 60–70% in the most favorable cases. The by-products are mainly cyclosilanes, $(RR'Si)_n$ where $n = 4–6$. The molecular weight distributions of the polymers obtained by this procedure are usually bimodal, as shown in Figure 5.[74] Various attempts have been made to improve the sodium condensation, including sonication and the addition of crown ethers and other additives, with some success.[75,76]

Several studies of the mechanism of the sodium coupling reaction have been carried out, and a mechanistic model has emerged which accounts for most of the experimental observations.[6,77,78] The reaction chain appears to be anionic in nature. The first step is believed to be the slow reaction of the dichlorosilane with sodium to give an anion (equation 34). The chain-extending process is the reaction of polymer silyl anions with dichlorosilane molecules (equation 35), followed by rapid reduction of the chlorine-terminated polymer to the anion (equation 36). Reduction must take place at the surface of a sodium particle. As polymerization occurs, some molecules may break free from the sodium surface; once in solution away from the metal, chain extension would cease. This portion may give rise to the low-molecular weight polymer. Other molecules probably become entangled at the sodium surface and so cannot break free. They therefore continue to react with fresh dichlorosilane, and eventually

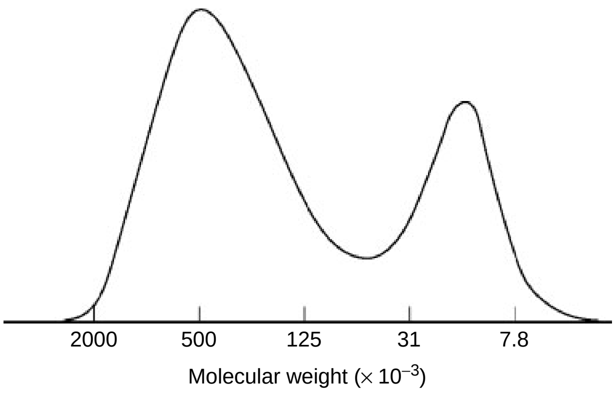

Figure 5 Gel permeation chromatograph of poly(methyl-*n*-hexylsilylene), showing bimodal molecular weight distribution

contribute the high molecular weight fraction.

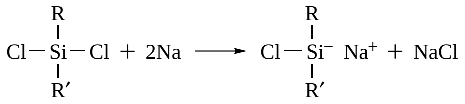

$$\mathrm{Cl{-}\overset{R}{\underset{R'}{Si}}{-}Cl + 2Na \longrightarrow Cl{-}\overset{R}{\underset{R'}{Si^{-}}}\ Na^{+} + NaCl} \qquad (34)$$

(very slow)

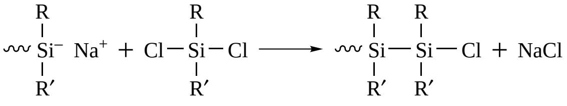

$$\mathrm{\sim\overset{R}{\underset{R'}{Si^{-}}}\ Na^{+} + Cl{-}\overset{R}{\underset{R'}{Si}}{-}Cl \longrightarrow \sim\overset{R}{\underset{R'}{Si}}{-}\overset{R}{\underset{R'}{Si}}{-}Cl + NaCl} \qquad (35)$$

(fast but rate-determining)

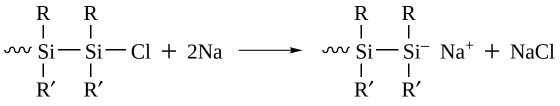

$$\mathrm{\sim\overset{R}{\underset{R'}{Si}}{-}\overset{R}{\underset{R'}{Si}}{-}Cl + 2Na \longrightarrow \sim\overset{R}{\underset{R'}{Si}}{-}\overset{R}{\underset{R'}{Si^{-}}}\ Na^{+} + NaCl} \qquad (36)$$

(very fast)

7.2 Polymerization of Masked Disilenes

Polyalkenes are invariably made by polymerization of alkenes. Why is an analogous route, the polymerization of disilenes, $R_2Si{=}SiR_2$, not used to make polysilanes? The reason is that the barrier to polymerization of disilenes is simply too low, so that in most cases they polymerize or oligomerize as soon as they are generated. Stable disilenes can be made and isolated, but only with very bulky substituents at the silicon which make the polymer less stable than the disilene.[79] An example is tetramesityldisilene (**7**), a highly reactive compound that undergoes many novel chemical reactions but does not polymerize.

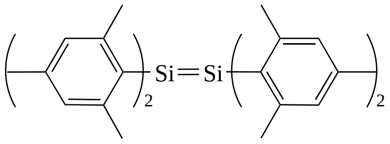

(**7**)

Anionic polymerization of 'masked disilenes' has been used for the synthesis of polysilanes.[80,81] The monomers are bridged disilabicyclooctadienes such as (**8**). Treatment of these with an organolithium compound converts them to 'living,' anionically terminated polysilanes (equation 37). The anionic ends of the polymers may be quenched with water, or used in further reactions, for instance, to generate block copolymers with other monomers such as styrene or butadiene. Polymerization of masked disilenes can also be used to obtain ordered polysilane copolymers, which are difficult to obtain by other methods.

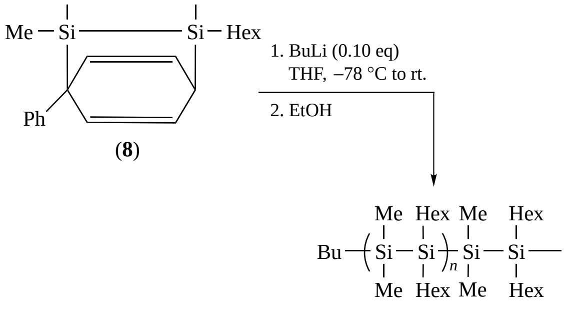

(37)

In addition to organolithium compounds, other reagents such as organomagnesium compounds and potassium alkoxides have also been used as initiator for anionic polymerization of masked disilenes.[82,83]

7.3 Ring-opening Polymerization

This method, which is the standard for polysiloxanes, is much less useful for polysilanes. One reason is that polysilane polymers are thermodynamically unstable compared to cyclosilanes. Thus, any method of polymerization leading to equilibration will produce cyclosilanes exclusively; the linear polymers can only be kinetic products.

Ring-opening polymerization can nevertheless be used to produce polysilanes, provided strained rings are used and the process does not proceed to equilibrium.[81] So far this method has been used to convert four-membered rings to polymers. Thermal ring opening transforms (MeSi-*n*-Hex)$_4$ to linear polymer (equation 38)[76] and anionic ring opening is effective for (PhSiMe)$_4$ (equation 39).[84,85] Photochemical technique has also been used recently for ring-opening polymerization to prepare polysilanes.[86]

$$(n\text{-HexSiMe})_4 \xrightarrow{\Delta} (n\text{-HexSiMe})_n \qquad (38)$$

$$(\mathrm{PhSiMe})_4 \xrightarrow{\mathrm{RLi}} (\mathrm{PhSiMe})_n \qquad (39)$$

7.4 Dehydrogenative Coupling

Condensation of diorganosilanes, $RR'SiH_2$, with loss of dihydrogen could provide a useful polysilane synthesis. Such dehydrogenative coupling, catalyzed by transition metals, has been extensively investigated.[87–89] The best catalysts are dialkyltitanocenes, Cp_2TiR_2, or zirconocene alkyls or hydrides, Cp_2ZrR_2 or Cp_2ZrH_2, however, late transition metal complexes (e.g. Wilkinson's catalyst) have also received attention lately. Diorganosilanes, R_2SiH_2, usually only undergo dimerization to $R_2SiH{-}SiHR_2$, but monoorganosilanes can be polymerized or oligomerized to moderate molecular weights. Arylsilanes are more reactive than alkyl derivatives, and the reaction has been best studied for phenylsilane (equation 40).

$$n\mathrm{RR'SiH_2} \xrightarrow{\text{catalyst}} \mathrm{H(SiRR')}_n\mathrm{H} + (n-1)\mathrm{H_2} \qquad (40)$$

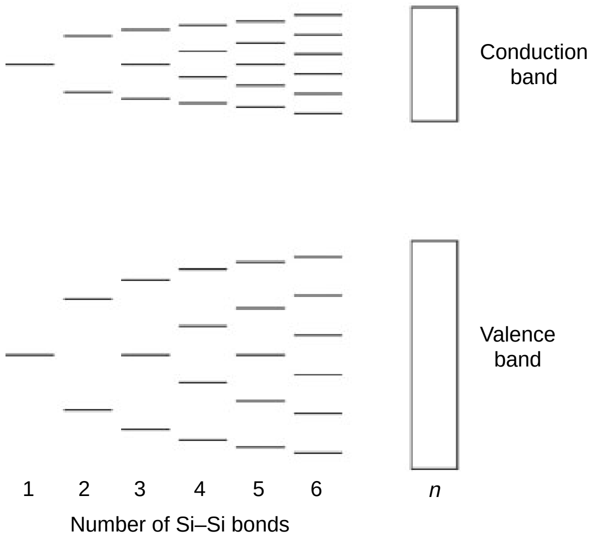

Figure 6 Schematic diagram showing splitting of filled and unfilled energy levels as the polysilane chain length increases, leading to formation of a valence band and a conduction band

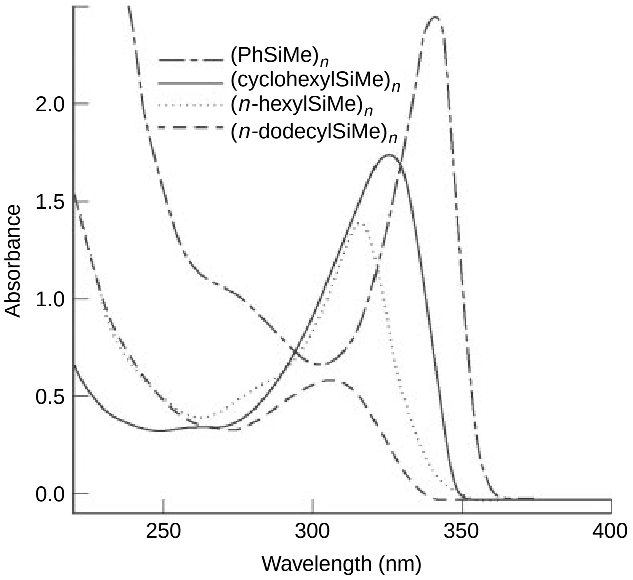

Figure 7 Typical UV spectra for polysilanes

8 POLYSILANES: ELECTRONIC PROPERTIES AND CONFORMATION

8.1 UV Absorption and Thermochromism

The σ-electron delocalization characteristic of polysilanes results in part from the low ionization potential for Si–Si σ electrons. The ionization potentials for polysilanes are often even lower than for alkenes. In addition, the resonance interaction between adjacent silicon orbitals is relatively large. The interaction can be viewed as one between neighboring Si–Si bonds, leading to an energy splitting. A similar interaction between antibonding Si–Si orbitals also takes place (Figure 6). As the number of silicon atoms increases, the energy gap between the filled σ and unfilled σ^* orbitals decreases. Eventually the filled orbitals combine to form a valence band, and the unfilled orbitals similarly generate a conduction band (*see Band Theory*).

The UV absorption by polysilanes involves promotion from the valence band to the conduction band, $\sigma \rightarrow \sigma^*$.[90] The absorption maxima for polysilanes typically lie between 300 and 400 nm (Figure 7), and are quite intense with $\varepsilon > 5000$ per Si–Si bond. In agreement with the model presented in Figure 6, the absorption maximum moves to a longer wavelength as the number of silicon atoms increases, eventually reaching a limit when the number of silicons is $\approx$30.

The polysilane σ–σ^* absorption wavelength, $\lambda_{\max}$, depends on the nature of the substituents, and depends quite strongly on the conformation of the polymer chain. The absorption band is shifted to a longer wavelength as the length of all-trans segments in the polymer chain increases. The number of trans junctions often increases with decreasing temperature, and as a result the polysilanes are often thermochromic (*see Thermochromism*), both in solution and as solids.[91] Sometimes the thermochromism is manifested by a gradual shift of the absorption band to lower energy; in other cases an abrupt thermochromic transition can be observed over a rather narrow temperature range. An example is shown in Figure 8 for poly(di-n-butylsilylene). This observation indicates that two forms of the polymer with different conformations are present in equilibrium, a surprising result. Thermochromism in polysilanes have been found to cause change in refractive index in polysilane films.[92] Thermochromism in polysilanes are found to be affected by the variation in side chain.[93] The UV absorption in polysilanes is affected by the solvent giving rise to solvatochromism.[93–96]

Another interesting behavior observed in polysilane films is ionochromism where the thermochromic frequency shift is either inhibited (negative inonochromism) or accelerated (positive ionochromism) upon addition of lithium salts.[97]

8.2 Conformation and Configuration

The solid-state structures of symmetrical di-n-alkylpolysilanes $(R_2Si)_n$ have been studied in some detail by X-ray crystallography, vibrational spectroscopy, and so on, and a partial summary is given in Table 4.

The lower members of the series, where $R =$ methyl to n-propyl, have all-trans conformations in the solid at ordinary temperatures, as do the polymers where $R = n$-hexyl, n-heptyl, and n-octyl. The two polymers with intermediate chain length, $R = n$-butyl and n-pentyl, instead have a 7/3 helical structure at room temperature.[7,98] Yet another conformation, alternating *trans–gauche* (TG–TG′), is found for the polymer where $R = n$-tetradecyl.[76] Above some

Table 4 Structures of Some polysilane polymers at 25 °C

Polymer	Structure	Torsion angle (°)	Polymer	Structure	Torsion angle (°)
$(Me_2Si)_n$	TT	180	$(n\text{-BuSi-}n\text{-Hex})_n$	Mesophase	–
$(n\text{-Pr}_2Si)_n$	TT	180	$(n\text{-Hex}_2Si)_n$	TT	180
$(n\text{-Bu}_2Si)_n$	7/3 helix	154	$(n\text{-Oct}_2Si)_n$	TT	180
$(n\text{-Pen}_2Si)_n$	7/3 helix	154	$[(n\text{-}C_{14}H_{29})_2Si]_n$	TGTG′	180, ≈90

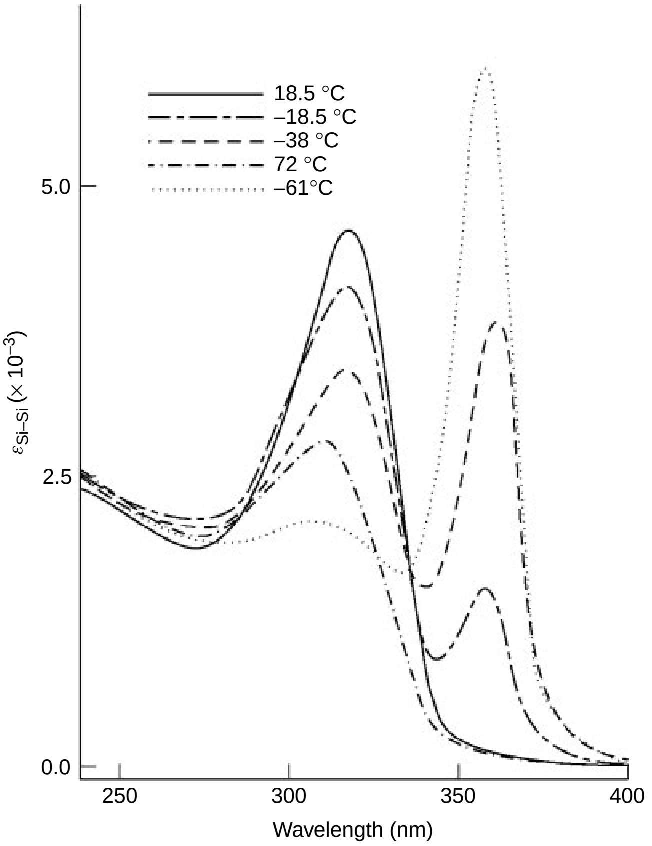

Figure 8 The UV spectrum for $(n\text{-butyl}_2Si)_n$ solutions in hexane as a function of temperature, showing an abrupt thermochromic transition

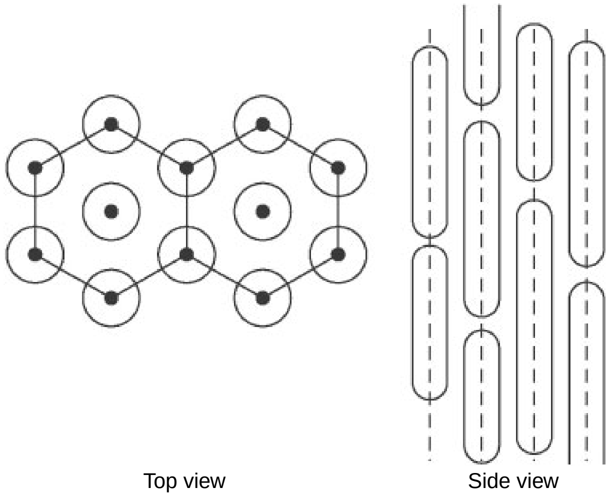

Figure 9 Schematic drawings showing the proposed arrangement of polysilane molecules in a hexagonal columnar liquid crystalline phase

transition temperature, many of the dialkylpolysilanes adopt a hexagonal, columnar liquid crystalline structure (Figure 9). For instance in poly(di-n-hexylsilylene), this transition takes place at 42 °C. Very recent studies indicate that polysilanes can exist in a variety of stable chain conformations.[99,100]

Polymers with two different alkyl substituents, $(RR'Si)_n$, are less crystalline. When the groups are very different in size the polymers are amorphous, as is the case for $(MeSi\text{-}n\text{-Hex})_n$, $(MeSi\text{-}n\text{-Bu})_n$, and $(MeSiPh)_n$. With groups of more nearly equal size, for example $(n\text{-BuSi-}n\text{-Hex})_n$, the columnar liquid crystalline structure is favored.[6,101] Copolymers, for example $(n\text{-Pr}_2Si)_n(n\text{-Hex}_2Si)_m$, $n/m \sim 1$, often also take the liquid crystalline arrangement. The many different structures which are observed for polysilanes reflects the great conformation flexibility in this class of polymers, consistent with theoretical calculations which indicate that the conformational preference is slight.

Less is known about the configurations of polysilane polymers. Dialkylpolysilanes such as $(MeSi\text{-}n\text{-Bu})_n$ made by sodium condensation appear to be atactic, from ^{29}Si NMR studies,[8] but arylalkylpolysilanes made by the same procedure appear to be partially tactic. Anionic ring-opening polymerization of $(PhSiMe)_4$ (Section 7.3) leads to a $(PhSiMe)_n$ polymer with greater, but still incomplete, stereoregularity.

8.3 Photophysics and Photochemistry

The polysilanes can be regarded as a series of loosely coupled chromophoric segments with mostly trans arrangement, separated by more pronounced kinks which break up the σ-conjugation. Transfer of energy from one segment to another in the polymer seems to be rapid, and the excitation thereby tends to become concentrated in the longer trans segments. Although the principal low-energy excitation is σ–σ^*, other excited states are undoubtedly present.[90]

The polysilanes generally exhibit intense, short-lived fluorescence. Competing with the fluorescence are photochemical reactions, of which three are most important. At high photon energy, the main reactions are silylene elimination (equation 41) and chain breaking to give silyl radicals (equation 42). A minor, but significant photoreaction is chain cleavage, with substituent migration to form a silylene (equation 43). At longer wavelengths, equation (41) does not take place and chain cleavage predominates.[102] The cross section (probability) for chain scission depends on the substituent groups, and is much greater in solution than in the solid state.

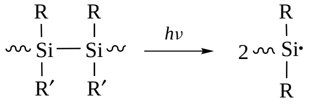

$$\sim\!\!\underset{R'}{\overset{R}{Si}}-\underset{R'}{\overset{R}{Si}}\!\!\sim \xrightarrow{h\nu} 2\sim\!\!\underset{R}{\overset{R}{Si}}\cdot \qquad (41)$$

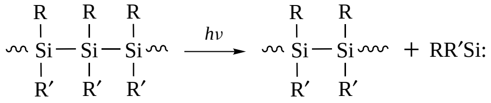

$$\sim\!\!\underset{R'}{\overset{R}{Si}}-\underset{R'}{\overset{R}{Si}}-\underset{R'}{\overset{R}{Si}}\!\!\sim \xrightarrow{h\nu} \sim\!\!\underset{R'}{\overset{R}{Si}}-\underset{R'}{\overset{R}{Si}}\!\!\sim + RR'Si: \qquad (42)$$

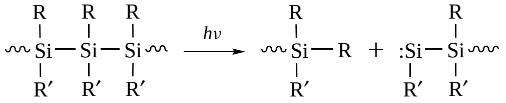

$$\sim\!\!\underset{R'}{\overset{R}{Si}}-\underset{R'}{\overset{R}{Si}}-\underset{R'}{\overset{R}{Si}}\!\!\sim \xrightarrow{h\nu} \sim\!\!\underset{R'}{\overset{R}{Si}}-R + :\underset{R'}{Si}-\underset{R'}{\overset{R}{Si}}\!\!\sim \qquad (43)$$

The various photoprocesses are important for several potential applications of polysilanes. Because of their intense fluorescence they have been suggested as scintillation materials for radiation detection. The chain-breaking reactions mean that polysilanes can be degraded by UV light; it is this property that makes them useful as photoresist materials.

9 TECHNOLOGICAL APPLICATIONS OF POLYSILANES

9.1 Silicon Carbide from Polysilanes

Polysilanes are now employed commercially as precursors for the synthesis of silicon carbide ceramics, either as fibers, foams, coatings, or solid monolithic objects.[7,8,55,56,103–106] This technology was initiated by the discovery in 1975 that silicon carbide could be made from $(Me_2Si)_n$, the original polysilane polymer.[2,10] In this process, $(Me_2Si)_n$ or the six-membered ring oligomer $(Me_2Si)_6$, are heated to near 450 °C. At this temperature complex rearrangement reactions take place. Methylene groups from the methyl substituents become inserted into the Si–Si bonds, so that the polysilane is largely transformed into a polymer with alternating silicon and carbon atoms, a polycarbosilane. This product is fractionated and can then be melt-spun into fibers. These are, however, meltable, so they must be rigidified by heating in air to form a thin coating of SiO_2 on the fiber surface. The heat-treated fibers are then reheated to high temperatures to obtain silicon carbide, with loss of CH_4 and H_2 (Scheme 4). Transformation to amorphous SiC is complete at about 280 °C; at still higher temperatures crystallites of β-SiC grow in the fiber, reinforcing and strengthening them. Maximum tensile strength is achieved at about 1300 °C.

This process is carried out in Japan by Nippon Carbon Co. to make NICALON silicon carbide fibers, with high tensile strength and excellent temperature and oxidation resistance. It can also be used to generate coatings and solid objects. Modifications of the basic process include the addition of borosiloxanes as catalysts, and the incorporation of titanium, in the form of titanium alkoxides, to produce fibers containing titanium and oxygen as well as silicon and carbon.

Of the other polysilanes which have been used as silicon carbide precursors, perhaps the best studied is ‘polysilasytrene’ (**6**). This polymer is used as a binder for finely divided silicon carbide powder, giving a mixture which can be injection molded. Firing then converts the molded object to silicon carbide.[6] The ceramic so produced is not fully dense, containing about 25% of void space from the hydrogen and hydrocarbons reheated during the firing. Although this reduces the ultimate strength somewhat, the microscopic ‘bubbles’ limit the growth of cracks, so that silicon carbide made by this process can be machined on a lathe.

Other more complex polymers have been employed as silicon carbide precursors. For instance, the mixture of methylchlorodisilanes obtained as a by-product in the direct synthesis of Me_2SiCl_2 can be redistributed with catalysts to give a polycyclic, partially cross-linked polymer with the approximate composition shown in equation (44). Pyrolysis of this precursor produces silicon carbide in good yield.[53] Partially cross-linked polymers made by condensing vinylmethyldichlorosilane and other methylchlorosilanes with sodium also are efficient precursors for silicon carbide.

Polysilanes have been used to prepare composite foams containing silicon carbide with aluminum nitride[103] or silicon nitride.[107]

$$MeCl_2SiSiCl_2Me + MeCl_2SiSiClMe_2 \xrightarrow[250^\circ]{Bu_4P^+Cl^-}$$

$$[(Me_2Si)_3(MeSi)_{17}Cl_5] \xrightarrow{\Delta} SiC \qquad (44)$$

9.2 Polysilanes as Photoresists for Microelectronics

In the manufacture of microchips and other microelectronic devices, the topography of the device is built up by sequential microlithography. A thin film of photosensitive material, a photoresist, is laid down on the substrate, usually a silicon wafer. The desired pattern is then transferred by exposing the wafer to light which causes a change in the photoresist layer. Because polysilanes are degraded by UV light, they are useful as positive-working photoresists.[7,108]

One application of polysilanes is in a bilayer construction, as shown in Figure 10. To cover existing topography on the wafer, a thin planarizing layer of a nonphotoactive polymer is deposited, followed by a very thin photoresist layer, about 0.5 to 0.2 μm in thickness. The wafer is exposed through a mask,

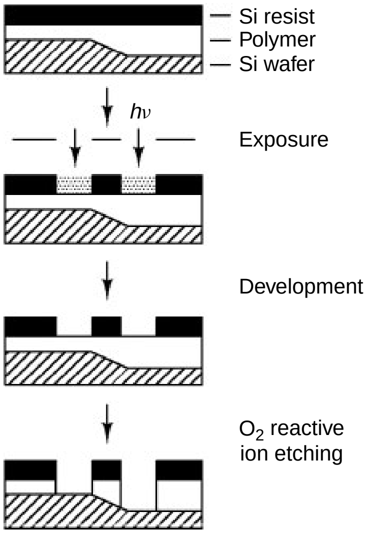

Figure 10 The use of a polysilane resist in a bilayer photolithographic process

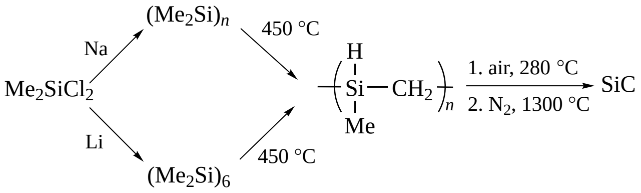

Scheme 4 Formation of silicon carbide from poly (dimethylsilylene)

with the result that the exposed portion of the polysilane is made more soluble than the unexposed polymer. The resist is then developed by a washing step in which the degraded polymer is removed, leaving the unexposed portion still in place. Next, the image is transferred through the planarizing layer by oxygen plasma etching. Polysilanes, and other silicon-containing photoresists, are advantageous because they form an inert coating of SiO_2 when contacted with the oxygen plasma, and so are not removed. The exposed planarizing layer is, however, etched away, down to the silicon surface, which can then be doped or otherwise altered. Following this processing all of the polymer can be removed, and the entire process repeated.

The wavelength of light used limits the resolution in microlithography, because at the present spacing of features diffraction effects are significant. The polysilanes, active in UV light, can provide greater resolution than visible-light photoresists. The light sensitivity of polysilanes is generally less than that of conventional photoresist materials which have light-amplifying properties. The polysilane light sensitivity can, however, be improved by careful design of the polymer and by the admixture of sensitizing additives.

9.3 Polysilanes as Photoinitiators

The photolytic cleavage of silanes to give silyl radicals can be used to induce radical chain reactions such as polymerization.[64,109] Several acrylate monomers have been polymerized with polysilanes as initiators, as well as styrene, and so on. The efficiency of polysilanes as radical photoinitiators is rather small, about an order of magnitude lower than conventional photoinitiators. The advantage of polysilanes lies in the fact that compared to most photoinitiators they are relatively insensitive to the effect of oxygen. This may be because oxygen-scavenging sites are generated along with radicals in the photolysis of polysilanes.[63]

9.4 Polysilanes as Hole Conductors in Electrophotography

In electrophotography, charges generated at a photoconductive surface are caused to migrate through a film under the influence of an electric field, and then used to produce an image. Because of the delocalization of Si–Si σ-electrons, the polysilanes show outstandingly good properties as hole conductors,[61] and are therefore promising materials for photocopying and printing applications.[62] Data for several materials are shown in Table 5. The films currently used in photocopiers are made of polycarbonate, doped with a triarylamine. The nitrogen atoms in the amine are the charge-carrying sites. Poly(phenylmethylsilylene) alone has hole mobility about as great as the materials now used commercially, and $(PhSiMe)_n$ with a triarylamine dopant added is about an order of magnitude faster.

By incorporating a charge-generating material onto a polysilane, a photoconductive film can be made. Very high photoconductivity has recently been observed for $(PhSiMe)_n$ doped with C_{60}, *Buckminsterfullerene*.[110] Photoconductive composite films of polysilane have been prepared by dispersing nanocrystalline silicon in the polymer.[111] Doping polysilanes with organic dyes have been used to prepare organic photoconductive films sensitive to particular wavelengths of light.[112]

The hole conducting property of silanes might made them very useful for preparing 'molecular wires'.[113]

Table 5 Charge mobility and activation energy for charge transport for electrophotographic polymers

Polymer	Hole mobility ($cm^2\,V^{-1}\,s^{-1}$)	Activation energy (eV)
Polyvinylcarbazole	10^{-8}	0.6
Amine-doped polycarbonate	10^{-4}	0.3–0.7
$(PhSiMe)_n$	$>10^{-4}$	0.28
Amine-doped $(PhSiMe)_n$	10^{-3}	–

10 RELATED ARTICLES

Hydrosilation Catalysis; Silicon: Organosilicon Chemistry.

11 REFERENCES

1. J. E. Mark, in 'Inorganic Polymers', eds. J. E. Mark, H. R. Allcock, and R. C. West, Prentice Hall, Englewood Cliffs, NJ, 1992.
2. F. O. Stark, J. R. Falender, and A. P. Wright, in 'Comprehensive Organometallic Chemistry', eds. G. Wilkinson, F. G. A. Stone, and E. W. Abel, Pergamon, Oxford, 1982, Vol. 2.
3. T. C. Kendrick, B. Parbhoo, and J. W. White, in 'The Chemistry of Organic Silicon Compounds', eds. S. Patai and Z. Rappoport, Wiley, New York, 1989, Vol. 2.
4. S. J. Clarson and J. A. Semlyen eds, 'Siloxane Polymers', Prentice Hall, Englewood Cliffs, NJ, 1993.
5. R. G. Jones, W. Ando, and J. Chojnowski eds, 'Silicon-Containing Polymers', Kluwer Academic Publishers, Dordrecht, 2000.
6. R. West, in 'Inorganic Polymers', eds. J. E. Mark, H. R. Allcock, and R. C. West, Prentice Hall, Englewood Cliffs, NJ, 1992, p. 186.
7. R. D. Miller and J. Michl, *Chem. Rev.*, 1989, **89**, 1359.
8. R. West, *J. Organomet. Chem.*, 1986, **300**, 327.
9. J. M. Zeigler and F. W. G. Fearon, *Adv. Chem. Ser.*, 1990, **224**, 1.
10. F. S. Kipping, *Proc. R. Soc. London*, 1937, **A159**, 139.
11. K. Feldner, 'Silicones: Chemistry and Technology', CRC Press, Boca Raton, FL, 1991, p. 7.
12. S. J. Clarson, in 'Synthesis and Properties of Silicones and Silicone-Modified Materials', ACS Symposium Series, eds. S. J. Clarson, J. J. Fitzgerald, M. J. Owen, S. D. Smith, and M. E. Van Dyke, ACS, Washington, DC, 2003, Vol. 838, p. 1.
13. E. G. Rochow, 'Silicon and Silicones', Springer-Verlag, Berlin, 1987.'',
14. L. N. Lewis, *J. Am. Chem. Soc.*, 1990, **112**, 5998.
15. J. M. Bablin, A. C. Crawford, D. C. DeMoulpied, and L. N. Lewis, *Ind. Eng. Chem. Res.*, 2003, **42**, 3555.
16. L. N. Lewis, *Polym. Prepr.*, 1998, **39**, 443.
17. M. Okamoto, S. Onodera, T. Okano, E. Suzuki, and Y. Ono, *J. Organomet. Chem.*, 1997, **531**, 67.
18. D. Seyferth, *Organometallics*, 2001, **20**, 4978.
19. J. L. Speier, *Adv. Organomet. Chem.*, 1979, **17**, 407.
20. B. Marciniec, *Silicon Chem.*, 2002, **1**, 155.
21. A. J. Chalk and J. F. Harrod, *J. Am. Chem. Soc.*, 1965, **87**, 16.
22. S. B. Duckett and R. N. Perutz, *Organometallics*, 1992, **11**, 90.
23. H. Brunner, *Angew. Chem., Int. Ed. Engl.*, 2004, **43**, 2749.
24. P. B. Glaser and T. D. Tilley, *J. Am. Chem. Soc.*, 2003, **125**, 13640.
25. Y. Otomaru and T. Hayashi, *Tetrahedron: Asymmetry*, 2004, **15**, 2647.
26. X.-X. Guo, J.-H. Xie, G.-H. Hou, W.-J. Shi, L.-X. Wang, and Q.-L. Zhou, *Tetrahedron: Asymmetry*, 2004, **15**, 2231.
27. D.-w. Lee and J. Yun, *Tetrahedron Lett.*, 2004, **45**, 5415.
28. V. Bette, A. Mortreux, F. Ferioli, G. Martelli, D. Savoia, and J.-F. Carpentier, *Eur. J. Org. Chem.*, 2004, 3040.
29. J. C. Saam, *Adv. Chem. Ser.*, 1990, **224**, 71.
30. C. J. Embery, S. R. Clarke, and J. G. Matisons, in 'Handbook of Organic-Inorganic Hybrid Materials and Nanocomposites', ed. H. S. Nalwa, American Scientific Publishers, Stevenson Ranch, CA, 2003, Vol. 2, p. 331.
31. C. J. Embery, J. G. Matisons, and S. R. Clarke, *ACS Symp. Ser.*, 2003, **838**, 26.
32. M. Fielden, L. G. Britcher, S. R. Clarke, C. J. Embery, and J. G. Matisons, *Polym. Prepr.*, 2001, **42**, 165.
33. M. Barrere, F. Ganachaud, D. Bendejacq, M.-A. Dourges, C. Maitre, and P. Hemery, *Polymer*, 2001, **42**, 7239.
34. A. De Gunzbourg, J.-C. Favier, and P. Hemery, *Polym. Int.*, 1994, **35**, 179.
35. S. J. Clarson, in 'Silicon-Containing Polymers', eds. R. G. Jones, W. Ando, and J. Chojnowski, Kluwer Academic Publishers, Dordrecht, 2000, p. 139.
36. W. Hechtl, 'Silicones: Chemistry and Technology', CRC Press, Boca Raton, FL, 1991, p. 45.
37. D. Wewers, 'Silicones: Chemistry and Technology', CRC Press, Boca Raton, FL, 1991, p. 75.
38. T. C. Kendrick, B. Parbhoo, and J. W. White, in 'Silicon-Heteroat. Bond', eds. S. Patai and Z. Rappoport, Wiley, Chichester, 1991, p. 67.
39. S. J. Clarson, J. J. Fitzgerald, M. J. S. Owen, D. Steven, and M. E. Van Dyke eds, 'Synthesis and Properties of Silicones and Silicone-Modified Materials', ACS, Washington, DC, 2003, Vol. 838; Symposium ACS National Meeting, San Diego, California, April 2–5, 2001.
40. C. L. Frye and J. M. Klosowski, *J. Am. Chem. Soc.*, 1971, **93**, 4599.
41. T. Takahashi, J. Kaschta, and H. Munstedt, *Rheol. Acta*, 2001, **40**, 490.
42. E. Lukevics, D. Pudova, and R. Sturkovich, 'Molecular Structure of Organosilicon Compounds', Ellis Horwood, Chichester, 1989, p. 191.
43. S. Grigoras and T. H. Lane, *Adv. Chem. Ser.*, 1990, **224**, 125.
44. R. West, L. S. Wilson, and D. L. Powell, *J. Organomet. Chem.*, 1979, **178**, 5.
45. B. D. Shepherd, *J. Am. Chem. Soc.*, 1991, **113**, 5581.

46. J. A. Tossell, J. H. Moore, K. McMillan, and M. A. Coplan, *J. Am. Chem. Soc.*, 1991, **113**, 1031.
47. M. J. Owen, *Adv. Chem. Ser.*, 1990, **224**, 705.
48. Y. Kawakami, *Polym. Adv. Technol.*, 2001, **12**, 658.
49. M. Murano, Y. Li, and Y. Kawakami, *Macromolecules*, 2000, **33**, 3940.
50. M. Oishi and Y. Kawakami, *Macromolecules*, 2000, **41**, 606.
51. J. C. Saam, *J. Inorg. Organomet. Polym.*, 1999, **9**, 3.
52. K. Tamao, R. West, and K. Tatsumi, *J. Organomet. Chem.*, 2003, **685**, 1.
53. R. H. Baney and G. Chandra, 'Encyclopedia of Polymer Science and Engineering', Wiley, New York, 1988, Vol. 13, p. 312.
54. X. Li and M. J. Edirisinghe, *Chem. Mater.*, 2004, **16**, 1111.
55. M. Narisawa, K. Okamura, T. Iseki, K. Oka, and T. Dohmaru, *Ceram. Trans.*, 2002, **144**, 141.
56. Y. C. Song, J. Wang, J. Liu, and C. X. Feng, *J. Mater. Sci. Lett.*, 2003, **22**, 679.
57. X. Bao and M. J. Edirisinghe, *J. Mater. Sci. Lett.*, 2003, **22**, 679.
58. C. K. Ober, Y.-J. Kwark, J.-P. Bravo-Vasquez, J. Dai, and A. Hamad, *Polym. Mater. Sci. Eng.*, 2004, **90**, 22.
59. Y. Sato, E. Shiobara, Y. Onishi, S. Yoshikawa, Y. Nakano, S. Hayase, and Y. Hamada, *J. Vac. Sci. Technol., B*, 2002, **20**, 909.
60. S. Seki, Y. Kunimi, Y. Sakurai, S. Tsuji, K. Maeda, and S. Tagawa, *J. Photopolym. Sci. Technol.*, 2000.
61. K. Yokoyama, S. Notsu, and M. Yokoyama, *J. Chem. Soc., Chem. Commun.*, 1990, 805.
62. M. A. Abkowitz, M. Stolka, R. J. Weagley, K. M. McGrane, and F. E. Knier, *Adv. Chem. Ser.*, 1990, **224**, 467.
63. A. R. Wolff and R. West, *Appl. Organomet. Chem.*, 1987, **1**, 7.
64. C. Peinado, A. Alonso, F. Catalina, and W. Schnabel, *Macromol. Chem. Phys.*, 2000, **201**, 1156.
65. P. Shukla, P. M. Cotts, R. D. Miller, S. Ducharme, R. Asthana, and J. Zavislan, *Mol. Cryst. Liq. Cryst. Sci. Technol.*, 1990, **183**, 241.
66. J. Li, Z. Li, H. Tang, H. Zeng, and J. Qin, *J. Organomet. Chem.*, 2003, **685**, 258.
67. W. E. Douglas, A. S. Kuzhelev, I. V. Yurasova, O. L. Antipov, L. G. Klapshina, V. V. Semenov, G. A. Domrachev, T. I. Lopatina, and D. M. H. Guy, *Phys. Chem., Chem. Phys.*, 2002, **4**, 109.
68. O. L. Antipov, G. A. Domrachev, W. E. Douglas, D. M. H. Guy, L. G. Klapshina, A. I. Koritin, A. S. Kuzhelev, and V. V. Semenov, *Appl. Organomet. Chem.*, 2000, **14**, 640.
69. A. Herman, *Mol. Elec. Mol. Elec. Dev.*, 1993, **1**, 31.
70. C. A. Burkhard, *J. Am. Chem. Soc.*, 1949, **71**, 963.
71. R. West, *Pure Appl. Chem.*, 1982, **54**, 1041.
72. S. Yajima, J. Hayashi, and M. Omori, *Chem. Lett.*, 1975, 931.
73. S. Yajima, K. Okamura, and J. Hayashi, *Chem. Lett.*, 1975, 1209.
74. D. Bratton, S. J. Holder, R. G. Jones, and W. K. C. Wong, *J. Organomet. Chem.*, 2003, **685**, 60.
75. H. K. Kim and K. Matyjaszewski, *J. Am. Chem. Soc.*, 1988, **110**, 3321.
76. R. H. Cragg, R. G. Jones, A. C. Swain, and S. J. Webb, *J. Chem. Soc., Chem. Commun.*, 1990, 1147.
77. S. Gauthier and D. J. Worsfold, *Macromolecules*, 1989, **22**, 2213.
78. D. J. Worsfold, *ACS Symp. Ser.*, 1988, **360**, 101.
79. R. West, *Angew. Chem., Int. Ed. Engl.*, 1987, **26**, 1201.
80. K. Sakamoto, K. Obata, H. Hirata, M. Nakajima, and H. Sakurai, *J. Am. Chem. Soc.*, 1989, **111**, 7641.
81. H. Sakurai and M. Yoshida, in 'Silicon-Containing Polymers', eds. R. G. Jones, W. Ando, and J. Chojnowski, Kluwer Academic Publishers, Dordrecht, 2000, p. 375.
82. T. Sanji, S. Isozaki, M. Yoshida, K. Sakamoto, and H. Sakurai, *J. Organomet. Chem.*, 2003, **685**, 65.
83. T. Sanji, K. Kawabata, and H. Sakurai, *J. Organomet. Chem.*, 2000, **611**, 32.
84. M. Cypryk, Y. Gupta, and K. Matyjaszewski, *J. Am. Chem. Soc.*, 1991, **113**, 1046.
85. H. Sakurai, T. Sanji, T. Sakai, and H. Hanao, *Phosphorus, Sulfur Silicon Relat. Elem.*, 1997, **124–125**, 173.
86. K. Obata, K. Sakamoto, and M. Kira, *Macromolecules*, 2001, **34**, 2739.
87. T. D. Tilley, *Acc. Chem. Res.*, 1993, **26**, 22.
88. L. Rosenberg and D. N. Kobus, *J. Organomet. Chem.*, 2003, **685**, 107.
89. L. Rosenberg, C. W. Davis, and J. Yao, *J. Am. Chem. Soc.*, 2001, **123**, 5120.
90. J. Michl, *Synth. Met.*, 1992, **50**, 367.
91. K. S. Schweizer, L. A. Harrah, and J. M. Zeigler, *Adv. Chem. Ser.*, 1990, **224**, 379.
92. T. Sato, N. Nagayama, and M. Yokoyama, *J. Mater. Chem.*, 2004, **14**, 287.
93. K. Furukawa, K. Ebata, D. Ichikawa, and N. Matsumoto, *Macromolecules*, 2003, **36**, 7681.
94. A. Saxena, M. Fujiki, M. Naito, K. Okoshi, and G. Kwak, *Macromolecules*, 2004, **37**, 5873.
95. H. Kato, T. Karatsu, A. Kaito, S. Matsuyama, and A. Kitamura, *Polymer*, 2003, **44**, 3269.
96. K. Oka, N. Fujiue, S. Nakanishi, T. Takata, R. West, and D. Takaaki, *J. Organomet. Chem.*, 2000, **611**, 45.
97. C.-H. Yuan and R. West, *Chem. Commun.*, 1997, 1825.
98. F. C. Schilling, F. A. Bovey, A. J. Lovinger, and J. M. Zeigler, *Adv. Chem. Ser.*, 1990, **224**, 341.
99. R. West, *J. Organomet. Chem.*, 2003, **685**, 6.

100. R. West, in ‘Chemistry of Organic Silicon Compounds’, eds. Z. Rappoport and Y. Apeloig, John Wiley & Sons, Chichester, 2001, Vol. 3, p. 541.
101. E. K. KariKari, A. J. Greso, B. L. Farmer, R. D. Miller, and J. F. Rabolt, *Macromolecules*, 1993, **26**, 3937.
102. T. Karatsu, R. D. Miller, R. Sooriyakumaran, and J. Michl, *J. Am. Chem. Soc.*, 1989, **111**, 1140.
103. X. Li and M. J. Edirisinghe, *J. Mater. Sci. Lett.*, 2002, **21**, 21.
104. M. R. Nangrejo, X. Bao, and M. J. Edirisinghe, *Int. J. Inorg. Mater.*, 2001, **3**, 37.
105. X. Bao, M. R. Nangrejo, and M. J. Edirisinghe, *J. Mater. Sci.*, 2000, **35**, 4365.
106. M. R. Nangrejo, X. Bao, and M. J. Edirisinghe, *J. Mater. Sci.*, 2000, **19**, 787.
107. M. R. Nangrejo, X. Bao, and M. J. Edirisinghe, *J. Eur. Ceram. Soc.*, 2000, **20**, 1777.
108. S. Hayase, Y. Nakano, S. Yoshikawa, H. S. Ohta, Y. Sato, E. Shiobara, S. Miyoshi, Y. Onishi, M. Abe, H. Matsuyama, and Y. Ohiwa, *Chem. Mater.*, 2001, **13**, 2186.
109. C. Peinado, A. Alonso, F. Catalina, and W. Schnabel, *J. Photochem. Photobiol., A*, 2001, **141**, 85.
110. Y. Wang, R. West, and C. H. Yuan, *J. Am. Chem. Soc.*, 1993, **115**, 3844.
111. M. Ando, Y. Ohsawa, H. Naito, and Y. Kanemitsu, *J. Organomet. Chem.*, 2003, **685**, 243.
112. S. Aihara, Y. Hirano, T. Tajima, K. Tanioka, M. Abe, N. Saito, N. Kamata, and D. Terunuma, *Appl. Phys. Lett.*, 2003, **82**, 511.
113. F. C. Grozema, L. D. A. Siebbeles, J. M. Warman, S. Seki, T. Seiichi, and U. Sche, *Adv. Mater.*, 2002, **14**, 228.

Quasicrystals

R. Bruce King
University of Georgia, Athens, GA, USA

1 Introduction 1
2 Related Articles 2
3 References 2

1 INTRODUCTION

Quasicrystals are solid materials exhibiting diffraction patterns with apparently sharp spots containing symmetry axes such as fivefold or eightfold axes, which are incompatible with the three-dimensional periodicity associated with crystal lattices.[1,2] Many such materials are aluminum alloys, which exhibit diffraction patterns with fivefold symmetry axes; such materials are called icosahedral quasicrystals.[3–7] Such quasicrystals[8–10] may be defined to have delta functions in their Fourier transforms, but their local point symmetries are incompatible with the periodic order of traditional crystallography. Structures with fivefold symmetry exhibit quasiperiodicity in two dimensions and periodicity in the third. Quasicrystals are thus seen to exhibit a lower order than in true crystals but a higher order than truly amorphous materials.

The structures of icosahedral quasicrystals may be viewed as three-dimensional analogues of Penrose tiling,[11–14] which is a geometric structure exhibiting fivefold symmetries and Bragg diffraction. Location of atoms in quasicrystals requires the use of six-dimensional crystallography,[15–18] in which the atoms correspond to three-dimensional hypersurfaces in six-dimensional periodic lattices rather than normal three-dimensional crystallography in which the atoms correspond to zero-dimensional points in three-dimensional periodic lattices. Note that in both the conventional three-dimensional crystallography used to determine the structures of regular crystals and in the six-dimensional crystallography required to determine the structures of quasicrystals, the dimensionality of the locations of the atoms is three less than the dimensionality of the lattice.

The complications of six-dimensional crystallography prevent the chemical structures of quasicrystals from being described in ways familiar to chemists. Instead, chemical models for quasicrystal structures are more readily developed by first considering closely related true crystalline materials, and then introducing appropriate perturbations destroying the periodic translational order but retaining the long-range translational and orientational order characteristics of quasicrystals.[5,6]

There are several classes of icosahedral quasicrystals with diverse compositions.[7,19] The following classes are the most important:

1. the i(Al–Mt) class (Mt = transition metal) including i($Al_{80}Mn_{20}$),[3] i($Al_{74}Mn_{20}Si_6$),[20,21] i($Al_{79}Cr_{17}Ru_4$),[22] and i($Al_{70}Pd_{20}Mn_{10}$);[23]
2. the i(AlZnMg) class including i($Al_{25}Zn_{38}Mg_{37}$),[24] i($Al_{44}Zn_{15}Cu_5Mg_{36}$),[25] and i($Al_{60}Cu_{10}Li_{30}$);[26]
3. the i(MMgRE) class (M = Zn or Cd; RE = rare earth metal) including $Zn_{60}Mg_{30}RE_{10}$[27] and $Cd_{65}Mg_{20}RE_{15}$;[28]
4. binary i(CdM) quasicrystals of approximate stoichiometry Cd_6M (M = Ca or Yb).[29]

Many of these phases contain relatively large amounts of aluminum suggesting the comparison of the structures of these materials with those of compounds with boron and gallium icosahedra including the icosahedral cage boranes, elemental boron, and boron-rich metal borides (*see* ***Borides: Solid-state Chemistry***), and gallium-rich intermetallic phases of alkali metals and gallium (*see* ***Gallium: Inorganic Chemistry***).

Consider the so-called T2 icosahedral quasicrystal i($Al_{60}Cu_{10}Li_{30}$) and related alloys containing aluminum, lithium, and copper and/or zinc, which have been studied by Audier and collaborators.[30] This system is significant since there are crystalline phases of stoichiometries similar to these T2 icosahedral quasicrystalline phases. Thus, the atom positions in the crystalline cubic R phase of approximate Al_5CuLi_3 stoichiometry are known so that the structure of this phase can provide some insight into the structure of the closely related T2 icosahedral phase of approximate stoichiometry $Al_{0.570}Cu_{0.108}Li_{0.322}$. Of interest in the structure of R-Al_5CuLi_3 is the presence of discrete Al_{12} icosahedra. Discrete molecules containing similar Al_{12} icosahedra are very rare although i-$Bu_{12}Al_{12}{}^{2-}$ containing an Al_{12} icosahedron, which is isoelectronic with $B_{12}H_{12}{}^{2-}$, has been reported as a low-yield product from the reduction of i-Bu_2AlCl with potassium metal.[31]

Audier and collaborators[20,32] have described a polyhedral shell structure for R-Al_5CuLi_3 using a number of polyhedra of icosahedral symmetry. This shell structure consists of the following layers:

1. a central $(Al,Cu)_{12}$ icosahedron;
2. an Li_{20} regular dodecahedron with the Li positions above the faces of the central $(Al,Cu)_{12}$ icosahedron (layer a) analogous to the construction of dual polyhedra (*see* ***Polyhedra***);
3. a larger $(Al,Cu)_{12}$ icosahedron formed from the external orbitals of the central $(Al,Cu)_{12}$ icosahedron (layer a) so that its atoms lie above the 12 faces of the Li_{20} dodecahedron in another 'polyhedral dual construction';
4. an $(Al,Cu)_{60}$ truncated icosahedron (Figure 1) distorted from I_h symmetry to O_h symmetry so that 12 vertices are of one type (circled in Figure 1) and 48 vertices are of another type (not circled in Figure 1). The atoms of

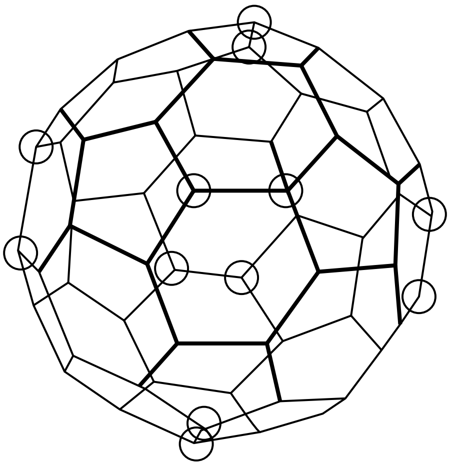

Figure 1 The two different types of vertices in the truncated icosahedron distorted from I_h to O_h symmetry as found in the structure of R-Al_5CuLi_3

this polyhedron lie above the midpoints of the faces of the omnicapped dodecahedron formed by combining the Li_{20} dodecahedron (layer b) with the larger $(Al,Cu)_{12}$ icosahedron (layer c) in still another 'polyhedral dual construction', since the truncated icosahedron is the dual of the omnicapped dodecahedron. Furthermore, the truncated icosahedron in layer d is the same polyhedron as that found in the structure of the C_{60} fullerene (*see* ***Carbon: Fullerenes***). The 84 atoms in layers a, c, and d taken together are known as a Samson complex.

A related model for quasicrystal structures has also been presented by Aslanov.**33**

The above discussion considers a model for the structure of the crystalline cubic R-Al_5CuLi_3. Now consider possible perturbations in this model to give the quasicrystalline T2-Al_5CuLi_3. In this connection, the 54-vertex Mackay icosahedron (Figure 2) appears as a structural unit in certain quasicrystals.**34** The Mackay icosahedron has a shell structure consisting of the following layers:

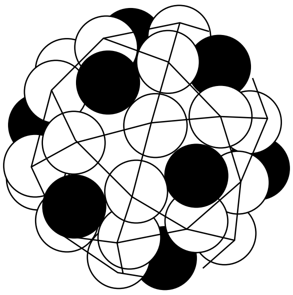

Figure 2 A view of the surface of a Mackay icosahedron showing the vertices of the larger icosahedron (layer b) as black circles and the vertices of the icosidodecahedron (layer c) as white circles. The vertices of the central icosahedron (layer a) are not visible

1. A central icosahedron (not visible in Figure 2);
2. A larger icosahedron formed from the external orbitals of the atoms in the central icosahedron (layer a) overlapping with an additional set of 12 atoms (black circles in Figure 2) that are located in the midpoints of the 12 pentagonal faces (6 visible) of the icosidodecahedron;
3. A 30-vertex icosidodecahedron formed by placing atoms above each of the 30 edges of the larger icosahedron (layer b). Layer c is shown as white circles in Figure 2.

Layers a and b of the Mackay icosahedron are identical to layers a and c in the Audier model for R-Al_5CuLi_3, whereas the outer icosidodecahedron layer of the Mackay icosahedron (layer c) has exactly half the number of atoms of the outer truncated icosahedron. Furthermore, the packing of the truncated icosahedra into the R-Al_5CuLi_3 lattice results in each of the peripheral truncated icosahedron atoms being shared between exactly two adjacent complexes (see above) so that a single Samson complex structural unit has the same 54 atoms as a corresponding Mackay icosahedron. This suggests a very close relationship between the packing of Samson complexes in the R-Al_5CuLi_3 crystal and a possible packing of Mackay icosahedra in a T2-Al_5CuLi_3 quasicrystal. In fact, a concerted 90° rotation about a tangential axis of each of the 30 edges connecting pairs of pentagonal faces in the peripheral truncated icosahedron in each Samson complex of the R-Al_5CuLi_3 crystalline lattice converts a lattice of 54-atom Samson complexes into a lattice of 54-atom Mackay icosahedra.

2 RELATED ARTICLES

Alloys; Aluminum: Inorganic Chemistry; Borides: Solid-state Chemistry; Boron: Polyhedral Carboranes; Carbon: Fullerenes; Gallium: Inorganic Chemistry; Polyhedra.

3 REFERENCES

1. D. Shechtman, I. Blech, D. Gratias, and J. W. Cahn, *Phys. Rev. Lett.*, 1984, **53**, 1951.
2. D. Shechtman and I. A. Blech, *Metall. Trans.*, 1985, **16A**, 105.
3. D. Shechtman, I. Blech, D. Gratias, and J. W. Cahn, *Phys. Rev. Lett.*, 1984, **53**, 1951.
4. D. Shechtman and I. A. Blech, *Metall. Trans.*, 1985, **16A**, 105.
5. C. Janot, 'Quasicrystals: A Primer', Clarendon Press, Oxford, 1994.
6. D. DiVicenzo and P. J. Steinhardt eds, 'Quasicrystals: the State of the Art', World Scientific Publishers, Singapore, 1999.
7. A.-P. Tsai, *Acc. Chem. Res.*, 2003, **36**, 31.
8. D. Levine and P. J. Steinhardt, *Phys. Rev. Lett.*, 1984, **53**, 2477.

9. D. Levine and P. J. Steinhardt, *Phys. Rev. B*, 1986, **34**, 596.
10. H.-R. Trebin ed., ‘Quasicrystals’, VCH, Weinheim, 2003.
11. N. de Bruijn, *Ned. Akad. Weten. Proc. Ser. A.*, 1981, **43**, 39.
12. N. de Bruijn, *Ned. Akad. Weten. Proc. Ser. A.*, 1981, **43**, 53.
13. A. L. Mackay, *Sov. Phys. Crystallogr.*, 1981, **26**, 517.
14. A. L. Mackay, *Phys. Status Solidi A*, 1982, **114**, 609.
15. V. Elser and C. L. Henley, *Phys. Rev. Lett.*, 1985, **55**, 2883.
16. P. Bak, *Phys. Rev. Lett*, 1986, **56**, 861.
17. R. K. Mandal and S. Lele, *Phys. Rev. Lett.*, 1989, **62**, 2695.
18. M. Senechal, ‘Quasicrystals and Geometry’, Cambridge University Press, Cambridge, 1995.
19. C. L. Henley, *Comments Cond. Mat. Phys.*, 1987, **13**, 59.
20. P. Guyot and M. Audier, *Philos. Mag.*, 1985, **B52**, L15.
21. L. A. Bendersky and M. J. Kaufman, *Philos. Mag.*, 1986, **B53**, L75.
22. P. A. Bancel and P. A. Heiney, *Phys. Rev. B*, 1986, **33**, 7919.
23. Y. Yokoyama, T. Miiura, A. P. Tsai, A. Inoue, and T. Masumoto, *Mater. Trans., JIM*, 1992, **33**, 97.
24. R. Ramachandrarao and G. V. S. Sastry, *Pramana*, 1985, **25**, L225.
25. N. K. Mukhopadhyay, G. N. Subbanna, S. Ranganathan, and K. Chattopadhyay, *Scr. Metall.*, 1986, **20**, 525.
26. P. Sainfort, B. Dubost, and A. Dubus, *Compt. Rend. Acad. Sci. Paris*, 1985, **301**, 689.
27. A. Niikura, A. P. Tsai, A. Inoue, and T. Masumoto, *Philos. Mag. Lett.*, 1994, **69**, 351.
28. J. Q. Guo, E. Abe, and A. P. Tsai, *Jpn. J. Appl. Phys.*, 2000, **39**, L770.
29. J. Q. Guo, E. Abe, and A. P. Tsai, *Phys. Rev.*, 2000, **B62**, R14605.
30. M. Audier, C. Janot, M. de Boissieu, and B. Dubost, *Philos. Mag.*, 1989, **B60**, 437.
31. W. Hiller, K.-W. Klinkhammer, W. Uhl, and J. Wagner, *Angew. Chem., Int. Ed. Engl.*, 1991, **30**, 179.
32. M. Audier, J. Pannetier, M. Leblanc, C. Janot, J.-M. Lang, and B. Dubost, *Phys. Status Solidi B*, 1988, **153**, 136.
33. L. A. Aslanov, *Acta Crystallogr.*, 1991, **A47**, 63.
34. P. Guyot, M. Audier, and R. Lequette, *J. Physiol. (Paris)*, 1986, **47**, C3.

Rhenium: Organometallic Chemistry

Carlos C. Romão
Instituto de Tecnologia Química e Biológica, Oeiras, Portugal

1	Introduction	1
2	Chemistry of the Re Carbonyl Derivatives	2
3	Chemistry of Re Hydrides	9
4	Chemistry of Re (η^1-Hydrocarbyl) Complexes	12
5	Chemistry of Re (η^2-Hydrocarbon) Complexes	21
6	Chemistry of Re (η^3-Hydrocarbyl) Complexes	22
7	Chemistry of Re (η^4-Hydrocarbon) Complexes	23
8	Chemistry of Re (η^5-Hydrocarbyl) Complexes	24
9	Chemistry of Re (η^6-Hydrocarbon) Complexes	33
10	Chemistry of Re (η^7-Hydrocarbon) Complexes	35
11	Chemistry of Re–Re Multiple Bonded Organometallic Complexes	35
12	Chemistry of Re Isocyanide Complexes	36
13	Chemistry of Re Nitrosyl Complexes	37
14	Polynuclear Re Organometallic Complexes	38
15	Bioorganometallic Chemistry of Rhenium	40
16	Related Articles	42
17	References	42

Glossary

Carbonylation: metal salt reduction by CO at high pressure with M–CO bond formation
Polyhydride: complex of the type L_nMH_x ($x > 3$)
Semibridging CO: unsymmetrically bridged CO
Wittig reaction: $R_3P{=}CR_2 + O{=}CR'_2 \longrightarrow R_3PO + R_2C{=}CR'_2$

Abbreviations

Ad = adamantyl; Ar = aryl; $[BarF]^- = [B\{3,5\text{-}(CF_3)_2C_6H_3\}_4]^-$; bipy = 2,2′-dipyridyl; COD = 1,5-cyclooctadiene; CVD = chemical vapor deposition; DAB = 1,4 diazabutadiene; DBU = 1,8-Diazabicyclo[5.4.0]undec-7-ene; DIPP = 2,6-*i*-$Pr_2C_6H_3$; DMF = dimethylformamide; DMSO = dimethylsulphoxide, $OSMe_2$; dppe = 1,2-diphenylphosphinoethane; dppf = 1,1′-bis(diphenylphosphino)ferrocene; dppm = diphenylphos-phinomethane; dppz = dipyrido[3,2-a:2′,3′-c]phenazine; FTIR = Fourier transform infrared spectroscopy; HBpin = pinacolborane, 4,4,5,5-tetramethyl-1,3,2-dioxaborolane; HDS = hydrodesulfurization; HMPA = hexamethylphos-phoramide, $OP\{N(Me_2)\}_3$; HOMO = Highest occupied molecular orbital; Ind = indenyl, η^5-C_9H_7; LUMO = Lowest unoccupied molecular orbital; MCPBA = *m*-chloroperbenzoic acid, 3-$ClC_6H_4C(O)OOH$; MeIm = 1-methylimidazole; MLCT = Metal to Ligand Charge Transfer; mq = 2-mercaptoquinoline; MTO = Methyltrioxorhenium, CH_3ReO_3; Np = neopentyl, CH_2-*t*-Bu; OTf = triflate, $CF_3SO_2O^-$; PPN = bis(triphenylphosphine)iminiumcation, $[(Ph_3P)_2N]^+$; py = pyridine; pyO = pyridine-*N*-oxide, ONC_5H_5; rt = room temperature; tacn = 1,4,7-triazacyclononane; TBP = trigonal bipyramidal; THF = tetrahydrofuran; TMS = trimethylsilyl, $SiMe_3$; Tp = hydrido(tris)pyrazolyl borate, $[HB(Pz)_3]^-$; triphos = $MeC(CH_2PPh_2)_3$.

1 INTRODUCTION

Rhenium organometallic chemistry has witnessed a very fast and important development during the last decade. Previously following upon the footsteps of Mn organometallic chemistry, it has gained full independence, creating a number of new and highly productive areas of research and applications. Although this course of progress was predicted one decade ago when the first edition of this Encyclopedia was written, in fact, it has well overridden any logical expectations mainly because the major developments emerged in zones barely above surface in those days.

From a more fundamental standpoint, large progress was made in the field of Re clusters and polynuclear complexes related to heterogeneous catalysis models, and in the study of the transformations of unsaturated hydrocarbons mediated by the $ReCp'(CO)_2$ and $[ReCp'(NO)(PPh_3)]^+$ fragments. For the latter case, a very sophisticated understanding of the stereochemical control of the reactivity of unsaturated C=C and C=O ligands has been reached falling very short from practical extensive use. Moreover, Re has excelled in stabilizing a number of elusive 'primeval' molecules like HNO, H_2CNH, H_2N_2, linear carbon allotropes, and others. However, the most spectacular progress was achieved on the side of more applied research topics. The research around the room-temperature luminescent derivatives of the *fac*-$Re(CO)_3$ fragment attained a fantastic sum of published work opening the perspective for short-term real applications in fields like molecular sensors, optical responsive materials, and many others. Practical applications are now commonly used in the field of oxidation and oxygen-transfer catalysis, which arose in the wake of the discovery of $ReMeO_3$ (MTO). Last, but very, very far from the least, is the astonishing growth of the research on Re bioorganometallic chemistry. This topic, a frail blossom 10 years ago, grew toward immediate applied targets as imaging, radiotherapy, biological assaying, and biomarking and was responsible for many spectacular results and applications while entailing a revolution of the whole synthetic establishment of Re organometallic chemistry. All taken together, these three areas account for the ca. 50% yearly increase in the publication rate of Re organometallic chemistry unabatedly registered from the mid-1990s onwards.

The following text is built upon the concept of descriptive organometallic chemistry, which uses the ligands rather than the oxidation states to organize the covered material. This includes all the material reviewed in the first edition[1] most of which is also covered by major comprehensive reference works until 1993.[2–4] All of the more recent material was taken directly from the primary literature as well as some annual surveys.[5–7] Therefore, in order to keep the number of references within an acceptable value, priority was given to the direct referencing of the material published from 1993, since the older material can be retrieved from the mentioned reference works and by cross referencing.

2 CHEMISTRY OF THE Re CARBONYL DERIVATIVES

2.1 Chemistry of $Re_2(CO)_{10}$

Dirhenium decacarbonyl $Re_2(CO)_{10}$ (**1**), the historical entry into the organometallic chemistry of Re, was discovered by Hieber and Fuchs in 1941. It can be prepared by carbonylation (*see also* ***Carbonyl Complexes of the Transition Metals***) of Re_2O_7, by reduction of $ReCl_5$ or K_2ReCl_6 under CO pressure, or at atmospheric pressure by the simple synthesis shown in equation (1).[8]

$$\mathrm{NaReO_4} \xrightarrow[\substack{\text{DIBAL-H} \\ \text{toluene } 80\,^\circ\text{C}}]{\text{CO 1 atm}} \mathrm{Re_2(CO)_{10}} \qquad (1)$$

(**1**) is a white, volatile, air-stable complex structurally isomorphous with its analogs $M_2(CO)_{10}$ (M = Mn, Tc). A single metal–metal bond joins two $M(CO)_5$ moieties in a staggered conformation with approximate D_{4d} symmetry, having the radial CO groups slightly bent away from the M–M bond (4–6°). The molecule is not fluxional (*see Fluxional Molecule*) at room temperature. $MnRe(CO)_{10}$ (**2**) is best prepared by reaction of $[Mn(CO)_5]Na$ with $ReBr(CO)_5$ (see Section 14). The value obtained for the Mn–Re *Bond Length* in (**2**), 2.909 Å, is close to the value of 2.9038 Å measured for the Mn–Mn distance and is clearly shorter than the 3.0413 Å in (**1**).

2.1.1 Homolytic Cleavage of $Re_2(CO)_{10}$ and the $Re(CO)_5$ Radical

In addition to the typical chemistry of binary metal carbonyls, which centers on substitution and redox reactions, the presence and fate of the M–M bond adds to the variety of reactions and mechanistic pathways available to the $M_2(CO)_{10}$ complexes, namely through the photochemical or thermal formation of reactive $M(CO)_5$ radicals. Photolysis of a gas-phase molecular beam of (**1**) with 300 nm light produces $Re(CO)_5$ radicals translationally polarized along the Re–Re bond; this is in agreement with bond rupture being caused by the $1(\sigma 2) \rightarrow (1\sigma\sigma^*)$ transition. However, in solution and low-temperature matrices the situation is more complex due to the competing Re–Re bond dissociation and CO loss as primary steps. This competition also occurs for $Mn_2(CO)_{10}$ and (**2**). A wavelength dependency of M–M homolysis and CO loss processes has been first ascertained for $Mn_2(CO)_{10}$, but it is common to all three $MM'(CO)_{10}$ complexes (M, M′ = Mn, Re). The primary photochemical reaction of $MM'(CO)_{10}$ in solution has been shown to result in (1) homolytic fission of the metal–metal σ bond to form $M(CO)_5$ radicals, (2) dissociation of a CO ligand to form $MM'(CO)_9$, (3) nondissociative relaxation to the electronic ground state, as summarized in Scheme 1.

The branching ratios have been found to depend on the excitation wavelength by which pathway (1) is favored by lower energy excitation, whereas pathway (2) is favored by higher energy excitation.[9]

The chemistry that follows the generation of the active species $Re(CO)_5$ or $Re_2(CO)_9$ is quite different. The primarily formed $Re_2(CO)_9$ has a vacant equatorial coordination site, *eq*-$Re_2(CO)_9$, but it may be converted to the axially vacant isomer, *ax*-$Re_2(CO)_9$ upon irradiation with 546 nm light. This vacant site may coordinate solvents (S) or other ligands (L) to form substituted complexes $Re_2(CO)_9(L)$ (equation 2).

$$\mathrm{M_2(CO)_{10}} + \mathrm{L} \xrightarrow{h\nu} \mathrm{M_2(CO)_9L} + \mathrm{CO} \qquad (2)$$

Flash photolysis of $MM'(CO)_{10}$ at 93 K leads to loss of CO and $MM'(CO)_9(S)$ as the sole net photochemical products.[10]

While $Mn_2(CO)_9(S)$ readily loses solvents at 93 K to form the semibridge form $Mn_2(CO)_8(\mu\text{-}\eta^1,\eta^2\text{-CO})$, $MnRe(CO)_9(S)$ only reverts to $MnRe(CO)_8(\mu\text{-}\eta^1,\eta^2\text{-CO})$ upon irradiation with visible light at 93 K. Upon warming

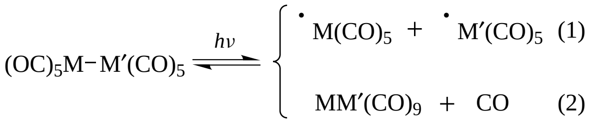

$$\mathrm{(OC)_5M{-}M'(CO)_5} \overset{h\nu}{\rightleftharpoons} \begin{cases} {}^{\bullet}\mathrm{M(CO)_5} + {}^{\bullet}\mathrm{M'(CO)_5} & (1) \\ \mathrm{MM'(CO)_9} + \mathrm{CO} & (2) \end{cases}$$

Scheme 1

of the glass, it recombines with CO to form $MnRe(CO)_{10}$. $Re_2(CO)_9(S)$ also reverts to (**1**) upon warming of the matrix but does not form any semibridged species upon irradiation either. A femtosecond infrared study of the dynamics of solvation and caging of these $Re(CO)_5$ (**3**) and *eq*-$Re(CO)_9$ (**4**) species is available.[9]

The $Re(CO)_5$ (**3**) radical, which may also be generated by several other methods, for example, deposition of Re atoms on a CO matrix at 10 K or *Pulse Radiolysis* of $ReBr(CO)_5$ in ethanol, has the theoretically predicted square-pyramidal structure that is maintained in solution at room temperature. Reactions where (**3**) may play a crucial role after photochemical generation from (**1**) include halogen abstraction, disproportionation, and electron transfer to an electron acceptor (EA) (Scheme 2).

Competition experiments established the reactivity order of radicals generated by M–M bond homolysis as $Re(CO)_5 > Mn(CO)_5 > CpW(CO)_3 > CpMo(CO)_3 > CpFe(CO)_2 > Co(CO)_4$.

Electron-transfer reactions (*see* ***Electron Transfer in Coordination Compounds***) are important because (**3**) behaves as a better oxidizing and reducing agent than (**1**).

Persistent $Re(CO)_3(PR_3)_2$ radicals have been spectroscopically and even crystallographically characterized, for example, $Re(CO)_3(PCy_3)_2$ (**5**), suggesting the square-pyramidal structure to be the most favored one (*see* ***Diffraction Methods in Inorganic Chemistry***). Subcarbonyls like $Re(CO)_2$ have been studied in rare gas matrices.

2.1.2 Substitution Reactions of $Re_2(CO)_{10}$

Since many substitution reactions of (**1**) are done under thermal or photolytic conditions where Re–Re bond rupture may occur, $Re(CO)_5$ was first regarded as an intermediate in both types of substitution reactions. However, the mechanistic studies of photochemically induced substitutions suggest that: (1) photochemical substitution may not occur through the monomeric $M(CO)_5$ but from the longer-lived primary photointermediate $M_2(CO)_9$ (equation 2); (2) both primary photointermediates may give the same reaction products; and (3) substitution of CO in $M(CO)_5$ is most probably associative and not dissociative as in most substitution reactions of 17- and 19-electron metal carbonyl complexes (*see* ***Mechanisms of Reaction of Organometallic Complexes*** and ***Paramagnetic Organometallic Complexes***).

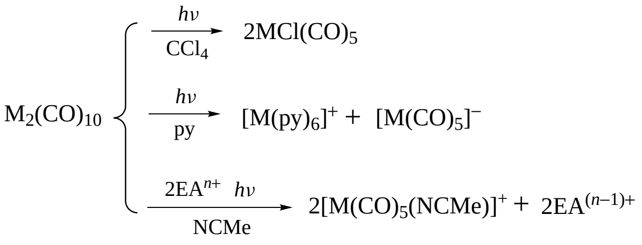
$M_2(CO)_{10}$
$\xrightarrow[CCl_4]{h\nu}$ $2MCl(CO)_5$
$\xrightarrow[py]{h\nu}$ $[M(py)_6]^+ + [M(CO)_5]^-$
$\xrightarrow[NCMe]{2EA^{n+}\ h\nu}$ $2[M(CO)_5(NCMe)]^+ + 2EA^{(n-1)+}$

Scheme 2

Independent of the mechanistic details involved, a host of *Ligand Substitution* products of (**1**) have been prepared. In monosubstituted products, $Re_2(CO)_9L$ ($L = PR_3$, py, NCMe), the axial position is normally occupied by the bulkier ligands (PPh_3) with equatorial substitution generally observed for the smaller ones, for example, py, PMe_3, and NCMe.

Coordination of the Si–H bond to $Re_2(CO)_9$ seems to be responsible for the catalytic activity of (**1**) in the synthesis of silyl ethers, $ROSiR'_3$ from R'_3SiH and ROH.[11]

Disubstituted complexes $Re_2(CO)_8L_2$ may have diaxial (**6**) or staggered transoid (**7**) isomers, while several other possibilities are found for trisubstituted $Re_2(CO)_7L_3$ ($L = PR_3$, CNR, $P(OR)_3$) (*see Isomer, Types of*).

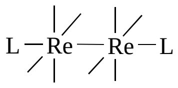

(**6**)

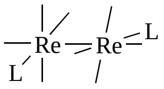

(**7**)

Further substitution with phosphines leads to monomeric radical products, for example, $Re(CO)_3(PR_3)_2$, but phosphite derivatives with a smaller *Cone Angle* may be prepared photolytically, for example, $Re_2(CO)_4\{P(OPh)_3\}_6$. In the bridged diphosphine complexes $Re_2(CO)_6(L–L)_2$ ($L–L = R_2P(CH_2)PR_2$), different photophysical properties arise because of the difficult breaking of the Re–Re bond. Photolysis of (**1**) in the presence of alkenes affords the dimers $[Re_2(\mu\text{-}H)(\mu\text{-}CH{=}CHR)(CO)_8]$ (**8**). These complexes are fluxional with the hydride and π-alkenyl bonds interchanging between the metals. The alkene in (**8**) may be displaced by two-electron ligands, for example, PR_3, $P(OR)_3$, alkenes, and H_2, in which case $[Re_2(\mu\text{-}H)_2(CO)_8]$ is formed. This type of reaction is quite general and photolysis of (**1**) with HX ($X = H$, OH, OMe, $C{\equiv}CPh$, C(O)Me, PR_2) gives the products with the structural framework (**9**), quite common in Re and Mn carbonyl chemistry.[12] Scheme 3 exemplifies some of the reactivity of complex (**9**: $X = PPh_2$).

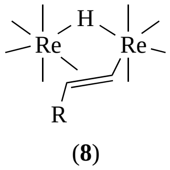

(**8**)

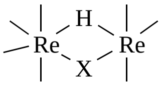

(**9**)

The complex (**9**; $X = CH_3$) prepared from $[Re_2(\mu\text{-}H)_2(CO)_8]$ and N_2CH_2, decomposes above −20 °C to liberate CH_4 and form 1,2-*eq*,*eq*-$[Re_2(CO)_8(THF)_2]$ (**10**). The lability of the THF ligand makes (**10**) a versatile precursor to other

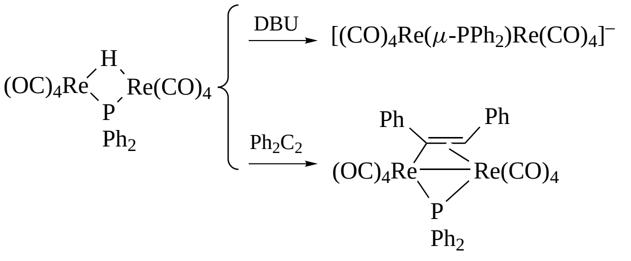

Scheme 3

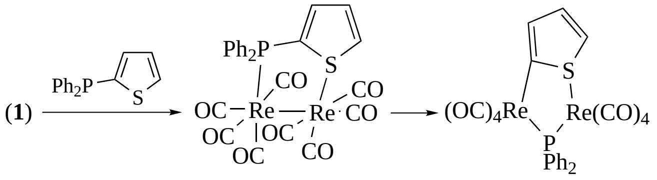

Scheme 4

complexes of type (**9**) by H–H and C–H activation, as well as polynuclear Re carbonyl hydride clusters (Section 3.2).[13]

Other bonds are cleaved by (**1**) under photolytic conditions, for example, the P–C bond in Scheme 4.

Thermal reaction of $Re_2(CO)_9(NCMe)$ with electrophilic alkynes $EtO_2C{\equiv}C(CO_2Et)$, $RC{\equiv}CCO_2R'$ inserts the alkyne across the Re–Re bond forming, for example, (**11**).[14]

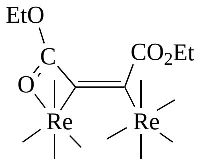

(**11**)

The thiethane complex $Re_2(CO)_9(SCH_2CH_2CH_2–)$ catalyzes the cyclooligomerization of thiethane to the sulfur macrocycles $12S_3$ and $24S_6$.[15]

The thermal substitution of CO is catalyzed by several supported transition metals and their oxides, for example, PdO (*see* ***Heterogeneous Catalysis by Metals*** and ***Oxide Catalysts in Solid-state Chemistry***).[16] Adsorption and reaction of (**1**) on MgO occurs according to Scheme 5.

The adsorption of (**1**) on Al_2O_3 is an important method of preparation of heterogeneous Re-containing catalysts, for example, hydrodesulfurization.[17]

(**10**) is an excellent starting material for the synthesis of molecular models of SiO_2-anchored Re carbonyls. An electron beam irradiation of (**1**) induces the formation of nanorods of Re (*see* ***Metallic Materials Deposition: Metal-organic Precursors***).

2.1.3 *Redox Reactions of $Re_2(CO)_{10}$*

Chemical oxidation of (**1**) with $NOPF_6$ in MeCN gives the cation $[Re(CO)_5(NCMe)]^+$ (**12**), a convenient starting material for other $[Re(CO)_5L]^+$ derivatives (e.g. $L = PR_3$, py). Oxidation with halogens in MeCN gives $ReX(CO)_5$ and (**12**). The order of reactivity within the $M_2(CO)_{10}$ family varies according to the nature of the oxidant, the type of electron-transfer step (inner or outer sphere) (*see Inner-sphere Reaction* and *Outer-sphere Reaction*), and the nature of the solvent (to which the reactions are very sensitive). Strong anionic oxidants, for example, $[Fe(CN)_6]^{3-}$, do not oxidize $M_2(CO)_{10}$ but oxidizing cations do.

The anion $[Re(CO)_5]^-$ (**13**) is formed by reduction of (**1**) with Na/Hg. This extremely reactive species yields a variety of Re carbonyl clusters (*see* ***Polynuclear Organometallic Cluster Complexes***). Further reduction to $[Re(CO)_4]^{3-}$ is possible with Na in HMPA. The electrochemistry of $M_2(CO)_{10}$ shows that these species oxidize at the same potential and, in MeCN, give $[M(CO)_5(MeCN)]^+$. However, (**1**) is more difficult to reduce than $Mn_2(CO)_{10}$ and electrochemical reduction leads to the typical clusters obtained from (**13**) under chemical conditions.

2.1.4 *Nucleophilic Attack on $Re_2(CO)_{10}$*

Reaction of Li alkyls with (**1**) gives acyl anions, which upon alkylation form Fischer-Type Carbene complexes (*see Fischer-type Carbene Complexes*) (Scheme 6).

This reactivity is very general for Re carbonyls. For instance, ($\mathbf{9}$; $X = PCy_2$) is not deprotonated by LiPh at −100 °C. Instead, the salt $Li[Re_2(\mu\text{-}H)(\mu\text{-}PCy_2)C(O)Ph]$ is obtained.[18]

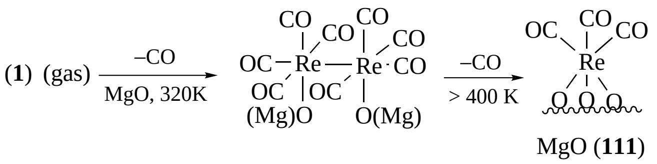

Scheme 5

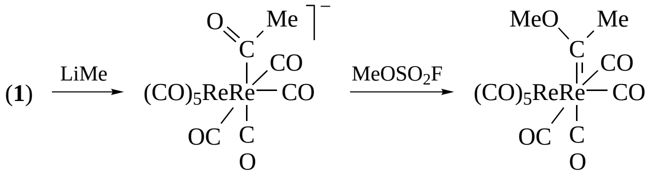

Scheme 6

In the context of the homogeneous modeling of the *Fischer-Tropsch Process*, the analogous formyls $[M_2(CO)_9(CHO)]Li$ were intensively studied. They were formed on addition of hydride (H^-) from $Li[BEt_3H]$ to $M_2(CO)_{10}$ (M = M, Re). The Re_2 derivative is the most stable of these rather sensitive complexes. They decarbonylate to $[Re_2(CO)_9H]^-$ via a radical chain mechanism and are stabilized by $SnBu_3H$, an H radical source. These formyls possess a strong hydridic character, that is, they behave as good H^- donors. $NaBH_4$ and OH^- additions to (**1**) lead to a wide variety of polynuclear Re carbonyl hydrides and Re carbonyl anions (see Section 3.2).

2.2 Chemistry of the Re Carbonyl Anions and Related Species

Among the mononuclear, $[Re(CO)_4]$ and $[Re(CO)_5]^-$ (**13**), and polynuclear, $[Re_2(CO)_9]^{2-}$ and $[Re_4(CO)_{16}]^{2-}$, carbonylate anions, (**13**) is the most important as it is a fundamental building block in Re organometallic chemistry. It is prepared by reduction of (**1**) with Na/Hg and may be conveniently metathesized to the unsolvated PPN salt, $[Re(CO)_5]PPN$.

This very strong nucleophile reacts with a variety of organic and inorganic substrates forming Re–C, Re–Re, and Re–M′ bonds, as discussed in Sections 4.1 and 14. The mechanistic simplicity of these substitutions, however, may be misleading because electron-transfer processes may be involved in the initial stage of the reaction because $[Re(CO)_5]^-$ is also a good reducing agent.**[19]**

One example of this complex behavior is given by the reaction of (**13**) with C_{60} that, under photolysis, ends in $[Re(CO)_4(\eta^2\text{-}C_{60})]^-$. Its Mn analogue has a very strong Mn–C_{60} bond.**[20]**

Complex (**13**) is very easily protonated to form Re carbonyl clusters of low nuclearity (as discussed in Section 3.2).

2.3 The Chemistry of the Re Carbonyl Cations $[Re(CO)_nL_{6-n}]^+$

The parent cation $[Re(CO)_6]^+$ is inert in substitution reactions, and CO replacement may only be achieved under forcing conditions and does not happen with labeled *CO. However, the positive charge in the complex enhances the reactivity of coordinated CO toward nucleophiles, as the labeling experiment in equation (3) shows.

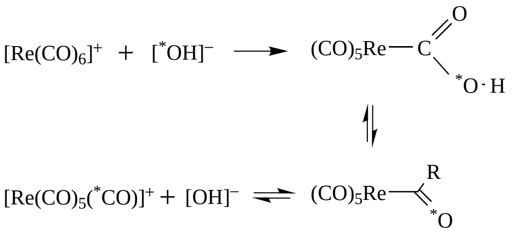

(3)

Nucleophilic attack of hydrazine, NH_2NH_2, or azide, N_3^-, on the coordinated CO of $[Re(CO)_6]^+$ is followed by rearrangement to give $Re(NCO)(CO)_5$ and NH_3 (or N_2). In a similar fashion to the first step in equation (3), OR^- and NHR_2 add to the CO of $[Re(CO)_nL_{5-n}]^+$ to give the adducts $[Re\{C(O)Z\}(CO)_3L_2]$ ($Z = OR$, NR_2). However, if the CO force constant is $<17 \times 10^{-8}$ N $Å^{-1}$ an equilibrium between reactants and adducts is observed. Structurally characterized neutral formyl complexes $[Re\{C(O)H\}(CO)_nL_{5-n}]$ result from H^- addition to the corresponding cations ($L = P(OR)_3$).

Substitutionally labile cations, $[Re(CO)_5(S)]^+$ (S = solvent) are available by oxidation of (**1**), by halide abstraction from $ReBr(CO)_5$ with Ag^+ salts, or by the reaction of $ReH(CO)_5$ or $ReMe(CO)_5$ with Ph_3CBF_4 or from the latter and HBF_4. The resulting $Re(CO)_5FBF_3$ is a strong Lewis acid that adds virtually any L donor to give $[Re(CO)_5L]^+$.**[21]**

Not unexpectedly, more reactive ligands like alkynes undergo acid-promoted transformations such as the cyclodimerization in equation (4) (*see* ***Oligomerization & Polymerization by Homogeneous Catalysis***).

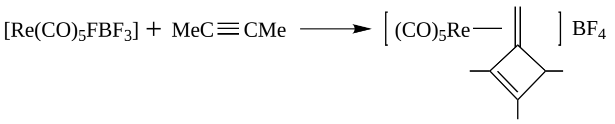

(4)

Complexes $[Re(CO)_4PR_3]^+$ stabilized by the $[BArF]^-$ counterion coordinate CH_2Cl_2, H_2, and Si–H bonds activating H_2 heterolysis and C–Cl bond breaking.**[22]**

$[Re(CO)_4(OEt_2)_2]^+$ is a useful reagent for the synthesis of a variety of $[Re(CO)_4L_2]^+$ complexes with weak donors, including $[Re(CO)_4(OH_2)_2]^+$.**[23]**

These chemical properties allow the stabilization of otherwise elusive ligands. The cations $[Re(CO)_n(PR_3)_{5-n}]Y$ react with hydrazine to form $[Re(H_2N{=}NH_2)(CO)_n(PR_3)_{5-n}]Y$. This can be oxidized to the 1,2-diazene species $[Re(\eta^1\text{-}HN{=}NH)(CO)_n(PR_3)_{5-n}]Y$, a rare example of a stabilized HN=NH ligand on a mononuclear complex. More interestingly, oxidation of $[Re(H_2N{=}NHCH_3)(CO)_n(PR_3)_{5-n}]Y$, also with $Pb(OAc)_4$, leads to the methylenimine complex $[Re(HN{=}CH_2)(CO)_n(PR_3)_{5-n}]Y$. This is only the second example of the stabilization of this extremely unstable yet fundamental molecule.**[24]** Other examples of Re complexes with this type of diazo ligands can be found in the Section on Substitution Reactions and in a review.**[25]** The elusive nitroxyl molecule (HN=O), isoelectronic with 1,2-diazenes and methylenimine, is also stabilized in the complex $[Re(CO)_3(PR_3)_2(NH{=}O)]OTf$ and in other similar species discussed in Section 13. Trisubstituted species $[Re(CO)_3L_2L']^+$ are produced by X^- abstraction from *fac*-$[ReX(CO)_3L_2]$ with the retention of *Stereochemistry*. $[Re(CO)_3L_3]^+$ ($L = MeCN$, NH_3, OH_2) are readily produced by arene displacement from $[Re(\eta^6\text{-}C_6H_5Me)(CO)_3]^+$, but they are now best prepared by the aqueous route described in Section 15. Rhenium carbonyl cations with higher degrees of substitution are uncommon, but $[Re(CO)_2(dppe)_2]^+$ can be made from $ReX(CO)_5$ under forcing conditions, or more mildly from $ReCl(N_2)(dppe)_2$.

2.4 Chemistry of the Re Carbonyl Derivatives $[ReX_x(CO)_yL_z]_n$

Complexes within this general class comprise a wide variety of uninegative (X) ligands and neutral two-electron donors and constitute the largest family of organorhenium complexes.[2]

2.4.1 The Re Carbonyl Halides $[ReX_x(CO)_y]_n$

The entry into this class of Re complexes is the family $ReX(CO)_5$ (**14**) (X = Cl, Br, I), prepared by oxidative addition of X_2 to (**1**) in hydrocarbons (equation 5).

$$\underset{(\mathbf{1})}{Re_2(CO)_{10}} + X_2 \longrightarrow \underset{(\mathbf{14})}{2\,ReX(CO)_5} \qquad (5)$$

The fluorides $ReF(CO)_5$ and $[Re(CO)_5F{\cdot}MF_5]$ (M = Re, I, As, Ta) have been reported and the crystal structure of $[Re(CO)_5F{\cdot}ReF_5]$, prepared from (**1**) and ReF_6 or XeF_2 in HF, is consistent with a bridge between $Re(CO)_5$ and ReF_6 radicals.

A number of other $[ReX_x(CO)_y]_n$ derivatives have been made for X = Cl, Br, I, and their schematic structures are represented in Figure 1.

Decarbonylation of (**14**), either thermally in boiling hexane (X = Cl, Br) or photochemically (X = I), gives the halide-bridged dimers $[ReX(CO)_4]_2$ (**15**) that catalyze Friedel–Crafts alkylation and acylation, as well as benzyl ester deprotection.[26]

Most of the other products (**16–22**), can be made directly from (**14**) and alkylammonium or phosphonium salts, R_4EX (E = N, P), under appropriate thermal and stoichiometric conditions. Mixed-halide derivatives have also been made. The preparation of the derivatives of the $[ReX(CO)_3]$ fragment, (**19**), (**20**), (**21**), and the tetrahedrane (**22**), require higher temperatures.

Nucleophilic addition of LiR or H^-, from $Li[BEt_3H]$, to (**14**) occurs at the *cis*-CO to give acyl or formyl anions $[Re\{C(O)R\}X(CO)_4]^-$, which may be protonated or alkylated to give the corresponding Fischer carbenes $[Re\{C(OR')R\}X(CO)_4]$. In contrast to the dinuclear formyls $[Re_2(CO)_9(CHO)]^-$, these are not stabilized by $SnBu_3H$ because rapid X^- loss produces $Re(CO)_4(CHO)$, which decomposes to $ReH(CO)_5$ or oxidatively adds the Sn–H bond.[3] Remarkably, double nucleophilic alkylation is possible without X^- replacement, and upon protonation bis(hydroxy)carbene complexes, for example, *fac*-$[ReX\{C(OH)Me\}_2(CO)_3]$ are obtained.[27]

Re carbonyl halides in higher oxidation states are rare. The paramagnetic *cis*-$[ReX_4(CO)_2]^-$ (X = Cl, Br) results from oxidative addition of X_2 to (**15**) or $[Re(CO)_3Br_3]^{2-}$. In

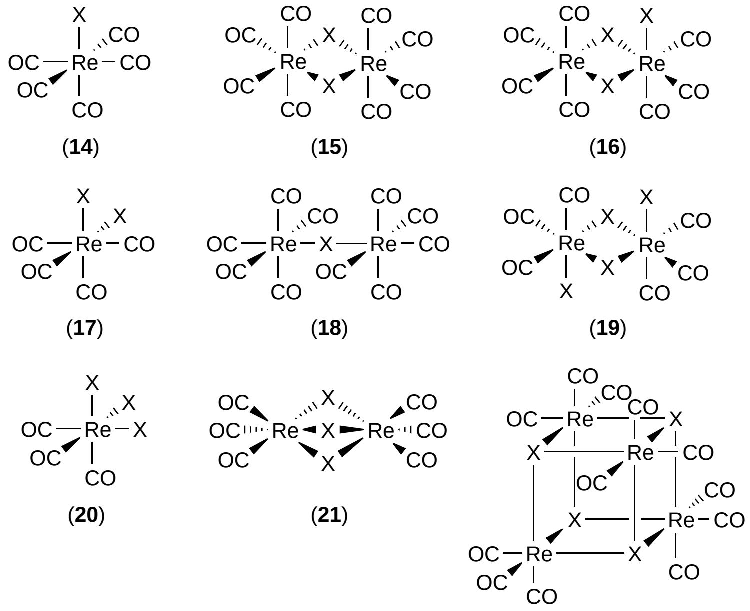

Figure 1 Schematic structures of $[Re^IX_n(CO)_m]^{x-}$ complexes; charges omitted

contrast, many oxidative additions of these types are known for the more electron-rich $[\mathrm{ReX(CO)}_n\mathrm{L}_{5-n}]$ analogs.

2.4.2 The Halide Derivatives $[\mathrm{ReX}_x\mathrm{(CO)}_n\mathrm{L}_{5-n}]$

The $\mathrm{Re^I}$ complexes $[\mathrm{ReX(CO)}_n\mathrm{L}_{5-n}]$ are generally prepared by straightforward CO substitution on (**14**), by ligand addition to the dimer (**15**), or by $\mathrm{X_2}$ addition to $\mathrm{Re_2(CO)_8L_2}$.

A wide variety of ligands form $[\mathrm{ReX(CO)_4L}]$ complexes ($\mathrm{L = PR_3}$, $\mathrm{AsR_3}$, $\mathrm{SR_2}$, $\mathrm{SeR_2}$, $\mathrm{OPR_3}$, $\mathrm{H_2O}$, THF, N-heterocycles, MeCN, MeNC) and $[\mathrm{ReX(CO)_3L_2}]$ complexes ($\mathrm{L = PR_3}$, $\mathrm{P(OR)_3}$, N-heterocycles, MeCN, MeNC; $\mathrm{L_2}$ = bipy, TMEDA, diimine). Carbonyl substitution in $\mathrm{ReX(CO)_5}$ is ca. 60 times slower than in $\mathrm{MnX(CO)_5}$ analogs. This is in agreement with a dissociative mechanism with cis labilization increasing in the order $\mathrm{I < Br < Cl}$ as revealed by kinetic experiments with $^{13}\mathrm{CO}$.

The second substitution proceeds by a similar dissociative mechanism, producing *fac*-$[\mathrm{ReX(CO)_3L_2}]$ which isomerizes to *mer,trans*-$[\mathrm{ReX(CO)_3L_2}]$ at higher temperatures. A cis-labilizing effect in the order $\mathrm{L = py > PPh_3 > P(OPh)_3 \sim CO}$ is responsible for the difficult preparation of $\mathrm{ReX(py)(CO)_4}$ and other N-heterocycle analogs. The decarbonylation product of (**14**) in THF, $[\mathrm{Re_2(\mu\text{-}X)_2(CO)_6(THF)_2}]$, provides an alternative mild route to *fac*-$[\mathrm{ReX(CO)_3L_2}]$ ($\mathrm{L = PR_3, NR_3}$, N-heterocycles), as does the dissolution of the tetramer (**22**) in donor solvents, for example, py. Wrighton's discovery of the luminescence of $\mathrm{ReCl(CO)_3(phen)}$ in solution at rt produced an extraordinary impact on inorganic photochemistry and in the development of the studies on *fac*-$[\mathrm{ReX(CO)_3L_2}]$ complexes (*see* ***Luminescence Behavior & Photochemistry of Organotransition Metal Compounds***). The literature spans several hundred articles on this topic studied from the photophysical, spectroscopic, and spectroelectrochemical aspects to very recent applications in molecular devices and solid-state materials as liquid crystals,[28] and photoresponsive materials.[29,30] A few references help highlighting the approaches used.[31–33]

An overwhelming number of different complexes bearing the $[\mathrm{Re(CO)_3}]^+$ fragment as $\mathrm{ReX(CO)_3L_2}$ or $[\mathrm{Re(CO)_3L_2L'}]^+$ have been studied and can by no means be covered here. Some of them can be found in reviews and most can be retrieved under $\mathrm{Re^I}$ and luminescence keywords.[34–36]

The largest families stem from substituted py, bipy, phen, and DAB but virtually any kind of O, N, S or P donor can be used. Both the nature of the ligands and their substituents as well as the nature of X (halide, alkoxide, alkyl, alkynyl) have been used as handles for tuning the photophysical properties of the excited state and emission of these complexes.

With regard to their excited state properties, $[\mathrm{Re(CO)_3X(N\text{–}N)}]$ (N–N = diimine) complexes are organometallic analogues of $[\mathrm{Ru(bipy)_3}]^{2+}$ and other octahedral d^6 low-spin metal complexes of Os, Rh, and Ir. They display long-wavelength MLCT ($\mathrm{Re'} \rightarrow$ diimine) absorptions in their electronic spectra. These bands exhibit solvatochromism tunable by the energy level of the diimine π^* orbitals. In analogy to $[\mathrm{Ru(bipy)_3}]^{2+}$, many (not all) of these rhenium complexes show an emission that originates from the lowest-energy MLCT triplet. This phosphorescence which appears in solution at rt can be quenched by electron and energy transfer. The MLCT excited states of both $[\mathrm{Ru(bipy)_3}]^{2+}$ and $\mathrm{Re(bipy)(CO)_3Cl}$ are inert to ligand substitution. Therefore, they are not inherently reactive but strongly emissive and susceptible to electron or energy transfer. $\mathrm{Re(bipy)(CO)_3Cl}$ catalyzes the photoreduction of $\mathrm{CO_2}$ to CO in the presence of an amine–electron donor, and this process is highly favored at high pressure.[37]

The poliynyl complexes $[\mathrm{Re(CO)_3(bipy)\{C{=}C{-}(C{=}C)_nR\}}]$ are highly luminescent at rt with an uncommon blue shift in energy emission upon extension of the carbon chain.[38]

Supramolecular systems based on $\mathrm{Re(CO)_3X}$ (**23**) and other fragments, generally called metallo-cyclophanes or molecular squares, are recent.[39]

The self-assembly of these squares (Scheme 7) from $\mathrm{Re(CO)_3X}$ is highly efficient and seems thermodynamically controlled (*see* ***Self-assembled Inorganic Architectures***).[40]

These supramolecular assemblies are being intensely studied with regard to host–guest behavior,[41] molecular, biologic[42] and ion sensors,[43,44] nanoporosity, and photo-switching.[45]

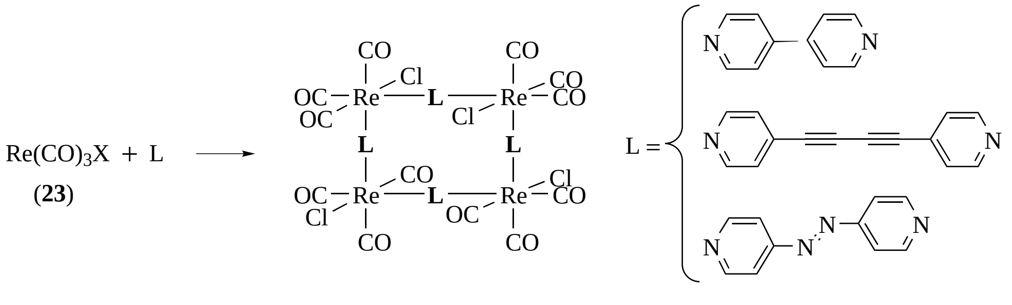

Scheme 7

Association of another light sensitive system with the $[Re(CO)_3(N\text{–}N)]^+$ chromophore leads to photoswitchable systems[46] or photoinduced electron transfer.[47]

Another class of halogen-bridged dimers is derived from reaction of (**14**) with bidentate ligands that bridge the two metal centers in the final product, as (**24**).

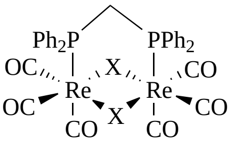

(**24**)

Trisubstitution from (**14**) with excess PR_3, $P(OPh)_3$, or tripodal phosphines gives the *mer*,*cis*-$[ReBr(CO)_2L_3]$, but further direct substitution from (**14**) or (**15**) requires bidentate phosphines (*trans*-$[ReX(CO)(dppe)_2]$) and forcing conditions. Alternatively, $[ReX(CO)L_4]$ ($L = PMe_2Ph$, diars) complexes are made via carbonylation reactions, for example, from *mer*-$[ReCl_3(PMe_2Ph)_3]$ to give *trans*-$[ReCl(CO)\{(PMe_2Ph)_3\}_4]$. The unprecedented MeECN (E = S, Se) sulfur bound ligands are obtained by methylation of the neutral $[Re(CO)_2(triphos)(ECN)]$ complexes at the E atom.[48]

Only a few Re^{II} octahedral, paramagnetic 17-electron complexes $[ReX_2(CO)_nL_{5-n}]$ are known, for example, all-*trans*-$[ReCl_2(CO)_2(PEt_3)_2]$, $[ReX(CO)(dppe)_2]^+$, and a few isocyanide analogs (see Section 14). The first compound is prepared by carbonylation of $Re_2X_4(PR_3)_4$ and the second by oxidation of the parent Re^I species. Electrochemical studies have shown these compounds to be strong oxidants and yet stable in solution.[49]

The Re^{III} complexes, generally prepared by X_2 oxidative addition to the parent Re^I species (equation 6), are normally seven coordinate and diamagnetic with a capped octahedron structure, but six-coordinate, 16-electron derivatives have been found, especially with isocyanide ligands.[50] (*see* ***Structure & Property Maps for Inorganic Solids***).

$$ReBr(CO)_3(PPhMe_2)_2 + Br_2 \longrightarrow ReBr_3(CO)_2(PPhMe_2)_2 \qquad (6)$$

2.4.3 *The Complexes $[ReX_x(CO)_y]_n$ (X = Pseudohalide, Uninegative Group 15 and 16 Ligands)*

The fundamental examples of this class of complexes, for example, cyanides, nitrates, thiocyanate, and the isocyanato derivatives are well known, and with the exception of the interesting, strong labilizing effect of the latter, which leads to fast decarbonylation to $[Re_2(\mu\text{-}NCO)_2(CO)_8]$, they do not have a special chemistry and are sometimes difficult to prepare. In any case, these difficulties have been removed by the use of $Re(CO)_5FBF_3$, which readily reacts with these types of anionic ligands to form the corresponding Re complexes.[21] A few structural analogs of (**14**) and (**15**), $Re(ER_2)(CO)_5$, $[Re_2(\mu\text{-}ER_2)_2(CO)_8]$, are known (E = P, As). These may be prepared, among other variations, by reaction of $HRe(CO)_5$ with E_2R_4 (e.g. $As_2(CF_3)_4$), $[Re(CO)_5]^-$ with XPR_2, or (**14**) with phosphide anions (e.g. $KPPh_2$).[2]

The coordination chemistry of the derivatives of the group 16 ligands, $[Re(AR)_x(CO)_y]_n$ (A = O, S, Se, Te) resembles that of the halides and group 15 anions, ER_2^-, namely the structural types (**14**), (**15**), and (**22**). No monomeric alkoxide $Re(CO)_5(OR)$ has been isolated, but $Re(CO)_5(OSi{\equiv}\text{anchored on }SiO_2)$,[51] $Re(CO)_5(OReO_3)$, and $Re(CO)_5(OTf)$ are stable compounds. The tetrahedrane (**22**, X = OH) is made by photolysis of (**1**) in H_2O and is active in *Alkene Metathesis*.[52] Reaction of OH^- with (**19**, X = Br) leads to $[Re_3(CO)_9(OH)_4]^-$, which corresponds to the removal of $[Re(CO)_3]^+$ from one corner of (**22**, X = OH). Reaction of the latter tetrahedrane with OH^- quantitatively forms (**20**, X = OH), an important compound in biomedical applications.[53]

$[Re_3(CO)_9(OH)_4]^-$ has been used as a tripodal ligand toward metal ions and fragments, for example, Mn^{II}, Cu^{II}, and $[PtMe_3]^+$. Basic alcoholysis of $[ReH_9]^{2-}$ gives triply bridged alkoxides $[Re_2(\mu\text{-}OR)_3(CO)_6]^-$with (**21**). A recent review on the chemistry of late transition metal alkoxides reports a series of $Re(OR)L_2(CO)_3$ ($L = PR_3$) complexes. They do not decompose by β-H elimination and react like anions producing $ReClL_2(CO)_3$ from acyl chlorides and $Re(EAr)L_2(CO)_3$ from HEAr (E = O, S, NH).

They insert CE_2 (E = O, S) but do not exchange OR groups between them. $Re(OR)(CO)_3(dppe)$ in benzene solution reversibly absorbs atmospheric CO_2.

Complexes of thiolates, selenates, and tellurates (AR) can be made either by reaction of their Na salts with (**14**) or by reaction of $ReH(CO)_5$ with the HAR to give either $Re(AR)(CO)_5$ or dimers with (**15**). The latter complexes, $[Re_2(\mu\text{-}AR)_2(CO)_8]$, are favored for R = alkyl, and the former for $R = CF_3$ or C_6F_5. Upon further heating, the tetrahedranes $[Re(AR)(CO)_3]_4$ are formed. Reaction of $[Re_2(\mu\text{-}AR)_2(CO)_8]$ with phosphines may lead to CO substitution, bridge cleavage, or both, depending on the reaction conditions. Potentially bidentate monoanionic ligands of the general formula $[E_2Y]^-$ (E = O, S, Se; Y = CR, COR, CNR_2, PR_2, AsR_2) form complexes with (**25**–**27**). Few complexes of type (**25**) have been directly prepared from (**14**), because its reaction with the anions $[E_2Y]^-$gives preferentially (**26**) and (**27**) as a result of the labilization effect of this type of ligand.

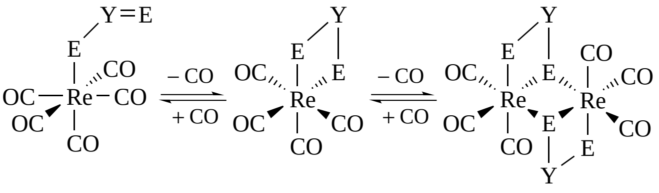

(**25**) (**26**) (**27**)

Carbonylation of (**26**) or (**27**) needs very high pressure, but the addition of PPh_3 is very easy and $Re(O_2CR)(CO)_3(PPh_3)$ is formed from $[Re(O_2CR)(CO)_3]_2$ at rt. Also favored in the PR_3 family of complexes, $ReX(CO)_3(PR_3)_2$, are the insertions of CE_2 into Re–H and Re–C bonds, yielding formates, carboxylates, and their S analogs, that is, $Re(E_2CR)(CO)(PR_3)_2$ (E = O, S; R = H, alkyls, phenyl) with (**27**). R_2PO_2, β-diketone derivatives, and other mixed O,S donors, for example, $HSCH_2CO_2Et$ also give complexes of related coordination types.[2] Derivatives in higher oxidation states are rare, but $Re(SR)_3(CO)_2$ is obtained by carbonylation of the parent MeCN derivative.

3 CHEMISTRY OF Re HYDRIDES

3.1 The Re Polyhydrides: $[ReH_9]^{2-}$ and $[ReH_xL_y]^{2-}$

Owing to their importance in many organometallic processes, *Polyhydrides* (*see* ***Hydride Complexes of the Transition Metals***) that are not strictly organometallic compounds justify being mentioned.[54] $[ReH_9]^{2-}$ prepared by reduction of $NaReO_4$ with Na in EtOH has a tricapped trigonal prism structure. It reacts with ER_3 (E = P, As) to give $[ReH_8(ER_3)]^-$, with CO to give $[Re_2(\mu\text{-}H)_3(CO)_6]^-$, and under basic conditions to give $[Re_2(\mu\text{-}OR)_3(CO)_6]^-$ With dppe, under N_2 atmosphere, the very useful precursor $[ReH(N_2)(dppe)_2]$ is obtained. Another central compound in this area is $ReH_7(PPh_3)_2$ (**28**) made from $ReOCl_3(PPh_3)_2$ and $LiAlH_4$.[55]

The main characteristic of the reactivity of $ReH_7(PR_3)_2$ and other polyhydrides is their ability to lose H_2 upon thermal, photochemical, or oxidative (electrophilic) activation. The resulting free coordination positions may then be occupied by two-electron donors, forming substitution products (equations 7 and 8) like $ReH_5(PR_3)_3$, $ReH_5(PR_3)_2L$, $ReH_3L(PR_3)_3$, and $ReHL_3(PR_3)_2$ (L is usually PR_3 or CO). Analogues with tripodal and bidentate phosphines also exist. $ReH_7(PR_3)_2$ can be protonated at low temperature to $[ReH_8(PR_3)_2]^+$, better formulated as the tautomer $[ReH_{8-x}(H_2)_x(PR_3)_2]^+$. These transformations are summarized in Scheme 8.

$$ReH_7(PR_3)_2 \xrightarrow{L} ReH_5(PR_3)_2L + H_2 \qquad (7)$$

$$ReH_7(PR_3)_2 \xrightarrow[NCMe]{HBF_4} [ReH(NCMe)_4(PR_3)_2]BF_4 + 3H_2 \qquad (8)$$

Cp and poly(pyrazolyl)borates also stabilize polyhydrides, for example, $ReCpH_4(PR_3)$ and $ReH_4\{\kappa^3\text{-}HB(OR)(3,5\text{-}Me_2pz)_2\}(PPh_3)$.[56] Nitrosyl hydrides, $ReH_x(NO)_yL_z$, are mentioned in Section 13.

Several polyhydrides dimerize producing dinuclear and a few higher nuclearity species like $[Re_2H_7(PR_3)_4L]^+$, $[Re_2H_6(PR_3)_5]$, and $[Re_2(\mu\text{-}H_4)H_4(PPh_3)_4]$ (**29**), the dimerization product of (**28**). The 'agno-hydrides' (**29**) and the pentahydrides are not very reactive, unless activated by *Electrophiles* such as H^+, or Ph_3C^+. In this way, $ReH_5(PPh_3)_3$ produces a number of substituted $[ReH_x(PPh_3)_2L_y]^{n+}$ derivatives (L = RCN, RNC). Similarly, paramagnetic, for example, $[Re_2H_7]^+$, and diamagnetic H bridged cores are prepared from (**29**).

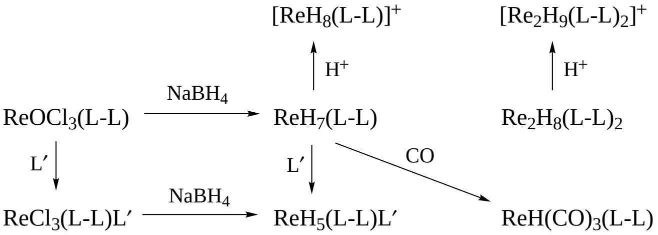

L-L = bidentate phosphine
L′ = monodentate phosphine

Scheme 8

NMR spectroscopy and neutron diffraction studies established the tautomeric formulation of many polyhydrides as dihydrogen (η^2-H_2 or H_2) complexes or *Nonclassical hydrides*. Examples are inter alia $ReH_5(H_2)\{P(o\text{-}tol)_3\}_2$, $[ReH_2(H_2)(PPh_3)_3]$, and $ReCl(H_2)(PMe_2Ph)_4$.[57] (**28**), but not $ReH_7(AsPh_3)$, may be considered borderline since it has one H–H stretched interaction and has been represented as $ReH_5(H\cdots H)(PPh_3)_2$. Electronic and steric factors seem to influence the extension of the H–H interactions and the balance between both tautomeric formulations that can be found in equilibrium in some cases like $[ReH_4(CO)\{(PMe_2Ph)_3\}_3]^+$. The borderline H_2 complex $[Re(\eta^2\text{-}H_2)\{N(C_2H_4NC_6F_5)_3\}]$ undergoes H/D exchange via a less usual oxidative addition process.[58]

Similarly, reaction of (**28**) with 2-hydroxypyridine or similar pyridine derivatives (HA) leads straight to $ReH(A)_2(PPh_3)_2$. With bulkier anions, for example, 2-mercaptoquinoline (mq), the intermediate $ReH_4(mq)(PPh_3)_2$ can be isolated.

Alkenes and dienes react smoothly with $ReH_7(PR_3)_2$ and a number of $ReH_3(\eta^4\text{-}diene)(PPh_3)_2$ and $ReH_3(\eta^2\text{-}alkene)_2(PPh_3)_2$ *Alkene Complexes* have been characterized. In the case of C_5H_6, a fast equilibrium between $ReH_3(\eta^4\text{-}C_5H_6)(PPh_3)_2$ and $ReH_2(\eta^3\text{-}C_5H_7)(PPh_3)_2$ is established. Addition of excess L produces $ReH(PPh_3)_2L_3$ or $ReH(PMe_3)_5$ (**30**) and cyclopentene. In agreement with this facile H migration from metal to ring, $ReCpH_2(PPh_3)_2$ undergoes substitution by PMe_3, under photolysis, via $ReH_2(\eta^3\text{-}C_5H_7)(PPh_3)$ as an intermediate.[59]

In spite of their high formal oxidation states, the polyhydrides behave as low-oxidation species because of the low charge on the metal, which is close to the charge found in the free metal. From the organometallic point of view, the most remarkable consequence of this reactivity is found in the reactions of polyhydrides with alkanes leading to alkane dehydrogenation, Alkane Activation or C–H Bond

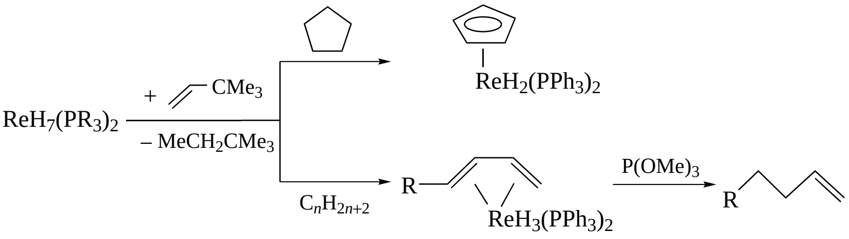

Scheme 9

Activation, with the formation of alkenes or dienes and H_2. For thermodynamic reasons, H_2 removal is effected by concomitant hydrogenation of *t*-butylethylene, as shown in Scheme 9, or by a flow gas.

[ReH_5(triphos)] is active for cyclooctene dehydrogenation but [$ReH_5(PPh_3)_3$] is not.

A remarkable property of the Re–H bonds in polyhydrides is their ability to establish a new kind of hydrogen bond, M–H···HX (X = O, N, C), called protonic-hydridic or dihydrogen bonds. Initially found in intramolecular systems, they can also be formed intermolecularly as established by neutron diffraction of the adduct $ReH_5(PPh_3)_2 \cdot C_8H_6\,NH \cdot C_6H_6$ formed in the cocrystallization of the hydride with indole in benzene.[60,61]

These bonds seem to play a crucial role in catalytic reactions involving M–H and X–H bonds.[55]

Several Re polyhydrides form heterobimetallic complexes with other transition and main-group metal fragments. Bimetallic complexes with a (μ-H_3) bridging system are common, although those having (μ-H_4), like (**29**), are rare due to geometric reasons. A clear-cut example is the formation of $[(PPh_3)_2H_3Re(\mu\text{-}H_3)M(CO)_3]^-$ from $[ReH_6(PPh_3)_2]^-$ and $L_3M(CO)_3$ (M = Cr, Mo, W). In many cases, M–M′ bonds are formed as discussed in Section 14.2.

3.2 The Re Carbonyl Hydrides, Clusters, and Related Complexes

The complexes in this section encompass a rich variety of structural types, from the simplest mononuclear $ReH(CO)_5$ (**31**) and its substituted analogs to high nuclearity clusters, for example, $[Re_8C(CO)_{24}]^{2-}$. Complex (**31**) was first prepared in 1961 by acidification of $[Re(CO)_5]^-$ generated from $Re_2(CO)_{10}$ and Na/Hg, but it may be prepared by H_2 reaction with $Re_2(CO)_{10}$ or H^- substitution on $ReX(CO)_5$. Complex (**31**) is rather inert in high purity and in the absence of light, but the presence of light induces ligand substitution by a radical chain mechanism and, therefore, derivatives such as $ReH(PPh_3)_2L_3$ or (**30**) are best prepared by alternative routes.[62] CO_2, CS_2, and fluorinated alkenes and alkynes insert into the Re–H bond. In NCMe solution, (**31**) has a pK_a value of 21.1 (14.1 for $MnH(CO)_5$) but reacts with thiols and carboxylic acids to give thiolates and carboxylates (see Section 2.4.3). The more *Electron-Rich Compound* (**30**) also cleaves C–H bonds.[62] (**31**) has been found to behave as a 'ligand', for example, in the reaction depicted in equation (9). This mode of coordination enhances the acidity of its H atom that can be removed by py.[63]

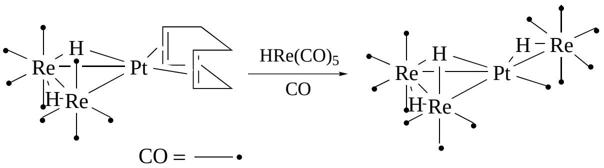

(9)

Labile H_2 complexes $[Re(\eta^2\text{-}H_2)(PR_3)_2L_3]^+$ (L = CO, CN-*t*-Bu) formed upon protonation of $ReH(PR_3)_2L_3$ are stabilized by large noncoordinating anions $[BAr_4]^-$ in comparison to $[BF_4]^-$. Similar W complexes have been widely investigated (*see* ***Tungsten: Organometallic Chemistry***).[64]

Reaction of $[Re(CO)_n(PMe_3)_{5-n}H]$ with $BH_3 \cdot THF$ gives the borohydride complexes $[Re(CO)_n(PMe_3)_{5-n}(\eta^2\text{-}BH_4)]$ ($n = 1, 2$).[65]

The first two preparative methods given above for (**31**) also produce tri- and tetranuclear clusters, a characteristic of all the reactions of (**1**) in protic basic media, including its own electrochemical reduction. Dinuclear species are depicted in Scheme 1, but under normal conditions more complex mixtures result from nucleophilic attack of BH_4^- and OH^- on (**1**), and these reactions are strongly dependent on reaction conditions. As an example of the complexity of the equilibria involved, the structurally characterized mononuclear dihydride $[ReH_2(CO)_4]^-$ protonates to $[Re_3H_3(CO)_{12}]$. The systematic exploration of these synthetic routes, together with hydrogenation of (**1**), led to the characterization of a large number of Re carbonyl hydride clusters $[Re_xH_y(CO)_z]^n$ (R = 3, 4; $n = 0, 1, 2$). This rich chemistry is summarized in Figure 2 and includes the geometry of the Re frameworks, the electron counts at Re, and specific examples. No parallel chemistry exists for Mn, as a result of weaker M–M bonds, but many similar compounds exist or might be expected for Tc. No CO *Bridging Ligands*, common in other metal clusters, are present due to the long Re–Re distance. In the clusters, the H atoms bridge the Re–Re bonds. Their absence in a given bond is reflected in a shorter Re–Re distance. The conjugate bases may be very basic. CO can be replaced by other ligands, for example, py, PPh_3, Hpz, and NCMe in several of the compounds in Figure 2.

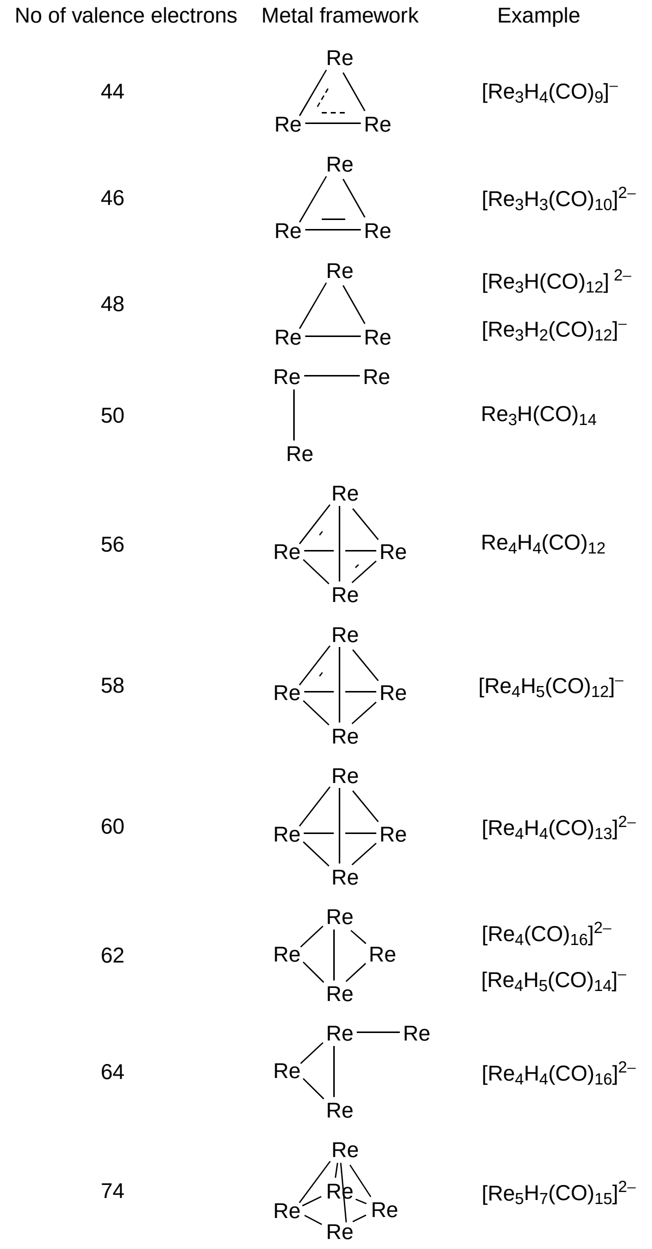

Figure 2 Schematic metal framework of rhenium carbonyl hydride clusters, electron counts, and selected examples

At the sites of Re unsaturation, ligands can be added. $\mathrm{Re_4H_4(CO)_{12}}$ adds NCMe to give $\mathrm{Re_4H_4(CO)_{12}(NCMe)_4}$, a 64 v.e. cluster. However, this is unstable and fragments to give $[\mathrm{Re_3H_4(CO)_9(NCMe)}]^-$. Equation (10) describes the similar fragmentation with DMF leading to a super-unsaturated anion cluster with 44 v.e. (**32**) that readily adds CO, py, NCMe, Hpz, and $\mathrm{PPh_3}$ to give $[\mathrm{Re_3H_4(CO)_9L}]^-$.

This fragmentation is also found with $\mathrm{Cl^-}$ and other weak donors. The cluster with L = Hpz presents an intramolecular dihydrogen bond between one N–H bond and a Re–H–Re bridge atom (see Section 3.1).[66]

$$\mathrm{Re_4H_4(CO)_{12}} \xrightarrow{\text{DMF}} \underset{(\mathbf{32})}{[\mathrm{Re_3H_4(CO)_9}]^-} + [\mathrm{Re(CO)_3(DMF)_3}]^+ \qquad (10)$$

The structure of the super-unsaturated cluster (**32**) is similar to that of $[\mathrm{Re_3H_4(\mu\text{-}H)_3(CO)_9(\mu_3\text{-}CH_3)}]^-$ where the methyl group bridges simultaneously the three Re atoms.

D'Alfonso and coworkers have studied the chemistry of $[\mathrm{Re_2(\mu\text{-}H)_2(CO)_8}]$ (**33**) exploring its 'ethylene-like' character. Indeed, $\mathrm{ReH(CO)_4}$ is isolobal with singlet $\mathrm{CH_2}$ making (**33**) an analogue to $\mathrm{C_2H_4}$. Addition of nucleophiles $\mathrm{X^-}$ ($\mathrm{X = Re(CO)_5}$, Cl) initially forms an L-shaped cluster (**34**) that initiates oligomerization of (**33**) to linear oligomers bearing XRe_n ($n = 4, 6, 8$) chains isolobal with the respective linear hydrocarbons (Scheme 10). Cyclic analogues of $(\mathrm{CH_2})_n$ have also been prepared with the general formula $[\mathrm{ReH(CO)_4}]_n$ ($n = 3, 4, 5, 6$). The $\mathrm{Re_5}$ member has an amplitude of ring puckering similar to that of cyclopentene itself and the $\mathrm{Re_6}$ member presents a typical cyclohexene chair conformation in the solid state.[67]

Heteroatoms (transition metals, main-group elements, and carbon) can be incorporated into the clusters (*see Metal Carbonyl Clusters*). For instance, carbides may be introduced in the clusters on pyrolytic reduction of (**1**) with Na, with $\mathrm{CO_2}$ production. High nuclearities become favored, for example, $[\mathrm{Re_5HC(CO)_{16}}]^{2-}$. High-temperature reactions of (**1**) with other elements, for example, In or heating of its substituted derivatives, for example, $\mathrm{Re_2(CO)_8(PPh_3)_2}$ provide a route to a wealth of clusters containing heteroatoms, as exemplified in Figure 3. $[\mathrm{Re_8C(CO)_{24}}]^{2-}$ can be considered as a homobicapped derivative of $[\mathrm{Re_6C(CO)_{18}}]^{4-}$ with two faces of the central $\mathrm{Re_6}$ octahedron capped by $[\mathrm{Re(CO)_3}]^+$. Similarly, $[\mathrm{Re_6C(CO)_{18}(Au(PPh_3)_2)}]^{2-}$ (**35**) has two $[\mathrm{Au(PPh_3)}]^+$ capping fragments. The C atom occupies the center of the octahedron coordinating six Re atoms.

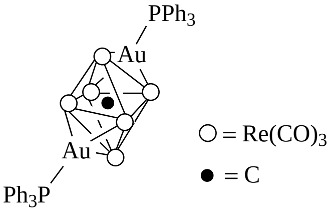

(**35**)

Decapping one face of $[\mathrm{Re_8C(CO)_{24}}]^{2-}$ originates $[\mathrm{Re_7C(CO)_{21}}]^{3-}$. This anion is isolobal with Cp and originates a wide range of heterobicapped derivatives represented in (**36**).[68]

The Ir atom can exchange positions with one Re atom of the central octahedral core.

A comprehensive review provides information on syntheses, reactivity, and NMR and a list of all structurally

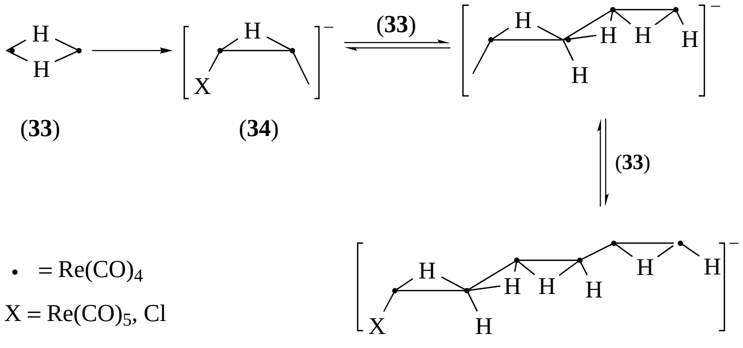

Scheme 10

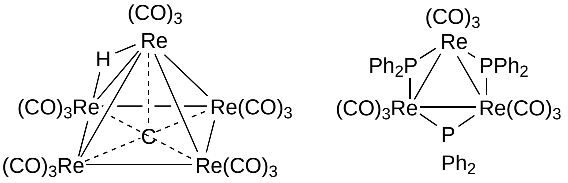

Figure 3 Structures of $HRe_5C(CO)_5$ and $Re_3(CO)_9(\mu\text{-}PPh_2)_3$

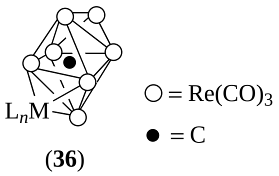

(**36**)

$ML_n = Ir(CO)_2$, $PtMe_3$, Pd(allyl), Tl, HgOAc, HgX, Hg, OH, HgSR, ZnCl, CdCl, CdSR

characterized $[Re_xH_yX_z(CO)_p]^{n-}$ clusters up to mid-1988 (*see **Cluster Compounds: Inorganometallic Compounds Containing Transition Metal & Main Group Elements***).**52**

4 CHEMISTRY OF Re (η^1-HYDROCARBYL) COMPLEXES

4.1 Re Carbonyl Alkyls, Aryls, Acyls, and Related Complexes

The title complexes are generally prepared by reaction of $[Re(CO)_5]^-$ (**13**) with organic halides (Scheme 11), affording a variety of alkyl, vinyl, acyl, aryl, and perfluoroalkyl and perfluoroacyl complexes.

The very strong nucleophile (**13**) is able to replace Cl^- from chlorofluoro hydrocarbons or F^- directly from perfluoroalkenes and activated alkynes, and is only second to $[FeCp(CO)_2]^-$ in the reactivity order of aromatic nucleophilic substitution on homo- and heterofluoroaromatics.

The interesting dimers $(CO)_5ReC(O)C(O)Re(CO)_5$ and $(CO)_5ReC{\equiv}CRe(CO)_5$ have been prepared, the former from (**13**) and oxalyl chloride and the latter by reaction of $[Re(CO)_5FBF_3]$ with HC≡CTMS and a base. $(CO)_5ReC{\equiv}CRe(CO)_5$ behaves as a common substituted acetylene in its coordination to M^+ ions (M = Cu, Ag, Au).**69**

The reverse route, that is, addition of R^- to either the cations $[Re(CO)_nL_{5-n}]^+$ or to $ReX(CO)_nL_{5-n}$, is of very limited value due to preferential nucleophilic addition of LiR to coordinated CO. Although not a general reaction, the decarbonylation shown in Scheme 11 has been used to prepare several alkyl and aryl derivatives including the hydrocarbon-bridged $[Re(CO)_5(\mu\text{-}C_xH_y)Re(CO)_5]$ that can also be made by reaction of (**13**) with $X(C_xH_y)X$ (X = Cl, OTf).**70**

Insertion of alkynes and perfluoroalkenes into the Re–H bond of (**31**) allows the preparation of β-hydrogen-substituted vinyl and fluoroalkyl derivatives, $Re\{C(CF_3){=}CH(CF_3)\}(CO)_5$ and $Re(CF_2CHF_2)(CO)_5$.

CO does not insert into $ReMe(CO)_5$ (**37**) before decomposition is observed (200 °C), whereas analogous formation of $Mn\{C(O)Me\}(CO)_5$ is facile at ca. 50 °C.**71**

The insertions in Scheme 12 combine two important driving forces for this reaction, namely the formation of a metallocycle and Lewis acid catalysis. Exceptional in this respect are the anions *cis*-$[Re\{C(O)R\}R(CO)_4]^-$ that readily form $[Re\{C(O)R\}\{C(O)R\}L(CO)_4]^-$ on addition of PR_3.**2**

More electrophilic substrates, such as CO_2, CS_2, fluoroalkenes, and fluoroalkynes, insert into the Re–Me bond of (**37**) but not so easily as into Re–H bonds. Electrophilic SO_2 insertion is facile, and gives O-bonded sulfinates $[Re\{OS(O)R\}(CO)_5]$, which rearrange to more stable S-bonded $[Re\{S(O)_2R\}(CO)_5]$, as in (**38**). Protonation of $MR(CO)_5$ (M = Mn, Re) with HSO_3Rf and an electrophilic attack with $[Ph_3C][BF_4]$ give $M(OSO_2Rf)(CO)_5$ and $[Re(CO)_5FBF_3]$, both excellent precursors of $[M(CO)_5]^+$ derivatives.**21** Formyl derivatives are mentioned in Sections 2.1.4, 2.3, and 8.1.2.

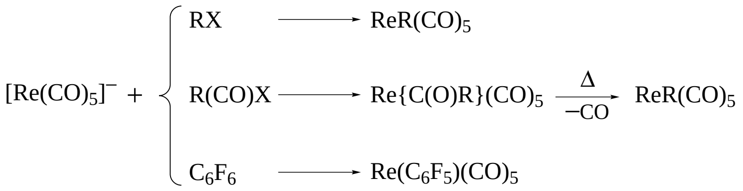

Scheme 11

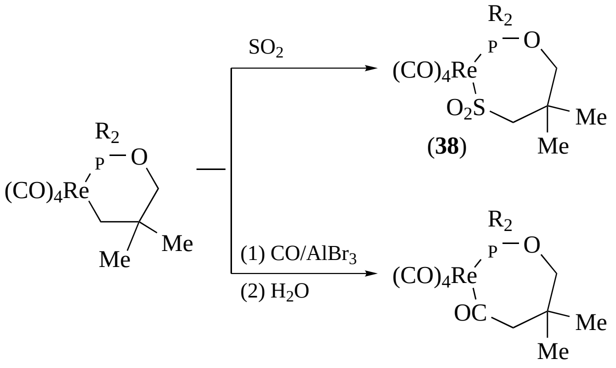

Scheme 12

Not unexpectedly, cationic complexes like $[Re(CO)_4(dppe)]^+$ react readily with $NaBH_4$ to give the formyl $[Re\{C(O)H\}(CO)_3(dppe)]^+$ that decarbonylates in solution to $[ReH(CO)_3(dppe)]$.

The acyl derivatives $[Re\{C(O)R\}(CO)_5]$ undergo nucleophilic addition of LiR to the *cis*-CO ligands, producing metalla-β-diketones. These may be protonated, complexed to other metal fragments or ions, and functionalized to imines by *Schiff-Base* condensation with amines (Scheme 13). A second attack forms *fac*-$[Re\{C(O)Me\}_3(CO)_3]Li_2$. Many such analogs of classical β-diketonates have been used as ligands for ML_n fragments and applied in imaging and biomedical uses with radiolabeled Re (see Section 15).[72]

The selected examples in equations (11–13) represent ways of generating *Metallacycles*, although other less predictable routes have been observed.[2,3]

The stabilization of the metallacycle is the driving force for some of the cyclizations shown. Analogous intermolecular reactions do not take place in the absence of a ring-closure process, namely the substitution in equation (11), the insertions forming (**39**) and (**40**), and the *Orthometalation* in equation (13).[73]

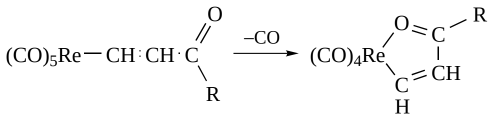

(11)

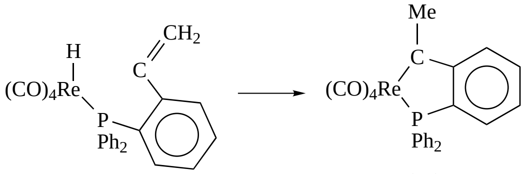

(12)

(**39**)

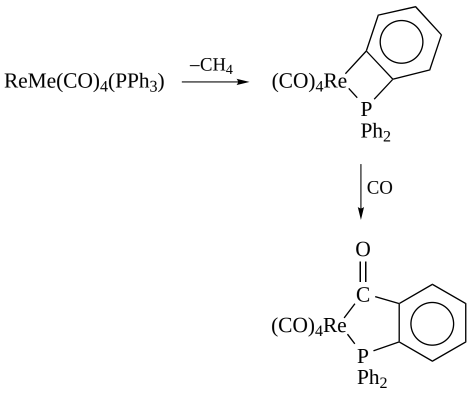

(13)

(**40**)

4.2 Homoleptic Re Alkyls and Aryls

Some early transition metals form homoleptic MMe_x complexes (*see Homoleptic Compound*), where x equals the highest oxidation state of the metal, for example, $TaMe_5$ and WMe_6. In the case of Re, probably as the result of a very unstable seven coordination, no corresponding d^0 Re alkyl has yet been observed. Instead, the deep-green, paramagnetic, explosive at rt, d^1 complex $ReMe_6$ (**41**), from alkylation of $Re(O)Me_4$ with $AlMe_3$ stands alone as a neutral homoleptic Re alkyl complex. It has a slightly distorted trigonal prismatic structure, which is intriguingly closer to D_{3h} symmetry than that of WMe_6. Complex (**41**) (or $ReOCl_4$) adds LiMe to give the square antiprismatic, paramagnetic dianion $[ReMe_8]^{2-}$ (**42**) with an almost perfect S_8 symmetry axis. (**42**) regenerates (**41**) on hydrolysis.[74]

A pronounced tendency toward the formation of Re–Re bonds in the lower oxidation states affords a number of di- and trinuclear Re alkyls, many of which have a structure analogous to the corresponding halides. Treatment of Re_3Cl_9 with MeMgCl in the presence of phosphine gives $Re_3(\mu\text{-}Me)_3(Me)_6(PR_3)_2$ with three bridging Me groups in the Re_3Me_3 plane and six other out-of-plane Me ligands.

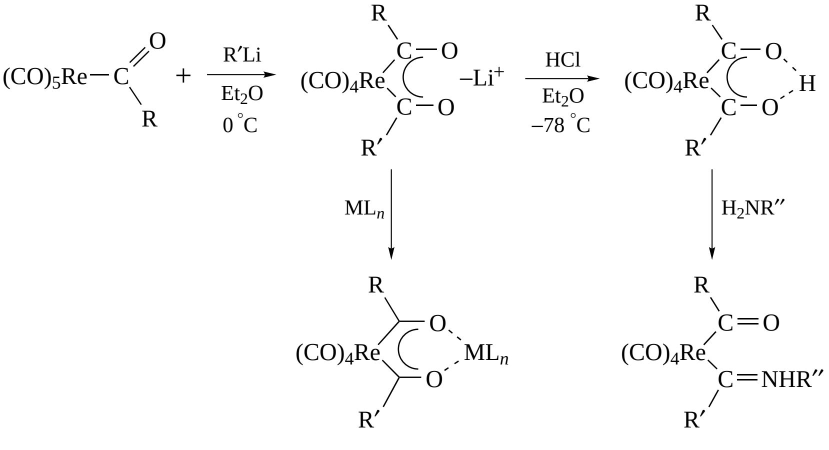

Scheme 13

Treatment of $ReCl_4(THF)_2$ with Grignard reagents gives volatile complexes $[Re_3R_{12}]$ (R = Me, CH_2TMS, $CH_2{}^tBu$) and in one case the dinitrogen complex $(ReR_4)_2N_2$ and a bridging-carbyne derivative, $Re_2(\mu\text{-}CTMS)_2(CH_2TMS)_4$. Indeed, alkyl ligands may undergo α-H abstraction to produce carbenes (alkylidenes) and carbynes (alkylidynes). In this respect, Schrock's complex $Re(\equiv CCMe_3)(=CHCMe_3)(CH_2CMe_3)_2$ is most remarkable since it contains simultaneously alkyl, alkylidene, and alkylidyne as sole ligands.[75]

Early attempts to prepare Re aryls using phosphine-stabilized Re halides, oxo halides, and nitrides yielded a number of adducts, of which $[ReAr_3(PR_3)_2]$ was shown to have a TBP coordination with apical PPh_3 ligands and almost coplanar equatorial phenyl rings. Improvements were only possible using bulkier aryls, a general strategy that has produced excellent results in the stabilization of reactive, coordinatively unsaturated species. This allowed the synthesis of the homoleptic d^3 Re aryl complex $Re(2\text{-}MeC_6H_4)_4$. It is monomeric with a slightly flattened tetrahedral structure similar to its Os^{IV} analog. The importance of the ring bulk is reflected in the fact that the above mentioned Re^{IV} alkyl, $[Re_3(CH_2TMS)_{12}]$, is trimeric even in the gaseous state. Upon reaction with basic small phosphines, for example, PMe_3, the air-stable benzyne complex (**43**) is formed (equation 14).[3]

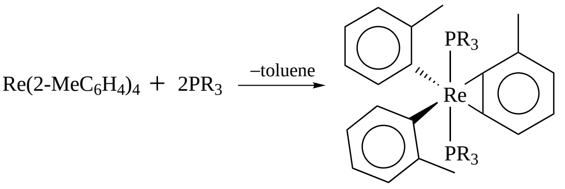

(14)

(**43**)

Complex (**43**) and its corresponding cation $[Re(\eta^2\text{-}2\text{-}MeC_6H_3)(2\text{-}MeC_6H_4)_2(PMe_2R)_2]^+$ have similar structures indicating a benzyne coordination of the rhenacyclopropene type as depicted.

4.3 Re Alkyl and Aryl Halides and Related Complexes

Reaction of Re_3Cl_9 with RMgX forms complexes $Re_3Cl_3R_6$ (**44**) (R = Me, CH_2TMS, CH_2CMe_3, CH_2Ph) with a structure based on an equilateral Re_3 triangle and three in-plane bridging Cl atoms, as determined for R = CH_2TMS. Addition of CO, H_2O, and py to (**44**) affords $Re_3Cl_3(R_6)L_3$ (**45**), but PMe_3 induces reductive cleavage to give $Re_2Cl_2(R_2)(PMe_3)_4$ with a quadruple Re–Re bond.

4.4 Re Carbene Complexes

The very important unsaturated carbene (CXR) or (CR_2) ligand appears in Re chemistry coordinated to different types of fragments. The classical examples, [M]{C(OR)R}, where [M] represents the fragments $Re_2(CO)_9$, $ReX(CO)_4$, and $ReCp(CO)_2$ (R = Me, Ar; R = H, Me, Et),[2] resulting from the two-step standard procedure to Fischer-type carbenes shown in Scheme 6. Fischer-type carbenes are electrophiles and are subject to nucleophilic attack, which seems to be frontier orbital rather than charge controlled (*see Frontier Orbitals*). This explains the preferential addition of nucleophiles to the LUMO located at the {C(OR)R} (or {C(X)Ph}) ligands, and not to the adjacent CO that bears the highest positive charge in the complex. In fact, other derivatives [M]{C(X)Ph} (X = NR_2, SR) may be obtained by reaction of alkoxycarbenes [M]{C(OR)R} with nucleophiles, for example, HNR_2 and HSR, with ROH elimination. Another method of preparing carbene complexes results from nucleophilic attack on carbynes $[L_nM(CR)]^+$. $ReCp(CO)_2\{C(X)Ph\}$ (X = CN, SCN, Me, H) and $[ReCp(CO)_2\{C(L)R\}]^+$ (L = PMe_3, CNMe) are prepared in this way (see also Section 4.5).

Another set of related carbenes are the five-membered cyclic aminooxy and dioxy derivatives (**46**) and (**47**) prepared from aziridines or epoxides and $ReX(CO)_5$ or $ReX(CO)_3(PPh_3)_2$.

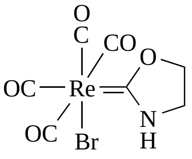

(**46**)

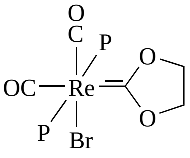

(**47**)

The reactions are catalyzed by X^-, and the mechanism, the results of substitution reactions, and several structures have been reported.[3] α-H abstraction from M–alkyl bonds with Ph_3C^+ generates the alkylidene or *Schrock-Type Carbene Complexes*, for example, $[ReCp(NO)(PPh_3)(CHR)]^+$. Even the simplest carbene, CH_2, is stabilized in $[ReCp^*(NO)(PPh_3)(CH_2)][BF_4]$ and air-stable $[ReCp_2(CH_2)][BPh_4]$ complexes, as discussed in Sections 8.1. Associated with the chemistry of high-oxidation states in the Re^{VII} imidoalkyls (Section 4.7), a number of alkylidenes have been prepared by intramolecular α-H abstraction reactions, for example $Re(NR)_2(CHR)(CH_2R)$ ($R = t$-Bu).[4] In a different approach, reaction of $[Re(O)(OR)_3(THF)_2]$ with 3,3-diphenylcyclopropene gives the oxo-vinylalkylidene $[Re(O)(=H–CH=CPh_2)(OR)_3(THF)]$ in high-yield ($R = O(CF_3)_2Me$).[76]

Vinylidene complexes $[M](=C=CHR)$,[77] may form on rearrangement of coordinated terminal alkynes. [M] represents $ReCl(dppe)_2$, $[Re(CO)_3(PR_3)_3]^+$ $ReCp(CO)_2$, $[ReCp(NO)(PPh_3)]^+$, and $[Re\,(CO)_2(P_3)]^+$ (P_3 = tripodal P ligand; see Section 8.2). The first example of the parent vinylidene complex was reported as $[ReCp(CO)_2(=C=CH_2)]$.[78]

A range of vinylidene complexes $[ReX(=C=CHR)(dppe)_2]$ (X = F, Cl) has been prepared by deprotonation of the corresponding carbynes $[ReX(\equiv C\text{-}CH_2R)(dppe)_2]^+$. The mechanism of the protonation of these complexes has shown that, depending on the reaction conditions, protonation occurs either directly at the vinylidene β-carbon or at the metal, followed by migration to the referred β-carbon.[79]

The fragment $ReCl(dppe)_2$ also adds to $PhC\equiv CMe$ to give the allene $[M](\eta^2\text{-}CH_2C=CHPh)$, which is protonated with HBF_4 to give the cationic metallacyclopropene, as shown in Scheme 14. Allenylidene $[Re(CO)_2(triphos)(=C=C=CRR')]^+$, hydroxyvinylidene, and hydroxycarbene complexes are formed from $[Re(CO)_2(triphos)]^+$ on reaction with propargyl alcohols. The allenylidene cation undergoes a nucleophilic addition of H^- and C, O, S nucleophiles at the γ-carbon according to Scheme 15. However, RSH and RNH_2 add across the $C\alpha$–$C\beta$ bond.[80]

The chemistry of allenylidenes and related cummulylidenes with many other transition metals has been reviewed.[77]

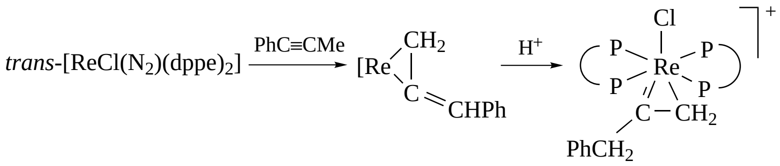

Scheme 14

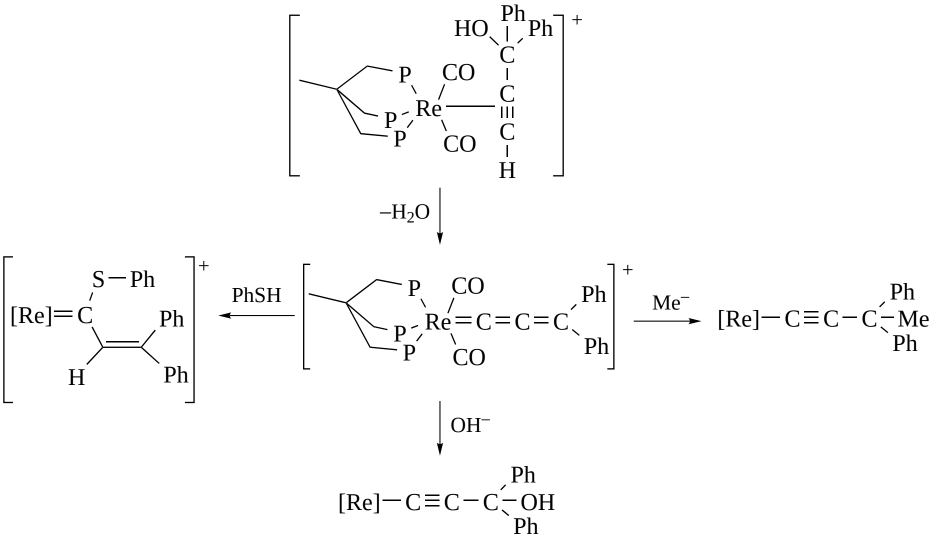

Scheme 15

The aminocarbenes derived from reactions of coordinated isocyanides are treated in Section 14 and bridging alkylidenes arising from C–H activation by Re atoms are presented in Section 9. The recent boom of metal complexes derived from simple ligand substitution with the stabilized N-heterocyclic carbenes has produced only a very limited number of Re complexes like the luminescent (**48**).[81]

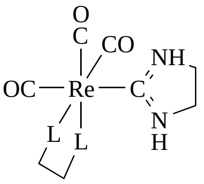

L-L = bipy, phen,

(**48**)

4.5 Re Carbyne Complexes

The oldest route to carbyne (CR) complexes involves a Lewis acid (A^+) attack on Fischer-type carbenes (equation 15). In this way, several Re carbyne derivatives under the general formula $[[Re](CR)]^{0,+}$ have been prepared. The leading examples are $[ReCp(CO)_2(CR)]^+$ (R = Ph, $SiPh_3$) because the analogous alkyl carbynes (alkylidynes) are much less stable due to facile deprotonation as elegantly shown by the spontaneous near-quantitative proton loss shown in equation (16).[78,82]

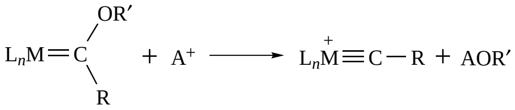

$$L_nM{=}C(OR')R + A^+ \longrightarrow L_n\overset{+}{M}{\equiv}C{-}R + AOR' \qquad (15)$$

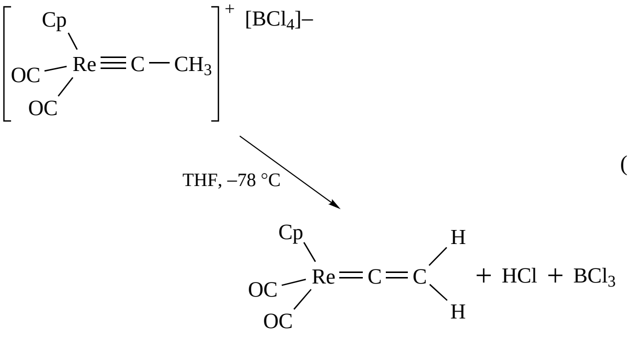

(16)

The molecular orbital analysis of the nucleophilic addition at the carbyne C atom infers the orbital control of the reaction since the C atom undergoing attack is the most negative one in the carbyne complex. [2 + 2] cycloadditions of $[ReCp(CO)_2(CPh)]^+$ with MeN=C(Ph)H, *t*-BuN=O, and ArN=NAr (Ar = aryl) but not with alkenes or alkynes, give the metallacycles. These reactions are driven by the nucleophilic attack of the lone pairs of the N atom at the electrophilic carbyne carbon atom.[83] These metallacycles are very stable and some may undergo nucleophilic attack of PMe_3 at the Cp ring as in Scheme 16.

Olefin oxides and sulfides also add to the carbyne carbon leading to ring opening and forming alkoxycarbenes and other products.[83]

The abstraction of 'O^{2-}' from the acyl group in $[Re(CO)_5(C(O)Ar)]$ with triflic anhydride leads to the carbyne $[Re(CO)_4(CAr)(OTf)][OTf]$ that opens the way to a number of other rare Re^V carbynes like $[Re(CO)_2(CAr)(OR)_2]$ (Ar = 2,4,6-$Me_3C_6H_2$).[84]

This same method was used to prepare a number of highly luminescent, similar Re^V carbynes with P and N donors.[85]

Protonation of the nucleophilic β-C of vinylidenes originated a one-pot synthesis of a range of carbyne complexes *trans*-$[ReF(dppe)_2(\equiv CCH_2R)]BF_4$ upon treating *trans*-$[ReCl(dppe)_2(N_2)]$ with HCCR, $[NH_4][BF_4]$, $[NH_4]Tl$, and light. $NH_4{}^+$ provides the protons necessary to the protonation of the vinylidene intermediates *trans*-$[ReCl(dppe)_2(=C=CHR)]$, whereas $BF_4{}^-$ provides the F^- ion that replaces Cl^-.[86]

Related aminocarbynes, $[ReX(\equiv CNRH)(dppe)_2]^+$, derived from CNR complexes are treated in Section 14.

Upon protonation of $ReH_4(mq)(PPh_3)_2$ with HPF_6, H^- is removed to form $[ReH_3(mq)(PPh_3)_2]+$ that reacts with alkynes forming hydrido-alkylidyne complexes in high-yield $[Re(\equiv CCH_2R)H_2(mq)(PPh_3)_2]^-$. The reaction involves fast and quantitative alkyne isomerization via η^2-allene intermediates.[87]

Re imidoalkyl chemistry in Section 4.7 ended up in several important carbynes, for example, $Re(CR)(CHR)L_2Cl_2$ (R = *t*-Bu; L = py) and $Re(CR)(CHR)(OR)_2$, the latter being active in alkene metathesis.[4] A remarkable preference for carbynes over carbenes is seen in complex $[Re(\equiv C\text{-}t\text{-}Bu)(=CH\text{-}t\text{-}Bu)(CH_2\text{-}t\text{-}Bu)_2]$ (**49**), which is preferred to its tautomer $Re(=CH\text{-}t\text{-}Bu)_3(CH_2\text{-}t\text{-}Bu)$ that would be an analogue to the utterly stable $[ReMeO_3]$.[75]

Protonation of (**49**) with HOTf yields $[Re(\equiv C\text{-}t\text{-}Bu)(CH_2\text{-}t\text{-}Bu)_3(OTf)]$. Addition of py leads to $[Re(\equiv C\text{-}t\text{-}Bu)(=CH\text{-}t\text{-}Bu)(CH_2\text{-}t\text{-}Bu)(OTf)(py)_2]$ (**50**) that reacts with $L_3 = Cp^-$, Tp^- or 1,4,7-trithiacyclononane to give $[Re(\equiv C\text{-}t\text{-}Bu)(=CH\text{-}t\text{-}Bu)(CH_2\text{-}t\text{-}Bu)L_3]^{0,+}$.[88]

Grafting (**49**) on a silica surface led to a 'well defined', highly active, heterogeneous olefin metathesis catalyst (**51**) fully characterized by solid-state NMR spectroscopy.[89]

4.6 Re Alkyl and Aryl Oxide Complexes

Organotransition metal oxides or organo oxo complexes (*see Oxo Complex*) represent a fast expanding area for early transition metals of groups 4 to 7, due to their relationship with catalytic species formed on the surface of oxides under catalytic conditions. Furthermore, they may also supply a convenient set of volatile starting materials for application in *Metal–Organic Chemical Vapor Deposition* and related techniques of solid-state and surface chemistry. Most of

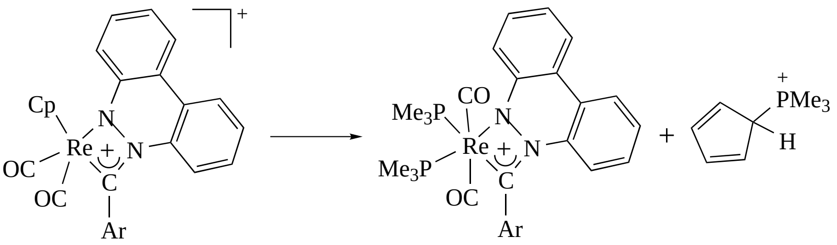

Scheme 16

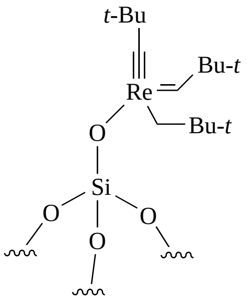

(**51**)

the fundamental work has been covered in comprehensive reviews.[4,90] Related examples are discussed in Sections 8.1.4 and 5.3.

Alkylation of $Re(O)Cl_4$ with MgRX proceeds through Re^V intermediates, $[R_4ReO]_2Mg(THF)_x$, that can be smoothly oxidized with H_2O_2 to give square-pyramidal, paramagnetic, d^1, $Re(O)R_4$ (R = Me, CH_2TMS). Simultaneously, the diamagnetic dimers (**52**) are formed in good yields. The trans conformation of the O=Re–O–Re=O unit with a linear Re–O–Re bond and partial multiple Re–O bond character is held responsible for the observed diamagnetism. They react with pyNO or Me_3NO to yield *cis*-$Re(O)_2R_3$ (**53**) quantitatively.

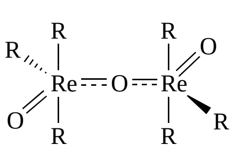

(**52**)

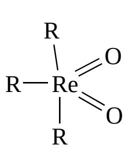

(**53**)

The dimer (**52**) splits upon addition of pyridine, establishing the equilibrium in equation (17). Addition of PPh_3 to the mixture consumes $ReO_2(CH_2TMS)_3$ but use of PMe_3 forms $OPMe_3$ and $ReO(PMe_3)(CH_2TMS)_3$ (**54**). Substituted alkynes readily replace PMe_3. However, acetylene inserts into the Re–P bond to give resonance stabilized ylides, $ReOR_3(CHCHPMe_3)$.[91] CO also inserts into a Re–C bond of (**54**) to give a rare example of a high-oxidation state acyl complex.[92]

$$Re_2O_3R_6 \xrightleftharpoons{py} Re(O)R_3py + Re(O)_2R_3 \xrightarrow{PPh_3} 2Re(O)R_3py + OPPh_3 \qquad (17)$$

The diamagnetic Re^{VI} dimers $Re_2O_4R_4$ (**55**) (R = Np, CH_2CMe_2Ph, CH_2TMS, Me, Et) result from the reduction of Re^{VII} species, for example $ReRO_3$, (see below). The structures may be described as dimers of the paramagnetic ReR_2O_2 fragment with a Re–Re bond. Reduction with the Li or Na amalgam gives the Re^V anions $[ReO_2Np_2]^-$, structurally characterized with several counterions, but reduction of $Re_2O_4Me_4$ with $CoCp_2$ gives a trimeric linear $Re(\mu\text{-}O)_2Re(\mu\text{-}O)_2Re$ framework.

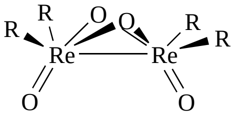

(**55**)

Oxidation of (**55**) with pyNO and with X_2 (X = Cl, Br) gives $[\{Re(O)_2R_2\}_2O]$ (**56**) or trigonal bipyramidal *cis*-$Re(O)_2Np_2X$ respectively. The latter may be alkylated to ReO_2Np_2R (R = Me, Np, CH_2TMS, Ph) (**57**),[93] or substituted to give *cis*-$Re(O)_2Np_2X$ (X = F, SR, OR).

The general reactions of the dioxo complexes (**53**) are oxygen abstraction by phosphines and photolytic conversion to the dimers (**55**), but in the case of (**57**; R = Np) the moderately air-stable carbene complex $Re(O)_2(CH\text{-}t\text{-}Bu)Np$ (**58**) is formed.[93]

For (**57**; R = Ph) the same photolysis, in pyridine, gives $ReO_2(Np)(py)_3$ that reacts with acetylene to give $ReO_2Np(RC{\equiv}CR)$.[93]

In the same vein, the primary event on broad-band UV-visible photolysis of matrix-isolated $(CH_3)_4ReO$ and (**53**; R = Me) is elimination of CH_4 and formation of methylene derivatives $H_2C{=}ReO(CH_3)_2$ and $H_2C{=}Re(CH_3)O_2$, respectively.[94]

The carbynes obtained by the transformations of (**58**) described in Scheme 17 form adducts with a series of ligands,

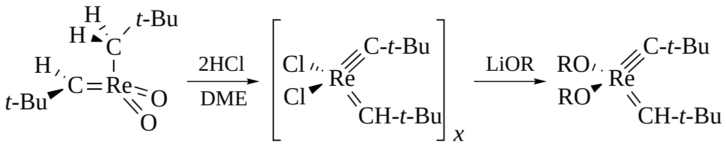

(**58**) (**59**)

Scheme 17

and the tetrahedral alkoxides (**59**) are the first homogeneous Re carbene alkene metathesis catalysts. The carbyne seems to play a spectator role in the reaction.[4]

A number of Re aryl oxides exist in some of the same structural classes described for the Re alkyl oxides. Examples are the paramagnetic d^1 $ReOAr_4$ (Ar = mesityl, *o*-tolyl, *o*-methoxyphenyl), the anionic $[ReO(mes)_4]^-$ and $[ReO_2(mes)_2]^-$. Paramagnetic $ReO_2(Ar)_2$ (Ar = mesityl, xylyl) do not have alkyl counterparts because of their avoided dimerization, but Mo and Os analogues are known.

So far, the trioxides $ReRO_3$ are the most important class of hydrocarbyl oxides of Re. A range of hydrocarbyl complexes $ReRO_3$ (**60**) has been prepared by reaction of Re_2O_7 with ZnR_2 or $SnR(n\text{-}Bu)_3$, including primary β-H-containing chains, for example, R = Et, Pr (no β-H elimination is observed (*see β-Elimination*)), aryls, cyclopropyl, vinyl, alkynyl, η^1-allyl, and η^1-indenyl. On the whole, the ReO_3 fragment can be considered as a general hydrocarbon substituent with an electronegativity close to that of $[PPh_3]^+$ or $[SMe_2]^+$. The chemistry of $ReR(O)_3$ complexes is very extensive and has been thoroughly reviewed.[90]

$ReMe(O)_3$ (**61**) is the most prominent member of this family. Initially prepared from Re_2O_7 and $SnMe_4$, (equation 18), it can be now obtained from cheaper ReO_4^- salts.[95]

$$Re_2O_7 + SnMe_4 \xrightarrow[\text{reflux}]{\text{THF}} ReMe(O)_3 + Re(O)_3OSnMe_3 \qquad (18)$$

The colorless, air-stable, volatile (**61**), usually abbreviated as MTO, has an outstanding thermal stability (dec > 300 °C) and is freely soluble in virtually any solvent from water to pentane. It is converted to ReO_4^- in basic aqueous solution.[96] In water at 70 °C, it forms an electrical conducting polymer of formula $[H_{0.5}\{Re(CH_3)_{0.92}O_3\}]\infty$. Photolysis homolyzes the Me–Re bond.[35] However, the primary reaction brought about by irradiation into the UV absorption near 260 nm in a solid Ar matrix involves tautomerization of MTO to the methylidene hydroxo derivative $H_2C{=}Re(O)_2OH$ (**62**).[97]

Chemical (thermal) trapping of this tautomer has been achieved by the combined reaction of py and $SnMe_2Cl_2$ to give $[\{(C_5H_5N\text{-}CH_2\text{-}Re(O)\text{-}O)\}_2SnMe_2Cl_2][ReO_4]_2$.[98]

This kind of intramolecular abstraction of αH by an oxo group has also been reported when the complexes ReTpO(R)OTf (R = Me, Et, *n*-Bu) are rapidly oxidized at ambient temperatures by pyO or DMSO to give $ReTpO_3$ and the corresponding aldehyde, RHCO.[99]

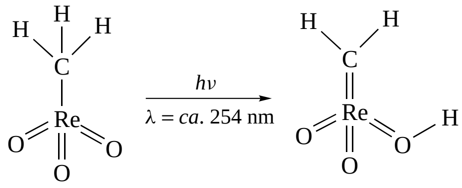

(**61**) (**62**)

MTO readily forms adducts with one or two N-donor ligands having trigonal bipyramidal (O ligands equatorial) or fac-octahedral structures respectively.[100]

A series of Re^V oxo complexes of general formula $Re(O)MeX_2(bipy)$ (X = alkyl, aryl, Cl, Br, OR) have been prepared either from $ReMeO_3(bipy)$.[101] MTO condenses with diols forming the diolates $[ReO_2Me(O,O)py]$. Reactions with arylthiols produce $Re(O)Me(SAr)_4$. However, when 1,2-ethanedithiol is used, the complex (**63**) is obtained by rearrangement of the intermediate $ReMe(O)(S_2C_2H_4)_2$. This represents the only example of Me transfer from a metal to a thiol ligand other than that of methylcobalamine and Co^{II} complexes related to vitamin B12.[102]

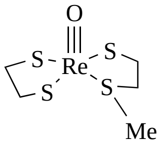

(**63**)

The related reaction with $1,2\text{-}C_6H_4(SH)(CH_2SH)$ ($mtpH_2$) forms $\{ReMe(O)(mtp)\}_2$ and disulfide. The dimer is split by L donors to, for example, $ReMe(O)(mtp)(PR_3)$ (**64**). This monomer is a catalyst for the oxygen-atom transfer reactions mimetic of those catalyzed by the biological Mo and W oxygen transfererases containing MO_2 fragments (equation 19).

$$XO + Y \longrightarrow YO + X \qquad (19)$$

$$XO = pyO,\ t\text{-}BuOOH,\ Me_2SO;\ Y = PPh_3$$

The postulated key intermediate $ReMe(O)_2(mtp)(XO)$ has been modeled from more stable 1,2-hydroxothiolate analogues.[103] (**64**) also catalyzes R_2S and thiophene oxidation to sulfoxides and sulfones with t-BuOOH.[104]

Oxygen abstraction from MTO with PPh_3 or H_3PO_2 forms the elusive $ReMeO_2$ that can be trapped with several ligands to give the Re^V derivatives, for example, $ReMeO_2(PPh_3)_2\cdot ReMeO_3$ and $ReMe(O)_2(\eta^2\text{-}RC{\equiv}CR)$.[105] The latter are efficient catalysts for the olefination of aldehydes.[106]

MTO is an astonishingly versatile catalyst particularly in oxidation and oxygen-transfer reactions. This varied research initiated by Herrmann and extensively developed by Espenson has been comprehensively reviewed up to 1999 but keeps growing.[107]

The first breakthrough was the identification of its end reaction product with H_2O_2, $ReMe(O_2)_2O$ (**65**) which, in spite of being explosive, was structurally characterized by gas-phase electron diffraction and as a solid adduct with H_2O or HMPA by X-ray diffraction.[108] Isolated (**65**) is active in olefin epoxidation. Reaction of MTO with H_2O_2 (1 equivalent) produces a monoperoxo species $ReMe(O_2)O_2$, but it was never isolated and exists in equilibrium with MTO and (**65**). In MTO-catalyzed alkene epoxidation with H_2O_2, both peroxo species may be active depending on the reaction conditions and concentration of H_2O_2 used. However, (**65**) seems to be active in a larger number of other oxidation reactions. Alkene epoxidation ensues at $-30\,^\circ C$ and can reach high turnover values. Even C_{60} can be converted to its epoxide. Experiments and calculations suggest that the oxygen transfer occurs through transition state (**66**).

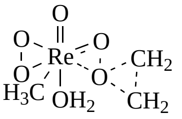

(**66**)

Epoxide opening and diol formation are suppressed by added Lewis bases, for example, py. Aromatic N-bases also lead to accelerated reactions with high selectivity allowing for oxidation of functionalized olefins in a now largely used protocol in organic synthesis. The complexes $ReMe(O)_3\cdot L_2$ (L_2 = bidentate N-donor) are also highly selective epoxidation catalysts.[100]

However, chiral amines only lead to modest enantiomeric excesses because of rapid decomplexation equilibria in solution.[109]

The MTO/H_2O_2 system is a general oxidizing system as can be seen from the variety of reactions in Table 1.

For catalytic purposes, MTO has also been supported on zeolites, niobia and polymers a useful means of preparing quinones in high yields (*see* ***Supported Organotransition Metal Compounds***).[110] Other useful variations use the urea-H_2O_2 adduct as an oxidant in water-free reactions or ionic liquids as solvents.[111]

Table 1 Oxidation products of the MTO/H_2O_2 system

Substrate	Product
Alkene, Dienes, 1,4-PBD, Allyl alcohols	Epoxide
5-Hydroxyalkenes	Tetrahydrofurans
RCH_2OH	Aldehyde or carboxylic acid[a]
R_2CHOH	Ketone
Furans	Enediones
2-hydroxymethylfurans	Pyranones
Silyl enol ethers	α-hydroxyketones
Internal alkynes	α-diketones and carboxylic acids
Terminal alkynes	α-ketoacids and carboxylic acids
Cyclic β-diketones	dicarboxylic acids
Ketene acetals	α-hydroxyesters
R_2S and thiophene	R_2SO or R_2SO_2[a]
RSSR	RS(O)SR and $RS(O)_2SR$[a]
Thioketones	$R_2C{=}S{=}O$
$XC_6H_4\ NH_2$ (X = H, Me, Cy, OMe, Cl)	XC_6H_4NO
p-$XC_6H_4NMe_2$	p-$XC_6H_4N(O)Me_2$
R_2NH	R_2HNO
RNH_2	RNO_2
$(RCH_2)_2NOH$	$RCH_2N(O){=}CHR$
$RHC{=}N\text{-}NMe_2$	RCN
$R_2C{=}N\text{-}NMe_2$	R_2CO
R_3E (E = P, As, Sb)	R_3EO
Ph_2CO	$Ph_2CH(OH)$
R_3SiH	$R_3SiOH + (R_3Si)_2O$
Naphthalenes, Phenanthrene, Anthracene	Corresponding quinones, for example Vitamin K
$(Me)_xC_6H_{6-x}$ ($x = 2, 3, 4$)	p-benzoquinones
p-$(RO)C_6H_4COH$	p-$(RO)C_6H_4OH$
Cl^-, Br^-	ClOH, BrOH
Cycloketones	Cyclolactones (Bayer-Villiger and Dakins)
$ReCp^*(CO)_3$	$ReCp^*O_3$

[a] Depending on specific reaction conditions or procedures.

Instead of O addition to the substrate, the reaction with silanes R_3SiH results in a clean and net insertion of O into a Si–H bond to give R_3SiOH via the computed transition state (**67**).[112]

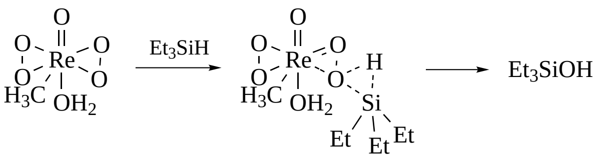

(**65**) (**67**)

Besides oxidation reactions, MTO supported on Al_2O_3/SiO_2, niobia, or zeolites also catalyzes the metathesis of functionalized alkenes, 1,2 transposition of allylic alcohols, addition of epoxides to ketones, alkoxylation of epoxides, dehydration and amination of alcohols, and

Diels–Alder additions in water.[113] It also catalyzes aldehyde olefination with $N_2C(CO_2Et)_2$ and PPh_3 as oxygen sink. Its catalyzed decomposition of $N_2C(CO_2Et)_2$ leads to carbene transfer reactions allowing for the formation of epoxides from aldehydes and ketones, aziridines from imines and cyclopropanation.

4.7 Re Alkyl and Aryl Imido Complexes

The isoelectronic oxo and imido ligands (NR) expectedly build isostructural types of complexes whose chemistry is largely parallel and has been jointly reviewed.[4,90] However, a significant advantage of the imido over the oxo ligand is the possibility it offers of tuning the reactivity of the metal center by adequate manipulation of the electronic and steric properties of the R substituent. Further stabilization is attained by the stronger π-donor character of these ligands, which renders the metal less electrophilic. Steric protection favors monomeric reactive species. These factors are abundantly expressed in the alkene metathesis catalysts derived from imido complexes of Mo and W (*see* ***Molybdenum: Organometallic Chemistry*** and ***Tungsten: Organometallic Chemistry***). Most of the organometallic Re imido complexes known are Re^{VII} species of the two main types: $ReR_3(NR)_2$ (**68**) and $ReR(NR)_3$ (**69**) and derive from the work of Schrock or Herrmann. The preparation of complexes (**68**) was first achieved by alkylation of $Re(N\text{-}t\text{-}Bu)_2Cl_3$ or its aryl congener $Re(NAr)_2(py)Cl_3$ with the appropriate MR_n reagent ($MR_n = AlMe_3$, $PhCH_2MgCl$, $Zn(CH_2TMS)_2$).

A TBP structure isostructural with (**53**) has been assigned to these complexes with the N-t-Bu groups on the equatorial plane. Mixed halo alkyl derivatives $Re(NR')_2Np_2Cl$ and $Re(NR')_2NpCl_2$ may be prepared with rigorous control of the stoichiometry of the alkylating agent, although a better preparation of some of these complexes is shown in Scheme 18.[4]

Alkylation of $Re(NR)_2Cl_3$ with $ZnNp_2$ gives directly $Re(NR)_2(CH\text{-}t\text{-}Bu)Np$ (**70**) ($R = t$-Bu, Ar) isostructural with (**58**). Controlled hydrolysis of $Re(NAr)_2(CH\text{-}t\text{-}Bu)Np$ ($Ar =$ DIPP) gives an alternative preparation for (**58**), and a complex containing simultaneously M=O, M=N, and M=C double bonds, $Re(O)(NAr)(CH\text{-}t\text{-}Bu)Np$, is also isolated by this process.

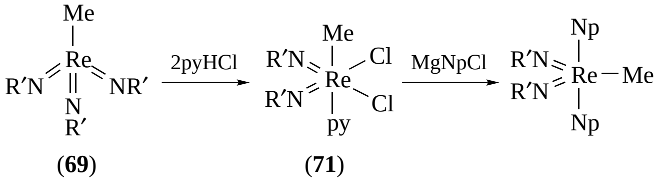

Scheme 18

The other main type of d^0 imido alkyl complexes are the red–purple derivatives (**69**). A number of examples have been prepared with different alkyls ($R = Me$, Et, Np, $1\text{-}C_3H_5$, $C{\equiv}CPh$; $R' = t$-Bu, DIPP) and aryls ($R = 2\text{-}MeC_6H_4$, $2,6\text{-}Me_2C_6H_3$, $2,4,6\text{-}Me_3C_6H_2$), by alkylation of $Re(NR')_3(OTMS)$ with either LiR or MgRX. These alkylations occur smoothly, in contrast to the similar reactions with $Re(O)_3(OTMS)$ where the same reagents lead to reduction, thus reflecting the increased electronic density at the metal in the $Re(NR')_3R$ complexes. Alkylation of $[Re(NR')_3]^-$ also produces $Re(NR')_3R$ and protonation produces the hydride $Re(NR')_3H$ (**71**) that does not have an oxo counterpart. The hydride (**71**) adds π-acceptor ligands L, like acetylenes, to produce $Re(NR')_2(NR'H)L$.[114]

The alternative conversion of $ReRO_3$ into $Re(NR)_3R$ with $R'NCO$ is limited to the methyl case due to the lesser stability of the other alkyl and aryl Re trioxides.[4]

As a result of the high electron density around the Re in $Re(NR')_3R$ complexes, the NR' groups are extremely sensitive to hydrolysis and protonation. This type of reaction occurs with HCl, catechol, or pyHCl and opens a new route into $Re(NR')_2R_xX_{3-x}$ complexes and from these into the mixed alkyls $Re(NR')_2R_xR''_{3-x}$ as exemplified in Scheme 18.

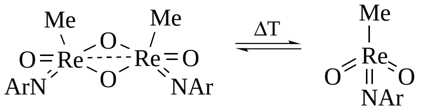

(**72**)

Mixed oxo–imido complexes $ReMeO_n(NR)_{3-n}$ exchange NR and O. $ReMeO_2(NAr)$ (**72**) is a dimer in the solid state and the monomer/dimer equilibrium in solution is temperature dependent.[115]

The complex $ReMe(NAd)_3$ exchanges NAd for O with aldehydes, not ketones, to form $ReMeO_3$ and RCH=NAd. It also exchanges NAd for NR' with imines $RCH{=}N'$ (imine metathesis).[116]

$ReMe(NAr)_2O$ reacts rapidly with $P(OMe)_3$ to form $OP(OMe)_3$ and $ReMe(NAr)_2\{P(OMe)_3\}_2$ (**73**). More basic phosphines react very slowly but replace $P(OMe)_3$ in (**73**). Interestingly, (**73**) under O_2 rapidly forms $ReMe(NAr)_2O$ and $OP(OR)_3$. This catalytic reaction is proposed to take place via the peroxo complex (**74**) that unveils the activation of molecular O_2 by a $ReMe(NAr)_2$ fragment. A parallel activation of O_2 with MTO is, however, less efficient.[117]

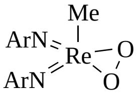

(**74**)

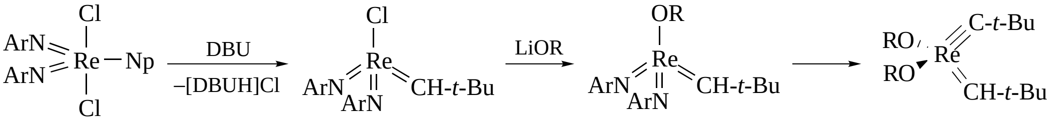

(75)

Scheme 19

Reduction of $Re(NAr)_2Cl_3(py)$ or $Re(NAr)Cl_3(Py)_2$ in the presence of acetylenes leads to $Re(NAr)_2(\eta^2\text{-}C_2R_2)Cl$ or $Re(NAr)(\eta^2\text{-}C_2R_2)_2Cl$ respectively. These can be further reduced to the anions $[Re(NAr)_2(\eta^2\text{-}C_2R_2)]^-$ and $[Re(NAr)(\eta^2\text{-}C_2R_2)_2]^-$, which are stronger nucleophiles than $[Re(N(Ar)_3)]^-$. Therefore, they undergo easy protonation and alkylation with alkyl halides to produce $Re(NAr)_2((\eta^2\text{-}C_2R_2)R'$ ($R' = H$, CH_2R') or $Re(NAr)(\eta^2\text{-}C_2R_2)_2R'$ ($R' = H$, CH_2R') with similar properties to the analogue oxo complexes (Section 5.3).[114]

The complex $Re(NAr)_2NpCl_2$ (Ar = DIPP) undergoes dehydrohalogenation with the strong base DBU, and the resulting halide can be further transformed into the alkoxide derivatives (**75**) with LiOR, for example, ($R = CH(CF_3)_2$, $CMe(CF_3)_2$) (Scheme 19). Contrary to earlier expectations, neither (**75**) nor its analogs, $Re(NAr)_2(CH\text{-}t\text{-}Bu)X$ (X = Cl, OR) and (**58**), are active for alkene metathesis or even polymerization of the very reactive norbornene.

5 CHEMISTRY OF Re (η^2-HYDROCARBON) COMPLEXES

5.1 Complexes with Alkenes

In comparison with late transition metals of groups 8 to 10, Re does not have an extensive chemistry with alkenes. Most of the complexes involving the fragments $Re(CO)_4$, $[Re(CO)_5]^+$, $ReCp(CO)_2$, $[ReCp(NO)(PPh_3)]^+$, *trans*-$[ReX(dppe)_2]^+$, $[Re\{N(C_2H_4NC_6F_5)_3\}]$,[58] and $ReH_x(PPh_3)_2$ are now known. An example of the oxidative addition of alkenes to (**1**) under photolytic conditions is the formation of the labile dimers (**8**). Reaction of $Re(CO)_5FBF_3$ with alkenes gives a variety of cations $[Re(CO)_5(\eta^2\text{-alkene})]^+$ and dications $[\{Re(CO)_5\}_2(\mu\text{-diene})]^{2+}$ in the cases of nonconjugated dienes, for example COD, which bridge the two Re atoms.[21]

Alkenes undergo nucleophilic addition when coordinated to cationic fragments, for example, $[Re(CO)_5]^+$ or $[ReCp(NO)(PPh_3)]^+$, and electrophilic abstractions when coordinated to the more electron-rich $ReCp(CO)_2$ fragment. One example is the formation of (**76**) from $[Re(CO)_5(\eta^2\text{-}C_4H_6)]^+$ and $[Re(CO)_5]^-$, but many others are known including the synthesis of α-aminoacids with organometallic side chains.[118]

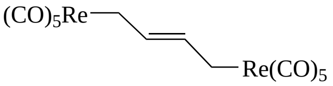

(76)

Section 8.1 contains examples pertaining to the $[ReCp(NO)(PPh_3)]^+$ fragment.

As already mentioned, $ReH_x(PR_3)_2$ ($x = 5, 7$) adds to and transforms alkenes and dienes. In this way, the complexes $ReH_3(\eta^2\text{-}C_2H_4)(PR_3)_3$ and $ReH_5(\eta^2\text{-}C_2H_4)(PR_3)_2$ are obtained from $ReH_7(PR_3)_2$ and C_2H_4 using $Pt(PR_3)_2$ as hydrogen abstractor. The allene *trans*-$[ReCl(\eta^2\text{-}H_2C{=}C{=}CHPh)(dppe)_2]$ is depicted in Scheme 14. Deprotonation of the allene ligand in $[ReCp(NO)(CO)(\eta^2\text{-}H_2C{=}C{=}CH_2)]^+$ leads to the neutral η^1-allenyl complex $[ReCp(NO)(CO)(\eta^1\text{-}HC{=}C{=}CH_2)]$.[119] Other alkene complexes of this metal fragment are treated in Section 8.1.2.

5.2 Complexes with η^2-aromatics

The coordination of aromatic molecules to certain strong metal π-bases leads to $(\eta^2\text{-aromatic})ML_n$ complexes (aromatic = arenes and aromatic heterocycles). This kind of η^2 coordination can activate the aromatic molecules toward an electrophilic attack since d → π back-donation into a π^*-orbital of the aromatic ligand disrupts its aromaticity. This dearomatization provides important synthetic pathways for the functionalization of aromatic compounds that are complementary to activation toward nucleophilic addition induced by their η^6-coordination to π-acid fragments (see Section 9). Induction of η^2-aromatic coordination by electron-rich metal fragments has its paramount example in $[Os(NH_3)_5]^{2+}$ (**77**), which provides the most stable η^2-aromatic complexes and the most useful functionalization reactions. However, this fragment suffers from several limitations that hamper its wider use, the most serious ones being its lack of chirality, the acidity of the ammonia ligands, and the reduced solubility due to its high positive charge. The development of Re^I surrogates to (**77**) attempted circumventing these handicaps.[120]

Indeed, Re^I complexes provide the best fragments for η^2-aromatic coordination after (**77**), although many are too labile to be of use (Figure 4).

The TpRe(CO)(L) fragment coordinates η^2-aromatics more strongly. While $\{TpRe(CO)_2\}$ binds naphthalene, furan, and *N*-methylpyrrole in a labile η^2 fashion,

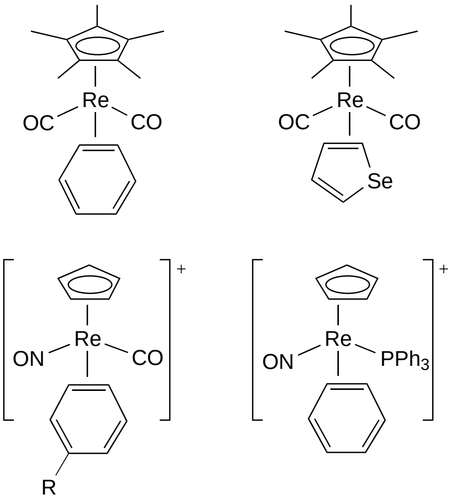

Figure 4 Some Re complexes with η^2-bonded aromatics

{TpRe(CO)(PMe$_3$)} produces a variety of stable η^2 complexes of the type TpRe(CO)(PMe$_3$)(η-L) (L = cyclohexene, cyclopentene, naphthalene, phenanthrene, thiophene, 2-methylthiophene, furan, or acetone).[121] They are obtained by reduction of the Re^{II} complex TpRe(CO)(PMe$_3$)(OTf) with Na/Hg in the presence of the unsaturated ligand.[122]

The {TpRe(CO)(PMe$_3$)} fragment is isoelectronic with [CpRe(NO)(PPh$_3$)]$^+$ and yet considerably more electron rich. This stronger π basic character is reflected in its capacity to bind naphthalene, diasterospecifically, in a η^2-coordination mode, to prefer η^2-thiophene over η^1-thiophene coordination and form stable π complexes with acetone rather than the more common σ-bonded species in, for example, [CpRe(NO)(PPh$_3$)(acetone)]$^+$.

The complex Re(Tp)(CO)(MeIm)(η^2-C$_6$H$_6$) is indeed able to effect dearomatization of the benzene ring allowing its uncoordinated ‘diene’ system to participate in Diels–Alder and other cycloadditions and, therefore, produce a synthetically useful protocol for benzene functionalization.[123]

5.3 Complexes with Alkynes

The chemistry of this class of complex parallels that of alkenes but, being more reactive and stronger donors, alkynes have a richer chemistry. The C–H addition of terminal alkynes to (**1**) forming bridging Re$_2$(μ-H)(μ-C≡CR)(CO)$_8$ dimers and the formation of vinylidenes on electron-rich fragments have already been mentioned (see Section 4.4 and the cyclization shown in equation 4). Internal alkynes RC≡CR bind in typical η^2 fashion to ReCp(CO)$_2$, [ReCp(NO)(PPh$_3$)]$^+$, and [Re(CO)$_4$]$^+$ fragments. The reactivity of the ReCp′(CO)$_2$(η^2-alkynes) has been explored in great detail and depth by the group of Casey and has produced a variety of very delicate structural rearrangements supported by the ReCp′(CO)$_2$ fragment.[124] For the rearrangement of putative ReCl(dppe)$_2$(η^2-MeC≡CPh) to η^2-allene and H$^-$ abstraction from coordinated 2-butyne, see Sections 5.1 and 6, respectively. The insertion of fluoroalkynes into Re–H and Re–C bonds, and related insertions involving ReCp$_2$H, are found in Sections 4.1 and 8.1.

A remarkable family of oxo alkyne complexes has been developed from Re(O)I(η^2-RC≡CR)$_2$ (**78**) (R = Me, Et). These complexes have an unusual electronic structure where the alkyne ligands do not rotate. Reaction of (**78**) with ZnR$'_2$ gives air-stable Re(O)R′(η^2-RC≡CR)$_2$ (R′ = Me, Et, *i*-Pr, η^1-C$_3$H$_5$) complexes (**79**), which are reversibly protonated at the O atom to give [Re(OH)R′(η^2-RC≡CR)$_2$]$^+$ and even further to liberate H$_2$O.[125]

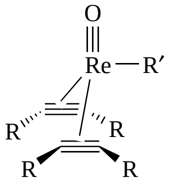

(**79**)

A rare oxo hydride, Re(O)H(η^2-RC≡CR)$_2$, and unsupported Re–Re bonded dimers [Re(O)(η^2-RC≡CR)$_2$]$_2$ reported in a series of papers by Mayer have been carefully compared in terms of structural and bonding properties.[126]

The oxo-hydride Re(O)H(η^2-RC≡CR)$_2$, is formed from Re(OH)(η^2-RC≡CR)$_3$, by intramolecular H migration from the hydroxo group to the metal followed by acetylene dissociation. Alkyl migrations from Re(OR)(η^2-RC≡CR)$_3$ to give (**79**) do not take place.[127] Analogous ReX(η^2-RC≡CR)$_3$ complexes have been made for X = Cl, OTf, NH$_2$, SH.

Related examples are the ReMe(O)$_2$(η^2-RC≡CR) derivatives obtained from (**68**) where alkyne rotation is only observed at ca. 100 °C and isomers exist at room temperature. Other alkyne complexes of high-oxidation state halides are essentially limited to ReCl$_4$(C$_2$Ph$_2$)·OPCl$_3$,[128] and derivatives of the ReCp* fragment mentioned in Sections 8.1.4 and 8.1.5.

6 CHEMISTRY OF Re (η^3-HYDROCARBYL) COMPLEXES

Homoleptic mononuclear Re-allyl complexes are not known. The closest is the triply bonded dimer Re$_2$(η^3-C$_3$H$_5$)$_4$ (see Section 12). In the absence of an autonomous chemistry, the allyl ligand appears associated with other fragments. Several Re(η^3-C$_3$H$_4$R)(CO)$_4$ compounds are conveniently prepared from ReBr(CO)$_5$ and SnMe$_3$allyl or by reaction of [Re(CO)$_4$]$^-$ with [Pd(η^3-C$_3$H$_4$R)Cl]$_2$. Protonation releases propene and forms the strong electrophilic solvent-stabilized [Re(CO)$_4$]$^+$ fragment that adds a wide range of ligands.[129]

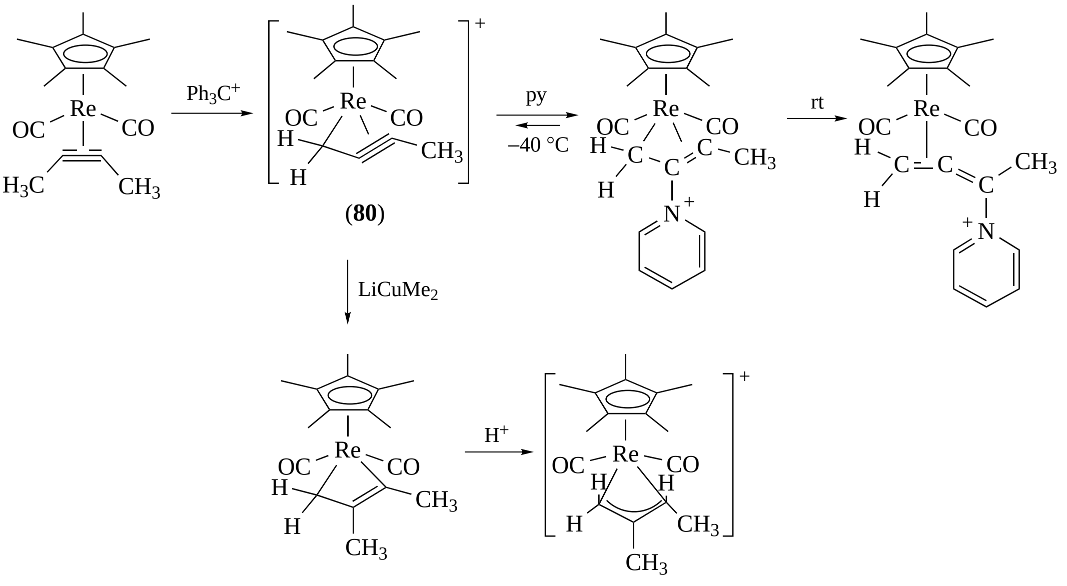

Scheme 20

Re(η^3-C_3H_5)$(CO)_4$ adds PPh_3, py, CNR, and NCR ligands to give Re(η^3-C_3H_5)$(CO)_3$L. Bidentate phosphines, bipy, and phen induce a $\eta^3 \rightarrow \eta^1$ shift forming Re(η^1-C_3H_5)$(CO)_3L_2$.[129]

The π-benzylic derivative Re(η^3-CPh_3)$(CO)_4$ is made from $[Re(CO)_5]^-$ and $[Ph_3C]^+$ and loses CO to give Re(η^5-$C_5H_5C{=}CPh_2$)$(CO)_3$. Addition of bulky PCy_3 leads to the radical $Re(CO)_3(PCy_3)_2$ but smaller phosphines lead to isolable Re(η^1-$C_5H_5C{=}CPh_2$)$(CO)_3L_2$.

Allylic complexes are intermediates in the reaction of $ReH_x(PR_3)_2$ and in the photolysis of (**1**) with dienes.[12] The photolysis of $ReH_7(PR_3)_2$ with propene gives ReH(η^3-C_3H_5)$_2$$(PPh_3)_2$, and the complex [$ReH_4$($\eta^3$-2-$i$-$PrC_3H_4$)(dppe)] is isolated from the reaction of ReH_7(dppe) with 2,3-dimethylbutadiene.

In a general method of preparation of allylic complexes, reaction of $ReCp(CO)_2$(THF) with dienes or allylic alcohol followed by protonation with HBF_4 produces allylic cations [ReCp(η^3-$C_3R_nH_{5-n}$)$(CO)_2]^+$. H^- abstraction from ReCp(CO)(η^2-C_3H_6) with $[Ph_3C]^+$ forms [$ReCp(CO)_2$(η^3-C_3H_5)$]^+$. Nucleophiles like H^-, $MeCO_2{}^-$, RS^-, MeO^-, Me_2HC^-, Ph^-, $N_3{}^-$, H_2N^-, and PMe_3 add at the terminal C atom of the allyl ligand in this cation, as predicted by the Davies–Green–Mingos Rules.[130] However, H^-, LiPh, and Grignard reagents react with [ReCpCl(CO)(η^3-C_3H_5)] to give [ReCpR(CO)(η^3-C_3H_5)]. Reaction of the hydride derivative with electrophiles (HX, NO^+, $MeOC_6H_4N_2{}^+$) forms propene complexes, for example, [ReCp(NO)(CO)(η^2-C_3H_6)$]^+$ and [ReCpHX(CO)(η^2-C_3H_6)].[131]

The recently reviewed chemistry of the η^3-allenyl and propargyl ligands has significant contributions from Re complexes.[132,133] η^3-propargyl derivatives of the $ReCp^*(CO)_2$ fragment (**80**) have been prepared either by H^- abstraction from alkyne complexes $ReCp^*(CO)_2(RC{\equiv}CR')$ or by protonation of the propargyl alcohol complexes $ReCp^*(CO)_2(RC{\equiv}CCHR'OH)$, (Scheme 20). Some fascinating structural rearrangements of these complexes have been examined in detail by Casey.[134]

These η^3-propargyl rhenium complexes undergo kinetic addition of nucleophiles at the central C atom to produce rhenacyclobutenes. The nucleophiles range from PR_3 to malonate, acetylides, pyridines, and water. The derivatives of the addition of pyridines, however, are unstable and undergo further rearrangements to allene or acetylene complexes.[135] Protonation of the metallacyclobutenes produces η^3-allyl complexes.

Electrophilic addition to the alkyne ligand in $ReCp'(CO)_2$ (η^2-$RC{\equiv}CR$) complexes leads to 1-metallacyclopropene cations similar to (**80**). These undergo a number of structural rearrangements eventually ending up in $ReCp'(CO)_2$(η^3-allyl) complexes.[124]

7 CHEMISTRY OF Re (η^4-HYDROCARBON) COMPLEXES

Like the alkenes, dienes have a very limited chemistry with Re. Photolytic reactions of (**1**) in the presence of dienes give complex mixtures of products, with η^3-allyl and bridging alkenyl structures, in a similar manner to the alkene dimers (**8**).[12] Reaction of $ReBr(CO)_3(THF)_2$ with the cyclooctateraene dianion $[C_8H_8]^{2-}$ produces a dimer $(CO)_3Re(\mu\text{-}C_8H_8)Re(CO)_3$ (**81**). Each Re atom is η^4 coordinated to ‘one half’ of the fluxional tetraene ligand.[136]

While the fragment $[Re(CO)_5]^+$ reacts with $MeC{\equiv}CMe$ to give the complex in equation (4), the fragment

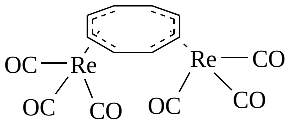

(**81**)

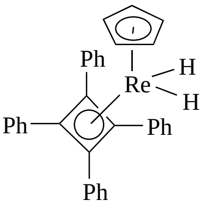

(**82**)

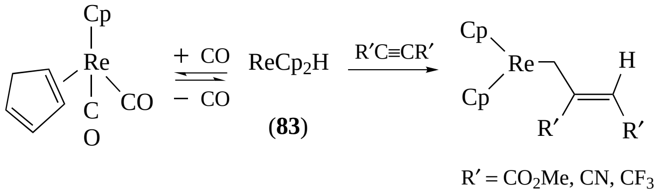

Scheme 21

$[Re(CO)_4]^+$ adds two MeC≡CMe ligands that undergo further cyclization to the cyclobutadiene complex $[Re(\eta^4\text{-}C_4Me_4)(CO)_4]^+$.[137] When heated at 80 °C, the complex $ReCpBr_2\{\eta^2\text{-}(4e)PhC{\equiv}CPh\}$ (with a 4e donor alkyne ligand) rearranges to the cyclobutadiene derivative $ReCp(\eta^4\text{-}C_4Ph_4)Br_2$. This can be transformed into the dihydride $ReCp(\eta^4\text{-}C_4Ph_4)H_2$ (**82**) that adds CF_3CO_2H, opening the cyclobutadiene ring to give $ReCp(\eta^4\text{-}1,3\text{-}C_4Ph_4H_2)H(O_2CCF_3)$.[138]

Reaction of $ReH_7(PR_3)_2$ or $ReH_5(PR_3)_2$ with dienes gives the fluxional $ReH_3(\eta^4\text{-diene})(PR_3)_2$ (diene = COD, C_4H_6, C_5H_6, C_6H_8).[54] Hydride migration to the ring is reversible, and the complexes are in equilibrium with $ReH_2(\eta^3\text{-allyl})(PR_3)_2$ or $ReH_2(\eta^5\text{-dienyl})(PR_3)_2$ species. Such complexes are intermediates in the C–H activation process of alkane dehydrogenation.[73] Some related chemistry arising from Re atom chemistry in benzene/diene mixtures is presented in Section 9.

8 CHEMISTRY OF Re (η^5-HYDROCARBYL) COMPLEXES

8.1 Bis(η^5-cyclopentadienyl)Re Complexes

The parent compound in this family, the rhenocene hydride $ReCp_2H$ (**83**) is a milestone in organometallic chemistry, since it was the first isolated carbonyl-free hydride and the first hydride to be characterized by ^1H NMR in 1958. However, it has a more limited chemistry compared to the other groups 4, 5, and 6 bent metallocenes (*see Metallocene Complexes*).[2,4]

Complex (**83**) is as basic as an organic amine and reversibly protonates in aqueous medium to give $[ReCp_2H_2]^+$, one of the earliest examples of metal complex basicity. Accordingly, (**83**) readily forms adducts with inorganic Lewis acids giving polynuclear complexes (Section 14). Reaction with C_3H_5Br and CCl_4 give $[ReCp_2(\eta^2\text{-}C_3H_6)]Br$ and $ReCp_2Cl$ respectively. Oxidation with halogens gives the d^2 cations $[ReCp_2X_2]^+$ (X = Cl, Br, I), but SbF_5 yields the Re^{VII} species $[ReCp_2X_2][SbF_6]_3$. Reactions with CO and alkynes are represented in Scheme 21.

CO addition probably involves a ring slippage toward η^1-Cp, followed by intramolecular reductive elimination; its reverse was established in low-temperature matrix studies. The alkyne insertion is kinetically controlled and leads to stereospecific trans insertion, as shown. Use of HC≡CR further established regioselectivity for β insertion. Deprotonation of (**83**) with LiBu, with or without the help of a chelating N base, affords the anion $[ReCp_2]^-$ (**84**) from which $ReCp_2R$ (R = Me, Et, Pr, $\eta^1\text{-}C_3H_5$) is easily obtained. Further reaction with MeI gives $[ReCp_2Me_2]^+$, which yields the diene derivative $ReCpMe_2(\eta^4\text{-}C_5MeH_5)$ on reaction with LiMe, a typical nucleophilic addition to a coordinated diene in a cationic complex. The rhenocene cation $[ReCp_2]^+$ is easily stabilized as an adduct with NCMe, CN-*t*-Bu, or HC≡CPh. Photolysis of $[ReCp_2(NCMe)]^+$ in the presence of C_6H_6 or thiophene leads to C–H activation forming the cations $[ReCp_2H(R)]^+$ (R = Ph, 2-C_4H_3S) in much the same way as described for the isoelectronic fragment WCp_2 (*see* ***Tungsten: Organometallic Chemistry***).[139]

Hydride abstraction from $[ReCp_2Me]$ with $[Ph_3C][BArF]$ quantitatively produces the air-stable methylene complex $[ReCp_2(CH_2)][BArF]$. This is another example of the ability of MCp_2 fragments to stabilize highly reactive molecular fragments. However, in the present case the outstanding stability of the compound depends on the size of the anion being high for $[BArF]^-$ and $[BPh_4]^-$ and marginal for $[BF_4]^-$ and $[PF_6]^-$. A tight association between the cation and the $[BArF]^-$ anion is proposed to operate preventing a bimolecular coupling of two $[ReCp_2(CH_2)]^+$ species that generate $[ReCp_2(C_2H_4)]^+$ and a solvent-stabilized cation $[ReCp_2(S)]^+$.[140]

The electrophilic methylene ligand undergoes nucleophilic additions with PPh_3, py, and CN-*t*-Bu. It reacts with O and S donors to give $[ReCp_2(\eta^2\text{-}H_2CE)]^+$ (E = O, S) and with N_2CHTMS to form the olefin complex $[ReCp_2(\eta^2\text{-}H_2C{=}CHTMS)]^+$.

Mild oxidation of (**84**) gives the Re–Re bonded dimer of rhenocene (**85**), which further reacts upon warming to form other dimers, such as the fulvalene derivative (**86**).

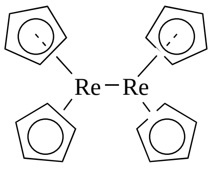

(**85**)

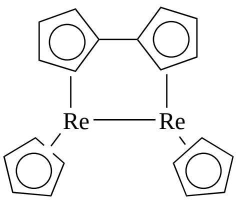

(**86**)

A similar chemistry is observed for MCp_2 ($M = Mo$, W), reflecting the instability of these metallocene complexes toward dimerization and C–H activation. Indeed, $ReCp_2$ can only be isolated in low-temperature CO and N_2 matrices by in situ UV irradiation of (**83**). Dimerization is prevented by use of Cp^*, thus enabling the isolation and full structural and spectroscopic characterization of $ReCp^*_2$ formed upon UV irradiation of $ReCp^*_2H$ (**87**). The rings are parallel and eclipsed. The hydride (**87**) is prepared by MVS techniques from Cp^*H and Re atoms in 10–15% yield.

The chemistry of (**87**) resembles that of (**83**), allowing isolation of the analogs $[ReCp^*_2H_2]^+$, $[ReCp^*_2]K$, $ReCp^*_2Cl$, and $ReCp^*_2Me$. C–H activation of the ring methyls, also common in other early transition metal MCp^*_2 metallocenes, arises upon irradiation of $ReCp^*_2Cl$ or oxidation of $ReCp^*_2$, for example, (**88**).[141]

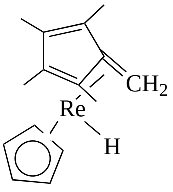

(**88**)

8.1.1 Chemistry of ReCp(CO)3

$ReCp(CO)_3$ (**89**), first prepared in 1968, and its analog $ReCp^*(CO)_3$ (**90**) represent, together with $Re_2(CO)_{10}$ and $Re(CO)_5X$, the most important entries into rhenium organometallic chemistry. Some ring-substituted congeners, for example, $C_5Me_nH_{5-n}$, indenyl, and fluorenyl, are also known, and the synthetic methods outlined in equations (20) and (21) are general and have good yields in most cases.[2]

$$ReBr(CO)_5 + NaCp \text{ or } SnCpRe_3 \xrightarrow{\Delta} ReCp(CO)_3 \quad (20)$$

$$Re_2(CO)_{10} + C_5Me_5H \xrightarrow{\Delta} ReCp^*(CO)_3 \quad (21)$$

The pentahapto coordination is attained from the first formed and isolable $Re(\eta^1\text{-}Cp)(CO)_5$. Added CO quantitatively reverses the reaction in the case of $Re(\eta^5\text{-}fluorenyl)(CO)_3$. Not unexpectedly, *fac*-$[Re(\eta^1\text{-}Cp)(CO)_3L_2]$ is obtained from $[ReXCO)_3L_2]$ and Cp^- ($L_2 =$ bidentate phosphines). Surprising, however, is irradiation of $Re(\eta^1\text{-}Cp)(CO)_5$, which only produces radicals by cleavage of the C–Re σ bond.

A variety of alternative methods for preparing $ReCp'(CO)_3$ where Cp' means a Cp ring substituted with bioactive molecules or with functions that enable binding of biomolecules, has been developed for biomedical applications (see Section 15).

Transformations of (**89**) may take place at the metal, the ring, or the coordinated carbonyls, engendering a variety of other monocyclopentadienylrhenium complexes, discussed in the following subsections.

Substitution Reactions. Thermal substitution is difficult to achieve both with (**89**) and the isoelectronic Mn analog. Thermal reaction of (**89**) with PMe_3 only yields $ReCp(CO)_2PMe_3$ under severe conditions. However, in refluxing hexane, the octahedral adduct *fac*-$Re(\eta^1\text{-}Cp)(CO)_3(PMe_3)_2$ is isolated. The intermediate $Re(\eta^3\text{-}Cp)(CO)_3PMe_3$ is unobserved but is kinetically required. Accordingly, the indenyl derivative $Re(\eta^5\text{-}Ind)(CO)_3$, which favors the $\eta^5 \rightarrow \eta^3$ ring slippage over the Cp, reacts much faster with PMe_3 but, again, only the final $Re(\eta^1\text{-}Ind)(CO)_3(L)_2$ is isolated. ReCp(CO)(NO)Me (see below) has a similar behavior.

Dissociatively photoinduced substitution is facile and extremely useful. Low-temperature photolysis in CO and N_2 matrices has identified the loss of one CO ligand as the primary step. Photolysis of (**89**) in hexane gives a good yield of the dimer $Re_2Cp_2(CO)_5$ with one bridging CO ligand by association of $ReCp(CO)_2$ with $ReCp(CO)_3$, whereas in benzene, structurally characterized $ReCp(CO)_2(\eta^2\text{-}C_6H_6)$ is first isolated but the reaction can be taken to completion producing $ReCp(\eta^6\text{-}C_6H_6)$. Photolysis of $ReCp^*(CO)_2(N_2)$ in 1,4-$C_6H_4F_2$ gives both the C–H activation product $ReCp^*(H)(C_6H_3F_2)(CO)_2$ and the coordinated arene $ReCp^*(CO)_2(\eta^2\text{-}C_6H_4F_2)$ in 5:9 ratio.[142]

The strong tendency of the $Cp'Re(CO)_2$ fragment to bind alkenes and η^2-arenes was mentioned in Section 5.2.

Ultrafast spectroscopy studies determined the oxidative addition of the Si–H bond to the unsaturated $ReCp(CO)_2$ fragment to be much faster (4.4 ps) than that of the C–H bond (230 ns).[143]

The photolytic generation of $ReCp^*(CO)_2$ in alkanes at low temperature forms the complexes $ReCp^*(CO)_2$(alkane). At rt the cyclopentane derivative, $ReCp^*(CO)_2(C_5H_{10})$, is the longest-lived alkane complex observed to date ($t = 125$ ms).[144] B–H bonds also coordinate unbroken as in $ReCp^*(CO)_2(\eta^2\text{-}HBpin)$.[145]

From a preparative point of view, the most useful substitution is achieved photochemically in THF ($\lambda < 300$ nm) to give $ReCp(CO)_2(THF)$ (**91**) or $ReCp^*(CO)_2(THF)$ (**92**). Replacement of labile THF leads to a variety of substitution products of general formula $ReCp(CO)_2(L)$ with two-electron donors, for example, PR_3, $AsPh_3$, $P(OR)_3$, py, N_2, $RC{\equiv}CR$, SR_2, and is responsible for the wide scope of the chemistry of the fragment $ReCp(CO)_2$.[3]

The simplicity of this preparative method, coupled with the versatile coordination ability of the $ReCp(CO)_2$ and $ReCp^*(CO)_2$ fragments, provides a good model for the studies on coordinative activation of less usual ligands and molecules, many of which do not have an autonomous existence as free molecular entities. One example is the formation of $ReCp(CO)_2(CE)$ ($E = S$, Se), together with $EPPh_3$, on reaction of (**89**) with CE_2 and PPh_3. Reaction of (**89**) with elemental sulfur (S_8) gives a mixture of several structurally characterized

S-bridged dimers and the monomeric complex $ReCp(CO)_2(S_2)$ (**93**). Stepwise oxidation of (**95**) with MCPBA produces many unusual complexes, for example, $ReCp^*(CO)_2(SSO)$ (**94**) and $ReCp^*(CO)_2(OSSO)$ (**95**).[3]

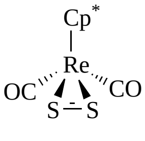
(**93**)

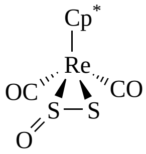
(**94**)

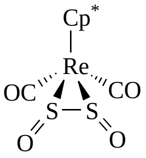
(**95**)

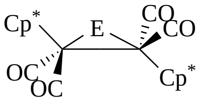
(**96**)

The series $[ReCp^*(CO)_2]_2(\mu\text{-}E)$ (**96**) (E = O, S, Se, Te) and related complexes have also been prepared from the elements or from EH_2 and (**92**). Slow decomposition of solid (**92**) in a glovebox produces the dimer $Cp^*Re(CO)_2{=}Re(CO)_2Cp^*$ (see Section 11). Reaction of (**91**) with $PhC{\equiv}CH$ gives the vinylidene $ReCp(CO)_2({=}C{=}CHPh)$, but the structure of the coordinated $PhC{\equiv}CPh$ in $ReCp(CO)_2(\eta^2\text{-}PhC{\equiv}CPh)$, in spite of being bent, has an almost unperturbed $C{\equiv}C$ bond with a rather short length. In contrast, the azobenzene derivative $ReCp(CO)_2(\eta^2\text{-}PhN{=}NPh)$ has an almost pure single N–N bond and is best described as a metallacyclic structure. The extensive research on the coordination of unsaturated N–N bonds to the fragment $[Re] = ReCp(CO)_2$ as related to N_2 reduction involving species sketched in Scheme 22 has been reviewed.[25]

The electron-rich $ReCp^*(PMe_3)_2(N_2)$ is protonated at the metal and not at N_2 in spite of its low ν (NN) vibration frequency. The aryldiazenido cations $[ReCp^*(CO)_2(N_2Ar)]^+$ undergo nucleophilic addition of R^- and H^- to give analogs of ligated N_2H, N_2H_2, and N_2H_3. Their somewhat unpredictable reaction with nucleophiles, for example, halides, CN^-, SCN^-, PPh_3, and $NaBH_4$, to yield the dinitrogen complex $ReCp'(CO)_2(N_2)$ actually proceeds by one-electron reduction ensuing a radical process.[146]

Electrophilic Attack and Oxidative Additions. Complex (**89**) cannot be protonated, but rapid H/D exchange of the ring protons is observed in CF_3CO_2D. The more electron-rich complex $ReCp(CO)_2PPh_3$, however, reacts in both ways giving faster H/D exchange and protonating at the metal to yield the isomers *cis*- and *trans*-$[ReHCp(CO)_2PPh_3]^+$, where the equilibrium favors the latter. Adducts with other Lewis acids, for example, $SnCl_4$ are known.[2]

Two other electrophiles give important reactions with (**89**) and (**90**) in terms of the vast chemistry of the resulting products: NO^+ and X_2. The former gives electrophilic substitution, yielding the cation $[ReCp(CO)_2(NO)]^+$ (**97**), while the latter gives $ReCpX_2(CO)_2$ (**98**; X = Br, I) with a four-legged piano stool structure. The diagonal (trans) and lateral (cis) isomers can be separated chromatographically. In boiling toluene solution, *lat*-(**98**) isomerizes to *diag*-(**98**) (X = Br). Heating in the solid state reverts *diag*-(**98**) back to *lat*-(**98**). This first example of a reversible phase-dependent isomerization reaction of one organometallic complex was further studied for other $ReCp(CO)LX_2$ (L = CO, $P(OMe)_3$) complexes adsorbed on a silica gel surface under visible light irradiation and found to be dependent on the nature of both X and L and the interaction with the surface hydroxyl groups.[147]

Internal alkynes displace both CO ligands to give $ReCpBr_2(\eta^2\text{-}(4e)RC{\equiv}CR)$.

The complexes $[ReCp^*(CO)_2X(NCMe)][BF_4]$, prepared from the parent dihalides and $AgBF_4$, react with $Et_3N{\cdot}3HF$ to produce the fulvene complex $[Re(\eta^6\text{-}C_5Me_5CH_2)X(CO)_2]$ (see Section 9).[148]

$ReCp(CO)_2(H)(MR_3)$ and $ReCp(CO)_2H_2$ are the products of photoinduced oxidative addition of (**89**) to H–MR_3 bonds (M = Si, Ge, Sn) (see Section 8.1.5). Photochemical activation of (**89**) or (**90**) in the presence of B_2pin_2 gave *cis* and *trans*-$ReCp'(CO)_2(Bpin)_2$, that is, oxidative addition to the B–B bond. Most remarkable, however, is the fact that further irradiation of this compound or of a mixture of (**90**) and B_2pin_2 in pentane led to regiospecific terminal C–H activation of the pentane with formation of $C_5H_{11}Bpin$ and HBpin. The mechanism of this elegant C–H activation process does not seem to take place via C–H activation on intermediate $ReCp'(CO)_2$.[149]

Photolysis of $ReCp^*(CO)_3$ in C_6F_6 does not lead to the $\eta^2\text{-}C_6F_6$ complex. Instead, both C–H and C–F activation take place leading inter alia to the fulvene complex $Re(\eta^6\text{-}C_6Me_5CH_2)(CO)_2(C_6F_5)$ and HF elimination (see Section 9).[150]

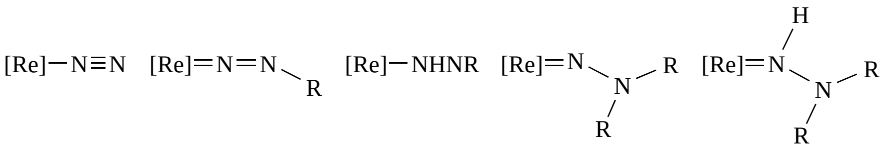

Scheme 22

The intramolecularly chelated $\mathrm{Re(C_5H_4CH_2CH_2NHMe)(CO)_2}$, being more electron rich than (**89**) undergoes facile oxidative additions of a variety of RX halocarbons to give $\mathrm{[Re(C_5H_4CH_2CH_2NHMe)R(CO)_2]X}$. They show a rich chemistry including CO insertion into Re–N bonds and CO activation.[151]

$\mathrm{ReCp(PMe_3)_3}$ is only accessible on reduction of *mer*-$\mathrm{[ReCl_3(PMe_3)_3]}$ with Na/Hg in the presence of $\mathrm{C_5H_6}$. Photolysis expels one $\mathrm{PMe_3}$ ligand and the orthometalation product $\mathrm{[ReCpH(2\text{-}CH_2PMe_2)(PMe_3)]}$ is formed. This extremely reactive species oxidatively adds to a series of hydrocarbons RH, including $\mathrm{CH_4}$, to generate $\mathrm{ReCp(H)(R)(PMe_3)_2}$. The reactivity order observed for the C–H activation is Ar $>$ cyclopropyl $\sim$ vinyl $>$ Me $>$ primary alkyl $>$ secondary alkyl. This type of C–H activation is also found in low-valent MCp (M = Rh, Ir) complexes.

Reactions with Bases. Reaction of (**89**) with lithium alkyls may deprotonate the Cp ring, generating metallates $\mathrm{Re(\eta^5\text{-}C_5H_4Li)(CO)_3}$. Reaction of these species with electrophiles such as XY ($\mathrm{X_2}$, XC(O)R, $\mathrm{SiXR_3}$, $\mathrm{(H_2CO)_n}$) forms ring-substituted derivatives, for example, $\mathrm{Re(\eta^5\text{-}C_5H_4Y)(CO)_3}$ with pendant organic functions that are useful for biomedical applications, for example, $\mathrm{Re(\eta^5\text{-}C_5H_4CH_2OH)(CO)_3}$.[152]

Disubstituted derivatives, $\mathrm{Re(\eta^5\text{-}C_5H_3Y_2)(CO)_3}$ can also be obtained by this method.

Nucleophilic Addition at the CO. The formation of the metal acyl $\mathrm{[ReCp(CO)_2\{C(O)Me\}]^-}$ (**99**) is a classic example of acylmetallate formation. The site of electrophilic alkylation of (**99**) is dependent on the hardness of the electrophile used. In fact, its reaction with the oxonium $\mathrm{[Me_3O]^+}$gives the expected Fischer carbene $\mathrm{[ReCp(CO)_2\{C(OMe)Me\}]}$, but the softer electrophile MeI attacks the Re, forming $\mathrm{[ReCpMe(CO)_2\{C(O)Me\}]}$ (**100**) (Scheme 23).

Oxidative Decarbonylation. First observed by adventitious air oxidation of (**92**), $\mathrm{ReCp^*O_3}$ (**101**) was later synthesized from (**90**) with $\mathrm{H_2O_2}$ (30%) in a two-phase water/benzene system with 80–85% yields.[90]

The detailed mechanism of this reaction is not known, but intermediates like (**96**) (E = O) and the dinuclear complex (**102**) have been characterized. This reaction is not general and cannot be used for the preparation of $\mathrm{ReCpO_3}$ from (**89**). In this context, is it worth mentioning the unusual result of the oxidation reaction in equation (22).[153] The chemistry of (**101**) is presented in Section 8.1.4.

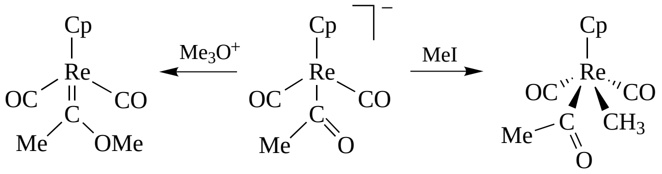

(**99**) (**100**)

Scheme 23

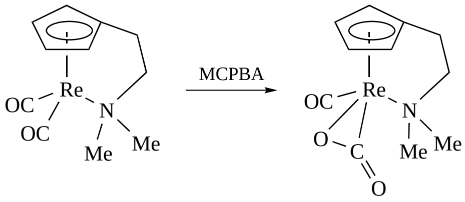

(22)

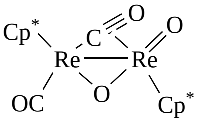

(**102**)

8.1.2 *Chemistry of $[\mathrm{ReCp(CO)_2NO}]^+$, $[\mathrm{ReCp(NO)(PPh_3)}]^+$, and Derivatives*

The cation, $\mathrm{[ReCp(CO)_2NO]^+}$ (**103**), with excess $\mathrm{I^-}$ undergoes ring slippage with Cp loss to $\mathrm{[Re(NO)(CO)_2I_3]^-}$. Hydrides, however, add to the CO, producing inter alia, the formyls ReCp(NO)(CO){C(O)H} (**104**) and $\mathrm{[ReCp(NO)\{C(O)H\}_2]}$. Double $\mathrm{H^-}$ attack at the same CO ligand, that is, at the formyl in (**104**), gives $\mathrm{ReCp(NO)(CO)CH_2OH}$, the first identified hydroxymethyl complex. This ligand represents an intermediate step in the reduction of coordinated CO to methyl. Reaction of (**104**) with $\mathrm{BH_3}$ completes reduction to give ReCp(NO)(CO)Me. Hydroxide addition to $\mathrm{[ReCp^*(CO)_2NO]^+}$ gives $\mathrm{[ReCp^*(NO)(CO)\{C(O)OH\}]}$, which originated a range of binuclear complexes $\mathrm{[ReCp^*(NO)(CO)(\mu\text{-}CO_2)\,ML_n]}$ with a $\mathrm{CO_2}$ bridge between the metals.[154]

Equation (23) describes a parallel behavior for $\mathrm{[ReCp(NO)(CO)(PPh_3)]^+}$, where the stable formyl $\mathrm{[ReCp(NO)(PPh_3)(CHO)]}$ has a rather short Re–C bond.

$$[\mathrm{ReCp(NO)(CO)(PPh_3)}]^+ \xrightarrow{\mathrm{H^-}} [\mathrm{ReCp(NO)(PPh_3)\{C(O)H\}}] \qquad (23)$$

Complex (**105**) is a pivotal compound in the development of a vast amount of chemistry of the fragment $\mathrm{[ReCp(NO)(PPh_3)]^+}$, hereafter abbreviated as $\mathrm{(Re)^+}$ for simplicity, which was recently reviewed.[155] Scheme 24 summarizes the fundamental set of reactions used to generate derivatives of this fragment.

The methylidene complex $\mathrm{[ReCp^*(NO)(PPh_3)CH_2]^+}$ is stable above 100 °C. Not surprisingly, (**106**) is less stable and decomposes to $\mathrm{[(Re)(\eta^2\text{-}C_2H_4)]^+}$ and $\mathrm{[(Re)(solvent)]^+}$ via a rate-determining dimerization process. It can, however, be trapped by a variety of nucleophiles to give both neutral and cationic derivatives (**107**). The alkyl complexes (Re)–CH_2CH_2R, obtained from (**106**) and $LiCH_2R$, generate new alkylidene species via predominant, but uncommon, H^- abstraction at C_α (equation 24). The C_β disubstituted (Re)-CH_2CHR_2 analogs undergo the normal β-H^- abstraction to give cationic alkene complexes $[(Re)(\eta^2\text{-}C_2R_2H_2)]^+$.

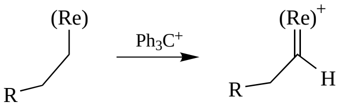

(24)

Evidence points to initial electron transfer between (Re)-CH_2R and Ph_3C^+ followed by H transfer to Ph_3C. For further chemistry of these alkylidene complexes, see Section 8.1.3.

The facile low-temperature protonation of (**105**) in chlorinated solvents provides an easy entry into the chemistry of the complexes $[(Re)–L]^+$ (**110**) *via* (**108**) and the alkyl halide intermediates (**109**) or its ClC_6H_5 analogue. Other alkyl halides, including $I(CH_2)M(CO)_5$ (M = Mn, Re), form similar adducts that undergo stereochemically controlled C–X bond cleavage in highly accelerated S_N2 reactions with inversion at C.**[156]**

The complexes (**110**) span a wide variety of donors L making the fragment $(Re)^+$ highly suited to study activation of coordinated ligands. More importantly, the 16-electron, pyramidal, Lewis acidic and π-basic $(Re)^+$ fragment has a remarkable stereochemical rigidity. The optically pure parent complex (**105**) can be easily prepared and all the transformations in Scheme 24 proceed with enantiomeric excesses >98%. Therefore, the $(Re)^+$ fragment behaves as a stereogenic center templating stereoselective binding and reactions of its coordinated ligands. The preferred geometry of the (Re)L complexes is dictated by the interaction of ligand p or π orbitals with the high-lying HOMO (**111**) of the fragment and by minimization of the steric interferences of the R substituents with Cp and PPh_3 as depicted in (**112**) to (**115**).

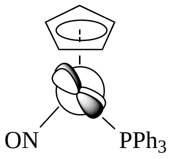

(**111**)

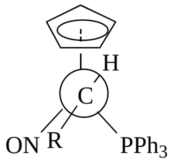

(**112**)

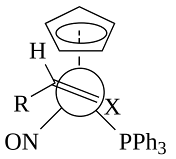

X = O, CH_2

(**113**)

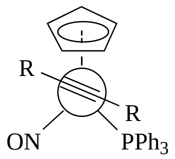

(**114**)

Because of the different degree of steric congestion in the interstices between the NO, Cp, and PPh_3 ligands (NO/PPh_3 most congested > Cp/PPh_3 > NO/Cp least congested), the chiral $(Re)^+$ fragment is able to discriminate between both faces of prochiral alkenes and aldehydes with high kinetic and thermodynamic selectivities. For example, the thermodynamic

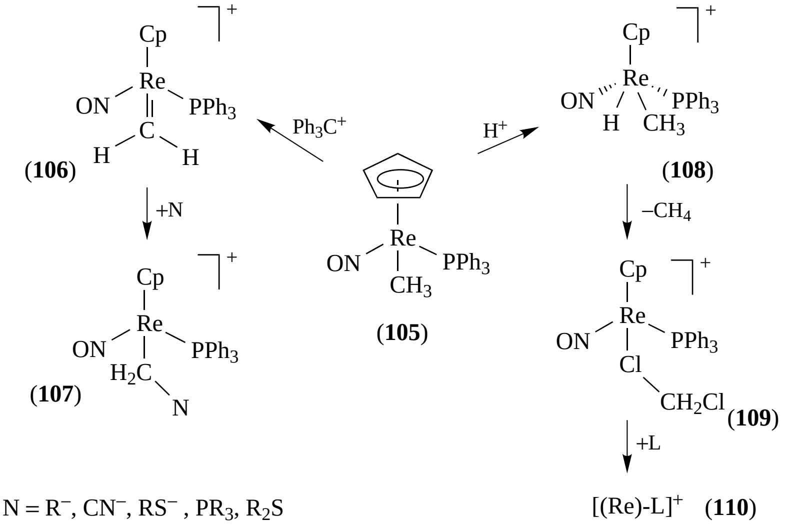

N = R^-, CN^-, RS^-, PR_3, R_2S

L = NCR, CO, $C_2H_2R_2$, C_2R_2, HRCO, R_2CO, PHR_2, $HN{=}CR_2$,
$H_2C{=}CR_2$, OR_2, SR_2, OSR_2, NHR_2, RCO_2R', pyrrolyl,
OR, NR_2, PR_2, CCH

Scheme 24

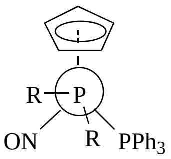

(**115**)

selectivity in monosubstituted alkenes and aliphatic aldehydes favors the diastereomer with the substituent in the least hindered interstice shown in (**113**) in a ca. 99:1 ratio. Ketones tend to bind in a σ fashion and show modest binding selectivities. This deep and extensive chiral recognition study methodically carried out mainly by Gladysz and collaborators with the (Re)$^+$ fragment over two decades has been revised by the author.**157**

This enantioselectivity translates into the outcome of the products resulting from nucleophilic addition to the [(Re)-(η^2-alkene)]$^+$ and [(Re)(η^2-aldehyde)]$^+$ cations. For example, addition of $LiCuMe_2$ to the alkene diastereomer in (**113**) results in (**116**) in >95:5 ratio.

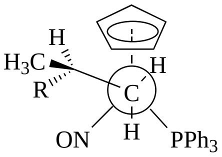

(**116**)

Chiral alkoxides are also obtained from the analogous aldehydes albeit with lower selectivity. Methyl ketones are selectively attacked on the face, unblocked by the bulky PPh_3. The obtained ee values match or exceed the ones found with other classic enantioselective reductants.

Other selected reactions of (Re)$^+$ derivatives include: the deprotonation of S-bound DMSO, $S(CH_2R)_2$ (R = sp^2 or sp^3 C) complexes at the Cα atom that are followed by stereospecific rearrangements; the deprotonation/reprotonation of [(Re)-(η^2-CH_2=CHR)]$^+$ to give [(Re)(=$CHCH_2R$)]$^+$; deprotonation of amine and phosphine derivatives [(Re)(EHR_2)]$^+$ to the amides and phosphides [(Re)(ER_2)]; epimerization of secondary alcohols catalyzed by [(Re)-(OMe)]; unprecedented transformation of N-bound pyrrolyl to C-bound pyrrolyl species.**155**

The configurationally robust [CpRe(NO)(PPh_3)X] complexes, easily obtained in an enantiomerically pure form (except for X = OR, NR_2), were used as building blocks for new chiral ligands with spectator chiral-at-metal fragments. Both chiral diphosphine (**117**) and diamine ligands (**118**) have been prepared and successfully tested in catalysis.**158**

The complexes (Re*)(C≡C)$_n$H) (n = 1, 2) have been used to produce binuclear species (Re*)(C≡C)$_n$(Re*) (**119**) bridged by linear sp carbon chains with lengths up to C_{20}.

With the increase in the value of n, the properties of the complexes approach those of a one-dimensional sp carbon allotrope. Both metal centers can be oxidized separately but the differences in the potentials almost fade out for C20 carbon chains. The monocations exhibit delocalized mixed valence and the dications exhibit cumulenic ground states, for example, $^+$Re=C=C=C=C=Re$^+$.**159**

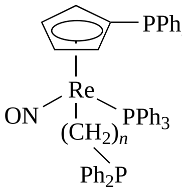

(**117**)

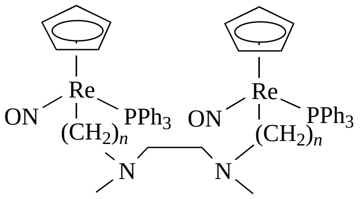

(**118**)

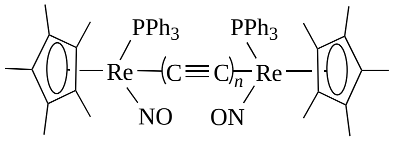

(**119**)

Some polynuclear complexes of general formula (Re*)C$_n$M′L$_m$ have been made.**155**

Deprotonation reactions of (Re)X derivatives have been clarified in terms of a general, initial kinetically controlled formation of Re(η^5-C_5H_4Li)(NO)(PPh_3)X. Fast migration of X to the ring occurs for X = C(O)R or SiR_3, leaving a metal-centered anion [Re(η^5-C_5H_4X)(NO)(PPh_3)]Li. No migration occurs for X = Me. For X = H, migration occurs above – 32 °C cleanly generating the synthetically useful anion [ReCp(NO)(PPh_3)]$^-$.**160**

8.1.3 Chemistry of [ReCp(CO)$_2$(carbene)] and [ReCp(NO)(PPh$_3$) (carbene)]$^+$ Complexes

The alkoxycarbenes ReCp(CO)$_2${C(OR′)R} have been known since 1968, but the first alkylidene analogs, ReCp(CO)$_2$(CHR) (**117**) (R = Me, $CH_2CH_2CMe_3$), were recently prepared by the unobvious, but effective, route shown in equation (25).

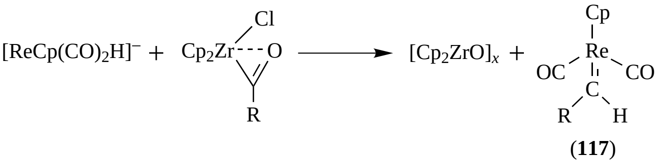

(**117**)

(25)

Complexes of type (**120**) are examples of an amphiphilic alkylidene, that is, the CHR ligand undergoes both electrophilic addition, typical of Schrock-type carbenes, and nucleophilic addition, typical of Fischer-type carbenes, as exemplified in Scheme 25.**161**

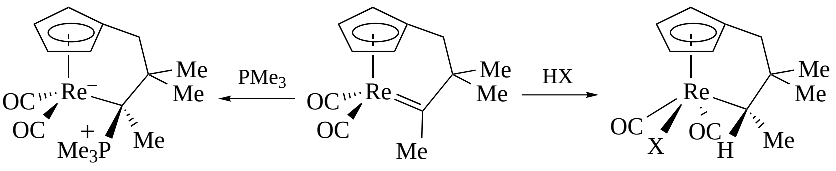

Scheme 25

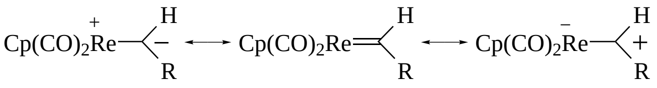

(**121**) (**120**) (**122**)

This rare feature is understood as the result of high polarizability of the Re=C bond, between the extreme contributors (**121**) and (**122**).

The same studies also revealed the first example of the interconversion of a hydroxycarbene (**123**) and its isomeric metal acyl hydride (**124**).[162]

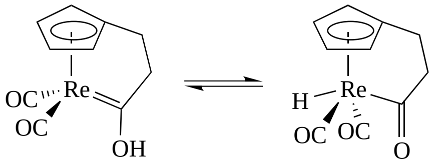

(**123**) (**124**)

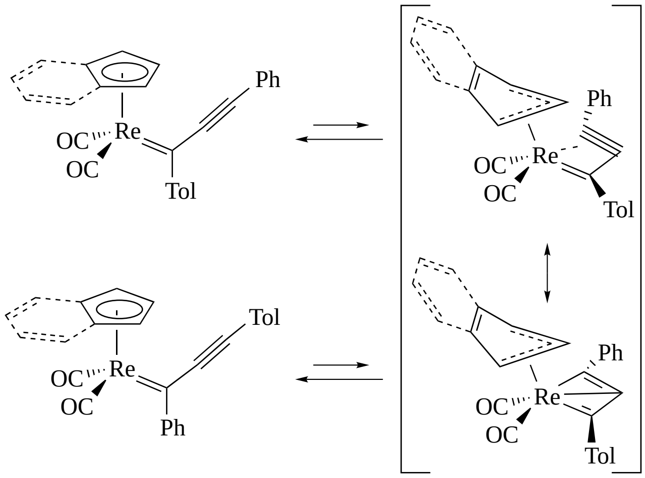

Scheme 26

The chemistry of the synthetically useful class of alkynylcarbene complexes represented in this context by the general formula [ReCp′(CO)$_2${=C(Tol)C≡C(*p*-XC$_6$H$_4$)}] (Cp′ = Cp, Cp*, Ind; X = H, NMe$_2$,CF$_3$, SO$_2$CF$_3$) undergoes an unprecedented kind of [1,3] metal shift under thermolysis at 120 °C to [ReCp′(CO)$_2${=C(*p*-XC$_6$H$_4$)C≡C(Tol)}] (Scheme 26), which is accelerated by electron-withdrawing substituents X and even more by ring slippage.[163]

However, the main product of this thermolysis results from a highly reactive carbene intermediate (**125**). This kind of species is responsible for a variety of intra and intermolecular reactions of alkynylcarbenes like those depicted in Scheme 27.[164]

Alkylidenes [ReCp(NO)(PPh$_3$)(CHR)]$^+$ and [(Re)CHR]$^+$ are readily formed via α-H$^-$abstraction from the corresponding

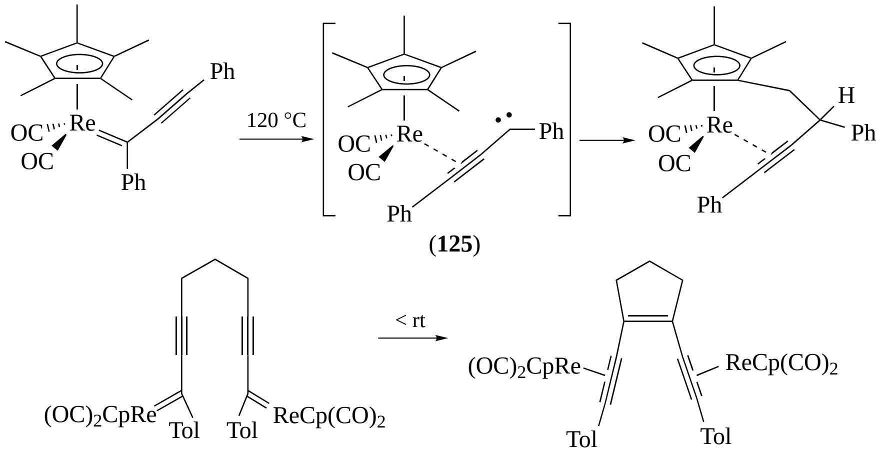

(**125**)

Scheme 27

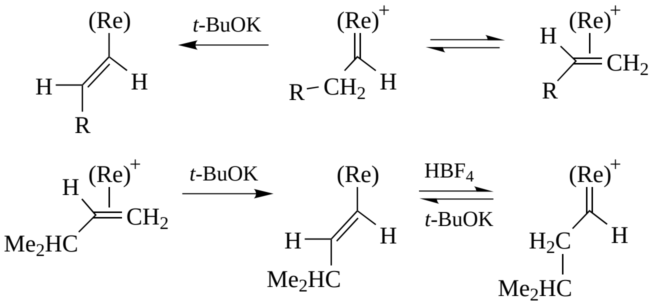

Scheme 28

alkyls. Some interconversions between alkylidene, vinyl, and alkene complexes on the (Re) fragment are summarized in Scheme 28. Vinylidene derivatives, $[\mathrm{(Re)({=}C{=}CRMe)}]^+$, are obtained by alkylation of the β-C of acetylides (Re)-C≡CR with $\mathrm{MeSO_3F}$ and undergo nucleophilic addition of $\mathrm{PMe_3}$ at the α-C.

Another type of carbenes, the vinylcyclopropenes play an important role in the transformations of alkynes coordinated to the $\mathrm{ReCp'(CO)_2}$ fragment as mentioned in Section 5.3.

8.1.4 *Chemistry of ReCp*O$_3$ and Related Derivatives*

The title complex (**126**) is greatly responsible for the recent expansion of high-oxidation state organometallic chemistry of Re and the neighboring metals, as seen in Section 4.2.[90] $\mathrm{ReCpO_3}$ has to be prepared by alkylation of $\mathrm{ReO_3(O_2CCF_3)}$ with $\mathrm{SnBu_3Cp}$ as the normal $\mathrm{ReRO_3}$ complexes. The O atoms in (**126**) are more electron rich than those in $\mathrm{ReMeO_3}$ as determined from a wealth of spectroscopic (^{17}O NMR and IR) and structural data. The crystal structure of $\mathrm{Re(\eta^5\text{-}C_5Me_4Et)}$ reveals rather long Re–C bonds to the symmetrically bound ring when compared to $\mathrm{ReCp(CO)_3}$ complexes. Nevertheless, its chemistry is dominated by reductive processes, with the Cp* ligand being lost in only a few cases.[90]

In the strict absence of $\mathrm{O_2}$, the reaction of (**126**) with $\mathrm{PPh_3}$ gives the $\mathrm{Re^V}$ dimer $[\mathrm{Re_2Cp^*_2(O)_2(\mu\text{-}O)_2}]$ (**127**).

In the presence of alkynes and $\mathrm{PPh_3}$, no $\mathrm{ReCp^*O_2(\eta^2\text{-}RC{\equiv}CR)}$ complex is formed, as in the $\mathrm{ReMeO_3}$ case. Cycloaddition of ketenes to (**126**) and (**127**) gives the $\mathrm{Re^V}$ species (**128**) and (**129**). No glycolates are formed in similar reactions with alkenes, in contrast to Tc analogs and $\mathrm{OsO_4}$, but the reverse reaction is possible. Indeed, glycolates (**130**) formed from vicinal diols and (**127**) extrude the alkene, reforming $\mathrm{ReCp^*O_3}$ in a stepwise mechanism (Scheme 29).[165]

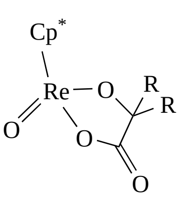

(**128**)

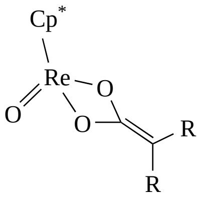

(**129**)

These two reactions were elegantly combined in the deoxydehydration of diols and polyols to alkenes and allylic alcohols catalyzed by $\mathrm{ReCp^*O_3/PPh_3}$, which provides a useful means of reducing oxygen-rich organics like carbohydrates.[166]

The system $\mathrm{ReCp^*O_3/PPh_3}$ is not efficient in catalytic deoxygenation of epoxides but its analogue $\mathrm{ReTpO_3}$ is and shows stereoselectivity.[167]

$\mathrm{ReCp^*OCl_2}$ (**131**) and other oxo halides (X = F, Cl, Br, I) have been prepared by reaction of HX or pyHI with (**127**). (**131**) can be alkylated with Grignard reagents to give the dialkyls $\mathrm{ReCp^*OR_2}$ (**132**) (R = Me, Ph, $\mathrm{CH_2Ph}$, Np). The crystal structures of complexes (**131**) and (**132**) reveal a remarkable asymmetrical coordination of the Cp* ligand attributed to a trans effect of the strong π-donor oxo ligand. A similar distortion of the Cp* ring, almost η^3-Cp*, is found in the imido complex $\mathrm{ReCp^*(N\text{-}\mathit{t}\text{-}Bu)Cl_2}$. The metallacycle (**133**), and the structural analogs $\mathrm{ReCp^*O(CO_3)}$ and $\mathrm{ReCp^*O(SO_4)}$, readily available from (**131**) easily eliminate $\mathrm{Me_2C{=}CH_2}$, $\mathrm{CO_2}$, and $\mathrm{SO_2}$ (reversibly in the latter case), respectively. Deoxygenation of (**131**) with $\mathrm{PMe_3}$ yields $\mathrm{ReCp^*Cl_2(PMe_3)_2}$. $\mathrm{ReCp^*Cl_4}$ is prepared by the deoxygenation/halogenation in equation (26).

$$\mathrm{ReCp^*O_3} \xrightarrow[\mathrm{Me_3SiX}]{\mathrm{PPh_3}} \mathrm{ReCp^*X_4} \qquad (26)$$

Use of $\mathrm{TiCpCl_3}$ provides both functions simultaneously and reaction with (**132**) gives $\mathrm{ReCp^*R_2Cl_2}$. However, in the case of $\mathrm{ReCp^*ONp_2}$, this reaction produces the paramagnetic carbyne $\mathrm{ReCp^*Cl_2(C\text{-}\mathit{t}\text{-}Bu)}$, which is reversibly oxidizable chemically.[3]

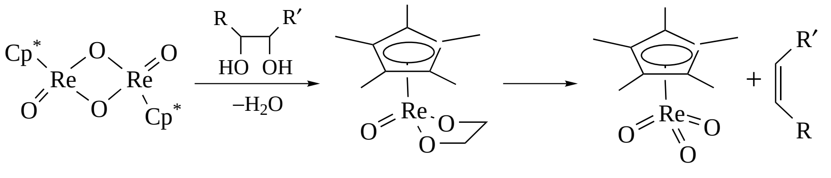

Scheme 29

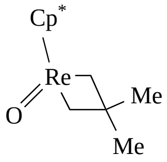

(**133**)

The first complex in this system to present the terminal Re=S bond (**134**) has been very recently reported in spite of the number of complexes of ReCp* with polysulfide rings (S3, S4) and thiolates previously known.**168**

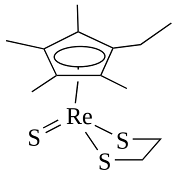

(**134**)

8.1.5 *Chemistry of ReCpX$_x$L$_y$ Complexes (X = Halides, Hydrocarbyls, and Hydrides)*

Complexes such as $ReCp(CO)_2Br_2$ (**135**) and $ReCp(CO)_2H_2$ are mentioned in Section 8.1.1. The latter is available from the former upon reaction with Ph_3SnH. $ReCp(CO)_2Me_2$ may be prepared by the reaction sequence in Scheme 30, whereas the analogues $ReCp^*(CO)_2R_2$ can be prepared from R_2CuLi and $ReCp^*(CO)_2Br_2$.

The nucleophilicity of $[ReCp(CO)_2H]^-$ is exemplified in equation (25). $ReCp(CO)_2MeX$ and the anion $[ReCp(CO)_2X]^-$ are mentioned in earlier literature as the result of alkylation reactions on (**135**) with LiR and MgRX. These are, however, not straightforward substitutions, since ring metalation and metal–halogen exchange take place under these circumstances. The study of $ReCp^*(CO)_2Br_2$ presents a thorough summary of the preceding chemistry in this field and shows that metal–halogen exchange with LiR or RMgX, to give isolable $[ReCp^*(CO)_2Br]^-$, is quantitative at −78 °C.**169**

Related $ReCp(PR_3)_2H_2$, $ReCp(PR_3)_2(H)R$, and $ReCp(CO)_2R\{C(O)R\}$ have already been referred to above.

All the other half-sandwich complexes in this section derive from the chemistry of $ReCp^*O_3$ and $ReCp^*Cl_4$ (**136**).**90** Complex (**136**) forms an octahedral adduct $ReCp^*Cl_4(PMe_3)$, but excess phosphine reduces it to $ReCp^*Cl_2(PMe_3)_2$. Hydrolysis and aminolysis form $ReCp^*OCl_2$and $ReCp^*(NR)Cl_2$ respectively. Stepwise reductive dehalogenation with $Al/HgCl_2$ affords the bridged halide dimers $[Re_2Cp^*_2Cl_4(\mu\text{-}Cl)_2]$ (Re–Re bond) and $[ReCp^*Cl(\mu\text{-}Cl)]_2$ (Re=Re bond).**4**

$$ReCp(CO)_2H_2 \xrightarrow{KOH} [ReCp(CO)_2]^- \xrightarrow{MeI} ReCp(CO)_2Me_2$$

Scheme 30

In the presence of dienes or alkynes, identical reduction of (**136**) yields $ReCp^*Cl_2$(diene) and $ReCp^*Cl_2(RC{\equiv}CR)$. The latter has an interesting chemistry which includes inter alia hydrolysis to form $ReCp^*(O)(RC{\equiv}CR)$, alkylation to give $ReCp^*Me_2(RC{\equiv}CR)$, and a series of H^+-catalyzed coupling reactions with alkenes to form $ReCp^*Cl_2$(diene) and $ReCp^*Cl$(dienyl).**4**

The bromides $ReCp^*Br_4$ and $[ReCp^*Br_2]_2$, the iodide $[ReCp^*I_3]_2$, and several substitution products of (**136**), for example, $ReCp^*(3,4\text{-}S_2C_6H_3Me)_2$ and $ReCp^*(O)S_4$, are also known. Monomethylation of (**136**) to form $ReCp^*MeCl_3$ occurs with $SnMe_4$, whereas $ReCp^*Me_4$ is obtained with MeMgCl. The complete family of mixed halo alkyls $ReCp^*Cl_xMe_{4-x}$ has been prepared in several steps from $ReCp^*Me_2Cl_2$. The reactions of $ReCp^*Me_3(OTf)$ with N_2H_4 and NHR_2 (R = H, Me) have been studied. The coordinated NH proton of $[ReCp^*Me_3(\eta^2\text{-}N_2H_4)]^+$ and $[ReCp^*Me_3(NHR_2)_2]^+$ can be removed with base to give imido complexes. Reduction of the hydrazine cation liberates ammonia.**4** The air-stable $ReCp^*H_6$ (**137**) is prepared from (**136**) by reaction of $LiAlH_4$ and methanolysis. Its thermal decomposition (>192 °C) gives the air-stable and structurally characterized dimer $[Re_2Cp^*_2H_4(\mu\text{-}H)_2]$. Photolysis of $ReCp^*H_6$ in the presence of PPh_3 gives $ReCp^*H_2(PPh_3)_2$. Besides (**137**), the reaction of $ReCp^*Cl_4$ with $LiBH_4$ gives the cluster $(ReCp^*H_2)_2B_4H_4$ (**138**). Reaction of this with $BH_3{\cdot}THF$ allows the synthesis of the $Re(Cp^*)_2B_nH_n$ ($n = 7–10$), a fascinating family of borane clusters that has many analogues with other transition metals.**170**

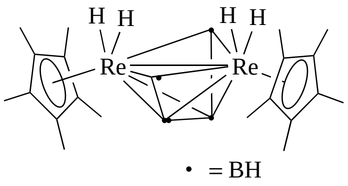

(**138**)

8.2 Miscellaneous Re (η^5-Pentadienyl) and Cyclopentadienyl Analog Complexes

A few Re complexes containing other η^5-dienyl ligands or analogs thereof have been reported. The open dienyl $Re(\eta^5\text{-}C_5H_7)(CO)_3$ undergoes a haptotropic shift to form $Re(\eta^1\text{-}C_5H_7)(CO)_3(L)_2$ on reaction with phosphines, a typical behavior for these complexes. Similar shifts are responsible for the formation of $Re(\eta^5\text{-}C_6H_5CPh_2)(CO)_3$ from its benzylic $Re(\eta^3\text{-}C_6H_5CPh_2)(CO)_4$ precursor and for the transient appearance of $Re(\eta^5\text{-}C_7H_7)(CO)_3$ in the photochemistry of $Re(\eta^1\text{-}C_7H_7)(CO)_5$ (see Section 10). The indenyl derivatives $Re(\eta^5\text{-}C_9R_7)(CO)_3$ are known (R = H, Me).

Photochemical removal of CO from Re(η^5-Ind)(CO)$_3$ in the presence of indene gives Re(η^5-Ind)(CO)$_2$(η^2-C$_9$H$_8$). This reacts with Ph$_3$C$^+$ to give [Re(η^5-Ind)(η^3-C$_9$H$_7$)(CO)$_2$]$^+$, isoelectronic with the bent indenyl complexes [M(η^5-Cp$'$)(η^3-Ind)(CO)$_2$] (M = Mo, W; Cp$'$ = Ind, Cp) (*see* ***Molybdenum: Organometallic Chemistry*** and ***Tungsten: Organometallic Chemistry***).**171**

[Re(η^5-Ind)Re(NO)(PPh$_3$)(X)]$^+$ complexes display several reactions similar to their Cp or Cp* analogues. Unexpected is the facile ring slippage caused by acetone and NCMe, which forms the adduct [Re(η^1-Ind)Re(NO)(CO)$_2$(OCMe$_2$)$_2$]$^+$ although it parallels related indenyl slippage in [M(η^5-Ind)(CO)$_2$L$_2$]$^+$, also favored by O and N π-donor ligands. A new insight into the indenyl ring slippage in the rather unreactive alkene and alkyne adducts of the fragment [Re(η^5-Ind)(CO)$_2$] led to the discovery of the alkyne assistance to CO-promoted indenyl slippage and ultimately to the new CO-catalyzed PPh$_3$ substitution in Re(η^5-Ind)(CO)$_2$(η^2-alkyne) to give Re(η^5-Ind)(CO)$_2$(PPh$_3$).**172**

A variety of η^5-hydrofullerene complexes having the Re(CO)fragment coordinated to a η^5-Cp like C$_{60}$ derivative has been disclosed. These compounds are made by Re$_2$(CO)$_{10}$-assisted hydrogenation of the fullerenes.**173**

Pyrrole reacts with ReH$_7$(PPh$_3$)$_2$ in the manner described for C$_5$H$_6$ or C$_5$H$_{10}$ to form Re(η-C$_4$H$_4$N)H$_2$(PPh$_3$)$_2$. Simple transformation to Re(η-C$_4$H$_4$N)HI(PPh$_3$)$_2$ activates the C-2 and C-5 positions for nucleophilic attack, resulting in a new stepwise preparation of mono- and difunctionalized pyrroles after ring decomplexation. Some η^5-dienyl complexes result from nucleophilic additions at coordinated arenes and rearrangements on Re^0 complexes as described in Section 9. Other classical formal analogs of cyclopentadienyl include the hydrido-tris-pyrazolylborate derivatives ReTp(CO)$_3$, and [Re(tacn)(CO)$_3$]$^+$, as described in Section 14, all of which are prepared from the ligands and ReX(CO)$_5$. The powerful π-basic fragment [ReTp(CO)(PMe$_3$)] was mentioned in Section 5.2. Phosphine derivatives of general formula [Re(P3)(CO)$_2$X] (P3 = tripodal HC(CCH$_2$PPh$_3$)$_3$ (triphos) or the macrocycle 12[ane]P3R3 (R = Et, i-Bu)) have been prepared from Re(CO)$_3$(PPh$_3$)$_2$Cl,**174** and by reduction of Re{12[ane]P3R3}Cl$_3$,**175** respectively. These [Re(P3)(CO)$_2$X] (X = Cl, H, OTf) complexes produce a variety of [Re(P3)(CO)$_2$L]$^+$derivatives with small molecules L = H$_2$, N$_2$, NCR. They originate vinylidenes [Re(P3)(CO)$_2$(C=C=HR)]$^+$ from terminal alkynes, and allenylidenes [Re(P3)(CO)$_2$(C=C=CRR$'$)]$^+$, carbenes, and vinylidenes from propargyl alcohols HC≡CRR$'$(OH).**176**

Another family of cyclopentadienyl analogs are the carborane derivatives the first of which, [Re(CO)$_3$(η^5-7,8-C$_2$B$_9$H$_{11}$)(CO)$_3$]$^-$, was reported in 1965. A few derivatives, [Re(η^5-7,8-R$_2$-7,8-C$_2$B$_9$H$_9$)(CO)$_3$]$^-$, [Re(NO)L$_2$(η^5-7,8-C$_2$B$_9$H$_{11}$)], and [Re(NO)(CO)(CR(OMe)(η^5-7,8-C$_2$B$_9$H$_{11}$}] are known.**177** The complex (**139**) presents intramolecular coordination of the pendant amine group and displays reactivity toward alkynes unprecedented in metallacarbaborane chemistry.**178**

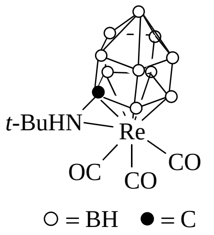

(**139**)

The novel monocarbon analogue dianion [Re(CO)$_3$(η^5-7-CB$_{10}$H$_{11}$)]$^{2-}$ was prepared with different organic cations and its chemistry generated a number of molecules with Re–M bonds (M = Pd, Pt, Rh, Ir).**179**

9 CHEMISTRY OF Re (η^6-HYDROCARBON) COMPLEXES

The bis-arene complexes [Re(η^6-C$_6$R$_6$)$_2$]$^+$ (R$_6$ = H$_6$, Me$_6$, 1,2,3-H$_3$Me$_3$) (**140**), prepared by the general Fischer–Hafner reaction (equation 27), were first reported in 1957, and the recognition of their sandwich structure similar to that of *Ferrocene*, gave decisive impetus to the then novel field of organotransition metal chemistry.**2**

$$3\text{ReCl}_5 + 4\text{Al} + 6\text{Arene} \xrightarrow[130\,^\circ\text{C}]{\text{AlCl}_3} 3[\text{Re}(\eta\text{-arene})_2][\text{AlCl}_4] + \text{AlCl}_3 \tag{27}$$

These light yellow, air- and water-stable cations can be isolated with a variety of counterions, for example, PF$_6$$^-$ and BPh$_4$$^-$ but, probably due to the very low yields, the chemistry of the complexes has been relatively unexplored.**2** Reduction by Na in liquid NH$_3$ or H$^-$ addition to (**140**) (R = H, Me) gives [Re(η^6-C$_6$R$_6$) (η^5-C$_6$R$_6$H-6-exo)]. A very unstable, paramagnetic complex, [Re(η^6-C$_6$Me$_6$)$_2$], has been isolated and identified by electron spin resonance (ESR) upon reduction of (**135**) (R = Me) with Li.

Also, the first reported yields of the cations [Re(η^6-C$_6$R$_6$)(CO)$_3$]$^+$ (**141**) were disappointingly low, especially in comparison to the higher yields obtained for the isoelectronic Mn$^{\text{I}}$ analogs. These low yields are a result of very fast product hydrolysis to [Re(H$_2$O)$_3$(CO)$_3$]$^+$. Improved high-yield preparations of a series of ring-substituted (**141**) complexes on the basis of avoiding oxygenated solvents, namely H$_2$O and THF (equation 28) are now available.

$$(\text{CO})_5\text{ReBr} + \text{AlBr}_3 \xrightarrow[120\,^\circ\text{C}]{\text{Arene}} [\text{Re}(\eta\text{-arene})(\text{CO})_3][\text{AlBr}_4] \tag{28}$$

The hydrolytic and solvolytic stability increases with the number of Me substituents. The penta- and hexamethyl derivatives can be treated in water.

The chemistry of complexes (**141**) is dominated by their electrophilicity. The products of nucleophilic attack depend on the nature of the nucleophile, which either reacts at the metal, to give substitution, or at the ring, to give additions, as summarized in Scheme 31.

Facile arene displacement is favored by hard donor solvents (L), particularly oxygenated ones like acetone, THF, and water. Reaction with MeCN shows second-order kinetics with activation parameters consistent with a S_N2 mechanism where the MeCN adds directly to the metal. This reaction is 104 times faster for Re than for the Mn analog, due to the larger size of Re, thus explaining why preparations employing hydrolytic work-up work well for Mn but not for Re.

Softer nucleophiles N, for example, H^- or PBu_3, add directly (reversibly in the latter case) to the exo face of the arene to give the $[Re(\eta^5\text{-}C_6R_6N\text{-}6\text{-}exo)(CO)_3]$ (**142**) complexes without any participation of the metal center. Attempted extension to Re complexes of the well-established methodology for double functionalization of arenes earlier developed for the Mn^I analogs on the basis of $[Mn(\eta^5\text{-}dienyl)(CO)_2(NO)]^+$ (*see* ***Manganese: Organometallic Chemistry***) is thwarted by the limitations found in the preparation of the cations $[Re(\eta^5\text{-}dienyl)(CO)_2(NO)]^+$.

Closely related to these arene carbonyl complexes are the cycloheptatriene derivatives, which, however, are prepared by insertion of C_7H_8 into a Re–C bond followed by H abstraction, with Ph_3C^+, as shown in Scheme 32.

Irradiation of $ReCp^*(CO)_3$ in the presence of C_8H_8 produces $ReCp^*(\eta^6\text{-}C_8H_8)$.**136**

Re arene complexes also result from application of the MVS technique to the extremely refractory Re metal (*see* ***Metal Vapor Synthesis of Transition Metal Compounds***). Cocondensation of pure benzene with Re atoms yields no tractable product, confirming the instability of $[Re(\eta^6\text{-}C_6H_6)_2]$. However, cocondensation of Re with a mixture of C_6H_6 and PMe_3 yields the Re–Re bonded dimer $[Re(\eta^6\text{-}C_6H_6)(PMe_3)_2]_2$ (**143**) in 30% yield. This complex can be protonated to give the dihydride $[\{Re(\eta^6\text{-}C_6H_6)H(PMe_3)_2\}_2]^{2+}$. Reduction of (**143**) with K followed by treatment with MeI gives $[Re(\eta^6\text{-}C_6H_6)(PMe_3)_2I]$ (**144**). $[Re(\eta^6\text{-}C_6H_6)(PMe_3)_2H]$ (**145**) is prepared by reaction of (**144**) with $LiAlH_4$, but its Mn analog results directly from the cocondensation of the metal with C_6H_6/PMe_3.**3** Underlining the parallel between the C–H activation of the $ReH_x(PR_3)_2$ polyhydrides and low-valent metal chemistry, cocondensation of Re atoms with cyclopentane and cyclohexane mixtures in the presence of PMe_3 gives $ReCpH_2(PMe_3)_2$ and (**145**), respectively.

When alkylarenes are cocondensed with Re atoms, C–H activation of the aliphatic side chains occurs and a variety of novel arene derivatives of Re with μ-arylidene and hydride bridges, $[Re_2(\eta^6\text{-}arene)_2(\mu\text{-}CHAr)(\mu\text{-}H)_2]$, are formed, for example, products containing *o*-xylyl ligands. Similar reactions are observed with saturated hydrocarbons, for example, cocondensation with CMe_4 gives (**146**).

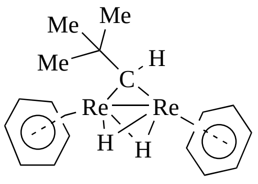

(**146**)

Cocondensation of Re with mixtures of benzene and unsaturated hydrocarbons gives a rich chemistry otherwise

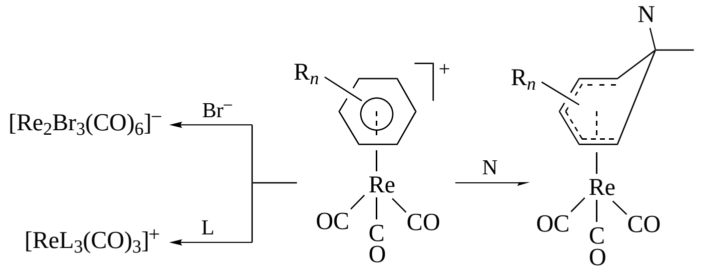

(**141**)

(**142**)

L = NCMe, Me_2CO, H_2O, NH_3

N = H^-, R^-, CN^-, PBu_3

Scheme 31

$$RePh(CO)_5 + C_7H_8 \longrightarrow Re(\eta^5\text{-}C_7H_8Ph)(CO)_3 \xrightarrow{Ph_3C^+} [Re(\eta^6\text{-}C_7H_7Ph)(CO)_3]^+$$

Scheme 32

impossible to obtain by more common synthetic methods. A few examples, resulting from the following mixtures, are given: C_6H_6/C_5H_6 gives $[Re(\eta^6\text{-}C_6H_6)Cp]$ and $ReCp_2H$; C_6H_6/indene forms $Re(\eta^5\text{-Ind})(\eta^6\text{-IndH})$; C_6H_6/C_6H_8 gives $[ReH(\eta^6\text{-}C_6H_6)(\eta^4\text{-}C_6H_8)]$ (**147**) and (**148**); and C_6H_6/C_7H_8 produces $[Re(\eta^6\text{-}C_6H_6)(\eta^5\text{-}C_7H_7)]$ and $[Re(\eta^6\text{-}C_6H_6)(\eta^5\text{-}C_7H_9)]$.

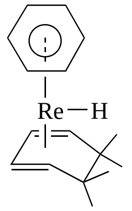

(**148**)

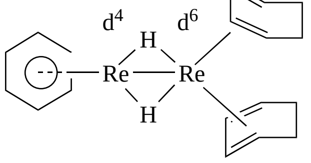

(**149**)

$[Re(\eta^6\text{-}C_6H_6)Cp]$ is a sandwich complex and (**147**) is a bent metallocene like $ReCp_2H$. Protonation of several of the reported complexes gives new Re hydrides, and complex $[Re(\eta^6\text{-}C_6H_6)Cp]$ has a remarkable chemistry in this respect. Compound (**149**) can be considered as a Re–Re bonded mixed valency d^4-d^6 species. Double-bond hydrogenation also occurs, for example, with (**148**).

The fulvene complex $Re(\eta^6\text{-}C_5Me_4CH_2)(CO)_2(C_6F_5)$ (see Section on Electrophilic Attack and Oxidative Additions) undergoes a nucleophilic attack at the *exo*-CH_2 group to give complexes like $[Re(C_5Me_4CH_2N)(CO)_2(C_6F_5)]^z$ (N = PMe_3, z = 0; N = OMe, z = −1). $Re(\eta^6\text{-}C_5Me_4CH_2)(CO)_2X)$ (X = C_6F_5, Cl, Br, I) react with HX′ (X′ = Cl, Br, I) to give$[Re(\eta^5\text{-}C_5Me_5)(CO)_2XX']$ and with X'_2 to give $[Re(\eta^5\text{-}C_5Me_4CH_2X)(CO)_2XX']$. The later reactions are initiated by an electrophilic H^+ or X^+ attack at the metal followed by a X^- attack at the CH_2 group.[148,180]

10 CHEMISTRY OF Re (η^7-HYDROCARBON) COMPLEXES

No such complex of this type has been isolated to date. In fact, attempts to photolyze the well-characterized $Re(\eta^1\text{-}C_7H_7)(CO)_5$ in order to induce haptotropic $\eta^1 \to \eta^7$ ring slippage leads to the dimer $[Re(\eta^5\text{-}C_7H_7)(CO)_2]_2$. Similarly, photolysis of (**1**) and C_7H_8 gives $Re(\eta^5\text{-}C_7H_7)(CO)_3$. However, the complex $Re(\eta^7\text{-}C_7H_7)(CO)_2$ is produced on photolysis of $Re(\eta^1\text{-}C_7H_7)(CO)_5$ in low-temperature matrices and stepwise ring slippage $\eta^1 \to \eta^3 \to \eta^5 \to \eta^7$ has been observed.[3] In the preceding section, the $(\eta^5\text{-}C_7H_7)$ derivative containing an uncoordinated double bond is mentioned.

11 CHEMISTRY OF Re–Re MULTIPLE BONDED ORGANOMETALLIC COMPLEXES

A number of organometallic complexes containing Re–Re multiple bonds, supported or not by bridging ligands, are known. Among the unsupported quadruply bonded species is the Re^{III} dianion $[Re_2Me_8]^{2-}$. This anion has an eclipsed conformation and has played an important role in the characterization of this type of multiple bond. Its reaction with excess acetic acid, forms $Re_2Me_2(\mu\text{-}O_2CMe)_2(O_2CMe)_2$. Other acetate-bridged complexes, such as $Re_2R_4(O_2CMe)_2$ (R = CH_2TMS, CH_2Ph, $CH_2\text{-}t\text{-Bu}$), are made from MgR_2 and $Re_2Cl_2(O_2CMe)_4$. A similar reaction with $Mg(2\text{-}MeOC_6H_4)_2$ gives $Re_2(2\text{-}MeOC_6H_4)_6$ with four bridging and two terminal $2\text{-}MeOC_6H_4$ bidentate ligands. Cleavage of the triangular clusters Re_3Me_9 with excess PR_3 leads to $Re_2Me_6(PR_3)_2$. However, the analogous chloroalkyl complex (**44**) undergoes reductive cleavage under the same conditions to give the triply bonded dimers $Re_2Cl_2R_2(PMe_3)_4$. These complexes cannot be made by direct alkylation of $Re_2Cl_4(PR_3)_4$. The latter complexes, however, give triply bonded $Re_2(\eta^3\text{-}C_3H_5)_4$ (**150**) on reaction with (allyl)MgX. This contrasts with the analogues $M_2(allyl)_4$ (M = Cr, Mo), since it has an unsupported Re–Re bond without bridging allyl ligands.

$Cp^*Re(CO)_2{=}Re(CO)_2Cp^*$ (**151**) is a rare example of a formal dimer of a 16e fragment in the case of $[ReCp^*(CO)_2]$, the other one being $[Re(\equiv C\text{-}t\text{-Bu})(O\text{-}t\text{-Bu})_2]_2$. Two of the CO ligands are terminal and the other two are semibridging. (**151**) is thermally stable to over 100 °C but is exceedingly reactive to H_2 addition giving $[ReCp^*(CO)_2)](\mu\text{-}H)_2$ and the addition of nucleophiles giving $[ReCp^*(CO)_2](\mu\text{-}CO)[ReCp^*(CO)L]$.[181] It reacts with enynes to give bridging alkenylidenes and with acetylenes to give a series of dimetallacycles in a cascade of thermal and photochemically induced rearrangements (Scheme 33).[182]

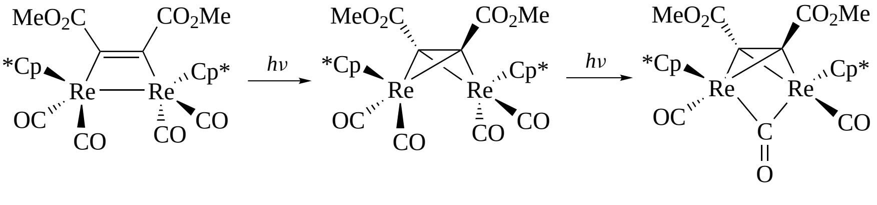

Scheme 33

It reacts with CH_2Cl_2 to give $[\{ReCp^*Cl\}_2(\mu\text{-}CO)_2]$ and $[\{ReCp^*(CO)_2\}_2(\mu\text{-}CH_2)]$ in contrast to its parent $ReCp^*(CO)_2(THF)$ that gives $ReCp^*(CO)_2Cl(CH_2Cl)$. It adds the P_2 fragment (from P_4) across the Re–Re bond (**152**) and reacts with Ph_2C_2 to give $ReCp^*(CO)(\eta^4\text{-}C_4Ph_4)$.[183] Interestingly, irradiation of (**89**) in the presence of a borylene complex gave the transfer of this rather inaccessible fragment isoelectronic with CR_2, forming $[\{ReCp(CO)_2\}_2\{\mu\text{-}B{=}N(SiMe_2)\}]$ isostructural with $[\{ReCp^*(CO)_2\}_2(\mu\text{-}CH_2)]$.[184]

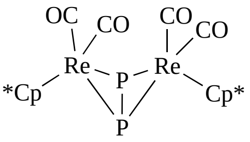

(**152**)

12 CHEMISTRY OF Re ISOCYANIDE COMPLEXES

The majority of Re isocyanide chemistry follows the structural patterns of the isoelectronic carbonyls and, in fact, many of them may be prepared by direct CNR substitution on parent Re carbonyl complexes. For example, $Re_2(CO)_{10-x}(CNR)_x$ ($x = 1-4$) and $MnRe(CO)_{10-x}(CNR)_x$ ($x = 1-4$) are prepared by PdO-catalyzed substitution. Mono- and disubstitution in $ReX(CO)_5$ and/or $[ReX(CO)_4]_2$ complexes, in THF, leads to $ReX(CO)_4(CNR)$ and *fac*-$[ReX(CO)_3(CNR)_2]$, with the decreasing orders of reactivities X = Cl > Br; R = aryl > alkyl. Under analogous conditions, $MnX(CO)_5$ reacts rapidly to give $[Mn(CNR)_6]^+$. Further substitution occurs under more forcing conditions, for example, refluxing toluene, and entails isomerization of *fac*-$[ReX(CO)_3(CNR)_2]$ to *mer,cis*-$[ReBr(CO)_2(CNMe)_3]$, and formation of $ReBr(CO)(CNR)_4$, $ReBr(CNR)_5$, and, in low yield, $[Re(CNR)_6]Cl$ (R = *p*-tolyl). PdO-catalyzed substitution of $ReX(CO)_4(PR_3)$ with CN-*t*-Bu leads to the mer- and fac- isomers of $ReX(CO)_3(PR_3)_2(CN\text{-}t\text{-}Bu)$. The fac isomer is favored at higher temperatures.[185]

Alternative high-yield preparations of many other derivatives were later developed, on the basis of the cleavage of Re–Re multiple bonded complexes, a reaction normally promoted by π-acceptors such as CO, NO, and CNR. In this way, homoleptic $[Re(CNR)_6]^+$ (**153**) derivatives (R = alkyl, aryl) and ReX(CNAr) are obtained in excellent yields from $Re_2(O_2CMe)_4Cl_2$. Mixed derivatives $[Re(CNR)_4(PR_3)_2]^+$ (**154**) are likewise prepared from $Re_2Cl_4(PR_3)_4$ and are not directly available from (**153**) because of its substitutional inertness. However, in the case of $Re_2Cl_4(LL)_2$ analogs (LL = dppm or dppe) where the diphosphine ligands bridge the two metals, reaction with CNR gives the adduct $Re_2Cl_4(LL)_2(CNR)$ with a bridging Cl atom. Additional CNR replaces Cl, giving $[Re_2Cl_3(LL)_2(CNR)_2]^+$, but the Re–Re bond retains its multiple character. This chemistry was later extended to CO and NCR and mixed-ligand analogs with emphasis on their structural characteristics.[186]

Alternatively, high yields of (**154**) are obtained by the reaction of the polyhydrides $ReH_7(PR_3)_2$ or $ReH_5(PR_3)_3$ with CNR. In Section 3.1, reference was made to a large number of complexes of the type $[ReH_x(PPh_3)_2(CNR)_y]^{n+}$. These compounds are prepared from polyhydrides and CNR, as illustrated in the reaction sequence of Scheme 34.

Pombeiro has shown that irradiation of $ReCl(N_2)(dppe)$ in the presence of a variety of CNR ligands leads to $ReCl(CNR)(dppe)_2$, which gives $[ReL(CNR)(dppe)_2]^+$ (L = CO, CNR) upon treatment with Tl^+ salts in the presence of ligand, L. Electrophilic reactions of these compounds have been used as models of *Nitrogen Fixation* by low-oxidation state metal centers and will be discussed below.

As mentioned in Section 2.4.2, 17-electron, mononuclear Re^{II} complexes are rare, in contrast to the multiply bonded $Re_2X_4(PR_3)_4$. A few representative examples were prepared by Walton either by oxidation of the parent Re^I complexes, for example, $[Re(CNAr)_6]^{2+}$ from $[Re(CNAr)_6]^+$, or by reduction of Re^{III} species with CNR.[3]

Re^{III} isocyanide derivatives are relatively abundant either as six- or seven-coordinate species. They may be prepared, as in the case of the carbonyls, by oxidative addition to Re^I precursors, for example, $ReBr_3(CNR)_4$ from $ReBr(CNR)_4(CO)$ and Br_2, by nonreductive cleavage of Re–Re bonds, by reacting $[Re_2Cl_8]_2$ or $Re_2Cl_6(PR_3)_2$ with CNR, giving $[ReX_2(CNR)_5]^+$ and $[ReX_2(CNR)_4(PR_3)]^+$, respectively, by substitution reactions, for example, from *mer*-$ReX_3(PR_3)_3$ to give $[ReX_2(CNR)_3(PR_3)_2]^+$ and by reduction of $ReOCl_2(PPh_3)_2$ with PPh_3 to give $ReCl_2(CNR)(PPh_3)_2$. $ReCl_3(CNMe)_3$ and trinuclear species $Re_3X_9(CNR)_3$ are also known.[50] In the mononuclear complexes, seven coordination achieves the 18-electron configuration and is typically a capped octahedron with a CNR ligand capping one of the faces. Upon loss of a two-electron ligand, octahedral 16-electron species are formed, of which all *trans*-$[ReCl_2(CN\text{-}i\text{-}Pr)_2(PMePh_2)_2]^+$ complexes were the first to be structurally characterized. This complex readily adds CO or CN-*i*-Pr to generate seven-coordinate species.[50] Re-CNR complexes in higher oxidation states, for example, $[ReCl_5(CNMe)]^-$ are very rare.[2]

$$ReH_5(PR_3)_3 \xrightarrow[\text{CNMe/NCMe}]{C_7H_7^+} ReH_4(PR_3)_3(CNMe) \underset{H^+}{\overset{NEt_3}{\rightleftharpoons}} ReH_3(PR_3)_3(CNMe)$$

Scheme 34

In contrast with the thermal substitutional inertness, photolysis of $[Re(CNAr)_6]^+$ in the presence of X^- gives $ReX(CNAr)_5$. Like the isoelectronic CO, coordinated CNR may undergo nucleophilic addition of Y^- to give the corresponding iminoacyls $[ML_n\{C(NR)Y\}]^-$ that produce Fischer-type carbenes $[ML_n\{{=}C(NR)(YR)\}]$. The electrophilicity of the coordinated C atom in CNR is obviously enhanced in cationic complexes and when electron-withdrawing R groups are present. Competition between nucleophilic addition at CO and CNR in the same metal has been studied on the basis of electronic effects, but the steric bulk of the R group also plays a role. Addition of H_2NR to $ReBr(CO)_4(CNR)$ confirmed attack at CNPh to form the diaminocarbene complex $ReBr(CO)_4\{{=}C(NHPh)(NHR)\}$.**187**

Stressing the importance of the charge and other electronic balances, $[Re(CO)_5(CN\text{-}t\text{-}Bu)]^+$ is found to react with nucleophiles, including amines, but preferentially at a *cis*-CO ligand to give the carbamoyl derivatives *cis*-$[Re(CO)_4(CNR)\{C(O)NHR\}]$. The complex $ReBr(CO)_3(CNPh)(CNN{=}CMe_2)$ (**155**) reacts with $H_2N\text{-}i\text{-}Pr$ preferentially at the N-isocyanoiminoalkane ligand to give $ReBr(CO)_3(CNPh)\{C(NH\text{-}i\text{-}Pr)(NHN{=}CMe_2)\}$, but a further attack at the CNPh ligand occurs readily to give the biscarbene $ReBr(CO)_3\{(C(NH\text{-}i\text{-}Pr)NHPh)\}\{C(NH\text{-}i\text{-}Pr)(NHN{=}CMe_2)\}$. (**155**) is obtained by the Wittig reaction of $ReBr(CO)_3(CNPh)(CNNPPh_3)$ with acetone.**188**

The $CNNPR_3$ ligand still has a rather undeveloped chemistry. The chemistry of aminocarbenes derived from isonitriles by nucleophilic addition has been reviewed.**189**

Electrophilic addition to coordinated CNR has been observed when it is ligated to very electron-rich metal centers. The structures of several of these complexes show severe bending of the C–N–R angle, between ca. 140 and 160°, and the (C≡N) stretching vibrations appear at rather low energies (ca. $1830\,cm^{-1}$) compared to normal linear CNR ligands of free CNR ($2150\,cm^{-1}$). Both effects are explained by the importance of the bonding structure (**157**) of the two bonding extremes, (**156**) and (**157**), which shows the carbene character of the Re–C bond in these complexes.

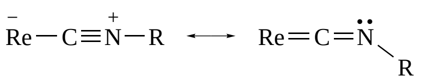

$$\overset{-}{Re}{-}C{\equiv}\overset{+}{N}{-}R \longleftrightarrow Re{=}C{=}\ddot{N}{\diagdown}R$$

(**156**) (**157**)

More pronounced bending is systematically observed when the ligand trans to a CNR ligand is not a π-acceptor, for example, CNR being trans to Cl in $ReCl(CNMe)_3(PMePh_2)_2$ (**158**) contrasted to being trans to NCMe in $[Re(NCMe)(CNMe)_3(PMePh_2)]^+$. The structure (**157**) also points to the nucleophilic character of the N atom that may be protonated to give aminocarbynes. The first such complex was reported in 1981 by the protonation of $(ReCl(CNR)(dppe)_2)$ with HBF_4 to give *trans*-$[ReCl(CNHMe)(dppe)_2]BF_4$. Examples formally derived from the protonation of (**158**), but actually prepared by Zn reduction of $[ReCl_2(CNR)_3(PMePh_2)_2]^+$ in the presence of traces of water, have been reported as fully characterized compounds and compared with analogs of other metals, for example, Mo, W, and Fe. The simplest aminocarbyne has also been characterized in $[ReCl({\equiv}CNH_2)(dppe)_2]BF_4$ as prepared from the parent CNH or CNTMS complexes.

The crystallographic data also stresses the important carbenic character of the aminocarbyne–metal bond ($Re{=}C{=}NHR$) inasmuch as the NHR group is planar and the C–N bond distance is appropriate for a C=N bond. The chemistry of aminocarbynes has been thoroughly reviewed.**190**

Protonation of the CNR ligand in complexes $Re\{N(CH_2CH_2S)_3\}(CNR)$ in aqueous HCl leads to the unprecedented transformation of CNR into CO producing $Re\{N(CH_2CH_2S)_3\}(CO)$ ($R = t\text{-}Bu, CH_2COOEt$). Again, the CNR ligand is strongly bent in these complexes and does not undergo nucleophilic addition at its C atom.**191**

13 CHEMISTRY OF Re NITROSYL COMPLEXES

The main role of the NO^+ ligand in organorhenium chemistry has been the replacement of CO in ML_nCO complexes to generate isoelectronic and isostructural metal nitrosyl complexes with one added unit of positive charge, for example, cationic $[ML_nNO]^+$ species. The effect of the π-acidity of NO^+ and an increased positive charge of the complex strongly activates the unsaturated ligands toward nucleophiles. The results of these effects are evident in the differences between the chemistries of $ReCp(CO)_2$ and the fragments $[ReCp(CO)(NO)]^+$ or $[ReCp(NO)(PPh_3)]^+$. In fact, while the alkenes in $[ReCp(CO)_2(\eta^2\text{-alkene})]$ undergo an electrophilic attack, in $[ReCp(NO)(PPh_3)(\eta^2\text{-alkene})]^+$ the reverse reaction, that is, nucleophilic addition, is observed. A complementary example of these ideas has been developed by Wieghardt from the systems $[Re(tacn)(CO)_3]^+$ (**159**) and $[Re(tacn)(CO)_2(NO)]^{2+}$ (**160**), which display a reactivity parallel to both isoelectronic cyclopentadienyl congeners. Complex (**159**) generates $[Re(tacn)O_3]^+$ with H_2O_2, and (**160**) reacts with $NaBH_4$ to give racemic $[Re(tacn)(CO)(NO)CH_3]^+$ (**161**), which has been resolved into its pure enantiomers.

The most useful precursors are the dimers $[ReCl_2(CO)_2(NO)]_2$, (**162**) $ReCl_2(OR)(PPh_3)_2(NO)$ (**163**), and $ReH_2(PPh_3)_3(NO)$ (**164**). Substitution or addition reactions on (**162**) give the dibromide, diiodide, and β-diketonate derivatives, $ReCl_2(CO)_2L(NO)$, $ReCl_2(CO)L_2(NO)$ complexes with a variety of two-electron ligands, L, and $ReR_2(CO)L_2(NO)$ ($R = H, Me$).**192**

Cationic complexes of formulae, $[Re(NO)XL_3(CO)]^+$ and $[Re(NO)L_4(CO)]^{2+}$ as well as the triflates $Re(NO)L_2(CO)(OTf)_2$ are obtained upon halide abstraction from $ReCl_2(CO)L_2(NO)$.**193**

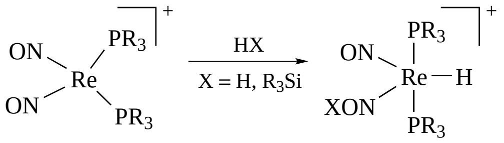

Scheme 35

Complex (**163**) reacts with other L ligands to give $ReCl_2(PPh_3)_2L(NO)$ and with $NaBH_4$ to afford (**164**). This latter compound reacts with CO to give $Re(CO)_2(PPh_3)_2(NO)$. With strong protic acids HX, in ROH, reaction of (**164**) forms $ReH(OR)(CO)(PPh_3)(NO)$ ($X = ClO_4$) and $ReHF(CO)(PPh_3)_2(NO)$ ($X = BF_4$). The spectroscopic and chemical properties of $ReH_2(NO)(CO)(PR_3)_2$ and similar complexes has been thoroughly studied by Berke. The high-yield synthesis of $[ReBr_5(NO)][NEt_4]_2$ provided the most recent entry to the chemistry of NO containing hydrides in several oxidation states. $Re(\eta^2\text{-}H_2)Br_2(NO)(PR_3)_3$, $ReH(BH_4)(NO)(PR_3)_2$, $ReH_2(NO)(PR_3)_3$, and $ReH_4(NO)(PR_3)_2$ $[ReH_3(NO)(PR_3)_2]^-$ are interrelated by simple chemical transformations (R = *i*-Pr, Cy). Reaction of $ReH(BH_4)(NO)(PR_3)_2$ with $NOBF_4$ leads to $ReH(NO)_2(PR_3)_2$ via the isolable intermediate $ReH(NO)(NOBF_3)(PR_3)_2$ (**165**).[194]

In most of the chemistry of the NO complexes, its influence has been considered as stemming from its outstanding π-acidity and from its noninnocent behavior as either a one (bent) or three (linear) ligand. However, (**165**) clearly reveals the Lewis basicity of the O atom of the NO ligand that is also shown to engage in hydrogen bonding with Re–H bonds.[61]

Indeed, the complexes *trans*-$Re(NO)(CO)_2(PR_3)_2$ are protonated by HCl at the NO to give the nitroxyl derivatives *trans*-$ReCl(HN{=}O)(CO)_2(PR_3)_2$ that are reversibly deprotonated by N-bases. This allowed the study of the properties of coordinated nitroxyl, a most unstable molecule.[195]

NO induces a strong hydridic polarization of the Re–H bond in nitrosyl hydrides, the 'nitrosyl effect'. The conjugation of these properties enables them to perform the heterolytic cleavage of H_2 and R_3Si–H bonds as depicted in Scheme 35 as well as the insertion of Re–H bonds into polar unsaturated organic substrates.[196]

A bent NO adduct of $ReCp^*_2$ is in agreement with the expected coupling of two radicals to form a two-electron Re–NO bond.[141]

The thionitrosyl $[Re(CO)_5(NS)]^{2+}$ adds halides to give $[Re(CO)_5(NSX)]+$ (X = F, Cl, Br).[197]

14 POLYNUCLEAR Re ORGANOMETALLIC COMPLEXES

Besides the classical donor atoms, C, O, N, P, S, and the halides, Re forms organometallic complexes containing practically all other metals and *Metalloids*, a class that may be broadly classified under the heading of *Polynuclear Complexes*. The number and structural variety of these species is overwhelming and has grown dramatically, along with the development of X-ray diffraction techniques as the ultimate tool for the characterization of often totally unexpected and/or new bonding modes and structural arrangements. The progress of the Re–CO cluster chemistry (Section 3.2) is paradigmatic. Among the several existing possibilities of subclassifications within this class of compounds, the existence of direct Re–M′ bonds (M′ = main group or d or f transition element) is adopted below. This classification has, however, rather weak boundaries. In fact, some Re–M′ bonds may be only formal or simply required by the *Effective Atomic Number Rule*, and complexes that have no such bonds may readily form them by simply losing a ligand, sometimes in a facile or reversible manner. Because of the extreme variety of compounds, only a few selected examples, mainly from the more recent literature, are presented. The use of other reviews is absolutely necessary to cover this field.[2–7]

14.1 Organometallic Polynuclear Re Complexes Containing Other Metals or Metalloid M′ without Re–M′ Bonds

These types of complexes have the general formula $L_nRe\text{–}Y\text{–}M'L'_n$ and at least one of the fragments is organometallic or the bridge has M–C bonds. They may be prepared in one of the following general, but not exclusive, ways: (1) a Re complex behaves as an electrophilic center for ligand substitution from an L'_mM' complex bearing nucleophilic ligands; (2) nucleophilic addition of L_nRe to an unsaturated ligand on the M′ complex; and (3) addition of the ligands in L_nRe to L'_mM'. Examples of each type are mentioned along the preceding sections.

The complexes $Re(CO)_3(HM'(pz)_3)$ (M′ = B, Ga) represent a trivial example of the first situation. However, the use of transition metal complexes as ligands is currently receiving more detailed attention, because of the possibility of either tuning the reactivity of the Re in the resulting complex by means of the influence of M′ on the ligand or by obtaining cooperative reactivity between the two metal centers. Reaction of ferrocenyl derived ligands, for example, $Fe(\eta^5\text{-}C_5H_4PR_2)_2(FcPPh_2)$ with $[ReX(CO)_4]_2$ affords *fac*-$[Re(CO)_3Cl(FcPPh_2)_2]$. Upon ferrocene-based oxidation, the Re electronic density is lowered, as shown by the increase in the ν(CO) vibration frequencies. The use of anionic organometallic ligands is also exemplified by the formation of $[W(CO)_5(\mu\text{-}PPh_2)Re(CO)_5]^-$ (**166**) from $ReX(CO)_5$ and $[W(CO)_5(PPh_2)]^-$. A related example is the formation of $Re(CO)_5(\mu\text{-}O)Re(O)_3$ from $Re(CO)_5FBF_3$ and $ReO_4{}^-$. The second method exploits the high nucleophilicity of $[Re(CO)_5]^-$, which adds to organometallic cations with unsaturated ligands in a similar fashion to R^- or H^- as extensively studied by Beck. Examples are the formation of complex (**167**) and analogs. The complexes formed from the ligands (**117**) and (**118**) are examples of the third method.

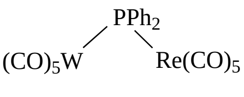

(**166**)

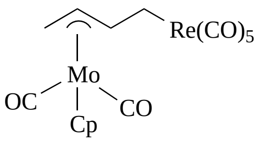

(**167**)

14.2 Organometallic Re Complexes Containing Re–M′ Bonds to Metals or Metalloid M′

This class of compound has a very high number of representatives for two main reasons: (1) the interest in cluster chemistry and the study of the systematic pathways for their construction; and (2) the fact that many reactions initially give products without M–M′ bonds, but subsequently form M–M′ bonded species to compensate for electronic deficiencies.

The extreme complexity of boron chemistry provides a wide variety of B–Re bonds, from simple $[Re(BH_3)(CO)_5][NEt_4]$ to more complex examples as (**138**) and (**139**).[2,3] Simple acid-base addition from $ReCp_2H$ to $AlMe_3$ gives an adduct with a Re–Al bond, while with Cu^I a tetranuclear species is formed. Reaction of Ga and In metals or compounds with $Re_2(CO)_{10}$ produce high nuclearity clusters.[2,52] ReM′ (M′ = Zn, Cd, Hg), as in $[Re(CO)_5]_2M'$, are well known. With the group 14 elements, many compounds are known. Oxidative addition of R_3M'–H bonds to $ReCp(CO)_3$ under photolysis gives $ReHCp(CO)_2(M'R_3)$ (M′ = Si, Ge, Sn). A number of Ge and Sn compounds of type $Re(CO)_5(M'R_3)$ and $Re(CO)_3(\alpha$-diimine$)(M'R_3)$ have been prepared from $[Re(CO)_3L_2]^-$ and $M'XR_3$ and their photophysics have been studied.[2] However, the most varied class of Re–M′ bonded complexes concerns the transition metals M′. According to Roberts and Geoffroy, these complexes are prepared by 17 synthetic methods divided into four main reaction categories: ligand substitution, addition, condensation, and bridge-assisted reactions.[2] This phenomenological classification does not account for mechanistic distinctions within each subcategory.

The use of carbonylate anions as nucleophiles in substitution reactions at metals has been used for a long time to prepare other Re–M′ metal-bonded derivatives, for example, $ReCo(CO)_9$ from $[Re(CO)_6]^+$ and $[Co(CO)_4]^-$ and (**168**) from $[ReBr(CO)_4]_2$ and $[Fe(CO)_4\{C(O)R\}][NMe_4]$.[198]

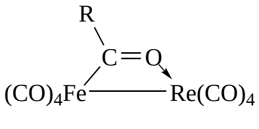

(**168**)

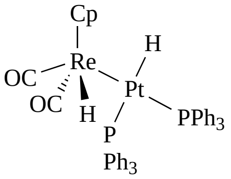

(**169**)

Addition of a metal fragment across a M–M or M–ligand bond is a very general and usually predictable method of preparing M–M′ bonded complexes. Among the latest Re complexes prepared by this method, (**169**) displays a rather interesting chemistry, hydrogenating alkynes to alkenes and providing the best route, so far, to $ReCp(CO)_2(\eta^2$-alkene) complexes. The mechanism of this kind of rare, effective cooperative catalysis in heterobimetallic complexes has been studied in detail.[199] The third general pathway, condensation reactions, forms a M–M bond through the elimination of a small molecule. Alkane elimination is quite useful and a classical example in Re chemistry is the formation of (**170**) from $ReCp_2H$ and $MnMe(CO)_5$ under elimination of CH_4.

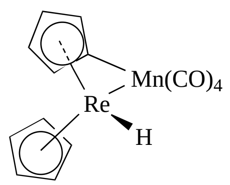

(**170**)

A more straightforward elimination is observed in the reaction of $MCp_2(THF)Me$ and $ReH_7(PPh_2)_2$ (M = Y, Lu), which gives $MCp_2(THF)(\mu$-$H)_2ReH_4(PPh_3)_2$. In this case, there is no M–M′ bond, although a close M–Re distance is measured.[200]

H_2 elimination is involved in the formation of $(PhMe_2P)_3(CO)ClRe(\mu$-H)Au(PPh3) with a rare Re–Au bond.[201] Polyhydrides react with unsaturated metal fragments to originate polynuclear complexes by addition, substitution with H_2 elimination, or redox processes. H_2 elimination accompanies the reaction between (**28**) and $[IrH_2(Me_2CO)_2(PPh_3)_2]^+$ to give $[(PPh_3)_2H_3Re(\mu$-$H_3)IrH(PPh_3)_2]^+$. (**171**) represents the product of the addition of $[AuPPh_3]^+$ to $[Re_3H_4(CO)_9(PPh_3)]^-$.[202]

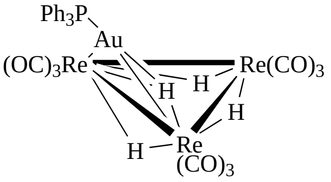

(**171**)

The central issue of the bridge-assisted mechanism is the presence of a ligand that brings the two metals together and favors the M–M′ bond formation by occupying a bridging position in the final product. The complex (**166**) is ‘en route’ to this mechanism and upon loss of a Re-bound CO forms a Re–W bond (**172**). Very important cases of the bridge-assisted M–M′ bond formation are the addition of $M'L_n$ fragments to $M{=}CR_2$ and $M{\equiv}CR$ fragments. This method provides the rationale for the construction of clusters with many metal combinations containing bridging carbene and carbyne ligands. Addition of $Re_2(CO)_{10}$ to $WCp(CO)_2(C{\equiv}Ar)$ (**173**), commonly used for this purpose, gives (**174**). However, again depending on the lability of the metal centers involved, reaction of (**173**) with $Re_2(\mu\text{-H})(\mu\text{-CH=CHBu})(CO)_8$ gives higher nuclearity structures due to the facile loss of 1-hexene. $[ReCp(CO)_2({\equiv}CAr)]^+$ has been used for the construction of related clusters. Nucleophilic addition of a wide range of metal-carbonylate anions to the alkylidyne C atom of this very sensitive and reactive cation, at low temperatures, is followed by rearrangements producing a variety of clusters with Re–M′ bonds. Carbonylates include, for example, $[M(CO)_5]^-$ (M = Mn, Re), $[Co(CO)_4]^-$, $[CpM(CO)_3]^-$ (M = Mo,W), $[CpFe(CO)_2]^-$, and some of the complexes formed are depicted in (**175–177**).

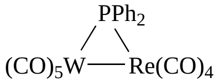

(**172**)

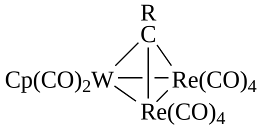

(**174**)

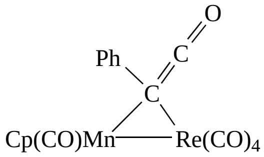

(**175**)

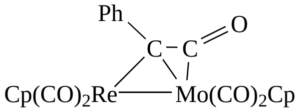

(**176**)

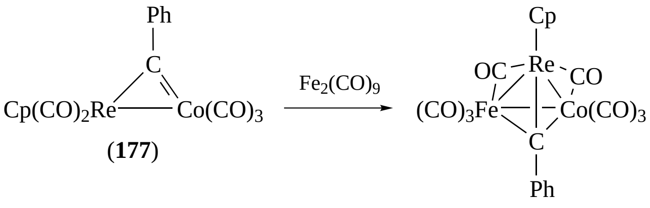

(**177**)

(**178**)

Further reactions of these complexes lead to higher nuclearity clusters, for example, (**178**).

Reactions with carbonylate dianions, for example, $[W(CO)_5]^{2-}$, $[Fe_2(CO)_8]^{2-}$, and others, also produce a rich cluster chemistry. Ligands other than CO can be included in the carbonylate anions, for example, NO, PR_3, SR, SCN, NCO, and CN increasing the scope of cluster derivatization of these synthetic procedures as in (**179**).[203]

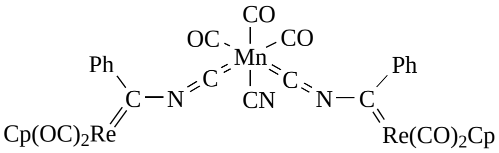

(**179**)

Of particular interest has been the study of Pt_xRe_y clusters due to their importance in petroleum refining where the Re seems to counteract the formation of unreactive coke, which poisons the Pt catalyst. A review covers this chemistry and structures (**180–183**) represent some examples.[204]

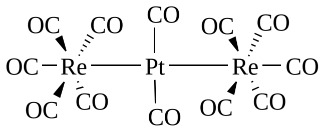

(**180**)

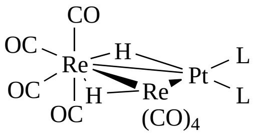

(**181**)

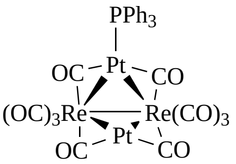

(**182**)

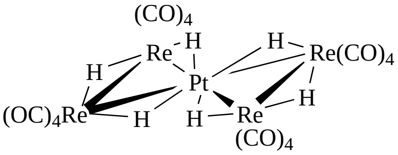

(**183**)

15 BIOORGANOMETALLIC CHEMISTRY OF RHENIUM

This fascinating and fast growing field, already amply reviewed,[205–209] takes advantage of the properties of a wide number of organometallic complexes using them as tools for biological applications. These range from metal immunoassays to drugs, radiopharmaceuticals for imaging and therapy passing through applications in peptide synthesis and peptide marking for X-ray diffraction, electronic microscopy, and other purposes. In the case of Re, one of the earliest examples was the condensation of Lukehart's rhenametalla-β-diketones (Scheme 13) with aminoacids to produce α-ketoimine complexes and, therefore provide for amino protection of those aminoacids. Later on, Jaouen and collaborators realized that the high stability of many CO-containing organometallics to air and to physiological conditions enabled their use in the carbonylmetalloimmunoassay (CMIA) technique. Taking advantage of their extremely intense CO vibrations in the IR region (1900–2100 cm^{-1}) where biological molecules do not absorb, steroids, hormones, or drugs labeled with $M(CO)_n$ fragments can be detected by FTIR in the 10^{-12} M range and are well recognized by their antibodies.

CMIA avoids radioisotopes and allows simultaneous parallel assays.[210]

The CMIA work with steroids marked with $Re(CO)_3$ led to the early recognition of the potential of this class of compounds for the diagnosis and therapy of steroid receptor-positive breast cancer. Complex (**184**) shows higher binding to estrogen receptors than the parent steroid. Complex (**185**) also binds to the tamoxyfen receptor and shows an antiproliferative action comparable to hydroxytamoxifen, a potent breast cancer drug.[211]

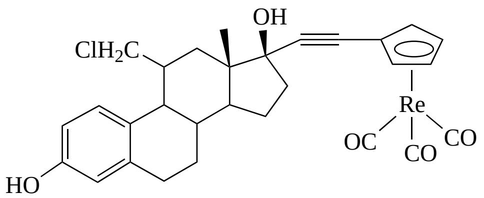

(**184**)

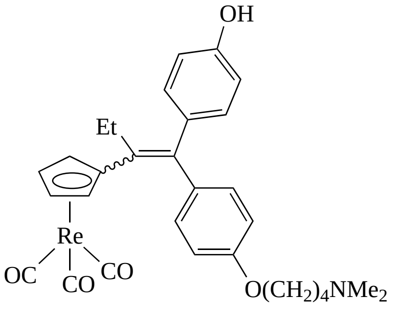

(**185**)

This great ability to selectively target metal pharmaceuticals has led to the possibility of using radioactive compounds to deliver radiation in specific receptors, tissues, organs, or cancer sites. The γ-ray emission and short half-lifetime make ^{99m}Tc the preferred element for imaging, whereas β-emitting ^{186}Re (5 mm range) and ^{188}Re (11 mm range) are preferred for radiotherapeutic purposes (tissue destruction).

As a consequence, Re chemistry has grown parallel to that of Tc using both organometallic and classical coordination complexes. A target-specific radiopharmaceutical must possess high affinity for the selected target but not for others. The 'unnatural' character of organometallic compounds might create distinct advantages compared with 'natural' drugs, which are often subject to unwanted rapid metabolism in vivo. Furthermore, the complex must by thermodynamically and kinetically stable to avoid decomposition and allow for rapid clearance in vivo. This is an advantage of the *fac*-$Re(CO)_3$ core over other Re^V classical complexes since it is particularly inert specially when bound to a fac-tripodal ligand system (L_3 or Cp) with an overall octahedral geometry.

Therefore, the bioorganometallic Re complexes comprise two main classes: the $(CpX)Re(CO)_3$ derivatives where CpX represents the Cp ligand substituted with a bioactive molecule with or without an appropriate spacer, for example, a steroid, a protein, a peptide; the *fac*-$Re(CO)_3L_3$ derivatives coordinated to classical N, P, O, S donors that may carry bioactive molecules of the types described above. (**186**; TROTEC-1) is a tropane derivative with an extremely high affinity for human dopamine transporter and (**187**) has a high affinity for the serotonergic receptors.

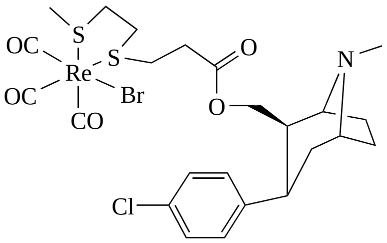

(**186**)

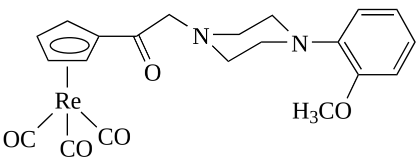

(**187**)

The synthesis of these complexes poses particular problems in the case of the $(CpX)Re(CO)_3$ derivatives because the methods to introduce delicate X functions either in a $CpRe(CO)_3$ complex or binding CpX to low-valent $Re(CO)_3$ precursors like (**1**) or $ReX(CO)_5$ require multistep procedures and/or reaction conditions incompatible with the presence of sensitive X groups. The situation becomes even more difficult when dealing with radioactive isotopes where fast, high-dilution and high-yield methods, and aqueous saline solutions are required.

This situation spurred the search for a number of alternative synthetic methods that have opened new avenues in the field of Re (and Tc) organometallic synthesis.

Still on classic grounds, the use of fulvenes or McMurry coupling to cymantrene ketyl to introduce substituents to the Cp ring in a mild fashion has produced several biologically labeled derivatives.[212]

Among several other methods, Katzenellenbogen developed one-pot reactions of three components like the one in Scheme 36.[213] Alternatively, $(CpX)SnBu_3$ can be generated and reacted in situ with $[Re(CO)_3Br(THF)]_2$.

A major development was introduced by Alberto with the generation of the $Re(CO)_3$ moiety in aqueous solution from $[ReO_4]^-$, BH_3, and 1 atom of CO. The resulting $[Re(CO)_3X_3]^{2-}$ (X = Cl, Br) is easily transformed into $[Re(CO)_3L_3]^+$ (L = NCMe, H_2O). Treatment of aqueous $[Re(CO)_3(H_2O)_3]^+$ with $[CpX]^-$ at pH 7.4 gives

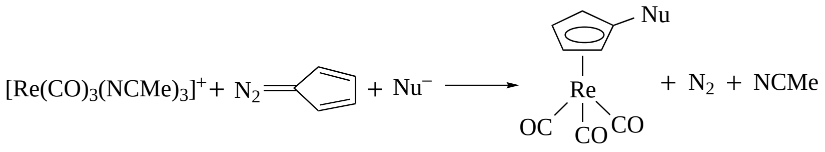

$Nu^- = R$ (from $RB(OH)_2$); RCOO; X

Scheme 36

$(CpX)Re(CO)_3$ where X is an acyl group (–COR) in which R carries the biomolecules of interest to target the $Re(CO)_3$ fragment to the required biological site.[214] The so-called double-ligand-transfer reactions also provide a mild synthesis of $(CpX)Re(CO)_3$ derivatized with biomolecules.[215]

Labelling of proteins and peptides with $CpRe(CO)_3$ fragments can be made by peptide bond formation with the carboxylic acid $Re(CpCOOH)(CO)_3$ or by acylation of free amine groups with organometallic succinimidyl esters.

Among the $[Re(CO)_3L_3]^+$ complexes bearing ligand systems (L_3) functionalized with biomolecules, recent advances include fatty acids attached to Schiff-base ligands for myocardial investigations,[216] peptides attached to histidine complexes,[217] (**188**) or glucose derivatives (**189**).[218] Luminescent complexes $[Re(CO)_3(N\text{-}N)(Py\text{-}spacer\text{-}biomolecule)]^+$ are powerful fluorophores for bioassays since the biomolecule does not interfere negatively with the luminescence from the metal fragment.[42]

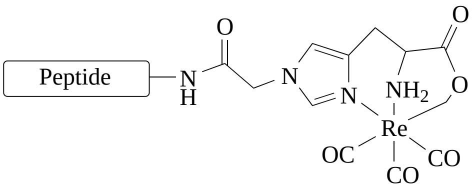

(**188**)

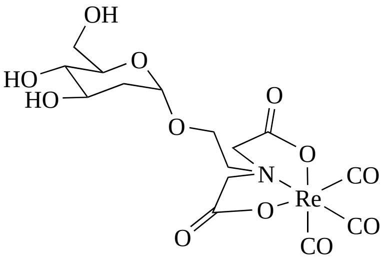

(**189**)

Organometallic compounds appear to be a serious alternative to state-of-the-art labeling techniques as shown in the ongoing preclinical and clinical studies with organometallic-labeled tumor affine peptides and single-chain antibody fragments.[219]

16 RELATED ARTICLES

Carbonyl Complexes of the Transition Metals; Dinuclear Organometallic Cluster Complexes; Hydride Complexes of the Transition Metals; Luminescence Behavior & Photochemistry of Organotransition Metal Compounds; Manganese: Organometallic Chemistry; Metal Vapor Synthesis of Transition Metal Compounds; Metathesis Polymerization Processes by Homogeneous Catalysis; Molybdenum: Organometallic Chemistry; Osmium: Organometallic Chemistry; Polynuclear Organometallic Cluster Complexes; Technetium: Organometallic Chemistry; Technetium & Rhenium: Inorganic & Coordination Chemistry; Tungsten: Organometallic Chemistry.

17 REFERENCES

1. C. C. Romão, in 'Encyclopedia of Inorganic Chemistry', ed. R. B. King, John Wiley & Sons, Chichester, 1994, Vol. 6, p. 3437.
2. N. M. Boag and H. D. Kaesz, in 'Comprehensive Organometallic Chemistry', eds. G. Wilkinson, F. G. A. Stone, and E. W. Abel, Pergamon, Oxford, 1982, Vol. 4, p. 161.
3. J. M. O'Connor, in 'Comprehensive Organometallic Chemistry-II', eds. E. W. Abel, F. G. A. Stone, and G. Wilkinson, Pergamon, Oxford, 1995, p. 167. Vol. 6.
4. D. M. Hoffman, in 'Comprehensive Organometallic Chemistry-II', eds. E. W. Abel, F. G. A. Stone, and G. Wilkinson, Pergamon, Oxford, 1995, Vol. 6, p. 231.
5. J. C. Vites and M. M. Lynam, *Coord. Chem. Rev.*, 1995, **146**, A207.
6. J. C. Vites and M. M. Lynam, *Coord. Chem. Rev.*, 1998, **169**, 201.
7. J. C. Vites and M. M. Lynam, *Coord. Chem. Rev.*, 1998, **172**, 357.
8. S. Top, P. Morel, H. Pankowski, and G. Jaouen, *J. Chem. Soc., Dalton Trans.*, 1996, 3611.
9. H. Yang, P. T. Snee, K. T. Kotz, C. K. Payne, and C. B. Harris, *J. Am. Chem. Soc.*, 2001, **123**, 4204.
10. T. L. Brown and S. L. Zhang, *Inorg. Chem.*, 1995, **34**, 1164.
11. D. H. R. Barton and M. J. Kelly, *Tetrahedron Lett.*, 1992, **33**, 5041.

12. C. G. Kreiter, *Adv. Organomet. Chem.*, 1986, **26**, 297.
13. L. Carlucci, D. M. Proserpio, and G. D'Alfonso, *Organometallics*, 1999, **18**, 2091.
14. R. D. Adams and L. F. Chen, *Organometallics*, 1994, **13**, 1264.
15. R. D. Adams, J. A. Queisser, and J. H. Yamamoto, *Organometallics*, 1996, **15**, 2489.
16. P. Johnston, G. J. Hutchings, and N. J. Coville, *J. Am. Chem. Soc.*, 1989, **111**, 1902.
17. A. Choplin and F. Quignard, *Coord. Chem. Rev.*, 1998, **180**, 1679.
18. H. J. Haupt, D. Petters, and U. Florke, *J. Organomet. Chem.*, 1998, **558**, 81.
19. T. M. Bockman and J. K. Kochi, *J. Phys. Org. Chem.*, 1997, **10**, 542.
20. D. M. Thompson, M. Bengough, and M. C. Baird, *Organometallics*, 2002, **21**, 4762.
21. W. Beck and K. Sünkel, *Chem. Rev.*, 1988, **88**, 1405.
22. X. G. Fang, B. L. Scott, K. D. John, and G. J. Kubas, *Organometallics*, 2000, **19**, 4141.
23. E. Lippmann, R. Kramer, and W. Beck, *J. Organomet. Chem.*, 1994, **466**, 167.
24. G. Albertin, S. Antoniutti, and M. T. Giorgi, *Eur. J. Inorg. Chem.*, 2003, 2855.
25. D. Sutton, *Chem. Rev.*, 1993, **93**, 995.
26. T. J. Davies, R. V. H. Jones, W. E. Lindsell, C. Miln, and P. N. Preston, *Tetrahedron Lett.*, 2002, **43**, 487.
27. C. M. Lukehart, *Adv. Organomet. Chem.*, 1986, **25**, 45.
28. M. A. Guillevic, T. Gelbrich, M. B. Hursthouse, and D. W. Bruce, *Mol. Cryst. Liq. Cryst.*, 2001, **362**, 147.
29. V. W. W. Yam, K. Z. Wang, C. R. Wang, Y. Yang, and K. K. Cheung, *Organometallics*, 1998, **17**, 2440.
30. L. S. M. Lam and W. K. Chan, *Chemphyschem*, 2001, **2**, 252.
31. L. C. Abbott, C. J. Arnold, T. Q. Ye, K. C. Gordon, R. N. Perutz, R. E. Hester, and J. N. Moore, *J. Phys. Chem. A*, 1998, **102**, 1252.
32. J. R. Schoonover and G. F. Strouse, *Chem. Rev.*, 1998, **98**, 1335.
33. B. D. Rossenaar, F. Hartl, and D. J. Stufkens, *Inorg. Chem.*, 1996, **35**, 6194.
34. D. J. Stufkens and A. Vlcek, *Coord. Chem. Rev.*, 1998, **177**, 127.
35. A. Vogler and H. Kunkely, *Coord. Chem. Rev.*, 2000, **200**, 991.
36. L. S. Forster, *Coord. Chem. Rev.*, 2002, **227**, 59.
37. H. Hori, Y. Takano, K. Koike, and Y. Sasaki, *Inorg. Chem. Commun.*, 2003, **6**, 300.
38. V. W. W. Yam, *Chem. Commun.*, 2001, 789.
39. K. E. Splan, M. H. Keefe, A. M. Massari, K. A. Walters, and J. T. Hupp, *Inorg. Chem.*, 2002, **41**, 619.
40. R. V. Slone, K. D. Benkstein, S. Belanger, J. T. Hupp, I. A. Guzei, and A. L. Rheingold, *Coord. Chem. Rev.*, 1998, **171**, 221.
41. S. Y. Chang and K. S. Jeong, *J. Org. Chem.*, 2003, **68**, 4014.
42. K. K. W. Lo, W. K. Hui, and D. C. M. Ng, *J. Am. Chem. Soc.*, 2002, **124**, 9344.
43. S. S. Sun, A. J. Lees, and P. Y. Zavalij, *Inorg. Chem.*, 2003, **42**, 3445.
44. P. D. Beer and J. B. Cooper, *Chem. Commun.*, 1998, 129.
45. S. S. Sun and A. J. Lees, *Coord. Chem. Rev.*, 2002, **230**, 171.
46. S. S. Sun and A. J. Lees, *Organometallics*, 2002, **21**, 39.
47. A. Gabrielsson, F. Hartl, J. R. L. Smith, and R. N. Perutz, *Chem. Commun.*, 2002, 950.
48. P. Bergamini, F. F. DeBiani, L. Marvelli, N. Mascellani, M. Peruzzini, R. Rossi, and P. Zanello, *New J. Chem.*, 1999, **23**, 207.
49. A. M. Bond, R. Colton, D. G. Humphrey, P. J. Mahon, G. A. Snook, V. Tedesco, and J. N. Walter, *Organometallics*, 1998, **17**, 2977.
50. S. Warner and S. J. Lippard, *Inorg. Chem.*, 1989, **28**, 3008.
51. G. D'Alfonso, D. Roberto, R. Ugo, C. L. Bianchi, and A. Sironi, *Organometallics*, 2000, **19**, 2564.
52. T. J. Henly, *Coord. Chem. Rev.*, 1989, **93**, 269.
53. D. Roberto, G. D'Alfonso, R. Ugo, and M. Vailati, *Organometallics*, 2001, **20**, 4307.
54. G. G. Hlatky and R. H. Crabtree, *Coord. Chem. Rev.*, 1985, **65**, 1.
55. K. Abdur-Rashid, A. J. Lough, and R. H. Morris, *Can. J. Chem.*, 2001, **79**, 964.
56. A. Paulo, J. Ascenso, A. Domingos, A. Galvao, and I. Santos, *J. Chem. Soc., Dalton Trans.*, 1999, 1293.
57. D. M. Heinekey and W. J. Oldham, *Chem. Rev.*, 1993, **93**, 913.
58. S. M. Reid, B. Neuner, R. R. Schrock, and W. M. Davis, *Organometallics*, 1998, **17**, 4077.
59. W. D. Jones, G. P. Rosini, and J. A. Maguire, *Organometallics*, 1999, **18**, 1754.
60. J. Wessel, J. C. Lee, E. Peris, G. P. A. Yap, J. B. Fortin, J. S. Ricci, G. Sini, A. Albinati, T. F. Koetzle, O. Eisenstein, A. L. Rheingold, and R. H. Crabtree, *Angew. Chem., Int. Ed. Engl.*, 1995, **34**, 2507.
61. A. Messmer, H. Jacobsen, and H. Berke, *Chem.-Eur. J.*, 1999, **5**, 3341.
62. D. L. Allen, M. L. H. Green, and J. A. Bandy, *J. Chem. Soc., Dalton Trans.*, 1990, 541.
63. M. Bergamo, T. Beringhelli, G. Dalfonso, G. Ciani, M. Moret, and A. Sironi, *Organometallics*, 1996, **15**, 1637.
64. G. Albertin, S. Antoniutti, S. Garcia-Fontan, R. Carballo, and F. Padoan, *J. Chem. Soc., Dalton Trans.*, 1998, 2071.
65. X. Y. Liu, S. Bouherour, H. Jacobsen, H. W. Schmalle, and H. Berke, *Inorg. Chim. Acta*, 2002, **330**, 250.

66. T. Beringhelli, G. D'Alfonso, M. Panigati, P. Mercandelli, and A. Sironi, *Chem.-Eur. J.*, 2002, **8**, 5340.
67. M. Bergamo, T. Beringhelli, G. D'Alfonso, P. Mercandelli, M. Moret, and A. Sironi, *Angew. Chem., Int. Ed. Engl.*, 1999, **38**, 3486.
68. C. A. Wright and J. R. Shapley, *Inorg. Chem.*, 2001, **40**, 6338.
69. S. Mihan, K. Sunkel, and W. Beck, *Chem.-Eur. J.*, 1999, **5**, 745.
70. J. A. M. Andersen and J. R. Moss, *Polyhedron*, 1995, **14**, 1881.
71. A. Derecskei-Kovacs and D. S. Marynick, *J. Am. Chem. Soc.*, 2000, **122**, 2078.
72. E. Lippmann, C. Robl, H. Berke, H. D. Kaesz, and W. Beck, *Chem. Ber.*, 1993, **126**, 933.
73. A. D. Ryabov, *Chem. Rev.*, 1990, **90**, 403.
74. V. Pfennig, N. Robertson, and K. Seppelt, *Angew. Chem., Int. Ed. Engl.*, 1997, **36**, 1350.
75. D. S. Edwards, L. V. Biondi, J. W. Ziller, M. R. Churchill, and R. R. Schrock, *Organometallics*, 1983, **2**, 1505.
76. B. T. Flatt, R. H. Grubbs, R. L. Blanski, J. C. Calabrese, and J. Feldman, *Organometallics*, 1994, **13**, 2728.
77. M. I. Bruce, *Chem. Rev.*, 1998, **98**, 2797.
78. M. R. Terry, L. A. Mercando, C. Kelley, G. L. Geoffroy, P. Nombel, N. Lugan, R. Mathieu, R. L. Ostrander, B. E. Owenswaltermire, and A. L. Rheingold, *Organometallics*, 1994, **13**, 843.
79. M. Carvalho, S. Almeida, A. J. L. Pombeiro, and R. A. Henderson, *Organometallics*, 1997, **16**, 5441.
80. N. Mantovani, L. Marvelli, R. Rossi, V. Bertolasi, C. Bianchini, I. de los Rios, and M. Peruzzini, *Organometallics*, 2002, **21**, 2382.
81. W. M. Xue, M. C. W. Chan, Z. M. Su, K. K. Cheung, S. T. Liu, and C. M. Che, *Organometallics*, 1998, **17**, 1622.
82. E. O. Fischer, C. Apostolidis, E. Dornberger, A. C. Filippou, B. Kanellakopulos, B. Lungwitz, J. Muller, B. Powietzka, J. Rebizant, and W. Roth, *Z. Naturforsch., B*, 1995, **50**, 1382.
83. L. A. Mercando, B. M. Handwerker, H. J. Macmillan, G. L. Geoffroy, A. L. Rheingold, and B. E. Owenswaltermire, *Organometallics*, 1993, **12**, 1559.
84. D. S. Williams and R. R. Schrock, *Organometallics*, 1994, **13**, 2101.
85. W. M. Xue, Y. Wang, M. C. W. Chan, Z. M. Su, K. K. Cheung, and C. M. Che, *Organometallics*, 1998, **17**, 1946.
86. S. Almeida and A. J. L. Pombeiro, *Organometallics*, 1997, **16**, 4469.
87. M. Leeaphon, A. L. Ondracek, R. J. Thomas, P. E. Fanwick, and R. A. Walton, *J. Am. Chem. Soc.*, 1995, **117**, 9715.
88. A. M. Lapointe and R. R. Schrock, *Organometallics*, 1995, **14**, 1875.
89. M. Chabanas, C. Coperet, and J. M. Basset, *Chem.-Eur. J.*, 2003, **9**, 971.
90. C. C. Romao, F. E. Kuhn, and W. A. Herrmann, *Chem. Rev.*, 1997, **97**, 3197.
91. D. M. Hoffman, J. C. Huffman, D. Lappas, and D. A. Wierda, *Organometallics*, 1993, **12**, 4312.
92. D. M. Hoffman, D. Lappas, and D. A. Wierda, *Polyhedron*, 1996, **15**, 3309.
93. S. Cai, D. M. Hoffman, and D. A. Wierda, *Organometallics*, 1996, **15**, 1023.
94. A. J. Downs, G. Dierker, J. C. Green, T. M. Greene, G. S. McGrady, L. J. Morris, S. D. Wolfgang, and P. Sirsch, *J. Chem. Soc., Dalton Trans.*, 2002, 3349.
95. W. A. Herrmann, R. M. Kratzer, and R. W. Fischer, *Angew. Chem., Int. Ed. Engl.*, 1997, **36**, 2652.
96. J. H. Espenson, H. S. Tan, S. Mollah, R. S. Houk, and M. D. Eager, *Inorg. Chem.*, 1998, **37**, 4621.
97. L. J. Morris, A. J. Downs, T. M. Greene, S. G. McGrady, W. A. Herrmann, P. Sirsch, W. Scherer, and O. Gropen, *Organometallics*, 2001, **20**, 2344.
98. C. G. Zhang, I. A. Guzei, and J. H. Espenson, *Organometallics*, 2000, **19**, 5257.
99. D. D. DuMez and J. M. Mayer, *J. Am. Chem. Soc.*, 1996, **118**, 12416.
100. P. Ferreira, W. M. Xue, E. Bencze, E. Herdtweck, and F. E. Kuhn, *Inorg. Chem.*, 2001, **40**, 5834.
101. W. A. Herrmann, M. U. Rauch, and P. W. Roesky, *J. Organomet. Chem.*, 1996, **511**, 299.
102. X. P. Shan, A. Ellern, and J. H. Espenson, *Angew. Chem., Int. Ed. Engl.*, 2002, **41**, 3807.
103. J. Dixon and J. H. Espenson, *Inorg. Chem.*, 2002, **41**, 4727.
104. Y. Wang, G. Lente, and J. H. Espenson, *Inorg. Chem.*, 2002, **41**, 1272.
105. J. H. Espenson and D. T. Y. Yiu, *Inorg. Chem*, 2000, **39**, 4113.
106. A. M. Santos, C. C. Romao, and F. E. Kuhn, *J. Am. Chem. Soc.*, 2003, **125**, 2414.
107. F. E. Kuhn and W. A. Herrmann, *Struct. Bonding*, 2000, **97**, 213.
108. W. A. Herrmann, R. W. Fischer, W. Scherer, and M. U. Rauch, *Angew. Chem., Int. Ed. Engl.*, 1993, **32**, 1157.
109. M. J. Sabater, M. E. Domine, and A. Corma, *J. Catal.*, 2002, **210**, 192.
110. R. Saladino, V. Neri, E. Mincione, and P. Filippone, *Tetrahedron*, 2002, **58**, 8493.
111. A. O. Bouh and J. H. Espenson, *J. Mol. Catal. A-Chem.*, 2003, **200**, 43.
112. H. S. Tan, A. Yoshikawa, M. S. Gordon, and J. H. Espenson, *Organometallics*, 1999, **18**, 4753.
113. F. E. Kühn and W. A. Herrmann, *Chemtracts-Org. Chem.*, 2001, **14**, 59.
114. D. S. Williams and R. R. Schrock, *Organometallics*, 1993, **12**, 1148.

115. W. A. Herrmann, H. Ding, F. E. Kuhn, and W. Scherer, *Organometallics*, 1998, **17**, 2751.
116. W. D. Wang and J. H. Espenson, *Organometallics*, 1999, **18**, 5170.
117. W. D. Wang and J. H. Espenson, *Inorg. Chem.*, 2001, **40**, 1323.
118. T. Ederer, K. Sunkel, and W. Beck, *Z. Anorg. Allg. Chem.*, 1999, **625**, 1202.
119. J. Q. Pu, T. S. Peng, A. M. Arif, and J. A. Gladysz, *Organometallics*, 1992, **11**, 3232.
120. B. C. Brooks, T. B. Gunnoe and W. D. Harman, 2000, **206**, 3.
121. T. B. Gunnoe, M. Sabat, and W. D. Harman, *J. Am. Chem. Soc.*, 1998, **120**, 8747.
122. T. B. Gunnoe, M. Sabat, and W. D. Harman, *Organometallics*, 2000, **19**, 728.
123. M. D. Chordia, P. L. Smith, S. H. Meiere, M. Sabat, and W. D. Harman, *J. Am. Chem. Soc.*, 2001, **123**, 10756.
124. C. P. Casey, J. T. Brady, T. M. Boller, F. Weinhold, and R. K. Hayashi, *J. Am. Chem. Soc.*, 1998, **120**, 12500.
125. Y. Han, C. J. Harlan, P. Stoessel, B. J. Frost, J. R. Norton, S. Miller, B. Bridgewater, and Q. Xu, *Inorg. Chem.*, 2001, **40**, 2942.
126. T. R. Cundari, R. R. Conry, E. Spaltenstein, S. C. Critchlow, K. A. Hall, S. K. Tahmassebi, and J. M. Mayer, *Organometallics*, 1994, **13**, 322.
127. S. K. Tahmassebi, W. S. McNeil, and J. M. Mayer, *Organometallics*, 1997, **16**, 5342.
128. G. Frenzen, D. W. Vongudenberg, and K. Dehnicke, *Z. Naturforsch., B*, 1993, **48**, 1019.
129. B. Aechter, K. Polborn, and W. Beck, *Z. Anorg. Allg. Chem.*, 2001, **627**, 43.
130. Y. X. He, R. J. Batchelor, F. W. B. Einstein, L. K. Peterson, and D. Sutton, *J. Organomet. Chem.*, 1997, **531**, 27.
131. Y. X. He and D. Sutton, *J. Organomet. Chem.*, 1999, **572**, 213.
132. A. Wojcicki, *Inorg. Chem. Commun.*, 2002, **5**, 82.
133. J. T. Chen, *Coord. Chem. Rev.*, 1999, **192**, 1143.
134. C. P. Casey, T. M. Boller, S. Kraft, and I. A. Guzei, *J. Am. Chem. Soc.*, 2002, **124**, 13215.
135. C. P. Casey, J. R. Nash, C. S. Yu, A. D. Selmeczy, S. Chung, D. R. Powell, and R. K. Hayashi, *J. Am. Chem. Soc.*, 1998, **120**, 722.
136. A. Hosang, U. Englert, A. Lorenz, U. Ruppli, and A. Salzer, *J. Organomet. Chem.*, 1999, **583**, 47.
137. E. Lippmann, T. Kerscher, B. Aechter, C. Robl, W. Beck, D. W. Price, M. Metz, and P. Hofmann, *J. Organomet. Chem.*, 1998, **556**, 207.
138. S. J. Dossett, M. Green, M. F. Mahon, J. M. McInnes, and C. Vaughan, *J. Chem. Soc., Dalton Trans.*, 1997, 3671.
139. H. Tobita, K. Hashidzume, K. Endo, and H. Ogino, *Organometallics*, 1998, **17**, 3405.
140. D. M. Heinekey and C. E. Radzewich, *Organometallics*, 1998, **17**, 51.
141. F. G. N. Cloke, J. P. Day, J. C. Green, C. P. Morley, and A. C. Swain, *J. Chem. Soc., Dalton Trans.*, 1991, 789.
142. J. J. Carbo, O. Eisenstein, C. L. Higgitt, A. H. Klahn, F. Maseras, B. Oelckers, and R. N. Perutz, *J. Chem. Soc., Dalton Trans.*, 2001, 1452.
143. H. Yang, M. C. Asplund, K. T. Kotz, M. J. Wilkens, H. Frei, and C. B. Harris, *J. Am. Chem. Soc.*, 1998, **120**, 10154.
144. G. I. Childs, C. S. Colley, J. Dyer, D. C. Grills, X. Z. Sun, J. X. Yang, and M. W. George, *J. Chem. Soc., Dalton Trans.*, 2000, 1901.
145. S. Schlecht and J. F. Hartwig, *J. Am. Chem. Soc.*, 2000, **122**, 9435.
146. A. Cusanelli and D. Sutton, *Organometallics*, 1995, **14**, 4651.
147. L. Cheng and N. J. Coville, *Organometallics*, 1997, **16**, 591.
148. F. Godoy, A. H. Klahn, and B. Oelckers, *J. Organomet. Chem.*, 2002, **662**, 130.
149. H. Y. Chen and J. F. Hartwig, *Angew. Chem., Int. Ed. Engl.*, 1999, **38**, 3391.
150. F. Godoy, C. L. Higgitt, A. H. Klahn, B. Oelckers, S. Parsons, and R. N. Perutz, *J. Chem. Soc., Dalton Trans.*, 1999, 2039.
151. T. F. Wang, C. C. Hwu, C. W. Tsai, and Y. S. Wen, *Organometallics*, 1999, **18**, 1553.
152. M. Herberhold and M. Biersack, *J. Organomet. Chem.*, 1995, **503**, 277.
153. T. F. Wang, C. C. Hwu, C. W. Tsai, and K. J. Lin, *Organometallics*, 1997, **16**, 3089.
154. D. H. Gibson, J. M. Mehta, M. S. Mashuta, and J. F. Richardson, *Organometallics*, 1997, **16**, 4828.
155. T. W. Hayton, P. Legzdins, and W. B. Sharp, *Chem. Rev.*, 2002, **102**, 935.
156. Y. L. Zhou and J. A. Gladysz, *Organometallics*, 1993, **12**, 1073.
157. J. A. Gladysz and B. J. Boone, *Angew. Chem., Int. Ed. Engl.*, 1997, **36**, 551.
158. L. J. Alvey, O. Delacroix, C. Wallner, O. Meyer, F. Hampel, S. Szafert, T. Lis, and J. A. Gladysz, *Organometallics*, 2001, **20**, 3087.
159. H. J. Jiao, K. Costuas, J. A. Gladysz, J. F. Halet, M. Guillemot, L. Toupet, F. Paul, and C. Lapinte, *J. Am. Chem. Soc.*, 2003, **125**, 9511.
160. M. C. Milletti and R. F. Fenske, *Organometallics*, 1989, **8**, 420.
161. C. P. Casey, C. J. Czerwinski, D. R. Powell, and R. K. Hayashi, *J. Am. Chem. Soc.*, 1997, **119**, 5750.
162. C. P. Casey, C. J. Czerwinski, and R. K. Hayashi, *J. Am. Chem. Soc.*, 1995, **117**, 4189.
163. C. P. Casey, S. Kraft, and D. R. Powell, *Organometallics*, 2001, **20**, 2651.
164. C. P. Casey, S. Kraft, and D. R. Powell, *J. Am. Chem. Soc.*, 2002, **124**, 2584.

165. K. P. Gable and J. J. J. Juliette, *J. Am. Chem. Soc.*, 1996, **118**, 2625.
166. G. K. Cook and M. A. Andrews, *J. Am. Chem. Soc.*, 1996, **118**, 9448.
167. K. P. Gable and E. C. Brown, *Organometallics*, 2000, **19**, 944.
168. S. H. Pawlicki, B. C. Noll, J. A. Kanney, and M. R. DuBois, *Inorg. Chem.*, 2003, **42**, 1556.
169. C. M. Nunn, A. H. Cowley, S. W. Lee, and M. G. Richmond, *Inorg. Chem.*, 1990, **29**, 2105.
170. S. Ghosh, M. Y. Shang, Y. P. Li, and T. P. Fehlner, *Angew. Chem., Int. Ed. Engl.*, 2001, **40**, 1125.
171. O. I. Trifonova, A. A. Borisenko, Y. A. Ustynyuk, and N. A. Ustynyuk, *Russ. Chem. Bull.*, 1993, **42**, 1222.
172. C. P. Casey, T. E. Vos, J. T. Brady, and R. K. Hayashi, *Organometallics*, 2003, **22**, 1183.
173. M. Toganoh, Y. Matsuo, and E. Nakamura, *Angew. Chem., Int. Ed. Engl.*, 2003, **42**, 3530.
174. C. Bianchini, A. Marchi, L. Marvelli, M. Peruzzini, A. Romerosa, R. Rossi, and A. Vacca, *Organometallics*, 1995, **14**, 3203.
175. R. J. Baker, P. G. Edwards, J. Garcia-Mora, F. Ingold, and K. M. A. Malik, *J. Chem. Soc., Dalton Trans.*, 2002, 3985.
176. C. Bianchini, N. Mantovani, A. Marchi, L. Marvelli, D. Masi, M. Peruzzini, R. Rossi, and A. Romerosa, *Organometallics*, 1999, **18**, 4501.
177. D. D. Ellis, P. A. Jelliss, and F. G. A. Stone, *Chem. Commun.*, 1999, 2385.
178. S. W. Du, J. A. Kautz, T. D. McGrath, and F. G. A. Stone, *Chem. Commun.*, 2002, 1004.
179. J. C. Jeffery, P. A. Jelliss, L. H. Rees, and F. G. A. Stone, *Organometallics*, 1998, **17**, 2258.
180. A. H. Klahn, B. Oelckers, F. Godoy, M. T. Garland, A. Vega, R. N. Perutz, and C. L. Higgitt, *J. Chem. Soc., Dalton Trans.*, 1998, 3079.
181. C. P. Casey, R. S. Carino, H. Sakaba, and R. K. Hayashi, *Organometallics*, 1996, **15**, 2640.
182. C. P. Casey, R. S. Carino, R. K. Hayashi, and K. D. Schladetzky, *J. Am. Chem. Soc.*, 1996, **118**, 1617.
183. O. J. Scherer, M. Ehses, and G. Wolmershauser, *J. Organomet. Chem.*, 1997, **531**, 217.
184. H. Braunschweig, M. Colling, C. Kollann, H. G. Stammler, and B. Neumann, *Angew. Chem., Int. Ed. Engl.*, 2001, **40**, 2298.
185. A. E. Leins and N. J. Coville, *J. Organomet. Chem.*, 1994, **464**, 183.
186. W. G. Wu, P. E. Fanwick, and R. A. Walton, *Inorg. Chim. Acta*, 1996, **242**, 81.
187. J. S. Fan, J. T. Lin, C. C. Chang, S. J. Chou, and K. L. Lu, *Organometallics*, 1995, **14**, 925.
188. J. S. Fan, F. Y. Lee, C. C. Chiang, H. C. Chen, S. H. Liu, Y. S. Wen, C. C. Chang, S. Y. Li, K. M. Chi, and K. L. Lu, *J. Organomet. Chem.*, 1999, **580**, 82.
189. R. A. Michelin, A. J. L. Pombeiro, M. Fatima, and C. G. da Silva, *Coord. Chem. Rev.*, 2001, **218**, 75.
190. A. J. L. Pombeiro, M. da Silva, and R. A. Michelin, *Coord. Chem. rev.*, 2001, **218**, 43.
191. M. Glaser, H. Spies, T. Lugger, and F. E. Hahn, *J. Organomet. Chem.*, 1995, **503**, C32.
192. H. U. Hund, U. Ruppli, and H. Berke, *Inorg. Chim. Acta*, 1993, **76**, 963.
193. D. Veghini and H. Berke, *Inorg. Chem.*, 1996, **35**, 4770.
194. D. Gusev, A. Llamazares, G. Artus, H. Jacobsen, and H. Berke, *Organometallics*, 1999, **18**, 75.
195. J. S. Southern, M. T. Green, G. L. Hillhouse, I. A. Guzei, and A. L. Rheingold, *Inorg. Chem.*, 2001, **40**, 6039.
196. A. Llamazares, H. W. Schmalle, and H. Berke, *Organometallics*, 2001, **20**, 5277.
197. C. Ruf, U. Behrens, E. Lork, and R. Mews, *Chem. Commun.*, 1996, 939.
198. D. Q. Xu, H. D. Kaesz, and S. I. Khan, *Inorg. Chem.*, 1991, **30**, 1341.
199. C. P. Casey, Y. Wang, R. S. Tanke, P. N. Hazin, and E. W. Rutter, *New J. Chem.*, 1994, **18**, 43.
200. D. Alvarez, K. G. Caulton, W. J. Evans, and J. W. Ziller, *Inorg. Chem.*, 1992, **31**, 5500.
201. S. Luo, C. J. Burns, G. J. Kubas, J. C. Bryan, and R. H. Crabtree, *J. Cluster Sci.*, 2000, **11**, 189.
202. T. Beringhelli, G. D'Alfonso, M. G. Garavaglia, M. Panigati, P. Mercandelli, and A. Sironi, *Organometallics*, 2002, **21**, 2705.
203. J. Chen and R. Wang, *Coord. Chem. Rev.*, 2002, **231**, 109.
204. J. L. Xiao and R. J. Puddephatt, *Coord. Chem. Rev.*, 1995, **143**, 457.
205. J. R. Dilworth and S. J. Parrott, *Chem. Soc. Rev.*, 1998, **27**, 43.
206. G. Jaouen, S. Top, A. Vessieres, and R. Alberto, *J. Organomet. Chem.*, 2000, **600**, 23.
207. F. Le Bideau, M. Salmain, S. Top, and G. Jaouen, *Chem. Eur. J.*, 2001, **7**, 2289.
208. R. Schibli and P. A. Schubiger, *Eur. J. Nucl. Med.*, 2002, **29**, 1529.
209. K. Severin, R. Bergs, and W. Beck, *Angew. Chem., Int. Ed. Engl.*, 1998, **37**, 1635.
210. G. Jaouen, A. Vessieres, and I. S. Butler, *Acc. Chem. Res.*, 1993, **26**, 361.
211. G. Jaouen, S. Top, A. Vessieres, P. Pigeon, G. Leclercq, and I. Laios, *Chem. Commun.*, 2001, 383.
212. S. Top, E. B. Kaloun, S. Toppi, A. Herrbach, M. J. McGlinchey, and G. Jaouen, *Organometallics*, 2001, **20**, 4554.
213. F. Minutolo and J. A. Katzenellenbogen, *Angew. Chem., Int. Ed. Engl.*, 1999, **38**, 1617.
214. J. Wald, R. Alberto, K. Ortner and L. Candreia, *Angew. Chem., Int. Ed. Engl.*, 2001, **40**, 3062.

215. R. R. Cesati, G. Tamagnan, R. M. Baldwin, S. S. Zoghbi, R. B. Innis, N. S. Kula, R. J. Baldessarini, and J. A. Katzenellenbogen, 2002, **13**, 29.

216. C. M. Jung, W. Kraus, P. Leibnitz, H. J. Pietzsch, J. Kropp, and H. Spies, *Eur. J. Inorg. Chem.*, 2002, 1219.

217. J. K. Pak, P. Benny, B. Spingler, K. Ortner, and R. Alberto, *Chem.-Eur. J.*, 2003, **9**, 2053.

218. J. Petrig, R. Schibli, C. Dumas, R. Alberto, and P. A. Schubiger, *Chem.-Eur. J.*, 2001, **7**, 1868.

219. T. Uehara, M. Koike, H. Nakata, S. Miyamoto, S. Motoishi, K. Hashimoto, N. Oku, M. Nakayama, and Y. Arano, *Nucl. Med. Biol.*, 2003, **30**, 327.

Rhodium: Inorganic & Coordination Chemistry

Fred H. Jardine
Washington State University, Pullman, WA, USA

1	Introduction	1
2	The Element and its Binary Compounds	2
3	The Lower Oxidation States	5
4	Rhodium(I) Complexes	5
5	Rhodium(II) Complexes	12
6	Rhodium(III) Complexes	15
7	The Higher Oxidation States	27
8	Nitrosyl Complexes	27
9	Related Articles	29
10	References	29

Glossary

Aqua regia: literally 'royal water', so called because it will dissolve gold; a mixture of three parts concentrated hydrochloric acid to one part concentrated nitric acid
Corundum structure: α-aluminum oxide structure
Electrochemical oxidation: oxidation of a solute by passing a direct electrical current through its solution (e.g. chlorine is produced industrially by the electrochemical oxidation of the chloride ion)
Ilmenite structure: the structure of the mineral $FeTiO_3$
Metathetical reaction: a common type of reaction, also known as a double decomposition reaction, in which the anions and cations of the reactants are interchanged in the products (e.g. $AX + BY \leftarrow AY + BX$)
Perovskite structure: the structure of the mineral $CaTiO_3$
Platinum metals: the six platinum metals are ruthenium, rhodium, palladium, osmium, iridium, and platinum
Radiolysis: decomposition of a compound by ionizing radiation such as X- or γ-rays or α-particles
Rutile structure: the structure of the mineral rutile, a form of TiO_2
Spinel structure: the structure of the mineral spinel, $MgAl_2O_4$
Zone refining: a modern method of refining where a narrow ring furnace melts a thin disk in a vertical rod of impure material under an inert atmosphere. Impurities are more soluble in the melt, and as the ring furnace traverses the rod the impurities are swept to the end for eventual discard. The process may be repeated until the desired degree of purity has been achieved

Abbreviations

cyclen = 1,4,7,10-tetraazacyclododecane; $C_8H_20N_4$; dmppe = 1,2-bis[methyl(phenyl)phosphino]ethane; MePhP$(CH_2)_2$PMePh; dpav = (Z)-1,2-bis(diphenylarsino)ethylene; $Ph_2AsCH{=}CHAsPh_2$; dppe = 1,2-bis(diphenylphosphino)ethane; $Ph_2PCH_2CH_2PPh_2$; dppm = *bis*(diphenylphosphino)methane; $Ph_2PCH_2PPh_2$; dppp = 1,3-bis(diphenylphosphino)propane $Ph_2P(CH_2)_3PPh_2$; dppv = (Z)-1,2-bis(diphenylphosphino)ethylene; $Ph_2PCH = CHPPh_2$; pz = pyrazolyl; $\Re$ = cross-linked polystyrene resin; res^+ = cross-linked polystyrene anion-exchange resin; tacn = 1,4,7-triazacyclononane; $C_6H_{15}N_3$; taud = 1,4,8,11-tetraazaundecane; $C_7H_{20}N_4$.

1 INTRODUCTION

Rhodium, a relatively rare and expensive metal, is hard, lustrous, high melting, and difficult to work. It is also resistant to chemical attack and its nobility is reflected both in the small number of binary compounds it forms and the ease with which several of these revert to the element.

The main application of rhodium is the production of catalytic alloys with other platinum metals. These alloys are used to reduce the emission of pollutants from automobile exhausts and to catalyze the formation of nitric acid from ammonia.

Despite its few binary compounds, the element gives rise to many complexes. Table 1 indicates the diversity of complexes formed. Several low oxidation state complexes of the element are important homogeneous catalysts, particularly in the oligomerization, isomerization, *Hydrogenation*, *Hydroformylation*, *Hydroboration*, or *Hydrosilation* of alkenes. Iodorhodium complexes catalyze the industrial-scale carbonylation of methanol to acetic acid.

Rhodium compounds are somewhat toxic and have been used in oncological chemotherapy, but they are less effective than platinum complexes. The expense and rarity of rhodium means that it is rarely a significant pollution hazard, particularly as it is of low inherent toxicity. The occupational exposure limit to dust is $1 mg m^{-3}$ and the LD_{50} for oral ingestion is $200\,mg\,kg^{-1}$ for several species. At these levels, rhodium and its compounds exhibit weak carcinogenicity and adverse reproductive effects have been observed.[1] Nevertheless, rhodium dust and water-soluble rhodium compounds are now found at roadsides as a result of erosion of automobile emission control catalysts.

The inorganic chemistry of rhodium is concerned principally with the complexes in which the element exhibits the oxidation states of I, II, or III, of which Rh^{III} is most common. Oxidation states of $-$I, 0, IV, and V are rare.

Table 1 Representative rhodium complexes

Oxidation state	d^n	Typical ligands	Examples	Geometry	Comments
−I	d^{10}	PF_3	$[Rh(PF_3)_4]$	Tetrahedral	Rare
0	d^9	PF_3	$[Rh_2(PF_3)_8]$	Linked TBP	Very rare
I	d^8	PR_3	$[RhCl(PPh_3)_3]$	Square planar[a]	Ubiquitous
		dppe	$[Rh(dppe)_2]X$	Square planar	Uncommon
		H, PR_3	$[RhH(PPh_3)_4]$	Monocapped tetrahedron	Common
		$P(OAr)_3$	$[Rh\{P(OAr)_3\}_5]X$	TBP	Uncommon
II	d^7	Cl, PR_3	$[RhCl_2(PCy_3)_2]$	Square planar	Rare
		$RCO_2{}^-$, L	$[Rh(O_2CR)_2py]_2$	Lantern[b]	Common
III	d^6	H, PR_3	$[RhH_2Cl(PPh_3)_2]$	Square pyramid	Uncommon
		NH_3, H_2O,	$[Rh(NH_3)_6]^{3+}$	Octahedral	Ubiquitous
		Cl, Br	$[RhCl_6]^{3-}$		
		ox^{2-}, en	$[Rh(ox)_3]^{3-}$		
IV	d^5	F, Cl	$[RhF_6]^{2-}$	Octahedral	Rare
V	d^4	F	$[RhF_6]^-$	Octahedral	Very rare

[a] Distorted. [b] Octahedrally coordinated rhodium.

Rhodium(III) complexes typically contain ammine, halo, or aqua ligands, or the important bidentate ligands 1,2-diaminoethane (en), oxalato, or pentane-2,4-dionato (acac) and are invariably octahedral. Their wide variety is in part a reflection of the slow reactions, which take place at the low-spin d^6 centers, which allow many intermediates, and geometrical or chiral isomers, to be isolated. It is fairly difficult to oxidize rhodium(III) complexes, but they may be reduced to rhodium(I) species in the presence of suitable ligands. However, there is little current work being carried out on the classical rhodium(III) complexes and even less on the higher oxidation states.

The $+1$ oxidation state has gained importance in the 40 years since its catalytic properties were discovered (*see* ***Rhodium: Organometallic Chemistry***). All isolable Rh^I complexes contain at least one *π-Acid Ligand*, which serves to protect the complexes against aerial oxidation or disproportionation. Reaction of Rh^IL_4 with H_2, HCl, MeI, or Cl_2 ($= XY$) often occurs via an *Oxidative Addition* reaction, to give rise to $Rh^{III}L_4XY$. Only powerful reducing agents such as potassium amalgam are capable of reducing rhodium(I) complexes.

Dimeric carboxylato complexes comprise virtually all the examples of rhodium(II) complexes. These species, of general formula $[Rh(O_2CR)_2L]_2$, adopt the lantern structure. Four carboxylato ligands bridge the two rhodium atoms; these bridges are supplemented by a single rhodium–rhodium bond. The neutral ligands take up the axial positions to complete the octahedral coordination around the rhodium(II) ion. Apart from metathetical reactions involving either carboxylate or axial ligands, the structure is quite stable and the complexes are neither readily oxidized nor reduced.

As noted above, the other oxidation states are not well represented; the -1 and zero oxidation states are exemplified by $[Rh(PF_3)_4]^-$ and the very similar $[Rh_2(PF_3)_8]$, respectively. Apart from a few ill-defined oxo species, octahedral hexafluororhodates comprise the bulk of the rhodium(IV) and -(V) complexes isolated.

The key reviews of the inorganic chemistry of rhodium and its complexes are now over a decade old.**[2,3]** With the possible exception of Griffith's book,**[4]** earlier reviews usually predate the discovery and application of the important low oxidation state complexes. The reader is referred to these**[2–4]** for more detailed coverage and references.

2 THE ELEMENT AND ITS BINARY COMPOUNDS

2.1 Occurrence and Applications

Rhodium occurs only to the extent of 10^{-9}% in the earth's crust. Fortunately, it is not evenly distributed, but is found, alloyed with the other platinum metals, to the extent of a few ppm (several grams per tonne) in its ores. The principal locations of these ore bodies are in the Urals near Ekaterinburg (the earliest commercial source) and in the Merensky reef near Pretoria in the Republic of South Africa. The latter is the major source today. Minor sources are found in North America and Zimbabwe. Many platinum metal resources, such as that at Sudbury in Ontario, contain very little rhodium. Various other minor sources are known, and in fact the element was first isolated by Wollaston in 1804 from impure platinum of South American origin.

Rhodium is separated from the other platinum metals either by classical chemical methods or, more recently, by solvent extraction. The latter has the advantage of a more rapid separation, which is financially advantageous with such expensive materials.

The world's supply of rhodium is in approximate balance with demand with erratic releases onto the world market from Russia being counterbalanced by national and industrial stockpiles. These fluctuations in availability are reflected in the spot price, which fell from US\$64 g^{-1} at the millennium to US\$17 g^{-1} by 2001. The current price in 2004 is US\$26 g^{-1}. Of the 2002 world production of 19.0 tonnes and recovered scrap from automobile catalysts of 3.1 tonnes, over 80% was used as rhodium alloy catalysts for automobile emission reduction. The rhodium component is vital in controlling NO_x emissions and looks set to increase in order to meet higher emission control standards.

Gauzes made from a similar alloy catalyze the oxidation of ammonia to nitric acid and represent the second most important application of the metal. Rhodium dies are used in the drawing of glass fibers. Each of these applications uses about 7% of annual metal production. The traditional rhodium/platinum thermocouple or furnace winding applications or electroplating other metals to increase their tarnish resistance or decrease their electrical contact resistance now account for merely 1% of the supply. Rhodium targets in the X-ray tube of X-ray fluorescence spectrometers are probably responsible for erroneous reports of rhodium in archeological samples. Erosion of catalytic gauzes and of thermocouples at high temperatures results in substantial irrecoverable losses. Nevertheless, rhodium is routinely recovered from virtually all materials.

Rhodium compounds and complexes are also commercially important catalysts. The hydroformylation of propene to butanal (a precursor of *bis*(2-ethylhexyl) phthalate, the PVC plasticizer) is catalyzed by hydridocarbonylrhodium(I) complexes. Iodo(carbonyl)rhodium(I) species catalyze the production of acetic acid from methanol. In the fine chemical industry, rhodium complexes with chiral ligands catalyze the production of L-DOPA, used in the treatment of Parkinson's disease. Rhodium(II) carboxylates are increasingly important as catalysts in the synthesis of cyclopropyl compounds from diazo compounds.**[5]** Many of the products are used as synthetic, pyrethroid insecticides. Hexacyanorhodate(III) salts are used to dope silver halides in photographic emulsions to reduce grain size and improve gradation.

There is little doubt that the catalytic properties of low-valent rhodium compounds have provided the driving force for the rapid expansion of interest in rhodium chemistry over the last four decades.

2.2 The Element

Rhodium was named by Wollaston after its rose colored salts. The hard, silvery, lustrous metal has a specific gravity of 12.41 and crystallizes in the face-centered cubic system ($a = 3.803$ Å). Modern work implies that there is no change in structure up to the melting point of 1960–1970 °C. Despite this structure, it is difficult to cold work and the rate of work hardening is high, although less so than for either osmium or iridium. It is best worked at 1200 °C.

Modern values for its physical properties are the more reliable since rhodium is difficult to obtain in a highly pure state because of reactions with refractory containers at or near its melting point. The purest samples have been obtained by zone refining. The differing standards of purity can be seen in the range of boiling points (3700–4500 °C) quoted.

Numerous isotopes of rhodium are known, but only ^{103}Rh is stable. The short half-lives of the remainder mean that few radiochemical applications exist. The heavy isotopes of the element feature among the fission products of uranium and the transuranic elements; they can also be made by neutron irradiation. Light isotopes result from α-bombardment of the metal, and those of high neutron deficiency from bombardment by very heavy ions.

The atomic mass of the single stable isotope is 102.9055. This has a nuclear spin of 1/2, which has proved invaluable in the NMR spectrometry of its diamagnetic complexes.

The *Ground-State* electronic configuration is $[Kr]4d^8 5s^1$. The first, second, and third ionization energies are 7.46, 18.1, and 31.1 eV, respectively.

The massive metal is inert, but very finely divided forms are more reactive, absorbing large quantities of either CO or H_2. While rhodium black or rhodium sponge dissolves in aqua regia or aqueous chlorine under pressure, larger pieces must be fused with sodium hydrogen sulfate to effect dissolution.

At 600 °C the metal reacts with oxygen to form Rh_2O_3, and with chlorine at 300 °C to form $RhCl_3$. The reaction is reversed at 318 °C without lower chlorides being formed.**[6]** Tri-, tetra-, penta-, or hexafluorides are formed by allowing the metal to react with fluorine under suitable conditions. Hexafluororhodates result from the action of fluorine in admixture with either oxygen or nitrosyl fluoride upon the metal (Scheme 1).

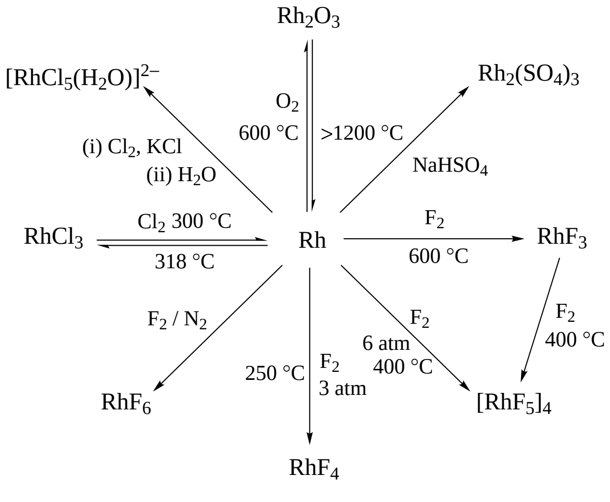

Scheme 1

Iodine vapor attacks the metal above 400 °C to form RhI_3. However, bromine gives an impure product. Pure $RhBr_3$ may be obtained by first allowing the metal to react with an HBr/Br_2 mixture and then brominating the first product at 400 °C.

2.3 Binary Compounds

The sesquioxide (Rh_2O_3) adopts the corundum structure at low temperatures and the perovskite structure at high temperatures. The latter form is usually obtained by heating the element or various compounds at 900–1000 °C. Prolonged heating of $Rh(NO_3)_3$ at 730 °C yields the low-temperature form.

If the sesquioxide is heated with oxygen under pressure, a dioxide is formed that has the rutile structure. Further heating causes reversion to the lower oxide, (equation 1).

$$Rh + O_2 \underset{1050\,°C}{\overset{600\,°C}{\rightleftharpoons}} Rh_2O_3 \underset{-O_2\ 850\,°C}{\overset{+O_2\ 35\,katm}{\rightleftharpoons}} RhO_2 \qquad (1)$$

Various 'rhodates' can be prepared by fusing Rh_2O_3 and other oxides or carbonates. The alkali metal compounds are of general formula M^IRhO_2 ($MI = Li, Na, K$). Spinels, $M^{II}Rh_2O_4$ ($M^{II} = Be, Mg, Zn, Cd, Mn$), can be made similarly, but this structure is not adopted by the alkaline-earth compounds, which are less well defined and of lower stability. Indium, yttrium, and lanthanoid rhodates, $M^{III}RhO_3$, have the perovskite structure, but $FeRhO_3$ has the ilmenite structure. Niobium or tantalum rhodates have the rutile structure.

Rhodium(III) hydroxide can be prepared by carefully treating aqueous rhodium trichloride with sodium hydroxide. A purer product can be obtained by dissolving the impure hydroxide in chloric(VII) acid and then reprecipitating the lemon-yellow hydroxide with alkali. The hydroxide is an important source of hydrated binary compounds of rhodium (Scheme 2).

The rhodium/sulfur system is complex and the best defined sulfide is the black Rh_2S_3. This compound can be prepared by heating rhodium and sulfur and subliming the product at 1100 °C.

Similar complexities are found in the Rh/Z ($Z = P$, As) systems, where the RhZ_3 phases have been found to crystallize with the cobalt triarsenide structure.

As we saw in Section 2.2, the halides are usually prepared by direct interaction of the elements. All four trihalides are known, together with the tetra-, penta-, and hexafluorides. No lower, binary halides are known.

The anhydrous trichloride, obtained by direct combination of the elements is of little use as a starting material for

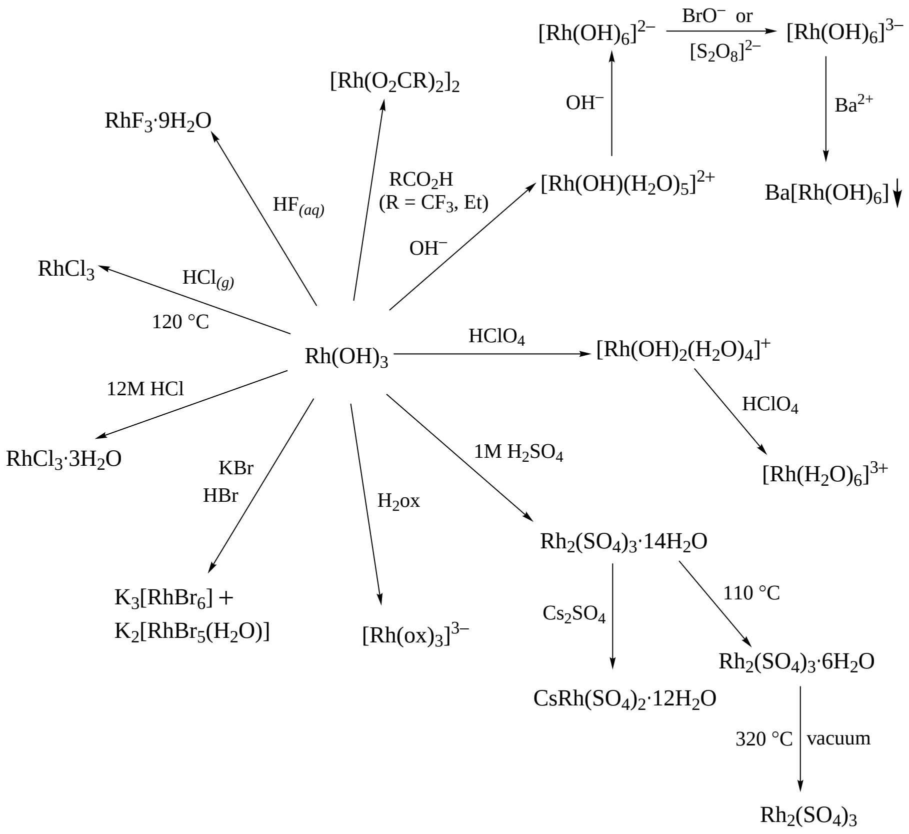

$[Rh(OH)_6]^{2-}$
BrO^- or
$[S_2O_8]^{2-}$
$[Rh(OH)_6]^{3-}$
$[Rh(O_2CR)_2]_2$
$RhF_3·9H_2O$
OH^-
Ba^{2+}
$HF_{(aq)}$
RCO_2H
($R = CF_3$, Et)
$[Rh(OH)(H_2O)_5]^{2+}$
$Ba[Rh(OH)_6]\downarrow$
OH^-
$RhCl_3$
$HCl_{(g)}$
120 °C
$Rh(OH)_3$
$HClO_4$
$[Rh(OH)_2(H_2O)_4]^+$
12M HCl
$HClO_4$
$RhCl_3·3H_2O$
KBr
HBr
1M H_2SO_4
$[Rh(H_2O)_6]^{3+}$
H_2ox
$Rh_2(SO_4)_3·14H_2O$
110 °C
$K_3[RhBr_6]$ +
$K_2[RhBr_5(H_2O)]$
Cs_2SO_4
$[Rh(ox)_3]^{3-}$
$Rh_2(SO_4)_3·6H_2O$
$CsRh(SO_4)_2·12H_2O$
320 °C
vacuum
$Rh_2(SO_4)_3$

Scheme 2

the preparation of other rhodium compounds since it is insoluble. To obtain a more synthetically useful trichloride, finely divided rhodium is ground with NaCl and the mixture chlorinated at 550 °C. Leaching the product with water yields $Na_2[RhCl_5(H_2O)]$ (equation 2), from which $Rh(OH)_3$ may be precipitated by careful addition of alkali. Dissolution of the hydroxide in the minimum quantity of 12 M HCl produces a dark red material approximating to $RhCl_3{\cdot}3H_2O$ upon evaporation to dryness. This is the source of nearly all rhodium compounds and complexes (Scheme 3). Additionally, it reacts with CO or alkenes to provide the starting materials for a host of organometallic compounds.

$$\mathrm{Rh} + \mathrm{NaCl} \xrightarrow[(ii)\mathrm{H_2O}]{(i)\mathrm{Cl_2}\ 550\,^\circ\mathrm{C}} \mathrm{K_2[RhCl_5(H_2O)]} \qquad (2)$$

3 THE LOWER OXIDATION STATES

Apart from the many carbonyls, very few complexes exist in the lowest oxidation state Rh−I, and its chemistry is essentially that of the tetrahedral anion $[Rh(PF_3)_4]^-$. This ligand also gives rise to a rare, authentic example of a noncarbonyl rhodium(0) complex. Orange–red, dimeric $[Rh_2(PF_3)_8]$ contains a rhodium–rhodium bond and has trigonal bipyramidal geometry around each metal atom. It can be reduced to $[Rh(PF_3)_4]^-$, which is isoelectronic with tetrahedral $[Co(CO)_4]^-$. The PF_2NMe_2 analog of the anionic complex is known. Reports of (triphenylphosphine)rhodium(0) complexes should be treated with caution, although $[Rh(dppe)_2]$ can be generated electrochemically. Some reactions of these complexes are shown in Scheme 4. Their characteristic property is their ability to form bonds between rhodium and the Group 14 elements.

4 RHODIUM(I) COMPLEXES

The outstanding feature of rhodium(I) chemistry is the general tendency to prefer four coordination to five. Very few five-coordinate, 18-electron complexes of general formula $[RhXL_4]$ or $[RhL_5]X$ have been prepared. The vast majority of rhodium(I) complexes are four-coordinate, 16-electron species. Some are important homogeneous catalysts for a variety of processes including hydrogenation, hydroformylation, homologation, hydrosilation, hydroboration, isomerization, or decarbonylation. The complexes are aided in their catalytic activity by their facile oxidation to rhodium(III) species which in turn undergo *Reductive Elimination* reactions, thus closing the catalytic cycles. Their potential catalytic applications have led to many new rhodium(I) complexes being prepared over the last 25 years.

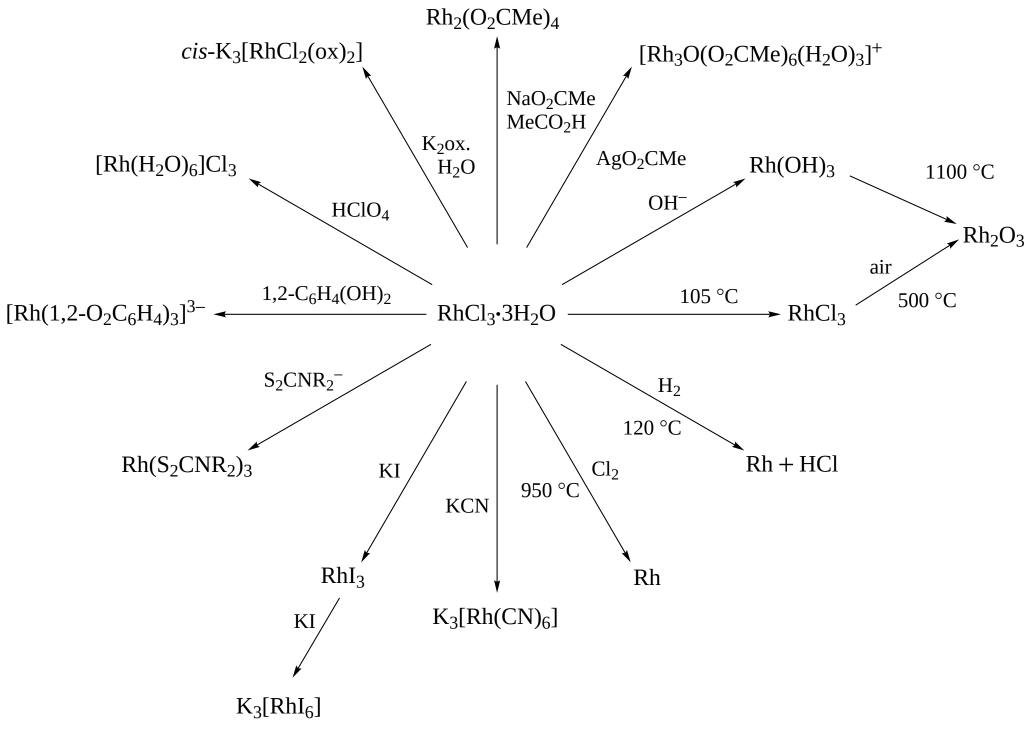

Scheme 3

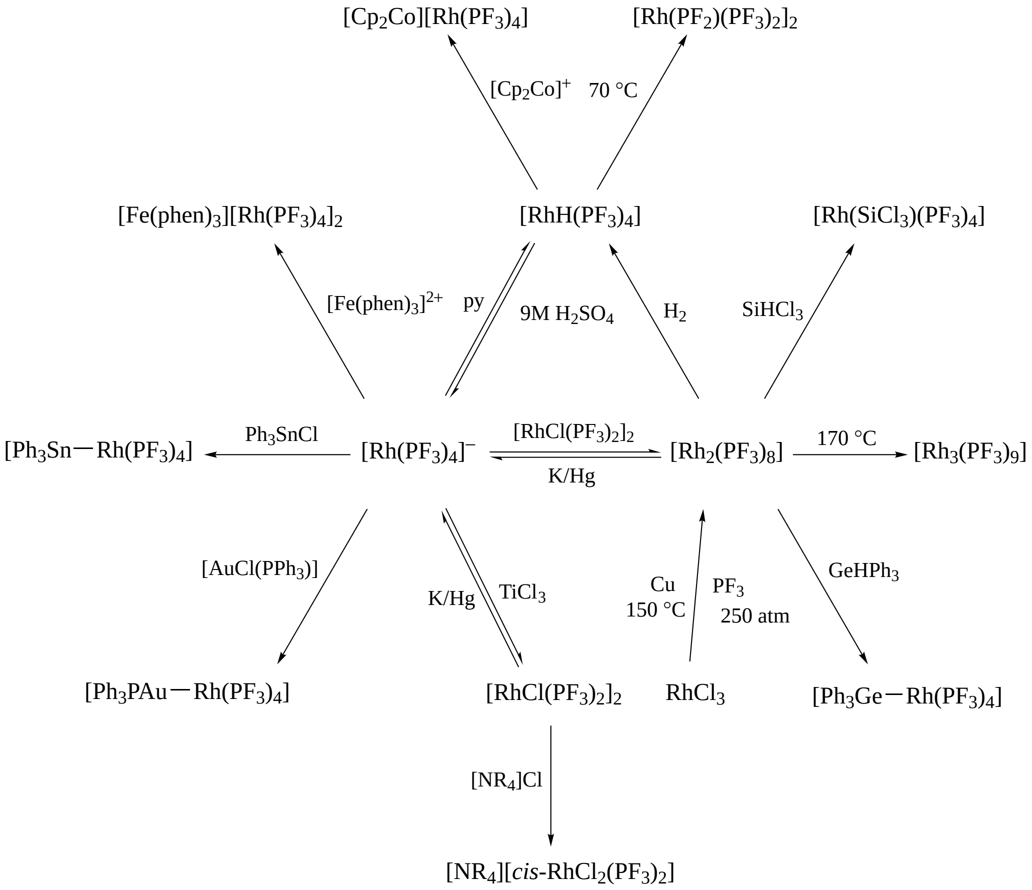
[Cp2Co][Rh(PF3)4]
[Rh(PF2)(PF3)2]2
[Cp2Co]+
70 °C
[Fe(phen)3][Rh(PF3)4]2
[RhH(PF3)4]
[Rh(SiCl3)(PF3)4]
[Fe(phen)3]2+
py
9M H2SO4
H2
SiHCl3
[Ph3Sn—Rh(PF3)4]
Ph3SnCl
[Rh(PF3)4]−
[RhCl(PF3)2]2
K/Hg
[Rh2(PF3)8]
170 °C
[Rh3(PF3)9]
[AuCl(PPh3)]
K/Hg
TiCl3
Cu
150 °C
PF3
250 atm
GeHPh3
[Ph3PAu—Rh(PF3)4]
[RhCl(PF3)2]2
RhCl3
[Ph3Ge—Rh(PF3)4]
[NR4]Cl
[NR4][cis-RhCl2(PF3)2]

Scheme 4

Stable rhodium(I) complexes usually require the presence of at least one π-acid ligand. The presence of bulky π-acid ligands tends to lead to coordinative unsaturation by ligand dissociation, which can enhance the catalytic activity. Tertiary phosphines meet both these requirements and have the added advantage of conferring solubility in organic solvents.

Although most rhodium(I) complexes in this section contain tertiary phosphines, there is an extensive chemistry of rhodium(I) with alkene or carbonyl ligands.

Anionic complexes are rare: there are a few containing PF_3 ligands and still fewer with PPh_3 ligands, and $SnCl_3^-$ forms the dimeric complex $[RhCl(SnCl_3)_2]_2^{4-}$.

4.1 Tricoordinate Complexes

All the isolable tricoordinate complexes such as $[RhX(PCy_3)_2]$ ($X = F, Cl, Br, I, N_3$), prepared via metathetical reactions of $[RhF(cod)]_2$, contain very large tertiary phosphine ligands. These complexes resemble transient intermediates in catalytic cycles. Triphenylphosphine complexes containing the large anionic ligands $N(SiMe_3)_2$ and $N{=}C(CF_3)_2$ are also known.

The 14-electron complexes are highly reactive and decompose even when stored in an inert atmosphere. They readily bind an additional small ligand. In particular, they react with dinitrogen under mild conditions. However, the dinitrogen ligand is easily lost and this property has been exploited in the preparation of other tricoordinate complexes (equations 3–5).

$$[RhF(cod)]_2 + 4PCy_3 \longrightarrow 2[RhF(PCy_3)_2]_2 \xrightarrow{NaX} [RhX(PCy_3)_2] \quad (X = Cl, Br, I, N_3) \tag{3}$$

$$[RhX(PCy_3)_2] + L \longrightarrow [RhX(PCy_3)L] + PCy_3 \quad (X = Cl, L = SO_2; X = Cl, Br, I, L = N_2) \tag{4}$$

$$[RhH(N_2)(PR_3)_2] \longrightarrow [RhH(PR_3)_2] + N_2 \quad (R_3 = Bu^t{}_3, Bu^t{}_2Ph) \tag{5}$$

$$[RhCl(PPh_3)_3] + Tl[ClO_4] \longrightarrow [Rh(PPh_3)_3][ClO_4] \tag{6}$$

There are several salts containing the $[Rh(PPh_3)_3]^+$ cation, such as the perchlorate, which can be obtained from

$[RhCl(PPh_3)_3]$ and $TlClO_4$ (equation 6). Another can be prepared similarly from $Tl[\textit{nido}\text{-}7\text{-}\{1\text{-}\textit{closo}\text{-}1,2\text{-}C_2B_{10}H_{11}\}\text{-}7,8\text{-}C_2B_9H_{11}]$. The crystal structures of the above complexes have been determined and both contain distorted T-shaped cations. The Rh–P bonds in the dicarbaborane complex are the longer.

The fluorocarbon acids $H_2C(SO_2CF_3)_2$, $PhCH(SO_2CF_3)_2$, $HN(SO_2CF_3)_2$, $H_2C(SO_2C_8F_{17})_2$, or $C_8F_7SO_3H$ also yield the appropriate $[Rh(PPh_3)_3]X$ salt when they react with hydridotetrakis(triphenylphosphine)rhodium(I). The stereochemically nonrigid cation readily coordinates an additional ligand.

4.2 Four-coordinate Complexes

This is by far the most populous subgroup of rhodium(I) complexes. The vast majority have the general formula $[RhXL_3]$, but two minor types also exist. The first contains a bidentate acido ligand; the second has bridging acido ligands. The complexes of bidentate acido ligands usually have rhodium bound to the two oxygen or sulfur atoms of the ligand, although some complexes of monothioanions are known where these ligands bind additionally through oxygen, nitrogen, or phosphorus. The complexes may be prepared either by cleaving bridged complexes (with or without bridge metathesis) or, more usually, by expelling the acido ligand and one neutral ligand from one of the numerous $[RhXL_3]$ complexes (equations 7–10).

$$[Rh(acac)L_2]_2 + 4PR_3 \longrightarrow 2[Rh(acac)(PR_3)_2] + 4L$$
$$(L = C_2H_4,\ R_3 = Ph_3,\ Ph_2Me;\ L = C_8H_{14},\ R_3 = F_2NEt_2,\ F(NMe_2)_2) \qquad (7)$$

$$[Rh(acac)(CO)_2] + 4PR_3 \longrightarrow [Rh(acac)(PR_3)_2] + 2CO$$
$$(R_3 = F_2NEt_2,\ F(NMe_2)_2) \qquad (8)$$

$$[RhXL_2]_2 + 2acacH \longrightarrow 2[Rh(acac)L_2] + 2HX$$
$$(X = Cl,\ Br,\ L = P(OPh)_3;\ X = Cl,\ L = PF_2NEt_2) \qquad (9)$$

$$[RhCl(PPh_3)_3] + M^IS_2Y \longrightarrow [Rh(S_2Y)(PPh_3)_2] + PPh_3 + M^ICl$$
$$(Y = PCy_2,\ P(OPh)_2,\ CNMe_2) \qquad (10)$$

There are many examples of dimeric complexes containing bridging halo ligands. Phosphorus ligands of high π-acidity tend to form complexes of this type. Their presence so lowers the electron density on the metal that a second, weakly nucleophilic, halo ligand is coordinated. Ligands of lower π-acidity tend to cleave the bridged starting materials, particularly when present in excess. Dimeric alkene or carbonyl complexes are frequently used as the starting materials to prepare this type of complex, in which case the organo ligands are displaced in the following order: ethylene > cycloocta-1,5-diene > carbonyl. This order also reflects the variety of complexes that can be prepared from each precursor (equations 11–13).

$$RhCl_3\cdot 3H_2O + PAr_3 \xrightarrow[78\,^\circ C]{EtOH} [RhCl(PAr_3)_2]_2$$
$$(Ar_3 = (C_6F_5)_3,\ Ph_2(C_6F_5),\ (C_6Cl_5)_3) \qquad (11)$$

$$[RhClL_2]_2 + 4L' \longrightarrow [RhClL'_2]_2 + 4L$$
$$(L = C_2H_4;\ L' = P(4\text{-}C_6H_4Me)_3,\ PPh_2\{CH_2CH_2SiMe(OMe)_2\},\ PF_2NMe_2,\ PF_2NEt_2;\ L = \tfrac{1}{2}cod,\ L' = P(OMe)_3,\ P(OPh)_3,\ PF_2(OPr);\ L = CO,\ L' = PF_3,\ P(OPh)_3,\ P(4\text{-}OC_6H_4Me)_3,\ P(4\text{-}OC_6H_4Cl)_3) \qquad (12)$$

$$2[RhCl(PAr_3)_3] \underset{+PAr_3}{\overset{C_6H_6\ 80\,^\circ C}{\rightleftharpoons}} [RhCl(PAr_3)_2]_2 + 2PAr_3$$
$$(Ar = Ph,\ 4\text{-}C_6H_4Me) \qquad (13)$$

When $[RhH(PPh_3)_4]$ reacts with 4-methoxyacetophenoneanilide in dioxane, orange crystals of $[Rh(OH)(PPh_3)_2]_2$ can be isolated. The anionic complex $[RhCl(SnCl_3)_2]_2{}^{4-}$ can be prepared from tin(II) chloride and $RhCl_3\cdot 3H_2O$. It is also possible to prepare this type of complex starting from $[RhXL_3]$ complexes, since the dimeric complexes are much less soluble than the monomers. This lower solubility may also assist the preferential isolation of dimers when hydrated rhodium trichloride reacts with certain tertiary phosphines in ethanolic solution. The halo complexes can serve as the starting materials for the preparation of many other rhodium(I) complexes (Scheme 5).

The structure of several dimers has been confirmed by X-ray crystallography. Unlike $[RhCl(CO)_2]_2$, they are not strongly puckered at the bridge; indeed, the central RhO_2Rh group of $[Rh(OH)(PPh_3)_2]_2$ is planar,**[6]** as is the $RhCl_2Rh$ core of $[RhCl(PPh_3)_2]_2\cdot MeCO_2Et$.

Halo-bridged, dimeric complexes containing bidentate neutral ligands may also be prepared, usually by displacement of organo ligands from dimeric complexes either by the bidentate ligand itself (equation 14) or by hydrogenation of a diene complex (equation 15). There is one instance of rhodium trichloride being reduced to a complex of this type.

$$[RhCl(cod)]_2 + (\mathbf{1}) \longrightarrow [RhCl(\mathbf{1})]_2 + 2cod \qquad (14)$$

$$[RhL(cod)]Cl + 2H_2 \longrightarrow [RhClL]_2 + 2C_8H_{14}$$
$$(L = dppe,\ DIOP,\ \mathbf{2}) \qquad (15)$$

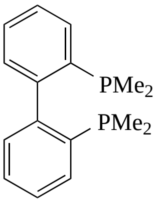

(1)

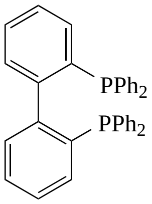

(2)

The $[RhXL_3]$ species are easily the most important rhodium(I) complexes because of the exceptional catalytic

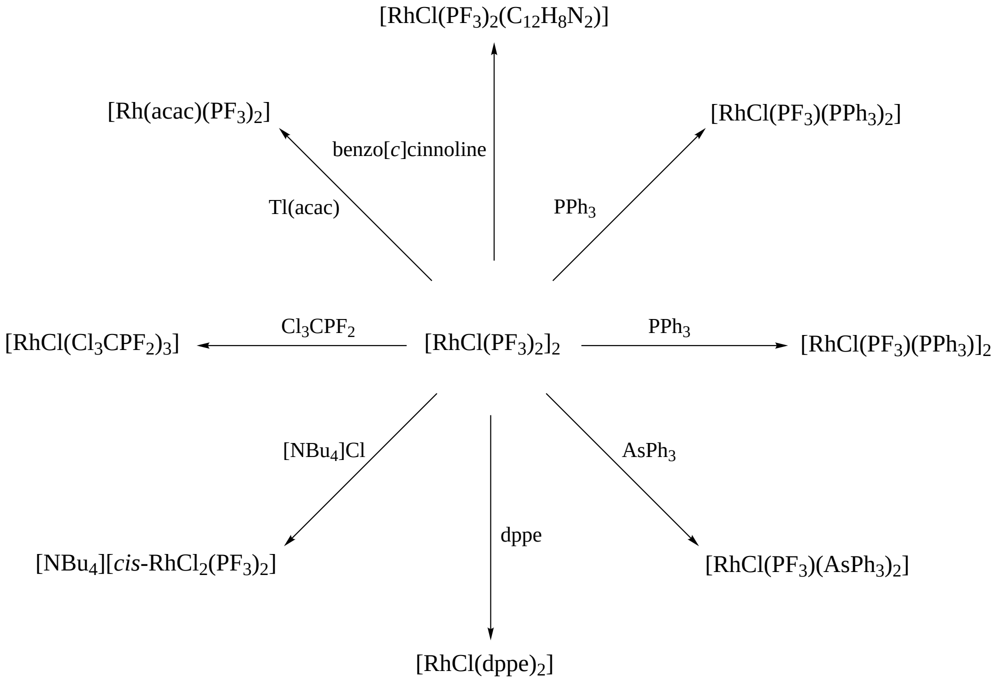

Scheme 5

properties of *Wilkinson's Catalyst*, [RhCl(PPh$_3$)$_3$], the first successful homogeneous hydrogenation catalyst for alkenes and alkynes. It was later shown to be effective for hydrosilation and decarbonylation reactions.[7]

Of the many different preparative methods known, the standard preparation of [RhCl(PPh$_3$)$_3$] is not of wide applicability to other phosphines (equation 16). The best general method for RhX(QR$_3$) (Q = P, As, Sb) is by displacement of alkene ligands from dimeric rhodium(I) complexes (equation 17). This method also avoids using rare and expensive tertiary phosphines as mere reductants.

$$\mathrm{RhCl_3{\cdot}3H_2O + 6PPh_3 \xrightarrow[N_2]{\text{EtOH } 78\,^\circ C} [RhCl(PPh_3)_3] + OPPh_3} \qquad (16)$$

$$\mathrm{[RhClL_2]_2 + 6L' \longrightarrow [RhClL'_3] + 4L}$$
$$\mathrm{(L = C_2H_4;\ L' = PPh_3,\ P(4\text{-}C_6H_4OMe)_3,\ P(4\text{-}C_6H_4F)_3,\ P(4\text{-}C_6H_4Me)_3,}$$
$$\mathrm{PHPh_2,\ PPh_2(CH_2CH_2SiCl_3),\ PPh_2Me,\ PPh_2Et,\ PPh_2(C_8H_{16}SiCl_3),}$$
$$\mathrm{PPh(C_4H_8NO)_2,\ PPh(C_5H_{10}N_2),\ \mathbf{3},\ \mathbf{4},\ PF_2NMe_2,\ AsEtPH_2,\ SPPh_3;}$$
$$\mathrm{L = C_8H_{14},\ L' = PF(NMe_2)_2,\ P(4\text{-}C_6H_4OMe)_3,\ P(4\text{-}C_6H_4Cl)_3)} \qquad (17)$$

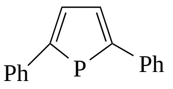

(3)

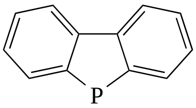

(4)

In addition to being a powerful and versatile catalyst, [RhCl(PPh$_3$)$_3$] is also the starting point for the preparation of numerous analogs that can be obtained by metathetical reactions. Schemes 6 and 7 show some replacement reactions of the chloro and triphenylphosphine ligands. Despite the $4d^8$ electronic configuration, these rhodium(I) complexes are seldom exactly square planar.

Tetrahydroborate or other hydridic anions produce [RhH(PPh$_3$)$_3$], widely used by Robinson's group as the starting point for the preparation of carboxylato and other complexes (equation 18). The IR spectra of [Rh(O$_2$CR)(PPh$_3$)$_3$] show that the carboxylate is monodentate and therefore Rh is four–coordinate; this has been confirmed by X-ray crystallography for the benzoate.

$$\mathrm{[RhH(PPh_3)_4] + RCO_2H \longrightarrow [Rh(OCOR)(PPh_3)_3] + H_2 + PPh_3}$$
$$\mathrm{(R = Me,\ Et,\ 4\text{-}C_6H_4NO_2,\ 4\text{-}C_6H_4Cl)} \qquad (18)$$

When neutral ligands replace PPh$_3$ in [RhCl(PPh$_3$)$_3$], the incoming ligand usually replaces the triphenylphosphine ligand trans to the chloro ligand (Scheme 7). Several of the complexes which can be prepared from [RhCl(PPh$_3$)$_3$] exhibit interesting structures, few more so than the *trans*-[RhCl(PPh$_3$)$_2$(P$_4$)] complex (**5**), which contains an η^2-tetrahedral P$_4$ ligand.

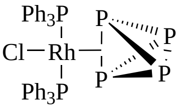

(5)

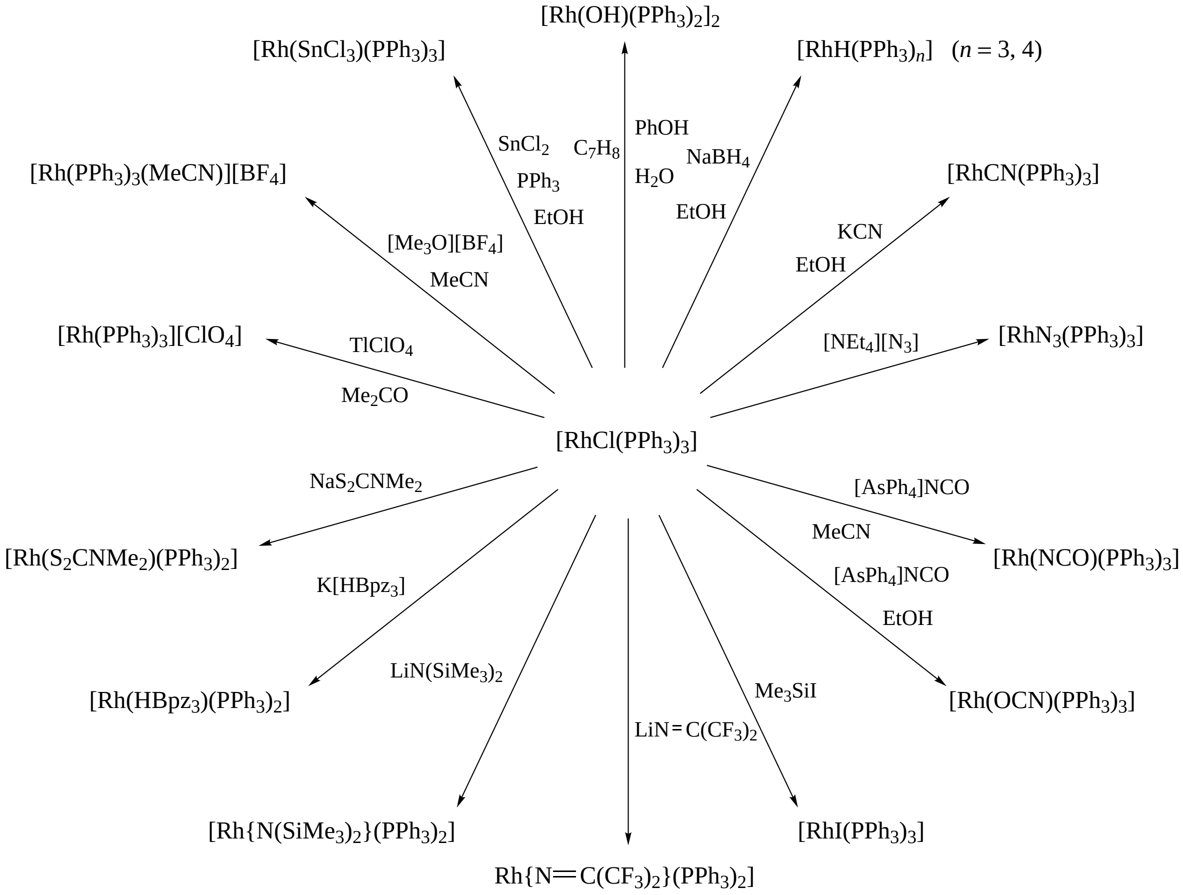
[Rh(OH)(PPh3)2]2
[Rh(SnCl3)(PPh3)3]
[RhH(PPh3)n] (n = 3, 4)
SnCl2
PPh3
EtOH
C7H8
PhOH
H2O
NaBH4
EtOH
[Rh(PPh3)3(MeCN)][BF4]
[RhCN(PPh3)3]
[Me3O][BF4]
MeCN
KCN
EtOH
[Rh(PPh3)3][ClO4]
TlClO4
Me2CO
[NEt4][N3]
[RhN3(PPh3)3]
[RhCl(PPh3)3]
NaS2CNMe2
[AsPh4]NCO
[Rh(S2CNMe2)(PPh3)2]
K[HBpz3]
MeCN
[AsPh4]NCO
[Rh(NCO)(PPh3)3]
EtOH
LiN(SiMe3)2
[Rh(HBpz3)(PPh3)2]
Me3SiI
[Rh(OCN)(PPh3)3]
LiN=C(CF3)2
[Rh{N(SiMe3)2}(PPh3)2]
[RhI(PPh3)3]
Rh{N=C(CF3)2}(PPh3)2]

Scheme 6

The PX=C(SiMe$_3$)$_2$ ligands (X = F, Cl) form η^1-complexes upon reaction with [RhCl(PPh$_3$)$_3$] in toluene solution. This contrasts with their reactions with d^{10} Ni^0 or Pt^0 species, where both oxidative addition and η^2-coordination may occur.

Another noteworthy species is [Rh(PPh$_3$)$_3$MeCN]$^+$, which can be prepared from [Rh$_2$(O$_2$CMe)$_2$(MeCN)$_6$][BF$_4$]$_2$ (equation 19). Although MeCN is normally a good leaving group, it is retained in some reactions (equation 20).

$$[\mathrm{Rh_2(O_2CMe)_2(MeCN)_6][BF_4]_2} + \mathrm{PPh_3} \longrightarrow \\ [\mathrm{Rh(PPh_3)_3(MeCN)][BF_4]} \qquad (19)$$

$$[\mathrm{Rh(PPh_3)_3(MeCN)}]^+ + \mathrm{P(OMe)_3} \longrightarrow \\ trans\text{-}[\mathrm{Rh(PPh_3)_2(MeCN)\{P(OMe)_3\}}]^+ + \mathrm{PPh_3} \qquad (20)$$

Replacement of PPh$_3$ by other tertiary phosphines can give important catalysts. Water-soluble analogs of [RhCl(PPh$_3$)$_3$] can be prepared by replacing all three PPh$_3$ ligands by Na[PPh$_2$(3-C$_6$H$_4$SO$_3$)$_3$] or Na$_3$[P(3-C$_6$H$_4$SO$_3$)$_3$]· xH$_2$O. These complexes find application in the hydrogenation of biologically important substrates, and also exhibit antitumor activity. One major problem in homogeneous catalysis is separating the catalyst from the product. This can be overcome by preparing a heterogenized catalyst, which may be achieved by binding a RhCl(PPh$_3$)$_2$ residue to a – PPh$_2$ group attached to a macromolecular support. Typical supports have included cross-linked polystyrene resins or silica. A recent development is the preparation of complexes containing fluorinated tertiary phosphine ligands for use in biphasic catalytic systems.

The mixed anhydrides of diphenylphosphinous acid and heavily substituted alkenoic acids displace one PPh$_3$ ligand from [RhCl(PPh$_3$)$_3$] to form a complex where the anhydride is coordinated through phosphorus. If these products are treated with thallium(I) or silver(I) salts, the anhydride coordinates additionally through the carbonyl oxygen and the chloro ligand is displaced.

There are relatively few complexes of the stoichiometry [RhL$_4$]X. Most of these contain small tertiary phosphines and anions of low coordinating power. The complexes of secondary phosphines are much in evidence and tertiary phosphite complexes are also known.

Much studied recently, [Rh(PMe$_3$)$_4$]Cl owes much of its reactivity to the facile loss of a PMe$_3$ ligand. The other

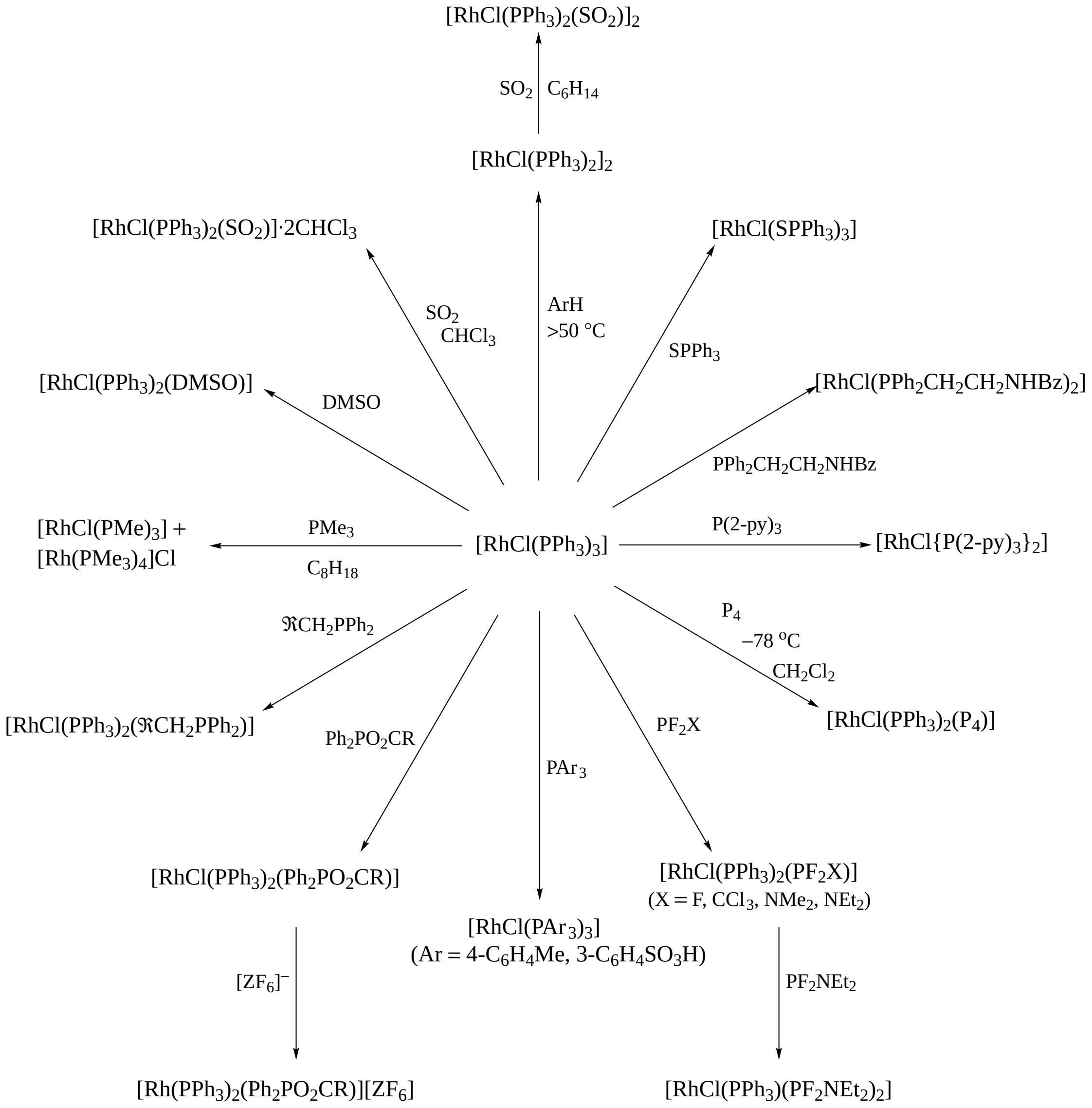

[RhCl(PPh3)2(SO2)]2
SO2 C6H14
[RhCl(PPh3)2]2
[RhCl(PPh3)2(SO2)]·2CHCl3
SO2 CHCl3
ArH >50 °C
[RhCl(SPPh3)3]
SPPh3
[RhCl(PPh3)2(DMSO)]
DMSO
[RhCl(PPh2CH2CH2NHBz)2]
PPh2CH2CH2NHBz
[RhCl(PMe)3] + [Rh(PMe3)4]Cl
PMe3
C8H18
[RhCl(PPh3)3]
P(2-py)3
[RhCl{P(2-py)3}2]
ℜCH2PPh2
[RhCl(PPh3)2(ℜCH2PPh2)]
P4 −78 °C CH2Cl2
[RhCl(PPh3)2(P4)]
Ph2PO2CR
PAr3
PF2X
[RhCl(PPh3)2(Ph2PO2CR)]
[RhCl(PPh3)2(PF2X)]
(X = F, CCl3, NMe2, NEt2)
[RhCl(PAr3)3]
(Ar = 4-C6H4Me, 3-C6H4SO3H)
[ZF6]−
PF2NEt2
[Rh(PPh3)2(Ph2PO2CR)][ZF6]
[RhCl(PPh3)(PF2NEt2)2]

Scheme 7

complexes are much less reactive (equations 21–23).

$$[\mathrm{RhCl(PPh_3)_3}] + 4\mathrm{PHPh_2} + \mathrm{M^IX} \xrightarrow[50\,^\circ\mathrm{C}]{\mathrm{MeOH}} [\mathrm{Rh(PHPh_2)_4}]\mathrm{X} + \mathrm{M^ICl}$$

$$(\mathrm{X} = \mathrm{BF_4, PF_6, ClO_4}) \qquad (21)$$

$$[\mathrm{Rh(PPh_3)_2(cod)}][\mathrm{PF_6}] + 10\mathrm{PR_3} \longrightarrow [\mathrm{Rh(PR_3)_4}][\mathrm{PF_6}]$$

$$(\mathrm{R_3} = \mathrm{Ph_2Me, Me_2Ph, Ph(OMe)_2}) \qquad (22)$$

$$[\mathrm{Rh(PMe_3)_4}]\mathrm{Cl} + \mathrm{KX} \longrightarrow [\mathrm{Rh(PMe_3)_3}]\mathrm{X} + \mathrm{PMe_3} + \mathrm{KCl}$$

$$(\mathrm{X} = \mathrm{BPh_4, PF_6}) \qquad (23)$$

The complexes are usually prepared by displacing ligands from other rhodium(I) complexes. Complexes containing two bidentate ligands may be prepared similarly. Additionally, simultaneous anion metathesis and ligand displacement may be employed when complexes containing poorly coordinating anions are sought.

There are numerous $[\mathrm{Rh(LL)_2}]\mathrm{X}$ complexes. Probably the most important of these are those complexes containing two chiral bidentate ligands (equations 24–26). The best known, containing the chiral ligand diop (**6**), have been widely employed in homogeneous asymmetric synthesis, where they have proved to be of increasing importance in the pharmaceutical industry (*see* ***Asymmetric Synthesis by Homogeneous Catalysis***).

$$[\mathrm{RhClL^1{}_2}]_2 + 4\mathrm{L^2} \longrightarrow 2[\mathrm{RhL^2{}_2}]\mathrm{Cl} + 4\mathrm{L^1}$$

$$(\mathrm{L^1} = \mathrm{C_8H_{14}},\ \mathrm{L^2} = \mathrm{dppm, dppp, dppb, (+)\text{-}DIOP};\ \mathrm{L^1} = \tfrac{1}{2}\mathrm{cod},$$

$$\mathrm{L^2} = \mathrm{dmppe, dppv, diars, dpav}) \qquad (24)$$

$$\mathrm{[RhCl(cod)]_2 + 4L \xrightarrow{MX} 2[RhL_2]X + 2cod + 2MCl}$$

$$\mathrm{(MX = NaBPh_4, L = Ph_2PCH_2CH_2SEt, Ph_2PCH_2CH_2SPh;}$$
$$\mathrm{MX = [NH_4][PF_6], L = (Bu^{\mathit{t}}CH_2)_2PCH_2CH_2P(CH_2Bu^{\mathit{t}});}$$
$$\mathrm{MX = Ag[PF_6], L = dmppe, dpav, diars)} \tag{25}$$

$$\mathrm{[RhCl(CO)_2]_2 + 4dpav + 2NaBF_4 \longrightarrow 2[RH(dpav)_2][BF_4] + 4CO + 2NaCl} \tag{26}$$

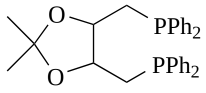
O
O
PPh$_2$
PPh$_2$

(**6**)

The reactions of $\mathrm{[Rh(dppe)_2]Cl}$ (Scheme 8) show that the major reaction is anion metathesis.

Pentacoordinate complexes adopt two stoichiometries. The neutral hydrido complexes are probably more numerous than the $\mathrm{[RhL_5]X}$ salts. The structures of the hydrido complexes are difficult to establish. X-ray crystallographic studies seldom locate the hydrido ligand and its position must be inferred from the disposition of the other ligands. In solution, ^{1}H NMR studies show the high-field line to be split into a weak multiplet by both rhodium and the phosphorus atoms present. On the evidence available, most complexes appear to have the monocapped tetrahedron structure. The phosphorus ligands found in the hydrido complexes include tertiary phosphines, ditertiary phosphines, and trialkyl phosphites. Chloro complexes are only known for small ligands of high π-acidity such as $\mathrm{PF_2(NMe_2)}$. Trialkyl phosphites appear to be the only ligands capable of forming $\mathrm{[RhL_5]^+}$ cations. This may again be due to their high π-acidity and their small *Cone Angles*. All the isolated complexes contain the large $\mathrm{[BPh_4]^-}$ counter ion, suggesting that the cations are unstable in the presence of small, polarizing anions. The white complexes can be prepared by displacement of alkene ligands from rhodium(I) complexes in the presence of $\mathrm{[BPh_4]^-}$ ions. As might be expected, the trialkyl phosphite ligands are easily lost.

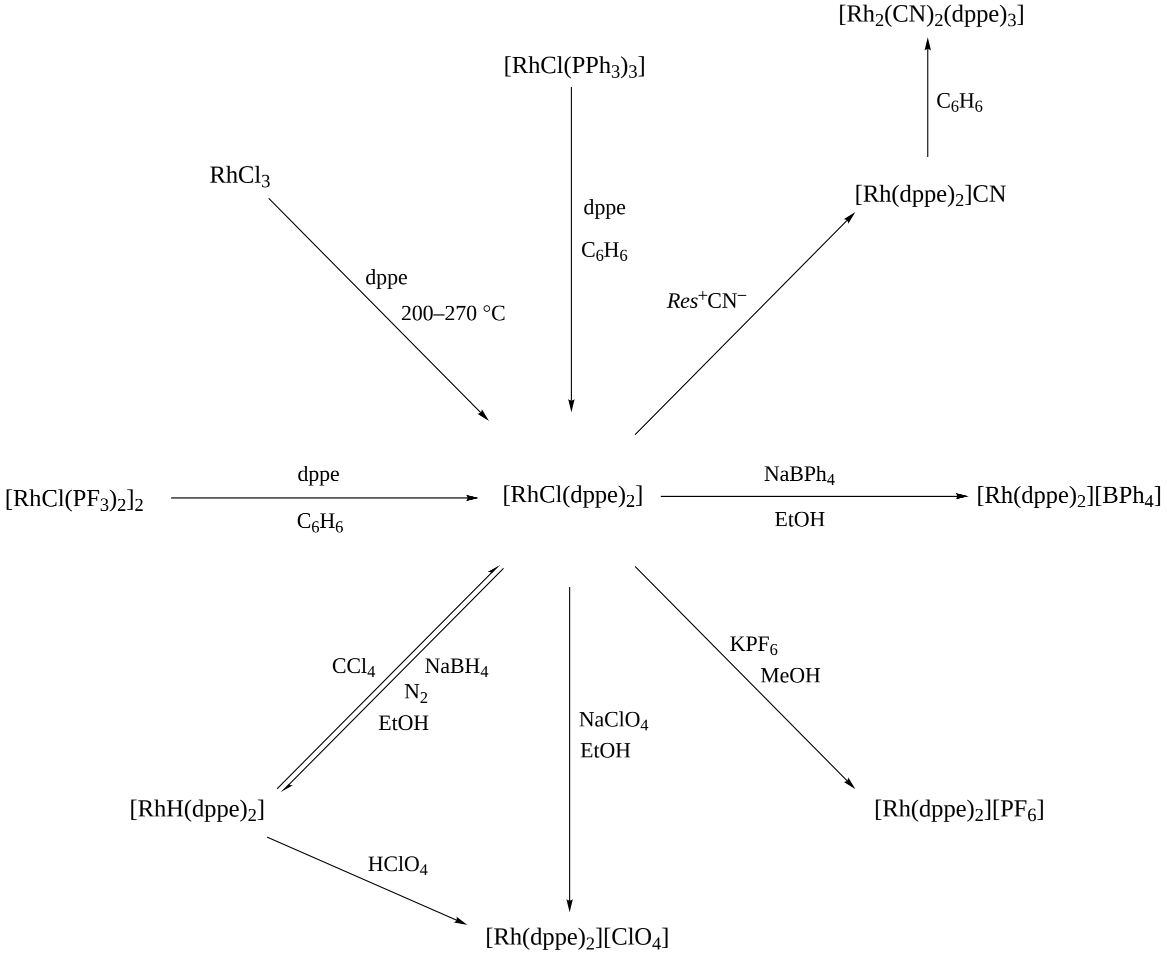
[Rh$_2$(CN)$_2$(dppe)$_3$]
[RhCl(PPh$_3$)$_3$]
C$_6$H$_6$
RhCl$_3$
[Rh(dppe)$_2$]CN
dppe
C$_6$H$_6$
dppe
200–270 °C
Res$^+$CN$^-$
[RhCl(PF$_3$)$_2$]$_2$
dppe
C$_6$H$_6$
[RhCl(dppe)$_2$]
NaBPh$_4$
EtOH
[Rh(dppe)$_2$][BPh$_4$]
CCl$_4$
NaBH$_4$
N$_2$
EtOH
KPF$_6$
MeOH
NaClO$_4$
EtOH
[RhH(dppe)$_2$]
[Rh(dppe)$_2$][PF$_6$]
HClO$_4$
[Rh(dppe)$_2$][ClO$_4$]

Scheme 8

5 RHODIUM(II) COMPLEXES

There are three types of rhodium(II) complex. By far the most common are the dimeric carboxylatorhodium(II) species. Octahedral complexes may also be generated by the radiolysis of aqueous solutions of classic rhodium(III) complexes. Square-planar complexes containing bulky tertiary phosphine ligands can be produced by careful reduction of hydrated rhodium trichloride. The chemistry of rhodium(II) differs very considerably from the well-known monomeric octahedral or tetrahedral cobalt(II) species because cobalt(II) complexes are high-spin d^7 species while rhodium(II) complexes are all low spin. No spin reorientation is required upon oxidation to rhodium(III), so monomeric rhodium(II) complexes are excellent reducing agents.

5.1 Monomeric Complexes

The complexes generated by photolysis or radiolysis of rhodium(III) precursors usually have very short lifetimes. The ammine complexes derived from radiolysis of aqueous solutions of $[RhCl(NH_3)_5]^{2+}$ are easily oxidized. The radiolysis of solutions of $[Rh(bipy)_3]^{3+}$ generates the corresponding rhodium(II) complex, which undergoes disproportionation to rhodium(III) and rhodium(I) complexes, the latter containing only two bipy ligands (equation 27).

$$[Rh(bipy)_3]^{3+} \rightsquigarrow [Rh(bipy)_3]^{2+} \xrightarrow{OH^-} \begin{array}{c}[Rh(bipy)_3]^{3+} \\ + \\ [Rh(bipy)_2]^{+}\end{array} \quad (27)$$

The best test for monomeric rhodium(II) complexes is their paramagnetism since both rhodium(I) and rhodium(III) complexes are diamagnetic. These complexes owe their stability either to the large size of the ligands or their electronic properties. Bulky ligands include porphyrins and tertiary phosphines. Typical tertiary phosphine ligands include tris(2-tolyl)phosphine, di-*t*-butyl(alkyl)phosphines, or tris(cyclohexyl)phosphine. These ligands reduce hydrated rhodium trichloride to the rhodium(II) complexes in ethanol at low temperatures (equation 28), rather than the reflux temperature required to bring about reduction to rhodium(I). Although no authentic rhodium(II) complexes containing tertiary arsines are known, tris(2-tolyl)stibine forms diamagnetic $[RhX_2\{Sb(2\text{-}C_6H_4Me)_3\}]$ complexes when it reacts with rhodium(III) halides. A dimeric structure has been proposed to account for the diamagnetism.

$$RhCl_3{\cdot}3H_2O + P(2\text{-}C_6H_4Me)_3 \xrightarrow[EtOH]{0\,^\circ C} [RhCl_2\{P(2\text{-}C_6H_4Me)_3\}_2] \quad (28)$$

Nonplanar or highly substituted Schiff bases also confer steric protection upon their rhodium(II) complexes. By contrast relatively simple thio ligands such as *N*,*N*-dialkyldithiocarbamates produce stable, square-planar rhodium(II) complexes of the type $[Rh(S_2CNR_2)_2]$ (R = Me, Et); similar anionic *bis*(maleonitriledithiolate) are also known. Neutral complexes are formed by the thiol containing amino acids cysteine, methyl cysteine, or penicillamine. It is noteworthy that these paramagnetic $[Rh(aminoacid)_2]$ complexes can easily be prepared from dimeric, diamagnetic $[Rh(O_2CMe)_2MeOH]_2$.**[8]**

5.2 Dimeric Complexes

The best-known complexes of this type are the carboxylates (**7**) and their derivatives (**8**). The four bridging carboxylato ligands are supplemented by a single rhodium–rhodium bond. The bond lengths in the cores of these structures are almost independent of the ligands present. In particular, the Rh–Rh bond length increases by only 0.08 Å upon changing the axial ligand, L, from methanol to $P(OMe)_3$ in the acetate complexes. Many other oxo-bridged dimers are known with similar Rh–Rh bond lengths. The principal reaction of the dimers is the substitution of the neutral axial ligands (Scheme 9). The propanoate reacts more rapidly than the acetate, which may partly explain its superior antitumor activity. Many different monodentate ligands can be bound to the axial sites. Oxygen donors, which form blue or green complexes, include water, the lower aliphatic alcohols, dimethyl sulfoxide, and tetrahydrofuran.

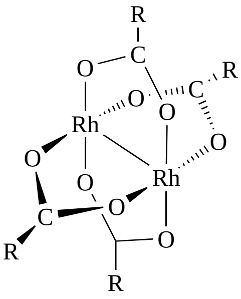

(**7**)

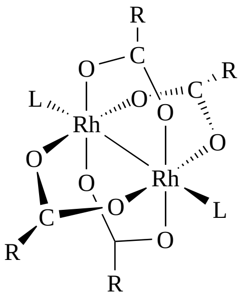

(**8**)

Thiols also bind to these sites, as does chloride ion in forming $[Rh(O_2CR)_2Cl]_2^{2-}$ anionic complexes. Nitrogenous ligands form many complexes, those of ammonia, pyridine, and both primary and secondary amines being well represented. Like the complexes of sulfur ligands, these are red or orange. Diamines also form complexes. Where the diamine geometry is favorable, for example, phenazine (**9**) or tetramethylphenylenediamine (**10**), they form polymeric chains of the type $[-LLRh(O_2CR)_4RhLLRh-]n$.

It has recently been shown that 2,2-bipyridine forms the complex (**11**). The importance of this structure is that it demonstrates the possibility of carboxylatorhodium(II) complexes acting in the same way as the well-known cisplatin (*cis*-$[PtCl_2(NH_3)_2]$) in cancer chemotherapy (*see*

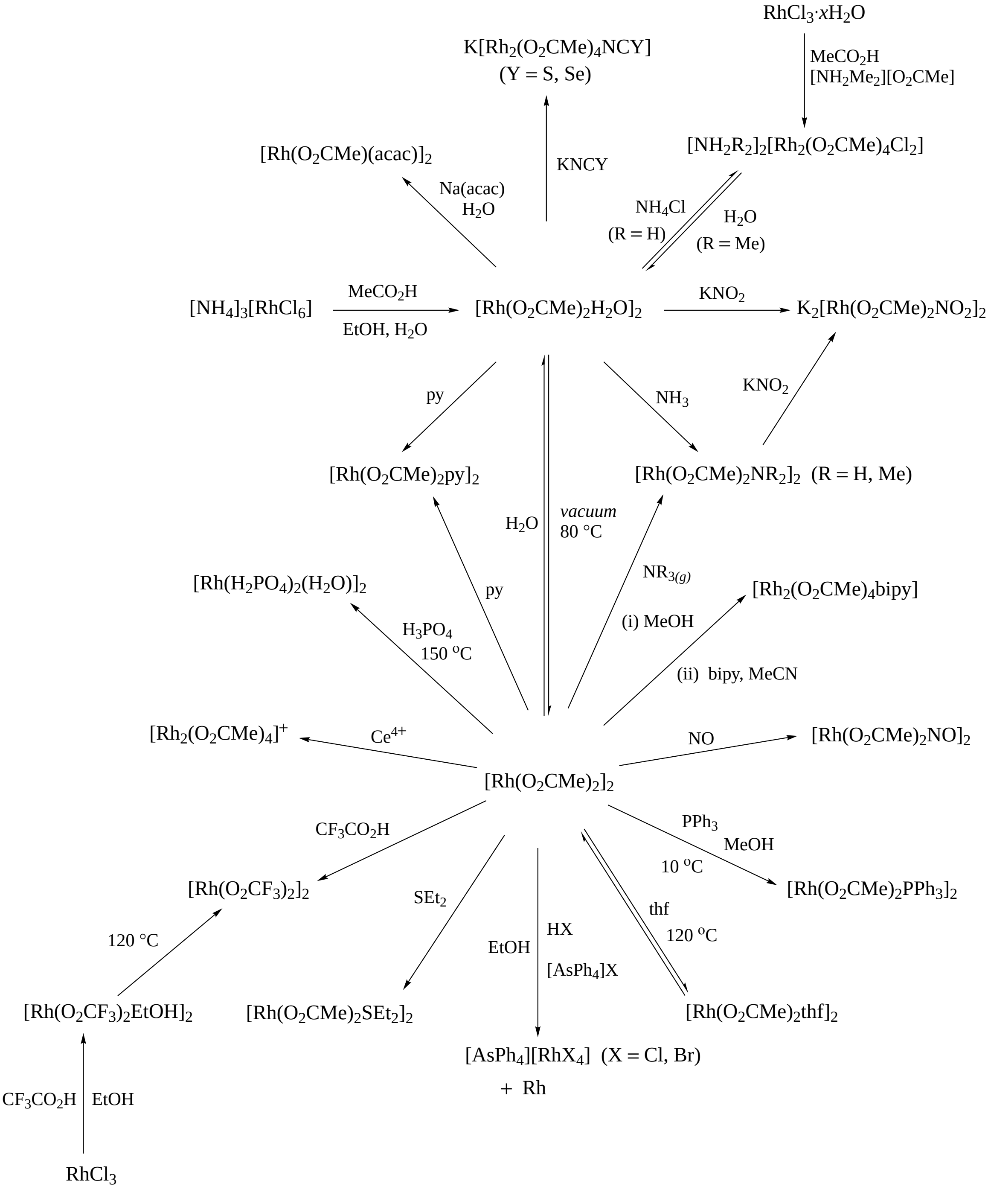
RhCl3·xH2O
MeCO2H
[NH2Me2][O2CMe]
[NH2R2]2[Rh2(O2CMe)4Cl2]
K[Rh2(O2CMe)4NCY]
(Y = S, Se)
KNCY
[Rh(O2CMe)(acac)]2
Na(acac)
H2O
NH4Cl
(R = H)
H2O
(R = Me)
[NH4]3[RhCl6]
MeCO2H
EtOH, H2O
[Rh(O2CMe)2H2O]2
KNO2
K2[Rh(O2CMe)2NO2]2
py
NH3
KNO2
[Rh(O2CMe)2py]2
[Rh(O2CMe)2NR2]2 (R = H, Me)
H2O
vacuum
80 °C
NR3(g)
[Rh(H2PO4)2(H2O)]2
py
[Rh2(O2CMe)4bipy]
H3PO4
150 °C
(i) MeOH
(ii) bipy, MeCN
[Rh2(O2CMe)4]+
Ce4+
NO
[Rh(O2CMe)2NO]2
[Rh(O2CMe)2]2
CF3CO2H
PPh3
MeOH
10 °C
[Rh(O2CF3)2]2
SEt2
[Rh(O2CMe)2PPh3]2
thf
120 °C
HX
EtOH
[AsPh4]X
120 °C
[Rh(O2CF3)2EtOH]2
[Rh(O2CMe)2SEt2]2
[Rh(O2CMe)2thf]2
[AsPh4][RhX4] (X = Cl, Br)
+ Rh
CF3CO2H
EtOH
RhCl3

Scheme 9

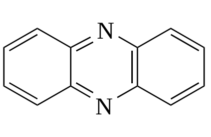

(**9**)

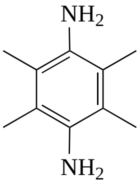

(**10**)

Platinum-based Anticancer Drugs). The latter disrupts mutant DNA by interstrand attachment to two adjacent guanine bases. Previously, it had been believed that the carboxylato complexes could not bind to DNA in this fashion. This may prompt further investigation of the antitumor activity of the rhodium complexes, which induce fewer harmful side effects than the platinum complexes.

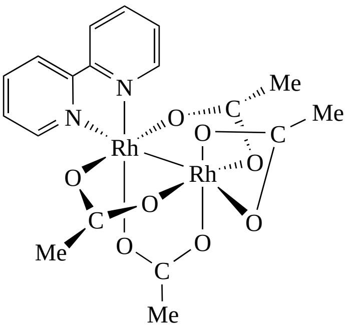

(**11**)

Tertiary phosphines or phosphites may also occupy the axial sites. Their high π-acidity lengthens the Rh–Rh bond, and the colors of their complexes range from red to yellow. Carbonyl, nitrosyl, or isocyanide ligands also lengthen the metal–metal bond. It should be noted that triphenylphosphine does not reduce the carboxylato complexes to rhodium(I) species. Polymeric complexes can be formed by α,ω-dinitriles linking the axial sites of two lantern units. Axial I_2 ligands can link $[Rh(O_2CCF_3)_2]_2$ units without oxidizing them.**[9]**

The carboxylato ligands also participate in metathetical reactions. These have been exploited to prepare homologous complexes. The carboxylato ligands can be replaced stepwise, and a few mixed carboxylato complexes have been isolated. The carboxylato complexes have been shown to be inefficient alkene hydrogenation catalysts.

Other bidentate ligands can bridge the two rhodium atoms. The complexes of the trifluoroacetamide anion, CF_3CNH^-, have been widely studied. Two isomeric products (**12**) and (**13**) are formed when the $[Rh(HNCOCF_3)_2]_2$ complex is allowed to react with 1,10-phenanthroline and $[NBu_4]Cl$ (equation 29). Of these, only the less symmetric (**12**) undergoes the further reaction with pyridine and $K[PF_6]$ (equation 30). These species again demonstrate the possible interaction between the dimeric complexes and DNA. However, carboxamide complexes show great promise as chiral cyclopropanation catalysts in the reactions between diazoesters and alkenes.**[10]** Attempts to fine tune the catalytic properties of the complexes make this a very active research area.

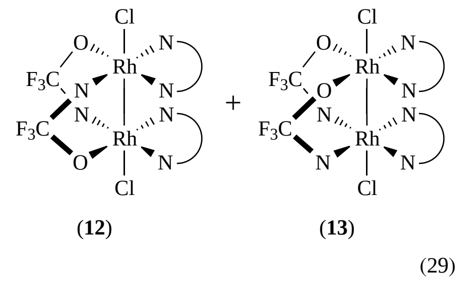

(**12**) (**13**)

(29)

$$[Rh(HNCOCF_3)Cl(phen)]_2 + 2K[PF_6] \xrightarrow{py} [Rh(HNCOCF_3)(phen)]_2[PF_6]_2 + 2KCl \qquad (30)$$

Another class of ligand that forms bridged dimeric complexes includes 6-methyl- or 6-halo-2-oxypyridines. The substituent at the 6-position is essential to discourage axial bonding, particularly when they are prepared via bridge metathesis, although they can be prepared directly from $RhCl_3{\cdot}3H_2O$. When a bidentate ligand coordinates through two different donor atoms the four isomers (**14**)–(**17**) are possible. These are designated the 4,0, 3,1, *cis*-2,2, and *trans*-2,2 isomers, respectively. Examples of all these isomers may be prepared from this class of ligand. Additionally, the 6-methyl-2-oxypyridine ligand can form a tetrameric complex when one of the four oxygen atoms increases its coordination number to four to bridge two 3,1-dimeric units.

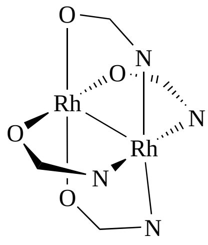

(**14**)

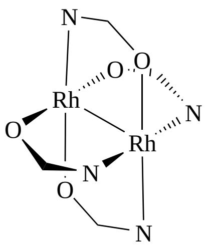

(**15**)

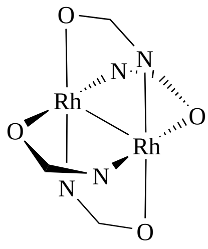

(**16**)

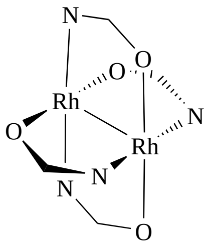

(**17**)

Despite the ubiquity of bridged species, several examples of dimeric unbridged rhodium(II) complexes are known. Heating $[Et_3O][BF_4]$ with $[Rh(O_2CCF_3)_2]_2$ in MeCN forms $[Rh_2(MeCN)_{10}][BF_4]_4$. The cation has Rh–Rh linked, staggered square-pyramidal units.**[11]** The aqua complex $[(H_2O)_5Rh–Rh(H_2O)_5]^{4+}$ is also known. Several inorganic oxo anions, for example, sulfate, carbonate, hydrogen carbonate, or dihydrogen phosphate, form bridged complexes with the aqua complex (equation 31).

$$[Rh_{2(aq)}]^{4+} + 4[H_2PO_4]^- \longrightarrow [Rh(H_2PO_4)_2(H_2O)]_2 \qquad (31)$$

The *bis*(octaethylporphyrin)dirhodium complex is also unbridged. The reduction of $[Rh(dmg)_2Cl_2]^-$ by tetrahydroborate in the presence of PPh_3 forms the unbridged rhodium(II) complex $[Rh(dmg)_2PPh_3]_2$ (**18**) (equation 32). This complex has axial PPh_3 ligands and a very long Rh–Rh bond of 2.936 Å. The parent complex can be prepared by the reaction of dmgH and $[Rh(O_2CMe)_2]_2$.

$$RhCl_3 + dmgH \xrightarrow{67\%EtOH} H[Rh(dmg)_2Cl_2] \xrightarrow[90\%EtOH]{KOH,\ PPh_3}$$

$$[Rh(dmg)_2Cl(PPh_3)] \xrightarrow[90\%MeOH]{NaBH_4} [Rh(dmg)_2(PPh_3)]_2 \qquad (32)$$

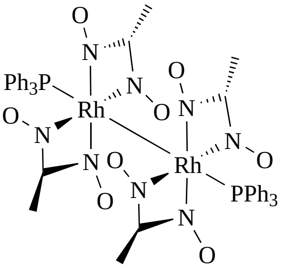

(**18**)

6 RHODIUM(III) COMPLEXES

The extensive chemistry of this oxidation state has two facets. The classical complexes containing σ-bonded ligands have been known for nearly two centuries. At the beginning of the twentieth century, they were widely used by Alfred Werner in his fundamental research into the constitution, stereochemistry, and isomerism of coordination compounds.

However, over the last 60 years a new type of chemistry has emerged. Although the first examples, tertiary arsine complexes, were initially prepared as an extension of classical rhodium(III) chemistry, the newer complexes containing π-bonding ligands have been a consequence of the intense interest in the catalytic properties of rhodium(I) complexes. Examples of these ligands also include tertiary phosphines and stibines, although it is debatable to what extent they act as π-acids when coordinated to rhodium(III).

This historical distinction is paralleled by the widely different chemistries exhibited by the two types of complex. The classical complexes are invariably octahedral and react so slowly that studies of their reactions are of kinetic rather than synthetic interest. They are impervious to both oxidation and reduction in aqueous solution.

On the other hand, rhodium(III) complexes containing π-bonded ligands are often pentacoordinate and undergo very rapid reductive elimination reactions. It is their ability to undergo this reaction that makes possible much of the important catalytic activity exhibited by lower oxidation state rhodium complexes.

6.1 Complexes of σ-bonding Ligands

A wide range of rhodium(III) complexes contain halo, aqua, ammine diaminoalkane, or dicarboxylato ligands. Rhodium(III) complexes whose net ionic charge varies from +3 to −3 are known. With complexes that react slowly, it is possible to isolate most intermediate complexes in the interconversions of $[Rh(H_2O)_6]^{3+}$ and $[RhCl_6]^{3-}$ (Scheme 10). The slow reaction rates of these complexes also allow geometrcal isomers to be isolated. Additionally, the *cis*-$[RhX_2(LL)_2]^+$ and $[Rh(LL)_3]^{n+}$ complexes containing bidentate ligands are chiral and may be resolved into their optical isomers.

The complexes of halo or pseudohalo ligands make a convenient starting point for the discussion of those complexes containing monodentate ligands. The hexaiodo complex is unknown, but the other $[RhX_6]^{3-}$ complexes (X = F, Cl, Br, CN, SCN, SeCN) are all well established. In contrast to rhodium(I) complexes, the SCN^- and $SeCN^-$ ions are chalcogenide bound. The stable hexafluororhodate(III) complex is low spin, unlike the corresponding Co^{III} complex, which is a rare d^6 high-spin complex and a powerful oxidizing agent. The hexanitrorhodate(III) ion can be prepared from $[RhCl_6]^{3-}$ (equation 33). The tripotassium salt, like its cobalt(III) analog, is insoluble in water. Di- and trihalo-bridged species, (**19**) and (**20**) respectively, can be formed from $[RhCl_6]^{3-}$ at high temperatures and from $[RhBr_6]^{3-}$ in solution.

$$K_3[RhCl_6] + 6KNO_2 \longrightarrow K_3[Rh(NO_2)_6] + 6KCl \qquad (33)$$

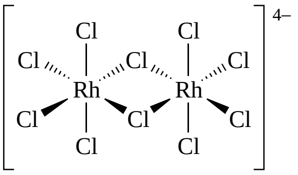

(**19**)

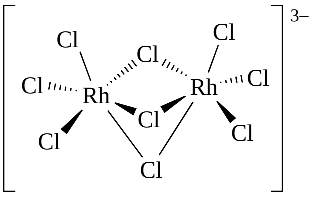

(**20**)

Aquation is the principal reaction in solution. As can be seen in Scheme 10, the trans labilizing effect of Cl^- is greater than that of the aqua ligand. Once the ligands trans to Cl^- are replaced by water, *fac*-$[RhCl_3(H_2O)_3]$ is inert to further aquation. It has also been found that the chloro ligand trans to water in $[RhCl_5(H_2O)]^{2-}$ has the shortest Rh–Cl bond.

The hexaaqua ion is virtually the sole example of a rhodium(III) ion complexed by six monodentate oxygen ligands. Solutions of this ion are acid due to hydrolysis (pKa = 3.3). Its principal reaction is anation, but it is difficult to isolate $[RhX(H_2O)_5]^{2+}$ intermediates since the formation of *trans*-$[RhX_2(H_2O)_4]^+$ is much more rapid. Hydrated rhodium trichloride, nominally $RhCl_3{\cdot}3H_2O$, is a mixture of several aquachloro complexes in which *fac*- and *mer*-$[RhCl_3(H_2O)_3]$ predominate. Since $BaCl_2$ gives no precipitate

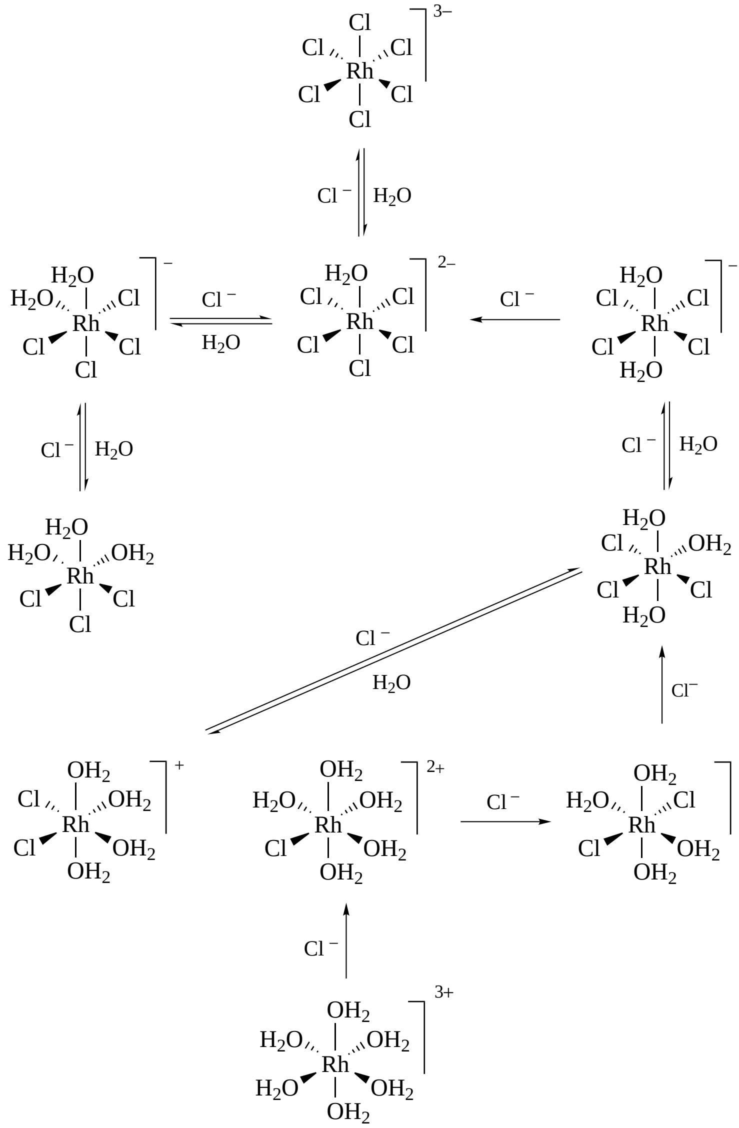

Scheme 10

with $Rh_2(SO_4)_3·6H_2O$, it is unlikely that it contains the $[Rh(H_2O)_6]^{3+}$ ion, more recent studies imply that dimeric cationic species are formed in aqueous solution. The only rhodium(III) carboxylate known is the unusual oxotrirhodium complex (**21**). This can be prepared either from silver(I) acetate and aqueous $RhCl_3·3H_2O$ (Scheme 3) or by ozonization of rhodium(II) acetate.

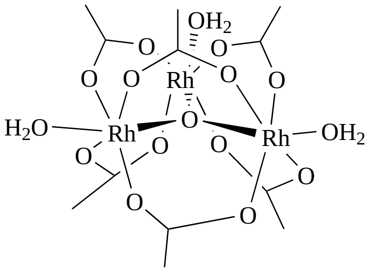

(**21**)

Several dialkyl sulfides form $[RhX_3(R_2S)_3]$ complexes. Some of these have been employed as alkene hydrogenation catalysts; however, they are only weakly active.

The hexaamine complex can only be prepared in sealed tube reactions (equation 34), unless the incorporation of the sixth ammine ligand is catalyzed by ethanol. In contrast, the pentaammine complexes are very accessible, and their anation and aquation reactions (Scheme 11) have been exhaustively studied. However, the exact mechanism of the anation reaction remains in doubt. While an interchange, I, mechanism is involved, conflicting arguments have been advanced for Ia or Id paths. The aquation reaction is catalyzed by Hg^{2+} or OH^-

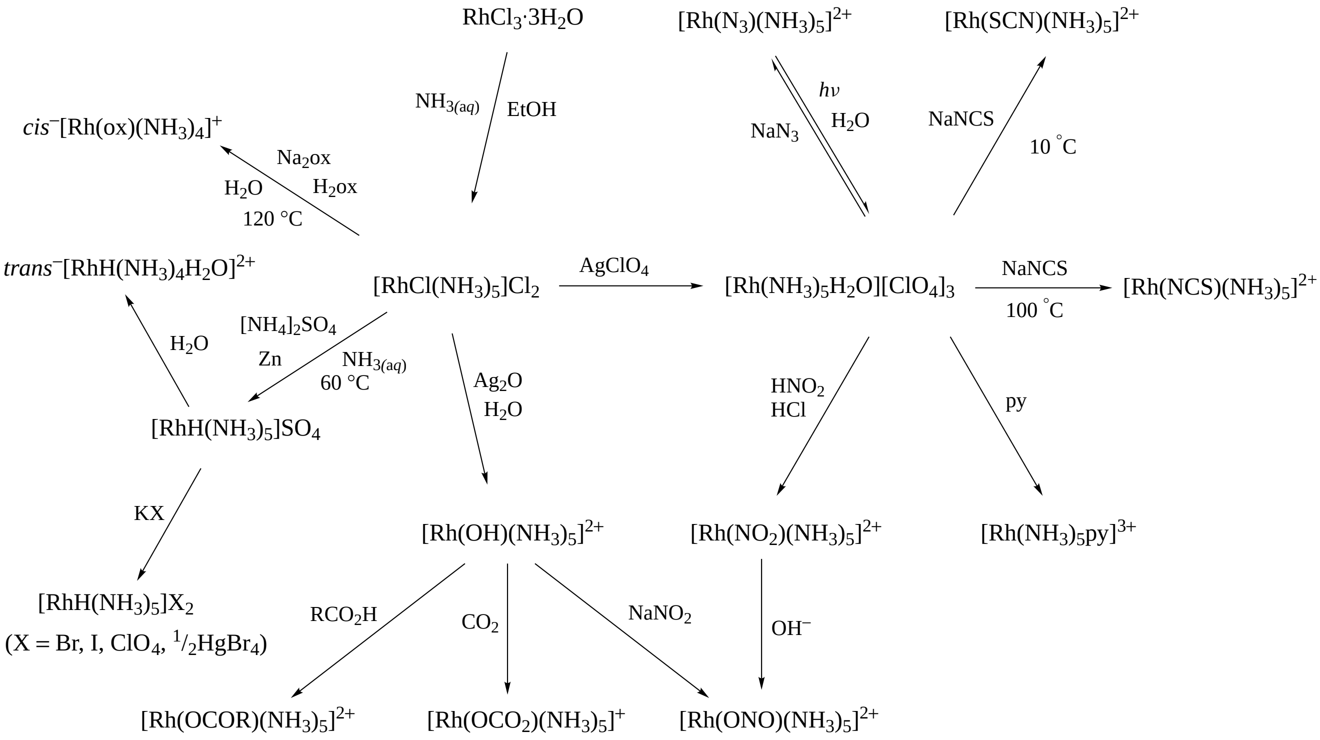

RhCl3·3H2O
NH3(aq)
EtOH
cis–[Rh(ox)(NH3)4]+
Na2ox
H2O
H2ox
120 °C
[Rh(N3)(NH3)5]2+
hν
H2O
NaN3
[Rh(SCN)(NH3)5]2+
NaNCS
10 °C
trans–[RhH(NH3)4H2O]2+
[RhCl(NH3)5]Cl2
AgClO4
[Rh(NH3)5H2O][ClO4]3
NaNCS
100 °C
[Rh(NCS)(NH3)5]2+
H2O
[NH4]2SO4
Zn
NH3(aq)
60 °C
[RhH(NH3)5]SO4
Ag2O
H2O
HNO2
HCl
py
KX
[Rh(OH)(NH3)5]2+
[Rh(NO2)(NH3)5]2+
[Rh(NH3)5py]3+
[RhH(NH3)5]X2
(X = Br, I, ClO4, 1/2HgBr4)
RCO2H
CO2
NaNO2
OH−
[Rh(OCOR)(NH3)5]2+
[Rh(OCO2)(NH3)5]+
[Rh(ONO)(NH3)5]2+

Scheme 11

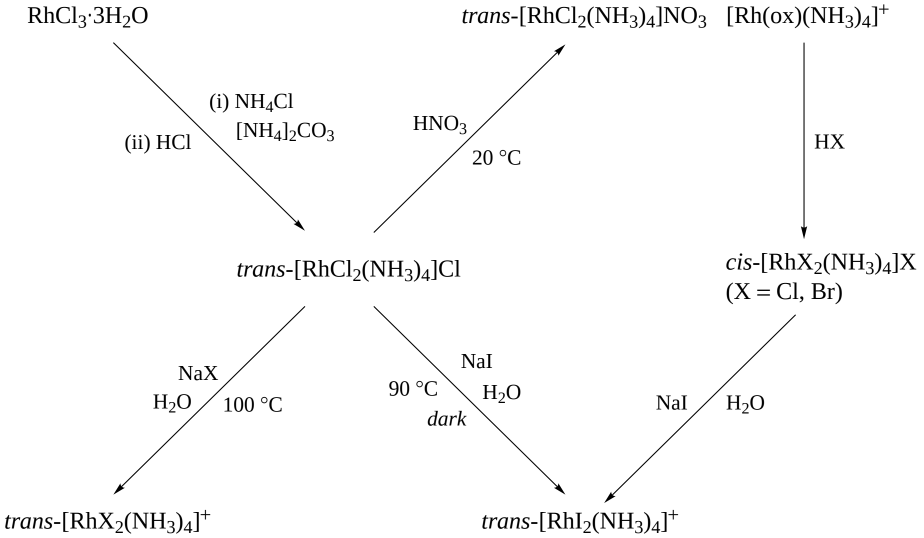

RhCl3·3H2O
trans-[RhCl2(NH3)4]NO3
[Rh(ox)(NH3)4]+
(i) NH4Cl
[NH4]2CO3
(ii) HCl
HNO3
20 °C
HX
trans-[RhCl2(NH3)4]Cl
cis-[RhX2(NH3)4]X
(X = Cl, Br)
NaX
H2O
100 °C
NaI
H2O
90 °C
dark
NaI
H2O
trans-[RhX2(NH3)4]+
trans-[RhI2(NH3)4]+

Scheme 12

ions.

$$RhCl_3{\cdot}3H_2O + NH_{3(aq)} \xrightarrow{120\,°C} [Rh(NH_3)_6]^{3+} \qquad (34)$$

The tetraammine complexes also undergo several substitution reactions (Scheme 12). Most of these reactions involve the trans isomers, possibly because these are less soluble and more easily isolated than the cis isomers. However, they are overshadowed by the more important $[RhX_2(N{-}N)_2]^+$ analogs (see below). The complex *trans*-$[RhCl_2py_4]Cl$ is an important starting material for other rhodium(III) complexes because of the ease with which the pyridine ligands may be replaced. Its anation reactions are also a source of other rhodium(III) complexes (Scheme 13).

Both *fac*- and *mer*-triammine complexes have been prepared. Di- and monoammine complexes are neither particularly stable nor important.

Bidentate oxygen ligands form numerous rhodium(III) complexes. Several tris(β-diketonato) complexes have been prepared from rhodium(III) nitrate (equation 35). The products are extraordinarily stable. They can be resolved into their optical isomers, and survive nitration and formylation reactions (equations 36 and 37). The tris(oxalato)rhodate(III) ion has also been resolved, but the enantiomers undergo slow racemization. Reaction of this complex with refluxing chloric(VII) acid leads to *cis*-$[Rh(ox)_2(H_2O)_2]$, which can be converted into *cis*- or *trans*-$[RhX_2(ox)_2]^{3-}$ complexes.

The important $[Rh(en)_3]^{3+}$ ion can be prepared by a variety of reactions (equations 38 and 39). The ion has been resolved and more recently the (-)-enantiomer has been shown to exist in the L configuration. Owing to its inertness, no ligand-substitution reactions have been reported. However, KNH_2 deprotonates the complex and allows its conversion to other species (equation 40). The tris(bipy) and $[Rh(phen)_3]^{3+}$ complexes have also been prepared and resolved.

$$Rh(NO_3)_3{\cdot}xH_2O + acaH \xrightarrow{pH4} [Rh(acac)_3] \qquad (35)$$

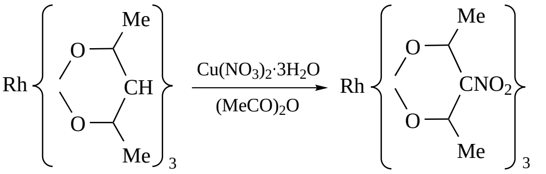
Rh
Me
O
CH
O
Me
3
Cu(NO3)2·3H2O
(MeCO)2O
Rh
Me
O
CNO2
O
Me
3

(36)

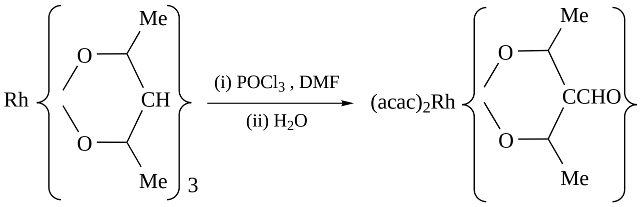
Rh
Me
O
CH
O
Me
3
(i) POCl3 , DMF
(ii) H2O
(acac)2Rh
Me
O
CCHO
O
Me

(37)

$$Na_3[RhCl_6] + en{\cdot}H_2O \longrightarrow [Rh(en)_3]^{3+} \qquad (38)$$

$$RhCl_3{\cdot}3H_2O + 3en \xrightarrow{EtOH/H_2O} [Rh(en)_3]^{3+} \qquad (39)$$

$$[Rh(en)_3]I_3 + KNH_2 \longrightarrow [Rh(en)(en\text{-}H)_2]I$$

$$\xrightarrow{BF_3} [Rh(en)(enBF_3)_2]I \qquad (40)$$

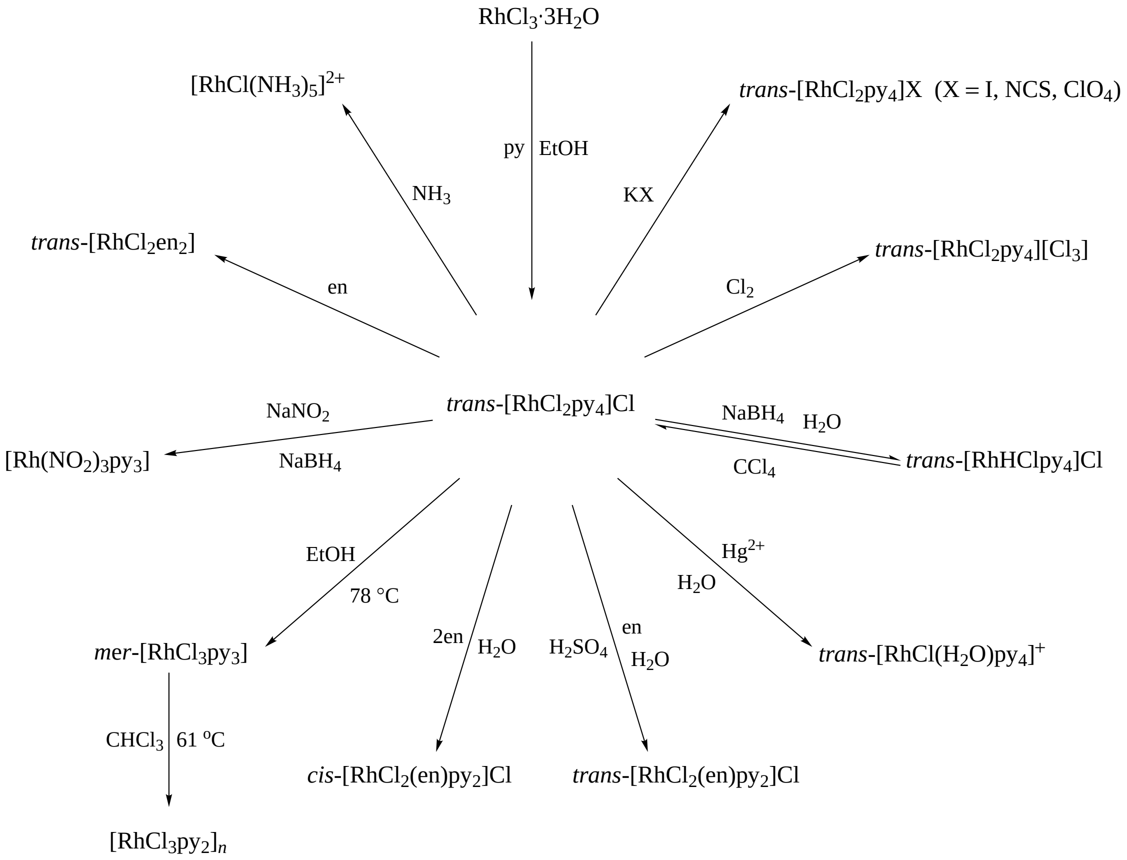
RhCl3·3H2O
py
EtOH
[RhCl(NH3)5]2+
NH3
trans-[RhCl2py4]X (X = I, NCS, ClO4)
KX
trans-[RhCl2en2]
en
trans-[RhCl2py4][Cl3]
Cl2
trans-[RhCl2py4]Cl
NaNO2
[Rh(NO2)3py3]
NaBH4
NaBH4
H2O
CCl4
trans-[RhHClpy4]Cl
EtOH
78 °C
mer-[RhCl3py3]
2en
H2O
H2SO4
en
H2O
Hg2+
H2O
trans-[RhCl(H2O)py4]+
CHCl3
61 °C
[RhCl3py2]n
cis-[RhCl2(en)py2]Cl
trans-[RhCl2(en)py2]Cl

Scheme 13

The *bis*(1,2-diaminoethane) complexes are more reactive, and their aquation and anation reactions have been widely studied (Scheme 14). The *cis*-$[RhX_2(en)_2]^+$ ion may be resolved, and (+)-$[Rh(ox)(en)_2]^+$ has been assigned the Δ configuration. The substitution reactions of the X_2 ligands proceed with retention of configuration.

Unlike the $[RhX_2(en)_2]^+$ ions, which can exist as either *cis* or trans isomers, both $[RhX_2(bipy)_2]^+$ and $[RhX_2(phen)_2]^+$ cations and their derivatives are exclusively *cis* (cf. the exclusively *trans*-$[RhCl_2py_4]^+$ ion above). Complexes of rhodium(III) with polydentate nitrogen ligands can also be prepared. Tridentate diethylenetriamine (**22**) forms $[Rh(dien)_2]I_3$ when allowed to react with rhodium trichloride in the presence of NaI. The trichloride salt can be obtained by metathesis with AgCl. The reactions of 1,4,7-triazacyclononane inorganic complexes are of current interest (Scheme 15).**[12]**

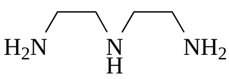

(**22**)

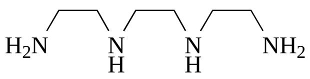

(**23**)

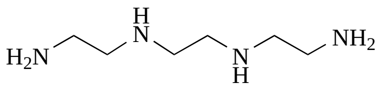

(**24**)

The quadridentate ligands trien (**23**), taud (**24**), 1,4,7,10-tetraazacyclododecane, and 1,4,8,11-tetraazacyclotetradecane all form rhodium(III) complexes. Both the cyclic ligands form predominantly *cis*-$[RhCl_2(N_4)]^+$ complexes when their hydrochlorides react with aqueous rhodium trichloride in the presence of a base. All three possible isomers (**25**)–(**27**) of the $[RhX_2(trien)]+$ cation have been characterized. The ligand (**24**) forms *trans*-$[RhCl_2(taud)]^+$, which may be prepared from either rhodium trichloride or *trans*-$[RhCl_2py_4]^+$. Both cis and trans products are formed from 1,4,8,11-tetraazacyclotetradecane and $RhCl_3{\cdot}3H_2O$. Each complex undergoes anation and metathetical reactions, and the cis complex can be resolved into its optical isomers. Other macrocyclic tetradentate ligands such as porphyrins or phthalocyanines form complexes where the four nitrogen atoms occupy the four equatorial coordination sites.

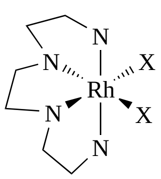

(**25**)

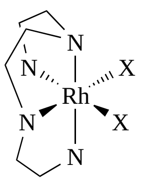

(**26**)

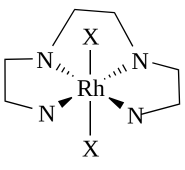

(**27**)

6.2 Complexes of π-bonding Ligands

Although some of these complexes are obtained from rhodium(III) precursors, most arise from oxidative additions to rhodium(I). An indication of the diversity of rhodium(III) complexes that can be obtained from $[RhCl(PPh_3)_3]$ is given in Scheme 16. Just as was the case with rhodium(I), there are very few anionic complexes containing π-bonding ligands. The general formula of the anions is $[RhX_4L_2]^-$. There are also some interesting complexes containing the thioarsine (**28**), in which the ligand occurs in both anion and cation.

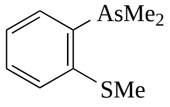

(**28**)

The majority of the pentacoordinate cationic complexes contain at least one hydrido ligand, although some are known to contain bulky neutral ligands. The latter may be regarded as the rhodium(III) analogs of the tricoordinate rhodium(I) complexes (see Section 4.1 above), from which most have been prepared by oxidative addition reactions.

The hydrido complexes, in turn, can be regarded as the analogs of the $[RhHL_2]$ complexes in which coordinative unsaturation is a consequence of the high trans effect of the H^- ligand. They exhibit either trigonal bipyramidal or square pyramid geometry. The hydrido ligand occupies the apical position in the *bis*(*t*-butyldipropylphosphine) complex (**29**), which can be prepared from $RhCl_3{\cdot}3H_2O$. More usually the complexes are prepared by oxidative addition of monohydrides to rhodium(I) complexes. Two very important catalyst types can be prepared by adding either a hydrosilane or borane**[13]** to $[RhCl(PPh_3)_3]$. The hydridocatecholborane derivative catalyzes the hydroboration of alkenes; oxidation and hydrolysis of the resulting boranes produces alcohols.

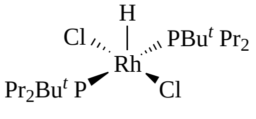

(**29**)

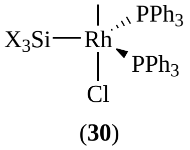

(**30**)

The numerous $[RhHCl(SiX_3)(PPh_3)_2]$ complexes (**30**) are potent hydrosilation catalysts for alkenes, alkynes, ketones, and other organic substrates containing either an active hydrogen or a multiple bond.**[7]** Many examples have been isolated in hydrosilation reactions. The complex $[RhHCl(SiAr_3)(PPr^i{}_3)_2]$ is square pyramidal but *mer*-$[RhHCl(SiHAr_2)(PMe_3)_3]$ complexes are formed from $[RhCl(PMe_3)_4]$ and $SiHAr_3$.**[14]** Besides being important catalysts, the complexes are also the source

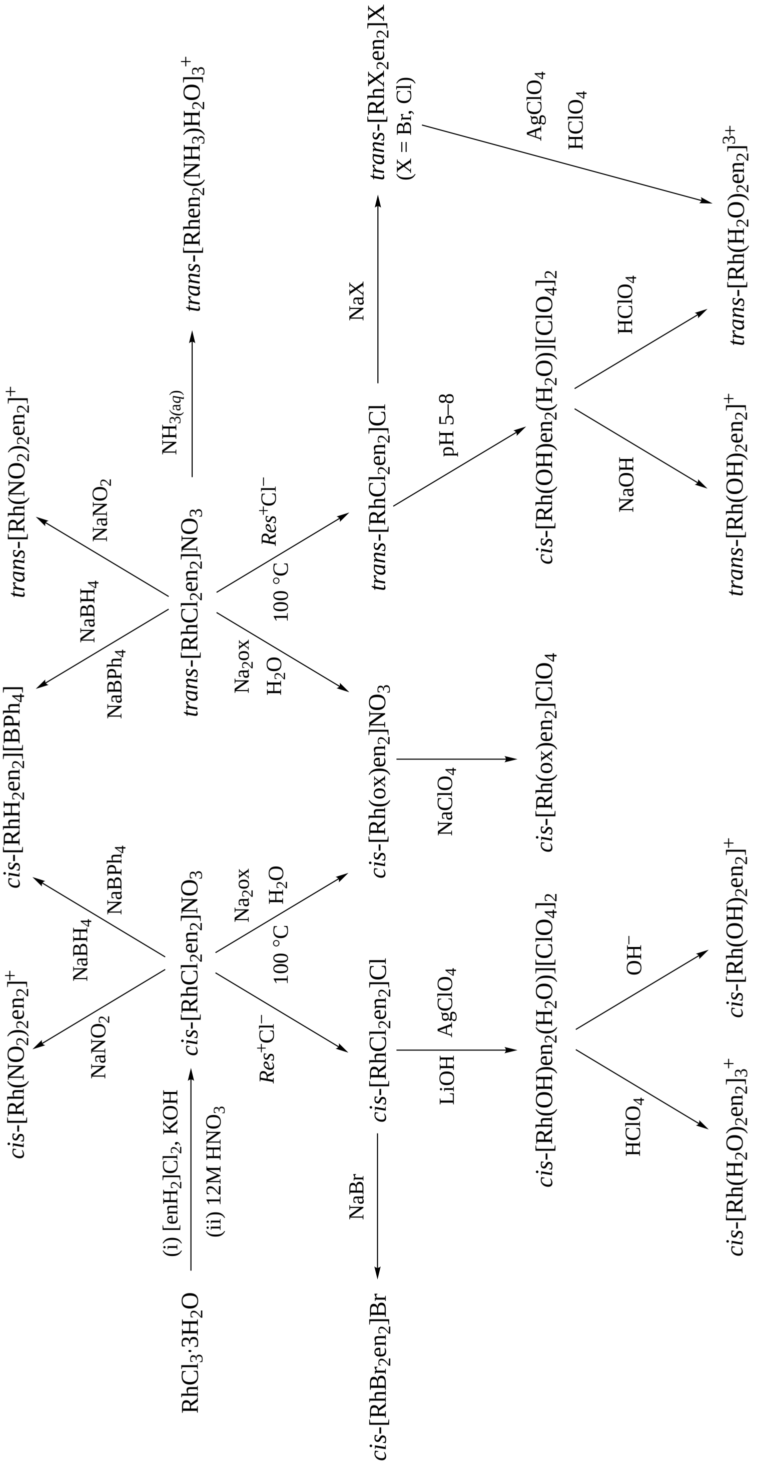
$RhCl_3·3H_2O$
(i) $[enH_2]Cl_2$, KOH
(ii) 12M HNO_3
cis-$[RhCl_2en_2]NO_3$
$NaNO_2$
cis-$[Rh(NO_2)_2en_2]^+$
$NaBH_4$
$NaBPh_4$
cis-$[RhH_2en_2][BPh_4]$
Res$^+Cl^-$
cis-$[RhCl_2en_2]Cl$
NaBr
cis-$[RhBr_2en_2]Br$
Na_2ox
H_2O
100 °C
cis-$[Rh(ox)en_2]NO_3$
$NaClO_4$
cis-$[Rh(ox)en_2]ClO_4$
LiOH
$AgClO_4$
cis-$[Rh(OH)en_2(H_2O)][ClO_4]_2$
$HClO_4$
cis-$[Rh(H_2O)_2en_2]_3^+$
OH^-
cis-$[Rh(OH)_2en_2]^+$
trans-$[RhCl_2en_2]NO_3$
$NaBH_4$
$NaBPh_4$
$NaNO_2$
trans-$[Rh(NO_2)_2en_2]^+$
$NH_{3(aq)}$
trans-$[Rhen_2(NH_3)H_2O]_3^+$
Na_2ox
H_2O
Res$^+Cl^-$
100 °C
trans-$[RhCl_2en_2]Cl$
NaX
trans-$[RhX_2en_2]X$
(X = Br, Cl)
pH 5–8
cis-$[Rh(OH)en_2(H_2O)][ClO_4]_2$
NaOH
trans-$[Rh(OH)_2en_2]^+$
$HClO_4$
trans-$[Rh(H_2O)_2en_2]^{3+}$
$AgClO_4$
$HClO_4$

Scheme 14

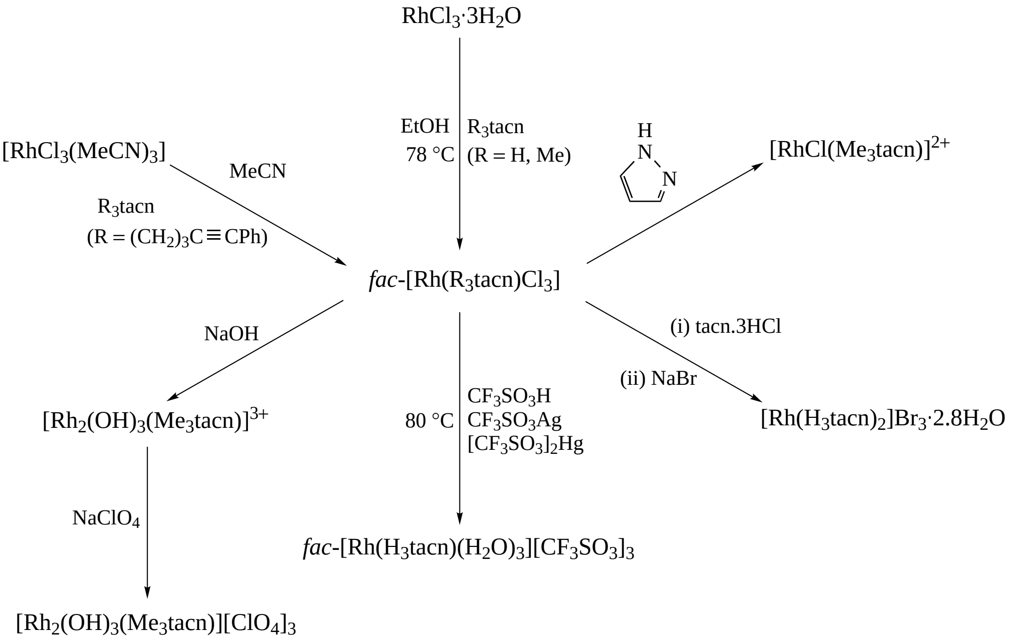

RhCl3·3H2O
EtOH 78 °C
R3tacn (R = H, Me)
[RhCl3(MeCN)3]
MeCN
R3tacn (R = (CH2)3C≡CPh)
fac-[Rh(R3tacn)Cl3]
[RhCl(Me3tacn)]2+
NaOH
[Rh2(OH)3(Me3tacn)]3+
80 °C
CF3SO3H
CF3SO3Ag
[CF3SO3]2Hg
(i) tacn.3HCl
(ii) NaBr
[Rh(H3tacn)2]Br3·2.8H2O
NaClO4
fac-[Rh(H3tacn)(H2O)3][CF3SO3]3
[Rh2(OH)3(Me3tacn)][ClO4]3

Scheme 15

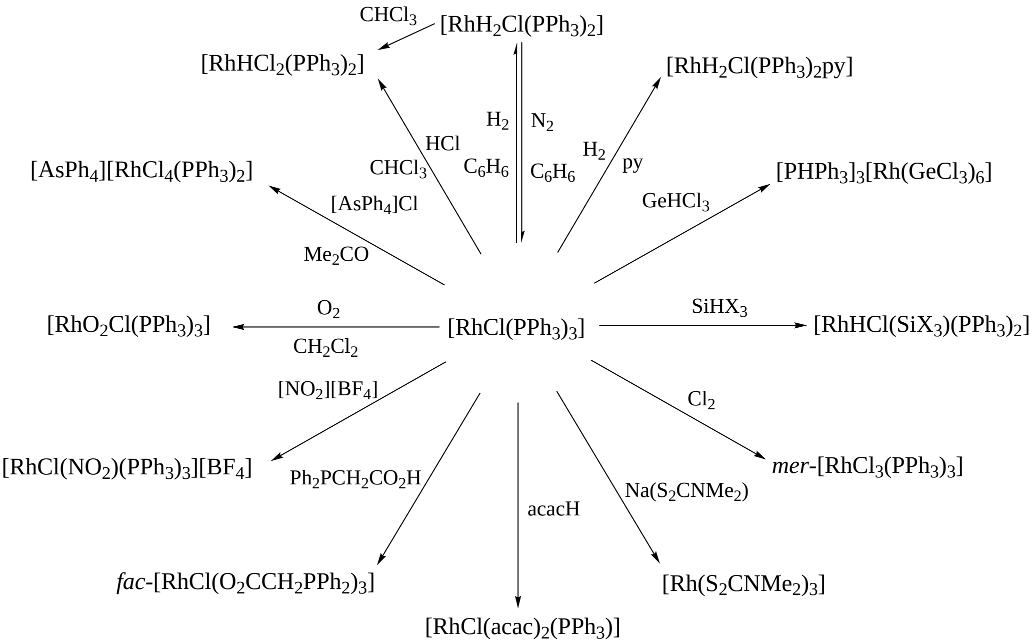

CHCl3
[RhH2Cl(PPh3)2]
[RhHCl2(PPh3)2]
[RhH2Cl(PPh3)2py]
H2
N2
HCl
CHCl3
C6H6
C6H6
H2
py
[AsPh4][RhCl4(PPh3)2]
[AsPh4]Cl
Me2CO
GeHCl3
[PHPh3]3[Rh(GeCl3)6]
O2
CH2Cl2
[RhO2Cl(PPh3)3]
[RhCl(PPh3)3]
SiHX3
[RhHCl(SiX3)(PPh3)2]
[NO2][BF4]
Cl2
[RhCl(NO2)(PPh3)3][BF4]
Ph2PCH2CO2H
acacH
Na(S2CNMe2)
mer-[RhCl3(PPh3)3]
fac-[RhCl(O2CCH2PPh2)3]
[Rh(S2CNMe2)3]
[RhCl(acac)2(PPh3)]

Scheme 16

of many other rhodium complexes (equations 41 and 42). Germyl analogs are known, but excess $GeHCl_3$ converts $[RhCl(PPh_3)_3]$ to the $[Rh(GeCl_3)_6]^{3-}$ anion.

$$[RhHCl\{Si(OEt)_3\}(PPh_3)_2] \xrightarrow{dppe} [RhCl(dppe)(PPh_3)] \quad (41)$$

$$[RhHCl\{Si(OEt)_3\}(PPh_3)_2] + HCl \longrightarrow [RhHCl_2(PPh_3)_2] + SiH(OEt)_3 \quad (42)$$

Another important subgroup of monohydrido complexes can be prepared by the oxidative addition of *nido*-heteroborane anions to $[RhCl(PPh_3)_3]$ (Scheme 17). Further, the *closo*-dicarborane complex is the starting material for the preparation of other rhodium(III) borane complexes (Scheme 18). They are also weakly active hydrogenation catalysts.

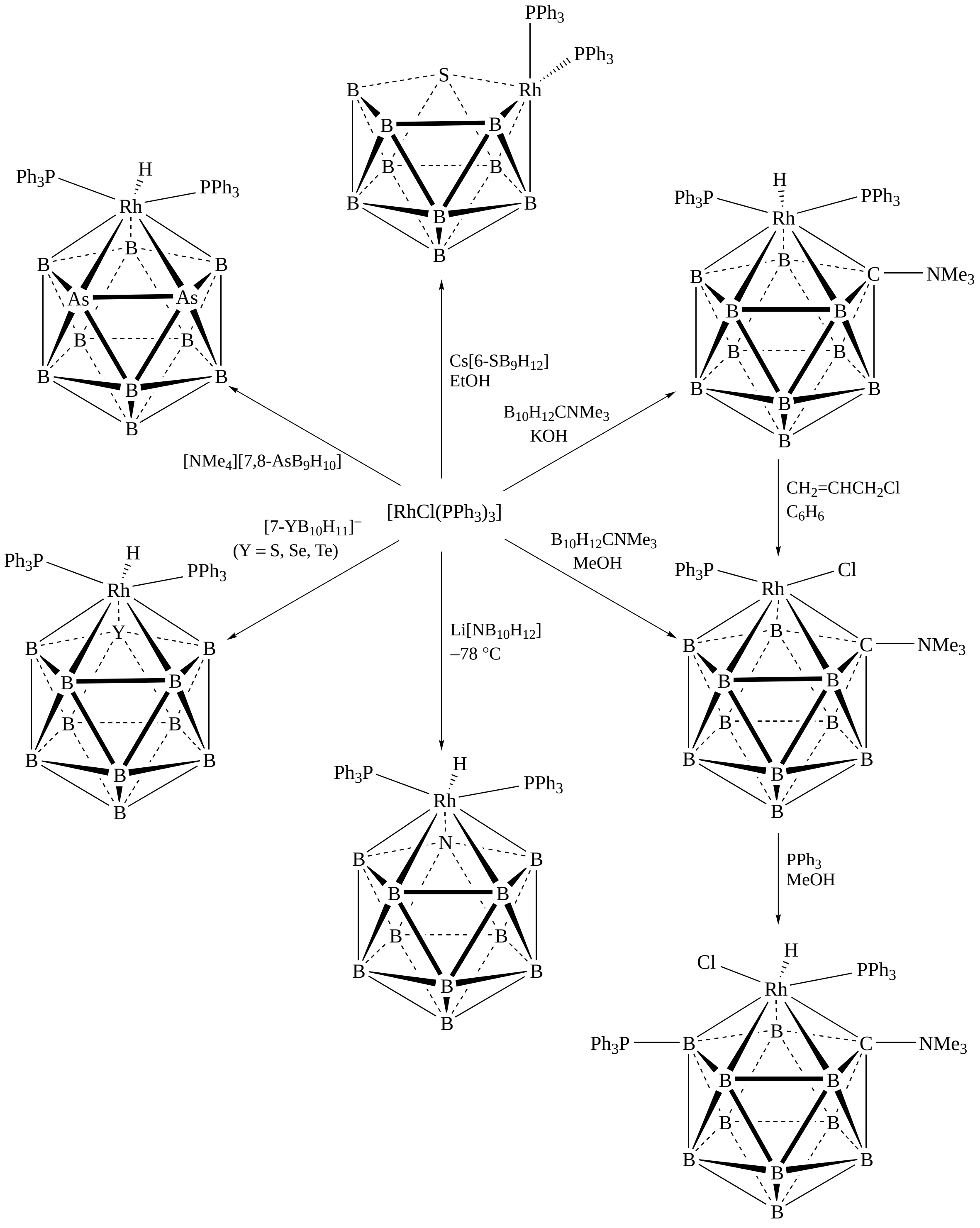
[RhCl(PPh3)3]
Cs[6-SB9H12]
EtOH
[NMe4][7,8-AsB9H10]
B10H12CNMe3
KOH
[7-YB10H11]−
(Y = S, Se, Te)
B10H12CNMe3
MeOH
Li[NB10H12]
−78 °C
CH2=CHCH2Cl
C6H6
PPh3
MeOH
Ph3P
PPh3
H
Rh
Cl
NMe3
S
As
Y
N
C
B

Scheme 17

Several pentacoordinate monohydrido complexes can add an additional, small, neutral ligand to form complexes of the type [$RhHX_2L_2L'$]. The dihydrido complexes are conveniently prepared by the oxidative addition of dihydrogen to rhodium(I) complexes dissolved in inert organic solvents. Chlorinated solvents are unsuitable since the hydrido complexes produced may reduce them with formation of HCl and contaminate the product with monohydrido complexes (see Scheme 16). A characteristic stoichiometric reaction of many dihydrides is the addition of a third neutral ligand to form [RhH_2XL_2L']

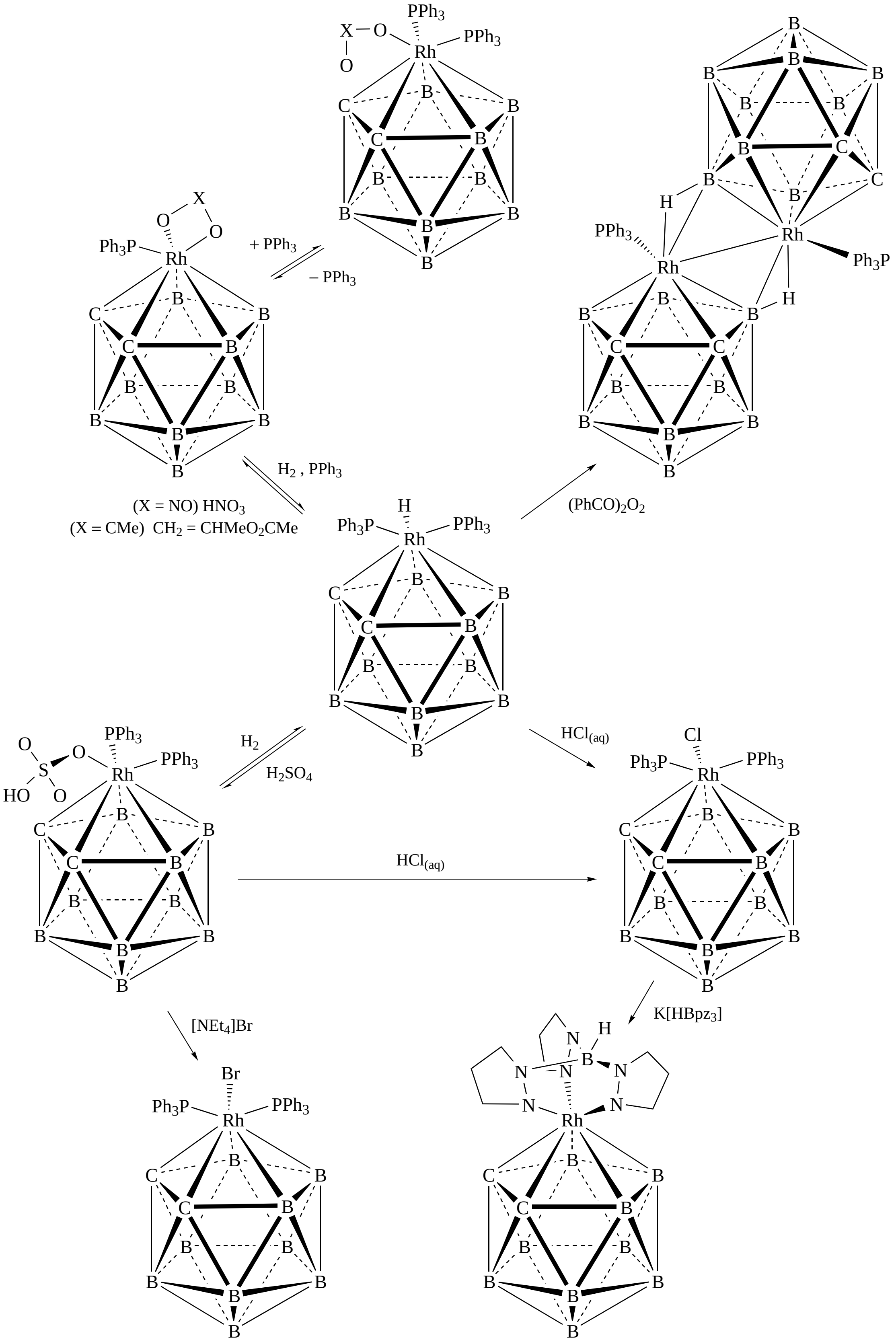
+ PPh3
− PPh3
H2 , PPh3
(X = NO) HNO3
(X = CMe) CH2 = CHMeO2CMe
(PhCO)2O2
H2
H2SO4
HCl(aq)
HCl(aq)
[NEt4]Br
K[HBpz3]

Scheme 18

complexes (equation 43). However, the principal reaction of the dihydrides is the catalytic reduction of C=C bonds. The hydrido complexes can be characterized by reference to the high-field line in their ^{1}H NMR spectra and the presence of a weak band at ca.2000 cm^{-1} in their IR spectra attributable to $\nu_{\text{Rh-H}}$.

$$[\text{RhH}_2\text{Cl}(\text{PPh}_3)_2] + \text{py} \longrightarrow [\text{RhH}_2\text{Cl}(\text{PPh}_3)_2\text{py}] \qquad (43)$$

Pentacoordinate complexes can also arise from reactions between rhodium(I) complexes and dioxygen. The reactions between the complexes and dioxygen under very slightly different conditions can, however, easily give rise to other products.

Chlorotris(triphenylphosphine)rhodium(I) forms $[\text{RhCl}(\text{O}_2)(\text{PPh}_3)_n]$ ($n = 2$, 3) or $[\text{RhCl}(\text{O}_2)(\text{PPh}_3)_2]_2$. The last complex is six coordinate and has structure (**31**). Ligand oxidation can also occur. A diagnostic test for the presence of O_2 ligands is a band at 870–900 cm^{-1}, attributable to $\nu_{\text{O-O}}$, in the IR spectrum.

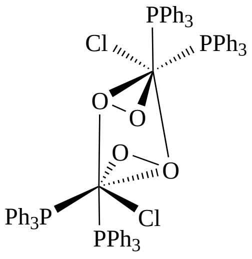

(**31**)

Another catalytically important type of pentacoordinate complex has recently been prepared by the oxidative addition of *bis*(benzoborazoles) to $[\text{RhCl}(\text{PPh}_3)_3]$. The boryl groups are labile – hence their complexes' ability to catalyze borylation of organic substrates – and can be replaced by other boryl groups (Scheme 19).**13** Trimethyl phosphine forms $[\text{RhCl}(\text{BO}_2\text{C}_6\text{H}_4)_2(\text{PMe}_3)_3]$ when allowed to react with $[\text{RhCl}(\text{BO}_2\text{C}_6\text{H}_4)_2(\text{PPh}_3)_2]$, but PEt_3 merely replaces the PPh_3 ligands to form a trigonal bipyramidal product.

Many complexes that appear to be pentacoordinate are actually six coordinate by virtue of the presence of a bidentate anion or an uncharacteristically bidentate neutral ligand. The former type are exemplified by complexes containing 1,3-diaryltriazenido (**32**) or disulfur anions. Both examples may be prepared by oxidative addition reactions. Those complexes of uncharacteristically bidentate ligands may be prepared by allowing rhodium(III) halides to react with a stoichiometric deficiency of the ligand. A second neutral ligand may become bidentate when a chloro complex undergoes a metathetical reaction with an anion of low coordinating power or isomerizes in a polar solvent (Scheme 20).

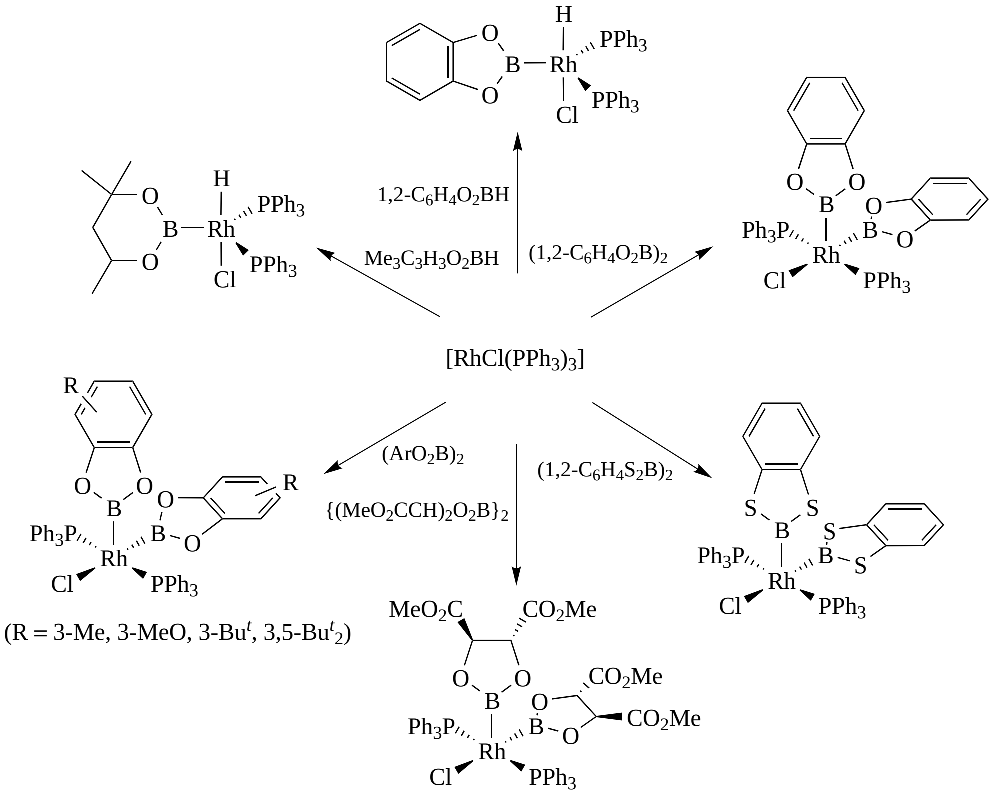

Scheme 19

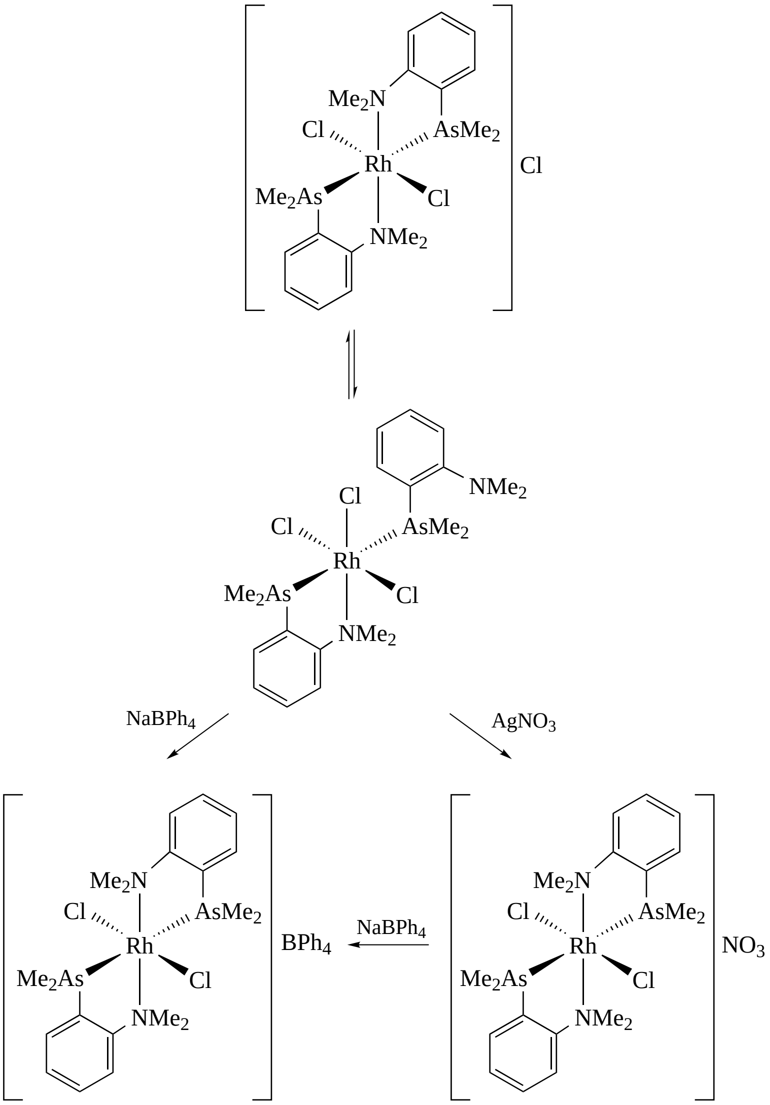

Scheme 20

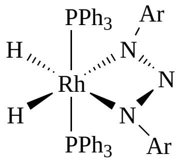

(**32**)

Dinuclear complexes can also have the same empirical formulas as pentacoordinate complexes. Their ^{31}P NMR spectra show that they adopt the noncentrosymmetric structure (**33**). Monomeric trialkylphosphine complexes are difficult to prepare and attempts at purification often lead to disproportionation (equation 44). The trihalo-bridged dimers adopt structure (**34**), in which each phosphorus atom is trans to a different chloro bridge.

$$3[RhCl_3(PBu_3)_2]_2 \longrightarrow [Rh_2Cl_6(PBu_3)_3] + mer\text{-}[RhCl_3(PBu_3)_3] \quad (44)$$

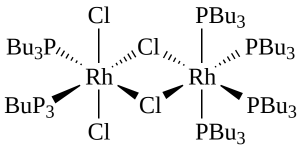

(**33**)

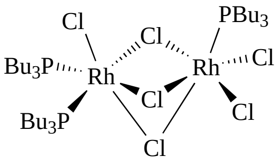

(**34**)

Despite the high trans effect of the hydrido ligand there are also many six-coordinate hydrido complexes of general formula $[RhHX_2(ZR_3)_3]$ (X = halide; Z = P, As). These complexes have two isomeric forms designated α and β and are shown in structures (**35**) and (**36**), respectively. They can be distinguished by means of IR or NMR spectrometry. The action of bases causes reductive elimination of hydrogen halide and the formation of a rhodium(I) complex (equation 45). Similarly, the $[\mathrm{RhX_3L_3}]$ complexes can exist as *fac* or *mer* isomers. The *fac* isomers are formed only by the smallest tertiary phosphines or arsines and are easily outnumbered by the meridional complexes. Virtually no attempts have been made to study the chemical reactions of the *fac* complexes.

$$[\mathrm{RhCl(PEtPh_2)_3}] \underset{\mathrm{PhNH_2}}{\overset{\mathrm{HCl}}{\rightleftharpoons}} \alpha\text{-}[\mathrm{RhHCl_2(PEtPh_2)_3}] \tag{45}$$

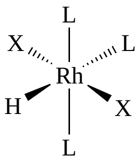

(**35**)

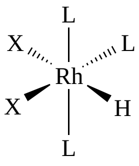

(**36**)

There are very few $[\mathrm{RhX_2L_4}]\mathrm{X}$ complexes, although numerous analogs containing two bidentate neutral ligands have been prepared (see below). Perhaps the most important are the dioxo complexes (**37**), arising from the addition of dioxygen to rhodium(I) complexes. The presence of a peroxo ligand has been confirmed by X-ray crystallography. Dioxygen complexes are well represented and indeed even disulfur analogs have been prepared from cyclo-octasulfur. The dioxygen complexes react with the lower oxides of nonmetals to form complexes containing oxyanions. Complexes containing ditertiary phosphines may be prepared from rhodium(III) halides, by displacing monodentate ligands from rhodium(III) complexes, or by oxidative addition to rhodium(I) complexes (Scheme 21). Strangely, there seem to be no *tris*(ditertiary phosphine or arsine) analogs of $[\mathrm{Rh(en)_3}]^{3+}$ or $[\mathrm{Rh(bipy)_3}]^{3+}$.

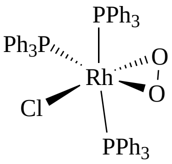
PPh3
Ph3P
O
Rh
O
Cl
PPh3

(**37**)

The tridentate ligands (**38**)–(**40**) form rhodium(I) complexes. The complexes of the first two ligands readily undergo oxidative addition to form rhodium(III) complexes. The complex [RhCl(**38**)] also adds either $\mathrm{SO_2}$ or $\mathrm{BF_3}$ to form pentacoordinate rhodium(I) complexes. The tetradentate ligands (**41**) (Z = P, As) and (**42**) and the hexadentate ligand (**43**) form both rhodium(I) and (III) complexes. By contrast, the tri(tertiary arsine) ligand (**44**) fails to reduce hydrated rhodium trichloride and forms both *fac*- and *mer*-trihalorhodium(III) complexes.

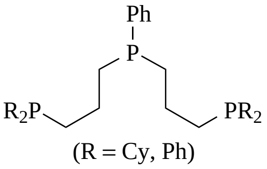
Ph
P
R2P
PR2
(R = Cy, Ph)

(**38**)

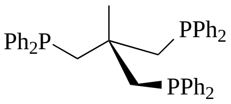
Ph2P
PPh2
PPh2

(**39**)

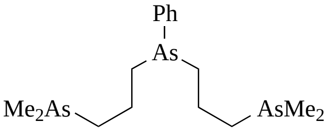
Ph
As
Me2As
AsMe2

(**40**)

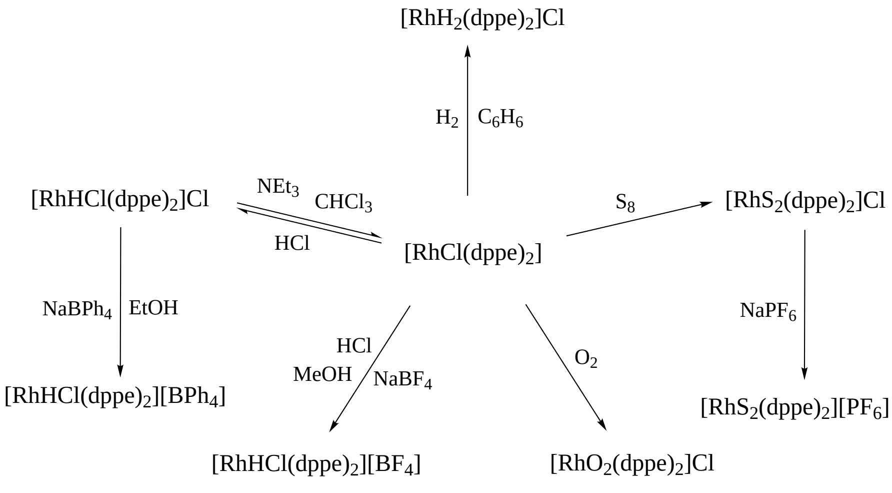
[RhH2(dppe)2]Cl
H2
C6H6
[RhHCl(dppe)2]Cl
NEt3
CHCl3
HCl
[RhCl(dppe)2]
S8
[RhS2(dppe)2]Cl
NaBPh4
EtOH
HCl
MeOH
NaBF4
O2
NaPF6
[RhHCl(dppe)2][BPh4]
[RhHCl(dppe)2][BF4]
[RhO2(dppe)2]Cl
[RhS2(dppe)2][PF6]

Scheme 21

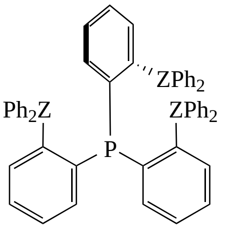

(**41**)

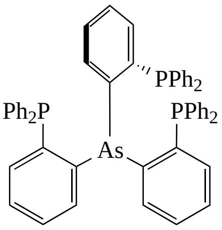

(**42**)

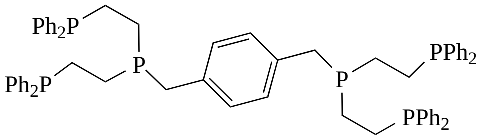

(**43**)

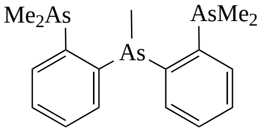

(**44**)

7 THE HIGHER OXIDATION STATES

The number and variety of compounds in oxidation states of four or greater is dramatically lower than for rhodium(III). Essentially only oxo and halo species are formed, and none of these are cationic.

Binary rhodium(IV) compounds are confined to the purple red tetrafluoride and the black dioxide. The hydrated dioxide may be prepared by oxidizing rhodium(III) compounds, either with chlorine or electrochemically. Attempts to dehydrate this material lead to decomposition. No cationic rhodium(IV) complexes have been characterized unambiguously, but both $[RhCl_6]^{2-}$and $[RhF_6]^{2-}$ are well established. The alkali metal salts of the hexafluororhodate(IV) ion are all isomorphous with their platinate(IV) analogs.

The hexahalorhodate(IV) complexes are best prepared by oxidizing the solid hexahalorhodate(III) species with the appropriate halogen. The hexafluororhodate ion is relatively easily hydrolyzed, but the hexachloro anion is a powerful oxidizing agent. In water, it disproportionates to chlorine and aquarhodium(III) species. Indeed, the blue species (Claus' blue) formed on oxidation of rhodium(III) species by chlorine, bromate(I), or ozone in aqueous solution have been shown to be peroxorhodium(III) compounds. Thus, only $Cs_2[RhCl_6]$ (obtained by oxidation with $[Ce(NO_3)_6]^{2-}$) can be precipitated from aqueous solution before decomposition occurs.**15** The hexachlororhodate(IV) ion is also very rapidly reduced via an *Outer-Sphere Reaction* when allowed to react with the $[Ru(phen)_3]^{2+}$ ion. The greater stability of the hexafluoro complex is exemplified by the solid-state preparations of $[O_2][RhF_6]$ and $[NO]_2[RhF_6]$. All the hexahalorhodate(IV) complexes are paramagnetic and are presumably low-spin d^5 species.

A number of poorly characterized materials such as $Na_2[RhO_3]$ or $Sr_4[RhO_6]$ have been reported in the literature. However, most of these materials have been found to be contaminated with rhodium(III) species.

Rhodium(V) is even less well represented than rhodium(IV). The only binary compound is the ruby red, tetrameric pentafluoride. The only complex is $[RhF_6]^-$. Bright yellow $M^I[RhF_6]$ salts (M^I = Na, K, Rb, Cs, but not Li) have been prepared by heating $RhCl_3$ and M^ICl in IF_5 or ClF_5. The sodium salt is paramagnetic and contains the low-spin d^4 rhodium(V) ion. Alkaline-earth salts can also be prepared if gaseous ClF_5 is used as the fluorinating agent. The anions are very moisture sensitive and require strictly anhydrous conditions. Nevertheless, they can be converted to salts of the $O_2{}^+$, NO^+, or $[YF_6]^+$ (Y = Kr, Xe) cations. The colors observed in $[BiO_3]^-$ oxidations of rhodium(III) salts have been associated with the +5 and even +6 oxidation states, but good evidence is lacking.

8 NITROSYL COMPLEXES

Although rhodium forms far fewer *Nitrosyl Complexes* than its neighbor in the *Periodic Table*, ruthenium, over 50 nitrosyl rhodium complexes are known, in addition to some ill-characterized ternary halorhodium nitrosyls. Three main series of complexes exist, with general formulas $[Rh(NO)L_3]$, $[RhX_2(NO)L_2]$, and $[Rh(NO)L_4]X$. There are also a few dinitrosyls of the type $[Rh(NO)_2L_2]X$.

8.1 [Rh(NO)L$_3$]Complexes

The most convenient preparation of the triarylphosphine complexes is from *N*-methyl-*N*-nitrosotoluene-4-sulfonamide and hydrated rhodium trichloride in the presence of the phosphine (equation 46). Other, less convenient, routes to this class of compound exist. The crimson-red crystals of the tris(triphenylphosphine) complex (**45**) contain three independent molecules, each of which has a bent nitrosyl group. In the gas phase or in solution $[Rh(NO)(PF_3)_3]$ appears to contain a linear Rh–N–O group, although this may be an artifact of the methods of structure determination. The very reactive triphenylphosphine compound converts other metal complexes to their nitrosyls (equations 47–49) and itself undergoes a variety of addition and ligand-substitution reactions (Scheme 22). The sulfur dioxide complex is noteworthy in that the ligand is bound through both sulfur and oxygen.

$$RhCl_3 \cdot 3H_2O + PPh_3 + 4\text{-}MeC_6H_4SO_2N(NO)Me \xrightarrow{NaBH_4} [Rh(NO)(PPh_3)_3] \qquad (46)$$

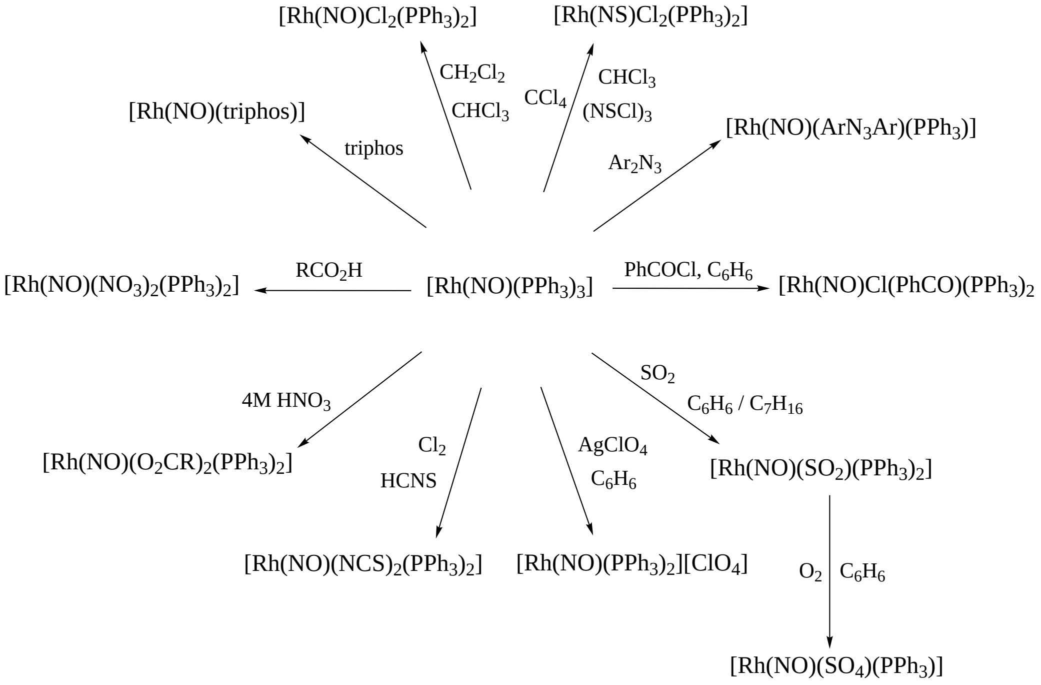
[Rh(NO)Cl$_2$(PPh$_3$)$_2$]
[Rh(NS)Cl$_2$(PPh$_3$)$_2$]
CH$_2$Cl$_2$
CHCl$_3$
CCl$_4$
CHCl$_3$
(NSCl)$_3$
[Rh(NO)(triphos)]
triphos
Ar$_2$N$_3$
[Rh(NO)(ArN$_3$Ar)(PPh$_3$)]
[Rh(NO)(NO$_3$)$_2$(PPh$_3$)$_2$]
RCO$_2$H
[Rh(NO)(PPh$_3$)$_3$]
PhCOCl, C$_6$H$_6$
[Rh(NO)Cl(PhCO)(PPh$_3$)$_2$
4M HNO$_3$
[Rh(NO)(O$_2$CR)$_2$(PPh$_3$)$_2$]
Cl$_2$
HCNS
AgClO$_4$
C$_6$H$_6$
SO$_2$
C$_6$H$_6$ / C$_7$H$_{16}$
[Rh(NO)(SO$_2$)(PPh$_3$)$_2$]
[Rh(NO)(NCS)$_2$(PPh$_3$)$_2$]
[Rh(NO)(PPh$_3$)$_2$][ClO$_4$]
O$_2$
C$_6$H$_6$
[Rh(NO)(SO$_4$)(PPh$_3$)]

Scheme 22

$$[\mathrm{Rh(NO)(PPh_3)_3}] + [\mathrm{FeCl_2(diphos)}] \xrightarrow{\text{thf}} [\mathrm{Fe(NO)_2(diphos)}] \quad (47)$$

$$[\mathrm{Rh(NO)(PPh_3)_3}] + [\mathrm{CoCl(PPh_3)_3}] \xrightarrow{\mathrm{C_6H_6}} [\mathrm{Co(NO)(PPh_3)_3}] \quad (48)$$

$$[\mathrm{Rh(NO)(PPh_3)_3}] + [\mathrm{NiCl_2(PPh_3)_2}] \xrightarrow{\mathrm{C_6H_6}} [\mathrm{Ni(NO)Cl(PPh_3)_3}] + [\mathrm{RhCl(PPh_3)_3}] \quad (49)$$

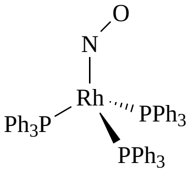

(**45**)

8.2 [RhX$_2$(NO)L$_2$] Complexes

The most convenient preparation of the archtypical complex [RhCl$_2$(NO)(PPh$_3$)$_2$] again involves the reaction between *N*-methyl-*N*-nitrosotoluene-4-sulfonamide and hydrated rhodium trichloride. Many other preparative methods exist; in particular, several other nitrosyl complexes can be converted to [RhCl$_2$(NO)(PPh$_3$)$_2$]. Dichloro(nitrosyl)*bis*(triphenylphosphine)rhodium has the square-pyramidal structure (**46**). The nitrosyl group is bent and both nitrogen and oxygen atoms lie on the RhP$_2$ plane. Surprisingly, the analogs of this complex cannot be obtained from it by metathetical reactions but must instead be prepared from the appropriate starting materials. Indeed, this class of compound is singularly unreactive, in marked contrast to [Rh(NO)L$_3$].

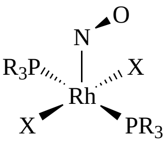

(**46**)

Analogs of the dichloro complex are prepared by a variety of methods, many of which are specific for single compounds. The dibromo complexes can be prepared using nitrosyl bromide or from *N*-methyl-*N*-nitrosotoluene-4-sulfonamide and rhodium tribromide. Replacement of the tribromide by the trichloride and an alkali metal iodide gives diiodo complexes (equations 50 and 51).

$$\mathrm{RhX_3{\cdot}}n\mathrm{H_2O} + \mathrm{4\text{-}MeC_6H_4SO_2N(NO)Me} \xrightarrow[\text{EtOH}]{\mathrm{N_2}} [\mathrm{RhX_2(NO)(PPh_3)_2}]$$
$$(\mathrm{X = Cl, Br}) \quad (50)$$

$$\mathrm{RhCl_3{\cdot}3H_2O} + \mathrm{MI} + \mathrm{PR_3} + \mathrm{4\text{-}MeC_6H_4SO_2N(NO)Me} \xrightarrow[\text{EtOH}]{\mathrm{N_2}} [\mathrm{RhI_2(NO)(PR_3)_2}]$$
$$(\mathrm{R = Et, Bu, Ph, 4\text{-}C_6H_4Me, 4\text{-}C_6H_4Cl}) \quad (51)$$

Nitric acid converts hydridorhodium(I) complexes to the *bis*(nitrato) complex (equation 52). Other examples of these complexes can be obtained from silver nitrate and a six-coordinate carbonyldichloronitrosyl complex. It is also possible to prepare a green chloro nitro complex from chlororhodium(I) complexes and oxides of nitrogen or NOCl (equations 53 and 54). However, no dinitro complex has yet been prepared. *Bis*(carboxylato) complexes are prepared very simply by the reaction of carboxylic acids with aerated solutions of $[Rh(NO)(PPh_3)_3]$ (equation 55). Most of these methods are equally applicable to the production of triphenylarsine complexes. The dihalo complexes may also be prepared from $AsPh_3$ and halonitrosylrhodium complexes. Although all these complexes are believed to have structure (**46**), *cis* basal ligands must be present in $[Rh(NO)Cl(NO_2)(dppe)]$ and $[Rh(NO)(SO_4)(PPh_3)_2]$. The latter structure has also been established for $[Rh(NO)Br_2\{P(OPh)_3\}_2]$. Some thionitrosyl complexes of this stoichiometry have also been prepared but are of doubtful provenance.

$$[RhH(PPh_3)_3] + HNO_3 \longrightarrow [Rh(NO_3)_2(NO)(PPh_3)_2] \quad (52)$$

$$[RhCl(PPh_3)_3] + 4NO \xrightarrow{C_6H_5Cl} [RhClNO_2(NO)(PPh_3)_2] \quad (53)$$

$$trans\text{-}[RhCl(CO)(PPh_3)_2] + NOCl \longrightarrow [RhClNO_2(NO)(PPh_3)_2] \quad (54)$$

$$[Rh(NO)(PPh_3)_3] + RCO_2H \xrightarrow[Me_2CO]{O_2} [Rh(NO)(OCOR)(PPh_3)_2]$$
$$(R = Me, Et, 4\text{-}C_6H_4Me, 4\text{-}C_6H_4NO_2, 4\text{-}C_6H_4Cl, CF_3, C_2F_5, C_6F_5) \quad (55)$$

8.3 Cationic Complexes

Both mono and dinitrosyl cations may be prepared. Salts of the tetrahedral dinitrosyl cation can be prepared either from rhodium nitrosyls (equation 56) or by addition of nitric oxide to ionic rhodium(I) complexes (equation 57). Both nitrosyl groups in complex (**47**) are bent. The action of dppe upon the *bis*(triphenylphosphine) complex produces N_2O. Penta- and hexacoordinate mononitrosyl cations are more common and are usually prepared by the action of $NOPF_6$ or $NOBF_4$ on rhodium(I) complexes in organonitrile solvents (equation 58). The principal reactions of the complexes are substitutions of the nitrile ligands (equations 59–61). A noteworthy feature of (**48**), $[Rh(NO)(MeCN)_3(PPh_3)_2]^+$, is that the MeCN ligand trans to the bent nitrosyl group is said to be bent.

$$[Rh(NO)(PPh_3)_3] + Ag[ClO_4] \xrightarrow{C_6H_6} [Rh(NO)_2(PPh_3)_2][ClO_4] \quad (56)$$

$$[Rh(nbd)(PPh_3)_2][PF_6] + 2NO \longrightarrow [Rh(NO)_2(PPh_3)_2][PF_6] \quad (57)$$

$$[Rh(cod)_2][PF_6] + NOPF_6 \xrightarrow{MeCN} [Rh(NO)(MeCN)_4][PF_6]_2 \quad (58)$$

$$[Rh(NO)(MeCN)_4][PF_6]_2 + Na_2S_2CNMe_2 \longrightarrow [Rh(NO)(S_2CNEt_2)_3][PF_6] \quad (59)$$

$$[Rh(NO)(MeCN)_4][PF_6]_2 + dppe \longrightarrow [Rh(NO)(dppe)_2][PF_6]_2 \quad (60)$$

$$[Rh(NO)(MeCN)_4][PF_6]_2 + PPh_3 \longrightarrow [Rh(NO)(MeCN)_2(PPh_3)_2][PF_6]_2 \quad (61)$$

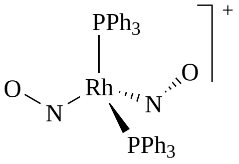

(**47**)

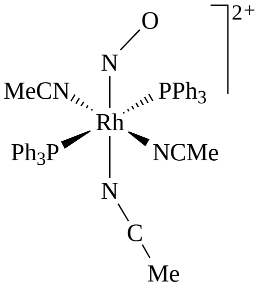

(**48**)

9 RELATED ARTICLES

Ammonia & N-donor Ligands; Asymmetric Synthesis by Homogeneous Catalysis; Decarbonylation Catalysis; Hydride Complexes of the Transition Metals; Hydroboration Catalysis; Hydrogenation & Isomerization of Alkenes; Hydrosilation Catalysis; P-donor Ligands; Rhodium: Organometallic Chemistry.

10 REFERENCES

1. S. Gangoli ed., 'Dictionary of Substances and their Effects', 2nd edn., Royal Society of Chemistry, Cambridge, UK, 1999, Vol. 6, p. 290.
2. L. Gmelins, 'Gmelins Handbuch der anorganischen Chemie', Rhodium, 8th edn., System No. 64, Verlag Chemie, Berlin, 1938, Supplement B1, 1982; Supplement B2, 1984; Supplement B3, 1984; Supplement A1, 1991.
3. F. H. Jardine and P. S. Sheridan, in 'Comprehensive Coordination Chemistry', ed. G. Wilkinson, Pergamon, Oxford, 1987, Vol. 4, Chap. 48, p. 901, references therein.
4. W. P. Griffith, 'The Chemistry of the Rarer Platinum Metals', Wiley, London, 1967.
5. H. M. L. Davies and R. J. Beckwith, *Chem. Rev.*, 2003, **103**, 2861.
6. J. K. Tagirov, E. V. Makarov, and V. A. Bryukvin, *Russ. J. Inorg. Chem.*, 1997, **42**, 919.
7. F. H. Jardine, *Prog. Inorg. Chem.*, 1981, **28**, 63, and references therein.
8. D. G. De Wit, *Coord. Chem. Rev.*, 1996, **147**, 209.
9. F. A. Cotton, E. V. Dikarev, and M. A. Petrukhina, *Angew. Chem., Int. Ed. Engl.*, 2000, **39**, 2362.

10. H. Brunner, *Angew. Chem., Int. Ed. Engl.*, 1992, **31**, 1183.
11. M. E. Prater, L. E. Pence, R. Clérac, G. M. Finniss, C. Campana, P. Auban-Senzier, D. Jérome, E. Canadell, and K. R. Dunbar, *J. Am. Chem. Soc.*, 1999, **121**, 8005.
12. F. Glasbøl, C. H. Petersen, and K. Simonsen, *Acta Chem. Scand.*, 1996, **50**, 567.
13. T. B. Marder, N. C. Norman, C. R. Rice, and E. G. Robins, *Chem. Commun. (Cambridge)*, 1997, 53.
14. K. Osakada, T. Koizume, S. Sarai, and T. Yamamoto, *Organometallics*, 1998, **17**, 1868.
15. I. J. Ellison and R. D. Gillard, *Polyhedron*, 1996, **15**, 339.

Rhodium: Organometallic Chemistry

Joel T. Mague
Tulane University, New Orleans, LA, USA

1	Introduction	1
2	Compounds with Rhodium–Carbon σ-Bonds	1
3	Compounds of Ligands Containing Localized π-Bonds	21
4	Compounds of Ligands Containing Delocalized π-Bonds	27
5	Miscellaneous Complexes	30
6	Related Articles	31
7	References	32

Abbreviations

Acac = acetyacetonate; $BAr_f{}^-$ = tetra(3,5-bis(trifluoromethyl)phenyl)borate anion; bridge = 1,3-diisocyanopropane; COD = cycloocta-1,5-diene; COE = cyclooctene; DFT = Density Functional Theory; dimen = 2,1,8-diisocyanomenthane; DMAD = dimethylacetylene dicarboxylate; DMSO = dimethylsulfoxide; dpmp = bis(diphenylphosphinomethyl) phenylphosphine; DPPB = 1,4-bis(diphenylphosphino)butane; DPPE = 1,2-bis(diphenylphosphino)ethane; DPPM = bis(diphenylphosphino)methane; en = 1,2-diaminoethane; hfac = hexafluoroacetylacetonate; HFB = hexafluorobut-2-yne; HOTf = trifluoromethanesulfonic acid (triflic acid); MLCT = Metal Ligand Charge Transfer; MO/MM = Molecular Orbital/Molecular Mechanics; NBD = bicyclo[2.2.1]heptadiene; OTf^- = trifluoromethanesulfonate (triflate) ion; OTs^- = *p*-toluenesulfonate (tosylate) ion; *p*-anis = *p*-$MeOC_6H_4$; pip = piperidine; pn = 1,2-diaminopropane; PPN^+ = bis(triphenylphosphine)iminium cation; *p*-tol = *p*-MeC_6H_4; pz = pyrazolate; QM/MM = Quantum Mechanics/Molecular Mechanics; TFB = tetrafluorobenzobarrelene; TM4 = 2,5-diisocyano-2,5-dimethylhexane; tn = 1,3-diaminopropane.

1 INTRODUCTION

The organometallic chemistry of rhodium continues to comprise a substantial portion of the field of organotransition metal chemistry. Some highlights of the work published since the appearance of the previous report[1] include substantial progress in the activation of C–H bonds in homogeneous systems, the synthesis of a large number of complexes containing vinylidene (=C=CRR′) and allenylidene (=C=C=CRR′) ligands and the chemistry of rhodium alkyl complexes containing tridentate nitrogen-donor ligands in place of the more traditional phosphine ligands.

A comprehensive work covering the organometallic chemistry of rhodium for the period 1982–1994[2] has appeared as have reviews of rhodium allenylidene complexes,[3] cationic rhodium arene complexes,[4] and the involvement of rhodium complexes in C–C coupling reactions.[5] Rhodium complexes are mentioned in a review of the use of ‘‘short bite’’ ligands (particularly DPPM) in cluster synthesis[6] and in reviews of the organometallic chemistry of porphyrin compounds,[7] complexes containing both heavy main group elements and transition metals,[8] complexes containing σ-π bridging vinyl, alkenyl, and related ligands,[9] complexes of polyynes,[10] homogeneous catalysis in water,[11] ‘‘very mixed’’ metal–carbonyl cluster compounds (e.g. $Cp_2Cr_2Rh(COD)(\mu_3\text{-}S)_2(\mu\text{-}SBu^t)(CO)_2)$,[12] and the transition metal assisted oligomerization of phosphaalkynes.[13]

The emphasis in the present chapter will be on recent developments in the area of organorhodium chemistry, and as there have been few reports of new synthetic methodologies, the new practitioner is referred to the previous report[1] for references to established procedures.

2 COMPOUNDS WITH RHODIUM–CARBON σ-BONDS

2.1 Alkyl and Aryl Complexes

In contrast to the impression that might be gained from earlier work, the presence of ‘‘soft’’ phosphine or arsine ligands is not required for the preparation of stable alkyl or aryl rhodium complexes. Considerable use has recently been made of the tridentate, nitrogen-donor ligands Cn (**1**, R = H (also called tacn)), Cn* (**1**, R = Me), and Tp′ (**2**, R = R′ = Me; R″ = H) in studying reactions of alkylrhodium complexes, particularly those involving reductive eliminations to form C–H bonds, where mounting evidence for the formation of σ-complexes (*see* ***Dihydrogen Complexes & Related Sigma Complexes***) of hydrocarbons with rhodium has been obtained. These ligands are considered to be analogs of the cyclopentadienyl ligands but with different steric and electronic properties.

Alkylation of $CnRhCl_3$ by standard methods (equation 1) yields $CnRhR_3$ (R = Me,

$$(Cn)RhCl_3 \xrightarrow{\text{xs RLi}} \xrightarrow{\text{MeOH}} (Cn)RhR_3 \qquad (1)$$

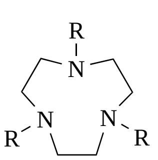

(**1**)

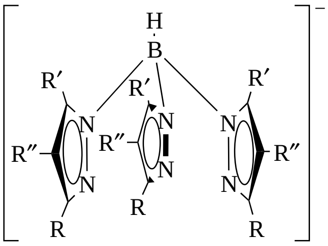

(**2**)

Et, Ph, vy, Bu^n, n-hexyl, n-decyl). Protonation of $CnRhR_3$ ($R = Me$, Et, Ph, Bu^n, n-hexyl, n-decyl) with two equivalents of HOTf followed by addition of a phosphorus ligand ($L = PMe_3$, $P(OMe)_3$) and reduction with $NaBH_4$ (equation 2) yields alkyl hydride (*see* ***Hydride Complexes of the Transition Metals***) complexes [CnRh(H)R(L)]Otf, which together with some Cn* analogs, were used to study the reductive elimination of alkane (RH). For $R = Me$, the half-life for the elimination of methane at 80 °C was 7 h indicating this to be a particularly stable alkyl hydride complex of rhodium. Heating [CnRh(H)R(L)]OTf ($R = n$-Bu, n-hexyl, n-decyl) in benzene forms $[CnRh(H)(C_6H_5)(L)]OTf$ via the activation of a C–H bond (*see* ***Alkane Carbon–Hydrogen Bond Activation***) of benzene by the reductive elimination product, {(Cn)Rh(L)}. The same process using [CnRh(D)R(L)]OTf led to deuterium incorporation into *both* terminal methyl groups of the product alkane leading to the proposal that the eliminated alkane remains associated with the {CnRh(L)} fragment, presumably via an Rh···H–C interaction (*see* ***Dihydrogen Complexes & Related Sigma Complexes***), and that the metal migrates down the alkane chain through a series of such interactions.[14]

$$\begin{tikzcd}
\mathrm{(Cn)RhR_3} + \mathrm{HOTf} \arrow[r] & \mathrm{(Cn)Rh(R)(OTf)_2} \arrow[dl, "L"'] \\
\mathrm{(Cn)Rh(R)((OTf)OTf} \arrow[r, "\mathrm{NaBH_4}"] & \mathrm{(Cn)Rh(R)((L)(H)OTf}
\end{tikzcd}$$

(2)

Protonation of $Cn^*Rh(vy)_3$ with HOTf yields the allyl complex $[Cn^*Rh(vy)(\eta^3\text{-}CH_2CHCHMe)]OTf$ (see also Section 4.1) in which coupling of two of the vinyl groups is proposed to proceed via an alkylidene intermediate (equation 3).[15]

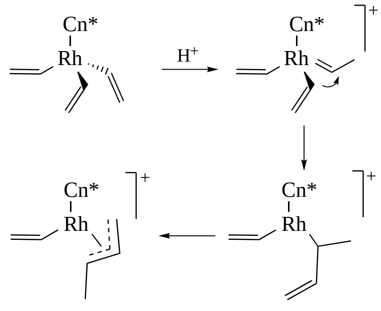

(3)

The starting point for the formation of alkylrhodium complexes containing the Tp′ ligand is $Tp'Rh(CNR')Cl_2$ ($R' = CH_2CMe_3$), which is prepared by replacement of the weakly bound acetonitrile ligand in $Tp'Rh(NCMe)Cl_2$ by the isocyanide. Conversion of this to the alkyl hydrides $Tp'Rh(CNR')(H)(R)$ ($R = CH_2CD_3$, Pr^n, Pr^i, vy, *cyclo*-C_3H_5) (*see* ***Hydride Complexes of the Transition Metals***) proceeds via equation (4). When $R = cyclo\text{-}C_3H_5$, rearrangement to the metallacylcobutane isomer occurs readily and is proposed to involve reductive elimination to give a σ-cyclopropane complex followed by insertion of the metal into a strained C–C bond. On heating, this rearranges again to the isomeric propene complex from which the olefin is liberated under photolysis with the solvent benzene undergoing C–H oxidative addition (*see* ***Alkane Carbon–Hydrogen Bond Activation***) to the reactive {Tp′Rh(CNR′)} fragment (equation 5).

$$\mathrm{Tp'Rh(CNR')Cl_2} \xrightarrow{\mathrm{RMgX}} \mathrm{Tp'Rh(CNR')(R)Cl} \xrightarrow{\mathrm{Cp_2ZrH_2}} \mathrm{Tp'Rh(CNR')(R)(H)} \qquad (4)$$

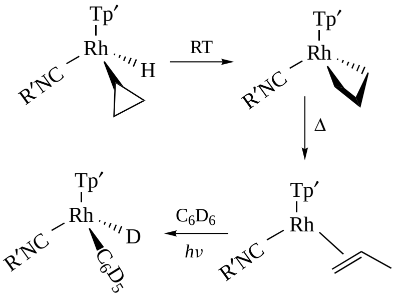

(5)

Reduction of $Tp'Rh(CNR')(vy)Cl$ with $CpZrH_2$ forms $Tp'Rh(CNR')(vy)(H)$, which rearranges at room temperature to the ethylene complex $Tp'Rh(CNR')(\eta^2\text{-}C_2H_4)$. To explore the regiochemistry of the C–H oxidative addition process in related systems, the {Tp′Rh(CNR′)} fragment was generated by photolysis of (**3**) in three liquid olefins. For $R = H$ and Me, oxidative addition occurs at a methyl C–H bond (*see* ***Alkane Carbon–Hydrogen Bond Activation***) to form the corresponding allyl hydride (equation 6). When $R = Me$, C–H reductive elimination occurs over three days at room temperature in benzene solution to form the propene complex

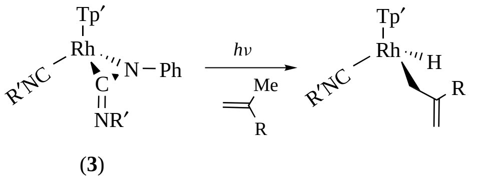

(**3**)

(6)

$Tp'Rh(CNR')(\eta^2\text{-}CH_2{=}CHMe)$, while for R = Me, the reductive elimination occurs more readily and the olefin complex is less stable so that the ultimate product is the benzene activation product $Tp'Rh(CNR')(H)(C_6H_5)$. Photolysis of (**3**) (*see* ***Photochemistry of Transition Metal Complexes***) in liquid *t*-butylethylene leads to oxidative addition of a vinylic C–H (*see* ***Alkane Carbon–Hydrogen Bond Activation***) bond yielding $Tp'Rh(CNR')(H)(CH{=}CHCMe_3)$, presumably because the bulk of the *t*-butyl group prevents this end of the molecule getting sufficiently close to the metal. This vinyl hydride complex is considerably more resistant to reductive elimination than the allyl hydride species and again the ultimate decomposition product is $Tp'Rh(CNR')(H)(C_6H_5)$. The methyl hydride complex $Tp'Rh(CNR')(H)(CH_3)$ in C_6D_6 solution at room temperature undergoes H/D exchange to initially form $Tp'Rh(CNR')(H)(CH_2D)$ and more slowly the solvent activation product $Tp'Rh(CNR')(D)(C_6D_5)$ plus CH_3D. The rate of reductive elimination of methane in C_6H_6/C_6F_6 mixtures depends on the concentration of benzene. Both observations are consistent with the presence of a rhodium–methane σ-complex (*see* ***Dihydrogen Complexes & Related Sigma Complexes***), which forms subsequent to the reductive elimination.[16]

Photolysis of $Tp'Rh(CO)_2$ in alkane solution (*see* ***Photochemistry of Transition Metal Complexes***) forms $Tp'Rh(CO)(H)(R)$ (R = *n*-pentyl, *n*-hexyl, *n*-heptyl, *i*-octyl) via oxidative addition of a C–H bond (*see* ***Alkane Carbon–Hydrogen Bond Activation***) to the reactive intermediate {$Tp'Rh(CO)$}. The wavelength dependence of the quantum yield suggests the involvement of two different excited states of differing reactivity. The lack of a thermal reaction in the dark suggests that a species with an η^2-Tp′ ligand is not involved. The analogous reaction with the modified tris(pyrazolylborate) ligand (**4**) resulted in oxidative addition of a C–H bond of the isopropyl substituent to the metal to form the pair of isomers shown in equation (7). These were shown to thermally interconvert via a rate-determining C–H reductive elimination/oxidative addition process within a single arm of the ligand, and without inversion of configuration at the metal.[17] The reaction of Lewis base ligands (L = py, MeCN) with $Tp'Rh(C_2H_4)_2$ and subsequent chemistry is outlined in equation (8). These results are interpreted as shown in equation (9).

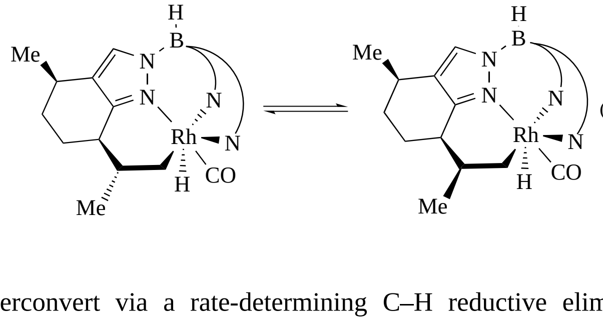

(7)

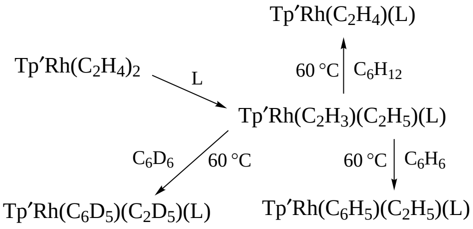

(8)

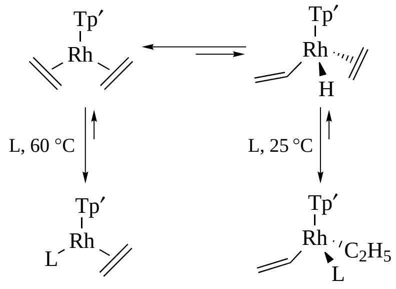

(9)

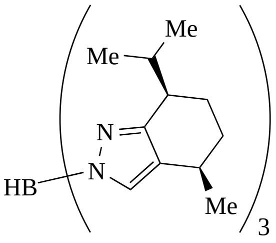

(**4**)

The key feature is the presence of a small equilibrium quantity of the vinyl hydride complex $Tp'Rh(H)(CH{=}CH_2)(\eta^2\text{-}C_2H_4)$ formed by C–H oxidative addition of one of the ethylene ligands. The formation of $Tp'Rh(C_2H_5)(C_6H_5)(L)$ and its deuterated analog are postulated to arise from coordination of benzene to the ethylene-loss species {$Tp'Rh(\eta^2\text{-}C_2H_4)$} followed by C–H oxidative addition (*see* ***Alkane Carbon–Hydrogen Bond Activation***).[18]

A series of more highly substituted (R = R′ = Me, CF_3; R′ = H. R = CF_3; R′ = Me; R″ = H. R = Me; (R,R′) = -$(CH_2)_3$-, -$(CH_2)_4$-) and unsymmetrical (R = Ph; R′ = Me; R″ = H on two pyrazolate rings and R,R′ = Me, Ph; Me,Me; Et,Et on the third), examples of (**2**) ($Tp^{R,R'}$) were used to prepare ($Tp^{R,R'}$) RhL_2 (L = CO, L_2 = COD). Experimental and theoretical studies of the structures and conformational preferences of these complexes were performed.[19]

Several further experimental and theoretical studies of the oxidative addition of methyl iodide to Rh(I) complexes have been reported, in part because of its importance in the rhodium-catalyzed carbonylation of methanol (*see* ***Carbonylation Processes by Homogeneous Catalysis***) to acetic acid (equation 10).

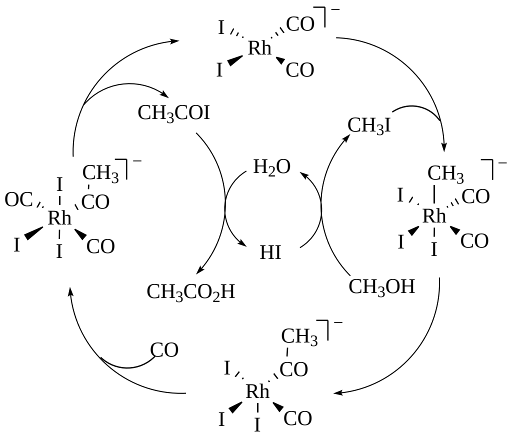

(10)

These include the reaction with (η^2-Tp′)Rh(L)(CO) (L = PMe_3, PMe_2Ph, $PMePh_2$, PPh_3) where the initial product is [(η^3-Tp′)Rh(L)(CO)Me]I, and slow conversion to the acyl derivative (η^3-Tp′)Rh(L)(C=(O)Me)(I) ensues. The second order kinetics, a correlation of rates with the basicity of L and a large negative value for $\Delta S^\ddagger$ indicate an associative activation process. The much lower reactivity of analogous bis(pyrazolyl)borate complexes suggests that the ability of Tp′ to change from η^2 to η^3 coordination at some point on the reaction coordinate is important to facilitating the process.**20** With $[\mathrm{Rh}(\mu\text{-Cl})(\mathrm{Pr}^i_3\mathrm{P})_2]_2$ and $\mathrm{RhCl}(\mathrm{PEt}_3)_3$ at −20 °C, methyl iodide (*see* ***Carbon–Carbon & Carbon–Heteroatom Activation***) forms 5- and 6-coordinate oxidative adducts, respectively, but with $(\mathrm{Pr}^i_3\mathrm{P})_2\mathrm{Rh}(\eta^2\text{-OTf})$, no reaction occurs at room temperature even in the presence of excess methyl iodide. Evidently, the nature of the anionic ligand (chloride is the better donor) and possibly the coordination number at Rh(I) are important factors for the success of the reaction.

A low (circa 1%) steady state concentration of $[\mathrm{Rh}(\mathrm{CH}_3)(\mathrm{CO})_2\mathrm{I}_3]^-$ has been detected spectroscopically when salts of $[\mathrm{RhI}_2(\mathrm{CO})_2]^-$ are dissolved in methyl iodide confirming the identity of the proposed initial oxidative adduct of methyl iodide to $[\mathrm{RhI}_2(\mathrm{CO})_2]^-$ in the methanol carbonylation process (*see* ***Carbonylation Processes by Homogeneous Catalysis***) (right side of equation 10). The transition state for this initial step has been explored by ab initio calculations (*see* ***Molecular Orbital Theory***) and two reasonable models were obtained. Both involve attack of the metal on the methyl group with the more energetically favored occurring opposite the iodine. This is the ''classical'' model for the transition state that leads to an inversion at carbon, and is also preferred on the basis of a comparison of the observed and calculated kinetic isotope effects of the reaction. The other plausible transition state involves attack adjacent to iodine and leads to retention at carbon.**21** Another computational study explored the conversion of $[\mathrm{Rh}(\mathrm{CH}_3)(\mathrm{CO})_2\mathrm{I}_3]^-$ to $[\mathrm{Rh}(\mathrm{C}(=\mathrm{O})\mathrm{CH}_3)(\mathrm{CO})\mathrm{I}_3]^-$ (lower right of equation 10) using DFT methods (*see* ***Molecular Orbital Theory***), from which it was concluded that it is a migratory insertion process with the methyl group migrating to a carbonyl ligand.**22** In a related study, spectroscopic and structural evidence for this migration of a methyl group between rhodium and a coordinated carbonyl ligand were obtained, as outlined in equation (11). In the first step, the diastereomer shown comprises 89% of the product acyl complex and the subsequent deinsertion/insertion processes occur stereospecifically indicating movement of the methyl group.**23** Both the oxidative addition and methyl migration steps have been independently studied in detail in the system depicted in equation (12).**24** Also reported is the cis oxidative addition of methyl iodide to both rhodium centers in $\mathrm{Pd}\{(\mu\text{-pz})(\mu\text{-SBu}^t)\mathrm{Rh}(\mathrm{CO})(\mathrm{P}(\mathrm{OMe})_3)\}_2$, which is followed by methyl migration to carbon monoxide on both centers such that the two acyl ligands formed are on the same side of the mean molecular plane.**25**

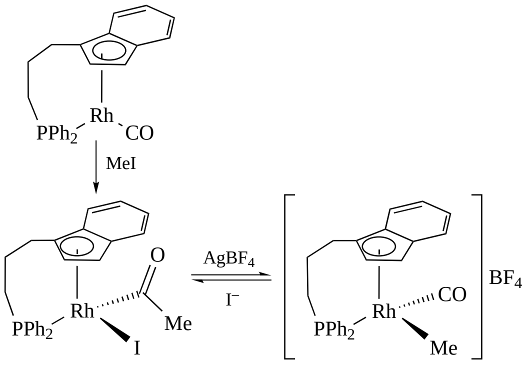

(11)

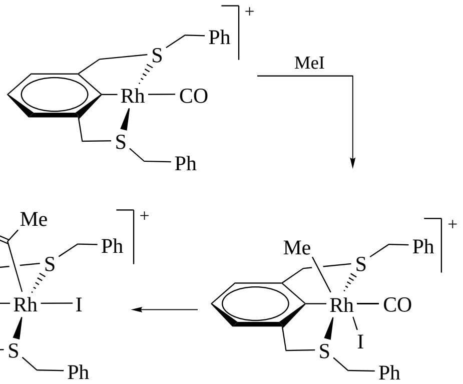

(12)

Laser flash photolysis (*see* ***Luminescence Behavior & Photochemistry of Organotransition Metal Compounds*** and ***Photochemistry of Transition Metal Complexes***) coupled with rapid infrared analysis of the solution species has proved a powerful tool for the detection of unstable intermediates, and has seen considerable application on experimental studies of the C–H oxidative addition reaction (*see* ***Alkane Carbon–Hydrogen Bond Activation***). Application to toluene solutions of $\mathrm{Cp}^*\mathrm{Rh}(\mathrm{PMe}_3)(\eta^2\text{-C}_2\mathrm{H}_4)$ has allowed detection of the intermediate $\mathrm{Cp}^*\mathrm{Rh}(\mathrm{PMe}_3)(\eta^2\text{-toluene})$, and by following the subsequent conversion to $\mathrm{Cp}^*\mathrm{Rh}(\mathrm{PMe}_3)(\mathrm{H})(\mathrm{C}_6\mathrm{H}_4\mathrm{Me})$, activation parameters for the C–H oxidative addition process have been derived. In a related study, the reductive elimination of this last species and analogous aryl hydride complexes showed that the activation barrier for the process increased and the transition state became ''looser'' as the substituents on the aryl group became more electron-withdrawing. It appears now that η^2-coordination of arenes to {Cp*Rh(PMe$_3$)} and related coordinatively unsaturated species precedes C–H oxidative addition, and control of the degree to which this occurs seems to depend on the extent to which the η^2-coordination disrupts the resonance stabilization of the arene.**[26]**

With the development of powerful methods for molecular orbital calculations (e.g. DFT) (*see* ***Molecular Orbital Theory***), several computational studies of the C–H oxidative addition (*see* ***Alkane Carbon–Hydrogen Bond Activation***) process have been undertaken. One has used {CpRh(PH$_3$)} to model the reactive intermediate {Cp*Rh(PMe$_3$)} proposed for the reaction shown in equation (13). The results suggest that reaction occurs from a singlet potential-energy surface via an initial σ-H–C$_3$H$_5$ complex through a single transition state to the cyclopropyl hydride complex, which is the kinetic product. They also indicate that the subsequent thermal rearrangement to the metallacyclobutane complex proceeds via C–H reductive elimination to the same σ-H–C$_3$H$_5$ complex followed by metal insertion into a C–C bond (*see* ***Carbon–Carbon & Carbon–Heteroatom Activation***) (see also equation 5).**[27]** In contrast, DFT calculations on the oxidative addition of methane to {CpM(L)} (M = Rh, Ir; L = CH$_2$, CO, SH$_2$, PH$_3$) suggest that C–H oxidative addition should proceed from the triplet state since it is said that the singlet-triplet splitting (*see* ***Electronic Structure of Organometallic Compounds***) correlates with both $\Delta H^\ddagger$ and ΔH for the process, but no comments are made in the previous paper about this difference.**[28]** A third study used ab initio methods to probe the preference for intermolecular C–H oxidative addition, as modeled by {CpRh(PH$_3$)} + CH$_4$, versus an intramolecular process involving a ligand substituent as modeled by {CpRh(PH$_2$R)} (R = Me, Et). The conclusion is that the intermolecular process has a lower activation barrier.**[29]** In an elaborate computational study, DFT methods that included quantization of vibrational energy, addition of zero-point energy and tunneling effects were used to probe the conversion of RhCl(η^2-H$_2$CH$_2$)(PH$_3$) to RhCl(H)(CH$_3$)(PH$_3$). At 200 K, the calculated rate constant was increased by a factor of 194 over that calculated using classical mechanics to describe the atomic motions along the reaction coordinate. So far there appear not to be sufficient experimental data for comparison.**[30]** A final paper used DFT methods to explore the C–H activation step in the Rh$_2$(OAc)$_4$ catalyzed coupling of a diazo compound with an alkane that finds significant application in organic synthesis (*see* ***Organic Synthesis Using Metal-mediated Coupling Reactions*** and ***Organic Synthesis using Transition Metal Carbonyl Complexes***). The results indicate that the diazo compound should coordinate to an axial site on the dinuclear complex via carbon with back-donation of electron density into the C–N σ^* orbital, facilitating extrusion of N$_2$ and formation of an intermediate carbene complex (see also Section 2.4 and ***Carbene Complexes***). The highly electrophilic carbene carbon then attracts the C–H bond of the alkane leading to the development of a three-center transition state (equation 14).**[31]**

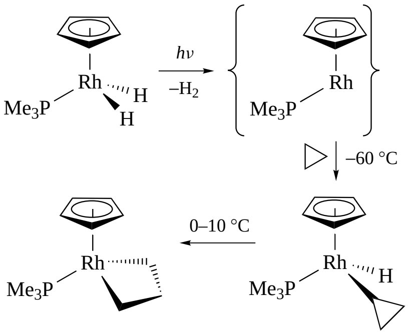

(13)

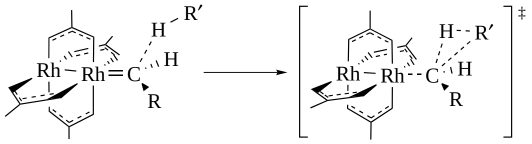

(14)

The early ideas that C–H oxidative addition (*see* ***Alkane Carbon–Hydrogen Bond Activation***) requires constraining the C–H bond to be close to the metal have been shown to be incorrect as many examples of unconstrained, intermolecular C–H oxidative addition are now known. Nevertheless, a considerable number of reports continue to appear on activation of C–H and C–C bonds in constrained, intramolecular systems. One series uses the ''pincer'' ligands (**5**) and (**6**). Reaction of (**5**) (R = Bu^t; R$_1$ = Et; R$_2$ = R$_3$ = H) with [Rh(μ-Cl)(L)$_2$]$_2$ (L = C$_2$H$_4$, COE) forms (**7**), which on prolonged heating converts to (**8**), conditions under which analogs with a methyl, trifluoromethyl, or β,β,β-trifluoroethyl group in place of the ethyl group were stable. This indicates (**8**) formed by β-H elimination, with the bulk of the tridentate ligand enforcing the necessary coordinative unsaturation in (**7**) and then enhancing the dissociation of the product olefin. Complex (**8**) can also be obtained directly from [Rh(μ-Cl)(L)$_2$]$_2$ (L = C$_2$H$_4$, COE) and (**5**) (R = Bu^t; R$_1$ = R$_2$ = R$_3$ = H) by oxidative addition of the C–R$_1$ (=H) bond. The insertion of Rh into the sp^2-sp^3 C–C bond (*see* ***Carbon–Carbon & Carbon–Heteroatom Activation***) in forming (**7**) rather than a C–H or a sp^3-sp^3 C–C bond is suggested to be kinetically controlled. To further explore the factors controlling preferences for C–H (*see* ***Alkane Carbon–Hydrogen Bond Activation***) versus C–C (*see* ***Carbon–Carbon & Carbon–Heteroatom Activation***) activation in these types of complexes, the reaction of (**6**) (X = OMe) with [Rh(COE)$_2$S$_n$]BF$_4$ (S = THF, MeOH, acetone) was performed leading to isolation of a mixture of (**9**) and (**10**), which on heating or on evaporation of the solvent converted to (**11**).

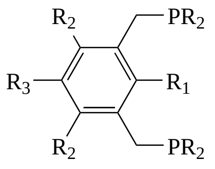
R2
PR2
R3
R1
R2
PR2

(**5**)

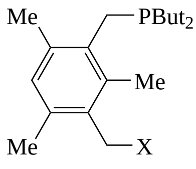
Me
PBut2
Me
Me
X

(**6**)

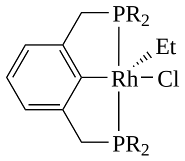
PR2
Et
Rh
Cl
PR2

(**7**)

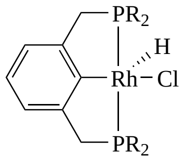
PR2
H
Rh
Cl
PR2

(**8**)

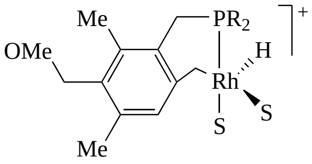
Me
PR2
+
OMe
H
Rh
S
S
Me

(**9**)

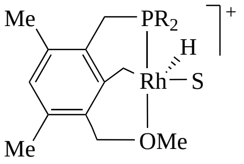
Me
PR2
+
H
Rh
S
OMe
Me

(**10**)

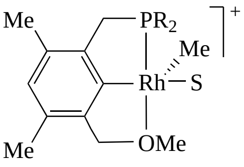
Me
PR2
+
Me
Rh
S
Me
OMe

(**11**)

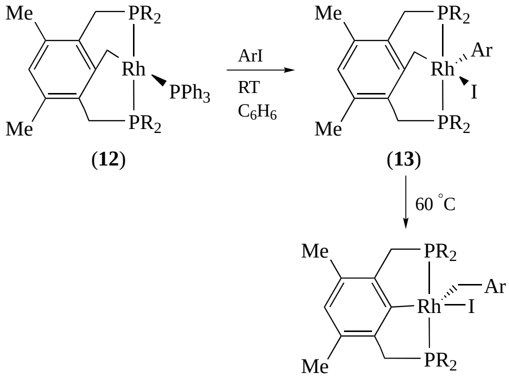
Me
PR2
Rh
PPh3
Me
PR2
(12)
ArI
RT
C6H6
Me
PR2
Rh
Ar
I
Me
PR2
(13)
60 °C
Me
PR2
Rh
Ar
I
Me
PR2
(14)

(15)

Molecular orbital calculations (*see* ***Molecular Orbital Theory***) indicate that the presence of a highly coordinatively unsaturated 14-electron Rh center is important for both C–C and C–H activation, but that for C–C activation to occur, the methoxy group of the ligand has to be coordinated to bring the central C–CH_3 bond close to the metal. Presumably, coordination of the solvent to the starting Rh(I) complex prevents (**6**) from binding as a bidentate ligand so this condition is not initially met. Removal of solvent permits additional binding of the methoxy substituent, and following reductive elimination, C–C activation occurs. In contrast to some of the computational studies mentioned earlier, a ''direct'' C–H oxidative addition (without initial formation of a σ-complex) is indicated by the calculations. Reaction of (**5**) (R = Ph; $R_1 = R_2 =$ Me; $R_3 =$ H) with $Rh(H)(PPh_3)_4$ forms the C–H activation product, (**12**), which oxidatively adds aryl iodides (Ar = Ph, *p*-XC_6H_4 (X = Me, OMe, CF_3), 3,5-$(CF_3)_2C_6H_3$) (equation 15). Complexes (**13**) on heating undergo transfer of a methylene group to form (**14**). This is proposed to occur via reductive elimination of the two Rh–C bonds in (**13**) followed by insertion of the metal into the C–CH_2Ar bond (*see* ***Carbon–Carbon & Carbon–Heteroatom Activation***). To probe the feasibility of the reverse transfer (**14** to **13**), an analog of (**12**) was reacted with $ArCH_2Br$ (Ar = *p*-$CF_3C_6H_4$) and then with phenyl lithium followed by triphenylphosphine (equation 16). The phenyl lithium replaces the bromide ligand to yield an intermediate with three Rh–C bonds, and coordination of the phosphine induces competitive reductive elimination of either the phenyl and benzyl groups to form the product pair on the left or the benzyl group with the Rh–C bond to the ligand. The latter process is followed by activation of a benzyl C–H bond and reductive elimination of benzene to form the product pair on the right.

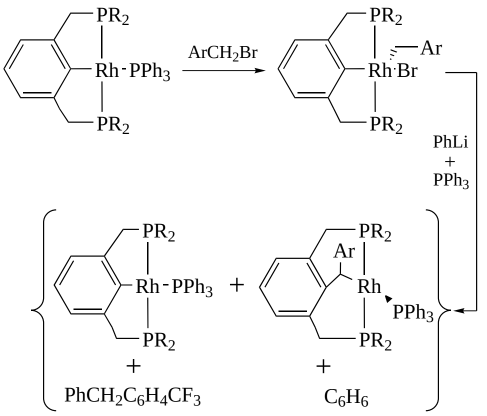
PR2
Rh
PPh3
PR2
ArCH2Br
PR2
Ar
Rh
Br
PR2
PhLi
+
PPh3
PR2
Rh
PPh3
PR2
+
PhCH2C6H4CF3
+
PR2
Ar
Rh
PPh3
PR2
+
C6H6

(16)

Reaction of (**5**) (R = Bu^t; R_1 = H; $R_2 = R_3$ = H, OMe) with $[Rh(\eta^2\text{-}C_2H_4)(CO)(THF)_{1,2}]OTf$ at room temperature forms a species formulated as (**15a**,**b**). The crystal structure shows the presence of an agostic hydrogen on the ring carbon adjacent to the metal indicating that oxidative addition of this C–H bond to the metal has not occurred, and so this is presumably a precursor to complexes like (**8**). That the agostic hydrogen is not in the plane of the attached ring is taken to indicate that this ring exhibits some degree of arenium

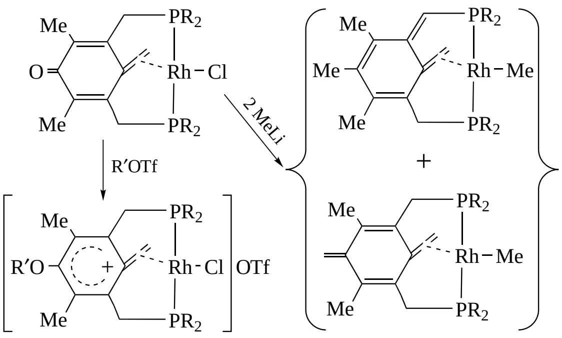

(17)

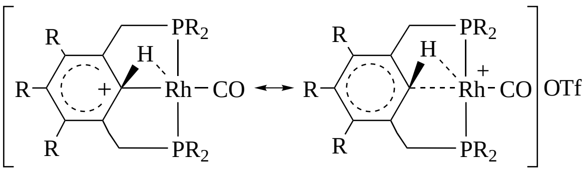

(**15a**) (**15b**)

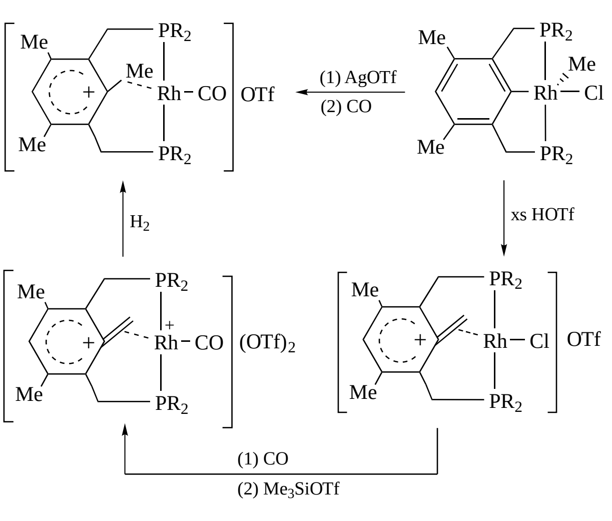

(18)

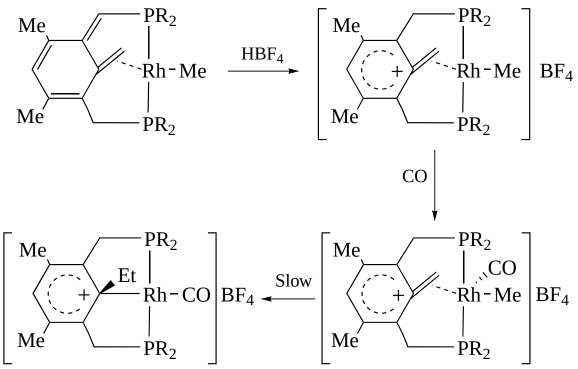

(19)

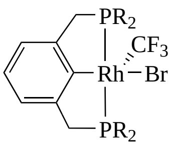

(**16**)

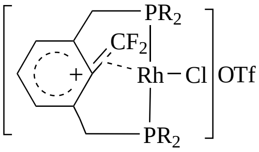

(**17**)

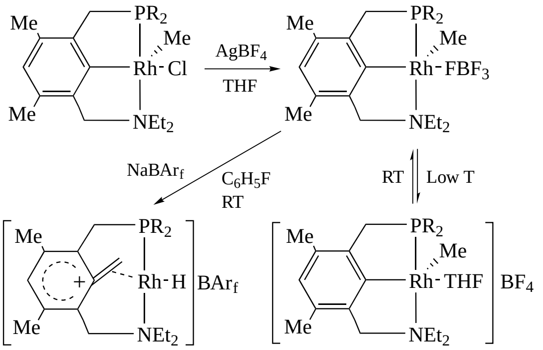

(20)

character. In deliberate attempts to generate arenium character in the central ring of the pincer ligand, the reaction sequence of equation (17) (R = Bu^t; R′ = H, $\mathrm{SiMe_3}$) was performed. The structure of the cationic complex showed a significant averaging of the C–C distances in the six-membered ring as compared with the quinoid precursor indicating it to be formulated as a methylene arenium cation. The two products of the reaction at the right of this scheme are characterized as metal stabilized xylylenes. Under forcing conditions, (**5**) (R = Bu^t; $\mathrm{R_1} = \mathrm{CF_3}$; $\mathrm{R_2} = \mathrm{R_3} = \mathrm{H}$) reacts with $[\mathrm{Rh}(\mu\text{-Cl})(\mathrm{L})_2]_2$ (L = $\mathrm{C_2H_4}$, COE) with cleavage of the C–$\mathrm{CF_3}$ bond to form (**16**). Protonation of (**16**) with HOTf yields the difluoromethylene arenium salt (**17**). Similar processes occur with the systems shown in equations (18) and (19), where both methylene arenium and methyl arenium cations were generated. The alkyl arenium compounds appear to have considerably less positive charge in the ring than do the methylene arenium analogs. This proposed to be the result of stabilization of the arene form via an agostic interaction of the $\mathrm{C_{ipso}}$–$\mathrm{C_{alkyl}}$ bond with the metal. The transformations depicted in equation (19) indicate that direct transfer of an alkyl group to the methylene arenium cation does not occur. Most recently, reaction of (**6**) (X = $\mathrm{NEt_2}$) with $[\mathrm{Rh}(\mu\text{-Cl})(\mathrm{COE})_2]_2$ has been reported to proceed via oxidative addition of the central methyl group to the metal as observed in related systems. Chemistry following chloride abstraction from the initial product in THF solution is outlined in equation (20). The formation of the methylene arenium cation in this instance is proposed to be the result of the noncoordinating character of the solvent fluorobenzene and the counterion $[\mathrm{BAr_f}]^-$ (*see **Boron: Organoboranes***) that forces a high degree of unsaturation upon the 14-electron metal leading to methyl transfer to the ring followed by β-H elimination.[32,33]

While ligands like (**5**) that force a C–H bond close to rhodium could be expected to facilitate C–H activation (*see*

Alkane Carbon–Hydrogen Bond Activation), such behavior might not be expected of a monophosphine. However, in the reaction of $[Rh(\mu\text{-Cl})(COE)_2]_2$ with four equivalents of $PhCH_2CH_2PBu^t{}_2$, this is observed as the product in (**18**) and conversion to (**19**) occurs on chloride abstraction (see also (**174**), Section 42).[34] A related situation is obtained when $[Rh(\mu\text{-Cl})(Bu^t{}_2PCH_2PBu^t{}_2)]_2$ is treated with neopentyl lithium where the highly unsaturated, 14-electron metal in the product, (**20**), is stabilized by an agostic interaction.[35]

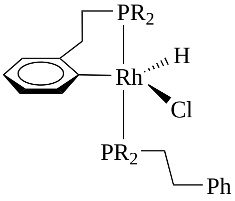
(**18**)

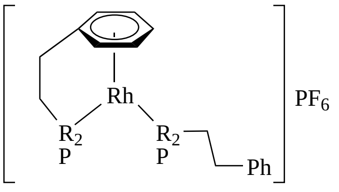
(**19**)

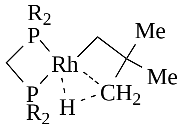
(**20**)

Recent work has also focused on the bis(oxazoline) ligands (**21**) ($R_1 = R_2 = Me$. $R_2 = H$; $R_1 = Me$, Et, Pr^i, Bu^i, Bu^t, Ph. $R' = H$, Me). Reaction with $RhCl_3{\cdot}3H_2O$ forms (**22**) in which there is an agostic interaction with the endo methyl group when $R_1 = R_2 = R' = Me$. On successive reactions with dimethyl zinc (*see* ***Zinc: Organometallic Chemistry***), AgOTf, and $NaBAr_f$, (**22**) ($R' = Me$, $R_2 = H$, $R_1 = Pr^i$) forms (**23**) where methyl migration to the aromatic ring (via C–C reductive elimination) occurs on reaction with neutral ligands to form (**24**) ($L = CO$, C_2H_4).[36]

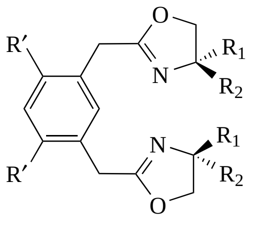
(**21**)

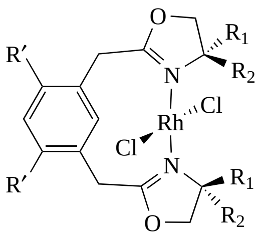
(**22**)

The migratory insertion reactions of ethylene into Rh–H and Rh–C bonds (*see* ***Organic Synthesis using Transition Metal Carbonyl Complexes***; ***Organic Synthesis using Transition Metal Complexes Containing π-Bonded Ligands***, and ***Organic Synthesis Using Metal-mediated Coupling Reactions***) have been explored by DFT calculations (*see* ***Molecular Orbital Theory***) on $[CpRh(PH_3)(C_2H_4)R]^+$ ($R =$ H, Me). Inclusion of relativistic effects was found to be important for results on the model to agree with experiment. For $R = H$, the calculated transition state was calculated to be close to the reactants, while for $R = Me$, the transition state is product-like. Both the ethyl and propyl products show an agostic interaction with a β-hydrogen.[37] A second study used DFT methods to explore the oxidative addition of the C–F bond in fluoromethane to unsaturated Rh(I) species modeled by $\{Rh(X)(PH_3)_2\}$ ($R = H$, Me, Cl). The activation barrier was found to correlate with the magnitude of the singlet-triplet splitting and to be lowered by the presence of π-donor ligands.[38]

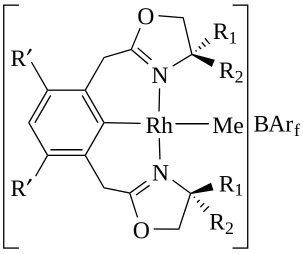
(**23**)

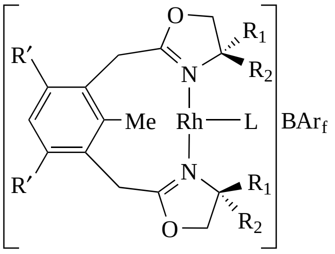
(**24**)

2.2 Dinuclear Complexes

Considerable interest continues to be shown in the chemistry of dinuclear complexes (*see* ***Dinuclear Organometallic Cluster Complexes***), particularly heterometallic species, containing metal–carbon σ-bonds to determine the extent to which the two metals may be involved in the cleavage and formation of C–H and C–C bonds (*see* ***Carbon–Carbon & Carbon–Heteroatom Activation*** and ***Alkane Carbon–Hydrogen Bond Activation***). With the symmetrical complex $[Rh(\mu\text{-pz})(CNBu^t)_2]_2$, methyl iodide adds (*see* ***Carbon–Carbon & Carbon–Heteroatom Activation***) to both metal centers forming $[Rh_2(\mu\text{-pz})_2(\mu\text{-I})(Me)_2(CNBu^t)_4]I$ but with $(COD)Rh(\mu\text{-pz})_2Rh(CNBu^t)_2$, only the metal coordinated to the isocyanide reacts. Evidently that metal is more basic. Similar results are seen with RCH_2Cl (R = vy, C(=O)Me, C(=O)OMe, Ph) where both metals are alkylated in the former complex but only one is alkylated in the latter complex. Both these results suggest that the metal atoms are acting independently in the oxidative addition. By contrast, addition of one equivalent of I_2 to $[Rh(\mu\text{-pz})(CNBu^t)_2]_2$ forms the *symmetrical* adduct $[Rh(\mu\text{-pz})I(CNBu^t)_2]_2$. The difference is attributed to the polarity of the C–I bond in methyl iodide, which makes it susceptible to attack by a nucleophilic metal while the nonpolar iodine functions more as a simple oxidizing agent. This is also suggested by the observation that $[Rh(\mu\text{-pz})(CNBu^t)_2]_2$ can be oxidized to $\{[Rh(\mu\text{-pz})(MeCN)(CNBu^t)_2]_2\}^{2+}$ by two equivalents of ferricinium hexafluorophosphate, and on reaction of the cation with iodide ion, $[Rh(\mu\text{-pz})I(CNBu^t)_2]_2$ is again formed. In the case of $RCHCl_2$ (R = H, C(=O)Me, C(=O)OMe, Ph), [Rh(μ-pz)(CNBu^t)$_2$]$_2$ forms Rh$_2$(μ-pz)$_2$(μ-CHR)Cl$_2$(CNBu^t)$_4$ and here the unsymmetrical dimer also gives an analogous product.[39]

Most numerous are reports on heterobimetallic complexes bridged by two DPPM ligands. The first example is (**25**) (X = BF$_4^-$, OTf$^-$). As depicted below, only the ligands in the equatorial plane of this and related complexes will be shown in the ensuing discussion for simplicity. Neutral ligands, L (=C$_2$H$_4$, various allenes) add to iridium in (**25**) to cause one carbonyl ligand to become semi-bridging while dimethylacetylene dicarboxylate (R = CO$_2$Me) oxidatively adds across both metals (equation 21). Allyl halides undergo simple oxidative addition (*see* ***Carbon–Carbon & Carbon–Heteroatom Activation***) to (**25**) at a low temperature but on warming, C–C coupling with the acetylide occurs (equation 22 (R = CH$_2$CHCH$_2$; Y = Cl, Br)). Protonation of (**25**) probably occurs initially at iridium, but the characterized product contains a bridging hydride ligand, which is induced to couple with the acetylide ligand and form a vinylidene-bridged species (equation 23). In contrast to internal alkynes, terminal alkynes undergo C–H oxidative addition (*see* ***Alkane Carbon–Hydrogen Bond Activation***) to the iridium center in (**25**) to form a bis-acetylide complex.[40]

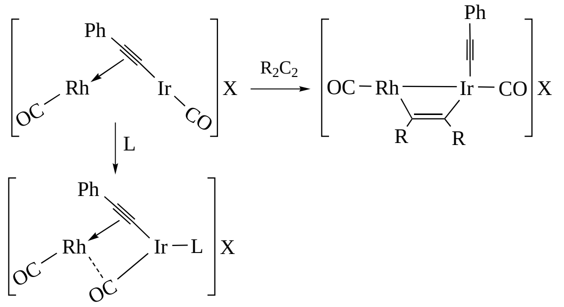

(21)

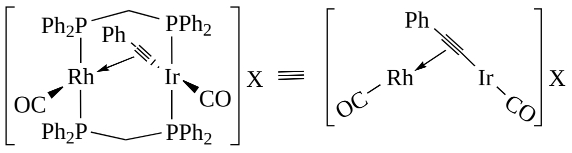

(**25**)

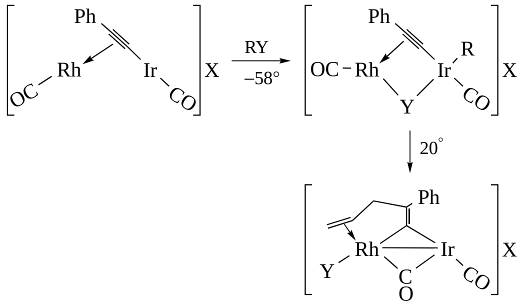

(22)

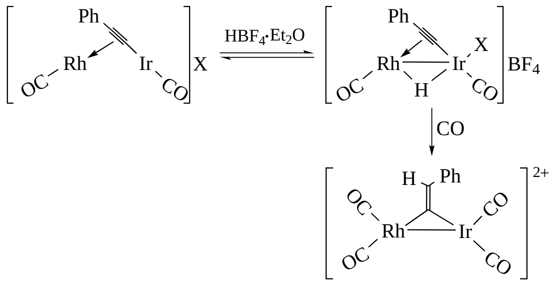

(23)

The neutral complex Rh(CO)(μ-DPPM)$_2$Ir(CO)$_2$ is unreactive toward even excess methyl iodide but is alkylated by MeOCH$_2$I and then methyl triflate (equation 24 (R = MeOCH$_2$)). It can, however, be methylated at iridium by methyl triflate and the subsequent reactions of this cationic methyl derivative with dihydrogen and with isocyanides are outlined in equations (25) and (26). The coupling of the methyl group with the isocyanide is of note particularly since, in the reaction of the methyl complex with acetylene, the alkyne oxidatively adds to both metals to initially form the dimetallated olefin complex but then couples with one of the DPPM ligands and not with the methyl group (equation 27).[41] By contrast, in the same reaction with dimethylacetylene

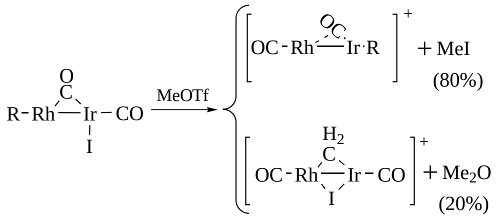

(24)

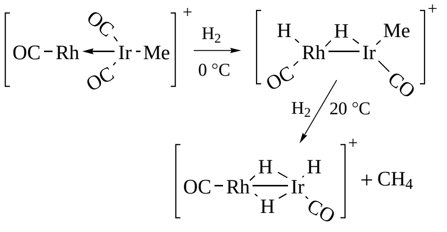

(25)

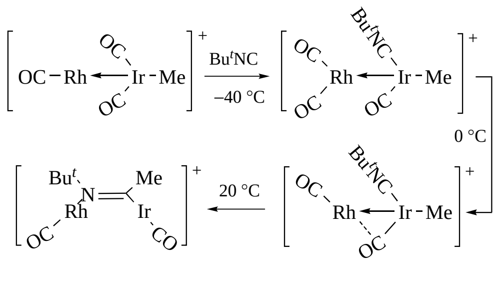

(26)

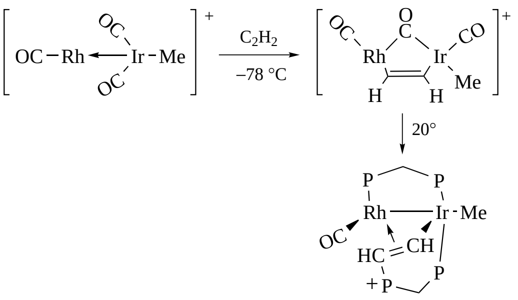

(27)

dicarboxylate, following the formation of an intermediate dimetallated olefin complex, coupling with the methyl group does occur. With phenyl acetylene, oxidative addition of the alkyne C–H bond to iridium occurs at a low temperature to form an acetylide hydride species, which on warming eliminates methane and ultimately reacts with a second alkyne by C–H oxidative addition to give $[Rh(CO)(\mu\text{-}H)(\mu\text{-}DPPM)_2(\mu\text{-}\eta^1{:}\,\eta^2\text{-}C{\equiv}CPh)Ir(C_2Ph)(CO)]^+$.**42**

At a low temperature, $Rh(CO)(\mu\text{-}DPPM)_2Mn(CO)_3$ oxidatively adds 3-butyne-2-one to form a dimetallated olefin complex, which rearranges on warming to the vinylidene-bridged isomer (equation 28 (R = C(=O)Me)). This last complex reacts

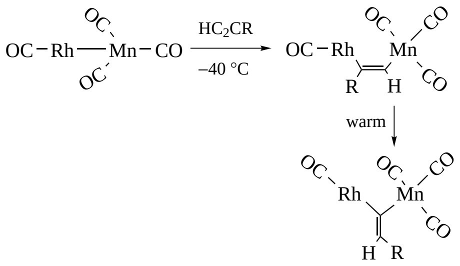

(28)

with triflic acid and methyl triflate as shown in equation (29). With the alkynes RC≡CR,

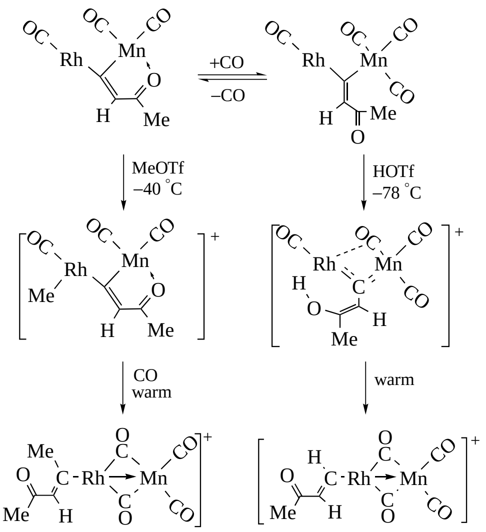

(29)

$Rh(CO)(\mu\text{-}DPPM)_2Mn(CO)_3$ also forms dimetallated olefin complexes, which can be converted to vinyl derivatives by protonation (equation 30 (R = CF_3, CO_2Me)).

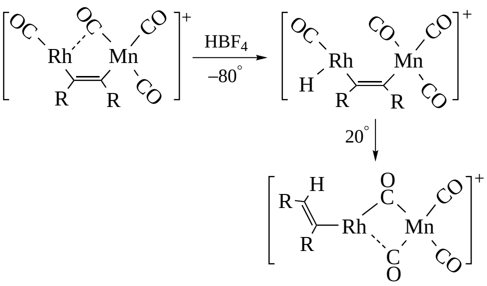

(30)

Protonation of $[Rh(CO)(\mu\text{-}DPPM)_2Os(CO)_3]^+$ by $HBF_4{\cdot}Et_2O$ in acetonitrile forms $[Rh(MeCN)(\mu\text{-}CO)(\mu\text{-}H)(\mu\text{-}DPPM)_2Os(CO)_2]^+$, some of whose chemistry is outlined in equations (31) and (32). The reaction of $[Rh(CO)(\mu\text{-}DPPM)_2Os(CO)_3]^+$ with *n*-butyl lithium

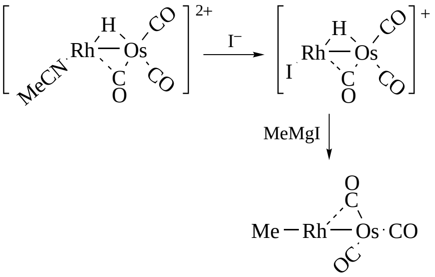

(31)

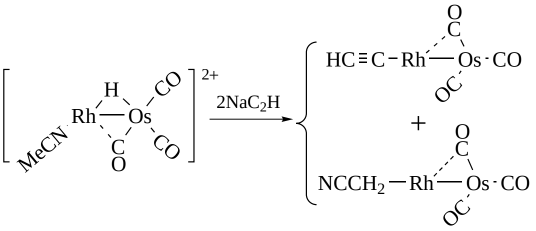

(32)

results in abstraction of a proton from the methylene carbon of one DPPM ligand rather than alkylation of one of the metal atoms, and the same product is obtained if the first step of equation (32) is performed under a CO atmosphere. Protonation of $Rh(Me)(\mu\text{-}DPPM)_2Os(CO)_3$ (see equation 31) at −80 °C occurs at osmium to form (**26**). On warming, the methyl group migrates to osmium via an intermediate in which the hydride ligand bridges both metals, methane is eliminated, and the resulting coordinatively unsaturated osmium atom undergoes oxidative addition of an *o*–C–H bond of one DPPM phenyl group to yield (**27**).

The neutral hydride complex $Rh(CO)(\mu\text{-}DPPM)_2Os(H)(CO)_2$ reacts with propyne and allenes to form vinyl derivatives (equation 33 (R = H, Me)). That the vinyl groups are

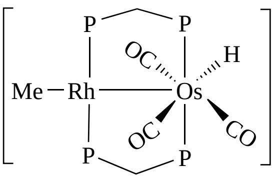

(**26**)

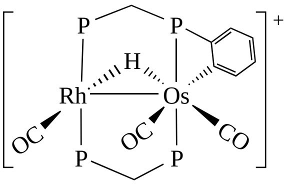

(**27**)

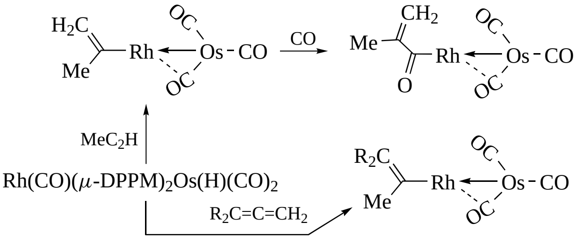

(33)

attached to rhodium despite the expectation of a stronger Os–C bond is attributed to the formal configuration Rh^I/Os^0 being favored. In the case of allene itself, a minor amount of $(\eta^3\text{-}C_3H_5)Rh(\mu\text{-DPPM})_2(CO)_3$ is also seen. All of the vinyl complexes react with one equivalent of H^+ or Me^+ at the osmium center, while a second equivalent of H^+ adds to the β-carbon of the vinyl group to convert this substituent to an alkylidene (equation 34) (see also Section 2.4).

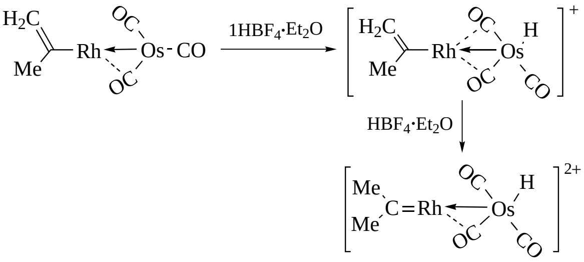

(34)

Vinyl complexes can also be obtained from the reaction of $Rh(CO)(\mu\text{-H})(\mu\text{-DPPM})_2M(CO)_3$ with alkynes (equation 35 (X = H; M = Mo: R′ = R′ = CF_3, CO_2Me. R′ = H; R″ = C(=O)Me, CO_2Me), while action of Grignard reagents on the chloride-bridged analogs forms related compounds (equation 35) (X = Cl; M = Mo; R = vy, Me, Ph,

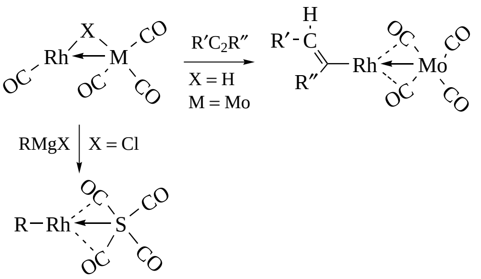

(35)

$CH_2CH{=}CH_2$. M = W; R = vy). With benzylmagnesium chloride under CO, this latter reaction forms the acyl complexes $Rh(C({=}O)CH_2Ph)(\mu\text{-DPPM})_2M(CO)_4$ M = Mo, W). The vinyl complex from equation (35) is protonated at a low temperature to give an ethylidene derivative, which on warming rearranges to an ethylene complex (equation 36).

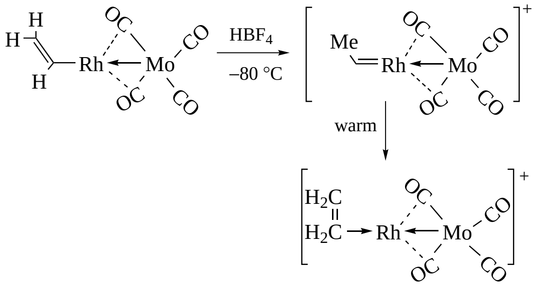

(36)

Because conversion of the ethylidene ligand to the ethylene ligand is facile, attempts to couple the ethylidene ligand with alkynes failed and only substitution of the olefin by the alkyne occurred.[42]

In the Rh/Mo and Rh/W complexes, it was hoped to study the effect that the two different metals might have on C–C and C–H coupling reactions (*see* ***Organic Synthesis Using Metal-mediated Coupling Reactions***), but in most instances, it proved impossible to put a hydride or a second organic ligand on one of the metal atoms. This goal was realized to some extent in the Rh/Ru system depicted in equation (37) (R = R′ = CO_2Me, CO_2Et, CF_3. R = Me; R′ = $CH(OEt)_2$, CH_2OH). It is

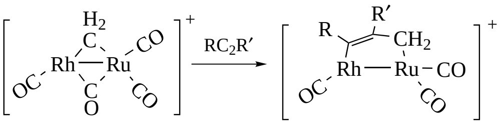

(37)

proposed that initial addition of the alkyne occurs at the coordinatively unsaturated rhodium center. Attempts to effect the coupling in the ‘‘reverse’’ direction by adding the methylene unit to an alkyne complex were unsuccessful, as C–C coupling did not occur (equation 38). Decarbonylation of the coupling product obtained from equation (37) forms

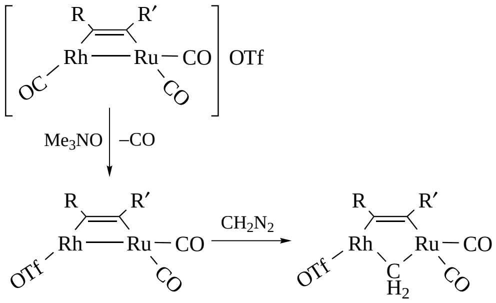

(38)

the alkylidene-bridged species (**28**), and only in the case where R = CH_2OH did more extensive coupling occur to give (**29**).[43]

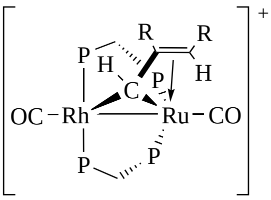

(28)

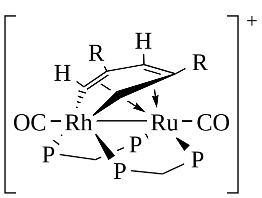

(29)

The dirhodium complex $Rh_2(CO)_3(\mu\text{-DPPM})_2$ reacts with methyl triflate to form the acetyl-bridged complex (**30**), which on heating loses a carbonyl ligand and undergoes methyl migration to the metal yielding $Rh_2(CO)(Me)(\mu\text{-CO})(\mu\text{-DPPM})_2$. This complex is fluxional via a methyl-bridged intermediate.[44] The carbonate-bridged complex (**31**) is formed when $(\eta^3\text{-}C_3H_5)Rh(\mathrm{Pr}^i{}_2PCH_2P\mathrm{Pr}^i{}_2)$ reacts with an excess of methyl formate.[45]

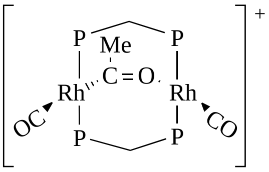

(30)

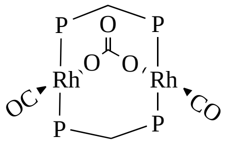

(31)

Diarylsilanes react with $[Rh(\mu\text{-H})(dippe)]_2$ to form $[Rh(\mu\text{-SiAr}_2)(dippe)]_2$, but with dimethylsilane the product is (**32**), which is a catalyst precursor for the dimerization of diphenylsilane (*see* ***Silicon: Inorganic Chemistry***).[46] The initial reaction of $[Cp^*_2Rh_2(\mu\text{-CH}_2)_2(\mu\text{-SH})]BPh_4$ with dimethylacetylene dicarboxylate is the insertion of one alkyne into the S–H bond but the second equivalent of alkyne couples with both methylene groups to form (**33**).[47]

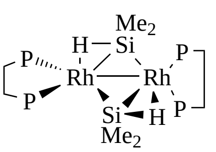

(32)

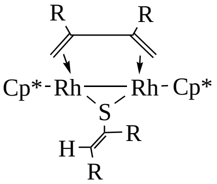

(33)

2.3 Vinylidene and Allenylidene Complexes

A considerable amount of work has been done in this area, which has been spurred in part by interest in the synthesis of multimetallic complexes in which the metal atoms are connected by unsaturated chains of several carbon atoms that may serve as ‘‘molecular’’ wires. The initial and still most widely employed synthetic route to vinylidene complexes involves addition of four equivalents of a trialkylphosphine ($L = \mathrm{PPr}^i_3$ hereafter unless otherwise specified) to $[Rh(\mu\text{-Cl})(COE)_2]_2$, forming the coordinatively unsaturated fragment $\{Rh(\mathrm{PPr}^i_3)_2\}$ (probably weakly solvated), which is reacted in situ with a terminal alkyne (equation 39 ($Y = H$; $R = CR'R''X$ (R', $R'' = H$, alkyl, aryl; $X = OH$, OMe, NH_2, Cl))). Depending on the conditions and the nature of R, some or all of the species shown can be isolated when $Y = H$, although often the whole transformation can be carried out in one pot. The C–H oxidative addition step can be initiated thermally or photochemically as can the conversion of the acetylide hydride to the vinylidene. More recently, an alternate route using silyl and stannyl alkynes (*see* ***Silicon: Inorganic Chemistry*** and ***Tin: Organometallic Chemistry***) has been developed that provides for a greater range of substituents on the vinylidene group. A third route uses $\{Rh(\mathrm{PPr}^i_3)_2\}$ together with $RR'C{=}CHCl$ ($R = Me$; $R' = Me$, Ph. $RR' = -(CH_2)_5-$) in the presence of sodium. This does not work with $Me_2C{=}C{=}C{=}CHCl$ as this allene simply coordinates unchanged to the rhodium via the central C=C. Expanding on the original route (equation 39), $\{Rh(\mathrm{PPr}^i_3)_2\}$ reacts with butadiyne to form (**34**) that is converted to (**35**) on heating.

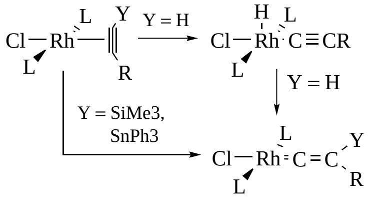

(39)

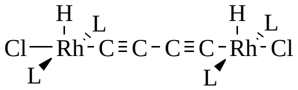

(34)

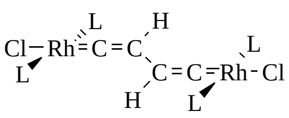

(35)

The reactivity of vinylidene complexes depends to a significant extent on the substituents of the β-carbon. For example, dehydration of (**36**) ($R = R' = Me$; $X = OH$, NH_2, Cl) with deactivated alumina forms the vinyl vinylidene complexes (**37**), but for $R = H$, Ph; $R' = Ph$; $X = OH$, the allenylidene complex (**38**) is the product. Diazomethane reacts with (**38**) ($R = Ph$; $R' = Ph$, CF_3, Bu^t) to couple a methylene fragment to the allenylidene ligand and form (**39**), which isomerizes to (**40**) on heating. Complex (**40**), with iodide in place of chloride, can be obtained directly from (**38**) on reaction with methyl iodide as the carbon source in the presence of KI and Na_2CO_3. In further investigations of C–C coupling processes (*see* ***Organic Synthesis Using Metal-mediated Coupling Reactions***), reaction of $(\eta^3\text{-}C_3H_5)Rh(\mathrm{PPr}^i_3)_2$ with two equivalents of $HC{\equiv}CCH(Ph)OH$ yielded the vinylidene acetylide complex (**41**) ($R = CH(Ph)OH$), but with $HC{\equiv}CCPh_2OH$, only the bis(acetylide), $Rh(H)(C{\equiv}CCPh_2OH)_2L_2$ forms. This reacts with a third equivalent of the alkyne to form (**42**) via (**43**) ($R = CPh_2OH$) as a proposed intermediate. Photolysis (*see **Photochemistry of Transition Metal Complexes***) of $Rh(H)(C{\equiv}CCPh_2OH)_2L_2$ promotes vinylidene formation (**41**), ($R = CPh_2OH$) where coupling (*see **Organic Synthesis Using Metal-mediated Coupling Reactions***) of the acetylide and vinylidene ligands is promoted by addition of neutral ligands to form (**44**) ($R = CPh_2OH$), while treatment of the hydride complex with deactivated alumina in the presence of chloride ion yields (**45**), possibly via the intermediacy of an acetylide allenylidene complex generated by the dehydration of an initially formed vinylidene species.

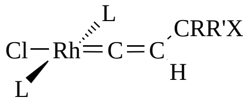
(**36**)

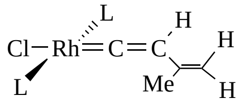
(**37**)

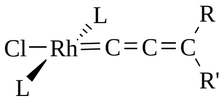
(**38**)

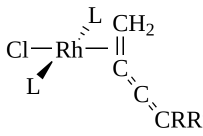
(**39**)

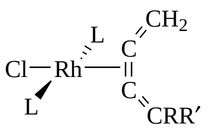
(**40**)

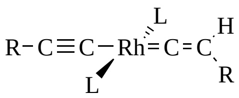
(**41**)

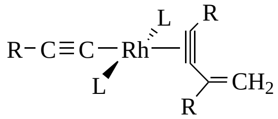
(**42**)

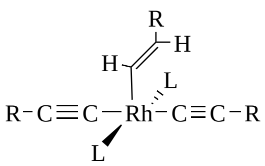
(**43**)

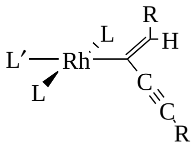
(**44**)

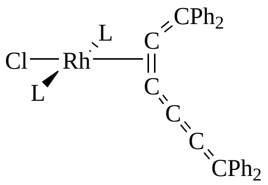
(**45**)

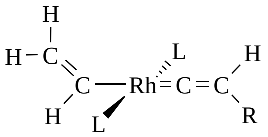
(**46**)

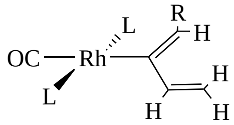
(**47**)

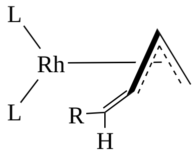
(**48**)

A stereoselective coupling (*see **Organic Synthesis Using Metal-mediated Coupling Reactions***) of alkyl, aryl, or vinyl groups to a vinylidene ligand and subsequent conversion to an allyl ligand has been achieved by the reaction of $Rh({=}C{=}CHR)ClL_2$ ($R = H$, Bu^t, Ph) with vinylmagnesium bromide to first form (**46**). This is converted to (**47**) by reaction with CO or to (**48**) (see Section 4.1) on mild heating in benzene solution.

More elaborate coupling reactions (*see **Organic Synthesis Using Metal-mediated Coupling Reactions***) include the reaction of $Rh({=}C{=}C{=}CRR')(N_3)L_2$ ($R = R' = Ph$, *p*-$MeOC_6H_4$. $R = Ph$, $R' = Bu^t$) with carbon monoxide which promotes migration of the azide group to the γ-carbon forming (**49**). This loses dinitrogen to give (**50**) and reacts with $[Me_3O]BF_4$ to yield $[\{Rh({=}C{=}C{=}CRR')L_2\}_2(\mu\text{-}N_3)]BF_4$. The fluoro analog of (**38**) ($R = Ph$; $R' = Bu^t$, Ph) reacts with $Ph_3Sn\text{-}C{\equiv}C\text{-}C{\equiv}C\text{-}SnPh_3$ to form $[(R(Ph)C{=}C{=}C{=})RhL_2]_2(\mu\text{-}C{\equiv}C\text{-}C{\equiv}C\text{-})$ and with $Ph_3Sn\text{-}C{\equiv}CPh$ (*see **Tin: Organometallic Chemistry***) to yield (**51**). Coupling of the acetylide and allenylidene fragments in (**51**) is initiated by addition of CO at a low temperature forming (**52**) and on warming CO, incorporation ensues to give (**53**). In a similar fashion, (**54**) converts to (**55**).

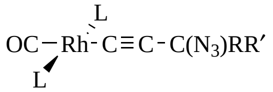
(**49**)

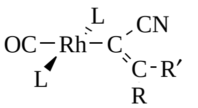
(**50**)

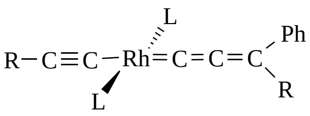

(**51**)

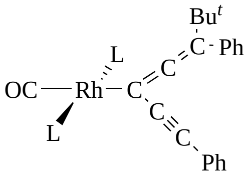

(**52**)

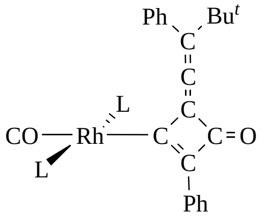

(**53**)

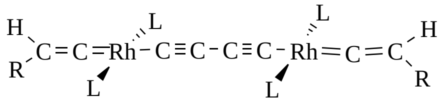

(**54**)

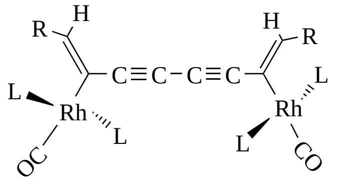

(**55**)

The migratory insertion of the allenylidene unit into Rh–O bonds occurs when Rh(=C=C=C(Ph)R)(OR$''$)L_2, prepared from (**38**) (R = Ph, *p*-tolyl; R$'$ = Ph) and K[OBu^t] in benzene/*t*-butanol followed by reaction with R$''$OH (R$''$ = Ph, MeC(=O)), is reacted with CO forming Rh{–C≡C–C(Ph)(OR$''$)R}(CO)L_2.

In transformations analogous to those in equation (39), {$Rh(PPr^i_3)_2$} fragments have been attached to the alkynyl substituents of 1,3,5-triethynylbenzene and various diethynylbenzenes and naphthalenes, and converted to vinylidenes as illustrated in (**56**) and (**57**).[48–50]

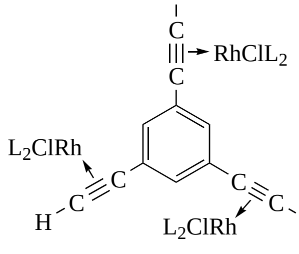

(**56**)

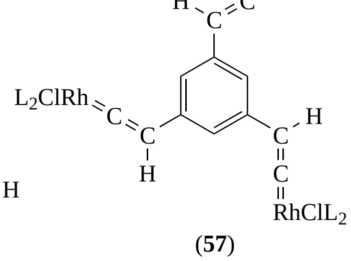

(**57**)

The process by which vinylidene complexes are formed from η^2-alkyne complexes has been explored by MP2 calculations (*see* ***Molecular Orbital Theory***) on $RhCl(PH_3)_2(\eta^2\text{-}C_2H_2)$ to model the steps depicted in the top row of equation (39). The C–H oxidative addition step appears facile but there is a high barrier for the migration of the hydrogen as H^+ to the β-carbon of the alkynyl ligand. Related MO/MM calculations on $Rh(H)Cl(C_2H)(PPr^i_3)_2$ indicate that for the second step, an intermolecular hydrogen transfer has a much lower barrier than does the intramolecular process. Similar calculations were done for $(PP_3)M^+$ (M = Co, Rh) interacting with acetylene, which also gave a low barrier for C–H oxidative addition where M=Rh. Since no vinylidene complexes were formed in this rhodium system, no calculations were performed for the acetylide to vinylidene transformation although in the cobalt analog it again appears that the hydrogen moves as a proton.[51,52] DFT calculations (*see* ***Molecular Orbital Theory***) have been used in conjunction with FT–Raman spectroscopy on the complexes *trans*-$[RhX(L)(PPr^i_3)_2]$ (X = F, Cl, Br, I, Me, C≡CPh; L = CO, =C=CH_2, =C=CHPh,) to obtain a trans influence series for the ligands X, which increase in the order shown.[53]

Protonation of (**58**) (L = Pcy_3; R = Ph, CO_2Me, $SiMe_3$) with $HBF_4{\cdot}Et_2O$ forms the vinylidene-bridged complex (**59**), while analogous protonation of the unsymmetrical isomer of (**58**) (R=C(OH)Ph_2) yields the allenylidene-bridged species (**60**).[54] A final route to a vinylidene-bridged dinuclear complex is the reaction of $[Rh(\mu\text{-pz})(CNBu^t)_2]_2$ with CH_3CCl_3 and triethylamine in benzene to yield $Rh_2(\mu\text{-C=CH}_2)\,(\mu\text{-pz})_2(CNBu^t)_4Cl_2$.[55]

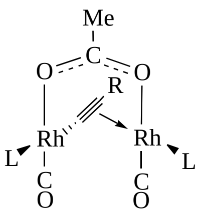

(**58**)

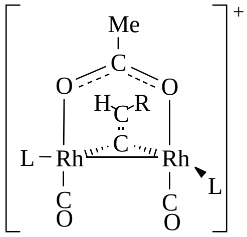

(**59**)

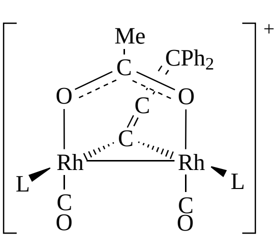

(**60**)

2.4 Carbene Complexes

The complex *trans*-$[RhCl(\eta^2\text{-}CH_2{=}CH_2)(SbPr^i_3)_2]$ has proven a suitable synthon for a variety of mono- and bimetallic

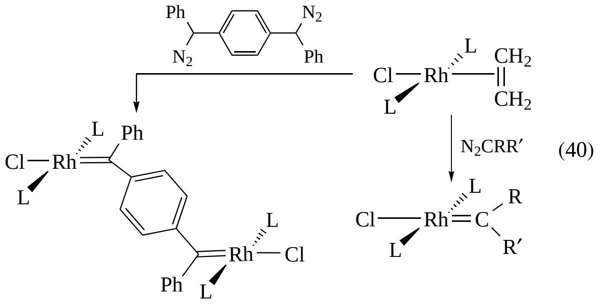

(40)

carbene complexes (*see* ***Carbene Complexes***) (equation 40 (L = SbPr$^i_3$: R = R′ = Ph, *p*-tol, *p*-anis. R = Ph; R′ = CF$_3$)). In the mononuclear complexes, the stibine ligands (*see* ***Antimony: Organometallic Chemistry***) can be replaced by trialkylphosphines and – arsines, and when R = R′ = Ph, the carbene moiety couples (*see* ***Organic Synthesis Using Metal-mediated Coupling Reactions***) with carbon monoxide, *t*-butylisocyanide, or ethylene to form, respectively, $Ph_2C{=}C{=}O$, $Ph_2C{=}C{=}NBu^t$, or $Ph_2CHCH{=}CH_2$. Heating Rh(=CRR′)ClL$_2$ (L = SbPr$^i_3$: R = R′ = Ph, *p*-tol. R = Ph; R′ = *p*-tol) forms dinuclear (**61**) containing a *bridging* tertiary stibine ligand. When R = R′ = Ph, (**61**) reacts with CO to form an apparently polymeric material formulated as $[Rh({=}CPh_2)Cl(CO)]_n$ but with *t*-butylisocyanide the product is (**62**). With one equivalent of Tl(acac), (**61**) converts to (**63**), in which the bridging stibine ligand can be replaced by trimethylphosphine giving (**64**). This is converted to (**65**) on reaction with chlorotrimethylsilane.

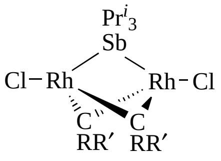

(**61**)

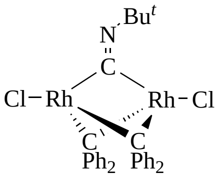

(**62**)

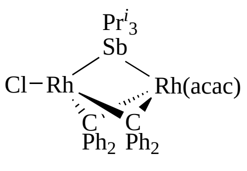

(**63**)

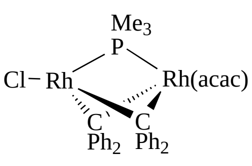

(**64**)

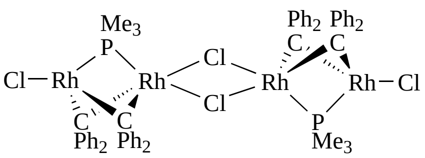

(**65**)

Treatment of Rh(=CRR′)ClL$_2$ (L = SbPr$^i_3$, PPr$^i_{3-n}$Ph$_n$ (n = 0–3); R = Ph; R′ = Ph, *p*-tol) with sodium cyclopentadienide forms CpRh(=CRR′)L in good yield. When L = SbPr$^i_3$, this ligand can be replaced with CO or CNBu^t, but when L = PPr$^i_3$, coupling of these molecules with the carbene ligand again occurs. In an attempt to generate a ketamine by a similar C–N coupling, CpRh(=CPh$_2$)L (L = SbPr$^i_3$, PPr$^i_3$) was reacted with an aryl azide but the product obtained was the tetraazadiene complex (**66**) (R = Ph, *p*-tol). The same complex (L = CO) reacts sequentially with CuCl and NaCp to form (**67**) while with L = PPr$^i_3$, protonation causes migration of the carbene moiety to the cyclopentadienyl ring to give (**68**) (R = Ph, *p*-tol; X = Cl, Br, I, O$_2$CCF$_3$). When the anion of the acid is noncoordinating (e.g. using HBF$_4$·Et$_2$O) or methylation is attempted with [Me$_3$O]BF$_4$, attack occurs on the carbene moiety in CpRh(=CPh$_2$)(L) (L = PPr$^i_3$) and the allyl complex (**69**) (Y = H. Me) is formed.[56,57] The indenyl complex (**70**) (L = SbPr$^i_3$, PPr$^i_3$) is prepared from Rh(=CPh$_2$)ClL$_2$ and indenylpotassium, and like its cyclopentadienyl analog, reacts with CO to transfer the carbene moiety to the indenyl ligand (**71**).[58]

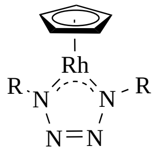

(**66**)

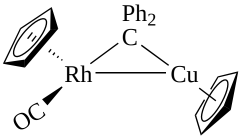

(**67**)

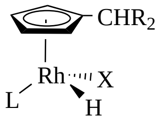

(**68**)

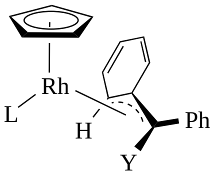

(**69**)

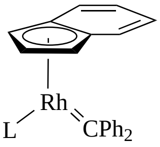

(**70**)

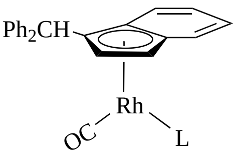

(**71**)

Photolysis (*see* ***Photochemistry of Transition Metal Complexes***) of a solution of CpRh(PMe$_3$)(η^2-CH$_2$=CH$_2$) in pentafluoroanisole initially forms CpRh(PMe$_3$)(η^2-C$_6$F$_5$OMe) (two isomers) and then (**72**). Hydride abstraction from (**72**) by trityl tetrafluoroborate generates the carbene complex (**73**).[59] Decarbonylation of (H$_2$B(3,5-Me$_2$pz)$_2$)Rh(CO)$_2$ with trimethylamine oxide in pyridine forms (H$_2$B(3,5-Me$_2$pz)$_2$)Rh(CO)(py), which in benzene solution adds methyl iodide to form (**74**). Heating (**74**) at 45 °C yields (**75**) by a rare example of a reverse α-hydrogen migration. It is proposed that the formation of (**74**) involves initial oxidative addition of methyl iodide (*see* ***Carbon–Carbon & Carbon–Heteroatom Activation***) to rhodium followed by migratory insertion of the methyl group which is facilitated by the coordination of the oxygen of the carbonyl group to the Lewis acid boron.[60]

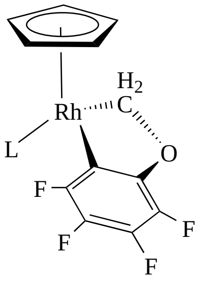

(**72**)

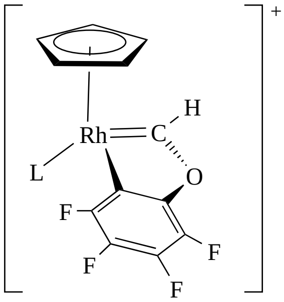

(**73**)

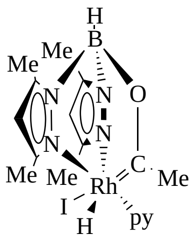

(**74**)

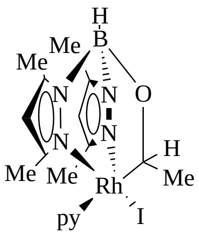

(**75**)

The neutral chloro analog of the ‘‘pincer’’ complex (**11**) (Section 2.1) can be reduced to a dinitrogen complex and on addition of phenyldiazomethane, a carbene complex results (equation 41 (R = Bu^t, R′ = Me)). An analogous product (**77**) is obtained at room temperature for the complex where R′ = H, but if the diazo compound is added at −70 °C, (**76**) is formed first and on warming converts to (**77**) plus the dinitrogen complex and *trans*-1,2-diphenylethylene. A series of DFT calculations (*see* ***Molecular Orbital Theory***) on the course of the reaction of the diazoalkane to form the carbene complex have been carried out from which it appears that with bulky substituents on phosphorus, conversion of (**76**) into an η^1-C-bound diazo complex is critical.[61] The phosphinocarbene (**78**) (R = NPr$^i{}_2$) forms the carbene complex $Rh(=C(PR_2)(2,6\text{-}(CF_3)_2C_6H_3))Cl(CO)_2$ when reacted with $[Rh(\mu\text{-}Cl)(CO)_2]_2$ at −50 °C, but on warming rearranges to the phosphorus-bound isomer $Rh(P(R)=C(R)(2,6\text{-}(CF_3)_2C_6H_3))Cl(CO)_2$. With $[Rh(\mu\text{-}Cl)(COD)]_2$, the analogous carbene complex $Rh(=C(PR_2)(2,6\text{-}(CF_3)_2C_6H_3))Cl(COD)$ is formed which appears to be more stable.[62]

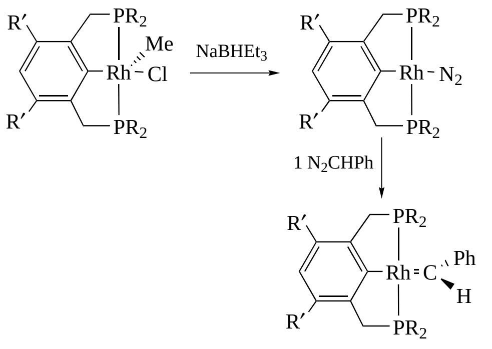

(41)

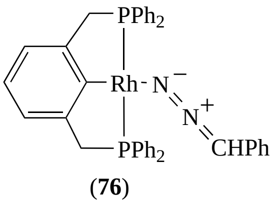

(**76**)

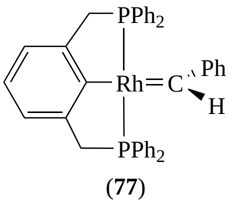

(**77**)

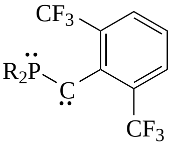

(**78**)

As the reaction of low-valent rhodium complexes with diazoalkanes is frequently used to prepare mono- and dinuclear carbene complexes (*see* ***Carbene Complexes***) (e.g. equation 41), it has been of interest to explore factors controlling the loss of dinitrogen from the initially formed metal complex of the diazoalkane (vide supra). To this end, complexes containing the $\{Rh(C(N_2)R)\}$ unit have been deliberately synthesized by reaction of $RhClL_n$ (L = PMe_3, $n = 4$; L = PEt_3, $n = 3$) with $Li[C(N_2)SiMe_3]$ to form $L_nRh(C(=N=N)SiMe_3)$. Photolysis of this product in benzene forms (**79**) (L = PEt_3) through the proposed intermediates (**80**) and (**81**). It is suggested that (**80**) exists in the singlet state because of the stabilizing influence of the neighboring low-spin, electron-rich $\{RhL_2\}$ unit, and as an electrophilic carbene, readily forms the ylide species (**81**).[63]

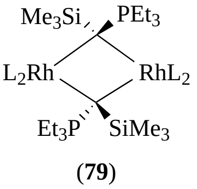

(**79**)

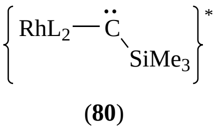

(**80**)

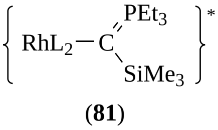

(**81**)

Mentioned in the previous edition[1] as a route to rhodium carbene complexes is the reaction of various low-valent complexes with electron-rich olefins like (**82**) (R = Et, bz). Reaction of $[Rh(\mu\text{-}Cl)(COD)]_2$ with (**82**) forms the tris-carbene complex $Rh(=C(N(R)CH_2CH_2N(R)\text{-})_3Cl)$, while with (**83**) the product is (**84**).[64] In related work, four equivalents of the imidazolium salt (**85**) (X = Br; R = bz) react with $[Rh(\mu\text{-}OEt)(COD)]_2$, prepared in situ from $[Rh(\mu\text{-}Cl)(COD)]_2$ and sodium ethoxide in ethanol to yield (**86**), and using the corresponding triazolium iodide, the same route furnishes (**87**), while with bis(diisopropylformamidinium)chloride the product is $[Rh(=C(NPr^i{}_2)_2)Cl(COD)]$. The last can also be prepared from $[Rh(\mu\text{-}Cl)(COD)]_2$ and bis(diisopropylamino)carbene.[65] An alternate synthesis of (**86**) (X = Cl; R = *p*-tol) involves the reaction of (**85**) with silver oxide to form an intermediate silver imidazolium carbene complex and the reaction of this with $[Rh(\mu\text{-}Cl)(COD)]_2$. The COD ligand can be replaced by two carbonyl ligands. This work has been extended to the chiral oxazoline-substituted imidazolium salts (**88**) (R = Me, Bu^t; R′ = Pr^i, bz), which on treatment with $LiOBu^t$ and $[Rh(\mu\text{-}Cl)(COD)]_2$ in THF form (**89**). Chloride abstraction from (**89**) with $TlPF_6$ then yields (**90**).[66] In related work, the bis(imidazolium) salts (**91**) (R = Bu^n; X = Br; Y = 1,2-C_6H_4. R = Pr^i, Bu^n; X = I; Y = CH_2) can be used to form (**92**) from $Rh_2(OAc)_4$ in acetonitrile (X = I) or from $[Rh(\mu\text{-}Cl(COD))]_2$, potassium iodide, and sodium acetate (X = Br). The complexes function as catalyst precursors for the hydrogenation of C=O and C=N bonds via hydrogen transfer from isopropanol.[67] Treatment of (**91**) (R = Bu^n; X = Br; Y = 2,6-C_6H_3N) with $[Rh(\mu\text{-}Cl(COD))]_2$ and triethylamine forms (**93**) (Z = RhBr(COD)) which is a catalyst precursor for olefin hydroformylation (*see* ***Carbonylation Processes by Homogeneous Catalysis***) and for which NMR studies indicate retention of the dinuclear structure under catalytic conditions.[68] Deprotonation of (**91**) (R = Bu^n; X = Cl; Y = 2,6-(-CH_2)C_6H_3N) with silver oxide forms (**93**) (Z = AgCl) and the {AgCl} units can be replaced by {RhCl(COD)}.[69] In neither example of (**93**) does coordination of the pyridyl nitrogen to rhodium occur, but when (**94**) (R = Pr^i, Bu^n, Bu^t) is reacted successively with $[Rh(\mu\text{-}Cl)(COE)_2]_2$ and carbon tetrachloride, the product is (**95**) (*see* ***Water & O-donor Ligands***) which contains a NCN ‘‘pincer’’ ligand (see also **5**–**8**). The water ligand can be replaced by an isocyanide ligand CNR′ (R′ = CO_2Me, SO_2(*p*-tol)) and this derivative in the presence of $KOBu^t$, undergoes an aldol condensation with aldehydes to form the carbene complex (**96**) (R″ = Bu^t, Ph).[70]

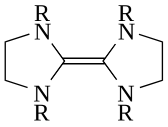
(**82**)

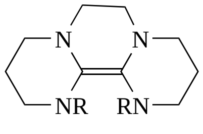
(**83**)

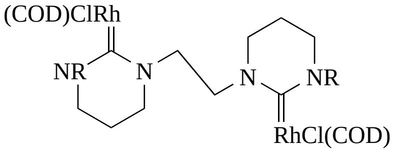
(**84**)

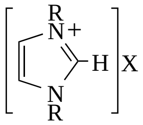
(**85**)

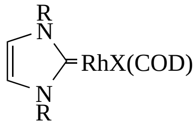
(**86**)

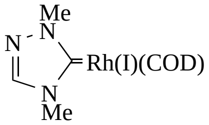
(**87**)

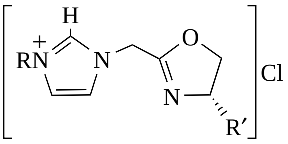
(**88**)

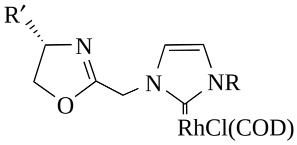
(**89**)

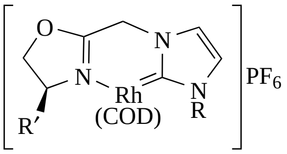
(**90**)

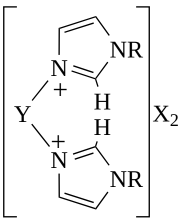
(**91**)

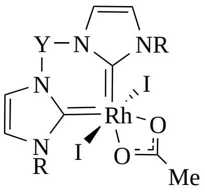
(**92**)

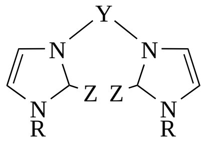
(**93**)

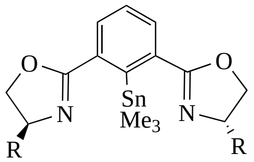
(**94**)

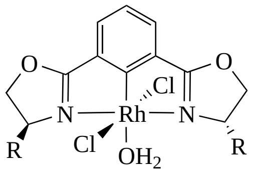
(**95**)

Complexes of the type $[Cp^*Rh(R)(\mu\text{-}CH_2)]_2$ have been studied to probe details of the coupling of alkyl and methylene groups that could be relevant to mechanisms for the Fischer–Tropsch process (*see* ***Organic Synthesis Using Metal-mediated Coupling Reactions***).[71] Reaction

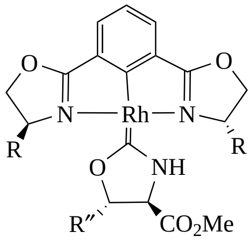

(96)

of $[Cp^*Rh(vy)(\mu\text{-}CH_2)]_2$ with HCl forms $Cp^*{}_2Rh_2Cl_2(\mu\text{-}CH_2)(\mu\text{-}CHMe)$ via coupling of one vinyl and one methylene group. Alkylation of this species with Grignard reagents yields $Cp^*{}_2Rh_2(R)_2(\mu\text{-}CH_2)(\mu\text{-}CHMe)$ (R = Me, Et, vy, Bu^n), which proved to be thermally robust. Oxidative decomposition of the dimethyl complex forms methane, propene, and but-1-ene by the process proposed in equation (42) (S = MeCN).[72]

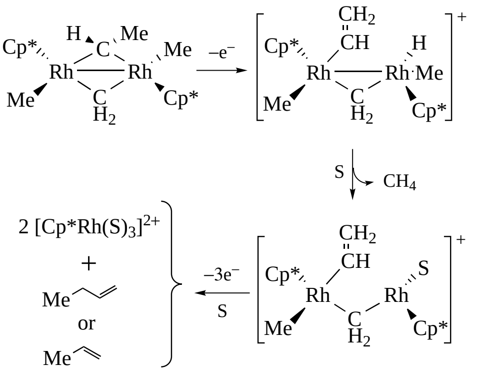

(42)

In the complex $Cp^*Rh(CpCo)_2(CO)_2(\mu\text{-}CH_2)$, NMR studies indicate that the methylene group is quite mobile (*see* ***Stability Constants & their Determination***) (equation 43) with the steps in which it moves

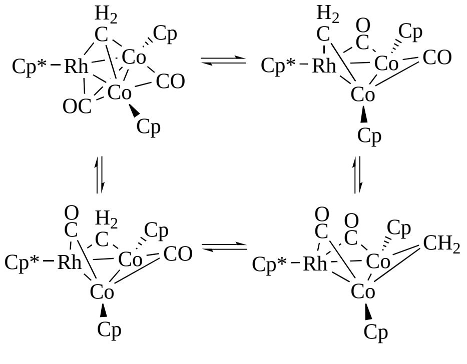

(43)

from a Rh–Co edge to the Co–Co edge thought to have a higher barrier than the other motions.[72]

2.5 Carbonyl Complexes

Carbonyl ligands are very prevalent in organometallic complexes of rhodium and may be either incidental to or necessary for the formation of complexes (*see* ***Carbonyl Complexes of the Transition Metals***) in which they are found. This section focuses primarily on carbonyl cluster complexes (*see* ***Polynuclear Organometallic Cluster Complexes***) in which carbonyl groups are the sole or at least the primary ligands. DFT calculations (*see* ***Molecular Orbital Theory***) on the unstable (in the absence of excess CO) $Rh_2(CO)_8$ molecule predict the lowest energy structure to be $Rh_2(CO)_6(\mu\text{-}CO)_2$ of the C_{2v} symmetry, which is the same as observed for the cobalt analog although unbridged structures are not much higher in energy. The C–O stretching frequencies calculated from this model agree well with experiment.[73]

Structures of $Rh_6(CO)_{15}L$ complexes ($L = P(OPh)_3$, $PBu_3{}^n$, $P(4\text{-}XC_6H_4)_3$ ($X = CF_3$, Cl, F, OMe), DMSO, MeCN, COE) have been determined and the structural effects of substitution are localized primarily in the vicinity of the substitution. In particular, in the triangle of rhodium atoms containing that bearing L, the Rh–Rh distances adjacent to the site of substitution are significantly lengthened and that opposite significantly shortened as compared to those remote from this site. This is attributed to an increase in electron density on the substituted metal as a result of substitution of CO by a ligand of lower π-acid character.[74] Heating of the fullerene (*see* ***Carbon: Fullerenes***) derivative of $Rh_6(CO)_{16}$ formulated as $Rh_6(CO)_9(DPPM)_2(\mu_3\text{-}\eta^2,\eta^2,\eta^2\text{-}C_{60})$ with excess C_{60} in chlorobenzene followed by reaction with benzylisocyanide leads to attachment of a second fullerene to the cluster and the product is $Rh_6(CO)_5(DPPM)_2(\mu_3\text{-}\eta^2,\eta^2,\eta^2\text{-}C_{60})_2$. The skeleton of the complex showing the locations of the fullerene substituents on opposite triangular faces of the metal octahedron is shown in (**97**). Cyclic voltammetric measurements show six well-separated, reversible, 1-electron reduction waves centered on the fullerene cages which are interpreted as the stepwise reduction to $(C_{60}{}^-)$ $Rh(C_{60})$, $(C_{60}{}^-)$ $Rh(C_{60}{}^-)$, and so on, implying an electronic communication between the cages (*see* ***Electrochemistry: Applications in Inorganic Chemistry***). The complex is thus proposed to be a model for carbon nanotubes connected by a heterogeneous inorganic junction of potential future use in electronic materials.[75]

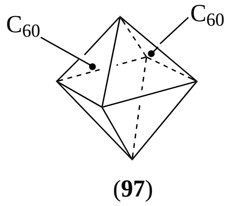

(97)

Reaction of $[Rh(\mu\text{-}Cl)(COD)]_2$ with p-toluidine and butyl lithium forms the tetrametallic imido cluster $Rh_4(\mu\text{-}NR)_2(COD)_4$ (R = p-tol) that is converted to $PPN[Rh_3(\mu_3\text{-}NR)_2(CO)_6]$ on treatment with CO and then [PPN]Cl. Oxidation of the carbonyl cluster with one equivalent of ferricinium hexafluorophosphate yields $[Rh_3(\mu_3\text{-}NR)_2(CO)_6]_2$ whose skeleton is depicted in (**98**). This is thought to arise from the dimerization of $[Rh_3(\mu_3\text{-}NR)_2(CO)_6]\cdot$ radicals formed by one-electron oxidation of the anionic trimetallic cluster.[76] One and two carbonyl ligands, respectively, in $[Rh_5(CO)_{15}]^-$ can be replaced by amines ($bzNH_2$, $Ph(CH_2)_3$ NH_2, pip) and diamines (en, pn, tn), while with $H_2N(CH_2)_4$ NH_2 (L_2) some $[\{Rh_5(CO)_{14}\}_2(\mu\text{-}L_2)]^{2-}$ is seen in addition to $[Rh_5(CO)_{13}(L_2)]^-$.[77]

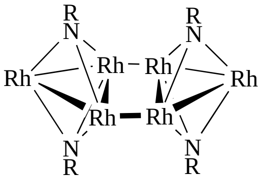
(**98**)

Interest continues in the synthesis of heterobimetallic carbonyl clusters (*see* ***Polynuclear Organometallic Cluster Complexes***) and most are prepared by the addition of carbonyl metallates to small- or medium-sized carbonyl clusters. For example, addition of four equivalents of $[HFe(CO)_4]^-$ to $[Rh(\mu\text{-}Cl)(CO)_2]_2$ forms $[Fe_2Rh(CO)_{10}]^-$, which is converted to (**99**) ($L = PPh_3$) by addition of the phosphine. Similarly, two equivalents of $[Rh(CO)_4]^-$ added to $Fe_2(CO)_9$ followed by refluxing in acetone forms $[Fe_2Rh_2(CO)_{10}]^{2-}$, which on reaction with $[Au(PPh_3)]^+$ gives (**100**) ($L = PPh_3$). Since $[Fe_2Rh(CO)_{10}]^-$ is a 46-electron cluster, it is coordinatively unsaturated which is reflected by its reactivity (equation 44). Combination of 2 mols of $[Rh(CO)_4]^-$ with 0.67 mol of $Ru_3(CO)_{12}$ gives $[Ru_2Rh_2(CO)_{12}]^{2-}$, which on further reaction with 1.3 mols of $Ru_3(CO)_{12}$ forms (**101**). Oxidation of $[RuRh_4(CO)_{15}]^{2-}$ with iodine yields (**102**) plus $[Rh(\mu\text{-}I)(CO)_2]_2$.[78] Condensation of $Rh_4(CO)_{12}$ with $Pt(PPh_3)_3$ provides a mixture of (**103**) and (**104**) ($L = PPh_3$). Complex (**104**) is an electron-deficient 58-electron cluster. Also, condensation of $[Rh(CO)_4]^-$ with $[PtCl(\mu\text{-}DPPM)]_2$ in methanol in a CO atmosphere forms (**105**) (phenyl groups of DPPM omitted for clarity). The same species can also be obtained, but in lower yield, from the reaction of $Pt_2(CO)_3(DPPM)_2$ and half an equivalent of $Rh_4(CO)_{12}$ under nitrogen in THF solution. Reaction of (**105**) with $Rh_6(CO)_{15}(MeCN)$ forms $\{Rh_6(CO)_{14}\}(\mu\text{-}CO)_2\{Pt_2Rh_2(CO)_5(DPPM)_2\}$via displacement of the weakly bound acetonitrile. The complex is proposed to contain a donor metal–metal bond from the Rh_6 unit to the Rh_2Pt_2 unit. The related reaction of $Pt_2(CO)_3(DPPM)_2$ directly with $Rh_6(CO)_{15}(MeCN)$ at a low temperature followed by warming to room temperature gives $\{Rh_6(CO)_{14}\}(\mu\text{-}CO)_2\{Pt_4(DPPM)_3\}$, where the skeleton is depicted as (**106**). In this instance, there is a dative metal–metal bond from platinum to rhodium.[79] A series of nickel/rhodium clusters have been prepared as indicated (equation 45) but most are rather unstable, and all attempts to observe Lewis acid/base and redox properties failed because of decomposition.[80]

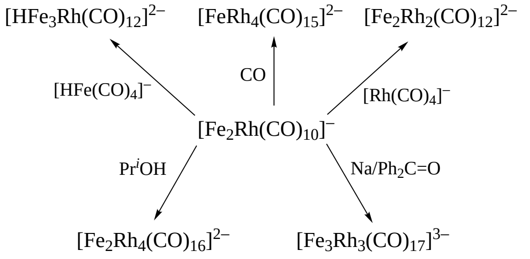
$[HFe_3Rh(CO)_{12}]^{2-}$
$[FeRh_4(CO)_{15}]^{2-}$
$[Fe_2Rh_2(CO)_{12}]^{2-}$
$[HFe(CO)_4]^-$
CO
$[Rh(CO)_4]^-$
$[Fe_2Rh(CO)_{10}]^-$
Pr^iOH
$Na/Ph_2C=O$
$[Fe_2Rh_4(CO)_{16}]^{2-}$
$[Fe_3Rh_3(CO)_{17}]^{3-}$

(44)

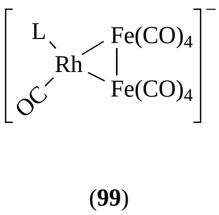
L
Rh
OC
$Fe(CO)_4$
$Fe(CO)_4$

(**99**)

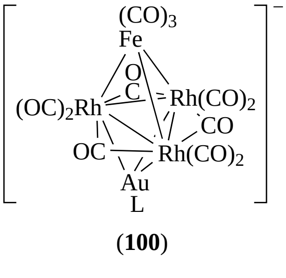
$(CO)_3$
Fe
O
C
$(OC)_2Rh$
$Rh(CO)_2$
CO
OC
$Rh(CO)_2$
Au
L

(**100**)

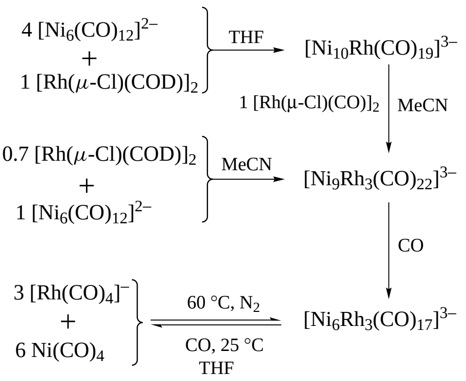
$4\ [Ni_6(CO)_{12}]^{2-}$
+
$1\ [Rh(\mu\text{-}Cl)(COD)]_2$
THF
$[Ni_{10}Rh(CO)_{19}]^{3-}$
$1\ [Rh(\mu\text{-}Cl)(CO)]_2$
MeCN
$0.7\ [Rh(\mu\text{-}Cl)(COD)]_2$
+
$1\ [Ni_6(CO)_{12}]^{2-}$
MeCN
$[Ni_9Rh_3(CO)_{22}]^{3-}$
CO
$3\ [Rh(CO)_4]^-$
+
$6\ Ni(CO)_4$
60 °C, N_2
CO, 25 °C
THF
$[Ni_6Rh_3(CO)_{17}]^{3-}$

(45)

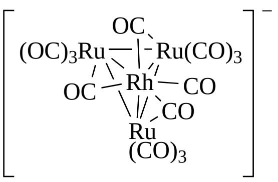
OC
$(OC)_3Ru$
$Ru(CO)_3$
OC
Rh
CO
CO
Ru
$(CO)_3$

(**101**)

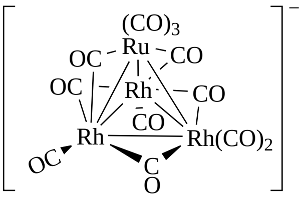
$(CO)_3$
OC
Ru
CO
OC
Rh
CO
CO
Rh
$Rh(CO)_2$
OC
C
O

(**102**)

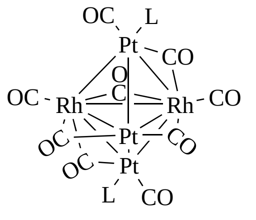
OC
L
Pt
CO
O
C
OC
Rh
Rh
CO
OC
Pt
CO
OC
Pt
L
CO

(**103**)

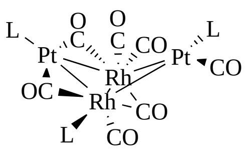
O
O
L
Pt
C
C
CO
Pt
L
CO
Rh
OC
Rh
CO
L
CO

(**104**)

Rhodium/rhenium clusters have been prepared by combination of $\mathrm{RhCl(CO)(PPh_3)_2}$ with $[\mathrm{Re_2(\mu\text{-}PR_2)(CO)_8}]^-$ (R = Ph, cy) under carbon monoxide and with $\mathrm{TlPF_6}$ as a halide abstraction agent. The initially obtained salt, $[\mathrm{Rh(CO)(PPh_3)_2}][\mathrm{Re_2(\mu\text{-}PR_2)(CO)_8}]$, loses a molecule of triphenylphosphine on standing in solution to give (**107**) ($\mathrm{L = PPh_3}$). If one starts with the preformed cationic rhodium complex $[\mathrm{Rh(COD)(PPh_3)_2}]\mathrm{BPh_4}$, a redox condensation occurs with $[\mathrm{Re_2(\mu\text{-}PR_2)(CO)_8}]^-$ in refluxing THF to form (**108**), which is said to have a rhenium–rhodium double bond.[81]

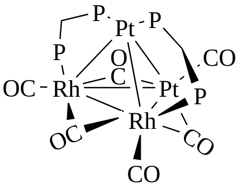

(**105**)

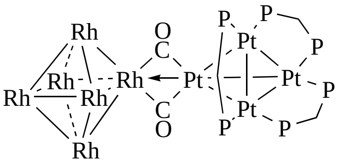

(**106**)

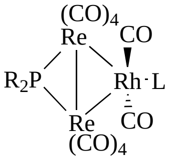

(**107**)

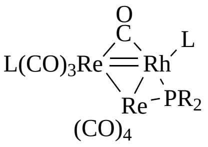

(**108**)

2.6 Isocyanide Complexes

As in the preceding section, the emphasis of this section will be on rhodium complexes containing isocyanide ligands, wherein the isocyanide ligand is the particular focus of the report. For example, there has been an extensive study of the spectroscopic and luminescent properties (*see* ***Luminescence Behavior & Photochemistry of Organotransition Metal Compounds*** and ***Electronic Structure of Organometallic Compounds***) of (**109**) ($\mathrm{L = CNBu}^t$. $\mathrm{X = Pt(CN)_2}$; $n = 1$. X = Ag, Au; $n = 2$). All show an intense singlet $d\sigma^* \rightarrow p\sigma$ absorption and molecular orbital calculations indicate that the $d\sigma^*$ orbital is mainly Rh $4d_{z^2}$ in character while the $p\sigma$ orbital is a combination of isocyanide π^* and Rh $5\mathrm{p_z}$ character. The absorption band therefore has significant $\mathrm{Rh} \rightarrow \pi^*$ charge transfer character. All complexes are phosphorescent.[82] Thermodynamic parameters for the disproportionation of the mixed-valence dimers $[\mathrm{Rh_2(\mu\text{-}L_2)_{4-\mathit{n}}(\mu\text{-}DPPM)_\mathit{n}}]^{3+}$ ($\mathrm{L_2}$ = TM4, $n = 0$; $\mathrm{L_2}$ = dimen; $n = 0$–2; $\mathrm{L_2}$ = bridge; $n = 2$) have been described and it appears that only when no DPPM ligands are present is this a facile process. The large difference in the tendency to disproportionate between this complex and those containing one or more DPPM ligands is attributed to large differences in the energies of the oxidized species within the series relative to those of the mixed-valence starting complexes. These energy differences are largely governed by the different affinities of the oxidized species for axial ligands as a function of the extent of substitution of diisocyanide ligands by DPPM.[83]

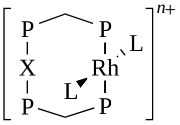

(**109**)

Addition of aryl azides to $\mathrm{CpRh(PMe_3)(CNMe)}$ results in coupling of the aryl nitrene with the isocyanide to form (**110**) (Ar = Ph, *p*-tol) which can be converted to (**111**) (R′ = H, Me), another example of a carbene complex (see also **73**, Section 2.4, ***Carbene Complexes***).[84] Replacement of COD in $\mathrm{Rh_2(COD)_2(\mu\text{-}Cl)(\mu\text{-}PBu^{\mathit{t}}_2)}$ by *t*-butylisocyanide yields $\mathrm{Rh_2(CNBu^{\mathit{t}})_4(\mu\text{-}Cl)(\mu\text{-}PBu^{\mathit{t}}_2)}$, which on treatment with one equivalent of lithium di(*t*-butyl)phosphide forms $[\mathrm{Rh(CNBu^{\mathit{t}})_2(\mu\text{-}PBu^{\mathit{t}}_2)}]_2$, which has a planar $\mathrm{Rh_2P_2}$ core and no Rh–Rh bond. In a chloroform solution, the last complex is slowly converted into a mixture of *cis*- and *trans*-$[\mathrm{RhCl(CNBu^{\mathit{t}})(\mu\text{-}PBu^{\mathit{t}}_2)}]_2$, while oxidation with ferricinium hexafluorophosphate yields $\{[\mathrm{Rh(CNBu^{\mathit{t}})_2(\mu\text{-}PBu^{\mathit{t}}_2)}]_2\}^{2+}$. Both of the oxidized dimers contain Rh–Rh bonds.[85]

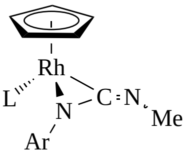

(**110**)

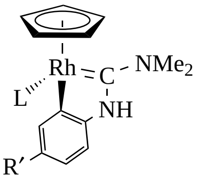

(**111**)

Cleavage of the chloride bridges in $[\mathrm{Cp^*RhCl(\mu\text{-}Cl)}]_2$ by 1,4-diisocyanobenzenes yields $\{\mathrm{Cp^*RhCl_2}\}_2(\mu\text{-CN-R-NC})$ (R = $\mathrm{2,3,5,6\text{-}Me_4C_6}$; $\mathrm{2,5\text{-}Me_2C_6H_2}$). Abstraction of one chloride ligand from each metal by silver triflate is followed by condensation of two of the resulting dications to form the metallamacrocycle (**112**). The larger cavity species (**113**) (X = CN-R-NC, 4,4′-bipyridyl) can be obtained by a second bridge-splitting reaction on (**112**) (see also Section 4.2).[86]

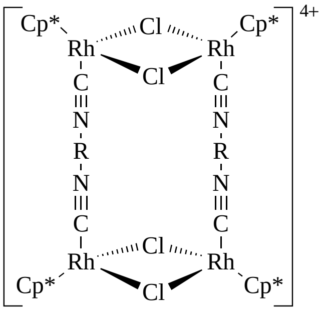

(**112**)

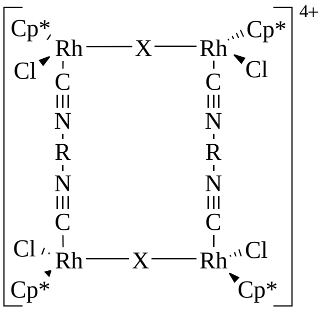

(**113**)

3 COMPOUNDS OF LIGANDS CONTAINING LOCALIZED π-BONDS

3.1 Complexes of Alkenes

Synthetic routes to alkene complexes remain primarily the same as in the preceding edition, but there has been significant interest shown in forming isolable complexes containing an alkene and either a hydride or an alkyl ligand, in order to study migratory insertions (*see* ***Oligomerization & Polymerization by Homogeneous Catalysis*** and ***Organic Synthesis Using Metal-mediated Coupling Reactions***). An interesting three-coordinate alkene complex, (**115**), results from the treatment of $[Rh(\mu\text{-}Cl)(COE)_2]_2$ with (**114**) (Ar $=$ 2,6-$X_2C_6H_3$ (X $=$ Me,Cl)), although when X $=$ Cl, there is an agostic interaction of one chlorine substituent with the metal to relieve the coordinative unsaturation. Complex (**115**) (X $=$ Me) adds dinitrogen and oxidatively adds dihydrogen. A low-temperature NMR study indicates the formation of a dihydrogen adduct (*see* ***Hydrogen Bonding & Dihydrogen Bonding***) prior to the generation of the dihydride species. The same complex is a catalyst for alkene hydrogenation (*see* ***Hydrogenation & Isomerization of Alkenes***) and the rate-determining step is considered to be either the conversion of the dihydrogen adduct to the dihydride or the migratory insertion of the alkene. Presumably, the combined bulk of the diimine and COE ligands permits the isolation of the three-coordinate (**115**), since with $[Rh(\mu\text{-}Cl)(COD)]_2$ and $[Rh(\mu\text{-}Cl)(C_2H_4)_2]_2$, four-coordinate products are obtained.[87] In related work, (**116**) (Ar $=$ 2,6-$Pr^i{}_2C_6H_3$) reacts with $[Rh(\mu\text{-}Cl)(C_2H_4)_2]_2$ followed by treatment with $NaBAr_f$ (*see* ***Boron: Organoboranes***) in the presence of ethylene to form (**117**). This oxidatively adds methyl iodide (*see* ***Carbon–Carbon & Carbon–Heteroatom Activation***) and subsequent abstraction of iodide with $AgBF_4$ in the presence of ethylene forms the cationic alkyl olefin complex (**118**), which was detected spectroscopically but not isolated in pure form. No evidence was found for ethylene polymerization (*see* ***Oligomerization & Polymerization by Homogeneous Catalysis***) in this system (presumably migratory insertion of ethylene into the Rh–methyl bond would be the initial step) in contrast to related systems containing the Cn-type ligands (see Section 2.1). The difference in reactivity between the two was attributed to the mer coordination of the supporting ligand here in contrast to the fac coordination of the Cn ligands.[88] Some success in facilitating alkene oligomerization (*see* ***Organic Synthesis Using Metal-mediated Coupling Reactions***) was realized with $Tp'Rh(C_2H_4)_2$ (see also Reference 18). Heating the solid compound at 60 °C forms a mixture of *exo*- and *endo*-$Tp'Rh(H)(\eta^3\text{-}C_3H_4Me)$, which on photolysis converts to the butadiene complex $Tp'Rh(\eta^2;\ \eta^2\text{-}CH_2{=}CHCH{=}CH_2)$. This last complex can also be generated, together with ethane from the reaction of $Tp'Rh(C_2H_4)_2$ with ethylene at room temperature, but if this is done at $-40\,°C$, the complexes $Tp'Rh(Et)(\eta^3\text{-}C_3H_4Me)$ and $Tp'Rh(\eta^2;\ \eta^2\text{-}CH_2{=}CHCH{=}CHC_2H_5)$ are also seen. The formation of the C–C coupling products is proposed to be initiated by the conversion of an ethylene ligand into a vinyl hydride complex (see also equation 9, section 2.1).[89] Protonation of $(acac)Rh(C_2H_4)_2$ with triflic acid in THF solution forms, predominantly, $(acac)Rh(C_2H_5)$, which was not isolated and is presumably solvated. Some but-2-enes were also detected implicating ethylene insertion into the Rh–Et bond, but no ethylene polymerization was detected. It is proposed that the putative rhodium–butyl complex undergoes β-hydride elimination with subsequent butene displacement by ethylene faster than the ethylene can insert into the rhodium–butyl bond.[90]

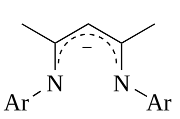

(**114**)

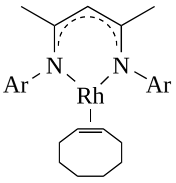

(**115**)

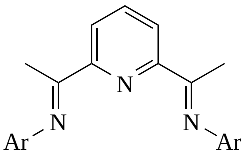

(**116**)

The calix[4]arene-based diphosphine (**119**) (R $=$ Me, Pr^i, Ph; R$'$ $=$ Pr^i) on reaction with $[Rh(\mu\text{-}Cl)(COD)]_2$ and then $TlPF_6$ forms the dinuclear species (**120**). These were tested as catalysts for hex-1-ene hydroformylation (*see* ***Carbonylation Processes by Homogeneous Catalysis***) and that with R $=$ Ph was best, but the performance was not better than extant systems and no special role for the calixarene moieties could be discerned.[91] Several papers have used DFT calculations as part of QM/MM studies (*see* ***Molecular Orbital Theory***) to probe the course of the hydroformylation process (*see* ***Carbonylation Processes***

by Homogeneous Catalysis) catalyzed by Rh(H)(CO)L_3 (L = tertiary phosphine) complexes with particular emphasis on the origin of the regioselectivity (straight vs. branched chain aldehyde). There are, however, enough differences between the models used and/or the restrictions on them that comparisons between the results are not easy to make. The first used Rh(H)(CO)(alkene)$(PH_3)_2$ to model the migratory insertion of ethylene and propylene into the Rh bond and the DFT-derived geometries with fixed coordination spheres were used in the MM stage with L = PPh_3 to model real systems based on diphosphine ligands. Reasonable predictions for the observed regioselectivities were provided by this model. The use of rigid coordination spheres in the MM stage has been criticized in a second study, which also begins with DFT calculations on Rh(H)(CO)(alkene)$(PH_3)_2$ but uses (**121**) (X = PPh, $SiMe_2$, S, CMe, C=CMe_2, NR, $(CH_2)_2$) as the ligand in the MM stage. It is concluded that here the regioselectivity is governed primarily by nonbonding interactions between the phenyl groups on phosphorus and the alkene. Changes in the ‘‘bite’’ angle of the diphosphine seem to have little effect. The most extensive study again used Rh(H)(CO)$(C_2H_4)(PH_3)_2$ for the QM portion and the sequence of equation (46) was proposed as the lowest energy path for the catalytic cycle. The results suggest that the migratory insertion of the carbonyl and ethyl groups is the rate-determining step, although experimentally it is thought that the oxidative addition of dihydrogen is rate-determining. Another peculiarity is the predicted generation of *cis*-Rh(H)(CO)L_2 following reductive elimination of aldehyde and the determination that cycles beginning with this isomer are energetically less favorable than those shown above. To explain this, it is suggested that the alkene adduct of *cis*-Rh(H)(CO)L_2 could undergo a Berry pseudorotation to generate the isomer shown at the top right of equation (46). These studies were extended to explore the alkene insertion steps for propylene where regiochemical information could be obtained. The possible conformations found for the transition states for propylene insertion are (**122**) and (**123**), with the former on the path to the linear product while the latter is on the path to the branched isomer. Both equatorial–equatorial (X = CO; Y = P) and axial–equatorial (X = P; Y = CO) propylene adduct precursors to these transition states were also examined with the conclusion that the axial–equatorial isomer predominated by a factor of 3 but that the equatorial–equatorial isomer was 15 times reactive. There are therefore two channels predicted for the hydroformylation process: linear aldehyde from the less reactive but more abundant alkene adduct through (**122**) (X = P; Y = CO) and branched product from the more reactive minor adduct through (**123**) (X = CO; Y = P). The experimentally observed regioselectivities are suggested to arise from ground-state discrimination between the two most stable isomers of the alkene adduct, and therefore, to be particularly sensitive to the steric profile of the phosphine ligands. This question was explored, unfortunately only with ethylene, in MM calculations on Rh(H)(CO)$(C_2H_4)L_2$ (L = PMe_3, PPh_3, P(*m*-$XC_6H_4)_3$, P(*p*-$XC_6H_4)_3$ (X = SO_3^-)). For all the aryl phosphine ligands, the presence of the aryl substituents renders the equatorial–equatorial transition state (cf. **122**) (X = CO; Y = P) more favorable and because of π-stacking interactions, the insertion product *cis*-Rh(Et)(CO)L_2 is preferred to the trans isomer.[92] Related DFT calculations on $Rh(H)(CO)_3(CH_2{=}CHMe)$ predict the most stable isomer to be the one having the alkene lying in the equatorial plane of the trigonal bipyramidal coordination sphere. From this, the calculated lowest energy path to aldehyde gives a ratio of linear to branched product comparable to that found experimentally, when $Rh_4(CO)_{12}$ is the catalyst precursor ($Rh(H)(CO)_3(CH_2{=}CHMe)$ is the presumed alkene adduct formed in the catalytic cycle). Polarizable and/or electron-withdrawing substituents on the alkene are predicted to favor branched product while bulky substituents favor the linear isomer.[93]

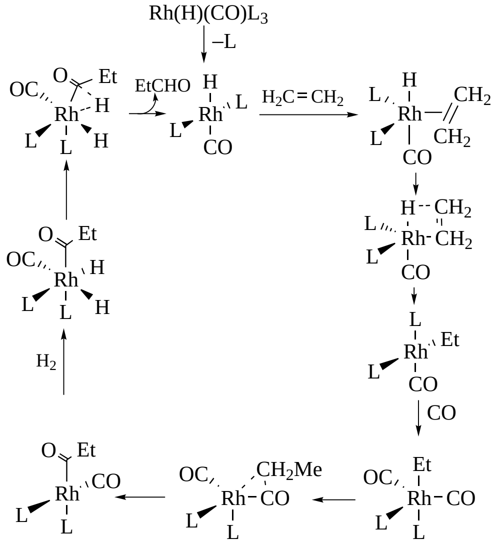

(46)

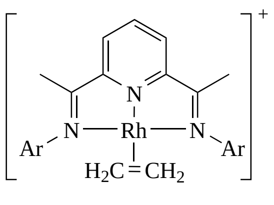

(**117**)

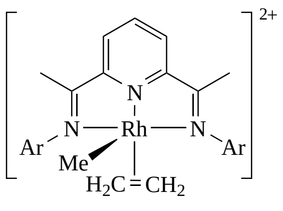

(**118**)

One computational study (*see* ***Molecular Orbital Theory***) has appeared using $\{RhCl(PH_3)_2\}$ to model the rhodium-catalyzed hydroboration of ethylene (*see* ***Hydroboration Catalysis***). Both associative and dissociative pathways were examined (equation 47). In the associative path, three possible

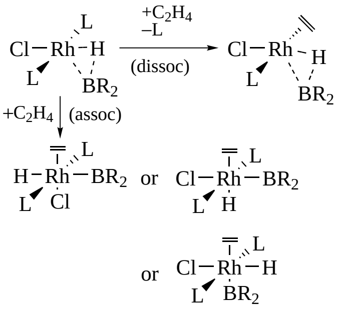

(47)

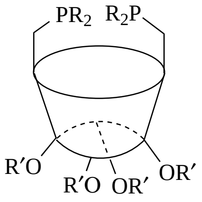

(**119**)

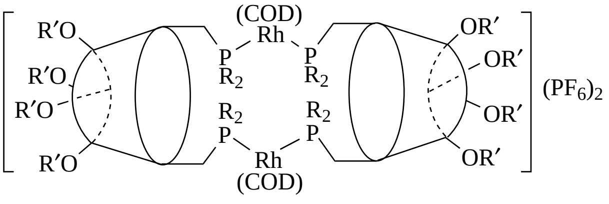

(**120**)

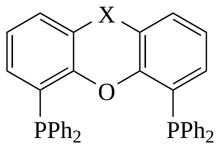

(**121**)

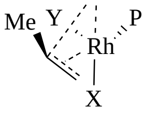

(**122**)

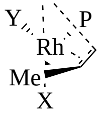

(**123**)

intermediates were considered to be on the reaction coordinate.[94] A related study on the hydrosilylation of alkenes (*see* ***Hydrosilation Catalysis***) using $RhCl(PH_3)_3$ as a catalyst model supports the modified Chalk–Harrod mechanism, namely oxidative addition of the Si–H bond to the metal followed by alkene coordination, insertion of the alkene into the Rh–Si bond, and C–H reductive elimination.[95]

The rhodium-catalyzed hydrogenation of alkenes (*see* ***Hydrogenation & Isomerization of Alkenes***) has also been the subject of several studies, both experimental and computational. The use of para-hydrogen-induced-polarization in the $RhCl(PPh_3)_3$-catalyzed hydrogenation of hex-1-ene and related alkenes demonstrated the presence of several species, heretofore, undetected. Two of these are (**124**) and (**125**). The latter is detected when the alkene is styrene or its derivatives, while the former is determined not to be in the catalytic cycle and so represents a path lowering the catalyst activity. Its formation can be inhibited by the presence of small amounts of free phosphine.[96] The factors responsible for the high enantioselectivity in the hydrogenation of prochiral alkenes (*see* ***Asymmetric Synthesis by Homogeneous Catalysis***), particularly (Z)-α-acetamidocinnamate esters catalyzed by cationic rhodium complexes of diphosphines have been explored by NMR and computational methods. There appears, from these results, to be considerable conformational mobility of the metal-complexed alkene so that a rigid chiral template is not established by the metal diphosphine framework. Instead, the primary enantiodiscriminating interaction is that between the plane of the enamide ester functionality and the proximal arene ring of the ligand. Molecular mechanics calculations were able to account for the diastereoselectivity of alkene binding but not the relative reactivities of the oxidative adducts of the alkene complexes with dihydrogen. This latter feature has been previously shown to be critical in determining the enantiomeric excess produced in the product. Some of the computational work suggested the possible importance of species such as (**126**) in the catalytic cycle.[97]

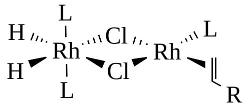

(**124**)

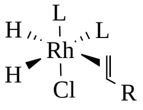

(**125**)

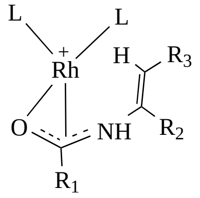

(**126**)

The classical Dewar-Chatt-Duncanson model for metal–alkene bonding has been revisited with a combination of X-ray structural data (*see* ***Diffraction Methods in Inorganic Chemistry***) and DFT calculations (*see* ***Molecular Orbital Theory***), particularly on complexes of the type $(acac)Rh(alkene)_2$. These indicate the existence of distortions from idealized geometry involving a ‘‘twist’’ (**127**), where the axis of the double bond is no longer perpendicular to the molecular plane and a ‘‘roll’’ (**128**), where the line joining the midpoint of the double bond to the metal is no longer in the molecular plane. The latter distortion is seen for unsymmetrically substituted alkenes and occurs so as to place the more nucleophilic carbon atom closer to the molecular plane.[98] The coordination geometries of (acac)Rh(C_2H_4)$_2$ and its hfac analog determined by X-ray structure analysis (*see* ***Diffraction Methods in Inorganic Chemistry***) are reproduced satisfactorily by DFT calculations. Similar calculations to determine ^{103}Rh chemical shifts in (acac)Rh(alkene)$_2$ complexes also agree well with experiment and with a correlation found previously between these chemical shifts and stability constants for these monoalkene complexes. Chelating and fluorinated alkenes do not follow this correlation presumably because of the chelate effect in the former and bonding more akin to a metallacyclopropane in the latter.[99]

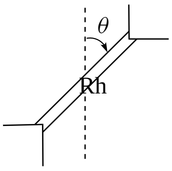

(**127**)

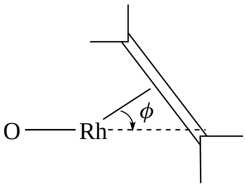

(**128**)

The complex [Cp*Rh(CH_3)(μ-CH_2)$_2$Rh(L)Cp*]PF_6 (L = η^2-C_2H_4) has been synthesized from the analog with L = MeCN by ligand exchange and obtained as a 2:1 mixture of trans and cis isomers. Decomposition above room temperature formed mainly methane and ethylene and small to trace amounts of ethane and propylene.[100] As another example that water is not necessarily incompatible with organotransition metal compounds (*see* ***Water & O-donor Ligands***), the complexes [Rh(L_2)(H_2O)$_2$]OTs (L_2 = COD, NBD, CH_2=C(Me)CH=CH_2, CH_2=C(Me)C(Me)=CH_2, (C_2H_4)$_2$) have been prepared from [Rh(μ-Cl)(L_2)]$_2$ and silver tosylate in water.[101] The unsubstituted double bond in mono-aryl allenes coordinates to rhodium in four-coordinate *trans*-RhClL_2(H_2C=C=CHAr) and five-coordinate RhClL_3(H_2C=C=CHAr) (L = PMe_3; Ar = Ph, *p*-FC_6H_4) (cf. **39, 45**) which are prepared, respectively, from [Rh(μ-Cl)L_2]$_2$ or RhClL_3 and approximately stoichiometric quantities of the allene. Particularly in the four-coordinate complex, there is an agostic interaction of an ortho hydrogen on the aryl group with a metal. If three equivalents of the allene are reacted with RhClL_3, coupling of two allene molecules occurs to form (**129**).[102] The unsymmetrical ligand $R_2PCH_2SbR_2$ (R = Pr^i) cleaves the chloride bridge in [Rh(μ-Cl(COD))]$_2$ to form RhCl(COD) ($R_2PCH_2SbR_2$) where the ligand coordinates only via phosphorus. Chelation can be achieved by abstraction of the chloride by $AgPF_6$, and addition of diazomethane to the resulting cationic complex forms (**130**) instead of the desired carbene complex.[103]

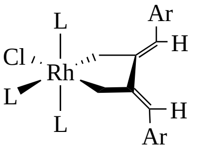

(**129**)

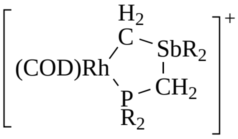

(**130**)

3.2 Complexes of Alkynes

Simple alkyne complexes continue to be reported, but the primary interest is in systems where the alkyne is transformed either by rearrangements (see Section 2.4 for conversion to vinylidenes and allenylidenes) or by coupling reactions between alkynes and/or other coordinated ligands (*see* ***Organic Synthesis Using Metal-mediated Coupling Reactions***). Terminal alkynes cleave a Co–Co bond in $Rh_nCo_{3-n}(CO)_{12}$ (n = 1, 2) to form the butterfly clusters $Rh_nCo_{3-n}(CO)_6(\mu\text{-}CO)_4(\mu_4,\eta^2\text{-}HC{\equiv}CR)$ (R = CpFe(η^5-C_5H_4), CH_2OH, $MeOC_{10}H_6C(HMe)C(O)OCH_2$) (*see* ***Polynuclear Organometallic Cluster Complexes***).[104]

The final product of the reaction of alkynes (PhC≡CH, PhC≡CPh, DMAD, HFB, HC≡CCO_2Me) with Cp*Rh(PMe_3)H_2 is the corresponding alkene complex Cp*Rh(PMe_3)(η^2-alkene) formed by hydrogenation of the C≡C bond. In the cases of HFB and methyl propiolate, intermediate vinyl hydride complexes could be detected.[105] Triethylgermane undergoes oxidative addition to (acac)Rh(COE)(Pcy_3) to form (**131**) (Y = $GeEt_3$; L = Pcy_3), which effects hydrogermylation (*see* ***Germanium: Organometallic Chemistry***) of terminal alkynes to yield (**132**) (R = CO_2Me, Ph). Complex (**131**) (Y = $SnPh_3$) is similarly obtained from triphenylstannane but only the hydride ligand can be transferred to an alkyne and (**133**) (R = CO_2Me, Ph) results. The difference is attributed to the greater strength of a C–Ge bond over a C–Sn bond coupled with the Rh–Sn bond being stronger than a Rh–Ge bond.[106] Aryl phosphines containing *o*-methoxy groups are often *O*-demethylated on reaction with transition metal complexes and this occurs in the reaction of [Cp*Rh(μ-Cl)Cl]$_2$ with $PPh_n(2,6\text{-}(MeO)_2C_6H_3)_{3-n}$ (n = 1, 2) to form (**134**) (R′ = Ph, 2,6-$(MeO)_2C_6H_3$). Alkyne coupling occurs with terminal alkynes (PhC≡CH, *p*-tolC≡CH) to give (**135**) (R′ = Ph; R_1 = R_4 = Ph, *p*-tol; R_2 = R_3 = H), while with R″C≡CCO_2R, the product is (**136**) (R′ = Ph, R = Me, Et; R″ = H, R = Me, R″ = CO_2Me).[107] Cou-

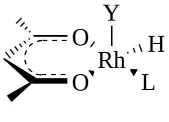

(**131**)

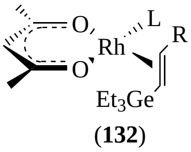

(**132**)

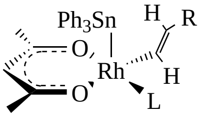

(**133**)

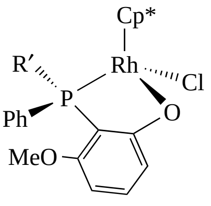
Cp*
Rh
Cl
R′
P
Ph
O
MeO

(**134**)

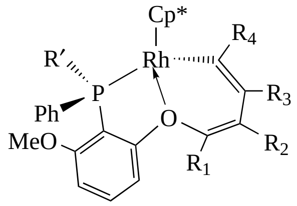
Cp*
Rh
R4
R′
P
R3
Ph
O
MeO
R2
R1

(**135**)

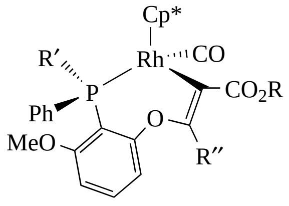
Cp*
R′
Rh
CO
CO2R
P
Ph
O
MeO
R″

(**136**)

pling of methyl propiolate with one of the bridging thiolate ligands (*see* ***Tellurium: Organotellurium Chemistry***) in $[Cp^*Rh(\mu\text{-}Cl)(\mu\text{-}SPr^i)_2]OTf$ yields (**137**) (R = CO_2Me), while $HC\equiv C(CH_2)_2OH$ forms the cyclic carbene (**138**).**108**

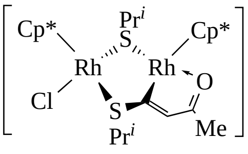
Cp*
Pr^i
Cp*
S
Rh
Rh
O
OTf
Cl
S
Pr^i
Me

(**137**)

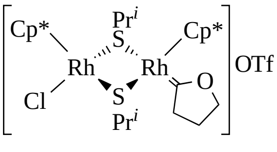
Cp*
Pr^i
Cp*
S
Rh
Rh
O
OTf
Cl
S
Pr^i

(**138**)

Complex (**139**) is prepared from $[Rh(\mu\text{-}Cl)(CO)_2]_2$ and a Cn derivative (**1** (R = $-(CH_2)_3C\equiv CMe$; Section 2.1)) by standard methods. Either thermal or photochemical conditions cause coupling of two alkynyl arms with a carbonyl group (*see* ***Organic Synthesis Using Metal-mediated Coupling Reactions***) to yield (**140**).**109** Cyclization with metallacycle formation (*see* ***Organic Synthesis Using Metal-mediated Coupling Reactions***) occurs when the diyne $O(CH_2C\equiv CCO_2Me)_2$ is reacted with the Rh(I) chloro complex of the bis(oxazoline) ligand (**141**) to yield (**142**),**110** while acidification of the dinuclear acetylide complex $[Cp^*Rh(C\equiv CR)(\mu\text{-}CH_2)]_2$ (R = Ph, *p*-tol) with HBF_4 initiates coupling of both acetylide ligands with the methylidene groups (*see* ***Organic Synthesis Using Metal-mediated Coupling Reactions***) to give (**143**) (X = H, Me) together with its anti isomer. Since HCl merely cleaves the acetylide ligand from $[Cp^*Rh(C\equiv CR)(\mu\text{-}CH_2)]_2$, the formation of (**143**) appears to require the presence of a noncoordinating anion and it is proposed that the reaction may proceed through (**144**) and (**145**) as intermediates although no vinylidene species could be detected even at a low temperature. In this instance, one alkynyl unit couples with one methylene unit but when phenyl acetylene reacts with $\{[Cp^*Rh(MeCN)(\mu\text{-}CH_2)]_2\}^{2+}$, both methylene units couple with two alkyne molecules (*see* ***Organic Synthesis Using Metal-mediated Coupling Reactions***) to form (**146**).**111**

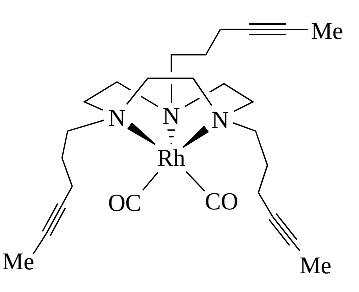
Me
N
N
N
Rh
OC
CO
Me
Me

(**139**)

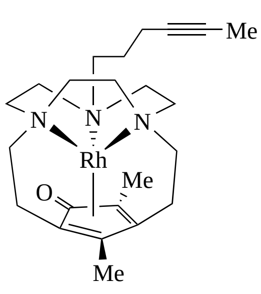
Me
N
N
N
Rh
Me
O
Me

(**140**)

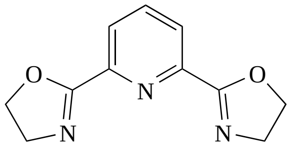

(**141**)

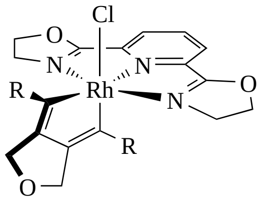
Cl
O
N
N
O
R
Rh
N
R
O

(**142**)

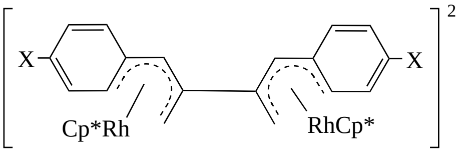
2+
X
X
Cp*Rh
RhCp*

(**143**)

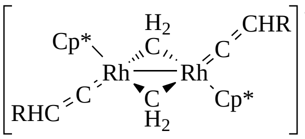
H2
2+
Cp*
C
CHR
C
Rh
Rh
C
RHC
C
Cp*
H2

(**144**)

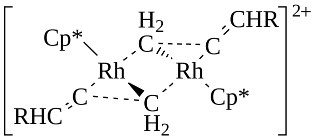
H2
2+
Cp*
C
CHR
C
Rh
Rh
C
RHC
C
Cp*
H2

(**145**)

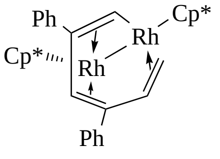
Ph
Cp*
Rh
Cp*
Rh
Ph

(**146**)

A considerable number of reactions of $CpRh(\mu\text{-}CO)(\mu\text{-}\eta^2\text{:}\eta^2\text{-}F_3CC\equiv CCF_3)RhCp$ have been reported which illustrates the diversity of products that can be obtained in transition metal alkyne chemistry (*see* ***Organic Synthesis Using Metal-mediated Coupling Reactions***). Reaction of this complex with dimethyldiazomethane forms a mixture of (**147**) and (**148**), and on recrystallization (**148**) converts to (**149**) by a 1,4 hydrogen shift. By contrast, CpRh(μ-CO)(μ-η^2:η^2-$F_3CC{\equiv}CCF_3$)RhCp with $N_2C(CO_2Me)_2$ forms (**150**) (R = CO_2Et) where the alkylidene unit couples with the alkyne to form (**151**). The formation of (**147**), one of a number of examples of the complexation of intact diazoalkanes, is taken to indicate that the first step of both reactions is coordination of the diazoalkane to the metal via nitrogen, with the subsequent course of the reaction being determined by both steric and electronic factors. Attempts to couple (CpMe)Mn$(CO)_2$(THF) (*see* ***Manganese: Organometallic Chemistry***) with CpRh(μ-CO)(μ-η^2:η^2-$F_3CC{\equiv}CCF_3$)RhCp in a photolytic reaction led instead to cleavage of the methylcyclopentadienyl ligand from manganese and the formation of (**152**).[112] The alkynyl phosphines $Ph_2PC{\equiv}CR$ (R = Me, Ph) act as simple phosphine ligands (L) toward CpRh(μ-CO)(μ-η^2:η^2-$F_3CC{\equiv}CCF_3$)RhCp to form CpRh(CO)(μ-η^1:η^1-$F_3CC{\equiv}CCF_3$)Rh(L)Cp, but on treatment of the initial product with alumina in the presence of oxygen, alkyne coupling occurs to form (**153**).[113] In a similar fashion, CpRh(CO)(μ-η^1:η^1-$F_3CC{\equiv}CCF_3$)Rh(L)Cp (L = SRR′ (R = R′ = Me, Et, Pr^n, bz. R = Me; R′ = Et) is formed with the addition of one equivalent of the disulfide, but when these products (R = R′ = Me, Et) are reacted with more of the same disulfide, (**154**) (R″ = Et, Bu^s) is formed in a metal-mediated Stevens rearrangement.[114] Complex (**155**) is formed from CpRh(CO)(μ-η^1:η^1-$F_3CC{\equiv}CCF_3$)Rh(L)Cp (L = η^1-DPPE) and CpPd(η^3-C_3H_5).[115]

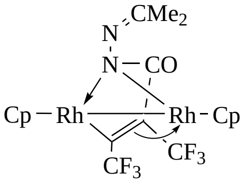
CMe2
N
N
CO
Cp
Rh
Rh
Cp
CF3
CF3

(**147**)

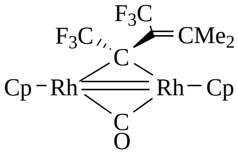
F3C
F3C
CMe2
C
Cp
Rh
Rh
Cp
C
O

(**148**)

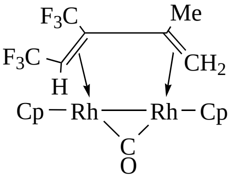
F3C
Me
F3C
CH2
H
Cp
Rh
Rh
Cp
C
O

(**149**)

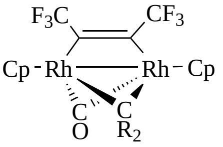
F3C
CF3
Cp
Rh
Rh
Cp
C
O
C
R2

(**150**)

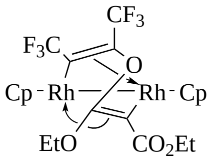
CF3
F3C
O
Cp
Rh
Rh
Cp
EtO
CO2Et

(**151**)

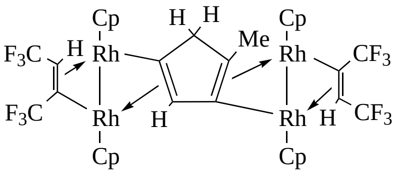
Cp
H
H
Cp
F3C
H
Rh
Me
Rh
CF3
F3C
Rh
H
Rh
H
CF3
Cp
Cp

(**152**)

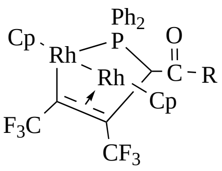
Ph2
Cp
P
O
Rh
Rh
C
R
Cp
F3C
CF3

(**153**)

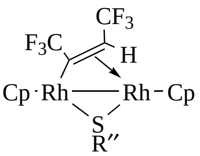
CF3
F3C
H
Cp
Rh
Rh
Cp
S
R″

(**154**)

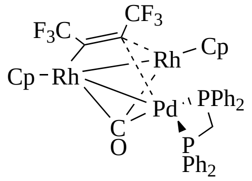
CF3
F3C
Rh
Cp
Cp
Rh
Pd
PPh2
C
O
P
Ph2

(**155**)

The reaction of $RhCl(PMe_3)_3$ with $Li(THF)_3[Si(SiMe_3)_3]$ in the presence of alkynes leads to Si–C coupling and metallacycle formation (equation 48 (L = PMe_3; R = Me, Ph)). It is proposed that $L_3Rh(Si(SiMe_3)_3)$ is formed initially and is converted to the silylene complex shown at the top left of equation (48) by a 1,2 migration of a trimethylsilyl group.[116]

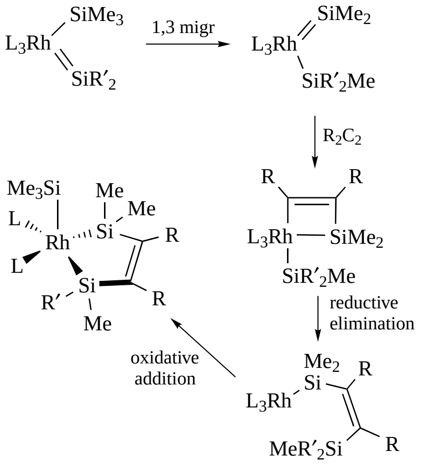
SiMe3
L3Rh
SiR′2
1,3 migr
SiMe2
L3Rh
SiR′2Me
R2C2
R
R
L3Rh
SiMe2
SiR′2Me
reductive elimination
Me2
Si
R
L3Rh
MeR′2Si
R
oxidative addition
Me3Si
Me
L
Me
Rh
Si
R
L
Si
R
R′
Me

(48)

As has been demonstrated repeatedly in the past, the reaction of alkynes with coordinatively unsaturated metal complexes frequently leads to a plethora of products resulting from the coupling of two or more alkyne molecules, sometimes also with inclusion of molecules present as ligands on the starting complex (*see* ***Organic Synthesis Using Metal-mediated Coupling Reactions***). Treatment of $[Rh(\mu\text{-}Cl)(COD)]_2$ with Pr^nLi and but-2-yne forms (**156**) (R = Me), but photolysis of CpRh(η^2-C_2H_4)$_2$ with RC≡CR (R = Me, Et) yields CpRh(η^2-RC≡CR)(η^2-C_2H_4), CpRh(η^4-C_6R_6), and (**157–160**) among other species. The oxygen atom in (**159**) is considered to result from hydrolysis during chromatographic workup of the crude reaction mixture while the formation of (**160**) suggests the intermediacy of a vinyl hydride species as has been found in the related Tp′ and Cn systems (see Section 2.1).[117] Coupling of a coordinated alkyne with an isocyanide occurs when CpRh(η^2-PhC≡CPh)(SbPr$^i_3$) with one equivalent of methyl isocyanide and (**161**) is formed. This reacts with a further two equivalents of an isocyanide to give the double insertion product (**162**) (R = Me, Bu^t).

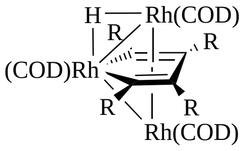
H
Rh(COD)
R
R
(COD)Rh
R
R
Rh(COD)

(**156**)

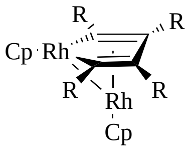
R
R
Cp Rh
R
R
Rh
Cp

(**157**)

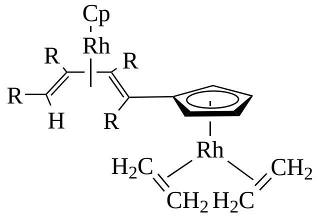
Cp
Rh
R
R
R
H
R
Rh
H$_2$C
CH$_2$
CH$_2$ H$_2$C

(**158**)

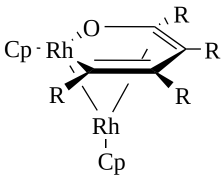
O
R
Cp Rh
R
R
R
Rh
Cp

(**159**)

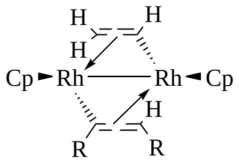
H
H
H
Cp
Rh
Rh
Cp
H
R
R

(**160**)

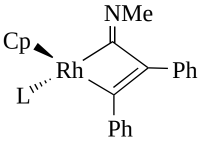
NMe
Cp
Rh
L
Ph
Ph

(**161**)

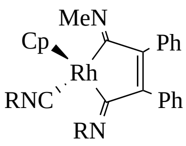
MeN
Cp
Ph
Rh
RNC
Ph
RN

(**162**)

Complex (**162**) (R = Me) can be obtained directly from CpRh(η^2-PhC≡CPh)(SbPr$^i_3$) and three equivalents of methyl isocyanide.[118]

Considerable use has been made of [Pt(C≡CR)$_4$]$^{2-}$ (R = Bu^t, SiMe$_3$) and *cis*-[(C$_5$F$_5$)$_2$Pt(C≡CR)$_2$]$^{2-}$ (R = Bu^t, Ph, SiMe$_3$) for the construction of multimetallic complexes via coordination of other metals to the C–C triple bonds. Thus, [Pt(C≡CR)$_4$]$^{2-}$ with [Rh(COD)(acetone)$_2$]$^+$ forms (**163**) (R = Bu^t, SiMe$_3$), while *cis*-M(C$_6$F$_5$)$_2$(THF)$_2$ (M = Pd, Pt) reacts with Cp*Rh(X)(C≡CR)(PEt$_3$) to give (**164**) (X = Cl, C≡CR; R = Bu^t, Ph; R′ = C$_6$F$_5$; M = Pd, Pt). Further reaction of (**164**) with an excess of [M′(C≡CPh)]$_n$ (M′ = Cu, Ag) forms (**165**). Similarly, *cis*-[(C$_5$F$_5$)$_2$Pt(C≡CR)$_2$]$^{2-}$ and [Rh(μ-Cl)(COD)]$_2$ give (**166**) while with [Rh(COD)(Et$_2$O)$_x$]$^+$ the bimetallic complex (**167**) is formed. Finally, acetylide ligand transfer from [Pt(C≡CR)$_4$]$^{2-}$ (R = Bu^t, SiMe$_3$) to rhodium occurs in its reaction with [Cp*Rh(PEt$_3$)(acetone)$_x$]$^{2+}$ and the product is (**168**) (L = PEt$_3$). Reaction of (**168**) with one equivalent of *cis*-Pt(C$_6$F$_5$)$_2$(THF)$_2$ attaches a {*cis*-Pt(C$_6$F$_5$)$_2$} fragment to the two acetylide ligands attached to Pt.[119]

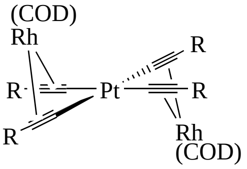
(COD)
Rh
R
R
Pt
R
R
Rh
(COD)

(**163**)

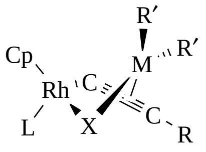
R′
Cp
M
R′
Rh
C
L
X
C
R

(**164**)

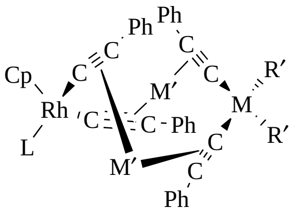
Ph
Ph
C
Cp
C
C
C
R′
Rh
M′
M
L
C
C - Ph
R′
C
M′
C
Ph

(**165**)

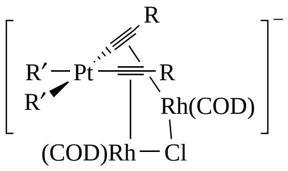
R
−
R′
Pt
R
R′
Rh(COD)
(COD)Rh
Cl

(**166**)

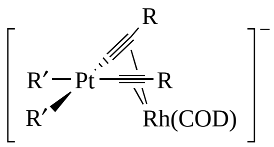
R
−
R′
Pt
R
R′
Rh(COD)

(**167**)

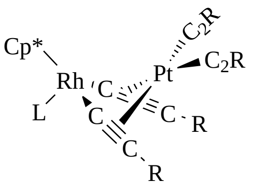
C$_2$R
Cp*
Pt
C$_2$R
Rh
C
L
C
C
R
C
R

(**168**)

4 COMPOUNDS OF LIGANDS CONTAINING DELOCALIZED π-BONDS

4.1 Allyl Complexes

Oxidative addition of allyl bromide (*see* ***Carbon–Carbon & Carbon–Heteroatom Activation***) to Tp′Rh(COE)(MeCN) initially yields Tp′Rh(η^1-CH$_2$CH=CH$_2$)(Br)(MeCN) but on heating in benzene solution it converts into Tp′Rh(η^3-C$_3$H$_5$)Br. This is an example of a typical procedure for the formation of η^3-allyl complexes, where the η^1-allyl complex is formed via oxidative addition of an allyl halide to a low-valent metal center or by metathesis of a metal halogen bond with an allyl Grignard or lithium reagent. Loss of a relatively labile two-electron donor ligand via thermolysis or photolysis converts the one-electron donor η^1-allyl ligand to a three-electron donor η^3-allyl ligand. Despite NMR evidence for significant electron deficiency in the allyl group in $\mathrm{Tp'Rh}(\eta^3\text{-}\mathrm{C_3H_5})\mathrm{Br}$, its reaction with MeMgBr replaces the bromide by a methyl group suggesting attack at the metal rather than at the allyl ligand as had been expected. Similarly, reaction with $\mathrm{LiBHEt_3}$ forms $\mathrm{Tp'Rh}(\eta^3\text{-}\mathrm{C_3H_5})(\mathrm{H})$, but when $\mathrm{LiBDEt_3}$ is used, incorporation of deuterium into the allyl ligand occurs to give $\mathrm{Tp'Rh}(\eta^3\text{-}\mathrm{CH_2CDCH_2})(\mathrm{H})$ in 92% isotopic purity. Also, reaction of $\mathrm{Tp'Rh}(\eta^3\text{-}\mathrm{CH_2CDCH_2})\mathrm{Br}$ with $\mathrm{LiBHEt_3}$ forms $\mathrm{Tp'Rh}(\eta^3\text{-}\mathrm{C_3H_5})(\mathrm{D})$ in 85% isotopic purity indicating that at least in this system, initial attack of hydride (or deuteride) occurs at the allyl ligand to form (**169**), which then undergoes β-hydride (or deuteride) elimination.[120] Multiple insertions of mono(aryl)allenes into the initially formed allyl complex occurs when an excess of the allene is reacted with $\mathrm{Rh(H)(PPh_3)_4}$ and (**170**) (Ar = p-$\mathrm{XC_6H_4}$ (X = H, Me, OMe, Bu^t, Cl, F); L = $\mathrm{PPh_3}$) is the product but with $\mathrm{Rh(H)(CO)(PPh_3)_3}$, only the initial allyl complex (**171**) results.[121] The majority of the phosphine-complexed rhodium in the solution resulting from the addition of DPPB to $[\mathrm{Rh}(\mu\text{-}\mathrm{H})(\mathrm{COD})]_4$ is $(\eta^3\text{-}\mathrm{C_8H_{13}})\mathrm{Rh(DPPB)}$ resulting from partial hydrogenation of the COD ligand. Hydrogenolysis of this complex in the presence of DPPB forms $\mathrm{Rh(H)(DPPB)_2}$ via the postulated intermediate Rh(H)(DPPB). This last species is considered to be the active catalytic species when a DPPB/$[\mathrm{Rh}(\mu\text{-}\mathrm{H})(\mathrm{COD})]_4$ mixture is used to catalyze the hydrogenation of carbon dioxide to formic acid (*see* ***Organic Synthesis using Transition Metal Carbonyl Complexes***).[122]

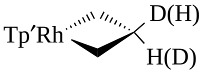

(**169**)

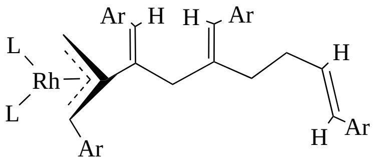

(**170**)

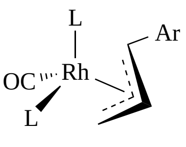

(**171**)

Two equivalents of the potassium enolate $\mathrm{K[PhC(O)CH_2]}$ react with $[\mathrm{Rh}(\mu\text{-}\mathrm{Cl})\mathrm{L_2}]_2$ to form the oxaallyl complex $(\eta^3\text{-}\mathrm{CH_2C(Ph)O})\mathrm{RhL_2}$ (L = $\mathrm{PPh_3}$), a rare example of a complex containing an unsupported oxaallyl ligand. Addition of an extra ligand causes an isomerization to the enolate complex $\mathrm{Rh(OC(Ph){=}CH_2)(L')L_2}$ (L′ = CO, Bu^tNC). The reactivity of the $(\eta^3\text{-}\mathrm{CH_2C(Bu^t)O})\mathrm{RhL_2}$ analog differs markedly in that with CO the products are pinacolone and $[\mathrm{Rh}(\mu\text{-}\mathrm{CO})(\mathrm{CO})\mathrm{L_2}]_2$, while with the isocyanide the oxaallyl ligand rearranges to the carbon-bound form in $\mathrm{Rh(CH_2C(O)Bu^t)L_2(CNBu^t)_2}$. The differences in reactivity as compared with analogous allyl complexes are attributed to the greater stability of the η^1-enolate form as compared with an η^1-allyl.[123] Following the standard procedure, $(\eta^3\text{-allyl})\mathrm{Rh(COD)}$ (allyl = $\mathrm{C_3H_5}$, 2-Me-$\mathrm{C_3H_4}$) is generated from reaction of (allyl)MgBr with $[\mathrm{Rh}(\mu\text{-}\mathrm{Cl})(\mathrm{COD})]_2$ and the COD can be replaced by various bis(phosphino)methane ligands giving $(\eta^3\text{-allyl})\mathrm{Rh(R_2CH_2PPr^{\mathit{i}}_2)}$ (R = Pr^i, cy, Ph). These initially add one carbonyl ligand to the metal but in the presence of excess CO undergo a reversible migratory insertion of CO into the allyl group to give the acyl complexes $\mathrm{Rh(C({=}O)CH_2C(R'){=}CH_2)(CO)_2(R_2CH_2PPr^{\mathit{i}}_2)}$ R′ = H, Me).[124] An attempt to generate an acyl carbene complex from the reaction of $[\mathrm{Rh}(\mu\text{-}\mathrm{Cl})(\mathrm{PPr^{\mathit{i}}_3})_2]_2$ and $\mathrm{PhC({=}O)CHN_2}$ led instead to the acyl ylide complex (**172**)[125] while action of vinylmagnesium bromide on the vinylidene complex *trans*-$\mathrm{Rh({=}C{=}CHR)Cl(PPr^{\mathit{i}}_3)_2}$ initially formed (**46**) (R = H, Bu^t, Ph; L = $\mathrm{PPr}^i{}_3$), but on standing in benzene solution this underwent coupling of the vinyl and vinylidene ligands to yield (**173**) (see also Section 2.3). Similarly, *trans*-$\mathrm{Rh({=}C{=}CHR)(Me)(PPr^{\mathit{i}}_3)_2}$, prepared in an analogous fashion at low temperature undergoes C–C coupling (*see* ***Organic Synthesis Using Metal-mediated Coupling Reactions***) at room temperature to form $(\eta^3\text{-}1\text{-R-}\mathrm{C_3H_4})\mathrm{Rh(PPr^{\mathit{i}}_3)_2}$ (R = H, Ph, Bu^t). For R = H, Ph the syn isomer forms, while R = Bu^t gives the anti.[126]

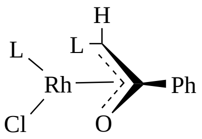

(**172**)

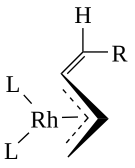

(**173**)

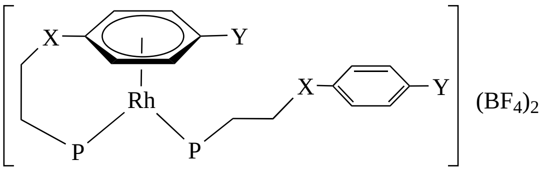

(**174**)

A series of DFT calculations (*see* ***Molecular Orbital Theory***) on $\mathrm{Rh}(\eta^3\text{-}\mathrm{C_3H_5})_3$ indicate that the ground-state structure has no symmetry. Calculated ionization energies agree well with values obtained from photoelectron spectra. The calculated potential-energy surface indicates the presence of three transition states, one of which involves an η^1-allyl ligand between the several minima that are found, and variable-temperature NMR measurements appear consistent with there being three distinct fluxional processes (*see* ***Stability Constants & their Determination***).[127]

4.2 Arene Complexes

Arene complexes figure prominently in a series of investigations into the synthesis of metallamacrocyclic complexes. The first report is on (**174**) (X = CH_2; Y = H, F. X = O; Y = H) that are obtained from $Ph_2PCH_2CH_2XC_6H_4Y$ and $[Rh(COE)(THF)_2]BF_4$, while an analogous route with 1,4-$(Ph_2PCH_2CH_2O)_2C_6R_4$ (R = Me) forms the dinuclear species (**175**). Using the more flexible ligand 1,4-$(Ph_2PCH_2CH_2CH_2O)_2C_6R_4$ (R = Me) allows for arene coordination and (**176**) is formed instead. Interestingly, with the ligand 4,4′-$(Ph_2PCH_2CH_2)_2C_6H_4C_6H_4$ arene coordination also occurs and (**177**) is formed. The coordination of the oxygen atoms in (**175**) and the arene groups in (**176**) and (**177**) serve to initially satisfy the coordination requirements of the metal and constitute a ‘‘weak link’’ approach to directing the synthesis in an efficient manner toward the final metallamacrocycle. Thus, successive reaction of (**176**) with acetonitrile and then carbon monoxide displaces the arene from the metal and forms (**178**) (R = Me). Similarly, the ‘‘weak links’’ in (**175**) and (**177**) are disrupted by carbon monoxide to form (**179**) ($n = 1$; R = Me. $n = 2$; R = H), while reaction of (**175**) with 1,4-diisocyanobenzene in acetonitrile forms the ‘‘occupied’’ metallamacrocycle (**180**).[128] The calix-shaped metallacyclophane (**181**) is formed from 9,10-bis(2-diphenylphosphinoethyl)anthracene and $[Rh(\mu\text{-Cl})(CO)_2]_2$ at a low temperature.[129]

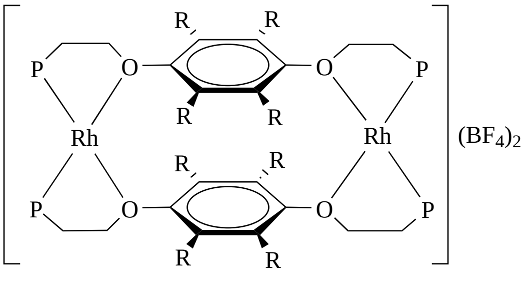

(**175**)

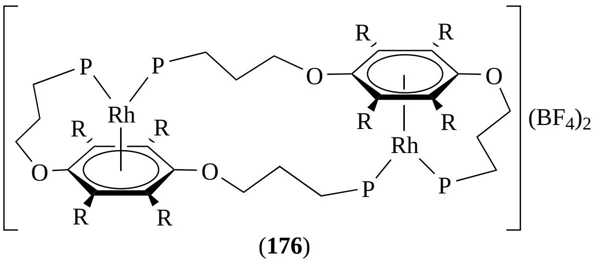

(**176**)

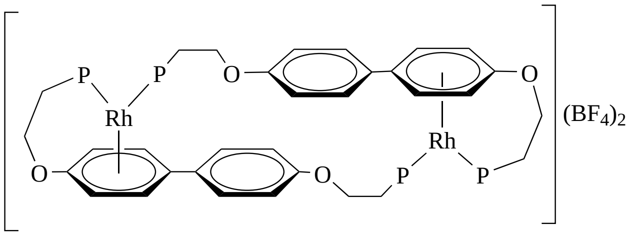

(**177**)

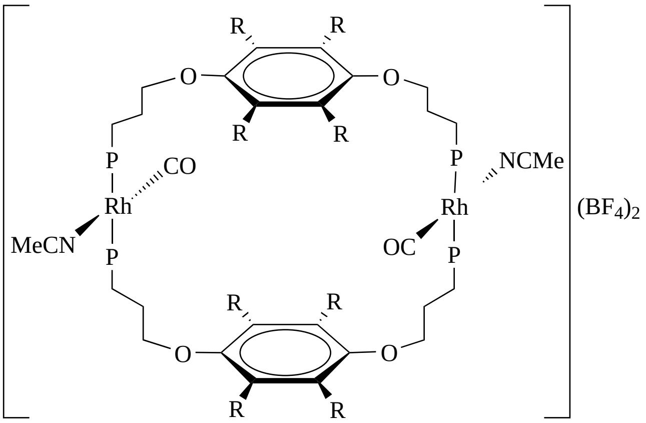

(**178**)

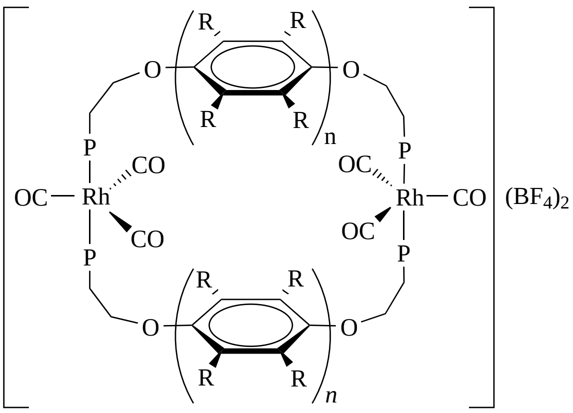

(**179**)

Complexes of formula $[(\eta^6\text{-arene})Rh(CO)L]PF_6$ (arene = C_6H_6, $C_6H_5CF_3$, C_6H_5OMe, mesitylene, 1,3,5-$(MeO)_3C_6H_3$; L = $PPr^i{}_3$) are readily formed by displacement of the weakly bound solvent from $[Rh(COE)(L)(acetone)_2]PF_6$ by the arene, and the COE ligand can be then replaced by the more strongly bonding alkene ethylene. Treatment of $[Rh(COE)(PPr^i_3)(acetone)_2]PF_6$ with $Pr^i{}_2P(CH_2)_nPh$ ($n = 2$, 3) forms (**182**) (L = COE) and analogs with L = C_2H_4, maleic anhydride, $EtO_2CC{\equiv}CH$, $SbPr^i_3$, and $Pr^i{}_2P(CH_2)_nPh$ can be prepared by substitution reactions.[130]

Photolysis (*see* ***Photochemistry of Transition Metal Complexes***) of a mixture of $CpRh(C_2H_4)_2$ and hexamethylbenzene in hexane solution forms a mixture of (**183**) and (**184**). Analogs are similarly formed with biphenyl under the same conditions.[131] The tetrameric borole complex $[Rh(\mu_3\text{-I})(\eta^5\text{-}C_4H_4BPh)]_4$ is converted to $[(\eta^5\text{-}C_4H_4BPh)Rh(MeCN)_3]BF_4$ by halide abstraction with $AgBF_4$. The acetonitrile can be

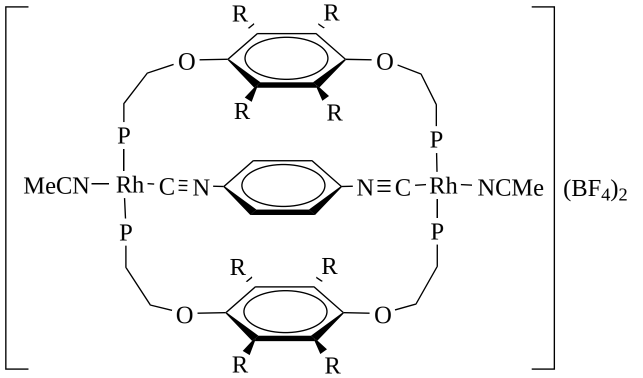

(**180**)

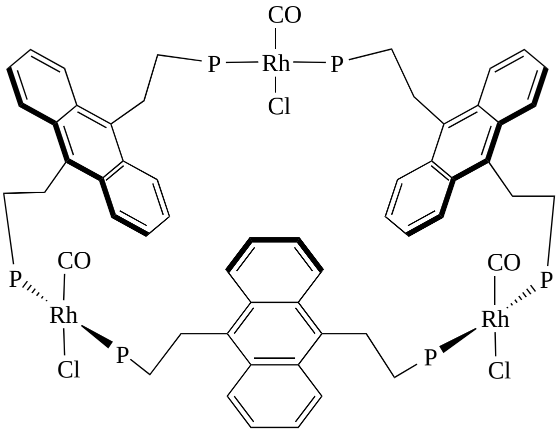

(**181**)

replaced by hexamethylbenzene to give $[(\eta^5\text{-}C_4H_4BPh)Rh(\eta^6\text{-}C_6Me_6)]BF_4$, but if the acetonitrile complex is taken to dryness it polymerizes to (**185**).[132] A final report on arene complexes concerns the chemistry of rhodium complexes containing η^6-coordinated tetraphenylborate ions (*see* ***Boron: Organoboranes***). For example, $(C_2H_4)_2Rh(\eta^6\text{-}C_6H_5BPh_3)$ plus $n-1$ equivalents of $(C_2H_4)_2Rh(OTf)$ forms $\{[(C_2H_4)_2Rh(\eta^6\text{-}C_6H_5)]_nBPh_{4-n}\}(OTf)_{n-1}$ ($n = 2$, 3). The complexes in THF or dichloromethane solution under dinitrogen decompose to form biphenyl, benzene, ethylbenzene, and styrene. The formation of the last two products indicates a process transferring a phenyl group to an ethylene ligand and the formation of a species such as $\{(C_2H_4)_2Rh(C_6H_5)\}$ is proposed.[133]

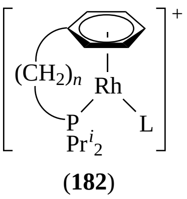

(**182**)

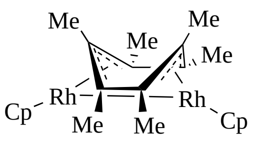

(**183**)

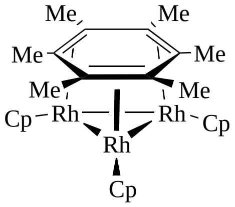

(**184**)

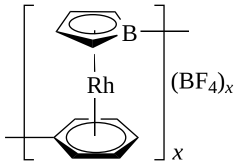

(**185**)

5 MISCELLANEOUS COMPLEXES

A new report on oxapentadienyl complexes includes the reaction of $[Rh(\mu\text{-}Cl)L_2]_2$ with several potassium oxapentadienides to form a mixture of the isomers (**186**) and (**187**) ($L = PMe_3, PEt_3$; $R = Me, H$). When $L = PEt_3$ and $R = Me$, reaction of (**186**) with methyl triflate forms (**188**), while with HBF_4 a mixture of (**189**) and (**190**) is obtained.[134] Reaction of diphenyl ketene with $[Rh(\mu\text{-}Cl)(COE)_2]_2$ and four equivalents of a phosphine forms *trans*-$RhCl(\eta^2\text{-}O{=}C{=}CPh_2)L_2$ ($L = PPr^i_3$, Pcy_3, PBu^t_2Me) where it is the C=O bond which is coordinated with the metal. In comparison to the iridium analog, there is less π-backbonding. The isotopically labeled complexes with $Ph_2C{=}^{13}C{=}O$ and $Ph_2C{=}C{=}^{18}O$ were also prepared and used to analyze the infrared spectrum leading to an identification of the C=O stretching vibration of the coordinated ketene.[135] Condensation of $[Cp^{tt}{}_2ZrS_2]^{2-}$ ($Cp^{tt} = 1,3\text{-}Bu^t{}_2C_5H_3$) with $[Rh(\mu\text{-}Cl)(L_2)]_2$ forms (**191**) (L_2 = COD, NBD, TFB). The same complex can also be synthesized from $Cp^{tt}{}_2Zr(SH)_2$ and $Rh(acac)(L_2)$. Replacement of the diolefin ligands in (**191**) with carbon monoxide occurs readily and one carbonyl ligand on each rhodium can then be replaced by a phosphine or a phosphite.[136] Hydrolysis of Cp^*TaMe_4 with two equivalents of $[Rh(\mu\text{-}OH)(COD)]_2$ forms (**192**) and this is further hydrolyzed by 4,6-dimethyl-2-hydroxy-3-cyanopyridine to yield (**193**).[137]

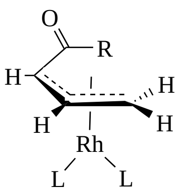

(**186**)

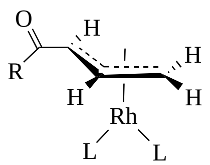

(**187**)

The uncoordinated phosphorus atoms in $[Pt_2(\mu\text{-}dpmp)_2L_2](PF_6)_2$ (L = xylylisocyanide) can bind a rhodium atom in

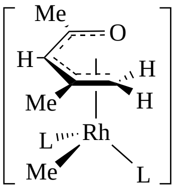

(188)

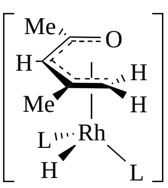

(189)

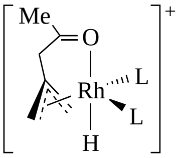

(190)

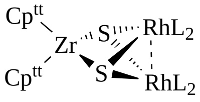

(191)

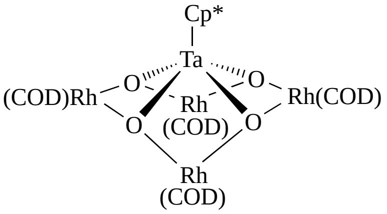

(192)

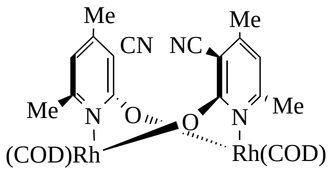

(193)

the reaction with [Rh(μ-Cl)(COD)]$_2$ to form a mixture of (**194**) and (**195**). Reaction of (**195**) with carbon monoxide forms (**196**) while with methyl propiolate (**197**) (R = Me) is the product.[138]

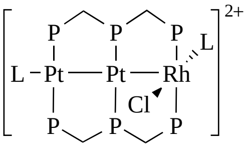

(194)

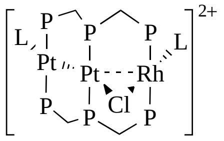

(195)

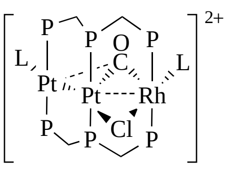

(196)

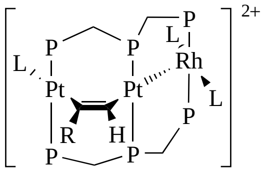

(197)

DFT calculations (*see* ***Molecular Orbital Theory***) on CpRh(CO)$_2$ and [RhCl$_2$(CO)$_2$]$^-$ have been used to determine the ground-state molecular structures, and these structures with symmetry-adapted cluster-configuration interaction calculations have been used to explore the nature of excited states (*see* ***Electronic Structure of Organometallic Compounds***). The ground state is predicted to be a singlet with the triplet state lying significantly above it. The activation process for the anion is predicted to be thermal dissociation of a carbonyl ligand but this process requires much more energy in the neutral complex. In the excited state of the anion, all strong absorptions are Rh → CO MLCT in nature while for CpRh(CO)$_2$ the Rh → CO MLCT and the Cp → {Rh + CO} absorptions are strongly mixed in the higher excited states with the latter having the greater oscillator strength. The results suggest that the low quantum efficiency for CpRh(CO)$_2$ to activate C–H and Si–H bonds can be attributed to a low proportion of MLCT excitation in the higher excited states (*see* ***Photochemistry of Transition Metal Complexes*** and ***Luminescence Behavior & Photochemistry of Organotransition Metal Compounds***).[139] Enthalpies of addition of CO, H$_2$, and Bu^{t}NC to [Rh(μ-Cl)(PPr$^i_3$)$_2$]$_2$ (which has been conclusively determined to be dimeric in solution) have been measured[140] (*see* ***Bonding Energetics of Organometallic Compounds***) and the analog [Rh(μ-Cl)(Bu$^t_2$PCH$_2$PBu$^t_2$)]$_2$ has been prepared. In solution, this latter species is thought to convert to the solvated monomer RhCl(Bu$^t_2$PCH$_2$PBu$^t_2$)(S) and is a catalyst precursor for the hydrosilylation of but-2-yne by HSi(OEt)$_3$ (*see* ***Hydrosilation Catalysis***). A much better system uses Rh(Me)(Bu$^t_2$PCH$_2$PBu$^t_2$)(PMe$_3$) which is prepared by addition of PMe$_3$ to RhCl(Bu$^t_2$PCH$_2$PBu$^t_2$)(S) followed by reaction with methyllithium. This system shows a high selectivity for the cis hydrosilylation product and the resting state of the catalyst is thought to be Rh(PMe$_3$)(Si(OEt)$_3$)(Bu$^t_2$PCH$_2$PBu$^t_2$), which could be isolated from reaction of Rh(Me)(Bu$^t_2$PCH$_2$PBu$^t_2$)(PMe$_3$) and the silane at low temperature.[141]

6 RELATED ARTICLES

Alkane Carbon–Hydrogen Bond Activation; Antimony: Organometallic Chemistry; Asymmetric Synthesis by Homogeneous Catalysis; Boron: Organoboranes; Carbene Complexes; Carbon–Carbon & Carbon–Heteroatom Activation; Carbon: Inorganic Chemistry; Carbonyl Complexes of the Transition Metals; Carbonylation Processes by Homogeneous Catalysis; Cluster Compounds: Inorganometallic Compounds Containing Transition Metal & Main Group Elements; Dihydrogen Complexes & Related Sigma Complexes; Dinuclear Organometallic Cluster Complexes; Electronic Structure of Organometallic Compounds; Hydride Complexes of the Transition Metals; Hydroboration Catalysis; Hydrogenation &

Isomerization of Alkenes; Hydrosilation Catalysis; Luminescence Behavior & Photochemistry of Organotransition Metal Compounds; Manganese: Organometallic Chemistry; Molecular Orbital Theory; Oligomerization & Polymerization by Homogeneous Catalysis; Organic Synthesis Using Metal-mediated Coupling Reactions; Organic Synthesis using Transition Metal Carbonyl Complexes; Organic Synthesis using Transition Metal Complexes Containing π-Bonded Ligands; P-donor Ligands; Photochemistry of Transition Metal Complexes; Photoelectron Spectroscopy of Transition Metal Systems; Polynuclear Organometallic Cluster Complexes; S-donor Ligands; Stability Constants & their Determination; Tin: Organometallic Chemistry; Transition Metal Carbonyls: Infrared Spectra; Water & O-donor Ligands.

7 REFERENCES

1. J. T. Mague, in ‘Encyclopedia of Inorganic Chemistry’, ed. R. B. King, John Wiley & Sons, Chichester, New York, 1994, p. 3489.
2. E. W. Abel, F. G. A. Stone and G. Wilkinson, eds., ‘Comprehensive Organometallic Chemistry II’, Pergamon Press, New York, 1995, Vol. 8.
3. H. Werner, *Chem. Commun.*, 1997, 903.
4. M. I. Rybinskaya, V. S. Kaganovich, and A. N. Nesmeyanov, *Izv. Akad. Nauk, Ser. Khim.*, 1993, 1186.
5. C. S. Chin., G. Won, D. Chong, M. Kim, and H. Lee, *Acc. Chem. Res.*, 2001, **35**, 218.
6. J. T. Mague, *J. Cluster Sci.*, 1995, **6**, 217.
7. P. J. Brothers, *Adv. Organomet. Chem.*, 2001, **46**, 223.
8. K. H. Whitmire, *Adv. Organomet. Chem.*, 1998, **42**, 1.
9. S. Lotz, P. H. van Rooyen, and R. Meyer, *Adv. Organomet. Chem.*, 1995, **37**, 219.
10. P. J. Low and M. I. Bruce, *Adv. Organomet. Chem.*, 2002, **48**, 71.
11. D. M. Roundhill, *Adv. Organomet. Chem.*, 1995, **38**, 155.
12. S. M. Waterman, N. T. Lucas, and M. G. Humphrey, *Adv. Organomet. Chem.*, 2000, **46**, 47.
13. L. Weber, *Adv. Organomet. Chem.*, 1997, **41**, 1.
14. T. C. Flood, K. E. Janak, M. Iimura, and H. Zhen, *J. Am. Chem. Soc.*, 2000, **122**, 6783.
15. H. Zhen, C. Wang, Y. Hu, and T. C. Flood, *Organometallics*, 1998, **17**, 5397.
16. D. D. Wick, K. A. Reynolds, and W. D. Jones, *J. Am. Chem. Soc.*, 199, **121**, 3974.
17. M. C. Keyes, V. G. Young Jr, and W. B. Tolman, *Organometallics*, 1996, **15**, 4133.
18. M. Paneque, P. J. Pérez, A. Pizzano, M. L. Poveda, S. Taboada, M. Trujillo, and E. Carmona, *Organometallics*, 1999, **18**, 4304.
19. T. Ruman, Z. Ciunik, A. M. Trzeciak, S. Wołowiec, and J. J. Ziołkowski, *Organometallics*, 2003, **22**, 1072.
20. V. Chauby, J.-C. Daran, C. Serra-Le Berre, F. Malbosc, P. Kalck, O. D. Gonzalez, C. E. Haslam, and A. Haynes, *Inorg. Chem.*, 2002, **41**, 3280.
21. R. Goikhman and D. Milstein, *Angew. Chem., Int. Ed. Engl.*, 2001, **40**, 1119.
22. M. Cheong, R. Schmid, and T. Ziegler, *Organometallics*, 2000, **19**, 1973.
23. Y. Kataoka, A. Shibahara, T. Yamagata, and K. Tani, *Organometallics*, 2001, **20**, 2431.
24. M. Bassetti, A. Capone, L. Mastrofrancesco, and M. Salamone, *Organometallics*, 2003, **22**, 2535.
25. M. T. Pinillos, A. Elduque, E. Martín, N. Navarro, L. A. Oro, A. Tiripicchio, and F. Ugozzoli, *Inorg. Chem.*, 1995, **34**, 3105.
26. A. D. Selmeczy, W. D. Jones, R. Osman, and R. N. Perutz, *Organometallics*, 1995, **14**, 5677.
27. C. E. Webster and M. M. B. Hall, *Organometallics*, 2001, **20**, 5606.
28. M.-D. Su and S.-Y. Chu, *Int. J. Quantum Chem.*, 1999, **72**, 405.
29. R. Jiménez-Cataño and M. B. Hall, *Organometallics*, 1996, **15**, 1889.
30. J. Espinosa-García, J. C. Corchado, and D. G. Truhlar, *J. Am. Chem. Soc.*, 1997, **119**, 9891.
31. E. Nakamura, N. Yoshikai, and M. Yamanaka, *J. Am. Chem. Soc.*, 2002, **124**, 7181.
32. M. E. van der Boom, C. L. Higgett, and D. Milstein, *Organometallics*, 1999, **18**, 2413.
33. M. Gandelman, L. Konstantinovski, H. Rozenberg, and D. Milstein, *Chem. – Eur. J.*, 2003, **9**, 2595.
34. G. Canepa, C. D. Brandt, and H. Werner, *Organometallics*, 2001, **20**, 604.
35. H. Urtel, C. Meier, F. Eisenträger, F. Romiger, J. P. Joschek, and P. Hofmann, *Angew. Chem., Int. Ed. Engl.*, 2001, **40**, 781.
36. M. Gerisch, J. R. Krumper, R. G. Bergman, and T. Don Tilley, *Organometallics*, 2003, **22**, 47.
37. Y. Han, L. Deng, and T. Ziegler, *J. Am. Chem. Soc.*, 1997, **119**, 5939.
38. M.-D. Su and S.-Y. Chu, *J. Am. Chem. Soc.*, 1997, **119**, 10178.
39. C. Tejel, M. A. Ciriano, L. A. Oro, A. Tiripicchio, and F. Ugozzoli, *Organometallics*, 2001, **20**, 1676.
40. D. S. A. George, R. W. Hilts, R. McDonald, and M. Cowie, *Organometallics*, 1999, **18**, 5330.
41. J. R. Torkelson, O. Oke, J. Muritu, R. McDonald, and M. Cowie, *Organometallics*, 2000, **19**, 854.
42. T. W. Graham, F. Van Gastel, R. McDonald, and M. Cowie, *Organometallics*, 1999, **18**, 2177.
43. B. D. Rowsell, R. McDonald, M. J. Ferguson, and M. Cowie, *Organometallics*, 2003, **22**, 2944.

44. F. Shafiq, K. W. Kramarz, and R. Eisenberg, *Inorg. Chim. Acta*, 1993, **213**, 111.
45. H. Werner, M. Manger, M. Laubender, M. Tiechert, and D. Stalke, *J. Organomet. Chem.*, 1998, **569**, 189.
46. L. Rosenberg, M. D. Fryzuk, and S. J. Rettig, *Organometallics*, 1999, **18**, 958.
47. Y. Kaneko, T. Suzuki, and K. Isobe, *Organometallics*, 1998, **17**, 996.
48. H. Werner, P. Bachmann, M. Laubender, and O. Gevert, *Eur. J. Inorg. Chem.*, 1998, 1217.
49. J. Gil-Rubio, M. Laubender, and H. Werner, *Organometallics*, 2000, **19**, 1365.
50. H. Werner, R. Wiedemann, M. Laubender, B. Windmüller, P. Steinert, O. Gevert, and J. Wolf, *J. Am. Chem. Soc.*, 2002, **124**, 6966.
51. E. Peréz-Carreño, P. Paoli, A. Ienco, and C. Mealli, *Eur. J. Inorg. Chem.*, 1999, 1315.
52. J. H. Moon, E. S. Choi, and S. K. Kang, *Bull. Korean Chem. Soc.*, 1998, **19**, 557.
53. D. Moigno, W. Kiefer, B. Callejas-Gaspar, J. Gil-Rubio, and H. Werner, *New J. Chem.*, 2001, **25**, 1389.
54. A. J. Edwards, M. A. Esteruelas, F. J. Lahoz, J. Modrego, L. A. Oro, and J. Schrickel, *Organometallics*, 1996, **15**, 3556.
55. C. Tejel, M. A. Ciriano, L. A. Oro, A. Tiripicchio, and F. Ugozzoli, *Organometallics*, 1994, **13**, 4153.
56. E. Bleuel, P. Schwab, P. M. Laubender, and H. Werner, *J. Chem. Soc., Dalton Trans.*, 2001, 266.
57. T. Pechmann, C. D. Brandt, C. Röger, and H. Werner, *Angew. Chem., Int. Ed. Engl.*, 2002, **41**, 2301.
58. E. Bleuel, O. Gevert, M. Laubender, and H. Werner, *Organometallics*, 2000, **19**, 3109.
59. M. Ballhorn, M. G. Partridge, R. N. Perutz, and M. K. Whittlesey, *Chem. Commun.*, 1996, 961.
60. J. S. Yeston and R. G. Bergman, *Organometallics*, 2000, **19**, 2947.
61. R. Cohen, B. Rybtchinski, M. Gandelman, H. Rozenberg, J. M. L. Martin, and D. Milstein, *J. Am. Chem. Soc.*, 2003, **125**, 6532.
62. E. Despagnet, K. Miqueu, H. Gornitzka, P. W. Dyer, D. Bourissou, and G. Bertrand, *J. Am. Chem. Soc.*, 2002, **124**, 11834.
63. E. Deydier, M.-J. Menu, M. Dartiguenave, Y. Dartiguenave, M. Simard, A. L. Beauchamp, J. C. Brewer, and H. B. Gray, *Organometallics*, 1996, **15**, 1166.
64. B. Çetinkaya, P. B. Hitchcock, M. F. Lappert, D. B. Shaw, K. Spyropoulos, and N. J. W. Warhurst, *J. Organomet. Chem.*, 1993, **459**, 311.
65. K. Denk, P. Sirsch, and W. A. Herrmann, *J. Organomet. Chem.*, 2002, **649**, 219.
66. A. R. Chianese, X. Li, M. C. Janzen, J. W. Faller, and R. H. Crabtree, *Organometallics*, 2003, **22**, 1663.
67. M. Albrecht, R. H. Crabtree, J. Mata, and E. Peris, *Chem. Commun.*, 2002, 32.
68. M. Poyatos, P. Uris, J. A. Mata, C. Claver, E. Fernandez, and E. Peris, *Organometallics*, 2003, **22**, 440.
69. R. S. Simons, P. Custer, C. A. Tessier, and W. J. Youngs, *Organometallics*, 2003, **22**, 1979.
70. Y. Motoyama, K. Shimozono, K. Aoki, and H. Nishiyama, *Organometallics*, 2002, **21**, 1684.
71. Z.-Q. Wang, J. Martínez, and P. M. Maitlis, *Inorg. Chim. Acta*, 1998, **280**, 62.
72. C. E. Barnes and F. H. Försterling, *Polyhedron*, 1998, **17**, 1045.
73. G. Aullón and S. Alvarez, *Eur. J. Inorg. Chem.*, 2001, 3031.
74. D. H. Farrar, E. V. Grachova, A. Lough, C. Patirana, A. J. Poë, and S. P. Tunik, *J. Chem. Soc., Dalton Trans.*, 2001, 2015.
75. K. Lee, H. Song, B. Kim, J. T. Park, S. Park, and M.-G. Choi, *J. Am. Chem. Soc.*, 2002, **124**, 2872.
76. C. Tejel, M. Bordonaba, M. A. Ciriano, F. J. Lahoz, and L. A. Oro, *Chem. Commun.*, 1999, 2387.
77. A. Fumagalli, M. C. Malatesta, A. Tentori, D. Monti, P. Macchi, and A. Sironi, *Inorg. Chem.*, 2002, **41**, 76.
78. A. Fumagalli, M. Bianchi, M. C. Malatesta, G. Ciani, M. Moret, and A. Sironi, *Inorg. Chem.*, 1998, **37**, 1324.
79. I. O. Koshevoy, S. P. Tunik, S. Jääskeläinen, M. Haukka, T. A. Pakkanen, and I. S. Podkorytov, *J. Chem. Soc., Dalton Trans.*, 2002, 2768.
80. C. Femoni, F. Demartin, M. C. Iapalucci, A. Lombardi, G. Longoni, C. Marin, and P. H. Svensson, *J. Organomet. Chem.*, 2000, **614–615**, 294.
81. H.-J. Haupt, U. Flörke, and H.-G. Beckers, *Inorg. Chem.*, 1994, **33**, 3481.
82. H.-K. Yip, H.-S. Lin, Y. Wang, and C.-M. Che, *Inorg. Chem.*, 1993, **32**, 3402.
83. M. G. Hill and K. R. Mann, *Inorg. Chim. Acta*, 1996, **243**, 219.
84. H. Werner, G. Hörlin, and N. Mahr, *J. Organomet. Chem.*, 1998, **551**, 367.
85. C. Tejel, M. Sommovigo, M. A. Ciriano, J. A. López, F. J. Lahoz, and L. A. Oro, *Angew. Chem., Int. Ed. Engl.*, 2000, **39**, 2336.
86. Y. Yamamoto, H. Suzuki, N. Tajima, and K. Tatsumi, *Chem. – Eur. J.*, 2002, **8**, 372.
87. P. H. M. Budzelaar, N. N. P. Moonen, R. De Gelder, J. M. M. Smits, and A. W. Gal, *Eur. J. Inorg. Chem.*, 2000, 753.
88. E. L. Dias, M. Brookhart, and P. S. White, *Organometallics*, 2000, **19**, 4995.
89. M. C. Nicasio, M. Paneque, P. J. Pérez, A. Pizzano, M. L. Poveda, L. Rey, S. Sirol, S. Taboada, M. Trujillo, A. Monge, C. Ruiz, and E. Carmona, *Inorg. Chem.*, 2000, **39**, 180.

90. L. Öhrström, S. Strömberg, J. Glaser, and K. Zetterberg, *J. Organomet. Chem.*, 1998, **558**, 123.
91. F. Plourde, K. Gilbert, J. Gagnon, and P. D. Harvey, *Organometallics*, 2003, **22**, 2862.
92. S. A. Decker and T. R. Cundari, *New J. Chem.*, 2002, **26**, 129.
93. G. Alagona, C. Ghio, R. Lazzaroni, and R. Settambolo, *Organometallics*, 2001, **20**, 5394.
94. C. Widauer, H. Grüzmacher, and T. Ziegler, *Organometallics*, 2000, **19**, 2907.
95. S. Sakaki, M. Sumimoto, M. Fukuhara, M. Sugimoto, H. Fujimoto, and S. Matsuzaki, *Organometallics*, 2002, **21**, 3788.
96. S. A. Colebrooke, S. B. Duckett, and J. A. B. Lohman, *Chem. Commun.*, 2000, 685.
97. A. Kless, A. Börner, D. Heller, and R. Selke, *Organometallics*, 1997, **16**, 2096.
98. D. W. Price, M. B. G. Drew, K. K. Hii, and J. M. Brown, *Chem. – Eur. J.*, 2000, **6**, 4587.
99. M. Bühl, M. Håkansson, A. H. Mahmoudkhani, and L. Öhrström, *Organometallics*, 2000, **19**, 5589.
100. Z.-Q. Wang, M. L. Turner, B. F. Taylor, and P. M. Maitlis, *Polyhedron*, 1995, **14**, 2767.
101. U. Kölle, R. Görissen, and T. Wagner, *Chem. Ber.*, 1995, **128**, 911.
102. J.-C. Choi, S. Sarai, T. Koizumi, K. Osakada, and T. Yamamoto, *Organometallics*, 1998, **17**, 2037.
103. M. Manger, J. Wolf, M. Laubender, M. Teichert, D. Stalke, and H. Werner, *Chem. – Eur. J.*, 1997, **3**, 1442.
104. B.-H. Zhu, W.-Q. Zhang, Q.-Y. Zhao, Z.-G. Bian, B. Hu, Y.-H. Zhang, Y.-Q. Yin, and J. Sun, *J. Organomet. Chem.*, 2002, **650**, 181.
105. A. D. Selmeczy and W. D. Jones, *Inorg. Chim. Acta*, 2000, **300–302**, 138.
106. M. A. Esteruelas, F. J. Lahoz, E. Oñate, L. A. Oro, and L. Rodríguez, *Organometallics*, 1996, **15**, 3670.
107. Y. Yamamoto, K. Sugawara, and X.-H. Han, *J. Chem. Soc., Dalton Trans.*, 2002, 195.
108. Y. Ishii, K. Ogio, M. Nishio, M. Retbøll, S. Kuwata, H. Matsuzaka, and M. Hidai, *J. Organomet. Chem.*, 2000, **599**, 221.
109. M. V. Baker, D. H. Brown, B. W. Skelton, and A. H. White, *J. Chem. Soc., Dalton Trans.*, 2002, 2595.
110. H. Nishiyama, E. Niwa, T. Inoue, Y. Ishima, and K. Aoki, *Organometallics*, 2002, **21**, 2572.
111. A. Castro, P. M. Maitlis, M. L. Turner, B. E. Mann, and H. Adams, *J. Organmet. Chem.*, 2002, **663**, 145.
112. R. S. Dickson, M. J. Liddell, B. W. Skelton, and A. H. White, *Aust. J. Chem.*, 1994, **47**, 1613.
113. R. S. Dickson, T. de Simone, R. J. Parker, and G. D. Fallon, *Organometallics*, 1997, **16**, 1531.
114. M. P. Devery, R. S. Dickson, G. D. Fallon, B. W. Skelton, and A. H. White, *J. Organomet. Chem.*, 1998, **551**, 195.
115. G. R. County, R. S. Dickson, and G. D. Fallon, *J. Organomet. Chem.*, 1998, **565**, 11.
116. G. P. Mitchell and T. D. Tilley, *Organometallics*, 1996, **15**, 3477.
117. J. Müller, T. Akhnoukh, P. E. Gaeda, A. Guo, P. Moran, and K. Quo, *J. Organomet. Chem.*, 1997, **541**, 207.
118. H. Werner, A. Heinemann, B. Windmüller, and P. Steinert, *Chem. Ber.*, 1996, **129**, 903.
119. I. Ara, J. R. Berenguer, E. Eguizábal, J. Forniés, E. Lalinde, and A. Martín, *Eur. J. Inorg. Chem.*, 2001, 1631.
120. S. Ikeda, Y. Maruyama, and F. Ozawa, *Organometallics*, 1998, **17**, 3770.
121. J. Choi, K. Osakada, and T. Yamamoto, *Organometallics*, 1998, **17**, 3044.
122. F. Gassner, E. Dinjus, H. Görls, and W. Leitner, *Organometallics*, 1996, **15**, 2078.
123. G. A. Slough, R. Hayashi, J. R. Ashbaugh, S. A. Shamblin, and A. M. Aukamp, *Organometallics*, 1994, **13**, 890.
124. M. Manger, J. Wolf, M. Teichert, D. Stalke, and H. Werner, *Organometallics*, 1998, **17**, 3210.
125. H. Werner, N. Mahr, G. Frenking, and V. Jonas, *Organometallics*, 1995, **14**, 619.
126. R. Wiedemann, J. Wolf, and H. Werner, *Angew. Chem., Int. Ed. Engl.*, 1995, **34**, 1244.
127. K. D. John, R. Michalczyk, G. Hernández, J. C. Green, R. L. Martin, R. T. Baker, and A. P. Sattelberger, *Organometallics*, 2002, **21**, 5757.
128. J. R. Farrell, A. H. Eisenberg, C. A. Mirkin, I. A. Guzei, L. M. Liable-Sands, C. D. Incarvito, A. L. Rheingold, and C. L. Stern, *Organometallics*, 1999, **18**, 4856.
129. F.-B. Xu, Q.-S. Li, X.-S. Zeng, X.-B. Leng, and Z.-Z. Zhang, *Organometallics*, 2002, **21**, 4894.
130. H. Werner, G. Canepa, K. Ilg, and J. Wolf, *Organometallics*, 2000, **19**, 4756.
131. J. Müller, C. Hirsch, A. Guo, and K. Qiao, *Z. Anorg. Allg. Chem.*, 2000, **626**, 2069.
132. G. Herberich, H. J. Eckenrath, and U. Englert, *Organometallics*, 1998, **17**, 519.
133. M. Aresta, E. Quaranta, I. Tommasi, S. Dérien, and E. Duñach, *Organometallics*, 1995, **14**, 3349.
134. J. R. Bleeke, E. Donnay, and N. P. Rath, *Organometallics*, 2002, **21**, 4099.
135. D. B. Grotjahn, L. S. B. Collins, M. Wolpert, G. A. Bikzhanova, H. C. Lo, D. Combs, and J. L. Hubbard, *J. Am. Chem. Soc.*, 2001, **123**, 8260.
136. M. A. F. Hernandez-Gruel, J. J. Pérez-Torrente, M. A. Ciriano, A. B. Rivas, F. J. Lahoz, I. T. Dobrinovitch, and L. A. Oro, *Organometallics*, 2003, **22**, 1237.

137. R. Fandos, C. Hernández, A. Otero, A. Rodríguez, M. J. Ruiz, J. L. G. Fierro, and P. Terreros, *Organometallics*, 1999, **18**, 2718.

138. T. Tanase, R. A. Begum, H. Toda, and Y. Yamamoto, *Organometallics*, 2001, **21**, 968.

139. Z. Hu, R. J. Boyd, and H. Nakatsuji, *J. Am. Chem. Soc.*, 2002, **124**, 2664.

140. K. Wang, G. P. Rosini, S. Nolan, and A. S. Goldman, *J. Am. Chem. Soc.*, 1995, **117**, 5082.

141. P. Hofmann, C. Meier, W. Hiller, M. Heckel, J. Riede, and M. U. Schmidt, *J. Organomet. Chem.*, 1995, **490**, 51.

Ruthenium: Inorganic & Coordination Chemistry

Sylviane Sabo-Etienne & Mary Grellier
Laboratory of Coordination Chemistry, Chimie de la Matière Condensée (CNRS), Toulouse, France

Based in part on the article Ruthenium: Inorganic & Coordination Chemistry by Bruno Chaudret & Sylviane Sabo-Etienne which appeared in the Encyclopedia of Inorganic Chemistry, First Edition.

1 Introduction 1
2 Ruthenium–Halide Complexes 1
3 Ruthenium Complexes of Oxygen-Donor Ligands 3
4 Ruthenium Complexes of Sulfur-Donor Ligands 5
5 Ruthenium Complexes of Nitrogen-Donor Ligands 6
6 Ruthenium Complexes of Phosphorus-Donor Ligands 12
7 Ruthenium Complexes of Group-14 Ligands 16
8 Ruthenium Hydride Complexes 17
9 Polynuclear Complexes of Ruthenium 19
10 Related Articles 19
11 References 19

Abbreviations

acacH = 2,4-pentanedione; BINAP = 2,2′-bis(diphenylphosphanyl)-1,1′-binaphthyl; bpy = 2,2′-bipyridine; cod = 1,5-cyclooctadiene; Cp = cyclopentadienyl; dcype = $Cy_2PCH_2CH_2PCy_2$; diop = 2,3-*O*-isopropylidene-2,3-dihydroxy-1,4-bis(diphenylphosphinobutane); dmpe = $Me_2P(CH_2)_2PMe_2$; DMSO = dimethyl sulfoxide; dpp = 2,9 diphenyl-1,10-phenanthroline; dppb = $Ph_2P(CH_2)_4PPh_2$; dppe = $Ph_2P(CH_2)_2PPh_2$; dppm = $Ph_2PCH_2PPh_2$; dppp = $Ph_2P(CH_2)_3PPh_2$; EDA = diazo ethylacetate; edta = ethylenediamine-*N*,*N*,*N*′,*N*′-tetraacetate; mnt = 1,2-dicyanoethylene dithiolato; mnts = bis(1,2-dicyano-2-mercaptoethylene)sulfide; NMO = *N*-methylmorpholine oxide; pac = polyamino carboxylate; phen = 1,10-phenanthroline; phi = phenanthrene-9,10-diimine; por = porphyrinato; py = pyridine; TEMPO = 2,2,6,6-tetramethylpiperidinooxy; terpy = 2,2′:6′,2″terpyridine; tmbp = 2,2′-Biphosphinines; TMP = tetramesitylporphyrin; tosyl = *p*-toluenesulfonyl; tppts = $(m\text{-}NaSO_3C_6H_4)_3P$; triphos = $MeC(CH_2CH_2PPh_2)_3$.

1 INTRODUCTION

Ruthenium was first recognized as a distinct metal in 1844 in Estonia by Clauss and was named after Ruthenia (Russia). However, its blue chloride solution had been previously observed by Vauquelin in Paris in 1804. Ruthenium is the least abundant platinum metal (10^{-3} to 10^{-4} ppm) after rhodium. In 2002, the demand for ruthenium was 11.6 tons, an increase of 1.8 tons compared to 2001, mainly because of increased sales of ruthenium paste to the electronics industry, for the manufacture of chip resistors and hybrid integrated circuits (HIC). Its atomic number is 44, its atomic weight 101.07, and its electronic configuration $[Kr]4d^7 5s^1$. Seven stable isotopes are known. Some physical data are reported in Table 1 (*see* ***Coordination Chemistry: History*** and ***Coordination Numbers & Geometries***).

Among the platinum metals, ruthenium shows the largest range of oxidation states, from −II to +VIII, with most of the inorganic chemistry taking place in the +II and +III states. The chemistry of ruthenium has been comprehensively reviewed in a monograph in 1984 and in '*Comprehensive Coordination Chemistry*' in 1987 and 2003.**[1–4]** In the most recent review, the results (including osmium chemistry) have been divided into two chapters referring to low- and high-oxidation states.**[3,4]**

This article represents an updated version of the one published in EIC-1. It is organize in the same way, with a survey of the coordination and inorganic chemistry of ruthenium, classified by the nature of the ligand, together with recent highlights in this field. Some old references will not be quoted and can be found in EIC-1. It is worth noting that the border with organometallic chemistry remains tenuous (see, for example, the use of classical coordination compounds for catalyzing organic reactions; *see* ***Ruthenium: Organometallic Chemistry***).

2 RUTHENIUM–HALIDE COMPLEXES

Compounds of the formulation RuX_3 are known for all four halides (X = F, Cl, Br, I). $RuCl_3$ exists as two well-characterized phases (α-$RuCl_3$ and β-$RuCl_3$), which

Table 1 Selected physical properties of ruthenium

Lattice structure	Close-packed hexagonal
Metallic radius for 12-coordination	0.134 nm
Density (20 °C)	12 450 kg m^{-3}
Melting point	2310 °C
Boiling point	3900 °C
Resistivity (0 °C)	6.80 μΩ cm
Ionization potential:	
1st	7.364 eV
2nd	16.76 eV
3rd	28.46 eV
^{96}Ru	I = 0 (12.62%)
^{98}Ru	I = 0 (5.51%)
^{99}Ru	I = 0 (1.87%)
^{100}Ru	I = 5/2 (12.72%)
^{101}Ru	I = 5/2 (17.07%)
^{102}Ru	I = 0 (31.61%)
^{104}Ru	I = 0 (18.58%)

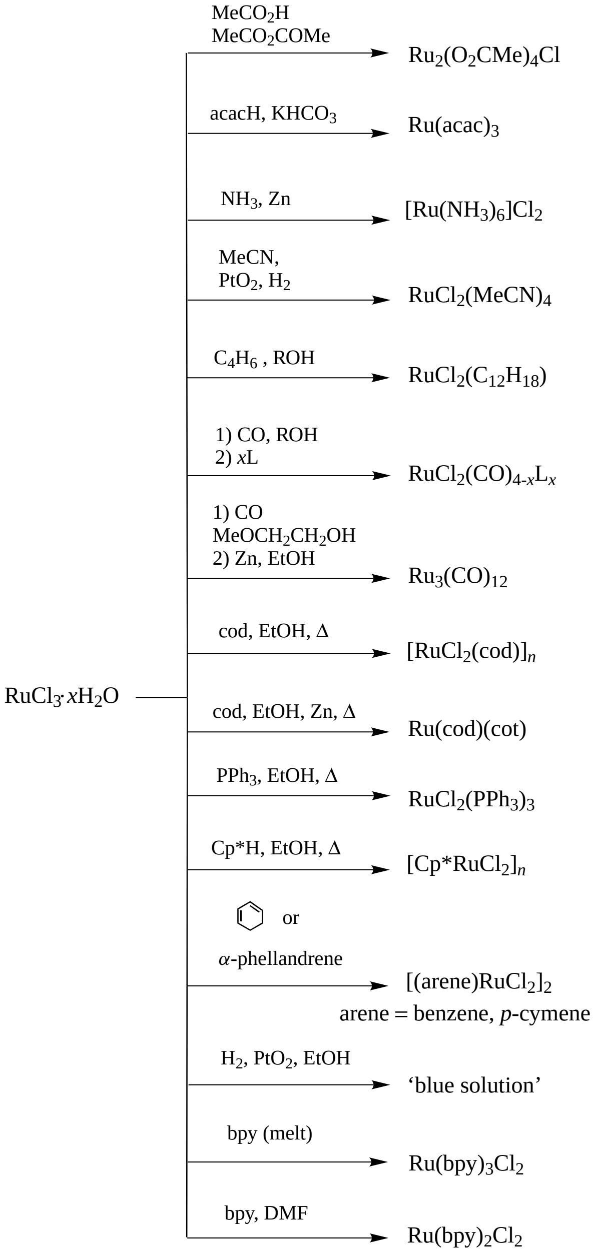
MeCO2H
MeCO2COMe
Ru2(O2CMe)4Cl
acacH, KHCO3
Ru(acac)3
NH3, Zn
[Ru(NH3)6]Cl2
MeCN,
PtO2, H2
RuCl2(MeCN)4
C4H6 , ROH
RuCl2(C12H18)
1) CO, ROH
2) xL
RuCl2(CO)4-xLx
1) CO
MeOCH2CH2OH
2) Zn, EtOH
Ru3(CO)12
cod, EtOH, Δ
[RuCl2(cod)]n
RuCl3·xH2O
cod, EtOH, Zn, Δ
Ru(cod)(cot)
PPh3, EtOH, Δ
RuCl2(PPh3)3
Cp*H, EtOH, Δ
[Cp*RuCl2]n
or
α-phellandrene
[(arene)RuCl2]2
arene = benzene, p-cymene
H2, PtO2, EtOH
'blue solution'
bpy (melt)
Ru(bpy)3Cl2
bpy, DMF
Ru(bpy)2Cl2

Scheme 1

are prepared by heating ruthenium metal in a stream of CO/Cl_2 at 600 to 700 °C and 330 to 340 °C, respectively. In contrast, the complex commonly known as 'hydrated ruthenium trichloride', or '$RuCl_3{\cdot}xH_2O$', is readily soluble in various polar solvents and is commercially available. It is by far the most common starting material in ruthenium chemistry, whether inorganic or organometallic (see Scheme 1 for selected examples of important compounds). However, it was demonstrated that this species actually corresponds to a mixture of different ruthenium compounds, mostly in the +IV oxidation state. Species such as $H_3[Cl_3Ru(\mu\text{-}OH)_3RuCl_3]$ and $H_3[Cl_3Ru(\mu\text{-}OH)_2(\mu\text{-}O)RuCl_3]$ have been shown to exist in the mixture. We will, nevertheless, refer to the common commercial name throughout this article.

A large number of mixed-ligand ruthenium(III) halides are known. One of the simplest is $K_2[RuCl_5(H_2O)]$, which is a valuable well-defined Ru^{III} starting material. A series of dinuclear complexes $Ru_2Cl_4(dppb)_2L$ can be obtained by electrolysis from the corresponding $RuCl_3(dppb)L$ complexes.**[5]** There is no strong evidence for the existence of any RuX_2 complexes. However, reduction of $RuCl_3{\cdot}3H_2O$ by various reagents (Zn, H_2/PtO_2, Na/Hg, Zn/Hg, etc.) in alcoholic or aqueous solutions affords a deep-blue solution (first observed by Vauquelin). The nature of such solutions is still controversial. Investigations by Rose and Wilkinson in the late 1960s have concluded in favor of the presence of the anionic cluster $[Ru_5Cl_{12}]^-$, although no X-ray evidence is as yet available on this compound. It was, nevertheless, found to be a valuable precursor for the synthesis of a large variety of ruthenium (II) derivatives. Bino and Cotton have shown that addition of tetraethylammonium chloride to the deep-blue solution obtained upon dissolving $Ru_2(OAc)_2Cl$ in 12 M HCl led to a green crystalline material, shown to be the homoleptic trimer $[Ru_3Cl_{12}]^{6-}$ containing Ru(III), Ru(II), and Ru(III) with short Ru–Ru distances (2.805(1) Å) in agreement with single Ru–Ru bonds.

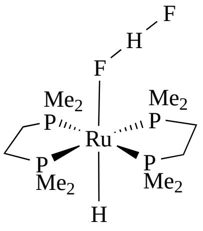
F
H
F
Me2
Me2
P
P
Ru
P
P
Me2
Me2
H

(**1**)

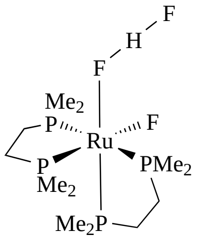
F
H
F
Me2
P
Ru
F
P
PMe2
Me2
Me2P

(**2**)

Some homoleptic fluorides of ruthenium are well characterized up to the oxidation state +VI: RuF_6 is a volatile dark-brown solid. Mixed-ligand complexes such as $RuOF_4$ are also known. RuF_4 has been isolated by treatment of AsF_5 with $[RuF_6]^{2-}$ in a HF solution.**[6]** With the other halides, the chemistry starts at the oxidation state IV. $RuCl_4$ can be observed in the gas phase between 400 and 800 °C, whereas the dianions $MX_6{}^{2-}$ ($X = F$, Cl, Br) are stable. During the last decade, considerable progress has been made in the field of transition metal–fluoride complexes. Several fluoride(carbonyl) complexes have been characterized (*see* ***Carbonyl Complexes of the Transition Metals***). A series of bifluoride HF_2 complexes incorporating mono- or diphosphines are now available.**[7]** In particular, two bifluoride complexes can be isolated from *cis*-$RuH_2(dmpe)_2$. The hydride complex *trans*-$RuH(HF_2)(dmpe)_2$ (**1**) was obtained by addition of $Et_3N{\cdot}3HF$ or by reaction with fluoroarenes as a result of C–F activation, whereas reaction with fluoroalkenes produced the fluoride complex *cis*-$RuF(HF_2)(dmpe)_2$ (**2**). The coordination mode of the fluoro ligand, terminal versus bridging, plays an important role in the stabilization of d^6 and d^8 complexes.[8]

3 RUTHENIUM COMPLEXES OF OXYGEN-DONOR LIGANDS (*See* ***Water & O-donor Ligands***)

3.1 Ruthenium Homoleptic Oxo Species

The ruthenium(VIII) complex RuO_4 and salts such as $K_n[RuO_4]$, derived by reduction ($n = 1-3$), have been reported in the literature. However, the compound originally thought to be the ruthenium(VI) oxide $[RuO_4]^{2-}$ has been identified by X-ray crystallography as $[RuO_3(OH)_2]^{2-}$. RuO_4 is a yellow, crystalline, low-melting (25.4 °C), and highly volatile solid. Care must be taken when using it since it is a highly toxic and powerful oxidizing agent. It reacts explosively with a variety of organic solvents. It is, nevertheless, a useful oxidizing reagent for organic substrates such as alcohol, amine, sulfide, and so on. The perruthenate $(^nPr_4N)RuO_4$ salt is a useful, mild, and selective oxidant of alcohols to aldehydes or ketones, even in allylic systems. O_2 or NMO is used as co-oxidant.[9] Interestingly, the salt can be recovered when using ionic liquids (*see* ***Oxidation Catalysis by Transition Metal Complexes***).[10] The ruthenium(IV) oxide, RuO_2, is a stable metallic oxide displaying a low chemical reactivity but interesting physical properties. Under high pressure, the rutile form of RuO_2 can be converted to a new cubic phase, which presents a very low compressibility (comparable to that of diamond).[11]

3.2 Mixed-ligand Oxo Derivatives

The study of mixed-ligand oxo derivatives is closely related to the use of these species in catalytic oxidation systems (including the epoxidation of alkenes and the oxidation of alkanes. *See* ***Oxidation Catalysis by Transition Metal Complexes***). In such complexes, the oxo group can be terminal, doubly bridging, or triply bridging.

The chemistry of triply bridging oxo(carboxylate) ruthenium clusters of general formula $[Ru_3(\mu_3\text{-}O)(\mu_2\text{-}O_2CR)_6(L)_3]^n$ (**3**) has been extensively developed. A rich chemistry is associated with the strong electronic and magnetic interactions involving Ru(II), Ru(III), and Ru(IV) centers. They are relevant to biomimetic systems, redox catalysis, and molecular devices.[12] A number of dinuclear ruthenium complexes incorporating a bridging oxygen have been isolated and used as a water oxidation catalyst. The μ-oxo(bipyridyl) dimer $[\{Ru(bpy)_2(OH_2)\}_2O]^{4+}$ (known as 'blue ruthenium dimer') is one of the most effective electrocatalytic reagents. The mechanism by which it oxidizes water to dioxygen is very complex (loss of 4e$^-$ and 4H$^+$) and has been extensively investigated by Meyer *et al.*[13]

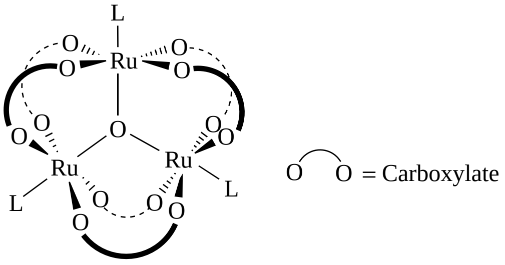

(**3**)

Monooxo and dioxo ruthenium (IV), (V), and (VI) complexes have been extensively studied. Che's group has been very active in this area, and a very detailed analysis of this field can be found in the chapter written by Che and Lau and published in '*Comprehensive Coordination Chemistry*'.[4] The chapter covers the various aspects of the chemistry (synthesis; characterization, including the Pourbaix diagrams for many representative species; reactivity; and catalysis). The most important classes of ligands for such $Ru(O)_n$ centers are (1) the porphyrins; (2) the macrocyclic tertiary amine ligands (*see* ***Macrocyclic Ligands***); and (3) the pyridine, polypyridyl, and related ligands. Most of the compounds are very active oxidants for a variety of organic and inorganic substrates.

Groves *et al.* isolated the first dioxoruthenium(VI) porphyrin complex $Ru(O)_2TMP$, able to efficiently catalyze the aerobic epoxidation of alkenes at ambient temperature and pressure.[14] A number of dioxo $[Ru(O)_2(por)]$ and oxo(imido) $[Ru(O)(por)(NR)]$ complexes of Ru (VI) with porphyrinato (por) ligands are now available. All these Ru(VI) complexes are diamagnetic. Complexes incorporating chiral porphyrins have also been isolated, and for example, enantioselective aerobic epoxidation of alkenes is achieved by complex (**4**). Recent developments involve the design of dendritic ruthenium porphyrins.[15] Similar high-oxidation oxo complexes can be prepared using various macrocyclic amine ligands such as [14]ane-N4 (**5**) or 14-tetramethylcyclam (TMC) and their 15- and 16-member analogs. A cis configuration, as in complex (**6**), can be obtained using a triazacyclononane ligand. (**6**) oxidizes disubstituted alkynes to 1,2 diketones in good yields.[16]

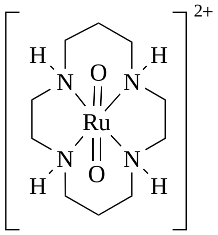

(**5**)

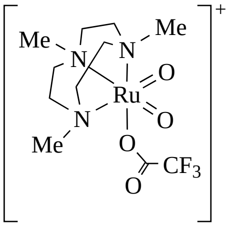

(**6**)

Bis-oxo-Ru(VI) complexes containing nonlabile oxidation-resistant nitrogen-donor ligands such as pyridine, bipyridine,

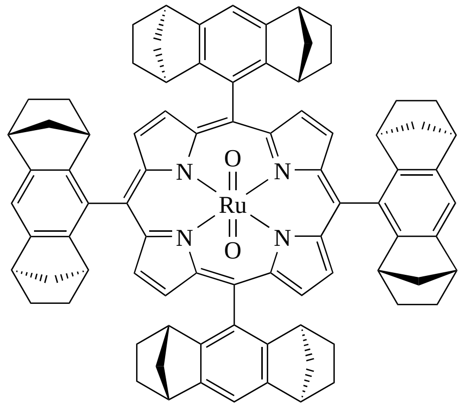

(**4**)

terpyridine, and related ligands are another important class of compounds that behave as four-electron oxidants and convert alcohols to aldehydes or ketones. The remarkable reactivity of high-oxidation-state ruthenium and osmium polypyridyl complexes has been recently reviewed by Meyer and Huynh.[17] The polypyridyl species are stronger oxidants than the macrocyclic family. The chemistry of periodato-derived species has been developed, and for example, the complex, $[Ru(O)_2(bpy)\{IO_3(OH)_3\}]$ (**7**), containing the triply protonated periodate ligand $[I(O)_3(OH)_3]^{2-}$ has been isolated. (**7**) behaves as a six-electron oxidant for the stoichiometric oxidation of alkenes.[18] Chloro and carboxylato dioxo complexes of Ru(VI) have been prepared and are also used as oxidants of halides, alcohols, sulfides, and even alkanes (*see* ***Oxidation Catalysis by Transition Metal Complexes***).

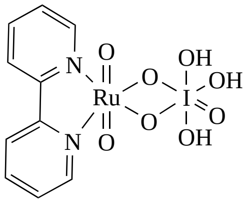

(**7**)

3.3 Carboxylate Ligands

The carboxylate group can act as a three-electron bridging or chelating ligand, as well as a one-electron monodentate ligand. This gives rise to a rich chemistry in which interconversion between the modes of coordination of the ligand and nuclearity of the complexes is facile. Examples of chelation are found in the phosphine adducts $Ru(OAc)_2(PPh_3)_2$ and $RuH(OAc)(PPh_3)_3$, which are prepared by metathetical exchange with chloride groups or by protonation of polyhydrides with acetic acid. The dicarboxylate complexes $Ru(OAc)_2(BINAP)$ are at the origin of all the chemistry developed by Noyori in asymmetric catalytic hydrogenation reactions (see Section 6.2). Similar complexes of the formula $Ru(O_2CCF_3)_2(ROH)_2(PP)$, incorporating various chiral phosphines (PP (diphosphines)), have also been characterized. The two carboxylates act as monodentate ligands, and two solvent molecules remain in the coordination sphere of the metal, in cis positions.[19]

Bridging carboxylates are mainly found in three types of structures: μ_3-oxo-bridged trimers, μ_2-oxo- or hydroxo-bridged dimers (see Section 3.2), and metal–metal multiply bonded dimers. Diruthenium tetracarboxylates exist as homovalent Ru_2(II,II) and mixed-valent Ru_2(II,III) species (*see* ***Mixed Valence Compounds***). They all adopt the familiar 'lantern' type motif (see structure (**8**)). The first dimers $[Ru_2(OCOR)_4Cl]$ were prepared by reaction of $RuCl_3{\cdot}3H_2O$ with a mixture of carboxylic acid/anhydride acid. The crystal structure of $[Ru_2(OCOMe)_4Cl]$ revealed the presence of infinite chains of Ru_2 units linked by Cl. Analogous complexes can be prepared using a variety of acids. Diadducts of the type $[Ru_2(OCOR)_4L_2]X$ incorporate L ligands such as H_2O, $OPPh_3$, THF, py, MeOH, and DMSO. The diruthenium carboxylate complexes display interesting magnetic and electronic properties as potential molecular materials and liquid crystals. They are now being tested as antitumor drugs.[20]

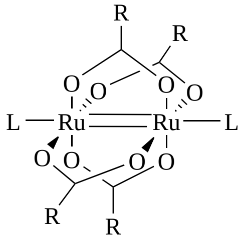

(**8**)

3.4 Other Oxygen-donor Ligands

Water reacts as a ligand in numerous inorganic and organometallic compounds. It normally behaves as a two-electron ligand on one ruthenium center, although some rare cases of water bridging two ruthenium centers are known. The homoleptic ruthenium(III) and ruthenium(II) complexes $[Ru(H_2O)_6]^{n+}$ have been known for nearly 40 years. In the course of their studies on Ring Opening Metathesis Polymerization (ROMP) reactions, Grubbs *et al.* explored the reactivity of $[Ru(H_2O)_6](tosyl)_2$ with acyclic- and monocyclic-functionalized alkenes (L), generating monoalkene adducts $[Ru(H_2O)_5L]^{2+}$ (*see* ***Water & O-donor Ligands***).[21]

Hydroxy ligands generally result from the protonation of oxo or deprotonation of aqua species and are thus found in systems similar to those described above. They occupy terminal or doubly or triply bridging positions. Alternative routes involve the metathetical exchange of Cl^- by OH^- or oxidative addition of H_2O. These routes have been used by Wilkinson *et al.* to prepare unsaturated trans hydroxo hydrido derivatives such as $RuH(OH)(PPh_3)_2(H_2O)$.[1,2] A series of alkoxide and hydroxide complexes have now been designed by Bergman *et al.*, and their properties and reactivities have been reviewed. The complexes, with a strongly polarized Ru–O bond, typically display nucleophilic reactivity (*see* ***Water & O-donor Ligands***).[22] The formation of an (alkoxy)ruthenium hydride and a piperidinyloxy species are postulated in the $RuCl_2(PPh_3)_3$/TEMPO-catalyzed aerobic oxidation of alcohols.[23]

$Ru(acac)_3$ is readily prepared from $RuCl_3{\cdot}3H_2O$, 2,4-pentanedione, and potassium hydrogencarbonate in hot water. Its structure has been determined by X-ray and neutron diffraction measurements at various temperatures.[24] This compound can be reduced to $[Ru(acac)_3]^-$. Protonation leads to liberation of acacH, thus making this compound a suitable starting material for ruthenium(III) chemistry. $Ru(acac)_3$-mediated oxidative di- and trimerization of 1,3-diamino benzene produce new diimine $Ru(acac)_2$ complexes.[25] Ruthenium complexes with the bulky $N(SPR_2)_2$ ligand, a sulfur analogue of acac, have been synthesized.[26]

4 RUTHENIUM COMPLEXES OF SULFUR-DONOR LIGANDS (*See S-donor Ligands*)

Ruthenium–sulfur systems have attracted attention, primarily owing to their relevance to biology and catalysis, in particular, for the hydrodesulfurization process. (*see* ***Hydrodesulfurization & Hydrodenitrogenation***). Soft sulfur ligands alone cannot stabilize Ru(VI) centers, and no Ru(V) complexes seem to have been reported with any sulfur ligands. Sulfide, thiolate, and thioether ligands are unique as they display versatile electronic properties: they can act as pure σ-donors, σ-donor π-acceptors, or even as σ-π-donors because of their lone pairs (*see* ***Subvalent Compounds***). The coordination chemistry of new mixed-donor ligands is now being investigated to benefit from the properties of the different atoms N, P, O, and S (*see* ***Sulfur: Inorganic Chemistry***).

4.1 Sulfides and Thiolato Ligands

Ruthenium sulfide (RuS_2) as well as other chalcogenides RuX_2 (X = Se, Te) adopt a cubic pyrite structure and should be regarded as Ru^{2+} $(S_2)^{2-}$. They are very stable compounds that are readily prepared by several routes, including direct combination of the elements. The chemistry of ruthenium complexes with bridging sulfide groups has been particularly examined by Matsumoto *et al.* The synthesis and properties of a family of complexes with a strong μ-donor ligand $(S_2)^{2-}$ bridging two Ru centers have been described. Of particular interest is the reaction of (**9**) with O_2. Amongst other products, oxidation of the sulfide ligand results in the formation of (**10**) with a unique bridging $S_2O_5{}^{2-}$ ligand.[27]

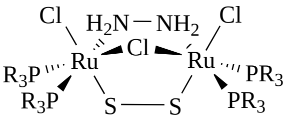

(**9**)

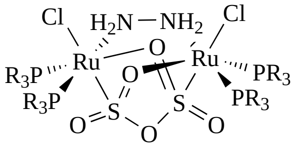

(**10**)

Numerous examples of complexes containing terminal or bridging thiolato ligands are known. For example, fluorinated thiolates Ru(II) and (III) species have been prepared in which $C_6F_5S^-$ acts either as a terminal ligand or as a bridging ligand between two ruthenium centers.[28] Trigonal-bipyramidal Ru(IV) thiolate complexes display a characteristic trigonal-planar $Ru(SR)_3$ core, and the organometallic reactivity of these species is now being explored.[29] The homoleptic complex $[Ru(mnt)_3]^{2-}$ (**11**) with only sulfur atoms in the coordination sphere of ruthenium has been isolated. (**11**) decomposes in the presence of light, leading to the formation of a compound $[Ru(mnts)_2]^{2-}$ containing a novel tridentate (mnts) ligand.[30] Various examples of hydrido(thiolate) complexes have been reported. Interestingly, protonation can occur at the metal, or at the hydride to form a dihydrogen complex, or at the sulfur site to give a thiol complex (see Section 8). The reactivity of the bis(dihydrogen) complex $RuH_2(H_2)_2(PCy_3)_2$ with sulfur heteroaromatic compounds leads to new compounds presenting different coordination modes of the S-substrates. As an example, C–S splitting in 2-acetylthiophene results in the formation of a dihydride metallocycle (**12**) with a new thiolato ligand η^2-(O,S) coordinated to ruthenium.[31]

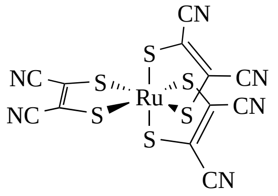

(**11**)

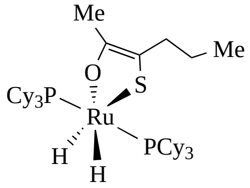

(**12**)

4.2 Thioethers and Analogous Derivatives

Numerous examples of complexes containing thioethers have been reported, including the first example by Sellmann *et al.* of a transition metal compound containing H_2S, namely, $Ru(SH_2)(PPh_3)(S_4)$ (S_4 = 2,2′-(ethylenedithio)bis(thiophenolate)). There is now an example of a room-temperature stable complex with a P–N ligand (see structure (**13**)).[32]

The remarkable complexing properties of cyclic thioethers, in particular, those exploited by Schröder's and Yoshida's groups, have stimulated a great interest in metal–thioether chemistry. These cyclic ligands bind preferentially to soft metal ions and have allowed the preparation of complexes displaying unusual stereochemistry and/or oxidation states. The most common thioethers involved are [9]ane-S_3,

[12]ane-S_3, [12]ane-S_4, [14]ane-S_4, [16]ane-S_4, and [18]ane-S_6. The affinity of ruthenium for these thioethers (see structure (**14**)) is evidenced by the loss of arene upon reaction of $[RuCl_2(arene)]_2$ with [9]ane-S_3, yielding the homoleptic derivative $[Ru([9]ane\text{-}S_3)]^{2+}$. Neutral (such as $[RuCl_2(PR_3)[9]ane\text{-}S_3]$), cationic ($[RuCl(L^1)(L^2)([9]ane\text{-}S_3)]^+$), or dicationic complexes ($[Ru(L^1)_2(L^2)([9]ane\text{-}S_3)]^{2+}$) can be prepared as well as dinuclear species.[33]

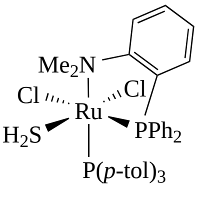

(**13**)

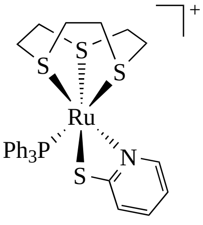

(**14**)

Sellmann *et al.* have extensively surveyed the coordination properties of tetra- and pentadentate ligands in the search for reduction of N_2 by metal–sulfur complexes under mild conditions (see structures (**15**) and (**16**)).[34] The Ru'S4' core is not always preserved and partial cleavage of S–C bonds can occur. To circumvent this problem, the ethylene bridge in 'S4' has been replaced by an *o*-phenylene bridge.[35]

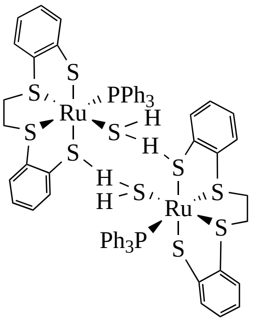

(**15**)

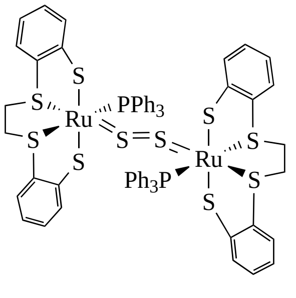

(**16**)

Pentaammine Ru(III) polarizes thiourea by complexing sulfur, and the complex $[Ru(NH_3)_5SC(NH_2)_2](S_2O_6)_{3/2}\cdot H_2O$ is isolated. The data are consistent with LMCT from a filled $p\pi$ sulfur orbital to the vacant $d_{xy}\pi$-orbital on Ru(III).[36]

4.3 Sulfoxides

Sulfoxide ruthenium complexes have received attention in part from the fact that they are useful starting materials for new organometallic and coordination compounds and in part from their role in biology and catalytic processes (*see* ***Metal-related Diseases of Genetic Origin***). Potential applications are found in medicinal chemistry, in particular as antitumor agents and as radiosensitizers. The complex Na{-*trans*[$RuCl_4$(DMSO)(Im)]} known as (NAMI), is the first ruthenium compound to enter clinical trials.[37–39]

$RuCl_2(DMSO)_4$ can be conveniently prepared by refluxing $RuCl_3\cdot 3H_2O$ in DMSO for a few minutes. This complex has found wide interest as a starting material, although DMSO is often difficult to eliminate. The sulfoxide ligand has two possible sites of coordination, sulfur and oxygen. Coordination to sulfur is generally observed in the case of ruthenium, and the $d\pi$-S back-bonding plays a major role. S to O linkage isomerization was first shown, by Taube *et al.*, to occur upon oxidation of $[Ru(NH_3)_5(DMSO)]^{2+}$. More recent studies demonstrate that DMSO can also be S-bonded to Ru(III) and Ru(IV) and suggest that the κS-(DMSO) σ-donation to Ru is extensive in Ru(II) and Ru(IV) states.[40] The complex $[Ru(bpy)_2(DMSO)_2]^{2+}$ is yellow and has two S-bound DMSO ligands. Upon irradiation, a color change to red is observed, which is attributed to linkage isomerization from S- to O-bound DMSO. The yellow color is slowly recovered in the dark.[41]

5 RUTHENIUM COMPLEXES OF NITROGEN-DONOR LIGANDS (*See* *Ammonia & N-donor Ligands*)

Supramolecular chemistry involving transition metal complexes has received increasing interest over the last decade. Photo-redox processes for solar energy conversion, information storage systems, biosensors, and complexes with antitumor activity are currently under investigation. In this area, the inorganic chemistry of ruthenium, largely dominated by the chemistry of nitrogen-donor ligands, plays a major role. Several important achievements in inorganic chemistry have involved nitrogen-donor ruthenium derivatives. These include (1) the first dinitrogen complexes, (2) the Creutz–Taube complex for the study of electron transfer and for the study of electron transfer in ruthenium-modified proteins, (3) the photochemistry of $[Ru(bpy)_3]^{2+}$ and all the applications of this and related complexes (from photovoltaic cells to DNA intercalation), and (4) the aerobic oxidation of alkenes in the presence of ruthenium–porphyrin derivatives using both oxygen atoms.

The chemistry of the higher oxidation states is dominated by metal–ligand multiple bonds, with the oxo ligand being the ligand of choice. There are no complexes of Ru(VIII) and Ru(VII) incorporating an imido or a nitrido ligand and almost no Ru(V) compounds. A number of nitrido Ru(VI) complexes exist with a variety of ligands, but the chemistry is much less matured than the analogous osmium chemistry (*see* ***Nitrides: Transition Metal Solid-state Chemistry***). There are no nitrido mononuclear Ru(IV) complexes, but a number of μ-nitrido species are known.

The simple amido complex $[Ru(NH_3)_5(NH_2)]^{2+}$ can be easily prepared by deprotonation of $[Ru(NH_3)_6]^{3+}$, and a series of hydrido(amido) ruthenium complexes have been recently reported.[22] The chemistry of Ru(VI) imido complexes is largely concentrated on oxo(porphyrins) compounds of general formula Ru(O)(NR)(por). Extensive work on oxo ruthenium(VI) complexes incorporating N-ligands has been performed, as already mentioned in Section 3.2. Three main classes of ligands can be distinguished: (1) the porphyrins, (2) the macrocyclic tertiary amine ligands, and (3) the pyridine, polypyridyl, and related ligands. The results show a rich electrochemistry, and numerous studies are connected to the use of these compounds as oxidants for a variety of substrates (*see* ***Oxidation Catalysis by Transition Metal Complexes***). Ruthenium porphyrins are efficient catalysts for a collection of organic reactions such as epoxidation and cyclopropanation of alkenes and hydroxylation and amidation of alkanes. For example, a dendritic ruthenium porphyrin efficiently catalyzes the EDA cyclopropanation of styrene.[15]

5.1 Ammine Salts

The hexaammine ruthenium(II) salt $[Ru(NH_3)_6]Cl_2$ is conveniently prepared by zinc reduction of $RuCl_3{\cdot}3H_2O$ in aqueous ammonia. It is readily oxidized in several ways to the corresponding ruthenium(III) derivative, $[Ru(NH_3)_6]^{3+}$. The ruthenium(II) complex is substitutionally very labile, unlike the ruthenium(III) analogue, and complexes of the general formula $[Ru(NH_3)_5(L)]^{2+}$ display a very rich photochemistry. $[Ru(NH_3)_5N_2]^{2+}$ was the first transition metal–dinitrogen complex, the discovery of which in 1965 stimulated the rapid development of nitrogen fixation chemistry (*see* ***Nitrogenase Catalysis & Assembly***). The first compound containing a bridging dinitrogen group, $[(NH_3)_5Ru(N_2)Ru(NH_3)_5]^{4+}$, was then obtained by mixing $[Ru(NH_3)_5N_2]^{2+}$ and $[Ru(NH_3)_5(H_2O)]^{2+}$.[1,2] Studies on the photochemistry of Ru(II) ammine complexes really started in 1969 with molecular nitrogen complexes. The photochemical reactions are dominated by substitution processes. The studies provide a better knowledge into the excited states reactivity of d^6 centers. The properties of the MLCT states in Ru(II)–ammine complexes depend on the nature of the L ligand. They can be varied by controlling the acidity of the medium and are solvent dependent. Several investigations have been focused on the prediction of electronic spectra and on identifying the extent of ruthenium–ligand electronic coupling in mononuclear and dinuclear species. The electronic spectra calculations are performed using modified INDO/s method (*see* ***Photochemistry of Transition Metal Complexes***; ***Photochemistry of Transition Metal Complexes: Theory***).[42–44]

Mixed-valence complexes exhibit interesting properties when significant electron coupling occurs between the donor and acceptor sites. Most of the systems are Ru(II)/Ru(III) species, but if electronic coupling is sufficient, there is a complete blending of oxidation states and the odd electron is delocalized over both sites. The μ-pyrazine-bridged dimer (**17**), also named the Creutz–Taube ion, was the first designed mixed-valence complex. The Nobel prize for chemistry was awarded to Taube in 1983 for his work on the mechanisms of electron transfer reactions (*see* ***Electron Transfer in Coordination Compounds*** and ***Electron Transfer Reactions: Theory***).[1–3] The electronic structure of (**17**) has been the subject of numerous studies. The complex is considered ‘delocalized’ but appears to have properties of both class II and class III in the Robin and Day classification. In particular, its spectroscopic properties show some residual localization. It should now be considered as the prototype of a new class of mixed-valence species, Class II–III, as evidenced by Meyer *et al.*[45] Medium effects on charge transfer in metal complexes have also been reviewed by Meyer *et al.*[46] Inventing new analogues of the Creutz–Taube ion remains a very active area of research.[47]

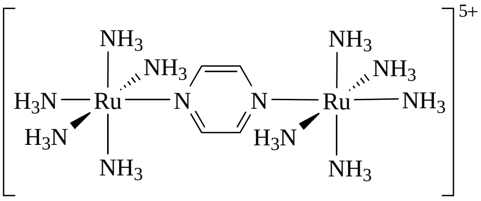

(**17**)

Long-distance intervalence electron transfer is now demonstrated with metal–metal distances up to 25 Å. Distance dependence of electron transfer has strong implications for the search of, for example, molecular switch devices or biosensors. The bridging ligand dicyanamidobenzene has been extensively studied, and for example, complex (**18**) exhibits a very strong coupling (0.32 eV) for a metal–metal distance of 19.5 Å.[48]

5.2 $[Ru(bpy)_3]^{2+}$ and Related Complexes. Some Selected Applications

A huge growth has been observed in $[Ru(bpy)_3]^{2+}$ chemistry over the last two decades as the complex displays a unique combination of air and thermal stability and redox and photophysical properties (*see* ***Electron Transfer in Coordination Compounds*** and ***Electron Transfer Reactions: Theory***). More generally, ruthenium complexes incorporating pyridine or multidentate ligands based on aromatic imines have attracted more attention than all the other classes of inorganic ruthenium derivatives (*see* ***Photochemistry of Transition Metal Complexes*** and ***Photochemistry of Transition Metal Complexes: Theory***).[3] An exhaustive database of bipyridine-containing molecules has now been reported.[49] Complexes of the general formula $[RuL_6]^{2+}$ ($L = py$; $L_2 = bpy$, phen, and derivatives; $L_3 = terpy$, etc.) can be prepared by a variety of

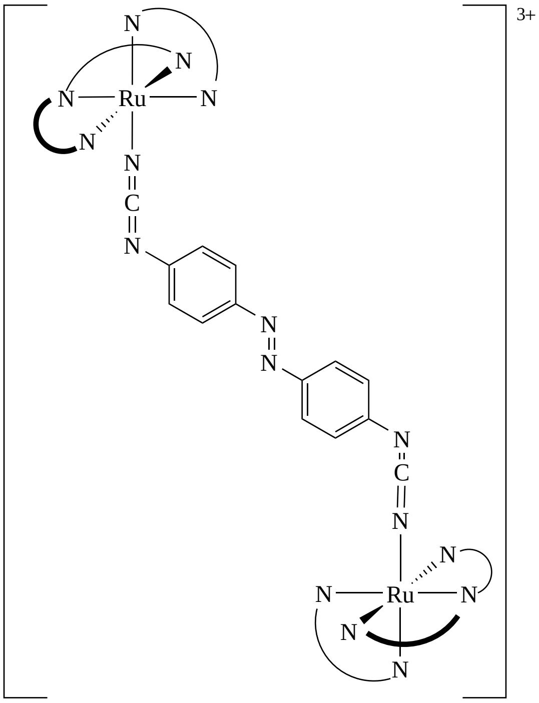

(**18**)

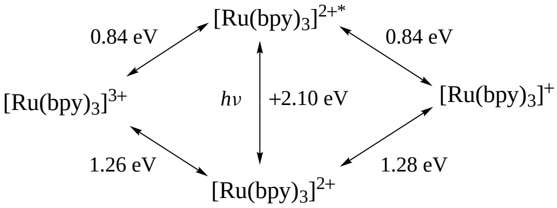

$$H_2O \xrightarrow{[Ru(bpy)_3]^{2+*}} H_2 + 1/2\ O_2$$

Scheme 2

methods.[1–3] In the case of $[Ru(bpy)_3]^{2+}$, a convenient method involves the reduction of $RuCl_3$ with H_2 over Pt black, followed by treatment with bpy in MeOH. The red crystals are obtained with 80% yield. It is out of the scope of this article to extensively review the photochemistry and photophysics studies on $[Ru(bpy)_3]^{2+}$ and related species, but we will give a few principles and highlight a few outstanding applications. Many investigations have benefited from the tremendous progress seen in various techniques (such as, for example, time-resolved femtosecond absorption spectroscopy).

$[Ru(bpy)_3]^{2+}$ possesses a luminescent excited state, $[Ru(bpy)_3]^{2+*}$, which can act as a reducing agent to give $[Ru(bpy)_3]^{3+}$ or as an oxidizing agent to give $[Ru(bpy)_3]^{+}$. Therefore, the energy-transfer process may be coupled to either an oxidizing or a reducing agent. The redox potentials for couples involving $[Ru(bpy)_3]^{2+}$ and the excited state $[Ru(bpy)_3]^{2+*}$ are shown in Scheme 2. Its redox potentials are in favor of water splitting.

The design of new molecules, aimed at controlling the transfer of energy and of electrons from the excited state, is still an active area of research. The current understanding of electron flow through proteins has been achieved mainly through the use of photoprobes, with photoactive Ru(II)-diimine complexes being in widespread use.[50]

A rich chemistry has flourished in the search for new luminescent systems (*see* ***Luminescence*** and ***Luminescence Behavior & Photochemistry of Organotransition Metal Compounds***). A great variety of inorganic architectures have been obtained, including helicates and large multicomponent arrays. As an example, rack-type polynuclear ruthenium complexes have been assembled by Lehn *et al.* These rack-type structures are based on tridentate ligands with pyrimidine and pyridine moieties. A fine tuning of the absorption and luminescence properties of these complexes can be performed by introducing substituents on the pyrimidine ring. These systems represent key structures for the development of photonic and electronic devices.[51] The control of the direction of the energy-transfer process in a multicomponent species offers new perspectives for artificial functions operating at the molecular level. The synthesis of multicomponent systems incorporating Ru(II) polypyridine and anthracene chromophores has been performed. The direction of the intercomponent energy-transfer process is reversed on passing from room temperature to 77 K.[52] Dentritic luminescent structures are now rather common as illustrated by the report in '*Inorganic Synthesis*', of a decanuclear ruthenium(II) polypyridine complex.[53,54]

Incorporation of the $Ru(bpy)_3$ moiety into acyclic, macrocyclic, and calixarene frameworks leads to a new class of anion receptors capable of optical and electrochemical sensing (see (**19**)).[55] The remarkable reactivity of high-oxidation-state ruthenium and osmium polypyridyl complexes has been recently reviewed by Meyer and Huynh,[17] whereas the significance of polypyridyl complexes as biomimetic models for the photosynthetic reaction center was analyzed by Dürr and Bossmann.[56] The viologen-linked $[Ru(bpy)_3]^{2+}$ system has been widely investigated, and a soluble polymer based on a polypyrrole–bisviologen-linked $[Ru(bpy)_3]^{2+}$ dyad is now available. The photostability of the dyad network in the presence of oxygen offers new possibilities in photoinduced redox processes (*see* ***Electrochemistry: Applications in Inorganic Chemistry***).[57]

5.2.1 Molecular Photovoltaics

The photochemical properties of bipyridine ruthenium compounds are at the origin of impressive results in the field of molecular photovoltaics. In 1991, Grätzel *et al.* prepared a molecular photovoltaic system by coating TiO_2 with a bipyridine complex linked to the surface

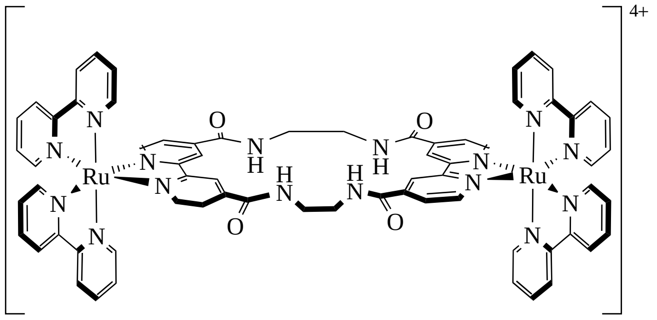

(**19**)

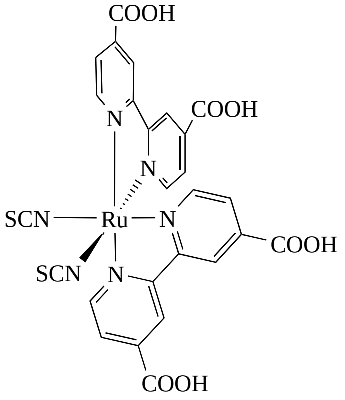

(**20**)

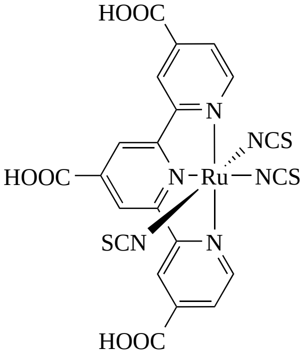

(**21**)

by carboxylate groups (*see* ***Semiconductor Interfaces*** and ***Superconductivity***). This system is able to inject one electron into the semiconductor conduction band extremely rapidly after photoexcitation. It is now admitted that the process occurs in the femtosecond time regime. By contrast, the back reaction of the electrons with the oxidized ruthenium complex is slow (microsecond to millisecond timescale). This first dye-sensitized nanocrystalline solar cell gave a conversion yield of 7%. Following this result, hundreds of other complexes have been synthesized and tested, but the polypyridyl–ruthenium complexes remain the precursors of choice for achieving the best photovoltaic performances. The best results are now obtained by complexes (**20**) and (**21**), known as N3 and black dye, respectively. The efficiency obtained with the black dye (**21**) is 10.4% under standard air mass 1.5 reporting conditions. The interaction between the carboxylic group and TiO_2 is of fundamental importance as the dye is attached via two carboxylates. Projects concerning molecular engineering with judicious substitutions of the carboxylic groups are under investigation. The ultimate goal is the splitting of water into dihydrogen and dioxygen by sunlight.[58,59] In photosynthesis, water oxidation is accomplished by photosystem II (PSII), which is a large membrane-bound protein. Several studies, aimed at mimicking the light-driven oxidation of water accomplished by PSII, involve the use of a photosensitizer, a ruthenium(II) complex incorporating bpy units, linked to manganese complexes (*see* ***Photosynthesis***).[60]

5.2.2 Molecular Machines

A special issue devoted to molecular machines appeared in ‘Accounts of Chemical Research’ in 2001. It reflects the current interest for this field in which ruthenium complexes act as important tools. Molecular machines are characterized by a mobile part and a stationary part. Photochemical and electrochemical inputs can make a machine work, offering the advantage of being switched on and off easily and rapidly. Mechanically interlocked molecules, such as rotaxanes and catenanes, are suitable candidates. Crown ethers, cyclophanes, and calixarenes are representative families of the cyclic component. The design of even more sophisticated molecular-level machines should open the way to a variety of applications. We have selected three examples to illustrate this fascinating field.

The design of a rotaxane is a synthetic challenge. One strategy is to combine a bifunctional ligand and two different metals, as demonstrated by Sauvage *et al.* The bifunctional ligand containing one dpp and two terpy units is treated with a preformed Cu(I)(dpp) macrocyclic complex to afford a prerotaxane complex with pendent terpyridines. The $[Ru(terpy)]^{2+}$ is then anchored to the pendent ligands. Selective removal of the cage Cu(I) template produces the rotaxane shown as structure (**22**).[61]

Another recent example also comes from Strasbourg’s group that prepared the first rotaxane with a $[Ru(diimine)_3]^{2+}$ core. The synthetic scheme consists of a ‘threading’ step followed by a stopping reaction: a ruthenium bisphenanthroline complex, acting as an axis, is threaded through a 35-membered ring macrocycle incorporating a bpy unit. The pseudorotaxane is shown in structure (**23**). The length of the threaded ring is too short and an isomer in which the axial ruthenium complex is attached in an exo fashion is also obtained (see structure (**24**)). A modified strategy has allowed the synthesis of a real rotaxane deriving from (**23**).[62]

The third example comes from Stoddart’s and Balzani’s groups. They prepared a photochemically driven molecular-level abacus by a four-step process. The system is made up of a photoactive unit P (a $[Ru(bpy)_3]^{2+}$-type complex serving as a stopper), two different π-electron acceptors A_1 and A_2 playing the role of stations for a π-electron-donor ring R (the BPP34C10 macrocycle), a rigid spacer S, and a tetraarylmethane group as second stopper T. The [2]rotaxane is shown as structure (**25**). The photochemically driven switching of the ring R between stations A_1 and A_2 is achieved by a mechanism involving a sacrificial electron donor.[63,64]

5.2.3 Interaction with DNA

Transition metal complexes can help target DNA sites with specificity, probe DNA, and furnish highly

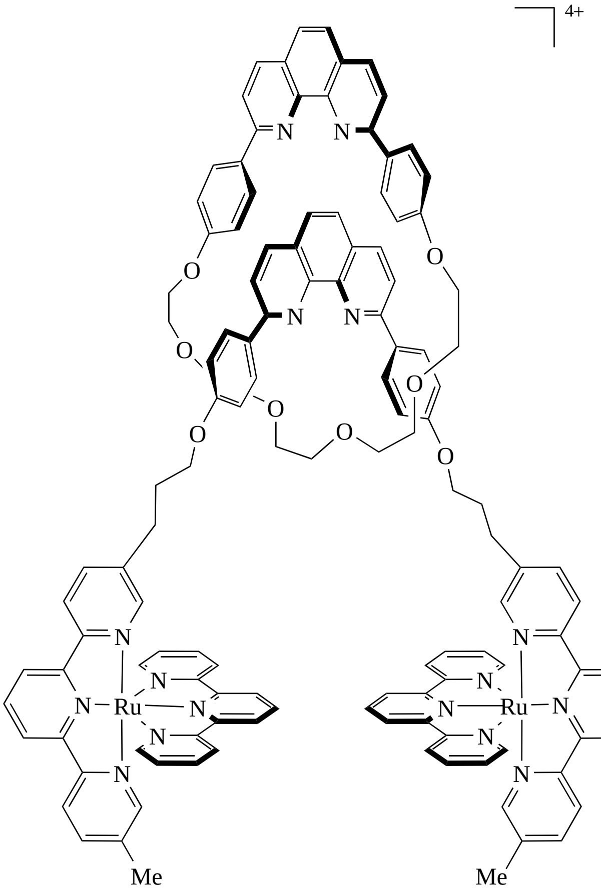

(**22**)

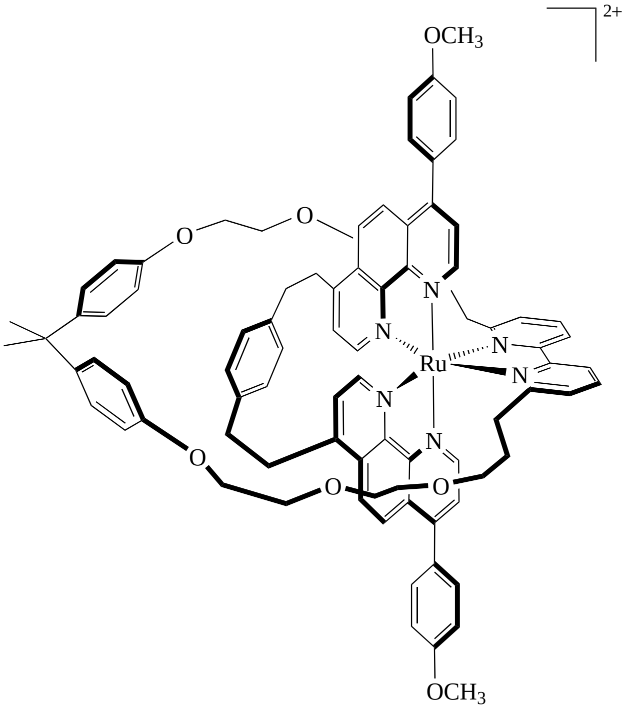

(**23**)

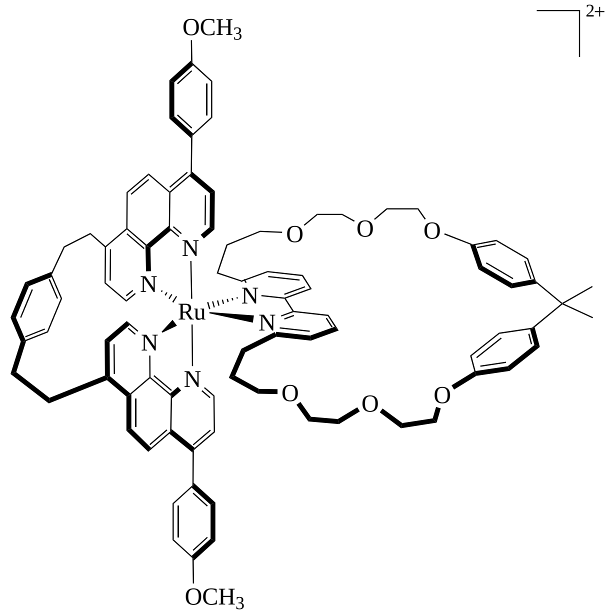

(**24**)

sensitive diagnostic agents. Metallointercalators contain planar aromatic heterocyclic groups able to insert and stack between the base pairs of double helical DNA (*see* ***Intercalation Chemistry*** and ***Nucleic Acid–Metal Ion Interactions***). Extensive work was performed by Barton *et al.*, and key features on recognition and reaction of metallointercalators with DNA have been reviewed in 1999.[65] One of the earliest examples concerned $[Ru(phen)_3]^{2+}$ existing, like any tris(diimine) ruthenium complex, as a mixture of enantiomers. In order to improve the complex binding affinities for DNA, the search for new ligands favoring intercalation was undertaken. Structures (**26–28**) are some typical examples. Minor changes in the ligand architecture and electronic structure can lead to profound influences on binding geometries.

The data concerning $[Ru(phen)_2(dppz)]^{2+}$ nicely illustrate the concept of ‘molecular light switch’ (dppz for **28**). When the complex is bound to DNA, the excited-state lifetime is approximately 200 ns, whereas without bounding, it is only 200 ps. This light-switch effect provides the basis for a valuable photophysical probe of nucleic acids. Luminescent characteristics of the complexes bound to DNA can also be used to illustrate the chiral discrimination associated with binding to the right-handed helix. Direct oxidation of DNA bases is also obtained by electrochemical activation of $[Ru(bpy)_3]^{2+}$. Recent developments concern the damage to DNA sites from a distance: site damage up to 200 Å away from the site of intercalation of the metal oxidant has been reported (*see* ***Long-range Electron Transfer in Biology***). One of the main challenges now is to use these molecules in vivo.[65,66]

The synthesis and properties of Ru(II) nucleosides and oligonucleotides have been recently reported using solid-phase

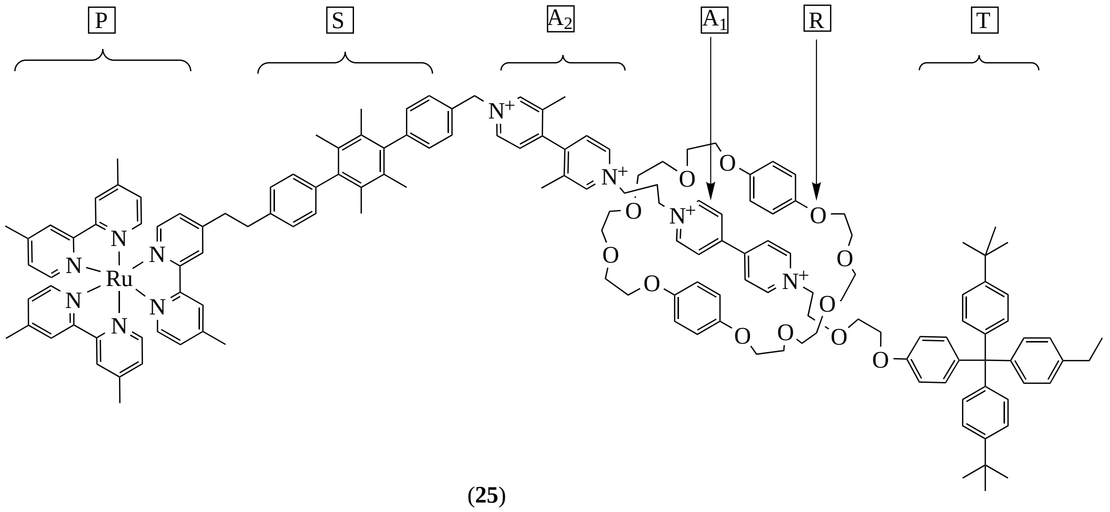

(**25**)

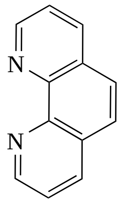

(**26**)

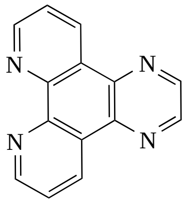

(**27**)

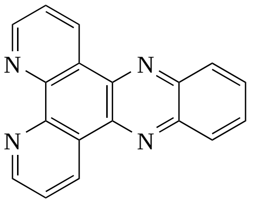

(**28**)

phosphoramidite chemistry. The first results offer interesting perspectives.**[67]**

5.3 Nitrosyl Ligands

The nitrosyl ligand can be combined with any other ligand (X, OH, H_2O, CO, PR_3, acac, NH_3, cyclam, *N*-aromatic heterocycles, NO_2, SO_2, DMSO, etc.) to form a wide range of nitrosyl ruthenium compounds (neutral, cationic, and anionic) with linear or bent NO ligands. This has been recently reviewed by Legzdins *et al.* and Housecroft.**[3,68]** The organometallic chemistry of nitrosyl ruthenium complexes is very rich, and various alkyl, acyl, alkene, carbene, and allyl complexes are known (*see* ***Nitrogen Monoxide (Nitric Oxide): Bioinorganic Chemistry*** and ***Ruthenium: Organometallic Chemistry***). The last decade has seen a renewed interest in understanding the chemistry of metal nitrosyl complexes, owing to the participation of NO in a wide range of physiological processes. The coordination and the release of NO by ruthenium dimethylsulfoxide**[39]** and ruthenium amine**[69]** complexes have been extensively investigated. Techniques such as X Ray, ^{15}N NMR, IR, EPR are very useful for determining the mode of bonding (i.e. N is deshielded by up to 450 ppm in bent form as compared to linear NO ligands). Spectroscopic methods associated with electrochemical techniques lead to a better understanding of the NO release mechanism. Studies of the reactivity of nitrosyl complexes are oriented toward reactions involving oxygen transfer to or from nitrosyl ligands and reduction of coordinated nitric oxide. For example, Shepherd *et al.* have studied, for the first time, a series of NO^+, $NO^{\cdot}$, and NO^- $[Ru(hedta)]^{n-}$ complexes by keeping a constant ligand–metal environment (see structure (**29**)). They found that the metal remained in the same oxidation state (II).**[68]**

The most common geometry displayed by ruthenium nitrosyl complexes is octahedral. However, some square-pyramidal and sawhorse geometries have been characterized. Chloride abstraction from $Ru(NO)Cl(CO)(PR_3)_2$ presenting a square-pyramidal geometry leads to $[Ru(NO)(CO)(PR_3)_2]^+$ (**30**) with a sawhorse structure, as a result of an intramolecular redox process. NO bending modification, from bent to linear, is concomitant with a formal decrease in the ruthenium oxidation state from +II to 0.**[68]** $[Ru(NO)_2Cl(PPh_3)_2]PF_6$ was the first complex containing the two modes of binding, that is, linear and bent (Ru–N–O axial, 138° Ru–N–O equat, 178° ν_{NO} linear, 1845 cm^{-1}; ν_{NO} bent, 1687 cm^{-1}).

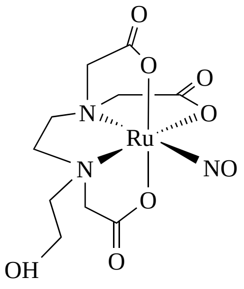

(**29**)

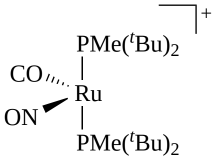

(**30**)

5.4 Miscellaneous Nitrogen Ligands

Although they have not yet attracted as much attention as the nitrosyl complexes, a large number of the isoelectronic thionitrosyl ones have been prepared. The most representative family is $Ru(NS)Cl_3L_2$, where L is phosphines, arsines, or stilbines. A linear bonding mode is observed.

We have previously mentioned in Section 4.2 the chemistry developed by Sellmann *et al.*, by using tetradentate or pentadentate ‘S4’ ligands. The use of such a ligand in nitrosyl ruthenium chemistry allowed the first conversion of a nitrosyl complex into a ruthenium HNO complex (**31**) by addition of $NaBH_4$ to $[Ru(NO)(py^{bu}S4)]Br$. The formation and decomposition of HNO complexes is often invoked in many processes such as combustion of fuels, oxidation of N_2, reduction of HNO_2, and so on.**[70]**

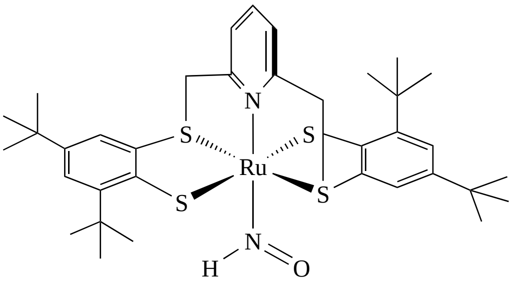

(**31**)

A large number of compounds with N-donor heterocyclic ligands have been prepared. Ruthenium complexes incorporating phthalocyanine or aza-macrocyclic ligands are known (*see* ***Macrocyclic Ligands***). In comparison to porphyrin chemistry, metallosalens and metallosalophens have received little attention, despite an easier synthetic access. A series of mononuclear and binuclear ruthenium derivatives with N_2O_2 Schiff base ligands are available. Some of them can act as supramolecular synthons.**[71]** α-Amino acids stabilize $Ru(bpy)_2$ moieties to produce the corresponding cations. The amino acid acts as a bidentate N,O-donor, leading to a five-membered metallocycle. A six-membered imine Ru(III) metallocycle was obtained by reduction of an oxime with $RuCl_2(PPh_3)_3$.**[72]**

The chemistry of ruthenium complexes incorporating edta, or related ligands such as pac, is generally based on substitution reactions of the water ligand present in the coordination sphere of the metal. The catalytic properties of these complexes in various organic transformations have been exploited, including electrocatalytic studies.**[73]**

The trispyrazolyl borate chemistry (*see* ***Boron–Nitrogen Compounds***) of ruthenium has prospered mainly during the last decade and is mostly restricted to ruthenium (II). The most common coordination mode of the tripyrazolylborates (Tp) ligand is the $\kappa^3(N,N',N'')$ mode (see structure (**32**)), but there are also some examples of the $\kappa^3(N,N',H)$ and κ^2(N,H) (see structure (**33**)) modes.**[74,75]** Two principal areas have been explored: the search for new polyhydrides and the organometallic reactivity of TpRu precursors. A rare example of a stable bis(dihydrogen) complex $Tp^*RuH(H_2)_2$ (**32**) could be isolated. Its chemistry is dominated by the electrophilic character of the hydride and dihydrogen ligands, as illustrated by the rapid exchange in deuterated solvents or by the absence of protonation by acids. A series of substituted complexes $[Tp^*RuH(H_2)L]$ could be obtained (L = PCy_3, tetrahydrothiophene (THT), py, $NHEt_2$). (**32**) catalyzes the reduction of ketones in mild conditions either by H_2 or by H_2 transfer from alcohols.**[74]** Cationic Tp complexes of the general formula $[TpRu(H_2)LL']^+$ were obtained by protonation of the corresponding hydrides.**[76]** TpRuCl(cod) is a precursor of choice for inducing a rich organometallic reactivity, which has been reviewed. Tp complexes accommodating carbon single or double bonds have been obtained and various catalytic coupling reactions were performed.**[77]** Another precursor of choice is $TpRuCl(PPh_3)_2$, whose synthesis has been described in ‘Inorganic Synthesis’.**[78]** BpRuH(cod) is a valuable precursor for a series of bispyrazolyl BpRu complexes in which the Bp ligand is able to coordinate with the ruthenium using three different modes: $\kappa^3(N,N',\mathrm{H})$, κ^2(N,H), or $\kappa^2(N,N')$.**[79]**

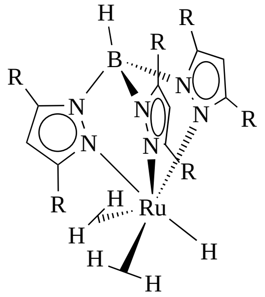

(**32**)

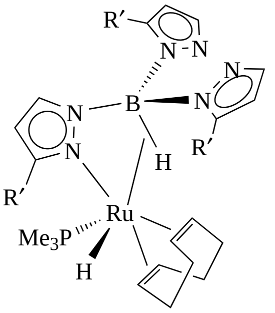

(**33**)

Nitriles, specifically acetonitrile, play an important role as solvents in inorganic chemistry. Nitriles are therefore found as co-ligands in various ruthenium complexes. $[RuCl_2(MeCN)_4]$ is readily prepared by reduction of $RuCl_3{\cdot}3H_2O$ in acetonitrile using different methods, a convenient one being the use of dihydrogen and Adam’s catalyst (PtO_2). This complex is an excellent well-defined ruthenium(II) starting material.

6 RUTHENIUM COMPLEXES OF PHOSPHORUS-DONOR LIGANDS (*See P-donor Ligands*)

The chemistry of ruthenium (II) complexes incorporating P-donor ligands, particularly phosphines and diphosphines, is flourishing. This class of compounds has given rise to a versatile organometallic reactivity. They are also found in many catalytic cycles, but decoordination of the phosphine from the coordination sphere of the metal is often required for the catalysis to proceed.

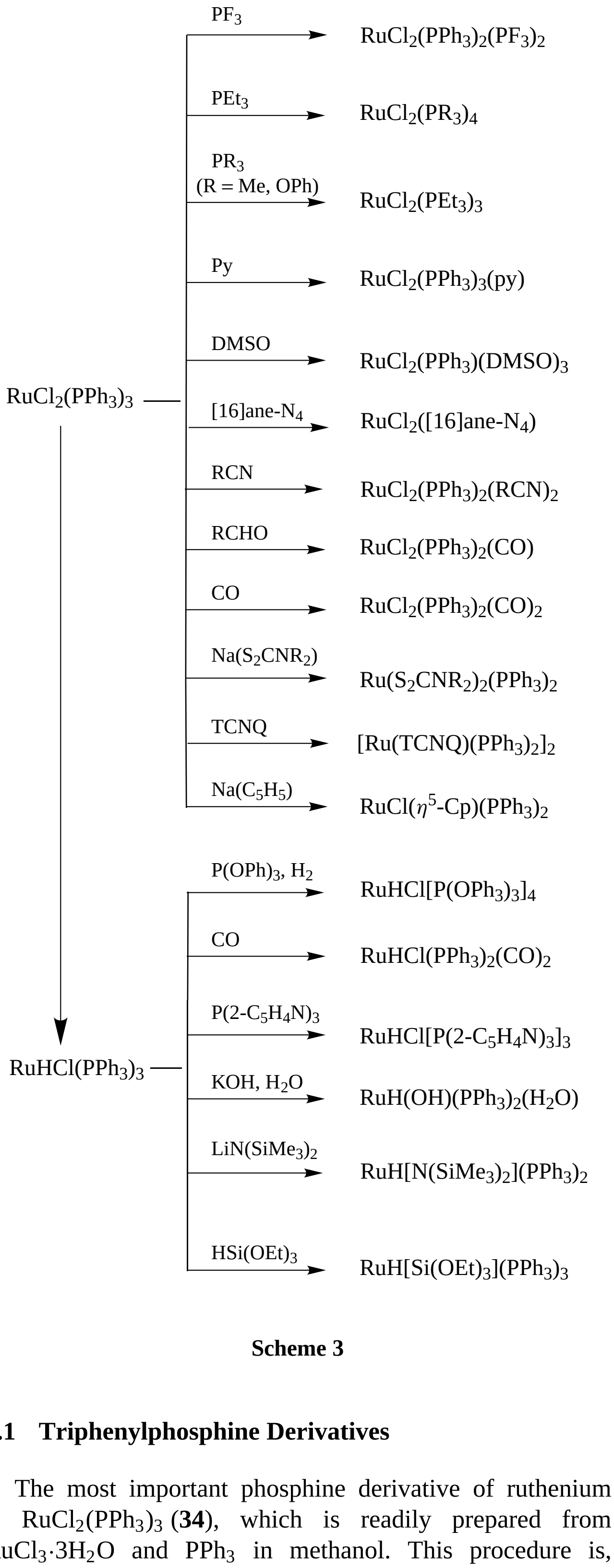
PF3
RuCl2(PPh3)2(PF3)2
PEt3
RuCl2(PR3)4
PR3
(R = Me, OPh)
RuCl2(PEt3)3
Py
RuCl2(PPh3)3(py)
DMSO
RuCl2(PPh3)(DMSO)3
RuCl2(PPh3)3
[16]ane-N4
RuCl2([16]ane-N4)
RCN
RuCl2(PPh3)2(RCN)2
RCHO
RuCl2(PPh3)2(CO)
CO
RuCl2(PPh3)2(CO)2
Na(S2CNR2)
Ru(S2CNR2)2(PPh3)2
TCNQ
[Ru(TCNQ)(PPh3)2]2
Na(C5H5)
RuCl(η5-Cp)(PPh3)2
P(OPh)3, H2
RuHCl[P(OPh3)3]4
CO
RuHCl(PPh3)2(CO)2
P(2-C5H4N)3
RuHCl[P(2-C5H4N)3]3
RuHCl(PPh3)3
KOH, H2O
RuH(OH)(PPh3)2(H2O)
LiN(SiMe3)2
RuH[N(SiMe3)2](PPh3)2
HSi(OEt)3
RuH[Si(OEt)3](PPh3)3

Scheme 3

6.1 Triphenylphosphine Derivatives

The most important phosphine derivative of ruthenium is $RuCl_2(PPh_3)_3$ (**34**), which is readily prepared from $RuCl_3{\cdot}3H_2O$ and PPh_3 in methanol. This procedure is, however, not generally used since large basic phosphines (P^iPr_3, PCy_3) lead to alcohol decarbonylation, whereas trichloro-bridged ruthenium(III) dimers are obtained by using small basic phosphines such as PMe_2Ph. $RuCl_2(PPh_3)_3$ (**34**) has found wide use as a precursor for other ruthenium(II) complexes and as a catalyst precursor for various reactions, essentially associated with hydrogenation or hydrogen transfer (*see* ***Hydrogenation & Isomerization of Alkenes***). $RuCl_2(PPh_3)_3$ can undergo three types of elementary reactions: (1) nucleophilic substitution of chloride groups, (2) addition of two-electron donor ligands, and (3) substitution of triphenylphosphine ligands and, usually, a combination of the three of them. Selected examples are shown in Scheme 3. The structure of (**34**) can be considered as octahedral, one hydrogen atom of a phenyl ring of a phosphine occupying the vacant coordination site. However, the Ru–H distance is long (2.59 Å), indicating a very weak agostic interaction. Additional structural information can be gained on (**34**) and related complexes by ^{31}P CP/MAS NMR spectroscopy.**[80]** It is remarkable that the use of ortho-methyl substituents has allowed the isolation of the first complex with two Ru···H–C agostic interactions $RuCl_2\{PPh_2(2,6\text{-}Me_2C_6H_3)\}_2$ (**35**), as demonstrated by NMR and X ray.**[81]** $RuCl_2(PPh_3)_3$ was one of the first transition metal complexes shown to activate dihydrogen heterolytically. The mechanism involves deprotonation from a transient unstable dihydrogen complex (*see* ***Dihydrogen Complexes & Related Sigma Complexes***). As shown in Scheme 3, some or all of the phosphine ligands can be substituted by various ligands. This includes diop, which leads to $[\{RuCl_2(diop)\}_2(\mu\text{-diop})]$, and various bidentate phosphines (L_2), leading to complexes of the general formula $RuCl_2L_2(PPh_3)_2$ or $RuCl_2(L_2)_2$.

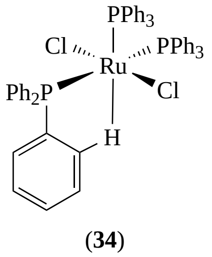
PPh3
Cl
PPh3
Ru
Ph2P
Cl
H

(**34**)

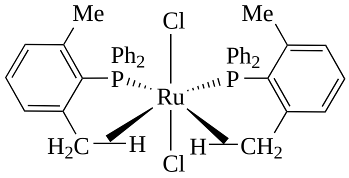
Me
Cl
Me
Ph2
P
Ph2
P
Ru
H2C
H
H
CH2
Cl

(**35**)

Phosphine substitution by water-soluble ligands has been used for the design of new catalysts that could be recovered from the aqueous phase. Extensive intra- and intermolecular hydrogen bonding are responsible of the high water solubility of a secondary–tertiary hydroxymethylphosphine complex, $[Ru\{P(CH_2OH)_3\}_2\{P(CH_2OH)_2H\}_2Cl_2]$.**[82]** The most important class of water-soluble ligands incorporates sodium sulfonate groups, with tppts being the preferred ligand. The complexes $RuCl_2(tppts)_3$, $[RuCl_2(tppts)_2]_2$, $RuHX(tppts)_3$ ($X = Cl$, I, OAc), and $RuH_2(tppts)_4$ can be prepared, and these display a reactivity in water similar to that of triphenylphosphine complexes in organic solvents, with, in some cases, an increase in activity and enhanced regioselectivity.**[83]**

The reaction of $RuCl_2(PPh_3)_3$ with diphenylcyclopropene led to the isolation of the alkylidene complex, whereas addition of an aryldiazoalkane allowed the formation of the benzylidene catalyst (see Scheme 4). These complexes are the first members of the $L_2X_2Ru{=}CHR$ family that has led to impressive developments, mainly by R. Grubbs' group, in the field of olefin metathesis (*see* ***Carbene Complexes***; ***Metathesis Polymerization Processes by Homogeneous Catalysis***; ***Organic Synthesis Using Metal-mediated Metathesis Reactions***, and ***Ruthenium: Organometallic Chemistry***).[84]

$RuCl_2(PPh_3)_3$ and $RuHCl(PPh_3)_3$ display a large catalytic activity. $RuHCl(PPh_3)_3$ is one of the most active alkene hydrogenation catalysts, while $RuCl_2(PPh_3)_3$ is of special use for hydrogen transfer reactions, in particular, the hydrogenation of bulky or functional compounds (equation 1) (*see* ***Hydrogenation & Isomerization of Alkenes***). $RuCl_2(PPh_3)_3$ is also a catalyst for hydrosilation (*see* ***Hydrosilation Catalysis***), although it is slow; chlorocarbon addition to alkenes; and even oxidation.

$$RR'CHOH + MeCH{=}CMeCO_2H \xrightarrow{RuCl_2(PPh_3)_3} RR'CO + MeCH_2CHMeCO_2H \qquad (1)$$

6.2 Diphosphine Complexes

A large number of bidentate phosphine ligands accommodate ruthenium in various oxidation states and in mono- or dinuclear structures. Some can be found in the same complex as both a monodentate and a bidentate ligand. The number of Ru(III) complexes is rather limited, but a series of $RuCl_3(P–P)L$ complexes have been prepared with $P–P$ = dppb or diop. In the case of $L = H_2O$, the X-ray structure shows that the aqua ligand forms hydrogen bonds with two chloro ligands of a neighboring molecule (*see* ***Hydrogen Bonding & Dihydrogen Bonding***). The exchange coupling between the two Ru III centers is evidenced by ESR data.[85] The most important family is represented by complexes of the general formulation $RuX_2(L–L)_2$. Since the earlier work by Chatt *et al.*, a wide range of cis and trans $RuX_2(L–L)_2$ complexes have been synthesized by the reaction of $RuCl_3{\cdot}3H_2O$, $RuCl_2(PPh_3)_3$, $RuCl_3(py)_4$, or $K_2RuCl_5(OH_2)$ with L–L in alcoholic solution (L–L = dppm, dppe, dppp, dmpe, etc.). Elegant studies involving laser flash photolysis and matrix isolation show the importance of $RuH_2(L–L)_2$ complexes in C–H bond activation. Dihydrogen loss and formation of square-planar $Ru(L–L)_2$ intermediates are induced by photolysis (*see* ***Photochemistry of Transition Metal Complexes*** and ***Alkane Carbon–Hydrogen Bond Activation***).[86] A few ruthenium complexes incorporating trans-spanning diphosphine ligands have been synthesized. However, the advantages of using such peculiar ligands remain to be demonstrated.[87]

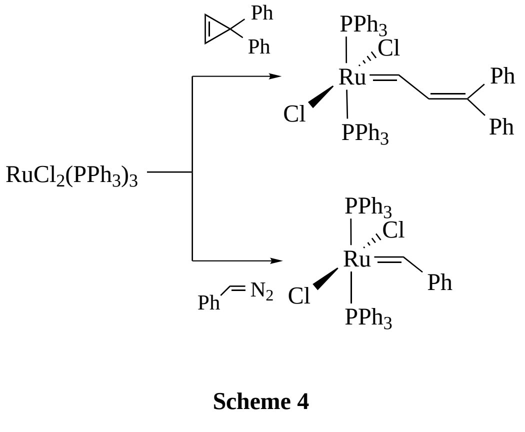

Scheme 4

The most significant industrial applications come from Noyori *et al.*, who have described ruthenium complexes bearing chiral BINAP ligands (*see* ***Asymmetric Synthesis by Homogeneous Catalysis***).[88,89] Noyori shared the Nobel Prize for chemistry in 2001 with Knowles and Sharpless for his achievements in asymmetric catalysis. BINAP–Ru dihalide catalysts have a very wide scope in industrial applications. The first key complexes, (**36**) and (**37**), were obtained in good yield by the reaction of $[RuCl_2(cod)]_n$ with (*S*)-or (*R*)-BINAP and triethylamine at 110 °C, followed by final treatment with sodium acetate in *t*-butyl alcohol at 80 °C. The crystal structure of $[Ru(OCO\text{-}{}^tBu)_2\{(S)\text{-BINAP}\}]$ indicates a C2 chirality. They are very effective catalysts in the hydrogenation of alkenes or ketones (*see* ***Hydrogenation & Isomerization of Alkenes***). For example, the synthesis of the anti-inflammatory drug Naproxen is achieved quantitatively in 97% optical yield.

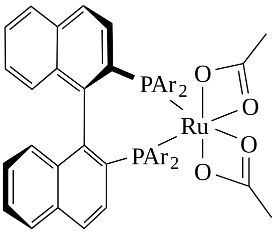

(**36**) (*R*)-BINAP Ru^{II} complex

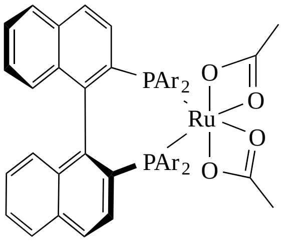

(**37**) (*S*)-BINAP Ru^{II} complex

These Ru-catalysts provide a practical way to prepare an intermediate for prostaglandin synthesis. Antibacterials and carbapenem antibiotics are now produced industrially. New achievements have been obtained with the introduction of diamine ligands, leading to the asymmetric synthesis of various pharmaceutical compounds. The catalyst mixture, as shown in Scheme 5, consists of a complex of the form $RuCl_2$(diamine)(diphosphine) with an alkoxide base, dihydrogen, and ketone in 2-propanol (*see* ***Asymmetric Synthesis by Homogeneous Catalysis***).[88,89] An in-depth mechanistic study was performed by Morris' group, leading to a better understanding of the catalytic cycle as depicted

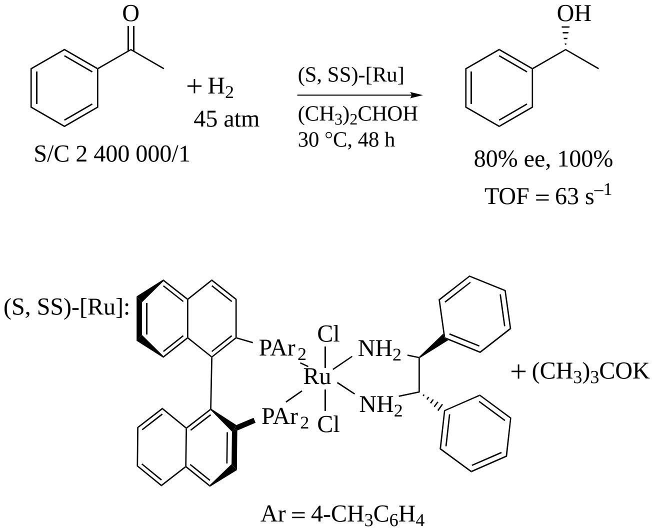

Scheme 5

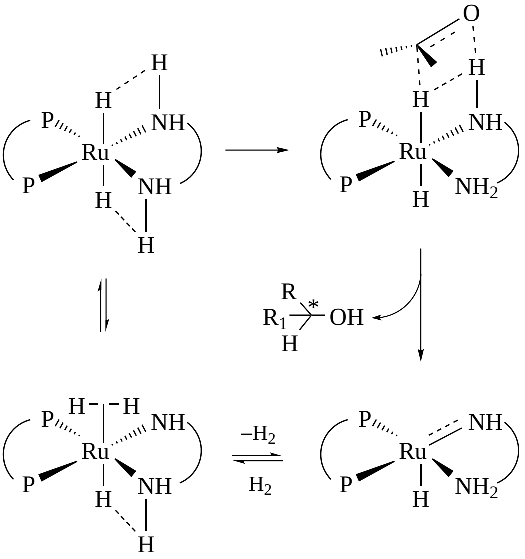

Scheme 6

in Scheme 6.[90] The use of the water-soluble dibenzofuran-based diphosphine ligands (BIFAPS) leads to high ee's in Ru-catalyzed hydrogenations (similar to BINAP).[91]

6.3 Polydentate Phosphines, Pincer Ligands, Phosphorus Heterocycles, and Phosphorus-based Hemilabile Ligands

The use of polydentate phosphines has received a renewed interest, with the search for new families of polyhydrides or molecular dihydrogen complexes (*see* ***Dihydrogen Complexes & Related Sigma Complexes***). For example, PP_3RuCl_2 ($PP_3 = P(CH_2CH_2PPh_2)_3$) was used as an entry to mono- and polyhydride ruthenium(II) complexes. The Ru (II) complex [(triphos)RuH(BH_4)] with the tripodal ligand triphos reacts with KO^{t}Bu to form the ruthenate complex [K(triphos)RuH_3]. The compound catalyzes benzothiophene hydrogenolysis into 2-ethylthiophenol.[92] Various ruthenium complexes containing a triphosphine ligand deriving from $PPh(CH_2CH_2PR_2)_2$ and $PPh(CH_2CH_2CH_2PR_2)_2$ have been prepared, including chiral ligands. The ability of the polydentate phosphine to control the stereochemistry and coordination number of the resulting complexes, and the presence of hydride and/or dihydrogen ligands provide access to unusual chemical (homogeneous catalysis) and structural properties.[93] A series of complexes incorporating a rigid allene-bridged polyphosphine exhibit room-temperature luminescence.[94]

During the past decade, the chemistry of complexes incorporating phosphine-based pincer ligands has rapidly developed. Most of these ligands are cyclometalated and thus will not be reviewed in this chapter. However, various complexes incorporating PNP ligands have been prepared and show interesting spectroscopic and catalytic properties (*see* ***Phosphorus–Nitrogen Compounds***).[3,95,96] The reactivity of the ligand $(R_2PCH_2SiMe_2)_2N$– on ruthenium has now appeared. The most striking result is the characterization of a four-coordinate, planar Ru(II) displaying a triplet state as a consequence of the low-coordination number and the lack of agostic interactions (see structure (**38**)).[97]

2,2′-Biphosphinines (tmbp) are analogous to bipyridines, albeit containing two phosphorus atoms (*see* ***Phosphorus: Organophosphorus Chemistry***). These ligands behave as excellent π acceptors, and chloro ruthenium complexes incorporating one or two tmbp could be isolated. The most significant result was obtained using the reduced ligand, and stabilization of a dianionic Ru complex was achieved. The complex $[Ru(tmbp)_2][Li(THF)_3]_2$ (**39**) presents a square-planar geometry with electrostatic interaction between Ru and Li centers.[98]

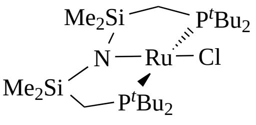

(**38**)

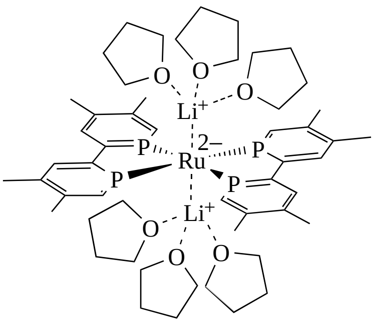

(**39**)

The synthesis of hemilabile ligands for the design of new catalysts is a very active area of research. Hemilabile ligands act as chelating ligands with one strongly and one weakly bonding group (see Structures (**40**) and (**41**)). The weakly bonding group can be easily displaced, offering new opportunities for catalytic applications. In this context, the chemistry of mixed phosphorus chelating ligands has been particularly examined (*see* ***Mixed Donor Ligands***). The most common type concerns the phosphorus–oxygen association, while systems with phosphorus–sulfur or phosphorus–nitrogen ligands are more limited. A common reaction involves PPh_3 substitution by the hemilabile ligand L from $RuCl_2(PPh_3)_3$ or from $RuHCl(PPh_3)_3$.[99]

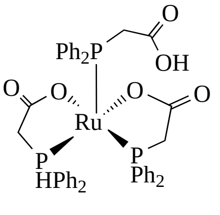

(**40**)

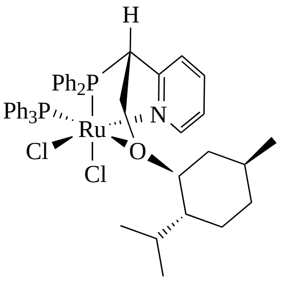

(**41**)

7 RUTHENIUM COMPLEXES OF GROUP-14 LIGANDS

Carbonyl complexes and complexes incorporating isocyanides are generally considered to be organometallic and are not reviewed in this article (*see* ***Ruthenium: Organometallic Chemistry*** and ***Carbonyl Complexes of the Transition Metals***). In contrast, cyanides are regarded as inorganic complexes (*see* ***Cyanide Complexes of the Transition Metals***). $K_4[Ru(CN)_6]$ was first prepared in 1896 through the action of KCN on $K_2[RuO_4]$ or $RuCl_3{\cdot}xH_2O$. Hexacyanide is found as a tetraanion with various cations or even as the tetracid. This complex undergoes a variety of substitution reactions and gives rise to cyano-bridged polynuclear compounds, either homo- or heteronuclear. Among the substitution reactions, a lot of interest has been devoted to the photophysical properties of mixed cyanide/diimine complexes.[100]

Silane activation by ruthenium complexes has been a field of intense activity over the past decade. This was made possible thanks, in particular, to the fantastic progress achieved in NMR and X-ray techniques, as well as in DFT calculations. A number of ruthenium complexes incorporating a silicon-attached ligand (*see* ***Silicon: Inorganic Chemistry***) are now available, with several variations of interactions between the silane and the metal.[101] Full oxidative addition can be observed leading to Si–H bond breaking and formation of the corresponding silyl or bis(silyl) complexes (**42**).[102] Arrested addition leads to the isolation of σ-silane complexes, analogous to the σ-dihydrogen complexes (*see* ***Dihydrogen Complexes & Related Sigma Complexes***).[103,104] Bridging and terminal SiR_2 groups (silylene complexes with Ru=Si bonds) can also be isolated.[101] The factors that promote the formation of the different structures are multiple, and the substituents on silicon and the electron density on ruthenium play a crucial role. Ruthenium complexes incorporating one, and even two, σ-Si–H bonds are now available, as shown by the general structure $[RuH_2\{(\eta^2\text{-}HSiR_2)_2X\}(PCy_3)_2]$ (**43**).[104] It is important to note that in these bis(silane) complexes, the establishment of secondary interactions between the silicon atoms and the classical hydrides stabilize the complexes and promote the unusual cis position of the bulky phosphines.[105]

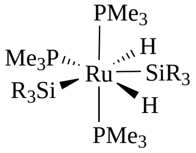

(**42**)

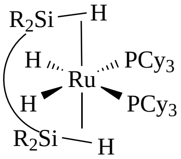

(**43**)

Unusual redistribution at silicon is observed by adding secondary silanes to the bis(dihydrogen) complex $RuH_2(H_2)_2(PCy_3)_2$ (see Section 8).[106] The complex $[RuH_2(PR_3)_2]_2(\mu\text{-}\eta^2:\eta^2:\eta^2:\eta^2\text{-}SiH_4)$ (**44**) (R = Cy, ^{i}Pr) is isolated with the SiH_4 ligand trapped in between the two metals. The silane is coordinated to the metals via four σ-Si–H bonds. Each interaction involves σ-donation to a ruthenium and back-bonding from the other ruthenium. A second redistribution process is observed after addition of an excess of $HSi(OMe)_3$ to (**44**). The dinuclear complex (**45**) is isolated, and the data show that the frontiers between true σ-Ru–H–Si interactions and more delocalized systems are not clear-cut (see Scheme 7).[106] Silyl and σ-silane complexes find important applications as catalyst precursors for Si–C coupling in hydrosilylation, dehydrogenative silylation, and dehydrocoupling for the formation of vinyl silanes and oligomeric carbosilanes, respectively (*see* ***Hydrosilation Catalysis***; ***Carbon–Carbon & Carbon–Heteroatom Activation***, and ***Polysiloxanes & Polysilanes***).

In comparison to Si, much less work has been published concerning Ge or Sn (*see* ***Germanium: Organometallic Chemistry*** and ***Tin: Organometallic Chemistry***). The complex $Ru(GeMe_3)_2(PMe_3)_4$ is an effective catalyst for the production

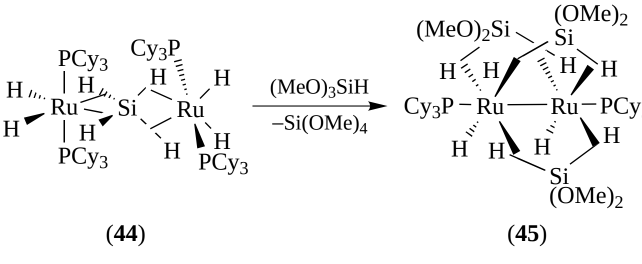

(**44**) (**45**)

Scheme 7

of high molecular weight polygermanes from $HGeMe_3$.[107] A number of complexes incorporating the $RuSnR_3$ moiety have been prepared. A rare example of a complex (**46**) containing a four-electron tridentate tin donor ligand was isolated,[108] and more recently, the complex $Ru(SnPh_3)_2(P_2C_2Ph_2)_2$ with two $SnPh_3$ units and a bis(diphosphabutadiene) ligand was reported.[109]

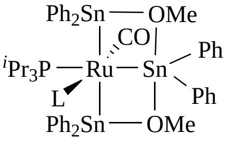

(**46**)

8 RUTHENIUM HYDRIDE COMPLEXES (*See Hydride Complexes of the Transition Metals* and *Dihydrogen Complexes & Related Sigma Complexes*)

The rich chemistry of ruthenium hydride developed rapidly after the preparation of $RuHCl(PPh_3)_3$.[1] The polyhydrides $RuH_2(PPh_3)_4$ and $RuH_4(PPh_3)_3$ were synthesized by reduction of $RuCl_2(PPh_3)_3$ with hydride donor reagents such as $NaBH_4$. The dihydride $RuH_2(PPh_3)_4$ can be used as an interesting alternative to conventional Lewis acid and base catalysts, as proven by its specific activity for nitrile activation.[110] Numerous hydrido derivatives containing other anionic functional ligands were prepared, either by anionic substitution of chloride on $RuHCl(PPh_3)_3$ or by reaction of the polyhydrides with acidic compounds (equation 2). The synthesis of hydride complexes, using $(BH_4)^-$ or $(AlH_4)^-$, may involve the formation of $Ru-BH_4$ or $Ru-AlH_4$ derivatives with one or two bridging hydrides. The method of preparation by reduction of chloride precursors has allowed the synthesis of derivatives of alkyl phosphines with a small cone angle, for example, $RuH_2(PBu_3)_4$. However, for bulky alkylphosphine derivatives, the preparation involves hydrogenation of the ruthenium(0) precursor $Ru(C_8H_{10})(C_8H_{12})$ (see equation 3).

$$RuH_2(L)(PPh_3)_3 + HX \longrightarrow RuHX(PPh_3)_3 + L + H_2 \qquad (2)$$

$$X = OCOR, SH, SR, Cl, etc; L = H_2, N_2, PPh_3$$

$$Ru(C_8H_{10})(C_8H_{12}) \xrightarrow{H_2,\ 2PCy_3} RuH_2(H_2)_2(PCy_3)_2 \qquad (3)$$

The discovery by Kubas of the coordination of dihydrogen without dissociation gave a new impetus to ruthenium hydride chemistry (*see* ***Dihydrogen Complexes & Related Sigma Complexes***).[111] As mentioned already in Section 7, considerable progress in NMR and X-ray techniques have allowed better characterization of many compounds and, in particular, better discrimination between a dihydride or a dihydrogen formulation. In addition, many more theoretical studies are now performed on polyhydrides and σ-complexes. Key information is thus gained, not only on the structures and energetics but also on the dynamic processes that are common in these systems.[105,112] $RuH_4(PPh_3)_3$ was mentioned as early as 1976 by Ashworth and Singleton as possibly containing undissociated dihydrogen. This was confirmed 10 years later by Crabtree and Hamilton who reformulated it as $RuH_2(H_2)(PPh_3)_3$. Similarly, $RuH_6(PCy_3)_2$ was reformulated as $RuH_2(H_2)_2(PCy_3)_2$ (**47**), a rare example of a thermally stable bis-dihydrogen complex (see equation 3). This complex displays a versatile reactivity, in some cases, similar to $RuH_2(H_2)(PPh_3)_3$ and $RuH_2(N_2)(PPh_3)_3$ (see Scheme 8). In particular, it reacts with halocarbons and thiols to give the corresponding 16-electron dihydrogen complexes, $RuH(H_2)X(PCy_3)_2$ ($X = Cl$, I, SR). The chemistry of (**47**) was reviewed in 1998 before the report of its X-ray crystal structure in 2000.[74,113] The reactivity of (**47**) with silanes leading to the formation of new σ-silane complexes and to interesting catalytic applications has been briefly described in Section 7.[103–106] It was also possible to activate various boranes, both stoichiometrically and catalytically (*see* ***Boron Hydrides***; ***Boron: Organoboranes***, and ***Hydroboration Catalysis***).[114,115] Remarkably, a complex incorporating two boron-attached ligands coordinated with two different bonding modes, $[RuH\{(\mu-H)_2Bpin\}(\sigma-HBpin)(PCy_3)_2]$, was isolated and proved to be an active species for catalytic formation of vinyl boranes or for selective hydroboration of olefins.[114] (**47**) is also a catalyst precursor for the hydrogenation of S- and N-heteroaromatic substrates (*see* ***Hydrodesulfurization & Hydrodenitrogenation***).[31,116] The presence of labile dihydrogen ligands is the key factor in the ability of (**47**) to catalyze, at room temperature, the Murai reaction (C–C bond coupling of an olefin with a functionalized aromatic compound. *See* ***Carbon–Carbon & Carbon–Heteroatom Activation*** and ***Ruthenium: Organometallic Chemistry***). In the case of acetophenone, the resulting orthometalated complex $RuH(H_2)(o-C_6H_4C(O)Me)(PCy_3)_2$ displays remarkable spectroscopic properties as exchange couplings between the hydride and the coordinated dihydrogen molecule can be detected by NMR.[117]

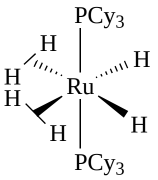

(**47**)

Ruthenium polyhydride complexes containing monophosphaferrocenes are now available.[118] In contrast to Cp ruthenium chemistry, the use of a trispyrazolyborate ligand favors the formation of dihydrogen structures: the chemistry of Tp

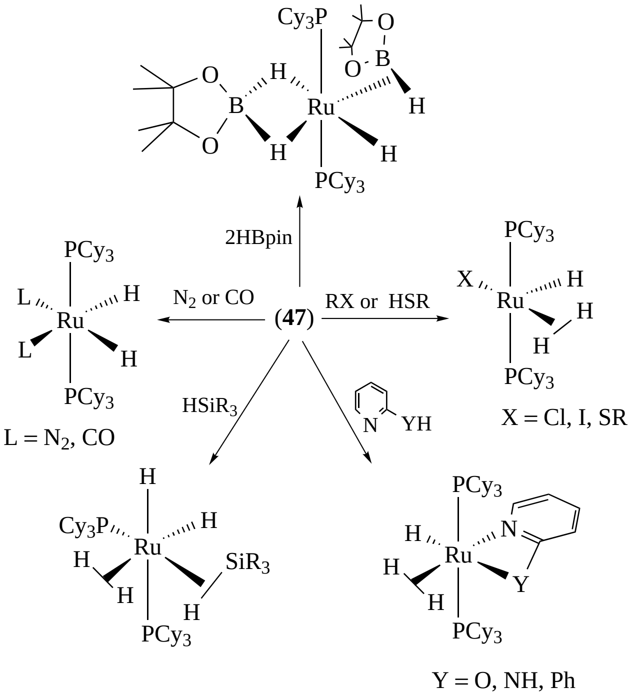

Scheme 8

and Bp ruthenium complexes has been briefly described in Section 5.4.[74–79]

Anionic polyhydride derivatives were obtained by reaction of potassium naphthalenide with $RuHCl(PPh_3)_3$ in THF. Addition of H_2 yields the trihydride $[RuH_3(PPh_3)_3]^-$, whereas the intermediacy of a diphenylbutadiene derivative is necessary to reach the pentahydride $[RuH_5(PPh_3)_2]^-$ after elimination of one phosphine ligand. A one-pot reaction was obtained by using a mixture of $RuCl_3$/2.5 P^iPr_3, KH, and a crown ether under a dihydrogen atmosphere. Interion proton hydride NH···HRu interactions exist in the salts $[K(Q)][RuH_5(P^iPr_3)_2]$ when Q is 1-aza-18-crown-6 or 1,10-diaza-18-crown-6.[119]

Cationic derivatives are prepared by protonation (which can lead to dihydrogen evolution) or by halide abstraction in the presence of dihydrogen. The cations $[RuH_3L_4]^+$ and $[RuH_5L_3]^+$ can be prepared by one of these methods. Most of the $[RuH_3L_4]^+$ complexes have now been reformulated as $[RuH(H_2)L_4]^+$. An important class of hydride derivatives contains chelating phosphorus-donor groups. Thus, the neutral $RuHX(L_2)_2$ ($X = H$, Cl; $L_2 =$ dppm, dppe, dcype, etc.) can adopt a cis or a trans configuration, but the corresponding cationic dihydrogen species ($[RuX(H_2)(L_2)_2]^+$) all display a trans configuration. These compounds were extensively studied, and $[RuH(H_2)(dppe)_2]^+$ (**48**) is one of the few complexes characterized by a neutron diffraction structure.[120] Dicationic complexes, as shown in structure (**49**), can also be prepared, and they display even more acidic properties than many cationic complexes.[121] The use of an acidic dihydrogen ruthenium complex as catalyst results in heterolytic cleavage of H_2 and, for example, in catalytic hydrogenolysis of trimethylsilyl enol ethers.[122] A review was published in 1998 on the properties of dihydrogen complexes as homogeneous reduction catalysts (*see* ***Hydrogenation & Isomerization of Alkenes***).[123] NMR methods play a major role in the characterization of polyhydrides (J_{H-D}, T_1; rate of intramolecular exchange; rate of exchange with other incoming ligands). The parahydrogen-induced polarization (PHIP) method is a relatively new NMR technique that can also bring valuable information on the detection of intermediates. It can be used as a mechanistic probe in highly fluxional systems, as was illustrated in ruthenium hydride carbonyl systems.[124]

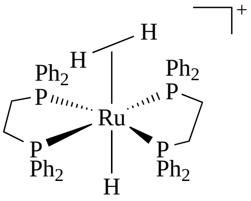

(48)

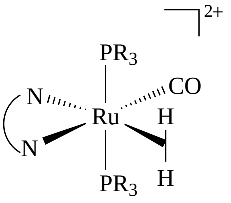

(49)

Unusual ruthenium porphyrin dihydrogen complexes were also obtained.[111] Dinuclear hydride or dihydrogen complexes generally result from the dimerization of hydride and/or chloride precursors. A number of bioctahedral complexes of central core $Ru(\mu\text{-}X)_3Ru$ have thus been prepared. The properties of the dinuclear complex $[RuHCl(P^iPr_3)_2]_2$ have been extensively studied by Caulton's group, and a rich organometallic chemistry has been reported.[125] Ruthenium hydride complexes have been used to prepare heterobimetallic complexes. Three strategies have been employed: (1) use of a ruthenium anion and reaction with transition metal chloride derivative or vice versa, (2) addition of Lewis acidic cations to ruthenium hydrides, and (3) use of bridging ligands. The mixture of *cis*- and *trans*-$RuH_2(dppm)_2$ is, for example, able to react with a variety of metallic fragments to yield mono- or bis-dppm-bridged hydrido species. An unusual example of a ruthenium–iridium complex, a mixed hydrido-alkoxide bridge, was reported.[126]

Hydrogen bonding is a well-known phenomenon that has led to major developments during the last decade in the field of polyhydrides. The formation of the so-called dihydrogen bond (M–H···H–X) can occur intermolecularly between a hydride and a weak acid (see equation 4) or intramolecularly between a hydride and a pendant ligand with an NH or OH group. This type of interaction is very important as it may control reactivity and selectivity in solution. A few examples have appeared in ruthenium chemistry.[127,128]

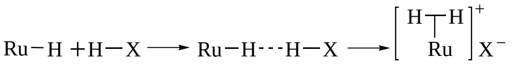

$$Ru{-}H + H{-}X \longrightarrow Ru{-}H{\cdots}H{-}X \longrightarrow \left[\overset{H-H}{Ru}\right]^+ X^- \qquad (4)$$

9 POLYNUCLEAR COMPLEXES OF RUTHENIUM

The chemistry of ruthenium carbonyl clusters is presented in ***Ruthenium: Organometallic Chemistry*** and ***Polynuclear Organometallic Cluster Complexes***, so the subject of metal particles deposited on supports will not be described in this article (*see* ***Ruthenium: Organometallic Chemistry*** and ***Polynuclear Organometallic Cluster Complexes***). The field concerning giant clusters and the molecular chemistry of metal particles in organic solutions has grown rapidly during the last decade. The ruthenium complex $Ru(C_8H_{10})(C_8H_{12})$, as shown by Chaudret *et al*., has been found to be a useful precursor for the controlled synthesis of well-dispersed nanoparticles stabilized by polymers or various ligands. Recent developments have shown that some of these compounds may be viewed as large inorganic clusters composed of a core of a few nanometers adopting the hcp structure of bulk ruthenium and a surface accommodating both ancillary ligands such as amines and thiols as well as active ligands such as hydrides. These species are active catalysts, in particular, for arene hydrogenation.[129,130] It is, in general, still difficult to distinguish between homogeneous and colloidal catalysis in such systems, although significant progress has recently been made, in particular, by Finke.[131]

10 RELATED ARTICLES

Asymmetric Synthesis by Homogeneous Catalysis; Coordination Chemistry: History; Coordination & Organometallic Chemistry: Principles; Dihydrogen Complexes & Related Sigma Complexes; Electron Transfer in Coordination Compounds; Electron Transfer Reactions: Theory; Heterogeneous Catalysis by Metals; Hydride Complexes of the Transition Metals; Luminescence; Luminescence Behavior & Photochemistry of Organotransition Metal Compounds; Photochemistry of Transition Metal Complexes; Ruthenium: Organometallic Chemistry.

11 REFERENCES

1. E. A. Seddon and K. R. Seddon, in ‘The Chemistry of Ruthenium’, ed. R. J. H. Clark, Elsevier, Amsterdam, 1984.
2. M. Schröder and T. A. Stephenson, in ‘Comprehensive Coordination Chemistry’, eds. G. Wilkinson, R. D. Gillard, and J. A. McCleverty, Pergamon Press, Oxford, 1987, Vol. 4, p. 277.
3. C. E. Housecroft, in ‘Comprehensive Coordination Chemistry II’, eds. T. J. Meyer and J. A. McCleverty, Pergamon Press, Oxford, 2003, Vol. 5, p. 555.
4. C.-M. Che and T.-C. Lau, in ‘Comprehensive Coordination Chemistry II’, eds. T. J. Meyer and J. A. McCleverty, Pergamon Press, Oxford, 2003, Vol. 5, p. 733.
5. K. Wohnrath, M. Peres de Araujo, L. R. Dinelli, A. A. Batista, I. de Sousa Moreira, E. E. Castellano, and J. Ellena, *J. Chem. Soc., Dalton Trans.*, 2000, 3383.
6. W. J. Casteel Jr, D. H. Lohmann, and N. Bartlett, *J. Fluorine Chem.*, 2001, **112**, 165.
7. N. A. Jasim, R. N. Perutz, and S. J. Archibald, *Dalton Trans.*, 2003, 2184.
8. C. Becker, I. Kieltsch, D. Broggini, and A. Mezzetti, *Inorg. Chem.*, 2003, **42**, 8417.
9. W. P. Griffith, *Chem. Soc. Rev.*, 1992, **21**, 179.
10. S. V. Ley, C. Ramarao, and M. D. Smith, *Chem. Commun.*, 2001, 2278.
11. J. Haines, J. M. Leger, M. W. Schmidt, J. P. Petitet, A. S. Pereira, J. A. H. Da Jordana, and S. Hull, *J. Phys. Chem. Solids*, 1998, **59**, 239.
12. H. E. Toma, K. Araki, A. D. P. Alexiou, S. Nikolaou, and S. Dovidauskas, *Coord. Chem. Rev.*, 2001, **219–221**, 187.
13. R. A. Binstead, C. W. Chronister, J. Ni, C. M. Hartshorn, and T. J. Meyer, *J. Am. Chem. Soc.*, 2000, **122**, 8464.
14. J. T. Groves, K. Shalyaev, and J. Lee, in ‘The Porphyrin Handbook’, eds. K. M. Kadish, K. M. Smith, and R. Guilard, Academic Press, San Diego, CA, 2000, Vol. 4, p. 17.
15. J.-L. Zhang, H.-B. Zhou, J.-S. Huang, and C. M. Che, *Chem. – Eur. J.*, 2002, **8**, 1554.
16. C. M. Che, W. Y. Yu, P. M. Chan, W. C. Cheng, S. M. Peng, K. C. Lau, and W. K. Li, *J. Am. Chem. Soc.*, 2000, **122**, 11380.
17. T. J. Meyer and M. H. V. Huynh, *Inorg. Chem.*, 2003, **42**, 8140.
18. A. J. Bailey, W. P. Griffith, and P. D. Savage, *J. Chem. Soc., Dalton Trans.*, 1995, 3537.
19. N. C. Zanetti, F. Spindler, J. Spencer, A. Togni, and G. Rihs, *Organometallics*, 1996, **15**, 860.
20. M. A. S. Aquino, *Coord. Chem. Rev.*, 1998, **170**, 141.
21. M. B. France, R. A. Paciello, and R. H. Grubbs, *Macromolecules*, 1993, **26**, 4739.
22. J. R. Fulton, A. W. Holland, D. J. Fox, and R. G. Bergman, *Acc. Chem. Res.*, 2002, **35**, 44.
23. R. A. Sheldon, I. W. C. E. Arends, G.-J. ten Brink, and A. Dijksman, *Acc. Chem. Res.*, 2002, **35**, 774.
24. P. A. Reynolds, J. W. Cable, A. N. Sobolev, and B. N. Figgis, *J. Chem. Soc., Dalton Trans.*, 1998, 559.
25. P. Majumdar, L. R. Falvello, M. Tómas, and S. Goswami, *Chem. – Eur. J.*, 2001, **7**, 5222.
26. W. H. Leung, H. G. Zheng, J. L. C. Chim, J. Chan, W. T. Wong, and I. D. Williams, *J. Chem. Soc., Dalton Trans.*, 2000, 423.
27. K. Matsumoto, T. Koyama, and Y. Koide, *J. Am. Chem. Soc.*, 1999, **121**, 10913.
28. H. Torrens, *Coord. Chem. Rev.*, 2000, **196**, 331.

29. Q.-F. Zhang, C.-Y. Lai, W.-Y. Wong, and W.-H. Leung, *Organometallics*, 2002, **21**, 4017.
30. R. Maiti, M. Shang, and A. G. Lappin, *Chem. Commun.*, 1999, 2349.
31. A. F. Borowski, S. Sabo-Etienne, B. Donnadieu, and B. Chaudret, *Organometallics*, 2003, **22**, 4803.
32. D. C. Mudalige, E. S. Ma, S. J. Rettig, B. R. James, and W. R. Cullen, *Inorg. Chem.*, 1997, **36**, 5426.
33. C. Landgrafe and W. S. Sheldrick, *J. Chem. Soc., Dalton Trans.*, 1996, 989.
34. D. Sellmann and J. Sutter, *Acc. Chem. Res.*, 1997, **30**, 460.
35. D. Sellmann, K. Engl, T. Gottschalk-Gaudig, and F. W. Heinemann, *Eur. J. Inorg. Chem.*, 1999, 333.
36. D. P. Fairlie, W. A. Wickramasinghe, K. A. Byriel, and H. Taube, *Inorg. Chem.*, 1997, **36**, 2242.
37. M. J. Clarke, *Coord. Chem. Rev.*, 2003, **236**, 209.
38. M. Calligaris and O. Carugo, *Coord. Chem. Rev.*, 1996, **153**, 83.
39. B. Serli, E. Zangrando, T. Gianferrara, L. Yellowlees, and E. Alessio, *Coord. Chem. Rev.*, 2003, **245**, 73.
40. J. J. Rack and H. B. Gray, *Inorg. Chem.*, 1999, **38**, 2.
41. M. K. Smith, J. A. Gibson, C. G. Young, J. A. Broomhead, P. C. Junk, and F. R. Keene, *Eur. J. Inorg. Chem.*, 2000, 1365.
42. E. Tfouni, *Coord. Chem. Rev.*, 2000, **196**, 281.
43. A. B. P. Lever and S. I. Gorelsky, *Coord. Chem. Rev.*, 2000, **208**, 153.
44. S. I. Gorelsky, E. S. Dodsworth, A. B. P. Lever, and A. A. Vleck, *Coord. Chem. Rev.*, 1998, **174**, 469.
45. K. D. Demadis, C. M. Hartshorn, and T. J. Meyer, *Chem. Rev.*, 2001, **101**, 2655.
46. P. Chen and T. J. Meyer, *Chem. Rev.*, 1998, **98**, 1439.
47. W. Kaim, A. Klein, and M. Glckle, *Acc. Chem. Res.*, 2000, **33**, 755.
48. J.-P. Launay, *Chem. Soc. Rev.*, 2001, **30**, 386.
49. C. Kaes, A. Katz, and M. W. Hosseini, *Chem. Rev.*, 2000, **100**, 3553.
50. A. R. Dunn, I. J. Dmochowski, A. M. Bilwes, H. B. Gray, and B. R. Crane, *Proc. Natl. Acad. Sci. U.S.A.*, 2001, **98**, 12420.
51. P. Ceroni, A. Credi, V. Balzani, S. Campagna, G. S. Hanan, C. R. Arana, and J.-M. Lehn, *Eur. J. Inorg. Chem.*, 1999, 1409.
52. S. Serroni, S. Campagna, R. Pistone Nascone, G. S. Hanan, G. J. E. Davidson, and J.-M. Lehn, *Chem.–Eur. J.*, 1999, **5**, 3523.
53. V. Balzani, S. Campagna, G. Denti, A. Juris, S. Serroni, and M. Venturi, *Acc. Chem. Res.*, 1998, **31**, 26.
54. S. Serroni, S. Campagna, F. Puntoriero, A. Juris, G. Denti, V. Balzani, and M. Venturi, *Inorg. Synth.*, 2002, **33**, 10.
55. P. D. Beer and J. Cadman, *Coord. Chem. Rev.*, 2000, **205**, 131.
56. H. Dürr and S. Bossmann, *Acc. Chem. Res.*, 2001, **34**, 905.
57. A. Martre, H. Laguitton-Pasquier, A. Deronzier, and A. Harriman, *J. Phys. Chem. B*, 2000, **107**, 2684.
58. A. Hagfeldt and M. Grätzel, *Acc. Chem. Res.*, 2000, **33**, 269.
59. M. Grätzel, *Nature*, 2001, **414**, 338.
60. L. Sun, L. Hammarstrom, B. Akermark, and S. Styring, *Chem. Soc. Rev.*, 2001, **30**, 36.
61. M.-J. Blanco, M. C. Jiménez, J.-C. Chambron, V. Heitz, M. Linke, and J.-P. Sauvage, *Chem. Soc. Rev.*, 1999, **28**, 293.
62. D. Pomeranc, D. Jouvenot, J.-C. Chambron, J.-P. Collin, V. Heitz, and J.-P. Sauvage, *Chem. Eur. J.*, 2003, **9**, 4247.
63. P. R. Ashton, R. Ballardini, V. Balzani, A. Credi, K. R. Dress, E. Ishow, C. J. Kleverlaan, O. Kocian, J. A. Preece, N. Spencer, J. F. Stoddart, M. Venturi, and S. Wenger, *Chem. – Eur. J.*, 2000, **6**, 3558.
64. R. Ballardini, V. Balzani, A. Credi, M. T. Gandolfi, and M. Venturi, *Acc. Chem. Res.*, 2001, **34**, 445.
65. K. E. Erkkila, D. T. Odom, and J. K. Barton, *Chem. Rev.*, 1999, **99**, 2777.
66. M. Pascaly, J. Yoo, and J. K. Barton, *J. Am. Chem. Soc.*, 2002, **124**, 9083.
67. D. J. Hurley and Y. Tor, *J. Am. Chem. Soc.*, 2002, **124**, 3749.
68. T. W. Hayton, P. Legzdins, and W. B. Sharp, *Chem. Rev.*, 2002, **102**, 935.
69. E. Tfouni, M. Krieger, B. R. McGarvey, and D. W. Franco, *Coord. Chem. Rev.*, 2003, **236**, 57.
70. D. Sellmann, T. Gottschalk-Gaudig, D. Häußinger, F. W. Heinemann, and B. A. Hess, *Chem. – Eur. J.*, 2001, **7**, 2099.
71. K. Chichak, U. Jacquemard, and N. R. Branda, *Eur. J. Inorg. Chem.*, 2002, 357.
72. K. Majumder, R. J. Butcher, and S. Bhattacharya, *Inorg. Chem.*, 2002, **41**, 4605.
73. D. Chatterjee, *Coord. Chem. Rev.*, 1998, **168**, 273.
74. S. Sabo-Etienne and B. Chaudret, *Coord. Chem. Rev.*, 1998, **178–180**, 381.
75. A. Caballero, F. Gómez de la Torre, F. A. Jalón, B. R. Manzano, A. M. Rodriguez, S. Trofimenko, and M. P. Sigalas, *J. Chem. Soc., Dalton Trans.* 2001, 427.
76. G. Jia and C.-P. Lau, *Coord. Chem. Rev.*, 1999, **190–192**, 83.
77. C. Slugovc, R. Schmid, and K. Kirchner, *Coord. Chem. Rev.*, 1999, **185–186**, 109.
78. A. F. Hill and J. D. E. T. Wilton-Ely, *Inorg. Synth.*, 2002, **33**, 206.
79. V. Rodriguez, I. Atheaux, B. Donnadieu, S. Sabo-Etienne, and B. Chaudret, *Organometallics*, 2000, **19**, 2916.
80. K. S. MacFarlane, A. M. Joshi, S. J. Rettig, and B. R. James, *Inorg. Chem.*, 1996, **35**, 7304.
81. W. Baratta, E. Herdtweck, and P. Rigo, *Angew. Chem., Int. Ed. Engl.*, 1999, **38**, 1629.
82. L. Higham, A. K. Powell, M. K. Whittlesey, S. Wocadlo, and P. T. Wood, *Chem. Commun.*, 1998, 1107.

83. M. Hernandez and Ph. Kalck, *J. Mol. Catal. A: Chem.*, 1997, **116**, 131.
84. T. M. Trnka and R. H. Grubbs, *Acc. Chem. Res.*, 2001, **34**, 18.
85. L. R. Dinelli, A. A. Batista, K. Wohnrath, M. P. de Araujo, S. L. Queiroz, M. R. Bonfadini, G. Oliva, O. R. Nascimento, P. W. Cyr, K. S. MacFarlane, and B. R. James, *Inorg. Chem.*, 1999, **38**, 5341.
86. L. Cronin, J. M. Carmen Nicasio, R. N. Perutz, R. G. Peters, D. M. Roddick, and M. K. Whittlesey, *J. Am. Chem. Soc.*, 1995, **117**, 10047.
87. C. A. Bessel, P. Aggarwal, A. C. Marschilok, and K. J. Takeuchi, *Chem. Rev.*, 2001, **101**, 1031.
88. R. Noyori and T. Ohkuma, *Angew. Chem., Int. Ed. Engl.*, 2001, **40**, 40.
89. R. Noyori, *Angew. Chem., Int. Ed. Engl.*, 2002, **41**, 2008.
90. K. Abdur-Rashid, S. E. Clapham, A. Hadzovic, J. N. Harvey, A. J. Lough, and R. H. Morris, *J. Am. Chem. Soc.*, 2002, **124**, 15104.
91. A. E. S. Gelpke, H. Kooijman, A. L. Spek, and H. Hiemstra, *Chem. – Eur. J.*, 1999, **5**, 2472.
92. C. Bianchini, A. Meli, S. Moneti, and F. Vizza, *Organometallics*, 1998, **17**, 2636.
93. H. M. Lee, C. Bianchini, G. Jia, and P. Barbaro, *Organometallics*, 1999, **18**, 1961.
94. B. Hong, S. R. Woodcock, S. K. Saito, and J. V. Ortega, *J. Chem. Soc., Dalton Trans.*, 1998, 2615.
95. H. Katayama, C. Wada, K. Taniguchi, and Fumiyuki. Ozawa, *Organometallics*, 2002, **21**, 3285.
96. G. Jia, H. M. Lee, I. D. Williams, C. P. Lau, and Y. Chen, *Organometallics*, 1997, **16**, 3941.
97. L. A. Watson, O. V. Ozerov, M. Pink, and K. G. Caulton, *J. Am. Chem. Soc.*, 2003, **125**, 8426.
98. P. Rosa, N. Mezailles, L. Ricard, F. Mathey, P. Le Floch, and Y. Jean, *Angew. Chem., Int. Ed. Engl.*, 2001, **40**, 1251.
99. C. S. Slone, D. A. Weinberger, and C. A. Mirkin, in 'Progress in Inorganic Chemistry', ed. K. D. Karlin, John Wiley & Sons, New York, 1999, Vol. 48, p. 233.
100. D. F. Mullica, P. K. Hayward, and E. L. Sappenfield, *Inorg. Chim. Acta*, 1996, **253**, 97.
101. J. Y. Corey and J. Braddock-Wilking, *Chem. Rev.*, 1999, **99**, 175.
102. V. K. Dioumaev, B. R. Yoo, L. J. Procopio, P. J. Caroll, and D. H. Berry, *J. Am. Chem. Soc.*, 2003, **125**, 8936.
103. S. Lachaize, S. Sabo-Etienne, B. Donnadieu, and B. Chaudret, *Chem. Commun.*, 2003, 214.
104. F. Delpech, S. Sabo-Etienne, J.-C. Daran, B. Chaudret, K. Hussein, C. J. Marsden, and J.-C. Barthelat, *J. Am. Chem. Soc.*, 1999, **121**, 6668.
105. I. Atheaux, F. Delpech, B. Donnadieu, S. Sabo-Etienne, B. Chaudret, K. Hussein, J.-C. Barthelat, T. Braun, S. B. Duckett, and R. N. Perutz, *Organometallics*, 2002, **21**, 5347.
106. R. Ben Said, K. Hussein, J.-C. Barthelat, I. Atheaux, S. Sabo-Etienne, M. Grellier, B. Donnadieu, and B. Chaudret, *Dalton Trans.*, 2003, 4139.
107. J. A. Reichl, C. M. Popoff, L. A. Gallagher, E. E. Remsen, and D. H. Berry, *J. Am. Chem. Soc.*, 1996, **118**, 9431.
108. M. L. Buil, M. A. Esteruelas, F. J. Lahoz, E. Oñate, and L. A. Oro, *J. Am. Chem. Soc.*, 1995, **117**, 3619.
109. A. Moores, N. Mézailles, L. Ricard, F. Mathey, and P. Le Floch, *Chem. Commun.*, 2003, 1914.
110. S.-I. Murahashi and H. Takaya, *Acc. Chem. Res.*, 2000, **33**, 225.
111. G. J. Kubas, 'Metal Dihydrogen and σ-bond Complexes', Kluwer Academic/Plenum Publishers, New York, 2001.
112. F. Maseras, A. Lledós, E. Clot, and O. Eisenstein, *Chem. Rev.*, 2000, **100**, 601.
113. A. F. Borowski, B. Donnadieu, J.-C. Daran, S. Sabo-Etienne, and B. Chaudret, *Chem. Commun.*, 2000, 543; A. F. Borowski, B. Donnadieu, J.-C. Daran, S. Sabo-Etienne, and B. Chaudret, *Chem. Commun.*, 2000, 1967.
114. V. Montiel-Palma, M. Lumbierres, B. Donnadieu, S. Sabo-Etienne, and B. Chaudret, *J. Am. Chem. Soc.*, 2002, **124**, 5624.
115. K. Essalah, J.-C. Barthelat, V. Montiel, S. Lachaize, B. Donnadieu, B. Chaudret, and S. Sabo-Etienne, *J. Organomet. Chem.*, 2003, **680**, 182.
116. A. F. Borowski, S. Sabo-Etienne, B. Donnadieu, and B. Chaudret, *Organometallics*, 2003, **22**, 1630.
117. S. Sabo-Etienne and B. Chaudret, *Chem. Rev.*, 1998, **98**, 2078.
118. A. J. Toner, B. Donnadieu, S. Sabo-Etienne, B. Chaudret, X. Sava, F. Mathey, and P. Le Floch, *Inorg. Chem.*, 2001, **40**, 3034.
119. K. Abdur-Rashid, D. G. Gusev, A. J. Lough, and R. H. Morris, *Organometallics*, 2000, **19**, 834.
120. A. Albinati, W. T. Klooster, T. F. Koetzle, J. B. Fortin, J. S. Ricci, J. Eckert, T. P. Fong, A. J. Lough, R. H. Morris, and A. P. Golombek, *Inorg. Chim. Acta*, 1997, **259**, 351.
121. T. A. Luther and D. M. Heinekey, *Inorg. Chem.*, 1998, **37**, 127.
122. Y. Nishibayashi, I. Takei, and M. Hidai, *Angew. Chem., Int. Ed. Engl.*, 1999, **38**, 3047.
123. M. A. Esteruelas and L. A. Oro, *Chem. Rev.*, 1998, **98**, 577.
124. S. B. Duckett and D. Blazina, *Eur. J. Inorg. Chem.*, 2003, 2901.
125. J. N. Coalter, III, J. C. Huffman, W. E. Streib and K. G. Caulton, *Inorg. Chem.* 2000, **39**, 3757.
126. M. L. Buil, M. A. Esteruelas, J. Modrego, and E. Onate, *New J. Chem.*, 1999, **23**, 403.
127. R. Custelcean and J. E. Jackson, *Chem. Rev.*, 2001, **101**, 1963.
128. E. I. Gutsul, N. V. Belkova, M. S. Sverdlov, L. M. Epstein, E. S. Shubina, V. I. Bakhmutov, T. N. Gribanova, R. M. Minyaev, C. Bianchini, M. Peruzzini, and F. Zanobini, *Chem. – Eur. J.*, 2003, **9**, 2219.

129. K. Philippot and B. Chaudret, *C. R. Chim.*, 2003, **6**, 1019.
130. C. Pan, K. Pelzer, K. Philippot, B. Chaudret, F. Dassenoy, P. Lecante, and M.-J. Casanove, *J. Am. Chem. Soc.*, 2001, **123**, 7584.
131. J. A. Widegren, M. A. Bennett, and R. G. Finke, *J. Am. Chem. Soc.*, 2003, **125**, 10301.

Ruthenium: Organometallic Chemistry

Rosemary E. White & Timothy P. Hanusa
Vanderbilt University, Nashville, TN, USA

Based in part on the article Ruthenium: Organometallic Chemistry by Ulrich Koelle which appeared in the Encyclopedia of Inorganic Chemistry, First Edition.

1	Introduction	1
2	Carbonyls	2
3	Alkene and Cycloalkene Complexes	14
4	Ruthenocene	18
5	(Arene)(Cyclopentadienyl) And Bis(Arene) Ruthenium Complexes	22
6	Half-sandwich Complexes	24
7	Related Articles	30
8	References	30

Abbreviations

acac = Acetylacetonate; allyl = η^3-C_3H_5, η^3-C_3R_5; arene = η^6-C_6R_6; bpy = 2,2′-bipyridine; cod = 1,5-cyclooctadiene; cot = Cyclooctatetraene; Cp = Cyclopentadiene (C_5H_5); Cp* = Pentamethylcyclopentadiene (C_5Me_5); dmbpy = 4,4′-dimethyl-2,2′-bipyridine; dppm = (diphenylphospino) methane; *p*-cymene = 1-isopropyl-4-methyl-C_6H_4; dad = Diazadienes, RN=CR′–CR′=NR; quin = 8-quinolate; nbd = Norbornadiene; OTf = Trifluoromethanesulfonate OTs = Tosylate; PPN = $(Ph_3P)_2N$; $RuCl_3$ = $RuCl_3\cdot 3H_2O$ (approximate); tmbpy = 4,4′,5,5′-tetramethyl-2,2′-bipyridine.

1 INTRODUCTION

Unlike iron, whose organometallic chemistry dates from the end of the nineteenth century (*see* ***Iron: Organometallic Chemistry***), that of its second-row transition metal congener ruthenium had to wait for the discovery of the sandwich compound ferrocene in 1951 (*see Ferrocene*). The impetus from that breakthrough stimulated all areas of organometallic research, and ruthenocene was reported the very next year.[1] More so than in its coordination chemistry (*see* ***Ruthenium: Inorganic & Coordination Chemistry***), it has become apparent that the organometallic chemistry of ruthenium has many features in common both with iron and with its heavier analog osmium (*see* ***Osmium: Organometallic Chemistry***). Thus, many complex types and reactions that are discussed below have counterparts with either iron or osmium or both. As is the case in all transition element groups, there is a tendency for substitution or addition (*see Oxidative Addition*) and elimination (*see Reductive Elimination*) reactions to be slower when proceeding down a group in the periodic table. The middle elements, in particular ruthenium and rhodium, profit from this trend, for example, hydride (*see Hydrides*) and alkyl bonds (*see Alkyl Complexes*) are generally more stable and consequently more abundant in ruthenium species than in analogous structures of iron. Conversely, rigid structures have been found in osmium complexes in cases where the ruthenium analogs are either unstable or highly fluxional (*see Fluxional Molecule*). Thus, ruthenium complexes in many instances are more stable than those of iron, yet are more mobile than the osmium equivalents.

Whereas the chemistry of the metallocenes (*see Metallocene Complexes*) is rather similar for the three elements, differences are obvious in their carbonyl chemistries (*see Carbonyl Compound*), which for ruthenium and osmium are based principally on the dodecacarbonyl $M_3(CO)_{12}$. The pentacarbonyl, a basic material for the carbonyl chemistry of iron, is readily available from daylight photolysis of $Ru_3(CO)_{12}$ (**1**) under CO in solution, but is far less common. Furthermore, carbonyl halides have played a role in the carbonyl chemistry of ruthenium, but analogous compounds of iron or even osmium are less frequently used. Among the iron group metals, cluster carbonyls that incorporate additional main group atoms, mostly hydrogen, carbon, and nitrogen, are broadly similar, although osmium shows the greatest diversity of compounds.

Owing to its higher position in the spectrochemical series (*see Spectrochemical Series*), ruthenium responds more strongly to changes in ligand field (*see Ligand Field Theory*) than iron. Consequently, the higher oxidation states Ru^{III} and Ru^{IV}, which are abundant in the coordination chemistry of the element, become strongly oxidizing in the presence of acceptor ligands, and are transformed into Ru^{II} (or even Ru^{I} or Ru^{0}) by mild reducing agents, such as alcohols. This property has been exploited in the synthesis of carbocyclic and alkenic π-complexes (*see Alkene Complexes*) of ruthenium where the halide $RuCl_3$ is treated with ligand or ligand precursors in alcohols with or without additional reducing agents. Hydrogenation/dehydrogenation reactions (*see Hydrogenation*) of poly- and cycloalkenic ligands are frequently observed in these reactions under mild conditions; a stable 18 valence electron coordination environment (*see Eighteen Electron Compounds*) is thereby produced.

The common starting material for nearly all preparations of ruthenium is a hydrated chloride ($RuCl_3$) of approximate composition $RuCl_3\cdot 3H_2O$, containing 36–42% Ru. Although the material from most sources is not very pure, for example, containing nitrosyls from prior contact with nitric acid, the presence of impurities in most cases is not a serious problem and the yields of conversion of '$RuCl_3\cdot 3H_2O$' can be nearly quantitative based on metal content.

The following article is organized according to basic complex types, where the preparation, structures, and properties of these complexes are described in some detail. Examples of other types of complexes derived from these most basic examples are discussed. Early reviews of the organometallic chemistry of ruthenium can be found in the comprehensive treatise by Seddon and Seddon,**2** and in the articles by Bruce, Bennett, and Matheson in *Comprehensive Organometallic Chemistry I*;**3** the latter have been updated.**4** A review of the 'Tentacular Chemistry of $[Cp^*Ru(OMe)]_2$' has also been published.**5**

2 CARBONYLS

2.1 General Characteristics

For a metal with eight valence electrons, 'electron precise' carbonyl structures (*see Electron Precise Compound*) are $M(CO)_5$ and $[M(CO)_4]_3$, which are known for all three metals of the iron group, albeit with quite different properties for the different metals. The next member, $[M(CO)_3]_6$, is not formed since a four-connected vertex requires more metal–metal bonding orbitals than can be arranged on the surface of a sphere. Bonding orbitals directed towards the inside of the cluster, however, form MOs that will accommodate more electrons than would be predicted by an 18 valence electron count for each metal (*see Eighteen Electron Compounds*), that is, 86 instead of 84 for a six-vertex *closo* cluster (*see Closo Cluster*). This situation is realized in the iron group by the anions $[M_6(CO)_{18}]^{2-}$, M = Fe, Ru, Os (isolectronic to $M_6(CO)_{16}$, M = Co, Rh, Ir).

An even-electron fragment, such as $M(CO)_n$ (M = Fe, Ru, Os), can form a three-connected vertex by incorporation of a one-electron ligand, such as hydrogen. Thus, the analog to the tetracarbonyls of the cobalt group $[M(CO)_3]_4$ in the iron group is represented by the $MH(CO)_3$ moiety, as in $[HRu(CO)_3]_4$, or as in the equivalence of two H or one H^- for one CO, giving $H_2Ru_4(CO)_{13}$ or $[HRu_3(CO)_{11}]^-$. The equivalence of one CO to two electrons generates species such as $M(CO)_4{}^{2-}$ or $[M_6(CO)_{18-n}]^{2(n+1)-}$ with $n = 0$, 1, and 2.

The most stable carbonyl for ruthenium is the trimeric tetracarbonyl $Ru_3(CO)_{12}$ (**1**), with $Ru(CO)_5$ (**2**) and $Ru_2(CO)_9$ (**3**) being much less stable. Compounds (**2**) and (**3**) are prepared from $Ru_3(CO)_{12}$ and revert to it on standing or irradiation. No neutral homoleptic (*see Homoleptic Compound*) ruthenium carbonyl of higher nuclearity, in particular no analog of $Os_6(CO)_{18}$, is known.

Known carbonyl hydrides of ruthenium include the unstable $HRu(CO)_4$, as well as the trinuclear $H_2Ru_3(CO)_{11}$, tetranuclear $H_2Ru_4(CO)_{13}$ and $H_4Ru_4(CO)_{12}$, and complexes of even higher nuclearity, as well as substitution and deprotonation derivatives. A special feature of ruthenium carbonyl chemistry is the existence of series of carbonyl halides of varying stability; many mono- and dinuclear carbonyl halides are known.

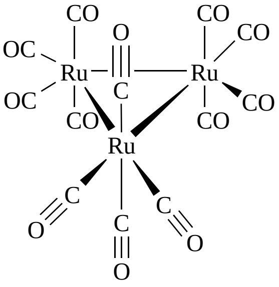

ν_{CO} 2061, 2032, 2015 cm^{-1}

(**1**)

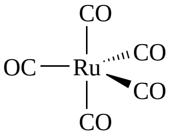

ν_{CO} 2035, 2000 cm^{-1}

(**2**)

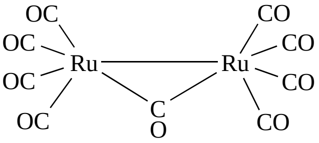

ν_{CO} 2077, 2018, 1814 cm^{-1}

(**3**)

2.1.1 $Ru_3(CO)_{12}$

As stated above, the one stable binary carbonyl of ruthenium is $Ru_3(CO)_{12}$ (**1**). This is readily formed from halides or coordination compounds of Ru^{III} by carbonylation at elevated temperature and pressure.**6–8** This commercially available carbonyl complex is an air-stable orange solid that is soluble in most organic solvents. Its structure consists, like the osmium analog but unlike $Fe_3(CO)_{12}$, of a regular Ru–Ru–Ru triangle with only terminal CO groups. Each $Ru(CO)_4$ corner is composed of two equatorial and two axial CO groups, with clearly different bonding parameters. Equatorial groups have shorter Ru–C bonds as well as C≡O bond distances in comparison to the axial CO groups, a difference that can be traced to a 'π-competition effect', that is, less back bonding (*see Back Bonding*) for the *trans* axial CO groups, which compete for metal electrons, whereas equatorial CO groups *trans* to a Ru–Ru bond can make full use of ruthenium d-electrons for back bonding.

Despite the absence of bridging CO ligands, exchange of axial and equatorial CO groups is rapid on the NMR timescale, giving rise to a single ^{13}CO signal down to −100 °C. It is found that when either two axial or equatorial positions are occupied by a donor ligand, CO exchange involving these positions is considerably slower. Thus, the pyrazine derivative depicted in Scheme 1 exhibits three bridging carbonyls; a low-temperature process occurs at −150 to −90 °C that affects bridging and equatorial CO groups only, and can be separated from the complete scrambling of all carbonyls at higher temperature. This process, designated as a 'merry-go-round' mechanism of

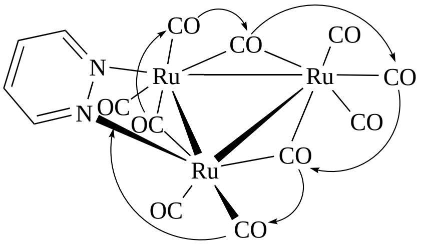

Scheme 1

CO interchange, can alternatively be viewed as the stepwise movement of the metal core (with the axial groups) by 60°.

2.1.2 *Ru(CO)$_5$*

$Ru(CO)_5$ (**2**) was first unambiguously characterized by Calderazzo in 1967.**[9]** The compound was obtained by carbonylating $Ru(acac)_3$ in heptane using a H_2/CO mixture. The ensuing heptane solution showed IR absorptions at 2035 and 1999 cm^{-1} from the newly formed pentacarbonyl. On standing, in particular under the action of light, (**2**) reverts to (**1**) with loss of CO, as can be readily monitored with IR spectroscopy (*see Infrared Spectroscopy*). $Ru(CO)_5$ can be prepared as a pure liquid (mp $-17\,°C$) by high-pressure carbonylation of (**1**), but the initially colorless liquid rapidly turns yellow on standing owing to the reformation of (**1**).

The $Ru_3(CO)_{12}/Ru(CO)_5$ equilibrium (equation 1) has been much investigated, and the thermodynamic parameters are presented in Scheme 2.**[10]** Establishment of the equilibrium is accelerated considerably by using a 2% admixture of H_2 to the CO. The reaction may proceed through one or more carbonyl hydride intermediates (Section 2.1.4). The value of the equilibrium constant suggests that (**2**) is stable at room temperature towards conversion into (**1**) under a few bar of CO. Substitution reactions of (**2**) proceed at or slightly above ambient temperature. ^{13}C NMR chemical shifts as well as ν_{CO} stretching frequencies in $M(CO)_5$ along the series iron, ruthenium, osmium suggest that backbonding from the metal decreases; this correlates with the lower thermal stability of the heavier pentacarbonyls.

$$\underset{(\mathbf{1})}{Ru_3(CO)_{12}} + 3CO \underset{<100°}{\overset{h\nu}{\rightleftharpoons}} \underset{(\mathbf{2})}{3Ru(CO)_5} \qquad (1)$$

$$K = \frac{[Ru(CO)_5]^3}{[Ru_3(CO)_{12}][CO]^3} = 36.6 \text{ at } 100\,°C;\ 13.0 \text{ at } 175\,°C$$

$$\Delta G^R = 5.12 \text{ kJ mol}^{-1}\ (25\,°C)$$

Scheme 2

2.1.3 *Ru$_2$(CO)$_9$*

The ruthenium analog (**3**) of $Fe_2(CO)_9$ is obtained as an elusive species through low-temperature UV irradiation of (**2**) in heptane. It loses CO much more readily than (**2**), converting into (**1**) at ambient temperature. Spectroscopic data have been obtained only in mixtures with (**1**), but the presence of a single absorption at 1814 cm^{-1} for bridging CO, along with bands at 2077 and 2018 cm^{-1} for terminal CO, is in accord with a structure similar to the osmium analog with one bridging and eight terminal CO groups. The more stable anion $[Ru_2(CO)_8]^{2-}$ (**4**) has been prepared from treatment of (**1**) with $Na_2[Ru(CO)_4]$; its structure is unique for complexes of this composition. Whereas the iron and osmium analogs show the expected one axial/three equatorial D_{2d} arrangement of CO groups, the structure of the ruthenium anion has only C_s molecular symmetry; the Ru–Ru vector occupies one equatorial position of a trigonal bipyramid (*see Trigonal Bipyramidal*) and one axial ligand of a square pyramid (*see Square Pyramidal*).**[11]**

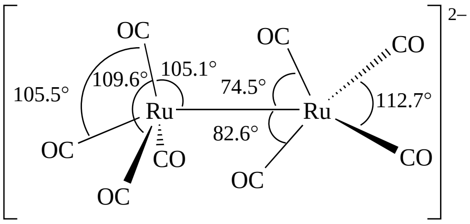

(**4**)

2.1.4 *Carbonyl Hydrides and Cluster Carbonylate Anions*[12,13]

Mono- and Dinuclear Compounds. The pentacarbonyl is a starting material for mononuclear ruthenium carbonyl complexes. As outlined in Scheme 3, reduction with sodium in liquid ammonia yields a pale-colored anion solution (**5**),

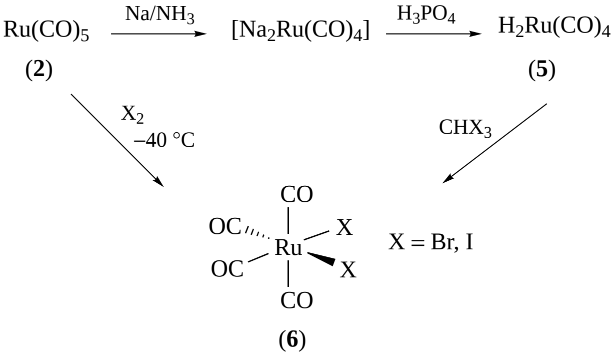

Scheme 3

from which the unstable *cis*-dihydride $H_2Ru(CO)_4$ is obtained by acidification with H_3PO_4. With haloforms, the dihydride converts to the same carbonyl halides (**6**) (Scheme 3) as are obtained from (**2**) with halogen or other halogenation reactions starting from (**1**) (Section 2.1.5).

Trinuclear Compounds. A versatile and much-studied compound is the hydrido ruthenium carbonyl anion $[HRu_3(CO)_{11}]^-$ (**7**), which is best obtained by treatment of (**1**) with $NaBH_4$ in THF and isolated as the Me_4N^+ salt.**14** Compound (**7**) has a bridging hydride and a bridging CO across the same edge of the $Ru_3(CO)_{10}$ triangle, which is shorter than the other two. The general trend for bridged metal–metal bond lengths is a shortening by CO bridges and widening by H bridges, where the former obviously has the larger effect in cases where they compete.

Reprotonation of (**7**) with strong acid occurs first at the bridging CO to give an elusive μ-C–OH intermediate that rearranges to the neutral dihydride (**8**) (Scheme 4). This is much less stable than the monoanion and decomposes at ambient temperature to (**1**) and the tetranuclear hydrides $H_2Ru_4(CO)_{13}$ (**9**) and $H_4Ru_4(CO)_{12}$ (**10**).

Tetrahedrane (**11**) is the ruthenium analog of the much-studied tricobaltnonacarbonyl clusters $Co_3(CO)_9CR$ (*see* ***Cobalt: Organometallic Chemistry***). The substitution chemistry of (**11**) has been studied.**15** A starting material is prepared from (**11**) by reaction with BX_3 (equation 2), which gives the chloro and bromo compounds (**12**). In addition, (**11**) can also be treated directly with compounds such as diynes to yield interesting substitution products. For example, when (**11**) is refluxed in THF with diphenylbutadiyne, cis- and trans-alkene isomers of two alkyne insertion regioisomers are formed (equation 3).**16** The product seems to arise from dehydrogenation of one end of the diyne to yield cis and trans enynes and an unsaturated monohydride cluster intermediate, which then reacts with the enynes to yield the allylic derivative products (**12**) and (**13**).

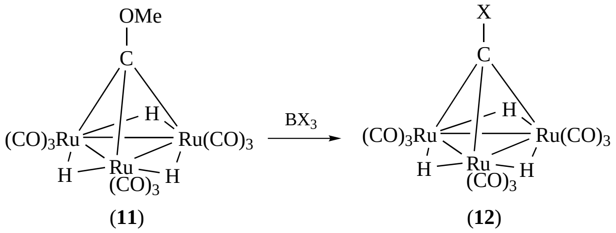

(2)

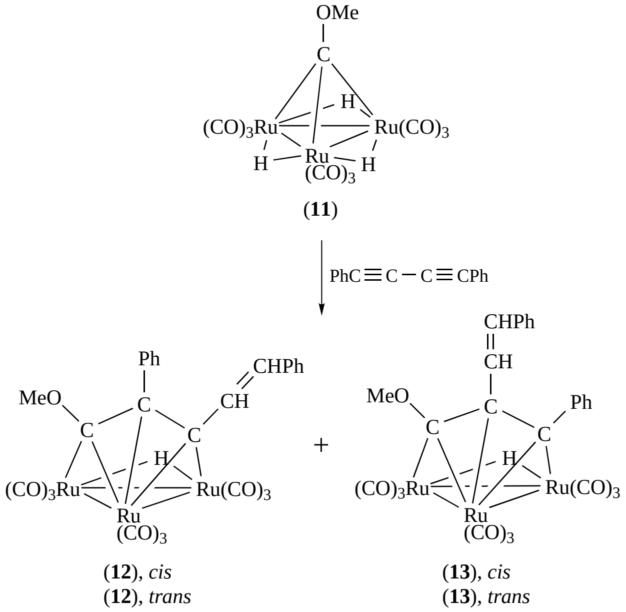

(3)

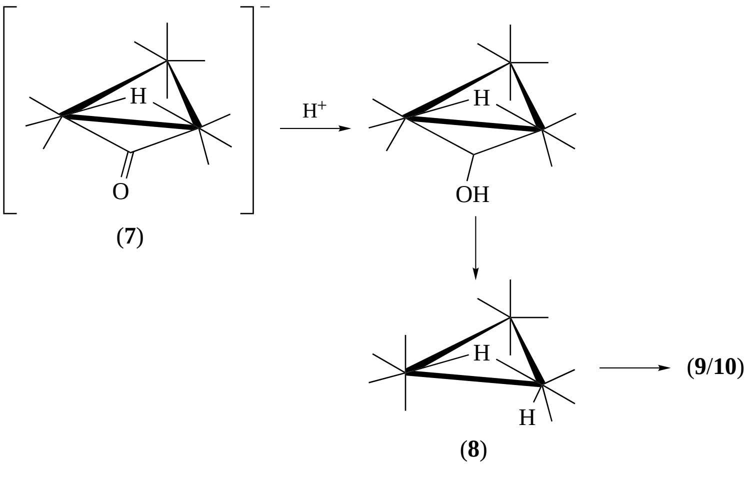

Scheme 4

The cluster anion (**7**) has been invoked as an intermediate in the water gas shift reaction (*see Water Gas Reaction*) catalyzed by (**1**).**17,18** In the cycle represented by equations (4–6), (**7**) is formed from (**1**) and hydroxide by a reaction that can be followed in THF and has been shown to generate CO_2 in this solvent (this is analogous to the well-studied reaction of (**1**) with methoxide). Hydrogen evolution from (**7**) is observed when CO is present, which leads to the assumption of a more easily protonated open-chain intermediate $[HRu_3(CO)_{12}]^-$ that closes the cycle (equation 6).

$$\underset{(\mathbf{1})}{Ru_3(CO)_{12}} + OH^- \longrightarrow \underset{(\mathbf{7})}{[HRu_3(CO)_{11}]^-} + CO_2 \qquad (4)$$

$$\underset{(\mathbf{7})}{[HRu_3(CO)_{11}]^-} + CO \longrightarrow [HRu_3(CO)_{12}]^- \qquad (5)$$

$$[HRu_3(CO)_{12}]^- + H_2O \longrightarrow Ru_3(CO)_{12} + H_2 + OH^- \qquad (6)$$

The interest in (**7**) as a hydroformylation (*see Hydroformylation*) catalyst comes from the fact that the unsubstituted (no phosphine ligands) trinuclear anion gives a very high linear/branched ratio of the resulting aldehyde, along with negligible alkene hydrogenation. This result is not easily achieved in other, mostly mononuclear, systems. Furthermore, this was the first system where the integrity of the trinuclear cluster throughout the catalytic cycle was proven;**19** deuteration experiments were used to establish this.

Higher Nuclearity Clusters. The three most thoroughly investigated carbonyl hydrides are $H_2Ru_4(CO)_{13}$ (**9**), $H_4Ru_4(CO)_{12}$ (**10**), and $H_2Ru_6(CO)_{18}$ (**14**). They are prepared by either direct reaction between $Ru_3(CO)_{12}$ and hydrogen, a method that gives the best yields of (**10**), by acidification of anions from alkali reduction of (**1**), or by complex reactions involving (**1**) and various alcohols, ketones, or amines, which induce valence disproportionation (*see Disproportionation*) and CO redistribution. Reaction of (**1**) with ethanol provides ready access to the dihydride (**9**). This in turn can be converted to the tetrahydride (**10**) with hydrogen gas (equation 7).

$$\underset{(\mathbf{1})}{Ru_3(CO)_{12}} \xrightarrow{EtOH} \underset{(\mathbf{9})}{H_2Ru_4(CO)_{13}} \xrightarrow{H_2} \underset{(\mathbf{10})}{H_4Ru_4(CO)_{12}} \qquad (7)$$

Treatment of (**10**) with KH in THF effects stepwise deprotonation to a mono- (**15**) and dianion (**16**); excess base gives (**17**) (Scheme 5). When (**1**) is treated with KOH followed by acidification with concentrated sulfuric acid in CH_2Cl_2, the purple neutral hydride (**14**) is produced.**20**

$H_2Ru_4(CO)_{13}$ (**9**) possesses 11 terminal and two semibridging CO groups that both bend towards a common $Ru(CO)_2$ apex. The tetrameric tetrahydride $H_4Ru_4(CO)_{12}$ (**10**) has four bridging hydrogens alongside four longer edges of a distorted tetrahedron. This generates two shorter Ru–Ru distances and a D_{2d} molecular symmetry. The disposition of the CO groups is eclipsed to a triangular face, with one of them *trans* to a nonbridged and two trans to a bridged Ru–Ru edge. Comparison of (**10**) with the structure of $H_2Ru_6(CO)_{18}$ (**14**) shows that the carbonyl orientation is different, with one CO *trans* to an octahedral face. This is because the two hydrogens in (**14**) are face bridging, and CO ligands will preferentially locate *trans* to a hydride ligand in accord with the established structural trans effect (*see Trans Effect*).**21**

$$\underset{(\mathbf{10})}{H_4Ru_4(CO)_{12}} \xrightarrow[THF]{KH} \underset{(\mathbf{15})}{[H_3Ru_4(CO)_{18}]^-} \xrightarrow[THF]{KH}$$

$$\underset{(\mathbf{16})}{[H_2Ru_4(CO)_{12}]^{2-}} \xrightarrow[THF]{KH} \underset{(\mathbf{17})}{K_4[Ru_4(CO)_{12}]}$$

$$\underset{(\mathbf{1})}{Ru_3(CO)_{12}} \xrightarrow[THF]{conc.\ KOH} \xrightarrow[CH_2Cl_2]{conc.\ H_2SO_4} \underset{(\mathbf{14})}{H_2Ru_6(CO)_{18}}$$

Scheme 5

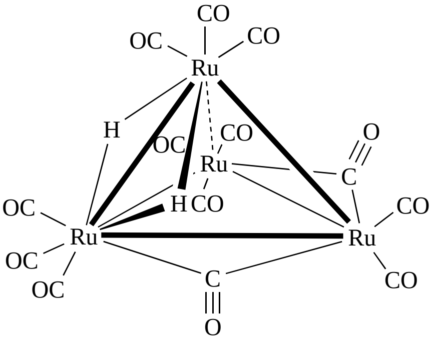

(**9**)

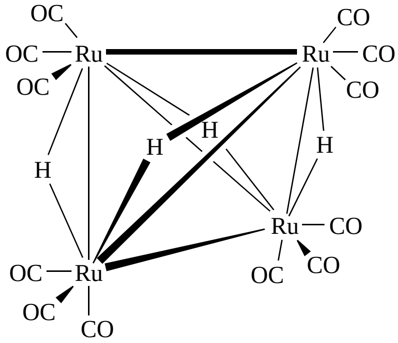

(**10**)

Ruthenium clusters with even higher nuclearity have also been isolated. When (**1**) is refluxed in ethanol for 18 h, the hexaruthenium hydrido complexes $[HRu_6(CO)_{18}]^-$ (**18**) and $[H_2Ru_{10}(CO)_{25}]^{2-}$ (**19**) are produced, along with metallic ruthenium (equation 8). The dihydride complex (**19**) represents the first noncarbido decaruthenium cluster. A trianion with 11 ruthenium centers (**20**) is synthesized by thermolysis of (**1**) in undried acetonitrile (equation 9), and

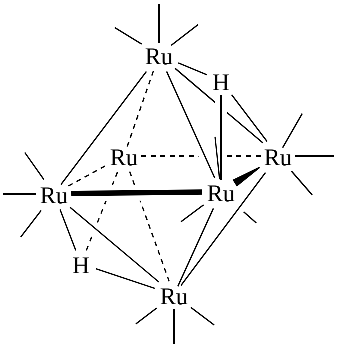

(14)

the relationships between these high-nuclearity ruthenium hydrido carbonyl clusters have been explored.[22]

$$\underset{(\mathbf{1})}{\mathrm{Ru_3(CO)_{12}}} \xrightarrow{\text{EtOH reflux}} \mathrm{Ru^0} + \underset{(\mathbf{18})}{[\mathrm{HRu_6(CO)_{18}}]^-} + \underset{(\mathbf{19})}{[\mathrm{H_2Ru_{10}(CO)_{25}}]^{2-}} \qquad (8)$$

$$\underset{(\mathbf{1})}{\mathrm{Ru_3(CO)_{12}}} \xrightarrow{\text{MeCN}} \underset{(\mathbf{18})}{[\mathrm{HRu_6(CO)_{18}}]^-} + \underset{(\mathbf{20})}{[\mathrm{HRu_{11}(CO)_{27}}]^{3-}} \qquad (9)$$

The clusters (**18**), (**19**), (**20**), and $[\mathrm{H_2Ru_8(CO)_{21}}]^{2-}$ (**21**) are all products from reacting $\mathrm{Ru_3(CO)_{12}}$ under different conditions. (**18**), the major product in the synthesis of all of these complexes, has an octahedral core of ruthenium atoms, with an interstitial hydride. The hydride seems to have some stabilizing effect on the octahedral complex, since all products of higher nuclearity are based on this octahedral framework. As seen in Scheme 6, the structure of the octaruthenium dihydride complex (**21**) resembles an octahedron with an additional $\mathrm{Ru_2}$ unit. Another $\mathrm{Ru_2}$ unit is added to this complex to produce the metal core of the decaruthenium (**19**); and another addition of a single ruthenium gives the core geometry of the undecaruthenium complex (**20**).[22]

2.1.5 Halocarbonyl Complexes of Ruthenium

Carbonyl halides of $\mathrm{Ru^{II}}$ are readily obtained, are stable for all halides, and thus lend themselves as valuable starting materials for the preparation of other ruthenium complexes, in particular those containing σ-donating ligands. The fluoride derivatives are the most outstanding, as there are few examples of fluorocarbonyl complexes in general. Carbonylation of tetrameric $\mathrm{RuF_5}$ or fluorination of (**1**) with $\mathrm{XeF_2}$ in Freon ($\mathrm{CClF_2CCl_2F}$) affords the tetrameric complex $[\mathrm{Ru(CO)_3F_2}]_4$ (**22**). It resembles that of $[\mathrm{RuF_5}]_4$, in which three fluorine atoms at each ruthenium are replaced by CO. Use of a larger excess of $\mathrm{XeF_2}$ in the fluorination of (**1**) gives the monomeric, paramagnetic $\mathrm{Ru^{III}}$ fluorocarbonyl $\mathrm{Ru(CO)_3F_3}$ (**23**). Solid-state susceptibility measurements are in accord with one unpaired electron in a low-spin, d^5 configuration.[23]

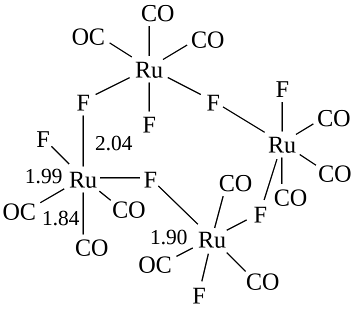

(22)

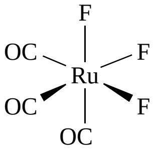

(23)

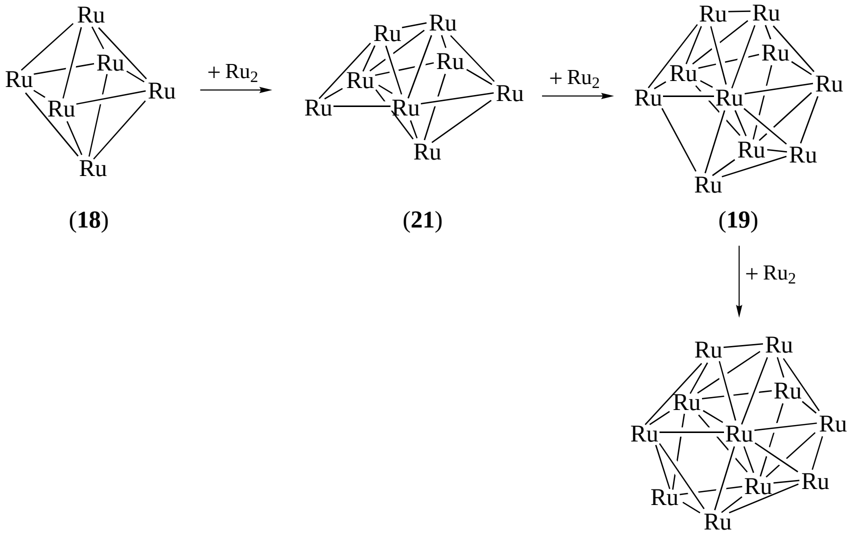

Scheme 6

The main types of halocarbonyl compounds found with the heavier halogens are depicted in Scheme 7. One example has already been presented in Scheme 3. Though methods of preparation other than those shown in Scheme 7 are also successful, reduction with formic acid/hydrohalic acid[24] gives a clear picture of the successive events leading to individual members of the series. Not all compounds listed for chlorine in Scheme 7 can be obtained for bromide and iodine, and in some cases stereoisomers are found with iodine only (cis/trans for $Ru(CO)_4I_2$).

Tetracarbonyl compounds $Ru(CO)_4X_2$ (**6**) (Scheme 3) have a *cis*-octahedral structure, established through an X-ray structure determination of the iodide. The second well-established group of halocarbonyls is dimeric tricarbonyls $[Ru(CO)_3X(\mu\text{-}X)]_2$ (cf. (**24**) in Scheme 7) with C_{2h} symmetry, as determined by X-ray crystallography (*see X-ray Crystallography*). Owing to its easy cleavage with even weak donor ligands (e.g. THF) and substitution to $Ru(CO)_2L_2X_2$, it is a useful starting material for ruthenium carbonyl chemistry. Treatment of (**6**) with an assortment of bidentate ligands has allowed the synthesis of a variety of carbonyl complexes, including $Ru(tmbpy)(CO)_2Cl_2$ (**25**) and $[Ru(dmbpy)(CO)_2Cl]_2$ (**26**). These substituted bipyridine ligands allow for control over the electronic and steric properties of the complex, and the monomeric complexes have been shown to be effective precursors for water gas shift and CO_2 reduction catalysts.[25]

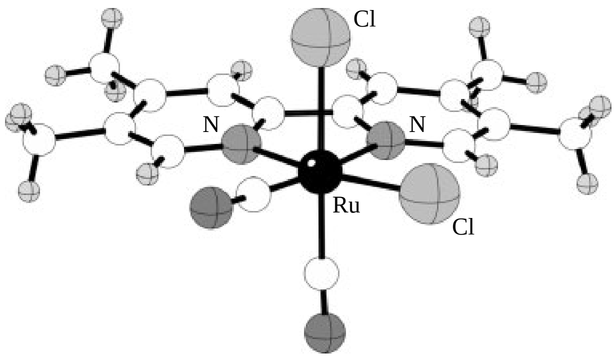

(**25**)

2.1.6 *Carbido and Nitrido Clusters*[13,26]

Several carbido clusters featuring a Ru_5C or Ru_6C core have been described and structurally characterized (*see* ***Cluster Compounds: Inorganometallic Compounds***

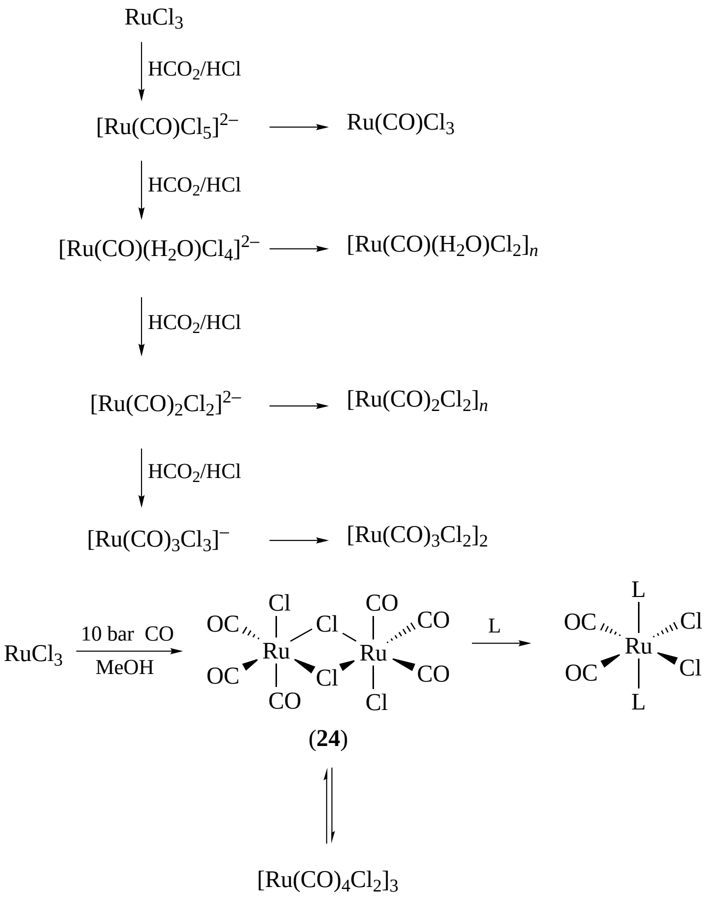
RuCl3
HCO2/HCl
[Ru(CO)Cl5]2–
Ru(CO)Cl3
HCO2/HCl
[Ru(CO)(H2O)Cl4]2–
[Ru(CO)(H2O)Cl2]n
HCO2/HCl
[Ru(CO)2Cl2]2–
[Ru(CO)2Cl2]n
HCO2/HCl
[Ru(CO)3Cl3]–
[Ru(CO)3Cl2]2
RuCl3
10 bar CO
MeOH
Cl
CO
OC
Cl
CO
Ru
Ru
OC
Cl
CO
CO
Cl
(24)
L
L
OC
Cl
Ru
OC
Cl
L
[Ru(CO)4Cl2]3

Scheme 7

Containing Transition Metal & Main Group Elements). Pyrolysis of (**1**) in arene solvents gives the carbido carbonyl $Ru_6C(CO)_{17}$ (**27**) together with $Ru_6C(CO)_{14}(\eta^6\text{-arene})$ in low yields (Scheme 8). Carbido clusters are also formed by heating (**1**) with $NaMn(CO)_5$ in refluxing diglyme. Under milder conditions, this reaction has furnished $[Ru_6(CO)_{18}]^{2-}$ (**28**). A brown suspension formed in an early stage of the reaction is believed to be this dianion, which then, on prolonged heating, is converted into red, soluble $[Ru_6C(CO)_{16}]^{2-}$ (**29**). At higher CO pressure, (**27**) is carbonylated to the pentaruthenium carbido carbonyl $Ru_5C(CO)_{15}$ (**30**) with formation of (**2**). Under argon pressure this reaction is reversible. Compound (**30**) is hydrogenated to a dihydride (**31**) or adds HX to give a halo carbido carbonyl (**32**).

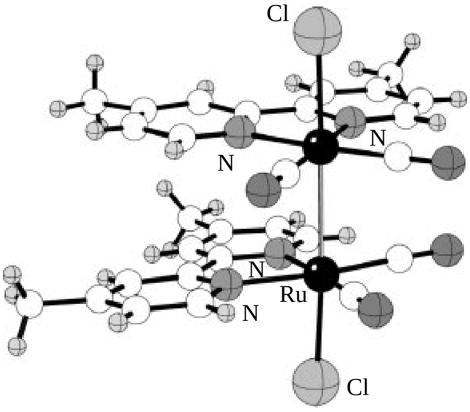
Cl
N
N
N
Ru
N
Cl

(**26**)

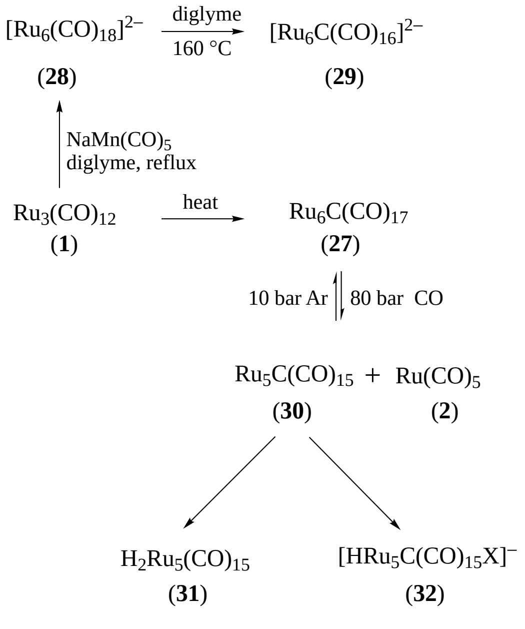
$[Ru_6(CO)_{18}]^{2-}$
diglyme
160 °C
$[Ru_6C(CO)_{16}]^{2-}$
(28)
(29)
$NaMn(CO)_5$
diglyme, reflux
$Ru_3(CO)_{12}$
heat
$Ru_6C(CO)_{17}$
(1)
(27)
10 bar Ar
80 bar CO
$Ru_5C(CO)_{15}$ + $Ru(CO)_5$
(30)
(2)
$H_2Ru_5(CO)_{15}$
$[HRu_5C(CO)_{15}X]^-$
(31)
(32)

Scheme 8

$Ru_5C(CO)_{15}$ (**30**) is a regular square pyramid with all CO groups terminal and has basically the same structure as the iron and osmium analogs. Interestingly, the nonparallel edges of the pyramid are at a minimum length in the ruthenium (2.3 Å) as compared to the iron (2.62 Å) and the osmium (2.85 Å) congeners. The carbon atom protrudes out of the basal Ru_4 plane by 0.11 Å (equation 10).

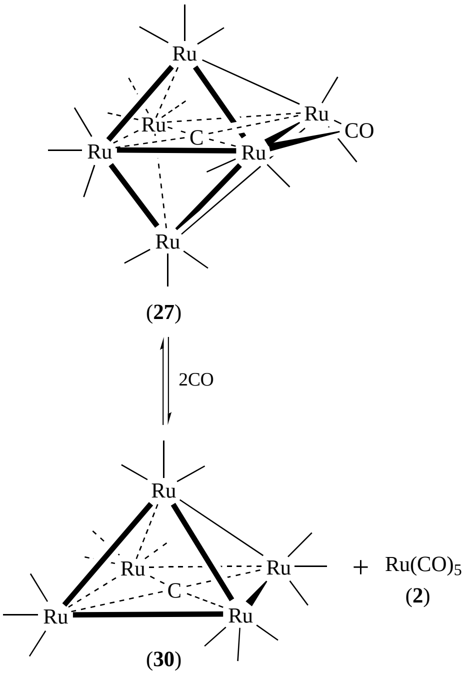
Ru
Ru
Ru
C
Ru
Ru
CO
Ru
(27)
2CO
Ru
Ru
Ru
C
Ru
Ru
+ $Ru(CO)_5$
(2)
(30)

(10)

Homoleptic hepta-, octa-, and nonaruthenium carbido clusters remain unknown. Two structurally similar decaruthenium clusters $[Ru_{10}C(CO)_{24}]^{2-}$ and $[HRu_{10}C(CO)_{24}]^-$ (**33**) were synthesized by treatment of (**1**) with mesitylene.[27] They are isostructural with the osmium analogs. The dicarbido cluster, $[Ru_{10}(C)_2(CO)_{24}]^{2-}$ (**34**), was formed by thermolysis of $[Ru_6(CO)_{18}]^{2-}$ in refluxing diglyme.[28] Synthesis of (**34**) was also accomplished by treatment of (**1**) with an excess of CaC_2.

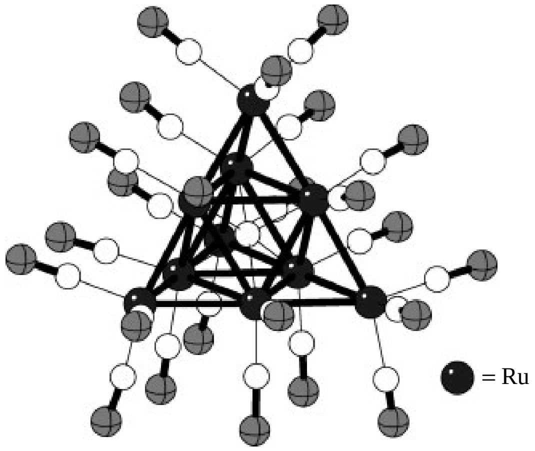

(**33**)

It is formed by the unusual cleavage of the C_2^{2-} dianion of CaC_2. The core of (**34**) consists of two octahedra that share one edge and each have an interstitial carbido atom.**[29]**

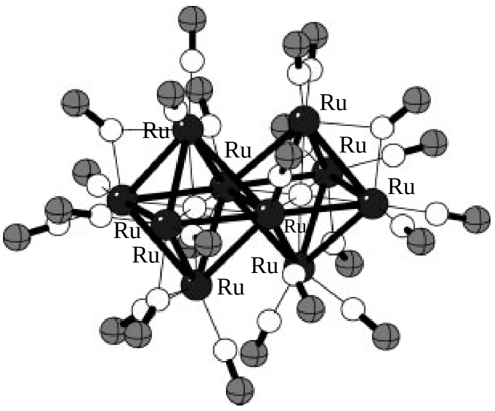

(**34**)

Nitrido clusters are known with a Ru_4N, Ru_5N, or Ru_6N core. As shown in Scheme 9, treatment of (**1**) with the PPN azide (PPN[N_3]) in THF, followed by evaporation of THF and redissolution in ether, the red complex $[Ru_4(NCO)(CO)_{13}]^-$ (**35**) is produced. One CO in (**35**) is easily displaced by H_2 giving $[H_2Ru_4(NCO)(CO)_{12}]^-$ (**36**), isolated as the PPN salt. Protonation of the latter gives neutral trihydride $H_3Ru_4(NCO)(CO)_{12}$ (**37**) and some nitrogen-free (hydrido)carbonyl by-products. Refluxing (**35**) in THF converts it to the nitride cluster anion $[Ru_4N(CO)_{12}]^-$ (**38**), which in turn can be protonated to the neutral hydride (**39**). The hexaruthenium nitride complex $[Ru_6N(CO)_{16}]^-$ (**40**) is obtained directly from (**1**) and PPN[N_3] in refluxing THF. Carbonylation under slight pressure (20 bar CO) cleaves (**40**) into (**1**) and the pentaruthenium nitrido anion $[Ru_5N(CO)_{14}]^-$ (**41**). Treatment of (**40**) with (**1**) yields the decaruthenium complex $[Ru_{10}N(CO)_{24}]^-$ (**42**) as shown in Scheme 9.

For nitrido clusters, open butterfly structures with a Ru_4 core are observed in (**38**) and the precursor molecules (**35**) or (**37**), where one nitride or isocyanate ligand bridges the open wings of the butterfly. Ru_5N cores, exemplified by $[Ru_5N(CO)_{14}]^-$ (**41**), are of a similar square pyramidal arrangement as Ru_5C clusters. The nitrido atom in the former is displaced out of the basal plane by as much as 0.21 Å (i.e. about twice as much as the carbon atom in (**30**)) making the transition to a distorted octahedron. The decanuclear complex (**42**) exists as a tetracapped octahedron, which is almost indistinguishable from the formally isoelectronic complex $[Ru_{10}HC(CO)_{24}]^-$. The hexaruthenium complex (**40**) has not yet been structurally characterized.

2.2 Substitution at Ruthenium Carbonyls

2.2.1 *Derivatives of $Ru(CO)_5$*

As previously mentioned, monosubstitution of $Ru(CO)_5$ (**2**) is thermally facile, and a range of the usual L-donor ligand substituted products $Ru(CO)_{5-n}L_n$ ($n = 1, 2$) is prepared in this way. If L is a phosphine, it occupies an axial position of the trigonal bipyramid (*see Trigonal Bipyramidal*) (with

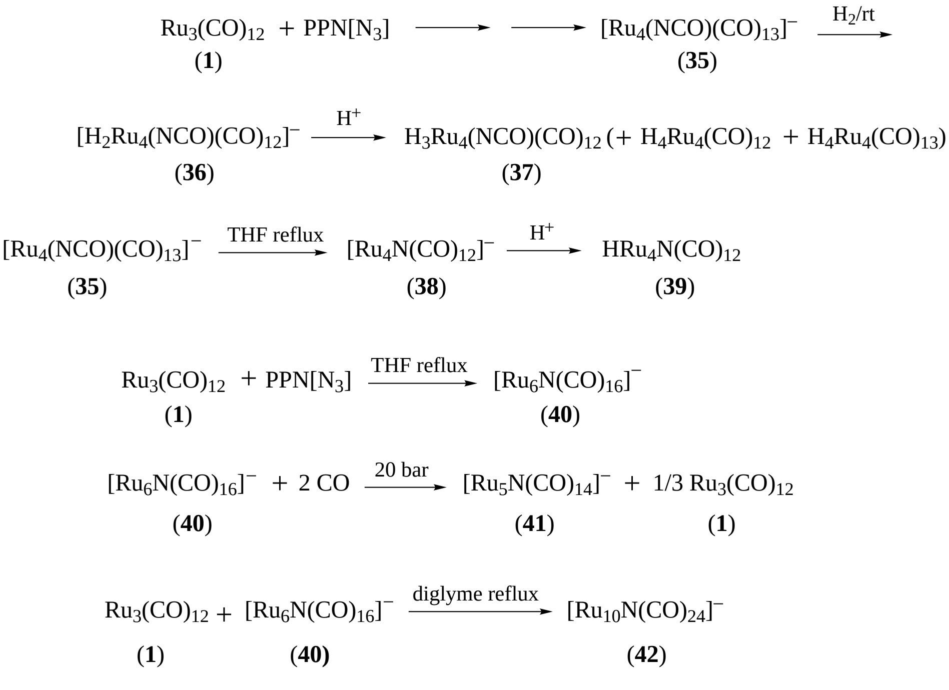

$$\underset{(\mathbf{1})}{Ru_3(CO)_{12}} + PPN[N_3] \longrightarrow \longrightarrow \underset{(\mathbf{35})}{[Ru_4(NCO)(CO)_{13}]^-} \xrightarrow{H_2/rt}$$

$$\underset{(\mathbf{36})}{[H_2Ru_4(NCO)(CO)_{12}]^-} \xrightarrow{H^+} \underset{(\mathbf{37})}{H_3Ru_4(NCO)(CO)_{12}} (+\ H_4Ru_4(CO)_{12} + H_4Ru_4(CO)_{13})$$

$$\underset{(\mathbf{35})}{[Ru_4(NCO)(CO)_{13}]^-} \xrightarrow{\text{THF reflux}} \underset{(\mathbf{38})}{[Ru_4N(CO)_{12}]^-} \xrightarrow{H^+} \underset{(\mathbf{39})}{HRu_4N(CO)_{12}}$$

$$\underset{(\mathbf{1})}{Ru_3(CO)_{12}} + PPN[N_3] \xrightarrow{\text{THF reflux}} \underset{(\mathbf{40})}{[Ru_6N(CO)_{16}]^-}$$

$$\underset{(\mathbf{40})}{[Ru_6N(CO)_{16}]^-} + 2\,CO \xrightarrow{\text{20 bar}} \underset{(\mathbf{41})}{[Ru_5N(CO)_{14}]^-} + 1/3\ \underset{(\mathbf{1})}{Ru_3(CO)_{12}}$$

$$\underset{(\mathbf{1})}{Ru_3(CO)_{12}} + \underset{(\mathbf{40})}{[Ru_6N(CO)_{16}]^-} \xrightarrow{\text{diglyme reflux}} \underset{(\mathbf{42})}{[Ru_{10}N(CO)_{24}]^-}$$

Scheme 9

exceptions found in chelating ligands). The preparation of $Ru(CO)_4PPh_3$ (**43**) and $Ru(CO)_3(PPh_3)_2$ (**44**) from (**2**) is shown in Scheme 10 as an example of one of the early studies of its reactivity.[30] Thermal substitution led to the bisphosphine derivative from which the dihydride was obtained under forcing conditions.

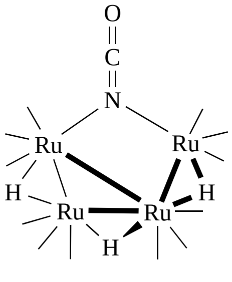

(**37**)

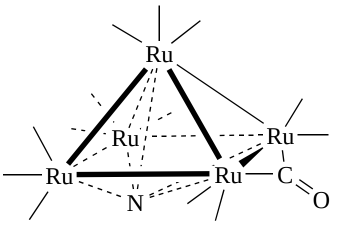

(**41**)

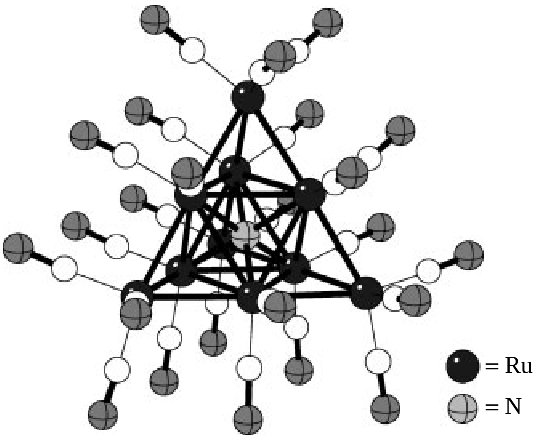

(**42**)

A route to phosphine- and similarly substituted derivatives that avoids the use of ruthenium carbonyl is performed by the direct reaction of hydrated $RuCl_3$ with PPh_3 in alcoholic solution in the presence of a source of CO. This general method consists of the reductive ligation (*see Reductive Ligation*) of the metal in the presence of ligand, notably PPh_3. The extent of reduction, to Ru^{II} or Ru^0 in this case, as well as the ligand set around the metal, depends on the particular conditions. The three complexes $RuHCl(CO)(PPh_3)_3$ (**45**), $RuH_2(CO)(PPh_3)_3$ (**46**), and $Ru(CO)_3(PPh_3)_2$ (**44**) (Scheme 11) are all obtained by the same basic procedure, with differences in alkali presence and reaction duration. $Ru(CO)_3(PPh_3)_2$ (**44**) and $RuH_2(CO)(PPh_3)_3$ (**46**) are active hydroformylation (*see Hydroformylation*) catalysts.[31]

Trisubstituted pentacoordinated complexes with phosphine ligands can be synthesized by reduction of $RuCl_2(CO)_2L_2$ (**47**) with magnesium in the presence of L, where $L = PPh_3$ (**48**), $PMePh_2$, PEt_3, or P^iPr_2Me (equation 11). The presence of L′ (L′ = PPh_3, $P(2\text{-furyl})_3$, or $AsPh_3$) in the magnesium reduction allows for the synthesis of mixed phosphine derivatives, such as the synthesis of (**50**) from (**49**) in equation (12).[32]

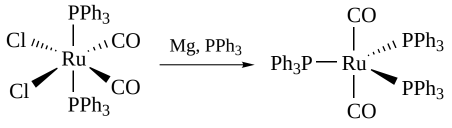

(**47**) (**48**) (11)

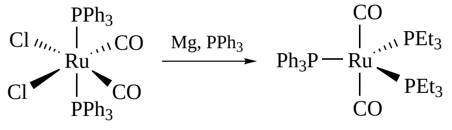

(**49**) (**50**) (12)

Another method for isolating complexes of the type $Ru(CO)_2L_3$ starts with the (hydrido)carbonyl halide complex (**50**). It can be dehalogenated by Ag^+ in the presence of a stabilizing intermediate ligand (e.g., acetonitrile). The cationic acetonitrile complex (**51**) substitutes easily to give the trisphosphine complex (**52**). Deprotonation of the latter with methoxide gives the neutral *trans*-dicarbonyltrisphosphine (**47**). One of the equatorial phosphine ligands is labile and exchanges with a variety of other ligands to form complexes (**53**), as indicated in Scheme 12. Of particular interest is the dioxygen adduct (**53**) ($L = O_2$), formed by exposure to

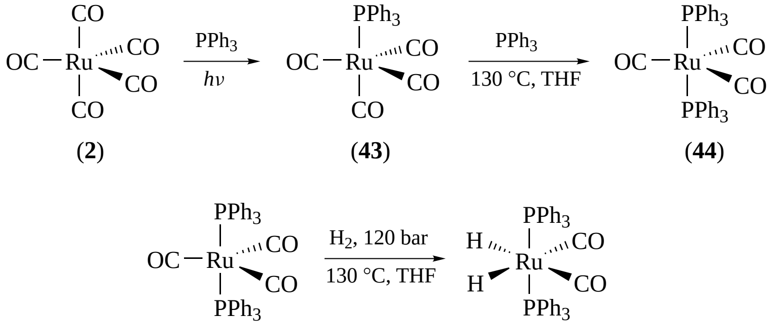

(**2**) (**43**) (**44**)

Scheme 10

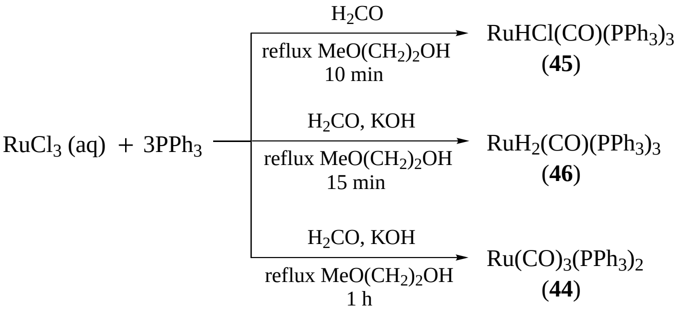

Scheme 11

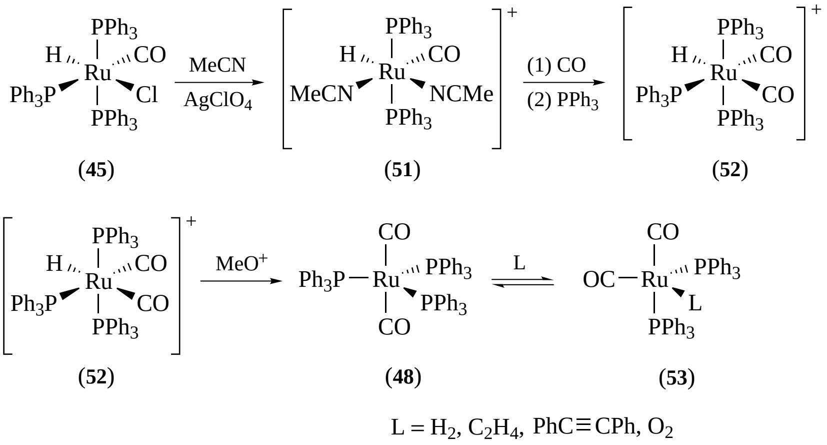

Scheme 12

oxygen. It can function as an oxygen transfer agent or as a catalyst in oxygenation reactions.

2.2.2 Derivatives of $Ru(CO)_4X_2$

A second large class of mononuclear ruthenium complexes is those formally derived from $Ru(CO)_4X_2$,that is, six-coordinated Ru^{II}. The synthesis often involves cleavage of carbonyl halide complexes or carbonyl phosphine halide complexes, which are directly obtained from $RuCl_3$ with a potential reducing agent and a CO donor, such as formic acid, in the presence of phosphine. The variation of ligands accommodated at a ruthenium center in these complexes is enormous, and is a characteristic of the general stability of octahedral low-spin d^6 complexes of the heavier transition metals. The high ligand field stabilization of Ru^{II} enables combinations of such π-acceptor ligands together with even the hardest σ-donors, such as carbonate, sulfate, or nitrate.[4] Ru^{II} carbonyl and phosphine complexes are known with myriad coligand combinations, having O (oxoanions mentioned, carboxylates, quinones), N (amines, amides, hydrazines, hydrazides, triazenes, formamidates, ureas), or S (thiocarbonyls, CS_2, thio- and dithiocarbonates, carbamates, thiophosphinates, thiophosphates) binding functionalities.

2.2.3 Derivatives of $Ru_2(CO)_9$

Although the parent carbonyl $Ru_2(CO)_9$ is virtually unknown, a number of complexes derived by substituting various CO groups of the dinuclear unit for one- or two-electron ligands are of interest owing to some unique transformations they exhibit. The syntheses of these materials begin with (**1**), which is cleaved by the appropriate ligands or reagents.

By treating (**1**) with hydrides $HE^{IV}R_3$ (E^{IV} = Si, Ge, Sn, Pb), Knox obtained the σ-$E^{IV}R_3$ derivatives $Ru(CO)_4(E^{IV}R_3)_2$ and $[Ru(CO)_4(E^{IV}R_3)]_2$,[33] the latter with a long unbridged Ru–Ru single bond, formally analogous to $Mn_2(CO)_{10}$ (*see* ***Manganese: Organometallic Chemistry***), and with some similarities in their reactivity pattern owing to the ready cleavage of the metal–metal bond in both complexes. Reactions were studied with cycloalkenes and are partly outlined in Section 3.3.

A system lacking π-ligands is obtained by cleavage of (**1**) with certain bisphosphines $R_2P–E–PR_2$, which lead to complexes $Ru_2(CO)_4(\mu\text{-}CO)(\mu\text{-}R_2P\text{–}E\text{–}PR_2)_2$ (**54**). These are formally related to $Ru_2(CO)_9$, in that four carbonyl groups are replaced by two bridging phosphines. A Ru–Ru bond is required to adjust the metal to the 18 valence electron rule (*see Eighteen Electron Compounds*), but this can be readily opened and closed in the course of substitution reactions when the so-called ‘A-frame’ is tightly held together by bridging phosphines. Moreover, the bridging carbonyl group is easily displaced to generate coordinatively unsaturated ruthenium centers, such as its replacement by hydrogen to give (**55**) (Scheme 13).**[34]** An intriguing case is provided if Ag^+ oxidation of (**54**) is followed by deprotonation. The resulting alkoxo (hydroxo) complex (**56**) rearranges by CO insertion to an η^2-formate or formic acid complex (**57**). This latter can be deprotonated to yield a complex with a $\mu_2 - \eta^2\text{-}CO_2$ bonding arrangement (**58**), an unusual bonding situation for CO_2 (Scheme 13).**[35]**

The reactions of an analogous A-frame type complex $[Ru_2(CO)_4(\mu\text{-dppm})_2(\mu\text{-}O_2CMe)]^+$ (**59**) have been studied extensively and are outlined in Scheme 14. When (**59**) is treated with $[Et_3O][BF_4]$ in MeCN, the dication (**60**) is formed, which readily converts to (**61**). Reaction of (**61**) with excess of an anion yields coordinatively unsaturated complexes instead of the expected substitution products $[Ru_2(\mu\text{-}CO)_2(\mu\text{-dppm})_2X_4]^{2-}$. The bond between the ruthenium centers is single, while the Ru–X bonds are multiple, probably double, as indicated by bond distances and angles in the crystal structure.**[36]** An interesting rearrangement occurs when (**59**) is treated with a bidentate ligand such as acetate, bpy, acac, or 8-quinolate (quin). The product is a complex with bridging carbonyls, where the new ligand binds in a bidentate fashion to only one of the ruthenium atoms and the acetate ligand migrates to a the opposite ruthenium (**62**). When a second equivalent of the bidentate ligand is added, the acetate is replaced to form (**63**).**[37]**

2.2.4 Derivatives of $Ru_3(CO)_{12}$

Substitution at (**1**) has been investigated extensively from a preparative as well as a mechanistic point of view, and most common substitution techniques, including photochemical activation and electron-transfer catalysis, have been employed. Simple thermal substitution leads to a mixture of products, but with special methods, up to 6 of the 12 CO ligands can be replaced without cleaving the trinuclear unit.

Numerous studies of photochemical substitution at (**1**) have been performed.**[38]** As observed for other polynuclear carbonyls, the photochemistry (*see Photochemistry*) of (**1**) is wavelength dependent. Irradiation at longer wavelength (close to the absorption maximum at 392 nm) presumably gives metal–metal bond cleavage as the primary photoevent, whereas short-wavelength irradiation around 300 nm effects clean CO substitution. At the longer wavelength there is mostly photofragmentation into mononuclear species, whereas at the shorter wavelength if any net change is observed then cluster substitution prevails. Photolysis of (**1**) at 405 nm under 1 atm CO, for example, quantitatively gives (**2**) with a solvent-dependent quantum yield of 0.028 mol einstein^{-1} in isooctane

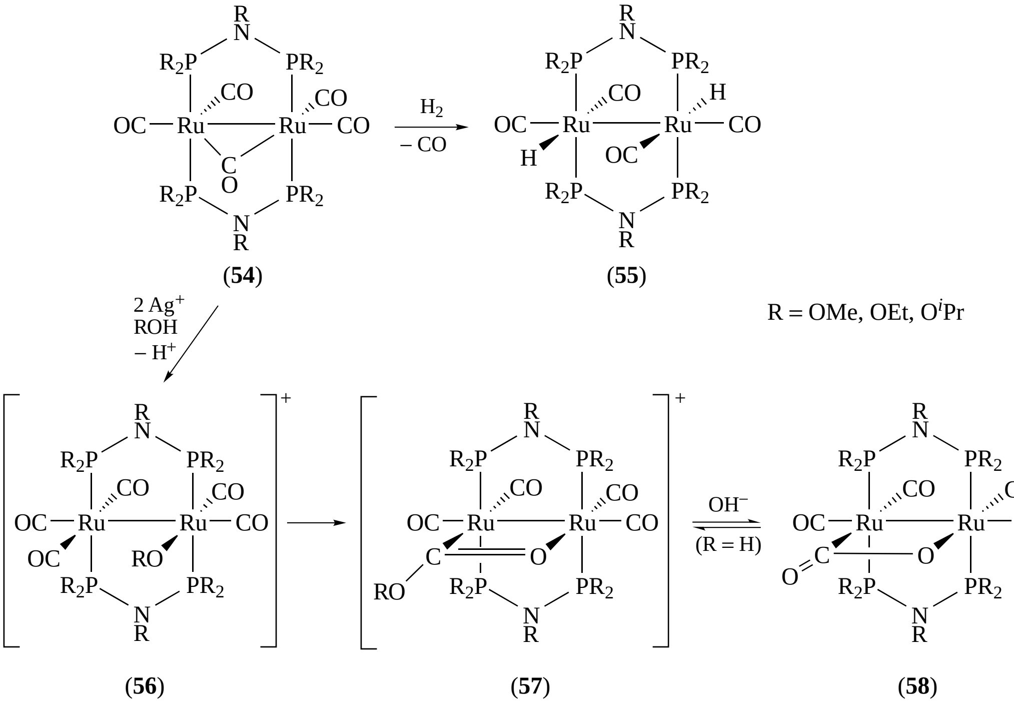

Scheme 13

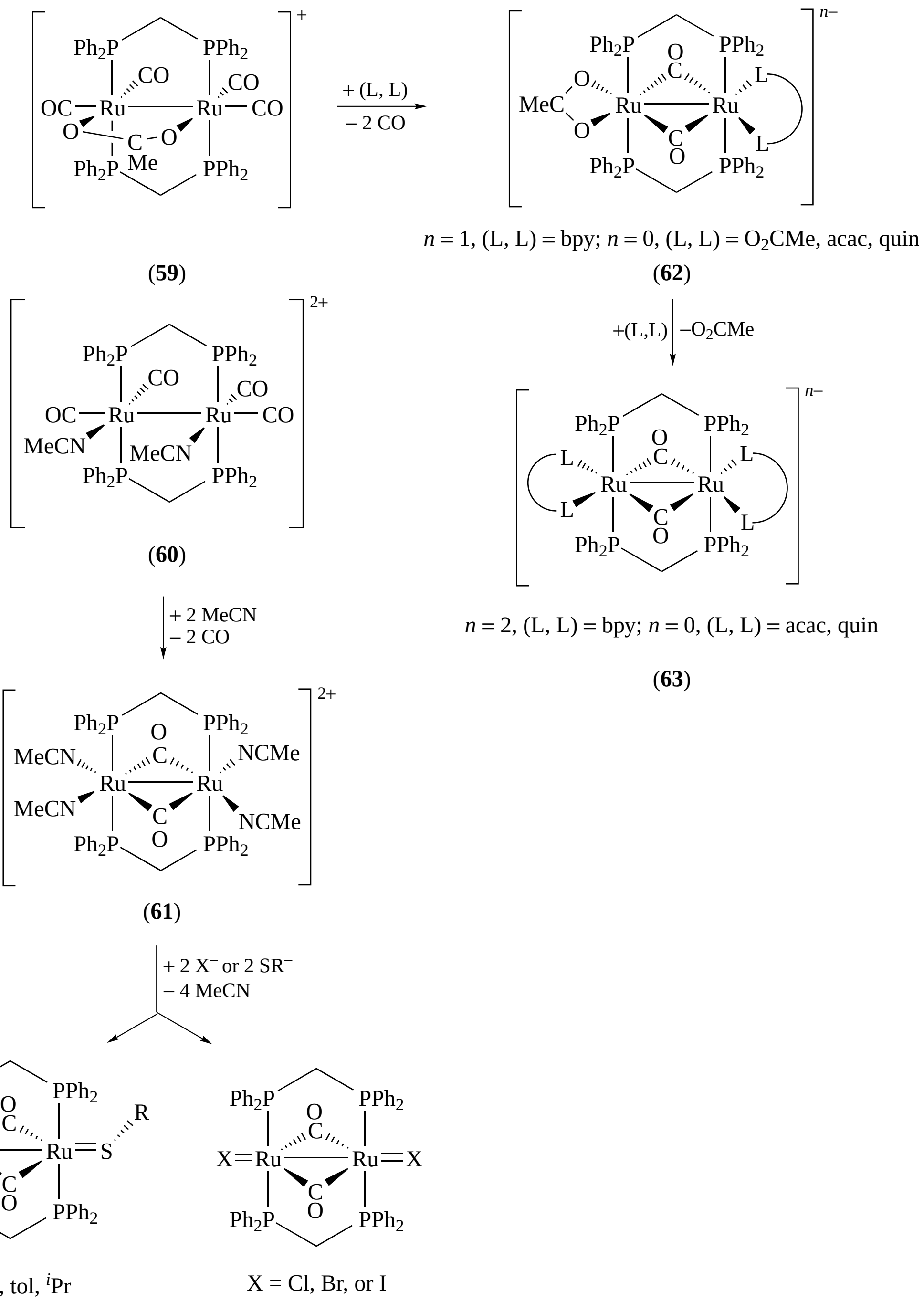
(59)
+ (L, L)
− 2 CO
n = 1, (L, L) = bpy; n = 0, (L, L) = O2CMe, acac, quin
(62)
+(L,L) −O2CMe
n = 2, (L, L) = bpy; n = 0, (L, L) = acac, quin
(63)
(60)
+ 2 MeCN
− 2 CO
(61)
+ 2 X− or 2 SR−
− 4 MeCN
R = H, tol, iPr
X = Cl, Br, or I

Scheme 14

(equation 13).

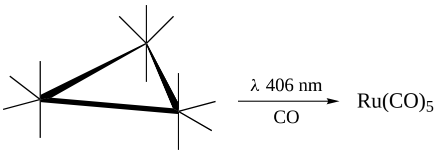
λ 406 nm
CO
Ru(CO)5
(1)
(2)

(13)

The synthesis of triruthenium derivatives via thermal substitution at (**1**) is complicated by the frequent formation of product mixtures. Thus, on heating (**1**) with a phosphine, phosphite, or a related Lewis basic ligand (*see Lewis Acids & Bases*), L, the products are either trinuclear tris- or bis-substituted complexes ($Ru_3(CO)_9L_3$ and $Ru_3(CO)_{10}L_2$), or mononuclear complexes (mostly $Ru(CO)_3L_2$), and often mixtures thereof. It appears that the first substitution step is the slowest, so the major product tends to be $Ru_3(CO)_9L_3$. A second problem with thermal substitution is the high temperatures that must be reached for substitution to occur.

A better approach to substitution at (**1**) is the use of catalytic routes. Induction with Me_3NO has proved successful for (**1**) in some cases, but of particular value for a clean reaction with (**1**) was electron-transfer catalyzed substitution using Ph_2CONa in low concentration as a reductive activator. The likely intermediate is the 49-electron species $[Ru_3(CO)_{12}]^-$, which quickly reacts to form $[Ru_3(CO)_{11}L]^-$. Electron-transfer occurs again to form $Ru_3(CO)_{11}L$ and to regenerate $[Ru_3(CO)_{12}]^-$ to repeat the cycle. The same type of reaction cycle can be induced with [PPN]X, where X = acetate, cyanide, or halides. The $[PPN][Ru_3(CO)_{12-n}X]$ ($n = 1$, 2, 3) species is the intermediate, and X is displaced by the appropriate ligand to obtain the substitution product.

The degree of substitution is determined by the initial ratio of (**1**) to ligand, and up to three (or in one instance, four) CO groups are replaced straightforwardly. This method can be employed sequentially, allowing for the preparation of mixed-ligand clusters. More forceful conditions must be employed to replace more CO ligands.

As a characteristic feature of (**1**), carbonyl substitution, even with some phosphines, is often accompanied by E–H, C–H, or even C–C bond cleavage; the substitution products are trinuclear or dinuclear units with bridging – ER groups and bridging hydrogen. Furthermore, CO groups in (**1**) are susceptible to nucleophilic attack by protic agents if a hydride bridge can be formed via a hydrogen shift. Thus, as given in Scheme 15, primary amines either add to a CO to give a formamidoyl bridge, as in (**64**), or just add across one Ru–Ru bond, substituting two CO groups, as with aniline in (**65**).[39] The adjacent functionalities NHR and CO are able to bridge a face of the triangle along with the formation of hydride bridges.[40]

Treatment of (**1**) with methylphenylsulfoximine (MePhS(O)NH) in THF yields the cluster $(\mu^2\text{-H})Ru_3(CO)_9[\mu^3\text{-}NS(O)MePh]$ (**66**). The product isolated is either enantiomerically pure or a racemic mixture, depending on whether (**1**) was reacted with optically pure or racemic starting material. Reversible carbonylation of (**66**) produces the cluster $(\mu^2\text{-H})Ru_3(CO)_9[\mu^2\text{-}NS(O)MePh]$ (**67**). Both of these optically active trinuclear clusters have potential as catalysts for enantioselective reactions.[41]

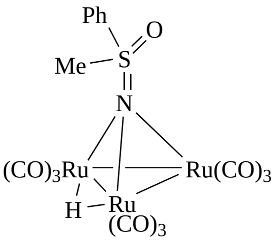

(**66**)

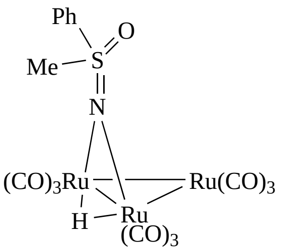

(**67**)

Reaction of (**1**) with α,β-diimines (such as Diazadienes (dad)) (Scheme 16) occurs mostly through the nitrogen atoms with some acceptor character imposed by the diene system. Products of the reaction of (**1**) with dad depend on the substituents on dad and on the reaction conditions. In contrast to the mononuclear complex $Ru(CO)_3$dad (**68**) and trinuclear $Ru_3(CO)_8$(dad) (**69**), where dad acts as an eight-electron ligand analogous to the iron congener, the dinuclear complex $Ru_2(CO)_6$(dad) (**70**) is obtained in which dad is coordinated in an unusual σ-/π-mode through both nitrogens and one carbon, thereby acting as a six-electron ligand.

3 ALKENE AND CYCLOALKENE COMPLEXES

3.1 Alkene Complexes of Ru^{II}

Ruthenium complexes of alkenes, dienes, or cyclodienes in oxidation states 0 and II are known. From a preparative view, an important class of compounds is the oligomeric or polymeric complexes of composition $[(\text{dialkene})RuX_2]_n$, which often serve as reagents for further transformations. Their synthesis is similar to the procedure that has been detailed for phosphine complexes; that is, when $RuCl_3$(aq) is refluxed in alcohol in the presence of the diene, an insoluble brown to orange oligomeric complex is deposited. However, the use of

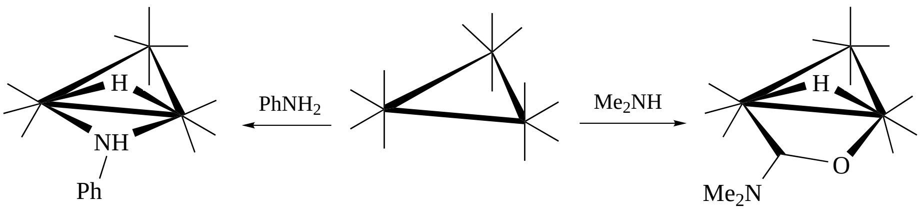

(**65**) (**1**) (**64**)

Scheme 15

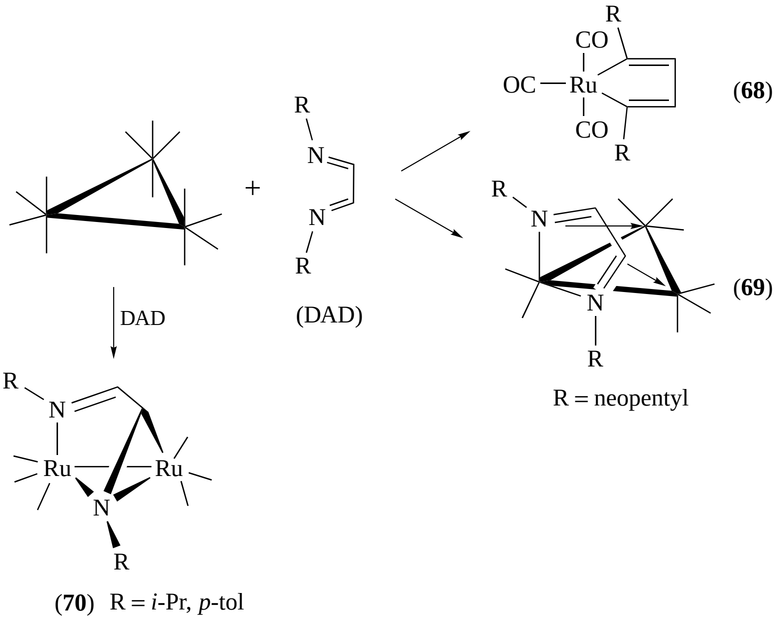

Scheme 16

cyclohexadiene produces the oligomer $[(C_6H_6)RuCl_2]_n$ (see Section 6.3). Because these polymers are formed in high yield directly from commercially available $RuCl_3$, this method is one of the best entries into organometallic ruthenium chemistry and is valuable in many cases where reaction of $Ru_3(CO)_{12}$ leads to product mixtures or is unsuitable for other reasons. The oligomers are cleaved by various donor ligands, L, notably amines or nitriles, to form soluble ionic or molecular monomers, ranging in composition from $[(\text{diene})RuLX_3]^-$ to $(\text{diene})RuL_2Cl_2$ and $[(\text{diene})RuL_4]^{2+}$.

A soluble dimer $[Ru(cod)Cl_2]_2$ (**71**), having the same formula as the insoluble polymer, has been isolated as a product from the reductive complexation of cod to ruthenium by Zn in EtOH/THF. The compound has been structurally characterized, and the Ru–Ru distance of 2.791 Å in this compound is in the range found for Ru–Ru single bonds, whereas a double bond would be required to satisfy the effective atomic number rule (*see Effective Atomic Number Rule*).**42**

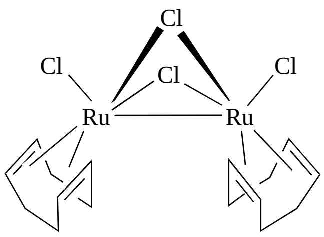

(**71**)

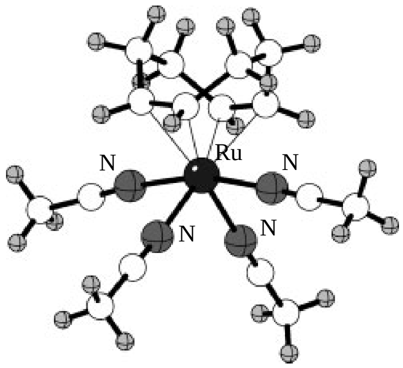

(**72**)

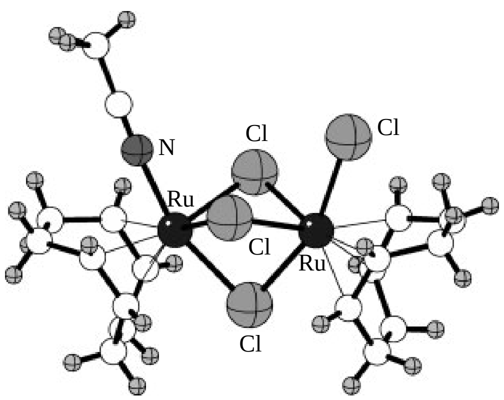

(**73**)

Refluxing (**71**) in cod and acetonitrile yields the monomeric complex $[(cod)Ru(CH_3CN)_4]^{2+}$ (**72**), which is useful in the synthesis of a variety of organometallic complexes owing to facile substitution of the acetonitriles.**43** Through a different synthetic method, a chloride-bridged diruthenium acetonitrile complex (**73**) is isolated. It was formed by reaction of (cod)Ru(cot) with naphthalene, followed by addition of acetonitrile. Compound (**73**) consists of two Ru^{II} centers with octahedral geometries. The complex undergoes two reversible one-electron oxidations, which is in contrast with other dimeric Ru^{II} complexes of this type.[**44**]

Another class of ruthenium alkene complexes contains those derived from the hexaaqua ion $[Ru(H_2O)_6]^{2+}$. The thermodynamically stable complex $[(cod)Ru(H_2O)_4]^{2+}$ (**74**) forms directly from $[Ru(H_2O)_6]^{2+}$ and cod in alcohol at ambient temperature (equation 14). In (**74**), the redox potential of Ru^{II} has shifted more positive for the oxidation to Ru^{III} and more negative for the reduction to Ru^{I} or Ru^{0}, so as to impose a high stability towards disproportionation (*see Disproportionation*) (in contrast to the readily disproportionating aqua ion $[Ru(H_2O)_6]^{2+}$). The X-ray crystal structure (*see X-ray Crystallography*) of the Tosylate $(Ots)^-$ salt disclosed quite different R–OH_2 distances of 2.095(2) and 2.156(2) Å for water *gauche* or trans to the alkene double bond, showing the structural trans effect (*see Trans Effect*) of the latter on a σ- (and π-) donor ligand trans to it.[**45**]

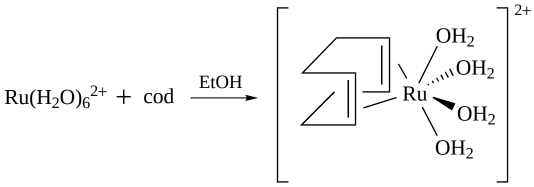

(14)

(**74**)

3.2 Alkene Complexes of Ru^0

Mononuclear carbonyl alkene complexes of Ru^0 exhibit moderate to low stability. The same is true for carbonyl phosphine complexes with unsubstituted alkenes, such as $Ru(CO)_2(PPh_3)_2(C_2H_4)$. An entry into the substitution chemistry of carbonyl alkene complexes is the thermal preparation of $(cod)Ru(CO)_3$ by refluxing (**1**) and cod in benzene. Isolation of the pure product requires double chromatography of a nearly colorless material of low-melting point and gives the product in about 60% yield.[**46**] Facile exchange of the cod ligand for conjugated dienes occurs in high yield.

A versatile reductive complexation method that leads directly to cycloalkene Ru^0 complexes consists of treatment of $RuCl_3$ with activated Zn in ethanol or methanol (or mixtures with THF) in the presence of an alkene (Scheme 17).[**47,48**] Starting from a diene, a dehydrogenation is required to provide the metal with 18 valence electrons (*see Eighteen Electron Compounds*), and this is accomplished by hydrogenating one of the cycloalkenes to a monoalkene, which as the weakest ligand is replaced by another diene. An extension of this method was found by prolonged refluxing of $RuCl_3$ in ethanol in the presence of Cyclooctatetraene (cot). The product was the insoluble oligomer $[(C_8H_{10})RuCl_2]_n$, where the cot ligand was hydrogenated to form cyclooctatriene. The same procedure also gives the analogous cycloheptatriene complexes.

3.3 Diene and Cyclodiene Complexes Derived from $Ru_3(CO)_{12}$

Simple alkene complexes, where one alkenic group replaces a carbonyl in (**1**) or (**2**) are unstable, as already stated, and have been characterized only in solution. For example, the monoethylene complex $Ru(CO)_4(\eta\text{-}C_2H_4)$ can be made photochemically in solution by irradiating (**1**) or (**2**) in the presence of an excess of ethylene. This compound decomposes below room temperature but its stability is enhanced in the presence of excess CO; presumably CO dissociation is the initial step of the decomposition. The compound serves as an intermediate for the preparation of more stable alkene complexes from electron-deficient alkenes by simple exchange at low temperature in solution. $Ru(CO)_4(\eta\text{-alkene})$ complexes with electrophilic alkenes can also be isolated from $Ru(CO)_4(\eta\text{-}C_2H_4)$ in this way.

A number of mono-, di-, and trinuclear carbonyl cycloalkene complexes derived from (**1**) have been prepared and studied, some in considerable detail owing to interesting modes of fluxionality of the cyclopolyene ligand. Reaction of $Ru_3(CO)_{12}$ with cycloalkenes gives products in which the triangle of ruthenium atoms is preserved and those in which it is cleaved into mono- and dinuclear units (e.g., (**75**) in equation 15). Products can also form by increasing the number of metal centers, such as the reaction of $Ru_3(CO)_{12}$ with C_8H_{14}, which forms the trinuclear cluster $[H_2Ru_3(CO)_9(\mu^3\text{-}\eta^2\text{-}C_8H_{12})]$ and the hexanuclear carbido-cluster $[Ru_6C(CO)_{15}(\mu^3\text{-}\eta^2\text{-}C_8H_{12})]$.[**49**]

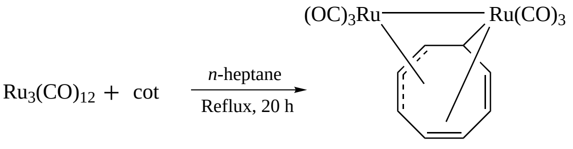

(15)

(**1**) (**75**)

Like all complexes of this type, (**75**) is fluxional (*see Fluxional Molecule*) at ambient temperature with respect to the cot ligand. The low-temperature limiting spectrum of (**75**) is in accord with the solid-state structure as inferred from the analogous iron compound that had been determined by X-ray analysis (*see X-ray Crystallography*), showing one allylic and one ‘en-ylic’ bound $Ru(CO)_3$ group with an interposed, noncomplexed double bond. This bonding mode is characteristic for many metal fragments coordinated to cot, cyclooctatriene, or other cyclotrienes.[**50**]

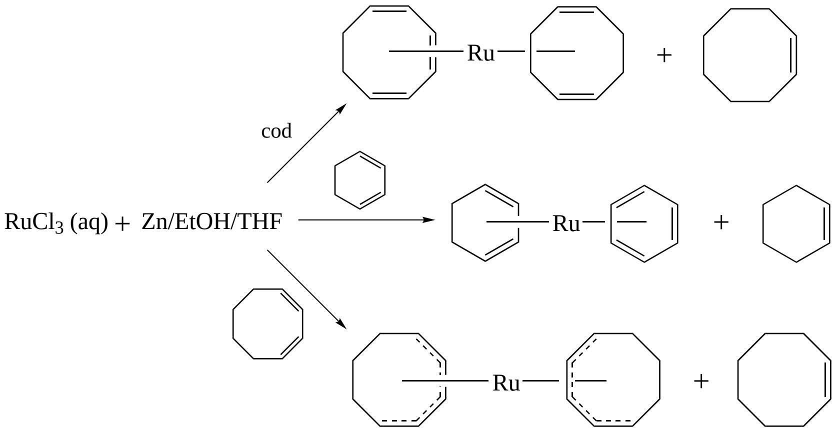

Scheme 17

Of particular interest is the bis(cot) compound (**76**) formed from reaction of $Ru_3(CO)_{12}$ and cot in *n*-octane reflux (equation 16). This molecule is fluxional (*see Fluxional Molecule*) at room temperature and below. A solid-state structure determination[51] established the near C_2 molecular symmetry (a C_2 axis passing through the carbonyl-free ruthenium atom and intersecting the opposite Ru–Ru vector). Only one enantiomer of the chiral molecule was found in the crystal, thus spontaneous resolution had occurred during crystallization (this could be accomplished by interconversion of enantiomers through the interchange of CO groups). One ruthenium atom is complexed only to alkenes, and the Ru–Ru distances to the other two metal atoms are longer than the bond between the two $Ru(CO)_2$ groups. Since the alkene is a weaker π-acceptor (*see π-Acid Ligand*) compared to CO, it takes less electron density out of the metal–metal antibonding HOMO.

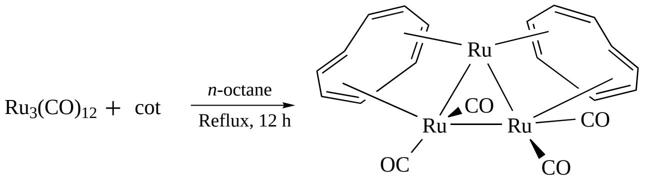

(**1**) (**76**)

(16)

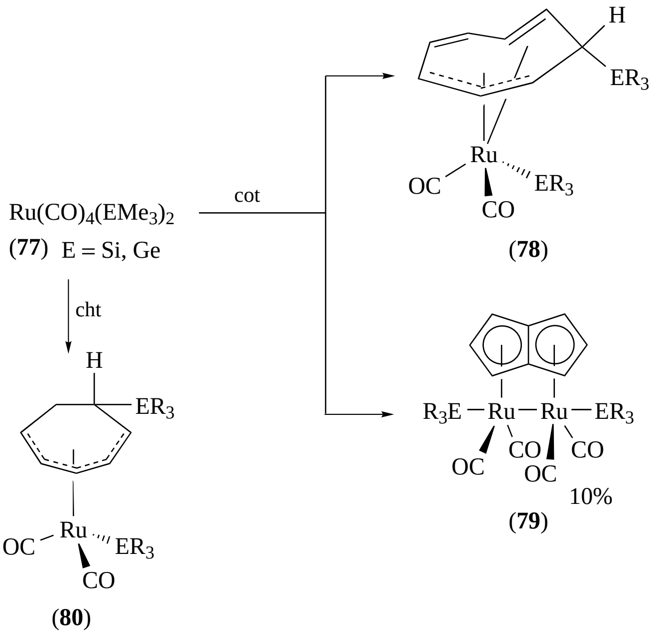

Scheme 18

In addition to hydrogen shifts, ring contraction is observed in reactions of cycloalkenes with ruthenium carbonyl centers containing E^{IV} ligand derivatives $Ru(CO)_4(ER_3)_2$ (**77**) and $[Ru(CO)_4ER_3]_2$. Heating of either (**77**) or $[Ru(CO)_4ER_3]_2$ with cot gives a mixture of two complexes (**78**) and (**79**) (Scheme 18), the latter in most cases in low yield.[52] In (**78**) one of the substituent groups ER_3 ($GeMe_3$ or $SiMe_3$) has migrated to the cot ring and is found stereospecifically in the *endo* position. For cot as the ligand, complexation is through an allyl fragment and an isolated double bond as shown in (**78**), leaving one uncomplexed double bond in between, whereas for the complex derived from cycloheptatriene (cht), a conjugated dienyl system is formed, as in (**80**).

The second major reaction product from the reaction of cot with (**77**) is the dinuclear complex (**79**) with a coordinated pentalene ligand (C_8H_6) that is highly unstable as a free hydrocarbon. In (**79**), the pentalene ligand has lost its substituent; however, since the pentalene complex can be generated from (**78**) in somewhat higher yield (about 30%) than in the direct reaction between (**77**)/$[Ru(CO)_4ER_3]_2$ and cot, it seems that (**78**) is an intermediate in the formation of (**79**). The ER_3 group appears to be a necessary prerequisite for dehydrogenative ring contraction. The exact mechanism of this reaction is not known.

4 RUTHENOCENE

4.1 General Properties and Preparation

The sandwich complex ruthenocene, $RuCp_2$ (**81**), is more stable than its iron analog ferrocene (*see Ferrocene*). With a decomposition temperature around 600 °C, ruthenocene is among the most stable organometallic compounds known. Similarities to ferrocene not only include structural features but also reactivity, such as facile electrophilic substitution at the cyclopentadiene ring. As a substituent, the ruthenocenyl group $RuCp(C_5H_4)$ (Rc) is slightly less electron releasing than ferrocene ($\sigma_\mathrm{p} - 0.05$ vs. -0.10 for ferrocene), but in direct metal–R interactions ruthenium forms stronger bonds. Thus, protonation of ferrocene with strong acids has yielded spectroscopic evidence for metal protonation at low temperature and rearrangement to a 16 valence electron $CpFe^+$ cation, whereas metal-protonated ruthenocenium cations, in particular those derived from penta- and decamethylruthenocene are readily isolated as salts.[53]

The common metathesis reactions for the preparation of metallocenes, treating a metal salt MX_2 with NaCp, are hampered in the case of ruthenium by the lack of suitable Ru^{II} salts. (RuI_2 is commercially available, but is still not commonly used in the synthesis of ruthenocene.) Thus, ruthenocene has been obtained from $Ru(acac)_3$ and NaCp in very low yield[1,54,55] and later from $RuCl_3$ and NaCp in 50–60% yield. It has now become apparent that alkene polymers, in particular $[Ru(nbd)Cl_2]_x$, but also $[Ru(cod)Cl_2]_x$ and hydrazine derivatives (Section 3.1), can serve as Ru^{II} precursors.[56] Equally successful in many cases is reductive complexation of cyclopentadiene in ethanol in the presence of Zn (Section 3.2), which furnishes the metallocene in about 80% yield. Decamethylruthenocene (**82**) was first obtained by the Zn reduction route in 20% yield,[57] but can now be prepared conveniently from halide complexes $[Cp^*RuCl_2]_2$[53] or $[Cp^*RuCl]_4$, a common method for the preparation of symmetrical and unsymmetrical sandwich compounds of ruthenium featuring one alkyl-substituted ligand.

4.2 Structure

The molecular and crystal structure of (**81**) is simpler than that of ferrocene as only one polymorph featuring eclipsed conformation of the cyclopentadienyl rings, has been found at ambient and low (100 K) temperature. The larger metal–carbon distance (2.186 Å in (**81**) vs. 2.03 or 2.06 Å in ferrocene) corresponds to the larger metal covalent radius (*see Covalent Radii*) and may also be responsible for the fact that an eclipsed conformation is found for the solid-state structure of decamethylruthenocene (**82**),[56] as opposed to decamethylferrocene where more closely spaced methyl groups impose the staggered D_{5d} conformation.

4.3 Redox Reactions and Bent Metallocenes (*see Bent Metallocenes*): $RuCp_2X^+$

Like ferrocene, ruthenocene is stable to reduction, and no anion or controlled reductive cleavage has yet been reported. One of the major differences between ruthenocene and ferrocene is their behavior in oxidation reactions. The facile and reversible one-electron oxidation of ferrocene is used as the principal electrochemical standard in nonaqueous solvents.[58] In contrast, an apparently irreversible two-electron oxidation of ruthenocene occurs under all but the most selective conditions. This behavior, at first sight in disagreement with the tendency of the heavier transition metals to stabilize higher oxidation states, is rationalized by considering the nature of the ^2E (d_{xy}) ground state of the radical cation (as proved by EPR (*see Electron Paramagnetic Resonance*)) for the cation $(\mathbf{82})^+$.[57] Since there is increasing ligand character in the degenerate $d_{xy}/d_{x^2-y^2}$ orbital pair with the 4d and 5d transition metals, single occupancy of these levels causes higher chemical reactivity.

For ruthenocene, the subsequent reaction (Scheme 19) is addition of a nucleophile (*see Nucleophile*) to the metal center. Generally, the nucleophile is a halide (X^-), but it can be mercury from a mercury electrode; a second oxidation then gives the cations $[RuCp_2X]^+$ (**83**) or $[Cp_2Ru–Hg–RuCp_2]^{2+}$, respectively. In the absence of a stabilizing nucleophile, disproportionation (*see Disproportionation*) prevails. The halide complexes are isolable, and the iodide and chloride cations $[RuCp_2X]^+$ have been structurally characterized.[59,60] The crystal structure of the bromide analog exists only with permethylated ligands.[61]

Bimolecular exchange between $[RuCp_2X]^+$ and $RuCp_2$ occurs as an inner-sphere (*see Inner-sphere Reaction*) electron transfer. The effects of varying the transferred atom (X), counterion, solvent, and substitution on the cyclopentadienyl ligands have been studied. It was found that the exchange rate constant is lowest with chlorine, and increases down the periodic table to iodine. Among complexes with the same halide, exchange rates increase with the number of methyl groups on the cyclopentadienyl ligands. This trend seems to be a consequence of the electronic effects of methylation on reaction energetics and shows that the mechanism is through the bridged transition state (Scheme 20).[62]

A different mode of stabilization for the monocations is dimerization. While the osmocene (*see Osmocene*)

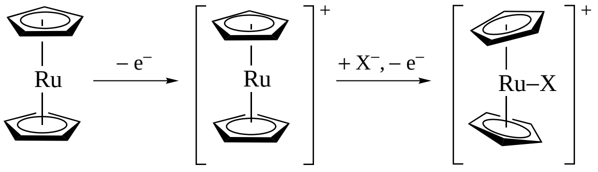

(**81**) $(\mathbf{81})^+$ (**83**)

Scheme 19

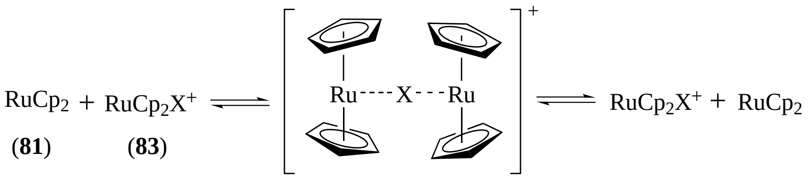

Scheme 20

dimer $[Cp_2Os–OsCp_2]^{2+}$, formed through one-electron oxidation, has been isolated and structurally characterized, the corresponding ruthenocenium dimer, although not structurally authenticated, has been studied. As indicated with CV experiments, the electrochemical oxidation of (**81**) produces mainly the dimer dication (**84**) in equilibrium with the monocation $(\mathbf{81})^+$ complex, as shown in equation (17). Complex (**84**) and the osmium analog represent the only two unbridged metal–metal bonded metallocenes.**[63]**

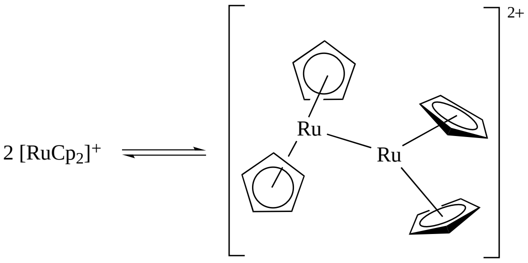

(17)

$(\mathbf{81})^+$ (**84**)

A reversible one-electron oxidation (equation 18) was observed with (**82**) in a nonnucleophilic solvent (such as CH_2Cl_2).**[57]** With rigorous exclusion of even the weakest nucleophiles (e.g., PF_6^-), using $[(3,5\text{-}(CF_3)_2C_6H_3)_4B]^-$ as the supporting electrolyte in cyclic voltammetry, a reversible one-electron oxidation of (**81**) is possible as well.**[64]**

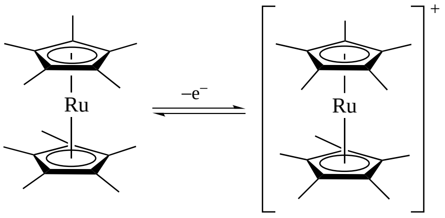

(18)

(**82**) $(\mathbf{82})^+$

4.4 Substitution

As mentioned above, ruthenocene is susceptible to electrophilic substitution in a manner similar to ferrocene. Thus, common reactions for activated aromatics, such as acylation ($RCOCl/AlCl_3$), sulfonation (SO_3 in dioxane), aminomethylation ($CH_2(NMe_2)_2$), Vilsmeier–Haack formylation ($DMF/POCl_3$), arylation via diazonium salts, as well as mercuration and lithiation, have been performed with (**81**).**[4,65]** The perhalogenated ruthenocene has commonly been obtained from the decaacetoxymercury derivative (**85**), which is formed as a highly insoluble product from mercuration of (**81**) with $Hg(OAc)_2$ in methylene chloride.**[66]** Halogenation of (**85**) with halogens (X_2) gives the perhaloruthenocenes (**86**) in one step, with yields from 40 to 70% depending on the halide. Repeated lithiation and successive quenching of the metallated ruthenocene with C_2Cl_4 to give finally perchlororuthenocene is another method for the synthesis of (**86**) (Scheme 21).

Although monolithiated metallocenes are well known, cyclopentadienyl ligands with higher lithiation are rare. Pentalithiocyclopentadienyl ligands have been isolated from the treatment of (**85**) or $Cp^*Ru[C_5(HgOAc)_5]$ (**87**) with methyllithium (Scheme 22). $Ru(C_5Li_5)_2$ and $Cp^*Ru(C_5Li_5)$ complexes have been isolated, respectively, with this synthetic route. They can easily be converted to halogenated complexes by treatment with electrophiles such as bromine or methyl iodide.**[67]** In addition to the lithiation method, ruthenocene complexes with unevenly substituted cyclopentadienyl ligands have been isolated using $RuCp(\eta^4\text{-butadiene})Cl$ (**88**). Refluxing (**88**) with $Tl(OC_6F_5)$ in THF yields $RuCp((2\text{–}6\text{-}\eta^5)\text{-}C_6F_5O)$, which is converted to the crystallographically characterized complex $RuCp(\eta^5\text{-}C_5F_5)$ with flash vacuum pyrolysis.**[68]**

A notable substitution product of ruthenocene is ethynylruthenocene, which can be bound to estradiol, a form of estrogen studied for breast cancer treatment. With the rigid alkyne spacer, the steroid's affinity to the estrogen receptor was surprisingly unchanged upon addition of the metallocene. The addition of organometallic complexes to biomolecules may allow for the selective tuning of properties of the molecule.**[69]**

Another interesting example of a substituted ruthenocene complex is produced upon the treatment of $Cp^*{}_2Ru_2Cl_4$ with excess Norbornadiene (nbd) in refluxing ethanol. The resulting $Cp^*Ru(\eta^5\text{-}C_5H_4C_9H_{11})$ complex has a cyclopentadienyl ring with a tricyclo$[4.2.1.0^{2,5}]$-non-7-en-3-yl substituent. This unique substituent is a result of nbd coupling, C–C bond cleavage, hydrogen migration, and hydrogen loss. The dimerization or trimerization of norbornadiene is common among transition metal complexes, but the formation of a substituted metallocene from the nbd coupling is unprecedented.**[70]**

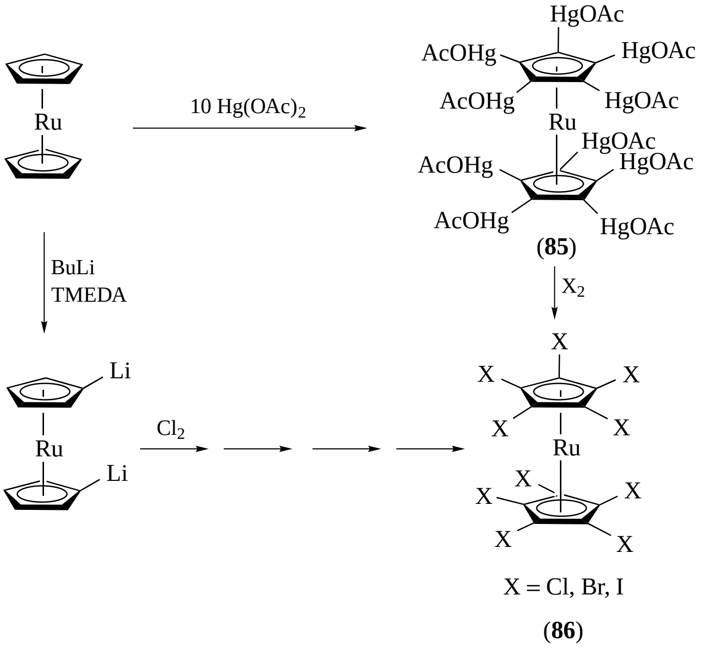

Scheme 21

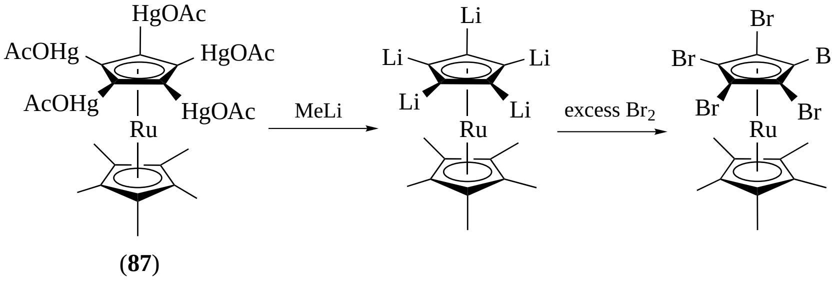

Scheme 22

4.5 α-Ruthenocenyl Carbonium Ions and η^6-Fulvene Complexes

Similar to ferrocene, the ruthenocene derivatives (**89**) substituted with a CR^1R^2 group are greatly stabilized in comparison to noncomplexed carbenes or carbonium ions. In fact, from the enhanced barrier to internal rotation in the α-ruthenocenyl carbonium ion Ru–$CHMe^+$ ($>130\,kJ\,mol^{-1}$) compared with the related ferrocene derivative ($70\,kJ\,mol^{-1}$), even greater stabilization in ruthenocene is expected.

The common preparative route to these cations by proton-cation induced OH abstraction from an α-hydroxymethyl group (equation 19) is complemented for methylruthenocenes by the direct and facile deprotonation of a ring methyl group in the cation (equation 20). Thus, oxidation of (**82**) in the presence of a halide ion rapidly converts the initially formed ruthenocenium cation $(\mathbf{82})^+$ into the respective fulvene, which is oxidized by excess $(\mathbf{82})^+$ to the fulvenyl or α-methylene cation (**90**). Complex (**90**) can also be obtained directly from (**82**) by hydride abstraction through Ph_3CBF_4 in high yield (equation 20).**[71]** An X-ray structure determination (*see X-ray Crystallography*) of (**90**) showed the existence of one shorter Ru–C bond, a displacement of ruthenium towards this bond, and inward bending of this atom from the otherwise planar C_5Me_4 ring.**[72]** Owing to their easy preparation and facile addition of various nucleophiles, these cationic fulvene complexes can be of high synthetic value. In an attempt to analyze the effect of end groups on charge localization of polymethines, the crystallographically characterized1,3-(diruthenocenyl)allylium cation was synthesized. It consists of a (η^6-fulvene)(η^5-cyclopentadienyl)ruthenium cation bridged by vinylene to a symmetrical ruthenocene. This is a unique molecule in that it is a symmetrically substituted species that adopts an unsymmetrical structure and localizes the charge at only one end.[73]

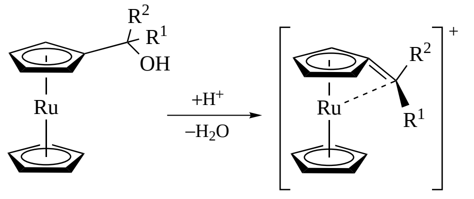

(**89**)

(19)

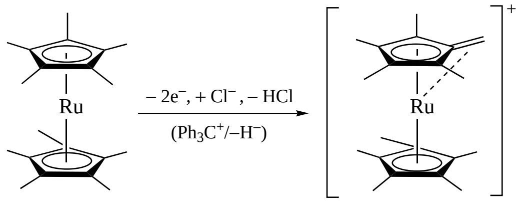

(**82**) (**90**)

(20)

4.6 Heteroruthenocenes and Ruthenocene-Related Dienyl Complexes

Among the few known heteroruthenocenes are cationic thiophene- and bis(thiophene)ruthenium, electronic analogs to arene ruthenium sandwich complexes (Section 5), and derivatives featuring a tetramethylpyrrole (tp) ligand, Cp*Ru(tp) (**91**) and Ru(tp)$_2$,[74] prepared by an adaptation of the Zn reduction method to the chloro complex [Cp*RuCl$_2$]$_2$ (**92**) (equation 21). The methyl groups are necessary to prevent σ-complexation of the pyrrole ligand; however, under suitable conditions ([Cp*Ru(acac)]$_2$/Zn^{2+}/pyrrole in ether), the preparation of at least Cp*Ru(pyrrole) (**93**) has been equally successful (equation 22).

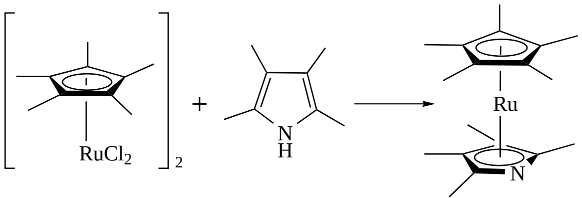

(**92**) (**91**)

(21)

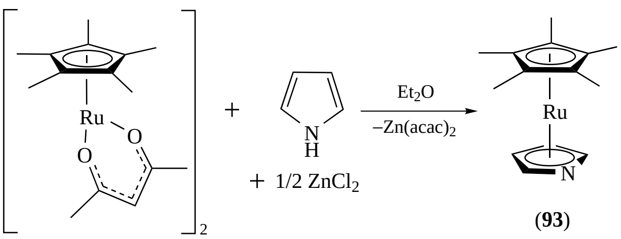

(**93**)

(22)

A series of so-called 'half-open ruthenocenes',[75] notably Cp*Ru(η^5-C$_5$R$_7$), are prepared similarly from Cp*Ru precursor complexes (Cp*RuCl)$_4$ or (Cp*RuOMe)$_2$ and dienyl alkali salts or dienes and a mild base to effect dehydrohalogenation. Half-open ruthenocenes are versatile, allowing for incorporation of substituents onto, as well as heteroatoms into, the pentadienyl fragment. X-ray crystallographic studies (*see X-ray Crystallography*) have found that the C$_5$R$_7$ ligands are essentially planar with rather short Ru–dienyl bond lengths (2.12–2.19 Å). Varying the composition of the pentadienyl ligand allows for adjustments to the chemistry of the complex. For example, oxodienyl complexes are generally more reactive than all-carbon analogs, owing to the weaker coordination of the oxygen.[76]

Open ruthenocenes, Ru(η^5-C$_5$R$_7$)$_2$, with asymmetric substitution of the pentadienyl ligands (*see Pentadienyl Ligand*) allow for the synthesis of diastereomeric products. The treatment of (**1**) with 2-methyl-4-phenylpentadiene and zinc dust yielded bis(2-methyl-4-phenylpentadienyl)ruthenium (**94**). The product consists of a pair of diastereomers, which were easily separated by fractional crystallization because of their substantially different solubilities. One isomer could exist as a pair of enantiomeric rotamers, each with C_1 symmetry (**94a**) and (**94b**), while the other could be a pair of diastereomeric rotamers, both with C_2 symmetry (**94c**) and (**94d**). Both of the former rotamers are observable, but (**94c**) is the only form of the latter, and interconversion to (**94d**) does not occur. The possibility of isomerization with photochemical initiation still remains to be investigated.[77]

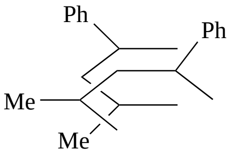

(**94a**)

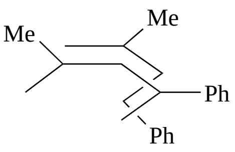

(**94b**)

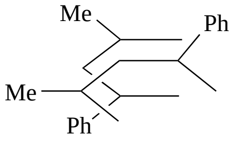

(**94c**)

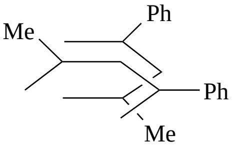

(**94d**)

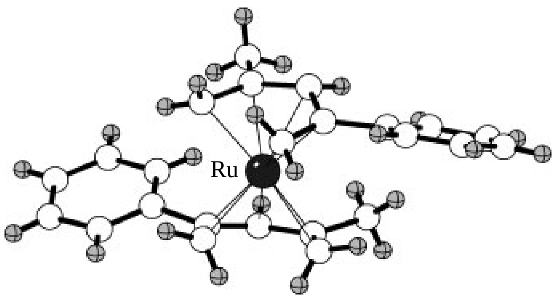

(**94**)

The tricarbadecaboranyl ligand (C$_3$B$_7$H$_{10}$) has been compared with the cyclopentadienyl anion, as both have the same charge and similar electron-donating ability. However, metal complexes with tricarbadecaboranyl exhibit greater oxidative, chemical, thermal, and hydrolytic stability compared to metallocenes. Nonetheless, the cage-slippage of the tricarbadecaboranyl ligand between η^6 and η^4 coordination modes mirrors a similar η^5 to η^3 slippage in metallocenes. The ruthenocene-like complex *commo-Ru*-(2-Me-*closo*-1,2,3,4-$RuC_3B_7H_9)_2$ (**95**) was synthesized by treating $RuCl_2(cod)_x$ with Li(6-Me-*nido*-5,6,9-$C_3B_7H_9$) in glyme.**[78]**

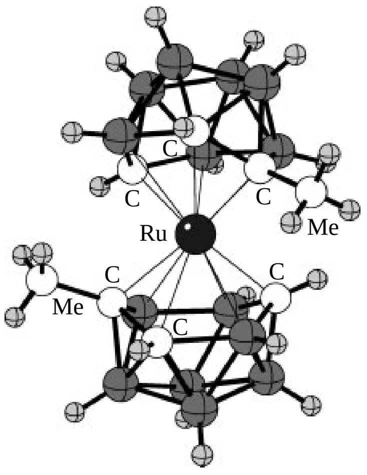

(**95**)

An interesting characteristic of ruthenocene is that it is a photoinitiator for the anionic polymerization of ethyl 2-cyanoacrylate. Solutions with millimolar concentrations of the complex in neat cyanoacrylate polymerize to a hard, plastic solid within seconds upon exposure to light. The low concentration of ruthenocene required for the polymerization makes it desirable in applications such as coating and adhesives that require solvent-free solutions of monomer.**[79]**

5 (ARENE)(CYCLOPENTADIENYL) AND BIS(ARENE) RUTHENIUM COMPLEXES

5.1 [Ru(arene)(cyclopentadienyl)]$^+$ Complexes

This type of sandwich complex, first reported with iron as the central metal, has now become widespread with ruthenium as well. Early routes to ruthenium complexes were modeled on iron chemistry, and used the $AlCl_3$-catalyzed exchange of a cyclopentadienyl ligand for an arene in ruthenocene, or reaction of $CpRu(CO)_2Cl$ with $AlCl_3$/arene. These methods are less successful with ruthenium than with iron, however, owing to the greater stability of ruthenocene. A mixture of arene, pentamethylcyclopentadiene, and $RuCl_3$ in the Zn reduction method gives good yields of the mixed-sandwich cations. A great variety of [Ru(arene)(cyclopentadienyl)]$^+$ complexes, including functionally substituted arenes, polyphenyls, and paracyclophanes, phenols, condensed polyaromatics, as well as the six-electron heterocycles thiophene and pyridines, have been complexed to ruthenium.

With the less tightly bound polyarenes or heteroarenes, displacement of the arene has been observed. Thus, sensitive dications with these types of ligands can only be prepared and handled in nonnucleophilic environments. Behavior in the pyridine complexes is particularly interesting. Here a rearrangement from the initially formed π-complex (**96a**) to a σ-complex (**96b**) occurs (equation 23).**[80]** However, heating of (**96b**) (L = acetonitrile) under vacuum gives (**96a**).**[81]** It thus appears that the pyridine π-complex is stable in the absence of additional σ-ligands, including excess pyridine.

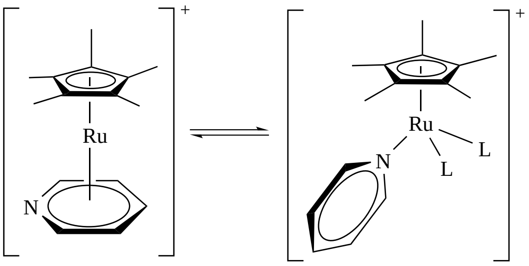

(23)

(**96a**) (**96b**)

Recently, organometallic ruthenium chemistry has found its way into biological applications. Treating $[Cp^*Ru(MeCN)_3][CF_3SO_3]$ with amino acids in THF yields η^6-coordinated amino acid complexes of the type $[Cp^*Ru(\eta^6\text{-}HaaOH)][CF_3SO_3]$, where HaaOH = L-HPheOH (phenylalanine) or L-HTrpOH (tryptophan), as shown in equation (24). Similarly, dipeptide and cyclopeptide complexes can be synthesized under parallel conditions. These types of complexes are essentially Cp^*Ru^{II} labeled peptides, which could have a notable impact on the analysis of protein receptor sites.**[82]**

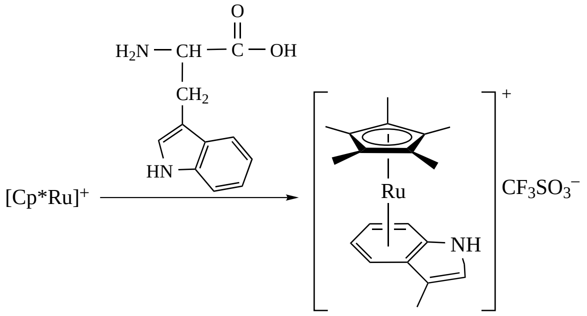

(24)

Ruthenocene derivatives have also been studied as potential second-order nonlinear optical materials. Using the $[Cp^*Ru]^+$ fragment, several aromatic systems have been synthesized and studied for this goal. The $[Cp^*Ru]^+$ fragment was synthesized by treating $[Cp^*Ru(OMe)]_2$ with triflic acid. Various aromatic complexes were then added to this reaction mixture to form sandwich derivatives of the type shown in equation (25).**83**

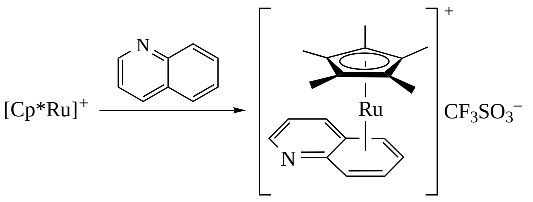

(25)

5.2 Neutral Ru(arene)(cyclopentadienyl) Complexes

An interesting derivative of the pyrrole ring that has found its way into ruthenocene chemistry is *meso*-octaethylporphyrinogen. The tetraanion is of interest because it allows for η^1, η^3, or η^5 binding and can donate from 8 to 24 electrons. It has an internal N_4 site that easily binds nickel(II). Treatment of the lithiated porphyrinogen with $Ru(Cl)(p\text{-cymene})_2(\mu\text{-}Cl)_2$ or $Ru(Cl)(cod)_2(\mu\text{-}Cl)_2$ binds one of the pyrrole rings to the Ru(p-cymene) (**97**) and the Ru(cod) fragments, respectively. Once the ruthenium is bound, the cod ligand undergoes rearrangement to form an η^5-cyclopentadienyl-like ligand (**98**). With a Ni^{II} and Ru^{II} center, it is an overall neutral molecule.**84**

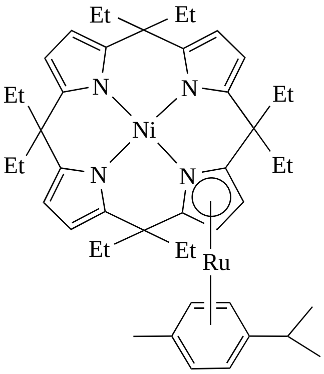

(**97**)

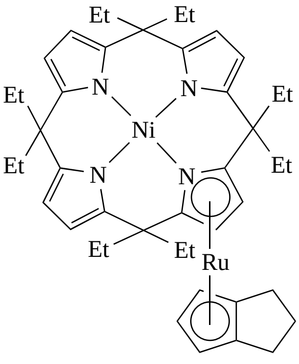

(**98**)

5.3 Bis(arene) Complexes

Bis(arene) complexes of ruthenium (**99**), first prepared in relatively low yield by the Fischer–Hafner synthesis (*see Fischer–Hafner Synthesis*) ($MCl_3/AlCl_3$/arene) are now readily available through solvento cations $[(arene)RuS]^{2+}$ (S = acetone, nitromethane), which in turn are made from the dimeric half-sandwich halides $[(arene)RuCl_2]_2$ (Section 6.3) with Ag^+ with the appropriate arene as solvent (Scheme 23). This method allows a whole range of functionalities to be incorporated to at least one of the arenes. The dications $(\mathbf{99})^{2+}$ are of relatively high solvolytic stability and are decomposed by DMSO only to form $[(arene)Ru(DMSO)_3]^{2+}$.

Whereas $[CpRu(arene)]^+$ cations are not easily reduced electrochemically (with $[CpRu(polyarene)]^+$ being an exception), the bis(arene) complexes have aroused interest owing to their two-electron redox change that converts one arene from an η^6- into a bent η^4-ligand. An electrochemical investigation of this process revealed that the second electron transfer is slower than the first one. In neutral Ru(η^6-arene)(η^4-arene) complexes (**99**), the bonding mode between η^4- and η^6-arene ligands interchanges, giving a new type of fluxionality ($\Delta G^\ddagger = 67\,\text{kJ mol}^{-1}$ for arene = C_6Me_6) as indicated in Scheme 23.

Bis(arene) ruthenium complexes $(\mathbf{99})^{2+}$ are electrophilic and add various nucleophiles (*see Nucleophile*), including hydride, to form (**100**) (Scheme 24). Methyl groups of methylated arene rings are acidic and can be deprotonated, giving the corresponding *exo*-methylene complexes (**101**). This is similar to the chemistry developed for analogous iron complexes, and is reminiscent of the α-ruthenocenyl carbonium ions (Section 4.5).

5.4 Triple-Decker Complexes

Ruthenium has played a central role in the development of 30 valence electron triple-decker cations of the iron group. These compounds were first prepared by Rybinskaya *et al.*,**85,86** through reaction of a 12 valence electron $[CpRu]^+$ fragment with a metallocene. The well-known photofragmentation of $[CpFe(arene)]^+$ was used to generate $[FeCp]^+$, which was then complexed to ruthenocene in situ. The structure of the triple-decker shows three exactly parallel rings, two of them (one outer and the inner) eclipsed and

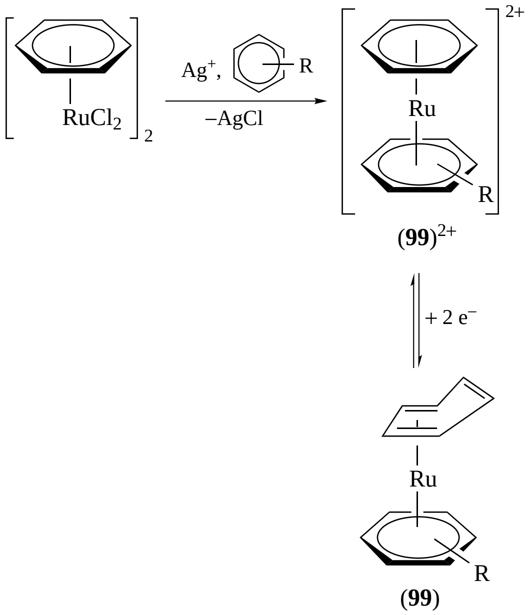

Scheme 23

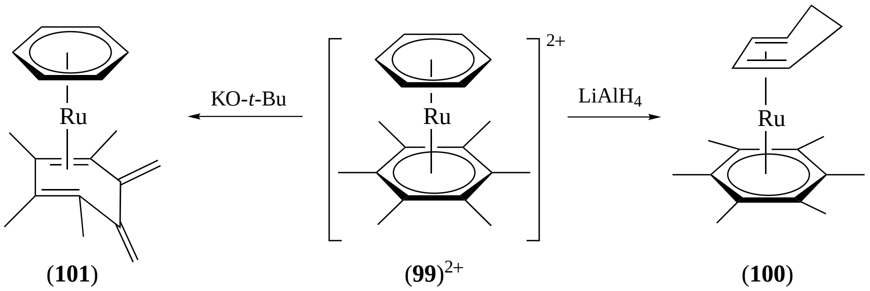

Scheme 24

perfectly staggered to the third one, with Ru–C and Ru–ring distances that on average do not differ significantly from those in ruthenocene or decamethylruthenocene (equation 26).

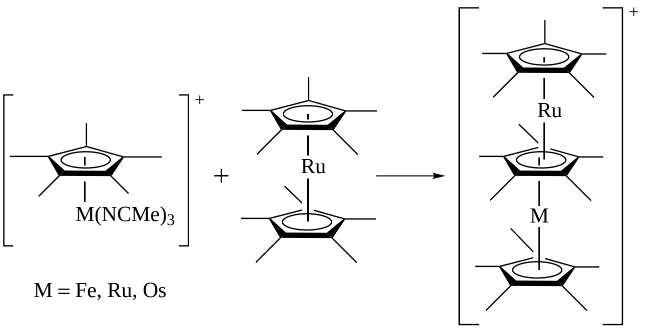

(26)

It was initially thought that the stability of the complexes required permethylation of the Cyclopentadiene (Cp) rings in the middle deck; however, careful choice of the stacking reagent allows for the preparation of partly methylated derivatives as well.[87] Thus, when $[Cp^{*}Ru]^{+}$ (as $(Cp^{*}RuOMe)/H^{+}$) is treated with either pentamethylruthenocene or ferrocene, attack is exclusively at the less-hindered site, making the Cp ring the bridging ligand (equation 27). The stacking reaction proceeds with kinetic control, and the activation barrier for attack at the substituted ring ligand appears to be considerably higher.

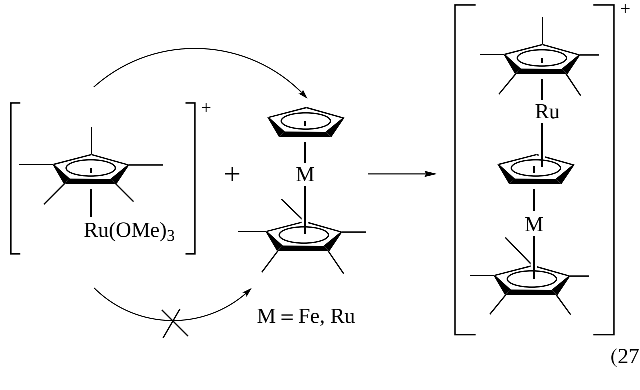

(27)

6 HALF-SANDWICH COMPLEXES (*See Half-sandwich Complexes*)

6.1 General Characteristics

Half-sandwich complexes of ruthenium are widespread with both Cp and arene ligands.[65] In the former, electron count considerations dictate the composition of $CpRuL_2X$ or $[CpRuL_2]_2$, where L are usually common π-acceptor ligands and X varies from fluorine to alkyl, hydride, and aryl ligands. If the binding atom in X contains lone pairs, these can substitute for L, leading to bridged structures, such as $[CpRuLX]_2$ or even $[CpRuX]_4$, the latter most common with X=S, SR, Se, and so on, but also exemplified by the chloro complex. The oxidation state of ruthenium can be Ru^{II}, Ru^{III}, and even partially Ru^{IV} in the tetrameric sulfur clusters (see Section 6.4).

It appears as if the potential ligands that can be accommodated in the (arene)Ru series may be even more extended than that in the CpRu series owing to the higher charge and the somewhat harder nature of the central metal, although the oxidation state is as yet confined to Ru^{II}. Apart from the molecular dimers $[(\eta\text{-arene})RuX_2]_2$, the most common starting materials for (η-arene)Ru chemistry are ionic complexes of the type $[(\eta\text{-arene})Ru(\mu\text{-}X)_3Ru(\eta\text{-arene})]^{+}$, similar to the closely related Cp* analogs of the cobalt group. Mononuclear complexes are of the type $(\eta\text{-arene})RuLX_2$, $[(\eta\text{-arene})RuL_2X]^{+}$, and $[(\eta\text{-arene})RuL_3]^{2+}$.

6.2 Half-Sandwich Complexes with Cyclopentadienyl Ligands

As outlined above, the most widespread complex type (similar to iron analogs) is $CpRuL_2X$ where L = CO, phosphines, dienes, or other similar ligands and X = hydride, alkyl groups, or halogens. Reaction of $Ru_3(CO)_{12}$ with cyclopentadiene in the absence of oxygen yields $CpRu(CO)_2H$; the presence of oxygen allows for the synthesis of dimeric $[CpRu(CO)_2]_2$ (Scheme 25). Halogenated complexes $CpRu(CO)_2X$, where X = Cl, Br, or I, are

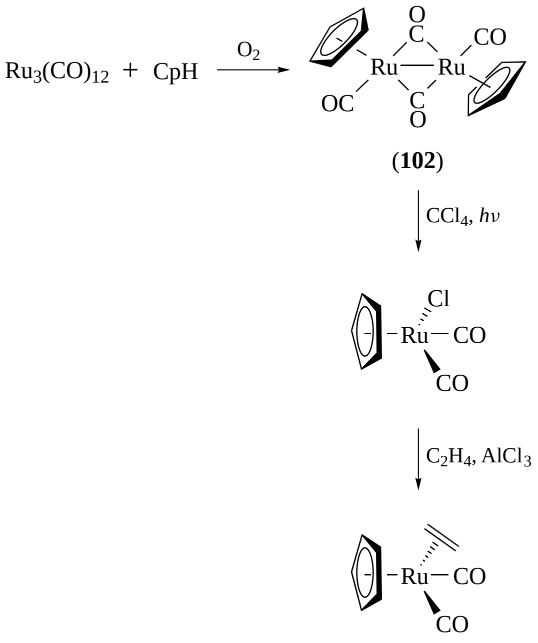

Scheme 25

formed upon treating $[CpRu(CO)_2]_2$ (**102**) with halogenated solvents. The halogen can be substituted with an olefin by reaction with olefins in the presence of AlX_3, yielding $CpRu(CO)_2L$, $L = C_2H_4$, $CH_2 = CHMe$, or cyclohexene (Scheme 25). Interestingly, the reaction of $Ru_3(CO)_{12}$ with cyclohexene results in a $Cp^{Me}Ru$ cluster derivative, where the cyclohexene undergoes ring contraction to form a methylcyclopentadienyl ligand on a hexaruthenium hydride cluster $[Ru_6(\mu_3\text{-H})(\mu_4\text{-}\eta^2\text{-CO})_2(CO)_{13}(\eta^5\text{-}C_5H_4Me)]$ (**103**).[88]

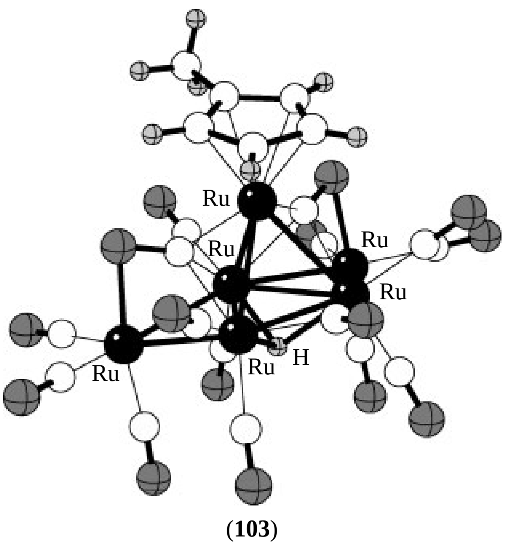

(**103**)

Whereas one CO group in complexes of type $CpRu(CO)_2Cl$ is readily substituted for phosphine, bis(phosphine) complexes, for example, $CpRu(PPh_3)_2Cl$, are best prepared in a one-step reaction from $RuCl_3$, CpH, and PPh_3 (equation 28). This air-stable crystalline solid provides a convenient starting point for further transformations.[89,90] The $CpRu(PR_3)_2$ fragment is more nucleophilic than $CpRu(CO)_2$; thus derivatives of $CpRu(PR_3)X$ with less electronegative (*see Electronegativity*) X ligands, like alkyl and hydride, are more highly stabilized compared to the respective derivatives of $CpRu(CO)_2Cl$.

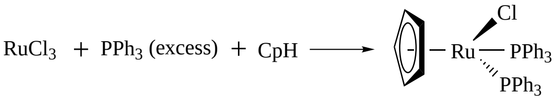

(28)

Reduction of (**102**) requires rather strong reducing agents and leads to the anion $[CpRu(CO)]^-$ (**104**) (equation 29). This reactivity is qualitatively similar to that of the iron analogs, but the ruthenium complexes are less nucleophilic. Analogous anions with a diene ligand have been prepared and are strong, highly reactive nucleophiles.[91] Substitution of CO by acceptor ligands leads to additional complexes of the same type. All these transformations are also known with substituted Cp ligands.[92]

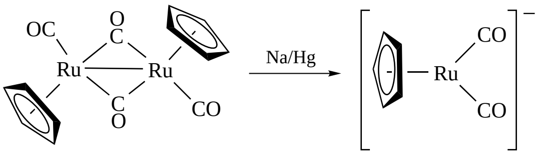

(**102**) (**104**) (29)

Half-sandwich ruthenium complexes have the ability to act as substrates for C–C bond cleavage or activation. Treatment of the methylated cyclopentadienyl complex $[Cp^*RuCl_2]_2$ with $LiAlH_4$ yields the tetrahydride-bridged complex $Cp^*Ru(\mu\text{-}H)_4RuCp^*$. Treating this complex with ethylene produces $Cp^*Ru(CH_2{=}CH_2)(CH{=}CH_2)_2RuCp^*$, which can undergo C–C coupling in toluene at 60 °C under 1 atm of ethylene to form the dinuclear ruthenacyclopentadiene complex $Cp^*Ru(CH_2{=}CH_2)(CMe{=}CHCH{=}CMe)RuCp^*$.[93]

The 1,5 cyclooctadiene complex $[Cp^*Ru(\eta^2:\eta^2\text{-}C_8H_{12})(CO)]OTf$ was isolated upon treatment of $Cp^*Ru(\eta^4\text{-butadiene})X$ ($X = Cl$, Br) with butadiene, AgOTf, and CO. A similar $[4+4]$ cycloaddition (a thermally forbidden reaction (*see Woodward–Hoffmann Rules*)) is observed when $Cp^*Ru(isoprene)Cl$ is treated with isoprene, AgOTf, and CO. Likewise, the reaction of 1,3-pentadiene with $Cp^*Ru(\eta^4\text{-1,3-pentadiene})Cl$ results in linear dimerization to form $[Cp^*Ru(4\text{-methyl-}(1,3\text{-}\eta\text{:}6\text{-}8\text{-}\eta^3)\text{-nonadienediyl})]OTf$. These types of dimerization occur with both stoichiometric and catalytic amounts of the ruthenium complex.[94]

The trinuclear pentahydride complex $[Cp^{*}Ru]_3(\mu\text{-}H)_3(\mu_3\text{-}H)_2$ (**105**) in Scheme 26 consists of ruthenium centers tightly bound by bridging hydrides. Treatment of the pentahydride complex with excess butadiene in THF results in a trinuclear 1-methyl-1,3-dimetalloallyl complex $[Cp^{*}Ru]_3(H)_4[\mu_3\text{-}\eta^3\text{-}C(Me)CHCH]$ (**106**). This interaction shows the cooperation of all three ruthenium centers as either coordination sites or activation sites. Similar results are found by treating (**105**) with isoprene.**[95]** Treatment of (**105**) with five equivalents of cyclopentadiene results in bond cleavage of the cyclopentadiene to form a dark purple crystalline solid $[Cp^{*}Ru(\mu\text{-}H)]_3[\mu_3\text{-}\eta_4\text{-}C(Me){=}CHCH{=}CH]$ (**107**). In this complex, two of the ruthenium centers act as a coordination site, while the third is an activation site.**[96]**

6.3 Half-Sandwich Complexes with Arene Ligands[97]

As mentioned in Section 3.1, reaction of 1,3- or 1,4-cyclohexadiene derivatives with $RuCl_3$ in ethanol yields a brown, highly insoluble polymer of composition $[(\eta\text{-}C_6R_6)RuCl_2]_x$ (equation 30). If this reaction is conducted at ambient temperature, most of the ensuing material is soluble in methylene chloride and consists of the dimer $[(\eta\text{-}C_6H_6)RuCl_2]_2$ (**108**).**[98]** An improvement of the method uses the readily available natural product α-phellandrene (5-*i*-propyl-2-methylcyclohexa-1,3-diene) as the cyclodiene in this reaction.**[99]** The ensuing complex $[(\eta\text{-}p\text{-cymene})RuCl_2]_2$ is not only soluble but also can exchange complexed *p*-cymene for other arene ligands, notably those with a higher degree of alkylation, as shown in equation (31) for hexamethylbenzene. However, not all functionalities seem not to be tolerated in these exchange processes.

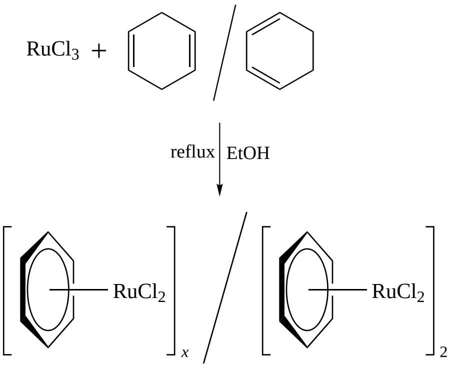

(**108**)

(30)

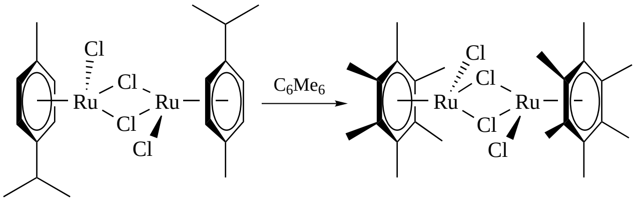

(31)

The reactivity patterns of the $(\eta\text{-arene})RuX_2$ moiety resemble those of the isoelectronic $Cp^{*}RhX_2$ unit. Thus,

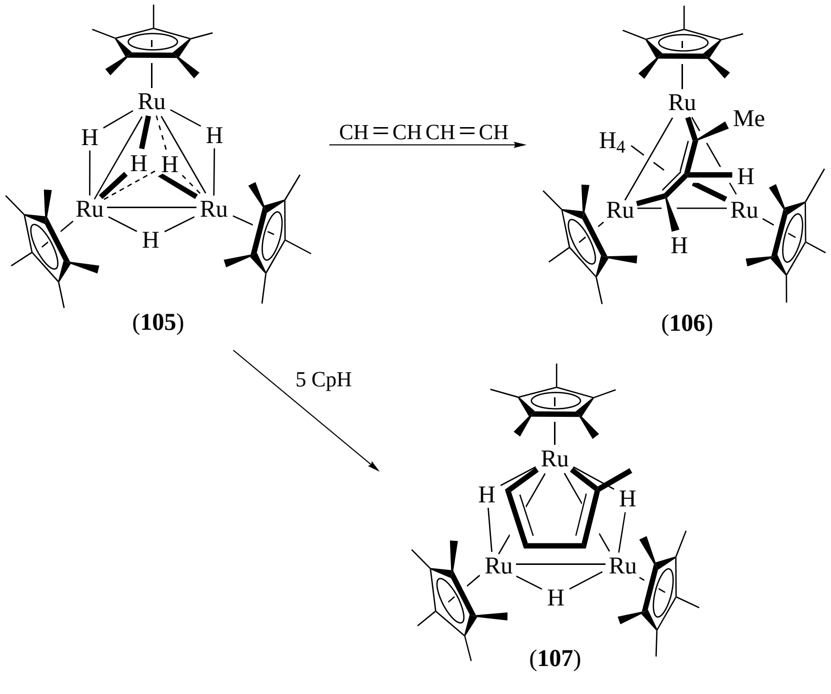

(**105**)

(**106**)

(**107**)

Scheme 26

ionization occurs in hot water to give the chloro-bridged cation (**109**), which can be precipitated as the PF_6^- salt (equation 32). The equilibrium in equation (33) is confirmed by NMR, UV, and cyclic voltammetry measurements.

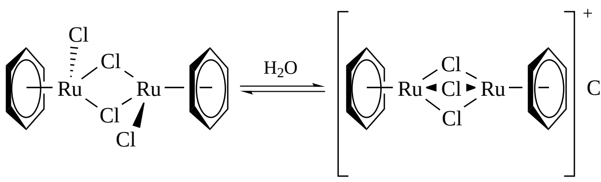

(**108**) (**109**)

(32)

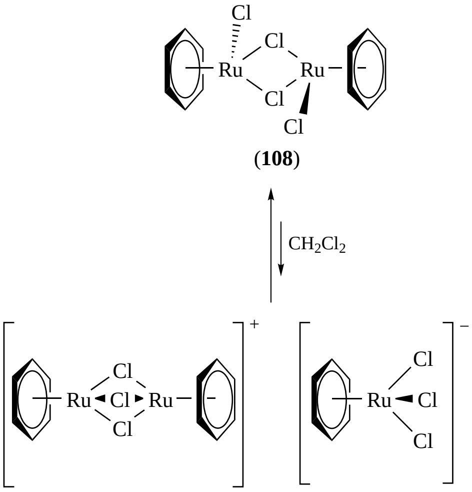

(**108**)

(33)

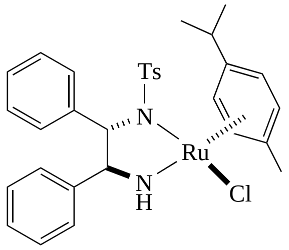

(**110**)

Cleavage of the dimer (**108**) proceeds easily with many donor and acceptor ligands and dehalogenation with Ag^+ ion in weakly coordinating solvents generates reactive solvent cations $[(\eta\text{-arene})Ru(solvent)_3]^{2+}$ for facile complexation. The (η-arene)Ru moiety accommodates all of the common classical σ-donor ligands along the spectrochemical series as coligands. The ability to bind such N- and O-ligands has been used to complex various amines, imines, Schiff bases, and amino acids to (η-C_6H_6)Ru, generating diastereomeric salts from substituted arene complexes. A notable example of this type is the complex (η-*p*-cymene)RuCl[(1S,2S)-*N*-*p*-toluenesulfonyl-1,2-diphenylethanediamine] (**110**). When chiral catalysts of this type are treated with formic acid/triethylamine, they asymmetrically reduce 1,2-diketones to enantiomerically pure chiral 1,2-diols (e.g., benzoins to benzils).[100] These optically active 1,2-diols are valuable in stereoselective organic syntheses and in the production of biologically active compounds.

It should be noted that there is organometallic chemistry associated with the (η-C_6H_6)Ru moiety itself, as exemplified by the orthometalation (*see Orthometalation*) of unsaturated arylphosphine complexes or by the transformations of the dimethyl complex (arene)$RuMe_2PR_3$ (**111a**), which on hydride abstraction rearranges into a cationic (hydrido)ethylene complex (**111b**) (Scheme 27). Much studied is the reaction of (arene)$RuCl_2PR_3$ with alkynes (Scheme 27). The primary acetylides (**112**) are attacked successively by protons and by nucleophiles, commonly alkoxide from a solvent alcohol, to give alkoxycarbene complexes (**113**). The sequence proceeds in one step if the alkyne is added in the presence of PF_6^- salt in alcohol solution. If the alkyne bears a hydroxyalkyl group, vinylvinylidene complexes are formed; this method has been extended to conjugated polyene derivatives (**114**).

A unique ruthenium arene complex is produced when $Ru_6C(CO)_{16}PPh_3$ is refluxed in chlorobenzene. The phosphine complex converts to the η-arene complex $Ru_6C(CO)_{13}[PPh_2(\mu\text{-}\eta^6\text{-}C_6H_5)]$ (**115**). In this reversible reaction, the tertiary phosphine ligand becomes η^6-coordinated to the adjacent ruthenium atom. Treatment of the complex with CO at room temperature drives the complex back to the P-bound form.[101]

The indenyl ligand is often viewed as a Cp analog in that it tends to bind to a metal center via its five-membered ring, as shown in (η^5-C_9H_7)RuCl(cod) (**116**). When (η^5-C_9H_7)Ru(dppm)H was treated with CF_3SO_3H or $HBF_4{\cdot}Et_2O$ at cool temperatures, the η^2-dihydrogen cation $[(\eta^5\text{-}C_9H_7)Ru(dppm)(H_2)]^+$ was produced. Under the same conditions, $(\eta^5\text{-}C_9H_7)Ru(PPh_3)_2H$ produces the dihydrogen cationic complex $[(\eta^5\text{-}C_9H_7)Ru(PPh_3)_2H_2]^+$. Warming either of these complexes to room temperature causes a proton to shift to the indenyl ligand, resulting in the migration of the metal to the six-membered ring of the indene; this is seen in $[(\eta^6\text{-}C_9H_8)Ru(dppm)(H)]^+$ (**117**). The proton migration to the indenyl ligand and rearrangement to the η^6-indene ruthenium complex is the first example of this type.[102]

A more recent addition to the half-sandwich chemistry of ruthenium is given by a number of complexes where the central metal obeys a 16 valence electron count. These coordinatively unsaturated (*see Coordinative Saturation & Unsaturation*) metal centers are widely invoked as intermediates or transition states in dissociative substitution processes or in catalytic transformations at transition metal centers. Such complexes are not, however, easily isolated. The most common way to stabilize such species is by coordinating sterically bulky ligands to the metal, thereby preventing further ligand addition. They can also be stabilized in the form of dimeric complexes.

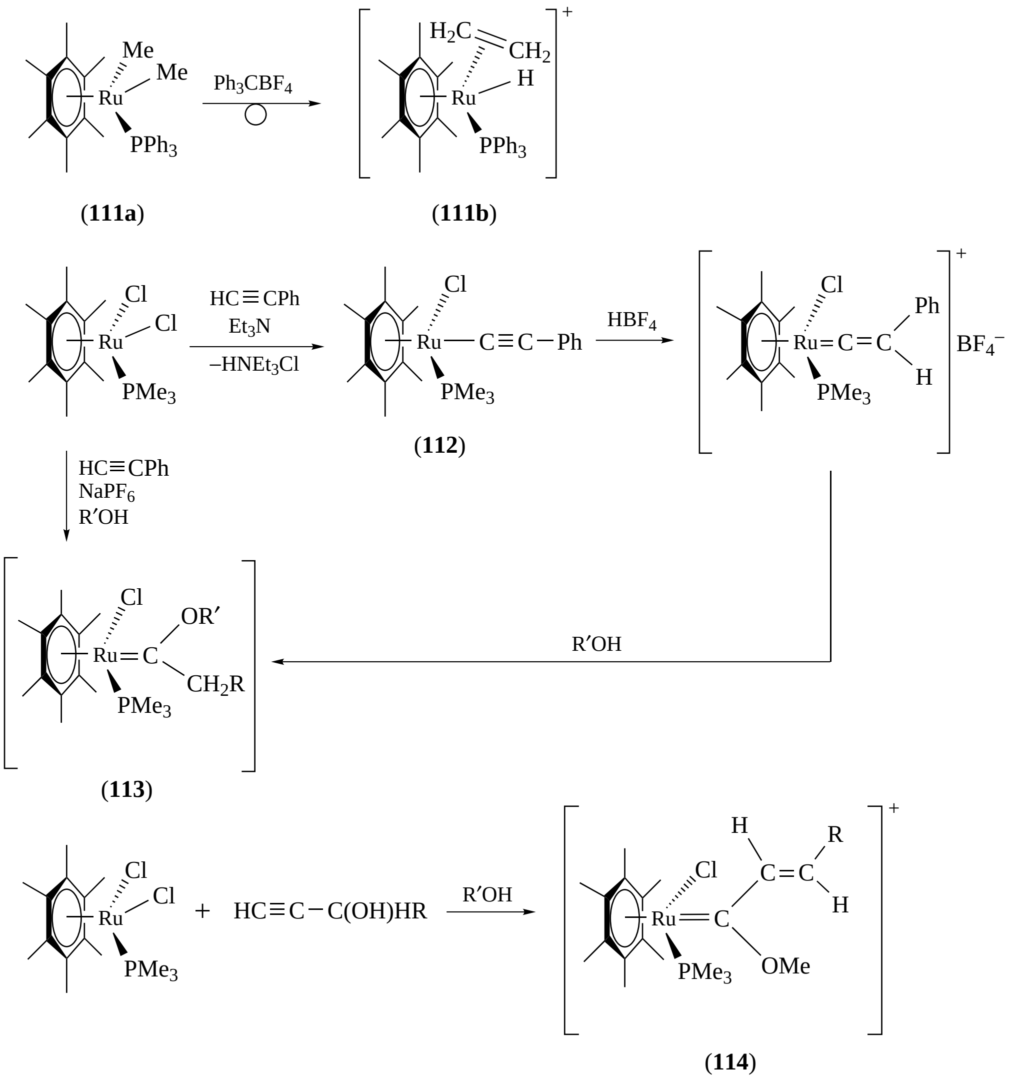

Scheme 27

A common feature of the dimers is a folded Ru–E–Ru–E core (E = O, S, or N) with a dihedral angle between the Ru-E-Ru planes of from 110 to 129°. The butterfly geometry observed in these dimeric complexes results from the retro π-overlap of lone electron pairs into empty metal orbitals and a second-order Jahn–Teller effect (*see Jahn–Teller Effect*) arising from the repulsive interaction of filled metal d-orbitals in a flat (D_{2h}) geometry. This type of geometry is exemplified by the crystallographically characterized complex $[(\eta\text{-}p\text{-cymene})\mathrm{Ru}(\mu_2\text{-2,6-di-isopropylphenylamido-}N,N)]_2$ (**118**).[103]

6.4 Higher Valent Half-Sandwich Complexes

Although the great majority of research involves ruthenium in oxidation states 0 to II, the organometallic half-sandwich chemistry of ruthenium also extends to oxidation states III and IV. The $\mathrm{Ru^{III}}$ complex (**119**) is formed in the same way as its rhodium analog, that is, by heating $RuCl_3$ with Cp*H in methanol or ethanol (Scheme 28).[104–106] This complex is the most widespread starting material in nearly all preparations containing alkylcyclopentadienyl ruthenium complexes. Complex (**119**) had long been considered a polymer before structural characterization revealed a chloride-bridged dimer. A unique feature of the solid-state structure of this compound, schematically indicated in Scheme 28, was the presence of two isomeric forms in the solid, a paramagnetic isomer with a long, nonbonding Ru–Ru separation of 3.75 Å, and one with a shorter Ru–Ru separation of 2.93 Å. In the latter isomer, the $\mathrm{Ru^{III}}$ d^5 centers strongly interact as shown by solid-state NMR to form a diamagnetic (*see Diamagnetism*) complex. In solution, these forms rapidly interconvert in a temperature-dependent equilibrium, as indicated by a large temperature-dependent chemical shift of the averaged Pentamethylcyclopentadiene (Cp*) signal (opposite to the temperature dependence of the magnetic susceptibility). This latter phenomenon has been used to prove the presence of similar isomers in solution in those cases where only one form is detected in the solid state.

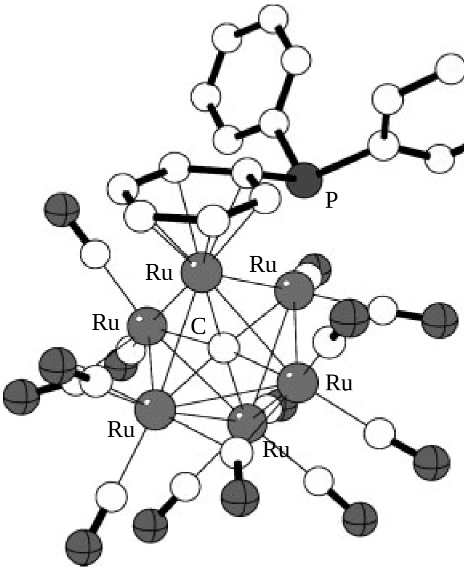

(**115**)

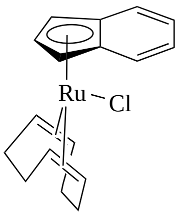

(**116**)

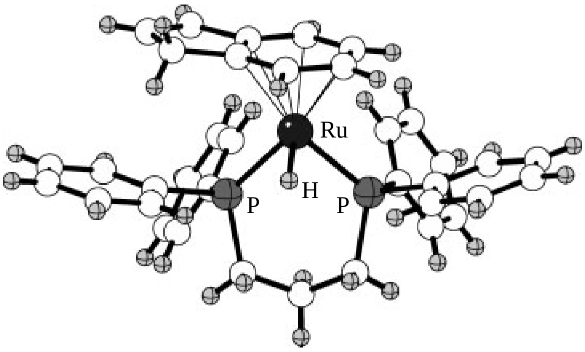

(**117**)

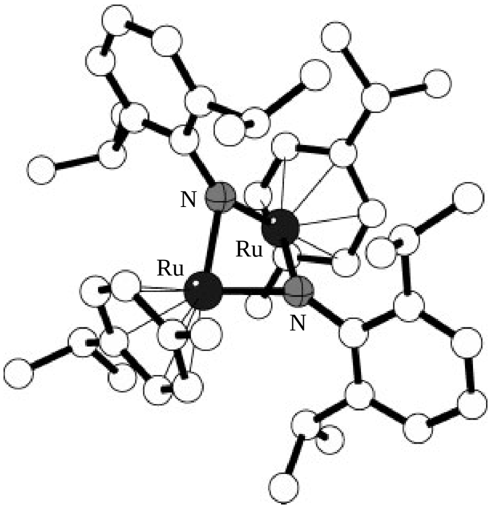

(**118**)

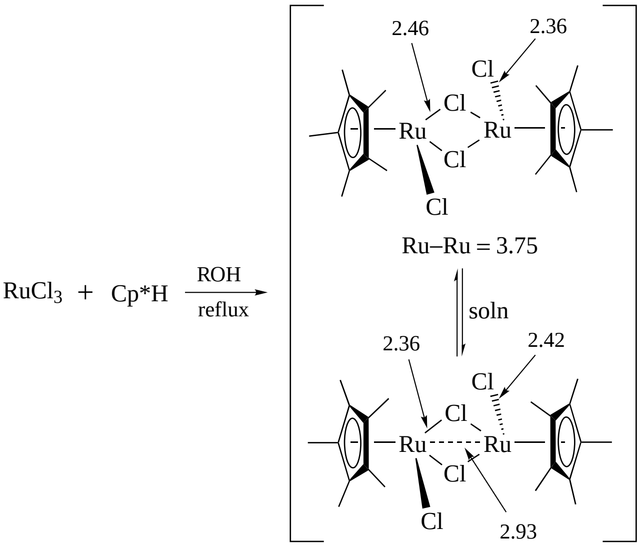

(**119**)

Scheme 28

A Ru^{IV} center has been encountered in Cp*Ru(η^4-2,3-disubstituted-1,3-butadiene)Br$_2$ complexes (**120**). These compounds are synthesized by the oxidative addition (*see Oxidative Addition*) of Br$_2$ to Cp*Ru(η^4-diene)Br complexes. Interestingly, when the diene in the starting material is 1,3-butadiene, or either monosubstituted- or 1,2-disubstituted-1,3-butadiene, a neutral dibromoruthenium(IV) (η^3-allyl) complex is formed. In this complex, the allyl assumes an *anti* conformation (**121**). When the starting material involves 1,4-disubstituted-1,3-butadiene, the same η^3-allyl complex is formed but with a *syn* configuration (**122**).[107] The complete series of trihalo ruthenium(IV) complexes (Cp*RuX$_3$)$_n$ (X = Cl, Br, I) are obtained from allowing (**119**) to react with the respective halogen.[108]

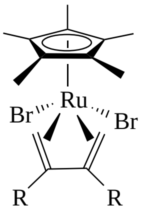

(**120**)

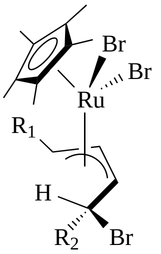

(**121**)

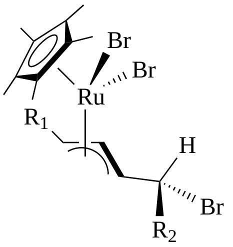

(**122**)

7 RELATED ARTICLES

Iron: Organometallic Chemistry; Osmium: Organometallic Chemistry; Rhodium: Organometallic Chemistry.

8 REFERENCES

1. G. Wilkinson, *J. Am. Chem. Soc.*, 1952, **74**, 6146.
2. E. A. Seddon and K. R. Seddon, ‘The Chemistry of Ruthenium’, Elsevier, Amsterdam, 1984.
3. M. I. Bruce, M. A. Bennett, and T. W. Matheson, in ‘Comprehensive Organometallic Chemistry’, eds. G. Wilkinson, F. G. A. Stone, and E. W. Abel, Pergamon, Oxford, 1982, Vol. 4, Chap. 32, p. 651.
4. M. I. Bruce, in ‘Comprehensive Organometallic Chemistry-II’, E. W. Abel, F. G. A. Stone, and G. Wilkinson, eds. Pergamon, Oxford, 1995, Vol. 7, Chap. 5, p. 291.
5. U. Koelle, *Chem. Rev.*, 1998, **98**, 1313.
6. B. F. G. Johnson and J. Lewis, *Inorg. Synth.*, 1972, **13**, 92.
7. A. Mantovani and S. Cenini, *Inorg. Synth.*, 1976, **16**, 47.
8. M. I. Bruce, C. M. Jensen, and N. L. Jones, *Inorg. Synth.*, 1989, **26**, 259.
9. F. Calderazzo and F. L’Eplattenier, *Inorg. Chem.*, 1967, **6**, 1220.
10. R. Koelliker and G. Bor, *J. Organomet. Chem.*, 1991, **417**, 439.
11. L.-Y. Hsu, N. Bhattacharyya, and S. G. Shore, *Organometallics*, 1985, **4**, 1483.
12. P. R. Raithby, in ‘Transition Metal Clusters’, ed. B. F. G. Johnson, Wiley, Chichester, 1980, p. 25.
13. J. S. Bradley, *Adv. Organomet. Chem.*, 1983, **22**, 1.
14. B. F. G. Johnson, J. Lewis, P. R. Raithby, and G. Süss, *J. Chem. Soc., Dalton Trans.*, 1979, 1356.
15. J. B. Keister and T. L. Horling, *Inorg. Chem.*, 1980, **19**, 2304.
16. J. A. Cabeza, I. da Silva, I. del Río, S. García-Granda, and V. Riera, *Inorg. Chim. Acta*, 2003, **347**, 107.
17. P. C. Ford, *Acc. Chem. Res.*, 1981, **14**, 31.
18. G. Süss-Fink and G. Herrmann, *J. Chem. Soc., Chem. Commun.*, 1985, 735.
19. G. Süss-Fink, *J. Organomet. Chem.*, 1980, **193**, C20.
20. C. R. Eady, P. F. Jackson, B. F. G. Johnson, J. Lewis, M. C. Malatesta, M. McPartlin, and W. J. H. Nelson, *J. Chem. Soc., Dalton Trans.*, 1980, 383.
21. R. D. Wilson, S. M. Wu, R. A. Love, and R. Bau, *Inorg. Chem.*, 1978, **17**, 1271.
22. P. J. Bailey, M. A. Beswick, B. F. G. Johnson, J. Lewis, M. McPartlin, P. R. Raithby, and M. C. Ramirez de Arellano, *J. Chem. Soc., Dalton Trans.*, 1996, 3515.
23. A. J. Hewitt, J. H. Holloway, R. D. Peacock, J. B. Raynor, and I. L. Wilson, *J. Chem. Soc., Dalton Trans.*, 1976, 579.
24. R. Colton and R. H. Farthing, *Aust. J. Chem.*, 1971, **24**, 903.
25. P. Homanen, M. Haukka, M. Ahlgrén, T. A. Pakkanen, P. N. W. Baxter, R. E. Benfield, and J. A. Connor, *J. Organomet. Chem.*, 1998, **552**, 205.
26. W. L. Gladfelter, *Adv. Organomet. Chem.*, 1985, **24**, 41.
27. P. J. Bailey, M. J. Duer, B. F. G. Johnson, J. Lewis, G. Conole, M. McPartlin, H. R. Powell, and C. E. Anson, *J. Organomet. Chem.*, 1990, **383**, 441.
28. C.-M. T. Hayward, J. R. Shapley, M. R. Churchill, C. Bueno, and A. L. Rheingold, *J. Am. Chem. Soc.*, 1982, **104**, 7347.
29. M. I. Bruce, N. N. Zaitseva, B. W. Skelton, and A. H. White, *J. Chem. Soc., Dalton Trans.*, 2002, 3879.
30. F. L’Eplattenier and F. Calderazzo, *Inorg. Chem.*, 1968, **7**, 1290.
31. P. Kalck, Y. Peres, and J. Jenck, *Adv. Organomet. Chem.*, 1991, **32**, 121.
32. M. Ogasawara, F. Maseras, N. Gallego-Planas, K. Kawamura, K. Ito, K. Toyota, W. E. Streib, S. Komiya, O. Eisenstein, and K. G. Caulton, *Organometallics*, 1997, **16**, 1979.
33. S. A. R. Knox and F. G. A. Stone, *J. Chem. Soc. A*, 1971, 2874.
34. J. S. Field, R. J. Haines, J. Sundermeyer, and S. F. Woollam, *J. Chem. Soc., Chem. Commun.*, 1991, 1382.
35. J. S. Field, R. J. Haines, J. Sundermeyer, and S. F. Woollam, *J. Chem. Soc., Chem. Commun.*, 1990, 985.
36. K.-B. Shiu, J.-Y. Chen, G.-H. Lee, F.-L. Liao, B.-T. Ko, Y. Wang, S.-L. Wang, and C.-C. Lin, *J. Organomet. Chem.*, 2002, **658**, 117.
37. K.-B. Shiu, S.-W. Jean, Y. Wang, and G.-H. Lee, *J. Organomet. Chem.*, 2002, **650**, 268.
38. M. F. Desrosiers, D. A. Wink, R. Trautman, A. E. Friedman, and P. C. Ford, *J. Am. Chem. Soc.*, 1986, **108**, 1917.
39. E. Sappa and L. Milone, *J. Organomet. Chem.*, 1973, **61**, 383.
40. T. Jenke, H. Stoeckli-Evans, U. Bodensieck, and G. Süss-Fink, *J. Organomet. Chem.*, 1991, **401**, 347.
41. G. Süss-Fink, G. Rheinwald, H. Stœckli-Evans, C. Bolm, and D. Kaufmann, *Inorg. Chem.*, 1996, **35**, 3081.
42. K.-M. Frosin and L. Dahlenburg, *Inorg. Chim. Acta*, 1990, **167**, 83.

43. J. A. Widegren, H. Weiner, S. M. Miller, and R. G. Finke, *J. Organomet. Chem.*, 2000, **610**, 112.
44. H. E. Selnau Jr, J. Mahmoud, and C. L. Porter, *Inorg. Chim. Acta*, 1994, **224**, 125.
45. U. Kölle, G. Flunkert, R. Görissen, M. U. Schmidt, and U. Englert, *Angew. Chem., Int. Ed. Engl.*, 1992, **31**, 440.
46. A. J. P. Domingos, J. A. S. Howell, B. F. G. Johnson, and J. Lewis, *Inorg. Synth.*, 1976, **16**, 103.
47. P. Pertici, G. Vitulli, M. Paci, and L. Porri, *J. Chem. Soc., Dalton Trans.*, 1980, 1961.
48. P. Pertici and G. Vitulli, *Inorg. Synth.*, 1983, **22**, 176.
49. D. B. Brown, B. F. G. Johnson, C. M. Martin, and S. Parsons, *J. Organomet. Chem.*, 1997, **536–537**, 285.
50. G. Deganello, 'Transition Metal Complexes of Cyclic Polyolefins', Academic Press, London, 1979, p. 156.
51. M. J. Bennett, F. A. Cotton, and P. Legzdins, *J. Am. Chem. Soc.*, 1968, **90**, 6335.
52. P. J. Harris, J. A. K. Howard, S. A. R. Knox, R. J. McKinney, R. P. Phillips, F. G. A. Stone, and P. Woodward, *J. Chem. Soc., Dalton Trans.*, 1978, 403.
53. P. G. Gassman and C. H. Winter, *J. Am. Chem. Soc.*, 1988, **110**, 6130.
54. O. Hofer and K. Schlögl, *J. Organomet. Chem.*, 1968, **13**, 443.
55. D. E. Bublitz, W. E. McEwen, and J. Kleinberg, *Org. Synth.*, 1961, **41**, 96.
56. M. O. Albers, D. C. Liles, D. J. Robinson, A. Shaver, E. Singleton, M. B. Wiege, J. C. A. Boeyens, and D. C. Levendis, *Organometallics*, 1986, **5**, 2321.
57. U. Koelle and A. Salzer, *J. Organomet. Chem.*, 1983, **243**, C27.
58. R. R. Gagné, C. A. Koval, and G. C. Lisensky, *Inorg. Chem.*, 1980, **19**, 2854.
59. Y. S. Sohn, A. W. Schlueter, D. N. Hendrickson, and H. B. Gray, *Inorg. Chem.*, 1974, **13**, 301.
60. M. Watanabe, I. Motoyama, M. Shimoi, and H. Sano, *J. Organomet. Chem.*, 1996, **517**, 115.
61. S. P. Deraniyagala and T. D. Westmoreland, *Organometallics*, 1994, **14**, 1239.
62. T. M. Shea and T. D. Westmoreland, *Inorg. Chem.*, 2000, **39**, 1573.
63. S. Trupia, A. Nafady, and W. E. Geiger, *Inorg. Chem.*, 2003, **42**, 5480.
64. M. G. Hill, W. M. Lamanna, and K. R. Mann, *Inorg. Chem.*, 1991, **30**, 4687.
65. M. O. Albers, D. J. Robinson, and E. Singleton, *Coord. Chem. Rev.*, 1987, **79**, 1.
66. C. H. Winter, Y.-H. Han, R. L. Ostrander, and A. L. Rheingold, *Angew. Chem., Int. Ed. Engl.*, 1993, **32**, 1161.
67. A. Bretschneider-Hurley and C. H. Winter, *J. Am. Chem. Soc.*, 1994, **116**, 6468.
68. R. P. Hughes, X. Zheng, R. L. Ostrander, and A. L. Rheingold, *Organometallics*, 1994, **13**, 1567.
69. S. Top, H. El Hafa, A. Vessières, M. Hunché, J. Vaissermann, and G. Jaouen, *Chem. – Eur. J.*, 2002, **8**, 5241.
70. J. L. Brumaghim and G. S. Girolami, *J. Organomet. Chem.*, 1999, **586**, 258.
71. U. Kölle and J. Grub, *J. Organomet. Chem.*, 1985, **289**, 133.
72. A. Z. Kreindlin, P. V. Petrovskii, M. I. Rybinskaya, A. I. Yanovskii, and Y. T. Struchkov, *J. Organomet. Chem.*, 1987, **319**, 229.
73. S. Barlow, L. M. Henling, M. W. Day, W. P. Schaefer, J. C. Green, T. Hascall, and S. R. Marder, *J. Am. Chem. Soc.*, 2002, **124**, 6285.
74. W. J. Kelly and W. E. Parthun, *Organometallics*, 1992, **11**, 4348.
75. R. D. Ernst, *Chem. Rev.*, 1988, **88**, 1255.
76. M. E. N. Clemente, P. J. Saavedra, M. C. Vásquez, and M. A. Paz-Sandoval, *Organometallics*, 2002, **21**, 592.
77. G. C. Turpin, A. L. Rheingold, and R. D. Ernst, *J. Organomet. Chem.*, 2003, **672**, 109.
78. B. M. Ramachandran, S. M. Trupia, W. E. Geiger, P. J. Carroll, and L. G. Sneddon, *Organometallics*, 2002, **21**, 5078.
79. C. T. Sanderson, B. J. Palmer, A. Morgan, M. Murphy, R. A. Dluhy, T. Mize, I. J. Amster, and C. Kutal, *Macromolecules*, 2002, **35**, 9648.
80. B. Chaudret, F. Jalón, M. Pérez-Manrique, F. Lahoz, F. J. Plou, and R. Sánchez-Delgado, *New J. Chem.*, 1990, **14**, 331.
81. R. H. Fish, H.-S. Kim, and R. H. Fong, *Organometallics*, 1991, **10**, 770.
82. A. J. Gleichmann, J. M. Wolff, and W. S. Sheldrick, *J. Chem. Soc., Dalton Trans.*, 1995, 1549.
83. D. W. Bruce, A. Thornton, B. Chaudret, S. Sabo-Etienne, T. L. Axon, and G. H. Cross, *Polyhedron*, 1995, **14**, 1765.
84. L. Bonomo, E. Solari, M. Latronico, R. Scopelliti, and C. Floriani, *Chem. – Eur. J.*, 1999, **5**, 2040.
85. A. R. Kudinov, M. I. Rybinskaya, Y. T. Struchkov, A. I. Yanovskii, and P. V. Petrovskii, *J. Organomet. Chem.*, 1987, **336**, 187.
86. P. O. Lumme, U. Turpeinen, A. R. Kudinov, and M. I. Rybinskaya, *Acta Crystallogr., Sect. C*, 1990, **C46**, 1410.
87. G. E. Herberich, U. Englert, F. Marken, and D. Hoffman, *Organometallics*, 1993, **12**, 4039.
88. D. B. Brown, P. J. Dyson, B. F. G. Johnson, C. M. Martin, D. G. Parker, and S. Parsons, *J. Chem. Soc., Dalton Trans.*, 1997, 1909.
89. M. I. Bruce and N. J. Windsor, *Aust. J. Chem.*, 1977, **30**, 1601.
90. M. I. Bruce, C. Hameister, A. G. Swincer, and R. C. Wallis, *Inorg. Synth.*, 1982, **21**, 79.

91. P. J. Fagan, W. S. Mahoney, J. C. Calabrese, and I. D. Williams, *Organometallics*, 1990, **9**, 1843.
92. G. Hogarth, *Organomet. Chem.*, 1995, **24**, 184.
93. H. Suzuki, H. Omori, D. H. Lee, Y. Yoshida, M. Fukushima, M. Tanaka, and Y. Moro-oka, *Organometallics*, 1994, **13**, 1129.
94. K. Itoh, K. Masuda, T. Fukahori, K. Nakano, K. Aoki, and H. Nagashima, *Organometallics*, 1994, **13**, 1020.
95. T. Takemori, H. Suzuki, and M. Tanaka, *Organometallics*, 1996, **15**, 4346.
96. H. Suzuki, Y. Takaya, T. Takemori, and M. Tanaka, *J. Am. Chem. Soc.*, 1994, **116**, 10779.
97. H. Le Bozec, D. Touchard, and P. H. Dixneuf, *Adv. Organomet. Chem.*, 1989, **29**, 163.
98. R. A. Zelonka and M. C. Baird, *Can. J. Chem.*, 1972, **50**, 3063.
99. M. A. Bennett, T.-N. Huang, T. W. Matheson, and A. K. Smith, *Inorg. Synth.*, 1982, **21**, 74.
100. K. Murata, K. Okano, M. Miyagi, H. Iwane, R. Noyori, and T. Ikariya, *Org. Lett.*, 1999, **1**, 1119.
101. H.-F. Hsu, S. R. Wilson, and J. R. Shapley, *Organometallics*, 1997, **16**, 4937.
102. M. Y. Hung, S. M. Ng, Z. Zhou, and C. P. Lau, *Organometallics*, 2000, **19**, 3692.
103. A. K. Berrell and A. J. Steedman, *J. Chem. Soc., Chem. Commun.*, 1995, **20**, 2109.
104. T. D. Tilley, R. H. Grubbs, and J. E. Bercaw, *Organometallics*, 1984, **3**, 274.
105. N. Oshima, H. Suzuki, and Y. Moro-oka, *Chem. Lett.*, 1984, 1161.
106. U. Koelle and J. Kossakowski, *J. Organomet. Chem.*, 1989, **362**, 383.
107. C. Gemel, K. Mereiter, R. Schmid, and K. Kirchner, *Organometallics*, 1996, **15**, 532.
108. N. Oshima, H. Suzuki, Y. Moro-oka, H. Nagashima, and K. Itoh, *J. Organomet. Chem.*, 1986, **314**, C46.

S-donor Ligands

Simon R. Collinson & Martin Schröder
University of Nottingham, Nottingham, UK

1 Introduction and General Features 1
2 H_2S, RSH, and HS^- Ligands 2
3 Sulfides: $S_N{}^{2-}$ 3
4 Thiolates: RS^- 10
5 Dithiolenes 15
6 Mixed S/O, S/N and P/S Ligands 17
7 Dithiocarbamates and Related Ligands 19
8 Thioethers: R_2S 20
9 Metalloenzymes 23
10 Related Articles 25
11 Further Reading 25
12 References 25

Glossary

S-Donor ligand: molecule in which a sulfur atom is directly bonded to a metal center

Abbreviations

porph = Porphyrin; pz = Pyrazine; [9]aneS_3 = 1,4,7-trithiacyclononane; [14]aneN_4 = 1,4,7,11-tetraazacyclotetradecane; [18]aneS_6 = 1,4,7,10,13,16-hexathiacyclooctadecane; [18]aneO_6 = 1,4,7,10,13,16-hexaoxacyclooctadecane; [9]aneN_3 = 1,4,7-triazacyclononane.

1 INTRODUCTION AND GENERAL FEATURES

A very extensive literature has developed concerning the chemistry of S-coordination compounds. A general feature of S-donor ligands is their ability to bind to a very wide variety of metal centers, particularly of the second and third row transition metals, to form mononuclear, polynuclear, and cluster compounds. Polysulfides $S_n{}^{2-}$, thiolates RS^-, and related anionic S-donors are generally regarded as strong σ- and π-donors. In addition, owing to their polarizability, these S-donor ligands can form a range of polynuclear complexes in which the S-atoms bridge between two metal ions, or face-cap three or more metal centers.**[1]** The formation of metal clusters is, therefore, a common and extremely important aspect of S-coordination chemistry, particularly since complexes of Fe, Mo, Cu, and Ni are present at the active sites of several metalloenzymes (*see* ***Iron–Sulfur Models of Protein Active Sites***; ***Iron–Sulfur Proteins***; ***Nickel Enzymes & Cofactors***; ***Nickel: Models of Protein Active Sites***; ***Nitrogenase: Metal Cluster Models*** and ***Polynuclear Organometallic Cluster Complexes***). Binding of soft anionic S-donors to soft metal centers is consistent with hard–soft acid–base principles, although covalency in metal–sulfur binding is also important. Thiolate RS^- and hydrosulfide HS^- ligands occur between F^- and Cl^- in the spectrochemical series reflecting their strong π-donor capacity and their abilities to stabilize relatively high metal oxidation states, for example, Mo^{VI}.

In contrast, thioethers of the type R_2S are generally poor donors to metals centers, the stability of complexes decreasing in the order $S^{2-} > RS^- > R_2S$ (Scheme 1). Macrocyclic ligands tend to form complexes of increased thermodynamic stability and kinetic inertness compared to their open-chain analogs (*see* ***Macrocyclic Ligands***).**[2–4]**

The relative π-acceptor and π-donor properties of thioether S-donors have been discussed (Scheme 2), and, although weak, their π-acceptor abilities can contribute to the stabilization of low-valent metal states,for example, Mo^0.**[2]** Thioether ligands, R_2S, are normally found between H_2O and NH_3 in the spectrochemical series, although certain macrocyclic thioether complexes appear to have ligand fields approaching those expected for tertiary phosphine ligands; macrocyclic ligands often impose specific bonding, stereochemical, and conformational restrictions upon the resultant complexes (see Section 8).**[2–4]**

A series of reviews on S-donor ligands has been published and these are referred to in the appropriate sections below. Reviews on general aspects of S-coordination chemistry have appeared,**[5,6]** while inorganic texts give good, general overviews on the subject.**[7]** Comprehensive accounts of S-donor ligands have been published.**[8]** A

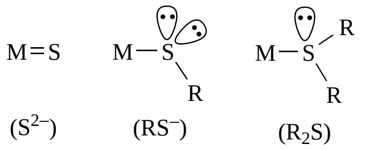

Scheme 1

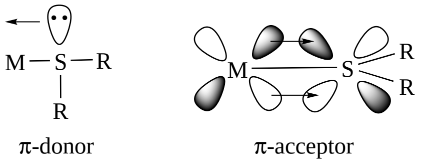

Scheme 2

review of sulfur donor ligands with transition metal complexes to generate homogeneous catalysts has recently appeared.**[9]**

2 H_2S, RSH, AND HS^- LIGANDS

Unlike H_2O, H_2S rarely forms simple complexes with transition metal ions owing to facile deprotonation to HS^- and S^{2-}. Additionally, reaction of H_2S with simple metal salts often leads to reduction of the metal and/or the formation of insoluble metal sulfides. A number of H_2S complexes have been reported including $[Mn(\eta\text{-}C_5H_5)(CO)_2(SH_2)]$ (**1**), $[W(CO)_5(SH_2)]$ (**2**), $[Ru(NH_3)_5(SH_2)]^{2+}$ (**3**), and the tetrahedral $[AlBr_3(SH_2)]$ (**4**). The coordinated H_2S ligand in $[W(CO)_5(SH_2)]$ can be alkylated with diazoalkanes to give the corresponding thioether complexes $[W(CO)_5(SR_2)]$ (R = Me, Et). The chemistry of hydrogen sulfide with palladium and ruthenium has been the subject of a short review.**[10]**

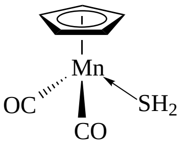

(**1**)

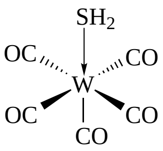

(**2**)

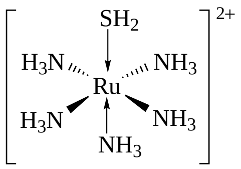

(**3**)

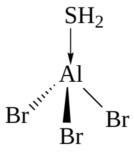

(**4**)

Syntheses of complexes incorporating the hydrosulfide HS^- ligand have to avoid the formation of S^{2-}, species which can oligomerize to give clusters and polymers. The modes of coordination of HS^- to metal centers are given in Scheme 3.

Deprotonation of coordinated H_2S occurs readily to afford species such as $[Ru(NH_3)_5(SH)]^{2+}$ (**5**), $[Ni(\eta\text{-}C_5H_5)(P\text{-}n\text{-}Bu_3)(SH)]$ (**6**), $[Cr(OH_2)_5(SH)]^{2+}$ (**7**), and $[W(CO)_5(SH)]^-$ (**8**). Oxidative addition of H_2S to Pt^0 starting materials affords trans-addition products such as *trans*-$[Pt(H)(PEt_3)_2(SH)]$ (**9**), while *trans*-$[Pt(PEt_3)_2(SH)_2]$ (**10**) has also been isolated.

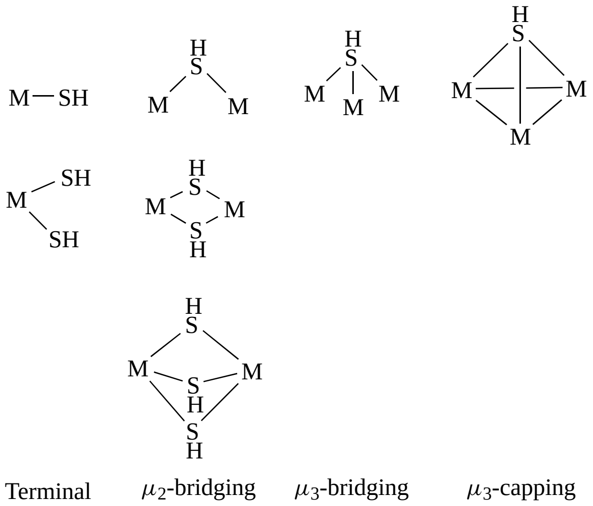

Scheme 3

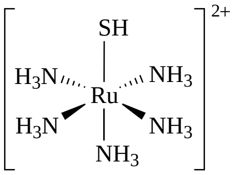

(**5**)

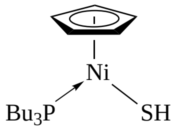

(**6**)

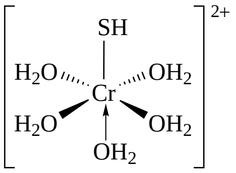

(**7**)

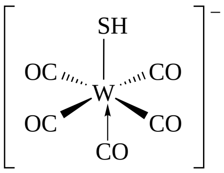

(**8**)

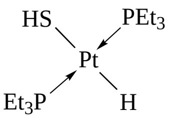

(**9**)

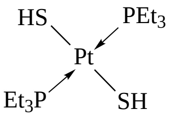

(**10**)

Binuclear and polynuclear species incorporating the HS^- ligand have been reported, including $[M_2(CO)_{10}(\mu\text{-SH})]^-$ (**11**; M = Cr, Mo, W), $[Mn_2(CO)_8(\mu\text{-SH})_2]$ (**12**), $[Fe_2(L)_2(\mu\text{-SH})_3]^+$ (**13**); L = bis(2-diphenylphosphinoethyl)phenylphosphine, and the proposed cubane complex $[PtMe_3(SH)]_4$ (**14**). Polymeric hydrosulfide complexes have been reported for the complex $[Co(SH)([14]aneN_4)](ClO_4)$ ($[14]aneN_4$ = 1,4,7,11-tetraazacyclotetradecane) where the macrocylic donors adopt the equatorial positions with the Co^{II} ions bridged by hydrosulfide anions positioned at the axial sites.**[11]** Hydrosulfido complexes of transition metals have been reviewed with emphasis being placed on the reactivities of hydrosulfido complexes, including nucleophilic reactions, oxidative coupling, and sulfide cluster formation.**[12]** The hydrogenation and hydrogenolysis of thiophenic molecules catalysed by soluble

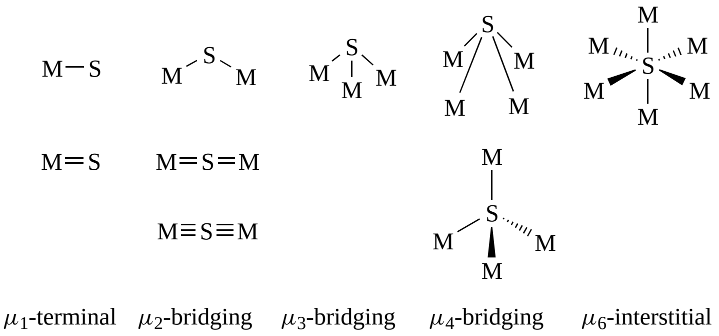

Scheme 4

metal complexes has been reviewed and the mechanistic information has been related to heterogeneous hydrodesulfurization catalysis.[13]

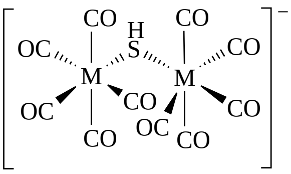

(**11**)

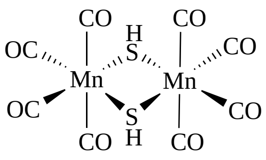

(**12**)

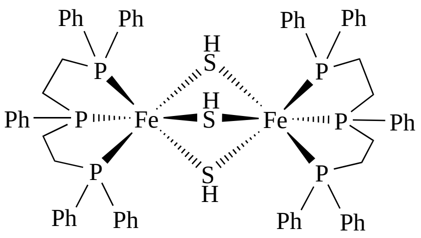

(**13**)

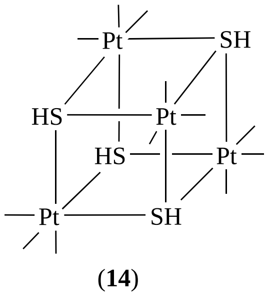

(**14**)

Complexes incorporating thiol RSH ligands are rare since deprotonation at the coordinated S-donor is relatively facile, although $[Ru(NH_3)_5(SHEt)]^{2+}$ and [Fe(TPP)(SPh)(SPhH)] have been reported.

3 SULFIDES: $S_N{}^{2-}$ (*See Sulfur: Inorganic Chemistry*)

3.1 Monosulfide: S^{2-}

The coordination chemistry of the sulfido ligand S^{2-} is very varied. Scheme 4 illustrates the modes of coordination of S^{2-} to transition metal ions. The monosulfido ligand can act as a two-electron, terminal or μ_2-bridging donor, or up to a six-electron donor if it binds as μ_4-bridging or interstitial donor. It is, therefore, not surprising that a wide variety of binuclear and polynuclear sulfido clusters complexes can be prepared.

Terminally bound sulfide S^{2-} is commonly found in a wide range of metallothio anions, particularly of d^0 metal centers for example $[MS_4]^{3-}$ (M = V, Nb, Ta), $[MS_4]^{2-}$ (M = Mo, W), and $[ReS_4]^-$. The mixed thiooxy and thioseleno anions $[MS_{4-x}O_x]^{n-}$ and $[MS_{4-x}Se_x]^{n-}$ have also been prepared. Additionally, metalloanions can coordinate to other metal centers, so behaving as ligands in their own right. Thus, a wide range of mixed metal clusters and oligomers incorporating bridging S^{2-} ligands can be prepared. Examples of metallothio anion complexes are given in Scheme 5.

Some complexes incorporating μ_2-, μ_3-, and μ_4-bridging S^{2-} ligands are illustrated in Scheme 6. Important examples include $[(OC)_2(Cp)Cr{\equiv}S{\equiv}Cr(Cp)(CO)_2]$ (**15**) incorporating a linear triply bonded Cr≡S≡Cr unit, Roussin's red anion $[Fe_2(NO)_4(\mu_2\text{-}S)_2]^{2-}$ (**16**), $[Fe_4S_4(Cp)_4]$ (**17**), and

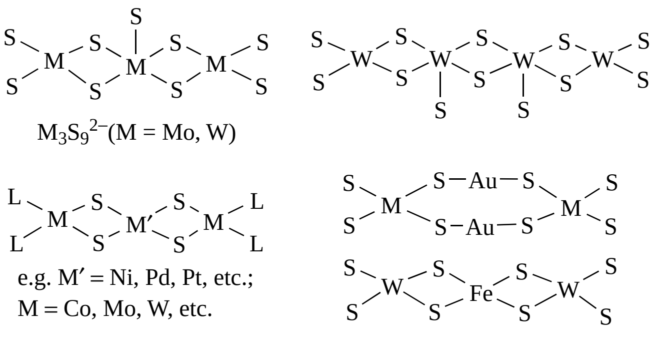

Scheme 5

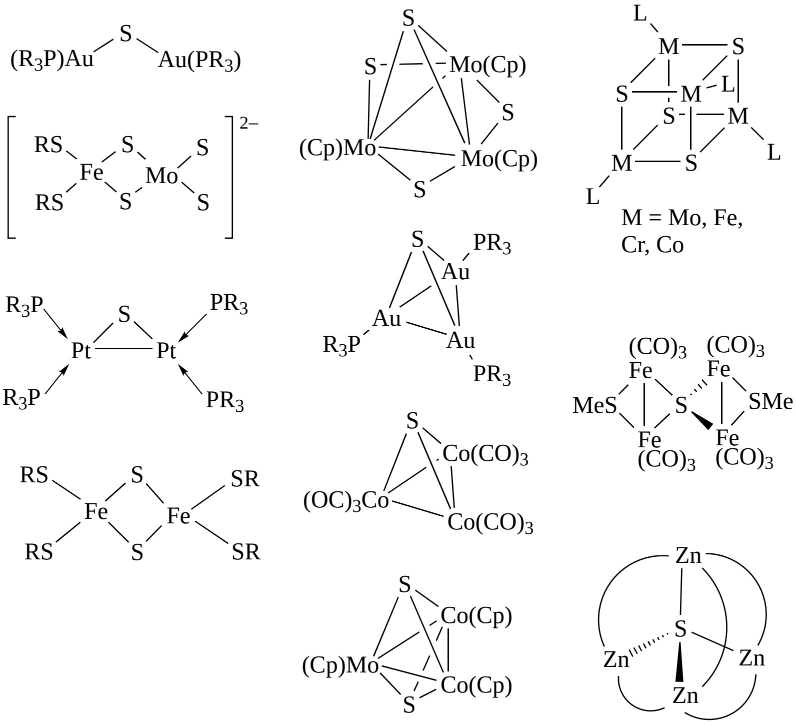

Scheme 6

$[Fe_4S_6(Cp)_4]$ incorporating S_2^- and S_2^{2-} moieties. Two reviews describing the use of $[Cp'_2M_2S_4]$ (where M = Fe or Ru and Cp′ = cyclopentadienyl or substituted cyclopentadienyl) as a building block for a host of multinuclear transition metal clusters have been published.[14,15]

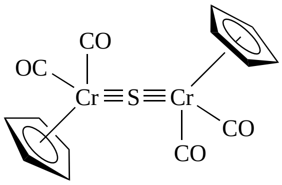

(**15**)

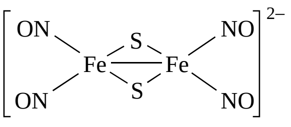

(**16**)

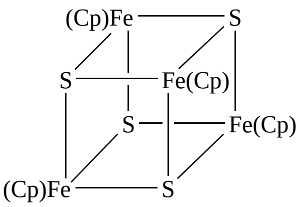

(**17**)

An enormous range of metal–sulfur cluster compounds derived from covalently linked cubane clusters and/or oligomers of metallothio anions has been prepared. Many have been found to be redox active and act as electron sinks via multielectron transfer processes. The electrochemistry of these systems has been comprehensively reviewed.[16]

One of the most important structural motifs in metal-sulfido cluster chemistry is the M_4S_4 cube. Fe_4S_4 cubane clusters have been studied in relation to biological systems in terms of substitution and redox chemistry. For example, the one-electron reduction of $[Fe_4S_4(SR)_4]^{2-}$ (**18**) to $[Fe_4S_4(SR)_4]^{3-}$ leads to a structural reorganization of the cubane structure from D_{2d} compressed to elongated D_{2d} (Scheme 7).[17] Scheme 8 shows subsite-specific reactions that have been reported at the $[Fe_4S_4]$ core.[18] The nature of the [4Fe–4S] and [3Fe–4S] cubane cluster in metalloenzymes such as ferrodoxins, aconitase, nitrogenase, hydrogenases, and sulfite reductase are major areas of research interest. The chemical interconversion of [4Fe–4S] and [3Fe–4S] clusters has allowed the synthesis of heteroatom clusters of type [3FeM′–4S] (equation 1).

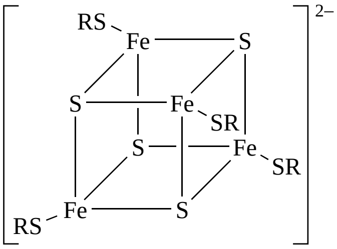

(**18**)

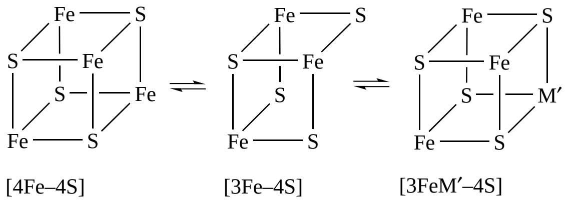
[4Fe–4S]
[3Fe–4S]
[3FeM′–4S]

(1)

A very wide range of higher metal–sulfur clusters has been prepared for example, $[Ni_9(\mu_4\text{-}S)_3(\mu_3\text{-}S)_6(PEt_3)_6]^{2+}$ (**19**),[**11**] $[Ni_3(\mu_3\text{-}S)_2(PEt_3)_6]^{2+}$ (**20**), and $[Ni_3(\mu_3\text{-}S)_2(SH)(PEt_3)_5]^{2+}$ (**21**).[**12**]

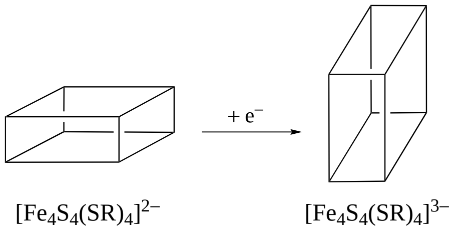
+ e⁻
[Fe4S4(SR)4]2–
[Fe4S4(SR)4]3–

Scheme 7

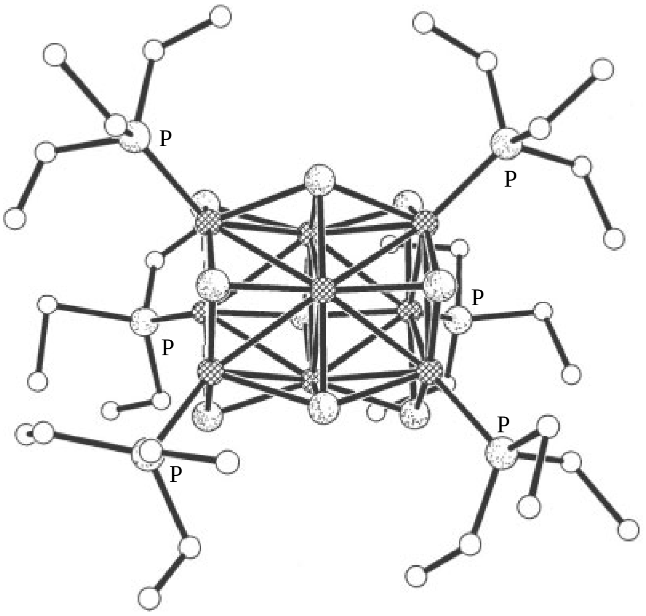

(19)

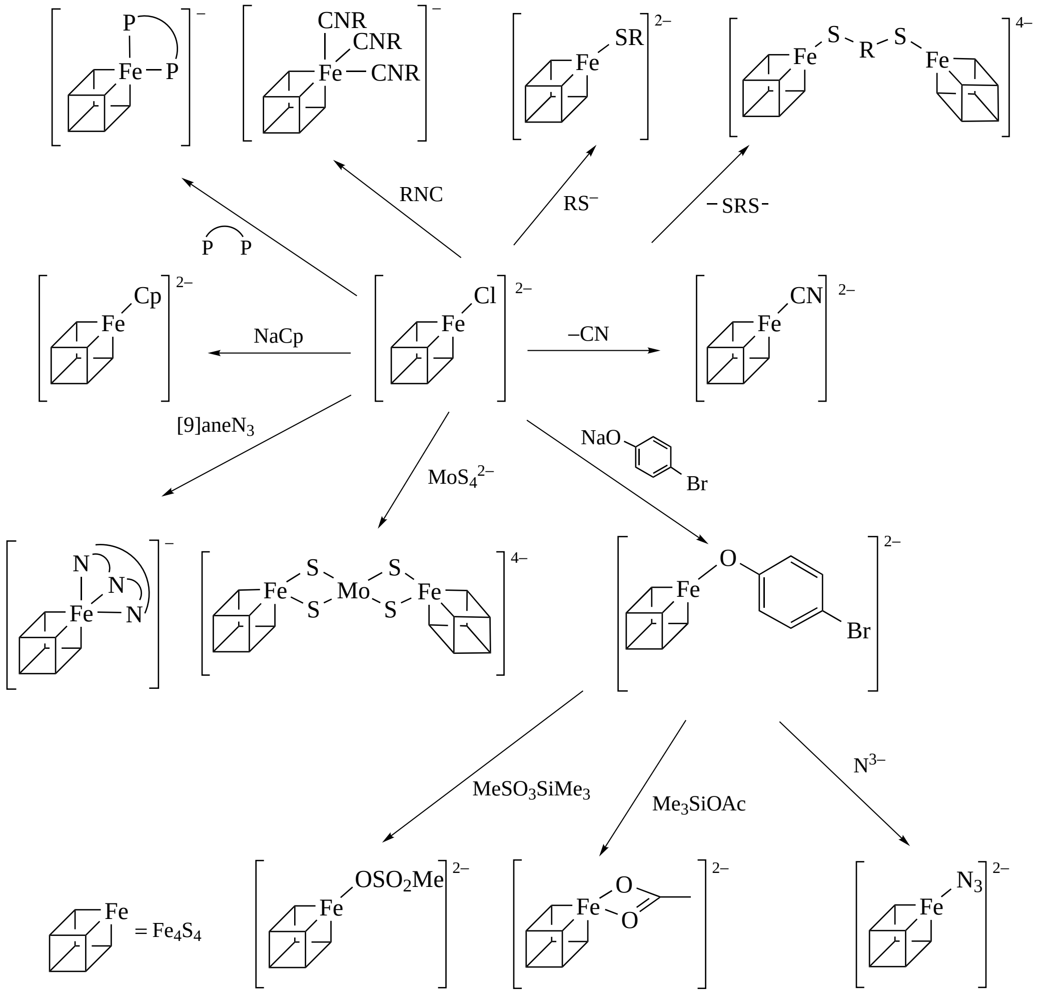
RNC
RS⁻
⁻SRS⁻
P P
NaCp
–CN
[9]aneN3
MoS4 2–
NaO–C6H4–Br
MeSO3SiMe3
Me3SiOAc
N3–
= Fe4S4

Scheme 8

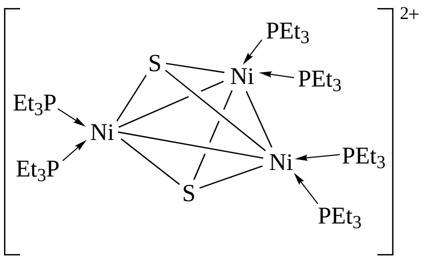

(**20**)

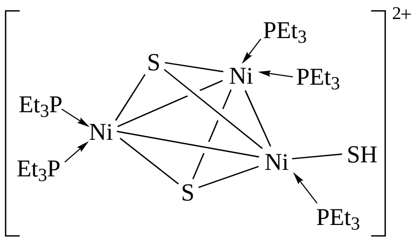

(**21**)

3.2 Disulfide: S_2^{2-}

In general, complexes of S_2^{2-} can be prepared by reaction of elemental sulfur with electron-rich metal centers, by high-temperature reaction of metal complexes with S_2Cl_2 and S_8, or by direct reaction of metal salts with polysulfides. The binding of S_2^{2-} to transition metals can be compared to the binding of O_2:σ-donation occurs from the filled π-orbital of the S_2^{2-} fragment coupled to π-donation from the π^*-antibonding orbital on S_2^{2-} to the metal d_π-orbitals (Scheme 9). Thus, coordination to a metal ion leads to a shortening of the S–S distance in S_2^{2-} and makes this fragment more susceptible to nucleophilic attack. The redox interconversion of coordinated S^{2-} and S_2^{2-} to give S_2 (equation 2) is of relevance to the action of desulfurization catalysts and to related biological processes.

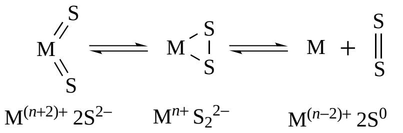

(2)

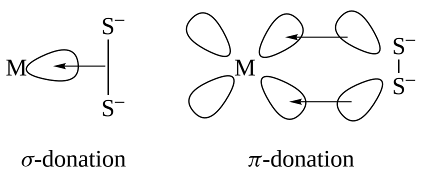

Scheme 9

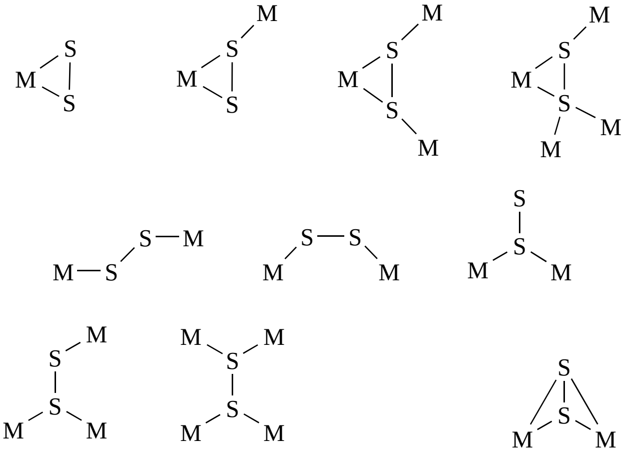

Scheme 10

Scheme 10 illustrates the range of coordination modes of S_2^{2-} to metal centers, while Scheme 11 illustrates some the complexes that have been characterized.

An unusual μ-η^1-S_2 ligand has been stabilized in the complex $[Fe_2(S_2)_3([9]aneN_3)_2]$ ($[9]aneN_3 = 1,4,7$-tri-azacyclononane). The persulfide ligands are stabilized via hydrogen-bonding to the amine hydrogen atoms, and the polarized structure for the persulfide ligands is supported by their reaction with methyliodide.[19]

3.3 Polysulfides: S_x^{2-}

The coordination chemistry of polysulfides has been reviewed[20] and has been developed for the synthesis of new chalcogenide materials.[21] Polysulfide ligands S_x^{2-} ($x = 2$–9) form a remarkable range of metal complexes which are usually prepared by reaction of metal salts with either elemental sulfur and/or with polysulfides. Scheme 12 illustrates some of the polysulfide complexes that have been prepared and characterized. The complex $[Ti(Cp)_2(S_5)]$ is a versatile starting material and reagent for the synthesis of a wide variety of compounds (Scheme 13). $[Ti(Cp)_2(S_5)]$ and $[Ti(Cp)_2(S_3)]$ are both fluxional in solution, showing a ring flipping of the polysulfide ring (equations 3 and 4).[22]

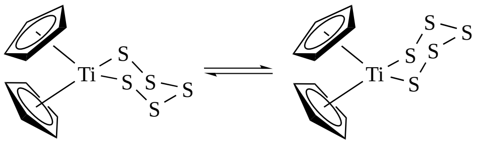

(3)

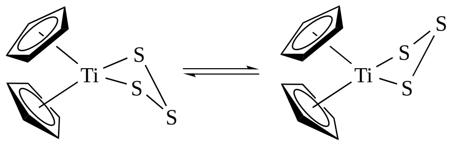

(4)

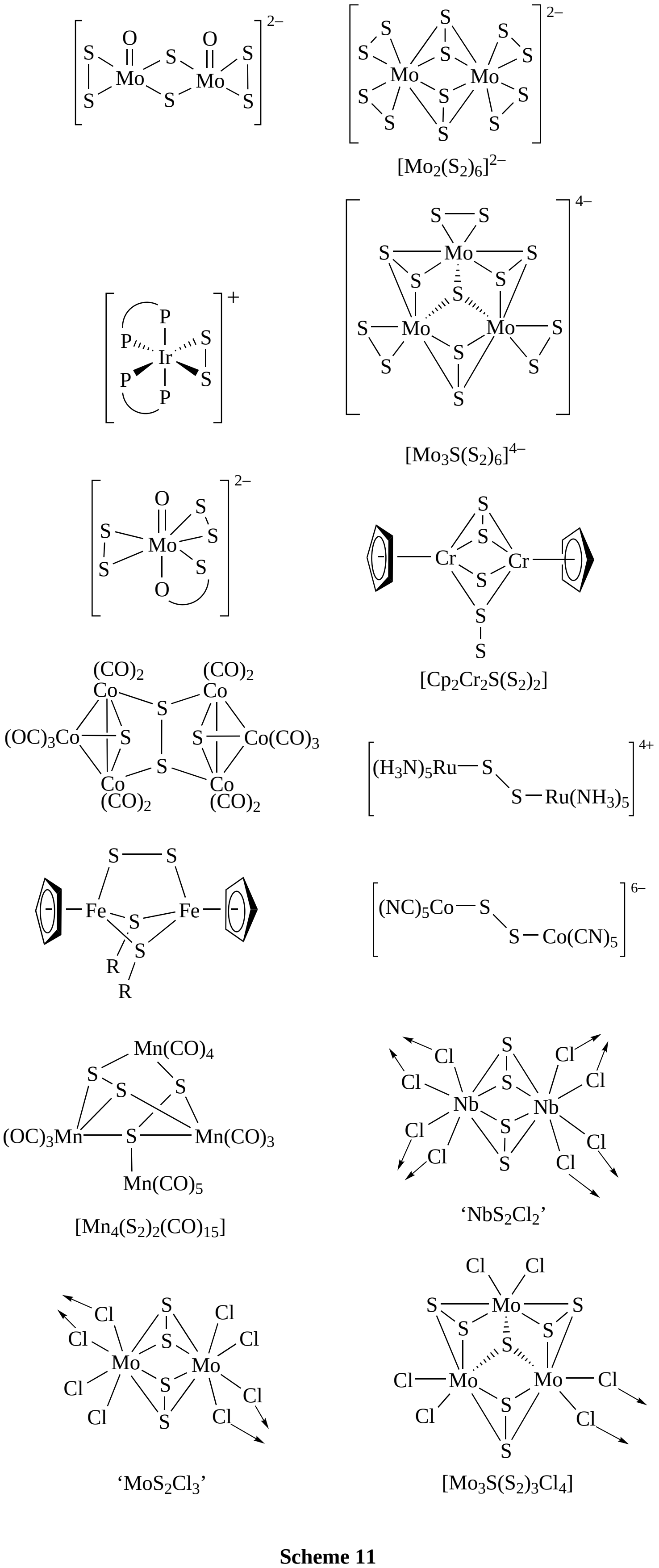
$[Mo_2(S_2)_6]^{2-}$
$[Mo_3S(S_2)_6]^{4-}$
$[Cp_2Cr_2S(S_2)_2]$
$[(H_3N)_5Ru—S—S—Ru(NH_3)_5]^{4+}$
$[(NC)_5Co—S—S—Co(CN)_5]^{6-}$
$[Mn_4(S_2)_2(CO)_{15}]$
‘NbS_2Cl_2’
‘MoS_2Cl_3’
$[Mo_3S(S_2)_3Cl_4]$

Scheme 11

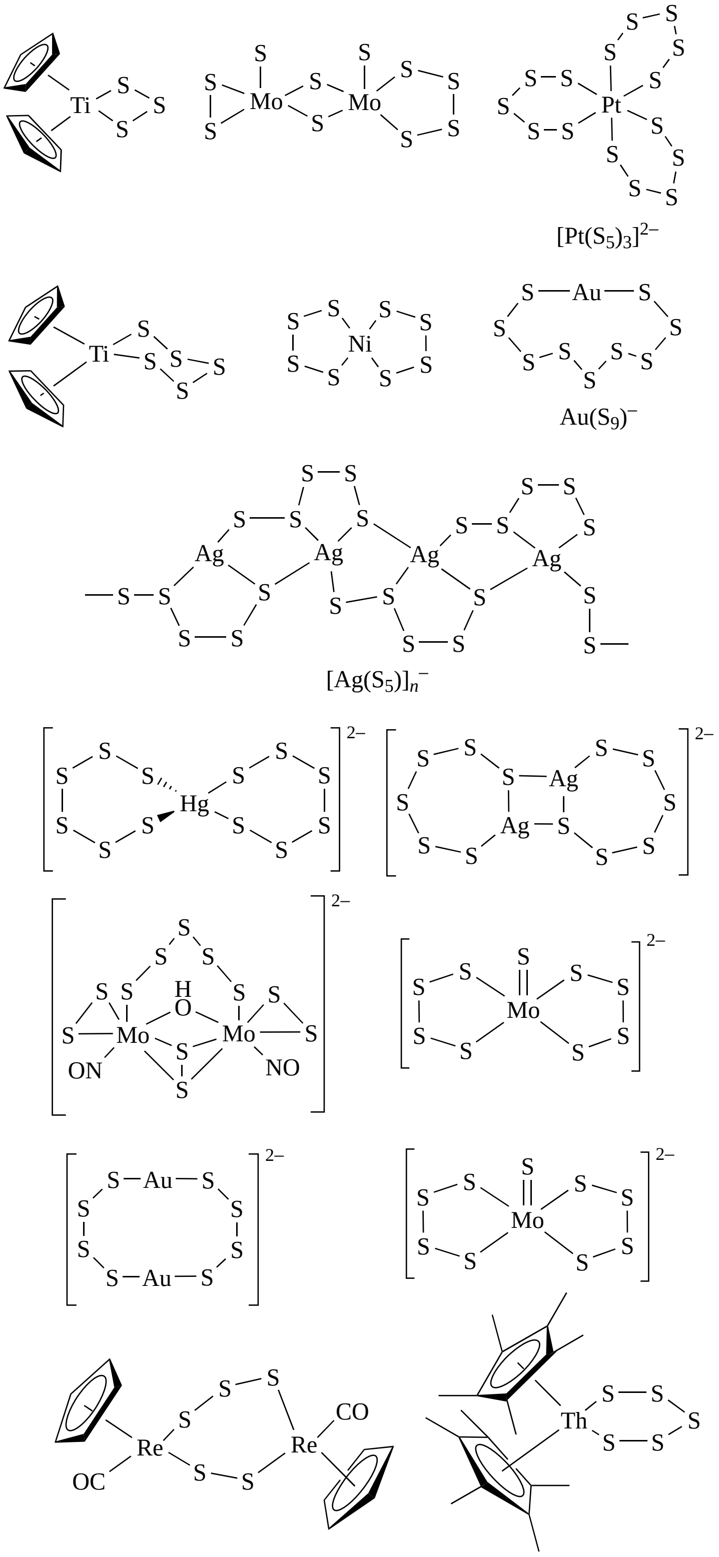
[Pt(S5)3]2–
Au(S9)–
[Ag(S5)]n–
2–
Ti
Mo
Pt
Ni
Au
Ag
Hg
Re
Th
CO
OC
ON
NO
H
O
S

Scheme 12

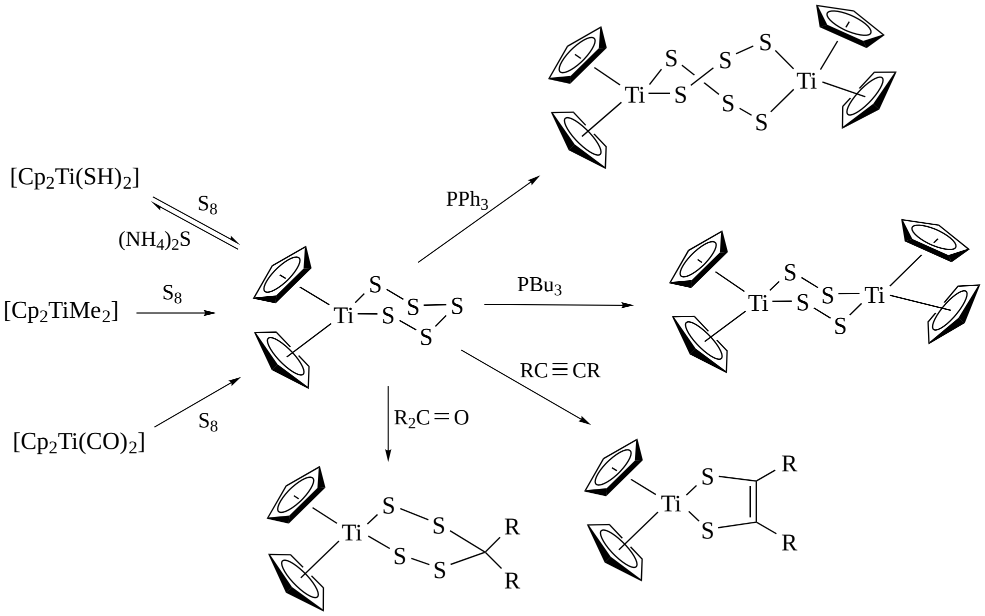

[Cp2Ti(SH)2]
S8
(NH4)2S
[Cp2TiMe2]
S8
[Cp2Ti(CO)2]
S8
PPh3
PBu3
RC≡CR
R2C=O
Ti
S
R

Scheme 13

Reaction of $[Os(PMe_3)_3(H)(CH_2PMe_2)]$ with elemental S affords two products $[Os(PMe_3)_3(S_6)]$ and $[Os(PMe_3)_3(S_7)]$ (**22**), the latter incorporating a tridentate S_7^{2-} ligand.[23] Likewise, reaction of $[Os(S_2CNR_2)_3]$ with elemental S affords $[Os_2(S_5)(S_3CNR_2)(S_2CNR_2)_5]$ (**23**; R = Et) in which an S_5^{2-} chelate has been formed, and an S has been incorporated into one of the dithiocarbamate, S_2CNR_2, ligands to give coordinated S_3CNR_2.[23] The dinuclear species $[Os_2(S_3CNEt_2)_2(S_2CNEt_2)_3]^+$ (**24**) has been isolated from the reaction of $[OsCl_6]^{2-}$ with NaS_2CNEt_2.

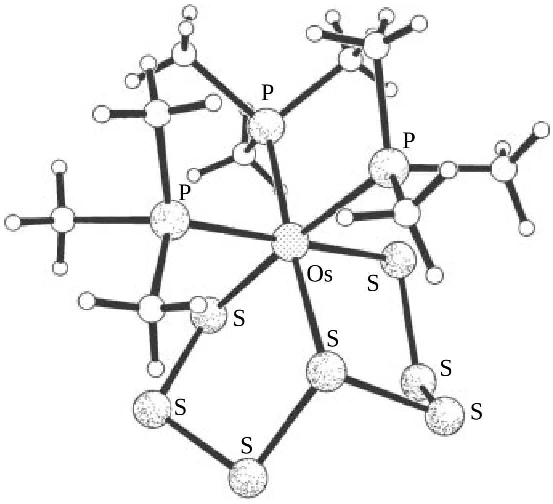

P
P
P
Os
S
S
S
S
S
S
S

(**22**)

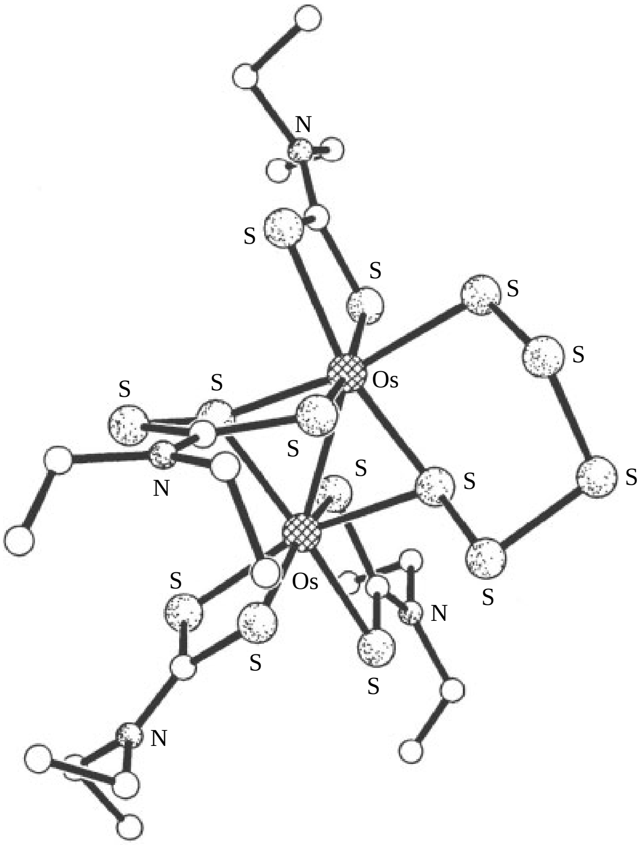

N
S
S
S
Os
S
S
S
S
N
S
S
S
S
Os
S
N
S
S
S
N

(**23**)

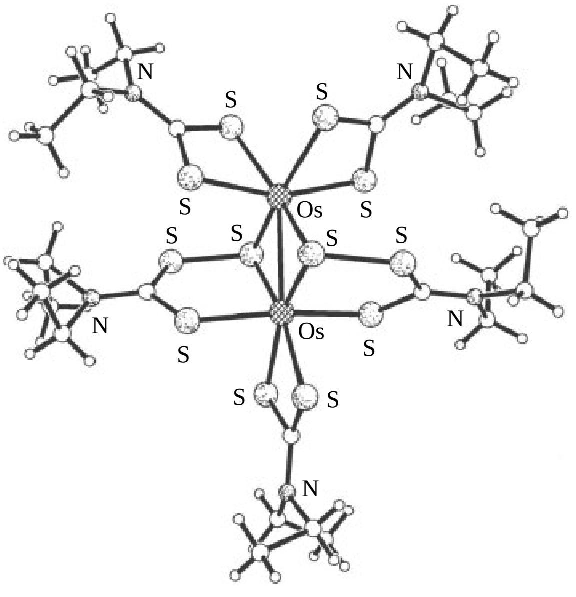

(**24**)

4 THIOLATES: RS$^-$

Comprehensive reviews on the coordination chemistry of thiolates and hindered thiolates have appeared.[24,25] One of the major problems in preparing complexes is oxidation of the thiolate to the corresponding disulfide. This can be more readily controlled with hindered thiolates, which can stabilize highly reactive, coordinatively unsaturated complexes. An important feature of thiolates is their ability to level charge within metal complexes. Thus, both π-acceptor (d-orbital on S, or S–C σ^*-orbital) and π-donor (lone pair on S) properties of thiolates have been discussed in relation to the degree of electron density at the metal center(s). The tendency for S$\cdots$S interactions and the polarizability of S-donors contrasts with the chemistry of the corresponding O-donor alkoxides. Scheme 14 illustrates the bonding modes of thiolates, RS$^-$, to transition metal centers.

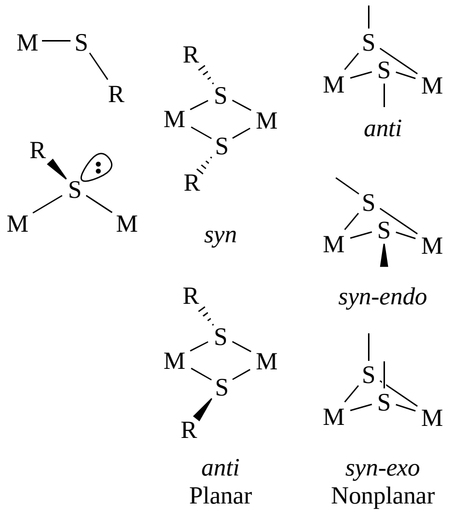

Scheme 14

Thiolates, RS$^-$, can bind terminally in octahedral [OsCl(PPhMe$_2$)$_3$(N$_2$)(SC$_6$F$_5$)] (**25**), tetrahedral [M(SR)$_4$]$^{2-}$ (**26**) (M = Fe, Co, Ni, Zn, Cd, Hg), square-planar [Pd(SR)$_4$]$^{2-}$ (**27**), trigonal planar [M(SPh)$_3$]$^-$ (**28**) (M = Cu, Hg), and linear structures [Hg(SR)$_2$] (**29**) (R = for example, Ph, SC$_6$F$_5$, SC$_6$Cl$_5$, SEt$_3$).

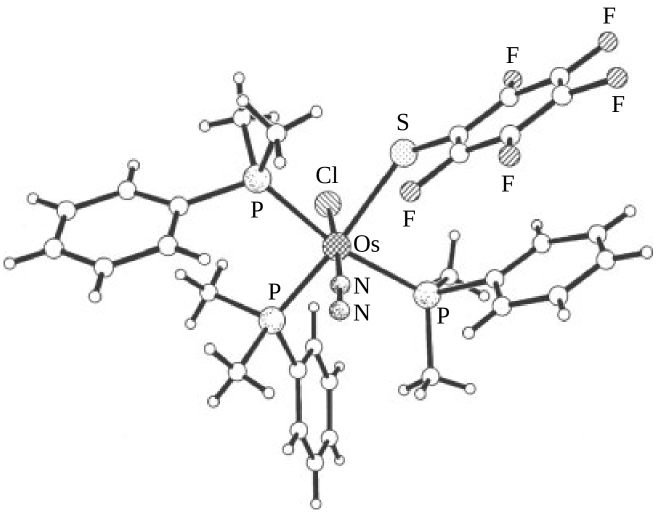

(**25**)

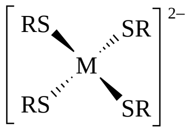

(**26**)

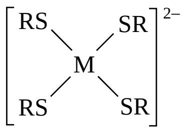

(**27**)

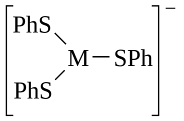

(**28**)

RS—Hg—SR

(**29**)

The synthesis, structures, and reactivities of metal thiolates with group 4 and 5 metals,[26] and the synthesis and study of copper-thiolates[27] have been reviewed. Hg^{II} thiolate chemistry has been reviewed and related to the binding of Hg^{II} in vivo by metalloregulatory proteins.[28] A range of two-, three-, and four-coordinate Hg^{II} thiolate complexes has been prepared, and comparisons with the metalloregulatory protein, Hg-MerR, suggest that the latter involves a trigonal planar $[Hg(SCys)_3]^-$ model. A ligand composed of *p*-*tert*-butylcalix[4]arene backbone bearing two thiol and two dodecyloxy- groups displays selective extraction of Hg^{II} from aqueous solution over Cd^{II} and Pb^{II}.**[29]** Scheme 15 illustrates some terminally bound thiolate complexes. Au^I thiosugar complexes and thiomalate complexes are used for the treatment of rheumatoid arthritis. Bridging thiolate ligands have been also observed and some complexes are given in Scheme 16.

Inversion at the S-donors of thiolates (Scheme 17) can be monitored by NMR spectroscopy and the activation energies for these fluxional processes have been assessed for a range of complexes (equation 5).**[30]**

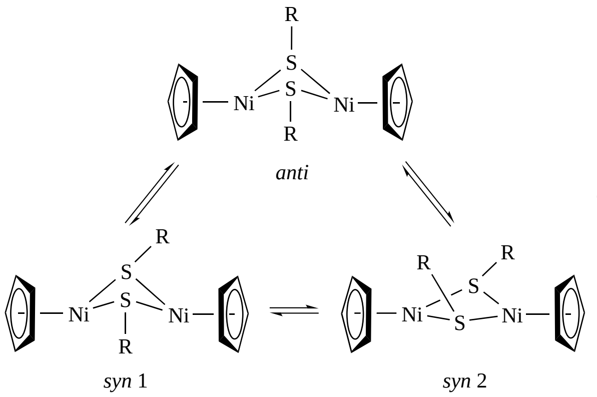

R
S
Ni
S
Ni
R
anti
R
S
Ni
S
Ni
R
syn 1
R
R
S
Ni
S
Ni
syn 2

(5)

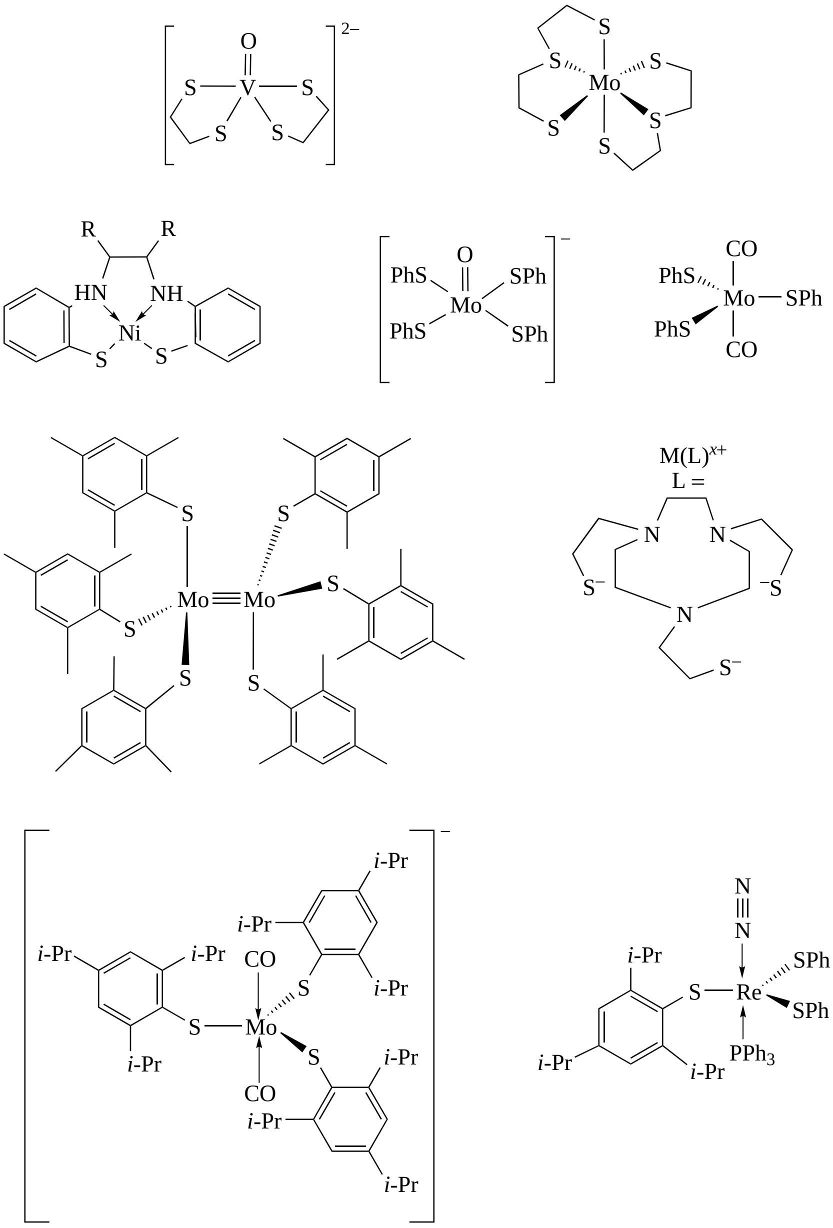

O
S
V
S
S
S
2–
S
S
S
Mo
S
S
S
R
R
HN
NH
Ni
S
S
O
PhS
SPh
Mo
PhS
SPh
–
CO
PhS
Mo
SPh
PhS
CO
S
S
S
Mo
Mo
S
S
S
M(L)^x+
L =
N
N
S⁻
⁻S
N
S⁻
i-Pr
i-Pr
i-Pr
i-Pr
CO
S
i-Pr
S
Mo
i-Pr
S
i-Pr
CO
i-Pr
i-Pr
–
N
N
i-Pr
SPh
S
Re
SPh
i-Pr
i-Pr
PPh3

Scheme 15

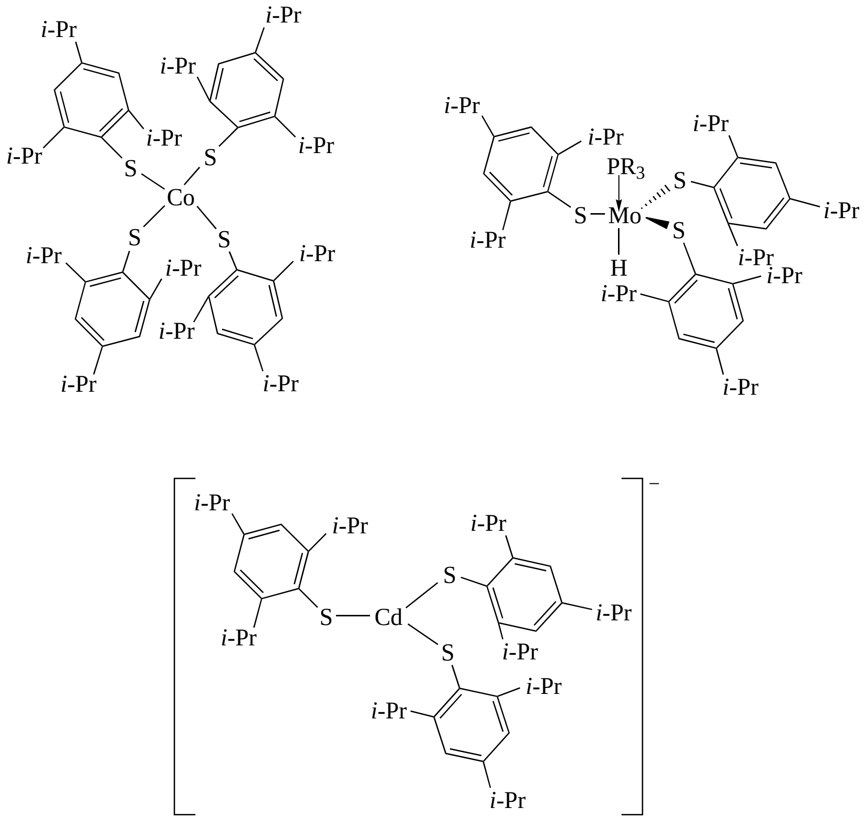

Scheme 15 cont'd

Pendant arm macrocycles with thiolate arms have been synthesized and shown to encapsulate Ga^{III} and In^{III} octahedrally.[31]

A recent major impetus for the study of S-donor complexes has been provided by the discovery of paramagnetic Ni centers in several biological systems (see Section 9). Several mixed N/S-donor complexes have been prepared and characterized, including $[Ni(terpy)(SPh)_2]_2$ (**30**), $[Ni(terpy)(SC_6F_5)_2(NCMe)]$ (**31**), $[Ni(terpy)(SR)_2]$ [R = 2,4,6-i-$Pr_3C_6H_2$ (**32**); 2,6-$Me_2C_6H_3$ (**33**)], and their chemical and redox properties have been related to the in vivo systems.[32]

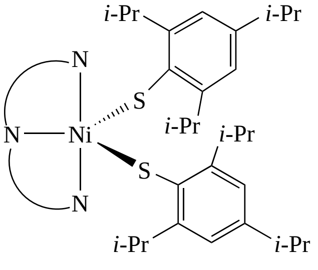

(**32**)

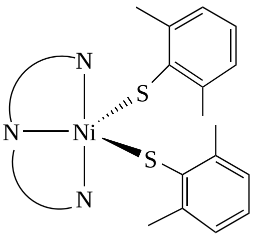

(**33**)

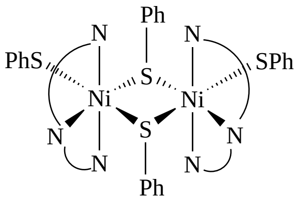

(**30**)

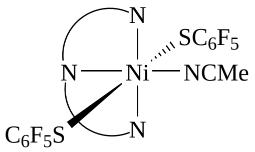

(**31**)

Holm and coworkers have investigated the structural and redox properties of a related series of mixed N/S-donor Ni^{II} complexes, for example (**34**) and (**35**), and have generated and studied the corresponding Ni^{III} species.[33] The binuclear nickel-thiolate macrocyclic complex (**36**) displays a one-electron oxidation to yield a $Ni^{III}.Ni^{II}$ species with significant delocalization of the unpaired electron density onto the bridging thiolate ligands but not onto the second nickel ion. Thus, the charge delocalization in this complex lies between the two redox extremes of nickel(III)-thiolate and nickel(II)-thiyl radical.[34] Redox studies on a series of metal bound thiolates such as (**37**) demonstrate their oxidation to sulfones and then to the sulfoxides. All the complexes display a reversible Ni^{II}-Ni^{I} reductive couple with the thiolate complexes also showing an irreversible ligand-based oxidation presumably to an unstable thiyl radical species. The

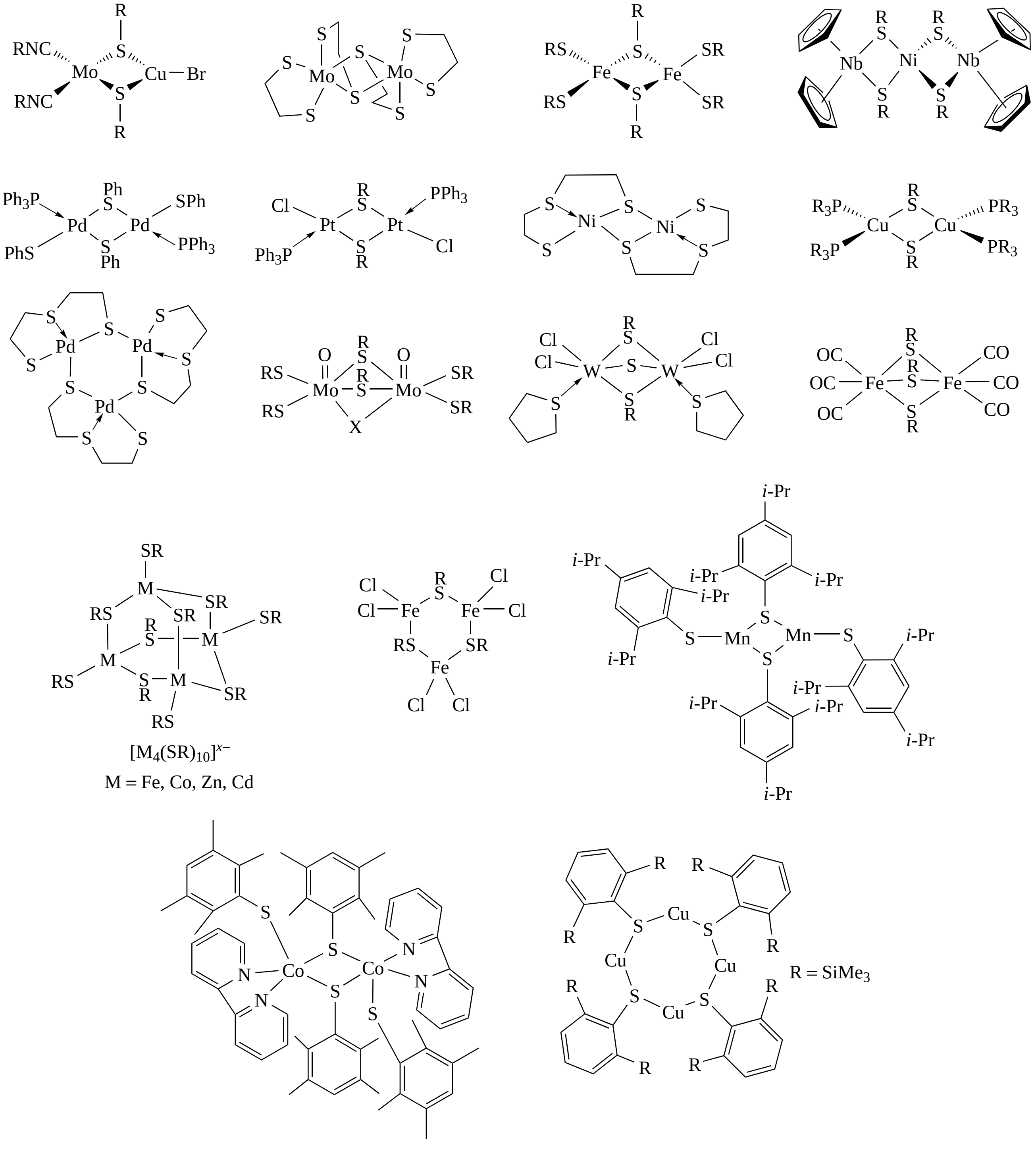

Scheme 16

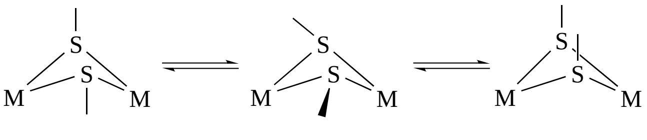

Scheme 17

bis(sulfone) complexes additionally show a reversible Ni^{II}-Ni^{III} oxidative process as do the analogous complexes where the sulfur has been alkylated. The possibility for a two centred Ni-SR site to function in oxidative-addition reactions was suggested as an intriguing solution by Nature to achieve this type of reactivity.[35]

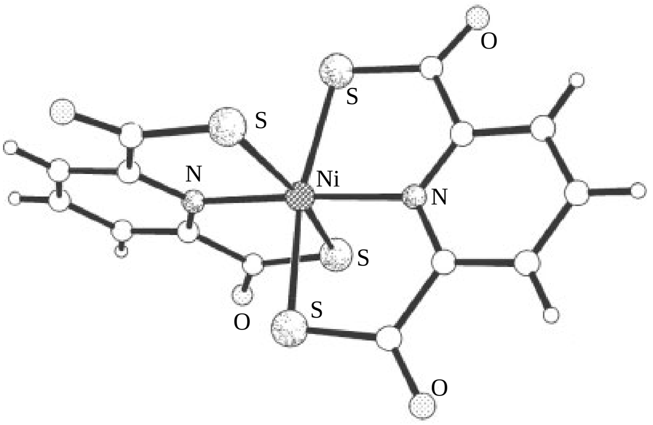

(**34**)

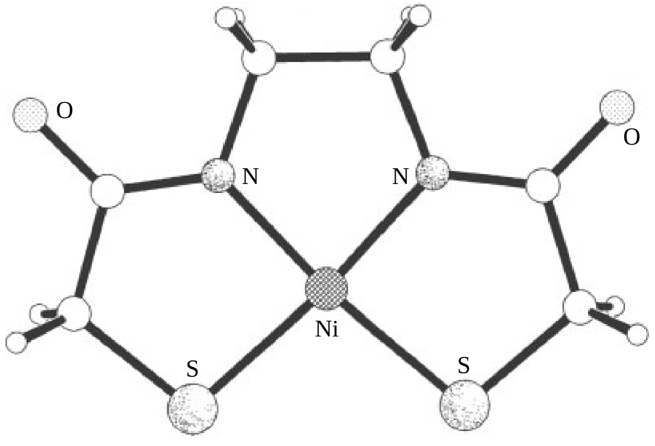

(**35**)

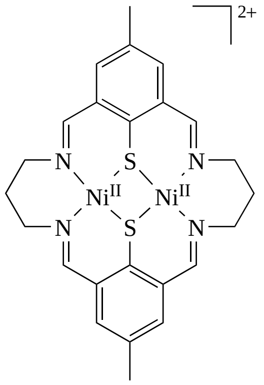

(**36**)

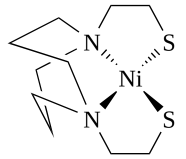

(**37**)

The Ru diazene binuclear complex (**38**) represents an important model for the activation of N_2 with N–H$\cdots$(S-thiolate)$_2$ interactions being vital to stabilisation of the diazene ligand.[36] Furthermore, the amino-thiolate Ru complex (**39**) incorporating bound dinitrogen can be prepared under mild conditions by exchange of a bound MeCN ligand.[37] Related Fe amino-thiolate complexes have also been shown to stabilize diazene fragments and the observed strong coupling of the H^+/e^- flux in these systems has been related to the mechanism of the nitrogenase FeMo cofactor.[38]

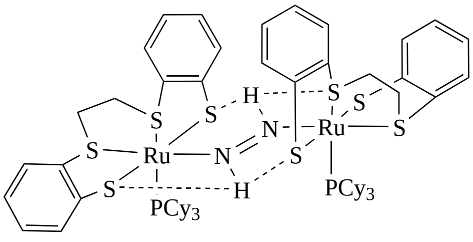

(**38**)

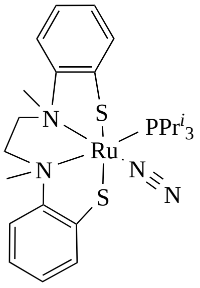

(**39**)

The Fe^{II} complex of 4,6-di-*tert*-butyl-2-aminothiophenol has been characterized crystallographically with the ligand in *o*-aminothiophenolate(1-), aromatic *o*-iminothiophenolate dianionic (2-) and open-shell *o*-iminothionebenzosemiquinonate (1-) forms. Zero-field Mossbauer spectroscopy unambiguously confirms the presence of high-spin ferrous ions throughout.[39]

The aggregation of Ni^{II} thiolate complexes yields homohexanuclear and heteropentanuclear complexes.[40,41] Fascinating pinwheel motifs have been observed with ligands such as (**40**) and (**41**) in which two Ni^{II} ions bridge four Ni^{II} amino-thiolate complexes. Alternatively, heteropentanuclear or heterohexanuclear complexes are realized where two Cu^{I}

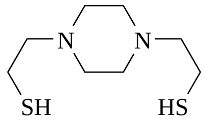

(**40**)

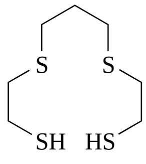

(**41**)

ions or two Pd^{II} ions bridge three or four Ni^{II} amino-thiolate complexes, respectively. Both the bite angle of the S^{-}-Ni-S^{-} unit and the choice of bridging metal ion influence whether a simple trinuclear aggregate or a higher motif is favored.

The isomers of $[Co(\text{L-cys})(en)_2](NO_3)\cdot AgNO_3$ have been structurally characterized. Significantly, the structure derived from Δ_L-$[Co(\text{L-cys})(en)_2]^{+}$ leads to a two-dimensional sheetlike structure, while Δ_L-$[Co(\text{L-cys})(en)_2]^{+}$ affords a one-dimensional left-handed helix, where the left-handed helicity is predetermined by the chiral configuration in the starting Co^{III} complex.**[42]**

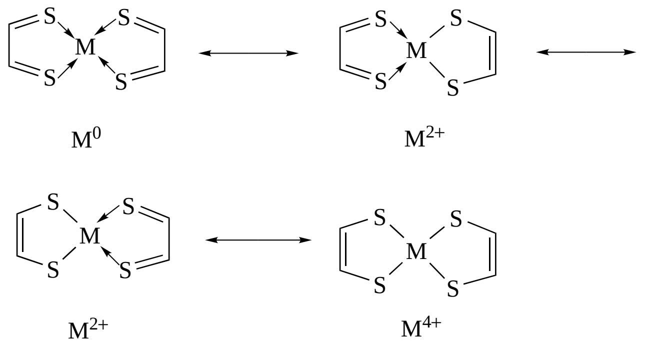

Scheme 18

5 DITHIOLENES

The coordination chemistry of 1,2-dithiolenes and related ligands has been reviewed.**[25,43]** 1,2-Dithiolenes are bidentate, redox-active ligands which can coordinate in the limit as dithiodiketones or dithiolates (Scheme 18). Scheme 19 illustrates the more common dithiolene ligands that have been investigated. Syntheses of these ligands are well established and are usually based upon derivatization of dihalo and ketonic starting materials (Scheme 20).

The coordination chemistry of dithiolenes is extensive with square-planar $[M(L)_2]^{x+}$ (**42**) and tris-chelate complexes $[M(L)_3]^{x+}$ (**43**) being prevalent. The latter are interesting since they tend to adopt trigonal prismatic rather than the much more common octahedral geometry, the driving force being thought to be attractive intraligand S–S interactions. The square-planar complexes $[M(L)_2]^{x+}$ can form five-coordinate adducts or oligomers via M–S bridges (equations 6 and 7). The formation of redox oligomers and related

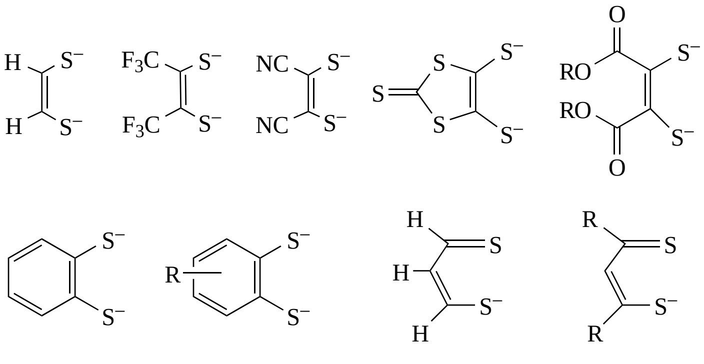

Scheme 19

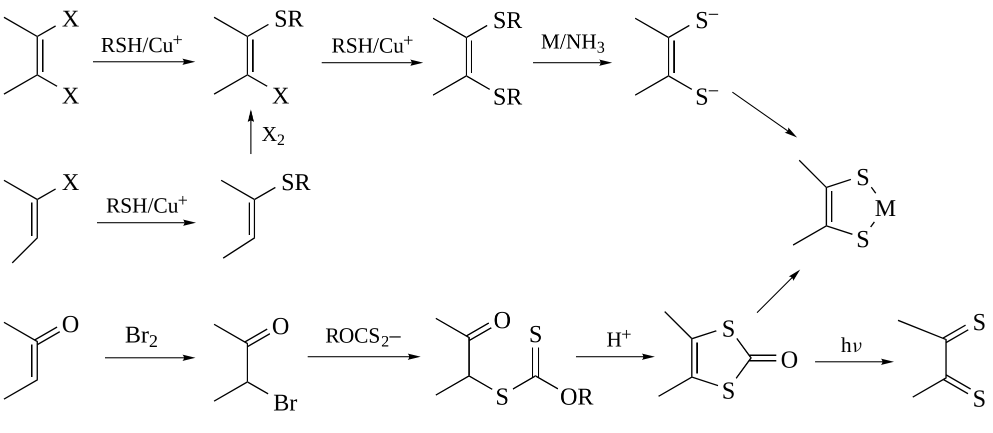

Scheme 20

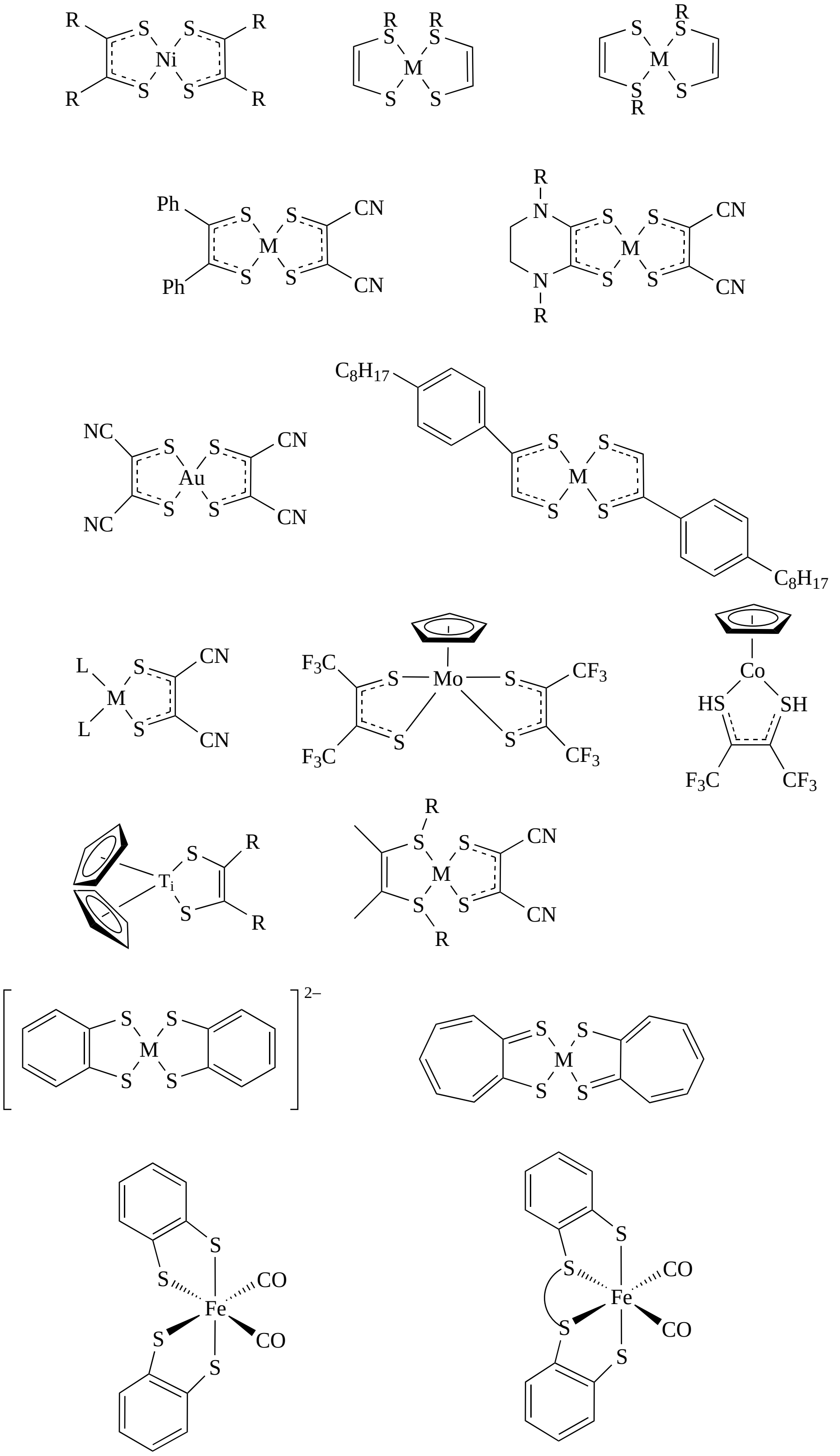
R S S R
Ni
R S S R
R R
S S
M
S S
R
S S
M
S S
R
Ph S S CN
M
Ph S S CN
R
N S S CN
M
N S S CN
R
C_8H_{17}
NC S S CN
Au
NC S S CN
S S
M
S S
C_8H_{17}
L S CN
M
L S CN
F_3C S Mo S CF_3
F_3C S S CF_3
Co
HS SH
F_3C CF_3
S R
Ti
S R
R
S S CN
M
S S CN
R
2–
S S
M
S S
S S
M
S S
S
S CO
Fe
S CO
S
S
S CO
Fe
S CO
S

Scheme 21

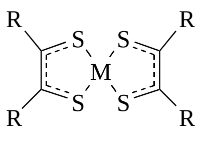

(42)

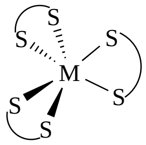

(43)

complexes showing stacked structures in the solid state has led to the formation of one-dimensional conductors, partially oxidized/reduced conducting polymers, and charge-transfer salts. Liquid crystal dithiolenes have also been prepared. Many dithiolene complexes are redox active, and the interpretation of these electron-transfer processes as being metal or ligand based has been controversial. The problems of assignment stem from the facile electron transfer of dithiolene ligands themselves, and delocalization of charge density across the ligand and metal centers.

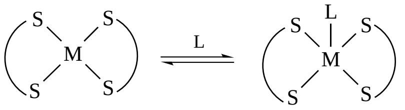

(6)

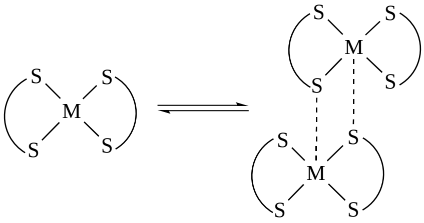

(7)

Scheme 21 illustrates some of the diothiolene complexes that have been prepared. The coordination chemistry of ligands derived from benzene-1,2-dithiolate has been investigated with Fe and Ru centers for the potential binding of N_2 and N_2H_4 as models for nitrogenase (*see* ***Nitrogenase: Metal Cluster Models***).[36,44]

Ni^{II} dithiolenes have been shown to be effective for the electrochemical separation of alkenes from complex streams. No poisoning was observed in the presence of H_2, CO, acetylene, or H_2S with binding of alkene to the sulfur ligands rather than to Ni (Scheme 22). This reflects the radical nature of dithiolenes in these complexes.[45] Metal bis-1,2-dithiolene complexes may also act as conducting or magnetic assemblies.[46]

A general route to asymmetric dithiolenes has been developed and has been used for the generation of the dithiolene complexes $[MO(dithiolene)_2]^{2-}$ (M = Mo or W).[47] These complexes have been developed to explore the chemistry of Mo and W when bound to pterin ligands in biology, for example in the molybdenum cofactor of DMSO reductase or in aldehyde oxidoreductase. A comprehensive study of 25 complexes $[W^{IV}(OC_6H_4\text{-}p\text{-}X')(S_2C_2(C_6H_4\text{-}p\text{-}X)_2)_2]^{1-}$ (X = Br, F, H, Me, OMe and X′ = CN, Br, H, NH_2) has been reported and their relevence to the mechanism of oxygen atom transfer in the DMSO reductase isoenzyme described. A stepwise oxo-transfer reaction is proposed in an early transition state in which primary W^{IV}-O(substrate) bond-making is rate-limiting. This is followed by a six-coordinate structure with another transition state involving both atom and electron transfer to yield an $W^{VI}=O$ group.[48] Monodithiolene complexes of Mo^V and Mo^{VI} have been synthesized as structural analogs of the oxidized form of the sulfite oxidase enzyme family.[49]

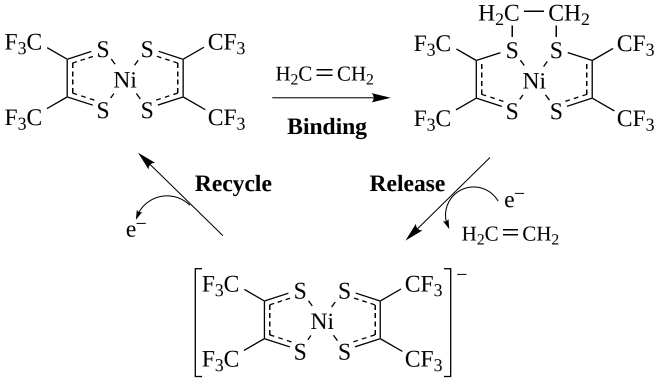

Scheme 22

6 MIXED S/O, S/N AND P/S LIGANDS

The coordination chemistry of NS (thionitrosyl), thiazate (NSO^-), disulfidothionitrate (S_3N^-), sulfur monoxide (SO), disulfur monoxide (S_2O), SO_2, DMSO, thiosulfate, sulfite, and thiourea ligands is extensive.[50–52] Scheme 23 illustrates their coordination modes and some of the complexes that can be generated.

The transition metal coordination chemistry of P/S ligands[53] and of thiophosphorus and thio arsenic ligands bound to transition metals and main group elements[54] have been summarized. An interpenetrating diamond-type framework has been prepared from the high-temperature solid-state reaction of U, P_2S_5, and S to yield UP_4S_{12}. This material contains U^{IV} ions linked by S,S′-bidentate $P_2S_6{}^{2-}$ molecular rods.[55] Extended S-donor ligand such as (**44**) can generate novel polymeric network materials.[56]

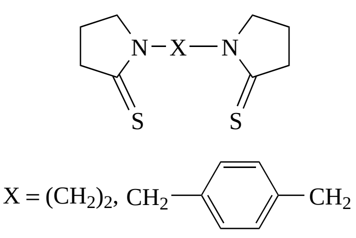

(44)

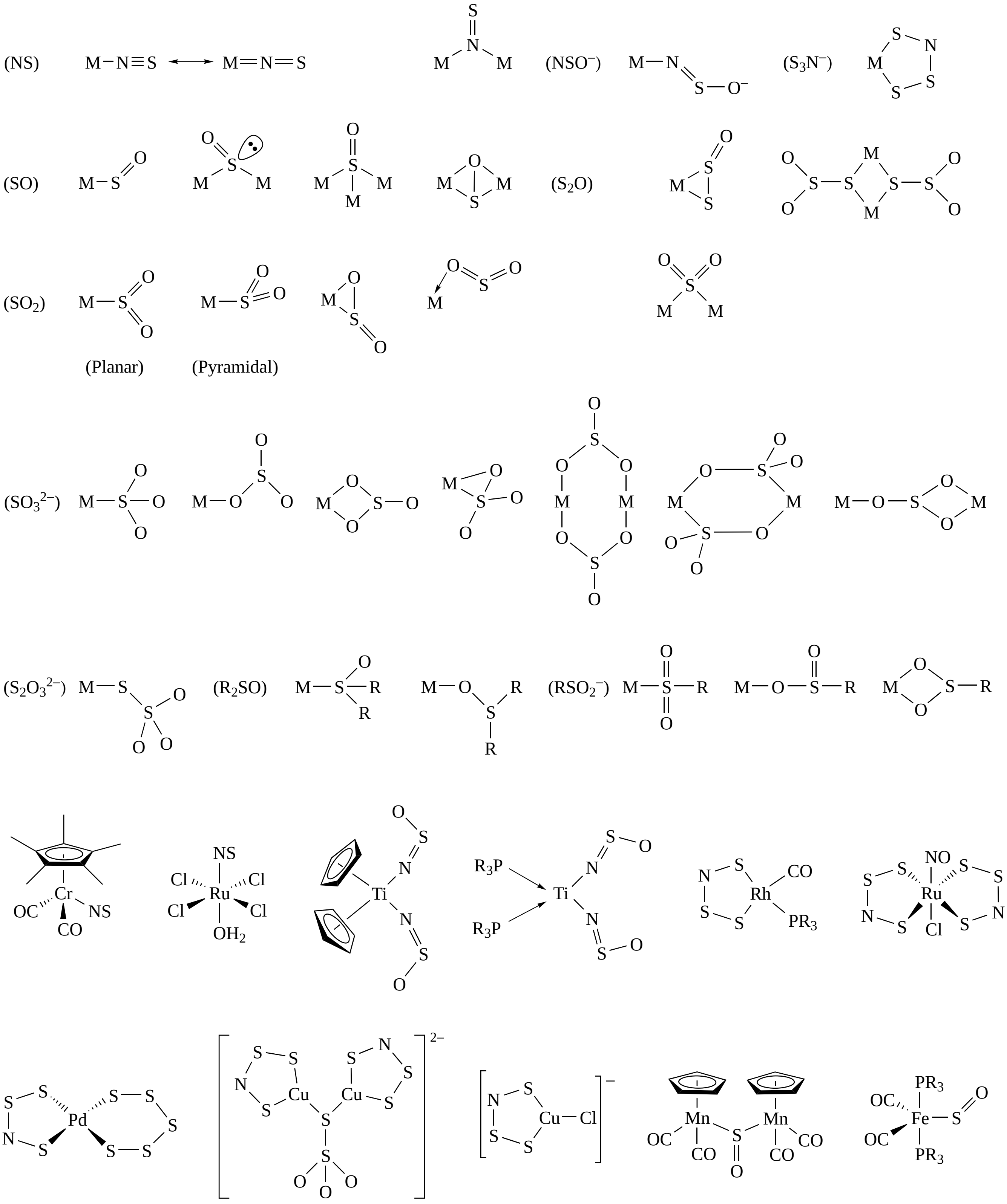
(NS)
(NSO⁻)
(S₃N⁻)
(SO)
(S₂O)
(SO₂)
(Planar)
(Pyramidal)
(SO₃²⁻)
(S₂O₃²⁻)
(R₂SO)
(RSO₂⁻)

Scheme 23

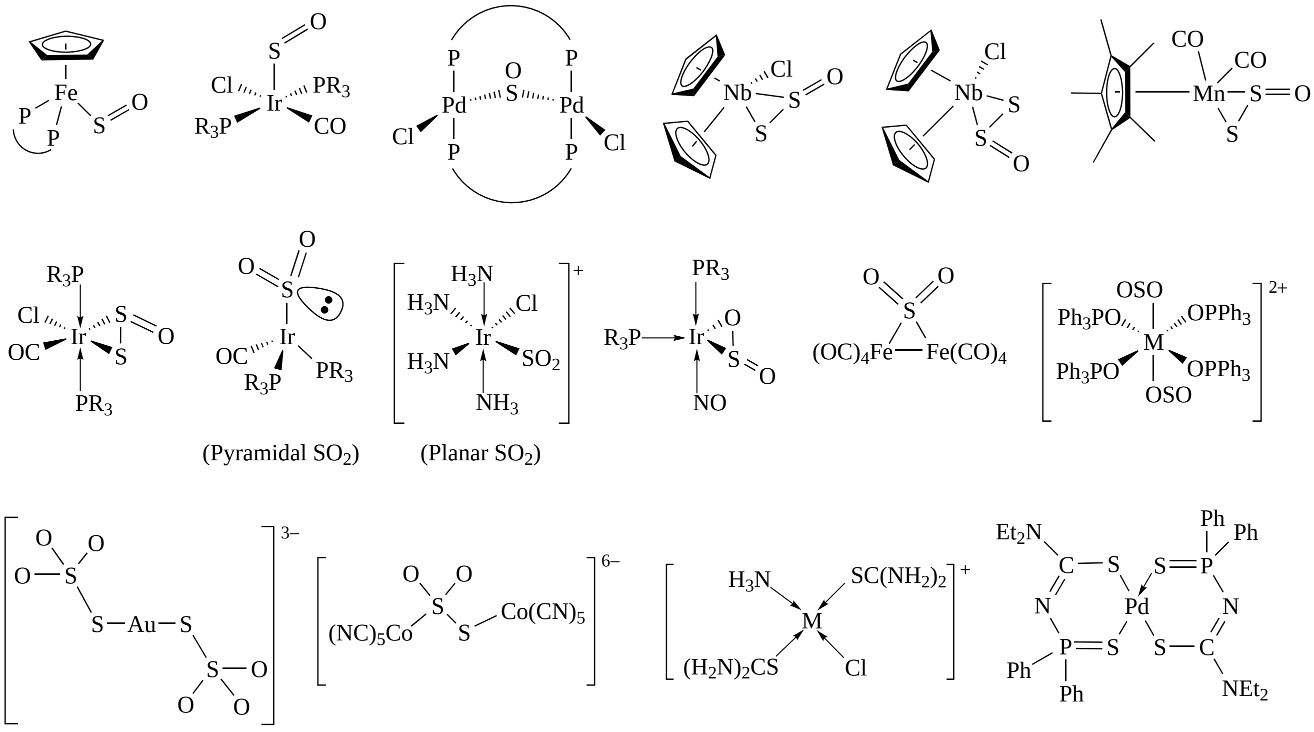

Scheme 23 cont'd

7 DITHIOCARBAMATES AND RELATED LIGANDS

The chemistry of dithiocarbamates, thioacids, and related ligands,[57] dithiolium and dithio-*β*-diketonate ligands,[58] thiooxalates,[59] and CS_2[60] has been reviewed. Scheme 24 illustrates the dithiocarbamate ligands that have been studied; complexes of monothio derivatives have also been investigated. The ligands are generally prepared by reaction of CS_2 or COS with the corresponding amine. A range of dithiocarbamate complexes, including $[M(S_2CNR_2)_2]$ (**45**) (M = Ni, Pd, Pt) and $[M(S_2CNR_2)_3]$ (**46**) (M = Fe, Ru, Os), have been prepared. Dithiocarbamates can also bridge between two metal ions, as in $[Ru_2(S_2CNR_2)_5]^+$, which exists as two isomers, the *α* form (**47**) and *β* form (**48**). The complexes $[Zn(S_2CNMe_2)_2]$ and $[Fe(S_2CNMe_2)_3]$ and the disodium salt $Na_2[S_2CNHCH_2CH_2NHCS_2]$ have been marketed as fungicides under the names Ziram, Ferbam, and Nabam, respectively.

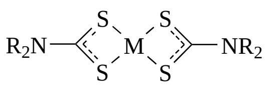

(**45**)

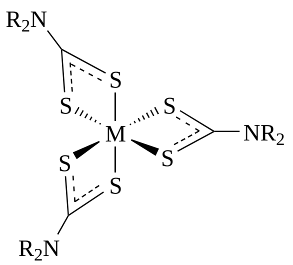

(**46**)

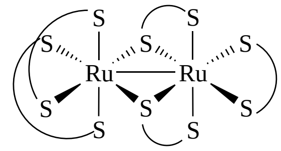

(**47**)

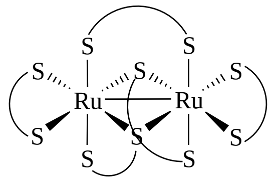

(**48**)

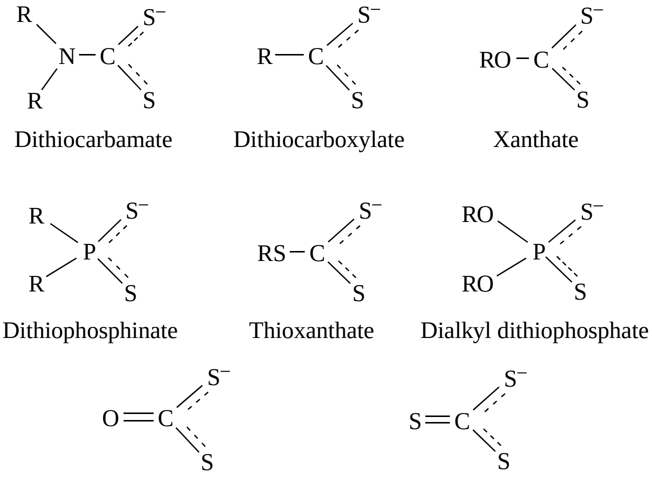

Dithiocarbamate
Dithiocarboxylate
Xanthate
Dithiophosphinate
Thioxanthate
Dialkyl dithiophosphate
Dithiocarbonate
Trithiocarbonate

Scheme 24

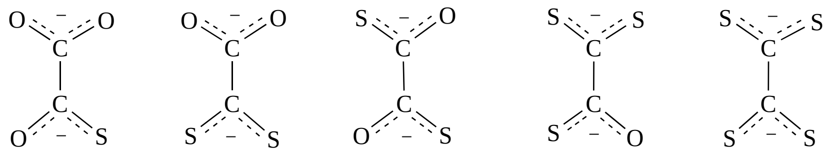

Scheme 25

Fe dithiocarbamates are enjoying a resurgence of interest in their chemistry following their application in the detection and analysis of biological NO produced endogenously from NO synthase.[61] Diothiocarbamates have been found to form complexes with Au^{II} ions as in binuclear complexes, $[Au_2(S_2CNR_2)_2X_2]$ and $[Au_2(S_2CNR_2)(CH_2PPh_2CH_2)X_2]$.[62]

Mono-, dithio-β-diketonate, and related ligands are effective chelates for a wide range of metal ions, forming complexes of the type $[M(L)_2]$ (**49**) (M = Co, Ni, Pd, Pt, Zn, Cd, Hg) and $[M(L)_3]$ (**50**) (M = Cr, Fe, Ru, Os, Co, Rh, Ir). The complexes are often redox active, and like those of dithiolenes, the location of redox activity in terms of metal- or ligand-based radicals has been the subject of much interest.

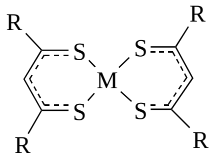

(**49**)

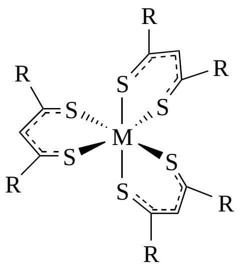

(**50**)

A wide range of mono-, di-, tri-, and tetrathiooxalate complexes have been prepared. These species can act as mono-, bi-, tri-, and tetradentate ligands and can also bridge between metal centers (Scheme 25).

CS_2 can bind in monodentate end-on, bidentate chelate, bridging, or η^2 forms (Scheme 26). Most complexes of CS_2 are low-valent electron-rich species, for example $[Mo(Cp)(CO)_2(\eta^2\text{-}CS_2)]$ (**51**), $[Ru(CO)_2(PPh_3)_2(\eta^2\text{-}CS_2)]$ (**52**), and $[Pt(PPh_3)_2(\eta^2\text{-}CS_2)]$ (**53**). Conversion of coordinated CS_2 to CS and CS_3 fragments can occur on coordination. The coordination chemistry of phosphine-carbon disulfide adducts (S_2CPR_3) has been reviewed; these versatile ligands can act as 2 to 8 electron donors to metal centres.[63]

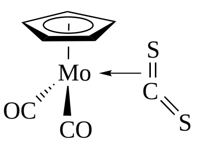

(**51**)

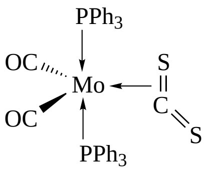

(**52**)

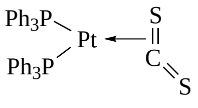

(**53**)

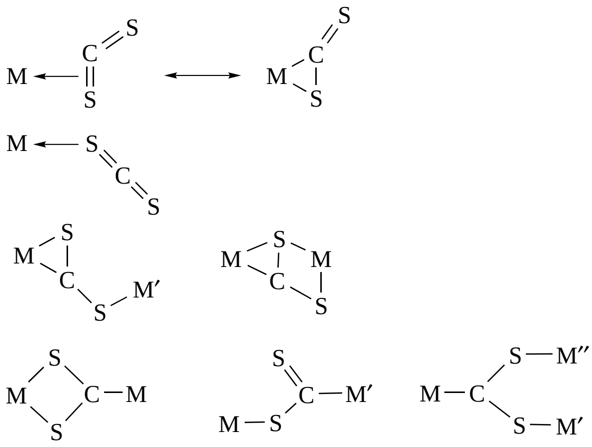

Scheme 26

8 THIOETHERS: R_2S

The coordination chemistry of thioethers has been reviewed.[2–4] They are generally poor ligands and highly labile, and so can be used as leaving groups for metal complex syntheses. For example, $[Au(tht)_2]^+$ (**54**; tht = tetrahydrothiophene) is an effective starting material

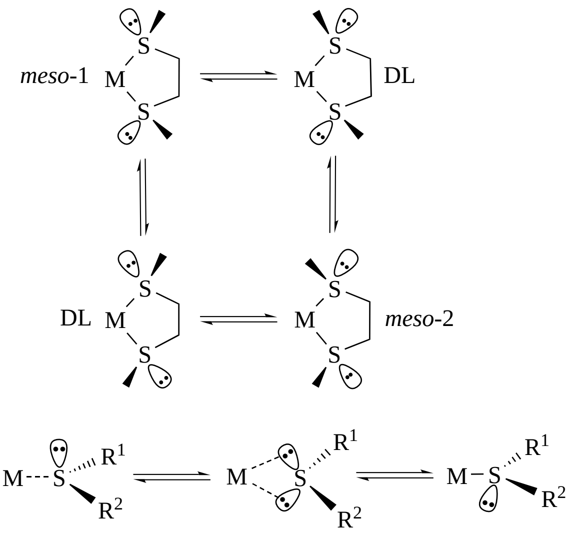

Scheme 27

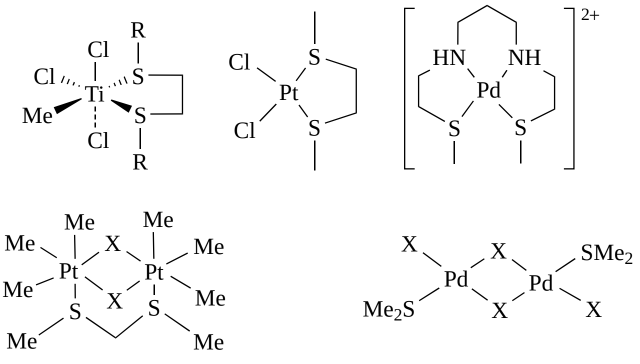

Scheme 28

for substitution reactions. Many thioether complexes are fluxional with inversion at the coordinated thioether S-center (Scheme 27). Scheme 28 illustrates some of the thioether complexes that have been prepared. The fluxionality of thioether and mixed thiolate/thioether ligands has been reviewed.[30] Reviews of complexes of groups 3–6 covering oxidation states greater than 3,[64] and of complexes of the p-block (groups 13–15)[65] with acyclic and macrocyclic thioethers have appeared.

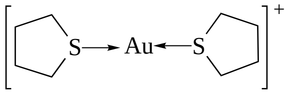

(**54**)

Thioether coordination chemistry has undergone a renaissance with the development of general syntheses of polythioether macrocyclic ligands. Scheme 29 illustrates some of the ligands that have been reported. The tridentate ligand

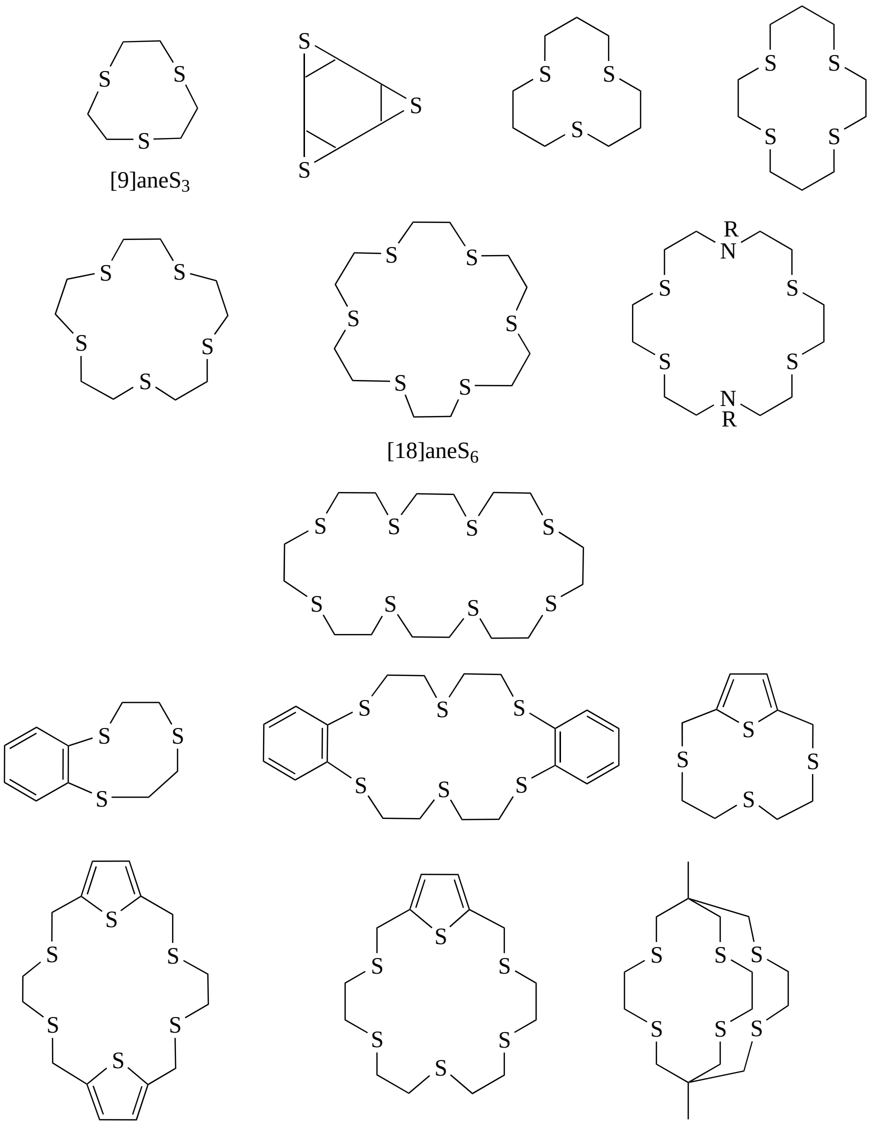

Scheme 29

[9]aneS$_3$ is unique in that it can be regarded as 'preorganized' for facial coordination, and indeed, this ligand forms a range of low-spin, bis-sandwich complexes $[\mathrm{M}([9]\mathrm{aneS}_3)_2]^{n+}$ (M = Cr, Fe, Ru, Os (**55**; $n = 2$), Co, Rh, Ir, Ni, Pd (**56**; $n = 2$), Pt, Zn, Ag, Au, Tl, In). Many of these complexes are redox active, and a series of mononuclear radical species of unusual metal oxidation states can be characterized and isolated, including the Pd$^{\mathrm{III}}$ radical complex $[\mathrm{Pd}([9]\mathrm{aneS}_3)_2]^{3+}$ (**57**).[66] The redox interconversion of Au$^{\mathrm{I}}$, Au$^{\mathrm{II}}$, and Au$^{\mathrm{III}}$ centers in $[\mathrm{Au}([9]\mathrm{aneS}_3)_2]^{+/2+/3+}$, (**58**), (**59**), (**60**), respectively, has been reported and illustrates the high coordinative flexibility of thioether crowns.[67]

The hexathioether ligand [18]aneS$_6$, the S-analog of 18-crown-6 ([18]aneO$_6$), can encapsulate M$^{\mathrm{II}}$ ions to form highly stable complexes $[\mathrm{M}([18]\mathrm{aneS}_6)]^{2+}$ (M = Fe; Co, Ni, Cu (**61**); Pd (**62**); Pt). The complexes of these ligands with d^8 metal ions such as Pd$^{\mathrm{II}}$, Pt$^{\mathrm{II}}$, and Au$^{\mathrm{III}}$ tend to show long-range M$\cdots$S interactions in the range 2.8–3.1 Å. This is reminiscent of the coordination at Cu sites in blue copper proteins such

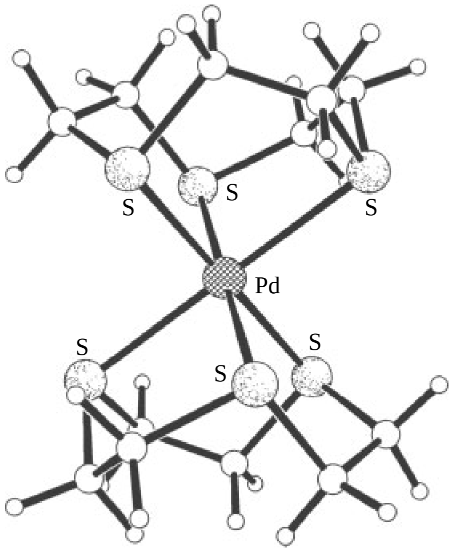

(**57**)

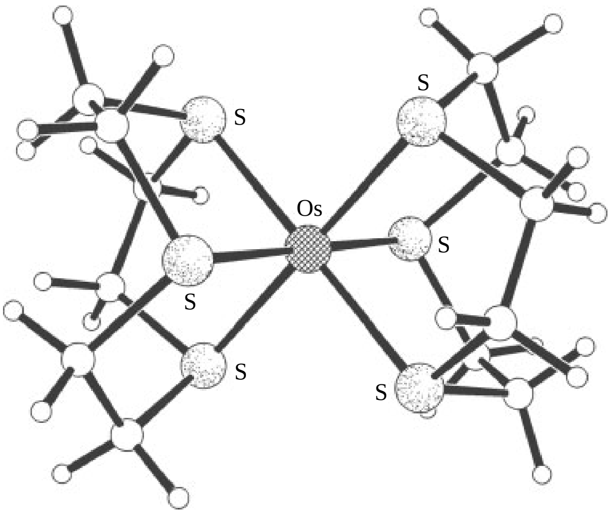

(**55**)

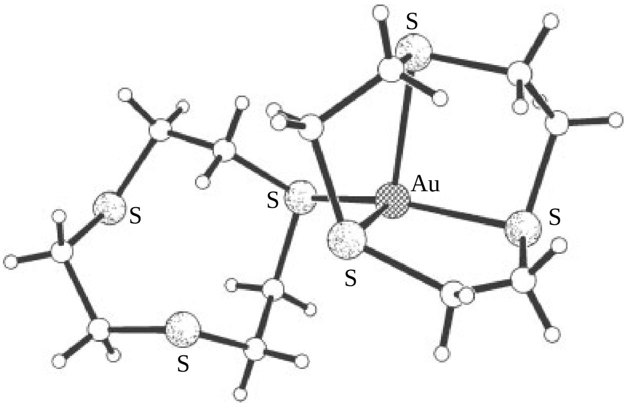

(**58**)

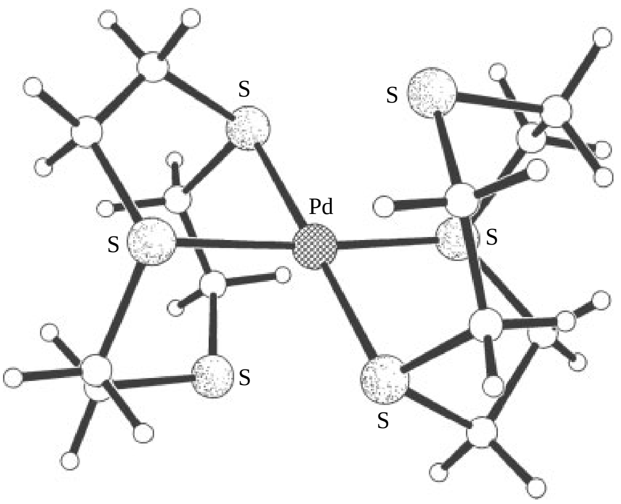

(**56**)

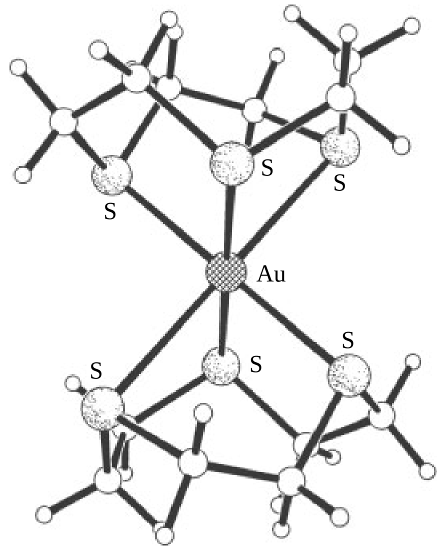

(**59**)

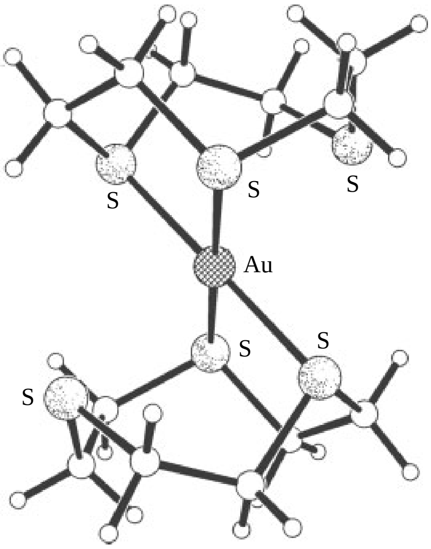

(**60**)

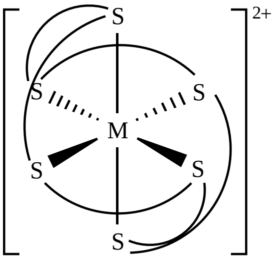

(**61**)

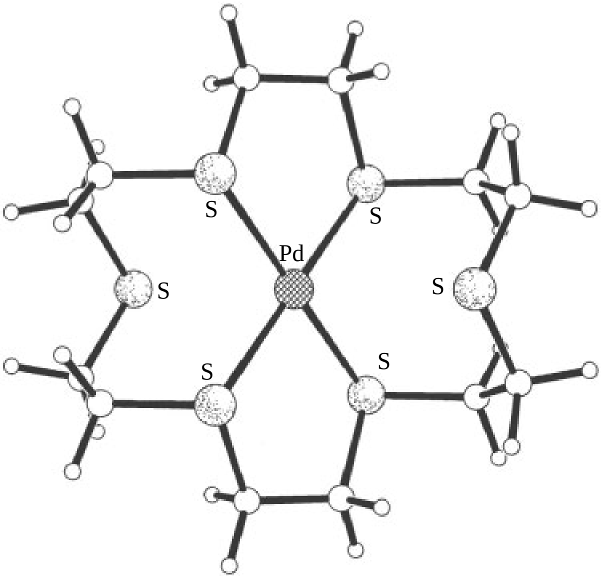

(**62**)

as azurin and plastocyanin, in which long-range thioether S to Cu distances of some 2.9 Å are observed. The binding of N_2 in the thioether complex *trans*-[Mo(N_2)$_2$(Me_8[16]aneS_4)] (**63**) has been reported and the ability of homoleptic thioether coordination at Mo^0 to stabilize N_2 binding has been discussed.**[68]**

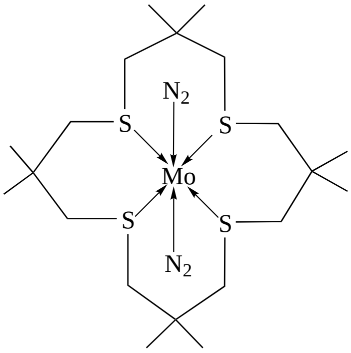

(**63**)

A range of half-sandwich complexes [Pd([9]aneS_3)Cl(L)](PF_6) (L = $2PPh_3$, $Ph_2PCH_2PPh_2$, $Ph_2PCH_2CH_2PPh_2$, $(Ph_2PCH_2)_3CMe$, 2,2′-bipyridine or 1,10-phenanthroline) show an approximately square-planar geometry at Pd^{II} with two sulfur donors and the ligand L; additionally, there is a weaker interaction to the other apical sulfur.**[69]**

The chemistry of tridentate mixed azathioether macrocyclic transition metal complexes has recently been reviewed in particular, focusing upon structural and redox properties,**[70]** and a series of acylurea pendant arm azathioether macrocycles have been developed as heteroditopic receptors for transition metal salts.**[71]** The first examples of mixed thio- and telluroethers [11]aneS_2Te, [12]aneS_2Te and [14]aneS_3Te, have been prepared. The complex [Ag([11]aneS_2Te)]BF_4 shows a one-dimensional polymeric chain adopted by the cation, in which the Ag^I ions are coordinated by three macrocyclic ligands.**[72]** The transition metal chemistry of alkylcycloarsathianes, in particular, of chain and macrocyclic As-S ligands has been reviewed.**[73]**

Thiacalixarenes have been observed to form complexes Cu_4L_2 (L = p-*tert*-butyltetrathiacalix[4]arene) with both S- and O-binding to Cu. This represents the first example of an intentionally synthesized paramagnetic koiland, that is hollow molecular building block.**[74]** Chiral thioether ligands have found applications in asymmetric catalysis of allylic substitution, hydrogenation, transfer hydrogenation, hydrosilation, Michael addition, 1,4-conjugate additions, and copolymerisations.**[75]**

9 METALLOENZYMES

Separate sections in this series are devoted to biological and bioinorganic chemistry (*see* ***Copper: Hemocyanin/Tyrosinase Models***; ***Copper Proteins with Dinuclear***

Active Sites; ***Copper Proteins: Oxidases***; ***Copper Proteins with Type 1 Sites***; ***Copper Proteins with Type 2 Sites***; ***Copper Enzymes in Denitrification***; ***Iron–Sulfur Models of Protein Active Sites***; ***Iron–Sulfur Proteins***; ***Nickel Enzymes & Cofactors***; and ***Nickel: Models of Protein Active Sites***). However, since many metalloenzymes have been found or postulated to incorporate metal−sulfur bonding, it is appropriate that a very short summary be included here.

The structural, electronic, biological, and magnetic properties of iron−sulfur clusters in metalloproteins has been reviewed focussing particularly on $[4Fe\text{-}4S^*]^{n+}$ ($n = 1{-}3$) centres,[76] and on synthetic $[Fe_3S_4]$ and heterometallic $[MFe_3S_4]$ clusters.[77] The chemistry and properties of aconitase have been reviewed in the context of its spectroscopic properties, structure, mechanistic function, and its relationship to the iron-regulatory protein.[78,79]

Metallothioneins are cysteine-rich proteins capable of binding a range of metal ions, such as Zn, Cu, Cd, and Hg, via thiolate coordination. The structure of a Zn/Cd metallothionein shows a triangular array of metals, each coordinated tetrahedrally to thiolate cysteines.

The blue copper proteins azurin, plastocyanin, stellacyanin, and umecyanin incorporate Cu bound to a combination of N/thiolate/thioether ligands. An important feature of these metalloenzymes is the facile copper(II)/(I) couple that these species exhibit, which is linked to the highly strained, asymmetric coordination geometry at the metal center. The synthesis of model complexes for these so-called Type 1 copper proteins has been reviewed.[80]

Cytochrome P_{450} catalyzes the oxidation of external substrates and particularly the incorporation of O from O_2 into C–H bonds. The active site involves an Fe-haem, with thiol ligation at an apical site from a S-donor cysteine residue being implicated in the mechanism of action. A short review of synthetic models for the active site of cytochrome P_{450} has appeared and discusses two kinds of iron porphyrins each with an axial thiolate ligand and hydroxyl groups inside the molecular cavity. A hydrogen bond to bound dioxygen has been observed in the oxy-form of a thiolate heme model system.[81] The electron-transfer metalloenzyme cytochrome *c* involves methionine S-coordination.

Rubredoxins are enzymes are found in anaerobic bacteria and are involved in redox reactions. They contain one Fe center bound to thiolate cysteine ligands, and are modeled by tetrahedral Fe^{II} $[Fe(SR)_4]^{2-}$ and Fe^{III} $[Fe(SR)_4]^{-}$ complexes.

Ferredoxins and high-potential iron proteins (HiPIPs) involve clusters of two, three, and four tetrahedral Fe centers bridged by sulfido S^{2-} donors. The coordination sphere at Fe is completed by thiolate cysteine ligands.

Nitrogenase converts N_2 to NH_3 in leguminous plants. Much work has been reported on the synthesis of model coordination compounds and clusters for nitrogenase. This complicated metalloenzyme contains an FeMo cofactor consisting of $[Fe_4S_3]$ and $[Fe_3MoS_3]$ cubanes linked together by two S^{2-} linkages and one O- or N-donor.[82] In addition, Fe_4S_4 cubes (so-called *P* clusters) are present and act as an electron-transfer agents.[83] The chemistry of Mo-sulfur complexes and clusters have been reviewed in relation to the nitrogenase FeMo cofactor.[84]

A range of chemical analogs of the catalytic centers of Mo and W dithiolene-containing enzymes (pterins) have been prepared.[85,86] In particular, the rich chemistry of multisulfur transition metal systems allows ligand redox, internal electron transfer, and intermediate redox states. Such redox flexibility may facilitate coupled proton/electron transfer and/or oxo-transfer mechanisms, which are employed by Mo and W enzymes.

Hydrogenase enzymes interconvert H_2 to $2H^+$ and involve thiolate binding at FeFe or NiFe active sites. The structure of [NiFe] hydrogenase comprises a heterobimetallic NiFe centre, with the Ni ligated by four cysteines, two of which are terminal and two of which bridge to Fe. The Fe centre is ligated further by two cyanide and one carbonyl ligands.[87] Activation of the enzyme is believed to involve loss of a bridging oxo-ligand and contraction of the nickel−iron separation to some 2.5−2.6 Å.[88] The application of hydrogenase for in vitro photoinduced H_2 evolution has been discussed.[89] A range of structural models for [NiFe] hydrogenase has been prepared,[90] and the reversible reduction of protons to dihydrogen in models for hydrogenase has been the subject of a recent review.[91]

The X-ray structure of methyl-coenzyme M reductase shows an octahedral Ni^{II} ion bound in a tetrapyrrole hydrocorphin ring and the oxygen from a glutamine residue at the fifth site. The sixth site is occupied by a thiol group of coenzyme M in the methyl-coenzyme M $\text{reductase}_{\text{ox1}-\text{silent}}$ structure and a sulfonate oxygen of coenzyme M in the methyl-coenzyme M $\text{reductase}_{\text{silent}}$ structure.[92]

The active site of carbon monoxide dehydrogenase has been shown to contain an asymmetric [Ni-4Fe-5S] cluster.[93] There have been two recent independent reports of X-ray structures for the bifunctional enzyme carbon monoxide dehydrogenase/acetyl-coenzyme A synthase. In both structures, Ni^{II} is also bound in the acetyl-coenzyme A synthase within a N_2S_2 environment originating from amide N- and thiolate S-donors. The latter donors bridge to either a Cu, Zn, or Ni, which in turn is connected to a 4Fe4S cluster.[94,95]

Zinc fingers are protein DNA-binding motifs have a finger structure, which is held together by Zn^{II} chelated by four cysteine S-donors. The binding and selectivity of Zn in proteins has been the subject of a short review.[96]

Compounds with S-centers such as sodium diethyldithiocarbamate and sodium thiosulfate have found use as protecting groups when used in combination with cisplatin in order to limit the toxicity associated with this anticancer drug. The mode of action remains a subject of debate.[97]

10 RELATED ARTICLES

Chalcogenides: Solid-state Chemistry; Copper Enzymes in Denitrification; Copper: Hemocyanin/Tyrosinase Models; Copper Proteins: Oxidases; Copper Proteins with Dinuclear Active Sites; Copper Proteins with Type 1 Sites; Copper Proteins with Type 2 Sites; Iron–Sulfur Models of Protein Active Sites; Iron–Sulfur Proteins; Nickel Enzymes & Cofactors; Nickel: Models of Protein Active Sites; Polynuclear Organometallic Cluster Complexes.

11 FURTHER READING

H. Vahrenkamp and L. F. Dahl, *Angew. Chem., Int. Ed. Engl.*, 1969, **8**, 144.

12 REFERENCES

1. P. J. Vergamini and G. J. Kubas, *Prog. Inorg. Chem.*, 1976, **21**, 261.
2. A. J. Blake and M. Schröder, *Adv. Inorg. Chem.*, 1990, **35**, 1.
3. G. Reid and M. Schröder, *Chem. Soc. Rev.*, 1990, **19**, 239.
4. S. C. Rawle and S. R. Cooper, *Struct. Bonding (Berlin)*, 1990, **72**, 1.
5. K. H. Schmidt and A. Müller, *Coord. Chem. Rev.*, 1974, **14**, 115; H. Vahrenkamp, *Angew. Chem., Int. Ed. Engl.*, 1975, **14**, 322; C. G. Kuehn and S. S. Isied, *Prog. Inorg. Chem.*, 1980, **27**, 153.
6. A. Müller, W. Jaegermann, and J. H. Enemark, *Coord. Chem. Rev.*, 1982, **46**, 245.
7. F. A. Cotton, G. Wilkinson, C. A. Murillo, and M. Bochmann, ‘Advanced Inorganic Chemistry’, 6th edn., Wiley Interscience, 1999.
8. G. Wilkinson, R. D. Gillard, and J. A. McCleverty eds, ‘Comprehensive Coordination Chemistry’, Pergamon, Oxford, 1987, Vol. 1; J. A. McCleverty and T. J. Meyer eds, ‘Comprehensive Coordination Chemistry’, 2nd edn., Pergamon, Oxford, 2003, Vol. 1.
9. J. C. Bayon, C. Claver, and A. M. Masdeu-Bulto, *Coord. Chem. Rev.*, 1999, **193**, 73.
10. B. R. James, *Pure Appl. Chem.*, 1997, **69**, 2213.
11. R. J. Pleus, H. Waden, W. Saak, D. Haase, and S. Pohl, *J. Chem. Soc., Dalton Trans.*, 1999, 2601.
12. S. Kuwata and M. Hidai, *Coord. Chem. Rev.*, 2001, **213**, 211; F. Cecconi, C. A. Ghilardi, and S. Midollini, *Inorg. Chem.*, 1983, **22**, 3802.
13. C. Bianchini and A. Meli, *J. Chem. Soc., Dalton Trans.*, 1996, 801.
14. H. Ogino, S. Inomata, and H. Tobita, *Chem. Rev.*, 1998, **98**, 2093.
15. M. Okazaki, M. Yuki, K. Kuge, and H. Ogino, *Coord. Chem. Rev.*, 2000, **198**, 367.
16. P. Zanello, *Coord. Chem. Rev.*, 1988, **87**, 1.
17. J. A. Ibers and R. H. Holm, *Science*, 1980, **209**, 223.
18. R. H. Holm, S. Ciurli, and J. A. Weigel, *Prog. Inorg. Chem.*, 1990, **38**, 1.
19. A. C. Moreland and T. B. Rauchfuss, *J. Am. Chem. Soc.*, 1998, **120**, 9376.
20. A. Müller and E. Diemann, *Adv. Inorg. Chem.*, 1987, **31**, 89.
21. S. A. Sunshine, D. Kang, and J. A. Ibers, *J. Am. Chem. Soc.*, 1987, **109**, 6202; M. G. Kanatzidis, *Chem. Mater.*, 1990, **2**, 353.
22. A. Shaver and J. M. McCall, *Organometallics*, 1984, **3**, 1823.
23. J. Götzig, A. L. Rheingold, and H. Werner, *Angew. Chem., Int. Ed. Engl.*, 1984, **23**, 814; L. J. Maheu and L. H. Pignolet, *J. Am. Chem. Soc.*, 1980, **102**, 3626.
24. J. R. Dilworth and J. Hu, *Adv. Inorg. Chem.*, 1994, **40**, 411.
25. J. P. Fackler Jr, *Prog. Inorg. Chem.*, 1976, **21**, 55.
26. D. W. Douglas and T. T. Nadasdi, *Coord. Chem. Rev.*, 1996, **147**, 147.
27. S. Mandal, G. Das, R. Singh, R. Shulka, and P. K. Bharadwaj, *Coord. Chem. Rev.*, 1997, **160**, 191.
28. J. G. Wright, M. J. Natan, F. M. MacDonnell, D. M. Ralston, and T. V. O’Halloran, *Prog. Inorg. Chem.*, 1990, **38**, 323.
29. P. Rao, O. Enger, E. Graf, M. W. Hosseini, A. De Cian, and J. Fischer, *Eur. J. Inorg. Chem.*, 2000, **7**, 1503.
30. E. W. Abel and K. G. Orrell, *Prog. Inorg. Chem.*, 1984, **32**, 1.
31. P. V. Bernhardt and G. A. Lawrence, *Coord. Chem. Rev.*, 1990, **104**, 297; D. A. Moore, P. E. Fanwick, and M. J. Welch, *Inorg. Chem.*, 1990, **29**, 672.
32. N. Baidya, M. M. Olmstead, J. P. Whitehead, C. Bagyinka, M. M. Maroney, and P. K. Mascharak, *Inorg. Chem.*, 1992, **31**, 3612.
33. H.-J. Krüger, G. Peng, and R. H. Holm, *Inorg. Chem.*, 1991, **30**, 734; H.-J. Krüger and R. H. Holm, *J. Am. Chem. Soc.*, 1990, **112**, 2955.
34. N. D. Branscombe, A. J. Atkins, A. Marin-Becerra, E. J. L. McInnes, F. E. Mabbs, J. McMaster, and M. Schröder, *Chem. Commun.*, 2003, 1098.
35. A. Grapperhaus and M. Y. Darensbourg, *Acc. Chem. Res.*, 1998, **31**, 451.
36. D. Sellmann, A. Fursattel, and J. Sutter, *Coord. Chem. Rev.*, 2000, **200**, 545.

37. D. Sellmann, B. Hautsch, A. Rosler, and F. W. Heineman, *Angew. Chem., Int. Ed. Engl.*, 2001, **40**, 1505.
38. D. Sellmann, J. Utz, N. Blum, and F. W. Heineman, *Coord. Chem. Rev.*, 1999, **192**, 607.
39. P. Ghosh, A. Begum, E. Bill, T. Weyhermuller, and K. Wieghardt, *Inorg. Chem.*, 2003, **42**, 3208.
40. A. J. Amoroso, S. S. M. Chung, D. J. E. Spencer, J. P. Danks, M. W. Glenny, A. J. Blake, P. A. Cooke, C. Wilson, and M. Schröder, *Chem. Commun.*, 2003, 2020.
41. P. J. Farmer, T. Solouki, D. K. Mills, T. Soma, D. H. Russell, J. H. Reibenspies, and M. Y. Darensbourg, *J. Am. Chem. Soc.*, 1992, **114**, 4601.
42. T. Konno, T. Yoshimura, K. Aoki, K. Okamoto, and M. Hirotsu, *Angew. Chem.*, 2001, **40**, 1765.
43. E. I. Stiefel, *Prog. Inorg. Chem.*, 1977, **22**, 1; R. Eisenberg, *Prog. Inorg. Chem.*, 1970, **12**, 295.
44. D. Sellmann, W. Soglowek, K. Knoch, G. Ritter, and J. Dengler, *Inorg. Chem.*, 1992, **31**, 3711; D. Sellmann, W. Soglowek, F. Knoch, and M. Moll, *Angew. Chem., Int. Ed. Engl.*, 1989, **28**, 1271.
45. K. Wang and E. I. Stiefel, *Science*, 2001, **291**, 106.
46. N. Robertson and L. Cronin, *Coord. Chem. Rev.*, 2002, **227**, 93.
47. E. S. Davies, G. M. Aston, R. L. Beddoes, D. Collison, A. Dinsmore, A. Docrat, J. A. Joule, C. R. Wilson, and C. D. Garner, *J. Chem. Soc., Dalton Trans.*, 1998, 3647.
48. K.-M. Sung and R. H. Holm, *J. Am. Chem. Soc.*, 2002, **124**, 4312.
49. B. S. Lim, M. W. Willer, M. Miao, and R. H. Holm, *J. Am. Chem. Soc.*, 2001, **123**, 8343.
50. K. K. Pandey, *Prog. Inorg. Chem.*, 1992, **40**, 445.
51. R. R. Ryan, G. J. Kubas, D. C. Moody, and P. G. Eller, *Struct. Bonding (Berlin)*, 1981, **46**, 48; W. A. Schenk, *Angew. Chem.*, 1987, **99**, 101.
52. W. L. Reynolds, *Prog. Inorg. Chem.*, 1970, **12**, 1.
53. J. R. Dilworth and N. Wheatley, *Coord. Chem. Rev.*, 2000, **199**, 89.
54. I. Haiduc, *Coord. Chem. Rev.*, 1997, **158**, 325.
55. C. Gieck, F. Rocker, V. Ksenofontov, P. Gütlich, and W. Tremel, *Angew. Chem.*, 2001, **40**, 908.
56. Z. Atherton, D. M. L. Goodgame, S. Menzer, and D. J. Williams, *Inorg. Chem.*, 1998, **37**, 849.
57. D. Coucouvanis, *Prog. Inorg. Chem.*, 1970, **11**, 233; D. Coucouvanis, *Prog. Inorg. Chem.*, 1979, **26**, 301.
58. T. N. Lockyer and R. L. Martin, *Prog. Inorg. Chem.*, 1980, **27**, 223.
59. W. Dietzsch, P. Strauch, and E. Hoyer, *Coord. Chem. Rev.*, 1992, **121**, 43.
60. P. V. Yanev, *Coord. Chem. Rev.*, 1977, **23**, 183; H. Werner, *Coord. Chem. Rev.*, 1982, **49**, 165.
61. S. Fujii and T. Yoshimura, *Coord. Chem. Rev.*, 2000, **198**, 89.
62. A. Laguna and M. Laguna, *Coord. Chem. Rev.*, 1999, **193**, 837.
63. A. Galindo and D. Miguel, *Coord. Chem. Rev.*, 1999, **193**, 643.
64. W. Levason and G. Reid, *J. Chem. Res.*, 2002, (S)467; (M)1001.
65. W. Levason and G. Reid, *J. Chem. Soc., Dalton Trans.*, 2001, 2953.
66. A. J. Blake, A. J. Holder, T. I. Hyde, and M. Schröder, *J. Chem. Soc., Chem. Commun.*, 1987, 987.
67. A. J. Blake, J. A. Greig, A. J. Holder, T. I. Hyde, A. Taylor, and M. Schröder, *Angew. Chem., Int. Ed. Engl.*, 1990, **29**, 203; A. J. Blake, R. O. Gould, J. A. Greig, A. J. Holder, T. I. Hyde, and M. Schröder, *J. Chem. Soc., Chem. Commun.*, 1989, 876.
68. T. Yoshida, T. Adachi, M. Kaminaka, T. Ueda, and T. Higuchi, *J. Am. Chem. Soc.*, 1988, **110**, 4872.
69. A. J. Blake, Y. V. Roberts, and M. Schröder, *J. Chem. Soc., Dalton Trans.*, 1996, 1885.
70. J. P. Danks, N. R. Champness, and M. Schröder, *Coord. Chem. Rev.*, 1998, **174**, 417.
71. J. B. Love, J. M. Vere, M. W. Glenny, A. J. Blake, and M. Schröder, *Chem. Commun.*, 2001, 2678.
72. W. Levason, S. D. Orchard, and G. Reid, *Chem. Commun.*, 2001, 427.
73. W. S. Sheldrick and I. M. Müller, *Coord. Chem. Rev.*, 1999, **182**, 125.
74. G. Mislin, E. Graf, M. W. Hosseini, A. Bilyk, A. K. Hall, J. M. Harrowfield, B. W. Skelton, and A. H. White, *Chem. Commun.*, 1999, 373.
75. A. M. Masdeu-Bulto, M. Dieguez, E. Martin, and M. Gomez, *Coord. Chem. Rev.*, 2003, **242**, 159.
76. J.-M. Mouesca and B. Lamotte, *Coord. Chem. Rev.*, 1998, **178–180**, 1573.
77. M. K. Johnson, R. E. Duderstadt, and E. C. Duin, *Adv. Inorg. Chem.*, 1999, **47**, 1.
78. H. Beinert, M. C. Kennedy, and C. D. Stout, *Chem. Rev.*, 1996, **96**, 2335.
79. D. H. Flint and R. M. Allen, *Chem. Rev.*, 1996, **96**, 2315.
80. E. Bouwman, W. L. Driessen, and J. Reedijk, *Coord. Chem. Rev.*, 1990, **104**, 143.
81. F. Tani, M.-U. Mikiya, S. Nakayama, and Y. Naruta, *Coord. Chem. Rev.*, 2002, **226**, 219.
82. J. Kim and D. C. Rees, *Nature*, 1992, **360**, 553; M. M. Georgiadis, H. Komiya, P. Chakrabarti, D. Woo, J. J. Kornuc, and D. C. Rees, *Science*, 1992, **257**, 1653; J. Kim and D. C. Rees, *Science*, 1992, **257**, 1677.
83. J. W. Peters, M. H. B. Stowell, S. M. Soltis, M. G. Finnegan, M. K. Johnson, and D. C. Rees, *Biochemistry*, 1997, **36**, 1181.
84. F. Barriere, *Coord. Chem. Rev.*, 2003, **236**, 71.
85. J. McMaster, J. M. Tunney, and C. D. Garner, *Prog. Inorg. Chem.*, 2003, **52**, 539.
86. E. I. Stiefel, *Pure Appl. Chem.*, 1998, **70**, 889.
87. A. Volbeda, M.-H. Charon, C. Piras, E. C. Hatchikian, M. Frey, and J. C. Fontecilla-Camps, *Nature*, 1995, **373**, 580; A. Volbeda, E. Garain, C. Piras, A. L. Delacey,

V. M. Fernandez, E. C. Hatchikian, M. Frey, and J. C. Fontecilla-Camps, *J. Am. Chem. Soc.*, 1996, **118**, 12989.

88. G. Davidson, S. B. Choudhury, Z. Gu, K. Bose, W. Roseboom, S. P. J. Albracht, and M. J. Maroney, *Biochemistry*, 2000, **39**, 7468.
89. I. Okura, *Coord. Chem. Rev.*, 1985, **68**, 53.
90. A. C. Marr, D. J. E. Spencer, and M. Schröder, *Coord. Chem. Rev.*, 2001, **219**, 1055.
91. D. J. Evans and C. J. Pickett, *Chem. Soc. Rev.*, 2003, **32**, 268.
92. U. Elmer, W. Grabarse, S. Shima, M. Goubeaud, and R. K. Thauer, *Science*, 1997, **278**, 1457; W. G. Grabarse, F. Mahlert, E. C. Duin, M. Goubeaud, S. Shima, R. K. Thauer, V. Lamzin, and U. Ermler, *J. Mol. Biol.*, 2001, **309**, 315.
93. H. Dobbek, V. Svetlitchnyi, L. Gremer, R. Huber, and O. Meyer, *Science*, 2001, **293**, 1281.
94. T. I. Doukov, T. M. Iverson, J. Seravalli, S. W. Ragsdale, and C. L. Drennan, *Science*, 2002, **298**, 567.
95. C. Darnault, A. Volbeda, E. J. Kim, P. Legrand, X. Vernede, P. A. Lindahl, and J. C. Fontecilla-Camps, *Nat. Struct. Biol.*, 2003, **10**, 271.
96. T. Dudev and C. Lim, *Chem. Rev.*, 2003, **103**, 773.
97. J. Reedijk, *Chem. Rev.*, 1999, **99**, 2499.

Scandium, Yttrium & the Lanthanides: Inorganic & Coordination Chemistry

Simon A. Cotton
Uppingham School, Uppingham, UK

1 Introduction 1
2 Scandium 2
3 Yttrium and the Lanthanides 6
4 Promethium 37
5 Lanthanides in Organic Synthesis 37
6 Uses of the Lanthanides 37
7 Toxicity of the Lanthanides 37
8 Related Articles 38
9 References 38

Abbreviations

bipyO$_2$ = 2,2′-bipyridyl *N*,*N*′-dioxide; 12-crown-4 = 1,4,7,10-tetraoxacyclododecane; 15-crown-5 = 1,4,7,10,13-pentaoxacyclopentadecane; 18-crown-6 = 1,4,7,10,13,16-hexaoxacyclododecane; dbm = Dibenzoylmethane; diglyme = Bis(2-methoxyethyl)ether; dipic = 2,6-pyridinedicarboxylate; dme = 1,2-dimethoxyethane; dmi = 1,3-dimethyl-2-imidazolidione; DMP = 2,6-dimethyl-4-pyrone; DOTA = 1,4,7,10-tetraaza-cyclododecane-*N*,*N*′,*N*″,*N*‴-tetraacetate; dpm = Dipivaloylmethane (= tmhd); dmpu = Dimethylpropylene urea; DTPA = Diethylenetriaminepentaacetate; DTPA-BMA = Dimethylamide of diethylenetriaminepentaacetic acid; EO2 = Diethylene glycol; EO3 = Triethylene glycol; EO4 = Tetraethylene glycol; EO5 = Pentaethylene glycol; facam = 3-trifluoroacetyl-d-camphor; fod = 2,2-dimethyl-6,6,7,7,7,8,8,8-heptafluorooctane-2,4-dione; hfac = 1,1,1,5,5,5-hexafluoropentane-2,4-dionate; Hhfip = Hexafluoroisopropanol; naph = 1,8-naphthyridine; pc = Phthalocyaninato; pmdien = *N*,*N*,*N*′,*N*″,*N*″-pentamethyldiethylenetriamine; pmhd = 1-phenyl-5-methylhexane-1,3-dionate; pu = Tetrahydro-2-pyrimidone; pyO = Pyridine N-oxide; terpy = 2,2′:6′,2″-terpyridyl; tetraglyme = Me(OCH$_2$CH$_2$)$_4$OMe; tmen = *N*,*N*,*N*′,*N*′-tetramethylethane-1,2-diamine; tmhd = 2,2,6,6-tetramethylheptane-3,5-dionato; tmu = -Tetramethylurea; Tp = Tris(pyrazolyl)borate; Tp$^{\mathrm{Bu}^t\mathrm{,Me}}$ = Hydrotris(3-*t*-butyl-5-methylpyrazolyl)borate; Tp$^{\mathrm{Me2}}$ = Tris(3,5-dimethylpyrazolyl)borate; tpa = Tris[(2-pyridyl)methyl]amine; tpza = Tris[(2-pyrazinyl)methyl]amine; tptz = 1,3,5-tri(2-pyridyl)-2,4,6-triazine; ttfa = Thenoyltrifluoroacetonato.

1 INTRODUCTION

These elements are generally grouped together in group 3 of the Periodic Table.[1–10] Scandium has considerably smaller atomic and ionic radii than the other metals and significantly different chemical properties, so it is treated separately in this article; the *Lanthanide Contraction* (*see Lanthanide Contraction*)means, however, that the later lanthanides are of similar size to yttrium, to which they bear a close chemical resemblance, and are thus often grouped together as the *Rare Earth Elements* (*see Rare Earth Elements*). The lanthanides resemble the group II metals, rather than the transition metals, in many respects – they have similar reactivities to Mg; the bonding in their complexes is essentially ionic in nature; coordination numbers are generally driven by steric considerations (and are usually high); most of the chemistry is in one oxidation state (+3). There is essentially no low oxidation-state organometallic chemistry, and they are not involved in multiple bonds, so there are no species like UO_2^{2+} or MnO_4^-. On the other hand, because of the gradual filling of the 4f subshell across the series, there are nuances in lanthanide chemistry owing to the gradual change in ionic radius – the partly filled 4f subshell leads most ions to be paramagnetic, and sometimes have visible colors; certain lanthanides (Ce, Eu, Sm, Yb in particular) have a significant chemistry in more than one oxidation state; and the complexes exhibit an exceptionally wide range in coordination numbers, often with subtle changes on passing from one lanthanide to another.

Lanthanide chemistry has its beginnings in Scandinavia.[3,11] In 1794, Johann Gadolin succeeded in obtaining an ‘earth’ (oxide) from a black mineral subsequently known as gadolinite, naming the earth yttria. Soon afterwards, M. H. Klaproth, J. J. Berzelius, and W. Hisinger obtained ceria, another earth, from cerite, but it was not until 1839–1843 that the Swede C. G. Mosander first separated these earths into their component oxides; thus ceria was resolved into the oxides of cerium and lanthanum and a mixed oxide ‘didymia’ (a mixture of the oxides of the metals from Pr through Gd), and likewise ‘yttria’ was separated into erbia, terbia, and yttria (though some 40 years later, the first two names were to be reversed!). Spectroscopic analysis aided the identification of further elements but also complicated matters with the erroneous identification of mixtures as over 70 ‘new’ elements. With the report of lutetium in 1907 by Urbain and von Welsbach, all the stable lanthanide elements had been discovered (von Welsbach’s alternative name of cassiopeium did not finally pass out of use until the 1950s), but Moseley showed (1913) the existence of an undiscovered element between Nd and Sm, leading to futile searches for the missing element. Counterclaims by both American and Italian researchers for element 61 (‘illinium’, ‘florentium’) were made in 1926. It was subsequently realized that element 61 would not have any stable isotopes and it was not until 1947 that it was identified in uranium fission products (and later named promethium).

Useful sources of information on these elements and their compounds include the 'Gmelin Handbook',[1] with extensive up-to-date coverage, and regular comprehensive reviews in the 'Handbook on the Physics and Chemistry of the Rare Earths'.[2] General accounts of the elements, their inorganic chemistry,[3] and coordination chemistry exist,[4,5] the latter being the most up-to-date. There are also recent monographs,[6–8] and compilations of in-depth and informed articles on different aspects of lanthanide chemistry and spectroscopy.[9,10]

When Mendeleev first published his Periodic Table in 1869, of these elements he included only lanthanum, cerium, didymium (now known to have been a mixture of Pr and Nd), another mixture in the form of erbia, and yttrium; unreliable information about atomic mass made correct positioning of these elements in the table difficult. Subsequently, it was not until the work of Bohr and of Moseley that it was known precisely how many of these elements there were. Most current versions of the Periodic Table place lanthanum under scandium and yttrium in group 3, though study of the periodic properties shows that lutetium bears a more compelling resemblance to Sc and Y, so that it has been cogently argued that these metals should appear in the same group, with lutetium preceded by the sequence La through Yb.[11]

In the traditional view, lanthanum is classed as a transition element; cerium, which has a 4f electron, is considered to be the first lanthanide, rather than lanthanum, which does not possess an electron in a 4f orbital (Table 1).

2 SCANDIUM

There are comprehensive accounts, covering the literature through 2002,[3–5,12,13] of the chemistry of scandium. References to it frequently occur in the context of the chemistry of the 4f metals.

In 1869, Mendeleev predicted the existence and certain properties of an element with atomic mass 45, terming it 'ekaboron'; within a decade, the Swede L. F. Nilsson and Frenchman P. T. Cleve independently isolated scandium oxide, subsequently preparing various other compounds. There are few ores where scandium is the main element (e.g. thortveitite, a silicate, $Sc_2Si_2O_7$, and sterrite, $ScPO_4{\cdot}2H_2O$) so that it is mainly obtained as a by-product from uranium extraction.

Scandium, a soft and silvery metal, was first isolated (1937) electrolytically, but it is generally obtained metallothermically, typically by reduction of the trifluoride with calcium. It is electropositive, tarnishing rapidly in air and reacting with water. It forms a wide range of binary compounds.

The ionic radius of Sc^{3+} is, at 0.745 Å (for six coordination) the largest of the 3d metals, so that high coordination numbers are frequently met with in its chemistry; examples between three and nine are known.

2.1 Binary Compounds of Scandium

2.1.1 Halides

All four scandium(III) halides are known, all but the fluoride (WO_3 structure) having the $FeCl_3$ structure. They can be obtained as white solids directly from the elements and in some cases by dehydration of the hydrated salts, as well as by thermal decomposition of $(NH_4)_3ScX_6$ (X = Cl, Br), a method also used for the lanthanides. Gas-phase studies have identified isolated planar ScF_3 molecules at 1750 K; $ScCl_3$ molecules with a very slight pyramidal distortion; and both monomers and dimers in ScI_3 vapour at 1050 K.

Table 1 Properties of scandium, yttrium, and the lanthanides

Element	Electronic configuration	Mp; bp (K)	Atomic radius (Å)	$E(M/M^{3+})$ (V)	EC M^{3+}	Ionic radius (Å)	Ground state	Magnetic moment (μ_B)	Color
Sc	$[Ar]3d^14s^2$	1814; 3104	1.606	2.03	[Ar]	0.745	$^1S_0$	0	
Y	$[Kr]4d^15s^2$	1795; 3611	1.81	2.37	[Kr]	0.901	$^1S_0$	0	
La	$[Xe]5d^16s^2$	1194; 3730	1.877	2.37	$[Xe]f^0$	1.032	$^1S_0$	0	
Ce	$[Xe]4f^26s^2$	1072; 3699	1.825	2.34	$[Xe]f^1$	1.01	$^2F_{5/2}$	2.56	
Pr	$[Xe]4f^36s^2$	1204; 3785	1.828	2.35	$[Xe]f^2$	0.99	$^3H_4$	3.62	Green
Nd	$[Xe]4f^46s^2$	1294; 3341	1.821	2.32	$[Xe]f^3$	0.983	$^4I_{9/2}$	3.68	Lilac red
Pm	$[Xe]4f^56s^2$	1441; c3000	1.81	2.29	$[Xe]f^4$	0.97	$^5I_4$	2.83	Pink
Sm	$[Xe]4f^66s^2$	1350; 2064	1.802	2.3	$[Xe]f^5$	0.958	$^6H_{5/2}$	1.55	Pale yellow
Eu	$[Xe]4f^76s^2$	1095; 1870	2.042	1.99	$[Xe]f^6$	0.947	$^7F_0$	3.4	
Gd	$[Xe]4f^75d^16s^2$	1586; 3539	1.802	2.29	$[Xe]f^7$	0.938	$^8S_{7/2}$	7.94	
Tb	$[Xe]4f^96s^2$	1629; 3396	1.782	2.3	$[Xe]f^8$	0.923	$^7F_6$	9.7	Very pale pink
Dy	$[Xe]4f^{10}6s^2$	1685; 2835	1.773	2.29	$[Xe]f^9$	0.912	$^6H_{15/2}$	10.6	Pale yellow
Ho	$[Xe]4f^{11}6s^2$	1747; 2968	1.766	2.33	$[Xe]f^{10}$	0.901	$^5I_8$	10.6	Yellow
Er	$[Xe]4f^{12}6s^2$	1802; 3136	1.757	2.31	$[Xe]f^{11}$	0.89	$^4I_{15/2}$	9.6	Rose pink
Tm	$[Xe]4f^{13}6s^2$	1818; 2220	1.746	2.31	$[Xe]f^{12}$	0.88	$^3H_6$	7.6	
Yb	$[Xe]4f^{14}6s^2$	1097; 1466	1.94	2.22	$[Xe]f^{13}$	0.868	$^2F_{7/2}$	4.54	
Lu	$[Xe]4f^{14}5d^16s^2$	1936; 3668	1.734	2.3	$[Xe]f^{14}$	0.861	$^1S_0$	0	

Scandium forms a number of well-defined lower halides,[14] especially chlorides. These are synthesized by high-temperature reaction of Sc with $ScCl_3$. Phases synthesized and characterized by diffraction methods are ScCl, Sc_2Cl_3 ('mouse fur'), Sc_5Cl_8, Sc_7Cl_{10}, and Sc_7Cl_{12}. They typically have chain structures with metal–metal bonding and octahedral clusters of scandiums (Figure 1). ScCl is isostructural with ZrBr, Sc_5Cl_8 contains infinite chains of Sc_6 octahedra sharing trans edges, while Sc_7Cl_{10} has two parallel chains of octahedra sharing a common edge. Sc_7Cl_{12} is regarded as made of Sc_6Cl_{12} octahedra with isolated scandium atoms in octahedral interstices. Sc_2Br_3 is also known.

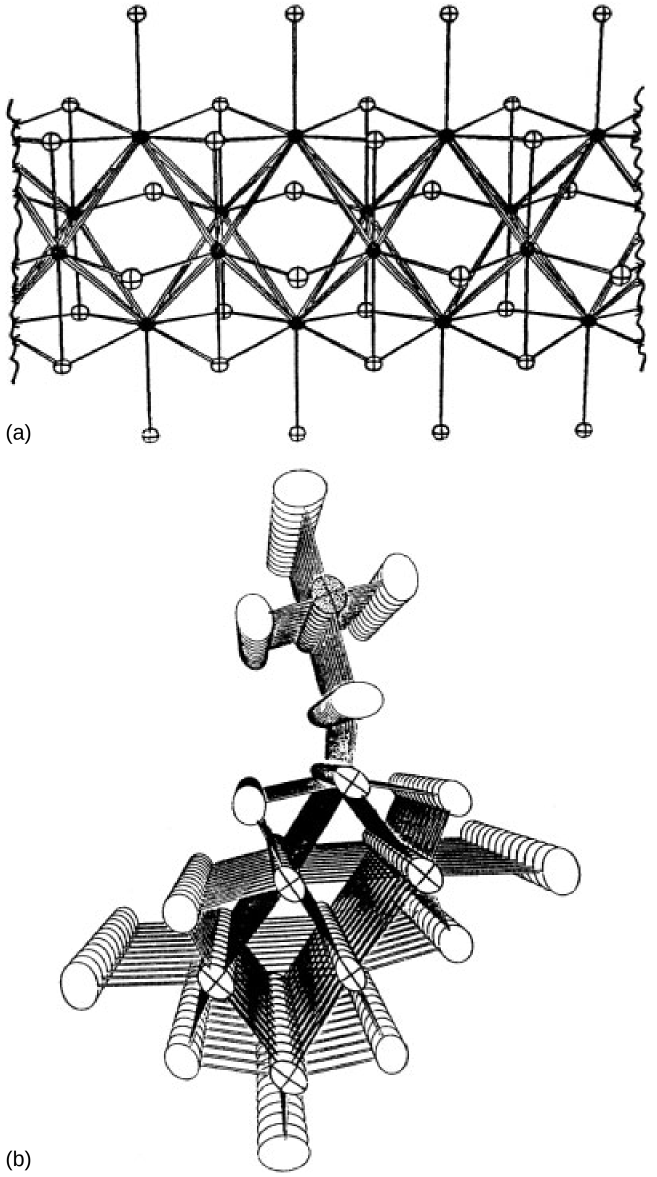

Figure 1 (a) The anionic polymetal chain in Sc_5Cl_8. (b) The structure of Sc_7Cl_{10} viewed almost along the chain axis. (Reprinted with permission from F.J. DiSalvo, J.V. Waszczak, W.M. Walsh, L.W. Rupp, and J.D. Corbett, *Inorg. Chem.*, 1985, **24**, 4624. © 1985 American Chemical Society)

2.1.2 *Other Binary Compounds*

Scandium oxide is a refractory white solid (mp 3100 °C) formed on ignition of either the metal or appropriate compounds such as the nitrate, sulfate, and hydroxide. It has amphoteric tendencies denoted by its solubility in excess alkali from which compounds like $K_3[Sc(OH)_6]$, containing octahedrally coordinated scandium, have been isolated. In the solid state it has six-coordinate scandium in the Mn_2O_3 structure.

Other significant binary compounds include the fcc dihydride ScH_2; unlike most of the lanthanides, scandium does not form a trihydride. This compound is conducting and is probably a scandium(III) compound of the type $Sc^{3+}(H^-)_2(e^-)$. The carbide ScC is cubic (NaCl structure) and other carbides Sc_3C, Sc_2C, Sc_4C_3, $Sc_{13}C_{10}$, and $Sc_{15}C_{19}$ are reported. Fullerene complexes (*see* ***Carbon: Fullerenes***) have been made: laser vaporization of scandium oxide–graphite mixtures followed by extraction of the resulting soot gives scandium–fullerene clusters, identified by MS to contain 1–3 scandiums, particularly paramagnetic $Sc_n@C_{82}$ ($n = 1,3$). The three pnictides ScQ (Q = N, P, As) exist with the nitride in particular being very high-melting (2600 °C), while there are two borides, ScB_2 and ScB_{12}.

2.2 The Aqua Ion and Hydrated Salts[15]

Although there was no real evidence for the coordination number of scandium in aqueous solution, it was been generally assumed for many years that the scandium aqua ion was $[Sc(H_2O)_6]^{3+}$, probably by analogy with the ions of the succeeding transition metals, all of which form $[M(H_2O)_6]^{3+}$ (M = Ti–Co). Against this was the fact that Sc^{3+} has an ionic radius much larger than that of the succeeding 3d metals (0.745 Å in six-coordination), intermediate between Ti^{3+} (0.670 Å) and the lanthanides ($La^{3+} = 1.032$ Å; $Lu^{3+} = 0.861$ Å). Since the lanthanides form $[Ln(H_2O)_9]^{3+}$ and $[Ln(H_2O)_8]^{3+}$ aqua ions, a coordination number intermediate between 6 and 8 could have been expected for scandium on steric grounds. Study of the Raman spectra of glasses of $ScCl_3$ and $Sc(ClO_4)_3$ led to the suggestion that the aqua ion was not a hexaaqua species. X-ray diffraction data[16] from scandium perchlorate solutions gave a sharp peak (suggesting that the Sc–O distances were all very similar) having a Sc–O distance of 2.180(7) Å with a coordination number of 7.4(4). X-ray absorption fine structure (XAFS) data from scandium triflate solutions also indicate a Sc–O distance of 2.18(2) Å, but no coordination number could be unambiguously obtained from the XAFS measurements. This Sc–O distance of 2.18 Å, nearly 0.1 Å longer than that found for six-coordination, fits well with the Sc-water distances found in the seven-coordinate $[Sc(H_2O)_7]^{3+}$ ions in the solid state. Considering all the data, it seems most likely that the predominant species present in rather acidic aqueous solution is a pentagonal bipyramidal $[Sc(H_2O)_7]^{3+}$ ion, with an average Sc–O distance around 2.18 Å. Study of the scandium aqua ion is handicapped by its ready hydrolysis and ability to complex with anions like chloride, nitrate, and even perchlorate. ^{45}Sc NMR studies on aqueous solutions of the chloride, nitrate, and formate were been interpreted in terms of the presence of both the aqua ion and mixed aqua/hydroxy species.

Among hydrated salts, scandium forms perchlorates $Sc(ClO_4)_3{\cdot}nH_2O$ ($n = 6$, 7); the hexahydrate is isostructural with the lanthanide analogues, thus containing octahedral $[Sc(H_2O)_6]^{3+}$ ions. The very soluble scandium triflate is isostructural with the lanthanide analogues $Ln(O_3SCF_3)_3{\cdot}9H_2O$, though there is evidence that the cation present is actually $[Sc(H_2O)_8]^{3+}$, rather than the nonaaqua species. When scandium halides (except the fluoride) are recrystallised from slightly acidified aqueous solution (to prevent the hydrolysis that could otherwise result in the hydroxy-bridged dimers discussed below), hydrated salts $ScX_3{\cdot}7H_2O$ (X = Cl, Br) and $ScI_3{\cdot}8H_2O$ are obtained. X-ray diffraction studies**[17]** show them all to contain $[Sc(H_2O)_7]^{3+}$ ions; in the chloride and iodide, the coordination geometry is essentially pentagonal bipyramidal, whilst in the iodide there is a substantial distortion (in view of the tendency of many of the hydrated lanthanide halides to contain coordinated halide ions, the chlorides in particular, the absence of halide from the coordination sphere of scandium in these compounds is remarkable). Reaction of refluxing aqueous $HC(SO_2CF_3)_3$ with scandium oxide yields the triflide salt $[Sc(H_2O)_7]\ (C(SO_2CF_3)_3)_3$. Though complicated by disorder, the structure shows two scandium-containing sites, with Sc–O distances falling in the range 2.113 (13)–2.222 (10) Å, averaging 2.17 Å. In contrast, the ytterbium analogue contains eight-coordinate $[Yb(H_2O)_8]^{3+}$ ions.

Overall, then, the existence of the three scandium-containing ions $[Sc(H_2O)_x]^{3+}$ ($x = 6,7,8$) in five different solid salts indicates that in itself X-ray diffraction data on solids cannot be relied upon to indicate the coordination number in aqueous solution. Ultimately, it is the solubility of a particular salt that determines which compound crystallises out from aqueous solution.

Other hydrated salts include $Sc_2(C_2O_4)_3{\cdot}6H_2O$, $Sc(NO_3)_3{\cdot}4H_2O$, and $Sc_2(SO_4)_3{\cdot}5H_2O$; the structure of the oxalate shows approximately dodecahedral coordination of scandium by two water molecules and six oxygens from bridging oxalates. The oxalate is, unlike lanthanide oxalates, slightly soluble in water and also dissolves in excess oxalate as $Sc(C_2O_4)_2^-$. No structural data are available for the nitrate, although it should be noted that eight-coordinate $Sc(NO_3)_3(H_2O)_2$ and nine-coordinate $Sc(NO_3)_3(H_2O)_3$ molecules are present in crown ether complexes, while the sulfate $Sc_2(SO_4)_3{\cdot}5H_2O$ has six-coordinate scandium. Both the nitrate and sulfate dehydrate on heating above 100 °C; at higher temperatures they change to the oxide. Structures are known of two other salts where water shares the coordination sphere of scandium with anions. Freshly precipitated $Sc(OH)_3$ reacts with picric acid (Hpic) forming a 1:1 adduct with picric acid, *trans*-$[Sc(H_2O)_4(pic)_2](pic)(HPic){\cdot}8.2\ H_2O$; scandium is present as part of a six-coordinate cation. In contrast to the benzenesulfonate, the p-toluenesulfonate salt $Sc(tosylate)_3{\cdot}6H_2O$ has coordinated anions in six-coordinate $[Sc(H_2O)_4(tosylate)_2]^+$ ions (the tosylates of the heavier lanthanides have six bound water molecules and two coordinated tosylates in eight-coordinate cations).

An important dimeric species is the $[(H_2O)_5Sc(OH)_2Sc(H_2O)_5]^{4+}$ ion (Figure 2), a cationic species with two hydroxy bridges, with approximately pentagonal bipyramidal coordination of scandium. It has been characterized as a benzene sulfonate salt,**[18]** and also as chlorides and bromides $[(H_2O)_5Sc(\mu\text{-}OH)_2Sc(H_2O)_5]\ X_4{\cdot}2H_2O$ (X = Cl, Br). The Sc–OH_2 and the Sc–OH bond lengths are similar in all three of these dimeric cations. These $[(H_2O)_5Sc(\mu\text{-}OH)_2Sc(H_2O)_5]^{4+}$ ions are significant in that they are believed to be formed in the first stage of the hydrolysis of the scandium aqua ion, and the coordination geometry involving scandium bound to seven water molecules and hydroxide ions can clearly derive from a $[Sc(H_2O)_7]^{3+}$ ion.

Among the carboxylates, scandium formate has a 2-D polymeric structure, whilst in the acetate, chains of Sc^{3+} ions are bridged by acetate groups (Figure 3) with essentially octahedral coordination of scandium. Similar bridging is found in the chloroacetate, where the six-coordination is in contrast with the nine-coordinate trimeric structure adopted by the heavier lanthanide ions. Scandium propynoate has

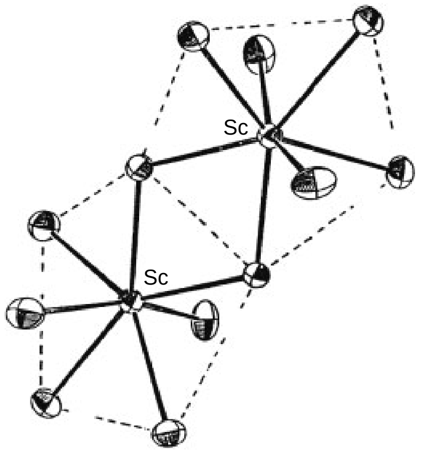

Figure 2 Structure of the dimeric cation $[(H_2O)_5Sc(OH)_2Sc(H_2O)_5]^{4+}$

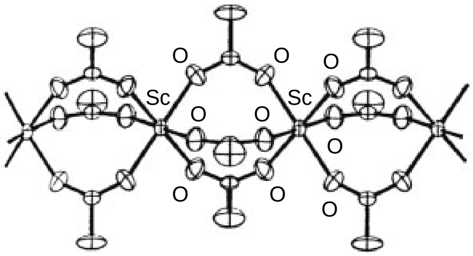

Figure 3 Chain structure in scandium acetate

an unusual three-dimensional polymeric structure (featuring six-coordinate scandium) that undergoes polymerization on γ-irradiation (probably with formation of a poly(propynoate)).[19]

2.3 Complexes[4,5]

A range of O-donor ligands (e.g. pyO, Me_2SO, HMPA, R_3PO) forms complexes with scandium, with two main series, ScL_3X_3 (where X is a coordinating anion such as chloride) and ScL_6X_3 (with anions such as perchlorate). With nitrate, higher coordination numbers are possible (because of the small 'bite' angle of bidentate nitrate).

A large number of complexes of phosphine and arsine oxides have been examined. $Sc(OTf)_3(Ph_3PO)_4$ has the structure *trans*-$[Sc(OTf)_2(Ph_3PO)_4]$ OTf, featuring octahedrally coordinated scandium (monodentate triflates), whilst $[Sc(NO_3)_3(Ph_3PO)_2]$ is eight-coordinate with symmetrically bidentate nitrates. Both $Sc(NO_3)_3(Ph_2MePO)_3$ and $Sc(NO_3)_3(Ph_2MePO)_4$ exist; the latter is $[Sc(NO_3)_2(Ph_2MePO)_4](NO_3)$ (bidentate nitrates). With Me_3PO, $[Sc(Me_3PO)_6](NO_3)_3$ is formed; similarly $[Sc(Me_3AsO)_6](NO_3)_3$ has octahedrally coordinated scandium. $Sc(NO_3)_3(Ph_3AsO)_3$ is seven-coordinate $[Sc(NO_3)_2(Ph_3AsO)_3]NO_3$. Among halide complexes, *trans*-$[ScBr_2(Ph_3PO)_4]Br$, *trans*-$[ScCl_2(Ph_3AsO)_4]Cl$ and $[Sc(Me_3AsO)_6]Br_3$ have all had structures confirmed by X-ray diffraction. Six-coordination is likewise found in *trans*-$[Sc(HMPA)_4(CF_3SO_3)_2]CF_3SO_3$ and the tetrahydro-2-pyrimidone complex $[Sc(pu)_6](CF_3SO_3)_3$, the latter unexpectedly having trigonal antiprismatic coordination of scandium, possibly partly induced by side-on interactions between pairs of pu ligands. Various complexes of N-oxide ligands $ScL_6(CF_3SO_3)_3$ (L = pyridine N-oxide, 2-picoline N-oxide, 3-picoline N-oxide, 4-picoline N-oxide) have been described, and all presumably contain octahedrally coordinated scandium, confirmed in $[ScCl_3(dme)(MeCN)]$ and $[ScCl_3(diglyme)]$.

$(NO^+)_2$ $[Sc(NO_3)_5]^{2-}$ contains a nine-coordinate pentakis(nitrato)scandate ion, one nitrate being monodentate, but in Rb_2 $[Sc(NO_3)_5]$ there are three bidentate and two monodentate nitrates, resulting in eight-coordinate scandium. These contrast with the lanthanide analogs which are ten-coordinate (the lanthanides also form 12-coordinate hexa(nitrato) complexes, see Section 3.7.7).

There are a number of complexes with diketonates, all probably octahedral like $Sc(acac)_3$ (X-ray); $Sc(tropolonate)_3$ also has six-coordinate scandium but eight-coordination also exists in $HSc(tropolonate)_4$ and probably in similar $Sc(diketonate)_4{}^-$ species. A number of crown ether complexes[20] like $Sc(NO_3)_3(H_2O)_2{\cdot}crown$ (crown = 15-crown-5, benzo-15-crown-5) do not involve direct crown ether–scandium bonding; instead they have hydrated scandium nitrate molecules linked to the crown ether by hydrogen bonds to the ether oxygens, However, reaction of $ScCl_3$ with halogen-extractor $SbCl_5$ and 18-crown-6 in acetonitrile gives $[ScCl_2(18\text{-crown-}6)](SbCl_6)$, in which the scandium is bound (Figure 4) to five ether oxygens and two chlorines in roughly pentagonal bipyramidal coordination.

Other $[ScCl_2(crown)]^+$ $[SbCl_6]^-$ species (crown = 15-crown-5, benzo-15-crown-5, and dibenzo-18-crown-6) complexes have been isolated, all believed to have a pentagonal bipyramidal coordination geometry, confirmed crystallographically for the benzo-15-crown-5 complex. Reaction of $ScCl_3(thf)_3$ and 1 mol of $SbCl_5$ with 1 mol of a larger crown ether yields the complexes $[ScCl_2(dibenzo\text{-}24\text{-crown-}8)(H_2O)]^+SbCl_6{}^-{\cdot}2$ MeCN and $[ScCl_2(dibenzo\text{-}30\text{-crown-}10)(H_2O)_2]^+SbCl_6{}^-{\cdot}MeCN{\cdot}H_2O$. The cavity in the smaller tetradentate 12-crown-4 ring is too small for a $[ScCl_2]^+$ ion to fit, so $[ScCl_2(12\text{-crown-}4)(MeCN)]^+SbCl_6{}^-$ is believed to have an 'extra-cavity' (half-sandwich) structure.

Use of excess $SbCl_5$ permits the extraction of further chlorides from the crown ether complexes. Thus reaction of $[ScCl_3(thf)_3]$ in MeCN with 3 mols of $SbCl_5$ and dibenzo-18-crown-6 leads to the complex $[ScCl(dibenzo\text{-}18\text{-crown-}6)(MeCN)]^{2+}$ $(SbCl_6{}^-)_2$. If $SbCl_5$ and $SbCl_3$ are used together, $[Sc(12\text{-crown-}4)_2]^{3+}$ $(Sb_2C_8)(SbCl_6)_2(MeCN)_2$ is obtained, with eight-coordinate Sc.

Few scandium alkoxides have been studied in detail, but monomeric three coordination is known in $[(2,6\text{-}(t\text{-Bu})_2\text{-}4\text{-}MeC_6H_2O)_3Sc]$, where the bulky ligand enforces steric

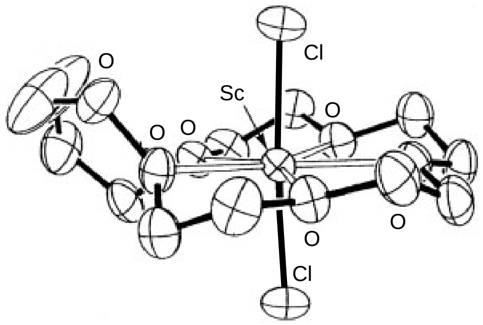

Figure 4 Seven-coordinate scandium in $[ScCl_2(18\text{-crown-}6)]$ $(SbCl_6)$

crowding. It will, however, expand its coordination sphere to form four-coordinate adducts with Ph_3PO and thf, unlike the corresponding three-coordinate silylamide. $Sc(OSi(t\text{-}Bu)_3)_3 \cdot L$ ($L =$ thf, py, NH_3) have also been prepared (the Lewis base cannot, however, be removed to afford the homoleptic siloxide; *see Homoleptic Compound*). The isopropoxide is pentanuclear $[Sc_5O(OPr^i)_{13}]$, similar to those formed by Y, Yb, and In, with the structure $[Sc_5(\mu_5\text{-}O)(\mu_3\text{-}OPr^i)_4(\mu_2\text{-}OPr^i)_4(OPr^i)_5]$. Anodic oxidation of scandium in aliphatic alcohols has been used as a pathway to scandium alkoxides $[Sc(OR)_3]$ ($R =$ Me, Et) and $[Sc_5O(OPr^i)_{13}]$. The elusive structure of the methoxide $[Sc(OMe)_3]$ is still not known; it appears not to contain an oxo ligand, and to be a polymer. Alcoholysis of $[Sc_5O(OPr^i)_{13}]$ leads to $[Sc(OR)_3]$ ($R =$ Me, Et, Bu^n), $[Sc_5O(OBu^s)_{13}]$ and $[Sc_5O(OPr^i)_8(OBu^t)_5]$.

Scandium complexes with ammonia have only been made by dry methods.[21] In $(NH_4)_2\ [Sc(NH_3)I_5]$, obtained from reaction of NH_4I and metallic scandium in a sealed tube at 500 °C, scandium has octahedral coordination with $Sc\text{–}N = 2.29\,(2)$ Å and $Sc\text{–}I = 2.856(5) - 2.899(5)$ Å. Reaction of Sc with NH_4Br in a sealed Ta vessel gives $[Sc(NH_3)_2Br_3]$ (isotypic with $Sc(NH_3)_2Cl_3$) having isolated dimers of bromide edge-connected [mer-Sc-$(NH_3)_3Br_3$] and $[Sc(NH_3)Br_5]$ octahedra. $[Sc(NH_3)Br_3]$, isotypic with $Sc(NH_3)Cl_3$, has zigzag chains of edge-connected $[Sc(NH_3)Br_5]$ octahedra as $[Sc(NH_3)_{1/1}Br_{1/1}Br_{4/2}]$.

Reaction of the anhydrous ScX_3 ($X =$ Cl, Br) with pyridine yields $Sc(py)_4X_3$, which possibly have one molecule of pyridine in the lattice, as it is lost in vacuo. $Sc(py)_3(NCS)_3$ also exists. Using bidentate ligands, ScL_2X_3 ($L =$ phen, bipy) have been made, sometimes in two forms; they are believed to be $[ScL_2X_2]^+X^-$ and it is possible that cis and trans-isomers may exist, but there is no structural confirmation. Similar ethylenediamine complexes have been made by removal of a ligand molecule in vacuo from $Sc(en)_3X_3$ ($X =$ Cl, Br). Of the complexes of tridentate N-donors, the best characterized is $Sc(terpy)(NO_3)_3$, which has nine-coordinate scandium, but with one rather long Sc–O bond.

A range of porphyrins and phthalocyanines exist; syntheses often involve the high-temperature routes typical of the transition metals but recently a high-yield low-temperature route has been utilized:

$$Li(OEP)^- + ScCl_3(THF)_3 \longrightarrow Sc(OEP)Cl + 2Cl^- + 3THF \quad (1)$$

The chloride can be replaced by alkoxy, alkylamide, alkyl, and cyclopentadienyl groups. Similar compounds with other porphyrins and with phthalocyanine have been made, as well as the oxo-bridged dimer $(OEP)Sc(\mu\text{-}O)Sc(OEP)$.

Scandium resembles the other 3d transition metals from titanium through cobalt in forming an unusual three-coordinate silylamide, $Sc[N(SiMe_3)_2]_3$, but unlike them its solid-state structure is pyramidal, not planar, in which respect it resembles the lanthanides and uranium. It does not form adducts with Lewis bases, presumably on steric grounds, the resemblance here being to the 3d metals. The less congested amide $[Sc\{N(SiHMe_2)_2\}_3]$ forms a thf adduct $[Sc\{N(SiHMe_2)_2\}_3(thf)]$, which has distorted tetrahedral coordination of scandium, with short solid-state $Sc\cdots Si$ contacts (this is in contrast to 5-coordinate $[Ln\{N(SiHMe_2)_2\}_3(thf)_2]$ ($Ln =$ La–Lu).

Like other M^{3+} ions, scandium forms strong complexes with EDTA and DTPA. In $NH_4\ [Sc(EDTA)(H_2O)_2]\cdot 3H_2O$, scandium is eight-coordinate with hexadentate EDTA and two coordinated water molecules), as expected in comparison with the smaller Fe^{3+} ion (forming seven-coordinate $[Fe(EDTA)(H_2O)]^-$) or larger La^{3+} ion (which forms nine-coordinate $[La(EDTA)(H_2O)_3]^-$). Again, scandium is eight-coordinate in $Mn[Sc(DTPA)]\cdot 4H_2O$, in which DTPA is octadentate but there are no coordinated water molecules, unlike the complex of the larger Gd^{3+} ion, $[Gd(DTPA)(H_2O)]^{2-}$, familiar as a magnetic resonance imaging (MRI) contrast agent (see Section ‘Magnetic Resonance Imaging and MRI Agents’), also in the $[Sc(DOTA)]^-$ ion found in $[[NaSc(DOTA)]_3\cdot NaOH\cdot 18H_2O]$, where the coordination geometry is twisted square antiprismatic. These compounds nicely illustrate the tendency of Sc^{3+} to adopt coordination numbers intermediate between those of the M^{3+} ions in the first transition series and those found for the lanthanides.

The best-defined halide complexes are the hexafluoroscandates, M_3ScF_6, which clearly contain $ScF_6{}^{3-}$ anions; Na_3ScF_6 adopts the cryolite structure, K_2NaScF_6 also has the cubic elpasolite structure, as does the high-temperature phase of Rb_2KScF_6; Sr_2ScF_7 has seven-coordinate scandium however. $KScF_4$ has a layered structure in which scandium acquires six-coordination by edge-sharing alternate cis- and trans-corners, whilst $(enH_2)_{0.5}ScF_4$ has corner-linked octahedral. Ba_2ScCl_7 is $Ba_2[ScCl_6]Cl$, whilst Na_3ScCl_6 again has the cryolite structure. $NaScCl_4$, is isostructural with $NaLuCl_4$, the structure being made up of *cis*- edge-sharing $ScCl_6$ octahedra. Na_3ScBr_6 has the Na_3CrCl_6 structure.

3 YTTRIUM AND THE LANTHANIDES[22]

The lanthanides exhibit a number of features in their chemistry that differentiate them from the d-block metals.

1. Reactivity significantly greater than the transition metals, akin to group 2 elements.
2. A wide range of coordination numbers (generally 6–12, but 2–5 are also known).
3. Coordination geometries determined by ligand steric factors rather than crystal-field effects.
4. The formation of labile ‘ionic’ complexes that undergo facile exchange of ligand.
5. The inability of the 4f orbitals (*see f-Orbitals*) in the Ln^{3+} ion to participate directly in bonding.[23] Their

spectroscopic and magnetic properties are thus largely uninfluenced by the ligand.

6. Small crystal-field splittings (*see Crystal Field Theory*) and very sharp electronic spectra in comparison with the d-block metals.
7. The preference for anionic ligands with donor atoms of rather high *Electronegativity* (e.g. O, F, *see Electronegativity*).
8. The ready formation of hydrated complexes (on account of the high hydration energy of the small Ln^{3+} ion) and this can cause uncertainty in assigning coordination numbers.
9. The insolubility of hydroxides which precipitate at neutral pH unless complexing agents are present.
10. The dominance of one (3+) oxidation state.
11. Their inability to form Ln=O or Ln≡N multiple bonds of the type known for many transition metals and certain actinides.
12. Unlike the transition metals, they do not form stable carbonyls, and have virtually no chemistry in the 0 oxidation state.

3.1 Ores and Extraction of the Metals[1,3,6]

In general, Y and the heavier lanthanides, Gd to Lu, are less abundant than the lighter lanthanides, La to Eu. However, there are two further complicating factors: one is that the elements with even atomic number are more abundant than those of odd atomic number, reflecting the greater stability of such nuclei. Secondly, some ores (e.g. bastnasite, monazite) are richer in the lighter metals while others (e.g. xenotime) have more of the heavier metals. The abundance of yttrium in the Earth's crust is 31 ppm while the total abundance of the lanthanides is some 180 ppm; cerium is the most abundant (66 ppm), while thulium and lutetium are the rarest (0.5 and 0.8 ppm, respectively).

Although over 150 minerals are known to contain lanthanides, the three most important (outside of China) are bastnasite ($LnFCO_3$), monazite ($LnPO_4$), and xenotime ($LnPO_4$). The main western source of bastnasite is California, USA, with some coming from Baiyunebo (inner Mongolia) where it is present as part of an iron ore. Monazite mainly comes from China and Australia (with important contributions from Malaysia, India, and Brazil), where the monazite contains 5–10% of ThO_2 (whose radioactivity presents an additional processing problem). Xenotime is likewise a phosphate containing rather more of the heavier metals and also containing thorium oxide with some U_3O_8 (main exporters are Australia, China, and Malaysia). Chinese rare earth reserves amount to over 70% of the known world total. Much of this is in the form of the ionic ores from southern provinces, of which the Longnan mineral contains a remarkable quantity of yttrium oxide (over 60%). These Chinese ion-absorption ores, weathered granites with lanthanides adsorbed on to the surface of aluminum silicates, are in some cases low in cerium and rich in the heavier lanthanides (Longnan), while the Xunwu deposits are rich in the lighter metals; the small particle size makes them easy to mine.

3.2 Extraction of the Lanthanides

As mined, Californian bastnasite contains around 8% lanthanide oxides. Flotation followed by dissolution of the calcite content in 10% HCl concentrates this to around 70%. The resulting concentrate is treated to oxidize Ce^{III} to Ce^{IV}, followed by reaction with hydrochloric acid to dissolve the oxides of the metals La and Pr through Gd, separating them from cerium (which is recovered as CeO_2). Solvent extraction of the resulting solution affords the individual lanthanides (europium can be separated from the mixture by zinc reduction to Eu^{II}, followed by precipitation as $EuSO_4$). Monazite is generally first treated with NaOH at 150 °C to remove phosphate as Na_3PO_4, leaving a mixture of the hydroxides of lanthanum and thorium. These can be separated either by selective precipitation of $Th(OH)_4$ while the Ln^{3+} ions remain in solution, or by selectively dissolving the lanthanides out of the hydroxide mixture. The resulting solution of Ln^{3+} ions is separated into the individual metal ions by solvent extraction.

Various other separation methods have been described, one recent one involving the use of supercritical carbon dioxide at 40 °C and 100 atm to convert the lanthanides into their carbonates, while the quadrivalent metals (e.g. Th and Ce) remain as their oxides.

For many years up to and immediately following the Second World War, isolation of the individual lanthanide compounds in a pure state was a problem that required innumerable fractional crystallizations of salts such as the bromates or magnesium double nitrates, exploiting slight solubility differences. As radioactive lanthanide isotopes are among the important fission products of uranium and because it was expected that the elements beyond plutonium would resemble the lanthanides, the development of ion-exchange chromatography was a highly important spin off from the Manhattan project and commercial separation processes based on cation exchange rapidly came into being. The later lanthanides with their smaller ionic radii conversely have the larger hydrated radii because of their greater tendency to attract water molecules. The separation relies on the use of complexing agents such as EDTA and HEDTA (hydroxyethylethylenediaminetriacetate), which form stronger complexes with the heavier lanthanides and elute them first (the original eluent was ammonium citrate).

The major disadvantage of ion exchange is that it is a slow process for large-scale separations. Solvent extraction has therefore come to be the process of choice, at least for the initial separation (up to the 99.9% purity level); it employs an automated continuous counter-current process using a two-solvent mixture, an acid (HCl or HNO_3) aqueous phase, and an organic phase, for which tributyl phosphate or similar compound with a P=O group is the usual complexing ligand.

This process is capable of giving individual lanthanides of sufficient purity for chemical use (99.9%), but for electronic or spectroscopic use (‘phosphor grade’) 99.999% purity is necessary, and further ion exchange is used for final purification to these levels.[24]

3.3 Preparation and Properties of the Metals[25]

Most of the elements are usually made by metallothermic reduction of the trifluoride, generally with calcium in excess of 1000 °C.

$$2MF_3 + 3Ca \longrightarrow 2M + 3CaF_2 \qquad (2)$$

The fluoride is chosen as it is both nonhygroscopic and also oxide-free. This method is not applicable to Sm, Eu, or Yb, which are only reduced to the difluorides; these metals are instead made by heating their oxides with lanthanum at 1000–1300 °C, the more volatile metal being removed by distillation at low pressure:

$$3La + M_2O_3 \longrightarrow 2M + La_2O_3 \qquad (3)$$

A third method, electrolysis of the mixed molten chlorides of the lighter lanthanides, is used to make the lanthanide mixture known as mischmetal. For some research applications, ultrapure metals are needed as even small quantities of light nonmetals such as carbon and hydrogen can have a marked effect on the properties of the metal. Thus if the LnF_3–Ca method is used the molten fluoride has to be treated with HF to ensure the absence of the oxyfluoride, while the calcium is twice redistilled under an ultrapure argon atmosphere before use. Further purification of the lanthanide can be achieved by methods including vacuum remelting, zone melting, and distillation.

These elements are silvery white reactive metals. The reactivity order is europium followed by lanthanum through lutetium, the exception being ytterbium, placed between Sm and Gd. Yttrium resembles terbium and dysprosium. Europium is quickly oxidized by air and the powdered metal can be pyrophoric; it reacts with water like calcium. Lighter lanthanides are oxidized readily at room temperature, especially in moist air, but the metals in the second half of the series tend to be fairly stable in dry air. All the metals dissolve rapidly in dilute acid and react slowly with the halogens at room temperature, rapidly on warming. Similar reactions occur with other nonmetals (S, C, N_2, Si, B, H_2) on heating. In their reactivity the metals resemble the alkaline earth metals; in the case of Eu and Yb the resemblance extends to forming dark blue solutions in liquid ammonia. The physical properties of the lanthanide metals follow a smooth pattern, with the exception of the metals with a tendency to divalency. The atomic radii of Eu and Yb are ca. 0.2 Å greater (and the densities correspondingly lower) than the other metals; samarium, ytterbium, and europium are considerably more volatile than the other lanthanides, implying that while most lanthanide metals can be represented as Ln^{3+} $(e^-)_3$, Eu and Yb should be regarded as Ln^{2+} $(e^-)_2$.

The lanthanides form a wide range of alloys, several of considerable importance. $LaNi_5$ readily absorbs hydrogen gas up to a composition $LaNi_5H_6$ and has been extensively studied for its potential for hydrogen removal and storage (as H_2 is desorbed on heating to about 140 °C), rechargeable batteries (as used in notebook PCs), electrode and fuel-cell materials, and in catalytic hydrogenation. Samarium–cobalt alloys have been widely used as $SmCo_5$ and Sm_2Co_{17} in permanent magnets. A ferrocerium alloy containing 25% iron and 75% mixed light lanthanides, mainly cerium (mischmetal), is used to make lighter flints; another use of mischmetal is for deoxidation and desulfurization of steels.

3.4 Oxidation States and Coordination Numbers[10]

The adoption of the (+3) oxidation state by the lanthanides in most of their chemistry is a consequence of the balance of a number of factors,[6,26,27] although many divalent and tetravalent compounds also exist. Nevertheless, in aqueous solution, only the lanthanide(III) ions are stable; Ce^{4+} is metastable whilst Eu^{2+} has a life of a few hours.

The ionic radius of the smallest lanthanide(III) ion, Lu^{III} is 0.861 Å (for six coordination), considerably greater than that of scandium and the 3d metals (corresponding values for lanthanum and yttrium are 1.032 and 0.900 Å, respectively). Purely on steric grounds, high coordination numbers would therefore be expected for Ln^{3+}, and in fact a range of values between 3 and 12 is known. The observed geometries are discussed in more detail in Section Magnetic Resonance Imaging and MRI Agents.

The lack of directional character of the essentially ionic bonding is a result of crystal-field effects being absent. The decreasing size of the lanthanide atoms and ions across the series, the *Lanthanide Contraction* (*see Lanthanide Contraction*), is due to the contraction of the $(5s^25p^6)$ configuration due to their penetration inside the 4f orbitals (a similar contraction is noted for the transition metals, although for a different reason).[28] Consequently a decrease in coordination number in a series of related compounds is often observed.

3.5 Magnetic and Spectroscopic Properties of the Ln^{3+} Ions[29,30]

These may be accounted for in terms of the Russell–Saunders coupling scheme in which the electron spins are coupled together separately from the coupling of the orbital angular momenta of the electrons and the orbital moment is unquenched. The ground state for a given lanthanide ion is unaffected by the ligands (and thus crystal-field splittings are weak) because of the shielding of the 4f electrons by the filled 5s and 5p orbitals. The strength of spin–orbit coupling means that the ground state is well separated from excited states, except for Sm^{3+} and Eu^{3+}, where contributions from low-lying paramagnetic excited states contribute to the magnetic moment. Thus, if the magnetic properties of the Eu^{3+} ion were solely determined by the $^7F_0$ ground state, its compounds would be diamagnetic, whereas contributions from thermally accessible levels such as $^7F_1$ and $^7F_2$ lead to the observed magnetic moments in the region of 3.5 μ_B. The magnetic moments in the second half of the series are greater than those in the first half, as $J = L + S$ for a shell greater than half-filled and $J = L - S$ for a less than half-filled shell. (Table 1 lists the magnetic moments for the tripositive lanthanide ions.) The magnetic moment of the Ln^{3+} ions are essentially independent of environment, from the practical viewpoint of the coordination chemist measuring bulk powder samples at around room temperature. The moments are given by the equation

$$\mu_{\text{eff}} = g_J\sqrt{J(J+1)} \tag{4}$$

where the Landé g factor is defined by

$$g_J = \frac{[S(S+1) - L(L+1) + 3J(J+1)]}{2J(J+1)} \tag{5}$$

The electronic spectra of lanthanide compounds resemble those of the free ions, in contrast to the norm in transition metal chemistry; the crystal-field (CF) splittings can be treated as a perturbation on the unsplit $^{2S+1}L_J$ levels. A further consequence of the weak CF splittings is the sharpness of the f–f transitions. The spectrum of the complex $Eu(NO_3)_3$(15-crown-5) shown in (Figure 5) displays this.

Certain transitions in the electronic spectra of some tripositive lanthanide ions (notably Nd, Ho, Er) exhibit ‘hypersensitivity’ to the environment, which can sometimes be used to indicate geometry, as in the case of the neodymium(III) aqua ion shown in Figure 6.

Study of the intensity and splitting pattern of certain transitions in the fluorescence spectra of compounds of Eu^{3+} and Tb^{3+} in particular can give a good deal of information about the environment of the lanthanide ion.[31,32] The $^7F_0$ ground state is unsplit, so that transitions to it give straightforward information about the excited state. Thus, since the $^5D_0$ state is also unsplit, if more than one component

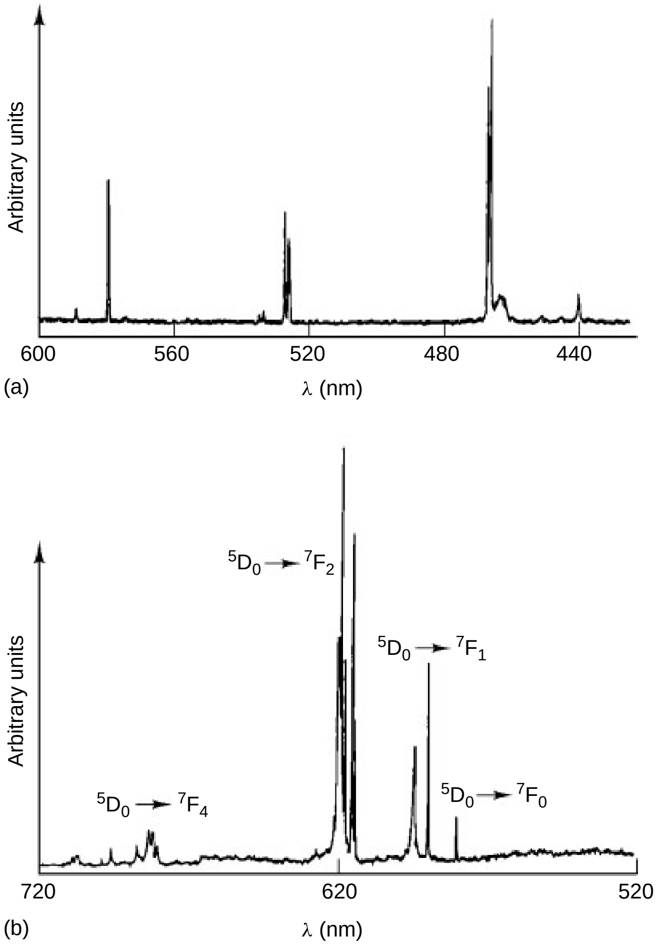

Figure 5 (a) Excitation spectrum at 77 K of $Eu(NO_3)_3$·15-crown-5 (λ_{anal} = 618 nm) (b) Fluorescence spectrum at 77 K (λ_{exc} = 397.7 nm). (Reprinted with permission from J.-C.G. Bunzli, B. Klein, G. Chapuis, and K.J. Schenk, *Inorg. Chem.*, 1982, **21**, 808. © 1982 American Chemical Society)

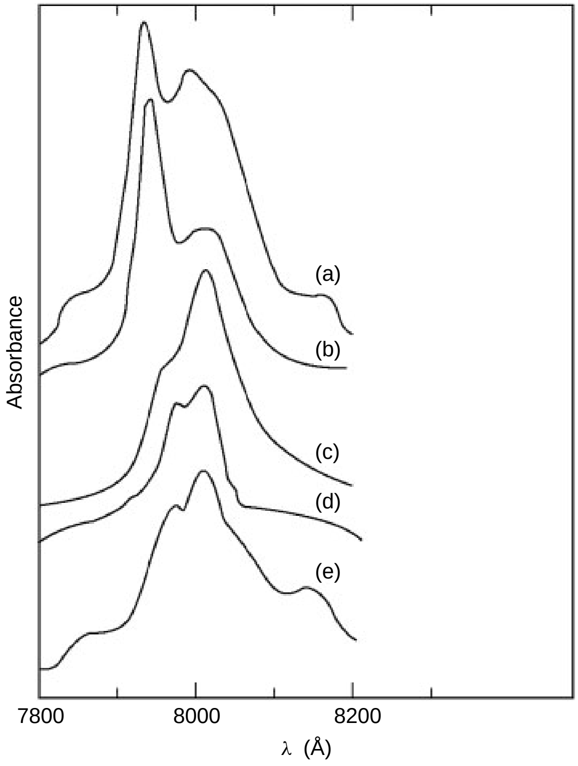

Figure 6 Spectra of the $Nd^{3+}\,^4I_{9/2} \rightarrow {}^2H_{9/2}$, $^4F_{5/2}$ transitions: (a) solid $Nd(BrO_3)_3 \cdot 9H_2O$; (b) 5.35×10^{-2} M Nd^{3+} (aq); (c) 5.35×10^{-2} M Nd^{3+} in 11.4 M HCl; (d) solid $NdCl_3 \cdot 6H_2O$; (e) $Nd_2(SO_4)_3 \cdot 8H_2O$. (Reprinted with permission from D.G. Karraker, *Inorg. Chem.*, 1968, **8**, 474. © 1968 American Chemical Society)

is seen for this transition, it shows more than one europium site; only one line is observed for the crown ether complex shown in Figure 5 so the sites are identical. This transition is electric-dipole allowed and only observed in low-symmetry environments (it is not seen in the emission spectrum of the $[EuCl_6]^{3-}$ ions in $Cs_2Li[EuCl_6]$ where they occupy sites with cubic symmetry) whereas the intensity of the magnetic-dipole transition from $^5D_0$ to $^7F_1$ is relatively insensitive to this; in the spectrum of the crown ether complex this transition appears as a doublet and singlet, a splitting consistent with the approximately pentagonal pseudosymmetry seen in its crystal structure (in a lower-symmetry environment, the doublet would be further split).

Study of these and other transitions can thus yield valuable information. Crystals of the nine-coordinate complex $[Eu(tmhd)_3(terpy)]$ contain two slightly different molecules present in the crystal, its luminescence spectrum showing a broad but unresolved $^5D_0 \rightarrow {}^7F_0$ transition. In solid $[Eu(tmhd)_3(Me_2phen)]$ (Ln = La, Eu, Tb, Ho), there are two different square-antiprismatic isomers in the unit cell, and in this case emissions from both isomers can be distinguished in the fluorescence spectrum of the europium complex, which shows an unusually high splitting of the $^5D_0 \rightarrow {}^7F_0$ transition.[33]

The paramagnetism of many lanthanide ions finds practical application in NMR shift reagents and, increasingly, in MRI contrast agents. EPR (*see Electron Paramagnetic Resonance*) spectra are only readily obtained from Gd^{3+}, with its ^8S ground state,[34] as yet there has been little study of the effects of environment upon the spectra.

The electronic spectra and magnetic susceptibility of lanthanide complexes thus cannot be used to give diagnostic information on the stereochemistry of lanthanide compounds as for the 3d transition metals. Ultimately, reliable stereochemical information can only be obtained from diffraction measurements.

The lanthanides form a series of ions of closely related size and bonding characteristics and in many respects resemble Ca^{2+}, for which they often substitute isomorphously in biological systems; since different Ln^{3+} ions can be probed with particular spectroscopic techniques (e.g. Eu^{3+} and Tb^{3+} fluorescence, Gd^{3+} ESR, Nd^{3+} electronic spectra), in favorable circumstances it should be possible to obtain information about the binding site of spectroscopically inactive Ca^{2+} in several ways.[35]

3.6 Binary Compounds of Yttrium and the Lanthanides

3.6.1 *Halides*[36,37]

These are the best characterized binary compounds of these metals; all the halides of the trivalent metals are well defined except EuI_3, whose existence is extremely uncertain. The insoluble fluorides are conveniently prepared by precipitation, followed by dehydration of the hydrate; this route is not generally open for the other anhydrous halides, as attempted dehydration of the hydrated halides tends to lead to oxyhalides. Reaction of the elements with the halogens or HX is often possible although a more convenient route involves heating the lanthanide oxide with the appropriate ammonium salt to afford $(NH_4)_3LnX_6$, followed by thermal decomposition. The halides may be purified by vacuum sublimation, with the caveat that the hot halides attack glass, forming the oxyhalide. The lanthanide trihalides very clearly demonstrate the effect of varying the cation and anion radii upon the structure type adopted (Table 2). As the radius of the lanthanide ion decreases on crossing the series from left to right, the coordination number of the metal in a given halide decreases; a similar effect is seen on descending group 17, as the radius of the halide ion increases.

The early fluorides feature the tysonite (LaF_3; Figure 7) structure in which the lanthanide has nine nearest-neighbor fluorides in a tricapped trigonal prismatic array (like the aqua ions), with two rather more distant neighbors capping the trigonal faces. From SmF_3 onwards the stable form is the

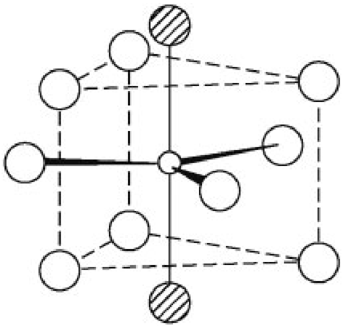

Figure 7 The LaF_3 structure

Table 2 Structures of the trihalides of yttrium and the lanthanides[a]

Halide	La	Ce	Pr	Nd	Pm	Sm	Eu	Gd	Tb	Dy	Ho	Er	Tm	Yb	Lu	Y
F	1	1	1	1	1	2	2	2	2	2	2	2	2	2	2	2
Cl	3	3	3	3	3	3	3	3	4	5	5	5	5	5	5	5
Br	3	3	3	4	4	4	4	6	6	6	6	6	6	6	6	6
I	4	4	4	4	4	6	?	6	6	6	6	6	6	6	6	6

[a] Abbreviations for structure types: 1 = LaF_3 (CN9 + 2); 2 = YF_3 (CN 9); 3 = UCl_3 (CN 9); 4 = $PuBr_3$ (CN 8); 5 = $AlCl_3$ (CN 6); 6 = $FeCl_3$ (CN 6).

'YF_3' structure in which there is a distorted tricapped trigonal prismatic array of fluorines round the metal. The trichlorides adopt successively the UCl_3 (nine-coordinate), $PuBr_3$ (eight-coordinate), and $AlCl_3$ (six-coordinate) structures. A similar sequence is found in the bromides, while nine-coordination is not found at all in the iodides; eight-coordination is the rule for the early metals as far as promethium with six-coordination for the later metals.

3.6.2 Lower Halides[14,38]

Whether an individual lanthanide forms a dihalide depends upon a number of factors, particularly the value of I_3, the third ionization energy.[39] There are three main types of lower halides.

1. The salt-like dihalides form the widest range. All MX_2 ($X = F, Cl, Br, I$) are formed by Eu, Sm, and Yb, the metals with the most stable divalent states; in addition, all except the difluoride are known for Nd, Dy, and Tm. They may typically be formed by reproportionation (comproportionation; see *Disproportionation*):

$$Nd + 2NdCl_3 \longrightarrow 3NdCl_2 \qquad (6)$$

   although hydrogen reduction is available for all the europium halides and all YbX_2 except YbF_2. They are nonconductors and have magnetic and spectroscopic properties consistent with the presence of M^{2+} ions. Only EuX_2 are stable for any length of time in aqueous solution. A range of solid-state structures is adopted; for example, all the difluorides have the fluorite structure.
2. Metallic diiodides are formed by La, Ce, Pr, and Gd, even though none of these lanthanides are well known in the divalent state. These have high conductivity, a metallic lustre, and are good reducing agents, reacting immediately with air and water. All the evidence supports the formulation Ln^{3+} $(I^-)_2(e^-)$ with the free electron in a conduction band. A high-pressure form of NdI_2 is also believed to be of this type. The 'reduced' halide Pr_2Br_5 is a Pr^{3+} compound with the extra electron in a d-band. Extra Pr can be incorporated into $PrCl_3$ to give a black solid, $Pr_{2.6}Cl_6$, whose electronic structure is uncertain.
3. Cluster compounds are exemplified by Gd_2Cl_3, which has a structure (Figure 8) based on Gd_6Cl_8 clusters sharing common edges in infinite chains. This, too, may be made by comproportionation; it is a semiconductor. Y_2Cl_3, Tb_2Cl_3, and Gd_2Br_3 have also been described. Many compounds hitherto thought to be reduced binary halides are now known to be clusters containing a third, interstitial, element as in YClH. An extensive range of mixed metal halides based on chain structures exist. Thus, La_4I_5Ru has metal octahedra linked into chains with edge-bridging iodines; parallel chains are also linked by iodine bridges, the whole structure having been described as a heterometal wire sheathed by iodine. Pr_3I_3Ru has a structure in which there are double chains of condensed, Ru-centered octahedra.

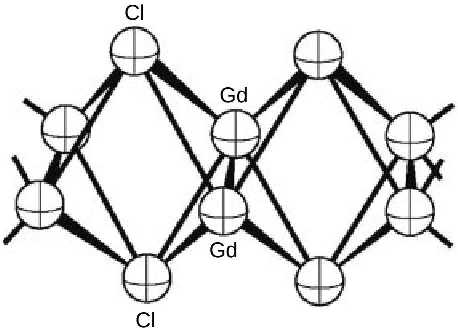

Figure 8 The Gd_2Cl_3 structure

3.6.3 M^IV Halides

The only tetrahalides isolated are the fluorides of Ce, Pr, and Tb. Only CeF_4 is made by direct fluorination of the metal (as well as CeX_3 ($X = Cl, F$)); the terbium compound is made by fluorination of TbF_3 while the more unstable PrF_4 is made by the reaction of Na_2PrF_6 with dry HF (it decomposes around 70 °C). $CeCl_4$, expected to be the most stable tetrachloride, has never been isolated (though Lewis base adducts have, cf. $PuCl_4$).

3.6.4 Oxides[40]

The most important of these compounds are the basic sesquioxides M_2O_3, readily prepared by heating oxysalts such as the carbonate or nitrate:

$$4Ln(NO_3)_3 \longrightarrow 2Ln_2O_3 + 12NO_2 + 3O_2 \qquad (7)$$

though metals with an accessible (+4) state need a reducing atmosphere. They adopt three types of structures; in the A-type structure (La to Sm) they have capped-octahedral seven-coordination, while in the B-type (Pr to Dy) face-capped trigonal prismatic seven-coordination and a distorted capped-octahedral structure coexist. Distorted octahedral coordination is found in the C-type structure, the most stable phase for most lanthanides.

Reduction of Eu_2O_3 with lanthanum or europium, as well as carbon, affords the stablest M^{II} oxide:

$$Eu + Eu_2O_3 \longrightarrow 3EuO \qquad (8)$$

Similar comproportionation has yielded NdO, SmO, and YbO, although in these cases it is necessary to work at high pressure. Europium and samarium also give mixed-valence oxides M_3O_4.

Of the Ln^{IV} compounds, CeO_2 is the most important. It is obtained as the product (white when pure, but usually yellow) of thermal decomposition of Ce^{III} oxy salts in air or by burning cerium metal. It has the fluorite structure. Additional phases, Ce_nO_{2n-2} ($n = 7$, 9, 10, 11), have been characterized. A hydrated yellow form is precipitated from aqueous solution. CeO_2 can be persuaded to dissolve in acid to afford Ce^{4+}, generally as a complex ion. Praseodymium and terbium usually form Pr_6O_{11} and Tb_4O_7 when corresponding aerial ignition is employed, but can be produced as stoichiometric dioxides by heating with atomic oxygen. They dissolve in acid but no Ln^{IV} aqua ion can be made.

Several mixed metal oxides involving lanthanides have been found to exhibit *Superconductivity* (*see Superconductivity in Solids*) since the 1986 report of a superconducting transition temperature of 30 K in $La_{2-x}Ba_xCuO_4$, the highest found at that date. Shortly afterwards, a T_c of 93 K, above the boiling point of liquid nitrogen, was determined for $YBa_2Cu_3O_7$. Another class of superconductors, though with lower T_c values (20 K), are of the type $Nd_{2-x}Ce_xCuO_4$. These superconductors are believed to function by the so-called *Cooper Pair* mechanism in which electron pairs move unhindered by lattice vibrations and impurities. The conduction electrons probably reside primarily on the oxygen atoms. The cuprate superconductors have a common feature of two-dimensional copper oxide planes along which the superconductivity occurs; inserted between these layers are planes of metal atoms (or metal/oxygen atoms) which fulfil the function of acting as charge reservoirs.

The $YBa_2Cu_3O_7$ compounds have been most extensively studied (Figure 9). Other, paramagnetic, lanthanide ions can be introduced in place of yttrium with little effect upon the conducting properties, arguing that the yttrium site has little involvement with the coppers but probably plays a supporting role. On the other hand, the presence of copper(II) is shown to be vital by other doping experiments. Above the superconducting region these compounds exhibit pronounced anisotropy in their resistance, it being greatest perpendicular to the CuO_2 planes.

The commercial implications of ‘warm’ superconductors have led to intense study of the magnetic properties of these materials and the investigation of reliable synthetic routes, including the preparation of thin films.

3.6.5 *Other Binary Compounds*

Hydrides are readily formed by union of these metals with hydrogen on gentle warming.[41] Apart from europium, which only forms EuH_2, both LnH_2 and LnH_3 exist, although the composition ranges can be considerable and the phase isolated is often nonstoichiometric (thus for yttrium the stability ranges are $YH_{1.90-2.23}$ and $YH_{2.77-3.0}$). Both types of hydride contain Ln^{3+} ions with the trihydrides as salt-like $Ln^{3+}(H^-)_3$ while the conducting dihydrides are $Ln^{3+}(H^-)_2(e^-)$. The important alloy hydride $LaNi_5H_6$ is discussed in Section 3.3.

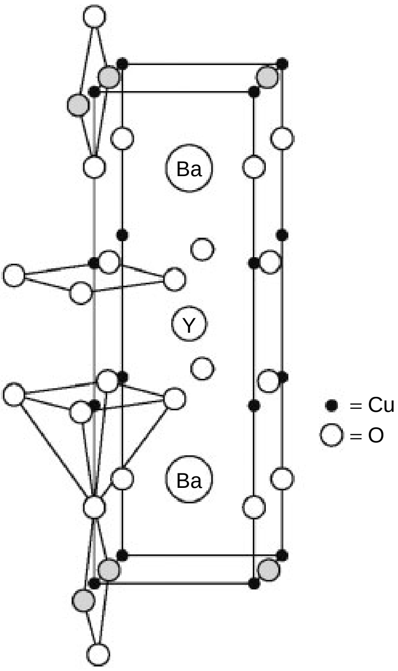

Figure 9 The structure of $YBa_2Cu_3O_7$; the shaded atoms are those removed to create oxygen-deficient phases up to $YBa_2Cu_3O_6$. (Ref. 6. Reproduced by permission of Palgrave Macmillan)

The lanthanides form a range of borides.[42] The most important of these is high-melting (2715 °C) LaB_6, widely used as a high-intensity thermal cathode in electron guns and in optical fibres. It has the CaB_6 structure and may be made by various routes, including La_2O_3 and B at 1500 °C. LaB_4(UB_4 type) and LaB_9 are also known. EuB_6 has been used as a neutron absorber in nuclear reactors; like YbB_6 it has Ln^{2+} ions, in contrast to the other hexaborides which contain Ln^{3+} ions, affording one electron from each lanthanide to provide a conduction band, and are metallic conductors. Many heavier lanthanides (above Gd) form MB_{12} (UB_{12} structure) and MB_{66} in which a B_{12} icosahedron is surrounded by 12 linked B_{12} icosahedra. A number of important ternary borides exist, particularly $Nd_2Fe_{14}B$, a high coercive-strength ferromagnet, while related compounds with other lanthanides are important in magnet technology. In addition to these, a number of $LnRh_4B_4$ compounds with the $CeCo_4B_4$ structure have been investigated for their superconducting properties.

An extensive array of sulfides has been obtained, and much research is still undertaken to clarify the picture.[43–45] The most important are sesquisulfides, M_2S_3, but other stoichiometries (MS, M_3S_4, and MS_2) also exist. A range of synthetic methods has been employed for the sesquisulfides (apart from the nonexistent Eu_2S_3); reaction of the lanthanide powders with sulfur in the presence of alkali-metal chlorides as a flux has found favor lately, as has reaction of the sesquioxide or reduced chloride or chloride hydrides with sulfur. These compounds do contain the Ln^{3+} ions and often exist in several crystalline forms, sometimes obtained from high-pressure/temperature synthesis. The α-form (La–Dy) has seven- and eight-coordinate metals, the high-temperature γ-form (La–Dy) involves eight-coordination; the δ-form (Y, Ho–Tm) has six- and seven-coordination, while the ε-form (Yb, Lu) has six-coordination only. M_3S_4(Th_3P_4 structure) are generally found for the early lanthanides (La–Sm); most have Ln^{3+} but Eu_3S_4 contains both di- and trivalent europium. The monosulfides LnS are mainly golden yellow solids (NaCl structure) with a metallic luster whose metallic conductivity indicates a structure Ln^{3+} $(S^{2-})(e^-)$, but the europium, ytterbium, and samarium compounds are insulators, $Ln^{2+}S^{2-}$.

Carbides are likewise formed in a number of stoichiometries.**[46]** LnC_2 are the most important; they can be made by direct synthesis from the elements as well as by heating the oxide or hydride with carbon. They have the CaC_2 structure with short C–C distances (around 1.28 Å) but have metallic conductivity and thus may be formulated Ln^{3+} $(C_2{}^{2-})(e^-)$. C_2 units are also found in Ln_2C_3 (Pu_2C_3 structure), while LnC, Ln_2C, and Ln_3C are also known. The carbides are readily hydrolyzed, affording a mixture of hydrocarbons whose composition depends on temperature.

Another kind of lanthanide−carbon binary compound recently discovered are the fullerenes (*see* ***Carbon: Fullerenes***); vaporization of graphite−Ln or graphite−Ln_2O_3 mixtures followed by toluene extraction of the resulting soot affords a number of clusters identifiable by mass spectroscopy, particularly $Ln@C_{82}$. ESR studies on the air-stable $La@C_{82}$ and $Y@C_{82}$ indicate the formulation $Ln^{3+}@(C_{82})^{3-}$; thus the spectrum of the lanthanum compound consists of eight lines of equal intensity due to hyperfine coupling to a single La ($I = 7/2$). An *Extended X-ray Absorption Fine Structure* (EXAFS) study on $Y@C_{82}$ indicated that yttrium has seven carbon neighbors (2.35 Å) and one yttrium (at 4.05 Å), suggesting a dimeric formulation.

Pnictides LnQ (Q = Group 15 element) having the NaCl structure are made by direct synthesis, with other routes for the nitrides including the reaction of the lanthanide hydride with either nitrogen or ammonia; like the carbides, they are readily hydrolyzed to the hydride QH_3.

3.6.6 The Hydroxides

These metals form genuine hydroxides (not hydrous oxides) by alkaline precipitation from aqueous solution, obtainable in crystalline form by hydrothermal methods (crystallization from hot Ln_2O_3/NaOH under pressure). All have the nine-coordinate UCl_3 structure, except for $Lu(OH)_3$ which adopts the six-coordinate $In(OH)_3$ structure. Like the oxides, their basicity extends to reaction with atmospheric CO_2, affording the carbonates.

Table 3 Stability constants for complexes of Sc, Y, La, and Lu**[49]**

	Sc^{3+}	Y^{3+}	La^{3+}	Lu^{3+}
F^- (1.0 M)	6.2[a]	3.6	2.67	3.61
Cl^- (1.0 M)	0	−0.1	−0.1	−0.4
Br^- (1.0 M)	−0.07	−0.15	–	–
$NO_3{}^-$ (1.0 M)	0.3	–	0.1	0.2
OH^- (0.5 M)	9.0	5.4	4.7	5.8
$acac^-$ (0.1 M)	8	5.89	4.94	6.15
$EDTA^{4-}$ (0.1 M)	23.1	18.1	15.46	19.8
$DTPA^{5-}$ (0.1 M)	24.4	22.1	19.5	22.4
Acetate (0.1 M)	–	1.68	1.82	1.85
Glycine (0.1 M)	–	3.5	3.1	3.9

[a] Data for solution of a slightly different ionic strength.

3.7 Coordination Chemistry of the +3 State[5,6,47,48]

Selected stability constants for scandium, yttrium, lanthanum, and lutetium are shown in (Table 3)**[49]** They show a preference for ‘hard’ donor atoms, as might be expected for the trivalent metals, but complexes with softer donor atoms like nitrogen can be isolated by operating in nonaqueous solvents.

3.7.1 Coordination Numbers and Geometries in Lanthanide Complexes[50]

As already noted, because of the large size of the lanthanide ion, it often occurs in high-coordination compounds (*see* ***Coordination Numbers & Geometries***). Application of a cone-packing model (*see Cone Angle*) to lanthanide complexes indicates that the coordination number adopted is a consequence of saturation in the coordination sphere. Analysis of the coordination numbers (*see* ***Coordination Numbers & Geometries***) for large numbers of coordination compounds of yttrium and the lanthanides indicates that coordination numbers of eight and nine are almost equally common, accounting for over 60% of the known structures. These are, of course, the coordination numbers associated with the aqua ions and related complexes.

Two coordination is known in the form of the monomeric (bent) alkyls $[Ln\{C(SiMe_3)_3\}_2]$ (Ln = Eu, Yb) which feature additional agostic interactions.**[51]** Coordination numbers of 3−5 are similarly associated with the use of bulky ligands, such as alkoxide (and related systems), bis(trimethylsilyl)amido, and the isolobal alkyl $CH(SiMe_3)_2$ (*see* ***Scandium, Yttrium & the Lanthanides: Organometallic Chemistry***). Several homoleptic three-coordinate LnX_3 systems are formed by these ligands, a few having the expected trigonal planar geometry, but usually they are pyramidal. The adoption of this geometry has, in the case of actinide trialkyls, been attributed to 6d involvement in the bonding; here it appears that weak agostic interactions are important in the solid state (the alkylamides have zero dipole moment in solution and thus appear to be planar there, though pyramidal in the solid state). Tetrahedral geometry is, as expected, found in the four-coordinate $[Lu(2,6\text{-dimethylphenyl})_4]^-$ ion and in $Ln[(N(SiMe_3)_2]_3(Ph_3PO)$; in the latter complex the ligands have high second-order steric effects (*see Fan Angle*), generating crowding round the lanthanide even though there are only four atoms bound to the lanthanide. In contrast, the adoption of six-coordination in the $LnCl_6{}^{3-}$ anion is the result of first-order crowding among the six chlorides bound to the lanthanide. The six-coordinate complexes are usually octahedral, though with bidentate S-donors distortion towards trigonal prismatic may be the result of steric interactions between ligands. The first lanthanide thiocyanate complex to be characterised was the six-coordinate $[Er(NCS)_6]^{3-}$ ion, as the tetrabutylammonium salt; since then, crystallographic study of many lanthanide thiocyanate complexes has shown that seven and eight-coordination are also possible with the coordination number adopted being the result of a subtle balance of factors including the counterion and solvent used (Section 3.7.10).

Among seven-coordinate structures, many involve diketonate complexes $Ln(diket)_3{\cdot}L$; these generally have either capped-octahedral or capped trigonal prismatic geometry. A considerable number of complexes with neutral donors (e.g. thf) of the type LnX_3L_4 ($X =$ halide, NCS), however, have structures closest to pentagonal bipyramidal, similarly found in the erbium perchlorate complex with 2,6-dimethyl-4-pyrone (Section 3.7.4).

Most eight-coordinate lanthanide complexes have dodecahedral or square-antiprismatic geometries; the energy difference between these is likely to be small. One exception is the $[La(bipyO_2)_4]^{3+}$ ion, which is cubic, possibly because of solid-state packing effects. Tricapped trigonal prismatic is the most familiar example of nine-coordinate geometry, adopted for the nonaqua ions of all lanthanides in a number of crystalline salts. This geometry is also often adopted where polydentate ligands are involved, such as the tris complexes with terpy and dipicolinate, even in $Eu(dpm)_3{\cdot}$ terpy.

Steric considerations (interdonor atom repulsions) make coordination numbers of 10 or more difficult, so fewer examples are known and, moreover, small differences between different types of polyhedra make assignment of a particular geometry difficult. Most examples involve nitrate, either alone (Section 3.7.7), or in combination with other polydentate ligands such as crown ethers (Section 3.7.8). Near-icosahedral geometries are found for regular 12-coordinate complexes such as $Pr(naph)_6{}^{3+}$ and $Ln(NO_3)_6{}^{3-}$.

Lanthanide complexes display a richness of coordination number and geometry unmatched by any other block of metals. It is becoming increasingly clear that in the absence of the strong ligand-field forces that often dictate coordination geometries in transition metal complexes, the coordination number adopted and the species formed in the solid state depends on the balance of a number of factors.

3.7.2 Aqua Ions and Simple Hydrated Salts[5,52]

Hydrated salts are readily prepared by reaction of the lanthanide oxide or carbonate with the acid. Salts of non coordinating anions most often crystallise as salts $[Ln(OH_2)_9]X_3$ (X e.g. bromate, triflate, ethylsulphate, tosylate). The tricapped trigonal prismatic structure was first established by X-ray diffraction in 1939 for the $[Nd(H_2O)_9]^{3+}$ ion in $[Nd(H_2O)_9]\ (BrO_3)_3$; this was an important structure historically, as it was the first clear indication that lanthanides could have high coordination numbers. It has since been verified for many other salts (Figure 10).

The crystals of the triflate contain columns of $[Ln(OH_2)_9]^{3+}$ cations and $CF_3SO_3{}^-$ ions, with a three-dimensional network of hydrogen bonds linking the columns. This presumably helps stabilise this structure favoring its isolation, even for the later lanthanides (Gd–Lu), where the eight-coordinate $[Ln(OH_2)_8]^{3+}$ ion predominates in solution (the $[Ln(OH_2)_8]^{3+}$ cation can be crystallised with certain other counter ions, for example, $[terpyH_2]_2[Tb(OH_2)_8]_7Cl_7{\cdot}8/3H_2O$, $[[Er(OH_2)_8](ClO_4)_3{\cdot}(dioxan){\cdot}2H_2O]$; $[[Eu(OH_2)_8]_2(V_{10}O_{28}){\cdot}8H_2O]$ and $[Lu(OH_2)_8]^{3+}$ in $[Lu(OH_2)_8]Cl_3{\cdot}1.5(12\text{-crown-}4){\cdot}2H_2O$, as well as in several hydrated iodides), and similar arguments are likely to apply to the ethylsulphates and bromates. The lanthanide–water distances for the positions capping the prism faces and at the vertices are different; as the lanthanide series is crossed, the Ln–O distance decreases from 2.62 to 2.50 Å for the three face-capping oxygens, but more steeply from ca. 2.52 to 2.29 Å for the six apical oxygens (data for the triflate salt[53]); the corresponding distances in the ethyl sulfates show a similar trend, with the Ln–O distances decreasing from 2.616 to 2.497 Å (face-capping) and from 2.517 to 2.318 Å (apical) on passing from La to Lu.

Octahedral six-coordination is, however, rather surprisingly found in the rather unstable perchlorates $[Ln(H_2O)_6]^{3+}(ClO_4{}^-)_3$ (X-ray, $Ln =$ La, Tb, Er), although the dioxane complexes $Ln(ClO_4)_3{\cdot}9H_2O{\cdot}4$ dioxane may contain the nonaaqua ions. The isolation of $Ln(ClO_4)_3{\cdot}6H_2O$ in the solid state must

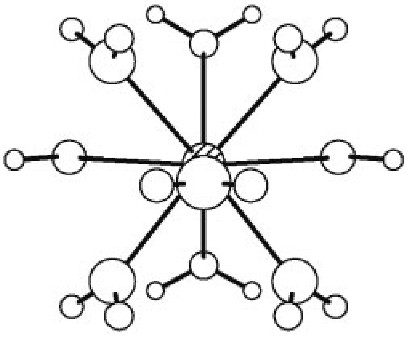

Figure 10 The structure of the nonaqualanthanide ion

reflect a balance of factors such as solubility and hydrogen-bonding in the solid state, as the close similarity between the EXAFS spectra of aqueous solutions of lanthanum perchlorate and the spectrum of solid $[Ln(H_2O)_9]\ (CF_3SO_3)_3$, indicates a coordination number of 9 for La^{3+} (aq) in the perchlorate solutions. Similarly, the fact that erbium is eight-coordinate in $[[Er(OH_2)_8](ClO_4)_3{\cdot}(dioxan){\cdot}2H_2O]$ shows the fine balance here. Lower hydrates than the hexahydrates exist. Partial dehydration of $Ln(ClO_4)_3{\cdot}6H_2O$ (Ln = Er, Lu) gives $Lu(ClO_4)_3{\cdot}3H_2O$ and $Er(ClO_4)_3{\cdot}H_2O$, both of which have eightfold coordination of the lanthanide. Similarly, $Yb(ClO_4)_3{\cdot}H_2O$ has been shown to have bi and tridentate perchlorate groups giving eight-coordinate ytterbium.

When anions can coordinate, a wide variety of species is obtained. Thus, whilst early lanthanides (La–Nd) form $[Ln(OH_2)_9](p\text{-}MeC_6H_4SO_3)_3$ with the usual trigonal prismatic coordination, the later lanthanide ions form the tosylates $Ln(p\text{-}MeC_6H_4SO_3)_3{\cdot}9\ H_2O$, which contain $[Ln(OH_2)_6(p\text{-}MeC_6H_4SO_3)_2]^+$ ions (Ln = Sm, Gd, Dy, Ho, Er, Yb, Y) in distorted dodecahedral eight-coordination.

A considerable number of nitrates $Ln(NO_3)_3{\cdot}nH_2O$ have been examined; in general, the coordination number of the lanthanide decreases with decreasing ionic radius and all nitrate groups are coordinated as bidentate ligands in these compounds, but the number of waters of crystallisation is no guide to how many are actually bound to the metal. Thus $Ln(NO_3)_3{\cdot}6H_2O$ are known for La–Dy and Y. Of these, the lanthanum and cerium compounds are $[Ln(NO_3)_3{\cdot}(H_2O)_5]{\cdot}H_2O$ (Ln = La, Ce) with 11-coordinate lanthanides, whilst the others are $[Ln(NO_3)_3{\cdot}(H_2O)_4]{\cdot}2H_2O$ (Ln = Pr–Dy, Y) with 10-coordination for the metal. $[Ln(NO_3)_3{\cdot}(H_2O)_4]$ molecules are also present in the pentahydrates $Ln(NO_3)_3{\cdot}5\ H_2O$ (Ln = Eu, Dy–Yb). Lutetium forms $Lu(NO_3)_3{\cdot}4H_2O$ and $Lu(NO_3)_3{\cdot}3H_2O$, isolated under very similar conditions, both of which contain nine-coordinate $[Lu(NO_3)_3{\cdot}(H_2O)_3]$ molecules. Nine-coordinate $Yb(NO_3)_3(H_2O)_3$ has also been identified. Additionally, $Ln(NO_3)_3(H_2O)_3$ molecules (Ln = Gd, Ho, Y, Lu) have been found in adducts with noncoordinating crown ether and bipy ligands.[54]

Among the halides, the chlorides of La and Ce, $LnCl_3{\cdot}7H_2O$ are dimeric $[(H_2O)_7Ln(\mu\text{-}Cl)_2Ln(OH_2)_7]\ Cl_4$ with what has been described as singly capped square-antiprismatic coordination of the metals (Figure 11) whilst $LnCl_3{\cdot}6H_2O$ (Ln = Ce–Lu) have antiprismatic $[LnCl_2(H_2O)_6]^+$ ions with the coordinated chlorides on opposite sides of the polyhedron. There are extensive hydrogen-bonding networks involving both coordinated and noncoordinated chlorides and water molecules.[55]

The hydrated bromides tend to resemble the chlorides; La and Ce form $LnBr_3{\cdot}7\ H_2O$, isomorphous with the corresponding chlorides and are dimeric $[(H_2O)_7Ln(\mu\text{-}Br)_2Ln(OH_2)_7]$ $Br_4{\cdot}LnBr_3{\cdot}6H_2O$ (Ln = Pr–Dy) are $[LnBr_2(H_2O)_6]Br$ whilst $LnBr_3{\cdot}8H_2O$ (Ln = Ho–Lu) which are $[Ln(H_2O)_8]\ Br_3$, with no bromide coordinated, and which resemble the hydrated iodides of the heavier lanthanides. Study of the hydrated iodides has been difficult because of their deliquescence and their tendency to oxidation in air. Iodide does not coordinate to the metal in any of them. The iodides of the earlier lanthanides are $LnX_3{\cdot}9H_2O$ (Ln = La–Ho),[56] containing the familiar tricapped trigonal prismatic $[Ln(OH_2)_9]^{3+}$ ions, but the range of Ln–O distances is much smaller than in the triflates and ethylsulphates, falling in the range 2.552–2.576 Å for Ln = La and similarly between 2.403 and 2.405 Å for the Ho complex. Heavier lanthanides (Ln = Er–Lu) form $LnI_3{\cdot}10H_2O$, containing square-antiprismatic $[Ln(OH_2)_8]^{3+}$ ions. The little-known thiocyanates form hexa- and heptahydrates; heptahydrates contain $Ln(NCS)_3(H_2O)_6$ molecules (Ln = La–Dy) and hexahydrates have $Ln(NCS)_3(H_2O)_5$ (Ln = Sm–Eu) molecules, in each case the crystal containing one uncoordinated water molecule.

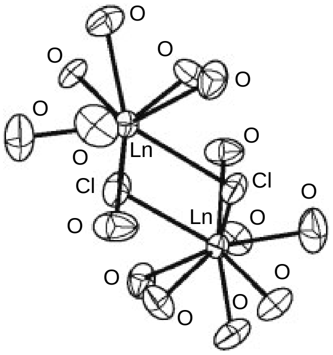

Figure 11 Structure of the dimeric cation $[(H_2O)_7LnCl_2Ln(H_2O)_7]^{4+}$

A number of hydrated sulfates exist. The nonahydrates of La and Ce have two distinct lanthanide sites, one nine-coordinate (six waters and three monodentatate sulfates) the other featuring 12-coordination (six waters and three bidentate sulfates). The other lanthanides form octahydrates with eight-coordination; the larger lanthanides also form pentahydrates such as $Nd_2(SO_4)_3{\cdot}5H_2O$ in which the metal is nine-coordinate (distorted trigonal prism) by seven sulfate oxygens and two water molecules.

The chloride, bromide, bromate, perchlorate, nitrate, acetate, and iodide salts are all soluble (the latter two types rather less than the others); the sulfates are sparingly soluble but the fluorides, carbonates, oxalates, and phosphates are insoluble.

3.7.3 *Aqua Ions*

The number of water molecules in the coordination sphere of the hydrated Ln^{3+} ion has been intensively studied for many years.[5] It now appears most probable that there is a change in coordination number from nine to eight for

$Ln(H_2O)_n{}^{3+}$ in mid-series, with the shape of the complex ion changing from tricapped trigonal prismatic nine-coordination for the lighter, larger, lanthanides to square-antiprismatic eight-coordination for the later metals, the changeover region (Sm to Tb) appearing to involve a mixture of eight- and nine-coordinate species. This view is based on information from a range of sources. A neutron-diffraction study of $Nd(ClO_4)_3$ and $Sm(ClO_4)_3$ in solution indicated coordination numbers of 9.0 and 8.5 respectively, with values of 7.9 for Dy and Lu, indicating that there are both eight- and nine-coordinate species present for samarium. EXAFS spectra (*see Extended X-ray Absorption Fine Structure*) of aqueous solutions of lanthanum perchlorate**[57]** are in close agreement with solid $[Ln(H_2O)_9]$ $(CF_3SO_3)_3$, suggesting a coordination number of 9 for La^{3+} (aq). In a study of chloride complexation by the lanthanides, EXAFS was used to determine hydration numbers of the aqua ions as 9.2 (La); 9.3 (Ce); 9.5 (Nd); 9.3 (Eu); 8.7 (Yb) and 9.7 (Y). Information from hydration studies of lanthanide ions by laser-induced fluorescence spectroscopy has been combined with other techniques to indicate a change in hydration number from 9 to 8 in the Eu–Tb region of the series. A luminescence study of lanthanide complexes reveals a linear correlation between the decay constant and the number of coordinated water molecules, used to calculate first coordination sphere hydration numbers of 9.0, 9.1, 8.3 and 8.4 for Sm^{3+}, Eu^{3+}, Tb^{3+}, and Dy^{3+}, respectively.

3.7.4 *Complexes of Other O-Donor Ligands*[4,5]

Complexes of ligands such as phosphine and arsine oxides were the first complexes of this type to be isolated from nonaqueous solvents. Among the studies of lanthanide halide complexes with these ligands, $[Ln(Ph_3PO)_5Cl]$ $(FeCl_4)_2$ (Ln = La–Nd, Sm–Er, Y) and $[Gd(Ph_3PO)_4Cl_2]$ $CuCl_3$ show that it is possible to pack several of these bulky ligands around a lanthanide. $YF_3{\cdot}0.5H_2O$ shows no signs of reaction with these ligands, but many complexes exist with other halides, most structurally confirmed examples involving yttrium, as in *trans*-$[YCl_2(Ph_3PO)_4]$ $Cl{\cdot}2.5EtOH{\cdot}H_2O$, *trans*-$[YBr_2(Ph_3PO)_4]$ $PF_6{\cdot}Et_2O$ and $[Y(Me_3PO)_6]$ Br_3, all with octahedrally coordinated yttrium. Other stoichiometries isolated include $[YX_3(Ph_2MePO)_3]$ (X = Cl, Br, I) and $[YCl(Ph_3PO)_5]$ $(SbCl_6)_2{\cdot}CeCl_3{\cdot}6H_2O$ reacts with Me_3PO in MeOH forming $[Ce(Me_3PO)_4Cl_3]{\cdot}4$ H_2O; on slow crystallisation of a $MeNO_2$ solution in air, crystals of $[Ce(Me_3PO)_4(H_2O)_4]Cl_3{\cdot}3H_2O$ result, cerium having triangulated dodecahedral coordination.

A considerable number of nitrate complexes have been examined.**[58]** The precise experimental conditions can be very important in their synthesis; thus the reaction of $Y(NO_3)_3{\cdot}6H_2O$ with 1 or 2 mols of Ph_3PO in boiling EtOH gives $[Y(NO_3)_3(Ph_3PO)_2(EtOH)]$ whilst 4 of triphenylphosphine oxide gives $Y(NO_3)_3(Ph_3PO)_3$, and reaction with 6 mols of Ph_3PO in cold ethanol affords $Y(NO_3)_3(Ph_3PO)_4$, the latter being $[Y(NO_3)_2(Ph_3PO)_4]$ NO_3. Lanthanide nitrates react with excess Ph_3PO in acetone forming $[Ln(NO_3)_3(Ph_3PO)_4]$ (Ln = La–Nd) which are $[Ln(\eta^2\text{-}NO_3)_2(\eta^1\text{-}NO_3)(Ph_3PO)_4]$, but in solution ($Me_2CO$ or CH_2Cl_2) they dissociate into $[Ln(NO_3)_3(Ph_3PO)_3]$ (the only product of reaction in ethanol) and Ph_3PO. $[La(NO_3)_3(Ph_3PO)_3]{\cdot}CHCl_3{\cdot}EtOH$ has three bidentate nitrate groups. $[Ln(NO_3)_3(Ph_3PO)_3]$ are the only products for the nitrates of Sm–Gd. The later lanthanide nitrates (Tb–Lu) give crystals of $[Ln(NO_3)_3(Ph_3PO)_3]{\cdot}2$ Me_2CO in propanone, but $[Ln(NO_3)_2(Ph_3PO)_4]$ NO_3 in cold ethanol.

A number of $[Ln(NO_3)_3(Ph_3PO)_2(EtOH)]$ Ln = Ce, Nd, Sm, Eu) have also been confirmed. With the less bulky Ph_2MePO, $[Ln(\eta^2\text{-}NO_3)_3(Ph_2MePO)_3]$ are isolated for all lanthanides, and $[La(\eta^2\text{-}NO_3)_3(Ph_2MePO)_4]$, for La only. Ph_3AsO forms $[La(NO_3)_2(Ph_3AsO)_4]$ NO_3, $[La(NO_3)_3(Ph_3AsO)_3]$, and $[La(NO_3)_3(Ph_3AsO)_2(EtOH)]$. A range of complexes have been made for the even less demanding Me_3AsO, such as $[La(Me_3AsO)_6](NO_3)_3$, $[La(\eta^2\text{-}NO_3)_2(\eta^1\text{-}NO_3)(Me_3AsO)_4]$ and $[Eu(NO_3)_3(Ph_3AsO)_3]$.

Lanthanide triflates reacts with Ph_3PO in ethanol forming $[Ln(OTf)_2(Ph_3PO)_4]$ OTf (Ln = La, Nd, Er, Lu). The erbium and lutetium compounds have octahedral coordination, with monodentate triflates, but the complexes of the larger La and Nd have seven-coordination with one triflate being bidentate.

Using hexamethylphosphoramide ($(Me_2N)_3PO$) as a ligand, two series are obtained in which the stoichiometry is maintained across the series, $Ln(HMPA)_6(ClO_4)_3$ and $Ln(HMPA)_3Cl_3$; these are verified crystallographically for $[Nd(HMPA)_6](ClO_4)_3$ and *mer*-$[Ln(HMPA)_3Cl_3]$ (Ln = Pr, Yb). Apart from the direct reaction between the ligand and the appropriate metal salt, such complexes have been made by an unusual ‘one-pot’ synthesis**[59]** by heating the ligand, metal (e.g. La), and the appropriate ammonium salt together in toluene, leading to the isolation of nine-coordinate $La(HMPA)_3(NO_3)_3$, seven-coordinate $La(HMPA)_4(NCS)_3$ (Figure 12), and $La(HMPA)_4Br_3$. Isomorphous *fac*-$[LnCl_3(HMPA)_3]$ (Ln = La, Pr, Nd, Sm, Eu, Gd) have also been synthesised to set alongside the *mer*-isomers; the isomerisation can be followed in solution by NMR, and is believed to occur by an associative mechanism.**[60]**

The application of a solution of SmI_2 in hexamethylphosphoramide as a one-electron reductant in organic syntheses has led to numerous studies of samarium complexes of HMPA. $[SmI_3(HMPA)_4]$, prepared from Sm and CH_2I_2 in HMPA/thf, scavenges traces of water forming $[Sm(HMPA)_2(H_2O)_5]I_3{\cdot}2$ HMPA and $[Sm(H_2O)_4(HMPA)_3]I_3$, both with pentagonal bipyramidally coordinated samarium. Other such complexes reported are $[Sm(H_2O)_5(HMPA)_2]$ $I_3(HMPA)_2$, $[Sm(H_2O)_3(HMPA)_4]$ I_3, $[SmBr_3(HMPA)_2(thf)]$, $[SmBr_2(HMPA)_4]$ $Br{\cdot}thf$, $[SmCl(H_2O)_4(HMPA)_2]$ $Cl_2{\cdot}thf$, $[SmCl(HMPA)_5]$ $(BPh_4)_2$, $[Sm(O_3SCF_3)_2(HMPA)_4]$ (O_3SCF_3), $[Sm(O_3SCF_3)_3(H_2O)(HMPA)_3]$ and $[Sm(HMPA)_3(\eta^2\text{-}NO_3)_3]$.**[61]**

Seven-coordination (distorted pentagonal bipyramidal) is found in the complex of 2,6-dimethylpyrone, Er

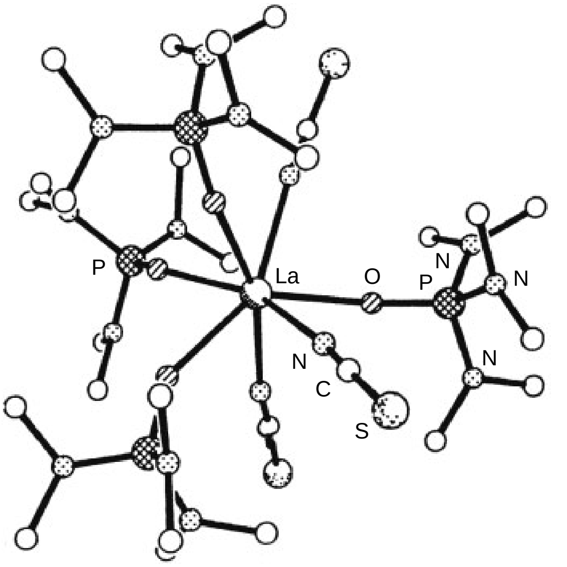

Figure 12 Structure of seven-coordinate $La(HMPA)_4(NCS)_3$

$(DMP)_7(ClO_4)_3$; with the earlier lanthanides this ligand forms $Ln(DMP)_8(ClO_4)_3$, presumably eight-coordinate.

Tetrahydrofuran complexes of the lanthanide chlorides are useful synthetic starting materials where a readily soluble form of the halide is needed, for example, in the synthesis of compounds such as alkoxides, aryloxides, alkylamides, and organometallics in general, though their stoichiometry can be uncertain owing to ready loss of the Lewis base. They are difficult to prepare from the hydrated chlorides; perhaps the best route is sonication of lanthanide powders and C_2Cl_6 in thf. There is a wide range of stoichiometry and structure,[59] with complexes $LnCl_3(thf)_x$ ($x = 2$, 2.5, 3, 3.5, 4) identified, and six different structure types confirmed. The compound actually isolated depends upon the reaction conditions, stoichiometry and the lanthanide concerned. Across the series, there is a decrease in coordination number from 8 (La) to 6 (Lu). Lanthanum is unique in forming $[LaCl_3(thf)_2]$ which is a single-stranded polymer $\ldots La(\mu\text{-}Cl)_3(thf)_2La(\mu\text{-}Cl)_3(thf)_2La\ldots$ with *cis*-thf molecules and square-antiprismatic eight-coordination of lanthanum. Compounds of the same stoichiometry, $[LnCl_3(thf)_2]$ are isolated for Ce–Nd, but have different structures, though again polymeric, in this case with seven-coordination $\ldots\ldots LnCl(thf)_2(\mu\text{-}Cl)_2LnCl(thf)_2(\mu\text{-}Cl)_2\ldots\ldots$ chains. $[LnCl_3(thf)_4]$ have been isolated for Nd–Gd, and are monomeric seven-coordinate complexes, having pentagonal bipyramidal structures with two axial halides. Complexes with the nominal formula $[LnCl_3(thf)_{3.5}]$ are formed from Gd to Tm. These in fact have an ionic structure $[LnCl_2(thf)_5]^+$ $[LnCl_4(thf)_2]^-$, containing a seven-coordinate cation and octahedrally coordinated six-coordinate anion, both with trans-geometries. Ytterbium forms a dimeric $[Cl_2(thf)_2Yb(\mu\text{-}Cl)_2Yb(thf)_2Cl_2]$, whilst both ytterbium and lutetium form a monomeric octahedral *mer*-$[LnCl_3(thf)_3]$ (Ln = Yb, Lu) like scandium. Yttrium forms '$YCl_3(thf)_{3.5}$' and $YCl_3(thf)_2$, which has a chain structure with double chlorine bridges, having pentagonal bipyramidal coordination. Structures have been reported for many individual compounds and far-i.r. spectra of the complexes have been correlated with structural type.[62] Little is known about the bromides, though $Ln(THF)_4Br_3$ (Ln = La, Ce, Nd) are[63] seven-coordinate pentagonal bipyramidal like the corresponding chlorides and $YbBr_3(thf)_3$ has *mer*-octahedral coordination. Iodide complexes $LnI_3(thf)_4$ [Ln = La, Pr] and $LnI_3(thf)_{3.5}$ [Ln = Nd, Sm, Gd, Dy, Er, Tm, Y] are prepared by reaction of the powdered metal and I_2 in thf, followed by Soxhlet extraction. Only two structure types have been identified so far, $PrI_3(thf)_4$ again has a pentagonal bipyramidal structure, whilst $LnI_3(thf)_{3.5}$ [Ln = Nd, Sm, Gd, Y, Yb] have the 'ion pair' structure $[LnI_2(thf)_5][LnI_4(thf)_2]$ (pentagonal bipyramidal cation, octahedral anion) also familiar from the chlorides.[64]

Thiocyanate complexes have been synthesised by metathesis, from $LnCl_3$ and KNCS in thf, followed by filtering off the KCl. The formula, $Ln(NCS)_3(thf)_4$, applies across the series, but falling into two types. The ytterbium compound is a monomer, having a pentagonal bipyramidal structure with two axial thiocyanates. For earlier lanthanides, the same stoichiometry $Ln(NCS)_3(thf)_4$ obtains, but there is association by $Ln\cdots SNC\text{-}Ln$ bridges so lanthanides are in eight-coordinate square-antiprismatic coordination. Ln–S interactions are in region 3.10 Å (Nd) to 3.26 Å (Er), increasing in length as Ln gets smaller suggesting that the interaction weakens as steric crowding increases. These compounds have been obtained for all Ln from Pr to Er.[65] A few nitrate complexes, $[Pr(thf)_4(NO_3)_3]$ and $[Ln(thf)_3(NO_3)_3]$ (Ln = Ho, Yb) have been reported. Some complexes of multidentate ethers exist, such as $[LnCl_3(dme)_2]$, a series made of two families, $[LnCl_3(dme)_2]_2$, dimers with the structure $[Cl_2(dme)_2Ln(\mu\text{-}Cl)_2LnCl_2(dme)_2]$ (Ln = La–Nd), and monomeric $[LnCl_3(dme)_2]$ (Nd–Lu).[66]

Among dimethyl sulfoxide complexes of lanthanide nitrates; early lanthanide nitrates form 10-coordinate $Ln(DMSO)_4(NO_3)_3$ (Ln = La–Gd) while the heavier metals form $Ln(DMSO)_3(NO_3)_3$ (Ln = Tb–Lu, Y). Studies of these complexes in solution indicate that the coordination number depends on the size of the lanthanide, with coordination numbers of 10 for lanthanum, decreasing to eight for Yb–Lu and also upon the DMSO concentration. A similar decrease was found for perchlorate complexes in solution; solid $Ln(DMSO)_8(ClO_4)_3$ compounds, where the perchlorate does not coordinate, have been isolated.[67] The EXAFS spectra of $[Ln(dmso)_8]$ $(CF_3SO_3)_3$ in both the solid state and in dmso solution are very similar, indicating the same coordination geometry in both. Similar pyridine *N*-oxide complexes have been made; with $Ln(pyO)_8(ClO_4)_3$ there is a change in coordination geometry of the $Ln(pyO)_8$ moiety with increasing ionic

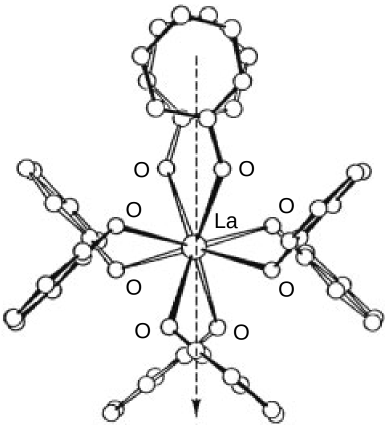

Figure 13 The structure of the $La(pyO)_8^{3+}$ ion

radius of the lanthanide, from square antiprismatic (Nd) to one intermediate between square antiprismatic and dodecahedral for the lanthanum compound (Figure 13).

3.7.5 *Complexes of β-Diketones*[68]

A wide variety of important complexes of *Diketones* (*see Diketones*), $Ln(R^1COCHCOR^2)_3$ has been synthesized and studied extensively. They came into prominence as *NMR Shift Reagents* in the early 1970s, but have subsequently found applications as precursors for high-temperature superconductors and chemical vapour deposition agents. The acetylacetonates (acac; $R = Me$) can be readily made from a lanthanide salt and the diketone with sodium hydroxide in a solvent such as methanol. They crystallize as hydrates, generally containing eight-coordinate $Ln(acac)_3(H_2O)_2$ (La–Ho, Y) (Figure 14) or seven-coordinate $Ln(acac)_3(H_2O)$ (e.g. Yb) molecules. The dihydrate of gadolinium is, however, reported to be a dimer. Some tri- and tetrahydrates are known, but these contain lattice water in addition to $Ln(acac)_3(H_2O)_2$ species (e.g. Eu, Ho). These water molecules can be hard to remove, and more sophisticated synthetic routes to β-diketonates in general begin with convenient starting materials like the oxides. The anhydrous acetylacetonates are not well defined, unlike the corresponding monomeric $M(acac)_3$ complexes formed by the d-block metals. The reasons for this are indicated in a careful study[69] of $Y(acac)_3$, which found that reaction of $[Y\{N(SiMe_3)_2\}_3]$ with Hacac gave hydrocarbon-soluble $[Y(acac)_3]_n$ (from NMR measurements, $n \sim 4$). Inadvertent hydrolysis on attempted slow crystallisation led to $[Y_4(OH)_2(acac)_{10}]$, a molecule with a diamond shaped Y_4 core, having μ_4-OH groups above and below the plane, and each acac terminal, affording eight-coordinate Y. Controlled vacuum thermolysis (85 °C) of $[Y(acac)_3(H_2O)_3]$ gives a product that can be crystallised from benzene to form $[Y_4(OH)_2(acac)_{10}]\cdot C_6H_6$. It is believed that hydrogen-bonding between water molecules and acac oxygens in $[Y(acac)_3(H_2O)_3]$ leads to the loss of acacH on thermolysis. In contrast, complexes of a bulkier ligand such as tmhd (dpm; $R = t$-Bu) readily form anhydrous $Ln(tmhd)_3$ which sublime in vacuo at 100–200 °C and are monomers in solution; they can be separated by gas chromatography. In the solid state they exist as dimers with seven-coordinate metals (La–Dy) and octahedral monomers (Dy–Lu, Y; trigonal prismatic coordination) which do hydrate readily (cf. capped trigonal prismatic $Dy(dpm)_3(H_2O)$).

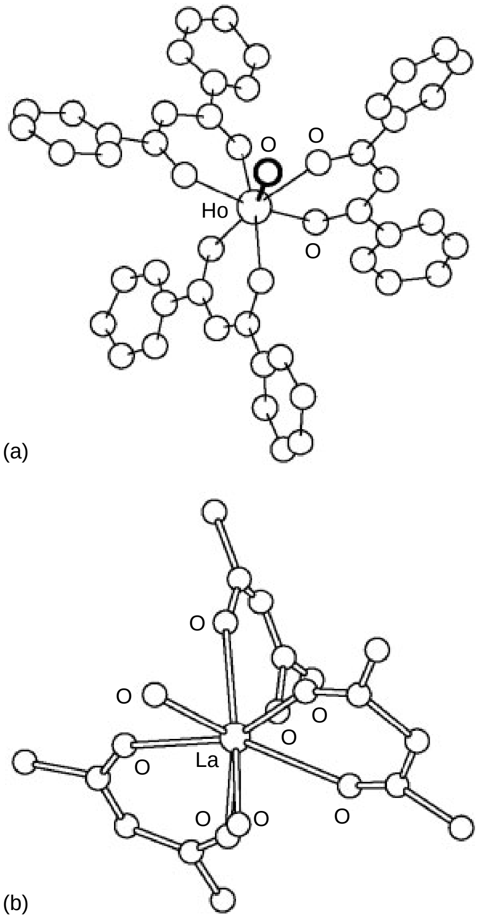

Figure 14 (a) The structure of $Ho(PhCOCHCOPh)_3(H_2O)$. (b) The structure of $La(acac)_3(H_2O)_2$

A similar pattern of decreasing coordination number with decreasing ionic radius is found in complexes of 2,2-dimethyl-6,6,7,7,8,8,8-heptafluorooctane-2,4-dione (fod). Thus $Pr(fod)_3\cdot H_2O$ is in fact dimeric, $[Pr_2(fod)_6(H_2O)]\cdot H_2O$, with eight-coordination completed by a bridging water, whereas $Lu(fod)_3\cdot H_2O$ is a seven-coordinate monomer. As prepared, the complexes are hydrates but can be dehydrated in vacuo and are volatile at 180–260 °C (though they do rehydrate avidly); trifluoro- and hexafluoroacetylacetonates are likewise generally obtained as hydrates which can be dehydrated in vacuo. Because the Ln(diketonate)$_3$ complexes are coordinatively unsaturated, they, as already noted, tend to complete their coordination sphere by forming adducts with Lewis bases, of which the hydrates have already been noted. For this reason, paramagnetic diketonates, especially some of the dpm and fod chelates, are of importance as NMR shift reagents (see Section 'β-Diketonates as NMR Shift Reagents[70–72]').

In addition to the neutral tris complexes, anionic [Ln(diketonate)$_4$]$^-$ species have been isolated for some of the less bulky ligands, such as antiprismatic [Eu(PhCOCHC OPh)$_4$]$^-$.

β-Diketonates as NMR Shift Reagents[70–72]. Paramagnetic lanthanide β-diketonate complexes produce shifts in the NMR spectra of Lewis base molecules capable of forming adducts with them and are thus often referred to as lanthanide shift reagents (LSR), although all paramagnetic lanthanide complexes can exhibit shifted resonances. The initial report (1969) concerned the ability of Eu(dpm)$_3$py$_2$ to induce considerable low-field shifts in the H spectrum of cholesterol; the magnitude of the proton shifts depended upon the distance of the proton from the site of coordination to the lanthanide ion. Subsequently it was realized that the diketonate complexes themselves were more effective than the pyridine adducts and that other lanthanide ions (e.g. Pr) could produce shifts in the opposite direction. Immense activity in this area resulted as the use of LSRs enabled simplification of the spectra of organic molecules (frequently to first order) without the use of high-frequency spectrometers. The spreading out of the spectrum and differential nature of the shifts removed degeneracies and overlaps while study of the shifts, particularly when more than one LSR was used, permitted spatial assignment of the protons (or other resonant nucleus) with concomitant structural information about the organic molecule.

Thus, to give but one example (Figure 15), the aromatic region of the proton NMR spectrum of benzyl alcohol is a singlet at 100 MHz, but on addition of Eu(dpm)$_3$, which coordinates at the OH group, the aromatic protons are shifted by amounts varying with their distance from the coordination site and become amenable to first-order analysis.

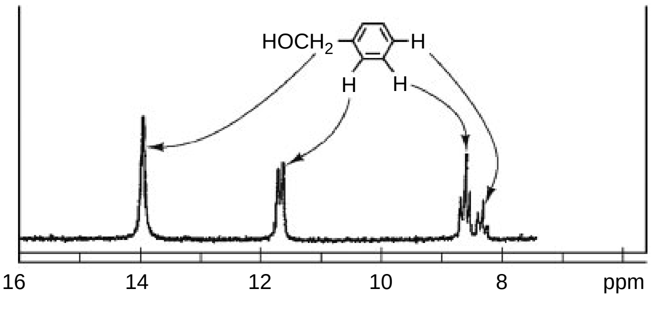

Figure 15 The proton NMR spectrum of benzyl alcohol in the presence of Eu(dpm)$_3$ (0.39 mol). (Reproduced by permission of The Royal Society of Chemistry from J.K.M. Sanders and D.H. Williams, *Chem. Commun.*, 1970, 422)

The lanthanide induced shifts (LIS) arise from the interaction of the magnetic nucleus with the magnetic field of the paramagnetic lanthanide ion. This could arise via two mechanisms: either a 'pseudocontact' (dipolar) through-space fashion involving a dipole–dipole interaction, or by a 'contact' mechanism with delocalization of unpaired spin density from the lanthanide f-orbitals via the lanthanide–substrate bond on to the organic molecule; the former is more important.

Adducts of Diketonates. Because of their involvement in NMR shift reagents, there has been considerable interest in the stoichiometry of the adducts formed between the diketonate complex and the Lewis base. Both 1:1 and 1:2 adducts are possible, the stoichiometry dependent upon the bulkiness of both the diketonate ligand and also upon that of the ligand. Since the species isolated in the solid state may not be the most abundant species in solution, complementary studies are necessary. Thus the M(fod)$_3$ chelates (Pr, Eu) have been found to form 1:1 and 1:2 adducts with a range of Lewis bases (even bulky ones like 2,4,6-Me$_3$py) in solution. The bulkier dpm chelates give isolable 2:1 adducts with pyridine and propylamine (Eu), but with the bulkier 3-picoline, only a 1:1 complex is isolated (Lu). Careful studies of Ho(dpm)$_3$ in solution have only given evidence for 1:1 adducts with bulky ligands such as triphenylphosphine oxide, camphor, and borneol. Some of the adducts vaporize unchanged; thus Ln(hfac)$_3$(Bu$_3$PO)$_2$ can be separated by gas chromatography. Adducts with polyethers have been studied as possible precursors for *Chemical Vapour Deposition* (*see Chemical Vapor Deposition*) as they often exhibit high volatility and good thermal stability. Thus La$_2$O$_3$ and Hhfac react together with tetraglyme in hexane forming [La(hfac)$_3$(tetraglyme)], an air-stable and volatile (95 °C, 10^{-4} mm Hg) substance.

Crystal structures have been determined for many of the adducts. Eu(acac)$_3$(phen) is antiprismatic, but Nd(ttfa)$_3$(Ph$_3$PO)$_2$, Eu(dpm)$_3$(py)$_2$, and Ho(dpm)$_3$(4-picoline)$_2$ are dodecahedral. Of the seven-coordinate adducts, Lu(dpm)$_3$(3-picoline) is a side-face capped trigonal prism and Eu(dpm)$_3$(quinuclidine) a capped octahedron. With the tridentate ligand terpyridyl, nine-coordination is possible as in Eu(dpm)$_3$(terpy); Pr(facam)$_3$(DMF)$_3$ is also nine-coordinate. What may be another case of nine-coordination are the acetylacetonate complexes Ln(acac)$_3$(Ph$_3$PO)$_3$ (Ln = Nd, Sm, Eu, Tb, Dy, Ho).

The geometric differences between one structure and another are often small, and a similar comment may also be made about the energy differences between one structure and another (e.g. square antiprismatic–dodecahedron). The structure adopted for an adduct in the solid state may be different to the one adopted in solution. The assumption of time-averaged axial symmetry for the monoadducts in solution in the interpretation of shifted NMR spectra seems frequently to be justified; however, study of bis adducts of substituted pyridines with $Ln(dpm)_3$ indicate biaxial magnetic anisotropy.

3.7.6 Carboxylates[73]

Carboxylate complexes of the lanthanides differ from those of many trivalent transition metals in that they do not adopt oxo-centered structures with M_3O cores. The hydrated acetates have a long history, with the first examples reported by Cleve in 1874; they can be synthesized by dissolving the oxides in acetic acid and the anhydrous compounds obtained by azeotropic distillation.

Anhydrous $[La(OAc)_3]$ has 10-coordinate La, involving both chelating and bridging acetates (the latter having one oxygen bound to two different lanthanum ions and the second oxygen just bound to one); the Ce analogue is isostructural. Both 9 and 10-coordinate praseodymium are found in $Pr(OAc)_3$; like $La(OAc)_3$, this has a three-dimensional network structure, whereas for the later metals $Ln(CH_3COO)_3$ adopt chain structures. Holmium acetate adopts a structure shared with other $Ln(OAc)_3$ (Ln = Sm–Er, Y); Ho occupies two slightly different eight-coordinate sites, whilst $Ln(OAc)_3$ (Ln = Tm–Lu) have the structure exemplified by $Lu(CH_3COO)_3$, in which Lu is seven-coordinate. On heating, both these structures change to the six-coordinate $Sc(CH_3COO)_3$ structure, this drop in coordination number being accompanied by an acetate group switching to a symmetrical bridging mode.[74]

Among the hydrated lanthanide acetates, mono- and sesquihydrates are found for the early metals (La–Nd); the heavier metals (from Nd) tend towards tetrahydrates, but some trihydrates are known (e.g. Eu, Tm) though for any given lanthanide there may be two or more phases with nearly equal stabilities under ambient conditions. The sesquihydrates $[Ln(CH_3COO)_3 \cdot 1.5H_2O]$ (Ln = La–Pr) have structures with acetate-bridged chains cross-linked by further acetate bridges; the lanthanides being 9 and 10-coordinated by bridging and chelating acetates. Monohydrates $[Ln(CH_3COO)_3 \cdot H_2O]$ (Ln = Ce–Nd) have one-dimensional polymeric structures with acetate bridges, the lanthanides being 9-coordinate in this case, whilst the tetrahydrates $[Ln(CH_3COO)_3 \cdot 4H_2O]$ (Ln = Sm–Lu) are acetate-bridged dimers, the lanthanides again being 9-coordinate. The bridging acetate groups in these compounds are often asymmetric, featuring one oxygen being bound to two lanthanide ions and the other oxygen bound to one lanthanide (this mode of bonding is common in lanthanide carboxylates). Among other carboxylates, $Pr(C_3H_7COO)_3 \cdot 3H_2O$ contains two distinctly different praseodymium sites. Each Pr is coordinated by four bidentate bridging carboxylates; additionally one is bound to three water molecules, the other is additionally bound to two bidentate propionates. $Nd(C_3H_7COO)_3(H_2O)$ has a zigzag chain structure containing 9-coordinate neodymium in capped square-antiprismatic coordination, there being two different neodymium sites. One neodymium is bound to four bridging tridentate carboxylates and one bridging bidentate group, as well as to two waters; the other neodymium is coordinated to four bridging tridentate carboxylates, one bridging bidentate carboxylate, and one chelating carboxylate. $[Ln(CF_3COO)_3 \cdot 3H_2O)]$ (Ln = La, Ce) are two-dimensional polymers containing eight-coordinate lanthanides, whilst $[Ln(CF_3COO)_3 \cdot 3H_2O]$ (Ln = Pr–Lu) have seven-coordinate lanthanides in dimeric units with four bridging carboxylates. $[La(CCl_3COO)_3 \cdot 5H_2O]$ and $[Ce(CCl_3COO)_3 \cdot 3H_2O]$ are linear one-dimensional polymers with nine and eight-coordinate lanthanides respectively. $[Ln(CCl_3COO)_3 \cdot 2H_2O]$ (Ln = Pr–Lu) are also linear polymers with a bridging water molecule rather than just carboxylate bridges. In these compounds the carboxylate groups act as bridging bidentate ligands or as terminal monodentate groups. Anhydrous europium methacrylate, $[Eu(H_2C{=}C(Me)CO_2)_3]$, has a chain structure in which Eu is eight-coordinate, one carboxylate acting as a bidentate bridging ligand and the other two also bridging, but with one oxygen bound to two europiums, the familiar chelate-bridging mode. Both this compound and the acrylates $[Ln(H_2C{=}CHCO_2)_3]$ (Ln = Eu, Tb) undergo radical-induced polymerisation.

Carbonate complexes are increasingly studied because of their importance in mobilising the actinides in the environment; lanthanide complexes are nonradioactive models for the later actinides. The first mononuclear lanthanide carbonate complex to be structurally characterised was $[N(CH_2)_3]_5[Nd(CO_3)_4]$. On the other hand, $[Co(NH_3)_6][Sm(CO_3)_3(H_2O)] \cdot 4H_2O$ has anions linked in a zigzag chain structure with μ-η^2-η^1 carbonate bridges affording nine-coordinate samarium. Similar bridges are found in the one-dimensional chains in $[Co(NH_3)_6]_6$ $[K_2(H_2O)_{10}]$ $[Nd_2(CO_3)_8]_2 \cdot 20H_2O$, formed on mixing solutions of $[Co(NH_3)_6]Cl_3$, $Nd(NO_3)_3$ and K_2CO_3.

The oxalates are very insoluble, affording quantitative precipitation of the lanthanide, a fact made use of in traditional quantitative analysis; on ignition, they are obtained as the oxide, the weighing form. In the solid state, structures show eight-coordination in the hexahydrates and nine-coordination in the nonahydrates such as $Nd_2(C_2O_4)_3 \cdot 9H_2O$.

Structures of the dialkylcarbamates $[Ln_4(O_2CNPr^i_2)_{12}]$ (Ln = Nd, Gd, Ho, Yb) indicate a steady contraction in Ln–O distances, averaging 14%, across the lanthanide series.

3.7.7 Nitrate Complexes

Nitrate complexes are of historical importance for their role in separation of the early lanthanides by fractional crystallization, when magnesium double nitrates, $Mg_3Ln_2(NO_3)_{12} \cdot 24H_2O$, were used. These complexes contain 12-coordinate $[Ln(NO_3)_6]^{3-}$ groups, also found in some crown ether complexes. Other nitrate complexes characterized include 10-coordinate $[Ln(NO_3)_5]^{2-}$, as salts with counterions like Ph_4As and Me_4N. Both these types of complex are characterized across the lanthanide series.

3.7.8 *Complexes of Crown Ethers*[75,76]

Crown ether (*see Crown Ethers*) complexes represent a very important area of lanthanide coordination chemistry that has undergone considerable development in recent years (*see Crown Ethers*). In contrast to the alkali metals, the lanthanides do not form such complexes readily in aqueous media, owing to the considerable hydration energy of the lanthanide ion, but are readily synthesized by operating in nonaqueous solvents. Complexes are obtained both with and without direct lanthanide-crown ether bonds as when $[Ln(NO_3)_3(H_2O)_3]$ is encapsulated by 18-crown-6. The choice is determined by the match between the size of the central cavity in the crown ether ring and the size of the lanthanide ion. Many of the studies have been made with lanthanide nitrate complexes, with the concomitant consequence of high coordination numbers in the resulting complexes on account of the proclivity for bidentate nitrate coordination. Thus 12-coordination is found in $La(NO_3)_3$(18-crown-6) (Figure 16), 11-coordination in $Eu(NO_3)_3$(15-crown-5), and 10-coordination in $Eu(NO_3)_3$(12-crown-4).

In addition to the 1:1 complexes, some other stoichiometries have been obtained; thus Nd(18-crown-6)$_{0.75}$ $(NO_3)_3$ is actually [Nd(18-crown-6)$(NO_3)_2]_3[Nd(NO_3)_6]$ with 10-coordination in the cation and 12-coordination in the anion.

The first crown ether complexes to be made were usually with lanthanide nitrates; when crown ethers complex with lanthanide nitrates, the two ligands generally combine to saturate the coordination sphere, but since chloride is a monodentate ligand, coordinative saturation is not always achieved that way and indeed chlorides are frequently displaced from the coordination sphere by water. Thus 12-crown 4 tends to give complexes of the type $[Ln(H_2O)_5$(12-C-4)] $Cl_3{\cdot}2H_2O$ (Ln e.g. Er) and $[LnCl_2(H_2O)_2$(12-C-4)] $Cl{\cdot}2H_2O$ (Ln e.g. Nd) but coordinating ability is affected by the presence of water and other solvents. The crown ether does not coordinate to the lanthanide at all in $[Lu(H_2O)_8]$ 1.5(12-C-4)$\cdot 2H_2O$, instead forming hydrogen bonds to coordinated water molecules. With the larger lanthanum ion, $[LaCl_3$(12-crown-4)(MeOH)] is eight-coordinate, owing to a molecule of solvent coordinating. 18-crown-6 forms two series of complexes with lanthanide chlorides $[LnCl(H_2O)_2$(18-crown-6)]$Cl_2{\cdot}2H_2O$ (Ln = Pr–Tb) and $[LnCl_2(H_2O)$ (18-crown-6)]$Cl{\cdot}2H_2O$ (Ln = La, Ce) although, depending upon conditions, $[LnCl_3$(18-crown-6)] can also be made. Its inability to form complexes with the chlorides of the smaller lanthanides is ascribed to a lack of flexibility found in polyethylene glycols, which can. By modifying conditions, different complexes can be isolated; thus in MeCN/MeOH, neodymium chloride and 15-crown-5 react to afford complexes where $[Nd(H_2O)_9]^{3+}$ and $[NdCl_2(H_2O)_6]^+$ ions are hydrogen-bonded to the crown ether, without direct lanthanide–crown ether bonding. However, by electrocrystallization the anhydrous eight-coordinate complex Nd(15-crown-5)Cl_3 with neodymium–crown ether bonding is obtained (Figure 17).

Unusually, chloride is found in the first coordination sphere of lanthanum as well as nitrate in the serendipitously discovered mixed anion complexes $[LaCl_2(NO_3)$(12-crown-4)$]_2$ and $[LaCl_2(NO_3)$(18-crown-6)]. A few complexes have been reported with other halides, such as $[SmI_3$(dibenzo-18-crown-6)] (tricapped trigonal prismatic) and $[LaBr_3$(12-crown-4)(acetone)] (distorted square antiprismatic). Lanthanide thiocyanate complexes of crown ethers are now starting to be studied. Several thiocyanate complexes of the

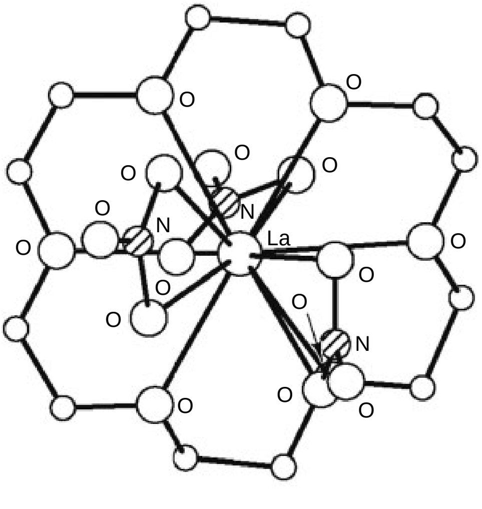

Figure 16 The structure of $La(NO_3)_3$(18-crown-6)

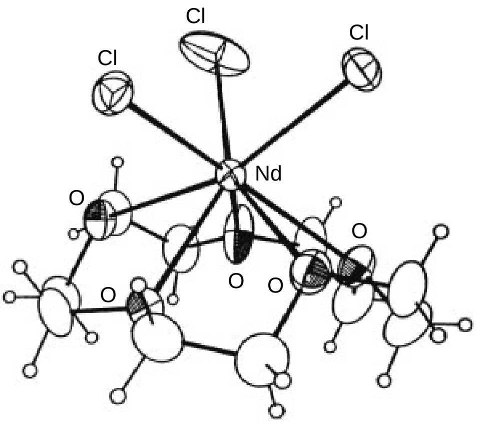

Figure 17 The structure of $NdCl_3$(15-crown-5)

tetradentate 13-crown-4 have been isolated in [Ln(NCS)$_3$(13-crown-4)(H$_2$O)$_2$] (Ln = La, Pr–Tb, Er–Yb) whilst lanthanum is 10-coordinate in [La(NCS)$_3$(18-crown-6)(dmf)] In the compounds [Ln(dibenzyldiaza-18-crown-6)(NCS)$_3$] (Ln = Ce, Nd, Eu), the lanthanide is bound to two nitrogens and four oxygens in the crown ether as well as three N-bonded thiocyanates. The CeN$_3$ (NCS) moiety exists as a trigonal planar arrangement at the centre of the macrocycle cavity with the trigonal plane perpendicular to the plane of the macrocycle. Steric factors can be important in complexation. Thus only the lighter, larger, lanthanides form stable complexes with 18-crown-6. Small crowns such as 12-crown-4 give 2:1 complexes with lanthanide perchlorates, although these are not obtained with lanthanide nitrates where the anion can readily coordinate.

Crown ethers have been used to stabilise alkyl complexes, in the form of [Ln(CH$_2$SiMe$_3$)$_3$(12-crown-4)] (Ln = Sc, Y, Sm, Gd, Tb, Dy, Ho, Er, Tm, Yb, Lu); structures of the Y and Lu complexes show facial coordination of the crown ether to the neutral lanthanide trialkyl unit. The cationic species [Ln(CH$_2$SiMe$_3$)$_2$(CE)(thf)$_n$]$^+$ [B(C$_6$X$_5$)$_3$(CH$_2$SiMe$_3$)]$^-$ (CE = [12]-crown-4, $n = 1$; CE = [15]-crown-5, [18]-crown-6, $n = 0$) have also been made.

Comparative studies between crown ethers and the noncyclic glymes (linear polyethers) suggest that glyme complexes are favoured, the chelate effect is thus more important than the macrocyclic effect. The ability of polyethylene glycols and glymes to wrap themselves round a lanthanide ion irrespective of size, and to accommodate water molecules and other small ligands (e.g. anions) more easily, makes them more flexible coordinating agents than crown ethers and giving a more favorable enthalpy change. Solubility effects may play a part too! The factors affecting the complexes formed by LnX$_3$, Ln(NCS)$_3$ and Ln(NO$_3$)$_3$ with polyethylene glycols have been examined; the chain length is the main factor controlling the coordination sphere and thus the number of additional inner-sphere ligands present. Pentaethylene glycol forms two series of nine-coordinate complexes with lanthanide chlorides, [LnCl$_2$(H$_2$O)(EO5)]Cl·2H$_2$O (Ln = La–Pr) and [Ln(H$_2$O)$_3$(EO5)]Cl$_3$·H$_2$O (Ln = Sm–Lu, Y). [Ln(EO3)$_3$]Cl$_3$ (Ln = Pr, Nd) are nine-coordinate, as are the lanthanides in [Ln(EO2)$_3$] (ClO$_4$)$_3$·3H$_2$O (Ln = Nd, Ho), whilst the lanthanide is 11-coordinate in [Nd(EO4)(NO$_3$)$_3$]. Cerium is nine-coordinate in [Ce(NCS)$_3$(EO4)(H$_2$O)].

Other significant complexes of this type, containing one or more lanthanides, are formed by calixarenes (*see Calixarenes*).[77,78] Much of this work has been prompted by their potential in separating lanthanides from uranium and other metals. A calixarene ligand with two amide substituents has been synthesised as an extractant for lanthanides; dimeric Sm and Eu and monomeric Lu complexes have been prepared. Another calixarene, with four phosphine oxides attached, has been fixed to silica particles and the resulting system has been found to give very efficient extraction of Eu^{3+} and Ce^{3+} from simulated waste. A calix[4]arene complex of Gd^{3+} binds noncovalently to human serum albumin and is a potential MRI contrast agent.

3.7.9 Halide Complexes[79]

Complexes with all the halides have been prepared, but the chlorides and particularly the fluorides are most stable and best characterized. The fluorides ALnF$_4$, A$_2$LnF$_5$, and A$_3$LnF$_6$ are known (A = alkali metal). The tetrafluoro complexes NaLnF$_4$ exist in two phases, the high-temperature form having eight-coordinate lanthanide (fluorite structure) while tricapped trigonal prismatic nine-coordination is found in the low-temperature form. Some hexafluoro complexes have the cryolite structure.

Six-coordinate chloride complexes Cs$_2$NaLnCl$_6$ with the cubic elpasolite structure have been made by fusion; the Ln^{3+} ions on the highly symmetric cubic sites exhibit very weak f–f transitions in their electronic spectra. (NH$_4$)$_3$YCl$_6$ and A$_3$LnCl$_6$ (Ln = Tb–Lu, Y) can be made similarly. Other hygroscopic complexes of the type (Ph$_3$PH)$_3$LnX$_6$ and (pyH)$_3$LnX$_6$ (X = Cl, Br, I) can be made by solution methods; the iodides are unusual and rather unstable. Octahedral YbCl$_6{}^{3-}$ units are found in (MeNH$_3$)$_4$YbCl$_7$. Compounds M$_2$LnCl$_5$ contain chains based on LnCl$_6$ octahedra sharing *cis* corners (X-ray for Cs$_2$DyCl$_5$; Ln = Y, heavy lanthanide). A different type of shared octahedra is found in a number of compounds M$_3$Ln$_2$X$_9$, where face sharing of octahedra obtains. A number of chlorides have been made (M = K or Cs) as well as several bromides and iodides such as Cs$_3$Y$_2$X$_9$ and Cs$_3$Er$_2$I$_9$.

3.7.10 Complexes of N-Donor Ligands[4,5]

Although pyridine and other amine-type ligands form adducts with lanthanide diketonates, few other lanthanide complexes have been made. However, the first homoleptic lanthanide ammine complexes, [Yb(NH$_3$)$_8$] [Cu(S$_4$)$_2$]·NH$_3$, [Yb(NH$_3$)$_8$] [Ag(S$_4$)$_2$]·2 NH$_3$, and [La(NH$_3$)$_9$] [Cu(S$_4$)$_2$], have been synthesised by reactions in aqueous ammonia.[80]

Direct reaction of the lanthanide halides with pyridine gives pyridine complexes of the lanthanides, with the synthesis of [YCl$_3$py$_4$] and [LnCl$_3$py$_4$]·0.5py (Ln = La, Er). These all have pentagonal bipyramidal structures, with two chlorines occupying the axial positions.[81] [MI$_3$py$_4$] (M = Ce, Nd) have also been reported. Various complexes of *N*-methylimidazole (*N*-Meim) have been made, [SmI$_3$(thf)$_3$] reacts with *N*-Meim forming square-antiprismatic [Sm(Meim)$_8$]I$_3$, whilst [YX$_2$(*N*-Meim)$_5$]$^+$X$^-$, (X = Cl, Br); [YCl$_2$(*N*-Meim)$_5$]$^+$ [YCl$_4$(*N*-Meim)$_2$]$^-$ and [Ce(NO$_3$)$_3$(*N*-Meim)$_4$] have also been prepared.

A number of MeCN complexes [Ln(MeCN)$_n$] X$_3$ have been made, with routes including the reaction of LnCl$_3$ with AlCl$_3$ in MeCN; reaction of the labile complexes La(OSO)$_x$(AsF$_6$)$_3$ with MeCN; and ultrasonication of mixtures of the lanthanide metal with AlCl$_3$ and MeCN in C$_2$Cl$_6$.

Structures of $[La(MeCN)_9]$ $(AsF_6)_3{\cdot}MeCN$; $[Sm(MeCN)_9]$ $(AsF_6)_3{\cdot}3MeCN$; $[Ln(MeCN)_9]$ $(AlCl_4)_3{\cdot}MeCN$ (Ln = Pr, Sm) and $[Yb(MeCN)_8]$ $(AlCl_4)_3$ are all known, the $[Ln(MeCN)_9]^{3+}$ ions having the familiar tricapped trigonal prismatic coordination of the lanthanide.[82]

The best studied monodentate N-donor is the thiocyanate ion, recent extensive studies[83] by Japanese workers showing it to participate in complexes with an interesting variety of stoichiometry and coordination geometry dependent upon counterion, solvent, and so on. They comprise $(Bu_4N)_3[M(NCS)_6]$ (M = Y, Pr–Yb) and $(Et_4N)_3[M(NCS)_6]{\cdot}$benzene (M = Er, Yb) with octahedrally coordinated lanthanide; $(Et_4N)_4[M(NCS)_7]{\cdot}$benzene (M = La, Pr with capped trigonal prismatic geometry) and $(Me_4N)_4[M(NCS)_7]$, (M = Dy, Er, Yb; pentagonal bipyramidal coordination); $(Et_4N)[M(NCS)_4(H_2O)_4]$ (M = Nd, Eu) and $(Me_4N)_3[M(NCS)_6(MeOH)(H_2O)]$ (M = La–Dy, Er), all square antiprismatic; $(Et_4N)_4[M(NCS)_7(H_2O)]$ (M = La–Nd, Dy, Er; cubic); and $(Me_4N)_5[M(NCS)_8]{\cdot}$benzene (M = La–Dy), intermediate between square antiprism and cubic.

A considerable number of complexes have been made using bidentate 1,10-phenanthroline, 2,2′-bipyridyl and similar ligands. Usually (but not invariably) phen and bipy form complexes with similar formulae and structures. Reaction of the hydrated lanthanide nitrate and the ligand in ethanol give complexes $LnL_2(NO_3)_3$ (L = phen, bipy), which have been studied in more detail than the others; both series are isomorphous throughout,[84] so all appear to possess 10-coordinate structures (Figure 18) with all nitrates present as coordinated bidentate groups (X-ray diffraction, L = bipy, Ln = La, Pr, Nd, Eu, Lu, Y; L = phen, Ln = La, Pr, Nd, Sm, Eu, Gd, Dy, Lu, Y) with a geometry approximating to a bicapped dodecahedron.[85] In the solid state, the individual complex molecules of $[Ln(phen)_2(NO_3)_3]$ associate by $\pi - \pi$ stacking into one-dimensional chains which themselves arrange into pseudo 1D close-packed patterns. Several tris complexes, $M(bipy)_3(NO_3)_3$, have been synthesised in a water-ethanol mixture, the Nd complex being shown to be $Nd(bipy)_2(NO_3)_3{\cdot}$bipy. In the presence of 15-crown-5, lanthanum nitrate reacts with bipy in MeOH-MeCN forming $[La(bipy)(NO_3)_3(H_2O)_2(MeOH)]{\cdot}$15-crown-5, which has 11-coordinate lanthanum. The presence of the coordinated MeOH molecule supplies a fifth hydrogen atom so that hydrogen bonds can be formed to all the crown ether oxygens. In another synthesis in the presence of a crown ether, a 10-coordinate complex, $[La(bipy)(NO_3)_3(H_2O)_2]{\cdot}$benzo-15-crown-5, is obtained. A complex of composition $La(phen)_4(NO_3)_3{\cdot}3H_2O$ is in fact $[La(phen)_2(H_2O)_2(NO_3)_2]{\cdot}NO_3.\,2\,phen.H_2O$ with intermolecular $\pi - \pi$ stacking (a phenomenon which is quite common in phen complexes of the lanthanides).

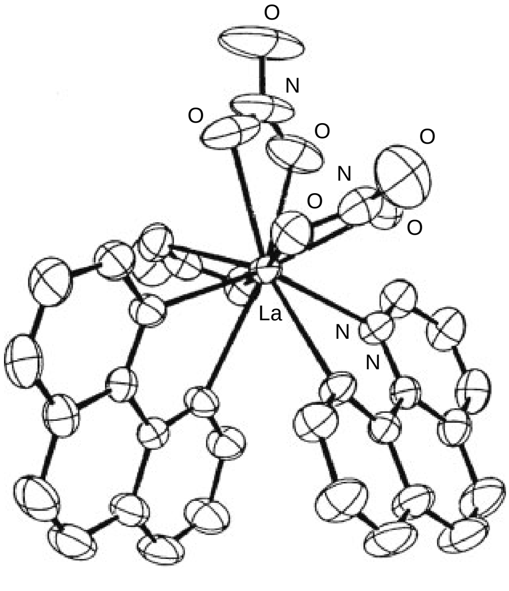

Figure 18 The structure of $La(phen)_2(NO_3)_3$

An extremely wide range of both 1:1 and 2:1 complexes of lanthanide chlorides with bipy and phen have lately received detailed and extensive crystallographic study.[86] For the 1:1 complexes of early lanthanides (La, Pr), the tendency seems to be for the formation of neutral complexes containing all available chloride ions, often binuclear in composition, usually containing at least two solvent molecules per lanthanide. By later in the series, mononuclear species tend to become more normal, and chloride ions are often excluded from the coordination sphere by solvent molecules. In the case of the 2:1 complexes, nine-coordination is possible at the start of the series in $[(bipy)_2Ln(OH_2)_4Cl]Cl_2{\cdot}2H_2O$, whilst by the end of the series ytterbium is seven-coordinate in $[(bipy)_2YbCl_3]$. M–N bond lengths contract from 2.724–2.787 Å in the lanthanum compound to 2.439–2.479 Å in the ytterbium compound. The situation has been described as 'a multidimensional jigsaw puzzle which still requires a great deal of work for its complete description'. Bipyridyl complexes of known structure include $[(bipy)_2Cl_2La(\mu\text{-}Cl)_2LaCl_2(bipy)_2]{\cdot}EtOH$, $[(bipy)_2Pr(OH_2)Cl_3]{\cdot}0.5EtOH$, $[(bipy)_2Ln(OH_2)Cl_3]{\cdot}EtOH$ (Ln = Nd, Eu) $[(bipy)Ln(OH_2)_6]Cl_3$ (Ln = Ho–Lu, Y), and $[(bipy)_2YbCl_3]$.; phen complexes include $[(phen)_2Ln(OH_2)Cl_3]{\cdot}MeOH$ (Ln = La, Pr, Nd, Eu), $[(phen)_2La(OH_2)_5]Cl_3{\cdot}phen{\cdot}4H_2O$ and $[(phen)_2Lu(OH_2)_4]Cl_3{\cdot}2H_2O$. An apparent 3:1 complex, $La(phen)_3Cl_3{\cdot}9H_2O$ has been shown to be $[La(phen)_2(OH_2)_5]Cl_3{\cdot}4H_2O{\cdot}phen$; the ability of phen molecules to be held in lattice sites by $\pi - \pi$ interaction with coordinated phenanthroline molecules is not uncommonly encountered. Complexes with lanthanide bromides do not seem to have received attention, but one iodide complex, $[CeI_3(bipy)_2(py)]{\cdot}5py{\cdot}bipy$ has been reported.

The thiocyanate complexes $Ln(phen)_3(NCS)_3$ (Ln = Pr, Nd) and $Pr(bipy)_3(NCS)_3$ are all nine-coordinate monomers.[85,87] A considerable number of bipy (and phen) adducts of lanthanide dithiocarbamates $[Ln(S_2CNR_2)_3(L)]$

have been synthesised, usually by one-pot syntheses involving a lanthanide salt, NaS_2CNR_2 and the neutral ligand. The interest here is in the potential of these compounds as precursors to lanthanide sulphides. Monomeric 8 coordinate structures are confirmed for $[Ln(S_2CNEt_2)_3(bipy)]$ (Ln = Pr, Sm, Eu, Er)[85] and $[Ln(S_2CNEt_2)_3(phen)]$ (Ln = Sm, Eu, Yb). $[Eu(L)(S_2PBu^i_2)_3]$ (L = phen, bipy) have also been made.

Carboxylate complexes are frequently dimeric. Thus $Lu(O_2CCH_3)_3\cdot(phen)\cdot H_2O$ is dinuclear $[(phen)(CH_3COO)Lu(\mu\text{-}O_2CCH_3)_4Lu(CH_3COO)(phen)]$. The terminal acetate groups are symmetrically bidentate; two of the bridging acetates are symmetrical, the other pair bridging in such a way that one of the two oxygens is bound to both lutetiums and the other is bound only to one lutetium. Similarly, $Ln(OAc)_3\cdot phen$ (Ln = Gd, Ce) are $[(AcO)(phen)Ln(\mu\text{-}OAc)_4Ln(phen)(OAc)]$ with two types of bridging acetate. The cerium compound gives a triplet EPR (*see Electron Paramagnetic Resonance*) spectrum at 4.2 K, showing an appreciable bridging interaction between the two ceriums ($D = 0.21\,cm^{-1}$); magnetic measurements to low temperatures on both compounds confirm weak interactions between the two metal ions. $[\{Pr(O_2CCMe_3)_3(bipy)\}_2]$ has two bidentate bridging and two tridentate cyclic bridging carboxylates; praesodymium is nine-coordinate.

The only complex with a non coordinating anion to be characterised fully is $[Ce(phen)_4(MeCN)_2]\ (ClO_4)_3\cdot 3MeCN$, which has 10-coordinate cerium in a bicapped square-antiprismatic geometry.

Another bidentate ligand whose complexes have been studied in some detail is 1,8-naphthyridine (naph) which, like nitrate, has a small bite angle and is similarly capable of affording high coordination numbers; two types of perchlorate complexes have been made, $M(naph)_6(ClO_4)_3$ (M = La–Pr) and $M(naph)_5(ClO_4)_3$ (M = Nd–Eu). The former complexes have 12-coordinate lanthanides, confirmed by diffraction methods for the praesodymium complex. The change in stoichiometry is doubtless a manifestation of the lanthanide contraction.

A number of complexes of 1,2-diaminoethane have been made. Infrared evidence for the complexes $Ln(en)_4(NO_3)_3$ indicated the presence of coordinated nitrate for the earlier metals, so that the complexes were formulated $[Ln(en)_4(NO_3)](NO_3)_2$ (La–Sm) and $[Ln(en)_4](NO_3)_3$ (Eu–Lu). Other complexes isolated include perchlorates $[Ln(en)_4](ClO_4)_3$ (Ln = La–Nd), chlorides, $Ln(en)_4Cl_3$, $[La(en)_4Cl]\ In_2Te_4$ and $[Y(en)_4](SH)_{2.72}I_{0.28}$, the latter two having nine- and eight- coordination respectively.

Complexes of the lanthanides with the rather similar terdentate ligands 2,2′:6′,2″-terpyridyl (terpy), 2,4,6-tris-2-pyridyl-1,3,5-triazine (tptz), 4-amino-bis(2,6-(2-pyridyl))-1,3,5-triazine (abptz), and related ligands have been studied in considerable detail and number, as these terdentate N-donor ligands are efficient in separating actinides from lanthanides selectively by solvent extraction, of obvious relevance to processing nuclear waste.

Reaction of aqueous lanthanide chlorides with alcoholic solutions of terpy affords complexes $Ln(terpy)Cl_3\cdot xH_2O$ ($x = 6-8$). They contain $[Ln(terpy)Cl(H_2O)_n]^{2+}$ ions (Ln = La–Nd, $n = 5$; Ln = Sm–Lu, $n = 4$). Within these two families of cations, there are the expected contractions in bond length with increasing atomic number (and decreasing ionic radius). Thus on going from La to Nd in the series of $[Ln(terpy)Cl(H_2O)_5]^{2+}$ ions, there are contractions in Ln–Cl, from 2.903 (2) to 2.855 (1) Å; in average Ln–N distance, from 2.688 to 2.616 Å; and in average Ln–O distance, from 2.561 to 2.505 Å. Similarly, in the $[Ln(terpy)Cl(H_2O)_4]^{2+}$ ions, on passing from Sm to Lu, there are decreases in Ln–Cl, from 2.794 (2) to 2.665 (2) Å; in the average Ln–N distance, from 2.513 to 2.457 Å; and in average Ln–O distance, from 2.475 to 2.317 Å. There are two families of bromide complexes, nine-coordinate $[Ln(terpy)(H_2O)_6]Br_3\cdot H_2O$ (Ln = La–Er) and eight-coordinate $[Ln(terpy)(H_2O)_5]Br_3\cdot 3H_2O$ (Ln = TmLu) all isolated from water-ethanol mixtures. Unlike in the chlorides, there is no bromide in the coordination sphere, a reflection of the weaker σ-donor power of bromide (though no studies have been reported in nonaqueous solvents). A hydroxy-bridged dimeric species to be formed with the heavier lanthanides, but usually acidification converts it into the mononuclear complex. The dimers contain bridging hydroxy groups, not halides, again reflecting the decreasing coordinating power of bromide. Iodide complexes have been isolated using nonpolar solvents, thus terpy reacts with solutions of LnI_3 in anhydrous pyridine forming eight-coordinate $[Ln(terpy)_2I_2]I$ (Ln = Ce, Nd), whilst $[Ce(terpy)_2I_2]I$ crystallises from slightly damp solvents forming nine-coordinate $[Ce(terpy)_2I_2(H_2O)]$ I. A comparison of structural data for $[Ce(terpy)_2I_2(H_2O)]I$ and $[U(terpy)_2I_2(py)]I$ indicates that the average U-N distance is shorter by about 0.05 Å, though on size grounds they would be expected to be very similar. This shortening may reflect a π back-bonding interaction between the 5f orbitals of uranium and the terpyridyl ligand which is absent in the lanthanide complex. Thiocyanate complexes $[Ln(terpy)_2(NCS)_3]$ (Ln = Pr, Nd), contain nine-coordinate lanthanides.[87]

Reaction of terpy with lanthanide perchlorates in MeCN affords $[La(terpy)_3](ClO_4)_3\cdot 2MeCN\cdot 0.67H_2O$, $[Ln(terpy)_3](ClO_4)_3\cdot MeCN.H_2O$ (Ln = Ce, Pr, Sm, Eu), $[Ln(terpy)_3](ClO_4)_3$ (Eu, Lu, Y); all of these have nine-coordinate $[Ln(terpy)_3]^{3+}$ cations with near-D_3 symmetry,[88] a structure originally deduced from the fluorescence spectrum of the europium complex and subsequently confirmed by X-ray diffraction (Figure 19).

Complexes of 4-alkylated terpyridyls, $[Ln(4\text{-}Rterpy)_3](ClO_4)_3$ (Ln = La, Eu, Tb; R = Et, Bu^t) have much higher luminescence efficiency, possibly due to the bulk of the alkyl group preventing approach of deactivating molecules, as well as their electronic effects.

The chemistry of lanthanide nitrate complexes of terpy is complicated;[89,90] various formulae occur, depending not

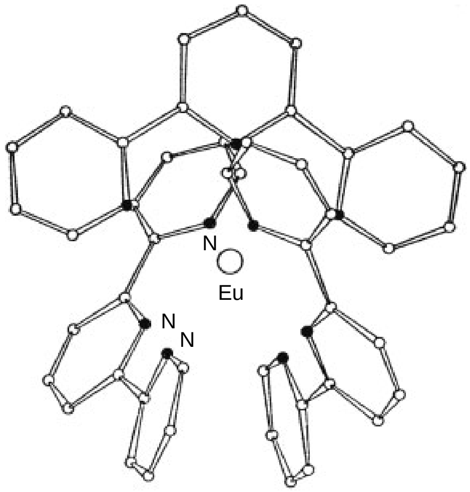

Figure 19 The structure of $Eu(terpy)_3{}^{3+}$

least upon the solvent used. Reaction of a 1:1 molar ratio of the hydrated lanthanide nitrate with terpy in MeCN, the initial products are $[Ln(terpy)(NO_3)_3(H_2O)_x]$. For the later lanthanides, $Ln(terpy)(NO_3)_3(H_2O)\cdot terpy$ (Ln = Ho, Er, Tm, Yb) can be obtained when an excess of terpy is used. Simple 1:1 complexes $Ln(terpy)(NO_3)_3(H_2O)$ (Ln = Nd, Eu, Tb) and $Ln(terpy)(NO_3)_3$ (Ln = Yb, Lu) have been described. All these complexes feature solely bidentate nitrates. In $[Lu(terpy)(NO_3)_3]$, the Lu–N distances are 2.379–2.407 Å and Lu–O bonds fall into the range 2.350–2.440 Å, so that even with the smallest lanthanide ion, all the nitrates are symmetrically bidentate. In contrast to the early lanthanides, where the same complex is obtained from synthesis in either acetonitrile or ethanol, the choice of solvent affects the structure for the 1:1 complexes of later lanthanides, with $[Ln(terpy)(NO_3)_3\cdot(C_2H_5OH)]$ (Ln = Y, Ho–Lu) being obtained from ethanol. These contain contains two bidentate nitrates and one monodentate nitrate as well as a coordinated ethanol, the lanthanide being nine-coordinate. Replacement of a bidentate nitrate trans- to the terpy by a coordinated ethanol and a monodentate nitrate causes a little reorganization in the coordination sphere; the $Lu–O(ONO_2)$ distance is 2.279 (3) Å, showing that the Lu–O bond is about 0.1 Å shorter than for an oxygen atom in a bidentate nitrate group. A second oxygen in this monodentate nitrate is hydrogen-bonded to the coordinated ethanol molecule (Lu–O = 2.297 (3) Å). Another feature of these compounds is short C–H···O interactions involving nitrate oxygens and hydrogens of the terpyridyl ligand in other molecules. Use of methanol as the reaction solvent results in a different product for La and Ce only, 11-coordinate $[La(NO_3)_3(terpy)(MeOH)_2]$ (Ln = La, Ce). If the hydrated lanthanide nitrates are reacted with 1 mol of terpy in MeCN, followed by recrystallisation of the initial complex from water, different complexes are obtained, 10-coordinate $[Ln(terpy)(NO_3)_2(H_2O)_3]\ NO_3$ (Ln = La–Gd) and nine-coordinate $[Ln(terpy)(NO_3)_2(H_2O)_2]\ NO_3\cdot 2H_2O$ (Ln = Tb, Lu, Y). They result from solvolysis by water of a nitrate group in $[Ln(terpy)(NO_3)_3(H_2O)_x]$. Structures show a girdle of ligands comprising a virtually planar terdentate terpy ligand and two or three water molecules coordinated round the lanthanide, with bidentate nitrates completing the coordination sphere above and below the metal ion.

Most lanthanide nitrate complexes have a 1:1 metal:terpy ratio. However, the complex $Ln(terpy)_{1.5}(NO_3)_3$ was isolated from a MeCN solution with a 8:1 terpy:La ratio and was found to be $[Ln(terpy)_2(NO_3)_2]^+\ [Ln(terpy)(NO_3)_4]^-$. Reaction of hydrated lanthanide nitrates with up to 4 mols of terpy in CH_3CN afford complexes with a similar 1.5:1 stoichiometry, $[Ln(terpy)_2(NO_3)_2]^+\ [Ln(terpy)(NO_3)_4]^-$ (Ln = Nd, Sm, Tb, Dy, Ho). In these, the lanthanide is 10-coordinate in both the cation and the anion, one nitrate group in the anion being monodentate, in contrast to the anion in the 1.5:1 complex of the larger lanthanum ion, where all nitrates are bidentate, this is evidently a consequence of congestion arising around the smaller lanthanide ions. Ce is also 11-coordinate in $(Hpy)[Ce(NO_3)_4(terpy)]\cdot py$. The $[Sm(terpy)(NO_3)_4]^-$ anion has also been isolated as the $(terpyH_2)^{2+}$ salt, this has an 11-coordinate anion with four bidentate nitrates, in contrast to the three bidentate and one monodentate group in the $[Sm(terpy)_2(NO_3)_2]^+$ salt, so solid-state packing effects seem important in determining coordination geometry.

A few lanthanide carboxylate complexes of terpy have been made, such as mononuclear $[Yb(O_2CCCl_3)_3\cdot(terpy)\cdot MeOH]$ in which coordinated methanol and two unidentate carboxylates and one bidentate carboxylate afford eight-coordinate ytterbium; in dimeric $[Ln(O_2CCCl_3)_3\cdot(terpy)\cdot(H_2O)]_2$ (Ln = La–Nd) the lanthanides are nine-coordinate. Some mixed-ligand quaternary complexes involving terpy, $[Ln(terpy)(NO_3)_2(acac)(H_2O)_n]$ (Ln = La, Pr, $n = 1$; Ln = Nd–Lu, $n = 0$), exhibit three different solid-state structures. $[La(terpy)(NO_3)_2(acac)(H_2O)]$ is 10-coordinate, with two bidentate nitrates and a chelating diketonate and a coordinated water; $[Pr(terpy)(NO_3)_2(acac)(H_2O)]$ is nine-coordinate, with one monodentate and one bidentate nitrate and a chelating diketonate and a coordinated water; and the remainder are $[Ln(terpy)(NO_3)_2(acac)]$ (Nd–Lu) with two bidentate nitrates and a chelating diketonate.

Structures are known of three types of complex of $tptz\cdot[Sm(tptz)(NO_3)_3(H_2O)]\cdot 2H_2O$ has 10-coordinate Sm with all nitrates bidentate; $[Eu(tptz)Cl_3(MeOH)_2]\cdot 2MeOH$ features eight-coordinate europium, and in dimeric $[Pr(tptz)(OAc)_3]_2\cdot 2MeOH$ praseodymium achieves 10-coordination through forming double (η^2,μ-1,1) acetate bridges familiar in other lanthanide carboxylate complexes. A study[91] of complexes of 4-amino-bis(2,6-(2-pyridyl))-1,3,5-triazine (abptz) with all the lanthanide nitrates gives a good deal of insight into how the stoichiometry and structure of complexes depend upon factors such as the radius of the metal ion, the composition of the reaction mixture and the solvent employed. Complexes whose structures are known are $[La(abptz)(NO_3)_3(H_2O)_2]$ (11-coordinate), $[Ln(abptz)(NO_3)_3(H_2O)]$ (Ln = La, Pr–Sm; 10-coordinate), $[Ln(abptz)(NO_3)_3(H_2O)]$ (Ln = Yb, Y; nine-coordinate, with one monodentate nitrate), $[Ln(abptz)(NO_3)_2(H_2O)_3]NO_3$ (Ln = Nd, Sm; 10- coordinate) and $[Ln(abptz)(NO_3)_2(H_2O)_2]$ NO_3(Ln = Eu–Lu; nine-coordinate). Unlike the succeeding metals, La forms 10 and 11-coordinate $[La(abptz)(NO_3)_3(H_2O)_n]$ ($n = 1, 2$), showing that the position of lanthanum as the largest lanthanide ion sometimes causes it to behave atypically; these complexes have similar solubilities and crystallize from the same reaction mixture. If the structures of these two complexes are compared, it can be seen that the decrease in coordination number from 11 to 10 is accompanied by a decrease in La–O (water) distance from 2.589 (4) and 2.610 (4) Å to 2.483 (5) Å; similarly, the La–N distances decrease from 2.739 (4), 2.755 (5) and 2.805 (6) in the 11-coordinate compound to 2.576 (5), 2.625 (5) and 2.641 (5) Å in 10-coordinate $[La(abptz)(NO_3)_3(H_2O)]$. The range of La–O (nitrate) distances decreases from 2.628 (4) – 2.702 (5) Å (with an outlying member at 2.805 (6) Å) in $[La(abptz)(NO_3)_3(H_2O)_2]$, to 2.525 (5) – 2.620 (5) Å in $[La(abptz)(NO_3)_3(H_2O)]$, indication of the congestion in the coordination sphere in the 11-coordinate complex. It indicates how nitrate is a versatile ligand in enabling lanthanide ions to achieve high coordination numbers. $[Ln(abptz)(NO_3)_2(H_2O)_3]$ NO_3 (Ln = Nd, Sm; 10-coordinate) and $[Ln(abptz)(NO_3)_2(H_2O)_2]$ NO_3 (Ln = Eu–Lu) are clearly analogous to terpy complexes mentioned above. On the other hand, the fact that abptz forms nine-coordinate $[Ln(abptz)(NO_3)_3(H_2O)]$ (Ln = Yb, Y) are, with one monodentate nitrate, rather than the alternative $[Ln(abptz)(NO_3)_3]$, with three bidentate nitrates, analogous to $[Ln(terpy)(NO_3)_3]$ (Ln = Er–Lu) indicates the subtle factors that can be responsible for the adoption of a particular geometry in a lanthanide complex.

Other ligands of the type whose complexation has been examined in detail include a range of 2,6-bis(5, 6-dialkyl-1,2,4-triazin-3-yl)pyridines, 2,6-bis(benzimidazol-2′-yl)pyridine (bzimpy) and N,N,N',N'-tetraethylpyridine-2,6-dicarboxamide. In some cases, segmental ligands have been employed to obtain complexes with stranded helical structures.

Among tetradentate ligands, complexes of the tripodal tpza and tpa have been explored. $[Ln(tpa)Cl_3]$ (Ln = Eu, Tb, Lu) have seven-coordination, whilst the larger neodymium ion can accommodate a coordinated solvent molecule in the eight-coordinate Nd analogue, $[Nd(tpa)Cl_3(MeOH)]$. Eight-coordinate lanthanum iodide complexes $[La(tpza)I_3(NCMe)]$ and $[La(tpza)I_3(thf)]$ exist. When lanthanide ions complex with the tripodal ligand tris(2-benzimidazol-2-ylmethyl)amine (ntb), bis complexes $[Ln(ntb)_2]^{3+}$ are formed where the ligand encapsulates the metal – to the exclusion of chloride from the coordination sphere, even when a deficit of ligand is used. Strong $\pi - \pi$ interactions between the benzimidazole rings may be responsible. However, 1:1 complexes $[Ln(ntb)(NO_3)_3]\cdot H_2O$ (Ln = La, Ce, Nd, Sm–Dy, Er) are formed when nitrate, with its stronger coordinating tendencies, is present. A chiral tris(2-pyridylmethyl)amine ligand has been used to form complexes $[Ln(L)](CF_3SO_3)_3$ (Ln = Eu and Tb) whose emission spectra of the europium complex in particular are most sensitive in both intensity and in line shape to the presence of a wide range of anions ($X = I^-$, Br^-, Cl^-, F^-, $ClO_4{}^-$, $NO_3{}^-$, SCN^-, $CH_3CO_2{}^-$, $HSO_4{}^-$ and $H_2PO_4{}^-$), working most effectively as a nitrate-specific luminescent sensor.**92**

The tetradentate quaterpyridine and hexadentate sexipyridine ligands form 1:1 complexes with yttrium and europium nitrates, respectively; the first-named ligand generates nine-coordinate $[Y(qtpy)(NO_3)_2(H_2O)]^+$ cations while the latter produces 10-coordinate $[Eu(spy)(NO_3)_2]^+$ cations where the ligand twists itself helically round the metal.**93**

3.7.11 Complexes of Porphyrins, Phthalocyanines, Aza Macrocycles, Texaphyrins, and Related Ligands

Reaction of $Ln(acac)_3$ with H_2TPP and other porphyrins (*see Porphyrin*) in solvents like trichlorobenzene (TCB) have been reported to give complexes Ln(acac)(porph), although for the early lanthanides $LnH(porph)_2$ seems to be the more usual product (on extended reflux, the double-decker sandwich $Ln_2(porph)_3$ may be obtained). Thus, refluxing $[Eu(acac)_3]$ with H_2OEP in 1,2,4-trichlorobenzene for 4 h leads to a mixture of $[Eu(OEP)_2]$ and $[Eu_2(OEP)_3]$ (along with a small amount of $[Eu(OEP)(OAc)]$), the former being a good deal more soluble in organic solvents, so that the mixture is separable by crystallisation.**94** Other, less forcing, methods have been described, such as when $[LuR_3]$ ($R = CH(SiMe_3)_2$) reacts with H_2OEP in toluene forming $[Ln(OEP)CH(SiMe_3)_2]$, which has a square-pyramidal structure with a highly dished porphyrin skeleton.**95** Among adducts of porphyrins, a rare example of seven-coordination is found in $[Ln(TPP)Cl(dme)]$ (Ln = Ho, Er, Tm, Yb) where the metal sits about 1.1 Å above the N_4 plane.**96** Bis(porphyrin) complexes with sandwich structures have also been synthesized. In general they are formally regarded as complexes of the trivalent lanthanide where one of the porphyrin ligands is a dianion and the other the oxidized cation radical. Genuine cerium(IV) complexes of both porphyrins and phthalocyanines have, however, been made. Phthalocyanine complexes can be made by heating a lanthanide compound such as the acetate with 1,2-dicyanobenzene.

A number of other complexes involve the lanthanide bonding to nitrogens in rings, either in aza crowns or in more classic macrocycles like cyclen. 1,4,7,10,13-pentaazacyclopentadecane (L) forms nitrate complexes $[Ln(L)(NO_3)_3]$ (Ln = Y, La–Yb except Ce, Pm, Ho); the structure of $[La(L)(NO_3)_3]$ shows it to have 11-coordinate lanthanum. As another example of structurally characterised complex of a N-donor macrocycle, $[Nd([18]aneN_6)(NO_3)_3]$ has two monodentate and one bidentate nitrate giving 10-coordination.

Cryptate complexes with macrobicyclic ligands containing three bipy units, in which the Ln^{3+} ion is contained within a ligand cavity, have been synthesized.[97] Such ligands will complex Ln^{2+} ions, such as Eu^{2+} and Sm^{2+}, under conditions where Ln^{3+} ions are not. An application has been using lanthanide cryptates of the early lanthanides (La, Ce, Eu) as catalysts in the hydrolysis of phosphate monoesters, diesters, and triesters. Schiff base complexes can be synthesized by the reaction of a lanthanide salt with a diamine and a suitable carbonyl derivative such as 2,6-diacetylpyridine.

Complexes, particularly of gadolinium, of ligands with a N_4-donor macrocyclic backbone that also supports carboxylate groups have assumed importance in the context of MRI contrast agents (see Section Magnetic Resonance Imaging and MRI Agents and *see also* ***Metal-based Imaging Agents***). The potentially octadentate ligand DOTA (1,4,7,10-tetra(carboxymethyl)-1,4,7,10-tetraazacyclododecane) has been widely studied. It forms very stable lanthanide complexes (one water usually molecule coordinated) $[Ln(DOTA)(H_2O)]^-$. These have slightly higher stability constants than the DTPA complexes; thus log K for $[Gd(DOTA)(H_2O)]^-$ is ~24.7, in comparison with 22.46 for $[Gd(DTPA)(H_2O)]^{2-}$. $[Gd(DOTA)(H_2O)]^-$, (Figure 20) is in clinical use (gadoterate meglumine; Dotarem™).[98] The structures of several lanthanide complexes of DOTA have been examined. Na $[Ln(DOTA)(H_2O)]\cdot 4H_2O$ all contain nine-coordinate $[Ln(DOTA)(H_2O)]^-$ ions (Ln = Pr, Nd, Eu, Gd, Ho, Lu) with twisted square-antiprismatic arrangements of the antiprism (on which the coordinated water molecule is superimposed), whilst $K[Tm(DOTA)]\cdot 6H_2O$ contains no coordinated water, showing the role of the counterion in determining the species crystallizing.

If one carboxylic acid side chain in H_4DOTA is replaced by hydrogen, the resulting acid, H_3DO3A, forms neutral lanthanide complexes. In solution, they are believed to have two water molecules coordinated so that the species present is $Gd(DO3A)(H_2O)_2\cdot[Eu(DO3A)(H_2O)_n]$ is known to exhibit a hydration equilibrium with $n = 1$, 2, strongly weighed towards $[Eu(DO3A)(H_2O)_2]$. Other derivatives have been made in which the fourth carboxylic acid group is replaced by hydroxyalkyl groups that are marketed and approved for use ($-CH_2CH(CH_3)OH$ = ProHance™; $-CH(CH_2OH)CH(OH)CH_2OH$ = Gadovist™). These compounds have a side-chain hydroxyalkyl group coordinated, in addition to four nitrogens, three carboxylate oxygens, and a water molecule (Figure 21).

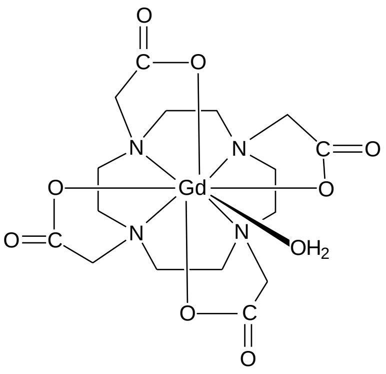

Figure 20 The MRI agent $[Gd(DOTA)(H_2O)]^-$

Quite apart from use as MRI contrast agents, there is considerable interest in applications of lanthanide complexes of DOTA and related complexing agents as spectroscopic probes.[99]

Examples of this include some Tb and Eu macrocyclic complexes, immobilised in a sol-gel glass, whose emission is made pH-dependent and can thus be used as narrow range pH sensors, and a terbium complex which behaves as a molecular logic gate; the output (a terbium emission line) is only observed when the 'inputs' (the presence of proteins and the absence of oxygen) are both satisfied. (Figure 22).

Texaphyrins. A new type of complex is provided by the texaphyrins, compounds of 'extended' porphyrins where

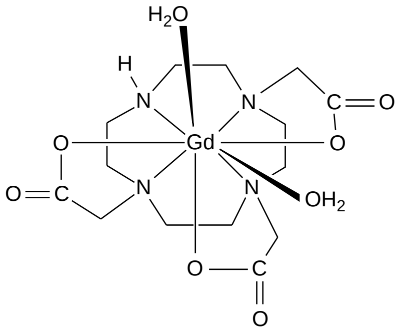

Figure 21 The neutral complex $[Gd(DO3A)(H_2O)2]$

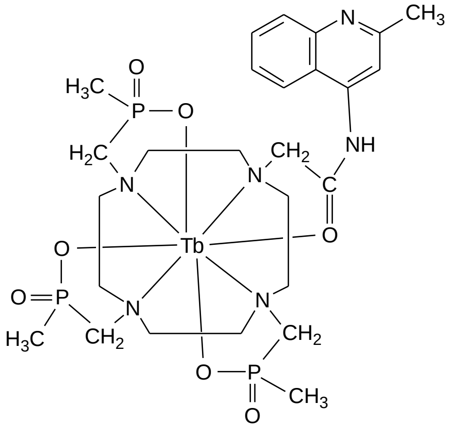

Figure 22 A terbium complex that acts as a 'logic gate'

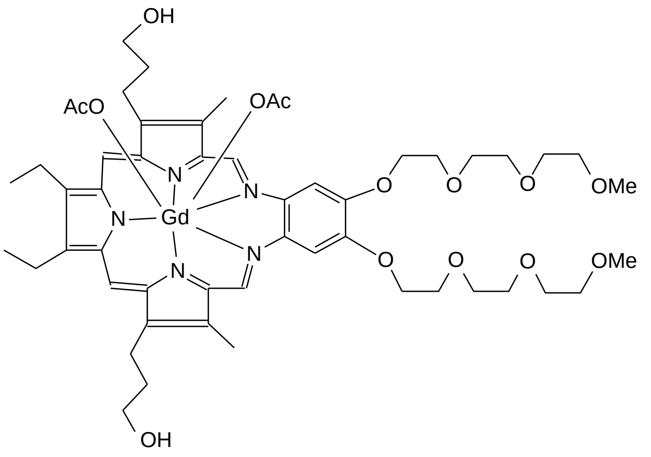

Figure 23 The gadolinium texaphyrin complex ‘Gd-tex’

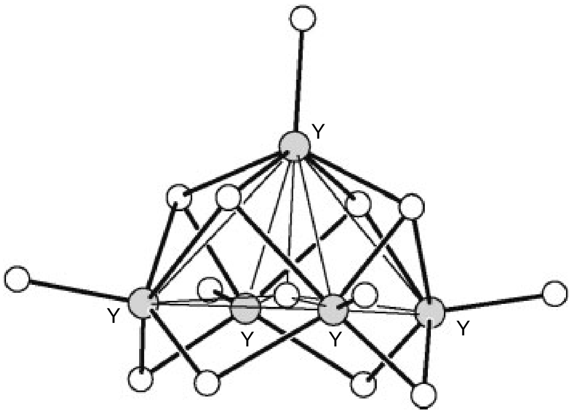

Figure 24 The structure of $Y_5O(O\text{-}i\text{-}Pr)_{13}$

the ring contains five donor nitrogens. These have attracted considerable interest because of their possible medicinal applications.[100] Two texaphyrin complexes are undergoing clinical trials; a gadolinium compound (Gd-tex; XCYTRIN™) is an effective radiation sensitiser for tumour cells (Figure 23). It assists the production of reactive oxygen-containing species, whilst the presence of the Gd^{3+} ion means that the cancerous lesions to which it localises can be studied by MRI. One form of the lutetium analogue (LUTRIN™), is being developed for photodynamic therapy for breast cancer, and another, (ANTRIN™) is being developed for photoangioplasty, where it has potential for treating arteriosclerosis.

3.7.12 Other Ligands

Alkoxides and Aryloxides[101]. Some of these compounds have been known for over 30 years, but interest in the former has been stimulated recently by their potential use as precursors for deposition of metal oxides using the sol–gel (*see* ***Sol–Gel Synthesis of Solids***) or Metal Organic Chemical Vapour Deposition (MOCVD) process (*see Metal–Organic Chemical Vapor Deposition*) In the case of alkoxides and aryloxides, it is harder to get monomers with low coordination numbers than with alkyl (and aryl-) amides, since –OR ligands by their own nature exert less second-order influence in the coordination sphere than the corresponding $–NR_2$, and, for the same reason, –OR groups are much more likely to be found in bridging positions. Thus, because of oligomerization and/or the presence of solvent in the coordination sphere, $Ln(OR)_3$ species are frequently not three-coordinate.

Simple methoxides like $La(OMe)_3$ are ill-defined structurally but are oligomeric; attempted isolation of corresponding isopropoxides has yielded the clusters $Ln_5O(O\text{-}i\text{-}Pr)_{13}$ (Figure 24) (Ln = Y, Yb) with a square-pyramidal core, $Nd_5O(O\text{-}i\text{-}Pr)_{13}(i\text{-}PrOH)_2$ (trigonal bipyramidal core), and $Nd_6(O\text{-}i\text{-}Pr)_{17}Cl$. Under other circumstances, a binuclear solvate, $[Nd(OCHPr^i_2)_3(thf)]_2$, with the structure $[(Pr^i_2CHO)_2(thf)Nd(\mu\text{-}OCHPr^i_2)_2Nd(thf)(OCHPr^i_2)_2]$ has been obtained. Similarly, the neopentoxides $Ln(OCH_2Bu^t)_3$ (Ln = La, Nd) are tetrameric $[Ln(OCH_2Bu^t)_3]_4$ based on a square of lanthanides with each lanthanide bound to one terminal and four bridging alkoxides. Using the bulkier t-butoxide ligand to minimize association gave $La_3(O\text{-}t\text{-}Bu)_9(thf)_2$ and $Ce(O\text{-}t\text{-}Bu)_3$ (believed to be monomeric); the latter undergoes thermolysis in high yield:

$$2Ce(O\text{-}t\text{-}Bu)_3 \longrightarrow [Ce(OCH\text{-}t\text{-}Bu_2)_3]_2 + 6C_4H_8 \tag{9}$$

The product is an alkoxy-bridged dimer with four-coordinate cerium. Dimeric structures are also exhibited by $[Ln(OQPh)_3]_2$(Ln = La, Ce, Y; Q = C, Si), although the bridges are cleaved by Lewis bases forming adducts such as $Ln(OSiPh)_3(thf)_3$ (*fac*-octahedral; Ln = Y, La, Ce) and $Y(OSiPh)_3(OPBu_3)_2$ (trigonal bipyramidal). An unusual cyclic decameric structure is exhibited by $[Y(OC_2H_4OMe)_3]_{10}$ (Figure 25).

Synthesis of alkoxides from $LnCl_3$ is often complicated by chloride retention from the starting material, and for this reason they are often made by alcoholysis of $Ln(N(SiMe_3)_2)_3$.

A range of aryloxides exists. With 2,6-dimethylphenoxide, six-coordinate $Y(OR)_3(thf)_3$ (and dimeric $[Y(OR)_3(thf)]_2$ with five- coordination) are formed; replacement of methyl by phenyl substituents leads to the isolation of the 2,6-diphenylphenolates $[Ln(OC_6H_3Ph_2\text{-}2,6)_3]$ (Ln = La, Ce, Pr, Nd, Gd, Ho, Er, Lu, Y), which have monomeric structures with the lanthanide slightly out of the O_3 plane, but with some additional ring-metal interactions. $[Ln(OC_6H_3Ph_2\text{-}2,6)_3(thf)_2]\cdot 2thf$ (Ln = La, Nd) have conventional five-coordinate trigonal bipyramidal coordination of the metal with one axial and one equatorial thf; in contrast, $[Nd(OC_6H_3Ph_2\text{-}2,6)_3(thf)]$ has pseudo-tbp coordination with three equatorial

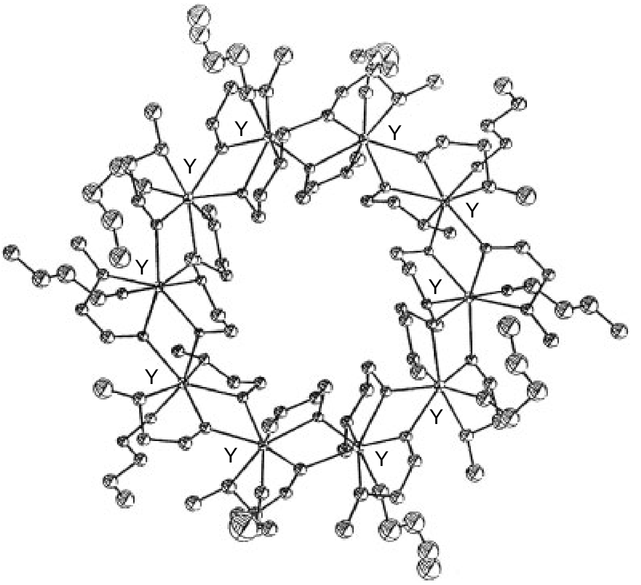

Figure 25 Cyclic decameric structure of [Y(OC$_2$H$_4$OMe)$_3$]$_{10}$

phenoxides, an apical thf and an apical position occupied by a phenyl group. Using the 2,6-diisopropylphenolate ligand leads to unsolvated Ln(OC$_6$H$_3$Pr$^i_2$-2,6)$_3$ species which are in fact η^6-arene bridged dimers Ln$_2$(OC$_6$H$_3$Pr$^i_2$-2,6)$_6$; in thf, they form conventional trigonal bipyramidal thf adducts [Ln(OC$_6$H$_3$Pr$^i_2$-2,6)$_3$(thf)$_2$] (Ln = Pr, Nd, Sm, Gd, Er, Yb, Lu). When the bulk of the aryloxide is increased by putting two t-butyl groups into the 2,6-positions of the benzene ring, three-coordinate aryloxides, Ln(O-2,6-t-Bu$_2$-4-R-C$_6$H$_2$)$_3$, can be isolated (R = H, Ln = Y, La, Sm; R = Me, Ln = Y, La, Ce, Pr, Nd, Dy–Er, Yb). Trigonal planar geometry is found in Y(O-t-Bu$_2$C$_6$H$_3$)$_3$ but a pyramidal structure is adopted in Ce(O-2,6-t-Bu$_2$-4-Me-C$_6$H$_2$)$_3$. Possibly the balance of small and variable 'agostic' and Van der Waals forces, whether within the lattice or within the complex species, is the determining factor in determining the form of three-coordination. Alkyl and aryloxides have proved useful synthetic precursors.

Alkylamides. The volatile air-sensitive silylamides are the best characterized alkylamides. They are made by salt-elimination reactions:

$$\mathrm{LnCl_3 + 3Li\ N(SiMe_3)_2 \longrightarrow Ln(N(SiMe_3)_2)_3 + 3LiCl} \tag{10}$$

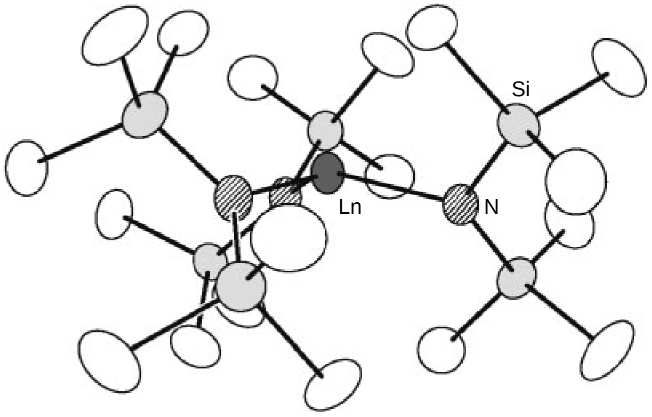

Figure 26 Three-coordinate Ln[N(SiMe$_3$)$_2$]$_3$

They are volatile in vacuo at 100 °C and dissolve in hydrocarbons; the first three-coordinate lanthanide compounds to be characterized, they have unusual pyramidal structures (Figure 26) in the solid state (similar structures have been reported for Y, Ce, Nd, Sm, Eu, Dy, Er, and Yb), but are believed to be planar in solution. Careful examination of the crystal structure of [Sm{(N(SiMe$_3$)$_2$)$_3$}] shows that one methyl group in each amide is placed above the pyramid relatively close to the samarium (Sm–C 3.003(4) Å; compare Sm–N 2.284(3) Å) suggesting the presence of agostic interactions (*see Agostic Bonding*). DFT (Density Field Theory) calculations on it support this view, indicating the presence of β-Si–C agostic interactions.**[102]** Ln(N(SiMe$_3$)$_2$)$_3$ form stable four-coordinate Ph$_3$PO and Ph$_2$CO adducts; when excess phosphine oxide is used, five-coordinate peroxide-bridged dimers are obtained. Eu[N(SiMe$_3$)$_2$]$_3$ forms both 1:1 and 1:2 adducts with Me$_3$PO. [Ln(N(SiMe$_3$)$_2$)$_3$] react with CyNC (Cy = cyclohexyl) forming trigonal bipyramidal five-coordinate adducts [Ln(N(SiMe$_3$)$_2$)$_3$(CyNC)$_2$] (axial nitriles). [Y(N(SiMe$_3$)$_2$)$_3$(PhCN)$_2$] has a similar structure.

When a deficit of the lithium alkylamide is used, dimeric chloride-bridged silylamides are obtained which are useful synthetic intermediates (Figure 27);**[103]** they can also be prepared by redistribution reactions between LnCl$_3$ and [Ln(N(SiMe$_3$)$_2$)$_3$; some bromo- and iodo- analogues have been reported.

Anhydrous lanthanide triflates are an alternative to the chlorides as starting materials for the synthesis of [Ln(N(SiMe$_3$)$_2$)$_3$] as they obviate problems of chloride retention in the product, which can lead to several products, as reaction of YbCl$_3$ and NaN(SiMe$_3$)$_2$ in a 1:2 molar ratio gives [Yb(N(SiMe$_3$)$_2$)$_3$], [Yb(N(SiMe$_3$)$_2$)$_2$(μ-Cl)(thf)]$_2$ and [Yb$_3$Cl$_4$O((N(SiMe$_3$)$_2$)$_3$(thf)$_3$)]. The latter is a trinuclear cluster with a triangle of ytterbiums, where Yb is octahedrally coordinated by an amide nitrogen, a thf, two μ_2-chlorine atoms and a μ_3-chlorine and μ_3-oxygen.

The amide Er{NBu^t(SiMe$_2$H)}$_3$, which has an unexpectedly high vapour pressure, displays three agostic Er–H–Si interactions in the solid state. Other alkylamides Ln(N-i-Pr$_2$)$_3$ (Ln = Y, La, Nd, Yb, Lu,) are obtained with the less hindered isopropylamide ligand; the neodymium compound forms

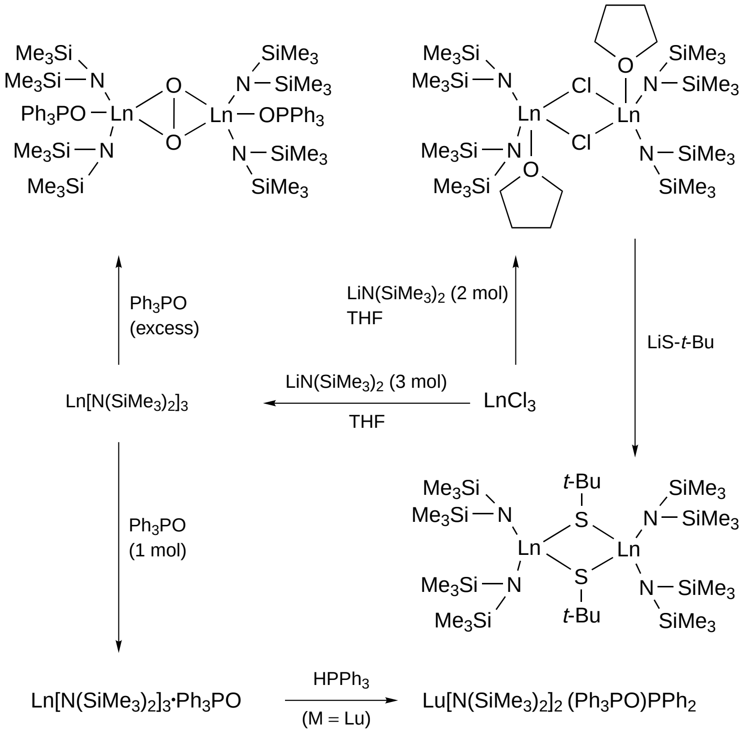

Figure 27 Reactions of lanthanide bis(trimethylsilyl)amide complexes. (Ref. 6. Reproduced by permission of Palgrave Macmillan)

a stable thf adduct [Nd(N-*i*-Pr$_2$)$_3$(thf)]. [Sm(Ncy$_2$)$_3$(thf)] is similar. In contrast to the three-coordinate silylamides and diisopropylamides, the lanthanides do not form simple homoleptic dimethylamides. Reaction of NdCl$_3$ with LiNMe$_2$ gives an adduct [Nd(NMe$_2$)$_3$(LiCl)$_3$], which with MMe$_3$ (M = Al, Ga) gives bridged [Nd(NMe$_2$)$_3$(MMe$_3$)$_3$].

Trigonal bipyramidal [Ln{N(SiHMe$_2$)$_2$}$_3$(thf)$_2$] (Ln = Y, La–Lu) are isostructural; these amides have been anchored to the internal walls of the mesoporous silicate MCM-41 as potential catalyst precursors.

Rather less is known about lanthanide arylamides. Reaction of NdCl$_3$ with KNHAr (Ar = Ph) leads to [Nd(NHPh)$_3$·3KCl], reminiscent of the adducts of the dimethylamides. Using the sterically demanding 2,6-Pr^i_2C$_6$H$_3$ group leads to octahedral [Nd(NH-2,6-Pr^i_2C$_6$H$_3$)$_3$(thf)$_3$] and trigonal bipyramidal [Ln(NH-2,6-Pr^i_2C$_6$H$_3$)$_3$(thf)$_2$] (Ln = Y, Yb).

Several compounds with highly fluorinated amides have been synthesized; [Sm(N(SiMe$_3$)(C$_6$F$_5$))$_3$] (Figure 28) contains three significant Sm···F and three Sm–C–H agostic interactions, which seem to be common in these compounds; the thf adduct [Sm(N(C$_6$F$_5$)(SiMe$_3$))$_3$(thf)] has two Sm···F and one Sm–C agostic interaction. The toluene adduct [(η^6-C$_6$H$_5$Me)Nd(N(C$_6$F$_5$)$_2$)$_3$] has a η^6-bonded toluene molecule with a distorted piano-stool geometry. Tetrahedral anionic species [Li(thf)Ln(N-*i*-Pr$_2$)$_4$] (Ln = La, Y, Lu) and [Li(thf)$_4$][Ln(NPh$_2$)$_4$] (Ln = Er, Yb) have also been made.

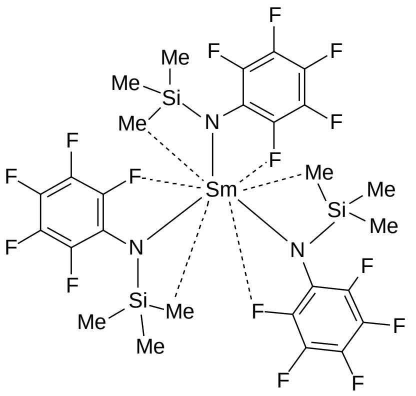

Figure 28 The samarium amide [Sm(N(SiMe$_3$)(C$_6$F$_5$))$_3$], showing the agostic interactions

Polypyrazolylborates. This area of chemistry has developed considerably.[104] [LnTp$_3$] have nine-coordinate structures for early lanthanides (e.g. Pr, Nd), but eight-coordinate for the later metals (e.g. Yb). Seven-coordinate bis complexes [Ln(Tp)$_2$Cl] are formed using totally moisture-free conditions, but these readily add a Lewis base, for example, water forming [Ln(Tp)$_2$Cl(H$_2$O)]. A very wide range of compounds, many of Sm, Eu, and Yb, in both the +2 and +3 states, has been synthesized with Tp$^{\text{Me2}}$, this time with a maximum of two Tp$^{\text{Me2}}$ bound. In triflate complexes

$Ln(Tp^{Me2})_2(OTf)$, triflate coordinates for the lighter lanthanides, as in $[Nd(Tp^{Me2})_2(O_3SCF_3)]$ whereas the smaller lanthanides form ionic $[Ln(Tp^{Me2})_2]$ O_3SCF_3, as in the ytterbium compound. The triflates form mono(MeCN) adducts, the MeCN being bound in $[La(Tp^{Me2})_2(MeCN)]$ O_3SCF_3 but not in $[Nd(Tp^{Me2})_2(O_3SCF_3)]\cdot MeCN$. This can be regarded as a type of ionisation isomerism. In a range of $Sm(Tp^{Me2})_2X$ compounds, where X = F, Cl, these have monomeric seven-coordinate molecular structures, but for X = I and BPh_4, the compounds are $[Sm(Tp^{Me2})_2]^+X^-$. A comparison of the ytterbium(II) and (III) compounds $[Yb(Tp^{Me2})_2]$ and $[Yb(Tp^{Me2})_2]$ O_3SCF_3 show six-coordination for ytterbium in both cases, with Yb–N bond lengths ca. 0.16 A longer in the Yb(II) compound.

Simple Alkyls. These are primarily dealt with elsewhere (*see* ***Scandium, Yttrium & the Lanthanides: Organometallic Chemistry***) but the structural similarity of the distorted three-coordinate trigonal pyramidal structures of the alkyls $[Ln((CH(SiMe_3)_2)_3)]$ to the alkylamides $[Ln((N(SiMe_3)_2)_3)]$ (Ln = La–Lu) is notable. Density Functional Theory calculations indicate that β-Si–C agostic interactions are important in these structures (*see Agostic Bonding*), but that the hitherto favoured γ C–H agostic interactions are in fact repulsive. Another family of alkyls with simple coordination geometries is $[Ln(CH_2SiMe_3)_3(thf)_n]$. These appear to be very unstable for lanthanides larger than samarium, but $[Ln(CH_2SiMe_3)_3(thf)_3]$ (Ln = Sm, Y) have *fac*-octahedral structures, whilst $[Ln(CH_2SiMe_3)_3(thf)_2]$ (Ln = Er, Yb, Lu) all have five-coordinate trigonal bipyramidal structures (axial thf ligands). The $[Ln(CH_3)_6]^{3-}$ ions (all lanthanides except Eu) have the expected octahedral structures.**[105]**

Thiolates and Related Systems. Lanthanide thiolates have only been characterized in detail recently. Monomeric species have been obtained using bulky ligands, such as the three-coordinate (pyramidal) $Sm(SC_6H_2$-*t*-Bu-2,4,6$)_3$ (Figure 29).**[106]**

The intensively reactive $[Ln(SBu^t)_3]$ (Ln = La, Ce, Pr, Nd, Eu, Yb, Y) are made**[107]** from $[Ln\{N(SiMe_3)_2\}_3]$ and $HSBu^t$; their reactivity is doubtless due to coordinative unsaturation. Some thiophenolates have been isolated as Lewis base adducts. $[Ln(SPh)_3(py)_3]_2$ (Ln = Ho, Tm) have two thiolate bridges with seven-coordinate lanthanides; $[Sm(SPh)_3(py)_2]_4$ has a linear arrangement of four seven-coordinate samariums with 3, 2, and 3 μ_2-bridging thiolates and $[Sm(SPh)_3(thf)]_{4n}$ is a polymer. Use of SC_6F_5 as a ligand gives stabler (even to air) and more hydrocarbon-soluble products, also obtained as Lewis base adducts. The large Ce^{3+} ion forms the seven-coordinate dimer $[Ce(SC_6F_5)_3(thf)_3]_2$ with thiolate bridges, whilst Ho and Er give monomeric $[Ln(SC_6F_5)_3(thf)_3]$ (Ln = Ho, Er). Other adducts $[Ln(SC_6F_5)_3(py)_4]$ (Ln = Sm, Yb) and $[Er(SC_6F_5)_3(dme)_2]$ have also been isolated. Many of these compounds feature $Ln\cdots F$ interactions, of the type noted in lanthanide amides. Another synthetic approach has utilized the reaction of lanthanide metals with disulphides and diselenides. Thus molecules such as $[Yb(SAr)_3(py)_3]$ (Ar = 2,4,6-triisopropylphenyl) and $Ln(SePh)_3py_3$ (Ln = Ho, Tm, Yb) have been made; the selenolates are dimeric with seven-coordinate lanthanides. In contrast, $[Yb(SPh)_3py_3]$ has a meridional, structure, whilst $[Ln(SePh)_3(thf)_3]$ (Ln = Tm, Ho, Er) have monomeric *fac*-octahedral structures. $[Sm(SePh)_3(py)_3]_2$ has two selenothiolate bridges with seven-coordinate samarium. An important reaction of these compounds is that they react with free chalcogens forming clusters. Thf solutions of thiolates $Ln(SPh)_3$ reacts with S forming octanuclear clusters $[Ln_8S_6(SPh)_{12}(thf)_8]$ (Ln = Ce- Sm, Gd–Er), their structure is based on a cube of lanthanides, edge bridged by mercaptides and face-bridged by sulphur; analogous pyridine clusters $[Ln_8S_6(SPh)_{12}(py)_8]$ (Ln = Nd, Sm, Er) have also been isolated. Reaction of Sm with PhSeSePh in thf gives a cluster $[Sm_8Se_6(SePh)_{12}(thf)_8]$ whilst $Sm(SePh)_3$ reacts with S in dme affording $[Sm_7S_7(SePh)_6(dme)_7]^+$ $[Hg_3(SePh)_7]^-\cdot Nd(SePh)_3$ reacts with Se in pyridine to form $[Nd_8Se_6(SePh)_{12}(py)_8]$. Reaction of later lanthanides with mixtures of I_2 and PhSeSePh in thf, followed by reaction with Se in pyridine affords iodine-containing clusters $[(thf)_6Ln_4I_2(SeSe)_4(\mu_4\text{-Se})]\cdot thf$ (Ln = Ho–Yb). These contain a square array of Ln(III) ions connected through a single (μ_4-Se) ligand. Another such cluster is $[Yb_6Se_6I_6(thf)_{10}]$. On thermolysis, these selenium rich compounds give iodine-free Ln_2Se_3.**[108]**

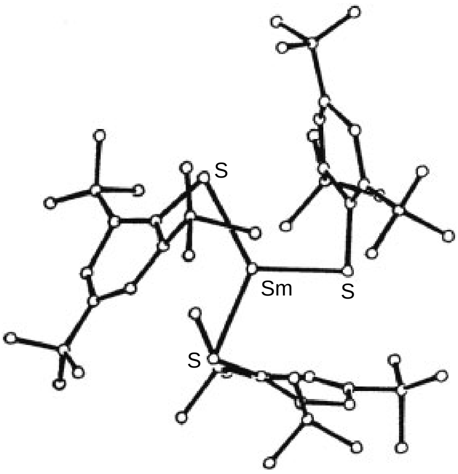

Figure 29 Structure of three-coordinate Sm in $Sm(SC_6H_2(Bu\text{-}t)_3$ -2,4,6$)_3$

Much of this work has been directed towards materials-based applications, as volatile compounds might be CVD precursors (*see Chemical Vapor Deposition*) and the ability of the thiolates and their fellows to react with the free chalcogens may assist doping lanthanide ions into optical and electrical materials. Thus, thermolysis of the $[Ln(SePh)_3(thf)_3]$ (Ln =

Tm, Ho, Er) gives Ln_2Se_3 (Ln = Tm, Yb) and a mixture of MSe and MSe_2 (M = Ho).

3.7.13 Complexes of N,O-Donors

Complexes of Polyaminepolycarboxylic Acids[**4,5**]. Ligands like EDTA form stable lanthanide complexes; complexation is facilitated by the considerable entropy change, the enthalpy change being small (and endothermic):

$$[Ln(H_2O)_9]^{3+} + EDTA^{4-} \longrightarrow Ln(EDTA)(H_2O)_3]^{3-} + 6H_2O \quad (11)$$

In general, the early lanthanides form triaqua species $[Ln(EDTA)(H_2O)_3]^{3-}$ with nine-coordinate metal (Figure 30), but metals from erbium form eight-coordinate $[Ln(EDTA)(H_2O)_2]^-$ following the 'lanthanide contraction'. Thus, $Na[Ln(EDTA)(H_2O)_3]5H_2O$ (Ln = La–Dy) are isostructural, with nine-coordinate lanthanides; as are $K[Ln(EDTA)(H_2O)_3]$(Ln = La, Nd); $K[Yb(edta)(OH_2)_2]{\cdot}5H_2O$ and Cs $[Yb(edta)(OH_2)_2]{\cdot}5H_2O$ contain eight-coordinate ytterbium. Comparison with other structures show there to be a dependence upon the alkali-metal cation present in some cases. Thus, $Cs[Dy(edta)(OH_2)_2]{\cdot}3H_2O$ and $Cs[Ho(edta)(OH_2)_2]{\cdot}3H_2O$ have eight-coordinate lanthanides (unlike the nine-coordinate Na salt), whilst $Na[Er(edta)(OH_2)_3]{\cdot}5H_2O$, $K[Ho(edta)(OH_2)_3]{\cdot}2H_2O$, Cs $[Nd(edta)(OH_2)_3]{\cdot}3.5\ H_2O$, $Cs[Sm(edta)(OH_2)_3]{\cdot}4H_2O$ and $Cs[Gd(edta)(OH_2)_3]{\cdot}4H_2O$ all have nine-coordinate lanthanides. Evidently there is a region towards the end of the lanthanide series where the eight and nine-coordinate anions have similar stabilities, and it is the solubility of the compound that determines which anion is isolated. The EDTA complexes are prototypes for a number of complexes of polyaminepolycarboxylic acids; they are historically important as an early established example of high coordination numbers for lanthanide complexes.

The potentially octadentate DTPA likewise forms stable complexes. These have lately attracted considerable interest with the use of its gadolinium complex as a contrast enhancing agent for body scanners (MRI, *see* ***Metal-based Imaging Agents***), probably the most important new application of lanthanide compounds to emerge in the last 20 years. The introduction of lanthanide-based contrast agents has revolutionised diagnostics, assisting doctors in distinguishing between normal and diseased tissue and thus improving prognosis.

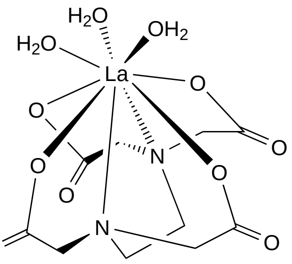

Figure 30 The structure of $La(EDTA)(H_2O)_3{}^-$

Magnetic Resonance Imaging and MRI Agents[**109,110**]. MRI relies on detecting the NMR signals of water molecules in the body as a function of space. Spatial information is obtained by making the ^1H resonance frequency position-dependent. The imaging agent enhances the contrast to distinguish between healthy and diseased tissue; the paramagnetic contrast agent, which shortens the relaxation time (T_1) for the protons in water molecules in that tissue and enhances the signal intensity. A number of factors have to be taken into account in designing a good MRI agents; they include (a) low toxicity; (b) high magnetic moment; (c) coordinated water molecules; (d) long electron-spin relaxation time; (e) osmolarity similar to serum; (f) water solubility; (g) targeting tissue. Gd^{3+} ions have a large number of unpaired electrons (S = 7/2) and high magnetic moment, additionally its magnetic properties are isotropic. Its electron-spin relaxation time $\sim 10^{-9}$ s, and is more suitable than other very paramagnetic lanthanide ions in the second half of the series, such as Dy^{3+}, Eu^{3+} and Yb^{3+} ($\sim 10^{-13}$ s). All these magnetic properties are desirable. The toxicity of the gadolinium aqua ion is too great for it to be used directly the LD50 is ∼0.1 mmol/kg, which is less than the imaging dose, which is normally of the order of 5 g for a human, so complexed Gd^{3+} is used, using a ligand that forms a very stable complex in vivo (this can also avoid precipitation as the hydroxide at physiological pH) so a gadolinium complex is used, with a ligand that forms a very stable complex.

Complexes of polyaminocarboxylic acids such as $[Gd(DTPA)(H_2O)]^{2-}$ (Figure 31; gadopentetate dimeglumine; Magnevist) or $[Gd(DOTA)(H_2O)]^-$ (gadoterate meglumine;

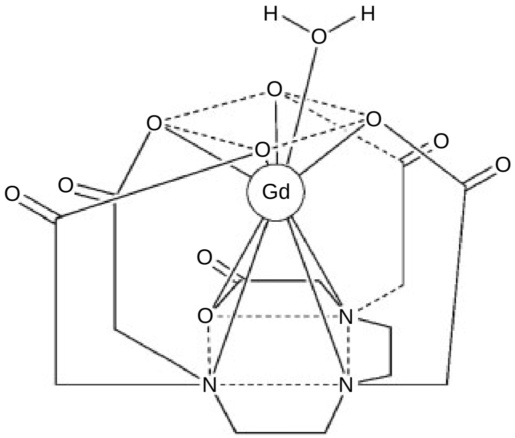

Figure 31 The structure of $Gd(DTPA)(H_2O)^-$

Dotarem) have been widely used; these meet most of the above criteria. Both neutral and charged complexes are used, the former having less osmotic effect and the latter being more hydrophilic, so that amide derivatives like [Gd(DTPA-BMA)(H_2O)] (gadodiamide; Omniscan) have advantages.

This complex again has a nine-coordinate lanthanide; because of the greater denticity of DTPA compared to EDTA, only one water molecule is coordinated in the solid-state structures of Na_2[Gd(dtpa)(H_2O)] Similar ions are present in the Ba[Gd(dtpa)(H_2O)] and (CN_3H_6)$_2$[Gd(dtpa)(H_2O)] and in Ba[Nd(dtpa)(H_2O)]. On the other hand, a few salts are known, like (NH_4)$_2$[Gd(dtpa)](H_2O), which have no water coordinated in the solid state. In (NH_4)$_2$[Gd(dtpa)](H_2O), a hydrogen-bonding network involving the ammonium ions causes Gd(dtpa) units to associate into dimers, in contrast to the monomeric nature of Na_2[Gd(dtpa)(H_2O)]. Similarly, Cs_4 [Dy(dtpa)]$_2$ has an unusual dimeric structure in which Dy is nine-coordinate (as in other dtpa complexes) but with the ninth coordination position occupied by a bridging carboxylate, rather than a water molecule. These disparate solid-state structures reflect the fine balance of forces influencing which species crystallises.

The structure found in salts like Na_2[Gd(dtpa)(H_2O)] is thought to represent the species found in solution – data from a number of measurements on solutions containing $[Ln(dtpa)(H_2O)_n]^{2-}$ species, such as luminescence spectra of the Eu and Tb analogues, indicate that one water molecule is coordinated. A wide variety of complexes of amide derivatives of DTPA have also been synthesised, in order to create neutral species.[111,112] Using $[Gd(DTPA)(H_2O)]^{2-}$ it has been shown that these complexes get absorbed by the DNA of the cell they have been used to locate and that they could act as an agent for neutron capture cancer therapy.

Dipicolinates (pyridine-2,6-dicarboxylates) have been investigated in some detail with structures determined for several tris complexes such as Na_3[Nd(dipic)$_3$]·15H_2O and Na_3[Yb(dipic)$_3$]·13H_2O, typical of the early and later lanthanides, respectively. The lanthanides have essentially tricapped trigonal prismatic coordination geometries, isostructural along the lanthanide series; they have been the subject of important solution NMR studies. Mono and bis complexes can also be synthesized; the mono complex [Nd(dipic)(H_2O)$_4$] ClO_4 has a polymeric structure in which each picolinate is bound to three different (nine-coordinate) neodymium ions.

3.7.14 Other Complexes of S-Donors[4,5]

As relatively hard acids, Ln^{3+} ions would not be expected to complex readily with soft donor atoms like sulfur. Apart from the thiolates discussed in (see Section 'Polypyrazolylborates'), several types of complex with chelating ligands such as dithiophosphates and dithiocarbamates have been synthesized by reaction in nonpolar solvents. These fall into two main classes, Ln(S_2Q)$_3$ and $[Ln(S_2Q)_4]^-$ (Q = R_2NC (dithiocarbamate) or R_2P (dithiophosphate)). Several crystal structures have been determined; [Ln(S_2PCy_2)$_3$] (Ln = Sm, Pr) have distorted trigonal prismatic six-coordination, whereas on passing to the Dy and Lu analogs the geometry tends more towards octahedral. In Et_4N[La(S_2CNEt_2)$_4$], the geometry is distorted dodecahedral while (Ph_4P)[Pr(S_2PMe_2)$_4$] is reported to have a distorted square-antiprismatic coordination geometry. (Ph_4As)[M(S_2PEt_2)$_4$] (M = La, Er) have a near-perfect dodecahedral coordination, as does Na [Eu(S_2CNMe_2)$_4$]. Eight-coordination is also confirmed for (Ph_4P)[Eu($S_2P(OEt)_2$)$_4$] and [Me_2NH_2] [Nd(S_2CNMe_2)$_4$]. A number of adducts have been synthesised in which coordination is primarily by sulphur, Ln(S_2CNR_2)$_3$(bipy) and Ln(S_2CNR_2)$_3$(phen); these are discussed in (Section 3.7.10).

A few complexes with sulfur-based crown ether ligands have been characterized, with reaction of LaI_3(thf)$_3$ with 9S3 in MeCN affording eight-coordinate [LaI_3(9S3)(MeCN)$_2$].[113]

3.8 Coordination Chemistry of the +2 and +4 States

Although relatively limited compared to that of the tripositive metal, these have remained relatively undeveloped until recently; with increasing emphasis on the use of nonaqueous solvents, many discoveries in the +2 state for Eu, Sm, and Yb in particular probably remain to be made.[4,5]

3.8.1 The +2 State

The zinc reduction of Eu^{3+} to Eu^{2+}, followed by its precipitation as the sulfate, is a traditional step in the separation of europium from other lanthanides. In general, the solubilities of the 'inorganic' compounds of the Ln^{2+} ions resemble those of the corresponding compounds of the alkaline earth metals (insoluble sulfate, carbonate, hydroxide, oxalate). Both europium and the Sm^{2+} and Yb^{2+} ions can also be prepared by other methods (e.g. electrolysis), although these solutions of the latter two metals tend to be short-lived and oxygen-sensitive in particular. Eu^{2+} is the only divalent aqua ion with any real stability in solution. Several divalent lanthanides can, however, be stabilized by the use of nonaqueous solvents such as HMPA and THF, in which they have characteristic colors, quite distinct from those for the isoelectronic trivalent ions on account of the decreased term separations.

3.8.2 Complexes

A large number of complexes of O-donors, particularly of SmI_2 have been examined, on account of the widespread use of SmI_2 as a 1-electron reductant in organic synthesis. HMPA has been widely used as the solvent, as it brings about a large increase in rate; HMPA is suspected to be a carcinogen, therefore alternative solvents (and ligands) have been investigated, so the structures of a number of complexes, both of hmpa and other O-donors, have been investigated, shedding light on SmI_2-promoted reactions. As a rule, these compounds of amide ligands have a coordination number 6, suggesting steric effects at work, in addition to pointing to strong electron-donating power of the ligands; the coordination number of samarium(II) is usually in the range 7–9. Starting materials for these iodide complexes are usually [$LnI_2(thf)_n$] (Ln = Sm, Yb, Eu) are useful starting materials; these can readily be made from the lanthanide and ICH_2CH_2I.

Changing reaction conditions and the solvent used can alter the stoichiometry of the product. The initial product of crystallisation of SmI_2 from thf is pentagonal bipyramidal [$SmI_2(thf)_5$]; other seven-coordinate complexes obtained using mixtures of thf and dimethoxyethane are [$SmI_2(thf)_3(dme)$] and [$SmI_2(thf)(dme)_2$]. YbI_2 reacts with 4.5 mols HMPA in thf forming [$Yb(HMPA)_4(thf)_2$] I_2; a similar reaction with SmI_2 affords [$Sm(HMPA)_4I_2$]. Excess HMPA gives [$Sm(HMPA)_6$]I_2·$SmI_2(thf)_2$ reacts with 2 mols of tetramethylurea forming all-*trans*-[$SmI_2(tmu)_2(thf)_2$], but excess tmu does not replace the other thf ligands. Another complex to be isolated is *trans*-[$SmI_2(dmi)_4$] here all the thf groups have been substituted. On the other hand, use of 4 mols (i.e. a deficit on the stoichiometric amount) of dmpu causes displacement of the iodides from $SmI_2(thf)_2$ forming [$Sm(dmpu)_6$] I_2 where the cation has a distorted trigonal antiprismatic geometry; Sm–O distances are 2.475–2.488 Å; however, if just 2 mols of dmpu are used in the reaction, [$SmI_2(dmpu)_3(thf)$] results, in which the iodides are trans- and the dmpu ligands have a mer- arrangement. These compounds all have six-coordinate Ln^{II}. Some simple complexes of N-donor ligands have not dissimilar structures. [$SmI_2(thf)_2$] reacts with *N*-methylimidazole (*N*-Meim) forming [SmI_2(*N*-Meim)$_4$]. On recrystallisation from hot thf, this loses a molecule of *N*-Meim and dimerises, forming [{SmI(μ-I)(*N*-Meim)$_3$}$_2$]. Eu behaves similarly in forming [EuI_2(*N*-Meim)$_4$] and [{EuI(μ-I)(*N*-Meim)$_3$}$_2$]. LnI_2 (Ln = Sm, Yb) reacts with substituted pyridines in thf forming [$LnI_2(pyridine)_4$]; [LnI_2(3,5-lutidine)$_4$] (Ln = Sm, Yb) and [YbI_2(4-*t*-Butpy)$_4$] were determined; all have trans-structures.

The developing coordination chemistry of Sm(II) has thrown up interesting cases of isomerism. Reaction of $SmI_2(thf)_2$ with diglyme results in the isolation of *trans*-[$SmI_2\{O(CH_2CH_2OMe)_2\}_2$], whilst the *cis*-isomer was obtained as a by-product in the reaction of SmI_2 with *t*-BuOK in diglyme. These were the first examples to be isolated of geometric isomers in an eight-coordinate complex.[114] The Sm–O distances in *cis*-[SmI_2\{diglyme\}$_2$], fall into the range 2,653–2.699 Å, averaging 2.68 Å, which is slightly shorter than the value for the trans-isomer. The Sm–I distances in the *cis*-isomer, however, at 3.332–3.333 Å, are significantly longer than those in *trans*-[SmI_2\{diglyme\}$_2$] (3.265 Å). In another study, reaction of SmI_2 with 1,2-diiodoethane at 50 °C yields [$SmI_2(dme)_3$]. Crystallisation at −20 °C affords racemic [$SmI_2(dme)_3$], whilst crystallisation from solution at ambient temperature yields a mixture of crystals of the two different enantiomers. It was suggested that interactions between methyl groups prevent ready interconversion.

The ytterbium (II) complex [$Yb(NCS)_2(thf)_2$] exhibits a rich range of oxidative addition reactions[115] affording complexes such as $Yb(NCS)_3(thf)_4$, $Yb(NCS)_3(Odpp)(thf)_3$ (HOdpp = 2,6-diphenylphenol), and $Yb(NCS)_2(Cp)(thf)_3$. It reacts with CCl_3CCl_3 forming $Yb(NCS)_2Cl(thf)_4$, which turns out to have the solid-state structure $[YbCl_2(thf)_5]^+$ $[Yb(NCS)_4(thf)_3]^-$ in contrast to the monomer $Yb(NCS)_3(thf)_4$. Oxidation of $Yb(NCS)_2(thf)_2$ with TlO_2CPh initially affords a solvated form of $Yb(NCS)_2(O_2CPh)$ which then gives a mixture of $Yb(NCS)_3(thf)_4$ and dimeric [[$Yb(NCS)(O_2CPh)_2(thf)_2$]$_2$]. The thf ligands in $Yb(NCS)_2(thf)_2$ can be replaced by dme forming 8-coordinate $Yb(NCS)_2(dme)_3$.

The first simple Tm(II), Nd(II) and Dy(II) complexes have been synthesised recently. Reaction of Nd and Dy with I_2 at 1500 °C followed by dissolution of the product affords [$LnI_2(dme)_3$] and [$LnI_2(thf)_5$] (Ln = Nd, Dy). [$NdI_2(thf)_5$] has the familiar pentagonal bipyramidal structure with axial iodines. [$TmI_2(dme)_2(thf)$] has a similar coordination geometry.[116]

Among complexes with multidentate ligands, a few lanthanide(II) diketonates are known. [$Eu(tmhd)_2(dme)_2$], has been made by reaction of [$EuI_2(thf)_2$] with Kthd in thf, evaporation and crystallisation from DME; [$Sm(tmhd)_2(dme)_2$] is made by a similar route.

A number of crown ether complexes exist. Thus [Eu(benzo-15-crown-5)$_2$] $(ClO_4)_2$ has been synthesised by electrochemical reduction of a solution of $Eu(ClO_4)_3$ and benzo-15-crown-5 in MeOH/H_2O. It contains 10-coordinate europium, with Eu–O distances in the range 2.662 (3)–2.728 (4) Å. This compound exhibits strong luminescence, taking on a violet hue in daylight. [Eu(12-crown-4)$(H_2O)_3$Cl]Cl has eight-coordinate Eu; europium is 10-coordinate in the [Eu((15-crown-5)$_2$)]$^{2+}$ ion and in [Eu(18-crown-6)$(ClO_4)_2$]. Two Sm(II) complexes have been made. [Sm(15-crown-5)$_2$] $(ClO_4)_2$ has a sandwich structure with samarium bound to two 15-crown-5 molecules, whilst in [Sm(18-crown-6)$(ClO_4)_2$] the metal cation is again 10-coordinate, bound to six oxygen atoms of the crown ligand and four oxygen atoms from two perchlorates.[117]

The Eu(II) edta complex Na_3[Eu(edta)]Cl·7H_2O is in fact polymeric in the solid state with europium bound to two nitrogens and to six carboxylate oxygens. $[(NH_2)_3]_3$ [Eu^{II}(dtpa)(H_2O)]·8H_2O is isostructural with the Sr analogue. Perhaps unexpectedly, in solution, [Eu^{II}(dtpa)(H_2O)]$^{3-}$ is less stable to oxidation than Eu^{2+} (aq).

A number of aryloxides employing bulky ligands have been explored in some detail. The thf adducts Yb(O2, 6-Bu^t_2-4-Me-C_6H_2)$_2$(thf)$_2$ are tetrahedral while Yb(O2,6-Bu^t_2-4-Me-C_6H_2)$_2$(thf)$_3$ are five- coordinate with square-pyramidal structures. [Sm(O-2,6-$Bu^t_2C_6H_3$)$_2$(thf)$_3$]·thf and [Sm($OC_6H_3Bu^t_2$-2,6-Me-4)$_2$(thf)$_3$] are both five-coordinate trigonal bipyramidal.

The bis(silylamide) complexes Ln\{$N(SiMe_3)_2$\}$_2$ and their adducts with Lewis bases such as thf and tertiary phosphines tend to be three- and four-coordinate. $Yb\{N(SiMe_3)_2\}_2$ is a dimer with two bridging alkylamides, giving three-coordination and $[Eu\{N(SiMe_3)_2\}_3]^-$ likewise is three-coordinate (surprisingly, planar, unlike the Eu^{III} analog), while $M\{N(SiMe_3)_2\}_2L_2$ ($L = PBu_3$, thf; $L_2 =$ dmpe) are four-coordinate and $Eu\{N(SiMe_3)_2\}_2(glyme)_2$ is six-coordinate. $[Sm(N(SiMe_3)_2)_2(thf)_2]$ has significant short-Sm$\cdots$C distances, evidence for agostic interactions (*see Agostic Bonding*). In $[Sm(NPh_2)_2(thf)_4]$, the coordination geometry approximates to trigonal prismatic (*see Trigonal Prism*).

Polypyrazolylborates have been extensively investigated.[104] $[Ln(Tp)_2(thf)_2]$ and $[Ln(Tp^{Me2})_2]$ (Ln = Eu, Sm, and Yb) have been synthesised; the latter are very insoluble and are usually purified by sublimation in the cases of the Eu and Yb compounds. The six-coordinate $[Sm(Tp^{Me2})_2]$ undergoes a range of 1- electron transfer reactions. In its wide range of oxidations, it forms $[Sm(Tp^{Me2})_2X]$ (X = Cl, Br, F) by halogen abstraction from organic compounds, and $[Sm(Tp^{Me2})_2]$ I by iodine oxidation. Reaction with $TlBPh_4$ gives $[Sm(Tp^{Me2})_2]$ $BPh_4\cdot[Sm(Tp^{Me2})_2]$ cleaves dichalcogenides REER forming $[Sm(Tp^{Me2})_2(ER)]$ (R e.g. Ph, E = S, Se), and reacts with azobenzene forming $[Sm(Tp^{Me2})_2(N_2Ph_2)]$ where the Tp^{Me2} ligands remain tridentate. $[Sm\{Tp^{Me2}\}_2]$ reacts with dioxygen forming the first lanthanide superoxo complex $[Sm\{Tp^{Me2}\}_2(\eta^2\text{-}O_2)]$. It undergoes a one-electron oxidation with $[Hg(C{\equiv}CPh)_2]$ forming monomeric seven-coordinate $[Sm(Tp^{Me2})_2(C{\equiv}CPh)]$. Using the bulkier hydrotris(3-t-butyl-5-methylpyrazolyl) borate ligand ($Tp^{^tBu,Me}$), it is still possible to obtain bis complexes with $Tp^{^tBu,Me}$, but $[Ln(Tp^{^tBu,Me})_2]$ (Ln = Sm, Yb) shows two different mode of ligand bonding; one is a conventional η^3-ligand, the other is bound via two nitrogen atoms and an agostic B–H$\cdots$Sm interaction. The NMR spectrum of $[Yb(Tp^{^tBu,Me})_2]$ shows ^{171}Yb–HB coupling, confirming that the agostic interaction persists in solution.

A number of organophosphides and organoarsenides of divalent lanthanides have been synthesised, with a certain similarity to the amides. $[YbI_2(thf)_2]$ and $[Yb\{N(SiMe_3)_2\}_2(thf)_2]$ react with $KPPh_2$ forming $[Yb(PPh_2)_2(thf)_4]$; the thf can be displaced by N-methylimidazole forming *trans*-$[Yb(PPh_2)_2(N\text{-Methylimidazole})_4]$. These compounds, together with $[Eu(PPh_2)_2(N\text{-Methylimidazole})_4]$, $[Sm(PPh_2)_2(N\text{-Methylimidazole})_4]$, $[Yb(P(mesityl)_2)_2(thf)_4]$, $[Sm(P(mesityl)_2)_2(thf)_4]$ and $[Sm(As(mesityl)_2)_2(thf)_4]$ all having trans-octahedral structures.

Some compounds with heavier group 16 donor atoms have lately been reported, of the type $Yb(SAr)_2(DME)_2$ (six-coordinate) and $Ln(QMes)_2(thf)_n$ (Ln = Yb, Sm, Eu; Q = Se, Te). Transmetallation of Sm and Eu with $Hg(SC_6F_5)_2$ affords $Sm(SC_6F_5)_3$ and $Eu(SC_6F_5)_2$ respectively; these have the solid-state structures $[(thf)_2Sm(\mu_2\text{-}SC_6F_5)(SC_6F_5)_2]_2$ and $[(thf)_2Eu(\mu_2\text{-}SC_6F_5)_2]_n$, the latter being a 1-dimensional polymer; these undergo thermal decomposition to LnF_3. Ytterbium reacts with organic disulphides forming $[Yb(SAr)_2(py)_2]$ (Ar = 2,4,6-triisopropylphenyl). A sterically crowded Yb^{II} thiolate $[Yb(SAr^*)_2(thf)_4]$ ($Ar^* = 2,6\text{-}Trip_2C_6H_3$, where Trip is $2,4,6\text{-}^iPr_3C_6H_2$) has the trans-structure now becoming familiar for these Ln^{II} systems. The overcrowding caused by the sterically encumbered Ar^* ligands is reflected in the large Yb–S–C angle of 151.16°. The unsolvated compound is formally two-coordinate, but there are η^6-π-interactions present. Lanthanide(II) selenolate and tellurolate complexes, usually obtained as etherates, are possible precursors to lanthanide monochalcogenides. $M(TePh)_2$ (M = Yb, Eu) crystallize as 1-dimensional polymers like $[(thf)_2Eu(TePh)_2]_\infty$ and $[(thf)_2Yb(TePh)_2\cdot 0.5(thf)]_\infty$. $[Ln(ESi(SiMe_3)_3)_2(tmeda)_2]$ (Ln = Eu, Yb; E = Se, Te) have been reported; the ytterbium tmeda complexes eliminate $E(Si(SiMe_3)_3)_2$ at 200 °C affording YbSe and YbTe. $Ln(SePh)_2$ reacts with selenium (rather as the trivalent analogues do) in dme forming heterovalent clusters $[Ln_4Se(SePh)_8(dme)_4]$ (Ln = Sm, Yb, Nd^{III}/Yb^{II}, Sm^{III}/Yb^{II}) which contain a square of lanthanide ions with a capping selenide.

A variety of halometallates exist. For example, Rb_4TmI_6, synthesised by heating a mixture of RbI, Tm, and HgI_2, has the K_4CdI_6 structure with trigonal antiprismatic coordination of Tm. $RbYbI_3$ has a structure based on edge-sharing $[YbI_6]$ octahedra. Reduction of MX_3 (M = Sm, Dy, Tm, Yb; X = Br, I) with alkali metals, In and Tl (A) leads in general to the ternary compounds AMX_3 and AM_2X_5; some similar compounds with divalent metals (Ca, Sr, Ba) have also been made. $LiDy_2Br_5$, prepared by reduction of $DyBr_3$ with Li metal at 700 °C, is isostructural with $LiDy_2Cl_5$, $LiYb_2Cl_5$ and $LiLn_2Br_5$ (Ln = Sm, Tm).

3.8.3 The +4 State

Cerium is the only lanthanide with an extensive chemistry in this oxidation state. The cerium(+4) aqua ion, obtained by acid dissolution of CeO_2, is thermodynamically unstable ($E = 1.6$ V in 1 M HNO_3); the reduction potential is anion-sensitive, indicating that complexes are present rather than a simple aqua ion. The salts $Ce(NO_3)_4\cdot 5H_2O$ and $CeSO_4\cdot 4H_2O$ can be crystallized from solution, the former probably having 11-coordinate $Ce(NO_3)_4(H_2O)_3$ molecules like the thorium analog. The most familiar nitrate complex is $(NH_4)_2Ce(NO_3)_6$, a traditional oxidizing agent in titrimetry and in organic chemistry as well as a convenient synthetic starting material. The $Ce(NO_3)_6{}^{2-}$ ion has 12-coordinate cerium while cerium is 10-coordinate in the $Ce(CO_3)_5{}^{6-}$ ion. $MgCe(NO_3)_6\cdot 8H_2O$ and $K_2Ce(NO_3)_6$ containing 12-coordinate $[Ce(NO_3)_6]^{2-}$ ions too. Hydrated cerium(IV) triflate dehydrates on stirring with triflic anhydride. It is potentially a valuable source of other Ce^{IV} compounds. The iodates $Ce^{IV}HIO_6\cdot 4H_2O$ and $MCe^{IV}IO_6\cdot nH_2O$ (M = alkali metal) have also been made.

A number of fluoride complexes have been made, both by crystallization for the ammonium salts like $(NH_4)_4CeF_8$, which has square-antiprismatic coordination of cerium, also found in the $(CeF_6{}^{2-})_\infty$ chains in $(NH_4)_2CeF_6$, its thermal decomposition product. $(NH_4)_3CeF_7\cdot H_2O$ acquires dodecahedral eight-coordination by dimerization. $(NH_4)_4[CeF_8]$ can also be made by fluorination of cerium oxide with NH_4HF_2. Alkali-metal cerates M_2CeF_6 and M_3CeF_7 (M = alkali metal) are moisture sensitive and are made by fluorination of MCl/CeO_2 mixtures. Several hexachlorocerate(IV) salts are known, perhaps the most convenient starting material for further syntheses being the $(H_2\ \mathrm{diglyme}_3)^+$ salt, made from the reaction of CeO_2 with $SOCl_2$ in diglyme; these react with HBr to give moisture-sensitive $CeBr_6{}^{2-}$ salts. Ce^{IV} is presumably too strongly oxidizing to coexist with I^- as no corresponding iodocerates have been made.

A number of neutral complexes of O-donor Lewis bases have been made, such as 10-coordinate $Ce(NO_3)_4(Ph_3PO)_2$, and octahedral $CeCl_4L_2$ (L = Ph_3PO, Ph_3AsO, HMPA, urea, t-Bu_2SO). The Ph_3PO complex is *cis*, like the uranium analog, while X-ray diffraction study of the (*trans*) HMPA complex shows a close structural correspondence to the corresponding U^{IV} compound.

Cerium(III) tris(β-diketonate) complexes are readily oxidized to the cerium(IV) compounds. They are volatile with vapor pressures high enough for MOCVD use. A number of diketonates are now better characterised, prompted by the possibility of using them as CVD materials and petrol additives, as well as a source of cerium oxide as an oxygen store for catalytic converters. $[Ce\{Me_3CCOCHCOCMe_2(OMe)\}_4]$, $Ce(acac)_4$ (Figure 32), $Ce(dbm)_4$, $[Ce(pmhd)_4]$, and $Ce(tmhd)_4$ all have square-antiprismatic coordination of cerium (in the $[Ce(catecholate)_4]^{4-}$ ion the coordination is dodecahedral).

The alkoxides $Ce(OR)_4$ are another well-developed class of Ce^{IV} compounds. The alkoxide group plays an important role in stabilising the Ce(IV) state, witness the existence of $[CeCp_2(OBu^t)_2]$ and $[CeCp_3(OBu^t)]$, when other Ce(IV) organometallics cannot be isolated. The isopropoxide is volatile in vacuo below 200 °C (its bis(isopropanol) adduct has six-coordinate cerium). General methods are available to make many $Ce(OR)_4$ (R e.g. Me, Et, OPr^i, n-C_8H_{17}):-

$$(NH_4)_2Ce(NO_3)_6 + 4ROH + 4NH_3 \longrightarrow Ce(OR)_4 + 6NH_4NO_3 \tag{12}$$

$$(NH_4)_2Ce(NO_3)_6 + 4ROH + 6NaOMe \longrightarrow Ce(OR)_4 + 6NaNO_3 + 2NH_3 + 6MeOH \tag{13}$$

As usual, many of these are oligomers, though coordinative saturation can be achieved by adduct formation. Crystals of $[Ce(OSiPh_3)_4(DME)]$ display octahedral coordination of cerium with Ce–O (Si) 2.10–2.14 Å and two rather long Ce–O (ether) bonds at 2.58–2.59 Å. Although the solid is air- and moisture-stable, it undergoes immediate reaction with Hacac forming $Ce(acac)_4$. Thermal desolvation of $[Ce(OPr^i)_4(HOPr^i)_2]$ affords $[Ce_4O(OPr^i)_{14}]$, which has the structure $[Ce_4(\mu_4\text{-}O)(\mu_3\text{-}OPr^i)_2(\mu\text{-}OPr^i)_8(OPr^i)_{14}]$. $(NH_4)_2Ce(NO_3)_6$ reacts with $NaOCMe_3$ forming various products, including $Na_2Ce(OCMe_3)_6(DME)_2$ which has octahedral $[Ce(OCMe_3)_6]^{2-}$ ions surrounded by $Na(DME)^+$ ions.

The first Ln(IV) amides have been made.**[118]** Although it cannot be oxidised with Cl_2, $[Ce(N(SiMe_3)_2)_3]$ reacts with $TeCl_4$ forming $[CeCl(N(SiMe_3)_2)_3]$; this has a trigonal pyramidal structure, with Ce 0.36 Å out of the N_3 basal plane (and, interestingly a 0.05 Å lengthening of the N–Si bond). PPh_3Br_2 reacts with $[Ce(N(SiMe_3)_2)_3]$ forming the isostructural $[CeBr(N(SiMe_3)_2)_3]$. Another Ce(IV) amide was synthesised by iodine oxidation of a cerium(III) compound of a triamidoamine, affording a notable compound with a rare Ce^{IV}-I linkage; analogous oxidation with X_2 (X = Cl, Br) yields mixed-valence dimers (Figure 33).**[119]**

2,4,6-tri-t-butylpyridyl-1,3,5-triazine (L) reacts with $(NH_4)_2[Ce(NO_3)_6]$ forming 11-coordinate $[Ce(L)(NO_3)_4]$. In contrast to the other lanthanides, cerium forms genuine bis(porphyrin) and bis(phthalocyanine) complexes with the metal in the +4 oxidation state. Solution NMR shows that the two porphyrin rings do not rotate with respect to each other even at 140 °C.

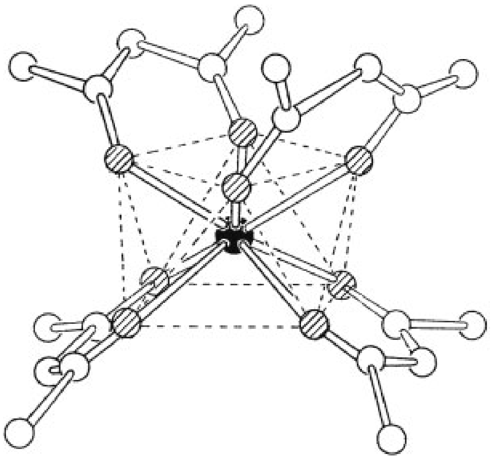

Figure 32 The structure of $Ce(acac)_4$

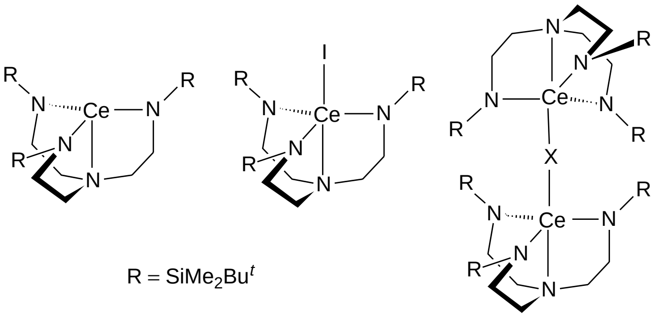

Figure 33 Cerium complexes of a tripodal triamidoamine ligand

4 PROMETHIUM

On account of this element's rarity, a separate account of it is desirable.[120,121] Although the existence of promethium was predicted as early as 1913, it was not definitely discovered until 1945, since all isotopes are radioactive with the longest-lived isotope having a half-life of 17.7 years (^{145}Pm). It is a fission product of ^{238}U and is thus obtained on work-up of reprocessing wastes.

Although early attempts to identify it in lanthanide ores were not successful, it has been detected at the level of 4×10^{-15} g kg^{-1} in Congolese pitchblende. It has also been detected at a low level in apatite (10^{-11} g from 6 million kg mineral), although it may have originated there from neutron irradiation of neodymium or by spontaneous fission of ^{238}U.

Relatively little is known about the chemistry of promethium, although the established facts highlight the resemblance of promethium to the lanthanides that flank it. The halides are well defined, and have been shown to have the expected structures (Table 2). Thus in a recent study, starting with some 100 μg of Pm_2O_3, the halides were synthesized microchemically, using the reaction with fluorine for PmF_3 and the reaction with HX (X = Cl, Br) for the chloride and bromide; the latter two reacted with HI to give the iodide. Pm_2O_3 is one of the few lanthanide oxides to crystallize in three modifications.[122]

It would be expected that promethium would form some stable compounds in the +2 oxidation state, but no definite evidence has yet been obtained since studies have been hindered both by the small quantities available and by its radioactivity.

5 LANTHANIDES IN ORGANIC SYNTHESIS

Lanthanide complexes have increasingly been used as reagents,[123,124] two of the main areas being SmI_2 as a one-electron reducing agent[125,126] and the use of lanthanide triflates (and scandium triflate especially) as reusable water-soluble Lewis Acid catalysts.[127,128]

6 USES OF THE LANTHANIDES[3,129,130]

There are increasingly numerous uses of these metals that make use of particular electronic, magnetic, and optical properties of individual lanthanides; most current applications involve the earlier rather than the later metals, there being no major uses for the metals Ho–Lu at present.

The main optical uses are in lasers, phosphors, and lenses. The single most important phosphors contain europium(III) in a yttrium host such as Y_2O_2S, which is used for the red phosphor in TV color screens; other phosphors are used (Tm, Tb) in X-ray image intensifying screens. Neodymium-doped yttrium–aluminum garnet (YAG) is an important laser material, whilst erbium-YAG lasers are starting to be used in cosmetic skin resurfacing. Erbium-doped fibre amplifiers are becoming significant in telecommunications. Neodymium-containing glass is used in protective goggles, owing to its absorption around 580 nm. while La_2O_3 is used in manufacturing optical glass of a high refractivity. CeO_2 is used in polishing glass and also in decolourising glass.

Principal magnetic uses employ either the samarium–cobalt or $Nd_2Fe_{14}B$ permanent magnet materials. The latter give slightly stronger products and employ materials with more assured supply, but the samarium magnets can be used at much higher temperatures.

There are a number of current optical and magnetooptical applications and several at the development stage. The use of LaB_6 in electron guns has long been established, as has that of yttrium–iron garnet (YIG) in microwave devices, while gadolinium–gallium garnet is used for bubble memory storage devices. Developing uses include yttrium-stabilized zirconia (YSZ) in particular as a solid electrolyte and as an oxygen-sensor in automobile exhaust systems, rare-earth-doped barium titanates in thermistors, and $LaNi_5$ in rechargeable batteries. Yttrium–barium copper oxide and other lanthanide-containing oxides are likely to become important commercially in warm superconductors.

Probably the biggest use in terms of quantity is that of lanthanide-exchanged zeolites as cracking catalysts in the petrochemical industry (mainly La and Ce), using about 500 t a day in the USA alone.

Because of its high refractive index and hardness, YSZ is a superior material for artificial diamonds to YAG, also used for this purpose. The praesodymium–neodymium mixture known as didymium is traditionally used to color welders' goggles (as well as a strengthening agent for Mg-based alloys). Several lanthanide oxides, particularly Nd_2O_3, are used as glass-coloring agents. CeO_2 has been used as an ingredient of automobile catalytic converters and in self-cleaning ovens as an oxidation catalyst whose oxygen storage role is presumably a consequence of the ability of cerium to switch oxidation states.

Medical applications are so far limited in number, but gadolinium complexes of DTPA and other ligands have become highly important injectible MRI contrast agents (*see* ***Metal-based Imaging Agents***). The luminescent properties of the lanthanides are becoming exploited in luminescent sensors and bioassays.

7 TOXICITY OF THE LANTHANIDES[35,131]

The lanthanides are generally not regarded as particularly toxic. Studies on animals indicate that the toxicity depends on how the lanthanide was introduced. Little appears to be absorbed in oral ingestion although it appears considerably more toxic in intravenous administration. Inhalation of vapor and dust should be avoided as solid compounds if inhaled tend to remain in the lungs and are only slowly ingested on account of their insolubility (This could be an occupational hazard in lanthanide refining and in 'new' lanthanide industries.) Lanthanides tend to accumulate in the liver, spleen, kidneys, and bone.

The use of complexed Gd^{3+} in MRI relies on the high stability of the Gd–DTPA complex to maintain an extremely low level of free Gd^{3+}, but some side-effects have been observed using such ionic compounds, prompting current research to produce nonionic contrast agents.

8 RELATED ARTICLES

Actinides: Inorganic & Coordination Chemistry; Scandium, Yttrium & the Lanthanides: Organometallic Chemistry.

9 REFERENCES

1. 'Gmelin Handbook of Inorganic Chemistry', System No. 39, Part A, History, Occurrence; Part B, The Elements; Part C, The Compounds; Part D, Coordination Compounds; 1938, onwards.
2. K. A. Gschneidner Jr and L. E. Eyring eds, 'Handbook on the Physics and Chemistry of the Rare Earths', North-Holland, Amsterdam, 32 Vols, 1978, onwards.
3. T. Moeller, in 'Comprehensive Inorganic Chemistry', ed. J. C. Bailar, Pergamon, Oxford, 1973, Vol. 4, p. 1.
4. F. A. Hart, in 'Comprehensive Coordination Chemistry', ed. G. Wilkinson, Pergamon, Oxford, 1987, Vol. 3, p. 1059.
5. S. A. Cotton, in 'Comprehensive Coordination Chemistry-II', eds. J. A. McCleverty and T. J. Meyer, Pergamon, Oxford, 2004, Vol. 3, p. 93.
6. S. A. Cotton, 'Lanthanides and Actinides', Macmillan, London, 1991.
7. H. C. Aspinall, 'Chemistry of the F-block Elements', Gordon and Breach, 2001.
8. N. Kaltsoyannis and P. Scott, 'The F Elements', Oxford University Press, Oxford, 1999.
9. J.-C. G. Bunzli and G. R. Choppin eds, 'Lanthanide Probes in Life, Chemical and Earth Sciences', Elsevier, Amsterdam, 1989.
10. S. P. Sinha ed., 'Systematics and Properties of the Lanthanides', Reidel, Dordrecht, 1983.
11. C. H. Evans, *Chem. Br.*, 1989, 880.
12. C. T. Horowitz ed., 'Scandium', Academic Press, New York, 1975.
13. S. A. Cotton, *Polyhedron*, 1999, **18**, 1691.
14. J. D. Corbett, *Pure Appl. Chem.*, 1992, **64**, 1395.
15. S. A. Cotton, *Comments Inorg. Chem.*, 1999, **21**, 165.
16. T. Yamaguchi, M. Niihara, T. Takamuru, H. Wakita, and H. Kanno, *Chem. Phys. Lett.*, 1997, **274**, 485.
17. K. C. Lim, B. W. Skelton, and A. H. White, *Aust. J. Chem.*, 2000, **53**, 875.
18. F. Matsumoto, Y. Ohki, Y. Suzuki, and A. Ouchi, *Bull. Chem. Soc. Jpn.*, 1989, **62**, 2081.
19. J. S. Brodkin and B. M. Foxman, *J. Chem. Soc., Chem. Commun.*, 1991, 1073.
20. G. R. Willey, P. R. Meehan, M. D. Rudd, and M. G. B. Drew, *J. Chem. Soc., Dalton Trans.*, 1995, 811.
21. G. Meyer, N. Cesur, and I. Pantenburg, *Acta Crystallogr., Sect. E*, 2003, **E59**, i145.
22. T. Moeller, *J. Chem. Educ.*, 1970, **47**, 417.
23. G. L. Breneman, *J. Chem. Educ.*, 1988, **65**, 31.
24. K. A. Gschneidner, in 'Fine Chemicals for the Electronics Industry II: Chemical Applications for the 1990s', eds. D. J. Ando and M. G. Pellatt, Royal Society of Chemistry, Cambridge, 1991, p. 63.
25. 'Gmelin Handbook of Inorganic Chemistry', Part B, Sect. 2–3, 1974–6.
26. D. A. Johnson, *Adv. Inorg. Chem.*, 1977, **20**, 1.
27. B. P. Hay, *Inorg. Chem.*, 1991, **30**, 2876.
28. D. R. Lloyd, *J. Chem. Educ.*, 1986, **63**, 502.
29. S. Hufner, in 'Systematics and Properties of the Lanthanides', ed. S. P. Sinha, Reidel, Dordrecht, 1983, p. 313.
30. W. T. Carnall, J. V. Beitz, H. Crosswhite, K. Rajnak, and J. B. Mann, in 'Systematics and Properties of the Lanthanides', ed. S. P. Sinha, Reidel, Dordrecht, 1983, p. 389.
31. S. P. Sinha, in 'Systematics and Properties of the Lanthanides', ed. S. P. Sinha, Reidel, Dordrecht, 1983, p. 451.
32. J.-C. G. Bunzli, in 'Lanthanide Probes in Life, Chemical and Earth Sciences', eds, J.-C. G. Bunzli and G. R. Choppin Elsevier, Amsterdam, 1989, p. 219.
33. R. C. Holz and L. C. Thompson, *Inorg. Chem.*, 1993, **32**, 5251.
34. E. M. Stephens, in 'Lanthanide Probes in Life, Chemical and Earth Sciences', eds, J.-C. G. Bunzli and G. R. Choppin Elsevier, Amsterdam, 1989, p. 181.
35. C. H. Evans, 'Biochemistry of the Lanthanides', Plenum, London, 1990.
36. 'Gmelin Handbook of Inorganic Chemistry', Part C, Sect. 3 (1976: fluorides), 4a, b (1982: chlorides), and 6 (1978: bromides and iodides).
37. J. Burgess and J. Kijorski, *Adv. Inorg. Chem. Radiochem.*, 1981, **24**, 51 (halides).
38. G. Meyer and H.-J. Meyer, *Chem. Mater.*, 1992, **4**, 1157.

39. S. A. Cotton, ‘Lanthanides and Actinides’, Macmillan, London, 1991, p. 22.
40. ‘Gmelin Handbook of Inorganic Chemistry’, 1974, Part C, Sect. 1.
41. ‘Gmelin Handbook of Inorganic Chemistry’, 1974, Part C, Sect. 1.
42. ‘Gmelin Handbook of Inorganic Chemistry’, 1990, Part C, Sect. 11 a, b.
43. ‘Gmelin Handbook of Inorganic Chemistry’, 1983, Part C, Sect. 7.
44. T. Schleid and F. Lissner, *J. Alloys Compd.*, 1992, **189**, 69.
45. K. Mitchell and J. A. Ibers, *Chem. Rev.*, 2002, **102**, 1929.
46. G. Adachi, N. Imanaka, and Z. Fuzhong, in ‘Handbook on the Physics and Chemistry of the Rare Earths’, eds. K. A. Gschneidner Jr and L. E. Eyring, North-Holland, Amsterdam, 1978, onwards, Vol. 15, p. 61.
47. ‘Gmelin Handbook of Inorganic Chemistry’, Part D, Sect. 1–5.
48. D. G. Karraker, *J. Chem. Educ.*, 1970, **47**, 424.
49. A. E. Martell and R. M. Smith, ‘Critical Stability Constants’, Plenum, New York, 1974–89, Vols. 1–6.
50. G. J. Palenik, in ‘Systematics and Properties of the Lanthanides’, ed. S. P. Sinha, Reidel, Dordrecht, 1983, p. 153.
51. C. Eaborn, P. B. Hitchcock, K. Izod, Z.-R. Lu, and J. D. Smith, *Organometallics*, 1996, **15**, 4783.
52. L. Niinsto, in ‘Systematics and Properties of the Lanthanides’, ed. S. P. Sinha, Reidel, Dordrecht, 1983, p. 125.
53. A. Chatterjee, E. N. Maslen, and K. J. Watson, *Acta Crystallogr., Sect. B*, 1988, **44**, 381.
54. P. C. Junk, D. L. Kepert, B. W. Skelton, and A. H. White, *Aust. J. Chem.*, 1999, **52**, 497.
55. C. J. Kepert, B. W. Skelton, and A. H. White, *Aust. J. Chem.*, 1994, **47**, 385.
56. K. C. Lim, B. W. Skelton, and A. H. White, *Aust. J. Chem.*, 2000, **53**, 867.
57. J. Näslund, P. Lindqvist-Reis, I. Persson, and M. Sandström, *Inorg. Chem.*, 2000, **39**, 4006.
58. N. J. Hill, W. Levason, M. C. Popham, G. Reid, and M. Webster, *Polyhedron*, 2002, **21**, 445.
59. D. Barr, A. T. Brooker, M. J. Doyle, S. R. Drake, P. R. Raithby, R. Snaith, and D. S. Wright, *Angew. Chem., Int. Ed. Engl.*, 1990, **29**, 285.
60. S. Petricek, A. Demšar, L. Golic, and J. Košmrlj, *Polyhedron*, 2000, **19**, 199.
61. K. Asakura and T. Imamoto, *Bull. Chem. Soc. Jpn.*, 2001, **74**, 731.
62. G. B. Deacon, T. Feng, P. C. Junk, B. W. Skelton, A. N. Sobolev, and A. H. White, *Aust. J. Chem.*, 1998, **51**, 75.
63. G. B. Deacon, T. Feng, P. C. Junk, G. Meyer, N. M. Scott, B. W. Skelton, and A. H. White, *Aust. J. Chem.*, 2000, **53**, 853.
64. K. Izod, S. T. Liddle, and W. Clegg, *Inorg. Chem.*, 2004, **43**, 214.
65. G. Depaoli, P. Ganis, P. L. Zanonato, and G. Valle, *Polyhedron*, 1993, **12**, 1933.
66. U. Baisch, D. B. Dell‘Amico, F. Calderazzo, R. Conti, L. Labella, F. Marchetti, and E. A. Quadrelli, *Inorg. Chim. Acta*, 2004, **357**, 1538.
67. A. Milicic-Tang and J.-C. G. Bunzli, *Inorg. Chim. Acta*, 1992, **192**, 201.
68. ‘Gmelin Handbook of Inorganic Chemistry’, 1981, Part D3.
69. E. H. Barash, P. S. Coan, E. B. Lobkovsky, W. E. Streib, and K. G. Caulton, *Inorg. Chem.*, 1993, **32**, 497.
70. T. J. Wenzel, ‘NMR Shift Reagents’, CRC, Boca Raton, FL, 1988.
71. A. D. Sherry and C. F. G. C. Geraldes, in ‘Lanthanide Probes in Life, Chemical and Earth Sciences’, eds. J.-C. G. Bunzli and G. R. Choppin, Elsevier, Amsterdam, 1989, p. 93.
72. R. E. Sievers, ‘Nuclear Magnetic Shift Reagents’, Academic Press, New York, 1973.
73. ‘Gmelin Handbook of Inorganic Chemistry’, 1984, Vol. D5.
74. A. Lossin and G. Meyer, *Z. Anorg. Allg. Chem.*, 1994, **620**, 438.
75. R. D. Rogers, R. D. Etzenhouser, J. S. Murdoch, and E. Reyes, *Inorg. Chem.*, 1991, **30**, 1445.
76. R. D. Rogers, A. N. Rollins, R. F. Henry, J. S. Murdoch, R. D. Etzenhouser, S. E. Huggins, and L. Nunez, *Inorg. Chem.*, 1991, **30**, 4946.
77. S. Fleming, C. D. Gutsche, J. M. Harrowfield, M. I. Ogden, B. W. Skelton, D. F. Stewart, and A. H. White, *J. Chem. Soc., Dalton Trans.*, 2003, 3319.
78. J. M. Harrowfield, M. I. Ogden, W. R. Richmond, and A. H. White, *J. Chem. Soc., Dalton Trans.*, 1991, 2153.
79. ‘Gmelin Handbook of Inorganic Chemistry’, 1977–8, Vols. C5–6.
80. D. M. Young, G. L. Schimek, and J. W. Kolis, *Inorg. Chem.*, 1996, **35**, 7620.
81. J.-S. Li, B. Neumuller, and K. Dehnicke, *Z. Anorg. Allg. Chem.*, 2002, **628**, 45.
82. G. B. Deacon, B. Görtler, P. C. Junk, E. Lork, R. Mews, J. Petersen, and B. Zemva, *J. Chem. Soc., Dalton Trans.*, 1998, 3887.
83. F. Matsumoto, T. Takeuchi, and A. Ouchi, *Bull. Chem. Soc. Jpn.*, 1990, **63**, 620.
84. D. L. Kepert, L. I. Semenova, A. N. Sobolev, and A. H. White, *Aust. J. Chem.*, 1996, **49**, 1005.
85. J. F. Bower, S. A. Cotton, J. Fawcett, R. S. Hughes, and D. R. Russell, *Polyhedron*, 2003, **22**, 347.
86. L. I. Semenova and A. H. White, *Aust. J. Chem.*, 1999, **52**, 571.
87. S. A. Cotton, V. Franckevicius, R. E. How, B. Ahrens, L. L. Ooi, M. F. Mahon, P. R. Raithby, and S. J. Teat, *Polyhedron*, 2003, **22**, 1489.

88. L. I. Semenova, A. N. Sobolev, B. W. Skelton, and A. H. White, *Aust. J. Chem.*, 1999, **52**, 519.
89. M. G. B. Drew, P. B. Iveson, M. J. Hudson, J. O. Liljenzin, L. Spjuth, P.-Y. Cordier, A. A. Enarsson, C. Hill, and C. Madic, *J. Chem. Soc., Dalton Trans.*, 2000, 821.
90. B. Ahrens, S. A. Cotton, N. Feeder, O. E. Noy, P. R. Raithby, and S. J. Teat, *J. Chem. Soc., Dalton Trans.*, 2002, 2027.
91. M. G. B. Drew, M. J. Hudson, P. B. Iveson, C. Madic, and M. L. Russell, *J. Chem. Soc., Dalton Trans.*, 2000, 2711.
92. T. Yamada, S. Shinoda, and T. Tsukube, *Chem. Commun.*, 2002, 1218.
93. E. C. Constable, R. Chotalia, and D. A. Tocher, *J. Chem. Soc., Chem. Commun.*, 1992, 771.
94. J. W. Buchler, M. Kihn-Botulinski, J. Loffler, and B. Scharbert, *New J. Chem.*, 1992, **16**, 545.
95. C. J. Schaverien and A. G. Orpen, *Inorg. Chem.*, 1991, **30**, 4968.
96. T. J. Foley, K. A. Abboud, and J. M. Boncella, *Inorg. Chem.*, 2002, **41**, 1704.
97. I. Bkouche-Waksman, J. Guilhem, C. Pascard, B. Alpha, R. Deschenaux, and J.-M. Lehn, *Helv. Chim. Acta*, 1991, **74**, 1163.
98. F. Benetollo, G. Bombieri, L. Calabi, S. Aime, and M. Botta, *Inorg. Chem.*, 2003, **42**, 148.
99. D. Parker, R. S. Dickins, H. Puschmann, C. Crossland, and J. A. K. Howard, *Chem. Rev.*, 2002, **102**, 1977.
100. J. L. Sessler, N. A. Tvermoes, J. Davis, P. Anzenbacher Jr, K. Jursikova, W. Sato, D. Seidel, V. Lynch, C. B. Black, A. Try, B. Andrioletti, G. Hemmi, T. D. Mody, D. J. Magda, and V. Kral, *Pure Appl. Chem.*, 1999, **71**, 2009.
101. R. C. Mehrotra, A. Singh, and U. M. Tripathi, *Chem. Rev.*, 1991, **91**, 1287.
102. E. D. Brady, D. L. Clark, J. C. Gordon, P. J. Hay, D. W. Keogh, R. Poli, B. L. Scott, and J. G. Watkin, *Inorg. Chem.*, 2003, **42**, 6682.
103. H. C. Aspinall, S. R. Moore, and A. K. Smith, *J. Chem. Soc., Dalton Trans.*, 1992, 153.
104. N. Marques, A. Sella, and J. Takats, *Chem. Rev.*, 2002, **102**, 2137.
105. F. T. Edelmann, D. M. M. Freckmann, and H. Schumann, *Chem. Rev.*, 2002, **102**, 1851.
106. B. Cetinkaya, P. B. Hitchcock, M. F. Lappert, and R. G. Smith, *J. Chem. Soc., Chem. Commun.*, 1992, 932.
107. H. C. Aspinall, S. A. Cunningham, P. Maestro, and P. Macaudiere, *Inorg. Chem.*, 1998, **37**, 5396.
108. J. H. Melman, C. Rohde, T. J. Emge, and J. G. Brennan, *Inorg. Chem.*, 2002, **41**, 28.
109. R. B. Lauffer, *Chem. Rev.*, 1987, **87**, 901.
110. P. Caravan, J. J. Ellison, T. J. McMurry, and R. B. Lauffer, *Chem. Rev.*, 1999, **99**, 2293.
111. M. S. Konings, W. C. Dow, D. B. Love, K. N. Raymond, S. C. Quay, and S. M. Rocklage, *Inorg. Chem.*, 1990, **29**, 1488.
112. J. F. Carvalho, S.-H. Kim, and C. A. Chang, *Inorg. Chem.*, 1992, **31**, 4065.
113. L. Karmazin, M. Mazzanti, and J. Pécaut, *J. Chem. Soc., Chem. Commun.*, 2002, 654.
114. V. R. Chebolu, R. Whittle, and A. Sen, *Inorg. Chem.*, 1987, **26**, 1821.
115. G. B. Deacon, C. M. Forsyth, and D. L. Wilkinson, *Eur. Chem. J.*, 2001, **7**, 1784.
116. M. N. Bochkarev, I. L. Fedushkin, S. Dechert, A. A. Fagin, and H. Schumann, *Angew. Chem., Int. Ed. Engl.*, 2001, **40**, 3176.
117. P. Starynowicz, *J. Chem. Soc., Dalton Trans.*, 2004, 825.
118. P. B. Hitchcock, A. G. Hulkes, and M. F. Lappert, *Inorg. Chem.*, 2004, **42**, 1031.
119. C. Morton, N. W. Alcock, M. R. Lees, I. J. Munslow, C. J. Sanders, and P. Scott, *J. Am. Chem. Soc.*, 1999, **121**, 11255.
120. F. Weigel, *Chem. Zeitung*, 1978, **198**, 339.
121. S. A. Cotton, *Educ. Chem.*, 1999, **36**, 96.
122. W. R. Wilmarth, R. G. Haire, J. P. Young, D. W. Ramey, and J. R. Peterson, *J. Less-Common Met.*, 1988, **141**, 275.
123. S. Kobayashi, ‘Lanthanides: Chemistry and Use in Organic Synthesis’, Springer Verlag, Berlin, 1999.
124. T. Imamoto, ‘Lanthanides in Organic Synthesis’, Academic Press, 1994.
125. G. A. Molander, *Chem. Rev.*, 1992, **92**, 29.
126. G. A. Molander and C. R. Harris, *Chem. Rev.*, 1996, **96**, 307.
127. S. Kobayashi, *Eur. J. Org. Chem.*, 1999, 15.
128. S. Kobayashi, M. Sugiura, H. Kitagawa, and W. W.-L. Lam, *Chem. Rev.*, 2002, **102**, 2227.
129. J. Hecht, ‘The Laser Guidebook’, 2nd edn., McGraw-Hill, New York, 1992.
130. D. L. Andrews and A. A. Demydov eds, ‘An Introduction to Laser Spectroscopy’, Kluwer, Dordrecht, 2002.
131. E. Merian ed., ‘Metals and their Compounds in the Environment’, VCH, Weinheim, 1991.

Scandium, Yttrium & the Lanthanides: Organometallic Chemistry

Herbert Schumann[1] **& Igor L. Fedushkin**[2]

[1] *Institut für Chemie, Technische Universität Berlin, Berlin, Germany*
[2] *G. A. Razuvaev Institute of Organometallic Chemistry, Russian Academy of Sciences, Nizhny Novgorod, Russia*

Based in part on the article Scandium, Yttrium & the Lanthanides: Organometallic Chemistry by R. D. Köhn, G. Kociok-Köhn, & H. Schumann which appeared in the Encyclopedia of Inorganic Chemistry, First Edition.

1 Introduction 1
2 Lanthanide Complexes with σ-Bonded Hydrocarbyl Ligands 1
3 Alkene and Alkyne Complexes 10
4 Allyl and Allenyl Complexes 10
5 Diene Complexes 12
6 Pentadienyl Complexes 13
7 Cyclopentadienyl, Indenyl, & Fluorenyl Complexes 13
8 Arene Complexes 27
9 Cycloheptatrienyl Complexes 31
10 Cyclooctatetraenyl Complexes 31
11 Organolanthanides in the Oxidation State 0, +1, +2 and +4 34
12 Related Articles 50
13 Further Reading 50
14 References 50

Abbreviations

Cp = cyclopentadienyl (C_5H_5); Cp' = general substituted or unsubstituted Cp; Cp* = pentamethylcyclopentadienyl (C_5Me_5); X_nCp = Cp with n Hs substituted by X; Ind = indenyl (C_9H_7); COT = cyclooctateraenyl (C_8H_8); Mes = mesityl ($C_6H_2Me_3$); Cy = cyclohexyl C_6H_{11}; Ln = lanthanide and group 3 metals.

1 INTRODUCTION

Organometallic compounds of the rare earth metals have been a curiosity till only a few decades ago. That changed in the last 20 years of the twentieth century after the availability of modern preparative and analytical techniques and with the discovery of the high potential of those compounds, which are all extremely sensitive to oxygen and water, as reagents in organic synthesis and as very active catalysts. Following the discovery of the tricyclopentadienyl derivatives of the lanthanides by *Wilkinson* and *Birmingham* in 1954,[1] most of the organolanthanide compounds prepared during the first 20 years have been sandwich complexes (*see Sandwich Compound*), containing unsubstituted or substituted cyclopentadienyl ligands. In contrast, cyclopentadienyl-free organolanthanide compounds, like alkyl or aryl derivatives, alkenyl, alkynyl, allyl, hydrido, and carbene complexes, as well as cyclooctatetraenyl, pentadienyl derivatives, and lanthanidocenes with nitrogen and phosphorus containing heterocycles, which are incredibly active catalysts, developed new fields in organolanthanide chemistry recently, establishing a new area of organometallic chemistry.

The research in this field has been well documented in review articles[2–6] and a book.[7] Recent reviews concerning the state of the art in 2002 can be found in the special issue of Chemical Reviews: Frontiers in Lanthanide Chemistry.[8]

This article discusses the preparation, structure, and chemistry of rare earths complexes with bonds to carbon. An emphasis is given to compounds prepared and characterized after EIC1 appeared in 1994 up to the end of 2003, but only papers, which appeared after 2000, are cited in the reference list. Inorganic compounds that may be bonded through carbon, such as carbides (*see* ***Carbides: Transition Metal Solid-state Chemistry***) or cyanides (*see* ***Cyanide Complexes of the Transition Metals*** and ***Scandium, Yttrium & the Lanthanides: Inorganic & Coordination Chemistry***), are also excluded as well as the chemistry of rare earth cations with organic compounds in the gas phase. While at the moment of finishing this chapter for EIC-I most organo rare earth complexes have been cyclopentadienyl derivatives, the development of this area of organometallic chemistry produced new classes of compounds in the common oxidation state Ln(III) as well as in the more unusual oxidation states Ln(0), Ln(I), Ln(II), and Ln(IV) in recent years. Therefore the organization of this chapter is somewhat different compared to EIC1. The use of organolanthanides as reagents in organic synthesis as well as in catalysis is not covered here, although Ln to carbon bonds may be involved in these processes. Those subjects have been treated in comprehensive book articles recently, for example, for organolanthanides in organic synthesis[9] and in catalysis.[10]

2 LANTHANIDE COMPLEXES WITH σ-BONDED HYDROCARBYL LIGANDS

Over the years the homoleptic (*see Homoleptic Compound*) alkyl and aryl complexes were one of the major challenges in organolanthanide chemistry. The simplest organometallic compounds of the rare earths are the solvated or solvent-free species LnR_2 or LnR_3 with the rare earth metals in their common oxidation states Ln^{2+} and Ln^{3+}. This is usually insufficient to meet the lanthanides' demands of steric saturation through high coordination numbers. The isolation and characterization of compounds belonging to this class were achieved using bulky alkyl ligands. When less bulky alkyl ligands are used, *ate* complexes containing more then three alkyl ligands attached to the metal $[R_{3+n}Ln]^{n-}$ are often formed. Mono- and dialkylcomplexes of the lanthanides are more frequent than homoleptic complexes, because in those cases the bulky ancillary ligands were usually used for the coordinative saturation of the metal center. This section deals only with Ln(III)-alkyl derivatives, for alkyl complexes of the divalent lanthanides see Section 11. Two reviews appeared for work up to 1994[3] and up to 2001.[11]

2.1 Complexes with Three and More σ-Bonded Hydrocarbyls

The reactions of $LnCl_3$ (Ln = Y, La, Pr, Nd, Sm, Gd, Tb, Dy, Ho, Er, Tm, Yb, Lu) with MeLi in Et_2O in the presence of TMEDA or DME yields *ate* complexes $[Li(L)]_3[LnMe_6]$ (L = TMEDA, DME) (equation 1).

$$LnCl_3 + 6MeLi + 3TMEDA \xrightarrow[-3LiCl]{Et_2O} [Li(TMEDA)]_3[LnMe_6] \quad (1)$$

The crystal structure of $[Li(TMEDA)]_3[LnMe_6]$ (Ln = Ho, Er) and $[Li(DME)]_3[LuMe_6]$ shows an octahedral $LnMe_6$ arrangement with Me bridges to the Li atoms (Figure 1). Alkylation of $(L)LnCl_3$ (Ln = Sc, Y; L = 1,4,7-trimethyl-1,4,7-triazacyclononane) with MeLi in THF gives the corresponding species $(L)Ln(CH_3)_3$, and the reaction of $LuCl_3$ with NaCp* and LiMe in THF in the presence of TMEDA yields $[Li(TMEDA)_2][Cp^*LuMe_3]$, showing the Lu atom tetrahedrally coordinated by the Cp* ring and the three Me groups.[11]

Homoleptic (*see Homoleptic Compound*) complexes $Ln(CH_2SiMe_3)_3(THF)_n$ (M = Sm, Y, $n = 3$; Tb, Er, Yb, Lu, $n = 2$) were prepared by the reactions of the respective $LnCl_3$ with Me_3SiCH_2Li in THF (equation 2 and 3). $Yb(CH_2SiMe_3)_3(THF)_2$ and the related neopentyl derivative $Yb(CH_2{}^tBu)_3(THF)_2$ are formed by the reaction of ytterbium metal with ICH_2SiMe_3 or neopentyl iodide in THF.[12] X-ray structural analyses of the Sm, Er, Yb, and Lu derivatives show the Sm atom in a *fac*-octahedral coordination and the heavier lanthanides Er, Yb, and Lu trigonal bipyramidally coordinated with three alkyl ligands in equatorial and two THF molecules in axial positions (equation 2).[13] The tris(trimethylsilylmethyl)scandium and -yttrium derivatives are thermally unstable. The bulky $PhMe_2SiCH_2$ ligand allows the isolation of thermally more robust analogues $Ln(CH_2SiMe_2Ph)_3(THF)_2$ (M = Sc, Y).[14] Reaction of $Ln(CH_2SiMe_3)_3(THF)_2$ (Ln = Y, Lu) with $B(C_6X_5)_3$ (X = H, F) in the presence of crown ethers yields cationic lanthanide-alkyl complexes, for example, $[Ln(CH_2SiMe_3)_2(CE)(THF)_n]^+$ $[B(CH_2SiMe_3)(C_6X_5)_3]^-$ (CE = 12-crown-4, $n = 1$; CE = 15-crown-5 and 18-crown-6, $n = 0$) (equation 3).[15] The use of four equivalents of $LiCH_2SiMe_3$ results in the formation of *ate* complexes $[Li(TMEDA)_2][Ln(CH_2SiMe_3)_4]$ (Ln = Y, Er, Yb). Similar homoleptic tetrakis-alkyl anions are formed when YCl_3 reacted with 2 equiv. of $LiCH_2SiMe_3$ and 2 equiv. of $LiOCMe_3$ to yield $\{(Me_3SiCH_2)_x(Me_3CO)_{1-x}Y(\mu\text{-}OCMe_3)_4[Li(THF)]_4(\mu_4\text{-}Cl)\}^+$ $[Y(CH_2SiMe_3)_4]^-$.[11]

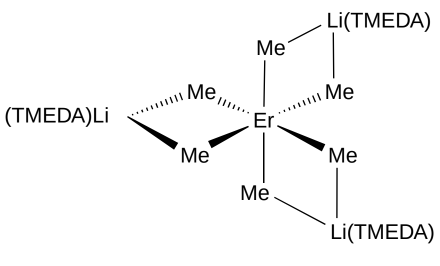

Figure 1 Structure of $[Li(TMEDA)]_3[ErMe_6]$

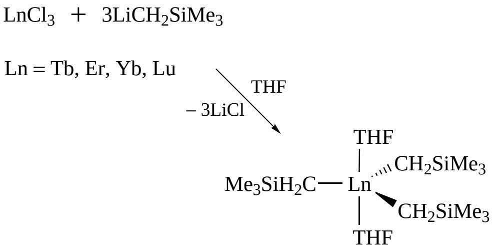

(2)

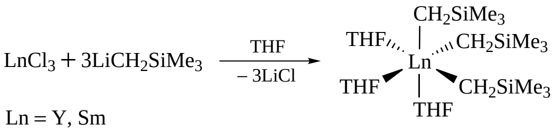

(3)

A number of analogous bis(trimethylsilyl)methyl lanthanide complexes have also been reported. $[(Et_2O)_3Li(\mu\text{-}Cl)Y\{CH(SiMe_3)_2\}_3]$ and the solvent-free $Y[CH(SiMe_3)_2]_3$ have been prepared and structurally characterized recently.[3,11]

Mixed lanthanide metal(III) alkyl complexes $R_3Ln(\mu\text{-}Me)Li(pmdeta)$ [Ln = La, Sm; R = $CH(SiMe_3)_2$; pmdeta = $MeN(CH_2CH_2NMe_2)_2$] were prepared from LnR_3, LiMe, and pmdeta. The reaction of $YbCl_3$ with 3-(dimethylamino) propyllithium in THF affords the *ate* complex $Li[(Me_2NCH_2CH_2CH_2)_4Yb]$, in which two Me_2N groups intramolecularly chelate the Yb atom whereas the other two donor functions are coordinated to lithium.

Homoleptic aryl-lanthanides are less studied then alkyl complexes. After the first lanthanide aryl complex $[Li(THF)_4][Lu(C_6H_3\text{-}2,6\text{-}Me_2)_4]$, neutral triphenyllanthanides $Ph_3Ln(THF)_3$ (Ln = Er, Tm, Yb) were synthesized in THF by reaction of metallic lanthanides with Ph_2Hg or

Ph_3Bi in the presence of catalytic amounts of LnI_2 or LnI_3. X-ray diffraction studies showed that these compounds represent monomeric complexes with a distorted *fac*-octahedral arrangement of ligands around the Ln atom. Transmetallation of $(C_{10}H_8)Yb(THF)_2$ with Ph_2Hg or Ph_3Bi in THF affords $Ph_2(THF)Yb(\mu\text{-}Ph)_3Yb(THF)_3$ (equation 4)

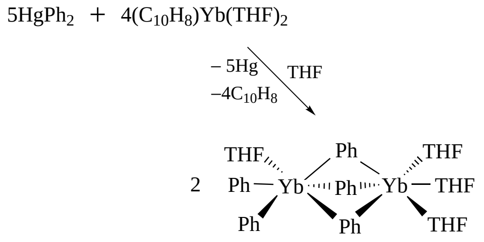
5HgPh₂ + 4(C₁₀H₈)Yb(THF)₂
– 5Hg
–4C₁₀H₈
THF
2
THF
Ph
Yb
Ph
Ph
Ph
Ph
Yb
THF
THF
THF

(4)

The X-ray crystal structure analysis of $Ph_3Sc(THF)_2$ reveals a trigonal-bipyramidal coordination sphere with the THF molecules in axial positions. The 1:1 or 2:1 reactions of $Li[C_6H_3\text{-}2,6\text{-}(O^iPr)_2]$ with anhydrous $SmCl_3$ in THF gave $[2,6\text{-}(^iPrO)_2C_6H_3]_3Sm$ exclusively, while the 3:1 reaction gave $[2,6\text{-}(^iPrO)_2C_6H_3]_4SmLi$ as the major product, which has been characterized by X-ray crystallography.[11]

2.2 Complexes with Two η^1-Bonded Hydrocarbyls

Dibenzylyttrium bromides like $[(TMEDA)(PhCH_2)_2\text{-}Y(\mu\text{-}Br)_2Li(TMEDA)]$ are formed from YBr_3 and $PhCH_2Li(TMEDA)$.[11] Different ancillary ligands provide stabilization of bis(alkyl)lanthanide derivatives such as described earlier in $Cp_2Lu(\mu\text{-}Me)_2Li(TMEDA)$, $[Cp^*{}_2\text{-}Lu(CH_2SiMe_3)_2][Li(DME)_2]$, and $[Cp_2Y(CH_2SiMe_3)_2]_2\text{-}Li_2(DME)_2(dioxane)$.[6] The reactions of $ScCl_3$ and $LuCl_3$ with one equiv. of $K[(S)\text{-}C_5H_4CHPhCH_2NMe_2]$ or $K[C_5H_4CH_2CH_2NMe_2]$ followed by two equiv. of $LiCH_2\text{-}SiMe_3$ yield the complexes $[(S)\text{-}C_5H_4CHPhCH_2NMe_2]\text{-}Ln(CH_2SiMe_3)_2$ (equation 5) and $(C_5H_4CH_2CH_2NMe_2)\text{-}Ln(CH_2SiMe_3)_2$ (equation 6), respectively.[16]

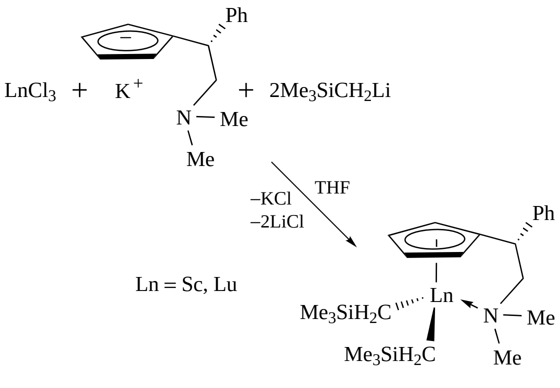
LnCl₃ + K⁺
Ph
N — Me
Me
+ 2Me₃SiCH₂Li
–KCl
–2LiCl
THF
Ln = Sc, Lu
Ph
Ln
Me₃SiH₂C
Me₃SiH₂C
N — Me
Me

(5)

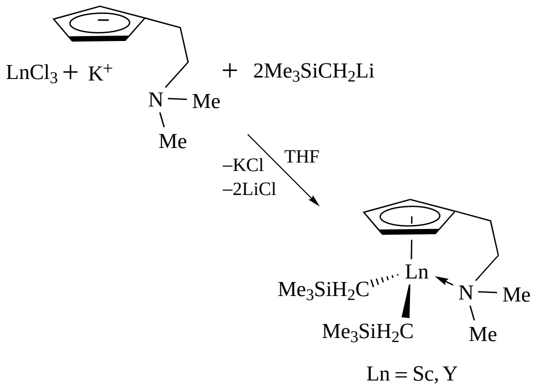
LnCl₃ + K⁺
N — Me
Me
+ 2Me₃SiCH₂Li
–KCl
–2LiCl
THF
Ln
Me₃SiH₂C
Me₃SiH₂C
N — Me
Me
Ln = Sc, Y

(6)

$SmBr_3$ and $GdBr_3$ react with $NaCH_2Ph$ and KCp^* in THF to give $[Cp^*{}_2Sm(CH_2Ph)_2K(THF)_2]_\infty$ and $Cp^*Gd(CH_2Ph)_2(THF)$, respectively.[11] Rare earth metal complexes of the type $Ln\{\eta^5{:}\eta^1\text{-}C_5Me_4SiMe_2(C_4H_3O\text{-}2)\}(CH_2SiMe_3)_2(THF)$ ($Ln = Y$, Lu) (Figure 2a) were prepared by alkane elimination reaction of $Ln(CH_2SiMe_3)_3(THF)_2$ with the 2-furyl-functionalized tetramethylcyclopentadiene. Reaction of these dialkyl complexes with BPh_3 in THF give thermally stable cations $[Ln\{\eta^5{:}\eta^1\text{-}C_5Me_4SiMe_2(C_4H_3O\text{-}2)\}(CH_2SiMe_3)(THF)_n]^+$.[17] The in situ generated $Sc(CH_2SiMe_3)_3(THF)_2$ reacts with the protonated hydrotris-pyrazolylborate ligands (*see Tris(pyrazolyl)borates*) $Tp^{Me,Me}H$ and $Tp^{tBu,Me}H$ affording $(Tp^{Me,Me})Sc(CH_2SiMe_3)_2$ and $(Tp^{tBu,Me})Sc(CH_2SiMe_3)_2$ (Figure 2b), respectively. Treatment of $(Cp_2YCl)_2$ with two equiv. of 2-dimethylaminomethylferrocenyl lithium Li(FcN) affords the heterotrimetallic complex $Li[Cp_2Y(FcN)_2]$ (Figure 2c).[6,11]

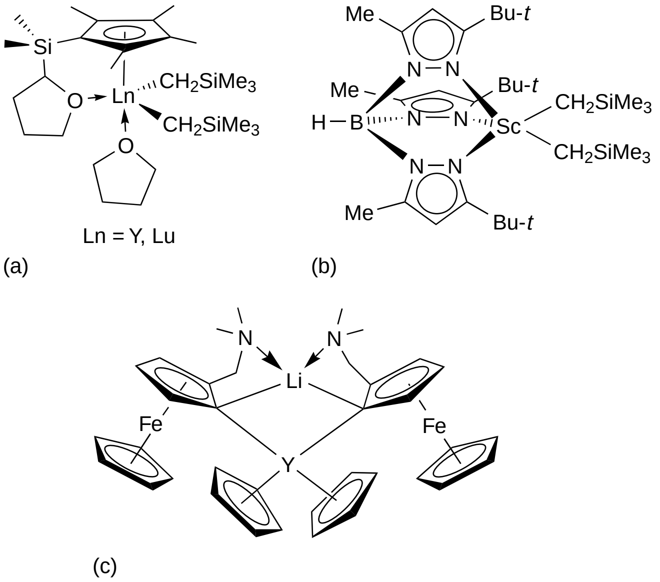
Si
O
Ln
CH₂SiMe₃
CH₂SiMe₃
O
Ln = Y, Lu
(a)
Me
Bu-t
N — N
Me
Bu-t
H — B
N — N
Sc
CH₂SiMe₃
CH₂SiMe₃
N — N
Me
Bu-t
(b)
N
N
Li
Fe
Fe
Y
(c)

Figure 2 (a) $Ln\{\eta^5{:}\eta^1\text{-}C_5Me_4SiMe_2(C_4H_3O\text{-}2)\}(CH_2SiMe_3)_2\text{-}(THF)$ ($Ln = Y$, Lu), (b) $(Tp^{tBu,Me})Sc(CH_2SiMe_3)_2$, and (c) $Li[Cp_2\text{-}Y(FcN)_2]$

Addition of RLi (R = Me, Et, and CH_2SiMe_3) to $ScCl_2(THF)[N(SiMe_2CH_2P^iPr_2)_2]$ gives bis-alkyl derivatives $R_2Sc[N(SiMe_2CH_2P^iPr_2)_2]$. The X-ray structural analysis of $Et_2Sc[N(SiMe_2CH_2P^iPr_2)_2]$ and $(Me_3SiCH_2)_2Sc$-$[N(SiMe_2CH_2P^iPr_2)_2]$ show mononuclear molecules with distorted trigonal-bipyramidal geometries.**[11]** The alkane elimination reaction between $Y(CH_2SiMe_2Ph)_3(THF)_2$ and 1 equiv. of salicylaldimine (LH) results in the formation of the dialkyl derivatives $LY(CH_2SiMe_2Ph)_2(THF)$ (Figure 3a).**[14]** Bis-alkyl derivatives $(L')Ln(CH_2SiMe_3)_2(THF)$ (Ln = Sc or Y) were obtained by the reaction of equimolar amounts of the related salicylaldimine ligand 2-(2,4,6-$Me_3C_6H_2N$=CH)(6-^{t}Bu)C_6H_3OH (L′H) with $Ln(CH_2SiMe_3)_3(THF)_3$. The trigonal-bipyramidal structure of the scandium dialkyl complex was confirmed crystallographically.**[11]** The scandium alkyl complexes are efficient catalysts for the ring-opening polymerization of ε-caprolactone.**[18]** The ß-diketiminate complex $(L)_2CeCl$ [L = N(R)C(Ph)C(H)C(Ph)NR; R = $SiMe_3$] reacts with either one or two equiv. of $Li(CHR_2)$ in Et_2O, forming $(L)Ce[CH(SiMe_3)_2]_2$ (Figure 3b).**[11]**

Several diorganoscandium complexes stabilized by the ß-diketiminato ligands (Ar)NC(R)CHC(R)N(Ar) (L′: Ar = 2,6-$^iPr_2C_6H_3$, R = CH_3; L″: Ar = 2,6-$^iPr_2C_6H_3$, R = ^{t}Bu) have been reported. Thus, reactions of the lithium salts of the ligands L′ and L″ with $ScCl_3(THF)_3$ lead to the complexes $(L')ScCl_2(THF)_n$ and $(L'')ScCl_2(THF)_n$, which are readily alkylated with various organolithium compounds or Grignard reagents to form the dialkyl derivatives $(L')ScR_2$ (R = $PhCH_2$, $^tBuCH_2$ and Me_3SiCH_2) and $(L'')ScR_2$ (R = CH_3, CH_3CH_2, $PhCH_2$, $^tBuCH_2$ and Me_3SiCH_2). Most of them are isolated as base-free, four-coordinate complexes and characterized via X-ray crystallography. Steric interactions between Ar and the Sc-alkyl groups force the scandium to adopt an out-of-plane bonding mode.**[19]** The reaction of $(L')ScMe_2$ with 1 equiv. of $B(C_6F_5)_3$ yields monomeric monomethyl cations $[(L)ScMe]^+$ $[MeB(C_6F_5)_3]^-$.**[20]** The reaction of $[(L)LuCl_2(\mu\text{-}Cl)(\mu\text{-}Li(THF)_2)]_2$ [L = 2,6-$(Me_2NCH_2)_2C_6H_3$] with Me_3SiCH_2Li gives the monoalkyl complex $[(L)Lu(\mu\text{-}Cl)(CH_2SiMe_3)]_2$, which reacts with a second equiv. of Me_3SiCH_2Li to produce the bis-alkyl complex $(L)Lu(CH_2SiMe_3)_2$ (Figure 4a).**[11]** YCl_3 reacts with the lithium salt of an anilido-imine ligand and 2 equiv. of $LiCH_2SiMe_2R$ (R = Me, Ph) yielding monomeric bis(alkyl)yttrium complexes $(L)Y(CH_2SiMe_2R)_2$ (R = Me, Ph) (Figure 4b).**[21]**

The sequential reaction of YCl_3 with $Li[^tBuC(N^iPr)_2]$ and 2 equiv. of $LiCH(SiMe_3)_2$ form the mono(amidinate) dialkyl yttrium complex $[^tBuC(N^iPr)_2]Y[CH(SiMe_3)_2]_2(\mu\text{-}Cl)Li(THF)_3$. Using the tridentate amidinate-amine ligand $PhC(NSiMe_3)N(CH_2)_2NMe_2$ (L) results in the formation of the salt-free dialkyl complex $(L)Y[CH(SiMe_3)_2]_2$ (Figure 5a). Attempts to prepare analogous benzyl or CH_2SiMe_3 complexes yielded the *ate* complexes $Li[(L)_2YR_2]$ (R = CH_2Ph, CH_2SiMe_3).**[22]** The reaction between aza-18-crown-6 (H-MAC) and $Y(CH_2SiMe_3)_3(THF)_2$ proceeded via elimination of $SiMe_4$, yielding $Y(MAC)(CH_2SiMe_3)_2$ (Figure 5b).**[11]** Yttrium dialkyl complexes supported by tetradentate ligands [*N*,*N*′-R_2-tacn-*N*″-$(CH_2)_2N^tBu$] (R = Me, tacn = 1,4,7-triazacyclononane) have been prepared analogously using H-tacn (Figure 5c).**[23]**

Mixed dialkyl-alkoxide complexes are also known, for example, $(Me_3SiCH_2)Sm[(\mu\text{-}OAr)(\mu\text{-}CH_2SiMe_3)Li(THF)]$-$[(\mu\text{-}OAr)_2Li(THF)]$ (Ar = 2,6-$^iPr_2C_6H_3$), containing a pentacoordinate Sm center ligated by one terminal and one bridging CH_2SiMe_3 and three bridging 2,6-$^iPr_2C_6H_3$ ligands. The anionic dialkyl–diaryloxide complex $[(Me_3SiCH_2)_2Lu(OC_6H_3{}^tBu_2\text{-}2,6)_2][Li(THF)_4](THF)_2$ has a distorted tetrahedral coordination geometry around both

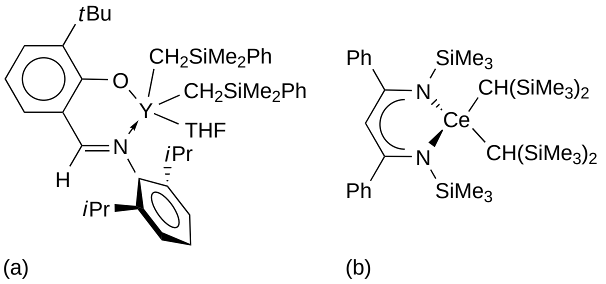

Figure 3 (a) $LY(CH_2SiMe_2R)_2(THF)_n$ and (b) $(L)Ce[CH(SiMe_3)_2]_2$

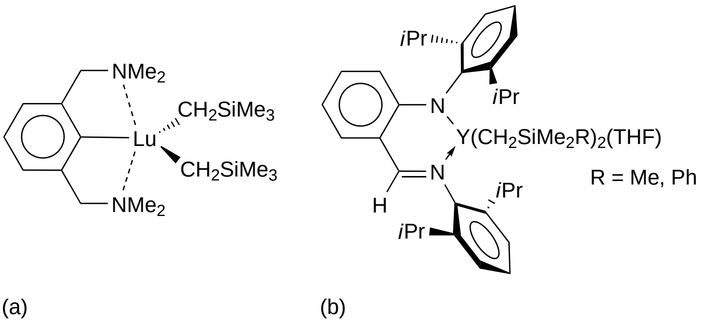

Figure 4 (a) $(L)Lu(CH_2SiMe_3)_2$ and (b) $(L)Y(CH_2SiMe_2R)_2$ (R = Me, Ph)

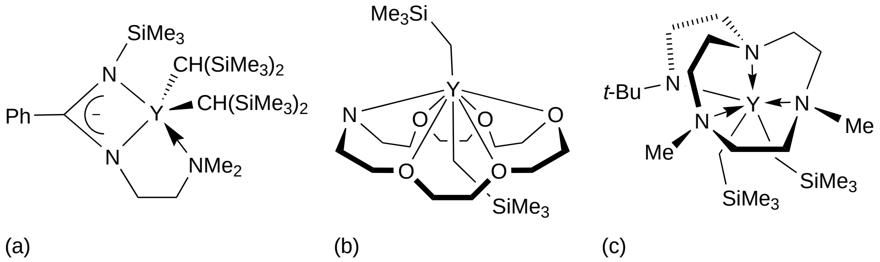

Figure 5 (a) $(L)Y[CH(SiMe_3)_2]_2$, (b) $Y(MAC)(CH_2SiMe_3)_2$, and (c) $[tacn]Y(CH_2SiMe_3)_2$

metals, whereas the related complex $[(Me_3Si)_2CH]_2Y(\mu\text{-}O^tBu)_2Li(THF)$ has a distorted tetrahedral coordinated yttrium and a trigonal planar lithium. The reaction of YCl_3 with 2 equiv. of $LiCH_2SiMe_3$ and 1 equiv. of $LiOC_6H_3{}^tBu_2$-2,6 in THF forms the neutral dialkyl aryloxide complex $(Me_3SiCH_2)_2Y(OC_6H_3{}^tBu_2\text{-}2,6)(THF)_2$. The coordination geometry around Y is distorted trigonal bipyramidal with the THF groups in the apical positions.[11]

2.3 Complexes with One η^1-Bonded Hydrocarbyl Ligand

Organolanthanides of this class, especially dicyclopentadienyl derivatives Cp_2LnR are the most effective catalysts for olefin polymerization and they are selective and effective reagents for organic synthesis.[9,24,25] They were prepared by alkylation of Cp_2LnCl or by treatment of methylaluminates $Cp_2Ln(\mu\text{-}Me)_2AlMe_2$ with equimolar amounts of pyridine.[6,25] More recently $[(C_5H_4SiMe_2R)_2Ln(\mu\text{-}Me)]_2$ ($R = {}^tBu$, Ln = Y, Sm, Lu; R = Me, Ln = Y, Sm, Lu), $[\eta^5\text{-}1,3\text{-}C_5H_3(SiMe_3)_2]_2LnMe(THF)$ (Ln = Sm, Lu),[26] $\{[1,3\text{-}(Me_3Si)_2C_5H_3]_2LnMe\}_2$ (Ln = Sm, Nd),[27] *rac*-$[O(CH_2CH_2C_9H_6)_2]LnCH_2SiMe_3$ (Ln = Y, Lu), $[Me_2Si(C_5Me_4)(C_5H_3CH_2CH_2NMe_2)]LnMe$ (Ln = Y, Ho, Lu) (Figure 6a), $Cp^*(C_5H_3CH_2CH_2NMe_2)ScMe$ (Figure 6b), $Cp^*(C_5H_3CH_2CH_2NMe_2)LnMe$ (Ln = Nd, Sm, Ho, Lu), $Cp^*(C_5H_3CH_2CH_2NMe_2)LuCH_2SiMe_3$, $(C_5H_4CH_2CH_2SEt)_2YMe$ (Figure 6c), and $Cp^*(C_5H_4CH_2CH_2SEt)LuMe$[28] have been described. Single-crystal X-ray structure analysis of the N- and S-donor functionalized complexes showed that donor atoms are intramolecularly coordinated to the metal. $\{[1,3\text{-}(Me_3Si)_2C_5H_3]_2LnMe\}_2$ (Ln = Sm, Nd) performs the living polymerization of methylmethacrylate and the block copolymerization of L-lactide with ε-caprolactone in high yields in the absence of any cocatalysts.[29] Lanthanidocene methyl complexes are effective precatalysts for the hydrosilylation of alkenes and alkynes.[24]

Dimeric $[(C_4Me_4P)_2LnCH(SiMe_3)_2]_2$ (Ln = Nd, Sm) supported by the 2,3,4,5-tetramethylphospholyl ligand can be prepared in a one-pot procedure starting from $LnCl_3$, $K(C_4Me_4P)$, and $LiCH(SiMe_3)_2$. Reaction of $(C_4Me_4P)_2LnCH(SiMe_3)_2$ with H_2 gives $(C_4Me_4P)_2NdH$ with Ln = Nd, in the case of Ln = Sm, reduction to $(C_4Me_4P)_2Sm$ takes place.[11]

$(Me_3Si)_2CH$ derivatives can be prepared as monomeric alkali salt- and solvent-free complexes, like $Cp^*{}_2LnCH(SiMe_3)_2$ (Ln = La, Nd, Sm, Lu), $(C_5Me_4Et)_2LnCH(SiMe_3)_2$ (Ln = Y, Nd, Sm), $(C_5Me_4{}^iPr)_2LnCH_3(THF)$ (Ln = Y, Sm), $(C_5Me_4{}^iPr)_2Ln\{CH(SiMe_3)_2\}$ (Ln = Y, Sm), $Me_2Si(C_5Me_4)_2LnCH(SiMe_3)_2$ (Ln = Y, Nd), $[R_2Si(C_5H_4)(C_5Me_4)]LnCH(SiMe_3)_2$ (Ln = Y, Lu), and (*R*)- and (*S*)-$Me_2Si(C_5Me_4)(C_5H_3R^*)LnCH(SiMe_3)_2$ [Ln = Y, Sm; R* = (+)-neomenthyl or (−)-menthyl]. However, alkylation of the bis(cyclopentadienyl)lanthanide halides with MeLi or Me_3SiCH_2Li often produces the *ate* complexes, for example, $Cp_2Ln(\mu\text{-}Me)_2Li(TMEDA)$, $Cp^*{}_2Ln(\mu\text{-}Me)_2Li(THF)_2$, $Cp^*{}_2Ln(\mu\text{-}Me)_2Li(THF)_2$, $Cp^*{}_2Ln(\mu\text{-}CH_2SiMe_3)_2Li(DME)_2$, and $(C_5H_4SiMe_3)_2Ln(\mu\text{-}Me)_2Li(THF)_2$.[8]

Compounds $Cp^*{}_2LnCH(SiMe_3)_2$ can be converted to the highly reactive hydrides $(Cp^*{}_2LnH)_2$ by reaction with

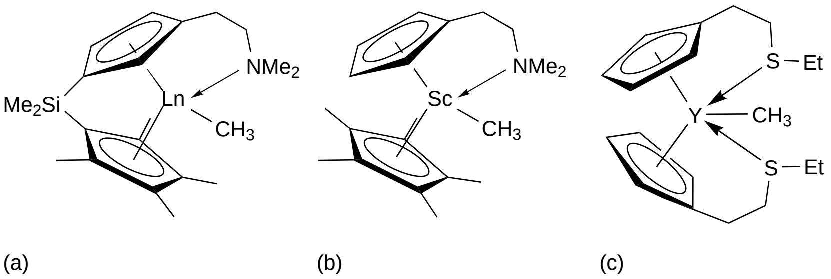

Figure 6 (a) $[Me_2Si(C_5Me_4)(C_5H_3CH_2CH_2NMe_2)]LnMe$, (b) $Cp^*(C_5H_3CH_2CH_2NMe_2)ScMe$, (c) $(C_5H_4CH_2CH_2SEt)_2YMe$

hydrogen. For instance, $(\mathrm{Cp^*_2YH})_2$ metalates pyridine selectively in *ortho*-position to yield $\mathrm{Cp^*_2Y}$(2-pyridyl), which further reacts with ethylene or propylene to give the monoinsertion products $\mathrm{Cp^*_2YCH_2CH_2(2\text{-}NC_5H_4)}$ and $\mathrm{Cp^*_2YCH_2CHMe(2\text{-}NC_5H_4)}$, respectively. With 2-butyne, the propargylic metallation product $\mathrm{Cp^*_2YCH_2C{\equiv}CMe}$ was obtained.

$\mathrm{[Me_2Si(N^tBu)(O^tBu)]_2YCH(SiMe_3)_2}$ reacts with $\mathrm{N{\equiv}CMe}$ via C–H activation forming $\mathrm{[\{Me_2Si(N^tBu)(O^tBu)]_2Y(\mu\text{-}(\mathit{N,N'})\text{-}NHCMe{=}CHCN)\}_2}$ (equation 7). With pyridine and picoline, the metallation of either cyclic or exocyclic positions yields pyridyl and picolyl complexes, $\mathrm{[Me_2Si(N^tBu)(O^tBu)]_2YR}$ (R = η^2-(C,N)-2-$\mathrm{NC_5H_4}$, η^2-(C,N)-$\mathrm{CH_2}$-2-$\mathrm{NC_5H_4}$, η^2-(C,N)-C(H)Me-2-$\mathrm{NC_5H_4}$, η^2-(C,N)-C(H)Me-2-$\mathrm{NC_5H_3}$-6-Me), respectively.

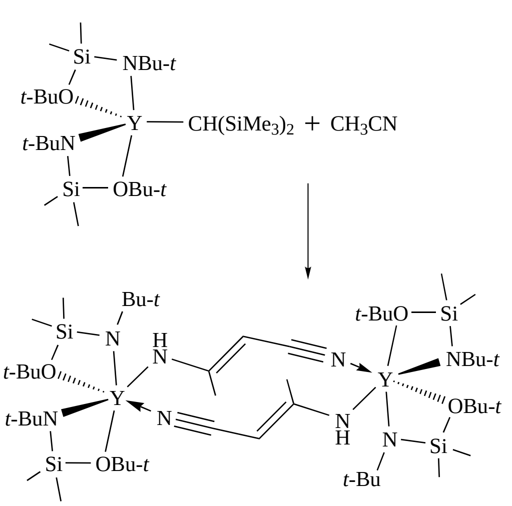

(7)

The reaction of the half-sandwich complex (*see Half-sandwich Complexes*) $(\eta^5{:}\eta^1\text{-}\mathrm{C_5Me_4SiMe_2N^tBu})\mathrm{Y(CH_2SiMe_3)(THF)}$ with furan and thiophene yields $[(\eta^5{:}\eta^1\text{-}\mathrm{C_5Me_4SiMe_2N^tBu})\mathrm{Y}(\mu_2\text{-}\mathrm{C_4H_3E})]_2$ (E = O, S) (Figure 7). In contrast to THF and pyridine, DME forms isolable, crystalline adducts $(\eta^5{:}\eta^1\text{-}\mathrm{C_5Me_4SiMe_2N^tBu})\mathrm{Y(2\text{-}C_4H_3E)(DME)}$. The reaction of $[\mathrm{Y}(\eta^5{:}\eta^1\text{-}\mathrm{C_5Me_4SiMe_2N^tBu})\mathrm{(CH_2SiMe_3)(THF)}]$ with excess DME yields the five-coordinate complex $[\mathrm{Y}(\eta^5{:}\eta^1\text{-}\mathrm{C_5Me_4SiMe_2N^tBu})\mathrm{(CH_2SiMe_3)(DME)}]$ that does not react with furan or thiophene, indicating an associative mechanism.[30]

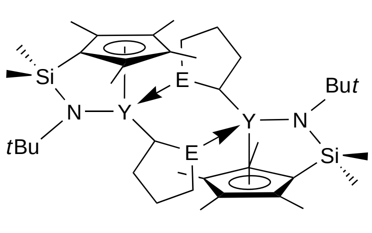

Figure 7 $[(\eta^5{:}\eta^1\text{-}\mathrm{C_5Me_4SiMe_2N^tBu})\mathrm{Y}(\mu_2\text{-}\mathrm{C_4H_3E})]_2$ (E = O, S)

The dimeric rare earth hydrides based on the same Cp/amide 'constrained geometry' ligand $[\mathrm{Ln}(\eta^5{:}\eta^1\text{-}\mathrm{C_5Me_4SiMe_2N^tBu})\mathrm{(THF)}(\mu\text{-}\mathrm{H})]_2$ (Ln = Y, Yb) react with an excess of α-olefins $\mathrm{H_2C{=}CHR}$ (R = Et, ^{n}Pr, ^{n}Bu) in a 1,2-insertion manner to give the series of THF-free dimeric *n*-alkyl complexes $[\mathrm{Ln}(\eta^5{:}\eta^1\text{-}\mathrm{C_5Me_4SiMe_2N^tBu})(\mu\text{-}\mathrm{CH_2CH_2R})]_2$. Single-crystal X-ray diffraction studies on $[\mathrm{Y}(\eta^5{:}\eta^1\text{-}\mathrm{C_5Me_4SiMe_2NCMe_2R'})(\mu\text{-}\mathrm{CH_2CH_2R})]_2$ (R′ = Me, R = Et, ^{n}Bu; R′ = Et, R = Et, ^{n}Pr) and $[\mathrm{Yb}(\eta^5{:}\eta^1\text{-}\mathrm{C_5Me_4SiMe_2N^tBu})(\mu\text{-}\mathrm{CH_2CH_2{}^nBu})]_2$ revealed that the centrosymmetric dimeric complexes consist of two trans arranged $[\mathrm{Ln}(\eta^5{:}\eta^1\text{-}\mathrm{C_5Me_4SiMe_2NCMe_2R'})]$ fragments connected by two μ-alkyl ligands, showing an agostic interaction (*see Agostic Bonding*) of the ß-$\mathrm{CH_2}$ hydrogen atoms of the *n*-alkyl groups with the formally 12-electron lanthanide metal center. α-Olefins having two or more substituents on the γ-carbon do not react with the hydride complexes.[31] The scandium complex $\mathrm{[C_5H_3(1\text{-}SiMe_2N^tBu)(3\text{-}CH_2CH_2NMe_2)]Sc(CH_2SiMe_3)}$ was prepared via alkane elimination by treatment of in situ generated $\mathrm{Sc(CH_2SiMe_3)_3}$ with the free ligand.

A number of chelating polydentate N-based ligands are useful to stabilize monoalkyl lanthanide complexes. The synthetic approach is alkane elimination from tris(alkyl)lanthanide precursors by treatment with protonated N-ligands. Deprotonation of *N*,*N*-dihydro-4,13-diaza-18-crown-6 ($\mathrm{H_2DAC}$) with $\mathrm{Y(CH_2SiMe_3)_3}$ yields the salt-free monoalkyl derivative $\mathrm{(DAC)Y(CH_2SiMe_3)}$ (Figure 8), which is related to $\mathrm{(MAC)Y(CH_2SiMe_3)_2}$ (Figure 5b).[11]

The reaction of $\mathrm{(DAC)Y(CH_2SiMe_3)}$ with $\mathrm{PhC{\equiv}CH}$ produces a mixture of the alkynide-coupled butatrienediyl complex $[(\mu\text{-}\mathrm{DAC})\mathrm{Y}]_2(\mu\text{-}(\mathrm{Z})\text{-}\mathrm{PhC{=}C{=}C{=}CPh})$ and the uncoupled bridging alkynide dimer $[\mathrm{(DAC)Y}(\mu\text{-}\mathrm{C{\equiv}CPh})]_2$. Reaction of $\mathrm{Lu[CH(SiMe_3)_2]_3}$ with octaethylporphyrin ($\mathrm{H_2OEP}$) affords $\mathrm{(OEP)Lu[CH(SiMe_3)_2]}$. Its crystal structure showed a highly bowl-shaped porphyrin skeleton with the square-pyramidal, five-coordinate lutetium atom 0.918 Å out of the $\mathrm{N_4}$ plane of the porphyrin ligand. Monoalkyl diamide complexes $\mathrm{(BDPPpyr)Ln(CH_2SiMe_3)(THF)}_n$ ($n = 1$, Ln = Sc (Figure 9a), Lu; $n = 2$, Ln = Y), $\mathrm{(BMespyr)Ln(CH_2SiMe_3)(THF)}_n$ ($n = 1$, Ln = Sc; $n = 2$, Ln = Lu), and $\mathrm{(BDPPoxyl)Ln(CH_2SiMe_3)(THF)}$ (Ln = Sc (Figure 9b), Lu, Y) were prepared from 2,6-bis[{(2,6-diisopropylphenyl)amino}methyl]pyridine ($\mathrm{H_2BDPPpyr}$), 2,6-bis[(mesitylamino)methyl]pyridine ($\mathrm{H_2BMespyr}$), or 1,2-bis[{(2,6-diisopropylphenyl)amino}methyl]benzene ($\mathrm{H_2BDPPoxyl}$) respectively using $\mathrm{Ln(CH_2SiMe_3)_3}$.[32]

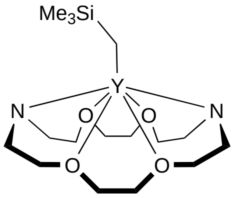

Figure 8 $\mathrm{(DAC)Y(CH_2SiMe_3)}$

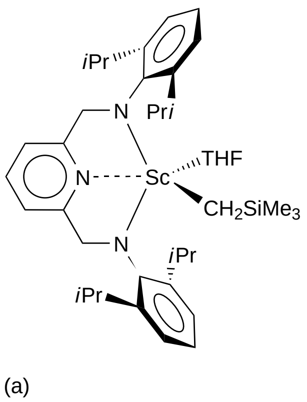

Figure 9 (a) $(BDPPpyr)Sc(CH_2SiMe_3)(THF)_n$ and (b) $(BDPPoxyl)Sc(CH_2SiMe_3)(THF)$

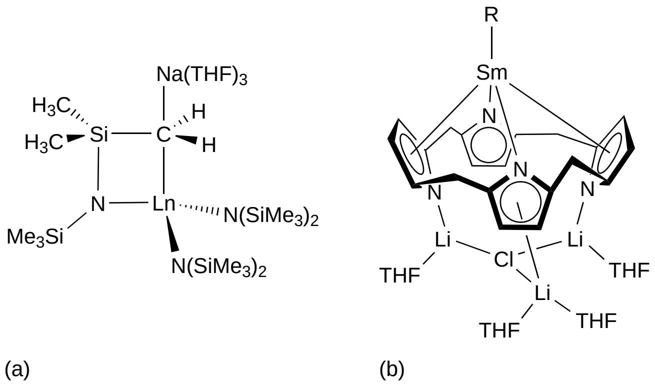

Figure 11 (a) $[(Me_3Si)_2N]_2LnN(SiMe_3)SiMe_2CH_2Na(THF)_3$ and (b) $(Et_8\text{-calix-pyrrole})(R)Sm(\mu_3\text{-}Cl)[Li(THF)]_2[Li(THF)_2]$ (R = Me, $CH{=}CH_2$)

$[ArN(CH_2)_3NAr]Y[CH(SiMe_3)_2](THF)$ (Ar = 2,6-$i$$Pr_2$-$C_6H_3$) is formed by alkali metal–salt elimination. The '*ate*-complex' is not formed because of the low solubility of KI and its complete precipitation.[33] Yttrium bis(silylamido)biphenyl complexes $[DADMB]YMe(THF)_2$ and $[DADMB]Y[CH(SiMe_3)_2](THF)(OEt_2)$ (DADMB = 2,2′-bis[(*tert*-butyldimethylsilyl)amido]-6,6′-dimethylbiphenyl) result from the reaction of $[DADMB]YCl(THF)_2$ and MeLi or $(Me_3Si)_2CHLi$, respectively. Both compounds react with $PhSiH_3$ or H_2 to give insoluble $\{[DADMB]Y(\mu\text{-}H)(THF)\}_2$, which reacts rapidly with ethene or 1-hexene to give a single insertion product.[11]

Amidinate ligands stabilize monoalkyl lanthanide derivatives like $[PhC(NSiMe_3)_2]_2YCH(SiMe_3)_2$, $[PhC(NSiMe_3)_2]$-$Y(\mu\text{-}Me)_2Li(TMEDA)$, $[p\text{-}MeOC_6H_4C(NSiMe_3)_2]_2YCH(SiMe_3)_2$, $[(Me_3Si)_2NC(N^iPr)_2]_2YCH(SiMe_3)_2$, $[(Me_3Si)_2NC(N^iPr)_2]_2Y(\mu\text{-}Me)_2Li(TMEDA)$, $[(Me_3Si)_2NC(N^iPr)_2]_2Y(^tBu)$,[34] $[Me_3SiNC(Ph)N(CH_2)_3NC(Ph)NSiMe_3]Y[CH(SiMe_3)_2](THF)$,[35] $\{CyNC[N(SiMe_3)_2]NCy\}_2LnCH(SiMe_3)_2$ (Ln = Sm, Yb), $[(Me_3Si)_2NC(N^iPr)_2]_2Ln(\mu\text{-}Me)_2Li(TMEDA)$ (Ln = Yb, Nd (Figure 10)),[36] $[PhC(NSiMe_3)_2]_2ScR$ (R = CH_2SiMe_3, Mes), and $[PhC(NSiMe_3)_2]_2ScMe(THF)$.

In THF, deprotonation of $Ln[N(SiMe_3)_2]_3$ (Ln = Sc, Yb, Lu) with $NaN(SiMe_3)_2$ leads to complexes containing a planar four-membered LnCSiN ring system with a linear Ln–C–Na arrangement (Figure 11a). Methyl- and vinyl-substituted Sm derivatives supported by a calix-tetrapyrrole ligand $(Et_8\text{-calix-pyrrole})(R)Sm(\mu_3\text{-}Cl)[Li(THF)]_2[Li(THF)_2]$ (R = Me, $CH{=}CH_2$) (Figure 11b) were prepared by the reaction of $(Et_8\text{-calix-pyrrole})(Cl)Sm[Li_2(THF)_3]$ with the corresponding organolithium reagents. The methyl derivative reacts with hydrogen affording the corresponding samarium hydride $(Et_8\text{-calix-pyrrole})(THF)Sm[Li(THF)]_2(\mu_3\text{-}H)$.[37]

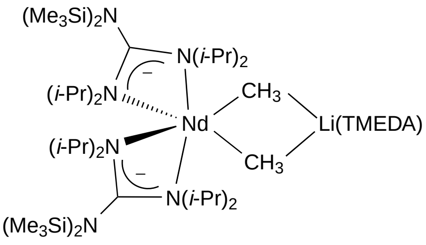

Figure 10 $[(Me_3Si)_2NC(N^iPr)_2]_2Nd(\mu\text{-}Me)_2Li(TMEDA)$

Monoalkyl complexes, $(L)LnCH_2SiMe_3$ (L = 1,3-di[2-(N-isopropylamino)troponimine]propane, Ln = La, Lu) (Figure 12a)[38] and a scandium alkyl complex bearing a diamide–diamine donor ligand (Figure 12b) are also known.[39,40]

The neutral monobenzyl compound $Cp^*_2Y(CH_2Ph)(THF)$ was obtained by the reaction of YBr_3 with benzylpotassium and KCp* in THF.[11] Terphenyl complexes $(Dmp)LnCl_2(THF)_n$ [Dmp = 2,6-di(mesityl)phenyl; Ln = Sc,

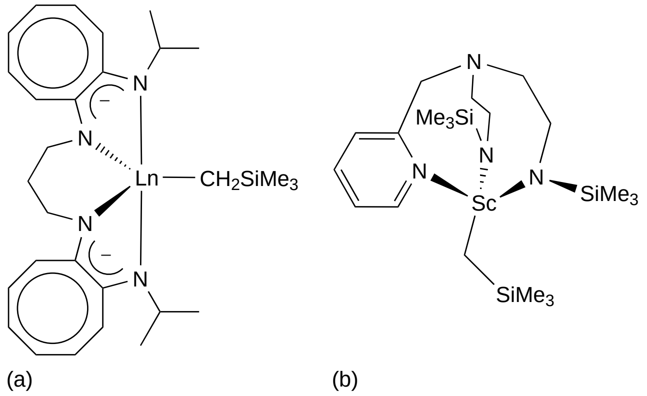

Figure 12 (a) $(^iPrNC_8H_6NCH_2CH_2NC_8H_6N^iPr)LnCH_2SiMe_3$ and (b) $[N(CH_2CH_2NSiMe_3)CH_2C_5H_4N]ScCH_2SiMe_3$

Yb, $n = 2$; Ln = Y, $n = 3$] and (Dnp)LnCl$_2$(THF)$_2$ [Dnp = 2,6-di(1-naphthyl)phenyl, Ln = Yb, Tm, Y] were prepared in THF from LnCl$_3$, and (Dmp)Li and (Dnp)Li, respectively. The Dnp complexes are monomeric with distorted trigonal-bipyramidal (Sc and Yb) or octahedral (Y) coordination geometry about the metal atom, with the two Cl atoms occupying the axial positions.[41] Complexes (Dnp)LnCl$_2$(THF)$_2$ (Ln = Yb, Tm, Y) exhibit distorted trigonal-bipyramidal coordination environments at the metal center, with the two O atoms of the THF ligands occupying the axial positions of a trigonal-bipyramidal coordination polyhedron.[42] The complexes with donor-functionalized terphenyl ligands [(Danip)Yb(μ-Cl)$_2$(μ_3-Cl)Li(THF)]$_2$ and [(Danip)Ln(μ_2-Cl)$_2$(μ_2-Cl)Li(THF)$_2$]$_2$ (Ln = Y, Sm; Danip = 2, 6-di(*o*-anisol)phenyl) are obtained from the reaction of equimolar amounts of (Danip)Li and LnCl$_3$ (Ln = Yb, Y, Sm) in THF. These complexes are dimeric and composed of lithium chloride–bridged (Danip)LnCl$_2$ moieties, stabilized through additional coordination of two methoxy functions to the lanthanide atom.[43] The structurally characterized lanthanidocene terphenyl derivatives (C$_5$H$_4$Me)$_2$YbR and Cp$_2$SmR [R = 2,6-(2,4,6-Me$_3$C$_6$H$_2$)$_2$C$_6$H$_3$] were obtained by the reaction of RLi with (C$_5$H$_4$Me)$_3$Yb or Cp$_3$Sm in toluene.[11]

Cp*$_2$SmPh(THF) is available by transmetalation between Cp*$_2$Sm(THF)$_2$ and Ph$_2$Hg. The solvent-free complex [Cp*$_2$SmPh]$_2$ thermally decomposes to yield benzene and the phenylene-bridged disamarium complex Cp*$_2$Sm(μ-1,4-C$_6$H$_4$)SmCp*$_2$.[44] SmBr$_3$ reacts with Li$^+{}_2$(biph)$^{2-}$ in THF to form dimeric [(quaph)SmBr(THF)$_2$]$_2$ (quaph = o-quaterphenyl) in which both Sm atoms are coordinated by a quaph ligand each and two THF molecules besides two bridging Br atoms resulting in a distorted octahedral coordination of the Sm atoms (Figure 13).[12]

Cp$_3$La(THF) reacts with Li[C$_6$H$_3$(CH$_2$NMe$_2$)$_2$-2,6] yielding Cp$_2$La[C$_6$H$_3$(CH$_2$NMe$_2$)$_2$-2,6] (Figure 14a); lanthanide complexes with the related mono-(Me$_2$N)-substituted phenyl ligand, (COT)Ln(THF)(C$_6$H$_4$CH$_2$NMe$_2$-2) (Ln = Er, Lu) and Cp$_2$Y(C$_6$H$_4$CH$_2$NMe$_2$-2), were prepared by alkylation of (COT)LnCl(THF) and Cp$_2$YCl, respectively, with LiC$_6$H$_4$CH$_2$NMe$_2$-2; reactions of LnCl$_3$ (M = Er, Yb, Lu) with 3 equiv. of LiC$_6$H$_4$CH$_2$NMe$_2$-2 gave the homoleptic tris(aryl)lanthanides Ln(C$_6$H$_4$CH$_2$NMe$_2$-2)$_3$; and treatment of (Cp*$_2$SmH)$_2$ with 2-phenyl-1-pyrroline causes orthometalation (*see Orthometalation*) resulting in the formation of Cp*$_2$SmC$_6$H$_4$(2-NC$_4$H$_6$) (Figure 14b).

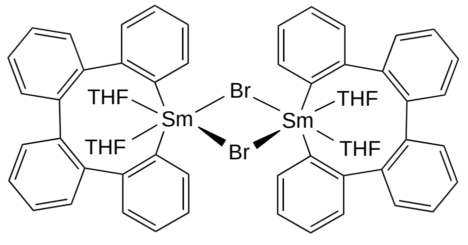

Figure 13 [(quaph)SmBr(THF)$_2$]$_2$ (quaph = o-quaterphenyl)

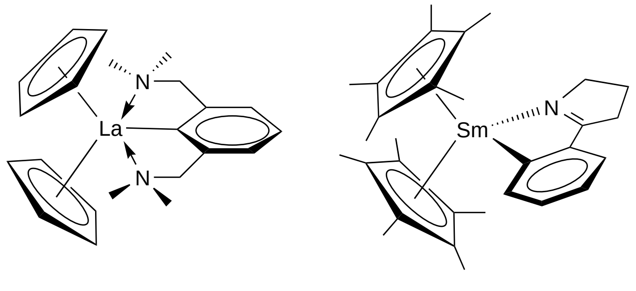

(a) (b)

Figure 14 (a) Cp$_2$LaC$_6$H$_3$(CH$_2$NMe$_2$)$_2$ and (b) Cp*$_2$SmC$_6$H$_4$-C$_4$H$_6$N-2

The first organolanthanide alkynide complexes [Cp$_2$Ln(μ-C≡C ^{t}Bu)]$_2$ (Ln = Er, Yb) were synthesized by the halide-free reactions of [Cp$_2$Ln(μ-Me)]$_2$ with HC≡C ^{t}Bu.[6] Alkynide bridged complexes [(^{t}BuCp)$_2$Ln(μ-C≡CPh)]$_2$ (Ln = Nd, Gd) were prepared similarly. According to X-ray data for the Er, Nd, and Gd complexes, the two Cp$_2$Ln units of the dimers are connected by asymmetric alkynide bridges. Dimeric [(MeC$_5$H$_4$)$_2$SmC≡C ^{t}Bu]$_2$ has been synthesized from (MeC$_5$H$_4$)$_2$SmCl and LiC≡C ^{t}Bu in THF. The early lanthanide alkyls Cp*$_2$LnCH(SiMe$_3$)$_2$ (Ln = Ce, La) react with terminal alkynes HC≡CR (R = Me, ^{t}Bu) to produce oligomeric acetylides [Cp*$_2$LnC≡CR]$_n$ (Ln = Ce, R = Me, ^{t}Bu; Ln = La, R = Me), which, in solution, rearrange to give the carbon–carbon coupled products, [Cp*$_2$Ln]$_2$(μ-η^2:η^2-R$_2$C$_4$) (Ln = Ce, R = Me, ^{t}Bu; Ln = La, R = Me). The X-ray structures of [Cp*$_2$Ce]$_2$(μ-η^2:η^2-R$_2$C$_4$) (R = Me, ^{t}Bu) show two Cp*$_2$Ce units bridged by a conjugated R$_2$C$_4$ group. The reaction of 2,4-dimethylpentadienylneodymium, (C$_7$H$_{11}$)$_3$Nd, with HC≡CPh in toluene also leads to dimeric phenylethynyl derivatives [(C$_7$H$_{11}$)$_2$NdC≡CPh]$_2$. The monomeric, solvent-free lanthanide alkynide tris(pyrazolyl)borate (TpMe$_2$) complex (TpMe$_2$)$_2$Sm(C≡CPh) results from the reaction of (TpMe$_2$)$_2$Sm with Hg(C≡CPh)$_2$ in THF.[45]

2.4 Lanthanide Alkylaluminates

Homoleptic (*see Homoleptic Compound*) alkylaluminates of the lanthanide metals like Nd[(μ-Me)$_2$AlMe$_2$]$_3$ are formed when an excess of AlMe$_3$ reacts with (Me$_2$N)$_3$Ln complexes (equation 8). Earlier Cp$_2$Ln(μ-R)$_2$AlR$_2$ (Ln = Sc, Y, Ga, Dy, Ho, Er, Tm, Yb, R = Me; Ln = Sc, Y, Ho, R = Et) have been prepared from (Cp$_2$LnCl)$_2$ with Li(AlR$_4$) or Mg(AlR$_4$)$_2$, as well as [Cp*$_2$Ln(μ-Me$_2$)MMe$_2$]$_2$ (Ln = Y, Yb; M = Al, Ga),[6] [Cp*$_2$Yb(μ-Me$_2$)AlMe$_2$]$_2$ and [Cp*$_2$Yb(S-*p*-tolyl)(Me$_3$Al)$_2$]$_2$,[46] and *rac*-Me$_2$Si(2-MeC$_9$H$_5$)$_2$Y(μ-R)$_2$AlR$_2$ (R = Me, Et, iso-Bu).[47]

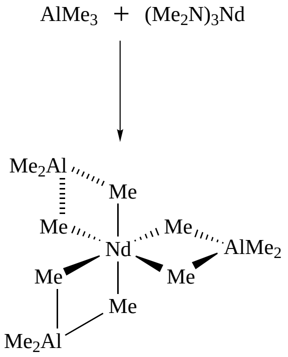

(8)

The reaction of $[Cp'_2Y(\mu\text{-Me})]_2$ ($Cp' = C_5H_5, C_5H_4SiMe_3$) with $B(C_6F_5)_3$ affords the complexes $Cp'_2Y\{MeB(C_6F_5)_3\}$. In $(\eta^5\text{-}Me_3SiC_5H_4)_2Y\{(\mu\text{-}FC_6F_4)(\mu\text{-}Me)B(C_6F_5)_2\}$, the yttrium atom is coordinated in a chelating fashion via one ortho-F atom and agostic interactions (*see Agostic Bonding*) to Me groups. The alkylation of $Ln(O^tBu)_3$ with $AlMe_3$ leads to the mixed-bridged alkyl–alkoxy complexes $Ln[(\mu\text{-}O^tBu)_3(\mu\text{-}Me)AlMe_2)]_3$ (Ln = Pr, Nd or Y). Bis-trialkylaluminum adducts $(ArO)Ln[(\mu\text{-}OAr)(\mu\text{-}R)AlR_2]_2$ (Ln = La, R = Me; Ln = La, R = Et; Ln = Sm, R = Et) were prepared by the reaction of $[Ln(OAr)_3]_2$ with four equiv. of trialkylaluminum.[48] Highly substituted lanthanide(III) aryloxide trimethylaluminum complexes are known. $Y(OC_6H_3{}^iPr_2\text{-}2,6)[(\mu\text{-}OC_6H_3{}^iPr_2\text{-}2,6)(\mu\text{-}Me)AlMe_2]_2$ and $Ln(OC_6H_3{}^tBu_2\text{-}2,6)_2[(\mu\text{-}Me)_2AlMe_2]$ (Ln = Y, Lu) have been characterized by X-ray structures.[49] The reaction of $Nd(NHPh)_3(KCl)_3$ with $AlMe_3$ afforded a heteroleptic mixed-metal complex $\{[Me_2Al(\mu\text{-}Me_2)]_2Nd(\mu_3\text{-}NPh)(\mu\text{-}Me)AlMe\}_2$. $Nd[(\mu\text{-}NMe_2)(\mu\text{-}Me)MMe_2]_3$ (M = Al, Ga) were prepared from $Nd(NMe_2)_3(LiCl)_3$ and 3 equiv. of MMe_3 (M = Al, Ga) and the reaction of $Nd(NMe_2)_3(LiCl)_3$ with excess of $GaMe_3$ gave homoleptic $Nd\{(\mu\text{-}Me)_2GaMe_2\}_3$. Aluminates $\{AlMe_2(O_2CC_6H_2{}^iPr_3\text{-}2,4,6)_2\}_2LnAlMe_4$ (Ln = Y, La, Nd, Lu), supported by carboxylate ligands, are available from lanthanide tris(carboxylates) and Me_3Al. These aliminates are highly active in the polymerization of isoprene forming more than 99% cis polymers.[50]

2.5 Lanthanide Complexes with Carbenes, Ylides, Bis(imino)phosphoranides, and Phosphomethanides

Imidazolin-2-ylidenes $C(NRCHR')_2$ react with coordinatively unsaturated organolanthanides and with THF or Lewis base stabilized organolanthanide complexes under replacement forming organolanthanide carbene adducts. Until now there are only a few examples of Ln(III) carbene adducts known, for example, $[(Me_2HSi)_2N]_3Y(C_3N_2H_2Me_2)_n$ ($C_3N_2\text{-}H_2Me_2$ = 1,3-dimethylimidazolin-2-ylidene, $n = 1,2$) (Figure 15a), $L_3Eu(C_3N_2Me_4)$ (L = 2,2,6,6-tetramethylheptan-3,5-dionate; $C_3N_2Me_4$ = 1,2,3,4-tetramethylimidazolin-2-ylidene), and the silylene derivative $Cp_3LnSi[\{N(CH_2{}^tBu)\}_2\text{-}C_6H_4\text{-}1,2]$ (Ln = Y, Yb).[51] For carbene complexes of Ln(II) compounds, see Section 11. $[(Me_3Si)_2N]_3Ln$ (Ln = La, Nd) and (COT)YCp* react with 1,3,4,5-tetramethylimidazoline-2-ylidene to yield the ylidic olefin complexes $[(Me_3Si)_2N]_3Ln\text{-}CH_2C(NMeCHMe)_2$ and $(COT)Cp^*YCH_2C(NMeCHMe)_2$ (Figure 15b) respectively.

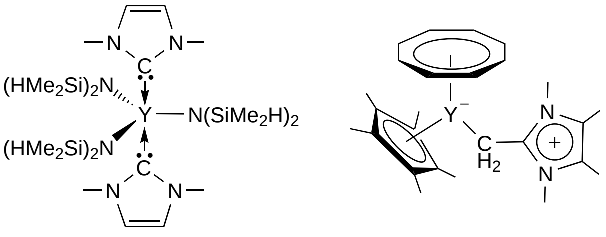

(a) (b)

Figure 15 (a) $[(Me_2HSi)_2N]_3Y(C_3N_2H_2Me_2)_2$ and (b) (COT)-$Cp^*YCH_2C(NMeCHMe)_2$

Organolanthanide-phosphorus ylide complexes $(C_5H_4R)_3NdCH_2P(Me)Ph_2$ (R = H, ^{t}Bu) and $(C_5H_4{}^tBu)_2Yb(Cl)\text{-}CH_2P(Me)Ph_2$ were synthesized from $Li[(CH_2)_2PPh_2]$ and the respective Cp_2LnCl precursors. Variable temperature $^{31}P\{^1H\}$ NMR spectroscopy indicates an equilibrium between $(C_5H_4R)_3NdCH_2P(Me)Ph_2$ and $[(C_5H_4R)_3Nd(THF) + CH_2{=}P(Me)Ph_2]$ in THF solution. The bisiminophosphorane $CH_2(Ph_2P{=}NSiMe_3)_2$ reacts with $Sm(NCy_2)_3(THF)$ in toluene to give $[(Ph_2P{=}NSiMe_3)_2C]Sm(NCy_2)(THF)$ (Figure 16).[52]

Phosphinomethanide complexes of the lanthanides $[Me_3SiC(PMe_2)_2]_3Lu(THF)$ and $[Me_3SiC(PMe_2)_2]_3Lu$ are prepared by reaction of $Lu(OSO_2CF_3)_3$ with $Li[Me_3SiC\text{-}(PMe_2)_2]$. Alkylation with MeLi forms $[Me_3SiC(PMe_2)_2]_2\text{-}Lu(Me)(THF)$ (Figure 17a). Reaction of $K\{CH(PPh_2NSiMe_3)_2\}$ with $LnCl_3$ forms $[\{CH(PPh_2NSiMe_3)_2\}LnCl_2]_2$ (Ln = Y, Sm, Er, Dy, Yb, Lu). Further reaction of the Y and Sm derivatives with $KNPh_2$ affords $[\{CH(PPh_2NSiMe_3)_2\}Ln\text{-}(NPh_2)_2]$ (Ln = Y, Sm).[53] The corresponding dicyclopentadienyl complexes $Cp_2Ln\{CH(PPh_2NSiMe_3)_2\}$ (Figure 17b)[54] are also known.

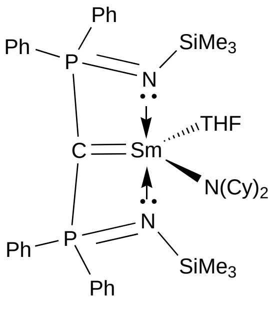

Figure 16 $[(Ph_2P{=}NSiMe_3)_2C]Sm(NCy_2)(THF)$

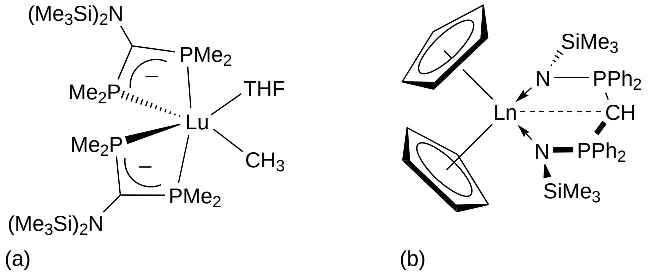

(a)

(b)

Figure 17 (a) $[Me_3SiC(PMe_2)_2]_2Lu(Me)(THF)$, (b) $Cp_2Ln\{CH(PPh_2NSiMe_3)_2\}$ (Ln = Y, Sm, Er)

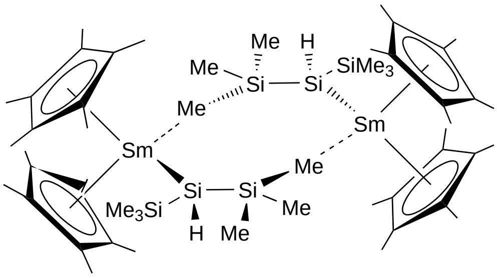

Figure 18 Dimeric $Cp^*_2LnSiH(SiMe_3)_2$

2.6 σ-Silyl-, Germyl-, and Stannyl-derivatives

$Cp^*_2LnCH(SiMe_3)_2$ (Ln = Sm, Nd, Y) and $(C_5Me_4Et)_2LnCH(SiMe_3)_2$ (Ln = Sm, Nd) react with $H_2Si(SiMe_3)_2$ to form the silyl complexes $Cp^*_2LnSiH(SiMe_3)_2$ (Ln = Sm, Nd, Y) and $(C_5Me_4Et)_2LnSiH(SiMe_3)_2$ (Ln = Sm, Nd), respectively. The X-ray crystal structure of $Cp^*_2LnSiH(SiMe_3)_2$ shows dimers in the solid state via intermolecular $Sm\cdots CH_3$–Si interactions (Figure 18). The samarium hydride $[Cp^*_2Sm(\mu\text{-}H)]_2$ reacts with *o*-$MeOC_6H_4SiH_3$ via Si–H activation affording $Cp^*_2SmSiH_2(OC_6H_4\text{-}OMe\text{-}2)$, which rapidly decomposes to the dimeric aryl complex $[Cp^*_2Sm(\mu\text{-}C_6H_4Me\text{-}2)]_2$,**[44]** and $[Cp^*_2Sm(\mu\text{-}H)]_2$ reacts with $PhSiH_3$ forming $[Cp^*_2SmSiH_3]_3$, which reacts with benzophenone yielding $Cp^*_2SmOCPh_2(SiH_3)$.**[55]** $[Li(DME)_3][Cp_2Ln(SiMe_3)_2]$ (Ln = Sm, Lu) was prepared from $Cp_2Ln(\mu\text{-}Cl_2)Na(DME)_2$ and Me_3SiLi in DME and the scandocene complexes $Cp_2Sc(ER_3)(THF)$ [ER_3 = $Si(SiMe_3)_3$, $Si(SiMe_3)_2Ph$, $Si(^tBu)Ph_2$, $SiPh_3$, $Ge(SiMe_3)_3$] were prepared by reacting the appropriate silyl- or germyllithium reagent with $(Cp_2ScCl)_2$.

3 ALKENE AND ALKYNE COMPLEXES

Organolanthanide(III) complexes with η^2 coordinated alkene or alkyne ligands are very rare. For alkene complexes of Ln(II) compounds, see Section 11. The coordination of the olefinic double bond to Y in $Cp^*_2YCH_2CH_2CMe_2CH{=}CH_2$ (equation 9) could be proved by NMR.

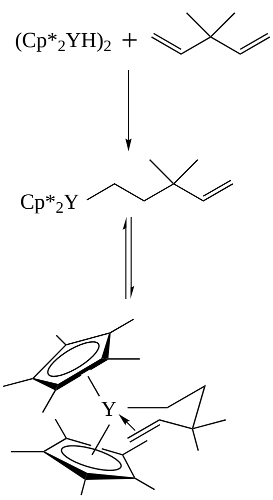

(9)

The reaction of *meso*-octaethylporphyrinogen (oepg) lanthanide complexes, $[\{(oepg)Ln\}Na(THF)_2]$ (L = Pr, Nd) with $NaC_{10}H_8$ in an ethene atmosphere in the presence of 18-crown-6 (*see Crown Ethers*) in THF yields dimeric species, where the metals are bridged by the $[C_2H_4]^{2-}$ anion. According to the X-ray crystal structure of the Nd derivative, the $[CH_2CH_2]^{2-}$ unit is side-on bonded to the two metal atoms (Figure 19a).

Similar reaction in an acetylene atmosphere gives the neutral dimers $[(oepg)Ln]_2[(\mu\text{-}C_2)(\mu\text{-}Na)_4]$. X-ray crystal structure analysis of the neodymium derivative (Figure 19b) shows the acetylide dianion end on bonded to the two metal centers.

The reaction of YCl_3 with $K_2(Ph_2C{=}CPh_2)$ followed by cation exchange with $NaBPh_4$ in THF yields $[Na(THF)_6][Y(Ph_2C{=}CPh_2)_2](THF)_2$. According to the X-ray crystal structure, the unit $[Y(Ph_2CCPh_2)_2]^-$ has a sandwich-like structure in which each $(Ph_2CCPh_2)^{2-}$ dianion has six carbon atoms oriented toward the metal center with Y–C distances between 2.518 and 2.689 Å.**[11]**

4 ALLYL AND ALLENYL COMPLEXES

Allyl complexes of the lanthanides are very efficient catalysts for stereospecific butadiene polymerization. The smaller size of the allyl anion compared to other ionic π-systems like Cp^- allows the formation of homoleptic anionic complexes of the type $[(allyl)_4Ln]^-$ with all four ligands η^3-bonded to the Ln metal. Complexes $[Li(dioxane)_n][Ln(\eta^3\text{-}C_3H_5)_4]$ (Ln = Ce, Pr, Nd, Sm, Gd, $n = 2$; Ln = Y, $n = 2.5$; Ln = La, $n = 3$), $[Li_2(THF)_n][Ln(\eta^3\text{-}C_3H_5)_5]$ (Ln = Y, La, $n = 2.5$; Ln = Ce, Pr, Nd, Sm, $n = 3$), and $[Li_2(dioxane)_n][Ln(\eta^3\text{-}C_3H_5)_5]$ (Ln = Ce, Nd, Sm, Gd, Dy, Ho, Er; $n = 1, 3$) are available by treatment of anhydrous lanthanide trichlorides with

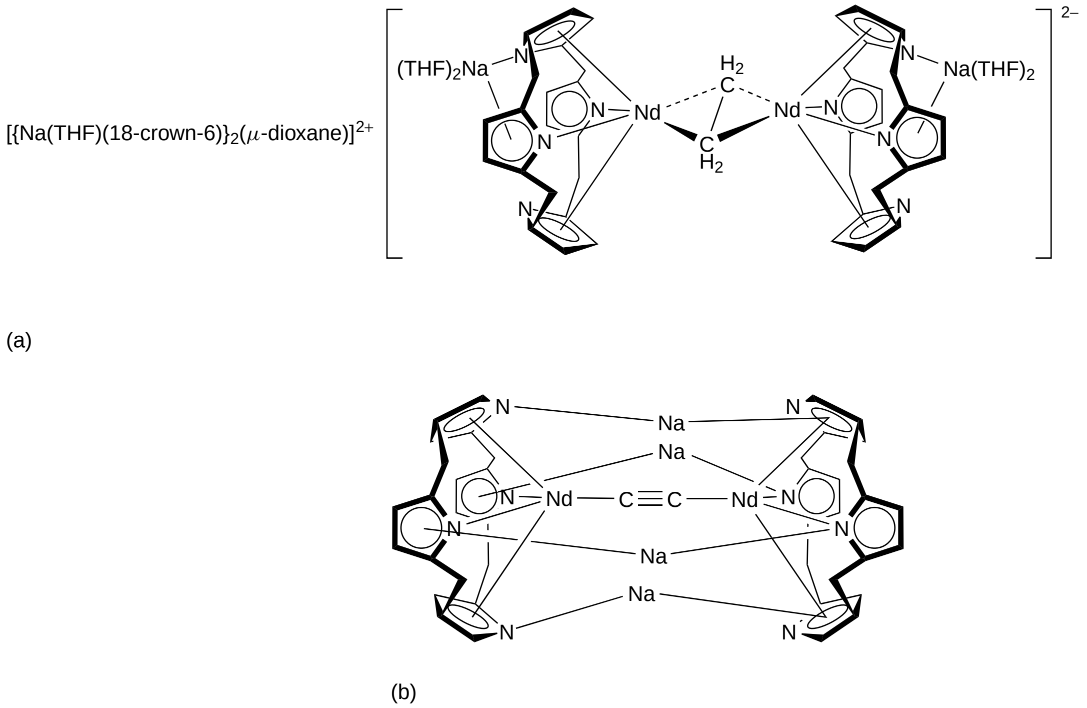

Figure 19 (a) $[\{Na(THF)(18\text{-crown-6})\}_2(\mu\text{-dioxane})][\{(oepg)Nd\}Na(THF)_2]$ and (b) $[(oepg)Nd]_2[(\mu\text{-}C_2)(\mu\text{-}Na)_4]$

allyllithium (equation 10). Neutral tris(allyl)lanthanide complexes $Ln(\eta^3\text{-}C_3H_5)_3(dioxane)_n$ ($Ln = La, n = 1.5; Ln = Nd, n = 1$) are prepared from $Li[Ln(C_3H_5)_4]$ ($Ln = La$ or Nd) via allyllithium abstraction with BEt_3 in dioxane. The La derivative is a dimer $[\{La(\eta^3\text{-}C_3H_5)_3(\eta^1\text{-dioxane})\}_2(\mu\text{-dioxane})]$, whereas the Nd derivative forms a coordination polymer $[Nd(\eta^3\text{-}C_3H_5)_3(\mu\text{-dioxane})]_n$. Bis(allyl)- and mono(allyl)neodymium(III) compounds $Cp^*Nd(\eta^3\text{-}C_3H_5)_2(dioxane)$ and $[Nd(\eta^3\text{-}C_3H_5)Cl(THF)_5][BPh_4](THF)$ were examined as catalysts for butadiene polymerization.[56]

$$NdCl_3 + 4Li(C_3H_5) \xrightarrow[\text{2) Et}_2\text{O/dioxane}]{\text{1) DME, 50 °C}} [Li(dioxane)_2][Nd(C_3H_5)_4] \qquad (10)$$

The bis- and mono(allyl)neodymium(III) chlorides, $Nd(\eta^3\text{-}C_3H_5)_2Cl(THF)_{1.5}$ and $Nd(\eta^3\text{-}C_3H_5)Cl_2(THF)_2$, were prepared by the reaction between $Nd(\eta^3\text{-}C_3H_5)_3(dioxane)$ and $NdCl_3(THF)_2$ in the corresponding molar ratio in THF. In combination with MAO, they catalyze the 1,4-*cis*-polymerization of butadiene in toluene and heptane, with extremely high activity and selectivity (≥98%). The bis(η^3-allyl)lanthanum(III) halides $La(\eta^3\text{-}C_3H_5)_2X(THF)_2$ ($X = Cl$, Br, I) are also available by partial protolysis of $La(\eta^3\text{-}C_3H_5)_3(dioxane)_{1.5}$ with Me_3NHX ($X = Cl$, Br, I) in THF.

The allyl complexes $[Cp'_2Sm(C_3H_5)]_n$ ($Cp' = {}^tBuC_5H_4$) and *ansa*-$Me_4C_2(\eta^5\text{-}C_5H_4)_2Sm(C_3H_5)_2Li(DME)$ were synthesized from $(Cp'_2SmCl)_2$ and *ansa*-$Me_4C_2(\eta^5\text{-}C_5H_4)_2SmCl\text{-}[MgCl_2(THF)_4]$, respectively. The mono-allyl complex $Cp^*{}_2Sm(\eta^3\text{-}C_3H_5)$ reacts with CO_2 in toluene at room temperature to form $[Cp^*{}_2Sm(\mu\text{-}O_2CCH_2CH{=}CH_2)]_2$. In THF it exists as solvated monometallic species $Cp^*{}_2Sm(\mu_2\text{-}O_2CCH_2CH{=}CH_2)(THF)$ but it crystallizes from hexane as a bimetallic complex that contains an eight-membered SmOCOSmOCO ring (equation 11).

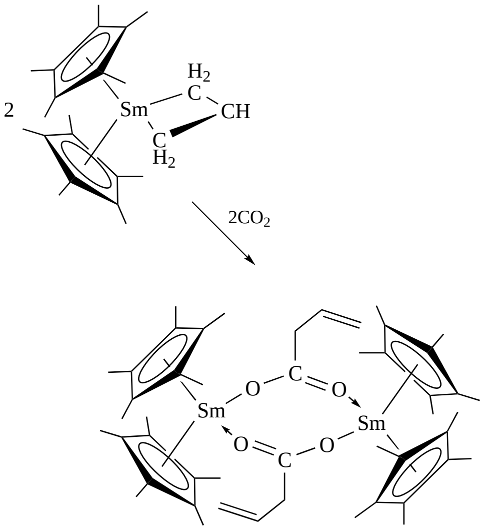

(11)

Variable temperature ^1H NMR spectroscopy of a series of Sc and Y metallocene allyl complexes indicates fluxional (*see Fluxional Molecule* and ***Structure & Property Maps for Inorganic Solids***) behavior involving C–C double-bond dissociation from the metal center, that is, an η^3 to η^1 change in coordination. Activation barriers to olefin dissociation were determined for η^5-$Cp^*_2Sc(C_3H_5)$, *meso*-$Me_2Si(\eta^5\text{-3-}^t BuC_5H_3)_2Sc(C_3H_5)$, *meso*-$Me_2Si(\eta^5\text{-2,4-}^i Pr_2C_5H_2)_2Sc(C_3H_5)$, *meso*-$Me_2Si\{\eta^5$-3-[2-(2-Me)adamantyl]$C_5H_3\}_2Sc(C_3H_5)$, *meso*-$Me_2Si\{\eta^5$-3-[2-(2-Me)adamantyl]$C_5H_3\}_2Y(C_3H_5)$, *rac*-$Me_2Si(\eta^5\text{-2,4-}^i Pr_2C_5H_2)_2Sc(C_3H_5)$, and (*R*)-$(C_{20}H_{12}O_2)Si(\eta^5\text{-2-SiMe}_3\text{-4-}^t BuC_5H_2)_2Sc(C_3H_5)$. It has been found that donor solvents do not significantly affect the rate of this process. X-ray structure analysis of *rac*-$Me_2Si(\eta^5\text{-2,4-}^i Pr_2C_5H_2)_2Sc(C_3H_5)$ showed the allyl ligand η^3 coordinated to the metal.[11]

The reaction of $Li_2[(Me_3Si)_2C_5H_2]SiMe_2(CHC{\equiv}CSiMe_3)$ with $SmCl_3$ yields the allenyl complex $\{[(Me_3Si)_2C_5H_2]SiMe_2(\eta^3\text{-CH=C=CSiMe}_3)\}SmCl_3Li_2(TMEDA)_2$, whereas the reaction of the dilithium salt of the triphenylsilyl substituted ligand with $SmCl_3$ yielded the η^1-propargyl derivative $\{[(Me_3Si)_2C_5H_2]SiMe_2(\eta^1\text{-CHC}{\equiv}\text{CSiPh}_3)\}Sm(TMEDA)[Cl_2Li(TMEDA)]$. A conversion of the bonding mode from η^1-propargyl to η^3-allenyl was observed when the later compound was treated with $(Me_3Si)_3CLi$/LiI to give the η^3-allenyl complex $\{[(Me_3Si)_2(C_5H_2)]SiMe_2(\eta^3\text{-CH=C=CSiPh}_3)\}SmI_2Li(TMEDA)$ (equation 12).[57]

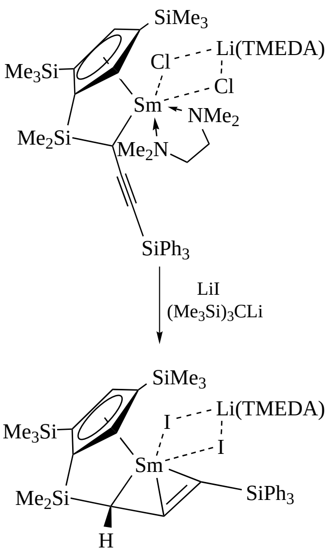

(12)

Thermal decomposition of $Me_2Si(C_5Me_4)(CH_2CH{=}CH_2)Y(CH_2SiMe_3)_2(THF)_2$, containing an allyl(dimethylsilyl)substituted cyclopentadienyl ligand, yields $[Y\{\eta^5{:}\eta^1\text{-C}_5\text{Me}_4\text{SiMe}_2(\mu\text{-}\eta^3\text{-C}_3\text{H}_3)\}L]_2$ (L = DME or THF). X-ray diffraction studies showed that the novel trianionic ligand bridges the two yttrium atoms by coordinating $\eta^5{:}\eta^1$ to one and η^3 to the other metal (Figure 20).[58]

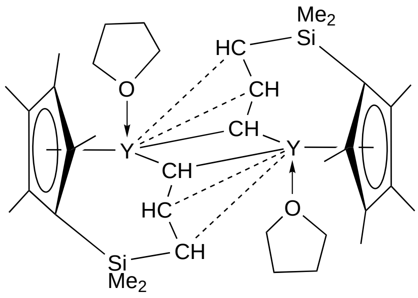

Figure 20 $[Y\{\eta^5{:}\eta^1\text{-C}_5\text{Me}_4\text{SiMe}_2(\mu\text{-}\eta^3\text{-C}_3\text{H}_3)\}\text{THF}]_2$

Several lanthanide(II) and lanthanide(III) complexes with aza-allyl ligands $Ln(L)_2X(THF)_n$ (L = $\eta^3\text{-Me}_3\text{SiN=C}(^t\text{Bu})\text{CHSiMe}_3$; X = Cl, $n = 1$, Ln = Ce or Nd; X = I, $n = 1$, Ln = Sm; X = I, $n = 0$, Ln = Yb), $Sm(L)_2(THF)$ and $Yb(L)_2$, were synthesized by the reaction of the appropriate lanthanide(II) or lanthanide(III) halides with two equiv. of 1,3-bis(trimethylsilyl)-1-aza-allylpotassium.

5 DIENE COMPLEXES

Lanthanide complexes with neutral coordinated diene ligands are unknown. In contrast, a few examples containing anionic diene ligands, for example, $[Cp^*_2La(THF)(\mu\text{-}\eta^1,\eta^3\text{-C}_4\text{H}_6)LaCp^*_2]$ and $[LaI_2(THF)_3]_2(\mu\text{-Ph}_2\text{C}_4\text{H}_4)$, have been described.[6] The related gadolinium complex $[GdCl_2(THF)_3]_2(\mu\text{-Ph}_2\text{C}_4\text{H}_4)$ was obtained by the reaction of $GdCl_3$ with potassium diphenylbutadienide generated in situ.[4] The structurally characterized lutetium compound $[(\mu\text{-PhCHCHCHCHPh})_2Lu(THF)_2K(THF)_2]_n$ contains two η^4-diphenylbutadiene ligands and two THF molecules coordinated to the central lutetium ion. The diphenylbutadiene is bonded in its *cis* conformation. In the crystal, a polymeric chain structure results from additional η^6-coordination of two phenyl rings to potassium. Since the oxidation state of lutetium is +3, the two diene ligands must be formally dianions to result in a monoanionic species with potassium as the counterion (Figure 21).[11]

Pentamethylcyclopentadienyllanthanide dichlorides Cp^*LnCl_2 (Ln = Sm, Lu) react with diarylbutadienes and lithium under elimination of the pentamethylcyclopentadienyl

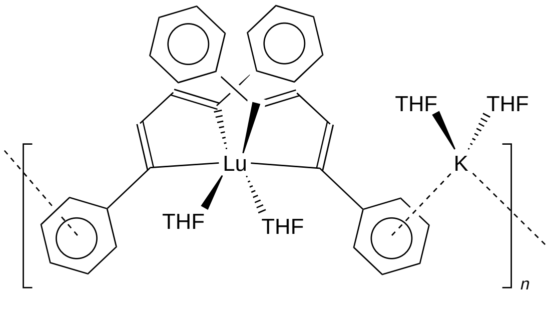

Figure 21 $[(\mu\text{-PhCHCHCHCHPh})_2Lu(THF)_2K(THF)_2]_n$

ligand and formation of anionic (butadiene)lanthanide complexes $[Li(THF)_3][Sm(1,4\text{-}Ph_2C_4H_4)_2]$ and $[Li(DME)][(1,4\text{-}Ar_2C_4H_4)LuCl_2]$ (in THF and DME, respectively). A slightly different lithium salt $[Li(THF)_3][Sm(1,4\text{-}Ph_2C_4H_4)_2]$ was isolated in the form of black–red crystals starting directly from $SmCl_3$. A mononuclear samarium complex $[1,4\text{-}(p\text{-}MeC_6H_4)_2C_4H_4]SmI(THF)_3$ containing a terminal 1,4-di-*p*-tolylbutadiene ligand results from the reaction of metallic samarium with iodine and the butadiene derivative in THF.

The reduction of diphenylacetylene with $[CpLu(C_{10}H_8)(DME)]^{2-}$ results in C–C coupling and formation of a dinuclear complex with a bridging $[C_4Ph_4]^{4-}$ ligand: $[CpLu(DME)]_2[\mu\text{-}\eta^4{:}\eta^4\text{-}PhCC(Ph){=}C(Ph)CPh]$. The crystallographic and spectral data suggest a dialkylidene bridging ligand in this complex.**[11]**

$CpLuCl_2(THF)_2$ reacts with 2 equiv. of $Na[PhCH{=}CHPh]$ in DME with dimerization of the stilbene radical anions to form $[Na(DME)_3][Cp_2Lu\{\mu\text{-}CH(Ph)CH(Ph)\text{-}CH(Ph)CH(Ph)\}]$ containing a dianionic 1,2,3,4-tetraphenylbutadiene ligand. X-ray crystal structure determination shows Lu coordinated to two Cp rings and the dianionic butadiene ligand in an η^5 and 1,4-diyl fashion.**[59]**

A nonreductive reaction pathway has been also used for coupling of alkynes to produce complexes with dianionic butadiene ligands. Thus, the reaction of $Cp^*{}_2LaCH(SiMe_3)_2$ with $PhC{\equiv}CH$ at room temperature yields the binuclear product $(Cp^*{}_2La)_2(\mu\text{-}Ph_2C_4)$ and $CH_2(SiMe_3)_2$. Although the uncoupled dimer $(Cp^*{}_2LaC_2{}^tBu)_2$ is formed in the reaction of $Cp^*{}_2LaCH(SiMe_3)_2$ with ${}^tBuC{\equiv}CH$ at 0 °C, it undergoes clean unimolecular conversion in toluene solution at 60 °C to the coupled dimer $(Cp^*{}_2La)_2(\mu\text{-}{}^tBu_2C_4)$. The related Sm(III) complex $(Cp^*{}_2Sm)_2(\mu\text{-}\eta^2{:}\eta^2\text{-}Ph_2C_4)$ has been prepared using both reductive and nonreductive conditions reacting $Cp^*{}_2Sm(THF)_2$ and $PhC{\equiv}C{-}C{\equiv}CPh$ or by thermolysis of $Cp^*{}_2Sm(C{\equiv}CPh)(THF)$ at 80–145 °C. The later compound can be prepared also from $PhC{\equiv}CH$ and $[Cp^*{}_2SmH]_2$ or $Cp^*{}_2Sm[CH(SiMe_3)_2]$.**[6]**

6 PENTADIENYL COMPLEXES

Owing to relationship between cyclopentadienyl and pentadienyl ligands, the complexes of the later ligand are often termed *open metallocenes*. Lanthanide derivatives with ‘open cyclopentadienyl ligands’ have been described since 1982, for example, Tris(2,4-dimethylpentadienyl)neodymium $Nd(C_7H_{11})_3$. The X-ray crystal structure shows three equivalent η^5-coordinated 2,4-dimethylpentadienyl ligands. The related complexes of La, Sm, Gd, Tb, and Lu are also known. Owing to the smaller ionic radius of Lu^{3+} only two 2,4-dimethylpentadienyl ligands are η^5-coordinated in the Lu derivative, while the third ligand is bonded to lutetium in an η^3-allyl-like fashion. Later work showed the formation of a minor by-product, which has been shown by X-ray crystallography to be $Lu(\eta^5\text{-}C_7H_{11})[\eta^5{:}\eta^3\text{-}MeC_5H_5CH_2CH_2CH(Me)C_3H_3(Me)]$, containing a dimeric chelate ligand derived from end-to-end fusion of two 2,4-dimethylpentadienyl groups (Figure 22).**[11]**

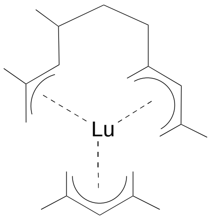

Figure 22 $Lu(\eta^5\text{-}C_7H_{11})(\eta^5{:}\eta^3\text{-}MeC_5H_5CH_2CH_2CHMeC_3H_3Me)$

Homoleptic tris(2,4-dimethylpentadienyl) derivatives of gadolinium and erbium have been used to synthesize phenylalkynyl derivatives via reactions with equimolar amounts of phenylacetylene (equation 13)

$$2Ln(C_7H_{11})_3 + 3PhCCH \xrightarrow{\text{toluene}} [(C_7H_{11})_2Ln(\mu\text{-}CCPh)]_2 + 2C_7H_{12} \qquad (13)$$

Several other pentadienyllanthanide complexes have been reported, including the mono(pentadienyl) derivatives $(\eta^5\text{-}C_7H_{11})LnCl_2(THF)_3$ (Ln = Nd, Sm, Gd) and bis(pentadienyl)lanthanide halides $(\eta^5\text{-}C_7H_{11})_2LnCl(THF)$ (Ln = Nd, Sm, Gd). The mono(pentadienyl) derivative $(\eta^5\text{-}C_7H_{11})NdCl_2$ is a hexamer $(\eta^5\text{-}C_7H_{11})_6Nd_6Cl_{12}(THF)_2$, which consists of two Nd_3Cl_5 entities connected via two chloro bridges. The structure of the Nd_3Cl_5 moiety contains a distorted hexagonal bipyramidal polyhedron with C_7H_{11} anions connected to the neodymium atoms in a η^5 fashion.**[11]** The reaction of $LnCl_3$ (Ln = Nd, Er) with K_2COT followed by treatment with $K(C_7H_{11})$ gave $(COT)Ln(\eta^5\text{-}C_7H_{11})(THF)$.

7 CYCLOPENTADIENYL, INDENYL, & FLUORENYL COMPLEXES

Most of all organometallic compounds of the rare earth metals known to date are cyclopentadienyl complexes. There is a large variety of cyclopentadienyl derivatives used as ligands such as mono-, bis-, and poly-substituted moieties; cyclopentadienides containing donor-functionalized substituents; bridged *bis*-cyclopentadienides forming ansa complexes; cyclopentadienide ligands with other adjacent π-coordinating ligands like carboranes or pyrroles; and annelated ligands with cyclopentadienyl segments such as indenyls and fluorenyls. A complete survey of this class of organolanthanides up to 1994 is given in Ref. 6. Later reviews are published in 2002.**[8]** This chapter deals only with tris(cyclopentadienyl)lanthanide complexes, bis(cyclopentadienyl)lanthanide and mono(cyclopentadienyl)lanthanide derivatives in which the lanthanide is bonded to elements other than carbon besides the cyclopentadienyl ligands, and corresponding complexes with annelated cyclopentadienyl ligands. For bis(cyclopentadienyl)lanthanide and mono(cyclopentadienyl)lanthanide alkyl, aryl, alkene, alkyne, or allyl complexes, see Sections 2 to 6.

7.1 Tris(cyclopentadienyl) Complexes

Tris(cyclopentadienyl)lanthanide complexes are prepared by salt elimination from the corresponding lanthanide trichlorides and NaCp or KCp in $\mathrm{Et_2O}$, THF, or benzene. In contrast to cyclopentadienyl complexes of the transition metals, the bonding of the lanthanide atoms to the cyclopentadienyl ring is best described as ionic with only little participation of covalency. Thus, the ^{151}Eu Moessbauer spectra of $\mathrm{CpEuCl_2(THF)_3}$, $\mathrm{CpEu(NCO)_2(THF)}$, and $\mathrm{CpEu(NCS)_2(THF)_3}$ have been measured at 4.2 K and show hyperfine parameters that are normal for organoeuropium(III) compounds, whereas the Moessbauer spectrum of $\mathrm{Cp_3Eu(THF)}$ is very different with a negative isomer shift of $-1.77\,\mathrm{mm\,s^{-1}}$ and a large negative quadrupole interaction of $-33.6\,\mathrm{mm\,s^{-1}}$. This isomer shift corresponds to the transfer of ca. 0.14 electrons from the cyclopentadienyl ligands into the 4f orbitals of europium via covalent bonding. Most tris(cyclopentadienyl)lanthanide complexes have been investigated by X-ray crystallography. The structure is highly dependent on the size of the metal. A strictly monomeric compound with three η^5-Cp ligands is found for Yb only. The smaller Sc and Lu (Figure 23) have a reduced formal coordination number of eight with two η^5-Cp ligands and two bridging η^1-Cp ligands so that a polymeric chain results. The larger metals increase their coordination number gradually by weak van der Waals interactions [Y, Er (Figure 24), Tm] or by increasing coordination [Nd: η^1-Cp; Pr: η^{1-2}-Cp; La: η^2-Cp (Figure 25)] to neighboring $\mathrm{Cp_3Ln}$ units so that polymeric chains are also formed.[6]

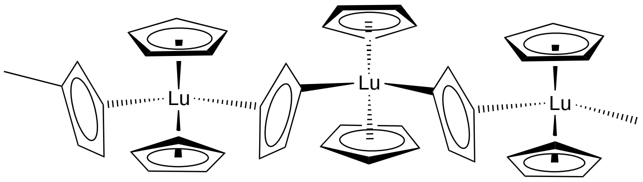

Figure 23 Structure of $\mathrm{Cp_3Lu}$

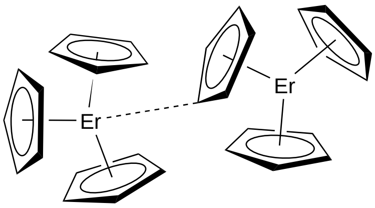

Figure 24 Structure of $\mathrm{Cp_3Er}$

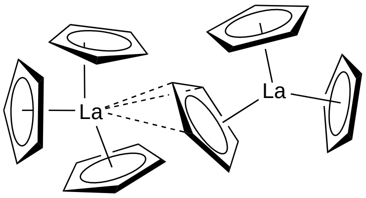

Figure 25 Structure of $\mathrm{Cp_3La}$

A series of homoleptic substituted tris(cyclopentadienyl) lanthanide(III) complexes $\mathrm{Cp}^{R}{}_{3}\mathrm{Ln}$ (Ln = La, Ce, Pr, Nd, Sm, Gd, Tb, Dy, Er, Tm, Yb), $\mathrm{Cp}^{t}{}_{3}\mathrm{Nd}$, $\mathrm{Cp}^{tt}{}_{3}\mathrm{Ce}$, $\mathrm{Cp}^{tt}{}_{3}\mathrm{Nd}$ [CpR = η^5-$\mathrm{C_5H_4CH(SiMe_3)_2}$, $\mathrm{Cp}^{t} = \eta^5$-$\mathrm{C_5H_4(SiMe_2{}^tBu)}$, $\mathrm{Cp}^{tt} = \eta^5$-$\mathrm{C_5H_3(SiMe_2{}^tBu)_2}$-1,3], and $\mathrm{[(Me_3Si)_2C_5H_3]_3Ln}$ (Ln = La, Nd, Sm, Gd or Dy) have been synthesized by reaction of anhydrous lanthanide(III) halides with the appropriate sodium or potassium cyclopentadienide in THF. Mixed cyclopentadienyl complexes $\mathrm{Cp^*{}_2CpLn}$ (Ln = La, Nd) were prepared by ring metathesis between $\mathrm{Cp^*{}_2Ca}$ and $\mathrm{Cp_3Ln}$ in toluene. Only one ring is exchanged between $\mathrm{Cp^*{}_2Ca(THF)}$ and $\mathrm{Cp_3La(THF)}$ in toluene to yield $\mathrm{Cp^*Cp_2La(THF)}$. The trichlorides of La, Nd, Sm, and Tb react with $\mathrm{Na(C_5HMe_4)}$ in THF to yield the homoleptic complexes $\mathrm{(C_5HMe_4)_3Ln}$ (Ln = La, Nd, Sm, Tb). On the other hand, the reactions of $\mathrm{HoCl_3}$, $\mathrm{TmCl_3}$, and $\mathrm{LuCl_3}$ with $\mathrm{Na(C_5HMe_4)}$ result only with formation of the dicyclopentadienyl complexes $\mathrm{(C_5HMe_4)_2LnCl(THF)}$ (Ln = Ho, Tm, Lu).

Tris(cyclopentadienyl)lanthanide complexes with sterically more crowded Cp ligands such as $\mathrm{C_5Me_4R}$ (R = Me, Et, ^{i}Pr, and $\mathrm{SiMe_3}$) are not assessable by simple metathesis between lanthanide trihalides and the respective alkali metal salt of the bulky Cp ligand. For instance, $\mathrm{Cp^*{}_3Sm}$, obtainable from $\mathrm{Cp^*{}_2Sm}$ and cyclooctatetraene, reacts with THF with ring-opening forming $\mathrm{Cp^*{}_2Sm[O(CH_2)_4Cp^*](THF)}$ (equation 14).

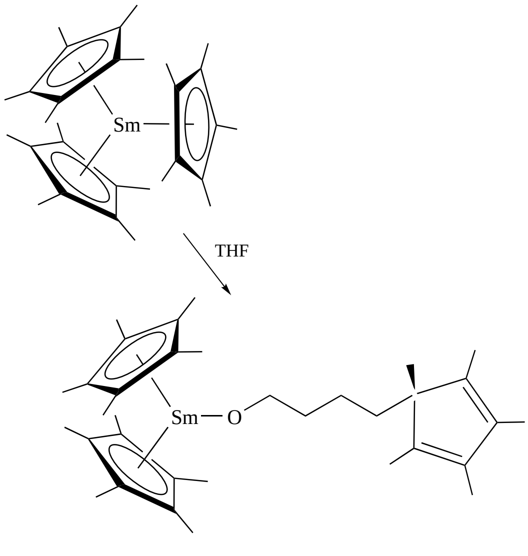

(14)

However, $Cp^*{}_2Sm(OEt_2)$ reacts cleanly with $Cp^*{}_2Pb$ to give $Cp^*{}_3Sm$ in >90% yield. This route has been used to synthesize the more sterically crowded $(C_5Me_4Et)_3Sm$. In general, $(C_5Me_4R)_3La$ ($R = Me$, Et, ^{i}Pr, and $SiMe_3$) complexes can be prepared in four steps by reaction of $LaCl_3$ with KC_5Me_4R to form $(C_5Me_4R)_2LaCl_2K(THF)_2$, followed by addition of allylmagnesium chloride to produce $(C_5Me_4R)_2La(C_3H_5)$, then protonolysis with Et_3NHBPh_4 yielding $[(C_5Me_4R)_2La][BPh_4]$, and finally by replacement of BPh_4^- with $C_5Me_4R^-$ using KC_5Me_4R affording $(C_5Me_4R)_3La$ (equation 15). X-ray crystallography shows monomer complexes $(C_5Me_4R)_3La$ ($R = Me$, Et, ^{i}Pr, $SiMe_3$) with three C_5Me_4R ring centroids defining a trigonal planar geometry around the La atom.**[60]**

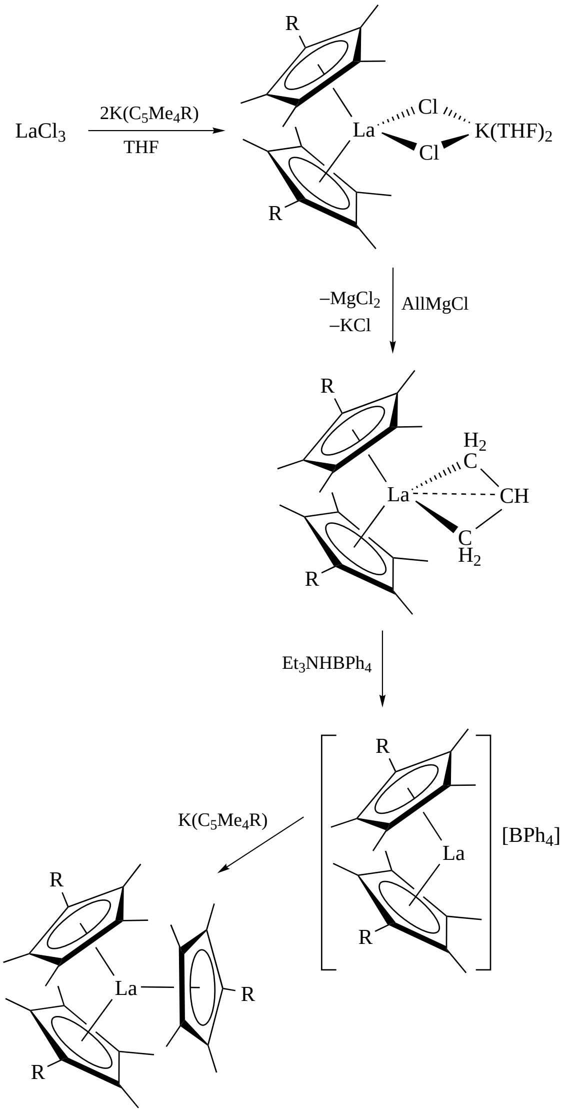

(15)

Related tris(peralkylcyclopentadienyl) complexes were also reported for smaller lanthanides than Nd and Sm. Such lanthanide(III) complexes behave as one-electron reductants, although the oxidation state of the metal retains +3. Thus, $Cp^*{}_3Nd$ reduces $Ph_3P{=}Se$ to Ph_3P forming $\{Cp^*{}_2Nd\}_2(\mu\text{-}\eta^2{:}\eta^2\text{-}Se_2)$ (equation 16). $Cp^*{}_3Sm$ reacts with a variety of substrates including CO, THF, ethylene, hydrogen, nitriles, isonitriles, isocyanates, cyclooctatetraene, azobenzene, and $Ph_3P{=}E$ ($E = O$, S, Se). Depending on the substrate, $Cp^*{}_3Sm$ can react either as a bulky alkyl complex $Cp^*{}_2SmR$ with $R = \eta^1\text{-}C_5Me_5$ or as zwitterionic $[Cp^*{}_2Sm]^+$ $[Cp^*]^-$ with the $[Cp^*]^-$ anion as the one-electron reductant.

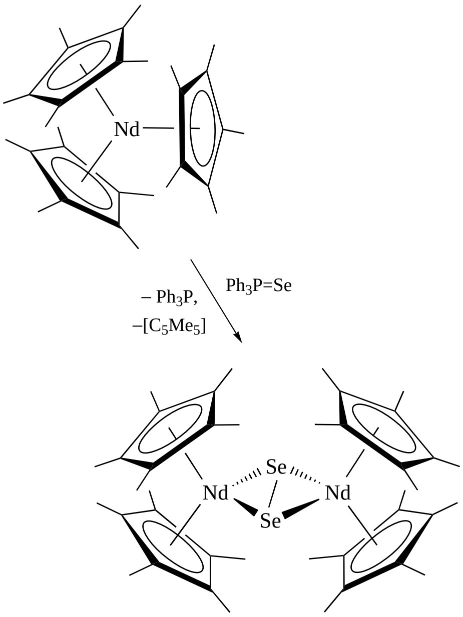

(16)

Tris(cyclopentadienyl)lanthanides form adducts with a variety of neutral Lewis bases such as THF; esters; sulfoxides; phospineoxides, for example, $(C_5H_4PPh_2)_3Ln(OPPh_3)$ ($Ln = La$, Pr, Nd, Sm, Er, Y); NH_3; various amines, for example, $Cp_3Ln(Nic)$ (Nic = (S)-(−)-nicotine)**[61]** and $Cp_3Yb(NC_4H_4N)YbCp_3$; phosphines, for example, $(C_5H_4Me)_3Yb(PMe_3)$; nitriles, for example, $Cp_3Sm(NCCH_3)$ and $Cp_3Pr(NC_6H_{11}\text{-}c)$; and anions like halides, for example, $[Cp_3Ln(\mu\text{-}Cl)LnCp_3]^-$ or azide, for example, $[Cp_3Sm(\mu\text{-}N_3)SmCp_3]^-$ (equation 17).

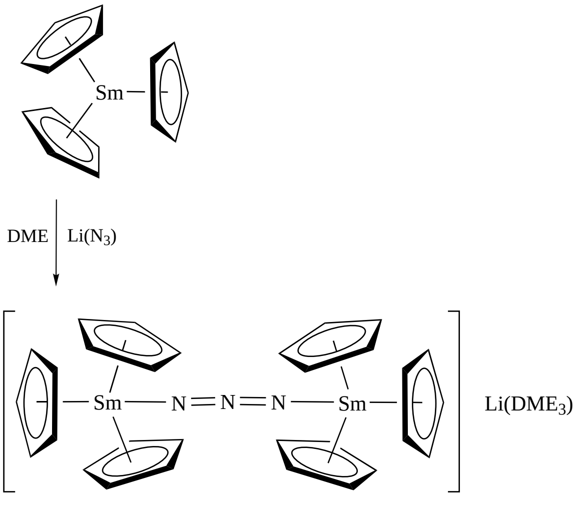

(17)

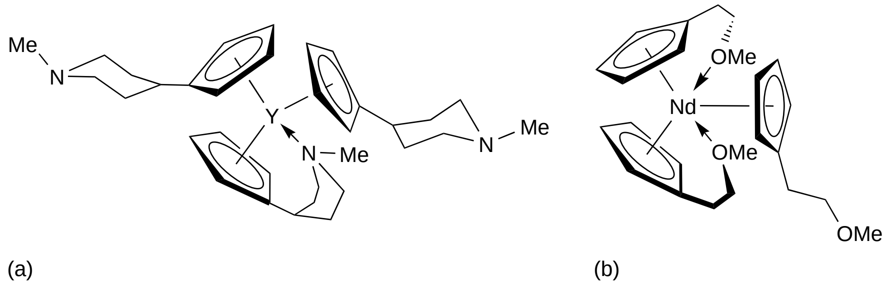

(a) (b)

Figure 26 (a) $[\eta^5\text{-}C_5H_4CH\{(CH_2)_2\}_2NMe_2]_3Y$ and (b) $(C_5H_4CH_2CH_2OMe)_3Nd$

Stabilization by Lewis base donors can also be achieved by using donor-substituted cyclopentadienyl ligands, as shown in $[\eta^5\text{-}C_5H_4CH\{(CH_2)_2\}_2NMe]_3Y$[62] (Figure 26a) or in $(C_5H_4CH_2CH_2OMe)_3Ln$ (Ln = La, Pr, Nd, Gd or Y) (Figure 26b). Crystal structure determinations revealed that, in these unsolvated monomeric metallocenes, the lanthanide metals are coordinated by three cyclopentadienyl rings and two oxygen atoms whereas the third oxygen atom is not coordinated. A similar situation is observed in the phosphorus-functionalized complex $[Cp(CH_2)_2PMe_2]_3La$.

Bis(pentamethylcyclopentadienyl)phospholyl and -arsolyl-samarium(III) complexes $Cp^*{}_2SmL$ ($L = C_4H_2Me_2P$, $C_4H_2{}^tBu_2P$, C_4Me_4P, $C_4H_2Me_2As$) are synthesized either by reaction of $Cp^*{}_2Sm(Et_2O)_x$ ($x = 0$, 1) with $(C_4H_2Me_2P)_2$, $(C_4H_2{}^tBu_2P)_2$, $(C_4Me_4P)_2$, $(C_4H_2Me_2As)_2$, or with Tl-$[C_4Me_4P]$ (equation 18).[63]

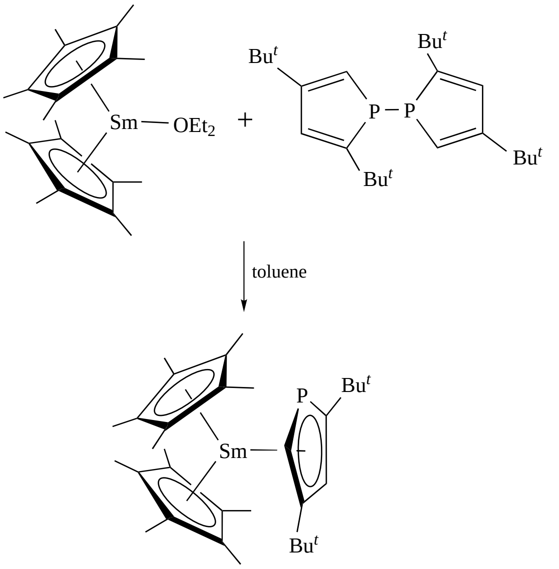

(18)

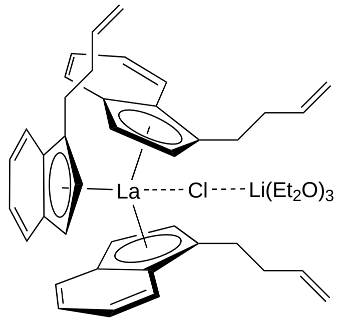

Figure 27 $(1\text{-}C_4H_7\text{-}4,7\text{-}Me_2C_9H_4)_3La(\mu\text{-}Cl)Li(Et_2O)_3$

Tris(indenyl)lanthanide complexes of all rare earth metals can be prepared analogously from the lanthanide trichlorides with alkali or magnesium indenyl salts.[6] All five-membered rings are η^5-bonded to the metal. They form base adducts with THF and pyridine, with (*S*)-(−)-nicotine,[61] and with bridging chloride or LiCl (Figure 27).[64]

7.2 Bis(cyclopentadienyl) Complexes

The organometallic chemistry of the rare earths deals mainly with bis(cyclopentadienyl) derivatives due to the easy available bis(cyclopentadienyl) rare earth chlorides and other halides via reaction of the rare earth trichlorides with two equivalents of a cyclopentadienyl alkali salt. Bis(cyclopentadienyl)lanthanide chlorides are formed as chloride-bridged dimers (Figure 28a), as monomers stabilized by a donor molecule like THF (Figure 28b) or as *ate* complexes with alkali halides (Figure 28c).

A lot of corresponding derivatives are known derived of substituted cyclopentadienyl ligands, for example, $(C_5H_4Me)_2LnCl$, $(C_5H_4{}^tBu)_2LnCl$, $(C_5HMe_4)_2LnCl$, $Cp^*{}_2$-LnCl, $(Me_3SiC_5H_4)_2LnCl$, $[(Me_3Si)_2C_5H_3]_2LnCl$, or $(PhCH_2C_5H_4)_2LnCl(THF)$ (Ln = Gd, Er). Bis(cyclopentadienyl) ytterbium and samarium halides can be prepared by oxidation of $Cp_2Ln(II)$, for example, $Cp_2YbX(THF)_n$ ($X = Cl$, $n = 0.5$; $X = Br$ or I, $n = 1$) oxidation of $Cp_2Yb(DME)$ with C_2Cl_6 or $(CH_2X)_2$ ($X = Br$ or I) in THF, and $(Cp_2YbX)_2$ analogously from unsolvated Cp_2Yb in petroleum ether.[6]

Hydrofluorination of $[(Me_3Si)_2C_5H_3]_3Ln$ or Cp_3Ln in THF with 1 equiv. of Me_3NHF gave $[\{(Me_3Si)_2C_5H_3\}_2LnF]_2$ (Ln = La, Nd, Sm, Gd) or $[Cp_2LnF(THF)]_2$ (Ln = Y, Yb),

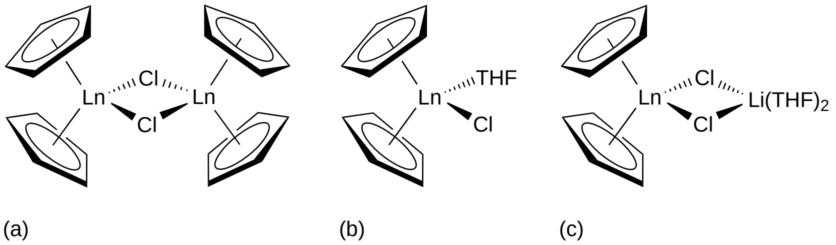

Figure 28 (a) $Cp_2Ln(\mu\text{-}Cl)_2LnCp_2$, (b) $Cp_2LnCl(THF)$, and (c) $Cp_2Ln(\mu\text{-}Cl)_2Li(THF)_2$

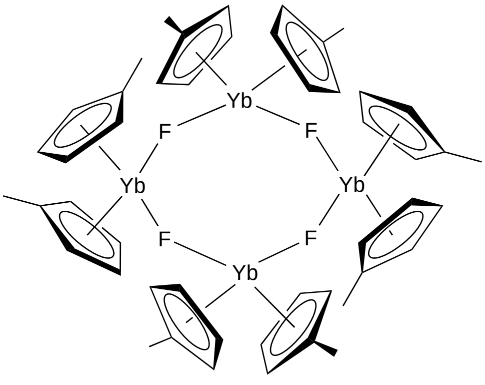

Figure 29 $[(C_5H_4Me)_2YbF]_4$

correspondingly. Oxidation of Cp_2Yb and $(C_5H_4Me)_2Yb$ with perfluoro(methylcyclohexane) or perfluorodecalin in DME gave unsolvated $(Cp_2YbF)_3$ and $[(C_5H_4Me)_2YbF]_4$, while in THF, the oxidation of $(C_5H_4Me)_2Yb$ provided the dimeric $[(C_5H_4Me)_2YbF(THF)]_2$. $(Cp_2YbF)_3$ is a trimer with formal eight-coordination for ytterbium and a planar $(YbF)_3$ ring, whereas $[(C_5H_4Me)_2YbF]_4$ is an eight-coordinate tetramer having a puckered $(YbF)_4$ unit (Figure 29).[65] The organosamarium fluoride $[(C_5H_4{}^tBu)_2Sm(\mu\text{-}F)]_3$ was generated by oxidation of $(C_5H_4{}^tBu)_2Sm(THF)_2$ with Me_3SnF.

$[(Me_3Si)_2C_5H_3]_2YbI(THF)$ was synthesized by the reaction of two equivalents of $Na[(Me_3Si)_2C_5H_3]$ with $YbI_3(THF)_2$.[66] Related complexes $[(Me_3Si)_2(C_5H_3]_2LnI(THF)$ (Ln = La, Sm, Y, Er, Lu) were prepared by treatment of $[\{(Me_3Si)_2C_5H_3\}_2LnCl]_2$ with excess of NaI in dry THF, or by reaction of a mixture of $LnCl_3$ and NaI with two equiv. of $Na[(Me_3Si)_2C_5H_3]$ in THF.

Lanthanide (+)-neomenthylcyclopentadienyl complexes $[Cp^{R}{}_2Ln(\mu\text{-}Cl)]_2$ (Ln = Sm, Yb, Y, Lu; Cp^R = (+)-neomenthylcyclopentadienyl) and $Cp^RLnX_2(THF)_3$ (X = Cl, Ln = Sm, Gd, Yb, Y, Lu; X = I, Ln = Sm, Yb) are available from $LnCl_3$ and the appropriate alkali metal (+)-neomenthylcyclopentadienyl complexes as chloride-bridged dimers. $Cp^RSmI_2(THF)_3$ is pseudo-octahedral with the two iodine atoms taking the trans positions.

$Cp^*{}_2Y(\mu\text{-}Cl)YCp^*{}_2Cl$ reacts with oxygen-containing substrates to form monomeric adducts $Cp^*{}_2YCl(L)$ (L = THF, benzophenone, methylmethacrylate, ε-caprolactone, hexamethylphosphoramide, ε-caprolactam, 1-methyl-2-pyrrolidinone, N,N'-dimethylpropyleneurea). A bis-adduct, $Cp^*{}_2YCl(\varepsilon\text{-caprolactam})_2$ was isolated when an excess of ε-caprolactam was used.[67]

Oxidation of $Cp^*{}_2Sm$ with $AgBPh_4$ in toluene yields $[Cp^*{}_2Sm][BPh_4]$, which in the solid state consists of a bent $Cp^*{}_2Sm$ unit oriented toward two of the Ph rings of the $[BPh_4]^-$ anion. Analogous Nd and Tm derivatives were prepared reacting $Cp^*{}_2Ln(\eta^3\text{-}CH_2CH{=}CH_2)$ (Ln = Nd, Tm) with $[Et_3NH][BPh_4]$ in benzene. $[(C_5H_4{}^tBu)_2Yb(THF)_2][BPh_4]$ has been synthesized from $(C_5H_4{}^tBu)_2Yb(THF)_2$ and $AgBPh_4$ followed by crystallization from THF. Related cationic organolanthanide compounds $[(C_5H_4R)_2Sm(THF)_2][BPh_4]$ (R = ^{t}Bu, $SiMe_3$), $[Pyr^*{}_2Sm(THF)][BPh_4]$ ($Pyr^* = NC_4H_2{}^tBu_2$-2,5) (Figure 30a), $[Cp^*{}_2Ln(THF)_2][BPh_4]$ (Ln = Y, Yb), and $[(C_5Me_4Et)_2Ln(THF)_2][BPh_4]$ (Ln = Y, Sm) have been synthesized by oxidation of the divalent metallocenes

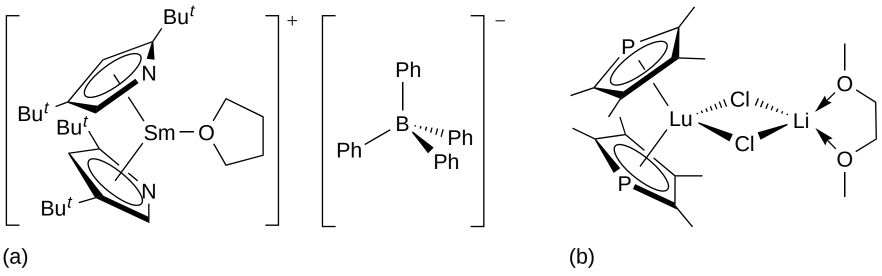

Figure 30 (a) $[Pyr^*{}_2Sm(THF)][BPh_4]$, (b) $(C_4Me_4P)_2Lu(\mu\text{-}Cl)_2Li(DME)$

with $AgBPh_4$ or by protolysis of the lanthanide alkyls $Cp^*_2YMe(THF)$, $Cp^*_2YbCH(SiMe_3)_2$, and $(C_5Me_4Et)_2LnCH(SiMe_3)_2$ (Ln = Y, Sm), respectively, by $[Et_3NH][BPh_4]$. Bis(phospholyl) chloride complexes of Y and Lu can be prepared as DME (Figure 30b) or Et_2O adducts.

Phosphinoethyl substituted cyclopentadienyl complexes $[CpCH_2CH_2PR_2]_2LnX$ (Ln = Y, Lu; R = Me, Cy, ^{t}Bu, Ph; X = Cl, CF_3SO_3) show a distorted trigonal bipyramid with two axial phosphino groups and two equatorial cyclopentadienyl moieties, and the third equatorial site being occupied by the halide or triflate ligand (Figure 31).[68]

The lanthanum complex $[(MeOCH_2CH_2C_5H_4)_2La(\mu\text{-}Cl)]_2$ with ether-functionalized Cp ligands is a chlorine-bridged dimer. Optically active metallocene complexes of Y, Sm, and Lu containing cyclopentadienyl ligands with chiral nonracemic N- or O-substituted side chains, for example, (*S*)-(2-methoxypropyl)cyclopentadienyl, (*S*)-[2-(dimethylamino)propyl]cyclopentadienyl, and (*S*)-[2-(dimethylamino)-1-(phenylethyl)]cyclopentadienyl were prepared by reaction of the potassium salts of those cyclopentadienyl systems with the trichlorides of Y, Sm, and Lu in a 2:1 molar ratio: $[(S)\text{-}\eta^5{:}\eta^1\text{-}C_5H_4(CH_2CH(Me)OMe)]_2LnCl$ (Ln = Y, Sm), $\{(S)\text{-}\eta^5{:}\eta^1\text{-}C_5H_4[CH_2CH(Me)NMe_2]\}_2LnCl$ (Ln = Y, Sm), and $\{(S)\text{-}\eta^5{:}\eta^1\text{-}C_5H_4[CH(Ph)CH_2NMe_2]\}_2LnCl$ (Ln = Y, Sm, Lu). The mixed chiral sandwich complexes $[(\eta^5\text{-}Cp^*)\{(S)\text{-}\eta^5{:}\eta^1\text{-}C_5H_4[CH_2CH(Me)NMe_2]\}LnCl]$ (Ln = Y, Lu) and $[(\eta^5\text{-}Cp^*)\{(S)\text{-}\eta^5{:}\eta^1\text{-}C_5H_4[CH(Ph)CH_2NMe_2]\}LnCl]$ (Ln = Y, Lu) were prepared by successive reaction of $LnCl_3$ with one equiv. of the potassium salt of the chiral nonracemic cyclopentadienyl ligand and one equiv. of Cp*Na. In all the cases, the N- and O-donor functions are coordinated by the metals (Figure 32). An intramolecular coordination of the oxygen atom has also been found in the chiral lanthanocene iodides $[(S)\text{-}Cp']_2LnI$ (Ln = La, Sm; $Cp' = C_5H_4CH_2CHMeOCH_2Ph$).

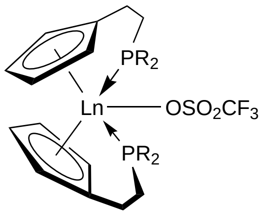

Figure 31 $[C_5H_4CH_2CH_2PR_2]_2LnOSO_2CF_3$

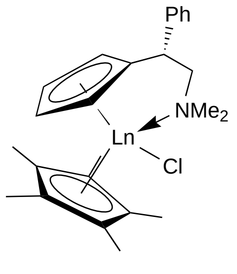

Figure 32 $[(Cp^*)\{(S)\text{-}\eta^5{:}\eta^1\text{-}C_5H_4(CHPhCH_2NMe_2)\}LnCl]$

Lanthanide complexes with vinyl-substituted cyclopentadienyl ligands $(CH_2{=}CHC_5Me_4)_2Ln(\mu\text{-}Cl)_2Li(Et_2O)_2$ (Ln = Y, Sm, Lu),[69] $[(CH_2{=}CHCH_2CH_2C_5Me_4)_2Ln(\mu\text{-}Cl)]_2$ (Ln = Y, Sm, Lu), and $(CH_2{=}CHCH_2CH_2C_5Me_4)_2LnCl(THF)$ (Ln = Y, Sm) were prepared by exchange reactions with the lithium and sodium salts of the appropriate Cp-ligands.[70] $(CH_2{=}CHC_5Me_4)_2Sm(\mu\text{-}Cl)_2Li(Et_2O)_2$ could be hydroborated with 9-BBN affording $(C_8H_{14}BCH_2CH_2C_5Me_4)_2Sm(\mu\text{-}Cl)_2Li(THF)_2$ (equation 19).[69]

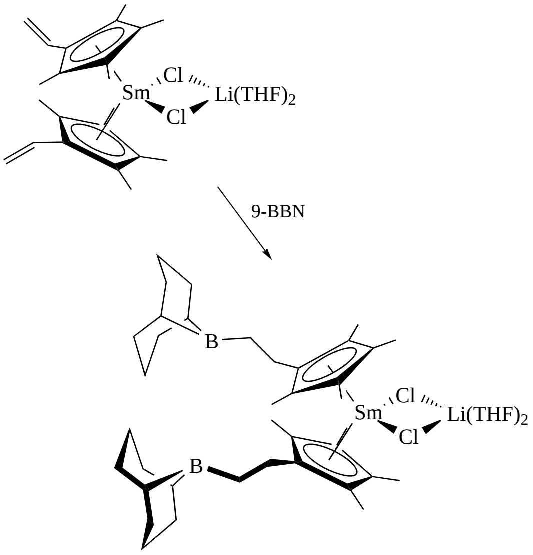

(19)

Many bis(cyclopentadienyl)lanthanide oxides, hydroxides, alkoxides, and carboxylates have been prepared mainly by protonolysis of tris(cyclopentadienyl)lanthanides and bis(cyclopentadienyl)lanthanide alkyls, or by alkali halide abstraction from bis(cyclopentadienyl)lanthanide chlorides and water, alcohols, acids, or the corresponding alkali metal salts, respectively;[6] for example, dinuclear $[Cp_2Yb(\mu\text{-}OCH_2CH_2CH_2CH_2CH_3)]_2$ (Figure 33a) and $[Cp_2Ln(\mu\text{-}OCH_2CH_2CHMe_2)]_2$ (Ln = Dy, Yb), $[Cp_2Ln(\mu\text{-}OPr)]_2$, monomeric $Cp_2Ln(THF)(OR^F)$ [Ln = Nd, Sm, Yb; R^F = 2,4,6-tris(trifluoromethyl)phenyl] (Figure 33b), $Cp_2Yb(\alpha\text{-naphthol})(THF)$ were prepared by reacting of Cp_3Ln with respective alcohols or phenols. Monomeric organolanthanide acetates $[(C_5Me_4{}^tBu)_2LnO_2CCH_3]$ (Ln = La, Lu) (Figure 33c) are prepared from $[(C_5Me_4{}^tBu)_2LnCl(THF)]$ (Ln = La, Lu) and NaO_2CCH_3.

Another approach to bis(cyclopentadienyl)lanthanide alkoxides is the cleavage of ethers by bis(cyclopentadienyl) lanthanide hydrides. Dialkyl ethers, ROR′, are cleaved by $(Cp^*_2LnH)_2$ (Ln = Y, La, Ce) to form Cp^*_2LnOR, Cp^*_2LnOR', R′H, and RH. The extent to which either of the C–O bonds of asymmetrically substituted dialkyl ethers ROR′

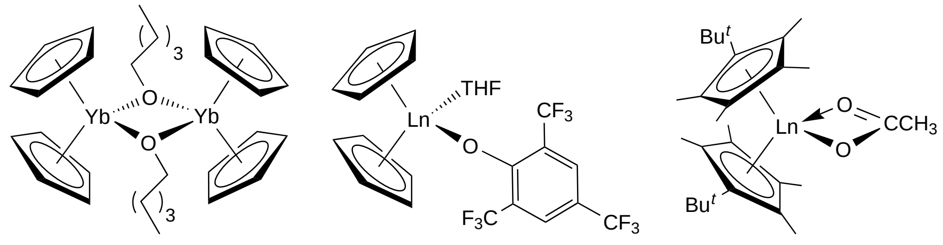

(a) (b) (c)

Figure 33 (a) $[Cp_2Yb(\mu\text{-}OCH_2CH_2CH_2CH_2CH_3)]_2$, (b) $Cp_2Ln(THF)(OR^F)$, (c) $[(C_5Me_4{}^tBu)_2LnO_2CCH_3]$

is attacked strongly depends on the alkyl substituents but is relatively insensitive to the nature of the metal. Ring opening is observed when THF or 1,4-dioxane reacted with hydrides to give $Cp^*{}_2YOBu$ and $(Cp^*{}_2Y)_2(\mu\text{-}OCH_2CH_2O)(THF)_2$, respectively. NMR studies in solution of the lanthanocene complexes containing a chiral alkoxide ligand, for example, $[Cp_2Ln(\mu\text{-}OCHRCHR^1NR^2R^3)]_2$ ($R = H$, $R^1 = Et$, R^2, $R^3 = Me$ and $Ln = Pr$, Nd, Sm, Yb, Lu) indicate an additional coordination of nitrogen to the lanthanide at room temperature for the Pr, Nd, and Sm complexes (Figure 34).

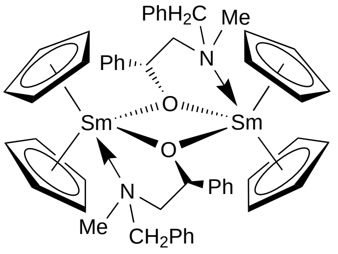

Figure 34 $[Cp_2Sm\{\mu\text{-}OCHPhCH_2NMeCH_2Ph\}]_2$

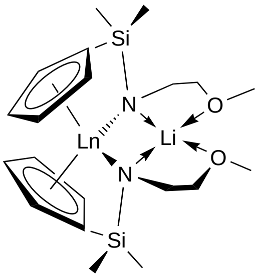

Figure 35 $Li[(\eta^5{:}\eta^1\text{-}C_5H_4SiMe_2NCH_2CH_2OMe)_2Ln]$

Reaction of two equiv. of $Li_2(C_5R_4SiMe_2NCH_2CH_2X)$ ($C_5R_4 = C_5Me_4$, $C_5H_3{}^tBu$; $X = OMe$, NMe_2) with $LnCl_3$ ($Ln = Y$, Lu) yields C_2-symmetric complexes $Li[(\eta^5{:}\eta^1\text{-}C_5R_4SiMe_2NCH_2CH_2X)_2Ln]$ (Figure 35). In the case of $Li[Y(\eta^5{:}\eta^1\text{-}C_5H_3{}^tBuSiMe_2NCH_2CH_2X)_2]$, a mixture of the two diastereomers in relative ratios depending on the reaction time are formed. The (R, S)-diastereomer is the kinetic product that rearranges to the thermodynamically preferred C_2-symmetric (R, R)-diastereomer in donor solvents such as THF.

Lanthanidocene silylamide complexes $(C_5HMe_4)_2YN(SiHMe_2)_2$, $Cp^*{}_2YN(SiHMe_2)_2$, and $(C_5HPh_4)_2LaN(SiHMe_2)_2$ were obtained by a silylamine elimination from $Ln[N(SiHMe_2)_2]_3(THF)_2$ ($Ln = Y$, La) and the respective cyclopentadienes. Deprotonation of tetraphenylcyclopentadiene was possible only in the case of La. The spectroscopic and structural data for these complexes revealed a strong agostic interaction (*see Agostic Bonding*) between the electron-deficient metal centers and the SiH moiety of the bis(dimethylsilyl)amide ligand (Figure 36a).[71] Amidolanthanidocenes $(C_5H_4Me)_2LnNC_5H_{10}$ ($Ln = Yb$, Er, Y; $NC_5H_{10} =$ piperidine) (Figure 36b) were prepared reacting $LnCl_3$ with NaC_5H_4Me, followed by treatment with $LiNC_5H_{10}$. The amidinate derivatives

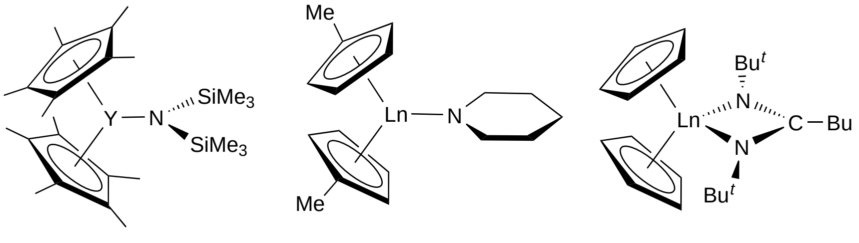

(a) (b) (c)

Figure 36 (a) $Cp^*{}_2YN(SiHMe_2)_2$, (b) $(C_5H_4Me)_2LnNC_5H_{10}$, (c) $Cp_2Ln[{}^tBuNCBuN{}^tBu]$

$Cp_2Ln[{}^tBuNC(Bu)N{}^tBu]$ (Ln = Er, Y, Gd) (Figure 36c) were prepared by reaction of Cp_2LnBu (generated in situ) with N,N'-di-*tert*-butylcarbodiimide that proceeds via monoinsertion of carbodiimide into the Ln–C σ-bond. The structurally characterized yttrium compound is a good catalyst for the cyclotrimerization of phenylisocyanate.[72]

Protonolysis of Cp_3Ln (Ln = Dy or Yb) with thiols, HSR (R = Pr or Bu) in THF yields dimeric thiolates $[Cp_2Ln(\mu\text{-}SR)]_2$ (R = Pr; Ln = Dy or Yb; R = Bu; Ln = Dy or Yb). $[Cp_2Yb(\mu\text{-}SBu)]_2$ has a planar Yb_2S_2 unit with the Bu groups antipositioned relative to the Yb_2S_2 ring (Figure 37a). Elemental Te readily inserts into the Sc–C bond of $Cp^*{}_2ScCH_2SiMe_3$ and $Cp^*{}_2ScCH_2Ph$ yielding the corresponding tellurates $Cp^*{}_2ScTeR$ (R = CH_2SiMe_3, CH_2Ph). The phosphide complex $Cp_2Lu[\mu\text{-}PPh_2]_2Li(TMEDA)$ (Figure 37b) was obtained from Ph_2PH and $Cp_2Lu(\mu\text{-}Me)_2Li(TMEDA)$[6] and the reaction of $[1,3\text{-}(Me_3Si)_2C_5H_3]_2YCl$ with $KPHSi{}^tBu_3$ yields $[1,3\text{-}(Me_3Si)_2C_5H_3]_2YPHSi{}^tBu_3$.[73]

Bimetallic complexes $Cp_2(THF)LuRu(CO)_2Cp$ (Figure 38a), $[1,3\text{-}(Me_3Si)_2C_5H_3]_2(THF)LuRu(CO)_2Cp$, and $Cp^*{}_2LuRu(CO)_2Cp$ were prepared by reaction of $Na[CpRu(CO)_2]$ with the respective cyclopentadienyllutetium halides in THF. An X-ray structural study of $(THF)Cp_2LuRu(CO)_2Cp$ revealed a direct Lu–Ru bond. Lanthanide–tungsten complexes $Cp^*{}_2Ln(C_5H_4)W(H)_2Cp$ (Ln = Y, Sm) (Figure 38b) were prepared reacting $(Cp^*{}_2LnH)_2$ with Cp_2WH_2.

Bis(indenyl)lanthanide complexes are also described. According to X-ray crystallographic investigations $(C_4H_7OCH_2C_9H_6)_2LnCl$ (Ln = Nd, Sm, Dy, Ho, Er, Yb) (Figure 39) are unsolvated nine-coordinate monomeric complexes with a trans arrangement of both the side arm and indenyl rings in the solid state.[74]

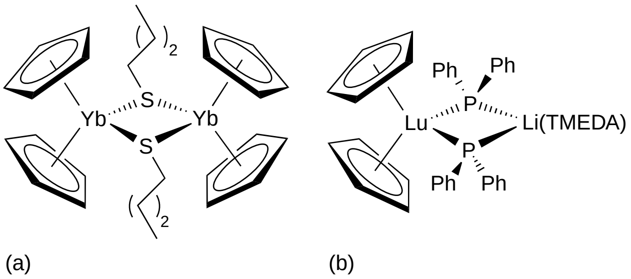

Figure 37 (a) $[Cp_2Yb(\mu\text{-}SBu)]_2$, (b) $Cp_2Lu[\mu\text{-}PPh_2]_2Li(TMEDA)$

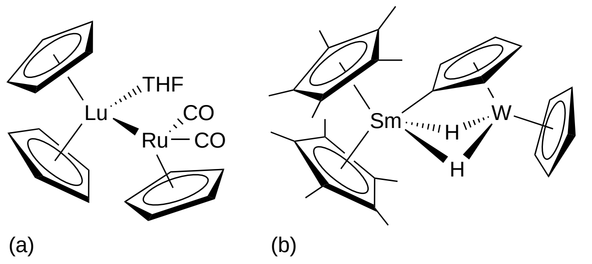

Figure 38 (a) $(THF)Cp_2LuRu(CO)_2Cp$, (b) $Cp^*{}_2Sm(C_5H_4)W(H)_2Cp$

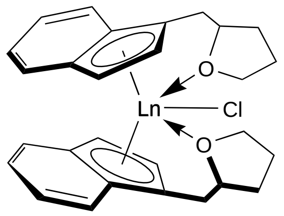

Figure 39 $(C_4H_7OCH_2C_9H_6)LnCl$

Similar structures were found for $(CH_3OCH_2CH_2C_9H_6)_2LnCl$ (Ln = Y, La, Nd, Gd, Ho, Lu). Neutral monomeric bis(indenyl) complexes containing alkenyl-functionalized ligands, for example, $(Ind')_2LnCl(THF)$ (Ln = Gd, Er; Ind′ = 1-Allyl-2,4,7-trimethyl-1H-indene) and $(Ind'')_2LnCl(THF)$ [Ln = Y, Lu; Ind″ = 1-(3-buten-1-yl)-4,7-dimethyl-1H-indene] were prepared by reaction of $LnCl_3$ with the lithium salts of the corresponding indenyl ligand. However, the trichlorides of the comparatively large Sm and La ions react with different molar amounts of Ind″Li in THF exclusively with formation of the tris(indenyl) complexes Ind''_3Sm and $Ind'_3La(\mu\text{-}Cl)Li(Et_2O)_3$, respectively. Single-crystal X-ray structural analyses show that the alkenyl groups of the indenyl side chains are not coordinated to the lanthanide atoms.[64]

7.3 *Ansa*-bis(cyclopentadienyl) Complexes

ansa-Lanthanidocene complexes are very important catalysts for a number of organic reactions such as hydrogenation (*see Hydrogenation*), hydrosilylation (*see Hydrosilation*), -amination, and -phosphination of unsaturated compounds, as well as for the polymerization of olefins and for ring-opening polymerization of cyclic esters. The nature of the *ansa*-metallocene ligands impacts dramatically activity and stereoselectivity of the Ln-based catalysts.

rac-, C_1-, and *meso*-*ansa*- Metallocene complexes (*see Metallocene Complexes*) of Y and Sm, for example, *rac*-$Me_2Si[2,4\text{-}(Me_3Si)_2C_5H_2]_2SmCl_2Li(THF)_2$, C_1-$Me_2Si[2,4\text{-}(Me_3Si)_2C_5H_2][3,4\text{-}(Me_3Si)_2C_5H_2]SmCl_2Li\text{-}(THF)_2$, C_1-$Ph_2Si[2,4\text{-}(Me_3Si)_2C_5H_2][3,4\text{-}(Me_3Si)_2C_5H_2]SmCl_2Li(THF)_2$, *meso*-$[1,2\text{-}(Me_2Si)(Me_2SiOSiMe_2)](4 - {}^tBuC_5H_2)_2SmCl_2Li(THF)_2$, *rac*-$Me_2Si[2,4\text{-}(Me_3Si)_2C_5H_2]_2YCl_2Li(THF)_2$, C_1-$Me_2Si[2,4\text{-}(Me_3Si)_2C_5H_2][3,4\text{-}(Me_3Si)_2C_5H_2]YCl_2Li(THF)_2$, *meso*-$[1,2\text{-}(Me_2Si)(Me_2SiOSiMe_2)](4\text{-}Me_3SiC_5H_2)_2YCl(THF)$ were prepared and structurally characterized. Their structures differ with respect to the bridging group and the position of the substituents on the cyclopentadienyl rings. The alkyl complexes C_1-$Me_2Si[2,4\text{-}(Me_3Si)_2C_5H_2][3,4\text{-}(Me_3Si)_2C_5H_2]SmCH(SiMe_3)_2$ (Figure 40) and C_1-$Me_2Si[2,4\text{-}(Me_3Si)_2C_5H_2][3,4\text{-}(Me_3Si)_2C_5H_2]YCH(SiMe_3)_2$ polymerize ethylene, giving high molecular weight polyethylenes.[75]

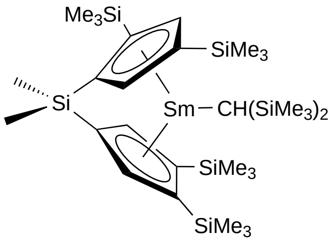

Figure 40 C_1-$Me_2Si[2,4$-$(Me_3Si)_2C_5H_2][3,4$-$(Me_3Si)_2C_5H_2]$-$SmCH(SiMe_3)_2$

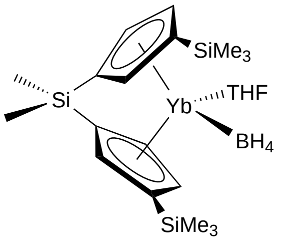

Figure 41 *meso*-$Me_2Si(3$-$Me_3SiC_5H_3)_2YbBH_4(THF)$

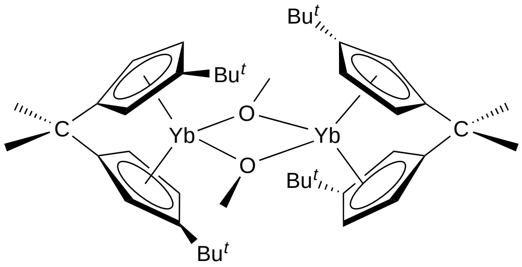

Figure 42 [*meso*-$Me_2C(3$-${}^tBuC_5H_3)_2Yb(\mu_2$-$OMe)]_2$

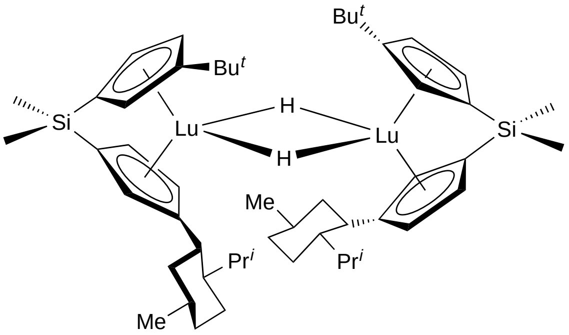

Figure 43 {[(R, S)-$Me_2Si(C_5H_3{}^tBu)(C_5H_3$-(+)-*neo*-Men)]LuH}$_2$

The *ansa*-ytterbocene(III) *meso*-$Me_2Si(3$-$Me_3SiC_5H_3)_2$-$YbCl(THF)$ undergoes desolvation during recrystallization from toluene yielding [*meso*-$Me_2Si(3$-$Me_3SiC_5H_3)_2Yb(\mu_2$-$Cl)]_2$. Treatment with $LiBH_4$ in Et_2O results in *meso*-$Me_2Si(3$-$Me_3SiC_5H_3)_2YbBH_4(THF)$ (Figure 41), in which ytterbium coordinates to three H atoms of the $BH_4{}^-$ anion.

Reaction of $\{Me_2Si[C_5H_2$-$2,4$-${}^iPr_2]_2\}Li_2$ with $ScCl_3$ and YCl_3 yields *rac*-$Me_2Si[C_5H_2$-$2,4$-${}^iPr_2]_2ScCl[LiCl(THF)_2]$, *meso*-$Me_2Si[C_5H_2$-$2,4$-${}^iPr_2]_2Sc(\mu_2$-$Cl)]_2$, *rac*-$Me_2Si[C_5H_2$-$2,4$-${}^iPr_2]_2YCl[LiCl(THF)_2]$, and *meso*-$Me_2Si[C_5H_2$-$2,4$-${}^iPr_2]_2Y(\mu_2$-$Cl)]_2$ in approximately 3:1 racemic:meso ratios. Treatment of the Sc compounds with allylmagnesium bromide affords the allyl complexes *rac*- and *meso*-$Me_2Si[C_5H_2$-$2,4$-${}^iPr_2]_2Sc(\eta^3$-$C_3H_5)$. Diastereomerically pure rac-compounds or pure meso dimers undergo spontaneous isomerization upon dissolution in THF-d_8 with reversion back to a 3:1 racemic:meso ratio. The complexes *rac*-$Me_2C(3$-${}^tBuC_5H_3)_2Yb(\mu_2$-$Cl)_2Li(OEt_2)_2$ and the monosolvate *meso*-$Me_2Si(3$-$Me_3SiC_5H_3)_2YbCl(THF)$ were prepared reacting $Me_2E(3$-$Me_3EC_5H_3)_2Li_2$ (E = C, Si) with $YbCl_3$, respectively. The reaction between $Me_2C(3-{}^tBuC_5H_3)_2Li_2$ and YbI_2 in DME proceeds with solvent cleavage to form the dimeric methoxide complex [*meso*-$Me_2C(3$-${}^tBuC_5H_3)_2Yb(\mu_2$-$OMe)]_2$ (Figure 42).

ansa-Metallocene complexes (R, S)-$Me_2Si({}^tBuC_5H_3)$ [(+)-*neo*-Men-Cp]$Ln(\mu$-$Cl)_2Li(OEt_2)_2$ (Ln = Y, Lu; (+)-*neo*-Men = (+)-*neo*-menthyl) were synthesized by reaction of the corresponding lanthanide trichlorides with the dilithium salt of the ligand and were isolated isomerically pure by crystallization from Et_2O. Alkylation of the (R, S)-epimers with $LiCH(SiMe_3)_2$ proceeds with retention of configuration at the lanthanide center, affording chiral hydrocarbyl complexes in high yield. Reaction of the Lu-hydrocarbyl with H_2 affords diastereomerically pure {(R, S)-$Me_2Si({}^tBuC_5H_3)$[(+)-*neo*-Men-Cp]LuH}$_2$ (Figure 43), an active catalyst for asymmetric olefin hydrogenation (*see* ***Asymmetric Synthesis by Homogeneous Catalysis***).

Disiloxane-bridged metallocenes $\{O(Me_2SiC_5H_4)_2\}PrCl$-$(THF)$ and $[\{O(Me_2SiC_5H_4)_2\}YbCl]_2$ (Figure 44a) were prepared from $LnCl_3$ (Ln = Pr or Yb) and $K_2[O(Me_2SiC_5H_4)_2]$ in THF. $[Me_2Si(C_5H_4)_2Yb(\mu$-$Br)]_2$ and $[Me_2Si(C_5H_4)_2Yb$-$(\mu$-$Cl)]_2$ are also dimers, like $[Me(R)Si(C_5H_4)(C_5Me_4)$-$LnCl]_2$ (R = Et, Ph; Ln = Y, La, Sm, Lu) and $[Me(Et)Si$-$(C_5H_4)(C_5Me_4)SmCl]_2$. Metallocenes with two cyclopentadienyl rings tethered by a 2,6-bis(methylene)pyridyl unit $[\{2,6$-$C_5H_3N(CH_2C_5H_4)_2\}Ln(\mu$-$O_2SOCF_3)]_2$ (Figure 44b) (Ln = Nd, Y, Yb) are also dimers with each triflate ligand bridging two Ln ions.**[76]**

$[MeO(CH_2)_5(Me)Si(C_5Me_4)_2]YCH(SiMe_3)_2$, containing a donor functionality in the Si bridge, exhibits low catalytic activity in such reactions as olefin hydrogenation, presumably because of the competition between the substrate (weak donor) and the donor functionality of the ansa ligand for the empty coordination site at the metal center. In contrast, for aminoalkene hydroamination/cyclization in which a strong amine donor is the substrate, catalytic activity is significantly enhanced while diastereoselectivity is essentially unchanged compared to nonfunctionalized analogs.

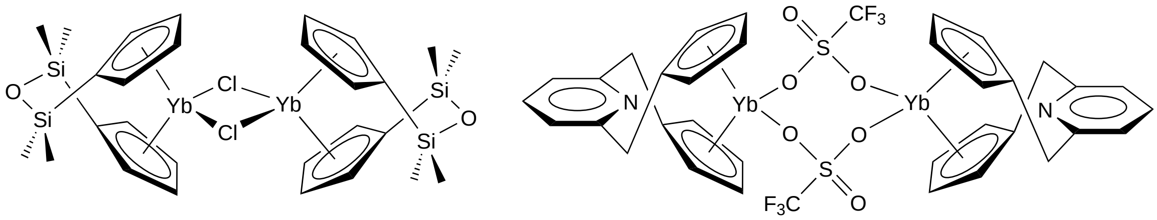

(a)

(b)

Figure 44 (a) $[\{O(Me_2SiC_5H_4)_2\}YbCl]_2$, (b) $[\{2,6\text{-}C_5H_3N(CH_2C_5H_4)_2\}Yb(\mu\text{-}O_2SOCF_3)]_2$

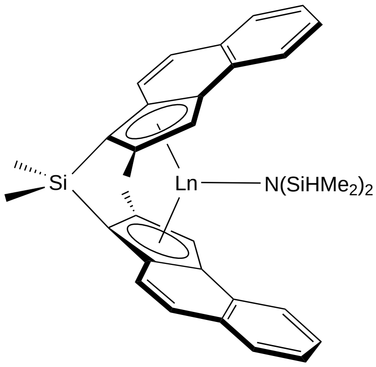

Figure 45 *rac*-$Me_2Si(2\text{-}Me\text{-}Benz\text{-}Ind)_2LnN(SiHMe_2)_2$

Brintzinger-type, indenyl-derived metallocene complexes *rac*-$Me_2Si(2\text{-}Me\text{-}Benz\text{-}Ind)_2LnN(SiHMe_2)_2$ (Figure 45) and *rac*-$Me_2Si(2\text{-}Me\text{-}C_9H_5)_2LnN(SiHMe_2)_2$ ($Ln = Y$, Lu) have been prepared by silylamine elimination of $Ln[N(SiHMe_2)_2]_3(THF)_2$ and linked, substituted indene systems, and isolated in racemic yields as high as 72%.[77]

1,2-Bis(indenyl)ethane-derived *ansa*-lanthanidocenes [*rac*- and *meso*-$(CH_2)_2(\eta^5\text{-}C_9H_6\text{-}1)_2LnCl][LiCl(Et_2O)_2]$ ($Ln =$ Yb, Lu) were synthesized from dilithiated 1,2-bis(indenyl)ethane with either $YbCl_3$ or $LuCl_3$ in THF followed by solvent exchange with Et_2O. In the Yb case, the major diastereomer formed is meso, while in the case of Lu, the rac diastereomer predominated.

1,1′- (3-Oxapentamethylene)-bridged bis(indenyl) *ansa*-lanthanidocenes $[O(CH_2CH_2C_9H_6)_2]LnCl(THF)$ ($Ln = Y$, Pr, Nd, Dy, Yb, Lu) were obtained as a rac/meso mixture by the reaction of $LnCl_3$ with $O(CH_2CH_2C_9H_6)_2K_2$ in THF. Direct amidation or alkylation of the rac/meso mixtures in toluene provided solely pure racemic *ansa*-lanthanidocene amides $[O(CH_2CH_2C_9H_6)_2]LnN(SiMe_3)_2$ ($Ln = Y$, Pr, Nd, Yb, Lu) and pure racemic *ansa*-lanthanidocene hydrocarbyls $[O(CH_2CH_2C_9H_6)_2]LnCH_2SiMe_3$ ($Ln = Dy$, Yb), correspondingly. The amide and hydrocarbyl complexes are efficient single-component catalysts for MMA polymerization.[78]

Me_2Si-bridged cyclopentadienyl/indenyl (donor-functionalized)-*ansa*-metallocenes $\{Me_2Si(C_5H_2\text{-}3,5\text{-}{}^tBuMe)[1\text{-}C_9H_5\text{-}3\text{-}(CH_2)_2NMe_2]\}LnCl$ ($Ln = Y$, Sm, Lu) are monomeric and solvent free with intramolecular coordination of the donor function to the metal as shown by X-ray crystallography of the Lu derivative (Figure 46).

A C_s-symmetric yttrocene complex, *ansa*-$Me_2Si(\eta^3\text{-}Flu)(\eta^5\text{-}C_5Me_4)YCl_2Li(OEt_2)_2$ ($Flu = C_{13}H_8$, fluorenyl), was prepared from YCl_3 and the dilithium salt of *ansa*-$Me_2Si(FluH)(C_5Me_4H)$. Treatment with $NaN(SiMe_3)_2$ yields the corresponding bis(trimethylsilyl)amide derivative *ansa*-$Me_2Si(Flu)(\eta^5\text{-}C_5Me_4)YN(SiMe_3)_2$ (Figure 47). In both complexes, the five-membered ring of the fluorenyl ligand is slipped from η^5 toward an η^3 coordination mode.

Lanthanide complexes with an unsymmetric cyclopentadienyl-fluorenyl ligand $[Me_2C(\eta^5\text{-}Flu)(\eta^5\text{-}Cp)]Ln(\eta^5\text{-}Cp)(FluH)CMe_2$ (Figure 48a) ($Ln = Y$, La, Nd) were prepared by amine elimination from $Ln[N(SiMe_3)_2]_3$ and ($CpH–CMe_2–FluH$). These ansa complexes feature very 'open' Cp(centroid)–Ln–Flu(centroid) bite angles ($Ln =$ La,

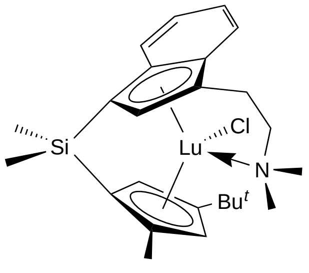

Figure 46 $\{Me_2Si(C_5H_2\text{-}3,5\text{-}{}^tBuMe)[1\text{-}C_9H_5\text{-}3\text{-}(CH_2)_2NMe_2]\}^-$ LuCl

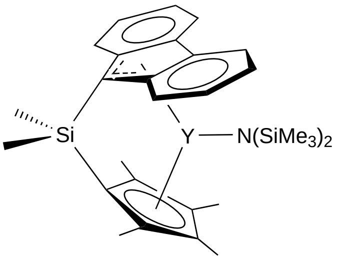

Figure 47 *ansa*-$Me_2Si(\eta^3\text{-}Flu)(\eta^5\text{-}C_5Me_4)YN(SiMe_3)_2$

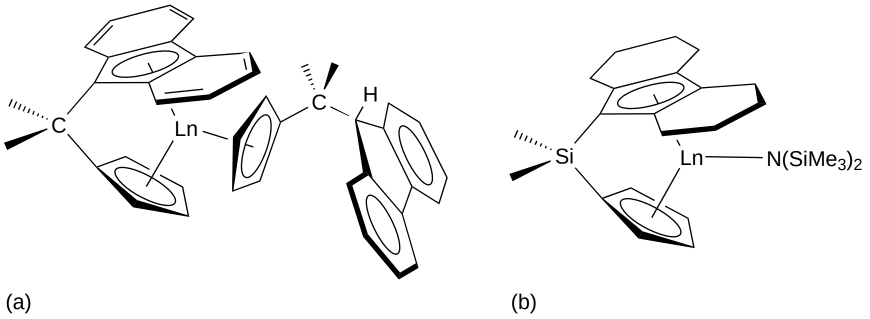

Figure 48 (a) $[Me_2C(\eta^5\text{-Flu})(\eta^5\text{-}C_5H_4)]Ln(\eta^5\text{-}C_5H_4)(FluH)CMe_2$, (b) $Me_2Si(OHF)(C_5H_3R)LnN(SiMe_3)_2$

103°; Nd, 105°).[79] The related Lu complex $[Ph_2C(\eta^5\text{-Flu})(\eta^5\text{-}Cp)]LuN(SiMe_3)_2$ exhibits intramolecular ß–C–Si agostic interaction with Lu. The complex was used as stereospecific catalyst in polymerization of MMA producing richly syndiotactic PMMA and in ring-opening polymerization of ε-caprolactone and δ-valerolactone producing polymers with moderate polydispersity.[80] Chiral C_1-symmetric *ansa*-metallocenes $Me_2Si(OHF)(C_5H_3R)LnN(SiMe_3)_2$ (Figure 48b) (OHF = η^5-octahydrofluorenyl; R* = (−)-menthyl; Ln = Sm,Y, Lu) exhibit catalytic activity for hydroamination/cyclization of aminoalkenes ($\leq$67% enantioselectivities) and for the hydrophosphination/cyclization of phosphinoalkenes ($\leq$96% diastereoselectivities).[81]

ansa-Metallocenes $(\eta^5{:}\eta^5\text{-}C_{24}H_{16})LnI(THF)$ (Figure 49) (Ln = Dy, Er, Tm, Lu) were prepared by in situ reactions of two equiv. of potassium acenaphthylenide K^+ $C_{12}H_8^-$ with LnI_3. Dimerization of two acenaphthylene radical anions produces a *rac*-*ansa*-metallocene structure with the Lu atom in a distorted tetrahedral geometry with two η^5-coordinated five-membered rings of the acenaphthylene ligands, the iodine and the THF.[82]

Tris(peralkylcyclopentadienyl)samarium complexes containing two rings bridged by a Me_2Si group were synthesized reacting SmI_3 first with $Me_2Si(C_5Me_4K)_2$ in THF followed by the reaction with KC_5Me_4R (R = Me, Et, ^{n}Pr, ^{i}Pr). When the second stage is carried out in toluene the solvent-free complexes $Me_2Si(C_5Me_4)_2SmCp^*$ (Figure 50a), $Me_2Si(C_5Me_4)_2Sm(C_5Me_4Et)$, $Me_2Si(C_5Me_4)_2Sm(C_5Me_4{}^n\text{Pr})$, and $Me_2Si(C_5Me_4)_2Sm(C_5Me_4\text{-}{}^i\text{Pr})$ were isolated. In contrast to the reactivity of Cp^*_3Sm, the complexes obtained do not cleave THF, do not reduce 1,3,5,7-C_8H_8 or $Ph_3P{=}Se$, and do not polymerize ethylene. Tris(cyclopentadienyl) compounds with two Cp rings linked by a tetramethylethano unit $Me_4C_2(C_5H_4)_2LnCp(THF)$ (Figure 50b) (Ln = Nd, Sm, Gd, Yb) were prepared by reaction of $Me_4C_2(C_5H_4MgCl)_2$ with $LnCl_3$ followed by CpNa in THF.

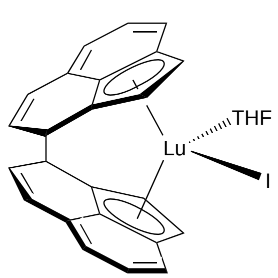

Figure 49 $(\eta^5{:}\eta^5\text{-}C_{24}H_{16})LuI(THF)$

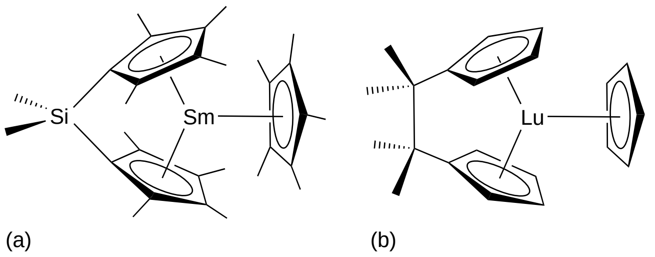

Figure 50 (a) $Me_2Si(C_5Me_4)_2SmCp^*$, (b) $Me_4C_2(C_5H_4)_2LuCp$ (THF)

7.4 Mono(cyclopentadienyl) Complexes

Monomeric half-sandwich complexes (*see Half-sandwich Complexes*) bearing double-N-functionalized cyclopentadienyl ligands $[C_5H_3(CH_2CH_2NMe_2)_2\text{-}1,2]LaI_2(THF)$ (Figure 51a) and $[C_5H_3(CH_2CH_2NMe_2)_2\text{-}1,3]LaI_2(THF)$ (Figure 51b), were prepared reacting LaI_3 with $K[1,2\text{-}C_5H_3(CH_2CH_2NMe_2)_2]$ and $K[1,3\text{-}C_5H_3(CH_2CH_2NMe_2)_2]$.

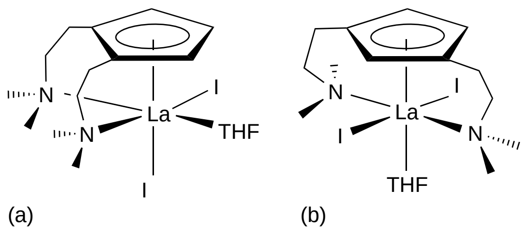

Figure 51 (a) $[C_5H_3(CH_2CH_2NMe_2)_2\text{-}1,2]LaI_2(THF)$, (b) $[C_5H_3(CH_2CH_2NMe_2)_2\text{-}1,3]LaI_2(THF)$

In both complexes, the La atoms have a distorted octahedral geometry. However, different coordination requirements of the tridentate 1,2- and 1,3-substituted cyclopentadienyl ligands cause different positions of the iodine atoms and the THF molecule around the metal.[83]

The (+)-neomenthylcyclopentadienyllanthanide complexes $\mathrm{Cp^RLnX_2(THF)_3}$ [X = Cl, Ln = Sm, Gd, Yb, Y, Lu; X = I, Ln = Sm, Yb; $\mathrm{Cp^R}$ = (+)-neomenthylcyclopentadienyl] were prepared by reaction of $\mathrm{LnCl_3}$ with appropriate alkali metal cyclopentadienyl derivatives. In the solid state, the monomeric $\mathrm{Cp^RSmI_2(THF)_3}$ adopts a pseudo-octahedral geometry with the two iodine atoms taking trans positions. A similar structure is found for $\mathrm{(Ind)GdCl_2(THF)_3}$.

Half-sandwich cyclopentadienyl lanthanide complexes $\{[(\eta^5\text{-}\mathrm{C_5H_4}{}^t\mathrm{Bu})\mathrm{Ln(THF)}]_2(\mu_2\text{-Cl})_2(\mu_3\text{-Cl})_3\mathrm{Na(THF)}\}_n$ (Ln = Nd, Sm, Gd, Yb) are available from the reaction of $\mathrm{LnCl_3}$ with $\mathrm{NaC_5H_4}{}^t\mathrm{Bu}$ in THF. The Sm complex reacts with $\mathrm{Na_2Se_5}$ yielding hexanuclear $[\mathrm{Na(THF)_6}]_2[(\eta^5\text{-}\mathrm{C_5H_4}{}^t\mathrm{Bu})_6\mathrm{Sm_6}(\mu_6\text{-Se})(\mu\text{-}\mathrm{Se_2})_6]$ (Figure 52).[84] Earlier described clusters containing monocyclopentadienylsamarium units are $[\mathrm{Cp_{12}Sm_{12}}(\mu_3\text{-Cl})_{24}]$, $[(\mathrm{Cp^*Sm})_6\mathrm{Se_{11}}]$, and $[(\mathrm{Cp^*Sm})_6\mathrm{Se_{11}}]$.

The reaction of $\mathrm{Sm(OAr)_3(THF)}$ (Ar = 2,6-$^t\mathrm{Bu_2C_6H_3}$) with one equiv. of LiCp* produces $\mathrm{Cp^*Sm(OAr)_2(THF)}$, which reveals a three-legged piano stool (*see Piano Stool Structure*) geometry. The monocyclopentadienyl yttrium complex containing a diamide ligand, $\mathrm{CpY\{ArN(CH_2)_3NAr\}(THF)}$ (Ar = 2,6-$^i\mathrm{Pr_2C_6H_3}$) (Figure 53) was obtained from alkali metal salts of the ligand and cyclopentadiene.[85]

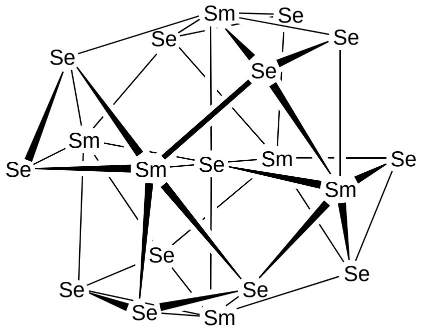

Figure 52 Structure of $[\mathrm{Na(THF)_6}]_2[(\eta^5\text{-}\mathrm{C_5H_4}{}^t\mathrm{Bu})_6\mathrm{Sm_6}(\mu_6\text{-Se})(\mu\text{-}\mathrm{Se_2})_6]$ (Cp ligands are omitted)

Besides the *ansa*-metallocene complexes with so-called *constrained geometry ligands* are used as effective catalysts in a number of important organic reactions. Constrained geometry ligands combine alkoxido-, amido- or other functions attached to the cyclopentadienyl ring. A variety of linkers between the Cp ring and the covalently bonded function, which both rigidly coordinate to the metal, enables the shaping of the free coordination sphere of the metal thus permitting a fine tuning of complex reactivity.[25,86] For alkyl lanthanide complexes supported by constrained geometry ligands see paragraph 2.3.

Reaction of $\mathrm{Y[N(SiMe_3)_2]_3}$ with $\mathrm{Me_2Si(C_5Me_4H)\ (N(H)\text{-}{}^tBu)}$ at 100° C results in elimination of 2 equiv. of $\mathrm{HN(SiMe_3)_2}$ and attachment of the Cp-amido ligand to yttrium. Later this synthetic approach was used for the preparation of related amide and alkyl complexes, for example, $[\mathrm{Me_2Si}(\eta^5\text{-}\mathrm{C_5Me_4})(\mathrm{N}{}^t\mathrm{Bu})]\mathrm{LnE(SiMe_3)_2}$ (Ln = Sm, Nd, Yb, Lu; E = CH, N) (Figure 54). They are significantly more active than the corresponding complexes $\mathrm{Cp^*{}_2LnE(SiMe_3)_2}$ as precatalysts for aminoalkene hydroamination/cyclization.

Yttrium alkyl complexes $\mathrm{Me_2Si}(\eta^5\text{-}\mathrm{C_5Me_4})(\eta^1\text{-}\mathrm{NCMe_2\text{-}R})\mathrm{Y(CH_2SiMe_3)(THF)}$ (R = Me, Et) and $\mathrm{Me_2Si}(\eta^5\text{-Ind})(\eta^1\text{-}\mathrm{N}{}^t\mathrm{Bu})\mathrm{Y(CH_2SiMe_3)(THF)}$ were prepared in high yields from $\mathrm{Y(CH_2SiMe_3)_3(THF)_2}$ and amino-functionalized cyclopentadienes or indene, respectively. According to single-crystal X-ray diffraction, $\mathrm{Me_2Si}(\eta^5\text{-}\mathrm{C_5Me_4})(\eta^1\text{-}\mathrm{NCMe_2Et})\mathrm{Y(CH_2SiMe_3)(THF)}$ has a three-legged piano stool geometry. Reaction of $\mathrm{Y(CH_2SiMe_3)_3(THF)_2}$ with the tridentate linked amido-cyclopentadienyl ligands $\mathrm{(C_5Me_4H)SiMe_2NHR}$ (R = $\mathrm{CH_2CH_2OMe}$, $\mathrm{CH_2CH_2NMe_2}$, $\mathrm{CH_2CH_2CH_2OMe}$, $\mathrm{CMe_2\text{-}CH_2OMe}$), which contain an additional donor functionality, results in the cleavage of the silicon-cyclopentadienyl bond and formation of $\mathrm{(C_5Me_4H)\{N(SiMe_2CH_2SiMe_3)(R)\}Y(CH_2\text{-}SiMe_3)(THF)}_n$ (n = 0, 1) (Figure 55a). The dimeric hydrido complexes $[\mathrm{Me_2Si(C_5Me_4)}(\eta^1\text{-}\mathrm{NCMe_2R})\mathrm{Y}(\mu\text{-H})\mathrm{(THF)}]_2$ were synthesized by hydrogenolysis of the corresponding alkyl derivatives. They polymerize ethylene, whereas styrene and 1-hexene were cleanly converted into the monoinsertion products. Styrene derivatives react with the hydrido complexes to give, for example, $\mathrm{Me_2Si(C_5Me_4)}(\eta^1\text{-}\mathrm{NCMe_2R})\mathrm{Y(CH_2C_6H_4}{}^t\mathrm{Bu)(THF)}$ (Figure 55b). The insertion product of 1-hexene initiates the polymerization of styrene

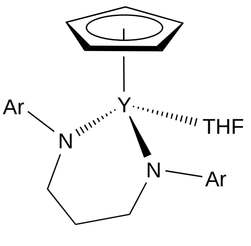

Figure 53 $\mathrm{CpY\{ArN(CH_2)_3NAr\}(THF)}$

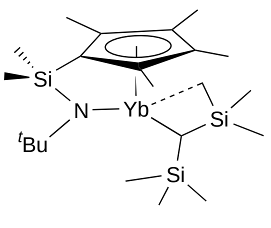

Figure 54 $[\mathrm{Me_2Si}(\eta^5\text{-}\mathrm{C_5Me_4})(\mathrm{N}{}^t\mathrm{Bu})]\mathrm{YbN(SiMe_3)_2}$

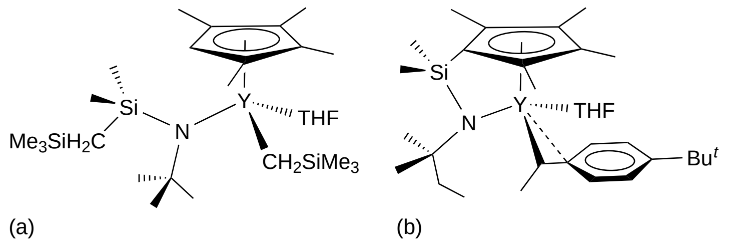

Figure 55 (a) $(C_5Me_4H)\{N(SiMe_2CH_2SiMe_3)(^tBu)\}Y(CH_2SiMe_3)(THF)_n$, (b) $Me_2Si(C_5Me_4)(\eta^1\text{-}NCMe_2Et)Y(CH_2C_6H_4{}^tBu)(THF)$

yielding atactic polystyrene with a narrow molecular weight distribution and microstructures enriched in syndiotacticity.[87]

Oxirane-ring opening of butylglycidyl ether with cyclopentadienylsodium or indenylsodium affords cyclopentadienyl- and indenyl-substituted alcohols $RCH_2\text{-}CH(OH)CH_2OBu$ ($R = C_5H_4$ or $3\text{-}C_9H_6$), which deprotonate with $Ln[N(SiMe_3)_2]_3$ to give corresponding lanthanide complexes $\{[(\eta^5\text{-}R)CH_2CH(\mu_2\text{-}\eta^1\text{-}O)CH_2OBu]LnN(SiMe_3)_2\}_2$ ($R = C_5H_4$, Ln = La, Pr, Er, Lu; $R = 1\text{-}C_9H_6$, Ln = La) (Figure 56). The coordination spheres of the metal atoms in these complexes involve simultaneously the η^5-cyclopentadienyl (indenyl), bridging alkoxide, and terminal amide ligands.[88]

Deprotonation of a CpH/OH ligand with $Y[N(SiMe_3)_2]_3$ yields the neutral chloride complex $[\eta^5{:}\eta^1\text{-}C_5H_4CH_2\{3,5\text{-}C_6H_3(CF_3)_2\}_2CO]_2YCl(THF)$, which is further converted to amide, alkoxide, or alkyl derivatives by reacting with one equiv. of $NaN(SiMe_3)_2$, $LiOC_6H_3{}^tBu_2\text{-}2,6$, and $LiCH(SiMe_3)_2$ respectively. The molecular structure of the amide[89] and phenoxide (Figure 57) derivatives were established by X-ray crystallography.[90]

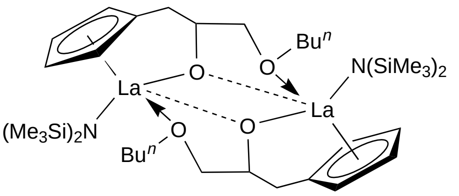

Figure 56 $\{[\eta^5\text{-}C_5H_4CH_2CH(\mu_2\text{-}\eta^1\text{-}O)CH_2OBu]La\text{-}N(SiMe_3)_2\}_2$

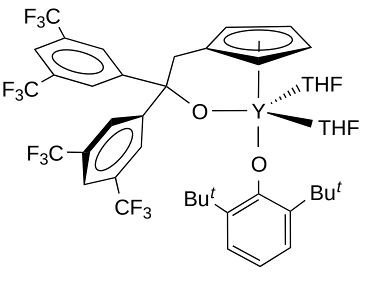

Figure 57 $[\eta^5{:}\eta^1\text{-}C_5H_4CH_2\{3,5\text{-}C_6H_3(CF_3)_2\}_2CO]Y(OC_6H_3\text{-}{}^tBu_2)(THF)_2$

Lanthanide(II) complexes $Me_2Si(C_5Me_4)(PAr)Ln\text{-}(THF)_3$ (Ln = Sm, Yb; $Ar = C_6H_2{}^tBu_3\text{-}2,4,6$) were prepared by reaction of SmI_2 and YbI_2, respectively, with $K_2[Me_2Si(C_5Me_4)(PHAr)]$. Oxidation of the Sm complex with benzophenone or ICH_2CH_2I in THF afforded $[Me_2Si(C_5Me_4)(PAr)Sm(THF)]_2(\mu\text{-}\eta^2\text{-}OCPh_2)$ (Figure 58a) and $[Me_2Si(C_5Me_4)(PAr)Sm(\mu\text{-}I)(THF)]_2$ (Figure 58b), respectively.[91]

7.5 Lanthanide Complexes with Carboranyl Ligands

A number of organolanthanide complexes with carboranes either bonded to the lanthanide metals via one carbon atom or with an open side as Cp analogs have been

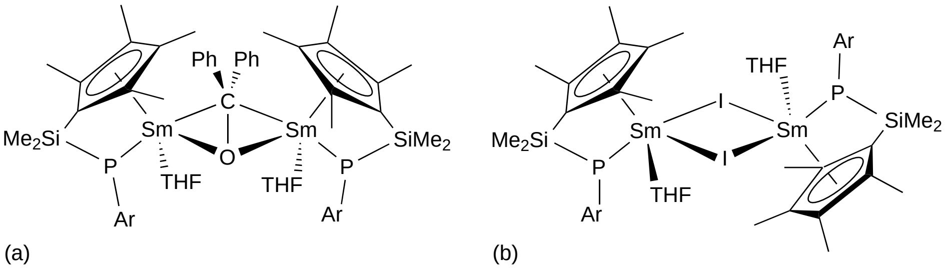

Figure 58 (a) $[Me_2Si(C_5Me_4)(PAr)Sm(THF)]_2(\mu\text{-}\eta^2\text{-}OCPh_2)$, (b) $[Me_2Si(C_5Me_4)(PAr)Sm(\mu\text{-}I)(THF)]_2$

described (see ***Boron, Metallocarboranes***). The dimethylsilyl bridged carboranyl/indenyl ligand $\mathrm{Me_2Si(Ind)(C_2B_{10}H_{11})}$ can be reduced to the monoanion $\mathrm{[Me_2Si(Ind)(C_2B_{10}H_{11})]^-}$, the dianion $\mathrm{[Me_2Si(Ind)(C_2B_{10}H_{10})]^{2-}}$, and the trianion $\mathrm{[Me_2Si(Ind)(C_2B_{10}H_{10})]^{3-}}$ by treatment with NaH or K in THF. Reaction of $\mathrm{LnCl_3}$ with one equiv. of $\mathrm{[Me_2Si(Ind)(C_2B_{10}H_{11})]Na}$ in THF yields $\mathrm{[Me_2Si(\eta^5\text{-}Ind)(C_2B_{10}H_{11})]LnCl_2(THF)_3}$ (Ln = Nd, Er). They further react with another equiv. of $\mathrm{[Me_2Si(Ind)(C_2B_{10}H_{11})]Na}$ to afford $\mathrm{[Me_2Si(\eta^5\text{-}Ind)(C_2B_{10}H_{11})]_2LnCl(THF)_2}$ (Ln = Ce, Nd, Sm, Er). $\mathrm{[Me_2Si(Ind)(C_2B_{10}H_{10})]K_3}$ reacts with $\mathrm{ErCl_3}$ forming $\mathrm{\eta^5{:}\eta^6\text{-}[Me_2Si(Ind)(C_2B_{10}H_{11})]Er(THF)_2}$ (Figure 59).

The related $\mathrm{Me_2C}$-bridged ligand $\mathrm{Me_2C(C_9H_7)(C_2B_{10}H_{11})}$ can be converted only into the monoanion $\mathrm{[Me_2C(Ind)(C_2B_{10}H_{11})]^-}$ and the dianion $\mathrm{[Me_2C(Ind)(C_2B_{10}H_{10})]^{2-}}$ by treatment with one or two equiv. of BuLi, respectively. Reaction of $\mathrm{LnCl_3}$ with one or two equiv. of the monoanionic salt yields $\mathrm{[Me_2C(\eta^5\text{-}Ind)(C_2B_{10}H_{11})]GdCl_2(THF)_2}$ and $\mathrm{[Me_2C(\eta^5\text{-}Ind)(C_2B_{10}H_{11})]_2LnCl(THF)(OEt_2)}$, respectively (Ln = Y, Yb).**92** Using $\mathrm{[Me_2C(C_5H_5)(C_2B_{10}H_{11})]Na}$, neutral $\mathrm{[Me_2C(\eta^5\text{-}C_5H_4)(C_2B_{10}H_{11})]_3Sm}$ (Figure 60) can be isolated besides $\mathrm{[Me_2C(\eta^5\text{-}C_5H_4)(C_2B_{10}H_{11})]SmCl_2(THF)_3}$ and $\mathrm{[Me_2C(\eta^5\text{-}C_5H_4)(C_2B_{10}H_{11})]_2SmCl(THF)_2}$.**93**

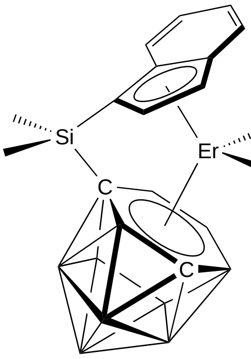

Figure 59 $\mathrm{[Me_2Si(Ind)(C_2B_{10}H_{11})]Er(THF)_2}$

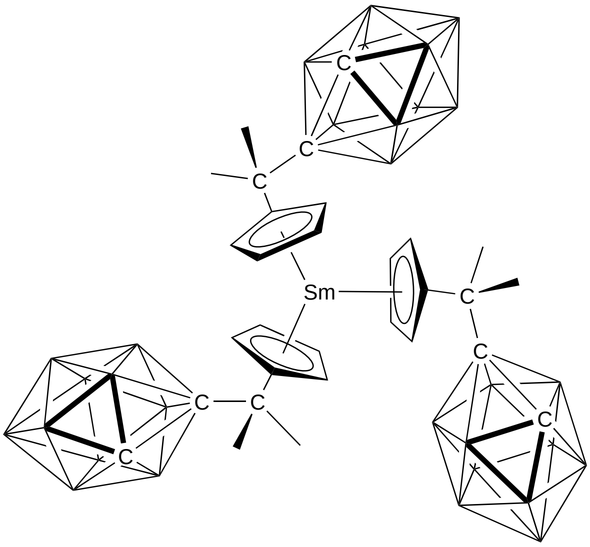

Figure 60 $\mathrm{[Me_2C(\eta^5\text{-}C_5H_4)(C_2B_{10}H_{11})]_3Sm}$

The first organolanthanide compound containing an η^7-carboranyl ligand, $\mathrm{[\{[Me_2C(\eta^5\text{-}C_5H_4)(\eta^7\text{-}C_2B_{10}H_{11})]Er\}_2\text{-}\{Na_4(THF)_9\}]_n}$ (Figure 61), was prepared by treatment of $\mathrm{[Me_2C(\eta^5\text{-}C_5H_4)(C_2B_{10}H_{11})]ErCl_2(THF)_3}$ or $\mathrm{[Me_2C(\eta^5\text{-}C_5H_4)(\eta^6\text{-}C_2B_{10}H_{11})]Er(THF)_2}$ with excess of Na in THF.

Silylamine elimination reactions of the boron-bridged ligand $\mathrm{{}^iPr_2NB(C_9H_7)(C_2B_{10}H_{11})}$ incorporating indenyl and carboranyl moieties and $\mathrm{Ln[N(SiHMe_2)_2]_3}$ resulted in the formation of $\mathrm{[{}^iPr_2NB(\eta^5\text{-}C_9H_6)(\eta^1\text{-}C_2B_{10}H_{10})]Ln\text{-}N(SiHMe_2)_2(THF)_2}$ (Ln = Nd, Er, Y) (Figure 62).**94**

Treatment of $\mathrm{1,2\text{-}(PhCH_2)_2\text{-}1,2\text{-}C_2B_{10}H_{10}}$ with excess Na or Li in THF followed by reaction with $\mathrm{LnCl_3}$ in the presence of excess alkali metal gave the 13-vertex closo-metallacarboranes $\mathrm{\{[(PhCH_2)_2C_2B_{10}H_{10}]Ln(THF)\}_2\text{-}\{Na(THF)_3\}_2}$ (Ln = Dy, Y, Er) or $\mathrm{[\{(PhCH_2)_2C_2B_{10}H_{10}\}\text{-}Ln(THF)]_2[Li(THF)_4]_2}$ (Figure 63) (Ln = Y, Er), respectively. The yttrium complexes were the first examples of d^0 metallacarboranes incorporating an η^7-carboranyl ligand. Density functional calculations indicate that the metal-carborane bonding is well delocalized and can be described as

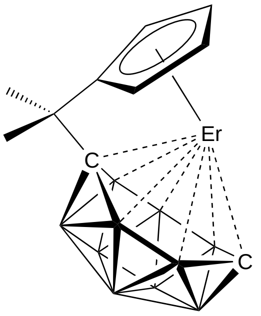

Figure 61 Structure of the dianionic fragment $\mathrm{[Me_2C(\eta^5\text{-}C_5H_4)\text{-}(\eta^7\text{-}C_2B_{10}H_{11})]Er}$

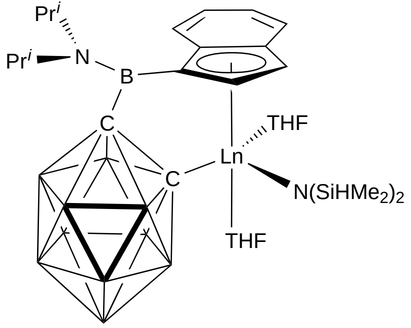

Figure 62 $\mathrm{[{}^iPr_2NB(\eta^5\text{-}C_9H_6)(\eta^1\text{-}C_2B_{10}H_{10})]LnN(SiHMe_2)_2\text{-}(THF)_2}$

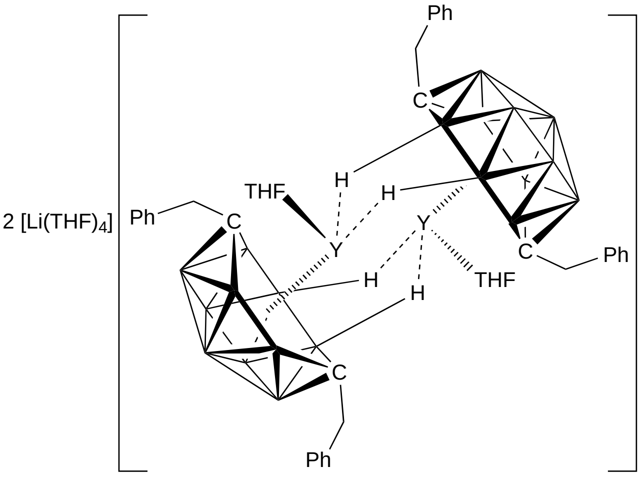

Figure 63 $[\{(PhCH_2)_2C_2B_{10}H_{10}\}Y(THF)]_2[Li(THF)_4]_2$

the orbital interactions between the metal's five d orbitals and the cage's five symmetry-adapted frontier orbitals. It is anticipated that only the d^0/f^n transition metal ion with the proper size is capable of being η^7-bound to an *arachno*-carboranyl ligand.[95]

Treatment of the sodium salt of the 'carbons-adjacent' *nido*-carborane anion $[\{\mu\text{-}1,2\text{-}[o\text{-}C_6H_4(CH_2)_2]\text{-}1,2\text{-}C_2B_{10}H_{10}\}_2Na_4(THF)_6]_n$ with two equiv. of $LnCl_3$ gave $[\eta^6\text{-}\{\mu\text{-}1,2\text{-}[o\text{-}C_6H_4(CH_2)_2]\text{-}1,2\text{-}C_2B_{10}H_{10}\}]LnCl(THF)_3$ (Ln = Nd, Er, Y). Further reactions with $NaBH_4$ and NaC_5H_5 resulted in $[\eta^6\text{-}\{\mu\text{-}1,2\text{-}[o\text{-}C_6H_4(CH_2)_2]\text{-}1,2\text{-}C_2B_{10}H_{10}\}]Nd[(\mu\text{-}H)_3\text{-}BH](THF)_3$ (Figure 64) and $[\eta^6\text{-}\{\mu\text{-}1,2\text{-}[o\text{-}C_6H_4(CH_2)_2]\text{-}1,2\text{-}C_2B_{10}H_{10}\}]Y(\eta^5\text{-}C_5H_5)(THF)$, respectively.[96]

The erbacarborane sandwich complex $2,2',4,4'\text{-}(Me_3Si)_4\text{-}3,6'\text{-}[(\mu\text{-}H)_2K(THF)_2]\text{-}1,1'\text{-}$*commo*-$Er(\eta^5\text{-}2,4\text{-}C_2B_4H_4)_2$ (Figure 65) results from the reaction of $1,2\text{-}(Me_3Si)_2\text{-}1,2\text{-}C_2B_4H_4$ with $ErCl_3$ and potassium in a 2:1:4 molar ratio, in the absence of an outside electron-transfer agent.[97]

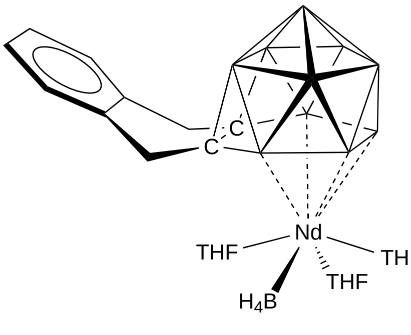

Figure 64 $[\eta^6\text{-}\{\mu\text{-}1,2\text{-}[o\text{-}C_6H_4(CH_2)_2]\text{-}1,2\text{-}C_2B_{10}H_{10}\}]$ $Nd[(\mu\text{-}H)_3BH](THF)_3$

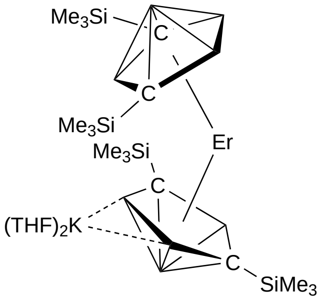

Figure 65 $2,2',4,4'\text{-}(Me_3Si)_4\text{-}3,6'\text{-}[(\mu\text{-}H)_2K(THF)_2]\text{-}1,1'\text{-}$*commo*-$Er(\eta^5\text{-}2,4\text{-}C_2B_4H_4)_2$

8 ARENE COMPLEXES

A comprehensive review covers the whole literature on arene complexes of the rare earth elements up to 2002.[98]

8.1 Complexes with Neutral Arene Ligands

Chloroaluminate complexes of the general formula $Ln(\eta^6\text{-}Arene)(\eta^2\text{-}AlCl_4)_3$ (equation 20) were prepared by reacting $AlCl_3$ with $LnCl_3$ in the corresponding aromatic solvent. In some cases, the reactions proceed only with addition of aluminum powder. The first compound of this type, $Sm(\eta^6\text{-}C_6Me_6)(AlCl_4)_3$, was reported in 1986.

$$3AlCl_3 + LnCl_3 \xrightarrow{\text{Arene}} Ln(\eta^6\text{-Arene})(\eta^2\text{-}AlCl_4)_3 \qquad (20)$$

Arene	**Lanthanide**
Benzene	La, Nd, Sm, Yb
Toluene	Sm, Nd, Gd ($[AlBr_4]^-$)
m-Xylene	Pr, Er
Mesitylene	Nd
Hexamethylbenzene	Nd, Sm, Gd, Yb

The molecular structure of $Sm(\eta^6\text{-}C_6Me_6)(AlCl_4)_3$ shows a distorted pentagonal bipyramid with the η^6-arene occupying an apical site. $Nd(\eta^6\text{-}C_6H_5Me)(AlCl_3Me)_3$ has been prepared by reaction of $Nd(\eta^6\text{-}C_6H_5Me)(AlCl_4)_3$ with $AlMe_3$. $(\eta^6\text{-}C_6H_6)Sm(AlCl_4)_2$ and $(\eta^6\text{-}C_6H_3Me_3)Sm(AlCl_4)_2$ were prepared by reduction of $SmCl_3$ with Na/Hg in the presence of $AlCl_3$ and the corresponding aromatic ligand. Single-crystal X-ray diffraction showed the Sm atom pentagonal-bipyramidal coordinated by the π-aromatic ligand and six Cl atoms. Analogoues Yb(II) chloroaluminates $(\eta^6\text{-}C_6H_6)_2Yb(AlCl_4)_2$ and $(\eta^6\text{-}C_6H_3Me_3)Yb(AlCl_4)_2$ have been synthesized by the same synthetic approach.

Abstraction of methide from the ß-diketiminato supported organoscandium complex $[LScMe_2]_2$ using $[Ph_3C][B(C_6F_5)_4]$ in arene solvents gives solvent separated ion pairs in which the arenes (C_6H_5Br, C_6H_6, C_6H_5Me, $1,3,5\text{-}Me_3C_6H_3$) are coordinated to the cationic scandium center in an η^6-fashion. Although the aromatic fragment in the bromobenzene

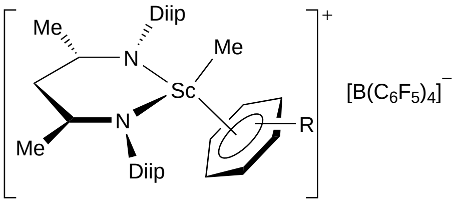

Figure 66 $[LSc(Me)(C_6H_5Br)][B(C_6F_5)_4]$ (Diip = 2,6-diisopropylphenyl, R = Br)

derivative $[LSc(Me)(C_6H_5Br)][B(C_6F_5)_4]$ (Figure 66) is η^6-bonded, steric interactions invoke significant ring tilting.[99]

The reaction of $Nd[N(SiMe_3)_2]_3$ with $(C_6F_5)_2NH$ in PhMe yields $[(\eta\text{-PhMe})Nd[N(C_6F_5)_2]_3]$ in which the Nd atom is η^6-bonded to a toluene solvent molecule.

η^6-Arene coordination between lanthanide ions and phenyl groups of certain phenolate and thiolate ligands have been detected in some unsolvated lanthanide complexes, for example, $Ln(SAr)_2$ (Ln = Eu, Yb; Ar = 2,6-$Trip_2C_6H_3$; Trip = 2,4,6-i-$Pr_3C_6H_2$), $[Eu_2(OAr)(\mu\text{-}OAr)_3]$ (OAr = 2,6-diphenylphenolate), and $Ln_2(O\text{-}2,6\text{-}(Me_2CH)_2C_6H_3)_6$ (Ln = Nd, Sm, Er), $[Sc(OArH)_3]$ (OAr = 2, 6-diphenylphenolate).[100] The reactions of the lanthanide metal powders with $Hg(C_6F_5)_2$ and 2,6-diphenylphenol in THF afford the lanthanide(III) phenoxides $Ln(2,6\text{-}OC_6H_3Ph_2)_3$ (Ln = Nd, Sm, Er, Yb, Lu) and the corresponding THF solvates. In the unsolvated compound $Yb(2,6\text{-}OC_6H_3Ph_2)_3$, one phenyl substituent is in a geometrically favorable position that allows this ring to engage in a novel π-interaction with the central ytterbium atom (Figure 67).

Reaction of 3 equiv. of 2,6-diisopropylaniline with $Sm[N(SiMe_3)_2]_3$ affords dimeric $[Sm(NHAr)_3]_2$, in which each metal center is engaged in an η^6-arene interaction with the aryl ring of an amide ligand attached to an adjacent samarium. IR spectroscopy indicates that the π-arene interactions are maintained in solution.[101]

8.2 Complexes with Anionic Arenes and Heterocyclic Aromatic Ligands

Treatment of Cp''_3Ln [Cp'' = 1,3-bis(trimethylsilyl) cyclopentadienide; Ln = La, Ce, Pr, Nd] with 2 equiv. of 18-crown-6 and 2 equiv. of potassium in benzene affords lanthanide complexes with C_6H_6 dianions. The molecular structure of the isomorphous La, Ce, and Nd salts $[K([18]\text{-}crown\text{-}6)][Ln\{\eta^5\text{-}C_5H_3(SiMe_3)_2\text{-}1,3\}_2(C_6H_6)]$ (Ln = La, Ce, Pr, Nd) shows a tight ion pair with a boat-shaped C_6H_6 dianion bridging the K and the Ln atoms (Figure 68).

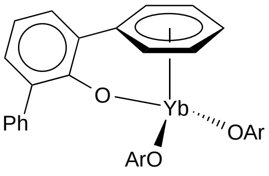

Figure 67 $Yb(2,6\text{-}OC_6H_3Ph_2)_3$ (Ar = 2,6-$OC_6H_3Ph_2$)

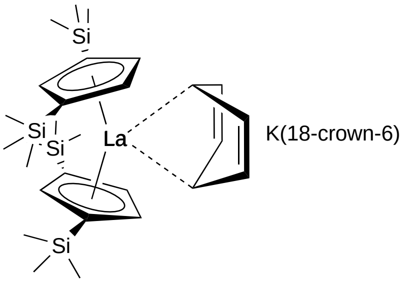

Figure 68 $[K([18]\text{-}crown\text{-}6)][La\{\eta^5\text{-}C_5H_3(SiMe_3)_2\text{-}1,3\}_2\text{-}(C_6H_6)]$

Phenylation of Y and Ho complexes $(LnL)_2(\mu\text{-}Cl)_2$ (Ln = Y, Ho; L = *syn*-$PhP[CH_2(SiMe_2)N(SiMe_2)CH_2]_2\text{-}PPh$) with PhLi in Et_2O/toluene results with coupling of two phenyl anions in binuclear compounds $[(L)Ln]_2(\mu\text{-}\eta^6\text{:}\eta^6\text{-}Ph_2)$ with a bridging diphenyl dianion. In these complexes, the Ln atoms are bonded to opposite sides of different rings of the biphenyl ligand, which retains its planarity (Figure 69).

In contrast, $(YbL)_2(\mu\text{-}Cl)_2$ reacts with PhLi yielding the paramagnetic monophenyl compound (L)YbPh.[102] Reduction of (L)LnCl(THF) (Ln = Y, Lu; L = *syn*-PhP $[CH_2(SiMe_2)N(SiMe_2)CH_2]_2PPh$) with KC_8 in toluene/ diethyl ether in the presence of naphthalene or 1-methylnaphthalene generates the dinuclear naphthalene-bridged species $[(L)Ln]_2(\mu\text{-}C_{10}H_7R)$ (R = H, Me; Ln = Y, Lu), in which each Ln atom has η^4-coordination to opposite sides of the dianionic naphthalene ligand. Similarly, reaction of anthracene with (L)LnCl(THF) (Ln = Y, Lu) in the presence of KC_8 yields $[(L)Ln]_2(\mu\text{-}C_{14}H_{10})$ (Ln = Y, Lu).[103] Related

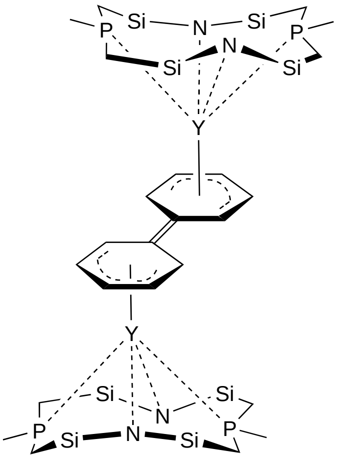

Figure 69 $[(syn\text{-}PhP[CH_2(SiMe_2)N(SiMe_2)CH_2]_2PPh)Y]_2(\mu\text{-}\eta^6\text{:}\eta^6\text{-}Ph_2)$ (Ph and Me groups are omitted)

lanthanide(III) complexes with a bridging naphthalene dianion $[(THF)_3LnI_2]_2(\mu\text{-}C_{10}H_8)$ (Ln = La, Ce, Pr, Nd) were synthesized by reaction of $LnI_3(THF)_3$ with equimolar amounts of Li metal and excess of $C_{10}H_8$ in THF. $[(DME)_2LnI]_2(\mu\text{-}C_{10}H_8)$ (Ln = Eu, Yb) were prepared in the same manner using LnI_2 in DME. The X-ray structure determination of the La and Eu complexes show two $LaI_2(THF)_3$ and $EuI(DME)_2$ moieties, respectively, bridged by η^4 bonded nonplanar naphthalene molecules. In contrast, reaction of TmI_2 with two equivalents of $Li[C_{10}H_8]$ in DME yields a binuclear Tm(III) complex with one bridging and two terminal naphthalene dianions $[Tm(DME)]_2(\eta^2\text{-}C_{10}H_8)_2(\mu^2\text{-}\eta^4{:}\eta^4\text{-}C_{10}H_8)$ (Figure 70).

Mononuclear lanthanide(III) complexes with terminal naphthalene dianions $CpLn(\eta^2\text{-}C_{10}H_8)(DME)$ (Ln = Y, Gd, Er, Tm, Lu) have been prepared by the reaction of $CpLnCl_2(THF)_3$ with $Na[C_{10}H_8]$ in DME (Figure 71a). The molecular structure of the yttrium and lutetium compound revealed that one naphthalene ring is bent, while the second one, which is not coordinated by the metal is planar. Two structurally related complexes of La(III) and Sm(III) with a bridging anthracene dianion $(Cp^*{}_2Ln)_2(\mu\text{-}\eta^3{:}\eta^3\text{-}C_{14}H_{10})$ (Ln = La, Sm) were prepared by reaction of $(Cp^*{}_2La)(\mu\text{-}Cl)_2K(DME)_2$ with disodium anthracenide and by direct reduction of anthracene with decamethylsamarocene in toluene, correspondingly. The molecules contain two $Cp^*{}_2Ln$ moieties, which are η^3-coordinated to two aromatic rings from opposite sides of the anthracene ligand (Figure 71b), which, in contrast to the complexes mentioned above, maintains its planarity. Bent anthracene dianions have also been found in $CpLu(\eta^2\text{-}C_{14}H_{10})(THF)_2$, $[Na^+(diglyme)_2][Cp_2Lu(\eta^2\text{-}C_{14}H_{10})]$, and $(DME)_2TmI(\eta^2\text{-}C_{14}H_{10})$.

2,3-benzanthracene and pyrene readily react with $Cp^*{}_2Sm$ to give $(Cp^*{}_2Sm)_2(\mu\text{-}\eta^3{:}\eta^3\text{-}Arene)$ (Arene = $C_{18}H_{12}$ and $C_{16}H_{10}$, respectively). In the benzanthracene derivative, two $Cp^*{}_2Sm$ fragments are coordinated at opposite edges of the nearly planar arene ligand and are located on the opposite faces of its plane in the manner similar to that in $(Cp^*{}_2Sm)_2(\mu\text{-}\eta^3{:}\eta^3\text{-}C_{14}H_{10})$. In contrast, the metallocene moieties in $(Cp^*{}_2Sm)_2(\mu\text{-}\eta^3{:}\eta^3\text{-}pyren)$ are coordinated at the neighboring edges of the pyrene ligand above and below its plane. Reaction of $(Cp^*LaCl)(\mu\text{-}Cl)_2Li(THF)_2$ with pyrene in toluene in the presence of potassium yields $(Cp^*LaCl)_3(\mu^3\text{-}C_{16}H_{10})(THF)$. All three Cp*LaCl moieties are located above one plane of the pyrene ligand and bridged by Cl atoms. Two La atoms are η^6-bonded to the arene ligand, whereas the third one is coordinated by one THF and has only two short La–C(pyrene) contacts (Figure 72).

Complexes of the lanthanides with heterocyclic aromatic ligands have been also reported, for example, $(Cp^*{}_2La)_2(\mu\text{-}Arene)$ (Arene = 2, 3-dimethylquinoxaline or phenazine). Phenazine is reduced by $Cp^*{}_2Sm$ yielding $(Cp^*{}_2Sm)_2(\mu\text{-}\eta^3{:}\eta^3\text{-}C_{12}H_8N_2)$ (Figure 73a), in which the samarocene fragments are in transoid orientation with respect to the $(C_{12}H_8N_2)^{2-}$ dianion. Three short contacts between the samarium atoms and the phenazine ligand suggest an allylic type of bonding. Reduction of acridine with $Cp^*{}_2Sm$, independent of the reagents ratio, results in dimerization of two arene ligands via C–C bond formation. An ytterbium complex containing the antiaromatic 2,2′-bipyridyl ligand has been prepared by reduction of 2,2′-bipyridine with $Yb(C_{10}H_8)(THF)_2$ as the cyclic trimer $[Yb(\mu^2\text{-}N_2C_{10}H_8)(THF)_2]_3$ in which the Yb atoms are bridged by 2,2′-bipy ligands (Figure 73b).

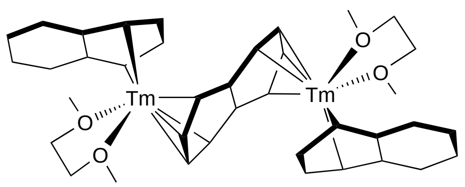

Figure 70 $[Tm(DME)]_2(\eta^2\text{-}C_{10}H_8)_2(\mu^2\text{-}\eta^4{:}\eta^4\text{-}C_{10}H_8)$

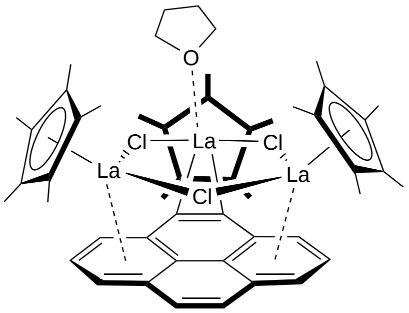

Figure 72 $(Cp^*LaCl)_3(\mu^3\text{-}C_{16}H_{10})(THF)$

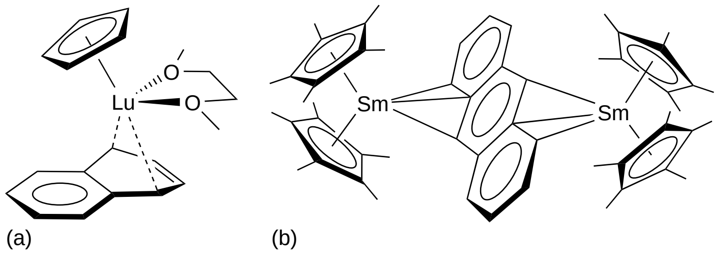

(a) (b)

Figure 71 (a) $CpLu(\eta^2\text{-}C_{10}H_8)(DME)$, (b) $(Cp^*{}_2Sm)_2(\mu\text{-}\eta^3{:}\eta^3\text{-}C_{14}H_{10})$

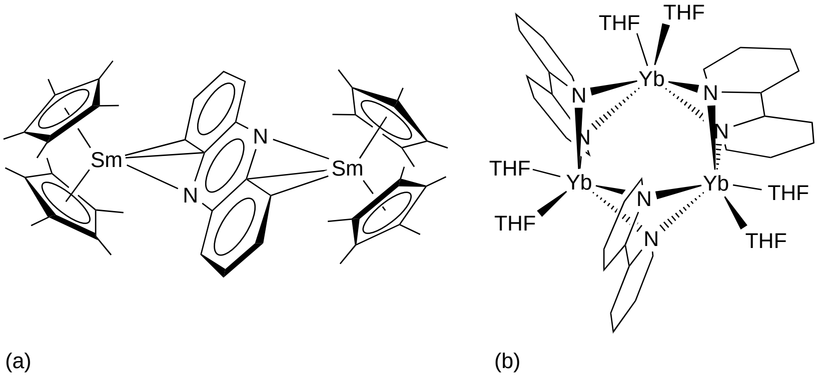

Figure 73 (a) $(Cp^*{}_2Sm)_2(\mu\text{-}\eta^3{:}\eta^3\text{-}C_{12}H_8N_2)$, (b) $[Yb(\mu^2\text{-}N_2C_{10}H_8)(THF)_2]_3$

8.3 Boratabenzene Complexes

Lithium 1-aminoboratabenzenes react with lanthanide trihalides in toluene to give the stepped ladder dimers $[(3{,}5\text{-}Me_2C_5H_3BNMe_2)_2Y(\mu\text{-}Cl)_2Li]_2$ (Figure 74a), $[(3{,}5\text{-}Me_2C_5H_3BNMe_2)_2Lu(\mu\text{-}Cl)_2Li]_2$, and the mononuclear complexes $YCl[3{,}5\text{-}Me_2C_5H_3BN(SiMe_3)_2]_2$, $LuCl[3{,}5\text{-}Me_2C_5H_3BN(SiMe_3)_2]_2$, and $ScCl(3{,}5\text{-}Me_2C_5H_3BN^iPr_2)_2$ (Figure 74b). The same reactions in THF or THP yield solvated complexes $(3{,}5\text{-}Me_2C_5H_3BNMe_2)_2Sm(\mu\text{-}Cl)_2Li(THF)$, $(3{,}5\text{-}Me_2C_5H_3BNMe_2)_2Y(\mu\text{-}Cl)_2Li(THP)$, $(3{,}5\text{-}Me_2C_5H_3BN^iPr_2)_2Y(\mu\text{-}Cl)_2Li(THF)_2$, $(3{,}5\text{-}Me_2C_5H_3BN^iPr_2)_2Sm(\mu\text{-}Cl)_2Li(THF)_2$, and the *ansa* complexes $[(3{,}5\text{-}Me_2C_5H_3BNMeCH_2)_2]Lu(\mu\text{-}Cl)_2Li(THF)_2$ and $[(3{,}5\text{-}Me_2C_5H_3BNMeCH_2)_2]Lu(\mu\text{-}Cl)_2Li(THP)_2$.[104]

Reaction of yttrium trichloride with lithium 1-methylboratabenzene in toluene affords donor-free dinuclear $[(C_5H_5BMe)_2Y(\mu\text{-}Cl)]_2$. Bis(boratabenzene)scandium complexes $[ScCl(C_5H_5BMe)_2]_2$, $[ScCl(3{,}5\text{-}Me_2C_5H_3BNMe_2)_2]_2$, and $ScCl[3{,}5\text{-}Me_2C_5H_3BN(SiMe_3)_2]_2$ were synthesized from solvent-free Li boratabenzenes and $ScCl_3$ in toluene. $[ScCl(C_5H_5BMe)_2]_2$ (Figure 75a) possesses a double chloro-bridged dinuclear structure with four facially coordinated boratabenzene ligands. In contrast, in $[ScCl(3{,}5\text{-}Me_2C_5H_3BNMe_2)_2]_2$, each Sc atom binds to one boratabenzene in an unprecedented N–B–C-2 coordination mode and facially to the second boratabenzene ligand (Figure 75b). $ScCl[3{,}5\text{-}Me_2C_5H_3BN(SiMe_3)_2]_2$ is mononuclear because of the bulkiness of its boratabenzene ligands. The

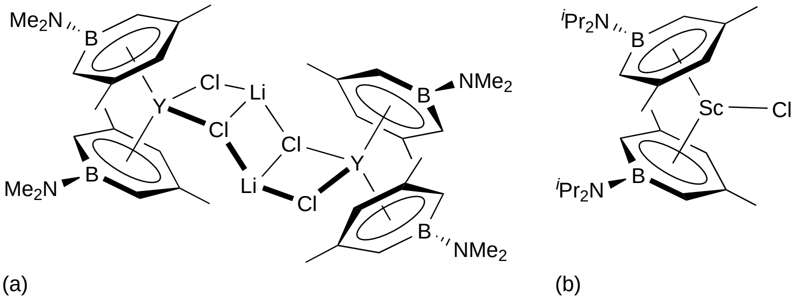

Figure 74 (a) $[(3{,}5\text{-}Me_2C_5H_3BNMe_2)_2Y(\mu\text{-}Cl)_2Li]_2$, (b) $ScCl(3{,}5\text{-}Me_2C_5H_3BN^iPr_2)_2$

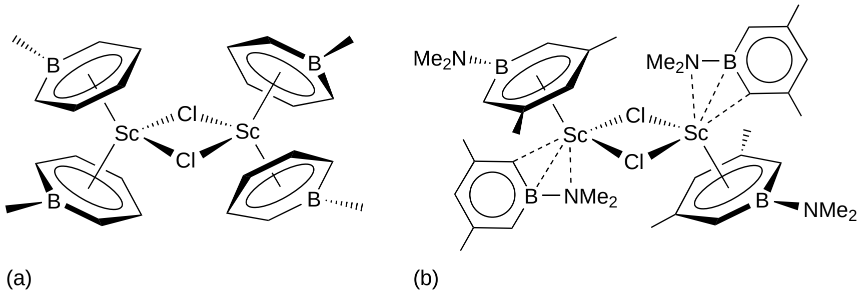

Figure 75 (a) $[ScCl(C_5H_5BMe)_2]_2$, (b) $[ScCl(3{,}5\text{-}Me_2C_5H_3BNMe_2)_2]_2$

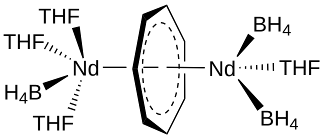

Figure 76 $(THF)(BH_4)_2Nd(\mu\text{-}\eta^7{:}\eta^7\text{-}C_7H_7)Nd(BH_4)(THF)_3$

reaction of $C_5H_5B{-}PMe_3$ with $Ph_3Sc(THF)_2$ provides $(C_5H_5B{-}Ph)ScPh_2(THF)$.

9 CYCLOHEPTATRIENYL COMPLEXES

Only one cycloheptatrienyl complex of the lanthanides is known until now. Reaction of $Nd(BH_4)_3(THF)_2$ with $K(C_7H_9)$ yields $(THF)(BH_4)_2Nd(\mu\text{-}\eta^7{:}\eta^7\text{-}C_7H_7)Nd(BH_4)(THF)_3$ (Figure 76). The X-ray structure determination shows a unique reverse-sandwich structure with both Nd atoms η^7 coordinated to the planar ligand.

10 CYCLOOCTATETRAENYL COMPLEXES

10.1 Mono(cyclooctatetraenyl) Complexes

Cyclooctatetraenyl lanthanide(III) halides of the type $[(COT)Ln(\mu\text{-}Cl)(THF)_2]_2$ (Figure 77a) are the most important precursors for the preparation of other half-sandwich (*see Half-sandwich Complexes*) and mixed sandwich complexes with cyclooctatetraenyl ligands. These complexes are readily accessible by reacting anhydrous lanthanide trichlorides with $K_2[COT]$ in a molar ratio of 1:1. The compounds consist of centrosymmetric, chloro-bridged dimers with η^8-coordinated cyclooctatetraenyl ligands. The use of the sterically demanding 1,4-bis(trimethylsilyl)cyclooctatetraenyl ligand allows the synthesis of a related series of organolanthanide halides $[Ln\{(1,4\text{-}(Me_3Si)_2C_8H_6)\}(\mu\text{-}Cl)(THF)]_2$ (Ln = Y, Sm, Ho, Lu). The anionic complex $[Li(diglyme)_2][(1,4\text{-}(Me_2SiC_6H_4NMe_2\text{-}o)_2C_8H_6)_2Sm_2(\mu\text{-}Cl)_3]$ (Figure 77b) has a triple chlorine bridge between two Sm atoms.

Mononuclear iodo complexes $(COT)LnI(THF)_n$ (Ln = La, Ce, Pr, $n = 3$; Ln = Nd, $n = 2$; Ln = Sm, $n = 1$) can be prepared either by reaction of LnI_3 with $K_2[COT]$ in THF (Ln = Nd, Sm), or directly from metal powders, iodine, and COT (Ln = La, Ce, Pr, Nd, Sm) in THF. The Tm complex $(COT)TmI(THF)_2$ is formed by reduction of COT with TmI_2 in THF. An improved solubility in polar organic solvents was also found for the corresponding mono(cyclooctatetraenyl)lanthanide triflates $[(COT)Ln(\mu\text{-}O_3SCF_3)(THF)_2]_2$. Mono(cyclooctatetraenyl) lanthanide complexes $(COT)Ln(BH_4)(THF)_n$ can be prepared from $Ln(BH_4)_3(THF)_3$ and $K_2[COT]$. $(COT)Nd(BH_4)(THF)_2$ looses one THF upon recrystallization forming the dimer $[(COT)Nd(\mu\text{-}BH_4)(THF)]_2$. Protonation of $(COT)Nd(BH_4)(THF)_2$ with $[NHEt_3][BPh_4]$ provides a convenient access to the cationic mono(cyclooctatetraenyl) neodymium(III) complex $[(COT)Nd(THF)_4][BPh_4]$. Its X-ray crystal structure reveals the presence of discrete cation–anion pairs in the solid state with the Nd ions being in a slightly distorted square-pyramidal coordination environment. Replacement of the THF ligands in $[(COT)Nd(THF)_4][BPh_4]$ with HMPA yields $[(COT)Nd(HMPA)_3][BPh_4]$.

Mono(cyclooctatetraenyl)lanthanide(III) complexes containing additional group 16 donor ligands $[(COT)Ln(\mu\text{-}OR)(THF)]_2$ (Ln = Y, Lu, R = Ph, 2,6-$C_6H_3Me_2$; Ln = Dy, R = $(CH_2)_3CH{=}CH_2$; Ln = Nd, R = Et) were prepared from $[(COT)Ln(\mu\text{-}Cl)(THF)_2]_2$ or $(COT)Ln(BH_4)(THF)_n$ and NaOR. Three representatives, $[(COT)Y(\mu\text{-}OPh)(THF)]_2$ (Figure 78a), $[(COT)Nd(\mu\text{-}OEt)(THF)]_2$, and $[(COT)Dy\{\mu\text{-}O(CH_2)_3CH{=}CH_2\}(THF)]_2$ have been structurally characterized. Other sterically more demanding alkoxides and

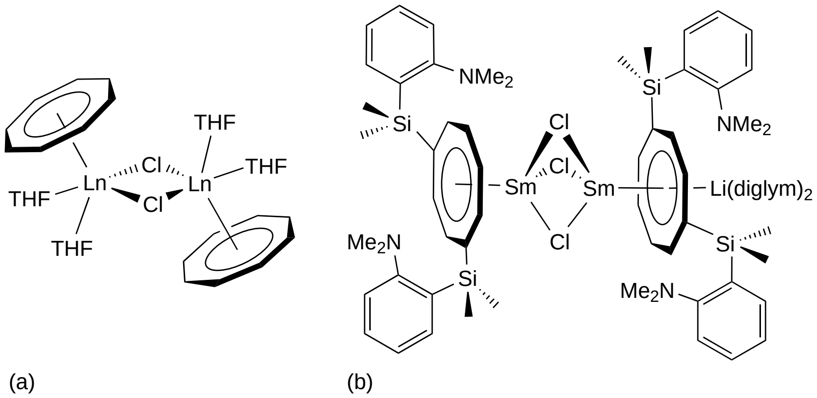

Figure 77 (a) $[(COT)Ln(\mu\text{-}Cl)(THF)_2]_2$, (b) $[Li(diglyme)_2][1,4\text{-}(Me_2SiC_6H_4NMe_2\text{-}o)_2(C_8H_6)_2Sm_2(\mu\text{-}Cl)_3]$

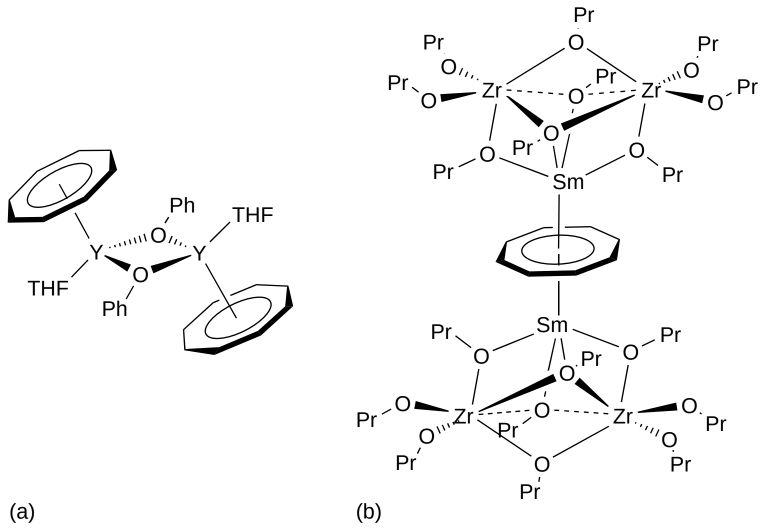

Figure 78 (a) [(COT)Y(μ-OPh)(THF)]$_2$, (b) {[Zr$_2$(O^{i}Pr)$_9$]Sm}$_2$(COT)

siloxides are (COT)Ln(OC^{t}Bu$_3$)(THF), (COT)Ln(OSiPh$_3$)(THF) (Ln = Y, Lu), Ln[1,4-(Me$_3$Si)$_2$C$_8$H$_6$](OC$_6$H$_2$-2,6-^{t}Bu$_2$-4-Me)(THF) (Ln = Sc, Y), [{1,4-(Me$_3$Si)$_2$C$_8$H$_6$}Sm(μ-OAr)]$_2$ (Ar = C$_6$H$_2$(^{t}Bu)$_2$-2,6,-Me-4), and {[Zr$_2$(O^{i}Pr)$_9$]Ln}$_2$(COT) (Ln = Sm, Yb) (Figure 78b).

The preparation of mono(cyclooctatetraenyl)samarium(III) thiolates and selenolates [(COT)Sm(μ-EAr)(THF)$_n$]$_2$ ($n = 1$, EAr = 2,4,6-SC$_6$H$_2$^{i}Pr$_3$; $n = 2$, EAr = SPh, SePh, 2,4,6-SC$_6$H$_2$^{i}Pr$_3$) has been achieved by the reaction of samarium powder with COT in THF in the presence of diaryl disulfides or diselenides. The molecular structure of [(COT)Sm(μ-SePh)(THF)$_2$]$_2$ reveals a dimeric molecule with phenylselenolate bridges. Monomeric organosamarium thiolates have been prepared in the same manner with use of either sterically demanding or potentially chelating thiolate ligands, for example, (COT)Sm(SC$_5$H$_4$N)[OP(NMe$_2$)$_3$]$_2$ (Figure 79a) or [Na(THF)$_2$][(COT)Nd(S-^{t}Bu)$_2$]. A number of lanthanide mono(cyclooctatetraenyl)/amide complexes (COT)Ln[N(SiMe$_3$)$_2$](THF) (Ln = Y, Gd, Er, Lu) has been synthesized by the reactions of [(COT)Ln(μ-Cl)(THF)$_2$]$_2$ with two equiv. of NaN(SiMe$_3$)$_2$. An unusual 'inverse sandwich complex' is obtained when the same reaction is carried out with [(COT)Sm(μ-Cl)(THF)$_2$]$_2$. [Sm{N(SiMe$_3$)$_2$}$_2$]$_2$(μ-COT) shows two Sm{N(SiMe$_3$)$_2$}$_2$ units symmetrically bridged by the cyclooctatetraenyl ligand (Figure 79b). A closely related 'inverse sandwich complex' of divalent samarium (μ-COT)[Sm{N(SiMe$_3$)$_2$}(THF)$_2$]$_2$ has a planar (COT)$^{2-}$ ring, sandwiched between two [{(Me$_3$Si)$_2$N}Sm(THF)$_2$]$^+$ cations. This structure is similar to that of the pentamethylcyclopentadienyl derivative [Cp*Ln(THF)$_2$]$_2$(μ-COT) (Ln = Sm, Eu, Yb), prepared by the reaction of [Cp*Ln(μ-I)(THF)$_2$]$_2$ (Ln = Sm, Eu, Yb) with one equiv. of K$_2$[C$_8$H$_8$] in toluene. Dissolvation of those complexes at 30 to 50° C under vacuum yields [Cp*Ln]$_2$(μ-η^8:η^8-COT) (Figure 79c).

The reaction of (COT)LnCl(THF)$_n$ compounds with the lithium, sodium, or potassium salts of C$_5$H$_6$,

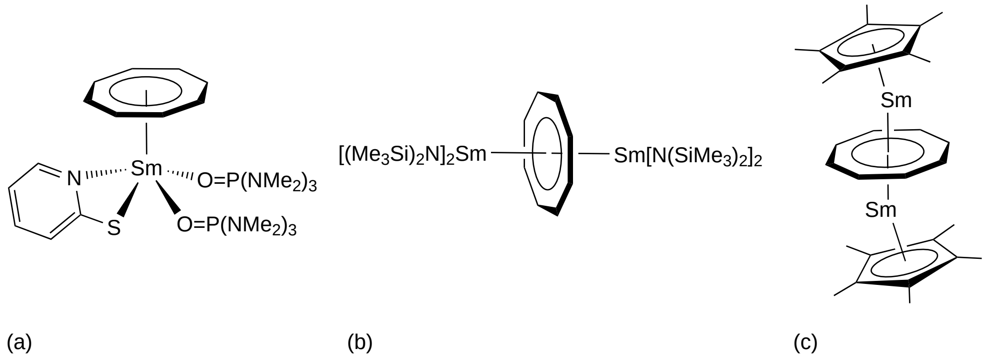

Figure 79 (a) (COT)Sm(SC$_5$H$_4$N)[OP(NMe$_2$)$_3$]$_2$, (b) [Sm{N(SiMe$_3$)$_2$}$_2$]$_2$ (μ-COT), (c) [Cp*Sm]$_2$(μ-COT)

$C_5H_2Me_4$, C_5HMe_5, C_5HMe_4Et, $C_5H_3(SiMe_3)_2$, C_5HPh_5, $C_5H_5CH_2Ph$, $C_5H_5C_5H_9$, or indene produces a number of mixed cyclopentadienyl(cyclooctatetraenyl)lanthanide complexes, such as (COT)Ln(C_5Me_4R)(THF)$_n$, (COT)Ln (Cp*), (COT)Pr(C_5Ph_5), (COT)Gd($C_6H_5CH_2C_5H_4$)(DME), [(COT)Nd(μ-η^8-COT)K(THF)(η^3-$C_6H_5CH_2$-μ^2-η^5-C_5H_4)-Nd(THF)$_2$(η^8-COT)], (COT)Ln($C_5H_9C_5H_4$)(THF)$_2$, (COT)-Gd($C_5H_9C_5H_4$)(THF), and (Ind)Ln(COT)(THF)$_2$.

Mixed chiral cyclooctatetraenyl cyclopentadienyl lanthanide complexes (COT)Sm{(*S*)-η^5:η^1-$C_5H_4CH_2CHMeO$-Me}, (COT)Ln{(*S*)-η^5:η^1-$C_5H_4CH_2CHMeNMe_2$}, (COT)-Ln{(*S*)-η^5:η^1-$C_5H_4CHPhCH_2NMe_2$} (Figure 80a), and achiral (COT)Ln(η^5:η^1-$C_5H_4CH_2CH_2NMe_2$) (Ln = Sm, Lu), which bear O- and N-donor-functionalized Cp-ligands, have been synthesized by reactions of [(COT)Ln(μ-Cl)(THF)]$_2$ (Ln = Sm, Lu) with respective cyclopentadienyl potassium salts.**[105]** Mixed COT/indenyl complexes with donor-functionalized indenyl ligands (η^5:η^1-$MeOCH_2CH_2C_9H_6$)Ln(COT)(THF)$_n$ (Figure 80b) (Ln = La, Nd, $n = 0$; Sm, Dy, Er, $n = 1$) and (η^5:η^1-$C_4H_7OCH_2C_9H_6$)-Ln(COT)(THF) (Ln = La, Nd, Sm, Dy, Er) were synthesized by the reactions of $LnCl_3$ with equimolar amounts of K_2[COT], followed by treatment with the corresponding potassium salt of ether-substituted indenide.**[106]**

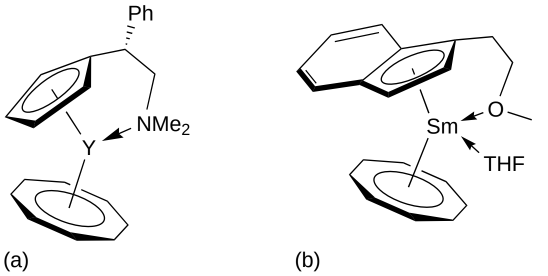

Figure 80 (a) (COT)Y{(*S*)-η^5:η^1-$C_5H_4CHPhCH_2NMe_2$}, (b) (η^5:η^1-$MeOCH_2CH_2C_9H_6$)Sm(COT)(THF)

Reactions of K[$C_5Me_4PMe_2$], Li[$C_5H_4PPh_2$], and K[$C_5Me_4PPh_2$] with [(COT)Sm(μ-Cl)(THF)$_2$]$_2$ yield a series of COT complexes (COT)Sm($C_5R_4PR'_2$)(THF)$_n$ (Figure 81a) (R = H or Me; R′ = Me or Ph; $n = 0$ or 2). They react with CpRh(CO)$_2$ affording phosphido-bridged bimetallic samarium(III)-rhodium(I) complexes (COT)Sm(μ-$C_5R_4PR'_2$)Rh(Cp)(CO) (R = H or Me; R′ = Me or Ph). 3,4-Dimethyl-2,5-bis(trimethylsilyl)phospholyl (Dsp) derivatives (COT)Sm(Dsp) and (COT)Nd(Dsp)(THF) (Figure 81b) have also been prepared.**[107]** COT/pyrolyl complexes (COT)Ln(η^5-pyr*)(THF)$_n$ (Figure 81c) (Ln = Sm, $n = 1$; Ln = Tm, Lu, $n = 0$) were prepared from [(COT)Ln(μ-Cl)(THF)]$_2$ and Na(pyr*) (pyr* = $NC_4H_2{}^tBu_2$-2,5).

Polydentate nitrogen ligands are very suited to stabilize mono(cyclooctatetraene) lanthanide(III) complexes. These include silylated benzamidinates [$RC_6H_4C(NSiMe_3)_2$]Ln-(COT)(THF) (Ln = Y, Ce, Pr, Nd, Sm, Tm, Lu; R = H, MeO, CF_3) (Figure 82a) and diiminophosphinates

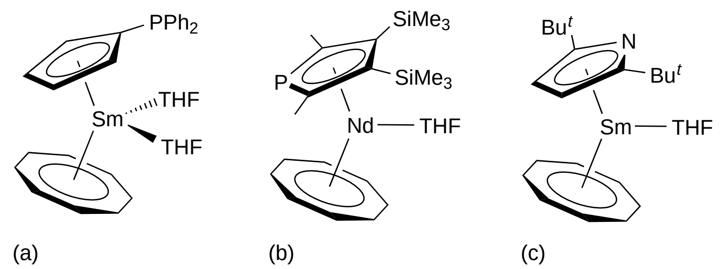

Figure 81 (a) (COT)Sm($C_5H_4PPh_2$)(THF)$_2$, (b) (COT)Nd(Dsp)(THF), (c) (COT)Sm(pyr*)(THF)

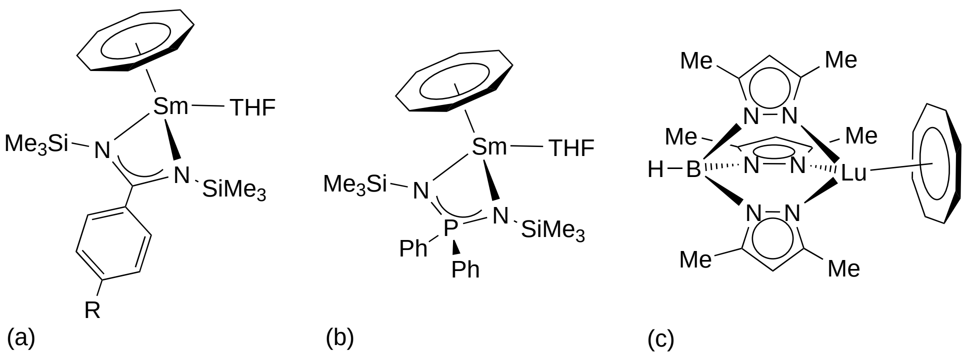

Figure 82 (a) [$RC_6H_4C(NSiMe_3)_2$]Sm(COT)(THF), (b) [$Ph_2P(NSiMe_3)_2$]Sm(COT)(THF), (c) [$HB(C_3N_2Me_2)_3$]Lu(COT)

$[Ph_2P(NSiMe_3)_2]Ln(COT)(THF)$ (Ln = Y, Ce, Pr, Nd, Sm) (Figure 82b), as well as tridentate pyrazolylborates $[HB(C_3N_2R_2)_3]Ln(COT)$ (Ln = Ce, Pr, Nd, Sm, Lu; R = H, Me) (Figure 82c).

Complexes of the type $[1,4\text{-}(Me_3Si)_2C_8H_6]Ln(DAD)$ (Ln = Sm, Yb; DAD = 1,4-diazadiene) have been prepared in a 'one-pot' reaction by treatment of elemental samarium or ytterbium with equimolar amounts of 1,4-bis(trimethylsilyl)cyclooctatriene and substituted 1,4-diazadiene ligands. ^1H and ^{171}Yb NMR data revealed that the Sm derivatives contain Sm^{3+} ions and coordinated DAD radical anions, while, in the case of Yb, the neutral DAD ligand is coordinated to divalent ytterbium. The ^{171}Yb NMR spectrum of $[1,4\text{-}(Me_3Si)_2C_8H_6]Yb[PhN{=}C(Me)C(Me){=}NPh]$ shows a single resonance at $\delta 224.3$ ppm, which is consistent with the presence of an Yb^{2+} complex. Recently a series of half-sandwich complexes containing the same ligand in combination with aminotroponiminates have been prepared and characterized (Figure 83).**108**

10.2 Bis(cyclooctatetraenyl) Complexes

Shortly after the synthesis of uranocene (*see Uranocene*), the first lanthanide complexes containing the cyclooctatetraenyl dianion, $K[Ln(COT)_2]$, have been prepared by the reaction of $K_2[COT]$ with lanthanide trichlorides (equation 21).

$$2K_2(COT) + LnCl_3 \xrightarrow[-3KCl]{solvent} [(solvent)K][Ln(\eta^8\text{-}COT)_2] \qquad (21)$$

They are thermally very robust, but decompose almost explosively upon contact with traces of oxygen. X-ray diffraction studies showed $[Li(THF)_4][Ln(COT)_2]$ (Ln = Ce, Sm) consisting of separated ions with the lithium cation being coordinated by four THF molecules. $[Na(THF)_3][Sm(COT)_2]$ (Figure 84a) forms a double sandwich with two COT ligands and the two metal ions arranged as a linear unit. A very similar molecular structure was reported for the solvated potassium salt $[K(diglyme)][Ce(COT)_2]$. The X-ray structure of $[(COT)Er(\mu\text{-}COT)K(\mu\text{-}COT)Er(\mu\text{-}COT)K(THF)_4]$ (Figure 84b) shows that the stacking of cyclooctatetraene ligands in organolanthanide complexes can be further extended.

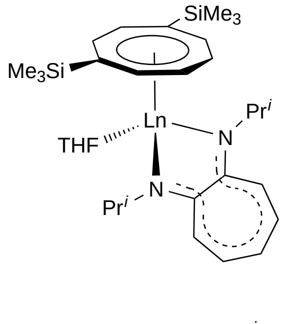

Figure 83 $[1,4\text{-}(Me_3Si)_2C_8H_6]\ Ln[C_7H_5(N^iPr)_2](THF)$

Several examples of anionic sandwich complexes containing substituted cyclooctatetraenyl ligands have been reported also, for example, $[Li(THF)_4][Ln\{1,4\text{-}(Me_3Si)_2C_8H_6\}_2]$ (Ln = Y, Ce, Pr, Nd, Sm). The very bulky 1,3,6-tris(trimethylsilyl)cyclooctatetraenyl ligand as well as functionally substituted cyclooctatetraenyl ligands $1,4\text{-}R_2C_8H_6$ ($R = o\text{-}Me_2NC_6H_4SiMe_2$) were also reported to form anionic sandwich complexes with nearly all rare earth elements. Alkali metal-free sandwich complexes $[Ln(COT)(HMPA)_n]^+[Ln(COT)_2]^-$ (Ln = La, $n = 4$; Ln = Sm, $n = 3$) were obtained by reaction of lanthanide metals with COT in the presence of a catalytic amount of iodine in THF containing HMPA. When a stoichiometric amount of iodine is used in this reaction, $[Sm(COT)(HMPA)_3]^+ (I)^-$ is isolated. Bimetallic complexes containing $[Ln(COT)_2]^-$ anions, for example, $[CoCp_2][Ce\{1,4\text{-}(Me_3Si)_2C_8H_6\}_2]$ (Figure 85a) and $[Yb(THF)_6][Ce\{1,3,6\text{-}(Me_3Si)_3C_8H_5\}_2]_2$ (Figure 85b) are also known.

11 ORGANOLANTHANIDES IN THE OXIDATION STATE 0, +1, +2 AND +4

11.1 Organolanthanides in the Oxidation State 0

There are just few examples of authentic lanthanide complexes in the oxidation state zero. Bis(arene) complexes of the lanthanides $(1,3,5\text{-}^tBu_3C_6H_3)_2Ln$ (Ln = Sc, Y, La, Nd, Pr, Sm, Gd, Tb, Dy, Ho, Er, Lu) have been synthesized by cocondensation of metal vapors (*see* ***Metal Vapor Synthesis of Transition Metal Compounds***) with 1,3,5-tri(*tert*-butyl)benzene at 75 K. A sandwich structure with coplanar arene ligands has been proven by X-ray crystal structure analysis of the Gd and Ho complexes (Figure 86a).

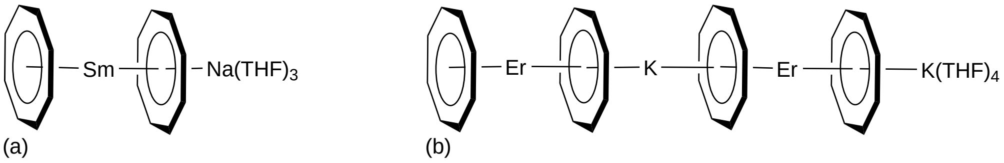

Figure 84 (a) $[Na(THF)_3][Sm(COT)_2]$, (b) $[(COT)Er(\mu\text{-}COT)K(\mu\text{-}COT)Er(\mu\text{-}COT)K(THF)_4]$

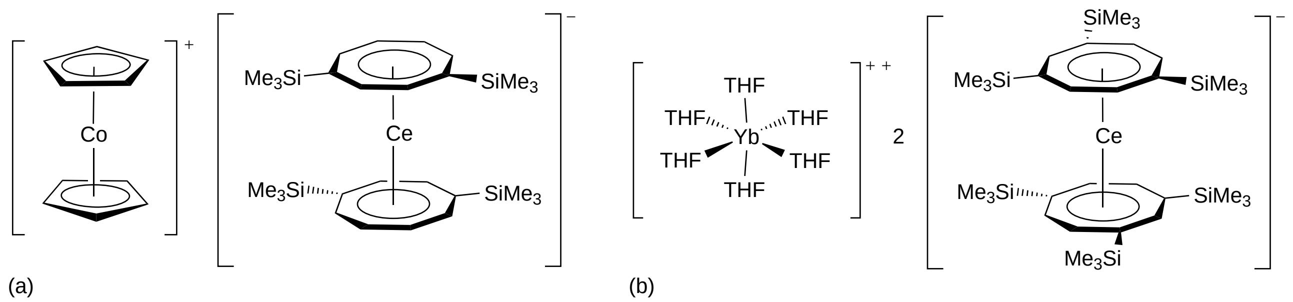

Figure 85 (a) $[\mathrm{CoCp_2}][\mathrm{Ce}\{1,4\text{-}(\mathrm{Me_3Si})_2\mathrm{C_8H_6}\}_2]$, (b) $[\mathrm{Yb(THF)_6}][\mathrm{Ce}\{1,3,6\text{-}(\mathrm{Me_3Si})_3\mathrm{C_8H_5}\}_2]_2$

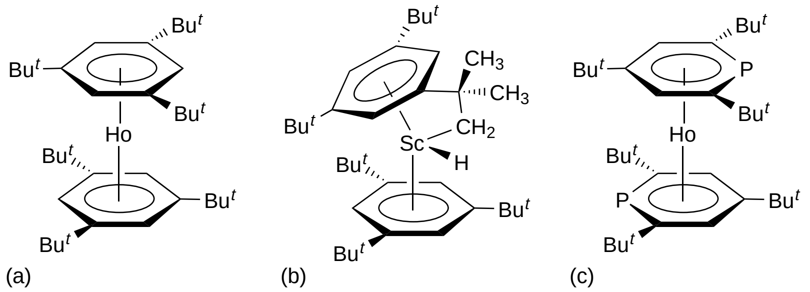

Figure 86 (a) $(^t\mathrm{Bu_3C_6H_3})_2\mathrm{Ho}$, (b) $(^t\mathrm{Bu_3C_6H_3})\mathrm{Sc(H)}[(^t\mathrm{Bu})_2(\mathrm{CMe_2CH_2})\mathrm{C_6H_3}]$, (c) $\mathrm{Ho}(\mathrm{PC_5H_2Bu}^t_3)_2$

An attempt to prepare the analogues complexes of Ce, Eu, Tm, and Yb failed, what has been explained on the basis of the difference in the promotion energy of $f^ns^2 \rightarrow f^{n-1}d^1s^2$ for different lanthanides. As in chloroaluminate lanthanide(III) complexes with neutral arene ligands, the stability of zerovalent bis(arene)lanthanides increases with increasing number and size of substituents at the aromatic ring. Cocondensation of Sc with tri-*tert*-butylbenzene results in the formation of the bis(arene)scandium complex together with $(\eta^6\text{-}^t\mathrm{Bu_3C_6H_3})\mathrm{Sc(H)}[(\eta^6{:}\eta^1\text{-}^t\mathrm{Bu})_2(\mathrm{CMe_2CH_2})\mathrm{C_6H_3}]$ (Figure 86b) via insertion of Sc into the C–H bond of one *tert*-butyl substituent. Cocondensation of Ho vapor with 2,4,6-tri-*tert*-butylphosphorin yields $\mathrm{Ho}(\eta^6\text{-}\mathrm{PC_5H_2Bu}^t_3\text{-}2,4,6)_2$ (Figure 86c), which sublimes with 90% recovery at 160°C/10^{-5} mbar.

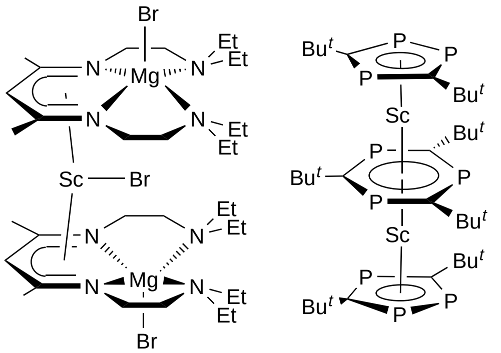

(**134**) (**135**)

Figure 87 (a) $[(\mathrm{Et_2NCH_2CH_2NCMeCHCMeNCH_2CH_2NEt_2})\mathrm{MgBr}]_2\mathrm{ScBr}$, (b) $(^t\mathrm{Bu_2C_2P_3})\mathrm{Sc}(\mu\text{-}^t\mathrm{Bu_3C_3P_3})\mathrm{Sc}(^t\mathrm{Bu_2C_2P_3})$

11.2 Organolanthanides in the Oxidation State 1

Organometallic compounds of the 4f-elements in the oxidation state +1 are not reported until now. There are only two examples of monovalent scandium complexes. Thus, the ß-diketiminato derivative of scandium, $\mathrm{LScBr_2}$ ($\mathrm{L = Et_2NCH_2CH_2NC(Me)CHC(Me)NCH_2CH_2NEt_2}$) reacts with $(\mathrm{C_3H_5})\mathrm{MgBr}$ yielding $(\mathrm{LMgBr})_2\mathrm{ScBr}$ (Figure 87a). X-ray structure, liquid and solid-state NMR, EPR-, UV-vis-spectroscopy, and magnetic measurements support a formal oxidation state of Sc(I) having no unpaired electrons.[109] Cocondensation of Sc vapor with 2,2-dimethylpropylidynephosphine, $\mathrm{Me_3CC{\equiv}P}$, affords the triple-decker sandwich complex $(\eta^5\text{-}^t\mathrm{Bu_2C_2P_3})\mathrm{Sc}(\mu\text{-}\eta^6{:}\eta^6\text{-}^t\mathrm{Bu_3C_3P_3})\mathrm{Sc}(\eta^5\text{-}^t\mathrm{Bu_2C_2P_3})$, which was characterized by X-ray crystallography (Figure 87b).

11.3 Organolanthanides in the Oxidation State 2

Organometallic compounds of the lanthanides in the oxidation state Ln(II) were first reported in the early 1980s and was limited to only Sm, Eu, and Yb. In 1997, the first divalent thulium complex (*see* ***Scandium, Yttrium & the Lanthanides: Inorganic & Coordination Chemistry***) was reported by Bochkarev *et al*. Since then, divalent Nd and Dy derivatives have been prepared and structurally characterized. The chemistry of those compounds is increasing because of their unique reactivity, which is associated with the reducing properties of the divalent lanthanide ions.

11.3.1 Divalent Alkyl Lanthanide Complexes

The reaction between LnI_2 (Ln = Eu, Yb) and $K[C(SiMe_3)_3]$ in benzene yields solvent-free monomeric $Ln[C(SiMe_3)_3]_2$. The Yb derivative reacts with Et_2O or iodomethane yielding $[Yb\{C(SiMe_3)_3\}(\mu\text{-OEt})(OEt_2)]_2$ and $[Yb\{C(SiMe_3)_3\}I]_2$, respectively, which are dimeric in the solid state. The Yb analogs of Grignard reagents, $Yb[C(SiMe_3)_2(SiMe_2X)]I(OEt_2)$ (X = Me, CH=CH_2, Ph, or OMe) were prepared from Yb metal and RI [R = $[C(SiMe_3)_2(SiMe_2X)]$, X = Me, CH=CH_2, or CH_2CH_2-OEt]. The alkylytterbium iodides crystallize from Et_2O as solvated iodide-bridged dimers in which the coordination at Yb is four when X = Me but is increased to five by chelation from the group X when X = OMe (Figure 88a). A redistribution yielding R_2Yb and YbI_2 is not observed when X = Me, but it takes place readily when X = Ph, CH=CH_2, or OMe. Reaction of $SmI_2(THF)_2$ with two equiv. of $K[C(SiMe_3)_2(SiMe_2OMe)]$ in THF results in the formation of $Sm[C(SiMe_3)_2(SiMe_2OMe)]_2(THF)$ (Figure 88b).

The ether-solvated bis(trimethylsilyl)methyl derivative $Yb\{CH(SiMe_3)_2\}_2(OEt_2)_2$ is prepared from YbI_2 and $Na[CH(SiMe_3)_2]$, the three-coordinate ytterbium(II) alkyl complex $[K(Yb\{CH(SiMe_3)_2\}_3)]_n$ from YbI_2 and three equiv. of $K[CH(SiMe_3)_2]$ in benzene, and the red *ate* complex $[Li(THF)_4][Yb\{CH(SiMe_3)_2\}_3]$ by the reaction of LiR, YbI_2, and two equiv. of $K[CH(SiMe_3)_2]$ in Et_2O in the presence of a small amount of THF. $[K(Yb\{CH(SiMe_3)_2\}_3)]_\infty$ consists in the solid state of double chains of $[(Yb\{CH(SiMe_3)_2\}_3)]^-$ anions linked by K^+ cations (Figure 89a), whereas $[Li(THF)_4][Yb\{CH(SiMe_3)_2\}_3]$ has an ionic structure with isolated $[Li(THF)_4]^+$ cations and $[Yb\{CH(SiMe_3)_2\}_3]^-$ anions (Figure 89b).**[110]** The mixed alkyl/alkoxy complexes $[Yb\{CH(SiMe_3)_2\}(OEt)(L)_n]$ (L = Et_2O, $n = 2$; L = THF, $n = 3$) were prepared from $[Yb(OEt)_2(L)_n]$ and $K[CH(SiMe_3)_2]$.

Only two crystallographically characterized aryl derivatives of divalent lanthanides are reported. Reaction of Eu

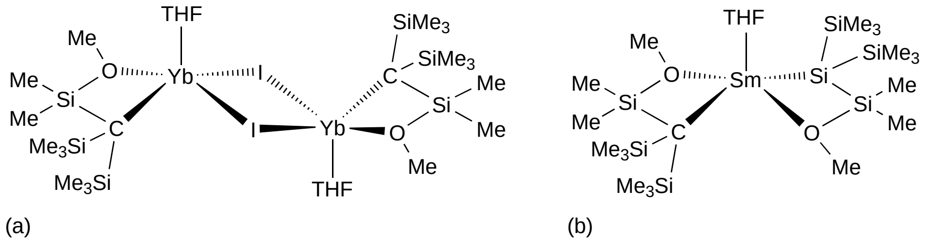
THF
Me
Me
Me
O
Si
Yb
I
C
Me3Si
Me3Si
I
Yb
THF
O
Me
SiMe3
SiMe3
C
Si
Me
Me
(a)
THF
Me
Me
Me
O
Sm
Si
C
Me3Si
Me3Si
SiMe3
SiMe3
Si
Si
Me
Me
O
Me
(b)

Figure 88 (a) $[YbC(SiMe_3)_2(SiMe_2OMe)(THF)]_2(\mu\text{-I})_2$, (b) $Sm[C(SiMe_3)_2(SiMe_2OMe)]_2(THF)$

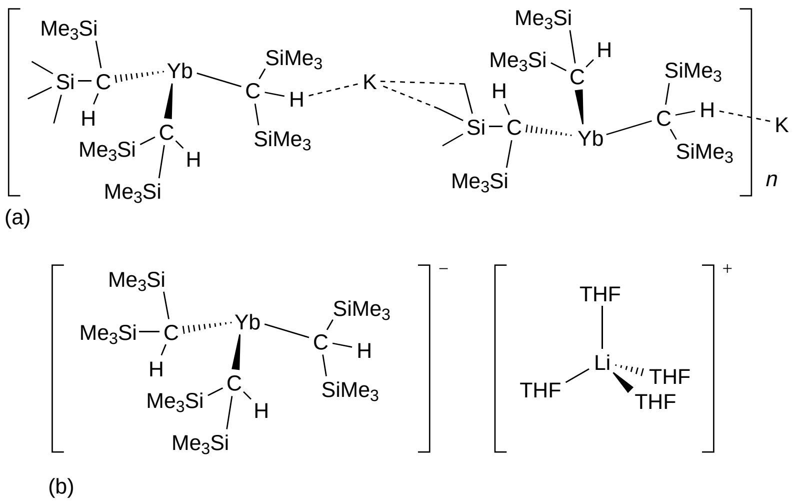
Me3Si
Si
C
H
Yb
C
Me3Si
H
Me3Si
SiMe3
C
H
SiMe3
K
Me3Si
Me3Si
H
C
H
Si
C
Yb
Me3Si
SiMe3
C
H
SiMe3
K
n
(a)
Me3Si
Me3Si
C
H
Yb
C
Me3Si
H
Me3Si
SiMe3
C
H
SiMe3
−
THF
Li
THF
THF
THF
+
(b)

Figure 89 (a) $[K(Yb\{CH(SiMe_3)_2\}_3)]_\infty$, (b) $[Li(THF)_4][Yb\{CH(SiMe_3)_2\}_3]$

metal with $Hg(C_6F_5)_2$ in THF, followed by crystallization from THF/light petroleum affords $Eu(C_6F_5)_2(THF)_5$, which reveals axial C_6F_5 and equatorial THF ligands bonded to a pentagonal-bipyramidal Eu center (Figure 90a).[111] *m*-Terphenyl derivatives $Yb(Dpp)I(THF)_3$ and $Eu(Dpp)_2(THF)_2$ ($Dpp = 2,6\text{-}Ph_2C_6H_3$) were obtained from reactions of DppI with lanthanides in THF.[112] In $Yb(Dpp)I(THF)_3$ (Figure 90b), the metal is bonded to the *ipso*-carbon atom of the terphenyl group, to the terminal iodo substituent, and to three THF molecules. $Eu(Dpp)_2(THF)_2$ shows an Eu center in a distorted tetrahedral coordination environment.

$(Ph_3Ge)_2Eu(DME)_3$ (Figure 91a) was synthesized by reacting Ph_3GeH with $C_{10}H_8$ $Eu(THF)_2$ in DME. The Eu atom is located in the center of the hexagonal bipyramid with axially positioned germyl ligands. Six oxygen atoms of the DME ligands form an equatorial plane. The interrelated stannyl derivative $(Ph_3Sn)_2Yb(THF)_4$ was prepared by reaction of Yb with either Ph_3SnCl, $PhSnCl_3$, or $Ph_3SnSnPh_3$. According to X-ray data, Sn is covalently bonded to Yb. Ph_2SnCl_2 reacts with Yb with formation of $[Yb_2Cl_2(DME)_6]^{2+}$ and $[(Ph_3Sn)_3Sn]^-$ ions (Figure 91b). In the solid state, it consists of $[(Ph_3Sn)_3Sn]^-$ anions separated by $[Yb_2Cl_2(DME)_6]^{2+}$ cations with μ_2-bridging chlorine atoms. A Sn–Sn bond formation also takes place when Sm or Yb reacts with Me_3SnCl in THF yielding $[(Me_3Sn)_3Sn]^-$ anions. However, in these cases, complexes with direct Ln–Sn bonds $[(Me_3Sn)_3Sn]_2Ln(THF)_4$ (Ln = Sm, Yb) were isolated. According to X-ray crystallography, both molecules have a distorted octahedral structure in which the central Ln (Ln = Sm, Yb) atom is bonded to four oxygen atoms of THF in equatorial positions and two tin atoms of the $(Me_3Sn)_3Sn$ groups in axial positions.

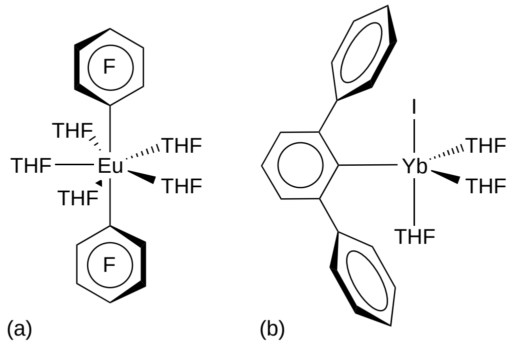

Figure 90 (a) $Eu(C_6F_5)_2(THF)_5$, (b) $Yb(Dpp)I(THF)_3$

$(Ph_3Si)_2Yb(THF)_4$ and $(Ph_3Ge)_2Yb(THF)_4$ (Figure 92a) were synthesized by reaction of Ph_3SiCl or Ph_3GeCl, respectively, with ytterbium in THF. Both compounds have octahedral structures with axial silyl and germyl groups. The reaction between YbI_2 and $K[Sn(CH_2{}^tBu)_3]$ affords diamagnetic $[({}^tBuCH_2)_3Sn]_2Yb(THF)_2$ (Figure 92b). Reaction with one equiv. of ArOH or Cp*H results in the formation of mixed-ligand complexes $(ArO)YbSn(CH_2{}^tBu)_3(THF)_2$ and $Cp^*YbSn(CH_2{}^tBu)_3(THF)_2$. $Cp^*YbSi(SiMe_3)_3(THF)_2$ was prepared by the reaction of $Cp^*_2Yb(OEt_2)$ with one equiv. of $Li[Si(SiMe_3)_3](THF)_3$ in toluene.

The reaction of $[(DME)_2YbI]_2(\mu\text{-}C_{10}H_8)$ with $PhC{\equiv}CH$ leads to the mixed iodo/ethynyl complex $[IYb(\mu\text{-}C{\equiv}CPh)(DME)_2]_2$ (Figure 93a). According to X-ray diffraction analysis, the molecule consists of two $YbI(DME)_2$ units bridged by two $C{\equiv}CPh$ groups. The central cyclic fragment Yb–C–Yb–C is planar. The homoleptic Yb(II)

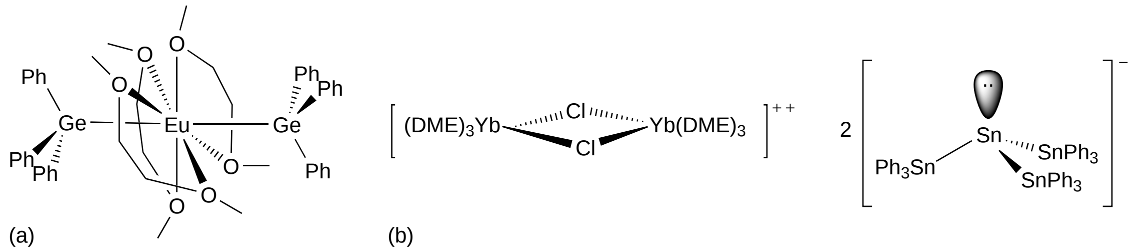

Figure 91 (a) $(Ph_3Ge)_2Eu(DME)_3$, (b) $[Yb_2Cl_2(DME)_6][(Ph_3Sn)_3Sn]_2$

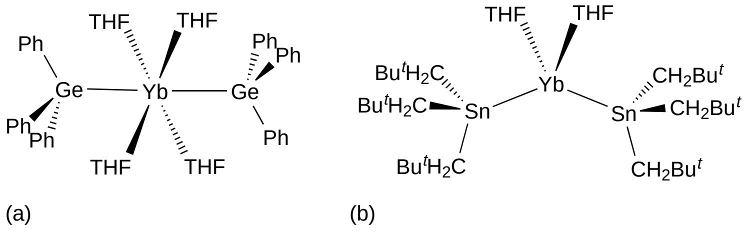

Figure 92 (a) $(Ph_3Ge)_2Yb(THF)_4$, (b) $[({}^tBuCH_2)_3Sn]_2Yb(THF)_2$

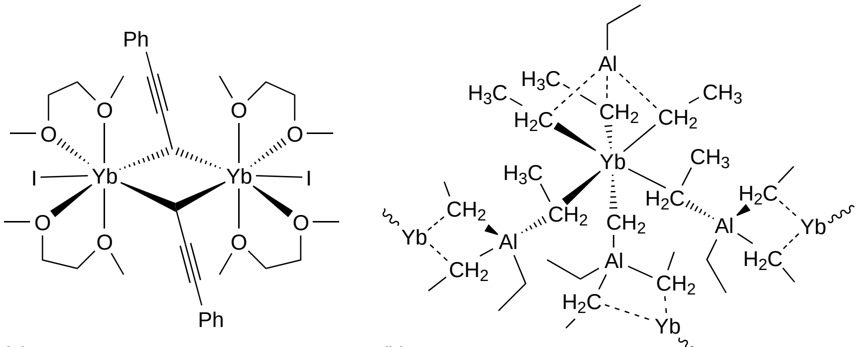

(a) (b)

Figure 93 (a) $[Yb(\mu\text{-}C{\equiv}CPh)(I)(DME)_2]_2$, (b) $\{Yb[AlEt_4]_2\}_n$

tetraalkylaluminate complexes $\{Yb[AlR_4]_2\}_n$ were obtained by silylamide elimination from $Yb[N(SiMe_3)_2]_2(THF)_2$ and excess AlR_3 (R = Me, Et, ^{i}Bu). In the solid state, $\{Yb[AlEt_4]_2\}_n$ (Figure 93b) is polymeric, constituted of $[Yb(AlEt_4)]^+$ and $[Yb(AlEt_4)_3]^-$ units, forming an intricacy three-dimensional network. Both fragments are linked by bridging α-C atoms and secondary $Yb\cdots H\text{–}C$ agostic interactions combining μ,η^1-,μ,η^2-, and μ,η^3-coordination modes that result in remarkably short $Yb\cdots Al$ (2.809 Å) and a large range of $Yb\cdots C$ (2.649-3.364 Å) distances.[113] The alkylaluminum adducts $Yb[N(SiMe_3)_2]_2(AlR_3)_2$ were prepared from $Yb[N(SiMe_3)_2]_2$ and AlR_3 (R = Me, Et).

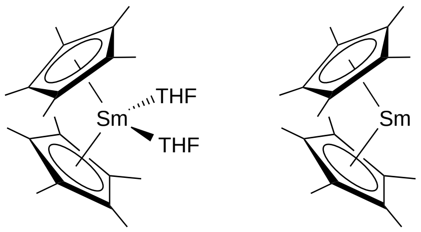

(a) (b)

Figure 94 (a) $Cp^*{}_2Sm(THF)_2$, (b) $Cp^*{}_2Sm$

11.3.2 *Divalent Lanthanidocenes and Related Compounds*

A variety of cyclopentadienyl, indenyl, fluorenyl, and other related ligands have been used for the synthesis of divalent lanthanidocenes. Most of the synthetic approaches employ metathetical reactions between lanthanide salts and alkali or alkaline-earth metal salts of the ligands. Till recently, only Ln(II) complexes have been known for Sm, Eu, and Yb.[114] However, the synthetic routes using lanthanide metals are also known. Europium and ytterbium metal dissolved in liquid ammonia react with Cp*H affording $Cp^*{}_2Ln(NH_3)(THF)$ (Ln = Eu, Yb). Transmetallation of $Tl(C_5D_5)$ or $(C_5H_4PPh_2)Tl$ with Yb metal in DME yields $(C_5D_5)_2Yb(DME)$ and $[(C_5H_4PPh_2)_2Yb(DME)]$, respectively. Diethylene glycol dimethyl ether (DIME) adducts $[(C_5H_4PPh_2)_2Eu(DIME)]$ and $[(C_5H_4PPh_2)_2Yb(DIME)]$ have been prepared analogously in THF, followed by crystallization from DME/DIME.

SmI_2 reacts with one or two equiv. of Cp*K in THF yielding $[Cp^*Sm(\mu\text{-}I)(THF)_2]_2$ and $Cp^*{}_2Sm(THF)_2$, respectively. $Cp^*{}_2Sm(THF)_2$ shows a bent metallocene (*see Bent Metallocenes*) structure in which the two Cp* ring centroids and the two oxygen atoms of the THF ligands (Figure 94a) are arranged roughly tetrahedral around Sm. $Cp^*{}_2Sm(THF)_2$ can be dissolvated at 75°C under high vacuum or under reflux in toluene to form $Cp^*{}_2Sm$, which was the first reported solvent-free bis(cyclopentadienyl) compound of Ln(II). Even in the absence of coordinating solvent molecules it has a bent structure (Figure 94b).

Bis(dihydropyran) and mono(tetrahydropyran) solvates of $Cp^*{}_2Sm$ have been prepared by displacing THF from $Cp^*{}_2Sm(THF)_2\cdot$ and $Cp^*{}_2Sm(DME)$ has been obtained as green crystals by the reaction of $SmCl_2$ with NaCp* in DME.

The reaction of LnI_2 with $Na(C_5Me_4{}^iPr)$ in THF yields $(C_5Me_4{}^iPr)_2Ln(THF)$ (Ln = Sm, Yb); base-free ytterbocenes $Cp^*{}_2Yb$, $(C_5HMe_4)_2Yb$, and $(C_5H_3{}^tBu_2)_2$-Yb have been prepared by refluxing their Et_2O adducts in toluene,[115] as well as bis(substituted cyclopentadienyl)lanthanide(II) complexes $[(Me_3Si)_2CHC_5H_4]_2Ln(THF)_2$ (Ln = Sm, Eu, Yb), $(Me_2{}^tBuSiC_5H_4)_2Yb(THF)_2$, $(\{Me_2{}^tBuSi\}_2C_5H_3)_2Ln(THF)_2$ (Ln = Sm, Yb), $[(Me_3Si)_2CHC_5H_4]_2Ln$ (Ln = Sm, Eu, Yb), $(Me_2{}^tBuSiC_5H_4)_2Yb$, $(\{Me_2{}^tBuSi\}_2C_5H_3)_2Ln$ (Ln = Sm, Yb), and $Me_2Si(C_5H_3CH\{SiMe_3\}_2)_2Yb(THF)_2$ were synthesized from the appropriate LnI_2 with the respective Na or K cyclopentadienide.[116] Other solvent stabilized lanthanidocenes are $(C_5H_3{}^tBu_2)_2Yb(OEt_2)$, $(C_5H_3{}^tBu_2)_2Sm(DME)$, $(C_5H_3{}^tBu_2)_2Yb(DME)$, and $(C_5H_2{}^tBu_3)_2Ln(L)$ (Ln = Sm, L = THF; Ln = Sm, Yb, L = 2, 6-$Me_2C_6H_3NC$).[117] Octa-isopropyllanthanidocenes, as well as hexa-*tert*-butyllanthanidocenes of Sm, Eu, and Yb show no tendency towards coordination of donor solvent molecules or alkali salts. Deca-isopropyllanthanidocenes have

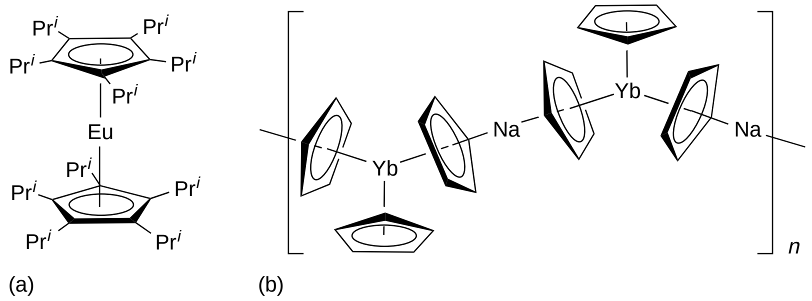

Figure 95 (a) $(C_5{}^iPr_5)_2Eu$, (b) $Na^+[YbCp_3]^-$

been synthesized from Sm, Eu, and Yb and free pentaisopropylcyclopentadienyl radicals (equation 22). The hexa-, octa-, and deca-isopropyleuropocenes show fluorescence in daylight or under UV irradiation. Crystals of $(C_5H_2{}^iPr_3)_2Eu$ and $(C_5H{}^iPr_4)_2Eu$ show bent-sandwich complexes, whereas $(C_5{}^iPr_5)_2Eu$ has an axial symmetry with parallel five-membered rings (Figure 95a).[118] Reduction of Cp_3Yb with $Na^+[C_{10}H_8]^-$ in THF yields $Na^+[YbCp_3]^-$ as a three-dimensional polymer in which μ-η^5:η^5-Cp groups link sodium and ytterbium (Figure 95b).

$$2[C_5(Pr^i)_5]^{\cdot} + Ln \xrightarrow{THF} [C_5(Pr^i)_5]_2Ln \qquad (22)$$

$$Ln = Sm, Eu, Yb$$

Coordinated THF in bis(cyclopentadienyl)lanthanides(II) can be replaced by so-called *Wanzlick-Arduengo carbenes*. $Cp^*{}_2Sm(THF)_2$ reacts with 1,3-diisopropyl-4,5-dimethylimidazoline-2-ylidene, $(C_3N_2Me_2{}^iPr_2)$, or 1,3,4,5-tetramethylimidazolin-2-ylidene, $(C_3N_2Me_4)$, in toluene with formation of $Cp^*{}_2Sm(C_3N_2Me_2{}^iPr_2)$ (Figure 96a),[119] and $Cp^*{}_2Sm(C_3N_2Me_4)_2$, respectively. Related 1,3-dimethylimidazoline-2-ylidene, $(C_3N_2H_2Me_2)$, adducts of divalent lanthanidocenes $(C_5Me_4Et)_2Ln(C_3N_2H_2Me_2)$ (Ln = Sm, Yb), $Cp^*{}_2Yb(C_3N_2H_2Me_2)$ and $(C_5H_3{}^tBu_2)_2Yb(C_3N_2H_2Me_2)$ were prepared analogously. The analogous silylene complex $Cp^*{}_2Sm[SiN{}^tBuCHCHN{}^tBu]$ has been synthesized by reaction of $Cp^*{}_2Sm$ with 1,3-di-*tert*-butyl-2,3-dihydro-1H-1,3,2-diazasilol-2-ylidene in toluene. The silylene ligand is located asymmetrically in the metallocene wedge with one ^{t}Bu group much closer to the metal than the other one (Figure 96b).[120]

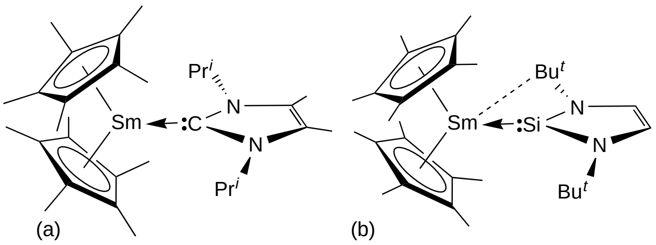

Figure 96 (a) $Cp^*{}_2Sm(C_3N_2Me_2{}^iPr_2)$, (b) $Cp^*{}_2Sm[SiN{}^tBuCH\text{-}CHN{}^tBu]$

Several heterometallic lanthanide(II)/transition metal complexes have been synthesized. $(THF)_2Yb(C_5H_4PPh_2)_2$-$PtMe_2$ was prepared by the reaction of $(C_5H_4PPh_2)_2Yb(THF)$ with (*cis*,*cis*-1,5-cyclooctadiene)dimethylplatinum in toluene. Similar reaction with $W(CO)_6$ in THF yields $[(THF)_3Yb(C_5H_4PPh_2)_2W(CO)_4]$, while $[(THF)Yb(C_5H_4$-$PPh_2)_2(\mu\text{-}OC)W(CO)_3]$ (Figure 97a) is obtained in toluene. In both molecules, the $(\eta^5\text{-}C_5H_4PPh_2)_2Yb$ units are bonded to W through the P atoms giving an octahedral *cis*-$W(CO)_4P_2$ arrangement. An isocarbonyl linkage (W–C=O–Yb) is found in $[(THF)Yb(C_5H_4PPh_2)_2(\mu\text{-}OC)W(CO)_3]$.[121] The reaction of $Cp^*{}_2Yb$ with $(dippe)PtMe_2$ (dippe = $^iPr_2P(CH_2)_2P{}^iPr_2$) results in the formation of $(dippe)Pt(\mu\text{-}Me)_2YbCp^*{}_2$ with

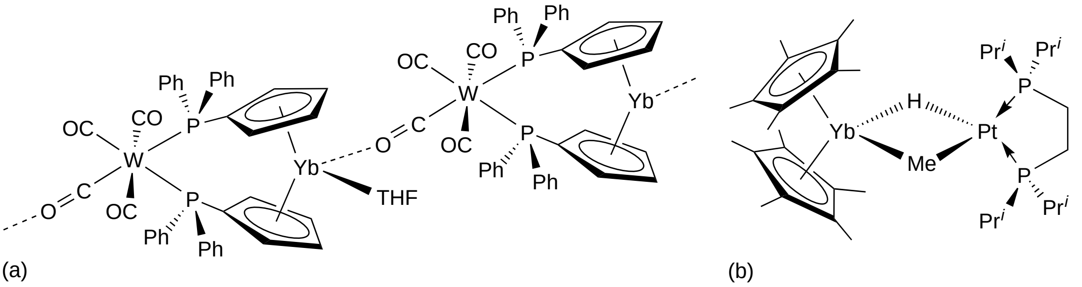

Figure 97 (a) $[(THF)Yb(C_5H_4PPh_2)_2(\mu\text{-}OC)W(CO)_3]$, (b) $(dippe)Pt(\mu\text{-}Me)(\mu\text{-}H)YbCp^*{}_2$

two Me groups bridging Pt and Yb. The solid-state structure of the adduct (dippe)Pt(μ-Me)(μ-H)YbCp*$_2$ (Figure 97b), which has been prepared analogously, showed an asymmetric (μ-Me)(μ-H) bridge between both metal atoms.

Mixed-ligand complexes CpLnCp$'$ are also known, for example, [$C_5H_2(SiMe_3)_3$][$C_5H_3(SiMe_3)_2$]Sm(THF) and ($C_5H_3{}^tBu_2$)(Cp*)Yb(THF) as bent sandwiches.

Reduction of dimethylfulvene with activated Sm or Yb in THF results in the formation of *ansa*-lanthanidocene complexes $Me_2C(C_5H_4)_2Ln(THF)_2$ (equation 23) and [($C_5H_2{}^tBu_2$-$C_5H_2{}^tBu_2$)Yb(THF)]$_2$ (Figure 98), and the analogous Sm derivative are formed by an electron-transfer reaction of Yb and Sm powder with tetra(*tert*-butyl)pentafulvalene in the presence of $HgCl_2$ in THF.

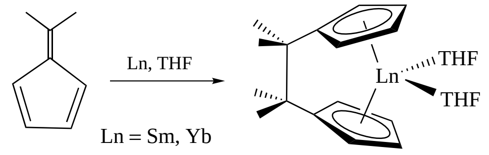
Ln, THF
Ln = Sm, Yb
Ln
THF
THF

(23)

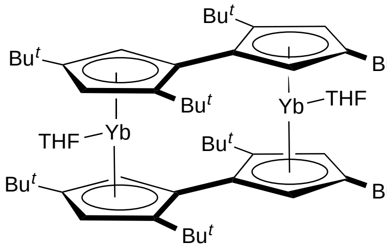
Bu^t
Bu^t
Bu^t
Bu^t
Yb
THF
THF
Yb
Bu^t
Bu^t
Bu^t
Bu^t

Figure 98 [($C_5H_2{}^tBu_2$-$C_5H_2{}^tBu_2$)Yb(THF)]$_2$

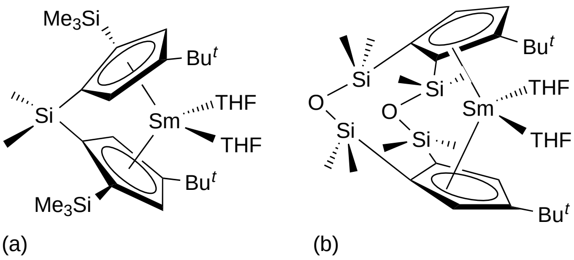
Me$_3$Si
Bu^t
Si
Sm
THF
THF
Bu^t
Me$_3$Si
(a)
Bu^t
Si
O
Si
O
Si
Si
Sm
THF
THF
Bu^t
(b)

Figure 99 (a) $Me_2Si(2\text{-}Me_3Si\text{-}4\text{-}{}^tBuC_5H_2)_2Sm(THF)_2$, (b) [1,2-$(Me_2SiOSiMe_2)_2$](3-^{t}BuC$_5H_2$)$_2$Sm(THF)$_2$

ansa-Metallocene complexes with oxygen bridged Cp ligands $O(CH_2CH_2C_5H_4)_2Ln(THF)_2$ (Ln = Sm, Yb) were synthesized by reduction of $O(CH_2CH_2C_5H_4)_2LnCl$ with Na metal in THF. Divalent samarium complexes with variously substituted Me_2Si-bridged *ansa*-bis(cyclopentadienyl) ligands were prepared and structurally characterized, for example, *rac*-$Me_2Si(2\text{-}Me_3Si\text{-}4\text{-}{}^tBuC_5H_2)_2Sm(THF)_2$ (Figure 99a), *rac*-$Me_2Si(2\text{-}Me_3Si\text{-}4\text{-}{}^tBuMe_2SiC_5H_2)_2Sm(THF)_2$, *meso*-[1,2-$(Me_2Si)(Me_2SiOSiMe_2)$](3-^{t}BuC$_5H_2$)$_2$Sm(THF)$_2$, and the C_{2v} symmetric [1,2-$(Me_2SiOSiMe_2)_2$](3-^{t}BuC$_5$H$_2$)$_2$Sm(THF)$_2$ (Figure 99b). They show high activity for the polymerization of ethylene and 1-olefins such as 1-pentene and 1-hexene. *rac*-$Me_2Si(2\text{-}Me_3Si\text{-}4\text{-}{}^tBuMe_2SiC_5H_2)_2Sm(THF)_2$ induces the cyclopolymerization of 1,5-hexadiene yielding poly(methylene-1,3-cyclopentane).

The X-ray crystal structure of [Cp*Sm(μ-I)(THF)$_2$]$_2$ shows two Cp*Sm(THF)$_2$ moieties bridged by iodine via a planar $Sm_2(\mu\text{-}I)_2$ unit, with the Cp* ring on one side of the plane and the THF molecules on the other one. The reaction of YbI_2 with two equiv. of Na[$C_5H_3(SiMe_3)_2$] in boiling toluene gives Na{[$C_5H_3(SiMe_3)_2$]$_2$Yb}$_2$(μ-I) (Figure 100a), containing an iodine bridged anion [{$C_5H_3(SiMe_3)_2$}$_2$Yb–I–Yb{$C_5H_3(SiMe_3)_2$}$_2$]$^-$. An unusual cyclic hexanuclear

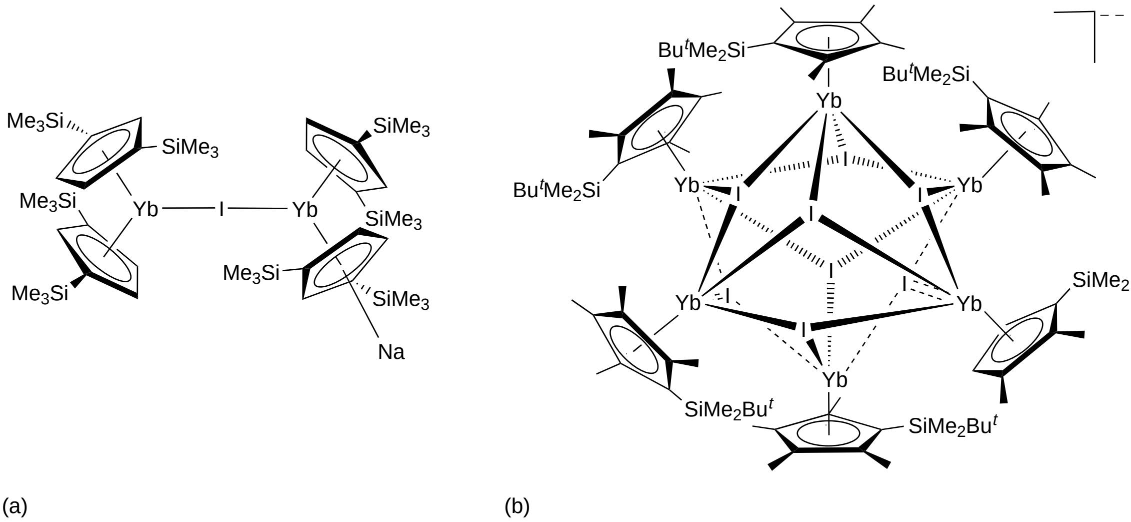
Me$_3$Si
SiMe$_3$
Me$_3$Si
Yb
I
Yb
SiMe$_3$
SiMe$_3$
Me$_3$Si
Me$_3$Si
SiMe$_3$
Na
(a)
Bu^{t}Me$_2$Si
Bu^{t}Me$_2$Si
Bu^{t}Me$_2$Si
Yb
Yb
Yb
I
I
I
I
I
I
I
I
Yb
Yb
Yb
SiMe$_2$Bu^t
SiMe$_2$Bu^t
SiMe$_2$Bu^t
2−
(b)

Figure 100 (a) Na{[$C_5H_3(SiMe_3)_2$]$_2$Yb}$_2$(μ-I), (b) [$Yb_6\{C_5Me_4(SiMe_2Bu^t)\}_6I_8$]$^{2-}$

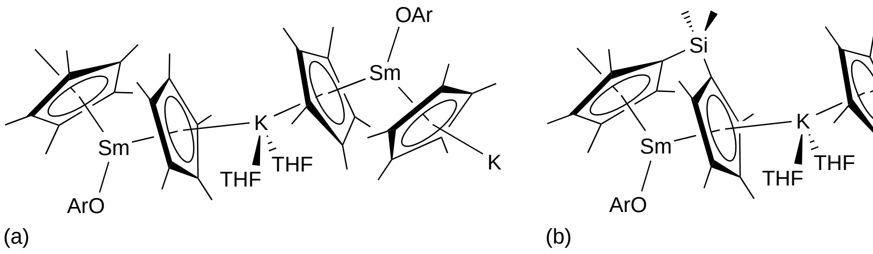

Figure 101 (a) $[Cp^{*}Sm(OAr)(\mu\text{-}Cp^{*})K(THF)_2]_\infty$, (b) $[Me_2Si(C_5Me_4)(\mu\text{-}C_5Me_4)K(THF)_2Sm(OAr)]_\infty$

Yb(II) octaiodo dianion $[Yb_6(\eta^5\text{-}Cp')_6I_8]^{2-}$ has been prepared by reaction of one equivalent of LiCp′ [Cp′ = $C_5Me_4(SiMe_2Bu^t)$] with YbI_2 (Figure 100b).

Reaction of $Cp^{*}_2Sm(THF)_2$ with one equiv. of ArOH (Ar = $C_6H_2{}^tBu_2$-2,6-R-4, R = H, Me, ^{t}Bu) produces unsolvated dimeric Sm(II) complexes $[Cp^{*}Sm(\mu\text{-}OAr)]_2$. Addition of four equiv. of HMPA to a THF solution of those complexes affords the corresponding HMPA-coordinated monomeric complexes $Cp^{*}Sm(OAr)(HMPA)_2$. The reaction with two equiv. of KCp* in THF yields polymeric Sm(II) complexes $[Cp^{*}Sm(OAr)(\mu\text{-}\eta^5\text{-}Cp^{*})K(THF)_2]_\infty$ (Figure 101a) in which the '$Cp^{*}K(THF)_2$' unit acts as a neutral coordinating ligand. Analogous complexes $[Cp^{*}Sm(XR)(\mu\text{-}Cp^{*})K(THF)_n]_\infty$ ($n = 1$ or 2; XR = $OC_6H_3{}^iPr_2$-2,6, $SC_6H_2{}^iPr_3$-2,4,6, $NHC_6H_2{}^tBu_3$-2,4,6, or $N(SiMe_3)_2$) have been synthesized in the same manner from $Cp^{*}_2Sm(THF)_2$ and KXR. Using $NaN(SiMe_3)_2$ instead of $KN(SiMe_3)_2$ affords the '$C_5Me_5Na(THF)_3$'-coordinated, 'monomeric' Ln(II) complexes $Cp^{*}Ln(N(SiMe_3)_2)(\mu\text{-}Cp^{*})\text{-}Na(THF)_3$ (Ln = Sm, Yb). The reaction of $Me_2Si(C_5Me_4)_2\text{-}Sm(THF)_2$ with one equiv. of KOAr in THF yields $[Me_2\text{-}Si(C_5Me_4)(\mu\text{-}C_5Me_4)K(THF)_nSm(OAr)]_\infty$ (Figure 101b) (Ar = $C_6H_2{}^tBu_2$-2,6-Me-4, $n = 2$; or $C_6H_3{}^tBu_2$-2,6, $n = 1$), which can be viewed as a C_5Me_4/OAr-ligated Sm(II) species coordinated by the silyl-linked neutral 'C_5Me_4K' ligand.

Reaction of $[Cp^{*}_2Yb(\mu\text{-}I)(THF)_2]_2$ with $K[N(SiMe_3)_2]$ generates $Cp^{*}Yb[N(SiMe_3)_2](THF)_2$ that crystallizes from toluene with a distorted piano stool (*see Piano Stool Structure*) geometry**[122]** and addition of $LnI_2(THF)_2$ (Ln = Sm, Yb) to $[Me_2Si(tacn)C_5Me_4]K$ (tacn = 1,4-diisopropyl-1,4,7-triazacyclononane) in THF yields monomeric solvent-free $[Me_2Si(tacn)C_5Me_4]SmI$ and $[Me_2Si(tacn)C_5Me_4]YbI$, in which all three N atoms of the triazacycle are coordinated to the metal (Figure 102).**[123]**

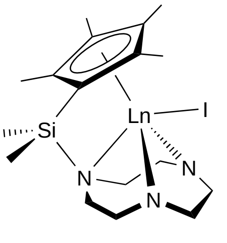

Figure 102 $[Me_2Si(tacn)C_5Me_4]LnI$

Structurally related Ln(II) alkyl complexes $[Cp^{*}Ln(CH(SiMe_3)_2)Cp^{*}K(THF)_2]_\infty$ (Ln = Sm, Eu, Yb) were prepared by reactions of $Cp^{*}_2Ln(THF)_2$ with one equiv. of $K[CH(SiMe_3)_2]$ in THF. In the presence of $PhSiH_3$, $[Cp^{*}Ln(SiH_3)Cp^{*}K(THF)_2]_\infty$ (Ln = Sm, Eu, Yb) are also isolated. $[Cp^{*}Sm(CH(SiMe_3)_2)Cp^{*}K(THF)_2]_\infty$ catalyzes the polymerization of ethylene and styrene.**[124]** Cp^{*}_2Yb can coordinate saturated hydrocarbons as in $Cp^{*}_2Yb(\mu\text{-}Me)BeCp^{*}$ (Figure 103a). The positions of the hydrogens on the bridging methyl group show that this is not a methyl bridge having a three-center-two-electron bond between Yb−C−Be. In contrast, trialkylaluminum forms Sm(III) complexes, for example, $[(C_5Me_4Et)_2Sm(\mu\text{-}Me)_2AlMe_2]_2$ (Figure 103b) in which Sm and Al are bridged by Sm–Me–Al three-center-two-electron bonds.

The use of crown ethers (*see Crown Ethers*) in organolanthanide chemistry often results in formation of solvent

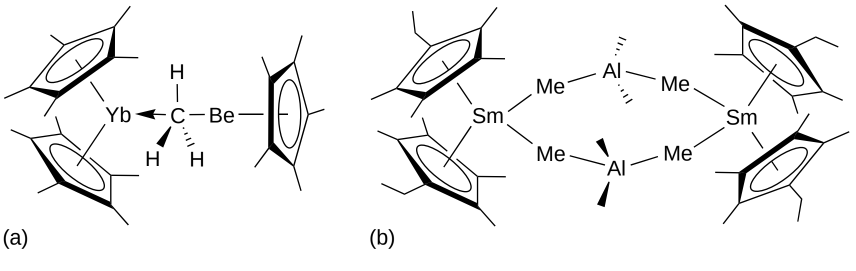

Figure 103 (a) $Cp^{*}_2Yb(\mu\text{-}Me)BeCp^{*}$, (b) $[(C_5Me_4Et)_2Sm(\mu\text{-}Me)_2AlMe_2]_2$

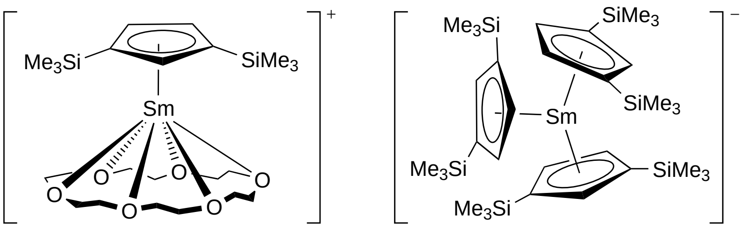

Figure 104 $[\{C_5H_3(SiMe_3)_2\}Sm([18]\text{-crown-6})][Sm\{C_5H_3(SiMe_3)_2\}_3]$

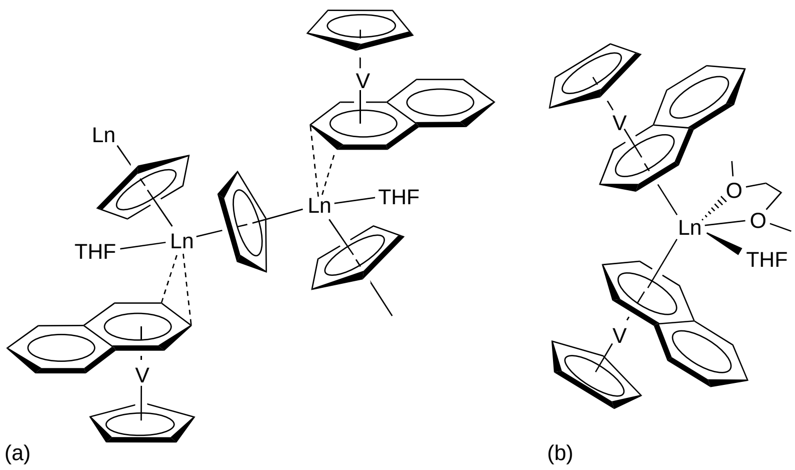

Figure 105 (a) $[CpV(C_{10}H_8)Ln(\mu\text{-}Cp)(THF)]_\infty$, (b) $[CpV(C_{10}H_8)]_2Ln(THF)(DME)$

separated ion pairs, like by treatment of $Ln[C_5H_3(SiMe_3)_2]_2$ ($Ln = Sm$, Yb) with [18]-crown-6 in benzene, yielding $[\{C_5H_3(SiMe_3)_2\}Sm([18]\text{-crown-6})][Sm\{C_5H_3(SiMe_3)_2\}_3]$ (Figure 104) and $[\{C_5H_3(SiMe_3)_2\}Yb([18]\text{-crown-6})][C_5H_3(SiMe_3)_2]$. Reduction of $[\{C_5H_3(SiMe_3)_2\}Sm([18]\text{-crown-6})][Sm\{C_5H_3(SiMe_3)_2\}_3]$ with K in toluene affords $[K([18]\text{-crown-6})(\eta^2\text{-}PhMe)_2][Sm\{C_5H_3(SiMe_3)_2\}_3]$.

Reduction of Cp_2V with an excess of $(C_{10}H_8)Yb(THF)_2$ in THF generates polymeric two-dimensional multidecker complexes $[CpV(C_{10}H_8)Ln(\mu\text{-}Cp)(THF)]_\infty$, which are also formed from the reaction of $YbI_2(THF)_2$ with an equimolar mixture of KCp and $K[CpV(C_{10}H_8)]$ in THF. The analogous Eu derivative has been prepared similarly using EuI_2. The crystals consist of infinite zigzag chains formed by $(\eta^5\text{-}Cp)Ln$ ($Ln = Eu$, Yb) moieties. Each Ln atom is η^2 coordinated by $(\eta^5\text{-}Cp)V(\eta^6\text{-}C_{10}H_8)$ anions via naphthalene (Figure 105a). Reaction of LnI_2 ($Ln = Eu$, Sm) with an equimolar mixture of KCp and $K[CpV(C_{10}H_8)]$ in DME forms bimetallic complexes $[CpV(C_{10}H_8)]_2Ln(THF)(DME)$ ($Ln = Eu$, Sm) containing $CpV(C_{10}H_8)$ units η^6-bonded to the lanthanide (Figure 105b).

A number of mono- and bis(cyclopentadienyl)lanthanide(II) complexes with donor-functionalized Cp ligands has been reported. $(MeOCH_2CH_2C_5H_4)_2Sm$ and $(MeOCH_2CH_2C_5H_4)_2Yb$ were synthesized by the reaction of $K[C_5H_4CH_2CH_2OMe)]$ with LnI_2 ($Ln = Sm$, Yb). Recrystallization of the Yb complex from THF produces the solvated $(MeOCH_2CH_2C_5H_4)_2Yb(THF)$ with coordination number 9 at Yb. Optically active metallocene complexes of Sm(II) and Yb(II) containing cyclopentadienyl systems with chiral N- or O-substituted side chains as ligands are available by reaction of the Na or K salts of the ligands with LnI_2, for example, $[Ln\{(S)\text{-}\eta^5{:}\eta^1\text{-}C_5H_4(CH_2CHROMe)\}_2]$ ($R = Me$, Ph; $Ln = Sm$, Yb), $[Ln\{(S)\text{-}\eta^5{:}\eta^1\text{-}C_5H_4(CH_2CHMeNMe_2)\}_2]$ ($Ln = Sm$, Yb) (Figure 106a), $[Ln\{(S)\text{-}\eta^5{:}\eta^1\text{-}C_5H_4(CHPhCH_2NMe_2)\}_2]$ ($Ln = Sm$, Yb), $[C_5H_4(CMe_2CH_2C_5H_4N\text{-}2)]_2Yb$, and $[C_5H_3(SiMe_3)(CMe_2CH_2C_5H_4N\text{-}2)\text{-}3]_2Yb$ (Figure 106b).

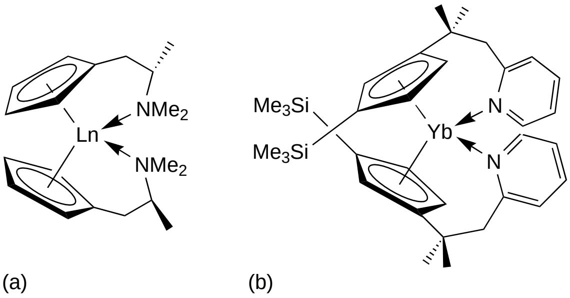

Figure 106 (a) $[Ln(S)\text{-}\eta^5{:}\eta^1\text{-}C_5H_4(CH_2CHMeNMe_2)\}_2]$, (b) $[C_5H_3(SiMe_3)(CMe_2CH_2C_5H_4N\text{-}2)\text{-}3]_2Yb$

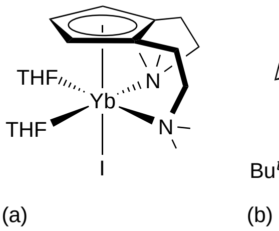

Figure 107 (a) $(C_5H_3(CH_2CH_2NMe_2)_2$-1,2)YbI(THF)$_2$, (b) $(C_5H_3(CH_2CH_2NMe_2)_2$-1,2)Yb($C_5H_4{}^t$Bu)

Analogous reactions of a mixture of the potassium salts of 1,2- and 1.3-bis[(dimethylamino)ethyl]cyclopentadiene with equimolar amounts of YbI_2 in THF allows only the isolation of crystalline (η^5:η^1:η^1-$C_5H_3(CH_2CH_2NMe_2)_2$-1,2)YbI(THF)$_2$ (Figure 107a). The reaction of this half-sandwich complex with KCp* and $NaC_5H_4{}^t$Bu results in the formation of (η^5:η^1:η^1-$C_5H_3(CH_2CH_2NMe_2)_2$-1,2)Yb(η^5-$C_5H_4{}^t$Bu) (Figure 107b) and (η^5:η^1:η^1-C_5H_3-$(CH_2CH_2NMe_2)_2$-1,2)Yb(Cp*) respectively.[83]

Linked cyclopentadienyl-anilido or amido lanthanide(II) complexes $Me_2Si(C_5Me_4)$(NPh)Ln(THF)$_n$ (Ln = Yb, $n = 3$; Ln = Sm, $n = 0$–1) are prepared from Ln[N(SiMe$_3$)$_2$]$_2$-(THF)$_2$ with 1 equiv. of $(C_5Me_4H)SiMe_2NHPh$. Recrystallization of $Me_2Si(C_5Me_4)$(NPh)Yb(THF)$_3$ from toluene/hexane yields [$Me_2Si(C_5Me_4)$(NPh)Yb(THF)]$_2$ as a dimer through an ‘intermolecular’ Yb–Ph π-interaction (Figure 108a). $Me_2Si(C_5Me_4)$(NPh)Yb(THF)$_3$ is oxidized in the presence of azobenzene or fluorenone yielding the Yb(III) complexes $Me_2Si(C_5Me_4)$(NPh)Yb(THF)(μ_2-η^2:η^3-N_2Ph_2)Yb(NPh)(C_5Me_4)SiMe$_2$ and $Me_2Si(C_5Me_4)$-(NPh)Yb(THF)$_2$($OC_{13}H_8$) respectively.[125] A tetranuclear Yb(II) complex with both alkoxy and ether functionalities in the Cp side chain {[(η^5-C_5H_4)CH_2CH(μ^3:η^1-O)$CH_2O{}^n$Bu]Yb}$_4$ was synthesized by the reaction of the potassium salt of the corresponding ligand and YbI_2(THF)$_2$. Redox transmetallation reaction of this complex with Me_2Hg yields the Yb(III) complex [(η^5-C_5H_4)CH_2CH(η^1-O)$CH_2O{}^n$Bu]YbMe(THF).[126] The dimeric Yb(II) half-sandwich complex [{(η^5-C_5Me_4)SiMe$_2$OSiMe$_2$(η^1-O)}-Yb(THF)]$_2$ (Figure 108b) containing the heterobifunctional tetramethylcyclopentadienyl-silanolate ligand has also been reported.

Half-sandwich (*see Half-sandwich Complexes*) indenyl complexes of Yb(II) have been prepared by reaction of (μ-$C_{10}H_8$)[YbI(DME)$_2$]$_2$ with indene. (Ind)YbI(DME)$_2$, is a monomer in the solid state and stable in DME solution, although it disproportionates in THF yielding (Ind)$_2$Yb(THF)$_2$ and YbI_2(THF)$_2$.[127] The reaction of samarium diiodide with potassium indenide and potassium fluorenide results in the formation of (Ind)$_2$Sm(THF)$_3$ (Figure 109a) and (Flu)$_2$Sm(THF)$_2$ (Figure 109b), respectively. Structural data indicate that, in both compounds, Sm has a more open coordination sphere compared to Cp*$_2$Sm(THF)$_2$.

ansa-Bis(indenyl) complexes (LCH_2CH_2L)Yb(THF)$_2$ (Figure 110a) (L = 1-indenyl and 4,7-dimethylindenyl) have been prepared from (LCH_2CH_2L)Li$_2$ and $YbCl_3$ in Et_2O with subsequent reduction by Na metal in THF. Solvent-free racemic bis(1-(2-dimethylaminoethyl)indenyl) complexes, $(Me_2NCH_2CH_2C_9H_6)_2$Sm and $(Me_2NCH_2CH_2C_9H_6)_2$Yb, (Figure 110b) have been synthesized by the reaction of $(Me_2NCH_2CH_2C_9H_6)$K with LnI_2 (Ln = Sm, Yb). The nitrogen atoms of both dimethylaminoethyl groups coordinate intramolecularly to Yb.

Fluorenyl complexes of divalent ytterbium [(Flu)$_2$Yb(L)$_n$] (Figure 111a) (L = THF, $n = 2$; L = DME, $n = 1$; L = ^{t}BuNCHCHN^{t}Bu, $n = 1$) have been prepared by reaction of YbI_2(THF)$_2$ with two equiv. of KFlu as well as

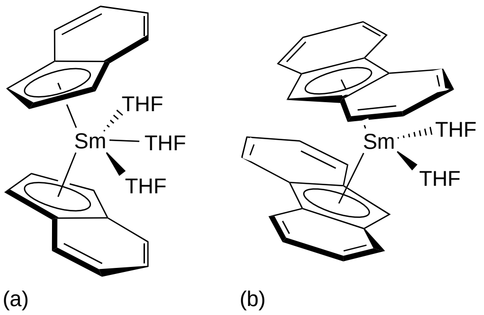

Figure 109 (a) (Ind)$_2$Sm(THF)$_3$, (b) (Flu)$_2$Sm(THF)$_2$

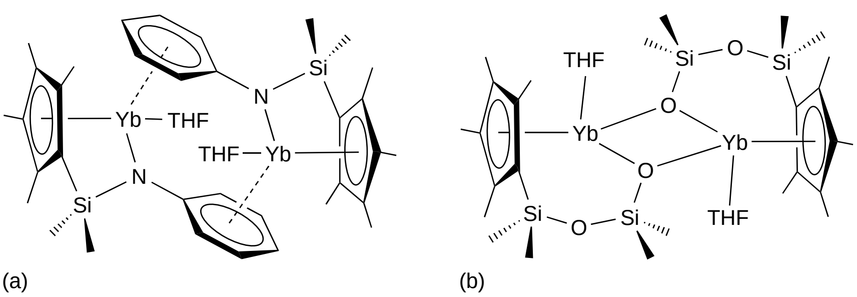

Figure 108 (a) [$Me_2Si(C_5Me_4)$(NPh)Yb(THF)]$_2$, (b) [(C_5H_4)SiMe$_2$OSiMe$_2$(η^1-O)Yb(THF)]$_2$

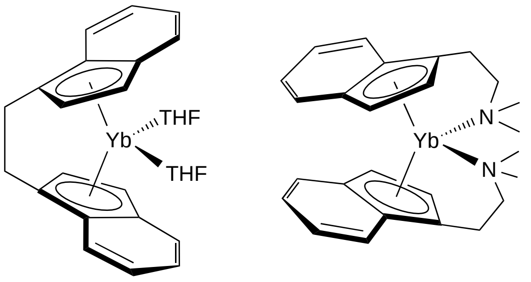

(a) (b)

Figure 110 (a) $(C_9H_6CH_2CH_2C_9H_6)Yb(THF)_2$, (b) $(Me_2NCH_2CH_2C_9H_6)_2Yb$

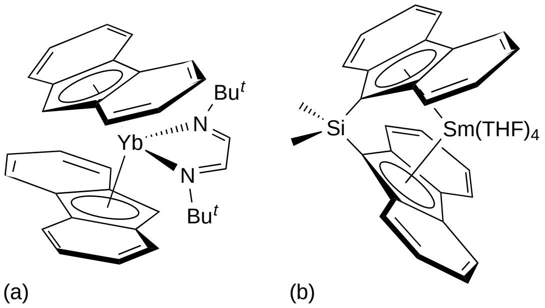

(a) (b)

Figure 111 (a) $(Flu)_2Yb(^tBuNCHCHN^tBu)$, (b) *ansa*-$Me_2Si(C_{13}H_8)_2Sm(THF)_4$

by reduction of fluorene with $(C_{10}H_8)Yb(THF)_2$ in THF. The mixed-ligand sandwich complex (Flu)(Cp*)Yb(DME) results from the reaction of $[YbI(DME)_2]_2(C_{10}H_8)$ with Cp*H and KFlu in DME. *ansa*-$Me_2Si(C_{13}H_8)_2Yb(THF)$ and *ansa*-$Me_2Si(C_{13}H_8)_2Sm(THF)_4$ (Figure 111b) were obtained by treatment of the appropriate Ln diiodides with [*ansa*-$Me_2Si(C_{13}H_9)_2]K_2$ in THF.[128]

$(Me_3SiC_{13}H_8)_2Sm(THF)_2$ reacts with an excess of AlR_3 (R = Me, Et, Pr, ^{i}Bu) and BEt_3 yielding $(Me_3SiC_{13}H_8\text{-}AlR_3)_2Sm$ and $(Me_3SiC_{13}H_8\text{-}BEt_3)_2Sm$, respectively in a reversible equilibrium (equation 24). In contrast, $(Me_3SiC_{13}H_8)_2Yb(THF)_2$ reacts with an excess of $AlMe_3$ yielding $(Me_3SiC_{13}H_8)(Me_3SiC_{13}H_8\text{-}AlMe_3)Yb$, in which, according to the X-ray crystal structure, only one $AlMe_3$ coordinates to the Yb atom through two Me groups via an agostic interaction. One of the Me_3Si-fluorenyl groups is η^5-coordinated, the other one η^6 (Figure 112). The bis(indenyl) derivative $(^iPrC_9H_6)_2Yb(THF)_2$ shows the same behavior.[129]

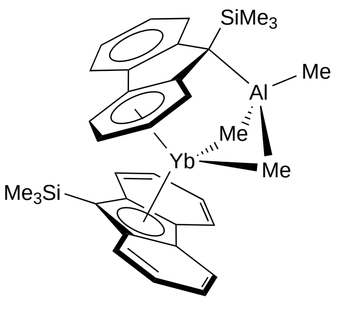

Figure 112 $(Me_3SiC_{13}H_8)(Me_3SiC_{13}H_8\text{-}AlMe_3)Yb$

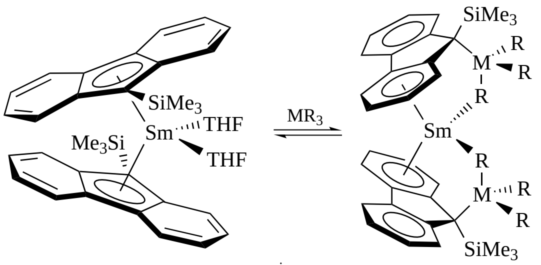

$MR_3 = Al^iBu_3, AlPr_3, BEt_3$

(24)

Divalent organolanthanide complexes Ln(COT) (Ln = Eu, Yb) were precipitated with COT from the metal solution in liquid ammonia. $(COT)Yb(py)_3$ (Figure 113a) crystallizes as a 3-legged piano stool. Ionic sandwich complexes like $[(DME)K]_2[Yb(COT)_2]$ (Figure 113b) are available in liquid ammonia by addition of a stoichiometric amount of K, Ln, and COT.

The reductive coupling (*see Reductive Coupling*) of acenaphthylene by activated metallic ytterbium and samarium yields *ansa*-lanthanidocenes $[(\eta^5\text{-}C_{12}H_8)_2Ln(THF)_2]$ (Ln = Yb, Sm) (equation 25).

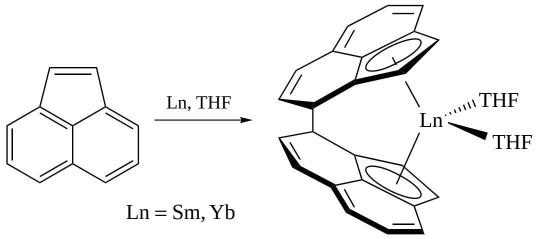

(25)

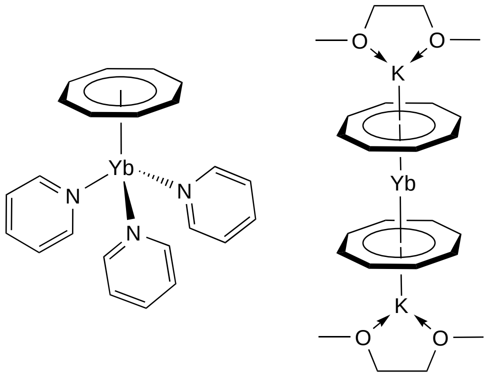

(a) (b)

Figure 113 (a) $(COT)Yb(py)_3$, (b) $[(DME)K]_2[Yb(COT)_2]$

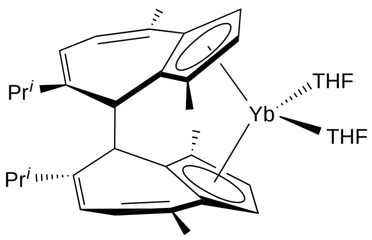

Figure 114 $(Gaz)_2Yb(THF)_2$

According to X-ray crystallography and NMR data, coupling of the radical anions of acenaphthylene in these reaction occurs stereoselectively affording exclusively C_2-symmetric *rac*-*ansa*-lanthanidocenes.[130] The related C_2-symmetric *rac*-*ansa*-ytterbocene complex $(Gaz)_2Yb(THF)_2$ (Gaz = guajazulene) (Figure 114) is isolated when GAZ is reacted with $(C_{10}H_8)Yb(THF)_2$.[131]

The chemistry of the lanthanide(II) complexes with pyrrolyl and pyrazolylborate ligands is unusual and provided surprising structures and unprecedented reactivity including dinitrogen reduction. The reactions of $SmI_2(THF)_2$ and $YbI_2(THF)_2$ with the alkali metal salts of 2,5-dimethylpyrrole led to the formation of divalent mono- and polynuclear complexes, for example, $(\mu\text{-}\eta^1{:}\eta^5\text{-}Me_2C_4H_2N)_3Sm(\mu\text{-}Cl)[Li(THF)_2]_2$ (Figure 115a), $\{[(Na(THF)_2)(\mu\text{-}\eta^1{:}\eta^5\text{-}Me_2C_4H_2N)_3Sm]_2(\mu\text{-}\eta^1{:}\eta^5\text{-}Me_2C_4N)_2\}(THF)_2$, $\{(\mu\text{-}\eta^1{:}\eta^5\text{-}Me_2C_4H_2N)_2Yb(\mu\text{-}Cl)[Li(OEt_2)]\}_2$, and $\{(\mu\text{-}\eta^1{:}\eta^5\text{-}Me_2C_4H_2N)_4[K(THF)]_2Yb\}_n$.[132] The reaction of diphenylbis(2-pyrrolyl)methane with KH and subsequent treatment with $YbI_2(THF)_2$ leads to $[Ph_2C(C_4H_3N)Yb]_8$ (Figure115b) as the major product.[133]

When the similar reaction has been carried out using $SmI_2(THF)_2$, a four-electron dinitrogen reduction is achieved, yielding $[\{[\mu\text{-}Ph_2C(\eta^1{:}\eta^5\text{-}C_4H_3N)_2]Sm\}_4(\mu\text{-}\eta^1{:}\eta^1{:}\eta^2{:}\eta^2\text{-}N_2)]$ (Figure 116).

Reaction of $[Sm\{N(SiMe_3)_2\}_2(THF)_2]$ with one equiv. of 1,1-di(α-pyrrolyl)cyclohexane in THF affords dark red $[\{[1,1\text{-}(\alpha\text{-}C_4H_3N)_2C_6H_{10}]Sm\}_8(THF)_4]$. It reacts rapidly with N_2 to form the dinitrogen complex $\{[(CH_2)_5C(C_4H_3N)_2]\text{-}Sm\}_4(THF)_2(\mu\text{-}N_2)$.[134] $SmCl_3(THF)_3$ reacts with 0.5 equiv. of $(Et_8\text{-calix-pyrrole})[Li(THF)]_4$ yielding $(Et_8\text{-calix-pyrrole})\text{-}Sm_2\{(\mu\text{-}Cl)_2[Li(THF)_2]\}_2$, which, by reduction with $LiAlH_4$,

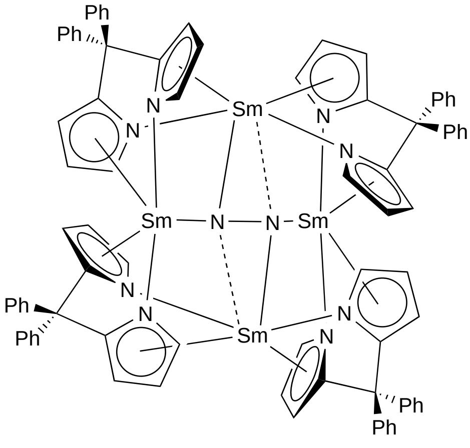

Figure 116 $[\{[\mu\text{-}Ph_2C(C_4H_3N)_2]Sm\}_4(N_2)]$

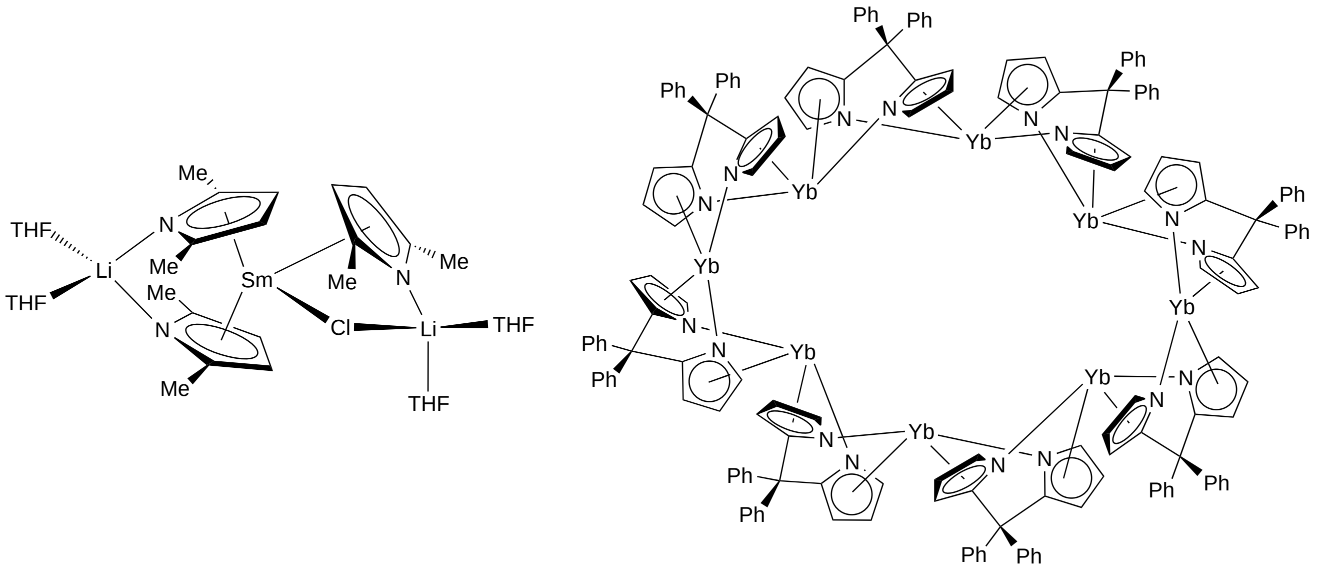

(a) (b)

Figure 115 (a) $(\mu\text{-}Me_2C_4H_2N)_3Sm(\mu\text{-}Cl)[Li(THF)_2]_2$, (b) $[Ph_2C(C_4H_3N)Yb]_8$

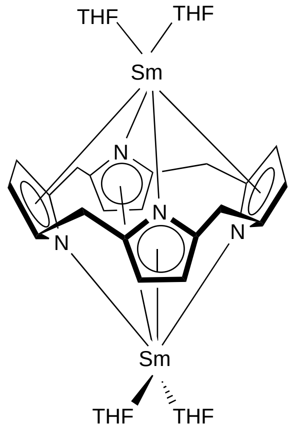

Figure 117 (Et$_8$-calix-pyrrole)Sm$_2$(THF)$_4$ (Et-groups are omitted for clarity)

produces either the mixed-valence (Et$_8$-calix-pyrrole)Sm$_2$-(THF)$_2$(μ-Cl)$_2$[Li(THF)$_2$] or the divalent (Et$_8$-calix-pyrrole)-Sm$_2$(THF)$_4$ (Figure 117), depending on the reaction conditions employed.**[135]**

Use of the sterically demanding hydrotris(3-^{t}Bu-5-Me-pyrazolyl)borate ligand (Tp^{t}Bu,Me) results in monomeric (Tp^{t}Bu,Me)YbI(THF) (Figure 118), which does not disproportionate to Yb(Tp^{t}Bu,Me)$_2$ and YbI$_2$. Reaction of [(Tp^{t}Bu,Me)YbH]$_2$ with C_5H_6 and $Me_3SiC_5H_5$ gave the corresponding mixed-ligand complexes (Tp^{t}Bu,Me)Yb(C_5H_4R) (R = H, SiMe$_3$). The solid-state structure of the SiMe$_3$-derivative exhibits an unusual distortion; one of the pyrazolyl rings is rotated in a way to bring both pyrazolyl nitrogens in bonding contact with Yb.**[136]**

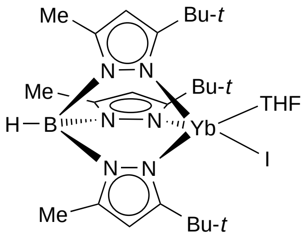

Figure 118 (Tp^{t}Bu,Me)YbI(THF)

Bis(η^5-phospholyl) or bis(η^5-arsolyl) complexes of Sm or Yb have been prepared from the metal or by metathesis from the metal iodides (equation 26). The coordinated THF molecules can be removed by heating a toluene solution in vacuo, in the case of the 2,3,4,5-tetramethylphospholyl or arsolyl, but not with the 2,5-diphenylphospholyl complexes.

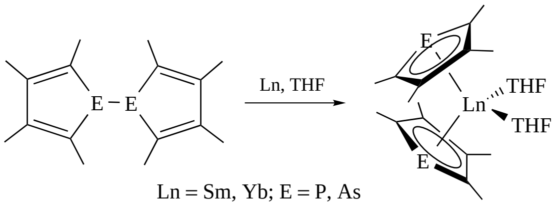

(26)

Related complexes [Yb(μ-Cl)(η^5-C$_4$Me$_4$P)(THF)$_2$]$_2$ and [Yb(μ-SPh)(η^5-C$_4$Me$_4$P)(THF)$_2$]$_2$ (Figure 119a) were prepared by direct cleavage of the P–Cl or P–S bonds of respective 1-chloro- and 1-phenylthio-2,3,4,5-tetramethylphosphole by ytterbium metal in THF at room temperature. Reaction of bis(η^5-tetramethylphospholyl)ytterbium(II) with RuH$_4$(PPh$_3$)$_3$ afforded heterometallic (THF)$_2$Yb[μ-η^5:η^1-C$_4$Me$_4$P]$_2$Ru(H)$_2$(PPh$_3$)$_2$ (Figure 119b).

Carboranyl complexes of Ln(II) like [Me$_2$-Si(C$_2$B$_{10}$H$_{11}$)(Cp)]Sm(THF)$_2$ are prepared by reaction of SmI$_2$ with 2 equiv. of [Me$_2$Si(C$_2$B$_{10}$H$_{11}$)(Cp)]Na in THF. In contrast, the reaction with YbI$_2$ afforded [Me$_2$Si(C$_2$B$_{10}$H$_{11}$)(Cp)]$_2$Yb(THF)$_2$ (Figure 120a). Treatment of LnI$_2$ with 1 equiv. of K$_2$[(PhCH$_2$)$_2$C$_2$B$_{10}$H$_{10}$] in THF yields after recrystallization from DME monomeric *exo-nido*-[(PhCH$_2$)$_2$C$_2$B$_{10}$H$_{10}$]Ln(DME)$_3$ (Ln = Sm, Yb). Using two equiv. of Na$_2$[(PhCH$_2$)$_2$C$_2$B$_9$H$_9$] results in dimeric complexes [*exo-nido*-{(PhCH$_2$)$_2$C$_2$B$_9$H$_9$}Ln(THF)$_3$]$_2$ (Ln = Sm, Yb) (Figure 120b).

Carboranyl/indenyl complexes of Yb(II) are formed by treatment of YbI$_2$ with Na[Me$_2$Si(Ind)(C$_2$B$_{10}$H$_{11}$)], resulting in [{Me$_2$Si(η^5-Ind)(C$_2$B$_{10}$H$_{11}$)}Yb(μ-I)(THF)$_2$]$_2$ (Figure 121a), which reacts with NaH yielding [Me$_2$Si(η^5-Ind)(σ-C$_2$B$_{10}$H$_{10}$)]Yb(THF)$_3$. Treatment with Na[Me$_2$Si-(Ind)(C$_2$B$_{10}$H$_{11}$)] in THF gave [Me$_2$Si(η^5-Ind)(C$_2$B$_{10}$H$_{11}$)]-Yb(THF)[Me$_2$Si(μ-η^5-Ind)(σ-C$_2$B$_{10}$H$_{10}$)]Na(THF)$_3$ (Figure 121b), which is also formed from YbI$_2$ and two equiv.

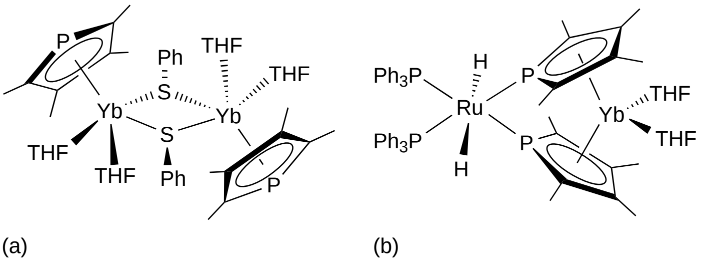

Figure 119 (a) [Yb(μ-SPh)(η^5-C$_4$Me$_4$P)(THF)$_2$]$_2$, (b) (THF)$_2$Yb[μ-C$_4$Me$_4$P]$_2$Ru(H)$_2$(PPh$_3$)$_2$

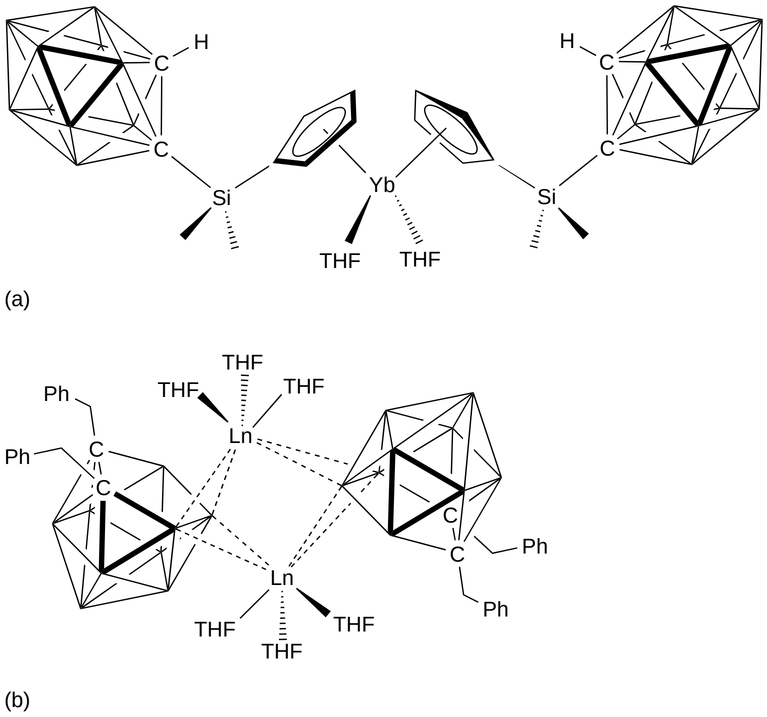
H
C
C
Si
Yb
THF
THF
H
C
C
Si
(a)
THF
THF
THF
Ph
Ph
C
C
Ln
Ln
THF
THF
THF
C
C
Ph
Ph
(b)

Figure 120 (a) [$Me_2Si(C_2B_{10}H_{11})(Cp)]_2Yb(THF)_2$, (b) [*exo*-*nido*-{$(PhCH_2)_2C_2B_9H_9$}$Ln(THF)_3]_2$ (Ln = Sm, Yb)

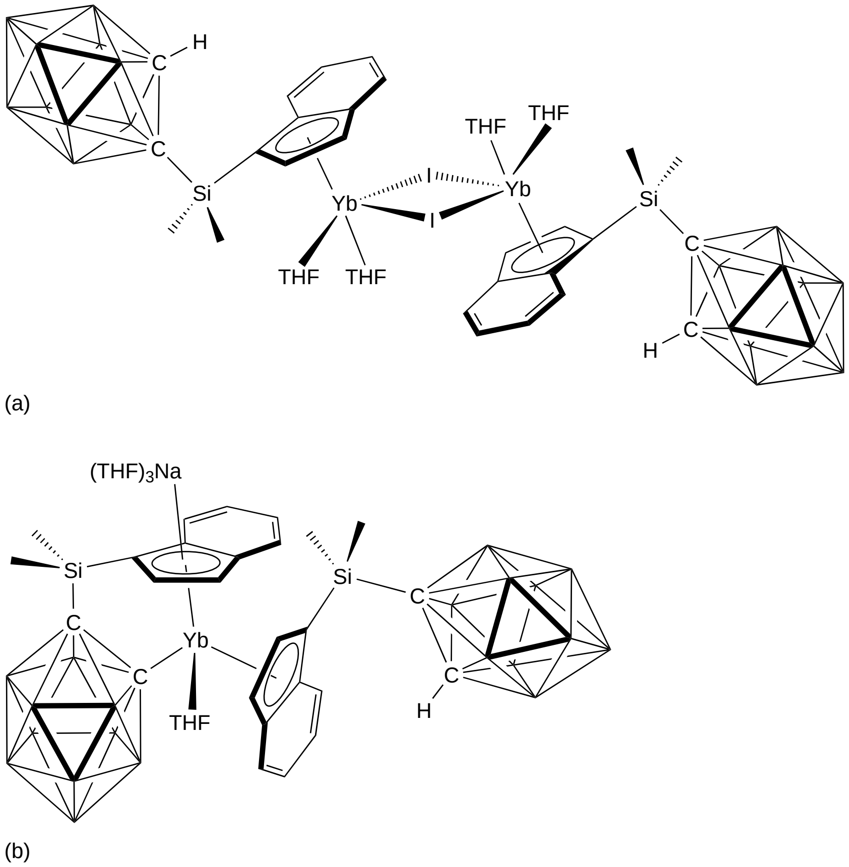
H
C
C
Si
Yb
THF
THF
I
I
THF
THF
Yb
Si
C
C
H
(a)
(THF)3Na
Si
C
C
Yb
THF
Si
C
C
H
(b)

Figure 121 (a) [{$Me_2Si(C_9H_6)(C_2B_{10}H_{11})$}Yb($\mu$-I)$(THF)_2]_2$, (b) [$Me_2Si(C_9H_6)(C_2B_{10}H_{11})$]Yb(THF)[$Me_2Si(C_9H_6)(C_2B_{10}H_{10})$]$Na(THF)_3$

of Na[$Me_2Si(Ind)(C_2B_{10}H_{11})$] in THF and reaction with NaH via intermediate [$Me_2Si(\eta^5$-Ind)($C_2B_{10}H_{11}$)]$_2$Yb(THF)$_2$.

Divalent [1,3-bis(trimethylsilyl)propenyl]$_2$Sm(THF)$_2$ (Figure 122) and (1,3-diphenylpropenyl)$_2$Sm(THF)$_2$ were synthesized by the reaction of potassium 1,3-bis(trimethylsilyl)propenide or potassium 1,3-diphenylpropenide with SmI_2.

Organometallic compounds of lanthanide metals other than Sm, Eu, and Yb are very rare until now. But the development of this chemistry became possible after the synthesis of divalent precursors of Tm, Dy, and Nd in the late 1990s, namely of their diiodides (*see* ***Scandium, Yttrium & the Lanthanides: Inorganic & Coordination Chemistry***) and by using ligands such as phospholyl or arsolyl, which stabilize divalent lanthanide ions.

The first organothulium(II) compound (η^5-1,3-($Me_3Si)_2$-$C_5H_3)_2$Tm(THF) (Figure 123a) was synthesized from K[$C_5H_3(SiMe_3)_2$-1,3] and $TmI_2(THF)_3$ in Et_2O or THF in Ar atmosphere. In contrast, DyI_2 and TmI_2 react with K[$C_5H_3(SiMe_3)_2$-1,3] under N_2 with reduction of N_2, yielding Ln(III) complexes like [{η^5-1,3-($ME_3Si)_2C_5H_3$}$_2$Dy]$_2$(μ-N_2).**[137]** $TmI_2(THF)_3$ reacts with K(L) (L = 2, 5-bis(trimethylsilyl)-3,4-dimethylphospholide or -arsolide; 2,5-di-*tert*-butyl-3,4-dimethylphospholide) forming the corresponding [η^5-$PC_4Me_2(SiMe_3)_2$]$_2$Tm(THF), [η^5-$AsC_4Me_2(SiMe_3)_2$]$_2$-Tm(THF) (Figure 123b), and [η^5-$PC_4Me_2(^tBu)_2$]$_2$-Tm(THF).**[138]**

The first example of a subvalent organolanthanum complex, [K([18]crown-6)(η^2-C_6H_6)$_2$][La{$C_5H_3(^tBu)_2$-1,3}$_2$]$_2$-(μ-C_6H_6) was prepared by reduction of La[$C_5H_3{}^tBu_2$]$_3$ with K in the presence of 18-crown-6 in benzene. The anion of this compound contains two [$C_5H_3{}^tBu_2$]$_2$La(II) moieties bridged by an η^6:η^6-benzenide monoanionic ligand (Figure 124). An alternative formulation of the anion with two [$C_5H_3{}^tBu_2$]$_2$La(III) moieties bridged by an [η^6-C_6H_6]$^{3-}$ seems less plausible.

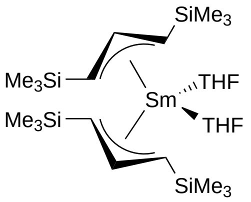

Figure 122 [1,3-($Me_3Si)_2C_3H_3$]$_2$Sm(THF)$_2$

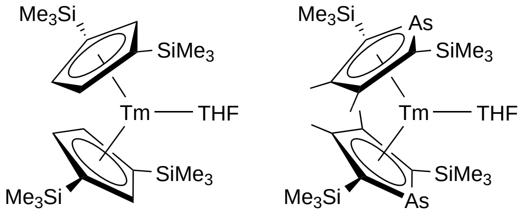

(a) (b)

Figure 123 (a) (1,3-($Me_3Si)_2C_5H_3)_2$Tm(THF), (b) [AsC_4Me_2 $(SiMe_3)_2$]$_2$Tm(THF)

11.3.3 Divalent Lanthanidocenes as Reducing Agents

Divalent organolanthanides, especially Cp*$_2$Sm(THF)$_2$, are widely used as reducing agents.**[114]** Decamethylsamarocene reduces a number of organic and inorganic substrates by one-electron transfer to give Sm(III) species, for example, as shown in equation (27).**[139]**

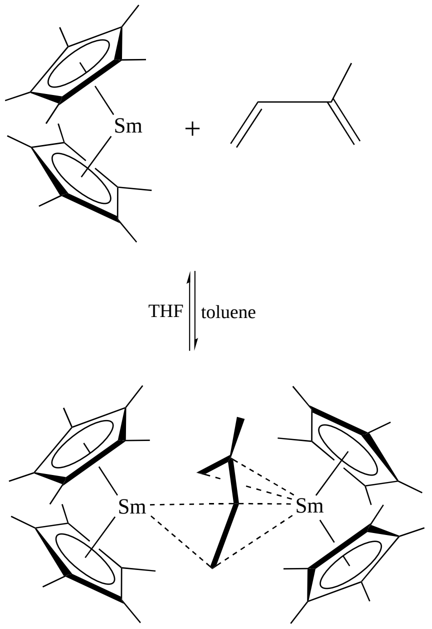

(27)

Divalent ytterbium has a lower reduction potential. Therefore, Yb(II) complexes reduce only substrates with relatively high electron affinity. That could be demonstrated by the isolation of several adducts between heterocyclic nitrogen bases and Cp*$_2$Yb. 1:1-Adducts of the type Cp*$_2$Yb(L) are formed with pyrazine, quinoxaline, 1,5- and 1,8-naphthyridine, 4,4′-bipyridine, phthalazine, and azobenzene. The adducts are paramagnetic, and their effective magnetic moments are consistent with the formulation Cp*$_2$Yb^{3+} ($L^{\cdot -}$) ($L^{\cdot -}$ = radical anion), in which spins on the individual units are uncoupled down to 5 K. Cp*$_2$Yb and pyridazine, phenazine, 2,2′-azopyridine, 2,2′-bipyrimidine, 2,2′-azobenzene, and 2,3-bis(2-pyridino)quinoxaline form (Cp*$_2$Yb)$_2$(μ-L) adducts. The crystal structure of (Cp*$_2$Yb)$_2$(μ-bipyrimidine) shows that two metallocenes are bridged by a planar bipyrimidine ligand. The effective magnetic moment of these 2:1 adducts shows that each [Cp*$_2$Yb(III)] fragment behaves as an isolated paramagnet; the bridging ligand is a diamagnetic dianion.**[140]** The 2,2′-bipyridyl and 1,3-diazadiene adducts Cp*$_2$Yb(bipy)

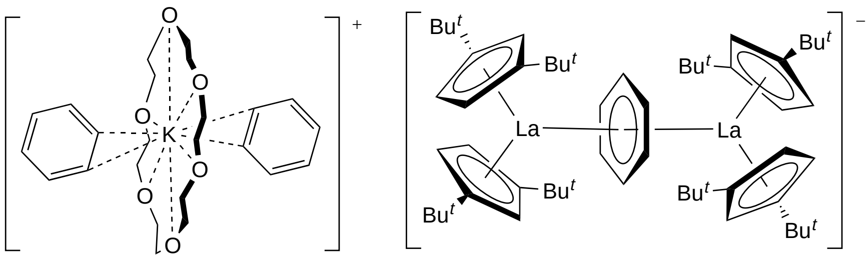

Figure 124 $[K([18]crown-6)(\eta^2-C_6H_6)_2][La\{C_5H_3(^tBu)_2-1,3\}_2]_2(\mu-C_6H_6)$

and $Cp_2Yb(DAD)$, respectively, are paramagnetic, containing radical anionic donor ligands.[141]

A new era in reductive chemistry of divalent lanthanides began with the synthesis of the first derivatives of divalent Nd, Dy, and Tm. The reaction of TmI_2 with Cp′K [Cp′ = Cp*, $C_5H_3(SiMe_3)_2$, $C_5H_4(SiMe_3)$] in Et_2O under nitrogen results in the formation of the dinitrogen reduction products $[(C_5Me_5)_2Tm]_2N_2$ (equation 28), $\{[C_5H_3(SiMe_3)_2]_2Tm\}_2N_2$, and $\{[C_5H_4(SiMe_3)]_2Tm(THF)\}_2N_2$ respectively.[142]

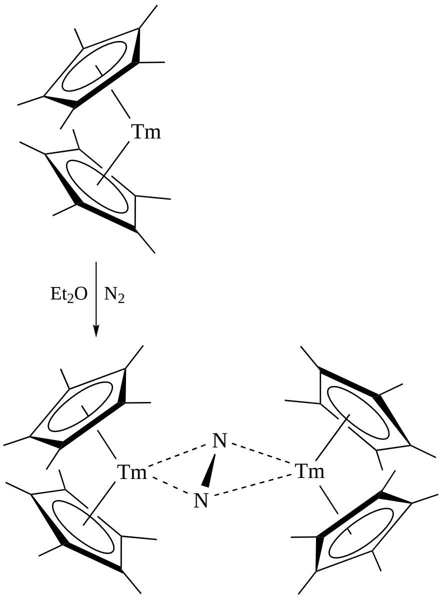

(28)

11.4 Tetravalent Organocerium Complexes

The most easily accessible tetravalent lanthanide is cerium. However, even Ce(IV) is a powerful oxidizing agent, and organic ligands are easily oxidized by it. Early reports of a Cp_4Ce and a number of other cyclopentadienylcerium(IV) complexes were claimed in the 1970s, but their existence could not be proved. Cerocene, $Ce(COT)_2$, and some related derivatives with substituted cyclooctatetraenyl ligands are available by reaction of $Ce(O^iPr)_4$ with an excess of COT and $AlEt_3$, or by oxidation of $K[Ce(C_8H_7Me)_2]$, $Li[Ce\{1,4-(Me_3Si)_2C_8H_6\}_2]$, and $K[Ce\{1,3,6-(Me_3Si)_3C_8H_5\}_2]$ with AgI (equation 29).

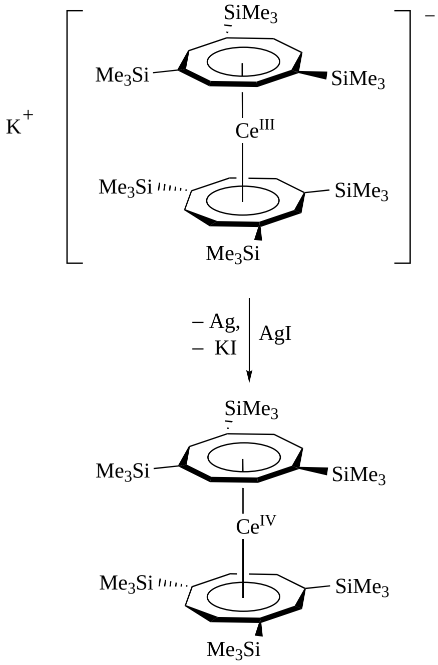

(29)

The X-ray structure analysis shows a soft bend sandwich complex for $Ce\{1,3,6-(Me_3Si)_3C_8H_5\}_2$ with an angle ring centroid-Ce-ring centroid of 176.1°. Ab initio calculations (*see Ab Initio Calculations*) on $Ce(COT)_2$, supported by X-ray absorption near-edge structure measurements (XANES), argue against a Ce(IV) complex, but, for a Ce(III) ion with $4f^1$ configuration, coordinated to two $(COT)^{1.5-}$ ligands.

The only one structurally characterized cyclopentadienyl derivative of Ce(IV), Cp_3CeO^tBu was prepared together with $Cp_2Ce(O^tBu)_2$ from $Ce(O^tBu)(NO_3)_3$ and NaCp according to equation (30).

$$Ce(OBu^t)(NO_3)_3(THF)_2 + 3CpNa \longrightarrow Cp_3Ce(OBu^t) + Cp_2Ce(OBu^t) + \text{other products} \quad (30)$$

12 RELATED ARTICLES

Actinides: Inorganic & Coordination Chemistry; Scandium, Yttrium & the Lanthanides: Inorganic & Coordination Chemistry; Zirconium & Hafnium: Organometallic Chemistry.

13 FURTHER READING

W. J. Evans and B. L. Davies, *Chem. Rev.*, 2002, **102**, 2119.

14 REFERENCES

1. G. Wilkinson and J. M. Birmingham, *J. Am. Chem. Soc.*, 1954, **76**, 6210.
2. H. Schumann, *Angew. Chem.*, 1984, **96**, 475; *Angew. Chem., Int. Ed. Engl.*, 1984, **23**, 474.
3. F. T. Edelmann, *Angew. Chem.*, 1995, **107**, 2647; *Angew. Chem., Int. Ed. Engl.*, 1995, **34**, 2466.
4. F. G. N. Cloke, Zero Oxidation State Complexes of Scandium, Yttrium and the Lanthanide Elements, in ‘Comprehensive Organometallic Chemistry II’, eds. F. G. A. Stone, G. Wilkinson, and E. W. Abel, Pergamon Press, Oxford, 1995, Vol. 4, Chap. 1 p. 1.
5. F. T. Edelmann, Scandium, Yttrium, and the Lanthanide and Actinide Elements, Excluding their Zero Oxidation State Complexes, in ‘Comprehensive Organometallic Chemistry II’, eds. F. G. A. Stone, G. Wilkinson, and E. W. Abel, Pergamon Press, Oxford, 1995, Vol. 4, Chap. 2 p. 11.
6. H. Schumann, J. A. Meese-Marktscheffel, and L. Esser, *Chem. Rev.*, 1995, **95**, 865.
7. M. N. Bochkarev, L. N. Zakharov, and G. S. Kalinina, ‘Organoderivatives of Rare Earth Elements’, Kluwer Academic Publishers, Dordrecht, 1995.
8. H. B. Kagan, Guest Editor: *Chem. Rev.*, 2002, **102**,(6), 1807.
9. S. Kobayashi, Volume Editor: Lanthanides: Chemistry and use in Organic Synthesis, in ‘Topics in Organometallic Chemistry 2’, eds. J. M. Brown, P. Dixneuf, A. Fürstner, L. S. Hegedus, P. Hofmann, P. Knochel, G. van Koten, T. J. Marks, S. Murai, and M. Reetz, Springer, Berlin, 1999.
10. B. Cornils and W. A. Herrmann, eds, ‘Applied Homogeneous Catalysis with Organometallic Compounds’, VCH Verlagsgesellschaft, Weinheim, 1996.
11. F. T. Edelmann, D. M. M. Freckmann, and H. Schumann, *Chem. Rev.*, 2002, **102**, 1851.
12. M. Niemeyer, *Z. Anorg. Allg. Chem.*, 2000, **626**, 1027.
13. H. Schumann, D. M. M. Freckmann, and S. Dechert, *Z. Anorg. Allg. Chem.*, 2002, **628**, 2422.
14. D. J. H. Emslie, W. E. Piers, M. Parvez, and R. McDonald, *Organometallics*, 2002, **21**, 4226.
15. S. Arndt, T. P. Spaniol, and J. Okuda, *Chem. Commun.*, 2002, 896.
16. H. Schumann, K. Herrmann, and F. Erbstein, *Z. Naturforsch.*, 2003, **58b**, 832.
17. S. Arndt, T. P. Spaniol, and J. Okuda, *Organometallics*, 2003, **22**, 775.
18. A. Lara-Sanchez, A. Rodriguez, D. L. Hughes, M. Schormann, and M. Bochmann, *J. Organomet. Chem.*, 2002, **663**, 63.
19. P. G. Hayes, W. E. Piers, L. W. Lee, L. K. Knight, M. Parvez, M. R. J. Elsegood, and W. Cleeg, *Organometallics*, 2001, **20**, 2533.
20. P. G. Hayes, W. E. Piers, and R. McDonald, *J. Am. Chem. Soc.*, 2002, **124**, 2132.
21. P. G. Hayes, G. C. Welch, D. J. H. Emslie C. L. Noak, W. E. Piers, and M. Parvez, *Organometallics*, 2003, **22**, 1577.
22. S. Bambirra, M. J. R. Brandsma, E. A. C. Brussee, A. Meetsma, B. Hessen, and J. Teuben, *Organometallics*, 2000, **19**, 3197.
23. S. Bambirra, D. van Leusen, B. Hessen, and J. H. Teuben, *Chem. Commun.*, 2001, 637.
24. G. A. Molander and J. A. C. Romero, *Chem. Rev.*, 2002, **102**, 2161.
25. J. Okuda, *J. Chem. Soc., Dalton Trans.*, 2003, 2367.
26. H. Schumann, M. R. Keitsch, and S. H. Mühle, *Z. Anorg. Allg. Chem.*, 2002, **628**, 1311.
27. Y. Satoh, N. Ikitake, Y. Nakayama, S. Okuno, and H. Yasuda, *J. Organomet. Chem.*, 2003, **667**, 42.
28. H. Schumann, K. Herrmann, S. H. Mühle, and S. Dechert, *Z. Anorg. Allg. Chem.*, 2003, **629**, 1184.
29. Y. Luo, Y. Yao, and Q. Shen, *Macromolecules*, 2002, **35**, 8670.
30. S. Arndt, A. Trifonov, T. P. Spaniol, J. Okuda, M. Kitamura, and T. Takahashi, *J. Organomet. Chem.*, 2002, **647**, 158.
31. P. Voth, S. Arndt, T. P. Spaniol, J. Okuda, L. L. Ackerman, and M. L. H. Green, *Organometallics*, 2003, **22**, 65.
32. F. Estler, G. Eickerling, E. Herdtweck, and R. Anwander, *Organometallics*, 2003, **22**, 1212.
33. F. G. N. Cloke, B. R. Elvidge, P. B. Hitchcock, and M. E. Vanessa, *J. Chem. Soc., Dalton Trans.*, 2002, 2413.
34. Z. Lu, G. P. A. Yap, and D. S. Richeson, *Organometallics*, 2001, **20**, 706.
35. S. Bambirra, A. Meetsma, B. Hessen, and J. H. Teuben, *Organometallics*, 2001, **20**, 782.
36. Y. Luo, Y. Yao, Q. Shen, K. Yu, and L. Weng, *Eur. J. Inorg. Chem.*, 2003, 318.
37. T. Dube, S. Gambarotta, and G. P. A. Yap, *Organometallics*, 2000, **19**, 121.
38. P. W. Roesky, *J. Organomet. Chem.*, 2000, **603**, 161.

39. M. E. G. Skinner and P. Mountford, *J. Chem. Soc., Dalton Trans.*, 2002, 1694.
40. B. D. Ward, S. R. Dubberley, A. Maisse-Francois, L. Gade, and P. Mountford, *J. Chem. Soc., Dalton Trans.*, 2002, 4649.
41. G. W. Rabe, C. D. Berube, G. P. A. Yap, K. C. Lam, T. E. Concolino, and A. L. Rheingold, *Inorg. Chem.*, 2002, **41**, 1446.
42. G. W. Rabe, C. D. Berube, and G. P. A. Yap, *Inorg. Chem.*, 2001, **40**, 2682.
43. G. W. Rabe, C. D. Berube, and G. P. A. Yap, *Inorg. Chem.*, 2001, **40**, 4780.
44. I. Castillo and T. D. Tilley, *J. Am. Chem. Soc.*, 2001, **123**, 10526.
45. G. Lin, R. McDonald, and J. Takats, *Organometallics*, 2000, **19**, 1814.
46. D. J. Berg and R. A. Andersen, *Organometallics*, 2003, **22**, 627.
47. M. G. Klimpel, J. Eppinger, P. Sirsch, W. Scherer, and R. Anwander, *Organometallics*, 2002, **21**, 4021.
48. G. R. Giesbrecht, J. C. Gordon, J. T. Brady, D. L. Clark, D. W. Keogh, R. Michalczyk, B. L. Scott, and J. G. Watkin, *Eur. J. Inorg. Chem.*, 2002, 723.
49. A. Fischbach, E. Herdtweck, R. Anwander, G. Eickerling, and W. Scherer, *Organometallics*, 2003, **22**, 499.
50. A. Fischbach, F. Perdih, P. Sirsch, W. Scherer, and R. Anwander, *Organometallics*, 2002, **21**, 4569.
51. X. Cai, B. Gehrhus, P. B. Hitchcock, and M. F. Lappert, *Can. J. Chem.*, 2000, **78**, 1484.
52. K. Aparna, M. Ferguson, and R. G. Cavell, *J. Am. Chem. Soc.*, 2000, **122**, 726.
53. M. T. Gamer, S. Dehnen, and P. W. Roesky, *Organometallics*, 2001, **20**, 4230.
54. M. T. Gamer and P. W. Roesky, *J. Organomet. Chem.*, 2002, **647**, 123.
55. I. Castillo and T. D. Tilley, *Organometallics*, 2000, **19**, 4733.
56. R. Taube, S. Maiwald, and J. Sieler, *J. Organomet. Chem.*, 2001, **621**, 327.
57. E. Ihara, M. Tanaka, H. Yasuda, N. Kanehisa, T. Maruo, and Y. Kai, *J. Organomet. Chem.*, 2000, **613**, 26.
58. W. J. Evans, J. C. Brady, and J. W. Ziller, *J. Am. Chem. Soc.*, 2001, **123**, 7711.
59. A. A. Trifonov, E. A. Fedorova, E. N. Kirillov, M. N. Bochkarev, F. Girgsdies, and H. Schumann, *Russ. Chem. Bull.*, 2000, **49**, 1436.
60. W. J. Evans, B. J. Davis, and J. W. Ziller, *Inorg. Chem.*, 2001, **40**, 6341.
61. J. Guan and R. D. Fischer, *Eur. J. Inorg. Chem.*, 2001, 2497.
62. M. M. Conradi, M. A. D. McGowan, P. C. McGowan, and M. Thornton-Pett, *Eur. J. Inorg. Chem.*, 2002, 2362.
63. F. Nief and L. Ricard, *Organometallics*, 2001, **18**, 3884.
64. H. Schumann, D. F. Karasiak, and S. H. Mühle, *Z. Anorg. Allg. Chem.*, 2000, **626**, 1434.
65. G. B. Deacon, G. Meyer, and D. Stellfeld, *Eur. J. Inorg. Chem.*, 2000, 1061.
66. P. B. Hitchcock, M. F. Lappert, and S. Prashar, *J. Organomet. Chem.*, 2000, **613**, 105.
67. W. J. Evans, C. H. Fujimoto, M. A. Johnston, and J. W. Ziller, *Organometallics*, 2002, **21**, 1825.
68. H. H. Karsch, V. W. Graf, and W. Scherer, *J. Organomet. Chem.*, 2000, **604**, 72.
69. H. Schumann, A. Heim, J. Demtschuk, and S. H. Mühle, *Organometallics*, 2003, **22**, 118.
70. H. Schumann, A. Heim, J. Demtschuk, and S. H. Mühle, *Organometallics*, 2002, **21**, 3323.
71. M. G. Klimpel, H. W. Gorlitzer, M. Tafipolsky, M. Spiegler, W. Scherer, and R. Anwander, *J. Organomet. Chem.*, 2002, **647**, 236.
72. J. Zhang, S. Ruan, Z. Shao, R. Cai, L. Weng, and X. Zhou, *Organometallics*, 2002, **21**, 1420.
73. M. Westerhausen, S. Schneiderbauer, M. Hartmann, M. Warchhold, and H. Nöth, *Z. Anorg. Allg. Chem.*, 2002, **628**, 330.
74. E. Ihara, S. Yoshioka, M. Furo, K. Katsura, H. Jasuda, S. Mohri, N. Kanehisa, and Y. Kai, *Organometallics*, 2001, **20**, 1752.
75. J. Cheng, D. Cui, W. Chen, T. Tang, and B. Huang, *J. Organomet. Chem.*, 2002, **658**, 153.
76. G. Paolucci, J. Zanon, V. Lucchini, W. E. Damrau, E. Siebel, and R. D. Fischer, *Organometallics*, 2002, **21** 1088.
77. J. Eppinger, M. Spiegler, W. Hieringer, W. A. Herrmann, and R. Anwander, *J. Am. Chem. Soc.*, 2000, **122**, 3080.
78. C. Qian, G. Zhou, Y. Chen, and J. Sun, *Organometallics*, 2001, **20**, 3106.
79. A. K. Dash, A. Razavi, A. Mortreux, C. W. Lehmann, and J. F. Carpentier, *Organometallics*, 2002, **21**, 3238.
80. C. Qian, W. Nie, Y. Chen, and J. Sun, *J. Organomet. Chem.*, 2002, **645**, 82.
81. M. R. Douglass, M. Ogasawara, S. Hong, M. V. Metz, and T. J. Marks, *Organometallics*, 2002, **21**, 283.
82. I. L. Fedushkin, Yu. A. Kurskii, C. I. Nevodchikov, M. N. Bochkarev, S. Mühle, and H. Schumann, *Russ. Chem. Bull.*, 2002, **51**, 160.
83. I. L. Fedushkin, S. Dechert, and H. Schumann, *Organometallics*, 2000, **19**, 4066.
84. Y. Cheng, Q. Shen, and Y. Li, *J. Organomet. Chem.*, 2001, **631**, 94.
85. P. W. Roesky, *Organometallics*, 2002, **21**, 4756.
86. S. Arndt and J. Okuda, *Chem. Rev.*, 2002, **102**, 1953.
87. K. C. Hultzsch, P. Voth, K. Beckerle, T. P. Spaniol, and J. Okuda, *Organometallics*, 2000, **19**, 228.

88. A. A. Trifonov, E. A. Fedorova, E. N. Kirillov, S. E. Nefedov, I. L. Eremenko, Yu. A. Kurskii, A. S. Shavyrin, and M. N. Bochkarev, *Russ. Chem. Bull.*, 2002, **51**, 684.
89. R. A. L. Gendron, D. J. Berg, and T. Barclay, *Can. J. Chem.*, 2002, **80**, 1285.
90. R. A. L. Gendron, D. J. Berg, P. Shao, and T. Barclay, *Organometallics*, 2001, **20**, 4279.
91. O. Tardif, Z. Hou, M. Nishiura, T. Koizumi, and Y. Wakatsuki, *Organometallics*, 2001, **20**, 4565.
92. S. Wang, Q. Yang, T. C. W. Mak, and Z. Xie, *Organometallics*, 2000, **19**, 334.
93. K. Chui, Q. Yang, T. C. W. Mak, and Z. Xie, *Organometallics*, 2000, **19**, 1391.
94. G. Zi, H. W. Li, and Z. Xie, *Organometallics*, 2002, **21**, 1136.
95. K. Chui, Q. Yang, T. C. W. Mak, W. H. Lam, Z. Lin, and Z. Xie, *J. Am. Chem. Soc.*, 2000, **122**, 5758.
96. G. Zi, H. W. Li, and Z. Xie, *Organometallics*, 2002, **21**, 3464.
97. J. Wang, S. Li, C. Zheng, J. A. Maguire, and N. S. Hosmane, *Organometallics*, 2002, **21**, 5149.
98. M. N. Bochkarev, *Chem. Rev.*, 2002, **102**, 2089.
99. P. G. Hayes, W. E. Piers, and M. Parvez, *J. Am. Chem. Soc.*, 2003, **125**, 5622.
100. G. B. Deacon, P. E. Fanwick, A. Gitlits, I. P. Rothwell, B. W. Skelton, and A. H. White, *Eur. J. Inorg. Chem.*, 2001, 1501.
101. J. C. Gordon, G. R. Giesbrecht, D. L. Clark, J. P. Hay, D. W. Keogh, R. Poli, B. L. Scott, and J. G. Watkin, *Organometallics*, 2002, **21**, 4726.
102. M. D. Fryzuk, L. Jafarpour, F. M. Kerton, J. B. Love, B. O. Patrick, and S. J. Rettig, *Organometallics*, 2001, **20**, 1387.
103. M. D. Fryzuk, L. Jafarpour, F. M. Kerton, J. B. Love, and S. J. Rettig, *Angew. Chem.*, 2000, **112**, 783; *Angew. Chem., Int. Ed. Engl.*, 2000, **39**, 767.
104. B. Wang, X. Zheng, and G. E. Herberich, *Eur. J. Inorg. Chem.*, 2002, 31.
105. H. Schumann, E. C. E. Rosenthal, J. Demtschuk, and S. Mühle, *Z. Anorg. Allg. Chem.*, 2000, **626**, 2161.
106. Q. Liu, X. Shen, J. Huang, Y. Qian, A. S. C. Chan, and W. T. Wong, *Polyhedron*, 2000, **19**, 453.
107. M. Visseaux, F. Nief, and L. Ricard, *J. Organomet. Chem.*, 2002, **647**, 139.
108. P. W. Roesky, *J. Organomet. Chem.*, 2001, **621**, 277.
109. A. N. Neculai, D. Neculai, H. W. Roesky, J. Magull, M. Baldus, O. Andronesi, and M. Jansen, *Organometallics*, 2002, **21**, 2590.
110. P. B. Hitchcock, A. V. Khvostov, and M. F. Lappert, *J. Organomet. Chem.*, 2002, **663**, 263.
111. C. M. Forsyth and G. B. Deacon, *Organometallics*, 2000, **19**, 1205.
112. G. Heckmann and M. Niemeyer, *J. Am. Chem. Soc.*, 2000, **122**, 4227.
113. M. G. Klimpel, R. Anwander, M. Tafipolsky, and W. Scherer, *Organometallics*, 2001, **20**, 3983.
114. W. J. Evans, *Coord. Chem. Rev.*, 2000, **206**, 263.
115. M. Schultz, C. J. Burns, D. J. Schwartz, and R. A. Andersen, *Organometallics*, 2000, **19**, 781.
116. P. B. Hitchcock, M. F. Lappert, and S. Tian, *Organometallics*, 2000, **19**, 3420.
117. F. Weber, H. Sitzmann, M. Schultz, C. D. Sofield, and R. A. Andersen, *Organometallics*, 2002, **21**, 3139.
118. H. Sitzmann, T. Dezember, O. Schmitt, F. Weber, G. Wolmershäuser, and M. Ruck, *Z. Anorg. Allg. Chem.*, 2000, **626**, 2241.
119. M. Glanz, S. Dechert, H. Schumann, D. Wolff, and J. Springer, *Z. Anorg. Allg. Chem.*, 2000, **626**, 2467.
120. W. J. Evans, J. M. Perotti, J. W. Ziller, D. F. Moser, and R. West, *Organometallics*, 2003, **22**, 1160.
121. K. Müller-Buschbaum, G. B. Deacon, and C. M. Forsyth, *Eur. J. Inorg. Chem.*, 2002, 3172.
122. W. J. Evans, M. A. Johnston, R. D. Clark, R. Anwander, and J. W. Ziller, *Polyhedron*, 2001, **20**, 2483.
123. G. R. Giesbrecht, C. Cui, A. Shafir, J. A. R. Schmidt, and J. Arnold, *Organometallics*, 2002, **21**, 3841.
124. Z. Hou, Y. Zhang, M. Nishiura, and Y. Wakatsuki, *Organometallics*, 2003, **22**, 129.
125. Z. Hou, T. Koizumi, M. Nishiura, and Y. Wakatsuki, *Organometallics*, 2001, **20**, 3323.
126. A. A. Trifonov, E. N. Kirillov, A. Fischer, F. T. Edelmann, and M. N. Bochkarev, *J. Organomet. Chem.*, 2002, **647**, 94.
127. A. A. Trifonov, E. N. Kirillov, S. Dechert, H. Schumann, and M. N. Bochkarev, *Eur. J. Inorg. Chem.*, 2001, 3055.
128. A. A. Trifonov, E. N. Kirillov, S. Dechert, H. Schumann, and M. N. Bochkarev, *Eur. J. Inorg. Chem.*, 2001, 2509.
129. H. Nakamura, Y. Nakayama, H. Yasuda, T. Maruo, N. Kanehisa, and Y. Kai, *Organometallics*, 2000, **19**, 5392.
130. I. L. Fedushkin, S. Dechert, and H. Schumann, *Angew. Chem.*, 2001, **113**, 584; *Angew. Chem., Int. Ed. Engl.*, 2001, **40**, 561.
131. I. L. Fedushkin, Yu. A. Kurskii, T. V. Balashova, M. N. Bochkarev, S. Dechert, S. Mühle, and H. Schumann, *Russ. Chem. Bull.*, 2003, **52**, 1363.
132. M. Ganesan, C. D. Gerube, S. Gambarotta, and G. P. A. Yap, *Organometallics*, 2002, **21**, 1707.
133. D. M. M. Freckmann, T. Dube, C. D. Berube, S. Gambarotta, and G. P. A. Yap, *Organometallics*, 2002, **21**, 1240.
134. M. Ganesan, S. Gambarotta, and G. P. A. Yap, *Angew. Chem.*, 2001, **113**, 788; *Angew. Chem., Int. Ed. Engl.*, 2001, **40**, 766.
135. T. Dube, S. Gambarotta, and G. P. A. Yap, *Organometallics*, 2000, **19**, 817.
136. G. M. Ferrence, R. McDonald, M. Morissette, and J. Takats, *J. Organomet. Chem.*, 2000, **596**, 95.

137. W. J. Evans, N. T. Allen, and J. W. Ziller, *Angew. Chem.*, 2002, **41**, 369; *Angew. Chem., Int. Ed. Engl.*, 2002, **41**, 359.
138. F. Nief, D. Turcitu, and L. Ricard, *Chem. Commun.*, 2002, 1646.
139. W. J. Evans, D. G. Giarikos, C. B. Robledo, V. S. Leong, and J. W. Ziller, *Organometallics*, 2001, **20**, 5648.
140. D. J. Berg, J. M. Boncella, and R. A. Andersen, *Organometallics*, 2002, **21**, 4622.
141. M. Schultz, J. M. Boncella, D. J. Berg, T. D. Tilley, and R. A. Andersen, *Organometallics*, 2002, **21**, 460.
142. W. J. Evans, N. T. Allen, and J. W. Ziller, *J. Am. Chem. Soc.*, 2001, **123**, 7927.

Acknowledgment

I. L. F. is grateful to the Alexander von Humboldt Foundation for the Friedrich Wilhelm Bessel Award, who made it possible to work on this part of EIC II during the stay at TU Berlin in 2003.

Selenium: Inorganic Chemistry

David A. Atwood
University of Kentucky, Lexington, KY, USA

Based in part on the article Selenium: Inorganic Chemistry by Bernt Krebs, Stefan Bonmann, & Illenora Eidenschink which appeared in the Encyclopedia of Inorganic Chemistry, First Edition.

1 Introduction 1
2 Polyatomic Cations 1
3 Halides and Related Compounds 6
4 Oxides 10
5 Haloselenates 12
6 Oxohaloselenates 16
7 Selenium and Nitrogen 17
8 Related Articles 20
9 References 20

1 INTRODUCTION

Selenium is the first member of the group 16 elements O, S, Se, Te, and Po that shows some metallic character. Among the several modifications of selenium, three nonmetallic ones contain Se_8 rings, whereas at least two others (gray metallic and amorphous black selenium) are semiconductors. Much of the current interest in the different allotropic modifications of selenium is connected with its extensive use in semiconductor applications, namely, in photocells, in xerography, and in rectifiers. Nanomaterials containing selenium are also becoming important targets. Selenium (and also tellurium) shares with sulfur the tendency to form homonuclear catenation in the element as well as in compound formation. The increasing metallic character in the series O, S, Se, Te, Po is reflected also in the lower electronegativity, in the less acid character of the oxides, and in the lower stability of the oxidation number +VI for selenium compared to sulfur.

Apart from the simple hydrogen chalcogenides of Se and Te (which are more acid and thermally less stable than the corresponding sulfur analogs) the most stable inorganic compounds of selenium (and its higher homologs) are: (1) the various chalcogenides and polychalcogenides with strongly positive counterions such as the alkali metals or the alkaline-earth metals, and those that are more covalently bonded to various transition metals; (2) a large variety of compounds of Se^{II}, Se^{IV}, and Se^{VI} with the electronegative elements O, F, Cl, and Br; (3) a number of homologous compounds belonging to the interesting class of sulfur–nitrogen compounds; and (4) a class of organoselenium compounds with other ligands such as Cl or Br as secondary ligands. All are somewhat less stable than the corresponding sulfur compounds. The tendency to form double bonds is smaller in selenium than sulfur, although the existence of strong Se=O bonds in oxo–halo selenium compounds such as $SeOCl_2$ or $[SeOCl_4]^{2-}$ indicate the ability to form significant (p–d)π bonding, quite in contrast to tellurium.

A well-known feature in the redox chemistry of selenium is its anomalous difficulty in attaining the highest oxidation number +VI. It shares this feature with its neighbors Ge, As, and Br, which immediately follow the 3d metals in the periodic table. The structural aspects and stereochemistry of selenium chemistry are quite diverse. In addition to normal two-valent geometries with bent coordination around the central Se (e.g. H_2 Se, $SeCl_2$, Se_2Cl_2), the following are known: three-coordinate pyramidal Se^{IV} compounds (e.g. H_2SeO_3, $SeCl_3{}^+$ in $SeCl_4$, polymeric SeO_2); four-coordinate 10-electron systems with ψ-trigonal bipyramidal coordination (e.g. SeF_4); five-coordinate 12-electron systems with ψ-octahedral coordination (e.g. $[SeOCl_4]^{2-}$); and hypervalent octahedral (distorted and undistorted, see below) coordination (e.g. $[SeCl_6]^{2-}$, $[SeBr_6]^{2-}$). The additional ability to form higher coordination with hypervalent bonding (described here as systems of three-center four-electron bonds, as in the hexahaloselenates) leads to many variations of intermolecular aggregation in the solid state, as exemplified by the cubane-like tetranuclear halides $[SeCl_4]_4$ and $[SeBr_4]_4$.

The present account will concentrate on the basic inorganic chemistry of inorganic selenium that will be useful to a reader or researcher exploring this subject for the first time. Thus, the review will describe the diverse range of cations oxo- and halo-compounds that selenium forms.

Other areas of selenium chemistry, such as selenium rings,[1,2] selenides,[3,4] organoselenium compounds,[5–7] and the focus of older, more comprehensive accounts of Se halide chemistry[8,9] will not be covered here. Additionally, the vast environmental chemistry of selenium, for example, its aqueous[10] and sediment[11] speciation,[12] plant uptake,[13,14] nutritional[15] and human health[16,17] aspects, and appearance in coal[18] and coal-derived ash,[19,20] are beyond the scope of this review. The previous reviews on Se-containing ligands,[21–24] biochemistry of selenium,[25] as well as other relevant aspects,[26,27] remain some of the most valuable sources for information on these subjects.

2 POLYATOMIC CATIONS

2.1 Homocyclic Selenium Cations

Several types of homocyclic structures of selenium atoms are known. Neutral selenium rings Se_n with $n = 5-10$ have been studied in the vapor phase by mass spectrometry. In solution, Se_n species with $n = 6-8$ have been observed by HPLC techniques. The crystal structure of Se_6 and three modifications of Se_8 have been determined by X-ray diffraction.[1,2]

It has been found that selenium may be oxidized by several different oxidizing agents to a variety of polyatomic cations. In 1827, Magnus observed that sulfuric acid dissolved selenium to give green or yellow solutions.[28] It has been shown that these solutions contain the polyatomic cations Se_4^{2+} and Se_8^{2+}.[29]

2.1.1 Se_4^{2+} Cation

In highly acidic and oxidizing solutions like fluorosulfuric, sulfuric, and disulfuric acids with additional oxidants like selenium dioxide, peroxydisulfuryl difluoride or SbF_5, Se_4^{2+} salts can be prepared (see equations 1–3). The products have been characterized by cryoscopic, conductometric, and spectroscopic experiments.[29,30]

$$4Se + 6H_2S_2O_7 \longrightarrow Se_4^{2+} + SO_2 + 2HS_3O_{10}^- + 5H_2SO_4 \quad (1)$$

$$7Se + SeO_2 + 6H_2SO_4 \longrightarrow 2Se_4^{2+} + 6HSO_4^- + 2H_3O^+ \quad (2)$$

$$4Se + S_2O_6F_2 \longrightarrow Se_4^{2+} + 2SO_3F^- \quad (3)$$

The yellow to orange compounds $Se_4(HS_2O_7)_2$, $Se_4(S_4O_{13})_2$, and $Se_4(Sb_2F_{11})_2$ have been prepared.[31] Crystallographic studies on $Se_4(HS_2O_7)_2$ have shown that the cation Se_4^{2+} has square-planar (D_{4h}) geometry.[32] The structure can be described by valence bond theory[33] in terms of four resonance structures equivalent to (**1a**), or by simple molecular orbital theory in which three of the four π molecular orbitals are filled.[34] The Se_4^{2+} ions are examples of six-π-electron systems, and they are thus examples of inorganic aromatic compounds (**1b**).

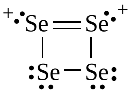

(**1a**)

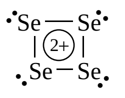

(**1b**)

Their π-bond order is 0.25; accordingly, the overall Se–Se bond length of 2.283 Å in $Se_4(HS_2O_7)_2$[32] is significantly shorter than the Se–Se distance of 2.34 Å in the Se_8 molecule. The intense yellow–orange color of the Se_4^{2+} ion (λ_{max} 410 nm, ε8000) is to be expected from the dipole-allowed excitation of an electron from the highest filled π-orbital which is of symmetry e_g and almost nonbonding, to the lowest empty π-orbital (b_{2u}). The square-planar arrangement is also consistent with magnetic circular dichroism of the Se_4^{2+} ion in solution.[35]

In crystals of $Se_4(Sb_2F_4)(Sb_2F_5)(SbF_6)_5$, prepared from Se and SbF_5 in liquid SO_2, and in $Se_4(AlCl_4)_2$,[36,37] the Se_4^{2+} ion has crystallographic inversion symmetry with average Se–Se distances of 2.260 and 2.286 Å.

Selenium can also be oxidized by arsenic pentafluoride to $Se_4(AsF_6)_2$ (equation 4) and by antimony pentafluoride to $Se_4(Sb_2F_{11})_2$ (equation 5) by heating the reactants in SO_2 for several days[31,38] With a trace of halogen (Cl_2, Br_2, I_2) or $AsCl_4AsF_6$, the reaction proceeds quantitatively in minutes.

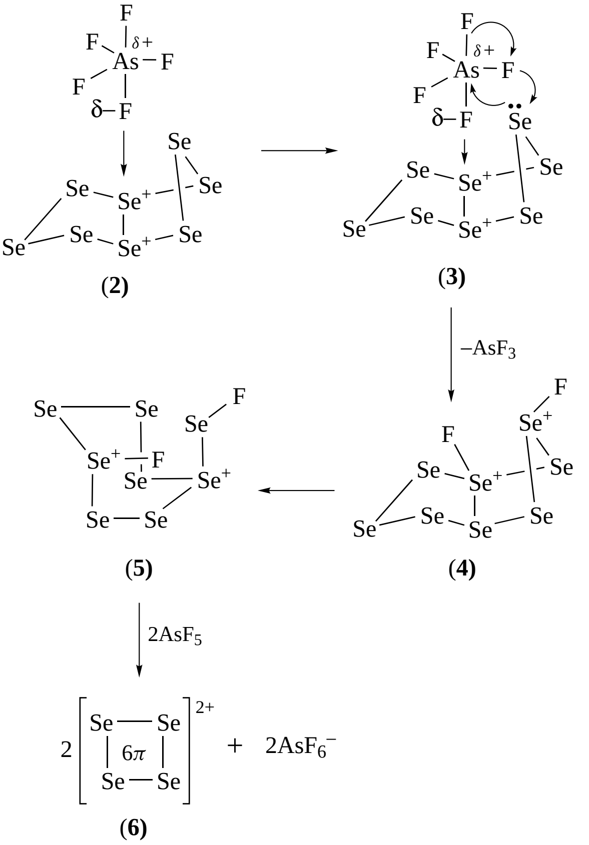

Scheme 1

They also propose[1] a reaction pathway for the oxidation of Se_8^{2+} to Se_4^{2+} by AsF_5 (Scheme 1).[39]

$$Se_8 + 6AsF_6 \xrightarrow{SO_2,\ 6\,d} 2Se_4(AsF_6)_2 + 2AsF_3 \quad (4)$$

$$Se_8 + 10SbF_5 \xrightarrow{SO_2,\ 12\,h} 2Se_4(Sb_2F_{11})_2 + 2SbF_3 \quad (5)$$

The Se_8^{2+} species may initially form a donor–acceptor adduct with AsF_5 (**2**) by the donation of an electron pair from the axial fluorine in AsF_5 to one of the positively charged three-coordinate selenium atoms. Another selenium atom of the ring donates an electron pair to the slightly positively charged arsenic atom, followed by rearrangement resulting in the formation of $Se_8F_2^{2+}$ (**3** → **4**). This species may rearrange to form (**5**). Finally, two AsF_5 molecules abstract two F^- to form two molecules of Se_4^{2+}(**5** → **6**).

Selenium reacts with an excess of SbF_5 in SO_2 at 363 K to form $(Se_4)_2(Sb_4F_{17})(SbF_6)_3$.[40] Two crystallographically independent Se_4^{2+} units with slight differences of Se–Se bond distances and angles (cation I, Se–Se 2.273, 2.276 Å, angles 90.5°, 89.5°; cation II, Se–Se 2.265, 2.276 Å, angles 90.7°, 89.3°) are found.[36]

None of these cations are stable in aqueous media or in any solvent containing small amounts of water, as they undergo disproportionation (equation 6).

They exist only in solvents with very low basicities, such as $H_2S_2O_7$, HSO_3F, SO_2, and AsF_5, and in the presence of anions such as SO_3F^-, $HS_2O_7^-$, SbF_6^-, $Sb_2F_{11}^-$, AsF_6^-, and $AlCl_4^-$, all of which are very weak bases of very strong corresponding acids.

$$2Se_4^{2+} + 6H_2O \longrightarrow 7Se + SeO_2 + H_3O^+ \tag{6}$$

2.1.2 *Se_8^{2+} Cation*

Conductivity measurements on solutions of selenium in highly acidic and oxidizing solutions indicate the formation of Se_8^{2+}.[10,12] Solutions of Se_8^{2+} in 100% H_2SO_4 are prepared by heating selenium in the acid at 50–60 °C (equation 7). Green solutions of Se_8^{2+} are also obtained by dissolving selenium in disulfuric acid (equation 8). The solutions are not stable, and further oxidation yields yellow solutions containing Se_4^{2+}. Salts of Se_8^{2+} are also obtained using SbF_5 or AsF_5 as oxidizing agents in an inert solvent such as SO_2 or HF (equation 9).[41,42]

$$8Se + 5H_2SO_4 \longrightarrow Se_8^{2+} + 2H_3O^+ + 4HSO_4^- + SO_2 \tag{7}$$

$$8Se + 6H_2S_2O_7 \longrightarrow Se_8^{2+} + 2H_2S_3O_{10}^- + 5H_2SO_4 + SO_2 \tag{8}$$

$$8Se + 3AsF_5 \xrightarrow[-23\,°C]{SO_2(l)} Se_8(AsF_6)_2 + AsF_3 \tag{9}$$

$$8Se + 5SbF_5 \xrightarrow[0\,°C]{HF} Se_8(Sb_2F_{11})_2 + SbF_3 \tag{10}$$

Both deep-green compounds undergo instant disproportionations in the presence of moist air (equation 6). Dissolution of $Se_8(AsF_6)_2$ or $Se_8(Sb_2F_{11})_2$ in 100% sulfuric acid, oleum, or fluorosulfuric acid, however, yields stable green solutions with typical absorption maxima at 295, 470, and 685 nm for the Se_8^{2+} cations.[29]

From phase diagram studies on the pseudobinary Se–($SeCl_4$ + $4AlCl_3$) system, the compounds $Se_4(AlCl_4)_2$ and $Se_8(AlCl_4)_2$ have been identified.[43,44] $Se_8(AlCl_4)_2$ alone was prepared from a stoichiometric mixture of Se, $SeCl_4$, and $AlCl_3$ after fusion at 250 °C for 3 h to produce black prismatic crystals (equation 11). $Se_8(AlCl_4)_2$ can also be prepared by the reaction of Se_2Cl_2 with $AlCl_3$ in SO_2 (equation 12)[45] The structure of $Se_8(AlCl_4)_2$ shows an endo–exo conformation of the eight-membered ring with approximate C_s symmetry (Figure 1).

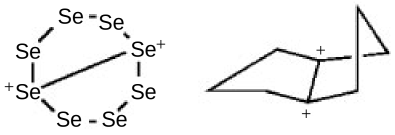

Figure 1 Structure of the bicyclic cation Se_8^{2+}

$$15Se + SeCl_4 + 4AlCl_3 \longrightarrow 2Se_8(AlCl_4)_2 \tag{11}$$

$$5Se_2Cl_2 + 4AlCl_3 \xrightarrow{SO_2(l)} Se_8(AlCl_4)_2 + 2SeCl_3(AlCl_4) \tag{12}$$

The bond lengths around the ring vary between 2.29 and 2.36 Å and do not differ significantly from those found in α and β selenium. The most striking difference between the Se_8^{2+} ion and the cyclic Se_8 molecules is the transannular bond, whose length of 2.84 Å is significantly shorter than the van der Waals contact separation of 4.0 Å.

The bond compensates for the removal of two electrons from Se_8 and is accompanied by the folding up of one end of the eight-membered ring. By removing two more electrons, the unknown Se_8^{4+} cation would result (decomposes to Se_4^{2+}). Interestingly, the structure of the isoelectronic Se_4N_4 molecule shows exactly the structure predicted for the hypothetical Se_8^{4+}, with the other end of the ring folding up and with a second transannular Se···Se bond. Thus, Se_8^{2+} appears to be the midpoint between the cage molecule of Se_4N_4 and the crown-shaped ring of Se_8 (Figure 2).[46]

2.1.3 *Se_{10}^{2+} Cation*

The hexafluoroarsenate and hexafluoroantimonate salts $Se_{10}(AsF_6)_2$ and $Se_{10}(SbF_6)_2$, containing the polyatomic

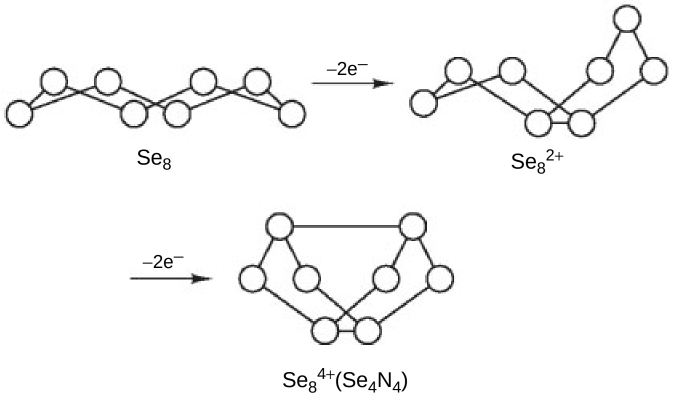

Figure 2 Gradual oxidation of Se_8 to 'Se_8^{4+}'

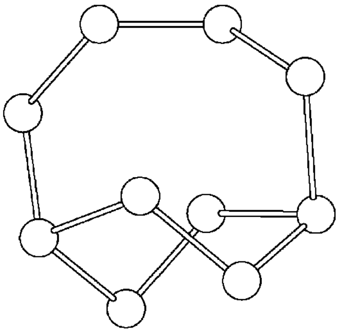

Figure 3 View of the Se_{10}^{2+} cation in $Se_{10}(SbF_6)_2$

cation Se_{10}^{2+}, were prepared by the reaction of excess selenium with AsF_5 or SbF_5 in SO_2 (equation 13) or the reaction of $Se_8(AsF_6)_2$ with elemental selenium in SO_2 (equation 14). $Se_{10}(SbF_6)_2$ can also be prepared similarly by disproportionation of $Se_8(AlCl_4)_2$ on washing with large quantities of SO_2 (equation 15).

$$10Se + MF_5 \longrightarrow Se_{10}(MF_6)_2 + 2MF_3 \qquad (13)$$

$$M = As, Sb$$

$$2Se + Se_8(AsF_6)_2 \longrightarrow Se_{10}(AsF_6)_2 \qquad (14)$$

$$4Se_8(AlCl_4)_2 \longrightarrow 3Se_{10}(AlCl_4)_2 + Se_2Cl_2 + 2AlCl_3 \qquad (15)$$

The structure of $Se_{10}(SbF_6)_2$ shows the cation to be of the bicyclo[4.2.2]decane type with approximate C_2 symmetry (Figure 3).[45] It consists of a six-membered, boat-shaped ring bridged by a chain of four selenium atoms to form an eight-membered ring. The six bonds to the three-coordinate atoms are the longest (2.41–2.44 Å). The adjacent bonds (2.24–2.26 Å) and the unique central bond in the bridging chain (2.35 Å) are shorter. The four short bonds are comparable to those in Se_4^{2+} salts, for example, in $Se_4(HS_2O_7)$ (2.28 Å) which have bond orders of 1.25 according to simple valence bond considerations. Spectrophotometric and potentiometric studies of cationic species of selenium in NaCl–$AlCl_3$ melts have been interpreted as indicating the presence of Se_{12}^{2+} and Se_{16}^{2+},[1,47] but the structures of these cations are unknown.

2.2 Derivatives of Selenium Rings

2.2.1 $Se_4I_4^{2+}$ Cation

The $Se_4I_4^{2+}$ cation is formed by the reaction of $Se_4(AsF_6)_2$ and I_2 in a 1:2 ratio.

Such solutions were studied by ^{77}Se NMR.[41] The coupling patterns are consistent with a four-membered ring or chain species. Ab initio energy calculations indicate a chain structure (**7**).

$$Se_4(AsF_6)_2 + 2I_2 \xrightarrow{SO_2} Se_4I_4(AsF_6)_2 \qquad (16)$$

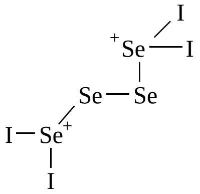

(**7**)

2.2.2 $Se_6I_2^{2+}$ and $(Se_6I^+)_n$ Cations

The salts $Se_6I_2(AsF_6)_2{\cdot}2SO_2$[48,49] and $(Se_6I)_n{\cdot}nAsF_6$,[49,50] containing stable selenium–iodine cations, have been prepared and characterized by X-ray crystallography. Both $Se_6I_2^{2+}$ and $(Se_6I^+)_n$ are derivatives of the chair form of Se_6, which exists as a metastable allotropic form of selenium.[1] $(Se_6I)_n{\cdot}nAsF_6$ is obtained quantitatively by reacting stoichiometric amounts of Se, I_2, and AsF_5 in SO_2 (equation 17). $Se_6I_2(AsF_6)_2{\cdot}2SO_2$ was prepared from SO_2 solutions (equation 18).

$$12Se + I_2 + 3AsF_5 \xrightarrow[11\,d]{SO_2,\ rt} 2/n(Se_6I)_n{\cdot}nAsF_6 + AsF_3 \qquad (17)$$

$$6Se + I_2 + 3AsF_5 \longrightarrow Se_6I_2(AsF_6)_2{\cdot}2SO_2 + AsF_3 \qquad (18)$$

$$2Se_8(AsF_6)_2 + 2SeI_3AsF_6 \longrightarrow 3Se_6I_2(AsF_6)_2{\cdot}2SO_2 \qquad (19)$$

The centrosymmetric $Se_6I_2^{2+}$ cation (Figure 4) contains hexaselenium rings with a chair conformation similar to Se_6.[48] The Se_6 ring is substituted in the 1,4-positions by two iodine atoms in an endo conformation. The tricoordinate selenium atoms in the $Se_6I_2^{2+}$ cation are positively charged. A Se–Se bond alternation between tri- and dicoordinate selenium atoms is observed, similar to other related rings and to the hexaselenium ring of Se_{10}^{2+}. The Se–I bonds (2.468 Å) are shorter than in SeI_3^+ (2.510 Å), implying $4p_\pi$–$4p_\pi$ and $4p_\pi$–$5p_\pi$ bonding. There are four intracationic I–Se contacts (average 3.714 Å; van der Waals radii 4.15 Å), leading to a distorted cube-like shape of the cation. This interaction must be attractive, otherwise the less sterically hindered *exo* conformation would be preferred.

The $(Se_6I^+)_n$ cation in $(Se_6I)_n{\cdot}nAsF_6$ has a two-dimensional polymeric structure. The geometry of the Se_6I_2

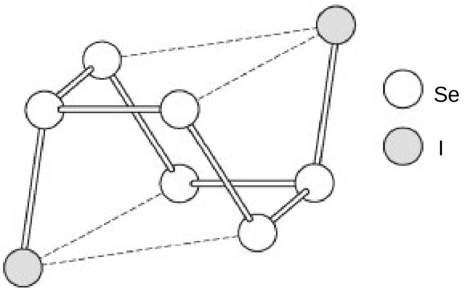

Figure 4 Structure of $Se_6I_2^{2+}$

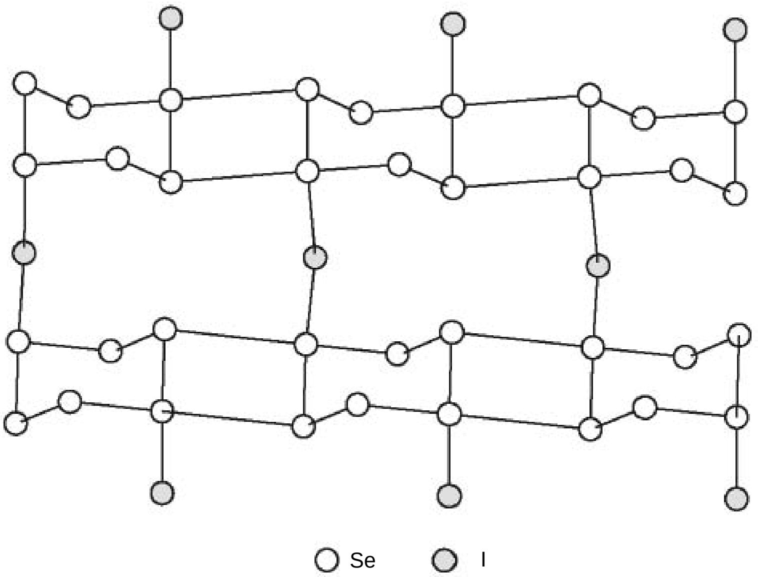

Figure 5 The polymeric $(Se_6I^+)_n$ cation

unit is similar to that in $Se_6I_2^{2+}$ (see above), with the iodine atoms bridging the Se_6 rings (Figure 5).**49** The bond alternation within the Se_6 ring is less pronounced than that in $Se_6I_2^{2+}$, consistent with the lower charge per ring.

2.2.3 $Ph_2Se_6^{2+}$ Cation

$Se_4(AsF_6)_2$ reacts with Ph_2Se_2 in liquid SO_2 at room temperature to give bright orange crystals of $Ph_2Se_6(AsF_6)_2 \cdot SO_2$.**42** This compound contains a six-membered selenium ring in a boat conformation with two phenyl groups in the 1,4-positions (Figure 6). The six-membered selenium rings Se_6, Se_6I^+, and $Se_6I_2^{2+}$ (see above) are all in the chair form. A reaction pathway was proposed (Scheme 2) with an initial trigonal prismatic intermediate or transition state, which rearranges to form the final boat conformation.**42**

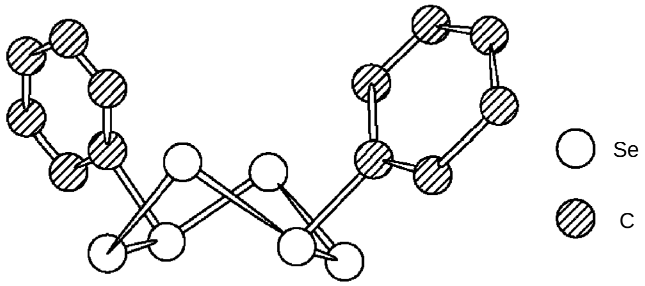

Figure 6 $Ph_2Se_6^{2+}$ cation in $Ph_2Se_6(AsF_6)_2 \cdot SO_2$

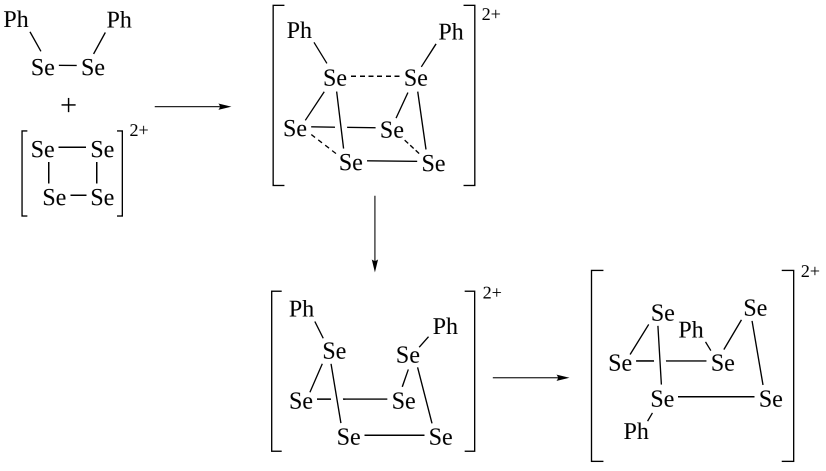

Scheme 2

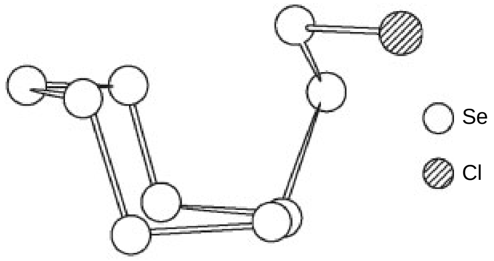

Figure 7 Se_9Cl^+ cation in $Se_9Cl(SbCl_6)$

2.2.4 *Se_9Cl^+ Cation*

The compound $Se_9Cl(SbCl_6)$ is prepared by the reaction of selenium with $NOSbCl_6$ in SO_2.[51] It is the first example of a seven-membered selenium ring (Figure 7). A Se_2Cl chain is joined to the ring which is in the chair conformation and in which the alternating Se–Se bond lengths around the ring vary from 2.270 to 2.430 Å.[52]

2.3 Acyclic Cationic Systems

$Se_2Br_5{}^+$, as the first reported example of a novel dinuclear cationic halogen−chalcogen species, was prepared as the deep-purple crystalline hexafluoroarsenate.[52] The cation consists of two trigonal pyramidal $SeBr_3$ units connected via a linear Se–Br–Se bridge. The formally positive Br^+ links two $SeBr_2$ molecules with formal oxidation number +2 for Se.

Reaction of selenium, bromine, and arsenic pentafluoride in liquid SO_2 leads to crystalline $(Se_3Br_3)(AsF_6)$. The crystal structure consists of discrete $Br_2Se^+SeSeBr$ and $AsF_6{}^-$ ions. The Se–Se bond lengths are 2.554 Å and 2.211 Å. The selenium−selenium bond alternation of 0.34 Å implies the presence of substantial partial $4p_\pi$–$4p_\pi$ bonding between the Se atoms in the Se–Se–Br unit.[53]

$Se_2I_4{}^{2+}$ has been reported recently as the first example of a novel type of diselenium tetraiodine(2+) cation.[54] It was synthesized by reaction of selenium with $[I_2][Sb_2F_{11}]$ in liquid SO_2. The cation consists of two $SeI_2{}^+$ units connected by a very weak Se–Se bond (2.841 Å) and has an eclipsed structure. The Se–Se bond length is comparable to the transannular bond in $Se_8{}^{2+}$.

2.4 Heterocyclic Selenium Cations

2.4.1 *S_3Se^{2+} Cation*

The heterochalcogen cations $S_xSe_{4-x}{}^{2+}$ ($x = 0$–3) have been characterized in SO_2 solution by ^{77}Se NMR studies. X-ray structural analysis of $(S_{3.0}Se_{1.0})_2(Sb_4F_{17})(SbF_6)_3$[55] have shown that the compound consists of two crystallographically independent $S_{3.0}Se_{1.0}{}^{2+}$ cations (for mixed Se/Te heterocyclic cations *see* ***Tellurium: Inorganic Chemistry***).

3 HALIDES AND RELATED COMPOUNDS

3.1 Monohalides

3.1.1 *SeF, SeCl, and SeBr Radicals*

Until recently, no selenium monohalide could be isolated; only the short-lived radicals SeF, SeCl, and SeBr were identified in the gas phase. SeF, can be produced by reaction of fluorine atoms (by passing CF_4 through a microwave discharge) with carbonyl selenide in a flow system. It has been detected by ESR spectroscopy[56,57] and the Se–F bond length (1.742 Å) is close to the value reported for SeF_2 (1.69 Å), deduced from infrared spectra.[9,58]

SeCl is formed by flash photolysis of $SeCl_2$ in the presence of N_2 or Ar. Addition of oxygen results in the formation of SeO.[59] Formation of SeCl is assumed when liquid selenium is in equilibrium with gaseous $SeCl_2$ at 280 °C (equation 20).[60] Gaseous SeBr was observed by its UV spectrum during the flash photolysis of Se_2Br_2 vapor at 50–55 °C in a mixture with nitrogen (75 mbar).[61] Both $SeCl_2$ and $SeBr_2$ are available as solutions in thf.[62]

$$Se(1) + SeCl_2(g) \longrightarrow 2SeCl \qquad (20)$$

3.1.2 *Se_2F_2, Se_2Cl_2, Se_2Br_2, and Se_2I_2*

A mixture of lower selenium fluorides is obtained by the reaction between heated selenium (210 °C) and fluorine, highly diluted with argon. FSeSeF and the other species are detected by IR spectroscopy. UV irradiation of matrix-isolated FSeSeF yields thermodynamically less stable $Se{=}SeF_2$.[63]

Selenium reacts with a stoichiometric amount of $SeCl_4$ to form reddish-brown liquid Se_2Cl_2. Se_2Br_2 can easily be prepared from the elements. Both have been characterized by X-ray structure analyses.[64] There are two different structure types (Se_2Cl_2, β-Se_2Br_2, and α-Se_2Br_2) containing X–Se–Se–X molecules with approximate C_2 symmetry and with dihedral angles of 87.4° (Se_2Cl_2) and 86.4° (Se_2Br_2). The average Se–X bond lengths are 2.202 Å (Se–Cl) and 2.364 Å (Se–Br). Different degrees of association of the molecules through Se···Se and Se···X contacts connect the molecules to layers and three-dimensional nets.

Orthorhombic α-Se_2Br_2 is thermodynamically stable compared to the monoclinic β-Se_2Br_2 modification. Monotropic exothermic transformation of the metastable into the stable form occurs in the range −40 to −5 °C.

In the gas phase, Se_2Cl_2 and Se_2Br_2 are not detectable because of dissociation into selenium and gaseous SeX_2. Se_2Cl_2 is able to form ionic complexes with strong Lewis acids.[65] Reaction of Se_2Cl_2 with BCl_3 and $SbCl_5$ in liquid sulfur dioxide at −40 °C forms $Se_2Cl_2{\cdot}BCl_3$ and $Se_2Cl_2{\cdot}SbCl_5$. Their IR spectra suggest ionic structures $[Se_2Cl]^+[BCl_4]^-$

and $[Se_2Cl]^+[SbCl_6]^-$. At room temperature, both compounds disproportionate to yield selenium and $SeCl_4{\cdot}BCl_3$ or $SeCl_4{\cdot}SbCl_5$.

An interesting reaction occurs between Se_2Cl_2 and S_4N_4 in the presence of thionyl chloride:[66] Thiatrithiazyl chloride, S_4N_3Cl, is formed, together with a compound of empirical formula $SeS_2N_2Cl_2$. From IR spectroscopy a structure corresponding to that of selenotrithiazyl haxachloroselenate(IV), $(SeS_3N_3)_2SeCl_6$, has been suggested. The cation in this salt may have the configurations (**8**) or (**9**).

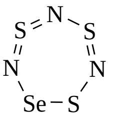

(**8**)

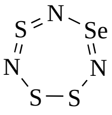

(**9**)

Simple binary selenium iodides are generally regarded as being nonexistent,[61] although several stable species with Se–I bonds have been reported: SeO_2I^-,[67] SeOClI,[68] areneselenium iodides,[69] $SeI_6{}^{2-}$,[70] $SeI_3{}^+$,[71] $(C_2F_5)SeI_2{}^+$,[71] $Se_2I_4{}^{2+}$,[54] $Se_4I_4{}^{2+}$,[41] $Se_6I_2{}^{2+}$,[48,49] and $(Se_6I)_n{}^{n+}$.[50,51] ^{77}Se NMR studies of solutions of selenium with iodine in carbon disulfide have been recently reviewed. These spectra indicate the presence of the selenium iodides Se_3I_2, Se_2I_2, and SeI_2 in such solutions, with Se_2I_2 as the main product.

3.2 Dihalides

Among the selenium dihalides, SeF_2, $SeCl_2$, and $SeBr_2$ are known to exist in the gas phase, while $SeCl_2$[62] and $SeBr_2$ are also known in solution. SeF_2 is obtained together with FSeSeF and SeF_4 by the reaction of heated selenium vapor with elemental fluorine diluted with argon (see above).[63] SeF_2 was also synthesized in good yield by UV photolysis of CF_3SeF_3 and isolated in an argon matrix:[72]

$$\mathrm{CF_3SeF_3} \xrightarrow{\lambda\,=\,208\,\mathrm{nm}} \mathrm{CF_4 + SeF_2} \tag{21}$$

IR spectra suggest the structure of the SeF_2 molecule to be nonlinear.[63] Photolysis of $SeCl_2$ as well as of $SeBr_2$ in an electrical discharge yields SeX· radicals.[59] In the case of the diselenium dihalides, only Se_2Br_2 gives detectable amounts of SeBr· species.[73]

Vapor pressure experiments and vibrational spectroscopic studies[74–77] show that $SeCl_2$ and $SeBr_2$ exist as dissociation products of the corresponding tetrahalides in the vapor phase or in organic solvents,[78] or as mixtures of SeO_2 and Se in aqueous HCl.[79] Their nonlinear structures were determined by photoelectron spectra and by electron diffraction.[80–82]

A remarkable stabilization of selenium dihalides is achieved if the central Se^{II} atom is coordinated with anionic (see Section 4.2) or neutral Lewis bases as ligands. $SeBr_2$ as well as $SeCl_2$ can be stabilized as crystalline tetramethylthiourea (tmtu) adducts, SeX_2(tmtu) (X = Cl, Br) (equations 22–23).[62,83]

$$\mathrm{RSeX_3 + tmtu \longrightarrow RX + SeX_2(tmtu)} \tag{22}$$

$$\mathrm{R = Me, Et}$$

$$\mathrm{SeX_4 + 3tmtu \longrightarrow (tmtu)_2X_2 + SeX_2(tmtu)} \tag{23}$$

$SeBr_2$(tmtu)[83] has a T-shaped heavy-atom $SSeBr_2$ framework (**10**), as previously suggested by IR spectroscopic studies.[84] The $SeBr_2$(tmtu) molecule can be described as a dimer with Se···Br contacts (3.34 Å) trans to sulfur that are shorter than the sum of the van der Waals radii (3.95 Å).[83] The arrangement around Se is distorted square planar.

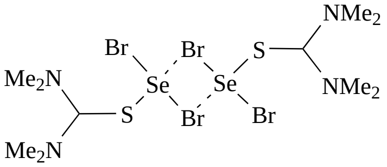

(**10**)

When triarylphosphane ligands are introduced as two-electron donors by the reaction of triarylphosphane selenide with Br_2, the product is T-shaped Ar_3PSeBr_2 with the Br ligands in the trans position.[85]

3.3 Tetrahalides

3.3.1 *Selenium Tetrafluoride*

Selenium tetrafluoride can be prepared in various reactions involving a fluorinating agent (AgF, ClF, ClF_3, CoF_3, SF_4, F_2, BrF_3) acting upon elemental selenium, SeO_2, $SeCl_2$, or $SeCl_4$. Another convenient method of preparation[86] uses SeF_4 itself as the reaction medium during the fluorination (equation 24).

$$\mathrm{3Se + 4ClF_3 \longrightarrow 3SeF_4 + 2Cl_2} \tag{24}$$

SeF_4 is a useful fluorinating agent, especially in organic chemistry, as it has some advantages over SF_4. It permits milder conditions and, because of its convenient liquid temperature range, it can be employed at atmospheric pressure.[86] Dissolved SeF_4 molecules have a ψ-trigonal bipyramidal structure like SF_4. If the enhanced concentration is increased, gradual intermolecular association of the molecules is observed.[87]

An X-ray structure determination of SeF_4[88] essentially confirmed the results of detailed vibrational spectroscopic investigations.[89–91] There is significant intermolecular association of the ψ-trigonal bipyramidal SeF_4 molecules in the solid state; however, it is much weaker than in TeF_4 where

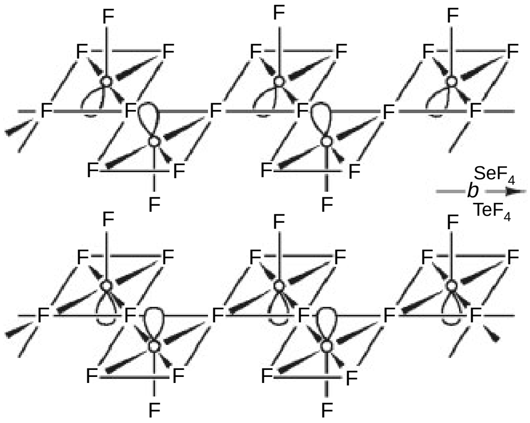

Figure 8 Polymeric structure of TeF$_4$ and the arrangement of monomeric SeF$_4$ subunits

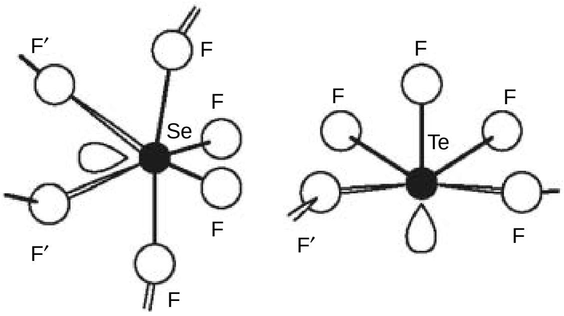

Figure 9 Coordination of selenium in crystalline SeF$_4$ as compared to the Te coordination in crystals of polymeric TeF$_4$

polymeric chains with square-pyramidal coordination of Te are formed (Figures 8 and 9).[92]

^{19}F NMR investigations have detected rapid intermolecular fluorine exchange in liquid SeF$_4$.[93] From conductometric measurements, SeF$_4$ in liquid hydrogen fluoride solution has been shown to be a weak base (equation 25).[94]

$$\mathrm{SeF_4 + HF \longrightarrow SeF_3{}^+ + HF_2{}^-} \tag{25}$$

The estimated value of the ionization constant ($K_b = 4 \times 10^{-4}$) indicates that SeF$_4$ is a weaker base in HF than SF$_4$ ($K_b = 4 \times 10^{-2}$).[95] The adducts of selenium tetrafluoride with Lewis acids are considered to be ionic compounds containing the SeF$_3{}^+$ cation. The systems of SeF$_4$ with BF$_3$, SbF$_5$, AsF$_5$, NbF$_5$, and TaF$_5$ have been studied.[94,96,97] Crystal structure determinations of SeF$_4$·NbF$_5$ and SeF$_4$·2NbF$_5$ show that they are composed of the SeF$_3{}^+$ and NbF$_6{}^-$ or Nb$_2$F$_{11}{}^-$ ions, respectively, although there is considerable interaction between the ions through fluorine bridging.[98,99] In the case of SeF$_3$·NbF$_6$, four formula units are linked to give Se and Nb atoms at alternate corners of a distorted cube, while for SeF$_3$·Nb$_2$F$_{11}$ the ions interact to form endless chains.

Conductometry and ^{19}F NMR spectroscopy have been used to study the systems of SeF$_4$ with BF$_3$ in HF.[94] Fluorine-bridged structures such as in SeF$_4$·NbF$_5$ and SeF$_4$·2NbF$_5$ with polymeric molecules and ions are present. The simplest equilibrium of this type involves the dimer (SeF$_4$·BF$_3$)$_2$, which may be either linear or cyclic.[94]

$$\mathrm{(SeF_4{\cdot}BF_3)_2 \rightleftharpoons (SeF_3)_2BF_4{}^+ + BF_4{}^-} \tag{26}$$

IR, Raman, and NMR studies of an adduct of SeF$_4$ with SO$_2$ in the solid and molten states are best interpreted as indicating a polymeric fluorosulfate-bridged structure.[100]

Adducts formed between SeF$_4$ and alkali metal fluorides[101] have been characterized by vibrational spectroscopy.[102] The observed Raman and IR spectra of CsSeF$_5$ indicate an ionic structure involving a square-pyramidal anion of C_{4v} symmetry.

3.3.2 Selenium Tetrachloride and Selenium Tetrabromide

Two characteristic structural and bonding features of the chlorine and bromine compounds of selenium(IV), in which the role of the inert pair determines much of stereochemistry and reactive properties of the entire class of compounds, are already evident in the simple binary halides.

1. Selenium(IV) as well as sulfur(IV) and tellurium(IV) tend to form a more or less distorted quasioctahedral (hypervalent) XY$_{3+3}$E or XY$_{4+2}$E coordination of six nearest neighbors in which there is a tendency to form stable trigonal pyramidal XY$_3{}^+$ subunits (X = Se, Y = Cl, Br, I; E is a more or less stereochemically active electron pair).
2. The harder (in Pearson's model[103]) or the more electronegative the ligand, the more pronounced the stereochemical activity of the inert electron pair localized at the chalcogen atom.

Selenium Tetrachloride. Selenium tetrachloride is usually prepared from the elements and decomposes thermally (equation 27).[104,105]

$$\mathrm{SeCl_4 \longrightarrow SeCl_2 + Cl_2} \tag{27}$$

As recent thermoanalytical and X-ray diffraction investigations show, SeCl$_4$ can be prepared in two polymorphic modifications, a metastable β-form[8,106,107] and a thermodynamically stable α-modification.[108,109] Crystallization from solvents such as POCl$_3$, sublimation of gaseous SeCl$_4$ into a zone with $T < 150\,^\circ\mathrm{C}$, or crystallization from the melt (360 °C) yields β-SeCl$_4$.

Increasing the sublimation and desublimation temperature ($T_d \sim 200\,^\circ\mathrm{C}$) causes the transformation of initial primary product, β-SeCl$_4$ into α-SeCl$_4$. Thus crystallization from the gas phase obeys Ostwald's rule.[106,110] α-SeCl$_4$ is also formed in the solid state by monotropic transformation above 180 °C. Stable selenium tetrachloride (α-$SeCl_4$)[109] contains Se_4Cl_{16} molecules.

β-$SeCl_4$ is isostructural with $TeCl_4$ and also contains tetrameric cubane-like Se_4Cl_{16} molecules with approximate T_d symmetry. Within the distorted $SeCl_{3+3}$ octahedra, the bonds to the triply bridging chlorine ligands are much longer than to the terminal chlorines. The bonding can be described either as covalent Se_4Cl_{16} molecules, or, in an ionic approximation, as $[(SeCl_3{}^+Cl^-)_4]$ with a certain degree of stereochemical activity of the lone pairs toward the center of the voluminous cubane center (Figure 10).[111,112] In the presence of strong Lewis acids, the $SeCl_4$ molecule ionizes and $[SeCl_3]^+$ ions are formed by chloride ion transfer (equation 28).[113]

$$SeCl_4 + HSO_3F \longrightarrow SeCl_3{}^+ + SO_3F^- + HCl \qquad (28)$$

The $[SeCl_3]^+$ ion is also formed in chlorosulfuric acid containing Se_2Cl_2[114] or selenium and chlorine.[115]

Solid compounds containing $[SeCl_3]^+$ cations have been well characterized. Thus in the case of the $SeCl_4{\cdot}AlCl_3$ adduct, the presence of discrete $[SeCl_3]^+$ and $[AlCl_4]^-$ ions has been shown by an X-ray structure determination.[116] The structure contains distorted $SeCl_6$ octahedra with three long and three short Se–Cl bonds of 3.04 and 2.11 Å (mean values). The spectra have been interpreted by assuming pyramidal $[SeCl_3]^+$ ions with C_{3v} symmetry.[117–121]

Selenium tetrachloride behaves as an ansolvo acid in an $SbCl_3$ melt (equation 29).

$$SeCl_4 + 2SbCl_3 \rightleftharpoons (SbCl_2)_2SeCl_6 \rightleftharpoons 2SbCl_2{}^+ + SeCl_6{}^{2-} \qquad (29)$$

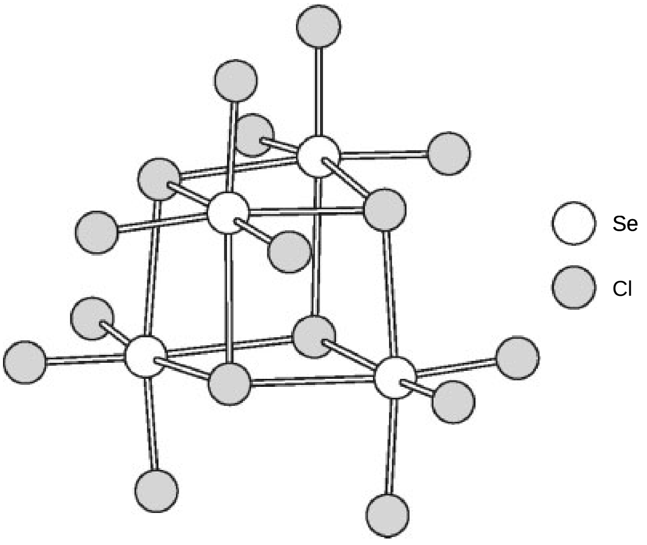

Figure 10 $Se_4Cl_{16}{}^-$ molecule in the structure of β-$SeCl_4$

Strong association of the ions was found by cryoscopy.[122] In the $SeCl_4$–$SbCl_5$ system, a compound of the composition $SeCl_4{\cdot}SbCl_5$ was concluded from the phase diagram.[123] $SeCl_4$ and excess $SbCl_5$ heated to 140–150 °C yield $SeCl_4{\cdot}SbCl_5$[97] ($SeCl_3{}^+SbCl_6{}^-$),[117] which is also obtained by reaction in $SOCl_2$ solution.[124]

Unlike SeF_4, which forms 1:1 ionic complexes containing the $SeF_5{}^-$ ion with alkali metal fluorides,[101,102] only octahedral ions of the type $[SeX_6]^{2-}$ are known for $SeCl_4$ and $SeBr_4$ (equation 30).

$$SeCl_4 + 2KCl \longrightarrow K_2SeCl_6 \qquad (30)$$

Some remarkable N-substituted derivatives of $SeCl_4$ with significant Se–N multiple bonding were reported from the reaction of Ph_3P–N–$SiMe_3$ with $SeCl_4$. The first product isolated was Ph_3P–N–$SeCl_3$, in which another chlorine can be replaced to give $(Ph_3P{=}N)_2SeCl_2$. On addition of $SbCl_5$ at −78 °C, one Cl is abstracted and $[(Ph_3P{=}N)_2SeCl^+]\,[SbCl_6{}^-]$ is formed.[125] $Cl_2Se{=}NTeF_5$, obtained as a reaction product from $SeCl_4$ and H_2NTeF_5,[126] is postulated to contain a Se=N double bond.

Selenium Tetrabromide. Selenium tetrabromide is mainly prepared by the reaction of the elements, either pure or dissolved in CS_2, using an excess of bromine. It occurs in two crystalline modifications, the thermodynamically stable α-$SeBr_4$ and the metastable β-$SeBr_4$. The latter forms first, in accordance with Ostwald's rule.

α-$SeBr_4$ crystallizes in the trigonal system and contains cubane-like $[SeBr_4]_4$ units.[106] Monoclinic β-$SeBr_4$ also consists of tetrameric cubane-like $[SeBr_4]_4$ molecules. β-$SeBr_4$ is isotypic with $TeCl_4$[127] and with β-$SeCl_4$; its chemical behavior and reactions are similar to $SeCl_4$.

3.3.3 *Reactions of the Tetrahalides*

Owing to their remarkable structural and bonding properties, their high general reactivity, and the significant influence of the lone pair on the reaction path and products, the reactions of the selenium(IV) halides are quite variable.

XY_4 + R^+Y^- $\longrightarrow$ haloselenates(IV)
+ selenium (IV)oxide $\longrightarrow$ selenium (IV)oxide halide
+ selenium (IV)oxide + R^+Y^- $\longrightarrow$ oxohaloselenates(IV)
+ reducing agents + R^+Y^- $\longrightarrow$ haloselenates(II)
+ alkyl(aryl)ating agents $\longrightarrow$ organoselenium(IV)halides
+ halides BY_n as Lewis acids / bases $\longrightarrow$ 'ionic' adducts
+ aqueous conc. HY $\longrightarrow$ hydronium haloselenates(IV)
+ superacids $\longrightarrow$ haloselenium polycations

Scheme 3

A wide variety of derivatives have been prepared according to the following reaction types (where Y = halogen, R^+ = metal ions or large cations such as tetraphenylphosphonium (arsonium)) (Scheme 3).

3.4 Hexahalides

3.4.1 *Selenium Hexafluoride*

SeF_6 can be prepared, stepwise directly from the elements (equation 31).[128] A patent claims the formation of selenium haxafluoride from selenium and chlorine monofluoride, ClF, at temperatures above 200 °C under substantially anhydrous conditions. Below 200 °C, SeF_4 is formed.[129] The rotational movements of the SeF_6 molecules in the plastic and liquid phases have been studied by ^{19}F NMR, IR, and Raman spectroscopy.[130]

$$\mathrm{Se}(s) + 3\mathrm{F_2(g)} \longrightarrow \mathrm{SeF_6(g)} \qquad (31)$$

X-ray measurements were made on polycrystalline material. It does not seem to be isotypic with the orthorhombic UF_6, as found by neutron diffraction.[131] SeF_6 is relatively inert to hydrolysis. It does not interact with water at room temperature over long periods, not even at elevated temperature.[132] The gas can be passed without change through aqueous 10% NaOH solution[133] and is resistant to aqueous 10% KOH solution as well.

3.4.2 *Selenium Pentafluoride Chloride*

Selenium pentafluoride chloride is the first compound isolated containing a stable Se–Cl bond. It was first obtained from SeF_4 and ClF,[134] but is best prepared from $CsSeF_5$ and $ClOSO_2F$:[135]

$$\mathrm{CsF + SeF_4 \rightleftharpoons CsSeF_5} \qquad (32)$$

$$\mathrm{CsSeF_5 + ClOSO_2F \rightleftharpoons SeF_5Cl + CsOSO_2F} \qquad (33)$$

Normal-coordinate analyses were carried out for SeF_5Cl.[136–138] There is a decrease of the stretching force constant values from SeF_6 to SeF_5Cl, demonstrating that the substitution of one fluorine atom in SeF_6 by the less electronegative chlorine atom causes an increased polarity of the remaining Se–F bonds.

4 OXIDES

4.1 Properties of the Se–O Bond

The bond parameters of the oxygen compounds of selenium compared to those of sulfur have been investigated.[139] The basic similarity between the bonding in these compounds, related to the model of a p_π–d_π bond system, has been confirmed by means of a linear relationship between the SeO and SO valence force constants.[140] A similar linear relationship has also been found between the valence force constants and the length of the SeO bond.[141] The influence of electronegative substituents on the frequencies of XO bonds in IR spectra has been verified for compounds of the type A–SeO–B.[142]

4.2 Selenium Dioxide

In the solid state, SeO_2 has a polymeric structure of corner-linked flattened SeO_3 pyramids, each carrying a pendant terminal O atom.[143] Mass spectrometric studies of the vapor over solid SeO_2 at 400 K indicate small amounts (1%) of dimeric SeO_2 in the gaseous phase.[144] A normal-coordinate calculation for the four possible symmetries of $(SeO_2)_2$ prove the centrosymmetric C_{2h} chair configuration (**11**) for the dimeric molecule.[145]

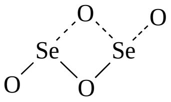

(**11**)

Selenium dioxide dissolves in $H_2S_2O_7$[146] to yield a colorless solution. From conductometry and cryoscopy measurements, it has been shown that, at low concentrations, SeO_2 may be protonated in $H_2S_2O_7$[124] in a similar manner as for H_2SO_4 solutions (equation 34).[147]

$$\mathrm{SeO_2 + 2H_2S_2O_7 \rightleftharpoons SeO(OH)^+ + HS_3O_{10}{}^- + H_2SO_4} \qquad (34)$$

The complex $H_2S_2O_7{\cdot}Se_2O_4$ is proposed in concentrated solutions.[146] SeO_2 is also very soluble in water producing selenous acid (H_2SeO_3), from which it can be recovered by dehydration. It is readily reduced to the element by NH_3, N_2H_4, or aqueous SO_2. Thus it also finds use as an oxidizing agent in organic chemistry.

4.3 Selenium Trioxide

The structure of the trioxide consists of tetrameric cyclic molecules $(SeO_3)_4$ of S_4 symmetry.[148] The mean Se–O distances are 1.55 Å for nonbridging oxygen and 1.77 Å for bridging oxygen. Electron diffraction[149] and mass spectrometry[144] of the vapor indicates that there is appreciable dissociation to the monomer at 120 °C. The Se–O distances in the monomeric SeO_3 molecule are 1.69 Å. In the molten state, selenium trioxide is probably polymeric.[150,151]

Selenium trioxide shows the typical properties of a Lewis acid[152] and forms 1:1 complexes with organic bases[153] such as pyridine, γ-picoline, quinoline, morpholine, and triethylamine in liquid SO_2 or nitromethane. The complexes were found to be of donor–acceptor type, and IR spectroscopy suggests that selenium is coordinated via the nitrogen atom of the tertiary base. It has also been confirmed that the tetrameric ring of SeO_3 is retained in the adducts.

Lewis-base characteristics are also exhibited by SeO_3. Reaction with arsenic or antimony chlorides and selenium trioxide in liquid SO_2 produces $SeO_3{\cdot}AsCl_3$, $SeO_3{\cdot}SbCl_3$, $SeO_3{\cdot}SbCl_5$, and $2SeO_3{\cdot}AsCl_3$, and the existence of $2SeO_3{\cdot}SbCl_3$ has been assumed from conductometric measurements.[154] These crystalline adducts are stable below $-20\,°C$. According to the Raman spectra of $SeO_3{\cdot}AsCl_3$ and $2SeO_3{\cdot}AsCl_3$ the oxygen atom of selenium trioxide is the donor in these complexes and the As atom is the electron-pair acceptor.[155] A thermogravimetric and gas-volumetric study[156] has shown that the thermal decomposition of SeO_3 takes place in two stages, with the formation of an intermediate pentoxide and the evolution of oxygen. It was also observed that SeO_3 begins to decompose at a lower temperature in a nitrogen atmosphere than in oxygen.

4.4 Diselenium Pentoxide

Se_2O_5 is formed as an intermediate during the thermal two-stage decomposition of SeO_3.[157] This has been confirmed by a thermoanalytical study and measurements of the evolved oxygen (equations 35 and 36).[156]

$$2SeO_3 \xrightarrow{185\,°C} Se_2O_5 + \tfrac{1}{2}\,O_2 \qquad (35)$$

$$Se_2O_5 \xrightarrow{225\,°C} 2SeO_2 + \tfrac{1}{2}\,O_2 \qquad (36)$$

Diselenium pentoxide can also be formed as a product in the reaction of selenium dioxide difluoride with SeO_2. Measurements of molten Se_2O_5 suggest that $[SeO]^+$ and $[SeO_4]^{2-}$ ions are present.[157] The structure of crystalline Se_2O_5 is that of a linear polymer with alternating Se^{IV} and Se^{VI} atoms (**12**), which has been confirmed by means of Raman spectroscopy.

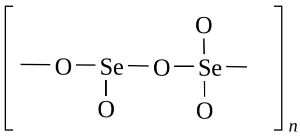

$$\left[\,-O-\underset{\underset{O}{|}}{Se}-O-\overset{\overset{O}{|}}{\underset{\underset{O}{|}}{Se}}-\,\right]_n$$

(12)

4.5 Selenium Oxide Halides

4.5.1 *$SeOF_2$, $SeOCl_2$, and $SeOBr_2$*

$SeOF_2$ has a trigonal pyramidal structure (C_s symmetry), as shown by microwave studies[158,159] and supported by the spectroscopic investigations of gaseous, liquid, and dissolved and solid $SeOF_2$.[160–163] In the gaseous state it is monomeric, as in the liquid, although there is some degree of intermolecular interaction. Fluorine and oxygen bridges are formed in the condensed phases, as confirmed by an X-ray structure determination.[164] Figure 11 shows the projection of the crystal structure of $SeOF_2$. $SeOF_2$ reacts with Lewis acids such as NbF_5, forming adducts of the type $SeOF_2{\cdot}NbF_5$.[165] The structure is reproduced in Figure 12.

$KSeOF_3$ is formed exothermally by reaction of $SeOF_2$ and KF.[166] The spectra confirm the expected geometry with two fluorine atoms at the apices of a pseudotrigonal bipyramid, in agreement with the prediction of the Valence Shell Electron Pair Repulsion (VSEPR) model.[167]

Like $SeOF_2$, $SeOCl_2$ molecules have a tendency to associate.[168] The monomers are in equilibrium with $(SeOCl_2)_2$ dimers in CS_2 solution. $SeOCl_2$ displays Lewis properties similar to other $SeOX_2$ compounds (X = F, Cl, Br, OMe, OEt). In donor–acceptor complexes of the type $D \rightarrow SeOX_2$, the Se atom always acts as the acceptor.[166] On the other

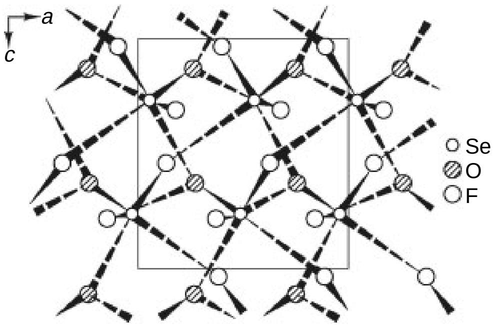

Figure 11 Projection of the crystal structure of $SeOF_2$

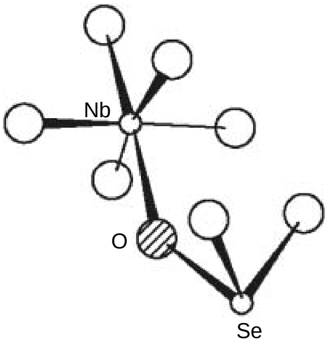

Figure 12 Atomic arrangement in $SeOF_2{\cdot}NbF_5$

hand, in complexes of the type $X_2SeO \rightarrow A$ the O atom is always the donor.[169–172] Reactions of $SeOCl_2$ with $S_2O_6F_2$ and $BrSO_3F$ yield, for example, a liquid of formula $SeO(SO_3F)_2$ as a product of both reactions.[173] This compound shows a partial temperature-dependent dissociation (equation 37). More recently, $SeOCl_2$ has been used as a selenium transfer agent.[174]

$$SeO(SO_3F)_2 \rightleftharpoons SeOSO_3F^+ + SO_3F^- \qquad (37)$$

Equimolar mixtures of $SeOCl_2$ and $SeOF_2$ react to form SeOClF, which is shown by ^{77}Se NMR[175] and Raman spectroscopy.[163] The reaction of $SeOCl_2$ with an equimolar amount of $SeOBr_2$ leads to red–orange liquid SeOBrCl.[163,175]

The $SeOBr_2$ molecule has a pyramidal structure (C_s symmetry), by analogy to $SeOF_2$ and $SeOCl_2$.[163] In the crystal structure, trigonal pyramidal $SeOBr_2$ molecules are associated with 3 + 3 coordinated selenium to polymeric double chains by oxygen and bromine bridges.[176]

4.5.2 SeO_2F_2

SeO_2F_2 is a very reactive gas, in contrast to SO_2F_2, due to the high oxidation power of selenium(VI) and the imperfect steric screening of the selenium atom by only four ligand atoms.[177] SeO_2F_2 has been used as a starting compound for the preparation of a large number of selenium–fluorine compounds. It reacts with dialkyl selenates to yield alkyl esters of fluoroselenic acid[178] and with N_2O_3 and N_2O_4 to yield nitrosonium and nitronium fluoroselenates.[179] When being fluorinated by HSO_3F, $HOSeF_5$ is formed.[180]

4.5.3 $SeOF_4$ and $Se_2O_2F_8$

$SeOF_4$ is prepared by vacuum decomposition of pure sodium pentafluoroorthoselenate (equation 38). The volatile rather unstable product is trapped at −196 °C.[181,182]

It can be assumed that $SeOF_4$ occurs as an intermediate in the decomposition of $As(OSeF_5)_3$,[183] $Ti(OSeF_5)_4$,[184] or $LiOSeF_5$[185] since the stable dimer of $SeOF_4$ is formed. In very small amounts, $SeOF_4$ is detected in the thermal decomposition of its dimer, $Se_2O_2F_8$, between 200 and 350 °C.[186,187]

$$NaOSeF_5 \xrightarrow{200\,^\circ C} NaF + SeOF_4 \qquad (38)$$

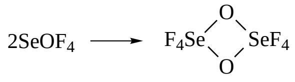

$$2SeOF_4 \longrightarrow F_4Se\overset{O}{\underset{O}{\diamond}}SeF_4 \qquad (39)$$

The $SeOF_4$ molecule is distorted trigonal bipyramidal, as shown by the IR, Raman,[181] and ^{19}F NMR spectra.[181,182] It is one of the few known hexavalent selenium compounds with fivefold coordination.[182] At temperatures above −100 °C the compound dimerizes to $Se_2O_2F_8$ (equation 39).[181,182] The compound is also prepared by pyrolysis of $NaOSeF_5$ via the intermediate formation of $SeOF_4$. The structure consists of two octahedra connected by a common O–O edge with a planar four-membered ring (Figure 13).[188] The dimer has only a slight tendency to split into the monomer even at elevated temperature.

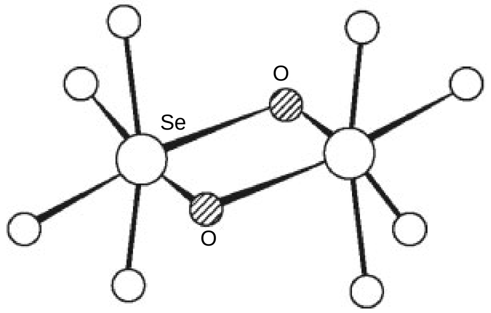

Figure 13 Molecular structure of $Se_2O_2F_8$

5 HALOSELENATES

5.1 Haloselenates(IV)

The nucleophilic stepwise degradation of the tetrameric Se_4X_{16} leads to tri-, di-, and mononuclear haloselenates(IV) (Figure 14).[8] In the case of the cubane-like Se_4Cl_{16}, the selenium atoms form three strong terminal bonds and three longer bridging bonds so that the bonding is close to an ionic formulation, $[(SeCl_3{}^+)_4(Cl^-)_4]$. As a general reaction scheme, it can be proposed that Cl^- ions attack the tetramer, eliminating one or two $SeCl_3{}^+$ groups in the form of neutral $SeCl_4$ species (equations 40 and 41). These products are obtained by reaction of stoichiometric amounts of the tetrahalides with R^+X^- (see

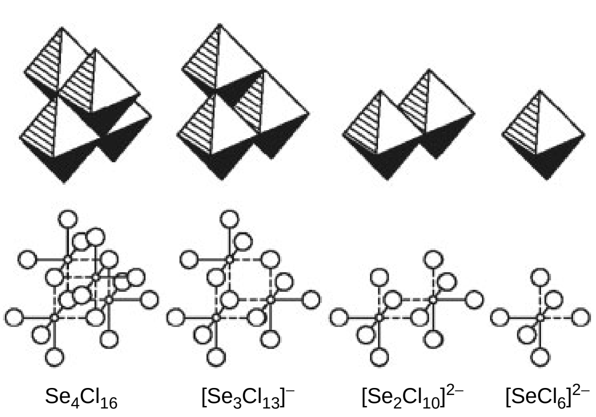

Figure 14 Degradation of the cubane-like tetrameric chalcogen(IV) halides exemplified by Se_4Cl_{16}

above) in organic solvents with low polarity.

$$Se_4Cl_{16} + R^+Cl^- \longrightarrow [R^+][Se_3Cl_{13}^-] + SeCl_4 \qquad (40)$$

$$Se_4Cl_{16} + 2R^+Cl^- \longrightarrow [R^+]_2[Se_2Cl_{10}^{2-}] + 2SeCl_4 \qquad (41)$$

5.1.1 Mononuclear Anions

The existence of $[SeF_6]^{2-}$ is doubtful because SeF_4 forms only $[SeF_5]^-$ anions with alkali fluorides.[101] The pentachloroselenate ion is present in a hydrochloric acid solution of selenium oxide at 0 °C[189] and in solid $[Et_4N][SeCl_5]$ or $[Ph_4As][SeCl_5]$.[190]

The hexahaloselenates(IV) $[SeX_6]^{2-}$ (X = Cl, Br) are the end-products of the nucleophilic degradation of the tetrahalides[8,61] (see Figure 14). The more or less ideal octahedral symmetry of these 14-electron SeX_6E systems cannot be described using simple models. They had been quoted as exceptions from the VSEPR theory.[167,191–193] From spectroscopic and theoretical studies, their bonding, structure, and their dynamic properties are well investigated.[61,194,195] Models to describe them extend from a simple $4p^34d^25s$ hybridization scheme,[196] with the inert pair shielding the bonding electrons, up to a molecular orbital-based model of three orthogonal three-center–four-electron bonds.[197]

5.1.2 Dinuclear and Trinuclear Anions

Decahaloselenates(IV) and tridecahaloselenates(IV) were isolated in salts such as $[Ph_4As]_2[Se_2Cl_{10}]$,[198] $[(C_{14}H_{13}ClN_3]_2[Se_2Cl_{10}]\cdot 2MeCN$,[199] $[Et_4N]_2[Se_2Br_{10}]$,[8] $[Ph_3C][Se_3Cl_{13}]$,[200] and $[Ph_3C][Se_3Br_{13}]$.[200] The dinuclear $[Se_2X_{10}]^{2-}$ structure consist of edge-sharing distorted octahedra. Also, as a fragment of Se_4X_{16} cubes, the anions $[Se_3X_{13}]^-$ consist of three edge-sharing octahedra with a central triply bridging chlorine or bromine atom (Figure 15).[200]

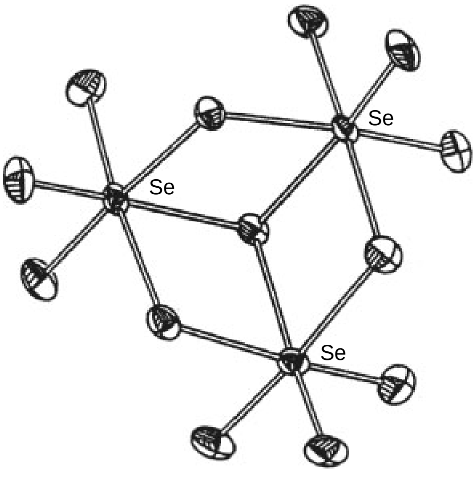

Figure 15 $[Se_3Cl_{13}]^-$ ion in $[Ph_3C][Se_3Cl_{13}]$

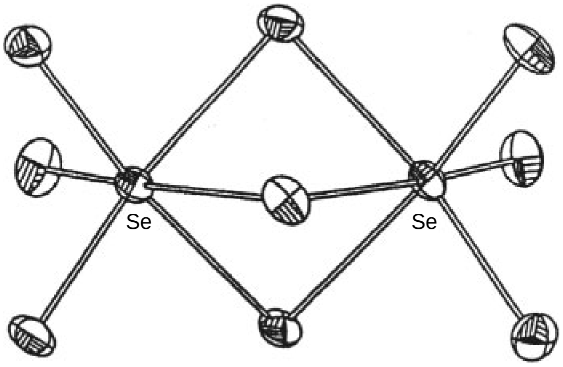

Figure 16 $[Se_2Br_9]^-$ ion in the crystal structure of $[EtPh_3P][Se_2Br_9]\cdot CH_2Cl_2$

The series of the decahaloselenates(IV) clearly demonstrates the stereochemical influence of the inert pair as a function of the halogen atom. The alkali metal pentafluoroselenates(IV) contain only the monomeric ψ-octahedral $[SeF_5]^-$ anions.[101,102]

If the degradation reaction of the tetramers is performed at slightly lower temperatures with very slow addition of halide as the nucleophilic agent, unexpected dinuclear nonahaloselenates(IV) are obtained. Their existence, together with evidence from their Raman spectra,[198] indicates the presence of an equilibrium between $[Se_2X_{10}]^{2-}$ and $[Se_2X_9]^-$ in aprotic solutions (equation 42).

$$[Se_2X_{10}]^{2-} \underset{+X^-}{\overset{-X^-}{\rightleftharpoons}} [Se_2X_9]^- \qquad (42)$$

The $[Se_2X_9]^-$ ions were isolated in $[Ph_4As][Se_2Cl_9]$,[198] $[EtPh_3P][Se_2Br_9]\cdot CH_2Cl_2$,[201] and in the double salts $[Et_4N]_4[Se_2Br_{10}(Se_2Br_9)_2]$[188] and $[Et_4N]_4[Se_2Cl_{10}(Se_2Cl_9)_2]$.[8,198] In Figure 16, the $[Se_2Br_9]^-$ anion is shown.[201] These nonahaloselenates(IV) contain three μ-bridging halogens, resulting in face-sharing of the two octahedral halves of the molecule.

5.1.3 Polynuclear Anions

$[S_4N_3]_n[SeCl_5]_n$[202] was obtained by diffusion of Se_2Cl_2 and S_4N_4 in $SOCl_2$ for several days. It contains polymeric $[SeCl_5^-]_n$ chains built from *cis* corner-sharing octahedra, resulting in $SeCl_{4+2}$ coordination (Figure 17a).

A compound with the empirical composition $[Me_3NH]_2[SeBr_8]$[4,203] was formed from $SeBr_4$ and trimethylammonium bromide in boiling aqueous HBr. It contains distorted $[SeBr_6]^{2-}$ anions which are in bonding contact to two *cis*-coordinated Br_2 molecules to form endless chains of composition $[SeBr_6^{2-}\cdot Br_2]_n$ (Figure 17b). The bond length in the Br_2 unit is significantly elongated compared to the free molecule, and the distortion of the $SeBr_6$ octahedron reflects the effect of intermolecular bonding.

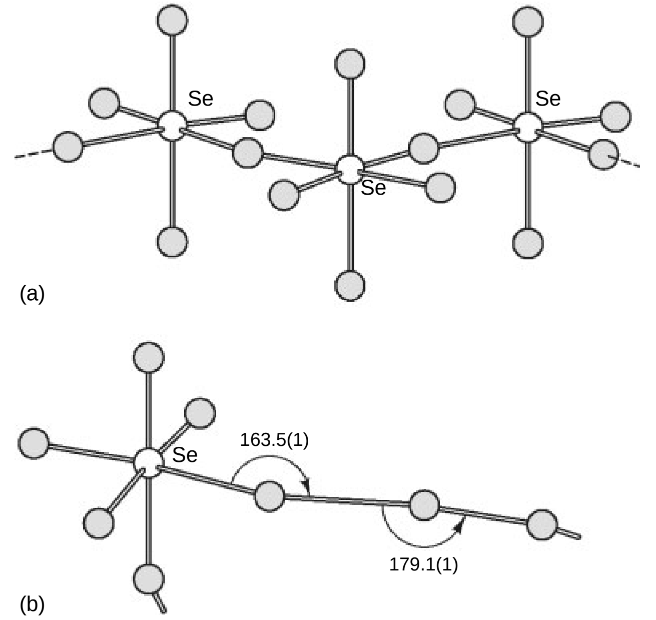

Figure 17 (a) Section of the polymeric $[SeCl_5^-]_n$ chain; (b) Section of the polymeric $[SeBr_6^{2-}\cdot Br_2]_n$ ion

5.2 Haloselenates(II)

5.2.1 *Mononuclear and Dinuclear Anions*

By symproportionation of elemental selenium and $SeCl_4$ in polar protic solvents, $[SeCl_4]^{2-}$ and $[Se_2Cl_6]^{2-}$ can be stabilized. They crystallize with voluminous organic cations (with $SeCl_2$:RCl ratios of 1:2 and 1:1) (equations 43–45).

$$SeCl_4 + Se \longrightarrow 2SeCl_2 \tag{43}$$

$$SeCl_2 + 2RCl \longrightarrow [R]_2[SeCl_4] \tag{44}$$

$$2SeCl_2 + 2RCl \longrightarrow [R]_2[Se_2Cl_6] \tag{45}$$

Using large organosubstituted countercations the anions could be isolated as $[Ph_3(C_2H_4OH)P]_2[SeCl_4]\cdot MeCN$ and $[Ph_4P]_2[Se_2Cl_6]$.[204] Also, the $S_4N_3^+$ cation is able to stabilize $[Se_2Cl_6]^{2-}$ in $[S_4N_3]_2[Se_2Cl_6]$.[202] Mononuclear planar haloselenates(II) are square-planar (ψ^2-octahedral) as predicted from VSEPR model considerations for these XY_4E_2 systems, which are isoelectronic with ICl_4^- or XeF_4. Their bonding can be described as a system of two four-electron–three-center bonds with a formal MO bond order of 0.5. The dinuclear planar $X_2Y_6^{2-}$ structure (isoelectronic with I_2Cl_6) consists of two edge-sharing distorted XY_4 squares. Tetrabromoselenate(II), $[SeBr_4]^{2-}$, and hexabromodiselenate(II), $[Se_2Br_6]^{2-}$, are formed in equilibrium mixtures of $SeOBr_2$ and/or $SeBr_4$ and their thermal reaction products in moderately polar organic solvents (equations 46–49).[205,206]

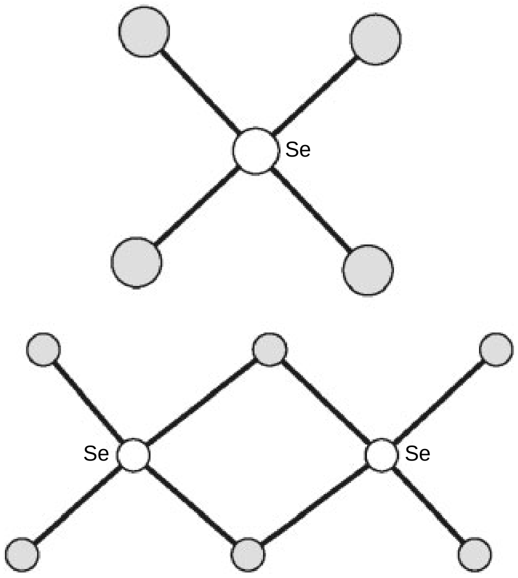

Figure 18 Structures of $[SeBr_4]^{2-}$ and $[Se_2Br_6]^{2-}$

$$2SeOBr_2 \xrightarrow[\text{MeCN}]{70\,^\circ\text{C}} SeBr_4 + SeO_2 \tag{46}$$

$$SeBr_4 \longrightarrow SeBr_2 + Br_2;\ 2SeBr_2 \longrightarrow Se_2Br_2 + Br_2 \tag{47}$$

$$SeBr_2 + Br_2 + SeO_2 + 4RBr \xrightarrow{\text{MeCN}} R_2[SeBr_4] + R[SeO_2Br] + RBr_3 \tag{48}$$

$$2SeBr_2 + 2Br_2 + 4RBr \xrightarrow[\text{MeCN}]{70\,^\circ\text{C}} R_2[Se_2Br_6] + 2RBr_3 \tag{49}$$

The structures of $[SeBr_4]^{2-}$ and $[Se_2Br_6]^{2-}$ are shown in Figure 18. From vibrational spectra it was concluded that the dimers dissociate in solution and form discrete T-shaped trihaloselenates(II).[207]

5.2.2 *Tri-, Tetra-, and Pentanuclear Anions*

Trinuclear $[Se_3Br_8]^{2-}$ was obtained in a 2-methyl propionitrile solution of $SeBr_4$, Se, and CuBr as the copper(I) salt $[(i\text{-PrCN})_4Cu]_2[Se_3Br_8]$.[203,208] The structure consists of a triangular arrangement of three planar $SeBr_4$ groups sharing a common edge (Figure 19a).

The tetranuclear $[Se_4Br_{14}]^{2-}$ anion was isolated as the ammonium salt $[Me_3PhN]_2[Se_4Br_{14}]$[209] and as the phosphonium salt $[EtPh_3P]_2[Se_4Br_{14}]$.[208] In these tetranuclear molecules, planar dinuclear Se_2Br_6 units are linked through two unusual nearly linear Se–Br–Se bridges. The bridging bromine atoms have the formal oxidation state +1. The Se–Br–Se bond angles are 175.9°[209] and 176.1°[208] (Figure 19b). If the ratio of $SeBr_2$ to R^+Br^- in the equilibrated

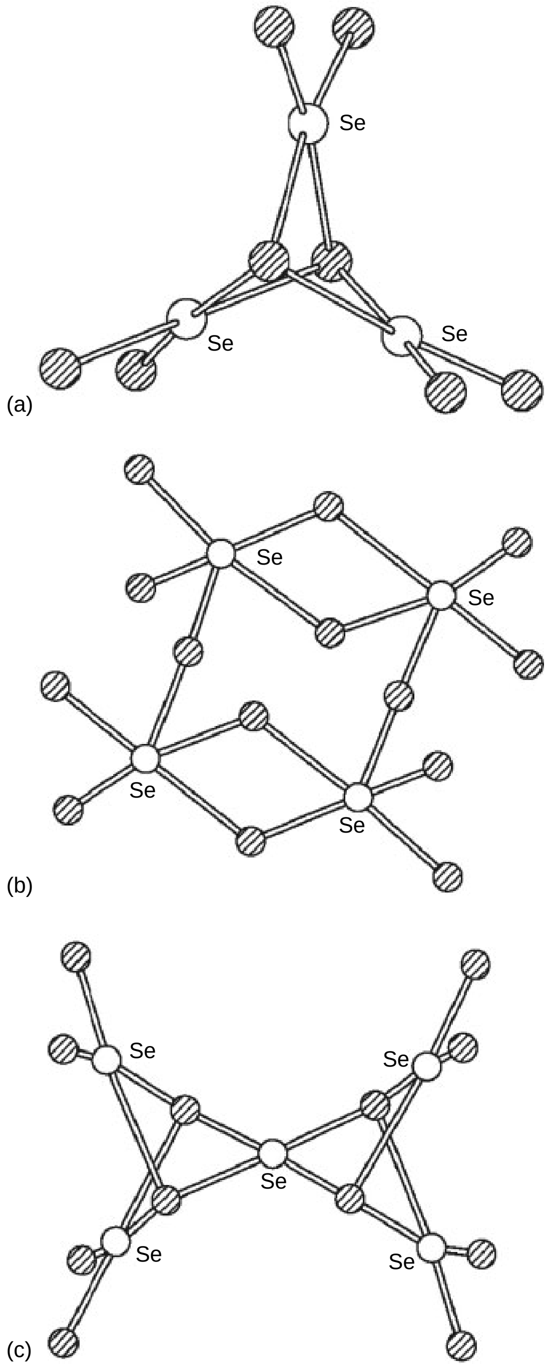

Figure 19 (a) $[Se_3Br_8]^{2-}$ anion, (b) $[Se_4Br_{14}]^{2-}$ anion, and (c) $[Se_5Br_{12}]^{2-}$ anion

reaction mixture is more than 2.5, the pentanuclear $[Se_5Br_{12}]^{2-}$ anion is formed.[208] It has D_{2h} symmetry and is composed of five planar $SeBr_4$ groups. Two pairs of two peripheral $SeBr_4$ units share one edge with one another and with the central unit (see Figure 19c). Because of the long Se–Br bonds from the terminal $SeBr_2$ groups to the μ_3-Br ligands, the bonding can also be approximated by the structural formula $[(SeBr_4{}^{2-})(SeBr_2)_4]$.

5.3 Mixed-Valence Haloselenates(II/IV)

From the complex reaction mixture of the redox system $SeBr_4/SeBr_2/Se/Br^-$ in aprotic solvents, di-, tri, and tetranuclear mixed-valence bromoselenates(II/IV) containing selenium in both oxidation states +2 and +4 were prepared: $[Se_2Br_8]^{2-}$, $[Se_3Br_{10}]^{2-}$, and $[Se_4Br_{12}]^{2-}$ (Figure 20).

In the $[Se^{II}Se^{IV}Br_8]^{2-}$ anion,[210,211] an octahedral $Se^{IV}Br_6$ group shares one edge with a square-planar $Se^{II}Br_4$ group. This coordination gives a clear assignment of the oxidation state of each selenium atom. The dihedral angles between the $Se^{II}Br_4$ plane and the basal plane of the $Se^{IV}Br_6$ octahedron are 34°[210] and 57°.[211]

By formal addition of a $SeBr_2$ group to this $[SeBr_8]^{2-}$ anion, the trinuclear decabromotriselenate(II/IV) $[Se_2{}^{II}Se^{IV}Br_{10}]^{2-}$ is formed, which was isolated as the n-propylammonium salt $[(n\text{-Pr})_4N]_2[Se_3Br_{10}]$.[210] In the centrosymmetric anion (see Figure 20b), a central $Se^{IV}Br_6$ octahedron is linked through two trans edges to two square-planar $Se^{II}Br_4$ groups with dihedral angles of 22° between the equatorial planes.

In the $[Se_3{}^{II}Se^{IV}Br_{12}]^{2-}$ ion,[210] two $SeBr_2$ moieties are coordinated via *cis* edges to the octahedral central $Se^{IV}Br_6$ unit. A third $SeBr_2$ group bridges one of the $Se^{IV}BrSe^{II}Br$ four-membered rings such that a short Se–Se distance of 3.335 Å results between Se(4) and Se(2) (see Figure 20c), indicating a

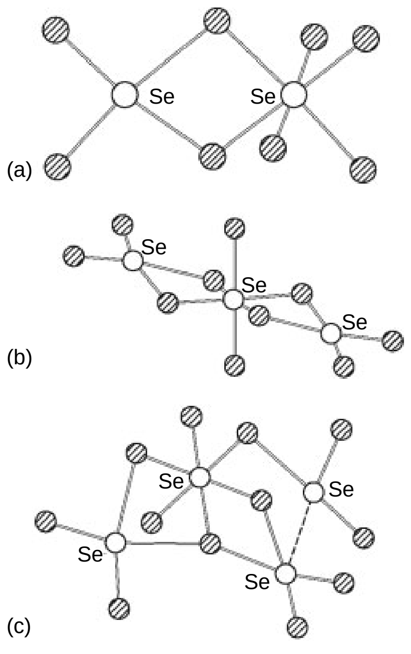

Figure 20 Mixed-valence bromoselenate(II/IV) anions: (a) $[Se_2Br_8]^{2-}$ in $[Et_4N]_2[Se_2Br_8]$; (b) $[Se_3Br_{10}]^{2-}$ in $[(n\text{-Pr})_4N]_2[Se_3Br_{10}]$; (c) $[Se_4Br_{12}]^{2-}$ in $[Ph_4P]_2[Se_4Br_{12}]\cdot CH_2Cl_2$

weak bonding interaction. Se(2) thereby completes the square-planar coordination geometry of Se(4).

The diamagnetic mixed-valence bromoselenates(II/IV) are to be assigned to class I in the Robin–Day scheme.**[212]** From the structural behavior, a significant valence exchange is not to be expected. The coordination geometries are always clear indications of different oxidation numbers.

6 OXOHALOSELENATES

6.1 Oxohaloselenates(IV)

Numerous oxohaloselenates(IV) with strong Se=O bonding are known. Three classes of these compounds can be prepared with stoichiometric compositions of $[SeO_2X]^-$, $[SeOX_3]^-$, and $[SeOX_4]^{2-}$ (X = F, Cl, Br).**[8,213–216]** The methods of preparation use nucleophilic addition reactions in different stoichiometric proportions of $SeOF_2$, $SeOCl_2$, or $SeOBr_2$ (or SeO_2 for oxygen-rich species, or SeX_4 + small amounts of H_2O) with the halide in aprotic solvents. $[SeO_2X]^-$ species had been predicted from spectroscopic considerations**[190]** and were confirmed by the preparation and structure of crystalline $[Me_4N][SeO_2Cl]$ and $[Ph_4P][SeO_2Br]$.**[176]** The structures of $[SeO_2Cl]^-$ and $[SeO_2Br]^-$ anions in these salts are shown in Figure 21. $[SeO_2Cl]^-$ is mononuclear, trigonal pyramidal, as expected for an $XY_2Y'E$ system. The closely related $[SeO_2Br]^-$, however, is associated through bridging bromine to polymeric chains. This shows once more the stereochemical flexibility and wide variability of the chalcogen inert-pair system as a function of the electronic environment.

This variability is also evident in the oxotrihaloselenates(IV). With different countercations, three isomers of the $[SeOX_3]^-$ anion could be prepared and structurally characterized (Figure 22).**[8]** A polymeric arrangement of $[SeOX_3{}^-]_n$ chains is found in $[C_9H_8NO][SeOCl_3]$.**[216]** The chains consist of distorted square $SeOCl_4$ pyramids with apical Se=O bonds (1.59 Å), two *cis* chlorines at 2.25 Å, and two bridging Cl at 2.96 and 2.99 Å from the selenium atom.

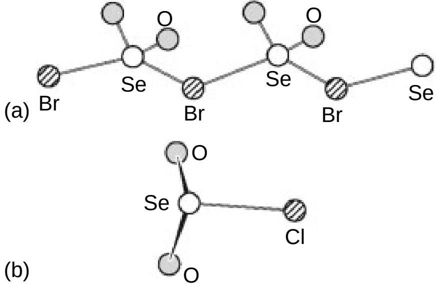

Figure 21 The two isomeric $[SeO_2Br^-]_n$ and $[SeO_2Cl]^-$ ions in (a) $[Ph_4P][SeO_2Br]$ and (b) $[Me_4N][SeO_2Cl]$

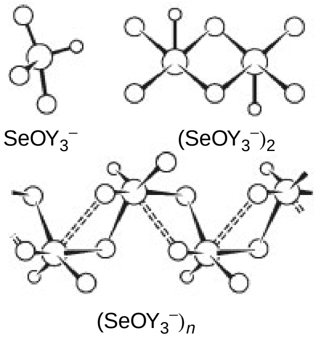

Figure 22 The three isomeric forms of oxotrichloroselenates(IV)

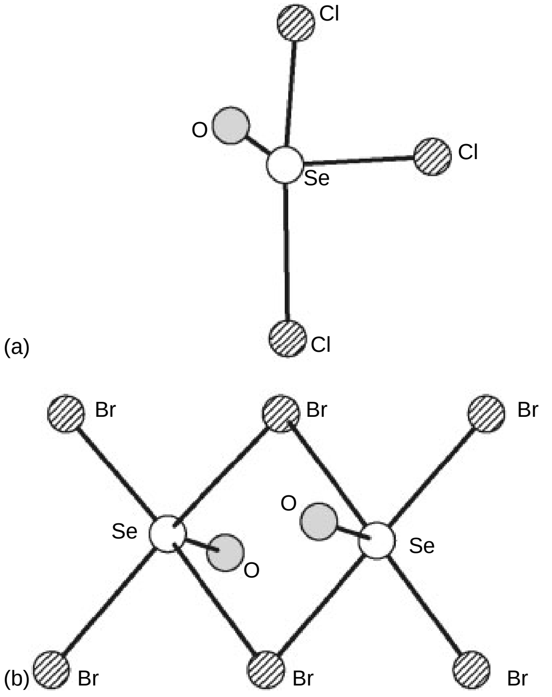

Figure 23 (a) Structure of the monomeric $[SeOCl_3]^-$ ion in $[Ph_4As][SeOCl_3]$ and (b) of the $[SeOCl_3{}^-]_2$ ion in $[Ph_4P][SeOCl_3]$

A monomeric $[SeOCl_3]^-$ anion with a trigonal bipyramidal structure is present in $[Ph_4As][SeOCl_3]$.**[217]** According to the VSEPR model, the oxygen (Se=O double bond) and the lone pair are located in the equatorial positions (Figure 23a). The third isomer is dinuclear; it can be isolated in the salts $[Et_4N][SeOCl_3]$,**[217]** $[Ph_4P][SeOCl_3]$, $[Ph_4P][SeOBr_3]$, and $[Ph_4As][SeOBr_3]$.**[218]** The centrosymmetric dianions consist of two edge-sharing tetragonal pyramidal $SeOX_4$ units with the inert pair at the selenium atom in trans positions to the strongly bonded axial oxygen atom (Figure 23b).

By formal exchange of one halogen for an oxygen atom, anions of the type $[SeO_2X_2]^{2-}$ are formed. The potassium salt $K_2SeO_2F_2$, which can be obtained by heating $KSeO_2F$

with an excess of KF to ≈300 °C or by decomposing $KSeO_2F$ in vacuum at 180 °C, contains the $[SeO_2F_2]^{2-}$ dianion. It is ψ-trigonal bipyramidal (C_{2v} symmetry) with the lone pair and the oxygen atoms in equatorial positions.[219]

The $[SeOCl_4]^{2-}$ anion is formed by nucleophilic attack of $SeOCl_2$ by two Cl^-:

$$SeOCl_2 \xrightarrow{+Cl^-} SeOCl_3{}^- \xrightarrow{+Cl^-} SeOCl_4{}^{2-} \qquad (50)$$

A regular pyramidal anion $[SeOCl_4]^{2-}$ is observed in the pyridinium double salt $[(C_5H_5NH)_4(H_3O)][(SeOCl_4)_2Cl] \cdot 11H_2O$[8,220] (Se=O 1.602 Å; Se–Cl 2.482 Å). In the dipyridinium salt $[C_{10}H_8N_2H_2]_2[SeOCl_4]$[221] (Se=O 1.63 Å; Se–Cl 2.25, 2.48, 2.48, 2.99 Å), the anions are distorted by participation of one of the Cl ligand atoms in strong Se–Cl···H–N hydrogen bridges to the cation. The ion is also present in $[Et_4N]_2[SeOCl_4]$, and $[Ph_4As]_2[SeOCl_4]$.[222]

A polynuclear $[Cl_2(SeOCl_2)_{10}]^{2-}$ unit is formed in $[Me_4N]_2[Cl_2(SeOCl_2)_{10}]$.[223] The two chloride ions are solvated by 10 $SeOCl_2$ molecules so that each Cl^- is octahedrally surrounded by six $SeOCl_2$ units, two of them sharing an adjacent octahedron (Figure 24).

6.2 Oxohaloselenates(VI)

The anion $[SeO_3F]^-$ is present in the compounds $MSeO_3F$ (M = alkali metal, NH_4, Ag, Tl, Cu, Zn, Cd, Co, Ni). It also occurs in the salts $[NO][SeO_3F]$[179] and $[NO_2][SeO_3F]$.[224] The corresponding acid $HSeO_3F$ is a clear, colorless liquid which hydrolyzes immediately.[225] It decomposes even at room temperature (equation 51).

$$2HSeO_3F \rightleftharpoons H_2SeO_4 + SeO_2F_2 \qquad (51)$$

$$SeO_2F_2 + 2HOSO_2F + KHF_2 \longrightarrow HOSeF_5 + KSO_3F + H_2SO_4 \qquad (52)$$

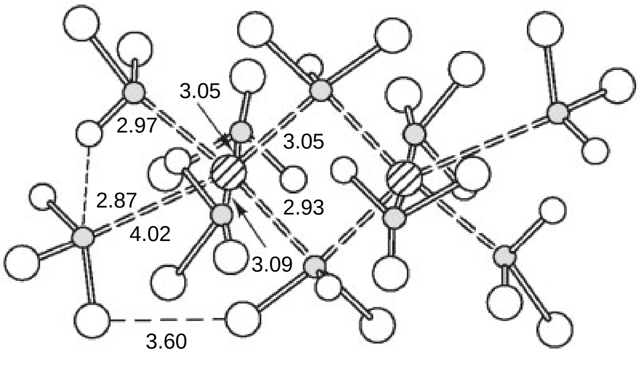

Figure 24 The arrangement of $SeOCl_2$ molecules around chloride ions in $[Me_4N]_2[Cl_2(SeOCl_2)_{10}]$ (distances in Å)

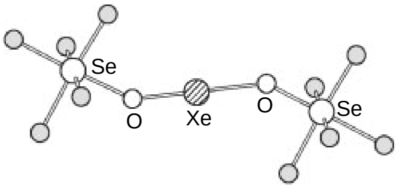

Figure 25 The structure of the $Xe[OSeF_5]_2$ molecule

The Raman and IR spectra of $[NO_2][SeO_3F]$ and $K[SeO_3F]$ can be assigned on the assumption of C_{3v} symmetry for the $[SeO_3F]^-$ anion.[224]

Pentafluoroselenic(VI) acid, $HOSeF_5$, was unexpectedly discovered during experiments to prepare the unknown $SeOF_4$.[202] It is best prepared from SeO_2F_2, $HOSO_2F$, and HF or KHF_2 (equation 52).

The anion $[OSeF_5]^-$ occurs in the pentafluoroorthoselenates $MOSeF_5$ (M = Li, K, Rb, Cs, NH_4,[226] Na,[181,226] NO_2[183,227]). The structure is octahedral, as derived from ^{19}F NMR, IR, and Raman spectra. The $OSeF_5$ group can best be characterized as a pseudohalogen or, more specifically, as a pseudofluorine. According to its reactions, this unit is more electronegative than fluorine. This is in line with the observation that the $OSeF_5$ groups in $F_nI[OSeF_5]_{5-n}$ occupy only equatorial positions.[228] The similarity to fluorine as a ligand is also shown in the ability of $[OSeF_5]^-$ to form the most stable xenon compound $Xe[OSeF_5]_2$[229] (Figure 25) besides the simple fluoride.

The extreme electronegativity of the $OSeF_5$ group is a result of the inductive effect of the five fluorines, thus additionally promoting p_π–d_π back-bonding from oxygen to the selenium atom.

7 SELENIUM AND NITROGEN

7.1 Selenium Nitrides

7.1.1 The SeN Radical

Selenium nitride, SeN, is formed by the reaction of selenium or selenium chlorides Se_2Cl_2 or $SeCl_4$[61] with active nitrogen produced by a high frequency discharge. To date, only the electron band spectra have been investigated.

7.1.2 Tetraselenium Tetranitride, Se_4N_4

Se_4N_4 is prepared by ammonolysis of selenium tetrahalides,[230–235] diselenium dichloride,[236] selenium dioxide,[232] or diethyl selenite.[226] It is rather unstable and decomposes explosively on heating or by sudden impact.

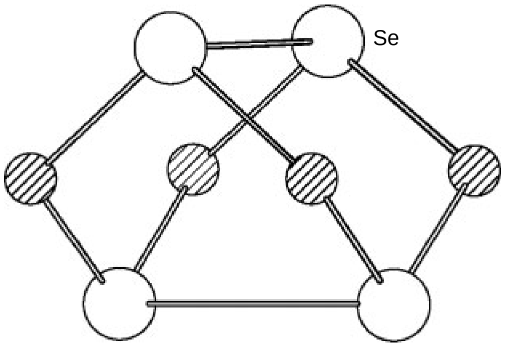

Figure 26 Structure of the Se_4N_4 molecule

In alkaline medium it is hydrolyzed to ammonia, elemental selenium, and selenium–oxygen compounds.

Se_4N_4 exists in at least two crystal modifications. The reaction of liquid NH_3 and $SeCl_4$, or $SeBr_4$, in an autoclave[232] yields crystals of the stable modification,[237] which is not isostructural with S_4N_4. It consists of discrete cage-like Se_4N_4 molecules. The eight-membered ring is puckered, the four selenium atoms being situated at the corners of a tetrahedron with the nitrogen atoms in a plane (Figure 26).

The metastable modification reverts to the first on heating.[238] Compounds of the type $(\overline{\text{SeNSeNSe}})_n(AsF_6)_2$, where n is 1 or 2, have been prepared by the reaction of stoichiometric quantities of $Se_4(AsF_6)_2$ ($n = 2$) or AsF_5 ($n = 1$ and 2) with Se_4N_4 in liquid sulfur dioxide.[239] ESR spectroscopy showed that $(\overline{\text{SeNSeNSe}})_2(AsF_6)_2$ contains the stable 7π radical $(\overline{\text{SeNSeNSe}})^{+}\cdot$ in solution while Raman and IR spectroscopy identified the 6π $(\overline{\text{SeNSeNSe}})^{2+}$ cation in $(\overline{\text{SeNSeNSe}})$ $(AsF_6)_2$. The structures of the solid species were characterized by X-ray structure determination. The reaction of Se_4N_4 with $[PtCl_2(PMe_2Ph)]_2$ in $CHCl_3$ gives $Pt(Se_3N)Cl(PMe_2PH)$ as the first example of a metal selenium–nitrogen complex. It contains the square-planar bidentate Se_3N^- ligand coordinated through two selenium atoms.[240]

7.1.3 *Se_4N_2*

In comparison to Se_4N_4, the recently synthesized Se_4N_2 molecule[241] is thermally more stable. It is formed by the reaction of Se_2Cl_2 with trimethylsilyl azide in CH_2Cl_2 (equation 53).

$$2Se_2Cl_2 + 4Me_3SiN_3 \longrightarrow Se_4N_2 + 5N_2 + 4Me_3SiCl \qquad (53)$$

According to its IR spectra the molecule has C_s symmetry with a chair configuration (**13**).

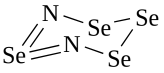

(13)

Two donor–acceptor complexes, $[SnCl_4(Se_4N_2)_2]$ and $[TiCl_4(Se_4N_2)]$, have been prepared by the reaction of Se_4N_2 with $SnCl_4$ and $TiCl_4$, respectively, in CH_2Cl_2 suspensions.[242] According to IR and ^{119}Sn Mössbauer spectra, in the tin complex both Se_4N_2 molecules are bonded with one of the nitrogen atoms at the tin atom in trans positions (**14**), whereas in the titanium complex both nitrogen atoms are assumed to be bonded in a chelating fashion at the titanium atom (**15**).

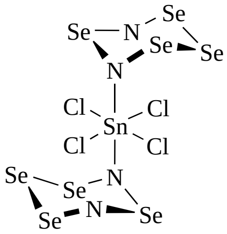

(14)

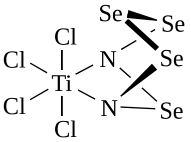

(15)

The reaction of tungsten hexachloride with Se_4N_2 leads to $[WCl_4(NSeCl)]_2$, which reacts with pyridine to form $[WCl_4(NSeCl)py]$, and with tetraphenylphosphonium chloride to form $PPh_4[WCl_5(NSeCl)]$.[243] The $[WCl_5(NSeCl)]^-$ ion contains an almost linear WNSe group.

7.1.4 *Selenium Chloride Nitrides*

Two stable chloride nitrides of selenium (with formal oxidation state +3 for Se), Se_2NCl_3 and $(Se_2NCl_2)(GaCl_4)$, have been synthesized.[244] The first structure consists of neutral Se_2NCl_3 units. The molecule is nearly planar with two linear Cl–Se–Cl moieties connected through a common bridging Cl atom. The nitrogen atom forms a second bridge between the two selenium atoms. The mean Se–N bond length of 1.738 Å and the Se–N–Se bond angle of 119.9° implies the presence of delocalized π-bonds between the Se atoms. The elimination of the bridging Cl atom with Lewis acids like $GaCl_3$ or $AlCl_3$ yields the cation $Se_2NCl_2{}^+$; it is nearly planar. The cation has approximately C_{2v} symmetry, with N–Se bond lengths of 1.695 Å, Se–Se distances of 2.147 Å, and bond angles of 146.6° (Se–N–Se) and 108.3° (Cl–Se–N).

7.1.5 *Related Selenium–nitrogen Rings*

Diselenium dichloride, Se_2Cl_2, and seleninyl chloride, $SeOCl_2$, react with a lithium salt of silylated t-butylamine with elimination of LiCl and Me_3SiCl or of LiCl, Me_3SiCl, and $(Me_3Si)_2O$, respectively, to form the cyclic compounds $(t\text{-Bu})_2N_2Se_6$ (**16**), a hexaselenadiazocin, and $(t\text{-Bu})_6N_6Se_9$

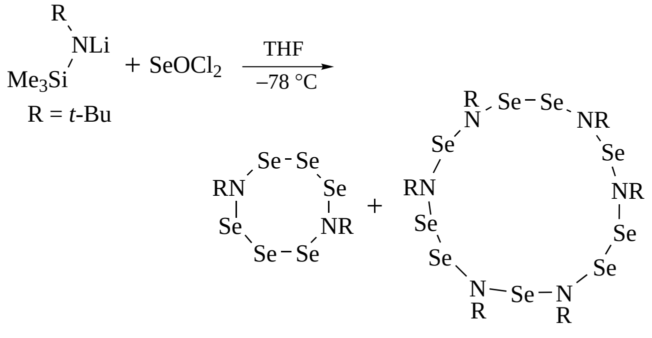

(16) **(17)**

(**17**), a nonaselenahexaazacyclopentadecane. The structures were established by X-ray diffraction.[245]

Another recently synthesized compound with a selenium atom coordinated by three nitrogen atoms is the tricyclic compound $SeSb_2Cl_2(NCMe_3)_4$, a product of the reaction between $[Se[NCMe_3(SiMe_3)]_2$ and $SbCl_3$.[246] According to an X-ray structure analysis, the six-membered $SeSb_2Cl_2(NCMe_3)_3$ ring is bonded to the triply bridging $NCMe_3$ moiety (Figure 27).

7.1.6 Selenium Imides

Newly available, pure, $SeCl_2$[62] was used, in combination with variable mole ratios of ${}^t\mathrm{BuNH_2}$, to prepare the structurally characterized imide compounds, acyclic $ClSe[N(t{-}Bu)Se]_{1\,\mathrm{and}\,2}Cl$, $Se_3(N^t\mathrm{Bu})_2$; and by combining $SeCl_4$ and ${}^t\mathrm{BuNH_2}$ with SO_2Cl_2 or $SeOCl_2$, c yclic ${}^t\mathrm{BuNSe}(\mu\text{-}t\text{-Bu})_2E$ ($E = SO_2$ and SeO).[247] The selenium-containing compounds were also studied by ^{77}Se NMR. The thermal decomposition of $Se(NAd)_2$ was studied by ^{77}Se NMR which indicated the presence of $Se_3(NAd)_3$, $Se(NAd)(\mu\text{-}NAd)_2SeO$ and $OSe(\mu\text{-}NAd)_2SeO$.[248] $Se_3(NAd)_2$ was isolated from the reaction and structurally characterized (Se–Se = 2.404(1) Å, Se–N = 1.873(4) Å).[249]

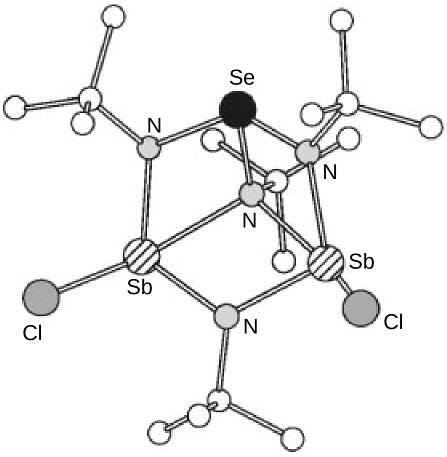

Figure 27 Structure of $SeSb_2Cl_2(NCMe)_4$

7.2 Amides of Selenious and Selenic Acid

7.2.1 Selenious Diamide, $SeO(NH_2)_2$, and Related Compounds

Selenious diamide is formed by reaction of ammonia with diethyl selenite or seleninyl bis(dimethylamide) (equation 54).[250]

$$(EtO)_2SeO + 2NH_3 \longrightarrow SeO(NH_2)_2 + 2EtOH \qquad (54)$$

$$(Me_2N)_2SeO + 2NH_3 \longrightarrow SeO(NH_2)_2 + 2Me_2NH \qquad (55)$$

The compound is sensitive to solvolysis and thermally unstable. $(NH)_2Se$ is formed by decomposition above −40 °C. Using methylamine or ethylenediamine instead of ammonia, seleninyl ethylenediamide, $(CH_2NH)_2SeO$, can be obtained by an analogous reaction. By the reaction of seleninyl bis(dimethylamide) with seleninyl chloride, a dimethylamide of chloroselenic(IV) acid results (equation 56).

$$(Me_2N)_2SeO + SeOCl_2 \longrightarrow 2Cl\text{–}SeO\text{–}NMe_2 \qquad (56)$$

7.2.2 Amidoselenic Acid, $HSeO_3NH_2$, and the $SeO_3NH_2{}^-$ Ion

The free acid $HSeO_3NH_2$ has not yet been prepared. The first salt of the acid was $NH_4SeO_3NH_2$, obtained by reaction of $C_5H_5N{\cdot}SeO_3$ with NH_3.[251] IR spectroscopy suggests C_s symmetry for the $SeO_3NH_2{}^-$ ion.[252,253]

In aqueous ammonia, $SeO_3NH_2{}^-$ anions react with excess Ag^+ ions to give two modifications of $AgSeO_3NAg_2$.[254] The crystal structure of α-Ag_3NSeO_3 consists of infinite chains of O_3SeNAg_3 molecules joined by O···Ag–N bridges,[255] in agreement with earlier IR results.[256] The molecules have almost regular tetrahedral configurations at each end and the Se–O and N–Ag bonds are almost eclipsed with a dihedral angle of 11.1°.[257]

7.2.3 Selenic Diamide, $SeO_2(NH_2)_2$

Selenic diamide, $SeO_2(NH_2)_2$, is formed by reaction of SeO_2F_2 and NH_3 in the gas phase or in inert solvents (e.g. CCl_4) among other selenium(VI)−nitrogen compounds.[177,257] In liquid ammonia, $SeO_2(NH_2)_2$ is thermally unstable (equation 57). It converts at −50 °C to the ammonium salts of cyclic triselenonylimide and at ambient temperature to the diamidopolyimidoselenic acids (equations 58−60).[258,259] Diamidoselenic acid hydrolyzes in water to form ammonium amidoselenate (equation 61).[258,259]

$$SeO_2F_2 + 4NH_3 \longrightarrow SeO_2(NH_2)_2 + 2NH_4F \qquad (57)$$

$$SeO_2(NH_2)_2 \longrightarrow SeO_2NH + NH_3 \qquad (58)$$

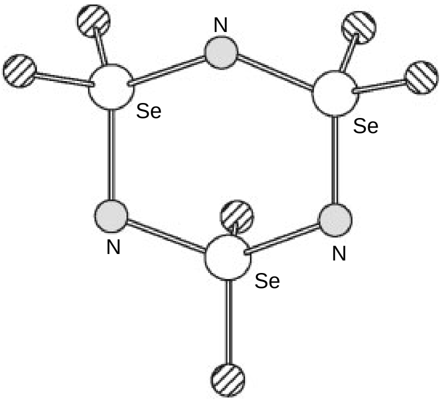

Figure 28 Molecular structure of $[SeO_2N]_3{}^{3-}$

$$3SeO_2NH + 3NH_3 \longrightarrow (NH_4)_3[SeO_2N]_3 \qquad (59)$$

$$nSeO_2NH + nNH_3 \longrightarrow NH_2SeO_2[SeO_2NNH_4]_{n-1}NH_2 \qquad (60)$$

$$SeO_2(NH_2)_2 + H_2O \longrightarrow NH_4SeO_3NH_2 \qquad (61)$$

7.3 Polymeric Anions of Selenonylimide

Selenonylimide, SeO_2NH, has not yet been isolated. The trimeric anion, $[SeO_2N]_3{}^{3-}$, occurs in some salts and the tetrameric anion, $[SeO_2N]_4{}^{4-}$, was identified by paper chromatography.

7.3.1 The $[SeO_2N]_3{}^{3-}$ Ion

The cyclic triselenonylimide ion, $[SeO_2N]_3{}^{3-}$, is present in the salts $M_3[SeO_2N]_3$ with M = K,[259–261] NH_4,[258–260] Ag, Tl^I.[260] All are highly explosive. The $[SeO_2N]_3{}^{3-}$ anion in the potassium salt (Figure 28) is a six-membered ring of approximate C_{3v} symmetry in a chair configuration with a considerably flattened Se_3N_3 skeleton. The Se–N distances indicate p_π–d_π delocalization over the individual Se–N–Se units.[261]

7.3.2 The $[SeO_2N]_4{}^{4-}$ Ion

The tetraselenonylimide ion, $[SeO_2N]_4{}^{4-}$, could only be detected in a paper chromatogram of the reaction products of SeO_2F_2 and NH_3.[257]

8 RELATED ARTICLES

Selenium: Organoselenium Chemistry; Selenium Proteins Containing Selenocysteine; Sulfur: Organic Polysulfanes; Tellurium: Inorganic Chemistry; Tellurium: Organotellurium Chemistry.

9 REFERENCES

1. R. J. Gillespie and J. Passmore, in ‘International Review of Science’, ed. V. Gutmann, Butterworth, London, 1974, Vol. 3, Chap. 4, p. 121.
2. R. Steudel and E. M. Strauss, *Adv. Inorg. Chem. Radiochem.*, 1984, **28**, 135.
3. J. Fenner, A. Rabenau, and G. Trageser, *Adv. Inorg. Chem. Radiochem.*, 1980, **23**, 329.
4. M. J. Atherton and J. H. Holloway, *Adv. Inorg. Chem. Radiochem.*, 1979, **22**, 171.
5. D. L. Klayman and W. H. H. Gunther eds, ‘Organic Selenium Compounds: Their Chemistry and Biology’, Wiley, New York, 1973.
6. D. L. J. Clive, *Tetrahedron*, 1978, **34**, 1049.
7. I. Omae, *Coord. Chem. Rev.*, 1982, **42**, 31.
8. B. Krebs and F.-P. Ahlers, *Adv. Inorg. Chem.*, 1990, **35**, 235.
9. A. Engelbrecht and F. Sladky, *Adv. Inorg. Chem. Radiochem.*, 1981, **24**, 189.
10. S. J. Hamilton, *Sci. Total Environ.*, 2004, **326**, 1.
11. P. T. Zawislanski, S. M. Benson, R. Terberg, and S. E. Borglin, *Environ. Sci. Technol.*, 2003, **37**, 2415.
12. S. Baoguo, M. Miroslav, and P. R. Haddad, *J. Chromatogr., A*, 2004, **1039**, 201.
13. K. M. Carvalho, M. T. Gallardo-Williams, R. F. Benson, and D. F. Martin, *J. Agric. Food Chem.*, 2003, **51**, 704.
14. P. Smrkolj and V. Stibilj, *Anal. Chim. Acta*, 2004, **512**, 11.
15. J. W. Finley, C. Ip, D. J. Lisk, C. D. Davis, K. J. Hintze, and P. D. Wanger, *J. Agric. Food Chem.*, 2001, **49**, 2679.
16. U. Schweizer, A. U. Brauer, J. Kohrle, R. Nitsch, and N. E. Savaskan, *Brain Res. Rev.*, 2004, **45**, 164.
17. P. Moreno, M. A. Quijano, A. M. Gutierrez, M. C. Perez-Conde, and C. Camara, *Anal. Chim. Acta*, 2004, **524**, 315.
18. R. Yan, D. Gauthier, G. Flamant, G. Peraudeau, J. Lu, and C. Zheng, *Environ. Sci. Technol.*, 2001, **35**, 1406.
19. B. P. Jackson and W. P. Miller, *Environ. Sci. Technol.*, 1999, **33**, 270.
20. M. Diaz-Somoano, M. A. Lopez-Anton, and M. R. Martinez-Tarazona, *Fuel*, 2004, **83**, 231.
21. S. G. Murray and F. R. Hartley, *Chem. Rev.*, 1981, **81**, 365.
22. B. Krebs, *Angew. Chem.*, 1983, **95**, 113; *Angew. Chem., Int. Ed. Engl.*, 1983, **22**, 113.
23. B. Walther, *Coord. Chem. Rev.*, 1984, **60**, 107.
24. E. W. Abel, S. K. Bhargava, and K. G. Orrell, *Prog. Inorg. Chem.*, 1984, **32**, 1.
25. J. D. Odom, *Struct. Bonding*, 1983, **54**, 1.
26. K. Seppelt, *Acc. Chem. Res.*, 1979, **12**, 211.
27. K. Dostal, in ‘International Review of Science’, ed. V. Gutmann, Butterworth, London, 1974, Vol. 3, Chap. 3, p. 85.

28. G. Magnus, *Ann. Phys. (Leipzig)*, 1827, **10**, 491; 1828, **14**, 323.
29. J. Barr, R. J. Gillespie, R. Kapoor, and K. C. Malhotra, *Can. J. Chem.*, 1968, **46**, 149.
30. R. J. H. Clark, T. J. Dines, and L. T. H. Ferris, *J. Chem. Soc., Dalton Trans.*, 1982, 2237.
31. J. Barr, D. B. Crump, R. J. Gillespie, R. Kapoor, and P. K. Ummat, *Can. J. Chem.*, 1968, **46**, 3607.
32. I. D. Brown, D. B. Crump, and R. J. Gillespie, *Inorg. Chem.*, 1971, **10**, 2319.
33. R. D. Harcourt, *J. Mol. Struct.*, 1985, **122**, 235.
34. K. Tanaka, T. Yamabe, H. Terama-e, and K. Fukui, *Inorg. Chem.*, 1979, **18**, 3591.
35. P. J. Stephens, *Chem. Commun.*, 1969, 1496.
36. G. Cardinal, R. J. Gillespie, J. F. Sawyer, and J. E. Vekris, *J. Chem. Soc., Dalton Trans.*, 1982, 765.
37. D. J. Prince, J. D. Corbett, and B. Garbisch, *Inorg. Chem.*, 1970, **9**, 2731.
38. P. A. W. Dean, R. J. Gillespie, and P. K. Ummat, *Inorg. Synth.*, 1974, **15**, 213.
39. M. P. Murchie, J. Passmore, G. W. Sutherland, and R. Kapoor, *J. Chem. Soc., Dalton Trans.*, 1992, 503.
40. R. Minkwitz, H. Borrmann, and J. Nowicki, *Z. Naturforsch.*, 1991, **46b**, 629.
41. M. M. Carnell, F. Grein, M. Murchie, J. Passmore, and C.-M. Wong, *J. Chem. Soc., Chem. Commun.*, 1986, 225.
42. R. Faggiani, R. J. Gillespie, and J. W. Kolis, *J. Chem. Soc., Chem. Commun.*, 1987, 592.
43. R. K. McMullan, D. J. Prince, and J. D. Corbett, *Inorg. Chem.*, 1971, **10**, 1749.
44. R. K. McMullan, D. J. Prince, and J. D. Corbett, *Chem. Commun.*, 1969, 1438.
45. R. C. Burns, W.-L. Chan, R. J. Gillespie, W.-C. Luk, J. F. Sawyer, and D. R. Slim, *Inorg. Chem.*, 1980, **19**, 1432.
46. K. Tanaka, T. Yamabe, H. Terama-e, and K. Fukui, *Nouv. J. Chim.*, 1979, **3**, 379.
47. R. Fehrmann and N. J. Bjerrum, *Inorg. Chem.*, 1977, **16**, 2089.
48. J. Passmore, P. S. White, and C.-M. Wong, *J. Chem. Soc., Chem. Commun.*, 1985, 1178.
49. W. A. S. Nandana, J. Passmore, P. S. White, and C.-M. Wong, *Inorg. Chem.*, 1989, **28**, 3320.
50. W. A. S. Nandana, J. Passmore, and P. S. White, *J. Chem. Soc., Chem. Commun.*, 1983, 526.
51. R. Faggiani, R. J. Gillespie, J. W. Kolis, and K. C. Malhotra, *J. Chem. Soc., Chem. Commun.*, 1987, 591.
52. M. Murchie, J. Passmore, and P. S. White, *Can. J. Chem.*, 1987, **65**, 1584.
53. J. Passmore, M. Tajik, and P. S. White, *J. Chem. Soc., Chem. Commun.*, 1988, 175.
54. W. A. S. Nandana, J. Passmore, P. S. White, and C.-M. Wong, *Inorg. Chem.*, 1990, **29**, 3529.
55. M. J. Collins, R. J. Gillespie, J. F. Sawyer, and G. J. Schrobilgen, *Inorg. Chem.*, 1986, **25**, 2053.
56. A. Carrington, G. N. Currie, and T. A. Miller, *J. Chem. Phys.*, 1969, **50**, 2726.
57. A. Carrington, G. N. Currie, P. N. Dyer, D. M. Levy, and T. A. Miller, *Chem. Commun.*, 1967, 641.
58. A. Haas and H. Willner, *Ber. Bunsen-Ges. Phys. Chem.*, 1978, **82**, 24.
59. S. Ciach, G. Power, and P. Thistlethwaite, *Chem. Phys. Lett.*, 1971, **9**, 349.
60. M. Lundqvist, *Acta Chem. Scand.*, 1968, **22**, 281.
61. ‘Gmelin Handbook of Inorganic Chemistry’, System No. 10, Selenium Suppl. Vol. B2, 8th edn., Springer, Berlin, 1984.
62. A. Maaninen, T. Chivers, M. Parvez, J. Pietikainen, and R. S. Laitinen, *Inorg. Chem.*, 1999, **38**, 4093.
63. A. Haas and H. Willner, *Z. Anorg. Allg. Chem.*, 1979, **454**, 17.
64. R. Kniep, L. Korte, and D. Mootz, *Z. Naturforsch.*, 1983, **38b**, 1.
65. R. C. Paul, R. D. Sharma, R. K. Verma, and K. C. Malhotra, *Indian J. Chem.*, 1972, **10**, 737.
66. A. J. Banister and J. S. Pandey, *J. Chem. Soc. A*, 1967, 1437.
67. S. Wasif and S. B. Salama, *J. Chem. Soc., Dalton Trans.*, 1975, 2239.
68. K. Neindorf and R. Paetzold, *J. Mol. Struct.*, 1973, **19**, 693.
69. W.-W. duMont, S. Kubiniok, K. Peters, and H.-G. von Schnering, *Angew. Chem.*, 1987, **99**, 820; *Angew. Chem., Int. Ed. Engl.*, 1987, **26**, 780.
70. N. N. Greenwood and B. P. Straughan, *J. Chem. Soc. A*, 1966, 962.
71. J. P. Johnson, M. Murchie, J. Passmore, M. Tajik, P. S. White, and C.-M. Wong, *Can. J. Chem.*, 1987, **65**, 2744.
72. D. M. De Leeuw, R. Mooyman, and C. A. De Lange, *Chem. Phys.*, 1979, **38**, 21.
73. G. A. Oldershaw and K. Robinson, *Trans. Faraday Soc.*, 1971, **67**, 907.
74. K. Högberg and M. Lundqvist, *Acta Chem. Scand.*, 1970, **24**, 255.
75. M. Lundqvist and M. Lellep, *Acta Chem. Scand.*, 1968, **22**, 291.
76. G. A. Ozin and A. Vander Voet, *Chem. Commun.*, 1970, 896.
77. E. Nagy-Felsobuki and J. B. Peel, *J. Chem. Soc., Faraday Trans. 2*, 1980, **76**, 148.
78. J. Milne, *Can. J. Chem.*, 1989, **67**, 1056.
79. M. Mahadevan and J. Milne, *Inorg. Chem.*, 1983, **22**, 1648.
80. P. A. Akishin, V. P. Spiridonov, and R. A. Mishulina, *Vestn. Mosk. Univ., Ser. II Khim.*, 1962, **17**, 23; *Chem. Abstr.*, 1962, **57**, 8166c.
81. L. Fernholt, A. Haaland, and R. Z. Seip, *Z. Naturforsch.*, 1983, **38b**, 1072.
82. E. Nagy-Felsobuki and J. B. Peel, *Chem. Phys.*, 1980, **45**, 189.

83. K. J. Wynne, P. S. Pearson, M. G. Newton, and J. Golen, *Inorg. Chem.*, 1972, **11**, 1192.
84. K. J. Wynne and P. S. Pearson, *Chem. Commun.*, 1971, 293.
85. D. J. Williams and K. J. Wynne, *Inorg. Chem.*, 1976, **15**, 1449.
86. G. A. Olah, M. Nojima, and I. Kerekes, *J. Am. Chem. Soc.*, 1974, **96**, 925.
87. K. Seppelt, *Z. Anorg. Allg. Chem.*, 1975, **416**, 12.
88. R. Kniep, L. Korte, R. Kryschi, and W. Poll, *Angew. Chem.*, 1984, **96**, 351; *Angew. Chem., Int. Ed. Engl.*, 1984, **23**, 388.
89. C. J. Adams and A. J. Downs, *Spectrochim. Acta*, 1972, **28A**, 1841.
90. L. E. Alexander and I. R. Beattie, *J. Chem. Soc., Dalton Trans.*, 1972, 1745.
91. I. C. Bowater, R. D. Brown, and F. R. Burden, *J. Mol. Spectrosc.*, 1968, **28**, 454.
92. A. J. Edwards and F. I. Hewaidi, *J. Chem. Soc. A*, 1968, 2977.
93. E. L. Muetterties and W. D. Phillips, *J. Chem. Phys.*, 1967, **46**, 2861.
94. M. Brownstein and R. J. Gillespie, *J. Chem. Soc., Dalton Trans.*, 1973, 67.
95. M. Azeem, M. Brownstein, and R. J. Gillespie, *Can. J. Chem.*, 1969, **47**, 4159.
96. J. A. Evans and D. A. Long, *J. Chem. Soc. A*, 1968, 1688.
97. R. J. Gillespie and W. A. Whitla, *Can. J. Chem.*, 1970, **48**, 657.
98. A. J. Edwards and G. R. Jones, *J. Chem. Soc. A*, 1970, 1491.
99. A. J. Edwards and G. R. Jones, *J. Chem. Soc. A*, 1970, 1891.
100. R. J. Gillespie and W. A. Whitla, *Can. J. Chem.*, 1969, **47**, 4153.
101. E. E. Aynsley, R. D. Peacock, and P. L. Robinson, *J. Chem. Soc.*, 1952, 1231.
102. K. O. Christe, E. C. Curtis, C. J. Schack, and D. Pilipovich, *Inorg. Chem.*, 1972, **11**, 1679.
103. R. G. Pearson, *Science*, 1966, **151**, 172.
104. G. Pannetier, P. Goudmand, O. Dessaux, and I. Arditi, *C. R. Hebd. Seances Acad. Sci.*, 1965, **260**, 2155.
105. G. Petropoulos, O. Dessaux, and P. Goudmand, *C. R. Hebd. Seances Acad. Sci.*, 1970, **C270**, 6.
106. P. Born, R. Kniep, D. Mootz, M. Hein, and B. Krebs, *Z. Naturforsch.*, 1981, **36b**, 1516.
107. R. Kniep, L. Korte, and D. Mootz, *Z. Kristallogr.*, 1981, **156**, 75.
108. G. V. Golubkova, E. S. Retrov, and T. I. Samsonova, *Zh. Strukt. Khim.*, 1976, **17**, 322.
109. R. Kniep, L. Korte, and D. Mootz, *Z. Naturforsch.*, 1981, **36b**, 1660.
110. A. W. Cordes, R. F. Kruh, E. K. Gordon, and M. K. Kemp, *Acta Crystallogr.*, 1964, **17**, 756.
111. B. Buss and B. Krebs, *Angew. Chem.*, 1970, **82**, 446; *Angew. Chem., Int. Ed. Engl.*, 1970, **9**, 463.
112. B. Buss and B. Krebs, *Inorg. Chem.*, 1971, **10**, 2795.
113. R. C. Paul, K. K. Paul, and K. C. Malhotra, *J. Inorg. Nucl. Chem.*, 1972, **34**, 2523.
114. R. C. Paul, D. S. Dhillon, D. Konwer, and J. K. Puri, *Indian J. Chem.*, 1980, **A19**, 473.
115. R. C. Paul, D. Konwer, and J. K. Puri, *Indian J. Chem.*, 1982, **A21**, 81.
116. B. A. Stork-Blaisse and C. Romers, *Acta Crystallogr.*, 1971, **B27**, 386.
117. W. Brockner and A. F. Demiray, *Z. Naturforsch.*, 1980, **35a**, 766.
118. W. Sawodny and K. Dehnicke, *Z. Anorg. Allg. Chem.*, 1967, **349**, 169.
119. H. Gerding and D. J. Stufkens, *Rev. Chim. Miner.*, 1969, **6**, 795; 1969, **6**, 807.
120. H. Gerding, D. J. Stufkens, and H. Gijben, *Recl. Trav. Chim. Pays-Bas*, 1970, **89**, 619.
121. R. Fehrmann, J. M. v. Barner, N. J. Bjerrum, and O. F. Nielsen, *Inorg. Chem.*, 1981, **20**, 1712.
122. G. Jander and K. H. Swart, *Z. Anorg. Allg. Chem.*, 1959, **299**, 252; 1959, **299**, 267.
123. N. D. Chikanov, *Russ. J. Inorg. Chem.*, 1972, **17**, 1338.
124. W. L. Groeneveld, Ph. D. Thesis, University of Leiden, 1953.
125. H. W. Roesky, K.-L. Weber, U. Seseke, W. Pinkert, M. Noltemeyer, W. Clegg, and G. M. Sheldrick, *J. Chem. Soc., Dalton Trans.*, 1985, 565.
126. H. Hartl, P. Huppmann, D. Lentz, and K. Seppelt, *Inorg. Chem.*, 1983, **22**, 2183.
127. P. Born, R. Kniep, and D. Mootz, *Z. Anorg. Allg. Chem.*, 1979, **451**, 12.
128. W. Hückel, *Nachr. Akad. Wiss. Gött. Math. Phys. Kl.*, 1946, 36.
129. C. Lau and J. Passmore, *J. Fluorine Chem.*, 1975, **6**, 77.
130. P. Rigny, M. Drifford, and J. Virlet, *J. Phys. (Paris) Colloq.*, 1971, 229.
131. J. Michel, M. Drifford, and P. Rigny, *J. Chim. Phys.*, 1970, **67**, 31.
132. U. Elgad and H. Selig, *Inorg. Chem.*, 1975, **14**, 140.
133. A. A. Banks and A. J. Rudge, *Nature*, 1953, **171**, 390.
134. S. Colton, J. L. Margrave, and P. W. Wilson, *Synth. React. Inorg. Met.-Org. Chem.*, 1971, **1**, 149.
135. C. J. Schack, R. D. Wilson, and J. F. Hohn, *Inorg. Chem.*, 1972, **11**, 208.
136. W. V. F. Brooks, M. Eshaque, C. Lau, and J. Passmore, *Can. J. Chem.*, 1976, **54**, 817.
137. K. O. Christe, C. J. Schack, and E. C. Curtis, *Inorg. Chem.*, 1972, **11**, 583.
138. S. P. So, K. K. Li, and L. K. Hung, *Bull. Soc. Chim. Belg.*, 1978, **87**, 411.
139. R. Paetzold, *Z. Chem.*, 1968, **4**, 321.

140. R. Paetzold, *Spectrochim. Acta*, 1968, **24A**, 717.
141. R. Paetzold, *Spectrochim. Acta*, 1970, **26A**, 577.
142. R. Steudel, *Z. Naturforsch.*, 1970, **25b**, 645.
143. J. D. Mc Cullough, *J. Am. Chem. Soc.*, 1937, **59**, 789.
144. P. J. Ficalora, J. C. Thompson, and J. L. Margrave, *J. Inorg. Nucl. Chem.*, 1969, **31**, 377.
145. G. A. Ozin and A. Vander Voet, *J. Mol. Struct.*, 1971, **10**, 173.
146. K. C. Malhotra and R. D. Sharma, *Indian J. Chem.*, 1972, **10**, 430.
147. R. J. Gillespie, R. H. Flavers, and E. A. Robinson, *J. Inorg. Nucl. Chem.*, 1959, **9**, 1.
148. F. C. Mijlhoff, *Acta Crystallogr.*, 1965, **18**, 795.
149. F. C. Mijlhoff, *Recl. Trav. Chim. Pays-Bas*, 1965, **84**, 74.
150. R. Paetzold and H. Amoulong, *Z. Anorg. Allg. Chem.*, 1965, **337**, 225.
151. F. C. Mijlhoff and R. Block, *Recl. Trav. Chim. Pays-Bas*, 1964, **83**, 799.
152. R. Paetzold, *Fortschr. Chem. Forsch.*, 1966, **5**, 590.
153. R. C. Paul, R. D. Sharma, and K. C. Malhotra, *Indian J. Chem.*, 1972, **10**, 428.
154. J. Touzin and M. Jaros, *Z. Chem.*, 1971, **11**, 469.
155. J. Touzin and P. Bauer, *Collect. Czech. Chem. Commun.*, 1975, **40**, 1296.
156. E. E. Sidorova, S. N. Kondrat'ev, K. N. Mochalov, G. I. Blagoveshchenskaya, and K. P. Pribylov, *Russ. J. Inorg. Chem.*, 1972, **17**, 157.
157. M. G. Jerschkewitz and K. Manning, *Z. Anorg. Allg. Chem.*, 1962, **319**, 83.
158. I. C. Bowater, R. D. Brown, and F. R. Burden, *J. Mol. Spectrosc.*, 1967, **23**, 272.
159. I. C. Bowater, R. D. Brown, and F. R. Burden, *J. Mol. Spectrosc.*, 1968, **28**, 461.
160. R. Paetzold, *Z. Chem.*, 1964, **4**, 272.
161. L. E. Alexander and I. R. Beattie, *J. Chem. Soc., Dalton Trans.*, 1972, 1745.
162. J. A. Rolfe and L. A. Woodward, *Trans. Faraday Soc.*, 1955, **51**, 778.
163. J. Milne, *Spectrochim. Acta*, 1982, **38A**, 569.
164. J. C. Dewan and A. J. Edwards, *J. Chem. Soc., Dalton Trans.*, 1976, 2433.
165. A. J. Edwards and G. R. Jones, *J. Chem. Soc. A*, 1968, 2858.
166. R. Paetzold and K. Aurich, *Z. Anorg. Allg. Chem.*, 1966, **348**, 94.
167. R. J. Gillespie, 'Molecular Geometry', Van Nostrand, London, 1972.
168. G. Hopf and R. Paetzold, *Z. Physiol. Chem.*, 1972, **251**, 273.
169. K. A. Jensen and V. Krishman, *Acta Chem. Scand.*, 1967, **21**, 1988.
170. R. Paetzold and G. Bochmann, *Z. Chem.*, 1968, **8**, 308.
171. R. Paetzold and G. Bochmann, *Z. Anorg. Allg. Chem.*, 1969, **368**, 203.
172. R. Paetzold and G. Bochmann, *Z. Anorg. Allg. Chem.*, 1971, **385**, 256.
173. H. A. Carter and F. Aubke, *Inorg. Nucl. Chem. Lett.*, 1969, **5**, 999.
174. R. R. Amaresh, M. V. Lahshmikantham, J. W. Baldwin, M. P. Cava, R. M. Metzger, and R. D. Rogers, *J. Org. Chem.*, 2002, **67**, 2453.
175. T. Birchall, R. J. Gillespie, and S. L. Vekris, *Can. J. Chem.*, 1965, **43**, 1672.
176. B. Krebs, M. Hucke, and A. Schäffer, *Z. Kristallogr.*, 1982, **159**, 84.
177. A. Engelbrecht and B. Stoll, *Z. Anorg. Allg. Chem.*, 1957, **292**, 20.
178. R. Paetzold, R. Kune, and G. Engelhardt, *Z. Anorg. Allg. Chem.*, 1967, **352**, 62.
179. K. Dostal and M. Cernik, *Z. Chem.*, 1966, **6**, 424.
180. K. Seppelt, *Angew. Chem.*, 1972, **84**, 212; *Angew. Chem., Int. Ed. Engl.*, 1972, **11**, 630.
181. K. Seppelt, *Z. Anorg. Allg. Chem.*, 1974, **406**, 287.
182. K. Seppelt, *Angew. Chem.*, 1974, **86**, 103; *Angew. Chem., Int. Ed. Engl.*, 1974, **13**, 91.
183. K. Seppelt, *Chem. Ber.*, 1977, **110**, 1470.
184. K. Seppelt, *Chem. Ber.*, 1975, **108**, 1823.
185. K. Seppelt, *Z. Anorg. Allg. Chem.*, 1977, **428**, 35.
186. M. J. Vasile, F. A. Stevie, and K. Seppelt, *J. Fluorine Chem.*, 1979, **13**, 408.
187. M. Willert-Porada, H. Willner, and K. Seppelt, *Spectrochim. Acta*, 1981, **37A**, 911.
188. M. J. Vasile, F. A. Stevie, and K. Seppelt, *J. Fluorine Chem.*, 1979, **13**, 487.
189. J. Milne and P. LaHaie, *Inorg. Chem.*, 1985, **24**, 840.
190. P. LaHaie and J. Milne, *Inorg. Chem.*, 1979, **18**, 632.
191. R. J. Gillespie, *Angew. Chem.*, 1967, **79**, 885; *Angew. Chem., Int. Ed. Engl.*, 1967, **6**, 629.
192. R. J. Gillespie, *J. Chem. Educ.*, 1974, **51**, 367.
193. R. J. Gillespie and R. S. Nyholm, *Q. Rev.*, 1957, **11**, 339.
194. D. L. Kepert, *Prog. Inorg. Chem.*, 1979, **25**, 41.
195. W. Abriel and E. J. Zehnder, *Z. Naturforsch.*, 1987, **42b**, 1273.
196. L. Pauling, 'The Nature of the Chemical Bond', 3rd edn., Cornell University Press, Ithaca, NY, 1960.
197. R. E. Rundle, *J. Am. Chem. Soc.*, 1963, **85**, 112.
198. B. Krebs, N. Rieskamp, and A. Schäffer, *Z. Anorg. Allg. Chem.*, 1986, **532**, 118.
199. A. J. Privett, S. L. Craig, D. Y. Jeter, A. W. Cordes, R. T. Oakley, and R. W. Reed, *Acta Crystallogr.*, 1987, **C43**, 2023.
200. F.-P. Ahlers, E. Lührs, and B. Krebs, *Z. Anorg. Allg. Chem.*, 1991, **594**, 7.
201. F.-P. Ahlers, Ph.D. Thesis, University of Münster, 1991.

202. H. G. Stammler and J. Weiss, *Z. Naturforsch.*, 1989, **44b**, 1483.
203. E. Lührs, Ph.D. Thesis, University of Münster, 1987.
204. B. Krebs, E. Lührs, R. Willmer, and F.-P. Ahlers, *Z. Anorg. Allg. Chem.*, 1991, **592**, 17.
205. B. Krebs, A. Schäffer, and S. Pohl, *Z. Naturforsch.*, 1984, **39b**, 1633.
206. S. Pohl, A. Schäffer, and B. Krebs, *Z. Kristallogr.*, 1982, **162**, 180.
207. K. J. Wynne and J. Golen, *Inorg. Chem.*, 1974, **13**, 185.
208. B. Krebs, F.-P. Ahlers, and E. Lührs, *Z. Anorg. Allg. Chem.*, 1991, **597**, 115.
209. S. Hauge, K. Marøy, and T. Odegård, *Acta Chem. Scand.*, 1988, **A42**, 51.
210. B. Krebs, E. Lührs, and F.-P. Ahlers, *Angew. Chem.*, 1989, **101**, 190; *Angew. Chem., Int. Ed. Engl.*, 1989, **28**, 187.
211. S. Hauge, K. Marøy, and T. Odegård, *Acta Chem. Scand.*, 1988, **A42**, 56.
212. M. B. Robin and P. Day, *Adv. Inorg. Chem. Radiochem.*, 1967, **10**, 247.
213. H. Kurbjuhn, Ph.D. Thesis, University of Jena, 1968.
214. R. Paetzold and K. Aurich, *Z. Anorg. Allg. Chem.*, 1965, **335**, 281.
215. E. J. Baran, *J. Fluorine Chem.*, 1977, **10**, 255.
216. A. W. Cordes, *Inorg. Chem.*, 1967, **6**, 1204.
217. B. Krebs, M. Hucke, M. Hein, and A. Schäffer, *Z. Naturforsch.*, 1983, **38b**, 20.
218. B. Krebs, A. Schäffer, and M. Hucke, *Z. Naturforsch.*, 1982, **37b**, 1410.
219. R. J. Gillespie, P. Spekkens, J. B. Milne, and D. Moffett, *J. Fluorine Chem.*, 1976, **7**, 43.
220. M. Hein, Ph.D. Thesis, University of Bielefeld, 1979.
221. B.-C. Wang and A. W. Cordes, *Inorg. Chem.*, 1970, **9**, 1643.
222. J. Milne, *Inorg. Chem.*, 1979, **18**, 2924.
223. Y. Hermodsson, *Acta Chem. Scand.*, 1967, **21**, 1328.
224. M. Cernik and K. Dostal, *Z. Anorg. Allg. Chem.*, 1976, **425**, 37.
225. H. Bartels and E. Class, *Helv. Chim. Acta*, 1962, **45**, 179.
226. K. Seppelt, *Chem. Ber.*, 1972, **105**, 2431.
227. K. Seppelt, *Chem. Ber.*, 1973, **106**, 1920.
228. D. Lentz and K. Seppelt, *Angew. Chem.*, 1978, **90**, 390; *Angew. Chem., Int. Ed. Engl.*, 1978, **17**, 355.
229. L. K. Templeton, D. H. Templeton, K. Seppelt, and N. Bartlett, *Inorg. Chem.*, 1976, **15**, 2718.
230. R. Espenschield, *Ann. Chem.*, 1860, **113**, 101.
231. J. Jander and V. Doetsch, *Angew. Chem.*, 1958, **70**, 704.
232. J. Jander and V. Doetsch, *Chem. Ber.*, 1960, **93**, 561.
233. W. Strecker and L. Claus, *Chem. Ber.*, 1923, **56**, 362.
234. A. Verneuil, *Bull. Soc. Chim. Fr.*, 1882, **38**, 548.
235. F. Wöhler and R. Espenschield, *Ann. Chem.*, 1859, **109**, 375.
236. H. B. Van Valkenburg and J. C. Bailar, *J. Am. Chem. Soc.*, 1925, **47**, 2136.
237. H. Bärnighausen, T. V. Volkmann, and J. Jander, *Acta Crystallogr.*, 1966, **21**, 571.
238. G. Wolmershäuser, C. R. Brulet, and G. B. Street, *Inorg. Chem.*, 1978, **17**, 3586.
239. E. G. Awere, J. Passmore, P. S. White, and T. Klapötke, *J. Chem. Soc., Chem. Commun.*, 1989, 1415.
240. P. F. Kelly, A. M. Z. Slawin, D. J. Williams, and J. D. Woollins, *J. Chem. Soc., Chem. Commun.*, 1989, 408.
241. K. Dehnicke, F. Schmock, K. F. Köhler, and G. Frenking, *Angew. Chem.*, 1991, **103**, 564; *Angew. Chem., Int. Ed. Engl.*, 1991, **30**, 577.
242. S. Vogeler, M. Schäfer, and K. Dehnicke, *Z. Anorg. Allg. Chem.*, 1991, **606**, 73.
243. S. Vogeler, W. Massa, and K. Dehnicke, *Z. Naturforsch.*, 1991, **46b**, 1625.
244. R. Wollert, A. Höllwarth, G. Frenking, D. Fenske, H. Goesmann, and K. Dehnicke, *Angew. Chem.*, 1992, **104**, 1216; *Angew. Chem., Int. Ed. Engl.*, 1992, **31**, 1251.
245. H. W. Roesky, K.-L. Weber, and J. W. Bats, *Chem. Ber.*, 1984, **117**, 2686.
246. M. Björgvinsson, H. W. Roesky, F. Pauer, and G. M. Sheldrick, *Chem. Ber.*, 1992, **125**, 767.
247. T. Maaninen, T. Chivers, R. Laitinen, G. Schatte, and M. Nissinen, *Inorg. Chem.*, 2000, **39**, 5341.
248. T. Maaninen, R. Laitinen, and T. Chivers, *Chem. Commun.*, 2002, 1812.
249. T. Maaninen, H. M. Tuononen, G. Schatte, R. Suontamo, J. Valkonen, R. Laitinen, and T. Chivers, *Inorg. Chem.*, 2004, **43**, 2097.
250. G. Hopf and R. Paetzold, *Z. Anorg. Allg. Chem.*, 1973, **401**, 179.
251. K. Dostal and J. Krejci, *Z. Anorg. Allg. Chem.*, 1958, **296**, 29.
252. R. Paetzold, K. Dostal, and A. Ruzicka, *Z. Anorg. Allg. Chem.*, 1969, **347**, 13.
253. J. Toutin, *Collect. Czech. Chem. Commun.*, 1973, **38**, 2384.
254. K. Dostal and A. Ruzicka, *Z. Anorg. Allg. Chem.*, 1965, **337**, 325.
255. J. K. Fawcett, V. Kocman, S. C. Nyburg, and R. J. O’Brien, *Chem. Commun.*, 1969, 1198.
256. R. Paetzold, K. Dostal, and A. Ruzicka, *Z. Anorg. Allg. Chem.*, 1966, **348**, 1.
257. A. Engelbrecht, *Monatsh. Chem.*, 1961, **92**, 1273.
258. K. Dostal and L. Zborilova, *Z. Chem.*, 1964, **4**, 353.
259. K. Dostal and L. Zborilova, *Collect. Czech. Chem. Commun.*, 1967, **32**, 2809.
260. A. Engelbrecht and F. Clementi, *Monatsh. Chem.*, 1961, **92**, 570.
261. V. Kocman and J. Rucklidge, *Acta Crystallogr.*, 1974, **B30**, 6.

Selenium: Organoselenium Chemistry

Thomas G. Back
University of Calgary, Calgary, AB, Canada

1 Introduction 1
2 Selenols and Selenolates 2
3 Selenides 2
4 Selenoxides and Selenones 3
5 Diselenides 4
6 Selenenyl Halides and Pseudohalides 6
7 Selenenic and Seleninic Acids and Derivatives 7
8 Selenocarbonyl Compounds 10
9 Chiral Organoselenium Compounds 11
10 Organic Conductors 12
11 Biologically Important Organoselenium Compounds 12
12 Related Articles 12
13 References 12

Glossary

Ad_E2 mechanism: a bimolecular 1,2-addition of an electrophilic reagent to an alkene via a cationic intermediate
Baeyer–Villiger reaction: the oxidation of a ketone to an ester or lactone, usually by means of a peroxy acid
Enone: an unsaturated ketone, usually α, β relative to the carbonyl group
Markovnikov orientation: the 1,2-addition of an unsymmetrical electrophilic reagent to an alkene with attachment of the more positive moiety of the reagent (H in the original definition) to the less substituted carbon
Michael addition: conjugate addition; addition of a nucleophile to the β-position of a carbon–carbon double or triple bond that is conjugated to a carbonyl or other electron-withdrawing group
Pummerer reaction: the reaction of a sulfoxide or selenoxide with an acidic or electrophilic reagent, with cleavage of the S–O or Se–O bond and formation of an S- or Se-stabilized carbenium ion that rearranges or reacts further with nucleophiles
S_N2 mechanism: a concerted, bimolecular nucleophilic substitution that occurs with inversion of configuration
$S_{RN}1$ mechanism: a nucleophilic substitution that proceeds by a chain mechanism via radical anion intermediates

Abbreviations

LDA = lithium diisopropylamide; MCPBA = *m*-chloroperbenzoic acid; DMF = *N*,*N*-dimethylformamide; HMPA = hexamethylphosphoric triamide.

1 INTRODUCTION

The element selenium was discovered by Berzelius in 1818, and reports of the first organoselenium compounds by Löwig, Wöhler, and others gradually appeared in the literature during the next 50 years. These compounds consisted mainly of simple aliphatic selenols (RSeH), selenides (RSeR), and diselenides (RSeSeR) that proved unpleasant to handle because of their highly malodorous nature. Difficulties in purification and the instability of certain derivatives also hampered early workers. Although the number and variety of known selenium compounds had grown dramatically by the 1950s, organoselenium chemistry remained a relatively arcane field of study until the 1970s. Around that time, the discovery of several useful new reactions and of a variety of novel structures with unusual properties began to attract more general interest in the discipline. This led to the appearance of several comprehensive texts on the chemical and biological properties of organoselenium compounds in the 1970s and 1980s.[1–6] Recent advances have also been driven by potential technological applications of, for example, selenium-containing organic conductors; by an increasing awareness of the biological importance of selenium compounds; and by the utility of organoselenium compounds in modern organic synthesis.[7,8] Today, a plethora of such species is known and key compounds are commercially available. Aryl-substituted derivatives and those containing selenium in higher oxidation states are generally less volatile and less offensive to handle than the original aliphatic compounds, and even the latter are now relatively easy to manipulate by modern techniques.

There are formal and behavioral resemblances between many types of organoselenium compounds and their sulfur and tellurium counterparts owing to their proximity in group 16 of the periodic table. For instance, selenols, selenides, diselenides, and selenoxides are in many ways analogous to thiols and tellurols, sulfides and tellurides, disulfides and ditellurides, and sulfoxides and telluroxides, respectively. However, despite formal similarities, there are also many differences between organoselenium, -sulfur, and -tellurium compounds with respect to their stabilities, properties, and reactions. The resemblance between organoselenium and oxygen compounds is considerably less pronounced because of the latter element's substantially higher electronegativity, lower polarizability, stronger bonds with carbon, and lack of available d orbitals for bonding.

2 SELENOLS AND SELENOLATES

Selenols (RSeH) are relatively strong acids (e.g. p$K_a = 5.9$ for PhSeH[9]) and so their conjugate bases, the selenolates (RSe$^-$), are readily formed in alkaline solutions. They are most commonly prepared by the reaction of Grignard reagents or alkyl- or aryllithiums with elemental selenium, followed by acidification. Alternatively, selenols and selenolates can be obtained by the monoalkylation of hydrogen selenide or the HSe$^-$ anion with alkyl halides or by the reduction of diselenides with reagents such as sodium borohydride, alkali metals, sodium or potassium hydride, sodium hydroxymethyl sulfoxylate (Rongalite), or hypophosphorous acid. The use of sodium borohydride results in the formation of a borane complex of the selenolate, which tends to suppress the reactivity of the selenolate. On the other hand, alkali metal selenolates in polar aprotic solvents such as DMF or HMPA display enhanced reactivity. The reduction or basic hydrolysis of selenocyanates (RSeCN) also affords selenols and selenolates. These processes are shown in Scheme 1. Both types of products react readily with oxygen to afford diselenides, and so they must be stored and handled under an inert atmosphere.

Although selenols and selenolates are weak bases, they are, nevertheless, powerful, soft nucleophiles[10–12] because of the high polarizability of the selenium atom. They therefore react readily with electrophilic compounds such as alkyl halides and tosylates to afford selenides, and with epoxides to give β-hydroxy selenides. These reactions occur via an S_N2 mechanism with an inversion of configuration at carbon. Aryl halides also undergo substitution with selenolates by means of an $S_{RN}1$ radical mechanism. Selenols are sufficiently acidic to protonate amines and form the corresponding ammonium selenolates. Attack by the highly nucleophilic selenolate anion upon an alkyl group of the ammonium cation of these species then affords the alkyl selenide and dealkylated amine.[9] Similar N-to-Se alkyl transfers have been carried out in the presence of ruthenium catalysts.[13] In contrast with most other nucleophiles, selenolates attack esters and lactones preferentially at the softer alkyl rather than the harder acyl carbon atom, with displacement of the corresponding carboxylate anion.[10–12] However, substitution at the acyl center of methyl esters can be achieved with the selenoalane $Me_2AlSeMe$,[14] to afford selenoesters. The cleavage of arylmethyl ethers and cyclopropanes with selenolates has also been reported. Selenols and selenolates perform Michael additions to enones and other activated alkenes and afford selenoacetals from aldehydes and ketones.[10–12] The selenoboranes $B(SePh)_3$ and $B(SeMe)_3$ are useful alternatives to selenols for this purpose.[15] These processes are illustrated in Scheme 2. Selenols and selenolates act as reducing agents toward a variety of organic functional groups, transforming vicinal dihalides into alkenes; α-halo carbonyl compounds into dehalogenated products; nitro, nitroso, azo, azoxy, and hydrazo compounds into primary amines; imino compounds into secondary amines; and sulfoxides into sulfides.[16,17] Selenolates have also been immobilized on solid supports, and several synthetic applications have been reported.[12]

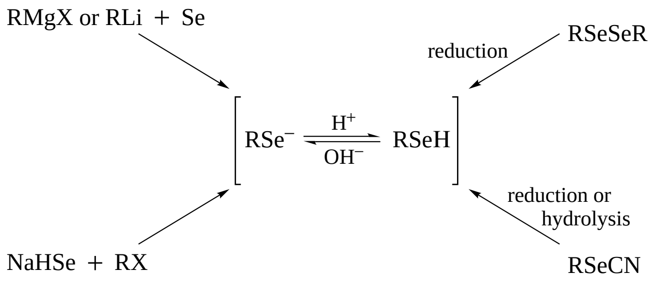

Scheme 1

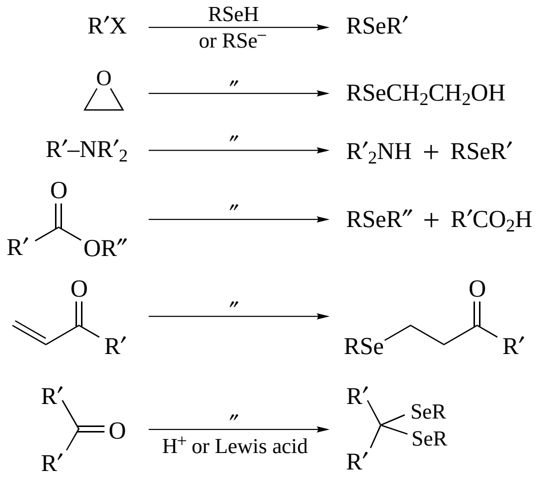

Scheme 2

3 SELENIDES

Acyclic alkyl and aryl selenides (RSeR) are generally stable and have a nonlinear structure. The C–Se–C bond angle of dimethyl selenide is 96.3° and the C–Se bond lengths are 1.945 Å, as determined by microwave spectroscopy.[18] A variety of cyclic selenides of varying stability are also known.[19] For example, episelenides (**1**) are highly labile and extrude selenium spontaneously to generate alkenes. Selenetane (**2**) is isolable but polymerizes easily, while its 3,3-dimethyl derivative is more stable. Several 1,3-diselenetanes (**3**), as well as a variety of relatively stable larger rings, have been prepared. Transannular interactions between the selenium atoms of oxidized cyclic bisselenides (e.g. **4**) have been studied[20] and several selenium analogs of crown ethers (e.g. **5**) have been reported.[21] Polymeric selenides such

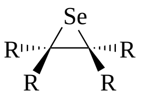

(**1**)

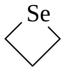

(**2**)

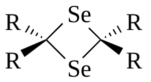

(**3**)

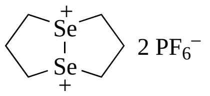

(**4**)

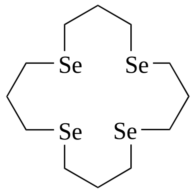

(**5**)

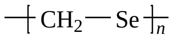

(**6**)

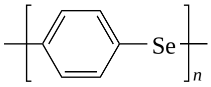

(**7**)

as (**6**) and (**7**) are available from the reactions of Na_2Se with methylene bromide and *p*-dibromobenzene, respectively.

Alkyl selenides are most conveniently prepared by the dialkylation of Na_2Se or by the monoalkylation of selenolates. Common routes to aryl derivatives include the reaction of a selenolate with a diazonium salt, the $S_{RN}1$ reactions described earlier, and the reaction of aryllithiums with aryl selenocyanates (ArSeCN). A different approach employs the reaction of alcohols with aryl selenocyanates or *N*-(phenylseleno)phthalimide (see Section 6) in the presence of tri-*n*-butylphosphine.[22] Similar conditions can also be used to convert carboxylic acids to selenoesters (**8**). These reactions are illustrated in Scheme 3.

Selenides are also nucleophilic and produce isolable selenonium salts (**9**) when treated with alkyl halides. They are easily oxidized to selenoxides (**10**) and further to selenones (**11**) under more forcing conditions (see Section 4). Reduction of selenides to the corresponding hydrocarbons is most conveniently achieved with nickel boride,[23] or with tri-*n*-butyl- or triphenyltin hydride under radical conditions.[24] Other reagents for reductive deselenization include Raney nickel, lithium triethylborohydride, and lithium in ethylamine (Scheme 4). Benzylic selenides undergo radical extrusion reactions under thermal or photolytic conditions to produce coupled hydrocarbon products, including highly strained products such as benzocyclobutane and paracyclophanes (e.g. equation 1).[25] Selenium-stabilized carbanions (**12**) are usually formed by treating selenoacetals with *n*-butyllithium, which cleaves the C–Se bond in preference to deprotonating the α-position. Alternatively, selenides containing α-hydrogens can be deprotonated by strong bases such as lithium diisopropylamide (LDA), although the presence of an additional anion-stabilizing group, apart from the selenium atom, is generally required.[26–29] The anions can then be alkylated, acylated, or added to the carbonyl groups of aldehydes and ketones. These reactions are summarized in Scheme 5.

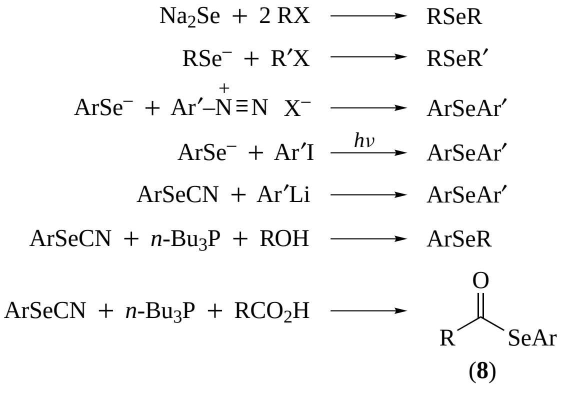

$$Na_2Se + 2\,RX \longrightarrow RSeR$$
$$RSe^- + R'X \longrightarrow RSeR'$$
$$ArSe^- + Ar'{-}\overset{+}{N}{\equiv}N\ X^- \longrightarrow ArSeAr'$$
$$ArSe^- + Ar'I \xrightarrow{h\nu} ArSeAr'$$
$$ArSeCN + Ar'Li \longrightarrow ArSeAr'$$
$$ArSeCN + n\text{-}Bu_3P + ROH \longrightarrow ArSeR$$
$$ArSeCN + n\text{-}Bu_3P + RCO_2H \longrightarrow RC(O)SeAr$$

Scheme 3

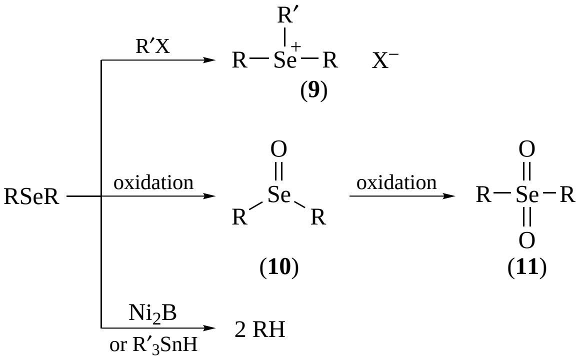

Scheme 4

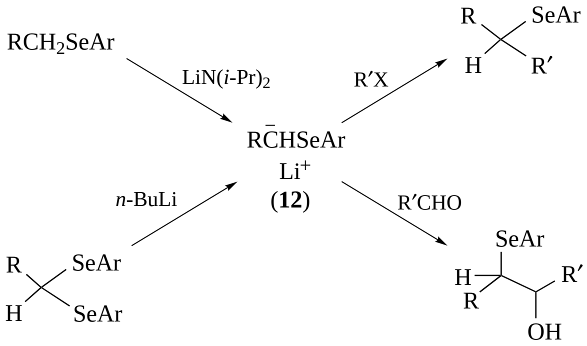

Scheme 5

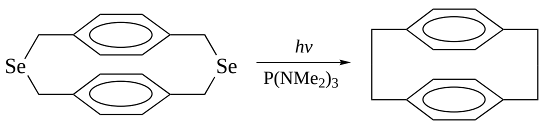

(1)

4 SELENOXIDES AND SELENONES

Selenoxides (**10**) are easily prepared by the oxidation of selenides with numerous types of oxidants, including hydrogen peroxide, peroxy acids, ozone, and sodium m-periodate. The reaction is easy to stop at this stage, and further oxidation to the selenone (**11**) requires strong oxidants such as peroxy acids and proceeds relatively slowly. This behavior contrasts with that of the analogous sulfur compounds, where the further oxidation of sulfoxides to sulfones is generally facile and often difficult to avoid.

Selenoxides derived from unsymmetrical selenides are chiral and stable toward pyramidal inversion at room or even higher temperatures.[30] They are produced enantioselectively by the use of chiral oxidants such as the Sharpless reagent[31] or camphor-derived oxaziridines[32] or diastereoselectively with achiral oxidants when one of the selenide substituents is itself chiral (see Section 9). Racemic selenoxides have been resolved by chromatography over chiral adsorbents.[33] Chiral selenoxides racemize readily in water,[30] particularly under acid-catalyzed conditions, presumably via the intermediacy of achiral selenoxide hydrates (equation 2).

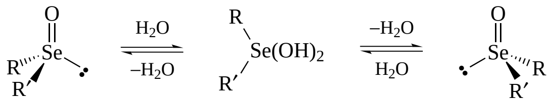
(2)

The syn elimination of selenoxides[34,35] containing β-hydrogens is an exceptionally mild alkene-forming reaction that generally takes place at or below room temperature (equation 3). The introduction of an arylseleno group into an organic substrate, followed by its oxidation and elimination, is therefore one of the most valuable synthetic transformations effected with selenium chemistry. The reaction is stereospecific, and the transition state requires all five participating centers to assume a coplanar geometry, with the O atom and the abstracted H atom on the same side of the C–C bond. When diastereotopic β-hydrogens are present, abstraction of the one leading to the trans alkene is favored. The reaction often displays good regioselectivity in those cases where several sites containing β-hydrogens are available. Thus, the double bond is formed preferentially at conjugated positions, away from oxygen substituents to give allylic rather than vinylic products, and toward the less substituted position in the absence of other factors. Vinylic selenoxides containing cis hydrogens produce acetylenes as the major products along with smaller amounts of allenes, while those lacking cis hydrogens afford only the latter products (equation 4). Allylic selenoxides undergo rapid [2,3] sigmatropic rearrangements to the corresponding selenenate esters (**13**).[35–37] The latter then decompose readily to allylic alcohols by hydrolysis (equation 5). It is interesting to note that the reverse process is favored in the analogous sulfur rearrangements, where the equilibrium shifts toward the corresponding sulfoxides instead of the sulfenate esters. Under acidic conditions, or in the presence of electrophiles such as acetic anhydride, selenoxides undergo Pummerer reactions (equation 6).

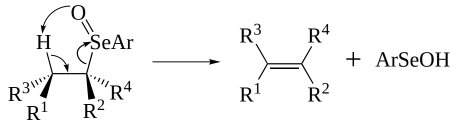
(3)

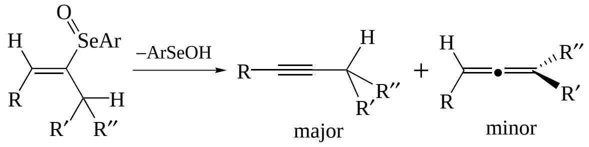
(4)

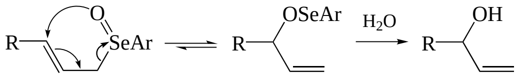
(**13**)

(5)

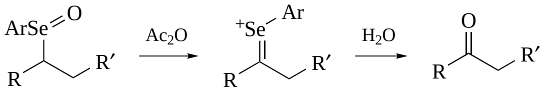
(6)

The chemistry of selenones[38] (**11**) has not been studied as extensively as that of selenoxides. However, it has been demonstrated that selenones function as good leaving groups, comparable to tosylates or halides.[39,40] For example, they are readily solvolyzed in methanol and produce rearranged products when β-substituents with high migratory aptitudes are present (equations 7 and 8). Vinylic selenones also act as Michael acceptors,[41] as in the first step of the process shown in equation (9).

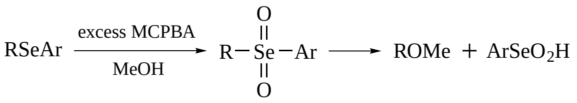

$$\mathrm{RSeAr}\xrightarrow[\text{MeOH}]{\text{excess MCPBA}}\mathrm{R{-}\overset{\overset{\Large O}{\|}}{\underset{\underset{\Large O}{\|}}{Se}}{-}Ar}\longrightarrow \mathrm{ROMe}+\mathrm{ArSeO_2H}\qquad(7)$$

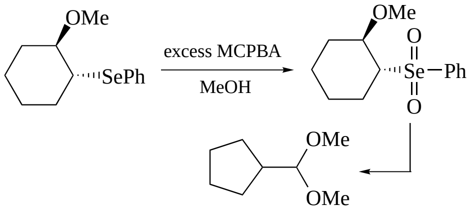
(8)

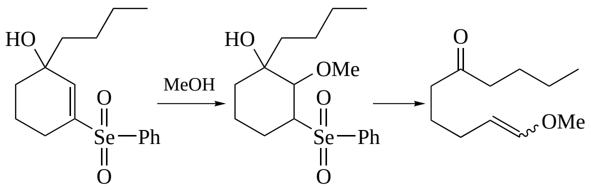
(9)

5 DISELENIDES

Acyclic diselenides (RSeSeR), like disulfides and peroxides, are nonplanar and exhibit large dihedral angles. An X-ray structure of diphenyl diselenide (PhSeSePh) revealed a dihedral angle of 82° and C–Se–Se angles of 104.6° and 107.5°, as well as Se–C and Se–Se bond lengths of 1.93 and 2.29 Å, respectively.[42] Bulky substituents increase the dihedral angle (e.g. 112.1° for *t*-$Bu_2CHSeSeCH$-*t*-Bu_2), lengthen the C–Se and Se–Se bonds, and result in bathochromic shifts in the UV spectrum,[43] while electronegative substituents shorten the diselenide bond. The preferred conformations of typical diselenides (roughly gauche with a dihedral angle of ca. 80°) are chiral but interconvert rapidly by rotation about the diselenide bond. The barrier to rotation in benzyl phenyl diselenide ($PhCH_2SeSePh$) has been measured to be 6.3 kcal mol^{-1} by dynamic NMR methods at low temperatures and is therefore 1.4 kcal mol^{-1} lower than that in the corresponding disulfide.[44] Simple cyclic diselenides such as (**14**) are known but tend to polymerize readily. A number of more complex cyclic diselenides have also been studied.[45] For example, the conformational properties of the paracyclophane diselenide (**15**) and its selenide counterpart were also investigated by dynamic NMR methods. The diselenide shows nonequivalent methylene protons at low temperatures and interconverts between syn conformers.[46] Theoretical, NMR, electrochemical, and photoelectron spectroscopic studies of cyclic diselenides and related 1,2-dichalcogenins have also been reported.[47,48]

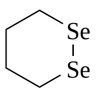

(**14**)

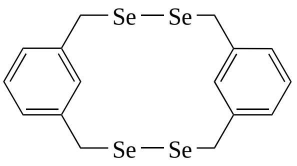

(**15**)

Diselenides are generally prepared by the aerial oxidation of selenols or selenolates (see Section 2) or by the reaction of Li_2Se_2, Na_2Se_2, or other $Se_2{}^{2-}$ species with alkyl or aryl halides. In the latter case, elevated temperatures and DMF as the solvent are recommended. Aryl diselenides may also be obtained from the reaction of $Se_2{}^{2-}$ with diazonium salts (Scheme 6). Relatively few unsymmetrical diselenides have been reported. Triselenides are also known but have not been as widely studied.

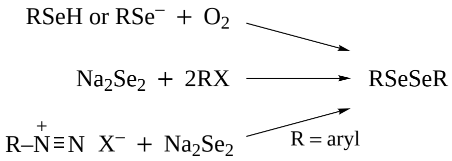

Scheme 6

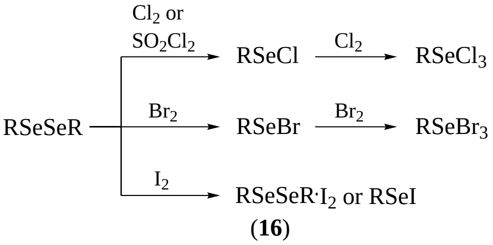

Scheme 7

As shown in Scheme 1, the reduction of diselenides generates selenols and selenolates, while their oxidation results in the formation of selenenic and seleninic acids and related compounds (see Section 7). Halogenation of diselenides with sulfuryl chloride, chlorine, or bromine affords selenenyl halides (RSeX) or, with a second mole of halogenating reagent, the corresponding selenium trihalides ($RSeX_3$). The reaction of diphenyl diselenide with iodine produces an adduct (**16**) that is probably a charge transfer complex instead of the selenenyl iodide.[49] This substance performs a number of typical reactions characteristic of a selenenyl halide, suggesting that free PhSeI may be present in solution. The more hindered bis(2,4,6-tri-*t*-butylphenyl) diselenide produced an authentic selenenyl iodide that was characterized by X-ray crystallography.[50] These processes are summarized in Scheme 7. The direct formation of selenenyl fluorides from the fluorination of diselenides has not yet been documented, but PhSeF, or an equivalent species, appears to be generated in situ from the sonication of PhSeBr or PhSeCl, in turn, obtained from halogenolysis of the corresponding diselenide, and AgF in a suitable solvent.[51] Similarly, the reaction of PhSeSePh with XeF_2 generates a species that behaves as the equivalent of PhSeF.[52] When photolyzed or pyrolyzed, diselenides undergo homolytic cleavage of the Se–Se bond, resulting in some interesting radical reactions,[53] such as radical 1,2-additions to acetylenes.[54,55] A palladium-catalyzed 1,2-addition of diselenides to acetylenes has also been reported, which can be performed in the presence of CO to afford (*Z*)-1,3-bis(arylseleno)-2-alken-1-ones.[56] Diazo compounds insert into the Se–Se bond and into a variety of selenium–heteroatom bonds.[57] Some examples of these processes are shown in Scheme 8. Benzylic diselenides extrude selenium under either photolytic or pyrolytic conditions to produce selenides (equation 10),[53] which in turn afford hydrocarbons from

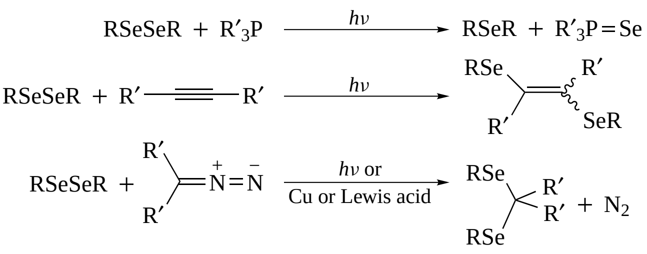

Scheme 8

further extrusion reactions, as indicated earlier.

$$\mathrm{ArCH_2SeSeCH_2Ar} \xrightarrow{h\nu \text{ or } \Delta} \mathrm{ArCH_2SeCH_2Ar} + \mathrm{ArCH_2CH_2Ar} + \mathrm{Se} \qquad (10)$$

6 SELENENYL HALIDES AND PSEUDOHALIDES

Selenenyl halides are relatively stable, though moisture sensitive, compounds that are generally prepared by the reactions shown in Scheme 7 and behave as electrophilic selenium species.[57–59] They react with ketones and aldehydes via their enols or enolates to afford α-seleno derivatives (e.g. (**17**) in equation 11). Similar α-selenenylations of β-dicarbonyl compounds, esters, and lactones can be performed, although the latter two types of compounds require prior formation of their enolates. Moreover, the α-selenenylation of anions stabilized by nitrile, nitro, sulfone, or various types of phosphorus substituents has also been reported (equation 12). In many such cases, the selenenylation step is followed by oxidation to the selenoxide and spontaneous syn elimination to provide a convenient method for the preparation of the corresponding α,β-unsaturated compound (e.g. **18** in equation 11). Enones react with benzeneselenenyl chloride (PhSeCl) and pyridine to afford α-phenylselenoenones (equation 13).

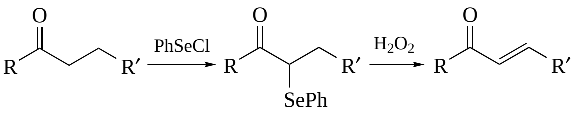

(**17**) (**18**)

(11)

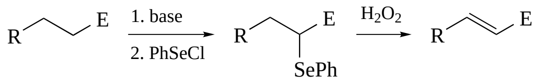

(12)

E = electron-withdrawing group (e.g. CO_2R, CN, NO_2, SO_2Ar, $Ph_2P(O)$, etc.)

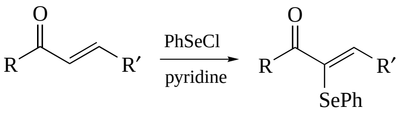

(13)

Selenenyl chlorides add to alkenes, often via an Ad_E2 mechanism involving a bridged seleniranium ion intermediate[60] (**19**) (equation 14). These reactions are therefore highly stereospecific, resulting in anti addition. The regiochemistry of the process can be under either kinetic or thermodynamic control. In some cases, initial anti-Markovnikov products were observed at low temperature and Markovnikov adducts dominated after further equilibration. Analogous electrophilic additions to acetylenes and allenes (Scheme 9) have also been reported. When selenenyl halides react with alkenes in the presence of other nucleophiles such as water, alcohols, nitriles, or azide or nitrite anions, a 1,2-addition of the selenium residue and the nucleophile to the C=C double bond is often observed (Scheme 9). When a nucleophilic group is present elsewhere in the alkenic substrate, the reaction is intramolecular, resulting in cyclization (e.g. equation 15).[58,59,61,62]

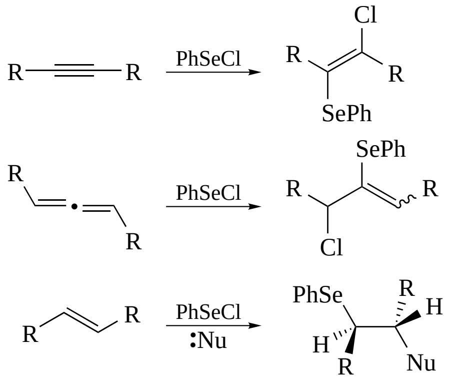

:Nu = OH, OR′, RCN, N_3, NO_2, etc.

Scheme 9

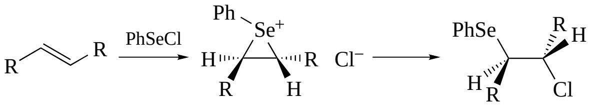

(**19**)

(14)

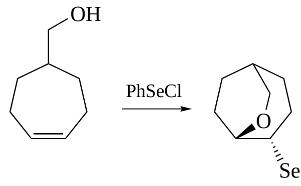

(15)

Other species of general structure RSeX, where X = a nonhalide leaving group, are also known and often show similar behavior to that of the selenenyl halides.[57–59] For example, benzeneselenenyl acetate (**20**), trifluoroacetate (**21**), and tosylate (**22**) can be generated in situ from the reactions of the selenenyl halides with silver acetate, trifluoroacetate, or tosylate, respectively (Scheme 10). The former two electrophiles react with enol acetates to produce α-seleno ketones and with alkenes and acetylenes to give 1,2-addition products, while the latter adds similarly to acetylenes. Examples are shown in equations (16) to (18).

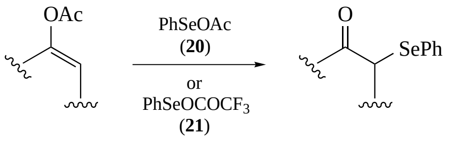

(16)

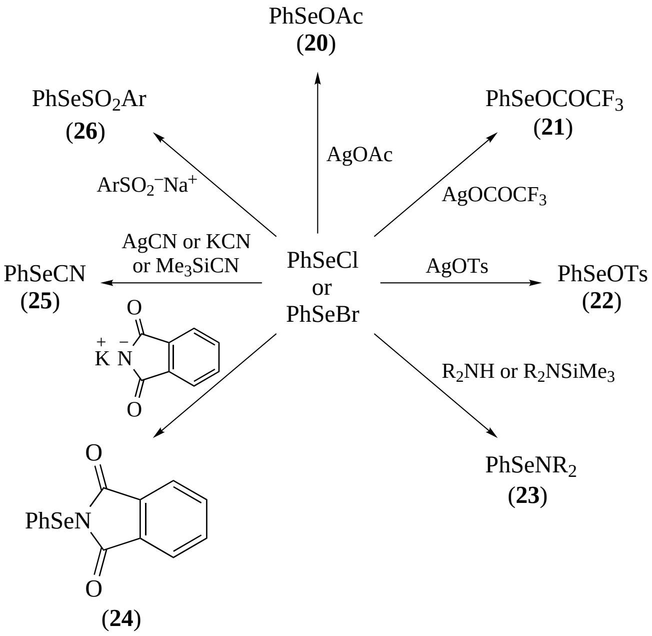

Scheme 10

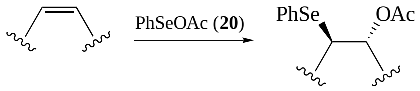

(17)

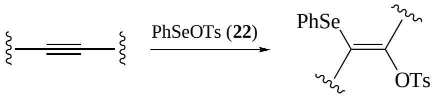

(18)

Selenenamides (**23**) are obtained by the substitution of selenenyl halides with amines[63] or by the metathesis of the former compounds with *N*-silylamines.[64] *N*-(Phenylseleno)phthalimide (**24**) is similarly obtained using potassium phthalimide (Scheme 10).[65] These compounds can be isolated but are prone to hydrolyze when exposed to moisture. Selenenamides react with aldehydes or β-dicarbonyl compounds to afford α-seleno derivatives (as in the process shown in equation 11), and add to activated double and triple bonds, as in the example in equation (19). The imide (**24**) is a useful alternative to PhSeCl in various selenenylation reactions, and to ArSeCN in the conversion of alcohols and carboxylic acids to selenides and selenoesters (**8**), as shown in Scheme 3.

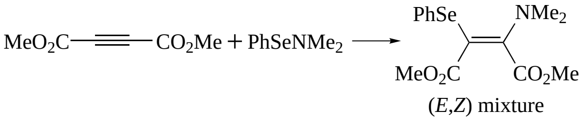

(19)

The preparation of selenocyanates[66] such as (**25**) can be achieved by the methods shown in Scheme 10, although a useful alternative employs the reaction of potassium selenocyanate (KSeCN) with alkyl halides or arenediazonium salts (equation 20).

$$\text{R–X or Ar–}\overset{+}{\text{N}}\equiv\text{N X}^- + \text{KSeCN} \longrightarrow \text{RSeCN or ArSeCN} \quad (20)$$

$$\text{X} = \text{halide}$$

Selenocyanates produce selenols or diselenides upon either reduction (e.g. with sodium borohydride) or hydrolysis (see Scheme 1). They undergo displacement of the cyanide ion by various nucleophiles and add to alkenes in a manner similar to selenenyl halides (see equation 14), except that catalysis with Lewis acids is required in the case of unactivated alkenes. The selenocyanates are also popular reagents for the preparation of selenides from alcohols, and (**8**) from carboxylic acids, as indicated in Scheme 3.

The selenosulfonates (**26**) comprise another class of selenenyl pseudohalides.[67] They are stable, crystalline compounds available from the reaction of selenenyl halides with sulfinate salts (Scheme 10) or more conveniently from the oxidation of either sulfonohydrazides ($ArSO_2NHNH_2$) or sulfinic acids ($ArSO_2H$) with benzeneseleninic acid (**27**) (equations 21 and 22). Selenosulfonates add to alkenes via an electrophilic mechanism catalyzed by boron trifluoride etherate, or via a radical mechanism initiated thermally or photolytically. The two reaction modes produce complementary regioselectivity, but only the electrophilic processes are stereospecific (anti). Similar radical additions to acetylenes and allenes have been reported, with the regio- and stereochemistry as shown in Scheme 11. When these selenosulfonation reactions are used in conjunction with subsequent selenoxide eliminations or [2,3] sigmatropic rearrangements, they provide access to a variety of unsaturated sulfone products.

$$\text{ArSO}_2\text{NHNH}_2 + \underset{(\mathbf{27})}{\text{PhSeO}_2\text{H}} \longrightarrow \underset{(\mathbf{26})}{\text{ArSO}_2\text{SePh}} + \text{N}_2 + 2\text{H}_2\text{O} \quad (21)$$

$$2\text{ArSO}_2\text{H} + \underset{(\mathbf{27})}{\text{PhSeO}_2\text{H}} \longrightarrow \underset{(\mathbf{26})}{\text{ArSO}_2\text{SePh}} + \text{ArSO}_3\text{H} + \text{H}_2\text{O} \quad (22)$$

Several types of electrophilic selenium species have been immobilized on solid supports, for more convenient application to organic synthesis. These include selenenyl halides,[68–71] selenocyanates,[72] and selenosulfonates.[73]

7 SELENENIC AND SELENINIC ACIDS AND DERIVATIVES

The partial oxidation of diselenides with appropriate oxidants such as hydrogen peroxide initially generates the corresponding selenenic acids (**29**) or anhydrides (**28**). Further oxidation leads to the corresponding seleninic acids (**31**) or

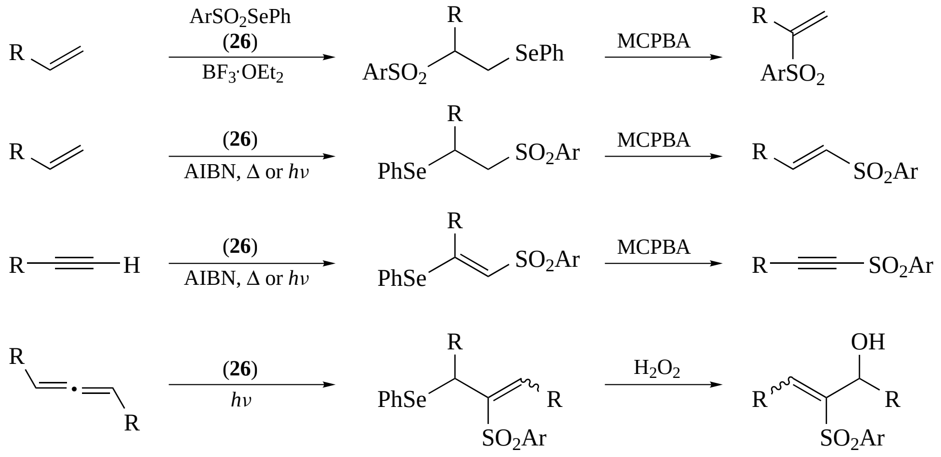

Scheme 11

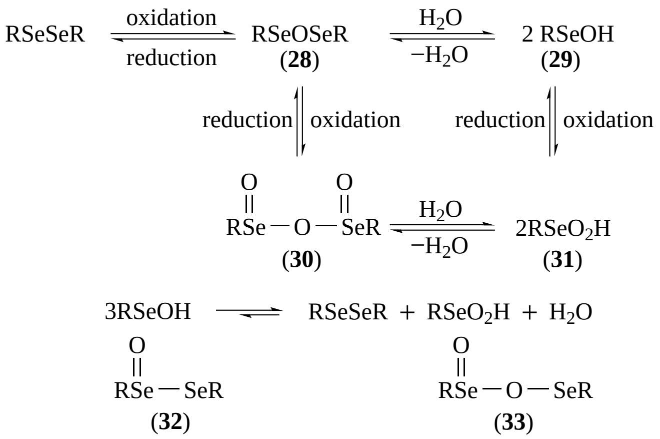

Scheme 12

anhydrides (**30**), as shown in Scheme 12. Though the seleninic compounds (**30**) and (**31**) are usually stable and isolable, their selenenic counterparts (**28**) and (**29**) are generally not and disproportionate to mixtures of the initial diselenide and the seleninic acid or anhydride. The disproportionation probably involves intermediates (**32**) and (**33**) (Scheme 12). Several early reports of isolable selenenic acids proved erroneous, although (**34**) has been characterized in solution.[74] More recently, selenenic acids (**35**)[75] and (**36**)[76] were isolated and characterized by X-ray crystallography. A few selenenic anhydrides have been prepared (e.g. **37** and **38**, which are stabilized by the ortho substituent).[77,78] The unstable selenolseleninate (**39**) was observed[79] when the corresponding cyclic diselenide was oxidized with 1 equiv of MCPBA (*m*-chloroperbenzoic acid) at low temperatures, and the similar oxidation of the 1,8-*peri*-diselenide of naphthalene produced a mixture of selenolseleninate (**40**) and selenenic anhydride (**41**).[80] The X-ray structure of an isolable selenolseleninate, structurally related to (**36**), has been reported.[76] Selenenic acids can also be generated in situ by the hydrolysis of selenenyl halides or other derivatives of the general structure RSeX, where X is a leaving group, and by the reduction of seleninic acids or anhydrides. The comproportionation of the latter with diselenides (i.e. the reverse of the disproportionation process in Scheme 12) also produces low equilibrium concentrations of (**28**) or (**29**). The continuous removal of (**28**) or (**29**) by their reaction with an appropriate substrate can, however, drive the reaction to completion.

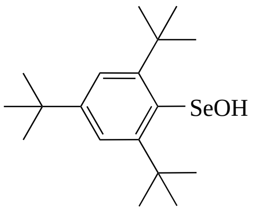

(**34**)

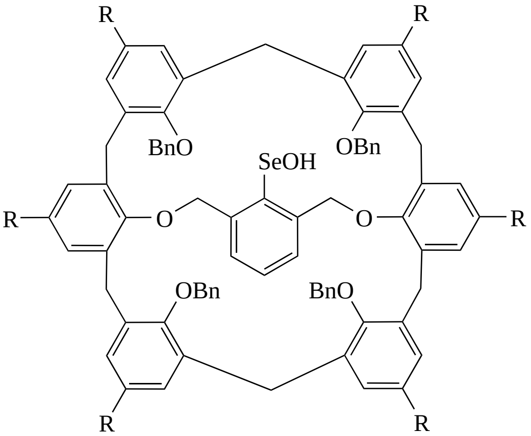

(**35**) R= *t*-Bu

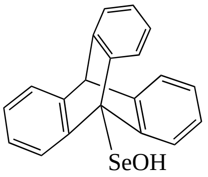

(**36**)

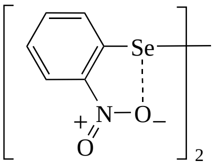

(**37**)

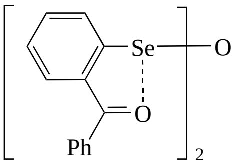

(**38**)

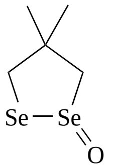

(**39**)

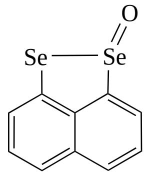

(**40**)

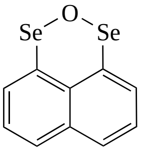

(**41**)

When selenenic acids are generated in the presence of alkenes, addition reactions similar to those of selenenyl halides occur. Oxidation and syn elimination of the adducts (**42**) provide a convenient synthesis of allylic alcohols (equation 23).$^{57–59}$

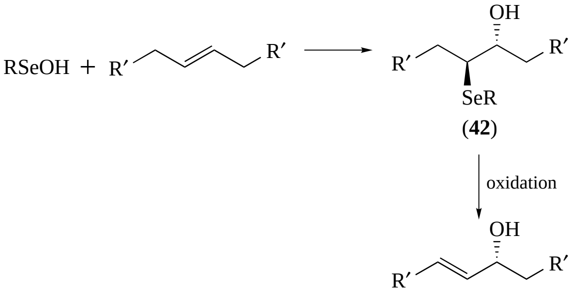

(23)

Benzeneseleninic acid (**27**) and the corresponding anhydride (**43**) are widely employed as oxidants in organic synthesis.^{81,82} The acid is conveniently prepared by the oxidation of diphenyl diselenide (PhSeSePh) with nitric acid, followed by neutralization of the resulting hydronitrate complex ($PhSeO_2H·HNO_3$) with a base. The anhydride is obtained by heating the acid in vacuo at ca. 120 to 130 °C. These reagents oxidize phenols to quinones, and primary and secondary alcohols to aldehydes and ketones, respectively. Amines afford imines and the corresponding ketones by subsequent hydrolysis, while hydrazine and its 1,2- and 1,1-disubstituted derivatives produce diimide, azo compounds, and tetrazenes, respectively. *N*-Acyl- and *N*-sulfonylhydrazines give selenoesters (**8**) and selenosulfonates (**26**) (see equation 21). These reagents are also useful in regenerating ketones from their hydrazones, oximes, semicarbazones, and dithioacetals. Thiones and other thiocarbonyl compounds are converted into the analogous ketones and other corresponding carbonyl compounds, and sulfinic acids afford (**26**) via equation (22). These processes are illustrated in Scheme 13. They augment the uses of inorganic selenium oxidants such as selenium dioxide (*see* ***Selenium: Inorganic Chemistry***).

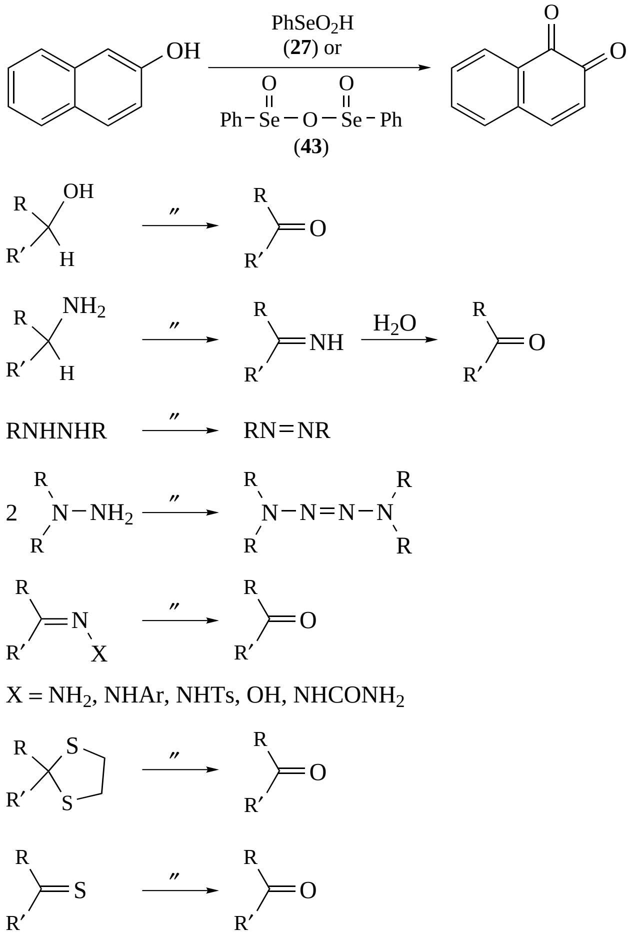

Scheme 13

The dehydrogenation of steroidal and other ketones can be accomplished with (**43**) at elevated temperatures.^{81,82} Similar reactions with lactones and lactams have also been reported. Other interesting oxidations include the angular hydroxylation of ketones and the oxidation of benzylic hydrocarbons, as shown in Scheme 14. In some cases, the selenium reagent may be employed catalytically in the presence of a less expensive cooxidant that reoxidizes Se^{II} by-products back to the required Se^{IV} oxidation state.

Seleninic acids can also be employed in epoxidation and Baeyer–Villiger reactions^{81,82} when used in conjunction with

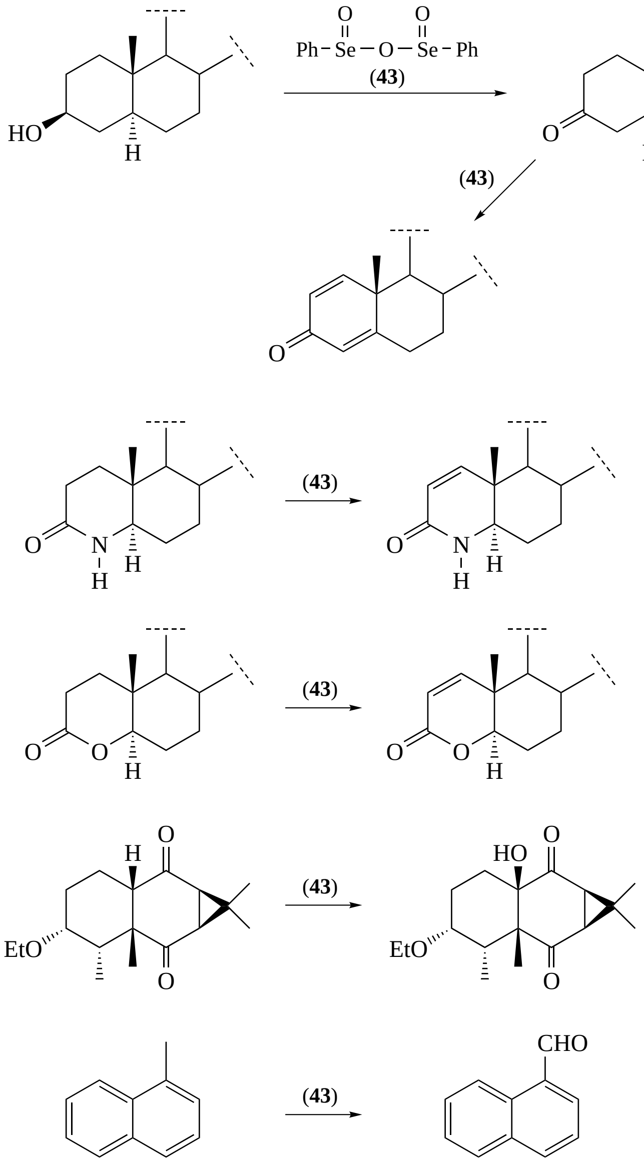

Scheme 14

hydrogen peroxide (Scheme 15). Intermediate peroxyseleninic acids (**44**) are likely intermediates in these processes.

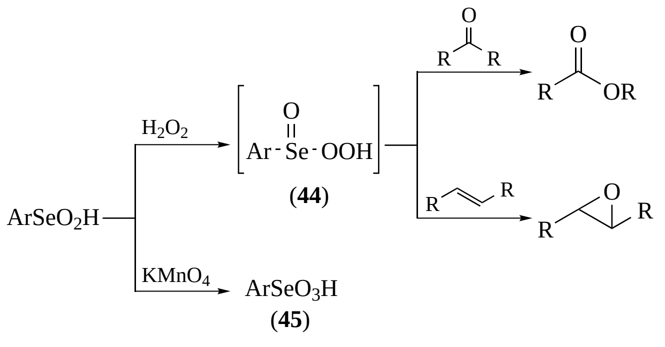

Scheme 15

Selenonic acids (**45**) have been little studied but can be produced by the further oxidation of seleninic acids with potassium permanganate.

8 SELENOCARBONYL COMPOUNDS

The relatively poor 2p–4p π-overlap of carbon–selenium double bonds makes selenocarbonyl groups less stable than the corresponding thiocarbonyl and carbonyl analogs. Until the mid-1970s, only those selenocarbonyl compounds where the bond order of the C=Se bond was lowered by coordination or resonance were known. However, the isolation of two deep blue, thermally stable selones (**46**) and (**47**) proved that such

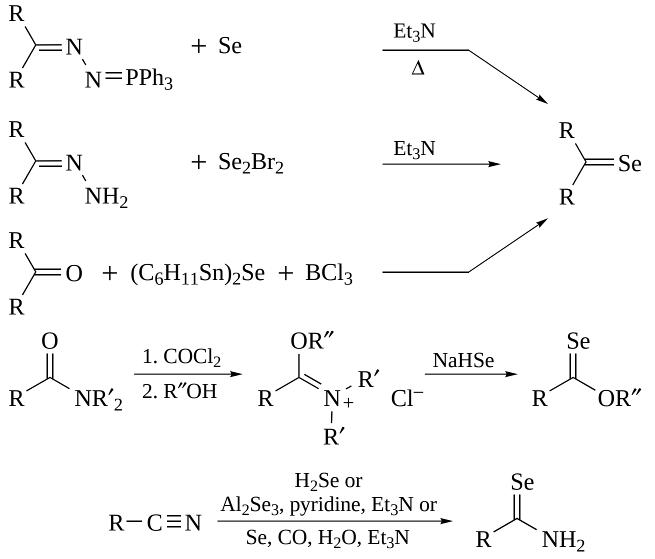

Scheme 16

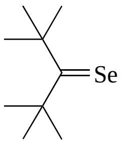

(**46**)

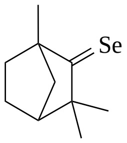

(**47**)

species could exist without electronic stabilization, provided that they were sterically protected.[83] Scheme 16 shows several methods for preparing selones and related selenocarbonyl compounds.[83–86] Perhaps their most notable chemical property involves their cycloaddition with diazo compounds to afford cycloadducts (**48**), which undergo twofold extrusion of N_2 and Se to afford alkenes (equation 24).[83] This method has been employed to produce some of the most hindered alkenes known to date.[83–86] Unlike ketones, selones are attacked by nucleophiles such as phenyllithium at the Se and not the C atom, producing selenium-stabilized carbanion intermediates. They act as spin-traps for radicals, which also attack at the selenium atom. Selones are easily reduced to diselenides by hydrogen selenide, by typical reducing agents such as sodium borohydride, or by photolysis. Less stable selones and selenoaldehydes have been trapped by cycloaddition with cyclopentadiene or other 1,3-dienes,[87] or isolated as the dimeric 1,3-diselenetanes (e.g. (**3**; R = Ph) from $Ph_2C{=}Se$)[88] or as higher oligomers or polymers. Selenoesters and selenoamides tend to be inherently more stable than selones because of resonance and can be prepared as shown in Scheme 16. A variety of other selenocarbonyl compounds, including carbon diselenide, carbon oxyselenide, selenoureas, selenocarbonates, selenoketenes, and others have also been reported.[84–86]

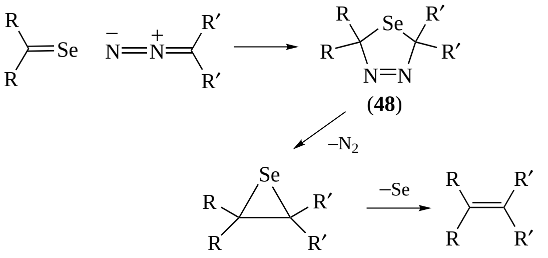

(24)

9 CHIRAL ORGANOSELENIUM COMPOUNDS

As indicated in Section 4, selenoxides bearing two different substituents are intrinsically chiral (i.e. the selenium atom itself is a stereocenter), although their resolution can be challenging. Certain other types of organoselenium compounds, such as selenonium salts (**9**) containing three different substituents, are also chiral and can sometimes be resolved into their respective enantiomers. Moreover, there is growing interest in organoselenium compounds that contain chiral auxiliary groups attached to the selenium atom. In this case, the selenium atom is not the stereocenter, which is instead present in the auxiliary.

A number of useful enantioselective syntheses can be performed by attaching a chiral auxiliary group to the selenium atom of an appropriate reagent.[89,90] Examples of such chiral auxiliaries include (**49–53**). Most of the asymmetric selenium reactions reported to date have involved inter- or intramolecular electrophilic additions to alkenes (i.e. enantioselective variations of processes such as shown in equations (23) and (15), respectively) but others include the desymmetrization of epoxides by ring-opening with chiral selenolates, asymmetric selenoxide eliminations to afford chiral allenes or cyclohexenes, and the enantioselective formation of allylic alcohols by [2,3]sigmatropic rearrangement of allylic selenoxides or related species.

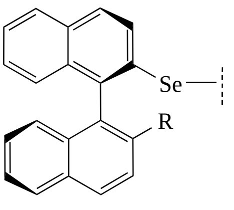

(**49**)

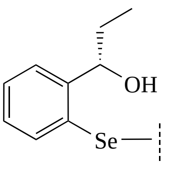

(**50**)

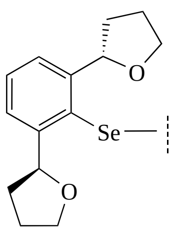

(**51**)

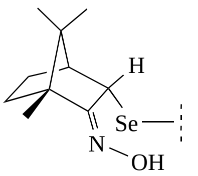

(**52**)

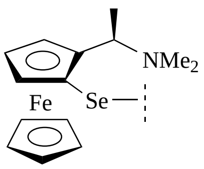

(**53**)

10 ORGANIC CONDUCTORS

A plethora of selenium-containing heterocycles are known to act as the donor component for donor−acceptor complexes that have properties as electrical conductors.[91–93] Two examples that have provoked widespread interest are tetraselenafulvalene (**54**) and tetraselenotetracene (**55**). A variety of selenium-containing polymers such as (**7**) are also of interest in this regard.

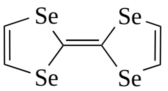

(**54**)

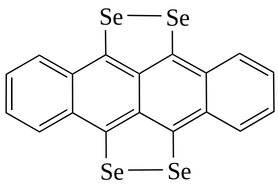

(**55**)

11 BIOLOGICALLY IMPORTANT ORGANOSELENIUM COMPOUNDS

Organoselenium compounds play several important biological roles.[2,94–98] They are generally toxic and so must be handled with appropriate care. Selenium intoxication symptoms in animals include 'alkali disease' and 'blind staggers', symptoms of which have been known for many years. On the other hand, selenium is also an essential trace element and its deficiency in the diet is severely detrimental to both animal and human health and has been implicated in white muscle disease and cardiac myopathy. Moreover, selenium compounds have been claimed to act as carcinogens, while other reports suggest that in appropriate doses they are anticarcinogens. Selenium compounds, in some cases acting synergistically with vitamin E, have apparent roles as anti-inflammatory agents, in maintaining the normal functioning of the immune system, and possibly in retarding the aging process. Much of the biological activity of selenium is associated with its incorporation into selenocysteine residues in the enzyme glutathione peroxidase (*see* ***Selenium Proteins Containing Selenocysteine***), which functions as an antioxidant. This protein catalyzes the reduction of harmful peroxides by glutathione. The peroxides are produced during the course of normal oxidative metabolism and result in damage to biologically important molecules, as well as to cell membranes. A variety of inflammatory conditions and other disease states are related to the undesired physiological effects of peroxides and the free radicals that are produced by them. A number of other selenium-containing proteins are known, along with the semisynthetic enzyme selenosubtilisin.[99] Several small-molecule synthetic compounds designed to mimic the antioxidant effects of glutathione peroxidase have been reported. These include ebselen (**56**),[100] a compound which has undergone clinical trials, as well as more recent compounds[98,101] (e.g. **57**−**61**), some displaying improved catalytic activity. Organoselenium compounds with antibacterial, antiviral, antifungal, antiparasitic, and antiradiation properties have also been reported, as well as selenium analogs of a variety of carbohydrates and nucleosides.

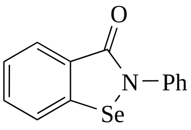

(**56**)

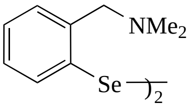

(**57**)

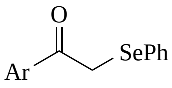

(**58**)

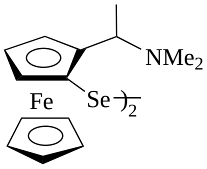

(**59**)

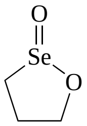

(**60**)

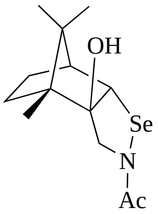

(**61**)

12 RELATED ARTICLES

Selenium: Inorganic Chemistry; Selenium Proteins Containing Selenocysteine; Tellurium: Organotellurium Chemistry.

13 REFERENCES

1. D. L. Klayman and W. H. H. Günther eds, 'Organic Selenium Compounds: Their Chemistry and Biology', John Wiley & Sons, New York, 1973.
2. R. J. Shamberger, 'Biochemistry of Selenium', Plenum Press, New York, 1983.
3. K. C. Nicolaou and N. A. Petasis, 'Selenium in Natural Products Synthesis', CIS, Philadelphia, PA, 1984.
4. C. Paulmier, 'Selenium Reagents and Intermediates in Organic Synthesis', Pergamon Press, Oxford, 1986.
5. D. Liotta ed., 'Organoselenium Chemistry', John Wiley & Sons, New York, 1987.
6. S. Patai and Z. Rappoport eds, 'The Chemistry of Organic Selenium and Tellurium Compounds', John Wiley & Sons, Chichester, 1986, Vol. 1; 1987 Vol. 2.
7. T. G. Back ed., 'Organoselenium Chemistry – A Practical Approach', Oxford University Press, Oxford, 1999.
8. T. Wirth ed., Organoselenium chemistry – modern developments in organic synthesis, in 'Topics in Current Chemistry', Springer-Verlag, Berlin, 2000, Vol. 208.

9. H. J. Reich and M. L. Cohen, *J. Org. Chem.*, 1979, **44**, 3148.
10. R. Monahan, D. Brown, L. Waykole, and D. Liotta, in ‘Organoselenium Chemistry’, ed. D. Liotta, John Wiley & Sons, New York, 1987, Chap. 4.
11. L. Engman and V. Gupta, in ‘Organoselenium Chemistry – A Practical Approach’, ed. T. G. Back, Oxford University Press, Oxford, 1999, Chap. 4.
12. M. Iwaoka and S. Tomoda, Organoselenium chemistry – modern developments in organic synthesis, in ‘Topics in Current Chemistry’, ed. T. Wirth, Springer-Verlag, Berlin, 2000, Vol. 208, pp. 55–80.
13. S. Murahashi and T. Yano, *J. Am. Chem. Soc.*, 1980, **102**, 2456.
14. A. P. Kozikowski and A. Ames, *J. Org. Chem.*, 1978, **43**, 2735.
15. D. L. J. Clive and S. M. Menchen, *J. Org. Chem.*, 1979, **44**, 4279.
16. T. G. Back, in ‘The Chemistry of Organic Selenium and Tellurium Compounds’, eds. S. Patai and Z. Rappoport, John Wiley & Sons, Chichester, 1987, Vol. 2, Chap. 3.
17. Y. Nishiyama and N. Sonoda, in ‘Organoselenium Chemistry – A Practical Approach’, ed. T. G. Back, Oxford University Press, Oxford, 1999, Chap. 6.
18. G. K. Pandey and H. Dreizler, *Z. Naturforsch.*, 1977, **32a**, 482.
19. M. Renson, in ‘The Chemistry of Organic Selenium and Tellurium Compounds’, eds. S. Patai and Z. Rappoport, John Wiley & Sons, Chichester, 1986, Vol. 1, Chap. 13.
20. H. Fujihara, R. Akaishi, T. Erata, and N. Furukawa, *J. Chem. Soc., Chem. Commun.*, 1989, 1789.
21. R. J. Batchelor, F. W. B. Einstein, I. D. Gay, J.-H. Gu, B. D. Johnston, and B. M. Pinto, *J. Am. Chem. Soc.*, 1989, **111**, 6582.
22. P. A. Grieco, S. Gilman, and M. Nishizawa, *J. Org. Chem.*, 1976, **41**, 1485.
23. T. G. Back, V. I. Birss, M. Edwards, and M. V. Krishna, *J. Org. Chem.*, 1988, **53**, 3815.
24. D. L. J. Clive, G. J. Chittattu, V. Farina, W. A. Kiel, S. M. Menchen, C. G. Russell, A. Singh, C. K. Wong, and N. J. Curtis, *J. Am. Chem. Soc.*, 1980, **102**, 4438.
25. H. Higuchi, M. Kugimiya, T. Otsubo, Y. Sakata, and S. Misumi, *Tetrahedron Lett.*, 1983, **24**, 2593.
26. H. J. Reich, in ‘Organoselenium Chemistry’, ed. D. Liotta, John Wiley & Sons, New York, 1987, Chap. 5.
27. A. Krief, in ‘The Chemistry of Organic Selenium and Tellurium Compounds’, eds. S. Patai and Z. Rappoport, John Wiley & Sons, Chichester, 1987, Vol. 2, Chap. 17.
28. A. Chieffi and J. V. Comasseto, in ‘Organoselenium Chemistry – A Practical Approach’, ed. T. G. Back, Oxford University Press, Oxford, 1999, Chap. 7.
29. S. Ponthieux and C. Paulmier, Organoselenium chemistry – modern developments in organic synthesis, in ‘Topics in Current Chemistry’, ed. T. Wirth, Springer-Verlag, Berlin, 2000, Vol. 208, pp. 113–142.
30. T. G. Back, N. Ibrahim, and D. J. McPhee, *J. Org. Chem.*, 1982, **47**, 3283.
31. T. Shimizu, M. Kobayashi, and N. Kamigata, *Bull. Chem. Soc. Jpn.*, 1989, **62**, 2099.
32. F. A. Davis, O. D. Stringer, and J. P. McCauley Jr, *Tetrahedron*, 1985, **41**, 4747.
33. T. Shimizu, M. Enomoto, H. Taka, and N. Kamigata, *J. Org. Chem.*, 1999, **64**, 8242.
34. T. G. Back, in ‘Organoselenium Chemistry – A Practical Approach’, ed. T. G. Back, Oxford University Press, Oxford, 1999, Chap. 2.
35. Y. Nishibayashi and S. Uemura, Organoselenium Chemistry – Modern Developments in Organic Synthesis, in ‘Topics in Current Chemistry’, ed. T. Wirth, Springer-Verlag, Berlin, 2000, Vol. 208, pp. 201–233.
36. H. J. Reich, in ‘Organoselenium Chemistry’, ed. D. Liotta, John Wiley & Sons, New York, 1987, Chap. 8.
37. Y. Nishibayashi and S. Uemura, in ‘Organoselenium Chemistry – A Practical Approach’, ed. T. G. Back, Oxford University Press, Oxford, 1999, Chap. 11.
38. A. Toshimitsu and S. Uemura, in ‘Organoselenium Chemistry – A Practical Approach’, ed. T. G. Back, Oxford University Press, Oxford, 1999, Chap. 13.
39. A. Krief, W. Dumont, and J.-N. Denis, *J. Chem. Soc., Chem. Commun.*, 1985, 571.
40. S. Uemura, S. Fukuzawa, and A. Toshimitsu, *J. Chem. Soc., Chem. Commun.*, 1983, 1501.
41. M. Shimizu, R. Ando, and I. Kuwajima, *J. Org. Chem.*, 1981, **46**, 5246.
42. R. E. Marsh, *Acta Crystallogr.*, 1952, **5**, 458.
43. T. G. Back and P. W. Codding, *Can. J. Chem.*, 1983, **61**, 2749.
44. J. E. Anderson and L. Henriksen, *J. Chem. Soc., Chem. Commun.*, 1985, 1397.
45. W. R. McWhinnie, in ‘The Chemistry of Organic Selenium and Tellurium Compounds’, eds. S. Patai and Z. Rappoport, John Wiley & Sons, Chichester, 1987, Vol. 2, Chap. 13.
46. K. R. Dixon and R. H. Mitchell, *Can. J. Chem.*, 1983, **61**, 1598.
47. E. Block, M. Birringer, R. DeOrazio, J. Fabian, R. S. Glass, C. Guo, C. He, E. Lorance, Q. Qian, T. B. Schroeder, Z. Shan, M. Thiruvazhi, G. S. Wilson, and X. Zhang, *J. Am. Chem. Soc.*, 2000, **122**, 5052.
48. R. S. Glass, N. E. Gruhn, D. L. Lichtenberger, E. Lorance, J. R. Pollard, M. Birringer, E. Block, R. DeOrazio, C. He, Z. Shan, and X. Zhang, *J. Am. Chem. Soc.*, 2000, **122**, 5065.
49. S. Kubiniok, W.-W. du Mont, S. Pohl, and W. Saak, *Angew. Chem., Int. Ed. Engl.*, 1988, **27**, 431.
50. W.-W. du Mont, K. Peters, and H.-G. von Schnering, *Angew. Chem., Int. Ed. Engl.*, 1987, **26**, 780.
51. Y. Usuki, M. Iwaoka, and S. Tomoda, *J. Chem. Soc., Chem. Commun.*, 1992, 1148.
52. K. Uneyama and M. Kanai, *Tetrahedron Lett.*, 1990, **31**, 3583.

53. T. G. Back, in ‘Organoselenium Chemistry’, ed. D. Liotta, John Wiley & Sons, New York, 1987, Chap. 7.
54. T. G. Back and M. V. Krishna, *J. Org. Chem.*, 1988, **53**, 2533.
55. A. Ogawa, H. Yokoyama, K. Yokoyama, T. Masawaki, N. Kambe, and N. Sonoda, *J. Org. Chem.*, 1991, **56**, 5721.
56. H. Kuniyasu, A. Ogawa, S.-I. Miyazaki, I. Ryu, N. Kambe, and N. Sonoda, *J. Am. Chem. Soc.*, 1991, **113**, 9796.
57. T. G. Back, in ‘Organoselenium Chemistry’, ed. D. Liotta, John Wiley & Sons, New York, 1987, Chap. 1.
58. P. L. Beaulieu and R. Déziel, in ‘Organoselenium Chemistry – A Practical Approach’, ed. T. G. Back, Oxford University Press, Oxford, 1999, Chap. 3.
59. M. Tiecco, Organoselenium chemistry – modern developments in organic synthesis, in ‘Topics in Current Chemistry’, ed. T. Wirth, Springer-Verlag, Berlin, 2000, Vol. 208, pp. 7–54.
60. G. H. Schmid and D. G. Garratt, in ‘The Chemistry of Double-Bonded Functional Groups’, ed. S. Patai, John Wiley & Sons, Chichester, 1977, Chap. 9, Supplement A, Part 2.
61. K. C. Nicolaou, N. A. Petasis, and D. A. Claremon, in ‘Organoselenium Chemistry’, ed. D. Liotta, John Wiley & Sons, New York, 1987, Chap. 2.
62. N. Petragnani, H. A. Stefani, and C. J. Valduga, *Tetrahedron*, 2001, **57**, 1411.
63. G. Kirsch and L. Christiaens, in ‘The Chemistry of Organic Selenium and Tellurium Compounds’, eds. S. Patai and Z. Rappoport, John Wiley & Sons, Chichester, 1987, Vol. 2, Chap. 11.
64. T. G. Back and R. G. Kerr, *Can. J. Chem.*, 1986, **64**, 308.
65. K. C. Nicolaou, D. A. Claremon, W. E. Barnette, and S. P. Seitz, *J. Am. Chem. Soc.*, 1979, **101**, 3704.
66. A. Toshimitsu and S. Uemura, in ‘The Chemistry of Organic Selenium and Tellurium Compounds’, eds. S. Patai and Z. Rappoport, John Wiley & Sons, Chichester, 1987, Vol. 2, Chap. 14.
67. T. G. Back, *Phosphorus, Sulfur Silicon Relat. Elem.*, 1992, **67**, 203.
68. K. C. Nicolaou, A. J. Roecker, J. A. Pfefferkorn, and G.-Q. Cao, *J. Am. Chem. Soc.*, 2000, **122**, 2966.
69. K. C. Nicolaou, J. A. Pfefferkorn, and G.-Q. Cao, *Angew. Chem., Int. Ed. Engl.*, 2000, **39**, 734.
70. K. C. Nicolaou, G.-Q. Cao, and J. A. Pfefferkorn, *Angew. Chem., Int. Ed. Engl.*, 2000, **39**, 739.
71. K. C. Nicolaou, N. Winssinger, R. Hughes, C. Smethurst, and S. Y. Cho, *Angew. Chem., Int. Ed. Engl.*, 2000, **39**, 1084.
72. K. Fujita, K. Watanabe, A. Oishi, Y. Ikeda, and Y. Taguchi, *Synlett*, 1999, 1760.
73. H. Qian and X. Huang, *Tetrahedron Lett.*, 2002, **43**, 1059.
74. H. J. Reich and C. P. Jasperse, *J. Org. Chem.*, 1988, **53**, 2389.
75. T. Saiki, K. Goto, and R. Okazaki, *Angew. Chem., Int. Ed. Engl.*, 1997, **36**, 2223.
76. A. Ishii, S. Matsubayashi, T. Takahashi, and J. Nakayama, *J. Org. Chem.*, 1999, **64**, 1084.
77. J. L. Kice, F. McAfee, and H. Slebocka-Tilk, *J. Org. Chem.*, 1984, **49**, 3100.
78. H. J. Reich, W. W. Willis Jr, and S. Wollowitz, *Tetrahedron Lett.*, 1982, **23**, 3319.
79. H. J. Reich, C. A. Hoeger, and W. W. Willis Jr, *J. Am. Chem. Soc.*, 1982, **104**, 2936.
80. J. L. Kice, Y.-H. Kang, and M. B. Manek, *J. Org. Chem.*, 1988, **53**, 2435.
81. S. V. Ley, in ‘Organoselenium Chemistry’, ed. D. Liotta, John Wiley & Sons, New York, 1987, Chap. 3.
82. T. G. Back, in ‘Organoselenium Chemistry – A Practical Approach’, ed. T. G. Back, Oxford University Press, Oxford, 1999, Chap. 5.
83. T. G. Back, D. H. R. Barton, M. R. Britten-Kelly, and F. S. Guziec Jr, *J. Chem. Soc., Perkin Trans. 1*, 1976, 2079.
84. F. S. Guziec Jr, in ‘Organoselenium Chemistry’, ed. D. Liotta, John Wiley & Sons, New York, 1987, Chap. 6.
85. F. S. Guziec Jr, in ‘The Chemistry of Organic Selenium and Tellurium Compounds’, eds. S. Patai and Z. Rappoport, John Wiley & Sons, Chichester, 1987, Vol. 2, Chap. 4.
86. T. Murai and S. Kato, Organoselenium chemistry – modern developments in organic synthesis, in ‘Topics in Current Chemistry’, ed. T. Wirth, Springer-Verlag, Berlin, 2000, Vol. 208, pp. 177–199.
87. P. T. Meinke and G. A. Krafft, *J. Am. Chem. Soc.*, 1988, **110**, 8671.
88. G. Erker, R. Hock, C. Krüger, S. Werner, F.-G. Klärner, and U. Artschwager-Perl, *Angew. Chem., Int. Ed. Engl.*, 1990, **29**, 1067.
89. T. Wirth, *Angew. Chem., Int. Ed. Engl.*, 2000, **39**, 3740.
90. T. Wirth, *Tetrahedron*, 1999, **55**, 1.
91. F. Wudl, in ‘Organoselenium Chemistry’, ed. D. Liotta, John Wiley & Sons, New York, 1987, Chap. 9.
92. D. Cowan and A. Kini, in ‘The Chemistry of Organic Selenium and Tellurium Compounds’, eds. S. Patai and Z. Rappoport, John Wiley & Sons, Chichester, 1987, Vol. 2, Chap. 12.
93. F. Ogura and K. Takimiya, in ‘Organoselenium Chemistry – A Practical Approach’, ed. T. G. Back, Oxford University Press, Oxford, 1999, Chap. 14.
94. R. F. Burk ed., ‘Selenium in Biology and Human Health’, Springer-Verlag, New York, 1994.
95. K. Soda, H. Tanaka, and N. Esaki, in ‘The Chemistry of Organic Selenium and Tellurium Compounds’, eds. S. Patai and Z. Rappoport, John Wiley & Sons, Chichester, 1987, Vol. 2, Chap. 7.
96. T. Sadeh, in ‘The Chemistry of Organic Selenium and Tellurium Compounds’, eds. S. Patai and Z. Rappoport, John Wiley & Sons, Chichester, 1987, Vol. 2, Chap. 8.

97. T. Masukawa, in ‘The Chemistry of Organic Selenium and Tellurium Compounds’, eds. S. Patai and Z. Rappoport, John Wiley & Sons, Chichester, 1987, Vol. 2, Chap. 9.

98. G. Mugesh, W.-W. du Mont, and H. Sies, *Chem. Rev.*, 2001, **101**, 2125.

99. Z.-P. Wu and D. Hilvert, *J. Am. Chem. Soc.*, 1990, **112**, 5647.

100. A. Müller, E. Cadenas, P. Graf, and H. Sies, *Biochem. Pharmacol.*, 1984, **33**, 3235.

101. G. Mugesh and H. B. Singh, *Chem. Soc. Rev.*, 2000, **29**, 347.

Selenium Proteins Containing Selenocysteine

August Böck
Department Biologie 1, University of Munich, Munich, Germany

1 Introduction 1
2 Prokaryotic Selenoproteins 1
3 Eukaryal Selenoproteins 3
4 Catalytic Role of Selenocysteine 5
5 Incorporation of Selenocysteine 6
6 Design of New Selenoproteins 9
7 Related Articles 9
8 References 9

1 INTRODUCTION

As a member of group 6 of the periodic table of elements, selenium shares many chemical properties with its neighboring homolog, sulfur (*see* ***Selenium: Inorganic Chemistry***; ***Selenium: Organoselenium Chemistry***). Both elements occur in the same oxidation states -2, 0, $+2$, $+4$, and $+6$ and they both enter biological macromolecules (protein; tRNA) in the -2 state. However, selenium also differs from sulfur in a number of important properties. The most significant one is that selenol is a more powerful nucleophile than thiol. Since the –SeH group of selenocysteine in proteins exhibits a pK of about 5.2, it is mostly dissociated at the physiological pH, whereas the –SH group with an average pK of 8.6 is predominantly protonated. Therefore, as has been shown for several enzymes, the incorporation of a chemically more reactive selenol group into the active center instead of a thiol confers a dramatic catalytic advantage. This review deals with enzymes from prokaryotes and eukaryotes, which contain a covalent selenocysteine residue, and also describes the present knowledge of its biosynthesis and mode of incorporation. The topic has been covered in several reviews concentrating on the biochemical, the nutritional and physiological, the molecular biological, and the biomedical aspects.[1–6] A comprehensive treatise has been compiled recently by Hatfield.[7]

2 PROKARYOTIC SELENOPROTEINS

2.1 Formate Dehydrogenases

Selenocysteine-containing formate dehydrogenases occur widely in nature. Operationally, they can be differentiated into two groups: enzymes that unidirectionally cleave formate into CO_2 and reducing equivalents, and enzymes that can act bidirectionally by interconverting formate and CO_2 plus reducing equivalents.

2.1.1 Unidirectionally Acting Formate Dehydrogenases

Unidirectionally operating formate dehydrogenases couple formate oxidation to the reduction of endogenously formed or exogenously added electron acceptors. Well-studied examples are the three formate dehydrogenase isoenzymes from *Escherichia coli* or the F_{420}-reducing formate dehydrogenases from archaea.

Under fermentative conditions, *E. coli* synthesizes the so-called formate hydrogenylase complex, which consists of formate dehydrogenase H, several electron carriers, and hydrogenase 3. The formate dehydrogenase H component consists of an 80-kDa selenopolypeptide encoded by the *fdhF* gene and catalyzes the reaction[1]

$$HCO_2H \longrightarrow CO_2 + 2e^- + 2H^+ \tag{1}$$

The *fdhF* gene product has been purified and subjected to a detailed biochemical and structural analysis.[8,9] It contains an Fe_4S_4 cluster, two molybdopterin–guanine dinucleotide cofactors and a selenocysteine in the active site, and it displays ping-pong bi-bi kinetics for the substrate formate and the artificial one-electron acceptor benzylviologen. The pH profile of inactivation by alkylation follows exactly the dissociation state of the selenol and indicates that selenocysteine is participating in the binding of formate.[8,9]

During anaerobic growth in the presence of nitrate, *E. coli* synthesizes formate dehydrogenase N, which couples formate oxidation to nitrate reduction:

$$HCO_2H + NO_3^- \longrightarrow CO_2 + NO_2^- + H_2O \tag{2}$$

The enzyme has been first purified by Enoch and Lester[10] and recently shown by X-ray analysis to be a 510-kDa membrane-bound complex of $(\alpha\beta\gamma)_3$ structure.[11] It channels the electrons withdrawn from formate by the α-subunit, which is a selenopolypeptide of 110-kDa molecular mass[12] via 11 redox centers consisting of molybdopterin–guanine dinucleotides and five Fe_4S_4 centers in a single unbranched chain to two heme b groups in the γ-subunit, which also contains a quinone binding site. The formate-binding site is located at the periplasmic side, the quinone reduction site at the opposite side of the cytoplasmic membrane.

Formate dehydrogenase O is present in *E. coli* cells grown aerobically or anaerobically in the presence of nitrate.[13] It is the least well-studied of the three isoenzymes, although it is this system for which a biological role of the element selenium was first demonstrated.[14] Formate dehydrogenase O appears to act as an oxidoreductase coupling formate oxidation with quinone reduction, but a detailed analysis of its structure and redox partners has not yet been carried out.

Depending on the selenium status of the growth medium, *Methanococcus vannielii* synthesizes either one of the two formate dehydrogenases.[15] In the absence of selenium, cells contain a formate dehydrogenase activity that is associated with a 105-kDa polypeptide, which carries a molybdenum cofactor and Fe/S center(s) (1 Mo and 10 FeS), but lacks selenium. When selenite is added to the medium, a 100-kDa selenocysteine-containing polypeptide is formed, which is associated with the 105-kDa polypeptide carrying the Mo–FeS centers. This enzyme complex exhibits a higher catalytic activity than the 105-kDa species alone.[15] Both catalytic species couple formate oxidation to the reduction of the 8-hydroxy-5-deazaflavin cofactor (F_{420}) present in methanogenic bacteria.

2.1.2 Bidirectionally Acting Formate Dehydrogenases

Acetogenic bacteria such as *Clostridium (Cl.) thermoaceticum* or *Cl. formicoaceticum* catalyze an $NADPH_2$-driven CO_2 reduction to formate, which is further reduced via the tetrahydrofolate pathway to the $–CH_3$ oxidation state, as the methyl is finally incorporated into acetic acid. This ‘anabolic’ formate dehydrogenase has long been known to depend on the presence of Se in the medium for its formation.[16] The enzyme is an $\alpha_2\beta_2$ heterooligomer of 340 kDa; the complex contains two selenocysteine residues, two moles of a tungsten cofactor, and Fe/S centers.[17]

2.2 Hydrogenases

Hydrogenases that catalyze the reversible oxidation of molecular hydrogen into protons and electrons can be classified based on their metal cofactor content into ‘Fe-only’ hydrogenases and [NiFe] hydrogenases, which also include [NiFeSe] hydrogenases.[18] The amino acid position occupied by the selenocysteine residue in [NiFeSe] hydrogenases is taken by a cysteine residue in [NiFe] hydrogenases. [NiFeSe] hydrogenases are formed by methanogenic bacteria, such as *Methanococcus* (*M.*) *vannielii*,[19] *M. voltae*,[20] *M. jannaschii*,[21] and *M. maripaludis*,[3] and by several sulfate-reducing bacteria such as *Desulfomicrobium* (*D.*) *baculatum*.[18] The [NiFeSe] hydrogenase of *D. baculatum* exhibits the classical $\alpha\beta$ heterodimeric structure of Ni-containing hydrogenases[18] with the large (α) subunit displaying a molecular mass of 62 kDa and the small (β) one a mass of 32 kDa. The large subunit is the selenocysteine-containing polypeptide and also carries the Ni in a 1:1 ratio to Se. Fe/S centers are present in both subunits.[18] EPR spectroscopy of the ^{77}Se-enriched enzyme and Ni and Se EXAFS studies revealed a direct coordination of the nickel atom to selenium,[22] which indicates that one of the four thiolate ligands of the metal center in [NiFe] enzymes is replaced by a selenocysteyl moiety in [NiFeSe] enzymes.

2.3 Glycine Reductase

A number of obligate anaerobic bacteria can ferment amino acids or purine bases by using glycine as the electron acceptor. The key enzyme for this fermentation pathway is glycine reductase; it is unique since it is the only reduction reaction known, which is coupled with energy generation via a substrate-level phosphorylation.[23] The overall balance of the fermentation of an alanine/glycine pair by Stickland organisms like *Cl. sticklandii* or *Eubacterium* (*E.*) *acidaminophilum* is given by equation (3), and that of the purine degradation intermediate formiminoglycine by *Cl. purinolyticum* or *Cl. cylindrosporum* by equation (4).

$$\text{Alanine} + 2\text{ glycine} + 3\text{ADP} + 3\text{P}_i \longrightarrow 3\text{ Acetate} + \text{CO}_2 + 3\text{NH}_4{}^+ + 3\text{ATP} \qquad (3)$$

$$\text{Formiminoglycine} + 2\text{ADP} + 2\text{P}_i \longrightarrow \text{Acetate} + \text{CO}_2 + 2\text{NH}_4{}^+ + 2\text{ATP} \qquad (4)$$

Three proteins, termed P_A, P_B, and P_C, contribute to the formation of the membrane-bound glycine reductase complex.[1,2] P_A is a 12.5-kDa acidic glycoprotein containing a single selenocysteine (U) residue in a sequence context (CxxU) also present in thioredoxins. P_A actually was the first protein for which the organoselenium compound selenocysteine was identified.[24] Protein P_B also contains a single selenocysteine residue[25] and appears to function in the activation of the specific substrate. Finally, P_C is an $\alpha_4\beta_4$ oligomer where β (48 kDa) carries an acetyl-accepting SH group and α (57 kDa) serves as a membrane anchor for the total glycine reductase complex.

The reaction cycle (Figure 1) initiates by the formation of a Schiff base between glycine and a pyruvoyl group carried by protein P_B. The Schiff base is then attacked by the selenol of protein P_A, resulting in formation of a Se–carboxymethyl intermediate. The next step has not yet been clearly resolved, but on completion, results in the transfer of an acetyl group to the thiol of the β-subunit of protein P_C to yield an acetyl-thioester of P_C and leaving protein P_A in an intramolecular selenadisulfide form. The acetyl-thioester is then cleaved phosphoroclastically with acetylphosphate being released,[23] and the oxidized protein P_A can be reduced involving a redox chain from $NADH_2$, thioredoxin reductase, and thioredoxin.[26]

2.4 Selenoenzymes Involved in Methanogenesis

The analysis of the genome of methanogenic bacteria, in particular, of *M. jannaschii*, disclosed the existence of a number of selenoenzymes involved in the reduction of CO_2 into CH_4.[3,21] Apart from the two classes of hydrogenases (F_{420}-reducing and F_{420}-nonreducing hydrogenases) and the formate dehydrogenase mentioned above, these are formylmethanofuran dehydrogenase and heterodisulfide reductase. Since these enzymes are essential for energy generation, the organism displays an obligate growth requirement for selenium. Intriguingly, growth of the closely related methanogen *M. maripaludis* on H_2 and CO_2 is independent of the availability of selenium since it possesses a 'backup' system of homologs, which contain a cysteine residue in the position of selenocysteine.[27] An exception is formate dehydrogenase for which no such sulfur homolog exists and consequently growth at the expense of formate requires a supply of selenium. When *M. maripaludis* is cultivated under selenium-adequate conditions, the sulfur enzymes are not synthesized; therefore, selenium or a follow-up product in its metabolism must exert a repressive effect on their formation.[27]

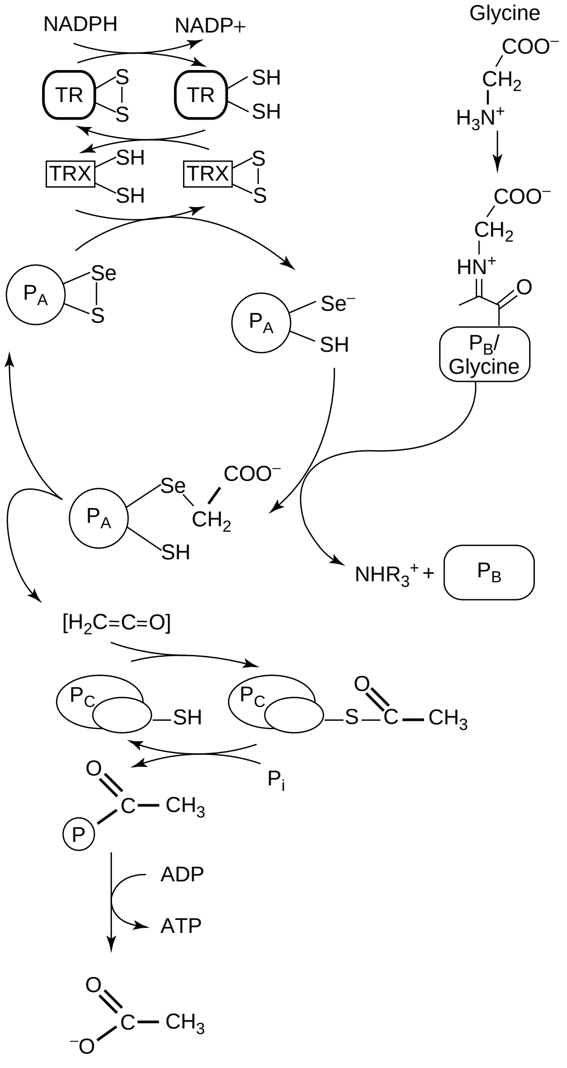

Figure 1 Reactions involved in the glycine reduction pathway by *Clostridia*. P_A, P_B, and P_C denote the components of the glycine reduction complex where P_B is specific for the substrate (e.g. glycine, betaine, sarcosine). The reduction of oxidized protein P_A occurs via a redox chain involving thioredoxin reductase (TR) and thioredoxin (TRX). The involvement of ketene as an intermediate has not yet been proven

3 EUKARYAL SELENOPROTEINS

A recent computational screen of the human genome resulted in the identification of 25 open reading frames as coding for putative selenoproteins.[28] Because of space limitation, this review concentrates only on the discussion of those proteins for which a biochemical function or an important physiological role had been attributed.

3.1 Glutathione Peroxidases

Four different classes of selenium-dependent glutathione peroxidases are known at present: cytoplasmic glutathione peroxidases, plasma glutathione peroxidases, gastrointestinal glutathione peroxidase, and phospholipid hydroperoxide glutathione peroxidases. They all catalyze the reduction of hydroperoxide and organic hydroperoxides by reduced glutathione:

$$\mathrm{ROOH} + 2\mathrm{GSH} \longrightarrow \mathrm{ROH} + \mathrm{H_2O} + \mathrm{GSSG} \qquad (5)$$

Cytoplasmic glutathione peroxidase is by far the most thoroughly studied species and has been extensively reviewed.[29] It was also the first selenoenzyme to be purified and demonstrated to contain covalently bound selenium.[30] The enzyme is present in the tissues of all mammalia and birds studied. Depending on the species, the molecular mass of the enzyme ranges between 76 and 94 kDa. It is composed of four identical constituent subunits that contain a single selenocysteine residue each.

A detailed kinetic analysis and the modeling of enzyme–substrate complexes with the aid of the 3D structure[31] have led to the suggestion of the reaction mechanism detailed in Figure 2.

According to this model, the dissociated selenol of the selenocysteine in the active center reacts with the

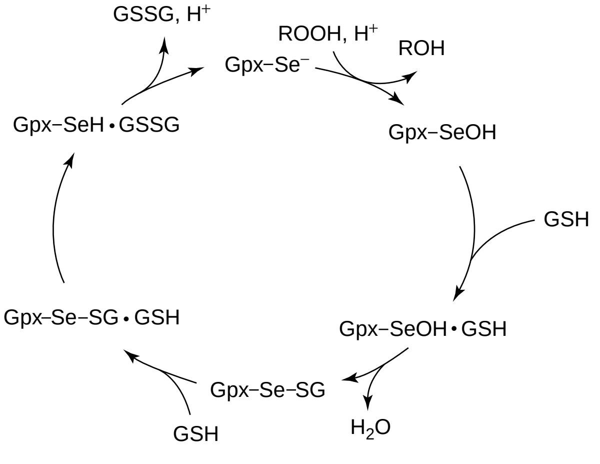

Figure 2 Reaction cycle catalyzed by glutathione peroxidase. GSH and GSSG denote reduced and oxidized glutathione, respectively

hydroperoxide (ROOH), which is reduced to the alcohol state. The selenolate, however, is oxidized to selenic acid, which can now react with reduced glutathione to form a mixed protein–glutathione–selenadisulfide. Experimentally, such an intermediate has been demonstrated to exist. In a consecutive and final step, the mixed selenadisulfide is reduced by a second glutathione molecule, regenerating the protein with a free selenol and producing oxidized glutathione. The efficiency of this regeneration depends on the glutathione concentration, a high concentration in the mM range being crucial, since the rate of this reaction is about two orders of magnitude lower than that of the hydroperoxide with the selenolate. According to the suggested model, selenium changes its oxidation state during the reaction cycle.

A glutathione peroxidase, distinct from the cellular enzyme species, has been purified from human plasma.[32] Its molecular mass was determined to be approximately 100 kDa and it was shown to be a tetrameric protein of identical subunits. Like the cytoplasmic form, it contains four atoms of selenium per mole of protein. In contrast to its cellular counterpart, however, the plasma protein is glycosylated. It catalyzes the reduction of both H_2O_2 and organic hydroperoxides, its affinity for glutathione being an order of magnitude lower than that of the cytoplasmic enzyme. Since the concentration of glutathione in plasma is far below the affinity of the enzyme, it is questionable whether glutathione is the natural substrate. Whereas the cellular enzymes from different species or tissues generally share sequence similarities between 80–95%, the plasma enzyme is evolutionarily more distant.

Ursini and collaborators purified a glutathione peroxidase from pig heart and pig liver that reduced phospholipid hydroperoxides with glutathione as a reductant, especially in the presence of a detergent.[33] Cellular and plasma glutathione peroxidases do not attack lipid hydroperoxides in vitro even in the presence of detergents. The enzyme is a 21-kDa monomer and contains a single selenocysteine residue.[34] The enzyme, termed ‘phospholipid hydroperoxide glutathione peroxidase’ (PHGPx), is believed to be the major determinant that protects membrane phospholipids from oxidative damage. Apart from this protective effect, PHGPx is involved in the modulation of inflammatory processes by regulating the biosynthesis of leukotrienes and prostaglandins, and may downregulate cytokine-induced transcription activation.[35]

PHGPx also fulfills a fascinating structural role during spermatogenesis It is an active peroxidase in the spermatids and develops into a major structural protein of the mitochondrial capsule of the spermatozoa. The formation of the capsule involves the H_2O_2-stimulated formation of keratin-like protein polymers linked via intramolecular and also intermolecular selenadisulfides with thiols of other proteins. It appears that PHGPx, which is present in extraordinarily high levels and also in different forms in the testes, is responsible for the long-known selenium dependence of male fertility.[36]

3.2 Tetraiodothyronine Deiodinases

3,3′,5,5′-Tetraiodothyronine (T_4; thyroxine) is synthesized in the thyroid gland and converted into 3,3′,5-triiodothyronine (T_3) and 3,3′,5′-triiodothyronine (reverse T_3, rT_3) by tetraiodothyronine deiodinases in nonendocrine organs.[37] The type I deiodinase is formed in the liver and the kidney, and catalyzes the formation of T_3 and rT_3; this class of deiodinase is responsible for producing the major part of T_3 present in the plasma. The type II enzyme is present in other tissues such as the central nervous system and is thought to contribute most of the rT_3 of the plasma. A third deiodinase (type III) is responsible for converting T_4 into hormonally inactive T_3 metabolites. All three deiodinases are selenoenzymes[37–39] with a single selenocysteine residue each. They are encoded by different genes and they control the tissue-specific availability of the endocrine hormone T3.[40]

The reaction cycle depicted in Figure 3 proposes that the enzyme with a free selenolate reacts with T_4 to produce T_3 and an enzyme–iodide intermediate. The selenolate is regenerated and the iodide released by reaction with reduced glutathione. The model also explains the inhibitory actions of gold thioglucose, which reacts with the selenolate, and of propylthiouracil, which releases the iodide from the enzyme–iodide intermediate and forms an enzyme–propylthiouracil–selenadisulfide.

3.3 Thioredoxin Reductase

In 1996, Tamura and Stadtman showed that thioredoxin reductase from mammalia – in contrast to the bacterial homologs – is a selenoprotein, and that selenocysteine is the penultimate C-terminal amino acid residue.[41] Selenium-containing isoenzymes, which are tissue specific, have later on been characterized biochemically, or the existence of such isoforms was suggested by in-silico methods.[4,28,42] The substrate of thioredoxin reductase is thioredoxin, which is the key regulator of the redox status within cells. Thioredoxin catalyzes thiol-disulfide exchange reactions in proteins and peptides; it is involved as redox mediator in the

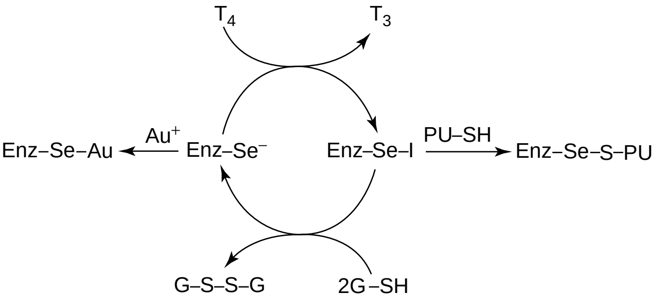

Figure 3 Reaction cycle catalyzed by the type I tetraiodothyronine deiodinase. T_4 = 3,3′,5,5′-tetraiodothyronine; T_3 = 3,3′,5-triiodothyronine; Au^+ = gold thioglucose; PU-SH = propylthiouracil

reaction of ribonucleotide reductase and in the activation of transcription factors and nuclear receptors. Thus, thioredoxin reductase regulates a multitude of metabolic processes and is involved in regulatory cascades within the eukaryal cell.[43] The enzyme is a homodimer with a head-to-tail orientation of the two subunits that form an intersubunit catalytic center.[44] The required reducing equivalents are derived from NADPH and transferred via FAD to a central CysXXXXCys motif of the protein, which in its oxidized form interacts with the selenocysteine of the opposite subunit via a selenadisulfide bond with the concomitant transfer of the reducing equivalents to the oxidized thioredoxin[45] (Figure 4). Both thioredoxin and thioredoxin reductase are essential proteins; the knock out of their genes causes embryonic lethality.

3.4 Methionine Sulfoxide Reductase

Mammalia contain two methionine sulfoxide reductases, forms A and B. Methionine sulfoxide reductase B is a selenoprotein, which reduces the R form of free or protein-bound methionine sulfoxides to methionine with thioredoxin as the reductant.[46] Together with isoform A (which does not contain selenium), the enzyme can repair oxidatively damaged protein and thus contributes to the antioxidant system of the cell.[47]

3.5 Plasma Selenoprotein P

Plasma from mammalia contains a selenoprotein that carries more than 50% of the selenium present. In rat, about 8% of the total selenium content is associated with this protein, selenoprotein P.[48] A change in the selenium status of the rat leads to a rapid change of the selenium level attached to selenoprotein P, preferential to changes of other selenoproteins such as plasma glutathione peroxidase.[48]

Selenoprotein P is a glycoprotein; the sequence of the protein moiety within it, having a molecular mass of about 41 kDa, was deduced from the nucleotide sequence of the rat gene.[49] It is unique since, dependent on the organism, it contains more than a dozen selenocysteine residues per monomer. The sequence also contains histidine- and cysteine-rich stretches, which could be involved in metal binding. Other putative functions discussed for selenoprotein P are selenium transport and tissue-specific delivery or a reducing role.[50]

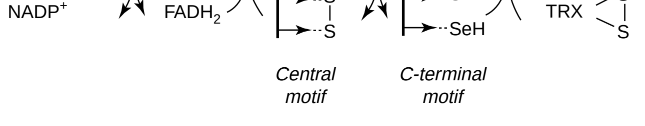

Figure 4 Cascade of redox reactions catalyzed by mammalian thioredoxin reductase

3.6 Selenophosphate Synthetase

Selenophosphate synthetase (SPS) catalyzes the synthesis of the activated selenium species required for the biosynthesis of selenocysteine (see below). The enzyme from *E. coli*, which was isolated first does not contain selenium.[51] It turned out, however, that in most other organisms, SPS is a selenocysteine-containing protein of about 37 kDa in which the selenocysteine occupies the position of a cysteine (Cys-17) in the *E. coli* homolog. Most mammalia possess two types of SPS homologs, one designated SPS II, which is a selenoprotein and possesses SPS activity; the other one, SPS I, has a threonine or arginine residue in the position of Cys-17 (*E. coli* nomenclature) and at least the arginine homolog lacks this activity. The actual function of SPS I is unknown. The reaction catalyzed by SPS is postulated to follow the sequence presented in equations (6) and (7).

$$\mathrm{ATP} + \mathrm{SPS} \longrightarrow \mathrm{SPS\text{-}P} \sim [\mathrm{ADP}] \qquad (6)$$

$$\mathrm{SPS\text{-}P} \sim [\mathrm{ADP}] + \mathrm{HSe}^{-} \longrightarrow \mathrm{HSe\text{-}PO_3H_2} + \mathrm{AMP} + \mathrm{P_i} \qquad (7)$$

Thus, the γ-phosphate group of ATP is transferred to some group of the protein and the enzyme phosphoryl intermediate is attacked by the selenide generating the only known direct phosphorus–selenium bond in biology. The ADP, which stays complexed to the enzyme is concomitantly hydrolyzed to AMP, and thus thermodynamically drives the overall reaction.[51] Sulfide does not serve as a substrate even at high concentrations, so SPS is one of the few enzymes that can discriminate between its Se substrate and the sulfur homolog. Recent evidence also indicates that the actual substrate is not free selenide but rather some selenium species generated from selenocysteine via the activity of one of the selenocysteine lyases present in the cell.[52]

4 CATALYTIC ROLE OF SELENOCYSTEINE

A question of particular interest concerns the catalytic advantage that a selenol in the active site of an enzyme has in comparison to a thiol group. It has been approached by replacing the selenocysteine in the formate dehydrogenase H by a cysteine residue and by determining the catalytic parameters of the Se-wild-type species with the mutant S-species. Table 1 presents the data obtained. They show that k_{cat} of the Se enzyme is more than 300-fold higher than that of the S variant and that the affinity to the substrate is only marginally affected.[53] Similar replacements of selenocysteine by cysteine in other enzymes like the deiodinase type I or methionine sulfoxide reductase B corroborated these results.

Table 1 Comparison of catalytic parameters of formate dehydrogenases

Enzyme	K_m (mM formate)	k_{cat} (min^{-1})	k_{cat}/K_m ($mM^{-1}\ min^{-1}$)
E. coli, N[10]	0.12	33 800	2.8×10^5
E. coli, H			
Se form[9]	26	170 000	6.5×10^3
S form[9]	9	540	6.0×10^1
M. formicicum[54]	not known	3100	–

In *Methanobacterim formicicum*, the formate dehydrogenase can be considered as a natural S variant of the *E. coli* formate dehydrogenase H since it has 46% sequence similarity and a cysteine residue in the position where the *E. coli* enzyme contains a selenocysteine residue.[1,54] Its k_{cat}, although being sixfold higher than the *E. coli* S species, is almost 50-fold lower compared to the Se form. This protein makes about 3% of the total cellular protein of the methanogen, so it appears that the organism compensates for the low turnover number by synthesizing an increased amount of the enzyme.[54]

In several enzymes, the selenolate group of the selenocysteine residue participates in the coordination of a metal. The catalytic advantage of the liganding of the Ni in the active center of NiFe-hydrogenases via a selenolate to the protein backbone is still not clear since no isogenic mutant forms are available. A comparison of the catalytic performance of [NiFeSe] hydrogenases with [NiFe] hydrogenases led only to some suggestions: (1) [NiFeSe] enzymes may be more efficient in H_2 evolution; (2) they may be activated more easily; (3) the stability of a nickel-bound hydride intermediate may be decreased by the less electronegative selenium, which would increase the probability of a double H^+ exchange.[22] In formate dehydrogenases, the molybdenum, which bridges two pterin guanine dinucleotides, is coordinated to the selenolate of the selenocysteine of the α subunit. In this case, the selenolate appears to directly participate in the reaction by facilitating the abstraction of a proton from the substrate.[9,11]

5 INCORPORATION OF SELENOCYSTEINE

5.1 A UGA Codon Directs Selenocysteine Insertion

A result emerging from the genetic analysis of selenoproteins was the discovery that selenocysteine is the 21st amino acid encoded in DNA.[55] Its insertion is directed by an in-frame UGA codon in the selenoprotein mRNA. UGA is used for this purpose in all three lines of descent (bacteria, archaea, and eukarya): The consistent use of UGA as a signal points to a common evolutionary origin of the selenocysteine coding system.

In the universal genetic code, UGA is one of the three stop codons that signal termination of polypeptide formation. Questions of basic biological relevance emerged from the use of this codon as the selenocysteine insertion signal: (1) What are the mechanisms which warrant that selenocysteine be inserted only at the position of this particular UGA codon, and not at the site of ordinary UGA termination codons? (2) Why does this particular codon not function as a termination signal? The investigation of the sequence context around this UGA did not reveal any peculiar features, which might contribute to its specificity. Rather, a secondary structure downstream of the UGA was found to be crucial (see below).

The existence of a special codon for selenocysteine implied that the amino acid is inserted cotranslationally. This was proved by means of gene fusions in which the 5′ terminal portion of the fusion was derived from the formate dehydrogenase gene (including the TGA) and the 3′ terminal portion was the *lacZ* reporter gene. The *lacZ* portion was translated into β-galactosidase only when the medium was supplemented with selenium although a full-length transcript was present in each case. Ribosomes, therefore, require selenocysteine to move into the *lacZ* mRNA portion.

5.2 tRNA^{Sec} is Responsible for Decoding the UGA

A cotranslational mode of selenocysteine insertion necessitates the existence of a tRNA that carries this amino acid. This tRNA was identified during a screening for *E. coli* mutants blocked in selenoprotein formation.[55] The genes and the function of the gene products found to be involved in selenoprotein synthesis are listed in Table 2.

The product of the *selC* gene, tRNA^{Sec}, was identified as a novel tRNA species. Its structure differs from the features of all elongator tRNAs.[56] With 95 nucleotides, it is the longest tRNA known to date. It has a variable loop of 22 nucleotides, an eight-base-pair aminoacyl acceptor stem, and a number of deviations from tRNA consensus structure. tRNA^{Sec} is charged with L-serine by the cellular seryl–tRNA synthetase, which is responsible for aminoacylation of the serine isoacceptor species. Thus, selenocysteine is formed from a serine residue charged to tRNA^{Sec}.

By chemical and enzymatic probing, the solution structure of this tRNA was analyzed. tRNA^{Sec} is identical to other tRNAs concerning the T-arm and anticodon arm conformations, and the joining of the D- and T-loops by

Table 2 *E. coli* genes and their products with a function in selenoprotein synthesis

Gene	Product function	Size
SelA	Selenocysteine synthase	10 × 50 kDa
SelB	Translation factor	69 kDa (monomer)
SelC	tRNA^{Sec}	95 nucleotides
SelD	Selenium activation	37 kDa (monomer)

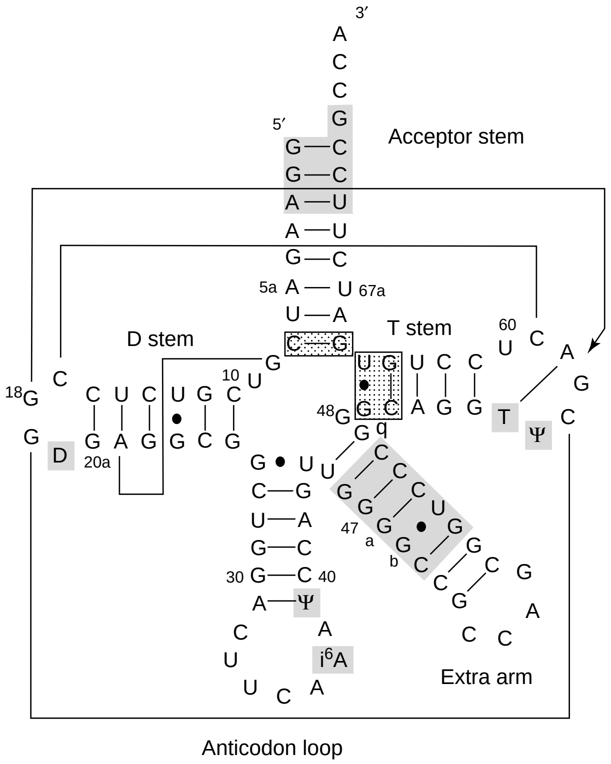

Figure 5 Structural features of the $tRNA^{Sec}$ from *E. coli*. Elements involved in recognition by seryl-tRNA synthetase are shaded, antideterminants against recognition by EF-Tu are hatched. The modified bases are: D: dihydrouridine; Ψ: pseudouridine; i^6A: isopentenyl-adenosine; T: ribothymidine. Tertiary interactions involving base pairing are indicated by lines, those with intercalations by arrows

a tertiary Watson–Crick G19–C56 interaction. Its extra-long arm is double-stranded and closed by a four-nucleotide loop. It possesses novel interactions, namely, a G8–A21–U14 triple pair and an interaction between C16 of the D-loop and C59 of the T-loop. The D-arm has six base pairs instead of three, with the D-loop containing only four nucleotides. The interactions within the $tRNA^{Sec}$ and for comparison, the ${tRNA^{Ser}}_1$ structures are presented in Figure 5. Altogether, the results show that although $tRNA^{Sec}$ displays the canonical L-shape in the three-dimensional structure, nature has used different sets of tertiary interactions to reach this structure.

5.3 Selenocysteine Biosynthesis

Displacement of the OH group of seryl–$tRNA^{Sec}$ by an –SeH group to yield selenocysteyl–tRNA requires the activation of the hydroxyl. When the *selA* gene product was purified, it was found that the protein contains pyridoxal phosphate as a prosthetic group. Accordingly, the reaction mechanism involves the formation of a Schiff base between the carbonyl of the pyridoxal moiety and the α-amino group of serine followed by 2,3-elimination of a water molecule, resulting in the formation of dehydroalanyl–$tRNA^{Sec}$. Nucleophilic addition of selenide from selenophosphate as the selenium donor molecule then delivers selenocysteyl-tRNA.[1,55] Selenocysteine synthase is a decamer of 50 kDa subunits. Two of these subunits bind one seryl–$tRNA^{Sec}$ molecule. Electron microscopy at 20 nm resolution showed that the subunits are arranged with pentameric symmetry and that one tRNA molecule binds peripherally to two subunits.

In summary, selenocysteine is synthesized by the sequence of the reactions

$$\text{L-Serine} + \text{ATP} + \text{tRNA}^{\text{Sec}} \xrightarrow{\text{SerS}} \text{Seryl-tRNA}^{\text{Sec}} + \text{AMP} + \text{PP}_i \tag{8}$$

$$\text{L-Seryl-tRNA}^{\text{Sec}} + \text{SS} \longrightarrow \text{SS-Dehydroalanyl-tRNA}^{\text{Sec}} + \text{H}_2\text{O} \tag{9}$$

$$\text{HSe}^- + \text{ATP} \xrightarrow{\text{SelD}} \text{AMP} + \text{P}_i\,(\beta) + \text{H}_3\text{PO}_3\,\text{Se} \tag{10}$$

$$\text{SS-Dehydroalanyl-tRNA}^{\text{Sec}} + \text{H}_3\text{PO}_3\,\text{Se} \longrightarrow \text{SS} + \text{Selenocysteyl-tRNA}^{\text{Sec}} + \text{H}_3\text{PO}_4 \tag{11}$$

where SS = selenocysteine synthase and SerS = seryl–tRNA synthetase. Selenophosphate synthesized by SSP (the *selD* gene product) also serves as an activated selenium species for another type of reaction, the conversion of 5-methylaminomethyl-2-thiouridine into 5-methylaminomethyl-2-selenouridine. This modified nucleoside is present in position 34 of the anticodon of $tRNA^{Glu}$ and $tRNA^{Lys}$ acceptor species, both from prokaryotes and eukaryotes.[2]

With regard to selenocysteine biosynthesis in archaea and eukarya, a tRNA has been known for some time, which accepts L-serine and possesses an anticodon complementary to UGA.[5] It shares a number of structural features with $tRNA^{Sec}$ from *E. coli*, such as extended aminoacyl acceptor and D-arms. In eukarya, the serine residue attached to this tRNA can be phosphorylated by a specific kinase and it was first assumed that this tRNA inserts phosphoserine into proteins. However, closer examination revealed that this tRNA carries selenocysteine in vivo and certainly is the pendant to $tRNA^{Sec}$ from *E. coli*. It is still elusive whether *O*-phosphoseryl–tRNA is the biosynthetic intermediate for selenocysteyl-tRNA formation in eukaryotes; also, there is no evidence yet of an eukaryal and archaeal enzyme, equivalent in its function to selenocysteine synthase from bacteria.

5.4 SelB, a New Translation Factor

Mutants of *E. coli* with a lesion in the *selB* gene were unable to synthesize selenoproteins although they accumulated selenocysteyl–$tRNA^{Sec}$ in vivo. This indicated a function of SelB in the decoding process itself. The following experimental results revealed that SelB is a translation factor, specialized for selenocysteyl–$tRNA^{Sec}$: (1) SelB, over its N-terminal two-thirds, displays sequence homology with translation factors such as EF-Tu and IF2α; (2) SelB, like other translation factors, is a guanine nucleotide-binding protein; (3) SelB binds selenocysteyl–tRNA^{Sec}. The precursor species, seryl–tRNA^{Sec} is not recognized, a fact which contributes to the specificity of insertion. EF-Tu binds selenocysteyl–tRNA with less than 1% of the affinity with which it binds aminoacyl–tRNAs of one of the 20 classical amino acids. This indicates that SelB has a function which is distinct from that of EF-Tu. Thus, EF-Tu forms a ternary complex with one of the 20 standard amino acids and GTP, whereas SelB forms an equivalent complex with selenocysteyl–tRNA and GTP.[57]

Regarding the structural features that enable EF-Tu and SelB to distinguish 'their' tRNAs, an extensive mutational analysis was performed and synthetic RNA 'minihelices' were analyzed for binding to EF-Tu and SelB. It was found that both the length of the aminoacyl–tRNA acceptor stem and the basal helical part of the acceptor arm were crucial.[58]

5.5 mRNA Determinants Required for Decoding UGA with Selenocysteine

In those genes that code for selenoproteins, TGA (UGA) directs the insertion of selenocysteine in all biological systems studied. The question of the recognition of the UGA as a signal for selenocysteine insertion was approached by a mutational analysis. Deletions introduced upstream and downstream of the UGA within the formate dehydrogenase H and N genes revealed the requirement of a segment of 40 nucleotides downstream of the codon.[59] A stable RNA hairpin structure (the SECIS element) can be formed within this RNA segment. The functional role of this hairpin in the selenocysteine decoding process has been proved by genetic and biochemical strategies. It was found that an intact secondary structure with a sequence determinant residing within a single-stranded (loop) region serves as a recognition element for differentiating the selenocysteine-specific UGA codons, thus providing evidence that it is the mRNA context that directs tRNA^{Sec} to decode this position. The nature of the codon/anticodon sequence is irrelevant, the only requirement is that they are complementary.

On the basis of a dual function of UGA as a codon for selenocysteine insertion and for translation termination within a single cell, it has to be assured (1) that this UGA codon is not used as a termination signal and (2) that selenocysteyl–tRNA is directed only to this position. The results of a biochemical analysis indeed revealed that this is achieved by the formation of a complex between SelB, selenocysteyl–tRNA, and the stem–loop structure downstream of the UGA. The binding to the SECIS element was shown to involve an ultimate 17-kDa C-terminal domain of SelB.

The interaction of SelB with its ligands was analyzed by stopped flow methods. The main finding was that binding of the two RNA ligands (selenocysteyl-tRNA and the SECIS element) confers to the SelB protein, a conformation that renders it compatible for interaction with the ribosome. Upon this interaction, GTP is hydrolyzed and the charged tRNA is released in the vicinity of the ribosomal A site. This scenario explains why ordinary UGA stop codons are not translated: since they lack a SECIS element in their vicinity, SelB (which is not complexed to the mRNA) does not possess the productive conformation for the decoding process.[57]

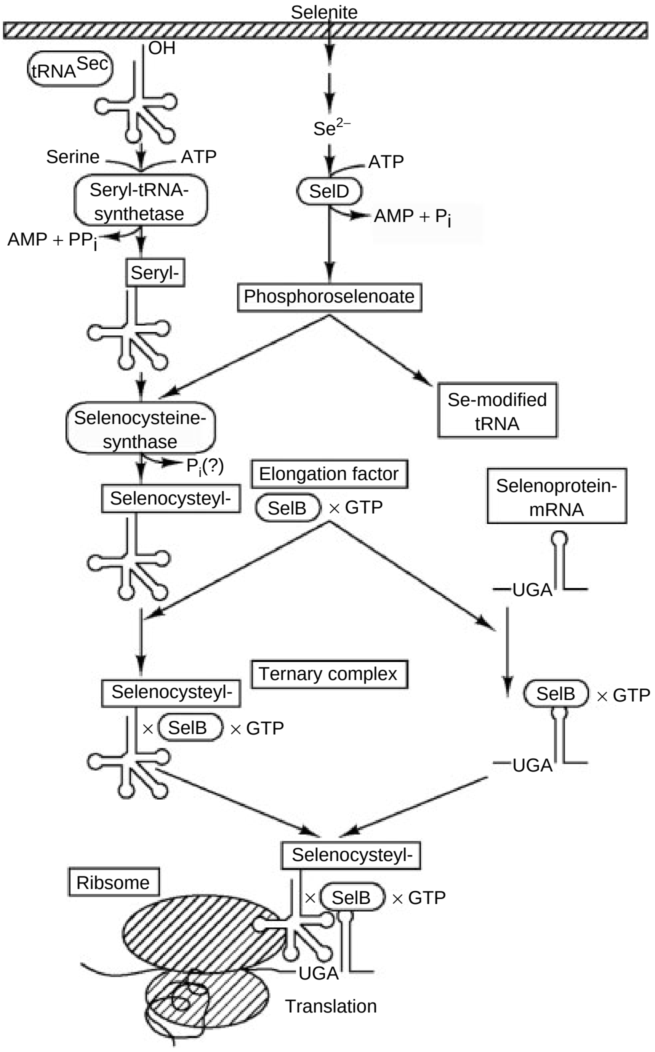

Figure 6 Pathway of selenocysteine biosynthesis and incorporation into protein as resolved for *E. coli*; for details, see text

Figure 6 summarizes the steps of selenocysteine synthesis and incorporation, as elucidated for the *E. coli* system.

In mammalia, a recognition element of selenoprotein mRNAs (SECIS) exists within the 3′ untranslated region, and the UGA within the selenoprotein mRNAs is decoded with selenocysteine only when the 3′ untranslated region is present.[5] Substitution of the homologous 3′ region by that of another selenoprotein mRNA allows selenocysteine insertion again. The eukaryal SECIS element is the binding target for a protein designated SBP2 (SECIS element binding protein 2). SBP2 undergoes protein–protein interaction with a eukaryal homolog of the bacterial translation factor SelB.**[6]** This interaction is stabilized in the presence of selenocysteyl-tRNA.**[60]** Therefore, in analogy to the bacterial system, the function of SelB is taken over by two proteins and their stable interaction requires the binding of the charged tRNA thus resembling the formation of the stabilized quaternary complex of SelB.

6 DESIGN OF NEW SELENOPROTEINS

The construction of synthetic selenocysteine-containing proteins or selenium-containing proteins attracts considerable interest at present, mainly for the reason that it can be used to solve the phase problem in X-ray crystallography. Selenomethionine incorporation has been used mostly until now for this purpose. There are also two reports on new synthetic selenocysteine-containing proteins. In one case, the active site serine of subtilisin has been converted into a selenocysteine residue by chemical means, with the result that the enzyme gains a predominant esterase instead of protease activity. In the second case, automated peptide synthesis was carried out to produce a peptide in which all seven-cysteine residues of the *Neurospora crassa* metallothionein (Cu) were replaced by selenocysteine. The replacement resulted in an alteration of both the stoichiometry and the affinity of copper binding.**[2]**

Future investigations will concentrate on the replacement of cysteine residues by selenocysteine using biological methods. Thus, a system has been established to substitute all cysteine residues of a protein in an overexpression system and it has been used successfully in structural analysis of cysteine-rich proteins and also to replace an active site cysteine by selenocysteine.**[61,62]** A strategy for the replacement of both methionine and cysteine by their selenium homologs has also been developed recently.**[63]** It may also be possible, however, to use the information on selenoprotein synthesis in bacteria to achieve targeted replacement of a selected, single cysteine residue. In rare cases, a change of the mRNA sequence by the introduction of silent mutations may be possible to create the determinants necessary for interaction with the translation factor SelB. To this end, a cysteine codon has to be changed to a UGA codon and the $3'$ flanking region has to be altered such that the stem-loop structure determining selenocysteine incorporation is generated. This approach, of course, suffers from the strict sequence constraints that may preclude the formation of this mRNA recognition element and may be open for application only in special cases. Thus, the methionine sulfoxide reductase gene from mammalia has been engineered such that the UGA is followed by the *E. coli* consensus SECIS element in the mRNA and in this way recombinant production of the eukaryal enzyme in *E. coli* could be achieved.**[64]** Also, recombinant mammalian thioredoxin reductase (in which the selenocysteine is the penultimate C-terminal amino acid residue) could be produced in *E. coli* by fusing the *E. coli* SECIS element downstream of the termination codon of the thioredoxin reductase gene.**[65]**

7 RELATED ARTICLES

Metallocenter Biosynthesis & Assembly; Metallochaperones & Metal Ion Homeostasis; Metalloprotein Design & Engineering; Molybdenum: MPT-containing Enzymes; Nickel Enzymes & Cofactors; Selenium: Inorganic Chemistry; Selenium: Organoselenium Chemistry; Sulfur: Inorganic Chemistry.

8 REFERENCES

1. J. Heider and A. Böck, *Adv. Microb. Physiol.*, 1993, **35**, 71.
2. T. C. Stadtman, *Annu. Rev. Biochem.*, 1996, **65**, 83.
3. M. Rother, A. Resch, R. Wilting, and A. Böck, *BioFactors*, 2000, **14**, 75.
4. M. Birringer, S. Pilawa, and L. Flohé, *Nat. Prod. Rep.*, 2002, **19**, 693.
5. D. L. Hatfield and V. N. Gladyshev, *Mol. Cell. Biol.*, 2002, **22**, 3565.
6. D. M. Driscoll and P. R. Copeland, *Annu. Rev. Nutr.*, 2003, **23**, 17.
7. D. L. Hatfield, *Selenium*, 'Its Molecular Biology and Role in Human Health', Kluwer Academic Publishers, Boston, Dordrecht, London, 2000.
8. M. J. Axley, D. A. Grahame, and T. C. Stadtman, *J. Biol. Chem.*, 1990, **265**, 8213.
9. J. C. Boyington, V. N. Gladyshev, S. V. Khangulov, T. C. Stadtman, and P. D. Sun, *Science*, 1997, **275**, 1305.
10. H. G. Enoch and R. L. Lester, *J. Biol. Chem.*, 1975, **250**, 6693.
11. M. Jormakka, S. Törnroth, B. Byrne, and S. Iwata, *Science*, 2002, **295**, 1863.
12. B. L. Berg, C. Baron, and V. Stewart, *J. Biol. Chem.*, 1991, **266**, 22386.
13. G. Sawers, J. Heider, E. Zehelein, and A. Böck, *J. Bacteriol.*, 1991, **173**, 4983.
14. J. Pinsent, *Biochem. J.*, 1954, **57**, 10.
15. J. B. Jones and T. C. Stadtman, *J. Biol. Chem.*, 1981, **256**, 656.
16. J. R. Andreesen and L. G. Ljungdahl, *J. Bacteriol.*, 1973, **116**, 867.
17. I. Yamamoto, T. Saiki, S.-M. Liu, and L. G. Ljungdahl, *J. Biol. Chem.*, 1982, **258**, 1826.
18. P. M. Vignais, B. Billoud, and J. Meyer, *FEMS Microbiol. Rev.*, 2001, **25**, 455.

19. S. Yamazaki, *J. Biol. Chem.*, 1982, **257**, 7926.
20. S. Halboth and A. Klein, *Mol. Gen. Genet.*, 1992, **233**, 217.
21. R. Wilting, S. Schorling, B. C. Persson, and A. Böck, *J. Mol. Biol.*, 1997, **266**, 637.
22. S. H. He, M. Teixeira, J. LeGall, D. S. Patil, I. Moura, J. J. G. Moura, D. V. DerVartanian, B. H. Huynh, and H. D. Peck Jr, *J. Biol. Chem.*, 1989, **264**, 2678; M. K. Eidsness, R. A. Scott, B. C. Prickril, D. V. DerVartanian, J. LeGall, I. Moura, J. J. G. Moura, and H. D. Peck Jr, *Proc. Natl. Acad. Sci. U.S.A.*, 1989, **86**, 147.
23. R. A. Arkowitz and R. H. Abeles, *Biochemistry*, 1991, **30**, 4090.
24. J. E. Cone, R. Martín del Río, and T. C. Stadtman, *Proc. Natl. Acad. Sci. U.S.A.*, 1976, **73**, 2659.
25. M. Wagner, D. Sonntag, R. Grimm, A. Pich C. Eckerskorn, B. Söhling, and J. R. Andreesen, *Eur. J. Biochem.*, 1999, **260**, 38.
26. T. Schräder and J. R. Andreesen, *Eur. J. Biochem.*, 1992, **206**, 79.
27. M. Rother, I. Mathes, F. Lottspeich, and A. Böck, *J. Bacteriol.*, 2003, **185**, 107.
28. G. V. Kryukov, S. Castellano, S. V. Novoselov, A. V. Lobanov, O. Zehtab, R. Gulgo, and V. N. Gladyshev, *Science*, 2003, **300**, 1439.
29. F. Ursini, M. Maiorino, R. Brigelius-Flohé, K. D. Aumann, A. Roveri, D. Schomburg, and L. Flohé, *Methods Enzymol.*, 1995, **252**, 38.
30. L. Flohé, W. A. Günzler, and H. H. Schock, *FEBS Lett.*, 1973, **32**, 132.
31. R. Ladenstein, O. Epp, K. Bartels, A. Jones, R. Huber, and A. Wendel, *J. Mol. Biol.*, 1979, **134**, 199.
32. K. Takahasi, N. Avissar, J. Whitin, and H. Cohen, *Arch. Biochem. Biophys.*, 1987, **256**, 677.
33. F. Ursini, M. Maiorino, M. Valent, and C. Gregolin, *Biochim. Biophys. Acta*, 1982, **839**, 62.
34. R. Schuckelt, R. Brigelius-Flohé, M. Maiorino, A. Roveri, J. Reumkens, W. Straburger, F. Ursini, B. Wolf, and L. Flohé, *Free Radical Res. Commun.*, 1991, **14**, 343.
35. R. Brigelius-Flohé, *Free Radical Biol. Med.*, 1999, **27**, 951.
36. F. Ursini, S. Heim, M. Kiess, M. Maiorino, A. Roveri, J. Wising, and L. Flohé, *Science*, 1999, **285**, 1393.
37. M. J. Berry and P. R. Larsen, *Endocr. Rev.*, 1992, **13**, 207.
38. D. Behne, H. Hilmert, S. Scheid, H. Gessner, and W. Elger, *Biochim. Biophys. Acta*, 1988, **966**, 12.
39. D. Behne, A. Kyriakopoulos, H. Meinhold, and J. Köhrle, *Biochem. Biophys. Res. Commun.*, 1990, **173**, 1143.
40. J. Köhrle, *Mol. Cell. Endocrinol.*, 2000, **151**, 103.
41. T. Tamura and T. C. Stadtman, *Proc. Natl. Acad. Sci. U.S.A.*, 1996, **93**, 1006.
42. A. Lescure, D. Gautheret, P. Carbon, and A. Krol, *J. Biol. Chem.*, 1999, **274**, 38147.
43. A. Holmgren, *BioFactors*, 2000, **11**, 63.
44. L. Zhong, E. S. Arner, and A. Holmgren, *Proc. Natl. Acad. Sci. U.S.A.*, 2000, **97**, 5854.
45. S. R. Lee, S. Bar-Noy, J. Kwon, R. Levine, T. C. Stadtman, and S. G. Rhee, *Proc. Natl. Acad. Sci. U.S.A.*, 2000, **97**, 2521.
46. G. V. Kryukov, R. A. Kumar, A. Koc, Z. Sun, and V. N. Gladyshev, *Proc. Natl. Acad. Sci. U.S.A.*, 2002, **99**, 4245.
47. J. Moskovitz and E. R. Stadtman, *Proc. Natl. Acad. Sci. U.S.A.*, 20003, **100**, 7486.
48. R. F. Burk, *FASEB J.*, 1991, **5**, 2274.
49. K. E. Hill, R. S. Lloyd, J.-G. Yang, R. Read, and R. F. Burk, *J. Biol. Chem.*, 1991, **266**, 10050.
50. L. Schomburg, U. Schweizer, B. Holtmann, L. Flohé, M. Sendtner, and J. Köhrle, *Biochem. J.*, 2003, **370**, 397.
51. G. M. Lacourciere, in ‘Selenium, its Molecular Biology and Role in Human Health’, ed. D. L. Hatfield, Kluwer Academic Publishers, Boston, Dordrecht, London, 2000, p. 33.
52. H. Mihara, S. Kato, G. M. Lacourciere, T. C. Stadtman, R. A. J. D. Kennedy, T. Kurihara, U. Tokumoto, Y. Takahashi, and N. Esaki, *Proc. Natl. Acad. Sci. U.S.A.*, 2002, **9**, 6679.
53. T. C. Stadtman, ‘Selenium., its Molecular Biology and Role in Human Health’, ed. D. L. Hatfield, Kluwer Academic Publishers, Boston, Dordrecht, London, 2000, p. 115.
54. N. L. Schauer and J. G. Ferry, *J. Bacteriol.*, 1986, **165**, 405.
55. A. Böck, K. Forchhammer, J. Heider, W. Leinfelder, G. Sawers, B. Veprek, and F. Zinoni, *Mol. Microbiol.*, 1991, **5**, 515.
56. S. Commans and A. Böck, *FEMS Microbiol. Rev.*, 1999, **23**, 335.
57. M. Thanbichler and A. Böck, *BioFactors*, 2000, **14**, 53.
58. J. Rudinger, R. Hillenbrandt, M. Sprinzl, and R. Giege, *EMBO J.*, 1996, **15**, 650.
59. A. Krol, *Biochimie*, 2002, **84**, 765.
60. A. M. Zavacki, J. B. Mansell, M. Chung, B. Klimovitsky, J. W. Harney, and M. J. Berry, *Mol. Cell*, 2003, **11**, 773.
61. G. Müller, H. Senn, B. Gsell, W. Vetter, C. Baron, and A. Böck, *Biochemistry*, 1994, **33**, 3404.
62. S. Boschi-Muller, S. Müller, A. van Dorsselaer, A. Böck, and G. Branlant, *FEBS Lett.*, 1998, **439**, 241.
63. M.-P. Strub, F. Hoh, J.-F. Sanchez, J. M. Strub, A. Böck, A. Aumelas, and Ch. Dumas, *Structure*, 2003, **11**, 1359.
64. S. Bar-Noy and J. Moskovitz, *Biochem. Biophys. Res. Commun.*, 2002, **4**, 956.
65. E. S. J. Arner, H. Sarioglu, F. Lottspeich, A. Holmgren, and A. Böck, *J. Mol. Biol.*, 1999, **292**, 1003.

Semiconductor Interfaces

Ming X. Tan, Ashish Bansal, Iver Lauermann, Gary A. Shreve & Nathan S. Lewis
California Institute of Technology, Pasadena, CA, USA

1 Introduction 2
2 Equilibrium State at a Semiconductor Junction 2
3 Charge Transfer at a Semiconductor Junction 11
4 Summary 16
5 Related Articles 16
6 References 16

Glossary

Accumulation region: the region near a semiconductor interface where negative charges (for an *n*-type semiconductor) accumulate
Band bending diagram: electric potential energy versus distance diagram of a semiconductor contact
Barrier height energy: the energy difference between the bottom of the conduction band of the semiconductor at the interface and the Fermi level of the contacting phase. It is the activation energy required to transfer charge from the contacting phase to the semiconductor
Built-in voltage: the absolute value of the difference between the electric potential of an electron at the semiconductor surface and an electron in the bulk of the semiconductor
Current–voltage properties: dependence of the observed current on the applied potential
Depletion approximation: an approximation that assumes that the net concentration of charges in the depletion region is equal to the dopant concentration. This concentration is constant throughout the depletion region. Furthermore, there are no uncompensated charges in the quasineutral region
Depletion region: a charged region of width W at the semiconductor interface consisting of fixed positive charges (for an *n*-type semiconductor)
Depletion width: the depth of the depletion region in a semiconductor
Diode equation: the equation that describes the relationship between the applied bias and the resulting current of a semiconductor contact. It is generally of the form $I = -I_0(\exp(-qV/kT)-1)$ where I_0 is the equilibrium exchange current and V is the applied bias
Electrochemical potential: quantity that describes the thermodynamic tendency of a phase to gain or lose electrons to another phase
Exchange current: the microscopic current crossing a semiconductor interface in either direction at equilibrium
Fermi level: the energy level where the probability of finding an electron is 1/2
Fermi level pinning: the ability of surface states to ‘buffer’ the Fermi level of the semiconductor from changes in the electrochemical potential of the contacting phase
Forward bias: the sign of the applied potential that results in an exponential increase in the current passing through a semiconductor junction
Homojunction: a junction formed between two identical semiconductors of different doping densities or dopant atoms
Quasineutral region: the region in a semiconductor where the net charge density is zero
Rectification: the asymmetric current–voltage characteristics of a semiconductor junction, in which charge-carrier flow is impeded in one direction, but not in the other direction
Reverse bias: the sign of the applied potential opposite to forward bias. In reverse bias, the current through a diode is essentially independent of the applied potential
Schottky barrier: a rectifying semiconductor/metal junction
Surface states: energy levels arising from atoms at the semiconductor surface
Work function: the minimum energy required to remove an electron from a phase to vacuum

Abbreviations

A_s = surface area of a semiconductor contact; $[A^-]$ = concentration of the reduced form of a redox couple in solution; $[A]$ = concentration of the oxidized form of a redox couple in solution; A^{**} = effective Richardson constant; $E(A/A^-)$ = electrochemical potential of a solution; E_{cb} = energy of the conduction band edge; E_F = Fermi level; $E_{F,m}$ = Fermi level of a metal; $E_{F,sc}$ = Fermi level of a semiconductor; $E(A/A^-)$ = redox potential of a solution; $E^{\circ'}(A/A^-)$ = formal redox potential of a solution; $\mathcal{E}$ = electric field; $\mathcal{E}_{max}$ = maximum electric field at a semiconductor interface; e = number of electrons transferred per molecule oxidized or reduced; F = Faraday constant; I = current; I_0 = exchange current; k = Boltzmann constant; k_{et} = intrinsic rate constant for electron transfer at a semiconductor/liquid interface; k_n = forward electron transfer rate constant; k_n^{-1} = reverse electron transfer rate constant; N_d = concentration of donor atoms in an *n*-type semiconductor; NHE = normal hydrogen electrode; n = electron concentration; n_b = electron concentration in the bulk of a semiconductor; n_s = electron concentration at a semiconductor surface; n_{so} = electron concentration at the surface of a semiconductor under equilibrium conditions; Q = charge per unit area; q = elementary charge; R = gas constant; SCE = saturated calomel electrode; sc = semiconductor; T = temperature; V = electric potential; V_{bi} = built-in voltage; V_n = the potential difference between the Fermi level and the conduction band energy in the semiconductor bulk; W = depletion width in a semiconductor; x = distance; ε_s = static dielectric constant; $\varphi =$ work function; $\phi_b =$ barrier height; $\lambda =$ nuclear reorganization energy for an interfacial electron transfer process.

---

1 INTRODUCTION

Semiconductors are technologically important, in large part due to their unique electrical and optical characteristics (*see* ***Semiconductors***). However, the construction of practical devices from semiconductors generally requires the formation of electrical contacts. The nature of these biphasic electrical contacts can modify, and can sometimes completely determine, the electrical and optical characteristics of the resulting device.[1] For example, contacting n-type Si with indium yields an ohmic, resistive electrical contact that freely passes current in both directions, whereas contacting n-type Si with gold yields a rectifying contact that passes current freely in one direction but effectively prevents its flow in the other direction.[2] Similarly, Si/HF(aq) junctions are useful for lithographically patterning and etching Si, while Si/methanol junctions provide the basis for efficient, stable, photoelectrochemical solar energy conversion devices.[3,4] Clearly, an understanding of the chemistry of semiconductor surfaces, and of contacts to these surfaces with other phases, is an important component in the design of any semiconductor-based device.[5–8] This article is therefore devoted to a description of the basic chemical and physical properties of semiconductor contacts.

The distinguishing feature of a semiconductor contact is the electric field that is present in the vicinity of the junction. Whenever two phases are brought into contact, charge must flow across the interface until the electrochemical potential of both phases is identical at all points in space. For example, when two metals are brought into contact, charge flows in response to the contact potential difference between the two phases. After this equilibration process has occurred, the physical characteristics of the metallic phases are essentially unchanged, because any excess charge at the metal/metal interface is screened in the first atomic layers of the metals (Figure 1). For contacts to semiconductors, however, the charge is not completely screened at the semiconductor surface, and an electric field is present in the semiconductor. A large interfacial electric field will generally induce a change in the charge-carrier concentration near the semiconductor surface. A large electric field will also direct and accelerate the motion of charge carriers, and can produce a nonzero flux of charge carriers toward the junction. Such effects can dramatically change the properties of the resulting semiconductor devices. For these reasons, chemical control over the electric fields at semiconductor contacts is desirable in essentially all semiconductor devices.

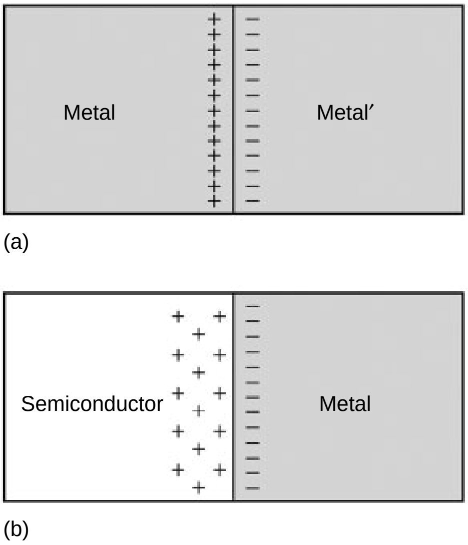

Figure 1 Charge transfer equilibration processes. (a) At a metal/metal′ junction; all the required charge is held within the first few layers of the junction. (b) At a metal/semiconductor junction; the charge arises from the ionization of dopant atoms, and produces an electric field in the bulk of the semiconductor

The focus of this article will be to describe, first qualitatively and then quantitatively, the electrical properties of semiconductor contacts. The goal is to understand the origin of the electric field at semiconductor contacts, to describe the field strength as a function of distance into the semiconductor bulk, and to understand the effects of the interfacial field on the current–voltage characteristics of the device. This discussion will be presented from a general perspective, and will be applicable to semiconductor/metal, semiconductor/liquid, semiconductor/semiconductor, and semiconductor/conducting polymer contacts. The discussion will provide an understanding of the principles behind the operation of diodes, transistors, photovoltaic cells, photoelectrochemical cells, light-emitting devices, and other technologically important semiconductor devices.

2 EQUILIBRIUM STATE AT A SEMICONDUCTOR JUNCTION

In its simplest terms, the charge transfer between a semiconductor and a contacting phase is no different from the charge transfer between atoms to form an ionic bond. For example, chemists realize that a neutral sodium atom will transfer charge when it encounters a neutral chlorine atom, because Na has a low electronegativity and Cl has a high electronegativity. The bond formation between these atoms results in an equilibrium state in which the compound NaCl is best represented with an ionic bond, that is, Na^+Cl^-. It is also obvious to chemists that the difference in electronegativities of the atoms will determine the degree of charge transfer in the molecule, with HCl having a much more covalent bond than NaCl.

The charge transfer reaction between two phases is governed by similar principles. However, the controlling factor in this situation is the electrochemical potential. Whenever two phases of differing electrochemical potentials are brought into contact, the phase that has a more negative electrochemical potential will tend to lose electrons to the phase with a more positive electrochemical potential (*see* ***Semiconductors*** for the sign convention on the electrochemical energy scale). Net charge transfer between the two phases will then occur until equilibrium is established.

At equilibrium, one phase will have an excess of positive charge, and the other phase will have an excess of negative charge. The initial difference in electrochemical potentials between the two phases will determine the degree of charge transfer across the phase boundary, much as the difference in electronegativity indicates the degree of bond ionicity in molecules formed from neutral atoms. The only conceptual difference between the molecular case and the semiconductor contact is that a physical junction between the semiconductor and the contacting phase provides an obvious dividing line to separate the phase that loses electrons from the phase that gains them.

In most of our examples, the semiconducting solid will be one of the phases that is undergoing charge transfer. A metal, with its high density of electronic states available to accept or donate charges, will be the other phase. An analogous treatment can be used to describe the charge transfer at semiconductor/liquid, semiconductor/polymer, and semiconductor/semiconductor contacts, but the semiconductor/metal contact is the simplest to describe conceptually. These different contacts have quantitative differences in the actual degree of charge transferred upon equilibration, but the qualitative principles are the same in all cases. Whenever possible, the discussion will be generalized to cover all of the junction types, with specific features of the different junctions discussed where appropriate.

2.1 Depletion

2.1.1 *Qualitative Description of Interfacial Charge Equilibration*

The simplest case to consider is the situation that describes the contact between an n-type semiconductor and a metal. As discussed above, the factor that controls the charge transfer process is the electrochemical potential, or Fermi level, E_F, of each phase.[9] The initial difference in the electrochemical potentials of the two phases indicates that, after contact, charge must flow between the phases in order to reach equilibrium. We will consider the case where the electrochemical potential of an isolated n-type semiconductor ($E_{F,sc}$) is more negative than the electrochemical potential of an isolated metal phase ($E_{F,m}$) (Figures 2a and c). In this situation, charge will leave the semiconductor, because it has a more negative initial electrochemical potential ($E_{F,sc} < E_{F,m}$). This charge will be accepted by the metal phase, which has a more positive electrochemical potential.

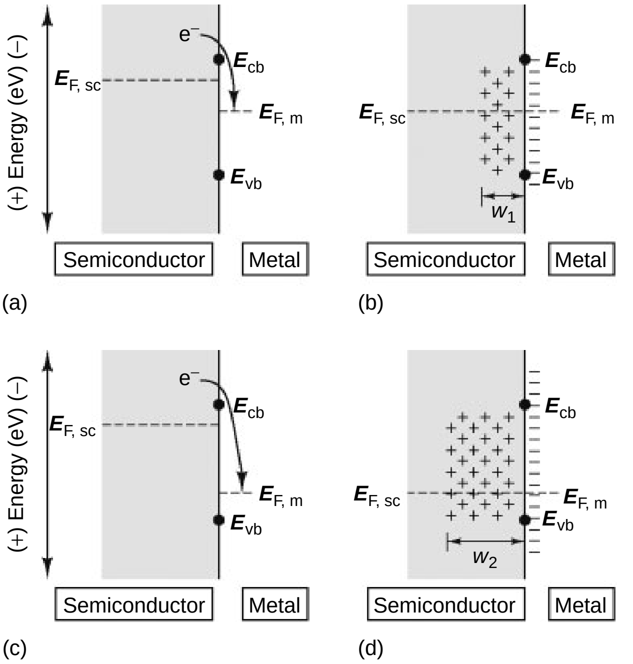

Figure 2 Charge transfer equilibration processes at semiconductor/metal junctions. (a) Before equilibrium is established, the entire semiconductor is neutral. (b) At equilibrium, a positively charged region of width W_1 is present in the semiconductor. (c) Similar to (a), except that the Fermi level in the metal ($E_{F,m}$) is farther from vacuum (more positive) than in (a). (d) Similar to (b), but the charged region extends deeper into the semiconductor ($W_2 > W_1$), because the number of charges that must cross the semiconductor/metal interface is greater. In both (b) and (d), the positions of the conduction and valence band edges are unchanged by the charge equilibration processes

As a result of this initial difference in electrochemical potentials, the transfer of electrons across the semiconductor/metal junction disrupts the original charge neutrality of the semiconductor and the metal. This interfacial charge-transfer process produces an excess of positive charges in the semiconductor and an excess of negative charges in the metal (Figures 2b and d). In essence, a capacitor is charged during this process, and the components of the capacitor are the electrons in the metallic phase and the positive charges in the semiconducting phase. This charging process continues until the initial difference in electrochemical potentials is neutralized, that is, until the capacitor is sufficiently charged that no further net charge transfer is thermodynamically possible. At this point, equilibrium is attained between the two phases. At equilibrium, electric fields and electric potential gradients are present in both the semiconducting and metallic phases, since neither phase is electrically neutral.[10]

In general, the addition of excess negative charges to a phase will tend to decrease the value of its electrochemical potential (i.e. shift E_F more negative). This can be rationalized because it is easier to ionize a phase with excess negative charges than one without such an excess. For an arbitrary phase in contact with a semiconductor, it is not always possible to predict a priori whether the Fermi level of the semiconducting phase will move more or less than that of the contacting phase. However, for semiconductor/metal contacts, it is possible to predict what will occur. The number of available electronic states per unit energy in the metal far exceeds the number present in a semiconductor, because the semiconductor has essentially no available states in its band gap region.**[9]** Consequently, the capacitance of the metal phase is much larger than the capacitance of the semiconductor phase. Thus, during the equilibration process, a relatively small percentage of the available states in the metal are filled and there is little negative movement of the electrochemical potential of the metal. The Fermi level of the n-type semiconductor, however, shifts positively until it reaches the value of the metal Fermi level. In chemical terms, the metal acts as an excellent ‘buffer’ of energy with respect to the excess charge. This situation is analogous to aqueous buffers that resist changes in pH when mixed with nonbuffered solutions that contain small amounts of H^+.

The equilibrium positions of the Fermi level for both the semiconducting and the metallic phases are therefore essentially equal to the initial value of the electrochemical potential of the metal, $E_{F,m}$ (Figure 2). When sufficient charge has transferred across the interface to produce this change in $E_{F,sc}$, equilibrium is reached, and no further net flow of charge across the metallurgical boundary will occur.

Without any additional quantitative information, some important chemical trends in junction behavior can be clearly understood. In a molecule, a large difference in electronegativity between bonded atoms leads to a large degree of ionicity in the bond. A greater initial difference in the electrochemical potentials of the isolated semiconducting and metallic phases should therefore produce a greater propensity for interfacial charge transfer at the semiconductor/metal junction. Using our example of an n-type semiconductor, metals with more positive electrochemical potentials produce greater initial contact potentials to a given semiconductor surface. These metals would thus be expected to produce larger degrees of interfacial charge transfer than metals with less positive electrochemical potentials (Figure 2). Similarly, an n-type semiconductor with a more negative Fermi level, that is, either a more highly doped sample of a given material, or a semiconductor with a more negative conduction band edge at a similar doping level, would be expected to produce a greater degree of charge transfer when placed in contact with a given metal. This chemical control over the charge-transfer process is one of the key experimental features of semiconductor contacts.

2.1.2 Depletion Width

An important quantity, the depletion width (W), can also be understood using these qualitative concepts. For a doped semiconductor, charge-transfer equilibration removes carriers from the sites that are most easily ionized. Thus, charge is typically removed from the dopant atoms, as opposed to being removed from atoms of the semiconductor material. For example, in phosphorous-doped n-type Si, charge-transfer equilibration would be accomplished by transferring the easily ionizable fifth valence electron from the P dopant atoms, as opposed to transferring electrons arising from ionization of the Si lattice atoms (*see* ***Semiconductors***). In order to reach charge transfer equilibrium, a certain number of charges must be pulled out of the semiconducting solid. The number of charges is generally far larger than the number of dopant atoms present in one atomic layer of the semiconductor.**[1]** Thus, as depicted in Figures 2(b) and (d), greater degrees of charge transfer require that we ‘reach further into’ the bulk of the semiconductor to obtain the proper number of ionizable charges from the semiconductor.

The depth over which dopants are ionized can be readily calculated. For an n-type semiconductor of majority carrier density N_d, a good first approximation is that charge transfer produces a fixed concentration of charged dopant atoms for a depth W. Within this depth, essentially all of the electrons donated by the available dopants have been removed from the semiconductor, and the ionized dopant atoms are left in this region as fixed positive charges. Beyond this depth, however, essentially no electrons have been removed, and the ionized dopants are neutralized by the surrounding electrons. This approximation is called the depletion approximation.**[10]** In the semiconductor, the charged region of width W is called the depletion region.

With this approximation, W is readily calculated if the amount of charge transferred per unit area, Q, is known. The value of W is then simply Q/N_d. When a higher dopant density is available for donating electrons to the metal, one needs to ‘reach in’ less deeply into the semiconductor to achieve the same degree of charge transfer. Thus, for a given initial contact potential, the value of W becomes smaller as the dopant density increases. W will be an important quantity to understand when considering the effects of various chemical modifications on the behavior of semiconductor/metal interfaces. An accurate calculation of W, using the depletion approximation, depends only on a prediction of the amount of charge per unit area, Q, that must be transferred to equilibrate the desired semiconductor/metal interface.

2.1.3 Quantitative Description of Interfacial Charge Equilibration

It is also important to understand quantitatively the strength of the electric field, and the values of the electric potential that are produced as a result of this charge-transfer equilibration process. Simple electrostatic considerations suggest that an electric field and an electric potential will be present in the semiconductor, because the interfacial charge transfer has removed negative charges from an initially neutral phase to produce a net positive charge density in the semiconductor portion of the junction.[11] Our goal now is to describe quantitatively the electric field and electric potential at a semiconductor junction.

The relationship between the charge density and the electric field strength is obtained from electrostatics. Consider a negative test charge that we will bring through the semiconductor and toward the semiconductor/metal interface. Within the bulk of the semiconductor, the negative charges on the metal side of the interface are offset (i.e. screened) by an approximately equal number of positive charges in the depletion region of the semiconductor. Thus, negligible electric fields are experienced by this test charge. This region is called the quasineutral region of the semiconductor, as a negative test charge in the bulk of the semiconductor is not influenced by the presence or absence of charge transfer at the semiconductor/metal interface.

As we move our negative test charge closer to the semiconductor/metal interface, it will penetrate the depletion region. This negative test charge will then be repelled from the interface, because it will experience the repulsion of those negative charges in the metal, which are not screened by the positive charges in the semiconductor. Another way of thinking about this situation is that there is now a net dipole acting on the test charge, and this dipole repels the charge from the interface. This net dipole arises from the excess of negative charges that are sensed by the test charge when it is located within the depletion region.

The presence of this electric dipole implies that work is required to push this negative test charge toward the interface. We can quantitatively express this work either in terms of the electric field strength at each position in the semiconductor, or in terms of the electric potential at each position of the system. According to electrostatics, the electric field is proportional to the integral of any excess charge density along the path of interest.[11] Thus, using the depletion approximation, which states that the charge density is simply the dopant density for all values of distance, x, up to the depletion width, we calculate that:

$$\mathcal{E}(x) = \left(\frac{qN_\mathrm{d}}{\varepsilon_\mathrm{s}}\right) x \tag{1}$$

where $\mathcal{E}(x)$ is the electric field at position x in the semiconductor, ε_s is the static dielectric constant of the semiconductor, q is the elementary charge, and N_d is the dopant density of the n-semiconductor. In equation (1), the origin of the x-axis has been defined as the position that separates the depletion region from the quasineutral region; therefore, the semiconductor/metal interface is at a distance W ($W > 0$) from the origin (Figure 3).

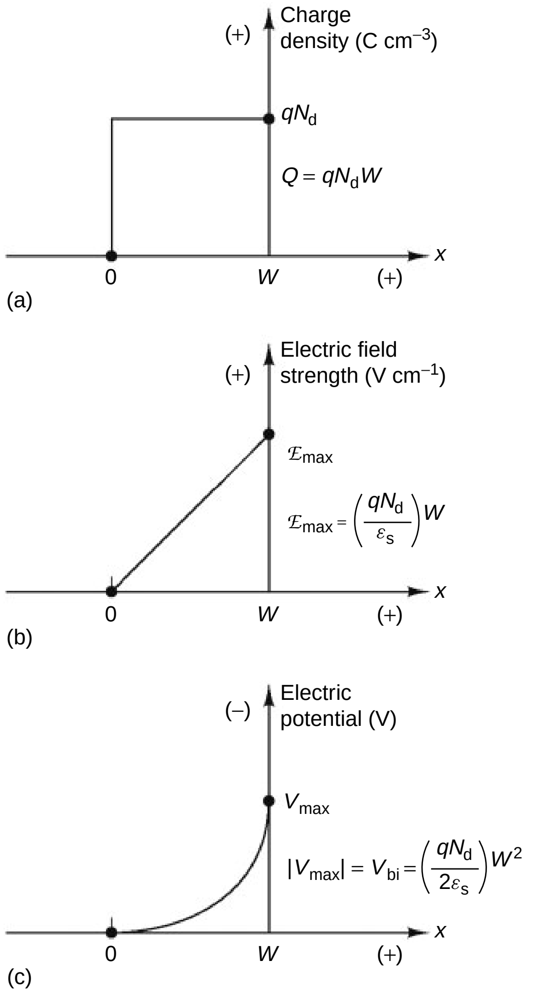

Figure 3 The spatial dependence of the charge density, the electric field, and the electric potential in the semiconductor at equilibrium for an n-type semiconductor/metal junction, where all of the voltage is dropped in the semiconductor space-charge region. The origin of the x-axis is chosen for convenience as the point closest to the interface where the net charge in the semiconductor equals zero. (a) The distance dependence of the charge density under the depletion approximation. (b) The electric field as a function of distance. Note that the maximum electric field occurs at the semiconductor interface. (c) The distance dependence of the electric potential. The electric potential in the bulk of the semiconductor has been defined as zero. Because the sign of the electric field strength is positive, the electric potential at the interface is more negative than in the bulk

As given in equation (1), since the depletion approximation ensures that the charge density in the depletion region is independent of distance, the electric field in this region increases linearly as it approaches the semiconductor/metal junction. The maximum electric field in the semiconductor ($\mathcal{E}_\mathrm{max}$) is obtained at the position $x = W$:

$$\mathcal{E}_\mathrm{max} = \left(\frac{qN_\mathrm{d}}{\varepsilon_\mathrm{s}}\right) W \tag{2}$$

Thus, the maximum electric field in a semiconductor/metal junction is located at the interface. This is an important feature for constructing numerous devices using semiconductor junctions, because the maximum ability for charge separation by the electric field occurs at the junction.

An alternate and convenient method of expressing the work required to push the negative test charge toward the interface is given by the electric potential at each point in the semiconductor. Electrostatics states that the electric potential is equal to the negative integral of the electric field over the path of interest.[11] Thus, integrating the linear electric field (equation 1) from the bulk of the semiconductor toward the semiconductor/metal interface yields a quadratic expression for the electric potential in the semiconductor phase:

$$V(x) = -\left(\frac{qN_\mathrm{d}}{2\varepsilon_\mathrm{s}}\right)x^2 \tag{3}$$

The electric potential of an electron near the interface is thus higher than that of an electron in the bulk. The negative sign in equation (3) merely indicates that the electric potential at the interface is more negative than that in the bulk. This makes sense, because work is required to push the negative test charge toward the interface. The difference in electric potential between the quasineutral region and any other position is a quantitative measure of the work required to move this test charge in the semiconductor.

A similar treatment can be used to calculate the electric field and the electric potential in the metal. However, in a metal, both the electric field and the electric potential drop to zero at a very short distance from the semiconductor/metal interface.[2] This occurs because metals do not support electric fields, and all of the excess charge density resides on the surface of the metallic phase.[9] The surface dipole layer is therefore effectively screened from test charges at any finite distance into the metallic phase, and the width of the electric potential gradient is extremely small. Because charge carriers can pass freely through this extremely thin barrier, only the electric field in the semiconductor significantly affects the electrical properties of semiconductor/metal contacts.

Combining all of these concepts, we can concisely express the electrostatic situation for any semiconductor/metal contact at equilibrium. Figure 3 contains plots of the charge density, electric field, and electric potential versus distance for such a semiconductor/metal junction. Because these diagrams are all related to each other, only one type of diagram is often depicted when a particular semiconductor/metal interface is discussed. The most convenient diagram is that of the electric potential energy versus distance, because the electric potential energy can be directly related to the potential energy of an electron at any point in the system. The potential energy of an electron at each position in the semiconductor can be obtained by multiplying the electric potential by the charge on an electron.

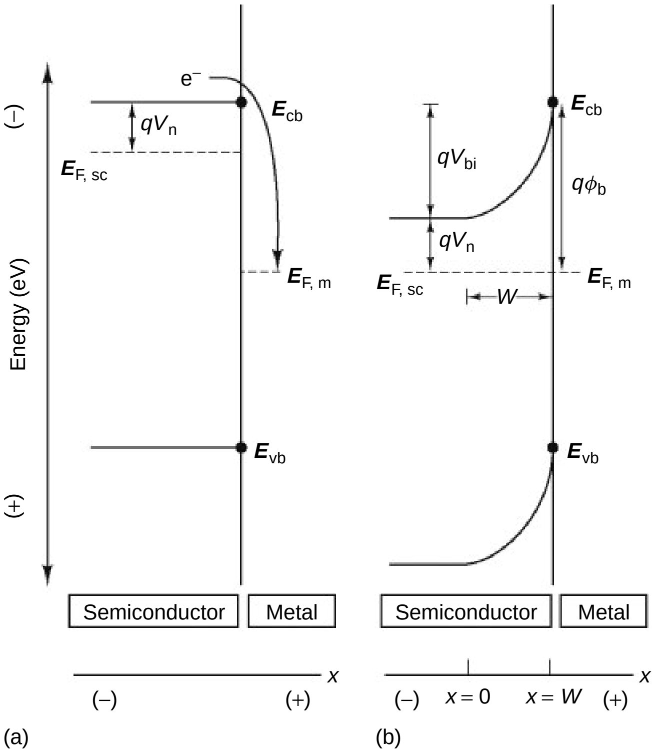

Figure 4 An energy diagram of an n-type semiconductor/metal junction. (a) Before charge equilibration occurs, the energy levels of the semiconductor conduction and valence bands are uniform at all points along the x-axis. (b) After charge equilibration has occurred, a depletion layer (W) is formed in the semiconductor. The electric potential energy levels of E_cb and E_vb are dependent on the distance into the depletion region. However, at equilibrium, the electrochemical potential is the same in the metal and at all points in the semiconductor (i.e. $E_\mathrm{F,m} = E_\mathrm{F,sc}$). qV_n is defined as the difference between $E_\mathrm{F,sc}$ and E_cb in the bulk of the semiconductor. V_bi is the built-in voltage of the junction and ϕ_b, the barrier height, is defined as $\phi_\mathrm{b} = V_\mathrm{n} + V_\mathrm{bi}$

A schematic of the energy versus distance relationship for a semiconductor/metal junction before and after equilibration is depicted in Figure 4. These potential energy versus distance diagrams are often called band bending diagrams. The electric potential gradient leads to a quadratic increase in the potential energy of an electron in the semiconductor as it approaches the semiconductor/metal junction. Both the conduction and valence bands are shown bent because the electric field acts equally well on test charges that are in either band. Note also that on these diagrams, the distance between the bottom of the conduction band and the top of the valence band always remains constant. This situation results because the presence of an electric field has a negligible effect on the value of the band gap for most semiconductors.[9]

Another chemical analogy is useful in elucidating the meaning of band bending diagrams. Chemists are quite comfortable with reaction coordinate diagrams, in which the free energy of the system is plotted versus some (typically unknown) reaction coordinate for a chemical reaction. A similar interpretation is possible for band bending diagrams (Figure 4b). These diagrams can be interpreted as representing the activation energy required to move a negative charge along a reaction coordinate toward the interface. This movement will require energy, because of the repulsion due to the unscreened negative charges on the metallic side of the semiconductor/metal junction. The difference between the common chemical reaction coordinate diagram and a band bending diagram is that if the amount of charge is known, the electric potential (equation 3), and therefore the electric potential energy of the system, can be calculated precisely at each point along the reaction coordinate. In contrast, typical chemical reaction coordinates are schematic in both energy and in direction along the bond coordinates.

A few quantitative values are worth deriving in order to complete the diagrams of Figure 4. According to equation (3), the absolute value of the electric potential reaches its maximum at the interface ($x = W$). The absolute value of this potential difference between the interface and the semiconductor bulk is called the built-in voltage (V_{bi}). The built-in voltage is a direct result of the initial electrochemical potential difference between the semiconductor and the metal, with $V_{\mathrm{bi}} = (|E_{\mathrm{F,sc}} - E_{\mathrm{F,m}}|)/q$ (Figure 4). This quantity is the total change in electric potential that would be experienced upon moving a test charge from the back of the semiconducting solid ($x = -\infty$) all the way to the interface between the semiconductor and the metal ($x = W$). The quantity V_{bi} is called the built-in voltage because this voltage is 'built-in' to the semiconductor as a result of equilibration of the semiconductor Fermi level with the electrochemical potential of the metal. V_{bi} can be related to the amount of charge transferred, and therefore, to the depletion width, W, using the equations developed above. From equation (3):

$$V_{\mathrm{bi}} = \left(\frac{qN_{\mathrm{d}}}{2\varepsilon_{\mathrm{s}}}\right) W^2 \tag{4}$$

$$W = \sqrt{\frac{2\varepsilon_{\mathrm{s}} V_{\mathrm{bi}}}{qN_{\mathrm{d}}}} \tag{5}$$

Another quantity of interest on the band bending diagrams refers to the bulk of the semiconductor. In the semiconductor quasineutral region where no electric fields are present, the difference between the Fermi level and the energy of the bottom of the conduction band remains the same as it was in the neutral semiconductor before equilibration with the metal. Thus, we can define $V_{\mathrm{n}} \equiv (E_{\mathrm{F,sc}} - E_{\mathrm{cb}})/q$ as the potential difference between the Fermi level and the conduction band energy in the semiconductor bulk, as shown on the band bending diagram in Figure 4.

The difference between the equilibrium Fermi level energy and the energy of the bottom of the conduction band at the semiconductor/metal interface is also an important quantity often mentioned in literature.[10] This difference is called the barrier height energy of the junction and is generally abbreviated as $q\phi_{\mathrm{b}}$, where ϕ_{b} is the barrier height in V, and $q\phi_{\mathrm{b}}$ is the barrier height energy in eV, that is, $q\phi_{\mathrm{b}} = E_{\mathrm{F,m}} - E_{\mathrm{cb}}$ (at the electrode surface). From Figure 4(b) and from the definitions of V_{bi} and V_{n}, it can also be seen that $\phi_{\mathrm{b}} = V_{\mathrm{n}} + V_{\mathrm{bi}}$. It is generally convenient to use ϕ_{b} to characterize the barrier height of semiconductor/metal contacts, because unlike V_{n} and V_{bi}, ϕ_{b} is independent of the doping level of the semiconductor. In fact, the magnitude of ϕ_{b} depends only on the initial position of the semiconductor conduction band, E_{cb}, and on the initial electrochemical potential of the metal, $E_{\mathrm{F,m}}$.

A final quantitative aspect of band bending diagrams concerns the equilibrium concentration of electrons at different positions in the semiconductor. Again we will refer to semiconductor/metal contacts in developing the equations, but analogous expressions are available for the other types of contacts as well. Before contact with another phase, the carrier concentration is equal at all points in the semiconductor. For a moderately doped semiconductor with completely ionized dopants, this carrier concentration is simply given by the quantity N_{d}. However, for a depleted n-type semiconductor/metal contact, the presence of unshielded negative charge on the metallic side of the interface will make it energetically difficult to support the negatively charged electrons in the semiconductor depletion region. Because the screening of interfacial charge is a function of distance away from the semiconductor/metal junction, the actual majority carrier concentration in a depleted semiconductor is expected to be a function of distance from the semiconductor/metal interface.

To obtain an expression for this carrier concentration versus distance relationship, we need to consider the potential energy difference between various points in the semiconducting solid. The relationship between the bulk carrier concentration, n_{b}, and the carrier concentration at any other position in the semiconductor can be obtained simply by using the Boltzmann equation:

$$n(x) = n_{\mathrm{b}} \exp\left(\frac{qV(x)}{kT}\right) \tag{6}$$

where $V(x)$ is the electric potential at any position of interest relative to the bulk semiconductor. The concentration of electrons in the bulk is the same as that in the neutral material, so $n_{\mathrm{b}} = N_{\mathrm{d}}$. The quantity $V(x)$ is negative with respect to the potential of the conduction band in the quasineutral region of the semiconductor (Figure 3c, equation 3). Therefore, as the semiconductor/metal interface is approached, $n(x)$ decreases exponentially from the bulk electron concentration. An identical expression can be applied to semiconductor/semiconductor and to semiconductor/liquid contacts, once $V(x)$ is known for the system of interest.

From equation (6), it can be seen that $n(x)$ reaches a minimum at the semiconductor surface. The concentration of electrons at the surface, n_s, is given by

$$n_s = n_b \exp\left(-\frac{qV_{bi}}{kT}\right) \tag{7}$$

where V_{bi} is the absolute value of $V(x)$ at $x = W$. This expression clearly shows that V_{bi} represents the total electric potential barrier for electrons to move from the bulk of the semiconductor to the metal. As will be discussed in later sections, the surface concentration of electrons (n_s) is an important factor that controls the charge transfer events between the semiconductor and the contacting phase. Thus, V_{bi} directly affects the current–voltage properties of a semiconductor/metal junction.

2.1.4 Trends in Contact Properties

The values of V_{bi} and ϕ_b are key experimental quantities that are used to characterize the physical properties of semiconductor/metal interfaces. If V_{bi} or ϕ_b can be determined, then W, Q, $\mathcal{E}(x)$, and most of the other important thermodynamic quantities that are relevant to the electrical properties of the semiconductor contact can be readily calculated using the simple equations that have been presented above. Methods to determine these important parameters can be found in the literature.[2] However, it would be useful at this point in the discussion to consider what values of ϕ_b and V_{bi} are expected theoretically for a given semiconductor/metal interface. By definition, $\phi_b = (E_{F,m} - E_{cb})/q$ at the electrode surface (Figure 4b). Thus, in principle, the barrier height can be predicted if the energies of the semiconductor band edges and the electrochemical potential of the metal can be determined with respect to a common reference energy.

In the literature, the work function of a metal, φ (in eV), is often used to estimate the degree of charge transfer at semiconductor/metal junctions.[12] The work function of a metal is defined as the minimum potential experienced by an electron as it is removed from the metal into a vacuum. The work function φ is often used in lieu of the electrochemical potential of a metal, because the electrochemical potential of a metal is difficult to determine experimentally, whereas φ is readily accessible from vacuum photoemission data.[12] Additionally, the original model of semiconductor/metal contacts, advanced by Schottky, utilized differences in work functions, as opposed to differences in electrochemical potentials, to describe the electrical properties of semiconductor/metal interfaces.[13] A more positive work function for a metal (or more rigorously, a more positive Fermi level for a metal) would therefore be expected to produce a greater amount of charge transfer for an n-type semiconductor/metal contact.[2] Therefore, use of metals with a range of φ (or $E_{F,m}$) values should, in principle, allow control over the electrical properties of semiconductor/metal contacts.

To this point, we have restricted the specifics of our discussion to semiconductor/metal contacts. However, a similar description of the interfacial equilibration process also applies to contacts between two dissimilar types of semiconductors. The most common form of these types of junctions is obtained when an n-type semiconductor is contacted with a semiconducting layer that has been doped p-type. When the two materials differ only in the type of doping, such junctions are called p–n homojunctions. To control the electric field in the n-type semiconductor, the p-type semiconductor is usually highly doped. The conductivity, and capacitance, of the highly doped p-type phase is then much larger than that of the n-type phase. In this situation, the electrostatics of the p–n homojunction closely resemble those of n-type semiconductor/metal contacts.

The biggest advantage of semiconductor homojunctions is the lack of a metallurgical junction between two structurally dissimilar solid phases. A homojunction provides an interface that is more perfect structurally, as well as less chemically reactive, than the junction between a semiconductor and a metal. Another advantage of a homojunction is that control over the Fermi level of the contacting phase is readily accomplished through changes in its dopant density. In contrast, for semiconductor/metal junctions, changing the Fermi level of the contacting phase requires a change in the nature of the metal, and thereby produces entirely new chemical interactions at the semiconductor interface. Because of their high electrical quality and ease of fabrication, homojunctions are used in a variety of technological applications in the semiconductor industry. The equations describing their performance are well-documented, and will not be described in more detail here.[10,14] However, the electrostatics of charge-transfer equilibration are readily obtained using slight modifications of the description presented above in equations (1–7).

A third type of semiconductor junction uses a conducting liquid to contact the semiconductor. Generally, the solvent and electrolyte do not participate in the charge-transfer process. Therefore, to control the Fermi level of the liquid phase, a donor/acceptor pair (a 'redox couple') must be added to the solution. The electrochemical potential, or Fermi level, of the solution phase is then given by the Nernst equation (equation 8):

$$E\left(\frac{\mathrm{A}}{\mathrm{A}^-}\right) = E^{\circ'}\left(\frac{\mathrm{A}}{\mathrm{A}^-}\right) + \frac{RT}{eF}\ln\frac{\mathrm{A}}{\mathrm{A}^-} \tag{8}$$

where $E^{\circ\prime}(\mathrm{A/A^-})$ is the formal redox potential of the redox couple, $[\mathrm{A}]$ and $[\mathrm{A}^-]$ are the concentrations of the oxidized and reduced forms of the redox couple, R is the gas constant, F is Faraday's constant, and e is the number of electrons per molecule oxidized or reduced in the reduction/oxidation process. The redox potential of the solution ($E(\mathrm{A/A^-})$) is related to the electrochemical potential by $E(\mathrm{A/A^-}) = E(\mathrm{A/A^-})/q$.

The electrostatics of charge transfer for semiconductor/liquid interfaces closely resemble those for semiconductor/metal contacts.[15] In the common experimental situation of a liquid with a high concentration of a supporting electrolyte and with a significant concentration of electroactive reagents, the equilibrium electrochemical potential of the semiconductor/liquid contact is dictated by the initial electrochemical potential of the solution phase. This occurs because the liquid phase has a large capacity to accept charge with a minimal change in energy, in an analogous fashion to the metal portion of a semiconductor/metal contact. In addition, the significant capacitance of a liquid phase with a high concentration of supporting electrolyte dictates that essentially all of the voltage drop will occur in the semiconductor. This is also analogous to the situation for a semiconductor/metal contact. Under these conditions, equations (1–7) can therefore be directly applied to the electrostatic situation at a semiconductor/liquid contact, even though they were developed in our discussion during consideration of a semiconductor/metal contact.

As for semiconductor/metal contacts, a change in the Fermi level of the liquid phase should result in a different amount of charge transferred across the semiconductor/liquid junction. For semiconductor/liquid junctions, the important energetic trends for a series of different liquid contacts can thus be determined by measuring the solution redox potential relative to a standard reference electrode system. Within this model, solutions with more positive redox potentials should induce greater charge transfer in contact with n-type semiconductors.

Unfortunately, a problem arises when attempting to compare the electrochemical potential of the solution and the electrochemical potential of the semiconductor. Like most electronic energy levels for molecules, the Fermi level of the semiconductor is usually determined relative to the vacuum level. Experimental measurements to determine $E_{\mathrm{F,sc}}$ for semiconductors (generally through determination of the semiconductor work function and dopant density) yield values that can be related to the energy of an electron in vacuum.[16] However, electrochemical potentials of liquid phases can only be measured as potential differences between the test solution and a solution that is used as a reference.[15] Since it is not possible to measure directly the energy of an individual redox couple relative to the vacuum level, it is not possible to determine directly the desired relationship between the energy level on the solid side of the junction and that on the liquid side.

Typically, the reference level for the solution redox potential is chosen to be the normal hydrogen electrode (NHE). Some tabulations use the saturated calomel electrode (SCE) as the reference level with the difference between these two scales well-known to be NHE $= -0.2412$ V versus SCE.[15] The fundamental problem lies in the determination of the absolute energy of the NHE relative to vacuum. Although a method to determine directly the absolute electrochemical potential of an NHE has not yet been described, a recent indirect measurement has indicated that it is approximately 4.4 eV below the vacuum level.[17,18] This value is often used to relate the solution electrochemical potential scale to the solid electrochemical potential scale. It provides the best approximation that is presently available to calculate the values of ϕ_{b} and V_{bi} for semiconductor/liquid contacts, based only on the values of E_{cb} and $E(\mathrm{A/A^-})$.

2.2 Accumulation

We have described above the relevant physics and electrostatics for a depleted semiconductor/metal contact. It is also possible, however, that the initial electrochemical potential of the metal will be more negative than the Fermi level of the semiconductor. During the approach to equilibrium, electrons will then tend to flow into the semiconductor from the metallic phase. This flow of electrons into the semiconductor leads to a qualitatively different energetic situation at the semiconductor/metal junction relative to the situation in depletion. This situation is technologically desirable to form ohmic, electrically resistive contacts to semiconductors. We discuss the charge-transfer equilibration for these types of contacts in this section.

When electrons from the metallic phase are transferred into the n-type semiconductor, these electrons are not confined to dopant atom sites. Instead, the majority carriers exist as mobile charges in the conduction band. Because these excess majority carriers need not reside on dopant atoms, but can

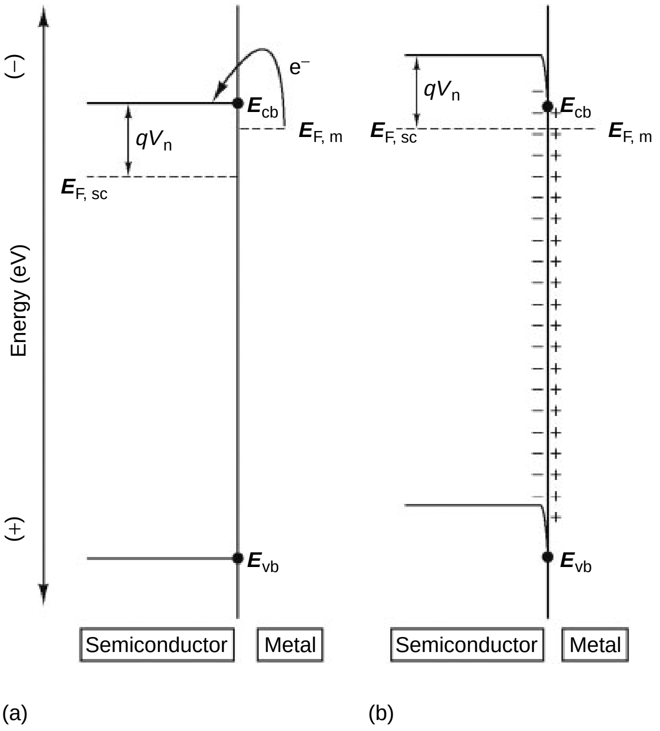

Figure 5 An energy diagram of a semiconductor/metal junction in accumulation. (a) Before charge equilibration occurs, the electrochemical potential of the semiconductor ($E_{\mathrm{F,sc}}$) is more positive than the Fermi level of metal ($E_{\mathrm{F,m}}$), and electrons will flow from the metal into the semiconductor. (b) After charge equilibration has occurred, an accumulation layer containing negative charges is formed in the semiconductor

also reside on lattice atoms of the semiconductor, the charge density that can be supported in accumulation is not limited by the dopant density. Instead, it is more closely approximated by the atom density in the crystal lattice. The spatial region in the semiconductor where the negative charges accumulate is called the accumulation region (Figure 5). The thickness of an accumulation region is therefore far smaller than that of a depletion region, for the same material and same amount of charge transferred across the interface. The width of an accumulation layer is typically less than 100 Å,[19] while the width of the depletion region is usually on the order of micrometers.[1]

Experimentally, the thin width of an accumulation layer implies that the electric potential gradient will not extend significantly into the semiconductor. The discussion in Section 3 will demonstrate that semiconductors in depletion act as rectifiers to current flow, selectively passing charge carriers in one direction while impeding their flow in the opposite direction. In accumulation, however, the lack of a significant barrier to charge flow implies that the semiconductor contact will be resistive, but not rectifying, to current flow. Thus, semiconductor/metal interfaces in accumulation are not useful for applications that require rectification. They are quite useful, however, for a variety of devices in which ohmic electrical contacts are required. They are also useful for basic investigations of the electrostatics of junction formation.[20]

2.3 Fermi Level Pinning

In discussing the behavior of semiconductor/metal junctions in depletion, it has been assumed that if the energy of the conduction band edge, E_{cb}, and the electrochemical potential of the contacting phase were known, their difference would yield a quantitative prediction of the barrier height for a given interface (Figure 4). Furthermore, even if the absolute magnitude of ϕ_{b} is not known, it should still be the case that a change in the electrochemical potential of the contacting phase should yield a defined change in the barrier height, and also in the built-in voltage, of the resulting semiconductor junction. The scenario in which these conditions apply is often called the 'ideal' behavior of a semiconductor contact. However, for many semiconductor contacts, this ideal behavior is not observed experimentally. In fact, in some systems, especially semiconductor/metal contacts, changes in the electrochemical potential of the contacting phase do not yield *any* change in properties of the junction. In the remainder of this section we describe how this important class of exceptions to ideal behavior can be understood, and we also describe the implications of this nonideal junction behavior for chemical control of device properties.

The key experimental observation is that the built-in voltage in the semiconductor, V_{bi}, often does not change as the electrochemical potential of the contacting phase is varied.[21] Attaining equilibrium between two phases requires that different degrees of interfacial charge transfer must occur when the initial electrochemical potential difference between these phases is changed. The experimental observation therefore indicates that another source or sink for charge must exist in the real interfacial system. These sources and sinks for charges are often referred to as surface states. Their ability to 'buffer' the semiconductor from changes in the electrochemical potential of the contacting phase is referred to as Fermi level pinning.

Surface states can arise simply because the atomic bonding at a semiconductor surface is necessarily different from that in the bulk. For example, in a Si lattice, the bonds at the Si surface are not fully coordinatively saturated. To relieve this unsaturation, either a surface reconstruction can occur and/or bonds to the metallic material can be formed. This distinct type of surface bonding results in a localized electronic structure for the surface which is different from that in the bulk. The energies of these localized surface orbitals are not restricted to reside in the bands of the bulk material, and can often be located at energies that are inside the band gap of the semiconductor. Orbitals that reside in this forbidden gap region are particularly important, because they will require modifications of our ideal model of charge equilibration at semiconductor/metal interfaces.[12]

To understand Fermi level pinning, we need to reconsider the charge equilibration process when the semiconductor/metal junction has a high density of surface states. As an example, we will consider a situation in which the surface states are half-filled when in equilibrium with a given metal and a semiconductor. The relevant question in this example concerns the change in V_{bi} when the electrochemical potential of the metal is made more positive. In the ideal model, the required charge had to be transferred by removing electrons from dopant atoms further into the semiconductor (Figure 2). As described above, this process required increases in both W and V_{bi}.

However, owing to the presence of occupied surface states, another source of charge is available in our nonideal system. If the charge required to equilibrate the junction is extracted from the surface states, and if the surface state density is sufficiently high to supply all of the required charges, then the junction can come to equilibrium without producing any change in V_{bi}. This situation occurs because no additional dopants have been ionized in the semiconductor. Instead, the additional charge is provided by the surface states. This situation is called Fermi level pinning; such terminology is used when the position of the semiconductor Fermi level is controlled by the occupancy of the surface states, as opposed to being controlled by the electrochemical potential of the metal.[12]

Quantitative calculations of the number of surface states that are needed to achieve Fermi level pinning will not be described here. However, such calculations show that even surface state densities as low as 10% of a monolayer (10^{14} states cm^{-2}) can provide sufficient charge to induce complete

Fermi pinning at semiconductor/metal contacts.[21] In other words, for a 1–2 V change in the work function of the metal, this density of surface states is sufficient that the values of W and V_{bi} will not change.

Lower surface state densities will, of course, produce less of a Fermi level pinning effect. This will result in an increased sensitivity of V_{bi} to changes in $E_{F,m}$. A quantitative measure of the degree of ideality of a junction can be obtained by plotting changes in V_{bi} (or ϕ_b) as a function of changes in $E_{F,m}$. Generally, however, as discussed above, values for $E_{F,m}$ are not available, so the work function φ is used instead. When the slope of a plot of V_{bi} versus φ is 1.0, the ideal situation is attained. When the slope of such plots is $\sim$0, complete Fermi level pinning is present. Intermediate situations, with $0 <$ slope < 1.0, or nonlinear behavior of V_{bi} vs. φ, are often referred to as partial Fermi level pinning.[1,12]

Fermi level pinning is generally an undesirable feature of semiconductor contacts. Its presence implies that there is a lack of chemical control over the electric field strength in the semiconductor. Some reports have appeared in the literature describing the preparations of semiconductor surfaces with acceptably low levels of deleterious surface states.[22] In others, surface modification procedures have been explored with the aim of forming bonds to the defects to remove the surface states.[23,24] Such efforts are extremely important, as the problem of Fermi level pinning remains a key challenge to chemists interested in manipulating the properties of semiconductors.

3 CHARGE TRANSFER AT A SEMICONDUCTOR JUNCTION

Up to this point, we have considered the charge flow that occurs to produce the equilibrium state between a semiconductor and a contacting phase. This type of charge flow is a prerequisite for the use of semiconductor junctions in essentially any technological application. However, understanding this transient charge flow is not sufficient to describe the electrical properties of semiconductor junctions under steady state, nonequilibrium conditions. Ultimately, the steady-state current–voltage behavior is the practical characteristic that generally determines the figure of merit of a particular semiconductor device, and therefore determines its suitability for a particular application. For instance, excellent steady-state rectification is desired for energy conversion devices, photonic detectors, and some other devices, while ohmic contacts are necessary for most transistor applications as well as for various other devices.[1] Our goal in this section is to establish a framework for describing the current–voltage behavior of a given semiconductor contact, and to establish a basis for choosing a particular type of contact for a particular type of application.

3.1 Current–voltage Behavior of a Semiconductor/metal Junction

In describing the steady-state current–voltage properties of semiconductor contacts, we will use, with no loss of generality, n-type semiconductor/metal contacts as our specific example for discussion. A balanced chemical equation that represents the interfacial charge transfer at a semiconductor/metal contact is

$$\begin{aligned}&\text{electron in the semiconductor} + \text{acceptor state in the metal}\\ &= \text{electron vacancy in the semiconductor} + \text{donor state in the metal}\end{aligned} \tag{9}$$

In equation (9), the forward reaction represents the transfer of electrons from the semiconductor into the contacting phase, and the reverse reaction represents the transfer of charge in the opposite direction. This equation, in combination with a simple kinetic model, can be used to obtain an expression for the current–voltage properties of a semiconductor contact.

In any chemical system, no net formation of products or net destruction of reactants occurs at equilibrium. There is, however, always some rate of conversion of an individual set of reactant molecules into a set of product molecules, and vice versa. At equilibrium, these rates cancel each other exactly. An analogous situation holds for charge transfer at a semiconductor/metal interface: at equilibrium, the rate of electrons flowing from the semiconductor into the metal must exactly equal the rate at which electrons flow into the semiconductor from the metal. Away from equilibrium, the rate constants for these processes will remain fixed for the interface of interest. However, the concentrations of the reactants and products will differ from their equilibrium values, and a net current can therefore be sustained through the interface. Our strategy in describing current flow is to evaluate the currents at equilibrium in accord with equation (9), and then to modify this treatment to include nonequilibrium conditions.

3.1.1 *Charge Transfer at Equilibrium*

The simplest model of electron transfer across a semiconductor/metal interface assumes that the current depends linearly on the concentration of electrons at the semiconductor surface, n_s. It also assumes that the concentrations of acceptor and donor states in a metal are extremely large;[9] thus, these variables can be assumed to be constant and can be incorporated as time-independent quantities into the appropriate rate equations. This assumption is extremely reasonable for the moderate current densities that flow through typical semiconductor/metal interfaces.[1]

At a semiconductor/metal contact, the rate of direct electron transfer from an n-type semiconductor to the metal can therefore be expressed as

$$\text{rate of electron injection into the metal} = k_n n_s \tag{10}$$

where k_n is the rate constant for the electron transfer. This expression represents the rate law for the forward chemical rate, that is, it represents the rate of formation of products for the chemical reaction in equation (9).

To maintain equilibrium, there must also be a current in the opposite direction that opposes this forward rate, that is, electrons must also be able to leave the metal phase and enter the semiconductor conduction band. Because the electrons enter the empty states of the semiconductor, the concentration of these empty states can be taken as a constant. This leads to the expression

$$\text{rate of electron transfer from the metal} = k_n^{-1} \tag{11}$$

In equation (11), k_n^{-1} is the reverse reaction rate constant, and it is independent of n_s. The concentration of vacant states in the semiconductor and the concentration of filled states in the metal has been incorporated into the value of k_n^{-1}. This rate is called the reverse rate, because it represents the formation of the species on the left-hand side of the reaction represented in equation (9). At equilibrium (when $n_s \equiv n_{so}$), these rates must be equal to each other ($k_n^{-1} = k_n n_{so}$).

The net rate of electron transfer into the metal, $-\mathrm{d}n/\mathrm{d}t$, is always the forward rate minus the reverse rate. From equations (9–11), we then obtain the general relationships

$$-\frac{\mathrm{d}n}{\mathrm{d}t} = k_n n_s - k_n^{-1} \tag{12}$$

$$-\frac{\mathrm{d}n}{\mathrm{d}t} = k_n (n_s - n_{so}) \tag{13}$$

Equations (12) and (13) were obtained by treating charge transfer across a semiconductor/metal interface as we would treat any other simple chemical kinetics problem. It states that the net rate at which charge crosses the semiconductor/metal interface is the rate of product formation minus the rate of reactant formation. Although equation (13) is exactly equivalent to equation (12), the form that we have adopted for equation (13) will be extremely useful in deriving concise expressions for the current–voltage relationship of a semiconductor/metal contact. This is because equation (13) expresses the net rate of charge transfer relative to the situation at equilibrium, where no current flows across the interface. According to equation (13), $-\mathrm{d}n/\mathrm{d}t = 0$ at equilibrium (as must be the case, because $n_s = n_{so}$ by definition). Away from equilibrium, $n_s \neq n_{so}$, so charge will cross the interface, and thus $-\mathrm{d}n/\mathrm{d}t \neq 0$.

3.1.2 The Current–voltage Characteristics of a Junction

It is now a simple task to describe the interfacial current as a function of applied voltage. Since the current is merely the electron transfer rate multiplied by the charge on an electron and by the surface area of the electrode, A_s, the interfacial electron transfer current can be written as:

$$I = -qA_s\left(-\frac{\mathrm{d}n}{\mathrm{d}t}\right) = -qA_s k_n (n_s - n_{so}) \tag{14}$$

In this notation, the current, I, is defined to be negative when electrons flow from the semiconductor to the metal. This notation is consistent with the electrochemical definition of a reduction current (electrons leaving the electrode). The dependence of the current on the applied voltage is implicit in n_s. To obtain this voltage dependence explicitly, we need to remember that the electron concentration at the surface of a semiconductor is related to the electron concentration in the bulk. As given in equation (7), the surface electron concentration at equilibrium is given by

$$n_{so} = n_b \exp\left(-\frac{qV_{bi}}{kT}\right) \tag{15}$$

Similarly, when a voltage V is applied across a semiconductor/metal junction, the total voltage drop in the semiconductor depletion region is $V_{bi} + V$, so we obtain an analogous Boltzmann relationship away from equilibrium:

$$n_s = n_b \exp\left[-\frac{q(V_{bi} + V)}{kT}\right] \tag{16}$$

This equation represents the physical situation that the electron concentration at the semiconductor surface can be either increased or decreased through the use of an additional voltage. This applied voltage controls the surface carrier concentration in the same fashion as the built-in voltage, so the same Boltzmann relationship applies.

Substituting equations (15) and (16) into equation (14), we obtain the desired relationship between the current and the voltage of a semiconductor/metal junction:

$$I = -I_0\left[\exp\left(-\frac{qV}{kT}\right) - 1\right] \tag{17}$$

where $I_0 = qA_s k_n n_{so}$. I_0 is called the exchange current, because it is the value of the current that is present at equilibrium. I_0 is responsible for transforming reactants into products, and vice versa, at a semiconductor/metal interface at equilibrium. For convenience, I_0 is defined as a positive quantity. I_0 is clearly dependent on the value of the equilibrium surface electron concentration, because a smaller exchange current should flow at equilibrium if there are fewer electrons available to exchange with a particular contacting phase.

We are now in a position to examine the properties of the current–voltage (I–V) behavior of a semiconductor/metal contact in detail. Equation (17) predicts that the current is exponentially dependent on the voltage for $V < 0$, but is independent of voltage, and of opposite sign, when $V > 0$. This can be understood qualitatively by reference to the elementary rate processes that result from equations (12) and (13). The net current across the semiconductor/metal interface is always given by the difference of the forward and reverse interfacial charge transfer rates, that is, by the rate of the reaction going to the right minus the rate going to the left, as written in equation (12). For voltages that reduce the surface electron concentration below its equilibrium value, Le Chatelier's principle implies that the reaction should proceed to the left as written in equation (9). Physically, a value of $V > 0$ will yield a larger electric potential drop in the semiconductor, which will exponentially reduce the surface concentration of electrons. This lower surface electron concentration will reduce the rate of electrons leaving the semiconductor (Figure 6a). However, the rate of electrons entering the semiconductor, that is, the rate of reactant formation, will remain unchanged. Therefore, for this direction of voltage change, the net current will be independent of voltage. This direction of the applied voltage is called reverse bias. In reverse bias, the reaction proceeds to the left as written in equation (9), and electrons are injected into the semiconductor from the metal.

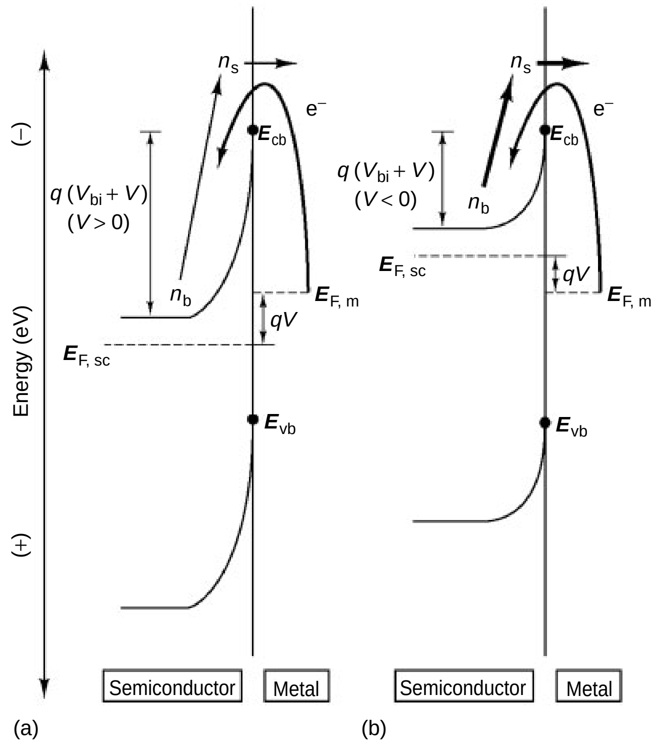

Figure 6 An energy diagram of the charge-transfer process at an n-type semiconductor/metal interface when an external potential (V) is applied across the semiconductor electrode. The applied potential changes the electric potential difference between the semiconductor surface and the bulk region. This perturbs the concentration of electrons at the surface of the semiconductor (n_s), and a net current flows through the semiconductor/metal interface. The forward reaction represents the transfer of electrons from the semiconductor to the metal and the reverse reaction represents the injection of electrons into the semiconductor from the metal. The width of the arrows indicates schematically the relative magnitude of the current. (a) The reverse bias condition for an n-type semiconductor ($V > 0$). The forward reaction rate is reduced relative to its equilibrium value, while the reverse reaction rate remains constant. A net positive current exists at the electrode surface. (b) The forward bias condition ($V < 0$), the forward reaction rate increases compared to its equilibrium value, while the reverse reaction rate remains unaffected. A net negative current exists at the electrode surface

For voltages that increase the surface electron concentration above its equilibrium value ($V < 0$), the sign of the current will be opposite to that of the current obtained at reverse bias. Le Chatelier's principle now implies that the reaction will go to the right as written in equation (9), so there will be a net transfer of electrons to the metal phase. Through the Boltzmann relationship, in forward bias ($V < 0$ for our n-type semiconductor example) the surface concentration of electrons increases exponentially with increased bias. This increased concentration of reactants results in an exponential increase in the forward rate of interfacial charge transfer, but has no effect on the reverse rate of charge transfer (Figure 6b). Because the rate of electrons leaving the semiconductor at high forward bias dominates the rate at which they enter it, the net current will depend exponentially on the applied voltage (specifically, when $\exp(-qV/kT) \gg 1$), as indicated by equation (17).

The current–voltage characteristic described by equation (17), where the current can flow predominantly in only one direction under an applied potential, is called rectification. The rectification characteristic is typical of electrical diodes.**1** Equations that have the form of equation (17) are therefore generally called diode equations. We have shown that a semiconductor/metal interface is expected to obey the diode equation when interfacial electron transfer is the rate-determining step for charge movement. In this situation, the applied voltage changes the electron concentration at the interface of the semiconductor, and this is directly reflected in the current versus voltage relationship of a semiconductor/metal interface (Figure 7). This behavior is a direct result of the Boltzmann relationships of equations (15) and (16).

Up to this point, there has been no explicit discussion of the role of the metal phase in the current–voltage behavior. For ideal semiconductor/metal junctions, it is relatively straightforward to evaluate I_0 in terms of the thermodynamic properties of the metal contact. Referring to equations (12–17), knowledge of either k_n or k_n^{-1} is sufficient to fully describe I_0. It is intuitively easier to appreciate the quantities incorporated into k_n^{-1}, which represents the rate constant for injection of electrons from the metal into the semiconductor. This charge-transfer process can be broken down conceptually into two steps. First, electrons in the metal must overcome the activation energy to enter the conduction band of the semiconductor. Because the highest occupied state in the metal is at the Fermi level, $E_{F,m}$, and the lowest unoccupied state at the semiconductor surface has an energy of E_{cb}, the electron transfer process will have an activation energy of $E_{F,m} - E_{cb} = q\phi_b$. Using a simple Arrhenius treatment of

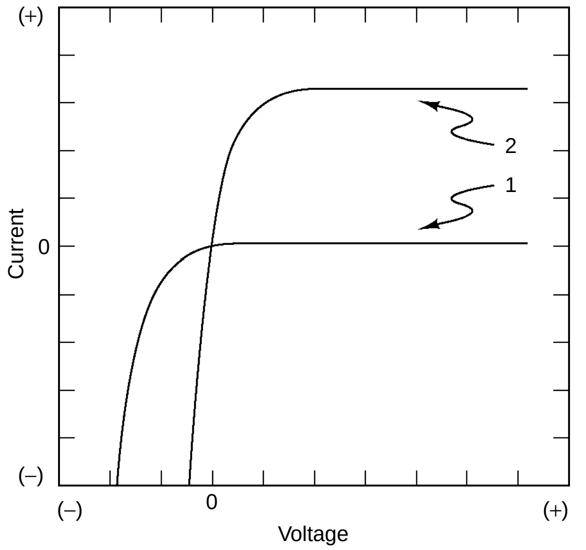

Figure 7 The current–voltage (I–V) behavior of an n-type semiconductor/metal junction in the dark. The shape of the I–V curve is described by the diode equation (equation 17); thus, such a curve is referred to as a diode curve. The difference between curves 1 and 2 is that the equilibrium exchange current, I_0, is greater for curve 2

this rate constant,[25] I_0 can therefore be written as

$$I_0 = qA_s k_n^{-1} = \text{constant} \times \exp\left(-\frac{q\phi_b}{kT}\right) \tag{18}$$

In the second conceptual step of this process, electrons with the appropriate energy must actually cross the semiconductor/metal interface, as opposed to thermalizing and remaining in the metal. A chemical analog of this event is that, once a set of reactants reaches the transition state, there is a defined probability that the reagents will proceed to form products, as opposed to reverting back to reactants. The constant in equation (18) therefore contains the probability of an actual interfacial charge transfer event. This constant also includes parameters that describe the maximum frequency for electron transfer events at the particular semiconductor/metal interface under consideration. Taken together, these two quantities closely resemble the preexponential factor in an Eyring rate expression for a chemical reaction.[25]

For a semiconductor/metal contact, it can be shown that the constant in equation (18) has a weak temperature dependence, that is, constant $\propto T^2$.[1] This temperature dependence is generally written explicitly in the expression for I_0, so the conventional form of the exchange current for a semiconductor/metal contact is

$$I_0 = A_s A^{**} T^2 \exp\left(-\frac{q\phi_b}{kT}\right) \tag{19}$$

where A_s is the area of the contact, and A^{**} is the effective Richardson constant. The constant A^{**} typically has a value of $10^2\ \text{A cm}^{-2}\ \text{K}^{-2}$.[1] The value of A^{**} is dependent on the type of semiconductor and type of metal at the particular contact of interest, but fortunately the values of A^{**} for common n-type semiconductor/metal contacts are relatively constant.[1,2] The major factor that determines the magnitude of I_0 is clearly the exponential term, which depends on the barrier height of the contact.

The role of $E_{\text{F,m}}$ in determining the electrical properties of a semiconductor/metal contact is now obvious. Physically, a more positive electrochemical potential of the metal will produce a larger barrier height and, according to equation (19), will produce a larger activation energy for electron transfer. This will produce a smaller exchange current at the semiconductor/metal contact. This effect on the exchange current can also be seen by considering the influence of $E_{\text{F,m}}$ on the semiconductor phase. In the semiconductor, a larger value of ϕ_b will produce a larger built-in voltage at an n-type semiconductor/metal interface (see Figures 2 and 4). This increased band bending decreases the equilibrium electron concentration at the surface (n_{so}), and leads to a smaller exchange current for this semiconductor/metal junction. Control over ϕ_b therefore produces control over I_0, and thus produces control over the rectification properties of semiconductor/metal contacts.

The rectification properties of semiconductor interfaces are the most important electrical characteristic of semiconductor contacts. Certain types of devices, such as transistors, require both ohmic and rectifying contacts on a given semiconductor surface, whereas other devices, such as Schottky barriers, are based on the inherent rectification properties of semiconductor/metal junctions. Numerous photonic devices, such as photon detectors and photovoltaic cells, require rectification at a semiconductor junction, and light-emitting diodes require both ohmic contacts and rectifying junctions in a well-defined geometry. Thus, successful fabrication of a desired device structure depends entirely on the electrical properties of the specific semiconductor contacts that are formed in the process. The principles described above allow the rational fabrication of contacts with the desired properties, and also describe the operation of the resulting devices within a simple, chemically intuitive, kinetic framework.

Although the discussion to this point has specifically focused on semiconductor/metal contacts, an identical formalism and analogous rate equations can also be used to describe the electrical properties of semiconductor/liquid contacts. Again the important factor is control over I_0, and again the energetic properties of the interface are the key factors that control the rectification properties of the system. In a semiconductor/liquid junction, it is the difference between the electrochemical potential of the solution and the energy of the conduction band edge ($E(\text{A/A}^-) - E_{\text{cb}}$) which defines the barrier height energy of the system.

For liquids, the only major difference in the kinetic equations lies in the analog of the Richardson constant. The probability of interfacial charge transfer at a semiconductor/liquid interface clearly depends on the chemical nature of the donor/acceptor pair that participates in the electron transfer event. For semiconductor/liquid contacts the exchange current is typically written as $I_0 = A_s[\mathrm{A}]n_{so}k_{et}$, where A_s is the area of the contact, [A] is the concentration of the acceptor in the solution and k_{et} is the intrinsic rate constant for electron transfer at the semiconductor/liquid interface of interest.[19] The electron transfer rate constant is a very important parameter in the kinetics of electron transfer at a semiconductor/liquid junction, and k_{et} appears in most of the equations that utilize kinetic models for I_0. Theoretical expressions for k_{et} have been derived by Morrison and by Gerischer.[19,26,27] These treatments have been reviewed extensively in the literature, and are primarily based on the Marcus theory for electron transfer at metal electrodes.[7,28–30]

The interfacial kinetics processes at semiconductor/liquid contacts for reactions with one-electron, outer-sphere, redox species can be understood in a conventional theoretical framework. The rate constant k_n can be broken down into a term representing the attempt frequency, ν_n, a term representing the electronic coupling between the electrons in the conduction band of the semiconductor and the redox acceptor state, κ_{el}, and a term representing the nuclear reorganization energy in the transition state from reactants to products, κ_n.[29] For outer-sphere electron transfer processes, the nuclear term is well-known to be:

$$\kappa_n = \exp\left[\frac{(-E_{cb} - qE^{o\prime}(\mathrm{A/A^-}) + \lambda)^2}{4\lambda kT}\right] \tag{20}$$

where λ is the nuclear reorganization energy.[29] The attempt frequency, ν_n, is generally on the order of $10^{13}\ \mathrm{s^{-1}}$, being related to the vibrational frequency of the nuclear motions that drive the reaction to the transitional state. For a random distribution of nonadsorbing outer sphere acceptors in the solution, the electronic term, κ_{el}, theoretically has a value on the order of $10^{-31}\ \mathrm{cm^4}$.[31] Hence the theoretical maximum interfacial charge transfer rate constant for a nonadsorbing, weakly coupled outer-sphere redox system to a semiconductor is expected to be on the order of $10^{-17}\ \mathrm{cm^4\ s^{-1}}$. An alternative evaluation, using a Fermi Golden Rule approach to evaluate the maximum value expected for k_{et}, yields a similar value.[32]

Recent experimental studies have confirmed these theoretical expectations for several exemplary semiconductor/liquid interfaces.[31] Detailed rate measurements on n-Si/CH_3OH-viologen$^{2+/+}$ and n-InP/CH_3OH interfaces have validated the dependence of k_n on driving force, as predicted by equation (20), and have indicated that the value of k_n at optimal exoergicity is approximately $10^{-17}\ \mathrm{cm^4\ s^{-1}}$. Scanning electrochemical microscopy measurements of the kinetics at p-WSe_2/H_2O-$Ru(NH_3)^{63+/2+}$ interfaces have yielded an interfacial charge-transfer rate constant of $5.7 \times 10^{-17}\ \mathrm{cm^4\ s^{-1}}$, and estimates of the nuclear terms for this reaction result in a rate constant at optimal exoergicity of $2 \times 10^{-16}\ \mathrm{cm^4\ s^{-1}}$. Hence it appears that these types of processes seem to be reasonably well-understood both experimentally and theoretically. In contrast, inner-sphere electron transfer processes, and processes involving adsorbed redox species, are not well-understood at present.

Even for inner sphere processes and adsorbed species, owing to the dependence of n_s on barrier height, for an n-type semiconductor, more positive redox potentials generally yield smaller values of I_0, and produce highly rectifying behavior.

The electrical behavior of semiconductor/liquid contacts is thus very similar to that of semiconductor/metal contacts. For an n-type semiconductor, more positive redox potentials will yield smaller values of I_0, and will produce highly rectifying diode behavior. In contrast, more negative redox potentials will yield larger values of I_0, and will produce poorly rectifying diode behavior. Thus, one goal in constructing semiconductor/liquid junctions is to insure that chemical control is maintained over the $I-V$ properties of semiconductor/liquid contacts. Changes in the solution redox potential are therefore one of the most important methods of manipulating the $I-V$ properties of semiconductor/liquid interfaces.

Similar behavior is also obtained for semiconductor/semiconductor interfaces. For homojunctions, the interfacial energetics are fixed by the nature of the solid, but the degree of charge transfer, and therefore the degree of rectification, is determined by the doping levels of each portion of the semiconductor device. In this situation, I_0 is a function of the dopant density of each phase. For such devices, I_0 is also a function of other physical properties of the material, such as the lifetime and diffusion coefficients of the charge carriers in the sample of interest. The particular equations that govern the current–voltage properties of homojunctions are well-known in the solid-state physics literature and will not be discussed in detail here.[1] However the fundamental operating principles of these types of devices are also readily grasped by application of the equations discussed above.

Although the diode behavior of a semiconductor/metal and a semiconductor/liquid junction have been derived by assuming that electron transfer is the important charge flow process across the interface, the diode equation is generally applicable to semiconductor/contact devices even when other processes are rate limiting, as is often the case for semiconductor/liquid junctions. A similar derivation can be performed for other possible charge flow mechanisms, such as recombination of carriers at the surface and/or in the bulk of the semiconductor. It can be shown that the $I-V$ relationships for these mechanisms almost all adopt the form of equation (17).[2,6] The major difference between the various mechanisms is the value of I_0 for each system. Mechanistic studies of semiconductor junctions therefore generally reduce to investigations of the various factors that control I_0. Such studies also involve quantitative comparisons of the magnitude of I_0 with the value expected for a specific charge transport mechanism. These types of investigations have yielded a detailed level of understanding of many semiconductor interfaces. Recent reviews, describing more details of this work on semiconductor/liquid interfaces, have been written by Koval[7] and by Lewis.[30,31] However, regardless of mechanism, the key point is that chemical control over I_0, and over the rectification properties of semiconductor contacts, is the ultimate goal of semiconductor contact chemistry.

4 SUMMARY

Using a very simple, qualitative approach, the fundamental properties of semiconductor contacts that are responsible for the operation of rectifiers, transistors, photovoltaic devices, and light-emitting diodes have been described. The charge-transfer processes across semiconductor interfaces are ultimately responsible for this behavior; thus, control over the interfacial charge-transfer reactions is crucial to control over the properties of semiconductor contacts. The penetration of the electric field and the electric potential into a bulk semiconductor phase yields a nonuniform carrier concentration in the sample, and produces contacts that either attract or repel specific types of charge carriers. Chemical control over these electric fields is crucial to the technology of semiconductor contacts. In principle, such control can be established through a simple variation in the electrochemical potential of the contacting phase. In practice, this ideal model often does not apply, and other factors influence or completely determine the interfacial electric field strength. The basis for semiconductor contact chemistry can, however, be understood in a straightforward fashion once the nature of the interface is successfully elucidated. These principles can be applied in a quite general fashion to semiconductor/semiconductor, semiconductor/metal, semiconductor/liquid and semiconductor/polymer contacts, making the approach valuable for understanding the operational principles of a variety of technologically important semiconductor devices.

5 RELATED ARTICLES

Electronic Structure of Solids; Semiconductors.

6 REFERENCES

1. S. M. Sze, ‘The Physics of Semiconductor Devices’, 2nd edn., Wiley, New York, 1981.
2. E. H. Rhoderick and R. H. Williams, ‘Metal-Semiconductor Contacts’, 2nd edn., Oxford University Press, New York, 1988.
3. P. J. Holmes, ‘The Electrochemistry of Semiconductors’, Academic Press, New York, 1962.
4. N. S. Lewis, M. L. Rosenbluth, L. G. Casagrande, and B. J. Tufts, in ‘Homogeneous and Heterogeneous Photocatalysis’, eds. E. Pelizzetti and N. Serpone, Reidel, Dordrecht, 1986.
5. H. O. Finklea, ‘Semiconductor Electrodes’, Elsevier Biomedical, Amsterdam, NY, 1988.
6. S. J. Fonash, ‘Solar Cell Device Physics’, Academic Press, New York, 1981.
7. C. A. Koval and J. N. Howard, *Chem. Rev.*, 1992, **92**, 411.
8. R. H. Fahrenbruch and A. L. Bube, ‘Fundamentals of Solar Cells’, Academic Press, New York, 1983.
9. C. Kittel, ‘Introduction to Solid State Physics’, 6th edn., Wiley, New York, 1986.
10. G. W. Neudeck, ‘The PN Junction Diode’, 2nd edn., Addison-Wesley, Reading, MA, 1989.
11. D. Halliday and R. Resnick, ‘Physics’, 3rd edn., Wiley, New York, 1978.
12. L. J. Brillson, *Surf. Sci. Rep.*, 1982, **2**, 123.
13. W. Schottky, *Z. Phys.*, 1939, **113**, 367.
14. W. Shockley, *Bell Syst. Tech. J.*, 1949, **28**, 435.
15. A. J. Bard and L. R. Faulkner, ‘Electrochemical Methods: Fundamentals and Applications’, Wiley, New York, 1980.
16. A. Many, Y. Goldstein, and N. B. Grover, ‘Semiconductor Surfaces’, North-Holland, New York, 1965.
17. A. J. Bard, R. Memming, and B. Miller, *Pure Appl. Chem.*, 1991, **63**, 569.
18. H. Reiss and A. Heller, *J. Phys. Chem.*, 1985, **89**, 4207.
19. S. R. Morrison, ‘Electrochemistry at Semiconductor and Oxidized Metal Electrodes’, Plenum, New York, 1980.
20. C. Hilsum ed., ‘Device Physics’, North-Holland, Amsterdam, NY, 1981.
21. J. Bardeen, *Phys. Rev.*, 1947, **71**, 717.
22. L. J. Brillson, R. E. Viturro, C. Mailiot, J. L. Shaw, and N. Tache, *J. Vac. Sci. Technol. B*, 1988, **6**, 1263.
23. K. C. Mandal and O. Savadogo, *J. Mater. Sci.*, 1992, **27**, 2355.
24. B. A. Parkinson, *Inorg. Chem.*, 1988, **24**, 4028.
25. P. W. Atkins, ‘Physical Chemistry’, 3rd edn., Freeman, New York, 1986.
26. H. Gerischer, *Z. Phys. Chem. (Frankfurt/Main)*, 1960, **26**, 223.
27. H. Gerischer, *Adv. Electrochem. Electrochem. Eng.*, 1961, **1**, 139.
28. R. A. Marcus, *J. Chem. Phys.*, 1965, **43**, 679.
29. R. A. Marcus and N. Sutin, *Biochim. Biophys. Acta*, 1985, **811**, 265.
30. N. S. Lewis, *Annu. Rev. Phys. Chem.*, 1991, **42**, 543.
31. N. S. Lewis, *J. Phys. Chem. B.*, 1998, **102**, 4843.
32. W. Royea, A. Fajado, and N. S. Lewis, *J. Phys. Chem. B.*, 1997, **101**, 11152.

Acknowledgments

We acknowledge the National Science Foundation, grant CHE-8814694, and the Department of Energy, Office of Basic Energy Sciences, grant DE-FG03-88ER13932 for support of work in photoelectrochemistry. IL acknowledges a postdoctoral research grant provided by the NATO Science Council through the DAAD. This is contribution 8756 from the Caltech Division of Chemistry and Chemical Engineering.

Semiconductors

Colby E. Stanton, SonBinh T. Nguyen, Janet M. Kesselman, Paul E. Laibinis & Nathan S. Lewis
California Institute of Technology, Pasadena, CA, USA

1 Introduction 2
2 Crystal Structures of Selected Semiconductors 2
3 Band Structure and Optical Properties of Semiconductors 4
4 Carrier Statistics for Semiconductors 9
5 Summary 15
6 Related Articles 15
7 References 15

Glossary

Absorption coefficient: a parameter that characterizes the ability of a solid to absorb light of a given wavelength
Acceptor: an impurity that scavenges an electron from the semiconductor; acceptors produce a hole in the valence band and a negative charge on the dopant atom
Charge carrier: either an electron or a hole, both of which are capable of conducting electrical charge in a semiconductor
Common anion rule: a general guideline, which states that the lattice anion controls the position of the valence band edge of a semiconductor
Conduction band: the lowest unfilled energy band in a solid
Conduction band edge: the bottom of the lowest unfilled energy band in a solid
Deep dopant: a dopant whose energy level is close to the middle of the semiconductor band gap
Direct band gap semiconductors: semiconductors that display a fully allowed electronic transition between the valence and conduction bands
Donor: an impurity that is readily ionized to produce an electron in the conduction band and a positive charge on the dopant atom
Dopant atoms: chemical impurities that are deliberately introduced into the semiconductor lattice to provide control over the conductivity and Fermi level of the solid
Doping: the introduction of specific chemical impurities into a semiconductor lattice to control the conductivity and the Fermi level of the semiconductor
Effective density of states: the number of electronic states within $3kT$ of the edge of an energy band, where k is the Boltzmann constant and T is the temperature
Energy bands: a cluster of orbitals in which the individual molecular orbitals are packed closely together to form an almost continuous distribution of energy levels
Fermi level: the energy level at which the probability of finding an electron is 1/2. This quantity characterizes the tendency of a semiconductor to transfer charges to other phases
Hole: an electronic vacancy in the valence band of a solid
Indirect band gap semiconductors: semiconductors in which the lowest energy electronic transition between the valence and conduction bands is formally optically forbidden
Intrinsic semiconductor: an undoped semiconductor
Majority carrier: the predominant charge carrier in the bulk of a doped semiconductor
Minority carrier: the less abundant charge carrier in the bulk of a doped semiconductor
n-type semiconductor: a semiconductor sample, doped with donors, that has an excess of free electrons relative to the intrinsic sample
Optical penetration depth: the distance into the semiconductor at which the transmitted light intensity reaches $1/e$ of the incident light intensity at the surface of the semiconductor
p-type semiconductor: a semiconductor sample, doped with acceptors, that has an excess of free holes relative to the intrinsic sample
Semiconductor band gap: the energy difference between the top of the valence band and the bottom of the conduction band in a semiconductor
Shallow dopant: a dopant whose energy level is close to either the valence band or the conduction band
Valence band: the highest filled energy band in a solid
Valence band edge: the top of the highest filled energy band in a solid

Abbreviations

A = Absorbance; α = Absorption coefficient; a = Acceleration of an electron due to an electric field; c = Concentration of absorbing material; $\mathcal{E}$ = Electric field; E = energy; ε = Molar extinction coefficient; E_{cb} = energy of the conduction band edge; E_{F} = Fermi level; E_{Fi} = Fermi level position in an intrinsic semiconductor; E_{g} = band gap energy; E_{vb} = energy of the valence band edge; F = Force; h = Planck's constant; I = Transmitted light intensity; I_0 = Incident light intensity; l = Optical path length; m_{e}^* = effective mass of an electron; m_{h}^* effective mass of a hole; n = Electron concentration; $N_{\mathrm{cb}}(E)$ = density of electronic states in the conduction band as a function of energy; N_{c} = Effective density of states in the conduction band; N_{d} = Concentration of donor atoms in a semiconductor lattice; n_{i} = Electron concentration in an intrinsic semiconductor at equilibrium; N_{v} = Effective density of states in the valence band; p = Hole concentration in a semiconductor; p_{i} = Hole concentration in an intrinsic semiconductor at equilibrium; q = Charge on a carrier; σ = Electrical conductivity of a semiconductor; T = Transmittance; τ_{m} = Mean free time for scattering; ν_{d} = Drift velocity; μ = Charge carrier mobility; μ_n = Mobility of an electron in a semiconductor lattice; μ_p = Mobility of a hole in a semiconductor lattice;

---

1 INTRODUCTION

Semiconductors constitute one of the most important classes of materials of the twentieth century. Their unique optical, electronic, and thermal properties make them well-suited for a variety of applications in the modern electronics industry. Semiconductors are of increasing interest to chemists owing to their applications in solar energy conversion,[1–5] organic synthesis,[6,7] and waste water treatment.[8,9] Common semiconductors can be formed from a variety of starting materials. Si and Ge are elemental semiconductors, whereas other semiconductors may be binary compounds (e.g. GaAs, CdS, and TiO_2), ternary compounds (e.g. $Hg_{0.2}Cd_{0.8}Te$ and $Ga_{0.8}As_{0.2}P$), or quaternary materials (e.g. $In_{0.2}Ga_{0.8}As_{0.7}P_{0.3}$) (*see Compound Semiconductor*). The unifying characteristic of semiconductors is their level of electrical conductivity. A semiconductor is generally defined as a material that has an electrical conductivity, σ, between 10^{-9} ohm^{-1} cm^{-1} and 10^2 ohm^{-1} cm^{-1}.[10] Thus, semiconductors comprise the class of materials whose electrical conductivities are higher than those of insulators and lower than those of metals. Another, more useful experimental definition is that the conductivity of a semiconductor increases exponentially with increasing temperature. As described below, the conductivity of a semiconductor is ultimately determined by its chemical and electronic structure. The focus of this chapter is to describe the important chemical structures, optical characteristics, and electrical properties of semiconducting solids.

The conductivity of semiconductors can be deliberately manipulated through the introduction of specific chemical impurities. This process is known as doping. These chemical impurities, or dopants, can either donate additional charges to the semiconductor, or can accept charges from the solid. The introduction of dopants can greatly modify the electrical properties of semiconductors. In fact, in some cases, doping can effect changes of over eight orders of magnitude in the electrical conductivity of a semiconductor![11] The factors involved in the choice of a particular dopant, and understanding the behavior of different dopant atoms in semiconductors, are two other chemical issues that will be discussed in this chapter.

Another important characteristic of semiconductors is their optical absorption properties. The optical properties of semiconductors are crucial to their uses as photovoltaic energy conversion devices, photonic detectors, light-emitting diodes, solid state lasers, and optical switches[11] (*see* ***Semiconductor Interfaces***). Some semiconductors absorb both visible and ultraviolet light, while others only absorb photons in the near-ultraviolet portion of the electromagnetic spectrum. The thickness of material required to absorb photons effectively can also vary widely in semiconductors, with strong absorbers requiring as little as 100 Å of material and weak absorbers requiring as much as 0.1 cm of material. The important optical properties of a semiconductor can also be understood from their chemical and electronic properties. Thus, a final goal of this chapter is to elucidate the chemical basis of the optical characteristics of semiconducting solids.

2 CRYSTAL STRUCTURES OF SELECTED SEMICONDUCTORS

To discuss the properties of semiconductors from a chemical perspective, it is important to first understand the structures of semiconducting solids. Semiconductors comprise a diverse group of inorganic materials and exhibit a variety of different *Crystal Structures*. The most basic semiconductor structure is based on the interpenetration of two face-centered cubic (fcc) lattices. A familiar, nonsemiconducting solid that adopts this structure is NaCl, where the Na^+ cations constitute one fcc lattice and the Cl^- anions constitute the other (Figure 1(a)). Many specific crystal structures of semiconductors are related to this basic face-centered cubic lattice.

Covalent semiconductors, such as the elemental semiconductors Si and Ge, have structures in which the atoms achieve maximum bonding between nearest neighbor atoms. For Si and Ge, each atom prefers sp^3-based tetrahedral bonding. Thus, these atoms will prefer a lattice in which tetrahedrally bonded atoms are positioned as closely as possible within the face-centered cubic structure. Si and Ge therefore adopt the cubic diamond lattice, in which half of the tetrahedral positions in the face-centered cubic lattice are filled with atoms (Figure 1(b)). A related structure is adopted by covalent, binary semiconducting solids having elements of similar electronegativities. For example, GaAs adopts the zinc blende structure, which is simply the cubic diamond structure with adjacent atoms throughout the structure alternating in type (Figure 1(c)). InAs, InP, and GaP are other examples of common covalent binary semiconductors that adopt the zinc blende structure.

In certain cases, when the semiconductor is composed of elements with very different radii and electronegativities, the lattice site in the tetrahedral position of a face-centered cubic structure becomes too small to accommodate one of the ions in the semiconductor. To maintain a lattice with a 1:1 cation:anion stoichiometry, the solid adopts a structure in which the atoms are instead hexagonally close-packed. As in the zinc blende structure, only half of the possible tetrahedral sites in this hexagonal structure are filled with atoms. This arrangement, which is adopted by semiconductors such as ZnO and CdSe (Figure 1(d)), is called the wurtzite structure.

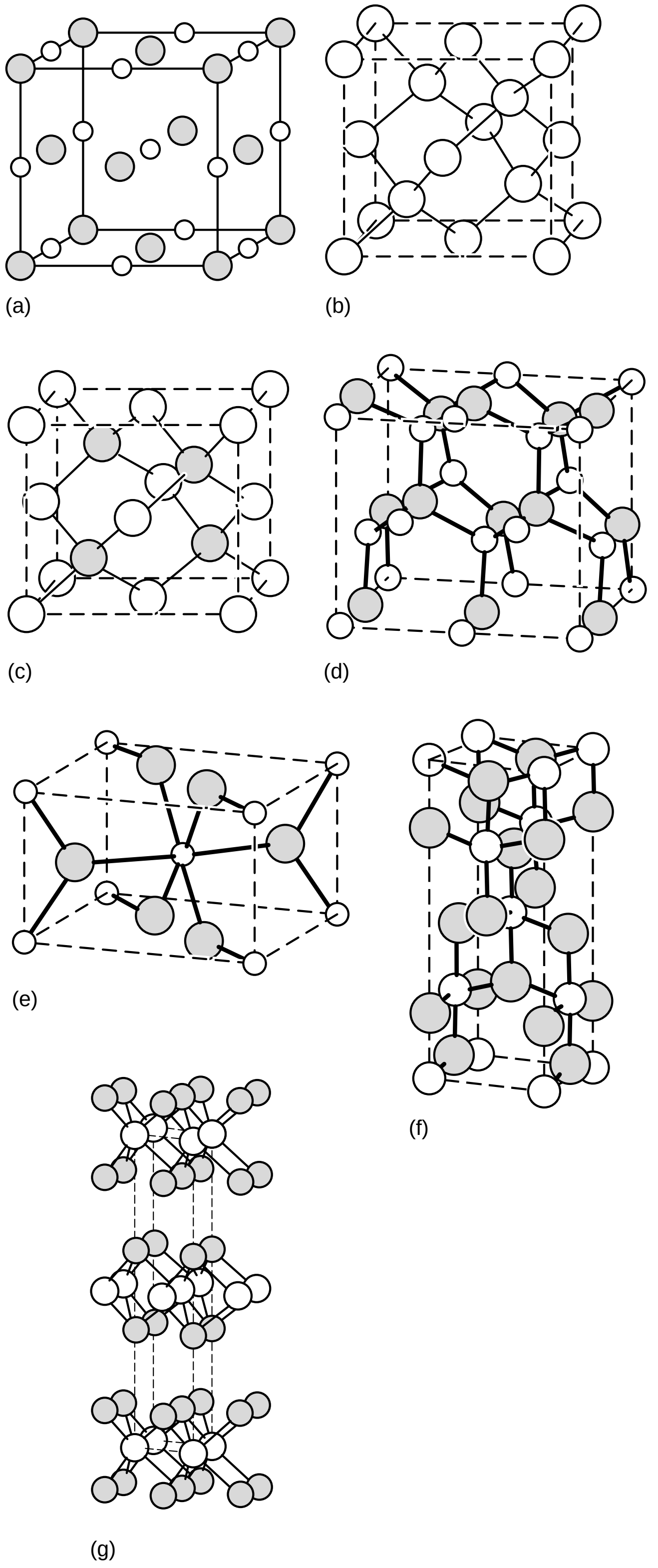

Figure 1 Structures of some common crystal lattices: (a) NaCl, (b) Si, (c) GaAs, (d) ZnO wurtzite, (e) TiO_2 rutile, (f) TiO_2 anatase, (g) MoS_2. For the binary materials, the shaded circles represent the more electronegative elements (i.e. Cl, As, O, and S) and the empty circles represent the less electronegative elements (i.e. Na, Ga, Zn, Ti, and Mo)

Some materials, such as ZnS, can be found in either the zinc blende or the wurtzite structure. Comparison between these lattices shows that the wurtzite structure is more open, and the bonding more ionic, than is the zinc blende structure.

Taken together, these three structures (cubic diamond, zinc blende, and wurtzite) encompass the majority of the common semiconductor materials in use today. These structures, which share the common feature of having an average of four valence electrons per atom, are called adamantine solids.[12]

In several semiconducting solids, steric, or electronic factors can result in the adoption of nonadamantine structures. Semiconductors that adopt nonadamantine structures include metal oxides such as TiO_2 and $SrTiO_3$, and transition metal dichalcogenides such as MoS_2, WS_2, and WSe_2. TiO_2, an important semiconductor, occurs in three forms: brookite, rutile, and anatase, but only rutile and anatase are commonly used.[2] Figures 1(e),(f) show the structures of the two common forms of TiO_2. The rutile lattice is derived from a body-centered cubic structure, where one-half of the trigonal-planar sites are occupied by anions to maintain a 1:2 cation:anion stoichiometry. The anatase lattice is derived from the NaCl structure with only one-half of the sites in one fcc lattice occupied by the Ti^{4+} cations. To date, large single crystals of TiO_2 have only been prepared in the rutile structure, while TiO_2 powders commonly contain both anatase and rutile components.[2]

Figure 1(g) illustrates a structure that is commonly found for transition metal dichalcogenide compounds such as MoS_2, WS_2, and WSe_2. These semiconductors adopt a layered structure in which the transition metal is 'sandwiched' between two layers of chalcogenide atoms. This arrangement produces a van der Waals structure, because there is no covalent bonding between adjacent chalcogenide layers. A useful feature of this structure is that the weak interactions between these planes allow high quality surfaces of van der Waals crystals to be prepared merely by peeling layers of the crystalline sample apart, as opposed to the extensive chemical and/or mechanical etching procedures that are required to produce desired surfaces in the more covalent semiconductor structures.

The surface properties of semiconductors often depend on the nature of the exposed crystal face. By convention, the orientation of a semiconductor surface is defined by the crystal plane that lies perpendicular to the normal of the surface. The conventional notation for this plane is obtained using Miller indices.[10,13] First, it is necessary to identify the intercepts of the surface plane with the crystallographic axes. The reciprocals of these intercepts are then reduced to Miller indices, which are integers that have the same ratios as the reciprocals themselves. For example, the plane ABCD in Figure 2 has formal intercepts of $\{1, \infty, \infty\}$ on the axes; thus, in the Miller index notation it is designated as the (1/1, $1/\infty$, $1/\infty$), or (100) plane. When a plane has a negative axis intercept, a bar is placed over the corresponding Miller index. For example, the plane that intercepts the axes at $x = -1$, $y = \infty$, $z = \infty$ would be designated as the $(\bar{1}00)$ plane.

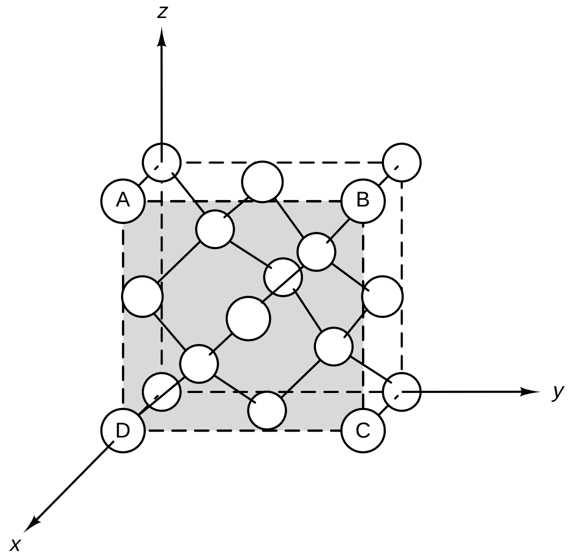

Figure 2 A schematic representation of Miller indices, imposed upon the Si crystal lattice. The x-, y-, and z-axes are indicated on the Si lattice, with the Si (100) face shaded

In the Miller index notation, the convention for denoting a direction perpendicular to a particular plane is to put square brackets around the numbers denoting that plane. The x-axis in Figure 2, for instance, is the [100] direction.

In some structures, several planes and directions may be equivalent by symmetry. For example, this is the case for the (100), (010), (001), $(\bar{1}00)$, $(0\bar{1}0)$, and $(00\bar{1})$ planes in the diamond cubic structure. Equivalent directions are denoted concisely as a group by using angular brackets. Thus, the (100) directions in a diamond cubic lattice include all of the directions that are perpendicular to the six planes noted above. The Miller index notation thus provides a concise designation for describing the surfaces of semiconductor crystals.

3 BAND STRUCTURE AND OPTICAL PROPERTIES OF SEMICONDUCTORS

The structure of semiconducting solids provides a convenient basis for understanding the important electronic properties of these materials. The important optical and electrical characteristics of semiconducting solids arise from the delocalized electronic properties of these materials. To understand the origin of this electronic delocalization, we must consider the nature of the bonding within semiconductor crystals. The basic model that has been successfully used to describe the electronic structure of semiconductors is derived from the *Band Theory* of solids. Our treatment of band theory will be qualitative, and the interested reader is encouraged to supplement our discussion with the excellent reviews by Hoffmann,[14–16] and with the classic texts by Ashcroft and Mermin,[17] Harrison,[18] Kittel,[10,19] Seitz,[20] and Goodstein.[21]

3.1 Molecular Orbital Description of Semiconducting Solids

The process of obtaining delocalized molecular orbitals for solids is similar to the approach that chemists use to describe the bonding in simple diatomic molecules. However, when orbital theory is used to describe the electronic properties of a collection of atoms within a solid lattice, a different terminology is generally used. The process is first illustrated on a chemically familiar system consisting of polyenes of varying chain lengths. This methodology is then generalized to include the bonding description of inorganic semiconducting solids.

3.1.1 Band Structure in Linear Conjugated Polyenes

An orbital description of the bonding in ethylene, which is the repeating unit in a straight chain polyene, is described first. In the Hückel molecular orbital (MO) description of ethylene (*see Hückel Theory*), the carbon atoms are sp^2 hybridized into a σ-orbital framework. The remaining carbon p-orbitals interact to yield two orbitals of π-symmetry, one of which is bonding and the other antibonding with respect to the C–C interaction. This situation is qualitatively represented in Figure 3. In the ground state of ethylene, the bonding π-orbital is occupied by two electrons, and this orbital is lower in energy than the empty antibonding orbital. A discrete optical transition exists between the highest occupied molecular orbital (HOMO) and the lowest unoccupied molecular orbital (LUMO) of ethylene, because a well-defined energy gap separates these two orbitals (*see HOMO–LUMO Gap*).

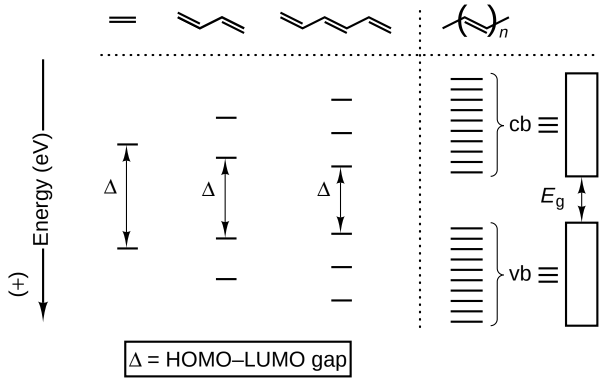

Figure 3 The development of a polyene band structure from the molecular orbitals (MOs) of ethylene.[14,15] From left to right, the molecular orbitals progressively develop into a band structure as the length of the conjugated chain is increased. For shorter polyene chains, Δ represents the HOMO–LUMO gap. For the infinite polyene chain, vb and cb denote the valence band and the conduction band, respectively, and E_g is the band gap

As the basic ethylene units are coupled together to form a larger molecule, the π-bonding will become more delocalized, and more atomic orbitals must be included in the overall molecular orbital description (Figure 3). When an infinite one-dimensional polyene chain is formed, it will contain an infinite number of bonding and antibonding molecular orbitals. In this infinite chain, the bonding orbitals will tend to cluster together into a tightly packed group, while the antibonding orbitals will cluster into another tightly packed group. It can be shown that these orbital clusters are separated by a well-defined HOMO–LUMO energy gap, just as in the cases of ethylene, 1,3-butadiene, 1,3,5-hexatriene, and other molecular oligomers that are precursors to the infinite chain polyene (Figure 3).[14,15]

Because the fully developed polyene has an extremely large number of molecular orbitals, a description of the π-bonding in this molecule can be simplified by considering groups of orbitals together as sets. Even though each of the molecular orbital distributions in the polyene consists of a large number of orbitals that are packed tightly together into a finite energy interval, we can ignore the energy spacing between the individual orbitals for most purposes. We can therefore consider the orbitals to form ‘continuous’ bands of energy levels (*see Energy Bands*). A shorthand notation for this assumption is to draw each band as a single block in energy. In this notation, there is an implicit understanding that there are actually a large number of states clustered together within this block (Figure 3). Under this scheme, the HOMO–LUMO gap is called the *Band Gap*.

3.1.2 Band Structure in Semiconducting Crystals

The band structure of a three-dimensional solid, such as a semiconductor crystal, can be obtained in a similar fashion to that of a polyene. Localized molecular orbitals are constructed based on an appropriate set of valence atomic orbitals, and the effects of delocalization are then incorporated into the molecular orbital as the number of repeat units in the crystal lattice is increased to infinity. This process is widely known to the chemical community as extended Hückel theory (*see Extended Hückel Molecular Orbital Theory*). It is also called tight binding theory by physicists who apply these methods to calculate the band structures of semiconducting and metallic solids.

We will not describe this process in detail for semiconducting solids, because there are complications that result from the different symmetry types of various unit cells, as well as from spin–orbit coupling considerations. These factors tend to increase the complexity of the MO description of inorganic solids relative to the simple MO treatment of polyenes. However, the principles of the procedure are the same as those outlined for the polyene example, with each individual atom in the lattice contributing a set of atomic orbitals toward the formation of crystal orbitals. These crystal orbitals will extend throughout the solid, and will yield discrete energy bands when represented on an energy diagram, just as in our polyene example (Figure 4). By definition, the highest filled band is called the valence band of the semiconductor. Similarly, the lowest unfilled band is called the conduction band. Thus, we obtain energy diagrams for semiconductor crystals that are similar to the one presented in Figure 3 for the organic polyenes, with bands of orbitals representing the HOMO and LUMO for the material of concern (Figure 4).

In semiconductor terminology, the top of the valence band and the bottom of the conduction band are called the valence band edge and the conduction band edge, respectively. The energy of the conduction band edge is denoted as E_{cb}; similarly, the energy of the valence band edge is denoted as E_{vb}. The energy difference between these levels is called the semiconductor band gap. The size of this band gap, E_{g}, is perhaps the most important characteristic of a semiconducting solid, as it influences many electronic properties of semiconductors. In general, semiconducting solids have band gaps that range from 0.5 to 3.5 eV; Table 1 lists the values of E_{g} for a variety of common semiconductors.

It should be noted that the positions of the crystal orbitals on the energy scale in Figures 3 and 4 are located with respect to the vacuum level as reference. The vacuum level is defined

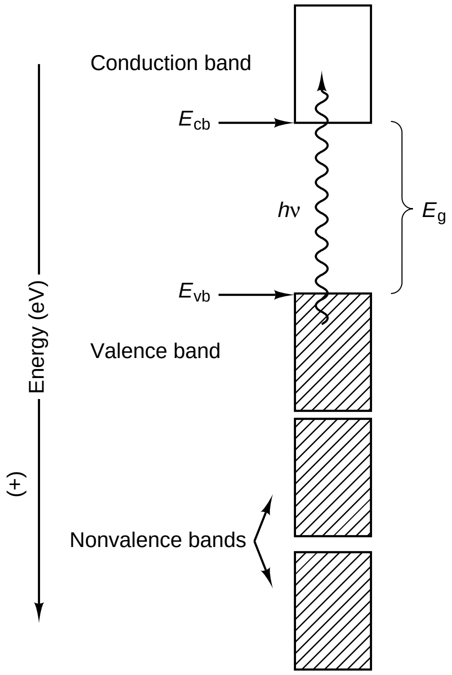

Figure 4 A schematic representation of the band structure of a semiconductor. The shaded area denotes a fully occupied band and the unshaded area denotes an empty band. Two nonvalence bands are also drawn to stress the point that the valence band of a semiconductor is the highest occupied band. E_{cb} and E_{vb} represent the conduction band edge and the valence band edge, respectively, and E_{g} is the band gap. When photons with energy greater than the band gap are absorbed by the semiconductor, electrons are excited from the semiconductor valence band into the conduction band

Table 1 Properties of some common semiconductors[a]

Semiconductor	Crystal structure	Band gap (eV)[b]	Type of band gap
Si	Diamond	1.12	Indirect
Ge	Diamond	0.66	Indirect
Se	Hexagonal	1.77	Direct
GaP	Zinc blende	2.26	Indirect
GaAs	Zinc blende	1.42	Direct
InP	Zinc blende	1.35	Direct
InAs	Zinc blende	0.36	Direct
ZnS	Zinc blende	3.58	Direct
	Wurtzite	3.70	Direct
ZnSe	Wurtzite	2.67	Direct
ZnTe	Wurtzite	2.26	Direct
CdS	Wurtzite	2.42	Direct
CdSe	Wurtzite	1.70	Direct
CdTe	Zinc blende	1.56	Direct
MoS_2	van der Waals	1.17	Indirect
$MoSe_2$	van der Waals	1.06	Indirect
$MoTe_2$	van der Waals	1.00	Indirect
WS_2	van der Waals	1.30	Indirect
WSe_2	van der Waals	1.16	Indirect
ZnO	Wurtzite	3.35	Direct
TiO_2	Rutile	3.02	Indirect
	Anatase	3.2	Indirect
$BaTiO_3$	Perovskite	3.3	Indirect
$SrTiO_3$	Perovskite	3.2	Indirect
$Al_{0.8}Ga_{0.2}As$	Zinc blende	2.00	Indirect
$GaAs_{0.7}P_{0.3}$	Zinc blende	1.77	Direct
$(Al_{0.2}Ga_{0.8})_{0.47}In_{0.53}As$	Zinc blende	0.84	–
WO_3	Perovskite	2.7	Indirect

[a]Data compiled from Refs. 2,11,22–24, and 25. [b]At 300 K.

as the energy level of an electron in vacuum, and is taken to be zero eV on the energy scale. Note also that although the physics convention assigns more negative energies to electrons that are more tightly bound relative to vacuum (for example, the energy of a 1s orbital in the H atom is -13.6 eV), the energy scale used by most electrochemists is opposite in sign, with more tightly bound electrons having more positive energies relative to the vacuum level. The assignment on the electrochemical energy scale is based on a 'work function' convention, which refers to the energy required to remove an electron from a particular electronic state in the solid.

3.1.3 *Density of States in the Energy Bands of a Semiconductor*

An important numerical quantity that describes the electronic structure of a semiconductor is the density of electronic states within a band. The density of electronic states per unit of energy can be obtained in a qualitative fashion by assuming that the crystal acts like a potential well and by treating the electron as a particle in a box.**[11,17,19]** Since the motions of electrons in a crystal are restricted by the delocalized orbital structure of the solid, the apparent mass of the electron is different from its mass in a vacuum. This 'effective' mass, m_e^*, describes the movement of an electron under the influence of the periodic potential in the lattice. The value of m_e^* can be calculated from the band structure of the semiconducting solid, and can also be measured experimentally using cyclotron methods.**[10]**

When the value of the effective electron mass is known, the resulting expression for the density of states in the conduction band is

$$N_{cb}(E) = \frac{4\pi(2m_e^*)^{3/2}}{h^3}(E_{cb} - E)^{1/2} \qquad (E \leq E_{cb}) \tag{1}$$

where h is Planck's constant and $N_{cb}(E)$ describes the density of electronic states in the conduction band as a function of energy, E. In this formalism, the influence of the periodic lattice potential on $N_{cb}(E)$ is contained in the value of the effective mass, m_e^*. A similar expression can be obtained to describe the density of electronic states in the valence band, and in all other bands, of the semiconducting solid.

The density of states is useful to our discussion because it allows the calculation of an extremely important numerical quantity, the effective density of states in the conduction band of the semiconductor, N_c. As a first approximation, N_c can be considered to be the number of electronic states in the conduction band of the semiconductor that are available to accept electrons from a donor. N_c is more formally defined as the number of electronic states, $N(E)$, for all energy E within $3kT$ of the conduction band edge $[|(E_{cb} - E)| < 3kT]$. Given the density of states per unit energy (equation 1), and using Fermi–Dirac statistics to describe the distribution of electrons as a function of energy, it can be shown that**[10,11,17]**

$$N_c = 2\left(\frac{2\pi m_e^* kT}{h^2}\right)^{3/2} \tag{2}$$

Typically, $N_c \approx 10^{19}$ states cm^{-3}. A similar equation can be derived for the valence band, and the effective density of states in the valence band, N_v, is also $\approx 10^{19}$ states cm^{-3}.

3.1.4 *Chemical and Electronic Properties of Semiconductors*

In general, semiconductors can have different types of valence band and conduction band structures. These differences can affect the chemical reactivity of the various types of semiconducting solids. For example, in a covalent solid such as Si, the valence and conduction bands can be considered as crystal orbitals that are either bonding or antibonding combinations of hybridized Si atomic orbitals. This situation is closely related to our polyene example, where the valence band consisted of bonding π-orbitals and the conduction band consisted of antibonding $\pi*$-orbitals. However, in an ionic crystal such as TiO_2, the valence band is composed of crystal orbitals that are derived from the filled O^{2-} 2p orbitals, while the conduction band is composed of crystal orbitals that are derived from the empty 3d orbitals of Ti^{4+}.[26–29] In this case, the band gap is not an energy gap between bonding and antibonding bands of the same symmetry. Rather, it is the energy gap between two very different types of bands.

The electronic band structure of solids is also useful in explaining many chemical properties of semiconductors. For example, ionic semiconductors are generally more stable towards corrosion and passivation than covalent semiconductors. This observation can easily be rationalized using the frontier molecular orbital argument (*see Frontier Orbitals*), which states that chemical reactivities are often controlled by the size of the HOMO–LUMO gap.[30,31] For semiconductors, the HOMO–LUMO gap is the band gap, and therefore the chemical reactivity of semiconductors should be related to the value of E_g. In a covalent semiconductor, the crystal orbitals that comprise the valence band and the conduction band are reasonably close in energy. The band gaps of these materials are relatively small, and these semiconductors are thus expected to be chemically reactive. This prediction is in agreement with experiment. In fact, one of the key problems in using small band gap semiconductors in energy conversion applications is their tendency to undergo corrosion and passivation reactions.[2] In contrast, the crystal orbitals that make up the valence and conduction bands of ionic semiconductors (TiO_2, $SrTiO_3$, etc.) are generally very different in energy, so their band gaps are usually very large. These solids should therefore be less prone to undergo oxidation or corrosion reactions. This prediction is also consistent with experimental results, and accounts for the emphasis on the use of metal oxides in water photoelectrolysis.[32–34]

The orbital character of the valence and conduction bands can also be used to understand trends in the electronic properties of semiconductors. For example, even though the value of E_g varies a great deal in metal oxide semiconductors (Table 1), the energies of the valence band edges are quite similar throughout this series of solids. This similarity can be understood from our MO/band structure treatment, as the valence bands of these semiconductors are constructed predominantly from the 2p orbitals of O^{2-}. The MOs that arise from these atomic orbitals should therefore be similar in bonding character and in energy. Within this framework, changes in the lattice cation will primarily affect the energy of the conduction band edge. This prediction is consistent with experimental data for metal oxide semiconductors.[35–39]

This latter behavior has been generalized to extend beyond the metal oxide semiconductor series. A general guideline has been proposed that the valence band character of most semiconductors is dominated by orbitals that are derived from atomic orbitals of the lattice anion.[40] To the extent that this generalization is valid, it predicts that semiconductors with a given lattice anion will have valence band edge energies similar to other materials with the same lattice anion. This rule also predicts that changes in the lattice cation will be reflected primarily in the energy of the conduction band edge (and therefore also in the band gap energy). This generalization is called the *Common Anion Rule*.[40] Although the common anion rule has received some experimental and theoretical support,[38,41–48] it is at best a rough generalization of chemical and electronic behavior. This generalization is not expected to be rigorously valid for any wide series of materials, especially for solids with different crystal structures or lattice stoichiometries.

Another analogy to chemical systems can be made when considering the reactivity of excited states of semiconductors. In molecular systems, it is well known that the types of orbitals in the HOMO and LUMO can determine the chemical reactivity of the excited electronic states of a molecule. A similar argument can be applied to predict the reactivity of different semiconductors. For example, it has been suggested that van der Waals semiconductors such as MoS_2 should be more stable towards corrosion and passivation reactions than II–VI semiconductors such as CdS.[49,50] This prediction was based on calculations that revealed that the valence and conduction bands of MoS_2 are both largely Mo 3d in character. For MoS_2, excitation of an electron is expected to result in the transfer of an electron from one metal-derived orbital set (in the valence band) to another metal-derived orbital set (in the conduction band), so no photocorrosion processes should be initiated. In contrast, the valence band of CdS is S^{2-} in character, and the conduction band is Cd^{2+} in character. For CdS, excitation of an electron from the valence band to the conduction band is expected to remove an electron from the S^2-derived orbitals, and should provide an initial step towards the dissolution of the lattice anion as the neutral S^0 species. These predictions have been partially verified by experiment, as metal dichalcogenide electrodes are often more stable in contact with aqueous solutions than are II–VI compounds.[2]

3.2 Optical Characteristics of Semiconductor Materials

In a semiconductor, some of the most important electronic transitions arise from the optical excitation of an electron across the semiconductor band gap. This excitation leads to the promotion of an electron from an orbital in the valence band to an orbital in the conduction band. This fundamental and extremely important process is crucial to the use of semiconductors as photovoltaic devices, photonic detectors, and optical switches. It is possible to understand the optical properties of semiconductors using the band structure formalism described above.

The light absorption process in semiconductors has an energy threshold. The value of this threshold is the band gap energy, E_g. Only photons with energies greater than or equal to the band gap energy can induce an electronic transition in the semiconductor. Large band gap materials such as TiO_2 will therefore only absorb light at short wavelengths, whereas small band gap materials such as Si and GaAs will respond to larger portions of the electromagnetic spectrum.

The band gaps of common semiconductors can vary from near-zero ($E_g = 0.1$ eV for $Hg_{0.8}Cd_{0.2}Te$) to greater than 3 eV ($E_g = 3.2$ eV for $SrTiO_3$).

From Beer's law, the absorbance and transmittance of a material can be expressed as

$$A = \ln \frac{I_0}{I} = \varepsilon c l \text{ and } T = \frac{I}{I_0} = \exp(-\varepsilon c l) \qquad (3)$$

where I is thetransmitted light intensity, I_0 is the incident light intensity, ε is the molar extinction coefficient, l is the optical path length, and c is the concentration of absorbing material. For solids, the concentration of the absorber is a constant, so Beer's law can be rewritten as

$$A = \ln \frac{I_0}{I} = \alpha l \text{ and } T = \frac{I}{I_0} = \exp(-\alpha l) \qquad (4)$$

where $\alpha \equiv \varepsilon c$ is the absorption coefficient of the material. This latter expression is usually used for expressing light absorption in solids. In this expression, α is a function of the wavelength at which the light absorption is measured.

For molecules, the extinction coefficient, ε, of an electronic transition can vary over a wide range of values, depending on whether the transition is optically and/or spin allowed. For semiconductors, the same restrictions apply. At the wavelength of interest, the electronic transition from one band to another must be optically and spin allowed to have a high extinction coefficient, that is to have a large absorption coefficient, α. Semiconductors that display a fully allowed transition between the valence band and the conduction band are referred to as direct band gap semiconductors. In these materials, such as GaAs and CdTe, the absorption coefficients are large, and the light is strongly absorbed close to the surface of the solid. Typical values of α for these materials are 10^4–10^5 cm^{-1}. Figure 5 depicts a plot of the absorption coefficient versus wavelength for a typical direct band gap semiconductor, GaAs.

For other semiconductors, such as Si, the lowest energy electronic transition between the valence band and the conduction band is formally optically forbidden. These materials are said to have an indirect band gap. Indirect band gap materials generally display small absorption coefficients for photons near the band gap energy. This behavior is analogous to a d–d electronic absorption band in an octahedral transition metal complex, which is formally optically forbidden owing to the inversion symmetry of the d orbitals. In such complexes, d–d transitions are generally observed experimentally, albeit with weak extinction coefficients, because other mechanisms allow the light absorption process to conserve momentum when the entire molecular wavefunction is considered. Similarly, for indirect band gap semiconductors, light absorption is allowed only when the momentum of the photon is coupled to vibrations of the crystal lattice and to the lowest energy electronic transition. Because of this requirement, the photon absorption process is less likely to occur, and indirect band gap semiconductors therefore have small absorption coefficients. For example, although the band gap energy for Si is 1.12 eV, the absorption coefficient at photon energies of 1.3 eV is still only 10^2 cm^{-1} (Figure 5). This contrasts with the value of 10^4 cm^{-1} that is typically displayed by direct band gap materials at photon energies 0.1–0.2 eV higher than E_g.[11] Examples of other indirect band gap semiconductors include GaP and TiO_2.

For direct band gap materials, the absorption coefficient generally increases rapidly when $h\nu$ is approximately equal to E_g, and it then remains at large values when $h\nu$ is much greater than E_g. For indirect band gap materials, the absorption coefficient is generally a much more slowly rising function of energy, with $\alpha \propto (h\nu - E_g)^2$ (for $h\nu \geq E_g$) being a typical dependence of the absorption coefficient on the energy of the incident photon.[11] In both cases, all of the incident light can be absorbed if the sample is sufficiently thick, because, as indicated by equation (4), increases in l will produce increases in absorbance. Note, however, that as the photon energy increases, the indirect band gap material will eventually enter a regime where it absorbs light almost as effectively as a material with a direct band gap.

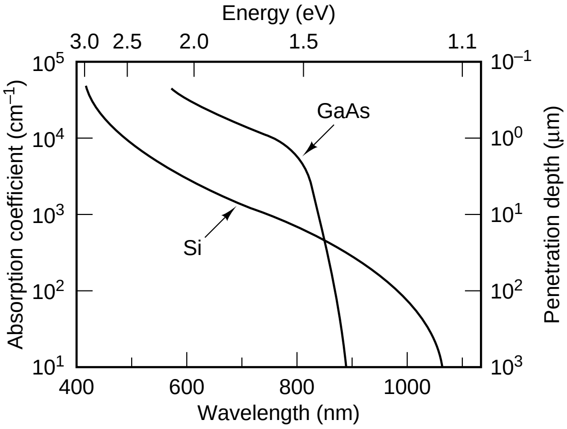

Figure 5 A plot of absorption coefficient versus photon wavelength for Si and GaAs.[24] A direct band gap semiconductor, such as GaAs ($E_g = 1.42$ eV), has a sharp onset of absorption at photon energy = E_g and a large absorption coefficient for $h\nu > E_g$. The indirect band gap semiconductor Si ($E_g = 1.12$ eV) has a broad, weak onset of absorption, which begins at photon energies $\leq E_g$ owing to vibrational coupling with the crystal lattice. For Si, note the low value of the absorption coefficient at photon energies substantially higher than the band gap energy

A related, useful quantity for characterizing the absorption of light by semiconductors is the optical penetration depth (Figure 5). This quantity is defined as the inverse of the absorption coefficient; that is, penetration depth $\equiv \alpha^{-1}$. From equation (4), it can be seen that the penetration depth is the distance into the semiconductor at which the transmitted light intensity reaches $1/e$ of the incident light intensity at the surface of the solid. In general, when compared to direct band gap semiconductors, indirect band gap semiconductors have larger penetration depths, and therefore require thicker samples to fully absorb the incident light.

One important optoelectronic application of semiconductors is as photovoltaic energy conversion devices. For efficient solar energy conversion, a semiconductor needs to be thick enough to absorb essentially all the incident photons with energies greater than E_g. For example, Si, an indirect gap semiconductor, has a value of α equal to 10^2 cm^{-1} for photon energies near E_g (Figure 5). This value implies that greater than 100 μm of Si must be used to absorb the incident light effectively in this energy range. This value places severe restrictions on the type of cells, and on the quality of crystals, that must be used in any efficient Si-based solar energy conversion device. This situation contrasts with that for the direct band gap semiconductor GaAs, in which α is approximately 10^4 cm^{-1} near E_g (Figure 5). The large absorption coefficient of this direct band gap semiconductor implies that only 1–2 μm of GaAs are needed to harvest the incident photons effectively near the GaAs band gap energy. Similar considerations apply, of course, to the use of semiconductors in other optical applications, such as in photonic detectors and optical switching applications.

4 CARRIER STATISTICS FOR SEMICONDUCTORS

With the above description of the band structure and optical properties of semiconductors, it is now possible to describe the remaining key characteristic of semiconductors: electrical conductivity. The electrical conductivity of semiconductors forms the basis for most of the modern electronics industry. Without precise control over the electrical conductivity of semiconductors, many modern electronic devices would not perform satisfactorily. The goal of this section is to understand the chemical basis for the electrical properties of semiconducting solids.

4.1 Carrier Concentrations in an Intrinsic Semiconductor

First, the properties of the undoped, intrinsic semiconductor (i.e. the pure semiconductor) must be considered. Although semiconductors have been described as having a filled HOMO (the valence band) and an empty LUMO (the conduction band), this condition is only rigorously true at absolute zero. At any finite, nonzero temperature, thermal excitation within the solid will result in promotion of carriers from one band to the other. This promotion of carriers produces a nonzero conductivity of the semiconductor. This situation is described quantitatively in this section.

Before proceeding with this discussion, it is important to realize that there are two different types of charge carriers in a semiconductor: electrons and holes. The promotion of an electron from the valence band into the conduction band, either by thermal or optical excitation, produces a free electron in the conduction band and an electronic vacancy in the valence band. This electronic vacancy is commonly referred to as a hole. Although the motion of holes is actually a representation of the motion of the remaining collection of valence band electrons, a hole can formally be treated as a discrete particle with a positive electronic charge. In general, most of the properties of electrons in the valence band can also be calculated formally as properties of holes. For example, the effective mass of a hole can be calculated similarly to that of an electron. However, owing to differences between the electronic structures of the valence and conduction bands, it is important to realize that the effective mass of a hole in the valence band may be quite different from the effective mass of an electron in the conduction band. The hole formalism is, however, quite useful in concisely describing the charge carrier motion in the valence band of a semiconductor.

Like an electron, a hole can act as a charge carrier. For example, a hole moving towards a contact is physically identical to an electron in the valence band moving away from that contact. Because both electrons and holes contribute to the current in a semiconductor sample, we will use the more general term charge carriers to refer to either electrons or holes in a semiconductor.

To describe the conductivity of an intrinsic semiconductor sample quantitatively, we need to calculate the concentrations of both types of charge carriers in the solid. The key quantity that controls the equilibrium concentration of electrons and holes in an intrinsic semiconductor is the band gap. Because the thermal excitation energy required to produce an electron and a hole is equal to E_g, the intrinsic carrier concentrations can be related to E_g using the Boltzmann relationship:[51]

$$n_i p_i = \text{constant} \times \exp\left(-\frac{E_g}{kT}\right) \tag{5}$$

In this equation, k is the Boltzmann constant, T is the absolute temperature, and n_i and p_i are the electron and hole concentrations at equilibrium in the intrinsic semiconductor, respectively. Both n_i and p_i are expressed as particles cm^{-3}, which is often abbreviated as ‘cm^{-3}’. The constant in equation (5) is actually a function of the band structure of the solid and is numerically equal to the product of N_c and N_v.[51] It is clear that this type of Boltzmann relationship should correctly describe the concentrations of electrons in the conduction band and of holes in the valence band that exist as a result of thermal excitation across the band gap at any given temperature.

Realizing that the thermal excitation to promote an electron into the conduction band must also result in the formation of a hole in the valence band, we can set $p_i = n_i$. This equivalence leads to the following relationship between n_i and E_g:

$$n_\mathrm{i}{}^2 = N_\mathrm{c}N_\mathrm{v}\exp\left(-\frac{E_\mathrm{g}}{kT}\right) \qquad (6)$$

This equation is essentially an equilibrium constant relationship between the electron and hole concentrations in the semiconductor. It is much like the ionization constant expression for the dissociation of water, which can be related to the concentrations of H^+(aq) and OH^-(aq) through the relationship $[H^+][OH^-] = K_\mathrm{w} = 1 \times 10^{-14}$ M^2. The only difference between these two expressions is that the temperature dependence of the water dissociation equilibrium constant is contained implicitly in the value of K_w, but is explicit in the relationship expressed by equations (5) and (6). The most important point to remember is that increases in the sample temperature will produce exponential increases in the electron and hole concentrations for an intrinsic semiconductor. Thus, the conductivity of intrinsic semiconductors increases exponentially with temperature. In contrast, the conductivity of metals decreases with increasing temperature.**[10]**

We can now estimate the intrinsic carrier concentrations for many semiconductors. We merely use equation (6) with the appropriate values of N_c and N_v for each material. As described above, N_c and N_v have similar values and are typically $\approx 10^{19}\,\mathrm{cm}^{-3}$. If these values are not known, they can be calculated from the band structure according to equation (2). For Si ($E_\mathrm{g} = 1.12$ eV), n_i is only $1.45 \times 10^{10}\,\mathrm{cm}^{-3}$. In general, samples with higher band gap energies will typically have lower values of n_i^2. For example, considering GaAs ($E_\mathrm{g} = 1.42$ eV) and using the actual values of N_c and N_v for GaAs at $T = 300$ K in equation (6), we calculate that the equilibrium concentrations of electrons and of holes at room temperature are $1.79 \times 10^6\,\mathrm{cm}^{-3}$.

For most semiconductors, kT (0.0259 eV at 300 K) is much smaller than E_g. Thus, few electrons and holes are produced at room temperature in such semiconductors. Intrinsic samples are far too resistive for many applications; additionally, in actual semiconductor samples, the concentration of unwanted impurities often exceeds the intrinsic carrier concentrations. Under these conditions, it is difficult to maintain quality control over the electrical properties of semiconductors. For these reasons, the conductivity of semiconductors is generally deliberately controlled through a process known as doping.

4.2 Carrier Concentrations in a Doped Semiconductor

Because the intrinsic carrier concentrations in semiconductors are so low, even impurity concentrations at the level of one part per billion can have a profound effect on the electrical properties of a semiconductor sample. To increase the sample conductivity and to control other electronic properties of the semiconductor, low concentrations of specific impurity atoms are often introduced into the crystal lattice. This process, which is called doping, serves to decrease the resistance of the crystal. Doping also allows control over the Fermi level (i.e. the electrochemical potential) of the semiconductor phase. The strategy for introducing dopant atoms, as well as some quantitative properties of doping statistics, is described in this section.

4.2.1 Chemistry of Dopants: Donors versus Acceptors

Dopant atoms can be either donors or acceptors. Donors are readily ionized to produce electrons in the conduction band and positive charges on the dopant atoms; acceptors scavenge electrons to produce holes in the valence band and negative charges on the dopant sites. A material that has been doped with donors is called an n-type semiconductor, while one that has been doped with acceptors is called a p-type semiconductor. These designations can be easily remembered by the sign of the predominant charge carrier. Donors create free electrons, which have a *n*egative charge, so the sample is denoted n-type. Similarly, acceptors create holes, which have a *p*ositive charge, so the sample is denoted p-type. The predominant charge carrier is called the majority carrier, so electrons are the majority carriers in an n-type sample and holes are the majority carriers in a p-type semiconductor.

Figure 6 displays the energy levels of common donors and acceptors with reference to the band edges of two semiconductors. If the energy levels of these donors and acceptors are close to the conduction or valence bands, respectively, they are called shallow donors or acceptors. Dopants with energy levels that are further away from either band are called deep dopants. While ionization of shallow dopants is usually complete at room temperature, ionization of deep dopants generally does not occur at room temperature. Shallow dopant materials are considered primarily in the remainder of this section.

The properties of most common dopants can be surmised from simple atomic ionization energies and from trends in the periodic properties of the elements. For example, in Si, which is a group 14 element, group 15 elements such as P or As (which have lower ionization energies than Si) will act as donors. Since only four of the five valence electrons in P are required for tetrahedral bonding in the crystal, the fifth valence electron will be donated to the conduction band at room temperature. This situation will produce an n-type semiconductor, in which the majority carriers are electrons. To a good approximation, the group 15 atom in the Si lattice could be considered as being a positively charged P core with a loosely bound electron, as depicted in Figure 7(a).

Conversely, group 13 elements such as B or Al are acceptors in Si, since they require an additional electron from the valence band to satisfy the tetrahedral bonding requirement. The group 13 atom in the Si lattice can be considered as a negatively charged B core with a loosely bound hole (Figure 7(b)). Since the trapping of an electron by the group 13 dopant atom results in the ionization of an electron from a lattice Si site, the doping process with the group 13 element produces an excess number

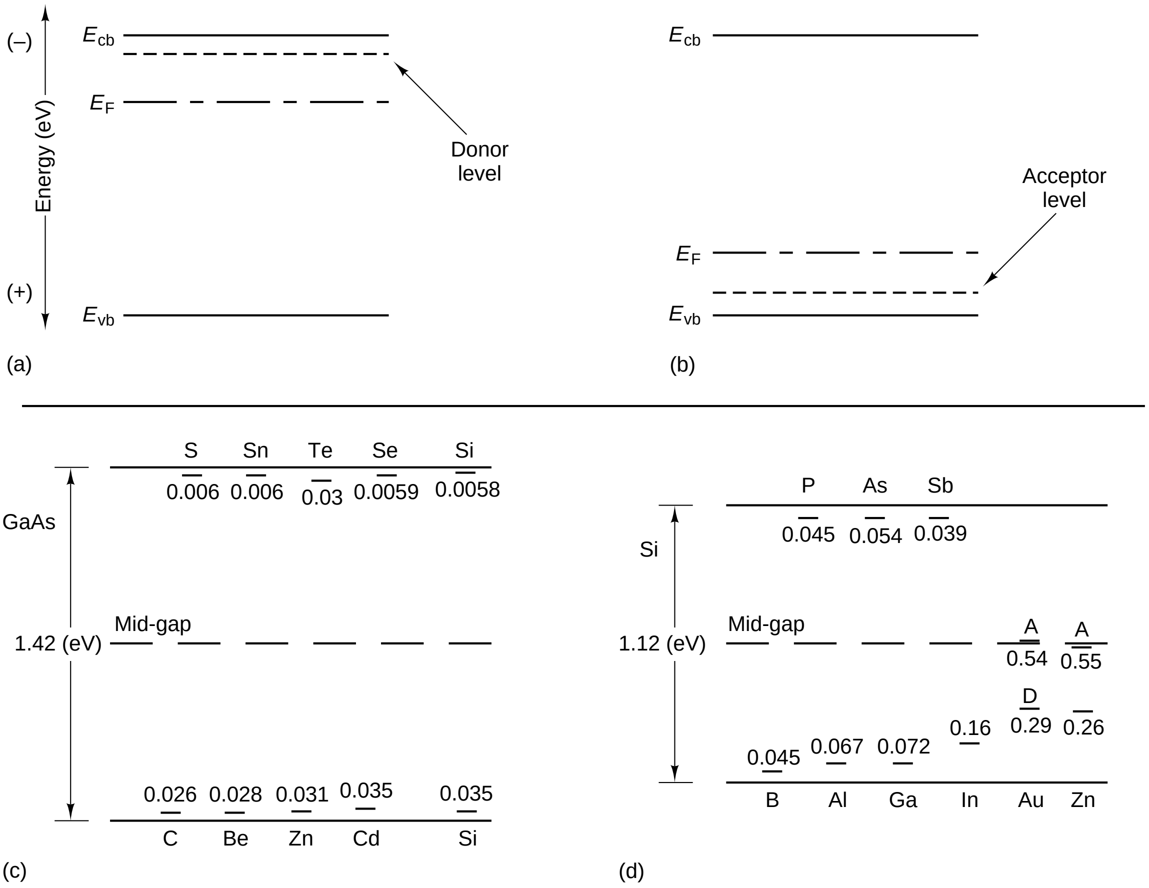

Figure 6 Above: schematic drawing of the energy levels of 'shallow' (a) donor and (b) acceptor dopants. E_{cb} and E_{vb} represent the conduction band edge and the valence band edge, respectively. E_F is the Fermi level. For a semiconductor doped with donors, the Fermi level is closer to the conduction band edge, while E_F is closer to the valence band edge for a semiconductor doped with acceptors. Below: representation of typical dopant levels for (c) GaAs and (d) Si in relation to the band edges.[11] The numbers near these levels denote the difference in energy (eV) away from the nearest band edge. Dopant levels that are close to the middle of the band gap are referred to as 'deep' dopant levels. In (d), an example of a compensator, Au, is shown, with an acceptor energy level above the donor, so that any Au dopant renders the Si crystal 'more intrinsic'. The two dopant levels of Zn are also represented

of holes in the valence band. Doping Si with B thus leads to a p-type Si sample. In such a p-type sample, the holes are the majority carriers, while the electrons are the minority carriers.

In some special cases, such as when Si is used as a dopant in GaAs, dopants are amphoteric. Amphoteric dopants can either be donors (Si in Ga sites of GaAs) or acceptors (Si in As sites of GaAs), depending on the crystal growth conditions (Figure 6(c)). Au in Si can best be described as a compensator, because its incorporation always reduces the number of free carriers in the sample. This occurs because Au has both a donor level and an acceptor level, with the acceptor level higher in energy (closer to vacuum) than the donor level (Figure 6(d)). Ionization of the gold dopant levels will therefore tend to make Si samples more intrinsic, regardless of whether the Si is initially n-type or p-type.

Other impurity atoms, such as transition metals, can have deep levels or multiple levels. An example of this situation is Zn in Si. Zn differs from Si by two valence electrons, so the Zn dopants can accept either one or two electrons from the Si valence band. However, owing to Coulombic repulsion and reorganization of the lattice atoms around the dopant, the energy of the singly charged state is different from that of the doubly charged state. This difference produces two distinct dopant energy levels for Zn in Si (Figure 6(d)).

Interstitial atoms and crystal defects can also behave as dopants. This type of doping is important for n-type CdS. Typical growth conditions for CdS yield S vacancies in the lattice, and the excess Cd then acts as an n-type dopant. For this reason, no p-type CdS has yet been prepared. CdSe and CdTe, however, have been grown in p-type forms, because they can be obtained in more defect-free crystalline phases and thus doping is more effective in controlling the carrier concentration of these purer solids.

The introduction of crystal defects such as oxygen vacancies is also an important mechanism for doping metal oxides. In fact, many of the n-type doping processes for

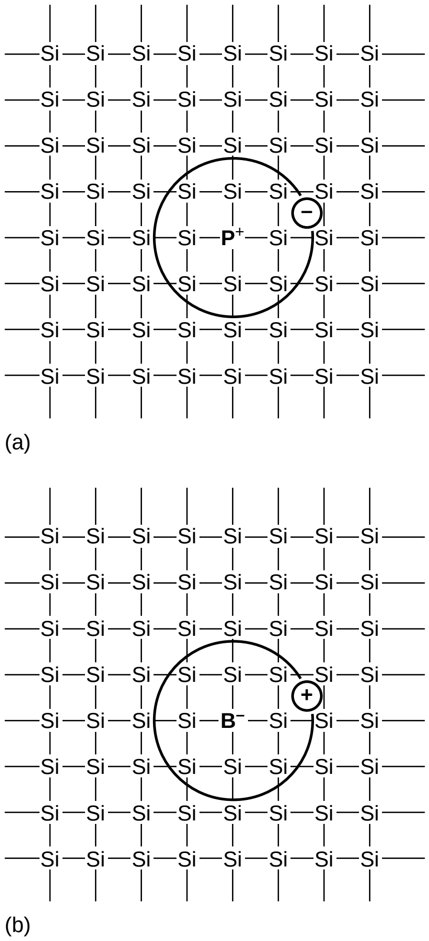

Figure 7 A schematic representation of dopant atoms in a Si lattice: (a) P-doped Si lattice, and (b) B-doped Si lattice. The dopant atoms are shown as replacing a Si atom in the crystal lattice. The circles represent schematic Bohr radii of the carrier (i.e. an electron (−) or a hole (+)) around the dopant atom. Note that these orbits are not drawn to scale; in reality, the first Bohr radius of these carriers is about 12 Å,[57] and a single carrier is spread over about 10^3 Si atoms

materials such as ZnO and TiO_2, which involve 'reduction' with H_2, actually create oxygen vacancies in the lattice.[2] The actual role of the H_2 is to combine with the lattice anions to form H_2O, which is expelled from the crystal. The reaction with H_2 creates the desired oxygen vacancies in the metal oxide lattice. These anion vacancies leave the surrounding lattice cations uncompensated. The electrons from these uncompensated metal ions then act as dopants, and make the entire crystal n-type in electrical properties. Formation of interstitials is also a possible mechanism for doping oxide semiconductors such as TiO_2. However, oxygen vacancies are generally viewed as the dominant doping process at low temperatures and higher oxygen partial pressures, while Ti interstitials may dominate the TiO_2 doping process at high temperatures and lower oxygen partial pressures.[2]

All of these factors can significantly affect the electronic properties of a semiconducting material, even if the dopant atoms exist in the crystal in concentrations of parts per billion. The manufacturing and processing of most semiconductor materials and devices are therefore conducted under conditions of excruciating cleanliness in order to minimize the incorporation of unwanted impurities. For most samples of technological importance, doping is performed using the straightforward concepts that have been described above. For certain applications, impurities with deep levels are incorporated into the semiconductor to control properties that cannot be easily manipulated by shallow dopants.[11,23,52]

4.2.2 Carrier Concentrations in a Doped Semiconductor

Because shallow dopant atoms are readily ionized at room temperature, the electron concentration, n, in an n-type semiconductor is closely approximated by the concentration of donor atoms, N_d, in the lattice. Rigorously, the electron concentration is given by the sum of the electrons thermally generated from the Si atoms and those generated by the thermal ionization of dopants. However, because n_i is so small for most common semiconductors, $n = n_i + N_d \approx N_d$ for any reasonable dopant concentration (10^{14}–10^{18} dopant atoms cm^{-3}). Similarly, for a p-type semiconductor, the hole concentration is approximately equal to the acceptor concentration, N_a. This approximation holds because shallow acceptors are essentially all ionized at room temperature, and the intrinsic hole concentration, p_i, is generally negligible compared to the number of holes that are generated by the dopants. Clearly, control over the dopant density of a semiconductor allows the manipulation of the carrier concentrations.

It is also important to calculate the equilibrium concentration of holes in a doped n-type semiconductor and of electrons in a doped p-type semiconductor. These minority carrier concentrations are readily obtained using the concepts described above, because equations (5) and (6) are actually more general than has been indicated. As mentioned above, the relationship between n_i and p_i in equation (5) is actually an equilibrium constant relationship between the electron and hole concentrations in the solid. In the discussion above, this expression was derived under the special constraint that $n_i = p_i$, that is under thermal excitation conditions. However, the equilibrium constant relationship on the right-hand side of equations (5) and (6) must hold regardless of the source of electrons and holes, so it applies to both doped and intrinsic semiconductor samples. We thus obtain

$$np = n_i^2 = N_c N_v \exp\left(-\frac{E_g}{kT}\right) \qquad (7)$$

as the general relationship between the electron and hole concentrations in any given semiconductor. In equation (7), n and p denote the equilibrium majority and minority carrier concentrations, respectively, in an n-type semiconductor, or vice versa in a p-type semiconductor.

This relationship is often called the *law of mass action* when applied to semiconductor doping statistics.[11] The situation is again conceptually identical to that for the equilibrium constant relationship for aqueous acid/base dissociation. The relationship $K_w = [H^+(aq)][OH^-(aq)]$ holds not only for the neutral liquid (i.e. the 'intrinsic', pH $= 7$ sample), but also for the proton and hydroxide concentrations in the presence of externally added sources of H^+ (aq) or OH^-(aq) (i.e. the extrinsic or 'doped' liquid). In the doped semiconductor, we are merely adding electrons or holes to control the carrier concentrations in the same way that the pH of water can be manipulated through the addition of acid or base.

4.2.3 Conductivity

The most important feature of the doping process is that it affects the electrical conductivity of the semiconductor sample. However, the doping process directly produces changes in the concentration of free charge carriers in the semiconductor, and indirectly produces changes in the electrical conductivity of the specimen. To understand the relationship between the charge carrier concentration and the electrical conductivity of a semiconductor, it is necessary to describe the macroscopic motion of charge carriers through the semiconducting solid. To describe this process, we first need to consider the motion of charge carriers when no electric field is present in the solid. We will then modify this discussion to incorporate the effects of electric fields in the system.

As described above, the electrons in a semiconductor can be described classically with an effective mass, m_e^*, which is usually less than the free electron mass. When no gradients in temperature, potential, concentration, and so on are present, the conduction electrons will move in random directions in the crystal. The average time that an electron travels between scattering events is the mean free time, τ_m. Carrier scattering can arise from the collisions with the crystal lattice, impurities, or other electrons. However, during this random walk, the thermal motion is completely random, and these scattering processes will therefore produce no net motion of charge carriers on a macroscopic scale.

Now we consider the charge carrier motion when an electric field is applied to the semiconducting solid. The electric field, $\mathcal{E}$, will result in a force, $F = -q\mathcal{E} = m_e^*$a, on the electron, where a is the acceleration of the electron due to the electric field. Under these conditions, the electron will still move with its average thermal velocity. However, in the presence of the electric field, the electron will also acquire a drift velocity, v_d. The drift velocity will be directed in the opposite direction from the electric field, and this directed motion will propel the electrons through the crystal even though they still undergo scattering events (Figure 8).[51] The drift velocity and the electric field can be related through the mean free time between scattering events, τ_m:

$$v_d = a\tau_m = -q\left(\frac{\tau_m}{m_e^*}\right)\mathcal{E} \tag{8}$$

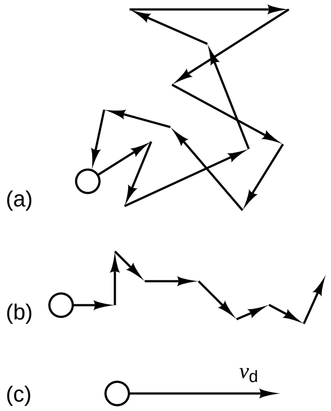

Figure 8 A schematic representation of the motion of charge carriers in a semiconductor lattice.[51] (a) A charge carrier in the absence of any external field. The thermal motion is random, and will not lead to any motion of the charge carrier on a macroscopic level. (b) A charge carrier in the presence of an electric field. The charge carrier motion due to the electric field is imposed upon its thermal motion. (c) The carrier drift shown at the macroscopic level. The random thermal motion of the charge carrier again leads to no motion on the macroscopic level. The charge carriers are propelled by the electric field at a constant velocity, v_d, either parallel or antiparallel to the applied field

A similar equation can be used to describe the motion of holes, except that holes will move toward the electric field rather than away from it.

The proportionality constant between the applied electric field and the resulting drift velocity is called the charge carrier mobility, μ. For electrons, $\mu_n = q(\tau_m/m_e^*)$; for holes, $\mu_p = q(\tau_m/m_h^*)$. It should be noted that, owing to differences in the effective masses of electrons and holes, their mobilities within a semiconductor may be markedly different. The electrical conductivity, σ, of a semiconductor is related to the free carrier concentrations by:

$$\sigma = qn\mu_n + qp\mu_p \tag{9}$$

This equation states that the electrical conductivity due to a free carrier is the product of the charge on the carrier, q, its concentration in the solid, and its mobility, μ. Since semiconductors have two different types of mobile charge carriers, electrons, and holes, the total sample conductivity, σ, is simply the sum of the individual conductivities due to each carrier type. It should be noted that the conductivity depends only on the absolute number of carriers, and therefore is not affected by the signs of the carriers themselves. Carrier mobilities for electrons and holes in a variety of semiconductors can be measured experimentally. These values have been tabulated in various reference books[10,11,22,23] and are available for many semiconductors of interest. Doping of a semiconductor therefore allows precise control over the conductivity of the semiconductor sample.

4.3 Fermi Levels and the Energetics of Semiconductor Samples

The last quantity that is needed to describe the important properties of an isolated semiconductor phase is the electrochemical potential, or *Fermi Level* (E_F), of the material. The Fermi level determines the tendency of the semiconductor to transfer charges to other phases. As formally defined in statistical mechanics, the Fermi level of any phase is the energy level where the probability of finding an electron is 1/2. In an intrinsic semiconductor crystal at absolute zero, the Fermi level would be located near the middle of the band gap (Figure 9(a)). At absolute zero, the energy states in the valence band would be totally occupied, while the states in the conduction band would be completely empty. The probability of finding an electron would therefore go from 1.0 in the valence band to 0.0 in the conduction band, and would reach a value of 1/2 at mid-gap (even though there are no actual electronic states at this energy).

For a doped semiconductor, the Fermi level position will be shifted from mid-gap, because the doping process will vary the tendency of the solid to either gain or lose electrons. For example, if donors are added to an intrinsic semiconductor, the material will be more likely to lose electrons. The Fermi level of an n-type semiconductor will thus move closer to the vacuum level (i.e. will become more negative on the electrochemical potential scale) (Figure 9(b)). Similarly, if acceptors are added to an intrinsic material, the Fermi level will become more positive, because this phase will now have an increased tendency to accept electrons from another phase (Figure 9(c)).

The Fermi level of a semiconductor phase can be written as

$$E_\mathrm{F} = E_\mathrm{Fi} - kT \ln\left(\frac{n}{n_\mathrm{i}}\right) \tag{10}$$

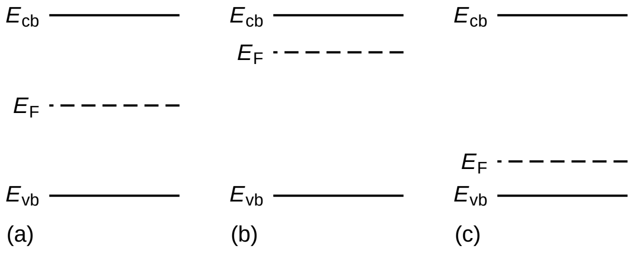

Figure 9 A schematic representation of the Fermi level position in a semiconductor. (a) The Fermi level in an intrinsic semiconductor at absolute zero is approximately at mid-band gap. (b) In an n-type semiconductor, the electron concentration in the conduction band is greater than in an intrinsic sample. The Fermi level is thus closer to the conduction band for an n-type sample. (c) In a p-type semiconductor, the Fermi level position is moved closer to the valence band. Thus, a p-type semiconductor is more likely to accept electrons from another phase than is the corresponding n-type semiconductor

or

$$E_\mathrm{F} = E_\mathrm{Fi} + kT \ln\left(\frac{p}{p_\mathrm{i}}\right) \tag{11}$$

In these equations, the term E_Fi represents the Fermi level position in the intrinsic semiconductor (i.e. when $n = n_\mathrm{i}$ in equation (10) or $p = p_\mathrm{i}$ in equation 11). This value serves as a reference energy, much as pH = 7 serves as a reference value for changes in the pH of a neutral aqueous solution. Physically, equation (10) states that doping a semiconductor with donors will produce a more negative Fermi level because $n > n_\mathrm{i}$. Similarly, the doping of a semiconductor with acceptors yields a more positive Fermi level, as given by equation (11) with $p > p_\mathrm{i}$. Of course, since $np = n_\mathrm{i}^2$, equations (10) and (11) can be used interchangeably to solve for E_F of a doped semiconductor if either n or p is known. Both expressions will yield identical numerical values for E_F. More rigorous equations can be obtained by using Fermi–Dirac statistics on the electron occupancy of the filled and empty states of a semiconductor.[11,52] However, the final results of such a treatment are identical to equations (10) and (11) for most doping conditions.

It is often convenient to refer the Fermi level to reference levels that are close to the band edge energies. If we were to fill up the conduction band with electrons to a value equal to the effective density of states in the conduction band, N_c, then the Fermi level would shift until it was exactly equal to the energy of the bottom of the conduction band, E_cb. Our new reference level would then be the energy of the Fermi level at the bottom of the conduction band, that is, $E_\mathrm{F} = E_\mathrm{cb}$. That is,

$$E_\mathrm{F} = E_\mathrm{cb} - kT \ln\left(\frac{n}{N_\mathrm{c}}\right) \tag{12}$$

In essence, this is analogous to shifting the reference level of an aqueous solution to pH = 0. Changes in pH could then be calculated relative to the amount of acid in a 1.0 M H^+ solution, as opposed to calculating pH changes relative to a 10^{-7} M H^+ solution for neutral water. The result for the Fermi level position versus electron concentration is, of course, identical no matter which formula is used. It is only a matter of convenience as to which reference level is used in the calculation of E_F. Similarly, we could choose to refer the Fermi level position to the energy of the top of the valence band, E_vb. In this case, the expression for E_F is:

$$E_\mathrm{F} = E_\mathrm{vb} + kT \ln\left(\frac{p}{N_\mathrm{v}}\right) \tag{13}$$

The forms used in equations (12) and (13) are often found in the solid-state physics and chemistry literature.

4.4 Chemical and Electrical Effects of Doping Semiconductors

We have seen that doping is useful for several purposes, in that it allows both the electrical conductivity and the Fermi level position of a semiconductor sample to be controlled readily. Various types of electronic devices can be obtained when the carrier concentrations are manipulated through doping. The conductivity of Si can vary from 10^{-4} ohm^{-1} cm^{-1} for nearly intrinsic Si to greater than 10^2 ohm^{-1} cm^{-1} for highly doped n-type or p-type samples. These levels of conductivity correspond to a range of doping levels in Si, for example, from 10^{12} to 10^{21} cm^{-3}.[11] The ability to control the electrical properties of these materials allows fabrication of rectifiers, transistors, physical, and chemical sensors, and other electronic devices from semiconducting materials. Further information on the specific doping geometry of electronic devices can be found in numerous textbooks.[11,53–55] It is clear, however, that deliberate manipulation of the electrical conductivity of semiconducting solids is a key feature of doping.

Doping also affects the Fermi levels of semiconducting solids, and therefore affects the chemical reactivity of these phases. The Fermi level is the electrochemical potential of the material, and materials with differing electrochemical potentials must react differently. For example, selective etchants can etch p-type Si, while leaving n-type Si untouched. Another example is the behavior of Si electrodes in contact with aqueous HF solution. Although p-type Si anodes corrode in contact with aqueous HF in the dark, n-type Si anodes are chemically inert in this system unless they are illuminated with photons above the Si band gap energy.[56] These chemical differences are a direct consequence of the different Fermi level positions that are obtained through doping. The Fermi level position is also of importance in semiconductor contacts, and in the formation of numerous other electronic devices. Thus, doping of semiconductors is critical for numerous fundamental and technological reasons.

5 SUMMARY

To this point, we have seen how the structural, electronic, optical, and electrical properties of semiconductors can be treated within a common framework. The bonding in the lattice determines the structure of the solid, and the structure of the lattice in turn affects the band structure. This band structure then can be used to describe the chemical, optical, and electrical properties of the semiconducting solid. Thus, chemical control over the electronic properties of semiconductors is an important component of modern research in solid-state chemistry and solid-state physics. The concepts described above enable this process to be understood from a relatively qualitative, chemically based viewpoint. Further details on specific topics can be obtained in specialized textbooks in solid-state chemistry and physics, but this introduction to the relevant concepts should suffice to provide the inorganic chemist with access to the terminology and concepts of the field.

6 RELATED ARTICLES

Electronic Structure of Solids; Germanium: Inorganic Chemistry; Semiconductor Interfaces; Silicon: Inorganic Chemistry.

7 REFERENCES

1. R. H. Fahrenbruch and A. L. Bube, ‘Fundamentals of Solar Cells’, Academic Press, New York, 1983.
2. H. O. Finklea, in ‘Semiconductor Electrodes’, ed. H. O. Finklea, Elsevier, Amsterdam, 1988.
3. A. Heller, *Acc. Chem. Res.*, 1981, **14**, 154.
4. B. Parkinson, *Acc. Chem. Res.*, 1984, **17**, 431.
5. M. S. Wrighton, *Acc. Chem. Res.*, 1979, **12**, 303.
6. M. A. Fox, *Acc. Chem. Res.*, 1983, **16**, 314.
7. M. A. Fox, in ‘Topics in Current Chemistry’, ed. E. Steckhan, Springer Verlag, New York, 1987.
8. Y. M. Xu, P. E. Ménassa, and C. H. Langford, *Chemosphere*, 1988, **17**, 1971.
9. H. Al-Ekabi, A. Safarzadeh-Amiri, W. Sifton, and J. Story, *Int. J. Environ. Pollut.*, 1991, **1**, 125.
10. C. Kittel, ‘Introduction to Solid State Physics’, 6th edn., Wiley, New York, 1986.
11. S. M. Sze, ‘The Physics of Semiconductor Devices’, 2nd edn., Wiley, New York, 1981.
12. N. S. Lewis and M. Rosenbluth, in ‘Photocatalysis: Fundamentals and Applications’, eds. N. Serpone and E. Pelizzetti, Wiley, New York, 1989.
13. P. W. Atkins, ‘Physical Chemistry’, 3rd edn., Freeman, New York, 1986.
14. R. Hoffmann, *Angew. Chem., Int. Ed. Engl.*, 1987, **26**, 846.
15. R. Hoffmann, ‘Solids and Surfaces – A Chemist’s View of Bonding in Extended Structures’, VCH, New York, 1988.
16. R. Hoffmann, *Rev. Mod. Phys.*, 1988, **60**, 601.
17. N. W. Ashcroft and N. D. Mermin, ‘Solid State Physics’, Holt, Rhinehart, and Winston, New York, 1976.
18. W. A. Harrison, ‘Solid State Theory’, Dover, New York, 1980.
19. C. Kittel and H. Kroemer, ‘Thermal Physics’, 2nd edn., Freeman, New York, 1980.

20. F. Seitz, ‘The Modern Theory of Solids’, Dover, New York, 1987.
21. D. R. Goodstein, ‘States of Matter’, Dover, New York, 1980.
22. R. C. Weast, M. J. Astle, and W. H. Bayer, ‘Handbook of Chemistry and Physics’, 71st edn., CRC Press, Boca Raton, FL, 1991.
23. J. I. Pankove, ‘Optical Processes in Semiconductors’, Dover, New York, 1975.
24. S. J. Fonash, ‘Solar Cell Device Physics’, Academic Press, New York, 1981.
25. C. R. Stanley, D. Welch, G. W. Wicks, C. E. C. Wood, C. Palmstrom, F. H. Pollack, and P. Parayanthal, in ‘Gallium Arsenide and Related Compounds, 1982’, ed. G. E. Stillman, Institute of Physics, Bristol, 1983.
26. S. Munnix and M. Schmeits, *Phys. Rev. Sect. B*, 1983, **28**, 7342.
27. K. Vos, *J. Phys. C: Solid State Phys.*, 1977, **10**, 3917.
28. J. B. Goodenough, *Prog. Solid State Chem.*, 1971, **5**, 145.
29. N. Daude, C. Gout, and C. Jouanim, *Phys. Rev. Sect. B*, 1977, **15**, 3229.
30. T. H. Lowry and K. S. Richardson, ‘Mechanism and Theory in Organic Chemistry’, 3rd edn., Harper & Row, New York, 1987.
31. J. P. Lowe, ‘Quantum Chemistry’, Academic Press, Orlando, FL, 1978.
32. A. Fujishima and K. Honda, *Bull. Chem. Soc. Jpn.*, 1971, **44**, 1148.
33. A. Fujishima and K. Honda, *Nature (London)*, 1972, **238**, 37.
34. M. S. Wrighton, A. B. Ellis, P. T. Wolczanski, D. L. Morse, H. B. Abrahamson, and D. S. Ginley, *J. Am. Chem. Soc.*, 1976, **98**, 2774.
35. H. Harada, T. Ueda, and T. Sakata, *J. Phys. Chem.*, 1989, **93**, 1542.
36. R. D. Rauh, J. M. Buzby, T. F. Reise, and S. A. Alkaitis, *J. Phys. Chem.*, 1979, **83**, 2221.
37. D. E. Aspnes and A. Heller, *J. Phys. Chem.*, 1983, **87**, 4919.
38. M. A. Butler and D. S. Ginley, *J. Electrochem. Soc.*, 1978, **125**, 228.
39. H. H. Kung, H. S. Jarett, A. W. Sleight, and A. Ferretti, *J. Appl. Phys.*, 1977, **48**, 2463.
40. J. O. McCaldin, T. C. McGill, and C. A. Mead, *J. Vac. Sci. Technol.*, 1976, **13**, 802.
41. M. Aven and C. A. Mead, *Appl. Phys. Lett.*, 1965, **7**, 8.
42. R. K. Swank, *Phys. Rev.*, 1967, **153**, 844.
43. K. Kajiyama, Y. Mizushimo, and S. Sakata, *Appl. Phys. Lett.*, 1973, **23**, 458.
44. J. O. McCaldin, T. C. McGill, and C. A. Mead, *Phys. Rev. Lett.*, 1976, **36**, 56.
45. R. Dingle, W. Wiegman, and C. H. Henry, *Phys. Rev. Lett.*, 1974, **33**, 827.
46. M. A. Butler and D. S. Ginley, *Chem. Phys. Lett.*, 1977, **47**, 319.
47. K. W. Frese Jr, *J. Vac. Sci. Technol.*, 1979, **16**, 1042.
48. A. H. Nethercot Jr, *Phys. Rev. Lett.*, 1974, **33**, 1088.
49. H. Tributsch, *Z. Naturforsch.*, 1977, **32A**, 972.
50. H. Tributsch, *Ber. Bunsen-Ges. Phys. Chem.*, 1977, **81**, 361.
51. R. F. Pierret, ‘Semiconductor Fundamentals’, 2nd edn., Addison-Wesley, Reading, MA, 1988.
52. J. S. Blakemore, ‘Semiconductor Statistics’, Dover, New York, 1987.
53. R. S. Muller and T. I. Kamins, ‘Device Electronics for Integrated Circuits’, Wiley, New York, 1977.
54. E. S. Yang, ‘Fundamentals of Semiconductor Devices’, McGraw-Hill, New York, 1978.
55. M. Zambuto, ‘Semiconductor Devices’, McGraw-Hill, New York, 1989.
56. D. J. Turner, in ‘The Electrochemistry of Semiconductors’, ed. P. J. Holmes, Academic Press, London, 1962.
57. H. Ibach and H. Luth, ‘Solid-State Physics’, Springer Verlag, Berlin, 1990.

Acknowledgments

We acknowledge the National Science Foundation, grant CHE-8814694, and the Department of Energy, Office of Basic Energy Sciences, grant DE-FG03-88ER13932, for support of work in photoelectrochemistry. Janet M. Kesselman acknowledges the National Science Foundation and SonBinh T. Nguyen acknowledges the Department of Defense, Office of Army Research for pre-doctoral fellowships. This is contribution 8755 from the Caltech Division of Chemistry and Chemical Engineering.

Short-lived Intermediates

Matthew J. Almond & Samantha L. Jenkins
University of Reading, Reading, UK

1	Introduction	1
2	Generation of Short-Lived Molecules	1
3	Methods of Detection of Short-Lived Intermediates	2
4	Structural Information from Spectroscopic Measurements	4
5	Photochemistry of Transition Metal Carbonyls	10
6	Main Group Molecules in High-Temperature Vapors	18
7	References	29

1 INTRODUCTION

Why study short-lived molecules?**[1]** Those who carry out such studies are perhaps driven by two main ambitions. First, to investigate the structures of compounds with unusual coordination numbers or oxidation states. We can thus make small molecules, for example, AlCl or OPCl (to take just two of very many examples), that are not stable under ambient conditions. In transition metal chemistry, it is becoming apparent that we cannot predict the structures of 'open shell' molecules simply by looking at the structures of 'closed shell' species, for example, we cannot predict what structure the unsaturated 16-electron carbonyl $Cr(CO)_5$ will adopt, simply by knowing that saturated 18-electron $Cr(CO)_6$ is octahedral. The second point is to study reaction mechanism. We must know about structures of intermediates fully to understand reaction pathways; *kinetics* alone is not enough.

In considering what we mean by 'short-lived molecules', we must be careful to distinguish between thermodynamic stability and kinetic inertness. A compound that is thermodynamically unstable need not be short-lived, provided a high activation barrier exists towards reaction. Such a molecule is said to be kinetically inert. A species that survives for only short periods is said to be *labile*. Thus most of those short-lived species that we will consider in this chapter have a degree of thermodynamic instability coupled with kinetic lability. An added complication arises when we consider photochemical systems. Here the ability of a molecule to absorb light at a particular wavelength and the quantum yield for reaction will determine, to some extent, its lifetime. The broad definition adopted in this article is that a short-lived molecule is one whose concentration decays, under ambient conditions, on a timescale ranging from nanoseconds or even picoseconds to a few seconds.

A comprehensive selection of the relevant chemistry is covered, supported by experiments that highlight two of the main areas of study of short-lived intermediates, namely photochemical reactions and high-temperature systems.

2 GENERATION OF SHORT-LIVED MOLECULES

Various means exist for the generation of short-lived intermediates. The first are 'high energy' systems such as high-temperature vapors or plasmas, the chemistry of which is often quite complex. The thermodynamics of the system under investigation must be considered carefully before predictions can be made as to what species will be present in the vapor. Thus, for example, evaporation of silica, SiO_2, yields SiO rather than SiO_2 molecules. This observation reflects the greater thermodynamic stability of the monoxide over the dioxide at the temperature (ca. 2000 K) at which vaporization takes place. Many other similar examples are known; sometimes the nature of the vapor-phase species depends upon the material of the vessel from which the species are evaporated. Thus evaporation of sodium phosphate (Na_3PO_4 or $Na_5P_3O_{10}$) from a boat made of a reducing metal such as Mo or Ta yields sodium phosphite ($NaPO_2$) molecules in the vapor. Reduction of phosphorus also occurs if $OPCl_3$ vapor is passed over silver heated to 1100 K. Here the gaseous product is OPCl.

Two other systems that produce 'high-temperature' molecules should be mentioned: shock waves and flames. Shock waves are typically formed by the rapid release of a high pressure of gas in a shock-tube apparatus. A shock wave is formed that can travel at several times the speed of sound; temperatures as high as 20 000 K have been produced in shock tubes. Thus the method is ideal for monitoring pyrolysis and oxidation reactions. Flames are gaseous systems where a flow of gas combines with a self-supporting reaction to produce a steady-state situation. Again, oxidation reactions are amenable to this approach. In particular, short-lived intermediates in hydrocarbon oxidation, such as C_2, OH, and CHO^+, have been identified in flames.

Plasmas are another example of a 'high energy' gas-phase system. The flow discharge, excited by microwave, radio frequency, or electric discharge, has been much used by chemists to generate reactive species. The system operates at low pressure and at moderate temperatures (ca. 600 K). The plasma contains electrons, ions (positive and negative), and neutral species (atoms, free *radicals* and molecules). Secondary reaction products may sometimes be formed in a plasma, for example, via the intermediacy of fluorine atoms formed when CF_4 or NF_3 gas is flowed through a discharge. Such a method has been used, for example, to generate methyl radicals:

$$F(g) + CH_4(g) \longrightarrow CH_3(g) + HF(g) \qquad (1)$$

A rather different route to short-lived intermediates is to irradiate a suitable precursor with radiation of an appropriate energy. Most common is UV–visible photolysis. Section 5 discusses some of the rich photochemistry displayed by transition metal carbonyls, these being very amenable to UV–visible photolysis. Thus unsaturated carbonyl fragments may be produced:[2,3]

$$\mathrm{Cr(CO)_6} \xrightarrow[h\nu]{\text{Ar matrix, 12 K}} \mathrm{Cr(CO)_5} + \mathrm{CO} \tag{2}$$

$$\mathrm{Fe(CO)_5} \xrightarrow[h\nu]{\text{Ar matrix, 12 K}} \mathrm{Fe(CO)_4} + \mathrm{CO} \tag{3}$$

For some reactions, however, higher energy radiation is required. Vacuum UV photolysis may be useful to initiate reactions of molecules that only absorb at short wavelengths. To form matrix-isolated radical cations of various aromatic compounds, for example, (**1**) and (**2**). Andrews and coworkers have devised a system for windowless photolysis of a low-temperature matrix (since most window materials will absorb vacuum UV light). A glow discharge of Ar or H_2 is used (the latter has strong emission centered at 121.6 nm) and the excited species emanating from the discharge are cocondensed with the molecules under investigation. The success of the method is demonstrated by the spectra shown in Figure 1. Here the yields of the *p*-dichlorobenzene cation using standard UV–visible or ‘windowless’ vacuum UV photolysis are contrasted. The latter approach is shown to produce an enormously enhanced yield.

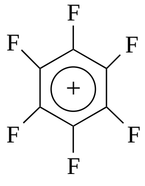

(**1**)

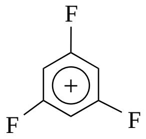

(**2**)

X-ray irradiation is another good way to produce radicals in low-temperature solids. To take just one example, the methoxyl radical MeO• is generated by X-ray irradiation of solid methanol-d_1 at 4.2 K:

$$\mathrm{MeOD} \xrightarrow[4.2\,\mathrm{K}]{\text{X-ray}} \mathrm{MeO\bullet} + \mathrm{D\bullet} \tag{4}$$

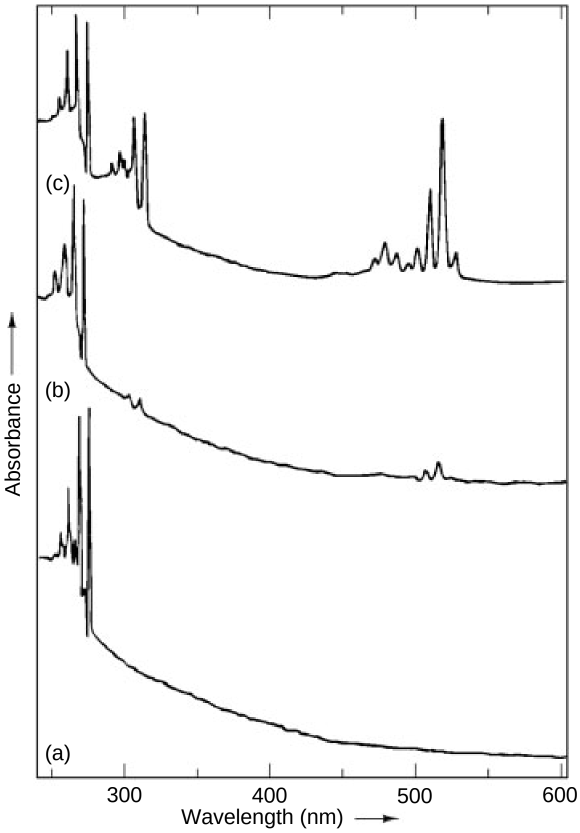

Figure 1 UV–visible absorption spectra of matrix-isolated *p*-dichlorobenzene and of its radical cation: (a) spectrum of *p*-dichlorobenzene before photolysis; (b) spectrum after 15 min photolysis at = 220–1000 nm; (c) spectrum after 15 min Ar resonance photolysis. The much increased yield of product upon vacuum UV photolysis can clearly be seen. (Reprinted with permission from Friedman *et al.*, *J. Phys. Chem.*, 1984, **88**, 1944. © 1984 American Chemical Society)

It has been the view of many chemists that ionizing radiation represents a ‘sledgehammer’ that will break molecules indiscriminately into a wide variety of products. However, it has become increasingly apparent that, for properly controlled systems, the products are often simpler and more readily predictable than those formed by UV light. Thus γ-rays may be used to produce a wide range of radicals and ions (equation 5 for example).

$$\mathrm{Me_2Te} \xrightarrow[\mathrm{CFCl_3},\ 77\,\mathrm{K}]{\gamma\text{-ray}} \mathrm{Me_2Te^+} \tag{5}$$

The ‘freon’ $CFCl_3$ is used as the solid host here since it has an ionization potential of ca. 11.8 eV, while the ionization potential of Me_2Te is 7.9 eV. Thus ionization of the guest is favored over that of the host.

3 METHODS OF DETECTION OF SHORT-LIVED INTERMEDIATES

This section addresses the question: how is it possible to obtain spectra of species whose lifetimes are only a small fraction of a second? It is only within the past 60 or so years that direct observation of short-lived molecules has been possible.

Nowadays such studies are relatively commonplace and three quite distinct methods are typically used: (i) flow techniques, (ii) flash photolysis, and (iii) matrix isolation. The oldest of these approaches is the flow method developed independently in the 1920s by Paneth, for demonstrating the existence and reactivity of gaseous free radicals, and by Hartridge and Roughton, for studying biochemical liquid-phase processes. Flash photolysis was first reported by Norrish and Porter in 1949, while matrix isolation, an invention of George Pimentel, was first used in 1953. To complement these methods, brief mention is made of two approaches that allow the presence of a reactive intermediate to be inferred without direct observation. These are (i) kinetic measurements and (ii) chemical trapping experiments, where a reagent is added to the reaction mixture, which forms a stable product with the intermediate and which is particularly characteristic of that intermediate.

3.1 Flow Techniques

If an unstable species is generated continuously in a flow system, its decay establishes steady-state concentrations that decrease with distance downstream from the point of generation. It is thus possible to detect spectroscopically the unstable intermediate, though, of course, the spectra will necessarily be complicated by the presence of unreacted reagents or carrier material. Flow methods may be used to look at unstable species in the gas phase or in solution. They are ideally suited to kinetic measurements since, if the velocity of the flow of gas or liquid is known, it is possible to measure the rate of decay of the species under investigation. Early experiments used UV–visible absorption or emission to monitor the species in the flow; however, such methods give only limited structural data. A more modern innovation is the use of tunable IR lasers to obtain high-resolution vibrational spectra.

Flow systems lend themselves to several other methods of detection. Radicals such as Me• or MeO• have been studied by flowing them through the cavity of an ESR spectrometer. The deflection of a beam of molecules in an electric field may give information about any permanent *Dipole Moment* of the species under investigation. Mass spectrometric detection and even structural measurements by gas electron diffraction may be made on the vapor.

It is pertinent to consider briefly the supersonic molecular beam. Here, a flow of gas is expanded through a nozzle into a vacuum in such a way that the flow diverges and becomes supersonic. As the gas expands, so the temperature falls, thus molecules within the beam may be studied at very low temperatures and essentially free from molecular interactions.

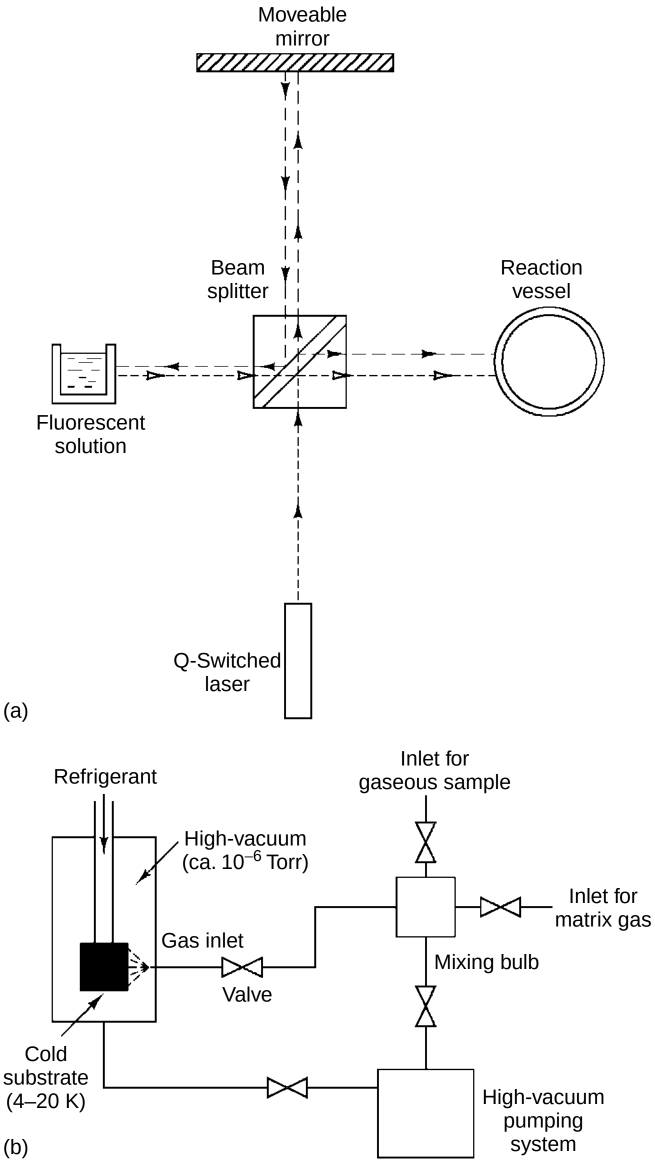

Figure 2 (a) An arrangement for nanosecond flash photolysis. (b) A schematic diagram of a matrix-isolation apparatus

3.2 Flash Photolysis

If a short-lived species is suddenly generated in a nonflowing sample it is possible to monitor the species spectroscopically some time after its generation, but before its decay is complete, provided that a very fast detection technique is available. Early systems used high-intensity UV lamps to generate the species and UV–visible spectroscopy to monitor their decay. Modern flash photolysis experiments generally use lasers. An arrangement for ‘nanosecond’ flash photolysis is shown schematically in Figure 2(a). In this case one laser only is used. Light from the laser initiates photolysis but some light is directed by means of a beam splitter to a vessel containing a fluorescent solution. Fluorescence from the solution gives a continuum of light over a region of the visible spectrum and this is used as the spectroscopic source for monitoring the decay of the reaction intermediates. It is possible to use a second (normally tunable) laser for this purpose. An IR laser can be used; thus it is possible to build up point-by-point IR spectra of the intermediates. However, the process is laborious. A large number of points are needed to cover even a relatively small part of the spectrum such as the ν(CO) region.

3.3 Matrix Isolation

This technique consists of trapping reactive molecules in a cold, solid, inert environment, where bimolecular reactions are prevented (provided that the sample is at sufficiently high dilution) and where the low temperatures greatly reduce the possibility of unimolecular decomposition.**[4]** In Figure 2(b) is shown a standard arrangement for a matrix-isolation apparatus. The low temperatures are often attained by the use of microrefrigerators using helium as the working fluid. The cold substrate, the nature of which depends upon the type of spectroscopy being used to monitor the sample, is enclosed in a shroud that is maintained at high vacuum.

Preparation of matrix-isolated samples generally follows one of two routes. Either the short-lived species is formed in the gas phase (by photolysis, pyrolysis, or the action of a discharge) then condensed with a large excess (typically thousandfold) of the matrix material, or a stable precursor is trapped within the matrix and the unstable species are generated in situ by photolysis or radiolysis.

Matrix isolation has the potential of tailoring the detection method to the problem. A large number of spectroscopic techniques are employed for matrix-isolated samples. Matrix isolation is thus an excellent method for studying the structures of short-lived molecules. However, it does have its drawbacks. Firstly, it can give no kinetic information. Secondly, the question must be asked: to what extent are species seen in a matrix analogous to those in more ‘normal’ chemical environments?

It is possible to address these points by studying reactive intermediates in low-temperature liquid solution, a typical solvent being liquid xenon. Here the molecules are retarded, rather than stopped so that, while conventional spectroscopic monitoring is possible, kinetic information about the species may also be obtained. In this way a ‘bridge’ is formed between flash photolysis work and matrix isolation.

4 STRUCTURAL INFORMATION FROM SPECTROSCOPIC MEASUREMENTS[5]

4.1 Nuclear Magnetic Resonance Spectroscopy

This technique is of immense potential importance but so far has been of very limited applicability towards short-lived intermediates. It is too slow for use in flash photolysis and there are extreme problems of sensitivity in matrix-isolation experiments. Although the feat of obtaining ^{1}H and ^{13}C nuclear magnetic resonance (NMR) spectra of stable matrix-isolated molecules was first achieved some time ago, it is only relatively recently that short-lived species have been detected in this way. Thus two-dimensional solid-state NMR has been used to study the intermediate 3,4-dimethylenethiophene (**4**) generated by photolysis of the parent diazo compound (**3**) in a 2-methyltetrahydrofuran glass at 77 K (equation 6).

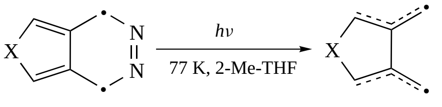

(6)

(**3**) a, X = S; b, X = O; • = ^{13}C (**4**)

It is not pertinent here to go into details of 2D NMR spectroscopy; such material is adequately covered elsewhere.**[6]** Suffice it to say that, in this instance, computer simulation of the dipolar coupled ^{13}C sideband patterns allowed estimates to be made of the C–H bond distances and the H–C–H bond angles. Such information is of extreme importance. A great shortcoming of matrix isolation is the lack of *Bond Length* information. Two techniques have been developed that will give these data: one is NMR, the other is extended X-ray absorption fine structure (EXAFS) (see Section 4.6).

4.2 Electron Spin Resonance (ESR) Spectroscopy

Electron Spin Resonance (ESR) spectroscopy is a very powerful method for studying species with *unpaired electrons*. It has been used to investigate short-lived intermediates in flow systems and in matrices. The two main data of interest from an ESR Experiment are the g values and the hyperfine splittings. The latter are important in providing information about the delocalization of the unpaired electrons within the molecule. For an electron with some s character, coupling between electron and nuclear spin magnetic moments occurs by the so-called Fermi contact interaction. Coupling to a single nucleus with spin $n/2$ gives $n+1$ lines that are of equal intensity and are equally spaced. Coupling to n equivalent nuclei of spin 1/2 again gives $n+1$ lines but here the intensities follow the binomial distribution. Low-temperature matrices are anisotropic systems; thus the situation is complicated in that both g values and hyperfine splitting constants must be considered as tensors. Three principal terms are obtained (for g values these may be labeled g_x, g_y and g_z). For systems with cubic or spherical symmetry these are equal; for those with at least axial symmetry there are two terms (labeled $g_{\parallel}$ and $g_{\perp}$); for lower symmetries all three terms are different. In Figure 3(a) is shown the ESR spectrum of the $^{15}N_2CO^+$ cation in a neon matrix at 4 K, formed by the reaction of CO^+ with $^{15}N_2$. Both parallel and perpendicular components can be seen: each forms a doublet of doublets, which points to the interaction of the unpaired electron with two inequivalent $I = 1/2$ ^{15}N nuclei. Thus, the structure of the cation may be deduced as (**5**).

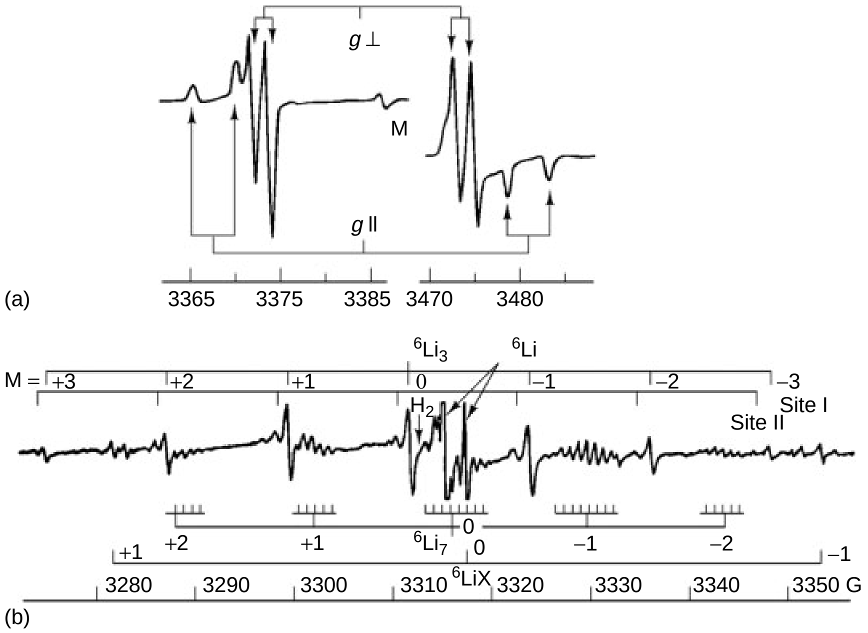

Figure 3 (a) ESR spectrum of the cation $^{15}N_2CO^+$ in a neon matrix at 4 K. (Reproduced by permission of the American Chemical Society from Knight Jr, *Acc. Chem. Res.*, 1986, **19**, 313) (b) ESR spectrum of pseudorotating $^6Li_3$ in an argon matrix at 28.5 K. (Reproduced by permission of American Institute of Physics from Garland and Lindsay, *J. Chem. Phys.*, 1983, **78**, 2814)

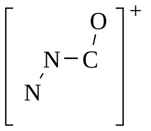

(5)

Figure 3(b) shows the ESR spectrum of the trimer $^6Li_3$ in an argon matrix at 28.5 K. Despite complications due to the presence of the heptamer $^6Li_7$ and an unknown impurity ^{6}LiX, seven equally spaced signals can be seen. These have the correct intensity ratio to belong to a molecule with three equivalent ^{6}Li nuclei ($I = 1$). It appears that the Li_3 trimer is rapidly pseudorotating in an argon matrix at this temperature; thus the system behaves as an isotropic one and only one set of g values are seen.

In this brief discussion, only radicals that have just one unpaired electron are mentioned. Obviously there are many systems that have several unpaired electrons but, especially for anisotropic systems, the ESR spectra for such species can be extremely complicated. More information on aspects of ESR spectroscopy of short-lived intermediates is given in two excellent reviews on the subject.[6,7]

4.3 Rotational Spectroscopy

For short-lived molecules this technique is only really of use for flow systems, where tunable lasers are employed to record high-resolution spectra; thus rotational fine structure can be seen. In Figure 4 is shown the high-resolution rotation–vibration spectrum, recorded using a tunable IR laser, of the Q-branch of the bending vibration of FO_2 prepared in a flow tube reaction. The band is centered near 578 cm^{-1} and the whole spectrum shown covers only 1.5 cm^{-1}. Analysis of the rotational fine structure of electronic bands is also possible. Much information about unstable diatomic molecules has been derived in this way: the rotation constant of a diatomic molecule may be calculated for each of many vibrational states of each electronic state involved in the transition. Much less information has been forthcoming for larger molecules, in part because it is difficult to attain the resolution needed to observe rotational fine structure on an electronic band in these cases. More fundamentally, the fine structure is often not defined because the excited state has a very short lifetime, with a consequent uncertainty in energy levels due to the uncertainty principle. By their nature, solid matrices are not amenable to rotational spectroscopy for the simple reason that all but the smallest molecules cannot rotate within these rigid media.

The most important use of rotational spectroscopy is the determination of rotation constants. A problem besetting rotational spectroscopy is centrifugal distortion; however, it is possible to take account of this if precise data over a range of quantum numbers is available.

Having once obtained rotational constants it is possible to define molecular structures via the corresponding moments of inertia. Both bond lengths and bond angles can be obtained, but the process is not always straightforward and, for polyatomics, can be laborious; detailed descriptions of these procedures are given by Hollas.[8]

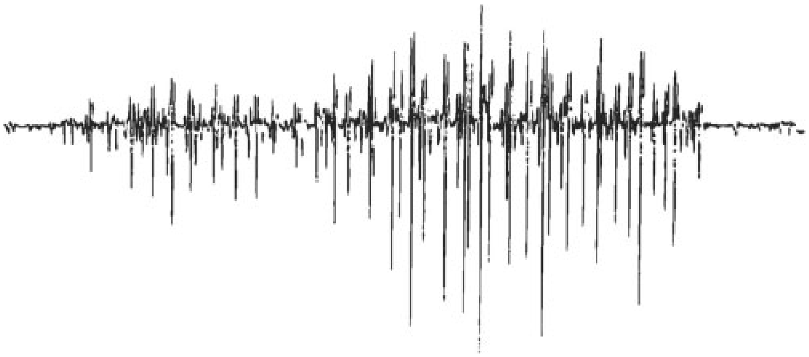

Figure 4 The Q-branch of the bending vibration of FO_2 prepared in a flow tube reaction. The band is centered near 578 cm^{-1} and the whole spectrum shown covers only 1.5 cm^{-1}. (Reproduced by permission of American Institute of Physics from Yamada and Hirota, *J. Chem. Phys.*, 1984, **80**, 4694)

Isotopic substitution may help us to obtain rotation constants. It also allows us to define atom positions within a molecule precisely (the effect of change of mass is small if the substituted atom is close to the center of mass, and zero if it is at the center of mass, for example, the rotation constants of BCl_3 are unaffected by the boron isotopic mass), and may confirm the presence of a particular type of atom in the molecule. This latter point is of particular value in studying unstable species where elemental analysis is impracticable. For example, in order to prove that a species under investigation is an oxide we may observe a shift in the position of rotational lines when ^{18}O replaces ^{16}O.

4.4 Vibrational Spectroscopy

Over the years, infrared (IR) absorption spectroscopy (*see Infrared Spectroscopy*) has been one of the mainstays of matrix isolation and it is nowadays being used increasingly (utilizing IR lasers) for monitoring the intermediates of flash photolysis reactions.

The main information to be obtained from IR spectroscopy concerns the presence of various groups within a molecule. Thus the presence of a nonclassically bound η^2-H_2 group in the complex $H_2Cr(CO)_5$ in low-temperature liquid xenon solution may be demonstrated by the presence of an IR band at ca. 3020 cm^{-1} corresponding to the ν(H–H) vibration.**[9]** Since the number of IR active vibrations depends upon the symmetry of the molecule under investigation, it is also possible to learn much about the number and geometry of groups within the molecule by analysis of the IR spectrum. A classical example is provided by matrix-isolated metal carbonyl fragments. Thus, for example, it should be straightforward to distinguish between C_{2v} (**6**) and D_{4h} (**7**) (*Square Planar*) symmetries for an $M(CO)_4$ fragment, since the former should show four IR active ν(CO) modes and the latter only one. However, the most unambiguous results are obtained when isotopic substitution is employed. For metal carbonyls partial enrichment in ^{13}CO is normally used, so that all isotopomers of the type $M(^{12}CO)_x(^{13}CO)_{n-x}$ are produced. For low values of n it is a relatively easy matter to determine the identity of the $M(CO)_n$ fragment from the spectra of the isotopic species. The molecule chromyl carbonyl, $O_2Cr(CO)_2$ (**8**), has a nonlinear C_{2v} $Cr(CO)_2$ fragment. Thus, the IR spectrum of the molecule, when enriched 50% in ^{13}CO, shows two triplets of bands each with a 1:2:1 intensity ratio, corresponding to the symmetric and antisymmetric ν(CO) modes of the $Cr(^{12}CO)_2$, $Cr(^{12}CO)(^{13}CO)$, and $Cr(^{13}CO)_2$ isotopomers.**[10]**

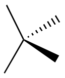

(**6**) C_{2v}

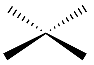

(**7**) D_{4h}

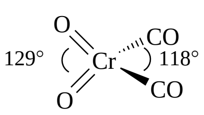

(**8**)

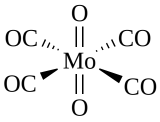

(**9**)

For more complex examples, it is necessary to model the IR spectrum using different possible geometries for the $M(CO)_n$ fragment and estimated stretching and interaction force constants. If the $M(CO)_n$ fragment has high symmetry, the results are usually unambiguous, for example, the square planar structure of the $Mo(CO)_4$ fragment of *trans*-$O_2Mo(CO)_4$ (**9**) is clear from the results of ^{13}CO substitution.**[11]** For this experiment, different degrees of ^{13}CO enrichment (33, 55, and 65%) were used. As shown in Figure 5, the spectra obtained can clearly be used to distinguish between a D_{4h} $M(CO)_4$ and D_{3h} $M(CO)_3$ fragments, either of which geometries would account for the IR spectrum of the unenriched molecule. For less symmetric species, unambiguous results may be obtained, though here it is necessary to pay careful attention to the matching of both the intensities and positions of peaks in the observed and calculated spectra.

Bond angles may be calculated from IR spectra in two distinct ways: (i) intensity measurements and (ii) isotopic shift calculations. For a molecule such as $O_2Cr(CO)_2$ (**8**), it is a relatively simple matter to calculate the C–Cr–C bond angle

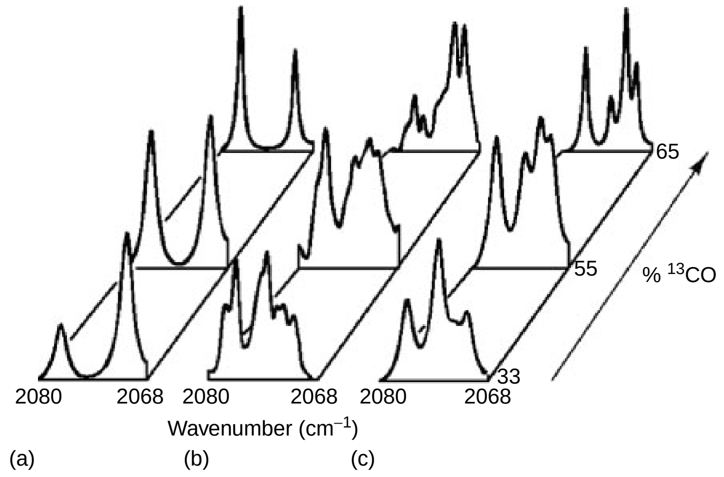

Figure 5 Stacked plot showing observed and predicted IR absorption spectra for *trans*-$O_2Mo(CO)_4$ in the region 2068–2080 cm^{-1} upon 33, 55, and 65% ^{13}CO enrichment: (a) predicted spectrum assuming a D_{3h} $Mo(CO)_3$ moiety; (b) observed spectrum; (c) predicted spectrum assuming a D_{4h} $Mo(CO)_4$ moiety. (Reprinted with permission from Ref. 11a. © 1984 American Chemical Society)

(θ). If we assume that there is no coupling between ν(CO) and any other vibration in the molecule, then we may estimate the bond angle from measured intensities of the bands arising from the symmetric and antisymmetric carbonyl stretching fundamentals using the relationship

$$\frac{I_{\text{sym}}}{I_{\text{asym}}} = \tan^2(\theta/2) \tag{7}$$

Nor is it difficult to modify this procedure to take account of the motion of a central atom, for example, to estimate the Mn–O–Mn bond angle (θ) of the O-bridged molecule Mn_2O_7. Here θ is calculated from the intensities of symmetric and antisymmetric ν(Mn–O–Mn) fundamentals using the relationship

$$\frac{I_{\text{asym}}}{I_{\text{sym}}} = \tan^2(\theta/2)\left[\frac{(m(\text{O}) + 2m(\text{Mn})\sin^2(\theta/2))}{(m(\text{O}) + 2m(\text{Mn})\cos^2(\theta/2))}\right] \tag{8}$$

where m(O) and m(Mn) are the atomic masses of oxygen and manganese, respectively. For Mn_2O_7, this value will be somewhat inaccurate because of coupling between bridging and terminal ν(Mn–O) vibrations. It is also rendered somewhat inaccurate by the anharmonicity of the vibrations involved.

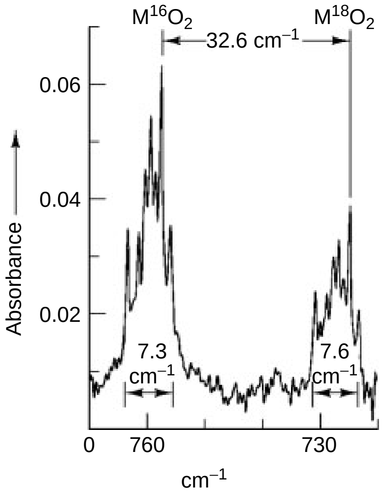

Figure 6 The 780–720 cm^{-1} of the IR absorption spectrum of *trans*-$O_2Mo(CO)_4$. The two bands are assigned to $\nu_{\text{as}}(^{16}\text{O}{=}\text{Mo}{=}^{16}\text{O})$ and $\nu_{\text{as}}(^{16}\text{O}{=}\text{Mo}{=}^{16}\text{O})$. Both clearly exhibit Mo isotope structure. (Reprinted with permission from Ref. 11a © 1984 American Chemical Society)

This last point is emphasized if we rely upon shifts in peak position upon isotopic substitution to calculate bond angles. It is possible to calculate the A–B–A bond angle of a molecule A_2B by isotopic substitution of either A or B. In Figure 6 is shown the IR spectrum arising from the antisymmetric $\nu(MoO_2)$ vibration of matrix-isolated (**9**), ca. 45% enriched in $^{18}O_2$. The isotopic splittings due to the natural abundance of the isotopes of Mo and due to $^{16}O_2$ and $^{18}O_2$ can be seen. It is possible to calculate O–Mo–O bond angles from either isotope splitting assuming that the O–Mo–O group behaves as an isolated harmonic triatomic oscillator. In fact, the observed frequencies are necessarily anharmonic. Thus, the isotopic substitution

$$^{16}\text{OMo}^{16}\text{O} \longrightarrow {}^{18}\text{OMo}^{18}\text{O} \tag{9}$$

gives an upper limit θ_u for the bond angle from

$$\sin\left(\frac{\theta_{\text{u}}}{2}\right) = \left[\frac{m(\text{Mo})\{m(^{16}\text{O}) - m(^{18}\text{O})R_1\}}{2(m(^{16}\text{O}))(m(^{18}\text{O}))(R_1 - 1)}\right]^{1/2} \tag{10}$$

where $m(\mathrm{X})$ is the atomic mass of X and

$$R_1 = \left[\frac{\nu(\mathrm{Mo}^{18}\mathrm{O}_2)}{\nu(^{16}\mathrm{MoO}_2)}\right]^2 \tag{11}$$

Similarly, the isotopic substitution

$$\mathrm{O}^x\mathrm{MoO} \longrightarrow \mathrm{O}^y\mathrm{MoO} \tag{12}$$

gives a lower limit, θ_1, from

$$\sin\left(\frac{\theta_1}{2}\right) = \left[\frac{(m(^x\mathrm{Mo}))(m(^y\mathrm{Mo}))(1 - R_2)}{2(m(\mathrm{O}))\{R_2(\mathrm{M}(^y\mathrm{Mo})) - m(^x\mathrm{Mo})\}}\right]^{1/2} \tag{13}$$

where

$$R_2 = \left[\frac{\nu(^y\mathrm{MoO}_2)}{\nu(^x\mathrm{MoO}_2)}\right]^2 \tag{14}$$

As well as providing information on bond angles, isotopic substitution experiments may tell us about the mode of coordination of atoms within a molecule. Again the example taken is that of oxo species although, of course, the technique may as well be applied to other chemical entities. For oxo species it is necessary to distinguish between the modes of coordination (**10**), (**11**), and (**12**), where M = metal or other atom. Typically, (**10**) shows ν(O–O) in the region 1000–1200 cm^{-1}, whereas ν(O–O) and ν(M=O) of (**11**) and (**12**), respectively, both occur in the typical range 750–1000 cm^{-1}, at least when M is a transition metal. A clear distinction between (**10**), (**11**), and (**12**) may be made by enrichment of the molecules with ^{18}O. Structure (**10**) is easily distinguished since two IR bands result from ν(O–O) of the mixed $^{16}\mathrm{O}^{18}\mathrm{O}$ isotopomers owing to the possibility of two distinct modes of coordination, that is, M–^{16}O–^{18}O and M–^{18}O–^{16}O. The IR spectra shown in Figure 7 illustrate this point for the molecule cyclopentadiene-*O*-oxide (**14**), formed when (**13**) is subjected to photolysis in a 10% O_2-doped N_2 matrix. To distinguish between (**11**) and (**12**) is again more difficult. In principle, (**12**) should show two ν(M=O) absorptions but (**11**) should show only one ν(O–O) absorption. In practice, often only one ν(M=O) band is seen for (**12**) either because one feature is obscured, or because $\nu_{\mathrm{sym}}(\mathrm{MO}_2)$ is weak owing to a wide O–M–O bond angle. When generated from a mixture of $^{16}\mathrm{O}_2$, $^{16}\mathrm{O}^{18}\mathrm{O}$, and $^{18}\mathrm{O}_2$, however, the absorption associated with ν(O–O) of (**11**) takes the form of a single symmetrical triplet; under similar circumstances, (**12**) is expected to display one or two unsymmetrical triplets, derived from the antisymmetric and symmetric MO_2 stretching fundamentals. The unsymmetrical pattern results from strong coupling between the two stretching modes of the $^{16}\mathrm{O}$=M=$^{18}\mathrm{O}$ unit since the reduction in local symmetry allows mixing between the two stretching vibrations that otherwise (on symmetry grounds) cannot mix. The effect is illustrated schematically in Figure 8.

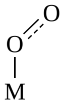

(**10**)

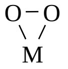

(**11**)

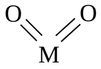

(**12**)

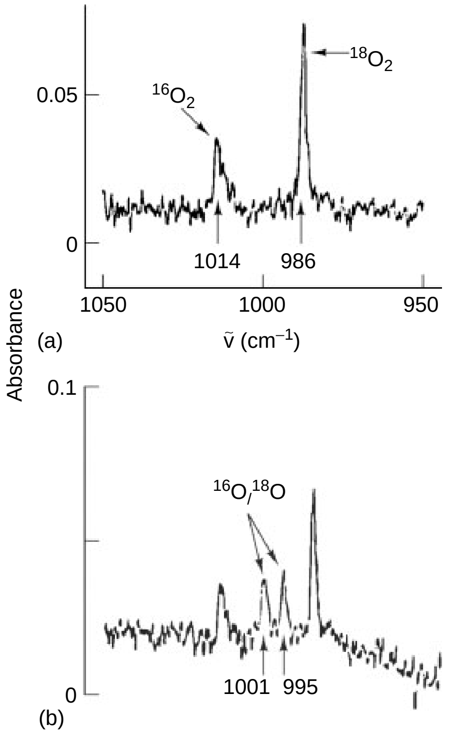

Figure 7 IR spectra recorded after photolysis of diazocyclopentadiene in O_2-doped N_2 matrices: (a) $^{16}\mathrm{O}_2$ and $^{18}\mathrm{O}_2$ present; (b) $^{16}\mathrm{O}_2$, $^{16}\mathrm{O}^{18}\mathrm{O}$ and $^{18}\mathrm{O}_2$ present. (Reproduced by permission of The Royal Society of Chemistry from Bell *et al.*, *J. Chem. Soc., Chem. Commun.*, 1983, 1213)

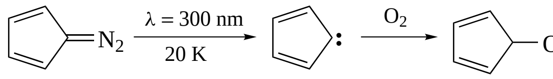

(**13**) (**14**)

It is always desirable to back up IR absorption spectroscopy with *Raman* measurements. The different selection rules for the two techniques means that, at least for symmetric species, it is often necessary to have data from both types of measurement to have a full picture of the vibrational spectrum. Raman spectroscopy has been used to study many matrix-isolated species although there are problems regarding intensity and photosensitivity. An excellent review exists on the subject that highlights both the applications and difficulties of the method.**[12]** A molecule that has been well characterized by both IR and Raman spectroscopy is the matrix-isolated species $\mathrm{Mo(CO)_5(N_2)}$ (**15**).**[13]** Spectra for (**15**) are illustrated

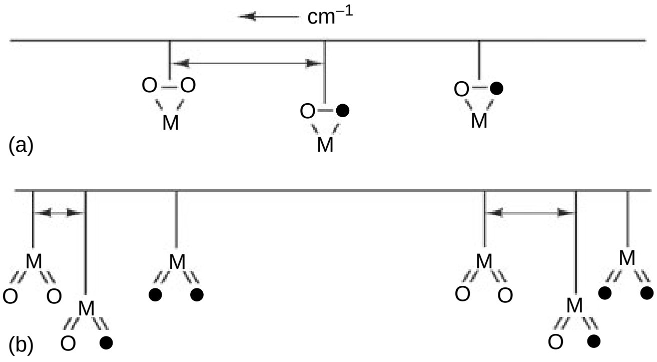

Figure 8 Predicted ^{18}O isotopic splitting patterns in the IR spectra of (a) the ν(O–O) band of a dioxygen complex and (b) the symmetric and antisymmetric ν(M=O) bands of a bent dioxometal complex assuming a scrambled 1:2:1 $^{16}O_2$, $^{16}O^{18}O$, $^{18}O_2$ mixture (O = ^{16}O, ● = ^{18}O)

in Figure 9. From the coincidence of the two a_1 ν(CO) modes (assigned to the a_1 symmetry class on the basis of polarization studies on the Raman lines) and the noncoincidence of the other two ν(CO) features, C_{4v} symmetry was assigned to the molecule, implying the structure (**15**) with a linear Mo–N–N unit.

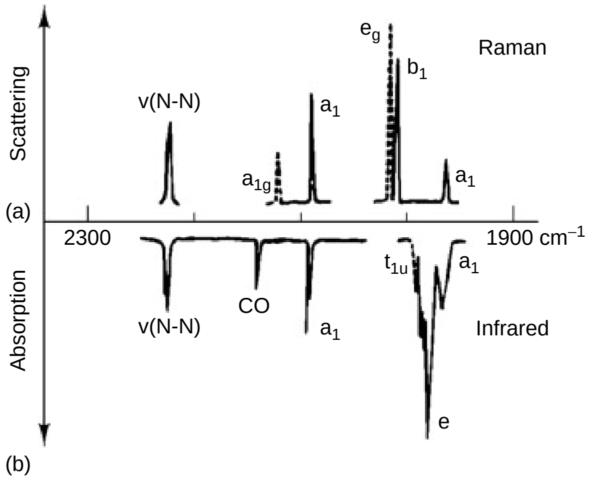

Figure 9 (a) Raman and (b) IR spectra of matrix-isolated $MO(CO)_5(N_2)$. The peaks drawn as dashed lines are due to unreacted $Mo(CO)_6$. (Reprinted with permission from Ref. 13 © 1978 American Chemical Society)

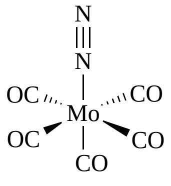

(**15**)

4.5 Electronic Spectroscopy

Electronic spectroscopy (*see Electronic Spectroscopy*), in one form or another, has been the principal method used for the detection of short-lived intermediates. UV–visible absorption was the initial spectroscopic method used with flash photolysis and flow systems, and for each of these methods it remains the most commonly used approach. For species in low-temperature matrices, many varieties of electronic spectroscopy have been used. These include UV–visible absorption and emission, fluorescence, magnetic circular dichroism (MCD) and magnetic linear dichroism, and photoelectron spectroscopy. It is unfortunate, therefore, that in many cases electronic spectroscopy yields little or no structural information. The exceptions are high-resolution spectra, where vibrational or rotational fine structure may be seen.

4.6 Extended X-ray Absorption Fine Structure (EXAFS)

EXAFS (*see Extended X-ray Absorption Fine Structure*) has been used to study a number of matrix-isolated species. EXAFS occurs when an X-ray photon with sufficient energy is absorbed by an atom so that a core electron is ejected. This electron may be represented as an outgoing spherical wave originating at the absorbing atom. If the atom has neighbors, backscattering from them causes interference with the outgoing wave. The outcome is that there are variations in the absorption coefficient that depend on the spatial relationship of the central atom and its neighbors. Thus, by measuring the EXAFS spectrum it is possible to measure bond distances and angles around the central atom. The EXAFS experiment involves measuring the absorption spectrum in the vicinity of the absorption edge for the chosen element. Almost universally, synchrotron radiation is used as the source. EXAFS has been used to study various matrix-isolated metal clusters; the first example of a combined in situ Fourier transform infrared (FTIR) and EXAFS study of a matrix-isolated molecule was reported for dibromomethane, (CH_2Br_2). This work has now been extended to a number of metal carbonyl halide and other molecules.**14** In Figure 10 is given the EXAFS spectrum and Fourier transforms for $FeCl_2$ isolated in solid CO; the observed curves are compared with calculated curves for the molecule *trans*-$Fe(CO)_4Cl_2$ (**16**). A very good fit is obtained; thus bond lengths may be calculated: Fe–C, 1.85(3) Å Fe–O, 2.96(4) Å; Fe–Cl, 2.25(3) Å. As with NMR, the allure of this method lies in deriving of bond lengths for matrix-isolated species.

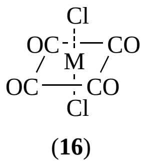

(**16**)

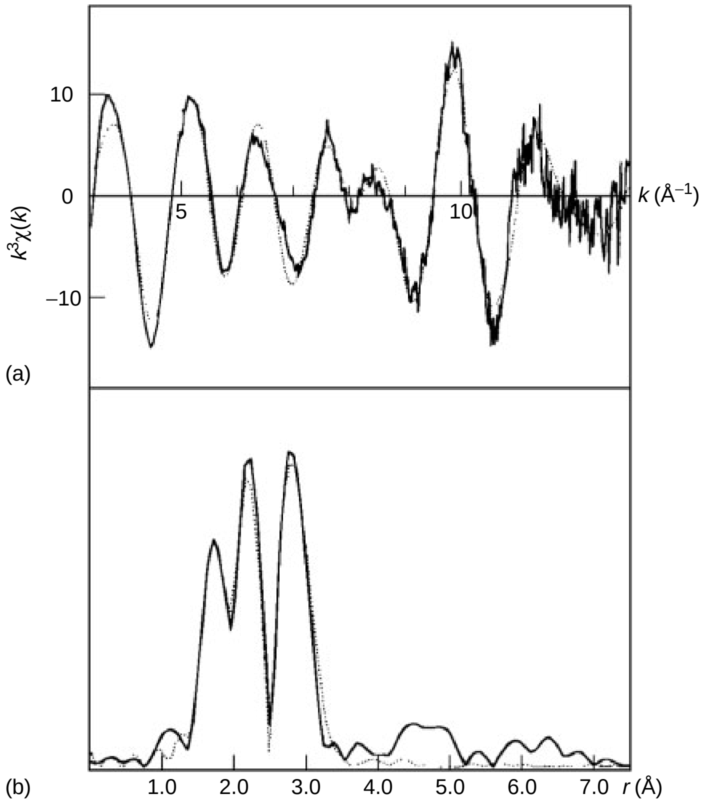

Figure 10 (a) EXAFS spectrum and (b) Fourier transforms for $FeCl_2$ isolated in solid CO: (—) experiment; (· · ·) curved wave multiple scattering theory for *trans*-$Cl_2Fe(CO)_4$. (Reprinted with permission from Ref. 14. © 1992 American Chemical Society)

4.7 Mössbauer Spectroscopy

Mössbauer spectroscopy (*see Mössbauer Spectroscopy*) has been used to look at a number of matrix-isolated species. However, the absence of structural information makes it appropriate to combine Mössbauer spectroscopy with other methods. Peden *et al*. report combined IR and Mössbauer spectra for the products of condensing iron vapor with CO: $Fe(CO)_x$ ($x = 1–5$) and $Fe_2(CO)_y$ ($y = 8$ or 9). The Mössbauer spectra also reveal the presence of unreacted iron atoms in the solid CO, which, of course, cannot be seen in IR absorption.

4.8 Quantum Calculations

Most current matrix-isolation studies involve the use of computational calculations to back up experimental results. It is beyond the scope of this chapter, however, to discuss these in any detail. Such calculations, typically using ab initio methods although sometimes adopting the density functional approximation, are used not only to model stable molecules, but also short-lived intermediates and transition states. In this way calculations may provide information about molecules and reactions that is impossible to obtain through experiment alone. In other cases calculations are used to back up, or confirm experimental findings. Typically geometries, energies and vibrational frequencies and intensities are calculated for a species of interest. A number of specific examples are quoted in the following sections of this chapter.

5 PHOTOCHEMISTRY OF TRANSITION METAL CARBONYLS

It is not surprising that transition metal carbonyls rank amongst the most well-studied of photochemical reactants (*see* ***Photochemistry of Transition Metal Complexes: Theory***). They are almost ideal candidates for such work since they have high quantum yields for photochemical reactions (in particular for substitution of carbonyl groups). They also show UV absorptions with large extinction coefficients and are strong IR absorbers and Raman scatterers (especially in the 1600–2200 cm^{-1} region, associated with CO stretching fundamentals), so that electronic and vibrational spectroscopy can readily be applied to monitor reactions of these molecules. Moreover they are generally volatile and readily soluble in nonpolar solvents so that sampling is rarely a problem.

There are very many known photochemical reactions of metal carbonyls; two classic examples are the substitution of a CO group by a donor ligand, for example, a phosphine:

$$Cr(CO)_6 + PPh_3 \xrightarrow[\text{cyclohexane}]{h\nu} Cr(CO)_5PPh_3 + CO \qquad (15)$$

and the deposition of solid $Fe_2(CO)_9$ when solutions of $Fe(CO)_5$ are irradiated:

$$2Fe(CO)_5 \xrightarrow[\text{glacial acetic acid}]{h\nu} Fe_2(CO)_9 + CO \qquad (16)$$

Some of the earliest systematic studies of related reactions were carried out in the early 1960s by Sheline and his coworkers at Florida State University. They studied the replacement of carbonyl groups of metal carbonyls by electron donor and *π-acceptor* molecules; a further aim was to develop an understanding of the mechanism of such reactions. They found that exposure to UV light of a colorless solution of $W(CO)_6$ in n-hexane containing acetonitrile resulted in the solution turning bright yellow almost immediately. At the same time, new IR absorptions in the 1700–2200 cm^{-1} region appeared that could be assigned to the molecules $W(CO)_5(MeCN)$, $W(CO)_4(MeCN)_2$, and $W(CO)_3(MeCN)_3$. Not surprisingly, the distribution of these products was affected by the time of photolysis. After 20 s, $W(CO)_5(MeCN)$ was the principal product and only a low yield of $W(CO)_3(MeCN)_3$ was seen. The yield of $W(CO)_3(MeCN)_3$ was increased substantially if the photolysis time was increased to 150 s. Perhaps more interesting is the observation that $W(CO)_6$ is regenerated if the photolyzed solution is allowed to stand unphotolyzed for 180 s. These workers postulated that the 16-electron intermediate $W(CO)_5$ is involved in the reaction. However, other plausible interpretations are possible. Firstly, an associative or a dissociative mechanism could operate. Secondly, if a dissociative mechanism is preferred, it is conceivable that this could proceed via a radical or an ionic pathway. The observations of Sheline *et al.* provided circumstantial evidence in favor of the radical dissociative process. What was needed was firm evidence to establish the presence of the pentacarbonyl intermediate.

5.1 The Search for 'Unsaturated' Metal Carbonyl Molecules

Early experiments to search for the $Cr(CO)_5$ molecule involved flash photolysis of cyclohexane solutions of $Cr(CO)_6$ with UV–visible detection. Problems arose owing to impurities in the solvent interacting with unsaturated intermediates. Although some evidence was obtained for 'naked' $Cr(CO)_5$ it was not possible to confirm the existence of this species nor to distinguish between square pyramidal, C_{4v} (**17**), and trigonal bipyramidal, D_{3h} (**18**), geometries (*see Isomer, Types of*).

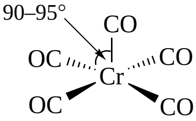

(**17**)

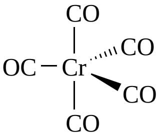

(**18**)

These findings indicate general difficulties in interpreting the results of flash photolysis experiments with UV–visible detection. First, no detailed structural information can be obtained. Second, minute traces of impurity in the solvent interfere strongly with the spectral behavior. It has now become clear that $Cr(CO)_5$ (and other unsaturated carbonyls) are almost always complexed by solvent or matrix molecules or atoms. Even in a neon matrix there is some interaction to produce the species $Ne\cdots Cr(CO)_5$. 'Naked' $Cr(CO)_5$ can be made in the gas phase, and by some rather cunning time-resolved solution experiments. Here, solvated $Cr(CO)_5$ is formed by UV photolysis of $Cr(CO)_6$, then the solvating molecule is removed by visible photolysis. Fast time-resolved spectroscopy allows the decay of the naked $Cr(CO)_5$, as it resolvates, to be monitored. It is clear that this decay is extremely rapid.

The use of tunable IR lasers means that nowadays structural information is more readily derived from flash photolysis experiments, and it is often of much interest to study molecular interactions of metal carbonyls in solution. It is now possible to make an estimate of the strengths of alkane$\cdots$Cr bonds in species such as $(CO)_5Cr\cdots X$ (X = alkane). Even neutral saturated metal carbonyls may show quite strong solvent interactions and such interactions may provide clues to any subsequent photochemical reactions. IR spectra have been obtained that provide strong evidence for intermolecular H-bonding between the 18-electron species $[Cp^*Ir(CO)_2]$ and the sterically crowded fluoroalcohol $(C_3F_7)(CF_3)_2COH$ in n-heptane solution (**19**).[15] A similar interaction might explain why O–H activation of MeOH is seen upon UV photolysis of cryogenic liquid xenon solutions of MeOH and $[Cp^*Ir(PMe_3)H_2]$.

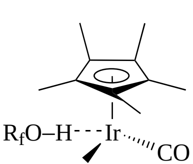

(**19**)

It is still of much interest to consider the early experiments in which molecules such as $Cr(CO)_5$ were studied in hydrocarbon glasses and inert gas matrices, since it is from these experiments that structural data on these species (albeit necessarily in their weakly solvated forms) was derived. IR detection of $M(CO)_5$ (M = Cr, Mo, or W) molecules trapped in a frozen hydrocarbon glass at 100 K showed three IR active ν(CO) absorptions whose relative intensities are indicative of C_{4v} symmetry (**17**) for the species. The effect of any possible distortion may be minimized by moving to a frozen inert gas matrix. In 1971, Graham, Poliakoff, and Turner published the results of experiments in which they succeeded in producing $M(CO)_5$ molecules by photolysis of $M(CO)_6$ in argon or methane matrices at 20 K. A pattern of IR bands corresponding to C_{4v} (**17**) symmetry for the molecules was again seen. A detailed analysis of the IR spectrum of $Cr(CO)_5$ produced on photolysis of randomly substituted $Cr(^{13}CO)_x(^{12}CO)_{6-x}$ containing ca. 50% ^{13}CO gave an accurate fit to a C_{4v} structure. From intensity data, axial–radial bond angles (α) of 90–95° were calculated.

Even in such an inert environment it soon became clear that the $M(CO)_5$ molecules are not completely free from interaction with the host material. On moving from a frozen hydrocarbon glass to a methane matrix the shifts in the position of the IR bands of $Cr(CO)_5$ are relatively modest (4–6 cm^{-1}). By contrast, quite a large shift in the position of the visible band of $Cr(CO)_5$ is seen upon changing the host material. This feature is centered at 489 nm when methane is employed as host, but shifts to 487 nm for xenon, 545 nm for argon, 560 nm for sulfur hexafluoride, and a high value of 624 nm for neon. In a mixed Ne/Xe matrix, two bands are seen, demonstrating that a specific interaction with each noble gas occurs since a generalized solvent effect would lead to a single absorption located somewhere between the positions of the absorptions in the pure matrices. Photochemical experiments show that a reversible photochromic reaction takes place (equation 17). It is presumed that neon has the weakest interaction with the metal carbonyl fragment and therefore that the situation in a neon matrix most closely resembles the gas phase.

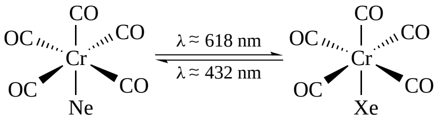

λ_{max} = 628 nm λ_{max} = 487 nm (17)

It is possible to make naked $Cr(CO)_5$ in the gas phase. Pulsed laser excitation at 249 nm of $Cr(CO)_6$ vapor yields $Cr(CO)_5$ and CO. Time-resolved IR spectroscopy reveals that the structure of gaseous $Cr(CO)_5$ is the same as that adopted in a solid matrix, that is, (**17**). Thus, the square pyramidal structure for ground state $Cr(CO)_5$ is confirmed. Photons of wavelength 249 nm are sufficiently energetic to rupture more than one M–C bond. Thus, after only 0.5 µs, the yield of $Cr(CO)_5$ decays and $Cr(CO)_4$ is seen as the principal product. If the wavelength of the exciting radiation is reduced to 193 nm then a high yield of $Cr(CO)_3$ is seen after 0.5 µs. The gaseous molecules $Cr(CO)_4$ and $Cr(CO)_3$ are found to adopt C_{2v} (**20**) and C_{3v} (**21**) symmetries, respectively.

It is rather more difficult to generate high yields of the molecules $M(CO)_4$ and $M(CO)_3$ (M = Cr, Mo, or W) in a

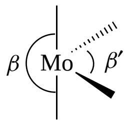

(**20**)

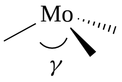

(**21**)

low-temperature matrix since energy transfer is much more efficient than in low-pressure gas-phase systems. Prolonged photolysis is required, but the molecules may be produced and isotopic studies using ^{13}CO show that the structures of these molecules are the same as in the gas phase. For $Mo(CO)_4$, the angles β and β' are calculated as 174° and 107°, respectively; for $Mo(CO)_3$ $\gamma = 105°$.

It is of interest to compare the structure of the d^6 molecule $Mo(CO)_4$ with that of the d^8 species $Fe(CO)_4$ generated by UV photolysis of matrix-isolated $Fe(CO)_5 \cdot {}^3Fe(CO)_4$ also adopts C_{2v} symmetry with $\beta = 150°$ and $\beta' = 120°$. A simple consideration of the d orbital splitting pattern for a d^8 species of C_{2v} symmetry suggests the presence of two unpaired electrons; this hypothesis was proved by the experimental observation of a temperature-dependent MCD spectrum for $Fe(CO)_4$ (diamagnetic species do not show any temperature dependence of their MCD signals). Thus, $Fe(CO)_4$ is the first binary transition metal carbonyl shown to have a high-spin electronic ground state. An interesting point about the structures of these unsaturated metal carbonyls is that none of them are much distorted from the structures that would be obtained by selective removal of CO groups from an octahedron. It is possible that an overriding factor in determining these structures is the maximization of overlap between filled ligand orbitals and unfilled metal d orbitals (*see High-spin & Low-spin Compounds* and *Ligand Field Theory*).

Differences between matrix-isolation and gas-phase photochemistry become more distinct when dinuclear and trinuclear carbonyls are considered. For a simple metal–metal bonded dinuclear carbonyl such as $Mn_2(CO)_{10}$, two primary photochemical steps are possible, namely M–CO dissociation or M–M bond rupture. In solution both processes occur, whereas in rigid media CO loss is seen as the sole discernible primary photolysis step, presumably because $Mn(CO)_5$ radicals readily recombine in the matrix cage. In argon matrices, photolysis of $Mn_2(CO)_{10}$ yields $Mn_2(CO)_9$, a molecule with a semibridging carbonyl group (with ν(CO) at 1764 cm^{-1}) that is shown by polarization studies to lie at about 45° to the Mn–Mn axis (**22**). By contrast, $Re_2(CO)_{10}$ gives rise to two unbridged isomers of $Re_2(CO)_9$ with the CO vacancy in equatorial (**23a**) or axial (**23b**) positions. The two isomers may be interconverted by UV irradiation. In a similar vein, $M_3(CO)_{12}$ (M = Fe or Ru) molecules, when trapped in methylcyclohexane glass at 90 K, show CO loss as the primary photolytic step, although the reaction sequence is complicated by the presence of different isomers of the photoproduct $M_3(CO)_{11}$. By contrast, in hydrocarbon solution, photofragmentation of the cluster takes place. In fluid media, bimolecular reactions involving large fragments may occur, which are prevented in rigid matrices. An example is provided by the formation of a species $Cr_2(CO)_{10}$ (whose structure remains unknown) upon photolysis of gaseous $Cr(CO)_6$, presumably by a reaction of the type

$$Cr(CO)_6 + Cr(CO)_4 \longrightarrow Cr_2(CO)_{10} \qquad (18)$$

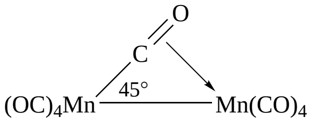

(22)

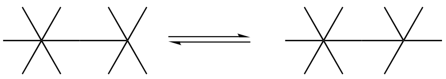

(23a) **(23b)**

The photochemistry of more complex carbonyls that contain ligands other than CO has been studied in some detail. Time-resolved IR spectroscopy has been used to study the photochemistry of the dinuclear carbonyl $[CpFe(CO)_2]_2$ (*see Cyclopentadienyl*) in solution and the results of these experiments have been compared with those obtained from earlier matrix-isolation work.**16**

In a CH_4 matrix at 12 K, (**24**) yields, upon UV photolysis, the CO-bridged dimer (**25**). When (**24**) is subjected to flash photolysis in cyclohexane solution at room temperature, time-resolved IR studies show that both (**25**) and the mononuclear radical $[CpFe(CO)_2]$ are formed within 5 µs. The radical has a half-life of <25 µs while (**25**) has a half-life of 1.5 ms under the experimental conditions. If the cyclohexane solution is doped with the two-electron donor molecule MeCN it is possible to monitor the formation of the substitution product $[Cp_2Fe_2(CO)_3L]$ (L = MeCN) (equation 19).

$$[CpFe(CO)_2]_2 + L \xrightarrow[\text{cyclohexane}]{h\nu} [Cp_2Fe_2(CO)_3L] + CO \qquad (19)$$

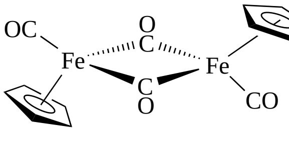

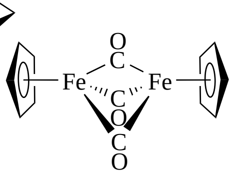

(24) **(25)**

Kinetic studies, as illustrated by the spectra in Figure 11, leave little doubt that the principal intermediate in the photosubstitution is not the radical but rather the dinuclear species (**25**). This situation is not true, however, for all ligands. When the hydrocarbon solution is doped with the phosphine $P(OMe)_3$ in place of MeCN, a reaction with the radical is seen:

$$[CpFe(CO)_2] + P(OMe)_3 \longrightarrow [CpFe(CO)\{P(OMe)_3\}] + CO \qquad (20)$$

The different pathways are reflected by the magnitudes of the bimolecular rate constants at 25 °C: L = MeCN, $k_2 \sim 7.6 \times 10^5\ dm^3\ mol^{-1}\ s^{-1}$; L = $P(OMe)_3$, $k_2 \sim 8.9 \times 10^8\ dm^3\ mol^{-1}\ s^{-1}$. The latter value is only about one order of magnitude slower than the diffusion controlled limit. These studies show the value of time-resolved IR spectroscopy for obtaining kinetic data.

When the photochemistry of carbonyls that also contain ligands other than CO is considered, it is not always the case that loss of CO predominates as the principal reaction pathway. For example, irradiation of $[CpMo(CO)_3Et]$ (M = Mo or W) generates $[CpM(CO)_3H]$ by loss of C_2H_4 (*see Alkene Complexes*). Scheme 1 presents a plausible mechanism for this process, which has been studied in *n*-heptane solution by time-resolved IR spectroscopy and in low-temperature matrices. Two distinct dicarbonyl species (**26**) and (**27**) are seen. In a matrix, (**26**) and (**27**) may be interconverted by photolysis at selected wavelengths. The reaction then proceeds via cis and trans isomers of $[CpM(CO)_2(C_2H_4)H]$. The results suggest that, in this system, β-hydrogen transfer is a facile process; they have important implications for the current interest in *agostic* hydrogen interactions.

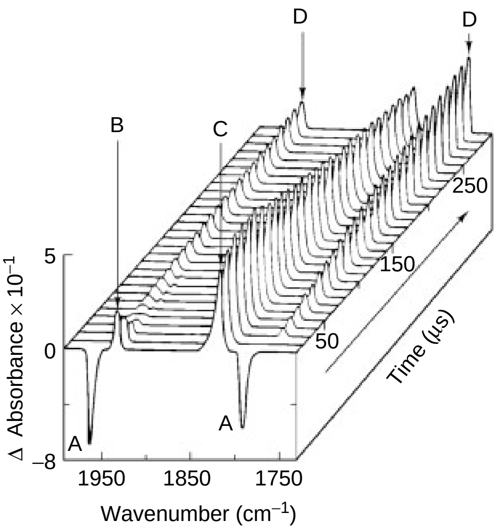

Figure 11 Time-resolved IR spectrum obtained after flash photolysis of $[CpFe(CO)_2]_2$ and MeCN in cyclohexane solution. Two intermediates, B = $CpFe(CO)_2$ and C = $CpFe(\mu\text{-}CO)_3$, are seen. D is the reaction product $Cp_2Fe_2(CO)_3(MeCN)$. (Reproduced by permission of The Royal Society of Chemistry from Dixon *et al.*, *J. Chem. Soc., Chem. Commun.*, 1986, 994)

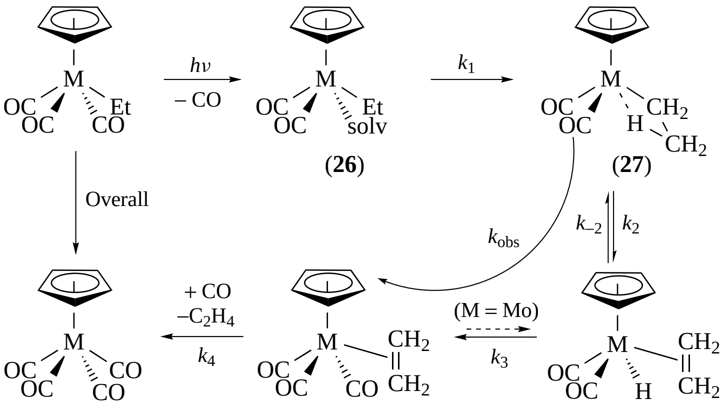

Scheme 1 Photochemistry of [CpMEt(CO)$_3$](M = Mo, W)

5.2 Reactions of Unsaturated Metal Carbonyls with CO, N$_2$, and H$_2$

Unsaturated metal carbonyls are necessarily prone towards addition reactions. Thus 16-electron species such as $M(CO)_5$ (M = Cr, Mo, or W) and $Fe(CO)_4$ will readily react with two-electron donor ligands. A large number of such reactions are known. Here details of three examples are considered, namely, the addition of CO, N_2, and H_2 molecules (*see **Hydride Complexes of the Transition Metals***).

Sheline's early experiments showed that $M(CO)_6$ molecules could be regenerated when photolyzed solutions of the hexacarbonyl were left to stand. Matrix-isolated $M(CO)_6$ may be obtained from $M(CO)_5$ only by annealing or upon *photolysis* into the visible absorption band of the pentacarbonyl:

$$M(CO)_5 + CO \xrightarrow{h\nu\text{(visible) or anneal}} M(CO)_6 \qquad (21)$$

The mechanism of the photochemical reaction has been the subject of some elegant experiments involving polarized light both for photolysis and for spectroscopic measurements.[17] Unpolarized UV photolysis of $Cr(CO)_6$ in pure methane matrices yields randomly oriented $Cr(CO)_5\cdots CH_4$ molecules. Polarized visible photolysis leads to specifically oriented $Cr(CO)_5\cdots CH_4$ molecules, as evidenced by the development of linear dichroism in the visible absorption band. The direction of the spectral dichroism depends upon the direction of polarization of the irradiating beam (equation 22).

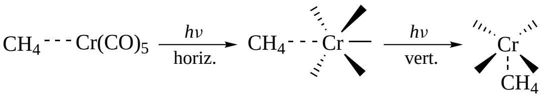

(22)

These experiments show that the matrix holds the $Cr(CO)_5$ fragment rigid at the beginning and end of the photolysis period, but that mobility is possible during irradiation. The most likely explanation is that visible photolysis causes the $Cr(CO)_5$ fragment to be excited from the ground state C_{4v} configuration to a D_{3h} excited state. The excited state can then relax back to a C_{4v} geometry, but reorientation of the molecule may occur (equation 23).

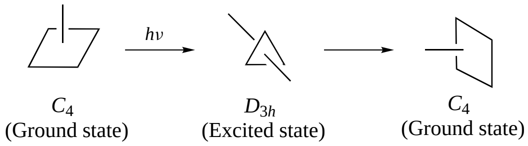

(23)

It is of course possible to propose a mechanism by which an $M(CO)_5$ fragment may take up a free CO molecule on visible photolysis to form $M(CO)_6$. This is via photoreorientation causing the vacant site of $M(CO)_5$ to move around the molecule, such that it may be directed towards any adjacent CO molecule trapped within the matrix cage. In this way a chemical bond will be formed between CO and the $M(CO)_5$ fragment. Alternatively, if the vacant site of the final product is directed towards a methane molecule, $Cr(CO)_5\cdots CH_4$ will be formed. This product is, however, still labile to visible photolysis, so reorientation may continue. Thus a reaction is possible with any CO molecule that is adjacent to the $M(CO)_5$ fragment. To backup this hypothesis it would be desirable to observe excited-state $Cr(CO)_5$ directly. Very recent solution experiments have been directed towards this end, but as yet such a species has defied unequivocal identification.

In a similar vein, near-IR photolysis of matrix-isolated $Fe(CO)_4$ promotes a reaction with photoejected CO to regenerate $Fe(CO)_5$:

$$Fe(CO)_4 + CO \xrightarrow[20\,K]{h\nu\text{(near IR)}} Fe(CO)_5 \qquad (24)$$

This finding led to an interesting study by Turner, Poliakoff *et al.* on the laser-induced isomerization of $Fe(CO)_4$. A statistical mixture of the different isotopomers of $Fe(^{12}C^{16}O)_{4-x}(^{13}C^{18}O)_x$ was formed in an argon matrix at 20 K by UV photolysis of matrix-isolated $Fe(CO)_5$

that had been 40% enriched with $^{13}C^{18}O$. These isotopomers are readily distinguished by their different IR absorption bands in the ν(CO) region. In all, there are seven possible isotopomers of $Fe(^{12}C^{16}O)_{4-x}(^{13}C^{18}O)_x$: two each of $Fe(^{12}C^{16}O)_{4-x}(^{13}C^{18}O)_x$ and three of $Fe(^{12}C^{16}O)_{4-x}(^{13}C^{18}O)_x$. It was found that irradiation of the matrix with the output of a tunable IR laser at a frequency corresponding to one particular isotopomer promoted a selective rearrangement as shown in Scheme 2. These interconversions may clearly be described as pseudorotations but the results show that the permutational mode is not that expected for the normal *Berry Pseudorotation* seen, for example, in the thermal rearrangement of SF_4. Thus the isomerization of $Fe(CO)_4$ was the first reported example of a non-Berry pseudorotation.

Visible photolysis of $Mo(CO)_5$ trapped in matrices containing N_2 results, not only in the regeneration of $Mo(CO)_6$, but also in the formation of a *dinitrogen complex* $Mo(CO)_5(N_2)$ (Scheme 3).**13** This molecule has been characterized by IR and Raman spectroscopy. Studies involving isotopic substitution with $^{15}N_2$, $^{15}N^{14}N$, and ^{13}CO have confirmed that the molecule has C_{4v} symmetry and thus a linear Mo–N–N unit is implied (**15**). Similar reactions are known for $Cr(CO)_5$, $W(CO)_5$, $Fe(CO)_4$, and $Ni(CO)_3$.

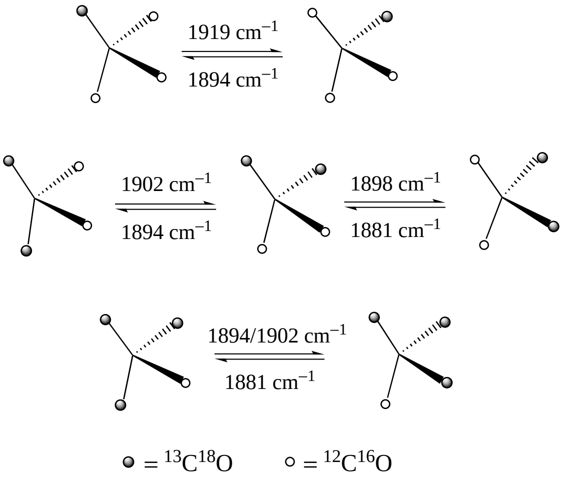

Scheme 2 Selective intramolecular rearrangement of isotopomers of $Fe(CO)_4$ partially enriched in ^{13}CO via a non-Berry pseudorotation

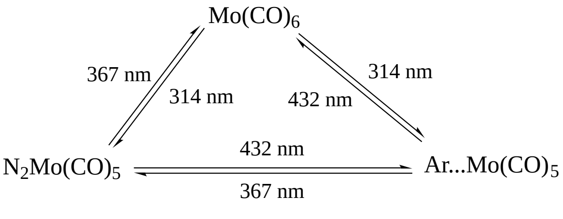

Scheme 3

The photochemical reaction of the binuclear carbonyl $Re_2(CO)_{10}$ with N_2 has been studied by matrix isolation. In an N_2 matrix at 10 K, $Re_2(CO)_{10}$ yields $Re_2(CO)_9$ upon UV photolysis. When the matrix is annealed to 15–20 K the equatorial isomer $Re_2(CO)_9(N_2)$ (**28**) is generated by a bimolecular reaction. Irradiation of the matrix with visible light ($\lambda = 546$ nm) converts (**28**) to the axial isomer (**29**), while (**29**) can be reconverted to (**28**) on UV irradiation at 313 nm.

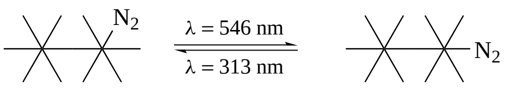

(**28**) (**29**)

Although providing valuable structural information, such matrix experiments tell us little or nothing about the thermal stability of these dinitrogen complexes nor of the strength of the M–N bond. Experiments have sought to address this problem by looking at similar reactions in low-temperature inert solvents such as liquid xenon. It is shown that the molecule $Cr(CO)_5(N_2)$ survives at temperatures as high as $-35\,°C$. For the related molecule $Ni(CO)_3(N_2)$, kinetic studies of its dissociation have been possible, giving an estimate of about $40\,kJ\,mol^{-1}$ for the activation enthalpy of the dissociative process:

$$Ni(CO)_3(N_2) \xrightarrow[\text{slow}]{-N_2} Ni(CO)_3 \xrightarrow[\text{fast}]{CO} Ni(CO)_4 \qquad (25)$$

Thus it is possible to estimate the enthalpy of the Ni–N bond (*see Bond Energies*).

The reactions between unsaturated metal carbonyls and dihydrogen have attracted much interest. Sweany discovered that a reversible interconversion between $Fe(CO)_4$ and $Fe(CO)_4H_2$ could be initiated by selective photolysis:

$$Fe(CO)_4 + H_2 \xrightleftharpoons[\text{UV-visible}]{\text{IR}} Fe(CO)_4H_2 \qquad (26)$$

In this case, there is no reason to suppose that hydrogen is coordinated in any way other than the classical dihydride manner (**30**) (*see* ***Hydrides: Solid State Transition Metal Complexes***). However, similar experiments using $Cr(CO)_5$ gave a product $Cr(CO)_5H_2$ for which strong circumstantial evidence pointed towards the nonclassical dihydrogen structure (**31**). Unfortunately, in low-temperature matrices

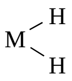

(**30**)

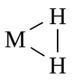

(**31**)

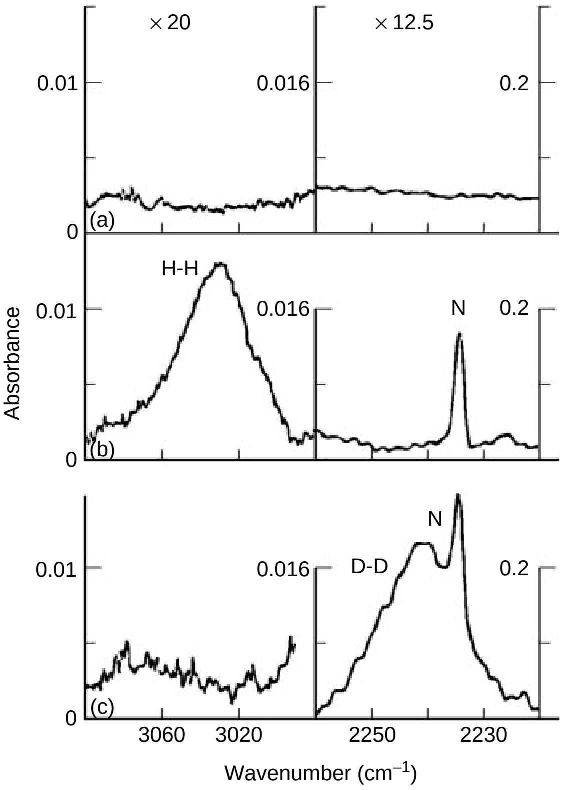

Figure 12 IR spectra of $Cr(CO)_6$ in hydrogen-doped liquid xenon solution: (a) before photolysis; (b) after photolysis in H_2-doped Xe; (c) after photolysis in D_2-doped Xe. N is an impurity band. (Reproduced by permission of The Royal Society of Chemistry from Upmacis *et al.*, *J. Chem. Soc., Chem. Commun.*, 1985, 27)

the ν(H–H) mode was too weak to be observed. This problem was overcome by Poliakoff, Turner and coworkers who repeated the experiment in liquid xenon solution at 200 K.[9] Taking advantage of the long path length (27 mm) of their cell, they were able to obtain the spectra illustrated in Figure 12 in which the ν(H–H) vibration and its counterpart when D_2 replaces H_2 as reactant are clearly visible. Interest in such complexes continues. The Nottingham group have shown that photolysis of $[CpV(CO)_4]$ in liquid xenon solution doped with H_2 generates the nonclassical complex $[CpV(CO)_3(\eta^2\text{-}H_2)]$. By contrast, under similar conditions, $[CpTa(CO)_4]$ yields a classical dihydride $[CpTa(CO)_3(H)_2]$ while $[CpNb(CO)_4]$ gives rise to a temperature-dependent equilibrium between the classical $[CpNb(CO)_3(H)_2]$ and nonclassical $[CpNb(CO)_3(H_2)]$ compounds. This equilibrium has been investigated by the use of time-resolved IR spectroscopy. Thus, we see a smooth trend where dihydrogen coordination is favored at the top of the group and the dihydride at the bottom.

The reactions of $M(CO)_6$ (M = Cr, Mo or W), $(\eta^6\text{-}C_6H_3Me_3)M(CO)_3$ (M = Cr or Mo) and $W(CO)_5CS$ with H_2 and N_2 in polyethylene matrices have been investigated.[17] A high pressure (5000 lb in^{-2}) and low-temperature (30 K) cell was utilized to carry out these reactions, an approach that allows some of the advantages of 'traditional' matrix isolation to be combined with some of the advantages of low-temperature solution work. UV photolysis of $M(CO)_6$ gives: under N_2, $M(CO)_5N_2$ and on prolonged photolysis $M(CO)_{6-x}(N_2)_x$ ($x = 2 - 4$); under H_2, $M(CO)_5(\eta^2\text{-}H_2)$, and *cis*-$M(CO)_4(\eta^2\text{-}H_2)_2$ – the disubstituted products being previously unknown for W or Mo. One of the interesting features of this experimental arrangement is that the construction of the cell allows gases to be exchanged during a single experiment. Thus, thermal exchange between coordinated N_2 and H_2 ligands in $M(CO)_5L$ compounds may be studied. It was found that the order of reactivity follows the sequence Mo > Cr > W. UV irradiation of $(\eta^6\text{-}C_6H_3Me_3)M(CO)_3$ (M = Cr or Mo) and $W(CO)_5CS$ also leads to hitherto uncharacterized N_2 and H_2 complexes.

5.3 Photochemical Reactions of Metal Carbonyls with Dioxygen

UV irradiation of matrices containing $M(CO)_6$ molecules (M = Cr, Mo, or W) and O_2 leads to the formation of oxocarbonyl species with fewer than five coordinated carbonyl groups that also contain, in one form or another, coordinated oxygen. Apparently the most stable oxocarbonyl molecule to be produced by photooxidation (*see Oxo Complex* and ***Dioxygen & Related Ligands***) of matrix-isolated $Cr(CO)_6$ is chromyl carbonyl (**8**).[18] The IR spectra of this species show clearly that the O–O bond has been cleaved. The C–Cr–C (from intensity measurements) and O–Cr–O (from ^{16}O–^{18}O isotopic shifts) bond angles are estimated at approximately 118° and 129°, respectively. This molecule attracts interest because it was the first example of a stable chromium(IV) carbonyl compound (*see Oxidation Number*), and yet it appears to be one of the most stable intermediates to be formed during photooxidation of $Cr(CO)_6$. The high energies of the ν(CO) vibrations (2125 and 2063 cm^{-1}) reflect the minimal capacity of the metal center to engage in back donation to the π-antibonding (*see Back Bonding*) orbitals of the CO groups.

The discovery of chromyl carbonyl prompted a search for analogs of the other group 16 metals, namely molybdenum and tungsten. However, it was soon found that the photooxidation of $Mo(CO)_6$ and $W(CO)_6$ proceeds in a somewhat different manner. Here the molecules $O_2M(CO)_2$ (M = Mo or W) are seen in only low yield and the most abundant oxocarbonyl species seen are the previously unknown complexes *trans*-dioxotetracarbonylmolybdenum and *trans*-dioxotetracarbonyltungsten (**9**).[11] These species were characterized by IR and Raman spectroscopy, including isotopic substitution with ^{13}CO and ^{18}O. Crucial evidence for the *trans* O=Mo=O formulation came from the observed splitting of the $\nu_{as}(MoO_2)$ IR absorption arising from the natural abundance of the different isotopes of molybdenum (see Figure 6).

For each of the group 16 hexacarbonyls, it is apparent that common to each reaction is an intermediate (η^2-O_2)M$(CO)_4$ (**32**). Upon UV photolysis the O–O bond is cleaved and CO groups are lost from the metal center yielding, upon prolonged photolysis, binary metal oxide molecules. Thus, $Cr(CO)_6$ yields as the final oxidation product CrO_2, while $Mo(CO)_6$ forms a mixture of MoO_2 and MoO_3. The formation of binary tungsten oxides from $W(CO)_6$ is somewhat more complex. The final product is WO_3 but this appears to be formed not from free WO_2, but rather from the molecule (η^2-O_2)WO_2 by loss of an O atom:

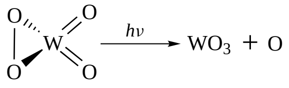

(27)

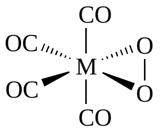

(**32**)

On the basis of these matrix-isolation experiments, a more-or-less complete mechanism for the photooxidation of the binary carbonyls $M(CO)_6$ (M = Cr, Mo, or W) in Ar matrices containing O_2 at 20 K can be proposed (Scheme 4): (i) Cr, 544 nm, Mo 403 nm, W, 435 nm; (ii) Cr, W 367 nm, Mo 314 nm; (iii) Mo and W only, Mo 403 nm or anneal at 35 K, W anneal at 35 K; (iv) Cr 314 nm or anneal at 35 K; Mo, W 314 nm; (v) Cr and Mo only.

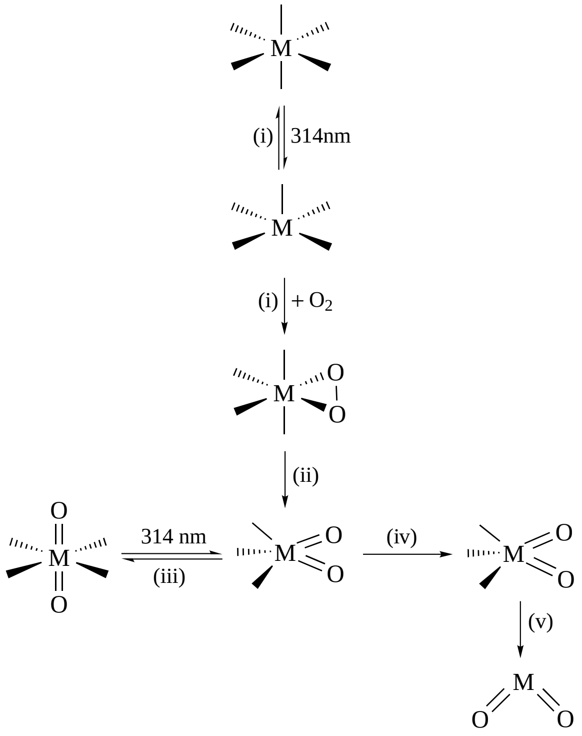

Scheme 4

One distinctive feature of these photochemical reactions is the clear photoselectivity displayed. Thus, by using different wavelengths of light it is possible to build up the concentrations of individual species at the expense of others. For example, a high yield of the peroxo complex (η^2-O_2)M$(CO)_4$ (where M = Mo or W) is generated upon visible (blue or green) photolysis, while near-UV photolysis promotes rupture of the O–O bond and loss of CO to form the dioxo species $O_2M(CO)_3$.

Iron pentacarbonyl ($Fe(CO)_5$) may be photooxidized in a similar manner. Although no fewer than five distinct iron carbonyl intermediates are seen, there is no sign of any photoselectivity in this reaction sequence.[18] It is possible, however, to build up reasonable concentrations, at least of the early intermediates, by carefully controlling the time of photolysis. Hence, it appears that the first oxidation product is (η^2-O_2)$Fe(CO)_4$, where the O_2 ligand occupies a basal site in a square pyramidal framework (**33**).

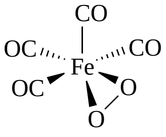

(**33**)

Photolysis then proceeds by rupture of the O–O bond and loss of CO to generate $O_2Fe(CO)_3$. Later oxocarbonyl intermediates are difficult to characterize since they are invariably formed only in meagre quantities. However, the nature of the final molecular binary oxide products does appear to have been resolved. They are the peroxo iron(II) species (η^2-O_2)Fe and the planar (or near planar) iron(VI) oxide FeO_3. Taken together the results point to the reaction scheme shown in Scheme 5 for the matrix photooxidation of $Fe(CO)_5$ in Ar or CH_4 matrices containing O_2 at 20 K.

Attention turned to the dinuclear carbonyls $Mn_2(CO)_{10}$, $Re_2(CO)_{10}$, and $Co_2(CO)_8$. Regarding mechanistic information, the study of $Re_2(CO)_{10}$ has been the most fruitful. Here two distinct oxocarbonyl species, which appear to contain only one rhenium atom each, are formed. The final product of the reaction is the O-bridged oxide Re_2O_7. In a similar vein, $Mn_2(CO)_{10}$ yields Mn_2O_7 upon matrix photooxidation, although there is no hint of any intermediate in this process, no matter what steps are taken to produce such species. The photooxidation of $Co_2(CO)_8$ is likely to follow a pathway even more complex than that of $Mn_2(CO)_{10}$ or $Re_2(CO)_{10}$. In this case not only is there competition between M–C and M–M bond rupture as the primary photochemical step, but there is also the complication of photoisomerism of the molecule.

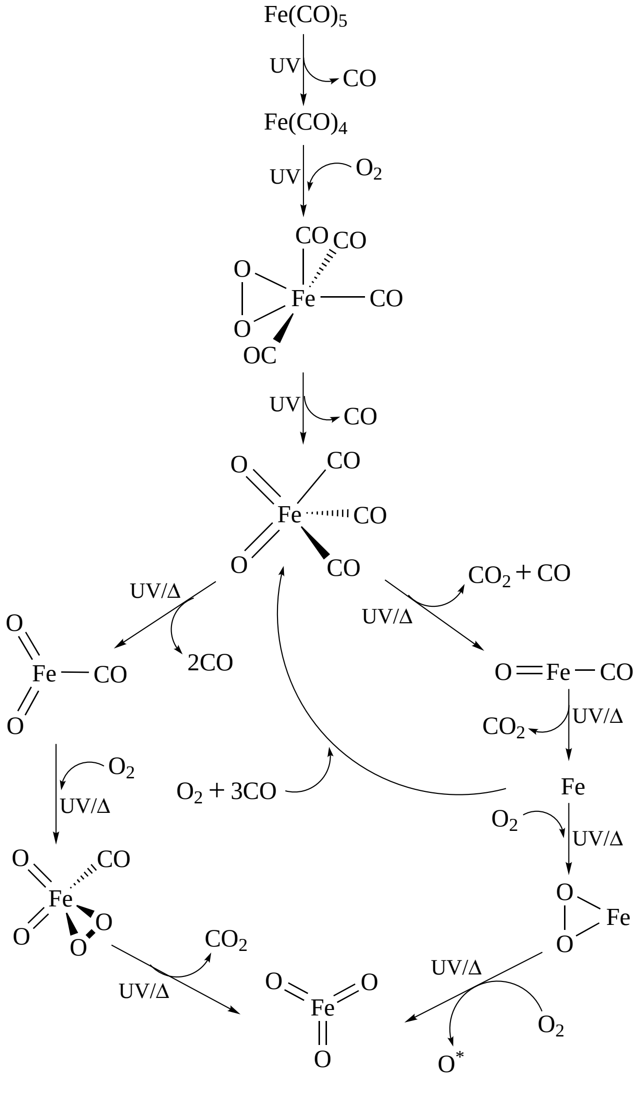

Scheme 5

Three isomers of $Co_2(CO)_8$, one with CO bridges, have been identified in low-temperature matrices and these readily interconvert upon UV–visible photolysis. In the event, two mononuclear peroxocobalt carbonyls, $(\eta^2\text{-}O_2)Co(CO)_3$ (**34**) and $(\eta^2\text{-}O_2)Co(CO)_4$ (**35**), are formed; they have been identified by comparison of their IR spectra with those of the same products formed by cocondensation of Co atoms with mixtures of CO and O_2.

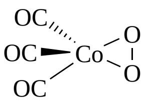

(**34**)

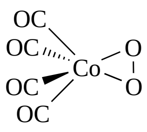

(**35**)

6 MAIN GROUP MOLECULES IN HIGH-TEMPERATURE VAPORS

6.1 Background

Many chemical molecules that are not stable under normal conditions at room temperature are found in high-temperature vapors. These include gaseous molecular forms of compounds such as metal oxides or chlorides that are normally encountered as solids at room temperature. Other species found in high-temperature vapors have unusual valencies and coordination numbers. Examples are the molecules OPCl and O_2PCl, which contain unusual two-coordinate trivalent and three-coordinate pentavalent phosphorus atoms, respectively. It is of interest to study such species to extend our knowledge of the structure and bonding of small molecules to new regions of the periodic table. Moreover, many such species are proposed chemical reaction intermediates.

Some methods of characterization of high-temperature molecules rely on direct flow-system vapor-phase measurements, for example, mass spectrometric and electron diffraction studies. Matrix isolation also plays a significant role in that vapor species may be trapped by rapid quenching. The most unambiguous results have perhaps been drawn from a combination of the two approaches.

6.2 Group 13

Monovalent compounds of the higher members of group 13 tend not to be stable. However, such species have been proposed as reaction intermediates (*see* ***Aluminum: Inorganic Chemistry*** and ***Boron Hydrides***). Thus, the reaction, discovered by Alfred Stock, in which B_2Cl_4 may be produced by the zinc discharge reduction of BCl_3, is believed to proceed via the intermediacy of BCl, which *inserts* into a B–Cl bond of a second BCl_3 molecule:

$$Zn^* + BCl_3 \xrightarrow{\text{discharge}} ZnCl_2 + [BCl] \qquad (28)$$

$$[BCl] + BCl_3 \longrightarrow B_2Cl_4 \qquad (29)$$

Similarly, higher boron subhalides (e.g. the pale-yellow tetrahedral molecule B_4Cl_4, the yellow–orange B_9Cl_9, and the red B_9Br_9) may be built up in discharge reactions of BCl_3 or BBr_3, presumably again via BCl or BBr molecules, although the exact reaction mechanisms remain obscure. Monovalent molecules akin to BCl are stable in high-temperature vapors; they may be studied by gas-phase or matrix-isolation methods. Particularly well-studied are the aluminum monohalides.

These molecules can be generated in a variety of chemical systems. Thus, AlCl is formed when Al vapor, at about 1000 K, is allowed to react with $AlCl_3$ vapor, at about 350 K,[19] while AlBr may be generated in a number of ways, for example,

$$2Al(g) + MgBr_2(g) \xrightarrow{1500\,K} 2AlBr(g) + Mg(g) \qquad (30)$$

$$2Al(v) + Br_2(g) \xrightarrow{1250\,K} 2AlBr(g) \qquad (31)$$

Aluminum monofluoride is formed by the reaction of Al vapor with HF at 1100 K. All of these molecules have been studied in both the gas-phase and in low-temperature matrices. It is found that the neon matrix gives IR spectra that most closely resemble those obtained from the gas phase.

These monohalide molecules are prone to aggregation in matrices; thus cyclic dimers such as (**36**) are formed. Two possible routes available to monovalent Al molecules to achieve the more stable trivalent state are addition of a two-electron donor, or insertion into a two-electron bond. Unsurprisingly, therefore, AlF reacts with O atoms in a matrix to form the linear molecule OAlF, a product that is itself prone to dimerization, forming (**37**). The structures of (**38**) and (**37**) have been investigated by isotopic substitution experiments involving ^{18}O and also by theoretical calculations. The structure of (**38**) is similar to that adopted by the stable solid $(SAlCl)_2$ (**39**), which is formed when $AlCl_3$ and Al_2S_3 are heated together at around 600 K:

$$2AlCl_3 + 2Al_2S_3 \xrightarrow{600\,K} 3(SAlCl)_2 \qquad (32)$$

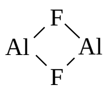

(**36**)

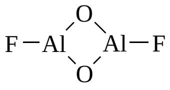

(**37**)

$O{=}Al{-}F$

(**38**)

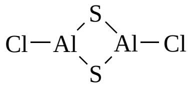

(**39**)

An example of an insertion reaction of an aluminium monohalide (cf. the insertion reactions of BCl mentioned earlier) is provided by the formation of planar $HAlCl_2$ (**40**) from AlCl and HCl in a low-temperature matrix. Similarly, GaCl will insert into HCl or H_2 to form the matrix-isolated chlorogallanes $HGaCl_2$ and H_2GaCl, respectively.

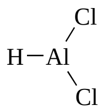

(**40**)

Aluminum monochloride may be generated in sufficient quantities to be used on a preparative scale. Cocondensation of AlCl vapor and dimethylacetylene at 77 K leads, upon warming the mixture to room temperature,[20] to the formation of an air- and moisture-sensitive product. This product shows an Al:Cl ratio of 1:1 while mass spectrometry suggests a molecular formula of $Al_4Cl_4C_{16}H_{24}$. A room-temperature single crystal X-ray diffraction study reveals the nature of the product. It consists of two dimeric 1,4-dialumina-2,5-cyclohexadiene rings (**41**) joined by a π-interaction between the Al atoms of one ring and the C=C bonds of the other (**42**). The C=C bonds are somewhat longer (136.7 pm) than an uncoordinated C=C bond, while the mean Al–C distance of 235.4 pm is approximately 10% greater than the Pt–C distance in the well-known alkene complex *Zeise's Salt*, $K[Pt(C_2H_4)Cl_3]$. The product is of interest as it might well be akin to intermediates in reactions of organoaluminum compounds; perhaps even in polymerization reactions catalyzed by Ziegler–Natta catalysts.

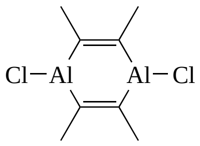

(**41**)

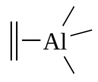

(**42**)

Interest in the reactions of monovalent aluminium compounds in low-temperature matrices has continued. Monomeric AlCl reacts, upon photoactivation, with acetylene in an argon matrix via insertion to give the acetylide species Cl(H)AlCCH.[21] IR spectroscopy with isotopic substitution was used to identify the product. This work provides an example of the use of quantum chemical calculations in probing the structure of unstable matrix-isolated compounds. Since the early 1990s almost all experimental matrix-isolation studies have been backed up by quantum calculations. These are used to predict structures of reactive species and to calculate minimum energies for these structures. Calculations may also be used to predict the IR spectrum of a particular species such that observed and calculated spectra may be compared. The work quoted here[21] is one example taken from many, but the principles of using experiment and calculation together are demonstrated. The energies of the acetylide product and of an alternative cyclic species are calculated, as are IR spectra for the species. As may be seen from Figure 13, there is an excellent match between the observed and calculated spectra. The work also illustrates the point that calculations do not replace experimental findings. It is still necessary to carry out isotopic substitution experiments and to compare observed and calculated IR spectra for the various isotopomers of the proposed product. This approach has been extended to the more complex reaction between photoactivated AlCl and 2-butyne; here two products are seen that are believed to be the insertion product $Cl(H)AlCH_2CCCH_3$ and the cyclic aluminacyclopropene isomer.[21] In a similar vein, AlF reacts with O_2 in an argon matrix to give peroxo and bis-superoxo complexes of aluminium, that is, $FAlO_2$ and $FAlO_4$.[22] The IR spectra shown in Figure 14 illustrate very nicely the importance of isotopic substitution in investigating systems such as this. It may be seen that when prepared from a mixture of $^{16}O_2$ and $^{18}O_2$ $FAlO_2$ shows a doublet of bands in the ν(O–O) region. This same product, however, gives a *triplet* of bands when a *scrambled* mixture of $^{16}O_2$, $^{16}O^{18}O$, and $^{18}O_2$ are used. $FAlO_4$ gives a triplet with unscrambled $^{16}O_2$ and $^{18}O_2$ – showing the

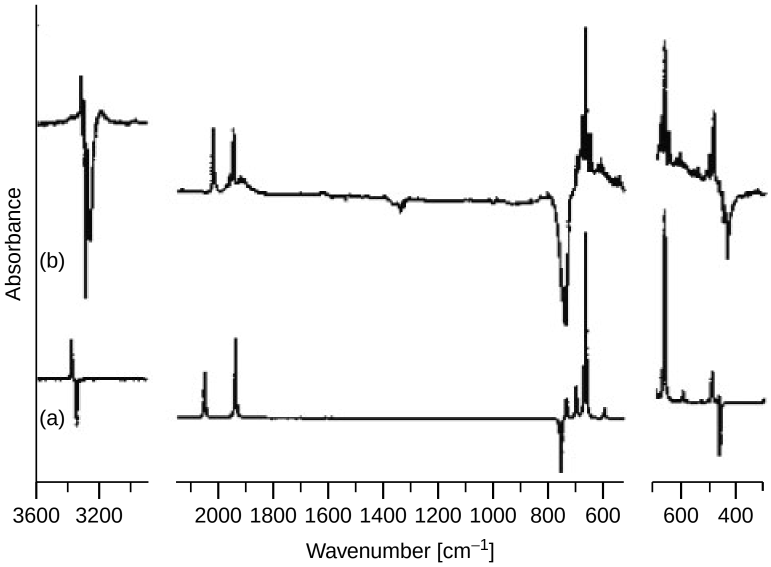

Figure 13 (a) Difference between the IR spectrum taken following photolysis of Ar matrix containing AlCl and C_2H_2 and the IR spectrum taken immediately upon deposition. (b) Difference between the simulated IR spectrum of Cl(H)AlCCH and those of C_2H_2 and AlCl. (Reprinted with permission from Ref. 21 © 2003 American Chemical Society)

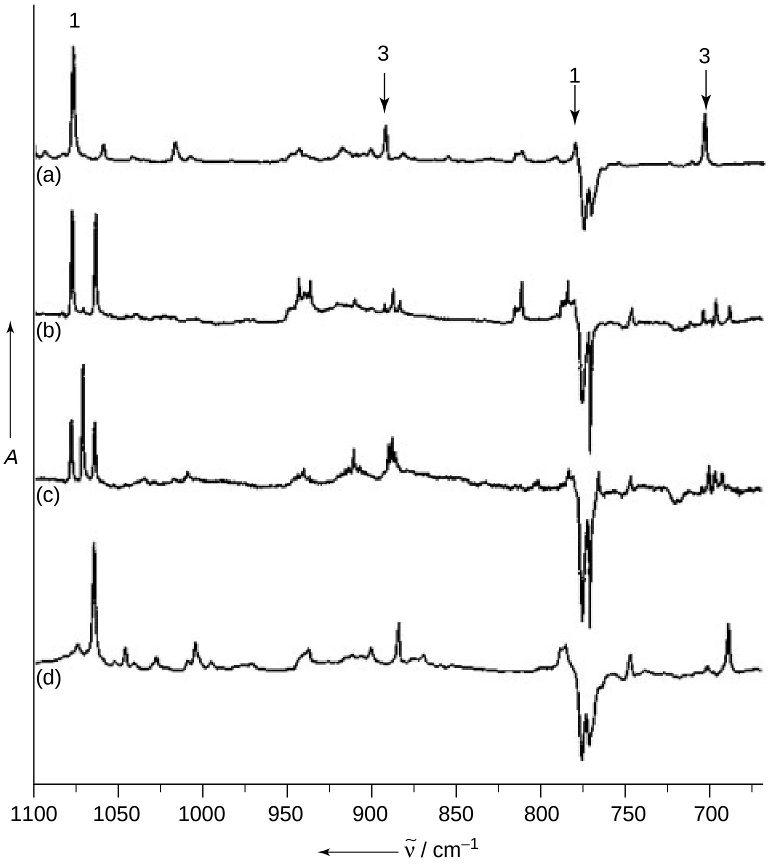

Figure 14 IR spectrum recorded after cocondensation of molecular AlF together with O_2 in a solid argon matrix followed by photolysis of the matrix with UV light ($\lambda_{max} = 254$ nm): (a) $^{16}O_2$, (b) $^{16}O_2/^{18}O_2$ (1:1 mixture), (c) $^{16}O_2/^{16}O^{18}O/^{18}O_2$ (1:2:1 mixture), (d) $^{18}O_2$. (Ref. 22. Reproduced by permission of Wiley-VCH)

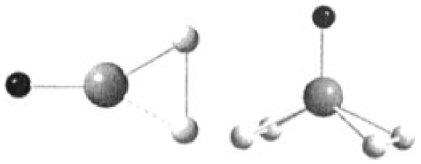

Figure 15 Structures of $FAlO_2$ and $FAlO_4$. (Ref. 22. Reproduced by permission of Wiley-VCH)

presence of two O_2 molecules. Once again Density functional theory (DFT) calculation back up the experimental studies (Figure 15).

In this area of chemistry, the use of *laser ablation* to generate metal atoms that may be cocondensed with a wide range of reagents has been particularly useful. Laser ablation often allows monomeric species to be produced when traditional thermal methods for generating metal vapors lead to dimers or oligomers. In this way, the aluminium carbonyls $Al(CO)_2$ and $Al_2(CO)_2$ – a cyclic molecule that shows some degree of aromaticity – have been prepared.[23] Recent developments in refrigeration techniques have allowed matrix temperatures of 3.5 K to be attained, which, in turn, has allowed pure hydrogen matrices to be deposited. The combination of utilizing laser ablation to generate metal atoms and depositing pure hydrogen as the matrix material has led to the development of new areas of metal hydride chemistry. When laser-ablated aluminium atoms are cocondensed with H_2 at 3.5 K and the mixture is subjected to ultraviolet irradiation and annealing to 6.5 K the product is the elusive molecule Al_2H_6.[24] Under normal conditions the only known aluminium hydride is the polymer $(AlH_3)_n$. A combination of IR spectroscopy and quantum chemical calculations show that this molecule is isostructural with diborane, B_2H_6. This study may be contrasted with a study of gallium hydrides utilizing more traditional methods of evaporation of gallium vapor from a resistively heated cell and cocondensation of the vapor with ca. 1% H_2-doped Ar.[25] In this case, the cyclic molecule $Ga(\mu\text{-}H)_2Ga$ is formed.

Laser-ablated aluminium, gallium, indium, or thallium atoms all react with HCN in excess argon.[26] Here both cyanide and isocyanide products viz MCN and MNC are seen (M = Al, Ga, In or Tl). No H-containing products are seen. These findings contrast with the results of experiments where laser-ablated group 2 atoms are cocondensed with HCN-doped argon.[27] Beryllium atoms give rise to HBeCN and HBeNC alongside BeCN and BeNC. Magnesium, calcium, strontium, and barium yield neither any H-containing products nor any cyanides. Only the isocyanides MNC (M = Mg, Ca, Sr or Ba) are formed. Why should the group 2 and 13 atoms behave so differently here? It appears that two mechanisms operate, namely insertion into the C–H bond or attack at the N atom. Calculations suggest that only Be and Al will insert into the C–H bond. With beryllium the H-containing product is seen, but rearrangement to the isocyanide also occurs. For aluminium direct insertion into C–H gives AlCN by loss of an H atom. All of the heavier atoms react by attack at the N atom to yield the isocyanides MNC. When M is a group 2 atom this product is stable, but when M is a group 13 atom the isocyanide rearranges to the more stable cyanide.

6.3 Group 14

Isoelectronic with monovalent group 13 molecules are divalent molecules of group 14 elements (*see* ***Germanium: Inorganic Chemistry***; ***Silicon: Inorganic Chemistry*** and ***Silicon: Organosilicon Chemistry***). The most populous class of these species are the silylenes, divalent compounds of silicon. It is not appropriate here to provide a detailed review of silicon chemistry since such material is more expertly and comprehensively covered elsewhere. However, it is pertinent to this discussion to make some mention of silylene chemistry.[28]

Silylenes are often generated by pyrolysis. Indeed, the simplest silylene of all, SiH_2, may be formed by pyrolysis of SiH_4. The presence of SiH_2 as an intermediate in this reaction, which yields ultimately Si_2H_6 and H_2, was first suggested over 30 years ago by Purnell and Walsh as a result of their kinetic studies:

$$SiH_4 \xrightarrow{\Delta} [SiH_2] + H_2 \qquad (33)$$

$$[SiH_2] + SiH_4 \longrightarrow Si_2H_6 \qquad (34)$$

the disilane Si_2H_6 being formed by an insertion reaction into the Si–H bond of SiH_4. As for isoelectronic group 13 molecules such as BCl and AlCl, it is not surprising to find that silylenes are prone towards insertion.

Silylene, SiH_2, was originally studied by electronic spectroscopy in the gas phase. Dubois *et al.*,[29] obtained its spectrum in 1968 and from it were able to estimate values for the bending vibrations of the second electronically excited ($^1A_1$) and ground ($^1B_1$) states of ~860 and ~1004 cm^{-1}, respectively. A rotational analysis of the fine structure of these bands afforded bond angles of 92° and 123° and r(Si–H) bond lengths of 1.516 and 1.487 Å for the $^1A_1$ and $^1B_1$ states of silylene. IR detection of silylene awaited the formation of the molecule in a low-temperature matrix. Good yields of this species were obtained by Fredin *et al.*, who cocondensed Si atoms with H_2. A spontaneous insertion reaction then yields SiH_2:

$$Si + H_2 \longrightarrow SiH_2 \qquad (35)$$

They obtained a value of 994.8 cm^{-1} for the wavenumber of the bending mode, in reasonable agreement with the gas-phase value.

Dimethylsilylene, Me_2Si, long postulated as a reaction intermediate, was first observed directly in 1979; it was formed photochemically. It is now known to be generated also in high-temperature vapors, for example, pyrolysis of

1-methylsilacyclobutane (**43**) in a tenfold excess of butadiene at 1000 K yields 1,1-dimethylsilacyclopent-3-ene (**44**) as a major product (equation 36).

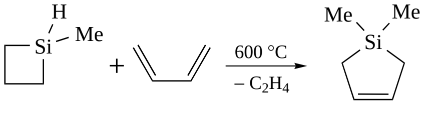

(**43**) (**44**)

(36)

The favored reaction mechanism is that which yields methylsilene and ethylene upon pyrolysis (equation 37).

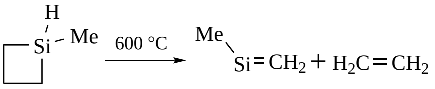

(37)

and the methylsilene rapidly isomerizes to dimethylsilylene (equation 38), which then adds to butadiene to yield the product (**44**).

$$MeSi{=}CH_2 \xrightarrow{\Delta} Me_2Si \qquad (38)$$

The isomerization of methylsilene and dimethylsilylene is now a well-known reaction in low-temperature matrices. It is a photochromic process that may be reversed upon irradiation of the matrix at selected wavelengths. Warming to temperatures as low as 100 K promotes the formation of the more thermally stable silylene (equation 39).

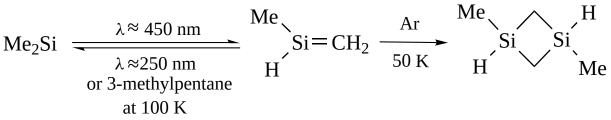

(39)

Thermochemical calculations show that the principal vapor species in the silicon/oxygen system is the monoxide SiO. This is the most stable molecule to contain a Si–O multiple bond. In 1969, Anderson and Ogden reported the results of matrix-isolation experiments in which the vapor over heated silica, SiO_2, (at 2000 K) or overheated silica/silicon mixtures (at 1600 K) was cocondensed with excess Ar or N_2. These results show that alongside the monomer, SiO, the dimer Si_2O_2 (**45**) and trimer Si_3O_3 (**46**) are also trapped in the matrix.

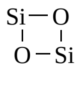

(**45**)

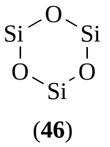

(**46**)

A point to be resolved is the extent to which the abundances of the matrix-isolated species reflect the composition of the high-temperature vapor. Mass spectrometric studies indicate that Si_2O_2 but not Si_3O_3 is present in the vapor. Thus it is presumed that Si_3O_3 is formed during the freezing of the matrix. A reinvestigation of this system has shown that if the temperature of the heated SiO_2 is raised above 1500 K, then the monomer is the most abundant gaseous species; at relatively high concentration, however, dimerization proceeds readily within the matrix. Normal coordinate analysis of the observed frequencies of the IR absorptions and ab initio self consistent field (SCF) calculations have been carried out for Si_2O_2 and are consistent with the cyclic planar structure (**45**).

Several reactions of matrix-isolated SiO are known. Irradiation of an argon matrix containing SiO and Cl_2 leads, via an insertion reaction, to the product $OSiCl_2$, the silicon analog of phosgene:

$$SiO + Cl_2 \xrightarrow[\text{Ar, 20 K}]{h\nu} O{=}SiCl_2 \qquad (40)$$

The IR spectrum of this molecule shows it to be planar with a force constant indicating an Si=O double bond, which is, however, somewhat weaker than the corresponding C=O double bond in phosgene itself.

Molecular SiO_2 is prepared by reacting matrix-isolated SiO with O atoms. Thus codeposition of SiO molecules with microwave-excited O_2 and excess argon yields a species that shows a prominent IR band at 1416.5 cm^{-1}.[30] Isotopic substitution experiments allow this feature to be assigned to the asymmetric stretch of a linear SiO_2 molecule. Force constant calculations show that the Si=O bonds of SiO_2 are rather weaker than the C=O bonds of CO_2. Similarly, matrix-isolated Si_2O_2 will react with O_2 to yield (**47**), the dimer of SiO_2, whose structure has been determined by isotopic substitution with ^{18}O, and the natural abundance of ^{28}Si, ^{29}Si, and ^{30}Si isotopes.

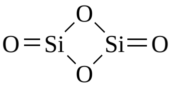

(**47**)

Silicon monosulfide, SiS, is formed if CS_2 gas is passed over silicon heated to 1270 K. Its matrix chemistry shows a strong resemblance to that of SiO. Thus, it reacts with Cl_2 to yield $SSiCl_2$ and with O atoms to form OSiS, the silicon analog of carbonyl sulfide. The latter molecule is of interest since it is shown to contain both Si=O and Si=S double bonds, while both experimental observations and ab initio calculations confirm the double bond nature of the Si=S linkage in $SSiCl_2$.

In 1992, Andrews and his coworkers[31] attempted to characterize small high-temperature molecules in the germanium/oxygen/sulfur system. In this system, only the monooxide, GeO, and the monosulfide, GeS, are well-known, both having been studied in the gas phase by a variety of methods including electronic absorption and emission, microwave absorption, and IR emission spectroscopy. They have also been observed in low-temperature matrices, while GeO_2 has been detected only in matrices. Andrews' approach has been to pass vapor-phase reagents through a microwave discharge. The systems studied are: (i) germane + sulfur; (ii) germanium + sulfur; (iii) germanium + oxygen + sulfur. The species present in each system are characterized by their behavior upon annealing the matrix and by isotopic substitution experiments. Thus, the new molecules SGeS and SGeO are seen. Like GeO_2, these are both linear; force constant calculations indicate some multiple bonding between Ge and S atoms although, as expected, such bonding is weak. Another molecule to show Ge=S multiple bonding is $Me_2Ge{=}S$. Michl *et al.* reported the first matrix-isolation study of this molecule, formed either by pyrolysis of the trimer $(Me_2GeS)_3$ or by the interaction of S atoms with dimethylgermylene (Me_2Ge). The vibration of most significance is the Ge=S stretch, which occurs at $604.5\,\mathrm{cm^{-1}}$. It is attributable to a highly polar true double bond, since single bond Ge–S stretching vibrations typically occur around $410\,\mathrm{cm^{-1}}$.

As in group 13 chemistry, laser ablation of metal sources has recently been used to allow new areas of group 14 chemistry to be explored. Again the use of dihydrogen matrices gives a route to group 14 metal hydrides. When laser-ablated silicon atoms are cocondensed with H_2-doped neon or argon a wide range of hydrides are formed, namely the monomeric species $SiH_{1,2,3,4}$ and the dimers $Si_2H_{2,4,6}$.[32] In pure deuterium matrices the major product is SiD_4 with smaller amounts of SiD_3, Si_2D_6 and Si_2D_4, but no SiD or SiD_2 was seen. Laser-ablated germanium atoms give, in H_2-doped neon or argon matrices, all four monomeric hydrides ($GeH_{1,2,3,4}$). Likewise all four monomeric germanium deuterides are seen in solid pure D_2. This suggests that the activation barrier for further reactions of GeD and GeD_2 might be higher than for the corresponding reactions of SiD and SiD_2.[33] Laser-ablated silicon and germanium atoms also react with ammonia to form 1:1 complexes that exhibit an interesting photochemistry.[34] Upon irradiation at $\lambda = 290\,\mathrm{nm}$, the insertion product $HSiNH_2$ is formed, while photolysis in the region 250–280 nm destroys $HSiNH_2$ and produces $SiNH_2$. Experiments utilizing thermally generated silicon atoms from a graphite cell heated to 1450–1650 °C have also been performed.[35] When Si atoms, formed in this way, are cocondensed with Me_2O or MeOH and the mixture is photolyzed a wide range of products are formed. These include the silylene MeOSiMe and the silanones $Me_2Si{=}O$ and $Me(H)Si{=}O$. The direct observation of silanones in detectable quantities under these conditions suggests that such reactions may be useful as a new route for the generation of these transient species.

6.4 Group 15

Small phosphorus (*see* ***Phosphorus: Inorganic Chemistry*** and ***Phosphorus–Nitrogen Compounds***) molecules with unusual valencies and coordination numbers are found in high-temperature vapors. An example is the phosphaethylene $CH_2{=}PCl$. This species has been prepared by pyrolysis of methyl dichlorophosphite (equation 41)

$$MeOPCl_2 \xrightarrow{\Delta} H_2C{=}PCl + HOCl \qquad (41)$$

and has been studied in the gas phase by microwave spectroscopy. It is thus shown to have a C=P distance close to 165.5 pm, a P–Cl distance close to 206.0 pm, and a C–P–Cl bond angle of 103.3° (**48**).

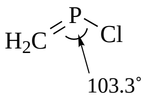

(**48**)

Isoelectronic with $CH_2{=}PCl$ is OPCl. This molecule has been prepared by two separate routes:

$$POCl_3(g) + Ag(s) \xrightarrow{1100\,K} OPCl(g) + 2AgCl(s) \qquad (42)$$

$$PCl_3(g) + H_2O(g) \xrightarrow{700\,K} OPCl(g) + 2HCl(g) \qquad (43)$$

It has been studied by IR spectroscopy (when trapped in a low-temperature matrix) and by mass spectrometric studies on the vapor. Isotopic studies ($^{35}Cl/^{37}Cl$ and $^{16}O/^{18}O$) allow the O–P–Cl bond angle to be calculated from the IR spectra at ca. 105° (i.e. close to the bond angle of CH_2PCl). From the observed appearance potential (20.9 eV) of P^+ [$AP(P^+)$] in the mass spectrum of OPCl, it is possible to estimate the enthalpy of atomization of $OPCl_{(g)}$ via the Born–Haber cycle (Scheme 6). Hence, since the standard enthalpies of formation of $P_{(g)}$, $O_{(g)}$, and $Cl_{(g)}$ are all known, the standard enthalpy of formation of $OPCl_{(g)}$ [$\Delta H^{\circ}_{f298}(OPCl)$] may be estimated as $-250.7\,\mathrm{kJ\,mol^{-1}}$.

A reaction similar to that with $OPCl_3$ occurs between $OPFX_2$ vapor (X = Cl or Br) and silver to produce OPF, a molecule that is isoelectronic with SiF_2 and SO_2. IR studies of Ar matrices and mass spectrometric studies of the vapor indicate that the O–P–F bond angle $= 109 \pm 5°$ and $\Delta H^{\circ}_{f298}(OPF_{(g)}) = -404.4\,\mathrm{kJ\,mol^{-1}}$.

Even more uncommon than molecules containing trivalent two-coordinate phosphorus are those that contain pentavalent

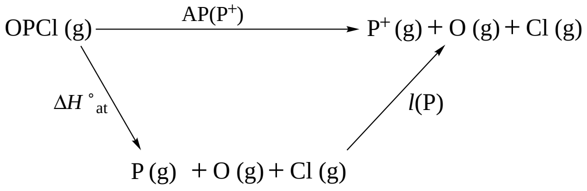

Scheme 6

three-coordinate phosphorus. The molecule O_2PCl may be prepared cleanly by UV irradiation of an Ar matrix containing OPCl and O_3:

$$\mathrm{OPCl} + \mathrm{O_3} \xrightarrow[\text{Ar matrix}]{h\nu} \mathrm{O_2PCl} + \mathrm{O_2} \qquad (44)$$

The formation of O_2PCl from OPCl is illustrated by the spectra shown in Figure 16. IR spectra show O_2PCl to be a planar molecule (**49**) with a relatively wide O–P–O bond angle (~135°) and an unusually strong P–Cl bond (with a stretching force constant of $370\,\mathrm{N\,m^{-1}}$). These observations may be rationalized by ab initio calculations.

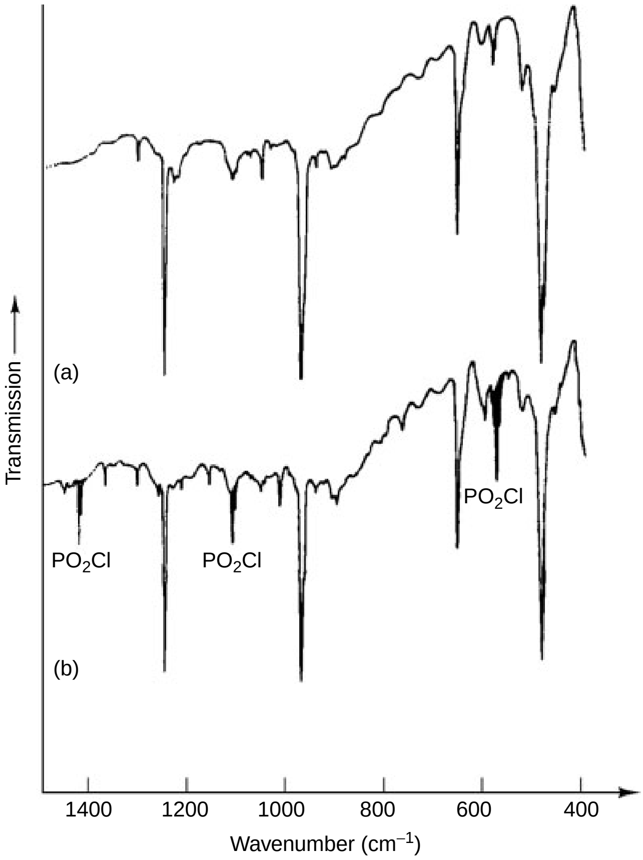

Figure 16 (a) IR spectrum of OPCl (derived from the reaction of $OPCl_3$ with Ag) cocondensed with $^{18}O_3$ in an argon matrix at ca. 15 K; (b) IR spectrum of the sample following UV irradiation for 15 min, showing the formation of the photoproduct O_2PCl. (Reprinted with permission from Ahlrichs *et al.*, *J. Am. Chem. Soc.*, 1986, 108, 3596. © 1986 American Chemical Society)

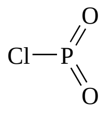

(**49**)

Several analogs of OPCl, produced in high-temperature vapors, have likewise been the subjects of matrix-isolation experiments. For example, SPCl can be made by the high-temperature reaction of $SPCl_3$ with Ag. It has an SPCl bond angle of about 110°. Preparation of OAsCl presents a more difficult challenge since the obvious precursor, $OAsCl_3$, does not survive long, even at normal temperatures. However, OAsCl can be generated if a gaseous $AsCl_3/O_2$ mixture is passed over silver heated to about 1350 K. Less successful have been attempts to study OSbCl. Although a reaction occurs between $SbCl_3$, O_2, and Ag at about 1350 K, Sb_4O_6 is a ubiquitous product alongside OSbCl, and IR absorptions of the binary oxide mask those of the ternary species.

The phosphorus nitride radical PN, isoelectronic with SiO, has recently been detected in interstellar space. It is readily prepared in high-temperature vapors either by heating solid P_3N_5 to 1100 K or by dehalogenation of cyclic $(NPCl_2)_3$ with Ag:

$$\mathrm{P_3N_5(s)} \xrightarrow{1100\,\mathrm{K}} \mathrm{3PN(g)} + \mathrm{N_2(g)} \qquad (45)$$

$$\mathrm{(NPCl_2)_3(g)} + \mathrm{6Ag(l)} \xrightarrow{1300\,\mathrm{K}} \mathrm{3PN(g)} + \mathrm{6AgCl(g)} \qquad (46)$$

When the vapor containing PN is cocondensed with excess krypton at 10 K the PN monomer and P_3N_3 trimer are seen, but there is no hint of the dimer P_2N_2. The monomer is readily converted into the trimer, as illustrated by the spectra shown in Figure 17, if the matrix is annealed to 35 K. Isotopic substitution with ^{15}N and ab initio SCF calculations show that P_3N_3 has a planar cyclic structure (**50**).

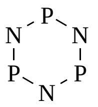

(**50**)

The formation of P_3N_3 from P_2 and N_2 molecules is shown to be an endothermic process, while the formation of P_3N_3 from three molecules of PN is found to be strongly favored. PN reacts with silver atoms in hydrocarbon glasses at 77 K. The product, as determined by ESR spectroscopy, is AgPN. Local density functional calculations suggest that Ag bonds exclusively to the P nucleus of PN in a bent geometry with an Ag–P–N bond angle close to 97.4°. An interaction is also found between copper(I) chloride and PN molecules in solid argon. Here the interaction appears to be between the Cu and N atoms and the product is a linear species ClCuNP.[36]

Various routes have been used to generate matrix-isolated phosphorus oxide radicals, for example, PO_2 and PO_3. These are: (i) codeposition of phosphine with O atoms from a microwave discharge source; (ii) the matrix reaction of P_2 (generated by heating GaP) and O_3; (iii) laser ablation of P_4O_{10}; (iv) laser ablation of red P in a stream of O_2. Both

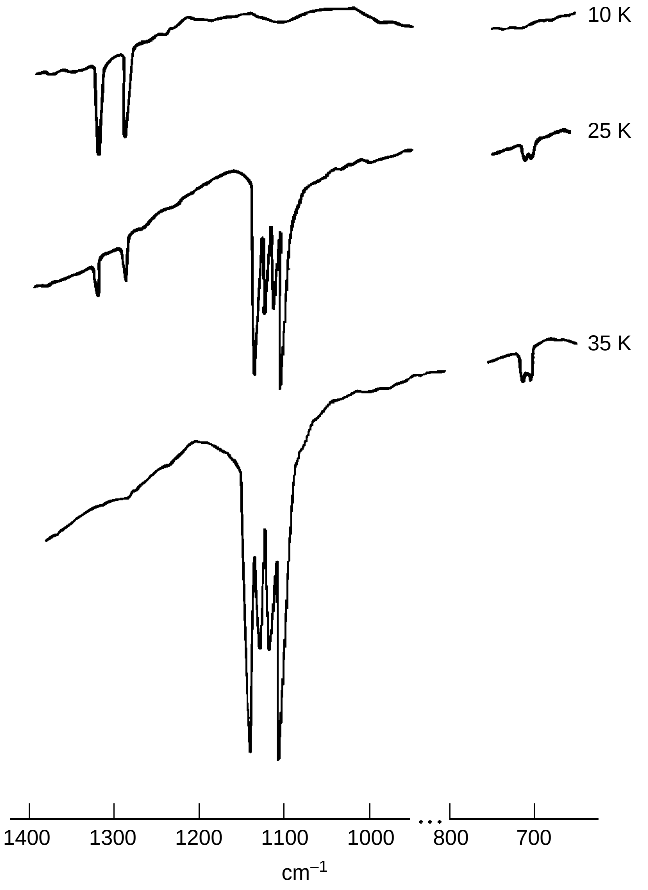

Figure 17 IR spectra of the $^{14}N/^{15}N$ isotopomers of PN and P_3N_3 (formed from PN upon annealing the matrix to 25–35 K) in a krypton matrix. (Reprinted from Ref. 36a © 1977, with permission from Elsevier)

PO_2 and PO_3 are seen in all four systems; these are highly reactive species so it is not surprising to see P_2O_5 also, formed by reaction of PO_2 with PO_3 upon diffusion. The reaction of the high-temperature molecule P_2 with O_3 yields the new molecule P_2O alongside cyclic P_4O_2, while the reaction of PH_3 with O generates also the H-containing species HPO, HOPO, H_2PO, and HPOH. The nature of the products formed by the laser ablation of P_4O_{10} depends upon the nature of the solid material used. The hexagonal form, the commercially available variety, gives mainly molecular P_4O_{10} with some P_2O_5 and PO_2. By contrast, the polymeric orthorhombic form yields little molecular P_4O_{10} but much higher quantities of PO, PO_2, P_2O, and P_2O_5. A similar distribution of products is obtained if red phosphorus is laser-ablated in a stream of O_2.

The phosphorus sulfides PS, P_2S, and PS_2 have been made by allowing P_4 and S_8 vapors to react in an Ar discharge.[37] Isotopic substitution studies show that P_2S is linear like P_2O and N_2O, while PS_2 is bent like PO_2 and NO_2. The species in the vapor above heated P_4S_{10} have been the focus of some controversy. It has been claimed that P_4S_{10} sublimes undissociated. However, matrix-isolation experiments reveal that the molecule P_4S_9 is also present in the vapor even at temperatures as low as 450 K. Some P_2S_5 is also formed upon vaporization of P_4O_{10}. By contrast, volatilization of pure P_4S_9 solid at 450 K yields no vapor-phase P_4S_9; rather, P_4S_7 and P_4S_{10} are generated by disproportionation.

The vapor species formed upon heating arsenic(V) oxide in vacuo include the four decomposition products As_4O_n ($n = 6$ to 9) as well as As_4O_{10} (**51**), which has been characterized by its IR spectrum.

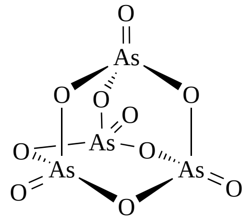

(**51**)

6.5 Group 16: Oxides and Oxy Salts

Several routes exist to molecular metal oxides. These include reactions of metal atoms with oxygen or photolysis of a suitable precursor, for example, a metal carbonyl in the presence of O_2 (see Section 5.3). Both of these methods lend themselves particularly well to trapping and detection by matrix isolation. A third means of generating molecular metal oxides is to heat a solid oxide sample, thus producing molecules in the vapor. The resulting gaseous species can then be studied either directly in the gas phase, or, following freezing with excess inert gas, in a matrix. A wide range of matrix-isolated metal monoxide molecules have been made in this way.

Higher oxides may also be formed. When WO_3 is heated to 1250–1700 K, the vapor contains a number of species of which the principal one appears to be the trimer W_3O_9. Gas electron diffraction studies suggest that the most likely structure of this species is one containing a six-membered ring (**52**). Mass spectrometry confirms the presence of W_3O_9 in the vapor and suggests also that the dimer W_2O_6 and tetramer W_4O_{12} are present. In order to make monomeric WO_3, a different technique must be employed. This is sputtering of a W electrode in a mixture of O_2 and an inert gas followed by rapid freezing of the products. IR experiments employing isotopic substitution show that WO_3 has planar D_{3h} symmetry (**53**).

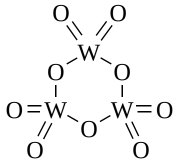

(**52**)

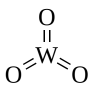

(**53**)

Dimanganese heptoxide, Mn_2O_7, is a volatile liquid and readily sublimes undissociated. The heavier congener, Re_2O_7, is less volatile and only vaporizes upon heating to about 400 K. It appears to sublime without dissociation, though an unidentified IR band ubiquitously appears in the spectrum of the matrix-isolated compound. This band has been variously attributed to: (i) aggregates of Re_2O_7; (ii) ReO_3 formed by loss of O_2 from Re_2O_7 and dissociation upon heating; (iii) $HReO_4$ formed by reaction of Re_2O_7 with traces of moisture. A definitive solution to this problem is not yet forthcoming, and the situation is complicated by the known rather complex behavior of rhenium oxides at high temperature. Upon volatilization at ca. 750 K, ReO_3 generates Re_2O_7 via the disproportionation reaction

$$3ReO_3(s) \xrightarrow{\Delta} ReO_2(s) + Re_2O_7(g) \tag{47}$$

which generates Re_2O_7 in the gas phase while leaving a residue of solid, involatile ReO_2. What mass spectrometric and matrix-isolation studies have so far failed to confirm is whether or not the Re_2O_7 is accompanied by ReO_3 in the vapor. Again the situation is complicated by the presence of $HReO_4$ whenever any traces of water are found.

Many structural studies have been made on the species present in the vapors above oxysalts such as alkali metal nitrates, chlorates, perrhenates, and so on. In part, the interest in such work lies in determining the mode of coordination of the metal atom to the oxyanion in the monomeric vapor species. Both gas electron diffraction and matrix isolation have been employed to seek an answer to this question.

Three plausible structures may be envisaged (**54–56**) for a simple monomeric metal nitrate such as $TlNO_3$. Electron diffraction studies indicate that the bidentate structure (**55**) is preferred, a mode of ligation that is also adopted by $MReO_4$ and $MClO_4$ ($M = Li$, K, Cs, or Tl). Such structures may readily be determined by IR spectroscopy involving isotopic substitution with ^{18}O. In Figure 18 are illustrated IR spectra for $CsReO_4$, 50% enriched in ^{18}O,**[38]** assuming bidentate coordination. Other metal oxysalts showing bidentate coordination are metal phosphates (MPO_3) and phosphites (MPO_2) and their arsenic analogs (**57, 58**). Metal sulfates and their selenium analogs also tend to show bidentate coordination. Molecular thallium sulfate has been prepared in situ in low-temperature matrices by cocondensing Tl_2O vapor with SO_2 and excess Ar:

$$Tl_2O + SO_2 \xrightarrow[\text{excess Ar}]{\text{cocondense}} Tl_2SO_3 \tag{48}$$

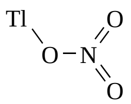

(**54**)

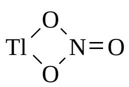

(**55**)

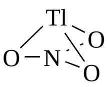

(**56**)

Alkali metal sulfates or selenates are generated in the gas phase by heating the appropriate solid material. Both adopt a bis-bidentate D_{2d} structure (**59**). For the molecular metal selenites,**[39]** it appears that the selenite anion has an unsymmetrical structure. As shown in Figure 19, the best fit between observed and calculated IR spectra is found for O–Se–O bond angles of 101, 115, and 115°. This finding suggests the possibility of monodentate (**60**) or a combination of mono- and bidentate (**61**) coordination of the cation to the central selenite pyramid.

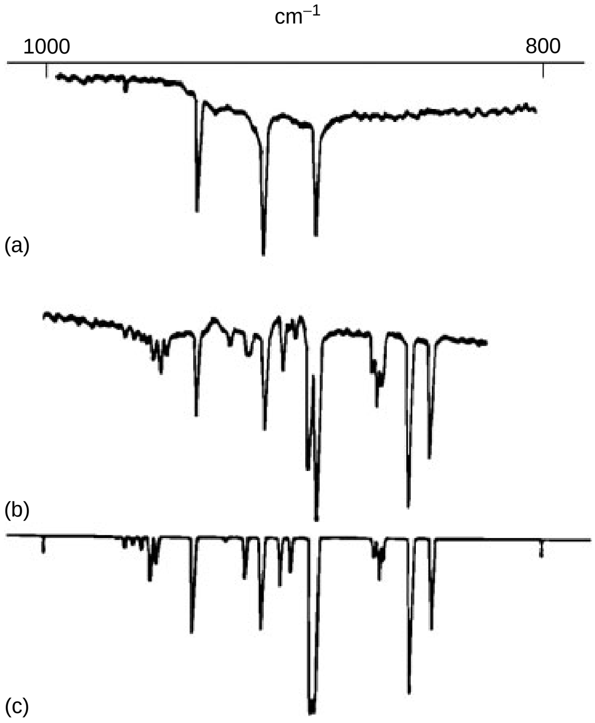

Figure 18 IR spectra of $CsReO_4$ in nitrogen matrices: (a) $CsRe^{16}O_4$; (b) $CsReO_4$ 50% enriched in ^{18}O; (c) calculated spectrum assuming a bidentate structure. (Ref. 38a. Reproduced by permission of The Royal Society of Chemistry)

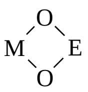

(**57**) E = P or As

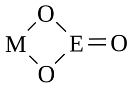

(**58**)

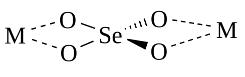

(**59**)

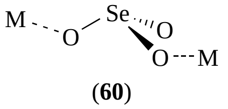

(**60**)

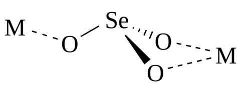

(**61**)

In contrast to the above molecules, cesium chlorate, $CsClO_3$, provides a rare example of tridentate coordination of a metal cation to an oxyanion (**62**).

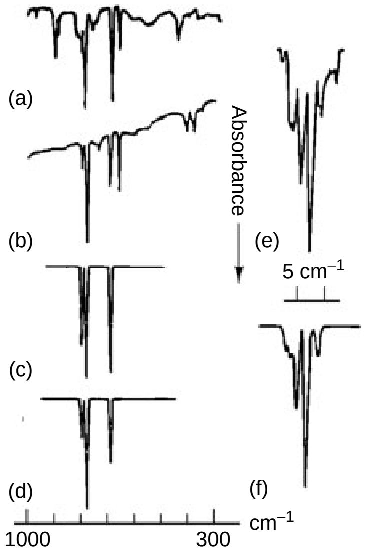

Figure 19 Matrix IR spectra obtained from the vaporization of alkali metal selenites: (a) spectrum obtained from Na_2SeO_3; (b) spectrum obtained from Cs_2SeO_3; (c) calculated spectrum assuming all the O–Se–O angles are 101°; (d) calculated spectrum assuming the three O–Se–O angles are 101, 115, and 115°; (e) high-resolution spectrum of the A″ band of Cs_2SeO_3; (f) calculated spectrum as in (d). (Reprinted with permission from Ref. 39 © 1991 American Chemical Society)

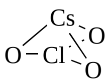

(**62**)

Devlin has reported some interesting results regarding the solvation of $LiNO_3$ molecules in a low-temperature matrix.**[40]** In a pure Ar matrix, $LiNO_3$ adopts structure (**55**) and the degenerate ν_3 mode of the trigonal nitrate ion is split into two components separated by 262 cm^{-1}. However, if $LiNO_3$ is cocondensed with Ar-containing Lewis bases such as water or Tetrahydrofuran (THF) then the Lewis base molecules coordinate to the lithium ion. The splitting of ν_3 thus decreases in regular steps corresponding to an increase in coordination number of the Li ion. In Figure 20 are illustrated the IR spectra of $LiNO_3$ in Ar matrices doped with concentrations of THF ranging from 1 to 25%. One remarkable feature of these experiments is that the coordination number of the Li ion reaches a higher value in the matrix than it does in solution!

6.6 Group 17: Halides

Simple alkali metal halide molecules, for example NaCl and KCl, are found in the vapors above heated samples of the solid compounds. These vapor species have been studied by IR spectroscopy of gases and matrices, and by gas electron diffraction. The studies show that planar rhombic dimers are also present.

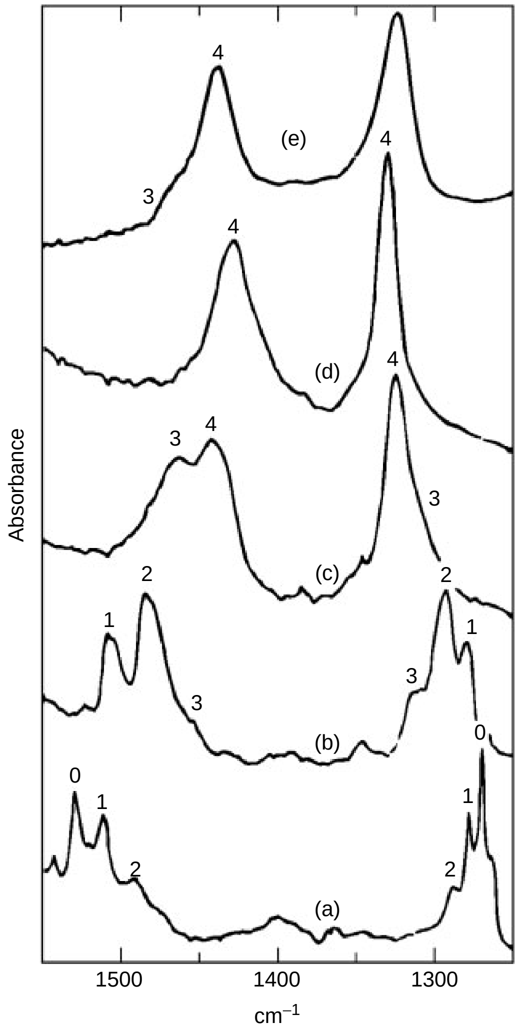

Figure 20 IR spectra of $LiNO_3$ in (a) 1% THF-doped solid argon; (b) 7% THF-doped solid argon; (c) 25% THF-doped solid argon; (d) pure solid THF (all at 25 K); (e) pure THF solution at 298 K. The numbers refer to n in $LiNO_3{\cdot}(THF)_n$. (Reproduced by permission of American Institute of Physics from Ritzhaupt *et al., J. Chem. Phys.,* 1985, **82**, 1167)

There has, over the years, been some controversy regarding the structure adopted by the dihalide molecules MCl_2 (M = Ca, Cr, Mn, Fe, Co, Ni, and Zn). One school of thought has it that these molecules are linear, a view supported by the results of gas electron diffraction, and molecular beam deflection studies. In N_2 matrices, however, $CoCl_2$ and $NiCl_2$ are strongly bent, probably owing to interactions with the N_2 host, and even in Ar matrices there is evidence that $FeCl_2$, $CoCl_2$, and $NiCl_2$ are all slightly bent with bond angles around 160°. Those who follow the results of matrix-isolation spectroscopy will be reminded of the controversy that once attended the structure of molecular $AlCl_3$. Gas electron diffraction supported the expected planar geometry. Matrix-isolation studies were in conflict, one group preferring a pyramidal shape while another, that of Beattie and Ogden, a

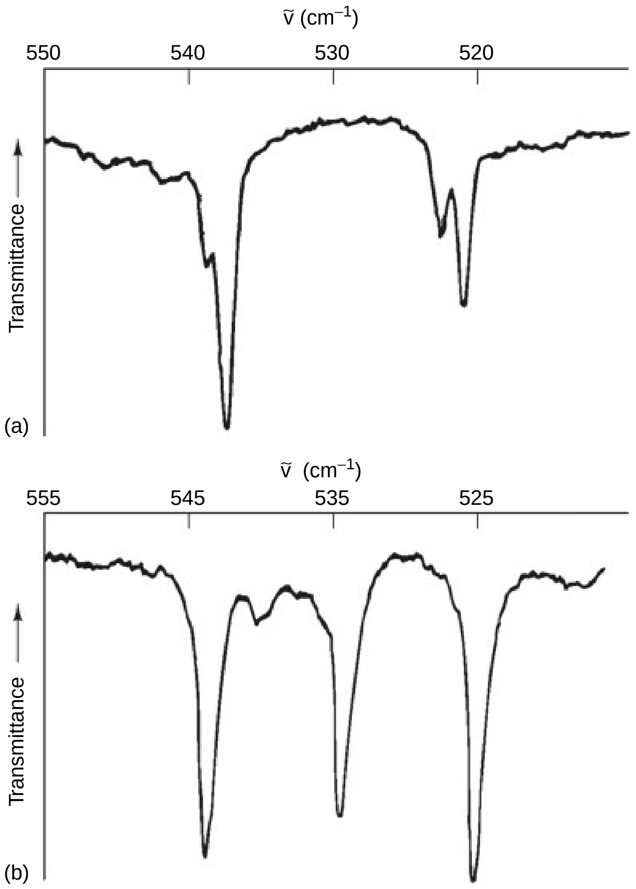

Figure 21 IR spectra of $CsUF_6$: (a) in an argon matrix; (b) in a nitrogen matrix (both at 14 K). (Reproduced by permission of The Royal Society of Chemistry from Arthers *et al.*, *J. Chem. Soc., Dalton Trans.*, 1984, 711)

planar molecule. The discrepancy was finally resolved when it was realized that the nonplanarity of $AlCl_3$ in some matrices results from weak complex formation.

It is clear that interactions between guest molecules and the matrix host can, in certain instances, cause significant structural perturbations to the guest species. An exemplary case is provided by $CsUF_6$. The spectra of this molecule (Figure 21) look quite different in argon or nitrogen matrices. This difference appears to result from a change in coordination of the Cs^+ cation to the UF_6^- anion upon moving from one matrix to the other. In argon the interaction is tridentate (**63**), in nitrogen it is bidentate (**64**). Thus, the overall molecular symmetry is lowered from C_{3v} to C_{2v} upon moving from argon to nitrogen matrices.

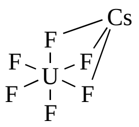

(**63**)

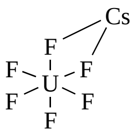

(**64**)

It is appropriate to end with the caveat that it is a weakness shared by many of these studies of high-temperature salt molecules that the IR characterization of the species does not extend to motions of the cation. Hence the location of the cation, or cations, has to be inferred circumstantially from the perturbation experienced by the anion. The basis of the argument does make the results vulnerable to misinterpretation, and there is no doubt that the surest results relate to molecules whose identities can be vouched for independently, for example by gas electron diffraction studies.

6.7 Group 18

One of the most interesting developments in the study of main group chemistry by matrix-isolation spectroscopy over the past few years has been the great expansion of the chemistry of the rare gases. Although the following work does not involve generation of reactive species in high-temperature vapors, it is included here because of its importance in the current understanding of rare gas chemistry. Much of this work has been done in the laboratories of Räsänen and his coworkers at Helsinki, Finland. In 1995 it was shown that irradiation of HI in a xenon matrix led to the formation of the species HXeI. This had charge transfer characteristics $[(HXe)^+I^-]$ and was identified by its strong H–Xe stretching vibration.[41] The list of such molecules has grown over the years and now includes krypton and argon species, for example, HKrCl and HArF and those with a wide range of electronegative components, for example, HXeOH, HXeSH, HXeH, HXeCN, HxeNC, and HXeNCO. It has been shown that these neutral rare gas compounds form from the neutral fragments $H + Y + Rg$ where H and Y fragments are produced by photolysis of the HY precursor and Rg is the rare gas. The intrinsic stability of the molecules is of great interest and it has been shown, for example, that HXeBr and HXeCl are stable in neon matrices, indicating intrinsic stability rather than a stability that depends upon the presence of a Xe (or Kr) matrix host. These molecules will form weak, but stable complexes in matrices. Thus HXeOH gives the complexes HXeOH-H_2O and HXeOH-$(H_2O)_2$ in H_2O-doped argon matrices while HArF, HKrF and HKrCl all form N_2 complexes in N_2-doped matrices. The yields of HRgY molecules are increased by annealing the matrix as the mobility of the H atoms formed by photodissociation of HY is increased. In this way the kinetics of the formation of HKrCl and DKrCl by annealing of krypton matrices containing H (or D) and Cl atoms (formed themselves by photodissociation of HCl or DCl) may be used as a measure of the mobility of H and D atoms in low-temperature matrices. Not surprisingly the D atoms are shown to migrate at a slower rate than H atoms under these conditions.

It must be remembered that there is an enormous amount of current research involving the chemistry of reactive intermediates. In this short review, it has been possible only to describe selected areas of work. It is hoped, however, that this will illustrate the principles of how such research is carried out and how the results of these studies have importance for a wide range of chemical and other scientific applications. The interdisciplinary nature of this research should also be noted. Work by spectroscopists – using a range of techniques – synthetic chemists, theoreticians, and kineticists is all brought together. The most successful findings in this area usually require input from those with a range of specialized interests.

7 REFERENCES

1. M. J. Almond, 'Short-Lived Molecules', Ellis Horwood, Chichester, 1990.
2. M. A. Graham, M. Poliakoff, and J. J. Turner, *J. Chem. Soc. A*, 1971, 2939; R. N. Perutz and J. J. Turner, *Inorg. Chem.*, 1974, **14**, 262.
3. M. Poliakoff, *Chem. Soc. Rev.*, 1978, **7**, 527; M. Poliakoff and E. Weitz, *Acc. Chem. Res.*, 1987, **20**, 408.
4. M. J. Almond and A. J. Downs, in 'Spectroscopy of Matrix-Isolated Species', eds. R. J. H. Clark and R. E. Hester, Wiley, Chichester, 1989; R. N. Perutz, *Ann. Rep. Prog. Chem. C*, 1985, **82**, 157; M. J. Almond and R. H. Orrin, *Ann. Rep. Prog. Chem. C*, 1993, **90**, 4; M. J. Almond, *Ann. Rep. Prog. Chem. C*, 1997, **93**, 3; M. J. Almond and K. S. Wiltshire, *Ann. Rep. Prog. Chem. C*, 2001, **97**, 3.
5. E. A. V. Ebsworth, D. W. H. Rankin, and S. Cradock, 'Structural Methods in Inorganic Chemistry', Blackwell, Oxford, 1987.
6. M. C. R. Symons, *Chem. Soc. Rev.*, 1982, **11**, 227.
7. L. B. Knight Jr, *Acc. Chem. Res.*, 1986, **19**, 313.
8. J. M. Hollas, 'Modern Spectroscopy', Wiley, Chichester, 1988.
9. R. K. Upmacis, G. E. Gadd, M. Poliakoff, M. B. Simpson, J. J. Turner, R. Whyman, and A. F. Simpson, *J. Chem. Soc., Chem. Commun.*, 1985, 27.
10. M. Poliakoff, K. P. Smith, J. J. Turner, and A. J. Wikinson, *J. Chem. Soc., Dalton Trans.*, 1982, 651.
11. (a) J. A. Crayston, M. J. Almond, A. J. Downs, M. Poliakoff, and J. J. Turner, *Inorg. Chem.*, 1984, **23**, 3051; (b) M. J. Almond, J. A. Crayston, A. J. Downs, M. Poliakoff, and J. J. Turner, *Inorg. Chem.*, 1986, **25**, 19.
12. A. J. Downs and M. Hawkins, in 'Advances in Infrared and Raman Spectroscopy', eds. R. J. H. Clark and R. E. Hester, Wiley, Chichester, 1983, Vol. 10, p. 1.
13. J. K. Burdett, A. J. Downs, G. P. Gaskill, M. A. Graham, J. J. Turner, and R. F. Turner, *Inorg. Chem.*, 1978, **17**, 523.
14. I. R. Beattie, P. J. Jones, and N. A. Young, *J. Am. Chem. Soc.*, 1992, **114**, 6146.
15. S. G. Kazarian, P. A. Hamley, and M. Poliakoff, *J. Chem. Soc., Chem. Commun.*, 1992, 994.
16. R. H. Hooker, K. A. Mahmoud, and A. J. Rest, *J. Chem. Soc., Chem. Commun.*, 1983, 1022; B. D. Moore, M. Poliakoff, M. B. Simpson, and J. J. Turner, *J. Phys. Chem.*, 1985, **89**, 850.
17. S. E. J. Goff, T. F. Nolan, M. W. George, and M. Poliakoff, *Organometallics*, 1998, **17**, 2730.
18. M. Fanfarillo, H. E. Cribb, A. J. Downs, T. M. Greene, and M. J. Almond, *Inorg. Chem.*, 1992, **31**, 2962; M. Fanfarillo, A. J. Downs, T. M. Greene, and M. J. Almond, *Inorg. Chem.*, 1992, **31**, 2973.
19. H. Schnöckel, *Z. Naturforsch. B*, 1976, **31**, 1291; H. Schnöckel, *J. Mol. Struct.*, 1978, **50**, 267; R. Koppe and H. Schnöckel, *J. Chem. Soc., Dalton Trans.*, 1992, 3393.
20. H. Schnöckel, M. Leimkuhler, R. Lotz, and R. Mattes, *Angew. Chem., Int. Ed. Engl.*, 1986, **25**, 921.
21. H. J. Himmel, *Organometallics*, 2003, **22**, 2679.
22. J. Bahlo, H. J. Himmel, and H. Schnöckel, *Angew. Chem., Int. Ed.*, 2001, **40**, 4696.
23. Q. Kong, M. Chen, J. Dong, Z. Li, K. Fan, and M. Zhou, *J. Phys. Chem. A*, 2002, **106**, 11709.
24. L. Andrews and X. Wang, *Science*, 2003, **299**, 2049.
25. H. J. Himmel, L. Manceron, A. J. Downs, and P. Pullumbi, *J. Am. Chem. Soc.*, 2002, **124**, 4448.
26. D. V. Lanzisera and L. Andrews, *J. Phys. Chem. A*, 1997, **101**, 9660.
27. D. V. Lanzisera and L. Andrews, *J. Phys. Chem. A*, 1997, **101**, 9666.
28. I. M. T. Davidson, *Ann. Rep. Prog. Chem., C*, 1985, **82**, 47; H. F. Schaeffer III, *Acc. Chem. Res.*, 1982, **15**, 283; G. Raabe and J. Michl, *Chem. Rev.*, 1985, **85**, 419.
29. I. Dubois, G. Herzberg, and R. D. Verma, *J. Chem. Phys.*, 1968, **46**, 2485.
30. J. S. Anderson and J. S. Ogden, *J. Chem. Phys.*, 1969, **51**, 4189; H. Schnöckel, *Angew. Chem., Int. Ed. Engl.*, 1978, **17**, 616; H. Schnöckel, *Angew. Chem., Int. Ed. Engl.*, 1980, **19**, 323.
31. P. Hassanzadeh and L. Andrews, *J. Phys. Chem.*, 1992, **96**, 6181.
32. L. Andrews and X. Wang, *J. Phys. Chem. A*, 2002, **106**, 7696.
33. X. Wang, L. Andrews, and G. P. Kushto, *J. Phys. Chem. A*, 2002, **106**, 5809.
34. M. Chen, A. Zheng, and M. Zhou, *J. Phys. Chem. A*, 2002, **106**, 3077.
35. V. N. Khabashesku, K. N. Kudin, J. L. Margrave, and L. Fredin, *J. Organomet. Chem.*, 2000, **595**, 248.
36. (a) R. M. Atkins and P. L. Timms, *Spectrochim. Acta, Part A*, 1977, **33**, 853; (b) R. Ahlrichs, M. Bar, H. S. Plitt, and H. Schnöckel, *Chem. Phys. Lett.*, 1989, **161**, 179; (c) J. A. Howard, R. Jones, J. S. Tse, M. Tomietto, P. L. Timms, and A. J. Seeley, *J. Phys. Chem.*, 1992, **96**, 9144.
37. Z. Mielke, G. D. Brabson, and L. Andrews, *J. Phys. Chem.*, 1991, **95**, 79.

38. (a) S. A. Arthers, I. R. Beattie, R. A. Gomme, P. J. Jones, and J. S. Ogden, *J. Chem. Soc., Dalton Trans.*, 1983, 1461; (b) I. R. Beattie and J. E. Parkinson, *J. Chem. Soc., Dalton Trans.*, 1984, 1363.
39. A. K. Brisdon, R. A. Gomme, and J. S. Ogden, *J. Phys. Chem.*, 1991, **95**, 2927.
40. G. Ritzhaupt, K. Consani, and J. P. Devlin, *J. Chem. Phys.*, 1985, **82**, 1167.
41. M. Pettersson, J. Lundell, and M. Räsänen, *J. Chem. Phys.*, 1995, **102**, 6423.

Silicon: Inorganic Chemistry

Paul D. Lickiss
Imperial College of Science, Technology & Medicine, London, UK

1 Introduction 1
2 One-Coordinate Compounds 4
3 Two-Coordinate Compounds 4
4 Three-Coordinate Compounds 7
5 Four-Coordinate Compounds 8
6 Transition Metal Silyl Complexes 29
7 Compounds Containing Silicon with Higher Coordination Numbers 35
8 Characterization and Analysis of Inorganic Silicon Compounds 41
9 Related Articles 41
10 References 41

Abbreviations

cod = 1,5-cyclooctadiene; MNDO = modified neglect of diatomic overlap; NMI = *N*-methylimidazole; $PPN^+ = [(Ph_3P)_2N]^+$; pyO = pyridine*N*-oxide.

1 INTRODUCTION

Silicon is the most abundant (≈27.7%) electropositive element in the Earth's crust and second only to oxygen in overall abundance, the two elements together accounting for approximately four out of every five atoms on the surface of the Earth. Elemental silicon does not seem to occur naturally but it is usually combined with oxygen to form the very wide variety of silicates (*see Silica* and ***Zeolites***) that make up many of the world's rocks. Silicon is not found to any appreciable extent in the atmosphere, and only relatively small amounts are found in the hydrosphere, although organisms such as diatoms and some plants are able to extract silicon in the form of silica or silicic acid from aqueous solutions and use solid deposits of silica as skeletal or protective material. For example, hydrated silica, $SiO_2{\cdot}nH_2O$, is used by a number of organisms for protection and strength, for example, in plant leaves and the teeth of limpets. For general reviews on silicon in biology, see References 1–3 and Section 1.2 below.

Despite the ubiquitous nature of silicate materials and humankind's historical use of them, elemental silicon was not isolated until the nineteenth century when Berzelius used potassium to reduce potassium hexafluorosilicate (equation 1). (For a review of the history of the discovery of the element and its occurrence, see Gmelin.[4])

$$K_2SiF_6 + 4K \longrightarrow Si + 6KF \tag{1}$$

The mid-nineteenth century also saw the preparation of simple, volatile, covalent compounds such as $(EtO)_4Si$, $SiCl_4$, and SiH_4 and the first organometallic silicon compound (Et_4Si) by Friedel and Crafts in 1863. Considerable growth in non-silicate silicon chemistry occurred in the first part of the twentieth century with Stock and Kipping working on silanes (Si–H containing compounds) and organosilicon compounds, respectively. This work then set the foundation for the enormous growth that silicon chemistry has seen since the 1940s, particularly in the fields of polymers containing silicon in their backbone, and organosilicon compounds that have been studied to see how their chemistry compares with that of carbon compounds. This article will deal only with the inorganic compounds of silicon and excludes all compounds containing a silicon to carbon bond (such organosilicon compounds may be found in the article ***Silicon: Organosilicon Chemistry***) except for silicon carbide and simple silyl cyanides in which the carbon may be viewed as 'inorganic'. Compounds that cannot be isolated under normal conditions and which are fleeting intermediates will be mentioned briefly but not discussed in detail. As in other areas of chemistry, computational work on silicon compounds has grown rapidly in recent years; an excellent comparative review of the theoretical aspects of Si, Ge, Sn, and Pb compounds can be found in Reference 5.

1.1 Elemental Silicon and its Production

The production of high purity silicon has become increasingly important during the last three decades as its semiconductor properties have been utilized in an enormous variety of electronic devices.[6] The early work on the chemical and physical properties of silicon and its simple inorganic compounds has been discussed in detail.[7] Large-scale production of silicon is achieved by reduction of quartz, SiO_2, with carbon at approximately 1700 °C (equation 2), that is, well above the melting point of silicon.

$$SiO_2 + 2C \xrightarrow{1700\,^\circ C} Si + 2CO \tag{2}$$

The silicon prepared by this route is known as metallurgical grade or ferrosilicon and contains varying amounts of iron which is derived from impurities in the silica used and by addition of iron to the reduction process. Leaching impurities from the ferrosilicon affords higher purity silicon (ca. 98.5%), containing Fe, Al, Ca, and O as main impurities, which can be used for chemical purposes such as the direct synthesis of organochlorosilanes (*see* ***Silicon: Organosilicon Chemistry***).

The preparation of high purity silicon for use in the electronics industry has been achieved using several methods relying on the formation, purification by distillation, and reduction of volatile silicon compounds such as SiF_4, $SiHCl_3$, and SiH_4 (for preparations of these compounds, see below). Scheme 1 outlines the basic features of the process to prepare single-crystal silicon using $HSiCl_3$ as the volatile silane, the low boiling point of which enables distillation to give a much higher purity starting material than in the SiO_2 reduction where physical separation of impurities is difficult.[6]

A second method of Si preparation involves the thermal decomposition of Na_2SiF_6 to give SiF_4, which is then reduced by sodium to give a mixture of NaF and Si. The sodium salts are then removed by aqueous acid leaching to give a high quality powder of Si.[8] A more recent and widely used method involves the thermal decomposition of SiH_4 (which can be obtained in higher purity than $SiHCl_3$ from redistribution reactions, Scheme 2) to give high purity polycrystalline rods.[9]

The high purity silicon prepared by the methods above is either polycrystalline or in the form of a microcrystalline powder. Two methods are used to prepare large, dislocation-free single-crystal silicon: the Czochralski method and the zone-refining or float zone method. The equipment used in the Czochralski method is shown in Figure 1. The graphite crucible is filled with polycrystalline pieces which are then melted. A seed crystal is dipped into the melt and then slowly withdrawn such that the silicon slowly crystallizes as it is removed from the hot zone. Both the graphite crucible and the pulling seed are rotated, often counter to each other, so that resistivity and oxygen content can be made uniform. Single crystals of 30-cm diameter and more than 1 m in length can be prepared in this way, but it is difficult to keep the large volume of molten silicon free from contamination by the silica container and from impurities in the inert gas blanket for the long periods of time required.[6]

Arc furnace reduction

$$SiO_2 + 2C \longrightarrow Si + 2CO$$

$$\downarrow$$

Formation of volatile silicon compound

$$Si + 3HCl \longrightarrow SiHCl_3 + H_2$$

$$\downarrow$$

Purification of $SiHCl_3$ (bp 31.8 °C) by distillation

$$\downarrow$$

Chemical vapor deposition of semiconductor (polycrystalline) silicon

$$\downarrow$$

Single crystal Si formation by Czochralski method or zone refining

Scheme 1

$$\begin{aligned}
2SiHCl_3 &\longrightarrow SiH_2Cl_2 + SiCl_4\\
2SiH_2Cl_2 &\longrightarrow SiH_3Cl + SiHCl_3\\
2SiH_3Cl &\longrightarrow SiH_4 + SiH_2Cl_2\\
SiH_4 &\longrightarrow Si + 2H_2
\end{aligned}$$

Scheme 2

The zone-refining method is shown in Figure 2. In this method, only a small band of the polycrystalline silicon rod is melted at any one time and the molten zone is moved along the length of the rod, and impurities dissolve preferentially in the molten phase and so are drawn to the end of the rod. Again, single-crystal silicon crystallizes on a seed crystal, and single-crystal growth continues as the melt zone is moved. This method also allows large single crystals to be prepared. Contamination is more easily controlled as only a small fraction of the silicon is molten at any one time and the liquid zone is not in contact with any solid container. The float zone method can be applied more than once to a silicon rod to increase purity. Table 1 gives a summary of some of the more important data associated with elemental silicon and the silicon atom.

The chemistry that can be carried out at a silicon surface has become more significant in recent years as the dimensions

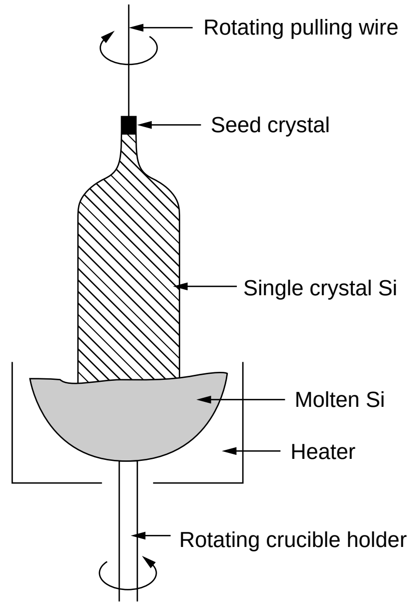

Figure 1 Schematic diagram of the Czochralski method of Si purification

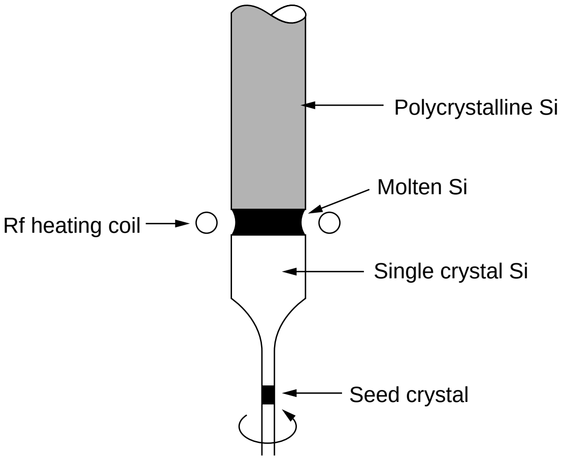

Figure 2 Schematic diagram of float zone or zone-refining method of Si purification

Table 1 Properties of silicon[10]

Melting point	1410 °C	
Boiling point	2355 °C	
Density	$2329\,\mathrm{kg\,m^{-3}}$ (at 0 °C) $2525\,\mathrm{kg\,m^{-3}}$ (liquid at mp)	
Atomic radius	1.17 Å	
Covalent radius	1.17 Å	
van der Waals radius	2.00 Å	
ΔH_{fusion}	$39.6\,\mathrm{kJ\,mol^{-1}}$	
ΔH_{vap}	$383.3\,\mathrm{kJ\,mol^{-1}}$	
Thermal conductivity	$148\,\mathrm{W\,m^{-1}\,K^{-1}}$ (at 27 °C)	
Electrical resistivity	$0.001\,\Omega\,\mathrm{m}$ (at 0 °C)	
Mass magnetic susceptibility	$-1.8 \times 10^{-9}\,\mathrm{kg^{-1}\,m^{3}}$	
Electronic configuration	$1s^22s^22p^63s^23p^2$	
Electron affinity	$133.6\,\mathrm{kJ\,mol^{-1}}$	
Ionization energies ($\mathrm{kJ\,mol^{-1}}$)		
$M \rightarrow M^+$	786.5	
$M^+ \rightarrow M^{2+}$	1577.1	
$M^{2+} \rightarrow M^{3+}$	3231.4	
$M^{3+} \rightarrow M^{4+}$	4355.5	
$M^{4+} \rightarrow M^{5+}$	16091	
Stable isotopes (mass and natural abundance)		
^{28}Si	27.976927	92.23%
^{29}Si	28.976495	4.67%
^{30}Si	29.973770	3.10%

of electronic devices based on crystalline silicon have become ever smaller. In addition to older methods such as doping, etching, and deposition of films to modify Si surfaces, newer studies have shown that reactions involving, for example, unsaturated species such as dienes, alkynes, and aromatic compounds can also occur and lead to Si–C bond formation. (These studies have been reviewed; see References 11 and 12). The reaction of elemental silicon, usually alloyed with copper, is the basis of the 'Direct Process' used for the preparation of simple alkylchlorosilanes (for a review see Reference 13).

The etching of silicon in the form, for example, of a wafer can be achieved in many ways and leads to a material known as 'porous silicon'. Etching can be achieved chemically, photochemically, or electrochemically using electrolytes usually comprising solutions of concentrated aqueous HF containing various additives. The size of the pores produced in the silicon can be varied from about 1×10^{-9} to 1×10^{-5} m, depending on the conditions used. The nature of the pores can also be varied greatly to include, for example, pores that are spongelike or cylindrical. The interest in porous silicon arises from its light-emitting properties such as photoluminescence and chemiluminescence and from its physical properties such as its high surface area (hundreds of square meters per cubic centimeter). If HF etching is used to prepare the porous silicon then the surface of the silicon is terminated by Si–H bonds and these can be used to carry out further chemistry at the surface such as oxidation to give Si–OH groups or hydrosilylation to give pendent organic groups. Such surface modification means that the materials may be used for bio- and chemical-sensing, new materials supports, and for mass spectrometry applications. The many methods of preparation and the potential uses of porous silicon have been reviewed.[14–17]

1.2 Silicon in Biology

Silica dissolves from the mineral environment into water to become bioavailable as silicic acid, $Si(OH)_4$, and can reach a concentration of up to 2 mM at near neutral pH. At higher concentrations, oligomerization takes place followed by the formation of colloidal particles of hydrated silica, $SiO_2.{\times}H_2O$. Silicic acid in water is used by organisms such as diatoms and radiolaria to build up complicated exoskeletons of hydrated silica and plants can take in silicic acid to build up silica materials that can strengthen stems and leaves or make protective spikes (*see* ***Biomineralization***). Thus, terrestrial plants can, at an average composition of 0.15% Si, contain more silicon than magnesium or phosphorus. Clearly, animals eating vegetation may consume large amounts of silicon in their normal diet. The effects of silicon in diet and silicon deficiency have been the subjects of several studies that have been reviewed.[18] It seems that although the silicon in higher animals plays neither a significant structural role nor participates in Si–C bond formation, it is useful in its interaction with toxic metals such as aluminum where it can affect the metal's bioavailability, distribution, and excretion. The bio-manipulation of silicic acid and its polycondensation into silica has been shown to involve several classes of proteins that have been named ‘frustulins’ (isolated from cell walls of diatoms), ‘silaffins’ (found occluded within biosilica) and ‘silicateins’ (also found occluded in silica needles). The mechanisms used by these biological controllers of silica production are of significant interest as they may be used to produce synthetic silica with high surface area and/or well-defined porosity.[19] Numerous reviews of the various aspects of biological silicon chemistry in plants, concerning, for example, silicon deposition in higher plants, the effects of silicon on plant growth and crop yield, and silicon resources for agriculture can be found in Reference 20.

2 ONE-COORDINATE COMPOUNDS

Compounds containing silicon bonded to only one other atom are unstable and are usually only generated and observed as reactive intermediates of short half-life. Silicon compounds subjected to flash photolysis or electrical discharges in the gas phase produce short-lived species SiX ($X = H$, F, Cl, Br, I, C, Si, etc.), the band structure of which have been studied in detail.[21] The structures, electronic configurations, and so on of SiX ($X = H$, F, Cl, Br, I, N, O, etc.) have also been the subject of MNDO (modified neglect of diatomic overlap) and other calculations.[22,23]

Silicon monoxide, SiO, is formed in a wide range of reactions such as those between SiO_2 and Si, SiO_2 and Mg, SiO_2 and CO, and $SiCl_4$ and O_2, at high temperatures. The reaction between Si and SiO_2 (equation 3) in an oxygen-free atmosphere may be troublesome in the high-temperature postoxidation annealing process used during the fabrication of semiconductor devices. However, the reaction is inhibited if O_2 is present (which presumably oxidizes SiO back to SiO_2 as it is formed) during the annealing process.[24] When quartz, SiO_2, is heated to sufficiently high temperatures for vaporization to occur, the predominant species in the gas phase is found to be SiO. Commercially SiO has been produced as a dark brown cokelike mass on a substrate from the reaction of Si with SiO_2 at 1250 to 1400 °C (for a review on the production, properties, and applications of SiO, see Reference 25). As a fine brown powder, freshly prepared SiO is pyrophoric and readily oxidizes to give SiO_2. Rapid cooling on to a cold surface, or condensation into an inert gas mixture, enables SiO to be isolated and studied spectroscopically. Thus condensation of an Ar/SiO mixture on to a cold copper surface allows IR spectroscopic identification of SiO, $(SiO)_2$, and $(SiO)_3$ with characteristic IR absorbances at 1226, 803 and 768, and 972 cm^{-1} respectively. The IR data suggest that $(SiO)_2$ has a cyclic structure.[26] Monomeric SiO can react in a matrix with metals, for example, reaction with Pd gives PdSiO the bonding in which is thought to be similar to the corresponding carbonyl, PdCO. The reactions of SiO in noble gas matrices have been reviewed.[27]

$$Si^{+\bullet} + HX \rightleftharpoons [SiHX]^{+\bullet *} \longrightarrow SiX^{+} + H^{\bullet}$$

$$X = Cl, OH, SH, NH_2$$

Scheme 3

$$Si + SiO_2 \longrightarrow 2SiO \qquad (3)$$

Silicon monosulfide, SiS, is formed in the high-temperature reaction between silicon and sulfur, or between SiO_2 and metal sulfides such as FeS or ZnS. It is also formed on passing H_2S over Si at 1500 K and it can be trapped in an argon matrix and analyzed by IR spectroscopy, showing a band at 739 cm^{-1} for SiS. The monosulfide reacts in the matrix with co-condensed COS to give linear SiS_2, which absorbs at about 900 cm^{-1}.[28]

There is continuing interest in the gas-phase reactions of silicon cations because of the increasing use of chemical vapor deposition in the semiconductor industry and the interest in the preparation of three-coordinate silicon cations in condensed phases. Atomic silicon cations, $Si^{+\bullet}$, react with a wide range of inorganic and organic species in the gas phase to give more complicated species that can be investigated by ion cyclotron resonance, flow tube techniques, or ion-trap techniques. Some simple examples of these reactions are shown in Scheme 3. Initially a long-lived intermediate form, it then breaks down to give the silicon-containing cation and $H^{\bullet}$. These and other reactions of $Si^{+\bullet}$ have been reviewed.[29]

Metal silicides such as NaSi, KSi, and $CaSi_2$ that appear from their empirical formulas to contain single-coordinate Si are, in fact, complicated three-dimensional solids. Metal silicides have found increasingly numerous applications in the semiconductor industry, in thermoelectric devices, and in structural applications. They may be prepared in numerous ways, for example, by depositing a layer of metal onto Si and then heating, by coevaporation of a metal and Si, or by chemical vapor deposition using a mixture of SiH_4, H_2, and a volatile metal complex. Metal silicides exhibit a wide variety of structures including isolated Si^{4-} ions such as in Mg_2Si, tetrahedral $Si_4{}^{4-}$ ions as in KSi, layers as in $CaSi_2$, and three-dimensional networks as in $SrSi_2$. These are beyond the scope of this review, but have been reviewed elsewhere.[30–33]

3 TWO-COORDINATE COMPOUNDS

Two-coordinate X_2Si: species are called silylenes (by analogy with carbenes) and are best described as reactive intermediates which may be trapped and observed spectroscopically at low temperatures in an inert matrix, but most of which have short lifetimes under normal conditions. The structures and electronic configurations of X_2Si: ($X = H$, F, Cl, Br, O, etc.) have been calculated by MNDO and other more sophisticated theoretical methods.[22,23,34,35] Experimental values for the X–Si–X angle in X_2Si: species have been found to be 92.5, 100.76, 102.8, and 102.7° respectively for X = H, F, Cl, and Br. This suggests that repulsions between the X groups as well as electronic effects may play an important part in determining the structure of silylenes.[36]

The simplest silylene H_2Si: is formed by the pyrolysis of SiH_4 and the higher perhydrosilanes and it undergoes two typical types of reaction: insertion and addition. Silylene readily inserts into Si–H bonds (Scheme 4) both in perhydro- and alkylsilanes (organosilanes such as Et_3SiH are often used as chemical traps for R_2Si: species).[37]

Silylene also undergoes nonstereospecific addition to a variety of conjugated dienes (Scheme 5).[37]

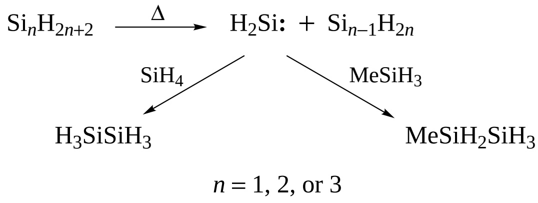

Si_nH_{2n+2}
Δ
$H_2Si: + Si_{n-1}H_{2n}$
SiH_4
$MeSiH_3$
H_3SiSiH_3
$MeSiH_2SiH_3$
n = 1, 2, or 3

Scheme 4

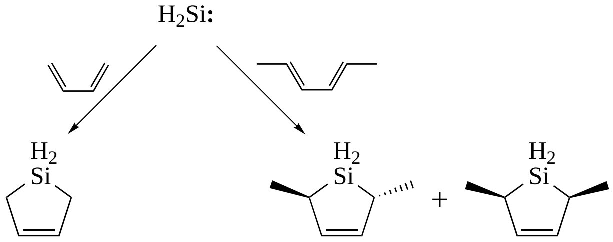

$H_2Si:$
H_2
Si
H_2
Si
+
H_2
Si

Scheme 5

Difluorosilylene is much more stable than other simple silylenes, having a half-life at room temperature of about two minutes, much longer than that of difluorocarbene (ca. 1 s), but much shorter than that of GeF_2 which is a stable solid. This has meant that much of the chemistry of F_2Si: has been investigated in the condensed rather than the gas phase. The silylene is readily prepared at high temperature, and in the absence of trapping agents forms oligo- and polyperfluorosilanes (equation 4).[37]

$$n\mathrm{Si} + n\mathrm{SiF_4} \xrightarrow{1200\,^{\circ}\mathrm{C}} 2n\mathrm{F_2Si:} \xrightarrow{-196\,^{\circ}\mathrm{C}} \mathrm{Si}_n\mathrm{F}_{2n+2} + \text{polymers} \tag{4}$$

As in the case of H_2Si:, difluorosilylene undergoes both insertion and addition reactions (Scheme 6), although in this case there is often more than one SiF_2 unit in the product, which is perhaps not surprising in view of the formation of Si_nF_{2n+2} species on condensation. Insertion reactions occur readily with fluoroalkenes, but addition occurs with other alkenes. This is presumably due to the high strength of the Si–F bond formed in the insertion which drives the reaction.[37]

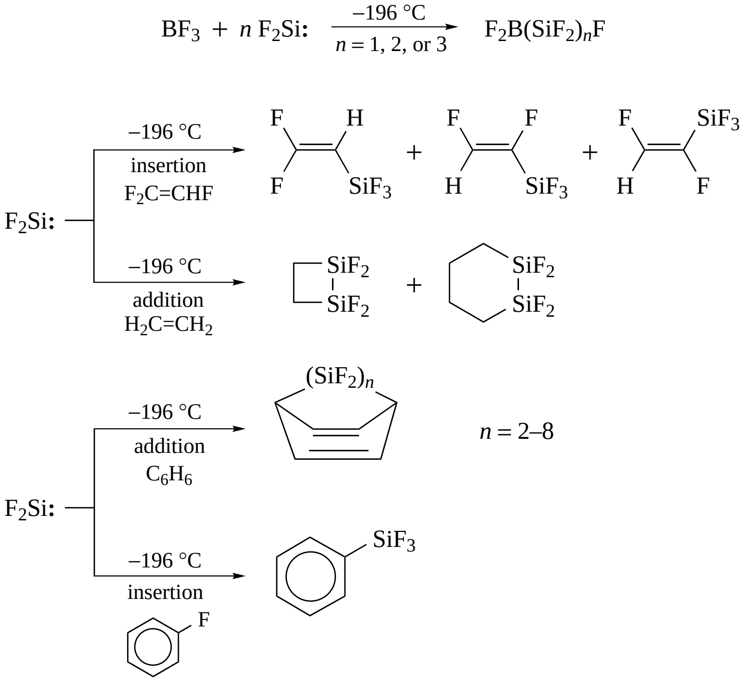

$BF_3 + n\,F_2Si:$
−196 °C
n = 1, 2, or 3
$F_2B(SiF_2)_nF$
−196 °C
insertion
$F_2C{=}CHF$
F
H
F
SiF_3
+
F
F
H
SiF_3
+
F
SiF_3
H
F
$F_2Si:$
−196 °C
addition
$H_2C{=}CH_2$
SiF_2
SiF_2
+
SiF_2
SiF_2
−196 °C
addition
C_6H_6
$(SiF_2)_n$
n = 2–8
$F_2Si:$
−196 °C
insertion
F
SiF_3

Scheme 6

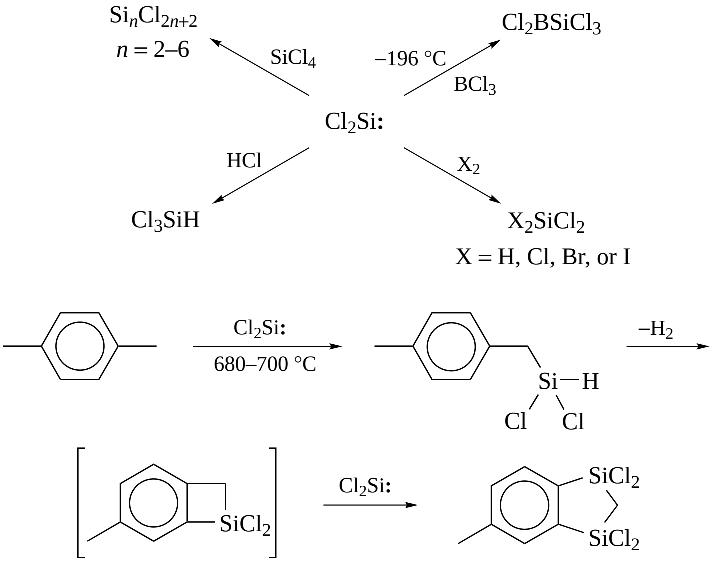
SinCl2n+2
n = 2–6
SiCl4
−196 °C
BCl3
Cl2BSiCl3
Cl2Si:
HCl
Cl3SiH
X2
X2SiCl2
X = H, Cl, Br, or I
Cl2Si:
680–700 °C
Si—H
Cl
Cl
−H2
SiCl2
Cl2Si:
SiCl2
SiCl2

Scheme 7

Dichlorosilylene may be prepared by pyrolysis of perchloropolysilanes and again undergoes both insertion and addition reactions. The insertion into a wide variety of bonds, including C–H bonds, has been studied (Scheme 7). At the elevated temperatures used in these reactions, elimination of H_2 and cyclization may also occur and, if the ring formed is strained, a further Cl_2Si: insertion may occur.**[37]**

As in the case of F_2Si:, addition of Cl_2Si: to alkenes occurs readily (Scheme 8), but the products rarely contain Si–Si bonds even if more than one Si atom is present in the product, due to dimerization.**[37,38]**

The flash photolysis of H_3SiX ($X = Cl$, Br or I) gives rise to HXSi:, the structures of which have been investigated by emission and absorption spectra. Like the X_2Si: species they have a singlet ground state with a relatively small angle at silicon.**[30]** Photolysis of H_3SiN_3 at 193 nm in an argon matrix at 10 K leads to the formation of HSi≡N that can be characterized by IR and UV spectroscopy at low temperature but which decomposes rapidly as it is warmed.**[39]** The co-condensation of SiO and O_2 in an argon matrix gives isolated, linear SiO_2 molecules (quite unlike the extended array of four-coordinate silicon atoms in SiO_2 in the form of quartz) having a characteristic IR band at $1400\,cm^{-1}$.**[40,41]** The mixed chalcogen species, SiOS may also be trapped from the reaction between SiS and O atoms.**[42]**

Although the chemistry of silylenes was for many years restricted to that of reactive species where the two substituents at Si were small, since the mid 1990s the realization that steric protection of the silylene center could enable stable silylenes to be isolated under normal laboratory conditions has led to a blossoming of new chemistry. Nitrogen substituted silylenes can be prepared by reduction of halosilane precursors as shown in Scheme 9. Reagents such as potassium in THF, potassium-graphite and finely divided magnesium can be used to effect the reduction and fluoro-, chloro-, or bromosilanes may be used as precursors. Although thermally stable, these

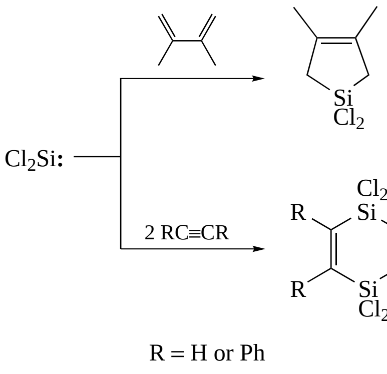
Cl2Si:
Si
Cl2
2 RC≡CR
Cl2
Si
R
R
R
R
Si
Cl2
R = H or Ph

Scheme 8

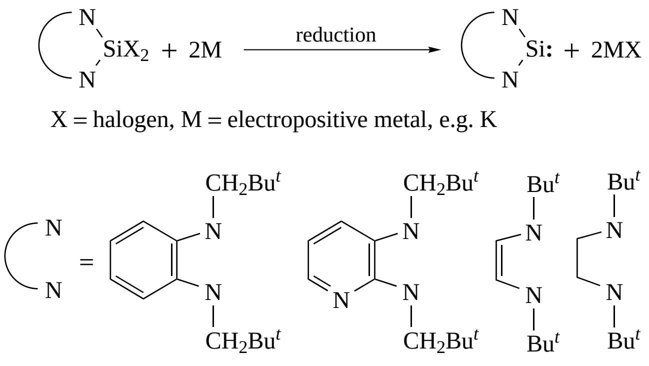
N
SiX2 + 2M
N
reduction
N
Si: + 2MX
N
X = halogen, M = electropositive metal, e.g. K
N
N
=
CH2But
N
N
CH2But
CH2But
N
N
N
CH2But
But
N
N
But
But
N
N
But

Scheme 9

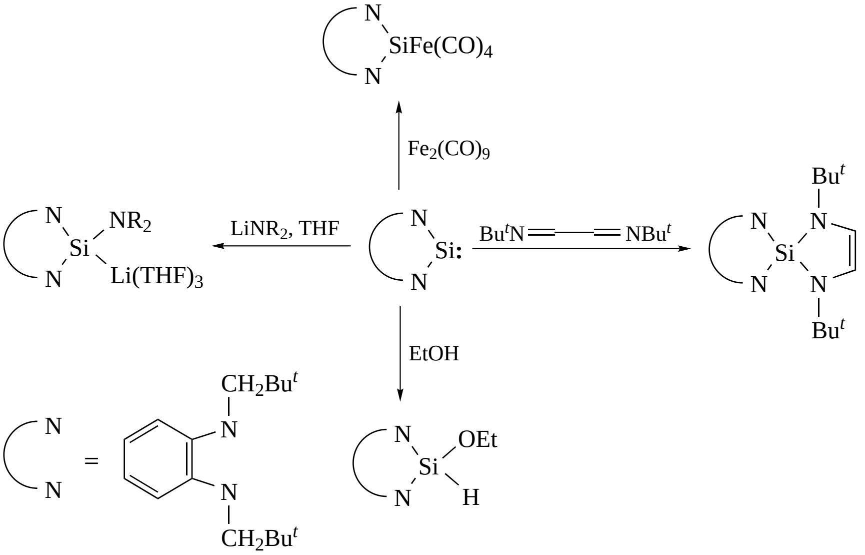

Scheme 10

silylenes are reactive towards a wide range of compounds and typically undergo reactions that involve nucleophilic addition to an unsaturated organic compound, insertion into polar bonds such as O–H, C–X (X = Cl, Br or I), or N–M (M = Li, Na or K), and reactions with transition metal centers. Examples of these reactions are shown in Scheme 10. The chemistry of these and related silylenes has been the subject of many publications, these have been reviewed recently.[43–46]

4 THREE-COORDINATE COMPOUNDS

The structural details of three-coordinate silicon compounds have, as their one- and two-coordinate analogs discussed above, mainly been obtained at either very high- or low temperatures or using very rapid spectroscopic techniques. This is due to their high reactivity and short half-lives, in turn due to the reluctance of silicon to form multiple bonds as, unlike carbon, it is usually much more thermodynamically advantageous to form two single bonds rather than one double bond to silicon. Early work on three-coordinate silicon compounds has been reviewed.[30] The structures of unsaturated Si–H containing compounds such as $H_2Si{=}SiH_2$ and other low-coordinate species such as silylenes have been the subject of much theoretical investigation. The calculated structures of these fascinating compounds and comparisons with experimentally derived data for them are available.[47]

Trivalent inorganic silicon cations are extremely rare in solution (but common in the gas phase[48]) and their existence has remained a matter of some dispute.[49–51] Many calculations on the structures and the stability of R_3Si^+, $R_3Si\bullet$, and R_3Si^- species have been carried out and are reviewed.[34,51] Silyl radicals, $R_3Si\bullet$, and silyl anions, R_3Si^-, may be prepared, although the radicals tend to have a short half-life. The inorganic radicals $R_3Si\bullet$ (R = H, F or Cl) are known, although organic-substituted silyl radicals are much more common and are used for radical reductions in organic chemistry. The radicals are usually prepared by UV photolysis of R_3Si–H compounds either alone or in the presence of radical initiators such as *t*-BuOOBu-*t*, and may be observed spectroscopically in inert gas matrices at low temperatures.[30]

An X-ray investigation of $MSiH_3$ (M = K, Rb, or Cs; for their preparation, see Section 5.1.3) shows that the compounds crystallize in the sodium chloride face-centered cubic lattice. This differs from the NiAs structure of KCH_3 and gives an effective ionic radius for SiH_3^- of about 2.26 Å.[52] The most widely studied of the compounds is $KSiH_3$, which also has an orthorhombic β-form[53] (see Section 5.1.3 for details of its reactions). The formation and use of the Cl_3Si^- ion by treatment of Cl_3SiH with tertiary amines or from $BrSiCl_3$ is discussed more fully in Section 5.2.3 Three-coordinate $SiOX_2$ (X = F or Cl) are formed in an argon matrix from the photolysis of SiO and X_2[41,54] while $SiOCl_2$ can be isolated in a matrix from the combustion of $SiCl_4$ with O_2.[55]

Stable compounds containing simple three-coordinate silicon atoms other than the alkali metal salts were not isolated until a range of transition metal silylene complexes were prepared. However, instead of having simple structures of the type $R_2Si = ML_n$, that is, analogous to their carbon analogs, the silicon atom is usually further coordinated by a donor ligand such as HMPA or THF. Some donor-free complexes have, however, been prepared in solution.

Displacement of a good leaving group from silicon in a noncoordinating solvent (equation 5) allows solvent-free complexes (**1**) to be prepared when the substituents on silicon are bound via sulfur. As would be expected by analogy with carbene complexes, the ^{29}Si NMR chemical shift for these complexes is at very low field (264.4 and 268.7 ppm, respectively, for R = S-*p*-tolyl and SEt, respectively) and they also react readily with donor molecules such as MeCN to give four-coordinate, donor stabilized silylene species.[56,57] (See Section 6 below for further details of transition metal silyl complexes.)

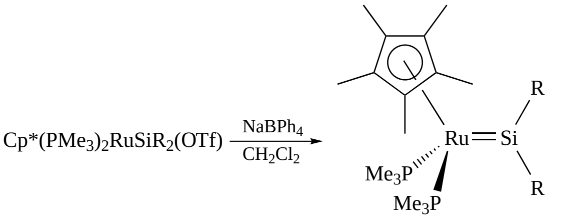

(5)

(**1**) R = S-*p*-tolyl or SEt

The salt elimination method (equation 6) may also be used to prepare silylene complexes and, again if sulfur ligands are present, a donor-free complex may be formed as shown, although it is only the minor product along with the donor stabilized complex (**2**) which it readily forms in the presence of excess HMPA. The donor-free complex is only stable below −30 °C and decomposes above this temperature to give $HFe_3(CO)_{11}^-$ and the polysilane $[(t\text{-BuS})_2Si]_n$.[58]

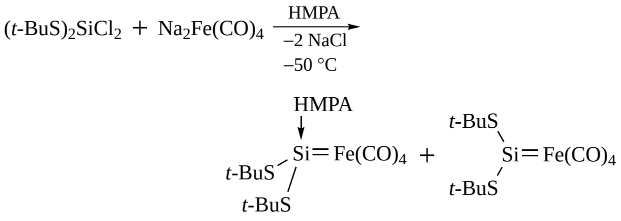

(**2**)

(6)

5 FOUR-COORDINATE COMPOUNDS

The chemistry of silicon is largely that of four-coordinate compounds although, as seen in Section 7, higher coordination is readily achieved and many stable compounds containing five- and six-coordinate silicon are known. Silicon forms unusually strong bonds to the electronegative elements such as the halogens, oxygen, and nitrogen; Table 2 shows typical bond energies in some representative four-coordinate compounds. The bonds to the halogens and to oxygen are even stronger than their carbon analogs, but, as will be seen in the following section, compounds containing such bonds are also usually much more reactive than their carbon analogs.

Table 2 Average covalent bond strengths and lengths in silicon compounds[59,60]

	Bond strength (kJ mol^{-1})	Bond length (Å)
Si–H	326	1.48
Si–F	582	1.55
Si–Cl	391	2.02
Si–C	301	1.87
Si–Si	226	2.32
Si–O	452	1.51

5.1 Perhydrosilanes

Although the chemistry of carbon, the near neighbor of silicon in the periodic table, is greatly dominated by the vast array of compounds containing C–H bonds, there are far fewer comparable silicon species. Generally speaking, the simple alkanes are rather unreactive and, even in more complicated compounds containing other functional groups, the C–H bonds are likely, along with C–C bonds, to be the least reactive in the molecule. Compounds containing Si–H bonds do not occur naturally and this is due to the high reactivity of the Si–H bond toward a wide variety of reagents. The Si–O bond is very strong and its formation is often the overriding factor in many reactions, and many of the compounds described in Section 6, including the hydrides, react with water or dilute aqueous acid or base to give Si–O containing products. Why then is the chemistry of silanes so different from that of alkanes? An important difference between carbon and silicon is their electronegativity, 2.5 and 1.8 (on the Pauling scale), respectively. The rather greater electropositive character of silicon means that in contrast to carbon, in which the C–H bond is polarized $C^{\delta-}$–$H^{\delta+}$, the Si–H bond is polarized in the opposite manner $Si^{\delta+}$–$H^{\delta-}$. This, combined with the relatively high ionic character of the Si–H bond, and the fact that it is about 90 kJ mol^{-1} weaker than the C–H bond, means that Si–H compounds are much more reactive than their carbon analogs. The Si–H bond also has greater ionic character than the C–H bond. The availability of d-orbitals on silicon means that five- or six-coordinate intermediates or transition states are readily accessible, and the larger size of silicon also means that incoming reagents have more space in which to attack than in comparable carbon compounds. The chemical and physical properties of hydrosilanes are discussed in detail elsewhere.[61,62]

5.1.1 *Preparation of Silicon Hydrides*

Several methods are available for the preparation of compounds containing Si–H bonds. Historically, the silicon hydrides $H(SiH_2)_nH$ ($n = 1, 2, 3$, etc.) were prepared by reaction of various metal silicides (such as those of Mg, Al, and Fe) with hydrochloric or phosphoric acid (equation 7).[63] For example, Mg_2Si addition to dilute phosphoric acid affords H_4Si, H_3SiSiH_3, $H_3SiSiH_2SiH_3$, Si_4H_{10}, and Si_5H_{12} (together

$$R_nSiX_{4-n} + (4-n)\,MH \xrightarrow{\text{ethereal solvent}} R_nSiH_{4-n} + (4-n)\,MX$$

R = alkyl, aryl, H, etc.; X = any halogen; MH = LiH, $LiAlH_4$, etc.;
$n = 0$–3; solvent usually = THF, Et_2O, or $(MeOCH_2CH_2)_2O$

$$2Cl_3SiSiCl_3 + 3LiAlH_4 \longrightarrow 2H_3SiSiH_3 + 3LiCl + 3AlCl_3$$

Scheme 11

with higher silanes) in an approximate ratio 8:6:3:2:1 but with only a 25% overall conversion of silicide to silane silicon. The yields from this type of reaction are low because of the hydrolysis of the Si–H bonds in the products by the aqueous environment. Better yields are obtained by treatment of Mg_2Si with NH_4Br in liquid ammonia (for the detailed preparation of silane from NH_4Br and Mg_2Si, see Brauer[64]) or with $H_2NNH_2{\cdot}2HCl$ in hydrazine. More recent analysis of the products from this type of reaction show that silanes containing up to nine silicon atoms are formed.[65]

$$Mg_2Si + \frac{H_2O}{H^+} \longrightarrow SiH_4 + Mg(OH)_2 \qquad (7)$$

These methods are no longer used because the separation of the mixtures formed leads to low yields of the individual silanes. A far more general method, and one that can conveniently be carried out on a laboratory scale, is the reduction of halosilanes using reagents such as $LiAlH_4$ or LiH (Scheme 11). Unfortunately, polyhalides cannot be partially reduced in this way, that is, $SiCl_4$ cannot be reduced to H_2SiCl_2. Silyl deuterides, Si_nD_{2n+2}, can be prepared in similar ways to the hydrides, that is, by D_2O/DCl decomposition of Mg_2Si or by reduction of halides with $LiAlD_4$.

Disilane, H_6Si_2, has also been produced cleanly by CO_2 laser irradiation of monosilane SiH_4[66] and a detailed procedure for the preparation of disilane, trisilane, and higher silanes by passage of an electric discharge through SiH_4 has also been reported.[67] Physical data for some silanes are given in Table 3 and, as would be expected by analogy with the alkanes, the small silanes are volatile gases and the larger ones are liquids with boiling points that increase as the molecular weight increases. Further properties of the higher silanes (NMR and Raman spectra, viscosity, and surface tension) are available,[68–70] and the physical and thermodynamic properties of SiH_4 have been reviewed.[71] There are also reviews of the manufacture and applications of SiH_4[62,72] and of the methods associated with analysis and purification of SiH_4.[62,73]

Table 3 Physical properties of perhydrosilanes[74]

	Mp (°C)	Bp (°C)	Density ($g\,cm^{-3}$)
SiH_4	−185	−112	1.44 $g\,L^{-1}$ (gas)
H_3SiSiH_3	−132.5	−14.5	0.685 at −25 °C
$H_3SiSiH_2SiH_3$	−117.4	52.9	0.739 at 20 °C
$H_3Si\,(SiH_2)_2SiH_3$	−88.2	107.4	0.792 at 20 °C
$(H_3Si)_3SiH$	−99.4	101.7	0.793 at 20 °C
$H_3Si\,(SiH_2)_3SiH_3$	−72.8	153.2	0.795 or 0.827, both at 20 °C
$(H_3Si)_2SiHSiH_2SiH_3$	−109.8	146.2	0.820 at 20 °C
$(H_3Si)_4Si$	−57.8	134.3	0.815 at 20 °C
$H_3Si(SiH_2)_4SiH_3$	−44.7	193.6	0.827 at 20 °C
$(H_3Si)_2SiHSiH_2SiH_2SiH_3$	−78.4	185.2	0.840 at 20 °C
$(H_3SiSiH_2)_2SiHSiH_3$	−69	179.5	0.843 at 20 °C

5.1.2 *Structure of Perhydrosilanes*

The structure of H_4Si and D_4Si has been investigated in the gas phase. Tetrahedral geometry is found as expected and the bond lengths are 1.49 and 1.47 Å, respectively, for the H and D compounds.[75] The structure of H_3SiSiH_3 has been determined by electron diffraction in the gas phase and shows an Si–Si bond length of 2.331 Å (which is slightly shorter than that found in elemental Si and in Si_2Me_6), an Si–H bond length of 1.492 Å, and an H–Si–Si angle of 101.3°.[76] Calculations on the structure of SiH_4 and related silanes are discussed in References 35 and 77.

5.1.3 *Reactions of Perhydrosilanes*

The perhydrosilanes are toxic and spontaneously flammable in air and form explosive mixtures with oxygen. The mechanism of SiH_4/O_2 explosions has been investigated, and the products from such reactions depend greatly on the initial composition of the mixture. For mixtures $>70\%$ O_2, the products are SiO_2 and H_2O, but for mixtures $>70\%$ SiH_4, the products are SiO_x (SiO deposited may be a mixture of SiO_2 and Si), Si, and H_2.[78] Extreme caution should, therefore, be exercised in their handling. Accidental release of silane into the atmosphere may lead to fire or explosion hazards, and spontaneous ignition of a SiH_4/N_2 mixture in air may occur above about 2.5 volume % SiH_4. (The problems associated with handling silane have been addressed.[79]) As has been stated above, highly pure silane undergoes thermal decomposition at about 570–670 °C to give highly pure silicon, and SiH_4 has therefore become an important gas used in the manufacture of integrated circuits and photovoltaic cells. There has been considerable discussion about the mechanisms of the plasma or thermal chemical vapor deposition of Si from SiH_4. Much work has suggested that the silyl radical $SiH_3{\cdot}$ is the dominant species responsible for deposition, but more recent work suggests that silylene, $H_2Si{:}$, is the most important species which, together with disilane (which is formed by insertion reaction as shown below), when adsorbed on to a surface, breaks down to give silicon.[80,81] The mechanism of deposition may also involve the adsorption of $H_2Si{:}$ on to a surface and then insertion of further $H_2Si{:}$ units into the Si–H bonds of the absorbed species; further insertions and loss of H_2 lead to the buildup of material containing Si–Si bonds (Scheme 12).[82] The use of SiH_4 and chlorosilanes for the deposition of Si has been discussed[83] and the reactions of SiH_4 to form transition metal complexes are described in Section 6.1. The ionization and

$$\begin{tikzcd}[column sep=small] \mathrm{SiH_4\,(g)} \arrow[r, "\mathrm{heat}"] & \mathrm{H_2\,(g) + H_2Si\!:\,(g)} \arrow[r] & \mathrm{H_2Si\!:\,(ads)} \arrow[d, "\mathrm{2H_2Si:}"] \\ & \mathrm{etc.} & \mathrm{(H_3Si)_2Si\!:\,(ads)} \arrow[l, "\mathrm{H_2Si:}"'] \end{tikzcd}$$

Scheme 12

ensuing fragmentation of SiH_4 gives $SiH_x^{+\bullet}$ (where $x = 1, 2,$ or 3) that can undergo hydride exchange reactions or clustering with neutral SiH_4. Reactions of these ions with inorganic and organic compounds have been reviewed.[29]

As stated above, the most obvious reaction of silanes is their oxidation by, for example, oxygen, water, and alcohols (in great contrast to the analogous alkanes). From this it follows that silanes are good reducing agents and organosilicon compounds (which are much easier to handle than the perhydro compounds) such as Et_3SiH have been used extensively to carry out reductions in organic chemistry. (For reductions in organic chemistry using $(EtO)_3SiH$, see Fieser.[84]) Although silanes do not appear to react with pure water or slightly acidic water under normal conditions, in slightly basic solution rapid and complete hydrolysis occurs with the evolution of hydrogen. The hydrolytic cleavage of a Si–Si bond also affords H_2, and this method can therefore be used to ascertain the number of Si–H and Si–Si bonds present in a molecule by measuring the volume of hydrogen evolved (Scheme 13).

Silane reacts with methanol to give the alkoxysilanes $(MeO)_nSiH_{4-n}$ ($n = 2, 3, 4$) and with higher alcohols in the presence of base to give tetraalkoxysilanes (equation 8).[85] This type of reaction is, however, rarely carried out as the alkoxysilanes produced are more conveniently prepared from alcohols and $SiCl_4$ (which is more readily available than SiH_4 and much more easily handled). Similarly, silyl esters, $Si(OCOR)_4$, are also usually prepared from polyhalogenosilanes rather than from silane and a carboxylic acid.

$$\mathrm{SiH_4 + 4ROH} \xrightarrow{\mathrm{RO^-}} \mathrm{Si(OR)_4 + 4H_2} \qquad (8)$$

$$\mathrm{R} = \mathrm{Et},\ n\text{-}\mathrm{Pr},\ n\text{-}\mathrm{Bu,\ etc.}$$

Silane reacts with alkali metals (Na, K, Rb, and Cs) over a period of between about a week for Cs, and two or three months for Na, to give H_3SiM species (see Section 4 for a description of their structures) in the ether solvents $MeOCH_2CH_2OMe$ or $(MeOCH_2CH_2)_2O$ by two different pathways depending on the stoichiometry of the reagents (Scheme 14).[86,87]

$$\mathrm{SiH_4 + 2KOH} \xrightarrow{\mathrm{H_2O}} \mathrm{K_2SiO_3 + 4H_2}$$

$$\mathrm{H_3Si{-}SiH_3 + 4KOH} \xrightarrow{\mathrm{H_2O}} \mathrm{2K_2SiO_3 + 7H_2}$$

Scheme 13

$$\mathrm{2SiH_4 + 2M} \longrightarrow \mathrm{2H_3SiM + H_2}$$

$$\mathrm{SiH_4 + 2M} \longrightarrow \mathrm{H_3SiM + MH}$$

Scheme 14

$$\begin{aligned} \mathrm{H_3SiK + MeI} &\longrightarrow \mathrm{H_3SiMe} \\ \mathrm{+\ Me_3MCl} &\longrightarrow \mathrm{H_3SiMMe_3} \\ \mathrm{+\ PhSiH_2Br} &\longrightarrow \mathrm{PhSiH_2SiH_3} \\ \mathrm{+\ PhGeBr_3} &\longrightarrow \mathrm{PhGe(SiH_3)_3} \end{aligned}$$

$$\mathrm{M = Si,\ Ge,\ or\ Sn}$$

Scheme 15

The most well known of the alkali metal derivatives is $KSiH_3$, which acts as a nucleophile in a wide range of displacement reactions, for example, with HCl to give SiH_4 and KCl, with MeCl to give H_3SiCH_3,[88] and with $PhCH_2Cl$ to give $PhCH_2SiH_3$,[89] or as a reducing agent, for example, reducing CO_2 to CO.[90] Silylpotassium reacts with various other halides to give silyl substituted products and a range of such reactions are depicted in Scheme 15.[91,92]

The reactions between $KSiH_3$ and perhydrosilanes (equation 9) afford various other silylpotassium reagents, which have also been used to prepare other functional oligosilanes in a manner similar to that shown in Scheme 15.[93,94]

$$\mathrm{H_3SiK + (H_3Si)_nSiH_{4-n}} \xrightarrow{\mathrm{MeOCH_2CH_2OMe}} \mathrm{(H_3Si)_nSiKH_{4-n-1}} \qquad (9)$$

$$n = 1, 2, \text{ or } 3$$

5.2 Silicon Halohydridosilanes, H_nSiX_{4-n} ($n = 1$–3, X = Halogen), etc.

These compounds are highly reactive like the perhydrosilanes and must be handled with care because of their ready hydrolysis in the atmosphere to give the corrosive and toxic hydrogen halides, HX (X = F, Cl, Br, or I). Again, this high reactivity is in great contrast to the relative inertness of common halohydroalkanes such as CH_2Cl_2 and $CHCl_3$. Of all the halohydrosilanes, trichlorosilane is by far the most important and the most widely studied because of its industrial uses, for example, in the preparation of high purity silicon as discussed earlier in Section 1.1 and in the preparation of organosilanes via the ***Hydrosilation Catalysis*** reaction.

5.2.1 *Preparation of Halohydrosilanes*

Trichlorosilane is produced and used on a large industrial scale and it is usually prepared from the reaction of Si with HCl at about 300 °C, which can also give H_2SiCl_2.[95] The preparation of $SiHBr_3$ and SiH_2Br_2 can be achieved in a similar manner from Si and HBr.[96] At 360 °C and above, Si reacts with HBr to give $SiHBr_3$ and $SiBr_4$ in varying proportions depending on the temperature, a higher temperature giving a greater proportion of $SiBr_4$.[97] Silicon tetrachloride can also be reduced with hydrogen to give $SiHCl_3$ (equation 10).[98]

$$\mathrm{SiCl_4 + H_2 \xrightarrow{525-650\,^{\circ}C} SiHCl_3 + HCl} \tag{10}$$

The monohalo- and the dihalosilanes H_3SiX and H_2SiX_2 ($X = Cl$, Br or I) may be prepared by the reaction between silane and one or two equivalents of HX respectively, catalyzed by the corresponding aluminum halide (equation 11).

$$\mathrm{H_4Si} + n\mathrm{HX} \xrightarrow{\mathrm{AlX_3}} \mathrm{H}_{4-n}\mathrm{SiX}_n + n\mathrm{H_2} \tag{11}$$

$$n = 1 \text{ or } 2$$

The fluorosilane H_3SiF cannot be prepared in this way but is readily available by halogen exchange reactions from, for example, the reaction between SbF_3 and H_3SiCl. The other fluorohydrosilanes H_2SiF_2 and $HSiF_3$ are similarly prepared by treatment of the corresponding chloro or bromo compound with a metal fluoride, for example, heating $SiHCl_3$ with TiF_4 at 100 to 200 °C affords $SiHF_3$.[99]

The iodosilane H_2SiI_2 can be prepared by cleavage of the Si–Ph bonds in Ph_2SiH_2 with HI[100] or more conveniently by treating $PhSiH_3$ with I_2 (Scheme 16).[101] (Cleavage of $PhSiH_3$ with HBr or HI similarly gives H_3SiBr or H_3SiI.[102,103])

Aryl groups such as Ph, *p*-tolyl, and α-naphthyl are all readily cleaved from silicon by HX/AlX_3 to give a variety of halohydrodisilanes (Scheme 17).[104] Similarly, an extensive range of halotrisilanes including most of the possible isomers of Si_3X_7H, $Si_3X_6H_2$, $Si_3X_5H_3$ ($X = Cl$, Br or I), $Si_3I_4H_4$, $Si_3I_3H_5$, and $Si_3I_2H_6$, can be prepared by cleavage of the Si-aryl bonds of corresponding arylsilanes using HX. Detailed NMR spectroscopic studies of these compounds have been carried out.[105]

Compounds containing Si–H bonds generally react readily with halogens; SiH_4 with Cl_2 or Br_2 gives explosive reactions but the vigor of these reactions is ameliorated at low temperature, and H_3SiBr and SiH_2Br_2 may be isolated from such reactions (equation 12).[106,107]

$$\mathrm{PhSiH_3 + I_2 \xrightarrow[\text{ethyl acetate}]{-78\ ^{\circ}C} PhSiH_2I + HI \longrightarrow H_2SiI_2 + C_6H_6}$$

Scheme 16

$$\left.\begin{array}{r}\mathrm{PhH_2SiSiH_2Ph}\\ \mathrm{Ph_2HSiSiHPh_2}\\ \mathrm{Ph_3SiSiH_3}\end{array}\right] \xrightarrow[\mathrm{HX}]{\mathrm{AlX_3}} \begin{array}{l}\mathrm{XH_2SiSiH_2X}\\ \mathrm{X_2HSiSiHX_2}\\ \mathrm{X_3SiSiH_3}\end{array}$$

$$X = \text{Br or I}$$

Scheme 17

$$\mathrm{SiH_4 + 2Br_2 \xrightarrow{-80\,^{\circ}C} SiH_2Br_2 + 2HBr} \tag{12}$$

The reaction of hydrogen halides with disilane gives halodisilanes but these, apart from IH_2SiSiH_3, tend to disproportionate. Reactions of the higher silanes with halogens also afford halohydrosilanes but such reactions are often accompanied by Si–Si bond cleavage; for example, the reaction of disilane with iodine gives not only H_3SiSiH_2I, $H_3SiSiHI_2$, and $H_2ISiSiIH_2$ but also SiH_2I_2 and $SiHI_3$ in significant yield.[108] For further details and discussion of this type of preparation, see MacDiarmid.[109,110] The triiodide can also usefully be prepared using the high reactivity of the Si–N bond, as shown in Scheme 18.[109,110]

The physical properties of some halohydrosilanes are shown in Table 4 and, as in the case of the perhydrosilanes, the compounds containing a small number of the lighter halogens

$$\begin{tikzcd}
\mathrm{SiHCl_3 + 6H_2NPh} \arrow[r] & \mathrm{SiH(NHPh)_3 + 3PhNH_3Cl} \arrow[d, "\mathrm{6HI}"] \\
 & \mathrm{SiHI_3 + 3PhNH_3I}
\end{tikzcd}$$

Scheme 18

Table 4 Physical Properties of halosilanes[74,111]

	Mp (°C)	Bp (°C)	Density ($g\,cm^{-3}$)
$SiBrCl_3$	−62	80.3	1.826
SiH_3Br	−94	1.9	1.533 at 0 °C
$SiBr_2Cl_2$	−45.5	104	2.172 at 25 °C
SiH_2Br_2	−70.1	66	2.17 at 0 °C
$SiBr_3Cl$	−20.8	126–128	2.497 at 25 °C
$SiBr_3H$	−73	109	2.7 at 17 °C
$SiBr_4$	5.4	154	2.7715
$Br_3SiSiBr_3$	95	265	–
$SiHCl_3$	−128.2, −126.5	33 or 31.8	1.331
Cl_3SiI	−60	113.5	–
Cl_4Si	−70	57.6	1.483
$Cl_3SiSiCl_3$	−1	147	1.5624
$(Cl_3Si)_2SiCl_2$	−67	216	1.61
$(Cl_3Si)_3SiCl$	59	68 at 0.05 mmHg	–
$(Cl_3Si)_4Si$	345	–	–
I_3SiH	8	220 (dec)	3.314
I_2SiH_2	−1	148–155	–
$ISiH_3$	−57	45.5	–
I_4Si	120.5	287.5	4.198 at −80 °C
$ClSiF_3$	−138	−70	–
F_4Si	−90.3	Subl. −95.7	1.598 at −80 °C
F_3SiSiF_3	−18.7	−19.1	–
$(F_3Si)_2SiF_2$	−1.2	42	–
$F_3Si(SiF_2)_2SiF_3$	66–68	85.1	–

are gases at room temperature and pressure while the others are liquids.

5.2.2 *Structure of Halohydrosilanes*

The molecular structures of several halohydrosilanes are known, and some of the structural parameters for them are shown in Table 5.

The structures of H_3SiF and H_3SiI in the solid state show clear intermolecular interactions. The molecules form chains (Figure 3), with both Si···F and Si···I distances being less than the sum of the respective van der Waals radii.[120]

5.2.3 *Reactions of Halohydrosilanes*

The halohydrosilanes disproportionate on heating as shown in Scheme 2 and react rapidly with protic reagents such as water, alcohols, and amines to give compounds containing Si–O and Si–N bonds, respectively. In the hydrolysis of such species the halogen is removed first (as HX) giving a hydroxysilane, for example, H_3SiOH, which then undergoes condensation to give a siloxane, for example, $H_3SiOSiH_3$, and finally the Si–H groups are hydrolyzed. Careful hydrolysis of Cl_3SiH affords a mixture of oligomeric silsesquioxanes of general formula $(HSiO_{1.5})_n$ ($n = 4–7$),[121] the structures of which are described in Section 5.5.1.

Table 5 Structural data for halohydrosilanes

Compound	Si–Si (Å)	Si–H (Å)	Si–X (Å)	Method^a
H_3SiSiH_2F[112]	2.332	–	1.598	M
H_3SiSiH_2I[112]	2.336	–	2.440	M
$HBr_2SiSiBr_2H$[112]	2.349	–	2.205	E
Cl_3SiH[112]	–	1.464	2.020	M
H_3SiF[113]	–	1.485	1.593	M
H_3SiCl[113]	–	1.485	2.049	M
H_3SiBr[113]	–	1.487	2.210	M
H_3SiI[113]	–	1.487	2.437	M
H_3SiF[114]	–	≈1.37	1.6045	X
Br_3SiH[115]	–	1.494	2.170	M
F_3SiH[116]	–	1.455	1.565	M
F_2SiH_2[117]	–	1.471	1.5767	M
I_2SiH_2[118]	–	1.470	2.423	E
Br_3SiH[119]	–	1.609	2.074	MO

^{a}E = electron diffraction; M = microwave; X = X-ray diffraction; MO = molecular orbital calculations.

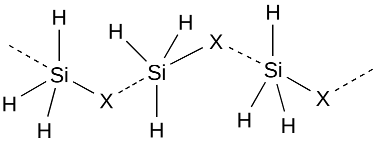

X = F or I

Figure 3 The chain structure of H_3SiX (X = F or I)

$$SiHCl_3 + R_3N \underset{}{\overset{\text{MeCN}}{\overset{\text{slow}}{\rightleftharpoons}}} [R_3\overset{+}{N}–H\overset{-}{Si}Cl_3] \overset{\text{fast}}{\rightleftharpoons} [R_3NH]^+[Cl_3Si]^-$$

R = *n*-Pr or *n*-Bu

Scheme 19

One of the most widely studied of the reactions of trichlorosilane is its interaction with tertiary amines in acetonitrile to give appreciable concentrations of Cl_3Si^- in solution, as shown in Scheme 19.[122]

The silyl anion, Cl_3Si^-, has been widely studied and reacts with a variety of compounds. The Cl_3SiH/R_3N system allows additions to multiple bonds (insertion into the Si–H bond, equation 13) and the formation of organosilicon compounds via the hydrosilation reaction.[122]

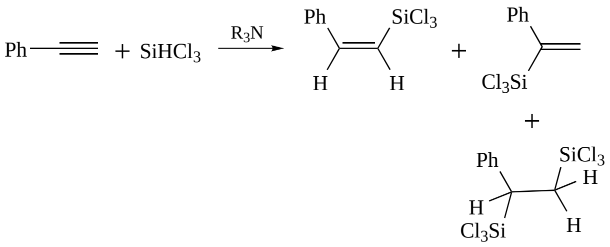

(13)

The trichlorosilyl anion also reacts with organic halides in several ways, the simplest of which involves substitution of the halide by an $SiCl_3$ group (Scheme 20).[122]

Unfortunately, organic halides with three or more chlorines on the same carbon undergo more complicated reactions with Cl_3Si^- and tend to give $SiCl_4$ as the main silicon-containing product.[122] With carbonyl compounds a so-called 'reductive silylation' occurs, in which the carbonyl oxygen is lost from the organic compound and is substituted by a Cl_3Si group and an H (Scheme 21).

In the reaction of Cl_3Si^- with acid chlorides, two trichlorosilyl groups are introduced (equation 14); this probably proceeds via a two-step mechanism. The first step involves reductive silylation and loss of the carbonyl group; the second involves a halide displacement as above. These trichlorosilyl compounds may be further treated with Grignard

$$p\text{-}ClC_6H_4CH_2Cl + SiHCl_3 \xrightarrow{n\text{-}Pr_3N} p\text{-}ClC_6H_4CH_2SiCl_3$$

$$PhCHCl_2 + SiHCl_3 \xrightarrow{n\text{-}Pr_3N} PhCH(SiCl_3)_2$$

Scheme 20

$$Ph_2CO + SiHCl_3 \xrightarrow{n\text{-}Pr_3N} Ph_2CHSiCl_3$$

$$2,6\text{-}Cl_2C_6H_3CHO + SiHCl_3 \xrightarrow{n\text{-}Pr_3N} 2,6\text{-}Cl_2C_6H_3CH_2SiCl_3$$

$$PhCONMe_2 + SiHCl_3 \xrightarrow{n\text{-}Pr_3N} PhCH(SiCl_3)NMe_2$$

Scheme 21

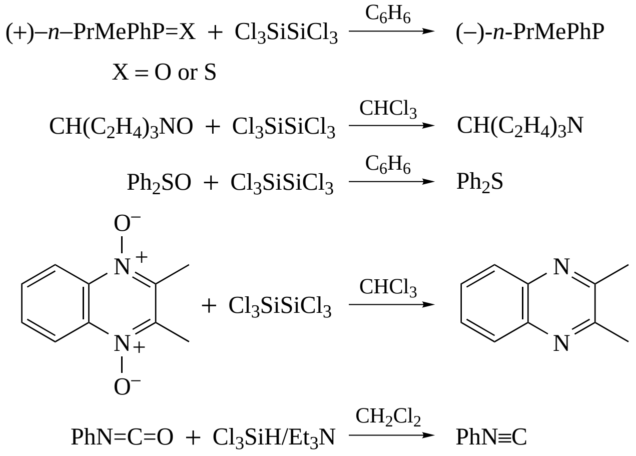
(+)–n–PrMePhP=X + Cl3SiSiCl3
C6H6
(–)-n-PrMePhP
X = O or S
CH(C2H4)3NO + Cl3SiSiCl3
CHCl3
CH(C2H4)3N
Ph2SO + Cl3SiSiCl3
C6H6
Ph2S
O−
N+
N+
O−
+ Cl3SiSiCl3
CHCl3
N
N
PhN=C=O + Cl3SiH/Et3N
CH2Cl2
PhN≡C

Scheme 22

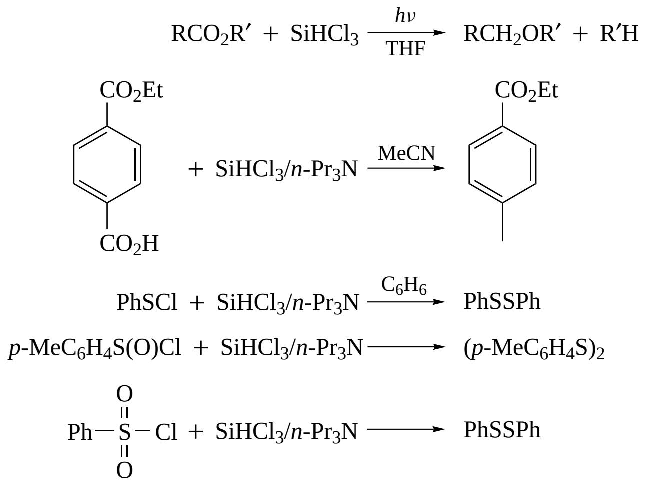
RCO2R′ + SiHCl3
hν
THF
RCH2OR′ + R′H
CO2Et
CO2H
+ SiHCl3/n-Pr3N
MeCN
CO2Et
PhSCl + SiHCl3/n-Pr3N
C6H6
PhSSPh
p-MeC6H4S(O)Cl + SiHCl3/n-Pr3N
(p-MeC6H4S)2
O
Ph–S–Cl + SiHCl3/n-Pr3N
O
PhSSPh

Scheme 23

or lithium reagents to give tetraorganosilanes.[122]

$$MeCOCl + SiHCl_3 \xrightarrow[n\text{-}Pr_3N]{MeCN} MeCH(SiCl_3)_2 \tag{14}$$

The strength of the Si–O (and the Si–S) bond and the stability of the Cl_3Si^- anion also allow the reduction of P^V to P^{III} compounds, S^{IV} to S^{II} compounds, and amine oxides to amines with either $Cl_3SiSiCl_3$ (or in some cases $SiHCl_3/R_3N$) in benzene or chloroform solution under mild conditions (Schemes 22 and 23).[123–126] The silicon-containing products are $SiCl_4$, $Cl_3SiXSiCl_3$ (X = O or S), and $(XSiCl_2)_n$ (X = O or S).

This type of reaction proceeds by a radical mechanism and the product distribution is very dependent on the R groups. Primary acetates give very predominantly ethers, secondary acetates give mixtures, and tertiary acetates give alkane as the exclusive product (Scheme 23).[127–129]

5.3 Tetrahalosilanes

The perhalosilanes X_4Si (X = F, Cl, Br, or I), the higher perhalosilanes, and compounds containing mixtures of halogens are all reactive compounds (as would be expected from the chemistry of the halohydrosilanes described above in Section 5.2.3) that hydrolyze readily to give HX in the atmosphere; they therefore require care in handling, preferably under a blanket of inert gas. The chloride Cl_4Si is by far the most widely used of these compounds and is available on a large scale.

5.3.1 Preparations of Perhalosilanes

The silicon tetrahalides SiX_4 may all be obtained by direct combination of the elements (equation 15). Silicon inflames in fluorine at room temperature to give SiF_4, but heating is required to bring about reactions with the other halogens; iodine vapor passed over silicon above 600 °C gives SiI_4. More conveniently, on a laboratory scale, cleavage of Si-aryl bonds may be used for synthesis, for example, reaction of $PhSiH_3$ with Br_2 affords $PhSiBr_3$, which when treated with $HBr/AlBr_3$ in benzene gives a near quantitative yield of $SiBr_4$.[130] A mixture of Cl_2 and Br_2 over Si at 700 °C affords the mixed halosilanes $SiCl_nBr_{4-n}$ $(n = 1–3)$,[110] as do the pyridine catalyzed redistribution reactions between $SiCl_4$ and $SiBr_4$.[131]

$$Si + 2X_2 \longrightarrow SiX_4 \quad X = F, Cl, Br, \text{or } I \tag{15}$$

Mixed tetrahalosilanes may be prepared by halogenation of a hydrohalosilane and by reaction of a tetrahalosilane with HX (Scheme 24). For example, $SiICl_3$ is formed from I_2 and $HSiCl_3$ and this subsequently reacts with the HI produced in the reaction to give SiI_2Cl_2.[132]

Redistribution reactions also readily occur, for example, mixtures of $SiCl_4$ and SiI_4 in the presence of pyridine afford

$$SiHCl_3 + I_2 \xrightarrow[\text{sealed bomb}]{250\,°C} SiICl_3 + HI \longrightarrow SiI_2Cl_2 + HCl$$

Scheme 24

statistical mixtures of $SiCl_nI_{4-n}$ ($n = 0-4$) under reflux at 61 °C.[133] Tetrafluorosilane reacts with $MgCl_2$ and $AlCl_3$ to give $SiCl_4$ and the mixed SiF_nCl_{4-n} ($n = 1-3$).[134] $HSiI_3$ undergoes halogen exchange reactions with, for example, $SiFBr_3$ to give $SiFBr_2I$, $SiFBr_2I$, $SiFBrI_2$, and $SiFI_3$.[135]

Hexafluorodisilane may be prepared by halogen exchange reactions of Si_2Cl_6 or Si_2Br_6 with a variety of metal fluorides but better yields (70–80%) may be obtained from the reaction between $(MeO)_3SiSi(OMe)_3$ and BF_3 in a sealed bomb at room temperature (equation 16).[136]

$$(MeO)_3SiSi(OMe)_3 + 6BF_3 \longrightarrow F_3SiSiF_3 + 6BF_2OMe \qquad (16)$$

The reaction of Si with SiF_4 at 1150 °C and low pressure gives $(SiF_2)_n$ polymer which, if heated under vacuum at 200 to 350 °C, breaks down to give perfluorosilanes Si_nF_{2n+2} where n is from 1 to 14 or more. The polymer is also broken down by aqueous HF to give silanes Si_nH_{2n+2} ($n = 1-6$).[137] The cleavage of Si_2F_6 with Br_2 affords SiF_3Br and SiF_2Br_2, while the fluorination of $SiBr_4$ with SbF_3 affords all three of the mixed halides.[138] Reaction of $[(MeO)_3Si]_2Si(OMe)_2$ with BF_3 in a sealed tube also gives $(F_3Si)_2SiF_2$ in a manner similar to equation (16).[139] Silicon tetraiodide when treated with silver powder at 208 °C gives I_3SiSiI_3.[140] The reaction between Si_2Cl_6 and Me_3N gives perchlorooligosilanes (equation 17), the exact product isolated, such as Si_5Cl_{12} and Si_6Cl_{14}, being dependent on the stoichiometry of the reagents used, and whether the volatile $SiCl_4$ formed as a coproduct is removed continuously from the reaction mixture.[141]

$$5Si_2Cl_6 + 0.1\%Me_3N \longrightarrow 4SiCl_4 + Si_6Cl_{14} \qquad (17)$$

This type of synthesis has clear advantages over the direct combination of elements method which gives complicated mixtures that need to be separated.[141] The higher perchlorosilanes $Cl_3Si(SiCl_2)_nSiCl_3$ ($n = 1-6$) can be prepared in low yield, along with $SiCl_4$, by passing chlorine over a mixture of $CaSi_2$ and $FeSi_2$ at 120 to 150 °C.[142] Perhalogenated silanes may also readily be made by cleavage of phenyl groups by HX/AlX_3, (X = Cl, Br or I) from either cyclic or acyclic perphenyl compounds (Scheme 25). The preparations and reactions of hydro- and halosilanes containing Si–Si bonds are discussed in more detail by Hengge.[143]

Straight chain perhalooligosilanes may also be prepared from the cyclic phenyl compounds by cleaving the ring first with halogen and subsequently cleaving the Si–Ph bonds with HX/AlX_3 (equation 18).[144–146]

$$(SiPh_2)_n + X_2 \longrightarrow X(SiPh_2)_nX \xrightarrow{HX/AlX_3} X(SiX_2)_nX + 2nC_6H_6$$
$$X = Br \text{ or } I;\ n = 4 \text{ or } 5 \qquad (18)$$

$$(SiPh_2)_n + 2nHX \xrightarrow[n = 4\text{–}6]{AlX_3} (SiX_2)_n + 2nC_6H_6$$

$$Si_nPh_{2n+2} + 2n{+}2\ HCl \xrightarrow[n = 2,\ 5,\ \text{or } 6]{AlX_3} Si_nCl_{2n+2} + 2n{+}2C_6H_6$$

Scheme 25

$$SiHCl_3 \xrightarrow[254\ \text{nm}]{h\nu} (Cl_3Si)_4Si \xleftarrow{Me_3N} (Cl_3Si)_2SiCl_2 \text{ or } Si_2Cl_6$$

Scheme 26

$$\begin{tikzcd}
2(X_3Si)_3SiH + t\text{-}Bu_2Hg \arrow[r] & {[(X_3Si)_3Si]_2Hg} \arrow[d, "h\nu"] \\
 & (X_3Si)_3Si\text{–}Si(SiX_3)_3
\end{tikzcd}$$

(**3**)

X = Cl or OMe

Scheme 27

The *neo*-pentasilane $(Cl_3Si)_4Si$ is formed along with $SiCl_4$, Si_2Cl_6, Si_3Cl_8, and Si_4Cl_{10} on mercury sensitized photolysis of Cl_3SiH[147] or by base-catalyzed disproportionation of Si_2Cl_6 or Si_3Cl_8 (Scheme 26).[141,148]

Ligand redistribution reactions occur when Si_2Cl_6 and Si_2Br_6 are heated together at 100 °C in a sealed tube, to give all of the mixed halodisilanes $Si_2Cl_nBr_{6-n}$ ($n = 1-5$). Unfortunately, the compounds cannot be separated by vacuum distillation because of further redistribution reactions. The mixed halide, $Br_3SiSiCl_3$, can be obtained pure by cleaving the Ph groups from $Cl_3SiSiPh_3$ using $HBr/AlBr_3$.[149] Reaction of $BrSiCl_3$ with the very hindered aryllithium reagent 2,4,6-t-$Bu_3C_6H_2Li$ at −78 °C leads to lithium/halogen exchange and formation of $LiSiCl_3$, which has a surprisingly long half-life at room temperature in THF/Et_2O of about 62 h. Little seems to have been done with $LiSiCl_3$, which could be a valuable reagent for the introduction of Cl_3Si groups.[150]

The tetrasilanes (**3**) react with t-Bu_2Hg to give the corresponding silylmercury derivatives, which break down on photolysis to give octasilanes (Scheme 27).[151]

5.3.2 *Reactions of Perhalosilanes*

Silicon halides (especially the readily available chlorides) are probably the most synthetically useful and versatile monomeric inorganic silicon compounds. They may readily be reduced to hydrides, hydrolyzed to silanols (and subsequently to siloxanes), treated with other protic species such as alcohols, carboxylic acids, amines, and thiols to give Si–OR, Si–OC(O)R, Si–NR_2, and Si–SR species respectively, used to make silyl pseudohalogen derivatives by treatment with silver or alkali metal salts, for example, treated with sodium derivatives of Group 15 elements to give Si–N, Si–P, or Si–As containing compounds, and form a wide range of adducts with amines, phosphines, and so on. They are also one of the main starting materials used for the formation of organosilicon compounds by using, for example, Grignard or organolithium compounds (*see* ***Silicon: Organosilicon Chemistry***). The reduction of silicon halides to give silicon hydrides is discussed in Section 5.1.1 and the reactions of halosilanes to give compounds containing Si–O and Si–N bonds are found in Sections 5.5.1 and 5.6.1.

All of the SiX_4 tetrahalides except the fluoride hydrolyze rapidly to give hydrated silica; the fluoride also undergoes partial hydrolysis but also forms the hexafluorosilicate ion (equation 19).

$$2SiF_4 + 2H_2O \xrightarrow{H_2O} SiO_2{\cdot}nH_2O + SiF_6^{2-} + 4H^+ + 2F^- \qquad (19)$$

Careful hydrolysis of $SiCl_4$ at −78 °C affords $(Cl_3Si)_2O$ and higher chlorinated siloxanes, $Cl_3Si(OSiCl_2)_nOSiCl_3$ ($n = 1-5$), as high boiling liquids.[152] These are formed by initial formation of Cl_3SiOH which rapidly condenses to give the disiloxane $(Cl_3Si)_2O$ which may react further with Cl_3SiOH to give the higher siloxanes. $(Cl_3Si)_2O$ may also be prepared by the reaction of $SiCl_4$ with O_2 at 960 to 990 °C.[153] The cyclic dimer $(Cl_2SiO)_2$ is not formed, unlike the S analog. The passage of a mixture of Br_2 and O_2 over Si at 700 °C affords bromosiloxanes such as $(Br_3Si)_2O$ and $(Br_2SiO)_4$; they are also formed on treatment of $SiBr_4$ with O_2 at 670 to 695 °C.[154] Reaction of $SiCl_4$ with H_2S at 900 to 950 °C affords Cl_3SiSH which can be distilled (unlike its oxygen analog Cl_3SiOH) at 95 °C at atmospheric pressure. The pure thiol does undergo condensation at high temperature to give $(Cl_3Si)_2S$, the cyclic compound $(Cl_2SiS)_2$, and $(SiCl_2S)_n$ polymer.[155] The reaction between $SiCl_4$ and AgS at 230 to 250 °C also affords $(Cl_3Si)_2S$.[156] The reaction between $SiCl_4$ and NEt_4SH affords $NEt_4[SiSCl_3]$, which contains four-coordinate near-tetrahedral $SiCl_3S$ units.[157]

The higher chlorosilanes, like $SiCl_4$, all hydrolyze readily and react with protic species; for example, $(Cl_3Si)_2SiCl_2$ reacts with $MeOH/Et_3N$ to give $[(MeO)_3Si]_2Si(OMe)_2$ and with Me_2NH to give $[(Me_2N)_3Si]_2Si(NMe_2)_2$.[158] The *neo*-pentasilane $(Cl_3Si)_4Si$ reacts with HCl to give the tetrasilane (**4**) and with MeOH to give (**5**) or (**6**) and (**7**) depending on the reaction conditions (Scheme 28). Compounds (**6**) and (**7**) react with BCl_3 or BF_3 to afford the corresponding halosilanes.[159–161]

The formation of the strong Si–O bond and an insoluble product (silica) occurs in the reaction between $SiCl_4$ and amines and acids to give amides (equation 20).[162]

$$2RCO_2H + 2R'NH_2 + SiCl_4 \longrightarrow 2RCONHR' + (SiO_2)_n + 4HCl$$
$$RR' = \text{MePh, PhPh, etc.} \qquad (20)$$

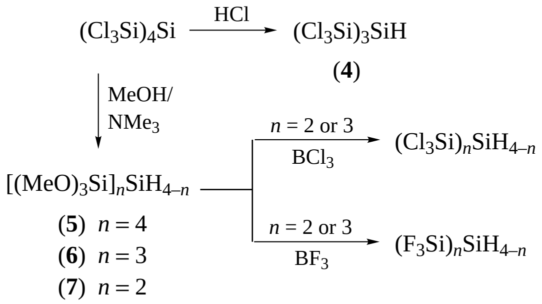

Scheme 28

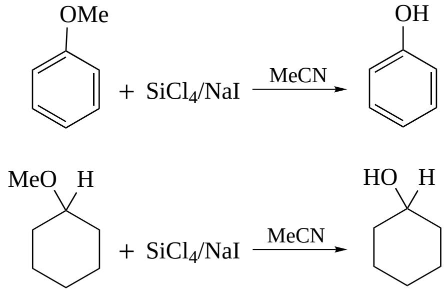

Scheme 29

The reaction of $SiCl_4$ with NaI in acetonitrile gives Cl_3SiI (Scheme 29), which is used in situ to cleave ethers to give (after hydrolysis of the initially formed silyl ether) alcohols and phenols.[163]

Silicon tetrafluoride reacts with epoxides in the presence of a tertiary amine to give fluorohydrins by a mechanism that probably involves five- or six-coordinate silicon species (equation 21).[164] The ionization of SiF_4 by electron impact affords $SiF_x^{+\bullet}$ (where $x = 1, 2$, or 3), which can form clusters with neutral SiF_4 and react with a range of small inorganic molecules.[29,165]

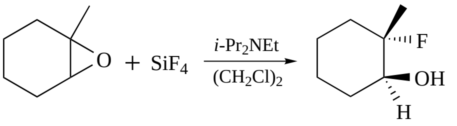

(21)

5.3.3 *Structures of Perhalosilanes*

The simple tetrahalides SiX_4 are tetrahedral, and bond lengths increase as the halogen gets larger. Some structural details for perhalosilanes are given in Table 6.

5.4 Silyl Pseudohalides

As might be expected, the silyl pseudohalides have chemical properties similar to the silyl halides although the structures of the pseudohalides have been studied in more detail and have been shown to be both interesting and novel.

Table 6 Structural data for tetrahalosilanes

Compound		Si–X (Å)	Method^a
F_4Si[166]		1.56	X
F_4Si[167]		1.552	E
Cl_4Si[168]		2.019	E
Cl_3SiF[169]	SiF	1.520	
	SiCl	2.019	M
Br_3SiF[170]	SiF	1.5607	
	SiBr	2.171	M
F_3SiCl[171]	SiF	1.560	
	SiCl	1.989	M
F_3SiBr[171]	SiF	1.560	
	SiBr	2.153	M
I_4Si^b	–		–

^{a}E = electron diffraction; M = microwave; X = X-ray diffraction.
^{b}For a discussion of the crystallization of SiI_4 see Kihara.[172]

5.4.1 *Silyl Isocyanates and Isothiocyanates*

Silyl isocyanates can readily be prepared by treatment of chlorosilanes (bromo- or iodosilanes would also work but are less readily available) with metal cyanates. With simple halosilanes the product is always the isocyanate isomer although in the case of highly sterically hindered organosilanes, normal cyanates (which thermally isomerize to isocyanates) may be formed using silver cyanate.[173] Thus $Si(NCO)_4$ is formed from the reaction between $SiCl_4$ and KOCN in liquid SO_2, AgOCN in C_6H_6, or $Pb(OCN)_2$ in C_6H_6.[174,175] Similarly, $Si(NCS)_4$ is formed in the reaction between $SiCl_4$ and a variety of thiocyanate salts (equation 22).[176] The Si–N bonds in $(H_3Si)_3N$ are cleaved by HOCN and HSCN to give H_3SiNCO and H_3SiNCS, respectively, providing a route to these compounds that does not involve metal salts.[177]

$$SiCl_4 + NH_4SCN \xrightarrow{C_6H_6} Si(NCS)_4 + 4NH_4Cl \qquad (22)$$

Treatment of $HSiCl_3$ with silver or potassium salts also gives $Si(NCE)_4$ (E = O or S) together with the expected $HSi(NCE)_3$ species, which are prepared in greater yield from $HSiI_3$ and the silver salts.[178] As in the case of the perhalo compounds, the pseudohalides also undergo redistribution reactions (Scheme 30).[179]

$$4SiHCl_3 + 3Si(NCO)_4 \xrightarrow[100\ ^\circ C]{4\ days} HSiCl_n(NCO)_{3-n} + H_2SiCl_2 + H_2SiCl(NCO),\ etc.$$
$$n = 0–3$$

$$SiCl_4 + Si(NCO)_4 \xrightarrow{600\ ^\circ C} SiCl_n(NCO)_{4-n}$$
$$n = 0–4$$

Scheme 30

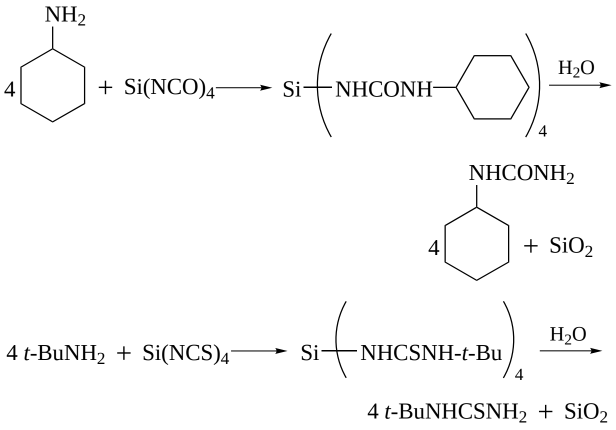

Scheme 31

The structures of the silyl species H_3SiX (X = NCO, NCS, N_3) have been examined in detail in electron diffraction and microwave spectroscopic studies. The microwave spectra of H_3SiNCO and H_3SiNCS suggest that the Si–N=C=O and Si–N=C=S linkages are linear, but electron diffraction studies show molecules that are bent at N. These data combined suggest that the ground state is linear but that the molecules are readily deformed, and in the gas phase at room temperature they spend most of their time bent.[120] In the solid state, the Si–N=C angle is 158° but this bent geometry appears to be due to weak but well-defined intermolecular Si···N interactions.[120] The structures of a range of silyl pseudohalides H_3SiR (R = N_3, NCO and NCS) have also been calculated, the results comparing well with those from experimental determinations (where these have been carried out) of the structures.[180–182] The linear (or near linear) arrangement in the silyl-isocyanate and -isothiocyanate has been attributed to p_π–d_π bonding involving the 3d orbitals of the silicon. The molecular structure of F_3SiNCO (prepared by passing F_3SiBr over AgOCN) in the gas phase also shows a bent Si–N=C angle of 160.7°.[183] The mixed halides/pseudohalides $SiCl_n(NCO)_{4-n}$ ($n = 1–3$) (prepared by heating a mixture of $SiCl_4$ and $Si(NCO)_4$) also have bent Si–N=C groups of 138, 136, and 145° for n = 3, 2, and 1, respectively.[184] The related disilyl species $H_3Si–N=C=N–SiH_3$ has a near linear Si–N=C=N–Si linkage, rather than the cyanamide structure $(H_3Si)_2NCN$.[185]

Isocyanates and isothiocyanates both react with water in a manner similar to the halosilanes to give hydrated silica. They also react with primary and secondary amines to give silylamines which, on hydrolysis, afford *N*-mono- and *N*,*N*-disubstituted ureas and thioureas (Scheme 31), which is a useful synthesis of these compounds.[186]

5.4.2 *Silyl Cyanides and Isocyanides*

The structure of H_3SiCN (prepared from H_3SiBr + AgCN) has been studied in detail. The gas-phase structure shows an

H–Si–C angle of 108.6° and in the solid phase 100.4° while the Si–C–N angle is linear and there are short intermolecular Si···N distances, indicating a donor–acceptor interaction which gives an almost linear chain formation that is not seen in the carbon analog, CH_3CN.[120,187]

Although the OCN and SCN groups are normally iso when attached to silicon, the CN group is usually attached via the carbon. However, the reaction between F_3SiBr or F_3SiI and AgCN affords both F_3SiCN and the silyl isocyanide F_3SiNC.[188] The reaction of the sterically hindered chlorosilane $(t\text{-BuO})_3SiCl$ with tetraethylammonium cyanide (equation 23) also affords a mixture of both the normal cyanide and the isocyanide, containing amounts of up to 6.5% of the latter. At 25 °C the equilibrium mixture contains 1.1% of the isocyanide isomer, apparently the only system that contains an appreciable amount of an isocyanide. The IR stretching frequencies for the C≡N and N≡C compounds are 2198 and 2103 cm^{-1}, respectively.[189]

$$(t\text{-BuO})_3SiCl + [Et_4N][CN] \xrightarrow{MeCN} (t\text{-BuO})_3SiCN + (t\text{-BuO})_3SiNC \tag{23}$$

5.4.3 *Silyl Azides*

The azide derivatives of silicon are generally more stable than organic azides although they may detonate on heating and should be handled with care. Silyl azides may be prepared by several routes (Scheme 32), the most important being hydrazoic acid cleavage of an Si–N bond and (in a manner similar to the other silyl pseudohalogens) by treatment of a silyl chloride with a metal azide.[190] In H_3SiN_3 the Si–N–N angle is about 127°.[191,192]

5.5 Silicon–oxygen Compounds

Although a significant fraction of the Earth's crust comprises material containing SiO_4 structural units arranged in three-dimensional arrays, the uses of discrete monomeric $Si(OR)_4$ species have only been widely studied since about the 1950s. Along with the chlorosilanes, the alkoxysilanes and siloxanes are very useful and widely available compounds that are produced in large quantities.

5.5.1 *Silanols and Siloxanes and Their Sulfur, Selenium, and Tellurium Analogs*

The propensity of silicon and oxygen to form materials in which the Si and O atoms alternate to form a polymer causes practical problems when preparations of small molecules containing the SiOH group are undertaken. Thus H_3SiOH, $H_2Si(OH)_2$, $HSi(OH)_3$, and H_3SiSiH_2OH have not been isolated in a pure form. The products obtained in attempted preparations of such species are invariably siloxanes owing to the condensation reaction that takes place very readily between two or more silanol molecules (Scheme 33). Hydrolysis of an $SiCl_3$ group attached to a transition metal may however lead to a stable $Si(OH)_3$ group (see Section 7 concerning transition metal complexes); also a wide variety of organosilanols $R_nSi(OH)_{4-n}$ ($n = 1$–3; R = alkyl or aryl) are known where the steric effect of the R groups tends to hinder condensation reactions.[193]

$$\begin{aligned}(H_3Si)_3N + 4HN_3 &\xrightarrow{n\text{-}Bu_2O} 3H_3SiN_3 + NH_4N_3\\ SiCl_4 + 4MN_3 &\xrightarrow{\quad\quad} Si(N_3)_4 + 4MX\end{aligned}$$

Scheme 32

The use of large, nitrogen-centered substituents at a silanetriol center does allow the isolation and characterization of stable silanetriols as shown in equation (24). These compounds can be used to prepare transition metal siloxide complexes (Scheme 34), still containing potentially moisture-sensitive Si–N bonds that may be precursors to metal-containing ceramics; for reviews of these compounds, see References 193–195.

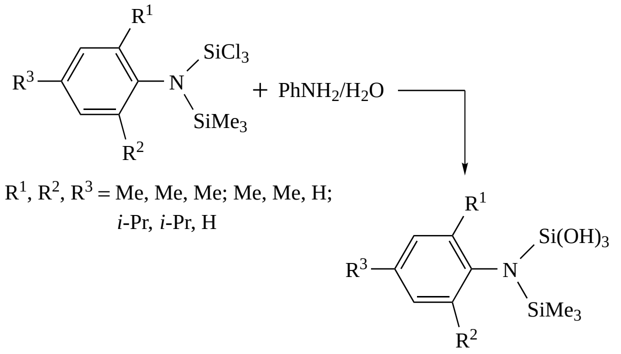

R^1, R^2, R^3 = Me, Me, Me; Me, Me, H; *i*-Pr, *i*-Pr, H

(24)

The wide range of silicon compounds that are readily hydrolyzed means that the siloxane $H_3SiOSiH_3$ is formed (probably via H_3SiOH) in numerous reactions (Scheme 35).[196]

Similarly, hydrolysis of halodisilanes tends to give siloxane rather than silanol products (Scheme 36).[196]

The compounds $(HSiO_{1.5})_n$ with $n = 4$–7 may, however, be isolated from the careful hydrolysis of Cl_3SiH. Figure 4 shows their polyhedral nature, which also suggests their other name of 'spherosiloxanes'.[121,197] The octasiloxane $(HSiO_{1.5})_8$ may be fully chlorinated to give $(ClSiO_{1.5})_8$, from which the methoxy derivative $(MeOSiO_{1.5})_8$ may be prepared by

$$\begin{aligned}2H_3SiOH &\xrightarrow{-H_2O} H_3SiOSiH_3\\ nH_2Si(OH)_2 &\xrightarrow{-n/2\ H_2O} (H_2SiO)_n\\ HSi(OH)_3 &\xrightarrow{-H_2O} \text{polymers and cage siloxanes}\end{aligned}$$

Scheme 33

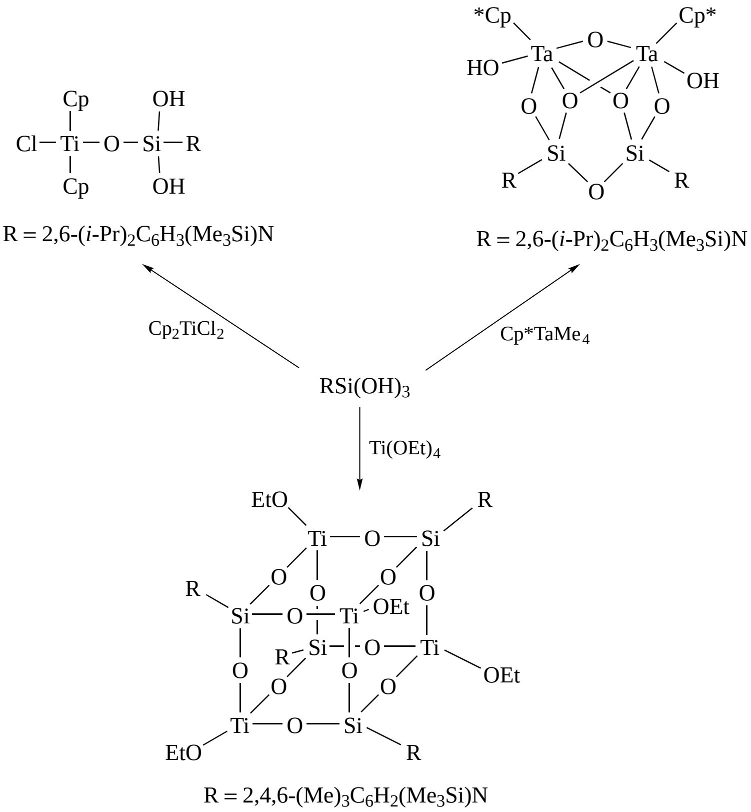
Cp
OH
Cl
Ti
O
Si
R
Cp
OH
R = 2,6-(i-Pr)2C6H3(Me3Si)N
*Cp
Cp*
Ta
O
Ta
HO
OH
Si
Si
R
R
R = 2,6-(i-Pr)2C6H3(Me3Si)N
Cp2TiCl2
Cp*TaMe4
RSi(OH)3
Ti(OEt)4
EtO
OEt
R = 2,4,6-(Me)3C6H2(Me3Si)N

Scheme 34

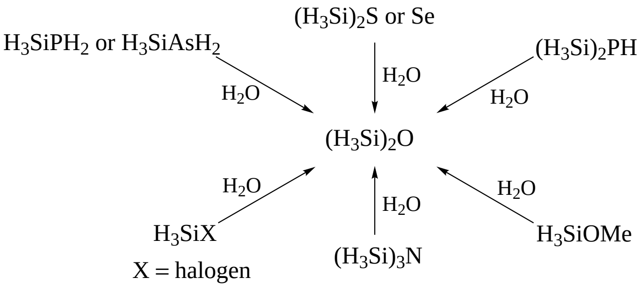
(H3Si)2S or Se
H3SiPH2 or H3SiAsH2
(H3Si)2PH
H2O
(H3Si)2O
H3SiX
X = halogen
(H3Si)3N
H3SiOMe

Scheme 35

$$H_3SiSiH_2I \xrightarrow{H_2O} (H_3SiSiH_2)_2O \xleftarrow{H_2O} H_2PSiH_2SiH_3$$

$$H_3SiI + H_3SiSiH_2Br \xrightarrow{H_2O} H_3SiOSiH_2SiH_3$$

Scheme 36

treatment with MeONO.[198] For the case of $n = 14$ two isomers, one of D_{3h} and one of C_{2v} symmetry, have been structurally characterized (Figure 5).[199] Larger silicates are treated elsewhere; reviews of the chemistry, preparation, and structures of the oligosilsesquioxanes are available.[200–202]

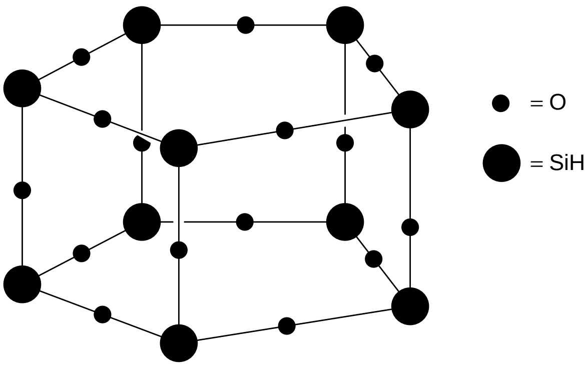

Figure 4 D_{5h} isomer of $(HSiO1.5)n$ for $n = 5$

The reactions of $(H_3Si)_2O$ fall into two general classes: those that proceed with Si–O bond cleavage, usually promoted by Lewis acids, and those that lead to condensation reactions, usually promoted by Lewis bases. Typical reactions are shown in Scheme 37.[196]

The preparation of the perchlorosiloxanes $Cl_3Si(OSiCl_2)_n$-$SiCl_3$ ($n = 0-5$) has been discussed above in the halosilanes section. The highly reactive Cl_3SiOH may, however, be generated by photochemical oxidation of $SiHCl_3$ by O_2 or O_3 at low temperature in either an argon matrix or

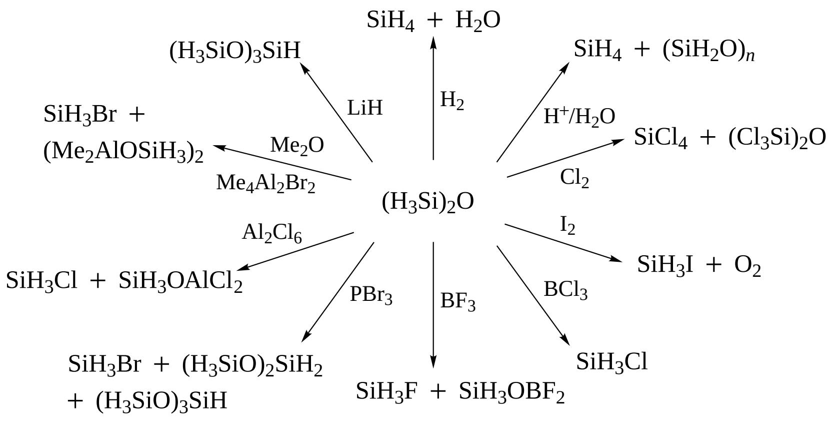
$SiH_4 + H_2O$
$(H_3SiO)_3SiH$
$SiH_4 + (SiH_2O)_n$
LiH
H_2
H^+/H_2O
$SiH_3Br +$
$(Me_2AlOSiH_3)_2$
Me_2O
$Me_4Al_2Br_2$
$SiCl_4 + (Cl_3Si)_2O$
Cl_2
$(H_3Si)_2O$
Al_2Cl_6
I_2
$SiH_3I + O_2$
$SiH_3Cl + SiH_3OAlCl_2$
PBr_3
BF_3
BCl_3
$SiH_3Br + (H_3SiO)_2SiH_2$
$+ (H_3SiO)_3SiH$
$SiH_3F + SiH_3OBF_2$
SiH_3Cl

Scheme 37

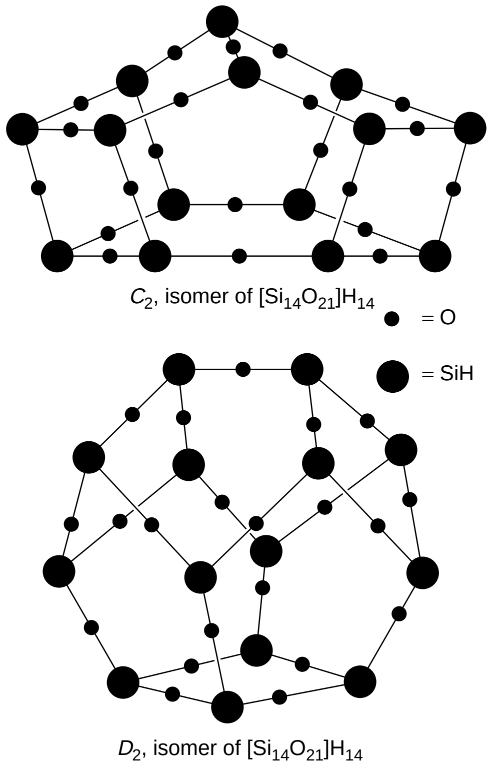
C_2, isomer of $[Si_{14}O_{21}]H_{14}$
● = O
● = SiH
D_2, isomer of $[Si_{14}O_{21}]H_{14}$

Figure 5 Structures of large spherosiloxanes

in $SiCl_4$. The compound cannot be isolated but is stable in dilute solution for several days.[203,204] Hydrolysis of H_3SiBr affords $H_3SiOSiH_3$, while reaction between H_3SiI and HgS, $Li[Al(SeH)_4]$ or Ag_2Se, and Li_2Te affords $(H_3Si)_2E$ (E = S, Se, and Te), respectively.[205–207] The lower disilyl chalcogenides hydrolyze to give $(H_3Si)_2O$ as shown, for example, in equation (25).[208]

$$(H_3Si)_2Se + H_2O \longrightarrow (H_3Si)_2O + H_2Se \qquad (25)$$

The reaction between Cl_3SiH or Cl_2SiH_2 and sulfur affords thiols such as Cl_3SiSH.[209,210] Disilyl sulfide undergoes a variety of reactions as shown in Scheme 38.[196]

The Si–O–Si angle in $(H_3Si)_2O$ in the solid phase is unusually wide at 144.1° (144° in the gas phase) for an sp^2 hybridized atom, but this is similar to other siloxanes, and again has been proposed to reflect p_π–d_π bonding between Si and O.[196] As in the simple silyl halides, there are close nonbonded intermolecular interactions in the siloxane with an $Si\cdots O$ distance of 3.05 Å and an O–Si–O angle close to 180°, giving a chain structure.[120] The bond shortening and wide Si–O–Si angles in siloxanes have been attributed to p_π–d_π interaction but molecular orbital calculations have suggested that these structural features are, in fact, the product of the unusually high ionic character of the Si–O bond, and that p_π–d_π bonding is of relatively little importance.[211] A useful discussion of the contributions of the bonding possibilities (p_π–d_π, Si–C σ^* interactions with Si–X bonds, and ionic factors) proposed for Si–X bonds (X = electronegative element) can be found in Reference 212. The solid-state structures of $(H_3Si)_2S$ and $(H_3Si)_2Se$ show angles at the chalcogen of 98.4 and 95.7°, respectively. As

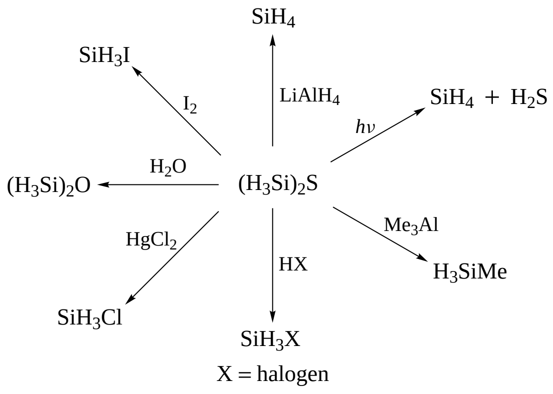
SiH_4
SiH_3I
I_2
$LiAlH_4$
$SiH_4 + H_2S$
$h\nu$
H_2O
$(H_3Si)_2O$
$(H_3Si)_2S$
$HgCl_2$
Me_3Al
HX
H_3SiMe
SiH_3Cl
SiH_3X
X = halogen

Scheme 38

for the oxygen analog, there are distinct though weaker intermolecular Si···S (or Se) interactions. However, in the siloxane case only, one silicon from each molecule is involved in intermolecular interactions, while in the S and Se analogs, both silicons show nonbonded interactions with the chalcogen giving all silicons five-coordination and the S and Se atoms tetrahedral coordination.[213]

The reaction of $(H_3Si)_2O$ with BX_3 (X = F or Cl) affords H_3SiOBX_2. These compounds together with other X_3SiOBX_2 species (X = H, F, or Cl) have had their structures calculated by MNDO methods. The compounds split into two types, one in which the Si–O–B angle is in the range from 140 to 152° (for X_3SiOBH_2 (X = H, F or Cl) and H_3SiOBF_2) and the second in which the Si–O–B angle is 180° ($X_3SiOBCl_2$ (X = H, F or Cl) and F_3SiOBF_2).[214]

Silanethiols are much more stable towards condensation reactions than their oxygen counterparts and may be isolated from insertion reactions of Si–H containing compounds with S at high temperature or by high-temperature reactions with H_2S (Scheme 39).[209,210]

The disilyl chalcogenides $(H_3Si)_2E$ (E = S, Se, Te) may be prepared from Li_2E and H_3SiBr. In the presence of H_2E an equilibrium is set up with H_3SiEH species (Scheme 40).[215]

$$X_3Si{-}H + S \xrightarrow{85\text{–}350\ °C} X_3SiSH$$

$$Cl_3Si{-}H + S \xrightarrow{690\ °C} Cl_3SiSH + H_2$$

$$Cl_2SiH_2 + S \xrightarrow{190\ °C} HCl_2SiSH + Cl_3SiSH,\ \text{etc.}$$

X = F, Br, or I

Scheme 39

$$Li_2E + 2SiH_3Br \xrightarrow[Me_2O]{-96\ °C} (H_3Si)_2E + 2LiBr$$

$$(H_3Si)_2E + H_2E \rightleftharpoons 2H_3SiEH$$

E = S, Se, or Te

Scheme 40

5.5.2 *Siloxene*

Siloxene is the name given to several materials that are prepared by the action of aqueous hydrochloric acid on calcium silicide, $CaSi_2$. Two main types of siloxene are available, the so-called 'Wohler' and 'Kautsky' materials named after the chemists who carried out the original preparations. The siloxenes are prepared as shown in equations (26) and (27), and the structures, that have been the subject of much discussion, are now thought to be as shown in Figure 6. The preparations are carried out in the dark and under argon as the siloxenes are both photosensitive and can be oxidized, the Wohler material being a bright yellow, layered material and the Kautsky material being grayish-green. The effects of the reaction conditions on rate of formation of siloxene have been investigated in detail.[216] The recent interest in siloxene has arisen because it exhibits a strong yellow-green photoluminescence, unlike crystalline silicon which does not emit visible light because of its small indirect bandgap. The presence of siloxene contamination in porous silicon has also been suggested to account for the strong visible photoluminescence from porous silicon. A large number of studies on the electronic and optical properties of siloxene have been published; see References 217–220 and references therein.

$$3CaSi_2 + 6HCl + x\ H_2O \xrightarrow{0\ °C,\ 3\ h} Si_6H_{6-x}(OH)x + 3CaCl_2 + x\ H_2 \tag{26}$$

$$3CaSi_2 + 6HCl + x\ H_2O \xrightarrow{EtOH,\ 0\ °C,\ 6\ h} Si_6H_6O_{2x/2} + 3CaCl_2 + x\ H_2 \tag{27}$$

5.5.3 *Silicon Chalcogenides: SiS_2, $SiSe_2$, and $SiTe_2$*

The disulfide, SiS_2, and the diselenide and $SiSe_2$, are isostructural in the crystalline phase and have the form of chains of edge-sharing distorted SiS_4 or $SiSe_4$ tetrahedra with Si–S and Si–Se bond lengths of 2.133 and 2.275 Å, respectively.[221] The structure of glassy $SiSe_2$ has been investigated by solid-state ^{29}Si NMR spectroscopy, which suggests that three Si environments are present (analogous to SiS_2) that differ in the number of edge-sharing tetrahedra involving each Si; these are shown in Figure 7.[222–224] Unlike SiO_2, SiS_2, $SiSe_2$, and $SiTe_2$ hydrolyze rapidly in air.[111]

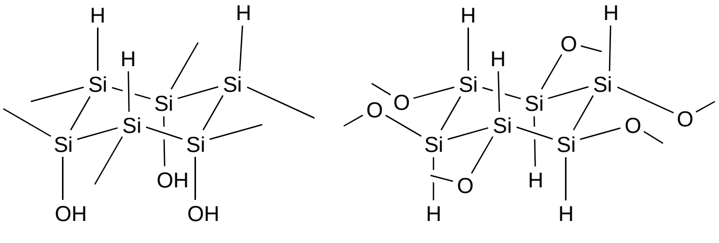

Figure 6 Structures of siloxene materials

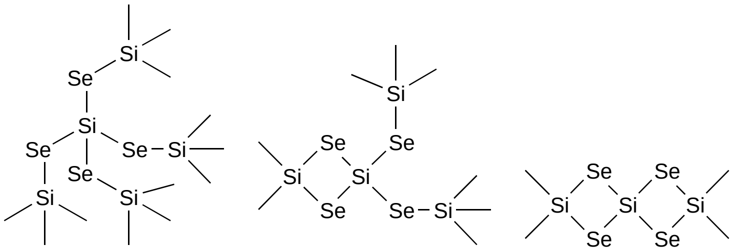
No shared edges

One edge shared

Two edges shared

Figure 7 Silicon environments in glassy $SiSe_2$

5.5.4 Silyl Alkoxides, Phenoxides, and Their Sulfur Analogs

Simple $(RO)_4Si$ compounds may readily be prepared by the reaction between a chlorosilane and an alcohol (or phenol) (Scheme 41). A problem in this type of reaction is that the HCl formed may cause unwanted side reactions. This may be minimized by blowing dry N_2 gas through the reaction mixture or heating the reaction so that HCl is driven off as it is formed, or a tertiary amine such as pyridine may be added to the reaction, which forms an amine hydrochloride salt that precipitates to remove the HCl.**[225]** Silicon alkoxides may also be made by reaction of a silicon halide and an alkali metal alkoxide (Scheme 41).**[226]**

The reaction between $Pb(SR)_2$ ($R = Me$, Et, or Ph) and $SiCl_4$ affords $Si(SR)_4$. If a deficiency of lead salt is used, partially substituted species such as $Cl_nSi(SEt)_{4-n}$ ($n = 1-3$) may be obtained which may subsequently be reduced by $LiAlH_4$ to give $H_nSi(SEt)_{4-n}$ compounds.**[227]**

A further method for the preparation of alkyl silicates involves using mineral silicates that contain discrete silicate anions such as $SiO_4{}^{4-}$ in γ-Ca_2SiO_4 or $Si_2O_7{}^{6-}$ in $Ca_2ZnSi_2O_7$ (hardystonite) rather than polymeric silicate networks. The anions are protonated and then treated with alcohol to form alkoxysilanes (Scheme 42). This method removes the energy intensive formation of elemental Si (see Section 2) but unfortunately does not give particularly good yields. Alkoxysilanes $(RO)_3SiH$ and $(RO)_4Si$ (R = Me, Et, n-Pr) are also formed in low yield from the direct reaction between Si/Cu alloy and ROH at 260–300 °C.**[228]**

An unfortunate side reaction in the conversion of $SiCl_4$ to $Si(OR)_4$ is that between the liberated HCl and the alcohol to give an alkyl chloride. This is particularly pronounced in the case of MeOH and higher alcohols such as isopropyl and butyl. (It should be noted that methoxysilanes such as $Si(OMe)_4$ are eye irritants and should be handled with care.) A more convenient route to such alkoxysilanes is via transesterification using $(EtO)_4Si$ (equation 28).

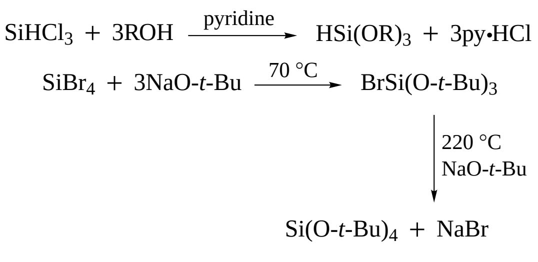

$$SiHCl_3 + 3ROH \xrightarrow{\text{pyridine}} HSi(OR)_3 + 3py{\bullet}HCl$$

$$SiBr_4 + 3NaO\text{-}t\text{-}Bu \xrightarrow{70\ ^\circ C} BrSi(O\text{-}t\text{-}Bu)_3 \xrightarrow[\text{NaO-}t\text{-Bu}]{220\ ^\circ C} Si(O\text{-}t\text{-}Bu)_4 + NaBr$$

Scheme 41

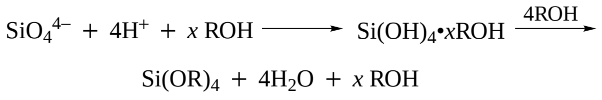

$$SiO_4{}^{4-} + 4H^+ + x\,ROH \longrightarrow Si(OH)_4{\bullet}x\,ROH \xrightarrow{4ROH} Si(OR)_4 + 4H_2O + x\,ROH$$

Scheme 42

$$Si(OEt)_4 + 4MeCO_2Pr \longrightarrow Si(OPr)_4 + 4MeCO_2Et \qquad (28)$$

The preparation of mixed alkoxysilanes may be achieved by, for example, treating $SiCl_4$ with two equivalents of EtOH to give $(EtO)_2SiCl_2$ and then with a second alcohol to give $(EtO)_2Si(OR)_2$. Aryl oxides do not suffer so readily from the reaction between ArOH and HCl and may easily be prepared from $SiCl_4$ and an appropriate phenol. The simplest phenoxysilane, $(PhO)_4Si$, is remarkable in that it may be distilled in air at over 400 °C. Careful hydrolysis of $Si(OR)_4$ affords silicate anions such as $Si_2O_7{}^{6-}$, and $Si_3O_{10}{}^{8-}$, and so on, or they may be formed during the reaction of an alcohol with $SiCl_4$ owing to the presence of some water. By analogy with $SiCl_4$, the reaction between $(Cl_3Si)_2O$, $Cl_3SiO(SiCl_2)OSiCl_3$, or $Cl_3SiSiCl_3$ with anhydrous alcohol gives $[(RO)_3Si]_2O$, $(RO)_3SiO[Si(OR)_2]OSi(OR)_3$, and $(RO)_3SiSi(OR)_3$, respectively.

The hydrolysis of $(EtO)_4Si$ (and the subsequent polycondensation of Si–OH containing molecules) has been the subject of considerable investigation because of its importance in the fabrication of glasses and colloidal silica via the sol–gel process (*see* ***Sol–Gel Synthesis of Solids***). Hydrolysis of the Si–O bond in alkoxysilanes is also very widely used to attach silicon compounds to surfaces and in coupling reactions.**[229,230]** The fundamental reaction types involved in the formation of polymeric silica materials (via, for example, cyclic oligomers similar to those shown in Figures 4 and 5) from monomeric $(RO)_4Si$ compounds are shown in Scheme 43.

$$(RO)_3Si{-}OR + H_2O \xrightleftharpoons{\text{hydrolysis}} (RO)_3Si{-}OH + ROH$$

$$(RO)_3Si{-}OR + HO{-}Si(OR)_3 \xrightleftharpoons{\text{alcohol condensation}} (RO)_3Si{-}O{-}Si(OR)_3 + ROH$$

$$(RO)_3Si{-}OH + HO{-}Si(OR)_3 \xrightleftharpoons{\text{water condensation}} (RO)_3Si{-}O{-}Si(OR)_3 + H_2O$$

Overall process

$$(RO)_4Si + 2H_2O \longrightarrow SiO_2 + 4ROH$$

Scheme 43

The reaction rates, the importance of various intermediates, and the properties of the end product of hydrolysis are highly dependent on the presence of catalysts (e.g., mineral acids or ammonia), the steric and inductive effects of the R groups, the water:alkoxysilane ratio, and the solvent. These factors together with a mechanistic analysis of the reaction have been discussed in detail.[231–234] In recent years, the hydrolysis of a wide range of compounds of the general form $RSiOR^1{}_3$ (where $R =$ an organic group and $R^1 =$ Me or Et) has been used to prepare organically modified silicas (ORMOSILs) which have a variety of interesting properties.[235]

Alkoxysilanes react with organometallic reagents such as Grignard reagents and organolithium compounds to give organosilicon compounds (*see* ***Silicon: Organosilicon Chemistry***) (Scheme 44) in a manner similar to the halosilanes. These reactions are, however, slower and less vigorous and are useful starting materials in the production of organosilanes.

Alkoxysilanes may be converted back to chlorosilanes by treatment with, for example, PCl_5 or $AlCl_3$, and they react with carboxylic acids RCO_2H to give esters $(RCO_2)_4Si$. Disilyl sulfide, $(H_3Si)_2S$, reacts with MeOH or PhOH to give $MeOSiH_3$ and $PhOSiH_3$, respectively.[236,237] The Si–O–C angles are 120.6(9) and 121(1)°, respectively, somewhat lower than in disilyl ether. The structure of $MeOSiF_3$ prepared by the route shown in equation (29) has also been investigated and has an Si–O–C angle of about 132°.[238]

$$SiCl_4 + MeOH \longrightarrow MeOSiCl_3 \xrightarrow{SbF_3} MeOSiF_3 \qquad (29)$$

The structures of these compounds and related materials have been discussed.[239] The structure of $(MeO)_4Si$ is of S_4 symmetry with an Si–O–C angle of 122.3°. As in $MeOSiF_3$, the Si–O bond length is shorter than normal owing to several electronegative substituents being present.[240]

$$2RMgX + (RO)_4Si \longrightarrow R_2Si(OR)_2 + 2MgXOR$$

$$4RLi + (RO)_4Si \longrightarrow R_4Si + 4ROLi$$

Scheme 44

5.5.5 *Silyl Esters and Thioesters*

Silyl esters may be formed using a variety of preparative routes as shown in Scheme 45.

Compounds containing both alkoxy and ester groups, $(RO)_nSi[(CO(O)R]_{4-n}$, may be made by redistribution reactions involving $Si(OR)_4$ and $(RCO)_2O$. Alkoxysilanes, $(RO)_4Si$, may also be prepared by passing dimethyl or diethyl carbonate over SiO_2/KOH at 500–600 K.[241] Silyl esters, $H_3SiO(C{=}O)R$, may also be prepared in the gas phase by reaction between $(H_3Si)_3N$ and RCO_2H or by reaction of H_3SiBr with n-$Bu_3SnO(C{=}O)R$ ($R =$ H, Me, CF_3 etc.). The thioacetate $H_3SiO(C{=}S)Me$ has also been prepared by the butyltin method.[242] Short intermolecular distances are also found in $H_3SiO(C{=}E)Me$ ($E =$ O or S), where zig-zag chains are formed in the solid state via Si···(E=C) interactions. The H_3Si group is *cis* to the carbonyl oxygen in both the solid and vapor phase.[120]

Silicon tetraacetate may be prepared by the reaction between $SiCl_4$ and acetic anhydride[243] and has a structure comprising discrete molecules with no bridging by acetate, although there is one short intramolecular distance between a carbonyl oxygen and the silicon in each molecule.[244,245] Silyl esters, $H_3SiOC(O)R$ ($R =$ H, He, CF_3, etc.), and the thioacetate $H_3SiOC(S)Me$ may be prepared by either gas-phase reaction of $(H_3Si)_3N$ with organic acids or from H_3SiBr and tributyltin acetate, equation (30).[242,246] Treatment of $LiSeSiH_3$ with MeC(O)Cl affords the analogous selenoacetate $H_3SiOC(Se)Me$, which is in equilibrium with its isomer $H_3SiSeC(O)Me$[247] while the difunctional $H_2Si(OCOH)_2$ may be prepared from H_2SiBr_2 and $Bu_3SnOCOH$.[248]

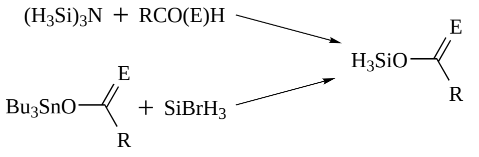

(30)

E = O or S

The structures of $H_3SiOCOH$ and $H_2Si(OCOH)_2$ have been determined in the gas phase.[242,249] In the monoformate the Si–O–C angle is 116.8° and the H_3Si group is twisted

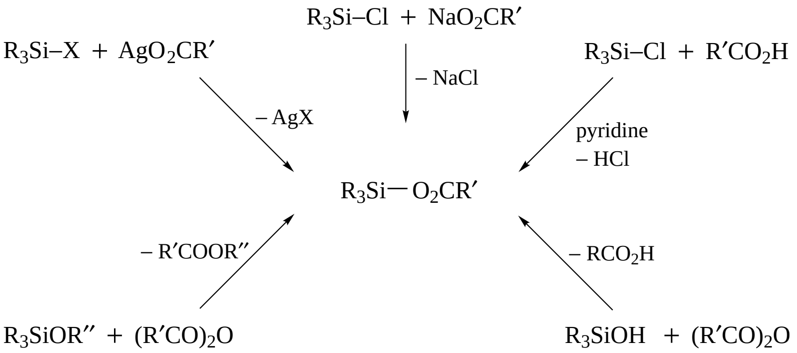
R3Si–Cl + NaO2CR′
R3Si–X + AgO2CR′
R3Si–Cl + R′CO2H
– NaCl
– AgX
pyridine
– HCl
R3Si—O2CR′
– R′COOR″
– RCO2H
R3SiOR″ + (R′CO)2O
R3SiOH + (R′CO)2O

Scheme 45

away from a planar cis arrangement by 21°. The diformate has an Si–O–C angle of 120.4° with one formate group in a cis and one in a trans arrangement about the Si–O bond, as shown in (**8**).

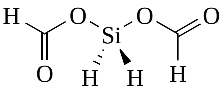

(**8**)

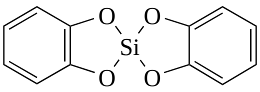

(**9**)

The reaction between catechol and Si/Cu alloy at high temperature and pressure affords the spiro compound (**9**) as a glassy white material.**[250]** The structure of (**9**) has been the subject of some dispute. Although it was originally thought to have a planar geometry at silicon this has not been confirmed, and it is likely that it has a normal tetrahedral arrangement as found in the related (**10**) and (**11**).**[251,252]**

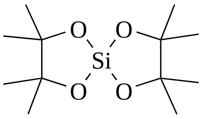

(**10**)

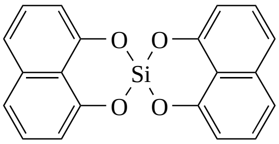

(**11**)

Compound (**10**) and the related spirocyclic compounds such as (**12**) and (**13**) may be conveniently prepared from the reaction between $(EtO)_4Si$ and a 1,2-, 1,3-, or 1,4-diol in the presence of a catalytic amount of metal alkoxide such as NaOMe or $(i\text{-PrO})_4Ti$.**[253]**

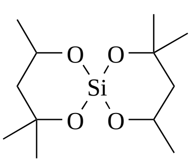

(**12**)

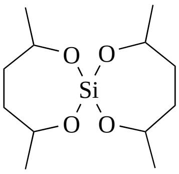

(**13**)

Tris(thioalkyl)silanes may be prepared by reaction between Cl_3SiH and thiols in a manner similar to the preparation of alkoxysilanes and are useful reagents for radical reductions of alkyl halides or alkenes in organic chemistry (Scheme 46).**[254]**

The reactions between $(H_3Si)_2E$ (E = S or Se) and H_2SiCl_2 or $HSiCl_3$ (Scheme 47) afford an interesting series of compounds containing several Si to chalcogen bonds such as $(HSi)_4S_6$ (**14**), which was found to have an adamantane-type structure.**[255]**

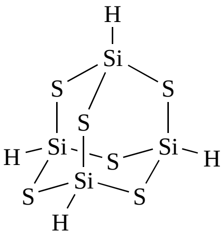

(**14**)

The reaction between $(CH_2SNa)_2$ and $SiCl_4$ gives the spirocyclic (**15**), which has a distorted tetrahedral arrangement

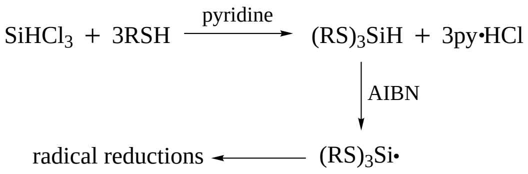
SiHCl3 + 3RSH
pyridine
(RS)3SiH + 3py•HCl
AIBN
radical reductions
(RS)3Si•

Scheme 46

$$(H_3Si)_2E + H_2SiCl_2 \longrightarrow H_3SiESiH_2Cl \xrightarrow{(H_3Si)_2E} (H_3SiE)_2SiH_2$$

$$(H_3Si)_2E + HSiCl_3 \longrightarrow (HSi)_4E_6$$

$$E = \text{S or Se}$$

Scheme 47

at silicon with the S–Si–S angles being in the range 100.1–124.7°.[256] The reaction of t-BuOH and SiS_2 gives a mixture of (t-BuO)$_2$Si(SH)$_2$, (t-BuO)$_3$SiSH, and (**16**) which, although planar, does not have a square Si_2S_2 ring but has endocyclic angles at Si and S of 97.8 and 82.2°, respectively.[257]

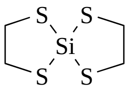

(**15**)

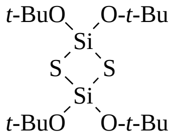

(**16**)

The (t-BuO)$_3$SiS group has been used as a ligand on various metals.[258] The bulky thiolate group is introduced by reaction of the thiol (t-BuO)$_3$SiSH with a suitable metal salt such as a nitrate or an oxide. The silver derivative is a cyclic tetramer, [(t-BuO)$_3$SiS]$_4$Ag, while the thallium and lead derivatives form planar and nonplanar cyclic dimers, [(t-BuO)$_3$SiSM]$_2$, respectively.[239] The reaction between (t-BuO)$_3$SiENa and (t-BuO)$_3$SiCl gives [(t-BuO)$_3$Si)]$_2$E (E = O or S), both of which are bent at the E atom.[259] By contrast, the Si–O–Si angle in the related peroxide, [(t-BuOO)$_3$Si]$_2$O, is 180°.[260]

5.6 Silicon–Nitrogen Compounds

The structures of simple silylamines have been the subject of much discussion and investigation. This has been due in large part to the finding that $(H_3Si)_3N$ is, unlike its pyramidal $(H_3C)_3N$ analog, planar at nitrogen. The silicon compound is also a much weaker Lewis base than the carbon analog and this has been attributed to p_π–d_π bonding between the lone pair of electrons on the nitrogen and the vacant d-orbitals on silicon but ionic contributions and Si–C σ^* interactions with the Si–N bond are probably also important (see Reference 212). Such bonding would increase the Si–N–Si angles to 120° and reduce the donor properties of the lone pair. The chemistry and physical properties of Si–N compounds (excluding Si_3N_4) have been discussed in detail.[261,262]

5.6.1 Preparations of Compounds Containing Si–N Bonds

The reaction between ammonia and H_3SiCl or H_3SiBr affords $(H_3Si)_3N$ as a low-boiling colorless liquid (equation 31).[196,263] Disilylamine, $(H_3Si)_2NH$, which is also planar at nitrogen, is unstable as a liquid and disproportionates to give trisilylamine and ammonia, but it may be made by reaction of Ph_2NSiH_3 and ammonia in a transammination reaction.[135] Similarly, H_3SiNH_2 also disproportionates, but it can be prepared at low pressure in the gas phase from the reaction between H_3SiI and ammonia.[264]

$$6H_3SiX + 2NH_3 \xrightarrow{-6\,HX} 2(H_3Si)_3N \xleftarrow{-NH_3} 3(H_3Si)_2NH \qquad (31)$$

The reaction between halosilanes and ammonia or primary or secondary amines is the most widely used synthetic route to compounds containing Si–N bonds. Such reactions are greatly controlled by steric effects: if large groups are present on either the silicon or the amine, then less than full substitution may occur. For example, ammonia reacts with chlorosilanes to give a variety of products depending on the size of the chlorosilane (equation 32).

$$NH_3 + R_3SiCl \longrightarrow NH_4Cl + (R_3Si)_3N \quad R = H \qquad (32)$$

$$R = Et,\ \text{product} = \text{mainly } (R_3Si)NH_2 + \text{some } (R_3Si)_2\,NH;$$

$$R = Ph,\ \text{product} = R_3SiNH_2 \text{ only}$$

This is also the case for the reaction of polyhalosilanes with amines, where small groups on the nitrogen allow a higher degree of substitution to be achieved (Scheme 48).

This type of reaction is usually carried out using chlorosilanes because of their ready availability, but bromo- or iodosilanes are more reactive and may give better yields. Reactions of fluorosilanes with amines tend to give, because of the relatively high Lewis acidity of fluorosilanes, stable donor–acceptor adducts such as $SiF_4{\cdot}HNR_2$. Heating such adducts, however, does give F_3SiNR_2 (R = Me, Pr, Bu) species in good yield. A successful method to overcome the steric problems encountered above is to use an alkali metal or magnesium amide to carry out a metathesis reaction. For example, although the tetraamidosilane Si(NHBu-t)$_4$ is not available by the silyl chloride plus amine route (see Scheme 48), it may be obtained using a magnesium amide (equation 33). Here again the use of the more reactive halogens allows successful substitution by the bulky groups. For a more detailed discussion of this type of reaction, and Si–N compounds in general, see Lappert *et al.*[262]

$$4\,t\text{-BuNHMgBr} + SiBr_4 \longrightarrow Si(NH\text{-}t\text{-Bu})_4 + 4MgBr_2 \qquad (33)$$

Tetraaminosilanes may be prepared by several methods using either a secondary amine or a metal amide (Scheme 49).[265] Mixed amides may also be prepared.

The reaction between Me_2NH and H_3SiBr gives Me_2NSiH_3, which has an unusually high melting point of 276 K, about 120 K higher than the closely related compounds $NMe_{3-x}(SiH_3)_x$ ($x = 0$–3). The surprising properties of Me_2NSiH_3 are associated with its unusual structure, which is pentameric with N atoms at the corners of a pentagon and SiH_3 groups midway along the pentagon sides (Figure 8).[120]

$$\begin{aligned}
&SiCl_4 + 8NHMe_2 \longrightarrow Si(NMe_2)_4 + Me_2NHCl\\
&SiCl_4 + 6NH_2\text{-}t\text{-Bu} \longrightarrow ClSi(NH\text{-}t\text{-Bu})_3 + 3t\text{-BuNH}_3Cl\\
&SiCl_4 + 4HN\text{-}i\text{-}Pr_2 \longrightarrow Cl_2Si(N\text{-}i\text{-}Pr_2)_2 + 2i\text{-}Pr_2NH_2Cl
\end{aligned}$$

Scheme 48

$$\begin{aligned}
&SiCl_4 + 8R_2NH \longrightarrow (R_2N)_4Si + 4R_2NH_2Cl\\
&SiCl_4 + n\,R_2NLi \longrightarrow Cl_{4-n}Si(NR_2)_n + LiCl \qquad n = 1\text{–}4\\
&SiCl_4 + 4R_2NMgBr \longrightarrow (R_2N)_4Si + 4MgBrCl\\
&R = Me, Et, n\text{-}Pr, i\text{-}Pr, etc.
\end{aligned}$$

Scheme 49

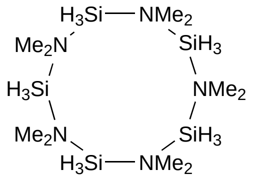

Figure 8 The pentameric structure of Me_2NSiH_3

The nitrogen atoms also have a pyramidal geometry rather than the planar $(H_3Si)_3N$, and the N–Si–N angles are about 177°.

The controlled reaction of two equivalents of ammonia with one of $SiCl_4$ gives a mixture of monomeric, oligomeric, and polymeric products which may undergo further reactions typical of Si–N compounds (Scheme 50).[266]

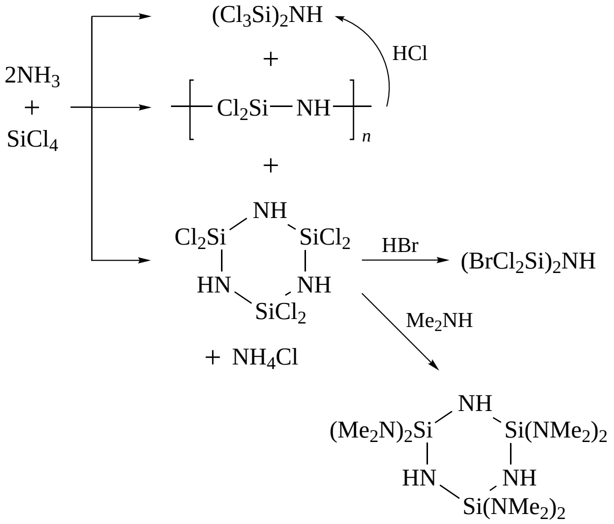

Scheme 50

The reaction between H_3SiBr and F_2PNH_2 in the vapor phase at room temperature gives $H_3SiNHPF_2$, which can be isolated and which reacts with a further equivalent of H_3SiBr to give $(H_3Si)_2NPF_2$.[267,268] The diphosphino compound $H_3SiN(PF_2)_2$ can be prepared in a similar manner (Scheme 51).[268] All three of the compounds are planar at nitrogen.[267,269]

The hexachloro monomer $(Cl_3Si)_2NH$ may react via $SiCl_3$, Cl, or H substitution reactions.[270] Heating the lithium compound (**17**) gives the cyclic dimer, presumably via elimination of LiCl and dimerization of the reactive intermediate $Cl_2Si{=}NSiCl_3$ (Scheme 52).

The cyclic trimer (**18**), formed by condensation reactions in a manner similar to cyclic siloxanes from SiOH compounds, has a planar Si_3N_3 skeleton with Si–N–Si and N–Si–N angles of 131 and 109°, respectively.[271]

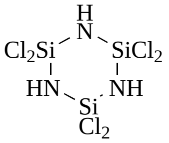

(**18**)

5.6.2 *Structures of Silyl Amines*

Structural data for several silyl amines are given in Table 7. Detailed discussions are given in appropriate places throughout this section.

5.6.3 *Reactions of Silyl Amines*

Silyl amines usually react readily with water or alcohols to give compounds containing Si–OR groups (R = H, Me, Et, etc.) and with HCl to give a chlorosilane. The poor donor properties of $(H_3Si)_3N$ mean that it does not form adducts as readily as Me_3N, no adduct is formed with Me_3B, and only weak adducts are formed with BF_3 or BCl_3. Reactions of $(H_3Si)_3N$ are summarized in Scheme 53.[196]

5.6.4 *Silicon Nitride, Si_3N_4*

Silicon forms the widely studied nitride Si_3N_4 when heated at high temperature (>1400 °C) in a nitrogen

$$SiBrH_3 + NH_2PF_2 \longrightarrow H_3SiNHPF_2 \xrightarrow[Me_3N]{H_3SiBr} (H_3Si)_2NPF_2 + NMe_3HBr$$

$$SiBrH_3 + HN(PF_2)_2 \xrightarrow{NMe_3} H_3SiN(PF_2)_2 + NMe_3HBr$$

Scheme 51

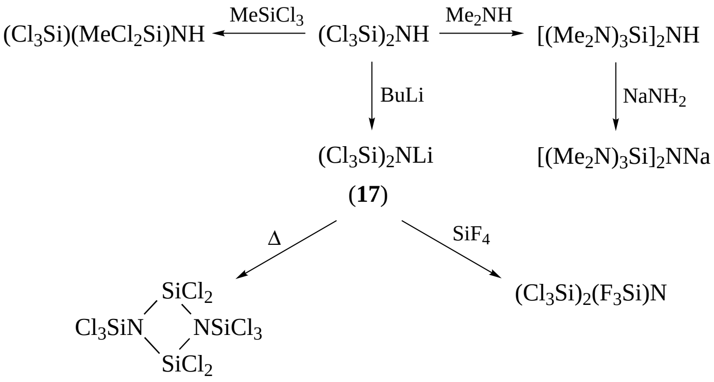
(Cl3Si)(MeCl2Si)NH
MeSiCl3
(Cl3Si)2NH
Me2NH
[(Me2N)3Si]2NH
BuLi
NaNH2
(Cl3Si)2NLi
(17)
[(Me2N)3Si]2NNa
Δ
SiF4
SiCl2
Cl3SiN
NSiCl3
SiCl2
(Cl3Si)2(F3Si)N

Scheme 52

Table 7 Structural details of several silylamines[112]

Compound	Structure	N–Si (Å)	Method[a]	Si–N–P, Si–N–Si, or Si–N–C angle (°)
$(H_3Si)_2NH$	Planar at N	1.725	E	127.7
$(H_3Si)_3N$	Planar at N	1.734	E	119.7(1)
$(H_3Si)(PF_2)NH$	Two gas-phase conformers	1.720	E	127.9
$(H_3Si)NMe_2$[272]	Nonplanar at N (gas phase)	1.715	E	120.0
	Pentameric, five-coord. Si	1.976	X	Si–N–Si 110 N–Si–N 177
F_3SiNMe_2	Planar at N	1.654	E	119.7
Cl_3SiNMe_2	Planar at N	1.657	E	123.1
$(H_3Si)_2NMe$	Planar at N	1.726	E	Si–N–Si 125.4 Si–N–C 117.3
$(H_3Si)_2NBF_2$	Planar at N and B	1.737	E	Si–N–Si 123.9
$(Me_2N)_3SiCl$	Planar at N	1.715	E	Cl–Si–N 113.5
$(Cl_2SiNH)_3$	Planar Si_3N_3 ring	1.68	E	Si–N–Si 131
$(H_3Si)_2NN(SiH_3)_2$[273]	Planar Si_2NN groups	1.731	E	Si–N–Si 129.5

[a] E = electron diffraction; X = X-ray diffraction.

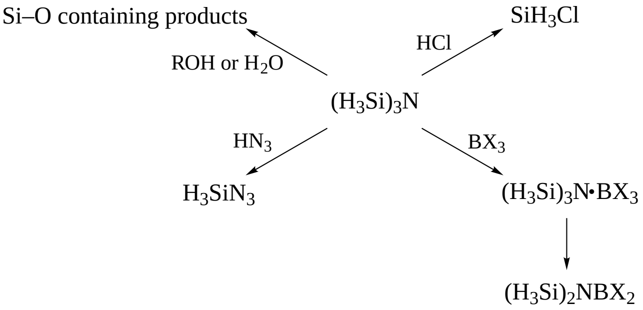
Si–O containing products
ROH or H2O
SiH3Cl
HCl
(H3Si)3N
HN3
BX3
H3SiN3
(H3Si)3N•BX3
(H3Si)2NBX2

Scheme 53

atmosphere. Interest in this ceramic material is due to its good refractory properties. The use of silicon nitride in the microelectronics industry and in the fabrication of solar cells has been discussed in detail.[274] Two main forms of Si_3N_4 are known, called α and β. Both structures are similar, comprising Si_4N tetrahedra, the difference being in how they are arranged in the crystal lattice. Interestingly, the NSi_3 groups within the structure are nearly planar, that is, similar to the arrangement found in $(H_3Si)_3N$.[275] Silicon nitride may be prepared in several ways, for example, Scheme 54.

5.7 Silicon, Phosphorus, Arsenic, and Antimony Compounds

Monosilyl compounds (H_3SiMH_2) of phosphorus and arsenic are known and they may be prepared in a variety of

$$3Si + 2N_2 \longrightarrow Si_3N_4$$
$$3SiO_2 + 6C + 2N_2 \longrightarrow Si_3N_4 + 6CO$$
$$3SiCl_4 + 4NH_3 \longrightarrow Si_3N_4 + 12HCl$$

Scheme 54

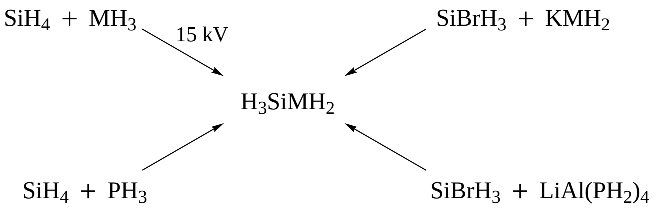

Scheme 55

ways (Scheme 55); similar preparative routes are successful in the preparation of $(H_3Si)_2EH$, $(H_3Si)_3E$, and $H_3SiSiH_2EH_2$ (E = P or As).[196]

The mercury sensitized photolysis of a mixture of F_3SiSiF_3 and PF_3 affords $P(SiF_3)_3$ as a colorless air-sensitive liquid. It reacts with a deficiency of water to give $(F_3Si)_2PH$ and F_3SiPH_2 and with bromine to give PBr_5 and F_3SiBr.[276]

There are many cyclic compounds known containing P and Si atoms in the ring but the majority have organic substituents on the silicon. (Details of the structures of such compounds are available.[112]) An exception is the spirocyclic compound (**19**), formed using an alkali metal-phosphorus derivative (equation 34).[277]

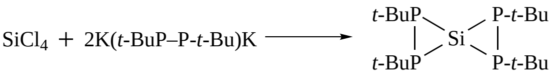

(34)

(**19**)

The lithium phosphide Li_3P_7 also reacts with silyl halides and with H_3SiX (X = Br or I) to form the tricyclic species (**20**).[278]

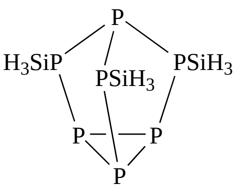

(**20**)

5.7.1 *Reactions of Silicon–Phosphorus, –Arsenic, and –Antimony Derivatives*

The reaction between SiH_4 and PH_3 gives H_3SiPH_2, which may be alkylated via H_3SiPLi_2 (Scheme 56).[279] Treatment of Si–H containing silylphosphines, however, leads to cleavage of an Si–P bond and alkylation at silicon. These reactions, and many other interesting cyclic and acyclic phosphines, most of which contain alkyl groups on silicon, are discussed in more detail by Fritz.[280]

$$H_3SiPH_2 + 2LiPEt_2 \longrightarrow 2HPEt_2 + H_3SiPLi_2 \xrightarrow{MeCl} H_3SiPMe_2$$
$$HSi(PEt)_3 + MeLi \longrightarrow MeSiH(PEt_2)_2 + LiPEt_2$$

Scheme 56

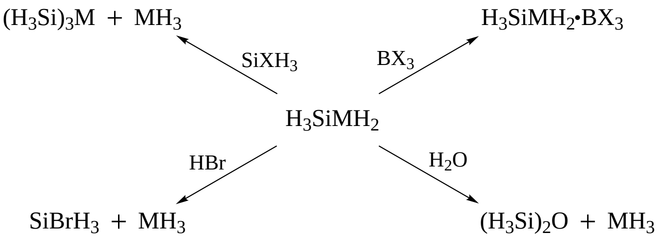

M = P or As

Scheme 57

$$MeLi + (H_3Si)_3E \longrightarrow (H_3Si)_2ELi + MeSiH_3$$
E = P or As
$$MeLi + (H_3Si)_2E \longrightarrow H_3SiELi + MeSiH_3$$
E = O, S, or Se

Scheme 58

The silyl phosphorus and arsenic compounds react with a variety of reagents and form adducts more readily with Lewis acids than the silyl amines (Scheme 57).[196]

The reaction of MeLi with Group 15 (but not N) and Group 16 silyl compounds affords metal derivatives (Scheme 58).

When the spirocyclic compound (**19**) is heated, dimerization occurs to give an unusual dispirocyclic compound containing three-, four-, and five-membered rings containing silicon (equation 35).[281]

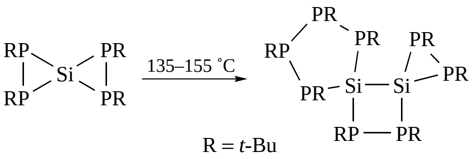

(35)

5.7.2 *Structures of Silicon–Phosphorus, –Arsenic, and –Antimony Derivatives*

Structural data for trisilyl compounds of the Group 15 elements are shown in Table 8. As would be expected, the

Table 8 Structural data for trisilyl compounds[196]

Compound	Si–H (Å)	Si–M (Å)	Si–M–Si (°)
$(H_3Si)_3N$	1.54	1.738	119.6
$(H_3Si)_3P$	1.50	2.247	95
$(H_3Si)_3As$	1.48	2.352	91.5
$(H_3Si)_3Sb$	1.394	2.557	88.6

Si–M bond length increases on going down the group. Only the amine is planar at nitrogen; the structures of $(H_3Si)_3E$ ($E = P$, As and Sb) show a steady decrease in Si–E–Si angle on going down the group,[282] any p_π–d_π interaction presumably being rather weaker on descending the group.[196] A more detailed discussion of these compounds is available.[112]

The structures of H_3Si–E derivatives ($E = Li$, Be, B, N, O, C, P, S, Cl, etc.) have been the subject of many theoretical investigations. Despite the fact that H_3SiNH_2 is unknown, it is calculated also to be planar at nitrogen.[283]

5.8 Compounds Containing Silicon to Boron Bonds

Compounds containing Si–B bonds are comparatively rare but the in situ coupling of $SiCl_4$ and $(MeO)_2BCl$ affords $Si[B(OMe)_2]_4$ which undergoes transesterification without cleavage of the Si–B bonds (equation 36).[284] The reaction between F_2Si: and BF_3 affords $F_3SiSiF_2BF_2$ and $F_3SiSiF_2SiF_2BF_2$.[285]

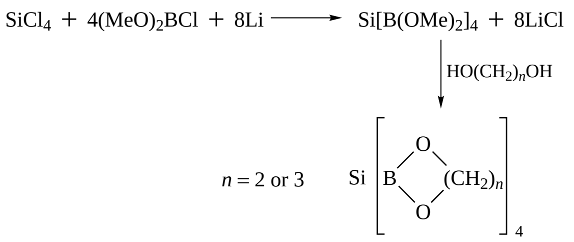

(36)

5.9 Compounds Containing Si–C and Si–Si Bonds

The vast majority of compounds containing Si–C bonds are dealt with in another article (*see **Silicon: Organosilicon Chemistry***), although silyl cyanides are treated in Section 5.4.2 above. The perhydrosilanes such as $H_3Si(SiH_2)_nSiH_3$ are covered in Section 5.1.

The photodecomposition of SiH_4/GeH_4 mixtures affords H_3SiSiH_3 and H_3SiGeH_3 by insertion of the initially formed H_2Si: into a Si–H or Ge–H bond of SiH_4 or GeH_4, respectively.[286]

Treatment of $SiCl_4$ with $LiSnMe_3$ affords $Si(SnMe_3)_4$, which reacts with MeLi to give (**21**); the latter is useful for introducing the $Si(SnMe_3)_3$ ligand (in an analogous fashion to the widely used $Si(SiMe_3)_3$ ligand) into complexes such as (**22**) (Scheme 59). The Si–W distance in the tungsten complex is 2.652 Å.[287]

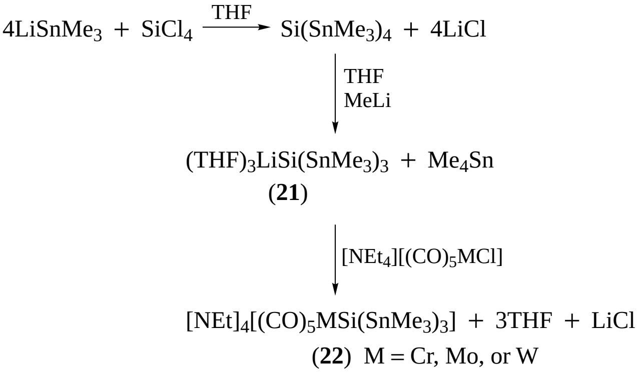

4LiSnMe3 + SiCl4 → Si(SnMe3)4 + 4LiCl
THF
THF
MeLi
(THF)3LiSi(SnMe3)3 + Me4Sn
(21)
[NEt4][(CO)5MCl]
[NEt]4[(CO)5MSi(SnMe3)3] + 3THF + LiCl
(22) M = Cr, Mo, or W

Scheme 59

Numerous Group 14 carborane complexes have been prepared, in which the main group metal interacts with a C_2B_3 fragment in an η^5-fashion. Such complexes are usually formed by reaction of an alkali metal carborane with a silicon chloride (equation 37). (For a more detailed discussion of this work see Hosmane and Maguire.[288])

$$SiCl_4 + 2Li_2[\mathit{nido}\text{-}7,8\text{-}C_2B_9H_{11}] \xrightarrow{C_6H_6} \mathit{commo}\text{-}3,3'\text{-}(3,1,2\text{-}SiC_2B_9H_{11})_2 + 4LiCl \qquad (37)$$

5.10 Silicon Carbide

The preparation, manufacture, and reactions of SiC have been discussed in detail in Gmelin,[289] as have the electrical, mechanical, and other properties of both crystalline and amorphous of SiC.[290] Silicon carbide results from the pyrolysis of a wide range of materials containing both silicon and carbon but it is manufactured on a large scale by the reduction of quartz in the presence of an excess of carbon (in the form of anthracite or coke), (Scheme 60), and more recently by the pyrolysis of polysilanes or polycarbosilanes (for a review, see Reference 291). Although it has a simple empirical formula, silicon carbide exists in at least 70 different crystalline forms based on either the hexagonal wurtzite (ZnS) structure α-SiC, or the cubic diamond (zinc blende) structure β-SiC. The structures differ in the way that the layers of atoms are stacked, with Si being four-coordinate in all cases.

The industrial interest in SiC derives from its high mechanical and chemical stability as well as its hardness (9.5 on the Moh scale), which makes it a useful abrasive. When pure, α-SiC is an intrinsic semiconductor, but it may be doped

$$SiO_2 + 2C \longrightarrow Si + 2CO$$

$$Si + C \xrightarrow{2000\text{–}2500\,^\circ C} SiC$$

Scheme 60

with various impurities to give an extrinsic semiconductor. β-SiC is also used as a high-temperature semiconductor.

6 TRANSITION METAL SILYL COMPLEXES

The interest in transition metal silyl derivatives stems largely from an interest in how such compounds compare with the very extensive organometallic chemistry of the transition elements and also because of the industrial importance of the *Hydrosilation* reaction used for the preparation of organosilicon compounds (*see* ***Silicon: Organosilicon Chemistry***). There is a variety of methods for preparing compounds containing transition metal to silicon bonds. The most common are oxidative addition of an Si–X bond (X is usually H) to a transition metal complex, the use of transition metal anions, and the use of silyl alkali metal derivatives (Scheme 61). There is a wide variety of compounds known and, as the principal focus of this article is silicon, they will be arranged according to the groups on silicon. Recent structural studies and developments in the chemistry of transition metal silyl compounds have been reviewed.[292–298]

6.1 Compounds Containing SiH_3 and Related Ligands

The Si–H bonds within a silane are generally more reactive toward *Oxidative Addition* than other Si–X bonds, for example, where X is halogen or SH. For example, the reactions between various H_3SiX species ($X = H$, Cl, or SiH_3) and *trans*-$[PtH_2\{P(C_6H_{11})_3\}_2]$ afford compounds (**23**) in which reaction at the Si–H rather than the Si–X bonds have occurred (equation 38).[299] The X-ray structure of (**23**; $X = H$) gives Pt–Si 2.382 Å; Si–H stretching frequencies are 2025 and 2020 cm^{-1}.

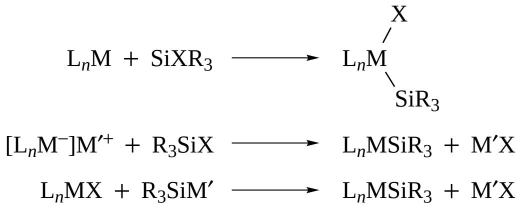

$$L_nM + SiXR_3 \longrightarrow L_nM\begin{matrix} X \\ \\ SiR_3\end{matrix}$$

$$[L_nM^-]M'^+ + R_3SiX \longrightarrow L_nMSiR_3 + M'X$$

$$L_nMX + R_3SiM' \longrightarrow L_nMSiR_3 + M'X$$

Scheme 61

$$SiH_3X + trans\text{-}[PtH_2\{P(C_6H_{11})_3\}_2] \longrightarrow trans\text{-}[PtH(SiH_2X)\{P(C_6H_{11})_3\}_2] + H_2$$
$$(\mathbf{23})\ X = H, Cl, \text{ or } SiH_3 \qquad (38)$$

Disilyl chalcogen compounds react in a similar manner (equation 39), to give both mononuclear complexes and bridged complexes (if excess platinum hydride precursor is used).[300]

$$(H_3Si)_2E + trans\text{-}[PtX(H)(PEt_3)_2] \longrightarrow trans[\text{-}PtX(PEt_3)_2(SiH_2ESiH_3)] + trans[\{\text{-}PtX(PEt_3)_2(SiH_2)\}_2E] + H_2$$
$$E = O, S, \text{ or } Se;\ X = Br \text{ or } I \qquad (39)$$

The silyl amines and phosphines also give similar complexes (Scheme 62).[301]

The salt elimination route is also a useful method, relying on the reaction between a silyl halide and a transition metal anion, for example, equation (40).[302] The IR spectra of such compounds are informative; values of 2141, 2136, and 2132 cm^{-1} for the disilyl compound and 2142 cm^{-1} for the silyl compound are found for the Si–H stretching frequencies.

$$H_3SiI + Na_2Fe(CO)_4 \longrightarrow (H_3Si)_2Fe(CO)_4 + (H_3Si)(H)Fe(CO)_4 \qquad (40)$$

In a similar manner, H_3SiI and H_2SiI_2 react with $NaCo(CO)_4$ to give silyl cobalt complexes (Scheme 63). The Si–Co bond in these complexes is cleaved by H–X species ($X = F$, Cl) and HgX_2 ($X = Cl$ or I) to give H_3SiX and either $HCo(CO)_4$ or $Hg[Co(CO)_4]_2$. The IR stretches for $H_3SiCo(CO)_4$ are at 2164, 2160, and 2154 cm^{-1}.[303] The reaction between H_3SiI and $NaMn(CO)_5$ proceeds in a similar manner.

The metal–Si bond is inert towards HCl and HgX_2 ($X = Cl$ or I) at room temperature. At higher temperatures, chlorosilyl derivatives are produced in the reaction with HCl (Scheme 64).[304] The thermal decomposition of the metal

$$(H_3Si)_2E + trans\text{-}[PtH(I)(PEt_3)_2] \longrightarrow trans\text{-}[PtI(PEt_3)_2\{H_2SiN(SiH_3)_2\}] + H_2$$
$$E = N \text{ or } P$$

$$\begin{matrix} PH_2(SiH_3) \\ \text{or } PH(SiH_3)_2 \end{matrix} + trans\text{-}[PtI(H)(PEt_3)_2] \longrightarrow trans\text{-}[PtI(PEt_3)_2(SiH_3)] + PH_3$$

Scheme 62

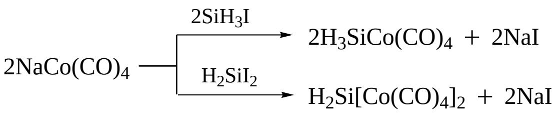
2SiH3I
H2SiI2
2NaCo(CO)4
2H3SiCo(CO)4 + 2NaI
H2Si[Co(CO)4]2 + 2NaI

Scheme 63

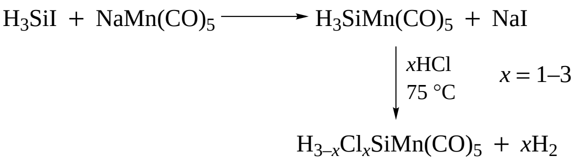
H3SiI + NaMn(CO)5
H3SiMn(CO)5 + NaI
xHCl
75 °C
x = 1–3
H3–xClxSiMn(CO)5 + xH2

Scheme 64

silyl complexes [$Co(CO)_4(SiH_3)$], [$Fe(CO)_4(SiH_3)_2$], and [$Mn(CO)_5(SiH_3)$] at 500 °C gives the metal silicides CoSi, β-$FeSi_2$, and MnSi–Mn_5Si_3, respectively.[305] In the presence of Lewis bases such as Me_3N and pyridine, 1:2 adducts $(H_3Si)(B)_2M(CO)_n$ ($M = $ Mn or Co, $n = 5$ or 4, respectively) are formed which are thought to have ionic structures of type $(H_3Si{\cdot}2B)^+ [M(CO)_n]^-$.[306]

If more than one Si–H group is present in the silane, then photolysis may lead to bridging H_2Si groups, for example, the manganese complex (**24**), which has an Si–Mn distance of 2.434 Å and an Mn–Si–Mn angle of 124.4°; (Scheme 65).[307] The reaction between H_3SiK and Cp_2TiCl_2 (Scheme 65) affords the olive-green bridged complex (**25**), presumably via the disilyl complex $Cp_2Ti(SiH_3)_2$.[308]

The molecular structures of $H_3SiMn(CO)_5$, $H_3SiRe(CO)_5$, and $H_3SiCo(CO)_4$ have all been determined in the gas phase.[309–311] The Si–M bond distances are 2.407, 2.562, and 2.381 Å for the Mn, Re, and Co complexes, respectively. Although it is difficult to estimate what might be expected for these distances, they all seem relatively short. This has been attributed to d → d π-bonding using the vacant d-orbitals on silicon. More detailed discussions of transition metal SiH_3 complexes have been published.[292–298]

Silyl complexes also result from the reaction between a silyl anion and a metal halide, for example, in the formation of (**26**), which has an Si–H stretching frequency of 2103 cm^{-1} (equation 41).[312]

$$(\eta^5\text{-}C_5H_5)Fe(CO)_2Br + H_3SiK \longrightarrow \underset{(\mathbf{26})}{(\eta^5\text{-}C_5H_5)Fe(CO)_2SiH_3} + KBr \tag{41}$$

The search for transition metal complexes that can activate alkanes has led to investigations into the potential of metal complexes to coordinate silanes. In 1995, the first SiH_4 complexes were prepared according to Scheme 66. These

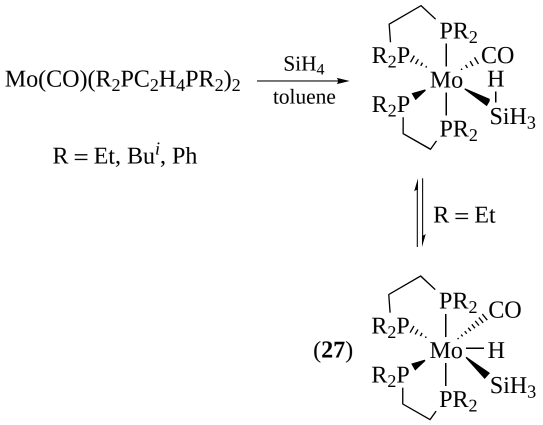
Mo(CO)(R2PC2H4PR2)2
SiH4
toluene
R = Et, Bui, Ph
PR2
R2P
CO
Mo
H
R2P
SiH3
PR2
R = Et
PR2
CO
R2P
Mo
H
R2P
SiH3
PR2

(**27**)

Scheme 66

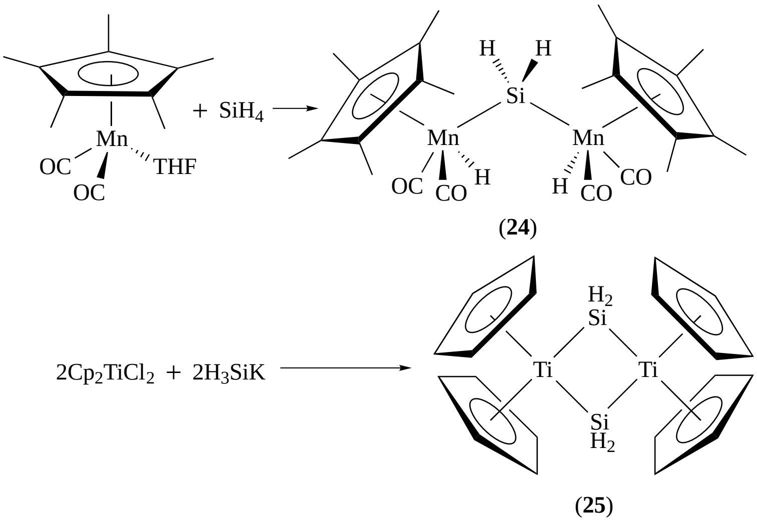
Mn
OC
THF
OC
+ SiH4
H
H
Si
Mn
Mn
OC
CO
H
H
CO
CO
2Cp2TiCl2 + 2H3SiK
H2
Si
Ti
Ti
Si
H2

(**24**)

(**25**)

Scheme 65

complexes have been characterized by multinuclear NMR spectroscopy and X-ray crystallography which show the metal center to have a distorted octahedral geometry and the CO and SiH_4 ligands to be cis to each other. For the complex containing the $(Et_2PCH_2)_2$ ligand an equilibrium between the η^2–SiH_4 complex and a hydrosilyl, (**27**), complex is found.[313] More recently, complexes, (**28**), in which an SiH_4 ligand bridges between two metals have been prepared, equation (42).[314] A variety of complexes are now known in which an Si–H bond is bound to the metal in an η^2–fashion; many of these contain organic substituents at Si, and their chemistry has been reviewed.[315–317]

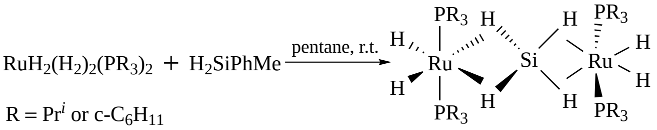
$RuH_2(H_2)_2(PR_3)_2$ + $H_2SiPhMe$
pentane, r.t.
R = Pr^i or c-C_6H_{11}
PR3
H
Ru
Si

(**28**)

(42)

6.2 SiX_3 Containing Ligands (X = F or Cl)

Hexafluorodisilane breaks down in a radiofrequency glow-discharge to give trifluorosilyl radicals that react with a variety of metal atoms when co-condensed on a cold surface (equation 43). This method allows the synthesis of a range of homoleptic SiF_3 metal derivatives (*see Homoleptic Compound*).[318]

$$F_3SiSiF_3 \xrightarrow[\text{glow discharge}]{\text{rf}} 2F_3Si\bullet \xrightarrow[-196\,^\circ\text{C surface}]{\text{M atoms}} (F_3Si)_nM \qquad (43)$$

$$n = 2,\ \text{M} = \text{Te or Hg};\ n = 3,\ \text{M} = \text{Sb or Bi}$$

If other ligands are also co-condensed or are added to coordinatively unsaturated F_3Si–M species, then further complexes may be prepared, for example, (η^6-toluene)$Ni(SiF_3)_2$, $(F_3Si)_2Pd(PMe_3)_2$, $(F_3Si)_2Cd\cdot$glyme, and $(F_3Si)_2Zn\cdot2$(pyridine). The bis F_3Si complex $(F_3Si)_2Ni(PMe_3)_2$ is also prepared in this way; it has a trigonal bipyramidal geometry with the F_3Si ligand occupying the axial positions and having an average Si–Ni bond length of 2.182 Å.[318] The arene complexes (η^6-toluene)$Ni(SiF_3)_2$ and (η^6-benzene)$Ni(SiCl_3)_2$ react with CO to give rare examples of nickel(II) carbonyl complexes, $(X_3Si)_2Ni(CO)_3$ (X = F or Cl). The Cl_3Si compound has trigonal bipyramidal geometry, with the $SiCl_3$ group in axial positions, and an average Si–Ni bond length of 2.286 Å; the fluorine analog is likely to have a similar structure.[319,320] Treatment of (η^6-toluene)$Ni(SiCl_3)_2$ with alkylammonium salts (Scheme 67) gives the bridged species (**29**), while treatment with wet di-*t*-butylpyridine affords (**30**), which has an average Ni–Si distance of 2.171 Å and an Si–N–Si bond angle of 89.9°.[321]

The X-ray structure of $F_3SiCo(CO)_4$ (prepared from F_3SiH and $Co_2(CO)_8$) shows a Si–Co bond length of 2.226 Å, that is, slightly shorter than that in the trichlorosilyl analog (2.254 Å).[322] The Fe–Si distance in (η^5-C_5H_5)$FeH(SiCl_3)_2(CO)$ is 2.252 Å.[323] The reaction of $(PPh_3)_3RhCl$ with Cl_3SiH gives $RhHCl(SiCl_3)(PPh_3)_2$, which crystallizes with disordered $HSiCl_3$ solvate molecules in the lattice. It has a short Rh–Si distance of 2.203 Å, which is again indicative of some back donation of electrons from the metal to the vacant d-orbitals on silicon to give some partial π-bonding.[324]

The UV photolysis of $M_3(CO)_{12}$ (M = Fe, Ru, or Os) with excess Cl_3SiH gives *cis*- and *trans*-$M(CO)_4(SiCl_3)_2$ (except for M = Ru, when only the cis isomer is formed). The CO ligands are readily substituted by PPh_3 or arene ligands to give, for example, *mer*-$Ru(CO)_3(SiCl_3)_2$ and (η^6-$Me_3C_6H_3$)$Ru(CO)(SiCl_3)_2$.[325] The structure of (η^6-*p*-*t*-$Bu_2C_6H_4$)$Ru(CO)(SiCl_3)_2$ is of the 'piano stool' type (*see Piano Stool Structure*) having Ru–Si distances averaging 2.339 Å.[326] If $M_3(CO)_{12}$ (M = Ru or Os) are heated at 70–75 °C with Cl_3SiH, then both $M(CO)_4(SiCl_3)_2$ and the trinuclear $M_3H_3(CO)_9(SiCl_3)_3$ are formed.[327]

Various other metal carbonyl complexes react with Cl_3SiH, with mononuclear silyl complexes being formed from dinuclear starting materials (Scheme 68).[328]

Similarly, photolysis of $(PR_3)Fe(CO)_4$ (R = Ph or OPh) with $HSiCl_3$ gives $H(SiCl_3)(PR_3)Fe(CO)_3$ (via addition

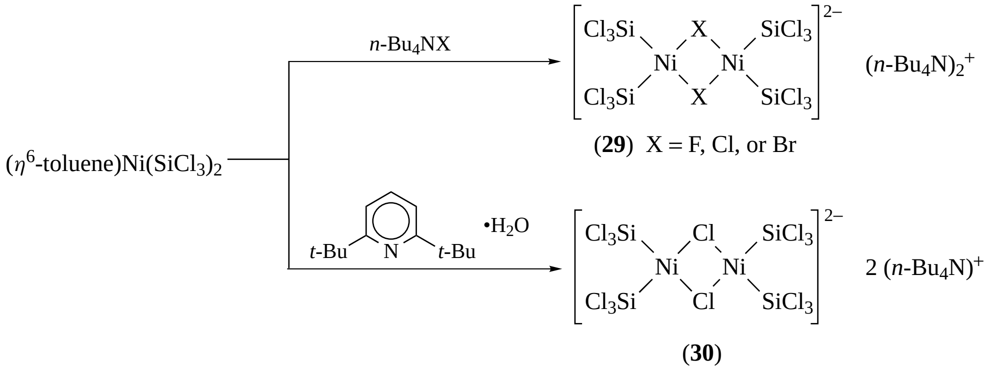

Scheme 67

$$M_2(CO)_{10} + 2Cl_3SiH \longrightarrow 2Cl_3SiM(CO)_5$$

M = Mn or Re

$$Fe(CO)_5 + Cl_3SiH \longrightarrow [Cl_2SiFe(CO)_4]_2$$

$$[Cp(CO)_nM]_2 + 2Cl_3SiH \longrightarrow 2Cl_3SiM(CO)_nCp$$

M = Mo, $n = 3$; M = Fe, $n = 2$; M = Ni, $n = 1$

Scheme 68

of Cl_3Si–H to the 16-electron species $(PPh_3)Fe(CO)_3)$, which when treated with PPNCl give PPN salts of $[(SiCl_3)(PR_3)Fe(CO)_3]^-$ anions. Both of the anions are trigonal bipyramidal with both the phosphorus and silicon ligands in axial positions, and Fe–Si distances of 2.197 and 2.206 Å for R = Ph and OPh, respectively.[329]

The structures of $(Cp)(CO)LM(H)SiR_3)$ complexes (R = Cl, L = CO, etc.), which are formed in photolytic experiments, are unusual in that they contain Mn–H–Si three-center bonds, for example, (**31**), in which the Si–H group may be regarded as being bound in an η^2-ligand position. (See Schubert[330] and References 315–317 for a more detailed discussion of η^2-coordination of Si–H bonds to transition metals.)

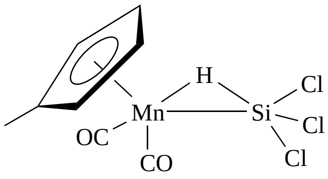
H
Mn
Si
Cl
Cl
Cl
OC
CO

(**31**)

The salt elimination reaction between transition metal anions and halosilanes also gives the trihalosilyl products (equation 44).[331]

$$[Cp(CO)_nM]Na + R_3SiX \longrightarrow [Cp(CO)_nMSiR_2X] + NaR \qquad (44)$$

$n = 3$, M = Mo or W, R = Cl, X = H

R = Cl = X

R = Br = X

$n = 2$, M = Fe, R = Cl, X = H

Some of these reactions are slow and give low yields, and Cl_3Si derivatives may more conveniently be prepared by chlorination of a $SiCl_2H$ ligand (equation 45).[332] The structure of $(\eta^5\text{-}C_5H_5)(CO)_2FeSiCl_3$ has an Fe–Si distance of 2.216 Å, while the related compound $(CO)_4CoSiCl_3$ has a trigonal bipyramidal structure with $SiCl_3$ in an axial position.[333,334]

$$Cp(CO)_nMSiHCl_2 \xrightarrow[50\,^\circ C]{CCl_4} Cp(CO)_nMSiCl_3 \qquad (45)$$

$n = 3$, M = Cr, Mo, or W; $n = 2$, M = Fe

The reaction between $MPhCl(CO)(PPh_3)_2$ species and Cl_3SiH also gives metal complexes. They undergo substitution reactions with alcohols and alkyllithium reagents to give SiR_3 species (Scheme 69).[335]

On treatment with three equivalents of water the osmium complex (**32**) affords the novel complex (**33**) containing an $Si(OH)_3$ ligand (Scheme 70). If only one equivalent of water is used, the bridging disiloxane complex (**34**) is formed (which is also formed from reaction between (**32**) and (**33**) with subsequent hydrolysis). The geometry of (**33**) is square pyramidal with the $Si(OH)_3$ group in the apical position and with an Si–Os distance of 2.319 Å.[336] The relatively recent interest in carrying out chemistry at such a coordinated SiX_3 ligand would seem to have great potential and further work

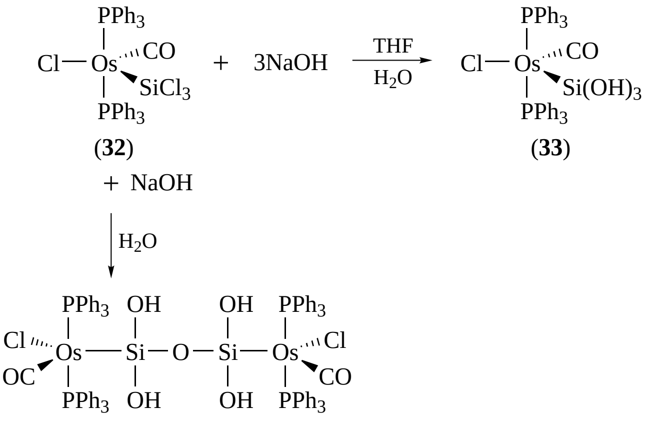
PPh3
Cl
Os
CO
SiCl3
PPh3
(32)
+ 3NaOH
THF
H2O
PPh3
Cl
Os
CO
Si(OH)3
PPh3
(33)
+ NaOH
H2O
PPh3 OH OH PPh3
Cl Os Si O Si Os Cl
OC CO
PPh3 OH OH PPh3
(34)

Scheme 70

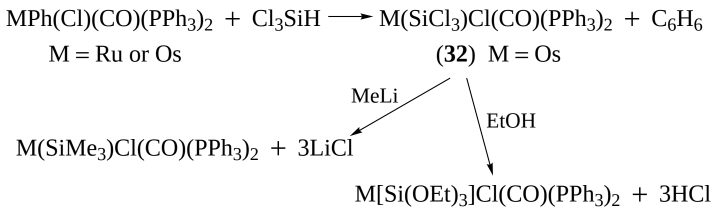
MPh(Cl)(CO)(PPh3)2 + Cl3SiH
M(SiCl3)Cl(CO)(PPh3)2 + C6H6
M = Ru or Os
(32) M = Os
MeLi
EtOH
M(SiMe3)Cl(CO)(PPh3)2 + 3LiCl
M[Si(OEt)3]Cl(CO)(PPh3)2 + 3HCl

Scheme 69

will undoubtedly see new synthetic routes to compounds unavailable by conventional methods of synthesis.[337]

6.3 Compounds Containing $Si(OR)_3$Ligands

The iron silyl compounds $K[Fe(CO)_3(\eta^1\text{-}Ph_2PCH_2PPh_2)\{Si(OMe)_3\}]$ and $[FeH(CO)_3(\eta^1\text{-}Ph_2PCH_2PPh_2)\{Si(OMe_3)\}]$ react with a variety of other transition metal complexes to give bimetallic compounds in which the $Si(OMe)_3$ group may act either to form an $\eta^2\text{-}\mu_2$-SiO bridge or remain as a simple terminal group. For example, reaction of the iron hydride with *trans*-$[PdCl_2(PhCN)_2]$ affords complex (**35**) in which the Si–Fe and Pd–O distances are 2.275 and 2.100 Å, respectively, while reaction with $[Cu(AsPh_3)_3]NO_3$ affords complex (**36**) which has an Si–Fe distance of 2.282 Å.[338,339]

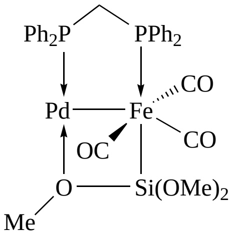

(**35**)

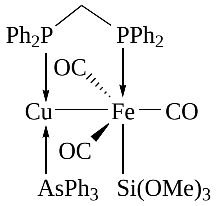

(**36**)

Oxidative addition of $(RO)_3SiH$ occurs (equation 46) when treated with $RhH(PPh_3)_4$ to give the silyl complexes (**37**).[340]

$$(RO)_3SiH + RhH(PPh_3)_4 \xrightarrow{-PPh_3} \underset{\textbf{(37)}}{(RO)_3SiRhH_2(PPh_3)_3} \qquad (46)$$

$$R = Me \text{ or } Et$$

Similarly, reaction between $(EtO)_3SiH$ and $RhX(PPh_3)_3$ (X = Cl, Br, or I) gives oxidative addition products (equation 47).[341]

$$(MPh_3)_3RhX + (EtO)_3SiH \xrightarrow{-MPh_3} (MPh_3)_2RhH[Si(OEt)_3]X \qquad (47)$$

$$M = P, As, \text{ or } Sb, X = Cl; M = P, X = Br \text{ or } I$$

Oxidative addition of alkoxysilanes to iron complexes also occurs.[342] On further treatment with $(RO)_3SiH$, a second carbonyl ligand is lost and a trihydro complex is formed (Scheme 71). The structure of the R = OEt complex is trigonal pyramidal with an Fe–Si distance of about 2.25 Å.[343]

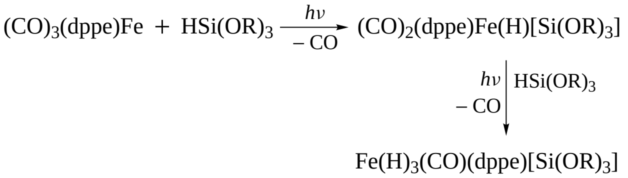

$$\begin{array}{c} (CO)_3(dppe)Fe + HSi(OR)_3 \xrightarrow[-CO]{h\nu} (CO)_2(dppe)Fe(H)[Si(OR)_3] \\ \Big\downarrow {\scriptstyle h\nu,\ -CO;\ HSi(OR)_3} \\ Fe(H)_3(CO)(dppe)[Si(OR)_3] \end{array}$$

Scheme 71

A less well-explored route to $Si(OR)_3$ containing complexes is by displacement of another silyl group from the transition metal center or by replacing an alkyl by an alkoxy group at silicon (Scheme 72).[344]

The preparation of transition metal complexes containing silanol groups as ligands can be achieved under mild conditions by oxidation of Si–H groups with dimethyldioxirane. For example, $Cp^*(CO)_2(PMe_3)WSiRH_2$ may be oxidized to $Cp^*(CO)_2(PMe_3)WSiR(OH)_2$ (where R = Me or OH) and, $Cp(CO)_2(PMe_3)MoSiH_3$ affords $Cp(CO)_2(PMe_3)MoSi(OH)_3$.[345–347]

6.4 Clusters Containing Silicon

Silicon forms a variety of compounds containing clusters of transition metal atoms that exhibit a wide range of structures. Disilane reacts with $Co_2(CO)_8$ to give the cobalt cluster (**38**) in which the silicon is coordinated to five Co atoms (equation 48). The Si···Si distance of 2.817 Å is too long for a bond (normally about 2.35 Å) and the Si–Co distances average 2.336 Å.[348]

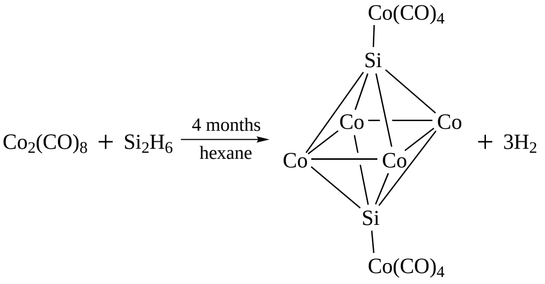

(48)

(**38**)

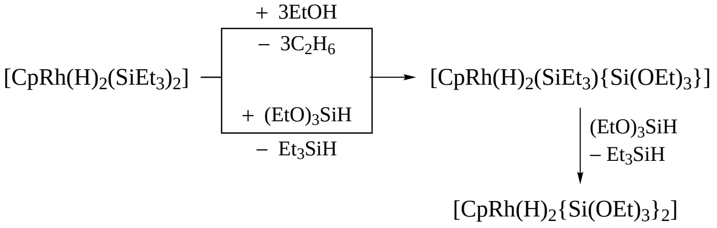

$$\begin{array}{c} [CpRh(H)_2(SiEt_3)_2] \xrightarrow[\substack{+\ (EtO)_3SiH \\ -\ Et_3SiH}]{\substack{+\ 3EtOH \\ -\ 3C_2H_6}} [CpRh(H)_2(SiEt_3)\{Si(OEt)_3\}] \\ \Big\downarrow {\scriptstyle (EtO)_3SiH;\ -\ Et_3SiH} \\ [CpRh(H)_2\{Si(OEt)_3\}_2] \end{array}$$

Scheme 72

The reaction between SiI_4 and $NaCo(CO)_4$ (equation 49) gives cobalt cluster (**39**) in which the silicon is coordinated to four cobalt atoms, the Si–$Co(CO)_3$ distances averaging 2.218 Å and the Si–$Co(CO)_4$ distance being 2.288 Å.[349] The reaction of SiH_4 with $Co_2(CO)_8$ (equation 50) gives the spiro complex (**40**) in which the Si–Co distance averages 2.288 Å.[350] Similarly, the reaction between SiI_4 and $NaM(CO)_5$ (M = Mn or Re) leads to tri- and tetra-substituted products (equation 51).[351]

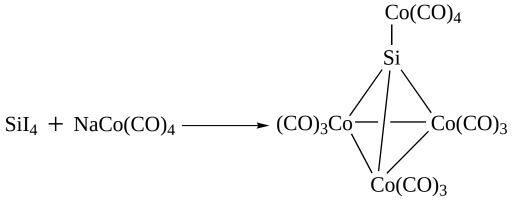
SiI4 + NaCo(CO)4
Co(CO)4
Si
(CO)3Co
Co(CO)3
Co(CO)3

(49)

(**39**)

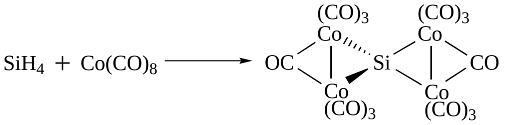
SiH4 + Co(CO)8
(CO)3
(CO)3
Co
Co
OC
Si
CO
Co
Co
(CO)3
(CO)3

(50)

(**40**)

$$nNaM(CO)_5 + SiI_4 \longrightarrow I_{4-n}Si[M(CO)_5]_n \qquad (51)$$

M = Mn or Re; n = 3 or 4

In a similar manner to the cobalt case, SiH_4 reacts with $Fe_2(CO)_9$ (equation 52) to give a spiro complex (**41**) containing no bridging COs and with an average Fe–Si distance of 2.345 Å.[352]

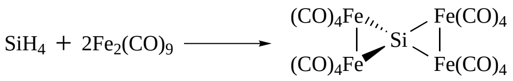
SiH4 + 2Fe2(CO)9
(CO)4Fe
Fe(CO)4
Si
(CO)4Fe
Fe(CO)4

(52)

(**41**)

Reaction of SiH_4 with a mixture of iron carbonyl complexes (equation 53) leads to a mixed ligand cluster (**42**) in good yield in which the average Si–$Fe(CO)_3$ distance is 2.306 Å and the Si–$Fe(CO_2Cp)$ average distance is 2.250 Å.[353]

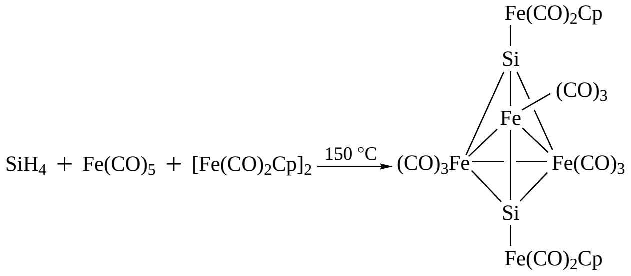
SiH4 + Fe(CO)5 + [Fe(CO)2Cp]2
150 °C
Fe(CO)2Cp
Si
(CO)3
Fe
(CO)3Fe
Fe(CO)3
Si
Fe(CO)2Cp

(**42**)

(53)

The reaction between μ_4-Si$[Co_2(CO)_7]_2$ and $[NEt_4][Co(CO)_4]$ affords an unusual mixed salt, $[NEt_4][\mu_8$-$SiCo_9(CO)_{21}][Co(CO)_4]$ (**43**). The silicon is encapsulated in the $[\mu_8$-$SiCo_9(CO)_{21}]^{2-}$ anion and lies almost equidistant from eight of the Co atoms in a capped square-antiprism with an average Si–Co distance of 2.299 Å.[354]

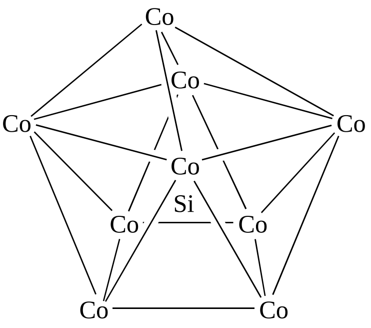
Co
Co
Co
Co
Co
Si
Co
Co
Co
Co

(**43**) A view of the $[\mu_8$-$SiCo_9(CO)_{21}]^{2-}$ anion (the CO groups are omitted for clarity)

6.5 Transition Metal Silylyne Complexes

Simple, terminal silylyne complexes, $L_nM{\equiv}SiR$, are very rare. However, as in the case of silylene ligands, the presence of a donor ligand at silicon greatly enhances the stability of such species. Thus, displacement of a good leaving group from silicon (equation 54) affords complexes (**44**) in which the silicon is coordinated by the bidentate donor ligands. The Si–Ru distance in the phenanthroline adduct is 2.269 Å which is, as would be expected, rather short although there are few compounds available with which to make comparisons. The Si···N distances are over 1.9 Å, which clearly indicates a dative coordination rather than the presence of an Si–N σ bond.[355]

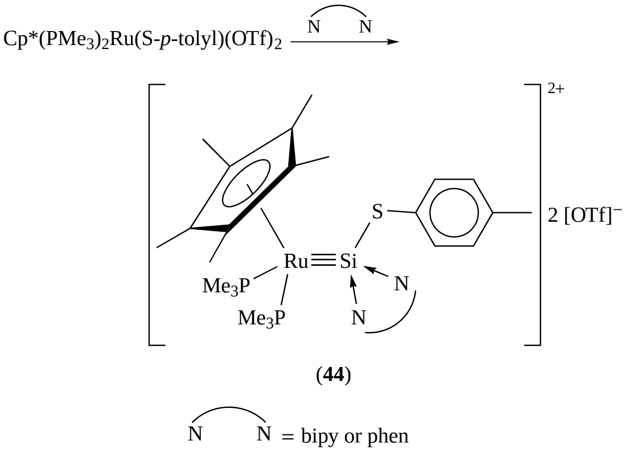
Cp*(PMe3)2Ru(S-p-tolyl)(OTf)2
N N
2+
S
2 [OTf]−
Ru
Si
Me3P
N
Me3P
N
N N = bipy or phen

(**44**)

(54)

6.6 Transition Metal Silylene Complexes

The preparation of several three-coordinate silylene complexes has been discussed in Section 4. A variety of four-coordinate complexes, (**45**), are also known in which the silicon is coordinated by a donor molecule such as HMPA or THF. These complexes are all formed by the salt elimination method, the dianions $[Fe(CO)_4]^{2-}$, $[Cr(CO)_5]^{2-}$, and $[W_2(CO)_{10}]^{2-}$ reacting with the appropriate R_2SiCl_2 compound. Treatment of $SiCl_4$ with two equivalents of $[Na_2Fe(CO)_4]$ similarly gives (**46**). These and other silylene complexes are discussed more fully elsewhere.[56,57,294,356]

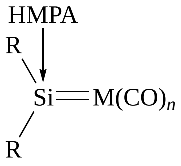

(**45**)

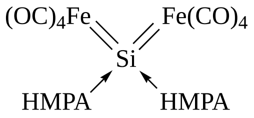

(**46**)

M = Fe, $n = 4$; R = O-*t*-Bu, S-*t*-Bu, or Cl
M = Cr, $n = 5$; R = O-*t*-Bu, Cl, or OCH_2-*t*-Bu
M = W, $n = 5$; R = O-*t*-Bu

The bulky stable silylenes described in Section 3 may be used as ligands in a range of transition metal complexes. The complexes are formed mostly via simple ligand displacement reactions as shown in Scheme 73 although in some cases reactions occur involving reduction of halogenometal complexes.[43]

The chemistry of silylene complexes has become much more developed in the past 10 years as silylene complexes have been found to be important intermediates in reactions such as the dehydrogenative coupling of hydrosilanes, redistribution reactions, and the 'Direct Process' for the production of simple chlorosilanes. For reviews of this work, see References 43, 44 and 294. Several complexes have now been prepared in which there is a silene or disilene ligand ($R_2C{=}SiR_2$ or $R_2Si{=}SiR_2$ species)[56,57] but, since all these contain several Si–C bonds, they will not be discussed further here.

7 COMPOUNDS CONTAINING SILICON WITH HIGHER COORDINATION NUMBERS

There are a large number of five- and six-coordinate silicon compounds, the extensive chemistry of which has been reviewed.[357–359] Many of these compounds contain Si–C bonds and so will not be described here. The study of such compounds is of interest because of the lack of analogous carbon chemistry and because of the intermediacy of species with greater than four-coordination in a variety of reaction mechanisms proposed for silicon. (Compounds containing seven-coordinate silicon are known; they usually have an Si–H group present and contain Si–C bonds. Such compounds are described in Reference 357.) There are also a small number of compounds containing silicon with even higher coordination number. For example, Mg_2Si has the antifluorite structure and eight-coordinate silicon and the cluster (**43**) in Section 6.4, contains Si coordinated by nine Co atoms.[354] Calculations on the structures of SiX_5 and SiX_6 species (X = H or alkali metal) are discussed in Reference 5.

7.1 Five-coordinate Compounds

The most widely studied of the neutral five-coordinate silicon compounds are the so-called 'silatranes' of general structure (**47**). They are of interest both because of their unusual structure, which incorporates a strong transannular N → Si bond, and because of their apparent physiological properties.[360]

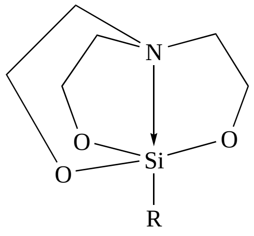

(**47**)

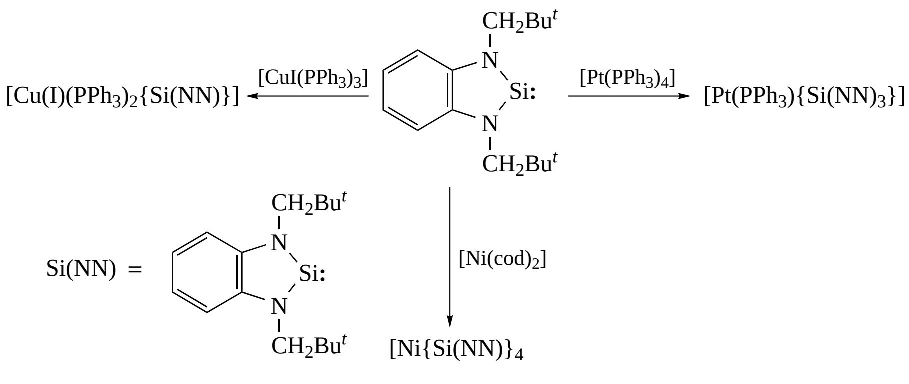

Scheme 73

The silatranes are generally prepared by reaction of $N(CH_2CH_2OH)_3$ with an $RSi(OR')_3$ species (R = alkyl, aryl, etc., R′ = Me or Et). Most of the silatranes have organic R groups and so will not be further discussed here. Silatranes may also be prepared by reaction of triethanolamine with a silsesquioxane $(RSiO_{1.5})_n$ in the presence of a catalytic amount of KOH.[361] The reaction of silatrane itself with *cis*-$[PtCl_2(PMe_2Ph)_2]$ gives complex (**48**), in which there is a very long Si· · ·N distance and a planar nitrogen (equation 55). This, together with IR data, suggests that there is no strong N → Si interaction in the complex and that the silicon is four coordinate.[362]

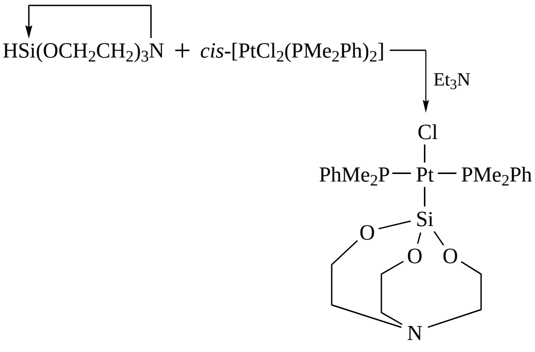

(55)

(**48**)

The reaction of $N(CH_2CH_2OH)_3$ with $(EtO)_4Si$ affords ethoxysilatrane (**49**), which is remarkably stable towards solvolysis. It does, however, undergo reaction (equation 56) with carboxylic acids to give esters (**50**).[363]

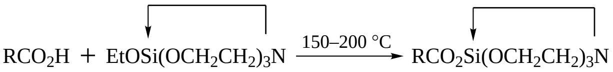

$$RCO_2H + EtOSi(OCH_2CH_2)_3N \xrightarrow{150\text{–}200\ °C} RCO_2Si(OCH_2CH_2)_3N$$

(**49**) (**50**)

R = Ph or Me

(56)

Reaction of ethoxysilatrane with a further equivalent of $N(CH_2CH_2OH)_3$ affords (**51**), which may be hydrolyzed to the silanol (**52**) (Scheme 74).[363]

The hydridosilane $HSi\overline{(CH_2CH_2O)_3}N$ may also be prepared in a similar manner from $HSi(OMe)_3$ and triethanolamine; the Si–H compound reacts with HF to give the fluorosilatrane.[364] The X-ray structure of 1-fluorosilatrane shows a N → Si distance of 2.042 Å, a little longer than that of 2.023 Å in the 1-chloro derivative.[365]

The interest in silatrane chemistry has led to the preparation of a range of related five-coordinate cyclic compounds that contain different coordination at the silicon or modification of the ring backbone. The synthesis of most of these compounds is achieved in the same way as the simple silatranes, that is, by the reaction of a trifunctional silane, $XSiY_3$ (where Y is a labile group such as halide, OMe, OAc) with a suitable trifunctional amine. (Representative examples of this interesting class of compounds are shown in Figure 9 below; their chemistry has been reviewed.[366])

Although no four-coordinate Si compounds have been found to have planar geometry, the five-coordinate anion (**53**), prepared as shown in equation (57), has a geometry at silicon distorted very much away from trigonal bipyramidal towards square pyramidal geometry. The O–Si–O angles across the spirocyclic ring are about 166°; and 143°.[363] The structures of numerous silatranes have been determined and are discussed elsewhere.[112]

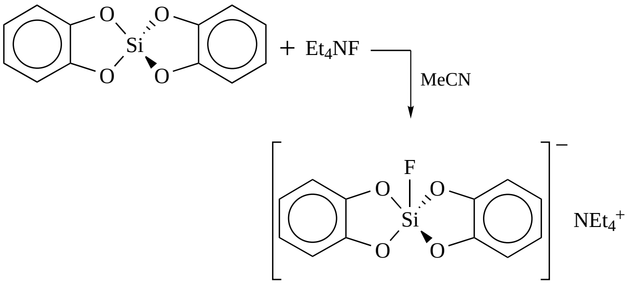

(**53**)

(57)

A variety of compounds derived from diethanolamine are also known and may be prepared in a similar way to the silatranes.[112] For example, equation (58) affords (**54**) in which

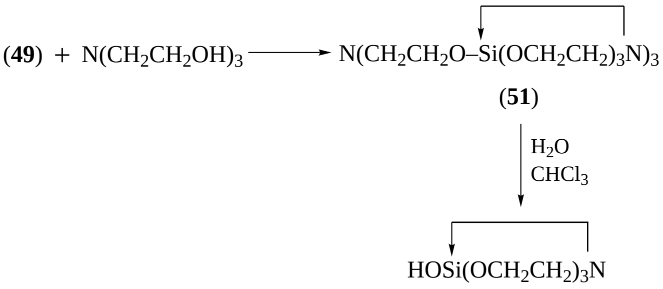

$$(\mathbf{49}) + N(CH_2CH_2OH)_3 \longrightarrow N(CH_2CH_2O\text{–}Si(OCH_2CH_2)_3N)_3$$

(**51**)

$$\xrightarrow[CHCl_3]{H_2O} HOSi(OCH_2CH_2)_3N$$

(**52**)

Scheme 74

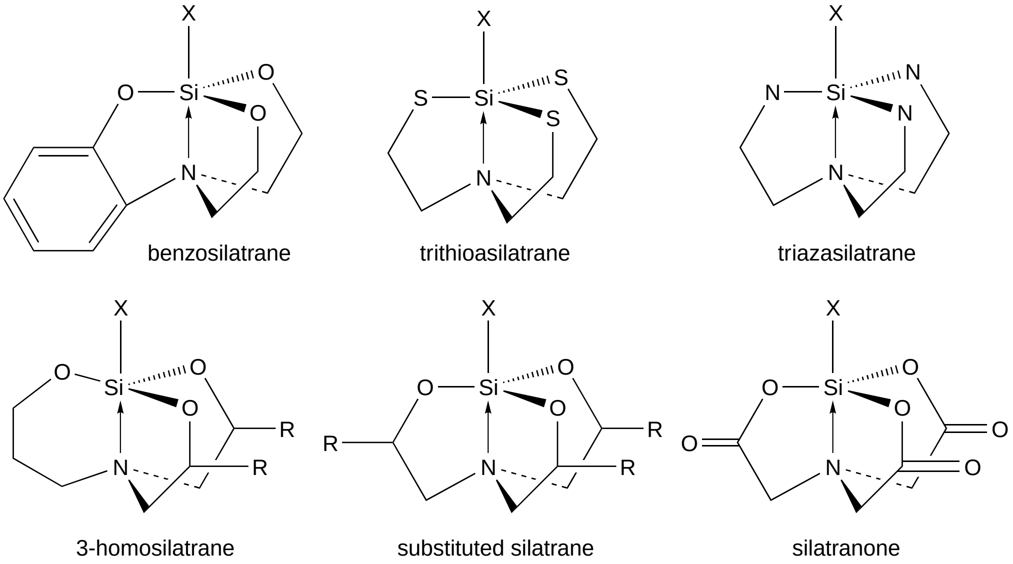
X
O
Si
O
O
N
benzosilatrane
S
Si
S
S
N
trithioasilatrane
N
Si
N
N
N
triazasilatrane
O
Si
O
O
N
R
R
3-homosilatrane
R
substituted silatrane
O
silatranone

R = organic group, X = H, halide, organic group etc.

Figure 9 Cyclic structures related to silatranes

the N → Si distance is rather short, 2.004 Å.[367]

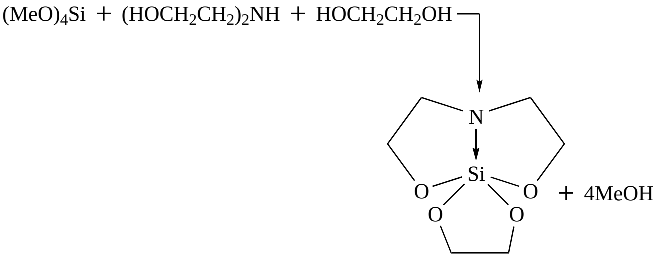
$(MeO)_4Si + (HOCH_2CH_2)_2NH + HOCH_2CH_2OH$
N
Si
O
O
O
O
+ 4MeOH

(54)

(58)

The reaction (equation 59) between lithium amides and $SiCl_4$ affords *N*-substituted silanes. The crystal structures of (**55**; X = F, Cl) clearly shows the intramolecular coordination of an aromatic nitrogen atom. As would be expected, the Si–N σ bonds are rather shorter (1.732 and 1.737 Å) than the N → Si distances (1.969 and 1.9484 Å for the fluoro and chloro derivatives, respectively).[112]

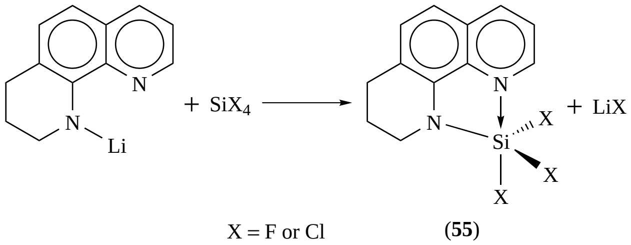
N
N
Li
+ SiX_4
N
N
Si
X
X
X
+ LiX

X = F or Cl **(55)**

(59)

In a similar way, reaction of (**56**) with SiF_4 (equation 60) affords (**57**), in which the Si–N and N → Si distances are again significantly different, being 1.701 and 1.974 Å, respectively.[368]

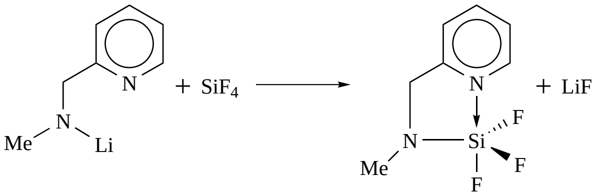
N
N
Me
Li
+ SiF_4
N
N
Me
Si
F
F
F
+ LiF

(56) **(57)**

(60)

The reaction of H_2SiCl_2 with Me_2NH gives ClH_2SiNMe_2, which is a monomer with four-coordinate Si in the gas phase. However, in the solid state it forms a centrosymmetric dimer in which the silicons are five-coordinate and in which there are two short (1.814 Å) and two long (2.054 Å) Si–N distances.[369] The phosphinimine (**58**) may be formed in two ways (Scheme 75) and in the solid state is shown to be a dimer, again with five-coordinate silicon atoms. The Si_2N_2 ring is planar with trigonal bipyramidal geometry at Si and has Si–N distances of 1.736 and 1.857 Å.[370,371]

The addition of a fluoride ion to various fluorosilanes gives salts with a five-coordinate silicon. Thus R_4NF addition to SiF_4 affords $[R_4N][SiF_5]$ (R = Et or Pr).[372] A crystallographic study of $[PhCH_2NMe_3][SiF_5]$ shows the silicon to have trigonal bipyramidal geometry.[373]

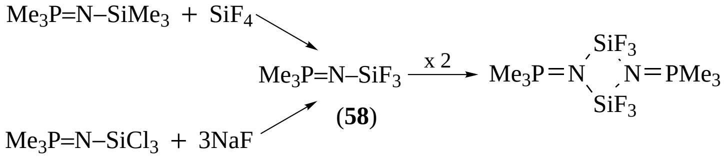

Scheme 75

7.2 Six-coordinate Compounds

A wide range of adducts between halosilanes and tertiary amines are known. They are formed by mixing the amine and the halosilane and are usually white solids. For example, SiF_4 and $SiCl_4$ form 1:2 adducts with pyridine, SiH_2Br_2 forms a 1:4 adduct with pyridine, H_2SiH_2 forms a 1:1 adduct with Et_3N, and $HSiCl_3$ forms a 1:1 adduct with $(Me_2NCH_2)_2$.[374] Many of these adducts are ionic; for example, $SiH_2I_2 \cdot 4py$ may better be represented as $[SiH_2 \cdot 4py]^{2+}2I^-$, but the fluorosilane compounds are neutral adducts.[375]

The molecular structure of $SiF_4 \cdot 2py$ (**59**) shows a centrosymmetric octahedral geometry at silicon with the pyridine molecules trans to each other and an Si–N distance of 1.93 Å.[376] Hexacoordinate geometry may also occur when using a chelating ligand such as bipyridine as in complex (**60**), where the N → Si distance averages 1.977 Å.[377]

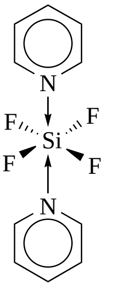

(**59**)

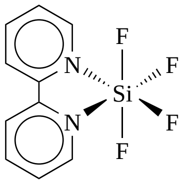

(**60**)

The alkali metal salts of the six-coordinate anion (**61**) may readily be prepared (equation 61) by using SiO_2 (or $Si(OMe)_4$) as starting material, thus forming monomeric silicon compounds from the polymeric SiO_2 without the need for the isolation of elemental silicon.[378]

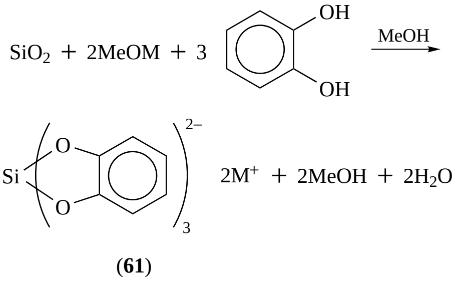

(**61**)

M = Na or K

(61)

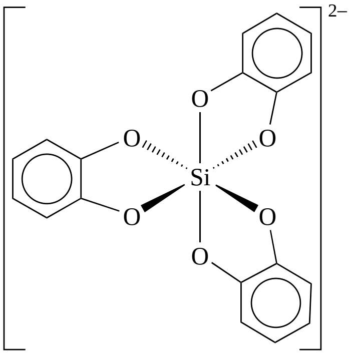

(**61**)

The catechol derivatives (**64**) are versatile synthetic intermediates and they form readily with Grignard or alkyllithium reagents (equation 62). The products formed depend on the solvent and the nature of the R group but species (**62**) or (**63**) may be produced, the latter being formed when R is allyl, vinyl, alkynyl, or phenyl.[378]

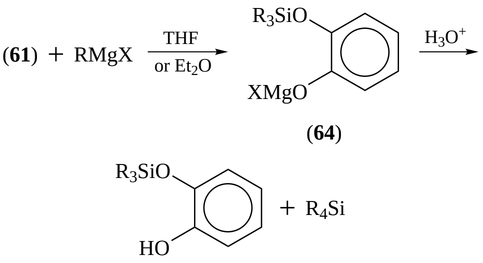

(62)

The catechol derivatives (**64**) are useful synthetic intermediates as they react with a variety of readily available reagents to give products as shown in Scheme 76.[378]

The tris(catecholate) complex (**61**) also reacts with $LiAlH_4$ to give SiH_4.[378] The structure of the tris(catecholate) complex $[C_5H_5NH]_2[(C_6H_4O_2)_3Si]$ has a slightly distorted octahedral symmetry for the dianion, with the O–Si–O angles being slightly less than 90°.[379]

Silicon, like many other elements, readily forms acetylacetonato (acac) complexes. Thus, reaction of $SiCl_4$ with 2,4-pentanedione (Scheme 77) affords the six-coordinate monocation (**65**). Other complexes may readily be prepared by addition of appropriate metal salts.[380]

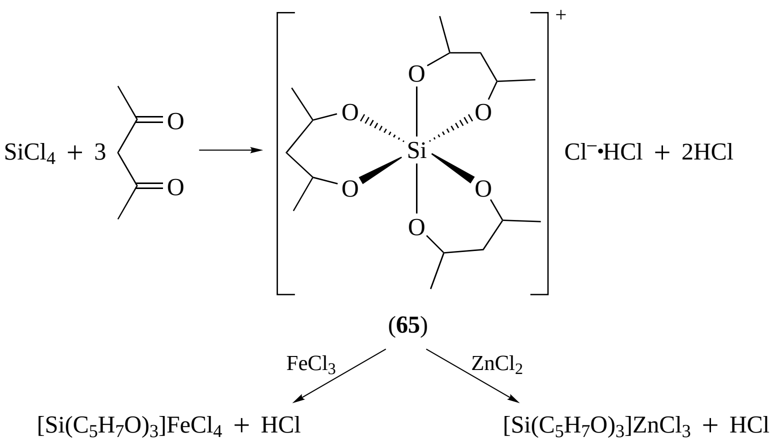

Scheme 77

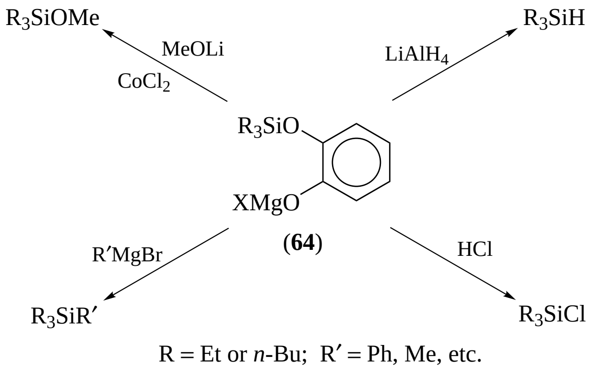

Scheme 76

The tris(oxalate) complex (**66**), which is very soluble in MeOH, may also be readily prepared (equation 63) using silver oxalate.[381]

$$\mathrm{SiCl_4 + 2Et_4NBr + 3Ag_2C_2O_4 \xrightarrow{acetone} \underset{(\mathbf{66})}{[Si(C_2O_4)_3]^{2-}}\,[Et_4N]_2{}^{+} + 4AgCl + 2AgBr} \qquad (63)$$

Tris chelate complexes such as $[(acac)_3Si]^+$ and (**61**) are potentially optically active and may be resolved by crystallization of suitable tartrate salts.[382,383] The reaction of $[NF_4][HF_2]$ with SiF_4 (equation 64) affords the six-coordinate (**67**) as a white crystalline solid that is stable at room temperature but decomposes at 90 °C.[384]

$$\mathrm{2[NF_4][HF_2]{\bullet}}n\mathrm{HF + SiF_4 \longrightarrow \underset{(\mathbf{67})}{[NF_4]_2[SiF_6]} + 2(}n\mathrm{ + 1)HF} \qquad (64)$$

The partial hydrolysis of $SiI_4(bipy)_2$ affords $[Si(OH)_2(bipy)_2]I_2{\cdot}2H_2O$, in which the cation has *cis* octahedral geometry and each OH group is hydrogen bonded to one of the water molecules.[385]

The mixing of silicon tetrahalides with simple Lewis bases such as NMe_3 (NH_3 would react with Si, Cl, Br, or I bonds) or PMe_3 leads to the formation of a variety of both five- and six-coordinate complexes, for example, $SiF_4{\cdot}nB$ ($n = 1$ or 2, B = PMe_3 or NMe_3), $SiCl_4{\cdot}2Me_3P$, $SiCl_4{\cdot}NMe_3$, and $Br_4Si{\cdot}2Me_3P$. The geometry of these compounds has been studied in detail by IR and Raman spectroscopy, which suggest that the five-coordinate complexes are trigonal bipyramidal and the six-coordinate are trans octahedral.[386,387] An X-ray structural study of $SiCl_4{\cdot}2PMe_3$ confirmed the trans octahedral geometry, showing Si–Cl bonds of about 2.25 Å and the Si–P distance as 2.26 Å.[388] However, an IR study of $SiF_4{\cdot}2\,NH_3$ and $SiF_4{\cdot}2N_2H_4$ suggests a cis octahedral structure for these adducts.[389] Compounds such as $SiF_4{\cdot}$bipy or $SiF_4{\cdot}$en containing bidentate chelating ligands are clearly constrained by the ligand geometry to be cis complexes. Perhalodisilanes and Si_3Cl_8 also react with chelating ligands to give 1:1 complexes such as $Si_2X_6{\cdot}$bipy (X = F, Cl, or Br), $Si_2X_6{\cdot}$phen (X = Cl or Br), and $Si_3Cl_8{\cdot}$bipy. IR and NMR studies suggest that the plane of the chelating ligand is perpendicular to that of the Si–Si axis. In Si_3Cl_8, the bipyridyl ligand coordinates to the more Lewis acidic, $SiCl_2$, silicon.[390]

A range of diiodosilanes react (equation 65) with 2,2′-bipyridine to give ionic complexes (**68**).[391]

$$\mathrm{SiXYI_2 + 2bipy \xrightarrow{CHCl_3} \underset{(\mathbf{68})}{[SiXY{\bullet}2\,bipy]^{2+}[I^-]_2}} \qquad (65)$$

$$\mathrm{XY = Cl_2, H_2, HCl, HI, or\ H(OMe)}$$

Si^{4+} ions are found in octahedral complexes containing six neutral ligands such as $[Si(pyO)_6]I_4$ (equation 66).[392]

$$\mathrm{SiI_4 + 6pyO \xrightarrow{CHCl_3} [Si(pyO)_6]I_4} \qquad (66)$$

Phenylene *N*-oxide also forms six-coordinate chelated complexes with SiX_4 (X = F, Cl, Br, and I).[393] Six-coordinate

$$\mathrm{SiI_4 + 3L_2 \longrightarrow [Si(L_2)_3]I_4}$$
$$\mathrm{L = bipy\ or\ phen}$$
$$\mathrm{SiI_4 + 6NMI \longrightarrow [Si(NMI)_6]I_4}$$

Scheme 78

$$\mathrm{2SiF_4{\bullet}2NHMe_2 \xrightarrow{-\,2\,HF} 2SiF_3NMe_2 + 2NHMe_2}$$
$$\mathrm{2SiF_4{\bullet}2NHMe_2 \xrightarrow{-\,4\,HF} SiF_2(NMe_2)_2}$$
$$\mathrm{2SiF_4{\bullet}2NH_2R \xrightarrow{-\,2\,HF} (SiF_3)_2NR}$$
$$\mathrm{R = H\ or\ Et}$$

Scheme 79

Si^{4+} complexes may also be formed by reacting SiI_4 with bipyridine or phenanthroline in the melt (Scheme 78). 1-Methylimidazole reacts with SiI_4 to give a similar complex (Scheme 78).[394]

Tetrafluorosilane is the strongest Lewis acid of the halosilanes and is capable of forming stable adducts with primary and secondary amines without loss of HX, which would occur with chloro-, bromo-, or iodosilanes (Scheme 79). The adducts are, however, broken down at high temperatures and in the presence of reagents such as $LiAlH_4$, B_2H_6, and $NaBH_4$.[262,395]

Both Na_2SiF_6 and $(NH_4)_2SiF_6$ may be used for the conversion of organosilicon chlorides to fluorides (equation 67).[396]

$$\mathrm{R}_n\mathrm{SiCl}_{4-n} + \mathrm{Na_2SiF_6\ or\ (NH_4)_2SiF_6} \longrightarrow \mathrm{R}_n\mathrm{SiF}_{4-n} \qquad (67)$$
$$n = 1, 2, \text{ or } 3;\ \mathrm{R} = \text{alkyl or aryl}$$

Porphyrin ligands may also be used to prepare a range of neutral, six-coordinate silicon compounds. Thus, deprotonation of a porphyrin with $LiN(SiMe_3)_2$ affords dianions that react readily with $HSiCl_3$ to give the corresponding dichlorides (**69**). These can then be treated with a variety of salts to give further derivatives (Scheme 80).[397]

Silicon-containing phthalocycanines (**70**) can form stacks and have interesting optical[398] and conducting properties.[399] The individual macrocycles can be connected via oxygen bridges from the silicon center, organic bridges, or by direct Si–Si bonds.[400]

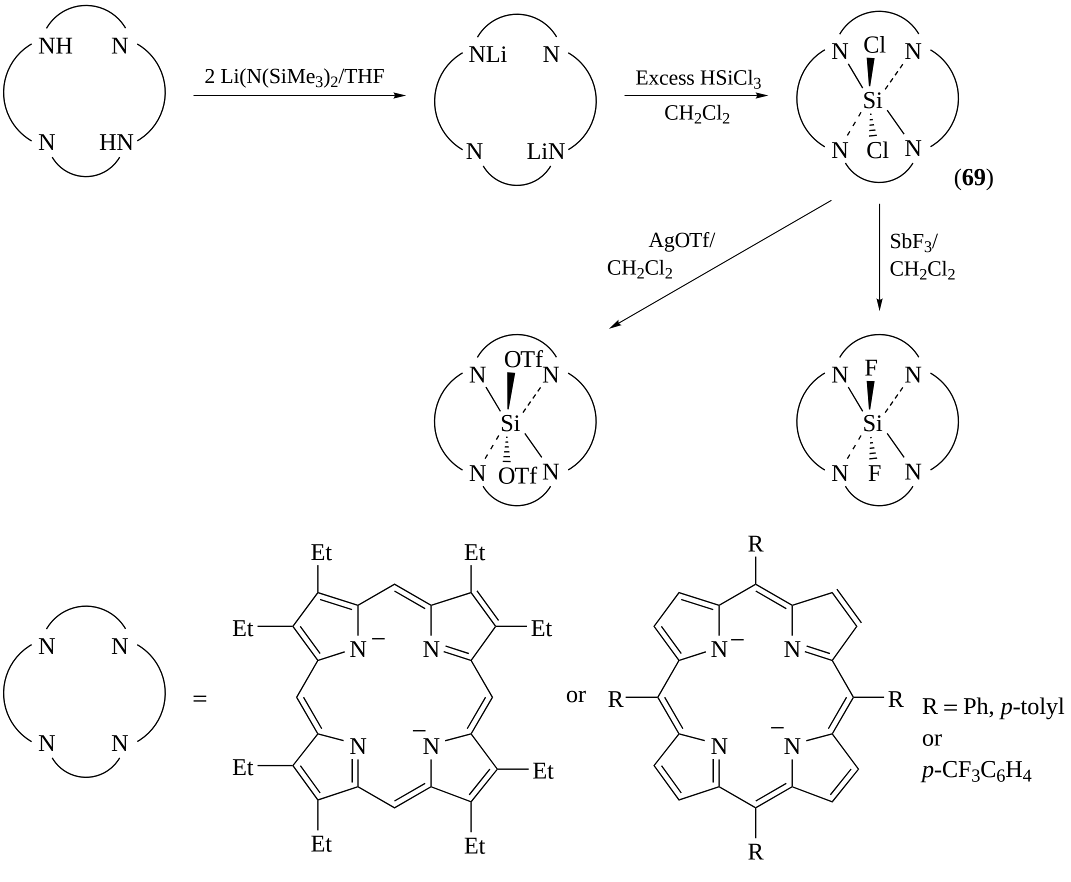

(**69**)

Scheme 80

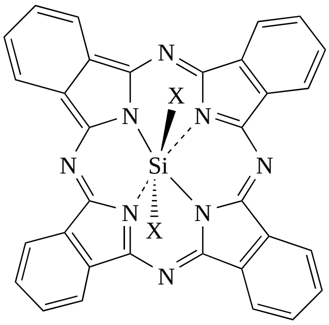

X = Cl or OH etc.

(**70**)

8 CHARACTERIZATION AND ANALYSIS OF INORGANIC SILICON COMPOUNDS

The compounds of silicon described in this article are generally monomeric and soluble in common solvents. They are, therefore, amenable to study by all of the commonly available methods for molecular characterization such as IR, UV, and NMR spectroscopy, mass spectrometry, and X-ray crystallography. Two of these methods, IR and ^{29}Si NMR spectroscopy, have been used with particular success.

The characteristic stretching frequencies for all of the common Si–X bonds have been studied in detail but perhaps the most useful is that of the Si–H bond. The Si–H stretch is usually strong and sharp and it occurs in the 2280−2080 cm^{-1} region of the IR spectrum, well away from most other bands. The precise position of the Si–H band is sensitive to the electronegativity of the substituents and a more detailed discussion of its position and that of bands due to other Si–X bonds can be found elsewhere.[401]

Silicon only has one naturally occurring isotope (^{29}Si) with a nonzero nuclear spin and ^{29}Si NMR spectroscopy has become one of the most widely used techniques for the identification of silicon compounds. Unfortunately, the natural abundance of ^{29}Si is only 4.7%, which combined with its long spin−lattice relaxation times, means that relatively long acquisition times may be needed to obtain high quality spectra. ^{29}Si NMR spectroscopy has been the subject of a number of reviews and tables of chemical shift data and coupling constants are available.[402–404]

Various methods for the determination of silicon, particularly from biological samples are available. The techniques usually involve decomposition of the compound to give silica or a silicate by either wet combustion or fusion with sodium peroxide. The silicate formed can then be determined colorimetrically, volumetrically, or gravimetrically.[401] Acidified ammonium heptamolybdate reacts only with monomeric Si(OH)$_4$ and not its oligomers to give a yellow silicomolybdic acid complex that can be determined spectrophotometrically. This method works for concentrations in the 1 to 1000 ppm range but concentrations down to 0.1 ppm can be determined if the yellow silicomolybdic acid is reduced to blue silicomolybdic acid.[405,406]

9 RELATED ARTICLES

Biomineralization; Hydrosilation Catalysis; Silicon: Organosilicon Chemistry; Zeolites.

10 REFERENCES

1. S. Mann, *J. Chem. Soc., Dalton Trans.*, 1993, 1.
2. C. C. Perry, in ‘Chemistry and Technology of Silicon and Tin’, eds. V. G. K. Kumar Das, N. S. Weng, and M. Gielen, Oxford University Press, Oxford, 1992, Chap. 27, p. 353.
3. C. C. Perry, in ‘Biomineralisation, Chemical and Biochemical Perspectives’, eds. S. Mann, J. Webb, and R. J. P. Williams, VCH, Weinheim, 1989, Chap. 8, p. 223.
4. K. Rumpf, eds. H. J. Emeléus and W. Lippert, ‘Gmelin Handbuch der Anorganischen Chemie’, 8th edn., System No. 15, 1984, Part A, Sect. 1.
5. M. Karni, Y. Apeloig, J. Kapp, and Pv. R. Schleyer, in ‘The Chemistry of Organic Silicon Compounds’, eds. Z. Rappoport and Y. Apeloig, John Wiley, Chichester, 2001, Vol. 3, p. 1.
6. T. Abe, in ‘VLSI Electronics Microstructure Science, Vol. 12, Silicon Materials’, eds. N. G. Einspruch and H. Huff, Academic Press, Orlando, FL, 1985, Chap. 1, p. 3.
7. ‘Gmelin Handbuch der Anorganischen Chemie’, 8th edn., System No. 15, 1959, Part B.
8. A. Sanjurjo, L. Nanis, K. Sancier, R. Bartlett, and V. Kapur, *J. Electrochem. Soc.*, 1981, **128**, 179.
9. S. K. Iya, *J. Cryst. Growth*, 1986, **75**, 88.
10. J. Emsley, ‘The Elements’, 2nd edn., Oxford University Press, Oxford, 1991.
11. C. H. Choi and M. S. Gordon, in ‘The Chemistry of Organic Silicon Compounds’, eds. Z. Rappoport and Y. Apeloig, John Wiley, Chichester, 2001, Vol. 3, p. 821.
12. H. N. Waltenburg and J. T. Yates Jr, *Chem. Rev.*, 1995, **95**, 1589.
13. L. N. Lewis, ‘The Chemistry of Organic Silicon Compounds’, John Wiley, Chichester, 1998, Vol. 2, p. 1581.
14. M. P. Stewart and J. M. Buriak, *Adv. Mater.*, 2000, **12**, 859.
15. H. Foell, M. Christophersen, J. Carstensen, and G. Hasse, *Mater. Sci. Eng. Rep.*, 2002, **R39**, 93.

16. D. F. Thomas, in ‘Handbook of Nanostructured Materials and Nanotechnology’, ed. H. S. Nalwa, Academic Press, San Diego, CA, 2000, p. 159.
17. L. T. Canham ed., ‘Properties of Porous Silicon’, INSPEC, London, 1997.
18. J. D. Birchall, *Chem. Soc. Rev.*, 1995, **24**, 351.
19. D. E. Morse, in ‘The Chemistry of Organic Silicon Compounds’, eds. Z. Rappoport and Y. Apeloig, John Wiley, Chichester, 2001, Vol. 3, p. 805.
20. L. E. Datnoff, G. H. Snyder, and G. H. Körndorfer eds, ‘Silicon In Agriculture’, Elsevier, Amsterdam, 2001.
21. K. P. Huber and G. Herzberg, ‘Molecular Spectra and Molecular Structure IV. Constants of Diatomic Molecules’, Van Nostrand, New York, 1979.
22. M. J. S. Dewar and C. Jie, *Organometallics*, 1987, **6**, 1486.
23. J. Sauer, P. Carsky, and R. Zahradnik, *Coll. Czech. Chem. Commun.*, 1982, **47**, 1149.
24. K. Hoffman, G. W. Rubloff, M. Liehr, and D. R. Young, *Appl. Surf. Sci.*, 1987, **30**, 25.
25. H.-D. Klein and F. König, in ‘Tailor-made Silicon-Oxygen Compounds, From Molecules to Materials’, eds. R. Corriu and P. Jutzi, Vieweg, Braunschweig, 1996, p. 141.
26. H. Schnöckel, T. Mehner, H. S. Plitt, and S. Schunck, *J. Am. Chem. Soc.*, 1989, **111**, 4578.
27. H. Schnöckel, in ‘Tailor-made Silicon-Oxygen Compounds, From Molecules to Materials’, eds. R. Corriu and P. Jutzi, Vieweg, Braunschweig, 1996, p. 131.
28. H. Schnöckel and R. Köppe, *J. Am. Chem. Soc.*, 1989, **111**, 4583.
29. S. Forniarini, in ‘The Chemistry of Organic Silicon Compounds’, eds. Z. Rappoport and Y. Apeloig, John Wiley, Chichester, 2001, Vol. 3, p. 1027.
30. H. Bürger and R. Eujen, *Top. Curr. Chem.*, 1974, **50**, 1.
31. A. F. Wells, ‘Structural Inorganic Chemistry’, 5th edn., Oxford University Press, Oxford, 1984, p. 982.
32. K. Maex and M. van Rossum eds, ‘Properties of Metal Silicides, (EMIS Datareviews series no. 14)’, INSPEC, London, 1995.
33. V. E. Borisenko ed., ‘Semiconductor Silicides: Basics, Formation, Properties’, (Springer Series in Materials Science), Springer-Verlag, Berlin 2000.
34. Y. Apeloig, in ‘The Chemistry of Organic Silicon Compounds’, eds. S. Patai and Z. Rappoport, Wiley, Chichester, 1989, Part 1, Chap. 2, p. 57.
35. M. Karni, Y. Apeloig, J. Kapp, and Pv. R. Schleyer, ‘The Chemistry of Organic Silicon Compounds’, John Wiley, Chichester, 2001, Vol. 3, p. 1.
36. W. S. Sheldrick, in ‘The Chemistry of Organic Silicon Compounds’, eds. S. Patai and Z. Rappoport, Wiley, Chichester, 1989, Part 1, Chap. 3, p. 227.
37. C.-S. Liu and T.-L. Hwang, *Adv. Inorg. Radiochem.*, 1985, **29**, 1.
38. E. A. Chernyshev, N. G. Komalenkova, and S. A. Bashkirova, *J. Organomet. Chem.*, 1984, **271**, 129.
39. G. Maier and J. Glatthaar, *Angew. Chem., Int. Ed. Engl.*, 1994, **33**, 473.
40. H. Schnöckel, *Angew. Chem., Int. Ed. Engl.*, 1978, **17**, 616.
41. H. Schnöckel, *Z. Anorg. Allg. Chem.*, 1980, **460**, 37.
42. H. Schnöckel, *Angew. Chem., Int. Ed. Engl.*, 1980, **19**, 323.
43. B. Gehrhus and M. F. Lappert, *J. Organomet. Chem.*, 2001, **617–618**, 209.
44. M. Okazaki, H. Tobita, and H. Ogino, *J. Chem. Soc., Dalton Trans.*, 2003, 493.
45. M. Haaf, T. A. Schmedake, and R. West, *Acc. Chem. Res*, 2000, **33**, 704.
46. N. Tokitoh and R. Okazaki, *Coord. Chem. Rev.*, 2000, **210**, 251.
47. R. S. Grev, *Adv. Organomet. Chem.*, 1991, **33**, 125.
48. H. Schwarz, in ‘The Chemistry of Organic Silicon Compounds’, eds. S. Patai and Z. Rappoport, Wiley, Chichester, 1989, Part 1, Chap. 7, p. 445.
49. P. D. Lickiss, *J. Chem. Soc., Dalton Trans.*, 1992, 1333.
50. P. D. Lickiss, in ‘The Chemistry of Organic Silicon Compounds’, eds. Z. Rappoport and Y. Apeloig, John Wiley, Chichester, 1998, p. 557.
51. C. Maerker and P. v. R. Schleyer, in ‘The Chemistry of Organic Silicon Compounds’, eds. Z. Rappoport, and Y. Apeloig, John Wiley, Chichester, 1998, p. 513.
52. E. Weiss, G. Hencken, and H. Kühr, *Chem. Ber.*, 1970, **103**, 2868.
53. O. Mundt, G. Becker, H. M. Hartmann, and W. Scharz, *Z. Anorg. Allg. Chem.*, 1989, **572**, 75.
54. H. Schnöckel, *J. Mol. Struct.*, 1980, **65**, 115.
55. M. Junker, A. Wilkening, M. Binnewies, and H. Schnöckel, *Eur. J. Inorg. Chem.*, 1999, 1531.
56. P. D. Lickiss, *Chem. Soc. Rev.*, 1992, **21**, 271.
57. D. A. Straus, S. D. Grumbine, and T. D. Tilley, *J. Am. Chem. Soc.*, 1990, **112**, 7801.
58. C. Leis, C. Zybill, J. Lachmann, and G. Müller, *Polyhedron*, 1991, **10**, 1163.
59. R. Walsh, *Acc. Chem. Res.*, 1981, **14**, 246.
60. R. Walsh, in ‘The Chemistry of Organic Silicon Compounds’, eds. S. Patai and Z. Rappoport, Wiley, Chichester, 1989, Part 1, Chap. 5, p. 371.
61. E. Hengge, eds. H. Keller-Rudek, D. Koschel, U. Krüerke and P. Merlet, ‘Gmelin Handbuch der Anorganischen Chemie’, 8th edn., System No. 15, 1982, Suppl. Vol. B 1.
62. B. Arkles, eds. J. I. Kroschwitz and M. Howe-Grant, ‘Kirk-othmer Encyclopedia of Chemical Technology’, 4th edn., Wiley Interscience, New York, 1997, Vol. 22, p. 38.

63. E. Wiberg and E. Amberger, ‘Hydrides of the Elements of Main Groups I–IV’, Elsevier, Amsterdam, 1971.
64. P. W. Schenk, in ‘Handbook of Preparative Inorganic Chemistry’, 2nd edn., ed. G. Brauer, Academic Press, New York, 1963, Vol. 1, p. 679.
65. F. Fehér, H. Baier, B. Enders, M. Krancher, J. Laakmann, F. J. Ocklenberg, and D. Skrodski, *Z. Anorg. Allg. Chem.*, 1985, **530**, 191.
66. J. Zavelovich and J. L. Lyman, *J. Phys. Chem.*, 1989, **93**, 5740.
67. S. D. Gokhale, J. E. Drake, and W. L. Jolly, *J. Inorg. Nucl. Chem.*, 1965, **27**, 1911.
68. F. Feher, P. Hadicke, and H. Frings, *Inorg. Nucl. Chem. Lett.*, 1973, **9**, 931.
69. F. Feher and R. Freund, *Inorg. Nucl. Chem. Lett.*, 1973, **9**, 937.
70. F. Feher and D. Skrodski, *Inorg. Nucl. Chem. Lett.*, 1974, **10**, 577.
71. R. W. Borreson, C. L. Yaws, G. Hsu, and R. Lutwack, *Solid State Tech.*, 1978, **21**, 43.
72. P. A. Taylor, *Solid State Tech.*, 1987, **30**, (7), 53.
73. P. A. Taylor, *J. Cryst. Growth.*, 1988, **89**, 28.
74. J. E. Macintyre ed., ‘Dictionary of Inorganic Compounds’, Chapman & Hall, London, 1992.
75. E. Lukevics, O. Pudova, and R. Sturkovich, ‘Molecular Structure of Organosilicon Compounds’, Ellis Horwood, Chichester, 1989, Sect. 1, p. 11.
76. B. Beagley, A. R. Conrad, J. M. Freeman, J. J. Monaghan, B. G. Norton, and G. C. Holywell, *J. Mol. Struct.*, 1972, **11**, 371.
77. C. Maerker, J. Kapp, and P. v. R. Schleyer, in ‘Organosilicon Chemistry II’, eds. N. Auner and J. Weis, Wiley-VCH, Weinheim, 1996, p. 329.
78. J. R. Hartman, J. Famil-Ghiriha, M. A. Ring, and H. E. O’Neal, *Combust. Flame*, 1987, **68**, 43.
79. V. M. Fthenakis and P. D. Moskowitz, *Solid State Tech.*, 1990, **33**, 81.
80. M. J. Kushner, *J. Appl. Phys.*, 1988, **63**, 2532.
81. S. Veprek, *Thin Solid Films*, 1989, **175**, 129.
82. A. M. Hodge, A. G. Morpeth, and P. C. Stevens, in ‘Fine Chemicals for the Electronics Industry II: Chemical Applications for the 1990’s’, eds. D. J. Ando and M. G. Pellatt, Royal Society of Chemistry, Cambridge, MA, 1991, p. 3.
83. P. A. Taylor, *Solid State Tech.*, 1989, **32**, 143.
84. M. Fieser, ‘Reagents for Organic Synthesis’, Wiley, New York, 1984, Vol. 11, p. 554.
85. J. S. Peake, W. H. Nebergall, and Y. T. Chen, *J. Am. Chem. Soc.*, 1952, **74**, 1526.
86. E. Amberger, R. Romer, and A. Layer, *J. Organomet. Chem.*, 1968, **12**, 417.
87. F. Feher and M. Krancher, *Z. Anorg. Allg. Chem.*, 1984, **509**, 95.
88. M. A. Ring and D. M. Ritter, *J. Am. Chem. Soc.*, 1961, **83**, 802.
89. F. Fehér, G. Betzen, and M. Krancher, *Z. Anorg. Allg. Chem.*, 1981, **475**, 81.
90. V. A. Williams and D. M. Ritter, *Inorg. Chem.*, 1985, **24**, 3278.
91. E. Amberger and E. Muhlhofer, *J. Organomet. Chem.*, 1968, **12**, 55.
92. F. Feher, P. Plichta, and R. Guilery, *Tetrahedron Lett.*, 1970, **11**, 4443.
93. F. Feher and M. Krancher, *Z. Naturforsch.*, 1985, **40B**, 1010.
94. F. Feher and M. Krancher, *Z. Naturforsch.*, 1985, **40B**, 1301.
95. P. W. Schenk, in ‘Handbook of Preparative Inorganic Chemistry’, 2nd edn., ed. G. Brauer, Academic Press, New York, 1963, Vol. 1, p. 691.
96. P. W. Schenk, ‘Handbook of Preparative Inorganic Chemistry’, 2nd edn., ed. G. Brauer, Academic Press, New York, 1963, Vol. 1, p. 692.
97. W. C. Schumb and R. C. Young, *J. Am. Chem. Soc.*, 1930, **52**, 1464.
98. W. M. Ingle and M. S. Peffley, *J. Electrochem. Soc.*, 1985, **132**, 1236.
99. W. Kwasnik, in ‘Handbook of Preparative Inorganic Chemistry’, 2nd edn., ed. G. Brauer, Academic Press, New York, 1963, Vol. 1, p. 214.
100. G. Fritz and D. Kummer, *Chem. Ber.*, 1961, **94**, 1143.
101. E. Keinan and D. Perez, *J. Org. Chem.*, 1987, **52**, 4846.
102. J. E. Drake, B. M. Glavincevski, R. T. Hemmings, and H. E. Henderson, *Inorg. Synth.*, 1979, **19**, 268.
103. L. G. L. Ward, *Inorg. Synth.*, 1968, **11**, 159.
104. K. Hassler and M. Pöschl, *J. Organomet. Chem.*, 1990, **398**, 225.
105. K. Hassler, W. Köll, and U. Pöschl, in ‘Organosilicon Chemistry III’, eds. N. Auner and J. Weis, Wiley-VCH, Weinheim, 1998, p. 301.
106. A. Stock, ‘Hydrides of Boron and Silicon’, Cornell University Press, Ithaca, 1933.
107. F. G. A. Stone, ‘Hydrogen Compounds of the Group IV Elements’, Prentice Hall, London, 1962.
108. F. Fehér, P. Plichta, and R. Guillery, *Chem. Ber.*, 1970, **103**, 3028.
109. A. G. MacDiarmid, *Adv. Inorg. Radiochem.*, 1961, **3**, 207.
110. A. G. MacDiarmid, *Prep. Inorg. React.*, 1964, **1**, 165.
111. E. G. Rochow, in ‘Comprehensive Inorganic Chemistry’, ed. A. F. Trotman-Dickenson, Pergamon Press, Oxford, 1973, Vol. 1, p. 1323.
112. E. Lukevics, O. Pudova, and R. Sturkovich, ‘Molecular Structure of Organosilicon Compounds’, Ellis Horwood, Chichester, 1989, Sect. 3, p. 231.

113. R. Kewley, P. M. McKinney, and A. G. Robiette, *J. Mol. Spectrosc.*, 1970, **34**, 390.
114. A. J. Blake, E. A. V. Ebsworth, S. G. D. Henderson, and A. J. Welch, *Acta Crystallogr.*, 1985, **C41**, 1141.
115. M. Mitzlaff, R. Holm, and H. Hartmann, *Z. Naturforsch.*, 1968, **23A**, 65.
116. G. A. Heath, L. F. Thomas, and J. Sheridan, *Trans. Faraday Soc.*, 1954, **50**, 779.
117. V. W. Laurie, *J. Chem. Phys.*, 1957, **26**, 1359.
118. A. Ben Altabef and H. Oberhammer, *J. Mol. Struct.*, 2002, **641**, 259.
119. J. Bunnell and T. A. Ford, *Spectrochim. Acta*, 1986, **42A**, 543.
120. E. A. V. Ebsworth, *Acc. Chem. Res.*, 1987, **20**, 295.
121. P. A. Agaskar, *Inorg. Chem.*, 1991, **30**, 2707.
122. R. A. Benkeser, *Acc. Chem. Res.*, 1971, **4**, 94.
123. K. Naumann, G. Zon, and K. Mislow, *J. Am. Chem. Soc.*, 1969, **91**, 7012.
124. G. Zon, K. E. DeBruin, K. Naumann, and K. Mislow, *J. Am. Chem. Soc.*, 1969, **91**, 7023.
125. F. R. Homaidan and C. H. Issidorides, *Heterocycles*, 1981, **16**, 411.
126. J. E. Baldwin, J. C. Bottaro, P. D. Riordan, and A. E. Derome, *J. Chem. Soc., Chem. Commun.*, 1982, 942.
127. S. W. Baldwin and S. A. Haut, *J. Org. Chem.*, 1975, **40**, 3885.
128. R. A. Benkeser and D. F. Ehler, *J. Org. Chem.*, 1973, **38**, 3660.
129. T. H. Chan, J. P. Montillier, W. F. Van Horn, and D. N. Harpp, *J. Am. Chem. Soc.*, 1970, **92**, 7224.
130. H.-G. Horn and D. Kuczkowiak, *Z. Anorg. Allg. Chem.*, 1996, **622**, 1083.
131. O. Bechstein and D. Hass, *Z. Anorg. Allg. Chem.*, 1991, **594**, 202.
132. R. West and E. G. Rochow, *Inorg. Synth.*, 1953, **4**, 41.
133. H. Stade, W. Wieker, and G. Garzo, *Z. Chem.*, 1981, **21**, 237.
134. W. C. Schumb and D. W. Breck, *J. Am. Chem. Soc.*, 1952, **74**, 1754.
135. F. Höfler and H. D. Pletka, *Monatsh. Chem.*, 1973, **104**, 1.
136. E. Hengge and S. Walkhör, *Z. Naturforsch.*, 1974, **29B**, 437.
137. P. L. Timms, R. A. Kent, T. C. Ehlert, and J. L. Margrave, *J. Am. Chem. Soc.*, 1965, **87**, 2824.
138. W. C. Schumb and H. H. Anderson, *J. Am. Chem. Soc.*, 1936, **58**, 994.
139. F. Höfler and R. Jannach, *Monatsh. Chem.*, 1976, **107**, 731.
140. P. W. Schenk, in 'Handbook of Preparative Inorganic Chemistry', 2nd edn., ed. G. Brauer, Academic Press, New York, 1963, Vol. 1, p. 689.
141. G. Urry, *Acc. Chem. Res.*, 1970, **3**, 306.
142. W. C. Schumb and E. L. Gamble, *Inorg. Synth.*, 1939, **1**, 42.
143. E. Hengge, *Top. Curr. Chem.*, 1974, **51**, 1.
144. K. Hassler, D. Kovar, H. Söllradl, and E. Hengge, *Z. Anorg. Allg. Chem.*, 1982, **488**, 27.
145. E. Hengge and D. Kovar, *Ang. Chem., Int. Ed. Engl.*, 1981, **20**, 678.
146. E. Hengge and D. Kovar, *J. Organomet. Chem.*, 1977, **125**, C29.
147. K. G. Sharp, P. A. Sutor, T. C. Farrar, and K. Ishibitsu, *J. Am. Chem. Soc.*, 1975, **97**, 5612.
148. C. Knopf, U. Herzog, G. Roewer, E. Brendler, G. Rheinwald, and H. Lang, *J. Organomet. Chem.*, 2002, **662**, 14.
149. H. Schmölzer and E. Hengge, *J. Organomet. Chem.*, 1982, **225**, 171.
150. H. Oehme and H. Weiss, *J. Organomet. Chem.*, 1987, **319**, C16.
151. W. Raml and E. Hengge, *Monatsh. Chem.*, 1979, **110**, 1257.
152. W. C. Schumb and A. J. Stevens, *J. Am. Chem. Soc.*, 1950, **72**, 3178.
153. B. A. Grigor and C. J. Wilkins, *Inorg. Synth.*, 1963, **7**, 23.
154. W. C. Schumb and C. H. Klein, *J. Am. Chem. Soc.*, 1937, **59**, 261.
155. D. J. Panckhurst and C. J. Wilkins, *Inorg Synth.*, 1963, **7**, 28.
156. W. C. Schumb and W. J. Bernard, *J. Am. Chem. Soc.*, 1955, **77**, 862.
157. U. Müller and V. Krug, *Z. Naturforsch.*, 1985, **40B**, 1015.
158. F. Höfler, *Monatsh. Chem.*, 1973, **104**, 694.
159. F. Höfler and R. Jannach, *Z. Anorg. Allg. Chem.*, 1975, **413**, 285.
160. F. Höfler, R. Jannach, and W. Raml, *Z. Anorg. Allg. Chem.*, 1977, **428**, 75.
161. F. Höfler and R. Jannach, *Inorg. Nucl. Chem. Lett.*, 1974, **10**, 711.
162. T. H. Chan and L. T. L. Wong, *J. Org. Chem.*, 1969, **34**, 2766.
163. M. V. Bhatt and S. S. El-Morey, *Synthesis*, 1982, 1048.
164. M. Fieser, 'Reagents for Organic Synthesis', Wiley, New York, 1990, Vol. 15, p. 286.
165. K. Hiraoki, M. Nasu, A. Minarnitsu, D. Oomori, and S. Yamabe, *J. Phys. Chem. A*, 1999, **103**, 568.
166. M. Atoji and W. N. Lipscomb, *Acta Crystallogr.*, 1954, **7**, 597.
167. K. Hagen and K. Hedberg, *J. Chem. Phys.*, 1973, **59**, 1549.
168. R. R. Ryan and K. Hedberg, *J. Chem. Phys.*, 1969, **50**, 4986.
169. R. Holm, M. Mitzlaff, and H. Hartmann, *Z. Naturforsch.*, 1967, **22A**, 1287.
170. M. Mitzlaff, R. Holm, and H. Hartmann, *Z. Naturforsch.*, 1968, **23A**, 1819.
171. J. Sheridan and W. Gordy, *J. Chem. Phys.*, 1951, **19**, 965.
172. T. Kihara, *Acta Crystallogr.*, 1981, **A37**, 46.
173. C. Eaborn, Y. Y. El-Kaddar, and P. D. Lickiss, *Inorg. Chim. Acta*, 1992, **198–200**, 337.
174. J. S. Thrasher, *Inorg. Synth.*, 1986, **24**, 99.

175. R. G. Neville and J. J. McGee, *Inorg. Synth.*, 1966, **8**, 23.

176. R. G. Neville and J. J. McGee, *Inorg. Synth.*, 1966, **8**, 27.

177. A. G. MacDiarmid ed., 'The Bond to Halogens and Halogenoids', Dekker, New York, 1972, Vol. 2, Part 1.

178. F. Höfler, G. Jägerhuber, and W. Veigl, *Monatsh. Chem.*, 1974, **105**, 539.

179. H. H. Anderson, *J. Am. Chem. Soc.*, 1944, **66**, 934.

180. M. H. Palmer and M. F. Guest, *Chem. Phys. Lett.*, 1992, **196**, 183.

181. M. H. Palmer, *J. Mol. Struct.*, 1991, **246**, 321.

182. C. Glidewell and H. D. Holden, *THEOCHEM*, 1982, **6**, 325.

183. W. Airey, C. Glidewell, A. G. Robiette, and G. M. Sheldrick, *J. Mol. Struct.*, 1971, **8**, 435.

184. R. L. Hilderbrandt and S. H. Bauer, *J. Mol. Struct.*, 1969, **3**, 325.

185. C. Glidewell and A. G. Robiette, *Chem. Phys. Lett.*, 1974, **28**, 290.

186. R. G. Neville and J. J. McGee, 'Organic Syntheses', Wiley, New York, 1973, Collective Vol. 5, p. 801.

187. P. D. Blair, A. J. Blake, R. W. Cockman, S. Cradock, E. A. V. Ebsworth, and D. W. H. Rankin, *J. Mol. Struct.*, 1989, **193**, 279.

188. A. P. Cox, A. D. Couch, I. M. Hedgecock, and S. G. Clement, *Chem. Phys. Lett.*, 1989, **158**, 6.

189. W. R. Hertler, D. A. Dixon, E. W. Matthews, F. Davidson, and F. G. Kitson, *J. Am. Chem. Soc.*, 1987, **109**, 6532.

190. U. Wannagat, *Adv. Inorg. Radiochem.*, 1964, **6**, 225.

191. C. Glidewell, A. G. Robiette, and G. M. Sheldrick, *Chem. Phys. Lett.*, 1972, **16**, 526.

192. C. Glidewell and A. G. Robiette, *Chem. Phys. Lett.*, 1974, **28**, 290.

193. P. D. Lickiss, in 'The Chemistry of Organic Silicon Compounds', eds. Z. Rappoport and Y. Apeloig, John Wiley, Chichester, 2001, Vol. 3, p. 695.

194. R. Murugavel, A. Voigt, M. G. Walawalker, and H. W. Roesky, *Chem. Rev.*, 1996, **96**, 2205.

195. R. Murugavel, M. Bhattacharjee, and H. W. Roesky, *Appl. Organomet. Chem.*, 1999, **13**, 227.

196. J. E. Drake and C. Riddle, *Quart. Rev.*, 1970, **24**, 263.

197. P. A. Agaskar and W. G. Klemperer, *Inorg. Chim. Acta*, 1995, **229**, 355.

198. V. W. Day, W. G. Klemperer, V. V. Mainz, and D. M. Millar, *J. Am. Chem. Soc.*, 1985, **107**, 8262.

199. P. A. Agaskar, V. W. Day, and W. G. Klemperer, *J. Am. Chem. Soc.*, 1987, **109**, 5554.

200. M. G. Voronkov and V. I. Laurent'yev, *Top. Curr. Chem.*, 1982, **102**, 199.

201. R. H. Baney, M. Itoh, A. Sakakibara, and T. Suzuki, *Chem. Rev.*, 1995, **95**, 1409.

202. D. A. Loy and K. J. Shea, *Chem. Rev.*, 1995, **95**, 1431.

203. A. E. Shirk and J. S. Shirk, *J. Mol. Spectrosc.*, 1982, **92**, 218.

204. R. Gooden, *Inorg. Chem.*, 1983, **22**, 2272.

205. J. E. Drake, B. M. Glavincevski, and R. T. Hemmings, *Can. J. Chem.*, 1980, **58**, 2161.

206. R. T. Hemmings and H. E. Henderson, *Inorg. Synth.*, 1979, **19**, 274.

207. J. E. Drake and B. M. Glavincevski, *Inorg. Synth.*, 1986, **24**, 127.

208. H. J. Emeleus, A. G. MacDiarmid, and A. G. Maddock, *J. Inorg. Nucl. Chem.*, 1955, **1**, 194.

209. H. G. Horn and M. Hemeke, *Chem. Ztg.*, 1985, **109**, 1; *Chem. Abstr.*, 1985, **102**, 142.

210. H. G. Horn, B. Toepfer, and M. Hemeke, *Chem. Ztg.*, 1991, **115**, 15; *Chem. Abstr.*, 1991, **114**, 258.

211. H. Oberhammer and J. E. Boggs, *J. Am. Chem. Soc.*, 1980, **102**, 7241.

212. M. A. Brook, 'Silicon in Organic, Organometallic and Polymer Chemistry', Wiley Interscience, New York, 2000, p. 31.

213. M. J. Barrow and E. A. V. Ebsworth, *J. Chem. Soc., Dalton Trans.*, 1982, 211.

214. C. Glidewell, *J. Mol. Struct. THEOCHEM*, 1981, **2**, 373.

215. C. Glidewell, D. W. H. Rankin, and G. M. Sheldrick, *Trans. Faraday Soc.*, 1969, **65**, 1409.

216. G. Vogg, M. S. Brandt, and M. Stutzmann, *Chem. Mater.*, 2003, **15**, 910.

217. M. S. Brandt, T. Puchert, and M. Stutzmann, in 'Tailor-made Silicon-Oxygen Compounds, From Molecules to Materials', eds. R. Corriu and P. Jutzi, Vieweg, Braunschweig, 1996, p. 117.

218. W. Hönle, U. Dettlaff-Weglikowska, S. Finkbeiner, A. Molassioti, and J. Weber, in 'Tailor-made Silicon-Oxygen Compounds, From Molecules to Materials', eds. R. Corriu and P. Jutzi, Vieweg, Braunschweig, 1996, p. 99.

219. E. F. Hengge and A. Kleewein, in 'Tailor-made Silicon-Oxygen Compounds, From Molecules to Materials', eds. R. Corriu and P. Jutzi, Vieweg, Braunschweig, 1996, p. 89.

220. E. Z. Kurmaev, S. N. Shamin, D. L. Ederer, U. Dettlaff-Weglikowska, and J. Weber, *J. Mater. Res.*, 1999, **14**, 1235.

221. J. Peters and B. Krebs, *Acta Crystallogr.*, 1982, **B38**, 1270.

222. K. Moran, R. Shibao, and H. Eckert, *Hyperfine Interac.*, 1990, **62**, 55.

223. M. Tenhover, R. D. Boyer, R. S. Henderson, T. E. Hammond, and G. A. Shreve, *Solid State Commun.*, 1988, **65**, 1517.

224. J. E. Griffiths, M. Malyj, G. P. Espinosa, and J. P. Remeika, *Phys. Rev. B*, 1984, **30**, 6978.

225. H. C. Kaufman, *J. Chem. Eng. Data*, 1962, **7**, 556.

226. H. Breederveld and H. I. Waterman, *Recl. Trav. Chim. Pays-Bas*, 1954, **73**, 871.

227. M. Schmeisser and H. Müller, *Angew. Chem.*, 1957, **69**, 781.

228. W. E. Newton and E. G. Rochow, *Inorg. Chem.*, 1970, **9**, 1071.
229. K. L. Mittal ed., 'Silanes and Other Coupling Agents', VSP, Utrecht, 1992.
230. K. L. Mittal ed., 'Silanes and Other Coupling Agents', VSP Utrecht, 2001.
231. J. Chojnowski, M. Cypryk, K. Kazmierski, and K. Rozga, *J. Non-Cryst. Solids*, 1990, **125**, 40.
232. C. J. Brinker, *J. Non-Cryst. Solids*, 1988, **100**, 31.
233. I. Hasegawa and S. Sakka, *J. Non-Cryst. Solids*, 1988, **100**, 201.
234. L. L. Hench, 'Sol-gel Silica: Properties, Processing and Technology Transfer', Noyes Publications, Westwood, NJ, 1999.
235. D. Avnir, L. C. Klein, D. Levy, and U. Schubert, in 'The Chemistry of Organic Silicon Compounds', eds. Z. Rappoport and Y. Apeloig, John Wiley, Chichester, 1998, Vol. 2, p. 2317.
236. C. Glidewell, D. W. H. Rankin, A. G. Robiette, G. M. Sheldrick, B. Beagley, and J. M. Freeman, *J. Mol. Struct.*, 1970, **5**, 417.
237. C. Glidewell, D. W. H. Rankin, A. G. Robiette, G. M. Sheldrick, B. Beagley, and J. M. Freeman, *Trans. Faraday Soc.*, 1969, **65**, 2621.
238. J. D. Odom, E. J. Stampf, V. S. Li, and J. R. Durig, *J. Mol. Struct.*, 1978, **49**, 1.
239. E. Lukevics, O. Pudova, and R. Sturkovich, 'Molecular Structure of Organosilicon Compounds', Ellis Horwood, Chichester, 1989, p. 222.
240. L. H. Boonstra, F. C. Mijlhoff, G. Renes, A. Spelbos, and I. Hargittai, *J. Mol. Struct.*, 1975, **28**, 129.
241. E. Suzuki, M. Akiyama, and Y. Ono, *J. Chem. Soc., Chem. Commun.*, 1992, 136.
242. W. Bett and S. Cradock, *Monatsh. Chem.*, 1980, **111**, 193.
243. J. H. Balthis, *Inorg. Synth.*, 1953, **4**, 45.
244. B. Kamenar and M. Bruvo, *Z. Kristallogr.*, 1975, **141**, 97.
245. L. Wicke, E. Alig, H. W. Lerner, and M. Bolte, *Acta Crystallogr.*, 2002, **E58**, o927.
246. E. A. V. Ebsworth and J. C. Thompson, *J. Chem. Soc. A*, 1967, 69.
247. S. Cradock, E. A. V. Ebsworth, D. W. H. Rankin, and W. J. Savage, *J. Chem. Soc., Dalton Trans.*, 1976, 1661.
248. D. G. Anderson and S. Cradock, *J. Chem. Soc., Dalton Trans.*, 1986, 113.
249. W. Bett, S. Cradock, and D. W. H. Rankin, *J. Mol. Struct.*, 1980, **66**, 159.
250. J. J. Zuckerman, *J. Chem. Soc.*, 1962, 873.
251. D. Schomburg, *Angew. Chem., Int. Ed. Engl.*, 1983, **22**, 65.
252. W. Bibber, C. L. Barnes, D. van der Helm, and J. J. Zuckerman, *Angew. Chem., Int. Ed. Engl.*, 1983, **22**, 501.
253. C. L. Frye, *J. Org. Chem.*, 1969, **34**, 2496.
254. C. Chatgilialoglu, M. Guerra, A. Guerrini, G. Seconi, K. B. Clark, D. Griller, J. Kanabus-Kaminska, and J. A. Martinho-Simões, *J. Org. Chem.*, 1992, **57**, 2427.
255. A. Haas, R. Hitze, C. Krüger, and K. Angermund, *Z. Naturforsch.*, 1984, **39B**, 890.
256. W. Wojnowski, K. Peters, M. C. Böhm, and H. G. von Schnering, *Z. Anorg. Allg. Chem.*, 1985, **523**, 169.
257. W. Wojnowski, K. Peters, D. Weber, and H. G. von Schnering, *Z. Anorg. Allg. Chem.*, 1984, **519**, 134.
258. B. Becker, A. Pladzyk, A. Konitz, and W. Wojnowski, *Appl. Organomet. Chem.*, 2002, **16**, 517.
259. W. Wojnowski, W. Bochenska, K. Peters, E. M. Peters, and H. G. von Schnering, *Z. Anorg. Allg. Chem.*, 1986, **533**, 165.
260. V. E. Shklover, Yu. T. Struchkov, A. V. Ganyushkin, V. A. Yablokov, and G. A. Razuvaev, *Dokl. Akad. Nauk. SSSR*, 1980, **253**, 341.
261. P. Eigen, H. Keller-Rudek, W. Kurtz, P. Merlet, H. Schäfer and F. Schröder, eds. H. Katscher, H. Keller-Rudek, P. Merlet, H. Schäfer, F. Schröder and H. Jehn, 'Gmelin Handbuch der Anorganischen Chemie', 8th edn., System No. 15, 1989, Suppl. Vol. 4.
262. M. F. Lappert, P. P. Power, A. R. Sanger, and R. C. Srivastava, 'Metal and Metalloid Amides', Ellis Horwood, Chichester, 1980, Chap. 5, p. 235.
263. L. G. L. Ward, *Inorg. Synth.*, 1968, **11**, 168.
264. D. B. Beach, *Inorg. Chem.*, 1992, **31**, 4174.
265. G. Kannengiesser and F. Damm, *Bull. Chem. Soc. Fr.*, 1967, 2492.
266. U. Wannagat, P. Schmidt, and M. Schulze, *Angew. Chem., Int. Ed. Engl.*, 1967, **6**, 446.
267. D. E. J. Arnold, E. A. V. Ebsworth, H. F. Jessep, and D. W. H. Rankin, *J. Chem. Soc., Dalton Trans.*, 1972, 1681.
268. E. A. V. Ebsworth, D. W. H. Rankin, and J. G. Wright, *J. Chem. Soc., Dalton Trans.*, 1979, 1065.
269. G. S. Laurenson and D. W. H. Rankin, *J. Chem. Soc., Dalton Trans.*, 1981, 425.
270. U. Wannagat, P. Schmidt, and M. Schulze, *Angew. Chem., Int. Ed. Engl.*, 1967, **6**, 447.
271. D. Mootz, J. Fayos, and A. Zinnius, *Angew. Chem., Int. Ed. Engl.*, 1972, **11**, 58.
272. A. J. Blake, E. A. V. Ebsworth, and A. J. Welch, *Acta Crystallogr.*, 1984, **C40**, 895.
273. C. Glidewell, D. W. H. Rankin, A. G. Robiette, and G. M. Sheldrick, *J. Chem. Soc. A*, 1970, 318.
274. E. F. Krimmel and R. Hezel, eds. A. Pebler and F. Schrödere, 'Gmelin Handbuch der Anorganischen Chemie', 8th edn., System No. 15, 1991, Suppl. Vol. B 5c.
275. R. Grün, *Acta Crystallogr.*, 1979, **B35**, 800.
276. K. G. Sharp, *J. Chem. Soc., Chem. Commun.*, 1977, 564.
277. M. Baudler and Th. Pontzen, *Z. Anorg. Allg. Chem.*, 1983, **491**, 27.

278. G. Fritz, K. D. Hoppe, W. Hönle, D. Weber, C. Mujica, V. Manriquez, and H. G. W. Schnering, *J. Organomet. Chem.*, 1983, **249**, 63.

279. G. Fritz, *Z. Naturforsch.*, 1953, **8B**, 776.

280. G. Fritz, *Adv. Inorg. Chem.*, 1987, **31**, 171.

281. M. Baudler, T. Pontzen, U. Schings, K.-F. Tebbe, and M. Fehér, *Angew. Chem., Int. Ed. Engl.*, 1983, **22**, 775.

282. B. Beagley and A. R. Medwid, *J. Mol. Struct.*, 1977, **38**, 239.

283. B. T. Luke, J. A. Pople, M. B. Krogh-Jespersen, Y. Apeloig, J. Chandrasekhar, and P. von Rague-Schleyer, *J. Am. Chem. Soc.*, 1986, **108**, 260.

284. R. J. Wilcsek, D. S. Matteson, and J. G. Douglas, *J. Chem. Soc., Chem. Commun.*, 1976, 401.

285. J. L. Margrave and P. W. Wilson, *Acc. Chem. Res.*, 1971, **4**, 145.

286. P. Zhu, M. Piserchio, and F. W. Lampe, *J. Phys. Chem.*, 1985, **89**, 5344.

287. R. H. Heyn and T. D. Tilley, *Inorg. Chem.*, 1990, **29**, 4051.

288. N. S. Hosmane and J. A. Maguire, *Adv. Organomet. Chem.*, 1990, **30**, 99.

289. V. Haase, G. Kirschstein, H. List, S. Ruprecht, R. Sangster, F. Schröder, W. Töpper and H. Vanacek, eds. H. Katscher, R. Sangster and F. Schröder, 'Gmelin Handbuch der Anorganischen Chemie', 8th ed., System No. 15, 1986, Suppl. Vol. B 3.

290. J. Schlichting, G. Czack, E. Koch-Bienemann, P. Kuhn and F. Schröder, eds. G. Kirschstein and D. Koschel, 'Gmelin Handbuch der Anorganischen Chemie', 8th edn., System No. 15, Suppl. 1984, Vol. B 2.

291. R. M. Laine and A. Sellinger, in 'The Chemistry of Organic Silicon Compounds', eds. Z. Rappoport and Y. Apeloig, John Wiley, Chichester, 1998, Vol. 2, p. 2245.

292. J. F. Harrod, *Coord. Chem. Rev.*, 2000, **206–207**, 493.

293. P. Braunstein, M. Knorr, and C. Stern, *Coord. Chem. Rev.*, 1998, **178–180**, 903.

294. M. S. Eisen, in 'The Chemistry of Organic Silicon Compounds', eds. Z. Rappoport and Y. Apeloig, John Wiley, Chichester, 1998, Vol. 2, p. 2037.

295. H. K. Sharma and K. H. Pannell, *Chem. Rev.*, 1995, **95**, 1351.

296. U. Schubert, *Transition Met. Chem.*, 1991, **16**, 136.

297. T. D. Tilley, in 'The Chemistry of Organic Silicon Compounds', eds. S. Patai and Z. Rappoport, Wiley, Chichester, 1989, Part 2, Chap. 24, p. 1415.

298. T. D. Tilley, in 'The Silicon–hetroatom Bond', eds. S. Patai and Z. Rappoport, Wiley, Chichester, 1991, Chap. 10, p. 309.

299. E. A. V. Ebsworth, V. M. Marganian, F. J. S. Reed, and R. O. Gould, *J. Chem. Soc., Dalton Trans.*, 1978, 1167.

300. E. A. V. Ebsworth, J. M. Edward, and D. W. H. Rankin, *J. Chem. Soc., Dalton Trans.*, 1976, 1667.

301. E. A. V. Ebsworth, J. M. Edward, and D. W. H. Rankin, *J. Chem. Soc., Dalton Trans.*, 1976, 1673.

302. B. J. Aylett, J. M. Campbell, and A. Walton, *J. Chem. Soc. A*, 1969, 2110.

303. B. J. Aylett and J. M. Campbell, *J. Chem. Soc. A*, 1969, 1910.

304. B. J. Aylett and J. M. Campbell, *J. Chem. Soc. A*, 1969, 1916.

305. B. J. Aylett and H. M. Colquhoun, *J. Chem. Soc., Dalton Trans.*, 1977, 2058.

306. B. J. Aylett and J. M. Campbell, *J. Chem. Soc. A*, 1969, 1920.

307. W. A. Herrmann, E. Voss, E. Guggolz, and M. L. Ziegler, *J. Organomet. Chem.*, 1985, **284**, 47.

308. G. Hencken and E. Weiss, *Chem. Ber.*, 1973, **106**, 1747.

309. D. W. H. Rankin and A. Robertson, *J. Organomet. Chem.*, 1975, **85**, 225.

310. D. W. H. Rankin and A. Robertson, *J. Organomet. Chem.*, 1976, **105**, 331.

311. A. G. Robiette, G. A. Sheldrick, R. N. F. Simpson, B. J. Aylett, and J. A. Campbell, *J. Organomet. Chem.*, 1968, **14**, 279.

312. E. Amberger, E. Muhlhoer, and H. Stern, *J. Organomet. Chem.*, 1969, **17**, P5.

313. X.-L. Luo, G. J. Kubas, C. J. Burns, J. C. Bryan, and C. L. Unkefer, *J. Am. Chem. Soc.*, 1995, **117**, 1159.

314. I. Atheaux, B. Donnadieu, V. Rodriguez, S. Sabo-Etienne, B. Chaudret, K. Hussein, and J.-C. Barthelat, *J. Am. Chem. Soc.*, 2000, **122**, 5664.

315. Z. Lin, *Chem. Soc. Rev.*, 2002, **31**, 239.

316. G. J. Kubas, *J. Organomet. Chem.*, 2000, **635**, 37.

317. J. Y. Corey and J. Braddock-Wilking, *Chem. Rev.*, 1999, **99**, 175.

318. T. R. Bierschenk, M. A. Guerra, T. J. Juhlke, S. B. Larson, and R. J. Lagow, *J. Am. Chem. Soc.*, 1987, **109**, 4855.

319. T. J. Groshens and K. J. Klabunde, *J. Organomet. Chem.*, 1983, **259**, 337.

320. S. K. Janikowski, L. J. Radonovich, T. J. Groshens, and K. J. Klabunde, *Organometallics*, 1985, **4**, 396.

321. M. M. Brezinski, J. Schneider, L. J. Radonovich, and K. J. Klabunde, *Inorg. Chem.*, 1989, **28**, 2414.

322. K. Emerson, P. R. Ireland, and W. T. Robinson, *Inorg. Chem.*, 1970, **9**, 436.

323. L. Manojlovic-Muir, K. W. Muir, and J. A. Ibers, *Inorg. Chem.*, 1970, **9**, 447.

324. K. W. Muir and J. A. Ibers, *Inorg. Chem.*, 1970, **9**, 440.

325. R. K. Pomeroy, *J. Organomet. Chem.*, 1979, **177**, C27.

326. F. W. B. Einstein and T. Jones, *Inorg. Chem.*, 1982, **21**, 987.

327. G. N. Van Buuren, A. C. Willis, F. W. B. Einstein, L. K. Peterson, R. K. Pomeroy, and D. Sutton, *Inorg. Chem.*, 1981, **20**, 4361.

328. W. Jetz and W. A. G. Graham, *J. Am. Chem. Soc.*, 1967, **89**, 2773.

329. J. W. Connolly, A. H. Cowley, and C. M. Nunn, *Polyhederon*, 1990, **9**, 1337.

330. U. Schubert, *Adv. Organomet. Chem.*, 1990, **30**, 151.
331. W. Malisch and M. Kuhn, *Chem. Ber.*, 1974, **107**, 979.
332. W. Malisch and M. Kuhn, *Chem. Ber.*, 1974, **107**, 2835.
333. U. Schubert, G. Kraft, and E. Walther, *Z. Anorg. Allg. Chem.*, 1984, **519**, 96.
334. W. T. Robinson and J. A. Ibers, *Inorg. Chem.*, 1967, **6**, 1208.
335. G. R. Clark, C. E. F. Rickard, W. R. Roper, D. M. Salter, and L. J. Wright, *Pure Appl. Chem.*, 1990, **62**, 1039.
336. C. E. F. Rickard, W. R. Roper, D. M. Salter, and L. J. Wright, *J. Am. Chem. Soc.*, 1992, **114**, 9682.
337. W. Malisch, H.-U. Wekel, I. Grob, and F. H. Köhler, *Z. Naturforsch.*, 1982, **37B**, 601.
338. P. Braunstein, M. Knorr, A. Tiripicchio, and M. Tiripicchio Camellini, *Angew. Chem., Int. Ed. Engl.*, 1989, **28**, 1361.
339. P. Braunstein, M. Knorr, B. E. Villarroya, and J. Fischer, *New J. Chem.*, 1990, **14**, 583.
340. H. Kono, N. Wakao, I. Ojima, and Y. Nagai, *Chem. Lett.*, 1975, 189.
341. R. N. Haszeldine, R. V. Parish, and D. J. Parry, *J. Chem. Soc. A*, 1969, 683.
342. M. Knorr, J. Müller, and U. Schubert, *Chem. Ber.*, 1987, **120**, 879.
343. M. Knorr, S. Gilbert, and U. Schubert, *J. Organomet. Chem.*, 1988, **347**, C17.
344. J. Ruiz and P. M. Maitlis, *J. Chem. Soc., Chem. Commun.*, 1986, 862.
345. W. Malisch, S. Schmitzer, G. Kaupp, K. Hindahl, H. Käb, and U. Wachtler, in ‘Organosilicon Chemistry, From Molecules to Materials’, eds. N. Auner and J. Weis, VCH, Weinheim, 1994, p. 185.
346. W. Malisch, R. Lankat, S. Schmitzer, and J. Reising, *Inorg. Chem.*, 1995, **34**, 5701.
347. W. Malisch, R. Lankat, O. Fey, J. Reising, and S. Schmitzer, *J. Chem. Soc., Chem. Commun.*, 1995, 1917.
348. M. Van Tiel, K. M. Mackay, and B. K. Nicholson, *J. Organomet. Chem.*, 1987, **326**, C101.
349. G. Schmid, V. Bätzel, and G. Etzrodt, *J. Organomet. Chem.*, 1976, **112**, 345.
350. K. M. Mackay, B. K. Nicholson, A. W. Sims, and C. C. Tan, *Acta Crystallogr.*, 1987, **C43**, 633.
351. B. J. Aylett and M. T. Taghipour, *J. Organomet. Chem.*, 1983, **249**, 55.
352. S. G. Anema, G. C. Barris, K. M. Mackay, and B. Nicholson, *J. Organomet. Chem.*, 1988, **350**, 207.
353. S. G. Anema, K. M. Mackay, B. K. Nicholson, and M. Van Tiel, *Organometallics*, 1990, **9**, 2436.
354. K. M. Mackay, B. K. Nicholson, W. T. Robinson, and A. W. Sims, *J. Chem. Soc., Chem. Commun.*, 1984, 1276.
355. S. D. Grumbine, R. K. Chadha, and T. D. Tilley, *J. Am. Chem. Soc.*, 1992, **114**, 1518.
356. M. Okazaki, H. Tobita, and H. Ogino, *J. Chem. Soc., Dalton Trans.*, 2003, 493.
357. D. Kost and I. Kalikhman, in ‘The Chemistry of Organic Silicon Compounds’, eds. Z. Rappoport and Y. Apeloig, John Wiley, Chichester, 1998, Vol. 2, p. 1339.
358. R. J. P. Corriu, C. Guerin, and J. J. E. Moreau, in ‘The Chemistry of Organic Silicon Compounds’, eds. S. Patai and Z. Rappoport, Wiley, Chichester, 1989, Part 1, p. 305.
359. S. N. Tandura, M. G. Voronkov, and N. V. Alekseev, *Top. Curr. Chem.*, 1985, **131**, 99.
360. M. G. Voronkow, *Top. Curr. Chem.*, 1979, **84**, 77.
361. M. G. Voronkow, *Pure Appl. Chem.*, 1966, **13**, 35.
362. C. Eaborn, K. J. Odell, A. Pidcock, and G. R. Scollary, *J. Chem. Soc., Chem. Commun.*, 1976, 317.
363. J. L. Harland, R. O. Day, J. F. Vollano, A. C. Sau, and R. R. Holmes, *J. Am. Chem. Soc.*, 1981, **103**, 5269.
364. C. L. Frye, G. A. Vincent, and W. A. Finzel, *J. Am. Chem. Soc.*, 1971, **93**, 6805.
365. L. Párkányi, P. Hencsei, L. Bihátsi, and T. Müller, *J. Organomet. Chem.*, 1984, **269**, 1.
366. V. Pestunovich, S. Kiripichenko, and M. Voronkov, ‘The Chemistry of Organic Silicon Compounds’, John Wiley, Chichester, 1998, Vol. 2, p. 1447.
367. V. D. Schomburg, *Z. Anorg. Allg. Chem.*, 1982, **493**, 53.
368. G. Klebe, M. Nix, and K. Hensen, *Chem. Ber.*, 1984, **117**, 797.
369. D. G. Anderson, A. J. Blake, S. Cradock, E. A. V. Ebsworth, D. W. H. Rankin, and A. J. Welch, *Angew. Chem., Int. Ed. Engl.*, 1986, **25**, 107.
370. W. S. Sheldrick and W. Wolfsberger, *Z. Naturforsch.*, 1977, **32B**, 22.
371. W. Wolfsberger, H.-H. Pickel, and H. Schmidbaur, *Chem. Ber.*, 1971, **104**, 1830.
372. F. Klanberg and E. L. Muetterties, *Inorg. Chem.*, 1968, **7**, 155.
373. D. Schomberg and R. Krebs, *Inorg. Chem.*, 1984, **23**, 1378.
374. H. J. Campbell-Ferguson and E. A. V. Ebsworth, *J. Chem. Soc. A*, 1966, 1508.
375. H. J. Campbell-Ferguson and E. A. V. Ebsworth, *J. Chem. Soc. A*, 1967, 705.
376. V. A. Bain, R. C. G. Killean, and M. Webster, *Acta Crystallogr.*, 1969, **B25**, 156.
377. A. D. Adley, P. H. Bird, A. R. Fraser, and M. Onyszchuk, *Inorg. Chem.*, 1972, **11**, 1402.
378. A. Boudin, G. Cerveau, C. Chuit, R. J. P. Corriu, and C. Reye, *Organometallics*, 1988, **7**, 1165.
379. J. J. Flynn and F. P. Boer, *J. Am. Chem. Soc.*, 1969, **91**, 5756.
380. R. F. Riley, R. Weat, and R. Barbarin, *Inorg. Synth.*, 1963, **7**, 30.
381. P. A. W. Dean, D. F. Evans, and R. F. Phillips, *J. Chem Soc. A*, 1969, 363.
382. E. Larsen, S. F. Mason, and G. H. Searle, *Acta Chem. Scand.*, 1966, **20**, 191.

383. D. R. Harvey and A. Weiss, *Angew. Chem., Int. Ed. Engl.*, 1965, **4**, 357.

384. K. O. Christe, W. W. Wilson, C. J. Schack, and R. D. Wilson, *Inorg. Synth.*, 1986, **24**, 46.

385. G. Sawitzki, H. G. von Schnering, D. Kummer, and T. Seshadri, *Chem. Ber.*, 1978, **111**, 3705.

386. I. R. Beattie, *J. Chem. Soc. A*, 1969, 2267.

387. I. R. Beatie and G. A. Ozin, *J. Chem. Soc. A*, 1970, 370.

388. H. E. Blayden and M. Webster, *Inorg. Nucl. Chem. Lett.*, 1970, **6**, 703.

389. R. C. Aggarwal and M. Onyszchuk, *Can. J. Chem.*, 1963, **41**, 876.

390. D. Kummer, A. Balkir, and H. Köster, *J. Organomet. Chem.*, 1979, **178**, 29.

391. D. Kummer, K.-E. Gaisser, and T. Seshadri, *Chem. Ber.*, 1977, **110**, 1950.

392. D. Kummer and T. Seshadri, *Z. Anorg. Allg. Chem.*, 1977, **432**, 147.

393. D. Kummer and T. Seshadri, *Z. Anorg. Allg. Chem.*, 1977, **432**, 153.

394. D. Kummer, K. E. Gaisser, J. Seifert, and R. Wagner, *Z. Anorg. Allg. Chem.*, 1979, **459**, 145.

395. M. Allan, B. J. Aylett, and I. A. Ellis, *Inorg. Nucl. Chem. Lett.*, 1966, **2**, 261.

396. R. Damrauer, R. A. Simon, and B. Kanner, *Organometallics*, 1988, **7**, 1161.

397. K. M. Kane, C. R. Lorenz, D. M. Heilman, and F. R. Lemke, *Inorg. Chem.*, 1998, **37**, 669.

398. P. P. S. Lee, T. Ngai, J.-D. Huang, C. Wu, W.-P. Fong, and D. K. P. Ng, *Macromolecules*, 2003, **36**, 7527.

399. C. Li and M. Lieberman, *Inorg. Chem.*, 2001, **40**, 932.

400. N. Kobayashi, F. Furuya, G.-C. Yug, H. Wakita, M. Yokomizo, and N. Ishikawa, *Chem. Eur. J.*, 2002, **8**, 1474.

401. T. R. Crompton, in 'The Chemistry of Organic Silicon Compounds', eds. S. Patai and Z. Rappoport, Wiley, Chichester, 1989, Part 1, p. 393.

402. J. Schraml, in 'The Chemistry of Organic Silicon Compounds', eds. Z. Rappoport and Y. Apeloig, John Wiley, Chichester, 2001, Vol. 3, p. 223.

403. Y. Takeuchi and T. Takayama, in 'The Chemistry of Organic Silicon Compounds', eds. Z. Rappoport and Y. Apeloig, John Wiley, Chichester, 1998, Vol. 2, p. 267.

404. E. A. Williams, in 'The Chemistry of Organic Silicon Compounds', eds. S. Patai and Z. Rappoport, Wiley, Chichester, 1989, Part 1, p. 511.

405. G. H. Snyder, in 'Silicon in Agriculture', eds. L. E. Datnoff, G. H. Snyder, and G. H. Körndorfer, Elsevier, Amsterdam, 2001, p. 185.

406. C. T. G. Knight and S. D. Kinrade, in 'Silicon in Agriculture', eds. L. E. Datnoff, G. H. Snyder, and G. H. Körndorfer, Elsevier, Amsterdam, 2001, p. 57.

Silicon: Organosilicon Chemistry

Hideki Sakurai
Tohoku University, Sendai, Japan

1 Introduction 1
2 Classes of Compounds and Nomenclature 1
3 Synthesis 2
4 Structure and Bonding 9
5 Reactions and Reactive Intermediates 12
6 Applications 22
7 References 27

1 INTRODUCTION

Silicon exists as the second most abundant element after oxygen, in the form of silicates in the Earth's crust. Berzelius first isolated the element silicon in 1823. In the periodic table, silicon has the position just below carbon. Carbon can be found in nature in a pure state or in a variety of forms of organic compounds, whereas silicon cannot be found in a pure state and constitutes mineral compounds. Thus carbon and silicon characterize the organic and inorganic worlds, respectively. Fundamental atomic properties can be compared with other group 14 elements; some are given in Table 1 (*see also* ***Silicon: Inorganic Chemistry***). Silicon can be described as having an outer electron configuration $3s^2p^2$.

Organosilicon compounds can be defined as chemical species having carbon–silicon bond(s). Since there are no organosilicon compounds in nature, all organosilicon compounds are artificial and therefore we can say that human wisdom built organosilicon compounds. Historically, organosilicon compounds have been known since Friedel and Crafts prepared tetraethylsilane by the reaction of diethylzinc and silicon tetrachloride in 1863.

$$2(C_2H_5)_2Zn + SiCl_4 \longrightarrow (C_2H_5)_4Si + 2ZnCl_2 \qquad (1)$$

Kipping, who has been frequently mentioned as the founder of organosilicon chemistry, used the Grignard reagents for the preparation of a variety of organosilicon compounds and investigated the properties of a wide range of compounds during the years 1898–1939. This period may be regarded as the first generation in organosilicon chemistry. Kipping summarized his investigation in rather a depressing tone that 'as moreover the few that are known are very limited in their reactions, the prospect of any immediate and important advance in this section of organic chemistry does not seem to be very hopeful' (Bakerian Lecture, 1936).

It was only after a short time that Eugene Rochow (US) and Richard Müller (Germany) simultaneously discovered the direct synthesis of methylchlorosilanes, in 1941–1942, that led to the booming silicone industry. New reactions and compounds have emerged since then. Perhaps the development until the late 1960s can be called the second generation of organosilicon chemistry. In that time, almost all known types of organosilicon compounds (silicon-functional compounds) were prepared and many fundamental reactions were described.

However, nothing was known of organosilicon reactive intermediates, double- and triple-bonded species, photochemistry, high-molecular weight polysilanes, and silicon polyhedranes. It was not until the late 1960s that organosilicon compounds received much interest as intermediates in organic synthesis. The nature of the effects that organosilicon groups exert on organic compounds was also systematically studied only in the past three decades. The author designates the period after 1970 as the third generation of organosilicon chemistry. Development of the organosilicon chemistry towards materials science is a notable fact from the end of the twentieth century.

The author will try, in this section, to introduce a concise summary of the basic organosilicon chemistry and an essence of the recent development.**[1]**

2 CLASSES OF COMPOUNDS AND NOMENCLATURE

The nomenclature of organosilicon compounds is based on the derivatives of silane, disilane, and higher polysilanes. When the silicon group is used as a substituent (silicon-containing radical), silyl, disilanyl, trisilanyl, and polysilanyl are used:

SiH_4 = silane, H_3Si- = silyl
SiH_3SiH_3 = disilane, H_3SiSiH_2- = disilanyl
$SiH_3SiH_2SiH_3$ = trisilane, $H_3SiSiH_2SiH_2-$ = trisilanyl

Note that for H_3SiSiH_2- and $H_3SiSiH_2SiH_2$-, disilanyl and trisilanyl should be used instead of disilyl and trisilyl. The latter means two and three silyl groups, respectively. For substituted silanes, substituents are arranged in alphabetical order. Me_2SiCl_2 and $ClCH_2SiMe_3$ are named as dichlorodimethylsilane and chloromethyltrimethylsilane. However, Me_3SiCl may be named as either chlorotrimethylsilane or trimethylsilyl chloride. Since hydrogen attached to silicon is a functional group capable of reduction of inorganic as well as organic compounds and *Hydrosilation*, compounds such as $Ph_3Si–H$ and $Et_3Si–H$ are referred to as organosilicon hydrides, specifically as triphenylsilyl hydride and triethylsilyl hydride. The

Table 1 Some fundamental properties of group 14 elements

	C	Si	Ge	Sn	Pb
Valence electrons	$2s^2 2p^2$	$3s^2 3p^2(3d)$	$4s^2 4p^2(4d)$	$5s^2 5p^2(5d)$	$6s^2 6p^2(6d)$
First ionization potentials (kcal mol^{-1})	260	188	182	169	171
Covalent radii (Å)	0.772	1.176	1.225	1.405	(1.750)
M−M bond energies (kcal mol^{-1})	82.6	46.4	38.2	39	
Relative electron densities [Atomic number/(covalent radii)^3]	13.1	8.6	17.4	17.8	15.3
Electronegativity (Pauling)	2.55	1.90	2.01	1.96	2.33
Electronegativity (Allred-Rochow)	2.50	1.74	2.02	1.72	1.55

general name of organosilane does not indicate the presence of the Si–H group.

Compounds having the general formula $H_3Si(XSiH_2)_n XSiH_3$ have the generic names silazanes ($X = NH$), silthianes ($X = S$), and siloxanes ($X = O$). The name silmethylenes ($X = CH_2$) may also be used. Examples are:

- $Me_3Si–NH–SiMe_3$ hexamethyldisilazane
- $H_3Si–S–SiH_2–S–SiH_3$ trisilthiane
- $Me_3Si–O–SiMe_3$ hexamethyldisiloxane
- $Me_3Si–CH_2–SiMe_2–CH_2–SiMe_3$ octamethyltrisilmethylene

Cyclic compounds having the formula $(SiH_2X)_n$ are called cyclosilazanes, cyclosilthianes, cyclosiloxanes, and cyclosilmethylenes for compounds with X = NH, S, O, and CH_2. The oxa-aza convention can be used for complex systems. For example, $Me_3Si–CHPh–SiMe(CH{=}CH_2)–O–SiMe_3$ may be named 2,2,4,6,6-pentamethyl-5-phenyl-4-vinyl-3-oxa-2,4,6-trisilaheptane.

Simple hydroxy derivatives are named as silanol:

Me_3SiOH trimethylsilanol
$PhSi(OH)_3$ phenylsilanetriol

Silicon-functional compounds are named by using appropriate prefixes or suffixes. Me_3SiNH_2 is trimethylsilylamine or aminotrimethylsilane. Organic compounds with silyl substituent(s) are usually named by organic nomenclature. Thus Me_3SiCH_2CN is named trimethylsilylacetonitrile. In organic chemistry, trimethylsilyl is often abbreviated as TMS. Thus TMSOEt indicates ethoxytrimethylsilane.

For commercially important methylsiloxanes and polymethylsiloxanes (silicones), a shorthand siloxane notation is used. Mono- di-, tri-, and tetra- (quarternary) functional $Me_3SiO_{1/2}$-, $–O_{l/2}SiMe_2O_{1/2}$-, $MeSi(O_{1/2}\text{-})_3$, and $Si(O_{1/2})_4$ groups are abbreviated as M, D, T, and Q. Therefore $Me_3Si–O–SiMe_3$, $Me_3Si–(OSiMe_2)_8–O–SiMe_3$, and $(Me_2SiO)_3$, are, for example, represented as M_2, MD_8M, and D_3, respectively.

Table 2 lists representative classes of organosilicon compounds with a typical example. The same classes of organic compounds are compared in the table.

3 SYNTHESIS

The following five types of reactions may prepare organosilicon compounds.

1. Silicon−carbon bond forming reactions.
2. Cleavage of the silicon−carbon bond to give silicon-functionalized silanes.
3. Substitution reactions on silicon to give silicon-functionalized silanes.
4. Preparation of carbon functionalized silanes.
5. Synthesis of polysilanes (silicon−silicon bond formation).

3.1 Silicon–carbon Bond Forming Reactions

3.1.1 Direct Synthesis (The Rochow Process)

Direct synthesis is the reaction of alkyl or aryl chloride and silicon in the presence of a proper catalyst. Mostly, methyl chloride is subjected to the reaction at 250−350 °C in a fluid bed with fine particles of silicon mixed with a copper catalyst (equation 2).**2**

$$MeCl + Si \xrightarrow{Cu} Me_nSiCl_{4-n} \qquad (2)$$

Operating conditions are usually optimized to give dichlorodimethylsilane, Me_2SiCl_2, required for the production of methylsilicones. Nevertheless, mixtures of chlorosilanes are always obtained, as listed in Table 3. Boiling points being very close each other, an extensive fractionating system is employed to separate these chlorosilanes in the silicone industry.

3.1.2 Reactions of Organometallic Reagents and Si–X

The most important laboratory method of the preparation of particular organosilicon compounds is the reaction of an appropriate chlorosilane and a Grignard reagent (equation 3).

$$R_3SiCl + R'MgBr \longrightarrow R_3SiR' \qquad (3)$$

Table 2 Comparisons of representative classes of Si and C compounds

Carbon		Silicon	
Single bonded compounds			
R_3C–H	Alkane	R_3Si–H	Silane
R_3C–F	Fluoroalkane	R_3Si–F	Fluorosilane
R_3C–CI	Chloroalkane	R_3Si–I	Chlorosilane
R_3C–Br	Bromoalkane	R_3Si–Br	Bromosilane
R_3C–OH	Alcohol	R_3Si–H	Silanol
R_3C–SH	Thiol	R_3Si–SH	Silanethiol
R_3C–OR	Ether	R_3Si–OR	Alkoxysilane
R_3C–NH_2	Amine	R_3Si–NH_2	Aminosilane
R_3C–COOH	Carboxylic acid	R_3Si–COOH	Silanecarboxylic acid
Double bonded compounds			
$>C{=}C<$	Alkene	$>Si{=}C<$	Silene
		$>Si{=}Si<$	Disilene
$>C{=}O$	Ketone	$>Si{=}O$	Silanone
$>C{=}NR$	Imine	$>Si{=}NR$	Silanimine
$RC{\equiv}CR$	Alkyne	$RSi{\equiv}CR$	Silyne
		$RSi{\equiv}SiR$	Disilyne

Table 3 Monomer composition of the direct synthesis products

Compound	% composition[a]	Bp (·C)
Me_4Si	0.01–0.5	26.6
$MeSiHCl_2$	1–6	41
Me_3SiCl	1–5	58
$MeSiCl_3$	3–10	66
Me_2SiCl_2	75–93	70

[a] Composition of the products depends on operating conditions.

$SiCl_4$, $SiHCl_3$, and various methylchlorosilanes are used in the reaction. When silicon carries more than two chlorine atoms, stepwise reaction occurs. Therefore partial alkylation (or arylation) is possible under carefully controlled conditions but, for that purpose, alkoxysilanes can conveniently be used because the reactivity of the last alkoxy group toward Grignard reagents is very low (equation 4).

$$MeSi(OEt)_3 + 2RMgBr \longrightarrow MeR_2SiOEt \qquad (4)$$

The relative reactivity of SiX toward Grignard reagent is shown in the following order: Si–CN > SiCl > SiOR > Si–OSi > SiH. Poly-Grignard reagents from X–$(CH_2)_n$–X give normal products when n is larger than 4. In the case of $n = 1$, in situ Grignard reactions can be utilized (equation 5).

$$2Me_3SiCl + CH_2Cl_2 \xrightarrow[\text{THF}]{\text{Li (in situ)}} (Me_3Si)_2CH_2 \qquad (5)$$

Organolithium compounds can also be used conveniently for the preparation of silanes. Reactivity of the lithium reagents is higher than the corresponding Grignard reagents, as demonstrated by the following example. The reaction of $HSiCl_3$ and i-PrMgCl results in the formation of i-Pr_2SiHCl, but the reaction with i-PrLi gives rise to i-Pr_3SiH. Preparation of t-butyldimethylchlorosilane from dimethyldichlorosilane requires the use of t-BuLi but an interesting accelerating effect of CN^- has been observed for the reaction of chlorosilanes with bulky t-BuMgCl. The reaction may proceed through a pentacoordinate intermediate (equation 6).**3**

$$Me_2SiCl_2 + t\text{-BuMgCl} \xrightarrow[\text{THF, reflux}]{\text{CuCN}} t\text{- BuMe}_2\text{SiCl} \qquad (6)$$

Dilithium reagents derived by reductive coupling of alkenes such as styrene and 1,1-diphenylethylene are important for the preparation of ring compounds (equation 7).

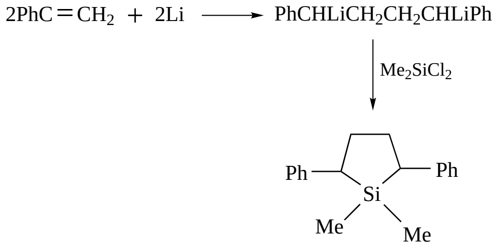

(7)

A similar dilithium reagent derived from 1,1-bis(trimethyl silyl)ethylene has been used for the protecting ligand of the first monomeric stannylene**4** (equation 8) and later, of various kinetically stabilized species (vide infra). Cyclooctatetraene undergoes 1,4-disilylation as shown below (equation 9).

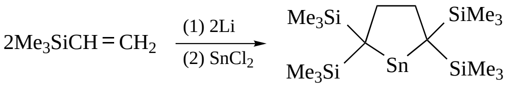

(8)

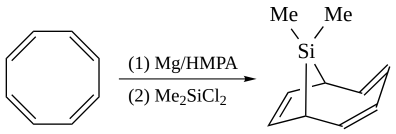

(9)

Closely related to the Birch reduction, benzene, and other aromatic compounds afforded reduction-silylation products (equation 10).[5] Electron-transfer reactions of bis(phenylethynyl)dimethylsilane gives 2,5-dianion of 3,4-diphenylsilole that is a useful intermediate to variously substituted siloles (equation 11).[6]

Examples using other organometallic reagents are illustrated in equations (12) and (13).

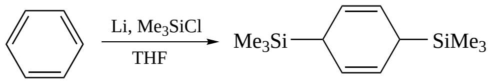

(10)

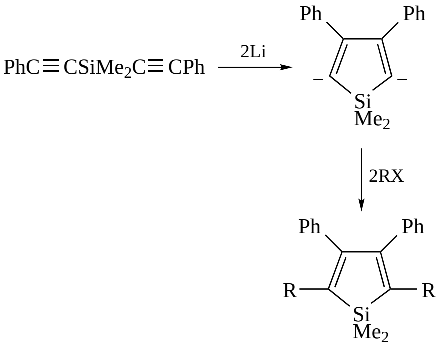

(11)

$$Me_3SiCl + o\text{-}Cl\text{–}C_6H_4Me + 2Na \longrightarrow o\text{-}(Me_3Si)C_6H_4Me + 2NaCl \quad (12)$$

$$Me_3SiCl + BrCH_2CO_2Et \xrightarrow{Zn} Me_3SiCH_2CO_2Et \quad (13)$$

3.1.3 *Reactions of Silylmetals*

Since silicon is a positive element, covalent bonds of most silicon compounds polarize as $Si^+\text{-}X^-$. However, silicon can form bonds with alkaline and alkaline earth metals to give silylmetals in which silicon compounds polarize as $Si^-\text{-}M^+$. These silylmetals are the source of silyl anions and react with haloalkanes to give the corresponding organosilanes (equation 14).

$$Me_3SiNa + C_5H_{11}Cl \xrightarrow[DMI]{} Me_3SiC_5H_{11} \quad (14)$$

Preparation of phenyl-substituted silyl anion is a simple process either from chlorosilanes or disilanes (equation 15).[7] Trimethylsilyl anions can he prepared from hexamethyldisilane by reaction with RM (RM=MeONa,[8] MeLi[9]) in a strongly basic solvent such as HMPA (hexamethyl phosphoramide).

$$2PhMe_2SiCl \xrightarrow{2Li} PhMe_2SiSiMe_2Ph \xrightarrow{2Li} 2PhMe_2SiLi \quad (15)$$

$$Me_3SiSiMe_3 + RM \longrightarrow Me_3SiM + Me_3SiR \quad (16)$$

$$RM = MeONa,\ MeLi$$

For the purpose of preparing trimethylsilylmetals, DMI (N,N-dimethylimidazolidinone) has been introduced as an efficient aprotic solvent. In fact, the choice of the solvent is important for the reaction (equation 14). In HMPA, electron transfer predominates to give products only in low yield, while in DMI the yield is almost quantitative.[10]

Silyllithium compounds may also be prepared by the transmetalation reaction between silylmercury and Li. The requisite silylmercury may be prepared from the corresponding chlorosilane or hydrosilane. The latter can be applied to the synthesis of polysilanyllithium. Equation (17) is an example.[11]

$$(Me_3SiSiMe_2)_2Hg \xrightarrow{2Li} 2Me_3SiSiMe_2Li \quad (17)$$

Diethylamino-substituted silyllithium is prepared successfully and used for the preparation of silicon-functional compounds (equation 18).[12]

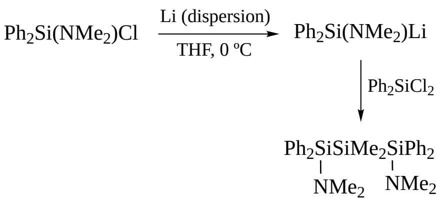

$$Ph_2Si(NMe_2)Cl \xrightarrow[\text{THF, 0 °C}]{\text{Li (dispersion)}} Ph_2Si(NMe_2)Li \xrightarrow{Ph_2SiCl_2} \underset{NMe_2}{Ph_2Si}SiMe_2\underset{NMe_2}{SiPh_2}$$

(18)

A combination of trimethylsilyllithium, MeMgBr, and a manganese salt is reported to be equivalent to $(Me_3Si)_2MnMe$ that shows an interesting reaction (equation 19). Further recent development on silyl anion chemistry will be described in Section 5.1.

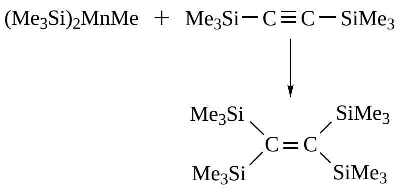

(19)

3.1.4 *Hydrosilation (Addition of Hydrosilane to Alkenes and Alkynes)*

Addition reactions of hydrosilanes to alkenes shown in the following general scheme are one of the most frequently utilized reactions for the preparation of organosilanes (equation 20).[13]

$$R_3SiH + R'CH{=}CH_2 \longrightarrow R_3SiCH_2CH_2R' \quad (20)$$

The reactions are further classified into three major categories: radical chain reactions, transition metal catalyzed reactions, and base-catalyzed reactions. In the radical chain reactions, dibenzoyl peroxide, di-t-butyl peroxide and α,α'-azobisisobutyronitrile (AIBN) are used most frequently as an

$$HSiCl_3 + In\cdot \longrightarrow Cl_3Si\cdot + InH$$

$$Cl_3Si\cdot + R{-}CH{=}CH_2 \longrightarrow R\dot{C}HCH_2SiCl_3$$

$$R\dot{C}HCH_2SiCl_3 + HSiCl_3 \longrightarrow RCH_2CH_2SiCl_3$$

Scheme 1

initiator. The characteristics of the reaction follow general free-radical reactions. Thus the regiochemistry of addition is an anti-Markovnikov fashion to produce the more stable radical. The trans-addition is generally observed for addition. Relative reactivity of hydrosilanes is determined by the polarity and bond dissociation energy of the Si–H bond. The order of the reactivity is: $HSiCl_3 > HSiRCl_2 > HSiR_2Cl > HSiR_3$. Reactive hydrosilanes such as $HSiCl_3$ are used most commonly (Scheme 1, and equations 21 and 22).

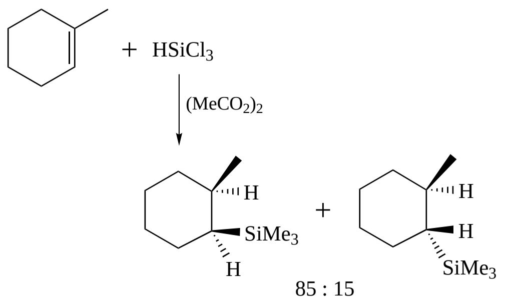

(21)

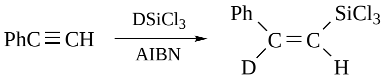

(22)

Hydrosilation reactions catalyzed by transition metal complexes have wide scope and applicability and hence used most conveniently for the silicon–carbon bond formation. Chloroplatinic acid, platinum on carbon or alumina, platinum(II) and platinum(0) complexes, $Co_2(CO)_8$, $NiCl_2{\cdot}(PPh_3)_2$ and $RhCl(PPh_3)_3$ are effective catalysts, among others. In particular, chloroplatinic acid, $H_2PtCl_6{\cdot}6H_2O$, known as Speier's catalyst, is the most commonly used and efficient catalyst, especially for the hydrosilation of alkenes. This catalyst, which is used as a solution in isopropyl alcohol, is quite efficient, only a minute amount in the range $10^{-5}–10^{-8}$ mole per mole of hydrosilane being necessary. Therefore the catalyst is not normally recovered from the product in the commercial process even though platinum is a precious metal. The Pt^0 catalyst, $Pt_2(H_2C{=}CSiMe_2OSiMe_2CH{=}CH_2)$, is also used extensively.

The reaction is also utilized for cross-linking between vinyl-substituted siloxanes and oligomeric hydrosilanes in the production of room-temperature vulcanizable silicone rubber. Reaction can be carried out without solvents, but common solvents such as benzene, toluene, dichloromethane, THF, and acetonitrile can be employed as well. A wide variety of 1-alkenes are hydrosilated regiospecifically to give the corresponding terminal addition products in high yields. Usually, reactions take place exothermically (equation 23).

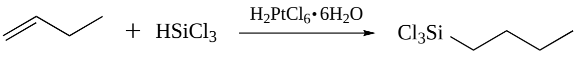

(23)

Regiospecificity of the reaction is normally high but with some alkenes, such as styrene, considerable amount of the β-isomer (38.5%) is produced exceptionally in addition to the α-isomer (58.7%). Interestingly, alkenes having an inner double bond undergo hydrosilation with isomerization to give exclusively terminal products, as shown in equation (24).

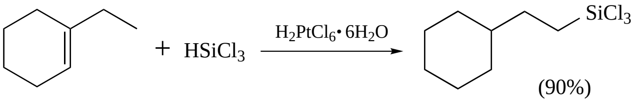

(24)

Isomerization does not take place on the products. No isomerization of alkenes occurs with the action of chloroplatinic acid alone, but recovered alkenes from a silane-alkene mixture often contain isomers of the alkene. D-H exchange is observed for the recovered hydrosilane from the hydrosilation mixture with $DSiCl_3$. These facts suggest the mechanism outlined in Scheme 2, which is known as the Chalk-Harrod mechanism.**[14]** The mechanism involves oxidative addition of hydrosilane to the active species of the catalyst, coordination of alkene, followed by $\sigma - \pi$ conversion, and reductive elimination of the product.

The Chalk-Harrod mechanism has been accepted for many years as a typical example of a homogeneous catalysis process. However, it has been recently suggested that the formation of colloidal platinum could be the key step in the action of Speier's catalyst.**[15]** Hydrosilation reactions with other catalysts such as $Co_2(CO)_8$, $NiCl_2(PPh_3)_2$, and $RhCl(PPh_3)_3$ are definitely homogeneous and probably follow the Chalk-Harrod mechanism. The step of reductive elimination is indicated to go with retention of configuration on carbon, the overall stereochemistry at silicon being also retention. Acetylenes gave syn addition products as shown in equations (22) and (25).

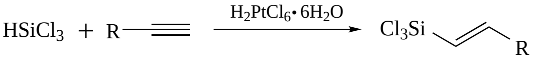

(25)

Alkenes with a variety of substituents such as acetal, amine, amide, carbamate, ester, ether, isocyanate, ketone, oxirane, and sulfide can be hydrosilated, usually without affecting the functional group. However, this is not always true; for example, allyl chloride gives a considerable amount of the reduction product (see equation 26). Table 4 lists representative examples of hydrosilation. It is not so remarkable in the case of radical hydrosilation, but reactivity is high for hydrosilane, which has electronegative group in the case of transition metal catalyzed hydrosilation.

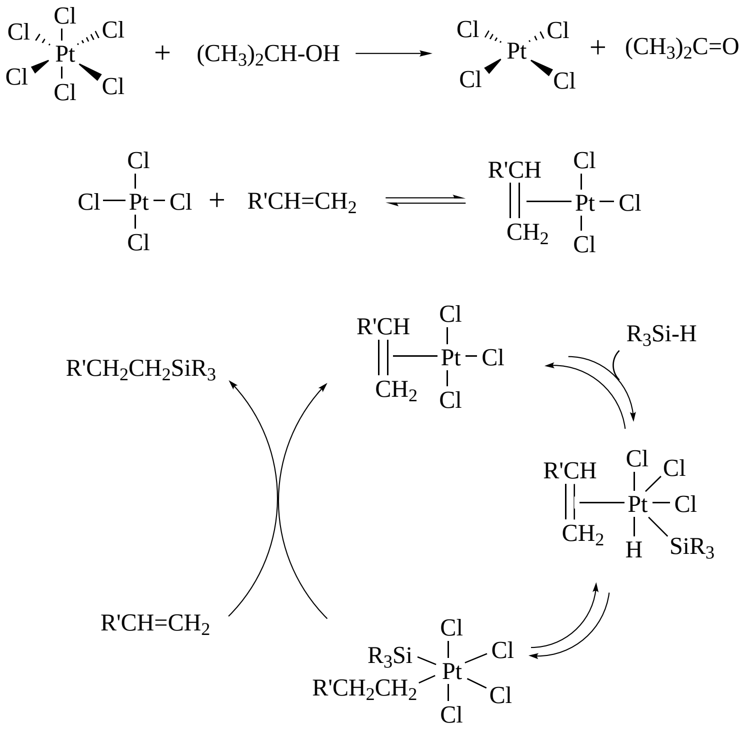

Scheme 2

Table 4 Hydrosilation of unsaturated compounds

Unsaturated compound	Hydrosilane	Catalyst	Product (% yield)
$CH_2{=}CH_2$	$HSiCl_3$	Pt/C	$CH_3CH_2SiCl_3$ (97)
$CH{\equiv}CH$	$HMeSiCl_2$	H_2PtCl_6	$MeCl_2SiCH{=}CH_2$ (81)
$CH_2{=}CHCN$	$HSiCl_3$	H_2PtCl_6	$Cl_3SiCH_2CH_2CN$ (99)
$CH_2{=}CHCH_2NO_2$	$HSiCl_3$	H_2PtCl_6	$Cl_3Si(CH_2)_3NO_2$ (92)
$CH_2{=}CH\,(CH_2)_2COMe$	$HMeSiCl_2$	H_2PtCl_6	$Cl_2MeSi(CH_2)_4COMe$ (84)
$CH_2{=}CHPh$	$HSiCl_3$	H_2PtCl_6	$Cl_3SiCH_2CH_2Ph$ (59) + $Cl_3SiCH(Me)Ph$(39)
$CH_2{=}CHCH{=}CH_2$	$HSiCl_3$	Pd + PPh_3	$MeCH{=}HCH_2SiCl_3$ (cis and trans, 94)
$CH_2{=}CHOPh$	$HEtSiCl_2$	H_2PtCl_6	$Cl_2EtSi(CH_2)_2OPh$ (77)
$CH_2{=}CHSPh$	$HSiMeEt_2$	H_2PtCl_6	$EtMeSi(CH_2)_2SPh$ (30)
$CH_2{=}CHCH_2\,NH_2$	$HSiEt_3$	H_2PtCl_6	$Et_3Si(CH_2)_3\,NH_2$ (62)
$CH_2{=}CHCH_2OCH_2CH{-}CH_2O$	$HSi(OEt)_3$	H_2PtCl_6	$(EtO)_3SiCH_2CH_2CH_2OCH_2CH{-}CH_2O$ (100)

$$HSiCl_3 + CH_2{=}CHCH_2Cl \xrightarrow{H_2PtCl_6\cdot 6H_2O} Cl_3Si(CH_2)_3Cl + CH_2{=}CHCH_3 \qquad (26)$$

The $[2\sigma + 2\pi]$ addition reaction of disilanes and acetylenes is closely related to hydrosilation. The prototype of the reaction is shown in the next example (equation 27).[16,17] The cis addition is established similar to hydrosilation.

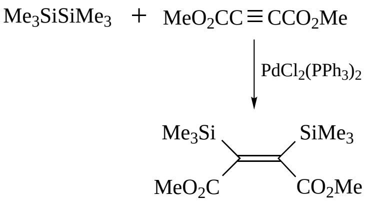

(27)

Base-catalyzed addition is almost limited to the addition of trichlorosilane to acrylonitrile. *t*-Amines and phosphines are used as catalysts (equation 28).

$$HSiCl_3 + CH_2{=}CHCN \xrightarrow{\text{base}} Cl_3SiCH_2CH_2CN \qquad (28)$$

3.1.5 *Condensation of Hydrosilanes with Hydrocarbons and Halogenated Hydrocarbons*

Trichlorosilane reacts with benzene in the vapor phase at 400–500 °C to give trichlorophenylsilane. Reaction temperature falls to 270–350 °C and yield improves by addition of a catalyst such as BF_3 and BCl_3 (equation 29).

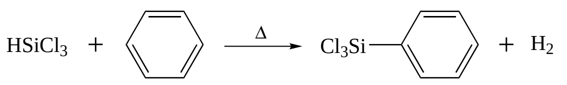

(29)

Under UV irradiation, Cl_2 catalyzes the reaction of trichlorosilane and benzene to give phenyltrichlorosilane in yield higher than 87%. The reaction of benzene with dichloromethylsilane gives $CH_3(C_6H_5)SiCl_2$ under the similar conditions in 65% yield. It is suggested that a radical process is involved in the reaction. Silation of aromatic compounds with well-defined silyl radicals generated in solution gives detailed information about the nature of homolytic aromatic silation.**[18]** It is noteworthy that the addition of silyl radicals to aromatics is a reversible process and therefore, product distribution depends on the reaction temperature**[19]** (Scheme 3).

Dehydrochlorinative coupling of hydrosilane with aryl or alkenyl chloride is utilized in the industrial synthesis of trichlorophenylsilane, methyldichlorophenylsilane, trichlorovinylsilane, and dichloromethylvinylsilane (equations 30 and 31). These reactions are usually carried out in the vapor phase at high temperature and accompanied by side reactions such as redistribution and reduction.

$$\mathrm{HSiCl_3 + C_6H_5Cl \xrightarrow{500-600\,^{\circ}C} C_6H_5SiCl_3 + HCl} \qquad (30)$$

$$\mathrm{HSiCl_3 + CH_2{=}CHCl \xrightarrow{500-600\,^{\circ}C} CH_2{=}CHSiCl_3 + HCl} \qquad (31)$$

The reaction of 2-chloropropene, trichlorosilane, and amine in the presence of a catalytic amount of copper(1) chloride proceeds smoothly under mild conditions to give allyltrichlorosilane in high yield**[20]** (equation 32).

$$\mathrm{HSiCl_3 + CH_2{=}CHCH_2Cl \xrightarrow[R_3N]{CuCl} CH_2{=}CH_2CHSiCl_3} \qquad (32)$$

3.1.6 Other Reactions

A variety of reactions generate new silicon–carbon bonds, although most of them are not utilized in the systematic synthesis of organosilicon compounds. Representative and interesting examples are shown in the following.

(Chloromethyl)trichlorosilane is formed in 60% yield by the reaction of tetrachlorosilane and diazomethane in ether at low temperature (equation 33).

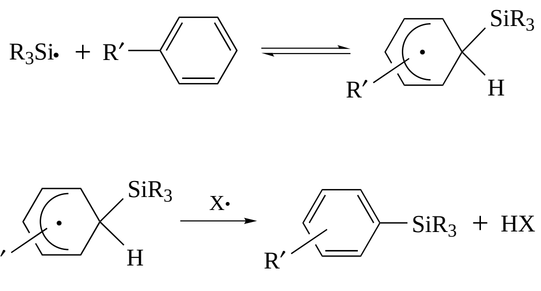

Scheme 3

$$\mathrm{SiCl_4 + CH_2N_2 \longrightarrow Cl_3SiCH_2Cl + N_2} \qquad (33)$$

Second and third methylenations are possible but with increasing difficulty. The reaction of trialkylsilane with a Simmons-Smith reagent gave the methylenation product. The reactivity of tri-n-butylsilane toward iodomethylzinc iodide is much higher than cyclohexene. Indeed, trialkytsilanes are good trapping reagents for divalent species such as carbene and silylene (equations 34 and 35).

$$\mathrm{Et_3SiH + ICH_2ZnI \longrightarrow Et_3SiCH_3 + ZnI_2} \qquad (34)$$

$$\mathrm{Me_2Si\colon + Et_3Si\text{-}H \longrightarrow Et_3Si\text{–}SiMe_2\text{–}H} \qquad (35)$$

Methylene insertion into a silicon–silicon bond is also possible for a reactive Si–Si bond (equation 36). Insertion reactions of divalent silicon species, silylene, also occur to the same substrate. Silylene forms a new silicon–carbon bond with a variety of substrates, which will be described later.

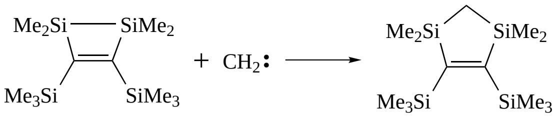

(36)

3.2 Synthesis of Silicon-functionalized Silanes by Cleavage of the Silicon–Carbon Bond

Silicon–carbon bonds are cleaved by the action of various reagents, and electronegative groups such as halogen and alkoxy are introduced into the silicon part. Therefore these reactions are utilized for introduction of functionality into silicon. Cleavage of the Ar–Si bonds is simple with electrophilic reagents. Halodesilation is important for the preparation of chlorosilanes (equation 37).

$$\mathrm{Ph_3SiLi + Me_3SiCl \longrightarrow Ph_3SiSiMe_3 \xrightarrow{HCl/AlCl_3} Cl_3SiSiMe_3} \qquad (37)$$

Arylsilanes undergo ipso-desilylation by electrophilic attack with E–Nu to give Ar–E and Nu–SiR_3. The reaction is useful for the preparation of both aryl derivatives and silicon-functionalized silanes (equation 38).

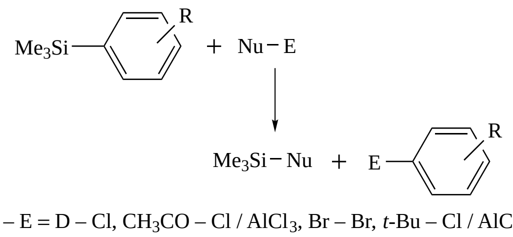

(38)

Nu – E = D – Cl, CH_3CO – Cl / $AlCl_3$, Br – Br, *t*-Bu – Cl / $AlCl_3$, NO_2 – OH / Ac_2O, etc

The chlorodemethylation reaction with a 1:1 mixture of acetyl chloride and aluminum chloride is a standard procedure for the preparation of chlorosilanes in the laboratory (equation 39).

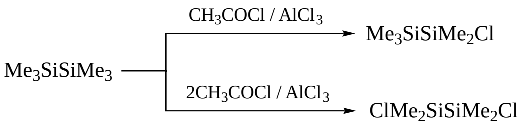

$$Me_3SiSiMe_3 \xrightarrow{CH_3COCl\,/\,AlCl_3} Me_3SiSiMe_2Cl \qquad Me_3SiSiMe_3 \xrightarrow{2CH_3COCl\,/\,AlCl_3} ClMe_2SiSiMe_2Cl \tag{39}$$

In the presence of a catalytic amount of aluminum chloride, hydrogen chloride, or trimethylchlorosilane also undergoes cleavage of the Si–C bond. The latter is an example of a redistribution reaction (equation 40). Facile cleavage of the allyl-silicon bond has been utilized for the preparation of iodotrimethylsilane (equation 41).**[21]**

$$Me_3SiSiMe_3 + Me_3SiCl \xrightarrow{AlCl_3} Me_3SiSiMe_2Cl + Me_4Si \tag{40}$$

$$CH_2{=}CHCH_2SiMe_3 + I_2 \longrightarrow CH_2{=}CHCH_2I + Me_3SiI \tag{41}$$

The silicon–carbon bond can also be cleaved by strong nucleophiles to give the corresponding carbanions, which may be utilized as the source of carbon nucleophiles in synthesis (equations 42 and 43).

$$(Me_3Si)_2CH_2 + NaOMe \xrightarrow{HMPA} Me_3SiCH_2{}^-Na^+ + Me_3SiOMe \tag{42}$$

$$CH_2{=}CHCH_2SiMe_3 + F^- \longrightarrow CH_2{=}CHCH_2{}^- + Me_3SiF \tag{43}$$

3.3 Synthesis of Silicon-functional Silanes by the Substitution Reactions on Silicon

Silicon centers having electronegative group(s) (leaving group(s)) receive nucleophilic attack easily to give the substitution products. Chloro, alkoxy, and sometimes hydride groups are common leaving groups on silicon. Substitution reactions with carbon nucleophiles serve for the formation of carbon–silicon bonds as described in Section 3.1.2. These reactions are mechanistically related to the corresponding reactions at the carbon center, so that S_N1 and S_N2 notations are frequently used also for the reaction at silicon center. However, rigorously speaking, it should be noted that S_N reactions are defined to the carbon centers. Accordingly, for example, the reaction of Me_3SiCl with $PhCH_2Li$ to give Me_3SiCH_2Ph should be designated as the S_E reaction at the carbon center. It is convenient, however, to assign this reaction as S_N2 at the silicon center. To give a clear and accurate explanation, these reactions may be designated as $S_N2(Si)$ or S_N2-Si. Hydrosilanes also undergo radical chlorination (equation 45). Mechanism and reactive intermediates of these reactions will be described later; here, synthetically useful examples are listed (equations 44–52).

$$Et_3SiCl \xrightarrow{LiAlH_4} Et_3SiH \tag{44}$$

$$R_3SiH + CCl_4 \xrightarrow{(PhCO_2)_2} R_3SiCl + CHCl_3 \tag{45}$$

$$Et_3SiH + I_2 \longrightarrow Et_3SiI + HI \tag{46}$$

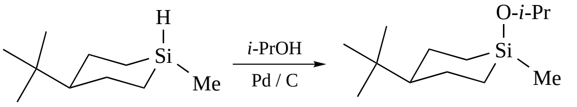

(47)

$$Me_3SiCl + H_2O \longrightarrow Me_3SiOH + HCl \tag{48}$$

$$Ph_2Si(OEt)_2 + 2PhCOCl \longrightarrow Ph_2SiCl_2 + 2PhCO_2Et \tag{49}$$

$$Me_3SiCl + 3NH_3 \longrightarrow Me_3SiNHSiMe_3 + 2NH_4Cl \tag{50}$$

$$Me_3SiCl + AgCN \longrightarrow Me_3SiCN + AgCl \tag{51}$$

$$MePhSiCl_2 + 2MeOH \longrightarrow MePhSi(OMe)_2 + 2HCl \tag{52}$$

3.4 Preparation of Carbon Functional Silanes

Carbon functional silanes are compounds having substituent(s) with functional group(s) on carbon(s). Me_3SiCH_2Cl, $Me_3SiCH_2CH_2CH_2\ NH_2$, and $Ph_3SiCOPh$ are examples. Preparations of these compounds are classified in two ways: (1) introduction of an organic group with functional group(s) to the silicon center, and (2) introduction of functional group(s) to a hydrocarbon substituent of silanes. The former is typically shown in the next two examples. In principle, any group can be introduced into the silicon center, provided that the corresponding lithium or Grignard reagents can be derived for those groups (equations 53 and 54).

$$MeOCH_2CH_2CH_2MgCl + Me_3SiCl \longrightarrow MeOCH_2CH_2CH_2SiMe_3 \tag{53}$$

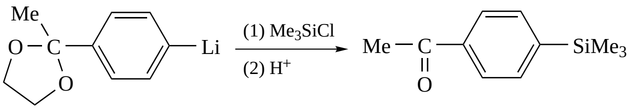

(54)

The latter is essentially an organic transformation, and all the known reactions can be applied. However, one should bear in mind that the elimination reaction involving the organosilyl group is rather facile with both strong electrophiles and nucleophiles and that the trialkylsilyl group exerts specific electronic effects, which will be described later.

3.5 Silicon–Silicon Bond Formation

The formation of the Si–Si bond occupies a special position in organosilicon chemistry. Silicon is one of the few elements, which can form stable catenated compounds. Besides high-molecular weight polysilanes, oligomeric polysilanes are a very important class of compounds that are related to silylenes,

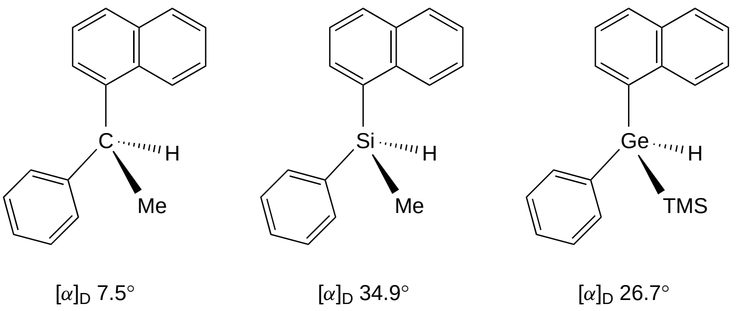

Figure 1 Isoconfigurational series

organosilylmetals, silicon–silicon double-bonded species, and photochemistry.

Wurtz coupling reactions of chlorosilanes are the main route to the silicon–silicon bonded compounds. For example, hexamethyldisilane can be prepared by refluxing trimethylchlorosilane with lithium sand in THF (97%). Lithium may be substituted by sodium by using a mixture of HMPA–THF as the solvent. Linear and branched oligosilanes can be prepared by the same method (equations 55–57).

$$2Me_3SiCl + 2Li \xrightarrow[THF]{} Me_3SiSiMe_3 + 2LiCl \qquad (55)$$

$$4Me_3SiCl + SiCl_4 \xrightarrow[THF]{Li} (Me_3Si)_4Si \qquad (56)$$

$$Me_3SiCl + n\ Me_2SiCl_2 \xrightarrow[THF]{Li} Me_3Si(Me_2Si)_nSiMe_3 \qquad (57)$$

The intermediate of the reaction may be the silyl-alkali metal species, so that the reaction of the silyl-alkali metal derivatives with chlorosilane resulted in the formation of the silicon–silicon bonded compound (equation 58).

$$Ph_3SiLi + Me_3SiCl \longrightarrow Ph_3SiSiMe_3 + LiCl \qquad (58)$$

Silylene insertion into the Si–H bond as well as silylene insertion into the Si–Si bond forms new silicon–silicon bonds (equations 59 and 60).

$$Et_3SiH + Me_2Si\colon \longrightarrow Et_3SiSiMe_2H \qquad (59)$$

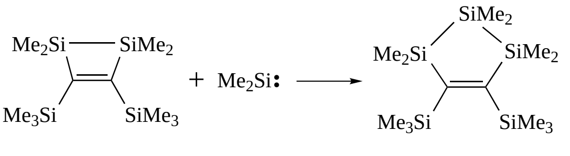

(60)

Finally, the coupling reaction of two silyl radicals gives the corresponding disilane. In this respect, mercury sensitized dehydrogenative coupling of hydrosilane is noteworthy. Other methods of forming polysilanes, related to the formation of high-molecular weight polysilanes, will be described later.

4 STRUCTURE AND BONDING

4.1 Tetrahedral Compounds

The geometry of most organosilanes is tetrahedral using the sp^3 hybridized orbitals on silicon. Like carbon, optically active silanes are possible when central chirality exists. A series of monofunctional optically active silanes can be prepared and used for stereochemical studies. These are the methyl(naphthyl)phenylsilyl derivatives, which are commonly abbreviated to R_3Si^*X.[22] Together with the similar germanium compound, the isoconfigurational series of compounds are shown in Figure 1.

4.2 Penta- and Hexacoordination

Contrary to carbon, silicon can form penta- or hexacoordinated compounds. The formation of such higher coordinated silicon compounds is frequently explained in terms of incorporation of d orbitals to form either sp^3d or sp^3d^2. However, a three-center four-electron bond can also describe the bonding. Both descriptions require electronegative substituents for stable complexes. Indeed, higher coordinated silicon compounds are made with electronegative substituents such as Cl, F, NR_2, and RO (Figure 2).

Electronegative atoms adjacent to silicon would contract the d orbitals and transfer electrons to form a dative bond. This concept is called $p\pi$-$d\pi$ or (p-d)π bonding (*see* $p_\pi - d_\pi$ *Bonding*) and has been used to explain a number of unique

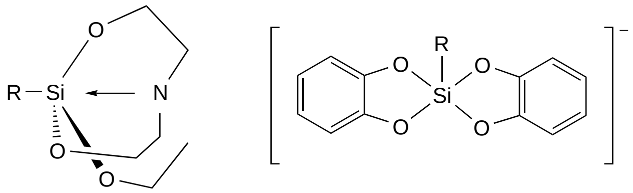

$[CH_2{=}CH\text{-}CH_2\text{-}SiF_4]^-$ $[C_6H_5SiF_5]^{2-}$

Figure 2 Penta- and hexacoordinated silicon compounds

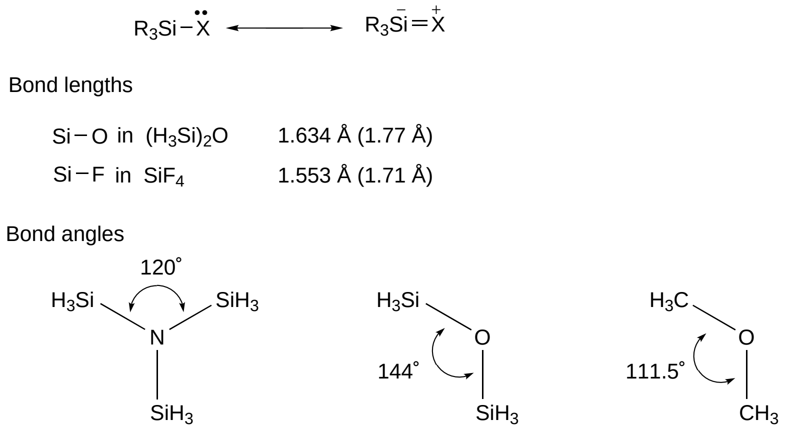

Figure 3 Examples of anomalous bond lengths and angles. Numbers in parentheses are calculated values

structural features such as shorter experimental bond lengths than calculated for Si–O and Si–F, planarity about nitrogen of $(H_3Si)_3N$, and the wider bond angle of disilazane than dimethylamine.[23] However, there is controversy over the theoretical proposals of (p-d)π bonding. The shorter bond lengths of silicon to electronegative elements may be explained by a larger contribution of ionic structures such as R_3Si^+ X^-. Thus contribution of $\sigma^*-\pi$ conjugation may also be significant (Figure 3), as will be described later.

4.3 σ–π Conjugation

Organosilicon reactions, which involve carbenium ion formation or development β to silicon, are much accelerated (β effect). This substituent effect of the silyl group is referred as hyperconjugation or $\sigma-\pi$ conjugation. This effect is extremely important in controlling the regiochemistry and reactivity in a number of reactions in which a positive charge is developing. Reactions of allylsilanes are typical examples and are used extensively in organic synthesis (Scheme 4).[24]

The $\sigma-\pi$ conjugation effect is spectroscopically best documented in a number of compounds such as allylic and benzylic silanes. The following examples demonstrate the effect most convincingly. Thus ionization potentials (IP) of 1-trimethylsilylindan, where $\sigma-\pi$ conjugation due to the trimethylsilyl group is possible, is lower than that of 2-silaindan in which the carbon–silicon bond is placed in the π nodal plane and hence $\sigma-\pi$ conjugation is impossible (Figure 4).

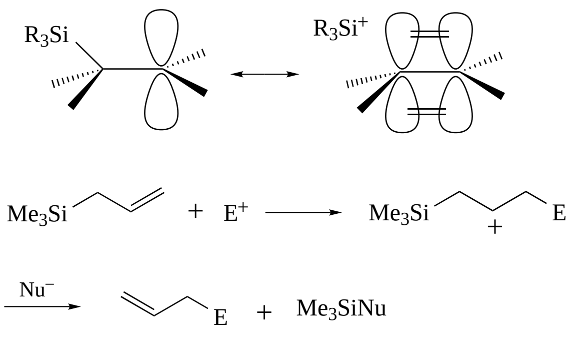

Scheme 4

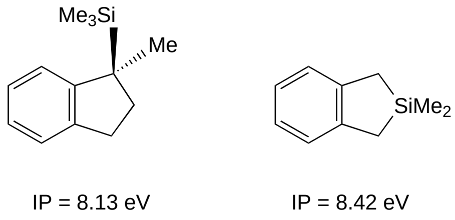

Figure 4 Stereoelectronic effect in $\sigma-\pi$ conjugation

The σ(Si–Si)-π conjugation is equally important. The effect was first evidenced by the discovery of unusually large bathochromic shifts in UV spectra of pentamethylvinyldisilane ($\lambda_{max} = 223\,nm$) and phenylpentamethyldisilane ($\lambda_{max} = 231\,nm$) compared with those of trimethylvinylsilane ($\lambda_{max} = 178\,nm$) and trimethylphenylsilane ($\lambda_{max} = 211\,nm$), respectively.[17,25] The importance of σ(Si–Si)-π conjugation has been demonstrated also in charge transfer and photoelectron spectra and finally confirmed by the stereoelectronic effect.[26] 1,1,2.2-Tetramethyl-3,4-benzo-1,2-disila-3-cyclopentene has both C–Si and Si–Si bonds in the nodal plane of the π system, so that no $\sigma-\pi$ conjugation is possible. Indeed, the characteristic ^1L_a band of Ph–Si–Si at 231 nm disappeared (Figure 5).

4.4 σ^*–π Conjugation

Silicon can stabilize α-carbanions or polarized α-metalloids in spite of the electropositive nature of silicon. Such stabilization has been accounted for involving (p-d)π bonding.

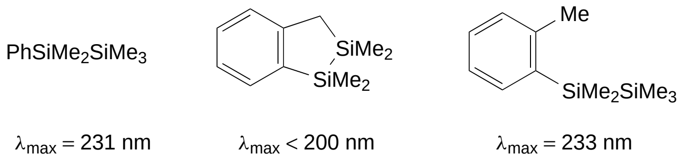

Figure 5 UV spectra of phenyldisilane derivatives showing σ(SiSi)$-\pi$ conjugation

However, more recently, stabilization for α-carbanions or polarized α-metalloids is explained in terms of the $\sigma^*-\pi$ conjugation (Scheme 5).

α-Carbanions or α-metalloids are important as a source of carbanions and are used frequently in organic synthesis (vide infra).

The trialkylsilyl group exerts effects to appropriately substituted π-electron systems in two ways as electron donor and acceptor. The R_3SiCH_2-group shows a strong electron-donating effect to the adjacent π-electron systems by the mechanism of σ(Si–C)-π hyperconjugation. For example, photoelectron spectroscopy indicated that the HOMO energy level of trimethylallylsilane was raised from ethylene. On the other hand, the trialkylsilyl group can behave as an electron acceptor to directly bonded π-electron systems owing to $\sigma^*-\pi$ conjugation. In planar silyl-substituted alkenes, no strong σ(Si–C)-π conjugation exists but a lowering effect to the LUMO was indicated by electron-transmission spectra for vinyltrimethylsilane.

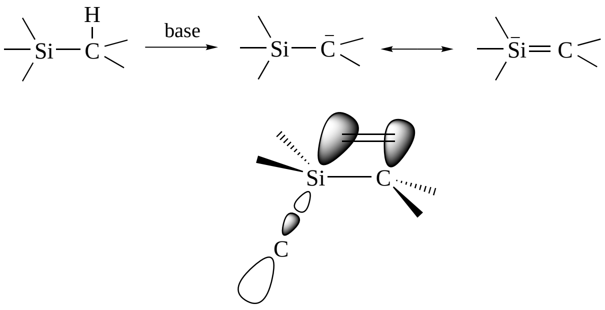

Scheme 5

Figure 6 shows relative orbital energies of trimethylvinylsilane and allyltrimethylsilane compared with ethylene.[27] The fact that IP of trimethylvinylsilane is lower than that of ethylene indicates the electron-donating effect of the trialkylsilyl group that is due to the lower electronegativity of silicon than carbon. But at the same time, the LUMO of trimethylvinylsilane is lowered. The HOMO of allyltrimethylsilane is raised relative to ethylene. These facts give the grounds that trimethylvinylsilane is susceptible to nucleophilic attack, whereas allyltrimethylsilane is reactive towards electrophiles.

The steric effect of the trimethylsilyl group is rather small when it stands singly but the cumulative steric effects should

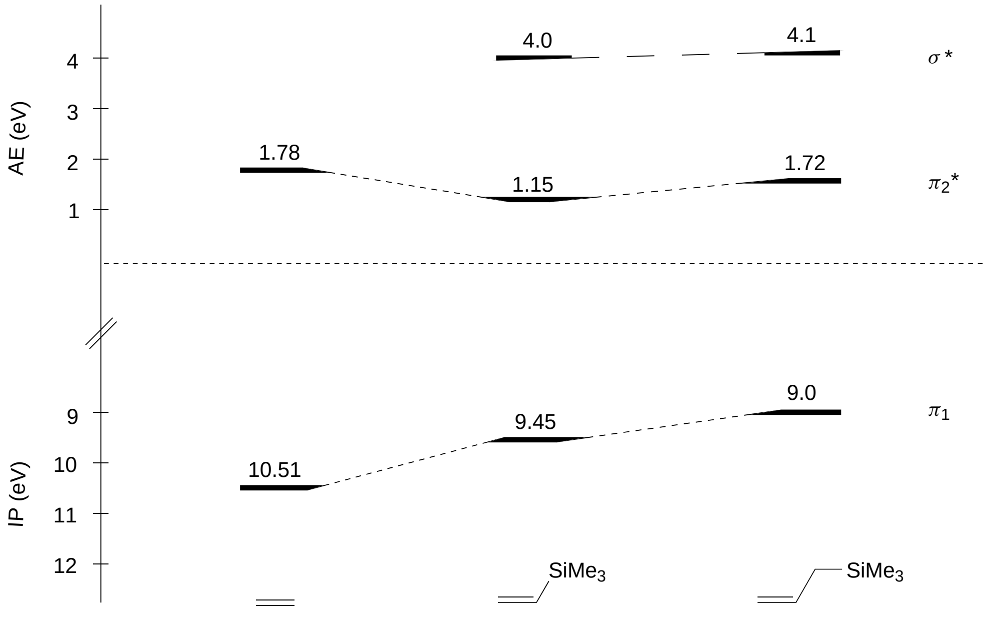

Figure 6 Relative HOMO–LUMO ievels determined by ionization energy (lP) andattachment energy (AE)

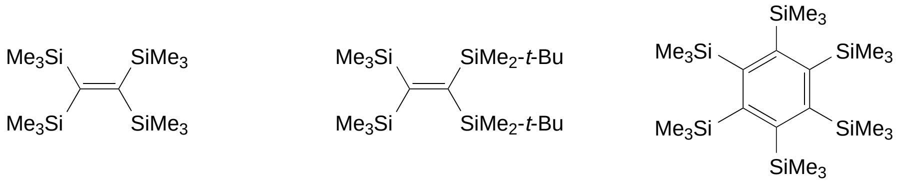
Double bond is twisted by 29.5°. Double bond is twisted by 49.6°. Boat form benzene

Figure 7 Over-crowded π-electron systems

be very large when the trimethylsilyl group substitutes the molecule extensively. Both tetrakis(trimethylsilyl)ethylene[28] and hexakis(trimethylsilyl)benzene[29] cannot maintain the π-systems planar to show interesting chemical and physical properties. Olefinic carbons of both tetrakis(trimethylsilyl)ethylene and 1,1-bis(t-butyldimethylsilyl)-bis(trimethylsilyl)ethylene are strictly coplanar with silicon substituents but twist of double bonds are 29.5° and 49.6°, respectively. These are most twisted olefins. Hexakis(trimethylsilyl)benzene is a boat-form benzene and undergoes facile isomerization (Figure 7).

4.5 Bond Lengths and Bond Energies

Table 5 lists selected bond lengths of tetracoordinated silicon-element and the corresponding carbon-element bonds. As noted before, the bond lengths for silicon bonded to elements more electronegative than carbon tend to be shorter than the calculated values.

Bond lengths of silicon can also be affected by the coordination number of the compound to some extent. The representative values are listed in Table 6. All the Si–X bonds become longer in higher coordinated states.

Selected bond dissociation energies are compiled in Table 7. Although bond lengths of silicon compounds are longer than the corresponding carbon compounds, silicon forms stronger bonds than carbon.[30]

5 REACTIONS AND REACTIVE INTERMEDIATES

Organosilicon compounds receive attack of nucleophilic, electrophilic, and homolytic reagents. The latter is related to the formation of radicals and divalent species. Organosilicon reactive intermediates corresponding to free radicals, carbenium ions, carbanions, and carbenes play important roles in these reactions. These are silyl radicals,[31] silylium

Table 5 Selected bond lengths for Si–X and C–X

Bond	Bond length (Å)	Bond	Bond length (Å)
$D_3Si–H$	1.48	$D_3C–H$	1.09
$H_3Si–CH_3$	1.87	$H_3C–CH_3$	1.53
$H_3Si–N(SiH_3)_2$	1.74	$H_3C–NH_2$	1.47
$H_3Si–OSiH_3$	1.63	$H_3C–OH$	1.4l
$H_3Si–F$	1.59	$H_3C–F$	1.38
$H_3Si–SiH_3$	2.33	$H_3C–SiH_3$	1.87
$H_3Si–PH_2$	2.25	$H_3C–PH_2$	1.86
$H_3Si–SSiH_3$	2.14	$H_3C–SH$	1.82
$H_3Si–Cl$	2.05	$H_3C–Cl$	1.78
$H_3Si–Br$	2.21	$H_3C–Br$	1.94
$H_3Si–I$	2.44	$H_3C–I$	2.14

Table 6 Selected Si–X bond lengths at different coordination numbers

Coordination number	Bond					
	Si–C	Si–N	Si–O	Si–F	Si–Si	Si–Cl
4	1.872	1.721	1.610	1.500	2.391	2.026
5	1.973	1.823	1.711	1.602	2.492	2.128
6	2.056	1.906	1.794	1.685	2.576	2.21l

Table 7 Selected bond dissociation energies of Si–X and C–X

X	Me_3Si–X	Me_3C–X	X	H_3Si–X	H_3C–X
H	90.3	92	H	90.3	105
CH_3	89.4	82	CH_3	82.1	90.4
$NHCH_3$	100	80	NH_2	(98.7)	84.9
OH	128	91	OH	108	92.3
F	(160)	104	F	135	109.9
$SiMe_3$	80.5	–	SiH_3	74	82.1
SBu	99	71	SH	70	74
Cl	113	80	Cl	91	84.6

ions,[32] silyl anions,[33] and silylenes.[34] Reaction patterns and reactivities of these reactive intermediates largely resemble those of carbon intermediates. The stereochemistry and mechanism of substitution reactions at silicon can be compared with those at carbon but are much more complicated.

5.1 Ionic Reactions

Silylium ions or silico cations are formed more readily than carbenium ions in the vapor phase by electron impact, as evidenced by the fact that the base peak of the mass spectra of trimethylsilyl derivatives is almost always the trimethylsilylium. This means that silicon can support a positive charge more strongly than carbon owing to its more electropositive nature. However, there is too little evidence of the formation of trivalent silylium ions in solution. Two factors may account for the facts: the counter anions normally used to the stabilized carbenium ions (such as perchlorate and tetrafluoroborate) bind to silicon strongly (silicophilic), and bond lengths of silicon and substituents are 1.5 times longer than those of the corresponding carbon compounds, so that the requisite steric congestion for the $S_N1(Si)$ over the $S_N2(Si)$ mechanism is lacking. A recent study shows that the attempted generation of silylium ions with nonnucleophilic borate counter anions resulted in the formation of silylium ion-solvent complexes. However, these results do not exclude the generation of 'free' silylium ions under proper conditions. Indeed, the crystal structure of Et_3Si^+ BAr_4 (Ar=C_6F_5) has been determined, where the interaction of the 'silylium ion' with the solvent toluene is minimal (equation 61).[35]

$$R_3SiH + Ph_3C^+BAr_4^- \xrightarrow{Ph_3CH} [R_3SiOEt_2]^+BAr_4^- \qquad (61)$$

A solvent-free but delocalized silylium ion has been prepared recently.[36] Interestingly, the silylium ion undergoes reversible redox reaction to give the corresponding radical and anion (equation 62).[37] The silylium ion is indicated to be a homotrisilacyclopropenium ion. In fact, 1,3-length of the silylium ion is much shorter than that of the corresponding radical.[38]

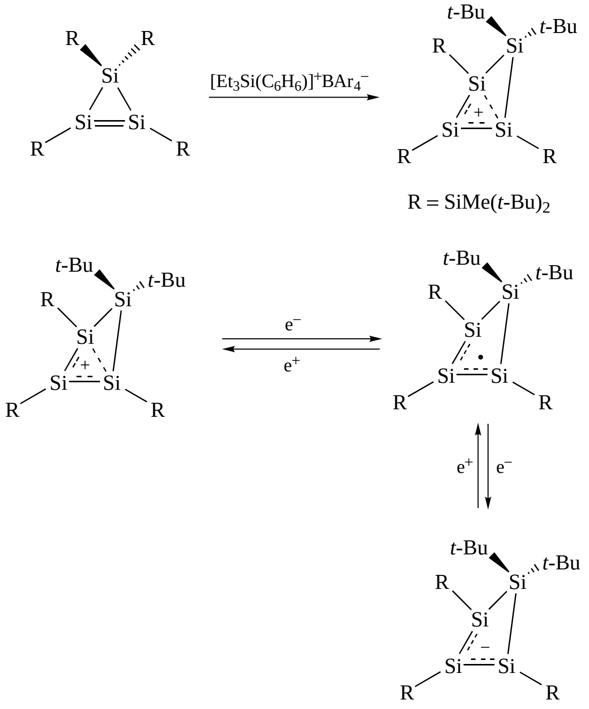

(62)

With a bulkier substituent (2,4,6-trimethylphenyl = Mes), Mes_3Si^+ $B(C_6F_5)_3$ is indicated as an isolated silylium in solution[39] and very recently the cation is proved to be a completely free silylenium ion (equation 63).[40]

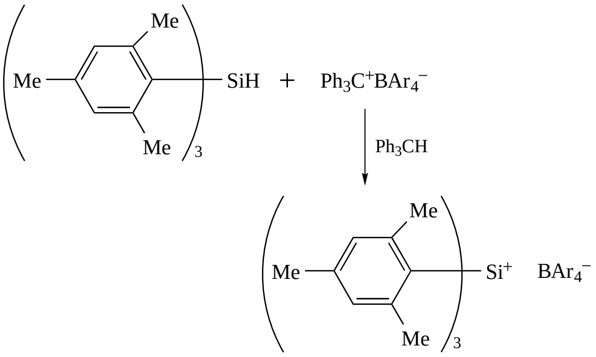

(63)

The $S_N2(Si)$ mechanism at silicon is quite common. However, the fundamental difference between carbon and silicon in the S_N2 mechanism is the fact that the pentacoordinate structure with attacking and leaving nucleophiles is not the transition state but an intermediate in silicon, contrary to carbon. In fact, in some cases, stable silicon compounds with the pentacoordinate structure can be isolated (see Figure 2). This fact is mainly due to the longer bond lengths of silicon compounds, where five ligands can be accommodated around the silicon atom.[41] Existence of stable pentacoordinate intermediates makes the stereochemistry of $S_N2(Si)$ reactions very complicated; not all S_N2 reactions at silicon occur with inversion, while at carbon inversion of the configuration is observed without exception. Thus, the larger size of silicon compared with carbon permits the attack of nucleophiles (*see Nucleophile*) from different directions, not only from the back side to result in inversion but from the flank side to give the retention product (Table 8).

Generally speaking,[42] reactions of silicon compounds with poor leaving groups such as H and OR result in retention of configuration. Inversion occurs only with strongly charge-delocalized reagents such as Ph_2CHLi (soft nucleophiles), whereas with a good leaving groups like Cl or Br, inversion is observed. The leaving groups F and SR show intermediate behavior, leading to either inversion or retention according to the attacking nucleophiles: inversion with allyllithium, benzyllithium, and $LiAlH_4$ (soft nucleophiles), but retention with alkyllithium and alkoxides (hard nucleophiles) (Hard & Soft Acid-base Theory).

The results are best explained in terms of interaction between the HOMO of the nucleophile and the LUMO of the substrate.[43] As shown in Figure 8, the flank-side attack to give the retention product corresponds to the interaction of the nucleophile with the large lobe on silicon. This attack corresponds, at the same time, to interaction with the orbital of the leaving group in an unfavorable out-of-phase fashion. The back-side attack with inversion involves interaction with the small lobe on silicon but no out-of-phase interaction. Determination of the stereochemistry depends on the equilibrium between these two directions. Hard nucleophiles have small, contracted, and high lying valence orbitals, so that overlap with the orbital of the leaving group

Table 8 Stereochemical behavior of $R_3Si^*–X$ in the reaction with nucleophiles

X	Nucleophile (solvent)	Product	Stereochemistry[a]
H	KOH (xylene)	$R_3Si^*–OK$	RN
	RLi (R = Me, Bu, THF)	$R_3Si^*–R$	RN
	Ph_2CHLi	$R_3Si^*–CHPh_2$	IN
OMe	RLi (R = Me, Bu)	$R_3Si^*–R$	RN
	Ph_2CHLi	$R_3Si^*–CHPh_2$	IN
Cl (Br, I)	RLi (THF)	$R_3Si^*–R$	IN
	RCOOH (Et_2O)	$R_3Si^*–OOCR$	IN
	H_2O	$R_3Si^*–OH$	IN
F	$LiAlH_4$ (Et_2O)	$R_3Si^*–H$	IN
	RLi (R = Me, Bu)	$R_3Si^*–R$	RN
	$PhCH_2Li$	$R_3Si^*–CH_2Ph$	IN
SMe	$LiAlH_4$ (Et_2O)	$R_3Si^*–H$	IN
	RLi (R = Me, Bu)	$R_3Si^*–R$	RN
	$PhCH_2Li$	$R_3Si^*–CH_2Ph$	IN

[a] RN = retention, IN = inversion.

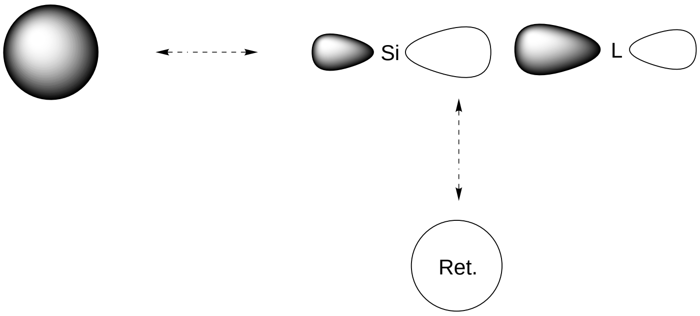

Figure 8 Frontier orbital interactions at S_N2 reactions of silicon

is very small to result in the flank-side attack. On the other hand, soft nucleophiles have usually large, diffused, low-lying delocalized orbitals, which may interact equally with orbitals of substrate and leaving group when the flank-side attack occurs. Therefore the back-side attack predominates to favor inversion products.

Silyl anions (silyl-alkali metal derivatives) have been prepared as described in equations (15–17). Reactions of triphenylsilyl anions with electrophiles give the expected products.[44] Silyl anions have a considerable configurational stability (equation 64).

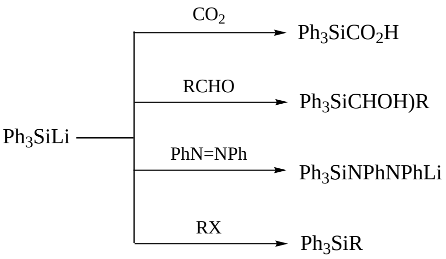

(64)

Trimethylsilyl anions also give the substitution products by the reaction with alkyl chloride in almost quantitative yield (equation 14), but considerable amounts of electron-transfer products are produced as well in HMPA. Indeed, Me_3SiNa/HMPA is an excellent reagent to produce anion radicals (Table 9) from aromatic hydrocarbons for ESR (electron spin resonance) studies (equation 65).[45]

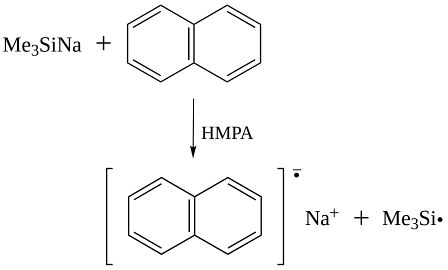

(65)

Silyllithium forms polymeric structures in the solid state, the structure being dependent on the nature of the silyl group. Trimethylsilyllithium is hexameric with a Li_6 skeleton of a highly folded chair in the solid state.[46] Pentamethyldisilanyllithium is tetrameric with a tetrahedral Li_4 skeleton. Four pentamethyldisilanyl groups occupy the center of the face to interact with three lithium atoms.[47] The structure of non-solvated monomeric silyllithium, $(t\text{-}Bu_2MeSi)_3SiLi$, is nearly planar. The Si–Si bond lengths are significantly shortened (av. 2.3632 Å) relative to those of $(t\text{-}Bu_2MeSi)_3SiH$ (av. 2.450 Å), indicating the existence of hyperconjugation between the central anionic p orbital and adjacent Si–Cσ*-orbitals.[48] Probably, this is also the origin of planarity of the silyl anion similar to the case of trisilylamine.

Silicon-functional silyllithium should be interesting intermediates to a variety of silicon-functional compounds. Chlorine substituted silyllithium is unstable to undergo α-elimination to give silylenes. Alkoxy-substituted silyllithium may be generated *in situ* reaction conditions and undergoes useful substitution reaction (equation 66).[49]

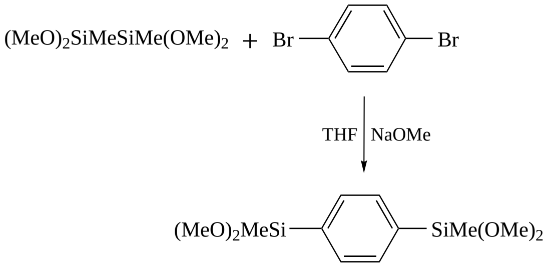

(66)

Diethylamino-substituted silyllithium is much more stable and useful for the preparation of silicon-functional compounds as described before (equation 18).

1,2-Dilithiosilanes have been known.[50] 1,1-Dilithiosilanes are interesting species and silole dianion was first reported.[51]

Table 9 ESR parameters for silyl radicals[31,55,57]

		Coupling constants (mT)			
Radical	g value	α-H	β-H	γ-H	^{29}Si
$H_3Si\cdot$	2.0032	0.784			19.0
$MeH_2Si\cdot$	2.0032	1.211	0.821		18.1
$Me_2HSi\cdot$	2.0031	1.729	0.730		18.3
$Me_3Si\cdot$	2.0031		0.634		18.3
$Et_3Si\cdot$	2.0030		0.569	0.016	
$Me_3SiSiMe_2\cdot$	2.0037		0.821	0.047	13.7
$Me_3SiSiMeH\cdot$	2.0037	1.630	0.815	0.030	
$(Me_3Si)_2SiMe\cdot$	2.0045		0.936	0.047	7.1
$(Me_3Si)_3Si\cdot$	2.0050			0.044	6.5
$(Et_3Si)_3Si\cdot$	2.0063				5.72
$(i\text{-}Pr_3Si)_3Si\cdot$	2.0061				5.56
$(t\text{-}Bu_2MeSi)_3Si$	2.0056				5.80

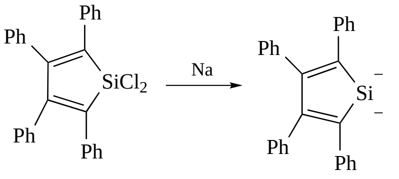

(67)

1,1-Dilithiosilanes with bulky substituents such as Tbt(Dip)$SiLi_2$ (Tbt = 2,4,6-tris[bis(trimethylsilyl)methyl] phenyl, Dip = 2,6-diisopropylphenyl)[52] and $(i\text{-}Pr_3Si)_2SiLi_2$[53] have been reported recently.

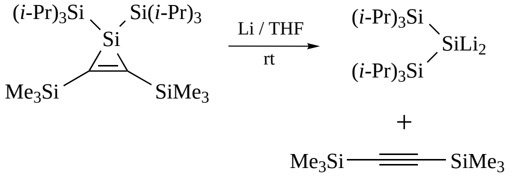

(68)

5.2 Homolytic Reactions (Silyl Radicals and Silylenes)

Silyl radicals can be generated most conveniently by hydrogen abstraction from the corresponding hydrosilane.[29]

$$R_3SiH + t\text{-}BuO\bullet \longrightarrow R_3Si\bullet + t\text{-}BuOH \qquad (69)$$

ESR spectra of several silyl radicals have been recorded and the ^{29}Si hyperfine coupling constants indicate that silyl radicals are nonplanar, contrary to organic radicals. Table 8 lists ESR data of representative silyl radicals. Comparison of ESR data of $Ar_3M\cdot$ (Ar = 3, 5-di-t-butylphenyl, M = C, Si, and Ge), which give relatively stable radicals, is interesting. The g values and hyperfine coupling constants, A_{o-H} and A_{p-H} (in Gauss), are as follows: $Ar_3C\cdot$ (−40 °C), 2.0026, 2.58, 2.80; $Ar_3Si\cdot$ (−50 °C), 2.0027, 0.95, 1.17; $Ar_3Ge\cdot$ (−70 °C), 2.0056, 0.60, 0.95. The spin densities at the central atoms of $Ar_3M\cdot$ are estimated to be 0.50 (M = C), 0.78 (M = Si), and 0.82 (M = Ge), indicating increasing nonplanarity with increasing localizing spin density on the central atom from carbon to germanium (equation 70).[54]

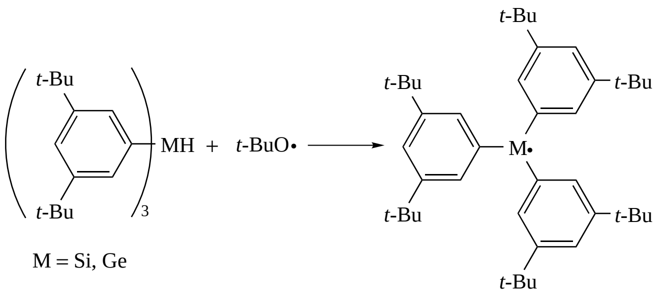

(70)

$$R_3Si\bullet + R'\text{-}Br \longrightarrow R_3SiBr + R'\bullet \qquad (71)$$

Generation of stable (persistent) silyl radicals has been an interesting target. $Ph_3Si\cdot$ is, contrary to $Ph_3C\cdot$, not persistent owing to longer Si–C bond lengths and tendency to undergo *ipso*-substitution. The trimesitylsilyl radical is fairly persistent to be able to observe good ESR spectra (equation 70). According to the general trick to elongate the lifetime of the free radicals, introduction of bulkier substituents produces longer-lived radicals such as triisopropylsilyl radical.[55] The $(t\text{-}BuMe_2Si)_3Si\cdot$ radical is shown to be much more persistent in solution[56] and finally $(t\text{-}Bu_2MeSi)_3Si\cdot$ has been isolated as a crystal.[57] The molecular structure is shown to be planar. One-electron oxidation of the corresponding silyl anion or one-electron reduction of the corresponding bromosilane is better than hydrogen abstraction to produce radicals because of lesser steric requirement in the reaction.

The reaction of silyl radicals with haloalkanes constitutes the H/halogen exchange reaction together with the hydrogen abstraction reaction (equations 69 and 71) but, alternatively, the reaction is also convenient for the production of alkyl radicals. A number of alkyl radicals have been generated and studied by ESR. Interestingly, the silyl radicals derived from an optically active hydrosilane undergo chlorine abstraction reaction mostly with retention of configuration.[58]

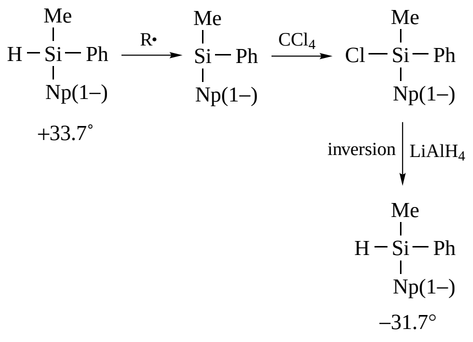

(72)

The configurational stability of the silyl radical may be best explained in terms of the pyramid structure and slower rate of inversion than abstraction of chlorine. The origin of the pyramidality of the silyl radical is the difference between electronegativities of central and substituent elements. This argument may be supported by the following evidence. Thus in the case of fluorinated methyl radicals, $\bullet CH_3$, $\bullet CH_2F$, $\bullet CHF_2$, and $\cdot CF_3$, structures change from planar to almost tetrahedral.[59] The planar structure (and low inversion barrier) of $(t\text{-}Bu_2MeSi)_3Si\cdot$ may depend on there being no difference in electronegativities between central and substituent elements. Delocalization of unpaired electron owing to σ^*-p conjugation should contribute to some extent. On this matter, it is noteworthy that chiral disilanyl radical undergoes chlorine abstraction from carbon tetrachloride with retention of configuration but in low optical yield.[60]

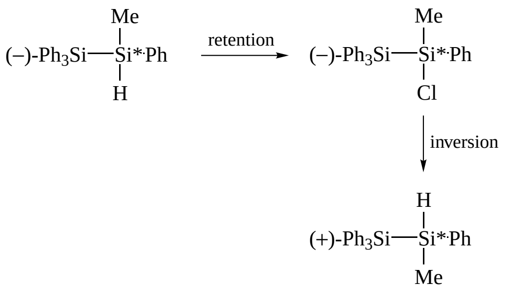
Me
(−)-Ph3Si—Si*Ph
H
retention
Me
(−)-Ph3Si—Si*Ph
Cl
inversion
H
(+)-Ph3Si—Si*Ph
Me

(73)

Addition of the silyl radical to carbon–carbon double bonds is an elementary reaction of radical hydrosilation (Scheme 1). Homolytic aromatic silation also occurs involving silyl radicals. Silyl radicals are nucleophilic owing to the high SOMO energy, as evidenced by the directive effects in the hemolytic aromatic substitution.[17,61] The intermediate cyclohexadienyl radicals have been observed by ESR.

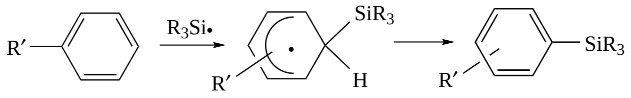
R′
R3Si•
SiR3
R′
H
SiR3
R′

(74)

Addition of the silyl radicals to carbonyl compounds occurs at the oxygen site (equations 75 and 76). The latter reaction is utilized also for spin trapping of silyl radicals (equation 76).

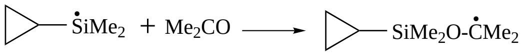
SiMe2
+ Me2CO
SiMe2O-CMe2

(75)

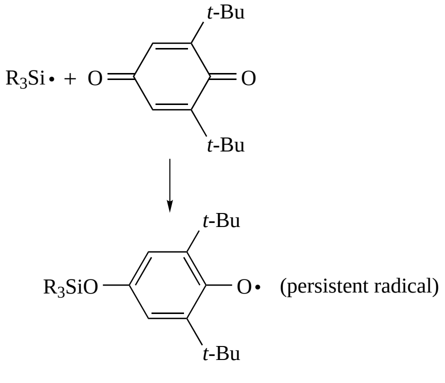
t-Bu
R3Si• + O
O
t-Bu
t-Bu
R3SiO
O•
(persistent radical)
t-Bu

(76)

Recently, radicals have increasingly been used in organic synthesis, especially for cyclization of alkenyl radicals generated from the corresponding halides. Tin hydrides have been used for this purpose before but $(Me_3Si)_3SiH$ is now used because it is environmentally safer.

Silylenes, the silicon analogs of carbenes, may be generated thermally[62] and photochemically[63] from appropriate polysilanes (equations 77 and 78).

$$MeOSiMe_2SiMe_2OMe \xrightarrow{\Delta} Me_2Si\colon + (MeO)_2SiMe_2 \qquad (77)$$

$$(SiMe_2)_6 \xrightarrow{h\nu} Me_2Si\colon + (SiMe_2)_5 \qquad (78)$$

Other important reactions for generating silylenes are shown in equations (79),[64] (80)[65] and (81).[66]

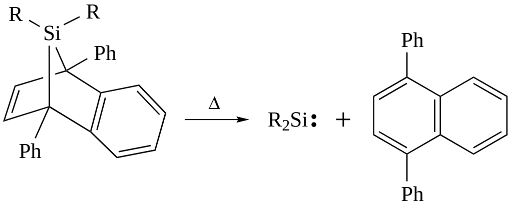
R
R
Si
Ph
Ph
Δ
R2Si:
+
Ph
Ph

(79)

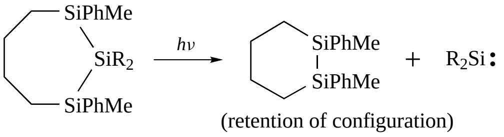
SiPhMe
SiR2
SiPhMe
hν
SiPhMe
SiPhMe
+
R2Si:

(retention of configuration)

(80)

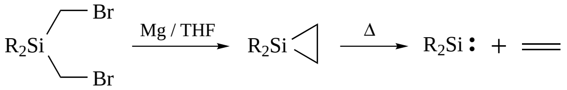
R2Si
Br
Br
Mg / THF
R2Si
Δ
R2Si:
+

(81)

Major reaction patterns of silylenes are insertion into the O–H (equation 82), Si–H (equation 59) and Si–Si bonds (equation 60), addition to multiple bonds (equation 83), rearrangement (equation 84), and dimerization. Dimerization of the bis(mesityl)silylene (equation 85) opened a pathway to the first isolable disilene.[67]

$$R_2Si\colon + R'OH \longrightarrow R_2Si(OR')H \qquad (82)$$

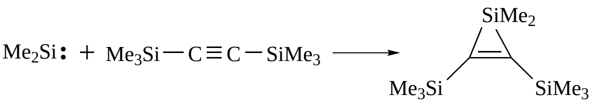
Me2Si:
+
Me3Si—C≡C—SiMe3
SiMe2
Me3Si
SiMe3

(83)

$$Me_3Si{-}SiMe_2{-}\ddot{Si}Me \xrightarrow{\bigcirc} Me_2Si{=}SiMe{-}SiMe_3 \qquad (84)$$

$$2Ar_2Si\colon \longrightarrow Ar_2Si{=}SiAr_2 \qquad (85)$$

Ar = mesityl (2,4,6-trimethylphenyl)

Silylenes with two different substituents, R^1R^2Si, are prochiral, and insertion into an alcoholic RO–H bond should create chirality on the silicon. In particular, if one of the two substituents is chiral, a diastereotopic face can be defined and diastereoselective addition can be expected. Quite recently, the first example of diastreoselective addition of alcohol to diastereotopic silylene has been reported.[68]

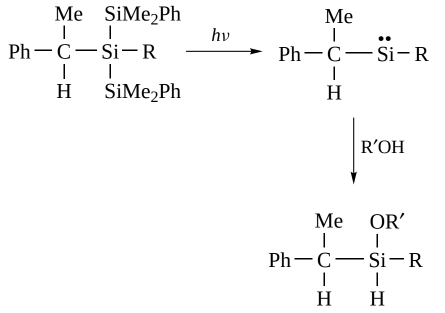

(86)

Even if it is not as stable as heavier members of the 14 group elements, divalent silicon species has some stability. Isolation of stable silylenes has been an interesting target in organosilicon chemistry. The first stable Si(II) species is silicocene, $(Me_5C_5)_2Si$, shown below.[69]

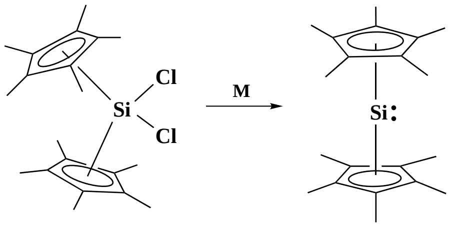

(87)

More recently, remarkably stable five-membered silylenes are reported (Figure 9).[70]

In these silylenes, electron donation to the vacant orbital of the silylenes from adjacent nitrogen atoms (n-π conjugation) should be the important factor in addition to the steric protection by bulky groups. It is interesting to argue whether stabilization owing to the aromaticity (6π electron system) for the unsaturated cyclic silylene (4 electrons from 2 nitrogen lone pair and 2π electrons from the double bond) really exists. It is suggested that unsaturated silylene is 58 kJmol^{-1} more stable than the saturated analog. Nonetheless, the saturated cyclic silylene is a fairly stable and unreactive species.

Similar cyclic and sterically protected silylene has been prepared recently (equation 88).[71] The silylene must be stabilized to some extent by σ-π conjugation instead of n-π conjugation for other stable cyclic silylenes shown in Figure 9. Indeed the silylene undergoes facile rearrangement (equation 88).

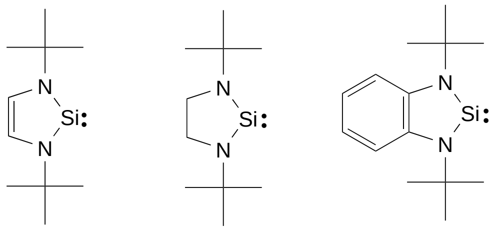

Figure 9 Stable five-membered silylenes

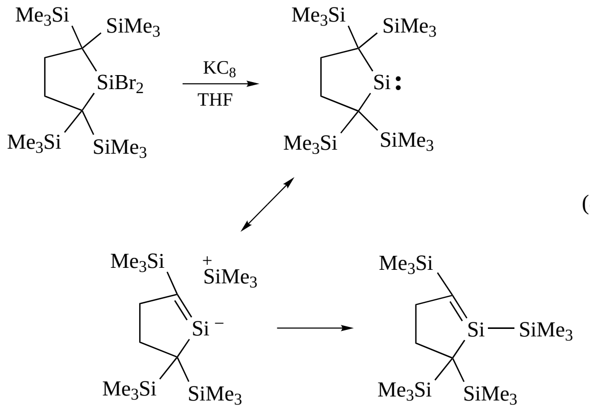

(88)

The carbon analog of silylenes, carbenes R_2C, can be either singlet or triplet electronic ground state depending on the electronic and steric characteristics of the substituents on the carbene center. Silylenes behave mostly as singlet species. In spite of several efforts, no clear evidence for the possibility of a triplet ground state of silylenes.[72] Bulky substituents should widen the bond angle to stabilize the triplet state. Thus it is predicted by computational studies that $(t\text{-}Bu_3Si)_2Si$: has a triplet ground state.[73] According to this prediction, very recently, $(t\text{-}Bu_3Si)_2Si$: has been generated by the photolysis of the corresponding silacyclopropene (equation 89). The ESR spectra as well as its chemical behavior indicate a triplet ground state for the silylene.[74]

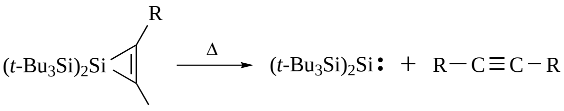

(89)

R = Me, Et

5.3 Formation and Reactions of Multiply Bonded Species

Because of the close relationship between silicon and carbon, many attempts have been made to try to synthesize species containing multiple bonds to silicon (Si=C, Si=O, Si=Si, etc.). However, it was not until 1967 that compelling evidence was presented that Si=C might exist in the thermal reaction of 1,1-dimethyl-1-silacyclobutane (equation 90).[75] The first evidence for the existence of Si=Si as transient intermediate was provided in the thermolysis of bridged disilane derivatives (equation 91).[76] Since then, many studies have been published on these unsaturated species, but it was in 1981 that synthesis and characterization of relatively stable crystalline compounds containing Si=C (silene) (equation 92)[77] and Si=Si (disilene) (equation 85) were reported (equations 90–92).

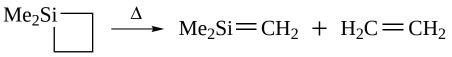

(90)

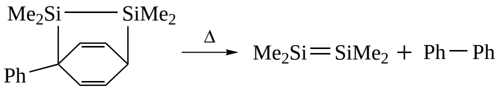
Me2Si
SiMe2
Ph
Δ
Me2Si=SiMe2 + Ph—Ph

(91)

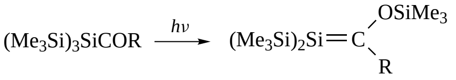

$$(Me_3Si)_3SiCOR \xrightarrow{h\nu} (Me_3Si)_2Si{=}C(OSiMe_3)R$$

(92)

R = 1-adamantyl, CEt_3

Until now, the chemistry of multiply bonded silicon has developed explosively. Methods of generation, reactivity, and structure of compounds containing multiply bonded silicon are well documented in reviews.[78] These are $R_2Si{=}SiR_2$ (disilene), $R_2Si{=}CR_2$ (silene), $R_2Si{=}NR$ (silanimine), $R_2Si{=}O$ (silanone), $R_2Si{=}P$ (silaphosphene), and $R_2Si{=}S$ (silanethione). Typical reactions of disilenes and silenes are summarized in Schemes (6) and (7).

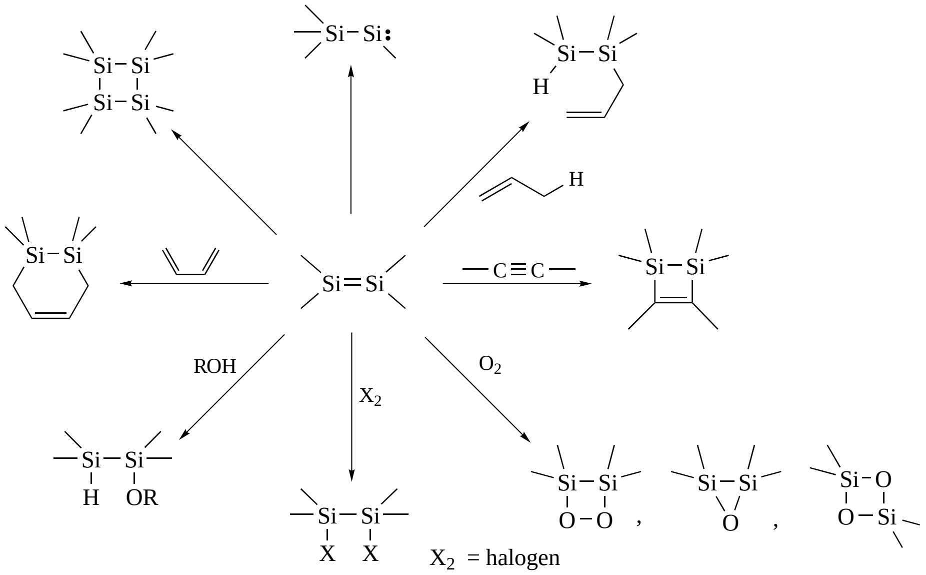
Si=Si
—C≡C—
ROH
X2
O2
H
X2 = halogen

Scheme 6

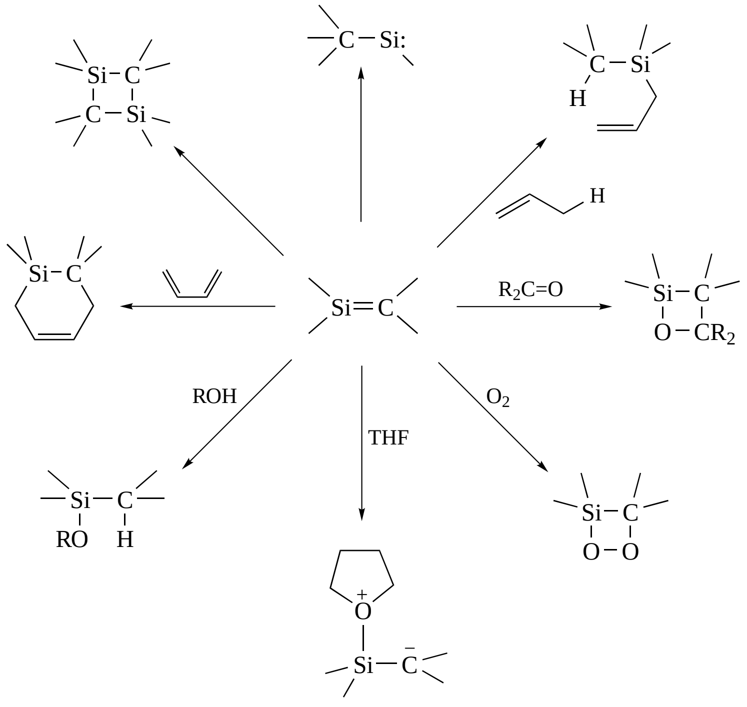
Si=C
R2C=O
ROH
THF
O2
H

Scheme 7

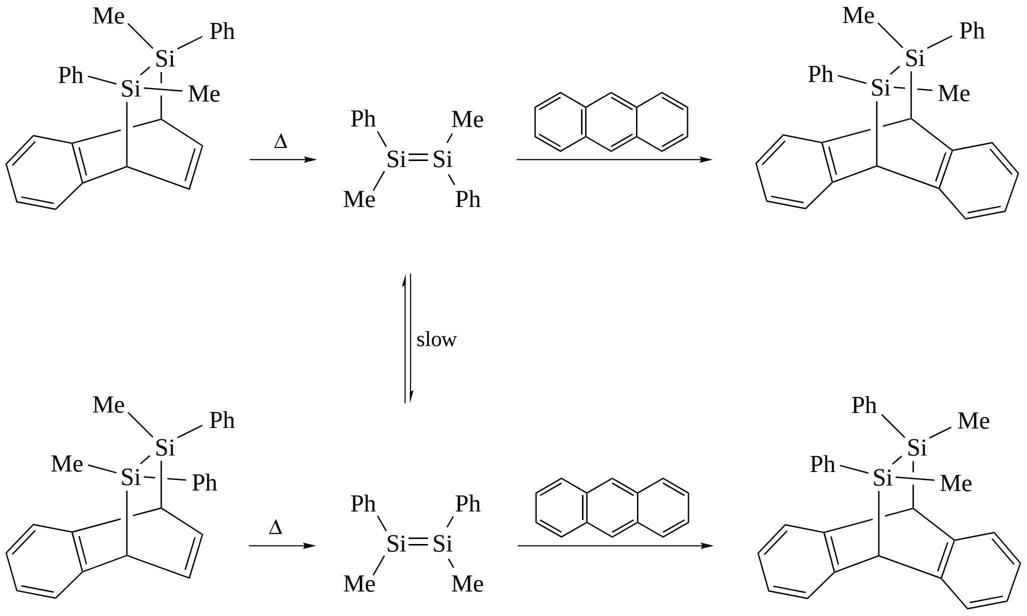

Scheme 8

Existence of geometric isomerism and estimate of the rotational barrier are fundamental properties of double bonds. Not only thermally stable disilenes but reactive disilenes such as cis- and *trans*-PhMeSi=SiPhMe can retain geometrical configuration during the reaction.[79] As shown in Scheme 8, *trans*-1,2-diphenyldimethyldisilene can be trapped with anthracene with retention of configuration (96:4) at 300 °C. A similar result was obtained with the cis precursor to give the product of configurational retention (94:6). Slightly less stereospecific results were obtained by increasing the temperature to 350 °C. Activation energy of at least $25.8 \pm 5\,\mathrm{kcal\,mol^{-1}}$ is calculated for the cis-trans isomerization.[80]

Notable advances in the last decade are isolation of kinetically stabilized silicon-containing double-bonded species.[81] As we have seen already, a variety of sterically bulky substituents have been utilized to stabilize silicon-centered reactive intermediates. This kinetic stabilization is the key issue also to isolate silicon double-bonded species. For example, the synthesis of isolable silicon analog of benzene and other aromatic compounds has been a target for a long time. One example is shown below for the generation of transient silabenezene.[82]

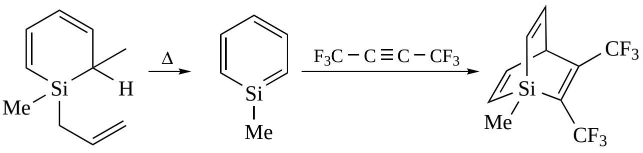

(93)

By using a very bulky substituent, Tbt (2,4,6-tris[bis(trimethylsilyl)methyl]phenyl), 2-silanaphthalene,[83] silabenzene[84] and other related compounds are prepared (Figure 10).

Tetrasilabutadiene,[85] trisilacyclopropene (cyclotrisilene), and tetrasilacyclobutene (cyclotetrasilene) are isolated and the structures are determined by X-ray crystallography.[86]

Compounds of triply bonded silicon or *sp*-hybridized silicon have been indicated as intermediates in some reactions,[87] but they have been elusive for a long time. Very recently, a trisilaallene derivative with a formally *sp*-hybridized silicon atom has been isolated as a stable crystalline compound (equation 94).[88] Contrary to linear original allenes, the trisilaallene is a bent molecule.

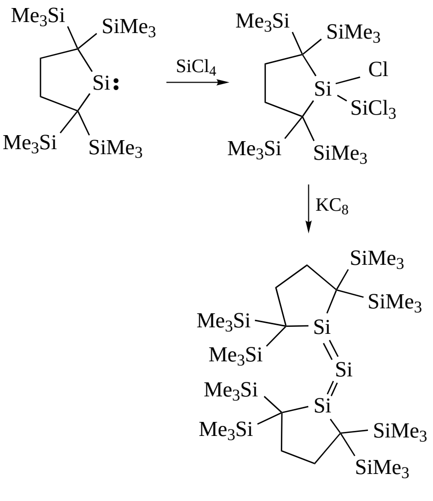

(94)

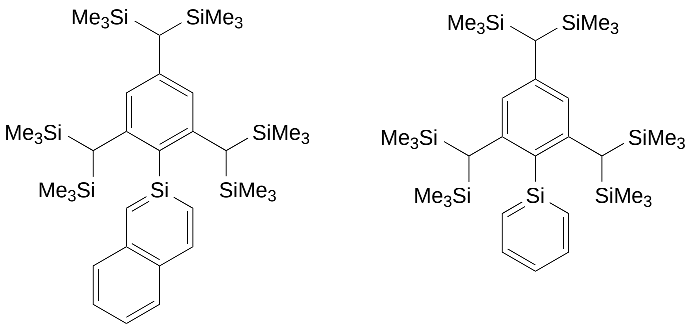

Figure 10 Kinetically stabilized silaaromatics

More recently, a stable compound containing a silicon–silicon triple bond (disilyne) has been isolated as emerald green crystals (equation 95).[89] 1,1,4,4-Tetrakis[bis(trimethylsilyl)methyl]-1,4-diisopropyl-2-tetrasilyne is thermally stable up to 100 °C in the absence of air. The observed Si–Si triple bond length is 2.0622(9) Å, which is shorter than the average Si–Si (2.39 Å, Table 6) and Si=Si (2.14 Å)[81] but the degree of shortening is smaller than those observed for carbon analogs. In fact, the disilyne is not a linear molecule as acetylene but has a trans bent structure with a bond angle of 137.44(4)°. The disilyne is reactive and reacts with two equivalent of bromine at room temperature to give the starting tetrabromide in 94% yield.

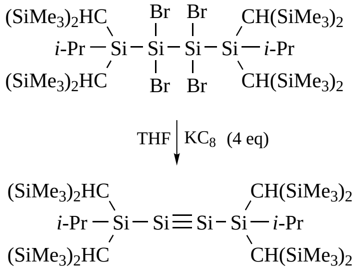

$$i\text{-Pr}-\underset{(SiMe_3)_2HC}{\overset{(SiMe_3)_2HC}{Si}}-\underset{Br}{\overset{Br}{Si}}-\underset{Br}{\overset{Br}{Si}}-\underset{CH(SiMe_3)_2}{\overset{CH(SiMe_3)_2}{Si}}-i\text{-Pr}\;\xrightarrow[\text{THF}]{\text{KC}_8\ (4\ \text{eq})}\; i\text{-Pr}-\underset{(SiMe_3)_2HC}{\overset{(SiMe_3)_2HC}{Si}}-Si\equiv Si-\underset{CH(SiMe_3)_2}{\overset{CH(SiMe_3)_2}{Si}}-i\text{-Pr} \qquad (95)$$

5.4 Silicon Polyhedranes

Closely related to disilynes, $(RSi)_2$, silicon polyhedranes of the type $(RSi)_{2n}$ are also interesting molecules for synthesis. A theoretical consideration of Croup 14 polyhedral compounds, X_nH_n, on the level of HF/6-31G*, where $n = 4$ (tetrahedrane), $n = 6$ (prismane), and $n = 8$ (cubane), suggested that the cubane and prismane structures possess a lower degree of strain energy than the carbon analogs.[90] Thus it may be reasonable to assume that the cubane and prismane analogs of the heavier atoms should be accessible and therefore they are appropriate synthetic targets. However, for the synthesis of strained polyhedranes, proper choice of both starting compounds with a suitable bulky substituent and metals as reducing reagent is of crucial importance, and therefore hexasilaprismane and octasilacubane have been synthesized rather recently.[91] The crystal structures of tetrakis(tri-*t*-butylsilyl)tetrasilatetrahedrane,[92] hexakis(2,6-diisopropylphenyl)hexasilaprismane[93] and octakis(2,6-diethylphenyl)octasilacubane[94] were determined (Figure 11).

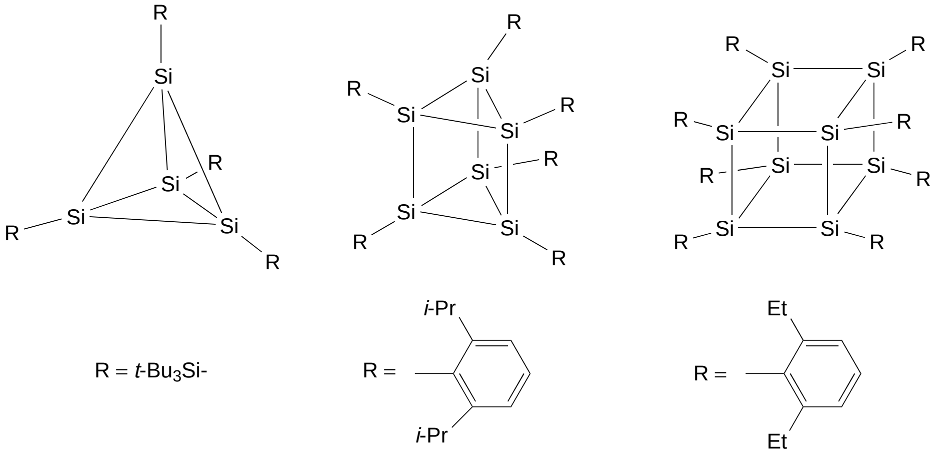

Figure 11 Silapolyhedranes

6 APPLICATIONS

Organosilicon chemistry has several areas of important applications. Owing to the limitation of the scope of this section, those will be described briefly.

6.1 Polymers

6.1.1 Silicones

Silicones are polymers with a polysiloxane backbone. The simplest one is polydimethylsiloxane, MD_nM, exhibiting the basic structure of the silicones. The methyl group may be substituted by another one such as phenyl, vinyl, and hydrogen. Wohler, who assumed that oxygen was bound to silicon by a double bond similar to that in ketones, introduced the name silicone. Silicones are fluids, resins, or elastomers; they can be greases or rubbers. Silicone oils mostly have the structure of MD_nM. Rubbers are of the same composition as oils but the degree of polymerization in rubbers is several thousands, much higher than oils. Resins contain T units for the three-dimensional network structure. The initial process of silicone production is hydrolysis of chlorosilanes. Hydrolysis of trimethylchlorosilane gives trimethylsilanol (equation 48) followed by the formation of MM. Hydrolysis of dimethyldichlorosilane is very rapid to give linear and cyclic polysiloxanes depending upon reaction conditions.

$$2Me_3SiOH \longrightarrow Me_3SiOSiMe_3(MM) + H_2O \qquad (96)$$

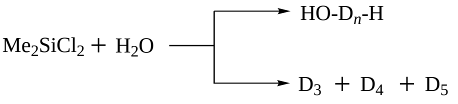

$$Me_2SiCl_2 + H_2O \longrightarrow \begin{cases} HO\text{-}D_n\text{-}H \\ D_3 + D_4 + D_5 \end{cases} \qquad (97)$$

Elastomers and nonsilanol terminated fluids are produced by base-catalyzed polymerization of low-molecular weight siloxanes. Polydimethylsiloxanes are also produced by ring opening polymerization of D_3, D_4, and D_5. In the presence of MM or MDDM (endcapper), silicones MD_nM are formed; otherwise, silanol terminated polysiloxanes may be obtained.

The polydimethylsiloxanes (PDMS) exhibit characteristic properties useful for practical applications: transparent, colorless, thermal stability, oxidative stability, chemical stability, shear stability, dielectric stability, low viscosity change on temperature, nonflammability, low surface tension, high compressibility, water repellant, biologically inactive, and so on. They are used in adhesives, cosmetics, electrical systems, as damping oils, lubricants, polishing oils, in heat exchange, diffusion pumps, textile finishing, and so on. A part of the methyl group of silicones can be replaced by other groups to produce modified silicones, which are now used in almost all industrial products.[95,96]

Silicone rubbers are made by adding an inert filler (mostly silica) to highly viscous PDMS gum, followed by curing in the presence of catalysts. The cure process is a cross-linking reaction of silicone chains and initiated by peroxide (radical process), typically benzoyl peroxide, *m*-chlorobenzoyl peroxide, and di-*t*-butyl peroxide. Major reactions responsible to the cross-linking are generation of free radical and coupling (equation 98). Generation of the $SiCH_2\cdot$ requires hydrogen abstraction and becomes more difficult when the system becomes more viscous. Then some group such as vinyl is introduced to facilitate the reaction. This process is called heat cure or high-temperature vulcanization (HTV) and the resulting rubber is used in electric, mechanical, automobile, medical, and food industries.

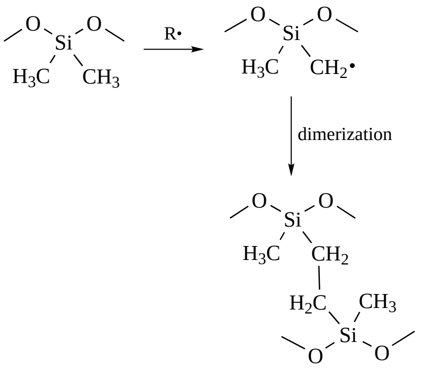

(98)

Silicone rubber has a very characteristic and useful way of vulcanization at low temperature. Liquid silicone rubbers of low viscosity polysiloxanes having reactive functional groups, undergo cross-linking by condensation or addition reactions. Cross-linking (curing) can be done at room temperature so that these rubbers are called RTV (room temperature vulcanizing) rubbers. Some typical reactions utilized for the production of RTV are shown in Scheme 9. They find a wide range of applications in molding, sealing, electrical insulation, and so on. People may be familiar with RTV at the dentist for the molding of an artificial tooth and/or inlay.

Silicones are exceptionally thermally stable without acidic or basic substances. Silicones are now used increasingly in cosmetics and personal care fields. Therefore, the fate of silicones (mostly dimethylsilicones) under ambient conditions may be a matter of environmental concern. Fortunately, it is shown that $M\text{-}D_n\text{-}M$ polymers depolymerize to $Me_2Si(OH)_2$ rather rapidly in soil and water under high dilution conditions. Then $Me_2Si(OH)_2$ undergoes stepwise demethylation to T units and finally to Q units (silicic acid). The final degradation of $Me_2Si(OH)_2$ to SiO_2 and CO_2 occurs within a few months to year.[97] Therefore, silicones are concluded to be quite safe materials.

$$R_3SiOH + HOSiR_3 \longrightarrow R_3SiOSIR_3 + H_2O$$

$$R_3SiOH + ROSiR_3 \longrightarrow R_3SiOSIR_3 + ROH$$

$$2R_3SiOR + H_2O \longrightarrow R_3SiOSIR_3 + 2ROH$$

$$2R_3SiOCOCH_3 + H_2O \longrightarrow R_3SiOSIR_3 + 2CH_3COOH$$

$$2R_3SiON{=}C(CH_3)_2 + H_2O \longrightarrow R_3SiOSIR_3 + 2(CH_3)_2C{=}NOH$$

$$2R_3SiOC(CH_3){=}CH_2 + H_2O \longrightarrow R_3SiOSIR_3 + 2(CH_3)_2C{=}O$$

Scheme 9

6.1.2 *Polysilylenes (Polysilanes)*

Permethylpolysilylene was prepared in 1949 by the sodium condensation of Me_2SiCl_2, but the products were insoluble, infusible, and intractable. As a result, these polymers have been neglected until the finding that polydimethyisilylene can be converted to polycarbosilane (PCS) at high temperature by thermal rearrangement. PCS is soluble and meltable. Melt spun PCS fibers can be converted to silicon carbide fibers, which are the most heat-resistant fibers so far.[98] Inspired by this observation, many studies on polysilylenes have been carried out and it was found that homopolysilylenes having substituents other than methyl and most copolymers are soluble. Since then, polysilylenes have been investigated extensively in the past decade because of their potential applications in the field of materials science.[99] The polysilylenes exhibit characteristic properties useful for practical applications. Applications of polysilylenes in SiC precursors, microlithography,[100] and reprography[101] show that polysilylenes are promising as advanced materials for the high technology of the next generation.

The Si–Si bonds in polysilylenes can also react with a variety of reagents. Typical examples are shown in Scheme 10 in which reactions of hexamethyldisilane, as a model compound, are indicated.

Polysilylenes are usually prepared by the Wurtz-type reductive coupling of dichlorosilanes with alkali metals.

$$R_2SiCl_2 + 2Na \longrightarrow (R_2Si)_n + 2NaCl \qquad (99)$$

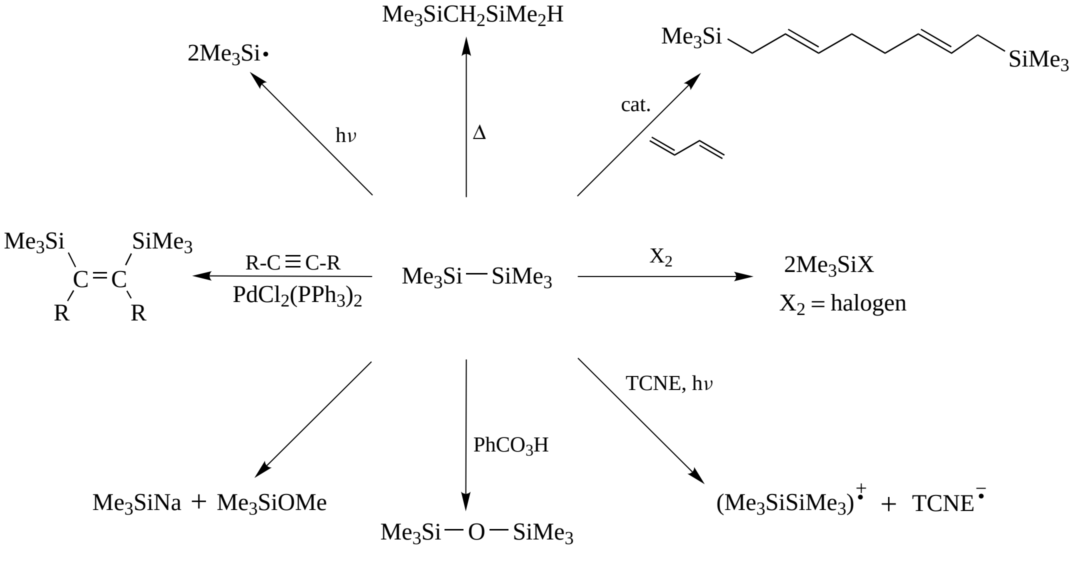

Scheme 10

Although many kinds of polysilylene have been prepared by this method, the structure of the polymers is difficult to control.[102] Molecular weight and polydispersity are also unmanageable.[103]

Recently, several new methods of preparing polysilylenes have been reported. Transition metal catalyzed dehydrogenative coupling of hydrosilanes, especially of $RSiH_3$, is promising (equation 100), although at this moment only oligomeric polysilylenes are available.[104]

$$RSiH_3 \xrightarrow{\text{cat.}} (RSiH)_n + H_2 \qquad (100)$$

The anionic polymerization of masked disilenes, that is, l-phenyl-7,8-disilabicyclo[2.2.2]octa-2,5-diene derivatives, is

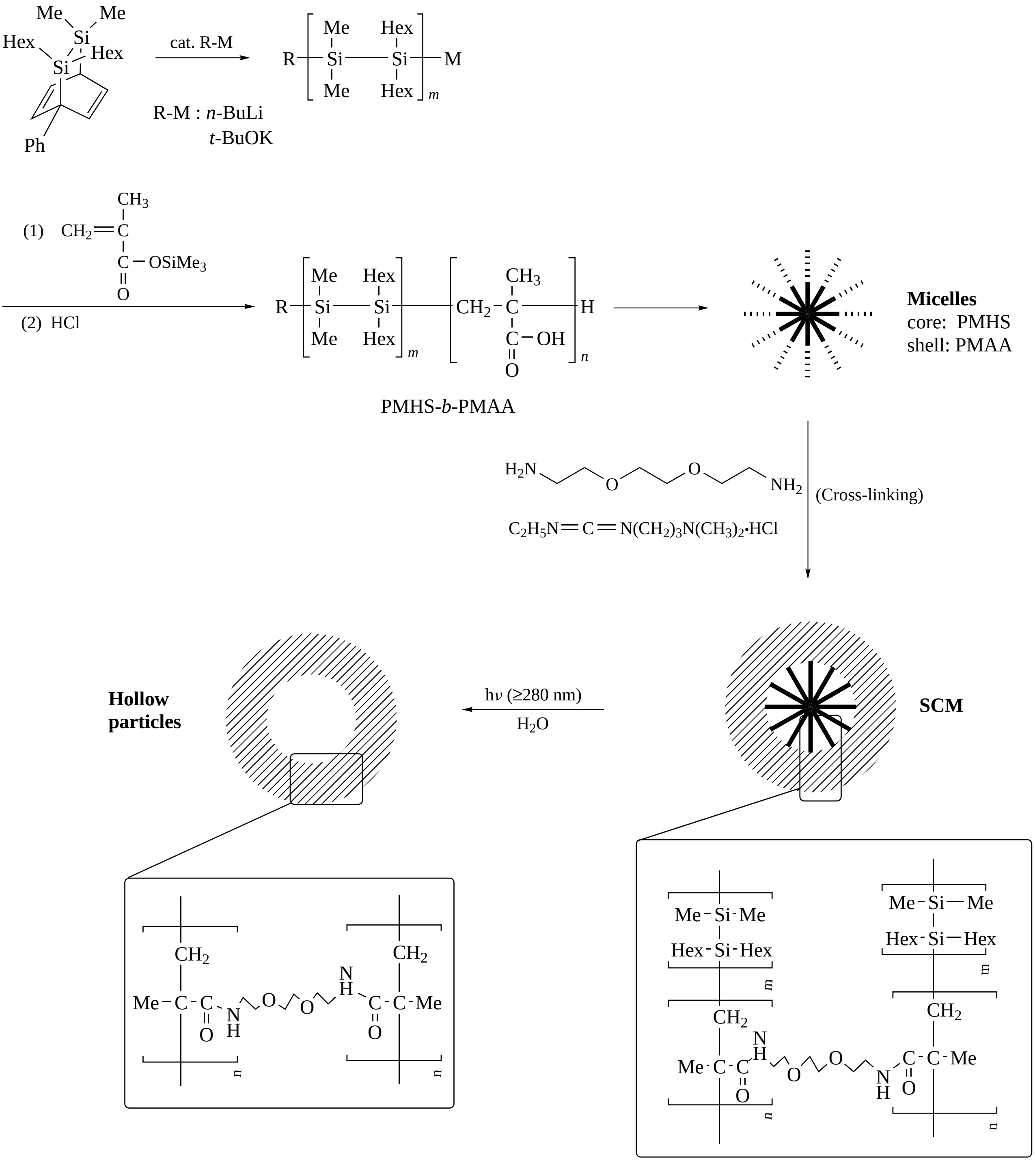

Me
Me
Hex
Si
Hex
Si
Ph
cat. R-M
R-M : n-BuLi
t-BuOK
R
Me
Hex
Si
Si
Me
Hex
M
m
(1) CH2=C(CH3)C(=O)OSiMe3
(2) HCl
CH3
CH2
C
C–OH
O
H
n
PMHS-b-PMAA
Micelles
core: PMHS
shell: PMAA
H2N
O
O
NH2
C2H5N=C=N(CH2)3N(CH3)2•HCl
(Cross-linking)
SCM
hν (≥280 nm)
H2O
Hollow particles
Me-C-C
N
H
Me-Si-Me
Hex-Si-Hex
CH2

Scheme 11

also a new promising method for preparing polysilylenes with highly controlled structures (equation 101).[105] Indeed, a highly ordered alternating polysilylene copolymer, poly(1,1-dihexyl-2,2-dimethyldisilene) $(SiHex_2SiMe_2)_n$ (PMHS), has been synthesized for the first time by this method; an interesting thermochromism was observed for alternating polysilylene copolymers with a highly ordered structure.[106]

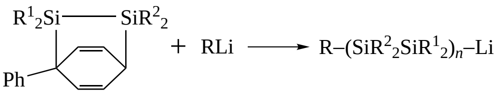

(101)

The anionic polymerization of masked disilenes proceeds *via* living anions, and therefore block copolymerization with a conventional vinyl monomer is possible. Recently, interesting hydrophobic block copolymer of PMHS with poly(2-hydroxyethyl methacrylate) (PHEMA) and poly(methacrylic acid) (PMMA) have been prepared (Scheme 11). These polymers can be self-assembled and are transformed into polysilane micelles,[107] shell cross-linked micelles (SCM),[108] and nanometer-sized hollow particles.[109]

6.2 Organic Synthesis

Applications of organosilicon compounds in organic synthesis are growing very rapidly. This topic has been discussed by several extensive reviews[110] and only some typical examples are listed here. However, it is meaningful to emphasize the importance of factors with which organosilicon compounds can be used for organic synthesis. These are: (a) silyl groups as proton substitutes, (b) stabilization of b carbocations by σ-π conjugation, and (c) stabilization of a carbanions by σ^*–π conjugation. The nature of the latter two factors is discussed in Section 4.

6.2.1 Silicon as Proton Substitutes

Historically, silation of ROH to $ROSiR_3$, was the first successful application of organosilicon compounds in organic chemistry. This kind of derivatization procedure has been used extensively for hydroxylic compounds such as sugars to give volatility in GLC (gas-liquid chromatography) and MS (mass spectrometry) applications.[111] In the beginning, the reaction of ROH with trimethylchlorosilane (TMSCl) in the presence of a stoichiometric amount of pyridine in toluene or benzene is employed for silation. A combination ofhexamethyldisilazane (HMDS) and TMSCl in a nonpolar solvent is more effective reagents.

$$3ROH + (Me_3Si)_2\,NH + Me_3SiCl \longrightarrow 3ROSiMe_3 + NH_4Cl \qquad (102)$$

Other commonly used trimethylsilation reagents are: *N*,*O*-bis(trimethylsilyl)acetamide (BSA), *N*-trimethylsilylacetamide, *N*-trimethylsilylimidazole (TMSI), and *N*,*N*-bis(trimethylsilyl)urea (BSU) (Figure 12).

The rate of hydrolysis of $ROSiR'_3$, that is, the hydrolytic stability of silylated compounds, depends on the steric bulkiness of R′. An approximate order of steric bulkiness of common silyl groups is as follows: (Note that the order depends on the nature of the reaction and alcohols).[112] Me_3Si (TMS) < $PhMe_2Si$ < Et_3Si (TES) < t-$BuMe_2Si$ (TBDMS) < i-Pr_3Si (TIPS) < t-$BuPh_2Si$ (TBDPS) < t-Bu_3Si (supersilyl) < $(cyclohexyl)_3Si$. Therefore, t-$BuMe_2Si$- and t-$BuPh_2Si$- are frequently used as strong protecting groups in organic synthesis.

Hydrosilanes, R_3SiH, can be viewed as ‘silylated hydrogen’ and used as a reducing reagent. Hydrosilation (equation 20) resembles hydrogenation in this sense. Reduction of prochiral ketones through hydrosilation has been investigated extensively with platinum and rhodium complexes having

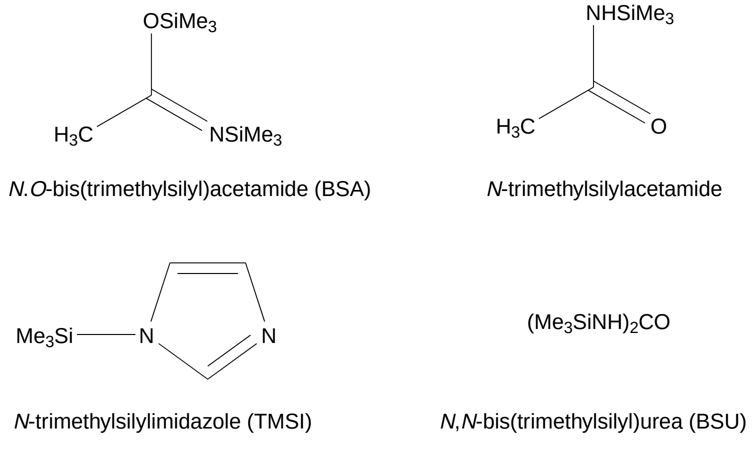

N.O-bis(trimethylsilyl)acetamide (BSA)

N-trimethylsilylacetamide

N-trimethylsilylimidazole (TMSI)

N,*N*-bis(trimethylsilyl)urea (BSU)

Figure 12 Commonly used trimethylsilation reagents

chiral ligand(s).[113]

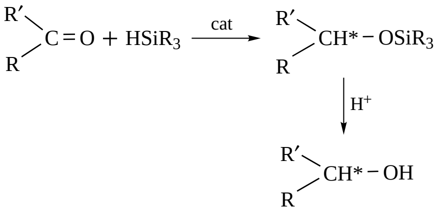
(103)

Trimethylsilyl cyanide (TMSCN) and trimethylsilyl azide ($TMSN_3$) are safe and convenient replacements for hydrogen cyanide and hydrogen azide, respectively, which are otherwise inconvenient or hazardous to handle.

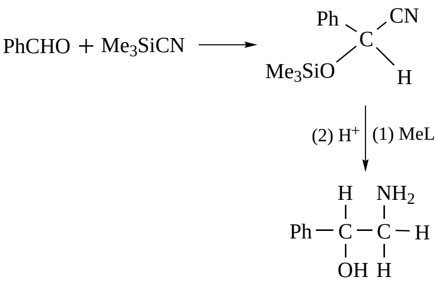
(104)

Trimethylsilyl esters of Bronsted acids such as trimethylsilyl triflate and trimethylsilyl iodide are useful as catalysts for trimethylsilyl transfer reactions. An example is given in equation (105).

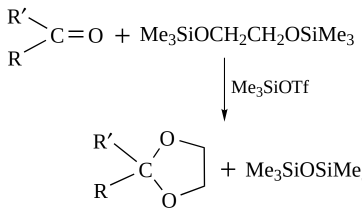
(105)

6.2.2 *Stabilization of β Carbocations*

The most important and representative examples of this category are the reactions of allylsilanes (Scheme 4 and equations 106 and 107).

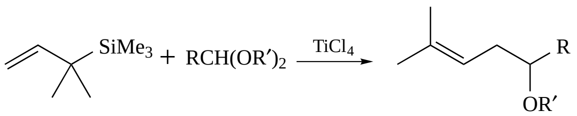
(106)

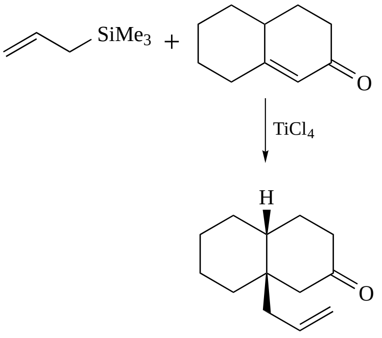
(107)

The regiochemistry of electrophilic attack to vinylsilanes is also controlled by the trimethylsilyl group.

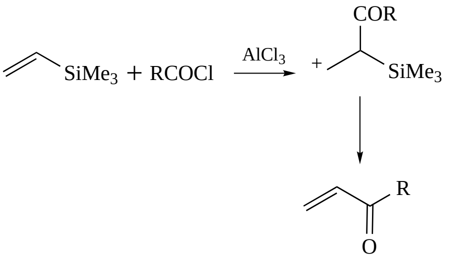
(108)

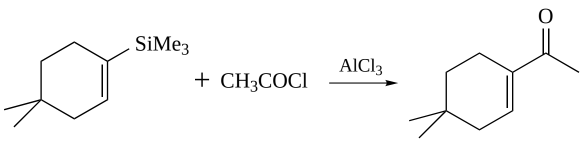
(109)

Silyl enol ethers are useful for regioselective aldol-type condensation.[114]

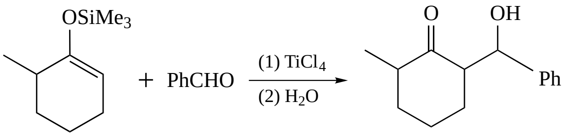
(110)

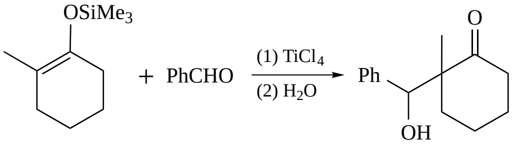
(111)

6.2.3 *Stabilization of α Carbanions*

α-Metalated organosilanes can be prepared by addition of an organometallic compound to vinylsilanes, proton abstraction, halogen-metal exchange, and transmetalation (equations 42, 112–114).

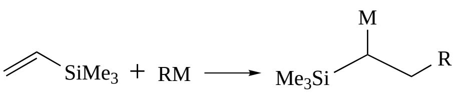
(112)

$$Me_3SiCH_2\text{-}H + BuLi \xrightarrow[\text{TMEDA}]{} Me_3SiCH_2Li \qquad (113)$$

$$Me_3SiCH_2\text{-}Cl + Mg \longrightarrow Me_3SiCH_2\text{-}MgCl \qquad (114)$$

These α metalated organosilanes react with carbonyl compounds to give methylenated products.[115]

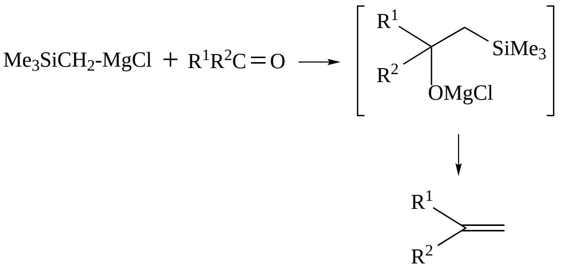

(115)

7 REFERENCES

1. For general references, see: C. Eaborn, ‘Organosilicon Compounds’, Butterworths, London, 1960; ‘The Chemistry of Organic Silicon Compounds’, eds. S. Patai and Z. Rappoport, Wiley, Chichester, 1989, Part 1 and 2; ‘The Chemistry of Organic Silicon Compounds’ eds. Z. Rappoport and Y. Apeloig, Wiley, Chichester, 1998, Vol. 2, Part 1,2, and 3; M. A. Brook, ‘Silicon in Organic, Organometallic, and Polymer Chemistry’, Wiley-Interscience, New York, 2000.
2. R. J. H. Voorhoeve, ‘Organosilanes, Precursors to Silicones’, Elsevier, Amsterdam, 1967.
3. A. Shirahata, *Tetrahedron Lett.*, 1989, **30**, 6393; P. J. Lennon, D. P. Mack and Q. E. Thompson, *Organometallics*, 1989, **8**, 1121.
4. M. Kira, R. Yauchibara, R. Hirano, C. Kabuto, and H. Sakurai, *J. Am. Chem. Soc.*, 1991, **113**, 7785.
5. J. Dunogues, C. Biran, and M. Laguerre, in ‘Organosilicon and Bioorganosilicon Chemistry’, ed. H. Sakurai, E. Horwood, John Wiley & Sons, Chichester, 1985, Chapt. 15, p. 157.
6. K. Tamao and S. Yamaguchi, *Pure Appl. Chem.*, 1996, **68**, 139.
7. D. Wittenberg and H. Gilman, *Q. Rev.*, 1959, **13**, 116.
8. H. Sakurai, A. Okada, M. Kira, and K. Yonezawa, *Tetrahedron Lett.*, 1971, 1511.
9. W. C. Still, *J. Org. Chem.*, 1976, **41**, 3062.
10. H. Sakurai and F. Kondo, *J. Organomet. Chem.*, 1975, **92**, C46.
11. A. Sekiguchi, M. Nanjo, C. Kabuto, and H. Sakurai, *Angew. Chem., Int. Ed. Engl.*, 1997, **36**, 113; M. Nanjo, A. Sekiguchi, and H. Sakurai, *Bull. Chem. Soc. Jpn.*, 1998, **71**, 741.
12. A. Kawachi and K. Tamao, *Bull. Chem. Soc. Jpn.*, 1997, **70**, 945.
13. B. Marciniec, J. Gulinski, W. Urbaniak, and Z. W. Kornetka, ‘Comprehensive Handbook of Hydrosilylation Chemistry’, Pergamon, Oxford, 1992.
14. J. F. Harrod and A. J. Chalk, *J. Am. Chem. Soc.*, 1966, **88**, 3491.
15. L. N. Lewis and N. Lewis, *J. Am. Chem. Soc.*, 1986, **108**, 7228; L. N. Lewis, *J. Am. Chem. Soc.*, 1990, **112**, 5998.
16. H. Sakurai, Y. Kamiyama, and Y. Nakadaira, *J. Am. Chem. Soc.*, 1975, **97**, 931.
17. For a review of [$\sigma + \pi$] reactions, see: H. Sakurai, *J. Organomet. Chem.*, 1980, **200**, 261.
18. H. Sakurai and A. Hosomi, *J. Am. Chem. Soc.*, 1971, **93**, 1709.
19. M. Kira, H. Sugiyama, and H. Sakurai, *J. Am. Chem. Soc.*, 1983, **l05**, 6436.
20. N. Furuya and T. Sukawa, *J. Organomet. Chem.*, 1975, **96**, C1.
21. M. Jung and T. A. Blumenkopf, *Tetrahedron Lett.*, 1978, 3657.
22. L. H. Sommer, ‘Stereochemistry, Mechanism & Silicon’, McGraw Hill, New York, 1965.
23. H. Kwart and K. King, ‘d-Orbitals in the Chemistry of Silicon, Phosphorus, and Sulfur’, Springer Verlag, Berlin, 1977.
24. H. Sakurai, *Pure Appl. Chem.*, 1982, **54**, l.
25. H. Sakurai and M. Kumada, *Bull. Chem. Soc. Jpn.*, 1964, **37**, 1894.
26. H. Sakurai, S. Tasaka, and M. Kira, *J. Am. Chem. Soc.*, 1972, **94**, 9285.
27. J. C. Giordan and J. H. Moore, *J. Am. Chem. Soc.*, 1983, **105**, 6543.
28. H. Sakurai, Y. Nakadaira, M. Kira, and H. Tobita, *Tetrahedron Lett.*, 1980, **21**, 3077; H. Sakurai, Y. Nakadaira, H. Tobita, T. Ito, K. Toriumi, and H. Ito, *J. Am. Chem. Soc.*, 1982, **104**, 300.
29. H. Sakurai, K. Ebata, C. Kabuto, and A. Sekiguchi, *J. Am. Chem. Soc.*, 1990, **112**, 1799.
30. R. Walsh, *Acc. Chem. Res.*, 1981, **14**, 246.
31. H. Sakurai, in ‘Free Radicals’, ed. J. K. Kochi, Wiley, New York, 1973, Vol. 2, p. 741; C. Chatgilialoglu, *Chem. Rev.*, 1995, **95**, 1229.
32. R. J. P. Corriu and M. Henner, *J. Organomet. Chem.*, 1974, **74**, 1; H. Schwarz, in ‘The Chemistry of Organic Silicon Compounds’, eds. S. Patai, Z. Rappoport, John Wiley & Sons, 1989, Part 1, Chapt 7; J. B. Lambert and W. J. Schulz, Jr, ‘The Chemistry of Organic Silicon Compounds’, eds. S. Patai, Z. Rappoport, John Wiley & Sons, 1989, Part 2, Chap. 16; J. B. Lambert, L. Kania, and S. Zhang, *Chem. Rev.*, 1995, **95**, 1191; Pv. R. Schleyer, *Science*, 1997, **275**, 39; J. Belzner, *Angew. Chem., Int. Ed. Engl.*, 1997, **36**, 1277; C. A. Reed, *Acc. Chem. Res.*, 1998, **31**, 325; C. Maerker and P. V. R. Schleyer, in ‘The Chemistry of Organic Silicon Compounds’; eds. Z. Rappoport, Y. Apeloig, John Wiley & Sons, 1998, Vol. 2, Part 1. Chap. 10; P. D. Lickiss, in ‘The Chemistry of Organic

Silicon Compounds', eds. Z. Rappoport, Y. Apeloig, John Wiley & Sons, 1998, Vol. 2, Part 1, Chap. 11.

33. K. Tamao and A. Kawachi, *Adv. Organomet. Chem.*, 1995, **38**, 1.
34. P. P. Gaspar and R. West, in 'The Chemistry of Organic Silicon Compounds', eds. Z. Rappoport and Y. Apeloig, Wiley, Chichester, 1998, Vol. 2, Part 3, p. 2463.
35. J. B. Lambert, S. Zhang, C. L. Stem, and J. C. Huffman, *Science*, 1993, **260**, 1917.
36. A. Sekiguchi, T. Matsuo, and M. Ichinohe, *J. Am. Chem. Soc.*, 2000, **122**, 11250.
37. T. Matsuo, M. Ichinohe, and A. Sekiguchi, *Angew. Chem., Int. Ed. Engl.*, 2004, **41**, 1575.
38. A. Sekiguchi, T. Matsuo, and M. Ichinohe, *J. Am. Chem. Soc.*, 2001, **123**, 12436.
39. J. B. Lambert, Y. Zao, H. Wu, W. C. Tze, and B. Kuhimann, *J. Am. Chem. Soc.*, 1999, **121**, 5001, and references cited therein.
40. K.-C. Kim, C. A. Reed, D. W. Elliot, L. J. Mueller, F. Tham, L. Lin, and J. B. Lambert, *Science*, 2002, **297**, 825.
41. M. J. S. Dewar and E. Healey, *Organometallics*, 1982, **1**, 103; Y. Apeloig, in 'The Chemistry of Organosilicon Compounds', eds. S. Patai and Z. Rappoport, Wiley, Chichester, 1989, Part I, Chap. 2.
42. R. J. P. Corriu, C. Guerin, and J. E. Moreau, in 'The Chemistry of Organosilicon Compounds', eds. S. Patai and Z. Rappoport, Wiley, Chichester, 1989, Part I, Chap. 4; A. R. Bassindale, and P. G. Taylor, in 'The Chemistry of Organosilicon Compounds', eds. S. Patai and Z. Rappoport, Wiley, Chichester, 1989, Chap.13.
43. N. T. Anh and C. Minot, *J. Am. Chem. Soc.*, 1980, **102**, 103.
44. D. Wittenberg and H. Gilman, *Q. Rev.*, 1959, **13**, 116.
45. H. Sakurai, A. Okada, H. Umino, and M. Kira, *J. Am. Chem. Soc.*, 1973, **95**, 955.
46. W. Ilsley, T. F. Schaaf, M. D. Click, and J. P. Oliver, *J. Am. Chem. Soc.*, 1980, **102**, 3769.
47. M. Nanjo, A. Sekiguchi, and H. Sakurai, *Bull. Chem. Soc. Jpn.*, 1998, **71**, 741.
48. M. Nakamoto, T. Fukawa, V. Ya Lee, and A. Sekiguchi, *J. Am. Chem. Soc.*, 2002, **124**, 15160.
49. H. Watanabe, K. Higuchi, M. Kobayashi, M. Hara, Y. Koike, T. Kitahara, and Y. Nagai, *J. Chem. Soc., Chem. Commun.*, 1977, 534.
50. M. Kira, T. Iwamoto, D. Yin, T. Maruyama, and H. Sakurai, *Chem. Lett.*, 2001, 910, and references cited therein.
51. W.-C. Joo, J.-H. Hong, S.-B. Choi, and H.-E. Son, *J. Organomet. Chem.*, 1990, **391**, 27; J.-H. Hong, P. Boudjouk, S. Castellino, *Organometallics*, 1995, **13**, 3387.
52. N. Tokitoh, K. Hatano, T. Sadahiro, and R. Okazaki, *Chem. Lett.*, 1999, 931.
53. A. Sekiguchi, M. Ichinohe, and S. Yamaguchi, *J. Am. Chem. Soc.*, 1999, **121**, 10231.
54. H. Sakurai, H. Umino, and H. Sugiyama, *J. Am. Chem. Soc.*, 1980, **102**, 6837.
55. S. Kyushin, H. Sakurai, T. Betsuyaku, and H. Matsumoto, *Organometallics*, 1997, **16**, 5386.
56. M. Kira, T. Obata, I. Kon, H. Hashimoto, M. Ichinohe, H. Sakurai, S. Kyushin, and H. Matsumoto, *Chem. Lett.*, 1998, 1097.
57. A. Sekiguchi, T. Fukawa, M. Nakamoto, V. Ya Lee, and M. Ichinohe, *J. Am. Chem. Soc.*, 2002, **124**, 9865.
58. H. Sakurai, M. Murakami, and M. Kumada, *J. Am. Chem. Soc.*, 1969, **91**, 519; A. G. Brook and J. H. Duff, *J. Am. Chem. Soc.*, 1969, **91**, 2119.
59. R. W. Fessenden and R. H. Schuler, *J. Chem. Phys.*, 1965, **43**, 2704.
60. H. Sakurai and M. Murakami, *Chem. Lett.*, 1972, 7.
61. I. Fleming, 'Frontier Orbitals and Organic Chemical Reactions', Wiley, Chichester, 1976, Chap. 5.
62. W. H. Attwell and D. R. Weyenberg, *Angew. Chem., Int. Ed. Engl.*, 1969, **8**, 469.
63. M. Ishikawa and M. Kumada, *Chem. Commun.*, 1970, 612; 1971, 489.
64. H. Sakurai, H. Sakaba, and Y. Nakadaira, *J. Am. Chem. Soc.*, 1982, **104**, 6156.
65. H. Sakurai, Y. Kobayashi, and Y. Nakadaira, *J. Am. Chem. Soc.*, 1971, **93**, 5272; H. Sakurai, Y. Kobayashi, and Y. Nakadaira, *J. Am. Chem. Soc.*, 1974, **96**, 2656.
66. R. L. Lambert Jr and D. Seyferth, *J. Am. Chem. Soc.*, 1972, **94**, 9246.
67. R. West, M. J. Fink, and J. Michl, *Science*, 1981, **214**, 1343.
68. T. Sanji, H. Fujiyama, K. Yoshida, and H. Sakurai, *J. Am. Chem. Soc.*, 2003, **125**, 3216.
69. P. Jutzi, in 'The Chemistry of Organic Silicon Compounds', eds. Z. Rappoport and Y. Apeloig, Wiley, Chichester, 1998, Vol. 2, Part 3, Chap. 36.
70. M. Denk, R. Lennon, R. Hayashi, R. West, A. V. Belyakov, H. P. Verne, A. Haaland, M. Wagner, and N. Metzler, *J. Am. Chem. Soc.*, 1994, **116**, 2691; M. Denk, R. Hayashi, and R. West, *J. Am. Chem. Soc.*, 1994, **116**, 10813.
71. M. Kira, S. Ishida, T. iwamoto, and C. Kabuto, *J. Am. Chem. Soc.*, 1999, **121**, 9722.
72. Y. Apeloig, in 'The Chemistry of Organic Silicon Compounds', eds. S. Patai and Z. Rappoport, John Wiley & Sons, New York, 1989, Part 1, Chap. 2; P. P. Gaspar and R. West, in 'The Chemistry of Organic Silicon Compounds II', eds. Z. Rappoport and Y. Apeloig, John Wiley & Sons. New York, 1998, Vol. 2, Part 3, Chap. 43; P. P. Gaspar, M. Xiao, D. H. Pae, D. J. Berger, T. Haile, T. Chen, D. Lei, W. R. Winchester, P. Jiang, *J. Organomet. Chem.*, 2002, **646**, 68.
73. M. C. Holthause, W. Koch, and Y. Apeloig, *J. Am. Chem. Soc.*, 1999, **121**, 2623.
74. A. Sekiguchi, T. Tanaka, M. Ichinohe, K. Akiyama, and S. Tero-Kubota, *J. Am. Chem. Soc.*, 2003, **125**, 4962.

75. L. E. Gusel'nikov and M. C. Flowers, *Chem. Commun.*, 1967, 864.

76. D. N. Roark and G. J. D. Peddle, *J. Am. Chem. Soc.*, 1971, **94**, 5837.

77. A. G. Brook, F. Abdesaken, B. Gutekunst, G. Gutekunst, and R. K. M. Kallury, *J. Chem. Soc., Chem. Commun.*, 1981, 191.

78. L. E. Cusel'nikov and N. S. Nametkin, *Chem. Rev.*, 1979, **79**, 529; G. Raabe and J. Michl, *Chem. Rev.*, 1985, **85**, 419; G. Raabe and J. Michl, in 'The Chemistry of Organic Silicon Compounds', eds. S. Patai and Z. Rappoport, Wiley, Chichester, 1989, Part 2, Chap. 17.

79. H. Sakurai, Y. Nakadaira, and T. Kobayashi, *J. Am. Chem. Soc.*, 1979, **101**, 487.

80. G. Olbrich, P. Potzinger, B. Reimann, and R. Walsh, *Organometallics*, 1984, **3**, 1267.

81. R. Okazaki and R. West, *Adv. Organomet. Chem.*, 1996, **39**, 231; N. Tokitoh and R. Okazaki, *Adv. Organomet. Chem.*, 2001, **47**, 121.

82. T. J. Barton and G. T. Burns, *J. Am. Chem. Soc.*, 1978, **100**, 5246.

83. N. Tokitoh, K. Wakita, R. Okazaki, S. Nagase, P. V. R. Schleyer, and H. Jiao, *J. Am. Chem. Soc.*, 1997, **119**, 6951.

84. K. Wakita, N. Tokitoh, R. Okazaki, and S. Nagase, *Angew. Chem., Int. Ed. Engl.*, 2000, **39**, 636; K. Wakita, N. Tokitoh, R. Okazaki, N. Takagi, and S. Nagase, *J. Am. Chem. Soc.*, 2000, **122**, 5648.

85. M. Weidenbruch, S. Willms, W. Saak, and G. Henckel, *Angew. Chem., Int. Ed. Engl.*, 1997, **36**, 2503.

86. A. Sekiguchi and V. Ya. Lee, *Chem. Rev.*, 2003, **103**, 1429.

87. J. Escudie, H. Ranaivonjatovo, and L. Rigon, *Chem. Rev.*, 2000, **100**, 3639.

88. S. Ishida, T. Iwamoto, C. Kabuto, and M. Kira, *Nature*, 2003, **321**, 725.

89. A. Sekiguchi, R. Kinjo, and M. Ichinohe, *Science*, 2004, **305**, 1755.

90. S. Nagase, M. Nakano, and T. Kudo, *J. Chem. Soc., Chem. Commun.*, 1987, 60; S. Nagase, *Angew Chem., Int. Ed. Engl.*, 1989, **28**, 329.

91. A. Sekiguchi and H. Sakurai, *Adv. Organomet. Chem.*, 1994, **37**, 1; A. Sekiguchi and S. Nagase, in 'The Chemistry of Organic Silicon Compounds', eds. Z. Rappoport, Y. Apeloig, John Wiley & Sons, 1998, Vol. 2, Part 1. Chap. 3.

92. N. Wiberg, C. M. M. Finger, and K. Polbom, *Angew. Chem., Int. Ed. Engl.*, 1993, **32**, 1054.

93. A. Sekiguchi, T. Yatabe, C. Kabuto, and H. Sakurai, *J. Am. Chem. Soc.*, 1993, **115**, 5853.

94. A. Sekiguchi, T. Yatabe, H. Kamatani, and H. Sakurai, *J. Am. Chem. Soc.*, 1992, **114**, 6260; K. Furukawa, M. Fujino, and N. Matsumoto, *Appl. Phys. Lett.*, 1992, **60**, 2744; H. Matsumoto, K. Higuchi, S. Kyushin, and M. Goto, *Angew. Chem., Int. Ed. Engl.*, 1992, **31**, 1354.

95. J. M. Zeigler and F. W. C. Fearon, 'Silicon-Based Polymer Science', ACS Symposium Series, No. 224, American Chemical Society, Washington, DC, 1990.

96. R. G. Jones, W. Ando, and J. Chojnowski eds, 'Silicon-Containing Polymers', Kluwer Academic Publishers, Dordrecht, 2000.

97. M. A. Brook, 'Silicon in Organic, Organometallic, and Polymer Chemistry', Wiley-Interscience, New York, 2000, p. 466.

98. S. Yajima, J. Hayashi, and M. Omori, *Chem. Lett.*, 1975, 931; S. Yajima, K. Okamura, and J. Hayashi, *Chem. Lett.*, 1975, 1200.

99. R. West, *J. Organomet. Chem.*, 1986, **300**, 327; R. D. Miller and J. Michl, *Chem. Rev.*, 1989, **89**, 1359; R. West, in 'Comprehensive Organometallic Chemistry', eds. G. Wilkinson, F. G. A. Stone, E. W. Abel, Pergamon, Oxford, 1982, Vol. 2, Chapt. 9.4.

100. G. C. Gobbi, W. W. Fleming, R. Sooriyakumaran, and R. D. Miller, *J. Am. Chem. Soc.*, 1986, **108**, 5624; R. West, *Macromolecules*, 1990, **23**, 4492.

101. M. Abkowitz, F. E. Knier, H. J. Yuh, R. J. Weagley, and M. Stolka, *Solid State Commun.*, 1987, **62**, 547.

102. M. Fujino and N. Matsumoto, *J. Polym. Sci., Part C: Polym. Lett.*, 1988, **26**, 109; R. Menescal and R. West, *Macromolecules*, 1990, **23**, 4492.

103. R. D. Miller, D. Thompson, R. Sooriyakumaran, and G. N. Ficks, *J. Polym. Sci., Part A: Polym. Chem.*, 1991, **29**, 813.

104. C. T. Aitken, J. F. Harrod, E. Samuell, *J. Am. Chem. Soc.*, 1986, **108**, 4059; G. M. Gray, and J. Y. Corey, in 'Silicon-Containing Polymers', eds. R. G. Jones, W. Ando, and J. Chojnowski, Kluwer Academic Publishers, Dordrecht, 2000, Chap. 14.

105. K. Sakamoto, K. Obata, H. Hirata, M. Nakajima, H. Sakurai, H. Sakurai, and M. Yoshida, *J. Am. Chem. Soc.*, 1989, **111**, 7641; in 'Silicon-Containing Polymers', eds. R. G. Jones, W. Ando, and J. Chojnowski, Kluwer Academic Publishers, Dordrecht, 2000, Chapt. 13.

106. K. Sakamoto, M. Yoshida, and H. Sakurai, *Macromolecules*, 1990, **23**, 4494.

107. T. Sanji, F. Kitayama, and H. Sakurai, *Macromolecules*, 1999, **32**, 5718.

108. T. Sanji, Y. Nakatsuka, F. Kitayama, and H. Sakurai, *Chem. Commun.*, 1999, 2201.

109. T. Sanji, Y. Nakatsuka, S. Ohnishi, and H. Sakurai, *Macromolecules*, 2000, **33**, 8524.

110. E. W. Colvin, 'Silicon in Organic Synthesis', Butterworth, London, 1980; W. P. Weber, 'Silicon Reagents for Organic Synthesis', Springer Verlag, Berlin, 1983; I. Fleming, in 'Comprehensive Organic Chemistry', eds. D. Barton and W. D. Ollis, Pergamon Press, New York, 1979, Vol 3, Chap. 13; G. L. Larson, in 'The Chemistry of Organosilicon Compounds', eds. S. Patai and Z. Rappoport, Wiley, Chichester, 1989, Part l, Chap. I l. 47; A. E. Pierce,

‘Silylation of Organic Compounds’, Pierce Chemical Company, Rockford, IL, 1968.

111. A. E. Pierce, ‘Silylation of Organic Compounds’, Pierce Chemical Company, Rockford, IL, 1968.

112. J. R. Hwe, S.-C. Tsay, and B.-L. Cheng, in ‘The Chemistry of Organic Silicon Compounds’, eds. Z. Rappoport and Y. Apeloig, Wiley, Chichester, 1998, Vol. 2, Chapt 8.

113. I. Ojima, ‘The Chemistry of Organosilicon Compounds’, eds. S. Patai and Z. Rappoport, Wiley, Chichester, 1989, Part 2, Chap. 25.

114. T. Mukaiyama, *Angew Chem., Int. Ed. Engl.*, 1977, **16**, 817.

115. D. J. Peterson, *J. Org. Chem.*, 1968, **33**, 780.

Silver: Inorganic & Coordination Chemistry

Thomas C. W. Mak & Xiao-Li Zhao
The Chinese University of Hong Kong, Hong Kong Special Administrative Region, People's Republic of China

Based in part on the article Silver: Inorganic & Coordination Chemistry by W. Ewen Smith which appeared in the Encyclopedia of Inorganic Chemistry, First Edition.

1	Introduction	1
2	Subvalent Silver Compounds	1
3	Silver(I) Compounds	1
4	Silver(II) Compounds	5
5	Silver(III) and Silver(IV) Compounds	6
6	Catalysis	7
7	Related Articles	8
8	References	8

1 INTRODUCTION

The chemical symbol Ag is derived from the Latin *argentum*, which in turn originates from the Greek ἀργός, meaning shiny or glistening. Silver is a rather rare element in the earth's crust, and its abundance is only about 0.07 part per million. Native silver as a compact mass and 'horn silver' (chlorargyrite, AgCl), originating from chemical reduction and the action of salt water, often occur among sulfidic ores such as acanthite (Ag_2S, the chief mineral), stromeyerite (CuAgS), proustite ($3Ag_2S{\cdot}As_2S_3$), stephanite ($5Ag_2S{\cdot}Sb_2S_3$), and margyrite ($Ag_2S{\cdot}Sb_2S_3$). Nowadays about 60% of silver is produced as a by-product in the processing of nonferrous metal ores such as galena (PbS) and copper pyrite ($CuFeS_2$), and the rest by cyanide leaching of silver ores and recovery from coins and industrial scrap. Final purification is usually carried out by electrolysis.[1]

The photographic film industry accounts for about one-third of the world's consumption of silver. It is also used in making jewelry, silverware, artwork, mirrors, electrical and electronic contact points, and high-capacity Ag–Zn and Ag–Cd batteries. The metal and its compounds are useful as catalysts in organic synthesis. In medicine, silver sulfadiazine is effective for the treatment of burns.

Silver has a cubic close-packed structure ($a = 408.626$ pm, space group $Fm\bar{3}m$) and is the best conductor of heat and electricity among all metals. Being ductile and very malleable, it can be hammered into thin foils, which transmit blue-green light.

The chemistry of silver is in accord with its electronic configuration $4d^{10}5s^1$.[1–3] Silver is chemically less reactive than copper except toward sulfur and hydrogen sulfide, which rapidly tarnish lustrous silver surfaces. Silver is immune to nonoxidizing acids such as hydrochloric acid, but it dissolves readily in dilute nitric acid. However, concentrated nitric and sulfuric acids attack it only at higher temperatures owing to the formation of a rather insoluble protective layer of $AgNO_3$ or Ag_2SO_4. It dissolves easily in cyanide solutions in the presence of oxygen owing to a large shift in the silver potential (from $+0.80$ V to -0.31 V) in forming the complex $[Ag(CN)_2]^-$. Some important properties of silver are listed in Table 1.[3,4]

2 SUBVALENT SILVER COMPOUNDS

Silver having a formal oxidation state smaller than one occurs in compounds with the most electronegative elements, namely, fluorine and oxygen. Disilver monofluoride (silver subfluoride), Ag_2F, is formed in the reaction between finely divided silver and AgF in liquid hydrogen fluoride. It can also be obtained electrolytically from AgF at low current densities, crystallizing on the silver cathode as bronze-colored platelets. Ag_2F decomposes into Ag and AgF above 100 °C. It has an *anti*-CdI_2 structure in which double layers of Ag ('metallic' $Ag\cdots Ag$ bond lengths lie in the range 2.814–2.996 Å) alternate with layers of AgF (Ag–F bond length is 2.451 Å). The compound is a good electrical conductor.

Trisilver oxide (silver suboxide), Ag_3O, which conducts electricity, is made by heating AgO to 80 °C in a silver vessel in the presence of H_2O under a pressure of 4×10^8 Pa. Ag_3O has an *anti*-BiI_3 structure in which oxygen occupies 2/3 of the octahedral holes in a hexagonal close-packed array of silver, in which the Ag–O bonds are 2.29 Å, while the $Ag\cdots Ag$ bonds are about 2.88 Å. Pentasilver orthosilicate, Ag_5SiO_4, is formed by hydrothermal reaction of silver powder with amorphous SiO_2 under high oxygen pressure.[5] Crystal-structure analysis showed that it should be formulated as $[Ag_6]^{4+}(Ag^+)_4(SiO_4{}^{4-})_2$, being composed of a packing of octahedral $Ag_6{}^{4+}$ clusters along with isolated Ag^+ and tetrahedral $SiO_4{}^{4-}$ ions. Silver also forms rare zero-valent carbonyl compounds $Ag(CO)_3$ and $Ag_2(CO)_6$, which exist only at low temperatures (10 and 30 K, respectively).

3 SILVER(I) COMPOUNDS

This is the dominant oxidation state of silver, and the Ag(I) ion with spherically symmetric configuration $4d^{10}$ exhibits a range of coordination numbers from 2 to 6. Silver(I) is stable in aqueous solution as $[Ag(H_2O)_2]^+$. However, the soft Ag(I) cation has a relatively low affinity

Table 1 Properties of elemental silver

Atomic number	47
Number of naturally occurring isotopes	2
Atomic weight	107.8682(2)
Electronic configuration	[Kr]$4d^{10}5s^1$
Metal radius (12-coordinate)/pm	144
Ionic radii (six-coordinate compounds)/pm	Ag^{I}115 Ag^{II}94 Ag^{III}75
van der Waals radius/pm	170
Ionization potential/kJ mol^{-1}	1st 730.8 2nd 2072.6 3rd 3359.4
Electronegativity	1.93 (Pauling), 1.42 (Allred)
Melting point/K	1235.08
Boiling point/K	2485
Δ H_{fusion}/kJ mol^{-1}	11.3
Δ H_{vap}/kJ mol^{-1}	255.1
Density (293 K)/kg m^{-3}	10500
Electrical resistivity (293 K)/Ω m	1.59×10^{-8}
Mass magnetic susceptibility/kg^{-1} m^3	-2.27×10^{-9} (s)
Molar volume/cm^3	10.27
Coefficient of linear thermal expansion/K^{-1}	19.2×10^{-6}

for the hard aqua ligand, so nearly all its crystalline inorganic salts are anhydrous except for AgF and $AgClO_4$.

Silver alkyls and aryls, together with silver(I) complexes of cyclic polyenes and alkynyl ligands, are generally classified under organometallic compounds. Stable silver(I) carbonyl complexes that have been characterized by X-ray analysis include $[Ag(CO)\{B(OTeF_5)_4\}]$, $[Ag(CO)_2\{B(OTeF_5)_4\}]$, and $[Ag(CO)\{HB[3,5\text{-}(CF_3)_2pz]_3\}]$.**[6]** Silver acetylide (Ag_2C_2) complexes are described in Section 3.6.

3.1 Halides and Pseudohalides

Silver halides can be prepared directly by addition of X^- to Ag^+ solutions, although AgF is usually prepared from silver oxide and hydrofluoric acid. The color and insolubility of silver halides in water increase in the order Cl < Br < I. Both AgCl and AgBr have the rock salt structure, though they are insulators. AgI has both zinc blende and wurtzite forms. The ultrahigh light-sensitivity of these halides (AgF only to the ultraviolet), particularly AgBr, is the basis for their use in photography. The formation of the linear $[H_3N\text{–}Ag\text{–}NH_3]^+$ complex can be used for the separation of mixed silver halides. Aqueous ammonium carbonate is sufficient to dissolve AgCl to give $[Ag(NH_3)_2]Cl$, while AgBr can be extracted with aqueous ammonia, in which AgI is sparingly soluble.

The halides AgX (X = Cl, Br, I) react with halide anions X^- to give a series of discrete anionic complexes $[Ag_mX_n]^{(n-m)-}$.**[7–9]** Examples of such iodo complexes are shown in Figure 1.

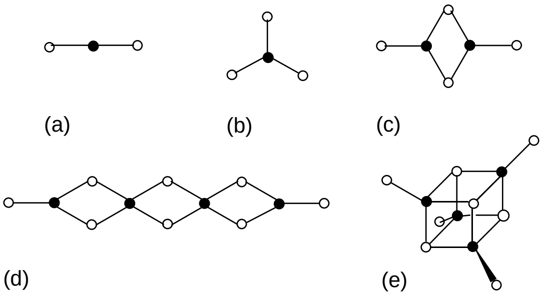

Figure 1 Structures of discrete iodoargentate complexes: (a) $[AgI_2]^-$; (b) $[AgI_3]^{2-}$; (c) $[Ag_2I_4]^{2-}$; (d) chain-like $[Ag_4I_8]^{4-}$; (e) cubane-like $[Ag_4I_8]^{4-}$

Polymeric species $[(Ag_mX_n)^{(n-m)-}]_\infty$ (X = Cl, Br, I) have been identified in several crystal structures.**[10]** Silver complexes with mixed halide ligands have also been prepared, for example, discrete $[Ag_2Br_4Cl_2]^{4-}$ and polymeric $[(Ag_6X_2I_6)^{2-}]_\infty$ (X = Cl, Br).**[11]**

The related pseudohalides AgCN, AgNCO, and AgSCN all have infinite chain structures. The Ag^+ ion in AgN_3 is coordinated tetrahedrally by four azide groups, each being surrounded in turn by four Ag^+ ions in a pseudotetrahedral arrangement.

3.2 Phosphorus Donor Ligands

With monophosphines, the complexes are mainly of the type $[AgX(PR_3)_n]$ ($n = 1-4$). The 1:1 compounds are tetrameric, with either cubane or chair structures depending on the steric requirements of both X and PR_3. $[AgX(PPh_2Bu)]$ (X = Cl, Br, I) have been shown to possess a Ag_4X_4-cubane core.**[12]** By using $PR^1{}_2R^2$ ligands of intermediate size between Pcy_3 (which forms two-coordinate Ag^+ species) and PPh_3 (which forms four-coordinate species), several three-coordinate (R^1 = Ph; R^2 = Ph, cy, C_5H_9) or two-coordinate ($R^1 = C_5H_9$, cy; R^2 = Ph) complexes have been generated.**[13]**

Heterobimetallic complexes of platinum, rhodium, or group 6 metals and silver with bridged bis(diphenylphosphanyl) methane (dppm) have been obtained.**[14]** The reaction of $[CoCl_2(PR_3)_2]$ ($PR_3 = PPh_3$, PPh_2CH_2COPh) with $AgBF_4$ gives $[Ag(PR_3)_2]Cl$, but the triphenylphosphine cobalt complex in the presence of excess PPh_3 gives the heterotrimetallic complex $[Ag_2CoCl_4(PPh_3)_4]$.**[15]**

Silver complexes with bidentate diphosphines tend to be bridged dimers or tetramers (Figure 2). A common $[Ag_2(dppm)_2]^{2+}$ core occurs in $[Ag_2X_2(dppm)_2]$ (X = NO_3, O_2CH_2Ph, O_2CMe, CH_3COO). The complexes $[Ag_3Cl_2(dppm)_3]X$ (X = ClO_4, $SnPh_2(NO_3)Cl$), $[Ag_3I_2(dppm)_3]I$ and $[Ag_4(\mu\text{-dppm})_4(\mu_4\text{-E})](OTf)_2$ (E = S, Se, Te) contain tri- or tetranuclear species. Also, a series of hexanuclear and heptanuclear silver(I) chalcogenolate complexes with bridging dppm ligands, $[Ag_6(\mu\text{-dppm})_4(\mu_3\text{-EAr})_4](PF_6)_2$ (EAr = SPh, SC_6H_4Me-p, SePh, SeC_6H_4Cl-p)

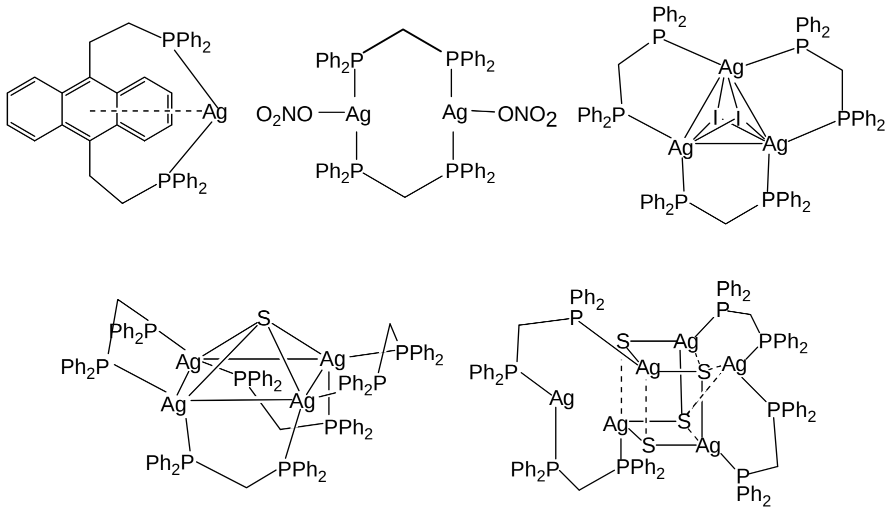

Figure 2 Structures of some silver(I) complexes with bridging bidentate diphosphines

and $[Ag_7(SPh)_7(dppm)_3]$, have been synthesized and characterized.[16] With some bulky diphosphines, such as 9,10-bis{(2-diphenylphosphanyl)ethyl}anthracene, mononuclear complexes can be obtained.[17]

3.3 Nitrogen Donor Ligands

There is considerable recent interest in the development of synthetic routes to supramolecular architecture from the self-assembly of silver(I) with multifunctional ligands under controlled reaction conditions.[18] Advances in this field have made use of nitrogen donors such as cyanide, thiocyanate, bipyridine, oligopyridines, aza-crowns, cryptands, tripodal imidazoles, and azide, leading to the rational synthesis of functional solid-state supramolecular silver(I) complexes with helical,[19] honeycomb channel,[20] interwoven diamondoid,[21] and other kinds of novel frameworks. The assembly process involves the interplay of various intermolecular interactions, which include hydrogen bonding, $\pi-\pi$ stacking, host-guest interaction, van der Waals forces, metallophilicity, and Coulombic attractions. Some examples of supramolecular silver(I) complexes consolidated by nitrogen donor ligands are shown in Figure 3.

3.4 Oxygen Donor Ligands

The most important classes of oxygen donor ligands for complexation of silver(I) are β-diketonates, carboxylates, crown ethers, and calixarenes.

Silver(I) β-diketonates are generally obtained by the reaction of Ag_2O with a β-diketonate in the presence of other ligands, or by treatment of $AgNO_3$ with the diketone in dry methanol and acetonitrile. They are of significant interest owing to the ease with which they can be reduced to the metal by metal-organic chemical vapor deposition (MOCVD), and volatility and stability problems have been overcome with new techniques such as supercritical fluid transport chemical vapor deposition (SFTCVD) and aerosol-assisted chemical vapor deposition (AACVD), as well as spray pyrolysis.[22]

Silver carboxylate compounds are light-sensitive and generally insoluble in most solvents, making it difficult for their structural characterization. In contrast, the zwitterionic betaine ligands $R_3N^+(CH_2)_nCO_2^-$ form stable silver complexes that are soluble in water and ethanol, and a variety of discrete dimers or polymeric chain/network structures constructed by the linkage of dimeric subunits have been obtained.[23]

Several silver(I) complexes with crown ethers and calixarenes have been synthesized. In the design of discrete molecules and infinite chains in silver acetylide chemistry, crown ethers function as blocking groups or protective cordons around a polyhedral $C_2@Ag_n$ cage so that the isolation of lower-dimensional supramolecular entities can be achieved.[24]

3.5 Chalcogen Donor Ligands

Silver(I) form numerous complexes with ligands containing soft S, Se, and Te donor atoms. The principal types of sulfur ligands are the thiolates, which give oligomers $(AgSR)_n$, dithiolates, thiocarbamates, dithiocarbamates, thiocyanate, thioureas, and thioethers. The complex $[Ag_4(SPh)_4(PPh_3)_4]$ takes the chair configuration. Silver(I) also binds to peptides and proteins, with a preference for –SR and imidazole nitrogen functionalities. Silver(I) thia-crown complexes have been used as templates for the synthesis of extended polyiodide networks, or as building blocks for the formation of coordination polymers.[25a–d] Silver(I) complexes with macrocyclic selenoethers are also known.[25e]

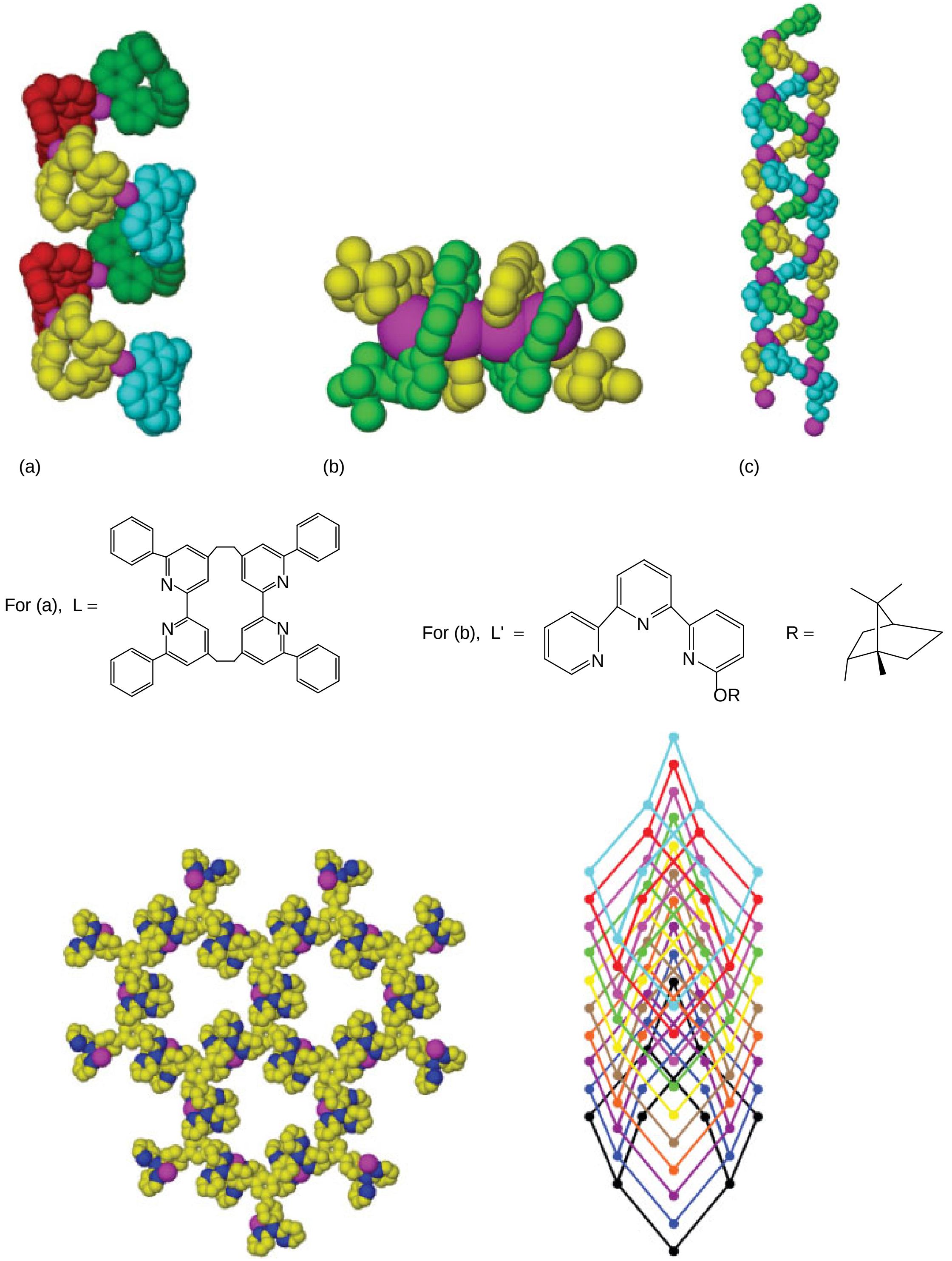

Figure 3 Structures of some supramolecular silver(I) coordination complexes with nitrogen donor ligands. (a) Helical polymeric cation in $[AgL]_n(PF_6)_n$. Different colors used for consecutive L ligands clearly reveal the pitch of the helix.[19a] (b) Tetranuclear M, M-$[\{Ag_2L'_2\}_2]^{4+}$ bis(double helices) in $[Ag_2(L')_2][PF_6]_2{\cdot}Me_2CO$.[19b] (c) Triple helical polymer in $Ag(3\text{-amp})ClO_4$ (3-amp = 3-aminomethylpyridines) showing the pitch along the *b* axis.[19c] (d) Space-filling model of single honeycomb-shaped cavity in $[\{[Ag(CF_3SO_3)]_{1.5}(tdapb)\}_n]$ (tdapb = 1, 3, 5-tris(4-(2, 2′-dipyridylamino)-phenyl)benzene).[20a] Color code: silver, purple; nitrogen, dark blue; carbon, yellow. (e) Schematic view of the 10-fold interpenetration in the coordination network of $[Ag(ddn)_2]NO_3$ (ddn = 1,12-dodecanedinitrile)[21a]

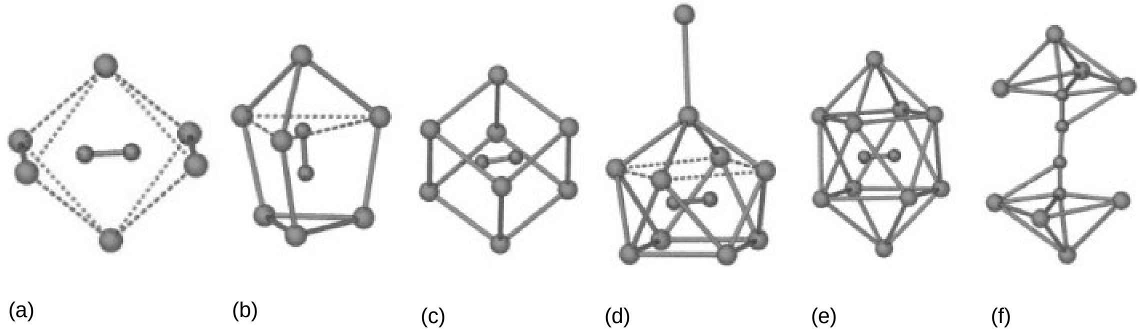

Figure 4 Silver polyhedra with embedded acetylenediide: (a) $C_2@Ag_6$ in $Ag_2C_2{\cdot}AgNO_3$.[27a] (b) $C_2@Ag_7$ in $2Ag_2C_2{\cdot}AgF{\cdot}4AgCF_3SO_3{\cdot}CH_3CN$.[27d] (c) $C_2@Ag_8$ in $[Ag_8(C_2)(CF_3CO_2)_6(L)_6]$ (L = 4-hydroxyquinoline).[27g] (d) $C_2@Ag_9$ in $Ag_2C_2{\cdot}8AgF$.[27b] (e) $C_2@Ag_{10}$ in $(L_2H)_4[Ag_{10}(C_2)(CF_3CO_2)_{12}(L)_2]{\cdot}5H_2O$ (L = 4-hydroxyquinoline).[27g] (f) $Ag_4C_4Ag_4$ aggregate in $Ag_2C_4{\cdot}6AgNO_3{\cdot}nH_2O$ ($n = 2, 3$)[27i]

3.6 Silver-rich Compounds

The significance of argentophilicity, that is, the $d^{10}–d^{10}$ closed-shell attraction that promotes the aggregation of silver(I) centers, has been substantiated by recent spectroscopic and structural evidence.[26]

3.6.1 Complexes Containing Silver Acetylide or 1,3-Butadiynediide

The general occurrence of $C_2@Ag_n$ polyhedra ($n = 6–10$; each with an embedded C_2^{2-} dianion) and fused double cages $(C_2)_2@Ag_{2n-m}$ (n vertexes, m shared atoms) has been established in a series of double, triple, and quadruple salts containing silver(I) acetylide (IUPAC name is acetylenediide), Ag_2C_2.[27a–e] The geometries of some $C_2@Ag_n$ polyhedra are illustrated in Figure 4. The exploration of $C_2@Ag_n$ polyhedra as building blocks for supramolecular assembly via functional linkages between the agglomerated components has led to the generation of a variety of new coordination frameworks.[27f–h] Replacement of C_2^{2-} by its higher homolog C_4^{2-} disrupts the convex $C_2@Ag_n$ cage, as found in two hydrated double salts $Ag_2C_4{\cdot}6AgNO_3{\cdot}nH_2O$ ($n = 2, 3$).[27i]

3.6.2 Halide-centered Ag_n Cages

The mixed-metal cluster $[Ni^{II}_6Ag^{I}_8(D\text{-pen})_{12}Cl]^{5-}$ (pen = penicillamine) has a central skeleton consisting of silver atoms at the corners of a cube with the chloride ion in its center.[28a] In the series of tetradecanuclear complexes $[Ag_{14}(C{\equiv}C^tBu)_{12}X]Y$ (X = F, Cl, Br; Y = OH, BF_4),[28b,c] the central cage is also a cubic array of silver atoms with an encapsulated halide ion, and the stabilization of these compounds is attributable to the argentophilic Ag···Ag interaction (Figure 5a). The halide-centered Ag^I_8 cubic cluster also occurs in $\{Ag_8(\mu_8\text{-}X)\ [Se_2P(OR)_2]_6(PF_6)\}$ (R = Et, Pr, ^{i}Pr; X = Cl, Br).[28d,e] The isostructural silver(I) triple salts $AgCN{\cdot}AgF{\cdot}4AgCF_3CO_2{\cdot}2L$ (L = MeCN or H_2O) have a layer structure in which the fluoride-centered octahedral cage $F@Ag_6$ are interconnected by $\kappa C, \kappa C : \kappa N, \kappa N$-cyanide and $\mu\text{-}O,\ O{:}O'O'$-trifluoroacetato bridges.[28f]

3.6.3 Silver–Chalcogenide Clusters

Examples of silver-rich chalcogenide 'supercluster' complexes include $[NHEt_3]_4[Ag_{50}S_7(SC_6H_4tBu)_{40}]$,[29a] $[Ag_{70}S_{20}(SPh)_{28}(dppm)_{10}](CF_3CO_2)_2$ and $[Ag_{262}S_{100}(StBu)_{62}(dppb)_6]$,[29b] and $[Ag_{70}S_{16}(SPh)_{34}(PhCO_2)(triphos)_4]$ and $[Ag_{188}S_{94}(PR_3)_{30}]$ (R = nPr, nBu).[29c] Similar very large Ag–Se and Ag–Te clusters such as $[Ag_{172}Se_{40}(SenBu)_{92}(dppp)_4]$,[29d] $[Ag_{38}Te_{13}(TetBu)_{12}(dppe)_6]$[29e] and $[Ag_{124}Se_{57}(SePtBu_2)_4Cl_6(tBu_2P(CH_2)_3PtBu_2)_{12}]$[29f] have been reported (triphos = 1, 1, 1-tris(diphenylphosphanylmethyl)ethane, dppb = bis(diphenylphosphanyl)butane, dppp = 1, 3-bis(diphenylphosphanyl)propane, dppe = 1, 2-bis(diphenylphosphanyl)ethane).

3.6.4 Silver–Gold Clusters

Taking advantage of argentophilicity and aurophilicity, large ternary M–Ag–Au clusters have been prepared: for example, $[(Ph_3P)_{10}Au_{12}Ag_{12}PtCl_7]C1$[30a] (Figure 5b), $[(Ph_3P)_{10}Au_{12}Ag_{12}NiCl_7](SbF_6)$[30b] and $[(Ph_3P)_6Au_6Ag_6Pt(AgI_3)_2](THF)_2$.[30c]

4 SILVER(II) COMPOUNDS

The Ag^{2+} ion is produced as an orange transient species $[Ag(H_2O)_6]^{2+}$ via oxidation of silver(I) salts with ozone in strongly acidic solution. It readily oxidizes water to oxygen. Silver(II) fluoride, AgF_2, is formed by the highly exothermic reaction of fluorine with very finely divided silver. AgF_2 is antiferromagnetic, with a magnetic moment well below

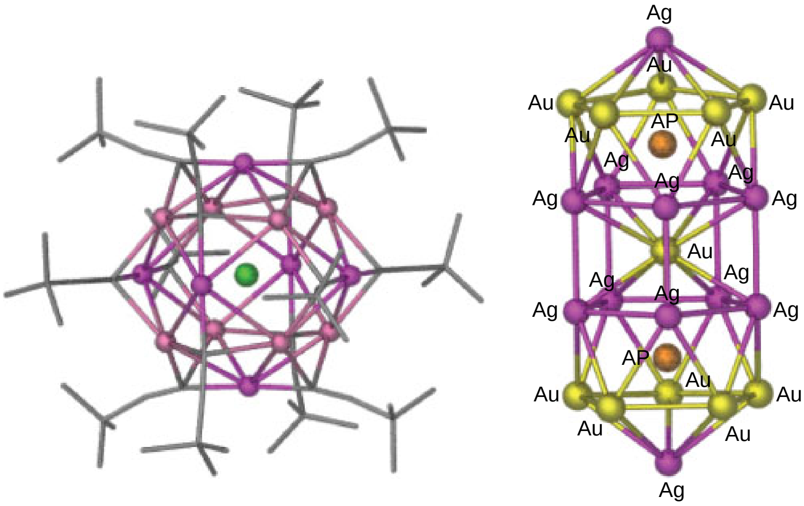

(a) (b)

Figure 5 (a) Structure of silver cage complexes $[Ag_{14}(C\equiv C^tBu)_{12}X]OH$ ($X = Cl, Br$) showing the rhombic dodecahedron of silver atoms (solid bonds) and the encapsulation of a halide anion at the center of an octahedron of type 2 silver atoms. Silver atoms of types 1 and 3 cap the faces of this octahedron and define a cubic array.[28b] (b) Mixed-metal $Au_{12}Ag_{12}Pt$ core in $[(Ph_3P)_{10}Au_{12}Ag_{12}PtCl_7]Cl$; the Pt atom and one Au atom randomly occupy the pair of AP sites[30b]

that expected for one unpaired electron. It can conveniently be used as a good source of fluorine in chemical reactions. Silver has a remarkable catalytic effect on reactions of many gases with fluorine, owing to the formation of AgF_2 as an intermediate. Fluoride ions and AgF_2 form the fluorocomplexes AgF_3^-, blue-violet AgF_4^{2-} and AgF_6^{4-}; in each case the Ag^{2+} ion is octahedrally coordinated by F^- with some tetragonal distortion. The octahedra share either opposite faces (in AgF_3^-) or edges (in AgF_4^{2-}) to form an infinite chain, or exist as discrete species (in AgF_6^{4-}). Silver fluorosulfate $Ag(OSO_2F)_2$ is made by heating the metal with $S_2O_6F_2$ at 70 °C and is stable to 210 °C.

Silver(II) forms stable complexes with a variety of nitrogen donor ligands such as pyridine, substituted bipyridine, phenanthroline, or citrazinic acid. They are usually obtained by reaction of a silver(I) salt with peroxodisulfate in the presence of the ligand.[31]

Disproportionation of Ag(I) to silver metal and Ag(II) in the presence of tetraaza macrocyclic ligands depends upon the ring size of the macrocycle; thus while 14-, 15-, and 16-membered rings generally cause disproportionation, larger rings do not. Two mixed-valence complexes $[Ag^{II}(tmc)(BF_4)][Ag^I_6(C_2)(CF_3CO_2)_5(H_2O)]\cdot H_2O$ and $[Ag^{II}(tmc)][Ag^{II}(tmc)(H_2O)]_2[Ag^I_{11}(C_2)(CF_3CO_2)_{12}(H_2O)_4]_2$ (tmc = 1,4,8,11-tetramethyl-1,4,8,11-tetraazacyclotetradecane) have been prepared. In the former, a $[Ag^{II}(tmc)(BF_4)]^{+1}_{\infty}$ cationic column induces the assembly of an anionic zigzag chain constructed from edge-sharing of silver(I) triangulated dodecahedra each enclosing a C_2^{2-} species. As to the latter, $[Ag^{II}(tmc)]^{2+}$ and $[Ag^{II}(tmc)(H_2O)]^{2+}$ complex cations together induce the self-assembly of a centrosymmetric anionic cluster dimer from the Ag(I), C_2^{2-} and $CF_3CO_2^-$ species.[32]

The porphyrins constitute another class of nitrogen donor ligands which favor Ag(II) over Ag(I). Their macrocyclic structure provides strong in-plane ligand fields, which facilitate oxidation of the metal.[33] Phthalocyanine complexes of Ag(II) are very stable and can be oxidized electrochemically to Ag(III); further oxidation gives a Ag(III) phthalocyanine cation radical. The oxidation of Ag(I) complexes of sulfur macrocycles also leads reversibly to Ag(II) complexes.[34]

Silver(II) complexes in the gas phase have been prepared with several nitrogen- and oxygen-donor ligands including pyridine, tetrahydrofuran, benzene, and CO_2. The complexes are of the type $[AgL_n]^{2+}$, and the compound $[Ag(CO_2)_4]^{2+}$ is particularly stable.[35]

5 SILVER(III) AND SILVER(IV) COMPOUNDS

The anodic oxidation of neutral aqueous solutions of $AgClO_4$ or $AgBF_4$ yields black, metallic lustrous crystals of Ag_2O_3, which contain square-planar Ag(III). Oxidation at lower potentials leads to the black, semiconducting monoxide AgO, which is actually diamagnetic $Ag^IAg^{III}O_2$; it can also be obtained by oxidation of Ag_2O with $S_2O_8^{2-}$ in alkaline solution. Trisilver tetroxide, Ag_3O_4, contains both divalent and trivalent silver, as indicated by the formula $Ag^{II}Ag^{III}{}_2O_4$.

Oxidation of Ag(I) by $S_2O_8{}^{2-}$ in a strong alkaline solution of periodate or tellurate yields a yellow, diamagnetic silver(III) complex, for example, $K_5[Ag(IO_6H)_2]$ and $Na_5[Ag(TeO_6H_2)_2]$.

Oxidation of a mixture of potassium and silver(I) halides with fluorine in alkaline solution produces yellow potassium tetrafluoroargentate, $KAgF_4$, which is very sensitive to moisture. The corresponding yellow sodium and cesium salts are also known. All contain the diamagnetic square-planar $[AgF_4]^-$ ion. There are mixed-metal salts such as KCs_2AgF_6, which contains the octahedral $[AgF_6]^{3-}$ ion. Fluorination of a mixture of CsCl and AgCl under pressure yields a complex salt of tetravalent silver $Cs_2[Ag^{IV}F_6]$.

A mixed-valence silver(I)-silver(III) cryptate complex has been synthesized by condensation of tris(3-aminopropyl)amine and terephthaldehyde in the presence of $AgNO_3$. Other pyridine silver(III) complexes have been obtained by oxidation of silver nitrate and ammonia with ammonium peroxydisulfate in aqueous ammonia solution. An air-stable diamagnetic silver(III) complex of a N-confused tetraphenylporphyrin, 5,10,15,20-tetraphenyl-2-aza-21-carboporphyrin argentate(III), has been described.[36]

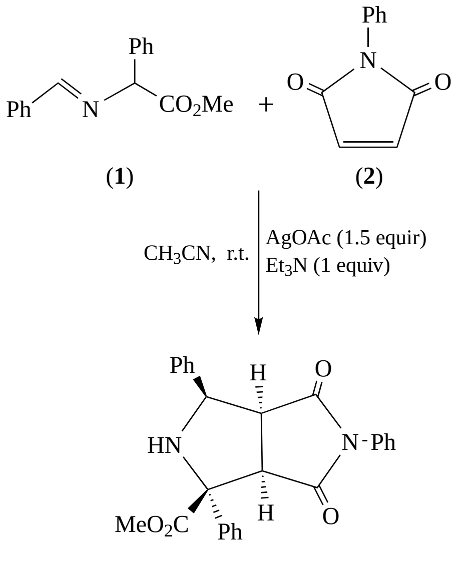

6 CATALYSIS

The metal is useful as a catalyst, particularly in the partial oxidation of ethylene to ethylene oxide. Silver(I) salts have mild Lewis acidity, rendering them useful as promoters and catalysts in organic synthesis.[37] Achiral silver(I) compounds, especially $AgBF_4$ and AgOTf, have been widely used in organic synthesis and numerous selective carbon–carbon bond-forming reactions, including cycloaddition, rearrangement, arylation and alkylation.[38] For example, AgOAc catalyzes the cycloaddition of (**1**), an arylidene imine of an α-amino acid ester, to dipolarophile (**2**), to give the proline derivative (**3**) in 71% yield.[39]

A catalytic amount of $AgBF_4$ promotes the rearrangement of housane (**4**) to the diastereomeric cyclopentenes (**5**) (*endo*-CD_3 group migration, 86% yield) and (**6**) (*exo*-CD_3 group migration, 14% yield).[40]

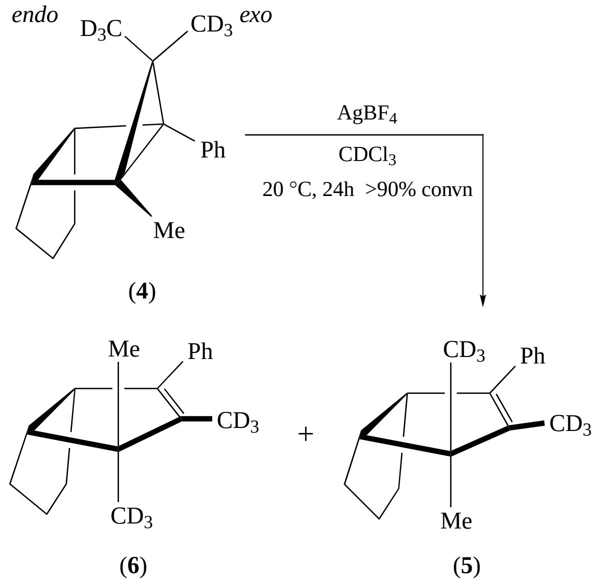

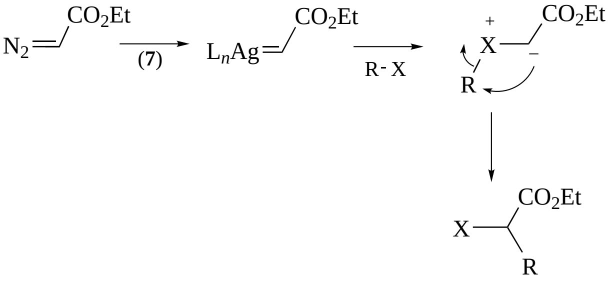

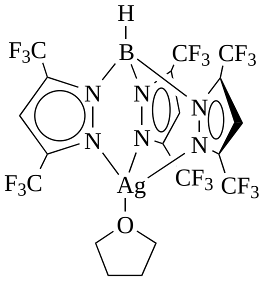

(**7**)

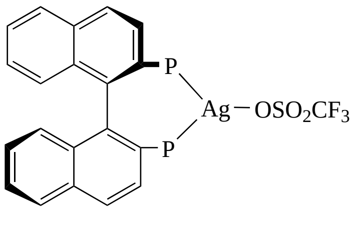

(*R*)-BINAP·AgOTf (**8**)

The complex $[HB\{3,5\text{-}(CF_3)_2pz\}_3]Ag(THF)$ (**7**) has been employed in the silver-catalyzed activation of carbon-halogen bonds through a carbene insertion process that occurs at room temperature, resulting in formation of a new sp^3–sp^3 carbon–carbon bond.[41]

The remarkable affinity of the silver ion for halides can be conveniently applied to accelerate the chiral palladium-catalyzed Heck reaction and other reactions.[42] Enantioselectivity of these reactions is generally increased by addition of silver salts, and hence silver(I) compounds in combination with chiral ligands hold much promise as chiral Lewis acid catalysts for asymmetric synthesis. Employing the BINAP·silver(I) complex (**8**) as a chiral catalyst, the enantioselective aldol addition of tributyltin enolates (**9**) to aldehydes (**10**) has been developed.[43] This catalyst is also effective in the promotion of enantioselective allylation, Mannich, ene, and hetero Diels–Alder reactions.

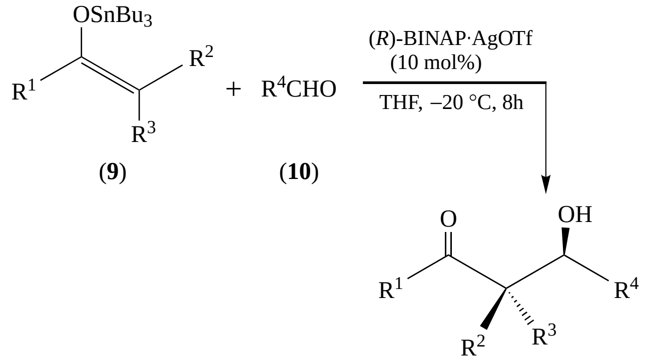

7 RELATED ARTICLES

Coordination Chemistry: History; Coordination Numbers & Geometries; Copper: Inorganic & Coordination Chemistry; Gold: Organometallic Chemistry; Halides: Solid-state Chemistry; Photochemistry of Transition Metal Complexes.

8 REFERENCES

1. N. Wiberg, ‘Holleman-Wiberg: Inorganic Chemistry’, Academic Press, San Diego, CA, 2001, p. 1265.
2. F. A. Cotton, G. Wilkinson, C. A. Murillo, and M. Bochmann, ‘Advanced Inorganic Chemistry’, 6th edn., Wiley, New York, 1999, p. 1084.
3. N. N. Greenwood and A. Earnshaw, ‘Chemistry of the Elements’, 2nd edn., Butterworth-Heinemann, Boston, MA, 1997, p. 1173.
4. J. Emsley, ‘The Elements’, 3rd edn., Clarendon Press, Oxford, 1998, p. 192.
5. C. Linke and M. Jansen, *Inorg. Chem.*, 1994, **33**, 2614.
6. H. V. R. Dias and W. Jin, *J. Am. Chem. Soc.*, 1995, **117**, 11381.
7. (a) G. Helgesson and S. Jagner, *Inorg. Chem.*, 1991, **30**, 2574; (b) S. K. Schneider, W. A. Herrmann, and E. Herdtweck, *Z. Anorg. Allg. Chem.*, 2003, **629**, 2363; (c) D. J. Darensbourg, M. J. Adams, J. C. Yarbrough, and A. L. Phelps, *Inorg. Chem.*, 2003, **42**, 7809.
8. (a) G. Helgesson and S. Jagner, *Dalton Trans.*, 1993, 1069; (b) H. Paulsson, M. Berggrund, A. Fischer, and L. Kloo, *Eur. J. Inorg. Chem.*, 2003, 2352; (c) A. Hassan, S. R. Breeze, S. Courtenay, C. Deslippe, and S.-N. Wang, *Organometallics*, 1996, **15**, 5613; (d) B. Neumuller, S. Chitsaz, and K. Dehnicke, *Z. Anorg. Allg. Chem.*, 2002, **628**, 523; (e) H.-W. Hou, X.-R. Ye, X.-Q. Xin, Z.-M. Wang, S.-X. Liu, and J.-L. Huang, *Acta Crystallogr., Sect. C: Cryst. Struct. Commun.*, 1995, **51**, 2013.
9. (a) S. Olson, G. Helgesson, and S. Jagner, *Inorg. Chim. Acta*, 1994, **217**, 15; (b) G. Helgesson and S. Jagner, *Dalton Trans.*, 1990, 2413.
10. (a) B. Ahrens, S. Friedrichs, R. Herbst-Irmer, and P. G. Jones, *Eur. J. Inorg. Chem.*, 2000, 2017; (b) G. Helgesson and S. Jagner, *Acta Crystallogr., Sect. C: Cryst. Struct. Commun.*, 1988, **44**, 2059; (c) W.-Z. Chen and F.-H. Liu, *J. Organomet. Chem.*, 2003, **673**, 5; (d) X.-G. Jin, K.-L. Tang, W.-D. Liu, and Y.-Q. Tang, *Heteroat. Chem.*, 1995, **6**, 41.
11. (a) M. Mayr, K. Wurst, K.-H. Ongania, and M. R. Buchmeiser, *Chem. Eur. J.*, 2004, **10**, 1256; (b) G. A. Bowmaker, Effendy, J. D. Kildea, B. W. Skelton, and A. H. White, *Aust. J. Chem.*, 1990, **43**, 2113.
12. R. J. Bowen, D. Camp, Effendy, P. C. Healy, B. W. Skelton, and A. H. White, *Aust. J. Chem.*, 1994, **47**, 693.
13. (a) A. Baiada, F. H. Jardine, and R. D. Willett, *Inorg. Chem.*, 1990, **29**, 4805; (b) A. Baiada, F. H. Jardine, and R. D. Willett, *Inorg. Chem.*, 1990, **29**, 3042.
14. (a) C.-F. Xu, G. K. Anderson, L. Brammer, J. Braddock-Wilking, and N. P. Rath, *Organometallics*, 1996, **15**, 3972; (b) S. A. Al-Jibori, *Transition Met. Chem.*, 1995, **20**, 523; (c) H.-K. Yip, H.-M. Lin, K.-K. Cheung, C.-M. Che, and Y. Wang, *Inorg. Chem.*, 1994, **33**, 1644.
15. P. Braunstein, D. G. Kelly, Y. Dusausoy, D. Bayeul, M. Lanfranchi, and A. Tiripicchio, *Inorg. Chem.*, 1994, **33**, 233.
16. (a) F. Caruso, M. Camalli, H. Rimml, and L. M. Venanzi, *Inorg. Chem.*, 1995, **34**, 673; (b) M.-C. Hong, D.-X. Wu, H.-Q. Liu, T. C. W. Mak, Z.-Z. Zhou, D.-D. Wu, and S.-L. Li, *Polyhedron*, 1997, **16**, 1957; (c) T. C. Deivaraj and J. J. Vittal, *Dalton Trans.*, 2001, 322; (d) D. M. Ho and R. Bau, *Inorg. Chem.*, 1983, **22**, 4073; (e) W.-B. Zhou, Z.-C. Dong, J.-L. Song, H.-Y. Zeng, R. Cao, G.-C. Guo, J.-S. Huang, and J. Li, *J. Cluster Sci.*, 2002, **13**, 119; (f) V. W.-W. Yam, K. K.-W. Lo, C.-R. Wang, and K.-K. Cheung, *Inorg. Chem.*, 1996, **35**, 5116; (g) V. W.-W. Yam, E. C.-C. Cheng, and N.-Y. Zhu, *New J. Chem.*, 2002, **26**, 279.
17. (a) D. A. Atwood, A. H. Cowley, and S. M. Dennis, *Inorg. Chem.*, 1993, **32**, 1527; (b) M. C. Gimeno, P. G. Jones, A. Laguna, and C. Sarroca, *Dalton Trans.*, 1995, 1473; (c) F.-B. Xu, Q.-S. Li, L.-Z. Wu, X.-B. Leng, Z.-C. Li, X.-S. Zeng, Y. L. Chow, and Z.-Z. Zhang, *Organometallics*, 2003, **22**, 633.

18. (a) A. G. Sykes, *Adv. Inorg. Chem.*, 1999, **46**, 174; (b) J. A. McCleverty and T. J. Meyer eds, 'Comprehensive Coordination Chemistry II', Elsevier Pergamon, Boston, MA, 2004, Vol. 6, p. 911.

19. (a) C. Kaes, M. W. Hosseini, C. E. F. Rickard, B. W. Skelton, and A. H. White, *Angew. Chem., Int. Ed. Engl.*, 1998, **37**, 920; (b) G. Baum, E. C. Constable, D. Fenske, C. E. Housecroft, and T. Kulke, *Chem. Commun.*, 1998, 2659; (c) S. Sailaja and M. V. Rajasekharan, *Inorg. Chem.*, 2000, **39**, 4586; (d) M. D. Ward, J. A. McCleverty, and J. C. Jeffery, *Coord. Chem. Rev.*, 2001, **222**, 251; (e) M. Albrecht, *Chem. Rev.*, 2001, **101**, 3457; (f) G. F. Swiegers and T. J. Malefetse, *Chem. Rev.*, 2000, **100**, 3483.

20. (a) C. Seward, W.-L. Jia, R.-Y. Wang, G. D. Enright, and S.-N. Wang, *Angew. Chem., Int. Ed. Engl.*, 2004, **43**, 2933; (b) J. A. Theobald, N. S. Oxtoby, M. A. Phillips, N. R. Champness, and P. H. Beton, *Nature*, 2003, **424**(6952), 1029; (c) S. Muthu, J. H. K. Yip, and J. J. Vittal, *Dalton Trans.*, 2002, 4561.

21. (a) L. Carlucci, G. Ciani, D. M. Proserpio, and S. Rizzato, *Chem. Eur. J.*, 2002, **8**, 1519; (b) L. Carlucci, G. Ciani, D. M. Proserpio, and S. Rizzato, *Cryst. Eng. Commun.*, 2002, **4**, 413; (c) S. Ferlay, S. Koenig, M. W. Hosseini, J. Pansanel, A. D. Cian, and N. Kyritsakas, *Chem. Commun.*, 2002, 218.

22. (a) M. G. Fragalà and O. Puglisi, *Chem. Mater.*, 2000, **12**, 290; (b) J. A. Darr, M. Ploiakoff, A. J. Blake, and W. S. Li, *Inorg. Chem.*, 1998, **37**, 5491; (c) T. H. Baum and C. E. Larson, Ligand Stabilised $+1$ Metal β-diketonates Coordination Complexes and their Use in Chemical Vapour Deposition of Metal thin Films. U. S. Patent 5,096,737, March 17, 1992.

23. (a) A. Michaelides, S. Skoulika, V. Kiritsis, and A. Aubry, *Chem. Commun.*, 1995, 1415; (b) F. Jaber, F. Charbonnier, and R. Faure, *J. Chem. Crystallogr.*, 1997, **27**, 397; (c) S.-L. Li and T. C. W. Mak, *Struct. Chem.*, 1997, **8**, 49; (d) D.-D. Wu and T. C. W. Mak, *Dalton Trans.*, 1995, 2671; (e) P.-R. Wei, Q. Li, B.-M. Wu, and T. C. W. Mak, *Polyhedron*, 1997, **16**, 153; (f) K. Nomiya, S. Takahashi, and R. Noguchi, *Dalton Trans.*, 2000, 1343.

24. (a) H. J. Buschmann and E. Schollmeyer, *J. Electroanal. Chem.*, 1999, **474**, 188; (b) H. J. Buschmann, A. Wego, and E. Schollmeyer, *Inorg. Chem. Commun.*, 2001, **4**, 9; (c) M. Wei, M. Munakata, Y. Suenaga, T. Kuroda-Sowa, and M. Makawa, *Inorg. Chim. Acta*, 2002, **332**, 18; (d) Q.-M. Wang and T. C. W. Mak, *Angew. Chem., Int. Ed. Engl.*, 2001, **40**, 1130; (e) Q.-M. Wang and T. C. W. Mak, *Chem. Eur. J.*, 2003, **9**, 43; (f) M. Munakata, L.-P. Wu, T. Kuroda-Sowa, M. Maekawa, Y. Suenaga, K. Sugimoto, and I. Ino, *Dalton Trans.*, 1999, 373.

25. (a) A. J. Blake, R. O. Gould, W.-S. Li, V. Lippolis, S. Parsons, C. Radek, and M. Schröder, *Inorg. Chem.*, 1998, **37**, 5070; (b) A. J. Blake, R. O. Gould, S. Parsons, C. Radek, and M. Schröder, *Angew. Chem., Int. Ed. Engl.*, 1995, **34**, 2374; (c) A. J. Blake, N. R. Champness, S. M. Howdle, and P. B. Webb, *Inorg. Chem.*, 2000, **39**, 1035; (d) K. Saito, S. Murakami, A. Muromatsu, and E. Sekido, *Polyhedron*, 1993, **12**, 1587; (e) D. G. Booth, W. Levason, J. J. Quirk, G. Reid, and S. M. Smith, *Dalton Trans.*, 1997, 3493.

26. (a) P. Pyykkö, *Chem. Rev.*, 1997, **97**, 597; (b) M. A. Omary, T. R. Webb, Z. Assefa, G. E. Shankle, and H. H. Patterson, *Inorg. Chem.*, 1998, **37**, 1380; (c) G.-C. Guo and T. C. W. Mak, *Angew. Chem., Int. Ed. Engl.*, 1998, **37**, 3183; (d) C.-M. Che, M.-C. Tse, M. C.-W. Chan, K.-K. Cheung, D. L. Phillips, and K.-H. Leung, *J. Am. Chem. Soc.*, 2000, **122**, 2464; (e) M. A. Rawashdeh-Omary, M. A. Omary, and H. H. Patterson, *J. Am. Chem. Soc.*, 2000, **122**, 10371.

27. (a) G.-C. Guo, G.-D. Zhou, and T. C. W. Mak, *J. Am. Chem. Soc.*, 1999, **21**, 3136; (b) G. C. Guo, G.-D. Zhou, Q.-G. Wang, and T. C. W. Mak, *Angew. Chem., Int. Ed. Engl.*, 1998, **37**, 630; (c) G.-C. Guo, Q.-G. Wang, G.-D. Zhou, and T. C. W. Mak, *Chem. Commun.*, 1998, 339; (d) Q.-M. Wang and T. C. W. Mak, *J. Am. Chem. Soc.*, 2000, **122**, 7608; (e) Q.-M. Wang and T. C. W. Mak, *J. Am. Chem. Soc.*, 2001, **123**, 1501; (f) Q.-M. Wang and T. C. W. Mak, *Inorg. Chem.*, 2003, **42**, 1637; (g) X.-L. Zhao, Q.-M. Wang, and T. C. W. Mak, *Inorg. Chem.*, 2003, **42**, 7872; (h) X.-L. Zhao and T. C. W. Mak, *Dalton Trans.*, 2004, 3212; (i) L. Zhao and T. C. W. Mak, *J. Am. Chem. Soc.*, 2004, **126**, 6852; (j) For a convenient summary, see M. I. Bruce and P. J. Low, *Adv. Organomet. Chem.*, 2004, **50**, 217, 399, 443.

28. (a) P. J. M. W. L. Birker, J. Reedijk, and G. C. Verschoor, *Inorg. Chem.*, 1981, **20**, 2877; (b) D. Rais, J. Yau, D. M. P. Mingos, A. J. P. White, and D. J. Williams, *Angew. Chem., Int. Ed. Engl.*, 2001, **40**, 3464; (c) D. Rais, D. M. P. Mingos, R. Vilar, A. J. P. White, and D. J. Williams, *J. Organomet. Chem.*, 2002, **652**, 87; (d) C.-W. Liu, H.-C. Haia, C.-M. Hung, B. K. Santra, B.-J. Liaw, and Z.-Y. Lin, *Inorg. Chem.*, 2004, **43**, 4464; (e) C.-W. Liu, C.-M. Hung, H.-C. Haia, B.-J. Liaw, L.-S. Liou, Y.-F. Tsai, and J.-C. Wang, *Chem. Commun.*, 2003, 976; (f) Q.-M. Wang and T. C. W. Mak, *Chem. Commun.*, 2000, 1435.

29. (a) K. Tang, X. Xie, Y. Zhang, X. Zhao, and X. Jin, *Chem. Commun.*, 2002, 1024; (b) D. Fenske, C. Persau, S. Dehnen, and C. E. Anson, *Angew. Chem., Int. Ed. Engl.*, 2003, **37**, 630; (c) X. J. Wang, T. Langetepe, C. Persm, B. S. Kang, G. S. Sheldrick, and D. Fenske, *Angew. Chem., Int. Ed. Engl.*, 2002, **41**, 3818; (d) D. Fenske, N. Zhu, and T. Langetepe, *Angew. Chem., Int. Ed. Engl.*, 1998, **37**, 2639; (e) T. Langetepe and D. Fenske, *Z. Anorg. Allg. Chem.*, 2001, **627**, 820; (f) D. Fenske and T. Langetepe, *Angew. Chem., Int. Ed. Engl.*, 2002, **41**, 300.

30. (a) B. K. Teo, H. Zhang, and X.-B. Shi, *Inorg. Chem.*, 1994, **33**, 4086; (b) B. K. Teo, H. Zhang, and X.-B. Shi, *J. Am. Chem. Soc.*, 1993, **115**, 8489; (c) B. K. Teo and H. Zhang, *J. Cluster Sci.*, 2001, **12**, 349.

31. (a) H. Firouzabadi, P. Salehi, and I. Mohammadpourbaltork, *Bull. Chem. Soc. Jpn.*, 1992, **65**, 2878; (b) H. C. Rai and V. Kumari, *Asian J. Chem.*, 1995, **7**, 881.

32. (a) Q.-M. Wang and T. C. W. Mak, *Chem. Commun.*, 2001, 807; (b) Q.-M. Wang, H. K. Lee, and T. C. W. Mak, *New J. Chem.*, 2002, **26**, 513.

33. (a) S. Naylor, C. A. Hunter, J. A. Cowan, J. H. Lamb, and J. K. M. Sanders, *J. Am. Chem. Soc.*, 1990, **112**, 6507; (b) A. Giradeau, J. P. Gisselbrecht, M. Gross, and J. Weiss, *Dalton Trans.*, 1993, 1103.

34. (a) G.-Y. Fu, Y.-S. Fu, K. Jayaraj, and A. B. P. Lever, *Inorg. Chem.*, 1990, **29**, 4090; (b) A. J. Blake, D. Collison, R. O. Gould, G. Reid, and M. Schröder, *Dalton Trans.*, 1993, 521.

35. N. R. Walker, R. R. Wright, and A. J. Stace, *J. Am. Chem. Soc.*, 1999, **121**, 4837.

36. (a) A. Kahani, M. Abedini, and M. Farnia, *J. Coord. Chem.*, 2001, **53**, 1; (b) H. Furuta, T. Ogawa, Y. Uwatoko, and K. Araki, *Inorg. Chem.*, 1999, **38**, 2676.

37. A. Yanagisawa, in ‘Lewis Acids in Organic Synthesis’, ed. H. Yamamoto, Wiley-VCH, Weinheim, 2000, Vol. 2, Chap. 13, p. 575.

38. (a) R. S. Orugunty, D. L. Wright, M. A. Battiste, R. J. Helmich, and K. Abboud, *J. Org. Chem.*, 2004, **69**, 406; (b) P. Merino, T. Tejero, M. Laguna, E. Cerrada, A. Moreno, and J. A. Lopez, *Org. Biomol. Chem.*, 2003, **1**, 2336; (c) X.-Q. Yao and C.-J. Li, *J. Am. Chem. Soc.*, 2004, **126**, 6884; (d) Y. Yamaguchi, S. Kobayashi, T. Wakamiya, Y. Matsubara, and Z.-I. Yoshida, *J. Am. Chem. Soc.*, 2000, **122**, 7404.

39. D. A. Barr, R. Grigg, H. Q. N. Gunaratne, J. Kemp, P. McMeekin, and V. Sridharan, *Tetrahedron*, 1998, **44**, 557.

40. W. Adam, C. P. Librera, F.-G. Klärner, and F. Wurche, *J. Am. Chem. Soc.*, 2003, **125**, 995.

41. H. V. R. Dias, R. G. Browning, S. A. Polach, H. V. K. Diyabalanage, and C. J. Lovely, *J. Am. Chem. Soc.*, 2003, **125**, 9270.

42. (a) A. Ashimori, B. Bachand, M. A. Calter, S. P. Govek, L. E. Overman, and D. J. Poon, *J. Am. Chem. Soc.*, 1998, **120**, 6488; (b) T. Matsuura, L. E. Overman, and D. J. Poon, *J. Am. Chem. Soc.*, 1998, **120**, 6500; (c) L. E. Overman and D. J. Poon, *Angew. Chem., Int. Ed. Engl.*, 1997, **36**, 518; (d) E. Hagiwara, A. Fujii, and M. Sodeoka, *J. Am. Chem. Soc.*, 1998, **120**, 2474.

43. A. Yanagisawa, Y. Matsumoto, H. Nakashima, K. Asakawa, and H. Yamamoto, *J. Am. Chem. Soc.*, 1997, **119**, 9319.

Silver: Organometallic Chemistry

John P. Fackler, Jr
Texas A&M University, College Station, TX, USA

1 Introduction 1
2 Alkyl and Aryl Compounds 1
3 Alkenyl and Alkynyl Silver(I) Compounds 2
4 π-Bonded Compounds 3
5 Cyanides, Isocyanates, and Related Compounds 3
6 Stabilized Organosilver Compounds 4
7 Carbenes 5
8 Miscellaneous Compounds 6
9 Related Articles 6
10 References 6

1 INTRODUCTION

The synthesis of organometallic compounds of silver has long been rather limited owing to the low thermal stability of the resulting compounds, which are generally less stable than their copper analogs. Furthermore, organometallic silver compounds are generally photosensitive, a fact that further limits their synthesis. The first alkylsilver compounds were reported[1] in 1941, although π and acetylene complexes were known prior to this time.[2] Fluoroalkyls have been used to prepare much more stable alkyl silver complexes, although most of these compounds are also air, moisture, and light sensitive. Surprisingly high thermal stability has been realized with ylide (*see Ylide*) complexes of silver. However, even these compounds tend to be photosensitive and often deposit a silver mirror. Although this lack of thermal and photostability has hampered structural studies of organometallic silver complexes, some X-ray structural results have been obtained. A few organometallic clusters also have been characterized structurally. A thorough review of silver organometallic compounds appeared in 1995.[3] Perhaps, the single most active area of organometallic silver chemistry during the past decade has been the study of carbene complexes. Although they were first reported[4] in 1991 by Arduengo, considerable progress has been made in understanding the synthesis, reactivity, and bonding of these compounds. Arnold reviewed advances in this chemistry in 2002.[5]

The relatively small energy separation[6] (about one-half the value for $\mathrm{Cd^{II}}$) between the filled d orbitals and the 5s orbital tends to cause the coordination about $\mathrm{Ag^{I}}$ to be linear with strongly donating ligands such as are found in organometallic species. $\mathrm{Ag^{II}}$ or $\mathrm{Ag^{III}}$ organometallic species are also much more difficult to obtain than similar copper and gold compounds. No organometallic compounds have been reported to date that have been crystallographically characterized which contain silver in one of these well-established higher oxidation states.

The $I = 1/2$ nuclear spins of $^{109}\mathrm{Ag}$ and $^{107}\mathrm{Ag}$ have made it possible to study organometallic silver complexes by NMR (a tool that has been less successfully used with similar copper complexes), although the sensitivity of the silver nuclei is rather low.

Organometallic silver complexes do not require special handling techniques aside from taking precautions regarding light, atmosphere, and thermal sensitivities typical of organometallic compounds. The well-known antibacterial properties of silver and its compounds suggest that new materials be handled cautiously. Contact with skin generally leads to brown–black stain deposits, which take a considerable time to vanish.

2 ALKYL AND ARYL COMPOUNDS

The use of organozinc compounds to prepare alkylsilver species was attempted as early as 1859. Success in synthesizing alkylsilver compounds, however, was not achieved until 1941 when Semerano and Riccoboni[1] found that tetraalkyllead could be used as a starting material (equation 1).

$$\mathrm{R_4Pb + AgNO_3 \xrightleftharpoons{-80\,^{\circ}C} RAg + R_3PbNO_3} \qquad (1)$$

The much more stable arylsilver compounds had been obtained by Krause and Schmitz[7] in 1919. Taking advantage of the thermodynamically favorable formation of $\mathrm{Et_3PbONO_2}$, various unsymmetrical $\mathrm{Et_3PbR}$ compounds were used by Glocking[8] to prepare a number of different silver compounds, such as $\mathrm{PhCH_2Ag}$, p-$\mathrm{CF_3C_6H_4Ag}$, p-$\mathrm{Me_2NC_6H_4Ag}$, and the more stable alkenyl compound $\mathrm{PhCH{=}CHAg}$. Glocking noted that these reactions occurred by a single ligand transfer with exclusive transfer of the special ligand, and that the most stable organosilver compounds were those with R groups in which the radical, R•, has the least stability. At −80 °C, the alkylsilver(I) compounds were found to be stable for several hours. Higher temperatures lead to quick decomposition. A listing of a few alkylsilver compounds is presented in Table 1. The thermal stability decreases as the alkyl group becomes larger; at −30 °C, for example, $\mathrm{CH_3Ag}$, a polymeric species, is stable for a short time while $\mathrm{CH_3CH_2CH_2Ag}$ decomposes quickly at −60 °C.

Table 1 Representative alkyl and aryl silver(I) compounds

		Thermal stability[a]	
Compound	Appearance	Slow dec.	Fast dec.
MeAg[1,3]	Yellow	−80 to −50[b]	−30
MeAg·AgNO$_3$[1,3]	Light yellow	[c]	–
EtAg[1,9]	Red-brown	−80[d]	−50
PhCH$_2$Ag[8]		−78[e]	–
PhAg[10–13]	Dark brown	25[f]	–
2PhAg·AgNO$_3$[6]	Bright yellow[g]	50	80–100
2,5-Me$_2$C$_6$H$_4$Ag[10]	Rust	25	–

[a] Temperature in °C. [b] Half-life times for pure dry powder are 6 months at −50 °C but only 4 h at −30 °C. [c] Somewhat more stable than MeAg. [d] Half-life times in ethanol are 3 h at −40 °C and 19 min at −20 °C. [e] Only a transient existence. [f] Ether suspension. [g] Light sensitive.

Phenylsilver was made by Krause[10] and by Reich[11] from a Grignard reagent in the dark (equation 2).

$$\mathrm{AgCl + PhMgBr \xrightarrow{dark} PhAg + MgBrCl} \qquad (2)$$

The dark brown phenylsilver compound exhibits slow decomposition at 25 °C. While the compound is sensitive to both air and nitrogen atmospheres, it is not particularly light sensitive. Hasimoto and Nanako[12] studied the decomposition and proposed a radical decomposition mechanism. The addition of *p*-benzoquinone decreased the formation of biaryl products in ether or pyridine.

Gilman *et al.*[13] found that the Grignard reaction with AgBr was considerably accelerated by light (equation 3).

$$\mathrm{AgBr + PhMgBr \xrightarrow[Et_2O]{\substack{h\nu \\ -18\,^{\circ}C}} PhAg + MgBr_2} \qquad (3)$$

Phenylsilver was found to react readily with acetyl chloride, allyl bromide, and phenyl isocyanate to give MeCOPh, $CH_2{=}CHCH_2Ph$, and $(PhNCO)_3$ respectively, but better yields and cleaner reactions occur with phenylcopper. Although symmetrical tetraalkyllead and tin compounds do not react with $AgNO_3$, the unsymmetrical Ph_3EtM (M = Pb, Sn) species do react[6] to give $2PhAg{\cdot}AgNO_3$ and $EtPh_2MONO_2$, with Pb reacting more quickly than Sn. The silver compound is very light sensitive, decomposing in a few minutes in daylight. A few of the arylsilver compounds are listed in Table 1.

The first structural report of an arylsilver complex appeared in 1983. Floriani and coworkers[14] prepared (mesityl)Ag from the Grignard reagent MesMgBr and AgCl under N_2 in the absence of light. The product is a crystalline tetramer, $Ag_4(Mes)_4$ (**1**) with Ag…Ag distances of 3.97 and 3.79 Å, well outside bonding distances. The mesityl group sterically shields the Ag^I atoms, which are two coordinate. This ligand is not subject to orthometallation (*see Orthometalation*). The Cu^I and Au^I mesityl compounds have different structures from the Ag^I species.

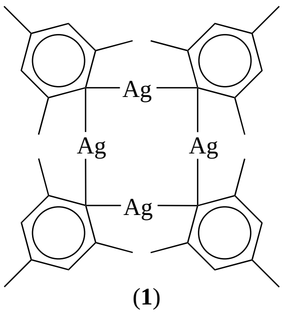

(**1**)

Unfortunately, the compound thought to be an example of a mono-coordinate Ag(I) complex,[15] the species reported to be Ag[Triph], (**2**) (Triph = $–C_6H_2$-2,4,6-Ph_3) apparently is the bromide starting material, TriphBr.[16] In a very nice paper by Power,[17] the syntheses and structures of lithium organoargentate salts $[Li(THF)_4][Ag(Triph)_2]{\cdot}THF$ and $[Li(THF)_4][Ag(C_6H_3\text{-}2,6\text{-}Mes_2)_2]{\cdot}1/8OEt_2$ (Mes = C_6H_2-2,4,6-Me_3) have been reported. These structures show Ag−C distances, 2.05−2.11 Å, that are longer than those of the Cu(I) analogues, as expected, further supporting the conclusions of Haaland[16] regarding the supposed mono-coordinate Ag(I) (and Cu(I)) species.

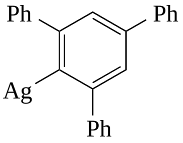

(**2**)

3 ALKENYL AND ALKYNYL SILVER(I) COMPOUNDS

Alkenylsilver compounds have been prepared from more electropositive element organometals, such as tetraalkenyllead.[18,19] While these compounds are more stable thermally than the alkylsilver species, they are air and moisture sensitive (Table 2). Complete decomposition of styrenylsilver,[18] for example, takes several days at room temperature. Metallic silver and polystyrene are formed.

Silver acetylides are readily prepared from silver salts such as the nitrate or perchlorate and the alkyne in aqueous or methanolic ammonia. They have been known[22] since the mid-1800s. In neutral solutions, a mixed salt, $AgC{\equiv}CR{\cdot}nAgNO_3$, is obtained.[24] Acetylene gives[20] the silver carbide, Ag_2C_2, and

Table 2 Examples of alkynylsilver compounds

Compound	Appearance	Decomposition temp. (°C)
$AgC\equiv CAg$[20]	White, shock sens.	140–190
$AgC\equiv CAg\cdot AgNO_3$[20]	White needles	210–230
$[KC\equiv CAg]_n$[21]	Polymeric	–
$HC\equiv CAg$[21]	Intense yellow	0
$MeC\equiv CAg$[21,22]	White crystalline	70
$PhC\equiv CAg$[22]	White crystalline	100
$PhC\equiv CAg\cdot AgNO_3$[22]	White needles	–
$[PhC\equiv CAgPMe_3]_n$[23]	Polymeric cryst.	130–140

mixed salts such as $Ag_2C_2\cdot nAgNO_3$, depending upon specific reaction conditions.

Acetylene and its derivatives react with trialkyl or triaryl phosphite complexes of AgCl to produce[25] the corresponding alkynyl complexes (equation 4).

$$RC\equiv CH + ClAgP(OR')_3 \longrightarrow RC\equiv CAg + HPO(OR')_2 + R'Cl$$

$$R = H, Ph, PhO, p\text{-}BrC_6H_4O, Me_3Si;\ R' = Et, Ph \qquad (4)$$

The insolubility of alkynylsilver compounds indicates coordination polymerization. These acetylides are thermally rather stable, decomposing[24,26] between 100 and 200 °C. The lowering of the triple bond $C\equiv C$ stretch frequency in the IR spectrum also suggests that the triple bond interacts directly with Ag through π-bonding in the solid state. Addition of strong donor ligands results in the breakdown of the polymer. The resulting solid product from phenylethynylsilver, R, and trimethylphosphine, L, is a linear chain of metal atoms with alternating $[L_2Ag]^+$ and $[R_2Ag]^-$ moieties. The crystal structure[23] reveals that the coordinated alkyne also residually π-bonds to an adjacent Ag atom in the cation (**3**). The Ag···Ag distance is 3.033 Å.

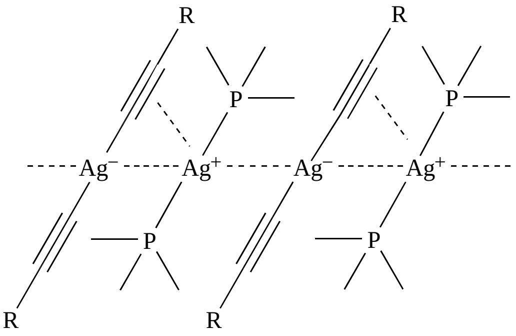

(**3**)

Silver tetranuclear clusters of luminescent silver(I) arylacetylides have been synthesized, characterized structurally, and studied for their photophysical properties.[27] Interesting rhombohedral silver-alkynyl cage compounds $[Ag_{14}(C\equiv C^tBu)_2(X)][BF_4]$ (X = F, Cl, Br) with O_h molecular symmetry, apparently form templates around the halide ions.[28] The silver...silver edge distances are about 2.9 Å, similar to the silver...silver distances observed in the tetranuclear clusters.

Complex anionic silver acetylides, $K[Ag(CCR)_2]$ (R = H, Me, Ph), are known and are prepared from the appropriate alkynylsilver and the potassium acetylide in a polar solvent.[21] They are colorless crystalline solids that are sensitive to light and that decompose in solution. They apparently are not explosive.

4 π-BONDED COMPOUNDS

Alkene interactions with Ag^I are well known, and chromatographic columns containing silver salts have long been used to separate alkenes. An early crystal structure[29] was that of 1,3,5,7-cyclooctatetraenesilver(I) nitrate, a pale yellow crystalline material that melts with decomposition at 173–174 °C. The structure of the benzenesilver(I) perchlorate was described by Rundle[30] in 1950 and again by Smith and Rundle[31] in 1958. The structure consists of chains of benzene and Ag^+, with Ag^+ also sitting above and below the benzene rings, giving a three-dimensional polymeric network. The syntheses of alkene(β-diketonato)silver(I) compounds are described[32] in *Inorganic Syntheses*. The compounds all lose the alkene when stored in air. The use of silver catalysts for the epoxidation of olefins[33] has been the primary focus of olefin–silver studies in recent years although separations of olefins using silver substrates on supports also has produced a number of patents and papers.[34]

5 CYANIDES, ISOCYANATES, AND RELATED COMPOUNDS

Elsewhere in this encyclopedia, there is a general discussion of cyanide complexes of the transition metals (*see* ***Cyanide Complexes of the Transition Metals***). AgCN has a chain structure with a linear N–Ag–C coordination.[6] Addition of alkali metal cyanides to AgCN produces the stable, linear $[NC\text{–}Ag\text{–}CN]^-$ anion. Much work has been related to the photophysics of these species that show exciplex formation in solution.[35] Reaction of alkyl iodides with AgCN produces isocyanides, Ag(CN)(CNR), from which the RNC can be removed upon heating with KCN. The bis(isocyanide)Ag^I cationic complexes $[Ag(CNC_6H_4Me\text{-}p)_2]X$ ($X = ClO_4, NO_3$) were studied by IR spectroscopy and found to have a higher NC stretching frequency than the uncoordinated ligands.[36]

Isocyanides of the general formula $[AgC(OR){=}NR']_3$ can be prepared according[37] to equation (5).

$$(ArNC)AgCl + ROH + KOH \longrightarrow H_2O + KCl + \frac{1}{3}[AgC(OR){=}NAr']_3$$
$$Ar = p\text{-}MeC_6H_4\ (R = Me, Et, n\text{-}Pr) \qquad (5)$$

Unlike the analogous isocyanide Au^I complexes, which react with alcohols or amines to form carbenes, the Ag^I complexes rearrange to the formamidate (RN=CHOR′) or formamidine (RNHCH=NR′) species, which are all probably cyclic oligomers such as (**4**).

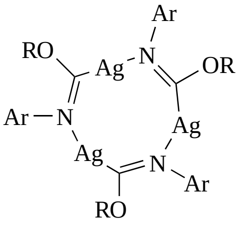

(**4**)

These trimers are sensitive to heat and light, but at the time they were first made they were some of the most stable nonfluorinated σ-bonded organometallic Ag^I compounds known. The ligand can be transferred to other metals by metathesis; hence, they are synthetically useful reagents.

6 STABILIZED ORGANOSILVER COMPOUNDS

Several different approaches have been taken to form stabilized σ-bonded Ag^I organometallic compounds. One of the earliest was to use perfluoroalkyls. In 1968, it was shown[38] that AgF will react directly with a fluorinated alkene such as $CF_2{=}CFCF_3$ in MeCN at 25 °C to form $AgCF(CF_3)_2$, a product which darkens slowly upon standing at room temperature. The 1-chloroperfluoroisopropyl and perfluoro-1,1-dimethylbutyl derivatives were also synthesized in this manner. In general, perfluorocarbanions will react[39] with silver salts such as silver acetate to form the perfluorinated organometallic compound. The perfluoro carbanions are formed from alkali metal fluorides and fluoroalkenes. The perfluorinated organosilver compounds are air, moisture, and light sensitive. Reaction of $AgCF(CF_3)_2$ with O_2, for example, gives hexafluoroacetone. Thermal decomposition generally occurs at temperatures under 100 °C. It was reported that bis(trifluoromethyl)ketene reacts with AgF to produce the perfluoroaldehyde complex $AgC(CF_3)_2C(O)F$.[40] Excess alkali or alkaline earth halides can suppress thermal decomposition of organosilver compounds. Thus butylsilver, formed from AgBr·2LiBr using Grignard or alkyllithium reagents, decomposes at −10 °C compared with the −60 °C decomposition temperature of the nonstabilized species. The structure of (acetonitrile)perfluoroisopropylsilver(I) has been reported by Burch and Calabrese.[41]

Chelation has been used to stabilize organosilver compounds.[42] The compound {2-[(dimethylamino)methyl]-phenyl}silver, a chelate involving N and C coordination, melts at 180 °C. The adduct with AgBr is light and air stable for 10 days. The product from LiBr was the first example[43] to contain bridging phenyl groups. It decomposes at 180 °C but is air and moisture sensitive.

Whitesides and Casey[44] demonstrated that alkylsilver compounds could be stabilized by phosphine coordination to the Ag^I. The mechanism of decomposition of these complexes was investigated by Whitesides and his students over several years.[45] Radical processes generally are involved. Thus, thermal decomposition of $n\text{-}BuAgP(n\text{-}Bu)_3$ gives 93% C_8H_{18}, 5% C_4H_{10}, and lesser amounts of other products along with elemental silver and free phosphine. Photolysis gave a different product distribution. With s-butyl(tri-n-butylphosphine)silver(I), the product distribution suggested silver hydride formation; however, no general mechanism for decomposition was discernible.

Remarkable stability of the Ag^I–C σ-bond has been observed with a broad class of organic ligands called ylides (*see Ylide*) (**5**). These neutral or anionic ligands are believed to contribute stability[46] to the metal–carbon bond by delocalization of charge away from the metal atom to the ligand. The stability of the uncoordinated ligand itself accommodates metal–carbon bond rupture without radical formation. Schmidbaur and his coworkers[47] pioneered the use of these ligands to form stable organometallic species and were the first to synthesize organometallic ylide complexes of silver (6). Chlorinated hydrocarbon solvents used for syntheses only slowly attack the organometallics. Isolated compounds show remarkable thermal stability, melting without decomposition at 192–194 °C (R = H), 118–120 °C (R = Me), and 124–126 °C (R = i-Pr) and decomposing at temperatures above 200 °C. While air and moisture stable, they all appear to be photosensitive.

$$AgCl + 2CH(R)PR'_3 \longrightarrow [R'_3PC(R)H\text{-}Ag\text{-}CH(R)PR'_3]Cl \qquad (6)$$
$$R = H, Me, i\text{-}Pr$$

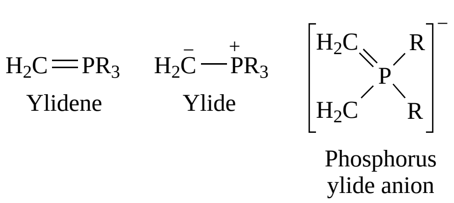

(**5**)

The ^1H NMR spectra of these ylide silver compounds showed coupling to ^{107}Ag and ^{109}Ag with $^2J(Ag\text{–}H)$ at about 12 Hz. The $^{31}P\{^1H\}$ spectrum is a doublet with $^3J(P–Ag) = 9.1$ Hz. Both silver isotopes (*see Isotopes & Isotope Labeling*) couple nearly equivalently, and hence only a doublet appears. The $^{13}C\{^1H\}$ spectra were the first to demonstrate $^{13}C–^{107,109}Ag$ spin–spin coupling. The neutral one-to-one adducts of CH_2PPh_3 with AgCl also were obtained by Schmidbaur and his coworkers[48] as monomeric species in solution, a result different from that obtained with the analogous copper(I) species that are polymeric. The pale yellow solid Ph_3PCH_2AgCl melts at 166–169 °C and is thermally stable up to 150 °C, although it is subject to decomposition in halocarbon solvents and in light.

At the same time, the synthesis of mononuclear silver ylide complexes were achieved, Schmidbaur and his colleagues[47] discovered that the ylide anions produced dinuclear species, $Ag_2[(CH_2)_2PMe_2]$. The remarkably stable methyl compound melts at 153–155 °C and can be sublimed at 150 °C and 0.1 atm. Mass spectral and ^1H and $^{31}P\{^1H\}$ NMR studies demonstrated the ring structure of the compound, although no structural analysis could be performed due to the photosensitivity of the compound. The synthesis of the dinuclear silver(I) ylide complex (**6**) is described[47] in *Inorganic Syntheses*, and although colorless crystals are obtained, no X-ray structure was possible due to sample decomposition in the X-ray beam.

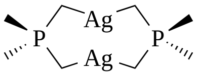

(**6**)

The first structural report of a silver–ylide complex appeared[49] in 1988. This compound, $C_6F_5–Ag–CH_2PPh_3$, shows that the C–Ag–C geometry is linear with a Ag–CH_2 distance of about 2.2 Å. Additional structural reports have appeared.[50]

Five general types of silver(I) ylide complexes have been described (Table 3). They are all remarkably stable thermally but decompose in halohydrocarbon solvents and they are generally photosensitive. The intramolecular Ag···Ag distances in the dinuclear compounds are 2.9–3.0 Å and they generally range from colorless to yellow. The $[AgCH_2P(S)Ph_2]_2$ complex luminesces yellow at 77 K when subjected to UV radiation and is a linear chain polymer in the solid state with an intermolecular Ag···Ag distance of 3.1 Å. The compound also displays a dynamical NMR pattern (*see* ***Structure & Property Maps for Inorganic Solids***) in solution in which a $^2J(Ag–H)$ coupling is observed only at −60 °C. Rapid isomerism was suggested as the cause of the absence of $^{13}C–^{107,109}Ag$ coupling in $[Ag(CH_2)_2PMePh]_2$. A similar suggestion was made for the NMR pattern of $[AgCH_2P(S)Ph_2]_2$. Such an isomerization has been established for $[Au(CH_2)_2PMePh]_2$ where the trans isomer has been obtained by crystallization and studied crystallographically (*see* ***Gold: Organometallic Chemistry***). The mixed Cu, Ag dimer can be obtained by mixing the dinuclear copper(I) and silver(I) complexes in solution.

Table 3 Types of Ylide Complexes

	Type	Examples
I[46]	RAgY	Y = CH_2PPh_2, CH_2AsPh_2 R = C_6F_5
II[46]	[YAgY]X	Y = CH_2PPh_3, $CH_2S(O)Me_2$, $CHMePPh_3$, $Me_3PCH(SiMe_3)$, $Ph_3PCHCOR'$ (R′ = OMe, OEt, Me) X = NO_3^-, Cl^-
III[46,47]	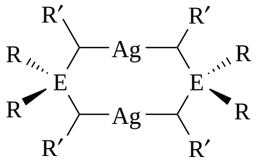	E = P, As R = Me, Ph R′ = Me
IV[49]	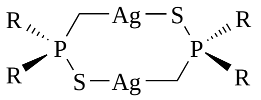	R = Ph
V[49]	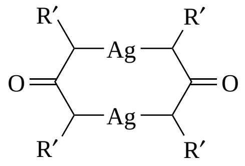	R′ = PPh_3

In addition to the phosphorus ylide complexes, arsenic and sulfur ylide complexes of silver have been obtained,[51] although no structural reports exist. While the arsenic derivatives match the phosphorus ylide complexes for stability of the Ag^I products, the sulfoxonium ylide complexes are somewhat less stable.

7 CARBENES

The ‘bottleable’ carbenes[5] formed by deprotonation of dialkyl imidazolium salts have produced a number of new compounds and clusters in which there is a Ag–C bond. There is good evidence that the singlet carbenes are dative-bonded[5] to silver through the C lone pair of electrons, with little, if any, metal-ligand π-bonding. Although discovered by Arduengo,[4] the synthesis from Ag_2O as developed by Lin[52] has proved to be sufficiently straightforward that a considerable new carbene chemistry has resulted.[5] An example of this is the work of Catalano,[53] who has found a new trinuclear cluster in which the carbenes bridge the silver atoms with the Ag_3 core seen here (**7**).

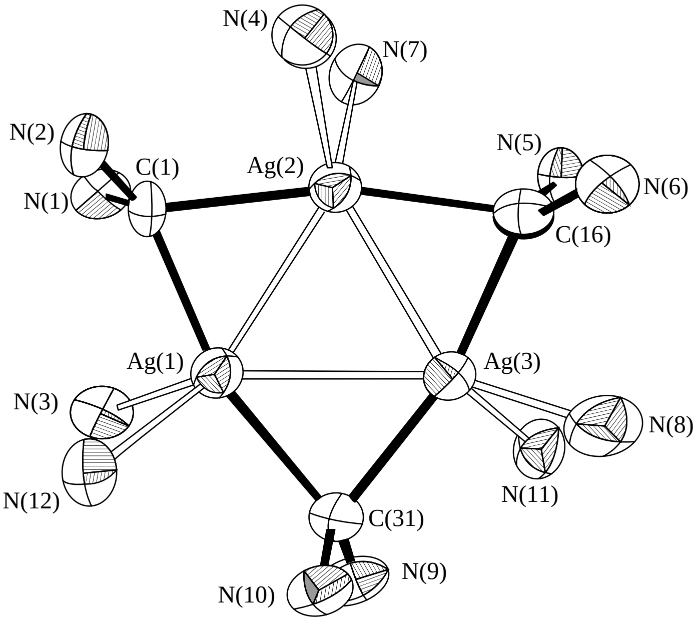

(**7**)

8 MISCELLANEOUS COMPOUNDS

A few interesting and unusual organometallic compounds of silver have been reported structurally that are categorized as miscellaneous. For example, a carbonyl complex has been obtained with a tetrakis(pentafluorotelluroxy)borate ligand.**[43]** Some unusual carbonyl clusters have been characterized, which contain bridging CO bonded to Ag with Os**[44]** and Ru**[45]** carbonyl components. Several cyano complexes also have been structurally characterized, such as bis(3,4;3′,4′-bis(ethylenedithio)-2,2′,5,5′-tetrathiofulvalenium)dicyanosilver(I) monohydrate, a compound of interest in studies of conducting materials.**[46]** In 2002, Mak reported**[54]** the structure of a silver cluster formed from Ag_2C_2 in which the C_2 unit is encapsulated within a Ag_8 square antiprism. These units are fused together into a polymeric column by edge-sharing of four of the Ag atoms of the Ag_7C_2 core structure. The dry starting material, Ag_2C_2, unfortunately detonates easily with thermal shock. Special silver(III) alkyl compounds such as $Ag(CF_3)_3L$, L = phosphine, and even $[Ag(CF_3)_4]^-$ have been reported. A detailed review of the synthesis of organometallic silver compounds appeared in 2004.**[55]**

9 RELATED ARTICLES

Copper: Organometallic Chemistry; Gold: Organometallic Chemistry.

10 REFERENCES

1. G. Semerano and L. Riccoboni, *Rec. Sci.*, 1943, **11**, 269.
2. F. R. Hartley, *Chem. Rev.*, 1973, **73**, 163.
3. G. Van Koten, S. L. James, and J. T. B. H. Jastrzebski, in ‘Comprehensive Organometallic Chemistry II’, eds. E. W. Abel, F. G. A. Stone, and G. Wilkinson, Elsevier Science, Kidlington, Oxford, 1995, Vol 3.
4. A. J. Arduengo, R. L. Harlow, and M. Kline, *J. Am. Chem. Soc.*, 1991, **113**, 361.
5. P. L. Arnold, *Heteratom Chem.*, 2002, **13**, 534.
6. F. A. Cotton, G. Wilkinson, C. A. Murillo, and M. Bochmann, ‘Advanced Inorganic Chemistry’, 6th edn., Wiley, New York, 1999.
7. E. Krause and M. Schmitz, *Ber. Dtsch. Chem. Ges.*, 1919, **52**, 2159.
8. (a) F. Glocking and D. Kingston, *J. Chem. Soc.*, 1959, 3001; (b) F. Glocking, *J. Chem. Soc.*, 1955, 716.
9. C. E. H. Bawn and R. Johnson, *J. Chem. Soc.*, 1960, 3923.
10. E. Krause and B. Wendt, *Ber. Dtsch. Chem. Ges.*, 1923, 2064.
11. R. Reich, *Compt. Rend. Acad. Sci.*, 1923, **177**, 322.
12. H. Hashimoto and T. Nanako, *J. Org. Chem.*, 1966, **31**, 891.
13. H. Gilman and J. Straley, *Recl. Trav. Chim. Pays-Bas*, 1936, **55**, 821.
14. E. M. Meyer, S. Gambarotta, C. Floriani, A. Chiesi-Villa, and C. Guastini, *Organometallics*, 1989, **8**, 1067; S. Gambarotta and C. Floriani, *J. Chem. Soc., Chem. Commun.*, 1983, 1087.
15. R. Lingnau and J. Strähle, *Angew. Chem., Int. Ed. Engl.*, 1988, **27**, 436.

16. A. Haaland, K. Rypdal, H. P. Verne, W. Scherer, and W. R. Theil, *Angew. Chem. Int. Ed. Engl.*, 1994, **33**, 2443.
17. C.-S. Hwang and P. P. Power, *J. Organomet. Chem.*, 1999, **589**, 234.
18. F. Glocking and D. Kingston, *J. Chem. Soc.*, 1959, 3001.
19. A. K. Holliday and R. E. Pendlebury, *J. Organomet. Chem.*, 1967, **7**, 281.
20. R. Vestin and A. Somersalo, *Acta Chem. Scand.*, 1949, **3**, 125; J. Shaw and E. Fisher, *J. Am. Chem. Soc.*, 1946, **68**, 2745.
21. R. Nast and H. Schindel, *Z. Anorg. Allg. Chem.*, 1963, **326**, 201.
22. C. Liebermann, *Justus Liebigs Ann. Chem.*, 1865, **135**, 268; C. Liebermann and F. Damerov, *Ber. Dtsch. Chem. Ges.*, 1892, **25**, 1096.
23. P. W. R. Corfield and H. M. M. Shearer, *Acta Crystallogr.*, 1966, **20**, 502.
24. C. D. M. Beverwijk, G. J. M. van der Kerk, A. J. Leusink, and J. G. Noltes, *Organomet. Chem. Rev. A*, 1970, **5**, 215.
25. M. Shostakovskii, L. Polyakova, L. Vasil'eve, and A. Polyakov, *Zh. Org. Khim.*, 1966, **2**, 2257.
26. A. M. Sladkov and L. Yu. Ukhin, *Russ. Chem. Rev. (Engl. Transl.)*, 1968, **37**, 748; A. M. Sladkov and I. R. Gol'ding, *Russ. Chem. Rev. (Engl. Transl.)*, 1970, **48**, 868.
27. Y.-Y. Lin, S.-W. Lai, C.-M. Che, K.-K. Chueng, and Z.-Y. Zhou, *Organometallics*, 2002, **21**, 2275.
28. D. Rais, D. M. P. Mingos, R. Vilar, A. J. P. White, and D. J. Williams, *J. Organomet. Chem.*, 2002, **652**, 87.
29. F. S. Mathews and W. N. Lipscomb, *J. Am. Chem. Soc.*, 1958, **80**, 4745.
30. R. E. Rundle and J. H. Goring, *J. Am. Chem. Soc.*, 1950, **72**, 5337.
31. H. G. Smith and R. E. Rundle, *J. Am. Chem. Soc.*, 1958, **80**, 5075.
32. W. Partenheimer and E. H. Johnson, *Inorg. Synth.*, 1976, **16**, 117.
33. M. A. Barteau, *Top. Catal.*, 2003, **22**, 3.
34. See for example: J. H. Kim, B. R. Min, J. Won, and Y. S. Kang, *Macromolecules*, 2003, **36**, 4577.
35. M. A. Rawashdeh-Omary, M. A. Omary, H. H. Patterson, and J. P. Fackler Jr, *J. Am. Chem. Soc.*, 2001, **123**, 11237.
36. F. A. Cotton and F. Zingales, *J. Am. Chem. Soc.*, 1961, **83**, 351.
37. G. Minghetti, F. Bonati, and M. Massobrio, *J. Chem. Soc., Chem. Commun.*, 1973, 260; *Inorg. Chem.*, 1975, **14**, 1974.
38. W. Miller and R. Burnard, *J. Am. Chem. Soc.*, 1968, **90**, 7367.
39. B. L. Dyathin, B. Martynov, L. Martynova, N. Kizim, Z. A. Stumbrevichute, and L. A. Federov, *J. Organomet. Chem.*, 1973, **57**, 423.
40. H. Westmijze, H. Kleijn, and P. Vermeer, *J. Organomet. Chem.*, 1979, **172**, 377.
41. R. R. Burch and J. C. Calabrese, *J. Am. Chem. Soc.*, 1986, **108**, 5359.
42. A. Luesink, G. Van Koten, and J. Noltes, *J. Organomet. Chem.*, 1973, **56**, 379.
43. A. Luesink, G. Van Koten, J. Marsman, and J. Noltes, *J. Organomet. Chem.*, 1973, **55**, 419.
44. G. Whitesides and C. Casey, *J. Am. Chem. Soc.*, 1966, **88**, 4541.
45. G. Whitesides, C. Casey, and J. Kreiger, *J. Am. Chem. Soc.*, 1971, **93**, 1379.
46. J. Stein, J. P. Fackler Jr, C. Paparizos, and H.-W. Chen, *J. Am. Chem. Soc.*, 1981, **103**, 2192.
47. H. Schmidbaur, J. Adlkofer, and W. Buchner, *Angew. Chem., Int. Ed. Engl.*, 1973, **12**, 415; Y. Yamamoto and H. Schmidbaur, *J. Organomet. Chem.*, 1975, **96**, 133; H. Schmidbaur, J. Adlkofer, and W. Herrmann, *Chem. Ber.*, 1974, **107**, 3699.
48. H. Schmidbaur and J. Adlkofer, *Inorg. Synth.*, 1978, **18**, 142.
49. R. Uson, A. Laguna, P. G. Jones, and K. Meyer-Bäse, *J. Chem. Soc., Dalton Trans.*, 1988, 341.
50. J. Vincente, M. Teresa Chicote, I. Saura-Llamos, and P. G. Jones, *Organometallics*, 1989, **8**, 767; S. Wang, J. P. Fackler Jr, and T. F. Carlson, *Organometallics*, 1990, **9**, 1973.
51. R. J. Meyer, E. A. Pietsch, and A. Kotowski, 'Gmelin Handbuch der Anorganischen Chemie', Springer-Verlag, Berlin, 1975.
52. H. M. J. Wang and I. J. B. Lin, *Organometallics*, 1998, **17**, 972; I. J. B. Lin and C. S. Vasam, *Comments on Inorganic Chemistry*, 2004, **25**, 75.
53. V. J. Catalano and M. A. Malwitz, *Inorg. Chem.*, 2003, **42**, 5483.
54. Q.-M. Wang and T. C. W. Mak, *Chem. Commun.*, 2002, 2682.
55. J. P. Fackler and C. W. Liu, in 'Science of Synthesis', ed. I. A. O'Neil, Georg Theime Verlag, Stuttgart, 2004, Vol. 3, p. 663.

Sol–Gel Synthesis of Solids

Thibaud Coradin & Jacques Livage
Chimie de la Matière Condensée (CNRS) and Collège de France, Université Pierre et Marie Curie, Paris, France

1 Introduction 1
2 Basic Principles of Sol–Gel Chemistry 1
3 Hybrid Organic–Inorganic Materials 5
4 Conclusion 10
5 Related Articles 11
6 References 11

1 INTRODUCTION

In 1845, M. Ebelmen, a French chemist, observed that tetraethyl orthosilicate reacts slowly with moisture to give a glassy solid. This was actually the first synthesis of an inorganic material (silica) from a metal–organic molecular precursor. It then took more than a century before this sol–gel synthesis began to attract academic and industrial interest. The first sol–gel products appeared on the market in 1953. Large-scale production by Schott Glaswerke started in 1959 with automotive rear-view mirrors and continued with antireflecting coatings in 1964. In the early 1960s, the sol–gel process was used for the production of ThO_2 and UO_2 microspheres in the nuclear industry. Since then, hundreds of scientists have become involved in this field and sol–gel science is now reaching its maturity.[1]

Glasses and ceramics are inorganic materials that have been produced for thousands of years (*see* ***Oxides: Solid-state Chemistry*** and ***Noncrystalline Solids***). Traditionally they are made from natural raw minerals such as clays or sand. Crystalline ceramics are shaped by adding water to clays in order to produce a plastic material and then heated in a furnace. Amorphous glasses are made from the melt and shaped by moulding near their softening temperature. In both cases, high temperatures are required.

In the sol–gel process, a solution of molecular precursors is converted by a chemical reaction into a sol or a gel which on drying and densification gives a solid material. This allows the production of single or multicomponent materials with high purity, novel compositions, tailored microstructures, and potentially greater chemical homogeneity at lower temperature. Moreover, films or fibres can be obtained directly from sols or gels by such techniques as dip-coating, spin-coating, spray, or drawing.[2]

The sol–gel process was first focused on silica glasses and then on multicomponent ceramics. The aim was to develop cheaper processing routes and to improve the properties of these materials. Nowadays, the major advance of sol–gel processes is undoubtedly the synthesis of hybrid organic–inorganic materials.[3]

This article describes the basic chemical reactions involved in the sol–gel synthesis of solid materials using molecular alkoxide precursors and reviews recent advances in hybrid materials preparation and properties.

2 BASIC PRINCIPLES OF SOL–GEL CHEMISTRY

2.1 Synthesis and Reactivity of Metal Alkoxides

Metal alkoxides $M(OR)_z$, where R is typically an alkyl group (R = Me, Et, etc.), have been known for a long time.[4,5] Many of them (M = Si, Al, Ti, etc.) are now commercially available. They can be synthesized via the reaction of metal chlorides with alcohol as follows:

$$MCl_z + h\,ROH \longrightarrow MCl_{z-h}(OR)_h + h\,HCl \qquad (1)$$

Most transition metal chlorides undergo only partial alcoholysis leading to chloroalkoxides $MCl_{z-h}(OR)_h$. Therefore the reaction has to be driven to completion by adding a base such as ammonia or sodium alkoxide.

The reaction of metal chloride with alcohol is not the only way to synthesize alkoxides. Other inorganic compounds such as oxides can also be used as precursors for the synthesis of metal alkoxides:

$$P_2O_5 + 3EtOH \longrightarrow PO(OH)(OEt)_2 + PO(OH)_2(OEt) \qquad (2)$$

Alkaline and alkaline-earth metals (*see* ***Alkali Metals: Inorganic Chemistry*** and ***Alkaline Earth Metals: Inorganic Chemistry***) are oxidized directly by alcohol:

$$Na + MeOH \longrightarrow NaOMe + \tfrac{1}{2}H_2 \qquad (3)$$

Alkoxy groups are rather hard π-donor ligands. They stabilize the highest oxidation number of the metal. Therefore alkoxides of main group elements and d^0 transition metals are well known, while those corresponding to soft d^n late transition metals have been much less studied. The number and stability of metal alkoxides decrease from left to right across the *periodic table*.

For coordinatively saturated metals the hydrolysis and condensation of metal alkoxides $M(OR)_z$ corresponds to the nucleophilic substitution of alkoxy ligands by hydroxylated species XOH:

$$M(OR)_z + x\,XOH \longrightarrow [M(OR)_{z-x}(OX)_x] + x\,ROH \qquad (4)$$

where X stands for hydrogen (hydrolysis), a metal atom (condensation), or even an organic or inorganic *Ligand* (complexation).

These reactions can be described by a S_N2 mechanism, as follows:

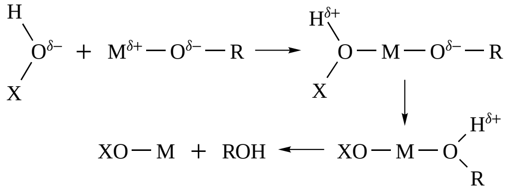

(5)

The reaction starts with the nucleophilic addition of negatively charged $HO^{\delta-}$ groups on to the positively charged metal atom, $M^{\delta+}$, leading to an increase of the coordination number of the metal atom in the transition state. The positively charged proton is then transferred toward an alkoxy group and the positively charged protonated ROH ligand is finally removed.**[6]**

The chemical reactivity of metal alkoxides toward hydrolysis and condensation mainly depends on the positive charge of the metal atom δ_M, and its ability to increase its coordination number N (*see* ***Coordination Numbers & Geometries***). As a general rule, the *Electronegativity* of metal atoms decreases and their size increases when going from the top right of the *periodic table* to the bottom left. The corresponding alkoxides become progressively more reactive toward hydrolysis and condensation. Silicon alkoxides are rather stable while cerium alkoxides are very sensitive to moisture. Alkoxides of electropositive metals must be handled with care under a dry atmosphere, otherwise precipitation occurs as soon as water is present. Alkoxides of highly electronegative elements such as $PO(OEt)_3$ (*see* ***Phosphorus: Inorganic Chemistry***) cannot be hydrolyzed under ambient conditions, whereas the corresponding vanadium derivatives $VO(OEt)_3$ (*see* ***Vanadium: Inorganic & Coordination Chemistry***) are readily hydrolyzed into vanadium pentoxide gels.

2.2 Molecular Structure of Metal Alkoxides

All silicon alkoxides $Si(OR)_4$ are monomeric and tetrahedral, but the situation is completely different with other metal alkoxides $M(OR)_z$. The coordination number 'N' of metal ions in $MO_{z/2}$ oxides is usually larger than their oxidation state Z. Therefore most metal alkoxides are not coordinatively saturated and coordination expansion is a general tendency of the sol-gel chemistry of metal alkoxides $M(OR)_z$. This is currently achieved by oligomerization via the formation of alkoxy (OR) or oxo (O) bridges and metal alkoxides often exhibit oligomeric molecular structures $[M(OR)_z]_n$. The degree of oligomerization increases with the size of the metal atom, its electropositive character and the 'N–Z' difference. As a general rule, it increases with the atomic number and decreases with the oxidation state. Large electropositive metals are known to give oxo-alkoxides such as $Pb_4O(OEt)_6$ in which oxo bridges favor coordination expansion. Oxo-alkoxides are more stable than the corresponding alkoxides and, of course, are less reactive toward hydrolysis and condensation.**[7]**

Alkoxide precursors are usually dissolved in a solvent so that coordination expansion can also occur via solvation. Solvate formation is often observed when alkoxides are dissolved in their parent alcohol. The stability of such solvates increases with the size and the electropositive character of the metal, that is, when going down the *periodic table*. At room temperature monomeric $Ti(OPr^i)_4$ (**1**) is not solvated by isopropanol whereas solvated dimeric species $[Zr(OPr^i)_4(Pr^iOH)]_2$ (**2**) and $[Ce(OPr^i)_4,Pr^iOH]_2$ are formed in alcoholic solutions (*see* ***Titanium: Inorganic & Coordination Chemistry***; ***Zirconium & Hafnium: Inorganic & Coordination Chemistry***, and ***Actinides: Inorganic & Coordination Chemistry***). (Figure 1). The degree of oligomerization of metal alkoxides can be tailored by an appropriate choice of the solvent. $[Zr(OPr^n)_4]_n$ oligomers are formed ($n \leq 4$) in nonpolar solvents such as cyclohexane allowing slow hydrolysis rates and the formation of clear gels. Less condensed solvates are formed in propanol ($n = 2$), hydrolysis becomes much faster leading to precipitation rather than gelation.

The molecular structure of metal alkoxides also depends on the steric hindrance of alkoxy groups. Bulky secondary or tertiary alkoxy groups tend to prevent oligomerization whereas most methanolates $M(OCH_3)_z$ form insoluble high polymers. $Ti(OBu^n)_4$ is currently used as a commercial precursor for TiO_2. It does not react too fast with water and can be handled without too much care. Because n-Bu, with four carbon atoms, is the largest alkoxy group that does not prevent oligomerization. It gives mainly $[Ti(OBu^n)_4]_3$ trimers (**3**) in

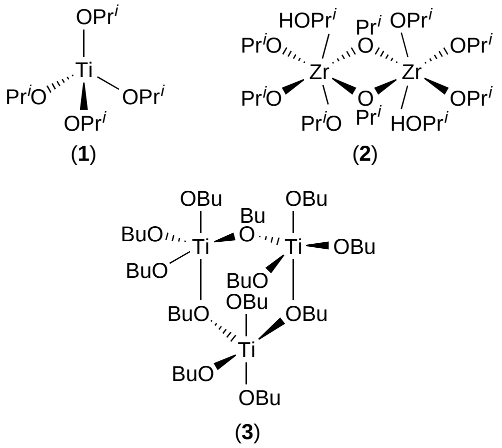

(**1**) (**2**) (**3**)

Figure 1 Molecular structure of some transition metal alkoxides: $Ti(OPr^i)_4$ monomer (**1**); $[Zr(OPr^i)_4(Pr^iOH)]_2$ dimer (**2**); $[Ti(OEt)_4]_3$ trimer (**3**)

benzene and $[Ti(OBu^n)_4,BuOH]_2$ dimers in its parent alcohol (Figure 1).

Hydrolysis and condensation rates depend on the molecular structure of metal alkoxides and alkoxide precursors have to be chosen as a function of the desired material final product. In the case of TiO_2, for instance, monomeric precursors such as $Ti(OPr^i)_4$, in which Ti is fourfold coordinated, react very quickly with water leading to the uncontrolled precipitation of polydispersed TiO_2. The reaction is much slower with oligomeric precursors such as $[Ti(OEt)_4]_n$ in which Ti has a higher coordination number. Spherical monodispersed TiO_2 powders can be produced via the controlled hydrolysis of diluted solutions of $Ti(OEt)_4$ in EtOH. On the contrary, monomeric precursors are more convenient for the sol-gel synthesis of multicomponent oxides. The perovskite phase $BaTiO_3$ is formed upon heating around 800 °C when $[Ti(OEt)_4]_n$ is used as a precursor. This temperature decreases down to 600 °C with the monomeric precursor $Ti(OPr^i)_4$ which favors the formation of Ti–O–Ba bonds.**[8]**

The tendency of metal ions to increase their coordination number via oligomerization depends on their oxidation state. Large monovalent (Li^+, Na^+, K^+) and divalent (Ba^{2+}, Ca^{2+}, Cu^{2+}, Zn^{2+}, etc.) metal ions give insoluble polymeric derivatives that can no longer be used as precursors for sol-gel syntheses. Oligomerization has then to be prevented by adding the metal powder directly in the alcoholic solution of another metal alkoxide. The alkaline alkoxide reacts readily with other precursors in the solution, giving rise to soluble heterometallic alkoxides rather than high polymers.**[9]**

Soluble low-valent metal alkoxides can also be synthesized by replacing small alkoxy group OR by bulky polydentate ligands such as 2-methoxyethanol $CH_3OC_2H_4OH$. This solvent is currently used to prevent polymerization and get soluble molecular precursors with low-valent metal cations such as Cu^{2+} in the sol–gel synthesis of advanced ceramics such as high T_c superconductors $YBa_2Cu_3O_{7-x}$ (*see* ***Sulfur: Organic Polysulfanes***).**[10]**

2.3 Chemical Control of Alkoxides Structure and Reactivity

Because of coordination expansion, most metal alkoxides, other than silicon, are highly reactive toward hydrolysis and condensation. Precipitation occurs as soon as water is added. Therefore their chemical reactivity has to be decreased in order to avoid uncontrolled precipitation. This can be performed via the chemical modification of the molecular precursor prior to hydrolysis.**[11]** Nucleophilic chemical additives are currently employed in order to stabilize highly reactive metal alkoxides and control the formation of condensed species.

Metal alkoxides react with hydroxylated compounds XOH such as carboxylic acids or β-diketones leading to the elimination of alkoxy groups, following equation (4). These complexing XOH species behave as bridging (acetate, AcO^-) (**4**) or chelating (acetylacetonate, acac) (**5**) bidentate ligands (Figure 2). They increase the coordination number of the metal atom. The new precursor has a different molecular structure, a reduced functionality, and therefore a different chemical reactivity toward hydrolysis and condensation. Complexed alkoxides are usually much less sensitive toward hydrolysis and condensation. Complexing ligands such as β-diketones are currently added to the alkoxide solution prior to hydrolysis, allowing a better control over the formation of oxide particles.

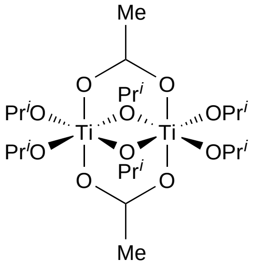

(**4**)

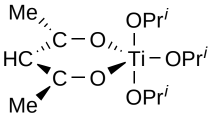

(**5**)

Figure 2 Chemical modification of $Ti(OPr^i)_4$: with acetic acid $[Ti(OPr^i)_3(OAc)]_2$ (**4**); with acetylacetone $[Ti(OPr^i)_3(acac)]$ (**5**)

TiO_2 powders can be readily obtained from the hydrolysis and condensation of titanium alkoxides. However such precursors are highly reactive, leading to the uncontrolled precipitation of polydispersed powders upon addition of water. The formation of TiO_2 can be controlled chemically by adding acetylacetone to the alkoxide $Ti(OBu^n)_4$. This leads to the formation of $Ti(OBu^n)_{3-x}(acac)_x$ species. This modified precursor can then be hydrolyzed by adding a given amount of water. The hydrolysis of alkoxy ligands gives reactive Ti–OH groups allowing condensation to proceed whereas acac groups act as polymerization lockers preventing condensation. The condensation of these molecular precursors can then be chemically controlled, by varying these two chemical parameters. Molecular clusters, colloidal particles, gels, or precipitates can be formed depending on the relative amount of hydrolysis ($h = H_2O/Ti$) and complexation ($x = acac/Ti$).

Fine powders can be obtained in the h/x range where colloidal sols are formed (*see* ***Semiconductor Nanocrystal Quantum Dots***). Amorphous colloidal particles are obtained when more water is added. Their mean diameter increases when h increases and x decreases. Monodispersed crystalline anatase TiO_2 particles are formed by heating the colloidal solution at 60 °C in the presence of an organic acid such as PTSA (ParaToluene Sulfonic Acid). Ti–acac bonds are then dissociated, allowing the formation of Ti–O–Ti bonds and the crystallization of the titanium oxide. Some organic groups (acac and PTSA) remain bonded to the surface of the colloids preventing their aggregation. Stable nonaggregated TiO_2 sols are then obtained. They can be dried to give nanopowders and even redispersed without aggregation in water–alcohol solutions at concentrations higher than 1 M, and deposited onto glass substrates in order to make antireflecting TiO_2

coatings. Crystalline zirconia nanoparticles synthesized from chemically modified zirconium alkoxides have been used for the production of microporous ceramic membranes.[12]

The sol–gel chemistry of silicon alkoxides is much simpler (*see* ***Silicon: Inorganic Chemistry***).[13] Si^{IV} is fourfold coordinated ($N = z = 4$) in the precursor as well as in the oxide so that coordination expansion does not occur. The electronegativity of Si is rather high compared to transition metals. Silicon alkoxides are therefore not very sensitive toward hydrolysis. Their reactivity decreases when the size of the alkoxy groups increases. This is mainly due to steric hindrance, which prevents the formation of hypervalent silicon intermediates (*see* ***Hypervalent Compounds***). Silicon alkoxides, $Si(OR)_4$, are always monomeric. Heterometallic alkoxides have never been obtained via the reaction of a silicon alkoxide with another alkoxide. Silicon alkoxides have to be prehydrolyzed before Si–O–M bonds can be formed.

Hydrolysis and condensation rates of silicon alkoxides have to be enhanced by acid or base *catalysis*, otherwise gelation would take several days (Table 1). Inorganic acids reversibly protonate negatively charged alkoxide ligands and increase the reaction kinetics by producing better leaving groups. Basic catalysis provides better nucleophilic OH^- groups for hydrolysis, whereas deprotonated silanol groups ($Si–O^-$) enhance condensation rates.

Catalysis not only enhances hydrolysis and condensation rates, but it also leads to polymeric species of different shapes. The negative charge of the OR groups increases as the electron-providing power of oxo and alkoxo ligands increases. The ease of protonation of OR groups, therefore, decreases as the connectivity of the adjacent Si atom increases. Acid-catalyzed condensation is directed preferentially toward the ends of oligomeric species, resulting in chain polymers. The positive partial charge δ_{Si} increases with its connectivity so that nucleophilic addition of $Si–O^-$ is directed preferentially toward the middles of oligomers, giving more compact, highly branched species that lead to the formation of monodispersed colloids.

The chemical reactivity of silicon alkoxides can also be increased by nucleophilic activation in the presence of chemical species, such as DMAP (dimethylaminopyridine), n-Bu_4 NF, or NaF, which behave as Lewis bases. A pentavalent intermediate is reversibly formed with F^- that stretches and weakens the surrounding Si–OR bonds. The positive charge δ_{Si} increases, rendering the silicon atom more prone to nucleophilic attack. This nucleophilic activation is efficient for both hydrolysis and condensation reactions.

Table 1 pH and gelation time Tg of a solution of $Si(OEt)_4$ (0.5 M) in the presence of various acid-base catalysts[6]

Catalyst	pH	Tg (h)
No catalyst	5	1000
HF	1.9	12
HCl	0.05	92
HNO_3	0.05	100
CH_3COOH	3.7	72
NH_4OH	9.9	107

2.4 Inorganic Precursors

Inorganic precursors are much cheaper and easier to handle than metal alkoxides. Therefore the industrial production of oxide powders for ceramics and catalysts is mainly based on the precipitation or coprecipitation of inorganic salts from aqueous solutions. Gibbsite, $Al(OH)_3$, (*see* ***Aluminum: Inorganic Chemistry***) is precipitated from aluminate solutions. TiO_2 powders are made via the controlled hydrolysis of titanium salts. Stabilized zirconia is coprecipitated from aqueous solutions of zirconium oxychloride, $ZrOCl_2$, and yttrium nitrate, $Y(NO_3)_3$.

Water, however, behaves both as a solvent of ionic compounds and a chemical reagent for the hydrolysis of molecular precursors (*see* ***Water & O-donor Ligands***). Hydrolysis and condensation reactions are therefore more difficult to control. Several monomeric or oligomeric solute species are often formed simultaneously when a metal salt is dissolved in water. These species are in rapid equilibrium and it is not easy to know which one is going to nucleate the solid phase. There are considerable data in the literature about the hydrolysis of metal cations in dilute solutions but very little is known about the formation of polynuclear species at concentrations greater than about 1 M, although these conditions are generally relevant to the synthesis of solid phases. Moreover, anions are known to play an important role even when they do not seem to be chemically involved in the hydrolysis and condensation of metal cations. As for the chemical modification of metal alkoxides by organic ligands, anions are able to form complexes with cationic precursors to provide a chemical control of the hydrolysis and condensation reactions.

The reactivity of inorganic precursors in aqueous solutions has been recently extensively described by Jolivet and will not be discussed in further detail here.[14] It is, however, worth mentioning that, in the presence of an excess of water, metal alkoxides lead to molecular or condensed species similar to those synthesized from aqueous precursors.

2.5 Recent Developments

The hydrolysis of trialkoxysilane $HSi(OR)_3$ under acidic conditions provides access to gels of composition $HSiO_{1.5}$. Because of Si–H bonds remaining at the gel surface, these compounds are hydrophobic, in contrast to silica gels bearing hydrophilic silanol groups. Thermal treatment of $HSiO_{1.5}$ under an NH_3 atmosphere leads to silicon oxynitrides $N(SiO_{1.5})_3$. Under oxidizing conditions, SiO_2 is obtained via the formation of silicon sesquioxide Si_2O_3 containing Si–Si bonds. Si_2O_3 can also be obtained from the hydrolysis of Si_2Cl_6.

Metal halides MX_n (M = Si, Al, Ti) can also be used in the formation of nonhydrolytic gels (NHG). When added to oxygen donors such as ethers, aldehydes or, for Al and Ti, parent metallic alkoxides in organic media, gels are formed. In the case of alumina, because no water is present in the reaction process, low-temperature hydrated crystalline phases, such as boehmite (AlO(OH)) cannot be formed so that gels remain amorphous over a larger range of temperature than for gels obtained via the hydrolytic process. Accordingly, the nature of the oxygen donor can control the high-temperature anatase-rutile transformation for titania NHG.[15]

3 HYBRID ORGANIC–INORGANIC MATERIALS

Sol-gel synthesis not only provides a new route to glasses and ceramics, but the 'chimie douce' conditions involved in the reaction process allow the incorporation of organic moieties into inorganic materials. These organic groups can be introduced in the precursor solution to control the sol–gel process and eliminated upon completion of solid formation. Alternatively, they can be retained within the inorganic framework, leading to hybrid organic-inorganic materials, also known as ORMOCERs (ORganically MOdified CERamics) or ORMOSILs (Organically MOdified SILicates)

3.1 Organic-templated Porous Materials

Organics can be used as catalysts, network modifiers or templating agents during the gel formation. Further washing, calcination or photodegradation treatments lead to purely inorganic solids. Recent developments in this field include the synthesis of meso-organized materials (*see* ***Porous Inorganic Materials***).[16] In contrast to microporous zeolites (*see* ***Zeolites***) obtained in hydrothermal conditions, these materials are obtained near room temperature using molecular or polymer surfactants as structure directing agents. Polymerization of inorganic precursors via the sol–gel process takes place at the interface with self-assembled templates (*see* ***Selenium Proteins Containing Selenocysteine***). Withdrawing the surfactants leaves empty pores in the inorganic network whose size, shape, and organization replicate the initial organic structure (Figure 3). Because surfactants can assemble as spherical or cylindrical micelles, which can aggregate as hexagonal, cubic, or lamellar liquid crystal phases, a wide range of pore size (2–50 nm) and organization can be obtained. Moreover, this self-assembly process is partially controlled by the interactions between the templating agent and the inorganic precursor. Therefore, the reactivity of the metal alkoxide is a key parameter for mesostructure formation, less stable transition metal precursors (Ti, V, etc.) lead to poorer organization than silicon alkoxides. Nevertheless, although this approach was pioneered for silica-based materials, numerous mesostructured oxides M_xO_y (M = Al, Ti, Zr, V, Nb, etc.) as well as nonoxides have been synthesized.[17] In addition to this chemical diversity, a wide range of shapes, such as powder, monoliths, fibres, films, and nanoparticles are now accessible, which should find applications in catalysis, optics, drug release (see Section 3.3). The most recent studies focus on hierarchically structured materials that would associate micro-, meso-, and macroporosity using micromoulding approaches, biotemplates (*see* ***Biomineralization***), and organogelators.[18]

3.2 Sol–Gel Approaches to Hybrid Nanocomposites

The sol-gel process allows the intimate mixing of inorganic and organic moieties at the molecular level. Based on the nature of the organomineral interface, hybrid organic-inorganic materials are conveniently divided in two classes.[19] Class I corresponds to systems in which organic components are simply embedded in an inorganic matrix. In contrast, Class II hybrids involve covalent or iono-covalent bonding between the organic and inorganic components.

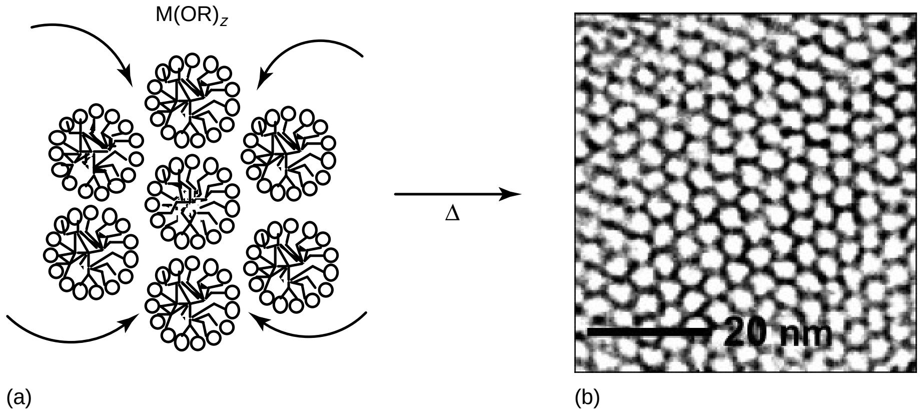

Figure 3 Synthesis of mesoporous metal oxides: (a) hexagonal assemblies of micellar systems are used as templates for the hydrolysis/condensation of $M(OR)_z$ alkoxides; (b) after calcination, the corresponding oxide exhibits an hexagonal array of mesopores

3.2.1 *Class I Hybrid Materials*

A wide variety of organic species can be dissolved with metal alkoxides in a common solvent. Hydrolysis and condensation reactions lead to the formation of an oxide network in which organic molecules remain trapped. However, the synthetic routes often have to be adapted to the properties of the immobilized species.

This is particularly true for biomolecules which are highly sensitive to pH and alcohol. The typical sol-gel procedure, which involves the homogenization of water and alkoxides mixtures by adding the parent alcohol as a cosolvent, as well as an acid-catalyzed hydrolysis step (HCl, $\mathrm{pH} \approx 2.$), is therefore not compatible with their entrapment. Actually, it was shown that the alcohol released during the alkoxide hydrolysis reaction was sufficient to rapidly homogenize the aqueous precursor solution. Moreover, the addition of a buffer to the hydrolyzed solution raises the pH above 5, allowing further mixing with the aqueous suspension of proteins. The pH buffer being close to 7, condensation occurs rapidly under basic conditions, embedding the biomolecules within the oxide network.[20]

In the case of polymer-oxide hybrids, a good homogeneity of the material is difficult to achieve unless weak interactions between both phases favor their mutual interpenetration at the molecular level. This can be achieved by taking advantage of the Brönsted acidity exhibited by M–OH hydroxyl groups produced via $\mathrm{M(OR)}_n$ alkoxide hydrolysis. These groups can form hydrogen bonds with amide carbonyl groups of polyamides polymers. Based on this principle, polymers such as poly(N-vinyl pyrrolidone) (PVP) or poly(N,N-dimethylacrylamide) (PDMAAm) could be associated with silica forming colorless, homogeneous, and transparent gels (Figure 4a).[21]

Alternatively, a suitable polymer-silica blend can be obtained by in situ polymerization of organic monomers. This can be achieved either by impregnation of a preformed gel, or by adding these monomers to the alkoxide solution. In this case, the simultaneous polymerization of organic and inorganic precursors leads to IPN (Interpenetrating Polymer Network) hybrids where both cross-linked gels are associated at the molecular level, as demonstrated for PDMAAm- and polystyrene-silica materials (Figure 4b).[22]

3.2.2 *Class II Hybrid Materials*

Organic species can also be chemically bonded to the oxide network via Si–C bonds. Many organoalkoxysilane precursors, $\mathrm{R}'_{4-x}\mathrm{Si(OR)}_x$, are commercially available. They contain nonhydrolyzable Si–C bonds, so that organic moieties are not removed upon hydrolysis. Depending on the nature and amount of organic and inorganic components, it becomes possible to tailor the microstructure and even obtain multifunctional materials.

The sol–gel synthesis of hybrid organic–inorganic compounds usually involves a mixture of di- or trifunctional organosilanes, which introduce Si–C bonds, with metal alkoxides, mainly $\mathrm{Si(OR)}_4$, as cross-linking reagents to build the inorganic network.[23,24]

- Trifunctional alkoxides, $\mathrm{R'Si(OR)}_3$, are the usual precursors used to introduce organic groups within an inorganic network. Careful control of polymerization reactions can lead to a homogeneous distribution of organic R′ groups within the silica network. These precursors can be used as such to modify silica surface properties such as hydrophobicity using long chain alkyl groups $\mathrm{(RO)_3{-}Si{-}C}_n\mathrm{H}_{2n+1}$, or fluoroalkyl silanes, $\mathrm{(RO)_3{-}Si{-}(CH_2)_2(CF_2)}_n\mathrm{CF_3}$, finding application in water-repellent coatings on metals or glasses. R′ can also be a polymerizable organic group, such as vinyl, epoxy, or methacrylate, leading

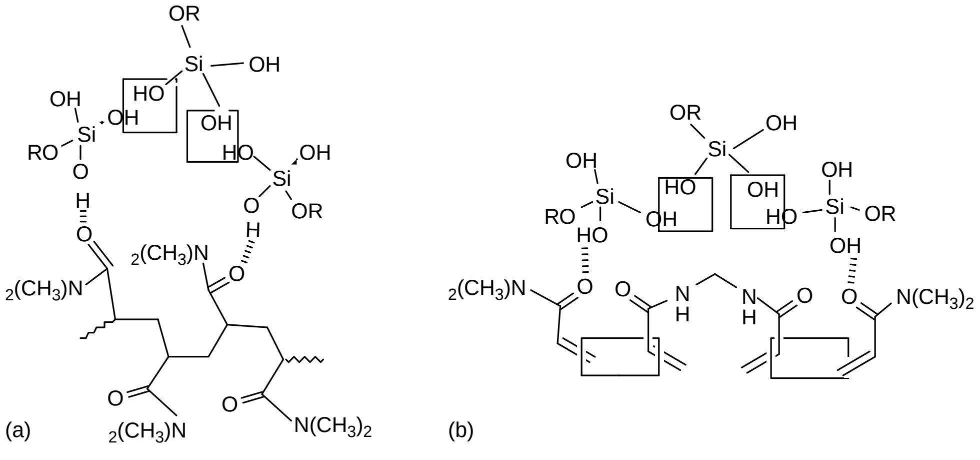

Figure 4 Polymer-silica hybrid materials: hydrogen bonding between silanol groups of hydrolyzed silicon alkoxides and carboxylate groups of preformed poly(N,N-dimethylacrylamide) (a) or in situ polymerized N,N-dimethylacrylamide/methylene bisacrylamide precursors (b) favors the formation of homogeneous organic–inorganic networks

to a polymer-silica hybrid. Starting from *N*-3-trimethoxysilyl-propyl-pyrrole (**6**), polypyrrole-silica materials were obtained exhibiting high electrical conductivity (Figure 5). Alternatively, R′ can provide a reactive site for further binding of ions, organics, and biomolecules.

- Difunctional alkoxides, $R'_2Si(OR)_2$, such as diethoxydimethylsilane (DEDMS), cannot act as network formers. However, their tendency to form chains is currently used to impart some flexibility to the oxide network. Polydimethylsiloxane (PDMS) (**7**) with terminal hydroxyl groups has also been used in this role instead of DEDMS (Figure 5). Polymers of various molecular weights lead to a whole set of hybrid materials ranging from viscous liquids to brittle glasses (*see* ***Polysiloxanes & Polysilanes***).
- Metal alkoxides act as cross-linking agents between organosilicon units, increasing the hardness of the materials. Tetrafunctional silicon alkoxides are more commonly employed, but transition metal alkoxides $M(OR)_n$ ($M = Ti$, Zr, etc.) can also be used. They not only serve as cross-linking reagents, but can also increase the refractive index or catalyze condensation.

Polyfunctional precursors can also be used to design hybrid organic–inorganic materials. Monomers consisting of a variable organic bridging group and two or more trifunctional silyl groups can undergo hydrolysis and condensation reactions, leading to bridged polysilsequioxanes (**8**) (Figure 5). Because of the increased number of reactive functions, the gelation process is much faster than for tetraethoxysilane (TEOS) at equivalent concentration. Monitoring the size, shape, rigidity, and functionality of the spacer allows the control of the material porosity, optical properties, and thermal stability. Bridged polysilsequioxanes are used for surface modification and coating formulations, and could find application in catalysis and separation media.[25]

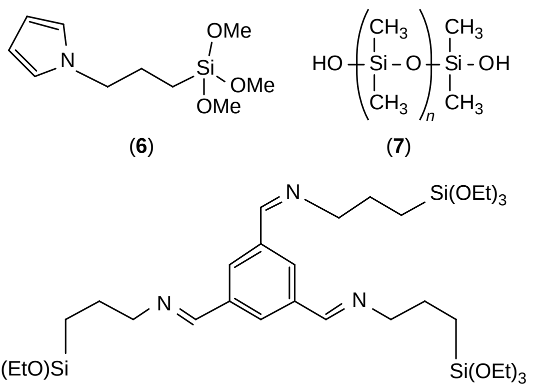

(**6**) (**7**)

(**8**)

Figure 5 Molecular structure of selected organoalkoxysilanes: trifunctional *N*-3-trimethoxy-silyl-propyl-pyrrole (**6**); difunctional polydimethylsiloxane (**7**); a multifunctional bridged polysilsesquioxane (**8**)

3.2.3 The Nanobuilding Blocks Approach

As an alternative to molecular precursors, the use of preformed objects, such as clusters (*see* ***Polynuclear Organometallic Cluster Complexes***) or nanoparticles (*see* ***Semiconductor Nanocrystal Quantum Dots***), that keep their integrity in the final material constitutes a convenient and fruitful method to control the organic-inorganic interface as well as the hybrid architecture. A wide range of Nano Building Blocks (NBBs), including polysilsesquioxane, organotin, polyoxometallates, and metal-oxo clusters, have been used, which can be functionalized with polymerizable ligands (vinyl, styryl, methacryl) or organic bridging spacers (telechelic molecules, polymers, dendrimers). Class I or II hybrids are obtained, depending on the anchoring interactions between the inorganic core and the organic moieties. The hybrid structure at the macromolecular scale is defined by the nature and number of functional groups. Using the monofunctional $R–Si(c\text{-}C_6H_{11}Si)_7O_{12}$ polyhedral oligosilsesquioxane, with R = styryl, 3-propylmethacrylate (**9**), or 2-ethylnorbornyl, linear polymeric backbones are obtained, exhibiting pendant silsequioxane cubes (Figure 6). In similar systems, the good dispersion of the NBB as well as its covalent anchoring to the organic network increase the polymer glass transition up to 200 °C. The oxo-hydroxo butyltin macrocation $(BuSn)_{12}O_{14}OH_{62}{}^{+}$ can be functionalized with two polymerizable anions 2-acrylamido-2-methyl-1-propanesulfonate. Copolymerization of these NBB with methylacrylate in toluene leads to homogeneous gels, which can be redissolved in DMSO owing to the electrostatic interactions responsible

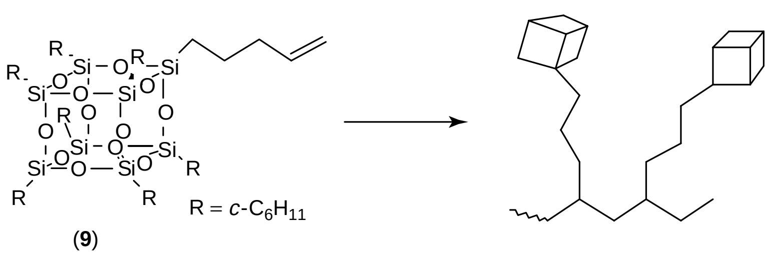

(**9**)

Figure 6 The nano building block approach to hybrid materials: polymerization of $R–Si(c\text{-}C_6H_{11}Si)_7O_{12}$ polyhedral oligosilsesquioxane, with R = 3-propylmethacrylate, (**9**), leads to linear polymeric backbones, exhibiting pendant silsequioxane cubes

for the cross-linking. Glassy transparent xerogels could be obtained by the association of $Ti_{16}O_{16}(OEt)_{32}$ oxo clusters with carboxylate- or alcoholate-functionalized dendrimers. Covalent bonds are formed, leading to a stable ordered dispersion of clusters at the 10 nm range. The cross-linking of water-soluble poly(acrylamide) with the $[\gamma\text{-SiW}_{10}O_{36}(RSiO)_4]^{4-}$ polyoxometalate, where $R = CH_2{=}C(Me)C(O)OPr^-$, allows the synthesis of hydrogels with swelling properties similar to those of super absorbent materials. Finally, silica, alumina, zirconia, and titania nanoparticles functionalized with alkylmethacrylate groups, are used to design reactive ceramic fillers for PMMA-based composites. The above-illustrated high versatility of this approach constitutes a promising tool for the future design of multiscale and/or multifunctional hybrid materials.[26]

3.3 Properties and Applications

The sol–gel process allows the synthesis of tailored-made inorganic or hybrid materials, with many different shapes and microstructures, while being compatible with a wide range of molecules, polymers, nano-objects as well as biospecies. These materials can be used as such, as filtration membranes or coatings, and constitute suitable hosts for organic/organometallic reactions, electrochemical process, photochemistry or bioactivity. It is therefore not surprising that the possible applications of organic–inorganic hybrids cover the whole field of materials science.[27]

3.3.1 Organic–Inorganic Hybrid Catalysts

Immobilization of organic (or organometallic) catalysts onto solids allows their easy recovery from reaction media and improves their recyclability. In case of preformed porous silica surfaces, direct grafting of the organic moiety can be achieved if an organosilane derivative incorporating the desirable functional groups can be synthesized. The commercially available aminopropyl-silanes have been widely used to design base catalysts for the Knoevenagel reaction. Alternatively, the support can be first functionalized with an appropriate reactive moiety that constitutes an anchoring site for further grafting. Imine-supported silicas could be prepared from amino-grafted supports and used for Michael addition *Catalysis*.

Nevertheless, the grafting approach presents several drawbacks, particularly: (1) the catalyst is linked to the silica surface via an external Si–O–Si bridging bond, whose stability can be incompatible with certain reaction conditions; (2) the accessibility of the pore surface to organosilane reagents in amorphous solids can be limited, leading to poor loading as well as heterogeneous distribution of the catalytic groups. The latter problem can be partially overcome if ordered porous materials are used. Although this approach was studied for microporous zeolites, its efficiency was more clearly revealed with mesoporous supports exhibiting larger surface area and pore size. In parallel, direct incorporation of the catalyst by cocondensation of the corresponding organosilane with network-forming tetrafunctional silicon alkoxides allows the elimination of the former limitation. Thus, a large variety of functional groups (amine, epoxide, thiol, etc.) can be introduced that remain accessible for further reaction. Incorporated in mesoporous materials, vinyl and methacrylate moieties can be postbrominated in situ whereas cyclodextrins maintain their chelating properties. Bifunctional materials are also obtained when a mixture of organosilanes is used. Sulfonic acid moieties act as catalysts for monoglyceride synthesis from glycerol and fatty acids. The cocondensation of the corresponding organosilane with hydrophobic methyltrimethoxysilane increases the catalytic activity of the bifunctionalized mesoporous materials by three when compared to the monofunctionalized support (Figure 7).[28]

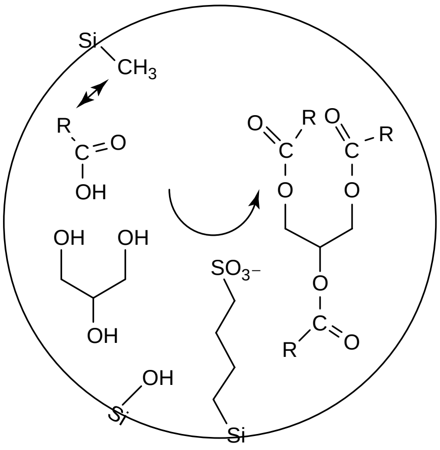

Figure 7 Mesoporous silica grafting for catalysis: enhanced activity towards glycerol esterification is obtained when a hydrophobic methyl chain is cografted with the sulfonate function, providing favorable interactions with fatty acid reagents

Two recent approaches open up new possibilities to design more stable and efficient hybrid catalysts. The first one relies on the incorporation of the organic moiety within the walls of the mesoporous materials rather than into the network voids, using bridged bis(trialkoxysilyl)-organosilanes.[29] As far as catalyst selectivity is concerned, the molecular imprinting approach, already widely used in organic polymers, has also been applied to silica gels. In this case, the sol-gel process is performed in the presence of suitable substrates that control the three-dimensional organization of the functional groups during the porous network formation. Removing the substrate leaves an optimized configuration for following catalytic reactions, mimicking the high selectivity of enzyme active sites.[30]

3.3.2 ‘Sol–Gel Optics’

Incorporation of photoactive species within sol–gel matrices has been extensively studied for dye laser materials, rare-earth ion-doped glass devices, nonlinear optics (NLO), photochemical hole burning (PHB) as well as photochromism and electroluminescence.[31] Because the sol–gel process allows the optimization of host-guest interactions by the fine tuning of the dye environment, some of these materials have been commercialized as television screen coatings (Toshiba) or colored glassware.

Optimization of photochromic devices provides a nice illustration of the flexibility of the sol–gel approach. Spirooxazine (SO) dyes (**10**) can undertake a reversible color change by absorption of a photon associated with large structural changes (Figure 8). The efficiency and rate of the photochromic response as well as the thermal stability of the open form are highly dependent on the host flexibility, pore size, and hydrophobicity. Thus, even though Class I hybrid materials obtained by SO-doping of pure silica matrices were shown to exhibit photochromic properties, slow thermal fading was observed because of the stabilization of the polar open form by hydrogen bonding with Si–OH silanol surface groups of the host. Moreover, at high concentration, these dyes tend to aggregate, interfering with the photochromic reaction. The use of hydrophobic matrices, synthesized from cocondensation of $MeHSi(OR)_2$ and $HSi(OR)_3$, increases the thermal fading kinetics by two orders of magnitude. Incorporating aromatic groups on the matrix surface using $C_6H_5HSi(OR)_2$ precursors, allows a higher SO loading while avoiding its aggregation. Alternatively, the photochromic dyes can be grafted on the silica surface via an organic spacer whose length controls the rate of the photochromic response.

Apart from the tuning of the host-guest interactions, the elaboration of efficient optical devices also relies on the optimization of the matrix mechanical properties and thermal stability. This is clearly demonstrated in the development of hybrid materials for NLO, and especially second harmonic generation (SHG). These properties rely on their noncentrosymetric organization of organic chromophores in the condensed phase. Because incorporation in a silica matrix leads to a random distribution of dyes, electrical field poling technics are needed to align the organic molecules. Nevertheless, upon aging, orientational relaxation occurs, leading to the loss of chromophore alignment and therefore of SHG efficiency. There is therefore a need for matrices with improved rigidity, which can be achieved by improving the silica network cross-linking by increasing the sol aging time, using prepolymerized precursors, or by adding thermally stable polymers such as polyimides. In addition, similar to photochromic materials, Class II hybrids involving the covalent linking of the chromophore to the silica surface via functionalized trialkoxysilane lead to better time and thermal stability and allow higher loadings of photoactive molecules. Thus, organic-inorganic composites incorporating high polarizable diazobenzene chromophores such as Red17 or DR1 can be made with high thermal stability (80–100 °C) as well as nonlinearities comparable to those reported for inorganic solids and organic polymeric materials.

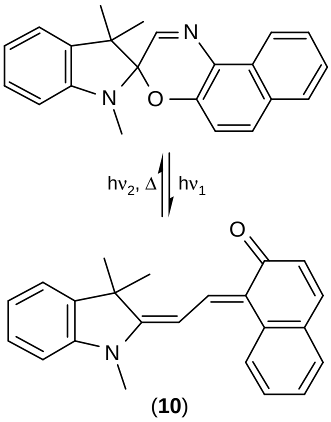

(**10**)

Figure 8 Molecular structure of spirooxazine (SO) dyes (**10**) and their light-driven equilibrium

3.3.3 *Bioencapsulation in Silica Gels*

The ability to form hybrid silica glasses under aqueous, room-temperature conditions (at which proteins and cells are active) opens up the possibility to extend sol-gel processing to the encapsulation of biologicals.[32] However, as mentioned earlier, the traditional sol–gel route using silicon alkoxides has to be adapted to avoid excess alcohol as well as low pH conditions (see section 3.2.1). Moreover, because biospecies could be denatured by covalent bonding, most bioorganic–inorganic composites are Class I hybrids.

Enzymes retain their biological activity when encapsulated within porous sol-gel glasses and can be used for the realization of biocatalysts or biosensors.[33] Glucose oxidase (GOD) is by far the most studied enzyme for applications in the field of medicine and food industry. GOD is capable of catalyzing the oxidation of D-glucose by molecular oxygen into D-gluconolactone and D-gluconic acid as follows:

$$\text{Glucose} + O_2 \xrightarrow{\text{GOD}} H_2O_2 + \text{Gluconic acid} \qquad (6)$$

The flexibility of the sol–gel process allows multiple approaches to enzymatic activity monitoring. The formation of hydrogen peroxide can be followed by optical measurements using another enzymatic reaction in which the oxidation of an organic dye is catalyzed by a peroxidase (HorseRadish Peroxidase HRP), coentrapped with GOD. The presence of glucose in the solution can also be detected via electrochemical means by following the redox reactions at the active site of GOD. However, because of the steric hindrance of the protein molecule, a ferrocene mediator has to be used in order to transfer electrons from the hidden active site to the electrode. Alternatively, oxygen consumption can be measured with a Clark electrode. The hybrid gel is deposited on a Pt cathode from a GOD and hydrolyzed tetramethoxysilane (TMOS) mixture. After d-glucose addition, oxygen concentration is measured by amperometric titration at imposed potential. All these experiments show that the catalytic activity of GOD is preserved within the gel and that their active sites remain accessible to the substrate. Moreover, upon encapsulation, the decrease of GOD catalytic activity with time is slowed up, suggesting that the silica matrix protects the enzyme against denaturation.

Sol–gel matrices can also provide a chemical surrounding that favors enzymatic reactions. Lipases act on ester bonds and are able to hydrolyze fats and oils into fatty acids and glycerol. These are interphase-active enzymes with lipophilic domains and the catalytic times reaction occurs at the water-lipid interface. Entrapped lipases can be almost 100 times more active when a chemically modified silica matrix is used. The cohydrolysis of $Si(OMe)_4$ and $RSi(OMe)_3$ precursors provides alkyl groups that offer a lipophilic environment that can interact with the active site of lipases and increase their catalytic activity. Such entrapped lipases are now commercially available and offer new possibilities for organic syntheses, food industry, and oil processing.[34]

Antigen-antibody reactions have also been performed within sol–gel matrices extending the field of sol–gel chemistry toward immunosensors. Specific haptens are used for the biodetection of chemicals such as atrazine, a widely used herbicide. Antiatrazine antibodies are trapped within the sol–gel matrix and nanograms of atrazine are applied on SiO_2 sol–gel columns doped with this antibody. Titration of eluted solutions shows that high amounts of atrazine remain bound to antiatrazine antibodies inside the silica gel. For medical applications, whole cell parasitic protozoa (*Leishmania donovani infantum*) have been trapped within sol–gel matrices and used as antigens for blood tests with human sera. Antigen–antibody interactions were followed by the so-called Enzyme-Linked Immunosorbent Assays (ELISA) and the presence of antibodies in the blood detected via a colored reaction, showing a clear-cut difference between negative and positive sera.[35]

The sol–gel encapsulation of whole cell bacteria *Escherichia coli* was first reported using the modified silicon alkoxide process. However, the release of alcohol during the hydrolysis step induces bacteria lysis. Using genetically engineered *E. coli* exhibiting stress-dependent luminescence properties, it was possible to optimize the sol–gel procedure (pH, water/TMOS ratio, drying time) for cell entrapment in silica thin films (*see* ***Thin Film Synthesis of Solids***). Moreover, the possibility to entrap simultaneously cells from two different strains was demonstrated, opening new possibilities for dual or multiple sensing. Alternatively, aqueous routes using a mixture of sodium silicate and colloidal, in the presence of organic additives, such as glycerol, allowed entrapped *E. coli* survival over one month (Figure 9). These studies also demonstrated that generic tests to assess bacteria viability in solution, such as culturability or glucose incorporation, could be transposed to cells entrapped in silica gels.

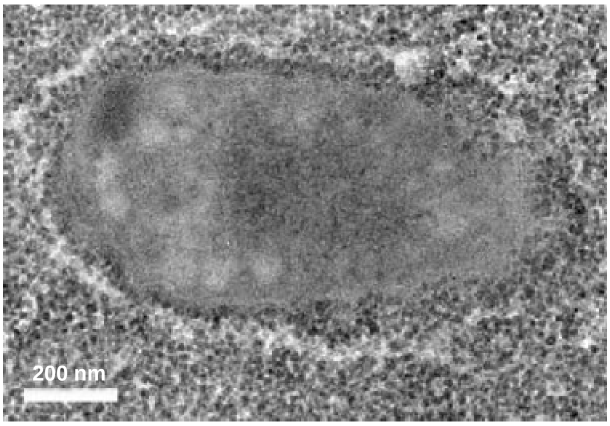

Figure 9 Transmission electron micrograph of an *E. coli* bacteria encapsulated in a silica gel

Mammalian tissues such as the pancreatic islets of Langerhans are known to produce insulin in response to glucose challenge. After encapsulation, they have been transplanted into a diabetic mouse where they retain their activity. The fine porosity of the gel protects transplanted islets against antibody aggression but permits nutrients to reach the cell and by-products to escape. Urinary excretion of glucose fell to almost zero within a few days of transplantation and remained close to zero for almost three months. In addition, both blood sugar and blood insulin concentrations were normal. After one month of transplantation, the surgically removed transplant showed no evidence of fibrosis. Such transplants, if viable for extended lengths of time, could emerge as a viable treatment for diabetes.[36]

4 CONCLUSION

Sol-gel chemistry has been extensively studied during the past decade. The basic reactions, hydrolysis, condensation, and complexation, involved in the formation of oxide networks from molecular precursors are now quite well described. The sol-gel process brings new opportunities in the field of materials science. It allows a powderless processing of glasses and ceramics. Coatings can be easily deposited directly from the solution onto a wide variety of substrates. Many patents have been taken and several products are now on the market. Other industrial applications will undoubtedly be developed during the next few years.

However, one of the main advantages of sol-gel chemistry will be to lead to new materials that cannot be obtained from the usual processing routes. At least three new fields are being explored taking advantage of soft chemistry to mix fragile organic molecules with hard oxide materials:

1. Mesoporous materials have been extensively studied since the discovery of mesoporous silica. The great progresses made in sol-gel chemistry open the way to the synthesis of hierarchically nanostructured porous materials.
2. New fields such as 'sol–gel optics' are based on the synthesis of hybrid organic-inorganic materials. They offer a new kind of materials ranging from polymers to glasses.
3. A new field is now emerging in which biomolecules or cells are trapped within sol-gel matrices. Silica gels offer many advantages and could compete in the near future with usual polymeric matrices. Rather few laboratories are involved in this field. More work is still required to make reproducible experiments, but some applications have already been developed.

5 RELATED ARTICLES

Biomineralization; Noncrystalline Solids; Polysiloxanes & Polysilanes; Porous Inorganic Materials; Semiconductor Nanocrystal Quantum Dots; Short-lived Intermediates; Silicon: Inorganic Chemistry.

6 REFERENCES

1. J. Livage, *Curr. Opin. Solid State Mater. Sci.*, 1997, **2**, 132.
2. J. D. Wright and N. A. J. M. Sommerdjik, 'Sol-Gel Materials. Chemistry and Applications', Gordon and Breach Science Publishers, Amsterdam, NY, 2001.
3. R. M. Laine, C. Sanchez, C. J. Brinker, and E. Giannelis eds., 'Organic/Inorganic Hybrid Materials-2000', Materials Research Society, Symposium Proceedings 628, Warrendale, PA, 2001.
4. D. C. Bradley, R. C. Mehrotra, and D. P. Gaur, 'Metal Alkoxides', Academic Press, London, 1978.
5. N. Y. Turova, E. P. Turevskaya, V. G. Kessler, and M. I. Yanovskaya, 'The Chemistry of Metal Alkoxides', Kluwer Academic Press, Norwell, MA, 2002.
6. C. J. Brinker and G. W. Scherer, 'Sol-Gel Science', Academic Press, San Diego, CA, 1990.
7. R. C. Mehrotra and A. Singh, *Chem. Soc. Rev.*, 1996, **25**, 1.
8. C. D. Chandler, C. Roger, and M. J. Hampden-Smith, *Chem. Rev.*, 1993, **93**, 1205.
9. L. G. Hubert-Pfalzgraf, *Polyhedron*, 1994, **13**, 1181.
10. M. Kakihana, *J. Sol.-Gel Sci. Technol.*, 1996, **5**, 7.
11. C. Sanchez, J. Livage, M. Henry, and F. Babonneau, *J. Non-Cryst. Solids*, 1988, **100**, 65.
12. C. G. Guizard, A. C. Julbe, and A. Ayral, *J. Mater. Chem.*, 1999, **9**, 55.
13. R. Corriu and P. Jutzi eds., 'Tailor-Made Silicon-Oxygen Compounds', Vieweg, Wiesbaden, 1996.
14. J. P. Jolivet, 'Metal Oxide Chemistry and Synthesis', John Wiley & Sons, Chichester, 2000.
15. R. J. P. Corriu and D. Leclerq, *Angew. Chem., Int. Ed.*, 1996, **35**, 1420.
16. J. S. Beck and J. C. Vartuli, *Curr. Opin. Solid State Mater. Sci.*, 1996, **1**, 76.
17. X. He and D. Antonelli, *Angew. Chem., Int. Ed.*, 2002, **41**, 214.
18. G. Jde. A. A. Soler-Illia, C. Sanchez, B. Lebeau, and J. Patarin, *Chem. Rev.*, 2002, **102**, 4093.
19. C. Sanchez and F. Ribot, *New J. Chem.*, 1994, **18**, 1007.
20. D. Avnir, S. Braun, O. Lev, and M. Ottolenghi, *Chem. Mater.*, 1994, **6**, 1605.
21. T. Saegusa, *Pure Appl. Chem.*, 1995, **67**, 1965.
22. Y. Chujo, *Curr. Opin. Solid State Mater. Sci.*, 1996, **1**, 806.
23. U. Schubert, N. Hüsing, and A. Lorenz, *Chem. Mater.*, 1995, **7**, 2010.
24. J. Wen and G. L. Wilkes, *Chem. Mater.*, 1996, **8**, 1667.
25. K. J. Shea and D. A. Loy, *Mater. Res. Soc. Bull.*, 2001, **26**, 368.
26. C. Sanchez, G. Jde. A. A. Soler-Illia, F. Ribot, T. Lalot, C. R. Mayer, and V. Cabuil, *Chem. Mater.*, 2001, **13**, 3061.
27. P. Gomez-Romero and C. Sanchez eds., 'Functional Hydrid Materials', Wiley-VCH, Weinheim, 2003.
28. A. P. Wight and M. E. Davis, *Chem. Rev.*, 2002, **102**, 3589.
29. T. Asefa, C. Yoshina-Ishii, M. J. MacLachlan, and G. A. Ozin, *J. Mater. Chem.*, 2000, **10**, 1751.
30. J. J. E. Moreau and M. Wong Chi Man, *Coord. Chem. Rev.*, 1998, **178–180**, 1073.
31. C. Sanchez and B. Lebeau, *Mater. Res. Soc. Bull.*, 2001, **26**, 377.
32. I. Gill and A. Ballesteros, *Trends Biotechnol.*, 2000, **18**, 282.
33. W. Jin and J. D. Brennan, *Anal. Chim. Acta*, 2002, **461**, 1.
34. M. T. Reetz, *Adv. Mater.*, 1997, **9**, 943.
35. J. Livage, T. Coradin, and C. Roux, *J. Phys.: Condens. Matter*, 2001, **13**, R673.
36. K. P. Peterson, C. M. Peterson, and E. J. A. Pope, *Proc. Soc. Exp. Biol. Med.*, 1998, **218**, 365.

Solids: Characterization by Powder Diffraction

Tom Vogt
Brookhaven National Laboratory, Upton, NY, USA

Based in part on the article Solids: Characterization by Powder Diffraction by Anthony K. Cheetham which appeared in the Encyclopedia of Inorganic Chemistry, First Edition.

1 Introduction 1
2 Neutron Powder Diffraction 2
3 X-ray and Synchrotron Radiation Powder Diffraction 3
4 Combined Neutron and X-ray High-resolution Powder Diffraction Studies of Catalysts 7
5 High-resolution X-ray and Neutron Diffraction in Magnetic Fields 9
6 Atomic Pair-distribution Functions and Nanocrystallography 10
7 High-pressure Neutron and Synchrotron X-ray Powder Diffraction 12
8 Outlook 16
9 References 16

1 INTRODUCTION

The driving force behind the rapid development of powder diffraction methods over the past 10 years is the increasing need for structural characterization of materials that are only available as powders. Examples are zeolite catalysts, magnets, metal hydrides, ceramics, battery and fuel cell electrodes, piezo- and ferroelectrics, and more recently pharmaceuticals and organic and molecular materials as well as biominerals. The emergence of nanoscience as an interdisciplinary research area will further increase the need for powder diffraction. pair-distribution function (PDF) analysis of powder diffraction pattern allows the refinement of structural models regardless of the crystalline quality of the sample and is therefore a very powerful structural characterization tool for nanomaterials and disordered complex materials.

Shortly after the discovery of X-ray diffraction by von Laue and von Knipping in 1910, Debye and Scherrer[1] (1916) in Germany and Hull[2] (1917) in the United States independently pioneered X-ray powder diffraction. Zachariasen[3,4] (1949) determined the first structures solely from powder diffraction data by using an intuition-based trial-and-error approach. The structures of UCl_3 as well as α- and β-UF_5 were solved this way. More than a decade later Zachariasen and Ellinger[5] (1963) used direct method procedures to solve the monoclinic structure of β-Pu. In direct methods, the crystallographic phase problem is solved using only the observed intensities by applying phase sum relationships. The first structure solved from powder data using Patterson methods was UO_2Cl_2 in 1968.[6] In the Patterson technique, an interatomic vector map (‘autocorrelation function’) is used to assign ‘heavy atoms’ that dominate the map and thereby determine atomic positions. These were however isolated one-off studies. The majority of structures were still being solved using single-crystal diffraction methods. Today, structure solution and refinements are no longer the exclusive domain of single-crystal diffraction. This shift towards using powder diffraction methods was triggered by (1) the advent of the application of least-squares fitting to powder diffraction pattern (Rietveld refinement method), (2) instrumental improvements of laboratory-based X-ray powder diffractometers, (3) the availability of user-friendly and dedicated high-resolution powder diffractometers at research reactors, neutron spallation sources and synchrotron radiation sources and (4) the increase of computing power. In recent years, the gap between laboratory and facility-based high-resolution diffractometers has closed and an increasing number of structures are now being solved using laboratory-based X-ray powder diffractometers. This has in turn led to a change in the use of facility-operated powder diffractometers, where ‘parametric studies’ of a sample as a function of sample environment such as temperature, pressure, and magnetic and electric fields are nowadays called for. Furthermore, powder diffraction studies are now increasingly used to probe mesoscopic structures beyond the atomic level such as texture, particle size, strain, and stacking faults. It has also come to the attention of the solid-state community that phase coexistence might be a necessary prerequisite for certain functionalities, that is, in giant magentoresistant oxides, magnetocaloric materials, and multifunctional catalysts. Therefore, the study of phase mixtures and their mesoscopic interplay will continue to challenge powder diffraction. Modern powder diffraction methods have developed from a mostly qualitative to a quantitative tool used to detect new phases and determine the atomic, magnetic, and mesoscopic structures. Langford and Louer wrote a substantial recent review of state-of-the-art powder diffraction techniques.[7]

Powder diffraction makes use of elastic scattering where the probe (neutron or X-ray photon) is deflected without energy transfer and located on a Debye-Scherrer cone at an angle θ according to Bragg’s law $n\lambda = 2d\sin\theta$. Scattering processes are often described using scattering triangles, where a scattering vector Q is defined by the vector relationship $Q=k-k'$, k and k' being the incident and diffracted spherical wavefronts. Simple trigonometric arguments show that in the case of elastic scattering $Q = 4\pi \sin\theta/\lambda$. If the probing particles interact with the scattering centers in such a way that the scattered waves have a phase relationship with each other, one speaks of coherent scattering. Diffraction or Bragg scattering is the simplest form of coherent scattering. In an incoherent scattering process, no interference is possible. The intensities therefore simply add up. In neutron scattering, the large incoherent scattering of hydrogen adds up to an effective absorption. Therefore hydrogen-containing samples need to be deuterated for neutron scattering experiments.

2 NEUTRON POWDER DIFFRACTION

Neutrons can be described by de Broglie's wave-particle formalism and a wavelength λ can be determined according to $\lambda = h/mv$ with h being Planck's constants and m and v being the mass and velocity respectively. The neutron's mean energy can be expressed as:

$$\mathrm{E(eV)} = 0.08617\mathrm{T(K)} = 5.227\ \mathrm{v}^2(\mathrm{kms}^{-1}) = \frac{81.81}{\lambda^2(\text{Å})} \qquad (1)$$

Neutrons used for research are made either in a fission or spallation process. Both processes create neutrons that need to be slowed down via a moderation process, that is, the neutrons adjust to the temperature of a hydrogen-containing moderator via inelastic neutron-proton collisions. In a research reactor, this moderation creates a distribution of neutrons between 1 and 3 Å. Using equation (1), one obtains a wavelength of 1.78 Å for a moderator temperature of 300 K, which is ideally suited for diffraction experiments. Neutrons interact with the atomic nucleus and not as X-rays do with the electrons. Nuclear forces have a very short range and the size of the nuclear scattering centers are about 10^5 times smaller than the probed interatomic distances. The nucleus is referred to as a 'point scatterer' and as a consequence the neutron is scattered isotropically. The neutron scattering length, b, which has dimensions of a length (given in fm) scatters independent of the scattering angle leading to strong nuclear Bragg intensities at high Q-values. This is in marked contrast to X-ray scattering, where the atomic form factor monotonically decreases the further one increases Q. Furthermore, the neutron scattering length does not, as in the case of X-rays, vary systematically with the atomic number Z, which leads to one of the attractive features of neutron scattering: light elements such as deuterium ($b = 6.671$ fm) or oxygen ($b[^{16}O] = 5.80$ fm) can scatter stronger than heavy elements such as W ($b = 4.86$ fm) or Ba ($b = 5.07$ fm). This is of tremendous advantage for the study of metal oxides and hydrides, where the scattering contribution of oxygen and hydrogen/deuterium is in general larger than in the corresponding X-ray scattering experiment and as mentioned above does not 'fall off' at high scattering angles. Neutron diffraction experiments in particular powder diffraction experiments with hydrogen-containing materials will be done using deuterium owing to the large incoherent scattering of hydrogen, which leads to a large neutron absorption. Another consequence of the nucleus-neutron interaction is that neighboring elements such as Mn ($Z = 25$), Fe ($Z = 26$) and Co ($Z = 27$) can have significantly different scattering lengths, namely, $b_{Mn} = -3.73$ fm, $b_{Fe} = 9.45$ fm and $b_{Co} = 2.5$ fm respectively. To distinguish Mn^{2+} from Fe^{3+} with X-rays, one needs to perform anomalous scattering experiments, whereas with neutrons a straightforward distinction is possible. Another useful property of the neutron-nucleus interaction is that the neutron scattering length is isotope dependent and can have negative values. The latter is due to a phase shift of the neutron during the interaction with the nucleus. The best-known example is hydrogen ($b = -3.74$ fm) and deuterium ($b = 6.674$ fm). Varying the ration of H_2O:D_2O can therefore make water 'invisible' in neutron scattering experiments. Similar 'zero-scattering isotope alloys' can be made for Ni ($b(^{58}Ni) = 14.4$ fm, $b(^{60}Ni) = 2.8$ fm, $b(^{61}Ni) = 7.60$ fm and $b(^{62}Ni) = -8.7$ fm) and Ti ($b(^{48}Ti) = -6.08$ fm and $b(^{50}Ti) = 6.18$ fm). In neutron high-pressure scattering experiments, a Ti–Zr zero-scattering alloy, which has an appreciable mechanical strength is used. The isotope specific neutron scattering length can be exploited in experiments to locate an atomic species, which is disordered over more than one site. Using four separate samples containing ^{nat}Ni, ^{58}Ni, ^{60}Ni and ^{62}Ni Henry *et al.* were able to determine the distribution of Ni^{2+} and Fe^{2+} over two metal sites in $Fe_2Ni(PO_4)_2$ using neutron powder diffraction.**[8]** A critical comparison of isotope substitution neutron powder diffraction and anomalous X-ray powder diffraction shows that the first is superior for distinguishing between Ni and Fe. Thus the unique neutron-nucleus interactions offer an investigative route for site-disordered solids provided the right isotopes are available.**[9]** However, the neutron-nucleus interaction is very weak compared to the X-ray-electron or electron–electron interaction. The energy of a 1 Å neutron is 82 meV whereas that of a 1 Å X-ray photon is 12 keV. Therefore, neutrons can penetrate deep into matter. A flux of neutrons with a wavelength of 1.78 Å is only attenuated to one half after 50 cm of Al, whereas half of the X-rays with 1.78 Å are already absorbed after 0.003 cm. As a consequence, it is very easy to penetrate sample environments (heat shields, pressure cells) using neutrons. However, the typical neutron fluxes are in the order of 10^8 neutrons/s. A standard sealed-tube X-ray diffractometer provides a flux of $\sim 2 \times 10^9$ photons/s and at a synchrotron 10^{12} photons/s can be routinely accessed for diffraction experiments. Another application of paramount importance is magnetic neutron scattering. Neutrons have a magnetic moment of $1.9132\,\mu_B$, which can interact via dipole–dipole interactions with the magnetic moments of unpaired electrons. Magnetic neutron scattering is the best method for the characterization of long-range-ordered spin structures. Nuclear and magnetic scattering have similar magnitudes, however, now that the neutron is interacting with an unpaired electron, which can no longer be approximated as a 'point scatterer' magnetic scattering – like X-ray scattering is not isotropic and therefore also has a Q-dependent form factor.

3 X-RAY AND SYNCHROTRON RADIATION POWDER DIFFRACTION

Synchrotron radiation is radiation emanating from charged particles (i.e. electrons or positrons) traveling at relativistic speeds in applied magnetic fields, which force them to travel along curved paths. Bending magnets keep the particles in a closed orbit. The two main insertion devices are wigglers and undulators in which an alternating magnetic field forces the electrons to oscillate and thereby produce synchrotron radiation.[10] The main advantages powder diffraction experiments using synchrotron radiation have over conventional X-rays is the high intensity, its narrow collimation and availability as a continuous spectrum. Many K- and L-absorption edges are accessible with synchrotron sources. This is exploited when performing anomalous powder diffraction experiments. This technique makes use of the modification of the atomic scattering amplitude occurring near an absorption edge. The atomic scattering factor f_i is dependent on the scattering vector Q and the incident photon energy E and can be written as: $f_i(Q,E) = f_i^{\circ}(Q) + f_i'(E) + if_i''(E)$.The nonresonant scattering factor $f_i^{\circ}(Q)$ is energy independent and neglects the electronic bonding effects and falls off with Q as mentioned above. The resonant part $f_i'(Q)$ and $if_i''(E)$ originates mainly from the core electrons and for the same arguments as made above for neutron scattering does not vary with Q and is strongly dependent on the chemical bonding and becomes significant only near absorption edges. Its value reaches a few electrons, that is, at its K edge f_i''(Fe) is increased by 5 electrons. This can be used to enhance the contrast between atoms.[11–13]

For the ab initio determination of structures, high Q-resolution is important to reduce the peak-overlap of Bragg reflections and be able to deconvolute their individual intensities. Using a so-called crystal-analyzer configuration pioneered by Hastings *et al.*,[14] an angular resolution of less than 0.01° full-width-at-half-maximum (FWHM) of Bragg reflections can be achieved. ($\Delta d/d \sim 5 \times 10^{-4}$). Using a linear position-sensitive detector,[15] angular resolutions of ∼0.03° FWHM can be reached ($\Delta d/d \sim 10^{-3}$). Alternatively image plates can be used and the spatial resolution of 100 μm leads to an angular resolution between 0.05 and 0.1°.

There are two principal experimental setups for diffraction experiments:

1. In the angle-dispersive or constant wavelength mode, one measures with a monochromatic beam obtained by making use of a single-crystal monochromator, which selects a narrow wavelength band $\Delta\lambda/\lambda$ via a Bragg condition. By varying the scattering angle horizontally or vertically, one then collects a section of the Debye-Scherrer cone as a diffraction pattern. In synchrotron X-ray powder diffraction, $\Delta\lambda/\lambda$ in the vertical is much smaller than in the horizontal and one therefore measures in the vertical direction to maximize resolution. A lot of commercial diffractometers employ the so-called Bragg-Brentano geometry (see Figure 1), where a divergent beam of X-rays coming from the line of focus of the X-ray tube passes through collimators and irradiates the flat surface of a specimen. All of the diffracted X-rays, which must fulfill the Bragg condition, converge to a line at a receiving slit and are then detected.

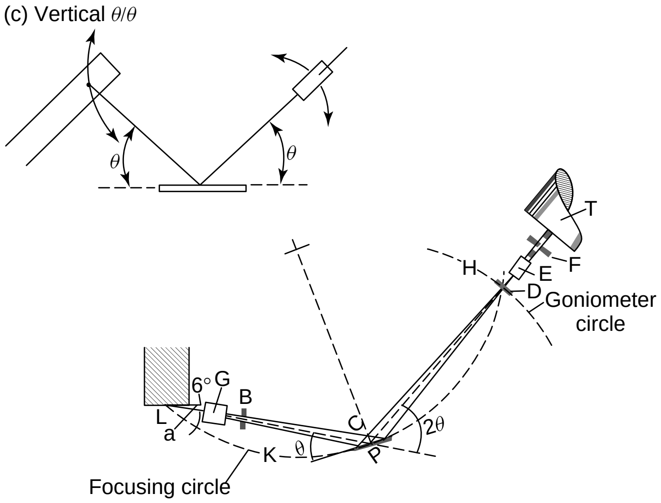

Figure 1 Bragg-Brentano geometry

2. If one leaves the scattering angle constant and uses a white beam with a very broad $\Delta\lambda/\lambda$ distribution, one is measuring in an energy-dispersive setup. In neutron scattering, this is also referred to as the time-of-flight technique since the time it takes a particle to travel from the source to the detector allows the separation of the Bragg peaks corresponding to their different d-spacings as follows: Combining de Broglie's law $\lambda = h/mv = ht/mL$ with Bragg's law one obtains: $d = ht/(2mL\sin\theta)$ [3]. If detectors are placed on locations defined by $L\sin\theta =$ constant, then the neutron scattered at different angles from one d-spacing will all be detected at the same time-of-flight. Neutron diffraction at spallation sources relies heavily on the time-of-flight mode.

What information can one obtain from a powder diffraction experiment?

1. **Position of the Bragg Reflections:** For constant wavelength diffractometers, the d-spacings can be obtained by measuring the angular position in 2θ corrected for the zero-point shift and then applying Bragg's law $d = \lambda/2\sin\theta$. In the case of a neutron time-of-flight experiment, $d = ht/2mL\sin\theta$ when the detectors are located on a functional so that $L\sin\theta$ is constant. Indexing unknown structures is the first hurdle that needs to be overcome in a

successful ab initio structure determination from powder diffraction data alone. Up to now the majority of indexing strategies rely on the above-mentioned extracting of peak positions. The most widely used indexing programs are ITO,[16] TREOR[17] and DIVCOL.[18] Recently, Kariuki *et al.* forwarded a new approach based on a full-profile fitting and global optimization using a genetic algorithm.[19] The genetic algorithm is used to explore a hypersurface of the reliability factor Rwp, which is a function of the unit-cell dimensions $\{a,b,c,\alpha,\beta,\gamma\}$. Other modern search strategies such as Monte Carlo and simulated annealing might also be employed. An efficient way to extract lattice parameters and d-spacings from powder diffraction data is to perform a cell-constrained full-profile refinement in which the individual Bragg intensities are treated as variables together with a zero-point shift in 2θ, various peak shape parameters and 'machine parameters', which determine the 2θ dependency of the FWHM. One thereby refines unit-cell parameters without reference to a structural model. The so obtained individual intensities of all Bragg reflections can then be used for structural solution attempts similar to intensities obtained from single-crystal diffraction experiments. Pawley pioneered these full-profile refinements.[20] LeBail[21] implemented a computationally more robust algorithm by iteratively adjusting the intensities. The correct assignments of errors to the intensities and the problem of completely overlapping reflections were addressed by David.[22] This method can also be used for data obtained from energy-dispersive diffraction.[23] The experimentally determined d-spacings of a material with unknown structure allow (1) the determination of unit-cell parameters using auto-indexing programs, (2) the calculation of precise lattice parameters as a function of temperature, pressure, electric, and magnetic fields, as well as (3) the residual stress in materials[24] to name just the most prominent uses. As an example, Figure 2 shows the temperature dependence of the unit-cell volume, the orthorhombic distortion, and individual cell parameters of $NdBaFe_2O_5$. This double perovskite undergoes a Fe^{2+}/Fe^{3+} charge-ordering transition at 216 K and a premonitory transition at 286 K, which is related to an orthorhombic deformation where a partial charge ordering into $Fe^{2.5+\delta}$ and $Fe^{2.5-\delta}$ takes place.[25] A very small enthalpy change and minute lattice distortion is associated with the latter. High-resolution synchrotron radiation powder diffraction data with a resolution of $\sim 10^{-3}$ in Δ d/d and closely stepped temperature intervals are required to detect such subtle unit-cell volume variations.

2. **Modification of the Peak Shape:**[26] The intrinsic peak shape (i.e. gaussian, lorentzian, and convolutions thereof) and FWHM after subtraction of the instrumental contribution by using a standard[27] such as LaB_6 or silicon permits:

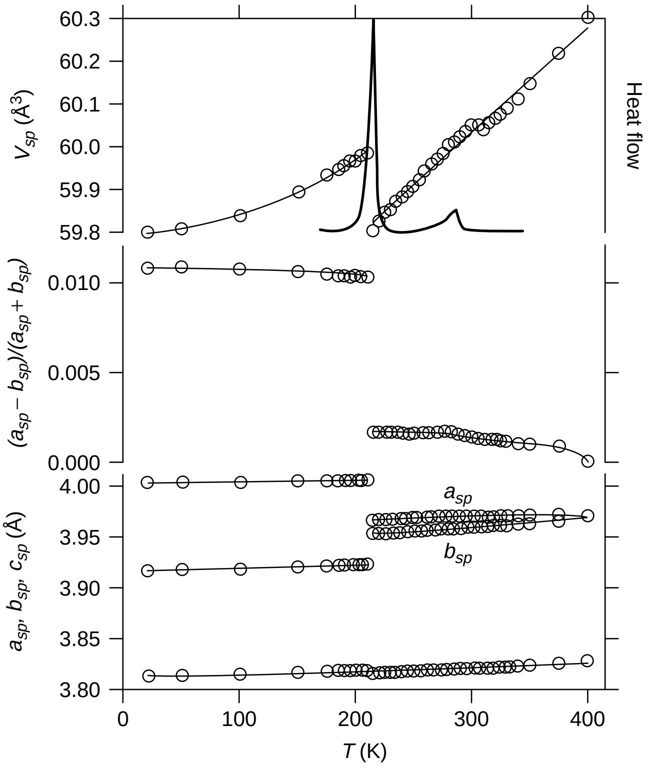

Figure 2 The variation of the unit-cell parameters of $NdBaFe_2O_5$ as a function of temperature revealing a very subtle phase transition near 286 K

- The determination of particle sizes using the Scherrer equation $\Delta(2\theta) = K\lambda/A\cos\theta$ [4] where A is the diameter of the coherently diffracting domain, K, a constant close to unit and $\Delta(2\theta)$ represents the broadening of the FWHM of the Bragg reflection in 2θ.
- The determination of stacking faults, which can lead to diffraction line broadening (i.e. twinning) and peak shifts as well.[28] Recent examples using X-rays are the examination of stacking faults in $Ni(OH)_2$, which can be related to the electrochemical behavior of this material[29] and neutron diffraction work by Berliner and Werner[30] on the 9R structure of lithium below 20 K.
- The local variation Δ d/d (microstrain) due to anisotropic strain in crystallites, lattice defects, and/or local compositional variations $\Delta(2\theta) = -2\Delta$ d/d $\tan\theta$ [5]. Figure 3 shows the comparison of the temperature-dependent behavior of two samples of $Nd_{0.5}Sr_{0.5}MnO_3$ with nominally the same composition. This material shows giant-magnetoresistive behavior.[31] The first sample phase separates into three coexisting macroscopic phases at low temperatures: a ferromagnetic phase that is orthorhombic and exists at high temperatures (HTO),

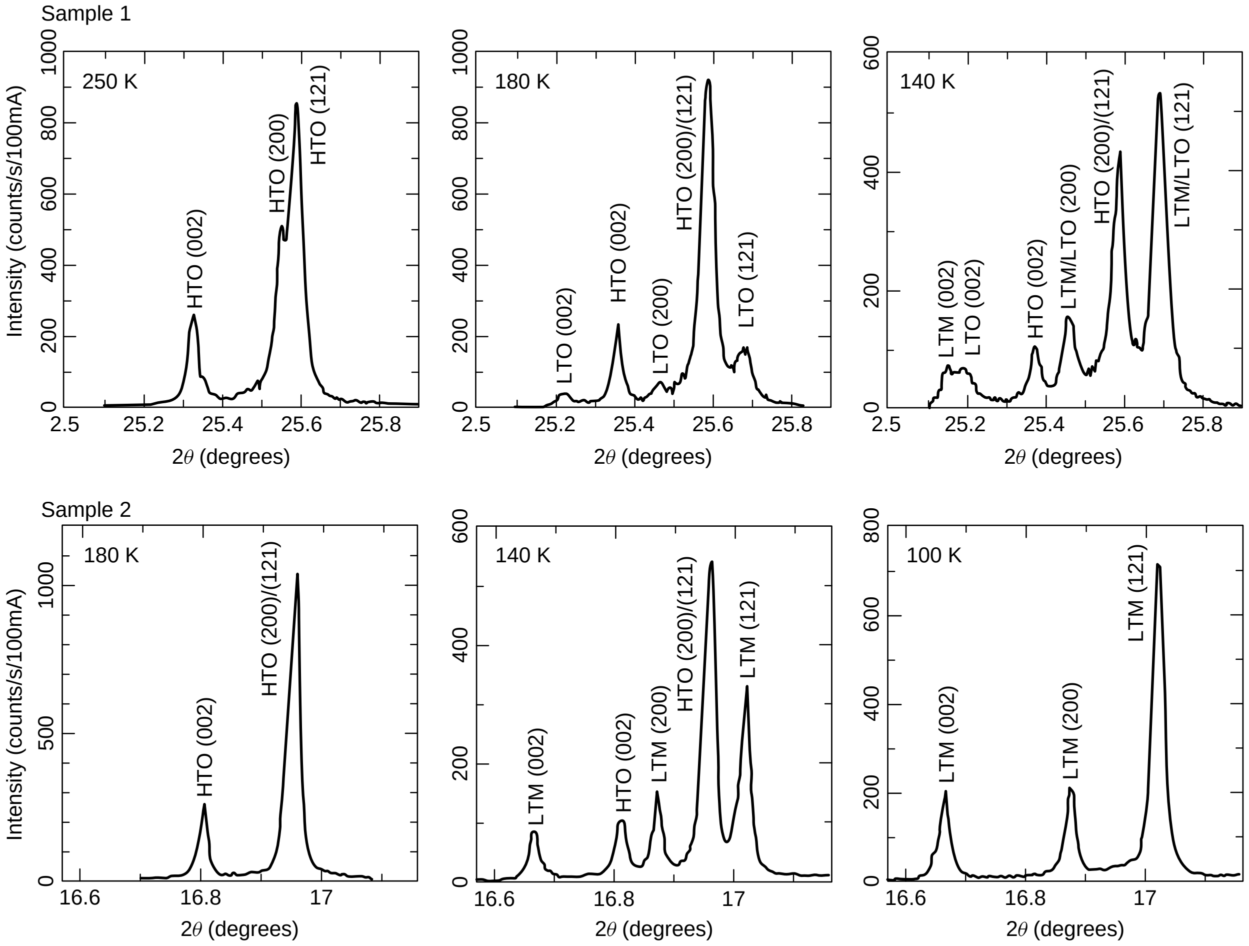

Figure 3 Temperature-dependent diffraction pattern of two samples of $Nd_{0.5}S\ r_{0.5}MnO_3$. The first sample was made using Mn_3O_4 as a starting material and phase separates at low temperatures into three coexisting phases owing to compositional variations. The second sample was made using MnO has a smaller compositional variation and shows only one phase at low temperature

an orthorhombic orbitally ordered antiferromagnetic low-temperature phase (LTO) and a monoclinic low-temperature phase, which is charge, orbital, and antiferromagnetically ordered (LTM). The second sample shows a clean transition from the HTO phase into the LTM phase with a small region of phase coexistence near 140 K. The first phase was made using Mn_3O_4 as starting material, the second using MnO.

The unusual behavior of the first sample is due to a slight excess of Mn^{4+} since Mn_3O_4 is a nonstoichiometric compound. As a result, a wider compositional range–range exists in this compound. At Mn^{4+}: Mn^{3+} ratios close to unity both electron delocalization and charge ordering occurs. This conclusion was obtained by analyzing a Williamson-Hall plot.[32] Combining the Scherrer equation with the above equation for microstrain broadening (equation 2) results in the following equality:

$$\mathrm{FWHM}_{\mathrm{corr}}\frac{\cos\theta}{\lambda} = \frac{1}{A} + \frac{K\Delta d/d\sin\theta}{\lambda} \qquad (2)$$

$\mathrm{FWHM}_{\mathrm{corr}}$ is corrected for the instrumental resolution and K varies with Δd/d and the FWHM. Setting the Scherrer constant K to unity one then plots $\mathrm{FWHM}_{\mathrm{corr}}\ \cos\theta$ against $\sin\theta$ as abscissa. One can then extract the scattering domain radius A from the intercept with the ordinate and Δd/d from the slope (see Figure 4).

An explanation for this extrinsic phase separation is thus to imagine each crystallite having its unit-cell parameters and stoichiometry controlled by its Mn^{4+}: Mn^{3+} ratio, which ultimately determines whether the HTO phase transforms into to orbitally ordered LTO phase or the charge-ordered LTM one, or not at all (see Figure 5).

In another example, Muller *et al.* have revealed a correlation between the mesoscopic structure and the dielectric

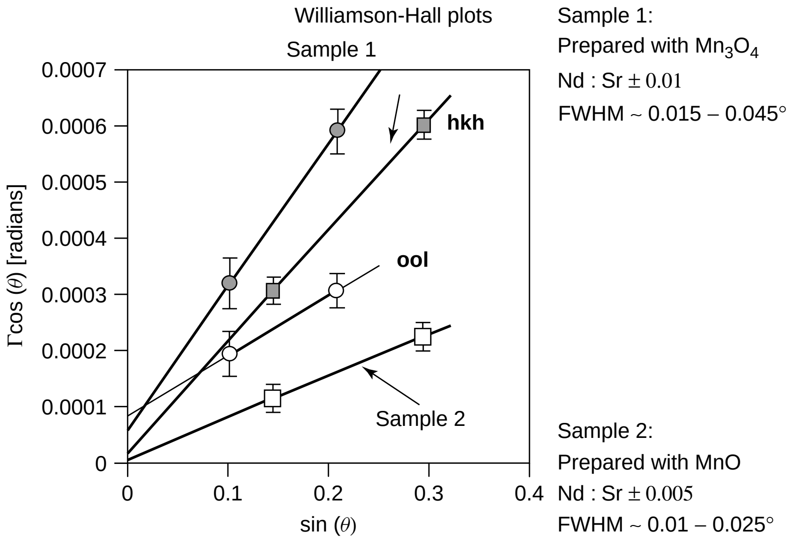

Figure 4 Williamson-Hall plot of the two samples of $Nd_{0.5}S\ r_{0.5}MnO_3$ indicating a larger compositional variation of sample 1

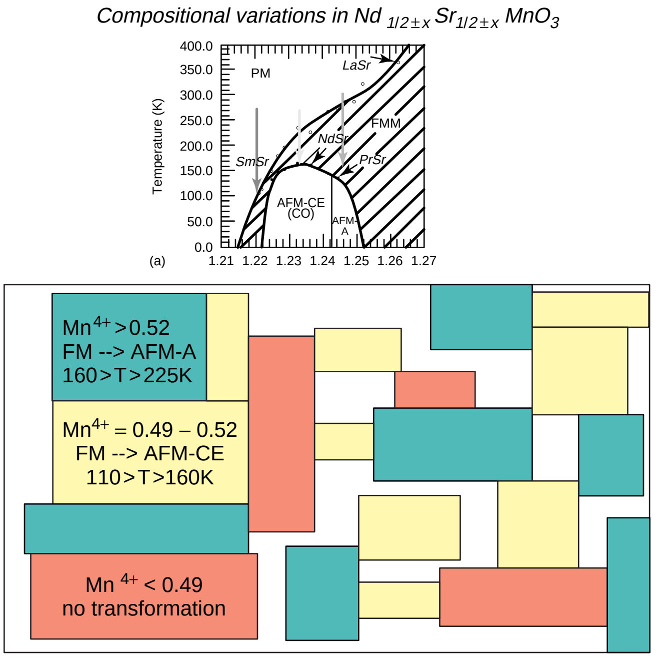

Figure 5 Phase diagram of $Nd_{0.5}S\ r_{0.5}MnO_3$ as a function of average A cation radius revealing how the Mn^{4+} concentration influences the phase transformation of each individual crystallite class. At Mn^{4+}:Mn^{3+} ratios close to unity, both electron delocalization and charge- ordering occurs

response of ferroelectric $SrBi_2Ta_2O_9$ (SBT) ceramics.[33] Using again high-resolution synchrotron X-ray powder diffraction data and evaluating the Williamson-Hall plot they showed that a mechanically ground sample has a three times larger strain Δd/d than one that was ground manually. As shown below, the shape as well as the position of the dielectric anomaly depends on the stoichiometry as well as the synthesis route used (see Figure 6). The mechanically ground sample was prepared by solid-state reaction between Bi_2O_3, Ta_2O_5 and $SrCO_3$ precursors, whereas the second sample was made by mechanically grinding the precursors in a ball-mill.

3. **Intensities of the Bragg Reflections:** The Rietveld method[34] of refining crystallographic models against the measured intensities of a powder diffraction pattern is based on the premise that the peak shape of Bragg reflections can be described analytically and their variation with the scattering vector Q can be expressed as a convolution of instrumental and sample related effects as described above. Modern powder methods[35] allow not only the refinement but also the determination of crystallographic structures.[36] For this the highest Q-resolution possible is needed to determine the unit cell of an unknown material and then apply structure solution methods (i.e. Patterson, direct methods) adapted to powder diffraction data and solve the phase problem. In recent years, more and more structures of molecular materials are being solved from powder diffraction data owing to the unavailability of good quality single crystals.[37] Innovative structure solution approaches are nowadays based on generalized Monte Carlo Methods,[38,39] simulated annealing,[40–42] and genetic algorithms.[43–45] Harris presents an overview of these recent developments in the structure determination of molecular materials. The program DASH written by David *et al.* uses modern simulated annealing techniques.[46] Recent highlights in molecular crystallography are the structure determination of lithium benzilate hemihydrate using DASH.[47] This monoclinic structure has 221 parameters and was refined using high-resolution synchrotron X-ray data.

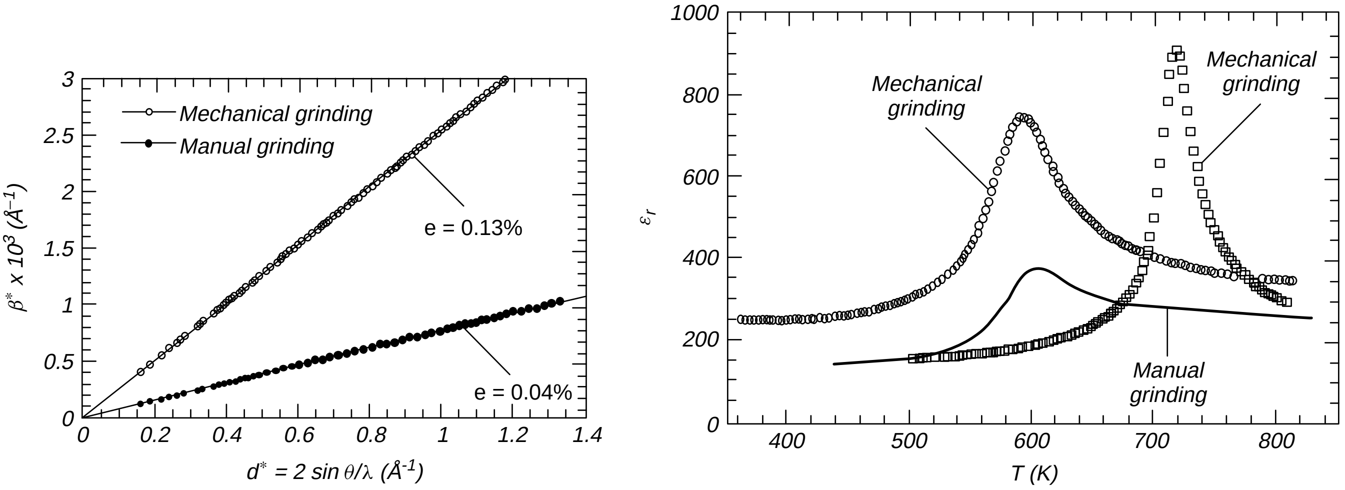

Figure 6 Williamson-Hall plot of SrBi$_2$Ta$_2$O$_9$ showing how the different strain influences the dielectric properties

4 COMBINED NEUTRON AND X-RAY HIGH-RESOLUTION POWDER DIFFRACTION STUDIES OF CATALYSTS

4.1 Structural Characterization of the M1 phase in the MoVNbTeO Propane Ammoxidation Catalyst

Of all catalytical reactions, the ammoxidation of propylene (C_3H_5) to acrylonitrile (C_2H_3CN) is one of the most important ones. The yearly worldwide production is above 10 billion pounds using the SOHIO/BP process. Current efforts in industrial research are focused on replacing propylene by the cheaper and more abundant propane. Propane (C_3H_8) ammoxidation catalysts for the production of acrylonitrile are mixed metal-oxide molybdenum systems. The best one is patented by Mitsubishi Chem. Ind. and composed of MoVNbTe-oxides. It provides a yield 59% yield with 63% selectivity. The catalytical reaction proceeds by first a hydrogen abstraction followed by an oxygen or NH insertion. V^{5+} has been identified as the important paraffin-activating element in paraffin oxidation and ammoxidation catalysts. To activate paraffins, the V^{5+} cations need to be in proximity to less electronegative metal cations such as Mo^{5+} or V^{4+}, so that the bridging oxygen is nucleophilic enough to abstract hydrogen. The hydrogen-abstracting element is Te^{4+} and the oxygen and/or NH insertion requires the presence of $(Mo^{6+})_2$. The latter two sites require close proximity and comprise the multifunctional catalytic moiety. To function properly, these catalytic centers need to be isolated. However, to achieve optimum activity they should be adjacent to reoxidation sites, so that they can communicate with each other over short distances.[48] This is achieved by four Nb^{5+} centers, each surrounded by five MoO_6 octahedra (see Figure 7). It was found when using the MoVNbTe-oxides that the active catalyst forms only under mildly reducing conditions and is made up of two prominent phases denoted M1 and M2. Recently, in a 'tour de force' the structures of both the M1 and M2 phase were determined by using a combination of transmission electron microscopy (TEM), high-resolution synchrotron, and neutron powder diffraction.[49,50] Predominantly single phase samples of M1 and M2 were synthesized. Initial models were obtained from TEM, in particular, selected area electron diffraction (SAED) and energy-dispersive spectroscopy (EDS). Then synchrotron X-ray powder diffraction data and neutron powder diffraction data were refined simultaneously. For the M1 phase, a total of 173 variables were refined against 2703 reflection in the neutron and 2441 reflections in the synchrotron powder diffraction data. The atomic structure of the M1 phase of this catalyst with the approximated stoichiometry of $Mo_{7.5}V_{1.5}NbTeO_{29}$ is shown in Figure 7. The unit cell of M1 is $a = 21.134(2)$ Å,$b = 26.658(2)$ Å and $c = 4.0146(3)$ Å (space group Pba2, $Z = 4$). The M2-phase has the approximate stoichiometry $Mo_{4.31}V_{1.36}Te_{1.81}Nb_{0.33}O_{19.81}$ and a unit cell with $a = 12.6294(6)$ Å, $b = 7.29156(30)$ Å and $c = 4.02010(7)$ Å (space group Pmm2, $Z = 4$).

The oxidation states of vanadium and its neighboring metals have been identified as critical factors in controlling the activity of the bridging oxygen. Bond valence calculations using the coordinates of the refined model suggest that this is the case in the M1 phase but not for the M2 phase. M1 fulfills all the requirements for a selective oxidation catalyst, whereas the M2 phase provides a catalytic moiety for propylene ammoxidation. Bond valence sum calculations are obtained using the relation $V_{ij} = \exp[(Ro-d_{ij})/0.37]$ with Ro being the ideal bond length between two atoms i and j and d_{ij} the actual distance between them.[51] In the M1 phase, the oxygen associated with the catalytic center for propane ammoxidation show significantly different Madelung site potentials when bound to V^{4+} and V^{5+} rather than Mo^{5+} and Mo^{6+}. The potential Φ_i of an ion I located on a site can be

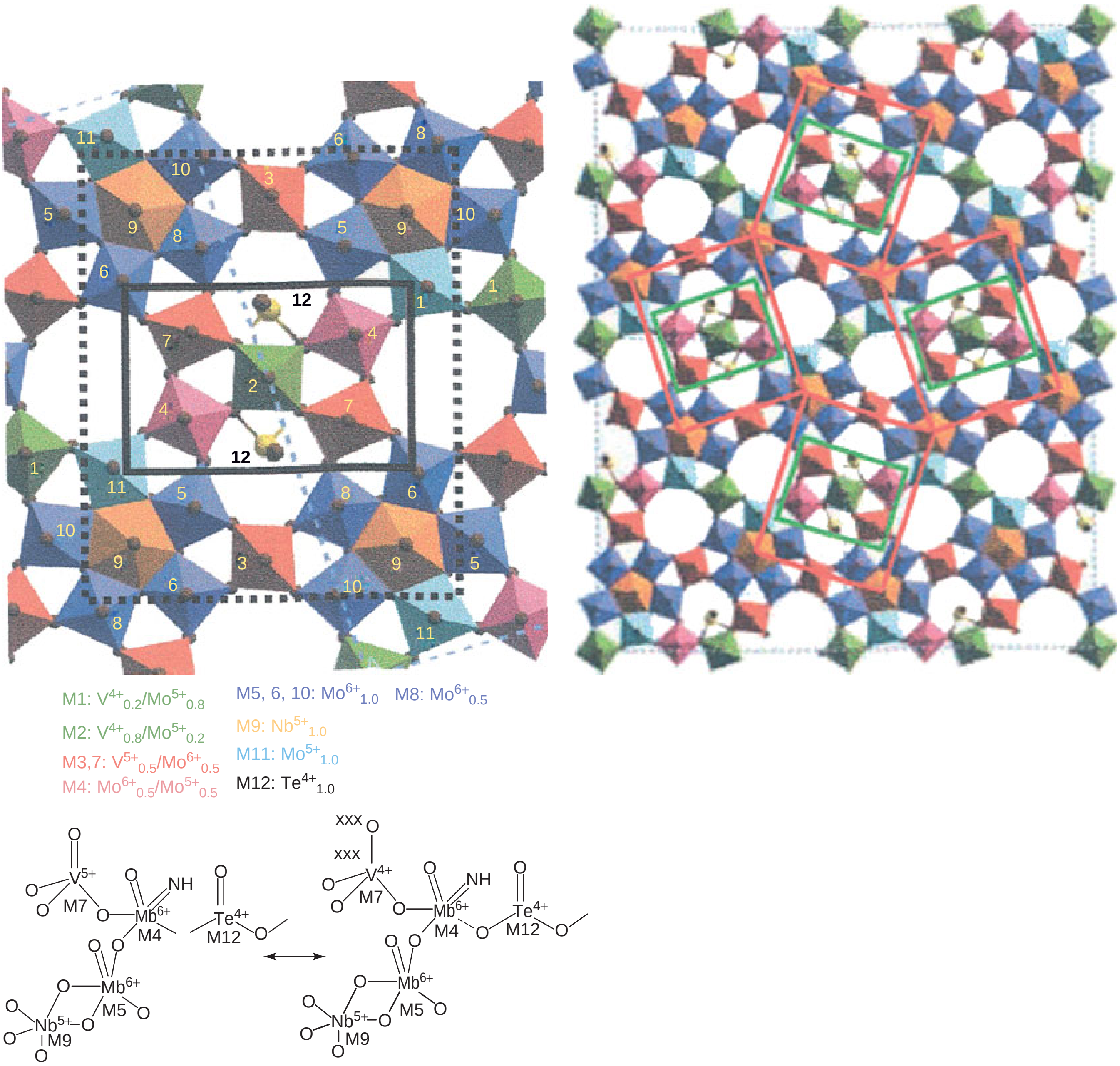

Figure 7 The average structure of $Mo_{7.5}V_{1.5}NbTeO_{29}$ in [001] projection and depictions of the active catalytic moiety. The right side shows how these active centers are isolated within the crystal structure

calculated from the Coulomb interactions between this ion and its neighbors using the charge obtained from bond valence sum calculations. In particular the apical oxygen O2 and O7 have much lower site potentials when vanadium partially occupies the Mo2 and Mo7 sites.

This structure reveals that the sites partially occupied by V^{5+} (red), V^{4+} (green), and Te^{4+} (light blue) cations are isolated providing sites for the propane amooxidation catalysis to occur on terminal [001] planes. In particular the ionicity of the metal–oxygen bonds in corner-sharing octahedra with a V^{5+} and V^{4+} /Mo^{4+} center provides a particularly nucleophilic bridging oxygen critical for propane activation. The Mo^{6+} sites have been shown to act as propane adsorption and nitrogen insertion sites in bismuth molybdates, which are also used for propane ammoxidation.

This structural characterization demonstrates how the multifunctionality required for an efficient and selective catalyst is based on the multielemental distribution within such complex oxide catalysts. Neutron powder diffraction is absolutely essential to be able to refine the oxygen positions in such large structures in the presence of high-Z metals. High-resolution synchrotron powder diffraction on the other hand provides unique information about the phase composition of such multicomponent catalysts. By providing even higher flux and smaller beams, it is conceivable that in the future one can isolate diffraction contributions from different phases originating from different grains and unravel the complex structure of the individual grains as well as the strain and texture effects that might be beneficial for catalytic processes. Furthermore, it is conceivable that in situ and time-resolved powder diffraction of ‘real’ catalytic processes provide an unprecedented wealth of understanding and lead to new approaches when designing novel multifunctional catalysts. Structural investigations of catalysts in particular zeolites have in the past been a prime motivation for instrumental developments in high-resolution powder diffraction.

4.2 The Location of Bronsted Acid Sites in Zeolites

Acidic zeolites are used in the chemical and oil industry as catalysts owing to their outstanding reaction selectivity as well as their outstanding chemical and thermal stability in processes such as the isomerization of xylenes, catalytical cracking, and paraffin hydroisomerization. Their functionality is based on the donation of Brønsted acid protons from bridging framework hydroxyls. These acid protons balance the negative framework charge, which is created by the substitution of Si^{4+} by Al^{3+} cations. In general zeolites are converted to their acidic form by ion exchanging with an NH_4^+ salt and subsequent calcinations to remove NH_3. The proton bonds covalently to one of the oxygen neighboring an Al^{3+} ion. The location of these acidic sites is a very difficult task using X-ray diffraction since one relies on indirect information, that is, the distortion of the average T–O distances (T = Si,Al), which are expected to increase upon protonation. On the basis of a comparison with T–O distances occurring in other acidic faujasites, Olson and Dempsey[52] suggested that the O1 and O3 sites in zeolite Y were protonated. This was experimentally shown to be correct by Czjzek *et al.*[53] in a high-resolution neutron powder diffraction experiment using both hydrogen and deuterium containing samples and taking advantage of the negative and positive scattering length for hydrogen and deuterium respectively. Cheetham *et al.*[54] performed neutron powder diffraction studies on the hydrated La containing form of zeolite Y and observed a Brønsted acid site as well as the hydrolyzed cation responsible for its formation. Neutron powder diffraction studies of the deuterated form of zeolite RHO revealed that the O1 site was preferentially protonated.[55] The same two acidic sites were found in the high silica zeolite CHA (SSZ-13)[56] as well as in the deuterated silico-alumino-phosphate analogue SAPO-34.[57] Martucci and coworkers reported two acidic sites in ferrierite (FER)[58] and 4 preferential sites in mordenite (MOR).[59] The highly complex zeolite ERS-7 (ESV) with 6 unique T sites, 14 unique oxygen, and altogether 56 independent positional parameters allowed the location of three acidic sites.[60] In this case, again a combined neutron and X-ray powder diffraction study took advantage of the scattering power of deuterium with neutrons and the high-resolution of synchrotron X-ray powder diffraction. In addition to the Bronsted acid sites, both X-ray and neutron powder difference Fourier maps identified a disordered oxygen site owing to varying local geometries of the Al in the neighboring site. Powder diffraction studies of zeolites will continue to be important in the future. The complexity of the structures will increase. To date, SSZ-58 is the most complex zeolites in terms of the number of atoms in the crystallographic asymmetric unit to be solved from powder diffraction data. It contains 38 individual atomic sites in an orthorhombic unit cell with a = 25.1106 Å, b = 12.4972 Å and c = 12.8596 Å.[61]

5 HIGH-RESOLUTION X-RAY AND NEUTRON DIFFRACTION IN MAGNETIC FIELDS

The interaction of a magnetic field with matter and in particular, the electronic properties are of fundamental and technological importance. Magnetic field–induced structural phase transitions can be probed using field-dependent measurements of the electrical resistance (magnetoresistance), magnetization, heat capacity (magnetocaloric effect) and strain (magnetostriction) and provide valuable macroscopic information. However, only the atomistic details will reveal the mechanism driving the phase transition.

5.1 Neutron Powder Diffraction in Magnetic Fields – Breaking Bonds in Magnetoresistive Materials

MnAs is a ferromagnet with a Curie temperature near 313 K[62] where simultaneously a metal-insulator transition occurs.[63] Above 313 K the structure is orthorhombic, below hexagonal. Mira *et al.*[64] have shown using neutron powder diffraction in magnetic fields that when heating and equilibrating MnAs at 321 K and then applying a magnetic field above 3.5 T one can fully restore the hexagonal phase (see Figure 8). Both field- and temperature induced phase transitions show a small region of phase coexistence. The field-induced phase transition is also accompanied by an enhanced magnetoresistance of ∼17% at 310 K. In the region of phase coexistence, the hexagonal ferromagnetic phase that is derived from the orthorhombic paramagnetic phase by a cooperative displacement of pairs of [1, −1,0] rows grows at the expense of the latter. It forms strong Mn–Mn bonds across octahedral-site edges, which run in zigzag chains within the basal planes while weakening the Mn–Mn bonds between planes. The orbitals of the Mn atoms in the basal planes are half-filled. As these spins are aligned according

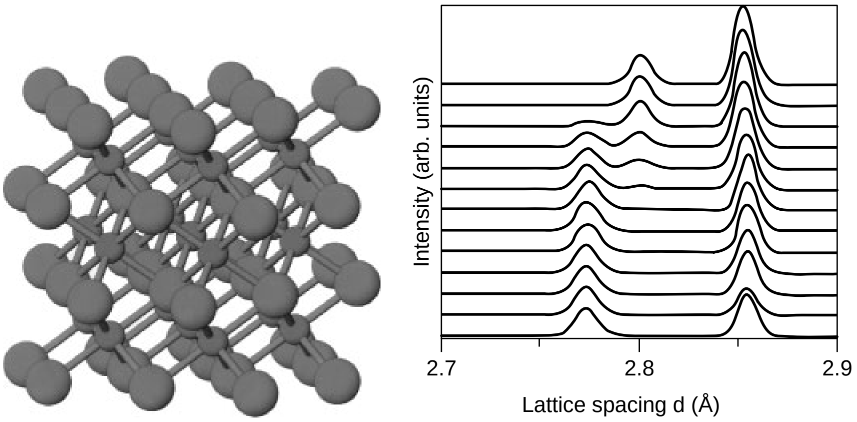

Figure 8 MnAs structure and the evolution from the orthogonal to hexagonal form as a function of increasing magnetic field strength along the y axis

to the Goodenough-Kanamori rules,**[65]** no bonding can occur between half-filled orbitals with parallel spins and therefore the high-spin ferromagnetic hexagonal phase is stabilized. Thus, this magnetic field–induced transition involves breaking of metal–metal bonds.

5.2 X-ray Powder Diffraction in Magnetic Fields – Strengthening Bonds in Magnetocaloric Materials

The inherent higher Q-resolution of X-ray powder diffraction allows the extraction of crystallographic details from highly complex magnetic structures. An example is Gd_5Ge_4 a giant magnetocaloric material,**[66]** which crystallizes in an orthorhombic structure with a primitive unit-cell volume above 800 Å^3. Magnetocaloric materials heat up when magnetized and cool down when demagnetized. They have the potential to be an alternative to cooling via the vapor-compression mechanism and would reduce the need for ozone depleting greenhouse chemicals. Gd_5Ge_4 orders antiferromagnetic below 130 K and the appearance of both magnetic and structural Bragg reflections would add further complexity to an already challenging neutron powder diffraction pattern. Furthermore, the prohibitive high absorption cross-section of natural Gd ($\sigma_{\text{abs}} = 49700$ barn for 0.0253 eV neutrons) and the exorbitant cost of the low absorbing isotopes ^{156}Gd ^{158}Gd and ^{160}Gd make neutron scattering experiments on this material unworkable. Pecharsky recently accomplished measuring X-ray powder diffraction pattern of Gd5Ge4 as a function of magnetic fields. His experimental setup is comprised of a standard Rigaku TTRAX system operating in Bragg-Brentano geometry with a theta/theta wide-angle goniometer and an 18 kW rotating anode X-ray generator providing monochromatic Mo Ka radiation. A custom-designed optical split-coil superconducting magnet allows the sample to be positioned at the center of the diffractometer and magnet, which gives uniform fields up to 35 kOe. Diffraction data up to a 2θ angle of 78 degrees enables the measurement of d-spacings larger than 0.564 Å. The samples are mixed with a nonreactive binder to prevent particle alignment with the easy magnetization axis parallel to the magnetic field, which would lead to preferred orientation.

Both the low-field(LF) and high-field (HF) structures of Gd_5Ge_4 have the same orthorhombic space group (Pnma) but slightly different structures (see Figure 9). The most prominent difference occurs in the interlayer Ge–Ge bonds. On transforming from the LF to the HF structure, a field-induced contraction and a concomitant strengthening of the Ge–Ge bonds between the layers occur. The intralayer distances vary up to a maximum of 5%, whereas the interlayer distances change as much as 27.6% (∼1Å). The layers themselves undergo very little structural changes under field. The magnetic field thus induces a 'martensitic-like' phase transition.**[67]** It was also discovered that even in a magnetically saturated sample a small amount (7%) of LF-phase is still present. This inhomogeneity of the sample is due to the balance between the works performed by the magnetic field to overcome the strain created by the 1.1% volume change of the unit cell. Magnetic work becomes insignificant near saturation but the strain remains extensive.

6 ATOMIC PAIR-DISTRIBUTION FUNCTIONS AND NANOCRYSTALLOGRAPHY

With a new generation of synchrotron sources being in various stages of planning and commissioning, it can be projected that the field of nanocrystallography using pair-distribution function analysis will be extended to smaller amounts of samples as well as smaller regions within complex

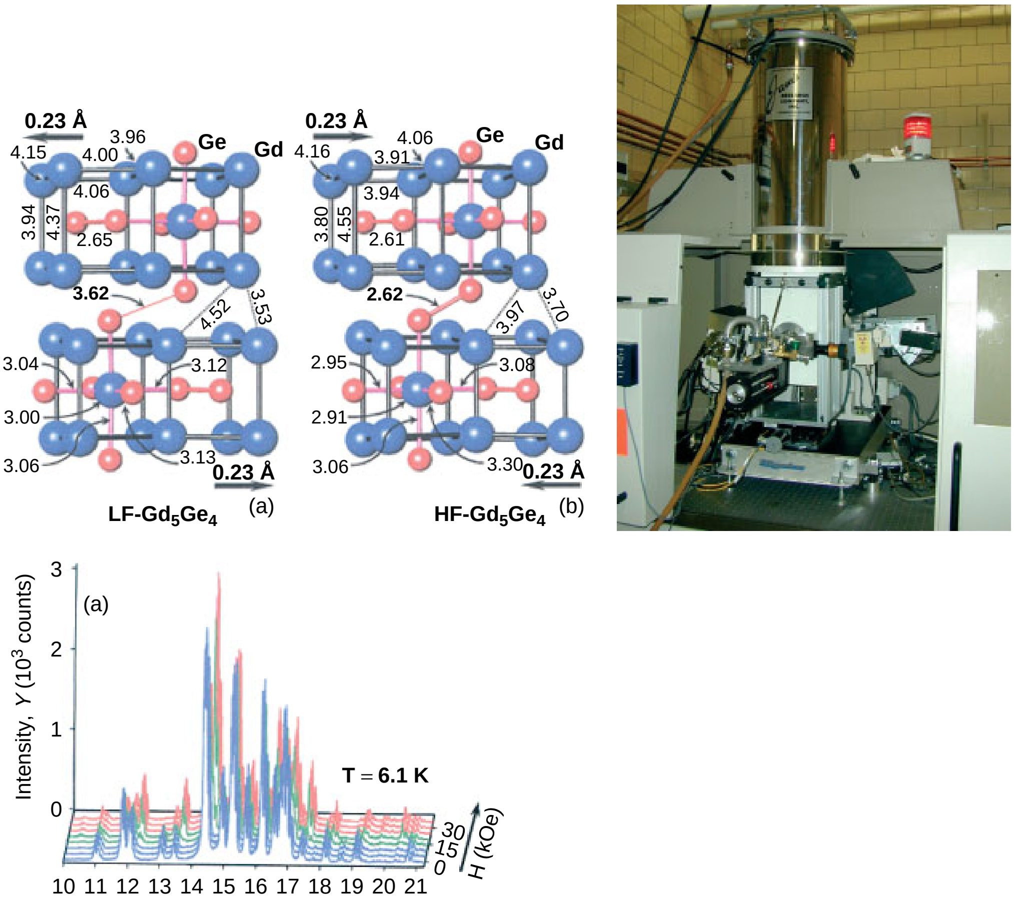

Figure 9 The antiferromagnetic low-field (LF) and ferromagnetic high-field (HF) Gd_5Ge_4 structures viewed along [001]. Under the influence of a magnetic field, the main changes occur in the interlayer distances. Below it is shown how the X-ray powder diffraction pattern changes at 6.1k as one increases the magnetic field. Blue indicates the LF, red the HF-Gd_5Ge_4 structure, and green the region of phase coexistence. On the right, the powder diffractometer (Bragg-Brentano geometry) equipped with an optical split-coil superconducting magnet is shown

materials. The focus of scientific attention on crystalline matter, and the use of symmetry to describe what are perforce only average structures do not adequately take into account the fact that real crystals are imperfect. Conventional crystallography encourages the view that atoms are to be placed within the context of symmetry elements even though they only react locally to physical forces. The advent of nanoscience and nanotechnology reminds us that structures are assembled locally. Recently, it has been realized that in complex materials there are conflicting forces, which compete locally *despite* the presence of a long-range-ordered structure. An adequate structural description of complex matter therefore has to go beyond classical crystallography and characterize both the local *and* average structure. Classical crystallography does also not take into account the fact that it is at the same time bulk and surface science. Nanoclusters comprised of fifty close-packed spheres have about 80% surface atoms and even a close-packed two thousand-atom grain still has about 20% surface atoms. The structural chemistry of nanomaterials as well as nanostructured complex materials often depends on the crystallography of internal surfaces in particular grains. Using atomic pair-distribution functions provides a means to obtain both the local *and* long-range atomic structure directly. In the PDF technique, both Bragg and diffuse scattering is Fourier transformed into real space. It therefore bridges the average crystallographic long-range structure generally obtained by standard Rietveld refinement and the local lattice distortions observable in TEM images and offers a stringent test for the validity of complex structure models.

6.1 The Pair-distribution Function

The diffraction experiments to collect pair-distribution functions (PDF) are typically done at synchrotrons or neutron spallation sources since high quality data at large momentum transfers $Q = 4\pi \sin\theta/\lambda > 20\,\text{Å}^{-1}$ are required to reduce termination errors at low real-space distances. The atomic PDF G(r) is defined as

$$G(r) = 4\pi r[\rho(r) - \rho_0] \quad (3)$$

where ρ_0 is the average atomic number density, $\rho(r)$ is the atomic pair-density and r is a radial distance. This function thus provides information about the number of atoms contained in a spherical section of a shell of unit thickness at distance r from a reference atom. The PDF is experimentally accessible since it is related to the total X-ray or neutron scattering S(Q) via its Fourier transform:

$$G(r) = \frac{2}{\pi} \int Q[S(Q) - 1] \sin(Qr)\, dQ \tag{4}$$

The quantity $Q[S(Q) - 1]$ is referred to as the reduced structure function. The total scattering structure function is related to the coherent part of the total diffracted intensity by:

$$S(Q) = \left[\frac{\left(I_{coh}(Q) - \sum c_i \left| f_i(Q)2 \right) \right.}{\left| \sum c_i f_i(Q) \right|} \right] + 1 \tag{5}$$

with Icoh(Q) being the total scattered intensity corrected for background and other experimental effects (i.e. absorption, multiple scattering) and normalized to the flux and number of atoms in the sample. Errors in these corrections result in peaks at unphysical low r values.[68] The atomic concentrations c_i and the individual atomic form factors f_i (or neutron scattering lengths b_i) of the individual species i are summed and in neutron scattering the different contributions of all isotopes and spin states (in neutron scattering) must also be included. The PDF is modeled by using the distance distribution via

$$G(r) + 4\pi\rho 0 = \frac{1}{r} \sum \sum \frac{(f_{0_i} f_{0_k})}{\langle f_0 \rangle^2 \delta(r\text{-}r_{ik})} \tag{6}$$

The form factors f_0 at $Q = 0$ are an approximation of the number of electrons Z of an atom. When modeling neutron PDFs, the appropriate nuclear scattering lengths or magnetic form factors replace these atomic form factors. In equation (6), r_{ik} is the distance between atoms i and k summed over all the atoms in the sample.

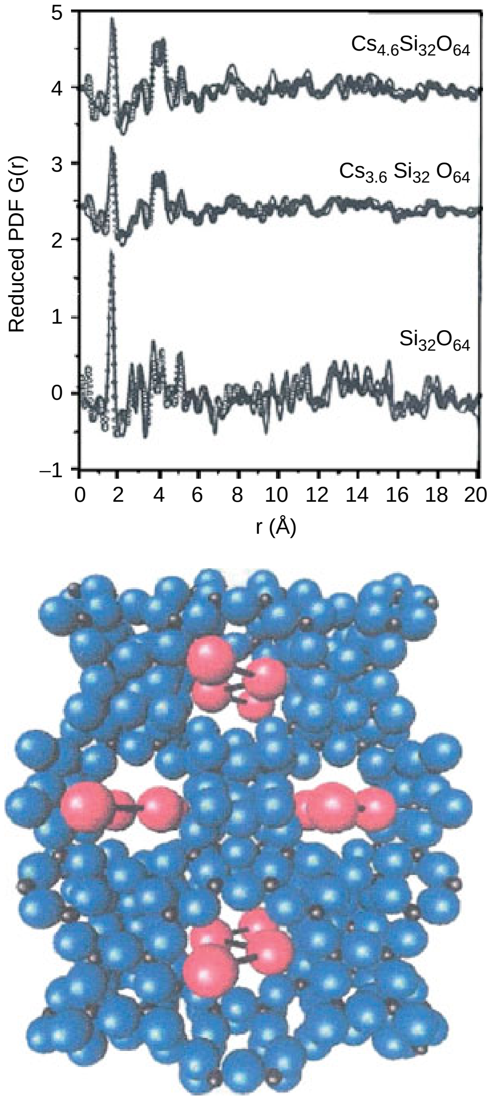

Figure 10 (a) Experimental (circles) and model (line) PDFs for $Cs_xSi_{32}O_{64}$ ($x = 0$, 3.6 and 4.6) (2) Fragment of the nanoscale structure of $Cs_xSi_{32}O_{64}$ where Cs^+ ions (red circles) in the nanopores are assembled in zigzag chains. Oxygen atoms are blue, silicon atoms black

6.2 Unique States of Matter – Room Temperature Electride

In electrides, electrons behave as anions. In a typical organic electride Cs^+ (15-crown-5)$_2$ e^-, the electrons occupy cavities connected by narrow channels. The first electride stable at room temperature was made by ionizing Cs into Cs^+ and e^- within the channels of an all-silica zeolite.[69] Petkov *et al.*[70] confirmed that Cs^+ and a low-density electron gas are present in the one-dimensional nanopores of the siliceous zeolite ITQ-4 ($Si_{32}O_{64}$). The PDF technique provided direct structural evidence that Cs intercalated in the form of Cs^+ ions arranged in short zigzag chains (see Figure 10). This structural model is now being used in electronic structure calculations to gain insight into this new nanoscale low-dimensional correlated electron material.

7 HIGH-PRESSURE NEUTRON AND SYNCHROTRON X-RAY POWDER DIFFRACTION

Pressure is a basic thermodynamic variable transforming matter from one state to another; when pressure is applied, atoms are brought closer together, ultimately altering a material's structural, electronic, and mechanical properties in radical and often unexpected ways. However, our knowledge of pressure-induced phase transformations is still very limited compared to the vast number of temperature-dependent phases we have characterized over the past decades. This is largely due to the experimental difficulties involved in both the need for specialized equipment and the development of expertise in the use of high-pressure cells. These limitations, coupled with the obvious interest in matter under numerous pressure-temperature conditions within planets, have led to the dominance of the field of high-pressure research by the Earth Sciences community. As an example, Loveday *et al.*[71] undertook a combined synchrotron X-ray and neutron powder diffraction of methane hydrate under high-pressure conditions up to 10 GPa. Structural phase transitions at about 1 and 2 GPa to new hydrate phases were discovered that remain stable to about 10 GPa. This explains how methane in the core of Titan remained in a stable phase throughout differentiation without being lost into the atmosphere, where photochemical processes would rapidly have destroyed it. Equally interesting phenomena occur in the more general areas of condensed matter physics, chemistry, and biology: pressure causes proteins to unfold, insulators to become metals or superconductors, materials to reach their yield strength and phase transitions to occur. The wider community of solid-state scientists now benefits from the technology and expertise developed by Earth Scientists. This opens up more unconventional conduits of research. Furthermore, pressure experiments provide one of the most fundamental properties of matter, the equation of state, which reveals how the unit-cell volume of a sample changes with pressure. This is predicted and used in various physical theories.

7.1 First Observation of Superhydration in a Zeolite

Upon hydrostatic pressure increase in a water-containing medium, the zeolite natrolite shows an abrupt volume expansion (ca. 2.5%) between 0.8–1.5 GPa. Rietveld refinements and subsequent Fourier difference maps using synchrotron X-ray powder diffraction data showed that this anomalous swelling is due to the selective sorption of water from the alcohol-based pressure-transmitting media into the expanded channels, giving rise to a 'superhydrated' phase of natrolite, $Na_{16}Al_{16}Si_{24}O_{80}\cdot 32H_2O$, which is distinct from natrolite at ambient conditions,[72] $Na_{16}Al_{16}Si_{24}O_{80}\cdot 16H_2O$ containing twice the amount of water.

Powdered samples were loaded into a diamond-anvil cell (DAC) at ambient pressure and room temperature along with a few small ruby chips (see Figure 11). The DAC employs two diamonds with 0.5 mm diameter culets mounted on tungsten-carbide supports. The X-rays are admitted by a 0.5 mm diameter circular aperture, and the exit beam leaves via a 0.5 × 3.0 mm rectangular tapered slit, oriented perpendicular to the horizontal plane of the diffractometer. The sample chamber is provided by a 200 or 350 μm hole formed in the center of a 300 μm thick stainless steel gasket, preindented to 100 μm thickness before spark-erosion drilling. A mixture of 16:3:1 by volume of methanol:ethanol:water is used as a pore-penetrating hydrostatic pressure transmission fluid, which is known to remain hydrostatic up to ∼10 GPa.[73] The pressure is measured ex situ by detecting the shift in the R1 emission line of the included ruby chips.[74] The structural evolution under pressure is analyzed using the Rietveld method.

The evolution of the unit-cell parameters of natrolite is shown as a function of the pressure in Figure 12. Between 0.8 and 1.5 GPa, the pressure-induced swelling is caused

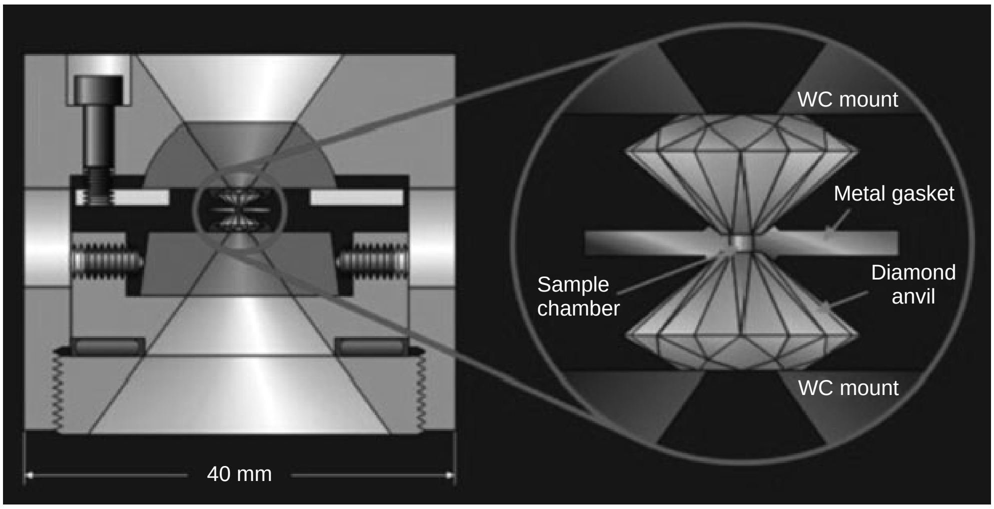

Figure 11 The diamond-anvil cell has emerged as the dominant and most versatile tool for achieving high pressures (up to millions times of the atmospheric pressure). It uses two diamond anvils, which exert pressure and serve as windows on the sample. A metal gasket confines the sample and supports the anvils. Because diamond is the strongest material known and is transparent over a wide range of the electromagnetic spectrum, various high-pressure experiments are performed using synchrotron radiation

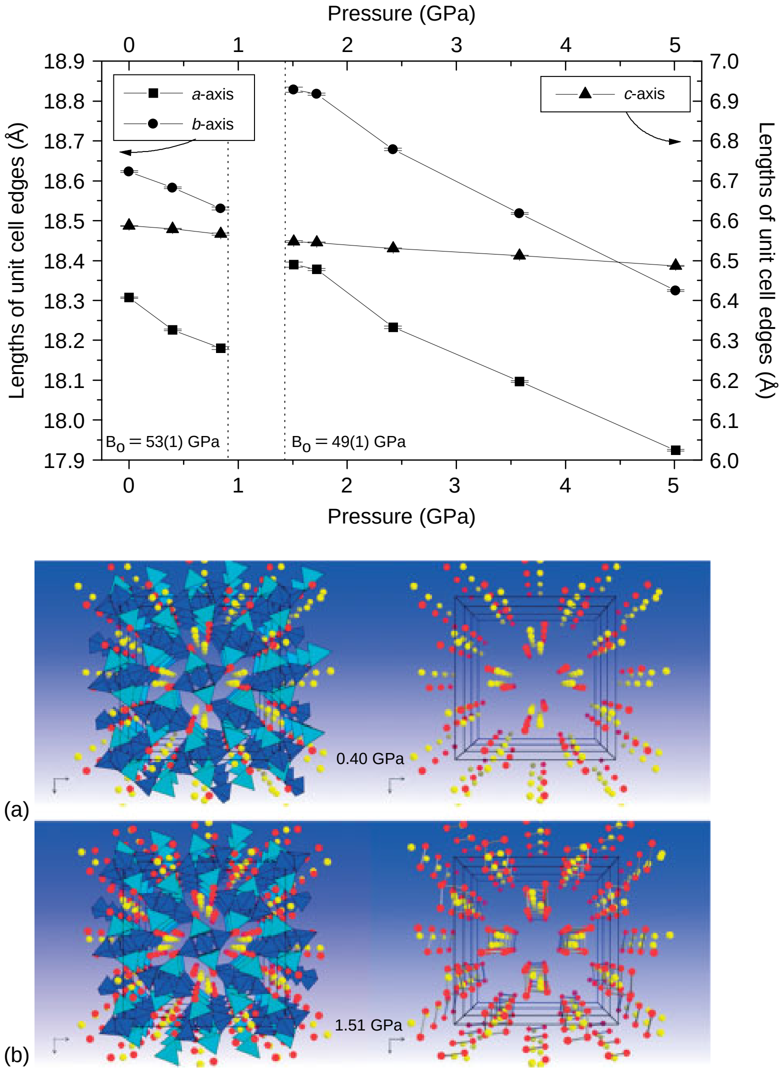

Figure 12 Changes in the unit-cell edge lengths (Å) of sodium aluminosilicate natrolite as a function of pressure. Polyhedral representations of natrolite at (a) 0.40 GPa and (b) 1.51 GPa viewed along [001], the chain/channel axis. Each representation is repeated on the right without the framework component to emphasize the channel contents. Note the formation of the hydrogen-bonded water nanotubes at 1.51 GPa. Red circles represent the oxygen of the water molecules; yellow ones sodium cations. Blue (azure) tetrahedra illustrate an ordered distribution of Si (Al) atoms in the framework

by the expansion of the unit cell along the a- and b-axes, whereas the c-axis shows the expected contraction throughout the volume expansion period. This anisotropic swelling suggests that the rotation of the tetrahedral chains along the c-axis and subsequent expansion of the channels in the (001) plane is responsible for the observed volume increase. The bulk modulus of the large-volume natrolite ($B_0 = 49(1)$ GPa) is slightly smaller than that of the normal natrolite ($B_0 = 53(1)$ GPa), illustrating an increased compressibility for the 'superhydrated' phase. The superhydration in sodium aluminosilicate natrolite is reversible. However, a synthetic analogue, potassium gallosilicate exhibits irreversible superhydration with retention of the high-pressure phase at ambient conditions.[75]

The two structural models for the phases before and after the volume expansion are shown below. After the volume expansion at 1.5 GPa, an additional fully occupied water site (OW2) appears along the channel, leading to 32 H_2O per unit cell. Unlike the chain of sodium and water in the low-pressure phase below 0.8 GPa, the superhydration at the OW2 site generates an infinite chain of hydrogen-bonded water nanotubes along the c-axis with O–O distances between 2.80(4) and 3.09(4) Å. The position of the sodium cation does not show any appreciable changes throughout the superhydration region. The ordered water nanotube in natrolite should be seen in light of theoretical water nanostructures proposed by Koga *et al.*[76] The presence of Na-ions within the water nanotubes should provide an incentive to study ion transport under pressure. Furthermore, these observations will also draw attention to a possible geophysical implication: superhydration conditions resemble regions of the cold lithosphere during subduction[77] implying a new possible mechanism for the storage and transport of water in framework structures in the Earth's upper mantle.

7.2 High-pressure Neutron Powder Diffraction Studies of Cristobalite

The high-pressure phase of cristobalite, one of the SiO_2 modifications, was studied with neutron time-of-flight powder diffraction using the PEARL beamline at the neutron spallation source ISIS at the Rutheford Appleton Laboratory (UK).[78] The high-pressure data were obtained using a Paris–Edinburgh-cell. This cell weighs about 50 kg and uses a 200 ton ram and fits into a 30 cm cube (Figure 13).[79] With a modified encapsulated gasket, it is now possible to measure under hydrostatic conditions up to 9 GPa.[80] The sample was mixed with Fluorinert™ as the pressure-transmitting medium and loaded in a circular gasket made of a Ti–Zr alloy, which has a zero coherent scattering length. This was then mounted between tungsten-carbide anvils and subsequently pressurized.

The diffraction pattern was collected in the time-of-flight mode. The starting model for the Rietveld refinement was obtained from ab initio density-functional theory (DFT) calculations. The crystal structure of the high-pressure form of cristobalite was found to be a monoclinic distortion of the cubic SiO_2 phase. As shown below, the structure is composed of puckered 6-membered rings composed of corner-sharing SiO_4 tetrahedra (see Figure 14). In the cubic phase these rings are perfect hexagons. The puckering is the result of relatively large rotations of the tetrahedra. The cubic structure is an average structure in which dynamic reorientations of the SiO_4 tetrahedra take place. The ambient phase is tetragonal. The question arose if the monoclinic phase is due to a distortion of the tetragonal or cubic parent phase. Using a theoretical approach referred to as 'rigid unit model',[81] a displacive

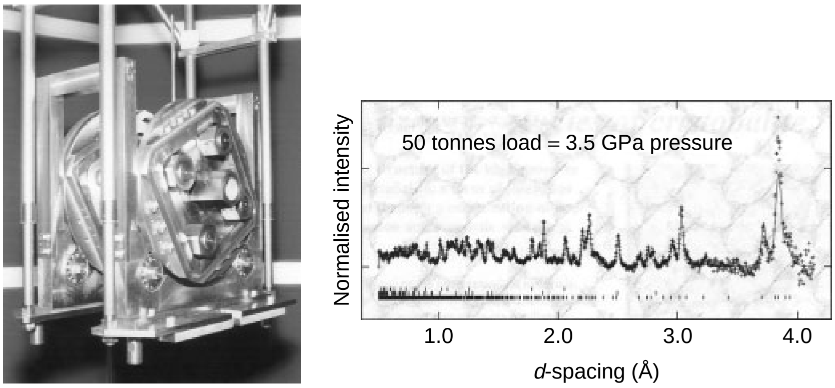

Figure 13 Paris–Edinburgh cell used for high-pressure neutron powder diffraction experiments. On the right neutron time-of-flight data of the high-pressure monoclinic form of cristobalite are shown

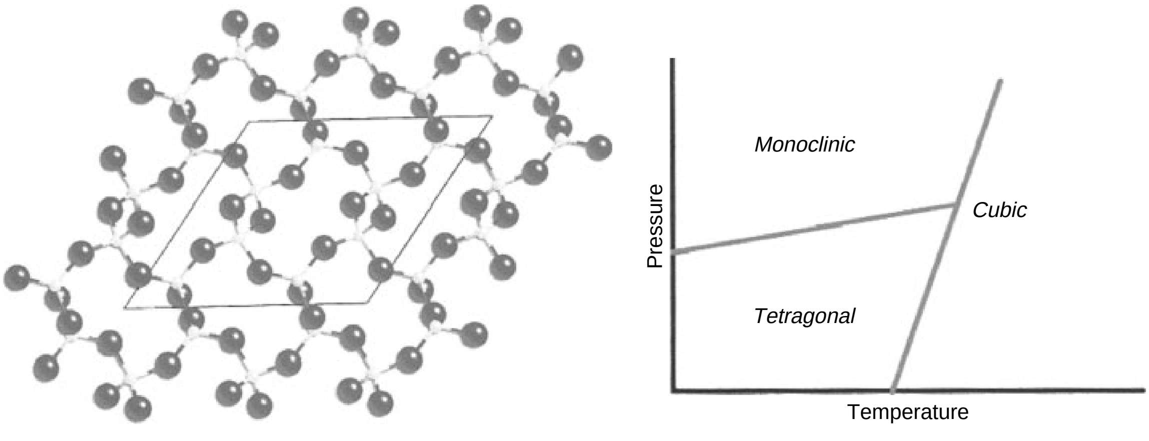

Figure 14 Structure of the monoclinic phase of cristobalite viewed down [010] revealing the puckered six-member rings of SiO_4 tetrahedra. On the right, a schematic pressure-temperature phase diagram

transition from the tetragonal phase seems unlikely. Rather, the monoclinic structure takes place owing to a so-called soft-mode in the cubic phase of cristobalite, which exists at high temperatures and pressures. This can also be inferred from the fact that the monoclinic space group $P2_1/c$ is not a subgroup of the tetragonal phase but of the cubic phase and therefore a displacive instability from the tetragonal phase is not possible.[82] This shows that high-pressure phase transitions can have more complex group-subgroup relationships than found in transitions caused by changing temperature.

8 OUTLOOK

New challenges and opportunities for powder diffraction are emerging. Powder diffraction is a very active field. As in the past, progress will benefit from advances in instrumentation and computing Examples are:

- The implementation of novel instrumental concepts and here, in particular, a new generation of neutron time-of-flight powder diffractometers. The General Materials Diffractometer (GEM) at ISIS is such a novel high-intensity, high-resolution neutron powder diffractometer ($\Delta d/d \sim 2 \times 10^{-3}$). When GEM is completed, it will have 7290 detector elements grouped in more than 98 modules. These detectors will cover scattering angles from 1.1° to 169.3°. The GEM scintillator detector system will contain 660,000 individual optic fibers, whose total length will be about 350 km.[83] The Spallation Neutron Source(SNS) currently being built at Oakridge National Laboratory will also provide access to a high-resolution GEM-type powder diffractometer.
- Another very active area of research is ultrafast time-resolved powder diffraction. Recent work at the European Synchrotron Radiation Facility (ESRF) by Teichert *et al.*[84] reported the direct observation of a photoinduced paraelectric-to-ferroelectric phase transition in a charge-transfer molecular material using a monochromatic 100 picosecond synchrotron pulse. The short-lived metastabile ionic state with long-range ferroelectric ordering was created by near-infrared light and more than 800 unique Bragg reflections were collected. With the start-up, the Sub-picosecond X-ray Pulse Source and the Linear Coherent Light Source (LCLS) at Stanford new horizons in single-shot diffraction and ultrafast time-resolved powder diffraction studies open up.
- A third area of research, which has the potential to revolutionize powder diffraction, is the focusing of X-rays into very small beams (‘nanobeams’). Nanoscience and modern synchrotron diffraction are engaged in a synergetic relationship in which on the one hand nanoscience requires nanoscale X-ray beams to probe nanometer size regions of matter and on the other hand, nanolithography tools such as electron beam writers are needed to pattern and manufacture optical devices such as zone plates, refractive lenses, and waveguides.
- With respect to developments in computing power and modeling capabilities, it can be taken for granted that both will continue to proliferate and increase at the current growth rate. This opens up new possibilities in real-space modeling and on-line data analysis for parametric studies. Parallel computing of Rietveld refinements has been already been demonstrated in the very popular General Structure Analysis Systems (GSAS) code. Using a modest cluster with seven processors reduced the time it takes to complete least-squares refinements between 2.5 and 5 times.[85] Remote-instrument control at user facilities is already being put into operation. Nanocrystallography requires both automated direct Fourier transformations in contrast to ‘manual’ processing as well as ‘smart’ interactive modeling tools to deal with future increases in the data acquisition rate. New methods and tools are emerging that will take advantage of unprecedented computational capabilities. Powder diffraction techniques will be able to investigate structures of a complexity deemed impossible just a few years ago.

9 REFERENCES

1. P. Debye and P. Scherrer, *Z. Phys.*, 1916, **17**, 277.
2. A. W. Hull, *Phys. Rev.*, 1917, **9**, 84.
3. W. H. Zachariasen, *Acta Crystallogr.*, 1948, **1**, 265.
4. W. H. Zachariasen, *Acta Crystallogr.*, 1949, **2**, 296.
5. W. H. Zachariasen and F. H. Ellinger, *Acta Crystallogr.*, 1963, **16**, 369.
6. P. C. Debets, *Acta Crystallogr.*, 1968, **B24**, 400.
7. J. I. Langford and D. Louer, *Rep. Prog. Phys.*, 1996, **59**(2), 131.
8. P. F. Henry, M. T. Weller, and C. C. Wilson, *J. Appl. Crystallogr.*, 2003, **36**, 1361.
9. A. J. Dianoux and G. Lander eds, ‘Neutron Data Booklet’, 1st edn., Institute Laue-Langevin, October 2001.
10. J. Als-Nielsen and D. McMorrow, ‘Elements of Modern X-Ray Physics’, John Wiley & Sons, 2001.
11. J. Attfield, *Mater. Sci. Forum*, 1996, **228–231**, 201.
12. D. Cox and A. Wilkinson, in ‘Resonant Anomalous X-ray Scattering, Theory and Applications’, eds. G. Materlick, C. J. Sparks, and K. Fischer, Elsevier Science, Amsterdam, 1994, p. 135.
13. J. L. Hodeau, V. Favre-Nicolin, S. Bos, H. Renevier, E. Lorenzo, and J. F. Berar, *Chem. Rev.*, 2001, **101**, 1843.
14. J. B. Hastings, W. Thomlinson, and D. E. Cox, *J. Appl. Crystallogr.*, 1984, **17**, 85.
15. A. P. Jephcoat, L. W. Finger, and D. E. Cox, *High Press. Res.*, 1992, **A310**, 667.

16. J. W. Visser, *J. Appl. Crystallogr.*, 1969, **2**, 89.
17. P. E. Werner, L. Eriksson, and M. Westdahl, *J. Appl. Crystallogr.*, 1985, **18**, 367.
18. A. Boultif and D. Louer, *J. Appl. Crystallogr.*, 1991, **24**, 987.
19. B. M. Kariuki, S. A. Belmonte, M. I. McMahon, R. L. Johnston, K. D. M. Harris, and R. J. Nelmes, *J. Synchrotron Radiat.*, 1999, **6**, 87.
20. G. S. Pawley, *J. Appl. Crystallogr.*, 1981, **14**, 357.
21. A. Lebail, H. Duroy, and J. L. Fourquet, *Mater. Res. Bull.*, 1988, **23**, 447.
22. W. I. F. David, *J. Appl. Crystallogr.*, 1987, **20**, 316.
23. Y. H. Dong, J. Liu, Y.-C. Li, and X. D. Li, *J. Appl. Crystallogr.*, 2003, **36**, 1123.
24. R. L. Snyder, J. Fiala, and H. J. Bunge, 'Defect and Microstructure Analysis by Diffraction', International Union of Crystallography, Oxford University Press, Oxford, 1999.
25. P. Karen, P. M. Woodward, P. N. Santosh, T. Vogt, P. W. Stephens, and S. Pagola, *J. Solid State Chem.*, 2002, **167**, 480.
26. P. W. Stephens, *J. Appl. Crystallogr.*, 1999, **32**, 281.
27. O. Masson, E. Dooryhee, and A. N. Fitch, *J. Appl. Crystallogr.*, 2003, **36**, 286.
28. A. J. C. Wilson, *Proc. R. Soc. London*, 1942, **A180**, 277; *Proc. R. Soc. London*, 1943, **A181**, 36.
29. C. Delmas and C. Tessier, *J. Mater. Chem.*, 1997, **7**, 1439.
30. R. Berliner and S. A. Werner, *Phys. Rev.*, 1986, **B34**, 3586.
31. S. Jin, M. McCormack, T. H. Teufel, and R. Ramesh, *J. Appl. Phys.*, 1994, **76**, 6929.
32. G. K. Williamson and W. H. Hall, *Acta Metall. Mater.*, 1953, **1**, 22.
33. Ch. Muller, F. Jacob, Y. Gagou, and E. Elkain, *J. Appl. Crystallogr.*, 2003, **36**, 880.
34. H. M. Rietveld, *Acta Crystallogr.*, 1967, **22**, 151; *J. Appl. Crystallogr.*, 1969, **2**, 65.
35. R. A. Young ed., 'The Rietveld Method', International Union of Crystallography Monographs on Crystallography No 5, IUCr/Oxford University Press, Oxford, 1993.
36. W. I. F. David, K. Shankland, L. M. McCusker, and Ch. Baerlocher eds, 'Structure Determination from Powder Diffraction Data', International Union of Crystallography Monographs on Crystallography No 13, IUCr/Oxford University Press, Oxford, 2002.
37. K. D. M. Harris and M. Tremayne, *Chem. Mater.*, 1996, **8**(11), 2554.
38. K. D. M. Harris, M. Tremayne, P. Lightfoot, and P. G. Bruce, *J. Am. Chem. Soc.*, 1994, **116**, 3543.
39. M. Tremayne, B. M. Kariuki, and K. D. M. Harris, *Angew. Chem., Int. Ed. Engl.*, 1997, **36**, 770.
40. D. Ramprasad, G. B. Pez, B. H. Toby, T. J. Markley, and R. M. Pearlstein, *J. Am. Chem. Soc.*, 1995, **117**, 10694.
41. Y. G. Andreev, G. S. MacGlashan, and P. G. Bruce, *Phys. Rev.*, 1997, **B55**, 12011.
42. A. M. T. Bell, J. N. B. Smith, J. P. Attfield, J. M. Rawson, K. Shankland, and W. I. F. David, *New J. Chem.*, 1999, **23**, 565.
43. B. M. Kariuki, H. Serrano-Gonzalez, R. L. Johnston, and K. D. M. Harris, *Chem. Phys. Lett.*, 1997, **189**, 280.
44. K. Shankland, W. I. F. David, and T. Csoka, *Z. Kristallogr.*, 1997, **212**, 550.
45. B. M. Kariuki, P. Calcagno, K. D. M. Harris, D. Philip, and R. L. Johnston, *Angew. Chem., Int. Ed. Engl.*, 1999, **38**, 831.
46. W. I. F. David, K. Shankland, J. Cole, S. Maginn, W. D. H. Motherwell, and R. Taylor, 'DASH User Manual', Cambridge Crystallographic Data Centre, Cambridge, 2001.
47. A. J. Mora, A. N. Fitch, B. M. Ramirez, G. E. Delgado, M. Brunelli, and J. Wright, *Acta Crystallogr.*, 2003, **B59**, 378.
48. R. K. Grasselli, J. D. Burrington, D. J. Buttrey, P. DeSanto Jr, C. G. Lugmair, A. F. Volpe, and T. Weingand, *Top. Catal.*, 2003, **23**(1–4), 5.
49. P. DeSanto Jr, D. J. Buttery, R. K. Grasselli, C. G. Lugmair, A. F. Volpe, B. H. Toby, and T. Vogt, *Top. Catal.*, 2003, **23**(1–4), 23.
50. P. DeSanto, D. J. Buttrey, R. K. Graselli, C. G. Lugmair, A. F.Volpe Jr, B. H. Toby, and T. Vogt, *Z. Kristallogr.*, 2004, **219**, 152.
51. I. D. Brown, 'The Chemical Bond in Inorganic Chemistry. The Bond Valence Model', International Union of Crystallography, Oxford University Press, Oxford, 2002.
52. D. H. Olson and E. Dempsey, *J. Catal.*, 1969, **13**, 221.
53. M. Czjzek, H. Jobic, A. N. Fitch, and T. Vogt, *J. Phys. Chem.*, 1992, **96**, 1535.
54. A. K. Cheetham, M. M. Eddy, and J. M. Thomas, *J. Chem. Soc., Chem. Commun.*, 1984, 1337.
55. R. X. Fischer, W. H. Baur, R. D. Shannon, R. H. Staley, L. Abrams, A. J. Vega, and J. D. Jorgensen, *Acta Crystallogr.*, 1988, **B44**, 321.
56. L. J. Smith, A. Davidson, and A. K. Cheetham, *Catal. Lett.*, 1997, **49**, 143.
57. L. J. Smith, A. K. Cheetham, R. E. Morris, L. Marchese, J. M. Thomas, and P. A. Wright, *J. Chen, Science*, 1996, **271**, 799.
58. A. Martucci, A. Alberti, G. Cruciani, P. Radaelli, P. Ciambelli, and M. Rapacciuolo, *Microporous Mesoporous Mater.*, 1999, **30**, 95.
59. A. Martucci, G. Cruciani, A. Alberti, C. Ritter, P. Ciambelli, and P. Rapacciuolo, *Microporous Mesoporous Mater.*, 1998, **29**, 1725.
60. B. J. Campbell, A. K. Cheetham, T. Vogt, L. Carluccio, W. O. Parker Jr, C. Flego, and R. Millini, *J. Phys. Chem.*, 2001, **B105**, 1947.
61. A. Burton, S. Elomari, R. C. Medrud, I. Y. Chan, C.-Y. Chen, L. M. Bull, and E. S. Vittoratos, *J. Am. Chem. Soc.*, 2003, **125**, 1633.

62. S. Hilpert and T. Dieckmann, *Ber. Dtsch. Chem. Ges.*, 1911, **A44**, 2378.
63. A. Serres, *J. Phys. Radium*, 1947, **8**, 146.
64. J. Mira, F. Rivadulla, J. Rivas, A. Fondado, T. Guidi, R. Caciuffo, F. Carsughi, P. G. Radaelli, and J. B. Goodenough, *Phys. Rev. Lett.*, 2003, **90**, 097203.
65. J. Goodenough, *Prog. Solid State Chem.*, 1963, **5**, 145.
66. V. K. Pecharsky and K. A. Gschneidner Jr, *Phys. Rev. Lett.*, 1997, **78**, 3299; *Adv. Mater.*, 2001, **13**, 683.
67. V. K. Pecharsky, A. P. Holm, K. A. Gschneidner Jr, and R. Rink, *Phys. Rev. Lett.*, 2003, **91**, 197203.
68. P. F. Peterson, E. S. Bozin, T. Proffen, and S. J. L. Billinge, *J. Appl. Crystallogr.*, 2003, **36**, 53.
69. A. S. Ichimura, J. L. Dye, M. A. Camblor, and L. A. Villaesusa, *J. Am. Chem. Soc.*, 2002, **124**, 1170.
70. V. Petkov, S. J. L. Billinge, T. Vogt, A. S. Ichimura, and J. L. Dye, *Phys. Rev. Lett.*, 2002, **89**(7), 075502.
71. J. S. Loveday, R. J. Nelmes, M. Guthrie, S. A. Belmonte, D. R. Allan, D. D. Klug, J. S. Tse, and Y. P. Handa, *Nature*, 2001, **410**, 661.
72. Y. Lee, J. A. Hriljac., T. Vogt., J. B. Parise, and G. Artioli, *J. Am. Chem. Soc.*, 2002, **124**, 5466.
73. R. M. Hazen and L. W. Finger, ‘Comparative Crystal Chemistry’, John Wiley & Sons, New York, 1982.
74. P. M. Bell and H. K. Mao, ‘Carnegie Institution of Washington Year Book’, Carnegie Institute of Washington, 1979, p. 665.
75. Y. Lee, T. Vogt, J. A. Hriljac, J. B. Parise, J. C. Hanson, and S. J. Kim, *Nature*, 2003, **420**, 485.
76. K. Koga, G. T. Gao., H. Tanaka, and C. X. Zeng, *Nature*, 2001, **412**, 802.
77. C. R. Bina and A. Navrotsky, *Nature*, 2000, **408**, 844.
78. M. T. Dove, M. S. Craig, D. A. Keen, W. G. Marshall, S. A. Redfern, K. O. Trachenko, and M. G. Tucker, *Mineral. Mag.*, 2000, **64**(3), 569.
79. J. M. Besson, R. J. Nelmes, G. Hamel, J. S. Loveday, G. Weill, and S. Hull, *Physica B*, 1992, **180**, 907.
80. W. G. Marshall and D. J. Francis, *J. Appl. Crystallogr.*, 2002, **35**, 122.
81. K. D. Hammond, M. T. Dove, A. P. Giddy, V. Heine, and B. Winkler, *Am. Mineral.*, 1996, **81**, 1057.
82. H. T. Stokes and D. M. Hatch, ‘Isotropy Subgroups of the 230 Crystallographic Space Groups’, World Scientific, Singapore, 1988.
83. W. G. Williams, R. M. Ibberson, P. Day, and J. E. Enderby, *Physica B*, 1998, **241–243**, 234.
84. E. Collet, M. H. Lemee-Cailleau, M. Buron-Le Cointe, H. Cailleau, M. Wulff, T. Luty, S.-Y. Koshihara, M. Meyer, L. Toupet, P. Rabiller, and S. Teichert, *Science*, 2003, **300**, 612.
85. T. R. Zeitler and B. H. Toby, *J. Appl. Crystallogr.*, 2002, **35**, 191.

Solids: Computer Modeling

Richard Catlow
Royal Institution of Great Britain, London, UK

1	Introduction	1
2	Methodologies	1
3	Applications	11
4	Summary	15
5	References	15

1 INTRODUCTION

Computational methods have had a major impact on almost all areas of science in recent years. The range of applications is now very broad, encompassing molecular biology, materials and surface science, mineralogy, and small molecule chemistry. This article focuses on the application of atomistic computer modeling techniques to materials science. We present a brief survey of the aims and scope of the field and short introduction to the main methodologies. We illustrate the current state of the art of computer modeling studies of materials by recent applications to bulk and surface properties of topical systems.

1.1 Range and Scope

Computer modeling is a distinct type of scientific technique that bridges fundamental theory with experimental observation on complex systems. Its success rests first on the fact that the basic physics controlling the behavior of matter at the atomic level has been established for over seventy years; secondly on the development over the last twenty years of approximate but effective methods for implementing this physics in complex systems; and thirdly on the ability of modern computers to handle the enormous demands regarding both processing power and memory required for realistic modeling of complex systems.

Computer simulation studies aim to provide reliable models at the atomistic level, which fulfill three main roles: first they can provide general insight and understanding of the systems simulated; secondly they can provide models, which can directly assist the interpretation of experimental data; and thirdly they can provide accurate numerical data on important parameters, which may be either difficult to measure or entirely inaccessible to experiment. As an example of the first role, we may cite the application of modeling techniques to the study of microporous materials[1] where they have given extensive insights into the structural and catalytic properties of these complex materials. The second role is illustrated by many applications in the science of defects and solids, where simulation tools have been used together with experiment to construct models of complex defect structures.[2] An excellent illustration of the third role is found in the field of high-pressure science, where computer modeling has enabled the accurate calculation of physical properties of materials under the enormous pressures present in the Earth's mantle and core.[3] The main characteristic of the present status of the field is its increasingly predictive nature and the growing complexity and realism of contemporary simulations, as will be illustrated in Section 3 of this chapter.

2 METHODOLOGIES

Two broad classes of technique are available for modeling matter at the atomic level. The first avoids the explicit solution of the Schrödinger equation by using *interatomic potentials* (*IP*), which express the energy of the system as a function of nuclear coordinates. Such methods are fast and effective within their domain of applicability and good interatomic potential functions are available for many materials. They are, however, limited as they cannot describe any properties and processes, which depend explicitly on the electronic structure of the material. In contrast, *electronic structure* calculations solve the Schrödinger equation at some level of approximation allowing direct simulation of, for example, spectroscopic properties and reaction mechanisms. We now present an introduction to interatomic potential-based methods (often referred to as atomistic simulations).

2.1 Atomistic Simulations

2.1.1 *Potential Functions and Their Evaluation*

The potential energy function $U(\mathbf{r}_1 \cdots \mathbf{r}_N)$ expresses the energy of an assembly of N atoms or ions as a function of the nuclear coordinates $\mathbf{r}_1 \cdots \mathbf{r}_N$. The Born-Oppenheimer approximation is, of course, implicit in the use of such functions but there is no explicit inclusion of the effects of the electronic structure of the system: such effects are subsumed into the potential function. The energy zero for such functions is normally taken to be that of the component atoms (or ions) at rest at infinity, that is, the self energies (electron-nuclear) of the atoms (or ions) are not included in U.

The potential function is commonly expanded as follows:

$$U = \frac{1}{2}\sum_{i}^{N}\sum_{j}^{N}{}'\varphi_{ij}(\mathbf{r}_i, \mathbf{r}_j) + \frac{1}{3}\sum_{i}^{N}\sum_{j}^{\infty}\sum_{k}^{\infty}{}'\varphi_{ijk}(\mathbf{r}_i, \mathbf{r}_j, \mathbf{r}_k) + \cdots \tag{1}$$

and the prime indicates that we only include terms $i \neq j$; where the φ_{ij} are 'two-body' functions that depend only on the positions of pairs of atoms i and j; φ_{ijk} are the 'three-body' terms depending explicitly on the positions of atoms i, j, and k and where the prime symbol again indicates that we only include terms $i \neq j \neq k$. The expansion extends to four-body terms φ_{ijkl} and higher order terms, which are, however, rarely included. Indeed it has been common to approximate U by including only the two-body component φ_{ij}, which may be usefully decomposed into Coulombic and non-Coulombic terms:

$$\varphi_{ij}(\mathbf{r}_i, \mathbf{r}_j) = \frac{q_i q_j}{\mathbf{r}_{ij}} + V_{ij}(\mathbf{r}_{ij}) \tag{2}$$

where r_{ij} is the distance between i and j and q_i is the charge on the atom or ion (and is normally treated as a point entity). The Coulombic term, which is purely two-body in nature, is handled by the procedures discussed after. The non-Coulombic, V_{ij}, is then usually approximated by analytical functions that generally include both attractive and repulsive components; the latter describes the Pauli repulsion arising from overlap of closed shell electron configurations, and the former attractive terms from dispersion (i.e. induced dipole-induced dipole) and covalence effects. Several such functions are available, notably the Lennard-Jones potential:

$$V(\mathbf{r}) = \mathrm{A}r^{-12} - \mathrm{B}\mathbf{r}^{-6}, \tag{3}$$

the Morse potential:

$$V(\mathbf{r}) = D\{1 - \exp[-\beta(\mathbf{r} - \mathbf{r}_\mathrm{e})]\}^2 \tag{4}$$

and the Buckingham potential:

$$V(\mathbf{r}) = \mathrm{A}\exp\left(\frac{-\mathbf{r}}{\rho}\right) - C\mathbf{r}^{-6}. \tag{5}$$

Lennard-Jones potentials have been used widely in modeling rare gas and molecular crystals. Morse potentials become more appropriate when covalent systems are being studied; D may then be interpreted as the covalent bond-dissociation energy and $\mathbf{r}_\mathrm{e}$ the equilibrium bond length. Buckingham potentials have been very widely used in the study of ionic and semi-ionic solids.[4]

Inclusion of many-body effects may be achieved by the use of angle dependent forces. For example, Sanders *et al.*[5] employed simple 'bond-bending' terms of the type,

$$E(\theta) = \tfrac{1}{2}k_\mathrm{B}(\theta - \theta_0)^2 \tag{6}$$

where θ is the angle subtended by three atoms and θ_0 is an equilibrium value; k_B is the appropriate force constant. The use of such terms is most appropriate in systems with directional covalent bonding, for example, silicates, where θ_0 will correspond to the tetrahedral angle subtended by O–Si–O bonds in the tetrahedral $\mathrm{SiO_4}$ groups.

Alternative, three-body functions are provided by the 'triple-dipole' formalism of Axilrod and Teller,[6] which takes the form:

$$V_{ijk} = \frac{k_\mathrm{T}(1 + 3\cos\theta_1\cos\theta_2\cos\theta_3)}{\mathbf{r}_{ij}^3\mathbf{r}_{jk}^3\mathbf{r}_{ik}^3} \tag{7}$$

where the angles and distances relate to the triangle defined by the three atoms i, j, and k. Such functions describe the three-body contributions to the induced dipole attractive forces, and have been shown by Meath and coworkers[7] to make important contributions to the cohesive energies of rare gas crystals. Work of Baetzold *et al.*[8] has shown that such terms may be of value in constructing potential models for the silver halide crystals.

Finally, we note that atomic and ionic polarization in solids is essentially a many-body effect. Moreover, in ionic materials polarization energies may be large, especially in the vicinity of charged defects and surfaces. Omission of polarization, while obviously leading to the failure to describe high frequency dielectric properties, also results in marked inadequacies in calculated phonon dispersion curves. The simplest way of modeling polarizability is to use the point polarizable ion (PPI) model, which assigns a linear constant of proportionality, that is, the polarizability, α, between the dipole moment μ and the field E acting on the atoms, that is:

$$\mu = \alpha E. \tag{8}$$

However, as the dipole is a point entity, it cannot describe the physical basis of polarizability, which is the displacement of the valence shell electron density in response to the applied field. Consequently, important physical effects, in particular, the coupling of polarizability and short-range repulsion, are omitted by these models, which fail badly in describing both dielectric and lattice dynamical properties of crystals, as discussed in greater detail in Reference 9. These deficiencies are largely overcome by the shell model originally proposed by Dick and Overhauser,[10] which describes the development of a dipole moment in terms of the displacement of a massless shell of charge Y (representing the valence shell electrons) from a core (representing the nucleus and core electrons). The core and the shell are connected by an harmonic restoring force for which the spring constant is k. The free atom polarizability, α, is then given by $\alpha = \mathrm{Y}^2/k$. Shell model potentials have been very widely used in studies of lattice dynamical and defect properties of ionic solids. Further discussion is given in Reference 9.

Having established the framework of the potential model to be used, it is next necessary to fix the variable parameters, that is, those used in the description of the short-range potential, $V(r)$, the shell model constants Y and k and the effective atomic charges q (although we note that in many modeling studies of ionic oxides, halides, and even silicates, these have been fixed at integral fully ionic values).

2.1.2 *Parameterization*

This is undertaken by two procedures: first, *empirical methods*, in which variable parameters are adjusted, generally *via* a least squares fitting procedure to observed crystal properties. The latter must include the crystal structure (and the procedure of 'fitting' to the structure has normally been achieved by minimizing the calculated forces acting on the atoms at their observed positions in the unit cell). Elastic constants should, where available, be included; and dielectric properties are required to parameterize the shell model constants. Phonon dispersion curves provide valuable information on interatomic forces; and *force constant* models (in which the variable parameters are first and second derivatives of the potential) are commonly fitted to lattice dynamical data. This has been less common in the fitting of parameters in *potential models*, which are our present concern as they are required for subsequent use in simulations. However, empirically derived potential models should always be tested against phonon dispersion curves when the latter are available.

An important aspect of empirical potential parameterization is the question of transferability. Are, for example, models derived in the study of binary oxides, transferable to ternary oxides? Considerable attention has been paid to this problem by Cormack *et al*.,**[11]** who have examined the use of potentials in spinel oxides, for example, $MgAl_2O_4$, $NiCr_2O_4$, and so on; in addition Parker and Price**[12,13]** have made a very careful study of silicates especially Mg_2SiO_4. These studies conclude that transferability works well in many cases. However, systematic modifications are needed when potentials are transferred to compounds with different coordination numbers. For example, the correct modeling of $MgAl_2O_4$ requires that the potential developed for MgO, in which the magnesium has octahedral coordination, be modified in view of the tetrahedral coordination of Mg in the ternary oxide. The correction factor is based on the difference $\Delta\mathbf{r}^{c}$ between the effective ionic radii for the different coordination numbers. If an exponential, Born-Mayer, repulsive term is used, the preexponential factor is modified as follows:

$$A' = A \exp\left(\frac{\Delta\mathbf{r}^{C}}{\rho}\right) \qquad (9)$$

where the unprimed and primed preexponential factors refer to original and modified coordination numbers. Cormack *et al*.**[11]** have shown that such procedures yield potentials that are successful in modeling spinels.

There are now several sets of empirical potential parameters for a range of solids. Parameter sets are available for organic, molecular solids (see, for example, the work of Williams**[14]** and of Kiselev**[15]**). Ionic solids have been widely studied in the last twenty years, and parameters are available for ionic halides,**[16]** oxides,**[17,18]** and silicates.**[12,13]**

Empirical procedures are still extensively used in developing potential parameters. They do, however, have obvious inadequacies: firstly, it is necessary to have a good range of accurate empirical data, which may not be possible when new systems are being studied; secondly, there is no guarantee of the validity of the potential function when used outside the range of interatomic spacings employed in the parameterization. For this reason there has been considerable incentive in recent years for the development of reliable theoretical procedures for calculating parameters. To date, such efforts have been directed largely towards parameterization of effective charges and of the short-range potential, V, and in a restricted number of cases, the three-body components of the potential. However it is still very difficult to calculate shell model parameters. Calculations of interatomic potentials have been of two types.

2.1.3 *Electron Gas Methods*

These methods are based on the electron gas description of the atom, which is used to calculate the interaction energies of pairs or in principle larger numbers of atoms (or ions) as a function of their nuclear coordinates. The method was established by Wedepohl**[19]** and by Gordon and Kim**[20]** and wide ranging and successful studies of ionic halides and oxides are reported by Mackrodt and coworkers (see, for example, References 21 and 22) (note also the compilation of parameters given in Reference 23). More recently, modified electron gas procedures developed by Cohen and coworkers**[24]** have enjoyed considerable success when applied to oxides and silicates.

As the electron gas method is now very standard and has been reviewed by the present author and others (References 9, 19, and 20), a more detailed discussion is not presented here; a summary of the essential features of the methodology is described in Reference 25.

2.1.4 *Explicit Quantum Mechanical Methods*

These are methods in which the Schrödinger equation is solved approximately for a cluster or periodic array of atoms in a variety of internuclear geometries; the resulting variation in the total energy is then fitted to an interatomic potential function. Ab initio Hartree-Fock (HF) methods are being increasingly used in such studies; examples are the early work of Mackrodt and coworkers,**[26]** and the more recent studies of Gale *et al*.**[27]** and Harrison *et al*.**[28]** The study of silicate systems has been particularly active, with calculation on clusters ranging from $Si(OH)_4$ to $Si_{15}O_{16}H_{12}$.**[29–31]**

In using such methods, care must be taken in the choice of basis sets (i.e. the atomic centred functions from which the LCAO-MOs are constructed). Unless good sets are used, then the resulting interatomic potential function will be inadequate owing to basis-set superposition errors. This subtle effect arises from the use by each atom in the many-atom calculation of basis functions on *other* atoms to reduce its own energy – an effect that invariably arises when incomplete sets are used. Correction procedures are available;[32] but, in general, high quality potentials need high quality basis sets. Secondly, it is important to note that wave functions in crystals differ from those of free ions. It is necessary therefore to include in such calculations a representation of the effects of the surrounding ions on the interacting atoms. A simple procedure commonly used in ionic solids is to employ point charges to reproduce the Madelung potential of the surrounding lattice. Thirdly, it should be recalled that the HF method does not include effects arising from electron correlation. More sophisticated and computationally expensive configurational interaction or perturbation methods are needed to describe correlation effects. Since, however, correlation is responsible for dispersive interactions, other methods are needed to calculate these terms. Alternative ab initio methods based on Density Functional Theory (DFT) discussed in Section 2.2 include directly certain of the effects of electron correlation, although they are still unable to model dispersive effects accurately. Perturbation theories following the original work of Mayer[33] may be used; but empirical methods may be needed for some time to come.

Ab initio techniques are generally far more expensive computationally than the electron gas techniques, and the cpu and disk requirements increase rapidly with the total number of electrons in the calculation. The former methods are, however, preferable, if high quality basis sets may be used, as they allow a more accurate description of atomic interactions, in particular the redistribution of electron densities consequent upon interaction. Electron gas methods clearly, however, provide a cheap, useful, and generally applicable technique for deriving short- range potential parameters, and as such they will have a continuing role in this field.

Finally we should note a valuable approach developed by Pyper and coworkers[34] for ionic solids in which HF methods are used first to obtain a set of crystal orbitals, the interactions between which are calculated as a function of distance including a full explicit evaluation of the exchange term (unlike the local density approximation used in the electron gas method). Estimates of the dispersive energy are then added to the resulting interaction energy. This approach is particularly successful for strongly ionic halides and oxides.

Having developed and parameterized potential models, the final stage before their use in a simulation study should be their *evaluation.* Nonempirically derived potentials should be evaluated by reference to their ability to predict empirical crystal properties. For empirical potentials, it is clearly necessary to use data outside the range employed in the parameterization. We have already referred to the use of lattice dynamical data. Comparison with the results of high-pressure studies, in particular the variation of structural and elastic properties with pressure, is also of great value; and in this context we should note the work of Harding and Stoneham,[35] who examined several potentials for simple ionic materials by comparison with 'Hugoniots', that is, pressure-volume trajectories obtained from shock wave studies. A further useful and demanding test is provided by the ability of potential models to predict crystal structures of polymorphs of a compound other than that used in the potential parameterization.

The development of improved potential models will continue to be a central feature of simulation studies. Progress will require the increased availability of accurate crystal data and refinements in theoretical procedures for calculating potentials.

2.1.5 Simulation Methodologies: Static Lattice Techniques

The characteristic features of these methods is that they do not include any explicit representation of thermal motions. Energies and entropies are calculated for the static lattice; the entropy calculations normally assume the harmonic approximation. High temperature properties can be calculated using the quasi-harmonic approximation, which simply evaluates energies and force constants for the high temperature lattice parameters. Within this framework, it is possible to predict lattice expansivity by calculating the free energy minimum as a function of lattice parameter for a series of temperatures. Calculations may be performed on both perfect and defective lattice configurations; both will now be reviewed.

2.1.6 Perfect Lattice Calculations

The most basic quantity open to calculation is the lattice energy. If we omit the zero-point vibrational energy (and four-body) and higher order terms, this may be written as:

$$E = U_{\mathrm{C}} + \frac{1}{2}\sum_{i=1}^{N}\sum_{j=1}^{\infty}{}' V_{ij}\mathbf{r}_{ij} + \frac{1}{3}\sum_{i=1}^{N}\sum_{j=1}^{\infty}\sum_{k=1}^{\infty}{}' \varphi_{ijk}(\mathbf{r}_i, \mathbf{r}_j, \mathbf{r}_k) \quad (10)$$

where U_{c} is the electrostatic energy which is obtained by summation of the coulomb term (see equation 2); this summation must not be truncated, and is usually handled by the Ewald procedure which involves a partial transformation into reciprocal space, as discussed, for example, in Reference 25. The summation conventions are as in equations (1) and the terms V_{ij} and φ_{ijk} are as defined in equations (1) and (2). We note that the great majority of lattice energy calculations only include the two-body contribution to the short-range energy. One important matter of definition is that the lattice energy gives the *energy of the crystal with respect to component ions at infinity.* If it is desired to express the energy with respect to atoms at infinity (for which the more appropriate term is then the *cohesive* energy), then the appropriate ionization energies and electron affinities will be added.

Lattice energy calculations are now routine, and may be carried out for very large unit cells containing several hundred atoms. The codes METAPOCS,**[36]** THBREL**[37]** and GULP**[38]** undertake lattice energy calculations including both two- and three-body terms, using both bond-bending and triple–dipole formalisms.

Lattice energy calculations provide valuable insight into the structure and stabilities of ionic and semi-ionic solids. The technique is most powerful when combined with energy minimization procedures, which generate the structure of minimum energy. These are discussed below after the calculation of entropies have been described. Good illustrations of the value of lattice energy studies are given in studies of the studies of the stabilities of microporous materials, discussed later in this chapter and in References 39 and 40.

In addition to calculating energies, it is also possible to calculate routinely a range of crystal properties, including the lattice stability, the elastic and dielectric and piezoelectric constants, and the phonon dispersion curves. The techniques used, which are quite standard, require knowledge of both first and second derivatives of the energy with respect to the atomic coordinates. Indeed it is useful to describe two quantities: first the vector, **g**, whose components $\mathbf{g}_i^{\alpha}$ are defined as:

$$\mathbf{g}_i^{\alpha} = \left[\frac{\partial E}{\partial x_i^{\alpha}}\right], \tag{11}$$

that is, the first derivative of the lattice energy with respect to a given Cartesian coordinate (α) of the ith atom. The second derivative matrix **W** has components $\mathbf{W}_{ij}^{\alpha\beta}$; defined by:

$$\mathbf{W}_{ij}^{\alpha\beta} = \left[\frac{\partial^2 E}{\partial x_i^{\alpha}\partial x_j^{\beta}}\right]. \tag{12}$$

The expressions used in calculating the properties referred to above from these derivatives are discussed in greater detail in Reference 9. For more detailed discussions of the calculation of phonon dispersion curves from the second derivative or 'dynamical' matrix W, the reader should consult References 41 and 42. Finally, we note that by the term 'lattice stability' we refer to the equilibrium conditions both for the atoms within the unit cell, and for the unit cell as a whole. The former are available from the gradient vector g, while the latter are described in terms of the six components $\varepsilon_1 \cdots \varepsilon_6$, which define the strain matrix ε, where

$$\varepsilon = \begin{bmatrix} \varepsilon_1 & \frac{1}{2}\varepsilon_4 & \frac{1}{2}\varepsilon_5 \\ \frac{1}{2}\varepsilon_4 & \varepsilon_2 & \frac{1}{2}\varepsilon_6 \\ \frac{1}{2}\varepsilon_5 & \frac{1}{2}\varepsilon_6 & \varepsilon_3 \end{bmatrix} \tag{13}$$

So when the unit cell as a whole is strained, we describe the modification of an arbitrary vector $\underline{\mathbf{r}}$ in the unstrained matrix to a vector $\underline{\mathbf{r}}'$ in the strained matrix, using the equation:

$$\mathbf{r}' = (1 + \varepsilon)\mathbf{r} \tag{14}$$

where 1 is the unit matrix. The six derivatives of energy with respect to strain, $[\partial E/\partial \varepsilon_i]$, therefore measure the forces acting on the unit cell. The equilibrium condition for the crystal therefore requires that $\mathbf{g} = 0$ and $[\partial E/\partial \varepsilon_i] = 0$ for all i.

2.1.7 Entropy Calculations

The entropy in a solid arises first from configurational terms that for a perfect solid are zero. However, for a solid showing orientational or translational disorder, configurational expressions based on the Boltzmann expression $S =$ kln(W) may be used. In this section, we shall pay more attention to the second term, which is arises from the population of the vibrational degrees of freedom of the solid. Thus the entropy of a solid may be written as:

$$S_{\text{vib}} = k\int_0^Q \mathrm{d}Q \sum_i \left\{\frac{h\nu_i}{kT}\left[\exp\left[\frac{h\nu_i}{kT}\right] - 1\right]^{-1} - \ln\left[1 - \exp\left[\frac{-h\nu_i}{kT}\right]\right]\right\} \tag{15}$$

where the sum is overall phonon frequencies and the integral is over the Brillouin zone. In practice, the integral is normally evaluated by sampling over the zone for which a variety of techniques are available.**[43]** Vibrational terms also give a contribution to the lattice energy of the crystal:

$$E_{\text{vib}} = kT\int_0^Q \mathrm{d}Q \sum_i \left\{\frac{h\nu_i}{2kT} + \frac{h\nu_i}{kT}\left[\exp\left[\frac{h\nu_i}{kT}\right] - 1\right]^{-1}\right\} \tag{16}$$

which results in the following expression for the crystal free energy with respect to ions at rest of infinity:

$$F = E + kT\int_0^Q \mathrm{d}Q \sum_i \left\{\frac{h\nu_i}{2kT} + \ln\left[1 - \exp\left[\frac{h\nu_i}{kT}\right]\right]\right\} \tag{17}$$

where E is the lattice energy (omitting vibrational terms) given by equation (10).

2.1.8 Energy Minimization

Having evaluated energies and free energies of a crystal structure, it is desirable to be able to use these in an energy (or free energy) minimization procedure. Let us consider first the simple case of minimization to constant volume (i.e. within fixed cell dimensions). We write the energy of the crystal as a Taylor expansion in the displacements of the atoms, d, from that current configuration giving:

$$E(\delta) = E_0 + \mathbf{g}\delta + \tfrac{1}{2}\delta\mathbf{W}\delta + \cdots\cdots \tag{18}$$

If we terminate this function at the second order term and minimize E with respect to d, we obtain for the energy minimum:

$$0 = \mathbf{g} + \mathbf{W}\delta \qquad i.e. \quad \delta = -\mathbf{g}\mathbf{W}^{-1} \tag{19}$$

Displacement of the coordinates by δ as given in equation (18) will generate the energy minimum configuration. Of course, in practice, it will not be valid to truncate the summation at the quadratic term, except when very close to the minimum. However, equation (19) provides the basis of an effective iterative procedure for attaining the minimum. Indeed this ‘Newton-Raphson’ method is widely used in both perfect and defect lattice energy minimization, as it is generally rapidly convergent. Its main disadvantage is that it requires the calculation, inversion, and storage of the second derivative matrix, W. Recalculation and inversion each iteration may be avoided by use of updating procedures due to Fletcher and Powell, which are discussed elsewhere.**[9,44–46]** The storage problem may become serious with very large structures owing to the high cpu memory requirements. Recourse may be made to gradient methods, for example, the well known conjugate gradients technique, which make use only of first derivatives. Such methods are, however, more slowly converging. The increasing availability of very large cpu memories is, however, reducing the difficulties associated with the storage of the W matrix.

For evaluation of the energy minimum with respect to constant pressure (i.e. with variable cell dimensions), first we note that we can define the six components of the mechanical pressure acting on the solid, corresponding to the six strain components, defined in equation (13), that is,

$$P^{\varepsilon_i} = \frac{1}{V}\left[\frac{\mathrm{d}E}{\mathrm{d}\varepsilon_i}\right] \tag{20}$$

where V is the unit cell volume. The strains can then be evaluated, using Hooke’s law,

$$\varepsilon = PC^{-1} \tag{21}$$

where C is the (6×6) elastic constant terms, which may be calculated from W. Substitution of these calculated strain components into equation (21) then yields the new cell dimensions and atomic coordinates. Again, the procedure is iterative, as it is only strictly valid in the region of applicability of the harmonic approximation. With a sensible starting point, however, only a small number of iterations (typically 2–5) is required.

The treatment above assumes that the pressure and corresponding strains are entirely mechanical in origin. However, at finite temperatures there will be a ‘kinetic pressure’ arising from the changes in the vibrational free energy with volume. These may be written as:

$$P^{\varepsilon_i}_{\mathrm{vib}} = \frac{1}{V}\left[\frac{\mathrm{d}F_{\mathrm{vib}}}{\mathrm{d}\varepsilon_i}\right] \tag{22}$$

where F_{vib} is the vibrational free energy. These kinetic pressures are most simply evaluated by applying small arbitrary strains to the structure and calculating the corresponding changes in F_{vib}. If P_{vib} is added to the mechanical pressure P in equation (20), it enables us to carry out free energy minimization. Parker and coworkers have written a general computer code, PAPAPOCS, for such calculations. Further discussion is given in Reference 42, which also describes how the techniques may be used to calculate lattice expansivity, either directly or by calculating the cell dimension as a function of temperature or by calculation of the thermal Gruneisen parameter.

2.1.9 Defect Simulations

Two techniques are available for calculating the properties of defects: first we may set up a periodic array of defects; second, we may embed the defect in an infinite representation of the surrounding crystal.

2.1.10 Supercell Methods

The simplest procedure for calculating the formation energies, entropies, and hence free energies of defects is to set up a defect supercell, that is, a large periodically repeating structure with the defect being at the centre of each unit cell. The techniques described in the previous section may then be employed. Thus, to evaluate the defect energy we perform a calculation on the perfect lattice, which may be equilibrated either to constant volume or pressure. The lattice energy E_{PERF} is then compared with the value E_{DEF} obtained under the same conditions for the defective lattice. Thus the defect formation energy E_{D} is simply written as:

$$E_{\mathrm{D}} = E_{\mathrm{DEF}} - E_{\mathrm{PERF}}. \tag{23}$$

A similar procedure is, of course, applicable for the entropies and hence free energies. The method is attractively simple, but has a number of drawbacks the principal one being the need for large supercells, especially if large complex defects are being considered. However, we note that supercells containing several hundred atoms are accessible to modern computers. A second drawback is that even with large supercells, the calculated defect energy will inevitably include a term arising from defect interaction as well as formation terms. In certain contexts, however, this may be an advantage, and indeed by calculating the defect energy for different sizes of the supercell, defect interactions may be calculated as a function of defect spacing. Such a study was performed by Cormack *et al.*[47] who investigated the interaction of the two-dimensional shear planes that form in nonstoichiometric oxides. Thirdly, there are problems in including charged defects. Either the defects must be neutralized by including a defect of opposite charge in the unit cell, in which case the isolated defect formation energy cannot be studied, or electroneutrality is achieved by adding a background neutralizing charge or by making small adjustments to the charges of the other atoms in the unit cell.

Despite these difficulties, supercell methods have found considerable application in defect studies,[47–49] and indeed the results compare well with those obtained using the alternative techniques described below.

2.1.11 *Mott–Littleton Methods*

In these calculations, the isolated defect or defect cluster is embedded in the crystal, which extends to infinity, and the contrast between this approach and that used in the supercell methods is illustrated diagrammatically in Figure 1. The normal procedure in a Mott–Littleton calculation is to relax all the atoms in a region of crystal surrounding the defect, containing typically 100–300 atoms, until all are at zero force. Newton–Raphson minimization methods are generally used. The relaxation of the remainder of the crystal is then described by more approximate methods in which the polarization, **P** at a point **r**, is calculated for crystals that have dielectric isotropy, from the expression:

$$\mathbf{P} = \frac{1}{4\pi}\frac{q\mathbf{r}}{r^3}(1-\varepsilon_0^{-1}) \tag{24}$$

where q is the charge on the defect, and ε_0 is the static constant. More complex expressions are used for dielectrically anisotropic crystals. In practice, an interface region is normally used between the two regions described above; in the interface, displacements are calculated using formulae of the type given above, but are evaluated as the sum of the response to individual defects in the inner region, rather than as a response to the net charge of the defect configuration, which is used for the remainder of the outer region. Short-range interactions between ions in the inner region and those in the interface are also calculated explicitly.

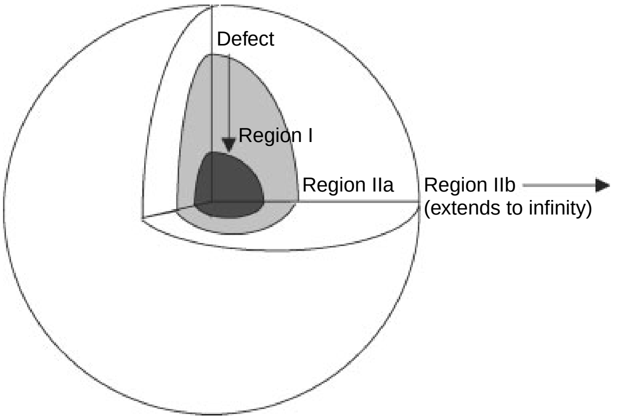

Figure 1 Schematic representation of the Mott–Littleton technique for treating relaxations around defects. (An interface region IIa is included between the inner and outer regions)

The methods have been widely discussed and reviewed in the literature.[9,46,50] Several good automated computer codes are available: the original HADES2 programme written by Norgett[51] was confined to crystals of cubic symmetry; the HADES3 code[52] extended the methodology to include crystals of any symmetry. Leslie[53] developed a program CASCADE, optimized for use on the CRAY vector processing supercomputers. The latest versions of this program permit the inclusion of many-body terms using bond-bending or triple-dipole formalisms. The GULP code written by Gale[38] also includes a Mott–Littleton module. A large number of applications of these techniques are now reported and reviewed in the references given above. Indeed, work using these techniques has helped to establish the quantitative reliability of simulation techniques in solid-state studies.

In addition to energies, defect entropies may also be calculated by related, although distinct, techniques. As with the case of the perfect lattice, defect entropies have two terms – configurational and vibrational – and the former can be calculated using simple combinatorial expressions. The latter arises from the perturbation of the vibrational frequency of the surrounding lattice atoms by the defect. The vibrational defect entropy S_{vib} is a function of the ratio of the perturbed to the unperturbed frequencies, that is,

$$S_{\text{vib}} = -k\ln\frac{\prod_{i=1}^{2N'}\omega_i'}{\prod_{i=1}^{3N}\omega_i} + 3k(N'-N)\left[1-\ln\left(\frac{\hbar}{kT}\right)\right] \tag{25}$$

To evaluate the perturbed frequencies, Greens function techniques may be used. However, Gillan and Jacobs[54] and Harding[55] have shown that embedded crystallite methods are more effective. Here the initial relaxation of the lattice surrounding the defect is undertaken as in the defect energy calculations. The perturbed force constant matrix for the relaxed region is then obtained. There are problems with the ‘convergence’ of the calculated entropy as a function of the size of the perturbed region; these may, however, be treated by the techniques discussed by Gillan and Jacobs.[54]

Work of Harding and coworkers[50,55] has clearly established the value of defect entropy calculations using these methods. Moreover, we note that comparisons have been made[56] between entropies and energies calculated using supercell and embedded crystallite techniques. It is reassuring that the techniques yield the same defect parameters for large sizes of the supercell and of the crystallite.

Both energy and entropy calculations of the type described above are generally performed at constant volume, or more precisely constant lattice parameter. These may, however, be converted to constant pressure values using the following expressions:

$$h_p = u_v - V\beta T\left[\frac{\mathrm{d}f_v}{\mathrm{d}V}\right], \tag{26}$$

$$s_p = s_v - V\beta\left[\frac{\mathrm{d}f_v}{\mathrm{d}V}\right], \tag{27}$$

where h_p and u_v are the constant pressure enthalpy and constant volume energy terms, s_p and s_v are the corresponding entropy terms, f_v is the constant volume free energy, the volume derivative of which may be calculated by studying the variation of u_v and s_v with lattice parameter; V is the unit cell volume and β is the expansivity of the solid. Discussion of these relationships is given in References 55 and 57. Work of Catlow *et al.*[58] on AgCl and Jackson *et al.*[59] on UO_2 has shown their value in studying high temperature, defect properties.

In concluding this section, we note that defect calculations may be used to study defect mobilities as well as defect formation and interaction processes. Assuming the validity of the hopping model of defect transport the frequency of defect jumps can then be written as:

$$\nu = \nu_0 \exp\left(\frac{-g_{\mathrm{ACT}}}{kT}\right) \tag{28}$$

where g_{ACT} is the activation free energy for the defect migration, that is, the difference between the free energies of the saddle point for the defect jump and that of its ground state. Saddle points may be identified by examining the potential energy surface for the migrating defect (although this may be difficult for crystals of low symmetry); once identified, the techniques discussed above may be used to calculate u_{ACT} and s_{ACT}.

Good discussions of the calculations of activation energies are given by Harding.[55] The validity of the hopping model, discussed in detail in Reference 60, requires generally that $u_{\mathrm{ACT}} \gg kT$ and that the 'jump time' for the migration process be far less than the 'residence time' of defects at individual sites. These conditions apply to the great majority of transport processes in solids. However, for materials with very high mobilities, the conditions may breakdown and it becomes necessary to use the dynamical simulation methods discussed in the next section.

2.1.12 *Molecular Dynamics Techniques*

In contrast to the static methods discussed in the previous section, molecular dynamics (MD) includes thermal energies explicitly. The method is conceptually simple: an ensemble of particles represents the system simulated and periodic boundary conditions (PBC) are normally applied to generate an infinite system. The particles are given positions and velocities, the latter being assigned in accordance with a target temperature. In simulations of crystalline solids, the simulation box will normally be a supercell of the basic unit cell. The system is then allowed to evolve in time by solving the classical equations of motion using a specified time step, t (which is typically 10^{-15}–10^{-14} s). A variety of updating algorithms are available, as discussed in detail by Allen and Tildesley.[61] In the limit of an infinitesimal time step, they all reduce to the simple classical equations of motion:

$$x(t+\tau) = x(t) + v(t)\tau, \tag{29}$$

$$v(t+\tau) = v(t) + \frac{f_i}{m_i}\tau, \tag{30}$$

where f_i is the force acting on the particle of mass m_i.

In the initial stages of the simulation, the ensemble equilibrates, that is, it achieves an equilibrium distribution of velocities and equipartition between potential and kinetic energy. After this period, which may take several thousand time steps, the simulation is run for as long a period as is computationally feasible, and the trajectories of all particles are, if possible, stored.

MD simulations yield rich and detailed information on the system simulated. Structural information is available from radial distribution functions (RDFs), and diffusion coefficients may be calculated from the mean square displacement $\langle \mathbf{r}_\alpha^2 \rangle$ of the particle as a function of time, using the relationship:

$$\mathrm{D}_\alpha = \frac{\langle \mathbf{r}_\alpha^2 \rangle}{6t} \tag{31}$$

where D_α is the diffusion coefficient of the particle of type α. Typical results are shown in Figure 2 for water in the CaF_2 and $CaCO_3$ mineral systems.[62] The increase of $\langle \mathbf{r}_\alpha^2 \rangle$ with t clearly shows that diffusion is occurring in the CaF_2 system. Calculation of the velocity auto-correlation function (VAF) and van Hove self-correlation function yields more detailed dynamical information that may be compared with the results

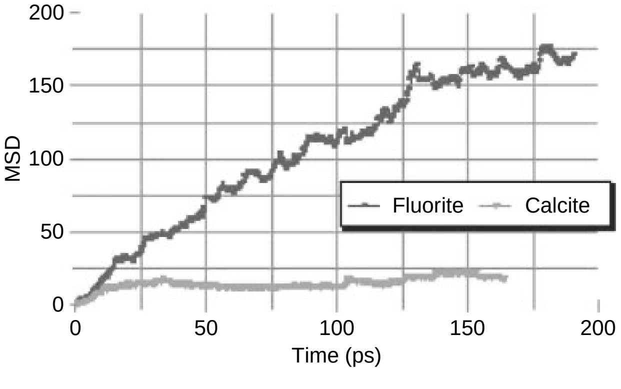

Figure 2 Mean square displacement versus time for H_2O at CaF_2 and $CaCO_3$ surfaces at 300 K

of inelastic neutron scattering studies. For further discussion, we refer to References 57, 61 and 63.

Despite its evident power, the technique has, however, serious limitations, the principal of which are as follows:

1. Even with modern supercomputers it is rarely possible to run simulations for longer than 10 ns. If the probabilities of the events of interest (e.g. a defect jump) are low in a period of this length, then the simulation may be of little value. Thus, in practice, with currently available computer power, diffusion can only be studied for values of the diffusion coefficient $D > 10^{-9}\,\mathrm{cm}^2\,s^{-1}$.
2. Inclusion of polarizability in the potential greatly increases the computational requirements for the simulation. For this reason, most MD simulations performed do not include this term, which may be a serious omission for ionic solids.
3. The calculation of thermodynamic properties is difficult using MD techniques. The case of defects is especially problematic and both formation and migration energies are far more effectively calculated using static simulation techniques.
4. In conventional MD, employing PBC, there are no surface effects. Thus, any process involving the generation or removal of species from the surface cannot be simulated. An example is provided by the generation of Schotty disorder in crystals, which requires displacement of ions to the surface. This cannot be simulated by conventional MD studies.

Despite these limitations, the scope of MD techniques is expanding rapidly mainly owing to the rapid growth in computer power, especially the development of parallel architecture systems. It is now possible to carry out routinely, simulations on several thousand particles, for periods of ∼100 ps. Moreover, the scope of the method has been expanded by a number of more specialized developments. The two following examples are of particular importance in the study of inorganic materials.

Constant Pressure MD. The conventional MD technique uses a fixed size for the simulation box, that is, the calculation is performed under constant volume conditions. Using methods developed by Parrinello and Rahman[64] and by Berendsen and coworkers,[65] it is now possible to undertake constant pressure simulations by allowing cell dimensions to vary during the simulation. Detailed discussions are given in Reference 61. The most obvious field of application of this technique is to the study of phase transitions, and useful applications have been reported to the study of melting and glass formation as discussed below.

MD Simulations of Glasses. Increasing use is being made of MD techniques to generate structural models for amorphous solids. The procedure used is simple: a molten system is generated and the simulation is then rapidly cooled to below the glass transition temperature. RDFs and other properties of the resulting simulated glass may then be calculated.

2.1.13 Monte Carlo Techniques

Like MD, Monte Carlo (MC) methods involve the generation of successive configurations of an ensemble of particles representing the system studied. However, unlike MD, there is no temporal connection between the different configurations. The aim of the technique is to generate a sufficient and representative number of configurations from which ensemble averages may then be calculated with acceptable accuracy.

A central feature of the procedure is the choice of a weighting scheme whereby configurations are included according to their probability. In particular, it is desirable to weight the probability of including a configuration according to its Boltzmann factor:

$$\mathbf{W} = \exp\left(\frac{-\Delta E}{kT}\right), \qquad (32)$$

where ΔE is the change in energy of the configuration. This may be achieved by an ingenious and simple procedure known as the Metropolis sampling method. Here the Boltzmann factor for a given configuration is calculated and compared with a random number P, which is generated in the range $0-1$. If $\mathbf{W} < P$, then the configuration is rejected, but if $\mathbf{W} > P$ it is accepted. It will be seen that, over a large number of configurations, the procedure weights the probability of their inclusion according to their Boltzmann factor. It necessarily involves the generation of configurations that, after evaluation of their energy, are rejected. A number of procedures are available to increase the efficiency of the method by reducing the number of rejected configurations.[61]

The manner in which the sequence of configurations is generated depends on the system studied. For example, in a collection of atoms, a given particle may be selected at random and displaced by a small amount. For molecules, displacement and rotation may be involved. Indeed, care must be exercised in generating configurations in order to maximize the sampling efficiency. One special type of system concerns vacancy disordered compounds in which we are interested in diffusional properties. Here the vacancies are selected at random as is their direction. The Boltzmann factor for the jump is then calculated (or obtained from a ‘look-up’ table) and compared with the random number P following the normal Metropolis procedure. Such methods have been extensively used by Murch and coworkers to study diffusion in alloys.[66] An application to oxygen diffusion in the superionic oxygen conductor $\mathrm{Y/CeO_2}$ was reported by Murray and coworkers.[67]

We note that a MC ‘move’ can consist of the insertion or deletion of a particle, to so-called Grand Canonical Monte Carlo technique, for detailed discussion of which and of other technical aspects of MC simulation we refer to Reference 61.

We also note an important class of applications that uses the MC method to explore complex energy surfaces and to find low energy regions, from which minima can subsequently be located by standard minimization procedures. *Simulated annealing* methods have been used with great effect in generating crystal structures from initial random configurations of atoms or ions. The ‘energy term’ in simulating annealing calculations may take a variety of forms. It is commonly a simple ‘cost function’ based on coordination numbers and connectivity. Lattice energies, calculated from Born model potentials, may of course be employed, but this procedure becomes computationally expensive. It should, however, be noted that simulated annealing procedures employing energies calculated by electronic structure techniques are becoming feasible. However, in practice it would seem to be more computationally efficient to use simpler procedures to calculate the energy (or cost function), and to refine the approximate configuration generated by simulated annealing by electronic structure methods when the use of such methods is needed.

The ‘temperature’ used in a simulated annealing study is normally a parameter with no real physical significance. Higher temperatures will result in the acceptance of an increasing number of high energy configurations, allowing the exploration of a wider range of the energy surface but, of course, at increased computational cost. In practice, the simulation usually starts with a high ‘temperature’, which is then reduced as the lower energy regions of the surface are identified. Simulated annealing like MC methods may also be adapted to the analysis of experimental data. In this case, the ‘energy term’ becomes the deviation between the calculated data (e.g. the calculated X-ray intensity versus scattering angle for a structural model) and experiment. Such techniques are described as ‘Reverse Monte Carlo’.**[68]**

2.2 Electronic Structure Techniques

The last 15 years has seen an enormous expansion in the applicability of electronic structure methods to problems in solid-state chemistry, and the techniques are now applied in an increasingly routine manner to complex systems. This growth owes more to developments in hardware, algorithms, and detailed aspects of the methodology (such as the functionals used in DFT as discussed below) than to any fundamental developments in theory. As such, it is typical of the way in which much of contemporary computational science has developed.

As we have noted, electronic structure techniques attempt to solve the Schrödinger equation. The traditional approach in quantum chemistry has been to use the Hartree Fock (HF) approximation, in which a determinantal, antisymmetrized wave function is optimized in accordance with the variational principle. The wave function is normally written as an expansion of atomic orbitals (the LCAO approximation). A major weakness of the HF method is that in its single determinantal form it omits electron correlation effects, which can be recovered at considerable expense by perturbation or multiconfigurational methods. The approach does have the advantage of accurately estimating exchange effects (within the limitations of the basis set used to express the wave function). Moreover, the approximations in the method are well defined and the procedures needed to progress to improved accuracy are well defined.

The alternative approach, which is now widely applied, is based on density functional theory (DFT) pioneered by Kohn, Hohenberg and Sham.**[69,70]** In DFT, the electron density has prime of place. Hohenberg and Kohn showed that the ground state energy of a system is a unique functional of the electron density. The total energy (E_T) is written as:

$$E_T = E^{KE}(\rho) + E^{C}(\rho) + E^{EC}(\rho) + E_{nn} \qquad (33)$$

Where the first term is the kinetic energy, the second term, the ‘classical Coulomb repulsion’ and the third, the ‘exchange – correlation’ energy; E_{nn} is the nuclear–nuclear repulsion energy. Evaluation of the first two terms is relatively straightforward. There is, however, no simple way of evaluating the exchange – correlation energy and in practice a range of approximate functionals are employed, as discussed below. Once this functional has been defined, the procedure is relatively straightforward. The variational principle is invoked and the energy minimized with respect to ρ. In practice, this is achieved using the Kohn Sham equations, which use a wave function to calculate ρ; the wavefunction is then optimized self – consistently in a manner akin to that used in HF theory.

Good recent accounts of both HF and DFT techniques are given by Abarenkov**[71]** and Harrison.**[72]** Here we confine our discussion to a number of general remarks, followed by some specific considerations for applications to solids.

General Considerations

1. *Electronic structure and interatomic potential methods.* There is no inherent superiority of electronic structure techniques. They do, of course, provide information that is inaccessible to interatomic potential methods, but they cannot explore systems of the size or timescales that are frequently needed. IP techniques provide accurate information on structure and transport properties and are often the appropriate technique, even when electronic structure methods are applicable. The simple and obvious guideline is that the appropriate technique is used for the particular problem at hand.
2. *HF and DFT methods.* DFT techniques have enjoyed considerable success in recent years and have been applied to a wide range of systems. However, in the present context, the following points should be made:
    (a) DFT is an approximate method, and although it is not semiempirical in the sense that it includes variable parameters that have been fitted to experimental data, the exchange correlation functionals have

commonly been evaluated by comparison with experimental data.

(b) DFT is a ground state theory. Although it may sometimes be used to make useful estimates of excited state properties (e.g. band gaps), such applications are necessarily limited and approximate.

(c) There is a continuing role for HF theory. The accurate calculation of exchange energies is a particular merit of the approach as is the ability, referred to above, to improve systematically the accuracy of the calculations.

Specific Issues for Solid-state Calculations

Again we refer to the articles of Harrison[72] and Abarenkov[71] for details; but here we note the following:

1. *Use of PBC techniques.* These are obviously the appropriate method for modeling crystalline solids. Moreover, there is an extensive range of high quality software for electronic structure studies based on PBC. The use of the approach becomes more problematic when investigating localized states (e.g. defects, impurities, and sorbed molecules.) In such calculations, the usual procedure is to place the localized state in the centre of a 'supercell' (which may comprise several basic unit cells) to which PBC are applied. The approach has the advantage of being straightforward; but, necessarily, interactions between defects and impurities in neighboring cells are included. This is often not a serious problem and indeed the magnitude of the interactions can be estimated. However if we are to apply the methods to studying, for example, problems in catalysis involving molecules adsorbed at active sites, then interactions between species in neighboring cells may become problematic, in which cases one of the alternative approaches outlined below should be used.
2. *Use of the molecular cluster approximation*. This is essentially the other extreme from the PBC approach – in which the region of interest is represented by a finite cluster, which, depending on the nature of the bonding, may be terminated with hydrogen atoms. The approach is clearly crude, as no long-range effects of the surrounding solid are included, but it is a useful method if the chemistry is predominantly local, and allows use of the wide range of software available for molecular quantum mechanical calculations.
3. *Use of embedding techniques.* With these, we attempt to remedy some of the deficiencies of the cluster method by including an approximate representation of the surrounding lattice using interatomic potential methods. There are several variants of the approach, but if implemented properly, such methods can overcome some of the difficulties of PBC methods, for example, catalytic reactions. A recent example of the use of this method is given in Section 3.3.

3 APPLICATIONS

In this section, we describe some topical recent examples of the applications of modeling techniques in solid-state chemistry. Our account cannot be detailed, but we aim to give an impression of the range of applicability of these techniques.

3.1 Prediction of the Structures of Microporous Materials

Microporous materials have been widely investigated over the last 50 years owing to their extensive range of applications in catalysis, gas separation, and ion exchange. Zeolites (originally observed as minerals, but now extensively available as synthetic materials) are all silica or silicate materials, based on fully corner shared networks of SiO_4 and AlO_4 tetrahedra, but with structures that contain channels pores and voids of molecular dimensions. Pore sizes are typically in the range 5–15 A. The aluminosilicate materials contain exchangeable cations, while the microporous structures give rise to the applications in molecular sieving and sorption. Exchange of protons into the materials creates acid sites that promote catalytic reactions including cracking, isomerization, and hydrocarbon synthesis; while metal ions in both framework and extra-framework locations can act as active sites for partial oxidation reactions.

Modeling techniques have been applied extensively and successfully to the study of microporous materials (see e.g. Reference 1). Furthermore, there have been a number of successful applications of minimization techniques to the accurate and indeed to the predictive modeling of microporous structures. Here we highlight a recent significant development, that is, the prediction of new hypothetical structures.

There have been many attempts to predict new microporous structures. Most of them have relied on the fact that the very definition of these materials is based on geometry, rather than on precise chemical composition, occurrence, or function. In order to be considered as a zeolite, or zeolite-type material (zeotype), a mineral or synthetic material must possess a three-dimensional four-connected inorganic framework, that is, a framework consisting of tetrahedra that are all corner-sharing. There is an additional criterion that the framework should enclose pores or cavities that are able to accommodate sorbed molecules or exchangeable cations, which leads to the exclusion of denser phases. Topologically, the zeolite frameworks may thus be considered as four-connected nets, in which each vertex is connected to its four closest neighbors. So far 139 zeolite framework types are known, either from the structures of natural minerals or from synthetically produced inorganic materials. In enumerating microporous structures, a number of fruitful approaches have been developed. Some have involved the decomposition of existing structures into their various structural subunits, and then recombining these in such ways as to generate novel frameworks. Methods that involve combinatorial, or systematic, searches of phase space have also been successfully deployed Recently, an approach based on mathematical tiling theory has also been reported.[73]

It was established that there are exactly 9, 117, and 926 topological types of four-connected uninodal (i.e. containing one topologically distinct type of vertex), binodal and trinodal networks, respectively, derived from simple tilings (tilings with vertex figures that are tetrahedra), and at least 145 additional uninodal networks derived from quasi-simple tilings (the vertex figures of which are derived from tetrahedra, but contain double edges). In principle, the tiling approach offers a complete solution to the problem of framework enumeration, although the number of possible nets is infinite.

Potentially therefore we may be able to generate an unlimited number of possible zeolitic frameworks. Of these, only a portion is likely to be of interest as having desirable properties, with an even smaller fraction being amenable to synthesis in any given composition. It is this last problem, the feasibility of hypothetical frameworks, which is the key question in any analysis of such structures. The answer is not a simple one, since the factors that govern the synthesis of such materials are not fully understood. Zeolites are metastable materials, as shown by the calculated lattice energies reported in Table 1. Aside from this thermodynamic constraint, the precise identity of the phase or phases formed during hydrothermal synthesis is said to be under ‘kinetic control’, although there is increasing sophistication in targeting certain types of framework using various templating methods, fluoride media, and other synthesis parameters. Additionally, certain structural motifs are more likely to formed within certain compositions, for example, double four rings in germanates, three rings in beryllium-containing compounds, and so on. A full characterization of any hypothetical zeolite must therefore include an analysis of framework topology and of the types of building unit present, as well as some estimate of the thermodynamic stability of the framework. Using an appropriate potential model, lattice energy minimization can, as shown above, provide a very good measure of this stability and well as optimizing structures to a high degree of accuracy.

Table 1 Relative energies (per mole) of microporous siliceous structures with respect to Quartz[39]

Structure	Energy (kJ mol^{-1})
Silicalite	11.2
Mordenite	20.52
Faujasite	21.4

In the method adopted by Foster *et al.*,[74] networks derived from tiling theory were first transformed into ‘virtual zeolites’ of composition SiO_2 by placing silicon atoms at the vertices of the nets, and bridging oxygens at the midpoints of connecting edges. The structures were then refined using the geometry-based distance least squares (DLS) procedure, before final optimization by lattice energy minimization. Among the 150 or so uninodal structures examined, all 18 known uninodal zeolite frameworks were found. Moreover, most of the unknown frameworks had been described by previous authors; in fact, there is a considerable degree of overlap between sets of uninodal structures generated by different methods. Most of the binodal and trinodal structures, however, are completely new. Using simulated lattice energy as an initial measure of feasibility, a number of the more interesting structures are illustrated in Figure 3. The challenge is now to synthesize these structures.

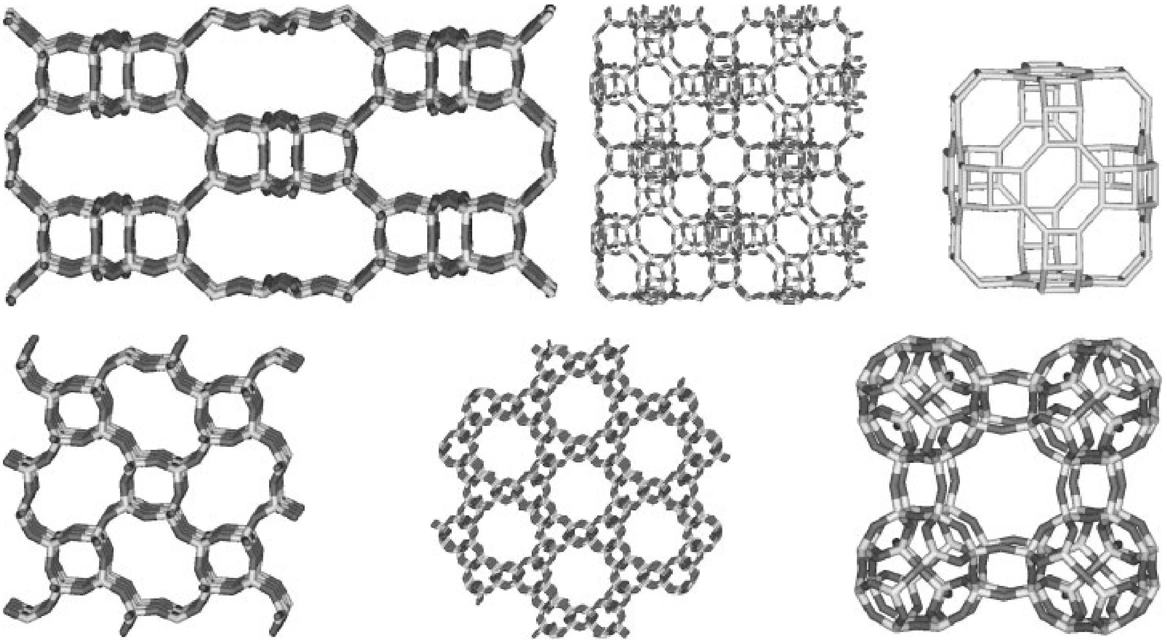

Figure 3 Illustrations of feasible uninodal zeolite structures generated by tiling theory and modelled using lattice energy minimization

3.2 Nanocluster Structures in ZnS

Our next example is an intriguing case study in cluster chemistry. As part of an extensive study aimed at identifying the structures of the critical growth nuclei in the growth of ZnS crystals Spano, Hamad, and Catlow[75,76] have identified a whole series of stable open cluster structures for $(ZnS)_n$ clusters with n ranging from 1 to 80. They have employed simulated annealing and minimization techniques using interatomic potentials but with critical structures also being modelled by DFT electronic structure methods (the results of which validate the interatomic potential-based simulations). The cluster structures have quite different topologies from bulk ZnS. A particularly interesting example is shown in Figure 4. It is an onion-like cluster with an inner core and outer shell. Work is in progress aimed at detecting these structures experimentally.

3.3 Reaction Mechanisms on the Surfaces of Zinc Oxide

A large quantity of methanol, in excess of 22 million tonnes worldwide, is produced annually using the multicomponent $Cu/ZnO/Al_2O_3$ catalyst and feed gas, $CO_2/CO/H_2$. Many experimental studies of this process have been performed but without any definite reaction mechanism for the production of methanol being established. However, it has long been acknowledged that the important rate-determining step is the hydrogenation of adsorbed intermediates, for example, the formate ion, at the active sites. Proposed mechanisms for methanol synthesis require the chemisorption of CO_2 before hydrogenation via formate to methanol. Theoretical studies of these systems have been hampered by the difficulty of modeling the catalytically active polar surfaces of ZnO, as well as the problems associated with the restrictions on the size of the system that can be modelled.

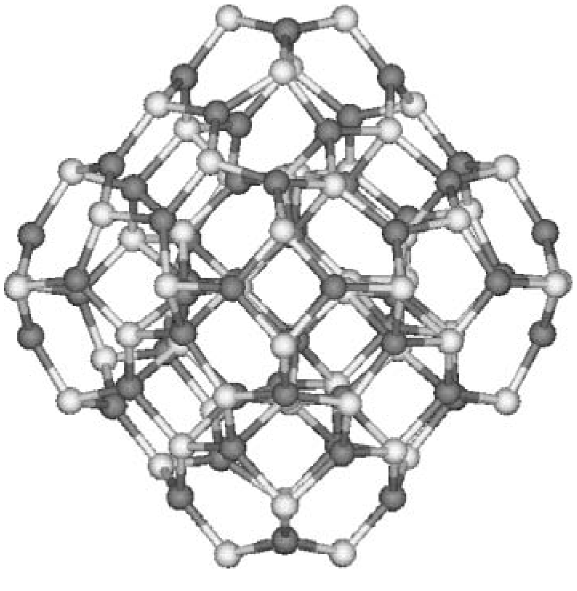

Figure 4 Predicted onion-like structure for $(ZnS)_{60}$

The nature of the active site for sorption/catalysis of CO_2 still remains unclear; as a test system or model catalyst, it has been proposed to use clean oxygen terminated surfaces of zincite. Temperature programmed desorption (TPD) studies have shown that the processes that occur at that particular surface are analogous to those on the industrial $Cu/ZnO/Al_2O_3$ catalyst.[77,78] In this study, we have therefore concentrated on the polar $(000\bar{1})$ oxygen terminated surface. In a given sample, the polar character of the surface necessitates a charge transfer between opposing polar surfaces, in order to quench surface induced polarization of the material, which may be achieved in zincite by abstracting ca. 25% of oxygen ions from the surface layer, thus creating *vacant oxygen interstitial surface sites*. The presence of such sites has been confirmed by optical and ESR spectroscopies;[79–81] they have, moreover, been suggested as the active catalytic sites for methanol synthesis and are therefore the focus of the investigation in the present article.

Recent work of French *et al.*[82] used novel solid-state embedding techniques in order to study important methanol precursors, including carbon dioxide, formate, and methoxy ions. Their study provides insight into the mechanism of methanol synthesis by calculating binding energies, bond lengths, and angles of these and related species. The hybrid approach implemented and applied in this work follows molecular embedded cluster methods developed to treat point defects and related localized states in ionic materials.[83–87]

At the heart of embedding approaches is a definition of a reference system and a single localized state, which causes only minor long-range perturbation of the reference system. In order to characterize the structural properties and interactions in the reference system, it is desirable to split it into structural elements. Zincite, as with many other important metal oxide catalysts, is a polar material; and many physical properties of these materials can be described using an ionic model. In this model, the strong long-range interactions are accounted for by Coulombic forces between nearly spherical ions. These ions, particularly negatively charged anions, are highly polarizable species. Upon perturbation of the reference system by a localized defect, two major effects are witnessed: (1) dramatic short-range effects (e.g. charge transfer and bond breaking) and (2) long-range polarization of electron groups owing to the field of the defect. Therefore, the model can be treated at two levels of approximation. In the present case, the short-range effects were dealt with fully ab initio, by DFT, while the long-range polarization effects were included through the use of the shell model of Dick and Overhauser.[10]

This methodology (details of which are given in Ref. 82) has been implemented within ChemShell, which is a computational chemistry environment, based on the Tcl programming language.[88] A DFT treatment, as implemented in the GAMESS-UK code,[89] was used. The study employed the B97-1[90] exchange correlation functional and TZV2P basis set on O and Zn, which has been reoptimized for the ionic state of ZnO, along with the standard 6-311 + (2p2d) basis set on all atoms of the adsorbates and a medium quality integration mesh.[89] In this work, interactions in region 2 and interface were dealt with using our recently developed atomistic potentials[91] within the GULP code.[38]

Detailed models of the $(000\bar{1})$–O terminated polar surfaces were investigated using interatomic potentials within the two-dimensional periodic slab model realized within the MARVIN code.[92] Two typical local environments were identified as terrace termination and interstitial vacancy sites; the latter has been used as the active site for the majority of calculations, as illustrated in Figure 5. The atoms highlighted in the figure indicate the surface embedded quantum region. For the calculations reported, region 1 consists of 12 atoms, the interface has 13 Zn sites, while region 2 comprises approximately 3000 atoms and 250 terminating point charges.

A probable reaction sequence for the conversion of the feed gas to methanol has been summarized by Chinchen[93] (Figure 6), where the gas phase and adsorbate species are indicated by (g) and (a) respectively. Reaction 4 is a complex process that includes multiple hydrogenation steps, which we have considered separately. The resulting species, which were not considered by Chinchen and others, were found to be stable, although they may possibly be transient and short lived.

The main catalytically active site that can facilitate the formation of anionic adsorbates is the *oxygen interstitial* site, as described above and illustrated in Figure 5. This site is able to trap an electron and thus adsorption can occur in two different ways; (1) neutral adsorbates approach the active site at which an electron is trapped, to form a surface anionic species and (2) transfer of an electron to the neutral active site occurs simultaneously with the adsorption of neutral adsorbates.

The proposed catalytic cycle is summarized in Figure 7, starting with the adsorption of CO_2 and H_2, CO_2 upon

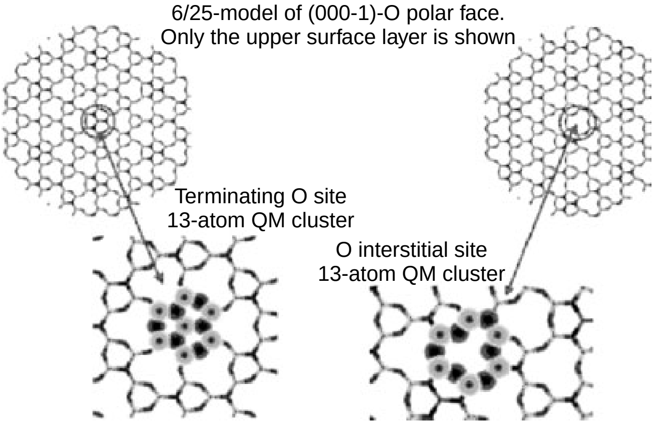

Figure 5 QM regions used for modeling of vacant oxygen interstitial surface sites. Only the upper surface layer is shown

$H_2(g) \rightarrow 2H(a)$
$CO_2(g) \rightarrow CO_2(a)$
$CO_2(a) + H(a) \rightarrow HCO_2(a)$
$HCO_2(a) + 2H(a) \rightarrow CH_3O(a) + O(a)$
$CH_3O(a) + H(a) \rightarrow CH_3OH(g)$
$CO(g) + O(a) \rightarrow CO_2(g)$
$H_2(g) + O(a) \rightarrow H_2O(g)$

Figure 6 Catalytic cycle; all reactants geometries are obtained by energy minimization of embedded clusters

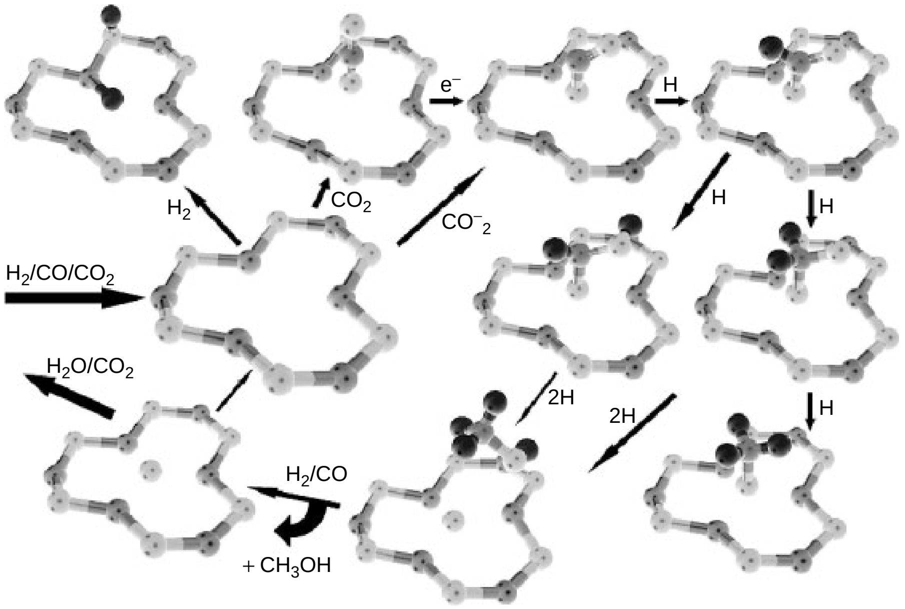

Figure 7 Calculated reaction energy profile for methanol synthesis over ZnO

adsorption in a neutral interstial site retains the linear structure exhibited in the gas phase. Upon adding an electron the neutral CO_2 molecule bends and the extraelectron populates an antibonding level, which leads to a rearrangement from an sp to an sp^2 hybridized configuration. The interaction with the surface stabilizes the radical $CO_2{}^-$ species.

The reaction then proceeds via the hydrogenation of the adsorbed $CO_2{}^-$, by surface hydrogen to the formate ion. The geometry resulting from the calculations is shown in Figure 7. The adsorption of hydrogen leads to a closed shell species. Further hydrogenation can proceed either through the formation of $H_2CO_2{}^-$ or $HCOOH^-$ as shown in Figure 7. TPD data do not detect these species, which suggests a short lifetime and therefore high reactivity. Computational techniques allow us to differentiate and investigate these different scenarios. Further hydrogenation and interactions of the resulting species with the surface and possible surface defects lead to a large variety of possible intermediates. We show examples of a methoxy ion (CH_3O^-) chemisorbed to the surface and physisorbed methanol. To complete the catalytic cycle, methanol is removed from the surface and the active site is recycled by desorption of carbon dioxide and water.

4 SUMMARY

Computer modeling techniques are now having a substantial impact on a broad range of problems in solid-state chemistry. They provide insight into structures and mechanisms at the atomic level and have an increasingly predictive role. Advances in techniques, algorithms, and computer power offer an exciting future with a great expansion in the predictive and explanatory capabilities of the methods in the future.

5 REFERENCES

1. C. R. A. Catlow, R. A. van Santen, and B. Smit, ‘Modelling of Microporous Materials’, Academic Press, London, 2003.
2. L. Minervini and R. W. Grimes, *J. Phys. Chem. Solids*, 1999, **60**, 235.
3. D. Alfe, G. D. Price, and M. J. Gillan, *Phys. Rev. B*, 2002, **65**, 165118.
4. A. M. Stoneham and J. H. Harding, *Annu. Rev. Phys. Chem.*, 1986, **37**, 37, 53.
5. M. J. Sanders, M. Leslie, and C. R. A. Catlow, *J. Chem. Soc. Chem. Commun.*, 1984, 1271.
6. B. M. Axilrod and E. Teller, *J. Chem. Phys.*, 1943, **11**, 299.
7. W. J. Meath and R. A. Aziz, *Mol. Phys.*, 1984, **52**, 225.
8. R. C. Baetzold, C. R. A. Catlow, J. Corish, F. M. Healy, P. W. M. Jacobs, M. Leslie, and Y. Tan, *J. Phys. Chem. Solids*, 1989, **50**, 791.
9. C. R. A. Catlow, Computer Modelling of Solids, in ‘Lecture Notes in Physics’, eds. C. R. A. Catlow and W. C. Mackrodt, Springer, Berlin, 1982, Vol. 166.
10. B. G. Dick and A. W. Overhauser, *Phys. Rev.*, 1958, **112**, 90.
11. A. N. Cormack, G. V. Lewis, S. C. Parker, and C. R. A. Catlow, *J. Phys. Chem. Solids*, 1988, **49**, 53.
12. S. C. Parker and G. D. Price, *Phys. Chem. Miner.*, 1984, **10**, 209.
13. G. D. Price, A. Wall, and S. C. Parker, *Philos. Trans. R. Soc. London*, 1989, **A328**, 391.
14. D. E. Williams, *Top. Curr. Phys.*, 1981, **26**, 3.
15. A. K. Kiselev, A. A. Lopatkin, and A. A. Shulga, *Zeolites*, 1985, **5**, 261.
16. C. R. A. Catlow, K. M. Diller, and M. J. Norgett, *J. Phys. C.*, 1977, **10**, 1395.
17. G. V. Lewis and C. R. A. Catlow, *J. Phys. C.*, 1985, **18**, 1149.
18. C. R. A. Catlow, C. M. Freemen, M. S. Islam, R. A. Jackson, M. Leslie, and S. M. Tomlinson, *Philos. Mag. A*, 1988, **58**, 123.
19. P. T. Wedepohl, *Proc. Phys. Soc.*, 1967, **92**, 79.
20. R. G. Gordon and Y. S. Kim, *J. Chem. Phys.*, 1972, **56**, 3122.
21. W. C. Mackrodt and R. F. Stewart, *J. Phys. C: Condens. Matter*, 1979, **12**, 431.
22. W. C. Mackrodt and R. F. Stewart, *J. Phys. C: Condens. Matter*, 1979, **12**, 5015.
23. A. M. Stoneham, UKAEA Report, AERE-R9598, 1981.
24. R. E. Cohen, L. L. Boyer, and M. J. Mehl, *Phys. Rev. B*, 1987, **35**, 5749.
25. C. R. A. Catlow, in ‘Solid State Chemistry: Techniques’, eds. A. K. Cheetham and P. Day, Oxford University Press, 1986.
26. W. C. Mackrodt, R. F. Stewart, J. C. Cambell, and I. H. Hillier, *J. Phys. (Paris)*, 1980, **41**, C764.
27. J. D. Gale, C. R. A. Catlow, and W. C. Mackrodt, *Modell. Simul. Mater. Sci. Eng.*, 1992, **1**, 73.
28. N. Harrison and M. Leslie, *Mol. Simul.*, 1992, **9**, 171.
29. K. P. Schroder and J. Sauer, *J. Phys. Chem.*, 1996, **100**, 11043.
30. B. W. H. van Beest, G. J. Kramer, and R. A. van Santen, *Phys. Rev. Lett.*, 1990, **60**, 1955.
31. J. Purton, R. Jones, M. Heggie, S. Oberg, and C. R. A. Catlow, *Phys. Chem. Miner.*, 1992, **18**, 389.
32. B. Johnson and B. Nelendar, *Chem. Phys.*, 1977, **25**, 263.
33. J. E. Mayer, *J. Chem. Phys.*, 1933, **1**, 270.
34. N. C. Pyper, in ‘Advances in Solid State Chemistry’, ed. C. R. A. Catlow, JAI Press, 1992, Vol II.
35. J. H. Harding and A. M. Stoneham, *J. Phys. C: Condens. Matter*, 1984, **17**, 3401.
36. S. C. Parker, C. R. A. Catlow, and A. N. Cormack, *Acta Crystallogr. B*, 1984, **40**, 200.

37. M. Leslie – Daresbury Laboratory Report, Warrington, WA4 4AD.
38. J. D. Gale, *J. Chem. Soc., Faraday Trans.*, 1997, **93**, 629.
39. G. Ooms, R. A. van Santen, C. J. J. den Ouden, R. A. Jackson, and C. R. A. Catlow, *J. Phys. C.*, 1988, **92**, 4462.
40. N. J. Henson, A. K. Cheetham, and J. D. Gale, *Chem. Mater.*, 1994, **6**, 1647.
41. W. Cochran, *Crit. Rev. Solid Sci.*, 1971, **2**, 1.
42. S. C. Parker and G. D. Price, in ‘Advances in Solid State Chemistry’, ed. C. R. A. Catlow, JAI Press, 1990, Vol I.
43. G. Filippini, C. M. Gramacciolli, M. Simonetta, and G. B. Suffritti, *Acta Crystallogr. A*, 1976, **32**, 259.
44. R. Fletcher and M. J. D. Powell, *Comput. J.*, 1963, **6**, 16.
45. M. J. Norgett and R. Fletcher, *J. Phys. C.: Condens. Matter*, 1970, **3**, L190.
46. C. R. A. Catlow ed., ‘Computer Modelling in Inorganic Crystallography’, Academic Press, London, 1997.
47. A. N. Cormack, R. M. Jones, P. W. Tasker, and C. R. A. Catlow, *J. Solid State Chem.*, 1982, **44**, 174.
48. M. Leslie and M. J. Gillan, *J. Phys. C: Condens. Matter*, 1985, **18**, 973.
49. N. L. Allan, W. C. Mackrodt, and M. Leslie, in ‘Advances in Ceramics’, eds. C. R. A. Catlow and W. C. Mackrodt, The American Ceramic Society, Westerville, Ohio, 1987, Vol. 23, p. 4257.
50. J. H. Harding, *Physica B*, 1985, **131**, 13.
51. M. J. Norgett, UKAEA Report, R7650, 1974.
52. C. R. A. Catlow, R. James, and W. C. Mackrodt, *Phys. Rev. B: Condens. Matter*, 1982, **25**, 1006.
53. M. Leslie, SERC Daresbury Laboratory Report, Rep. DL-SCI-TM31T, 1982.
54. M. J. Gillan and P. W. M. Jacobs, *Phys. Rev. B*, 1983, **28**, 759.
55. J. H. Harding, *Rep. Prog. Phys.*, 1990, **53**, 1403.
56. J. H. Harding and A. M. Stoneham, *Philos. Mag B.*, 1981, **43**, 705.
57. C. R. A. Catlow, *Annu. Rev. Mater. Sci.*, 1986, **16**, 517.
58. C. R. A. Catlow, J. Corish, P. W. M. Jacobs, and A. B. Lidiard, *J. Phys. C.*, 1981, **14**, L121.
59. R. A. Jackson, A. D. Murray, J. H. Harding, and C. R. A. Catlow, *Philos. Mag. A*, 1986, **53**, 27.
60. C. R. A. Catlow, *Solid State Ionics*, 1983, **8**, 89.
61. M. P. Allen and D. J. Tildesley, ‘Computer Simulation of Liquids’, Oxford University Press, 1987.
62. N. H. de Leeuw and S. C. Parker, *Mol. Simul.*, 2000, **24**, 71.
63. C. R. A. Catlow, *Solid State Ionics*, 1992, **53**, 955.
64. M. Parrinello and A. Rahman, *J. Chem. Phys.*, 1984, **80**, 860.
65. H. J. C. Berendsen, J. P. M. Postma, W. F. van Gunsteren, A. D. Nola, and J. R. Haak, *J. Chem. Phys.*, 1984, **81**, 3684.
66. G. E. Murch, *Philos. Mag. A*, 1982, **46**, 575.
67. A. D. Murray, G. E. Murch, and C. R. A. Catlow, *Solid State Ionics*, 1986, **18–19**, 196.
68. D. A. Keen and R. L. McGreevy, *Nature*, 1990, **344**, 423.
69. P. Hohenberg and W. Kohn, *Phys. Rev. B*, 1964, **136**, 864.
70. W. Kohn and L. J. Sham, *Phys. Rev. A*, 1956, 1133.
71. I. V. Abarenkov, in ‘Computational Materials Science’, Nato Science Series III, eds. C. R. A. Catlow and E. Kotomin, Kluwer, Amsterdam, 2003, Vol 187.
72. N. M. Harrison, in ‘Computational Materials Science’, Nato Science Series III, eds. C. R. A. Catlow and E. Kotomin, Kluwer, Amsterdam, 2003, Vol 187.
73. O. Delgado Friedrichs, A. W. M. Dress, D. H. Huson, J. Klinowski, and A. L. Mackay, *Nature*, **400**, 644.
74. M. D. Foster, A. Simpler, R. G. Bell, O. Delgado Friedrichs, F. A. Almeida Paz, and J. Klinowski, *Nature Mat.*, 2004, **3**, 234.
75. E. Spano, S. Hamad, and C. R. A. Catlow, *J. Phys. Chem. B*, 2003, **107**, 10337.
76. E. Spano, S. Hamad, and C. R. A. Catlow, *Chem. Commun.*, 2004, 864.
77. M. Bowker, H. Houghton, and K. C. Waugh, *J. Chem. Soc., Faraday Trans. 1*, 1981, **77**, 3023.
78. V. E. Heinrich and P. A. Cox, ‘The Surface Science of Metal Oxides’, Cambridge University Press, Cambridge, MA, 1996.
79. K. Vanheusden, C. H. Seager, W. L. Warren, D. R. Tallant, J. Caruso, M. J. Hampden-Smith, and T. T. Kodas, *J. Lumin.*, 1997, **75**, 11.
80. A. R. Gonzalez-Elipe and J. Soria, *J. Chem. Soc., Faraday Trans. 1*, 1988, **84**, 3961.
81. B. Yu, C. Zhu, F. Gan, and Y. Huang, *Mater. Lett.*, 1998, **33**, 247.
82. S. A. French, A. A. Sokol, S. T. Bromley, C. R. A. Catlow, S. C. Rogers, F. King, and P. Sherwood, *Angew. Chem., Int. Ed.*, 2001, **40**, 4437.
83. J. H. Harding, A. H. Harker, P. B. Keegstra, R. Pandey, J. M. Vail, and C. Woodward, *Physica B*, 1985, **131**, 151.
84. A. L. Shluger, E. A. Kotomin, and L. N. Kantorovich, *J. Phys. C*, 1986, **19**, 4183.
85. Z. Barandiarán and L. Seijo, *J. Chem. Phys.*, 1988, **89**, 5739.
86. M. N. Nygren, L. G. M. Petersson, Z. Barandiaran, and L. Seijo, *J. Chem. Phys.*, 1994, **100**, 2010.
87. P. V. Sushko, A. L. Shluger, and C. R. A. Catlow, *Surf. Sci.*, 2000, **450**, 153.
88. P. Sherwood, A. H. Devries, S. J. Collins, S. P. Greatbanks, N. A. Burton, M. A. Vincent, and I. H. Hillier, *Faraday Discuss.*, 1997, **106**, 79.
89. GAMESS-UK is a package of ab initio programs written by M. F. Guest, J. H. van Lenthe, J. Kendrick, K. Schoffel, and P. Sherwood, with contributions from R. D. Amos, R. J. Buenker, H. J. J. van Dam, M. Dupuis, N. C. Handy, I. H. Hillier, P. J. Knowles, V. Bonacic-Koutecky, W. von Niessen, R. J. Harrison, A. P. Rendell, V. R. Saunders,

A. J. Stone, D. J. Tozer, and A. H. de Vries. The package is derived from the original GAMESS code due to M. Dupuis, D. Spangler and J. Wendoloski, NRCC Software Catalog, Vol. 1, Program No. QG01 (GAMESS) 1980.

90. F. H. Hamprecht, A. J. Cohen, D. J. Tozer, and N. C. Handy, *J. Chem. Phys.*, 1998, **109**, 6264.

91. L. Whitmore, A. A. Sokol, and C. R. A. Catlow, *Surf. Sci.*, 2002, **498**, 135.

92. D. H. Gay and A. L. Rohl, *J. Chem. Soc., Faraday Trans.*, 1995, **91**, 92.

93. G. C. Chinchen, M. S. Spencer, K. C. Waugh, and D. A. Whan, *J. Chem. Soc., Faraday Trans. I*, 1987, **83**, 2193.

Acknowledgment

I am grateful to N.H. de Leeuw, A.A. Sokol, S.A. French, R.G. Bell, M. Foster and B. Slater for their contributions to the work described in this article. I wish to thank Accelrys for provision of software.

Stability Constants & their Determination

Alan T. Hutton & Peter W. Linder
University of Cape Town, Rondebosch, South Africa

Based in part on the article Stability Constants & Their Determination by Harry M. N. H. Irving which appeared in the Encyclopedia of Inorganic Chemistry, First Edition.

1 Introduction 1
2 Definition of Stability Constant 1
3 Experimental Approaches 3
4 Uses of Stability Constants 6
5 Stability Constants and Their Contribution to the Basic Ideas of Chemistry 6
6 Related Articles 7
7 References 7

1 INTRODUCTION

Stability constants, otherwise known as formation constants, constitute a particular type of equilibrium constant (*see Equilibrium Constant*), that is, for reactions in solution between metal ions or protons (*see Proton*) and ligands (*see Ligand*) or Lewis bases (*see Lewis Acids & Bases*) to form complexes. Following Rossotti and Rossotti,**[1]** we can define a complex as a species formed by the association of two or more simple species, each normally capable of independent existence. A broad definition of complex formation would not restrict this to a reaction between ions of opposite charge but would embrace association between any electron acceptor, such as the proton, H^+, a metal ion, M^{n+}, or other positively charged species, or even electron-deficient molecules (such as BF_3), and an electron donor such as water, ether, or thioether (*see* ***S-donor Ligands***); ammonia, pyridine, or other nitrogen base (*see* ***Ammonia & N-donor Ligands***); phosphine (*see* ***P-donor Ligands***) or arsine (*see* ***Arsenic: Organoarsenic Chemistry***); hydroxide (*see* ***Oxygen: Inorganic Chemistry***); cyanide (*see* ***Cyanide Complexes of the Transition Metals***); halide (*see* ***Chlorine, Bromine, Iodine, & Astatine: Inorganic Chemistry***); or pseudohalide (*see Pseudohalide*) ion. Since the emphasis in this article will be on the stability of metal complexes in aqueous solutions, important complexes such as $Ni(CO)_4$ or $Ni(PF_3)_4$, metal cyclopentadienyls (*see Cyclopentadienyl*), and many other organometallic compounds (*see Organometallic Complexes*) will not be considered.

Such reactions as $Ag^+ + NH_3 \rightleftharpoons Ag(NH_3)^+$, $Hg^{2+} + Cl^- \rightleftharpoons HgCl^+$, $H^+ + MeCO_2^- \rightleftharpoons MeCO_2H$, and $Cu^{2+} + NH_2CH_2CH_2NH_2 \rightleftharpoons Cu(NH_2CH_2CH_2NH_2)^{2+}$ are typical of 1:1 complex formation, while the reactions $Hg^{2+} + I^- \rightleftharpoons HgI^+$, $HgI^+ + I^- \rightleftharpoons HgI_2$, $HgI_2 + I^- \rightleftharpoons HgI_3^-$, and $HgI_3^- + I^- \rightleftharpoons HgI_4^{2-}$ show that complex formation between electron donors and electron acceptors can take place regardless of their formal charge. The successive coordination of three molecules of 1,10-phenanthroline (*see* ***Ammonia & N-donor Ligands***) with an iron(II) ion to give $Fe(phen)^{2+}$, $Fe(phen)_2^{2+}$, and $Fe(phen)_3^{2+}$ illustrates the buildup of a higher complex, ML_n, where the species M comprises the central atom to which the species L, usually referred to as the ligand (*see Ligand*), is bonded to form a coordination complex (*see Coordination Complexes*). We can generalize these reactions for simplicity as follows:

$$M + nL \rightleftharpoons ML_n \qquad (n = 1, 2, 3, \ldots) \tag{1}$$

(a) by omitting any reference to specific charges, and (b) by omitting any reference to the number of molecules of solvent that may be closely associated with each of the participating molecules in solution. The relevance of this omission will be more obvious in any later discussion of the chelate effect (*see Chelate Effect*). Polynuclear complexes, M_qL_p (for which $q > 1$, $p \geq 0$), are frequently encountered in aqueous solution chemistry, particularly in hydrolysis reactions where $L = OH^-$.**[1]**

This article considers the definition of stability constant, distinguishing between thermodynamic and stoichiometric constants as well as between stepwise and overall constants. Attention is given to methods of calculating stability constants from experimental data. This is followed by brief descriptions of experimental methods. Next, perspectives are presented on the uses of stability constants with special reference to determining chemical species distributions in systems that contain huge numbers of metal ion species, ligand species, and species of complex formed between them. Examples of such systems are biological, geological, and industrial fluids. Finally, a view is given of how studies of metal–ligand equilibria have contributed to some of the basic ideas of chemistry.

2 DEFINITION OF STABILITY CONSTANT

The activity of the complex species, ML_n, found in solution at a specified temperature (T) is related to the activities of the component species M and L by the equation

$$\{ML_n\} \rightleftharpoons {}^{T}\beta_n\{M\}\{L\}^n \tag{2}$$

where ${}^{T}\beta_n$ is the activity quotient or thermodynamic stability constant for the reaction

$$M + nL \rightleftharpoons ML_n \tag{3}$$

and is generally termed the *overall* (or *gross*) *stability constant*. Here and elsewhere the symbols [X], {X}, and γ_X refer to the concentration, the activity, and the activity coefficient, respectively, of the species X.

When the reaction can be represented as a series of discrete stages forming a sequence of complex ions

$$\mathrm{ML}_{n-1} + \mathrm{L} \rightleftharpoons \mathrm{ML}_n \qquad (4)$$

the activity quotient at each stage is defined by a thermodynamic stepwise stability constant, ${}^T\!K_n$ such that ${}^T\!\beta_0 = {}^T\!K_0 = 1$, ${}^T\!\beta_1 = {}^T\!K_1$, ${}^T\!\beta_2 = {}^T\!K_1 \times {}^T\!K_2$, and in general

$$^T\!\beta_n = {}^T\!K_1 \times {}^T\!K_2 \times {}^T\!K_3 \times \cdots \times {}^T\!K_n \qquad (5)$$

Ideally one would wish to measure the activities of all the reacting species in equation (4) but it is not possible to determine activities of single ionic species (at best, mean ionic activities may be determined in some cases) and the determination of activities of uncharged species is fraught with difficulties. However, modern experimental methods (see Section 3) can readily be applied to the determination of concentrations of at least some of the species concerned, leading to stoichiometric stability constants defined by

$$K_n = \frac{[\mathrm{ML}_n]}{[\mathrm{ML}_{n-1}][\mathrm{L}]} = {}^T\!K_n \times \left(\frac{\gamma_{\mathrm{ML}_{n-1}}\gamma_{\mathrm{L}}}{\gamma_{\mathrm{ML}}}\right) \qquad (6)$$

It must be emphasized that such stoichiometric stability constants are dependent, inter alia, upon the ionic strength of the solution, and, in reporting experimental results, the ionic strength of the experimental solutions should always be specified. Further, the numerical value of a stoichiometric constant will depend upon the units used, viz. mole fractions, molar, molal, millimole, and so on, and which is used should always be made clear.

If M_t and L_t are the total concentrations of metal and ligand in solution and [ML], [M], and [L] the concentrations of individual free species, then for the case where only one complex is present at equilibrium we can write:

$$\mathrm{M}_t = [\mathrm{M}] + [\mathrm{ML}] = \frac{\{\mathrm{M}\}}{\gamma_{\mathrm{M}}} + \frac{\{\mathrm{ML}\}}{\gamma_{\mathrm{ML}}} \qquad (7)$$

$$\mathrm{L}_t = [\mathrm{L}] + [\mathrm{ML}] = \frac{\{\mathrm{L}\}}{\gamma_{\mathrm{L}}} + \frac{\{\mathrm{ML}\}}{\gamma_{\mathrm{ML}}} \qquad (8)$$

Clearly, if M_t and L_t are known, it will only be necessary to obtain a value for one of the terms [M], [L], or [ML] to calculate the stoichiometric stability constant K_1.[2,3]

However, to calculate the thermodynamic stability constant, ${}^T\!K_1$, we would need reliable values for all the relevant activity coefficients. As indicated above, these are usually inaccessible directly from experimental measurements and, although some form of the Debye–Hückel equation has sometimes been used to calculate theoretical activity coefficients, certain difficulties often arise here, too. These difficulties and attempts to circumvent them are discussed by Linder, Torrington, and Williams.[4] Many workers have preferred to calculate thermodynamic stability constants by measuring K_n in solutions of different known ionic strengths and extrapolating to infinite dilution when all $\gamma \rightarrow 1$. The associated problems have been thoroughly discussed.[1,2,4,5]

A common procedure is to carry out all measurements in a medium of constant ionic strength, I, where, as Brønsted showed as early as 1927, 'small changes in the concentration of the solute have a negligible effect on its activity coefficients, provided that its concentration is never comparable to that of the 'background salt'.' Clearly the background salt must not form complexes with any of the ions involved in the complex formation being measured (*see Noncoordinating Anion or Cation*). 1 M Potassium nitrate, 1 M sodium chloride, 1 M and 2 M lithium perchlorate, and 3 M sodium perchlorate have been extensively used as inert background electrolytes, but the use of a perchlorate must be avoided with Hg^+, Fe^{2+}, and Ce^{3+} with which it forms complexes, and it gives insoluble complexes with ions such as $\mathrm{Ni(en)_3}^{2+}$. Potassium ions in the presence of perchlorate ought to be avoided since $\mathrm{KClO_4}$ has very low solubility and would potentially cause troublesome precipitation. Biochemists often prefer $I = 0.150$ M NaCl as being more comparable with conditions in the living cell.[6]

When several homonuclear complexes, ML_n ($n = 1, 2, 3, \ldots N$) are in equilibrium, equations (7) and (8) can be extended and generalized:

$$\begin{aligned}
\mathrm{M}_t &= [\mathrm{M}] + [\mathrm{ML}] + [\mathrm{ML}_2] + \cdots + [\mathrm{ML}_N] \\
&= [\mathrm{M}]\{1 + \beta_1[\mathrm{L}] + \beta_2[\mathrm{L}]^2 + \cdots + \beta_N[\mathrm{L}]^N\} \\
&= [\mathrm{M}]\left\{\sum_0^N \beta_n[\mathrm{L}]^n\right\} \qquad \text{with } \beta_0 = 1 \qquad (9)
\end{aligned}$$

$$\begin{aligned}
\mathrm{L}_t &= [\mathrm{L}] + [\mathrm{ML}] + 2[\mathrm{ML}_2] + \cdots + N[\mathrm{ML}_N] \\
&= [\mathrm{L}] + \beta_1[\mathrm{M}][\mathrm{L}] + 2\beta_2[\mathrm{M}][\mathrm{L}]^2 + \cdots + N\beta_N[\mathrm{M}][\mathrm{L}]^N \\
&= [\mathrm{L}] + [\mathrm{M}]\left\{\sum_1^N n\beta_n[\mathrm{L}]^n\right\} \qquad (10)
\end{aligned}$$

The average number of ligands bound to each central group is

$$\overline{n} = \frac{(\mathrm{L}_t - [\mathrm{L}])}{\mathrm{M}_t} = \frac{\sum_1^N n\beta_n[\mathrm{L}]^n}{\sum_0^N \beta_n[\mathrm{L}]^n} \qquad (11)$$

where $\overline{n}$ is generally termed the *degree of formation* and equation (11) can be written out as a polynomial in [L]:

$$\overline{n} + (\overline{n} - 1)\beta_1[\mathrm{L}] + (\overline{n} - 2)\beta_2[\mathrm{L}]^2 + \cdots + (\overline{n} - N)\beta_N[\mathrm{L}]^N = 0 \qquad (12)$$

It is important to note that, for a mononuclear complex, $\overline{n}$ is a function only of the free ligand concentration [L], and does not depend explicitly upon M_t, L_t, or [M].

A plot of $\overline{n}$ against pL (or $-\log[L]$) is called the *formation curve*.[3] If it approaches $\overline{n} = 1$ as $pL \rightarrow 0$, we can assume that only one complex, ML, is in equilibrium. If $\overline{n} \geq 1$ at the limiting value, we are assured of the presence of higher complexes. If $\overline{n}$ is found to be a function of [L] only and not dependent on M_t, then N sets of pairs of values ($\overline{n}$, [L]) are in principle sufficient for the computation of the N stability constants β_1, β_2, $\beta_3, \ldots$ and so on. However, experimental work generally gives rise to more than N data sets and, owing to experimental errors, the simultaneous equations formed from neighboring points are often ill-conditioned. In the early days, only graphical methods were available for evaluating experimental data;[1,2,5] but with the increasing availability of high-speed computers, the various curve-fitting methods of Sillén and Dyrssen[7,8] and Rossotti *et al.*,[9] the correction-term method of Irving and Rossotti[10] and the method of corresponding solutions[11,12] have become outmoded and values for stability constants and their statistical weight (standard deviations) can now be obtained by a wide variety of well-tried computer programs. Well-known examples of these computer programs are the early pit-mapping procedure of Sillén (LETAGROP),[13] the widely used MINIQUAD of Sabatini *et al.*,[14] the improved version, SUPERQUAD,[15] and its more recent development, HYPERQUAD,[16] both of Gans *et al.*, the ESTA suite of software developed by May and Murray[17–19] and BEST, a program advanced by Martell and Motekaitis.[20] This essential aspect of the determination of stability constants has been thoroughly discussed[5] and critically reviewed.[21]

3 EXPERIMENTAL APPROACHES

A great variety of experimental methods is encountered in the determination of stability constants,[1–3,5,20,22–24] and only a few types are selected here.

3.1 Potentiometry

If an electrode reversible to the ions of metal M is introduced into a solution of known M_t and L_t in a medium of constant ionic strength and the solution is combined with a reference electrode through a suitable conducting bridge (such as a 'Wilhelm' type electrode[25]), the measured emf at a temperature T K is given by the Nernst equation (*see Nernst Equation*):

$$E = E_{\text{const}} + \left(\frac{RT}{zF}\right) \ln[\text{M}] \qquad (13)$$

where E_{const} must be determined at the particular ionic strength of the experiment, and incorporates the intrinsic electrode parameter as well as relevant activity coefficients and liquid junction potentials. Suitable half-cells and various amalgam electrodes have been used to measure [M] and hence to obtain the stability constants of metal complexes of Cu^+, Cu^{2+}, Ag^+, Au^+, Zn^{2+}, Cd^{2+}, Hg^{2+}, $Hg_2{}^{2+}$, Co^{2+}, Ni^{2+}, Sn^{2+}, Pb^{2+}, Bi^{3+}, Fe^{2+}, Pd^{2+}, and other cations.[1] Ion-specific electrodes have been used in many cases, notably for Ca^{2+} and F^-.

3.2 Polarography and Anodic Stripping Voltammetry

Although the redox processes (*see Redox Properties & Processes*) occurring on the surface of a dropping mercury electrode are generally more complex than those in potentiometry, the simplicity of polarographic apparatus has led it to be widely used in equilibrium solution chemistry. If a reversible electrode process is assured, the half-wave electrode potential is given by the Heyrovsky–Ilkovic equation:

$$E = (E_{1/2})_{\text{s}} = \frac{\left(\dfrac{RT}{zF}\right) \ln i_{\text{d}}}{(i_{\text{d}} - i)} \qquad (14)$$

where z is the change in electron number, i_{d} is the diffusion current, and i the current strength at the half-wave potential $(E_{1/2})_{\text{s}}$. Complex formation shifts the half-wave potential toward more negative values; however, if complex formation occurs in steps that overlap, the plot of $E_{1/2}$ against log[L] varies continuously. DeFord and Hume[26] developed the equation

$$\text{antilog}\left(\frac{0.4343E}{RT}\right) \Delta E_{1/2} + \log\left(\frac{I_{\text{s}}}{I_{\text{c}}}\right) = \sum_{0}^{N} \beta_i [\text{L}]^i \qquad (15)$$

where I_{s} and I_{c} are the diffusion currents of the free metal ion and the complex equilibrium system at the value [L].[27]

Details of the application of polarography and various elaborations of this technique to the determination of stability constants are described by Heyrovsky and Kuta,[28] Nancollas,[29] Hartley *et al.*,[22] Beck and Nagypál,[5] and Cukrowski.[30] A major advantage of polarography is its usefulness as a complement to potentiometry for determining stability constants.[31]

Anodic stripping voltammetry (ASV) can be very useful in studies of metal complexation in natural aquatic systems.[32] The technique can be used, under favorable conditions, to determine metal concentrations as low as $10^{-11}\,\text{mol}\,\text{L}^{-1}$. Further, and again under appropriate conditions, stability constants may be determined in a manner analogous to that used in polarography. The principle of the technique involves deposition of a metal ion in reduced form on a static mercury electrode followed by reoxidation through reversal of the polarity. The reoxidation current is related to the metal concentration in the analyte. In the presence of a complexing ligand, the peak potential in the anodic stripping (i.e. reoxidation) step undergoes a shift in relation to the uncomplexed metal and the magnitude of this shift can be used to determine the corresponding stability constant.

3.3 pH Metric Equilibrium Studies

Besides the use of half-cells involving metal ions, special reference must be made to electrodes capable of measuring $[H^+]$ and especially to the modern glass electrode.**[4]** pH-metry is the most powerful method for the determination of stability constants – indeed, 90% or more of stability constant data have been obtained by this method.**[33]** Values of $[H^+]$ are readily obtained by a precalibration method.**[4,24,34]**

Many organic ligands are the conjugate bases of comparatively weak acids and their metal stability constants are readily obtained by pH-metric titrations after a preliminary determination of the important hydrogen-ion stability constants of the ligand acid itself.

For a polybasic acid, H_NL, we can write equation (16) for the total acidity:

$$\begin{aligned} H_t &= [H^+] - [OH^-] + [HL] + 2[H_2L] + \cdots + N[H_NL] \\ &= [H^+] - [OH^-] + [L]\sum_1^N \beta^H n[H]^n \end{aligned} \tag{16}$$

where $\beta^H = [H_nL]/[L][H^+]^n$ is the overall stability constant for a hydrogen–ligand complex, that is, the conjugate acid of the ligand L. $\bar{n}_H$ is the average number of protons bound to each ligand atom (that is not bound to a metal):

$$\begin{aligned} \bar{n}_H &= \frac{\{H_t - [H^+] + [OH^-]\}}{(L_t - \bar{n}M_t)} \\ &= \frac{\sum_0^N n\beta^H[H^+]^n}{\sum_0^N \beta^H[H^+]^n} \end{aligned} \tag{17}$$

If we have measured $[H^+]$ in a solution where M_t and L_t are known, we can calculate all β_n for the metal–ligand complexes from

$$\bar{n} = \frac{\{L_t - (H_t - [H^+] + [OH^-])/\bar{n}_H\}}{M_t} \tag{18}$$

This procedure, essentially based on competitive complexing of the ligand L by metal ions M and protons H^+, has been used very extensively.**[1–3,5,20,22–24]**

3.4 Competitive Equilibria

The stability of some metal complexes is very large. For example, with ethylenediaminetetraacetic acid (EDTA, Na_2H_2Y) and tripositive lanthanide ions, Ln^{3+}, values of K_{LnY} range from $10^{15.7}$ to $10^{20.0}$ and the equilibrium

$$Ln^{3+} + H_2Y^{2-} \rightleftharpoons LnY^- + 2H^+ \tag{19}$$

lies so far to the right that it would be useless to try to compute the concentration of the free metal ion, $[Ln^{3+}] = Ln_{tot} - 2[H^+]$, from the difference between these two large and nearly equal quantities. In such cases, it is preferable to introduce a second cation, M^{n+}, and to study the position of the new equilibrium, for example, $M^{2+} + LnY^- \rightleftharpoons MY^{2-} + Ln^{3+}$, where the new equilibrium constant is given by

$$\begin{aligned} K_c &= \frac{[MY][Ln]}{[M][LnY]} = \frac{[MY]}{[M][Y]} \times \frac{[Ln][Y]}{[LnY]} \\ &= \frac{K_{MY}}{K_{LnY}} \end{aligned} \tag{20}$$

Although there is no simple electrode with which to measure Ln^{3+}, the determination of a mixture of M, MY, and LnY can be carried out polarographically if the cation M^{n+} is chosen so that its reduction wave precedes and is sufficiently separated from those of all other species in solution and if, of course, $[M^{n+}]$ is proportional to the height of the polarographic wave. In studies of the aminopolycarboxylic acid ligands EDTA and cyclohexanediaminetetraacetic acid (CDTA), Schwarzenbach and Freitag**[35]** showed that the auxiliary cation M^{n+} could be Cu^{2+}, Cd^{2+}, or Pb^{2+}, and Irving and Conesa**[36]** extended this to studies of all the lanthanide complexes of propylenediaminetetraacetic acid. K_c can thus be obtained from polarographic measurements and since K_{MY} will be known from earlier experiments, K_{LnY} follows from equation (20).

3.5 Use of Cation Exchange Resins

The partition of a cationic species $ML_n{}^{z+}$ between an aqueous phase and the sodium ion form of a cation exchanger (*see Ion Exchange*) can be represented by

$$z(Na^+)_R + (ML_n{}^{z+}) \rightleftharpoons (ML_n{}^{z+})_R + z(Na^+) \tag{21}$$

where the subscript R distinguishes the resin phase. The stoichiometric partition coefficient for each metal species is given by

$$\phi = \frac{[ML_n{}^{z+}]_R}{[ML_n{}^{z+}]} = k\left(\frac{[Na^+]_R}{[Na^+]}\right)^z \tag{22}$$

and will be constant provided k and the ratio of sodium ion concentrations in the two phases are both constant, a condition that can be met if the resin load and the extent of exchange is low and if the aqueous phase contains a constant and high concentration of Na^+.[1] These conditions are greatly assisted if M_t is a low concentration of a suitable radioisotope (*see Isotopes & Isotope Labeling*). The overall distribution ratio is given by

$$\phi = \frac{\sum_0^N [ML_i]_R}{\sum_0^N [ML_i]} = \frac{\sum_0^N \phi_n \beta_n [L]^n}{\sum_0^N \beta_n [L]^n} \qquad (23)$$

which reduces to $\phi = \phi_0/\Sigma\beta_n[L]^n$ if only the uncomplexed metal ion exchanges with the resin. In this form, the procedure has been used for determining the stability constants of many transition metals with a variety of organic and inorganic ligands.[1] If both M and ML exchange with the resin, computation becomes more difficult, but the procedure has been widely used.[1] Carleson and Irving describe the use of ion-exchange resin for determining the stability constants of indium halides where In^{3+}, $In(hal)^{2+}$, and $In(hal)_2{}^+$ all exchange with sodium ions on the resin.[37]

3.6 Liquid–liquid Partition

Liquid–liquid partition is useful when one of the series of metal complexes, ML_n^0, has a zero charge and can partition into an immiscible organic phase according to Nernst's law, $p_n = [ML_n^0]_{org}/[ML_n^0]_{aq}$.[1,5] Equilibration of an aqueous phase with known M_t and L_t with this immiscible organic phase leads to an experimentally determinable distribution ratio:

$$p_d = \frac{[ML_n^0]}{\sum_0^N [ML_n]} = \frac{p_n \beta_n [L]^n}{\sum_0^N \beta_n [L]^n} \qquad (24)$$

from which values of the overall stability constants β_n can be computed. This is especially easy if M_t comprises a suitable radioisotope (*see Isotopes & Isotope Labeling*) of the metal M and is present at a low concentration. As L_t increases, p_d increases steadily to a value p_n; but if cationic complexes also occur in the equilibrium mixture, the distribution ratio passes through a maximum and then decreases, as in the system $MeHg^+/Br^-$/xylene, where the complex MeHgBr is the only extractable species but starts to be replaced by $MeHgBr_2{}^-$ in the aqueous phase as the bromide concentration increases.[38]

3.7 Spectrophotometric Methods

The absorbance of a species, ML_n, of concentration c in a cell of length d is given by $A = \varepsilon cd$, where ε is the molar absorption coefficient at a specified wavelength. Since $[ML_n] = A/\varepsilon d$, we can compute one of the terms needed to determine a series of overall stability constants provided its spectrum is sufficiently distinguishable from those of other species in solution. In a study of the equilibrium $pM + qL \rightleftharpoons M_pL_q$, a series of solutions can be made up for which $(M_t + L_t)$ is constant and the mole ratio $x = L_t/(M_t + L_t)$ varies from 0 to 1. Some property proportional to $[M_pL_q]$ (e.g. the absorbance in visible spectrophotometry) is measured and plotted against x to give two straight lines (for a stable complex) intersecting at $x = p/q$. For a less stable complex, more or less rounded curves with the same maximum are obtained. For a 1:1 complex, irrespective of the wavelength chosen, $x = 0.5$. While this procedure (Job's method[39]) and its various extensions have been widely used for determining the formula of a particular complex in solution, it is well adapted for determining reliable values of β_n for a series of complexes in equilibrium.[1,5]

3.8 Nuclear Magnetic Resonance Spectroscopy

The application of nuclear magnetic resonance (NMR) spectroscopy to the study of metal–ligand equilibria is growing rapidly. This technique can be used not only to determine stability constants but also to provide information on the structures of the complexes formed as well as the location of the binding sites on the ligand of the hydrogen and metal ions.[5]

In cases of slow exchange, the method comes into its own with simple sets of reactions forming mixed ligand complexes, for example, $AlCl_4{}^-$ and $AlBr_4{}^-$ in equilibrium with $AlBrCl_3{}^-$, $AlBr_2Cl_2{}^-$, and $AlBr_3Cl^-$.[40] Here, each species is clearly identified and integrated intensities unequivocally yield concentration ratios from which stability constants are directly calculated. Beck and Nagypál[5] describe the approach, with examples, in the cases of both slow and fast exchange. The identification of species present and the values of stability constants as determined by potentiometry and NMR spectroscopy are not always in agreement. Such was found to be the case by Crisponi *et al.*[41] in their study of cadmium(II)-ATP (adenosine-5′-triphosphate) equilibria. The discrepancies are attributed to ATP stacking at the higher concentrations required for the NMR measurements as well as to the inherently lower thermodynamic reliability of the NMR data.

An example of the identification, by NMR spectroscopy, of the protonation sites on multibasic ligands is described by Dhansay *et al.*[42]

3.9 Other Methods

Other physical methods often used include measurements of polarimetry, infrared (*see Infrared Spectroscopy*) and Raman (*see Raman Spectroscopy*) spectroscopy, conductivity, and colligative properties such as depression of the freezing point, solubility, and reaction kinetics. These topics and the extensive work carried out on mixed and polynuclear complexes is discussed in many of the books to which reference has already been made.[1,2,5,20,22,23]

4 USES OF STABILITY CONSTANTS

Numerical data on stability constants are needed in many aspects of technology such as extraction metallurgy and the nuclear energy industry, in planning analytical methods involving ion-exchange processes, separations of metals, chromatography, complexometric titrations, and for many aspects of academic, medical, environmental, and industrial research.[20,32,43–45] The toxic effect of some metals in the environment becomes enhanced when any derived complexes can be leached by underground water from a mine, land-fill site, or waste dump. On the other hand, very stable complexes can be effective detoxificants and it is important to be able to calculate the effect of definite concentrations of a particular ligand or mixture of ligands on the final composition of a wide range of elements and compounds in the natural environment[44] or to be able to model the selective action of drugs in the human system.[46,47] In agriculture, the transfer of an essential trace element from the soil to the growing plant and the use of synthetic agents to supplement or control plant nutrients, and many problems of technology, geochemistry, and of a biochemical nature can best be tackled with the aid of quantitative data on stability constants.[20]

Determination of the distribution of all the species (uncomplexed metal ions and ligands plus all the complexes coexisting in equilibrium) in a multicomponent system such as blood plasma, other biological fluids, sea-water, lakes, and other geological fluids is often referred to as *speciation*.[45] Arguably, the best way of carrying out speciation on a system is by calculation, making use of reliable stability constant values inserted into appropriate forms of mass action and mass balance equations.[46] Several databases have been constructed and several suitable computer programs have been developed for this purpose.[43] For example, a recent version of a blood plasma database incorporates 10 metal ion species, over 100 types of ligand and 10 000 complexation reactions between them.[47] Critically evaluated stability constants are to be found in several modern databases.[48–50]

5 STABILITY CONSTANTS AND THEIR CONTRIBUTION TO THE BASIC IDEAS OF CHEMISTRY

In 1941, Sidgwick summarized what he called the relative affinities of common ligands for acceptor molecules and ions; at the time, heats and entropies of compound formation were almost nonexistent and reliance had to be placed on qualitative comparisons. By 1953, stability constants for a number of metal complexes had been reported and it was feasible to ask the following questions: (1) For a given ligand, how does the stability constant vary with changes in the central metal atom? (2) How does the stability vary when the nature of the coordinating ligand, L, is changed? After reviewing all the data available in 1953, Irving and Williams showed that for divalent ions of the first transition series the stability always follows the order Mn < Fe < Co < Ni < Cu > Zn. This is now commonly called the *Irving–Williams Series* (*see Irving–Williams Series*).[51,52] For each cation, the stability increased when donor oxygen was replaced by donor nitrogen in either monodentate or bidentate ligands (see Figure 1). As the number of chelated rings increased so the stability increased, but it decreased with increase in ring size.[53]

The stability order $K_{n+1} < K_n$ was followed unless the added ligand produced changes in the electronic ground state (as with Fe^{2+} and phen), or introduced changes in coordination number (as with Ag^+ and the second molecule of ammonia, or Cd^{2+} and halides).[51–54]

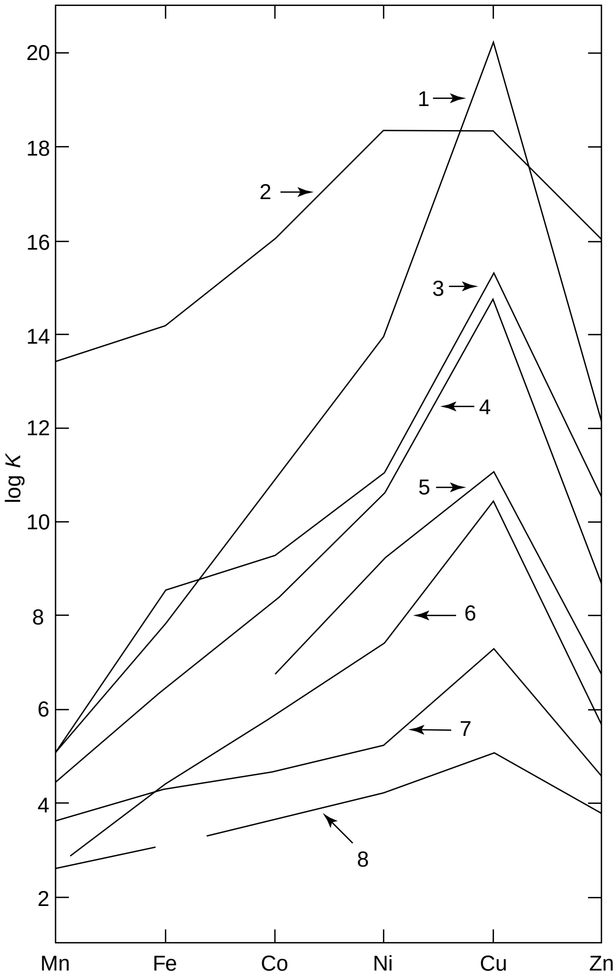

Figure 1 The stability of complexes of divalent transition metal cations. 1, Triethylenetetramine, $NH_2C_2H_4NHC_2H_4NHC_2H_4NH_2$; 2, EDTA, ethylenediaminetetraacetic acid; 3, diethylenetriamine, $NH_2C_2H_4NHC_2H_4NH_2$; 4, norleucine, $Me(CH_2)_3CH(NH_2)CO_2H$; 5, 1,2,3-triaminopropane, $NH_2CH_2CH(NH_2)CH_2NH_2$; 6, ethylenediamine, $NH_2C_2H_4NH_2$; 7, salicylaldehyde, 2-(HO)C_6H_4CHO; 8, oxalic acid, HO_2CCO_2H. For norleucine, 4, the values for log β_2 are plotted

In 1954, Carleson and Irving[37] noted that published data for the stability of a variety of metal halides separated them into two distinct groups. The order of decreasing stability $\mathrm{F}^- \gg \mathrm{Cl}^- > \mathrm{Br}^- > \mathrm{I}^-$ was followed by most cations (Group (i)), but was reversed for a few elements (Group (ii)) such as Ag^+, Cu^+, Hg^{2+}, and Tl^{3+}, for which the stability increased in the order $\mathrm{F}^- < \mathrm{Cl}^- < \mathrm{Br}^- < \mathrm{I}^-$ as shown in Figure 2.

These observations were in part a precursor of the well-known review of the relative affinities of ligand atoms for acceptor molecules and ions published by Ahrland, Chatt, and Davies in 1958.[55] By using quantitative measurements of stability constants measured for aqueous solutions and supplementing these by heats of dissociation (ΔH), association constants for metal complexes measured at specified temperatures $(1/K_p)$, and a mass of qualitative information, they noted two regularities: (1) There was, in general, a great difference between the coordinating affinities of the first and second element from each of three vertical groups of ligand atoms in the periodic table (*see* ***Periodic Table: Historical Aspects***), viz. between N and P, O and S, and between F and Cl. (2) There were two classes of acceptors (*see Class A & Class B Behavior*). The larger, class (a), which includes the hydrogen ion, forms its most stable complexes with the first ligand of each group, that is, N, O, or F. The characteristic of the less numerous group, class (b), is most pronounced in the central part of the periodic table in a roughly triangular region, with copper at its apex and extending to Ir and Hg at its base. In their lower oxidation states, these are also the elements that form stable alkene complexes and have electrons from the lower d-orbitals available for π-bonding.[55]

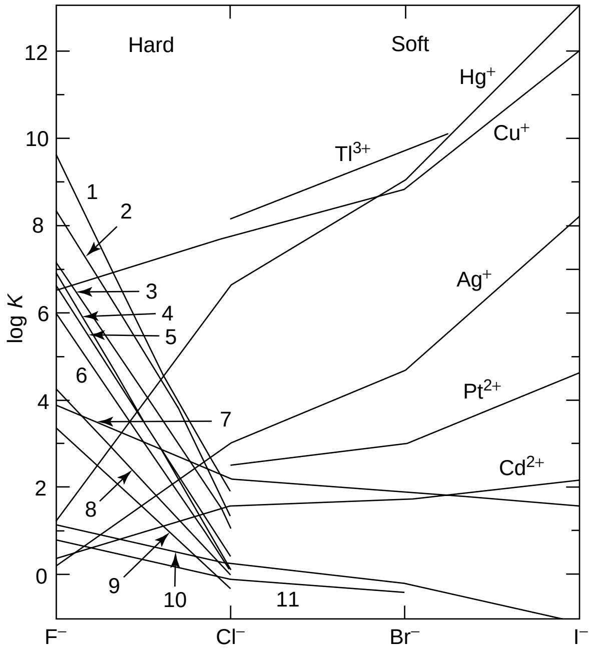

Figure 2 The stability of halogen complexes of various cations. 1, Zr^{4+}; 2, Th^{4+}; 3, Sc^{3+}; 4, Pu^{4+}; 5, Fe^{3+}; 6, $\mathrm{UO_2}^{2+}$; 7, Sn^{2+}; 8, In^{3+}; 9, La^{3+}; 10, Hg^{2+}; 11, Zn^{2+}

Later workers have correlated the classification of elements in class (a) and class (b) with Pearson's principle of hard and soft acids and bases (HSAB principle)[56] (*see* ***Hard & Soft Acids and Bases***) on the basis that class (a) metal ions are hard acids and class (b) are soft acids. Borderline elements in the Ahrland–Chatt–Davies classification tend to be harder in the higher oxidation states and softer in their lower oxidation states.

While the class (a)/class (b) approach and the HSAB principle of Pearson are excellent qualitative methods for interpreting and classifying the phenomena encountered in many donor–acceptor reactions, progress toward establishing a more quantitative basis for these theories has been slow.[5,57] Drago's E and C parameters[58] (*see Drago Parameters*) represent a quantitative approach to a related problem: they allow the heat of association for a given acid–base adduct to be estimated if the empirical E and C parameters are known for both acid and base (*see Drago–Wayland Scheme*). Building on this approach, the parametric correlation work of Hancock and Marsicano[59] has provided valuable insights into the nature of donor–acceptor reactions. Very recent work[60] involving density functional theory calculations augurs well for the prediction of stability constants of complexes of metal ions with monodentate ligands (*see Monodentate Ligand*), and may also lead to a quantitative foundation for theories of metal complex formation reactions.[61]

Discussions in other sections of this encyclopedia deal with the chelate (*see Chelate Effect*) and macrocyclic (*see Macrocycle*) effects, which are also pertinent to our understanding of metal complexation reactions. The factors contributing to these effects are admirably discussed in detail by Martell and Hancock.[62]

6 RELATED ARTICLES

Coordination & Organometallic Chemistry: Principles.

7 REFERENCES

1. F. J. C. Rossotti and H. Rossotti, 'The Determination of Stability Constants', McGraw-Hill, New York, 1961.
2. H. Rossotti, 'The Study of Ionic Equilibria', Longman, London, 1978.
3. J. Bjerrum, 'Metal Ammine Formation in Aqueous Solution', Haase, Copenhagen, 1941.
4. P. W. Linder, R. G. Torrington, and D. R. Williams, 'Analysis using Glass Electrodes', Open University, Milton Keynes, 1984.

5. M. T. Beck and I. Nagypál, ‘Chemistry of Complex Equilibria’, trans. D. A. Durham, Ellis Horwood, Chichester, 1990.
6. D. R. Williams, ‘Proceedings of the Summer School on Stability Constants, Bivigliano (Florence) 1974’, Edizioni Scuola Universitaria, Firenze, Italy, 1974.
7. L. G. Sillén, *Acta Chem. Scand.*, 1956, **10**, 186.
8. D. Dyrssen and L. G. Sillén, *Acta Chem. Scand.*, 1953, **7**, 663.
9. F. J. C. Rossotti, H. Rossotti, and L. G. Sillén, *Acta Chem. Scand.*, 1956, **10**, 203.
10. H. Irving and H. S. Rossotti, *J. Chem. Soc.*, 1953, 3397.
11. H. M. N. H. Irving and D. H. Mellor, *J. Chem. Soc.*, 1955, 3457.
12. H. M. N. H. Irving and K. Sharpe, *J. Inorg. Nucl. Chem.*, 1971, **33**, 203.
13. N. Ingri and L. G. Sillén, *Ark. Kemi*, 1964, **23**, 97.
14. A. Sabatini, A. Vacca, and P. Gans, *Talanta*, 1974, **21**, 53.
15. P. Gans, A. Sabatini, and A. Vacca, *J. Chem. Soc., Dalton Trans.*, 1985, 1195.
16. P. Gans, A. Sabatini, and A. Vacca, *Talanta*, 1996, **43**, 1739.
17. P. M. May, K. Murray, and D. R. Williams, *Talanta*, 1988, **35**, 825.
18. P. M. May and K. Murray, *Talanta*, 1988, **35**, 927.
19. P. M. May and K. Murray, *Talanta*, 1988, **35**, 933.
20. A. E. Martell and R. J. Motekaitis, ‘Determination and Use of Stability Constants’, VCH, New York, 1988.
21. D. Leggett, ‘Computational Methods for the Calculation of Stability Constants’, Plenum, New York, 1985.
22. F. R. Hartley, C. Burgess, and R. M. Alcock, ‘Solution Equilibria’, Ellis Horwood, Chichester, 1980.
23. M. Meloum, J. Havel, and E. Högfeldt, ‘Computation of Solution Equilibria’, Ellis Horwood, Chichester, 1988.
24. P. W. Linder, Experimental Techniques for Determining Complex Stability Constants, in ‘Handbook of Metal–Ligand Interactions in Biological Fluids’, ed. G. Berthon, Marcel Dekker Inc., New York, Basel, Hong Kong, 1995, Vol. 1, p. 524.
25. W. Forsling, S. Hietanen, and L. G. Sillén, *Acta Chem. Scand.*, 1952, **6**, 901.
26. D. D. DeFord and D. N. Hume, *J. Am. Chem. Soc.*, 1951, **73**, 5321.
27. H. M. N. H. Irving, in ‘Advances in Polarography’, ed. I. S. Langmuir, Pergamon, Oxford, 1960, Vol. 1, p. 42.
28. J. Heyrovsky and J. Kuta, ‘Principles of Polarography’, Academic Press, New York, 1966.
29. G. H. Nancollas, ‘Interactions in Electrolyte Solutions’, Elsevier Publishing Company, Amsterdam, London, New York, 1966.
30. I. Cukrowski, *Analyst*, 1997, **122**, 827.
31. B. Kurzak, J. Spychala, and J. Swiatek, *J. Coord. Chem.*, 1992, **25**, 95.
32. J. Buffle, ‘Complexation Reactions in Aquatic Systems. An Analytical Approach’, Ellis Horwood, Chichester, 1988.
33. A. E. Martell and R. J. Motekaitis, *Coord. Chem. Rev.*, 1990, **100**, 323.
34. H. M. N. H. Irving, M. G. Miles, and L. D. Pettit, *Anal. Chim. Acta*, 1967, **38**, 475.
35. G. Schwarzenbach and E. Freitag, *Helv. Chim. Acta*, 1951, **34**, 1503.
36. H. M. N. H. Irving and J. P. Conesa, *J. Inorg. Nucl. Chem.*, 1964, **26**, 1945.
37. B. G. F. Carleson and H. M. N. H. Irving, *J. Chem. Soc.*, 1954, 4390.
38. M. Jawaid, F. Ingman, and D. H. Liem, *Acta Chem. Scand.*, 1978, **A32**, 7.
39. P. Job, *Ann. Chim. Phys.*, 1928, **9**, 113.
40. D. E. H. Jones, *J. Chem. Soc., Dalton Trans.*, 1992, 567.
41. G. Crisponi, R. Caminiti, S. Biagini, M. Casu, and A. Lai, *Polyhedron*, 1984, **3**, 1105.
42. M. A. Dhansay, P. W. Linder, R. G. Torrington, and T. A. Modro, *J. Phys. Org. Chem.*, 1990, **3**, 248.
43. G. Berthon ed., ‘Handbook of Metal–Ligand Interactions in Biological Fluids’, Marcel Dekker Inc., New York, Basel, Hong Kong, 1995, Vols. 1 and 2.
44. A. M. Ure and C. M. Davidson, ‘Chemical Speciation in the Environment’, Blackie Academic and Professional, Glasgow, 1995.
45. J. A. C. Broekaert, Ş. Güçer, and F. Adams, ‘Metal Speciation in the Environment’, NATO ASI Series G: Ecological Sciences, Vol. 23, Springer-Verlag, Berlin, Heidelberg, New York, 1990.
46. P. M. May, P. W. Linder, and D. R. Williams, *J. Chem. Soc., Dalton Trans.*, 1977, 588.
47. P. M. May, Modelling Metal–Ligand Equilibria in Blood Plasma, in ‘Handbook of Metal–Ligand Interactions in Biological Fluids’, ed. G. Berthon, Marcel Dekker Inc., New York, Basel, Hong Kong, 1995, Vol. 2, p. 1184.
48. P. M. May and K. Murray, *Joint Expert Speciation System*, 2000, http://jess.murdoch.edu.au/jess/jess_home.htm.
49. A. E. Martell, R. M. Smith, and R. J. Motekaitis, ‘NIST Standard Reference Database 46: Critically Selected Stability Constants of Metal Complexes, Version 7’, National Institute of Standards and Technologies, Gaithersburg, MD, 2002, http://www.nist.gov/srd/nist46.htm.
50. L. D. Pettit and K. J. Powell, ‘IUPAC Stability Constants Database’, Academic Software, Timble, Otley, LS21 2PW, U.K., 2004, http://www.acadsoft.co.uk/scdbase/scdbase.htm.
51. H. M. N. H. Irving and R. J. P. Williams, *Nature*, 1948, **162**, 746.
52. H. M. N. H. Irving and R. J. P. Williams, *J. Chem. Soc.*, 1953, 3192.
53. H. M. N. H. Irving, R. J. P. Williams, D. F. Ferrett, and A. E. Williams, *J. Chem. Soc.*, 1954, 3494.
54. H. M. N. H. Irving and J. M. M. Griffiths, *J. Chem. Soc.*, 1954, 213.

55. S. Ahrland, J. Chatt, and N. R. Davies, *Q. Rev. Chem. Soc.*, 1958, **12**, 265.
56. R. G. Pearson, *J. Am. Chem. Soc.*, 1963, **85**, 3533.
57. J. Burgess, ‘Ions in Solution’, Ellis Horwood, Chichester, 1988.
58. R. S. Drago, N. Wong, C. Bilgrien, and G. C. Vogel, *Inorg. Chem.*, 1987, **26**, 9, and refs. cited.
59. R. D. Hancock and F. Marsicano, *Inorg. Chem.*, 1978, **17**, 560.
60. R. D. Hancock and L. J. Bartolotti, *Chem. Commun.*, 2004, 534.
61. R. G. Pearson, ‘Chemical Hardness’, Wiley-VCH, Weinheim, 1997.
62. A. E. Martell and R. D. Hancock, *ACS Symp. Ser.*, 1994, **565**, 240.

Stereochemical Nonrigidity of Organometallic Complexes

John W. Faller
Yale University, New Haven, CT, USA

1	Introduction	1
2	Alkene and Alkyne Rotations: Paradigms for Stereochemical Nonrigidity	4
3	Carbene Rotation	12
4	Hindered Rotation about Single Bonds	14
5	Hindered Rotations of η^6-Arenes, η^5-Cyclopentadienyl, and Similar Ligands	18
6	Nonrigidity in Hemilabile Ligands	19
7	Allyl Rearrangements	21
8	Haptotropic Rearrangements in Rings	23
9	Hydride–Alkene Complexes and Agostic Interactions	23
10	Hydride and Dihydrogen Complex Equilibria	24
11	Six-coordination and Nonrigidity	25
12	Ketone and Aldehyde complexes	25
13	Comments	26
14	Related Articles	27
15	References	27

Glossary

Dynamic NMR: NMR spectra in which broadening or averaging is observed owing to exchange of nuclei between different chemical environments. This is the method by which nonrigidity or fluxionality is generally detected
Fluxional molecule: a stereochemically nonrigid molecule in which all interconverting structures are equivalent
Stereochemically nonrigid compound: a compound that undergoes intramolecular rearrangements at rates that affect the NMR line shapes in generally accessible temperature ranges
Stereodynamics: dynamics associated with interconversion of stereoisomers or conformers

Abbreviations

DNMR = dynamic NMR; T_c = coalescence temperature; T_I = temperature at which initial broadening occurs in a DNMR spectrum; T_{LL} = low temperature at which broadening is no longer observed in a DNMR spectrum (usually 5–10 °C below T_I); T_1 = spin–lattice relaxation time; EXSY = 2D NMR method for evaluating exchange sites and rates; PSEXSY = phase-sensitive EXSY; HMQC = Indirect method for observing NMR of low abundance nuclei, such as ^{15}N, ^{57}Fe, ^{13}C, and so on, using the coupling to a sensitive nucleus, often ^{1}H; NOESY = Nuclear Overhauser Effect Spectroscopy, a 2D NMR method for assignment of resonances based on proximity; SIT = Spin Inversion Transfer; sp = square pyramidal; tbp = trigonal bipyramidal; Tp = hydrido(trispyrazolylborate); Tp′ = hydridotris(3,5-dimethylpyrazolylborate).

1 INTRODUCTION

Molecules that undergo intramolecular rearrangements at rates that affect the NMR line shapes in generally accessible temperature ranges are said to be stereochemically nonrigid. This terminology was originally proposed by Muetterties**[1,2]** and was popularized from 1966 when Cotton, Davison, and their coworkers produced a long series of articles entitled 'Stereochemically Nonrigid Organometallic Compounds.'**[3–8]** Cotton's retrospective description of these early developments provides a review of the early work.**[9]** Over the next eight years the use of NMR to study rearrangements of this type became sufficiently widespread, so that in 1975 an entire book was devoted to the subject of Dynamic Nuclear Magnetic Resonance Spectroscopy (abbreviated DNMR).**[10]** This book still provides the most comprehensive treatment of the subject and is a recommended starting point for further study. The fundamentals regarding the chemistry are treated well there, but the recent advances in multinuclear and two-dimensional NMR spectroscopy, such as EXSY and HMQC, have vastly improved the technology for detecting and investigating nonrigid processes.**[11,12]** Since that time, there have been a number of shorter reviews with particular emphasis on inorganic and organometallic chemistry that are recommended.**[13–24]** Although dating from 1988, the extensive review by Mann**[13]** is still a particularly valuable resource. Owing to the large number of references subsequent publications tend to focus on recent developments rather than being comprehensive. Orrell's review**[23]** includes many of the most recent references. Mann's book**[24]** includes abundant examples of applications of DNMR and illustrates the applications of more modern NMR techniques.

The subset of nonrigid molecules in which all observable interconverting species of a given type are structurally equivalent are designated as being fluxional.**[25,26]** Although this formal distinction was made previously, current usage often employs fluxional and stereochemical nonrigidity interchangeably. For example, as a static structure, separate resonances would be expected for the equatorial and apical positions of a trigonal bipyramidal molecule. The rapid rearrangement of the carbonyls in Fe(CO)$_5$ (**1**) is an example of a fluxional process, which gives rise to a single resonance in the room temperature ^{13}C NMR spectrum. Presumably, the formation of a square pyramidal intermediate provides a pathway for this interconversion, as shown in equation (1). There are, however, alternative paths that differ in the details by which nuclei are permuted among the sites. It was well known in 1966 that the variations in line-width in the NMR spectra allowed the determination of rates of rearrangement, but using NMR to distinguish possible mechanisms was first used**[3]** with the classic example of a fluxional organometallic, $Cp_2Fe(CO)_2$ (**2**). Although this molecule had been formulated as (η^5-Cp)Fe(CO)$_2$(η^1-Cp), only singlets were originally observed for the cyclopentadienyl ligands in the ^{1}H NMR spectrum.**[27]** Lowering the temperature resulted in broadening of one singlet, which eventually decoalesced into the AA′BB′X spectrum expected for the η^1-Cp ligand. The observation that the A portion of the spectrum broadened differently than that of the B portion provided definitive evidence that the path involved a rearrangement in which the iron moved from one carbon to the immediately adjacent carbon, rather than randomly to other positions, or across the ring (see equation 2). NMR line shape analysis often allows the elimination of some mechanisms or provides a consistency with a limited number of mechanisms. Nevertheless, the primary use of NMR line shape analysis has often been for the determination of rates of rearrangement and for evaluating barriers to rearrangements. The timescale of the NMR measurements generally allows evaluation of barriers between 40 and 80 kJ mol^{-1}.

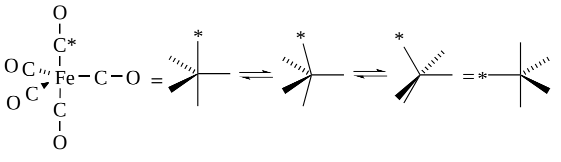

(**1**)

(1)

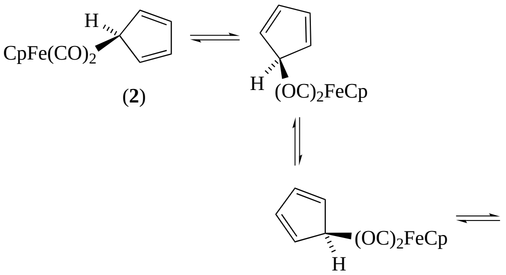

(**2**)

(2)

1.1 Measurement of Barriers to Interconversion

The magnitude of errors arising from neglect of coupling and chemical shift variations with temperature was not well recognized in the early- 1960s, and it is understandable that exceptionally large errors in activation energy were often obtained. Unfortunately, even after 40 years, many researchers fail to recognize the problems and often report barriers that may be in error by more than 100%. Since we will wish to compare rearrangement barriers, it will be necessary to establish the reliability of the data and determine a practical definition of barrier. That is, one may consider $\Delta G^{\ddagger}$, E_a, or a potential function maximum. Although one may debate which has the most theoretical significance, the practical situation is that $\Delta G^{\ddagger}$ is experimentally the most accessible, most reliable, and subject to the least experimental error.

Computer programs for calculation of line shapes are readily available.**[28–31]** Modern programs for personal computers, such as gNMR,**[31]** have user-friendly graphical interfaces that allow rapid calculation and display of spin-coupled spectra as a function of exchange rate. Careful line shape analysis, however, must include intrinsic variations of chemical shift with temperature and is a tedious procedure. Considering the rate ranges available (often less than a factor of 100), inaccuracies in E_a are sufficient to make comparison of results based on temperature variations questionable. It has been our experience that, for intramolecular reactions, significant activation entropies are not encountered, and that, in carefully executed experiments with large spans in rate (more than a factor of 1000), values between 12.3 and 13.5 are usually found for log A in Arrhenius plots. Values outside of this range usually indicate that the E_a is suspect. For example, the original alkene rotation barrier in the Rh−alkene complexes was reported to have log $A \sim 5$ and $E_a \sim 6\,\mathrm{kcal\,mol^{-1}}$ ($25\,\mathrm{kJ\,mol^{-1}}$),**[32]** whereas the more recent values are log $A = 12.5$ and $E_a = 15.0\,\mathrm{kcal\,mol^{-1}}$ ($62.7\,\mathrm{kJ\,mol^{-1}}$).**[33]** In principle, one could encounter a situation, particularly in coordinatively unsaturated systems, in which a major solvent reorganization in the transition state produced a major deviation. Nevertheless, this situation appears to be rare. In most situations, one can reasonably accurately reproduce the variations in rates with temperature in these nonrigid systems by assuming log $A = 12.8$ or assuming $\Delta G^{\ddagger}$ is independent of temperature.

Since in many situations the information of greatest interest is the relative rearrangement rates among complexes, the variations in rates reflected by differences in $\Delta G^{\ddagger}$ are adequate for most purposes. The greater reliability of $\Delta G^{\ddagger}$ determined from the most accurate rate obtained at a given temperature suggests that one should focus on comparisons of $\Delta G^{\ddagger}$ values.

The errors and problems in evaluating rates has been reviewed elsewhere,**[34–37]** but a convenient and accurate evaluation of the rate can be obtained as the resonances begin to broaden above the limiting low-temperature spectrum by using equation (3).

$$k = \pi W \qquad (3)$$

In this expression, k is the first-order rate constant for leaving one site and W is the broadening in excess of the natural line-width (in Hz). Thus, if one assumes that the low-temperature limit is reached when the excess broadening is $\approx$1 Hz, one can make a fairly accurate estimate of $\Delta G^{\ddagger}$ from this temperature (see Table 1). One might note for a rule of

Table 1 Approximate free energies of activation determined by the temperature at which a low-temperature limiting spectrum is reached[a]

T	kcal mol^{-1}	kJ mol^{-1}
−160	6.1	25
−140	7.3	30
−120	8.4	35
−100	9.5	40
−80	10.7	45
−60	11.8	49
−40	13.0	54
−20	14.2	59
0	15.3	64
20	16.5	69
40	17.6	74
60	18.8	79
80	20.0	84
100	21.2	89
120	22.3	93
140	23.5	98
160	24.7	103
180	25.9	108
200	27.0	113

[a] The best values are obtained at the temperature, T_I, when broadening just becomes perceptible in ^{1}H NMR. Since larger sweeps are used for ^{13}C and ^{31}P NMR, larger line-widths are needed to be perceptible and the free energy of activation may be slightly overestimated.

thumb that this corresponds to $64\,\mathrm{kJ\,mol^{-1}}$ at $T_\mathrm{I} = 0\,°\mathrm{C}$ and changes by $\approx 5\,\mathrm{kJ\,mol^{-1}}$ for each $20\,°\mathrm{C}$ interval.

Formulae also exist for the point at which two resonances of equal intensity coalesce to a single resonance upon raising the temperature,[38,39] and if from the Eyring rate equation (assuming a transmission coefficient of one) $k = (k_\mathrm{b}T/h)K^{\ddagger} = (k_\mathrm{b}T/h)\exp(-\Delta G^{\ddagger}/RT)$, then one obtains equation (4). Equation (5) follows from using the rate expression for NMR coalescence.

$$\Delta G^{\ddagger} = 2.303RT\left(10.32 + \log\frac{T}{k}\right) \tag{4}$$

$$\Delta G^{\ddagger} = -RT_\mathrm{c}\ln\pi\Delta\nu\left(\frac{h}{k_bT_c2^{1/2}}\right) \tag{5}$$

In equation (5), $\Delta\nu$ is the separation between the resonances, h is Planck's constant and k_b is Boltzmann's constant. The temperature at which this coalescence occurs is often reported as T_c. Since the rate depends on the chemical shift difference between the sites in the absence of exchange at that temperature, T_c varies with the field strength of the spectrometer. Since field strengths between 60 and 800 MHz are now in use and variations in chemical shift with temperature are often neglected, T_c can be a rather misleading indicator of barrier height, and its use is not recommended by this author. Furthermore, it should be noted that equation (4) only applies for the case of equal intensities and no coupling between the nuclei. There is also a persistent problem with the definition of k from equation (4) in chemical terms (see below). Thus T_I, the temperature where initial broadening ($\approx$1 Hz) is observed, will be reported here where possible. T_I is independent of field, and it provides an indication of the probable reliability of the energy barrier determination. This temperature is slightly above the temperature T_LL at which the 'limiting low-temperature' spectrum is obtained. Upon reaching this low limit, the rotation is often considered to be 'frozen out.' One should note that the motion has not actually stopped, but has merely slowed to the point where it no longer affects the NMR spectrum significantly (e.g. a rate constant $< \approx 0.03\mathrm{s}^{-1}$).

Most modern programs for the calculation of rates of exchange are cast in the form of matrices representing probabilities of transitions between sites and the relative populations of those sites. The 'rate constant' obtained from these programs often represents the sum of nuclei moving from all sites or an overall rate constant. It is the responsibility of the user of the program to deconvolute the 'rate' produced by the program into the rate for leaving a particular site or for the rate of the reaction expressed in chemical terms. This problem has been discussed for some complicated cases by Green *et al.*[39] and was covered in a previous review for simpler systems.[16] Green's approach focuses on an overall rate constant, k_chem, and there are alternative choices to that approach; nevertheless, a reliable check is provided by comparing results from computer calculations with those from equation (1) for an elementary step in the rearrangement. In most cases, difficulties can be eliminated by cleanly defining 'rate' in terms of a rate constant for departures of nuclei from a given site. A prudent investigator should consider careful definitions of (1) rate versus rate constant, and (2) probability versus population (both indicated as p). In complex cases, it is important to delineate nuclei that leave a given environment and go to a different one from those that return to the same environment.

Equation (4) is the expression for the free energy of activation in terms of coalescence temperature; however, the k used in the derivation may have the ambiguity of a factor of 2 as discussed above for relating 'rate' to rate constant. Furthermore, we have taken the transmission factor (f) in the Eyring expression to be 1. This has been a commonly recommended assumption,[38–40] although a case can be made for using a factor of 1/2 in the case of a symmetrical well with equal populations.[41] The choice of f as either 1 or $\approx 1/2$ produces a $0.4\,\mathrm{kcal\,mol^{-1}}$ or $1.7\,\mathrm{kJ\,mol^{-1}}$ difference in $\Delta G^{\ddagger}$. The evaluation of a conventional transmission factor in complicated cases can be more difficult. If the k has been defined in terms of nuclei leaving the site and going on to other sites, however, a transmission coefficient of 1 is appropriate. Several classic papers on obtaining energies from NMR data[37–40,42] provide further discussion of these points. The details of obtaining rates using computer calculations from line shapes are covered in several volumes.[37,43–45] One of the most commonly used is that developed by Binsch[46] or modern modifications thereof,[28–31] such as used in g-NMR.[31] Rate data can also be obtained *via* 2D methods and magnetization transfer methods. Similar problems in defining the exchange matrices used to obtain rates from EXSY experiments require an analysis of similar factors to those above.[47,48] Saturation transfer or magnetization transfer experiments also provide rate data in which clearly defined rate constants are important.[49–52]

Modern NMR spectrometers allow routine application of pulsed methods, which allow determination of rates and exchange patterns by alternatives to line shape analysis. Somewhat slower rates can be determined by magnetization transfer experiments, such as SST and SIT. In saturation transfer (SST) experiments,[49–52] a resonance is irradiated for sufficient time to saturate it and allow its magnetization to equilibrate with that of any nuclei with which it might exchange. This generally would result in a decrease in the intensity of resonances involved in the exchange and the fraction of the intensity that remains depends upon the rate of exchange and the relaxation time of the nuclei (equation 6). This is particularly effective for rate constants $\sim 0.1 - 1\,\text{sec}^{-1}$.

$$k = \left(\frac{1}{T_1}\right)\left(\frac{M_0}{M-1}\right) \tag{6}$$

The method requires the measurement of the relaxation time of the nuclei at the site to which saturation magnetization is transferred (site A). This can be easily determined when $k \ll 1/\text{T1}$ with a standard inversion-recovery (180°-τ-90°) sequence[52,53] that is available on most spectrometers. Since T_1 will vary somewhat with time, one can extrapolate T_1 into the region of interest or attempt to measure it. This is straightforward if the T_1 for that site ($T_{1\text{A}}$) is the same as the site saturated ($T_{1\text{B}}$) since both recover at the same rate. If $T_{1\text{A}}$ is very different than $T_{1\text{B}}$, analysis is much more difficult since nuclei from the faster relaxing site migrate to the slower relaxing site and *vice versa* during the measurements. Hence, the observed T_1's are composites of both and the T_1 for the slower relaxing site will be artificially shorter owing to magnetization being transferred into it. This is somewhat like the SIT experiment described below where only one resonance is inverted. Fortunately, most cases involve relaxation times that are similar. The case of metal-hydride-dihydrogen exchange is perhaps the most common situation in which the relaxation times are very different and mistakes are made evaluating T_1's for a particular site.

Potential errors arise from competing nuclear Overhauser effects, which can increase the intensities. Alternatively an nOe can be used to enhance the magnetization at a site and the enhancement can be transferred. This approach is more useful for ^{13}C and ^{31}P NMR. Saturation of a resonance is straightforward for ^{1}H NMR spectra since a second frequency can be readily set to allow saturation of a resonance before the 90° pulse is delivered to obtain the spectrum. For ^{13}C and ^{31}P NMR this can be achieved by setting the spectrometer frequency for the resonance, turning on the power at low level to saturate the resonance and then using a high-power 90° pulse.

An alternative is to use a ''soft pulse.'' The usual 90° pulse is several 10s of microseconds and results in a large bandwidth of frequencies. The soft pulse only affects a narrow range of frequencies and can be used to effectively produce a 180° pulse and invert a resonance. This inverted magnetization then recovers as in a T_1 experiment, but during the recovery, magnetization can be transferred to and from other nuclei. Unlike the SST experiment, this SIT experiment is followed with time and the intensities of the resonances depend upon the exchange rate and relaxation times. The method was originally developed for biochemical NMR[54] and several methods for producing the soft pulses are available[55,56] (UBURP256[56] being relatively popular). The intensities versus time are fitted to exponentials and the rates can be derived from them.[35,36,57] This approach was used in earlier studies of organometallics for observation of hydrides exchanging with carbenes and vinyls.[58,59] A recent study of ring inversion provides an example of its application including experimental parameters.[60] Other relaxation methods have been discussed in the review by Orrell.[23]

Modern spectrometers allow ready access to 2D spectra and menu-driven NOESY experiments are frequently used for assigning proton spectra based on correlations of Overhauser enhancements of intensity. Generally, proton spectra are plotted on both x and y axes and cross peaks are observed where nOe enhancements are large. These cross peaks allow assignments of nuclei, which are in close proximity. If exchange is occurring, cross ''peaks'' will also be observed between exchanging nuclei. By altering a time delay, one can emphasize the exchange peaks and then the experiment is often designated as an EXSY. Optimum results are often found for a fast exchange rate constant ($\sim 1\,\text{sec}^{-1}$) and short delay times. It is possible to delineate Overhauser effects from exchange effects using phase-sensitive experiments, although it is often convenient to discard phase information and use magnitudes. Frequently only a minor modification of NOESY parameters allows effective use of EXSY experiments to ascertain which nuclei are exchanging with which. One can obtain quantitative rate date by analyzing volumes of cross peaks,[12,35] but 1D methods would appear to give more accurate results.[36] Modern methods have most recently been reviewed by Bain.[37]

2 ALKENE AND ALKYNE ROTATIONS: PARADIGMS FOR STEREOCHEMICAL NONRIGIDITY

Conformational equilibria and rotational interconversion of conformers of metal–alkene complexes play a crucial role in asymmetric hydrogenation[61,62] and asymmetric hydroformylation.[63] Selectivity in reaction chemistry can be related intimately to relative stability of conformers;[64] hence there are practical reasons for studies of nonrigidity. As indicated in earlier reviews,[10,13,16] rotation about an axis from the metal to the midpoint of an η^2-alkene or η^2-alkyne is a commonly observed and generally accepted phenomenon and is sometimes called '*propeller rotation*.' DNMR spectra are the prime indicators of alkene rotation processes; however, only a limited number of experiments using complexes with chiral centers allow the distinction between rotation about the metal–alkene axis and a rotation about the carbon–carbon axis (see below). Nevertheless, except for intermolecular exchange, rotations or oscillations about metal–alkene or metal–alkyne bonds would appear to account for the vast majority of the DNMR spectra in these complexes. An extended discussion of stereochemical nonrigidity in alkene complexes will follow, since it provides an opportunity to examine pitfalls and provides caveats for interpretations of results for other nonrigid compounds.

Attention originally focused on analogs of Zeise's salt and corresponding $\mathrm{Rh^I}$ systems. Crystal structures of these compounds show that the C–C axis of the alkene is perpendicular to the coordination plane of the metal and the other ligands. Hence, a potential minimum is generally assumed for the alkene orientation in which the plane containing the metal and the alkene carbon atoms produces a dihedral angle of 90° with that defined by the metal and other ligands (see **3**).

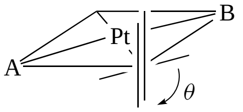

(**3**)

The first indications that the ethylene moiety was not rigidly fixed in the complex were the unusually large temperature factors for the carbon atoms in the X-ray structure determination of platinum–alkene derivatives and temperature dependence in the NMR spectra of the solids.[65–67] The early X-ray results implied an angular amplitude of oscillation of ≈20° in *trans*-$\mathrm{PtCl_2(C_2H_4)(NHMe_2)}$. Oscillations estimated from NMR results for $\mathrm{[PtCl_2(C_2H_4)]_2}$ and Zeise's salt indicated a 19° oscillation about the metal–alkene axis and a 29° oscillation about the C–C axis.

An AA′BB′ proton spectrum was observed in solutions at low temperature for the ethylene moieties in $(\eta^5\text{-}\mathrm{C_5H_5})\mathrm{Rh(C_2H_4)_2}$. The coalescence of this pattern upon raising the temperature led Cramer to ascribe these variations in the spectra to complete rotation of the alkene ligands. The analysis of the temperature dependence of the NMR spectra, which was carried out in 1964, implied barriers to rotation in $(\eta^5\text{-}\mathrm{C_5H_5})\mathrm{Rh(C_2H_4)_2}$ and $\mathrm{(acac)Rh(C_2H_4)_2}$ of ≈25 kJ mol^{-1}. This original study did not take into account the variations in chemical shifts with temperature and thus gave an anomalously low activation energy for a process which showed initial line broadening at $\approx -15\,^\circ$C and a coalescence temperature of ≈50 °C for resonances separated by 110 Hz.[32] A subsequent reevaluation of the activation energies, including approximations for coupling,[33] found an activation energy of 65 kJ mol^{-1} for $\eta^5\text{-}\mathrm{CpRh(C_2H_4)_2}$. The advantages of using initial broadening to estimate barriers is obvious as reference to Table 1 would have predicted a 60–65 kJ mol^{-1} barrier.

Few attempts have been made to map out accurately the potential function for the rotation of ethylene on a metal center from experiment. Most NMR studies report E_a or $\Delta G^\ddagger$ and consider the point no further. If one considers only differences in interactions with d_{xy} and d_{xz} on a square-planar metal, then a maximum at $\theta = 0°$ would be a reasonable assumption. Routine NMR methods of line shape analysis, however, provide only a measure of the highest point on the potential in the rotation. Hence, NMR generally yields no indication of local maxima or minima during the rotation. The details of potential functions and distortions from idealized structures have been discussed elsewhere.[20,68] Early molecular orbital calculations suggested that local minima may also be anticipated.[69] Thus, for $\mathrm{(NH_3)Cl_2Pt(C_2H_4)}$, a double minimum was obtained with a conformation of maximum energy at $\theta = 22.5°$ and minima at $\theta = 0°$ and 90° with a difference in energy between the minima of 106 kJ mol^{-1}.

MO calculations suggest that exceptional care must be taken in the interpretations and extrapolations from the 'barrier to rotation' obtained by NMR and a detailed description of the real potential function for rotation of an alkene. The barrier to rotation ($\Delta G^\ddagger$) can be readily determined and perhaps may best be viewed as a very useful correlation of interconversion rates as a function of temperature.

The Dewar, Chatt, and Duncanson[70,71] concept of the bonding of metal–alkene complexes (*see Dewar–Chatt–Duncanson Bonding Model*) provides an adequate theoretical framework for considering rotation of alkenes, even though other treatments suggest a somewhat more complicated situation.[72,73] It would appear that the σ-donation/π-back donation concept is essentially correct. Therefore, we may anticipate that a qualitative appreciation of rotational barrier heights should be derivable from considerations of relative degrees of σ-donor and π-acceptor ability of the alkene or alkyne ligands in various orientations.

2.1 Characterizing Rotations and Barriers

Before attempting to rationalize the experimentally determined barriers in terms of bonding theory, we must acknowledge the possible errors in NMR determinations of barriers and the one-parameter relationship of $\Delta G^\ddagger$ or E_a

to a potential function. Even for symmetrical alkenes it would not be prudent to attempt to describe the motion involved in an ‘alkene rotation’ in too great a detail. Thus any contortions, such as twisting, tilting, or skewing, that the alkene might execute are not realistically open to experimental verification. Nevertheless, the extent of idealization must be recognized. A rotation about an axis between the metal and a point midway in the C=C bond is probably a fairly accurate description of the movement in symmetrical alkenes. One must recognize, however, that some alkenes are severely distorted[68] and that an eccentric rotation would be anticipated.

A substituent often causes tilting or partial rotation of the alkene and displacement out of the coordination plane of the metal.[68] One of the more informative structures demonstrating these effects is that of $PtCl_2[Me(O)S(C_6H_4Me)](Me_2C{=}CH_2)$.[74] The alkene in this complex is rotated away from the perpendicular by ≈6°. Thus the minimum in the rotational potential is at $\theta = \approx 84°$. Furthermore, the alkene is displaced from the coordination plane such that the substituted carbon is slightly further from the plane. This effect is more pronounced with aromatic substitutents,[68] and can become extreme if conjugation or interaction of the substituents with the metal occur (e.g. vinyl alcohol).[75] In the vinyl alcohol derivative, the midpoint of the C=C bond lies 0.59 Å from the coordination plane.[75] Thus, if one assumes the axis of rotation is in the coordination plane, it might intercept the C=C axis closer to one end, rather than midway between the carbon atoms (Figure 1).

The nomenclature has not been consistent in attempts to describe deviations from the idealized configurations.[68] We will generally refer to a deviation in θ simply as partial rotation. The term twist has been used for this, but has often been used to describe rotational distortion about the C=C axis. Partial rotation about the remaining axis has been called *skewing*. The stereochemically nonrigid process of ‘alkene rotation’ primarily involves changes in θ, but would also include some variations in twist and skew as θ varies. As the motion also involves some eccentric motion (see above), one must recognize that the term propeller rotation is an idealized description of the process.

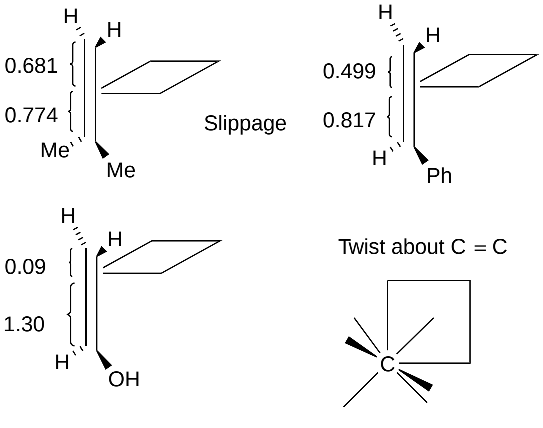

Figure 1 Slippage and twist in alkene complexes (distances in Å)

Substitution also introduces the possibilities of isomerism. In certain cases, conformers differing by a 180° rotation about θ are no longer energetically equivalent and produce further complications in the potential surface. Thus, viewing down the metal–alkene axis of an unsymmetrical complex of propylene, one can readily predict the nonequivalence of well depths for conformations with the methyl groups endo or exo to a substituent, for example, (**4**) or (**5**). Hence the minima will not be at exactly $\theta = 90°$ and 270° and they will not have the same energy.

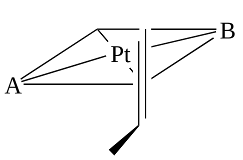

(**4**) *endo*

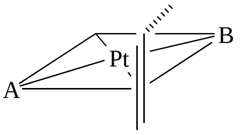

(**5**) *exo*

Although it is generally agreed that rotation about θ occurs in most cases, it is relatively difficult to prove this point and two caveats are in order: (1) intermolecular exchange can produce NMR spectra very similar in nature to rotation (especially in coordinatively unsaturated d^8 complexes); and (2) addition–elimination reactions can produce an identical interchange of protons. Retention of coupling constants to the spin of the metal in ^{195}Pt and ^{103}Rh complexes and those with ^{31}P in other ligands or failure to observe exchange with free ligand can eliminate intermolecular exchange as a pathway. This apparent rotation from addition–elimination, however, does not dissociate the alkene and may proceed as follows (in equation 7, Nu is a nucleophile, such as pyridine or phosphine). A $\pi \rightarrow \sigma$ interconversion has been demonstrated for the pyridine nucleophile[76] and could presumably also occur with electrophiles other than protons.[77]

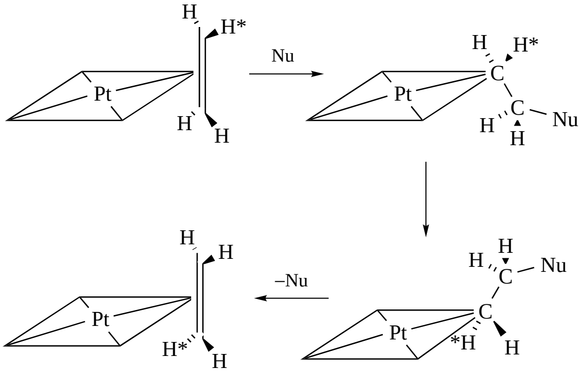

(7)

2.2 Factors Influencing Barrier Heights

Metal–alkene rotation in square complexes has been reviewed by Mann.**13** Examination of these results indicates that increasing steric interactions with cis ligands, substituting the alkene, particularly with fluorine, and using metals in the lower rows of the periodic table increases the barriers. These square-planar complexes provide models for alkene and alkyne rotation in all complexes and many trends carry over to other complexes. It is often difficult to assess the accuracy of barriers reported in the literature. Frequently, inappropriate approximations, such as neglect of coupling, gave rise to gross errors. It is the experience of this author that reference to Table 1 and estimating the initial broadening temperature often provides a more reliable and accurate barrier than that calculated in the original literature. Differences on the order of 1 kJ mol^{-1} generally cannot be given much credence. It is often difficult to reproduce temperatures accurately enough to achieve accuracy of this level. The best procedure is the comparison of rates at the same temperature using line shape analysis. Although checking the temperature using peak separations in methanol is in common use, this author recommends using an internal temperature standard such as $[\text{PhB(pz)}_3]_2\text{Co}$,**78** which has an enormous temperature dependence in the phenyl proton separations.

A large number of Pt^{II}–ethylene complexes have barriers reported to be between 44 and 58 kJ mol^{-1} and have coalescence temperatures below 0 °C. Comparisons of complexes with very bulky cis substituents show significant, although not large, increases. For example,**79** in the *cis*-Cl_2LPt(ethylene) series, there is an increase in the order Et_3As (46 kJ mol^{-1}), Ph_3As (49 kJ mol^{-1}), and $(2\text{-MeOC}_6\text{H}_4)_3\text{P}$ (58 kJ mol^{-1}). In these cases, the electronic influence is not as great as probed by the CO stretching frequency in the analogous $\text{PtCl}_2\text{L(CO)}$ complexes, for which values of 2101, 2106, and 2103 cm^{-1} are observed. Here also the increase in the size of arsenic compared to phosphorus is offset by the longer bond length, and the steric influence of the ligand substituents is enhanced by the shorter Pt–P distance. Thus, in a series of cis complexes, nonbonded interactions tend to dominate variations in barrier with cis ligands. The trans ligand cannot have an appreciable steric influence under normal circumstances; however, major changes in donor or acceptor strength can be anticipated to effect only modest changes in barriers. For example, replacement of a *trans*-chloride by trifluoroacetate produces a lowering of the barrier by ≈2.5 kJ mol^{-1} (a difference which might be considered of only marginal significance in the absence of very careful measurements).

The importance of steric interactions with cis ligands can be more clearly seen in alkene substituent effects. The barrier increases significantly in the PtCl(acac)(ene) series where ene = substituted ethylene compared to ene = ethylene. The *cis*-Cl_2(DMSO)Pt(alkene) series (**6**)–(**9**), studied by Boucher and Bosnich,**80** is particularly instructive. The rotation in the ethylene begins to produce broadening about −47 °C, whereas the propene conformers broaden at ≈ −20 °C and no broadening is observed in the *trans*-butene complex up to +50 °C. T_I's imply barriers of 53, 59, and >75 kJ mol^{-1}. This demonstrates the general increase in barrier observed upon alkyl substitution and can clearly be ascribed to steric effects. The dramatic increase in barrier in comparing propene to butene can be attributed to the interaction of the methyl group attached to the alkene and the bulky sulfoxide. The increased interaction is suggested by the differing stabilities of the endo and exo isomers of the propene complex. These two conformers can be interconverted by a ≈180 °C oscillation ($\theta = 90° \rightarrow 0° \rightarrow 270°$) with the propene methyl passing by the chloride. Presumably a 360° rotation would occur rapidly only at higher temperatures owing to interaction of the methyl group with the sulfoxide. Since the stereochemistry of *trans*-butene requires that a methyl group pass near the sulfoxide in a rotation, its barrier is dominated by that interaction. This suggests that, in the propene complex, the potential maximum in the 90° → 180° → 270° path is at least 12 kJ mol^{-1} more than in the 270° → 0° → 90° path. The contribution from the methyl group interaction with the halogen is also probably increased since the twisting possible in the propene complex may be suppressed in the butene complex.

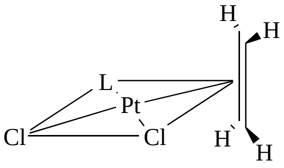
(**6**)

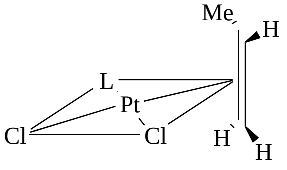
(**7**) $\theta = 90^\text{o}$

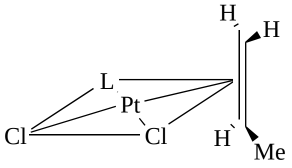
(**8**) $\theta = 270^\text{o}$

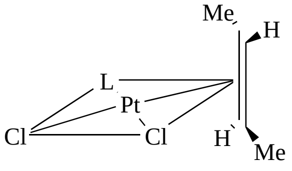
(**9**)

The most effective approach to interpreting the barriers for a wide range of compounds lies in the consideration of the relative interactions within the Dewar, Chatt, Ducanson model of metal–alkene bonding.**70,71** An extended Hückel MO approach has explored the interactions of the valence orbitals and examined the important interactions. A comprehensive extended Hückel MO treatment of ethylene bonding and rotational barriers by Albright, Hoffmann *et al.***81** presents an excellent analysis and the reader is referred to their paper for further discussion. We have found that the following approach, which considers only three orbitals on the metal and the π and π^* orbitals of the alkene, provides the essential elements for understanding the barriers to rotation. Naturally, steric effects and secondary interactions with other orbitals modulate these primary interactions.

The donor component of the metal–alkene bonding is a symmetric interaction and to a first approximation is independent of the orientation of the alkene relative to the other ligands (Figure 2). It is the back-bonding interaction, which is most sensitive to the orientation of the alkene. This is most cleanly illustrated in six-coordinate complexes, where one can readily predict preferred orientations by considering competitions for back donation of electron density.

In the absence of interaction with other ligands or orbitals, the back-bonding interaction in the *yz* plane for the $\theta = 90^\circ$ orientation would be degenerate with that in the *xz* plane for the $\theta = 0^\circ$ orientation. Thus, for the chromium and molybdenum derivatives $M(CO)_5$(ethylene), there would be no preference for either the *yz* or the *xz* plane. In fact, at this level of approximation, no barrier would be expected for a rotation from the *yz* to the *xz* plane, that is, the interaction with a linear combination of *xz* and *yz* would also be equivalent in energy.

If one of the cis carbonyls is substituted by a phosphine, the degeneracy is lifted and the preferred conformation is one in which the alkene lies along the O–C–M–P axis,[82,83] (**10**). If the phosphine is on the x axis, then the orientation along x involves a back-bonding competition for the electron density in the *xz* orbital between the ethylene π^*, the carbonyl π^*, and the phosphine unfilled d orbital, whereas orientation along y involves a competition between the ethylene π^* and two carbonyl π^* orbitals. The weaker acceptor ability of phosphine thus produces a richer back-bonding capability for the alkene in the *xz* plane than in the *yz* plane. Therefore, the bond is stronger when the alkene is oriented in the x direction. The barrier thus arises from the differential bonding in the two directions. This is an important feature: the overall strength of the metal–alkene bond will not correlate directly with barriers, since it is the differential strength, which is important. Hence, it is quite feasible to have a situation where a weakly bonded alkene could have a high barrier to rotation and a strongly bonded alkene could have a low barrier.

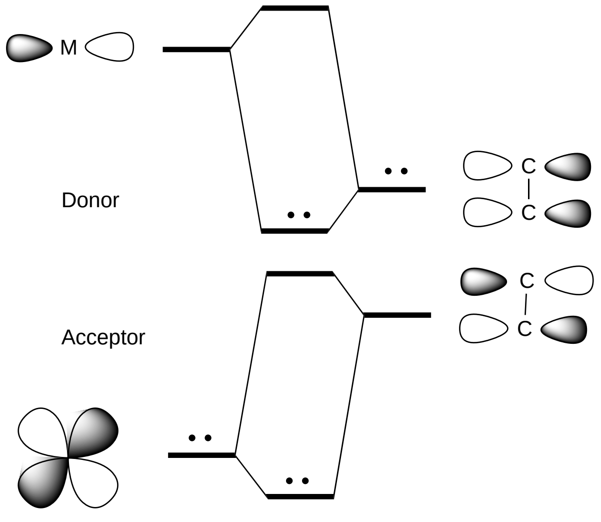

Figure 2 Donor and acceptor components of a metal–alkene bond

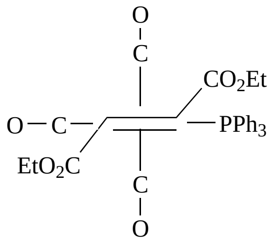

(**10**)

The origin of the differential interaction can also be illustrated in MO terminology by considering the effect of other ligand orbitals on the levels involved in back donation. An unfilled ligand orbital of the same symmetry would lower the bond order in the Mo–alkene π^* in proportion to the magnitude of its interaction. Thus, one can qualitatively estimate the effect on the barrier by considering the relative energies and overlap of the competing orbitals. Although these interactions are a major factor in the bonding, attempting to describe all barriers and orientational preferences to this limited set of interactions will obviously lead to failure when these effects do not dominate. For example, when a large differential in back-bonding capability in the *xz* and *yz* planes exists, as in the case of cis-phosphine-substituted alkene complexes, then one can confidently predict the preferred orientation. When the differential interaction diminishes, other effects may dominate and exert control over the orientation. Thus when the x and y orientation are degenerate, the simple model would predict that no preference should exist either for the x or y direction or anywhere in between. Nevertheless, there is a preference for lying parallel to the other ligands. This can be traced to an unfavorable interaction of the filled alkene π orbital with the filled metal *xy* orbital.[81]

As shown in (**10**), a large differential in back-bonding capability in the *xz* and *yz* planes exists in the alkene complexes *cis*-$(CO)_4(PMe_3)$W(ene) (**11**), $(CO)_3$(diphos)W(ene) (**12**), $(CO)_3(PMe_3)_2$ W(ene) (**13**), and (CO)$(PMe_2Ph)Cl_2$Ru(ene) (**14**). The horizontal (*xz*) is preferred to the vertical (*yz*) in each complex, illustrating that the plane containing the orbital with greatest back-bonding ability is preferred. Note also that the presence of an additional phosphine enhances the effect and raises the barrier by ≈40 kJ mol^{-1} in comparing (**11**) and (**13**) with ene = dimethyl fumarate, that is, $\Delta G^\ddagger$ of 40 and 80 kJ mol^{-1}.[79,80] Thus, any steric effect which might have been anticipated to destabilize the orientation parallel to the M–P bond is not sufficient to overcome the electronic control of conformational preference. The barrier for (**14**) is less than 40 kJ mol^{-1}.

A particularly interesting case is that of *trans*-bis(ethylene)Mo(diphos)$_2$, (**15**) in which the ethylene ligands are staggered but align themselves along the Mo–P bonds.[84,85] The alignment along the Mo–P bonds is attributable to the repulsive interaction of the filled π orbital of ethylene with the filled *xy* orbital of the metal. The staggering of the ethylenes

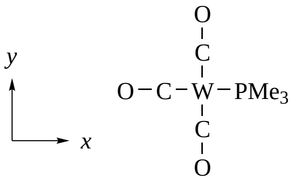

$$\begin{array}{ccccc} & & \mathrm{O} & & \\ & & | & & \\ & & \mathrm{C} & & \\ & & | & & \\ \mathrm{O}{-}\mathrm{C} & {-} & \mathrm{W} & {-} & \mathrm{PMe_3} \\ & & | & & \\ & & \mathrm{C} & & \\ & & | & & \\ & & \mathrm{O} & & \end{array}$$

(**11**)

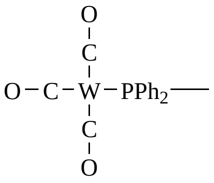

$$\begin{array}{ccccc} & & \mathrm{O} & & \\ & & | & & \\ & & \mathrm{C} & & \\ & & | & & \\ \mathrm{O}{-}\mathrm{C} & {-} & \mathrm{W} & {-} & \mathrm{PPh_2}{-} \\ & & | & & \\ & & \mathrm{C} & & \\ & & | & & \\ & & \mathrm{O} & & \end{array}$$

(**12**)

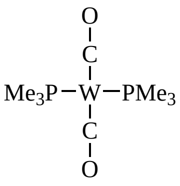

$$\begin{array}{ccccc} & & \mathrm{O} & & \\ & & | & & \\ & & \mathrm{C} & & \\ & & | & & \\ \mathrm{Me_3P} & {-} & \mathrm{W} & {-} & \mathrm{PMe_3} \\ & & | & & \\ & & \mathrm{C} & & \\ & & | & & \\ & & \mathrm{O} & & \end{array}$$

(**13**)

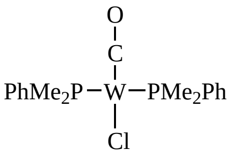

$$\begin{array}{ccccc} & & \mathrm{O} & & \\ & & | & & \\ & & \mathrm{C} & & \\ & & | & & \\ \mathrm{PhMe_2P} & {-} & \mathrm{W} & {-} & \mathrm{PMe_2Ph} \\ & & | & & \\ & & \mathrm{Cl} & & \end{array}$$

(**14**)

follows from the sharing of the electron density in the same d orbital in the eclipsed form relative to the effective utilization of both orbitals in the staggered form: one π^* to each d. Further analysis suggests that the rotations should be concerted, and that the motions of the top and bottom ethylene are concerted with the two ligands synchronously turning and remaining perpendicular to each other, as shown in equation (8).

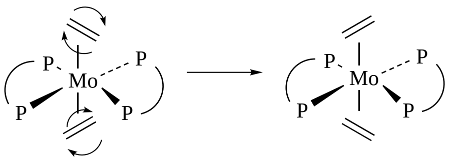

(**15**)

(8)

A more recent study[86] of series of $W(CO)_4(ene)_2$ complexes by ^{13}C NMR showed that from the highest barrier, for l-pentene rotation ($\Delta\ G^\ddagger = 45.8\,\mathrm{kJ\,mol^{-1}}$), to the lowest barrier, for cyclohexenone ($\Delta G^\ddagger = 38.8\,\mathrm{kJ\,mol^{-1}}$), there was only a difference of $\sim 7\,\mathrm{kJ\,mol^{-1}}$. It appears that the different steric effects of the alkenes in these complexes have little effect on the barrier to rotation.

Since Cramer's early studies on ethylene and tetrafluoroethylene complexes,[32,33] a rule of thumb developed that fluorinated alkenes would rotate much slower than the corresponding unfluorinated alkenes attached to the same metal fragment. High barriers to rotation are the norm for C_2F_4 and this has been attributed to increased back bonding and the formation of a metallacyclopropane-like structure.[87] One might note that, in $Rh(acac)(C_2H_4)(C_2F_4)$, the 56 MHz ^{19}F NMR spectrum showed a single environment for the fluorines, which could have been interpreted as fast rotation for the C_2F_4. At higher fields, however, an AA′BB′X pattern is observed, indicating that fluorinated ligand rotation is slow on the NMR timescale.[88]

2.3 Rotations of Alkenes in Cyclopentadienyl Complexes

For $CpRh(C_2H_4)(C_2F_4)$, the ethylene rotates rapidly on the NMR timescale but the C_2F_4 appears rigid. The $CpRh(C_2H_4)_2$ has an $E_a = 62.7\,\mathrm{kJ\,mol^{-1}}$ ($T_I = 0°$ and Table 1 would suggest $\Delta G^\ddagger = 64\,\mathrm{kJ\,mol^{-1}}$). $Cp^*Ir(C_2H_4)_2$ has a $T_I = 110°$ indicating $\Delta G^\ddagger = 86.5\,\mathrm{kJ\,mol^{-1}}$.[89] It is therefore surprising that Hughes has observed that $Cp^*Ru(trifluoroacac)(C_2F_4)$ and $Cp^*Ru(Cl)(t\text{-}BuNC)(C_2F_4)$ have relatively low barriers of $\Delta G^\ddagger = 53$ and $59\,\mathrm{kJ\,mol^{-1}}$, respectively, as determined by line shape analysis ($T_I \sim -30°$, $\Delta G^\ddagger = 56\,\mathrm{kJ\,mol^{-1}}$, Table 1). There is apparently only one other reference to a low barrier for C_2F_4,[90] but this could be an accidental equivalence. It thus appears that these Cp*Ru complexes are the first examples of low barriers for propeller rotation. Hughes' paper provides a summary of references to this area.[88]

A cyclopentadienyl group can be presumed to occupy three coordination positions; thus CpM(CO)X(alkene) complexes can be conveniently considered as octahedral systems. Reference to Mann's review[13] indicates that a wide range of barriers are observed in these extensively studied systems. The introduction of the cyclopentadienyl moiety as well as other ligands produces the possibility of several isomers. Thus a propene complex can exist in endo and exo forms,[91] as in (**16**) and (**17**), and a substituent on the alkene can be cis or trans to other ligands. The use of 'cis' and 'trans' is inconvenient owing to the nature of the interconversion via rapid rotation. Thus, in $[CpM(CO)(NO)(propene)]^+$ complexes, the rotation of the exo isomer with the methyl group cis to NO (**18**) produces the endo isomer with the methyl group trans to NO (**19**).[92] It should be noted that the rotation does not change the configuration at the metal or alkene stereogenic center. Since the chirality at the substituted carbon is retained during the rotation, it is most convenient to use chirality descriptors. (Note that the chirality at the metal center is given first, so that (**18**) is (R,S)-exo, whereas (**19**) is (R,S)-endo.) It should be noted that once the other two ligands are not the same, the stable conformation may not have the alkene exactly parallel with the ring (see below).

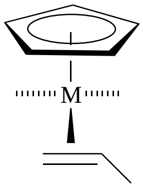

(**16**) *exo*

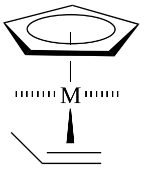

(**17**) *endo*

A single barrier is often reported for propene complexes; however, since the free energy of the endo isomer is usually less than that of the exo isomer, the direction of the path should be stipulated, that is, exo to endo, because the endo to exo barrier usually differs by 2 to $12\,\mathrm{kJ\,mol^{-1}}$. Secondly, there are two routes by which one can proceed from exo to

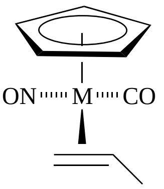

(**18**) (*R,S*)-*exo*

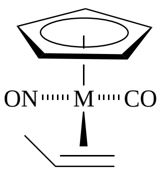

(**19**) (*R,S*)-*endo*

endo: a clockwise rotation and a counterclockwise rotation. One of these involves passing the methyl group by the cyclopentadienyl ring and the other less energetic path only requires a vinyl proton to interact with the ring. Only the lowest energy path is usually reported, although experiments can be designed to determine the differences.

In the symmetrical $CpM(CO)_2$ systems, endo–exo isomerism exists and the C=C is effectively parallel to the ring and bisects the coordinates on which the other ligands might be assumed to be located; this is the orientation shown in (**16**) and (**17**). The introduction of a group with a large difference in π-acceptor ability relative to carbonyl either enhances or depletes the back-bonding ability of the orbital parallel to the bond. It is most convenient to consider that the orbitals and the molecule are reoriented along a Cartesian system, as shown in Figure 3.

Again, in this situation, one would expect the alkene to try to align along the axis of greatest back-bonding capability. Thus, in a nitrosyl carbonyl complex, one would expect the alkene to align with the M–C–O bond.[81,91,92] The alignment is not perfect, owing to steric interactions and other orbital interactions; nevertheless, it has a profound effect on the stability of conformers and barrier heights.

For example, in $[CpFe(CO)_2(propene)]^+$, the equilibrium constant is $\approx$19 in favor of exo; however, in the $[CpMo(NO)(CO)(propene)]^+$ system, the constant is only 1.7. The orientational preference induced by the NO relieves the steric interaction of the methyl with the Cp ring in the endo isomer. The barrier is also significantly higher in the Mo complex, not only because the back bonding is greater (a neutral versus a positively charged complex), but because there is a large differential in the back-bonding capability in various orientations available to the alkene.[91–93]

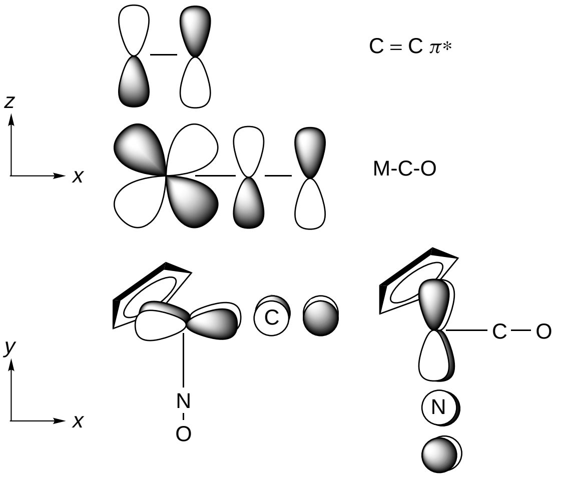

Figure 3 Orbital interactions for a CpM(NO)(CO) fragment

The use of prochiral alkenes such as propene,[91] 2-butene,[91] *trans*-dideutereoethylene,[94,95] dialkyl fumarates,[96] and *trans*-dimethoxyethylenes,[94] have allowed detailed structural and mechanistic studies of alkene complexes. The diastereomers produced upon binding of prochiral alkenes to CpM(CO)X centers provided the key complexes to prove that interconversions occurred by rotations about the metal–(C=C) axis. Thus observations[91,96] that neither the chirality at the metal nor at the alkene is changed in the rearrangement of a trans-substituted alkene provided proof that the nature of the dynamic process was a propeller rotation. Note that in equation (9) the equilibrium between (**20**) and (**21**) averages environments *b* and *d* separately from *a* and *c*. A key feature is that olefin rotation does not alter the chirality at the olefin because of the olefin-metal bond.

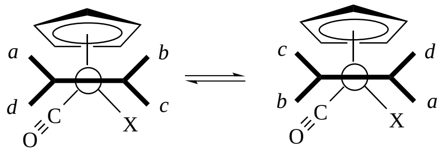

(**20**) (**21**) (9)

2.4 Alkene Nonrigidity Other than Rotation

Gladysz has carried out an investigation of $[CpRe(NO)(PPh_3)(alkene)]^+$ complexes[97] and has observed comparable results to those above in most cases. A $\Delta G^{\ddagger}_{369} = 68.6\,\mathrm{kJ\,mol^{-1}}$ was determined from the ^{13}C NMR spectra at T_c for $[CpRe(NO)(PPh_3)(C_2H_4)]^+$ and is typical of this system. A $T_I \sim 30\,°C$ suggests a barrier of $\approx 71\,\mathrm{kJ\,mol^{-1}}$. One might note that ^{13}C NMR provides advantages for determining barriers owing to the absence of coupling between ^{13}C nuclei. Unfortunately, however, the low sensitivity for broad resonances often makes it difficult to examine broad spectra. Use of equation (3) and initial NMR line broadening is recommended. As discussed above and by Hoffmann,[93] the preferred orientations can generally be predicted on the basis of π-interactions. Gladysz has cast his arguments in terms of interactions with the *d* orbital HOMO.[98,99] His papers serve as a source of recent references in this area.[98–101] The comprehensive study by Boone and Gladysz[101] provides a particularly useful summary of this area. There have also been recent studies[102,103] of fluxionality in $[Cp^*Ir(NO)(ethylene)]^+$, which are also consistent with propeller rotation of the olefin.

Prior to 1992, it was generally accepted that inversion of chirality in olefin binding would require complete dissociation of the olefin in an intermolecular process unless the olefin was tethered to a ligand. There is, however, a spectacular result[97] that showed that the chirality of the alkene is not maintained in some *intramolecular* rearrangements of CpRe(NO)(L)(alkene). Although the result could be interpreted as a rotation about the C–C axis of the alkene, the most reasonable interpretation is that the metal takes an end run around the alkene (equation 10). The barrier ($121\,\mathrm{kJ\,mol^{-1}}$) for the ''end-run'' pathway is above that which is accessible by NMR, but indicates that the process could occur with lower barriers in some cases. There is substantial evidence that C–H σ-bonds can interact strongly with rhenium and iridium in low oxidation states. Deuterium-exchange studies by Faller and Felkin[104] provided early evidence that suggested that *t*-butylethylene interacted via the C–H bond without prior coordination of the alkene. A number of σ-bond complexes of C–H bonds are now known, but are usually tethered to the metal and termed ''*agostic*;'' nevertheless, there is growing evidence that nonrigid processes involving σ-bonded C-H complexes should be observable by DNMR (this will be discussed below and in more detail in Section 9.2).

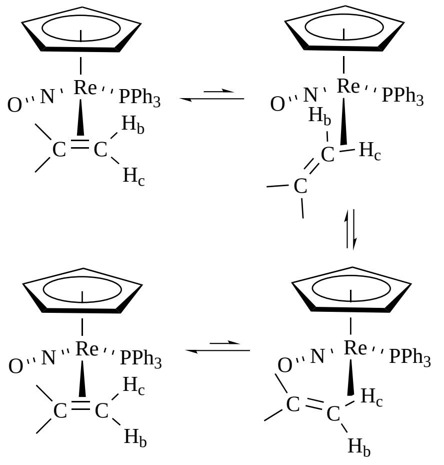

(10)

Harman has developed an analog of the CpRe(NO)(L)$^+$ systems using hydrido(tris)pyrazolylborate, Tp, complexes.[105–109] The [TpRe(CO)(PMe$_3$)] moiety is more electron rich than its counterpart and will even bind naphthalene in an η^2-fashion. Ethylene rotation in TpRe(CO)(L)(ene) has a barrier of $40.0\,\mathrm{kJ\,mol^{-1}}$ as determined by SST experiments. Substantial variation of barriers correlated with basicity were noted with different L groups: L = *t*-BuNC, $32\,\mathrm{kJ\,mol^{-1}}$ estimated from extensive broadening $\sim -85\,°\mathrm{C}$; L = py, $51.0\,\mathrm{kJ\,mol^{-1}}$ (SST); L = 1-methyl-imidazole = MeIm, $52.3\,\mathrm{kJ\,mol^{-1}}$.[108] Generally, olefin rotation occurred at lower barriers than for interfacial interconversion ($>84\,\mathrm{kJ\,mol^{-1}}$). A thorough study of binding of olefins with MeIm ligand was carried out.[105] Since the rhenium fragment is chiral diastereomers are formed with prochiral olefins; hence, rotamers interconvert faster than diastereomers. The interconversions of rotamers for propene are shown in Figure 4; diastereomer interconversions involve barriers of $\sim 134\,\mathrm{kJ\,mol^{-1}}$.

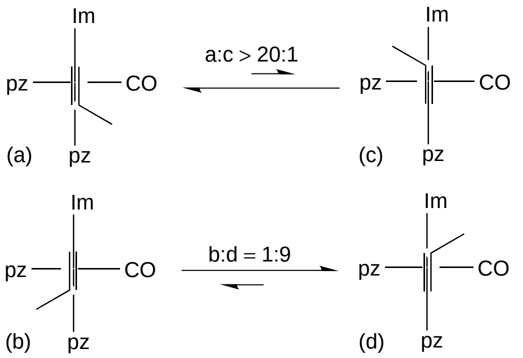

Figure 4 Interconversion of rotamers for TpRe(CO)(MeIm)(propene)

The TpRe(CO)(PMe$_3$)(thiophene) complex shows a selectivity of 3.2:2.0:1.0 for diastereomer (**22**) to (**23**) to an η^1-S isomer, as shown in Figure 5. This complex, as well as other thiophene complexes, offer the potential for an intramolecular face flip via formation of an η^1-S intermediate that could invert at sulfur to interconvert diastereomers. Nevertheless, SST experiments showed that the lowest energy path for interfacial exchange occurred *without* passing through an η^1-S intermediate.[109] The interfacial (face flip) for the thiophene complex (R=H) occurred with a $\Delta G^\ddagger = 79.4\,\mathrm{kJ\,mol^{-1}}$ whereas the intrafacial (ring-walk on the same face) occurred at higher energy, $\Delta G^\ddagger = 83.6\,\mathrm{kJ\,mol^{-1}}$. Many aromatics and heteroaromatics, in fact, underwent intramolecular interfacial interconversions at lower energies than migrations on the same face of the arene. A key feature is that this occurs in most of the arene systems at free energies of activation lower than those in the alkenes. It is therefore probable that these interconversions also involve agostic intermediates as suggested by Gladysz ''end-run'' olefin interconversions.

2.5 Rotations in Other Geometries

Eisenberg[110] has examined [Ir(^{13}CO)(diphos)(ethylene)$_2$]$^+$ by ^{1}H, ^{13}C, and ^{31}P DNMR.

At the slow exchange limit ($-90\,°\mathrm{C}$), four ethylene proton resonances are observed, see (**24**). Upon raising the temperature, a propeller rotation ($\Delta G^\ddagger \sim 38\,\mathrm{kJ\,mol^{-1}}$) in the trigonal bipyramidal complex averages two environments to yield an AA′BB′ pattern in the ^{1}H{^{31}P} spectrum. A second dynamic process averages the ^{31}P resonances ($T_c = -10\,°\mathrm{C}$) in the ^{31}P NMR and the ^{31}P-^{13}C coupling in the ^{13}C NMR at the same time that nonequivalent ^{1}H protons for the diphos backbone become equivalent ($\Delta G^\ddagger \sim 46\,\mathrm{kJ\,mol^{-1}}$). This can be attributed to a pseudorotation in the trigonal bipyramidal structure similar to that shown in equation (1). It should be noted that the pseudorotation favors certain permutations because this does not average the AA′BB′ pattern of the ethylenes. At higher temperatures, exchange with free ethylene occurs.

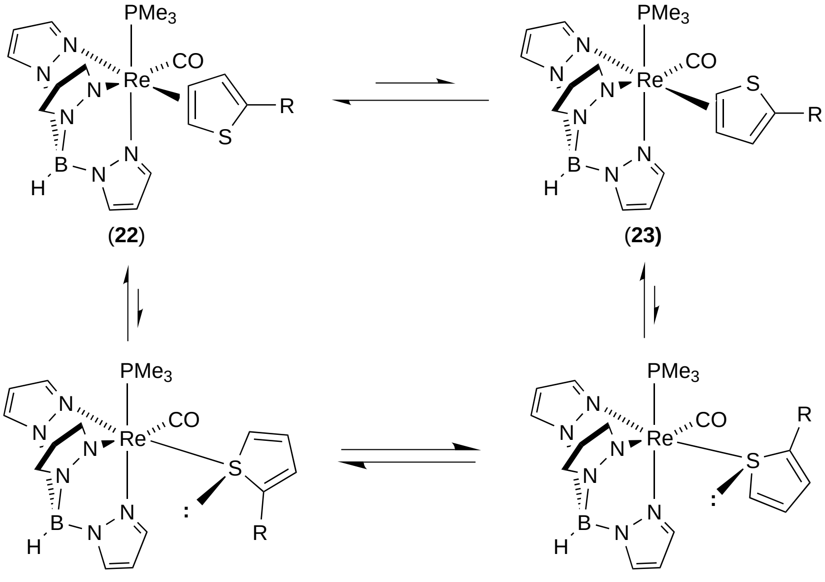

Figure 5 Diastereomer interconversion in TpRe(CO)(MeIm)(thiophene)

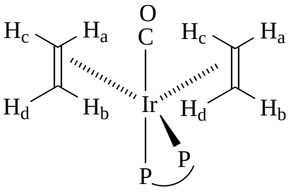

(**24**)

2.6 Rotations in Solids

Although some of the initial studies of olefin rotation employed solid-state methods, relatively few studies have been carried out recently. Studies of relaxation in the solid-state ^{2}H spectra of (acac)Rh(ethylene-d_4)$_2$ indicated a free energy of activation of 56.5 kJ mol^{-1}.[111] Olefin rotation in deuterated (Ph$_3$)$_2$Pt(ethylene) and K[Cl$_3$Pt(ethylene)] was characterized by long T_1's for the ^{2}H, which indicated slow rotation.[112] This indicates barriers in the solids of $>$80 kJ mol^{-1}. Measurements in solids can be influenced by nearest neighbor interactions and thus do not necessarily correlate with barriers measured in solution. It is possible, however, to measure very low barriers in solids and this can potentially overcome the practical lower limits that are imposed by solution studies. One should note, however, that, in certain cases, low barriers can be determined in solution using ^{1}H relaxation times rather than line shapes, SST, or EXSY spectra. The dipolar relaxation of the protons in complexes containing a ^{13}CH$_3$ group can be analyzed as a function of temperature to yield a barrier. For a variety of organometallics, the activation energy for methyl rotation is $\sim$12 kJ mol^{-1}.[113] ^{2}H relaxation studies give a 10.9 kJ mol^{-1} barrier for the three equatorial methyl groups in [Cp*WMe$_4$] PF$_6$.[114] The axial methyl group has one of the largest barriers known for methyl rotation of 26.8 kJ mol^{-1}. The measurement of motional barriers in solids has been reviewed by Duer.[115]

2.7 Rotations of Alkynes in Cyclopentadienyl Complexes

Alkyne complexes have behavior directly analogous to the alkene complexes,[13,20] except for having somewhat higher barriers, and will not be discussed in great detail. They do, however, present an example of the potential problems arising from assuming cationic species will have lower rotational barriers. For example, [CpMo(CO)(HOCH$_2$C≡CCH$_2$OH)$_2$]$^+$ has a barrier more than 42 kJ mol^{-1} higher than the neutral complex CpMo(Cl)(ClCH$_2$C≡CCH$_2$Cl)$_2$.[116] Thus replacement of CF$_3$C≡CCF$_3$ by PhC≡CPh in CpWCl(CF$_3$C≡CCF$_3$)$_2$ increases the barrier by 12 kJ mol^{-1}.[117] The orientation of one of the MeC≡CPh (Me cis or trans to Cl) produces a 6-kJ mol^{-1} differential in barrier of the other MeC≡CPh in CpMoCl(MeC=CPh)$_2$.[116]

Templeton has carried out extensive studies of rotational barriers of alkynes and has calculated a number of rotational energy profiles; his papers provide leading references to earlier work.[118] Pyrazolylborate analogues also show similar behavior[119] and this work as well as earlier reviews provides leading references.[13,20]

3 CARBENE ROTATION

Renewed interest in metal carbenes, particularly N-heterocyclic carbenes, has resulted from recent progress in ring closing metathesis[120–122] and the preparation of relatively stable carbenes that are active catalysts.[122] Recent reviews provide leading references for activity in physical aspects of the area.[123,124] Theoretical studies indicate that conformational equilibria play a key role in the catalysis.[125–129]

The symmetry of the *p*-orbital in a carbene ligand is directly analogous to that in the π^*-orbital of an alkene and, consequently, similar orientation effects are expected for carbene complexes as found in alkene complexes[93,130] in electronically asymmetric complexes, such as (**25**). The extensive studies of rotational barriers and conformational preferences by Brookhart[131] and Gladysz[132,133] provide leading references to earlier work. Typical examples of conformational isomerism are (**26**) and (**27**). The nomenclature can be easily confused, but (**26**) has been termed *synclinal* and (**27**) described as the *anticlinal* conformer.[131,132] Synclinal isomers have been shown to be more reactive than *anticlinal* isomers in $[\mathrm{CpFe(CO)(PR_3)(carbene)}]^+$ complexes.[131] The conformational isomers control the stereochemistry of reactions of the carbene.[133] Diastereomerically pure $\mathrm{CpMn(CO)(PR_3)(carbene)}$ complexes have also been prepared.[134] The electronic asymmetry in $[\mathrm{Tp'W(CO)(PhC_2Me)({=}CH_2)}]$ gives rise to a very high barrier (not detectable by NMR) for rotation of the methylene.[135,136] Rotational isomers are observed in the amido complexes $\mathrm{TpMo({=}CHR)(NAr)(CH_3)}$ (**28**), $\mathrm{TpMo({=}CHR)(NAr)(OCH_3)}$ (**29**), and TpMo(=CHR)(NAr) (OTf) (**30**).[137] The variations in ligands produces a significant variation in barriers to rotation: (**28**) > (**29**) > (**30**). Other arylamido complexes show increased rotational rates in alkylidenes as alkoxide substituents become more electron donating.[138–140] Vinylidenes with similar ligands, such as $[\mathrm{Cp^*(Ph_2PCH{=}CH_2)_2Ru{=}C{=}CH_2}]$, show a low barrier to hindered rotation ($<28\ \mathrm{kJ\,mol^{-1}}$) owing to a lack of electronic asymmetry.[141] Other examples are covered in a review.[123]

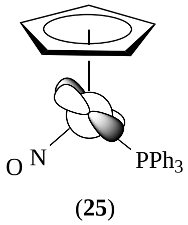

(**25**)

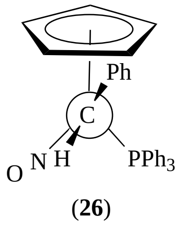

(**26**)

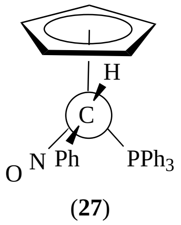

(**27**)

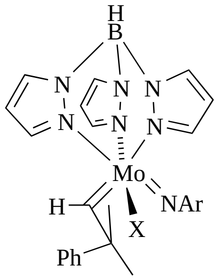

(**28**) X = Me

(**29**) X = OMe

(**30**) X = OTf

Barriers to carbene rotation in N-heterocyclic carbenes (NHC's) appear to be dominated by steric interactions, and they can also be observed in square-planar complexes using the diastereotopic protons in benzyl, butyl, and ethyl derivatives.[142] For example, the COD derivative (**31**) shows diastereotopic methylenes owing to a lack of a mirror plane through the Ir–C(carbene) plane. These do not average at high temperature indicating a barrier greater than $92\ \mathrm{kJ\,mol^{-1}}$. The carbonyl analogues (**32**) show averaging of the methylene protons that indicates a 65-kJ $\mathrm{mol^{-1}}$ barrier to rotation. Steric interactions influencing barriers have also been observed by Hermann.[143,144] With unsymmetrically substituted NHC's or triazolinylidenes, enantiomers, for example (**33**) and (**34**), are produced upon binding to the square-planar complex.[145,146] With chiral substituents, diastereomers can be separated when the rotational barrier is high and they have been used for asymmetric catalysis.[146] When two carbenes are present in a cis complex, the axial chirality allows three isomers (**35–37**). For some bis carbene complexes, the restricted rotation can cause broadening at room temperature in the proton NMR spectra.[147] An alternative to preventing rotation by steric interactions is to tether the carbene to a cyclopentadienyl group to prevent rotation (**38**).[148]

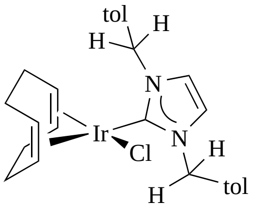

(**31**)

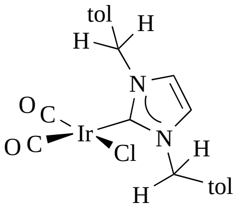

(**32**)

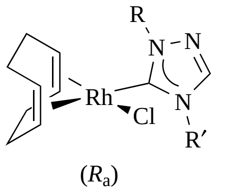

(R_a)

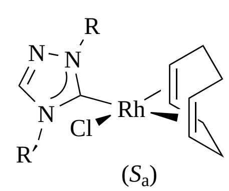

(S_a)

(**33**) (**34**)

Other types of hindered rotation besides rotation about the M=C can occur. Hindered rotation about the C–C bond between the α-carbon and ipso-carbon of the phenyl in the M=CHAr is observed in both iron and rhenium compounds with $\Delta G^\ddagger$ 42–50 $\mathrm{kJ\,mol^{-1}}$.[132,149]

Compounds such as $[\mathrm{Cp^*(Ph_2PCH{=}CH_2)_2Ru\ {=}C{=}CH_2}]$ show a low barrier to hindered rotation about the Ru=C;

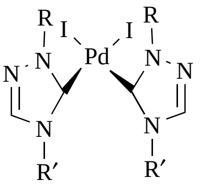

cis-syn-(R_a,S_a)

(**35**)

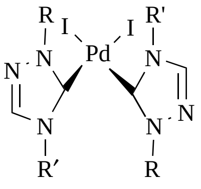

cis-anti-(R_a,R_a)

(**36**)

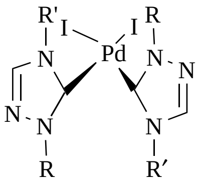

cis-anti-(S_a,S_a)

(**37**)

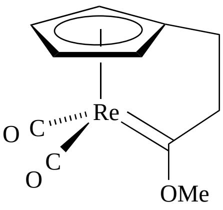

(**38**)

however, DNMR spectra are observed owing to restricted rotations about other single bonds, that is, Ru-P and P-C.[141]

4 HINDERED ROTATION ABOUT SINGLE BONDS

In investigations of diastereomers, there is a common problem wherein barriers are low enough that averaged spectra are observed at room temperature. Upon lowering the temperature, isomers can be observed, but it is difficult to tell whether these are the isomers or conformations that are frozen out owing to relatively high barriers to rotation about single bonds.[150] This is a particularly important distinction to be made when diastereomers are being used for asymmetric catalysis.

4.1 Restricted Rotation About M-P and P-C Bonds

Hindered rotations of M-P bonds involve barriers generally much less than $60\,\mathrm{kJ\,mol^{-1}}$ and with bulky phosphines may have barriers $\sim 40\,\mathrm{kJ\,mol^{-1}}$. Since the rate at which resonances will coalesce depends on the reciprocal square of the chemical shift difference, the increasing use of higher field NMR spectrometers yields many instances where conformational effects are a source of broadening that can be observed. Since conformational interconversions do occur at rates that can be studied by NMR, and although barriers are low, there have been extensive studies of hindered rotation in P–M bonds.[151–168] Generally these involve phosphines containing bulky substituents, such as *t*-butyl, *o*-tolyl, and mesityl groups. The barriers can be high enough ($\sim 60\,\mathrm{kJ\,mol^{-1}}$) to show broad resonances at room temperature in some cases, such as Pt(mesityl$_2$PH)$_2$(Et)(I).[166] Generally less-hindered phosphines have lower barriers, but in some cases they can be measured. Cp*Ir(pz)$_2$(PPh$_3$) shows hindered rotation about the Ir–P bond.[160] The silver derivative Cp*Ir(pz)$_3$Ag(PPh$_3$) shows Ag–P restricted rotation with a $\Delta H^{\ddagger} = 35\,\mathrm{kJ\,mol^{-1}}$ and $\Delta S^{\ddagger} = -55\,\mathrm{eu}$.[160] In some cases, π-stacking effects, rather than steric hindrance, has been attributed to the source of increased barriers. The *trans*-[PtX(Me$_2$-phen)(PPh$_3$)$_2$]X complexes, which contain a monocoordinated 2,9-dimethyl-1,10-phenanthroline, represent a rare case where triphenylphosphine shows a barrier higher than $42\,\mathrm{kJ\,mol^{-1}}$.[159] Usually barriers to rotation about M-PMe$_3$ bonds are low, but there are several recent cases of relatively high barriers in analogues of Cp*Ir(2-C$_6$BrF$_4$)Br(PMe$_3$).[168] The barrier for this compound is $39\,\mathrm{kJ\,mol^{-1}}$ and for the 2-C$_6$BrF$_4$ analogue it is $38\,\mathrm{kJ\,mol^{-1}}$. The highest value of $44\,\mathrm{kJ\,mol^{-1}}$ for $\Delta G^{\ddagger}$ was found for Cp*Rh(2-C$_6$IF$_4$)I(PMe$_3$).[168]

Hindered rotation about the P–C bonds in phosphine ligands can also produce conformational isomers and DNMR spectra below room temperature.[159,163,166–179] There have been moderately successful attempts to estimate relative conformational stability using molecular mechanics methods with force fields adjusted for metal compounds.[180–185] These different conformations can produce conformational isomers that are diastereomers in complexes with chiral metal centers, such as in (**39**) and (**40**).[186] Propeller chirality, which is designated as *P* and *M*, has also been studied in triphenylsilane and triphenylstannane.[187]

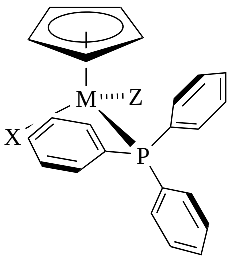

(**39**)-(*P*)

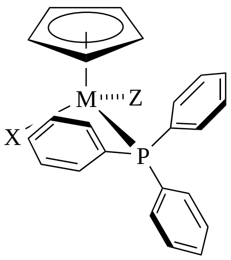

(**40**)-(*M*)

Generally one would expect the propeller chirality to be controlled by the chirality at the metal center, such that (**39**) or (**40**) would be preferred depending upon the interactions with the other ligands on the metal. There is, however, a strong influence of the conformations and configurations of the other ligands. For example, (**41**) is formed initially upon reduction of a carbene precursor and the (R)-stereochemistry at the metal center induces an (R) configuration at the carbon attached to the metal, which in turn induces a propeller chirality of (M) in the triphenylphosphine. This kinetic isomer can be isomerized to the thermodynamically stable isomer (**42**), which an (S) configuration at the carbon, but a propeller chirality of (P).[185] It is interesting to note that the sign of the rotation is positive for (**41**), but negative for (**42**).

The chirality associated with the PPh$_2$ analogue of this propeller-type chirality is particularly important with nonracemic chiral ligands, such as BINAP, since it influences

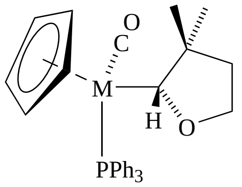

(**41**)-(R_{Fe},R_C,M)

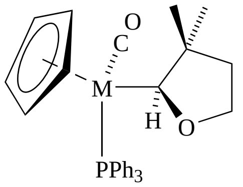

(**42**)-(R_{Fe},S_C,P)

the chiral environment when the complex is used as an asymmetric catalyst. Hindered phenyl rotation has been observed in several BINAP complexes.**[186,188,189]** In the case of (BINAP)$PdCl_2$, the inequivalent ortho and meta proton resonances of one phenyl group are near coalescence at 25 °C and only become sharp multiplets (at 400 MHz) on heating to 70 °C.**[186]** The hindered rotation of the axial phenyl group was implicated in determining the high stereoselectivity of the BINAP catalyst enantioselective hydroformylation.

4.2 Restricted Rotation About M-aryl Bonds

As observed with carbene rotations (see Section 3), conformations of aryls can introduce additional chirality into a complex. Aryls prefer to lie orthogonal to the coordination plane in square-planar complexes. Hindered rotation of aryls in these complexes can produce atropisomerism,**[190]** although this description is most commonly associated with restricted rotation about C–C single bonds in biaryls. An example of hindered rotation is found in (DIOP)Pt(3,5-$Br_2C_6H_3$)(I) (**43**) in Brown's paper which provides an excellent discussion and leading references.**[191]** The ortho protons of the dibromoaryl are diastereotopic owing to the chirality of the DIOP ligand. These protons can be identified by their coupling to ^{31}P (6.5 Hz) and ^{195}Pt (40 Hz), but they are broad at 25 °C and sharpen at -10 °C, suggesting a barrier for Pt-aryl rotation $\sim$64 kJ mol^{-1} using Table 1. One should note that the ^{195}Pt satellites are still somewhat broad at -10 °C. This, however, is due to chemical shift anisotropy relaxation of the ^{195}Pt nuclei rather than restricted rotation. This CSA relaxation often induces broadening in high field ^{1}H spectra where coupling to ^{195}Pt is present. This relaxation is field dependent and thus can be reduced or effectively eliminated by working at lower fields. It is important, however, to avoid mistaking CSA relaxation for hindered rotation.

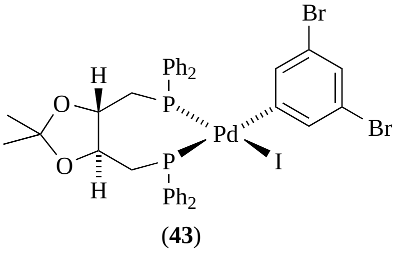

(**43**)

If the aryl is not C_2-symmetric in analogues of (**43**), diastereomeric rotamers will exist. Thus, the 2-MeO-phenyl analogue shows a 57:43 ratio of rotamers. When two aryls are present, syn and anti isomers can exist and were observed in nickel complexes.**[192]** The bis(2-methoxyphenyl)Pd(DIOP) (**44**) exhibits three sets of ^{31}P resonances in a ratio of 3:1:1 at ambient temperature.**[191]** There are two anti isomers and one syn isomer, which is readily identified owing to the nonequivalence of its ^{31}P resonances. The chirality of the bisphosphine ligand favors one of the anti isomers.

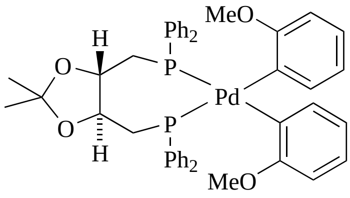

(**44**)

In (tmeda)PdBr{o-(CH_2CH_2OH)C_6H_4}, (**45**) aryl rotation is restricted and sharp spectra are observed in $CDCl_3$ up to 60 °C ($\Delta G^{\ddagger} > 79$ kJ mol^{-1}). A number of diastereotopic features are observed owing to the retention of chirality: the two methylene groups show diastereotopic protons; and four methyl resonances are observed for the NMe_2 groups in the tmeda. An X-ray structure shows that there is an H bond from the alcohol proton to the bromide, which may account for the particularly high barrier for aryl rotation. In methanol, the barrier is lower (63 kJ mol^{-1}) owing to ionization of the bromide.

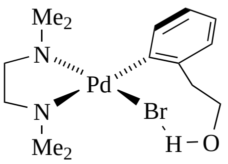

(**45**)

Atropisomerization in cis-[Pd(2-C_6BrF_4)$_2$(tetrahydrothiophene)$_2$] (**46**) also illustrates a situation in which dissociation can modify the barrier for syn-anti interconversion (equation 11).**[193,194]** In the presence of excess tetrahydrothiophene (tht), dissociation is suppressed and a syn to anti rate constant of 1.4 s^{-1} at 26 °C ($\Delta G^{\ddagger} \sim 70$ kJ mol^{-1}) was observed using a ^{19}F-SIT experiment. Considering rate changes with lower tht concentrations allowed determination of rate constants for a pathway involving dissociation and syn-anti interconversion via a 3-coordinate intermediate. Activation parameters (from a 40° temperature range) were obtained for the interconversion via the 4-coordinate ($\Delta H^{\ddagger} = 83 \pm 3$ kJ mol^{-1} and $\Delta S^{\ddagger} = 37 \pm 10$ J K-mol^{-1}) and 3-coordinate ($\Delta H^{\ddagger} = 77 \pm 3$ kJ mol^{-1} and $\Delta S^{\ddagger} = 28 \pm 10$ J K-mol^{-1}) complex. Note that a relatively large value of $\Delta S^{\ddagger}$ is even observed for the nondissociative path, which is unusual.

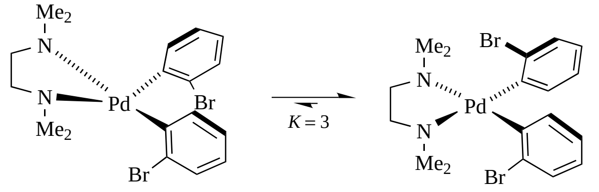

(**46**) *syn* (**46**) *anti*

(11)

There are a number of other complexes that show restricted rotation of fluorinated phenyl groups, both in square-planar and pseudooctahedral complexes.[195–201] Situations also exist where similar syn and anti isomers exist owing to aryls attached to ligands, for example, (**47**).[202]

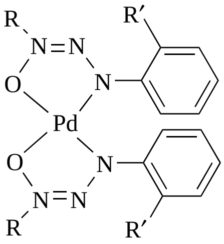

(**47**)

4.3 Restricted Rotation About M-py and M-heteroaryl bonds

Pyridine complexes can show analogous hindered rotation to that observed with metal–aryl complexes. This has been observed for over 30 years,[203] but recent interest in supramolecular chemistry, particularly by Fujita[203,204] and Stang,[205–209] wherein bipyridyls have been used as linkers has spurred renewed interest in the phenomenon. Several articles on dynamics provide leading references for applications of EXSY and other DNMR methods in these systems.[209–211] BINAP complexes with picolines and methyl-substituted isoquinolines, which show syn and anti isomerism, have been investigated, for example, (**48**), (**49**), and (**50**).[210]

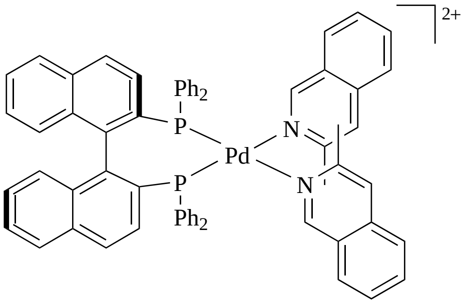

(**48**)

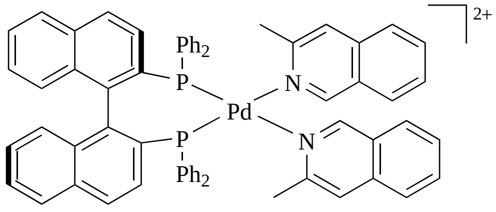

(**49**)

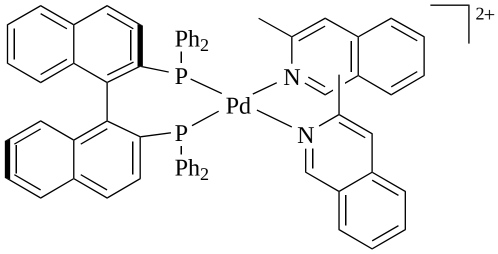

(**50**)

For [(BINAP)Pd(3-picoline)$_2$]$^{2+}$, $\Delta G^{\ddagger} \sim 50\,\mathrm{kJ\,mol^{-1}}$ was determined for restricted rotation about the Pd–N bonds. The barrier in the analogous platinum complexes were higher, $\Delta G^{\ddagger} \sim 58\,\mathrm{kJ\,mol^{-1}}$.[210] The general trend is that the barriers for the Pd–N bonds are somewhat lower than those for Pd–C bonds in analogous covalently bonded aryl complexes. This type of phenomena can also be flowed by ^{31}P NMR.[209] It would appear that one of the anti isomers is generally preferred in systems with a chiral bidentate ligand. Barriers are also observed in octahedral complexes and have been studied in ruthenium complexes.[212,213]

There has also been interest in restricted rotations in adenosine–Pt complexes in which lower temperatures reveal the effects of rotation in complexes such as (**51**).[214] Marzilli[215–217] has been particularly active in the analysis of dynamics of N-donor bioligands, but they have also emphasized studies of octahedral ruthenium complexes. More complicated N-donor ligands can produce multiple processes which can be observed by DNMR and in some cases hindered rotation in pendant rings can be observed.[218–220] There has been a recent review of DNMR methods applied to supramolecular systems.[221]

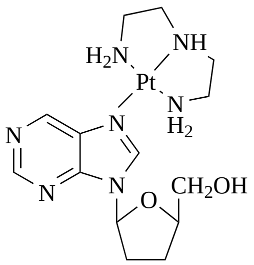

(**51**)

4.4 End to End Rotation About M-L Single Bonds

In the absence of steric hindrance, one would anticipate a low barrier to rotation about the single bond. The potential, however, exists for that bond to break and reform at another point on the ligand intramolecularly. Although it occurs at rates slower than observable by DNMR, N_2 has been shown to undergo an intramolecular end to end rotation using ^{15}N singly labeled dinitrogen ligand in $CpRe(CO)_2(N_2)$.**[222]** SIT experiments, however, demonstrated an intramolecular end to end rotation of FHF^- in *trans*-$[(PPh_3)_2Pt(Ph)(FHF)]$ which presumably occurred through a five-coordinate intermediates involving two Pt–F bonds.**[223]** It is also common for coordinated $BF_4{}^-$, $PF_6{}^-$, and $SbF_6{}^-$ to undergo intermolecular end to end rotation or spinning.**[224]** (see equation 12).

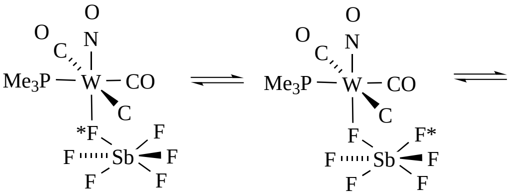

(12)

Our discussion has focused on barriers in the range available *via* the usual DNMR methods. There are specialized approaches that allow determination of lower barriers usually found in most single bond rotations,**[225]** such as methyl rotation.**[113,226,227]** Note that investigations of very low barriers involving groups with hydrogen nuclei may need to consider quantum tunneling effects.

4.5 Hindered C-C Rotation and Atropisomerism

The restricted rotation about C–C bonds in biaryls can allow the isolation of axially chiral complexes that do not racemize (atropisomers) or racemize slowly and this has led to the popularity and the extensive use of ligands such as BINAP. There has also been an interest in ligands with modest barriers to interconversion. In BIPHEP (**52**), the barrier for racemization can be measured by observing the exchange between diastereotopic nuclei in the phenyl groups.**[228]** This requires higher temperatures and the rotation about the phenyl C–P bonds are rapid at this temperature. Hence, there are separate resonances associated with the ortho protons of the diastereotopic phenyl groups. These average at high temperature yielding a barrier of 102 kJ mol^{-1} for racemization of the biphenyl backbone. The actual measurement was carried out with a sample deuterated in the meta and para positions; however, the barrier could also have been readily determined using ^{13}C DNMR for the ipso or ortho carbon atoms.

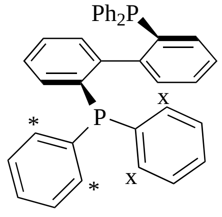

(**52**)

Hindered rotation of phenyl groups in planar ligands can also produce propeller chirality. McGlinchey has contributed a large number of publications in this area which are summarized in recent reviews.**[229,230]** An interesting example is shown in equation (13), where a 3:1 equilibrium of diastereomers in (**53**) is observed at −100 °C and the DNMR of ligand ($L = Me_2PPh$) resonances allow determination of the epimerization barrier ($\Delta G^{\ddagger} = 49\,\text{kJ mol}^{-1}$) involving $C_{Cp}–C_{Ph}$ rotation.**[231]** Similar processes are also well known for ethyl substituted η^6-arenes and reference to reviews**[229,232]** for a more complete description.

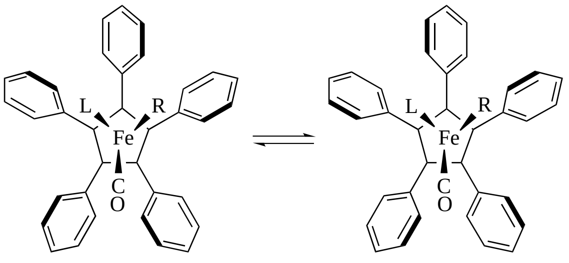

(**53**) *M* (**53**) *P*

(13)

High degrees of substitution are not required, as restricted rotation has been observed in para-substituted arenes. For example, in $(1,4\text{-}C_6H_4\text{-}Pr^i_2)Fe(CO)(SiCl_3)_2$ (**54**), there are two arene proton resonances observed at −120 °C, indicative of hindered rotation. At −40 °C, they have coalesced to a singlet indicating a barrier of 45 kJ mol^{-1}.**[233]** *p*-Cymene is frequently used with ruthenium complexes owing to the ready availability of $[(1,4\text{-}C_6H_4Me,Pr^i)RuCl_2]_2$. Hindered rotation of the arene has been observed in (*p*-cymene)Ru(pfc)Cl (**55**).**[234]** This is particularly important since hindered rotation for the ring produces diastereomers related to arene orientation, which might be mistaken for diastereomers from different configurations at the chiral metal center.**[150]**

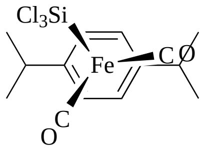

(**54**)

Atropisomers arising from hindered rotation of meso-aryl have been used in studies of metalloporphyrins. Barriers for a series of para and meta aryls in titanyl porphyrins and

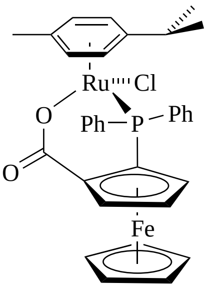

(**55**)

hydroporphyrins range from 61 to 77 kJ mol^{-1}.[233] Reference to this study will provide leading references.

5 HINDERED ROTATIONS OF η^6-ARENES, η^5-CYCLOPENTADIENYL, AND SIMILAR LIGANDS

Generally, one expects a very low barrier for rotation of a η^5-cyclopentadienyl ligand. The barrier is sufficiently low that it can rarely be measured in solution. When metals with unpaired electrons are prepared, the EPR can occasionally provide information on low barriers owing to the larger 'chemical shift' separations. In the case of 19-electron (η^5-C_5Ph_4H)Mo(CO)$_2$(bis-diphenylphosphinomaleic anhydride), where the electron resides predominantly on the ligand, the barrier for ring rotation was ~13 kJ mol^{-1} at 25 °C.[234] Suitable substitutions on the rings and metal can raise the barriers to heights sufficient for them to be measured by DNMR. McGlinchey has been very active in this area and reference to his reviews are recommended.[229,230] In the previous example related to phenyl orientation, (**53**), the fluxionality associated with the helical phenyl inversion is not correlated with the tripodal rotation of the Fe(CO)(L)(R) group which has a barrier of 36-kJ mol^{-1} compared to the 49-kJ mol^{-1} for the phenyl rotation. With unsymmetrical substitution of the ring, different rotamers can be observed in complexes such as (**56**), equation (14), at low temperature.[231]

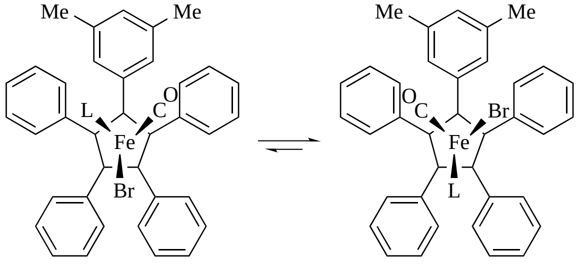

(**56**) *major* (**56**) *minor*

(14)

There have also been extensive studies of a η^4-diene rotation and rotamers that can be observed in complexes of dienes. In Cp complexes, the orientation relative to the Cp ligand gives rise to endo and exo isomers, for example, (**57**) and (**58**), the interconversion of which can be observed by DNMR.[235,236] Interconversions are particularly rapid when the parent structures are nonrigid. Thus the [CpMo(CO)$_2$(η^4-diene)]$^+$ complexes can be considered to be based on a square pyramid and are analogous to CpMo(CO)$_2$LX ligands, which are nonrigid themselves.[237]

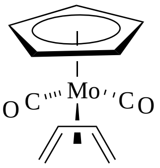

(**57**) *exo*

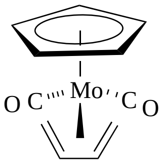

(**58**) *endo*

The stereodynamics[238–240] of (η^4-diene)Fe(CO)$_2$L (L = CO, phosphine, or phosphite) complexes are likely to be of importance in understanding the reactivity of the diene moiety, as these complexes are used in several synthetic strategies.[241,242] Theoretical analyses[243,244] have tended to consider the rearrangement in terms of rotation of the Fe(CO)$_2$L fragment relative to the diene. A number of (η^4-enone)Fe(CO)$_2$L complexes have also been investigated.[244,245] Three conformers, (**59**), (**60**), and (**61**), are expected for the unsymmetrically substituted diene complexes and analogous ones are expected for the enone complexes. The relative stabilities of the conformers can be determined by NMR (the ^{13}C for the two carbonyls are different in each conformer) and the rotamer populations are sensitive to substitution. Barriers are ~60 kJ mol^{-1} for these compounds, but one should note that six different $\Delta G^\ddagger$'s, as well the free energy differences between conformers, need to be considered. Several publications provide leading references.[243–251]

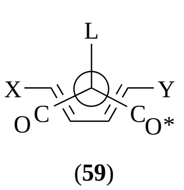

(**59**)

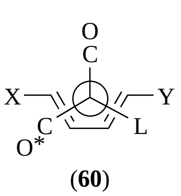

(**60**)

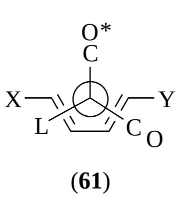

(**61**)

In complexes of this type, there is an effective rotation of the 1,3-diene. This should be distinguished from the *apparent* rotation often found for 1,5-dienes, such as COD, in which ligands are interchanged relative to double bonds by M–P or M–N bond rupture with hemilabile ligands (see Section 6).

6 NONRIGIDITY IN HEMILABILE LIGANDS

A fundamental aspect of using DNMR to study fluxional or nonrigid systems is that the observed effects should arise from an intramolecular rearrangement. Detection of an intermolecular process is most simply determined by observing resonances of the free ligand and noting whether there is an exchange with the ligand in the complex. With monodentate ligands it is not uncommon that a higher energy process will involve dissociation of a ligand, but lower energy intramolecular processes occur as well. A potential problem of adding free ligand is that a second-order process will start to occur at a sufficient rate that exceeds those of intramolecular processes that, in the absence of excess ligand, would be readily discerned. There tends to be a total focus on relative concentrations of complex and free ligand; whereas, useful important information can be obtained by following the effects of concentration by using dilutions of the solutions. Perhaps the most convenient technique is noting the retention of spin coupling with a ligand when a dynamic process is observed in the absence of an added ligand. This is most commonly used with ^{31}P coupling in phosphines or with metals having observable spin coupling, such as ^{195}Pt, ^{103}Rh, or ^{183}W. Coupling of other ligands to ^{31}P is averaged since when a ligand with a ^{31}P with spin $+1/2$ dissociates a ^{31}P with spin $-1/2$ can return and this produces an average of the components of the doublet arising from coupling to ^{31}P. In this context, one should note that if a ^{31}P with spin $+1/2$ returns, the frequency of the resonance would not change; hence, the coupled nucleus ‘‘would not know that anything had happened.’’ Hence, if broadening of a doublet from exchange of ^{31}P is involved, one may need to double the rate constant obtained from equations such as equation (3), to provide a chemically meaningful exchange rate.

If the donor that dissociates is tethered to the complex, for example, a bidentate ligand, then the same nucleus that departs, also returns to the metal so the coupling will be retained. This assumes that more rapid relaxation of the nucleus does not occur when free, which is usually the case. Consequently, unless that free:bound fraction is large (>100:1), there is little evidence that the dissociation is taking place. Thus, when donors are tethered to a complex in some way, it is quite difficult to determine if they dissociate on the NMR timescale.

There has been an increased interest in mixed-donor and hemilabile ligands owing to their successful use in catalysis owing to their electronic asymmetry or ability to provide access to an unsaturated site via dissociation of one of the termini.[252,253] Typical ligands used for catalysis that make use of their hemilability involve a phosphine and an oxygen donor, such as an ether.[254,255] A weak donor, such as an ether (if it binds at all), is relatively easily displaced, and rupture of the M–O bond and retention of the M–P bond is expected to provide an ideal hemilabile system. With *P*,*N*- ligands, either terminus could dissociate preferentially depending upon the hardness of the metal center. Since most of these systems do not involve a significant fraction of dissociated donor, it is difficult to demonstrate that a donor at a given terminus actually dissociates.

6.1 Arm-off Polydentate Ligands for Discerning Hemilability

In some mechanistic studies, the relative rates of flexible versus rigid backbone bis- phosphines[256–258] were used to provide indirect evidence for hemilability in bisphosphines. In complexes with a potentially tridentate ligand that is bound by only two donors, interchange of the free and bound donors can demonstrate an intramolecular exchange process and rupture of a given bond. This can be misleading, as the proximity of the tethered free donor (the ‘‘arm-off’’ donor) may make an associative process more likely than would occur in an isolated bidentate ligand, particularly in four-coordinate d^8 systems. One might expect that κ^3-bonding and *fac* complexes would prevail with tridentate ligands, such as Tp, HC(py)$_3$, and MeC(CH$_2$PPh$_2$)$_3$ = triphos. Some square complexes can favor κ^2-bonding with Tp and pz$_4$B$^-$. Taking PdCl(PEt$_3$)(κ^2-pz$_4$B) (**62**) as an example, there are two arm-off pyrazolyls and they show averaging with the bound pyrazolyls.[259,260] In fact, there are two processes observed. Bond rupture is promoted trans to the phosphine so that pyrazolyl broadens and starts to average with the free pyrazolyls before the pyrazolyl trans to the chloride (equation 15). This clearly shows that it is possible to rupture the Pd–N bond in an intramolecular process and the averaging with the arm-off donor allows the process to be detected. One should note that the process of rupture of the bond and the reformation is not detected by this experiment. One measures the rate of the overall process, which also involves the rotation of 3-arm-off pyrazolyl; hence it represents an upper limit of the barrier.

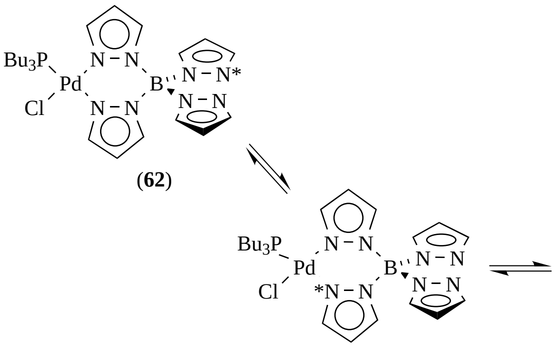

(**62**)

(15)

One might expect triphos to behave in a similar way; however, its most stable form tends to involve κ^3 bonding in a five-coordinate complex. For example, (triphos)Ir(CO)H (**63**) is trigonal bipyramidal with a carbonyl equatorial and the hydride axial.[261] The ^{31}P spectrum exhibits a singlet at room temperature, but a triplet at -10.1δ and doublet at $-15.8\ \delta$ are observed at $-110\,°$C. This does not necessary prove that a $\kappa^3-\kappa^2-\kappa^3$ process is involved, since a pseudorotation would also give the same result. Upon raising the temperature to $-80\,°$C, however, the -15δ resonance is sharp, whereas the -10.1δ resonance is broad. If this difference in width were not just the consequence of the differences in population (the spectra were not reproduced in the paper), it could be the result of averaging with a fraction of the κ^2 form ($\sim$5% estimated). The faster exchange of that P would follow from the expected greater lability of the phosphorus trans to hydride.

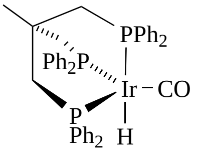

(**63**)

There have been a number of (triphos)Rh complexes that are fluxional and that could rearrange via formation of a κ^2-triphos or via the loss of another ligand.[262–264] In most cases, it is not clear which mechanism is dominant.

6.2 Pyrimidines and Triazines as Detectors of Hemilability in Analogs of Bipy

Ligand systems with pyrimidines have, in effect, internal ‘‘arm-off’’ donors that present less of a problem of potentially increasing the rate of Pd–N bond rupture via a second-order process from the proximate donor. Gogoll and Backvall[265] showed that 2-2′-bipyrimidyl (bpm) (**64**) was useful in this regard. Hence interconversion of the H-4 and H-6 is indicative of Pd–N bond rupture.[265]

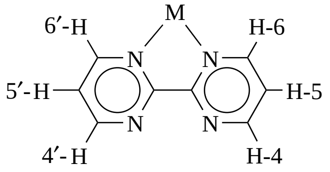

(**64**)

Pyrazolylpyrimidines (pzpm)[266–269] also provide a method for detecting the Pd–N bond rupture (see equation 16). This has been extended to tri-substituted triazines,[270] wherein Pd–N bond rupture can be detected, but which also allows the metal to pass around the entire ligand via a series of (1) metallotropic shifts involving retention of the triazene N–Pd bond and (2) pyrazolyl ligand assisted metal ‘‘hurdling’’ from one triazene N to another (see equation 17). The subject of metals shuttling from one nitrogen atom to another has been extensively investigated by Elguero[270,271] and Orrell.[23]

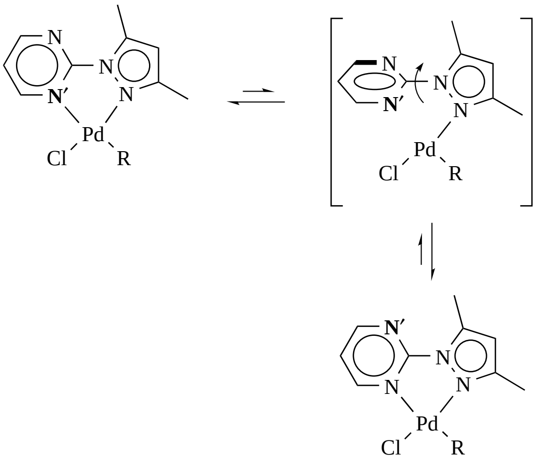

(16)

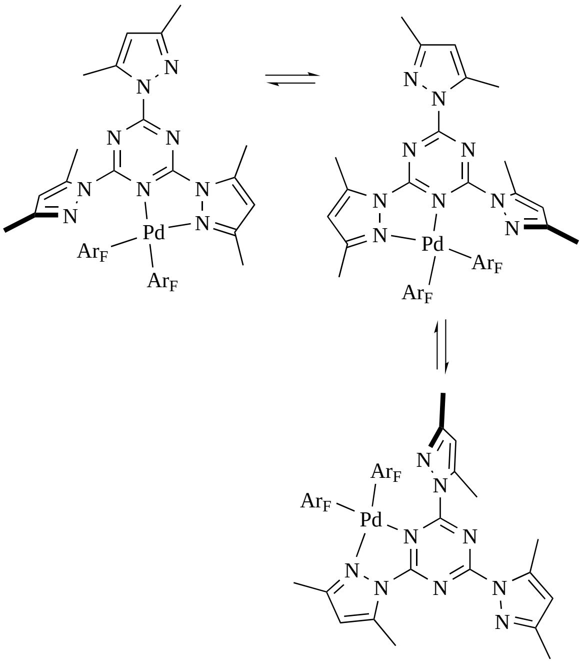

(17)

6.3 Amine Inversion as a Detector of Hemilability

One of the most reliable methods for detecting hemilability is available for ligands with dimethylamino groups as donors. In many cases, the methyl groups will be diastereotopic owing to an unsymmetrical substitution pattern in the complex. If the metal–nitrogen bond ruptures, rapid pyramidal inversion at the nitrogen interchanges the methyl groups and upon reforming the M–N bond, the chemical environments of the methyl groups are interchanged. Thus, even though an intermediate of lower hapticity might only be formed in minute quantity, it provides a pathway for equilibration of environments. (*Note that here again the k derived from equation (3) is one-half of the constant for bond rupture.*) An illustrative example is shown in equation (18), where a (PTTF)Pd(maleic anhydride) (**65**) shows a process that interconverts a major and minor conformer.[272,273] The methyl groups are diastereotopic in both conformers so that at low temperatures there are four N-methyl resonances. Two sets of the methyl groups exchange as the ligand rotations giving rise to two resonances corresponding the average of those above the coordination plane and those below it. At still higher temperatures (at 100 °C these resonances coalesce to a single broad resonance ($\Delta G^{\ddagger} \sim 73\,\mathrm{kJ\,mol^{-1}}$)), this averaging of the diastereotopic methyl groups can be attributed to Pd–N bond rupture.

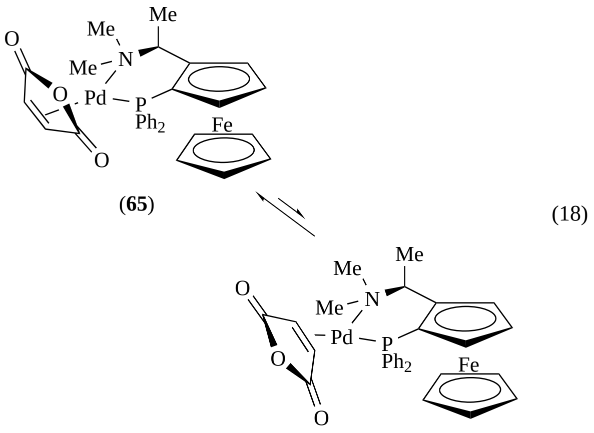

(**65**)

(18)

The *apparent* rotation of the ligands in (η^3-$C_{10}H_{15}$) Pd(Me_2NCH_2py) (**66**) has been investigated using EXSY (equation 19).[267] The important features are that: (1) the anti protons of the allyls exchange among themselves but not with the syn protons between isomers; (2) N-Methyl groups exchange between isomers, *but not within a given isomer*. This requires that the Pd–N bond is not ruptured. The observation can be accommodated by: (1) rupture of the py–N–Pd bond; (2) rotation about the Pd–N(Me_2) bond; (3) isomerization within the T-shaped intermediate; and (4) reformation of the py–N–Pd bond. It also can be accommodated by: (1) rupture of the more substituted Pd–allyl bond; (2) rotation about the Pd–CH_2 bond; (3) isomerization within the T-shaped intermediate; and (4) reformation of the allyl–Pd bond. Thus, this experiment shows that neither the Pd–CH_2 nor Pd–$N$$Me_2$ is broken in the process.

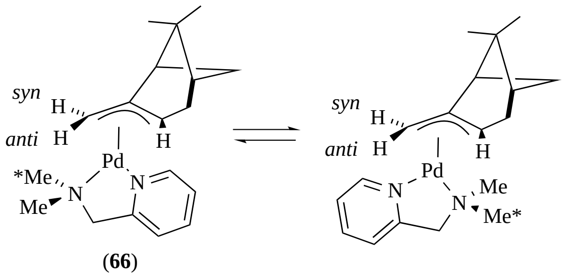

(**66**)

(19)

The *apparent* rotation of the ligands in (η^3-$C_{10}H_{15}$) Pd(TMEDA) (**67**) was also investigated using EXSY spectra.[265] The methyl groups were assigned using NOE experiments. Methyl groups on different nitrogen atoms were exchanging at 25 °C but not those on the same nitrogen atom. This was then consistent with cleavage of the Pd−allyl carbon bond, but showed that the Pd–N bonds did not rupture in the process. At higher temperatures, however, all four methyls showed mutual exchange. Addition of chloride increased the rate of exchange and, at −15 °C, exchange of the methyl groups on the same nitrogen occurred rapidly. This suggests that the chloride can promote Pd–N bond rupture and is consistent with the formation of a four-coordinate arm-off TMEDA complex.

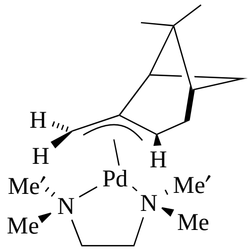

(**67**)

Studies of arm-off (COD)Rh[2,2′-$C_6H_3(CH_2NMe_2)_2$] (**68**) have also suggested interconversion proceeds *via* a T-shaped three-coordinate intermediate.[274] Other *apparent* rotations observed in $[(\mathrm{COD})\mathrm{Rh}(\mathrm{bidentate})]^+$ complexes appear to via breaking of Pd–N or Pd–P bonds.[275]

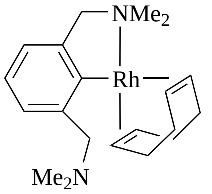

(**68**)

7 ALLYL REARRANGEMENTS

Allyl complexes were amongst the earliest studied nonrigid complexes, and there are a number of reviews on their rearrangements.[13,276,277] Interest has been particularly high owing to their importance in catalysis[277] and synthesis,[278] with palladium and molybdenum complexes playing leading roles.

$CpMo(CO)_2$(η^3-allyl) complexes show a planar allyl rotation analogous to that found for the diene in $[CpMo(CO)_2(\eta^4\text{-diene})]^+$ complexes.[279] Endo−exo isomerism is observed and interconversion occurs rapidly at room temperature

($\Delta G^{\ddagger}_{endo\rightarrow exo} = 63.5\,\mathrm{kJ\,mol^{-1}}$). In the electronically asymmetric complex [CpMo(CO)(NO)(η^3-allyl)]$^+$, however, this barrier increases dramatically to $\Delta G^{\ddagger}_{endo\rightarrow exo} = 94\,\mathrm{kJ\,mol^{-1}}$. This corresponds to an increase in room temperature half-life for interconversion of 10^{-2} s to 4×10^3 s; nevertheless, the principal path for interconversion is still a planar rotation.**280**

In the halide derivatives, for example, CpMo(NO)(Br)(η^3-allyl), however, an η^3–η^1–η^3 or π–σ–π rearrangement is the lowest energy path for endo–exo interconversion. These complexes show ‘static’ NMR spectra at ambient temperature and the temperature must be raised to observe broadening; $\Delta G^{\ddagger}_{endo\rightarrow exo} = 81.5\,\mathrm{kJ\,mol^{-1}}$ for CpMo(NO)(Br)(η^3-C_3H_5) (equation 20). Thus, when enantiomerically pure CpMo(NO)(X)(η^3-allyl)-type complexes are isolated, they do not racemize on a timescale of days, even though they are rearranging on a timescale of seconds. Another feature is that the electronic symmetry at the metal results in the σ-bond only being formed cis to the nitrosyl, as in (**70**). This has proven useful since the coordinatively unsaturated intermediate can bind to aldehydes and then go on to react to give homoallyllic alcohols in high enantiomeric purity.**281–284**

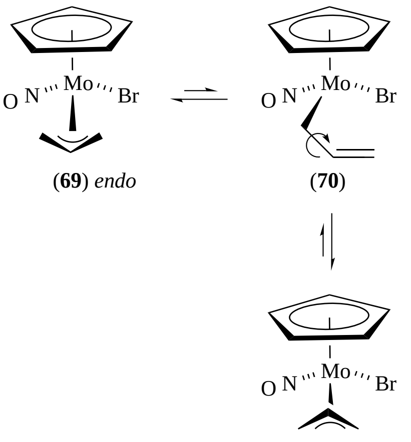

(**69**) *endo*

(**70**)

(**71**) *exo*

(20)

Virtually all of the stereochemical nonrigidity of the allyls in square-planar (η^3-allyl)Pd$^{\mathrm{II}}$ complexes derives from π–σ–π rearrangements rather than rotation. There are, however, *apparent rotations* which derive from hemilability of the nonallyl ligands rather than the allyl,**265,277,285,286** as was observed for other complexes (Section 6). In most cases, there is not a large preference for the σ-bond to form at one terminus or the other. Large trans effects from the other ligands in unsymmetrical (η^3-allyl)PdXY can produce a modest preference for breaking of the Pd-π-bond trans to one of the ligands.

In cases with similar trans-effect ligands, substituents on the terminus reduce the rate of σ-bond formation at the substituted terminus. Thus, one can expect an increase of 4–12 $\mathrm{kJ\,mol^{-1}}$ in $\Delta G^{\ddagger}$ per methyl substituent.**287** Two effects tend to produce a $\Delta\Delta G^{\ddagger}$ for σ-bond formation at the different termini of $\approx 20\,\mathrm{kJ\,mol^{-1}}$ in 1,1-dimethyl-substituted allyls: (1) the stability order of 1° > 2° > 3° M–C bond and (2) the decreased stability of π-M–C bonds on substitution. Hence, one would generally expect the ease of formation of the σ-bonded intermediate at the unsubstituted terminus to increase in the order 1,1-dimethylallyl < 1-methylallyl < allyl.

Another feature that is crucial in considering η^3–η^1–η^3 rearrangements in monosubstituted allyls is the effect on the chirality and stereochemistry. In crotyl complexes, formation of a σ-bond at the unsubstituted terminus provides a path for racemization for the stereogenic center at the substituted terminus (equation 21). Formation of the σ-bond at the monosubstituted terminus, however, results in conversion to a different isomer (equation 22). The most stable isomer is the syn isomer (**72**) and, in the absence of a substituent on the central carbon, the anti isomer (**74**) will only occur to the extent of ≈5%. Thus if one considers complexes like (acac)Pd(allyl), some racemize, whereas others only isomerize because there is no path for racemization (equation 23).**288** These concepts have been used effectively by Bosnich in the design of systems for asymmetric allylic alkylation.**289** These concepts also allow the rationalization of why certain substrates give low enantiomeric yields. It should be noted here that the planar rotation found in some of the molybdenum complexes retains the chirality in the allyl moiety.

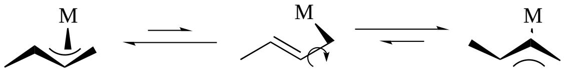

(**72**) (*S*) (**73**) (**74**) (*R*)

(21)

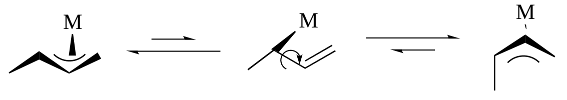

(**72**) *syn*-(*S*) (**75**) (**76**) *anti*-(*S*)

(22)

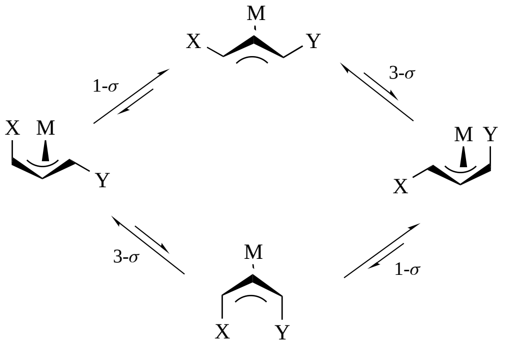

(23)

Exchange of the ligands in XYPd(allyl) can give the appearance of rotation of the allyl.**265,277,285,286** Although rearrangements in many allyl–Pd and – Rh complexes meet the requirement for intramolecularity to be classified as fluxional or stereochemically nonrigid, there are a number of intermolecular processes which can give rise to DNMR spectra. Multiple paths, some of which are second order, have been found in the palladium allyl systems.[276,283]

8 HAPTOTROPIC REARRANGEMENTS IN RINGS

The movement of metals about five-, seven-, and eight-membered rings has been studied extensively since the 1970s. Often, the lowest barrier process involves the metal migrating about on one side of the ring and moving to the immediately adjacent position, as seen with $(C_7H_7)Ru(CO)_3$ (**77**) (equation 24) and as discussed earlier for $CpFe(CO)_2(\eta^1\text{-}C_5H_5)$ (equation 2). Theoretical interest in these rearrangements[290,291] increased together with the study of sigmatropic rearrangements in organic chemistry in the 1970s and early- 1980s, so that early reviews are still the most comprehensive.[10,13] There was sufficient activity in the area that one review was devoted solely to η^1-Cp compounds with main group elements.[292] Fortunately, there has been a recent review which provides coverage up to 2000.[293] Several recent reports also provide some leading references.[294–296] The migration around the rings led to the slang term ''ring whizzers'', but *haptotropic* appears to be currently popular. Although (**77**) migrates via a series of 1,2-shifts, other substituents on the metals can make other processes feasible.[294] There is an interesting class of compounds that contain two migrating groups (*diatropic*) where a metal migrates on one side of a ring while a second group migrates on the other. A 1,2-shift of the iron accompanied by a shift of the boron in (**78**) is the lowest energy process ($E_a = 71\ \text{kJ mol}^{-1}$), but other migrations occur at higher temperature.[295] Although the Sn moiety migrates rapidly in $(C_7H_7)SnPh_3$ via a 1,4-shift, in the chromium tricarbonyl analogue (**79**) that migration path is blocked; nevertheless, a slower 1,3-shift of Sn occurs along with a 1,2-shift of Cr was observed by SST.[296] Owing to recent interest in chiral organometallics, these rearrangements that restrict the metal to one side of the ring or produce populations of isomers relative to specific substituents can become important. For example, the migrations observed in (η^1-indenyl) complexes result in racemization (equation 25). Generally one expects the metal to be restricted to one side of the ring; however, the results observed by Gladysz[97] for olefins and Harman[109] with aromatics indicate that there is a real possibility of migration to the opposite face via an agostic C–H intermediate.

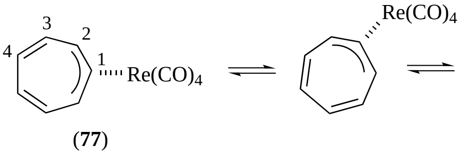

(**77**)

(24)

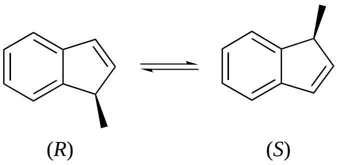

(25)

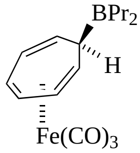

(**78**)

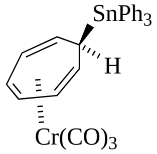

(**79**)

9 HYDRIDE–ALKENE COMPLEXES AND AGOSTIC INTERACTIONS

One of the most important reactions in organometallic chemistry is the *Insertion* of an alkene into a metal–hydride bond and its reverse, *β-Hydride Elimination* (equation 26). Brookhart has carried out extensive studies in this area where the process can be studied by DNMR.[297]

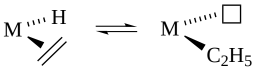

(26)

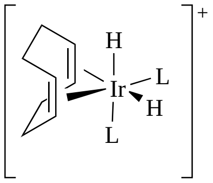

(**80**)

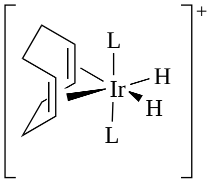

(**81**)

9.1 Hydride–Alkene Complexes

The hydride must be in the proper orientation relative to the alkene in order for it to insert. Thus, if the hydride is trans to the alkene or if it is cis to the alkene and the metal–H bond cannot get oriented properly to the C–C axis, it will not insert. Thus, the cis–cis isomer (**80**) allows insertion more readily than the cis–trans isomer (**81**) of $[(cod)(PPh_3)IrH_2]^+$.[298] Hydride migration was observed as early as 1971,[299] but the most interesting simple cases are those discovered by Werner[300,301] and developed by Brookhart,[302–304] that is, $[Cp^*Rh(L)(ethylene)(H)]^+$. For $L = (MeO)_3P$, the propeller rotation of the ethylene occurs with a barrier of $\approx 40\ \text{kJ mol}^{-1}$. Note that the rotation averages the ^{13}C resonances of the alkene, but since the Rh is chiral, the protons are diastereotopic and two sets average independently. At higher temperatures, however, the alkene protons average with the hydride, indicating a $\Delta G^{\ddagger}_{234} = 50.2\,\text{kJ mol}^{-1}$ for the β-migratory insertion.

9.2 Agostic Ethyl Complexes

For a wide range of phosphite and phosphine ligands in the $[\text{Cp}^*\text{Rh(L)(ethylene)(H)}]^+$ system, the stable structure is that of the terminal alkene hydride (**82**); however, stereochemical nonrigidity is observed. One would presume that there is a transition state in which the hydride being transferred is attached to both the metal and the alkene (**83**) (equation 27). When viewed as a metal interaction with the C–H σ-bond in the ethyl complex this is termed an *agostic interaction*. When L is another alkene rather than a phosphine or phosphite, however, the agostic complex is the ground state, as shown in equation (28). Thus, $[\text{Cp}^*\text{Rh(ethylene)}_2\text{H}]^+$ (**85**) is a transition state or intermediate in the stereochemical nonrigidity exhibited by $[\text{Cp}^*\text{Rh(ethylene)(CH}_2\text{CH}_2\text{-}\mu\text{-H)}]^+$ (**86**). The agostic hydrogen is readily characterized in these complexes by a reduced $^1J(^{13}\text{C}-^1\text{H})$ compared to that found in other Rh–alkene complexes and a reduced $^1J(^{103}\text{Rh}-^1\text{H})$ compared to a terminal rhodium hydride.

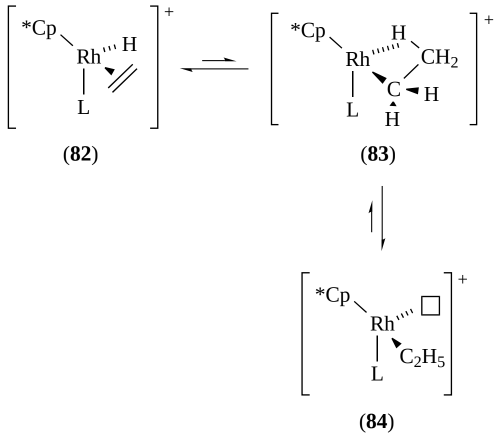

(27)

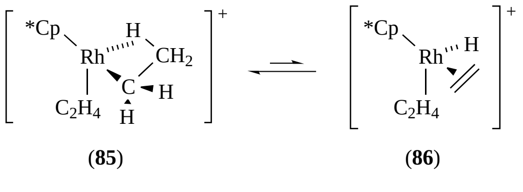

(28)

The conversion from agostic hydride to terminal hydride occurs with a $\Delta G^{\ddagger} < 15\,\text{kJ mol}^{-1}$. Averaging of the agostic hydride with the other protons of the methyl in the ethyl group occurs with a $\Delta G^{\ddagger} = 35.5\,\text{kJ mol}^{-1}$ and apparently occurs via opening of $[\text{Cp}^*\text{Rh(ethylene)(CH}_2\text{CH}_2\text{-}\mu\text{-H)}]^+$ to a normal ethyl complex $[\text{Cp}^*\text{Rh(ethylene)(CH}_2\text{CH}_3)]^+$ (**51**) having a low barrier to rotation of the methyl group. An 'in place' rotation of the agostic methyl could also occur.[304] This process only equilibrates the hydride with the methylene protons proximal to the hydride; ethylene rotation allows equilibration with both ends of the alkene.

9.3 Other Agostic Complexes

One would anticipate an analogous situation with allyl hydrides and propene complexes. Indeed, one can find allyl hydrides, propene complexes, agostic propene, propene hydrides, and isopropyl complexes. Green[36,58] has effectively reviewed this area in his analysis of the evaluation of rate constants in these systems. Substantial effort is required to examine the possible factors relating exchange rates.[58] Again it is necessary to be quite careful to delineate rate and rate constant, since mass balance requires the forward and reverse rates between two sites of different population to be the same, whereas the rate constants are proportional to reciprocal populations. The reader is referred to the original literature[36,58] for an exposition on the difficulties which can arise. Diene hydrides also show similar agostic systems for which a study by Bennett and Brookhart provides an excellent review of the literature in this area.[305]

10 HYDRIDE AND DIHYDROGEN COMPLEX EQUILIBRIA

Metal hydrides were among the earliest fluxional compounds to be studied. The more recent discovery of dihydrogen complexes and stereochemical nonrigidity in complexes containing both hydride and dihydrogen ligands has provided one of the areas of most intense interest in DNMR in recent years.[306–311]

Hydrides in complexes with coordination numbers of five and higher often show fluxional characteristics typical of other nonrigid complexes,[21] such as Fe(CO)_5 (equation 1). This area has been reviewed previously.[20,306–311] A feature that was not appreciated originally was that some ''polyhydrides'' actually existed as hydride–dihydrogen complexes. Extraordinarily stable dihydrogen ligands can be found with cationic complexes such as $[\text{Cp}^*\text{Ru(dppm)H}_2]^+$ ($\text{ddpm} = \text{Ph}_2\text{PCH}_2\text{PPh}_2$).[312] This complex has an H–H bond length ($r_{\text{HH}} = 1.10\,\text{Å}$) intermediate between that found in more weakly bound H_2 complexes ($r_{\text{HH}} < 1.00\,\text{Å}$) and dihydrides ($r_{\text{HH}} >\simeq 1.50\,\text{Å}$). The inverse correlation of J_{HD} and bond length has been used as a convenient measure r_{HH}, for example, $J_{\text{HD}} = 21\,\text{Hz}$ for $[\text{Cp}^*\text{Ru(dppm)H}_2]^+$.

In the case of hydride–dihydrogen complexes, one can observe stereochemical nonrigidity wherein the effects of scrambling of the nuclei between the hydride and dihydrogen ligands can be observed (equation 29). The first example of this was reported by Crabtree[313] for $[\text{(benzoquinolyl)(PPh}_3)_2\text{Ir(H}_2\text{)(H)}]^+$. In most cases it appears that the mechanism involves the formation of a very low concentration intermediate of trihydride, but the formation of an η^3-H_3 intermediate has been also suggested. The observation of temperature-dependent averaged J_{H-D} couplings are indications that an intermediate in modest concentration is formed in some cases, for example, $[(diphos)_2Os(H_2)(H)]^+$.[314] Both $[(CO)L_3ReH_4]^+$ and $[(CO)L_3ReH_2(\eta^2\text{-}H_2)]^+$ tautomers can be observed, and thus the mechanism of interconversion can be studied.[315] Perhaps the most comprehensive study of a single complex has been that of $L_3Fe(H)_2(\eta^2\text{-}H_2)$. This study encompasses theory and provides leading references.[316]

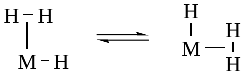
(29)

One should note that in these complexes there are multiple nonrigid processes: (1) the dihydrogen undergoes either a tunneling or spinning motion, with a low barrier (4–8 kJ mol^{-1}); (2) the parent seven-, eight-, or nine-coordinate structures are often fluxional themselves; and (3) hydride–dihydrogen equilibria occur. These studies are often complicated by several factors other than those discussed in earlier sections. The short H–H bonds in the dihydrogen complexes give rise to short T_1 relaxation times from dipolar effects. This can cause difficulties in spin saturation transfer experiments, as well as in-line shape analysis, owing to the effect on T_2, that is, it produces inherently broad natural line-widths, which are temperature dependent. In T_1 determinations, exchange with hydrides (SIT) can artificially lengthen the observed T_1. Furthermore, the effects of quadrupolar nuclei cannot always be ignored (this is particularly true with Re, Mn, and Co complexes). Finally, some trihydride species can give rise to bizarre quantum mechanical exchange phenomena which produce incredibly large couplings between the hydrogen nuclei.[317,318]

11 SIX-COORDINATION AND NONRIGIDITY

Just as one found that $Fe(CO)_5$ is fluxional (equation 1), one anticipates that most five-coordinate structures including hydrides would be fluxional. As expected, early ^1H and ^{31}P NMR studies showed that $HRhL_4$ complexes were fluxional.[306] For metals coordinated by seven or more ligands, stereochemical nonrigidity is generally observed. Although ML_7 compounds typically have barriers <17 kJ mol^{-1},[319] DNMR can be observed in pseudo-seven-coordinate complexes,[237] for example, $CpMo(CO)_2LH$ (assuming Cp occupies three coordination positions). As the coordination number increases, the number of possible rearrangement mechanisms increases and low barriers for fluxionality are the norm. The ‘rotation of polyhedral faces’ is a convenient starting point, but alternatives involving conversions of triangular faces to diamonds or squares have been suggested. The two or more environments expected for protons in $ReH_9{}^{2-}$, ReH_8L^-, and ReH_7L_2 have not been observed. With chelating tridentate phosphines, however, the tungsten analogs $W(L_3)H_6$ have yielded multiple barrier processes showing sequential averaging of environments (≈29 kJ mol^{-1} and 42 kJ mol^{-1}).[320] The complexes not only have the many rearrangement paths available for nine-coordinate complexes, but also have those available in lower coordination numbers by formation of eight- or seven-coordinate transient intermediates containing dihydrogen.

Most six-coordinate structures would be expected to be rigid. Isomerization rates of *cis* to *trans* $M(^{13}CO)(CO)_4(L)$ (M = Cr, W) are over 100 kJ mol^{-1} and the reactions are intramolecular, with the kinetics of the tungsten compound suggesting an internal twist mechanism for this higher barrier process.[321] Nevertheless, some six-coordinate dihydrides of iron and ruthenium show stereochemically nonrigid behavior.[322] For example, a low-temperature limiting spectrum is observed at −50 °C for $Fe[PPh(OEt)_2]_4H_2$ and shows both cis and trans isomers. Hydride–dihydrogen equilbria which allows conversion to five-coordination could also rationalize the low barriers for some octahedral dihydrides.[322] SST experiments have also indicated a dihydride intermediate in rearrangements of pseudooctahedral $Re(CO)(NO)L_2(H_2)$.[323]

Fluxionality has also been observed in chelated octahedral complexes.[21,324,325] In some cases, this can be attributed to hemilability of the ligands and rearrangement of a five-coordinate intermediate. Dithiolene chelates are an exception and tend to exist as trigonal prismatic compounds, but are still nonrigid.[326] One of the most interesting octahedral systems, where five-coordinate intermediates are less likely, involves the fluxionality of $Fe(CO)_4(SiMe_3)_2$ and the $Fe(CO)_4(SnMe_3)_2$ analogue.[327] Interestingly, $Fe(CO)_4(BCat)_2$, where BCat = $BO_2C_6H_3$-4-*t*-Bu, and $Fe(CO)_4(BCat)(SnMe_3)$ appear to be rigid at room temperature.[328]

12 KETONE AND ALDEHYDE COMPLEXES

The binding of organic carbonyl compounds to Lewis acids has a dramatic effect on the rates and selectivities of reactions at the carbonyl center. The use of organometallic Lewis acid centers promises to have significant advantages in catalysis of reactions of ketones and aldehydes.[329,330] Electronically asymmetric systems, such as $[CpRe(NO)(PPh_3)]^+$, provide preferred orientations (**87**) and (**88**) as a consequence of overlap of the *d* orbital HOMO (**25**) with the acceptor π^*-orbitals of the carbonyl. Unfavorable interactions with the Cp ring make the conformer with a N–Re–O–C torsion angle ≈0° significantly more favorable energetically.[331,332] Another feature, however, is a process by which the metal effectively migrates ‘from one lone pair to the other’ (equation 13). This might be considered as inversion of the lone pair or rehybridization of the orbitals as the metal moves. The barrier for this interconversion is quite low. There are relatively few examples where DNMR could be used to analyze this barrier. Decoalescence of the methyls in *trans*-$Cl_2(py)Pt(\eta^1$-$O{=}CMe_2)$ by ^1H and ^{13}C NMR**[333]** gives a $\Delta G^{\ddagger}_{199}$ of $\approx$40 kJ mol^{-1}. An even lower estimated $\Delta G^{\ddagger}_{199}$ of 25 kJ mol^{-1} is found from a T_c of $-140\,°C$ in the ^{13}C NMR for ^{13}C-enriched $[CpRe(NO)(PPh_3)(O{=}CMe_2)]^+$.**[332]** Although most strong Lewis acids tend to bind ketones as η^1 species, Harman showed in 2001, that TpRe(CO)(L) systems bind the ketones as η^2 species and thus tend to orient them as found with olefins in Section 2.

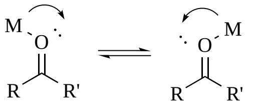

(30)

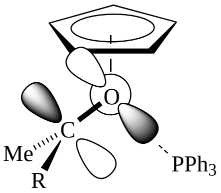

(**87**)

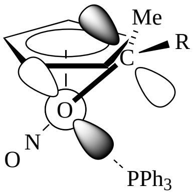

(**88**)

13 COMMENTS

This review has emphasized selected topics that illustrate principles rather than enumerating examples. Many topics of current interest, such as carbonyl rearrangements, metal–carbonyl cluster rearrangements, and naked metal-cluster rearrangements, were not covered. Topics were selected to illustrate the importance of stereochemical nonrigidity in reactivity and the potential for affecting stereochemistry in reaction products. Table 2 provides a brief list of sources for leading references for some additional topics. The reader is referred to earlier reviews for more comprehensive coverage.**[10,13,19–24,306,310]**

Equation (31) illustrates fluxionality in a bimetallic compound with a conventional ligand having an unusual bonding mode.**[334]** This provides a caveat regarding the potential for unexpected intermediates and the real need to consider other modes of binding when considering bidentate chelates. Biphep, BINAP, and similar ligands, for example, have shown bidentate binding modes that involve *P*,*C* rather than *P*,*P* coordination.**[363–370]**

Table 2 Leading references for additional selected topics on stereochemically nonrigid molecules

Metal–metal multiple bond hindered rotation	**335–337**
Ligand lone pair inversion	
Phosphide inversion	**338–340**
Sulfur inversion	**341–350**
Selenium and tellurium inversion	**341,351**
Rearrangements in bare metal clusters	**352**
Rearrangements in polynuclear transition metal clusters	**353–358**
Carbonyl scrambling and rearrangement	**13,14,354**
Atropisomeric ligand interconversion	**359,360**
Dynamics in solids	**115,356,361,362**

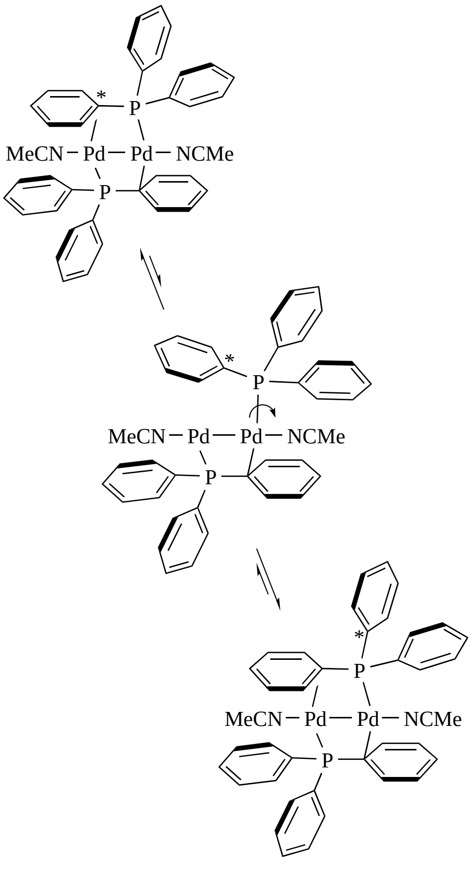

(31)

For those planning the use DNMR to evaluate barriers, the evaluations of sources of error covered in Section 1.1 and other published articles should be consulted.**[16,36,37,42,43]** A caveat to consider the definition of rate constant carefully is in order.**[16,39]** The author recommends the use of equation (3) and substitution into the Eyring equation as the most reliable method for obtaining an experimental value for $\Delta G^{\ddagger}$. Owing to the large errors, which can arise, the use of coalescence temperatures and rate expressions at T_c should be avoided at all costs. As primitive as it may seem, reference to Table 1 can provide a fairly accurate value for $\Delta G^{\ddagger}$ in most cases.

14 RELATED ARTICLES

Asymmetric Synthesis by Homogeneous Catalysis; Carbonyl Complexes of the Transition Metals; Hydride Complexes of the Transition Metals; Organic Synthesis using Transition Metal Complexes Containing π-Bonded Ligands; Polynuclear Organometallic Cluster Complexes.

15 REFERENCES

1. E. L. Muetterties, *Inorg. Chem.*, 1965, **4**, 769.
2. E. L. Muetterties, *Acc. Chem. Res.*, 1970, **3**, 266.
3. M. J. Bennet, F. A. Cotton, A. Davison, J. W. Faller, S. J. Lippard, and S. M. Morehouse, *J. Am. Chem. Soc.*, 1966, **88**, 4371.
4. F. A. Cotton, J. W. Faller, and A. Musco, *J. Am. Chem. Soc.*, 1966, **88**, 5406.
5. F. A. Cotton, A. Davison, and J. W. Faller, *J. Am. Chem. Soc.*, 1966, **88**, 4507.
6. F. A. Cotton, J. W. Faller, and A. Musco, *Inorg. Chem.*, 1967, **6**, 179.
7. J. W. Faller and A. Davison, *Inorg. Chem.*, 1967, **6**, 182.
8. D. J. Ciappenelli, F. A. Cotton, and L. Krucksinski, *J. Organomet. Chem.*, 1972, **42**, 159.
9. F. A. Cotton, *J. Organomet. Chem.*, 1975, **100**, 29.
10. L. M. Jackman and F. A. Cotton eds, ‘Dynamic Nuclear Magnetic Resonance’, Academic Press, New York, 1975.
11. P. S. Pregosin ed., ‘Transition Metal Nuclear Magnetic Resonance’, Elsevier, Amsterdam, NY, 1991.
12. C. L. Perrin and T. J. Dwyer, *Chem. Rev.*, 1990, **90**, 935.
13. B. E. Mann, *Adv. Organomet. Chem*, 1988, **28**, 397; An earlier review is also useful: B. E. Mann, in ‘Annual Reports on NMR Spectroscopy’, ed. G. A. Webb, Academic Press, London, 1982, Vol. 12, p. 263.
14. E. Bond and E. L. Muetterties, *Chem. Rev.*, 1978, **78**, 639.
15. D. W. Meek and T. J. Mazanec, *Acc. Chem. Res.*, 1981, **14**, 266.
16. J. W. Faller, *Adv. Organomet. Chem.*, 1977, **16**, 211.
17. J. Evans, *Adv. Organomet. Chem.*, 1977, **16**, 319.
18. A. Steigel, in ‘NMR, Basic Principles and Progress’, eds. P. Diehl, E. Fluck, and R. Kosfeld, Springer-Verlag, Berlin, 1978, Vol. 15, p. 1.
19. E. W. Abel and K. G. Orrell, in ‘Encyclopedia of Inorganic Chemistry’, ed. R. B. King, John Wiley & Sons, New York, 1994, p. 2581.
20. J. W. Faller, in ‘Encyclopedia of Inorganic Chemistry’, ed. R. B. King, John Wiley & Sons, New York, 1994, p. 3914.
21. R. C. Fay, *Coord. Chem. Rev.*, 1996, **154**, 99.
22. V. I. Minkin, I. E. Mikhailov, G. A. Duchenko, A. Zsunke, *Russ. Chem. Rev.*, 2003, **71**, 867.
23. K. G. Orrell, *Annu. Rep. NMR. Spectrosc.*, 1999, **37**, 1.
24. J. Akitt and B. E. Mann, ‘NMR and Chemistry’, 4th edn., Stanley Thornes, Cheltenham, 2000.
25. W. von, E. Doering, and W. R. Roth, *Angew. Chem., Int. Ed. Engl.*, 1963, **2**, 120. The original suggested spelling was ‘fluctional’ but this has generally been replaced by ‘fluxional’.
26. F. A. Cotton, *Acc. Chem. Res.*, 1968, **1**, 257.
27. T. S. Piper and G. Wilkinson, *J. Inorg. Nucl. Chem.*, 1956, **3**, 104.
28. D. S. Stephenson and G. Binsch, ‘DNMR5: Iterative Nuclear Magnetic Resonance Program for Unsaturated Exchange-Broadened Band Shapes’, Institute of Organic Chemistry, University of Munich, Munich FRG (QCPE 365 and 569).
29. J. H. Brown and C. H. Bushweller, *QCPE Bulletin*, 1983, **3**, 103, qcpe.chem.indiana.edu.
30. H. J. Reich, *J. Chem. Educ.*, 1995, **72**, 1086; *J. Chem. Educ. Software*, **3D2**.
31. P. H. M. Budzelaar, ‘gNMR, Adept Scientific’, 7909 Charleston Court, Bethesda, MD, 1999, p. 20817.
32. R. Cramer, *J. Am. Chem. Soc.*, 1964, **86**, 217.
33. R. Cramer, J. B. Kline, and J. D. Roberts, *J. Am. Chem. Soc.*, 1969, **91**, 2519.
34. G. Binsch and H. Kessler, *Angew. Chem., Int. Ed. Engl.*, 1980, **19**, 411.
35. K. G. Orrell, V. Sik, and D. Stephenson, *Prog. Nucl. Magn. Reson. Spectrosc.*, 1990, **22**, 141.
36. A. D. Bain and J. A. Cramer, *J. Magn. Reson. Ser. A*, 1996, **118**, 21.
37. A. D. Bain, *Prog. Nucl. Magn. Reson. Spectrosc.*, 2003, **43**, 63; see also A. D. Bain, D. M. Rex, and R. N. Smith, *Magn. Reson. Chem.*, 2001, **39**, 122.
38. L. W. Reeves, *Adv. Phys. Org. Chem.*, 1967, **3**, 18.
39. M. L. H. Green, L.-L. Wong, and A. Sella, *Organometallics*, 1992, **11**, 2660.
40. C. S. Johnson Jr, *Adv. Magn. Reson.*, 1965, **1**, 35.
41. J. E. Anderson and J. M. Lehn, *J. Am. Chem. Soc.*, 1967, **89**, 81.
42. A. Allerhand, H. S. Gutowsky, J. Jonas, and R. Meintzer, *J. Am. Chem. Soc.*, 1966, **88**, 3185.
43. G. Binsch, in ‘Dynamic Nuclear Magnetic Resonance’, eds. L. M. Jackman and F. A. Cotton, Academic Press, New York, 1975, p. 45.
44. J. I. Kaplan and G. Fraenkel, ‘NMR of Chemically Exchanging Systems’, Academic Press, New York, 1980.
45. J. Sandstrom, ‘Dynamic NMR Spectroscopy’, Academic Press, London, 1982.
46. D. S. Stephenson and G. Binsch, *J. Magn. Reson.*, 1978, **32**, 145.

47. E. W. Abel, T. P. J. Coston, K. G. Orrell, V. Sik, and D. Stephenson, *J. Magn. Reson.*, 1986, **70**, 34.
48. E. W. Abel, I. Moss, K. G. Orrell, V. Sik, and D. Stephenson, *J. Chem. Soc., Dalton Trans.*, 1987, 2695.
49. J. W. Faller, in 'Determination of Organic Structures by Physical Methods', eds. F. C. Nachod and J. Zuckerman, Academic Press, New York, 1973, Vol. V, p. 75.
50. G. A. Morris and R. Freeman, *J. Magn. Reson.*, 1978, **29**, 433.
51. R. A. Freeman, 'Handbook of Nuclear Magnetic Resonance', Longmans, Harlow, 1987.
52. R. L. Jarek, R. J. Flesher, and S. K. Shin, *J. Chem. Educ.*, 1997, **74**, 978. (Note T_1 calculations here do not take exchange effects into account and are only valid if T_1 in both sites are equal).
53. D. J. Wink, *J. Chem. Educ.*, 1989, **66**, 810.
54. J. R. Alger and J. H. Prestegard, *J. Magn. Reson.*, 1977, **27**, 137.
55. G. Robinson, P. W. Kuchel, B. E. Chapman, D. M. Doddrell, and M. G. Irving, *J. Magn. Reson.*, 1985, **63**, 314.
56. H. Geen and H. R. Freeman, *J. Magn. Reson.*, 1991, **93**, 93.
57. C. L. Perrin and R. E. Engler, *J. Magn. Reson. Ser. A* 1996, **123**, 188.
58. M. L. H. Green, A. Sella, and L. L. Wong, *Organometallics*, 1992, **11**, 2650.
59. R. S. Threlkel and J. E. Bercaw, *J. Am. Chem. Soc.*, 1981, **103**, 2650.
60. P. J. Heard, P. M. King, and D. A. Tocher, *J. Chem. Soc., Dalton Trans.*, 2000, **11**, 1769.
61. J. D. Morrison, W. F. Masler, and M. K. Newberg, *Adv. Catal.*, 1976, **25**, 81.
62. W. Tang and X. Zhang, *Chem. Rev.*, 2003, **103**, 3029.
63. P. Pino, G. Consiglio, C. Botteghi, and C. Salamon, in 'Homogeneous Catalysis II', ACS Advances in Chemistry Series, Vol. 132, eds. D. Forster and J. F. Roth, American Chemical Society, Washington, DC, 1974, p. 295.
64. M. D. Fryzuk and B. Bosnich, *J. Am. Chem. Soc.*, 1978, **100**, 5491; 1979, **101**, 3043.
65. L. W. Reeves, *Can. J. Chem.*, 1960, **38**, 736.
66. A. R. Luxmoore and M. R. Truter, *Acta Crystallogr.*, 1962, **15**, 1117.
67. S. Maricic, C. R. Redpath, and J. A. S. Smith, *J. Chem. Soc.*, 1963, 4905.
68. S. D. Ittel and J. A. Ibers, *Adv. Organomet. Chem.*, 1976, **14**, 33.
69. J. Howard, T. C. Waddington, and C. J. Wright, *J. Chem. Soc., Faraday Trans. 2*, 1976, **72**, 513.
70. M. J. S. Dewar, *Bull. Soc. Chim. Fr.*, 1951, **18**, C71.
71. J. Chatt and L. A. Duncanson, *J. Chem. Soc.*, 1953, 2939.
72. D. M. P. Mingos, *Adv. Organomet. Chem.*, 1977, **15**, 1.
73. D. M. P. Mingos, in 'Comprehensive Organometallic Chemistry', eds. G. Wilkinson, F. G. A. Stone, and E. W. Abel, Pergamon, Oxford, 1982, Vol. 3, p. 1.
74. R. G. Ball and N. C. Paine, *Inorg. Chem.*, 1977, **16**, 1871; 1976, **15**, 2494.
75. F. A. Cotton, J. N. Francis, B. A. Frenz, and M. Tsutsui, *J. Am. Chem. Soc.*, 1973, **95**, 2483.
76. P. D. Kaplan, P. Schmidt, and M. Orchin, *J. Am. Chem. Soc.*, 1968, **90**, 4175.
77. L. P. Seiwell, *Inorg. Chem.*, 1976, **15**, 2560.
78. D. L. White and J. W. Faller, *J. Am. Chem. Soc.*, 1982, **104**, 1548.
79. J. Ashley-Smith, I. Douek, B. F. G. Johnson, and J. Lewis, *J. Chem. Soc., Dalton Trans.*, 1972, 1776; 1974, 128.
80. H. Boucher and B. Bosnich, *Inorg. Chem.*, 1977, **16**, 717.
81. T. A. Albright, R. Hoffmann, J. C. Thibeault, and D. L. Thorn, *J. Am. Chem. Soc.*, 1979, **101**, 3801.
82. C. G. Kreiter and H. Strack, *Z. Naturforsch.*, 1975, **30B**, 748.
83. U. Koemm, C. G. Kreiter, and H. Strack, *J. Organomet. Chem.*, 1978, **148**, 179.
84. C. Bachman, J. Demuynck, and A. Veillard, *J. Am. Chem. Soc.*, 1978, **100**, 2366.
85. J. W. Byrne, H. V. Blazer, and J. A. Osborn, *J. Am. Chem. Soc.*, 1975, **97**, 3871.
86. M. Jaroszewski, T. SzymanskaBuzar, M. Wilgocki, and J. J. Ziolkowski, *J. Organomet. Chem*, 1996, **509**, 19.
87. L. J. Guggenberger and R. Cramer, *J. Am. Chem. Soc.*, 1972, **94**, 3779.
88. O. J. Curnow, R. P. Hughes, and A. L. Rheingold, *J. Am. Chem. Soc.*, 1992, **114**, 3153.
89. K. Moseley, J. W. Kang, and P. M. Maitlis, *J. Chem. Soc. A*, 1970, 2875.
90. J. A. K. Howard, S. A. R. Knox, N. J. Terrill, and M. I. Yates, *J. Chem. Soc., Chem. Commun.*, 1989, 640.
91. J. W. Faller, B. V. Johnson, and C. D. Schaeffer Jr, *J. Am. Chem. Soc.*, 1976, **98**, 1395.
92. R. D. Adams, D. F. Chodosh, J. W. Faller, and A. M. Rosan, *J. Am. Chem. Soc.*, 1979, **101**, 2570.
93. B. E. Schilling, R. Hoffmann, and J. W. Faller, *J. Am. Chem. Soc.*, 1979, **101**, 592.
94. M. Heberhold, G. Wiedersatz, and C. G. Kreiter, *J. Organomet. Chem.*, 1976, **104**, 209.
95. H. Alt, M. Herberhold, C. G. Kreiter, and H. Strack, *J. Organomet. Chem.*, 1974, **77**, 353.
96. A. Alt, M. Herberhold, C. G. Kreiter, and H. Strack, *J. Organomet. Chem.*, 1975, **102**, 491.
97. G. S. Bodner, T.-S. Peng, A. M. Arif, and J. A. Gladysz, *Organometallics*, 1990, **9**, 1191.
98. W. A. Kiel, G.-Y. Lin, A. G. Constable, F. B. McCormick, C. E. Strause, O. Eisenstein, and J. A. Gladysz, *J. Am. Chem. Soc.*, 1982, **104**, 4865.

99. T.-S. Peng and J. A. Gladysz, *J. Am. Chem. Soc.*, 1992, **114**, 4175.
100. J. Q. Pu, T. S. Peng, C. L. Mayne, A. M. Arif, and J. A. Gladysz, *Organometallics*, 1993, **12**, 2686.
101. J. A. Gladysz and B. J. Boone, *Angew. Chem., Int. Ed. Engl.*, 1997, **36**, 551.
102. X. Q. Yan, F. W. B. Einstein, and D. Sutton, *Can. J. Chem.*, 1995, **73**, 939.
103. R. J. Batchelor, F. W. B. Einstein, N. D. Lowe, B. A. Palm, X. Q. Yan, and D. Sutton, *Organometallics*, 1994, **13**, 2041.
104. J. W. Faller and H. Felkin, *Organometallics*, 1985, **4**, 1488.
105. L. A. Friedman, S. H. Meiere, B. C. Brooks, and W. D. Harman, *Organometallics*, 2001, **20**, 1699.
106. S. H. Meiere, B. C. Brooks, T. B. Gunnoe, E. H. Carrig, M. Sabat, and W. D. Harman, *Organometallics*, 2001, **20**, 3661.
107. S. H. Meiere and W. D. Harman, *Organometallics*, 2001, **20**, 3876.
108. T. B. Gunnoe, M. Sabat, and W. D. Harman, *Organometallics*, 2000, **19**, 728.
109. B. C. Brooks, S. H. Meiere, L. A. Freidman, E. H. Carrig, T. B. Gunnoe, and W. D. Harman, *J. Am. Chem. Soc.*, 2001, **123**, 3541.
110. P. J. Albietz, B. P. Cleary, W. Paw, and R. Eisenberg, *Inorg. Chem.*, 2002, **41**, 2095.
111. S. A. Vierkotter, C. E. Barnes, G. L. Garner, and L. G. Butler, *J. Am. Chem. Soc.*, 1994, **116**, 7445.
112. G. M. Bernard, R. E. Wasylishen, and A. D. Phillips, *J. Phys. Chem.*, 2000, **104**, 8131.
113. S. C. Mackie and M. C. Baird, *Organometallics*, 1992, **11**, 3712.
114. D. C. Maus, V. Copie, B. Q. Sun, J. M. Griffiths, R. G. Griffin, S. F. Luo, R. R. Schrock, A. H. Liu, S. W. Seidel, W. M. Davis, and A. Grohmann, *J. Am. Chem. Soc.*, 1996, **118**, 5665.
115. M. J. Duer, *Annu. Rep. NMR Spectrosc.*, 2001, **43**, 1.
116. J. W. Faller and H. H. Murray, *J. Organomet. Chem.*, 1979, **172**, 171.
117. F. G. A. Stone, J. L. Davidson, M. Green, and A. J. Welch, *J. Chem. Soc., Dalton Trans.*, 1976, 738.
118. M. J. McGeary, A. S. Gamble, and J. L. Templeton, *Organometallics*, 1988, **7**, 271.
119. M. Etienne, B. Donnadieu, R. Mathieu, J. F. Baeza, F. Jalon, A. Otero, and M. E. RodrigoBlanco, *Organometallics*, 1996, **15**, 4597.
120. K. J. Ivin, *J. Mol. Catal. A*, 1998, **133**, 1.
121. C. Pariya, K. N. Jayaprakash, and A. Sarkar, *Coord. Chem. Rev.*, 1998, **168**, 1.
122. Z. Wu, S. T. Nguyen, R. H. Grubbs, and J. W. Ziller, *J. Am. Chem. Soc.*, 1995, **117**, 5503.
123. J. W. Herndon, *Coord. Chem. Rev.*, 2003, **243**, 3.
124. C. F. Bernasconi, *Chem. Soc. Rev.*, 1997, **26**, 299.
125. O. M. Aagaard, R. J. Meier, and F. Buda, *J. Am. Chem. Soc.*, 1998, **120**, 7174.
126. T. R. Cundari and M. S. Gordon, *Organometallics*, 1992, **11**, 55.
127. C. Adhart and P. Chen, *Angew. Chem., Int. Ed. Engl.*, 2002, **41**, 4484.
128. S. F. Vyboishchikov and G. Frenking, *Chem. Eur. J.*, 1998, **4**, 1428.
129. R. J. Meier, O. M. Aagaard, and F. Buda, *J. Mol. Catal. A*, 2000, **160**, 189.
130. B. E. R. Schilling, R. Hoffmann, and D. L. Lichtenberger, *J. Am. Chem. Soc.*, 1979, **101**, 585.
131. M. Brookhart, Y. Liu, E. W. Goldman, D. A. Timmers, and G. D. Williams, *J. Am. Chem. Soc.*, 1991, **113**, 927.
132. W. A. Kiel, W. E. Buhro, and J. A. Gladysz, *Organometallics*, 1984, **3**, 879.
133. Y. Wang and J. A. Gladysz, *Chem. Ber.*, 1995, **128**, 213.
134. H. Fischer, K. Weissenbach, C. Karl, and A. Geyer, *Eur. J. Inorg. Chem.*, 1998, 339.
135. T. B. Gunnoe, M. Surgan, P. S. White, J. L. Templeton, and L. Casarrubios, *Organometallics*, 1997, **16**, 4865.
136. T. B. Gunnoe, P. S. White, J. L. Templeton, and L. Casarrubios, *J. Am. Chem. Soc.*, 1997, **119**, 3171.
137. W. M. Vaughan, K. A. Abboud, and J. M. Boncella, *Organometallics*, 1995, **14**, 1567.
138. H. D. Hansen and J. H. Nelson, *Inorg. Chim. Acta*, 2003, **352**, 4.
139. J. H. Oskam and R. R. Schrock, *J. Am. Chem. Soc.*, 1993, **115**, 11831.
140. J. H. Oskam and R. R. Schrock, *J. Am. Chem. Soc.*, 1992, **114**, 10680.
141. J. H. Oskam and R. R. Schrock, *J. Am. Chem. Soc.*, 1992, **114**, 7588.
142. A. R. Chianese, X. W. Li, M. C. Janzen, J. W. Faller, and R. H. Crabtree, *Organometallics*, 2003, **22**, 1663.
143. T. Weskamp, W. C. Schattenmann, M. Spiegler, and W. A. Herrmann, *Angew. Chem., Int. Ed. Engl.*, 1998, **37**, 2490.
144. W. A. Herrmann, L. J. Goossen, and M. Spiegler, *J. Organomet. Chem.*, 1997, **547**, 357.
145. D. Enders, H. Gielen, J. Runsink, K. Breuer, S. Brode, and K. Boehn, *Eur. J. Inorg. Chem.*, 1998, 913.
146. D. Enders and H. Gielen, *J. Organomet. Chem.*, 2001, **617**, 70.
147. D. S. McGuinness and K. J. Cavell, *Organometallics*, 2000, **19**, 741.
148. C. P. Casey, C. J. Czerwinski, and R. K. Hayashi, *J. Am. Chem. Soc.*, 1995, **117**, 4189.

149. M. Brookhart, J. R. Tucker, and G. R. Husk, *J. Organomet. Chem.*, 1980, **193**, C23.
150. J. W. Faller, J. Parr, and A. R. Lavoie, *New J. Chem.*, 2003, **27**, 899.
151. B. E. Mann, C. Masters, B. L. Shaw, and R. E. Stainbank, *J. Chem. Soc., Chem. Commun.*, 1971, 1103.
152. C. H. Bushweller and M. Z. Lourandos, *Inorg. Chem.*, 1974, **13**, 2514.
153. C. H. Bushweller, S. Hoogasian, A. D. English, J. S. Miller, and M. Z. Lourandos, *Inorg. Chem.*, 1981, **20**, 3448.
154. C. H. Bushweller, C. D. Rithner, and D. J. Butcher, *Inorg. Chem.*, 1986, **25**, 1610.
155. C. M. Dimeglio, K. J. Ahmed, L. A. Luck, E. E. Weltin, A. L. Rheingold, and C. H. Bushweller, *J. Phys. Chem.*, 1992, **96**, 8765.
156. B. E. Mann and A. Musco, *J. Organomet. Chem.*, 1979, **181**, 439.
157. G. Hunter, T. J. R. Weakley, and W. Weissensteiner, *J. Chem. Soc., Dalton Trans.*, 1987, 1545.
158. J. Q. Pu, T. S. Peng, C. L. Mayne, A. M. Arif, and J. A. Gladysz, *Organometallics*, 1993, **12**, 2686.
159. F. P. Fanizzi, M. Lanfranchi, G. Natiel, and A. Tiripicchio, *Inorg. Chem.*, 1994, **33**, 3331.
160. D. Carmona, L. A. Oro, M. P. Lamata, M. L. Jimeno, J. Elguero, A. Belguise, and P. Lux, *Inorg. Chem.*, 1994, **33**, 2196.
161. J. U. Notheis, R. H. Heyn, and K. G. Caulton, *Inorg. Chim. Acta*, 1995, **229**, 187.
162. H. Brunner, R. Oeschey, and B. Nuber, *Organometallics*, 1996, **15**, 3616.
163. R. A. Widenhoefer, H. A. Zhong, and S. L. Buchwald, *Organometallics*, 1996, **15**, 2745.
164. R. Giannandrea, P. Mastrorilli, M. Palma, F. P. Fanizzi, U. Englert, and C. F. Nobile, *Eur. J. Inorg. Chem.*, 2000, 2573.
165. J. Albert, R. Bosque, J. M. Cadena, S. Delgado, and J. Granell, *J. Organomet. Chem.*, 2001, **634**, 83.
166. E. M. Pelczar, E. A. Nytko, M. A. Zhuravel, J. M. Smith, D. S. Glueck, R. Sommer, C. D. Incarvito, and A. L. Rheingold, *Polyhedron*, 2002, **21**, 2409.
167. G. Canepa, C. D. Brandt, K. Ilg, J. Wolf, and H. Werner, *Chem. Eur. J.*, 2003, **9**, 2502.
168. R. P. Hughes, R. B. Laritchev, A. Williamson, C. D. Incarvito, L. N. Zakharov, and A. L. Rheingold, *Organometallics*, 2003, **22**, 2134.
169. J. W. Faller and B. V. Johnson, *J. Organomet. Chem.*, 1975, **96**, 99.
170. J. A. S. Howell, P. C. Yates, M. G. Palin, P. McArdle, D. Cunningham, Z. Goldschmidt, H. E. Gottlieb, and D. Hezronilangerman, *J. Chem. Soc., Dalton Trans.*, 1993, 2775.
171. J. A. S. Howell, M. G. Palin, P. McArdle, D. Cunningham, Z. Goldschmidt, H. E. Gottlieb, and D. Hezronilangerman, *Inorg. Chem.*, 1993, **32**, 3493.
172. J. A. S. Howell, M. G. Palin, P. McArdle, D. Cunningham, Z. Goldschmidt, H. E. Gottlieb, and D. Hezronilangerman, *Organometallics*, 1993, **12**, 1694.
173. J. Vicente, M. T. Chicote, M. C. Lagunas, P. G. Jones, and B. Ahrens, *Inorg. Chem.*, 1997, **36**, 4938.
174. M. S. Davies, G. W. Allen, M. J. Aroney, T. W. Hambley, and R. K. Pierens, *J. Mol. Struct.*, 1994, **326**, 81.
175. S. G. Davies, A. E. Derome, and J. P. McNally, *J. Am. Chem. Soc.*, 1991, **113**, 2854.
176. I. Kovacs and M. C. Baird, *Organometallics*, 1995, **14**, 4084.
177. W. D. Jones and F. J. Feher, *Inorg. Chem.*, 1984, **23**, 2376.
178. T. Daniel and H. Werner, *J. Chem. Soc., Dalton Trans.*, 1994, 221.
179. J. W. Faller and K. J. Chase, *Organometallics*, 1995, **14**, 1592.
180. S. C. Mackie and M. C. Baird, *Organometallics*, 1992, **11**, 3712.
181. J. Polowin, S. C. Mackie, and M. C. Baird, *Organometallics*, 1992, **11**, 3724.
182. J. Polowin and M. C. Baird, *J. Organomet. Chem.*, 1994, **478**, 45.
183. J. F. Costello and S. G. Davies, *J. Chem. Soc., Perkin Trans. 2*, 1998, 1683.
184. J. F. Costello, S. G. Davies, and D. McNally, *J. Chem. Soc., Perkin Trans. 2*, 1999, 465.
185. A. P. Ayscough, J. F. Costello, and S. G. Davies, *Tetrahedron-Asymmetry*, 2001, **12**, 1621.
186. C. J. Ammann, P. S. Pregosin, H. Ruegger, A. Albinati, F. Lianza, and R. W. Kunz, *J. Organomet. Chem.*, 1992, **423**, 415.
187. J. B. Lambert and L. J. Lin, *Magn. Reson. Chem.*, 2001, **39**, 714.
188. L. Kollar, P. Sandor, and G. Szalontai, *J. Mol. Catal.*, 1991, **67**, 191.
189. A. J. Deeming, D. M. Speel, and M. Stchedroff, *Organometallics*, 1997, **16**, 6004.
190. N. W. Alcock, J. M. Brown, and J. J. Pereztorrente, *Tetrahedron Lett.*, 1992, **33**, 389.
191. J. M. Brown, J. J. Pereztorrente, and N. W. Alcock, *Organometallics*, 1995, **14**, 1195.
192. K. Miki, M. Tanaka, N. Kasai, and M. Wada, *J. Organomet. Chem.*, 1988, **352**, 385.
193. P. L. Alsters, J. Boersma, W. J. J. Smeets, A. L. Spek, and G. Vankoten, *Organometallics*, 1993, **12**, 1639.
194. A. C. Albeniz, A. L. Casado, and P. Espinet, *Inorg. Chem.*, 1999, **38**, 2510.
196. A. D. Selmeczy, W. D. Jones, M. G. Partridge, and R. N. Perutz, *Organometallics*, 1994, **13**, 522.

195. A. C. Albeniz, A. L. Casado, and P. Espinet, *Organometallics*, 1997, **16**, 5416.

197. J. A. Casares, P. Espinet, J. M. MartinezIlarduya, and Y. S. Lin, *Organometallics*, 1997, **16**, 770.

198. J. A. Casares and P. Espinet, *Inorg. Chem.*, 1997, **36**, 5428.

199. L. U. Colmenares and R. S. H. Liu, *Tetrahedron*, 1996, **52**, 109.

200. M. C. Carrion, A. Diaz, A. Guerrero, F. A. Jalon, B. R. Manzano, and A. Rodriguez, *New J. Chem.*, 2002, **26**, 305.

201. M. C. Carrion, A. Guerrero, F. A. Jalon, B. R. Manzano, A. de la Hoz, R. M. Claramunt, V. Milata, and J. Elguero, *Inorg. Chem.*, 2003, **42**, 885.

202. Z. Ciunik, J. A. Wolny, M. F. Rudolf, and S. Wolowiec, *J. Chem. Soc., Dalton Trans.*, 2002, 885.

203. J. W. Faller and M. J. Mattina, *Inorg. Chem.*, 1972, **11**, 1296.

204. M. Fujita, J. Yazaki, and K. Ogura, *J. Am. Chem. Soc.*, 1990, **112**, 5645.

205. M. Fujita and K. Ogura, *Bull. Chem. Soc. Jpn.*, 1996, **69**, 1471.

206. P. J. Stang, D. H. Cao, S. Saito, and A. M. Arif, *J. Am. Chem. Soc.*, 1995, **117**, 6273.

207. C. J. Kuehl, S. D. Huang, and P. J. Stang, *J. Am. Chem. Soc.*, 2001, **123**, 9634.

208. S. Leininger, B. Olenyuk, and P. J. Stang, *Chem. Rev.*, 2000, **100**, 853.

209. P. J. Stang, B. Olenyuk, and A. M. Arif, *Organometallics*, 1995, **14**, 5281.

210. M. Fuss and H. U. Siehl, *Organometallics*, 1999, **18**, 758.

211. E. Rotondo, G. Bruschetta, G. Bruno, A. Rotondo, M. L. Di Pietro, and M. Cusumano, *Eur. J. Inorg. Chem.*, 2003, 2612.

212. A. H. Velders, A. C. G. Hotze, G. A. van Albada, J. G. Haasnoot, and J. Reedijk, *Inorg. Chem.*, 2000, **39**, 4073.

213. A. H. Velders, C. Massera, F. Ugozzoli, M. Biagini-Cingi, A. M. Manotti-Lanfredi, J. G. Haasnoot, and J. Reedijk, *Eur. J. Inorg. Chem.*, 2002, 193.

214. J. Arpalahti, K. D. Klika, R. Sillanpaa, and R. Kivekas, *J. Chem. Soc., Dalton Trans.*, 1998, 1397.

215. E. Alessio, L. Hansen, M. Iwamoto, and L. G. Marzilli, *J. Am. Chem. Soc.*, 1996, **118**, 7593.

216. E. Alessio, M. Calligaris, M. Iwamoto, and L. G. Marzilli, *Inorg. Chem.*, 1996, **35**, 2538.

217. E. Alessio, E. Iengo, E. Zangrando, S. Geremia, P. A. Marzilli, and M. Calligaris, *Eur. J. Inorg. Chem.*, 2000, 2207.

218. A. Gelling, K. G. Orrell, A. G. Osborne, and V. Sik, *J. Chem. Soc., Dalton Trans.*, 1998, 937.

219. A. Gelling, K. G. Orrell, A. G. Osborne, V. Sik, M. B. Hursthouse, D. E. Hibbs, and K. M. A. Malik, *Polyhedron*, 1998, **17**, 2141.

220. A. Gelling, K. G. Orrell, A. G. Osborne, V. Sik, M. B. Hursthouse, and S. J. Coles, *J. Chem. Soc., Dalton Trans.*, 1996, 203.

221. M. Pons and O. Millet, *Prog. Nucl. Magn. Reson. Spectrosc.*, 2001, **38**, 267.

222. A. Cusanelli and D. Sutton, *Organometallics*, 1996, **15**, 1457.

223. D. C. Roe, W. J. Marshall, F. Davidson, P. D. Soper, and V. V. Grushin, *Organometallics*, 2000, **19**, 4575.

224. R. V. Honeychuck and W. H. Hersh, *J. Am. Chem. Soc.*, 1989, **111**, 6056.

225. U. Berg and J. Sandstrom, *Adv. Phys. Org. Chem.*, 1989, **25**, 1.

226. A. J. Horsewill, *Prog. Nucl. Magn. Reson. Spectrosc.*, 1999, **35**, 359.

227. W. J. E. Parr and T. Schaefer, *Acc. Chem. Res.*, 1980, **13**, 400.

228. O. Desponds and M. Schlosser, *Tetrahedron Lett.*, 1996, **37**, 47.

229. S. Brydges, L. E. Harrington, and M. J. McGlinchey, *Coord. Chem. Rev.*, 2002, **233**, 75.

230. M. J. McGlinchey, *Can. J. Chem.*, 2001, **79**, 1295.

231. L. J. Li, A. Decken, B. G. Sayer, M. J. McGlinchey, P. Bregaint, J. Y. Thepot, L. Toupet, J. R. Hamon, and C. Lapinte, *Organometallics*, 1994, **13**, 682.

232. M. J. McGlinchey, *Adv. Organomet. Chem.*, 1992, **34**, 285.

233. A. M. Stolzenberg and G. S. Haymond, *Inorg. Chem.*, 2002, **41**, 300.

234. F. Mao, C. E. Philbin, T. J. R. Weakley, and D. R. Tyler, *Organometallics*, 1990, **9**, 1510.

235. J. W. Faller and A. M. Rosan, *J. Am. Chem. Soc.*, 1977, **99**, 4858.

236. J. W. Faller, H. H. Murray, D. L. White, and K. H. Chao, *Organometallics*, 1983, **2**, 400.

237. J. W. Faller and A. S. Anderson, *J. Am. Chem. Soc.*, 1970, **92**, 5852.

238. C. M. Adams, A. Hafner, M. Koller, A. Marcuzzi, R. Preivo, I. Solana, B. Vincent, and W. von Philipsborn, *Helv. Chim. Acta*, 1989, **72**, 1658.

239. J. A. S. Howell, G. Walton, M. C. Tirvengadum, A. D. Squibb, M. G. Palan, P. McArdle, D. Cunningham, A. Goldsmidt, H. E. Gottlieb, and G. Strul, *J. Organomet. Chem.*, 1991, **401**, 91.

240. L. Kruczynski and J. Takats, *Inorg. Chem.*, 1976, **15**, 3140.

241. A. J. Pearson, *Synlett*, 1990, 10.

242. H. J. Knolker, A. Braier, D. J. Brocher, S. Cammerer, W. Frohner, P. Gonser, H. Hermann, D. Herzberg, K. R. Reddy, and G. Rohde, *Pure Appl. Chem.*, 2001, **73**, 1075.

243. T. A. Albright, P. Hofmann, and R. Hoffmann, *J. Am. Chem. Soc.*, 1977, **99**, 7546.

244. M. J. Calhorda and E. J. S. Vichi, *Organometallics*, 1990, **9**, 1060.

245. J. A. S. Howell, D. T. Dixon, and J. C. Kole, *J. Organomet. Chem.*, 1984, **266**, 69.

246. L. Harland, G. R. Stephenson, and M. J. Whittaker, *J. Organomet. Chem.*, 1984, **263**, C30.

247. T. A. Albright, *Acc. Chem. Res.*, 1982, **15**, 149.

248. O. Gonzalez-Blanco, V. Branchadell, and R. Gree, *Chem. Eur. J.*, 1999, **5**, 1722.

249. P. McArdle, J. Skelton, and A. R. Manning, *J. Organomet. Chem.*, 1997, **538**, 9.

250. S. Ozkar, C. G. Kreiter, and M. Kotzian, *J. Organomet. Chem.*, 1995, **494**, 115.

251. C. Chardon, O. Eisenstein, T. Johnson, and K. G. Caulton, *New J. Chem.*, 1992, **16**, 781.

252. A. Bader and E. Lindner, *Coord. Chem. Rev.*, 1991, **108**, 27.

253. C. S. Slone, D. A. Weinberger, and C. A. Mirkin, *Prog. Inorg. Chem.*, 1999, **48**, 233.

254. P. Jutzi and U. Siemeling, *J. Organomet. Chem.*, 1995, **500**, 175.

255. E. Lindner, M. Schmid, P. Wegner, C. Nachtigal, M. Steimann, and R. Fawzi, *Inorg. Chim. Acta*, 1999, **296**, 103.

256. U. Fekl and K. I. Goldberg, *Adv. Inorg. Chem.*, 2003, **54**, 259.

257. D. M. Crumpton-Bregel and K. I. Goldberg, *J. Am. Chem. Soc.*, 2003, **125**, 9442.

258. D. D. Wick and K. I. Goldberg, *J. Am. Chem. Soc.*, 1997, **119**, 10235.

259. M. Onishi and K. Hiraki, *Inorg. Chim. Acta*, 1994, **224**, 131.

260. M. Onishi, K. Hiraki, A. Ueno, Y. Yamaguchi, and Y. Ohama, *Inorg. Chim. Acta-Art. Lett.*, 1984, **82**, 121.

261. P. Janser, L. M. Venanzi, and F. Bachechi, *J. Organomet. Chem.*, 1985, **296**, 229.

262. C. Landgrafe, W. S. Sheldrick, and H. Sudfeld, *Eur. J. Inorg. Chem.*, 1998, 407.

263. D. J. Rauscher, E. G. Thaler, J. C. Huffman, and K. G. Caulton, *Organometallics*, 1991, **10**, 2209.

264. E. G. Thaler, K. Folting, and K. G. Caulton, *J. Am. Chem. Soc.*, 1990, **112**, 2664.

265. A. Gogoll, J. Ornebro, H. Grennberg, and J. E. Backvall, *J. Am. Chem. Soc.*, 1994, **116**, 3631.

266. R. Fernandez-Galan, F. A. Jalon, B. R. Manzano, J. Rodriguez de la Fuente, M. Vrahami, B. Jedlicka, W. Weissensteiner, and G. Jogl, *Organometallics*, 1997, **16**, 3758.

267. A. Albinati, R. W. Kunz, C. J. Ammann, and P. S. Pregosin, *Organometallics*, 1991, **10**, 1800.

268. J. Elguero, A. Fruchier, A. delaHoz, F. A. Jalon, B. R. Manzano, A. Otero, and F. GomezdelaTorre, *Chem. Ber.*, 1996, **129**, 589.

269. J. Elguero, A. Guerrero, F. G. de la Torre, A. de la Hoz, F. A. Jalon, B. R. Manzano, and A. Rodriguez, *New J. Chem.*, 2001, **25**, 1050.

270. F. Gomez-de la Torre, A. de la Hoz, F. A. Jalon, B. R. Manzano, A. Otero, A. M. Rodriguez, M. C. Rodriguez-Perez, A. Echevarria, and J. Elguero, *Inorg. Chem.*, 1998, **37**, 6606.

271. M. C. Carrion, A. Guerrero, F. A. Jalon, B. R. Manzano, A. de la Hoz, R. M. Claramunt, V. Milata, and J. Elguero, *Inorg. Chem.*, 2003, **42**, 885.

272. F. Gomez-de la Torre, F. A. Jalon, A. Lopez-Agenjo, B. R. Manzano, and A. Rodriguez, *Organometallics*, 1998, **17**, 4634.

273. F. Gomez-de la Torre, F. A. Jalon, A. Lopez-Agenjo, B. R. Manzano, A. Rodriguez, T. Sturm, W. Weissensteiner, and M. Martinez-Ripoll, *Organometallics*, 1998, **17**, 5941.

274. A. A. H. Vanderzeijden, G. Vankoten, R. A. Nordemann, B. Kojicprodic, and A. L. Spek, *Organometallics*, 1988, **7**, 1957.

275. H. Valentini, K. Selvakumar, M. Worle, and P. S. Pregosin, *J. Organomet. Chem.*, 1999, **587**, 244.

276. K. Vrieze, in ‘Dynamic Nuclear Magnetic Resonance’, eds. L. M. Jackman and F. A. Cotton, Academic Press, New York, 1975, p. 441.

277. P. S. Pregosin and R. Salzmann, *Coord. Chem. Rev.*, 1996, **155**, 35.

278. B. M. Trost and M. L. Crawley, *Chem. Rev.*, 2003, **103**, 2921.

279. J. W. Faller, C. C. Chen, M. J. Mattina, and A. Jakubowski, *J. Organomet. Chem.*, 1973, **52**, 361.

280. J. W. Faller and A. M. Rosan, *J. Am. Chem. Soc.*, 1976, **98**, 3388.

281. J. W. Faller and D. Linebarrier, *J. Am. Chem. Soc.*, 1989, **111**, 1937.

282. J. W. Faller, J. A. John, and M. R. Mazzieri, *Tetrahedron Lett.*, 1989, **30**, 1769.

283. J. W. Faller, M. DiVerdi, and J. A. John, *Tetrahedron Lett.*, 1991, **32**, 1271.

284. J. W. Faller, J. T. Nguyen, W. Ellis, and M. R. Mazzieri, *Organometallics*, 1993, **12**, 1434.

285. J. W. Faller, H. L. Stokes-Huby, and M. A. Albrizzio, *Helv. Chim. Acta*, 2001, **84**, 3031.

286. J. Sprinz, M. Kiefer, G. Helmchen, G. Huttner, O. Walter, L. Zsolnai, and M. Reggelin, *Tetrahedron Lett.*, 1994, **35**, 1523.

287. J. W. Faller, M. E. Thomsen, and M. J. Mattina, *J. Am. Chem. Soc.*, 1971, **93**, 2642.

288. J. W. Faller and M. T. Tully, *J. Am. Chem. Soc.*, 1972, **94**, 2676.

289. B. Bosnich and P. B. Mackenzie, *Pure Appl. Chem.*, 1982, **54**, 189.

290. N. T. Anh, M. Elian, and R. Hoffmann, *J. Am. Chem. Soc.*, 1978, **100**, 110.

291. K. J. Karel, T. A. Albright, and M. Brookhart, *Organometallics*, 1982, **1**, 419.

292. P. Jutzi, *Chem. Rev.*, 1986, **86**, 983.

293. Y. F. Oprunenko, *Russ. Chem. Rev.*, 2000, **69**, 683.

294. D. R. Muhandiram, G. Y. Kiel, G. H. M. Aarts, I. M. Saez, J. G. A. Reuvers, D. M. Heinekey, W. A. G. Graham, J. Takats, and R. E. D. McClung, *Organometallics*, 2002, **21**, 2687.

295. I. D. Gridnev, O. L. Tok, M. E. Gurskii, and Y. N. Bubnov, *Chem. Eur. J.*, 1996, **2**, 1483.

296. I. D. Gridnev and O. L. Tok, *J. Am. Chem. Soc.*, 2003, **125**, 14700.

297. L. H. Shultz and M. Brookhart, *Organometallics*, 2001, **20**, 3975, references therein.

298. R. H. Crabtree, *Acc. Chem. Res.*, 1979, **12**, 331.

299. F. N. Tebbe and G. W. Parshall, *J. Am. Chem. Soc.*, 1971, **93**, 3793.

300. H. Werner and R. Feser, *Angew. Chem., Int. Ed. Engl.*, 1979, **18**, 157.

301. H. Werner and R. Feser, *J. Organomet. Chem.*, 1982, **232**, 351.

302. M. Brookhart and D. M. Lincoln, *J. Am. Chem. Soc.*, 1988, **110**, 8719.

303. M. Brookhart, D. M. Lincoln, M. A. Bennett, and S. Pelling, *J. Am. Chem. Soc.*, 1990, **112**, 2691.

304. M. Brookhart, D. Lincoln, A. F. Volpe, and G. F. Schmidt, *Organometallics*, 1989, **8**, 1212.

305. M. A. Bennett, I. J. McMahon, S. Pelling, M. Brookhart, and D. M. Lincoln, *Organometallics*, 1992, **11**, 127.

306. J. P. Jesson and E. L. Muetterties, in ‘Dynamic Nuclear Magnetic Resonance’, eds. L. M. Jackman and F. A. Cotton, Academic Press, New York, 1975, p. 253.

307. R. H. Crabtree and G. G. Hlatky, *Coord. Chem. Rev.*, 1985, **65**, 1.

308. D. M. Heinekey and W. J. Oldham Jr, *Chem. Rev.*, 1993, **93**, 913.

309. R. H. Morris and P. G. Jessop, *Coord. Chem. Rev.*, 1992, **121**, 155.

310. G. J. Kubas, ‘Metal Dihydrogen and σ-bond Complexes: Structure, Theory and Reactivity’, Kluwer, New York, 2001.

311. D. G. Gusev and H. Berke, *Chem. Ber.*, 1996, **129**, 1143.

312. J. K. Law, H. Mellows, and D. M. Heinekey, *J. Am. Chem. Soc.*, 2002, **124**, 1024.

313. R. H. Crabtree, M. Lavin, and L. Bonneviot, *J. Am. Chem. Soc.*, 1986, **108**, 4032.

314. K. E. Earl, G. Jia, P. A. Maltby, and R. H. Morris, *J. Am. Chem. Soc.*, 1991, **113**, 3027.

315. X. L. Luo and R. H. Crabtree, *J. Am. Chem. Soc.*, 1990, **112**, 6912.

316. L. S. Van Der Sluys, J. Eckert, O. Eisenstein, J. H. Hall, J. C. Huffman, S. A. Jackson, T. F. Koetzle, G. J. Kubas, P. J. Vergamini, and K. G. Caulton, *J. Am. Chem. Soc.*, 1990, **112**, 4831.

317. D. M. Heinekey, J. M. Millar, T. F. Koetzle, N. G. Payne, and K. W. Zilm, *J. Am. Chem. Soc.*, 1990, **112**, 909.

318. C. Scheure, R. Wiedenbruch, R. Meyer, R. R. Ernst, and D. M. Heinekey, *J. Chem. Phys.*, 1997, **106**, 1.

319. S. S. Wreford, *Organometallics*, 1982, **1**, 935.

320. D. Michos, X.-L. Luo, J. W. Faller, and R. H. Crabtree, *Inorg. Chem.*, 1993, **32**, 1370.

321. D. J. Darensbourg and R. L. Gray, *Inorg. Chem.*, 1984, **23**, 2993.

322. C. Soubra, Y. Oishi, T. A. Albright, and H. Fujimoto, *Inorg. Chem.*, 2001, **40**, 620.

323. V. Bakhmutov, T. Burgi, P. Burger, U. Ruppli, and H. Berke, *Organometallics*, 1994, **13**, 4203.

324. C. Y. Lee, Y. Wang, and C. S. Liu, *Inorg. Chem.*, 1991, **30**, 3893.

325. S. Azuma, M. Kojima, and Y. Yoshikawa, *Inorg. Chim. Acta*, 1998, **271**, 24.

326. D. Argyropoulos, C. A. Mitsopoulou, and D. Katakis, *Inorg. Chem.*, 1996, **35**, 5549.

327. R. K. Pomeroy, L. Vancea, H. P. Calhoun, and W. A. G. Graham, *Inorg. Chem.*, 1977, **16**, 1508.

328. X. M. He and J. F. Hartwig, *Organometallics*, 1996, **15**, 400.

329. W. Beck and K. Sünkel, *Chem. Rev.*, 1988, **88**, 1405.

330. J. W. Faller, B. J. Grimmond, and D. G. D’Alliessi, *J. Am. Chem. Soc.*, 2001, **123**, 2525, references therein.

331. Y.-H. Huang and J. A. Gladysz, *J. Chem. Educ.*, 1988, **65**, 298.

332. D. M. Dalton, J. M. Fernandez, K. Emerson, R. D. Larsen, A. M. Arif, and J. A. Gladysz, *J. Am. Chem. Soc.*, 1990, **112**, 9198.

333. J. Auffret, P. Courtot, R. Pichon, and J. Y. Salaun, *J. Chem. Soc., Dalton Trans.*, 1987, 1687.

334. H. Kurosawa and T. Murahashi, *Pure Appl. Chem.*, 2001, **73**, 295.

335. J. P. Collman, J. M. Garner, R. T. Hembre, and Y. Y. Ha, *J. Am. Chem. Soc.*, 1992, **114**, 1292.

336. J. P. Collman, S. T. Harford, S. Franzen, T. A. Eberspacher, R. K. Shoemaker, and W. H. Woodruff, *J. Am. Chem. Soc.*, 1998, **120**, 1456.

337. J. L. Eglin, L. T. Smith, and R. J. Staples, *Inorg. Chim. Acta*, 2003, **351**, 217.

338. N. Quiros Mendez, A. M. Arif, and J. A. Gladysz, *Organometallics*, 1991, **10**, 2199.

339. D. K. Wicht, D. S. Glueck, L. M. Liable-Sands, and A. L. Rheingold, *Organometallics*, 1999, **18**, 5130.

340. M. A. Zhuravel, D. S. Glueck, L. N. Zakharov, and A. L. Rheingold, *Organometallics*, 2002, **21**, 3208.

341. K. G. Orrell, *Coord. Chem. Rev.*, 1989, **96**, 1.

342. J. C. Bayon, C. Claver, and A. M. Masdeu-Bulto, *Coord. Chem. Rev.*, 1999, **195**, 73.

343. A. M. Masdeu-Bulto, M. Dieguez, E. Martin, and M. Gomez, *Coord. Chem. Rev.*, 2003, **242**, 159.

344. K. Ohkita, H. Kurosawa, T. Hirao, and I. Ikeda, *J. Organomet. Chem.*, 1994, **470**, 179.

345. M. G. Choi, L. M. Daniels, and R. J. Angelici, *Inorg. Chem.*, 1991, **30**, 3647.

346. J. S. L. Yeo, G. M. Li, W. H. Yip, W. Henderson, T. C. W. Mak, and T. S. A. Hor, *J. Chem. Soc., Dalton Trans.*, 1999, 435.
347. J. W. Guan, J. Stehr, and R. D. Fischer, *Chem. Eur. J.*, 1999, **5**, 1992.
348. A. Venturelli, T. B. Rauchfuss, and A. K. Verma, *Inorg. Chem.*, 1997, **36**, 1360.
349. E. W. Abel, K. G. Orrell, M. C. Poole, and V. Sik, *Polyhedron*, 1999, **18**, 1345.
350. T. B. Gunnoe, M. Sabat, and W. D. Harman, *Organometallics*, 2000, **19**, 728.
351. W. Levason, S. D. Orchard, and G. Reid, *Coord. Chem. Rev.*, 2002, **225**, 159.
352. J. D. Corbett, *Chem. Rev.*, 1985, **85**, 383.
353. J. Evans, *Adv. Organomet. Chem.*, 1977, **16**, 319.
354. B. E. Hanson, *Inorg. Chem.*, 1986, **25**, 4062.
355. A. Venturelli and T. B. Rauchfuss, *J. Am. Chem. Soc.*, 1994, **116**, 4824.
356. T. Eguchi and B. T. Heaton, *J. Chem. Soc., Dalton Trans.*, 1999, 3523.
357. H. ElAmouri and M. Gruselle, *Chem. Rev.*, 1996, **96**, 1077.
358. M. J. McGlinchey, L. Girard, and R. Ruffolo, *Coord. Chem. Rev.*, 1995, **143**, 331.
359. M. D. Tudor, J. J. Becker, P. S. White, and M. R. Gagne, *Organometallics*, 2000, **19**, 4376.
360. M. T. Ashby, S. S. Alguindigue, and M. A. Khan, *Organometallics*, 2000, **19**, 547.
361. A. J. Edwards, N. J. Burke, C. M. Dobson, K. Prout, and S. J. Heyes, *J. Am. Chem. Soc.*, 1995, **117**, 4637.
362. F. Grandjean and G. J. Long, *Inorg. Chem.*, 1996, **35**, 4532.
363. Y. Wang, X. Li, J. Sun, and K. L. Ding, *Organometallics*, 2003, **22**, 1856.
364. D. D. Pathak, H. Adams, N. A. Bailey, P. J. King, and C. White, *J. Organomet. Chem.*, 1994, **479**, 237.
365. P. Kocovsky, S. Vyskocil, I. Cisarova, J. Sejbal, I. Tislerova, M. Smrcina, G. C. Lloyd-Jones, S. C. Stephen, C. P. Butts, M. Murray, and V. Langer, *J. Am. Chem. Soc.*, 1999, **121**, 7714.
366. T. J. Geldbach and P. S. Pregosin, *Eur. J. Inorg. Chem.*, 2002, 1907.
367. N. Feiken, P. S. Pregosin, G. Trabesinger, and M. Scalone, *Organometallics*, 1997, **16**, 537.
368. T. Y. Cheng, D. J. Szalda, and R. M. Bullock, *Chem. Commun.*, 1999, 1629.
369. N. M. Brunkan and M. R. Gagne, *Organometallics*, 2002, **21**, 4711.
370. P. Dotta, P. G. A. Kumar, P. S. Pregosin, A. Albinati, and S. Rizzato, *Organometallics*, 2003, **22**, 5345.

Structure & Property Maps for Inorganic Solids

Jeremy K. Burdett & John R. Rodgers

[1]The University of Chicago, Chicago, IL, USA
[2]National Research Council Canada, Ottawa, ON, Canada

1	Introduction	1
2	Crystal Symmetry of Inorganic Solids	1
3	The Choice of Indices and Structure Maps	2
4	Thermodynamic Properties	10
5	Properties	13
6	Related Articles	18
7	References	18

1 INTRODUCTION

One of the major challenges to the solid-state chemist is the prediction of the properties of a material given its chemical formula. As examples of how poor present methodology is in this area, consider the following two cases. Was it possible to predict the crystal structure and properties of $YBa_2Cu_3O_7$ and $Nd_2Fe_{14}B$ before these two materials were synthesized? The structure of the first could perhaps have been anticipated from our knowledge of oxide chemistry (it has a defect perovskite structure), but the fact that it is a 95 K superconductor could not. For the second example, probably neither its structure nor its very interesting and commercially important magnetic properties could have been predicted before its synthesis and characterization. In a closely related problem, one is also constantly searching for new ways to classify and organize the properties of systems that are already known. Perhaps the largest area of activity has been in studies that attempt to organize and understand the crystal structures of known compounds. Pauling summarized[1] the ideas current in the structural chemical world in 1929 with his seminal paper containing a set of rules. Laves listed some more qualitative considerations as to how atoms pack in solids.[2] The first Pauling rule introduced the concept of an ionic radius and the idea of a coordination environment that is set by the ratio of anion to cation radii, r_+/r_-. Certain critical values, $(r_+/r_-)_{\mathrm{crit}}$, delineate the boundaries between four and six and between six and eight coordination. One way of exploring the validity of such an idea is shown[3] in Figure 1, a plot of pairs (r_+, r_-) and a symbol that identifies the lowest energy crystal structure. The database used is the collection of binary octet systems AB that are found in the B1 (rocksalt), B2 (CsCl), B3 (sphalerite or zincblende), or B4 (wurtzite) structure types. This is an example of a structure map that uses the values of r_+ and r_- as indices. In fact, as may be seen, although examples with higher coordination numbers are associated in general with larger values of r_+/r_-, the quantitative separation of structures using the solid lines, $(r_+/r_-)_{\mathrm{crit}}$ of Pauling's theory, is poor. A better separation is obtained by employing a Mendeleevian philosophy, by drawing the boundaries (the dashed lines) between one structure type and another without regard for any preconceived theory. This article will show the utility of such ideas in crystal chemistry, and will highlight the type of index that needs to be employed to accurately sort the properties of systems from each other. Many of the examples will be structure maps in that structures are being delineated, but other properties such as heats of formation and reaction, and other materials properties, will be discussed as well. Firstly, it is worthwhile to review the types of crystal structures adopted by inorganic solids.

2 CRYSTAL SYMMETRY OF INORGANIC SOLIDS

For crystal symmetry analysis, inorganics can be divided into two: compounds of ternary and higher oxides and compounds containing halides and noble gases are classed as inorganics, and the remainder are classed as intermetallics. One of Laves' principles[2] states that structures aim at the highest symmetry. Figure 2 shows the distribution of compounds by crystal system.[4,5]

The crystal symmetry population patterns for inorganics and intermetallics are different. For inorganic compounds, 50% fall into biaxial crystal systems (anorthic, monoclinic, and orthorhombic); for intermetallics this is 22%. The distribution of compounds by crystal symmetry class for inorganics and intermetallics is about the same (Figure 3). Sixty percent of inorganics belong to the following eight crystal symmetry classes: 2, 5, 7, 8, 15, 20, 27, and 32. For intermetallics, 70% of the compounds fall into seven crystal symmetry classes: 5, 8, 15, 20, 27, 31, and 32. In both cases, these classes belong to the highest symmetry class of the crystal system: (The highest symmetry classes for each crystal system are: $2 = \bar{1}$ anorthic, $5 = 2/m$ monoclinic, $7 = mm2$ orthorhombic, $8 = mmm$ orthorhombic, $15 = 4/mmm$ tetragonal, $20 = \bar{3}m$ rhombohedral, $27 = 6/mmm$ hexagonal, $31 = \bar{4}3m$ cubic, $32 = m3m$ cubic.)

Over 75% of inorganics and 95% of intermetallics crystallize in crystal structures having 90° and 120° interaxial angles of the unit cell. The residual compounds for inorganics are mainly oxides, halides, and sulfides, while those for the intermetallics are Se, Te, and S compounds. These compounds represent the 'boundary' compounds between the inorganics and the intermetallics.

Space group statistics for inorganic compounds (Figure 4(a)) show that 33% crystallize in eight space groups:

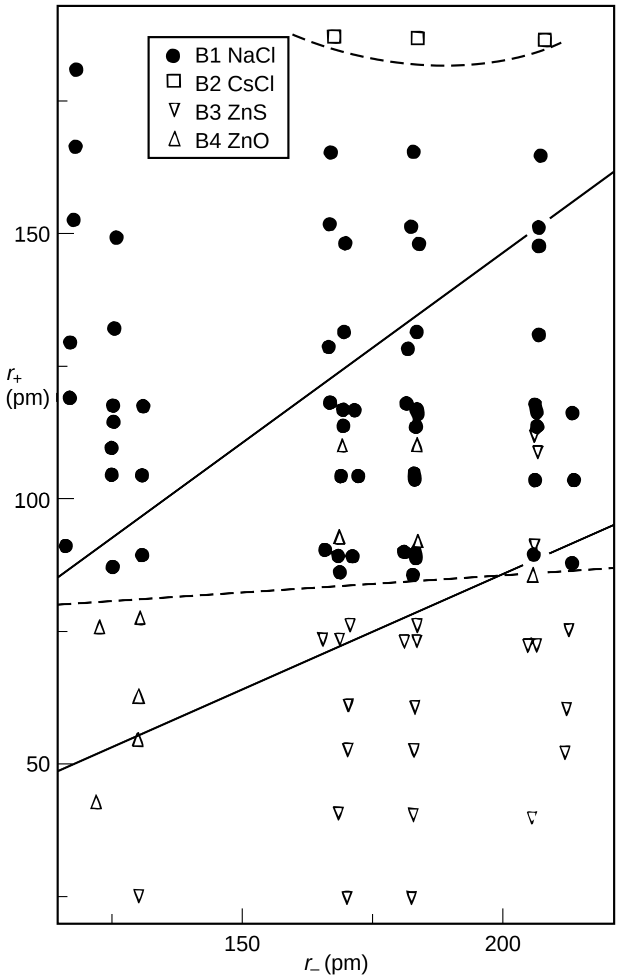

Figure 1 A structure map for the AB octets using the crystal radii, $r_\pm$, as indices

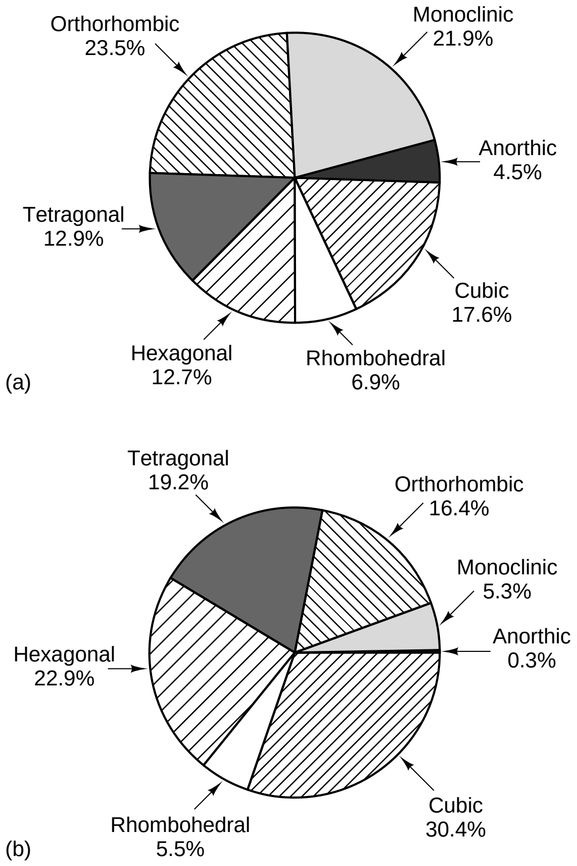

Figure 2 Distribution of compounds by crystal system for (a) inorganics and (b) intermetallics

2 ($P\bar{1}$), 12 ($C2/m$), 14 ($P2_1/c$), 15 ($C2/c$), 62 (*Pnma*), 194 ($P6_3/mmc$), 225 ($Fm3m$), and 227 ($Fd3m$), while those for intermetallics (Figure 4(b)) show that over 50% of all intermetallic compounds crystallize in the following eight space groups: 62 (*Pnma*), 139 ($I4/mmm$), 166 ($R\bar{3}m$), 191 ($P6/mmm$), 194 ($P6_3/mmc$), 221 ($Pm\bar{3}m$), 225 ($Fm\bar{3}m$), and 227 ($Fd\bar{3}m$).

For both classes of compounds (inorganics and intermetallics), their seven and eight space groups represent 3.0% and 3.5% of all 230 space groups, respectively. Each of the remaining space groups (223, 222) has less than 2%, most of them having a frequency of less than 1%. The only lower symmetry space group that is preferred for both classes is space group *Pnma* (Figure 4(b)).

The distribution of unaries (chemical elements) by their crystal systems is shown in Figure 5(a). Similar distributions of crystal systems for intermetallics are shown for binary, ternary, and quaternary compounds (Figures 5(b–d)). These figures show that for intermetallics, in the first approximation, alloying additional different elements to unaries, which then moves them to binaries, ternaries, and so on, does not significantly change the symmetry distribution.

3 THE CHOICE OF INDICES AND STRUCTURE MAPS

Much of the textbook organization of chemical properties relies heavily on the classification of the elements themselves as arranged in the periodic table. Thus, one useful set of indices is one that strings the elements together in a way that reflects this. Pettifor's index[6] makes use of the periodic classification and Figure 6 shows how the string is threaded. Figure 7 shows the separation[7] of the structures of the AB binaries using this index for both A and B. Of course, the 'Periodic Table' index includes in it details such as electron count, orbital ionization energy, ionic size, and so on, and indeed all properties that vary systematically in this way.

The first structure maps designed to sort the structures of solids did not use the concept of size per se, but used two different indices, those of AB electronegativity difference

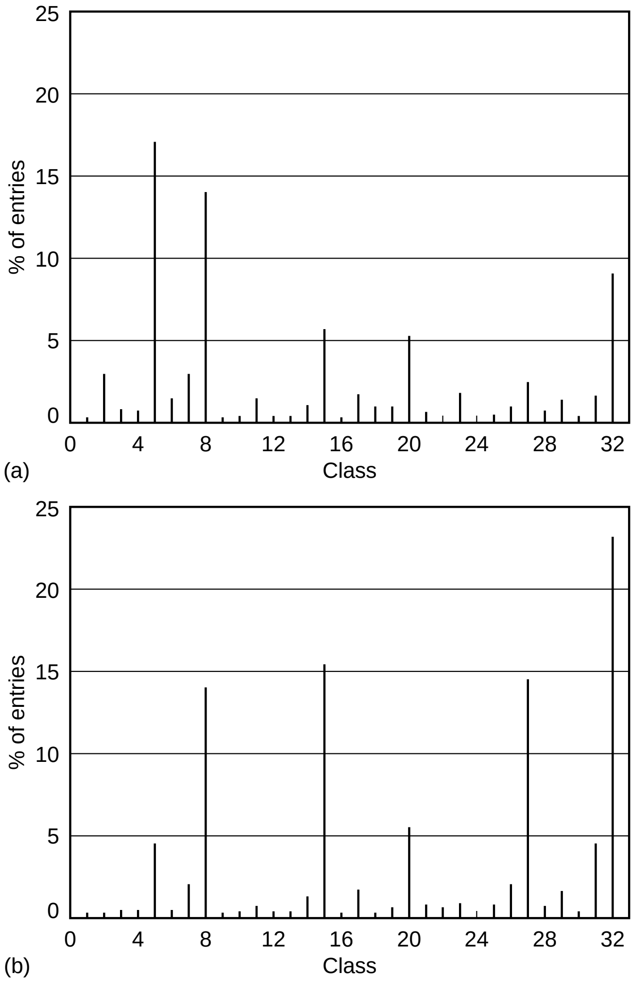

Figure 3 Distribution of compounds by crystal symmetry class for (a) inorganics and (b) intermetallics

($\Delta\chi$) and the average, $\tilde{n}$, of the principal quantum number, n, of the valence electrons on the A, B atoms. Two of these Mooser–Pearson diagrams[8] are shown in Figures 8 and 9. Notice that for the AB octets such indices sort the structures of the three different coordination number structures from each other well, and also separate the wurtzite structure from the sphalerite structure. The wurtzite structure is found for the more ionic examples.

The strikingly successful structure map for the octets of Phillips and van Vechten[9] used two indices that were derived from measured spectroscopic properties of solids. A virtually perfect separation for these materials was achieved by dividing the experimentally measured band gap into two parts that reflect chemical bonding ideas, namely, into 'covalent' (E_c) and 'ionic' (E_i) contributions. In order to understand the origin of the division, it is necessary to briefly examine the broad contributions to such energy gaps from simple orbital considerations. Consider the molecular orbital diagram of Figure 11 for a diatomic molecule (perhaps the hypothetical HHe species) in which one atom is more electronegative than the other. This implies that the α values (using the language of Hückel theory) of the 1s orbitals are not the same. A secular determinant needs to be solved to obtain the energy levels of the molecule. This is shown in equation (1), where β is the interaction integral between the orbitals on adjacent atoms.

$$\begin{pmatrix} \alpha_1 - E & \beta \\ \beta & \alpha_2 - E \end{pmatrix} = 0 \tag{1}$$

The roots of this determinant are $E \approx [(\alpha_1 + \alpha_2) \pm ((\alpha_1 - \alpha_2)^2 + 4\beta^2)^{1/2}]/2$. If Δ is written as the energy difference between bonding and antibonding levels, then this expression leads to the relationship $\Delta^2 = (\Delta E)^2 + 4\beta^2$. For the homonuclear case where $\Delta E = 0$, then $\Delta = 2\beta$. In the extended solid with energy bands rather than two individual levels, Δ is some average excitation from the bonding to

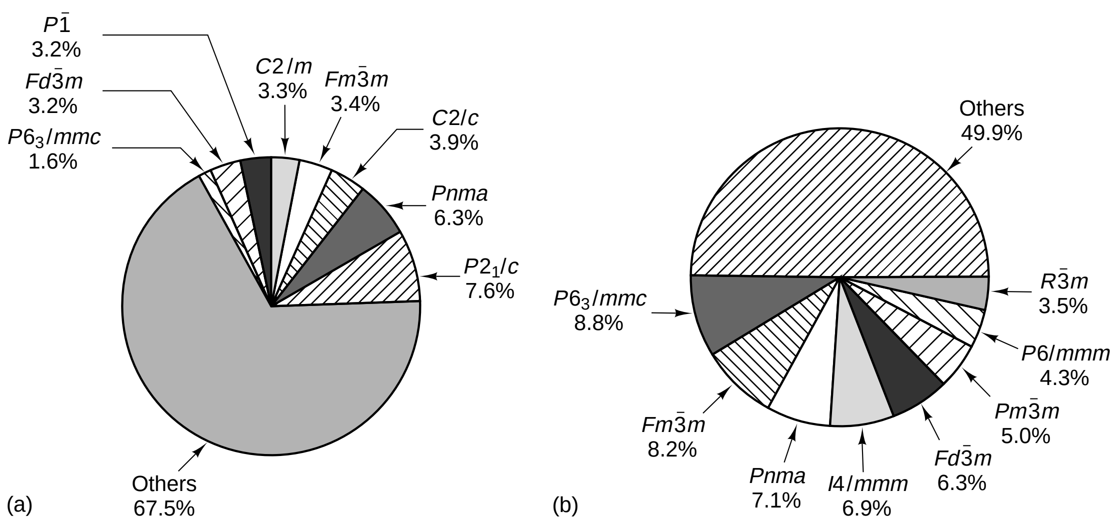

Figure 4 Distribution of the most frequently occurring space groups for (a) inorganics and (b) intermetallics

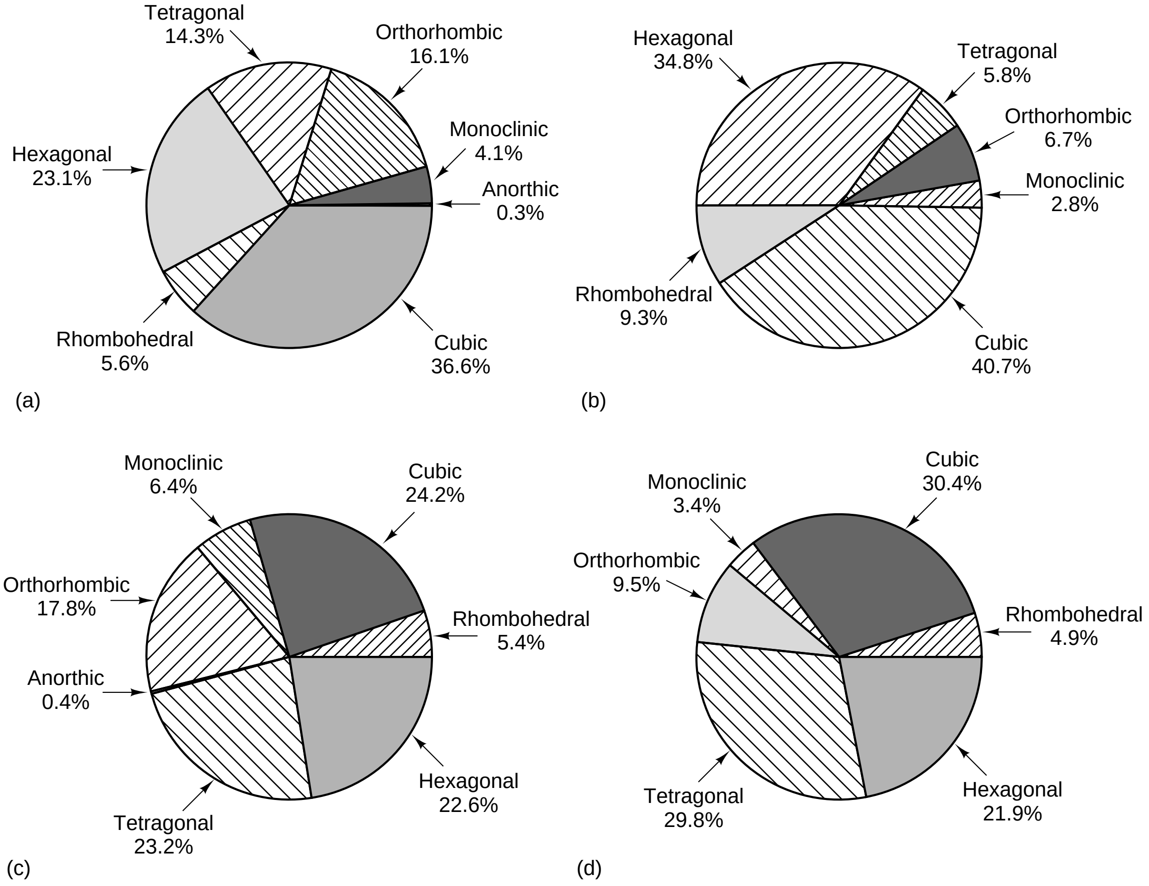

Figure 5 Distribution of intermetallic compounds by crystal system: (a) unaries (elements), (b) binaries, (c) ternaries, and (d) quaternaries

antibonding band rather than the actual band gap itself, extracted from spectral measurements. Using the measured values of Δ for the elements and assuming that the covalent contribution and the internuclear separation, d, are related by $E_c \approx d^{-2.5}$, leads to evaluation of values of E_c for all of the AB examples, and from measurement of Δ, for values of E_c and E_i for all the AB octets. The Phillips–van Vechten plot of these pairs is shown in Figure 10, and is extremely successful in sorting four- and six-coordinate structures.

The concept of atomic or ionic 'size' is one that has been debated for many years. The structure map of Figure 1 used the crystal radii of Shannon and Prewitt[10] and these are generally used today in place of Pauling's radii. Shannon and Prewitt's values come from examination of a large database of interatomic distances, assuming that internuclear separations are given simply by the sum of anion and cation radii. Whereas this is reasonably true for oxides and fluorides, it is much more difficult to generate a self-consistent set of radii for sulfides, for example.[11] A set of 'radii' independent of experimental input would be better. The pseudopotential radius is one such estimate of atomic or orbital size.

Figure 12 shows the idea[12] of the pseudopotential. The coulombic attraction of a valence electron by the nucleus is screened by the core. However, this still strong attraction is counterbalanced by the Pauli repulsion of the valence electrons by those of the core. The result is a fairly weak potential that has a minimum and a crossing point, the latter occurring where attractive and repulsive forces exactly cancel. This crossing point can be used as a measure of the 'size', r_l, of the orbital defined by the pseudopotential. For the valence orbitals of an atom, r_s, r_p, and (where appropriate) r_d are orbital parameters that define atomic properties. Figure 13(a) shows a structure map for the same AB octet database as in Figure 1. Here the value of r_σ is just the sum of the s and p radii (equation 2), the simplest estimate of atomic size.

$$r_\sigma = r_s + r_p \tag{2}$$

Clearly the separation into structural types is somewhat better than when using the ionic radii. The pseudopotential radius for orbital l is also related to other atomic parameters. Since ${r_l}^{-1}$ has units of energy, it is not surprising to find that it scales nicely with the spectroscopically observed multiplet-averaged ionization energy for that atomic orbital. Recalling the Mulliken definition of electronegativity, it is then easy to see that an estimate of an atomic electronegativity comes from

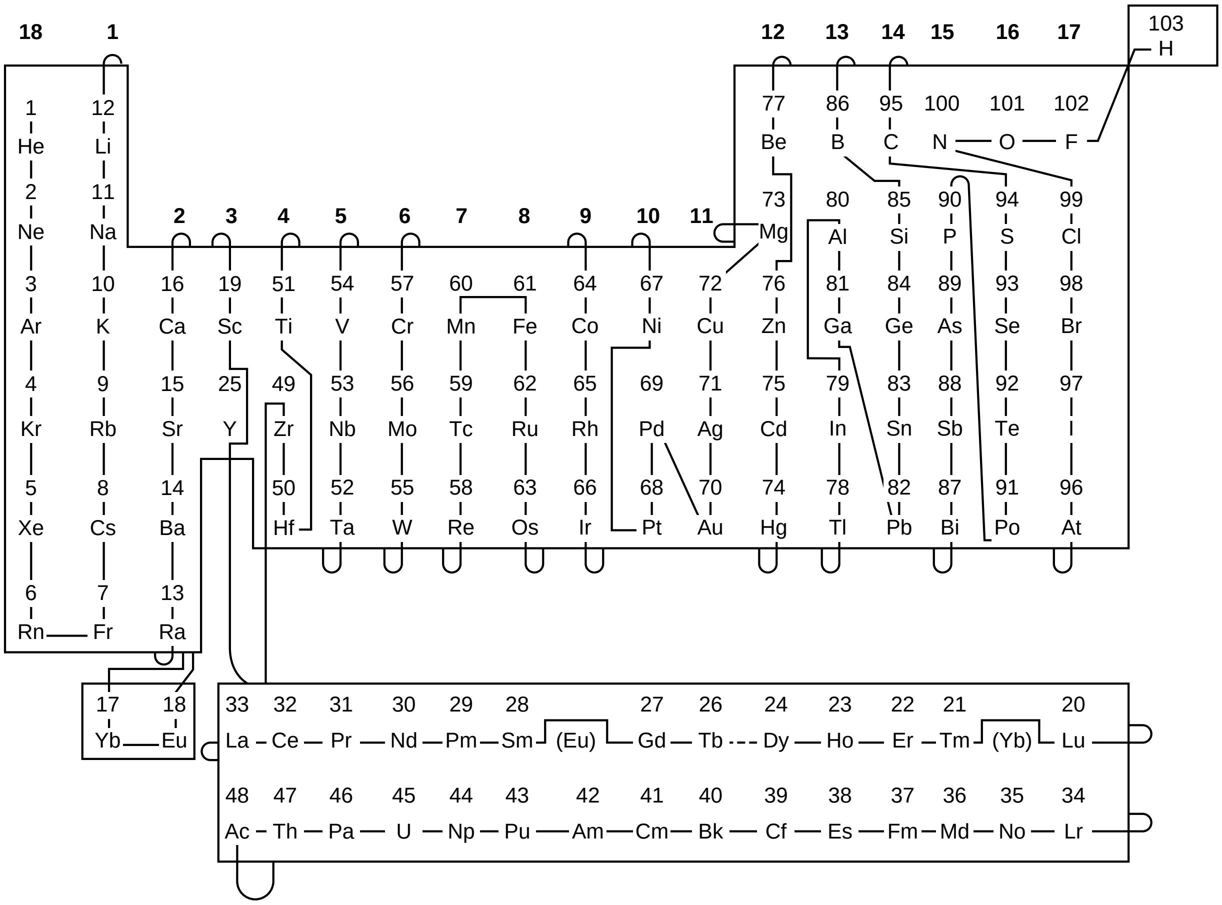
18
1
12
13
14
15
16
17
2
3
4
5
6
7
8
9
10
11
103 H
1 He
2 Ne
3 Ar
4 Kr
5 Xe
6 Rn
12 Li
11 Na
10 K
9 Rb
8 Cs
7 Fr
16 Ca
15 Sr
14 Ba
13 Ra
19 Sc
25 Y
51 Ti
49 Zr
50 Hf
54 V
53 Nb
52 Ta
57 Cr
56 Mo
55 W
60 Mn
59 Tc
58 Re
61 Fe
62 Ru
63 Os
64 Co
65 Rh
66 Ir
67 Ni
69 Pd
68 Pt
72 Cu
71 Ag
70 Au
77 Be
73 Mg
76 Zn
75 Cd
74 Hg
86 B
80 Al
81 Ga
79 In
78 Tl
95 C
85 Si
84 Ge
83 Sn
82 Pb
100 N
90 P
89 As
88 Sb
87 Bi
101 O
94 S
93 Se
92 Te
91 Po
102 F
99 Cl
98 Br
97 I
96 At
17 Yb
18 Eu
33 La
32 Ce
31 Pr
30 Nd
29 Pm
28 Sm
(Eu)
27 Gd
26 Tb
24 Dy
23 Ho
22 Er
21 Tm
(Yb)
20 Lu
48 Ac
47 Th
46 Pa
45 U
44 Np
43 Pu
42 Am
41 Cm
40 Bk
39 Cf
38 Es
37 Fm
36 Md
35 No
34 Lr

Figure 6 The ordering of elements used to define Pettifor's index. (Reproduced by permission of IPC from Pettifor[6])

an expression of the form shown in equation (3).

$$\chi = A(r_s)^{-1} + B(r_p)^{-1} + C(r_d)^{-1} \tag{3}$$

Figure 13(b) shows the structure map for the AB octets using such an electronegativity index with A = B, C = 0. The structural sorting[3,13] is just as good as that in Figure 13(a) and presents an interesting dilemma. Pauling presented his structural rules[1] in terms of the radius ratio of anion to cation, a mechanical model. This philosophy is fine for understanding the trends of Figure 13(a), but the ideas of electronegativity, especially in the Mulliken sense, are generally associated with electronic rather than with steric arguments. Thus, there will always be a problem in trying to answer the question why solids have the structures they do. Since size and electronegativity are so closely related, an argument cast in one language may be immediately transformed into one in the other. The pseudopotential radii may be used in the construction of two new, and very useful, indices, the Zunger–Cohen parameters, R_σ and R_π (equations 4 and 5),[14] and their closely related Bloch–Schattemann analogs, R_{H} and ΔR_{CT}, (equation 5).[15]

Zunger–Cohen
$$r_\sigma = r_s + r_p, \qquad r_\pi = |r_s - r_p| \\ R_\sigma = |r_\sigma^{\mathrm{A}} - r_\sigma^{\mathrm{B}}|, \qquad R_\pi = |r_\pi^{\mathrm{A}} + r_\pi^{\mathrm{B}}| \tag{4}$$

Bloch–Schattemann
$$\left.\begin{aligned} R_{\mathrm{H}} &= R_\sigma \\ R_{\mathrm{CT}} &= \left(r_s + \left(\frac{1}{2}\right) r_p - \left(\frac{1}{8}\right) r_d\right) \\ \Delta R_{\mathrm{CT}} &= |R_{\mathrm{CT}}^{\mathrm{A}} + R_{\mathrm{CT}}^{\mathrm{B}}| \end{aligned}\right\} \tag{5}$$

$R_{\mathrm{H}} = R_\sigma$ is a measure of the size mismatch or electronegativity difference between A and B. R_π is a measure of 'orbital nonlocality', namely, how different in spatial extent are the s and p orbitals located on the same atom. Figure 14 shows[15] a structure map for the binary octet compounds using R_σ and R_π as indices. Straight lines were used to separate one domain from the next. The separation is excellent. The octet compounds MgS and MgSe lie in the B3 region close to the border with the B1 (rocksalt) structure. There are similar problems sorting these two systems in Figures 13(a) and (b). However, the free energy of the B1–B3 phase transition is close to zero for these examples.

Four types of structure maps have been presented here for the octets. Ignoring those of Figures 1 and 13, which

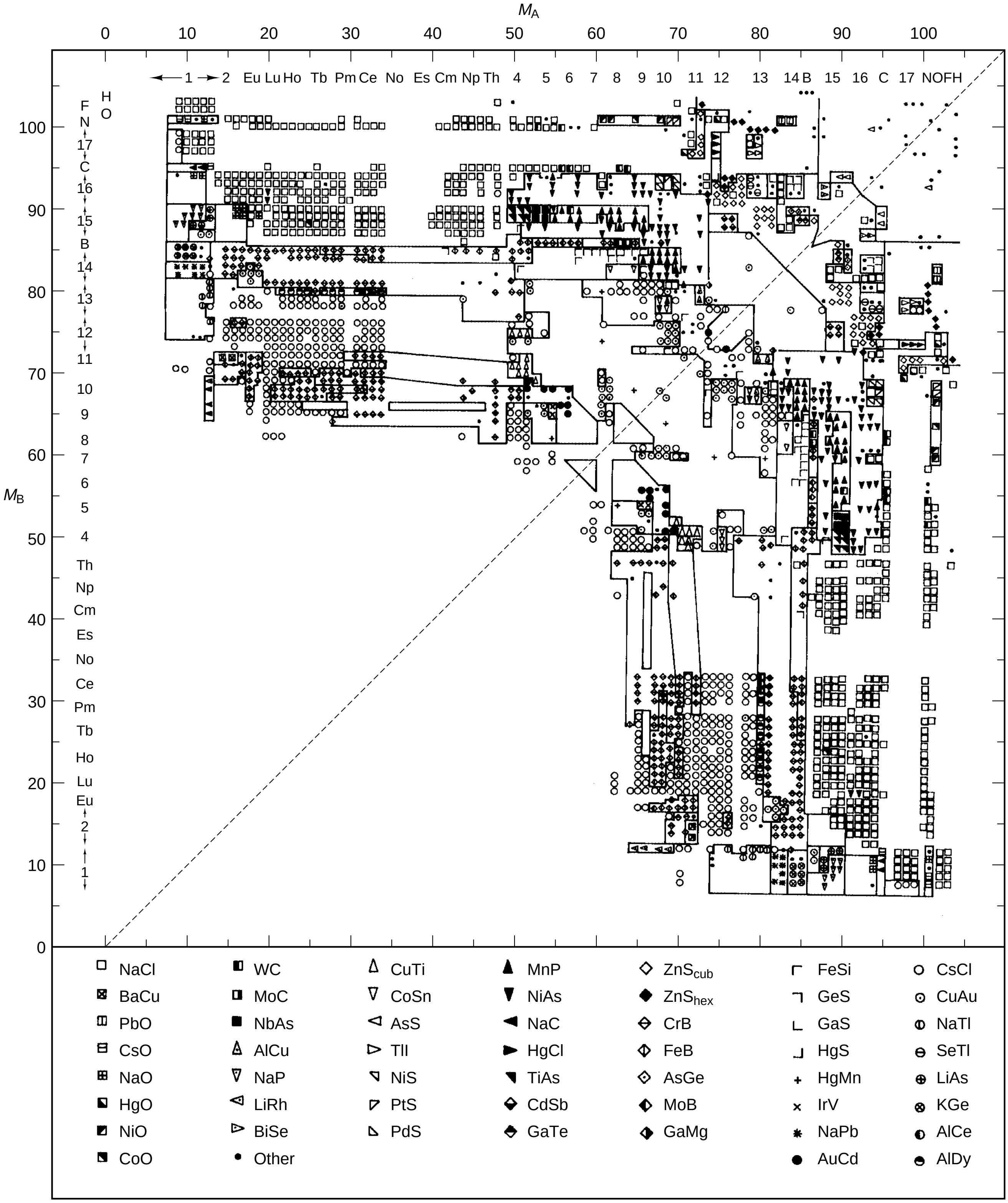

Figure 7 A structure map for the AB binaries using the Pettifor index. (Ref. 7. Reproduced by permission of Institute of Physics)

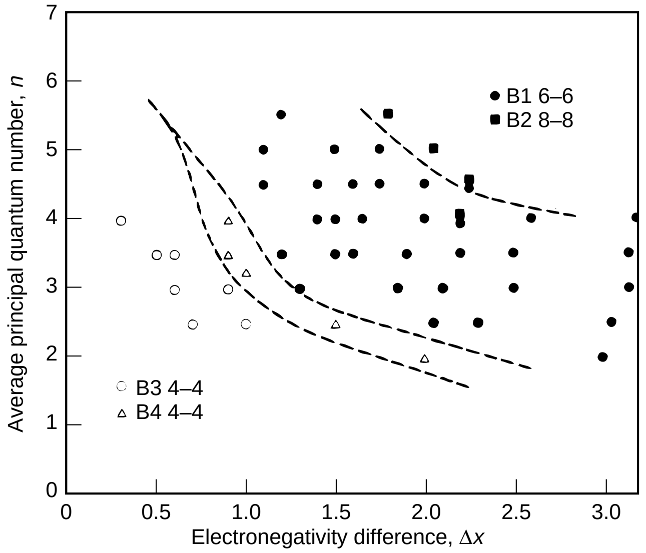

Figure 8 A structure map for the AB octets using the indices of Mooser and Pearson[8]

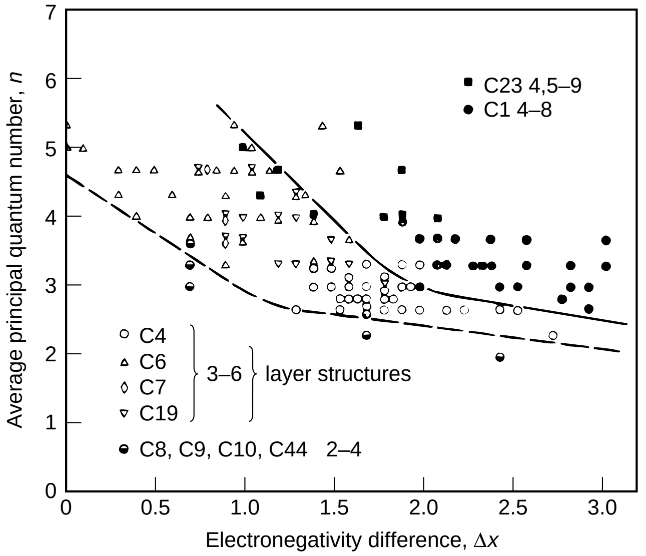

Figure 9 A structure map for the AB_2 binaries using the indices of Mooser and Pearson[8]

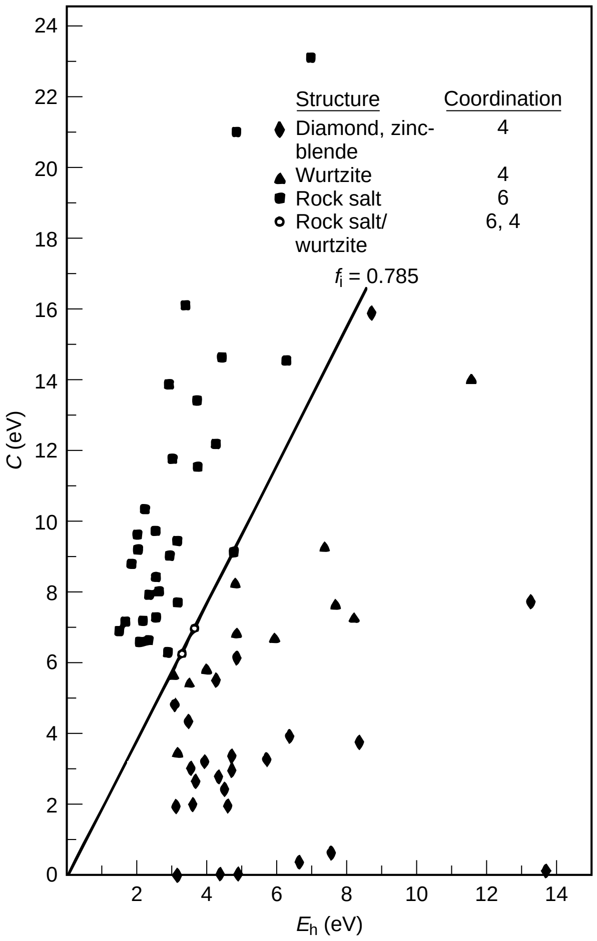

Figure 10 A structure map for the AB octets using the indices of Phillips and van Vechten. (Reprinted from Ref. 9. © 1981, with permission from Elsevier)

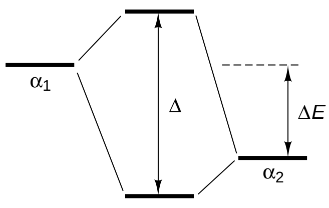

Figure 11 Orbital interaction diagram for two atomic orbitals of different electronegativity

have indices associated with one atom only, there are some interesting similarities between the other three plots. This is to be expected since E_i, $\Delta\chi$, and R_σ all measure the electronegativity difference. Certainly the orbital nonlocality, R_π, is expected to increase as the atoms become heavier and thus scale with $\tilde{n}$. E_c is expected to decrease as the elements become heavier and thus scale inversely with R_π and $\tilde{n}$. Figure 15 shows[15] a more adventurous structure map for 356 binary nonoctet compounds using R_σ and R_π. Straight lines were used to separate one domain from the next, as in Figure 14. The structural separation is quite impressive. The indices are, however, unable to separate the NiAs type ($B8_1$) from the MnP type (B31). The two structures are, however, closely related in geometrical terms. The distortion of the metal and nonmetal frameworks of NiAs gives the zig-zag metal and nonmetal chains in MnP. Similarly, the CrB (B33) and FeB (B27) types are not sorted one from another. These two structures are related by the mode of linkage of trigonal prisms of metal atoms. The occurrence of both pairs

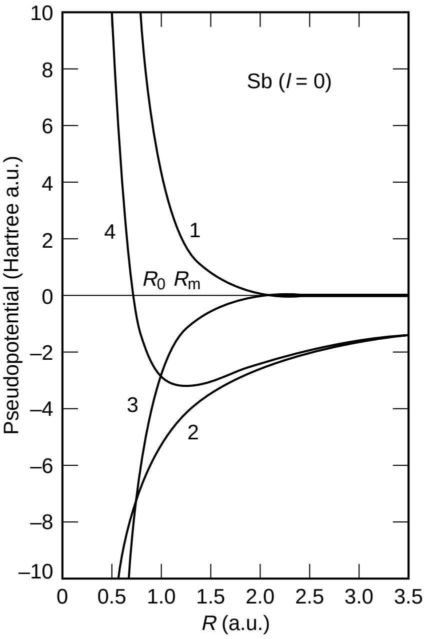

Figure 12 The various parts of the pseudopotential: (1) is the Pauli repulsion between the electrons in the valence orbital (Sb, $l = 0$ in this case) with the core; (2) is the coulomb attraction of the electrons for the nucleus screened by the core to give (3); (4), the pseudopotential, is the sum of (1) and (3); R_0 is the crossing point of the pseudopotential. (Reprinted from Ref. 12. © 1981, with permission from Elsevier)

of structural types depends critically on the number of valence electrons, which are not mimicked sufficiently by the variation in the pseudopotential radii. The separation is not perfect, but it turns out that some of the compounds listed in the existing database do not exist (CuF and FeC), or only have the structure indicated when small quantities of impurity are present. The true success of the sorting is around 2%. Figure 16 shows[15] structure maps for binary compounds with 9, 10, and 11 valence electrons. The structural sorting is more effective here if the indices $|r_p^A - r_p^B|$ and R_π^{-1} are used.

The identification of the ingredients that determine the adoption of either the normal or inverse spinel structure for oxides of formula AB_2O_4 is an old problem. The spinel structure may be envisaged as being a hybrid of sphalerite and rocksalt structures in that it is based on a cubic close-packed array of oxide ions in which the metal atoms occupy some of the octahedral and tetrahedral interstices. The normal and inverse variants are distinguished by which interstices the metal ions occupy. In the ‘normal’ arrangement, the A ions occupy one-eighth of the tetrahedral holes and the B atoms one-half of the octahedral holes. In the ‘inverse’ arrangement, all of the A ions and one-half of the B ions have changed places. In terms of structural popularity, most spinels are of the normal type, but there are several with the inverse structure. There are others where the best description is of a disordered variant somewhere between the two. Table 1 gives some examples. The traditional approach to the spinel problem[16] involves calculation of the *Crystal Field Stabilization Energy* (CFSE) for the relevant d electron configurations to give a value of the difference in CFSE, Δ(CFSE), which favors the inverse structure (A(oct)B(tet)B(oct)) over the normal one (A(tet)B_2(oct)). Naturally this approach is limited to solids containing ions that have an asymmetric d orbital occupancy. Thus d^0 (high spin), d^5, and d^{10} ions (in fact, the majority of the database) are excluded from consideration. The general view of transition metal–ligand interaction is one where the major interactions are between the ligand orbitals and the valence $(n+1)$s, p orbitals on the metal, with the d orbitals playing a smaller role. A similar picture emerges from the form of a structure map[17] using the s and p pseudopotential orbital radii of the A and B metals, namely, r_σ as an index (Figure 17). The normal and inverse structures are quite well separated by the use of these indices. Of the four ‘normal’ errors in the ‘inverse’ region, two correspond to poorly characterized systems and two are real errors. No such clean separation of structure type is achieved if the crystal radii of Shannon and Prewitt are used. One of the most interesting observations is that a mixture of normal and inverse examples is found at the boundary between the two regions. It turns out that for all of these, the variant actually found is the one predicted to be more stable from

Table 1 Some examples of materials with the spinel structure[a]

A					B_2				
	Al	Ga	In	Ti	V	Cr	Mn	Fe	Co
Mg	N	I	I	N	N	N	N	I	
	0.1	0.7–0.8	1.0	0.0	0.0	0.0	0–0.4	0.7	
Cu		N	I			N	N	I	
		0.4	1.0			0	0.2–0.4	0.7–1.0	
Zn		N	N		N	N	N	N	N
		1.0	1.0		1.0	1.0	1.0	1.0	1.0
Co	N	I			N	N	N	I	
	0.2	0.9			0	0	0–0.2	1.0	
Ni	I	I			N	I	I	I	
	0.75	1.0			0	0.74	1.0	1.0	

[a] Listed is the distribution parameter x, which determines the site occupancies in the normal structure (0.0), inverse structure (1.00), and structures in-between.

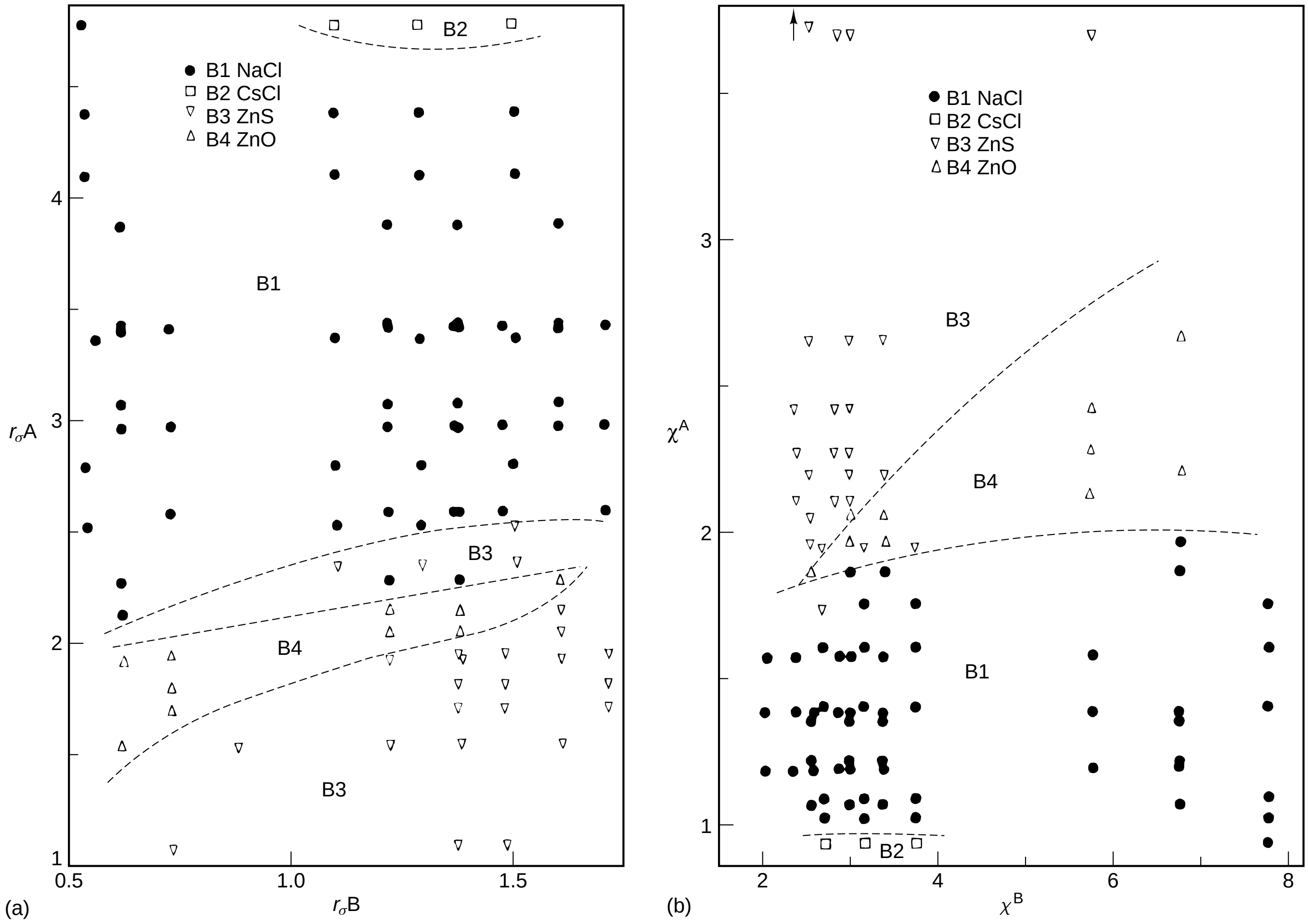

Figure 13 Structure maps for the AB octets (same database as in Figure 1) using (a) r_σ (equation 1) as an index and (b) the electronegativity (defined as in equation 3) as an index

consideration of Δ(CFSE). So the dominant effect is, as in main group octet compounds, associated with the electronic demands of the valence s and p orbitals. Only at the boundary between the two regions, where the energy difference that distinguishes one arrangement over the other is not large, are the forces associated with the d orbitals important. The structure map is a very useful way to gain insights into this problem. The spinels (around 187 known examples) are mainly oxides and chalcogenides, but some halides and cyanides adopt this structure too. There are, however, only 80 that contain asymmetric d orbital configurations for which the crystal field model can make a prediction with a success rate of 67/80 (13 errors). The structure map gives a total of four errors out of 187 examples.

Perhaps the most comprehensive analysis of structure type comes from the work of Villars and his collaborators.[18–20] The observation that different structure maps were required for different electron counts was noted earlier. Thus, the total number of electrons will be important as an index. The concept of atomic size as defined through the use of the pseudopotential radius has already been discussed. This will be the second index. The third index chosen by Villars is the electronegativity, defined not through the reciprocals of the pseudopotential radii, as in equation (3), but taken directly from the experimental values of the multiplet-averaged ionization energies of the atoms themselves. This is shown for the binary systems A_xB_y in equation (6).

$$\text{Villars}\qquad \left.\begin{aligned} \overline{N}_{\mathrm{v}} &= xN_{\mathrm{v,A}} + yN_{\mathrm{v,B}} \\ \Delta\chi &= 2x(\chi_{\mathrm{A}} - \chi_{\mathrm{B}}) \\ \Delta R &= 2x(R_{\mathrm{A}} - R_{\mathrm{B}}) \end{aligned}\right\} \qquad (6)$$

Figure 18 shows[21] a structure map for the octets using these indices. In fact, this is a slice through the three-dimensional plot using all three. Shown are both transition metal and main group examples. These indices are sufficient to sort both types of compound. The reader is referred to the literature cited in Villars,[22] where further aspects of structural sorting are

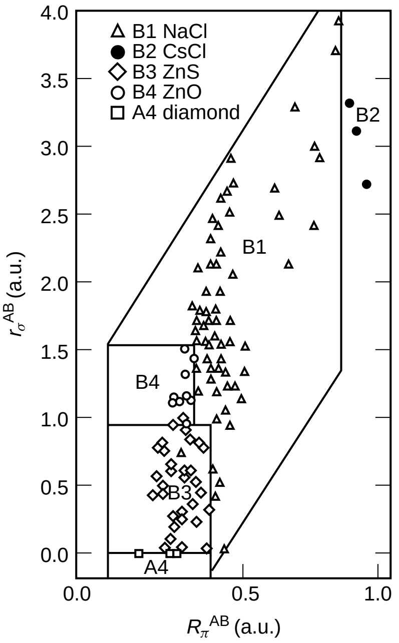

Figure 14 A structure map for the AB octets using the indices of Zunger and Cohen, R_σ and R_π. (Reprinted from Ref. 15. © 1981, with permission from Elsevier)

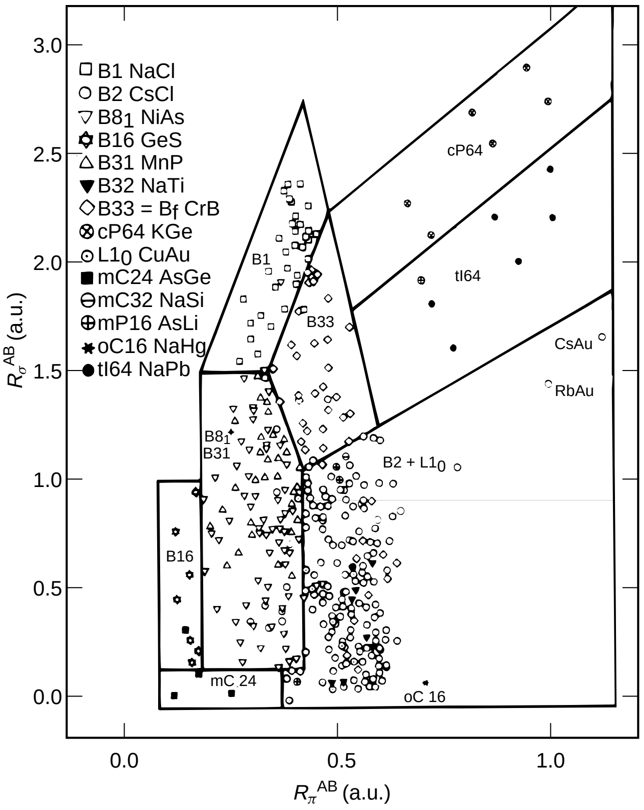

Figure 15 A structure map for 356 nonoctet AB compounds using the indices of Zunger and Cohen, R_σ and R_π. (Reprinted from Ref. 15. © 1981, with permission from Elsevier)

described. These diagrams are often referred to as quantum structural diagrams (QSD).

4 THERMODYNAMIC PROPERTIES

It is well known that the structural part of the energy of a solid, namely, the energy difference between two polymorphs, is considerably smaller than the heat of formation itself. For TiO_2, for example, the energy difference between the rutile and anatase forms is about 2 kcal mol^{-1}, whereas the heat of formation of rutile is close to 225 kcal mol^{-1}. One interesting feature of the structure maps, therefore, is that they contain energetic information too. With reference to Figure 19, the heat of the reaction, shown in equation (7)

$$AB + CD \longrightarrow AD + CB \tag{7}$$

is proportional[23] to the difference in the lengths of the heavy lines connecting the two pairs of compounds (equation 8)

$$\Delta H_R = a_x(d_{AD,CB} - d_{AB,CD}) = a_x \Delta d(\lambda) \tag{8}$$

where λ is a scaling factor between the R_σ and R_π scales shown in Figure 19 (equation 9).

$$d^2_{AB,CD} = |(R_\sigma^{AB} - R_\sigma^{CD})^2 + \lambda^2(R_\pi^{AB} - R_\pi^{CD})^2| \tag{9}$$

The agreement with experiment is good for the whole database of alkali halide and alkaline-earth oxides and

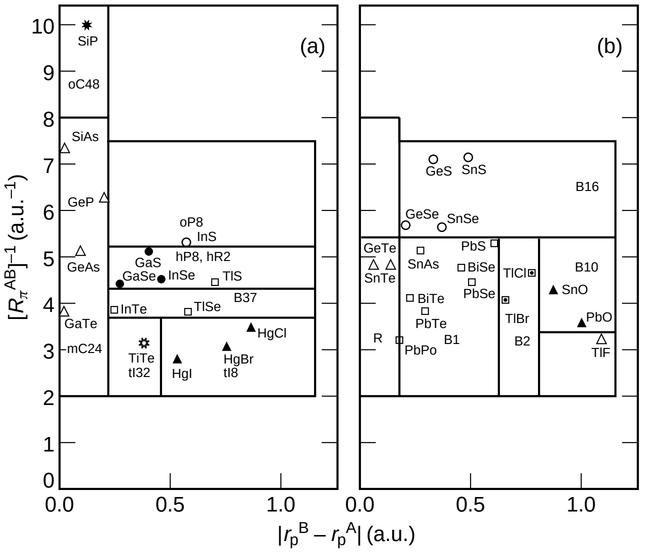

Figure 16 A structure map for 9-, 10-, and 11-electron AB compounds using the indices $|r_p^A - r_p^B|$ and R_π^{-1}. (Reprinted from Ref. 15. © 1981, with permission from Elsevier)

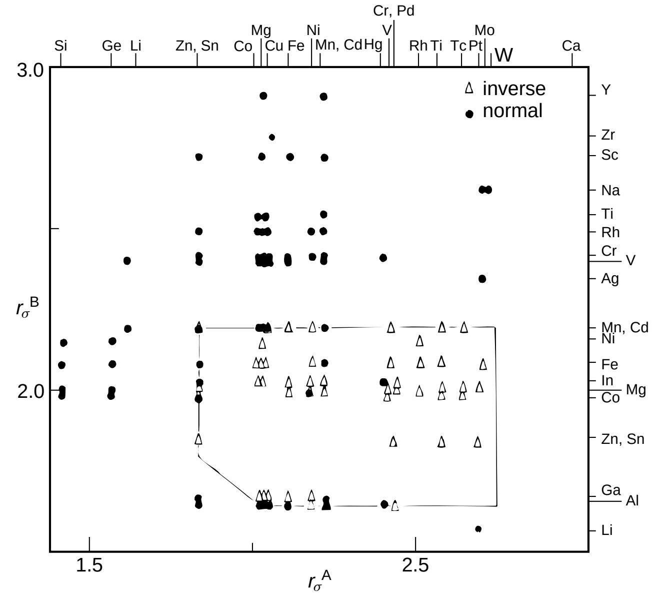

Figure 17 Structure maps for the AB_2O_4 spinels using r_σ (equation 2) as an index

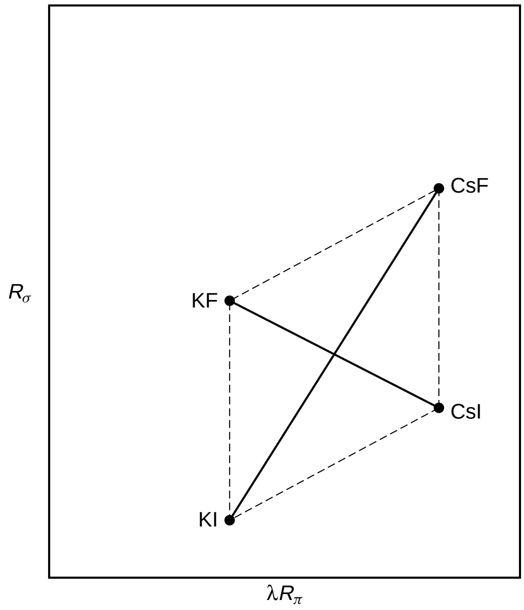

Figure 19 An R_σ/R_π plot and the heats of reaction of equation (7)

chalcogenides, with the exception of reactions involving BeO and to a lesser extent MgS and MgSe, three compounds, in fact, that are misplaced on the Zunger plot of Figure 13. Errors are also found for reactions involving LiF. The function χ^2 (equation 10) was minimized with respect to the parameter for all N reactions.

$$\chi^2 = \sum_{1}^{N} \left\{ \frac{(\Delta H_R^i - a_x \Delta^i(\lambda))}{E(\Delta H_R^i)} \right\}^2 \tag{10}$$

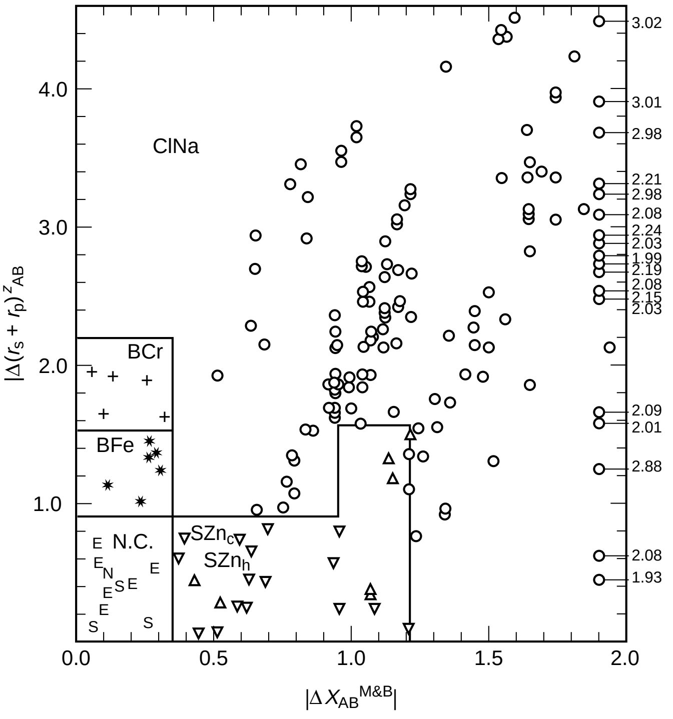

Figure 18 A structure map (or quantum structural diagram, QSD) for the AB octets using Villars' indices. (Reproduced by permission of Elsevier from Villars[21])

Table 2

Model	Δn	Δd
a_x or a_n (kcal mol^{-1})	2.08	8.28
λ	–	4.4
$N = 78$, $\chi^2 =$	81.3	37.7
$N = 100$, $\chi^2 =$	162.2	94.2
Total number predicted		
outside experimental error	29	22
involving BeO	4	4
involving MgX	5	4
involving LiF	11	9
others	9	5

ΔH_R^i is the experimentally determined heat of reaction, associated with an experimental error $E(\Delta H_R^i)$. The value of $\lambda = 4.4$ (Table 2) shows that both R_σ and R_π are important.

Perhaps the traditional way of looking at the energetics of such reactions uses the concept of hard and soft acids and bases and suggests an alternative expression for ΔH_R (equation 11)

$$\Delta H_R = a_x[(n_A + n_B) - (n_C + n_D)] \tag{11}$$

where n is the principal quantum number. As Table 2 shows, this is a much poorer model. As a final point, it is worth noting that although equation (9) works well for the group 1 and 2 systems with their group 17 and 16 counterparts, respectively, it is not applicable to differences in the heats of formation of transition metal-containing systems. It is interesting to find, therefore, that the heat of the reaction of equation (12) for the spinel minerals correlates with the differences in R_σ as shown in equation (13).

$$AB_2O_4 + CD_2O_4 \longrightarrow AD_2O_4 + CB_2O_4 \tag{12}$$

$$\Delta R = |R_\sigma^{AD_2O_4} - R_\sigma^{CB_2O_4}|^2 - |R_\sigma^{AB_2O_4} - R_\sigma^{CD_2O_4}|$$

where

$$R_\sigma^{AB_2O_4} = r_\sigma^B - r_\sigma^A (13)$$

The energetic correlation for the spinels is shown[24] in Figure 20, along with the corrections that follow from consideration of the d orbital occupation through the differences in CFSE.

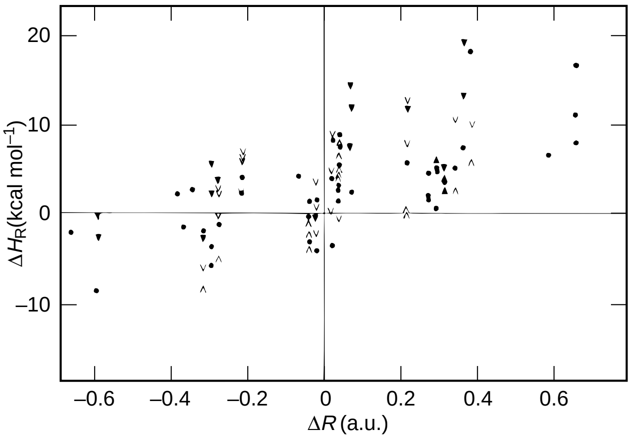

Figure 20 The heats of reaction of the spinel minerals from equation (13)

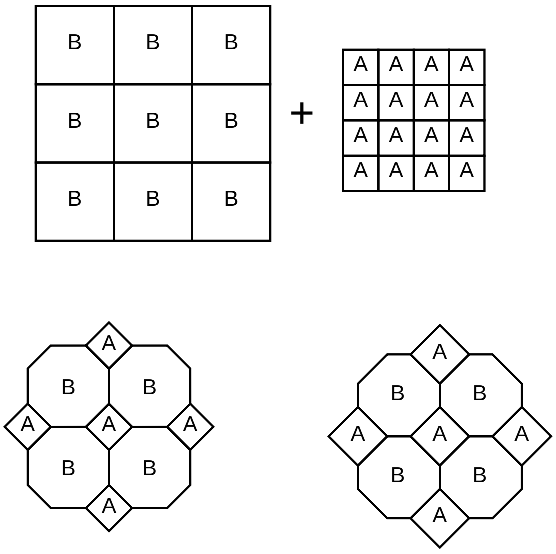

Figure 21 The 'macroscopic atom' model of Miedema. First, atomic cells are taken from each metal to form the alloy with a small change in shape but not volume. In the second step, the atomic volumes adjust to the new environment

Certainly one of the most basic properties of alloys is whether they actually exist, or, alternatively stated, have a positive or negative heat of formation. The scheme devised by Miedema[25] is a very impressive one in this regard. The model (Figure 21) is based on a 'macroscopic atom' view of alloy formation. The 'atomic cells' of the A and B components are first rearranged with a small change in shape but without any change in volume. There is a difference in chemical potential (identified with the chemist's concept of electronegativity) between the two metals, and as a result a small amount of charge transfer takes place. In response to this charge transfer, the atomic volumes change a little in a second step. The major suggestion of the theory is that the driving force for alloy formation arises via the transfer of electrons from the energy levels associated with the more electropositive metal to those of the more electronegative atom. One of the atomic indices of use in measuring this effect should then be associated with the electronegativity of the element. As a first approximation, the work function of the metal, ϕ, is used, although Miedema refined its value to give a better agreement with experiment. The contribution to the heat of formation from this source depends upon $-(\Delta\phi)^2$. There is a second contribution to the heat of formation. This is positive and thus represents an

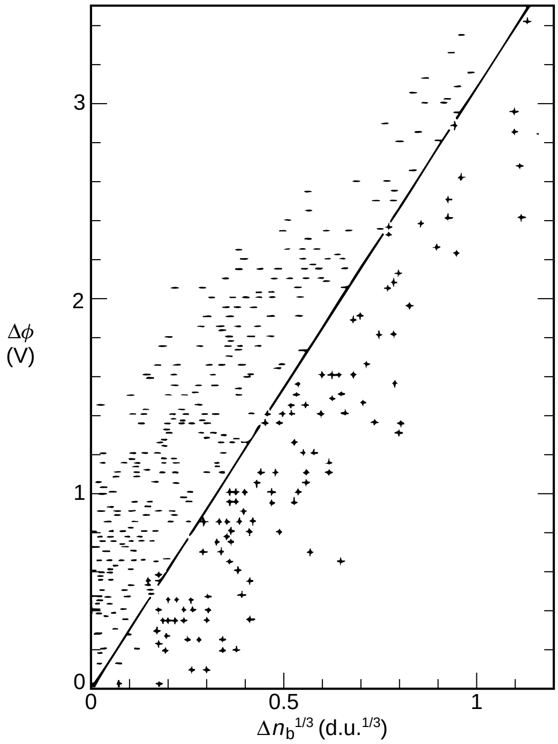

Figure 22 The correlation with experiment for equation (14). A minus sign indicates that there is at least one stable binary compound between the elements, that is, that $\Delta H < 0$. A plus sign indicates that there is no stable binary compound known and also that there is limited solubility (<10%) of the two metals

energy penalty on forming the alloy. Since electron density is continuous across the boundaries of the cells in the pure A and pure B systems, but certainly discontinuous for the AB alloy in the cell model of Figure 21, a readjustment of electron density at the cell boundaries is necessary for it to be continuous in the AB alloy too. The energy cost associated with this process is proportional to $+(\Delta n_b^{1/3})^2$ where Δn_b is visualized as the electron density discontinuity at the boundary between A and B cells. The term $\Delta n_b^{1/3}$ is a second index. The combination of the two effects leads to a heat of formation (equation 14) written as

$$\Delta H = f(c)[-P(\Delta\phi)^2 + Q(\Delta n_b^{1/3})^2] \tag{14}$$

where $f(c)$ is a term that allows for changes in stoichiometry. Irrespective of the physical origin of the indices, it is clear that the two indices for each element i, ϕ_i and $n_b^{1/3}$, may be regarded as two general parameters with which to represent the heat of formation. The agreement with experiment for transition metal–transition metal alloys is shown in Figure 22 and is very impressive. For transition metal–main group alloys, the theory has to be modified slightly,[22] but a good predictive model remains.

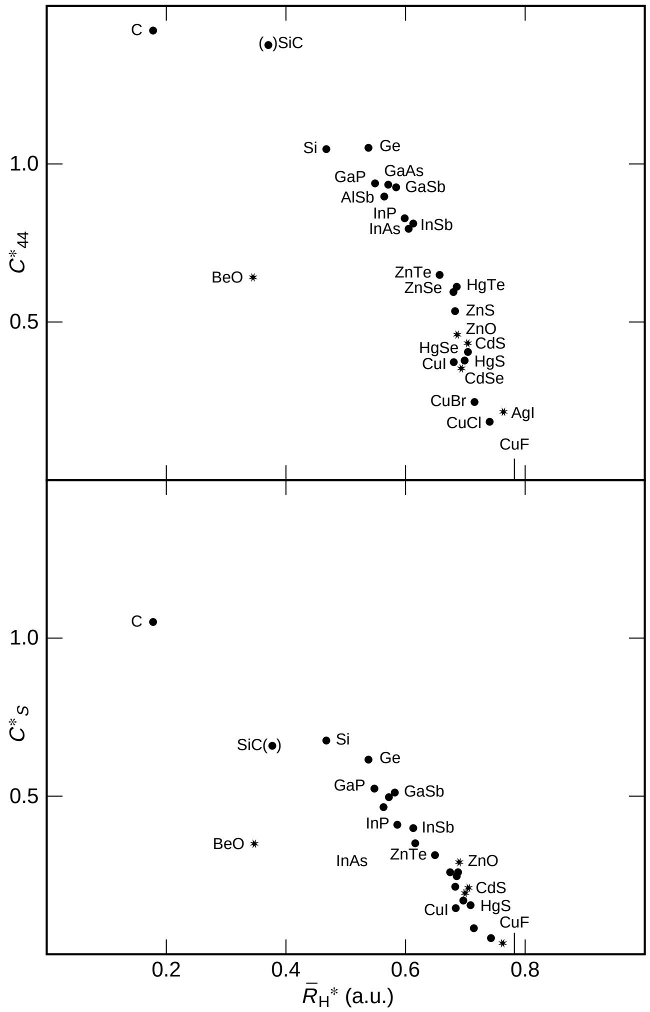

Figure 23 R_σ (R_H) versus cubic shear moduli of tetrahedrally coordinated octet solids. (Reprinted from Ref. 14. © 1981, with permission from Elsevier)

5 PROPERTIES

Industry is highly interested in new materials that possess new or improved properties. The use of structure maps and other diagrammatic tools aid in this quest. Below are described the uses of such maps in the search for property-specific materials. In the sections on stable quasicrystals, high-T_c superconductors, and ferroelectrics, the applications of the quantum structural diagrams (QSD) described above will be used. In these classes of materials, the analysis starts with the compilation of the diagrammatic coordinates as described in equation (6). For these unusual types of order, the existence of diagrammatic regularities implies, at least, that the same factors that control local structure and stability in ordinary compounds also determine the tendency to these types of order and probably a connection as well.

In terms of other indices, the parameter R_σ is a good one[14] for the correlation of the cubic shear moduli of solids, as shown in Figure 23. The variation in the axial ratios of compounds with the wurtzite structure are well correlated[14] (Figure 24) with the parameter ΔR_{CT}.

5.1 Stable Quasicrystals

Rabe and coworkers[22,26] have used QSDs to analyze stable ternary quasicrystals. They have plotted the 10 known stable quasicrystals: $CuLi_3Al_6$, $Ga_{20}Mg_{37}Zn_{43}$, $A_{15}Cu_{20}Al_{65}$ (A = Fe, Ru, Os), $Cu_{15}Co_{20}Al_{65}$, $Co_{15}Ni_{15}Al_{70}$, (Mn, Re)Pd_2Al_7, and the recently discovered $Al_{43}Mg_{43}Pd_{14}$.[27] For the first nine, the diagrammatic coordinates are computed and plotted on the QSD, as shown in Figure 25. All 10 quasicrystals, including $Al_{43}Mg_{43}Pd_{14}$, fall into the restricted range $-0.6 \le \overline{\Delta X} \le 0.3$ and $-0.2 \le \overline{\Delta R} \le 0.7$, which they designated the QSD quasicrystal condition. Predictions for new quasicrystals have been produced by screening two kinds of candidate composition lists: new combinations based on compositions of known quasicrystals[22,26,28,29] and known intermetallic compounds as possible crystalline approximants.[21,22] The predictions by Price,[24] based on the new combinations approach, led to the discovery of four new metastable quasicrystals.[28]

5.2 High-T_c Superconductors

Villars[30] and Phillips[31] have applied QSD to the systematization of compounds possessing high-T_c superconducting properties. These results are presented in Figure 26. Figure 26(a) shows the two-dimensional plot $\overline{\Delta X}$ versus $\overline{\Delta R}$ and Figure 26(b), the Mathias[32] plot T_c versus N_v. Figure 26(a) show three islands, A, B, and C, each being characterized by particular ranges of $\overline{\Delta X}$, $\overline{\Delta R}$, and N_v. Island A is dominated by binaries with the cP8 (Cr_3Si) (A15) structure type, but in addition has five other structure types. Island B contains compounds having the cF8 (NaCl) (Bl) structure type. These simple binary compounds (island B) are five times more likely to have $T_c > 10$ K than the binaries that have the NaCl structure type but that do not have the restriction of $\overline{\Delta R}$ and $\overline{\Delta X}$. Island C contains the Chevrel (M_xMo_6X, where X is usually a chalcogenide) and perovskite (ABO_3) phases and the ternary cuprate superconductors as well ($La_{2-x}Sr_xCuO_4$).

5.3 Ferroelectricity

In their analysis of ferroelectric compounds using QSD, Villars *et al.*[33] studied 175 ternary ferroelectric and antiferroelectric oxides. These compounds were divided into three sets: F_1 with $T_c > 500$ K with 50 representatives, F_2 with 22 compounds with $300\,\text{K} < T_c < 500$ K, and F_3 with 103 representatives containing pseudoternaries and quaternary oxides with $T_c > 500$ K. The calculation of $\overline{\Delta X}$ and $\overline{\Delta R}$ for the pseudoternaries and quaternaries with $T_c > 500$ K (set F_3) was performed by combining the two most chemically similar elements into a single 'element' with weighted average N_v, X, and R. Figure 27 shows that the resulting $\overline{\Delta X}$ and $\overline{\Delta R}$

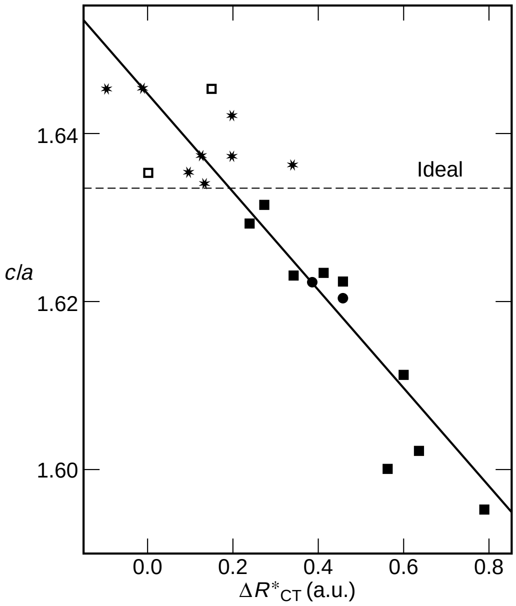

Figure 24 The variation in the axial ratios of compounds with the wurtzite structure with the parameter ΔR_{CT}. (Reprinted from Ref. 14. © 1981, with permission from Elsevier)

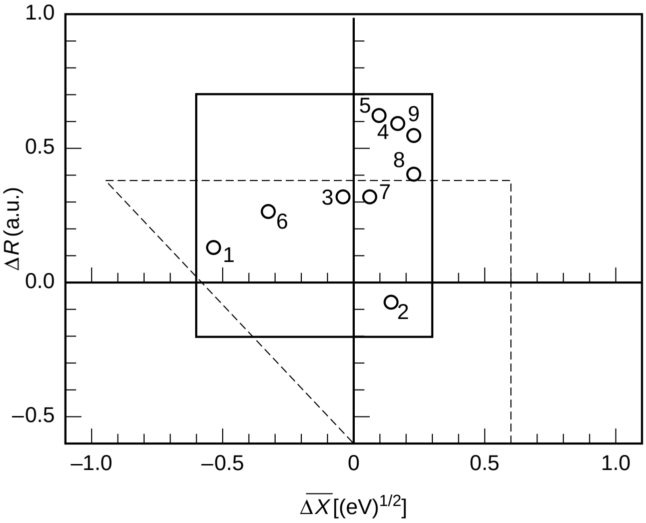

Figure 25 A QSD projection on the $\overline{\Delta X} - \overline{\Delta R}$ plan for nine quasicrystals (numbering given in Table 1 of Villars[22]). The dashed lines show segments of the boundary of the $\overline{\Delta X} - \overline{\Delta R}$ zone defining the quasicrystal conditions based on cI162 compounds.[28] (Reprinted with permission from K.M. Rabe, J.C. Phillips, P. Villars, and I.D. Brown, *Phys. Rev.*, 1992, **B45**, 7650. © American Physical Society. http://pra.aps.org)

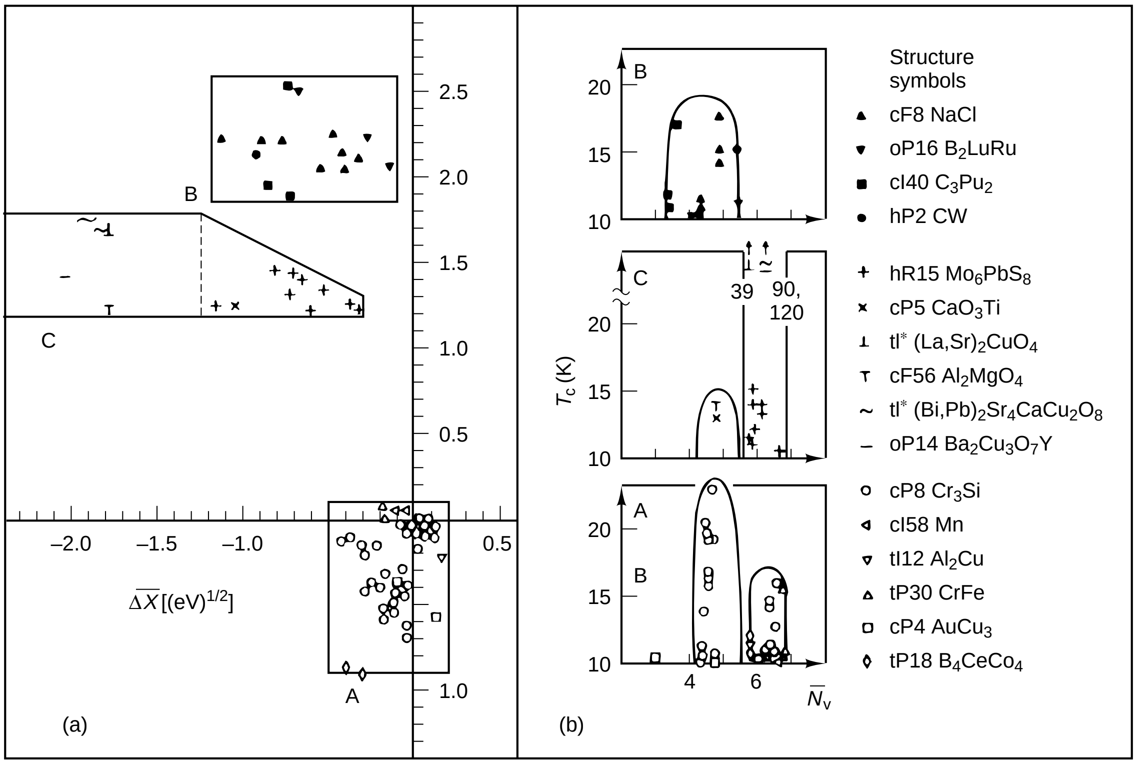

Figure 26 Plots for 67 high-T_c superconductors: (a) $\overline{\Delta X} - \overline{\Delta R}$ quantum structural diagrams, and (b) Mathias plot T_c versus N_v. See text for information on islands A, B, C. (Reproduced by permission of Academic Press from Phillips.[31])

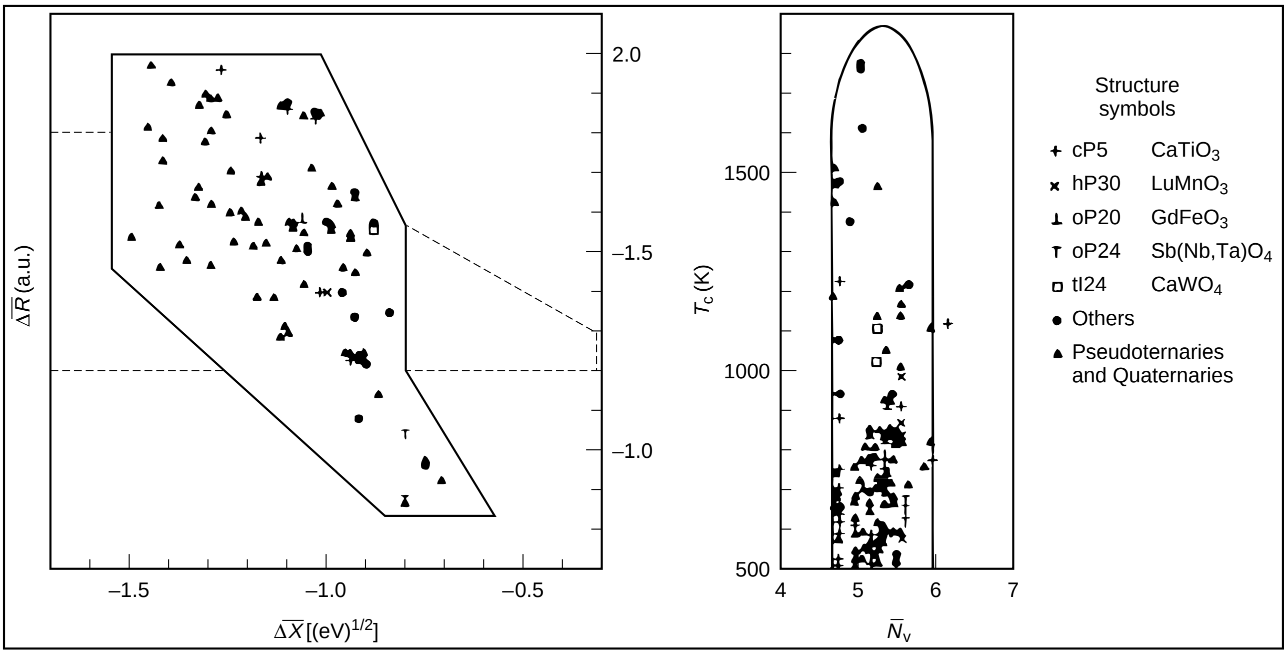

Figure 27 QSD and Mathias plots for 175 high-T_c ferroelectrics and antiferroelectrics. Pseudoternaries and quaternaries with $T_c > 500\,K$ (set F_3) are represented by solid triangles; the ternaries with $T_c > 500\,K$ (set F_1) are represented by a variety of symbols distinguishing different structure types, as shown in the legend (all scales are expanded by a factor of 2 relative to Figure 26). The outline for the island C from Figure 26 is shown as a dashed line to facilitate comparison of ferroelectric and superconducting domains. (Ref. 33. Reproduced by permission of Taylor & Francis)

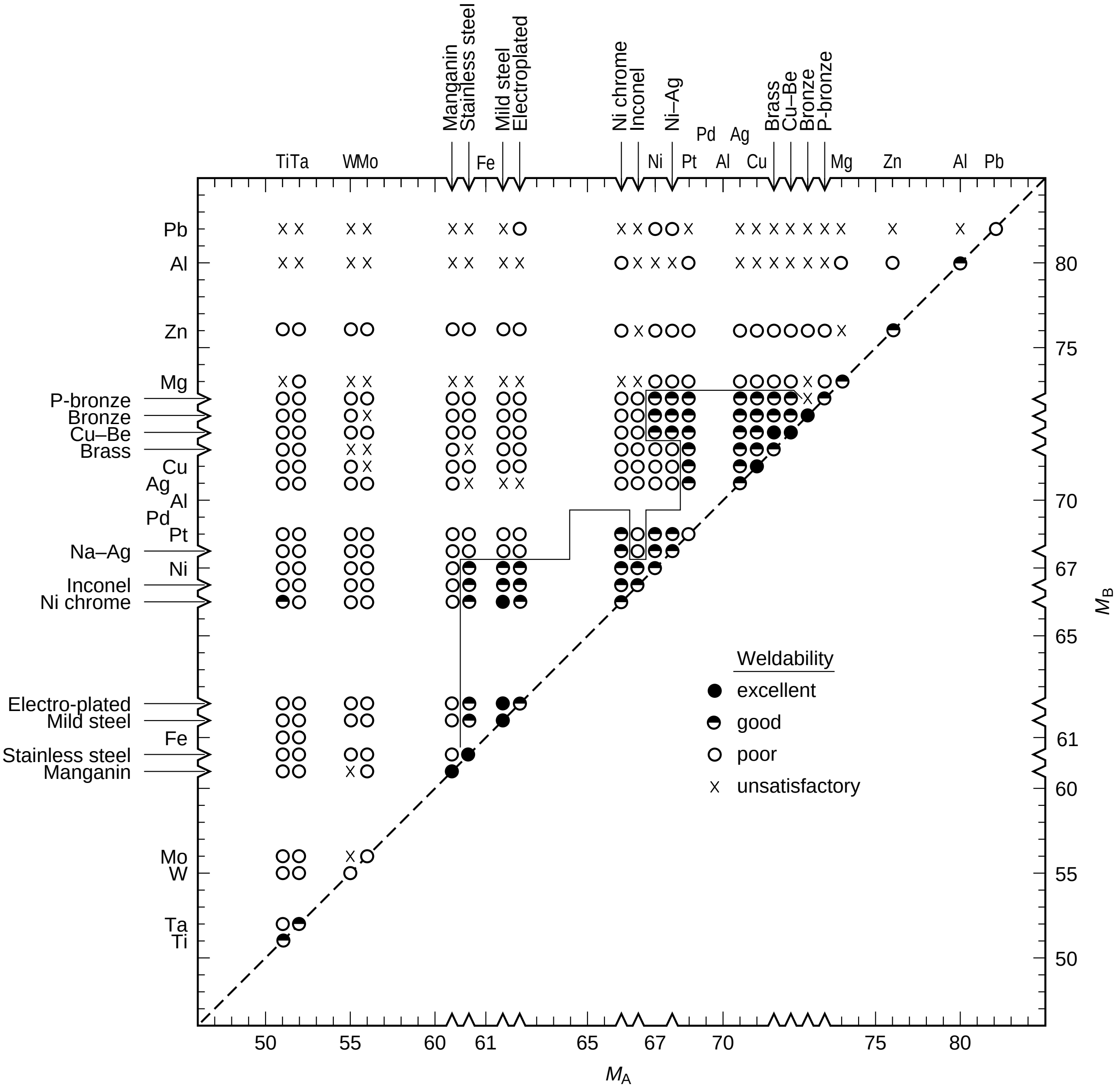

Figure 28 Weldability property plots. (Reproduced by permission of the Institute of Metals from Pettifor.[34])

values for the ternaries, pseudoternaries, and quaternaries with $T_c > 500\,\mathrm{K}$ (sets F_1 and F_3) are confined to one very small region of the QSD. The area occupied by the set F_1 is particularly small, while the inclusion of set F_3 requires a slight displacement of the left-hand boundary to larger values of $|\overline{\Delta X}|$. This figure also shows a Mathias population plot for T_c versus N_v for the 153 compounds belonging to the sets F_1 and F_3. This Mathias plot shows a very narrow peak, even narrower than is found for superconductors, for which such plots are usually made. The narrowness of this peak is consistent with the excellent localization in the $(\overline{\Delta X}, \overline{\Delta R})$ diagram, showing the conditions for high-T_c ferroelectricity are limited to a very small volume of QSD ($\bar{N}_v$, ΔX, ΔR space).

5.4 Weldability

Pettifor[34] shows, in a Mendeleev (M_A vs. M_B) weldability plot (Figure 28) for AB intermetallics, the separation between compounds having excellent, good, poor, and unsatisfactory weldability properties. It can be observed that domains of excellent weldability are clearly defined.

5.5 High-temperature, High-strength Materials

In the selection of materials for high-temperature structural applications, information on two properties is necessary.

These properties, which are insensitive to processing, are the melting temperature (T_m) and the specific gravity (ρ). Compounds with high T_m have high stiffness, high strength, and a low thermal expansion coefficient, while those with low ρ have high specific strength and specific stiffness.[35] Fleischer[35] has plotted T_m versus ρ for a series of intermetallic compounds grouped by structure type; two such plots are shown in Figure 29. These plots show that by using intermetallics crystallizing in certain structure types, new compounds can be designed, for example, intermetallics that have both high T_m and high ρ (aerospace applications). From these plots, it is clearly seen that cF8 NaCl-type intermetallics (Figure 29(a)) would be better suited for such aerospace applications than the cP4 $AuCu_3$ type (Figure 29(b)).

5.6 Electrical Conductivity

Kiang and Liu[36] have found a connection between the electrical conductivity (ϕ), the fractional number of bonds (n), and the electronegativity difference ($\Delta X_{\mathrm{Pauling}}$) for binary compounds. Figure 30 shows a projection of the electrical conductivity contours. This figure is intended to show the trend of the variation of the degree of ionicity and the degree of covalency of a bond in binary compounds.

5.7 Other Properties

Pettifor maps, two-dimensional plots (M_A vs. M_B) (see Figures 6 and 7), have lead to good structural separation of pseudobinary and ternary compounds. The following stoichiometries have been plotted and discussed elsewhere:[37] AB, AB_2, AB_3, AB_4, AB_5, AB_6, AB_{11}, AB_{12}, A_2B_3, A_2B_5, A_2B_{17}, A_3B_4, A_3B_5, A_3B_7, A_4B_5, and A_6B_{23}. These maps have been used by alloy designers to predict new ternary or quaternary systems with a desired structure type and property, for example, cubic Cu_3Au-type alloys, which have better mechanical properties at high temperature than the brittle noncubic Al_3Ti or $AiTi_3$ binary systems.[38] The two-dimensional maps[39] for A_2B_{17}, AB_{11}, AB_{12}, and AB_{13} structure types have been used to search for Fe-based

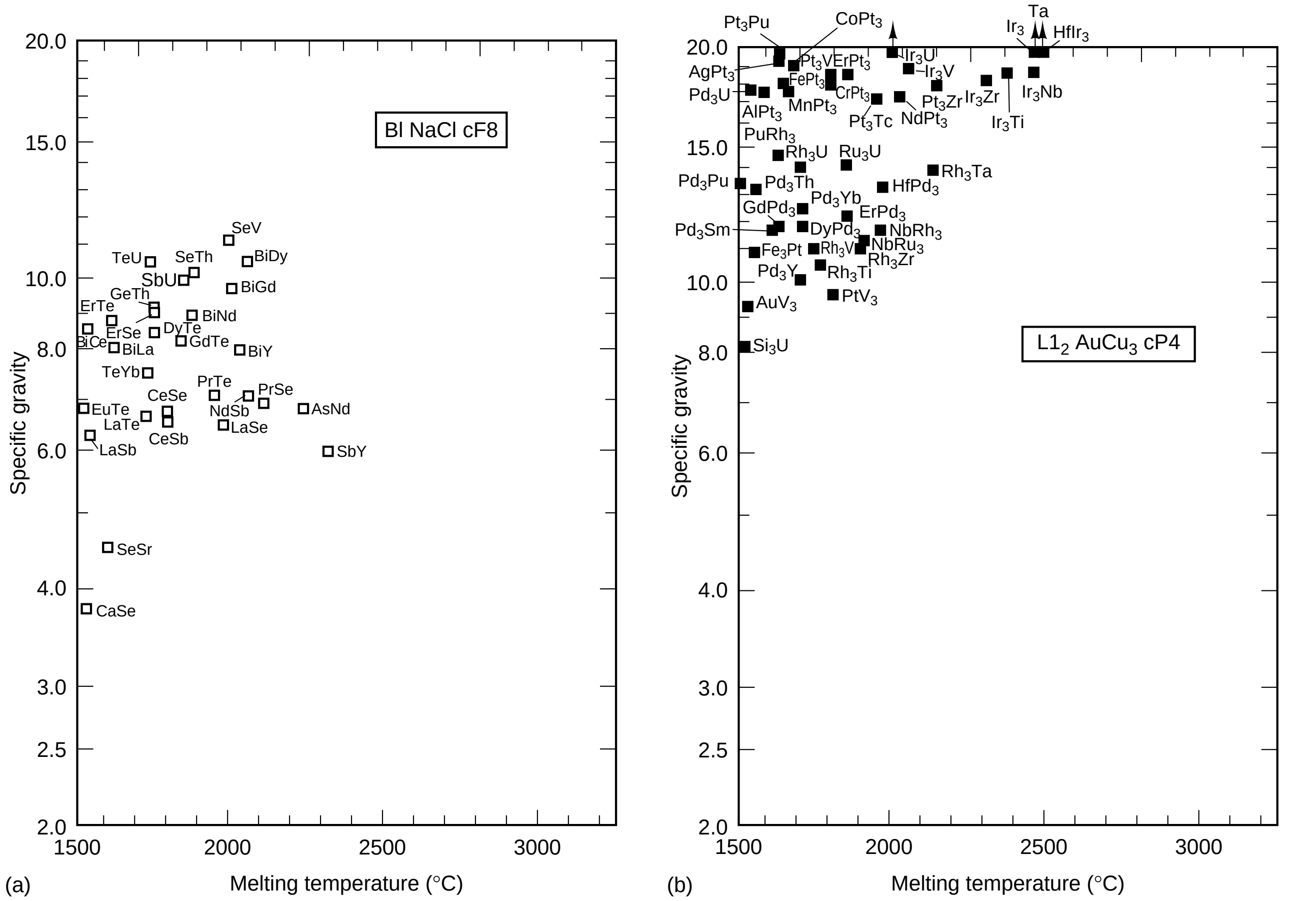

Figure 29 T_m versus ρ for (a) cF8 NaCl (B1) compounds and (b) cP4 $AuCu_3$ ($L1_2$) compounds. (Reproduced by permission of Chapman & Hall from Fleischer[35])

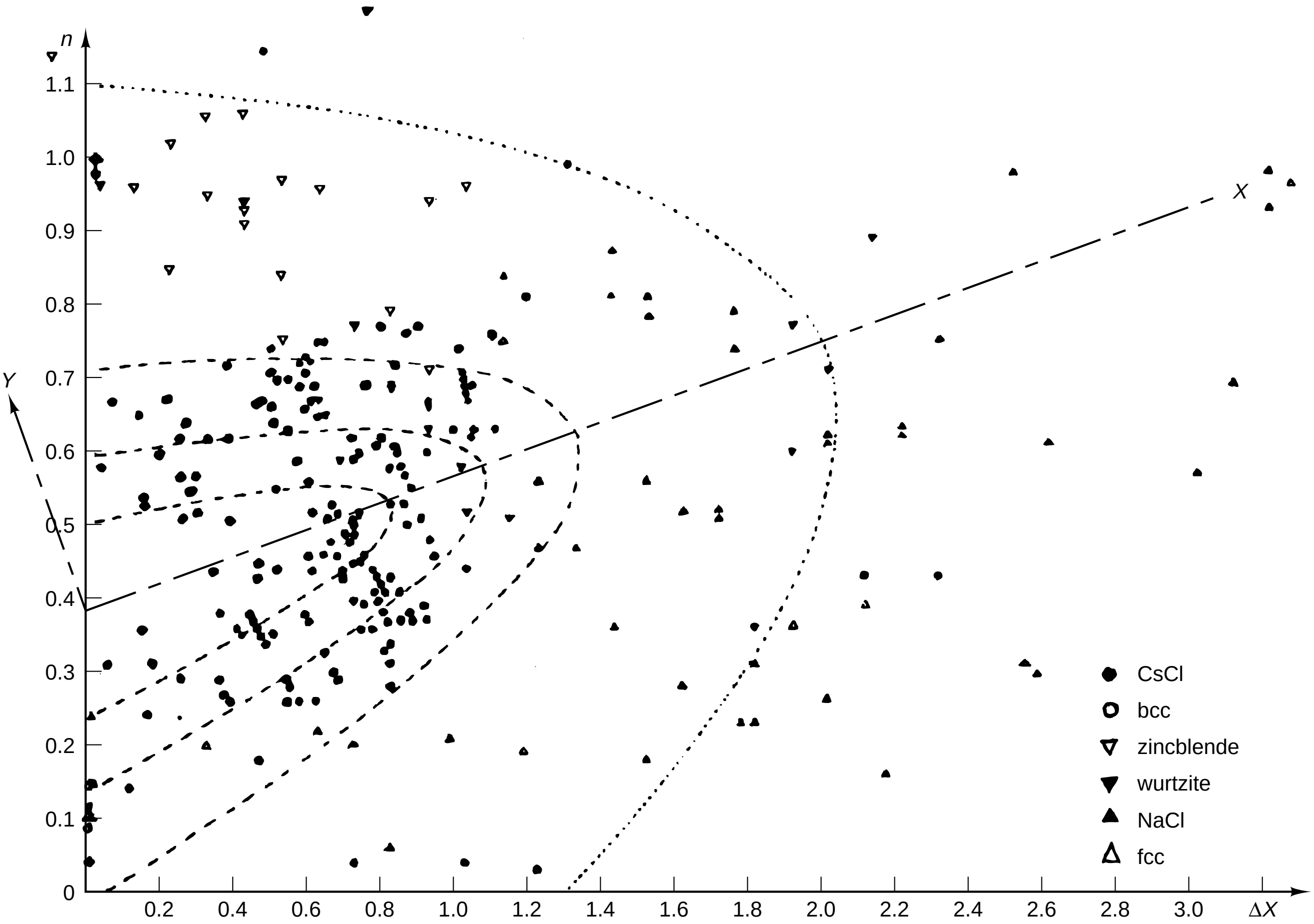

Figure 30 Electrical conductivity contours. Fraction number of bonds (n) versus electronegativity difference (ΔX). (Reproduced by permission of Elsevier from Kiang.[36])

permanent magnets with the tetragonal $BaCd_{11}$, $ThMn_{12}$, and $NaZn_{13}$ structure types.

6 RELATED ARTICLES

Superconductivity.

7 REFERENCES

1. L. Pauling, *J. Am. Chem. Soc.*, 1929, **51**, 1010.
2. F. Laves, 'Theory of Alloy Phases', American Society for Metals, Cleveland, 1956.
3. J. K. Burdett, S. L. Price, and G. D. Price, *Solid State Commun.*, 1981, **40**, 923.
4. A. D. Mighell and J. R. Rodgers, *Acta Crystallogr., Sect. A*, 1980, **A36**, 321.
5. J. R. Rodgers and P. Villars, *J. Alloys Compd.*, in press.
6. D. G. Pettifor, *New Sci.*, 1986, **110**, 48.
7. D. G. Pettifor, *J. Phys. C*, 1986, **19**, 285.
8. W. B. Pearson, 'Crystal Chemistry and Physics of Metals and Alloys', Wiley, New York, 1972.
9. J. C. Phillips, in 'Structure and Bonding in Crystals', eds. M. O'Keefe and A. Navrotsky, Academic Press, New York, 1981, Vol. 1.
10. R. D. Shannon, *Acta Crystallogr., Sect. A*, 1976, **A32**, 751.
11. R. D. Shannon, in 'Structure and Bonding in Crystals', eds. M. O'Keeffe and A. Navrotsky, Academic Press, New York, 1981, Vol. 2.
12. M. L. Cohen, in 'Structure and Bonding in Crystals', eds. M. O'Keeffe and A. Navrotsky, Academic Press, New York, 1981, Vol. 1.
13. J. K. Burdett, S. L. Price, and G. D. Price, *Phys. Rev.*, 1981, **B24**, 2903.
14. A. N. Bloch and G. C. Schattemann, in 'Structure and Bonding in Crystals', eds. M. O'Keeffe and A. Navrotsky, Academic Press, New York, 1981, Vol. 1.

15. A. Zunger, in ‘Structure and Bonding in Crystals’, eds. A. O’Keeffe and A. Navrotsky, Academic Press, New York, 1981, Vol. 1.
16. T. M. Dunn, D. S. McClure, and R. G. Pearson, ‘Some Aspects of Crystal Field Theory’, Harper & Row, New York, 1965.
17. J. K. Burdett, S. L. Price, and G. D. Price, *J. Am. Chem. Soc.*, 1982, **104**, 92.
18. P. Villars and F. Hulliger, *J. Less-Common Met.*, 1987, **132**, 284.
19. P. Villars, K. Mathis, and F. Hulliger, in ‘Structures of Binary Compounds’, eds. F. de Boer and D. Pettifor, North-Holland, Amsterdam, 1989, Vol. 2, p. 1.
20. P. Villars, *J. Less-Common Met.*, 1986, **119**, 175.
21. P. Villars, *J. Less-Common Met.*, 1983, **92**, 215.
22. K. M. Rabe, J. C. Phillips, P. Villars, and I. D. Brown, *Phys. Rev.*, 1992, **B45**, 7650.
23. J. K. Burdett and S. L. Price, *Phys. Rev.*, 1981, **B23**, 5642.
24. G. D. Price, S. L. Price, and J. K. Burdett, *Phys. Chem. Miner.*, 1982, **8**, 69.
25. A. R. Miedema and P. F. de Châtel, in ‘Theory of Alloy Phase Formation’, ed. L. H. Bennett, Metallurgical Society of the AIME, Warrendale, PA, 1980.
26. K. M. Rabe, A. R. Kortan, J. C. Phillips, and P. Villars, *Phys. Rev.*, 1991, **B43**, 6280.
27. N. Koshikawa, S. Sakamoto, K. Edagawa, and S. Takeuchi, *Jpn. J. Appl. Phys., Part 2*, 1992, **31**, L966.
28. P. Villars, J. C. Phillips, and H. S. Chen, *Phys. Rev. Lett.*, 1986, **57**, 3085.
29. J. Tartas and E. J. Knystautas, *J. Mater. Res.*, 1991, **6**, 1219.
30. P. Villars and J. C. Phillips, *Phys. Rev.*, 1987, **B37**, 2345.
31. J. C. Phillips, ‘Physics of High T_c Superconductors’, Academic Press, Boston, MA, 1989.
32. B. T. Mathias, *Phys. Today*, 1971, **24**, 23.
33. P. Villars, J. C. Phillips, K. M. Rabe, and I. D. Brown, *Ferroelectrics*, 1992, **130**, 129.
34. D. G. Pettifor, *Mater. Sci. Technol.*, 1988, **4**, 675.
35. R. L. Fleischer, *J. Mater. Sci.*, 1987, **22**, 2281.
36. L. I. Kiang and T. L. Liu, *Phys. Lett.*, 1980, **76A**, 181.
37. D. G. Pettifor, *J. Phys. C*, 1986, **19**, 285.
38. C. T. Liu, J. A. Horton, and D. G. Pettifor, *MRS Symp. Proc.*, 1989, **133**, 37.
39. D. G. Pettifor, *Physica B*, 1988, **149**, 3.

Sulfur: Inorganic Chemistry

J. Derek Woollins
University of St Andrews, St Andrews, UK

1	Introduction	1
2	Elemental Sulfur	1
3	Sulfur Oxides	9
4	Sulfanes	18
5	Sulfur Halides	22
6	Sulfur–Carbon Compounds	26
7	Main Group Rings and Cages	28
8	Inorganic Biological Sulfur Chemistry	31
9	Analysis of Inorganic Sulfur Compounds	32
10	Related Articles	33
11	References	33

1 INTRODUCTION

Sulfur has been known since ancient times. The German and Scandinavian words for sulfur (*schwefel*/*svovel*/*svavl*) derive from the Indo-European *suelphlos*, which is derived from *swel*, meaning to burn slowly. The Latin sulpur may have the same origin. Sulfur has also been thought to be derived from Sanskrit *sulveri*, meaning the enemy of copper. The Greeks burnt elemental sulfur to 'purify the atmosphere' and recognized its usefulness in medicine. Brimstone was a major force in the destruction of Sodom and Gomorrah. From the thirteenth to the mid-nineteenth century, gunpowder (made from $NaNO_3$, charcoal, and sulfur in 75:15:10 weight ratio) was important in military affairs although, subsequent to this, it was replaced by nitroglycerine and cordite. Metal sulfides were among the earliest inorganic pigments (e.g. ultramarine). The alchemists regarded metals as being derived from sulfur and mercury, with higher sulfur contents resulting in less metallic properties. Sulfur is an essential element for life, and is a minor constituent of a number of proteins; typical human consumption is ca. 100 mg per day. For many years the extent of the industrialization and gross national product of many countries could be closely equated with their sulfuric acid production. Important events in the history of sulfur chemistry are shown in Table 1. Physical properties of atomic sulfur are shown in Table 2.

The range of oxidation states and compounds available to sulfur includes S^{-2}, S^0, S^{II}, S^{IV}, and S^{VI}; examples of species in each of these categories are given in Table 3. Industrial uses are illustrated in Figure 1. There is an extensive bibliography of sulfur chemistry including Gmelin,[3] Mellor,[4] monographs,[5,6] and good coverage in advanced inorganic chemistry texts.[1,2,7]

2 ELEMENTAL SULFUR

2.1 Natural Occurrence

Sulfur is a relatively common element and occurs naturally as the element (in the caprock of salt domes and in the basin deposits in Poland), in metal sulfides (Table 4), and in sulfates such as gypsum. Furthermore, the sulfur deposits in natural gas and crude oil are now also becoming increasingly significant commercially. The world reserves of sulfur are believed to be in excess of 2×10^9 tonnes.[8,9]

2.2 Production

The production of sulfur parallels the development of chemistry. In the 1700s, sulfur mining was undertaken on a steadily increasing scale. In the nineteenth century, demand for sulfur increased dramatically with volcanic derived sulfur (mostly from Sicily) providing for the emergent chemical industry. The Frasch process revolutionized the production of sulfur and ensured a stable supply from the turn of the century. Worldwide production of sulfur is estimated to be in excess of 60 million tonnes annually; the three main sources of production are (1) recovery from crude oil and gas, (2) direct mining/Frasch recovery of the element, and (3) roasting of metal sulfides, in particular, pyrites. In addition, there is an increasingly large amount of sulfur obtained from SO_2 in flue gases.

Recovery of sulfur from crude oil is achieved by treating the H_2S using the Claus process. The H_2S is reacted with air/oxygen according to equation (1).

$$\begin{aligned} H_2S + 1.5O_2 &\longrightarrow SO_2 + H_2O \\ 2H_2S + SO_2 &\longrightarrow 3S + 2H_2O \end{aligned} \tag{1}$$

The remaining unconverted H_2S (up to 40%) is passed through a number of reactors containing alumina/copper/molybdenum catalysts to achieve full conversion of the hydrogen sulfide to sulfur.

Sulfur, which is present in the limes of America and Iran, can be obtained by the Frasch process, which involves pumping superheated steam (160–170 °C) deep into the sulfur-rich rocks. The sulfur becomes molten and is then forced up to the surface using compressed air (Figure 2). Between 2000 and 5000 gallons of water are needed for each ton of sulfur that is recovered. Once pumped up on to the surface, the molten sulfur is cooled in layers in gigantic 'sulfur vats' to give solid blocks up to 60 feet high.

Alternatively, heating iron pyrites (FeS_2) to 1200 °C with exclusion of air gives sulfur and liquid FeS by the 'Outokumpu' process.

As a consequence of environmental concerns associated with burning fossil fuels during the latter part of the twentieth century, greater efforts have been made to recover sulfur from

Table 1 History of the chemistry of sulfur[1]

Ancient times	Sulfur, in the guise of brimstone, referred to frequently in the Old Testament
800 BC	The ability of sulfur to fumigate mentioned by Homer
79 AD	Pliny the Elder mentions many uses of sulfur
1250	Bacon and Swartz independently discover gunpowder
1661	Evelyn describes the effects of SO_2 pollution in London to Charles II
1746	Roebuck introduces the lead chamber process for H_2SO_4
1777	Elemental nature of S proposed by Lavoisier
1781	Sulfur first detected in plants by Deyeux
1809	Although Humphrey Davy contends that oxygen and hydrogen are essential constituents of sulfur, Gay-Lussac and Thenard firmly establish it as an element
1813	Sulfur detected in animals by Vogel
1822	Xanthates (e.g. EtOCSSK) discovered by Zeise, who also prepares the first thiol (EtSH) in 1834
1831	Contact process for H_2SO_4 patented by Philips
1835	S_4N_4 made ($S_2Cl_2 + NH_3$)
1839	Vulcanization of natural rubber latex by heating it with sulfur discovered by Goodyear
1865	Prospectors boring for oil in Louisiana discover large sulfur deposits beneath a 150 m thick layer of quicksand
1891–4	Frasch develops process for recovery of sulfur
1912	Rhombohedral sulfur established as S_8
1926	Isotopes ^{33}S and ^{34}S discovered by Aston, who previously (1920) had only detected ^{32}S
1935	Molecular structure of *cyclo*-S_8 established by X-ray methods
1944	Sulfur first produced from the H_2S in natural gas
1950	SF_4 isolated by Silvery and Cady
1951	^{33}S NMR signals detected by Dharmatti and Weaver
1972	H_2SO_4 and S detected in the atmosphere of Venus by USSR Venera 8
1970s	Various S_n and $S_n{}^+$ synthesized and characterized
	Role of sulfur ligands in metalloproteins begins to be recognized
	Polymeric $(SN)_x$ shown to have metallic and superconducting properties, leading to much wild speculation
1980s	Alkali metal/sulfur battery developed
	Low-temperature syntheses of metal polysulfides emerge
1990s	II/VI Semiconductors thin-film technology

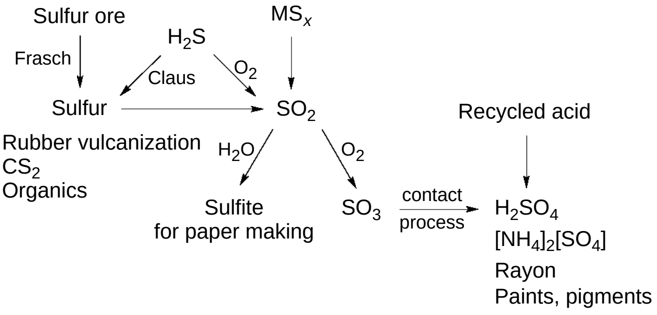

Figure 1 Industrial uses of sulfur

oil and gas. The majority of elemental sulfur is now obtained by this route rather than Frasch mining.

The industrial uses of sulfur have been discussed.[8,10,11]

2.3 Homocyclic Sulfur Compounds

2.3.1 Neutral Sulfur Homocycles

Preparation and Structure. There is a wide range of sulfur allotropes.[12,13] Apart from the many different crystalline forms of S_8, several other sulfur rings have been reported[14] and a new allotrope S_{14} was recently described[15] Historical names and properties of some of the common allotropes (*see Allotrope*) are given in Table 5.

Cyclo-S_8 crystallizes in orthorhombic (α) and two monoclinic (β, γ) forms (Figure 3 illustrates the packing in the α and γ forms). The α form is stable up to 96 °C; liquid sulfur above this temperature is usually cooled to give β sulfur. However, if liquid sulfur is quenched, the familiar plastic sulfur, believed to consist of S_n chains, is obtained.

The crown structure of *cyclo*-octasulfur, S_8, is only one member of an homologous series of S_n ($n = 6–26$) rings (Figure 4). Additionally, cyclic sulfur oxides[16] such as S_6O and S_7O_2 and mixed sulfur–selenium systems[17] are known. These latter compounds are of some commercial significance, with applications as diverse as antidandruff shampoos, fireworks, and polymerization inhibitors.

The preparation of S_n rings can be accomplished by a variety of routes (see equation 2).[14,18] Acid hydrolysis of thiosulfate was originally used for the preparation of S_6, which is separated from S_7 and S_8 by recrystallization from toluene. An alternative method is the thermal decomposition (at room temperature) of diiodosulfane, S_2I_2 (formed in

Table 2 Atomic properties of sulfur[2]

Nuclide	Natural abundance (%)	Half-life	Nuclear spin
^{32}S	95.02	Stable	0
^{33}S	0.75	Stable	3/2
^{34}S	4.21	Stable	0
^{35}S	0	8.72 days (β decay)	3/2
^{36}S	0.02	Stable	0

Radii	
covalent	104
van der Waals	185
atomic	104
S^{4+}	37
S^{6+}	29 pm
Pauling electronegativity	2.58
Electron affinity	200.4 kJ mol^{-1}
Ionization potentials	
1st	999.6
2nd	2251
3rd	3361
4th	4564
5th	7013
6th	8495 kJ mol^{-1}

^{33}S NMR magnetogyric ratio 2.0534×10^7 rad T^{-1} s^{-1}
Quadrupole moment -0.05×10^{-28} m^2
Receptivity/^{13}C 0.0973
Reference: sulfate.

Typical bonds	Length (pm)	Energy (kJ mol^{-1})
S–H	133.5	347
S–C	182	272
S=C	155	476
S–O	150	265
S=O	144	ca. 525
S–F	156	328
S–Cl	199	255
S–S	208	226

Table 4 Some common sulfide minerals

Name	Idealized formula	Name	Idealized formula
Molybdenite	MoS_2	Realgar	As_4S_4
Pyrite (fool's gold)	FeS_2	Orpiment	As_2S_3
Marcasite	FeS_2	Stibnite	Sb_2S_3
Pyrrhotite	$Fe_{1-x}S$	Chalcopyrite	$CuFeS_2$
Chalcocite (Cu glance)	Cu_2S	Bornite	Cu_5FeS_4
Sphalerite (Zn blende)	ZnS	Arsenopyrite	$FeAsS$
Cinnabar (vermilion)	HgS	Tetrahedrite	$Cu_{12}As_4S_{13}$
Galena (Pb glance)	PbS		

situ), which gives a 36% yield of S_6 and minor amounts of higher *cyclo*-sulfanes after purification (equation 3). S_6 is obtained as orange–red crystals that readily decompose at room temperature. Some of the larger rings are more stable and so can be prepared from molten S_8. For example, if commercial sulfur is heated to 200 °C, cooled to ca. 150 °C, and finally quenched by pouring into liquid nitrogen, a mixture of S_7, S_{12}, S_{18}, and S_{20} rings is obtained. The individual compounds are, however, only obtained after painstaking recrystallizations. An alternative route to S_{18} is the reaction of $S_{10}Cl_2$ with H_2S_8, but in this case the preparation of the starting materials is very tedious.**[19]**

$$Na_2S_2O_3 + 2HCl(aq) \longrightarrow \frac{1}{n}S_n + SO_2 + 2NaCl + H_2O \qquad (2)$$

$$S_2Cl_2 + 2KI \longrightarrow S_2I_2 + 2KCl \longrightarrow \frac{1}{n}S_{2n} + I_2 \qquad (3)$$

Fortunately, rational syntheses based upon reactions of Cp_2TiS_5 with chlorosulfanes (and consequent elimination of Cp_2TiCl_2, *see Metathesis*, salt elimination) have been developed (Figure 5).**[14,20]** The Cp_2Ti fragment is isolobal (*see Isolobal Analogy*) (*see also Isoelectronic*) with the sulfur

Table 3 Typical oxidation states and geometries for sulfur

Oxidation number	Coordination number	Geometry	Examples
−2	2	Angular	H_2S
−1	2	Angular	H_2S_2
0	2	Ring	S_n
I	2	Angular	S_2Cl_2, RSCl
II	2	Angular	Me_2S, H_2S
	3	Pyramidal	Me_3S^+
III	3	Angular	$S_2O_4{}^{2-}$
IV	2	Angular	SO_2
	3	Pyramidal	$SF_3{}^+$, OSF_2, $SO_3{}^{2-}$
	4	Ψ-Trigonal-bipyramidal	SF_4, RSF_3
		Tetrahedral	Me_3SO^+
	5	Square pyramidal	$SF_5{}^-$
V	6	Octahedral	S_2F_{10}
VI	3	Trigonal-planar	SO_3 (g)
	4	Tetrahedral	$SO_4{}^{2-}$, SO_3 (s), SO_2Cl_2, $S_2O_3{}^{2-}$
	5	Trigonal-bipyramidal	SOF_4
	6	Octahedral	RSF_5, SF_6

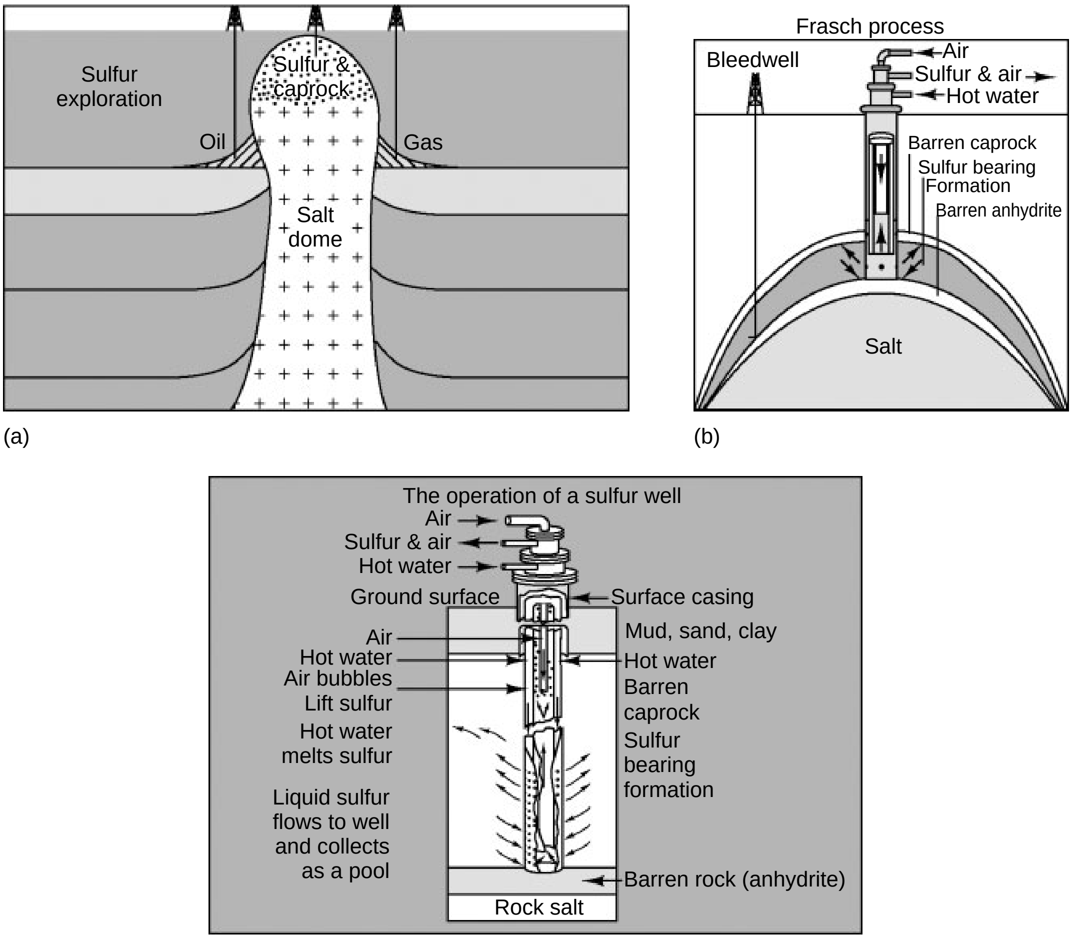
Sulfur exploration
Sulfur & caprock
Oil
Gas
Salt dome
Frasch process
Bleedwell
Air
Sulfur & air
Hot water
Barren caprock
Sulfur bearing Formation
Barren anhydrite
Salt
The operation of a sulfur well
Air
Sulfur & air
Hot water
Ground surface
Surface casing
Air
Hot water
Air bubbles
Lift sulfur
Hot water melts sulfur
Liquid sulfur flows to well and collects as a pool
Mud, sand, clay
Hot water
Barren caprock
Sulfur bearing formation
Barren rock (anhydrite)
Rock salt

(a) (b) (c)

Figure 2 The Frasch process. (Courtesy of Freeport McMoRan Copper & Gold, Inc)

atom, and thus this compound is actually a stable analog of S_6. This approach has been extended to enable the formation of Se_5S, Se_5S_2, and Se_7 by treatment of Cp_2TiSe_5 with SCl_2, S_2Cl_2, and Se_2Cl_2, respectively. The use of transition metal complexes as synthetic reagents in this way will no doubt be more widespread in the future. Surprisingly, the preparation of S_6 from Cp_2TiS_5 is not the best route (probably because pure SCl_2 is difficult to obtain). Reaction of S_2Cl_2 with H_2S_4 gives S_6 (equation 4) but H_2S_4 is difficult to obtain; the preferred route is reaction of S_2Cl_2 with KI as shown in equation (3).

$$S_2Cl_2 + H_2S_4 \longrightarrow \underset{85\%}{cyclo\text{-}S_6} + 2HCl \qquad (4)$$

Eight-membered, and larger, sulfur–selenium rings may be obtained from melts of the elements, by reaction of chlorosulfanes with hydrogen selenide (or vice versa), from selenous acid, or by decomposition of mixtures of Se_2I_2 and S_2I_2, although many of these reactions give rise to mixtures of isomers (equations 5–7).

$$Se_2Cl_2 + H_2S_n \longrightarrow Se_nS_{12-n} + 2HCl \qquad (5)$$

$$2H_2S + SeO_2(aq) \longrightarrow Se_nS_{8-n}\downarrow + 2H_2O \qquad (6)$$

$$\frac{S_2Cl_2}{Se_2Cl_2} + KI \longrightarrow \frac{S_2I_2}{Se_2I_2} + KCl \longrightarrow Se_nS_{8-n} + I_2 \qquad (7)$$

The cyclic sulfur oxides are normally prepared by oxidation of their parent sulfur rings using peroxyfluoroacetic acid (equations 8 and 9), although when S_8 is treated with excess acid, S_7O_2 and SO_2 are obtained, suggesting that ring contraction proceeds via a currently uncharacterized oxidized eight-membered ring.

$$S_n + CF_3CO_3H \longrightarrow S_nO + CF_3CO_2H \quad n = 6\text{–}10 \qquad (8)$$

$$S_n + 2CF_3CO_3H \longrightarrow S_nO_2 + CF_3CO_2H \quad n = 7, 9 \qquad (9)$$

As can be seen in Figure 4, all of the species consist of puckered rings with variable bond angles and distances.

Table 5 Names of allotropes of sulfur

Old and present names	Accepted name	Features
Rhombohedral sulfur Aten sulfur Engel sulfur ε-Sulfur ρ-Sulfur	Rhombohedral (ρ) sulfur	Crystalline *cyclo*-S_6 Space group $R3$
Rhombic sulfur α-Sulfur Orthorhombic sulfur Muthmann's sulfur I	Orthorhombic (α) sulfur	Crystalline *cyclo*-S_8 Space group $Fddd$
Monoclinic sulfur Prismatic sulfur β-Sulfur Muthmann's sulfur II	Monoclinic (β) sulfur	Crystalline *cyclo*-S_8 Space group $P2_1/c$
γ-Sulfur Nacreous sulfur Mother of pearl sulfur Muthmann's sulfur III Gernez's sulfur	Monoclinic (γ) sulfur	Crystalline *cyclo*-S_8 Space group $P2/n$
Fibrous sulfur Ψ-Sulfur	Fibrous sulfur	Crystalline *catena*-S_x Space group not known
Plastic sulfur Elastic sulfur ν-Sulfur η-Sulfur	Mixture	Probably *cyclo*-S_8 and *catena*-S_x
Insoluble sulfur Das sulfur	Insoluble (ω) sulfur, if crystallized	Probably *catena*-S X-ray pattern

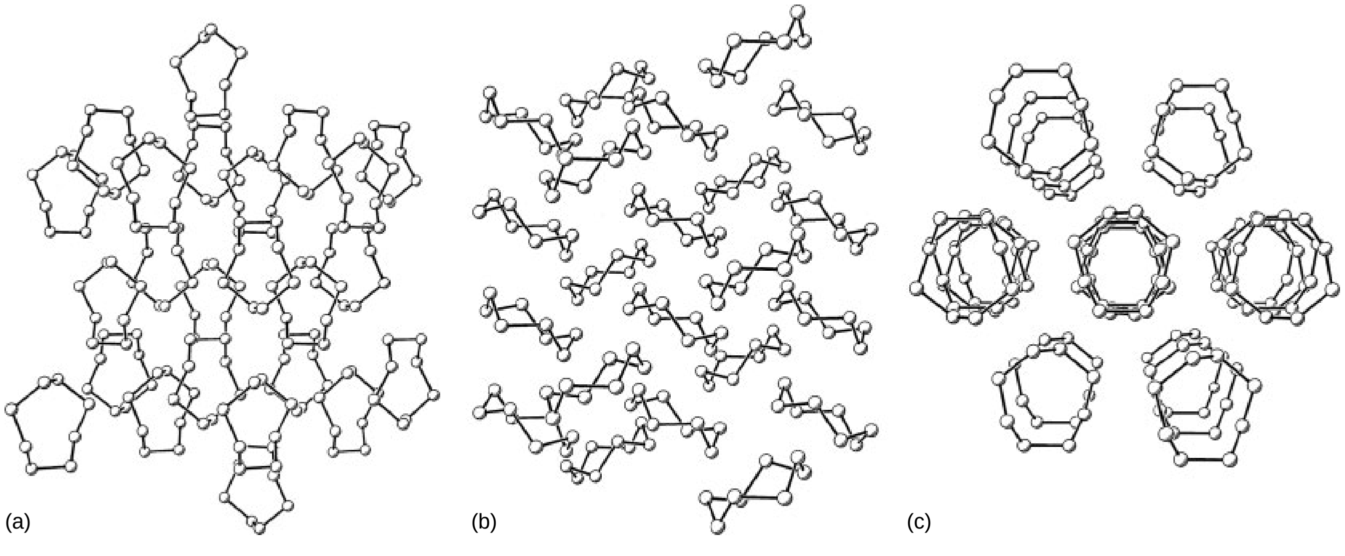

Figure 3 Packing of (a) α-$S_8$$b$-axis, (b) γ-$S_8$$b$-axis (c) γ-$S_8$$c$-axis

High symmetry rings such as S_8 or S_6 have normal S–S bond distances (ca. 2.05 Å) and torsional angles (ca. 85°); however, lower symmetry species can be quite distorted. The most interesting example in this regard is S_7, which would be expected to have C_2 symmetry like cycloheptane, but actually has C_s symmetry with four of the sulfur atoms in a plane and consequently one torsional angle of close to 0°. The S–S distances for the four coplanar sulfur atoms are unusually short, and this may imply some π bonding contributions.

An empirical rationalization of the structure of S_7 has been provided by Gillespie.[21] A convenient starting polyhedron is a cube. Figure 6 also shows how the structure of S_7O and S_7I^+ may be related to that of S_7.

The structures of mixed sulfur–selenium rings are similar to their sulfur analogs. Structures in which the number of

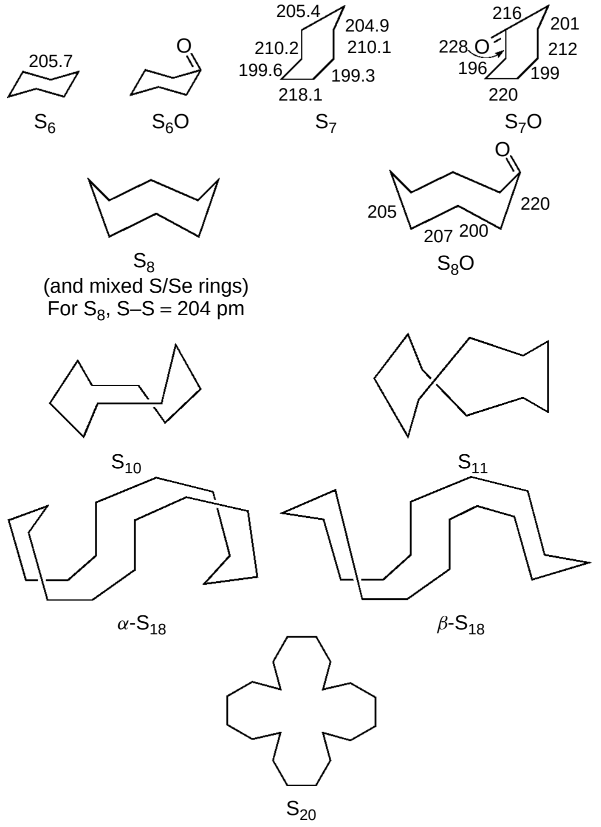
205.7
S6
S6O
205.4
204.9
210.2
210.1
199.6
199.3
218.1
S7
216
201
228
212
196
199
220
S7O
S8
(and mixed S/Se rings)
For S8, S–S = 204 pm
205
220
207
200
S8O
S10
S11
α-S18
β-S18
S20

Figure 4 The structures of S_n and S_nO rings

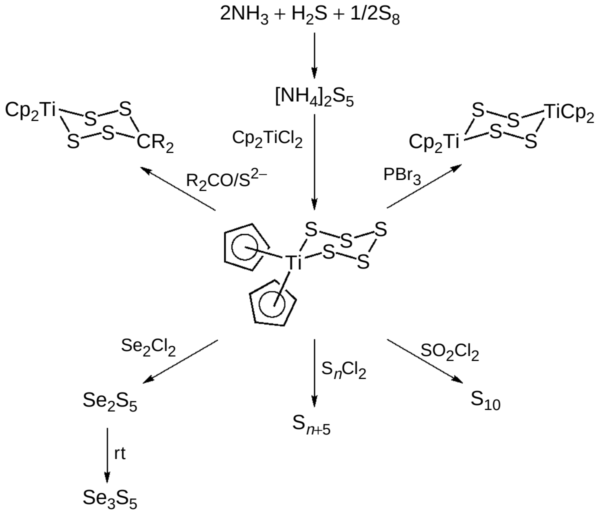
2NH3 + H2S + 1/2S8
[NH4]2S5
Cp2TiCl2
Cp2Ti
CR2
R2CO/S2–
TiCp2
PBr3
Ti
Se2Cl2
SnCl2
SO2Cl2
Se2S5
Sn+5
S10
rt
Se3S5

Figure 5 The preparation and some reactions of Cp_2TiS_5

S–Se bonds is minimized appear to be favored, and the rings thus consist of chains of sulfurs attached to chains of selenium atoms, in contrast to the *cyclo*-sulfur imides (*see* ***Sulfur–Nitrogen Compounds***) where S–N bonds are favored over N–N bonds.

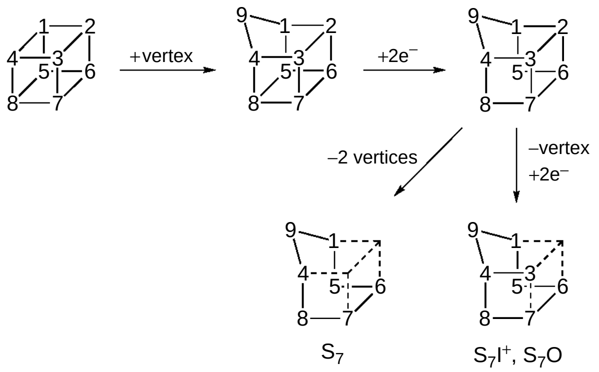
+vertex
+2e–
–2 vertices
–vertex
+2e–
S7
S7I+, S7O

Figure 6 Empirical rationalization of the structures of S_7, S_7O, and S_7I^+

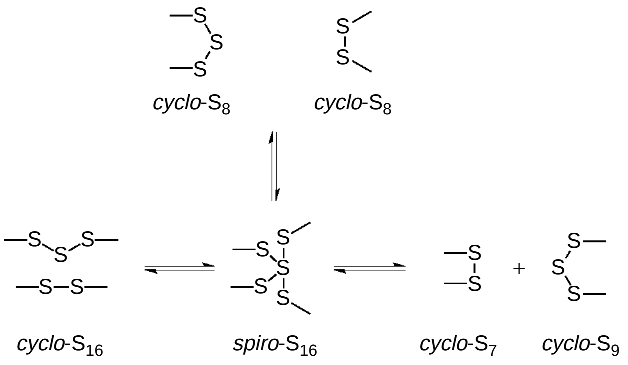
cyclo-S8
cyclo-S8
cyclo-S16
spiro-S16
cyclo-S7
cyclo-S9

Figure 7 Potential mechanism for the formation of S_7 and S_9 from S_8

Cyclo-sulfur rings are yellow or pale orange, low-melting solids (Table 6) of variable stability. For example, S_9 decomposes above 0 °C, while S_6 and S_7 are only moderately stable at room temperature. Their thermal stability decreases in the order S_{12}, S_{18}, S_{20} (years) $>$ S_6, S_9, S_{10}, S_{11}, S_{13} (days) $\gg$ S_7 (minutes). Their interconversion reactions ($S_n \rightarrow S_m, m \neq n$) have been studied in some detail. Thermal as well as photochemical reactions are possible, and a number of mechanisms have been proposed (Figure 7). (1) Radical, consisting of ring opening ($S_n^{\text{ring}} \rightarrow S_n^{\text{chain}}$), polymerization ($S_n^{\text{chain}} \rightarrow S_\infty^{\text{chain}}$), and depolymerization ($S_\infty^{\text{chain}} \rightarrow$ mixture of $S_m^{\text{ring}} + S_n^{\text{ring}}$). (2) Isomerization/transfer, which involves formation of an intermediate ($S_8 \rightarrow S_7S$) with a similar structure to S_7O followed by sulfur transfer ($S_7S + S_8 \rightarrow S_7 + S_9$). (3) Dimerization followed by dissociation. It seems likely that this latter pathway is important at moderate temperatures ($\leq$150 °C), while there is evidence for radical intermediates in photochemical reactions and at higher temperatures. The various sulfur rings may be analyzed by HPLC using a simple reverse-phase column and methanol as the eluent; the larger rings give longer retention times. In addition, each ring has a very characteristic Raman spectrum

Table 6 Molecular properties of sulfur allotropes

S_x	Colour	Space group	S–S bond (pm)	Bond angles (°)	Torsional angles (°)	Mp (°C)
S_6	Orange–red	$R3$	206.8	102.6	73.8	d > 50
γ-S_7	Yellow	$P2_1/c$	199.8–217.5	101.9–107.4	0.4–108.8	d 39
δ-S_7	Yellow	$P2_1/n$	199.5–218.2	101.5–107.5	0.3–108.0	d 39
α-S_8	Yellow	$Fddd$	204.6–205.2	107.3–109.0	98.5	112.8
β-S_8	Yellow	$P2_1/c$	204.7–205.7	105.8–108.3	96.4–101.3	119.6
γ-S_8	Light yellow	$P2/c$	202.3–206.0	106.8–108.5	97.9–100.1	106.8
S_{10}	Pale green	$C2/c$	203.3–207.8	103.3–110.2	75.4–123.7	d > 0
S_{12}	Pale yellow	$Pnnm$	204.8–205.7	105.4–107.4	86.0–89.4	148
S_{14}	Pale yellow	$P-1$	204.7–206.1	104.4–109.3	72.5–101.7	117
S_{18}	Lemon yellow	$P2_12_12_1$	204.4–206.7	103.8–108.3	79.5–89.0	128 m,d
S_{20}	Pale yellow	$Pbcn$	202.3–210.4	104.6–107.7	66.3–89.9	124 m,d

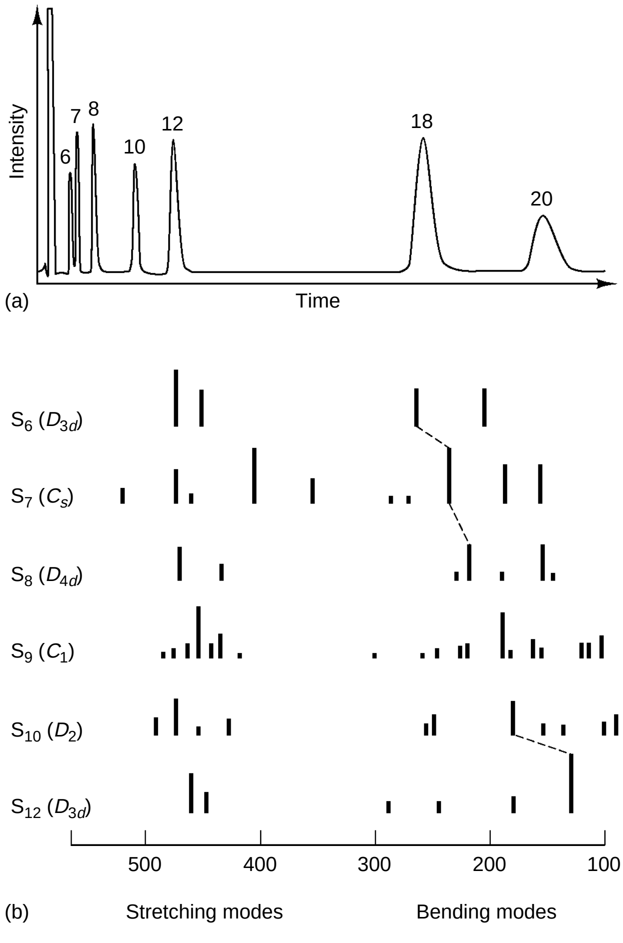

Figure 8 (a) HPLC showing the separation of *cyclo*-S_n rings and (b) typical characteristic Raman spectra of S_n rings. (For further details, see Steudel[16,18])

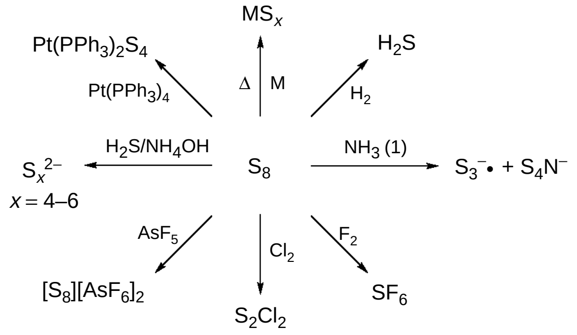

Figure 9 Reactions of S_8

(*see Raman Spectroscopy*) which allows detection in mixtures (Figure 8).[17]

Reactions. Sulfur is a relatively reactive element, with the majority of the reactions proceeding with cleavage of one or more S–S bonds, usually as a result of nucleophilic attack (Figure 9). It forms compounds by direct reaction with virtually every element (the exceptions being the noble gases, nitrogen, iodine, iridium, platinum, and gold). It burns in air with a blue flame, in fluorine to give SF_6, and in chlorine to give S_2Cl_2. Triplet sulfur (which is responsible for the blue flame of sulfur) can be formed by the photochemical activation of CS_2 or COS. Sulfur is not especially reactive with water (which does not wet it), but it does dissolve in liquid ammonia to give complex mixtures of anions (*see* ***Sulfur–Nitrogen Compounds***). *Cyclo*-S_6 is known to be more susceptible to nucleophilic attack than *cyclo*-S_8, and this feature may be of utility in organic synthesis. Oxidation reactions of sulfur rings have already been mentioned and the formation of cyclo cations is discussed below.

2.3.2 Homocyclic Cations

It was observed in 1804 that sulfur reacts in oleum to give intense blue, red, or yellow solutions depending on the time of reaction and the concentration. Tellurium and selenium also give rise to deeply colored solutions in concentrated sulfuric acid. The identity of the species responsible for these colors was in doubt until quite recently. In the past few years, some quite remarkable cations have been isolated.[21] Since

Table 7 Group 16 cations

M_4^{2+}	S_4^{2+}	Se_4^{2+}	Te_4^{2+}	$Te_2Se_2^{2+}$	
M_6^{2+}	–	–	–	S_3Se^{2+} $Te_2Se_4^{2+}$ $Te_3S_3^{2+}$	$Se_6Ph_2^{2+}$ Se_6I^+
M_6^{4+}	–	–	Te_6^{4+}	–	$Se_6I_2^{2+}$ S_7I^+ $(S_7I)_2I^{3+}$
M_8^{2+}	S_8^{2+}	Se_8^{2+}	–	$Se_6Te_2^{2+}$	– Se_9Cl^+
M_{10}^{2+}	–	Se_{10}^{2+}	–	–	–
M_{19}^{2+}	S_{19}^{2+}	–	–	–	–

the various cations down group 16 relate to each other in this section, examples from each element will be discussed. Table 7 gives examples of the known species. Many of the S_x^{n+} cations' electron counts fall between those of (group $16)_x$ and S–N molecules, for example S_8, S_8^{2+}, and S_4N_4 are 48, 46, and 44 electron species, respectively. Apart from the difficult synthetic chemistry, the various cations have thus presented substantial problems theoretically, and the empirical treatment developed to rationalize their structures has been discussed in an excellent review of this area.[21]

A number of synthetic routes are available (*see Superacid*). For success, the final anion has to be insufficiently basic to react with the cation. The cations are usually extremely sensitive to nucleophilic attack, and so solvents such as SO_2, AsF_3, and HSO_3F and counterions like $AlCl_4^-$, AsF_6^-, and SO_3F^- are essential. Typical oxidations are shown in Figure 10. Although many of the methods are logical, it is worth noting the preparation[22] of S_{19}^{2+}. Mixed cations may also be prepared by use of alloys, reaction of an element with a cation of a different element, or reaction between cations of two different elements. Halogen substituted monocations are obtained[23,24] if the oxidation is carried out in the presence of the halogen and by several other routes, for example, reaction of excess sulfur with $I_2Sb_2F_{11}$ or by reaction of I_2 with a previously prepared cation, $S_x(AsF_6)_2$ ($x \sim 19$).

Some solid-state structures are shown in Figure 10. The M_4^{2+} cations have a total electron count of $22e^-$ or 11 pairs. Using *Wade's Rules*, a planar cation can be derived from an octahedron by removal of two opposite vertices and may be described as *iso-arachno*. Support for a planar structure with extra electron density in the ring are the slightly short M–M bonds in M_4^{2+} (e.g. in S_4^{2+}, S–S = 1.98 Å, vs. 2.04 Å in S_8).

The $Te_3S_3^{2+}$ cation contains 34 electrons ($5n + 4$) and is based on a trigonal prism with two bonds broken or on P_4S_3 with one vertex removed. The Te_6^{4+} cation has, surprisingly, a symmetrical structure. This can be rationalized as a trigonal prism with any one of three bonds being broken (or all three broken to an equal extent). Figure 11 illustrates the relationship of M_6^{n+} structures; notice that more electrons result in more open geometries. The structure of S_7I^+ is analogous to that of S_7O. Two forms of M_8^{2+} cations have now been observed. $Te_2Se_6^{2+}$ is based upon a cube with three bonds broken, while S_8^{2+} is related to cuneane with three bonds broken. To rationalize the structure of S_{19}^{2+}, see an excellent review.[17]

The solution structures of group 16 cations have been probed by ^{77}Se and ^{125}Te NMR.[25,26] Both Se_8^{2+} and $Te_2Se_6^{2+}$ retain their (different) solid-state conformations in solution. However, the Se_{10}^{2+} cation does appear by ^{77}Se NMR to undergo structural isomerism with two resonances whose relative intensities are temperature dependent.

$$S_8 + 3AsF_5 \xrightarrow{SO_2} [S_8]^{2+}[AsF_6]_2 + AsF_3$$

$$4Se + S_2O_6F_2 \longrightarrow Se_4^{2+} + 2SO_3F^-$$

$$SeCl_4 + 15Se + 4AlCl_3 \xrightarrow{melt} 2[Se_8][AlCl_4]_2$$

$$28S + 5AsF_5 \longrightarrow [S_{19}^{2+}][AsF_6]_2$$

$$Te_4^{2+} + Se_8^{2+} \longrightarrow Te_3Se_3^{2+}$$

$$4S_8 + 2I_2 + 9AsF_5 \longrightarrow [(S_7I)_4][S_4][AsF_6]_6 + 3AsF_3$$

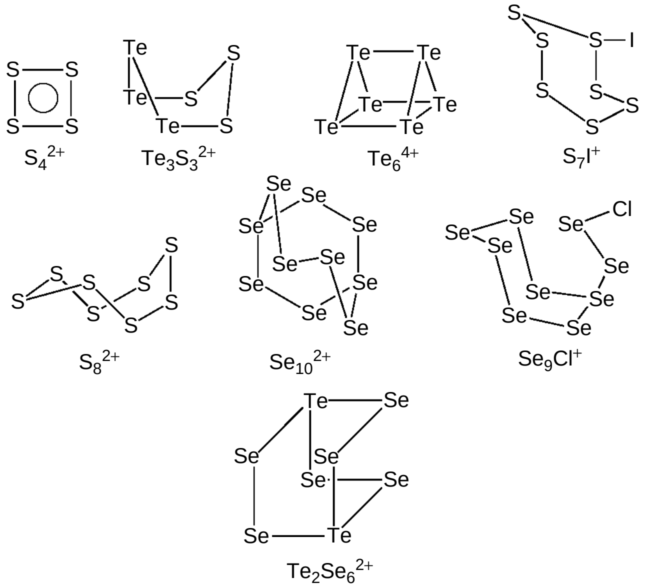

Figure 10 Preparation and structures of E_n^+

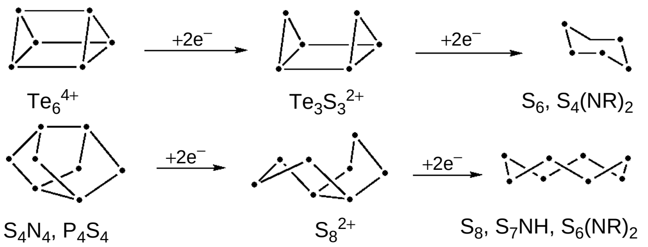

Figure 11 Relationship between the structures of some cyclic sulfur-containing molecules

The reaction of $[Se_4][AsF_6]_2$, $[Se_8][AsF_6]_2$, or $[Se_{10}][AsF_6]_2$ with $M(CO)_6$ (M = Mo or W) gives $[M_2(CO)_{10}Se_4][AsF_6]_2$ in which two $[M(CO)_5Se_2]^+$ cations are linked by long Se···Se bonds (3.015 Å).[27] The $Se_4{}^{2+}$ cation also provides a source of the Se_2 group in the synthesis[28] of $[FeW(CO)_8Se_2][SbF_6]_2$. Reaction of $Se_4{}^{2+}$ with PhSeSe Ph results in a boat conformation $Se_6Ph_2{}^{2+}$ ring. The usefulness of group 16 cations in organic synthesis has been described. For example, the preparation[29] of perfluorinated sulfides, selenides, and tellurides from C_2F_4 (equation 10).

$$[S_8][AsF_6]_2 + C_2F_4 \longrightarrow (C_2F_5)_2S_x \quad x = 2, 3 \qquad (10)$$

More recently, the oxidizing power of $S_n{}^{2+}$ cations has been demonstrated.[30] Reaction of $S_8{}^{2+}$ with hydrocarbons proceeds with insertion of sulfur into a C–H bond (e.g. CH_4 gives methanethiol); toluene is converted into a series of isomeric dimethylbiphenyls, while reaction with CO gives COS.

2.3.3 *Sulfur Vapor*

Sulfur vapor (generated from α-S_8, HgS, or electrochemically) contains a range of S_n species ($n = 1$–10).[31] At higher temperatures, significant amounts of S_2–S_6 are formed. There have been a number of spectroscopic studies on sulfur vapor; Raman studies identified bands due to S_6–S_8 and ionization potential measurements have been compared with UV/Vis studies (see), particularly for S_2, which is an important constituent at high temperatures and low pressures.

2.3.4 *Liquid Sulfur*

Liquid sulfur is a very complex equilibrium system.[32,33] For example, at the melting point it is a clear yellow color, but at its boiling point it is opaque and deep red. Furthermore, it undergoes viscosity changes as the temperature is raised, going through maxima at 159 °C and 185 °C. From EPR and magnetic susceptibility studies it appears that there are no radicals present at low temperature but significant quantities at high temperature. At its melting point, sulfur consists of mostly *cyclo*-S_8 and, as the temperature is raised, various chain length sulfur species are formed. The presence of long-chain S_n species accounts for the weak EPR, the intense color, and the viscosity of high-temperature liquid sulfur, but it is apparent from the literature that the system is still not fully characterized.

3 SULFUR OXIDES

The sulfur oxides include[34] the simplest species SO, SO_2, SO_3 through to very sulfur-rich species such as S_8O (Figure 12), although the di- and trioxide are undoubtedly the most important commercially. We have already mentioned (Section 2.3) that *cyclo*-S_n rings may be oxidized using peroxyfluoroacetic acid to give S_nO and S_nO_2.

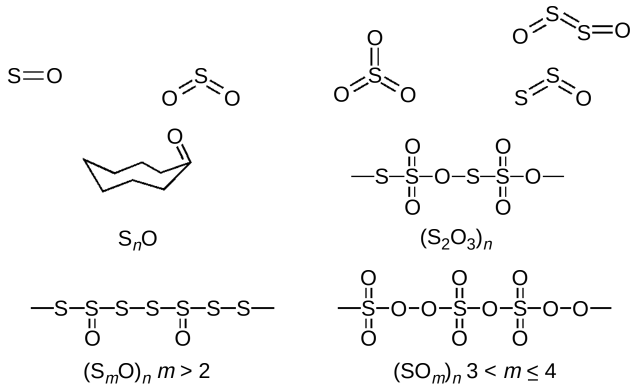

Figure 12 The range of sulfur oxides

3.1 Sulfur Dioxide

3.1.1 *Commercial Preparation*

SO_2 is obtained commercially most commonly by the combustion of sulfur, typically by spraying fine droplets of sulfur into a combustion chamber along with dry air (ΔH −297 kJ mol^{-1}). Both single- and two-stage combustion processes are used. Single-stage processes use an excess of O_2/air, whereas two-stage systems use ca. 90% of the required air in the first stage and add additional O_2 in the second combustion. The two-stage system produces SO_2 that contains virtually no nitrogen oxides.

SO_2 is also obtained commercially from metal sulfide ores by roasting in fluidized bed furnaces (equation 11). The reaction is carried out at 650–1100 °C, with the resultant SO_2 being filtered electrostatically to remove ash and then freed of As_2O_3 impurities before being used in the preparation of SO_3.

$$2FeS_2 + 5.5O_2 \longrightarrow Fe_2O_3 + 4SO_2 \qquad (11)$$

Sulfur dioxide is converted to SO_3 and ultimately to sulfuric acid using the double contact process, which is based upon the equilibrium between SO_2 and SO_3 (equation 12).

$$SO_2 + \tfrac{1}{2}O_2 \longrightarrow SO_3 \quad \Delta H = -99.0\ \text{kJ mol}^{-1} \qquad (12)$$

The equilibrium is slow except in the presence of a catalyst. Typically, vanadium catalysts, which consist of $VO(SO_4)$ supported on kieselguhr, are used to push the equilibrium to the right-hand side. Since the equilibrium shifts in favor of the starting materials with increasing temperature, as low a temperature as possible (ca. 425 °C) is employed, together with continuous removal of the SO_3 by absorption into sulfuric acid. The overall production of sulfuric acid from sulfur is very exothermic, and the energy produced is usually converted into superheated steam.

3.1.2 *Physical Properties, Molecular Structure, and Bonding*

SO_2 is a poisonous, colorless gas with a sharp odor (Table 8); it condenses (−10 °C) to give a colorless liquid and ultimately (ca. −76 °C) white crystals. It has a bent structure (S–O bond length 143.2 pm, O–S–O ca. 119.5° in the gas phase), and is dipolar (1.62 D). It is believed to be only slightly associated in the liquid state, and adopts an orthorhombic form as a solid. The bond lengths and angle in the solid agree well with those determined for the gas by microwave spectroscopy and electron diffraction. Valence bond and molecular orbital calculations agree with the observed bond length, being somewhat shorter than a simple S=O double bond. Vibrational spectroscopy reveals the three expected IR and Raman fundamental vibrations, and force constant calculations suggest a bond order of ca. 1.93.

3.1.3 *Reactions of SO_2 with Main Group Species*

The oxidation of SO_2 to SO_3 (equation 12) is undoubtedly the most important commercially, but there is also quite a large chemistry of SO_2 that merits mention (Figure 13).

With chlorine or fluorine, SO_2X_2 is obtained while I_2 and liquid SO_2 form a weak complex in which SO_2 acts as a Lewis acid. Larger mixed S–O–X species may also be formed (equation 13).

$$S_2O_6F_2 + SO_2 \longrightarrow S_3O_8F_2 \qquad (13)$$

Table 8 Physical properties of sulfur dioxide

(a) Gaseous Property	Temp. (°C)	Value
Melting point	−75.48	−75.48 °C(1.256 Torr)
Boiling point	−10.02	−10.02 °C
Enthalpy of melting	−75.48	1.769 kcal mol^{-1}
Enthalpy of vaporization	−10.02	5.955 kcal mol^{-1}
Standard entropy	25	59.40 cal deg^{-1} mol^{-1}
Molar heat	25	9.51 cal deg^{-1} mol^{-1}
Critical temperature	157.5	–
Critical pressure	–	77.7 atm
Critical density	–	0.51 g cm^{-3}
Vapor density	0/760 Torr	2.2630 (air = 1)
Weight per liter	0/760 Torr	2.9266 g
(b) Liquid Property	**Temp. (°C)**	**Value**
Freezing point	−72.45	−72.45 °C
Density	−10	1.46 g cm^{-3}
	0	1.435 g cm^{-3}
Specific heat	0 to 40	0.3254 cal g^{-1} deg^{-1}
Specific conductivity	−65 to 0	10^{-7} ohm^{-1} cm^{-1}
Vapor pressure	0	1163 Torr (1.52 atm)
Dipole moment	25	1.16 D
Ebullioscopic constant	–	1.45 deg mol^{-1}
Trouton constant	–	30.15 cal deg^{-1} mol^{-1}
Dielectric constant	−16.5	17.27

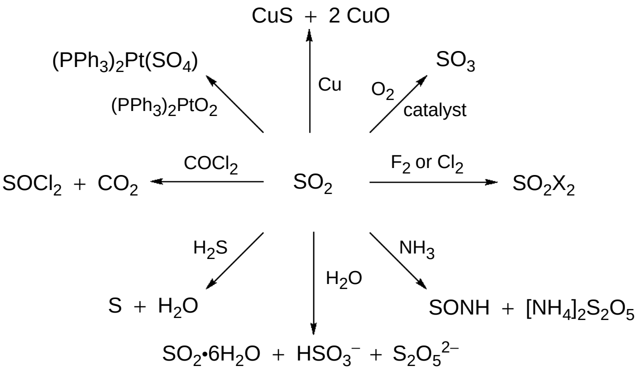

Figure 13 Reactions of SO_2

SO_2 is reduced by carbon at 350 °C to give sulfur, and by hydrogen (catalytically) to give H_2S and sulfur. Hydrogen sulfide also reduces SO_2 at high temperature (300 °C), as mentioned above in the Claus process. SO_2 is oxidized by $HClO_3$ to give sulfuric acid and ClO_2, and may be oxidized to $SOCl_2$ using PCl_5.

SO_2 dissolves in water to give ‘sulfurous acid’, which according to Raman spectroscopy contains large amounts of solvated SO_2 as well as $HSO_3{}^-$, H_3O^+, and $S_2O_5{}^{2-}$. With ammonia and amines, quite complex reactions, which are not fully understood, occur. In the gas phase, ammonia and SO_2 react according to equation (14).

$$3SO_2 + 3NH_3 \longrightarrow SONH + [NH_4]_2[S_2O_5] \qquad (14)$$

In solution, tertiary amines and SO_2 give simple complexes, with the SO_2 behaving as a Lewis acid. Hydrogen halides also react to form complexes of the formula $SO_2{\cdot}HX$, although it is thought that these are simple dipolar adducts.

SO_2 is oxidized by nitric oxides, as exemplified in the Lead Chamber Process (equation 15). This process is only operated in special cases nowadays, because of the low final acid concentration that is achievable (no more than 78%), although it only requires modest temperatures and so may be utilized again in the future.

$$SO_2 + 2NOHSO_4 + 2H_2O \longrightarrow 3H_2SO_4 + 2NO \qquad (15)$$

3.1.4 *Reactions of SO_2 with Metals and Metal Complexes*

The gas reacts with metals (As, Sb, Mg, Zn, Cd, Tl, Pb, Mn, Ni, Co, Ag, etc.) reductively to give metal sulfides and metal oxides, although secondary reactions often lead to sulfates or sulfur formation.

In aqueous solution, SO_2 is reduced to dithionite by a range of metals or sodium hydride. With metal halides, SO_2 forms complexes and may behave as an electron donor (e.g. with $AlCl_3$, $SnBr_4$, or $TiCl_4$) or undergo solvolysis (equation 16)

$$VF_5 + SO_2 \longrightarrow VOF_3 + SOF_2 \qquad (16)$$

or with alkali metal halides with formation of fluorosulfites, MSO_2F.

Sulfur dioxide was first obtained as a coordinated ligand by a hydroxide abstraction reaction of a bisulfite complex (equation 17) in 1936.[35]

$$[Ru(NH_3)_5(SO_3H)]^{-} \longrightarrow [Ru(NH_3)_5SO_2]^{2-} \qquad (17)$$

Subsequently, an enormous range of complexes of SO_2 has been prepared (mostly by simple displacement reactions of labile ligands) and it has been suggested that SO_2 displays one of the most extensive ranges of coordination mode for any ligand. Some examples of SO_2 coordination modes are given in Figure 14. The orbitals involved in the two most common modes are illustrated in Figure 15. The area has been reviewed;[36,37] organometallic aspects, especially involving migratory reactions (e.g. Figure 16), have been of particular interest in recent times.[38] There has also been substantial interest in the synthesis of analogs of SO_2 and Figure 14 illustrates some of these; the electronic factors influencing the stability of the various analogs have been discussed. In general, the replacement of one oxo group does not lead to major geometric changes, but the energies of the orbitals capable of donating to metal centers go up on replacement of the oxygen atom by other groups (Figure 17). For example, for HNSO and HNSNH, the nitrogen

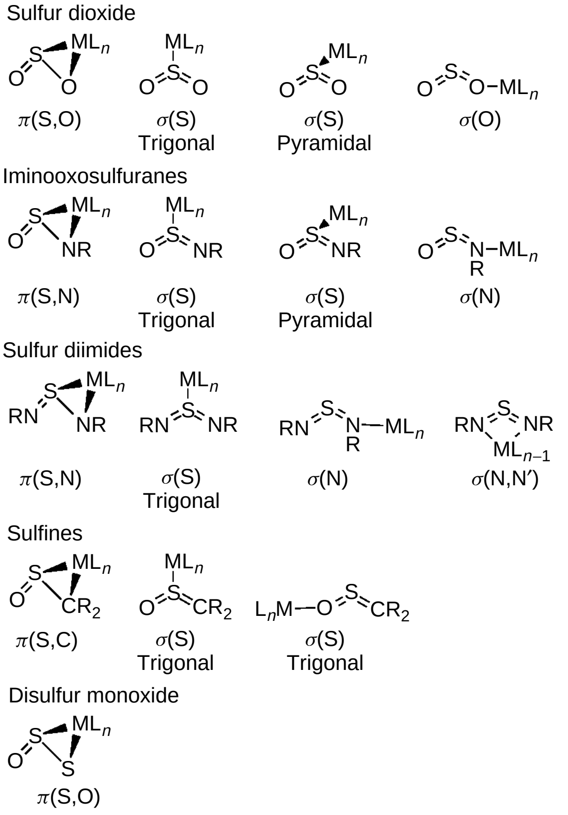
Sulfur dioxide
π(S,O)
σ(S) Trigonal
σ(S) Pyramidal
σ(O)
Iminooxosulfuranes
π(S,N)
σ(S) Trigonal
σ(S) Pyramidal
σ(N)
Sulfur diimides
π(S,N)
σ(S) Trigonal
σ(N)
σ(N,N′)
Sulfines
π(S,C)
σ(S) Trigonal
σ(S) Trigonal
Disulfur monoxide
π(S,O)

Figure 14 Coordination modes of SO_2 and related ligands

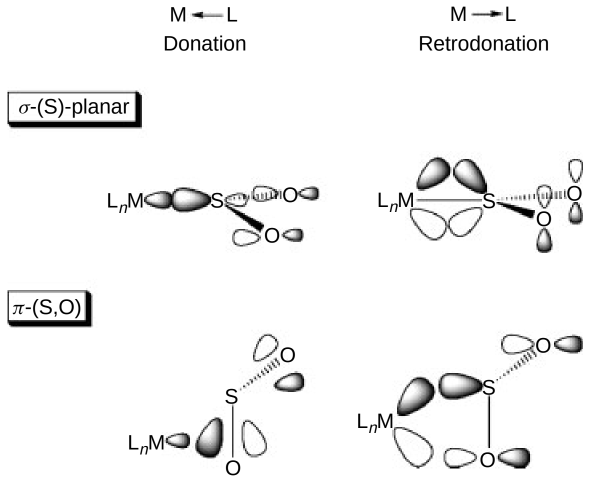
M ← L
Donation
M → L
Retrodonation
σ-(S)-planar
π-(S,O)
LnM
S
O

Figure 15 Orbitals involved in SO_2 coordination

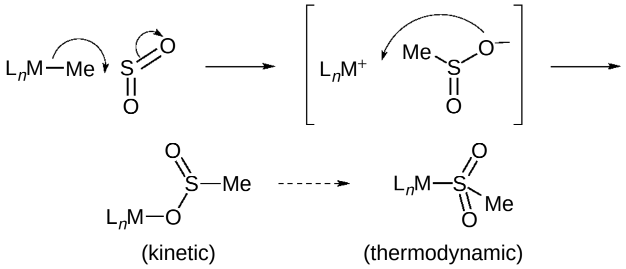
LnM—Me
LnM+
(kinetic)
(thermodynamic)

Figure 16 Mechanism for the insertion of SO_2 into transition metal alkyls

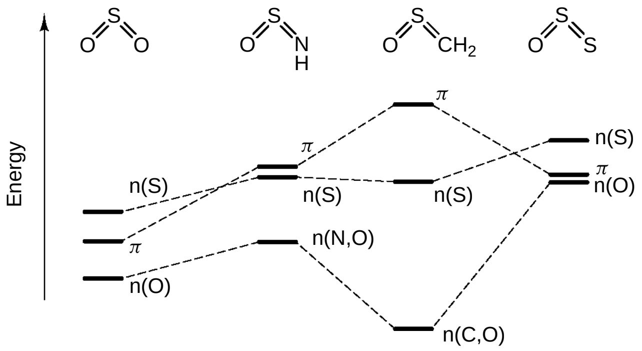
Energy
n(S)
π
n(O)
n(N,O)
n(C,O)
CH2

Figure 17 MO scheme for SO_2 and analogs

lone pair is more nucleophilic than the equivalent orbitals on oxygen.

3.2 Liquid SO_2 as a Solvent

Liquid SO_2 (Table 8) dissolves many inorganic and organic compounds;[39] generally, covalent compounds are the most soluble since the dielectric constant of SO_2 is much lower than that of water or ammonia. Although poisonous, SO_2 as the liquid may be handled without great difficulty using glassware equipped with rotary PTFE taps. It has been extensively used as a solvent for the preparation of group 16 cations[40] and S–N cations, as well as for the preparation of $(SN)_x$.[41]

3.3 Environmental Problems and SO_2

There is currently great concern about the environmental effects of airborne sulfur dioxide.[42–44] Although SO_2 is released into the atmosphere from natural sources such as volcanoes, the majority (ca. 200 million tonnes per year) is man-made either from industrial processes or domestic use such as coal and oil burning. The long-term consequences of large-scale release of SO_2 into the atmosphere are undoubtedly severe, and have been the subject of much public debate. The most objectionable aspect of the problem is that often the 'acid rain', which results from SO_2, occurs hundreds of miles from the source.

In the future, it seems likely that most processes that currently entail the discharge of SO_2 will have to be adapted with the introduction of 'scrubbers'. Two main methods can be employed for this: either the reduction of SO_2 to sulfur using the Claus process or, alternatively, neutralization using 'milk of lime' (equation 18) to give either calcium sulfite or, with complete oxidation, calcium sulfate (gypsum).

$$\begin{aligned} SO_2 + Ca(OH)_2 &\longrightarrow CaSO_3\cdot\tfrac{1}{2}H_2O + \tfrac{1}{2}H_2O \\ SO_2 + Ca(OH)_2 + \tfrac{1}{2}O_2 + H_2O &\longrightarrow CaSO_4\cdot 2H_2O \end{aligned} \tag{18}$$

Unfortunately, the gypsum produced by the latter process is inferior to natural gypsum and cannot be used as a substitute in all cases.

3.4 Sulfur Trioxide

3.4.1 *Commercial Preparation and Significance*

The commercial significance of SO_3 for the preparation of sulfuric acid has already been mentioned, and this is the most important aspect of its industrial chemistry. However, substantial amounts of pure SO_3 are prepared commercially for use in the manufacture of, for example, chloro- and fluorosulfonic acids, thionyl chloride, and as a sulfonating agent. Pure, liquid SO_3 is obtained industrially by distillation from oleum.

3.4.2 *Physical Properties, Molecular Structure, and Bonding*

Sulfur trioxide exists in at least three different solid modifications, as well as a liquid and a gas (Figure 18).

In the gas phase,[45] the molecule is mainly monomeric; it is trigonal planar (D_{3h}) with three equivalent bond lengths (ca. 1.43 Å from microwave spectroscopy), with a bond order that is formally greater than 2.

Liquid SO_3 may be prepared in the laboratory by a similar method to the industrial process. When completely dry, it remains as a liquid for many months but traces of water (as low as 10^{-3} mol%) catalyze the polymerization to β-SO_3. In the liquid, the monomeric[46] species is in equilibrium with a trimer, S_3O_9, which has a similar, nonplanar, structure to the trimer in γ-SO_3.

Three reasonably well-defined modifications of solid SO_3 exist. γ-SO_3, which is often described as 'ice-like', is orthorhombic[47] and consists of cyclic trimers with traces of monomeric SO_3 included. With even traces of water, γ-SO_3 or liquid SO_3 polymerize to give glistening needles of monoclinic β-SO_3.[48] This modification is believed to consist of a mixture of different chain length polymers; if warmed, it melts with depolymerization between 32–45 °C. α-SO_3 has a higher melting point than the other solid forms and consists of higher polymers, almost certainly in a layer structure.

3.4.3 *Reactions of Sulfur Trioxide*

Sulfur trioxide is extremely reactive, behaving as a powerful oxidant and Lewis acid. Indeed, many of its reactions involve initial adduct formation followed by rearrangement. We have already discussed the formation of sulfuric acid, and other typical reactions are shown in Figure 19. Chloro- and fluorosulfonic acids (XSO_3H) are used as mild chlorinating and fluorinating agents and, in the case of the latter, for polishing lead crystal.

3.5 Other Sulfur Oxides

3.5.1 *Lower Oxides*

Cyclic sulfur oxides S_nO ($n = 6$, 8, 9 10) are normally prepared by oxidation of their parent sulfur rings using peroxyfluoroacetic acid (equations 8 and 9) in an inert solvent

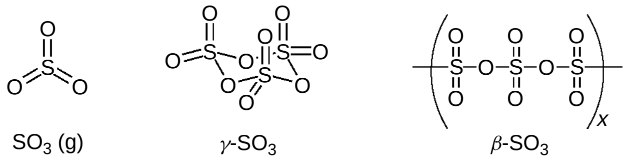

Figure 18 Modifications of SO_3

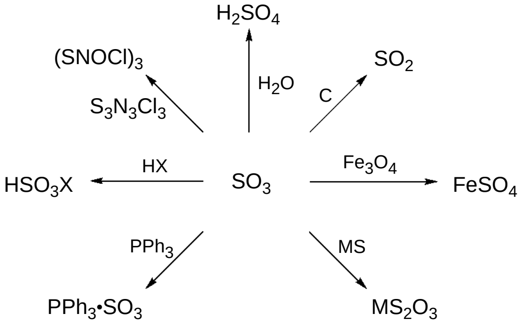
H_2SO_4
$(SNOCl)_3$
SO_2
$S_3N_3Cl_3$
H_2O
C
HX
Fe_3O_4
HSO_3X
SO_3
$FeSO_4$
PPh_3
MS
$PPh_3{\cdot}SO_3$
MS_2O_3

Figure 19 Reactions of SO_3

such as CS_2 or CH_2Cl_2, although in some cases the dioxide (e.g. S_7O_2) may also be obtained. S_8O has also been prepared by the reaction of thionyl chloride with H_2S_7 at −40 °C (equation 19).

$$SOCl_2 + H_2S_7 \longrightarrow S_8O + 2HCl \qquad (19)$$

The compounds whose structures are shown in Figure 4 are orange or dark yellow and decompose at, or around, room temperature to give sulfur and sulfur dioxide.

There are very few reactions known for S_nO species, although adducts with Lewis acids ($SnCl_4$, $SbCl_5$) have been prepared.[49] The structure of $[SnCl_4(S_8O)_2]$ is a distorted octahedral arrangement of four chlorine and two oxygen coordinated *cis*-S_8O ligands.[50]

Sulfur monoxide, obtained by the reaction of SO_2 and sulfur, has been observed in the gas phase but is very short lived.[51] S_2O_2 has a slightly longer lifetime (half-life a few seconds) and mixtures of both gases may be obtained by subjecting SO_2 to a microwave discharge. S_2O is one of the decomposition products of SO and may also be prepared by a number of other routes,[52] such as burning sulfur in low pressure of oxygen or passing SO_2 through a high voltage discharge.

SO, S_2O, and S_2O_2 are stabilized as ligands in metal complexes. The coordination chemistry of SO and S_2O has been developed by preparations that involve formation of the ligand from suitable precursor complexes. The most common method involves oxidation of a coordinated S_n ligand. The first example of an S_2O complex was reported by Schmidt and Ritter[53] and subsequently refined by Rauchfuss[54] (Figure 20), and extended to the corresponding S_2O_2 complex. A dinuclear complex of S_2O has been isolated. SO complexes may also be obtained by the reaction of thionyl chloride, *trans*-stilbene episulfoxide, or thiirane *S*-oxide with metal complexes.

The oxidation of S_2 complexes is a somewhat limited approach, and a more general route[55] may be the nucleophilic attack of H_2S upon iminooxosulfurane complexes, which has been developed by analogy with the equivalent hydrolysis reactions (Figure 21 and 22).

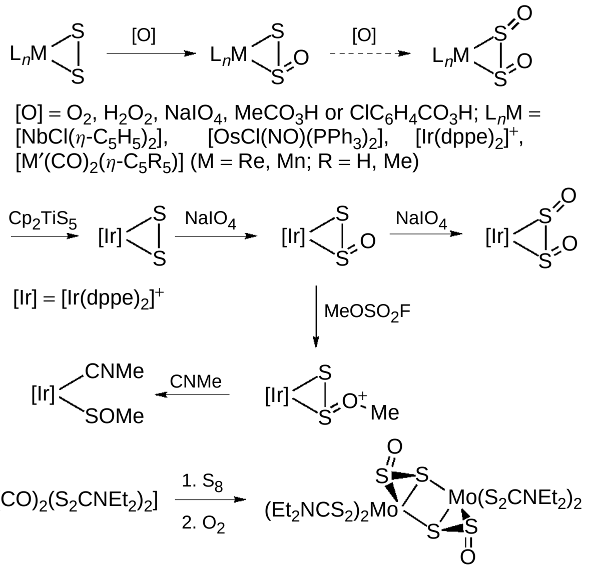
L_nM
[O]
[O]
[Ir]
Cp_2TiS_5
$NaIO_4$
$NaIO_4$
$MeOSO_2F$
CNMe
[Ir] = $[Ir(dppe)_2]^+$
$[Mo(CO)_2(S_2CNEt_2)_2]$
1. S_8
2. O_2
$(Et_2NCS_2)_2Mo$
$Mo(S_2CNEt_2)_2$

[O] = O_2, H_2O_2, $NaIO_4$, $MeCO_3H$ or $ClC_6H_4CO_3H$; L_nM = $[NbCl(\eta\text{-}C_5H_5)_2]$, $[OsCl(NO)(PPh_3)_2]$, $[Ir(dppe)_2]^+$, $[M'(CO)_2(\eta\text{-}C_5R_5)]$ (M = Re, Mn; R = H, Me)

Figure 20 Preparative routes to S_2O and S_2O_2 complexes

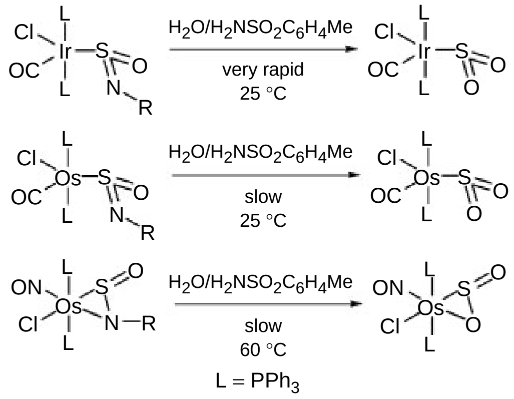
$H_2O/H_2NSO_2C_6H_4Me$
very rapid
25 °C
$H_2O/H_2NSO_2C_6H_4Me$
slow
25 °C
$H_2O/H_2NSO_2C_6H_4Me$
slow
60 °C
L = PPh_3

Figure 21 Reactions of iminooxosulfuranes with H_2O

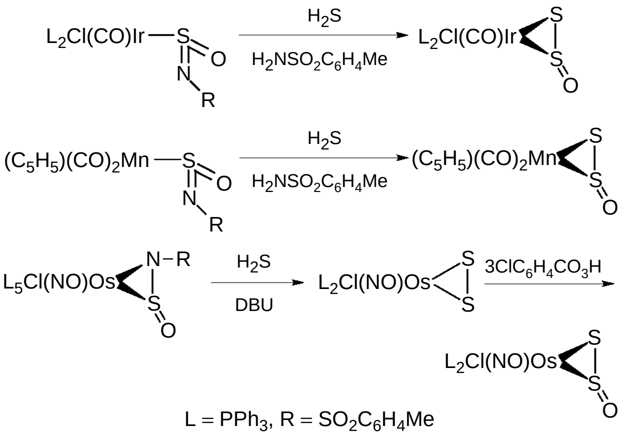
$L_2Cl(CO)Ir$
H_2S
$H_2NSO_2C_6H_4Me$
$(C_5H_5)(CO)_2Mn$
H_2S
$H_2NSO_2C_6H_4Me$
$L_5Cl(NO)Os$
H_2S
DBU
$L_2Cl(NO)Os$
$3ClC_6H_4CO_3H$
L = PPh_3, R = $SO_2C_6H_4Me$

Figure 22 Reactions of iminooxosulfuranes with H_2S

The chemistry of coordinated S_2O has yet to be studied in any real detail. Simple oxidation or reduction to coordinated S_2O_2 or S_2 is known. The bulk of the information is derived from the reactions of $[Ir(dppe)_2(S_2O)]^+$.[54] Reaction with PPh_3 gives phosphine oxide and phosphine sulfide, together with $[Ir(dppe)]^+$; the initial reactivity suggests that the exocyclic sulfur atom is the most electrophilic. Alkylation at this sulfur atom gives $[Ir(SSOMe)_2(dppe)_2]^{2+}$.

SO can coordinate in a number of modes;[56] apart from simple σ donation (bent), it may bridge two or three metal centers (via sulfur) and there is one example of a fully characterized edge-on bridging mode. From X-ray crystal structural studies[57] it appears that the coordinated S_2O ligand behaves as a π-acid, as it has a substantially lengthened S–S bond compared to the free S_2O.

3.5.2 Higher Oxides

A number of higher, polymeric oxides are known. In general, these are structurally related to β-SO_3 by random substitution of oxo bridges by peroxo bridges. Monomeric SO_4 has been studied by matrix isolation and is believed to have an O_2SOO (peroxo) structure.

3.6 Oxoacids

3.6.1 Sulfuric Acid and Sulfates

The oxoacids of sulfur are summarized in Table 9.

Industrially, sulfuric acid remains an extremely important material; world production is estimated at ca. 150 × 10^6

Table 9 The common oxoacids of sulfur

Formula	Name	Ox. states	Schematic structure[a]	Salt
H_2SO_4	Sulfuric	VI	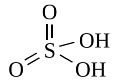	Sulfate, SO_4^{2-}; H-sulfate, $HOSO_3^-$
$H_2S_2O_7$	Disulfuric	VI	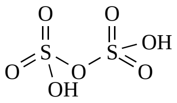	Disulfate, $O_3SOSO_3^{2-}$
$H_2S_2O_3$	Thiosulfuric	IV, 0, (or VI, -II)	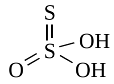	Thiosulfate, SSO_3^{2-}
H_2SO_5	Peroxomonosulfuric	VI	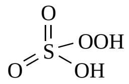	Peroxomonosulfate, $OOSO_3^{2-}$
$H_2S_2O_8$	Peroxydisulfuric	VI	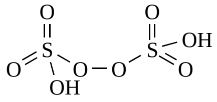	Peroxydisulfate, $O_3SOOSO_3^{2-}$
$H_2S_2O_6$	Dithionic[a]	V	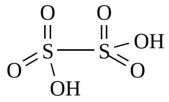	Dithionate, $O_3SSO_3^{2-}$
$H_2S_{n+2}O_6$	Polythionic	V, 0	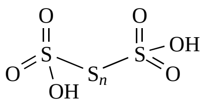	Polythionate, $O_3S(S)_nSO_3^{2-}$
H_2SO_3	Sulfurous[a]	IV	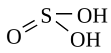	Sulfite, SO_3^{2-}; H-sulfite, $HOSO_2^-$
$H_2S_2O_5$	Disulfurous[a]	V, III	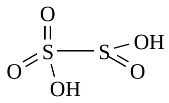	Disulfite, $O_3SSO_2^{2-}$
$H_2S_2O_4$	Dithionous[a]	III	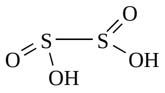	Dithionite, $O_2SSO_2^{2-}$

[a] Acids only exist as salts.

tonnes per year. The majority of this acid is prepared from SO_2, but increasingly, because of environmental considerations, sulfuric acid is recycled. If the levels of impurities are low, the acid is evaporated in stages to the appropriate concentration and any organic impurities destroyed by oxidation. Alternatively, if the acid is heavily contaminated, it is concentrated and thermally decomposed (to H_2O, SO_2, and O_2) under oxidative or reductive conditions, depending on the nature of the impurities. Oxidative processes have the advantage that they liberate CO_2. Metal sulfates also provide a source of sulfuric acid. For example, gypsum or calcium sulfate (from the manufacture of phosphoric acid) can be reacted with coal; the calcium oxide is utilized for the manufacture of Portland cement (equation 20).

$$4CaSO_4 + 2C \longrightarrow 4CaO + 4SO_2 + 2CO_2 \qquad (20)$$

Alternatively, sulfuric acid can be prepared from the iron(II) sulfate waste, which is obtained during the manufacture of TiO_2 (equation 21).

$$2FeSO_4{\cdot}7H_2O \longrightarrow Fe_2O_3 + 2SO_2 + \tfrac{1}{2}O_2 + 14H_2O \qquad (21)$$

Commercially, sulfuric acid has many important applications (Figure 23). The largest proportion is used in the manufacture of phosphorus and nitrogen based fertilizers. It is also used in the manufacture of inorganic sulfates, HF, B_2O_3, and a range of organic compounds, as well as in the petrochemical industry for the refining of raw paraffin.

Anhydrous sulfuric acid (Table 10) has a very high dielectric constant and electrical conductivity as a consequence of autoionization (equations 22 and 23), which occurs via two different equilibria.

$$2H_2SO_4 = H_3SO_4^+ + HSO_4^- \qquad (22)$$

$$2H_2SO_4 = H_3O^+ + HS_2O_7^- \qquad (23)$$

For equation (22), the equilibrium constant is ca. 3×10^{-4}, which is 10^{10} greater than the analogous reaction for water, and comparable with anhydrous H_3PO_4. Equation (23) can be considered as 'self-dehydration', and involves dissociation of the acid to H_2O and SO_3 with subsequent reaction of SO_3 and HSO_4^-. From these comments, it is clear that sulfuric acid is a complex mixture of species in equilibrium.

Table 10 Properties of sulfuric acid

Freezing point	10.371 °C
Boiling point	290–317 °C
Viscosity (25 °C)	24.54 cP
Density (d^{25}, 25 °C)	1.8269 g cm^{-3}
Dielectric constant (25 °C)	100
Specific conductance (25 °C)	1.0439×10^{-2} ohm^{-1} cm^{-1}
Heat capacity (25 °C)	0.3373 cal deg^{-1} g^{-1}
Heat of fusion (10.37 °C)	2560 cal mol^{-1}

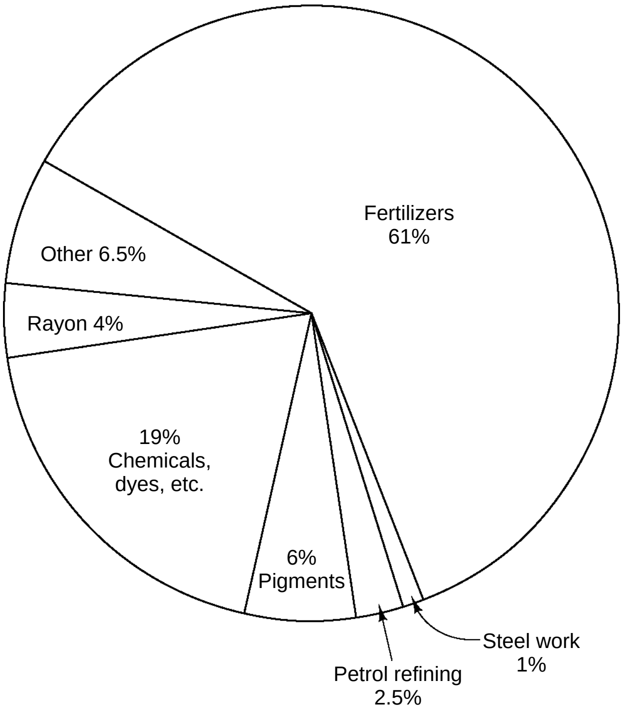

Figure 23 Uses of H_2SO_4

Aqueous sulfuric acid behaves as a strong acid in most systems and forms salts with most metals by a variety of routes, such as reaction of the acid with the metal, neutralization of a metal oxide or hydroxide, or decomposition of metal carbonates. In organic synthesis, it is most well known for its use with nitric acid as a reagent for the nitration of aromatics (equation 24) via the NO_2^+ cation.

$$2H_2SO_4 + HNO_3 \longrightarrow NO_2^+ + H_3O^+ + 2HSO_4^- \qquad (24)$$

Many metal sulfates are known, and often exist in Nature. Apart from gypsum ($CaSO_4$), Epsom salts ($MgSO_4{\cdot}7H_2O$) are a common feature of many households and were recommended by Mrs Beeton's book of household management for the treatment of constipation and as bath salts! The sulfate ion is tetrahedral and has a large coordination chemistry, forming monodentate (O coordinated) and bidentate (O,O′chelating or O,O′ bridging) complexes that have characteristic vibrational spectra.[58]

3.6.2 *Sulfurous Acid*

H_2SO_3 exists in trace amounts in aqueous solutions of SO_2 but has never been isolated. However, sulfites are well known and usually stable. Sodium sulfite is used extensively commercially. It is obtained by reacting SO_2 with NaOH

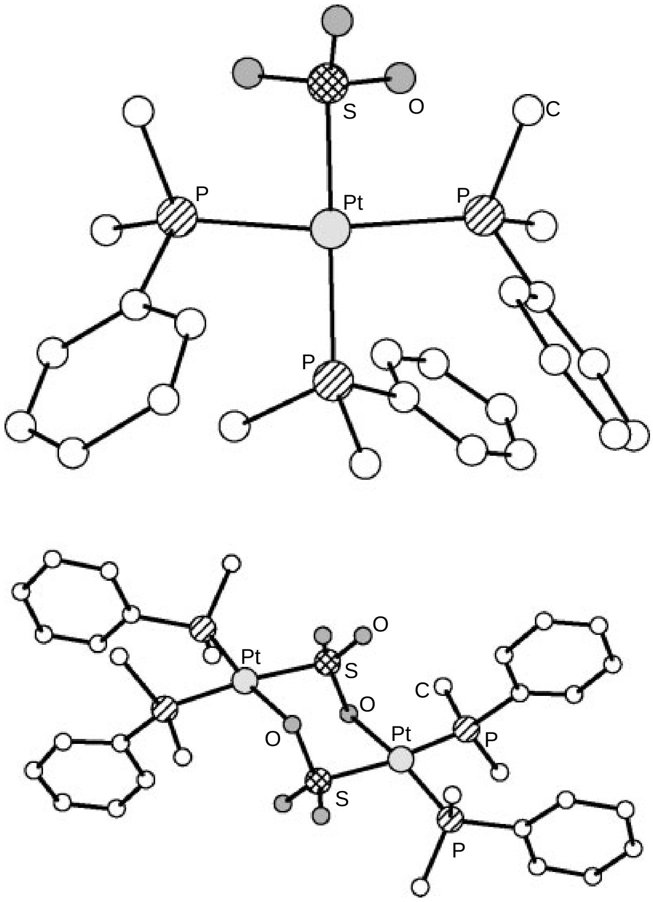

Figure 24 Monodentate and bridging SO_3^{2-} complexes[59]

and is used as a reducing agent in photography, for the preservation of foods, the treatment of boiler water, and in the textiles and paper industry. The sulfite ion is pyramidal and displays a number of coordination modes. Interestingly, apart from monodentate coordination through sulfur, and bidentate coordination through two oxygen atoms, dinuclear compounds with S=O coordination have recently been characterized (Figure 24).[59] Protonation of sulfite to give HSO_3^- appears to occur at the sulfur rather than at an oxygen atom. The sulfite and bisulfite anions are both moderately strong reducing agents, as exemplified by the well-known reaction (equation 25) used in volumetric analysis.

$$HSO_3^- + I_2 + H_2O \longrightarrow HSO_4^- + 2H^+ + 2I^- \qquad (25)$$

3.6.3 Thiosulfuric Acid

Anhydrous thiosulfuric acid may be obtained, at low temperatures, by a number of routes (equations 26 and 27), but attempts to prepare the aqueous acid by acidification of metal thiosulfates invariably fail as a result of the rapid decomposition of the acid by water.

$$Na_2S_2O_3 + 2HCl \xrightarrow{Et_2O/-78\,^\circ C} 2NaCl + H_2S_2O_3{\cdot}2Et_2O \qquad (26)$$

$$HSO_3Cl + H_2S \longrightarrow HCl + H_2S_2O_3 \qquad (27)$$

Stable thiosulfates can be obtained by a number of routes, such as addition of sulfur to a sulfite (equation 28), or the reduction of sulfides (equation 29).

$$\underset{(\text{or } NH_4^+)}{Na_2SO_3} + S \longrightarrow Na_2SO_4 \qquad (28)$$

$$2Na_2S + Na_2CO_3 + 4SO_2 \longrightarrow 3Na_2S_2O_3 + CO_2 \qquad (29)$$

The thiosulfate anion is structurally very similar to sulfate and has a range of coordination modes (Figure 25). Two examples of S-bonded thiosulfate complexes[60] are shown in Figure 26 and 27, and the substitution chemistry of $[OsO_2(S_2O_3)_2]^{2-}$ is summarized in Figure 28. Thiosulfates have a diverse range of applications. Both sodium and

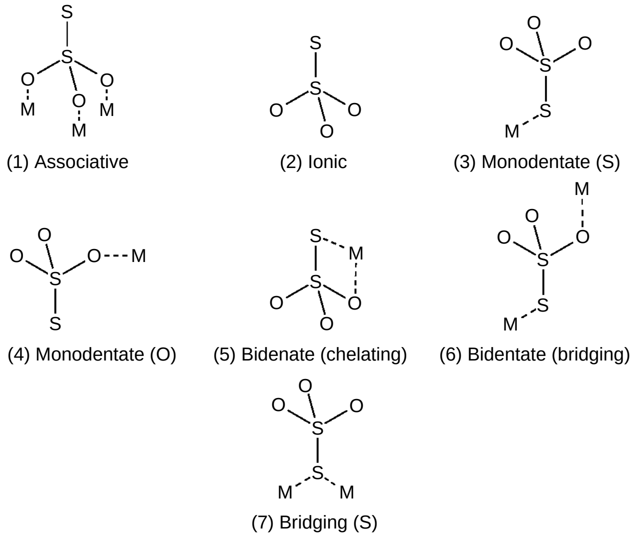

(1) Associative (2) Ionic (3) Monodentate (S)

(4) Monodentate (O) (5) Bidenate (chelating) (6) Bidentate (bridging)

(7) Bridging (S)

Figure 25 Modes of coordination of $S_2O_3^{2-}$

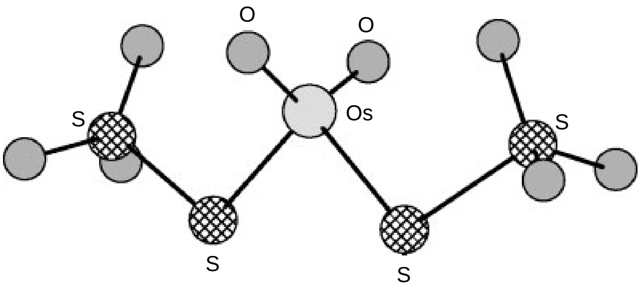

Figure 26 The X-ray crystal structure[60] of $[OsO_2(S_2O_3)_2]^{2-}$

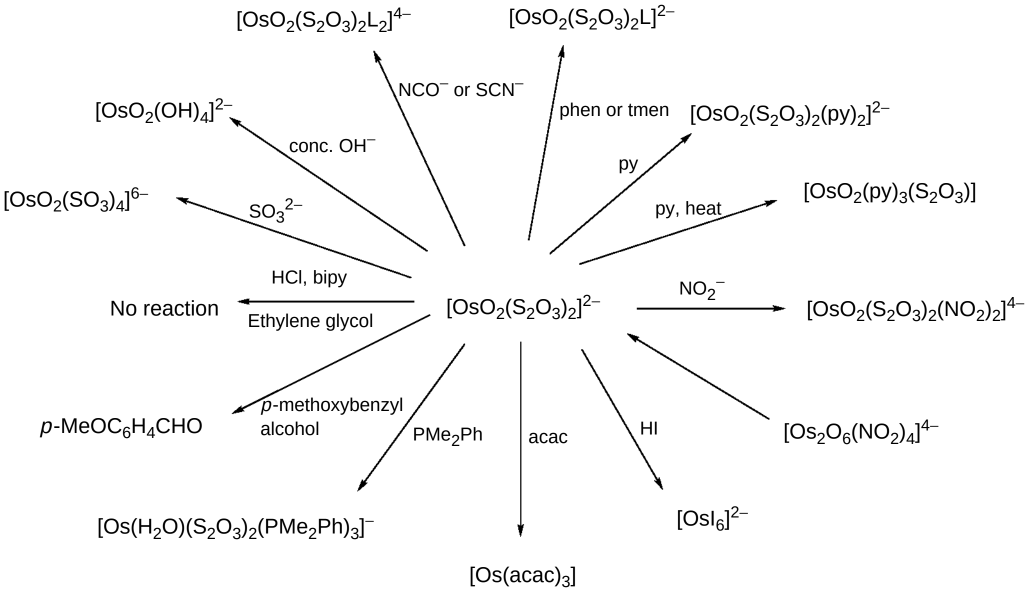
$[OsO_2(S_2O_3)_2L_2]^{4-}$
$[OsO_2(S_2O_3)_2L]^{2-}$
NCO^- or SCN^-
phen or tmen
$[OsO_2(OH)_4]^{2-}$
conc. OH^-
$[OsO_2(S_2O_3)_2(py)_2]^{2-}$
py
$[OsO_2(SO_3)_4]^{6-}$
SO_3^{2-}
py, heat
$[OsO_2(py)_3(S_2O_3)]$
HCl, bipy
No reaction
Ethylene glycol
$[OsO_2(S_2O_3)_2]^{2-}$
NO_2^-
$[OsO_2(S_2O_3)_2(NO_2)_2]^{4-}$
p-$MeOC_6H_4CHO$
p-methoxybenzyl alcohol
PMe_2Ph
acac
HI
$[Os_2O_6(NO_2)_4]^{4-}$
$[Os(H_2O)(S_2O_3)_2(PMe_2Ph)_3]^-$
$[OsI_6]^{2-}$
$[Os(acac)_3]$

Figure 28 Reactions of $[OsO_2(S_2O_3)_2]^{2-}$

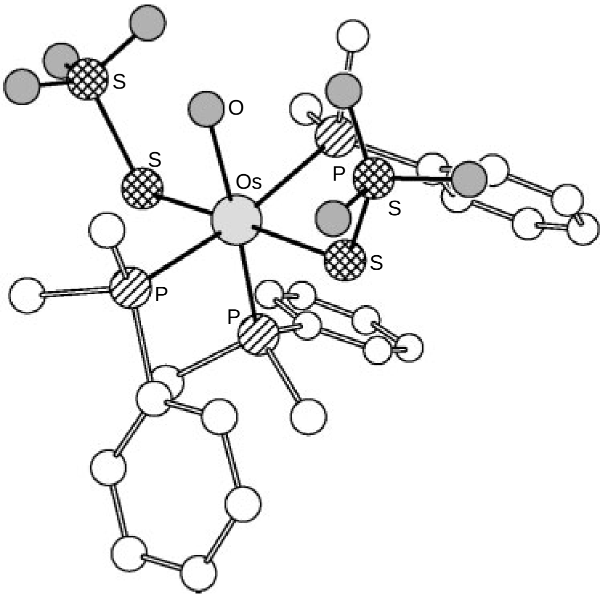
S
O
S
Os
P
S
S
P
P

Figure 27 The X-ray crystal structure[61] of $[OsO_2(H_2O)(S_2O_3)_2(PMe_2Ph)_3]^-$

ammonium thiosulfate are used for removing AgBr (fixing) in photography, although the ammonium salt has the advantage of shorter fixing and washing times. Silver thiosulfates may be used as flower preservatives and to inhibit ripening of fruit (it is believed that the thiosulfate disrupts the ethylene action that causes the onset of ripening). Sodium thiosulfate is also used to destroy excess chlorine in the bleaching industry, where it behaves as a moderate reducing agent (equation 30). The structure of the $[SeSO_3]^{2-}$ anion was recently determined with a central sulfur atom bound to the three oxygens and a selenium with a S-Se distance of 217 pm[61] Gold and silver thiosulfates are well-established materials for the treatment of arthritis, although the mechanism of action is not well understood.[62]

$$S_2O_3{}^{2-} + 4Cl_2 + 5H_2O \longrightarrow 2HSO_4{}^- + 8H^+ + 8Cl^- \qquad (30)$$

3.6.4 *Other Oxoacids*

There are a range of S–O acids that contain S–S bonds, reflecting in part the variety of oxidation states available to sulfur.

Dithionic acid, $H_2S_2O_6$, can be obtained in quite concentrated aqueous solutions (equation 31) from barium dithionate. The metal dithionates are usually obtained by oxidizing the corresponding sulfite or metathesis.

$$BaS_2O_6 + H_2SO_4 \longrightarrow H_2S_2O_6 + BaSO_4 \qquad (31)$$

Sodium dithionite, $Na_2S_2O_4$, is well known and used as a reducing agent. Like dithionate, it may be obtained from the sulfite, although commercially dithionites are usually prepared from SO_2 (equations 32 and 33). Dithionous acid is unknown.

$$Zn + 2SO_2 \longrightarrow ZnS_2O_4 \qquad (32)$$

$$HCOONa + 2SO_2 + NaOH \longrightarrow Na_2S_2O_4 + CO_2 + H_2O \qquad (33)$$

Although the dithionate anion usually adopts a staggered conformation, the dithionite anion has an eclipsed structure; they have quite different S–S bond lengths (215 vs. 239 pm).

Dithionite solutions display EPR signals, suggesting the presence of a monomer (radical) $\rightleftharpoons$ dimer equilibrium in solution. Dithionites are strong reducing agents and find applications in dyeing/printing, and in the precipitation of metals. In addition, sodium dithionite is used in the preparation of $HOCH_2SO_2Na$ (sodium hydroxymethanesulfinate), which is also used on a large scale in printing.

Apart from the well-known S–O anions mentioned above, there is a developing chemistry of the salts of the so-called polythionic acids, $H_2S_nO_6$. Some structures and synthetic routes to these species are shown in Figure 29 and 30. This is a complex, but fascinating, area that illustrates the difficulty of characterizing main group species. The original observations of the reactivity of SO_2 solutions with H_2S were made by Dalton, and systematically studied by Wackenroder in the 1840s, but it is only in relatively recent times that the structures of the various species have been elucidated. Further work is also now elucidating the synthetic routes and structures of complex mixed S/Se oxyanions such as $[Se(S_2O_3)_2]^{2-}$.[63]

There has recently been a report on the synthesis of the $[S_3O]^{2-}$ anion, obtained in the complex $[Pt(PPh3)_2(S_3O)]$ as a bidentate *S,S* complex – this complex may be important in the catalytic transformation of H_2S to sulfur.[64]

$$\begin{aligned}
MnO_2 + 2SO_2 &\longrightarrow MnS_2O_6\\
2KHSO_3 + SCl_2 &\longrightarrow K_2S_3O_6 + 2HCl\\
2H_2SO_3 + S_2Cl_2 &\longrightarrow H_2S_4O_6 + 2HCl\\
2S_2O_3^{2-} + I_2 &\longrightarrow S_4O_6^{2-} + 2I^-\\
2H_2S_2O_3 + SCl_2 &\longrightarrow H_2S_5O_6 + 2HCl\\
2H_2S_2O_3 + S_2Cl_2 &\longrightarrow H_2S_6O_6 + 2HCl
\end{aligned}$$

Figure 29 Preparative routes to polythionic acids

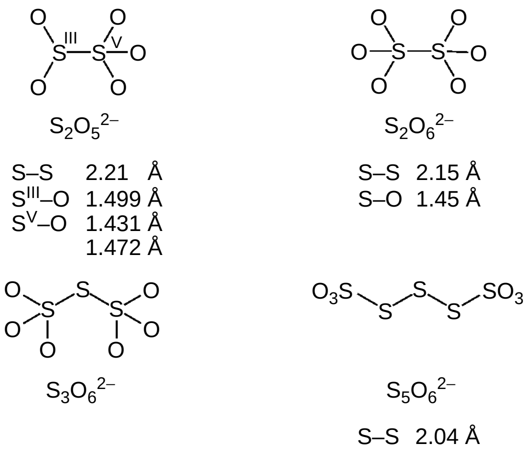

Figure 30 Structures of polythionic acids

4 SULFANES

4.1 Historical

The existence of the sulfanes has been recognized since the eighteenth century, both H_2S and 'persulfide of hydrogen' being studied; by the mid-nineteenth century, Thenard had shown that crude polysulfane solution was a mixture of variable composition.[65] In the early 1900s, significant progress was made with the separation, by vacuum distillation, of H_2S_2 and H_2S_3. Since 1940, very substantial progress has been made by Feher and coworkers, who have developed systematic preparative routes to a range of sulfanes and thoroughly characterized the compounds by a variety of physical techniques, including Raman spectroscopy. Notwithstanding these achievements, the polysulfanes remain a difficult group of compounds to prepare and separate pure and currently there is more work on polysulfides and metal complexes containing S_x^{2-} ligands than on the free acids.

4.2 Preparation

H_2S occurs in Nature, in small concentrations as a result of reduction of sulfate or sulfur-containing proteins by microorganisms. It is most prevalent in crude oil and natural gas, where the H_2S content can be as high as 10%.

Hydrogen sulfide is usually prepared by the acid hydrolysis of sulfides (e.g. using iron(II) sulfide and hydrochloric acid in the Kipps apparatus),[65] although industrially it is prepared by the reaction of hydrogen with molten sulfur at 350 °C in the presence of a catalyst. The higher sulfanes are not thermodynamically stable and are obtained by one of four routes.

Aqueous polysulfide solutions give, upon acidification, a crude oil that, from Raman spectroscopy,[66] contains a range of polysulfanes (H_2S_x, $x = 2-6$); $x = 2$ and 3 species are obtained from this oil by careful distillation/cracking of the mixture.[67] The products can then be purified further by fractional distillation.

Closely related to the above method is the formation of $x = 2-5$ species by the acidification of K_2S_x with formic acid under anhydrous conditions.[68] This nonaqueous method has the advantage of avoiding some of the side reactions associated with the aqueous route.

Crude polysulfanes with $x = 7-12$ can be obtained in up to 50% yield at the cathode by reduction of SO_2/H_2SO_4 solutions. The initial reaction product at the cathode is dithionous acid $H_2S_2O_4$, which decomposes in strong acid to give sulfurous acid and sulfane. Persulfate is obtained at the anode.

For sulfanes with $x > 6$, vacuum distillation is not practical and systematic condensation reactions at -50 °C developed by Feher and coworkers are used.[69] The most general form of the reaction is equation (34).

$$aH_2S_n + bS_mX_2 \longrightarrow (a-b)H_2S_x + 2bHX \qquad (34)$$

(where $x = (na + mb)/|(a - b)|$; $n = 1, 2, 3\ldots$; $m = 0, 1, 2, 3\ldots$; X = Cl, Br). When $a > b$ the reaction is used for the preparation of sulfanes, but when $b > a$ halosulfanes may be prepared, while if $a = b$, sulfur is formed. In a typical reaction, chain lengthening to give higher sulfanes can occur with a sequence illustrated in equation (35).

$$\begin{aligned} 2H_2S_2 + S_2Cl_2 &\longrightarrow H_2S_6 + 2HCl \\ 2H_2S_6 + S_2Cl_2 &\longrightarrow H_2S_{14} + 2HCl \end{aligned} \tag{35}$$

Assuming that the rates of reaction are comparable, it is possible to predict quite easily the relative proportions of different chain length sulfanes that will be obtained for any particular a/b ratio; and thus it is possible to prepare individual compounds in quite high purity.

4.3 Physical Properties and Molecular Structures

The physical properties of the polysulfanes are well defined (Table 11). Measurements of viscosity, molar volume, and density are convincing proof that the polysulfanes are a genuine homologous series. The molar volumes and densities increase in a simple additive way. The viscosities have been correlated with the square of the molecular weight, increasing with increasing molecular weight, although they do show a greater than predicted increase in mixtures of different chain lengths.

H_2S is bent in the gas, liquid, and solid state with H–S–H being 90° in the gas phase and 92.2° in the liquid phase; and H–S is 135 pm. The electronic spectra of sulfanes indicate some delocalization of electron density, probably by use of 3d orbitals; as chain length increases, the compounds exhibit deeper colors. In common with the homocyclic sulfur rings discussed in Section 2, Raman spectroscopy has proved to be extremely useful in the study of polysulfanes. Spectra have been reported for $x = 2-8$, and they are quite characteristic of chain length. The spectrum of H_2S_2 suggests that this compound has a structure similar to that of H_2O_2. The higher sulfanes exhibit hindered rotation about S–S bonds, and this leads to complex structures. Insight into the structures of polysulfanes can be gained by examination of the structures of the polysulfide anions.

Table 11 Physical properties of the sulfanes[a]

Sulfane	d^{20}	V	η^{20}	R
H_2S_2	1.344	49.6	1.631	17.7
H_2S_3	1.491	65.9	1.729	26.2
H_2S_4	1.582	82.3	1.791	34.9
H_2S_5	1.644	98.7	1.836	43.6
H_2S_6	1.688	115.2	1.867	52.2
H_2S_7	1.721	131.6	1.893	60.9
H_2S_8	1.747	148.0	1.912	69.5

[a] d^{20} = density (20 °C); V = molar volume; η = refractive index; R = molar refraction.

4.4 Reactions

Hydrogen sulfide is a weak acid ($pK_a = 6.88$), whereas the other sulfanes are considerably stronger, with pK_a decreasing as the chain length increases (for $x = 2$, 3, 4, 5 the first acid dissociation constants are 5.0, 4.2, 3.8 and 3.2, respectively). In neutral aqueous solution, the sulfanes decompose with formation of sulfur and H_2S, while they are stable under anhydrous conditions, in acid or in alkali (as the corresponding polysulfide anion). Reactions of H_2S are summarized in Figure 30. Commercially, the most important reactions are the formation of NaSH, Na_2S, and of organic sulfur compounds. HDS is used in the preparation of heavy water (equation 36).

$$HDS(g) + H_2O(l) \rightleftharpoons H_2S(g) + HDO(l) \tag{36}$$

In general, the sulfanes have a less well-developed chemistry, partly because of the difficulty in isolating them pure, although they have been used for the synthesis of some organosulfur compounds (*see* ***Sulfur: Organic Polysulfanes***).

4.5 Polysulfides

4.5.1 Free Anions

Simple sulfides are discussed elsewhere. However, the chemistry of polysulfides relates to that of the sulfanes, and some discussion is provided here.

In principle, deprotonation of any of the sulfanes gives polysulfide anions $S_x{}^{2-}$. In practice, this route is not employed and rather fewer anions are known compared with the sulfanes. It was established last century that sulfur dissolves in basic media to give intensely colored (often blue) solutions.[70] The well-known polysulfide solution $[NH_4]_2S_x$, which contains mostly $x = 4$ and 5, is obtained by bubbling H_2S through a suspension of sulfur in ammonium hydroxide. It is accepted nowadays that the blue coloration of many of these solutions is a consequence of the $S_3{}^{-\bullet}$ radical. This species has characteristic EPR, visible, and Raman spectra that have enabled its detection in a variety of solutions including liquid ammonia,[71] DMF, and HMPA. $S_2{}^{2-\bullet}$ can be introduced as an impurity into alkali metal halides. In lapis lazuli (lazurite that is made synthetically as ultramarine blue: $Na_8[A1_6Si_6O_{24}]S_n$, $n = 2-4$), the blue color is due to the presence of $S_3{}^{-\bullet}$ radicals, which has also been identified by *Resonance Raman Spectroscopy*.[72]

There is a range of polysulfide dianions $S_x{}^{2-}$ that can be obtained by reaction of sulfur with simple sulfides, by high-temperature reaction of an alkali metal with sulfur, or by reaction of alkali metals with sulfur in liquid ammonia. Often, once formed, the anions are in equilibrium in solution, but individual anions can be complexed successfully. Structures of the free polysulfide anions are shown in Figure 31.

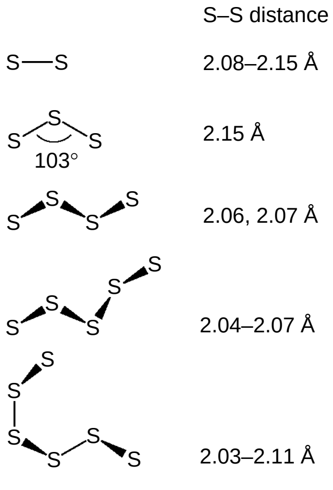

Figure 31 Structures of S_x^{2-} anions

4.5.2 *Metal Polysulfides*

This area continues to provide many new compounds and structures, reflecting the versatility and thermodynamic stability of polysulfide anions. Most of the compounds are described under the appropriate metal elsewhere in the Encyclopedia, some of the most elegant recent developments have been with other p-block elements such as tellurium, bismuth, and antimony.[73]

Preparation and Structure. Many minerals exist as sulfides, and these have been outlined in Section 2.1.1. The alkali and alkali earth metals form simple ionic sulfides that are water soluble. Many sulfides, polysulfides, and their complexes are known and there have been a number of reviews illustrating their structures,[73] catalytic uses,[74] and biological significance.[75] Excellent reviews illustrate the complexity of this area for the chemistry of Cr, Mo, and W sulfides.[76] Many of the sulfides exist in different phases depending upon the conditions used in their synthesis and they may be interconverted by annealing, etc. MoS_2 is used as a high-temperature lubricant.

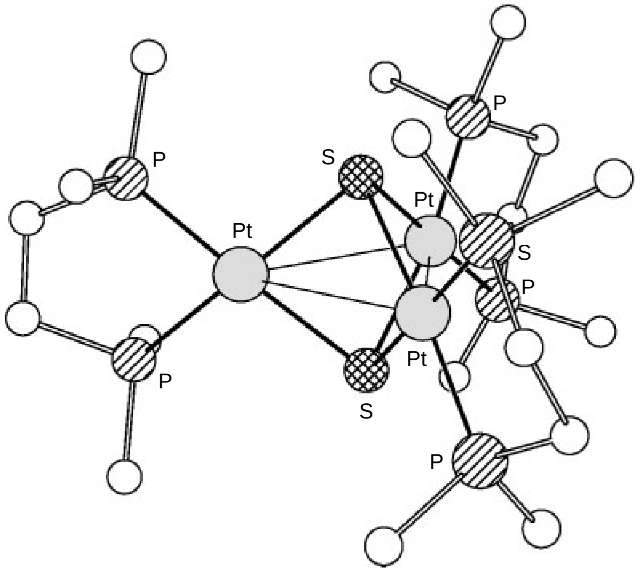

Figure 32 The X-ray crystal structure[78] of $[Pt_3(dppe)_3S_2]^{2+}$

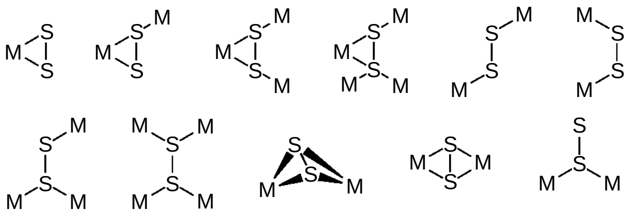

Figure 33 Coordination modes of S_2^{2-}

The coordination chemistry of S_x^{2-} is very diverse.[73,74] The monosulfide dianion has important coordination chemistry in biological systems (e.g. *see* ***Iron–Sulfur Proteins***). There has recently been a report of the crystal structure of the $[Pt_3(dppe)_3S_2]^{2+}$ dication, which contains two face capping S^{2-} anions (Figure 32).[77] The disulfide anion S_2^{2-} can coordinate edge-on (*see Side-on Coordination*), or bridge two or more central metal atoms The most common are illustrated in Figure 33. *End-On Coordination* of S_2^{2-} is not well established although, there has been a recent example with Cu(I)[78] As can be seen, a wide range of coordination types is known. An interesting example illustrating the types of structural motifs that are possible is the reaction of $[Mo_2S_{12}]^{2-}$ with PhS^-, which gives $[Mo_2S_{10}]^{2-}$ (equation 37). The starting dianion actually exists in two isomeric forms ($[Mo_2(S_2)_4(\mu\text{-}S_2)_2]^{2-}$ and $[(MoS)_2(S_4)_2(\mu\text{-}S_2)]^{2-}$); the latter form is desulfurated to give a species containing bridging and nonbridging coordination of the S_2^{2-} ligand.[79]

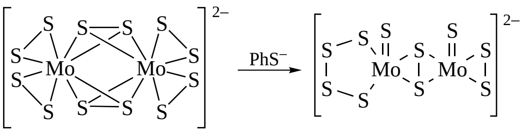

(37)

Dibenzyl trisulfide provides[80] a useful source of sulfur for the preparation of sulfide anions via oxidative replacement of RS^- ligands (equation 38). $[Fe_2(\mu\text{-}S_2)(S_5)_2]^{2-}$ contains two FeS_5 rings bridged by two S^{2-} anions.

$$[Fe(SPh)_4]^{2-} + xs\ Bz_2S_3 \longrightarrow [Fe_2(\mu\text{-}S)_2(S_5)_2]^{2-} \qquad (38)$$

Another, quite general route[81] is to prepare a sulfide in situ by reduction of sulfur using superhydride (equation 39).

$$2LiBHEt_3 + \frac{5}{8}S_8 \longrightarrow Li_2S_2 + H_2 + 2BEt_3$$

$$Cp_2TiCl_2 + Li_2S_2 \longrightarrow Cp_2TiS_5 + 2LiCl \qquad (39)$$

Interestingly, although the TiS_5 ring is quite stable for Cp_2TiS_5, there are significant steric effects upon substituting the Cp rings. Thus for C_5Me_5, monomeric $(C_5Me_5)_2TiS_3$ is known,[82] but for C_5H_4Me the dimeric $[(C_5H_4Me)_2TiS_3]_2$, containing bridging S_3^{2-} ligands, is observed.[83]

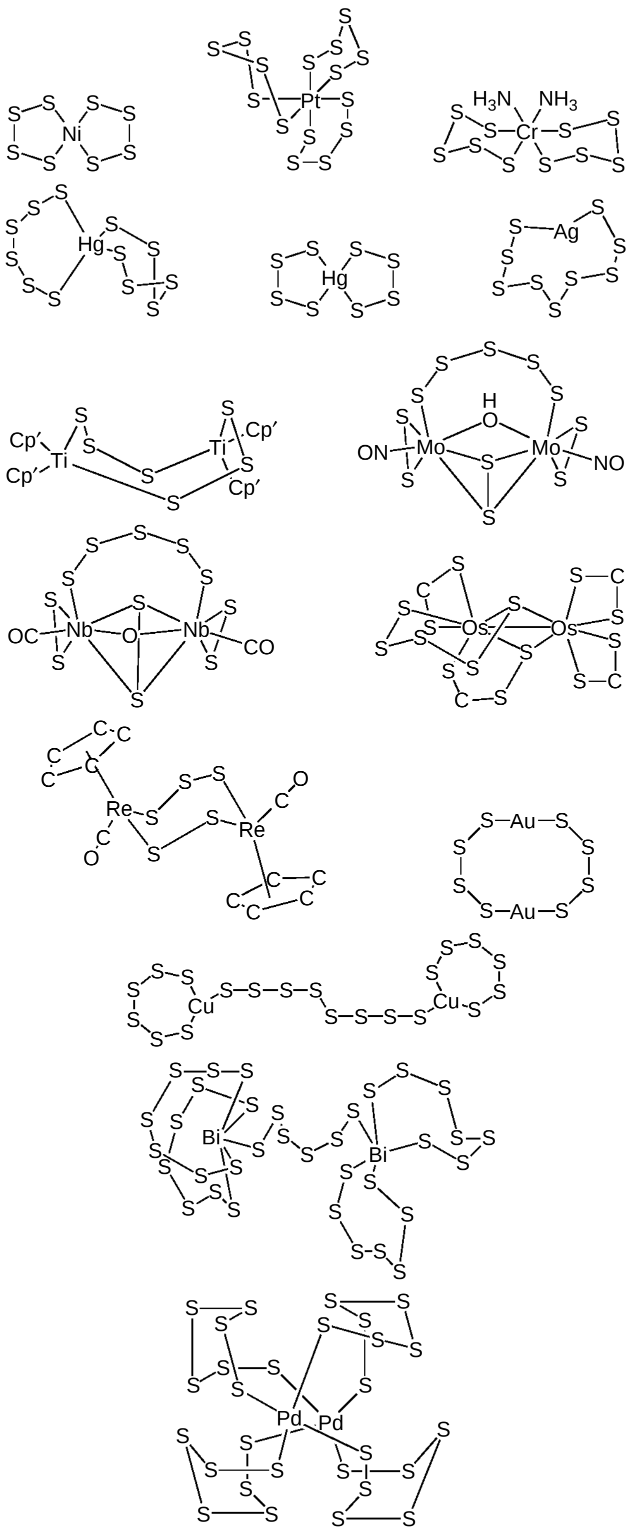

Figure 34 Examples of metal–polysulfide coordination modes

Larger S_x^{2-} ligands are known (Figure 34); the commonest sulfido complexes consist of MS_4 and MS_5 units, which probably reflects the stability of the anions in solution and even more so as coordinated ligands in MS_4 and MS_5 rings, although S_4^{2-} can also behave as a bridging ligand. Larger MS_x rings have been characterized (e.g. AuS_9^-), as have larger anions. Perhaps the most well-known polysulfide complex is Cp_2TiS_5, which has already been mentioned above; some of its reactions are illustrated in Figure 5.

Oxidative Addition reactions may also be employed. For example, reaction of $M(PPh_3)_4$ with sulfur (M = Pd, Pt) gives $M(PPh_3)_2S_4$.[84] Sulfur may be reacted without oxidation of the metal centre, for example with Cp_2TiMe_2 or $Cp_2Ti(SH)_2$ to give Cp_2TiS_5,[85] or with oxosulfur or sulfur anions such as $MoOS_3^{2-}$, WS_4^{2-}, and so on.[86] The majority of the homoleptic complexes have been obtained from reactions of S_x^{2-} solutions (water, ethanol, MeCN, or DMF) and some examples are included in Figure 35.

One interesting recent report illustrates the subtlety of this area.[87,88] Na_2E_4 (prepared by stirring the appropriate quantities of sodium and elemental S/Se/Te together in liquid ammonia) was stirred together with $M(CO)_6$ (M = Mo, W) in DMF. The contrasting reactivity of S and Se versus Te is immediately apparent from equations (40) and (41).

$$M(CO)_6 + S_4^{2-} \longrightarrow MS_4^{2-} \tag{40}$$

$$M(CO)_6 + Te_4^{2-} \longrightarrow [(CO)_4MTe_4]^{2-} \tag{41}$$

Molten salt routes have been employed[89,90] for the synthesis of a range of materials, with particular emphasis being directed towards obtaining systems with 'extended' structures. These reactions can be performed at surprisingly low temperatures (for example, M_2S_4 (M = Na, K) have melting points of ca. 160 °C), although most of the media have quite a wide liquid range (up to 600 °C), which offers the scope for great flexibility in the reaction conditions. Typically, a reaction medium (and reactant) is obtained by adding sulfur to a metal sulfide M_2S; another metal, metal sulfide, or halide is then added and the whole is ground together, sealed in a suitable vessel (usually made of quartz), heated to the desired temperature (for several hours or even days), and

$$2FeCl_2 + 12S + 6Na \xrightarrow{DMF} Na_2[Fe_2S_{12}] + 4NaCl$$

$$Cp_2MoCl_2 + Na_2S_2 \longrightarrow Cp_2Mo(S_2) + 2NaCl$$

$$MoO_4^{2-} + S_n^{2-} \longrightarrow [Mo_3S(S_2)_6]^{2-} + [Mo_2(S_2)_6]^{2-}$$

$$[NH_4]_2S_x + Cp_2TiCl_2 \longrightarrow Cp_2TiS_5$$

$$[NH_4]_2S_x + K_2PtCl_6 \longrightarrow [NH_4]_2[Pt(S_5)_3]$$

Figure 35 Preparation of metal polysulfide complexes from polysulfide solutions

slowly cooled. The products are usually obtained by removing unwanted, soluble M_2S_x. For example, transparent orange crystals of K_4TaS_{11} were obtained by reaction of K_2S, Ta, and S (3:2:5 ratio) at 800 °C.[89] Reaction of copper in molten K_2S_x (1:3 ratio) depends on the temperature employed. At high temperatures (350 °C), CuS is obtained; at 215 °C, α-$K[Cu_4S_3]$ is the product; while at 250 °C, β-$K[Cu_4S_3]$ is formed.[90] The molten salt route has been applied particularly to the formation of low-dimensional polychalcogenides rather than 'molecular' species. Especially interesting are the layer compounds (e.g. $[CuS_4]_n{}^{n-}$) that are emerging.

The structural chemistry associated with polysulfide molecules and materials reflects the stereochemical freedom of the sulfur atom; as mentioned above, disulfide ligands can coordinate in a number of ways. Similarly, larger rings may adopt a variety of geometries (from X-ray studies) and the evidence that is available suggests that many of the rings are fluxional in solution. Muller has classified and discussed some aspects of this problem for molecular species, but the rationalization of the structures adopted in solid-state materials is not yet complete.[73]

Reactions of Sulfido Complexes. Some reactions of polysulfide complexes have been studied. For example, $[Pt(S_5)_3]^{2-}$ reacts with CN^- with reduction[91] and loss of one ligand to give $[Pt(S_5)_2]^{2-}$, and with PPh_3 to give[92] $SPPh_3$ and $Pt(PPh_3)_2S_4$. We have already mentioned the oxidation of S_2 ligands for the formation of S_2O and S_2O_2 complexes, and illustrated the reactions of Cp_2TiS_5. Other important reactions include thermal decompositions (a) of $Cs_2[Mo_2(S_2)_6]\cdot nH_2O$ with elimination of S_2, which was identified by matrix-isolation spectroscopy,[93] and (b) of $[NH_4]_2[Mo_3S(S_2)_6]\cdot nH_2O$, which gives MoS_2 as the final product.[94] The reactions of polysulfide complexes with activated acetylenes (e.g. dimethyl acetylenedicarboxylate) proceed with insertion. Thus $(MeCp_2Ti)_2(S_2)_2$ gives $MeCp_2TiS_2(CCO_2Me)_2$ containing a TiS_2C_2 ring;[95] some molybdenum complexes behave in a similar fashion.[96]

The use of polysulfide complexes in catalysis has been discussed. Two major classes of reactions are apparent: (1) hydrogen activation and (2) electron transfers. For example, $[CpMo(S)(SH)]_2$ catalyzes the conversion of nitrobenzene to aniline at room temperature,[97] while $(CpMo(S))_2S_2CH_2$ catalyzes a number of reactions such as the conversion of bromoethylbenzene to ethylbenzene[98] and the reduction of acetyl chloride, as well as the reduction of alkynes to the corresponding *cis*-alkenes.[99] Electron transfer reactions (*see* ***Electron Transfer in Coordination Compounds***) have been studied because of their relevance to biological processes (in, for example, ferrodoxins), and these cluster compounds are dealt with in ***Iron–Sulfur Proteins***. Other studies include the use of metal polysulfide complexes as catalysts for the photolytic reduction of water by THF[100] and copper compounds for the hydration of acetylene to acetaldehyde.[101]

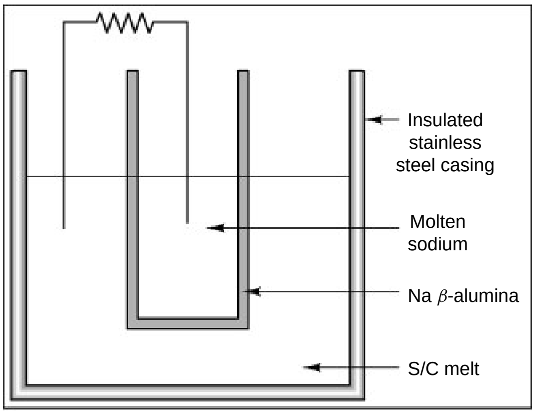

Figure 36 The sodium–sulfur battery

The Sodium Sulfur Battery. Lightweight, high-capacity batteries based upon alkali metals and sulfur have been the subject of much study, and are now commercialized. In contrast to conventional (lead–sulfuric acid) batteries, they consist of a solid electrolyte that separates the two liquid electrodes (molten sulfur is the anode and molten sodium the cathode) (Figure 36). The Na/S system can store up to five times the energy of an equivalent weight conventional battery but is more expensive to produce; it operates at ca. 300 °C and so must be well insulated to maintain the molten electrodes when not in use. In operation the sodium is oxidized to Na^+ and the sulfur reduced to polysulfide anions during the discharge of the battery, resulting in the formation of Na_2S_x, which is readily converted back into Na and S if the polarity of the cell is reversed. Typical systems suitable for road vehicles are expected to contain up to 1000 small cells, capable of providing 50 kWh at 100 V and fully rechargeable up to 1500 times. The chemistry associated with this type of electrochemical cell has been extensively studied.[102,103]

5 SULFUR HALIDES

As might be expected, there is a vast range of compounds containing sulfur–halogen bonds (Figure 37), and they play an important role in synthetic sulfur chemistry. For convenience, they are divided by oxidation state. The sulfur oxyhalides are also dealt with in this section.

5.1 Sulfur(VI)

5.1.1 Sulfur Hexafluorides and Derivatives

Apart from sulfur hexafluoride (and sulfuryl halides), the S^{VI} oxidation state is maintained[104,105] for species SF_5R and SF_4R_2. All of these compounds are octahedral and the latter species may adopt cis or trans configurations.

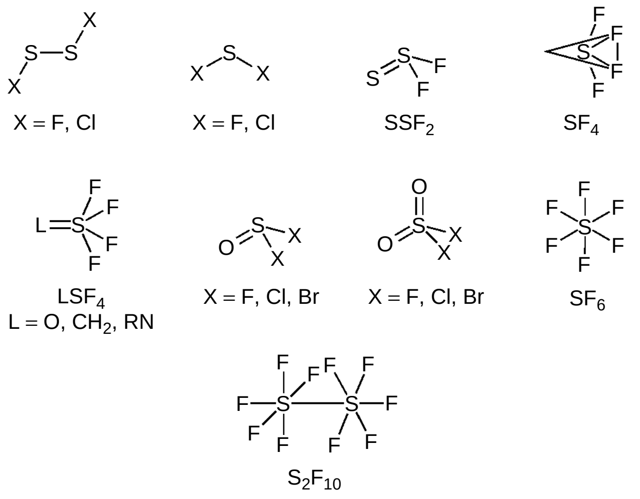

Figure 37 Structures of sulfur halides and oxohalides

Sulfur hexafluoride was first isolated and characterized in 1900; obtained by burning sulfur in a fluorine atmosphere, it is a colorless generally unreactive gas. This lack of reactivity has been put to use, with SF_6 being employed in tracer studies on flue gases from power stations, and as an insulating gas in transformers. Some reactions are possible, however. For example, treatment of SF_6 with SO_3 gives sulfuryl fluoride.[106] In general, however, SF_6 is not an especially useful starting material.

Disulfur decafluoride can be prepared in a similar fashion to SF_6, provided the reaction conditions are adjusted and carefully controlled, although a more convenient laboratory scale reaction is the photochemical reaction of SF_5Cl with H_2 (equation 42).[107]

$$SF_5Cl + H_2 \longrightarrow S_2F_{10} + 2HCl \qquad (42)$$

S_2F_{10} is a colorless liquid (bp 30 °C) that is extremely toxic and much more reactive than SF_6. Structurally, it should be noted that the two SF_5 groups are staggered with respect to each other (Figure 37). It disproportionates on heating to give SF_4 and SF_6. It is, as expected, a powerful oxidizing agent. Under carefully controlled conditions it reacts with ammonia to give NSF_3. With chlorine or bromine it forms SF_5X, and with SO_2, F_5SOSO_2F is formed (Figure 38).[108]

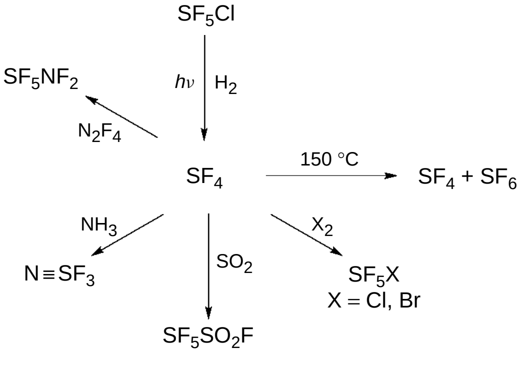

Figure 38 Reactions of S_2F_{10}

There are a number of SF_5L and SF_4L_2 species (Table 12). Perfluoroalkyl compounds are formed by oxidative fluorination of thiols.[109] ^{19}F NMR provides a simple and quick method for establishing the stereochemistry in the bis compounds; there does not appear to be any fluxionality.

SF_5Cl and SF_5Br are usually prepared by oxidation of SF_4 (equations 43 and 44).[110,111]

$$SF_4 + ClF \longrightarrow SF_5Cl \qquad (43)$$

$$SF_4 + Cl_2 + CsF \longrightarrow SF_5Cl + CsCl \qquad (44)$$

Both compounds are more reactive than SF_6 or S_2F_{10}. For example, they are hydrolyzed by aqueous alkali, and the bromide will even react with water. The increase in reactivity is probably a consequence of the dipolar S–X bond $[X(\delta+)]$ with initial attack being at X. This view is supported by the higher reactivity of the bromide versus the chloride. Some examples of SF_5L compounds prepared from SF_5X are given in Table 12. With organic alkenes, SF_5Cl reacts both photochemically and thermally.[112] It is a common feature of the chemistry of SF_5X to proceed via $SF_5\bullet$ radicals and a

Table 12 Physical properties of some S^{6+} compounds

Compound	Mp (°C)	Bp (°C)
SF_6	sublimes	−63.8
SF_5Cl	−64	−21
SF_5Br	−79	3.1
SF_5SF_5	−52.7	30
$C_2F_5SF_5$	–	11.3
$C_2F_5SF_4C_2F_5$	–	70
$SF_5CF_2SF_5$	–	60
$SF_5CF_2CF_2Cl$	−113	47
$SF_5[CF_2CF_2]_3Cl$	−5	142
SF_5OF	−86	−35.1
SF_5OSF_5	−118.5	31
SF_5OOSF_5	−95.4	49.4
$SF_5OSF_4OSF_5$	−82	−94.0
$SF_5OSO_2OSF_5$	−48	101.9
SF_5OCF_3	–	−10
SF_5OOCF_3	−136	7.7
$SF_5OCH_2CF_3$	−108	41.7
SF_5Oph	–	139
p-$SF_5OC_6H_4Me$	–	161
SF_5Ph	–	148.6
$SF_5CH{=}CH(OH)Me$ (*cis*)	–	144
$SF_5CH{=}CH(OH)Me$ (*trans*)	–	115
SO_2F_2	−120	−55
SO_2FCl	−25	7
SO_2Cl_2	−54	−69
SO_2FBr	−86	41

typical sequence is given in (equation 45).

$$\begin{tikzcd} SF_5Cl \arrow[r] & SF_5\bullet + Cl\bullet & \\ SF_5\bullet + C_2H_5 \arrow[r] & SF_5C_2H_4\bullet \arrow[r] \arrow[d, "SF_5Cl"] & SF_5(CH_2CH_2)_2 \\ & SF_5CH_2CH_2Cl + SF_5\bullet & \end{tikzcd} \quad (45)$$

5.1.2 *Sulfur Oxyfluorides and Oxychlorides*

SOF_4 is obtained by fluorination of thionyl fluoride (equation 46) or by the oxidation of SF_4.[113] It has a trigonal-bipyramidal structure with the S=O in the equatorial plane.[114]

$$SOF_2 + F_2 \longrightarrow SOF_4 \qquad (46)$$

It is easily hydrolyzed by water to sulfuryl fluoride and reacts with ammonia to give $NH{=}SOF_2$. With F_2/AgF_2, SF_5OF is obtained.

SF_5OF and the related compound bis(pentafluorosulfur) peroxide undergo facile decomposition to give radicals (equation 47) and are very powerful oxidizing agents. The radicals have been used in reactions with, for example, N_2F_4 to give SF_5ONF_2. With benzene, $PhOSF_5$ is obtained; the OSF_5 activates the ring to electrophilic substitution at the *para* position in a similar manner to fluorine.

$$F_5SOOSF_5 = SF_5O\bullet \qquad (47)$$

The sulfuryl halides are usually prepared by reaction of X_2 with SO_2. SO_2F_2 and SO_2Cl_2 are both tetrahedral in geometry; SO_2Br_2 is not well characterized and is probably unstable at room temperature. The S–X and S=O bonds are shorter than in the simple halides (SF_6 and S_2Cl_2) and the S=O is also shorter in SO_2F_2 than in SO_3 or SO_2Cl_2.

Sulfuryl fluoride is not especially reactive, whereas sulfuryl chloride is extensively used in industry.[8] It readily dissociates into SO_2 and chlorine, and is widely used for chlorination (particularly selective side-chain chlorination of aromatics) and sulfochlorination (introduction of SO_2Cl) in organic chemical manufacture for dyes, disinfectants, herbicides, and so on.

5.2 Sulfur(IV)

5.2.1 *Halides*

Only SF_4 is stable at room temperature, although $RSCl_3$ compounds are known. SF_4 may be prepared on a laboratory scale by reaction of sulfur dichloride with sodium fluoride in an aprotic solvent such as acetonitrile (equation 48).[115]

$$3SCl_2 + 4NaF \longrightarrow S_2Cl_2 + SF_4 + 4NaCl \qquad (48)$$

It is a colorless gas that condenses to give an associated liquid. Spectroscopic studies (IR/Raman, microwave, NMR)[116,117] suggest that the structure is based upon a trigonal bipyramid with one of the equatorial sites occupied by a lone pair. Its ^{19}F NMR spectrum consists of a singlet at room temperature and two triplets at −98 °C.[116]

SF_4 is rapidly hydrolyzed by water to give thionyl fluoride and hydrofluoric acid and so great care must be exercised when using it as a reagent. It can be used (Figure 39) as a powerful fluorinating agent (equations 49 and 50).

$$I_2O_5 + 5SF_4 \longrightarrow 2IF_5 + 5SOF_2 \qquad (49)$$

$$CsF + W(CO)_6 + xs\ SF_4 \longrightarrow CsWF_6 \qquad (50)$$

SF_4 forms adducts with main group inorganic fluorides, and these have been variously described as simple Lewis acid–base systems (with SF_4 behaving as the base) or as ionic systems such as $[SF_3]^+\ [BF_4]^-$. The reactions of SF_4 with organic molecules have been widely studied. The most important reaction is the conversion of a carbonyl group to a difluoride (equation 51).

$$R_2CO + SF_4 \longrightarrow R_2CF_2 + SOF_2 \qquad (51)$$

As expected, it undergoes oxidative addition with fluorine or ClF. With fluorinated peroxides $FSO_2OOSO_2F_2$, the SF_4 inserts into the O–O bond to give $SF_4(OSF_5)_2$.

As mentioned above, SCl_4 is unstable at room temperature. Sulfur dichloride reacts with liquid chlorine at −75 °C to give a white solid that has the empirical formula SCl_4, but decomposes above −30 °C. By analogy with PCl_5, it is postulated that the structure is $[SCl_3]Cl$.

Organic sulfur trihalides (RSX_3, X = Cl, F) are known.[118] The arylsulfur trifluorides can be obtained by oxidation of the disulfide with silver difluoride but this reaction fails for alkyl compounds. Fluoroalkenes provide a valuable source of compounds according to equation (52), which is catalyzed by cesium fluoride.

$$CF_3CFCF_2 + SF_4 \longrightarrow (CF_3)_2CFSF_3 \qquad (52)$$

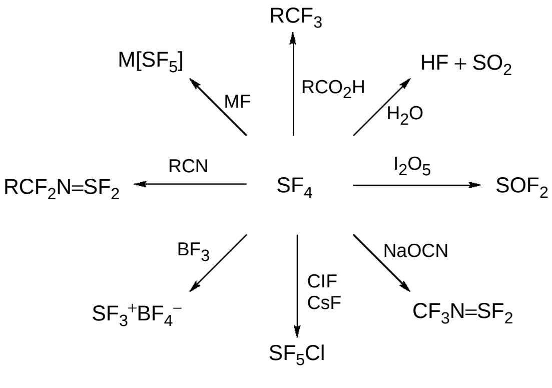

Figure 39 Reactions of SF_4

The trichloro compounds, like SCl_4, are less thermally stable than their fluoro analogs. Generally they are prepared by reaction of the appropriate sulfenyl chloride with chlorine (equation 53).

$$RSCl + Cl_2 \longrightarrow RSCl_3 \qquad (53)$$

5.2.2 *Thionyl Halides*

The known thionyl halides include SOX_2 ($X = F$, Cl, and Br; Table 13) as well as the mixed compound SOFCl. They are pyramidal in geometry, with the S=O bond being shorter in the fluoride than the chloride or bromide.**[119]** Thionyl chloride is prepared industrially by reacting sulfur dioxide or trioxide with sulfur dichloride or sulfur monochloride, or by the reaction of phosphorus trichloride with sulfuryl chloride (equations 54–57).

$$SO_3 + 2SCl_2 + Cl_2 \longrightarrow 3SOCl_2 \qquad (54)$$

$$2SO_2 + S_2Cl_2 + 3Cl_2 \longrightarrow 4SOCl_2 \qquad (55)$$

$$SO_3 + S_2Cl_2 + 2Cl_2 \longrightarrow 3SOCl_2 \qquad (56)$$

$$SO_2Cl_2 + PCl_3 \longrightarrow SOCl_2 + POCl_3 \qquad (57)$$

The other thionyl halides are obtained by treatment of thionyl chloride with appropriate halide exchange reagents (e.g. SbF_3, NaF, KBr).

The thionyl halides hydrolyze in water to give sulfur dioxide and HX. A common inorganic application of this reaction is for the preparation of anhydrous metal chlorides (although it can lead to difficulties for some metal chlorides). Industrially, thionyl chloride is used for the preparation of anhydrous metal halides and oxyhalides as well as in organic transformations, where it converts hydroxyl groups to chlorides. Over 50 000 tonnes a year are manufactured.

SOF_2 has not been studied as extensively as $SOCl_2$. It is used in reaction with $Me_2SnS_2N_2$ to give the five-membered heterocycle $(O)SS_2N_2$.

Iminosulfur difluorides, $RNSF_2$, are isoelectronic with SOF_2. They are obtained by the reaction of SF_4 with cyanates, nitriles, and amines (e.g. equations 58 and 59).

$$RNCO + SF_4 \longrightarrow RNSF_2 + COF_2 \qquad (58)$$

$$RNH_2 + SF_4 \longrightarrow RNSF_2 + [RNH_3]F \qquad (59)$$

Table 13 Properties of S^{IV} compounds

Compound	Mp (°C)	Bp (°C)
SF_4	−121	−38
SCl_4	−30d	–
OSF_2	−110	−44
OSFCl	−120	12
$OSCl_2$	−101	76
$OSBr_2$	−50	140
$MeN{=}SF_2$	−123	16
$EtN{=}SF_2$	129.5	42
$FCON{=}SF_2$	−94.7	49
CF_3SF_3	−110	−7
$(i\text{-}C_3F_7)_2SF_2$	<−78	111

Thiothionyl fluoride, $S{=}SF_2$ (an isomer of S_2F_2), is also known, although it is not especially stable;**[120]** it is often obtained mixed with disulfur difluoride, but may be obtained directly by reaction of NF_3 with sulfur or by the fluorination of S_2Cl_2 with KF in SO_2.

5.3 Sulfur(II)/(I)

The only established example of a sulfur(II) halide is SCl_2; we shall include the S^I halides in this section (Table 14).

Disulfur difluoride is prepared by several routes, including the reaction of sulfur with silver fluoride. It is a colorless liquid (bp 15 °C). Disulfur dichloride is obtained by reaction of the elements and the bromide is prepared by reaction of S_2Cl_2 with HBr. Industrially, S_2Cl_2 is continuously manufactured by passing Cl_2 into liquid sulfur.**[8]** Sulfur dichloride is obtained by further chlorination of S_2Cl_2. Disulfur dihalides have structures similar to that of hydrogen peroxide, while SCl_2 has the expected bent geometry.

The sulfur chlorides are poisonous yellow/orange liquids; pure SCl_2 is difficult to obtain since it readily disproportionates to give S_2Cl_2. Both chlorides hydrolyze with water and burn in oxygen. Most of their reactions are described in other sections, since the sulfur chlorides are useful reagents. Industrially, disulfur dichloride and sulfur dichloride are used for the manufacture of thionyl chloride and SF_4, as a catalyst for the chlorination of acetic acid, and in rubber vulcanization. Perhaps the most notorious use of sulfur chlorides is in the preparation of the highly toxic ‘mustard gases’ (equation 60).**[121]**

$$C_2H_4 + SCl_2 \longrightarrow ClC_2H_4SCl \xrightarrow{C_2H_4} (ClC_2H_4)_2S \qquad (60)$$

Sulfur dichloride reacts with Lewis acids with halide transfer (equation 61) and behaves as a typical acid chloride (equation 62).

$$SCl_2 + AlCl_3 \longrightarrow SCl^+AlCl_4^- \qquad (61)$$

$$SCl_2 + Hg(SCN)_2 \longrightarrow S(CN)_2 + HgCl_2 \qquad (62)$$

Table 14 Physical properties of $S^{II/I}$ halides

Compound	Mp (°C)	Bp (°C)
FSSF	−133	15
$S{=}SF_2$	−165	−11
SCl_2	−78	59 d
S_2Cl_2	−80	135.6
S_2Br_2	2.63	−40

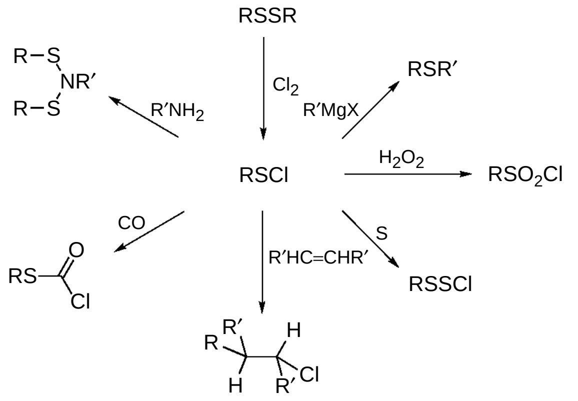
RSSR
Cl2
RSR′
R′MgX
R–S
NR′
R–S
R′NH2
RSCl
H2O2
RSO2Cl
CO
RS
O
Cl
R′HC=CHR′
S
RSSCl
R′
R
H
H
R′
Cl

Figure 40 Reactions of RSCl

A large class of compounds derived from sulfur dichlorides are the sulfenyl chlorides, RSCl. They are most commonly obtained by chlorination of a disulfide (RSSR) using Cl_2 or SO_2Cl_2. They have a large organic chemistry that has been reviewed;[122,123] selected reactions are illustrated in Figure 40.

6 SULFUR–CARBON COMPOUNDS

6.1 Neutral Carbon–Sulfur Compounds

There is an extensive chemistry of carbon sulfides.[124–126] The simplest neutral carbon sulfide is CS, which is obtained by treating a stream of CS_2 with a silent discharge. It has been spectroscopically characterized by *Matrix Isolation*; it polymerizes at 50 K to give brown $(CS)_x$ and reacts with chalcogens to give CSE (E = S, Se, Te).[127] Although free CS is substantially less stable than CO, like carbon monoxide it does behave as a ligand and this aspect of its chemistry has been thoroughly reviewed.[128] Some examples of the preparation and structures of CS complexes are given in Figure 41. Carbon monosulfide complexes may be prepared by a variety of routes. Direct cocondensation reaction of carbon monosulfide with nickel atoms gives $Ni(CS)_4$, but is a unique route.[129] Reaction of metal chlorocarbenes with SH^- proceeds with elimination of HCl. Many CS compounds are formed from carbon disulfides.[130,131] The CS_2 is methylated and then acidified. Alternatively, a route that makes use of the thiophilicity of phosphines is the use of PPh_3/CS_2. When reacted with an appropriate metal complex the CS_2 complex is initially formed, and this rapidly loses $SPPh_3$ to give the carbon monosulfide.[132] CS may also behave as a bridging ligand in a similar fashion to carbon monoxide,[133] as well as bridging with donation from the sulfur atom.[134]

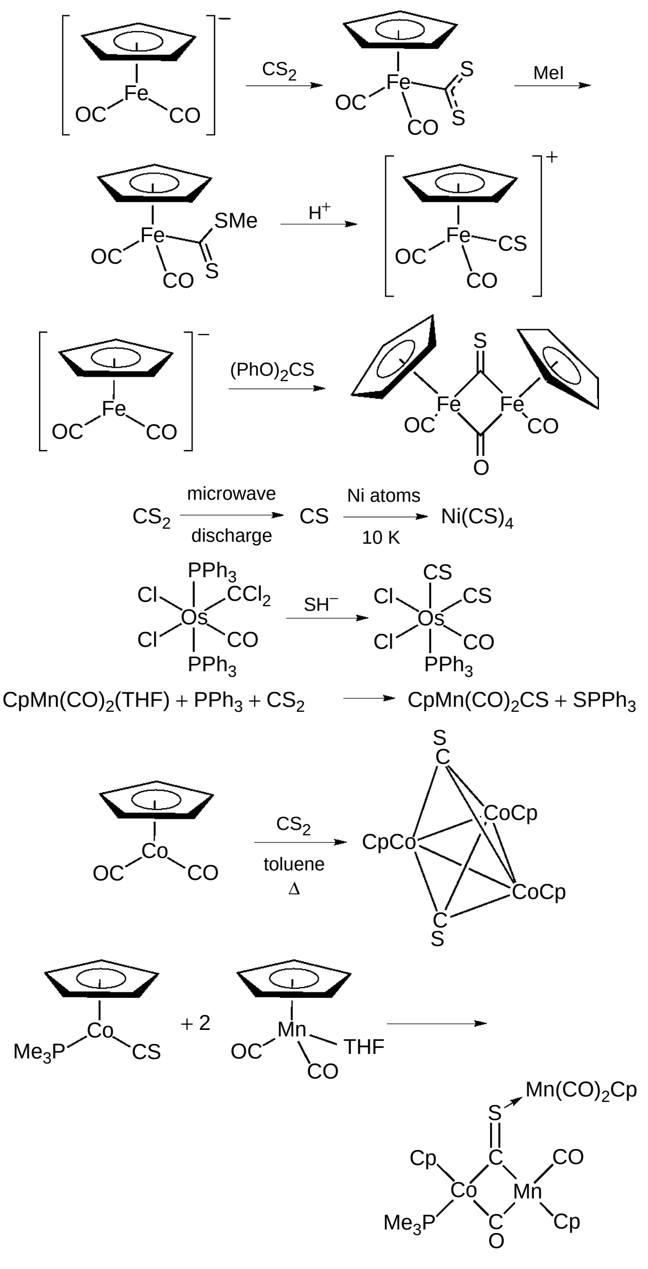
Fe
OC
CO
CS2
Fe
OC
CO
S
S
MeI
Fe
OC
CO
SMe
S
H+
Fe
OC
CO
CS
+
Fe
OC
CO
(PhO)2CS
S
Fe
Fe
OC
CO
O
CS2
microwave
discharge
CS
Ni atoms
10 K
Ni(CS)4
PPh3
Cl
CCl2
Os
Cl
CO
PPh3
SH−
CS
Cl
CS
Os
Cl
CO
PPh3
CpMn(CO)2(THF) + PPh3 + CS2
CpMn(CO)2CS + SPPh3
Co
OC
CO
CS2
toluene
Δ
S
C
CoCp
CpCo
CoCp
C
S
Co
Me3P
CS
+ 2
Mn
OC
THF
CO
Mn(CO)2Cp
S
Cp
C
CO
Co
Mn
Me3P
C
Cp
O

Figure 41 Complexes of carbon monosulfide

Carbon disulfide is prepared commercially by the reaction of charcoal with liquid sulfur at elevated temperatures, although the use of methane as a feedstock (equation 63) is gaining in importance.[8] It is a revolting smelling, volatile liquid that is easily ignited (flash point −30 °C).

$$\mathrm{CH_4} + \tfrac{1}{4}\mathrm{S_8} \longrightarrow \mathrm{CS_2} + 2\mathrm{H_2S} \tag{63}$$

Typical reactions of CS_2 are summarized in Figure 42. CS_2 forms a range of metal complexes,[135] making use of one, two, or all of its atoms (Figure 43). Commercially, the reaction with alcohol (cellulose) is used in the manufacture of viscose fiber; this use, together with the preparation of CCl_4, accounts for the majority of CS_2 manufacture, with lesser

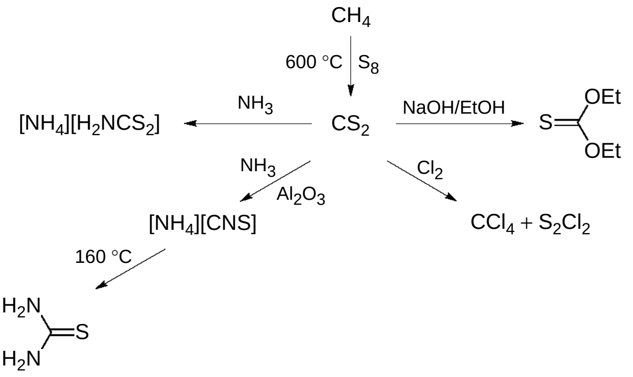
CH4
600 °C
S8
[NH4][H2NCS2]
NH3
CS2
NaOH/EtOH
OEt
S
OEt
NH3
Al2O3
Cl2
[NH4][CNS]
CCl4 + S2Cl2
160 °C
H2N
H2N
S

Figure 42 Reactions of carbon disulfide

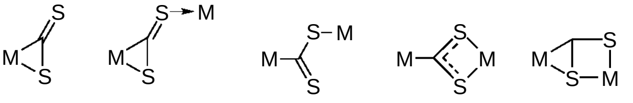
S
M
S
S
M
M
S
S–M
M
S
S
M
M
S
M
S
S–M

Figure 43 Coordination modes of CS_2

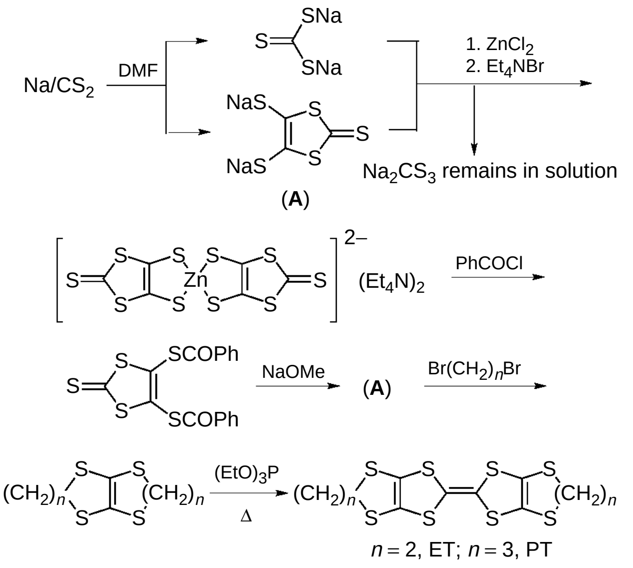
Na/CS2
DMF
SNa
S
SNa
NaS
S
S
NaS
S
(A)
1. ZnCl2
2. Et4NBr
Na2CS3 remains in solution
2–
Zn
(Et4N)2
PhCOCl
SCOPh
SCOPh
NaOMe
(A)
Br(CH2)nBr
(CH2)n
(EtO)3P
Δ
(CH2)n
n = 2, ET; n = 3, PT

Figure 44 Preparation of ET

amounts being used in the manufacture of rubber and the pharmaceutical industry. The reaction of CS_2 with NaOH/R_2NH to give dithiocarbamates has been studied in some detail, since these behave as ligands in a range of systems.[136] For a discussion of these related ligands, such as dithiolenes, *see* ***S-donor Ligands***.

Reduction of CS_2 gives[137] α-$C_3S_5^{2-}$, which is used in the preparation of bis(ethylene)dithiotetrathiafulvalene (ET) (Figure 44 and 45), which has itself been extensively studied as a constituent of organic metals.[137]

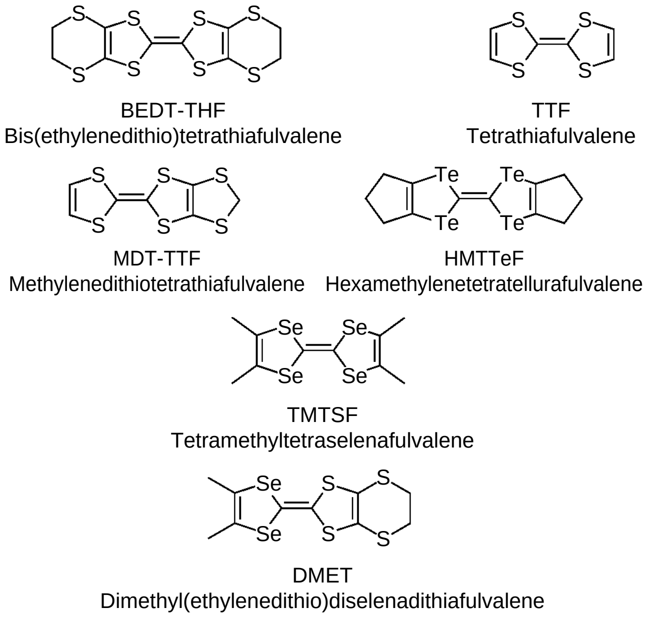
BEDT-THF
Bis(ethylenedithio)tetrathiafulvalene
TTF
Tetrathiafulvalene
MDT-TTF
Methylenedithiotetrathiafulvalene
HMTTeF
Hexamethylenetetratellurafulvalene
TMTSF
Tetramethyltetraselenafulvalene
DMET
Dimethyl(ethylenedithio)diselenadithiafulvalene

(a) Organic donor molecules

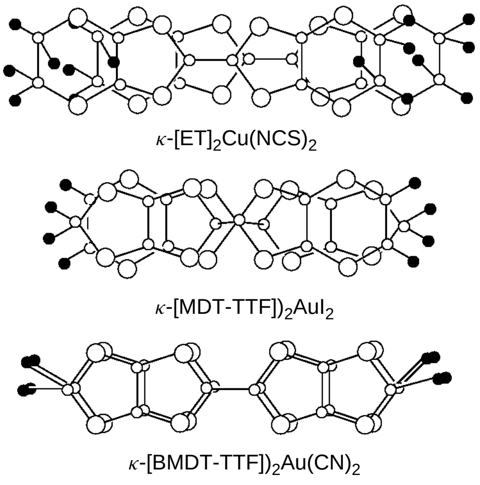
κ-[ET]2Cu(NCS)2
κ-[MDT-TTF])2AuI2
κ-[BMDT-TTF])2Au(CN)2

(b) Donor dimers

Figure 45 (a) Organosulfur compounds used in organic metals; (b) typical stacking motifs for organosulfur rings in organic metals

Higher binary C–S compounds are illustrated in Figure 46. The majority have been prepared from C–S anions, and the reactions used are described below. Quite recently C_2SO has been prepared in an argon matrix by irradiating (254 nm) a mixture of CS and CO at 10K[138]

6.2 Anionic Carbon Sulfides

Examples of anionic compounds are shown in Figure 46. $C_3S_3^{2-}$ is obtained by desilylation[139] of $C_3S(SC_2H_4SiMe_3)_2$; $C_4S_4^{2-}$ is obtained from squaric acid; and reduction of CS_2 gives α-$C_3S_5^{2-}$, which thermally rearranges to give the β

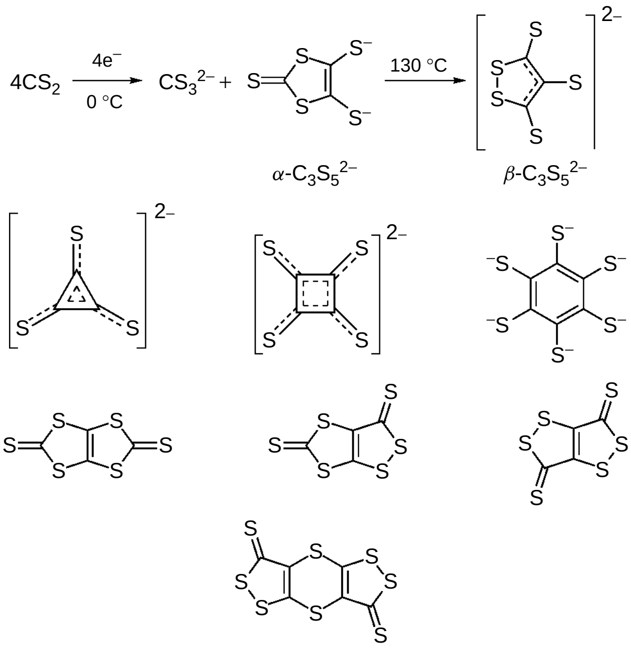

Figure 46 Binary carbon–sulfur compounds

isomer.[140] The $C_6S_6{}^{6-}$ anion is obtained[141] by reduction of $C_6(SCH_2Ph)_6$ with $Na/NH_3(liq)$. The anions may be complexed with metals such as zinc or with the Cp_2Ti unit. The metal complexes can then be reacted with simple halides in an analogous fashion to the reactions of Cp_2TiS_5 (equation 64).

$$[Zn(C_3S_5)_2]^{2-} + 2S_2Cl_2 \longrightarrow ZnCl_4{}^{2-} + \tfrac{1}{2}C_6H_{12} + C_3S_8 \qquad (64)$$

Reactions of thionyl chloride and sulfuryl chloride with zinc complexes of α- and β-C_3S_5 have been used[142] for the preparation of C_6S_8, $C_6S_{10}{\cdot}0.5CS_2$, and $(\beta\text{-}C_3S_5)_n$. Reaction of $C_6S_6{}^{6-}$ with thiophosgene gives C_9S_9. A second isomer of this empirical formula is also known.[143] A simple route to $[CS_3]^{2-}$ has been devised. Reaction of CS_2 in liquid ammonia followed by addition of $Pt(PR_3)_2Cl_2$ gives $Pt(PR_3)_2(CS_3)$ complexes in good yield.[144]

The chemistry of carbon sulfides is not especially well developed as yet, but some general trends in reactivity have been recognized.[126] (1) S–S bonds are usually able to be reductively cleaved to give anions; (2) S–S subunits will add to low-valent metals; (3) electrophilic alkenes and alkynes add across S–S bonds; (4) the sulfur atoms are most often nucleophilic.

Although binary carbon sulfides appear to be something of a curiosity at the moment, given their stability (especially compared to binary S–N compounds) and their usefulness in the synthesis of new organosulfur compounds and ligands that may be redox active, it is to be expected that their chemistry will develop rapidly over the next few years.

7 MAIN GROUP RINGS AND CAGES

7.1 Phosphorus–Sulfur Cages

There are believed to be 19 different binary phosphorus sulfides (including isomers) – the six well-established phosphorus sulfides[145] are shown in Figure 47, together with examples of mixed P–O–S cages. Closely related to these are mixed phosphorus–arsenic sulfides ($P_xAs_{4-x}S_3$) and phosphorus–sulfur selenides, $P_4S_xSe_{3-x}$. There have also been recent reports on the nmr characterization of two new binary phosphorus sulfides – both isomers of the previously elusive P_4S_6[146] the δ isomer contains a central P_4S_5 core with one terminal P═S bond while the ε isomer contains a central P_4S_4 core and two terminal P═S units. Structurally, all of the compounds can be derived from the P_4 tetrahedron by edge bridging or vertex addition of chalcogen atoms. In P_4S_4, the sulfur atoms are in a square plane with the phosphorus atoms in a P_4 tetrahedron above and below the plane. This viewpoint underlines the structural similarity of P_4S_4 with Se_4N_4 and S_4N_4. The structure of P_4S_5 is analogous to $S_4N_5{}^-$ but there is, as yet, no sulfur–nitrogen analog of P_4S_7. Though the gross geometries appear similar, there are significant differences in the bonding descriptions. All of the phosphorus sulfides may be adequately described by simple two-centre–two-electron bonds and there is no indication of additional cluster bonding. The situation for sulfur–nitrogen compounds is more complex and is discussed in ***Sulfur–Nitrogen Compounds***.

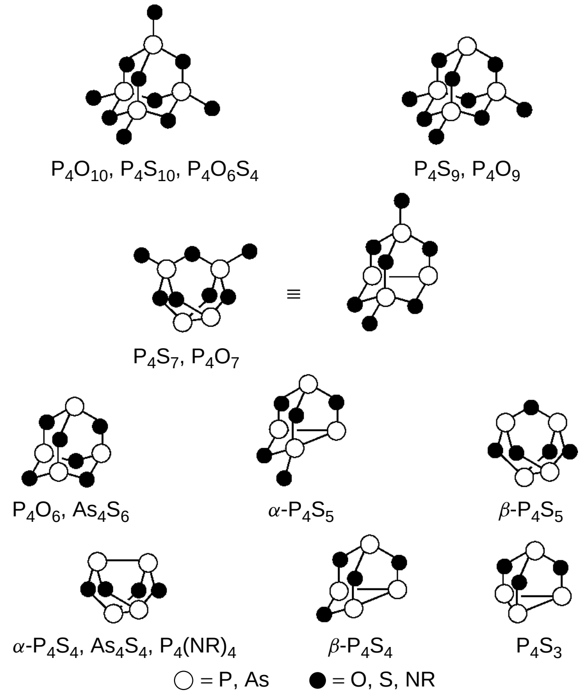

Figure 47 Phosphorus–sulfur and related cages

Originally, phosphorus–sulfides were prepared by direct combination of the elements and, for many compounds this is still a satisfactory procedure. P_4S_3, P_4S_7, and P_4S_{10} are made commercially by reaction of white phosphorus and sulfur at elevated temperatures (over 300 °C) under an inert atmosphere, with the products being distilled from the reactions. Convenient laboratory scale preparations use red phosphorus and sulfur, often in an inert solvent (e.g. xylene). There has recently been an nmr reinvestigation of the reaction of white phosphorus with sulfur that reveals that at 100 °C 12 of the known binary sulfides form[147] with the major product being P_4S_7. Combination of P_4S_{10} or P_4S_3 with the appropriate quantity of phosphorus or sulfur can be used to give P_4S_5, P_4S_7, and P_4S_9 (equation 65).[148]

$$P_4S_3 + \tfrac{1}{4}S_8 \longrightarrow P_4S_5 \qquad (65)$$

Some rather milder and more elegant strategies have been developed,[40] and these are useful for the thermally unstable compounds P_4S_5 and P_4S_4. Triphenylphosphine can be progressively used as a desulfurating agent and the tin reagent $(Me_3Sn)_2S$ is useful (equations 66 and 67).[149]

$$\begin{tikzcd}
P_4S_{10} + PPh_3 \arrow[r] & P_4S_9 + SPPh_3 \arrow[d, "2PPh_3"] \\
\beta\text{-}P_4S_5 & P_4S_7 + 2SPPh_3 \arrow[l]
\end{tikzcd} \qquad (66)$$

$$\begin{tikzcd}
P_4S_3 + I_2 \arrow[r] & \beta\text{-}P_4S_3I_2 \arrow[r] & \alpha\text{-}P_4S_3I_2 \arrow[d, "(Me_3Sn)_2S"] \\
 & & \alpha\text{-}P_4S_4 + 2Me_3SnI
\end{tikzcd} \qquad (67)$$

With the exception of P_4S_3, the phosphorus sulfides are moisture sensitive and readily hydrolyzable. The relative stability is sometimes used in its purification; the impure material is suspended in boiling water, which hydrolyzes the other compounds present (equation 68).

$$P_4S_{10} + 16H_2O \longrightarrow 4H_3PO_4 + 10H_2S \qquad (68)$$

All of the phosphorus sulfides burn readily in air, and P_4S_3 is still used (in combination with $KClO_4$ and binders) in ‘strike anywhere’ matches.

We have already mentioned the reaction of iodine with P_4S_3; this compound and the others that contain P–P bonds (P_4S_5 and P_4S_7) also react with bromine (equation 69).[150] The first stage of the reaction may be an opening of the P–P bond.

$$P_4S_7 + 3Br_2 \longrightarrow P_2S_6Br_2 + P_2S_5Br_4 \qquad (69)$$

Reactions with chlorine completely destroy the cages; P_4S_{10} gives S_2Cl_2, SCl_2, and PCl_5. P_4S_{10} reacts with anisole to give ‘Lawesson’s reagent’, which is extensively used as a reagent for the conversion of C=O into C=S. Interestingly, a *cis* analog of Lawesson’s reagent has recently been reported from the reaction of P_4S_{10} with bromonaphthalene (Figure 48).[151] This compound has been studied extensively in recent times both as a source of sulfur in thionation reactions and because it represents a useful entry into disubstituted naphthalenes. Reactions with alcohols lead to mono- and dialkoxy acids (equation 70).

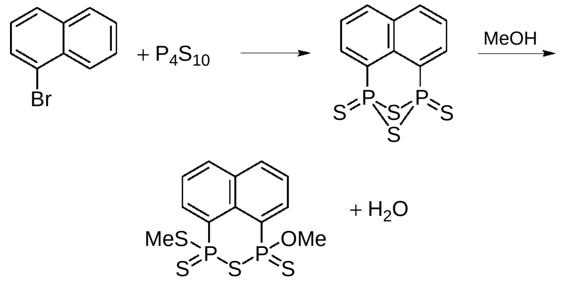

Figure 48 Organophosphorus–sulfur compounds

$$P_4S_{10} + 8ROH \longrightarrow 4(RO)_2PS(SH) + 2H_2S \qquad (70)$$

The dithiophosphoric acids are very important commercially for the preparation of pesticides such as malathion and in the manufacture of engine oil additives such as zinc dialkyldithiophosphates (ZDDPs). The structure of basic ZDDP was finally determined to be similar to beryllium acetate with a central Zn_4O core bridged along each edge by the dialkyldithiophosphate ligand[152] The coordination chemistry of dithio- and (more recently) monothiophosphoric acid derivatives has been studied as a consequence of the commercial importance of ZDDPs. The monothio derivatives can behave as bridging ligands with the hard oxygens bonding to hard metals such as zinc, and the soft sulfur atoms coordinating softer metals such as platinum (Figure 49).[153]

Reaction of P_4S_{10} with KCN/H_2S yields the trithiometaphosphate anion PS_3^-, which has been stabilized using the bulky cation Ph_4As^+ to stop dimerization to $P_2S_6^{2-}$. The latter can be prepared directly by heating together an alkali metal with the appropriate quantities of phosphorus and sulfur.

Treatment of P_4S_{10} with NaN_3 gives $P(N_3)_2S_2^-$; this reacts with additional P_4S_{10} to give $[P_4S_9N]^-$ in which an N^- has replaced a bridging sulfur atom.

7.2 Phosphorus–Sulfur Ligands

A number of metal complexes in which P_4S_3 acts as a donor ligand through its apical phosphorus have been prepared (equations 71 and 72).

$$Ni(\eta^3\text{-}C_3H_5)_2 + 4P_4S_3 \longrightarrow Ni(P_4S_3)_4 \qquad (71)$$

$$Mo(CO)_6 + P_4S_3 \longrightarrow Mo(CO)_5(P_4S_3) \qquad (72)$$

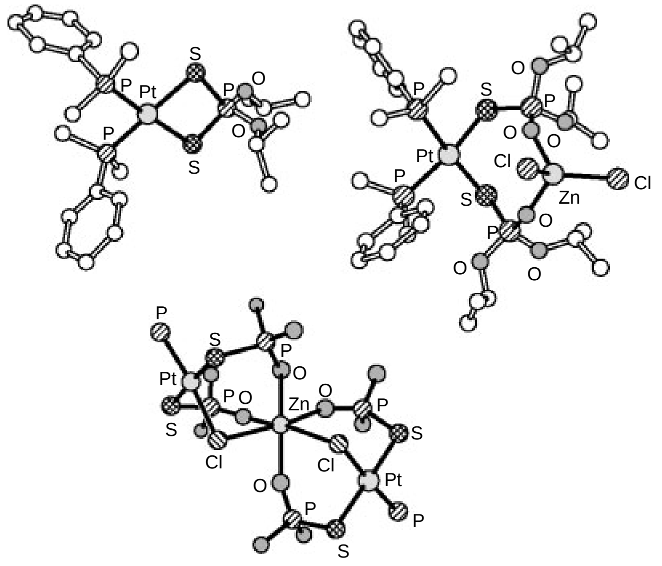

Figure 49 Mononuclear dithiophosphate and dinuclear and trinuclear complexes containing monothiophosphate ligands. In the trinuclear complex, the methyl substituents on phosphorus and the *i*-Pr groups on the oxygen atoms have been omitted for clarity

Insertion into the basal P–P bond is also possible. For example, in the oxidative addition reaction of P_4S_3 to Vaska's compound, *trans*-$Ir(CO)Cl(PPh_3)_2$ in benzene at 60 °C gives an octahedral Ir^{III} complex $[Ir(CO)Cl(P_4S_3)(PPh_3)]_2$ as a green air-stable solid. Related reactions have been described.[30,31] Metal centers can also be used to trap reactive arsenic–sulfur species (equation 73).

$$[(C_5Me_5)Co(CO)_2]_2 + As_4S_4 \xrightarrow[h\nu]{THF} [(C_5Me_5)_2Co_2(As_2S_3)] \tag{73}$$

7.3 Phosphorus–Sulfur Rings

The structural types observed for phosphorus–sulfur rings are rather more diverse than for the oxygen congeners. Figure 50 shows representative examples.

The most stable and well-known species are the four-membered rings $RP(S)S_2P(S)R$, in particular, Lawesson's reagent[154] ($R = MeOC_6H_4$), which is readily prepared from P_4S_{10} and is used in organic synthesis as a sulfurating agent (equation 74).

$$P_4S_{10} + 4PhOMe \longrightarrow 2[(MeOC_6H_4)PS_2]_2 + 2H_2S \tag{74}$$

Larger rings are known but only when large sterically demanding substituents (i.e. mesityl and 'supermesityl') are present (equations 75 and 76).[155,156]

$$(2,4,6\text{-}t\text{-}Bu_3C_6H_2)PCl_2 + Li_2S \longrightarrow [(2,4,6\text{-}t\text{-}Bu_3C_6H_2)PS]_3 + 2LiCl \tag{75}$$

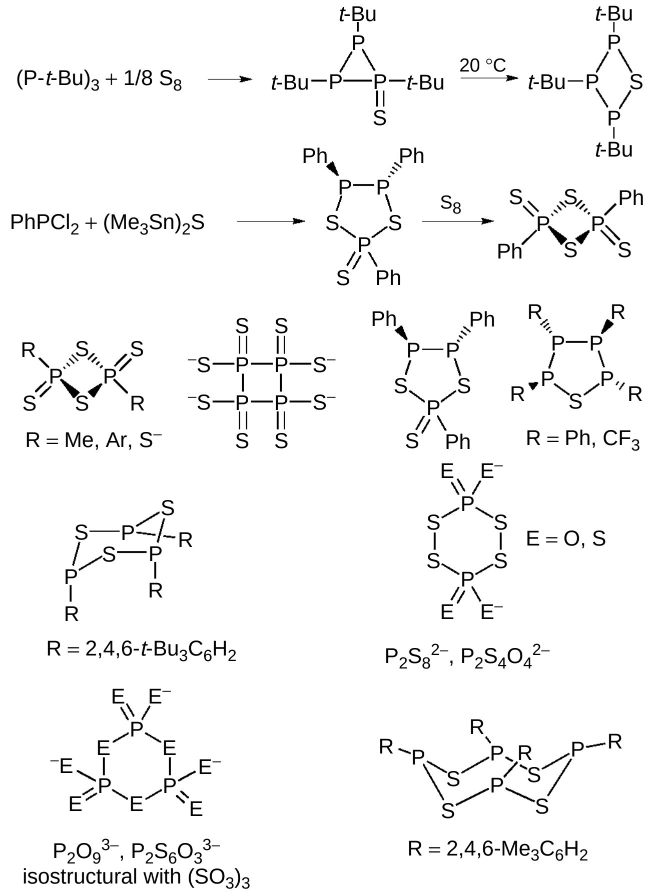

Figure 50 Phosphorus–sulfur rings

$$(2,4,6\text{-}Me_3C_6H_2)PCl_2 + (Me_3Si)_2S \longrightarrow [(2,4,6\text{-}Me_3C_6H_2)PS]_4 + 2Me_3SiCl \tag{76}$$

In comparison it is worth noting that use of a simple phenyl group allows formation of a five-membered ring with adjacent PPh groups and an exocyclic sulfur.[157] This five-membered ring readily reacts with sulfur to give $(PhPS_2)_2$.

The six-membered $(RPS)_3$ has a chair cyclohexane conformation, while $(RPS)_4$ has a crown (S_8) structure, which is as predicted from simple electron counting, since CH_2, RP, and S are isoelectronic. Although the six-membered ring is thermally stable, the eight-membered ring compound (which has smaller substituents on phosphorus) forms $(RPS_2)_2$ on standing in toluene solution.

7.4 Other Nonmetal Sulfides

Sulfur–nitrogen rings and cages are discussed in ***Sulfur–Nitrogen Compounds***. There are several boron–sulfur and silicon–sulfur rings[5] and examples are given in Figure 51.

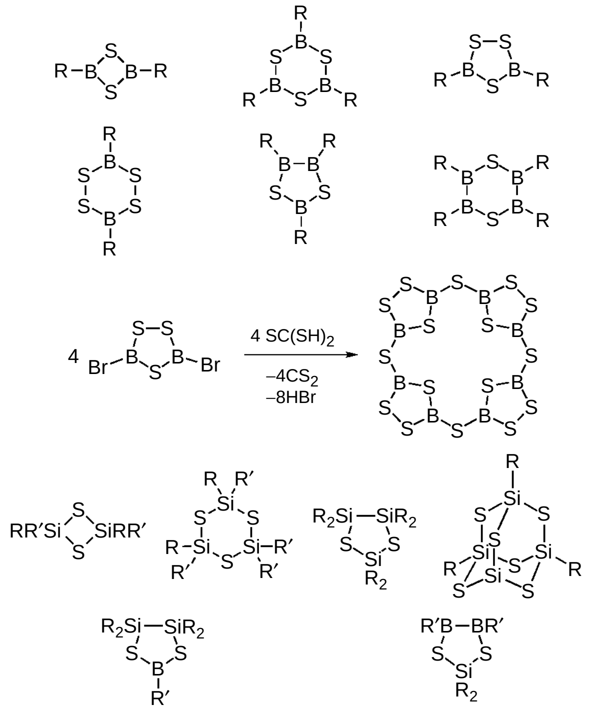

Figure 51 Examples of boron–sulfur and silicon–sulfur rings

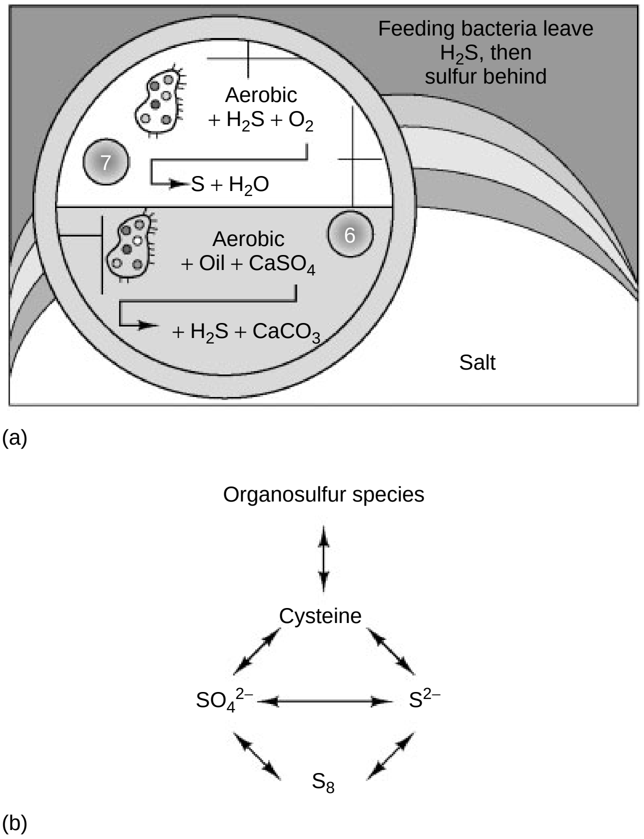

Figure 52 (a) Formation of sulfur in the cap rocks of lime. (b) The biological sulfur cycle

8 INORGANIC BIOLOGICAL SULFUR CHEMISTRY

Sulfur compounds are widespread in Nature in living organisms and this is also reflected in the geochemistry of sulfur. A constituent of amino acids (cysteine, methionine) and of cofactors such as biotin, thiamine, and coenzyme A, sulfur is essential for the maintenance of cells. Inorganic sulfur compounds, in the Earth's crust, the sea, and the atmosphere are converted by plants and microorganisms into organosulfur compounds, while the demands of animals and humans for sulfur is much lower and is usually met by the oxidation of amino acids.

Nature provides inorganic sulfur in a variety of forms. In seawater, the average concentration of sulfate is ca. 0.03 mol L^{-1}, although the concentrations in fresh water are much more variable and depend on local conditions. Freshwater may also contain sulfides. Soil samples can contain both of these sources of sulfur along with sulfate esters. Geological sulfur consists largely of sulfides and sulfates, although free sulfur is common. Figure 52 illustrates the cycle for the formation of sulfur in the salt domes of limes. Atmospheric SO$_2$ may be used by higher plants either directly, or after absorption through the soil. This process must account for the observation that, in some crops, the sulfur concentration is higher than is achievable based on the sulfur content of the soil alone.

The most important biological sulfur transformations[158] are illustrated in Figure 52(b). In general, plants and microorganisms convert inorganic sulfur into sulfur-containing organic molecules (sometimes described as 'reduced' sulfur), which then provide essential nutrition for animals. There are some exceptions to this generalization, most notably ruminants and birds (probably via symbiosis with microorganisms in their digestive system). The ability of plants to utilize inorganic sulfur is very markedly affected by the activities of the microflora in the local environment. In addition to the transformations in Figure 52, there is a range of metal–sulfur (e.g. iron–sulfur) proteins that are very important; examples of these are shown in Figure 53; more discussion of this aspect is provided in ***Iron–Sulfur Proteins***.

The key intermediates in the metabolism of inorganic sulfur are two sulfate containing nucleotides, adenylyl sulfate (APS), and 3′-phosphoadenylyl sulfate (PAPS, Figure 54). PAPS is biosynthesized from ATP by the enzymes ATP-sulfurylase and APS-kinase, and is a source of the sulfuryl group for a number of functions; the transfer usually being catalyzed by the sulfotransferases. Typical cycles are illustrated in Figure 54. PAPS is involved in the transport of sulfur for assimilatory and dissimilatory sulfate reduction (i.e. small-scale reduction to give sulfur-containing organic cell

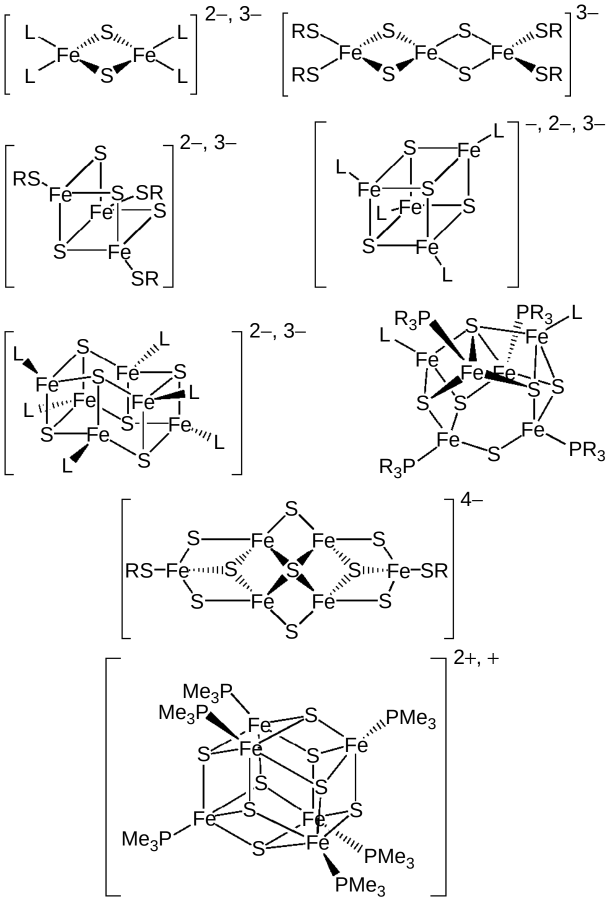

Figure 53 Examples of biologically important M–S clusters

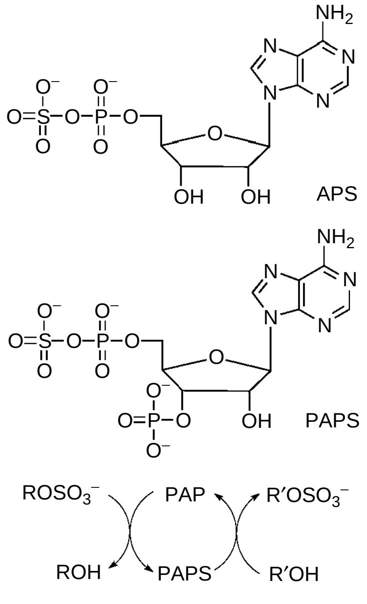

Figure 54 Adenylyl sulfate (APS) and 3′-phosphoadenylsulfate (PAPS) and a typical sulfur transfer cycle for PAPS

constituents and large-scale transformations to give sulfides as part of energy-yielding transformations, respectively). A detailed discussion of the biological processes involving sulfur is available.[158]

9 ANALYSIS OF INORGANIC SULFUR COMPOUNDS

Qualitative methods for the identification are given in Table 15.[159] Quantitative methods are well documented.[158,159] Sulfur compounds are readily studied by vibrational spectroscopy, both IR and Raman. The oxides and oxyanions have characteristic spectra[160] in the IR while the sulfanes and *cyclo*-sulfur compounds give strong Raman spectra as a result of their high polarizability. The only potentially useful NMR nucleus is ^{33}S, which is quadrupolar and low in abundance (Table 2). In general, measurements of ^{33}S NMR

Table 15 Qualitative analysis of sulfur anions

S^{2-}	$+HCl \rightarrow H_2S(\uparrow)$
	$AgNO_3 \rightarrow Ag_2S$ (sol. in hot dil. HNO_3)
	$2NaN_3 + I_2 \rightarrow 2NaI + 3N_2(\uparrow)$ (sensitivity 0.3 µg NaS)
$SO_3{}^{2-}$	$+HCl \rightarrow SO_2(\uparrow) + H_2O$
	$AgNO_3 \rightarrow Na(AgSO_3)$ (sol. in dil. HNO_3 or NH_4OH)
	Malachite Green decolorized (1 µg)
$SO_4{}^{2-}$	$BaCl_2 \rightarrow BaSO_4(\downarrow)$
	$AgNO_3 \rightarrow AgSO_4$ (sol. in H_2O)
$S_2O_4{}^{2-}$	$KI \rightarrow I_2$
	$AgNO_3 \rightarrow Ag_2O_2$
$S_2O_3{}^{2-}$	$+HCl \rightarrow S(\downarrow) + SO_3{}^{2-}$
	$AgNO_3 \rightarrow Na_3[Ag(S_2O_3)_2] \rightarrow\rightarrow Ag_2S$
	$[Ni(en)](NO_3)_2 \rightarrow [Ni(en)_3]S_2O_3(\downarrow)$ violet

Table 16 Typical ^{33}S NMR data

Species	$\delta(^{33}S)$ (ppm)	$\Delta W_i/2$ (Hz)	Solvent
Na_2SO_4	0	6.5	D_2O
$Na_2S_2O_3$	33.5	60	D_2O
CS_2	−332	320	Neat
SO_2	707	375	Neat
OCS	−260	594	Neat
$SOCl_2$	224	600	Neat
SO_2Cl_2	−45	600	Neat
SO_2F_2	−41	–	Neat
$SO_2(NH_2)_2$	−15.3	256	D_2O
SF_6	−176	Multiplet	Neat
H_2S	−503	–	Neat
$[WS_4]^{2-}$	159	13	H_2O
$[WS_3O]^{2-}$	57	140	H_2O
$[WS_2O_2]^{2-}$	−56	220	H_2O
$[WSO_3]^{2-}$	−166	300	H_2O
Na_2S	34	60	H_2O
ZnS	−100	53	Solid

spectra are achieved most readily with high-field solid-state machines that are capable of very rapid pulsing at high powers and of implementing sequences such as RIDES (to reduce ringing in the probe). Quite variable line widths, which can be related to the symmetry of the substituents about the nucleus, are observed. Notwithstanding the difficulties, ^{33}S NMR has become increasing widely used in recent years;[161–164] solid-state ^{33}S NMR has even been reported.[165] Although the lines can be very broad, the chemical shift range is still useful. Some examples of δ values and line widths are given in Table 16.

10 RELATED ARTICLES

Iron−Sulfur Proteins; Sulfur−Nitrogen Compounds; Sulfur: Organic Polysulfanes.

11 REFERENCES

1. N. N. Greenwood and A. Earnshaw, 'Chemistry of The Elements', 2nd edn., Pergamon, Oxford, 1997.
2. J. Emsley, 'The Elements', 2nd edn., Clarendon Press, Oxford, 1990.
3. 'Gmelin Handbook of Inorganic Chemistry', Springer, Berlin, includes the following: Sulfur A1 (History, 1942); A2 (Occurrence, Technology, 1953); A3 (The Element, 1953); B1 (Hydrides and Oxides, 1953); B2 (Sulfur−Oxygen Acids, 1960); B3 (Compounds, 1963); Sulfur Suppl. Vol. 1 (Thionyl Halides, 1978); Sulfur Suppl. Vol. 2 (Sulfur Halides, 1978); Sulfur Suppl. Vol. 3 (Sulfur Oxides, 1980); Sulfur Suppl. Vol. 4a/b (Sulfanes, 1983) as well as several volumes on S–N chemistry.
4. J. W. Mellor, 'A Comprehensive Treatise of Inorganic and Theoretical Chemistry', Longmans, London, 1930, and subsequent editions.
5. G. Nickless ed., 'Inorganic Sulfur Chemistry', Elsevier, Amsterdam, 1968; J. D. Woollins, 'Non-Metal Rings, Cages and Clusters', Wiley, Chichester, 1988; I. Haiduc and D. B. Sowerby eds, 'The Chemistry of Inorganic Homo and Heterocycles', Academic Press, London, 1987, Vols. 1 and 2.
6. B. Meyer ed., 'Elemental Sulfur, Chemistry and Physics', Wiley, New York, 1965.
7. F. A. Cotton and G. Wilkinson, 'Advanced Inorganic Chemistry', 5th edn., Wiley, New York, 1988.
8. W. Buchner, R. Schliebs, G. Winter, and K. Buchel, in 'Industrial Inorganic Chemistry', ed. D. R. Terrell, VCH, Weinheim, 1989.
9. D. W. Davis and R. A. Detro, 'Fire and Brimstone', Resource Information Series No. 8, Louisiana Geological Survey, Baton Rouge, LA, 1992.
10. J. R. West ed., 'New Uses of Sulfur', Advances in Chemistry Series, No. 140, American Chemical Society, Washington, DC, 1975.
11. D. J. Bourne ed., 'New Uses of Sulfur-II', Advances in Chemistry Series, No. 165, American Chemical Society, Washington, DC, 1978.
12. B. Meyer, *Chem. Rev.*, 1976, **76**, 367.
13. J. Donohue, 'The Structures of the Elements', Wiley, New York, 1974.
14. R. Steudel, *Top. Curr. Chem.*, 1982, **102**, 149.
15. R. Steudel, O. Schumann, J. Buschmann, and P. Luger, *Angew. Chem., Int. Ed. Engl.*, 1998, **37**, 2377.
16. R. Steudel, *Phosphorus Sulfur*, 1985, **23**, 33.
17. R. Steudel and R. Laitinen, *Top. Curr. Chem.*, 1982, **102**, 177.
18. R. Steudel, in 'The Chemistry of Inorganic Homo and Heterocycles', eds. I. Haiduc and D. B. Sowerby, Academic Press, London, 1987, Vol. 2.
19. H. J. Mausle and R. Steudel, *Z. Anorg. Allg. Chem.*, 1980, **463**, 27.
20. R. Steudel and R. Strauss, *J. Chem. Soc., Dalton Trans.*, 1984, 1775.
21. R. J. Gillespie, *Chem. Soc. Rev.*, 1979, **8**, 315.
22. R. C. Burns, R. J. Gillespie, and J. F. Sawyer, *Inorg. Chem.*, 1980, **19**, 1423.
23. J. Passmore, G. Sutherland, P. Taylor, T. K. Whidden, and P. S. White, *Inorg. Chem.*, 1981, **20**, 3839.
24. J. Passmore, G. Sutherland, and P. S. White, *Inorg. Chem.*, 1982, **21**, 2717.
25. M. J. Collins and R. J. Gillespie, *Inorg. Chem.*, 1984, **23**, 1975.
26. M. J. Collins, R. J. Gillespie, J. F. Sawyer, and G. J. Schrobilgen, *Inorg. Chem.*, 1986, **25**, 2053. see also 4465.
27. M. J. Collins, R. J. Gillespie, J. Kolis, and J. F. Sawyer, *Inorg. Chem.*, 1986, **25**, 2057.
28. D. J. Jones, T. Makani, and J. Roziere, *J. Chem. Soc., Chem. Commun.*, 1986, 1275.
29. C. D. Desjardins and J. Passmore, *J. Chem. Soc., Dalton Trans.*, 1973, 2314.
30. A. M. Rosan, *J. Chem. Soc., Chem. Commun.*, 1985, 377.
31. T. Chivers and I. Drummond, *Chem. Soc. Rev.*, 1973, **2**, 233.
32. R. Steudel, *Z. Anorg. Allg. Chem.*, 1981, **476**, 171.
33. H. J. Mausle and R. Steudel, *Z. Anorg. Allg. Chem.*, 1981, **478**, 177.
34. P. W. Schenk and R. Steudel, in 'Inorganic Sulfur Chemistry', ed. G. Nickless, Elsevier, Amsterdam, 1968, Chap. 11.
35. V. K. Gleu, W. Brunel, and K. Rehm, *Z. Anorg. Allg. Chem.*, 1938, **235**, 201, 211.
36. D. M. P. Mingos, *Transition Met. Chem.*, 1978, **3**, 1.
37. R. R. Ryan, G. J. Kubas, D. C. Moody, and P. G. Eller, *Struct. Bonding*, 1981, **46**, 47.
38. A. F. Hill, *Adv. Organomet. Chem.*, 1993, **35**, 1805.

39. T. C. Waddington, in ‘Non-Aqueous Solvent Systems’, ed. T. C. Waddington, Academic Press, London, 1965, Chap. 6.
40. J. Passmore, in ‘The Chemistry of Inorganic Ring Systems’, ed. R. Steudel, Elsevier, Amsterdam, 1992 Chap. 19; T. Klapotke, in ‘The Chemistry of Inorganic Ring Systems’, ed. R. Steudel, Elsevier, Amsterdam, 1992, Chap. 20.
41. A. J. Banister, Z. V. Hauptman, and A. G. Kendrick, *J. Chem. Soc., Chem. Commun.*, 1983, 1016.
42. B. Meyer, ‘Sulfur, Energy and the Environment’, Elsevier, Amsterdam, 1977.
43. J. O. Nriagu, ed., ‘Sulfur in the Environment’, Wiley, Chichester, 1979, Part 2.
44. L. R. Ember, *Chem. Eng. News*, 1981, **59**, 20.
45. R. J. Lovejoy, J. H. Colwell, D. F. Eggers, and G. D. Halsey, *J. Chem. Phys.*, 1962, **36**, 612.
46. K. Stopperka, *Z. Anorg. Allg. Chem.*, 1966, **345**, 277.
47. W. S. McDonald and D. W. J. Cruikshank, *Acta Crystallogr.*, 1967, **22**, 48.
48. R. Westrik and C. H. McGillavry, *Acta Crystallogr.*, 1954, **7**, 764.
49. R. Steudel, T. Sandow, and J. Steidel, *J. Chem. Soc., Chem. Commun.*, 1980, 180.
50. R. Steudel, J. Steidel, and T. Sandow, *Z. Naturforsch., Teil B*, 1986, **41**, 951.
51. P. W. Schenk and R. Steudel, *Angew. Chem., Int. Ed. Engl.*, 1965, **4**, 402.
52. P. W. Schenk and R. Steudel, *Angew. Chem., Int. Ed. Engl.*, 1964, **3**, 61.
53. G. Schmidt and G. Ritter, *Angew. Chem., Int. Ed. Engl.*, 1975, **14**, 645.
54. J. E. Hoots, D. A. Lesch, and T. B. Rauchfuss, *Inorg. Chem.*, 1984, **23**, 3130.
55. M. Heberhold and A. F. Hill, *J. Chem. Soc., Dalton Trans.*, 1988, 2027.
56. K. K. Pandey, *Prog. Inorg. Chem.*, 1992, **40**, 445.
57. M. Heberhold and B. Scmidkonz, *Angew. Chem., Int. Ed. Engl.*, 1985, **24**, 515; *J. Organomet. Chem.*, 1986, **308**, 35.
58. K. Nakamoto, ‘Infrared Spectra of Inorganic and Coordination Compounds’, Wiley, New York, 1970.
59. V. C. Ginn, P. F. Kelly, A. M. Z. Slawin, D. J. Williams, and J. D. Woollins, *J. Chem. Soc., Dalton Trans.*, 1992, 963; *J. Chem. Soc., Dalton Trans.*, 1992, 1135; *Polyhedron* 1994, **13**, 1501.
60. C. F. Edwards, W. P. Griffith, and D. J. Williams, *J. Chem. Soc., Dalton Trans.*, 1992, 145.
61. A. J. Blake, V. Costerdine, M. F. A. Dove, S. Lammas, and L. H. Thompson, *J. Chem. Soc., Dalton Trans.*, 1998, 3.
62. M. W. Whitehouse and W. R. Walker, *Agents Actions*, 1978, **8**, 85.
63. S. Rahim and J. Milne, *Can. J. Chem.*, 1996, **74**, 753.
64. A. Shaver, M. El-Khateeb, and A. M. Lebuis, *Angew. Chem., Int. Ed. Engl.*, 1996, **35**, 2362.
65. E. Noack, *Z. Anorg. Allg. Chem.*, 1925, **64**, 123.
66. F. Feher and M. Baudler, *Z. Anorg. Allg. Chem.*, 1947, **254**, 289.
67. F. Feher, W. Laue, and G. Winkhaus, *Z. Anorg. Allg. Chem.*, 1956, **288**, 103.
68. F. Feher and R. Berthold, *Z. Anorg. Allg. Chem.*, 1957, **290**, 251.
69. F. Feher, W. Laue, and J. Kraemer, *Z. Anorg. Allg. Chem.*, 1955, **281**, 151.
70. T. Chivers, in ‘Homoatomic Rings, Chains and Macromolecules of Main Group Elements’, ed. A. L. Rheingold, Elsevier, Amsterdam, 1977.
71. T. Chivers and C. Lau, *Inorg. Chem.*, 1982, **21**, 453.
72. R. J. H. Clark and D. G. Cobbold, *Inorg. Chem.*, 1978, **17**, 3169; R. J. H. Clark, T. J. Dines, and M. Kurmoo, *Inorg. Chem.*, 1982, **22**, 2766; S. Best, R. Clark, M. Daniels, and R. Withnall, *Chem. Br.*, 1993, 118.
73. U. Muller and W. Bubenheim, *Z. Anorg. Allg. Chem.* 1999, **625**, 1522; M. Schur and W. Bensch, *Z. Anorg. Allg. Chem.* 1998, **624**, 310; J. Wachter, *Angew. Chem., Int. Ed. Engl.*, 1998, **37**, 751; J. K. Burdett and E. L. Miller, *J. Am. Chem. Soc.*, 1987, **109**, 4081; M. Draganjac and T. B. Rauchfuss, *Angew. Chem., Int. Ed. Engl.*, 1985, **24**, 742; H. Vahrenkamp, *Angew. Chem., Int. Ed. Engl.*, 1975, **14**, 322; A. Muller and E. Diemann, *Adv. Inorg. Chem. Radiochem.*, 1987, **31**, 89.
74. M. Rakowski Dubois, *Chem. Rev.*, 1989, **89**, 1.
75. R. H. Holm, *Chem. Soc. Rev.*, 1981, **10**, 455; R. H. Holm, S. Ciurli, and J. A. Weigel, *Prog. Inorg. Chem.*, 1990, **38**, 1; A. X. Trautwein, E. Bill, E. L. Bominaar, and H. Winkler, *Struct. Bonding*, 1991, **78**, 1.
76. G. A. Tsigdinos, *Top. Curr. Chem.*, 1978, **76**, 65; G. Moh, *Top. Curr. Chem.*, 1978, **76**, 153.
77. M. J. Pilkington, A. M. Z. Slawin, D. J. Williams, and J. D. Woollins, *J. Chem. Soc., Dalton Trans.*, 1992, 2425.
78. P. Chen, P. P. Paul, Z. Tyeklar, R. D. Sommer, L. N. Zakharov, A. L. Rheingold, E. I. Solomon, and K. D. Karlin, *J. Am. Chem. Soc.*, 2003, **125**, 1160.
79. W. Clegg, G. Christou, C. D. Garner, and G. M. Sheldrick, *Inorg. Chem.*, 1981, **20**, 1562.
80. M. Draganjac, E. Simhon, L. T. Chan, M. Kanatzidis, N. C. Baenziger, and D. Coucouvanis, *Inorg. Chem.*, 1982, **21**, 3321.
81. J. M. McCall and A. Shaver, *J. Organomet. Chem.*, 1980, **193**, C37.
82. P. H. Bird, J. M. McCall, A. Shaver, and U. Siriwardane, *Angew. Chem., Int. Ed. Engl.*, 1982, **21**, 384.
83. C. M. Bolinger, T. B. Rauchfuss, and S. R. Wilson, *J. Am. Chem. Soc.*, 1981, **103**, 5620.
84. J. Chatt and D. M. P. Mingos, *J. Chem. Soc. A*, 1970, 1243.

85. H. Kopf, B. Block, and M. Schmidt, *Chem. Ber.*, 1968, **101**, 272; E. Samual and G. Gianotti, *J. Organomet. Chem.*, 1976, **113**, C17.
86. A. Muller, M. Romer, C. Romer, U. Reinsch-Vogell, U. Bogge, and U. Schimanski, *Monatsh. Chem.*, 1985, **116**, 711.
87. J. W. Kolis, *Coord. Chem. Rev.*, 1990, **105**, 195.
88. S. C. O'Neal and J. W. Kolis, *Inorg. Chem.*, 1989, **28**, 2780 and refs. therein.
89. S. Schreiner, L. E. Aleandri, D. A. Kang, and J. A. Ibers, *Inorg. Chem.*, 1989, **28**, 392.
90. Y. Park, D. C. Degroot, J. Schindler, C. R. Kannenwurf, and M. G. Kanatzidis, *Angew. Chem., Int. Ed. Engl.*, 1991, **30**, 1325.
91. M. Schmidt and G. G. Hoffmamm, *Z. Anorg. Allg. Chem.*, 1979, **452**, 112; A. E. Wickenden and R. A. Krause, *Inorg. Chem.*, 1969, **8**, 779.
92. B. Kreutzer, P. Kreutzer, and W. Beck, *Z. Naturforsch., Teil B*, 1972, **B27**, 461; D. Dudis and J. P. Fackler, Jr, *Inorg. Chem.*, 1982, **21**, 3577.
93. A. Muller, unpublished results, discussed in Ref. 73.
94. E. Diemann, A. Muller, and P. J. Aymonino, *Z. Anorg. Allg. Chem.*, 1981, **479**, 191.
95. C. M. Bolinger, J. E. Hoots, and T. B. Rauchfuss, *Organometallics*, 1982, **1**, 223.
96. M. Draganjac and D. Coucouvanis, *J. Am. Chem. Soc.*, 1983, **105**, 139.
97. C. J. Casewit, D. E. Koons, L. L. Wright, W. K. Miller, and M. Rakowski Dubois, *Organometallics*, 1986, **5**, 951.
98. R. Weberg, R. C. Haltiwanger, J. C. V. Laurie, and M. Rakowski Dubois, *J. Am. Chem. Soc.*, 1986, **108**, 6242.
99. M. McKenna, L. L. Wright, D. J. Miller, L. Tanner, R. C. Haltiwanger, and M. Rakowski Dubois, *J. Am. Chem. Soc.*, 1983, **105**, 5329.
100. R. Battaglia, R. Henning, B. Dinh-Ngog, W. Schlaman, and H. Kisch, *J. Mol. Catal.*, 1983, **21**, 239.
101. O. N. Temkin, G. K. Shestakov, and R. M. Flid, *Dokl. Chem.*, 1969, **184**, 43; *Chem. Abstr.*, 1969, **70**, 95 950s.
102. 'Fast Ion Transport in Solids: Electrodes and Electrolytes', eds. P. Vashita, J. N. Mundy, and G. K. Shenoy, North Holland, New York, 1979.
103. A. R. West, 'Basic Solid State Chemistry', Wiley, Chichester, 1988, p. 325.
104. R. A. Crawford, F. Dudley, and K. W. Hedberg, *J. Am. Chem. Soc.*, 1959, **81**, 5287.
105. N. Muller, P. C. Lauterbur, and C. F. Svatos, *J. Am. Chem. Soc.*, 1957, **79**, 1043.
106. M. T. Rogers and J. J. Katz, *J. Am. Chem. Soc.*, 1952, **74**, 1375.
107. H. L. Roberts, *J. Chem. Soc.*, 1962, 3183.
108. H. J. Emeleus and K. Packer, *J. Chem. Soc.*, 1962, 771.
109. 'Advances in Fluorine Chemistry', Butterworths, London, 1960, Vols. 1 and II.
110. F. Nyman and H. L. Roberts, *J. Chem. Soc.*, 1962, 3180.
111. C. W. Tullock, D. D. Coffman, and E. L. Muetterties, *J. Am. Chem. Soc.*, 1964, **86**, 357.
112. J. R. Case, N. H. Ray, and H. L. Roberts, *J. Chem. Soc.*, 1961, 2066.
113. F. B. Dudley, G. H. Cady, and D. F. Eggers, *J. Am. Chem. Soc.*, 1956, **78**, 1553.
114. G. Gundersen and K. Hedberg, *J. Chem. Phys.*, 1969, **51**, 2500.
115. C. W. Tullock, F. S. Fawcett, W. C. Smith, and D. D. Coffman, *J. Am. Chem. Soc.*, 1960, **82**, 539.
116. F. A. Cotton, J. W. George, and J. S. Vaughan, *J. Chem. Phys.*, 1958, **28**, 994; E. L. Muetterties and W. D. Phillips, *J. Am. Chem. Soc.*, 1959, **81**, 1084.
117. R. E. Dodd, H. L. Roberts, and L. A. Woodward, *Trans. Faraday Soc.*, 1956, **52**, 1052.
118. I. B. Douglas, K. R. Brower, and F. T. Martin, *J. Am. Chem. Soc.*, 1951, **73**, 5787.
119. P. Bender and J. M. Wood, *J. Chem. Phys.*, 1955, **23**, 1316; H. O'Loane and M. K. Wilson, *J. Chem. Phys.*, 1955, **23**, 1313.
120. F. Seel, *Adv. Inorg. Chem. Radiochem.*, 1974, **74**, 297.
121. W. Hahn and R. Strohe, 'Methoden der Organischen Chemie', 4th edn., Thieme, Stuttgart, 1962, p. 503, Vol. 5/3.
122. A. Senning ed., 'Sulfur in Organic and Inorganic Chemistry', Marcel Dekker, New York, 1971, Vol. 1, and other volumes in the following years.
123. E. Kuhle, 'The Chemistry of Sulfenic Acids', Thieme, Stuttgart, 1973.
124. G. Gattow and W. Behrendt, 'Carbon Sulfides and Their Inorganic and Complex Chemistry', Thieme, Stuttgart, 1977.
125. E. K. Moltzen, K. J. Klabunde, and A. Senning, *Chem. Rev.*, 1988, **88**, 391.
126. C. P. Galloway, T. B. Rauchfuss, and X. Yang, in 'The Chemistry of Inorganic Ring Systems', ed. R. Steudel, Elsevier, Amsterdam, 1992.
127. R. Steudel, *Z. Naturforsch., Teil B*, 1966, **B21**, 255; R. Steudel, *Angew. Chem., Int. Ed. Engl.*, 1967, **6**, 635.
128. P. V. Broadhurst, *Polyhedron*, 1985, **4**, 1801.
129. G. V. Calder, J. V. Verkade, and L. W. Yarbrough, *J. Chem. Soc., Chem. Commun.*, 1973, 705.
130. T. A. Wnuk and R. J. Angelici, *Inorg. Chem.*, 1977, **16**, 1173.
131. G. R. Clark, K. R. Grundy, R. O. Harris, S. M. James, and W. R. Roper, *J. Organomet. Chem.*, 1975, **90**, C37.
132. A. E. Fenster and I. S. Butler, *Inorg. Chem.*, 1974, **13**, 915.
133. H. Werner, *Coord. Chem. Rev.*, 1982, **43**, 165.
134. M. H. Quick and R. J. Angelici, *Inorg. Chem.*, 1982, **21**, 1674; B. D. Dombek and R. J. Angelici, *J. Am. Chem. Soc.*, 1974, **96**, 7568.

135. T. G. Southern, U. Oehmichen, J. Y. Le Marouille, H. Le Bozec, D. Grandjean, and P. H. Dixneuf, *Inorg. Chem.*, 1980, **19**, 2976; P. V. Broadhurst, B. F. G. Johnson, J. Lewis, and P. R. Raithby, *J. Chem. Soc., Chem. Commun.*, 1982, 140 and refs. therein.
136. G. D. Thorn and R. A. Ludwig, 'The Dithiocarbamates and Related Compounds', Elsevier, Amsterdam, 1962; D. Coucouvanis, *Prog. Inorg. Chem.*, 1970, **11**, 233.
137. P. Jeroschewski, *Z. Chem.*, 1981, **21**, 412; K. S. Varma, A. Bury, N. J. Harris, and A. E. Underhill, *Synthesis*, 1987, **9**, 837; J. M. Williams, H. H. Wang, T. J. Emge, U. Geiser, M. A. Beno, P. C. Leung, K. D. Carlson, R. J. Thorn, and A. J. Schultz, *Prog. Inorg. Chem.*, 1987, **35**, 1; J. M. Williams and K. Carneiro, *Adv. Inorg. Chem. Radiochem.*, 1985, **29**, 249.
138. G. Maier, H. P. Reisenhalter, and R. Ruppel, *Angew. Chem., Int. Ed. Engl.*, 1997, **36**, 1862.
139. G. Baum, F. J. Kaiser, W. Massa, and G. Seitz, *Angew. Chem., Int. Ed. Engl.*, 1987, **26**, 1163.
140. G. Steimecke, H. J. Sieler, R. Kirmse, W. Dietzsch, and E. Hoyer, *Phosphorus Sulfur*, 1982, **12**, 237.
141. A. M. Richter, V. Engels, N. Beye, and E. Fanghanel, *Z. Chem.*, 1989, **29**, 444.
142. X. Yang, PhD Thesis, University of Illinois at Urbana-Champaign, IL, 1991; B. Krebs and D. F. Koenig, *Acta Crystallogr.*, 1969, **B25**, 1022.
143. A. M. Richter, N. Beye, and E. Fanghanel, *Z. Chem.*, 1988, **28**, 284.
144. S. M. Aucott, A. M. Z. Slawin, and J. D. Woollins, *Polyhedron*, 2000, **19**, 499.
145. D. B. Sowerby, in 'The Chemistry of Inorganic Homo and Heterocycles', eds. I. Haiduc and D. B. Sowerby, Academic Press, London, 1987.
146. H. Nowottnick and R. Blacknik, *Z. Anorg. Allg. Chem.*, 1999, **625**, 1966.
147. M. E. Mason, T. Ngo, and S. Rahmann, *Inorg. Chem.*, 1997, **36**, 2633.
148. M. Meisel and H. Grunze, *Z. Anorg. Allg. Chem.*, 1970, **373**, 265.
149. A. M. Griffin, P. C. Minshall, and G. M. Sheldrick, *J. Chem. Soc., Chem. Commun.*, 1976, 809.
150. R. A. Cherkasov, G. A. Kutyrev, and A. N. Pudovik, *Tetrahedron*, 1985, **41**, 2567.
151. A. M. Z. Slawin, D. J. Williams, P. T. Wood, and J. D. Woollins, *J. Chem. Soc., Chem. Commun.*, 1987, 1741; M.-E. Eleftheriou, J. Novosad, D. J. Williams, and J. D. Woollins, *J. Chem. Soc., Chem. Commun.*, 1991, 116; M. R. St. J. Foreman, A. M. Z. Slawin and J. D. Woollins, *Heteroat. Chem.*, 1999, **10**, 651; P. Kilian, D. Philp, A. M. Z. Slawin, and J. D. Woollins, *Eur. J. Inorg. Chem*, 2003, 249; P. Kilian, A. M. Z. Slawin, J. D. Woollins, *Chem. Eur. J.*, 2003, **9**, 215; P. Kilian, A. M. Z. Slawin, and J. D. Woollins, *Chem. Commun.*, 2003, 1174.
152. S. Menzer, J. R. Phillips, A. M. Z. Slawin, D. J. Williams, and J. D. Woollins, *J. Chem. Soc., Dalton Trans.*, 2000, 3269.
153. J. C. Poat, A. M. Z. Slawin, D. J. Williams, and J. D. Woollins, *J. Chem. Soc., Chem. Commun.*, 1990, 1036; *Polyhedron*, 1992, **11**, 2125.
154. P. T. Wood and J. D. Woollins, *Transition Met. Chem.*, 1986, **9**, 358.
155. B. Cetinkaya, P. B. Hitchcock, M. F. Lappert, A. J. Thorne, and H. Goldwhite, *J. Chem. Soc., Chem. Commun.*, 1982, 691.
156. C. Lensch and G. M. Sheldrick, *J. Chem. Soc., Dalton Trans.*, 1984, 2855.
157. C. Lensch, W. Clegg, and G. M. Sheldrick, *J. Chem. Soc., Dalton Trans.*, 1984, 723.
158. A. B. Roy and P. A. Trudinger, 'The Biochemistry of Inorganic Compounds of Sulfur', Cambridge University Press, Cambridge, 1970.
159. A. I. Vogel, 'A Text Book of Macro and SemiMicro Qualitative Inorganic Analysis', 4th edn., Longmans, London, 1953.
160. K. Nakamoto, 'Infrared and Raman Spectroscopy of Inorganic and Coordination Compounds', 3rd edn., ed. K. Nakamoto, Wiley, New York, 1978.
161. H. C. E. McFarlane and W. McFarlane, in 'Multinuclear NMR', ed. J. Mason, Plenum, New York, 1987, Chap. 15.
162. P. S. Belton, I. J. Cox, and R. J. Harris, *J. Chem. Soc., Faraday Trans. 2*, 1981, 63.
163. P. S. Belton and J. D. Woollins, *Magn. Reson. Chem.*, 1986, **9**, 358.
164. R. E. Waylishen, C. Connor, and J. O. Friedrich, *Can. J. Chem.*, 1984, **62**, 981, 1181.
165. M. Haller, W. E. Hertler, O. Lutz, and A. Nolle, *Solid State Commun.*, 1980, **33**, 1051.

Sulfur–Nitrogen Compounds

Tristram Chivers
The University of Calgary, Calgary, AB, Canada

1 Introduction 1
2 Structure and Bonding 1
3 Thermal Stability 2
4 Physical Methods 2
5 Binary Sulfur–Nitrogen Compounds 4
6 Sulfur–Nitrogen Halides 10
7 Sulfur–Nitrogen Oxides 12
8 Heterocyclothiazenes 14
9 Sulfanuric Compounds 20
10 Cyclic Sulfur Imides 20
11 Sulfur–Nitrogen Chains and Polymers 21
12 Poly(Sulfur Nitride) 22
13 Related Articles 22
14 Further Reading 23
15 References 23

Glossary

π-Electron-rich compound: a compound in which the number of π-electrons exceeds the number of atoms
Heterocyclothiazene: an unsaturated sulfur–nitrogen ring system containing another element
Thiazene: a compound containing an unsaturated sulfur–nitrogen bond

Abbreviations

DFT = density functional theory; HMQC = heteronuclear multiple quantum coherence; SOMO = singly occupied molecular orbital; PES = photoelectron spectroscopy; CI = configuration interaction; LUMO = lowest unoccupied molecular orbital; HOMO = highest occupied molecular orbital; TLC = thin layer chromatography.

1 INTRODUCTION

Sulfur–nitrogen (S–N) compounds have a long history. The first example, S_4N_4, was discovered in 1835, but the intriguing cage structure (**1**) of this inorganic heterocycle was not established until 1963.**[1]** The related polymer, $(SN)_x$ (**2**), was first obtained in 1910 and its metallic character was noted. However, it was the discovery in 1975 that $(SN)_x$ is a superconductor at 0.26 K that excited considerable interest in S–N chemistry.**[2]**

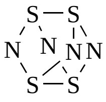
(**1**)

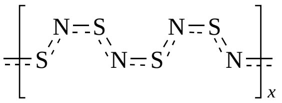
(**2**)

Three years earlier, in 1972, Banister had proposed that planar S–N heterocycles belong to a class of 'electron-rich aromatics', which conform to the Hückel $(4n+2)$ π-electron rule.**[3]** These two aspects of S–N chemistry have attracted the attention of both synthetic chemists and theoreticians. Since the 1970s, the field has reached maturity. Many new S–N compounds with unusual structures and properties have been characterized, and theoretical studies have provided reasonable rationalizations of the structure–reactivity relationships of these fascinating compounds.**[4,5]** The versatile behavior of S–N compounds as ligands in transition metal complexes has also been established.**[6,7]** Recent studies have focused on the magnetic and conducting properties of materials derived from C–S–N radicals.**[8,9]**

A book by Heal, published in 1980, is the only text devoted to inorganic S–N chemistry.**[10]** A more recent monograph contains substantial coverage of S–N compounds.**[11]** Specialized reviews of specific aspects of S–N chemistry are referred to in the appropriate sections of this article.

2 STRUCTURE AND BONDING

Banister's proposal that *planar* S–N ring systems obey the Hückel $(4n+2)\pi$-electron rule was based on the reasonable assumption that each sulfur contributes two electrons and each nitrogen one electron to the π system.**[3]** The heterocycles S_2N_2 (6π) (**3**), $S_4N_3{}^+$ (10π) (**4**), and $S_5N_5{}^+$ (14π) (**5**) were cited as examples to support this suggestion. These ring systems are referred to as π-electron-rich since the number of π-electrons exceeds the number of atomic centers in the ring.**[12]** However, this simple counting procedure belies the fact that the surplus of electrons is accommodated in π^* (or $n\pi$) orbitals. Consequently, the π-bond orders in S–N heterocycles are significantly lower than those in the corresponding aromatic hydrocarbons. The electronic structures of planar S–N rings have been discussed at the simple and extended Hückel levels**[13,14]** and for ab initio molecular orbital calculations**[5]** (*see* ***Molecular Orbital Theory***). These calculations provide a detailed description of the frontier orbitals of S–N heterocycles, which is essential for understanding their reactivity patterns and the nature of electronic transitions.

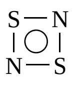
(3)

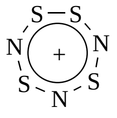
(4)

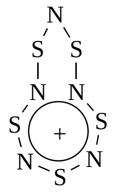
(5)

A characteristic feature of eight-membered (or larger) S–N heterocycles is the formation of folded structures with a transannular S–S interaction. The classic example is S_4N_4 (**1**) and the same structural feature is evident in the related ring systems $E_2N_4S_2$ (**6**) where $E = PR_2$ or $CNMe_2$. The S–S distance of ca. 250−260 pm in these compounds is substantially longer than the normal S–S single-bond length of 205 pm, indicating an unusual type of bonding. Molecular orbital calculations reveal that the folded structures result from an *intramolecular* $\pi^*-\pi^*$ interaction, as shown in Figure 1.[7] A similar type of bonding is found in S_8^{2+} (*see* ***Sulfur: Inorganic Chemistry***). *Intermolecular* $\pi^*-\pi^*$ bonding is also a significant feature of S–N compounds, as exemplified by the dimer $S_6N_4^{2+}$ (**7**), where two $S_3N_2^+$ rings (a 7π-electron system) are connected by weak S–S interactions [d(S–S) $= 300-310$ pm].[14]

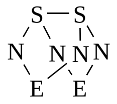
(6)

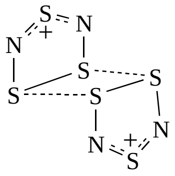
(7)

3 THERMAL STABILITY

Electron-rich S–N heterocycles are thermodynamically unstable with respect to the loss of N_2 and there is often a low kinetic barrier to decomposition. Consequently, caution must be exercised to avoid explosions when handling certain S–N compounds, for example, S_2N_2 (**3**), S_4N_4 (**1**), S_5N_6 (**8**), and alkali metal salts of the anions $S_3N_3^-$ (**9**) and $S_4N_5^-$ (**10**). These compounds may explode when subjected to mechanical or thermal stress, for example, on contact with a metal spatula or upon gentle heating.

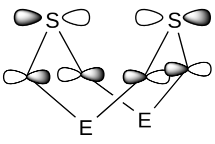

Figure 1 The $\pi^*-\pi^*$ interaction in $E_2N_4S_2$ ($E = CNMe_2$, PR_2)

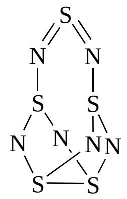
(8)

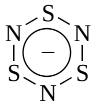
(9)

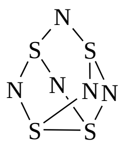
(10)

Under suitably controlled conditions, thermal decomposition may be used to prepare certain S–N compounds. For example, S_2N_2 is obtained by the mild thermolysis of a variety of S–N heterocycles (see Section 5.1.3); and heating solutions of $S_3N_3^-$ salts in boiling acetonitrile produces the acyclic $SSNSS^-$ anion (see Section 5.3.4). Bond enthalpies for S–N compounds can be estimated from S–N bond lengths.[15]

4 PHYSICAL METHODS

4.1 X-Ray Crystallography

The structures of many S–N compounds are often unpredictable. Furthermore, the reactions of these compounds frequently result in substantial reorganization of their structural frameworks, for example, ring contraction or expansion and the formation of acyclic products from ring systems (or vice versa), to give products with unexpected structures.

Spectroscopic methods are usually not sufficient to provide decisive structural information. Consequently, the ability to establish atomic arrangements rapidly by X-ray crystallography has been of paramount importance in the development of S–N chemistry (*see* ***Diffraction Methods in Inorganic Chemistry***). X-Ray crystallography also provides the details of intermolecular interactions in the solid state, which are important for understanding the physical properties, for example, conductivity and magnetic behavior of S–N compounds with extended structures.

4.2 $^{14}N/^{15}N$ NMR Spectroscopy

Although NMR spectroscopy played a minor role in the early development of S–N chemistry, the availability of high-field instruments with Fourier transform capabilities has facilitated nitrogen NMR investigations. Nitrogen has two nuclei, ^{14}N ($I = 1$, 99.6%) and ^{15}N ($I = 1/2$, 0.4%) that are amenable to NMR studies. The advantages of ^{15}N NMR are narrow, well-resolved lines and the potential ability to observe spin–spin coupling patterns. The disadvantages include lengthy acquisition times due to long spin-lattice relaxation times and the necessity to prepare isotopically enriched materials in order to observe the effects of spin–spin coupling.[16] On the other hand, the ^{14}N nucleus gives rise to relatively broad lines, poorer resolution, and loss of coupling information. To offset these disadvantages, very short delays between pulses are possible in view of the short spin-lattice relaxation times and good signal-to-noise ratios can be achieved in relatively short acquisition times when the appropriate experimental conditions are used.[17]

Some important examples of the application of ^{14}N NMR spectroscopy in S–N chemistry include (a) investigations of the $(NSCl)_3 \rightleftharpoons 3NSCl$ equilibrium in solution[18] and (b) identification of the S–N species present in solutions of sulfur in liquid ammonia.[19] The half-width of ^{14}N NMR resonances is dependent on the symmetry of the atomic environment as well as other factors, such as solvent viscosity. The values may vary from ca. 10 Hz for solutions of $NS_2^+ AsF_6^-$ in liquid SO_2 to >1000 Hz in metal–S–N complexes. However, the chemical shift range for S–N compounds is ca. 800 ppm, so that useful information may frequently be obtained despite the broad lines.[17] Liquid SO_2 is a particularly good solvent for ^{14}N NMR studies of cationic S–N species,[18] while liquid ammonia is well suited to investigations of S–N anions.[17,19]

^{15}N NMR spectroscopy has been applied to the identification of complex mixtures of S–N rings and cages formed from the air oxidation of $S_3{}^{15}N_3{}^-$ in acetonitrile[20] and to investigations of the dynamic behavior of the bicyclic compound $PhCN_5S_3$ (**11**), which undergoes 1,3-nitrogen shifts.[21]

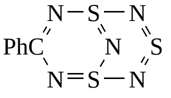

(**11**)

In S–N compounds containing ^1H directly bonded to nitrogen, reverse 2D $^1H\{^{15}N\}$ NMR spectroscopy can be applied to give ^{15}N chemical shifts and coupling constants involving ^{15}N nuclei using natural-abundance ^{15}N molecules.[22]

The only sulfur isotope with a nuclear spin is ^{33}S, which is quadrupolar ($I = 3/2$) and of low natural abundance (0.76%). Consequently, ^{33}S NMR spectroscopy has found very limited applications in S–N chemistry.

4.3 ESR Spectroscopy[23]

Many radicals containing the S–N linkage are persistent for more than several hours at room temperature. The majority of these radicals have semioccupied orbitals to which the sulfur and nitrogen p orbitals make a dominant contribution. In cyclic species, the unpaired electron often occupies a delocalized π-orbital, which may contribute to the stability of the species. ESR spectroscopy is an excellent technique for the characterization of S–N radicals and, in conjunction with MO calculations, provides unique information about their electronic structures.

The ^{14}N nucleus ($I = 1$, 99.6%) has a moderately large magnetic moment and hyperfine splittings from this nucleus are a distinctive feature of the ESR spectra. For example, the thermally unstable $S_4N_4{}^{-\bullet}$ radical anion has been identified by its characteristic nine-line ESR spectrum. For ^{33}S ($I = 3/2$, 0.76%), isotopic labeling is usually necessary to obtain information on electron spin density at sulfur.

The first radical containing S–N linkages, PhSNSPh (**12**), was produced in 1925. It was 50 years later when the ESR spectra of (**12**) and related radicals were reported.[24] Some of the more important S–N radicals include the 7π-electron system $S_3N_2{}^+$ (**13**) and the isoelectronic neutral radicals (**14**) and (**15**).

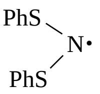

(**12**)

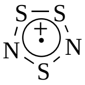

(**13**)

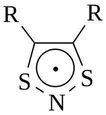

(**14**)

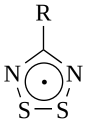

(**15**)

4.4 UV–Visible and Magnetic Circular Dichroism Spectroscopy

Electron-rich S–N heterocycles usually exhibit intense colors ranging from yellow to orange and red to blue. The colors are due to low-energy ($\pi^* \rightarrow \pi^*$ or $n \rightarrow \pi^*$) transitions.[4] For example, the 8π-electron heterocycles $R_2PN_3S_2$ (**16**) and $S_3N_3O_2{}^-$ (**17**) both have intense purple colors due to a visible absorption band at 550–560 nm attributed to the HOMO(π^*)–LUMO(π^*) transition.

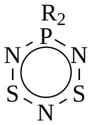

(**16**)

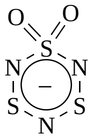

(**17**)

The experimental values of these excitation energies (from electronic spectra) have been correlated with those calculated by the transition-state method with considerable success.

Assignments of the UV–visible absorption bands to the appropriate electronic transitions can usually be made by comparing the calculated transition moments for the various alternatives. The technique of Magnetic Circular Dichroism (MCD) spectroscopy has also been applied to a variety of S–N ring systems in conjunction with π-electron calculations.[25] The MCD spectra can be interpreted in terms of $\pi^* \rightarrow \pi^*$ excitations and, in some cases, reveal transitions that are obscured in the electronic absorption spectra.

4.5 IR and Raman Spectroscopy

Several planar S–N heterocycles have been the subject of a complete vibrational analysis. For example, the IR and Raman spectra of S_2N_2, $S_3N_3^-$, and $S_4N_4^{2+}$ have been interpreted on the basis of D_{2h}, D_{3h}, and D_{4h} geometries, respectively.

The IR and Raman spectra of $S_4^{14}N_4$ and $S_4^{15}N_4$ have been assigned in accordance with the D_{2d} structure (**1**).[26] The method of ^{15}N enrichment has also been used to distinguish S–N from S–S vibrations in, for example, the $SSNSS^-$ and $SNSS^-$ anions.[20] The S–S vibration appears as a strong band in the Raman spectrum and this technique can be used to detect transannular (π^*–π^*) S–S interactions in bicyclic or cage S–N molecules or ions. The strong Raman-active S–S vibrations occur at frequencies in the range 185–270 cm^{-1} for S–S bond lengths of 240–270 pm.

The vibrational assignments for S_7NH and $S_4N_4H_4$ have been assigned with the aid of both ^{15}N and ^2H labeling, and the force constants for these molecules were determined.[27] Matrix isolation techniques combined with ^{15}N and ^{34}S labeling have provided the IR spectra of the unstable species NS, N_2S, and NS_2.[28]

4.6 Mass Spectrometry

Low ionizing potentials or soft ionization methods are necessary to observe the parent ions in the mass spectra of many S–N compounds because of their facile thermal decomposition. Indeed, mass spectrometry has been used to investigate the thermal breakdown of S_4N_4 (**1**) in connection with the mechanism of the formation of the polymer $(SN)_x$ (**2**).[29] On the basis of appearance and potential of various S_xN_y fragments, two important steps were identified: (a) the fragmentation of S_4N_4 to S_2N_2 and (b) the transformation of cyclic S_2N_2 to an open form, $(SN)_2$. The $S_3N_3^{\bullet}$ radical has been identified by MS (in conjunction with PES) as the major product of the vaporization of the $(SN)_x$ polymer.[30]

4.7 Electrochemical Studies[31]

Electrochemical studies provide important information about the redox states of S–N compounds that are potential neutral radical conductors, for example, $[RCN_2S_2]^{\bullet}$ (**15**) (see Section 8.1.1).[31] Electron-rich S–N heterocycles are good electron acceptors since the lowest unoccupied molecular orbitals (LUMOs) are low lying relative to those in aromatic hydrocarbons or cyclophosphazenes (*see* ***Phosphorus–Nitrogen Compounds***). Since the LUMOs are π^*-orbitals antibonding with respect to S–N linkages, the addition of electrons promotes ring opening to give either chains or ring-contracted products. For example, the electrochemical reduction of S_4N_4 at −0.93 V (vs. Ag/0.1 M $AgClO_4$) produces the anion radical $S_4N_4^-$, which decomposes above 0 °C to give the six-membered ring $S_3N_3^-$ (**9**).[32]

Electrochemical methods may also be used to promote the polymerization of S–N rings. Thus, the electrochemical reduction of salts of the $S_5N_5^+$ cation (**5**) in SO_2 or CH_2Cl_2 at low temperatures produces microcrystalline $(SN)_x$.[33]

4.8 Photoelectron Spectroscopy (*See Photoelectron Spectroscopy of Transition Metal Systems*)

Photoelectron spectra supply information about the energy of either inner-core (X-ray PES) or valence-level (UV-PES) electrons. The data obtained provide experimental support for MO calculations of electronic energy levels and atomic charges in various molecules. UV-PE spectra are most readily obtained for reasonably volatile compounds, and studies of S–N heterocycles have included S_2N_2 (**3**), S_4N_2 (**18**), S_4N_4 (**1**), and 1,5-$R_2C_2N_4S_2$ (**6**; E = CR).[4] The UV-PE spectrum of S_2N_2 shows that the two upper π-levels (π_S and π_N) are nearly degenerate. They are primarily nonbonding orbitals located on the sulfur atoms and nitrogen atoms, respectively, with π_S being of slightly higher energy than π_N. The UV-PE spectra of S_4N_4, S_4N_2, and 1,5-*t*-$Bu_2C_2N_4S_2$ provide ionization potentials that are in good agreement with calculated values.[4]

UV-PES studies of 1,2,4,6-thiatriazinyl $[R_2C_2N_3S]^{\bullet}$ and 1,2,3,5-dithidiazolyl $[RCN_2S_2]^{\bullet}$ (**15**) radicals have also provided ionization potentials that are in good agreement with modified neglect of differential overlap (MNDO) calculations.[34]

5 BINARY SULFUR–NITROGEN COMPOUNDS

5.1 Neutral Molecules

Sulfur analogues of the well-known nitrogen oxides NO and NO_2 (*see* ***Nitrogen: Inorganic Chemistry***) are thermally unstable and the most common binary sulfur nitride is the tetramer S_4N_4 (**1**). This reflects the tendency of multiply bonded species containing heavier main group elements to oligomerize in the absence of steric protection (*see* ***Electronic Structure of Main-group Compounds***).

5.1.1 *Thiazyl Monomer (Sulfur Nitride), NS*[35]

Thiazyl monomer is a radical with one unpaired electron. In contrast to nitric oxide, it polymerizes so readily that it cannot be isolated as a monomeric solid or liquid and has only a transient existence in the gas phase. Thiazyl monomer may be generated in a number of ways, including the volatilization of $(SN)_x$ (**2**) or pyrolysis of S_4N_4 (**1**) over quartz wool above 300 °C. The emission spectrum and ESR spectrum have been reported. The bond length is calculated to be 149.7 pm from its spectroscopic moment of inertia. This indicates a bond order of between two and three. The dissociation energy of this strong sulfur–nitrogen bond is estimated to be 463 $\mathrm{kJ\,mol^{-1}}$ from spectroscopic data. Nevertheless, like other sulfur nitrides, NS is endothermic and unstable with respect to its elements. Thiazyl monomer exhibits an IR band at 1209 $\mathrm{cm^{-1}}$.[28] The experimental dipole moment is 1.83 ± 0.03 D and the ionization potential is 9.85 eV.

Thiazyl monomer can be stabilized by coordination to a metal, and many thionitrosyl complexes with Cr, Mo, Re, Ru, Os, Co, Rh, Ir, and Pt are known.[6,7,35] Comparison of the spectroscopic properties and the electronic structures of M–NS and M–NO complexes indicates that NS is a better σ-donor and π-acceptor ligand than NO. Oxygen transfer from an NO_2 to an NS ligand on the same metal center occurs in ruthenium porphyrin complexes.[36]

Several routes are available for the preparation of thionitrosyl–metal complexes. These include (a) reaction of nitride complexes with sulfur or sulfur halides, (b) reaction of $(NSCl)_3$ with transition metal complexes, and (c) reaction of NS^+ salts with metal complexes. The first organometallic thionitrosyl complex was prepared by method (b) (equation 1).

$$\mathrm{Na[CpCr(CO)_3]} + \frac{1}{3}\mathrm{(NSCl)_3} \xrightarrow{\mathrm{THF}} \mathrm{CpCr(CO)_2(NS)} + \mathrm{CO} + \mathrm{NaCl} \qquad (1)$$

Two bonding modes, linear and bent, have been established for metal–thionitrosyl complexes. The characteristic stretching vibration for linear M–NS complexes occurs in the range 1150–1370 $\mathrm{cm^{-1}}$, while that for terminal bent complexes appears at lower frequencies.

5.1.2 *Dinitrogen Sulfide, N_2S*[37]

A variety of acyclic and cyclic S–N compounds decompose at moderate temperatures (100–150 °C) with the formal loss of a symmetrical NSN fragment, but this molecule has never been detected. Ab initio calculations indicate that linear NNS is the lowest energy of N_2S species. The molecule, N_2S, can be generated by flash vacuum pyrolysis of 5-phenyl-1,2,3,4-thiatriazole (equation 2).

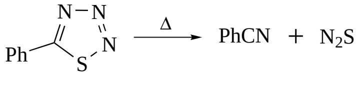

(2)

Unlike N_2O, which is a stable unreactive molecule, N_2S is only stable up to 160 K. The IR spectrum is dominated by a very strong band at 2040 $\mathrm{cm^{-1}}$ [υ(NN)].[28] The gaseous N_2S molecule has been detected by high-resolution mass spectrometry. The first ionization potential has been determined by PES to be 10.6 eV. These data indicate that N_2S resembles diazomethane, CH_2N_2 rather than N_2O. It decomposes to give N_2 and diatomic sulfur, S_2, and, hence, elemental sulfur, rather than monoatomic sulfur. The bond lengths of linear and cyclic N_2S have been determined by calculations.[38]

5.1.3 *Disulfur Dinitride, S_2N_2*[39]

S_2N_2 (**3**) forms large colorless crystals with an iodine-like smell. It detonates with friction or on heating above 30 °C, but can be sublimed at 10^{-2} Torr at 20 °C. It has a square planar structure with S–N bond distances of 165.4 ppm and bond angles of $90.0 \pm 0.4°$. It is prepared by the thermolysis of other cyclic S–N compounds, for example, S_4N_4 (over silver wool at 220 °C), $S_4N_3{}^+Cl^-$, or $Ph_3AsNS_3N_3$ at ca. 130 °C. S_2N_2 is a six II-electron system, but four of these electrons occupy non-bonding orbitals.[40] It exhibits significant diradical character.[41]

S_2N_2 dimerizes rapidly to S_4N_4 in the presence of nucleophiles and this process can be understood in terms of the frontier orbital interactions between the singly occupied molecular orbital (SOMO) of an $S_2N_2{}^{-\bullet}$ radical anion and the LUMO of an S_2N_2 molecule.[5] The polymerization of crystalline S_2N_2 is a nondiffusive process that produces a mixture of monoclinic (90%) and orthorhombic (10%) $(SN)_x$.[42]

S_2N_2 forms both mono- and diadducts, $S_2N_2{\cdot}L$ and $S_2N_2{\cdot}L_2$, with Lewis acids such as BCl_3 or $SbCl_5$, and with a variety of transition metal halides.[43] The S_2N_2 ligand is attached to the Lewis acid through nitrogen in these complexes and coordination has very little effect on the geometry of the four-membered ring. The formation of π-complexes, for example, $(\eta^4\text{-}S_2N_2)M(CO)_3$ ($M = Cr$, Mo, W), in which S_2N_2 acts as a 6π-electron ligand, has been proposed,[44] but only N-bonded adducts are observed.

5.1.4 *Trisulfur Trinitride, S_3N_3*[30]

The $S_3N_3^{\bullet}$ radical has been characterized by photoelectron and quadrupole mass spectroscopy as the major product from the vaporization of $(SN)_x$. In the condensed state, it reforms the polymer and other colored materials. Ab initio CI calculations indicate a planar geometry with close to D_{3h} symmetry for the $S_3N_3^{\bullet}$ radical.

5.1.5 *Tetrasulfur Dinitride, S_4N_2*[39]

S_4N_2 forms dark-red needles (mp 23 °C) upon recrystallization from diethyl ether. It sublimes readily at room temperature, but must be stored at −20 °C to avoid decomposition. Several methods are available for the preparation of S_4N_2. The decomposition of $Hg(S_7N)_2$ at room temperature gives the best yield (65%), while the reaction of S_2Cl_2 with aqueous ammonia is quick and cheap.

The S_4N_2 molecule consists of a six-membered ring in a half-chair conformation (**18**). There are long S–N bonds (168 pm) connecting the –SSS–and –N=S=N– units, which have S–N distances of 156 pm.[45] Few chemical reactions of S_4N_2 have been studied owing to their thermal instability.

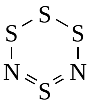

(**18**)

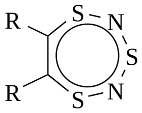

(**19**)

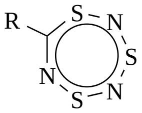

(**20**)

5.1.6 *Tetrasulfur Tetranitride, S_4N_4*[5,39]

Tetrasulfur tetranitride is orange–yellow at room temperature, but becomes almost colorless at −190 °C. In CS_2 solution, it is readily recognized by two strong, characteristic bands at 705 and 938 cm^{-1} in the IR spectrum. The standard synthesis of S_4N_4 involves the treatment of S_2Cl_2 with chlorine, followed by ammonia gas in carbon tetrachloride at 20–50 °C. Alternatively, S_4N_4 can be prepared by the reaction of $[(Me_3Si)_2N]_2S$ with an equimolar mixture of SCl_2 and SO_2Cl_2.[46] Crystalline S_4N_4 may explode when subjected to heat or friction.

Tetrasulfur tetranitride (**1**) adopts a cage structure with equal S–N bond lengths (162 pm) and two weak transannular S–S interactions of ca. 260 pm at room temperature. Although S_4N_4 is thermochromic (*see Thermochromism*), there is no significant difference between the value of the S–S distance and that found at 120 K. Rietveld analysis indicates that S_4N_4 undergoes a transition to a new orthorhombic phase at 397 K.[47] Theoretical and experimental charge densities reveal intermolecular attractions in S_4N_4 that correspond to molecular recognition in the solid state.[48] The unusual structure of S_4N_4, in which the sulfur atoms are three coordinate and the nitrogen atoms are two coordinate, is the inverse of that found for α-P_4S_4 and As_4S_4, where the more electronegative atoms occupy the lowest coordination sites. A planar (D_{4h}) S_4N_4 molecule would be a 12π-electron system with an open-shell configuration, unstable with respect to the Jahn–Teller distortion. Correlation of the molecular orbitals of the hypothetical planar molecule with those of the experimental (D_{2d}) conformation shows that the orbital degeneracy of the ground state is lost in the latter, and four of the previously π^* electrons are accommodated in S–S σ-bonds.[49]

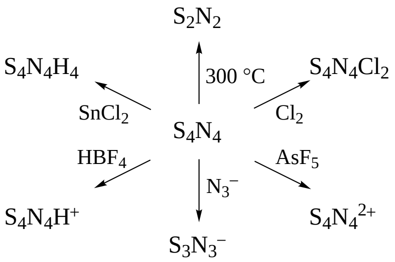

Scheme 1 Some reactions of S_4N_4

The S_4N_4 molecule exhibits a very versatile chemical behavior and is a source of many other S–N heterocycles, as shown in Scheme 1.[4] The synthesis of other S–N rings from S_4N_4 can be classified as follows: reactions with (a) halogens or other oxidizing agents, (b) nucleophiles or reducing agents, and (c) metal halides or organometallic reagents. The eight-membered ring is retained in 1,5-$S_4N_4Cl_2$ and $S_4N_4^{2+}$, the initial products of chlorination or oxidation of S_4N_4, respectively. Further chlorination or oxidation results in ring contraction to give $(NSCl)_3$ or the $S_6N_4^{2+}$ cation (**7**). The reaction of S_4N_4 with nucleophiles also leads to ring contraction. For example, the degradation of S_4N_4 by anionic nucleophiles produces $S_3N_3^-$ (**9**), while $Ph_3EN{-}S_3N_3$ (E = P, As) is obtained from S_4N_4 and triphenylphosphine or -arsine. N-Bonded adducts of the type $S_4N_4{\cdot}L$, where the eight-membered ring is flattened into a puckered boat with no cross-ring interactions, are formed with a variety of Lewis or Brønsted acids and some transition metal halides, for example, $FeCl_3$ and VCl_5. However, the reactions of S_4N_4 with metal halides or organometallic reagents more often give rise to cyclometallathiazenes in which the metal becomes part of the S–N ring (see Section 8.5).

The reactions of S_4N_4 with alkynes have also been investigated in considerable detail.[50] These reactions produce 1,3,5,2,4-trithiadiazepines (**19**) and 1,3,5,2,4,6-trithiatriazepines (**20**), both of which are planar, 10π-electron seven-membered rings, in addition to 1,2,5-thiadiazoles, which are the major products (see Section 8.1).

5.1.7 *Pentasulfur Hexanitride, S_5N_6*[39]

Pentasulfur hexanitride is an explosive, air-sensitive, orange solid, which is best prepared from $S_4N_4Cl_2$ (equation 3).[51] The structure of S_5N_6 (**8**) resembles a basket in which a –N=S=N–unit bridges two sulfur atoms of an S_4N_4 cradle via S–N single bonds. It decomposes in warm solvents to give S_4N_4. Because of its hazardous nature, very few reactions of S_5N_6 have been reported. An exception is the reaction with $[Ph_4P]_2[Pd_2Cl_6]$ to give $[Ph_4P]_2[Pd_2Cl_4(S_2N_3)]$, which contains a chelating $S_2N_3^-$ ligand.[52]

$$S_4N_4Cl_2 + Me_3SiNSNSiMe_3 \longrightarrow S_5N_6 + 2Me_3SiCl \qquad (3)$$

5.2 Sulfur–Nitrogen Cations

Investigations of binary S–N cations have played an important role in the development of S–N chemistry. The cyclic cations, $S_2N_3^+$, $S_3N_2^{2+}$, $S_4N_3^+$, $S_4N_4^{2+}$, and $S_5N_5^+$, are of interest in the context of Banister's proposal that planar S–N rings obey the Hückel $(4n + 2)\pi$-electron rule.[3] The simple cations, NS^+ and NS_2^+, are useful reagents for the synthesis of other S–N compounds.

5.2.1 The Thiazyl Cation, SN^{+}[35]

Thiazyl salts were first prepared in 1971 by the reaction of NSF with AsF_5 or SbF_5.[53] They are more conveniently prepared from $(NSCl)_3$ by reacting with (a) $AgAsF_6$ in liquid SO_2 (equation 4) or (b) $AlCl_3$ in CH_2Cl_2 under the influence of heat or ultrasound.

$$(NSCl)_3 + 3AgAsF_6 \xrightarrow{SO_2} 3[NS][AsF_6] + 3AgCl \qquad (4)$$

The S–N bond length in thiazyl salts is about 1.42 Å and the vibrational frequency [ν(S–N)] occurs at $1437\,cm^{-1}$ in $[NS][AsF_6]$. The NS^+ cation exhibits an ^{14}N NMR resonance at ca. 200 ppm, and this technique is useful for monitoring reactions of NS^+.[18]

The thiazyl cation is used for the preparation of other S–N compounds (see Scheme 2). For example, the insertion reactions with S_4N_4 and SCl_2 produce the $S_5N_5^+$ (**5**) and $ClSNSCl^+$ (**21**) cations respectively. Insertion of thiazyl cations into the metal–halogen bond of $Re(CO)_5X$ (X = Cl, Br) provides a route to thiazyl halide complexes.

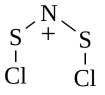

(**21**)

5.2.2 The Dithianitronium Cation, S_2N^{+}[54]

The S_2N^+ cation was first obtained in 1978 by the oxidation of S_7NH with $SbCl_5$.[55] Another route to S_2N^+ salts involves the reaction of AsF_5 with a mixture of S_4N_4 and sulfur in appropriate proportions. More conveniently, the reaction of in-situ–generated NS^+ salts with sulfur (see Scheme 2) or the reduction of the $ClSNSCl^+$ cation (**21**) with anhydrous tin(II) chloride in SO_2 or CH_2Cl_2 can be used to prepare NS_2^+ salts (equation 5).[56]

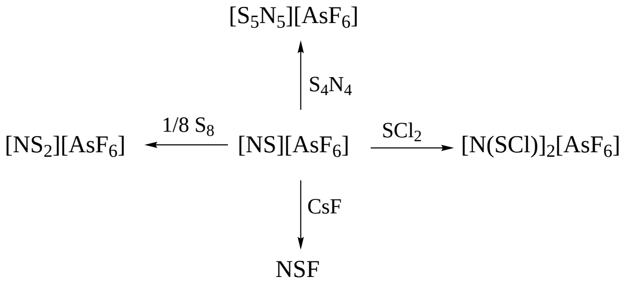

Scheme 2 Some reactions of $[NS][AsF_6]$

$$[N(SCl)_2][AlCl_4] + SnCl_2 \longrightarrow [SNS][AlCl_4] + SnCl_4 \qquad (5)$$

The SNS^+ cation is a linear species isoelectronic with CS_2. The S–N bond distances are 146–147 pm. The NS_2^+ cation exhibits a very narrow ^{14}N NMR resonance at −91 ppm ($\nu 1/2 = 8\,Hz$) in SO_2 and this technique is useful for monitoring reactions of the cation.[18]

The NS_2^+ cation is an important reagent in S–N chemistry, especially in thermally allowed cycloaddition reactions with organic nitriles and alkynes that give quantitative yields of heterocyclic cations (see Scheme 3).[54] The dominant orbital interaction in these cycloadditions is between the LUMO of S_2N^+ and the HOMO of the alkyne or nitrile (see Figure 2). Cycloaddition reactions also occur with alkenes, and colored charge-transfer complexes are formed with arenes.

5.2.3 The Dithiatriazyl Cation $S_2N_3^{+}$[57]

The cyclic $S_2N_3^+$ cation (**22**), a 6π-electron system, is the only example of a nitrogen-rich, binary S–N cation. The

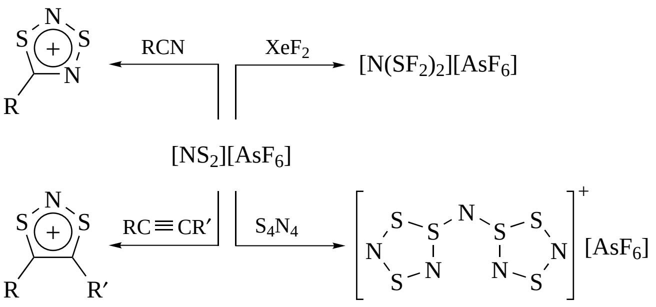

Scheme 3 Some reactions of $[NS_2][AsF_6]$

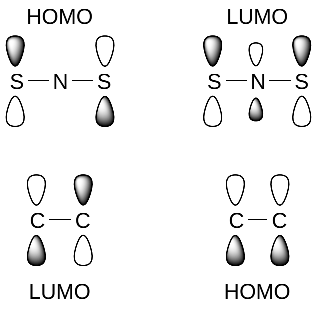

Figure 2 Frontier orbital interactions in the cycloaddition reaction of NS_2^+ with alkynes

thermally stable salt $[S_2N_3]_2[Hg_2Cl_6]$ is obtained from the reaction of $(NSCl)_3$ with $HgCl_2$ in CH_2Cl_2. The bond lengths in the five-membered ring indicate a delocalized π-bonding that is attenuated across the S–S bond.**57**

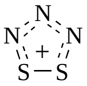

(**22**)

5.2.4 *The Thiodithiazyl Cations, $S_3N_2{}^{n+}$ (n = 1, 2), and Dimer, $S_6N_4{}^{2+}$*[39]

Although the $S_3N_2{}^{+\bullet}$ radical cation (**13**) has been well characterized in solution by its characteristic five-line (1:2:3:2:1) ESR signal ($g = 2.01$; $a_N = 3.15$ G),**23** this S–N heterocycle is usually found in the solid state as the dimeric cation $S_6N_4{}^{2+}$ (**7**), in which two 7π-electron $S_3N_2{}^+$ rings are associated via weak intermolecular S–S interactions [d(S–S) $= 300-310$ pm].

The 6π-electron $S_3N_2{}^{2+}$ dication has been prepared as the $AsF_6{}^-$ salt by the cycloaddition of NS^+ and $NS_2{}^+$ cations in SO_2 (equation 6) and structurally characterized.**58** It decomposes in solution to NS^+ and $NS_2{}^+$, with a calculated barrier to dissociation of 5.6 kJ mol^{-1}.**59**

$$[NS][AsF_6] + [NS_2][AsF_6] \rightleftharpoons [S_3N_2][AsF_6]_2 \qquad (6)$$

5.2.5 *The Cyclotrithiazyl Cation, $S_3N_3{}^+$*

The $S_3N_3{}^+$ cation is an interesting example of an antiaromatic 8π-electron system. Ab initio CI calculations indicate that a triplet cation, with a planar ring, is more stable than the singlet cation.**30** The $S_3N_3{}^+$ cation has been obtained as the norbornene adduct,**60** but salts of the free cation have not been isolated.

5.2.6 *The Thiotrithiazyl Cation, $S_4N_3{}^+$*[39]

The thiotrithiazyl cation in $[S_4N_3]Cl$ was one of the earliest S–N heterocycles to be prepared and structurally characterized. It is obtained as a reasonably air-stable, yellow solid by the reaction of S_4N_4 or $[S_3N_2Cl]Cl$ with S_2Cl_2 in CCl_4 (equation 7).

$$3[S_3N_2Cl]Cl + S_2Cl_2 \longrightarrow 2[S_4N_3]Cl + 3SCl_2 \qquad (7)$$

The $S_4N_3{}^+$ cation (**4**) is a planar seven-membered ring with approximately equal S–N bond lengths and an S–S bond. This cation is a 10π-electron system. The ^{15}N NMR spectrum shows the expected doublet–triplet pattern. The seven-membered ring fragments upon heating at ca. 250 °C give S_2N_2 and, hence, the polymer $(SN)_x$. The reduction of $[S_4N_3]Cl$ with metals such as iron or mercury gives S_4N_4.

5.2.7 *The Cyclotetrathiazyl Dication, $S_4N_4{}^{2+}$*[39]

The $S_4N_4{}^{2+}$ cation was first reported in 1977.**61** It is prepared by the oxidation of S_4N_4 with an excess of a Lewis acid, such as $SbCl_5$ or AsF_5, or with $S_2O_6F_2$ (equation 8).

$$S_4N_4 + S_2O_6F_2 \longrightarrow [S_4N_4][FSO_3]_2 \qquad (8)$$

The $S_4N_4{}^{2+}$ cation (**23**) is a planar eight-membered ring with equal S–N bond lengths (D_{4h}) of ca. 155 pm. It is a fully delocalized 10π-electron system with a strong π-network.

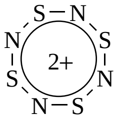

(**23**)

5.2.8 *The Tetrasulfur Pentanitride Cation, $S_4N_5{}^+$*[39]

The bicyclic $[S_4N_5]Cl$ is a yellow–orange, hygroscopic solid which decomposes violently on heating. It is readily prepared from $(NSCl)_3$ (equation 9).**62** The treatment of $[S_4N_5]Cl$ with AgF_2, $SbCl_5$, or $AgAsF_6$ gives $[S_4N_5]F$, $[S_4N_5][SbCl_6]$, or $[S_4N_5][AsF_6]$, respectively.

$$(NSCl)_3 + Me_3SiNSNSiMe_3 \longrightarrow [S_4N_5]Cl + 2Me_3SiCl \qquad (9)$$

$[S_4N_5]Cl$ has a polymeric, predominantly ionic structure in which $S_4N_5{}^+$ cations (**24**) are bridged by Cl^- ions with d(S–Cl) $= 281$ pm. The unbridged S–S distance is 401 pm (cf. 271 pm in the corresponding anion $S_4N_5{}^-$) (**10**). A number of covalent derivatives of the S_4N_5 cage have been prepared by the reaction of $[S_4N_5]Cl$ with various silylated reagents.

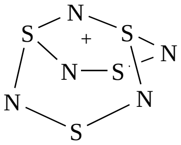

(**24**)

5.2.9 *The Cyclopentathiazyl Cation, $S_5N_5{}^+$*[39]

The first $S_5N_5{}^+$ salt was reported in 1969.**63** These salts are moisture sensitive, but they dissolve without decomposition in $SOCl_2$ or formic acid. The $S_5N_5{}^+$ cation is formed by the reaction of S_4N_4 with the NS^+ cation (see Scheme 2).

The $S_5N_5{}^+$ cation is a 14π-electron system. With the exception of $[S_5N_5]Cl$, which is red, salts of $S_5N_5{}^+$ are yellow. The planar, 10-membered ring usually has an azulene shape (**5**), with alternating sulfur and nitrogen atoms.**33**

5.3 Sulfur–Nitrogen Anions

Sulfur and nitrogen represent a versatile combination in the formulation of binary anions with cyclic, cage, or catenated structures, none of which have counterparts among the known N–O anions. In addition, several S–N anions are known only in complexes with transition metals (see Section 8.5).

5.3.1 The Sulfur Diimide Dianion, SN_2^{2-}[64]

The pale yellow salt, $K_2[SN_2]$, is prepared from bis(trimethylsilyl)sulfur diimide in boiling dimethoxyethane (equation 10). It reacts explosively with water. The dilithium salt, $Li_2[SN_2]$, is generated from $Me_3SnNSNSnMe_3$ and MeLi in the same solvent.[65] The SN_2^{2-} ion is also formed upon exhaustive electrochemical reduction of S_4N_4.

$$Me_3SiNSNSiMe_3 + 2KO\text{-}t\text{-}Bu \longrightarrow K_2[SN_2] + 2Me_3SiO\text{-}t\text{-}Bu \quad (10)$$

The SN_2^{2-} ion is isoelectronic with the thionylimide anion, NSO^-, and with sulfur dioxide, SO_2. The frequencies of the three fundamental vibrations are 1198, 1001, and 528 cm^{-1}. The salt $K_2[SN_2]$ is an important reagent for the preparation of other sulfur diimide derivatives when $Me_3SiNSNSiMe_3$ is not sufficiently reactive.[64] For example, both acyclic and cyclic arsenic(III) compounds, $t\text{-}Bu_2AsNSNAs\text{-}t\text{-}Bu_2$ and $t\text{-}BuAs(NSN)_2As\text{-}t\text{-}Bu$, have been obtained in this way.

Protonation of the anion SN_2^{2-} by acetic acid in diethyl ether produces the thermally unstable sulfur dimide $S(NH)_2$. Like all symmetrical sulfur diimides, the parent compound $S(NH)_2$ can exist as three isomers (see Scheme 4). Ab initio MO calculations indicate that the (cis, cis) configuration is somewhat more stable than the (cis, trans) isomer, while the (trans, trans) isomer is expected to possess considerably higher energy.

Salts of the sulfur diimide anions $RNSN^-$ (**25**; R = aryl, *t*-Bu, $SiMe_3$) are prepared by Si–N cleavage of $RNSNSiMe_3$ with $[(Me_2N)_3S][Me_3SiF_2]$.[66] The anions (**25**) adopt cis configurations with short terminal S–N bond lengths (144–149 pm), indicative of a thiazylamide anion. Anions of the type (**25**) exhibit well-separated ^{14}N NMR chemical shifts.[67]

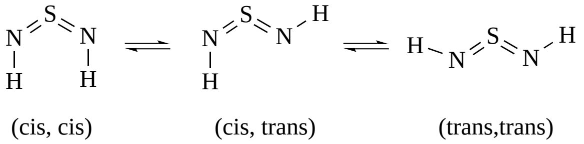
(cis, cis) (cis, trans) (trans,trans)

Scheme 4 Isomers of sulfur diimide, HNSNH

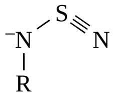
(**25**)

5.3.2 The $[S(Nt\text{–}Bu)_x]^{2-}$ Ions (x = 3,4)[68]

The dimer $[Li_2S(Nt\text{-}Bu)_3]_2$, prepared from $t\text{-}BuNSNt\text{-}Bu$ and $LiNHt\text{-}Bu$ in toluene (equation 11), has a hexagonal, prismatic structure.[68] It is readily oxidized to the deep blue radical $\{Li_3[S(Nt\text{-}Bu)_3]_2\}$.[69] The pyramidal $[S(Nt\text{-}Bu)_3]^{2-}$ anion is isoelectronic with sulfite, SO_3^{2-}. Oxidation with halogens provides easy access to $[S(Nt\text{-}Bu)]_3$, which is isoelectronic with SO_3. The tetrakisimidosulfate dianion $S(Nt\text{-}Bu)_4^{2-}$ can be prepared from $S(Nt\text{-}Bu)_3$ using methodology similar to that shown in equation (11).[70]

$$2S(Nt\text{-}Bu)_2 + 4LiNHt\text{-}Bu \longrightarrow [Li_2S(Nt\text{-}Bu)_3]_2 + 2H_2Nt\text{-}Bu \quad (11)$$

5.3.3 The $SSNS^-$ Ion[20]

The orange–red S_3N^- ion (λ_{max} 465 nm) is obtained by the addition of triphenylphosphine to a solution of a S_4N^- salt in acetonitrile. It can be isolated as a salt in combination with large counterions, for example, Ph_4As^+ or $N(PPh_3)_2^+$, but it is unstable with respect to the formation of the blue S_4N^- ion in solution or in the solid state under the influence of heat or pressure.[71]

Although the structure of the S_3N^- ion has not been established by X-ray crystallography, the vibrational spectra of 30% ^{15}N-enriched S_3N^- suggest an unbranched ($SNSS^-$) arrangement of atoms in contrast to the branched structure (D_{3h}) of the isoelectronic CS_3^{2-} ion and the isovalent NO_3^- ion. Many metal complexes are known where the S_3N^- ion is chelated to the metal by two sulfur atoms (see Section 8.5).[6,7]

5.3.4 The $SSNSS^-$ Ion[20]

The dark blue S_4N^- ion (λ_{max} 580 nm) was first obtained in 1972 by the decomposition of $[n\text{-}Bu_4N][S_7N]$, produced by deprotonation of S_7NH with $n\text{-}Bu_4NOH$ in diethyl ether at −78 °C.[20] It is more conveniently prepared by the thermolysis of salts of the $S_3N_3^-$ ion with large cations in boiling acetonitrile.[72] The S_4N^- ion is also formed in (a) the reaction of S_2Cl_2 with ammonia in polar solvents (the preparation of cyclic sulfur imides) (see Section 10), (b) solutions of sulfur in liquid ammonia, and (c) the reaction of sulfur with sodium azide in $(Me_2N)_3PO$.[20]

The S_4N^- ion (**26**) is a planar (*E*,*Z*) chain with nitrogen as the central atom and short, terminal S–S bonds [*d*(S–S) ∼190 pm], which give rise to strong bands at ca. 565 and 590 cm^{-1} in the Raman spectrum. The S_4N^- ion is an 8π-electron system and the intense visible absorption band near

580 nm has been assigned to a π^*(HOMO) → π^*(LUMO) transition.[72]

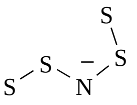

(**26**)

5.3.5 *The $S_2N_2H^-$ Ion*

The $S_2N_2H^-$ ion has been characterized by ^{14}N and ^{15}N NMR spectroscopy.[19] It is formed in liquid ammonia by treatment of $S_4N_4H_4$ with 2 mol. equiv. of potassium amide or by the reaction of the S_3N^- ion with potassium amide. Although it has not been isolated as a salt, the $S_2N_2H^-$ ion is well known in complexes with metals, for example, Ni, Pd, Pt, where it acts as a bidentate (S,N) ligand (see Section 8.5).[6,7]

5.3.6 *The Trisulfur Trinitride Ion, $S_3N_3^-$*[20]

The yellow $S_3N_3^-$ ion is formed, together with the $S_4N_5^-$ ion, from the reaction of S_4N_4 with a variety of nucleophilic reagents, for example, ionic azides, organolithium reagents, or secondary amines. The best preparation involves the reaction of S_4N_4 with an azide of a large cation, for example, $(Ph_3P)_2N^+$. The large cation is necessary to stabilize the anion; alkali metal salts of $S_3N_3^-$ are explosive. Two $S_3N_3^-$ salts with interesting solid-state structures are $[PhCN_2S_2][S_3N_3]$,[73] prepared from $[PhCN_2S_2]_2$ and $[S_5N_5]Cl$, and $[Cp_2Co][S_3N_3]$,[74] obtained by the reduction of S_4N_4 with cobaltocene (*see* ***Cobalt: Organometallic Chemistry***).

The $S_3N_3^-$ ion (**9**) is an essentially planar, six-membered ring with bond angles at nitrogen of ca. 123° and at sulfur of ca. 117° and almost equal S–N bond lengths.[75] The vibrational spectra of most alkali metal salts are consistent with D_{3h} symmetry for the anion. The $S_3N_3^-$ ion is an important example of a 10π-electron system. Although the π-orbital pattern is similar to that of benzene, the occupancy of the π-orbitals is very different (Figure 3). The presence of four electrons in the degenerate antibonding (π^*) orbitals dramatically weakens the S–N framework. The thermolysis of yellow solutions of $S_3N_3^-$ in boiling acetonitrile produces the deep blue S_4N^- ion. The yellow color (λ_{max} 360 nm) of $S_3N_3^-$ is assigned to a π^*(HOMO) → π^*(LUMO) transition and this assignment is confirmed by the MCD spectrum.

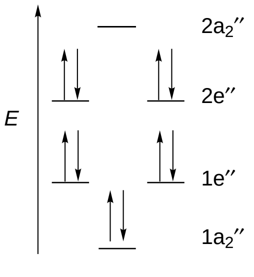

Figure 3 π-Energy levels of $S_3N_3^-$

5.3.7 *The Tetrasulfur Pentanitride Ion, $S_4N_5^-$*[20]

The yellow $S_4N_5^-$ ion was first reported in 1975 from the methanolysis of sulfur dimides (equation 12).[76] It can also be prepared by the treatment of S_4N_4 with certain nucleophiles, for example, secondary amines or azides of small alkali metals.[20]

$$t\text{-BuN=S=NSiMe}_3 \xrightarrow{\text{MeOH}} \text{NH}_4{}^+\text{S}_4\text{N}_5{}^- \qquad (12)$$

The structure of $S_4N_5^-$ (**10**) is closely related to that of S_4N_4. In $S_4N_5^-$, five of the six edges of the S_4 tetrahedron are bridged by nitrogen atoms. The S–S distance for the sixth edge is ca. 270 pm.

Alkali metal salts of $S_4N_5^-$ are explosive when subjected to heat or mechanical shock, but salts with large counterions, for example, Ph_4As^+ or $(Ph_3P)_2N^+$, are safe to handle in the solid state. The carefully controlled thermolysis of solutions of $S_4N_5^-$ salts in boiling acetonitrile generates $S_3N_3^-$ (**9**) and, subsequently, the S_4N^- ion (**26**). The reaction of $S_4N_5^-$ with bromine or iodine produces pentasulfur hexanitride S_5N_6 (**8**), whereas oxidation with chlorine yields $[S_4N_5]Cl$.

6 SULFUR–NITROGEN HALIDES

6.1 Thiazyl Halides, NSX (X = F, Cl, Br)

Thiazyl fluoride is a moisture-sensitive, thermally unstable gas.[77] It is conveniently generated by decomposition of $FC(O)NSF_2$ or $Hg(NSF_2)_2$. It may also be obtained from $[NS][AsF_6]$ and CsF or from $(NSCl)_3$ and KF in tetramethylene sulfone at 80 °C. The microwave spectrum of NSF indicates a bent structure. Thiazyl fluoride can be stabilized by coordination to a transition metal and such complexes, for example, $[M(NSF)_6][AsF_6]$ (M = Co, Ni), are conveniently prepared in liquid SO_2.[6,7]

Monomeric NSCl is formed as a greenish yellow gas by heating the cyclic trimer $(NSCl)_3$ under vacuum or in an inert gas stream. It trimerizes in the condensed state. The monomer NSCl may also be generated in solutions of $(NSCl)_3$ in liquid SO_2 at room temperature or in CCl_4 at 70 °C.[18] Numerous metal–NSCl complexes are known.[78] Typically, the preparation of these complexes involves the reaction of a high oxidation–state metal chloride with $(NSCl)_3$ in $POCl_3$ or CCl_4 (equation 13). Spectroscopic and X-ray structural data

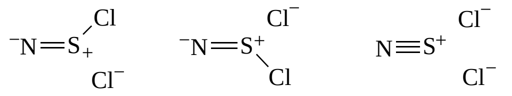

Scheme 5 Resonance structures of $\mathrm{NSCl_2}^-$

indicate M=N=S–bonding in these complexes.

$$2\mathrm{MCl_6} + \frac{2}{3}(\mathrm{NSCl})_3 \xrightarrow[\mathrm{M\,=\,Mo\ or\ W}]{} [\mathrm{MCl_4(NSCl)}]_2 + 2\mathrm{Cl_2} \tag{13}$$

Monomeric NSBr is generated in the gas phase by pyrolysis of $[\mathrm{S_4N_3}]\mathrm{Br}$. It has been characterized by its IR spectrum.

6.2 Thiazyl Halides, $\mathrm{NSX_2}^-$ (X = Cl, F)[79]

The $\mathrm{NSCl_2}^-$ anion, isoelectronic with $\mathrm{OSCl_2}$, is prepared by the addition of $[\mathrm{Ph_4P}]\mathrm{Cl}$ or $[\mathrm{Me_4N}]\mathrm{Cl}$ to a solution of $(\mathrm{NSCl})_3$ in $\mathrm{CH_2Cl_2}$.**[79]** The $\mathrm{NSCl_2}^-$ anion in the $[(\mathrm{Ph_3PN})_2\mathrm{SCl}]^+$ salt has a slightly distorted C_s structure with a very short S–N bond (144 pm) and two loosely bound chlorine atoms [d(S–Cl) = 242 pm]. The structure is best described by three resonance forms (see Scheme 5).

6.3 Thiazyl Trifluoride, $\mathrm{NSF_3}$[77]

Thiazyl trifluoride, a colorless gas with a pungent odor, is obtained by fluorination of NSF or $\mathrm{FC(O)NSF_2}$ with $\mathrm{AgF_2}$. On the basis of spectroscopic data, $\mathrm{NSF_3}$ has a distorted tetrahedral structure. A number of transition metal complexes of $\mathrm{NSF_3}$, for example, $[\mathrm{M(NSF_3)_4}][\mathrm{AsF_6}]_2$ (M = Mn, Fe, Co, Ni or Cu), are known.**[6]** The S–N bond distance in these complexes (136–137 pm) is extremely short. The thiazyl difluoride complex $[\mathrm{Ir(CO)ClF(NSF_2)(PPh_3)_2}]$ is prepared by oxidative addition of $\mathrm{NSF_3}$ to $[\mathrm{Ir(CO)Cl(PPh_3)_2}]$.**[80]**

6.4 Thiodithiazyl Dichloride, $[\mathrm{S_3N_2Cl}]\mathrm{Cl}$[39]

Thiodithiazyl dichloride is a rust-colored, moisture-sensitive solid, which is conveniently prepared by heating $\mathrm{S_2Cl_2}$ with dry, finely ground ammonium chloride (equation 14).

$$4\mathrm{S_2Cl_2} + 2\mathrm{NH_4Cl} \longrightarrow [\mathrm{S_3N_2Cl}]\mathrm{Cl} + 8\mathrm{HCl} + \frac{5}{8}\mathrm{S_8} \tag{14}$$

$[\mathrm{S_3N_2Cl}]\mathrm{Cl}$ reacts readily with chloride ion acceptors, for example, $\mathrm{AlCl_3}$ and $\mathrm{FeCl_3}$, to give salts of the $\mathrm{S_3N_2Cl}^+$ cation, which consists of a slightly puckered five-membered ring (**27**). $[\mathrm{S_3N_2Cl}]\mathrm{Cl}$ is a useful source of the sulfur–nitrogen oxides, $\mathrm{S_3N_2O}$ and $\mathrm{S_4N_4O_2}$, by reactions with anhydrous formic acid and $\mathrm{SO_2(NH_2)_2}$ respectively. Gentle heating of $[\mathrm{S_3N_2Cl}]\mathrm{Cl}$ under vacuum gives the dark green dimer $(\mathrm{S_3N_2Cl})_2$, which contains the $\mathrm{S_6N_4}^{2+}$ cation (**7**).

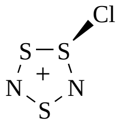

(**27**)

6.5 Cyclotrithiazyl Halides, $\mathrm{S_3N_3X_3}$[39]

The trimer $(\mathrm{NSCl})_3$ is obtained as pale yellow, moisture-sensitive crystals by the chlorination of $[\mathrm{S_3N_2Cl}]\mathrm{Cl}$ (equation 15).

$$3\mathrm{S_3N_2Cl_2} + 3\mathrm{SO_2Cl_2} \longrightarrow 2\mathrm{S_3N_3Cl_3} + 3\mathrm{SCl_2} + 3\mathrm{SO_2} \tag{15}$$

The six-membered ring in $(\mathrm{NSCl})_3$ adopts a chair conformation with all three chlorine atoms in axial positions (**28**). This arrangement is stabilized by the anomeric effect (delocalization of the nitrogen lone pair into an S–Cl σ^* orbital).**[81]**

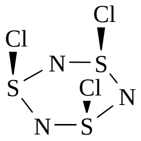

(**28**)

The cyclic trimer is an important reagent in S–N chemistry as a source of both cyclic and acyclic compounds (see Scheme 6).**[4,39]** In part, the synthetic utility of $(\mathrm{NSCl})_3$ stems from the ease with which it dissociates into monomeric NSCl in solution. Thus, the trimer provides a facile source of the NS^+ cation (see Section 5.2.1). Monomeric NSCl, generated from $(\mathrm{NSCl})_3$, undergoes a [2 + 4] cycloaddition reaction

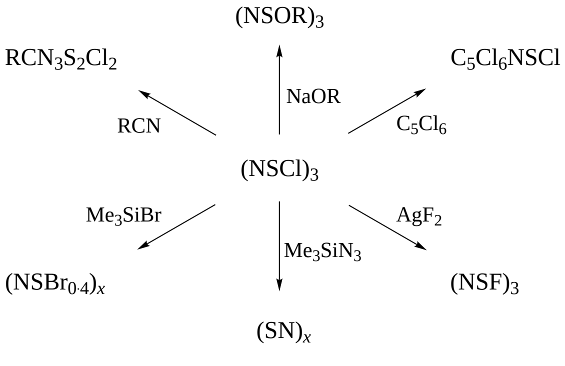

Scheme 6 Some reactions of $(\mathrm{NSCl})_3$

with hexafluorobutadiene to give a six-membered ring, but it reacts as a nitrene with fluorinated alkenes to give *N*-(chlorosulfenyl)aziridines.**[82]** The reactions of $(NSCl)_3$ with sodium alkoxides to give $(NSOR)_3$**[83]** or with AgF_2 to produce $(NSF)_3$ are two examples of transformations which occur with retention of the six-membered ring. Cyclotrithiazyl chloride is also a useful reagent in organic chemistry, for example, in the synthesis of 1,2,5-thiadiazoles and isothiazoles.**[84,85]**

The structure of $(NSF)_3$ is similar to that of the corresponding chloride (**28**).**[77]** The six-membered ring is retained in the formation of $[N_3S_3F_2][MF_6]$ from $(NSF)_3$ and MF_5 (M = As, Sb).

6.6 1,5-Dihalocyclotetrathiazenes, $S_4N_4X_2$[39]

The oxidative addition of one mole of X_2 (X = Cl, F) to S_4N_4 under mild conditions produces 1,5-$S_4N_4X_2$ as moisture-sensitive, thermally unstable compounds. The structure of 1,5-$S_4N_4Cl_2$ (**29**) consists of a folded eight-membered ring [d(S–S) = ca. 245 pm] with the exocyclic substituents in *exo, endo* positions. The halogen atoms in $S_4N_4Cl_2$ can be replaced by dialkylamino groups by using trimethylsilyl reagents.

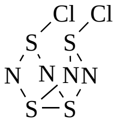
(**29**)

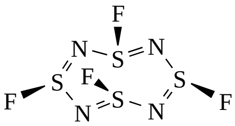
(**30**)

6.7 Tetrafluorocyclotetrathiazene, $S_4N_4F_4$[77]

The fluorination of S_4N_4 with an excess of AgF_2 in CCl_4 under reflux gives $S_4N_4F_4$. The heterocyclic ring of $S_4N_4F_4$ (**30**) is boat-shaped with alternate long (166 pm) and short (154 pm) S–N bonds as a result of Jahn–Teller distortion.**[86]** The fluorine substituents occupy alternate axial and equatorial positions. The structure of $S_4N_4[ON(CF_3)_2]_4$ is similar to that of (**30**). The tetramer $(NSF)_4$ dissociates into a NSF monomer when heated under vacuum at 300 °C. Treatment of $S_4N_4F_4$ with AsF_5 results in ring contraction to give $[S_3N_3F_2][AsF_6]$.

7 SULFUR–NITROGEN OXIDES[39]

7.1 Neutral Molecules

7.1.1 Thiodithiazyl Oxide, S_3N_2O

The sulfur–nitrogen oxide S_3N_2O is a red liquid. It was first prepared in 1975 by the reaction of $(Me_2SnS_2N_2)_2$ with SOF_2, but it is more conveniently prepared from $[S_3N_2Cl]Cl$ (equation 16).**[87]**

$$[S_3N_2Cl]Cl + HCO_2H \longrightarrow S_3N_2O + 2HCl + CO \qquad (16)$$

The ^{15}N NMR spectrum of S_3N_2O exhibits two resonances consistent with the five-membered ring structure (**31**). Lewis acids such as $SnCl_4$ form 2:1 adducts with S_3N_2O, in which the ligands are coordinated to tin in a cis configuration through their oxygen atoms.

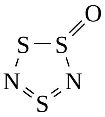
(**31**)

7.1.2 Trisulfur Dinitrogen Dioxide, $S_3N_2O_2$[88]

Trisulfur dinitrogen dioxide or bis(sulfinylimino) sulfide, $S(NSO)_2$, is a yellow, moisture-sensitive solid that has been known since 1953. It is conveniently prepared in high yields by the procedure described in equation (17).

$$2Me_3SiNSO + SCl_2 \longrightarrow S(NSO)_2 + 2Me_3SiCl \qquad (17)$$

$S(NSO)_2$ is a planar acyclic molecule with C_{2v} symmetry (**32**). The stability of the observed molecular conformation can be attributed to an electrostatic interaction between the negatively charged oxygen centers and the positively charged central sulfur atom. The central S–N distances are ca. 165 pm, while the S–N distances in the NSO group are ca. 153 pm.

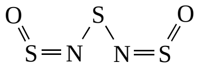
(**32**)

Complexes of $S(NSO)_2$ with silver(I) and zinc(II) where the ligand bonds to the metal through either oxygen or nitrogen atoms have been structurally characterized.

7.1.3 Cyclotetrathiazene Dioxide, $S_4N_4O_2$[39]

The dioxide $S_4N_4O_2$ is obtained as orange–yellow needles by the condensation of $[S_3N_2Cl]Cl$ with sulfamide $SO_2(NH_2)_2$. The S–N bond lengths in $S_4N_4O_2$ (**33**) indicate a structure in which two –N=S=N– units bridge a sulfur atom and a SO_2 group to form a boat-shaped eight-membered ring.**[87]** Sodium methoxide attacks $S_4N_4O_2$ at the sulfur atom opposite the SO_2 group to give $S_4N_4O_2(OMe)^-$, an eight-membered ring with a transannular S–S interaction. Other nucleophiles promote ring contraction. For example, the reaction of $S_4N_4O_2$ with azide ion in acetonitrile produces the purple $S_3N_3O_2^-$ ion (**17**).

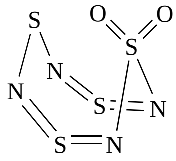

(**33**)

7.2 Anions

7.2.1 *The Thionyl Imide Ion, NSO⁻*

Thionyl imide, HNSO, is a thermally unstable gas, which polymerizes rapidly.[10] It can be prepared by the reaction of thionyl chloride with ammonia in the gas phase. It has a planar, cis structure according to IR and microwave spectra. Some transition metal complexes of thionyl imide, for example, $[M(CO)_5(HNSO)][AsF_6]$ (M = Mn, Re), are known.[7]

Potassium thionyl imide, K[NSO], is readily prepared from Me_3SiNSO and potassium *t*-butoxide in THF. Sodium, rubidium, and cesium salts are synthesized in a similar manner.[89] The more soluble $(Me_2N)_3S^+$ salt has also been prepared (equation 18).[90]

$$[(Me_2N)_3S][Me_3SiF_2] + Me_3SiNSO \longrightarrow [(Me_2N)_3S][NSO] + 2Me_3SiF \quad (18)$$

These salts can be used for the synthesis of both transition metal and main group element thionyl imides by metathetical reactions, for example, $Cp_2Ti(NSO)_2$ and $Ph_{3-x}As(NSO)_x$ ($x = 1$, 2), respectively.[64] The M–NSO group invariably adopts a cis geometry in these derivatives. A characteristic reaction of thionyl imides is the thermal or base-promoted elimination of SO_2 to give the corresponding sulfur diimide.[64]

7.2.2 *The Thionitrite and Perthionitrite Anions, SNO⁻, and SSNO⁻*[91]

The red $SSNO^-$ ion is produced by the reaction of an ionic nitrite with elemental sulfur or a polysulfide in acetone. It has been isolated as the $N(PPh_3)_2^+$ salt and shown to have a planar cis structure (**34**) with a short S–S bond distance (199 pm).[91] The $SSNO^-$ ion is probably involved as an intermediate in the gunpowder reaction, which entails the reaction of potassium nitrite (produced by reduction of potassium nitrate with charcoal) and sulfur.[92] The treatment of $SSNO^-$ with triphenylphosphine produces the thionitrite ion SNO^-, which has a bent structure with a bond angle of ca. 120° at nitrogen.[91] Ab initio MO calculations, including a correlation energy correction, indicate that the SNO^- ion is less stable than the isomer NSO^- by at least 38 kJ mol^{-1}.[93]

Organic derivatives RSNO (*S*-nitrosothiols), which have important roles in NO transport and regulation in biological systems,[94] have been characterized by X-ray crystallography, ^{15}N NMR, and IR spectra. Both syn and anti forms are present in solution. The barriers to rotation about the S–N bond are 11–12 kcal mol^{-1} and the S–N bond dissociation energies are estimated to be 20–30 kcal mol^{-1}.[95–98]

7.2.3 *The $SO_xN_3^-$ (x = 2,3) Anions*[99]

Yellow $(SO_2)_2N_3^-$ salts, obtained from SO_2 solutions of CsN_3 or $[Me_4N]N_3$, lose SO_2 to give the corresponding $SO_2N_3^-$ salts. The $SO_3N_3^-$ ion is prepared by the reaction of $CsSO_3Cl$ with trimethylsilyl azide (see equation 19). The S–N bond in $SO_2N_3^-$ is much weaker than that in $SO_3N_3^-$.

$$CsSO_3Cl + Me_3SiN_3 \longrightarrow CsSO_3N_3 + Me_3SiCl \quad (19)$$

7.2.4 *The $S_3N_3O_x^-$ Ions (x = 1,2,4)*[39]

The controlled oxidation of solutions of $S_3N_3^-$ in acetonitrile produces the red $S_3N_3O^-$ (**35**) and purple $S_3N_3O_2^-$ (**17**) ions.[20] The latter may also be obtained from $S_4N_4O_2$ (**33**) and azide ion. The yellow anion $S_3N_3O_4^-$ is produced as the $S_6N_4^{2+}$ salt, together with $S_3N_2O_5$, from the treatment of $S_4N_4O_2$ with SO_3.

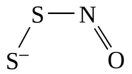

(**34**)

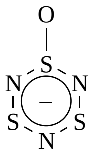

(**35**)

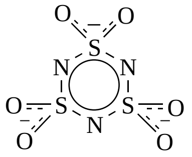

(**36**)

7.2.5 *The $S_3N_3O_6^{3-}$ Anion*

The $S_3N_3O_6^{3-}$ anion (**36**) in the ammonium salt has a chair conformation with approximately equal S–O bond lengths.[100]

7.2.6 *The $S_4N_5O_x^-$ Ions (x = 1,2)*

The yellow $S_4N_5O^-$ anion (**37**) is obtained as the water-soluble NH_4^+ salt from the reaction of $SOCl_2$ with liquid ammonia.[101] The oxygen atom in $S_4N_5O^-$ is attached to a sulfur atom that is connected to three nitrogen atoms. The $S_4N_5O_2^-$ ion has been prepared from $S_3N_3O_2^-$ (**17**) by oxidative addition with $PhICl_2$, followed by treatment with $Me_3SiNSNSiMe_3$.[5]

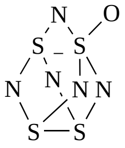
(37)

8 HETEROCYCLOTHIAZENES

Heterocyclothiazenes are S–N ring systems containing one (or more) other element(s). In view of the isolobal correspondence (*see Isolobal Analogy*) between S^+ and the groups RC or R_2P^V as substituents in an S–N ring, it is not surprising that C–N–S and P–N–S heterocycles have been the subject of recent investigations.**[5]** The replacement of one or more S^+ substituents in a binary S–N cation by RC or R_2P^V groups confers greater stability on the ring system, and in the case of the RC group, provides a link between these inorganic heterocycles and the benzenoid compounds. The introduction of R_2P^V groups supplies an informative, structural probe via ^{31}P NMR spectroscopy and generates heterocycles that are hybrids of π-electron-rich (S–N) and π-electron-precise ring systems (cyclophosphazenes, *see* ***Phosphorus–Nitrogen Compounds***).

8.1 Carbon–Sulfur–Nitrogen Rings

Activity in this area of S–N chemistry has been stimulated by the theoretical prediction that polymers of the type $(RCNSN)_x$ will have conducting properties similar to those of $(SN)_x$.**[102]** Consequently, there have been extensive investigations of C–S–N heterocycles as potential precursors for such polymers.**[5,50]** In addition, a new area of radical chemistry based on $RCN_2S_2^{\bullet}$ (dithiadiazolyl) systems has emerged.**[103]** These heterocycles and their selenium analogs exhibit considerable potential for the development of one-dimensional metals.

8.1.1 Five-Membered Rings[103]

The first examples of the 1,2,3,5-dithiadiazolium cation (**38**) were obtained in 1977 from the treatment of organic nitriles with $(NSCl)_3$. This reaction has subsequently been shown to proceed by the intermediate formation of S,S'-dichlorodithiatriazines (**39**).**[104]** Another route to (**38**) involves the cyclocondensation of trisilylated amidines with sulfur dichloride (equation 20). This method is readily extended to the synthesis of multidithiadiazolium cations, for example, 1,3,5-$C_6H_3(CNSSN)_3{}^{2+}$.**[103]**

$$RC(NSiMe_3)[N(SiMe_3)_2] + 2SCl_2 \longrightarrow [RCN_2S_2]Cl + 3Me_3SiCl \qquad (20)$$

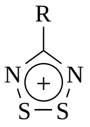
(38)

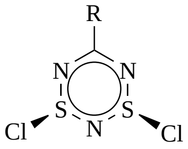
(39)

The isomeric 1,3,2,4-dithiadiazolium cation (**40**) is prepared by the $(4 + 2)\pi$ cycloaddition of the $NS_2{}^+$ cation to the C–N triple bond of organic nitriles (see Figure 2).**[54]** The $NS_2{}^+$ cation also reacts with polycyano compounds, for example, dicyano- and tricyanobenzenes, to give the corresponding bis- and tris(dithiadiazolium) cations.

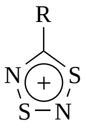
(40)

The color of salts containing the cations (**38**) or (**40**) depends markedly on the anion. Weak donor (hard) anions, for example, $AsF_6{}^-$, give yellow (**38**) or colorless (**40**) salts, whereas softer anions, for example, Br^- or I^-, bestow darker (burgundy or black) colors.

The $RCN_2S_2{}^+$ ring is a 6π-electron system, which is readily reduced to the corresponding 7π-electron radical $RCN_2S_2^{\bullet}$ (**15**). The structures of (**15**) are highly dependent on the nature of R. By changing R, it is possible to produce a monomer, a variety of cis, trans, and staggered dimers, or polymeric structures.**[103]** Thus when R = Ph, the rings are associated by two S–S interactions in a cis configuration (**41**), whereas both the Me_2N and CF_3 derivatives involve only one S–S interaction and the CN_2S_2 rings are twisted at ca. 90° to one another. Interestingly, the bulky t-Bu group prevents dimerization and t-BuCNSSN$^{\cdot}$ is a paramagnetic liquid at room temperature. The related dithiazole (**14**; R = CF_3) is also a paramagnetic liquid that vaporizes to give a blue gas.

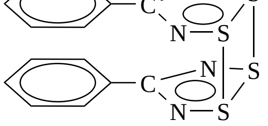
(41)

Dithiadiazolyl radicals are of interest in the design of molecular conductors. Multifunctional radicals, for example, 1,3,5-$C_6H_3(CN_2S_2)_3$, have been prepared.**[103,105]** Iodine doping increases the conductivity of these radical systems.**[106]** Materials with unique magnetic properties are produced by introducing substituents that inhibit the dimerization process.**[9]**

1,3,2,4-Dithiadiazoles are unstable with respect to isomerization to the 1,2,3,5-isomers, but several such structures have been isolated. An interesting example is the biradical p-$C_6H_4(CNSNS)_2$, which has a polymeric structure.[103] The isomerization is a photochemically symmetry-allowed process which is thermally symmetry forbidden. It can readily be monitored by ESR spectroscopy because the 1,3,2,4-dithiadiazoles exhibit a 1:1:1 triplet, whereas the 1,2,3,5-isomers give a 1:2:3:2:1 quintet. A bimolecular head-to-tail rearrangement has been proposed to account for this isomerization.[107]

The dimer $[PhCNSSN]_2$ (**41**) reacts with a variety of zerovalent metal complexes via ligand replacement and cleavage of the S–S bond.[108] For example, reaction with $Pt(PPh_3)_3$ produces the chelated complex (**42**).

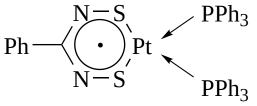

(**42**)

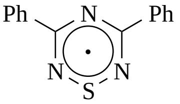

(**43**)

8.1.2 Six-Membered Rings

The thiatriazinyl system (**43**), prepared by the reduction of the corresponding S-chloro derivative, is also a 7π-electron radical. In the solid state, it exists as a cofacial dimer with an S–S distance of ca. 2.67 Å.[109] In solution, the ESR spectrum of (**43**) gives a seven-line pattern with equal hyperfine coupling constants to all three nitrogen atoms.

The dithiatriazine ring, prepared by the reduction of the corresponding S,S'-dichloro derivative, also exists as a cofacial dimer (**44**) in the solid state with an S–S separation of 253 pm.[110] MNDO calculations for the 8π-electron monomer (**44**; R = H) reveal a triplet ground state and the S–S bonds arise from intermolecular π^*–π^* interactions. The dimer (**44**) can also be prepared by reaction of the dithiadiazolyl dimer (**41**) with excited nitrogen atoms generated in a low-pressure direct current discharge.[103] Monomeric dithiatriazines can be stabilized by the formation of $1,3(S,S')$ adducts with electron-rich alkenes, for example, norbornadiene. The regiochemistry and kinetic control of these cycloadditions is governed by the interaction of the alkene HOMO with the LUMO of the dithiatriazine.[5]

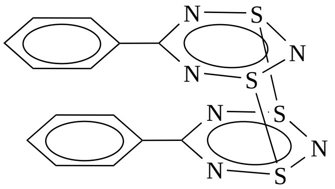

(**44**)

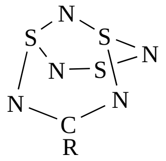

(**45**)

Bicyclic derivatives of the type RCS_3N_5 (**45**) may be prepared from S,S'-dichlorodithiatriazines (**39**) and $Me_3SiNSNSiMe_3$. ^{15}N NMR studies have demonstrated that (**45**; R = Ph) is a fluxional molecule that undergoes a series of degenerate 1,3-nitrogen shifts.[21]

1,3,5,2,4-Trithiadiazines (**46**), first obtained from S_4N_4 and diazoalkanes, are conveniently synthesized from 1,1-bis(sulfenyl chlorides) and $Me_3SiNSNSiMe_3$.[111] The 9π-electron radical $HCS_3N_2^{\bullet}$, isoelectronic with $S_3N_3^{\bullet}$, is formed on treatment of (**46**; R = H) with benzoyl peroxide.

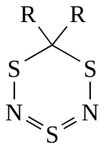

(**46**)

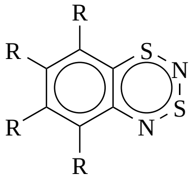

(**47**)

The antiaromatic 12π-electron benzodithiadiazine (**47**; R = H), an inorganic naphthalene analogue, is obtained as a volatile deep blue solid by the reaction of $PhNSNSiMe_3$ with SCl_2, followed by an intramolecular condensation of HCl.[5] The tetrafluoro derivative (**47**; R = F) is prepared by treatment of $C_6F_5SNSNSiMe_3$ with CsF in acetonitrile. In contrast to (**47**; R = H), which has an essentially planar structure in the solid state, the dithiadiazine ring in the tetrafluoro derivative is somewhat twisted. In the gas phase, electron diffraction studies show that (**47**) (R = F) is planar, whereas (**47**) (R = H) is nonplanar.[112,113]

8.1.3 Seven-Membered Rings

The seven-membered rings (**19**), a 1,3,5,2,4-trithiadiazepine, and (**20**), a 1,3,5,2,4,6-trithiatriazepine, are 10π-electron systems isoelectronic with $S_4N_3^+$.[50] 1,3,5,2,4-benzotrithiadiazepine is formed in 50% yield as bright yellow crystals by the reaction of benzo-1,2-bis(sulfenyl chloride) with $Me_3SiNSNSiMe_3$. The tetrafluoro analogue has been prepared by a similar procedure.[114] The isomeric 1,2,4,3,5-benzotrithiadiazepine is obtained from the reaction of $PhNSNSiMe_3$ and S_2Cl_2 followed by intramolecular cyclization.[115] The parent trithiadiazepine, (**19**; R = H), is planar and the bond lengths indicate complete π-delocalization. It is inert to protic and Lewis acids and, as befits an aromatic structure, it does not undergo cycloaddition reactions. Trithiadiazepine undergoes standard electrophilic aromatic-substitution reactions at carbon. For example, the 6-bromo and 6,7-dibromo derivatives are obtained in high yields upon treatment with N-bromosuccinimide.

The parent trithiatriazepine, (**20**; R = H), is obtained as a colorless solid of high thermal stability by carefully heating the ester, (**20**; R = CO_2Me), with aqueous HCl followed by decarboxylation of the carboxylic acid so formed. The ester has a planar, aromatic structure.

8.1.4 *Eight-Membered Rings*

1,5-Dithiatetrazocines, $R_2C_2N_4S_2$, were first reported in 1981.[116] These eight-membered rings were prepared by the cyclocondensation of a benzamidine or dimethylguanidine with SCl_2 in the presence of a base. The yields are low and improved methods have been devised.[117] Cyclophanes containing one or two $C_2N_4S_2$ rings have also been synthesized.[118]

The structures of 1,5-dithiatetrazocines are remarkably dependent upon the nature of the group attached to carbon. With (**48**; R = Ph), the heterocyclic ring is planar and the bond lengths indicate a fully delocalized 10π-electron aromatic system (cf. $S_4N_4{}^{2+}$). By contrast, the bis(dimethylamino) derivative (**6**; E = Me_2NC) adopts a folded structure with d(S–S) = 243 pm. This folding is explained by the destabilizing influence of the π-donor Me_2N substituents on the HOMO of the $C_2N_4S_2$ ring and subsequent second-order Jahn–Teller distortion.[5] 1,5-Dithiatetrazocines with exocyclic N(Me)Bu groups exhibit both cis/trans and ring inversion isomerism on the NMR timescale.[119]

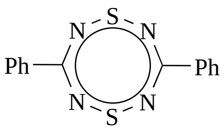

(**48**)

Consistent with its aromatic character, the planar ring (**48**) has high thermal stability and is chemically unreactive.[116] For example, it does not react with n-butyllithium or m-chloroperbenzoic acid and it exhibits no basic properties toward $HClO_4$. By contrast, the folded ring (**49**) is readily oxidized and provides an informative model for understanding the processes involved in the oxidation of heterocycles containing transannular S–S bonds, for example, S_4N_4.[5] Two types of stereochemistries are involved in these oxidation processes: reaction with Cl_2 or Br_2 produces an *exo–endo* geometry (as in **29**), whereas fluorination or reaction with $(CF_3)_2NO^{\bullet}$ results in an *exo–exo* substitution pattern. These substitution patterns are the result of polar and radical oxidation mechanisms, respectively. In electronic terms, they can be understood by viewing the S–S σ and σ^* orbitals of S_4N_4 to be isolobal with the π and π^* orbitals of an alkene. The polar oxidation route is thought to involve the attack of a halogen X_2 on the S–S σ-bonding orbital of S_4N_4. Subsequent uptake of X^- should then occur in a position trans to that of X^+.[5] The structural characterization of the asymmetrically bridged cation (**49**) provides support for the proposed polar oxidation mechanism. The addition of nucleophilic radicals, on the other hand, is considered to proceed by interaction of the SOMO of the radical with the S–S σ^*-LUMO.

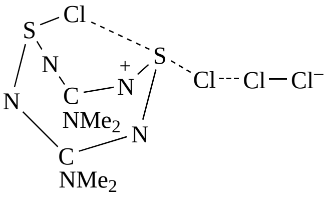

(**49**)

The folded ring system (**6**; E = Me_2NC) forms an $\eta^2 S,S'$ complex with platinum upon reaction with $Pt(PPh_3)_4$.[120]

8.2 Phosphorus(V)–Sulfur–Nitrogen Rings[121]

Heterocycles of the type $R_2PS_2N_3$ (**16**) (cyclophosphadithiatriazines) are of interest as examples of 8π-electron systems. The first derivative (R = Me_3SiNH) was obtained in 1976 from the reaction of S_4N_4 with $(Me_3Si)_2NP(NSiMe_3)_2$.[122] The reaction of R_2PPR_2 (R = Me, Ph) or Ph_2PH with S_4N_4 in boiling toluene also provides a source of (**16**; R = Ph, Me), together with the eight-membered rings 1,3-$R_4P_2N_4S_2$ (**50**) and 1,5-$R_4P_2N_4S_2$ (**51**). The best route to (**16**; R = Ph) is shown in equation (21).

$$Ph_2P(NSiMe_3)(NHSiMe_3) + \tfrac{1}{2}S_4N_4 \xrightarrow[110\,^{\circ}C]{\text{toluene}} Ph_2PS_2N_3 + (Me_3Si)_2NH \quad (21)$$

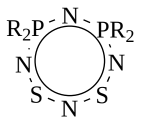

(**50**)

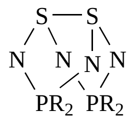

(**51**)

The compounds $R_2PS_2N_3$ are obtained as purple crystals (R = Me_3SiNH, Ph), or as a thermally unstable, purple oil (R = Me), which decomposes at room temperature to give 1,5-$Ph_4P_2N_4S_2$. The structure of (**16**; R = Ph) consists of a six-membered ring in which the phosphorus atom lies 26 pm out of the S_2N_3 plane.[123] The S–N bond lengths fall within a narrow range (156–158 pm). By contrast, the electron-donating Me_3SiNH group gives rise to localized π-bonding in the ring. Ab initio molecular orbital calculations confirm that the PS_2N_3 ring is an 8π-electron system. The purple color ($\lambda_{max} \sim 550$ nm) is attributed to the HOMO(π^*) $\rightarrow$ LUMO(π^*) transition.

The cyclophosphadithiatriazines (**16**) reversibly form white crystalline adducts with norbornadiene, where the alkene adds in a 1,3-fashion across the sulfur atoms to give the exo adduct.[123] This adduct formation provides a convenient way of characterizing the less-stable derivatives of (**16**; R = F, OPh, Me).

Bicyclic compounds of the type $R_2PS_3N_5$ (**52**) were first prepared by the reaction of PF_5 with $Me_3SiNSNSiMe_3$. They may also be obtained by the oxidative addition of Cl_2 to (**16**) followed by reaction of the *S*,*S*′-dichloro derivative with $Me_3SiNSNSiMe_3$.[39]

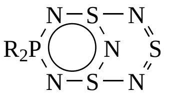

(**52**)

The diphosphadithiatetrazocines (**50**) and (**51**) contain one more R_2PN units in the ring than (**16**). The structure of the orange–red 1,3-isomer, (**50**; R = Ph), consists of an essentially planar S_2N_3 unit with phosphorus atoms located on opposite sides of the plane.[121] The isomer (**50**) forms a 1:1 adduct with norbornadiene via 1,3-addition across the sulfur atoms.

The 1,5-isomers (**51**) are colorless, air-stable solids. They are obtained by the cyclocondensation reaction of $R_2PN_2(SiMe_3)_3$ with sulfur dichloride or thionyl chloride. The structures of 1,5-$R_4P_2N_4S_2$ (R = alkyl, aryl) are folded eight-membered rings with a cross-ring S–S distance of ca. 250 pm. This structural feature is the result of an intramolecular $\pi^*-\pi^*$ interaction (Figure 1). It gives rise to anomalous ^{31}P NMR chemical shifts (110–140 ppm) (*see Intramolecular*) for the 1,5-isomers compared to other P–N–S rings or cyclophosphazenes. The dication $[Et_4P_2N_4S_2]^{2+}$ is planar.[124] Alkali metal derivatives of the dianion $[Ph_4P_2N_4S_2]^{2-}$ have been prepared, but not structurally characterized.[125] A methylene bridge can be inserted between the sulfur atoms of (**51**) by treatment of $Li_2[Ph_4P_2N_4S_2]$, generated from (**51**; R = Ph) and $Li[Et_3BH]$, with CH_2I_2.

The 1,5-diphosphadithiatetrazocines (**51**) serve as excellent models for determining the identity of the initial products formed in the reactions of S–N compounds.[126] The NPR_2N units act as a brace as well as a source of structural information through ^{31}P NMR spectroscopy. Thus, in contrast to S_4N_4, the integrity of the eight-membered ring in (**51**) is retained in reactions with either electrophiles or nucleophiles. The oxidative addition of halogens occurs smoothly to give the *exo, endo* dihalogenated derivatives 1,5-$Ph_4P_2N_4S_2X_2$ (cf. **29**). Oxidative addition also occurs with platinum(0) or palladium(0) reagents to give η^2-S,S′ complexes that involve synergic metal–ligand bonding analogous to that found in the classic metal–alkene complexes (*see Dewar–Chatt–Duncanson Bonding Model*). The 1,5-diphosphadithiatetrazocines behave as weak Lewis bases in forming N-bonded adducts with protic or Lewis acids and with platinum(II). The cross-ring S–S bond is retained in these adducts. The reaction of (**51**; R = Ph) with organolithium reagents proceeds smoothly to the lithium derivatives $Li[Ph_4P_2N_4S_2R]$. The reaction of $Li[Ph_4P_2N_4S_2Me]$ with MeI gives the *S*,*S*′-dimethyl derivative (**53**).

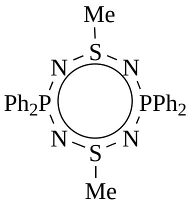

(**53**)

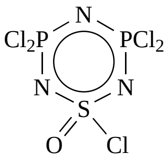

(**54**)

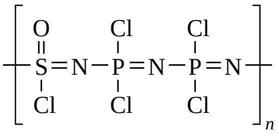

$$-\!\!\left[\underset{\text{Cl}}{\overset{\text{O}}{\text{S}}}=\text{N}-\underset{\text{Cl}}{\overset{\text{Cl}}{\text{P}}}=\text{N}-\underset{\text{Cl}}{\overset{\text{Cl}}{\text{P}}}=\text{N}\right]_n\!\!-$$

(**55**)

Six-membered rings containing two phosphorus atoms and one four-coordinate sulfur atom (**54**) have been known since 1972.[127] An ambient temperature reaction of (**54**) with $GaCl_3$ produces the high molecular weight poly(thionylphosphazene) (**55**) via ring-opening polymerization.[128] Subsequent reaction of (**55**) with *n*-$BuNH_2$ yields the hydrolytically stable polymer, $[NSO(NHBu)\{NP(NHBu)_2\}_2]_n$. Polymers with backbones of alternating S(O)=N and P=N units are prepared via a condensation route (equation 22).[129]

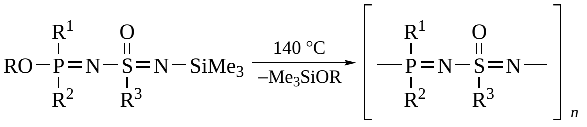

$$\text{RO}-\underset{R^2}{\overset{R^1}{\text{P}}}=\text{N}-\underset{R^3}{\overset{\text{O}}{\text{S}}}=\text{N}-\text{SiMe}_3 \xrightarrow[-\text{Me}_3\text{SiOR}]{140\ °\text{C}} \left[-\underset{R^2}{\overset{R^1}{\text{P}}}=\text{N}-\underset{R^3}{\overset{\text{O}}{\text{S}}}=\text{N}-\right]_n \tag{22}$$

8.3 Phosphorus(III)–and Arsenic(III)–Sulfur–Nitrogen Compounds

The RP^{III} and RAs^{III} groups are isoelectronic with a sulfur atom as a substituent in an S–N ring. Thus, it is reasonable to expect that ring systems where sulfur atoms have been replaced by these groups will exist. The first examples $MeAsN_2S_2$ (**56**; R = Me) and $(MeAs)_2N_4S_2$ (**57**; R = Me) were reported in 1970.[130] The SN_2^{2-} anion has been used to prepare the acyclic arsenic(III) derivative *t*-$Bu_2AsNSNAs$-*t*-Bu_2, and the eight-membered ring (**57**; R = *t*-Bu) from *t*-Bu_2AsCl and *t*-$BuAsCl_2$ respectively.[64] The S–N bond lengths in the boat-shaped ring (**57**; R = *t*-Bu) are typical of a sulfur diimide. Phosphorus(III) derivatives of the type $R_2PNSNPR_2$ are only stable if R is a bulky group such as *t*-butyl or if the phosphorus atoms are coordinated to a transition metal. The eight-membered ring $(RP)_2N_4S_2$ has been obtained in transition metal complexes, for example (**58**), in which the $P_2^{III}N_4S_2$ is essentially planar with localized sulfur diimide bonding.[131] Six-membered rings of the type RPNSNSNH have also been structurally characterized in transition metal complexes, for example, (**59**).[64,126]

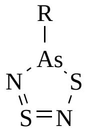

(**56**)

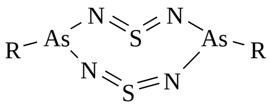

(**57**)

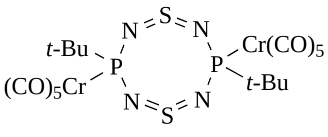

(**58**)

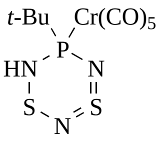

(**59**)

8.4 Sulfur–Nitrogen–Selenium Compounds

S–N compounds containing selenium provide an important bridge between binary S–N systems and their less-stable Se–N analogs (*see* ***Selenium: Inorganic Chemistry***). The compound $Se(NSO)_2$, prepared from a 1:1 mixture of Me_3SiNSO and selenium monochloride, is an important source of S–N–Se compounds.[132] For example, the reaction of $Se(NSO)_2$ with $TiCl_4$ produces the adduct $SeSN_2{\cdot}TiCl_4$ (**60**) and treatment with $POCl_3$ yields $SSe_2N_2Cl_2$. The acyclic reagent, $Me_3SiNSNSeNSNSiMe_3$, is prepared from $Me_3SiNSNSiMe_3$ and $SeCl_2$ (equation 23).[133] It can be used to prepare 1,5-$S_2Se_2N_4$ (**61**) (equation 24).

$$2Me_3SiNSNSiMe_3 + SeCl_2 \longrightarrow Me_3SiNSNSeNSNSiMe_3 + 2Me_3SiCl \tag{23}$$

$$Me_3SiNSNSeNSNSiMe_3 + SeCl_2 \longrightarrow 1{,}5\text{-}S_2Se_2N_4 + 2Me_3SiCl \tag{24}$$

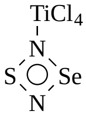

(**60**)

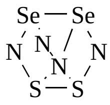

(**61**)

On the basis of vibrational and ^{77}Se NMR spectra, the hybrid sulfur/selenium nitride SeS_3N_2 has a cyclic structure in which the selenium atom is linked to two sulfur atoms (**62**).[134] The five-membered ring $[S_2SeN_2Cl]^+$ (**63**) can be used to prepare platinum complexes of the $SSeN_2{}^{2-}$ anion (**64**) by treatment with *cis*-$PtCl_2(PR_3)_2$ in liquid ammonia.[6]

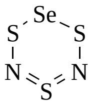

(**62**)

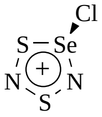

(**63**)

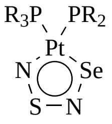

(**64**)

Salts of the sulfur–nitrogen–selenium cation radicals $[SnSe_{3-n}N_2]^{+\bullet}$ ($n = 1{,}2$) have dimeric structures similar to that of $S_6N_4{}^{2+}$ (**7**).[135,136]

8.5 Cyclometallathiazenes[6,7]

A cyclometallathiazene is a ring system consisting of only sulfur, nitrogen, and one (or more) metal atoms. As indicated in Table 1, cyclometallathiazenes can formally be considered as complexes between cationic metal fragments and binary S–N anions where, with the exception of the $S_2N_2H^-$ and $S_4N_4{}^{2-}$ ions, both the sulfur and nitrogen atoms are two coordinate (*see* ***Mixed Donor Ligands***).

Since only two of these ions, S_3N^- and $SN_2{}^{2-}$, have been isolated as salts, the synthesis of cyclometallathiazenes usually employs S_4N_4 (**1**) as a source of the S–N fragment. Some representative examples are shown in Scheme 7.

Complexes containing the $S_2N_2H^-$ ion comprise the best-characterized group of cyclometallathiazenes. The dark green nickel derivative $Ni(S_2N_2H)_2$ (**65**) is readily obtained in ca. 60% yields from the reaction of S_4N_4 with anhydrous $NiCl_2$ in methanol. The MS_2N_2H units in these complexes are planar. Compounds of the type $[Pt(S_2N_2H)(PR_3)_2]X$ are especially interesting since they form continuous stacking structures.[6] The NH groups in $M(S_2N_2H)$ complexes are readily deprotonated to give anions which can be converted to organic derivatives by treatment with organic halides.[7]

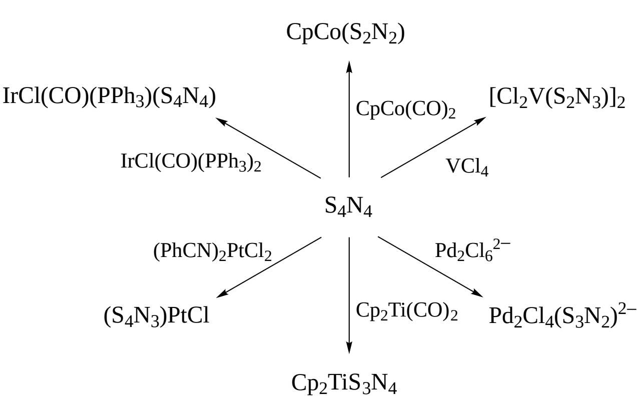

Scheme 7 Preparation of cyclometallathiazenes from S_4N_4

Table 1 Cyclometallathiazenes

Ring system	Corresponding S–N anion	Metal	Year of discovery (first X-ray structure)
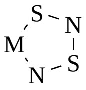	$S_2N_2^{2-}$	Co, Ir, Ni, Pd, Pt (Pb)	1982 (1982)
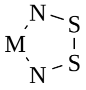	$S_2N_2^{4-}$	Re	1984 (1984)
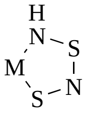	$[S_2N_2H]^-$	Co, Ni, Pd, Pt	1953 (1958)
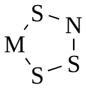	S_3N^-	Co, Ni, Pd, Pt, Cu, Ag, Au	1958 (1966)
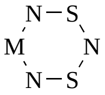	$S_2N_3^-$	Pd	1992 (1992)
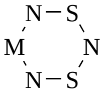	$S_2N_3^{3-}$	V, Mo, W	1983 (1983)
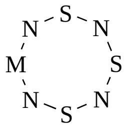	$S_3N_4^{2-}$	Ti	1983 (1983)
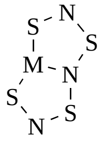	$S_4N_3^-$	Pt	1981 (1981)
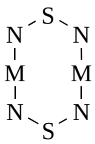	SN_2^{2-}	Hg, Zr, Hf	1904 (1984)
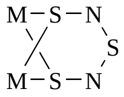	$S_3N_2^{2-}$	Pd	1966 (1982)
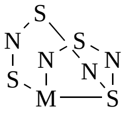	$S_4N_4^{2-}$	Ir, Pt	1970 (1986)

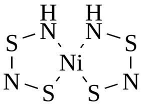

(**65**)

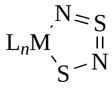

(**66**)

In addition to S_4N_4, a variety of S–N reagents, including $S_3N_3^-$, $S_4N_4H_4$/diazobicycloundecene, $[Me_2Sn(S_2N_2)]_2$, and solutions of $[S_4N_3]Cl$ in liquid ammonia, provide a source of $S_2N_2^{2-}$ for metal complexes. X-Ray structural data for MS_2N_2 complexes (**66**) indicate a localization of π-bonding within the NSN unit. The MS_2N_2 complexes are readily protonated at the nitrogen atom attached to the metal (equation 25).

$$Pt(S_2N_2)(PR_3)_2 + HBF_4 \longrightarrow [Pt(S_2N_2H)(PR_3)_2]BF_4 \qquad (25)$$

The first metal complex of the S_3N^- anion, $Ni(S_3N)_2$, was obtained in 0.04% yield (9 mg) from $NiCl_2$ and S_4N_4 (10 g) in methanol and correctly identified.[137] Such complexes are now obtained in acceptable yields via deprotonation of S_7NH in the presence of metal halides or by using the mercury complexes $Hg(S_7N)_2$ or $PhHg(S_7N)$ as a source of S_3N^-.[7] The formation of the trigonal bipyramidal anion $\{[Ni(S_3N)]_3S_2\}^-$ (**67**) by the former process is of particular interest.[138] In the $Cu(S_3N)(S_7N)^-$ anion, the S_7N ring is (partly) preserved and coordinated to copper through the nitrogen atom.[139]

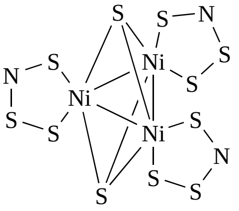

(**67**)

Reaction of high-oxidation state early-transition metal halides with S_4N_4, $(NSCl)_3$, or $[S_3N_2Cl]Cl$ generates the MS_2N_3 ring, for example, $[VCl_2(S_2N_3)]_n$, which may be viewed as a complex of the $S_2N_3{}^{3-}$ trianion.[140] The thiazene segment of the ring in MS_2N_3 is usually planar but, in some cases, the metal is tilted out of this plane. Complexes of the monoanion $S_2N_3{}^-$ can be obtained by the reactions of $[PPh_4]_2[Pd_2Cl_6]$ with S_5N_6 or, preferably, $Me_3SiNSNSNSNSiMe_3$.[52] The electronic structures of cyclometallathiazenes have been investigated by Density Functional Theory (DFT) calculations.[141]

Coordination of the dianion, $S_4N_4{}^{2-}$, as a tridentate ligand has been established in a few cases.[6] The complexes $IrCl(CO)(S_4N_4)PPh_3$[142] and $PtCl_3(S_4N_4)^-$[143] contain this ligand *facially* bonded to the metal through one nitrogen and two sulfur atoms (see Table 1). By contrast, the same ligand adopts a *meridional* (S,S,N) geometry in the complex $PtCl_2(S_4N_4)(PMe_2Ph)$, which according to ^{15}N NMR investigations, is converted to a *facial* S,N,N isomer in boiling chloroform (*see* ***Coordination Numbers & Geometries***).[144]

9 SULFANURIC COMPOUNDS[39]

These compounds contain the characteristic group –N=S(O)X– (where X = Cl, F, alkyl, aryl, or R_2N). Unlike the isoelectronic cyclophosphazenes, only six-membered rings have been well characterized. The sulfanuric halides are colorless solids (X = Cl) or liquids (X = F), which are stable in dry air. Sulfanuric chloride is best prepared by treatment of $SOCl_2$ with sodium azide (equation 26). It may also be obtained as a mixture of α- and β-isomers in a two-stage reaction from H_2NSO_3H and PCl_5. The fluoride, $[NS(O)F]_3$, is formed as a mixture of isomers by the fluorination of $[NS(O)Cl]_3$ with SbF_3.

$$SOCl_2 + NaN_3 \xrightarrow[-35\,°C]{MeCN} \frac{1}{3}\,[NS(O)Cl]_3 + NaCl + N_2 \qquad (26)$$

The isomer α-$[NS(O)Cl]_3$ (**68**) is a six-membered ring in the chair form with equal S–N bond lengths of 157 pm. The three chlorine atoms are in axial positions on the same side of the ring. The β-isomer has one equatorial and two axial chlorine atoms.[145] The metal-containing sulfanuric ring system (**69**) has been prepared from $PhS(O)N(SiMe_3)_2$ and $ClNMoCl_4$.[146]

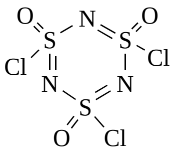

(**68**)

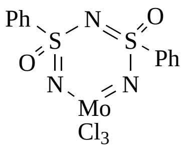

(**69**)

The fluoride $[NS(O)F]_3$ is more stable thermally and toward nucleophilic reagents than the corresponding chloride. For example, α-$[NS(O)Cl]_3$ is hydrolyzed by water to $NH(SO_2NH_2)_2$, whereas sulfanuric fluoride is unaffected by cold water. In warm water, however, hydrolysis occurs to give the $N_3S_3O_4F_2{}^-$ ion. All three fluorine atoms in $[NS(O)F]_3$ can be replaced by primary or secondary amines at 80−90 °C in the absence of a solvent.

High molecular weight polymers containing repetitive [N=S(O)R] (R = Me, Ph) units have been characterized.[147] These polymers are produced by the condensation process shown in equation (27).

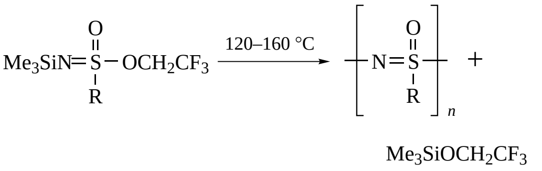

$$Me_3SiN{=}\overset{\displaystyle O}{\underset{\displaystyle R}{\overset{\|}{\underset{|}{S}}}}{-}OCH_2CF_3 \xrightarrow{120\text{–}160\ °C} \left[N{=}\overset{\displaystyle O}{\underset{\displaystyle R}{\overset{\|}{\underset{|}{S}}}} \right]_n + Me_3SiOCH_2CF_3 \qquad (27)$$

10 CYCLIC SULFUR IMIDES[10,39]

The best-known cyclic sulfur imides are saturated sulfur−nitrogen heterocycles, which are derived from *cyclo*-S_8 by the replacement of one or more sulfur atoms by an amido (NH) group. Derivatives containing adjacent NH groups are not found. Thus, the members of this series consist of S_7NH (**70**), three diimides 1,3-, 1,4- and 1,5-$S_6(NH)_2$, two triimides 1,3,5- and 1,3,6-$S_5(NH)_3$, and $S_4N_4H_4$ (**71**).

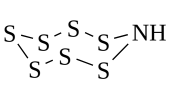

(**70**)

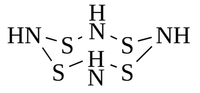

(**71**)

The standard preparation of cyclic sulfur imides, with the exception of $S_4N_4H_4$, involves the reaction of S_2Cl_2 with ammonia in DMF at ca. −10 °C, followed by hydrolysis with cold dilute hydrochloric acid. This method gives mainly S_7NH, but the three diimide isomers and very small amounts of 1,3,6-$S_5(NH)_3$ can be separated by chromatography of CS_2 solutions on silica gel. The reaction of sodium azide with elemental sulfur in $(Me_2N)_3PO$ is an excellent source of S_7NH, and it has been used for making a ^{15}N-enriched product. Both these methods proceed via the formation of the deep blue S_4N^- ion for the synthesis of S_7NH.**39** The reduction of S_4N_4 by hydrazine in CCl_4 is the only useful route to 1,3,5-$S_5(NH)_3$. The tetraimide $S_4(NH)_4$ is best prepared from S_4N_4 by using methanolic $SnCl_2{\cdot}2H_2O$ as the reducing agent.

The cyclic sulfur imides form colorless, air-stable crystals, which undergo slow photochemical decomposition to give elemental sulfur. They all adopt the crown configuration of *cyclo*-S_8 with S–S bond lengths in the range 204–206 pm.**10** The S–N bond distances (166–168 pm) are significantly shorter than a S–N single bond and the geometry around the nitrogen atoms is almost planar, indicating three-center π-bonding in the – S–N(H)–S– units. Electron deformation density measurements of (**71**) indicate bent S–N bonds with endocyclic maxima.**148**

TLC (thin layer chromatography) gives a quick indication of the composition of a mixture of imides. IR spectroscopy provides a better method for the analysis of such mixtures. The IR spectra of CS_2 solutions exhibit bands in the S–N stretching region (775–840 cm^{-1}) that are characteristic of the individual imides. The characteristic ^1H and ^{15}N NMR chemical shifts of all the imides have been determined by the HMQC method.**149** The values of $^1J(^{15}N–^1H)$ fall within the narrow range 93–96 Hz, consistent with sp^2-hybridized nitrogen atoms.

The cyclic sulfur imides are weak Brønsted acids that are readily deprotonated by strong bases. In the case of S_7NH, deprotonation produces the thermally unstable, yellow S_7N^- ion, which decomposes to the deep blue S_4N^- ion (equation 28).**20** Some covalent derivatives of S_7N^- have been isolated.**10** The most important are the mercury(II) compounds, $PhHgS_7N$ and $Hg(S_7N)_2$.

$$S_7NH + Bu_4NOH \xrightarrow{-78\,^\circ C} [Bu_4N][S_7N] \xrightarrow{>-50\,^\circ C} [Bu_4N][S_4N] + \frac{3}{8}S_8 \qquad (28)$$

Both S_7NH and the $S_6(NH)_2$ isomers decompose above their melting points to give mainly S_4N_4 and S_8. These cyclic sulfur imides readily undergo condensation reactions with sulfur halides in the presence of a base. For example, the reaction of S_7NH with dichlorosulfanes produces the series $(S_7N)_2S_x$ (x = 1, 2, 3, 5) and the treatment of 1,3-$S_6(NH)_2$ with S_5Cl_2 generates small amounts of the bicyclic compound $S_{11}N_2$.**10**

Complexes of the type $(S_4N_4H_4)M(CO)_5$ (M = Cr, W), in which the ligand is bonded to the metal by a sulfur atom, are formed by the reaction of the tetraimide with $(THF)M(CO)_5$ (*see* ***Carbonyl Complexes of the Transition Metals***).**7** The deprotonation of $S_4N_4H_4$ with strong bases produces the $S_2N_2H^-$ ion and, subsequently, $S_3N_3^-$.**19** Ring fragmentation also occurs in the reaction of $S_4N_4H_4$ with $Pt(PPh_3)_4$ to give $Pt(PPh_3)_2(S_2N_2)$.**6,7**

Nine- and ten-membered sulfur imides, S_8NH and S_9NH, respectively, are prepared by the oxidative addition of S_7NH to $Cp_2Ti(CO)_2$ to give $[Cp_2Ti(S_7NH)]$ followed by treatment with the appropriate dichlorosulfane (equation 29).**150** The structure of S_8NH is similar to that of *cyclo*-S_9 (*see* ***Sulfur: Inorganic Chemistry***), whereas the structure of S_9NH resembles the crown structure of *cyclo*-S_8 with the insertion of a SN(H) unit.

$$[Cp_2Ti(S_7NH)] + S_xCl_2 \longrightarrow Cp_2TiCl_2 + S_{7+x}NH \ (x = 1, 2) \qquad (29)$$

Six- and seven-membered sulfur imides, S_5NR and S_6NR (R = n-Oct), are obtained as yellow oils from $[Cp_2Ti(\mu\text{-}S_2)_2NR]$ and S_xCl_2 (x = 1, 2) by using the methodology shown in equation (29).**151** Molecular ions were observed in the EI mass spectra.

Monomeric sulfur imide SNH is not known, but a coordination compound $Fe_2(CO)_6(HNS)$ (**72**) has been isolated and converted to the corresponding anion $[Fe_2(CO)_6(\mu\text{-}SN)]^-$ with n-BuLi.**152** The complex (**72**) is obtained from the reaction of $Fe_3(CO)_{12}$ with $Me_3SiNSNSiMe_3$, followed by chromatography on silica. The HNS unit behaves as a six-electron ligand (*see Counting Electrons*). Mononuclear complexes of the type $(RNS)Cr(CO)_5$ (R = Me_2N, Ph_2N), in which the ligand is bonded to the metal via sulfur, have also been structurally characterized.**140**

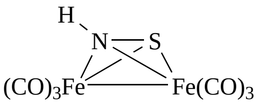

(**72**)

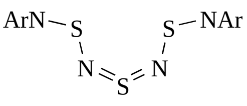

(**73**)

11 SULFUR–NITROGEN CHAINS AND POLYMERS[153]

The unusual properties of the polymer $(SN)_x$ have sparked interest in S–N polymers with organic groups in the backbone as well as S–N chains with terminal organic residues. The first reports of such S–N chains described the preparation of trithiadiazenes ArS_3N_2Ar (**73**), which adopt planar (cis, cis) conformations.**154,155** Since then, rational syntheses have been developed for chain lengths up to ArS_5N_4Ar (Ar = aryl) via condensation reactions involving the elimination of Me_3SiCl or $Me_3SiOSiMe_3$ (see Scheme 8).

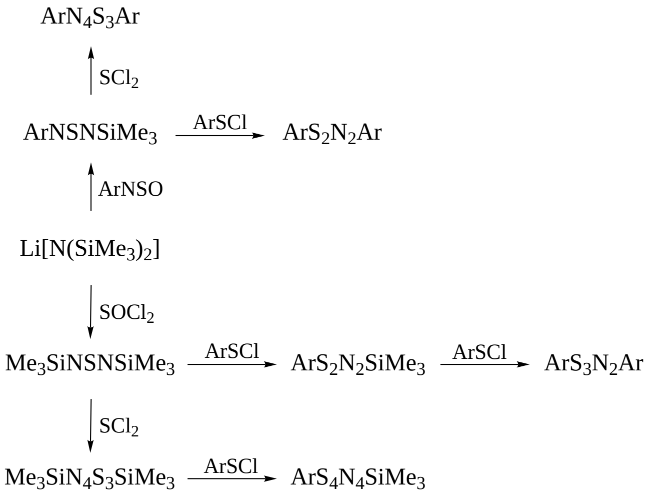

Scheme 8 Preparation of S–N chains

These S–N chains may be considered as small fragments of $(SN)_x$. In contrast to $(SN)_x$, however, they exhibit alternating long and short S–N bonds, as depicted in the structures of $Me_3SiN_4S_4C_6H_4NO_2$ (**74**) and ArS_5N_4Ar (**75**), consistent with a more localized structure. Cationic S–N chains, for example, $[ArS_4N_3Ar]^+$ (**76**), are also known.[156] Continuing interest in these oligomeric materials stems from their optical properties and possible applications as molecular wires. In general, the shorter chains tend to be brightly colored, yellow or orange, whereas the longer chains produce intense deep green, blue, or purple solutions and in the solid state, they have a metallic luster.

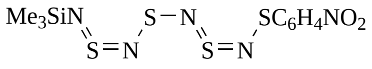

(**74**)

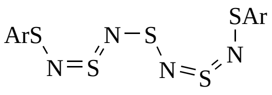

(**75**)

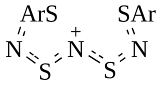

(**76**)

Conducting polymers with *p*-phenylene groups in the backbone can be prepared by the metathetical reaction shown in equation (30).[157] Doping of these polymers with acceptors such as I_2, Br_2, or AsF_5 increases the conductivity to ca. $10^{-4}\Omega^{-1}\,cm^{-1}$.

$$Me_3SiNSNC_6H_4NSNSiMe_3 + SCl_2 \longrightarrow \frac{1}{x}\,[–C_6H_4NSNSNSN–]_x \tag{30}$$

Polymers with $–C_6H_4SNSNSC_6H_4–$ or $–C_6H_4SNSNS C_6H_4SNSNSC_6H_4–$segments separated by flexible spacer groups have also been synthesized.[158] These insulators are converted to semiconductors (*see* ***Semiconductors***) when doped with Br_2.

12 POLY(SULFUR NITRIDE)[2]

Polymeric sulfur nitride (or polythiazyl) (**2**) was first reported in 1910. It is prepared by the solid-state polymerization of S_2N_2 at 0 °C over several days (see Section 5.1.3).[159] The polymer is also obtained in high yield from the reaction of $(NSCl)_3$ with trimethylsilyl azide in acetonitrile or by the electrochemical reduction of $S_5N_5^+$ salts.

Poly(sulfur nitride) is a shiny metallic solid consisting of highly oriented parallel fibers. The crystal structure reveals an almost planar cis,trans-polymer (**2**) with adjacent S–N bond lengths of 163 and 159 pm. The conductivity of $(SN)_x$ at room temperature along the fibers ($\sigma\|$) is $1–4 \times 10^3\Omega^{-1}\,cm^{-1}$ depending on the quality of the crystals, and this value increases by about two orders of magnitude at 4 K. The conductivity across the fibers ($\sigma\perp$) is much smaller. Typical values of the anisotropy ratio $\sigma\|/\sigma\perp$ are ≈ 50 at room temperature and ≈ 1000 at 40 K. The metallic properties of $(SN)_x$ are attributed to a half-filled conducting band.[2] Single crystals of $(SN)_x$ have been investigated as an electrode material.[160]

Partial bromination of $(SN)_x$ or powdered S_4N_4 with bromine vapor yields the blue–black polymer $(SNBr_{0.4})_x$ which has a room temperature conductivity of $2 \times 10^4\Omega^{-1}\,cm^{-1}$.[2] The bromine in this polymer is present as Br_3^- ions and intercalated Br_2 molecules. The polymer $(SNBr_{0.4})_x$ is also prepared by the reaction of $(NSCl)_3$ with Me_3SiBr in CH_2Cl_2 at $-60\,°C$. Similar highly conducting, nonstoichiometric polymers can be obtained by treating S_4N_4 with ICl, IBr, or I_2.

13 RELATED ARTICLES

Ammonia & N-donor Ligands; Electronic Structure of Main-group Compounds; Mixed Donor Ligands; Sulfur: Inorganic Chemistry; Sulfur: Organic Polysulfanes.

14 FURTHER READING

T. Chivers, ‘A Guide to Chalcogen–Nitrogen Chemistry’, World Scientific Publishing Co. Inc., New Jersey, 2004.

15 REFERENCES

1. H. W. Roesky, *Adv. Inorg. Chem. Radiochem.*, 1979, **22**, 239.
2. A. J. Banister and I. B. Gorrell, *Adv. Mater.*, 1998, **10**, 1415.
3. A. J. Banister, *Nature (London)*, 1972, **237**, 92.
4. T. Chivers, *Chem. Rev.*, 1985, **85**, 341.
5. R. T. Oakley, *Prog. Inorg. Chem.*, 1988, **36**, 299.
6. P. F. Kelly and J. D. Woollins, *Polyhedron*, 1986, **5**, 607.
7. T. Chivers and F. Edelmann, *Polyhedron*, 1986, **5**, 1661.
8. J. M. Rawson and G. D. McManus, *Coord. Chem. Rev.*, 1999, **189**, 135.
9. J. M. Rawson and F. Palacio, *Struct. Bonding (Berlin)*, 2001, **100**, 93.
10. H. G. Heal, ‘The Inorganic Heterocyclic Chemistry of Sulfur, Nitrogen and Phosphorus’, Academic Press, London, 1980.
11. J. D. Woollins, ‘Non-Metal Rings, Cages and Clusters’, John Wiley & Sons, Chichester, 1988, p. 89.
12. T. Chivers, *Acc. Chem. Res.*, 1984, **17**, 166.
13. B. M. Gimarc and N. Trinajstić, *Pure Appl. Chem.*, 1980, **52**, 1443.
14. R. Gleiter, *Angew. Chem., Int. Ed. Engl.*, 1981, **20**, 444.
15. S. Parsons and J. Passmore, *Inorg. Chem.*, 1992, **31**, 526.
16. T. Chivers, R. T. Oakley, O. J. Scherer, and G. Wolmershäuser, *Inorg. Chem.*, 1981, **20**, 914.
17. I. P. Parkin, J. D. Woollins, and P. S. Belton, *J. Chem. Soc., Dalton Trans.*, 1990, 511.
18. J. Passmore and M. J. Schriver, *Inorg. Chem.*, 1988, **27**, 2749.
19. T. Chivers and K. J. Schmidt, *Can. J. Chem.*, 1992, **70**, 710.
20. T. Chivers and R. T. Oakley, *Top. Curr. Chem.*, 1982, **102**, 117.
21. K. Bestari, R. T. Boeré, and R. T. Oakley, *J. Am. Chem. Soc.*, 1989, **111**, 1579.
22. B. Wrackmeyer, K. Schlamel, K. Guldner, and M. Herberhold, *Z. Naturforsch., Teil B*, 1987, **42B**, 703.
23. K. F. Preston and L. H. Sutcliffe, *Mag. Reson. Chem.*, 1990, **28**, 189.
24. Y. Miura, N. Makita, and M. Kinoshita, *Bull. Chem. Soc. Jpn.*, 1977, **50**, 482.
25. H.-P. Klein, R. T. Oakley, and J. Michl, *Inorg. Chem.*, 1986, **25**, 3194.
26. R. Steudel, *Z. Naturforsch., Teil A*, 1981, **36A**, 850.
27. R. Steudel, *J. Mol. Struct.*, 1982, **87**, 97.
28. P. Hassanzadeh and L. Andrews, *J. Am. Chem. Soc.*, 1992, **114**, 83.
29. E. Besenyei, G. K. Eigendorf, and D. C. Frost, *Inorg. Chem.*, 1986, **25**, 4404.
30. W. M. Lau, N. P. C. Westwood, and M. H. Palmer, *J. Am. Chem. Soc.*, 1986, **108**, 3229.
31. R. T. Boeré and T. L. Roemmele, *Coord. Chem. Rev.*, 2000, **210**, 369.
32. T. Chivers and M. Hojo, *Inorg. Chem.*, 1984, **23**, 1526.
33. A. J. Banister, Z. V. Hauptman, A. G. Kendrick, and R. W. H. Small, *J. Chem. Soc., Dalton Trans.*, 1987, 915.
34. R. T. Boeré, R. T. Oakley, R. W. Reed, and N. P. C. Westwood, *J. Am. Chem. Soc.*, 1989, **111**, 1180.
35. K. K. Pandey, *Prog. Inorg. Chem.*, 1992, **40**, 445.
36. D. S. Bohle, C.-H. Hung, A. K. Powell, B. D. Smith, and S. Wocadlo, *Inorg. Chem.*, 1997, **36**, 1992.
37. C. Wentrup and P. Kambouris, *Chem. Rev.*, 1991, **91**, 363.
38. R. D. Davy and H. F. Schaefer III, *J. Am. Chem. Soc.*, 1991, **113**, 1917.
39. T. Chivers, in ‘The Chemistry of Inorganic Homo- and Heterocycles’, eds. D. B. Sowerby and I. Haiduc, Academic Press, London, 1987, Vol. 2, Chap. 29, p. 793.
40. Y. Jung, T. Heine, P. V. R. Schleyer, and M. Head-Gordon, *J. Am. Chem. Soc.*, 2004, **126**, 3132.
41. H. M. Tuononen, R. Suontamo, J. Valkonen, and R. S. Laitinen, *J. Phys. Chem. A.*, 2004, **108**, 5670.
42. H. Müller, S. O. Svensson, J. Birch, and A. Kvick, *Inorg. Chem.*, 1997, **36**, 1488.
43. K. Dehnicke and U. Müller, *Transition Met. Chem.*, 1985, **10**, 361.
44. M. Bénard, *Nouv. J. Chim.*, 1986, **10**, 529.
45. T. Chivers, P. W. Codding, W. G. Laidlaw, S. W. Liblong, R. T. Oakley, and M. Trsic, *J. Am. Chem. Soc.*, 1983, **105**, 1186.
46. A. Maaninen, J. Siivari, R. S. Laitinen, and T. Chivers, *Inorg. Synth.*, 2002, **33**, 196.
47. S. H. Irsen, P. Jacobs, and R. Dronskowski, *Z. Anorg. Allg. Chem.*, 2001, **627**, 321.
48. W. Scherer, M. Spiegler, B. Pedersen, M. Tafipolsky, W. Hieringer, B. Reinhard, A. J. Downs, and G. S. McGrady, *Chem. Commun.*, 2000, 635.
49. R. Gleiter, *J. Chem. Soc. A*, 1970, 3174.
50. C. W. Rees, *J. Heterocycl. Chem.*, 1992, **29**, 639.
51. W. S. Sheldrick, M. N. S. Rao, and H. W. Roesky, *Inorg. Chem.*, 1980, **19**, 538.
52. P. F. Kelly, A. M. Z. Slawin, D. J. Williams, and J. D. Woollins, *Chem. Soc. Rev.*, 1992, 245.
53. O. Glemser and W. Koch, *Angew. Chem., Int. Ed. Engl.*, 1971, **10**, 127.
54. S. Parsons and J. Passmore, *Acc. Chem. Res.*, 1994, **27**, 101.

55. R. Faggiani, R. J. Gillespie, C. J. L. Lock, and J. D. Tyrer, *Inorg. Chem.*, 1978, **17**, 2975.
56. B. Ayres, A. J. Banister, P. D. Coates, M. I. Hansford, J. M. Rawson, C. E. F. Rickard, M. B. Hursthouse, K. M. A. Malik, and M. Motevalli, *J. Chem. Soc., Dalton Trans.*, 1992, 3097.
57. S. Herler, P. Mayer, H. Nöth, A. Schulz, M. Suter, and M. Vogt, *Angew. Chem., Int. Ed. Engl.*, 2001, **40**, 3173.
58. W. V. F. Brooks, T. S. Cameron, S. Parsons, J. Passmore, and M. J. Schriver, *Inorg. Chem.*, 1994, **33**, 6230.
59. F. Grein, *Can. J. Chem.*, 1993, **71**, 335.
60. A. Apblett, T. Chivers, A. W. Cordes, and R. Vollmerhaus, *Inorg. Chem.*, 1991, **30**, 1392.
61. R. J. Gillespie, D. R. Slim, and J. D. Tyrer, *J. Chem. Soc., Chem. Commun.*, 1977, 253.
62. T. Chivers, L. Fielding, W. G. Laidlaw, and M. Trsic, *Inorg. Chem.*, 1979, **18**, 3379.
63. A. J. Banister, P. J. Dainty, A. C. Hazell, R. G. Hazell, and J. G. Lomborg, *Chem. Commun.*, 1969, 1187.
64. M. Herberhold, *Comments Inorg. Chem.*, 1988, **7**, 53.
65. D. Hänssgen, H. Salz, S. Rheindorf, and C. Schrage, *J. Organomet. Chem.*, 1993, **443**, 61.
66. T. Borrmann, A. V. Zibarev, E. Lork, G. Knitter, S.-J. Chen, P. G. Watson, E. Cutin, M. M. Shakirov, W.-D. Stohrer, and R. Mews, *Inorg. Chem.*, 2000, **39**, 3999.
67. T. Borrmann, E. Lork, R. Mews, M. M. Shakirov, and A. V. Zibarev, *Eur. J. Inorg. Chem.*, 2004, **2004**, 2452.
68. R. Fleischer and D. Stalke, *Coord. Chem. Rev.*, 1998, **176**, 431.
69. R. Fleischer, S. Freitag, and D. Stalke, *J. Chem. Soc., Dalton Trans.*, 1998, 193.
70. R. Fleischer, A. Rothenberger, and D. Stalke, *Angew. Chem., Int. Ed. Engl.*, 1997, **36**, 1105.
71. J. Bojes, T. Chivers, W. G. Laidlaw, and M. Trsic, *J. Am. Chem. Soc.*, 1982, **104**, 4837.
72. T. Chivers, W. G. Laidlaw, R. T. Oakley, and M. Trsic, *J. Am. Chem. Soc.*, 1980, **102**, 5773.
73. A. J. Banister, M. I. Hansford, Z. V. Hauptman, A. W. Luke, S. T. Wait, W. Clegg, and K. A. Jorgensen, *J. Chem. Soc., Dalton Trans.*, 1990, 2793.
74. P. N. Jagg, P. F. Kelly, H. S. Rzepa, D. J. Williams, J. D. Woollins, and W. Wylie, *J. Chem. Soc., Chem. Commun.*, 1991, 942.
75. J. Bojes and T. Chivers, *J. Chem. Soc., Chem. Commun.*, 1978, 391.
76. O. J. Scherer and G. Wolmershäuser, *Angew. Chem., Int. Ed. Engl.*, 1975, **14**, 485.
77. O. Glemser and R. Mews, *Angew. Chem., Int. Ed. Engl.*, 1980, **19**, 883.
78. K. Dehnicke and U. Müller, *Comments Inorg. Chem.*, 1985, **4**, 213.
79. E. Kessenich, F. Kopp, P. Mayer, and A. Schulz, *Angew. Chem., Int. Ed. Engl.*, 2001, **40**, 1904.
80. P. G. Watson, E. Lork, and R. Mews, *J. Chem. Soc., Chem. Commun.*, 1994, 1069.
81. E. Jaudas-Prezel, R. Maggiulli, R. Mews, H. Oberhammer, and W.-D. Stohrer, *Chem. Ber.*, 1990, **123**, 2117.
82. A. Lork, G. Gard, M. Hare, R. Mews, W.-D. Stohrer, and R. Winter, *J. Chem. Soc., Chem. Commun.*, 1992, 898.
83. R. Jones, I. P. Parkin, D. J. Williams, and J. D. Woollins, *Polyhedron*, 1987, **6**, 2161.
84. X.-G. Duan and C. W. Rees, *Chem. Commun.*, 1997, 1493.
85. T. Torroba, *J. Prakt. Chem.*, 1999, **341**, 99.
86. D. Gregson, G. Klebe, and H. Fuess, *Acta Crystallogr.*, 1991, **C47**, 1784.
87. H. W. Roesky, W. Schaper, O. Petersen, and T. Müller, *Chem. Ber.*, 1977, **110**, 2695.
88. T. Chivers, *Sulfur Reports*, 1986, **7**, 89.
89. S. Mann and M. Jansen, *Z. Anorg. Allg. Chem.*, 1995, **621**, 153.
90. W. Heilemann and R. Mews, *Chem. Ber.*, 1988, **121**, 461.
91. F. Seel, R. Kuhn, G. Simon, M. Wagner, B. Krebs, and M. Dartmann, *Z. Naturforsch, Teil B*, 1985, **40B**, 1607.
92. F. Seel, in 'Sulfur–Its Significance for Chemistry, for the Geo-, Bio–and Cosmophere and Technology', eds. A. Müller and B. Krebs, Elsevier, Amsterdam, 1984, p. 55.
93. S. P. So, *Inorg. Chem.*, 1989, **28**, 2888.
94. D. L. H. Williams, *Acc. Chem. Res.*, 1999, **32**, 869.
95. N. Arulsamy, D. S. Bohle, J. A. Butt, G. J. Irvine, P. A. Jordan, and E. Sagan, *J. Am. Chem. Soc.*, 1999, **121**, 7115.
96. M. D. Bartberger, K. N. Houk, S. C. Powell, J. D. Mannion, K. Y. Lo, J.-S. Stamler, and E. J. Toone, *J. Am. Chem. Soc.*, 2000, **122**, 5889.
97. J.-M. Lü, J. M. Wittbrodt, K. Wang, Z. Wen, H. B. Schlegel, P. G. Wang, and J.-P. Cheng, *J. Am. Chem. Soc.*, 2001, **123**, 2903.
98. M. D. Bartberger, J. D. Mannion, S. C. Powell, J. S. Stamler, K. N. Houk, and E. J. Toone, *J. Am. Chem. Soc.*, 2001, **123**, 8868.
99. K. O. Christe, J. A. Boatz, M. Gerken, R. Haiges, S. Schneider, T. Schroer, F. S. Tham, A. Vij, V. Vij, R. I. Wagner, and W. W. Wilson, *Inorg. Chem.*, 2002, **41**, 4275.
100. C. Leben and M. Jansen, *Z. Naturforsch., Teil B*, 1999, **B54**, 757.
101. R. Steudel, P. Luger, and H. Bradaczek, *Angew. Chem., Int. Ed. Engl.*, 1973, **12**, 316.
102. M.-H. Whangbo, R. Hoffman, and R. B. Woodward, *Proc. R. Soc. London, Ser. A*, 1979, **366**, 23.
103. J. M. Rawson, A. J. Banister, and I. Lavender, *Adv. Heterocycl. Chem.*, 1995, **62**, 137.
104. A. Apblett and T. Chivers, *Inorg. Chem.*, 1989, **28**, 4544.
105. R. T. Oakley, *Can. J. Chem.*, 1993, **71**, 1775.
106. C. D. Bryan, A. W. Cordes, R. M. Fleming, N. A. George, S. H. Glarum, R. C. Haddon, R. T. Oakley, T. T. M. Palstra,

A. S. Perel, L. F. Schneemeyer, and J. V. Waszczak, *Nature*, 1993, **365**, 821.

107. J. Passmore and X. Sun, *Inorg. Chem.*, 1996, **35**, 1313.
108. A. J. Banister, I. May, J. M. Rawson, and J. N. B. Smith, *J. Organomet. Chem.*, 1998, **550**, 241.
109. P. J. Hayes, R. T. Oakley, A. W. Cordes, and W. T. Pennington, *J. Am. Chem. Soc.*, 1985, **107**, 1346.
110. R. T. Boeré, C. L. French, R. T. Oakley, A. W. Cordes, J. A. J. Privett, S. L. Craig, and J. B. Graham, *J. Am. Chem. Soc.*, 1985, **107**, 7710.
111. R. M. Bannister and C. W. Rees, *J. Chem. Soc., Perkin Trans. I*, 1990, 509.
112. F. Blockhuys, S. L. Hinchley, A. Y. Marakov, Y. V. Gatïlov, A. V. Zibarev, J. D. Woollins, and D. W. H. Rankin, *Chem. Eur. J.*, 2001, **7**, 3592.
113. A. Yu. Makarov, I. Yu. Bagryanskaya, F. Blockhuys, C. Van Alsenoy, Y. V. Gatilov, V. V. Knyazev, A. M. Maksimov, T. V. Mikhalina, V. E. Platonov, M. M. Shakirov, and A. V. Zibarev, *Eur. J. Inorg. Chem.*, 2003, 77.
114. I. Yu. Bagryanskaya, H. Bock, Y. V. Gatilov, A. Haas, M. M. Shakirov, B. Salouki, and A. V. Zibarev, *Chem. Ber.*, 1997, **130**, 247.
115. A. Yu. Makarov, M. M. Shakirov, K. V. Shuvaev, I. Yu. Bagryanskaya, Y. V. Gatilov, and A. V. Zibarev, *Chem. Commun.*, 2001, 1774.
116. I. Ernest, W. Holick, G. Rihs, D. Schomburg, G. Shoham, D. Wenkert, and R. B. Woodward, *J. Am. Chem. Soc.*, 1981, **103**, 1540.
117. A. D. Bond, D. A. Haynes, and J. M. Rawson, *Can. J. Chem.*, 2002, **80**, 1507.
118. S. Dell, D. M. Ho, and R. A. Pascal Jr, *Inorg. Chem.*, 1996, **35**, 2866.
119. R. A. Pascal Jr and R. P. L'Esperance, *J. Am. Chem. Soc.*, 1994, **116**, 5167.
120. T. Chivers, K. S. Dhathathreyan, and T. Ziegler, *J. Chem. Soc., Chem. Commun.*, 1989, 86.
121. N. Burford, T. Chivers, M. N. S. Rao, and J. F. Richardson, *ACS Symp. Ser.*, 1983, **232**, 81.
122. R. Appel and M. Halstenberg, *Angew. Chem., Int. Ed. Engl.*, 1976, **15**, 696.
123. N. Burford, T. Chivers, A. W. Cordes, W. G. Laidlaw, M. C. Noble, R. T. Oakley, and P. N. Swepston, *J. Am. Chem. Soc.*, 1982, **104**, 1282.
124. M. Brock, T. Chivers, M. Parvez, and R. Vollmerhaus, *Inorg. Chem.*, 1997, **36**, 485.
125. T. Chivers, M. Edwards, X. Gao, R. W. Hilts, M. Parvez, and R. Vollmerhaus, *Inorg. Chem.*, 1995, **34**, 5037.
126. T. Chivers and R. W. Hilts, *Coord. Chem. Rev.*, 1994, **137**, 201.
127. J. C. van de Grampel, *Coord. Chem. Rev.*, 1992, **112**, 247.
128. A. R. McWilliams, D. P. Gates, M. Edwards, L. M. Liable-Sands, I. Guzei, A. L. Rheingold, and I. Manners, *J. Am. Chem. Soc.*, 2000, **122**, 8848.
129. V. Chunechom, T. E. Vidal, H. Adams, and M. L. Turner, *Angew. Chem., Int. Ed. Engl.*, 1998, **37**, 1928.
130. O. J. Scherer and R. Wies, *Z. Naturforsch., Teil B*, 1970, **25B**, 1486.
131. T. Chivers, K. S. Dhathathreyan, C. Lensink, A. Meetsma, J. C. van de Grampel, and J. L. de Boer, *Inorg. Chem.*, 1989, **28**, 4150.
132. A. Haas, J. Kasprowski, K. Angermund, P. Betz, C. Krüger, Y.-H. Tsay, and S. Werner, *Chem. Ber.*, 1991, **124**, 1895.
133. J. Konu, A. Maaninen, K. Paananen, P. Ingman, R. S. Laitinen, T. Chivers, and J. Valkonen, *Inorg. Chem.*, 2002, **41**, 1430.
134. A. Maaninen, J. Siivari, R. J. Suontamo, J. Konu, R. S. Laitinen, and T. Chivers, *Inorg. Chem.*, 1997, **36**, 2170.
135. E. G. Awere, W. V. F. Brooks, J. Passmore, P. S. White, X. Sun, and T. S. Cameron, *J. Chem. Soc., Dalton Trans.*, 1993, 2439.
136. A. Maaninen, J. Konu, R. S. Laitinen, T. Chivers, G. Schatte, J. Pietkäinen, and M. Ahlgren, *Inorg. Chem.*, 2001, **40**, 3539.
137. T. S. Piper, *J. Am. Chem. Soc.*, 1958, **80**, 30.
138. J. Weiss, *Angew. Chem., Int. Ed. Engl.*, 1982, **21**, 705.
139. J. Weiss, *Z. Anorg. Allg. Chem.*, 1986, **532**, 184.
140. H. W. Roesky, *Chem. Soc. Rev.*, 1986, **15**, 309.
141. A. Sundermann and W. W. Schoeller, *Inorg. Chem.*, 1999, **38**, 6261.
142. F. Edelmann, H. W. Roesky, C. Spang, M. Noltemeyer, and G. M. Sheldrick, *Angew. Chem., Int. Ed. Engl.*, 1986, **25**, 931.
143. P. S. Belton, V. C. Ginn, P. F. Kelly, and J. D. Woollins, *J. Chem. Soc., Dalton Trans.*, 1992, 1135.
144. P. F. Kelly, R. N. Sheppard, and J. D. Woollins, *Polyhedron*, 1992, **11**, 2605.
145. E. Lork, V. Behrens, G. Steinke, and R. Mews, *Z. Naturforsch., Teil B*, 1994, **B49**, 437.
146. T. Lübben, M. Witt, H. W. Roesky, M. Noltemeyer, and H.-G. Schmidt, *Inorg. Chem.*, 1995, **34**, 4275.
147. A. K. Roy, G. T. Burns, G. C. Lie, and S. Grigoras, *J. Am. Chem. Soc.*, 1993, **115**, 2604.
148. D. Gregson, G. Klebe, and H. Fuess, *J. Am. Chem. Soc.*, 1988, **110**, 8488.
149. T. Chivers, M. Edwards, D. D. McIntyre, K. J. Schmidt, and H. J. Vogel, *Mag. Reson. Chem.*, 1992, **30**, 177.
150. R. Steudel, K. Bergemann, J. Buschmann, and P. Luger, *Angew. Chem., Int. Ed. Engl.*, 1996, **35**, 2537.
151. R. Steudel, O. Schumann, J. Buschmann, and P. Luger, *Angew. Chem., Int. Ed. Engl.*, 1998, **37**, 492.
152. M. Herberhold, U. Bertholdt, W. Milius, and B. Wrackmeyer, *Z. Naturforsch., Teil B*, 1996, **51**, 1283.
153. J. M. Rawson and J. J. Longridge, *Chem. Soc. Rev.*, 1997, 53.

154. E. M. Holt, S. L. Holt, and K. J. Watson, *J. Chem. Soc., Dalton Trans.*, 1974, 1357.
155. F. P. Olsen and J. C. Barrick, *Inorg. Chem.*, 1973, **12**, 1353.
156. J. A. K. Howard, I. Lavender, J. M. Rawson, and E. A. Swain, *Main Group Chem.*, 1996, **1**, 317.
157. O. J. Scherer, G. Wolmershäuser, and R. Jotter, *Z. Naturforsch., Teil B*, 1982, **B37**, 432.
158. J. C. W. Chien and S. Ramakrishnan, *Macromolecules*, 1988, **21**, 2007.
159. M. J. Cohen, A. F. Garito, A. J. Heeger, A. G. MacDiarmid, C. M. Mikulski, M. S. Saran, and J. Kleppinger, *J. Am. Chem. Soc.*, 1976, **98**, 3844.
160. H. B. Mark Jr, A. Voulgaropoulos, and C. A. Meyer, *J. Chem. Soc., Chem. Commun.*, 1981, 1021.

Sulfur: Organic Polysulfanes

Ralf Steudel
Technische Universität Berlin, Berlin, Germany

1	Introduction	1
2	Synthesis of Organic Polysulfanes	2
3	Structures of Organic Polysulfanes	15
4	Analysis of Organic Polysulfanes	17
5	Reactions of Organic Polysulfanes	20
6	Natural Occurrence of Organic Polysulfanes and Their Biological Activity	23
7	Applications of Organic Polysulfanes	26
8	Related Articles	28
9	References	28

1 INTRODUCTION

By definition, sulfanes or polysulfanes are compounds of type X–S_n–X with $n = 1, 2, \ldots$ and X being a univalent group such as hydrogen (sulfanes), halogen (halosulfanes), organic radical R (organic polysulfanes), and so on. In a certain sense, even elemental sulfur may be called a polysulfane, for example, S_8 is *cyclo*-octasulfane. H_2S_3 is termed trisulfane and S_2Cl_2 is dichlorodisulfane. Numerous compounds of these types are known since sulfur atoms tend to form homoatomic chains and rings owing to the high S–S bond energy ($265\,\mathrm{kJ\,mol^{-1}}$).[1–2] Table 1 presents an overview of which chain lengths or ring sizes have so far been observed for various polysulfane derivatives (*see* ***Sulfur: Inorganic Chemistry***).

The organic polysulfanes described in this article are compounds of the type R–S_n–R with $n > 2$; they may be chain-like or cyclic. The organic residues (alkyl or aryl) are linked to the sulfur chain via carbon atoms. These compounds are also known as organic polysulfides.

Sulfur-rich organic polysulfanes can be viewed as intermediate between organic and inorganic compounds. On one hand, they are characterized by organic substituents R, which terminate the sulfur chain or close this chain to form a ring. On the other hand, sulfur chains of three or more sulfur atoms are 'inorganic' enough to attract the interest of inorganic chemists who have contributed much to this area. Organic polysulfanes with up to 35 sulfur atoms in a chain have been prepared in mixtures, but only those with up to 16 atoms have been obtained as pure substances. The correct nomenclature for the compounds, R–S_n–R, is bis(organyl)polysulfanes. In this article, the more convenient term organic polysulfane will also be used. Mono(organyl)polysulfanes, R–S_n–H, are sometimes termed hydropersulfides or hydrodisulfides if $n = 2$. Organylchlorosulfanes, R–S_n–Cl, are homologs of the sulfenyl chlorides R–S–Cl and will be summarized under the latter name for the sake of brevity. In the older literature, they are also termed thiosulfenyl chlorides or chloro disulfides if $n = 2$. The International Union of Pure and Applied Chemistry (IUPAC) nomenclature is, however, always based on the name sulfane even for derivatives such as R_2S and R–S–Cl.

Organic polysulfanes, which play an important role in basic research and industry, are found as natural products in organisms and occur in the inanimate world. In the latter case, they are partly of biotic, partly of abiotic (geochemical) origin and are widespread in sulfur-rich fossil fuel. Some of the polysulfanes produced by algae, mushrooms, or ascidians show biological activity that makes them interesting for the pharmaceutical industry. The main importance of organic polysulfanes comes, however, from their role in the large scale industrial vulcanization of natural and synthetic rubber with elemental sulfur, which in the early stages of the reaction results in sulfur-rich polysulfanes as will be described later.

Since the chemistry of organic polysulfanes is closely related to their oxidized derivatives, Table 2 presents the well-characterized species with up to three sulfur atoms in the chain. The systematic nomenclature based on the IUPAC recommended name *sulfanes* is also given in Table 2. In addition, conventional names for some of these compounds are shown in brackets.

In this article, we will review the preparation, structure, modern analysis, basic reactions, natural occurrence, biological activity, and practical importance of organic polysulfanes with three or more neighboring sulfur atoms in a chain or ring. Previous reviews have also included disulfanes (R_2S_2) and the emphasis was usually on the latter. The preparation of R_2S_n ($n > 2$) was reviewed by Schöberl and Wagner[3] in 1955, by Wilson and Buchanan[4] in 1976, by Field[5] in 1977, and by Gundermann and Humke[6] in 1985. Laur[7] summarized the stereochemistry of (mainly) organic sulfur compounds in 1972. The analytical chemistry or organic polysulfanes was reviewed by Cardone[8] 1972. Reid[9] published a list of 76 organic polysulfanes ($n > 2$) known in 1960. A brief account on inorganic and organic polysulfanes by Pickering and Tobolsky[10] appeared in 1972. The most recent and most comprehensive review on organic polysulfanes was published in 2002 by Steudel (390 refs.).[11] Progress in the area of trisulfanes and their oxides has been reviewed by Clennan and Stensaas in 1998.[12]

Organometallic polysulfanes such as 1,2,3-trithia-[3]ferrocenophane have not been included in this article; their chemistry has been reviewed elsewhere.[12]

Table 1 Size of sulfur rings and chains

		Isolated	NMR, HPLC evidence	Indirect evidence
cyclo-Sulfanes	S_n:	6 . . . 20	up to 30	up to 80
Sulfanes	$H–S_n–H$	1 . . . 8	up to 35	–
Chlorosulfanes	$Cl–S_n–Cl$	1 . . . 8	up to 55	–
Organylsulfanes	$R–S_n–R$	1 . . . 9	up to 35	–
Polythionates	$^{-}O_3S–S_n–SO_3^{-}$	1 . . . 4	up to 22	up to 50
Polysulfides	S_n^{2-}	1 . . . 9	. . .	–
Sulfanemonosulfonates	$^{-}S_n–SO_3^{-}$	1	–	2 . . . 13
Bunte salts	$R–S_n–SO_3^{-}$	1	–	2
Organylpolysulfides	$R–S_n^{-}$	1	2	–

Table 2 Nomenclature of polysulfanes and their oxidized derivatives (trivial names are given in parentheses)

R–S–R Monosulfane (sulfide)	R–S–S–R Disulfane (disulfide)	R–S–S–S–R Trisulfane (trisulfide)
R–S(O)–R Monosulfane oxide (sulfoxide)	R–S(O)–S–R Disulfane monoxide (thiosulfinate)	R–S(O)–S–S–R Trisulfane 1-oxide
R–S–O–R Sulfenate	R–S(O)–S(O)–R Disulfane 1,2-dioxide	R–S(O)–S–S(O)–R Trisulfane 1,3-dioxide
R–S(O)–O–R Sulfinate	R–S(O_2)–S–R Disulfane 1,1-dioxide	R–S–S(O)–S–R Trisulfane 2-oxide (dithiosulfite)
R–S(O_2)–O–R Sulfonate	R–S–SO_3^{-} Thiosulfate (Bunte salt)	R–S(O_2)–S–S–R Trisulfane 1,1-dioxide (sulfenylthiosulfonate)
	R–S–S–SO_3^{-} Disulfanemonosulfonate	R–S(O_2)–S–S(O_2)–R Trisulfane 1,1,3,3-tetroxide

2 SYNTHESIS OF ORGANIC POLYSULFANES

There are numerous reactions to prepare organic polysulfanes, which will be grouped in several sections according to the reagents used. Although there is normally no difference in principle between the preparation of chainlike and cyclic polysulfanes $R_2–S_n$, for convenience, the two types will be treated separately. Which method to choose for the synthesis of a particular polysulfane will depend on the available reagents, on the chemical reactivity of the organic group R, on the possibility of separating the reaction mixture to produce pure substances, and on the amount of material needed. The following list of synthetic procedures is in arbitrary order and should not be taken as a measure of relative importance or general applicability.

2.1 Chainlike Organic Polysulfanes

2.1.1 *Reaction of Thiols, Thiolates, or Monoorganylsulfanes with Dichlorosulfanes*

Alkyl and aryl polysulfanes may be prepared by the classical reactions (equations 1–3).[3–6,13]

$$2RSH + S_xCl_2 \longrightarrow R–S_n–R + 2HCl \qquad (1)$$

$$2RSM + S_xCl_2 \longrightarrow R–S_n–R + 2MCl \qquad (2)$$

$$2RS_yH + S_xCl_2 \longrightarrow R–S_n–R + 2HCl \qquad (3)$$

However, since only SCl_2 and S_2Cl_2 are easily available, equations (1) and (2) are primarily used to make tri- and tetrasulfanes. Sulfur-rich dichlorosulfanes S_xCl_2 ($x > 2$) may be synthesized in analogous reactions from H_2S, H_2S_2, or H_2S_3 and excess SCl_2 or S_2Cl_2 (equation 4).

$$2Cl–S_x–Cl + H–S_y–H \longrightarrow Cl–S_{2x+y}–Cl + 2HCl \qquad (4)$$

The longer-chain species S_xCl_2 ($x = 6–8$) are best prepared by ring-opening chlorination of *cyclo*-S_n ($n = 6–8$) with Cl_2 in CCl_4 at 0 °C (equation 5).[14–16]

$$\textit{cyclo}–S_n + Cl_2 \longrightarrow Cl–S_n–Cl \quad n = 6–8 \qquad (5)$$

Reactions 1 and 3 are usually carried out in dry ether, or in a nonpolar solvent in the presence of a tertiary amine such as pyridine to bind HCl.[17–21] In reaction 2, lead thiolates have been found to be very useful.[4,6]

Substituted phenyl trisulfanes $(4\text{-}R'C_6H_4)_2S_3$ with $R' =$ NO_2, MeCO, EtOCO, MeS, MeO, and even NH_2 have been prepared by reaction 1. Since amino groups would also be attacked by SCl_2, this reaction was carried out in anhydrous acetic acid, resulting in protonation of the $–NH_2$ group to $–NH_3^{+}$, which is less reactive towards SCl_2.[21] The bisacetate obtained is converted to bis(4-aminophenyl)trisulfane by reaction with sodium hydroxide.[21]

Bifunctional thiols react with dichlorosulfanes to give cyclic organic polysulfanes (Section 2.2.1).

Reaction 2 has also been used to synthesize polysulfanes of thiocarbonic acids,[22,23] alkoxythiocarbonic acids,[24–27] (alkylthio)thiocarbonic acids,[24–26] or of alkoxydithiocarbonic acids (xanthates[28–31]) (reactions 6–8 with $M = H$, Na, K and $n = x + 2$).

$$2R\text{–}C(O)\text{–}SM + S_xCl_2 \longrightarrow R\text{–}C(O)\text{–}S_n\text{–}C(O)\text{–}R + 2MCl \qquad (6)$$

$$2RO\text{–}C(O)\text{–}SM + S_xCl_2 \longrightarrow RO\text{–}C(O)\text{–}S_n\text{–}C(O)\text{–}OR + 2MCl \qquad (7)$$

$$2RO\text{–}C(S)\text{–}SM + S_xCl_2 \longrightarrow RO\text{–}C(S)\text{–}S_n\text{–}C(S)\text{–}OR + 2MCl \qquad (8a)$$

$$2RS\text{–}C(O)\text{–}SM + S_xCl_2 \longrightarrow RS\text{–}C(O)\text{–}S_n\text{–}C(O)\text{–}SR + 2MCl \qquad (8b)$$

It should be noted that the polysulfanes obtained by equations (8a and 8b) are isomeric.

The monoorganylpolysulfanes RS_yH needed for equation (3) may be prepared from organylacylpolysulfanes by alcoholysis (equation 9, $n = 2$ or 3).[32]

$$R\text{–}C(O)\text{–}S_n\text{–}R' + R''OH \longrightarrow R'\text{–}S_n\text{–}H + RC(O)\text{–}OR'' \qquad (9)$$

2.1.2 Reaction of Thiols or Monoorganylpolysulfanes with Sulfenyl Chlorides

The condensation of thiols or monoorganylsulfanes with sulfenyl chlorides, usually carried out in dry ether at 20 °C, allows the synthesis of symmetrically or unsymmetrically substituted polysulfanes. R and R′ may be alkyl, aryl, or acyl groups;[4,6] yields can be as high as 90%.

CF_3SSH reacts at 20 °C without solvent with CF_3SCl to give $(CF_3)_2S_3$, and with CF_3SSCl to yield $(CF_3)_2S_4$.[33] Unsymmetrical trisulfanes with various alkyl and aryl substituents[34–36] have been synthesized by equation (10), and bis(sulfenyl chlorides) react similarly.[37]

$$R\text{–}S_x\text{–}H + Cl\text{–}S_y\text{–}R' \longrightarrow R\text{–}S_n\text{–}R' + HCl$$
$$x = 1, 2, \ldots;\ y = 1, 2, \ldots \qquad (10)$$

The sulfenyl chlorides[4] and their homologs needed for reaction 10 may be prepared by reactions (11–13). For the synthesis of alkoxycarbonyl compounds,[38] reactions (14–16) can be applied.

$$RSH + Cl_2 \longrightarrow RSCl + HCl \qquad (11)$$

$$RSH + SCl_2 \longrightarrow RS_2Cl + HCl \qquad (12)$$

$$RSH + S_2Cl_2 \longrightarrow RS_3Cl + HCl \qquad (13)$$

$$RC(O)SCl + RC(O)SH \longrightarrow [RC(O)]_2S_2 + HCl \qquad (14)$$

$$[RC(O)]_2S_2 + Cl_2 \longrightarrow RC(O)S_2Cl + RCOCl \qquad (15)$$

$$RC(O)S_2Cl + R'SH \longrightarrow RC(O)S_3R' + HCl \qquad (16)$$

Since the latter polysulfanes react with thiols in the presence of a base according to equation (17), they have been used to synthesize various unsymmetrical trisulfanes in good yields (25–100%).[39]

$$MeO\text{–}CO\text{–}S_3\text{–}R + R'SH \longrightarrow R\text{–}S_3\text{–}R' + MeOH + COS \qquad (17)$$

Since the reaction conditions (−78 to 0 °C; base: N-methylmorpholine, aniline, or N,N-dimethylaniline) are mild, even trisulfanes with unsaturated (allyl) or functionalized (–OH, $–NH_2$, $–CO_2H$) substituents may be prepared.[39]

2.1.3 Reaction of Sulfenyl Halides with H_2S, H_2S_2, or Their Salts

Aryl- and alkyltri- and -tetrasulfanes may be obtained in good yields by reactions of the type in equation (18).[4,6] 2-Nitrophenylsulfenyl bromide or related RSBr compounds react at 20 °C in benzene with HgS, PbS, Ag_2S, or Tl_2S to give the corresponding trisulfanes in a 80–100% yield.[40] Use of H_2S in ether, acetic acid, dioxane, or ethyl acetate produces the trisulfanes in lower yield.[41] Liquid CCl_3SCl reacts in low-yield with H_2S at 20 °C to give $(CCl_3)_2S_3$ and with H_2S_2 at 85 °C to yield $(CCl_3)_2S_4$; both polysulfanes form colorless crystals.[41]

$$2R\text{–}S\text{–}X + M_2S_x \longrightarrow R\text{–}S_n\text{–}R + 2MX_x$$
$$X = Cl, Br;\ M = H, Na, Ag, Hg, Tl, Pb;\ x = 1, 2 \qquad (18)$$

Bis(alkoxycarbonyl)polysulfanes ($n = 3$, 4) have been prepared from the sulfenyl chlorides ROC(O)SCl with H_2S_x ($x = 1$, 2)[24–26] or Na_2S_x ($x = 1$, 2).[24–26] It is, however, usually observed that equation (18) does not proceed in a clean way to give the tri- or tetrasulfane in high yield but, owing to secondary interconversion reactions catalyzed by SH compounds or sulfide ions (see Section 5.3), results in complex mixtures of polysulfanes R_2S_n, which can be detected by LC[42] or HPLC[24–26] (see Section 4).

The bifunctional sulfenyl chloride $ClS\text{–}C(O)\text{–}O\text{–}(CH_2)_4\text{–}O\text{–}C(O)\text{–}SCl$, dissolved in chloroform, reacts with aqueous Na_2S or Na_2S_2 at 20 °C to give corresponding polymers of the general formula $[\text{–}S_n\text{–}CO_2\text{–}(CH_2)_4\text{–}CO_2\text{–}S\text{–}]$.[43]

2.1.4 Reaction of Sulfenyl Chlorides with Ionic Iodides

Alkoxycarbonylsulfenyl chlorides react at 20 °C with aqueous potassium iodide primarily with halogen exchange. The sulfenyl iodides, RSI, are unstable and combine in a bimolecular reaction to give the disulfane and elemental iodine (equation 19), which is removed by washing the organic phase with sodium thiosulfate (equation 20).[24–26]

$$2R\text{–}S_x\text{–}Cl + 2KI \longrightarrow R\text{–}S_n\text{–}R + I_2 + 2KCl \qquad (19)$$

$$I_2 + 2Na_2S_2O_3 \longrightarrow 2NaI + Na_2S_4O_6 \qquad (20)$$

When organochlorodisulfanes are used, RS_2Cl (dissolved in dichloromethane), the product should be the corresponding tetrasulfane, but owing to secondary interconversion reactions (see Section 5), possibly catalyzed by iodine, a mixture of polysulfanes is observed (HPLC analysis; see Section 4) (equations 21 and 22).[24–26]

$$2\text{MeO–C(O)–S}_2\text{–I} \longrightarrow (\text{MeOCO})_2\text{S}_4 + \text{I}_2 \qquad (21)$$

$$2\text{R}_2\text{S}_4 \rightleftharpoons \text{R}_2\text{S}_3 + \text{R}_2\text{S}_5 \qquad (22)$$

Therefore, depending on the reaction conditions, either the trisulfane or the tetrasulfane is isolated as the main product.[24–27] The aqueous solution of NaI and $Na_2S_4O_6$ may also be used for halogen exchange reactions of the type shown in equation (19).[44]

2.1.5 *Reaction of Organic Halides or Sulfenyl Chlorides with Titanocene Polysulfides*

Titanocene dichloride, Cp_2TiCl_2, reacts with alkali polysulfides to give the chelate complexes (**1**) and (**2**). These air-stable products react with inorganic sulfur chlorides to give homocyclic S_n molecules[45] (*see* ***Sulfur: Inorganic Chemistry***). Analogously, organic sulfenyl chlorides and certain organic halides react with (**1**) or (**2**) as shown in equations (23–25).[46,47] These very clean sulfur transfer reactions take place at 0–20 °C in organic solvents (CS_2, CH_2Cl_2).

$$2\text{R–Cl} + \text{Cp}_2\text{TiS}_5 \longrightarrow \text{R–S}_5\text{–R} + \text{Cp}_2\text{TiCl}_2 \qquad (23)$$

$$2\text{R–S}_x\text{–Cl} + \text{Cp}_2\text{TiS}_5 \longrightarrow \text{R–S}_n\text{–R} + \text{Cp}_2\text{TiCl}_2$$
$$x = 1, 2;\ n = 2x + 5 \qquad (24)$$

$$4\text{R–S}_2\text{–Cl} + \text{Cp}'_4\text{Ti}_2\text{S}_4 \longrightarrow 2\text{R–S}_6\text{–R} + 2\text{Cp}'_2\text{TiCl}_2 \qquad (25)$$

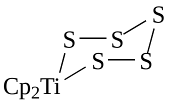
(**1**)

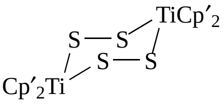
(**2**)

Bis(triphenylmethyl)pentasulfane was obtained in 83% yield from Ph_3CCl and Cp_2TiS_5 in CS_2 at 20 °C.[48] In an analogous manner, triphenylmethylsulfenyl chloride and the corresponding disulfane RS_2Cl react with Cp_2TiS_5 to give the hepta- and nonasulfanes R_2S_n (n = 7, 9).[49] These reactions, and the work-up procedure, can be most conveniently followed by HPLC analysis (see Section 4).

The dinuclear complex $Cp'_4Ti_2S_4$ reacts as a transfer reagent for S_2 units, and with certain organochlorodisulfanes one obtains hexasulfanes R_2S_6 (e.g. $R = Ph_3C$) (equation 25).[46,47,50] The Cp′ ligand (η^5-MeC_5H_4) is used because of the higher solubility of the corresponding dinuclear complex.

2.1.6 *Reaction of Thiols with Sulfur–Nitrogen Bonds in Sulfenamides*

Several sulfenamides and their homologs have been used as transfer reagents for S_1 or S_2 units as shown in equations (26) and (27). Examples include the bis(imidazolo)sulfane (**3**) and the bis(phthalimido)sulfane (**4**).[6] These compounds with one or two sulfur atoms bridging the nitrogen atoms may be prepared from the NH derivatives and SCl_2 or S_2Cl_2 in a molar ratio of 2:1 in the presence of a tertiary amine. When SCl_2 is applied in a molar ratio of 1:1, the sulfenyl chloride $R_2N–SCl$ may be isolated, from which the unsymmetrical sulfenamide needed in equation (27) is prepared by condensation with a thiol, R′SH. Alternatively, R_2NS_2R' may be prepared from R_2NH and $R'S_2Cl$.[35,51]

$$2\text{RSH} + \text{R}_2\text{N–S}_x\text{–NR}_2 \longrightarrow \text{R–S}_n\text{–R} + 2\text{R}_2\text{NH} \qquad (26)$$

$$\text{RS}_x\text{H} + \text{R}_2\text{N–S}_y\text{–R}' \longrightarrow \text{R–S}_n\text{–R}' + \text{R}_2\text{NH}$$
$$x = 1, 2;\ y = 1, 2;\ n = x + y \qquad (27)$$

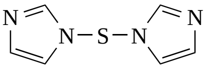
(**3**)

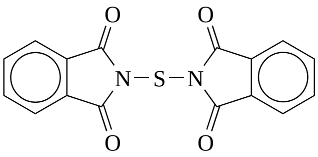
(**4**)

Symmetrical and unsymmetrical tri- and tetrasulfanes may be synthesized by equations (26) and (27) in high yield and under mild conditions (benzene, 20 °C). Since phthalimide is insoluble in benzene, it can be simply filtered off.[35,51,52] Various other azole derivatives have also been used successfully.[53]

2.1.7 *Reaction of Thiols with Sulfur–Oxygen Bonds of Bis(Alkoxy)Sulfanes*

Bis(alkoxy)sulfanes $(RO)_2S_n$, are easily accessible from the corresponding alcohol by reaction with either (**3**) or (**4**) or with the corresponding dichlorosulfane.[54–56] Using (**1**) as a sulfur transfer reagent and $RO–S_2–Cl$ as the alkoxy derivative, a chain length n of 9 in $(RO)_2S_n$ ($R = i$-Pr) has been achieved.[55] $(RO)_2S_n$ reacts with certain thiols at 20 °C according to equation (28), allowing the preparation of polysulfanes under mild conditions.[57] Bis(tetraacetylthioglucosyl)polysulfanes with up to 11 S atoms in a chain have been prepared in this way.[58] Equations (26–28) are typical nucleophilic displacement reactions (see Section 5).

$$2\text{R}'\text{SH} + \text{RO–S}_x\text{–OR} \longrightarrow \text{R}'\text{–S}_n\text{–R}' + 2\text{ROH}$$
$$x = 1 - 9;\ n = x + 2 \qquad (28)$$

2.1.8 *Reaction of Dichlorodisulfane with Aromatic Ethers*

Methoxybenzene (anisole), 1,2-dimethoxybenzene, and similar aromatic ethers react with S_2Cl_2 in dry ether or benzene at 0–20 °C within several days to give a mixture of bisarylsulfanes R_2S_n with $n = 1–3$ (equation 29). Anisole is substituted in the *para* position.[59]

$$\begin{gathered}2\text{R–H} + S_2Cl_2 \longrightarrow \text{R–S}_n\text{–R} + 2\text{HCl}\\ n = 1–3\end{gathered} \qquad (29)$$

2.1.9 *Reactions of Organic Halides, Thiols, Sulfenyl Chlorides, or Disulfanes with Elemental Sulfur or Inorganic Polysulfides*[6]

Alkyl chlorides, -bromides, and -iodides can be converted to tri- or tetrasulfanes by treatment with elemental sulfur at 20 °C in the presence of KOH and traces of water; methyl-, ethyl-, isopropyl-, and allylpolysulfanes have been prepared in this manner.[60,61] Sometimes hydrazine is added to reduce S_8 to polysulfide anions.[62]

Trifluoroiodomethane reacts at 310 °C with elemental sulfur in a steel autoclave to yield $(CF_3)_2S_2$ (yield 75%), $(CF_3)_2S_3$ (12%), and $(CF_3)_2S_4$ (1%).[63] Probably CF_3 radicals are primarily formed that attack the reactive sulfur molecules[64] present in elemental sulfur at 310 °C.

Bis(4-methyl-2-nitrophenyl)trisulfane is formed in 84% yield on reaction of 4-chloro-3-nitrotoluene with molten sodium polysulfide.[65] Other aryl halogenides have also been converted to trisulfanes by ionic polysulfides.[66,67]

Alkyltri- and -tetrasulfanes may be conveniently prepared from thiols and elemental sulfur in the presence of catalytic amounts of *n*-butylamine at 25–63 °C (equation 30 with $Y = H_2S$). The products formed are determined by the molar ratio RSH:S_8, the polarity of the solvent (CH_2Cl_2, MeOH), the reaction time, and the temperature;[68,69] *n*-, *i*-, and *t*-alkyl thiols as well as cycloalkyl thiols have also been applied.[68–71]

$$\begin{gathered}2\text{R–X} + xS_8 \longrightarrow \text{R–S}_n\text{–R} + \text{Y}\\ \text{X} = \text{Cl, Br, I, SH, SCl}\end{gathered} \qquad (30)$$

Trichloromethylsulfenyl chloride reacts with elemental sulfur at 220 °C to give $(CCl_3)_2S_2$ and S_2Cl_2; the disulfane may be converted to $(CCl_3)_2S_3$ by reaction with sulfur at 170 °C (equations 30 and 31).[72] Alkyltrisulfanes have also been prepared from disulfanes and elemental sulfur with the addition of H_2S and butylamine or triethylamine, or P_4S_{10}.[6]

$$\text{R–S}_2\text{–R} + xS_8 \longrightarrow \text{R–S}_n\text{–R} \qquad (31)$$

Diethylpentasulfane may be prepared from the trisulfane by heating with elemental sulfur to 200 °C followed by distillation in vacuum.[19,20]

See equation (32) for the preparation of organic trisulfanes from alkyl halides and alkali trisulfides;[19,20,71,73] for the preparation of polymeric polysulfanes by equation (32), see Section 7.

$$\begin{gathered}2\text{R–X} + K_2S_3 \longrightarrow \text{R–S}_3\text{–R} + 2\text{KX}\\ \text{X} = \text{Cl, Br}\end{gathered} \qquad (32)$$

2.1.10 *Organosilicon- and -Tin Reagents for Sulfur Transfer Reactions*

Silicon, germanium, and tin have a high affinity for chlorine and bromine, which is utilized in equations (33–36).[74–76]

$$2\text{RSSiR}'_2\text{Cl} + SCl_2 \longrightarrow R_2S_3 + 2\text{R}'_2\text{SiCl}_2 \qquad (33)$$

$$\begin{gathered}R_3\text{Sn–S–SnR}_3 + 2\text{R}'\text{SX} \longrightarrow \text{R}'_2S_3 + 2R_3\text{SnX}\\ \text{X} = \text{Cl, Br}\end{gathered} \qquad (34)$$

$$\frac{1}{3}(R_2\text{SnS})_3 + 2\text{R}'\text{SX} \longrightarrow \text{R}'_2S_3 + R_2\text{SnX}_2 \qquad (35)$$

$$\begin{gathered}2R_3\text{SnSR}' + S_xCl_2 \longrightarrow \text{R}'_2S_{x+2} + 2R_3\text{SnCl}\\ x = 1, 2\end{gathered} \qquad (36)$$

Diethyltrisulfane has been obtained in an 87% yield from ethylthiodimethylchlorosilane and SCl_2 at 20 °C (no solvent) followed by vacuum distillation (equation 33).[74] Symmetric diaryltri- and -tetrasulfanes may be prepared from triorganotin sulfides or thiolate complexes as shown in equations (34–36).[75] These reactions proceed smoothly in $CHCl_3$ or CCl_4 at 20 °C or slightly elevated temperatures and the products are obtained in yields of between 25 and 90%.[75,76] The organotin thiolates are prepared from R_3SnCl, R_3SnOH, or $(R_3Sn)_2O$ by reaction with the corresponding thiol (equations 37 and 38)[76] (*see* ***Tin: Organometallic Chemistry***).

$$\begin{gathered}R_3\text{SnX} + \text{R}'\text{SH} \xrightarrow{\text{NaOH}} R_3\text{Sn–SR}' + \text{HX}\\ \text{X} = \text{Cl, OH}\end{gathered} \qquad (37)$$

$$(R_3\text{Sn})_2\text{O} + 2\text{R}'\text{SH} \longrightarrow 2R_3\text{Sn–SR}' + H_2O \qquad (38)$$

Silicon is one of the most oxophilic elements (*see* ***Silicon: Organosilicon Chemistry***). Therefore, organosilicon sulfides react with certain sulfur–oxygen compounds, as shown in equations (39) and (40).[77]

$$R_3\text{Si–S–SiR}_3 + \text{R}'\text{–S(O)–S–R}' \longrightarrow \text{R}'_2S_3 + (R_3\text{Si})_2\text{O} \qquad (39)$$

$$R_3\text{Si–S–SiR}_3 + 2\text{R}'\text{–S(O)}_2\text{–S–R}' \longrightarrow \text{R}'_2S_3 + 2R_3\text{Si–O–S(O)–R}' \qquad (40)$$

Bis(trimethylsilyl) sulfide reacts with methyl, phenyl, or other thiosulfinates (disulfane oxides), R′S(O)SR′, in anhydrous chloroform at 60 °C to give the symmetrical trisulfane and hexamethyldisiloxane; the latter is removed together with the solvent by vacuum distillation, leaving almost pure R'_2S_3 (yields 70–90%).[77] In a similar reaction,

$EtSO_2SEt$ was converted to Et_2S_3 with a 95% yield (equation 40).[51]

2.1.11 *Reaction of Alkenes with Elemental Sulfur or Sulfur-Rich Compounds*

The reactions of alkenes with elemental sulfur is of great importance because of analogies to the vulcanization of natural or synthetic rubber by sulfur in the presence of various catalysts (accelerators). This technical process, and the related model reactions of simple alkenes with sulfur, will be described in Section 7.

Sulfur may react with alkenes either by addition to the C=C double bond or by substitution of H by S with the elimination of H_2S. In both cases polysulfanes are formed. Octafluoroisobutene, $(CF_3)_2C{=}CF_2$, reacts at 60–70 °C in dimethylformamide (DMF) and in the presence of cesium fluoride with elemental sulfur to give the thioketene dimer (**5**) and the trisulfane (**6**) (yield 21% and 35% based on the alkene). Use of KF instead of CsF also produced some tetrasulfane analogous to (**6**).[78]

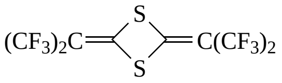

(**5**)

$(CF_3)_3C{-}S_3{-}C(CF_3)_3$

(**6**)

Acrylonitrile, $CH_2{=}CH{-}CN$, reacts at 80 °C in DMF in the presence of NH_3 to give 1,7-dicyano-3,4,5-trithiaheptane, $(NC{-}C_2H_4)_2S_3$, in a 49% yield.[73] The latter compound may be converted to the dicarbonic acid $(HO_2CC_2H_4)_2S_3$ by hydrolysis in hydrochloric acid (90% yield).[73] Tetrafluoroethylene, C_2F_4, may be sulfurized by reaction with solid $[S_8][AsF_6]_2$ at 20 °C; after 2 days, AsF_3 and a mixture of polysulfanes, $(C_2F_5)_2S_n$ with $n = 2$ (80%), 3 (19%), and 4 (0.5%), had formed.[79]

2.1.12 *Reaction of Thiols with Sulfur(IV) and Sulfur(VI) Compounds (SO_2, Tetrahalides, Thiosulfinates, Sulfinylimides, Bunte Salts, etc.)*

Thiols are powerful reducing agents, which may be oxidized by O_2, peroxides, halogens, sulfoxides, or metal ions in high oxidation states [$FeCl_3$, $Pb(O_2CMe)_4$]; usually disulfanes are formed in these reactions.[4,6] Oxidation of thiols by sulfur(IV) or sulfur(VI) compounds often results in mixtures of polysulfanes.

Liquid SO_2 oxidizes alkanethiols in the presence of triethylamine at 20 °C to a mixture of di- and trisulfanes (ratio ca. 7:3) (equations 41–43).[80]

$$RSH + SO_2 \longrightarrow R{-}S{-}S(O)OH \qquad (41)$$

$$RSS(O)OH + RSH \longrightarrow RS{-}S(O){-}SR + H_2O \qquad (42)$$

$$2RS{-}S(O){-}SR \xrightarrow{\text{base}} R_2S_2 + R_2S_3 + SO_2 \qquad (43)$$

The postulated intermediates RS–S(O)–OH and R_2S_3O could not be observed, but trisulfane 2-oxides $(RS)_2SO$, are known from the reaction of thiols with thionyl chloride (equation 44).[62–64]

$$2RSH + SOCl_2 \xrightarrow{\text{base}} (RS)_2SO + 2HCl \qquad (44)$$

Oxidation of trisulfanes by peroxo compounds sometimes also produces trisulfane 2-oxides; see below.

Substituted aromatic thiols are oxidized by *N*-sulfinylimides to yield equimolar mixtures of di- and trisulfanes (equation 45). This reaction proceeds via the intermediate 'adduct' R′–NH–SO–SR (**7**), which in favorable cases can be isolated (e.g. with $R' = 4\text{-}O_2NC_6H_4$).[85,86] Compound (**7**) reacts with thiols according to equation (46), allowing the preparation of symmetrical disulfanes and unsymmetrical trisulfanes.

$$4RSH + R'{-}N{=}S{=}O \longrightarrow R_2S_2 + R_2S_3 + R'NH_2 + H_2O \qquad (45)$$

$$R'{-}NH{-}SO{-}SR + 3R''SH \longrightarrow R''_2S_2 + R{-}S_3{-}R'' + R'NH_2 + H_2O \qquad (46)$$

Since (**7**) does not have to be isolated, the reaction of *N*-phenylsulfinylimide with benzenethiol at −15 °C in ether followed by addition of ethanethiol in acetone resulted in Et–S_3–Ph, which could be isolated in a 24% yield.[85,86] Other arylalkyltrisulfanes have been prepared by analogous reactions. The reaction of alkoxythionyl chloride with thiols also proceeds via reactive intermediates, and is therefore useful for the preparation of unsymmetrical trisulfanes (equations 47–49 with R = alkyl, R′ = aryl).[83]

$$RO{-}S(O){-}Cl + RSH \longrightarrow RO{-}S(O){-}SR + HCl \qquad (47)$$

$$RO{-}S(O){-}SR + R'SH \longrightarrow ROH + R'S{-}S(O){-}SR \qquad (48)$$

$$R'S{-}S(O){-}SR + 2R'SH \longrightarrow R'{-}S_3{-}R + R'_2S_2 + H_2O \qquad (49)$$

The reduction of sulfane oxides, R–S(O)–S–S–R, by thiols R′SH results in unsymmetrical di- and trisulfanes.[87]

SCl_4 and ethanethiol react in ether at −20 °C or below according to equation (50).[88]

$$SCl_4 + 4EtSH \longrightarrow Et_2S_2 + Et_2S_3 + 4HCl \qquad (50)$$

In a similar reaction, SF_4 and potassium ethyl xanthate yield the corresponding di- and trisulfanes in benzene at 20 °C (equation 51).[30,31]

$$SF_4 + 4EtOC(S)SK \longrightarrow [EtOC(S)]_2S_2 + [EtOC(S)]_2S_3 + 4KF \qquad (51)$$

2.1.13 *Reaction of Inorganic Polysulfides with Organic Sulfur–Oxygen Compounds (Thiosulfonates, Bunte Salts, Dimethyl Sulfate)*

Dimethyl sulfate is a strong methylating agent, which reacts at 20 °C with methanolic or ethanolic solutions of sodium polysulfides to give mixtures of dimethylpolysulfanes from which Me_2S_3 may be obtained by distillation in a 80% yield (equation 52).**[19,20,89]**

$$(MeO)_2SO_2 + Na_2S_n \longrightarrow Me_2S_2 + Na_2SO_4 \qquad (52)$$
$$n = 3 - 5$$

Organic thiosulfates, $RSSO_3M$ (M = Na, K, etc.), are called Bunte salts and may be obtained from organic halides or thiols with aqueous thiosulfate, by cleavage of disulfanes with sulfite ions, or by reaction of thiols with tetrathionate (equations 53–55).**[90–93]**

$$R\text{–}X + Na_2S_2O_3 \longrightarrow R\text{–}S_2O_3Na + NaX \qquad (53)$$
$$X = Cl, Br, SH$$
$$R\text{–}S\text{–}S\text{–}R + SO_3^{2-} \longrightarrow R\text{–}SSO_3^{-} + RS^{-} \qquad (54)$$
$$RSH + S_4O_6^{2-} \longrightarrow RSSO_3^{-} + HS_2O_3^{-} + \frac{1}{8}S_8 \qquad (55)$$

Bunte salts react with aqueous sulfide under mild conditions to give trisulfanes in high yield (equations 56 and 57).

$$RSSO_3^{-} + HS^{-} \longrightarrow RSS^{-} + SO_3^{2-} + H^{+} \qquad (56)$$
$$RSSO_3^{-} + RSSH \longrightarrow R_2S_3 + SO_3^{2-} + H^{+} \qquad (57)$$

Trisulfanes with R = methyl, ethyl, allyl, benzyl, phenacyl, 4-tolyl, and 2-methylpent-2-enyl have been prepared in this way. The pH of the solution is kept at 8 using a buffer and the trisulfane is extracted by ether or hexane.**[66,67,92,93]** To prevent the sulfite ions liberated in equations (56) and (57) from attacking the trisulfane with formation of disulfane and thiosulfate, the reaction is carried out in the presence of an excess of formaldehyde, which at pH ~8 traps the sulfite (equation 58).

$$SO_3^{2-} + CH_2O + H_2O \longrightarrow HOCH_2SO_3^{-} + OH^{-} \qquad (58)$$

In addition, saturation of the aqueous phase with NaCl lowers the solubility of R_2S_3, which is then more rapidly extracted into the organic phase.**[92,93]**

Thiosulfonates or disulfane 1,1-dioxides, $R\text{–}S\text{–}SO_2\text{–}R$, are thioalkylating agents as the S–S bond is weak and easily cleaved. Sulfide ions therefore react with thiosulfonates in a similar fashion as Bunte salts (see above), and symmetrical alkyl- and aryltrisulfanes may be prepared in high yields by equations (59) and (60).**[42]**

$$RSO_2SR + M_2S \longrightarrow RSO_2M + RSSM \qquad (59)$$
$$M = Na, K$$
$$RSSM + RSO_2SR \longrightarrow R_2S_3 + RSO_2M \qquad (60)$$

The reaction is carried out in methanol at 20 °C. It is apparent from equations (59) and (60) that the central sulfur atom originates from the sulfide. Cyclic thiosulfonates result in chainlike trisulfanes with chain-terminating $\text{–}SO_2^{-}$ groups (equation 61).**[94,95]**

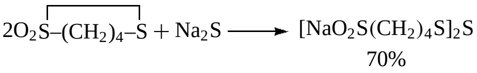

$$2O_2S\text{–}(CH_2)_4\text{–}S + Na_2S \longrightarrow \underset{70\%}{[NaO_2S(CH_2)_4S]_2S} \qquad (61)$$

Such sulfinate compounds are water soluble and may be used as antiradiation drugs (see Section 7.4).**[94–97]** Bis(sulfinato)trisulfanes may be converted to the corresponding bisalkyl esters by reaction with either diazomethane or a solution of BF_3 in diethyl ether.**[98,99]** When sodium polysulfide is applied in equation (59) the resulting polysulfanes (equation 60) contain up to six sulfur atoms. However, bis(sulfinato)polysulfanes with more than four catenated sulfur atoms are unstable in water, and elemental sulfur is slowly precipitated.**[96]** When the thiosulfonate $RS(O)\text{–}(CH_2)_2\text{–}SSO_2C_6H_4Me$ was used in equations (59) and (60), the bis(sulfoxido)trisulfane $[RS(O)\text{–}(CH_2)_2]_2S_3$ resulted.**[97]**

2.1.14 *Reduction of Sulfane Oxides by Triphenylphosphane*

Trisulfane 1,1,3,3-tetroxides, $RSO_2\text{–}S\text{–}SO_2R$, may be prepared by equation (62)**[100]** or by oxidation of trisulfanes by peroxy acids (equation 63).**[101]**

$$RSO_2SNa + R'SO_2Cl \longrightarrow RSO_2\text{–}S\text{–}SO_2R' + NaCl \qquad (62)$$
$$R_2S_3 + 4R\text{–}CO_3H \longrightarrow RSO_2\text{–}S\text{–}SO_2R + 4R\text{–}CO_2H \qquad (63)$$

Triphenylphosphane is an oxophilic compound that reduces sulfoxides (R_2SO), disulfane oxides (RS(O)SR), disulfane dioxides (sulfones) (RSO_2SR), and trisulfane tetroxides to the corresponding sulfanes. From the products prepared by equations (62) or (63), symmetrical or unsymmetrical aryl- or alkyltrisulfanes can be obtained in high yields (refluxing in ether or benzene) (equation 64).**[100]**

$$RSO_2\text{–}S\text{–}SO_2R' + 4Ph_3P \longrightarrow RS_3R' + 4Ph_3PO \qquad (64)$$

Sulfoxides are intermediates in the reaction shown in equation (64). An excess of Ph_3P converts the trisulfanes, via disulfanes, to monosulfanes, R_2S (see Section 5.3).**[100]**

2.1.15 Miscellaneous Reactions for the Preparation of Chainlike Polysulfanes

Carbon disulfide reacts with iodine pentafluoride in a sealed tube at 195 °C to give a mixture of CF_4, SF_4, $(CF_3)_2S_2$, $(CF_3)_3S_3$, and probably I_2. The trisulfane was isolated by vacuum distillation in a 7% yield.**[63]**

Cyanosulfanes, $S_n(CN)_2$, with $n = 3–8$ have been prepared by reaction of the corresponding dichlorosulfanes with $Hg(SCN)_2$ in CS_2, sometimes in the presence of EtBr as a polar solvent (equation 65).**[102–105]**

$$S_xCl_2 + Hg(SCN)_2 \longrightarrow S_n(CN)_2 + HgCl_2 \qquad (65)$$

$$x = 1 - 7;\ n = x + 2$$

While $S_3(CN)_2$, $S_6(CN)_2$ and $S_9(CN)_2$ are crystalline solids, the other dicyanosulfanes are oily liquids at 20 °C, but crystallize on cooling. The chainlike structures of $S_n(CN)_2$ with $n = 3$, 4, 6, and 9 have been established by X-ray diffraction on single crystals (see Section 3.1).

Aliphatic acid chlorides react with H_2S_3 in the presence of $ZnCl_2$ at 20 °C (no solvent) according to equation (66).**[22,23]**

$$2RCOCl + H_2S_3 \longrightarrow (RCO)_2S_3 + 2HCl \qquad (66)$$

Aliphatic ketones and aldehydes react with H_2S under pressure to give a mixture of geminal dithiols and tri- and tetrasulfanes according to equations (67–69).**[106]**

$$RCHO + 2H_2S \longrightarrow RCH(SH)_2 + H_2O \qquad (67)$$

$$R_2CO + 2H_2S \longrightarrow R_2C(SH)_2 + H_2O \qquad (68)$$

$$R_2CO \xrightarrow[-H_2O]{H_2S} (R_2CH)_2S_x \qquad (69)$$

$$x = 2 - 4$$

Polysulfane yields of up to 60% were obtained for this mixture. From acetylacetone, a cyclic trisulfane was prepared.**[106]**

Primary and secondary alkyltetrasulfanes may be prepared from ketones via hydrazones by reaction with H_2S (equations 70 and 71).**[107]** The mechanism and stoichiometry of equation (71) are unknown, but $MeCO_2H$ and $2NH_4^+$ are probably formed as by-products, in which case four equivalents of H_2S are needed, resulting in a tetrasulfane.

$$R–CO–R' + H_2N–NH–CO_2Me \longrightarrow RR'C{=}N–NH–CO_2Me + H_2O \qquad (70)$$

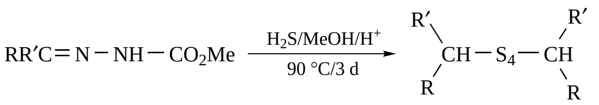

$$RR'C{=}N-NH-CO_2Me \xrightarrow[90\ ^\circ C/3\ d]{H_2S/MeOH/H^+} RR'CH-S_4-CHRR' \qquad (71)$$

Oxidation of monoorganyldisulfanes, RS_2H, by iodine in ethanol (equation 72), or by quinones in benzene produces tetrasulfanes in high yield.**[6]**

$$2RS_2H + I_2 \longrightarrow R_2S_4 + 2HI \qquad (72)$$

2.2 Cyclic Organic Polysulfanes

The Hantzsch–Widman system is often used for the nomenclature of organic rings. This indicates the ring size by specific suffixes; the first suffix given is used for saturated rings, the second for unsaturated rings:

- three-membered rings: -irane, -iren;
- four-membered rings: -etane, -ete;
- five-membered rings: -olane, -ole, -olen;
- six-membered rings: -ane, -in;
- seven-membered rings: -epane, -epin;
- eight-membered rings: -ocane, -ocin;
- nine-membered rings: -onane, -onin;
- ten-membered rings: -ecane, -ecin.

Examples will be presented in the following sections.

2.2.1 Reaction of Dithiols with Dichlorosulfanes

The reaction of organic dithiols with dichlorosulfanes may result in the formation of rings, of oligomeric rings, or of polymers (equations 73–75).

$$HS–R–SH + Cl–S_n–Cl \longrightarrow \overline{S–R–S–S_n} + 2HCl \qquad (73)$$

$$2HS–R–SH + 2Cl–S_n–Cl \longrightarrow \overline{SRS–S_n–SRS–S_n} + 4HCl \qquad (74)$$

$$nHS–R–SH + nCl–S_n–Cl \longrightarrow \left(S–R–S–S_n\right) + 2nHCl \qquad (75)$$

The formation of small rings (equation 73) is promoted by application of the dilution principle (simultaneous addition of both reagents to a large volume of solvent to keep the actual concentration low). Nevertheless, when the size of the desired ring is too small (≤ 5), the dimeric compound will form either exclusively, or in addition to, the monomeric ring (equation 74). Such reactions often are carried out in ether, which binds the HCl by strong hydrogen bonds, although a hydrocarbon solvent plus a tertiary amine may also be used. Rings with up to seven neighboring sulfur atoms have been synthesized by equation (73). Methanedithiol reacts with S_3Cl_2 to give pentathiane, CH_2S_5, and with S_5Cl_2 to give heptathiacyclooctane, CH_2S_7 (equation 76). Both compounds form yellow crystals,**[108,109]** the structure of which has been determined by X-ray diffraction (see Section 3.2).

$$CH_2(SH)_2 + S_nCl_2 \longrightarrow \textit{cyclo}\text{-}CH_2S_{n+2} + 2HCl \qquad (76)$$

$$n = 3, 5$$

Substituted methanedithiols also react with S_3Cl_2 according to equation (76).**[110]** However, when methanedithiol or substituted derivatives are reacted with SCl_2, an eight-membered cyclic bis-trisulfane is obtained, rather than a four-membered ring (equation 74 with $n = 1$).[110]

Numerous aliphatic and aromatic dithiols have been reacted with dichlorosulfanes, and cyclic polysulfanes have been obtained in yields of up to 80%.[111–116] Sometimes the sodium salt of the dithiol is used,[117] in which case the ring size obtained may be different from what was expected as the strongly nucleophilic RS^- ions catalyze interconversion reactions (see Section 5.1).

Despite the reactivity of dichlorosulfanes towards C=C double bonds, it has been possible to synthesize cyclic organic polysulfanes with alkenic double bonds by equation (73), for example, isothiazolepentasulfane,[117] pentathiepin, $C_2H_2S_5$,[118] and norbornenepentasulfane, $C_7H_8S_5$.[118] 3,6-Dimercapto-1,4-dimethyl-2,5-dioxopiperazine reacts with S_2Cl_2 without a base to give a stable, bicyclic epitetrasulfane,[119,120] which is related to the naturally-occurring antibiotic polysulfanes gliotoxin, sporidesmin, aranotin, and chaetocin II (see Section 6.2).

2.2.2 *Reaction of Bifunctional Organic Halides, Tosylates, or Esters with Sodium Polysulfide*

The reactions depicted in equations (77) and (78) are similar to those shown in equations (73–75): depending on the sizes of the organic group R and on the polysulfide anion S_x^{2-}, either a small ring, RS_n, or a larger ring (equation 78) will form. Since aqueous polysulfide consists of various anions in equilibrium, the resulting polysulfanes may contain several different $-S_n-$units. The strongly nucleophilic polysulfide ions substitute the halide ions Cl^-, Br^-, or I^-, the tosylate anion $MeC_6H_4SO_3{}^-$, or the alcoholate anion RO^-.

$$\text{X–R–X} + \text{Na}_2\text{S}_x \longrightarrow \overline{\text{R–S}_n} + 2\text{Nax} \qquad (77)$$

$$2\text{X–R–X} + 2\text{Na}_2\text{S}_x \longrightarrow \overline{\text{R–S}_n\text{–R–S}_m} + 4\text{NaX} \qquad (78)$$

Aqueous sodium polysulfide of average composition $Na_2S_{2.5}$ reacts at 20 °C with diiodomethane within 5 h to give 1,2,3,5,6-pentathiacycloheptane (lenthionine; see Section 6.2), which is extracted into chloroform and purified by LC (equation 79).[121,122]

$$2\text{CH}_2\text{I}_2 + \text{Na}_2\text{S}_2 + \text{Na}_2\text{S}_3 \longrightarrow \overline{\text{CH}_2\text{–S}_2\text{–CH}_2\text{–S}_3} + 4\ \text{NaI} \qquad (79)$$

When an excess of CH_2Cl_2 is stirred into aqueous $Na_2S_{2.5}$ at pH = 8, lenthionine and hexathiacycloheptane, CH_2S_6, are obtained. At pH = 12, 1,2,4,6-tetrathiacycloheptane (tetrathiepane) and 1,2,4-trithiacyclopentane (trithiolane) are obtained.[121,122]

Various aliphatic and aromatic dichlorides and -bromides have been used to synthesize tri- and tetrasulfanes by reaction with aqueous or alcoholic sodium polysulfide. For instance, the benzotrithiepin (**8**) was obtained from the corresponding dibromide,[123] the hydroxytrithiane (**9**) from glycerol-α,α'-dichlorohydrin,[124] and lenthionine (**10**) (1,2,3,5,6-pentathiepane) from dimethyldisulfane via bis-chloromethyldisulfane (equations 80–82).[125]

$$\text{MeSSMe} + 3\text{Cl}_2 \longrightarrow 2\text{ClCH}_2\text{SCl} + 2\text{HCl} \qquad (80)$$

$$2\text{ClCH}_2\text{SCl} + 2\text{KI} \longrightarrow \text{ClCH}_2\text{SSCH}_2\text{Cl} + 2\text{KCl} + \text{I}_2 \qquad (81)$$

$$\text{ClCH}_2\text{SSCH}_2\text{Cl} + \text{Na}_2\text{S}_x \longrightarrow \overline{\text{CH}_2\text{SSCH}_2\text{SSS}} + 2\text{NaCl} \qquad (82)$$

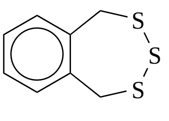

(**8**)

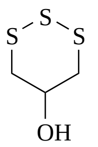

(**9**)

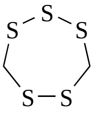

(**10**)

An epitetrasulfane of 2,5-piperazinedione has been prepared from the dibromide and Na_2S_x.[118]

Bifunctional mesityl ethers react with aqueous sodium polysulfide to give cyclic disulfanes and trisulfanes in high yields (equation 83).[114]

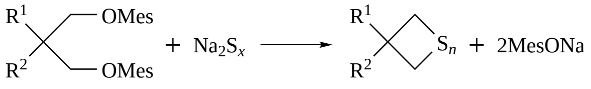

R^1 = Me, Et, *i*-Bu; $R^2 = R^1$, Ph, *neo*-C_5H_{11}; $n = 2, 3$

(83)

Similarly, bifunctional tosylates yield cyclic di-, tri-, and tetrasulfanes on treatment with sodium polysulfide (equation 84).[126]

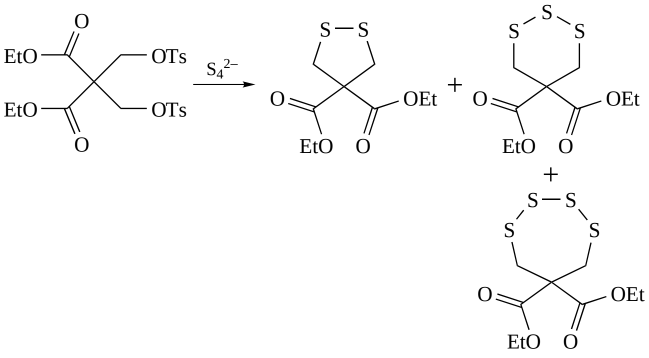

(84)

2.2.3 *Reaction of Organic Thiosulfates (Bunte Salts) or Thiosulfonates with Sodium Sulfide*

Bunte salts and thiosulfonates react with aqueous sulfide as shown in equations (56) and (57). When bifunctional Bunte salts are used, cyclic trisulfanes are obtained (equation 85).

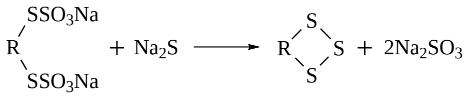

(85)

To prevent the sulfite from attacking the trisulfane (with formation of thiosulfate and disulfane), the reaction is carried out in the presence of formaldehyde at pH = 7 (see equation 58). Aromatic, aliphatic, and alkenic trisulfanes have been obtained in this way in high yields.[87,127]

Bifunctional thiosulfonates react similarly (no CH_2O is needed) and yield cyclic trisulfanes, also in high yields (equation 86).[87]

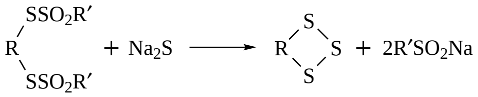

(86)

2.2.4 Reaction of Dihalides, Dithiols, or Thiocarbonates with Elemental Sulfur in the Presence of a Base

Aliphatic and aromatic dithiols react with elemental sulfur in liquid ammonia at 20 °C according to equation (87).[128–132]

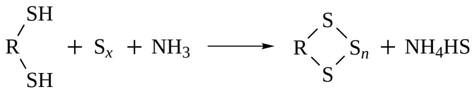

(87)

Various cyclic di-, tri-, tetra-, and pentasulfanes have been prepared by equation (87); examples are given in Figure 1.

Aromatic bistrithiocarbonates have been used to synthesize cyclic bis-polysulfanes as shown in equation (88) (R = OMe, OEt, O^{i}Pr, OCH_2Ph).[128–132]

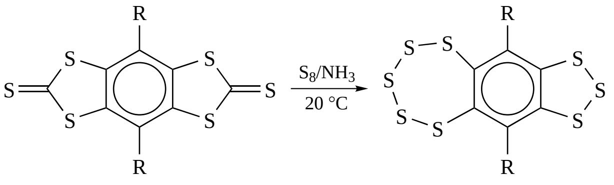

(88)

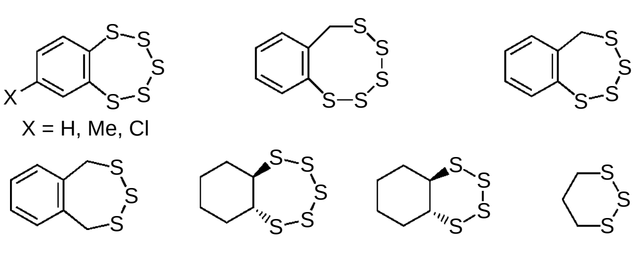

Figure 1 Cyclic polysulfanes prepared from organic dithiols and elemental sulfur in the presence of ammonia as a catalyst

Polycyclic polysulfanes may also be obtained from aromatic tetrahalides as shown in equation (89) (R = Me, Et, n = 1, 3).[128–132]

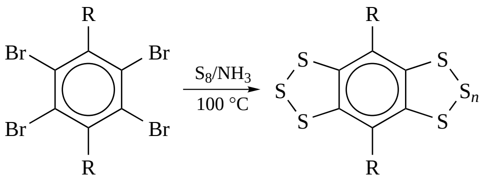

(89)

For a recent review on cyclic benzopolysulfanes, see ref.[133]

The preparation of 1,2,3-trithiane from $Br(CH_2)_3Br$ and elemental sulfur in the presence of KOH in THF has been described.[60,61]

2.2.5 Reactions of Alkenes with Elemental Sulfur

The reactions of sulfur with various types of organic compounds have been reviewed in 1987.[134]

Under certain conditions, alkenes react with elemental sulfur or sulfur-rich compounds to yield cyclic polysulfanes. Tetrafluorethylene, C_2F_4, reacts with boiling elemental sulfur (445 °C) to give tetrafluoro-1,2,3-trithiolane (yield 10%) and tetrafluoro-1,2,3,4-tetrathiane (60%); both compounds are malodorous oils.[135] Ordinary hydrocarbons would yield H_2S under these conditions, therefore, a catalyst or irradiation is applied to achieve milder reaction conditions. When a mixture of norbornene and S_8 in CS_2 is irradiated (wavelength 350 nm), besides other products, the trithiolane derivative (**11**) is formed (77% yield; equation 90).[136]

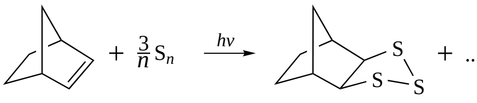

(90)

Since irradiation of S_8 in CS_2 results in various reactive sulfur molecules S_n ($n < 8$),[137,138] it is not clear which molecules S_n are reacting in equation (90). Cyclohexene reacts similarly to norbornene.[136]

Heating of norbornene, dicyclopentadiene (DCPD) or tricyclopentadiene with elemental sulfur in DMF in the presence of NH_3 or triethylamine also produces the corresponding 1,2,3-trithiolane derivatives in yields of 20–85%.[139,140] For the reaction of liquid sulfur with DCPD, see Section 7. A careful investigation of the reactions of sulfur with norbornene, norbornadiene, and DCPD showed that tri- and pentasulfanes are formed and may be isolated as pure materials; in the case of norbornene these are in equilibrium in solution at 20 °C (equation 91).[141]

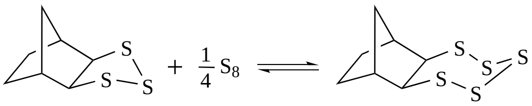

(**11**)

(91)

The DCPD polysulfanes with between four and eight sulfur atoms have been independently synthesized from titanocene polysulfides and DCPD sulfenyl chlorides by sulfur transfer reactions.[142]

Cycloheptatriene reacts with elemental sulfur in sulfolane at 70 °C and in the presence of pyridine in such a way that an S_3 unit is added across the 1,6-positions, resulting in 2,3,4-trithiabicyclo[4.3.1] deca-6,8-diene (21% yield).[143] Trimethylvinylsilane, $Me_3SiCH{=}CH_2$, and sulfur react at 55 °C in the presence of $Fe_3(CO)_{12}$ to give, *inter alia*, 1-trimethylsilyl-2,3,4,5,6-pentathiacycloheptane.[144] The preparation of cyclic trisulfanes from alkenes and S_8 has also been carried out by reduction with NaH in toluene in the presence of a phase transfer catalyst.[145] Indole fused pentathiepines were obtained by lithiation of indole or N-methylindole followed by thionation with elemental sulfur.[146,147]

Unusual unsaturated cyclic polysulfanes are obtained on reaction of tetraarylbutatrienes with elemental sulfur in DMF at 125 °C (equations 92 and 93).[148–150]

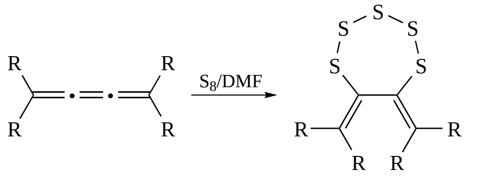

(92)

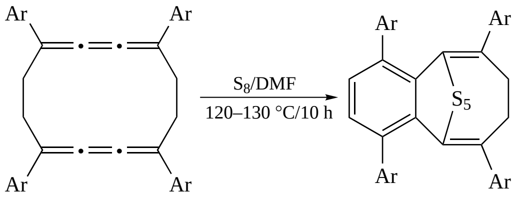

(93)

Ar = phenyl, 24%
Ar = *p*-tolyl, 24%

2.2.6 *Reactions of Alkenes with Sulfur Compounds: Sulfur Transfer Reactions*

The highly reactive S_2 molecule can be prepared by various routes in solution. Its intermediate presence has been deduced from trapping reactions with alkenes, which are turned into disulfanes,[151–154] however, tri- and tetrasulfanes are sometimes also formed; only the latter reactions will be reported here.

Cyclopentadiene epidisulfane reacts with norbornene, C_7H_{10}, on heating to give the trisulfane (**11**) in 61% yield (equation 94).[155]

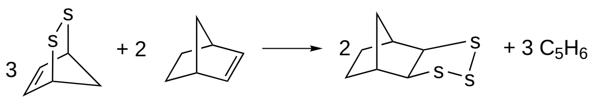

(**11**)

(94)

The same product (**11**) is obtained when S_2 is generated from $(R_3Ge)_2S_3$ by reaction with Ph_3PBr_2.[151–154] Analogously, the enes shown in Table 3 result in cyclic trisulfanes at the yields given.[151–154] The exact pathway of these reactions is unknown.

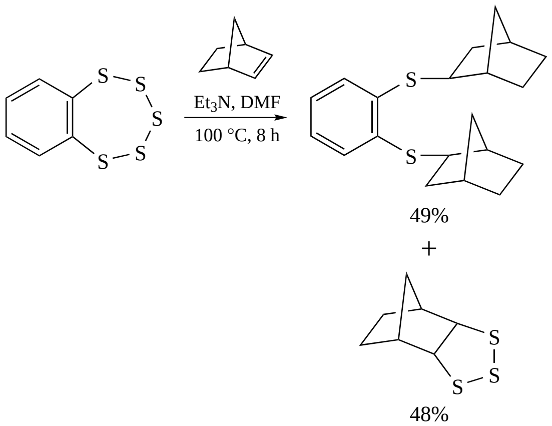

(95)

The formation of the 1,2,3-trithiolane (**11**) has also been observed when norbornene was heated with benzopentathiepin, 1,2-$C_6H_4S_5$, in DMF in the presence of triethylamine (yield 48%, at 100 °C) (equation 95).[156,157] Benzopentathiepin, heated in the presence of R_3N, apparently

Table 3 Products of the formal addition of S_2 to cyclic alkenes[151–154]

Ene	Product(s)	% Yield
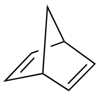	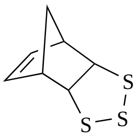	75
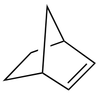	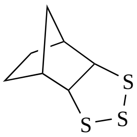	88
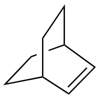	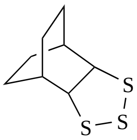	15
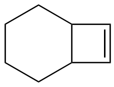	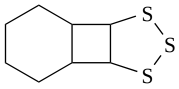	18
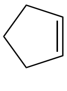	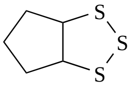	31
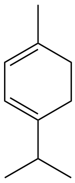	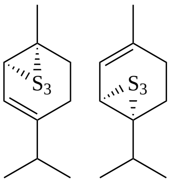	87, 13

splits into S_3 and 1,2-$C_6H_4S_2$, which have both been trapped by norbornene.[156,157] The analogous reactions of benzopentathiocin and the related benzotetrathiepin with various enes, dienes, and trienes in dimethylsulfoxide (DMSO) have been investigated, and di- or trisulfanes resulting from [2 + 3], [4 + 2], and [6 + 3] cycloaddition have been isolated in high yields.[156,157] These remarkable reactions show that on heating in polar solvents cyclic sulfur-rich polysulfanes may produce various reactive sulfur species that can be transferred to suitable alkenic acceptors; if less reactive alkenes such as cyclohexene or cyclooctene are used, elemental sulfur instead of cycloadducts is obtained.[156,157] For S_3 transfer reactions, see also Section 5.2.

Triphenylmethylchlorodisulfane reacts with 2,3-dimethyl-1,3-butadiene to give two polysulfanes that arise from the addition of S_2 (equations 96–98).[158]

$$\mathrm{Ph_3C{-}S_2{-}Cl} \longrightarrow \mathrm{Ph_3C{-}Cl} + \mathrm{S_2} \qquad (96)$$

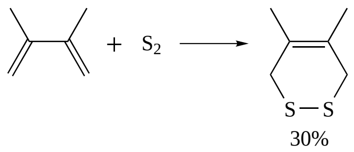

(97)

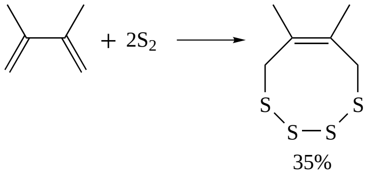

(98)

The actual mechanism, however, seems to involve addition of Ph_3CSSCl to the diene, with subsequent elimination of Ph_3CCl.[158] It should be remembered that the formation of free S_2 or S_3 molecules in all of the above reactions is only a working hypothesis as long as there is no direct evidence for S_2 and S_3, e.g. from spectroscopic measurements. Most of these reactions can also be explained by a direct reaction between the sulfur donor and the sulfur acceptor, without the intermediate presence of free S_2 or S_3 molecules.

2.2.7 *Reaction of Titanocene Chelate Complexes with Bis(Sulfenyl Chlorides)*

Titanocene pentasulfide (**1**) has been used as a transfer reagent for the S_5 unit to prepare numerous inorganic homo- and heterocycles.[159] More recently, cyclic organic polysulfanes have also been obtained from (**1**) by reaction with bis(sulfenyl chlorides) (equation 99).[46,47]

$$\mathrm{R(SCl_2)} + \mathrm{Cp_2TiS_5} \longrightarrow \overline{\mathrm{R{-}S_7}} + \mathrm{Cp_2TiCl_2} \qquad (99)$$

1,2-$C_2H_4(SCl)_2$ reacts with (**1**) to give the nine-membered ring $C_2H_4S_7$ in 31% yield.[48,50] Toluenebis(sulfenyl chloride), $MeC_6H_3(SCl)_2$, reacts similarly to give the bicyclic $MeC_6H_3S_7$.[48,50] Norbornanetrithiolan (**11**) on chlorination gives one of the two sulfenyl chlorides $C_7H_{10}(SCl)_2$ or $C_7H_{10}(SCl)(S_2Cl)$, depending on the reaction conditions. These react with (**1**) to give the previously unknown polysulfanes $C_7H_{10}S_7$ and $C_7H_{10}S_8$.[160] $C_7H_{10}S_7$ exists in solution as two conformers, as was shown by ^{1}H NMR (proton nuclear resonance) spectroscopy.[160] The DCPD polysulfanes $C_{10}H_{12}S_n$ with $n = 4–8$ were obtained using the polysulfido complexes (**1**) and $(Cp_2TiCl)_2S_3$, together with the sulfenyl chlorides $C_{10}H_{12}(S_mCl)(S_nCl)$ with $m, n = 1$ or 2.[160]

The reactions of equation (99) usually proceed quantitatively to the right and without any side reactions. The advantage of (**1**) over sodium pentasulfide is not only that it is soluble in organic solvents (CS_2, CH_2Cl_2) and does not equilibrate with other ring sizes, but also that it does not introduce nucleophilic polysulfide anions that catalyze decomposition and interconversion reactions (see Section 5.1).

On treatment with acetone and sodium sulfide, (**1**) is transformed to $Cp_2Ti(\mu\text{-}S_2)_2CMe_2$, which is also a transfer reagent. This reacts with S_2Cl_2 to give dimethylhexathiepin, Me_2CS_6 (30% yield), and with a mixture of dichlorosulfanes, S_nCl_2 ($n = 1–30$), to yield the corresponding mixture of heterocycles, Me_2CS_{n+4}, which has been analyzed by HPLC.[15,16]

Another valuable titanocene precursor is obtained by the action of CS_2 on $Cp_2Ti(CO)_2$ at 20 °C, resulting in $Cp_4Ti_2C_2S_4$.[161] This dinuclear complex contains the $C_2S_4{}^{4-}$ ligand, which may be used to synthesize the bicyclic polysulfanes shown in equations (100–102).[162–165]

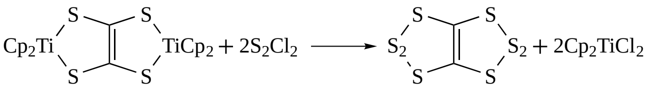

(100)

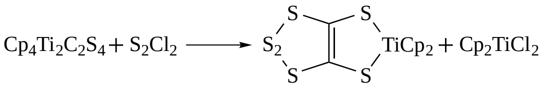

(101)

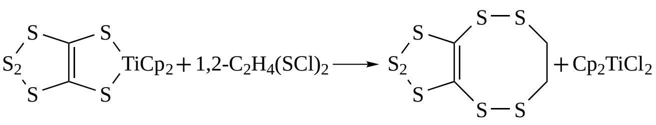

(102)

A similar reaction, shown in equation (103), yields a binary tricarbon octasulfide, C_3S_8, in a 15% yield[166,167] (rather than C_3S_7, which would be expected from the stoichiometry).

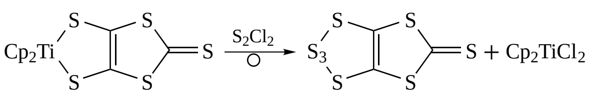

(103)

Equations (99–103) are carried out at 0 or 20 °C. At slightly elevated temperatures, Cp_2TiS_5 reacts even with certain C–Cl

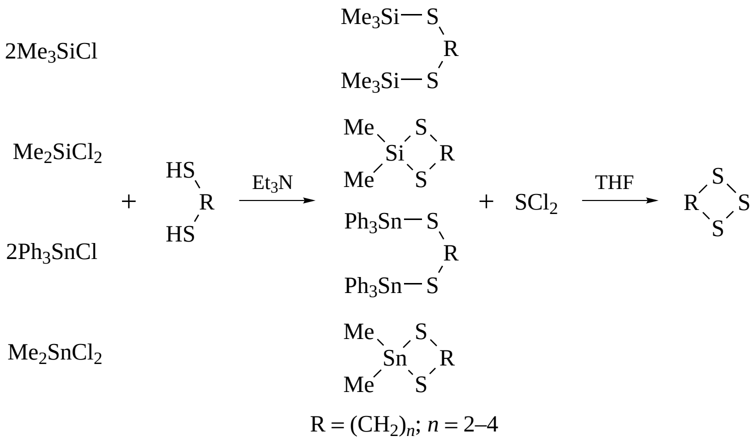

Scheme 1

bonds, as equation (104) shows. The product ($C_4O_4S_{10}$) forms yellow crystals consisting of 14-membered ring molecules (yield 48%).[168,169]

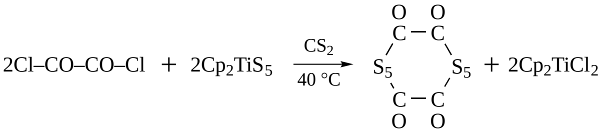

(104)

More recently, the hexasulfido zinc complex $[(TMEDA)Zn][S_6]$ has been used to prepare extremely sulfur-rich cyclic polysulfanes by reaction with 1,2-benzenebis(sulfenyl chloride).[170]

2.2.8 *Cyclic Polysulfanes from Organosilicon or Organotin Sulfides and Dichlorosulfanes*

As shown in Scheme 1, dithiols react with organic silicon and tin chlorides to give sulfides that can be cleaved by SCl_2 to synthesize cyclic trisulfanes.[171]

The best yields were obtained with $(Me_3SiS)_2R$ and $R = C_3H_6$ or C_4H_8. In the case of $R = C_2H_4$, oligomeric compounds were formed. The reaction with SCl_2 is carried out in THF followed by evaporation of the solvent and of Me_3SiCl and preparative TLC (Thin-layer Chromatography) separation with hexane as an eluent.

2.2.9 *Reaction of Benzothiadiazoles or Related Compounds with Elemental Sulfur*

1,2,3-Benzothiadiazoles are thermally stable up to 195 °C but in the presence of elemental sulfur evolution of nitrogen occurs at 160−170 °C and benzopentathiepins are formed (equation 105).[172,173]

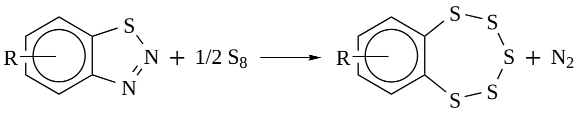

(105)

With R = H, Cl, CF_3, OMe, NMe_2, or Br, yields of up to 57% have been obtained if some diazabicyclo[2.2.2]octane (Dabco) is added.[172,173] In a similar reaction, the thiadiazole (**12**) when heated with elemental sulfur to 120 °C affords the corresponding cyclic tetra- and pentasulfanes in 18 and 22% yields, respectively (equation 106).[174–176]

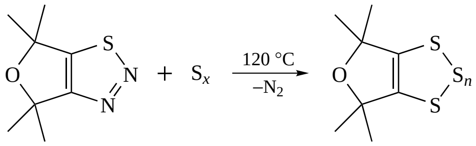

(**12**) $n = 2, 3$

(106)

Certain selenadiazoles also react with sulfur to yield cyclic polysulfanes (equation 107).[174–176]

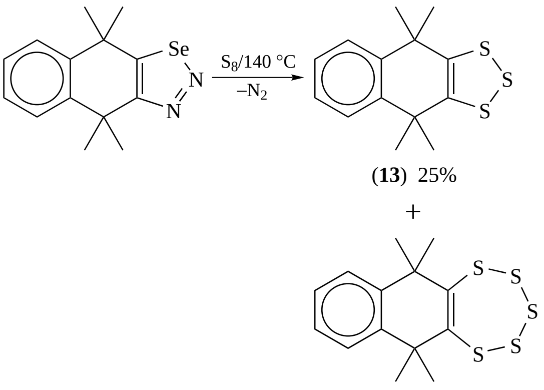

(**13**) 25%

+

(**14**) 11%

(107)

On heating or irradiation, (**14**) is converted to (**13**) and S_8.[174–176] When the selenadiazole (**15**) is heated with sulfur, a complicated mixture of sulfurization products was obtained from which the pure polysulfanes shown in equation (108) were obtained by chromatography and crystallization.[177]

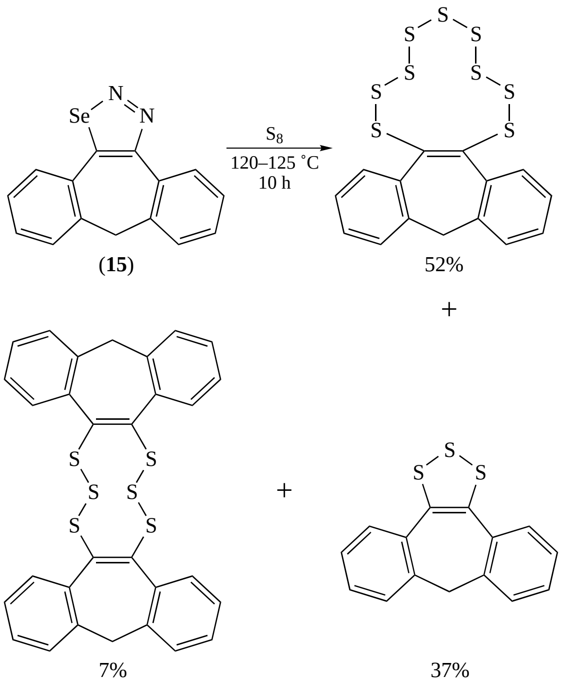

(**15**) 52% 7% 37%

(108)

An octathionane of type $RHCS_8$ has been obtained in a 25% yield on refluxing S_8 and the monosubstituted diazomethane $RHCN_2$ in benzene with R = 2, 4,6-tris[bis(trimethylsilyl)methyl]phenyl (equation 109).[178,179]

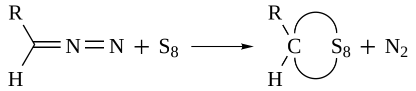

(109)

This cyclic octasulfane is stable at 20 °C, and even in a boiling EtOH/$CHCl_3$ mixture. Related to equation (109) is the reaction of hexafluoroacetone hydrazone with S_2Cl_2, which produces the hexathiepane $(CF_3)_2CS_6$ (equation 110).[178,179]

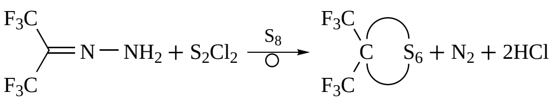

(110)

If the hydrazone is substituted with two bulky groups such as adamantyl or *t*-butyl, a tetrathiolane is obtained in the reaction with S_2Cl_2,[180] but with phenyl substituents pentathianes and hexathiepanes are formed.[181]

2.2.10 Miscellaneous Reactions for the Synthesis of Cyclic Polysulfanes

Electrochemical reduction of CS_2 in either DMF or MeCN yields the trithiocarbonate (**16**) and the 4,5-dimercapto-1,3-dithiole-2-thione (**17**) dianions, which on oxidation by iodine give the binary carbon sulfide C_3S_6 in good yields (equations 111 and 112).[182]

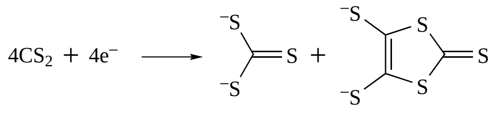

(**16**) (**17**) (111)

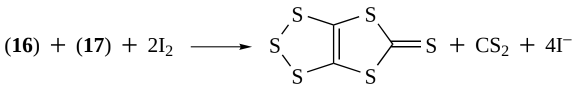

(112)

C_3S_6 is a yellow solid, sparingly soluble in CS_2.[118]

The use of *N*,*N*′-dibenzimidazolyl sulfide for the synthesis of cyclic polysulfanes by reaction with dithiols has been explored. In many cases, oligomers or low-molecular mass polymers are formed, however, *α*,*α*′-dimercaptoxylene yields the benzotrithiepin shown in equation (113) when stirred at 20 °C with the imidazolyl sulfide in benzene.[183]

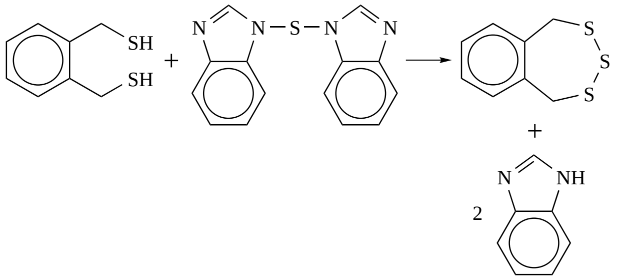

(113)

4-(*N*,*N*′-Dimethylamino)-1,2-dithiolane is transformed to the corresponding trithiane by reaction with sodium tetrathionate at 20 °C and pH = 7.8 (yield 65%) (equation 114).[184]

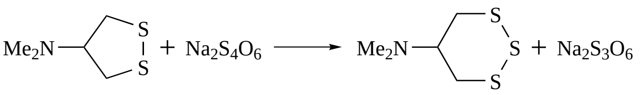

(114)

A mixture of S_8 and phosphorus(V) sulfide may also be used to sulfurize organic compounds: certain epidisulfanes are transformed to epitrisulfanes.[185,186] The reaction of SCl_2 with 1,4-diethoxybenzene, catalyzed by Al_2Cl_6, in CS_2 or $CHCl_3$, yields a bis-tetrasulfane in which two S_4 units bridge the two benzene rings.[187]

Acyclic and cyclic trisulfanes may be synthesized from sulfenyl thiocarbonates by nucleophilic displacement.

From 1,6-hexanedithiol and MeOC(O)SCl the bis-sulfenyl thiocarbonate shown on the left side of equation (115) was obtained, which on treatment with potassium *t*-butoxide in methanol resulted in a macrocyclic bis-trisulfane, (equation 115).[188]

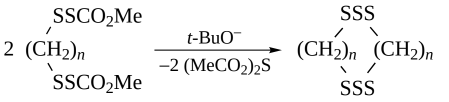

(115)

In this reaction, the alkoxide anion displaces the MeOCO group, generating an RSS$^-$ anion that attacks the neighboring molecule, producing a dimer that is attacked by another alkoxide ion, and so on until finally ring closure takes place. Similar reactions were observed for $n = 7$, 8, and 10, while for $n < 6$ only polymers were obtained.[188]

Certain ketones react with H_2S or sodium polysulfide to give cyclic polysulfanes. Formaldehyde and aqueous $Na_2S_{2.5}$ in the presence of chloroform result in 1,2,3,5,6-pentathiepin (lenthionine, see Section 6.2).[121,122] Cycloheptanone reacts with ammonium polysulfide at 20 °C to give the tricyclic pentathiepane derivative $C_{14}H_{24}S_5$ containing a disulfane and a trisulfane bridge between the two cycloalkyl units.[189] Various cyclic and acyclic tri- and tetrasulfanes have been obtained from the corresponding ketones, diketones, or aldehydes and H_2S at temperatures of 30−135 °C and pressures of 50−8500 bar.[106] The use of H_2S_2 for the transformation of dithiols or epidisulfanes into cyclic tri- and tetrasulfanes in good yields has also been reported.[190,191] When 1,2,4,5-tetrathiane is treated with Na_2S_4 in DMF at 20 °C, 1,2,3,5,6-pentathiepin (lenthionine) is formed in a 30% yield.[192] Substituted benzothiocarbonates may be converted to benzotrithioles by reaction with NaHS in DMSO.[193]

3 STRUCTURES OF ORGANIC POLYSULFANES

The stereochemistry of organic sulfur compounds was reviewed very extensively by Laur[7] in 1972 and that of organic polysulfides by Rahman *et al.*[194] in 1970. Since those days, however, considerable progress has been made. The molecular and crystal-structures of more than 60 cyclic and acyclic polysulfanes of type R–S$_n$–R have been determined by X-ray diffraction on single crystals. In rare cases, electron diffraction of the vapor of R–S$_n$–R molecules has been used to determine the structure (*see* ***Diffraction Methods in Inorganic Chemistry***). In addition, the structures of several acyclic polysulfane oxides such as RS–SO–SR[84,195,196] and RSO$_2$–S$_n$–SO$_2$R ($n = 1$, 2, 3),[197,198] and of the trisulfane cation $(MeS)_3{}^+$,[199,200] have been determined.

Chainlike organic polysulfanes with up to nine sulfur atoms have been characterized structurally, while in cyclic species the maximum number of sulfur atoms was 11, but the total number of sulfur atoms in the molecule can be as high as 16. In all cases, the –S$_n$– backbone was found to be unbranched. It may be characterized by the bond distances d_{SS}, the bond angles α_{SSS}, and the torsional angles τ_{SS}, which determine the overall conformation of the molecule. Typical values of these parameters in chainlike R–S$_n$–R are $d_{SS} = 205 \pm 4$ pm, $\alpha_{SSS} = 107 \pm 3°$, and $\tau_{SS} = 85 \pm 20°$. The torsional angles may be positive (clockwise rotation) or negative (counterclockwise rotation). A helical sulfur chain –S$_n$– may therefore be a right-handed (all τ positive) or a left-handed screw (all τ negative). The order of the signs of τ in such a chain is termed the motif. Thus, the motif of a helix is either $+ + + \cdots$ or $- - - - \cdots$. Less symmetrical –S$_n$– chains are usually obtained when the motif is less regular. In *cyclo*-octasulfane, S_8, the motif is $+ - + - \cdots$ or $(+-)_4$; in S_{12} it is $(+ + - -)_3$.[1]

Rotation around S–S bonds in acyclic organic disulfanes requires an energy of 25−40 kJ mol^{-1},[201] which is far too low to permit the isolation of the rotational isomers. In the case of R–S$_2$–R, these stereoisomers are mirror images or enantiomers. However, in favorable cases these stereoisomers crystallize from solutions as enantiopure single crystals (see below). The torsional barriers of organic polysulfanes R–S$_n$–R with $n > 2$ have not yet been accurately determined, but may be even lower than for disulfanes. This might be concluded from the results obtained for the inorganic species H_2S_n ($n = 2$−4)[202] and from the *Pseudorotation* of the cyclic S_n molecules ($n \geq 7$).[203] It therefore can be expected that acyclic organic polysulfanes show a rapid torsional isomerization in solution at 20 °C. The conformational properties of trisulfanes, R_2S_3, in the liquid and solid states have been studied by Raman spectroscopy (*see Raman Spectroscopy*).[204]

In the case of cyclic polysulfanes, it has repeatedly been observed by ^{1}H NMR spectroscopy that different conformational isomers exist in equilibrium with each other in solution.[116,160,205] However, as in the case of acyclic polysulfanes, the energy barriers between these isomers are too low to allow a preparative separation.[116]

No organic polysulfane has been observed that has a branched structure of the type –S–S(=S)–S–, however, molecules of this type have recently been subjects of sophisticated theoretical study. According to these results, branched species are considerably less stable than the unbranched isomers, and the barrier for isomerization is extremely high.[206,207]

3.1 Structures of Chainlike R–S$_n$– R Molecules

Table 4 compiles the structural parameters of the –S$_n$– backbone of 15 chainlike polysulfanes.[25,208–214] The only undisturbed free molecules investigated by electron diffraction of vapors are Me_2S_3, $(CF_3)_2S_3$, and $(CF_3)_2S_4$. All other data are derived from X-ray diffraction on single crystals. In the latter case, the molecular conformation may be influenced by intermolecular interaction (‘packing effects’). Many polysulfanes are chiral (helical chirality). While normally

Table 4 Structures of chain-like organic polysulfanes R–S_n–R

R	Method[b]	n	d_{SS} (pm)	α_{SSS} (°)	τ_{SS} (°)[c]
Me	ED[208]	3	200	104	n.d.[b]
F_3C	ED[32]	3	204.0	105.3	+89
ICH_2CH_2[a]	X[209]	3	205	113	+82
Cl_3C	X[210]	3	203.4, 203.4	106.0	+93, +95
CN[a]	X[211]	3	207.1	105.3	+87, −87
MeSC(O)[a]	X[25]	3	204.0	107.8	+83.1
n-$C_{18}H_{37}$	X[213]	3	202.3 203.0	106.3	+72.8, +67.3
F_3C	ED[32]	4	203.4, 205.4	106.8	+84, +98, −84
CN	X[212]	4	207.1, 201.7, 206.5	106.2, 106.7	+74.6, +84.8, +81.7
n-$C_{18}H_{37}$[a]	X[213]	4	201.8, 206.0	105.3	+75.9, +65.3
MeSC(O)[a]	X[25]	4	203.2, 205.5	106.2	+87.3, +78.8
Ph_3C	X[50]	5	204, 202, 205, 201	109, 106, 111	+97, +81, +76, +92
Ph_3C	X[50]	6	203.3, 207.0, 205.2, 206.1, 202.4	107.0, 104.8, 108.5, 108.5	+104.1, +99.1, −88.7, −95.5, +93.6
$(CH_2)_5NC(S)$	X[214]	6	201.6, 204.5, 204.0, 204.5, 201.1	107.3, 106.5, 107.4, 106.6	+81.8, +93.4, −96.4, +92.3, +82.4
CCl_3	X[215]	7	201.8−205.9	103.6−107.1	79.7−91.1
CN	X[212]	9	204.1−207.8	104.3−106.8	+84.3, +87.5, −80.2, −86.3, +87.3, +94.8, −94.2, +82.1

[a] Owing to the symmetry of the molecule, the number of independent molecular parameters is lower than the number of internal coordinates.

[b] ED, electron diffraction; X, X-ray diffraction on single crystal; n.d., not determined.

[c] Torsion angles along the sulfur chain. For chiral molecules, the torsion angles of the other enantiomer are obtained by changing all signs to the opposite.

chiral molecules crystallize in such a manner that the unit cell contains equal amounts of both enantiomers, there are some cases known in which enantiopure crystals have been obtained. For example, the nonasulfane $S_9(CN)_2$ crystallizes from CS_2/hexane solution as enantiopure crystals despite the many conformations this molecule can adopt.[212] It should be noted that the parameters cited in Table 4 have widely differing standard deviations.

Most trisulfanes adopt a *trans* conformation with a local symmetry of C_2 for the central X–S–S–S–X unit (motif ++ or −−). The term *trans* describes the position of the two substituents X with respect to the plane defined by the three sulfur atoms. Dicyanotrisulfane is the exception to the rule since this molecule adopts a *cis* conformation in the solid state, which seems to be the result of the weak interaction of the two nitrogen atoms with the central sulfur atom of a neighboring molecule.[211] The motif of $S_3(CN)_2$ is +− (or −+ for the enantiomer (*see Enantioselectivity*), which is present in equal amounts in the unit cell). Electron density measurements on gaseous Me_2S_3 have been interpreted by a mixture of mainly *trans*- and little *cis*-Me_2S_3.[216]

The only tetrasulfane investigated in the vapor phase is most probably of C_1 symmetry (*cis-trans*) with the motif + + −. This result is in agreement with ab initio MO calculations,[32] which indicate this conformer to be slightly more stable (by 1.2 kJ mol^{-1}) than the trans−trans conformer. Electron diffraction has shown that the analogous MeO–S–S–OMe also adopts a *cis-trans* conformation in the vapor, but a *trans−trans* structure in the solid state.[217] The three solid tetrasulfanes exist in a *trans−trans* conformation with all torsional angles of equal sign. The same holds for the only acyclic pentasulfane, which has been studied structurally and which has a helical S_n unit of motif + + ++. Interestingly, however, the two hexasulfanes listed in Table 4 do not adopt a helical but a more compact conformation with motifs + + − − + and + + − + +, respectively. It may well be that longer chain polysulfanes in the crystalline state have to have a motif of this type to allow for an efficient space-filling packing of the molecules in the crystal.

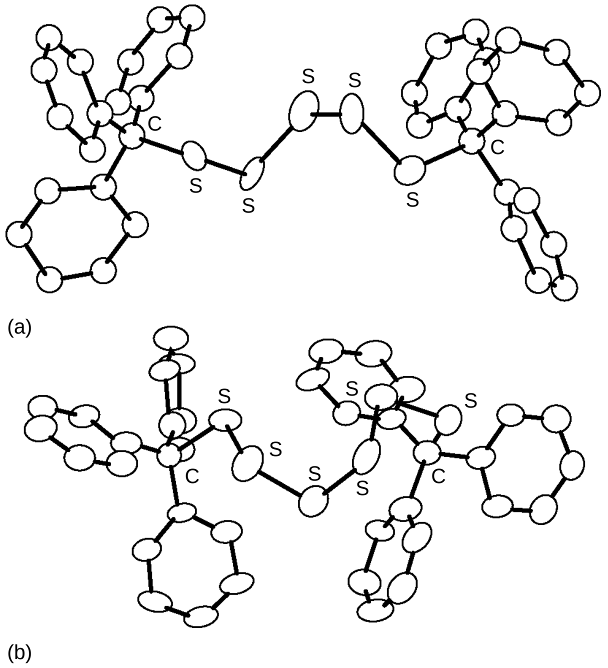

Figure 2 Molecular structures of bis(triphenylmethyl)pentasulfane (a) and -hexasulfane (b)[50]

In Figure 2, the molecular conformations of $(Ph_3C)_2S_5$ and $(Ph_3C)_2S_6$ are shown to illustrate the impact of the motif on the size and shape of the molecule.

The rotational isomerism that probably exists in solution may be responsible for the fact that so far no single crystals have been obtained for organic polysulfanes with more than nine sulfur atoms in a chain. However, cyclic polysulfanes with up to 11 neighboring sulfur atoms have been structurally elucidated (see below), and the structures of homocyclic sulfur molecules with up to 20 atoms are known.[45]

The molecular parameters in Table 4 show that the accurately determined SSS bond angles range from 105 to 108°, and the absolute values of the torsional angles at the SS bonds range from 75 to 99° with the exception of $(n\text{-}C_{18}H_{17})_2S_4$, which has one torsional angle of 65°, which may be a result of the large substituents. However, if more structures are considered, these ranges are slightly larger.[11]

3.2 Structures of Cyclic R–S_n–R Molecules

More than 40 cyclic polysulfanes have been investigated by X-ray diffraction on single crystals. These compounds are monocyclic or polycyclic. All ring sizes have been studied from 5 to 12 as well as 14, 16 and 20, and the number of sulfur atoms in the $-S_n-$ unit varies from 3 to 11. There are also systems with two independent $-S_n-$ units ($n = 2-8$) in one ring, bridged by carbon atoms. The following are leading references: trisulfanes;[124,131,132,166,167,172,173,218–220] bis-trisulfane;[221] tetrasulfanes;[222–225] bis-tetrasulfane;[226] pentasulfanes;[131,132,144,148–150,172,173,227–230] bis-pentasulfane;[168,169] hexasulfanes;[148–150,230] heptasulfane;[50] octasulfane;[178,179] nonasulfane,[177] undecasulfane.[231]

The geometrical parameters of the $-S_n-$ unit in cyclic organic polysulfanes may be quite different from those in chainlike polysulfur compounds since ring closure may enforce unusual valence and torsional angles and, as a consequence, the bond distances may be affected. This problem is well known from the structures of homocyclic sulfur molecules (*cyclo*-S_n), which exhibit torsional angles in the range of 0–140°, bond angles in the range of 101–111°, and bond distances in the range of 200–218 pm.[45]

The conformation of cyclic organic polysulfanes is usually as follows:

1. five-membered rings of composition C_2S_3 are envelope-shaped (four atoms C_2S_2 in a plane, one S atom out of plane);[131,132,172,173,218,220]
2. six-membered rings of composition C_3S_3, C_2S_4, or CS_5 are chairlike;[124,222,225,229,230]
3. seven-membered rings of composition C_2S_5 are chairlike as *cyclo*-S_7 or distorted (twisted) chairs;[131,132,144,148–150,172,173,219,227,228,230]
4. larger rings either resemble in shape the sulfur homocycles, like S_8, S_{10}, S_{11} and S_{12}, or are of lower symmetry.[166,167,174–179,221,223,224,226]

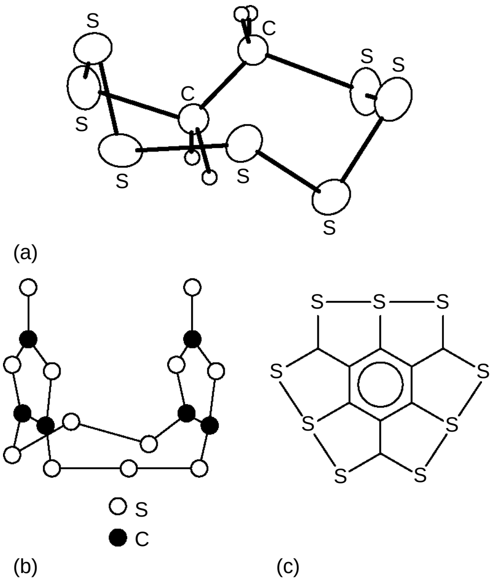

Figure 3 Molecular structures of the nine-membered ring $C_2H_4S_7$ [1,2,3,4,5,6,7-heptathionane] (a), of the tricyclic carbon sulfide C_6S_{12} (b), and of C_9S_9 (c)

The structures of some naturally-occurring organic polysulfanes will be discussed in Section 6 of this article.

To illustrate the types of cyclic structures known, the results of X-ray structural analyses of $C_2H_4S_7$ and of two binary carbon sulfides are shown in Figure 3. The structure of $C_2H_4S_7$ may be derived from the structure of S_8 by substitution of one sulfur atom by a *trans*-C_2H_4 group.[50] The carbon sulfide C_6S_{12} is a tricyclic molecule prepared only in 1989.[166,167] C_9S_9 is formally a thioketone,[232] but it contains three linear three-center bonds between adjacent sulfur atoms, resulting in an unusually symmetrical planar system of two 'concentric rings'. The structures and bonding in compounds of the latter type have been reviewed in 1976.[233]

4 ANALYSIS OF ORGANIC POLYSULFANES

A comprehensive review on the analytical chemistry of organic di- and polysulfanes was published in 1972 by Cardone (340 pages, 1200 references).[8] The latter review summarizes the physical properties (density, boiling point, refractive index, vapor pressure, molar refraction, parachor, dipole moment, viscosity, optical rotation, crystal data) as well as the application of analytical techniques (thermal analysis, mass spectroscopy, ^{1}H NMR spectroscopy, infrared (IR) and Raman spectroscopy, UV–Vis spectroscopy, polarography, liquid chromatography including TLC, paper chromatography, gel permeation and ion-exchange chromatography, partition chromatography, electrophoresis, and gas chromatography). In addition, the chemical treatment of polysulfane mixtures prior to analysis (pyrolysis, reduction to RSH and H_2S, oxidation by bromine, nucleophilic degradation by sulfite, cyanide, or tertiary phosphanes) are reviewed.[8]

The preparation of organic polysulfanes usually results in mixtures of R_2S_n molecules. Even after pure substances have been obtained these tend to decompose by equilibration with other chain lengths or ring sizes, and by formation of elemental sulfur (equations 116 and 117).

$$2R_2S_n \rightleftharpoons R_2S_{n+x} + R_2S_{n-x} \qquad (116)$$

$$R_2S_{n+x} \longrightarrow R_2S_n + S_x \qquad (117)$$

$$x = 6 - 8$$

These reactions are accelerated by light, heat, and numerous catalysts of which strong nucleophiles are most effective. In addition, silica gel, alumina, and other porous and finely divided solids catalyze the above reactions. Therefore, conventional liquid chromatography, including paper chromatography, may yield erroneous results. The same holds for gas chromatography since the low vapor pressure of many organic polysulfanes requires high injector and column temperatures. Equally doubtful is mass spectrometry (MS) if the sample has to be heated to evaporate or if a heated ion source is used. Reliable quantitative data about a mixture of organic polysulfanes can best be obtained by either ^{1}H NMR spectroscopy or reversed-phase high-pressure liquid chromatography (RP-HPLC).

In a chainlike compound R–S_n–R, the chemical shift of the protons of R will depend on the chain length n. This is most obvious from the NMR spectra of the inorganic sulfanes H_2S_n, which in this manner have been identified with n ranging up to 35.[234] In other words, the chemical shift of the chain-terminating hydrogen atoms depends on the chain length. Similar situations can be expected for alkyl-substituted sulfanes (methyl, t-butyl, i-propyl), which exhibit simple spectra.[235] In the case of aryl substituted or cyclic organic polysulfanes, the spectra may be too complex to analyze these mixtures of homologous compounds spectroscopically. In such cases, HPLC is the method of choice.

RP-HPLC is a particularly gentle separation technique that may be used for qualitative and quantitative analysis of mixtures of R_2S_n molecules. The resolution power of HPLC approaches that of gas chromatography if stationary phases of low particle size (10, 5, or 3 µm) are used. The most widely used stationary phase is the 'C18' phase, that is, silica gel covered by $-SiMe_2(C_{18}H_{37})$ groups that are linked to the surface by very strong disiloxane bonds (Si–O–Si). This surface modification is produced by reaction of silanol groups (SiOH) of silica gel with chlorosilanes (Cl–SiR_3).[236] The long alkyl chain of $C_{18}H_{37}$ renders the formerly polar surface of the silica gel totally unpolar, and if all OH groups have reacted, a chemically very inert but still highly porous material is obtained. The mobile phase then has to be polar and methanol or mixtures based on methanol are very often applied.[237,238]

All sulfanes have a very strong ultraviolet (UV) absorption near 220 nm, and therefore application of a UV absorbance detector operating at any wavelength between 220 and 260 nm is recommended. The high extinction coefficients of polysulfanes result in a very low detection limit, and very dilute samples may therefore be applied. In this way, no problems are to be expected with the low solubility of sulfur-rich species in the polar mobile phase. The total sample concentration may be as low as 0.1 mg L^{-1} using a 10 µL loop injector and a column of 8–10 mm inner diameter.

The main problem in HPLC is the peak assignment. LC–MS systems are available but are far from being standard equipment. Some help may be expected from a diode-array detector, which allows the measurement of the UV–Vis absorption spectrum, for example, in the range 200–800 nm, on-line during chromatographic separation. Unfortunately the absorption spectra of organic polysulfanes[17,18,32,160,239,240] are not very specific. The measurement of absorption spectra under static conditions cannot be recommended since polysulfanes rapidly decompose or react with the solvent on UV irradiation.

Peak identification normally requires reference substances. If a homologous series of compounds R_2S_n is to be analyzed, it is of great help that the retention behavior depends systematically on both R and on the number n of sulfur atoms in the ring or chain. For an unpolar molecule, the retention time t_R will be larger if either R or n is larger than in a reference molecule. It is probably the surface area of a molecule that determines the retention behavior,[236–238] in other words, t_R of Et_2S_3 is larger than that of Me_2S_3, and Me_2S_4 elutes later than Me_2S_3. Even the small size or surface area difference between isomeric alkyl groups (n-butyl, i-butyl, t-butyl) results in different retention times.

In this context, the capacity factor $k' = (t_R - t_0)/t_0$ is important: t_0 is the 'dead' time of the chromatographic system, roughly the time the pure eluent needs to travel from the injector to the detector. It may be determined by injection of a methanol/water mixture since H_2O does not show any significant retention in a C18 column. For cyclic[115,137,138,160] and acyclic[24–26,48,50,237,238] organic polysulfanes, it has been found that the logarithm of the capacity factor is a linear function of the number of sulfur atoms (equation 118).

$$\ln k' = a \times n + b \qquad (118)$$

This relationship was first observed in gas chromatography of alkylpolysulfanes.[92,93] As an example, experimental retention data of bis(triphenylmethyl)polysulfanes, $(Ph_3C)_2S_n$, are shown in Figure 4. These linear relationships are extremely helpful since they allow the identification of members of a homologous series by means of inter- and extrapolation. However, sometimes a long series is characterized by *two* linear relationships of slightly differing slope, one for the first three or four members and another one for the higher members.

The retention times and capacity factors depend, of course, on the chromatographic system and its operating

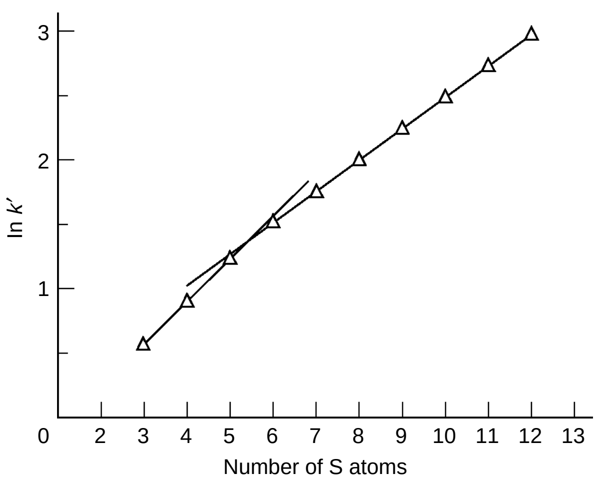

Figure 4 Relationship between the logarithm of the capacity factor k' and the number of sulfur atoms in $(Ph_3C)_2S_n$ molecules ($n = 3-13$)[50]

conditions (flow, eluent composition, temperature, column length, particle size, type of stationary phase, etc.). A more independent measure of the retention behavior is provided by the Kovats' retention indices, which are well known in gas chromatography. This index simply relates the retention time of a substance to the retention time of reference substances measured under identical conditions. The tremendous advantage of the retention index is that it is independent of the chromatographic system and only depends on the eluent composition, the type of stationary phase, and the temperature. Therefore the retention index is a similar characteristic parameter to the chemical shift in NMR spectroscopy, which is also related to the resonance signal of a reference substance.

A few retention index values of organic polysulfanes have been published.[46–48,160] They may be calculated as follows.[241] The homocyclic sulfur molecules S_6, S_8, S_9, and S_{10} are recommended as reference substances because they are easy to make (see below), have high extinction coefficients in the UV,[242] and retention times similar to those of organic polysulfanes.[243–244] To these molecules, the sulfur-based retention index values (RS values) of 600 (S_6), 800 (S_8), 900 (S_9), and 1000 (S_{10}) are assigned by definition.[241] A plot of $\ln k'$ of these four molecules versus these defined RS values gives a straight line according to equation (119).

$$\ln k' = a \times \text{RS} + b \qquad (119)$$

After the parameters a and b have been determined, they are used to derive the RS value of the unknown substance. This substance is measured under identical conditions as for the sulfur rings, the capacity factor is calculated, and $\ln k'$ is used to calculate the RS value of the unknown substance from equation (119). These RS data are practically identical when determined from retention data measured with different HPLC systems in different laboratories.

The necessary solution of S_6, S_8, S_9, and S_{10} in CS_2 is prepared as follows: commercial elemental sulfur (1 g) is heated in a test tube to near 200 °C (oil bath) for 2.5 h, cooled slowly to ca. 130 °C (freezing point 115 °C), and poured into liquid nitrogen, resulting in a fine yellow powder that is extracted by CS_2 at 20 °C. The yellow solution contains all sulfur rings from S_6 to S_{25} and is stable at 4 °C in the dark if not too concentrated.[64,243–245] The peak assignment is straightforward since S_8 gives the tallest peak (besides CS_2), which is preceded by S_6 and S_7 and followed by S_9, S_{10}, and so on.[243–244] However, S_7 is not used for the calculations of RS values since it does not fit equation (119) very well.

4.1 Examples

Chainlike homologous polysulfanes with between 2 and 23 sulfur atoms have been separated by RP-HPLC,[24–26,48,50,237,238,246] while cyclic isopropylpolysulfanes Me_2CS_n, with n ranging from 5 to 34, have been separated by the same technique.[16] Furthermore, alkoxythiocarbonylpolysulfanes, $[ROC(S)]_2S_n$ (xanthates),[247] and methylthiocarbonylpolysulfanes, $[RSC(O)]_2S_n$, as well as alkoxycarbonylpolysulfanes[57] may be analyzed by RP-HPLC. The separation of cyclic methylene sulfanes by RP-HPLC has also been reported and the impact of the ring size, number of sulfur atoms, and number of C–S bonds per molecule on the

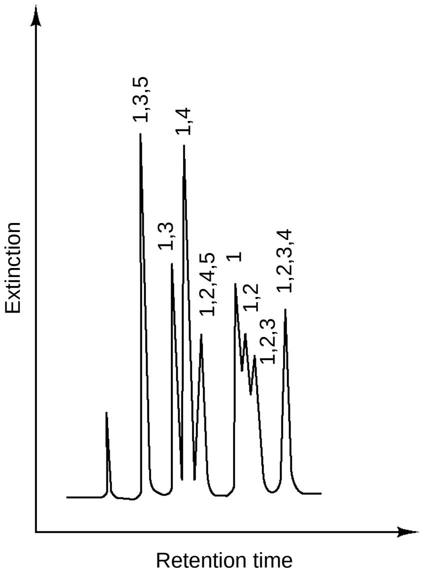

Figure 5 Chromatographic separation (RP-HPLC) of eight six-membered methylene sulfanes $(CH_2)_{6-n}S_n$ with $n = 1$, 2 (3 isomers), 3 (2 isomers), and 4 (2 isomers). The numbers give the positions of the S atoms in the ring, for example, '1,3' means '1,3-dithiane'. (Reproduced by permission of Verlag der Zeitschrift für Naturforschung from Steudel and Strauss[115])

retention time has been elucidated.[115] In Figure 5 the HPLC separation of six-membered methylene sulfanes, $(CH_2)_{6-n}S_n$ with $n = 1-5$, is shown: even the isomeric dithianes 1,2-, 1,3-, and 1,4-$(CH_2)_2S_4$ are well separated. Since the retention time is an unambiguous function of the ring size, of the number of S atoms, and of the number of heteronuclear bonds, the retention of new cyclo-methylenesulfanes can be predicted.[115]

It should be mentioned here that Raman and X-ray absorption near edge spectroscopy (XANES) spectroscopy are also suitable analytical techniques to analyze mixtures of organic polysulfanes.[11]

5 REACTIONS OF ORGANIC POLYSULFANES

Of the many reactions known for polysulfanes, only the following types will be dealt with since they are of general importance for inorganic and organic polysulfur compounds: interconversion and sulfur transfer reactions, nucleophilic displacement reactions, and oxidation reactions with conservation of chain length.

5.1 Interconversion Reactions

The formal exchange of sulfur atoms between like molecules containing S–S bonds is called interconversion; examples are given in equations (120) and (121).

$$2S_8 \rightleftharpoons S_7 + S_9 \tag{120}$$

$$2R_2S_4 \rightleftharpoons R_2S_3 + R_2S_5 \tag{121}$$

These reactions are reversible and proceed at moderate temperatures (0–120 °C) when compounds with cumulated S–S bonds (polysulfanes, elemental sulfur) are considered. The activation energy and therefore the rate of reaction at a certain temperature very much depend on the particular compound. Interconversion reactions are promoted by UV radiation as well as by cationic, anionic, and nucleophilic catalysts. The reaction mechanisms will, of course, be different in these various cases. The various reaction types possible under noncatalyzed conditions and with exclusion of light have been critically reviewed by Steudel in 1982.[248] Originally it had been thought that homolytic bond scission is the first and rate-determining step in all cases. Dissociation energies of cumulated S–S bonds[1–2] are, however, above 120 kJ mol^{-1}, while some interconversion reactions proceed slowly even at ambient or at only slightly elevated temperatures. Therefore, several alternatives for a formal exchange of S atoms between molecules have been proposed.[248]

Isomerization of an unbranched sulfur chain to form a branched structure is one possibility (equation 122) to start a sulfur transfer reaction.

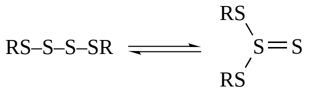

(122)

The terminal sulfur atom of the thiosulfoxide may then be transferred to a neighboring molecule (equation 123).

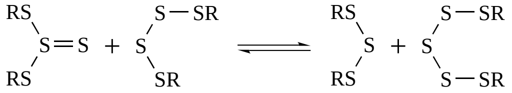

(123)

Such isomerization reactions are, of course, endothermic but the reaction energy in the case of sulfur-rich molecules is lower than ca. 60 kJ mol^{-1}.[206,207,249] Unfortunately, the activation energy is known only for disulfanes. However, in the case of ethylene episulfide a similar sulfur atom transfer has been shown to be the lowest energy pathway for the decomposition to elemental sulfur and an alkene with an activation enthalpy of 110 kJ mol$^{!1}$.[250] Compounds of type X–S(=S)–X are stable at 20 °C if X = F or OR.

Another route for the exchange of sulfur atoms between polysulfanes involves a σ-sulfurane type intermediate as shown in Scheme 2.

This potential pathway has recently been studied in detail.[251] Although sulfuranes of the type SX_4 are known in large numbers with X = F, Cl, OR, R (=organyl),[252–254] the reaction shown in Scheme 2 requires an activation energy of more than 250 kJ mol^{-1} and therefore cannot explain any interconversion reaction of organic polysulfanes at or near room temperature.[251]

Interconversion reactions at temperatures above 100 °C will probably proceed via a radical chain reaction mechanism,[248] as illustrated by equations (124–127).

$$\text{RS–S–S–SR} \rightleftharpoons 2\text{RS–S}\cdot \tag{124}$$

$$\text{RS–S}\bullet + R_2S_4 \rightleftharpoons R_2S_3 + \text{RS–S–S}\bullet \tag{125}$$

$$\text{RS–S–S}\bullet + \text{RS–S}\bullet \rightleftharpoons R_2S_5 \tag{126}$$

$$2\text{RS–S–S}\bullet \rightleftharpoons R_2S_6 \tag{127}$$

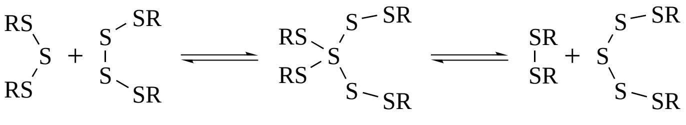

Scheme 2

Most likely, light-induced interconversion reactions also proceed by a radical chain reaction. The formation of radicals upon irradiation of elemental sulfur has been demonstrated by ESR (electron spin resonance) spectroscopy,[137,138] and the isomerization of chainlike S_2Cl_2 to the thiothionyl chloride isomer $Cl_2S{=}S$ has also been achieved by irradiation.

5.2 Sulfur Transfer Reactions

It has been known for some time that on heating certain organic di- or polysulfanes seemingly split off S_2, which may then add to a substrate to form another disulfane.[151–154] Only recently, transfer reactions for the S_3 and even the S_3O unit have been observed.[196] When a substituted ('labeled') norbornanetrisulfane is heated with norbornene in benzene to 100 °C, a clean transfer of the S_3 unit is observed for R = phenyl (equation 128).

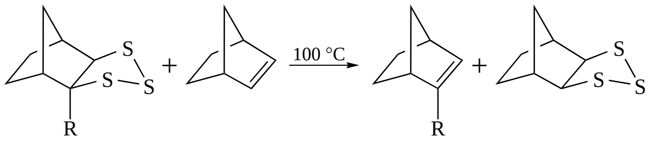

(128)

The rate and the yield of the reaction shown in equation (128) depend on the nature of R and of the alkene to which the S_3 unit is to be transferred. If this norbornene is also substituted in the 2-position the yields differ greatly depending on the substituent: phenyl results in high, methyl in low, and methoxycarbonyl in intermediate yields. When an unsymmetrically-substituted norbornadiene is used as acceptor molecule, the two double bonds react at the same rate to give equal amounts of the two trithiolanes. Most probably, the transfer reaction proceeds by a concerted bimolecular mechanism.

Norbornanetrisulfane may be oxidized by MCPBA (3-chloroperbenzoic acid) to give the two isomeric compounds trisulfane 1-oxide and 2-oxide.[196] The 2-oxide may also be prepared from norbornanedithiol and thionyl chloride. Heating the substituted 1-oxide in benzene with norbornene for 12 h to 100 °C resulted in a 50% S_3O transfer (equation 129).

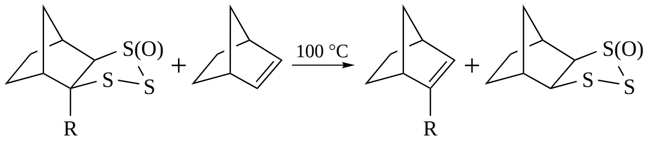

(129)

For other thermally induced sulfur transfer reactions, see Section 2.2.6.

5.3 Nucleophilic Displacement Reactions at the Sulfur–Sulfur Bond

A strong *Nucleophile* (Nu) may open an S–S bond as shown in equation (130).

$$\mathrm{Nu} + \mathrm{RS{-}S{-}S{-}SR} \rightleftharpoons \mathrm{Nu{-}\overset{+}{S}{-}SR} + \mathrm{RS{-}S^-} \qquad (130)$$

The anion RSS^- has been displaced. The relative strengths of various nucleophiles that determine the position of the equilibrium of equation (130) may be given by their 'thiophilicity'. This area has been pioneered by Foss and expertly reviewed by Davis.[255,256] The following species are very strong thiophiles that are able to open any sulfur–sulfur single bond in a polysulfane in a reaction of the type shown in equation (130): normal thiolates (RS^-), HS^-, S_n^{2-} ($n = 1, 2, \ldots$), SO_3^{2-}, CN^-, R_3P (R = alkyl, aryl, alkoxy, dialkylamino, etc.). The corresponding reactions are depicted in equations (131–135).

$$\mathrm{RS^- + R'_2S_3 \longrightarrow R'S^- + RR'S_3} \qquad (131)$$

$$\mathrm{HS^- + R_2S_3 \longrightarrow S_2{}^{2-} + H^+ + R_2S_2} \qquad (132)$$

$$\mathrm{2SO_3{}^{2-} + R_2S_4 \longrightarrow 2S_2O_3{}^{2-} + R_2S_2} \qquad (133)$$

$$\mathrm{2CN^- + R_2S_3 \longrightarrow 2SCN^- + R_2S} \qquad (134)$$

$$\mathrm{R_3P + R'_2S_3 \longrightarrow R_3PS + R'_2S_2} \qquad (135)$$

As is apparent, some reagents desulfurize to the level of disulfanes, while others even give monosulfanes, R_2S. In the case of R_3P, it depends on R whether di- or monosulfanes are formed (see below). Such reactions display second order kinetics. The rate very much depends on the steric requirements and on the strain of the S–S bonds to be broken. For example, methylsulfenyl thiocyanate reacts with cyanide according to equation (136).

$$\mathrm{Me{-}S{-}SCN + CN^- \longrightarrow Me{-}SCN + SCN^-} \qquad (136)$$

However, *t*-butylsulfenyl thiocyanate does not react with cyanide. Similar observations have been made with the reactions shown in equations (137) and (138), which have been studied using labeled sulfur atoms.

$$\mathrm{R{-}S{-}S{-}R + R\overset{*}{S}{}^- \rightleftharpoons R{-}S{-}\overset{*}{S}{-}R + RS^-} \qquad (137)$$

$$\mathrm{R{-}S{-}SO_3{}^- + \overset{*}{S}O_3{}^{2-} \rightleftharpoons R{-}S{-}\overset{*}{S}O_3{}^- + SO_3{}^{2-}} \qquad (138)$$

With R = *t*-butyl the relative rates are orders of magnitude smaller than with R = Me. Strained ring systems react much faster with thiolates than comparable chainlike compounds. For example, 1,2-dithiolane reacts about 5000 times faster with *n*-butylthiolate as does bis-*n*-butyldisulfane. The thiophilicity of thiolate ions (RS^-) very much depends on R: 2,4-dinitrophenylthiolate is much less thiophilic than phenylthiolate, which in turn is less thiophilic than ethylthiolate.[255,256] In unsymmetrical disulfanes, RSSR′, the less basic RS^- group is displaced by an incoming nucleophile like cyanide, sulfite, or thiolate.[255,256] The nucleophiles R_3N, OH^-, $S_2O_3{}^{2-}$, and SCN^- are too weak to open an ordinary S–S bond.

These reactivities can be explained by the oxidative dimerization potential E_o derived for equation (139) and the base strength of the nucleophile.

$$2XS^- \rightleftharpoons X–S–S–X + 2e^- \qquad (139)$$

According to a rule by Foss,[255,256] the anions of more positive E_o will displace anions of lower E_o. Aqueous thiosulfate is not able to open S–S bonds and therefore the equilibrium shown in equation (140) is completely to the left.[255,256]

$$S_2O_3{}^{2-} + R_2S_3 \rightleftharpoons S_3O_3{}^{2-} + R_2S_2 \qquad (140)$$

The situation with OH^- and R_3N is similar. Both nucleophiles are too weak thiophiles to open an S–S bond. However, sulfur chemists know that alkalies and amines tend to decompose polysulfur compounds very effectively. This is due to secondary reactions of these nucleophiles with the ubiquitous traces of either H_2S or SO_2, resulting in the formation of the strong thiophiles HS^- or $SO_3{}^{2-}$ (equations 141–144).[255,256]

$$H_2S + R_3N \rightleftharpoons HS^- + R_3NH^+ \qquad (141)$$

$$H_2S + OH^- \rightleftharpoons HS^- + H_2O \qquad (142)$$

$$SO_2 + 2OH^- \rightleftharpoons SO_3{}^{2-} + H_2O \qquad (143)$$

$$SO_2 + H_2O + 2R_3N \rightleftharpoons SO_3{}^{2-} + 2R_3NH^+ \qquad (144)$$

Sulfide and polysulfide ions have very high thiophilicities and will displace thiolate from aryldisulfanes. The reaction of sodium sulfide with S_8 in alkaline methanol is fast even at −78 °C![255,256]

The reactions of tertiary phosphanes with elemental sulfur have been studied kinetically in detail.[21] While trialkylphosphanes and, even more so, trialkoxyphosphanes react with great vigor, certain arylphosphanes react slowly enough for kinetic data to be measured. It was found that diphenyl(2-tolyl)phosphane reacts with homocyclic sulfur molecules S_n ($n = 6, 7, 8, 12$) in CS_2 at −12 to +35 °C in a second order reaction to give $R_2R'PS$. The activation energies (in $kJ\,mol^{-1}$) (*see Activation*) are: 51 (S_6), 40 (S_7), 69 (S_8), and 46 (S_{12}). At 20 °C, the relative reactivities ($S_8 = 1$) are as follows:

$$S_6{:}S_7{:}S_8{:}S_{12} = 10\,700{:}178{:}1{:}187.$$

Similar dramatic differences are to be expected for cyclic and linear polysulfanes as a function of ring size and inductive as well as steric effects of the substituents. In the case of cyclic species the first and rate-determining step will always be the opening of the ring, resulting in a highly reactive zwitterion, which is then rapidly degradated by additional phosphane molecules (equation 145).[255,256]

$$R_3P + S_8 \longrightarrow R_3\overset{+}{P}–S_7–\overset{-}{S} \xrightarrow{7R_3P} 8R_3PS \qquad (145)$$

The polarity of the solvent will also play an important role.

The desulfurization of di- and trisulfanes by a variety of tertiary phosphanes has repeatedly been studied in detail. In the case of trisulfanes, the initial step may be an attack of the phosphane on either the central sulfur atom or on one of the terminal S atoms (equations 146 and 147).[257,258] In both cases, a pair of ions is formed.

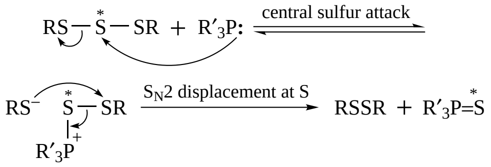

(146)

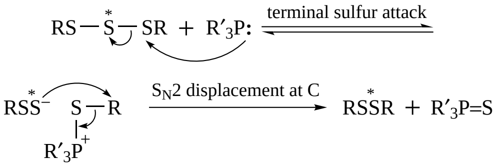

(147)

In the second and irreversible steps of these reactions, the anions induce a nucleophilic displacement at the cations as follows: in equation (146) the RS^- ion attacks the terminal sulfur with formation of R_2S_2, while in equation (147), the RSS^- ion attacks the carbon atom linked to the terminal sulfur. In the first case, the central sulfur atom is eliminated, while in the second case one of the terminal S atoms is eliminated. Radiochemical experiments which used trisulfanes containing the central S atom labelled by ^{35}S showed that desulfurization of dialkyltrisulfanes by triarylphosphanes results in 91–99% removal of central sulfur, essentially independent of solvent polarity (Et_2O or MeCN), reaction temperature (0–50 °C), type of trisulfane (dibenzyl or dipropyl), and *para* substituents on Ar_3P. In sharp contrast to this, desulfurization of dialkyltrisulfanes by tris(dialkylamino)phosphanes results in preferential removal of a terminal sulfur atom in Et_2O, while in MeCN more than the statistical amount (33%) of central sulfur is removed. When sterically-hindered trisulfanes are used, the rate of desulfurization decreases and the percentage of central sulfur atom removal increases, as expected.[255,256]

Initially, a phosphane attacks a trisulfane both at the central and the terminal sulfur atoms, and there is evidence that the two resulting phosphonium salts shown in equations (146) and (147) exchange their anions (equation 148).

$$[R'_3\overset{+}{P}–SR][RS\overset{-}{S}] + [R'_3\overset{+}{P}–SSR][R\overset{-}{S}] \rightleftharpoons [R'_3\overset{+}{P}–SR][R\overset{-}{S}] + [R'_3\overset{+}{P}–SSR][RS\overset{-}{S}] \qquad (148)$$

The ion pairs on the right side of equation (148) may dissociate into R_2S_2, R_2S_4, and $R_3'P$, and the formation of tetrasulfane was observed. In other words, tertiary phosphanes (including Ph_3P), like other strong nucleophiles, catalyze the exchange and interconversion (equations 149 and 150), which has been observed.[255,256]

$$\mathrm{RSSR} + \mathrm{R'SSR'} \rightleftharpoons 2\mathrm{RSSR'} \qquad (149)$$

$$2\mathrm{R_2S_3} \rightleftharpoons \mathrm{R_2S_2} + \mathrm{R_2S_4} \qquad (150)$$

It depends on the phosphane and the solvent whether equation (146) or (147) prevails, and whether the final product will be a di- or monosulfane. The latter are usually obtained using $(R_2N)_3P$, but only in the case of dialkylsulfanes.[255,256] Many examples of nucleophilic displacement reactions can be found in Section 2 of this article, for example, equations (54), (56), (61), (77)–(79), (82), (85), and (86).

It has been reported that $RhH(PPh_3)_4$ in the presence of 1,2-bis(diphenylphosphino)ethylene catalyzes the exchange of sulfur atoms between elemental sulfur and organic polysulfanes at room temperature.[259] During this reaction traces of phoshpine sulfides may be formed which are strong nucleophiles.

5.4 Oxidation of Polysulfanes to Polysulfane Oxides

Sulfane oxides are compounds of type $R_2S_nO_m$ ($n > 1$, $m = 1, 2, 3\ldots$) with the oxygen atoms present as sulfoxide or sulfone groups. For the nomenclature of organic sulfur-oxygen compounds see Table 2; for reviews on oxidized sulfur chains and rings, see Steudel.[260,261] Disulfane 1-oxides, RS(O)–SR, are also known as thiosulfinates and the 1,1-dioxides are usually termed as thiosulfonates. Trisulfane 1-oxides and 1,3-dioxides, as well as tetrasulfane 1-oxides and 1,4-dioxides, have been obtained by stepwise oxidation of the corresponding sulfanes by peroxy acids (equations 151–153).[67,101,123,127,262–265]

$$\mathrm{R_2S_3} + \mathrm{CF_3CO_3H} \begin{cases} \xrightarrow{1:1} \mathrm{R{-}SO{-}S{-}S{-}R} \\ \xrightarrow{1:2} \mathrm{R{-}SO{-}S{-}SO{-}R} \end{cases} \qquad (151)$$

$$\mathrm{R_2S_4} + \mathrm{CF_3CO_3H} \begin{cases} \xrightarrow{1:1} \mathrm{R{-}SO{-}S{-}S{-}S{-}R} \\ \xrightarrow{1:2} \mathrm{R{-}SO{-}S{-}S{-}SO{-}R} \end{cases} \qquad (152)$$

$$\mathrm{R_2S_3} + 4\mathrm{R'CO_3H} \longrightarrow \mathrm{R{-}SO_2{-}S{-}SO_2{-}R} + 4\mathrm{R'CO_2H} \qquad (153)$$

With bulky substituents, the oxidation of the central sulfur atom has been observed.[266] Dimethyldioxirane and ozone (at −78 °C) may also be used to prepare such sulfane oxides.[196,266,267]

The crystal and molecular structures of disulfane 1-oxides (R = 4-tolyl)[195] and of trisulfane 2-oxides[84,195,196] have been determined by X-ray diffraction. The latter compounds are usually obtained from thionyl chloride and thiols (RSH) in ether or in the presence of pyridine (equations 154 and 155).[81–83] Unsymmetrically-substituted trisulfane 2-oxides, RS–SO–SR′, are accessible by a stepwise condensation of $SOCl_2$ with first RSH and then R′SH; the intermediate RS–SO–Cl has been isolated as a yellow solid (R = 2-naphthyl). RSSOCl reacts at 0 °C in ether with thiols to give RS–SO–SR′.[83]

$$\mathrm{RSH} + \mathrm{Cl{-}SO{-}Cl} \longrightarrow \mathrm{R{-}S{-}SO{-}Cl} + \mathrm{HCl} \qquad (154)$$

$$\mathrm{R{-}S{-}SO{-}Cl} + \mathrm{HSR'} \longrightarrow \mathrm{R{-}S{-}SO{-}S{-}R'} + \mathrm{HCl} \qquad (155)$$

The structure of the $-S_3O-$ group of trisulfane 2-oxides is similar to the structure of $SOCl_2$ (symmetry C_s); the S–S bond distances are considerably longer (ca. 213 pm)[84,195] than in trisulfanes (ca. 204 pm); see Section 3.

Oxidation of organic polysulfanes by an excess of peroxy acid results in disulfones (polysulfane tetroxides) (equation 153).[101] Polysulfane 1,1-dioxides (monosulfones) may be prepared by reaction of monoorganylthiosulfates with sulfenyl chlorides (equation 156).[268–270]

$$\mathrm{R{-}SO_2{-}SK} + \mathrm{ClSR'} \longrightarrow \mathrm{R{-}SO_2{-}S{-}S{-}R'} \qquad (156)$$

The molecular structures of several polysulfane tetroxides of this type have been elucidated by X-ray diffraction on single crystals.[197,198] The S–S bonds between the sulfone groups and the neighboring sulfane sulfur are weaker (210–214 pm) than ordinary S–S single bonds (205 pm).[1]

6 NATURAL OCCURRENCE OF ORGANIC POLYSULFANES AND THEIR BIOLOGICAL ACTIVITY

It is well known that disulfane-containing compounds, such as proteins, hormones, lipoic acid, enzymes, and other products, occur naturally and many studies on their biochemical role have been published.[271] Protein folding influenced by –S–S– bridges of cystine has been studied intensively, and it is generally accepted now that introducing disulfane bonds into proteins thermally stabilizes the folded state.

It is less well known that tri-, tetra-, penta-, and even hexasulfanes also occur in organisms or materials produced from them, including peptides. In this section, a brief overview will be presented of chainlike and cyclic organic polysulfanes, which have so far been isolated from or detected in biological materials. For sulfur-rich peptides, see refs.[272,273]

An extensive review on organic sulfur compounds from marine organisms is available.[274]

6.1 Chainlike Organic Polysulfanes

Table 5 summarizes the chainlike polysulfanes $R{-}S_n{-}R$, which have been identified in various natural sources or materials prepared from them. The sulfur chain length varies

Table 5 Naturally occurring chainlike bis-organyl polysulfanes, $R^1-S_n-R^2$

R^1	R^2	n	Source
Me[275–277]	R^1	3, 4	Shiitake mushroom
Me[282]	R^1	3	Geotrichum candidum
Me[277]	R^1	3	Oil made from *Ferula asafoetida*
Me[277]	2-Bu	3	Oil made from *Ferula asafoetida*
2-Bu[277]	R^1	3, 4	Oil made from *Ferula asafoetida*
Me, Et, Pr[283]	Me, Et, Pr	3	Durian fruit
Allyl[278,279]	R^1	3–6	Garlic oil
Alanyl[280]	R^1	3, 4	Wool hydrolysate (acidic)
3-Oxoundecyl[281]	R^1	3, 4	*Dictyopteris plagiogramma* (Hawaiian alga)
Methyl[284]	Complex structure	3	Calichemicin *(Micromonospora echinospora)*

between 2 (not shown) and 6, while the organic residues R are saturated or unsaturated alkyl groups or derivatives of them.[275–281]

Asafetida is the oleogum resin exudate obtained from certain *Ferula* species. It has a characteristic strong odor and is used as a flavoring in a variety of foods. The volatile oil obtainable by steam distillation is abundant in sulfur compounds. The flavor of asafetida is largely due to 2-butyl 1-propenyl disulfane, 1-methylthiopropyl 1-propenyl disulfane and 2-butyl 3-methylthioallyl disulfane, but in addition the four tri- and tetrasulfanes mentioned in Table 5 have been identified as minor components by GC/MS analysis.[277]

The edible Shiitake mushrooms (*Lentinus edodes*) are another rich source of sulfur compounds, cyclic and noncyclic. Blending of the fresh mushrooms with water at $\mathrm{pH} = 7$ followed by pentane extraction and GC/MS analysis of the extract showed Me_2S_3 as one of the major constituents (besides various disulfanes).[275,276] When the blending was carried out at $\mathrm{pH} = 9.0$, at which enzymes have their maximum activity, additional S compounds like Me_2S_4 and cyclic species (see below) were extracted and detected by GC/MS.[275,276] This result clearly shows that the work-up procedure does influence the kind of products to be detected.

A large number of organic sulfur compounds have been detected in extracts or distillates prepared from garlic, onions, or other *Allium* species. This chemistry has been reviewed by Block.[278,279] Polysulfanes have been detected in many of these preparations but most recent results show that fresh extracts of garlic, prepared under mild conditions (20 °C), did not show any polysulfanes R–S_n–R ($n > 2$) when analyzed by RP-HPLC analysis.[278,279]

However, commercial garlic oil, prepared by steam distillation of garlic homogenizates, did show bis-allyl tri-, tetra-, penta-, and hexasulfanes (Table 5), detected by HPLC and GC/MS analysis. Detailed investigations showed that these polysulfanes probably originate from the very reactive bis-allyl disulfane by thermal cleavage of the S–S and C–S bonds and recombination of the RS· and RS_2· radicals as well as by interconversion of the polysulfanes in reactions of the type in equation (157).

$$2R_2S_n \rightleftharpoons R_2S_{n-x} + R_2S_{n+x} \qquad (157)$$

When garlic is extracted by methanol, allyl methyl trisulfane is formed.[275,279] Unsaturated polysulfanes from *Allium* species inhibit the growth of certain tumors.[278,279]

Tri- and tetrasulfanes with the unusually long, oxidized alkyl chain C_8H_{17}–CO–C_2H_4– as substituents have been isolated as colorless needles from methanol/chloroform extracts of a Hawaiian alga (Table 5) by LC on silical gel and gel permeation chromatography followed by crystallization.[281] These compounds were characterized by ^{1}H-NMR, MS, and UV spectroscopy.

It also should be mentioned that bis-alanyl tri- and, to a smaller degree, tetrasulfane have been detected in acidic wool hydrolysates, but it is not clear whether the corresponding amino acid, $[HO_2C–CH(NH_2)–CH_2–]_2S_3$, is part of the wool structure or is formed from cystine during hydrolysis.[280]

6.2 Cyclic Organic Polysulfanes

Lenthionine (1,2,3,5,6-pentathiepane) was the first cyclic polysulfane isolated from an organism, however, in the very first report it was stated that this compound is not present in Shiitake mushrooms, but is formed from an unknown precursor by the action of an enzyme when the mushroom was immersed in water overnight.[121,122] From 5 kg dried mushrooms, 0.44 g crystalline lenthionine (mp 61 °C) were obtained; the structure (see Table 6) was established by MS[121,122] and X-ray diffraction on a single crystal.[219] In addition, hexathiepane (Table 6) and 1,2,4,6-tetrathiepane were also isolated from the aqueous Lentinus edodes mushroom.[121,122] All three cyclic methylene sulfides can easily be prepared from CH_2Cl_2 and aqueous sodium polysulfide.[121,122] When fresh Lentinus edodes was directly extracted by chloroform (which inactivates the enzymes), fractionated by LC on silica gel, and analyzed by GC/MS or MS, the only polysulfanes detected were dimethyl trisulfane, 1,2,3,5-tetrathiane and lenthionine.[275,276] However, when the fresh mushrooms were blended at room temperature with water for 3 min and the pH adjusted to 9.0, chloroform extraction yielded 18 organic sulfur compounds including the ones mentioned above.[275,276] They all are believed to originate from lentinic acid by enzymic activity via CH_2S_2 as a reactive intermediate.[192,275,276]

Table 6 Naturally Occurring Cyclic Bis-organyl Polysulfanes

Compound	Source
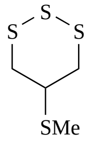 5-Methylthio-1,2,3-trithiane	*Chara globularia* (green alga)[285,286]
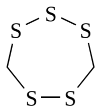 Lenthionine	*Chondria californica* (red alga)[285–287] *Parkia speciosa* (mimosaceae species)[288] *Lentinus edodes* (Shiitake mushroom)[114,203,241]
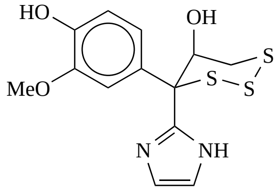	*Aplidium* sp. D (ascidian)[289]
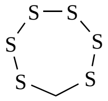 Hexathiepane 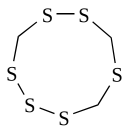 Hexathionane 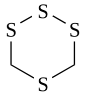 1,2,3,5-Tetrathinane	*Lentinus edodes* (Shiitake mushroom)[121,122,275,276]
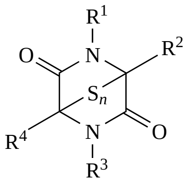 3,6-Epipolythiopiperazine-2,5-dione	
$n = 3$; $R^1 = R^3 = Me$; $R^2 = CH_2OH$; $R^4 = CH_2Ph$	Fungus
Sporidesmine E	*Pithomyces chartarum*[190,191,194,290]
$n = 4$; $R^1 = R^3 = Me$; $R^2 = CH_2OH$; $R^4 = CH_2Ph$	*Hyalodendron* sp. (fungus); *Penicillium turbatum*[289]
Sporidesmine G	*Pithomyces chartarum*[190,191,194]
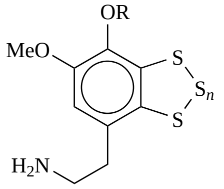	
$n = 3$; R = H Lissoclinotoxin A	*Lissoclinum perforatum* (ascidian)[291]
$n = 3$; R = Me Varacin	*Lissoclinum vareau* (ascidian)[292–294]

Lenthionine and related cyclic methylene disulfanes of ring sizes 6–12 have also been obtained from the alga *Chondria californica* and from the seed of the mimosacea *Parkia speciosa*.[287,288]

Derivatives of 1,2,3-trithiane as well as 1,2-dithiolane are known for their biological activity.[268–270,295] Two naturally occurring trithiane derivatives are shown in Table 6. 5-Methylthio-1,2,3-trithiane has been isolated by gas-phase isopentane extraction from the green alga *Chara globulares* and identified by GC/MS, ^{1}H-MR and UV spectra.[285,286] Its synthesis is straightforward.[285,286] The second natural trithiane derivative has been extracted by methanol/water from the New Zealand ascidian *Aplidium* sp. D and isolated after RP-HPLC as a yellow gum.[289] This compound shows anti-microbial, anti-leukemic, and cytotoxic properties in vitro.[289]

Chemically related to the trithianes is the benzo-1,2,3-trithiane derivative lissoclinotoxin A, shown at the bottom of Table 6. It has been obtained by methanol extraction of the tunicate *Lissoclinum perforatum* followed by preparative HPLC on SiO_2, and forms a yellow solid of mp 245–250 °C.[291] In vitro, this material exhibits potent antimicrobial, antifungal, and modest cytotoxic activities.[291] The benzopentathiepin derivative varacin (Table 6) has also been obtained from a tunicate; this compound bears obvious structural and biosynthetic relationships to dopamine.[292–294]

Sporidesmin is a naturally occurring polycyclic disulfane that contains the piperazinedione ring shown in Table 6. The corresponding trisulfane has been termed sporidesmin E. It has been obtained by extraction of *Pithomyces chartarum* followed by LC on silica gel.[194] From the same organism, sporidesmin G, the corresponding tetrasulfane, has been obtained.[190,191] These compounds are also biologically active.

The piperazinedione framework is also present in hyalodendrin, which is an epidisulfane with the substituents given in Table 6. The corresponding epitrisulfane has been isolated from cultures of an unidentified fungus,[290] while the epitetrasulfane was obtained from chloroform extracts of fermentations of *Hyalodendron* sp.[296,297] it is also produced by *Penicillium turbatum*.[296,297] In all cases, however, it is unknown whether these polysulfanes are present in the organisms, or resulted from the work-up procedure by decomposition of the corresponding disulfane. Such conversion reactions have in fact been observed.[296,297]

7 APPLICATIONS OF ORGANIC POLYSULFANES

For many years organic polysulfanes have been used as additives to high-pressure lubricants to prevent metals from welding together under extreme pressure.[298] At temperatures above 200 °C, the metals react with the additive to form sulfides, which have both a lower friction coefficient and a lower melting point than the metals themselves.

Organic polysulfanes are also important constituents of ‘polysulfide polymers’ of the Thiokol type, of vulcanized rubber, and of sulfur cement. In addition, there are a few special applications in the oil industry and in medicine. Sulfur-containing polymers have been extensively reviewed by Tobolsky and MacKnight in 1965 and by Duda and Penczek in 1987.[299,300]

7.1 Polysulfide Polymers

The preparation, properties, and uses of industrially-produced polysulfide polymers have been reviewed in detail by Ellerstein and Bertozzi in 1982 and by Lucke in 1992.[301,302] Synthesis is based on the reaction of aliphatic dichloro compounds with aqueous sodium polysulfide according to equation (158).

$$n\mathrm{Cl{-}R{-}Cl} + n\mathrm{Na_2S_{\mathit{x}}} \longrightarrow \left(\mathrm{R{-}S{-}S}\right)_n + 2n\ \mathrm{NaCl} \qquad (158)$$

Most of the polysulfide polymers are made from bis(2-chloroethyl)formal [bis(2-chloroethoxy)methane], which is synthesized from ethylene chlorohydrin [1-chloroethan-2-ol] and formaldehyde under acid catalysis according to equation (159).

$$\mathrm{2ClCH_2CH_2OH + CH_2O \xrightarrow{H^+} ClCH_2CH_2OCH_2OCH_2CH_2Cl + H_2O} \qquad (159)$$

Ethylene chlorohydrin is made from HCl and ethylene epoxide. When small amounts of 1,2,3-trichloropropane are added to the bis(2-chloroethyl)formal, some branching of the otherwise linear polymer structure is achieved.

The sodium polysulfide solution is customarily made by heating concentrated aqueous sodium hydroxide with elemental sulfur to 100–150 °C according to equation (160).

$$\mathrm{6NaOH} + \frac{2x+2}{8}\mathrm{S_8} \longrightarrow \mathrm{2Na_2S_{\mathit{x}} + Na_2S_2O_3 + 3H_2O} \qquad (160)$$

The thiosulfate by-product does not take part in the subsequent reactions with the organic chlorides. The x value in equation (160) is referred to as the rank of the sodium polysulfide; a typical value for x is 2.25. However, since aqueous sodium polysulfide is a complex mixture containing various polysulfide anions in equilibrium, the final polymer obtained in equation (158) may contain various structural units $-\mathrm{S}_n-$ ($n = 1$–4). In addition, the aqueous phase contains $\mathrm{OH^-}$, resulting in some terminal OH groups in the polymer. By applying an excess of sodium polysulfide (1.3 mol per mol $\mathrm{RCl_2}$), the number of chain-terminating OH groups is reduced (see equation 161).

$$\cdots\mathrm{{-}RSSR{-}OH + Na_2S_2} \longrightarrow \cdots\mathrm{{-}RSSNa + HORSSNa} \qquad (161)$$

At the end of the polymerization process, the polymers are washed free of sodium chloride, excess sodium polysulfide and solubilized hydroxy-containing terminals. The molecular mass of the resultant polymer is thought to be at least 5×10^5–10^6; the yield is 80%. The polymer forms as small dispersed spheres approximately 5–15 µm in diameter, which have a higher density than the aqueous phase in which they are produced, and therefore settle to the bottom of the reactor. The polymer is washed with hot water, followed by decantation, coagulation by acidification, and drying with heat, resulting in a solid, rubbery mass.

If a liquid polysulfide (LP) polymer is desired, a chemical reduction of some of the polysulfide groups to thiol terminals is carried out, after which the polymer is cleaned, coagulated, and dried to its final liquid form. The thiol-terminated version is by far the most common form of polysulfide polymers (molecular mass 700–8000; trade name LP Thiokol). A mixture of NaSH and $\mathrm{Na_2SO_3}$ is used to generate terminal SH groups from disulfane structural units (equation 162).

$$\begin{aligned} &\cdots\mathrm{{-}R{-}S{-}S{-}R{-}}\cdots + \mathrm{NaHS + Na_2SO_3 + H_2O} \\ &\longrightarrow 2\cdots\mathrm{{-}R{-}SH + Na_2S_2O_3 + NaOH} \end{aligned} \qquad (162)$$

The sulfite not only helps in the reduction of the disulfane group to thiol groups, but it also removes the polysulfanes of rank greater than 2 (equation 163).

$$\cdots\text{–R–S–S–S–R–}\cdots + \mathrm{Na_2SO_3} \longrightarrow \cdots\text{–R–S–S–R–}\cdots + \mathrm{Na_2S_2O_3} \tag{163}$$

The polymer is then in a stripped state in which no polysulfane group exceeds the disulfane stage. Thiokol FA is a copolymer of dichloroethane and the bis(2-chloroethyl)formal–sodium polysulfide reaction product.

The polysulfide polymers derive their utility from their unusually good resistance to solvents and to the environment and their good low-temperature properties. The solid elastomers in the vulcanized cure state are used in printing rolls, paint-spray hoses, solvent hoses, gaskets, and gas-meter diaphragms. LP polymers are used mainly in sealants, the largest application being sealants for double-pane insulating glass windows. Other applications are general sealants, and high quality sealants for construction, boat hulls and decks, printing rolls, aircraft bodies and integrated fuel tanks. The common way to convert the LP polymers to solid elastomers is to oxidize the terminal thiol groups to disulfanes. This is usually carried out in a formulation with fillers, plasticizers, and curing-rate modifiers (e.g. stearic acid). Both organic oxidizing agents, for example, *t*-butyl hydroperoxide, and inorganic oxidizing agents have been used, with most cures occurring at ambient temperature in a few hours.

7.2 Vulcanization of Rubber by Sulfur

By far the most important application for organic polysulfanes is the vulcanization of natural and synthetic rubber by elemental sulfur. More than 2 × 10^5 tonnes of sulfur are used for this process annually, partly in the form of polymeric sulfur (trade name 'Crystex'). The organic polymers to be vulcanized contain alkenic double bonds in varying environments (see Figure 6).

The vulcanization process involves heating the organic polymer with elemental sulfur in the presence of various accelerators and modifiers ('rubber chemicals'). A typical vulcanization mixture contains rubber (100 parts per weight), carbon black (50), zinc oxide (2–10), stearic acid (1–4), sulfur (0.5–4), and organic accelerators and antioxidants as well as retarders.[303] The vulcanization takes place at 140–160 °C and results in organic mono-, di-, and polysulfanes, some of which act as crosslinks to the polymer chains and thus generate the high-elastic properties of vulcanized rubbers (see Figure 7). The chemistry of vulcanization[304,305] and the importance of polysulfane crosslinks[306] have been reviewed. It should be recognized, however, that rubber mixtures are rather complex and difficult to analyze chemically, and the chemistry of vulcanization has therefore been worked out largely by using low-molecular mass analogs of the rubber structure (model alkenes) and then extrapolating the results to the polymeric system. These studies have considerably increased general knowledge about organic polysulfanes.[299,300,306] Several model studies have been published.[134,307–309]

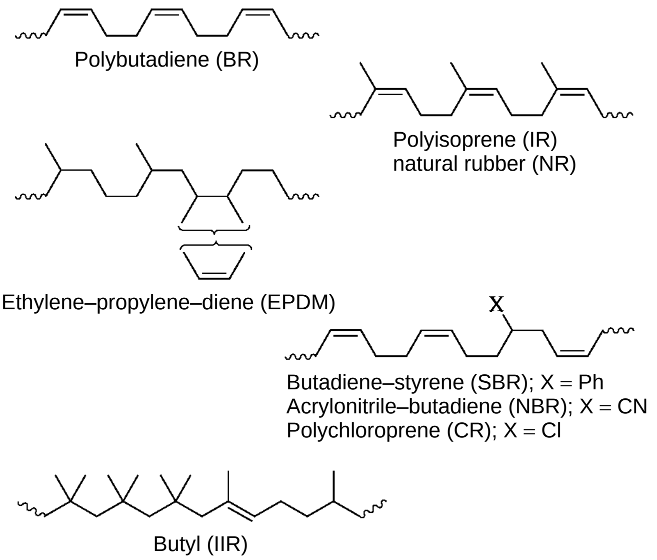
Polybutadiene (BR)
Polyisoprene (IR)
natural rubber (NR)
Ethylene–propylene–diene (EPDM)
X
Butadiene–styrene (SBR); X = Ph
Acrylonitrile–butadiene (NBR); X = CN
Polychloroprene (CR); X = Cl
Butyl (IIR)

Figure 6 Polymeric alkenes, which may be vulcanized by elemental sulfur or sulfur donors

7.3 Sulfur Cement and Sulfur Concrete

Elemental sulfur is an inexpensive material available in high purity and large quantities, and has repeatedly been suggested for 'new uses' in the civil engineering field. It is used as an extension to asphalt in road pavements and as an insulating material,[310] but use as a construction material requires 'modification' with additives designed to stop the embrittlement that occurs with pure elemental sulfur. If pure liquid sulfur is cooled to ambient temperature, monoclinic octasulfur (β-S_8) is instantaneously formed, which then slowly converts to orthorhombic α-S_8. Because of the difference in densities between α- and β-S_8, a brittle material results. Many additives have been proposed to modify elemental sulfur, nearly

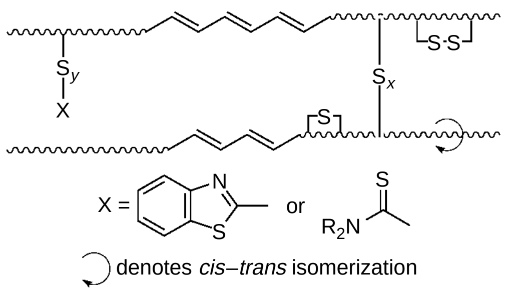

Figure 7 Schematic representation of rubber after vulcanization by sulfur, resulting in pendant groups ($-S_y-X$) as well as mono-, di-, and polysulfane bridges

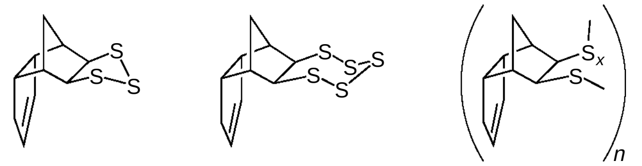

endo-DCPD-S_3 *endo*-DCPD-S_5 Low molecular mass polymer

Figure 8 Molecular and polymer polysulfanes formed in the reaction of *endo*-DCPD with elemental sulfur at elevated temperatures

all of them either organic polysulfanes or substances that will react with liquid sulfur to give in situ formation of polymeric polysulfanes, for example alkenes and certain thiokols.[311]

The most important alkene in this context is DCPD or a mixture of di- and tricyclopentadienes. The addition of 5–10% by mass to elemental sulfur, followed by heating to 140 °C results in a complex mixture of polysulfanes and sulfur, which after cooling to 20 °C is no longer brittle but of extremely high mechanical strength (sulfur cement). When the liquid sulfur cement is mixed with suitable pre-heated mineral fillers and cooled to ambient temperature a very useful construction material is obtained (sulfur concrete).[311] In contrast to Portland cement and conventional concrete, sulfur cement and sulfur concrete are resistant to aqueous acids and concentrated salt solutions.

The polysulfanes formed on reaction of DCPD with liquid sulfur have been studied by extraction of sulfur cement and analysis by LC, ^{1}H-NMR, MS, and other techniques.[299,300,311–313] The initial products are trisulfane and pentasulfane derived from DCPD by addition of S_3 or S_5 units to the norbornenyl double bond. These ‘monomers’ are believed to further react with elemental sulfur to form low-molecular mass polymers (CS_2 soluble), and on further heating form an insoluble material. The cyclopentenyl unsaturation of DCPD is much less reactive and is still present in the CS_2-soluble products. *endo*-DCPD reacts more slowly with liquid sulfur at 140 °C than *exo*-DCPD, while the cyclic trisulfanes of *endo*- and *exo*-DCPD react at almost the same rate with liquid sulfur at 140 °C.[272–274] The structures of DCPD-S_3, DCPD-S_5, and the likely structure of the low-molecular mass polymer, are shown in Figure 8.

The interaction of styrene with liquid sulfur has also been studied extensively.[299,300,312]

7.4 Organic Polysulfanes as Antiradiation Drugs

Field *et al.*[314] discovered that certain di- and trisulfanes, R–S_n–R′, terminated by sulfinate functions, –S(O)–O–, protect mice against otherwise lethal effects of ionizing radiation. The preparation of these compounds has been described in Section 2.1.13. The ionic sulfinate group makes these compounds partly hydrophilic and water soluble. Neither a trisulfane nor a sulfinate by itself are significantly radioprotective but the presence of a sulfur–sulfur bond is considered a key requirement since a thiol can be engendered by a neighboring group effect of an electron-donating group. One hypothesis suggests that this ‘protective thiol’ undergoes formation of mixed disulfanes with proteins in the cells, leading to a series of disturbances including decreased oxygen consumption, decreased carbohydrate utilization, and mitotic delay by temporary inhibition of DNA and RNA synthesis, along with cardiovascular, endocrine, and permeability changes. The mitotic delay allows time for repair processes to restore normal nucleic acid synthesis.[315]

8 RELATED ARTICLES

Hypervalent Compounds; Silicon: Organosilicon Chemistry; Sulfur: Inorganic Chemistry; Tin: Organometallic Chemistry; Titanium: Organometallic Chemistry.

9 REFERENCES

1. R. Steudel, *Angew. Chem.*, 1975, **87**, 683; *Angew. Chem. Int. Ed. Engl.*, 1975, **14**, 655.
2. S. W. Benson, *Chem. Rev.*, 1978, **78**, 23.
3. A. Schöberl and A. Wagner, in ‘Methoden der Organischen Chemie’, ed. E. Müller, Thieme, Stuttgart, 1955, Vol. IX, Chapt. 4.
4. R. M. Wilson and D. N. Buchanan, in ‘Methodicum Chimicum’, eds. H. Zimmer and K. Niedenzu, Thieme, New York, 1976, Vol. 7, Chap. 33.
5. L. Field, in ‘Organic Chemistry of Sulfur’, ed. S. Oae, Plenum, New York, 1977, p. 303.
6. K.-D. Gundermann and K. Hümke, in ‘Methoden der Organischen Chemie’, ed. D. Klamann, Thieme, Stuttgart, 1985, p. 148. Vol. E 11 (Teilband 1).
7. P. Laur, in ‘Sulfur in Organic and Inorganic Chemistry’, ed. A. Senning, Dekker, New York, 1972, p. 91. Vol. 3, p.
8. M. J. Cardone, in ‘The Analytical Chemistry of Sulfur and its Compounds’, ed. J. H. Karchmer, Wiley, New York, 1972, Part II, p. 89.
9. E. M. Reid, ‘Organic Chemistry of Bivalent Sulfur’, Chemical Publ., New York, 1960, p. 362.Vol. III, Chap. 7.
10. T. L. Pickering and A. V. Tobolsky, in ‘Sulfur in Organic and Inorganic Chemistry’, ed. A. Senning, Dekker, New York, 1972, p. 19. Vol. 3.
11. R. Steudel, *Chem. Rev.*, 2002, **102**, 3905.
12. E. L. Clennan and K. L. Stensaas, *Org. Prep. Proced. Int.*, 1998, **30**, 551.
13. E. Zysman-Colman and D. N. Harpp, *J. Org. Chem.*, 2003, **68**, 2487.

14. T. Sandow, J. Steidel, and R. Steudel, *Angew. Chem.*, 1982, **94**, 782; *Angew. Chem., Int. Ed. Engl.*, 1982, **10**, 794.
15. R. Steudel, J. Steidel, and T. Sandow, *Z. Naturforsch., Part B*, 1986, **41**, 958.
16. R. Steudel, R. Strauss, and D. Jensen, *Chem.-Ztg.*, 1985, **109**, 349.
17. J. Tsurugi and T. Nakabayashi, *J. Org. Chem.*, 1960, **25**, 1744.
18. J. Tsurugi and T. Nakabayashi, *J. Org. Chem.*, 1959, **24**, 807.
19. F. Fehér, G. Krause, and K. Vogelbruch, *Chem. Ber.*, 1957, **90**, 1570.
20. F. Fehér and E. Kiewert, *Z. Anorg. Allg. Chem.*, 1970, **377**, 152.
21. F. Fehér and D. Kurz, *Z. Naturforsch., Part B*, 1968, **23**, 1030.
22. I. Bloch and M. Bergmann, *Ber. Dtsch. Chem. Ges.*, 1920, **53**, 961.
23. M. V. Rao, C. B. Reese, and Z. Zhengyun, *Tetrahedron Lett.*, 1992, **33**, 4839.
24. G. Barany and A. W. Mott, *J. Org. Chem.*, 1984, **49**, 1043.
25. A. W. Mott and G. Barany, *J. Chem. Soc., Perkin Trans. 1*, 1984, 2615.
26. G. Barany, A. L. Schroll, A. W. Mott, and D. A. Halsrud, *J. Org. Chem.*, 1983, **48**, 4750.
27. F. Fehér, W. Becher, R. Kreutz and F. R. Minz, *Z. Naturforsch., Part B*, 1963, **18**, 507.
28. D. Twiss, *J. Am. Chem. Soc.*, 1927, **49**, 491.
29. W. Knoth and G. Gattow, *Z. Anorg. Allg. Chem.*, 1987, **552**, 181.
30. G. Winter, *Inorg. Nucl. Chem. Lett.*, 1975, **11**, 113.
31. G. Winter, *Rev. Inorg. Chem.*, 1980, **2**, 253.
32. T. Nakabayashi, J. Tsurugi, and T. Yabuta, *J. Org. Chem.*, 1964, **29**, 1236.
33. M. Gaensslen, R. Minkwitz, W. Molzbeck, and H. Oberhammer, *Inorg. Chem.*, 1992, **31**, 4147.
34. T. Nakabayashi and J. Tsurugi, *J. Org. Chem.*, 1961, **26**, 2482.
35. D. N. Harpp and D. K. Ash, *Int. J. Sulfur Chem., Ser. A*, 1971, **1**, 211.
36. O. Aberkane, J. L. Mieloszynski, D. Robert, M. Born, and D. Paquer, *Phosphorus, Sulfur, Silicon*, 1993, **79**, 245.
37. F. Fehér and W. Becher, *Z. Naturforsch., Part B*, 1965, **20**, 1126.
38. H. Böhme and H.-P. Steudel, *Liebigs Ann. Chem.*, 1969, **730**, 121.
39. A. W. Mott and G. Barany, *Synthesis*, 1984, **8**, 657.
40. L. R. M. Pitombo, *Chem. Ber.*, 1962, **95**, 2960.
41. F. Fehér and H. J. Berthold, *Chem. Ber.*, 1955, **88**, 1634.
42. J. D. Buckmann and L. Field, *J. Org. Chem.*, 1967, **32**, 454.
43. N. Kobayashi and T. Fujisawa, *J. Polym. Sci.*, 1972, **10**, 3317.
44. R. Steudel, J. Steidel, and J. Pickardt, *Angew. Chem.*, 1980, **92**, 313; *Angew. Chem., Int. Ed. Engl.*, 1980, **19**, 325.
45. R. Steudel and B. Eckert, *Top. Curr. Chem.*, 2003, **230**, 1.
46. R. Steudel, K. Hassenberg, V. Münchow, O. Schumann, and J. Pickardt, *Eur. J. Inorg. Chem.* 2000, 921.
47. V. Münchow and R. Steudel, *Eur. J. Inorg. Chem.* 2004, 718.
48. R. Steudel, S. Förster, and J. Albertsen, *Chem. Ber.*, 1991, **124**, 2357.
49. J. Albertsen, Synthesis and characteristics of new chalcogen-rich heterocycles with organoelement compounds of the 4th main group and purification of bisorganic polysulfanes using titanocene chalcogenide chelate complexes, Doctoral Dissertation, Technical University of Berlin, 1993.
50. M. Kustos, J. Pickardt, J. Albertsen, and R. Steudel, *Z. Naturforsch., Part B*, 1993, **48**, 928.
51. A. B. Sullivan and K. Boustany, *Int. J. Sulfur Chem., Ser. A*, 1971, **1**, 207.
52. D. N. Harpp, D. K. Ash, T. G. Back, J. G. Gleason, B. A. Orwig, W. F. VanHorn, and J. P. Snyder, *Tetrahedron Lett.*, 1970, **41**, 3551.
53. D. N. Harpp, K. Steliou, and T. H. Chan, *J. Am. Chem. Soc.*, 1978, **100**, 1222.
54. E. Baumeister, H. Oberhammer, H. Schmidt, and R. Steudel, *Heteroat. Chem.*, 1991, **2**, 633.
55. H. Schmidt and R. Steudel, *Z. Naturforsch., Part B*, 1990, **45**, 557.
56. E. Zysman-Colman, N. Nevins, N. Eghbali, J. P. Snyder, and D. N. Harpp, *J. Am. Chem. Soc.*, 2006, **128**, 291.
57. H. Kagami and S. Motoki, *J. Org. Chem.*, 1977, **42**, 4139.
58. R. Steudel and H. Schmidt, *Chem. Ber.*, 1994, **127**, 1219.
59. Z. S. Ariyan and L. A. Wiles, *J. Chem. Soc.*, 1962, 4709.
60. G. Morel, E. Marchand, and A. Foucand, *Synthesis*, 1980, 918.
61. P. Sinha, A. Kundu, S. Roy, S. Prabhakar, M. Vairamani, A. R. Sankar, and A. C. Kunvar, *Organometallics*, 2001, **20**, 157.
62. N. A. Korchevin, L. P. Turchaninovy, E. N. Deryagina, and M. G. Voronkov, *Zh. Obshch. Khim.*, 1989, **59**, 1785.
63. R. N. Haszeldine and J. M. Kidd, *J. Chem. Soc.*, 1953, 3219.
64. R. Steudel, R. Strauss, and L. Koch, *Angew. Chem.*, 1985, **97**, 58; *Angew. Chem., Int. Ed. Engl.*, 1985, **24**, 59.
65. R. L. Dannley and D. A. Zazaris, *Can. J. Chem.*, 1965, **43**, 2610.
66. K. Aghoramurthy, *Tetrahedron*, 1966, **22**, 415.
67. R. M. Dodson, V. Srinivasan, K. S. Sharma, and R. F. Sauers, *J. Org. Chem.*, 1972, **37**, 2367.
68. B. D. Vineyard, *J. Org. Chem.*, 1966, **31**, 601.
69. B. D. Vineyard, *J. Org. Chem.*, 1967, **32**, 3833.
70. C. D. Trivette and A. Y. Coran, *J. Org. Chem.*, 1966, **31**, 100.
71. A. J. Kolar and R. K. Olsen, *J. Org. Chem.*, 1971, **36**, 591.
72. P. Klason, *Ber. Dtsch. Chem. Ges.*, 1887, **20**, 2376.
73. P. Labuk, A. Duda, and S. Penczek, *Phosphorus Sulfur Silicon*, 1989, **42**, 107.
74. E. W. Abel and D. A. Armitage, *J. Chem. Soc.*, 1964, 5975.

75. J. L. Wardell and P. L. Clarke, *J. Organomet. Chem.*, 1971, **26**, 345.
76. R. Steudel and T. Göbel, unpublished results, T. Göbel, Synthesis and analysis of aliphatic (chain-forming) polysulfur compounds: Modeling metabolism of sulfur bacteria, Doctoral Dissertation, Technical University of Berlin, Berlin, 1988.
77. G. Capozzi, A. Capperucci, A. Deglinnocenti, R. D. Duce, and S. Menichetti, *Tetrahedron Lett.*, 1989, **30**, 2991.
78. C. G. Krespan and D. C. England, *J. Org. Chem.*, 1968, **33**, 1850.
79. H. L. Paige and J. Passmore, *Inorg. Chem.*, 1973, **12**, 593.
80. F. Akiyama, *J. Chem. Soc., Perkin Trans. 1*, 1978, 1046.
81. L. Field and W. B. Lacefield, *J. Org. Chem.*, 1966, **31**, 3555.
82. R. Steudel, P. W. Schenk, and J. Bilal, *Z. Anorg. Allg. Chem.*, 1967, **353**, 250.
83. R. Steudel and G. Scheller, *Z. Naturforsch., Part B*, 1969, **24**, 351.
84. R. Steudel, P. Luger, and H. Bradaczek, *Chem. Ber.*, 1977, **110**, 3553.
85. G. Kresze and H.-P. Patzschke, *Chem. Ber.*, 1960, **93**, 380.
86. B. Holmberg, *Ber. Dtsch. Chem. Ges.*, 1910, **43**, 226.
87. P. K. Singh, L. Field, and B. J. Sweetman, *J. Org. Chem.*, 1988, **53**, 2608. and references cited therein.
88. F. Fehér and K.-H. Schäfer, *Z. Naturforsch., Part B*, 1962, **17**, 849.
89. W. Strecker, *Ber. Dtsch. Chem. Ges.*, 1908, **41**, 1105.
90. R. Steudel and A. Albertsen, *J. Chromatogr.*, 1992 **606**,, 260.
91. R. Steudel, A. Albertsen, M. Kustos, and J. Pickardt, *Z. Naturforsch., Part B*, 1993, **48**, 555. references cited therein.
92. B. Milligan, B. Saville, and J. M. Swan, *J. Chem. Soc.*, 1961, 4850.
93. B. Milligan, B. Saville, and J. M. Swan, *J. Chem. Soc.*, 1963, 3608.
94. L. Field and Y. H. Khim, *J. Med. Chem.*, 1972, **15**, 312.
95. P. K. Srivastava and L. Field, *J. Med. Chem.*, 1975, **18**, 798.
96. L. Field and V. Eswarakrishnan, *J. Org. Chem.*, 1981, **46**, 2025.
97. R. Chandra and L. Field, *J. Org. Chem.*, 1986, **51**, 1844.
98. V. Eswarakrishnan and L. Field, *J. Org. Chem.*, 1981, **46**, 4182.
99. P. R. Srivastava and L. Field, *Phosphorus Sulfur*, 1985, **25**, 161.
100. S. Hayashi, M. Furukawa, J. Yamamoto, and K. Hamamura, *Chem. Pharm. Bull.*, 1967, **15**, 1310.
101. F. Fehér, K.-H. Schäfer, and W. Becher, *Z. Naturforsch., Part B*, 1962, **17**, 847.
102. F. Fehér and H. Weber, *Angew. Chem.*, 1955, **67**, 231.
103. F. Fehér and H. Weber, *Chem. Ber.*, 1958, **91**, 642.
104. R. Steudel, K. Bergemann, J. Buschmann, and P. Luger, *Angew. Chem.*, 1993, **105**, 1781; *Angew. Chem. Int. Ed. Engl.*, 1993, **32**, 1702.
105. R. Steudel, K. Bergemann, K. Buschmann, and P. Luger, *Inorg. Chem.*, 1996, **35**, 2184.
106. T. L. Cairns, G. L. Evans, A. W. Larchar, and B. C. McKusick, *J. Am. Chem. Soc.*, 1952, **74**, 3982.
107. R. Ballini, *Synthesis*, 1982, 834.
108. F. Fehér and W. Becher, *Z. Naturforsch., Part B*, 1965, **20**, 1125.
109. F. Fehér, B. Degen, and B. Söhngen, *Angew. Chem.*, 1968, **80**, 320.
110. F. Fehér and K. Glinka, *Z. Naturforsch., Part B*, 1979, **34**, 1031.
111. F. Fehér and B. Degen, *Angew. Chem.*, 1967, **79**, 689.
112. F. Fehér, K. Glinka, and F. Malcharek, *Angew. Chem.*, 1971, **83**, 439.
113. F. Fehér, M. Langer, and R. Volkert, *Z. Naturforsch., Part B*, 1972, **27**, 1006.
114. G. Goor and M. Anteunis, *Synthesis*, 1975, 329.
115. R. Steudel and E.-M. Strauss, *Z. Naturforsch., Part B*, 1983, **38**, 719.
116. H. G. Guttenberger, H. J. Bestmann, F. L. Dickert, F. S. Jorgensen, and J. P. Snyder, *J. Am. Chem. Soc.*, 1981, **103**, 159.
117. S. A. Vladuchick, T. Fukunaga, H. E. Simmons, and O. W. Webster, *J. Org. Chem.*, 1980, **45**, 5122.
118. F. Fehér and M. Langer, *Tetrahedron Lett.*, 1971, 2125.
119. H. Poisel and U. Schmidt, *Angew. Chem.*, 1971, **83**, 114.
120. H. Poisel and U. Schmidt, *Chem. Ber.*, 1971, **104**, 1714.
121. K. Morita and S. Kobayashi, *Tetrahedron Lett.*, 1966, 573.
122. K. Morita and S. Kobayashi, *Chem. Pharm. Bull.*, 1967, **15**, 988.
123. P. K. Singh, L. Field, and B. J. Sweetman, *Phosphorus Sulfur*, 1988, **39**, 61.
124. A. Kato, Y. Hashimoto, I. Otsuka, and K. Nakatsu, *Chem. Lett.*, 1978, 1219.
125. I. W. J. Still and G. W. Kutney, *Tetrahedron Lett.*, 1981, **22**, 1939.
126. L. Teuber and C. Christophersen, *Acta Chem. Scand., Part B*, 1988, **42**, 620. references cited therein.
127. B. Milligan and J. M. Swan, *J. Chem. Soc.*, 1965, 2901.
128. R. Sato, *Rev. Heteroat. Chem.*, 1990, **3**, 193.
129. R. Sato, S. Saito, H. Chiba, T. Goto, and M. Saito, *Bull. Chem. Soc. Jpn.*, 1988, **61**, 1647.
130. R. Sato, S. Saito, H. Chiba, T. Goto, and M. Saito, *Chem. Lett.*, 1986, 349.
131. R. Sato, T. Kimura, T. Goto, and M. Saito, *Tetrahedron Lett.*, 1988, **29**, 6291.

132. R. Sato, T. Kimura, T. Goto, M. Saito, and C. Kabuto, *Tetrahedron Lett.*, 1989, **30**, 3453.
133. R. Sato, *Rev. Heteroatom Chem.*, 2000, **22**, 121.
134. M. G. Voronkov, N. S. Vyazankin, E. N. Deryagina, A. S. Nakhmanovich, and V. A. Usov, in 'Reactions of Sulfur with Organic Compounds', ed. J. S. Pizey, Consultants Bureau, New York, 1987.
135. C. G. Krespan and W. R. Brasen, *J. Org. Chem.*, 1962, **27**, 3995.
136. S. Inoue, T. Tezuka, and S. Oae, *Phosphorus Sulfur*, 1978, **4**, 219.
137. E.-M. Strauss and R. Steudel, *Z. Naturforsch., Part B*, 1987, **42**, 682.
138. R. Steudel, J. Albertsen, and K. Zink, *Ber. Bunsenges. Phys. Chem.*, 1989, **93**, 502.
139. J. Emsley, D. W. Griffiths, and G. J. J. Jayne, *J. Chem. Soc., Perkin Trans. 1*, 1979, 228.
140. T. C. Shields and A. N. Kurtz, *J. Am. Chem. Soc.*, 1969, **91**, 5415.
141. P. D. Bartlett and T. Ghosh, *J. Org. Chem.*, 1987, **52**, 4937.
142. M. Kustos and R. Steudel, *J. Org. Chem.*, 1995, **60**, 8056.
143. H. Fritz and C. D. Weis, *Tetrahedron Lett.*, 1974, 1659.
144. E. A. Chernyshev, O. V. Kuzmin, A. V. Lebedev, A. I. Gusev, N. I. Kirillova, N. S. Nametkin, V. D. Tyurin, A. M. Krapivin, and N. A. Kubasova, *J. Organomet. Chem.*, 1983, **252**, 133.
145. K. Okuma, S. Kuge, Y. Koga, K. Shioji, H. Wakita, and T. Machiguchi, *Heterocycles*, 1998, **48**, 1519.
146. G. W. Rewcastle, T. Janosik, and J. Bergman, *Tetrahedron*, 2001, **57**, 7185.
147. J. Bergman and C. Stalhandske, *Tetrahedron Lett.*, 1994, **35**, 5279.
148. W. Ando, N. Tokitoh, and Y. Kabe, *Phosphorus Sulfur Silicon*, 1991, **58**, 179.
149. N. Tokitoh, M. Noguchi, Y. Kabe, and W. Ando, *Tetrahedron Lett.*, 1990, **31**, 7641.
150. N. Tokitoh, H. Hayakawa, M. Goto, and W. Ando, *Tetrahedron Lett.*, 1988, **29**, 1935.
151. K. Steliou, Y. Gareau, G. Milot, and P. Salama, *J. Am. Chem. Soc.*, 1990, **112**, 7819.
152. K. Steliou, *Acc. Chem. Res.*, 1991, **24**, 341.
153. K. Steliou, P. Salama, and X. Yu, *J. Am. Chem. Soc.*, 1992, **114**, 1456.
154. I. Abu-Yousef, *J. Sulfur Chem.*, 2006, **27**, 87.
155. T. L. Gilchrist and J. E. Wood, *J. Chem. Soc., Chem. Commun.*, 1992, 1460.
156. R. Sato, K. Chino, and M. Saito, *Sulfur Lett.*, 1990, **10**, 233.
157. R. Sato, S. Satoh, and M. Saito, *Chem. Lett.*, 1990, 139.
158. C. R. Williams and D. N. Harpp, *Tetrahedron Lett.*, 1991, **32**, 7651.
159. R. Steudel, in 'The Chemistry of Inorganic Ring Systems', ed. R. Steudel, Elsevier, Amsterdam, 1992, p. 233.
160. R. Steudel and M. Kustos, *Phosphorus Sulfur Silicon*, 1991, **62**, 127.
161. H. A. Harris, A. D. Rae and L. F. Dahl, *J. Am. Chem. Soc.*, 1987, **109**, 4739.
162. R. Steudel and U. Westphal, *Organomet. Chem.*, 1990, **388**, 89.
163. U. Westphal and R. Steudel, *Chem. Ber.*, 1991, **124**, 2141.
164. R. Steudel, U. Westphal, and J. Pickardt, *Chem. Ber.*, 1995, **128**, 561.
165. R. Steudel, M. Kustos, V. Münchow, and U. Westphal, *Chem. Ber.*, 1997, **130**, 757.
166. C. P. Galloway, T. B. Rauchfuss, and X. Yang, in 'The Chemistry of Inorganic Ring Systems', ed. R. Steudel, Elsevier, Amsterdam, 1992, p. 25.
167. X. Yang, T. B. Rauchfuss, and S. R. Wilson, *J. Am. Chem. Soc.*, 1989, **111**, 3465.
168. H. W. Roesky, H. Zamankhan, J. W. Bats, and H. Fuess, *Angew. Chem.*, 1980, **92**, 122.
169. H. W. Roesky, H. Zamankhan, J. W. Bats, and H. Fuess, *Angew. Chem., Int. Ed. Engl.*, 1980, **19**, 125.
170. R. Steudel, K. Hassenberg and J. Pickardt, *Eur. J. Org. Chem.* 2001, 2815.
171. N. Yamazaki, S. Nakahama, K. Yamaguchi, and T. Yamaguchi, *Chem. Lett.*, 1980, 1355.
172. B. L. Chenard and T. J. Miller, *J. Org. Chem.*, 1984, **49**, 1221.
173. B. L. Chenard, R. L. Harlow, A. L. Johnson, and S. A. Vladuchick, *J. Am. Chem. Soc.*, 1985, **107**, 3871.
174. W. Ando, Y. Kumamoto, and N. Tokitoh, *Tetrahedron Lett.*, 1987, **28**, 4833.
175. W. Ando and N. Tokitoh, in 'Heteroatom Chemistry', ed. E. Block, VCH, New York, 1990, p. 1.
176. N. Tokitoh, H. Ishizuka, and W. Ando, *Chem. Lett.*, 1988, 657.
177. N. Tokitoh, Y. Okano, W. Ando, M. Goto, and H. Maki, *Tetrahedron Lett.*, 1990, **31**, 5323.
178. N. Takeda, N. Tokitoh, T. Imakubo, M. Goto, and R. Okazaki, *Bull. Chem. Soc. Jpn.*, 1995, **68**, 2757.
179. R. Okazaki, K. Inoue, and N. Inamoto, *Bull. Chem. Soc. Jpn.*, 1981, **54**, 3541.
180. A. Ishii, J. Yinan, Y. Sugihara, and J. Nakayama, *Chem. Commun.*, 1996, 2681.
181. Y.-N. Jin, A. Ishii, Y. Sugihara, and J. Nakayama, *Heterocycles*, 1997, **44**, 255.
182. M. F. Hurley and J. Q. Chambers, *J. Org. Chem.*, 1981, **46**, 775.
183. D. N. Harpp, R. A. Smith, and K. Steliou, *J. Org. Chem.*, 1981, **46**, 2072.
184. H. Schubert, J. Heinicke, and H. Mühlstädt, *J. Prakt. Chem.*, 1991, **333**, 191.
185. R. Rahman, S. Safe, and A. Taylor, *J. Chem. Soc. C*, 1969, **12**, 1665.

186. D. Brewer, R. Rahman, S. Safe, and A. Taylor, *Chem. Commun.*, 1968, 1571.
187. Z. S. Ariyan and R. L. Martin, *Chem. Commun.*, 1969, 847.
188. D. N. Harpp and A. Granata, *J. Org. Chem.*, 1979, **44**, 4144.
189. A. Fredga, *Acta Chem. Scand.*, 1958, **12**, 891.
190. S. Safe and A. Taylor, *J. Chem. Soc. C*, 1970, **3**, 432.
191. E. Francis, R. Rahman, S. Safe, and A. Taylor, *J. Chem. Soc., Perkin Trans. 1*, 1972, 470.
192. Y. Takikawa, T. Makabe, N. Hirose, T. Hiratsuka, R. Takoh, and K. Shimada, *Chem. Lett.*, 1988, 1517.
193. K. Rasheed and J. D. Warkentin, *J. Org. Chem.*, 1980, **45**, 4806.
194. R. Rahman, S. Safe, and A. Taylor, *Quart. Rev.*, 1970, **24**, 208.
195. C. T. Kiers and A. Vos, *Recl. Trav. Chim. Pays-Bas*, 1978, **97**, 166.
196. T. Ghosh and P. D. Bartlett, *J. Am. Chem. Soc.*, 1988, **110**, 7499.
197. I. Chen and Y. Wang, *Acta Crystallogr., Sect. C*, 1984, **40**, 1890.
198. O. Foss, F. Kvammen, and K. Maroy, *J. Chem. Soc., Dalton Trans.*, 1985, 231.
199. R. Laitinen, R. Steudel, and R. Weiss, *J. Chem. Soc., Dalton Trans.*, 1986, 1095.
200. R. Minkwitz, R. Krause, and H. Preut, *Z. Anorg. Allg. Chem.* 1989, **571**, 133.
201. D. Jiao, M. Barfield, J. E. Combariza, and V. J. Hruby, *J. Am. Chem. Soc.*, 1992, **114**, 3639.
202. Y. Drozdova, K. Miaskiewicz, and R. Steudel, *Z. Naturforsch. Part B*, 1995, **50**, 889.
203. R. Steudel, *Z. Naturforsch., Part B*, 1983, **38**, 543.
204. M. T. Delvin, G. Barany, and I. W. Levin, *J. Mol. Struct.*, 1990, **238**, 119.
205. S. Kabuss, A. Lüttringhaus, H. Friebolin, and R. Mecke, *Z. Naturforsch., Part B*, 1966, **21**, 320.
206. R. Steudel, Y. Drozdova, K. Miaskiewicz, R. H. Hertwig, and W. Koch, *J. Am. Chem. Soc.*, 1997, **119**, 1990.
207. M. W. Wong, Y. Steudel, and R. Steudel, *Chem. Phys. Lett.*, 2002, **364**, 387.
208. J. Donohue and V. Schomaker, *J. Chem. Phys.*, 1948, **16**, 92.
209. J. Donohue, *J. Am. Chem. Soc.*, 1950, **72**, 2701.
210. H. J. Berthold, *Z. Anorg. Allg. Chem.*, 1963, **325**, 237.
211. J. W. Bats, *Acta Crystallogr., Sect. B*, 1977, **33**, 2264.
212. K. Bergemann, M. Kustos, and R. Steudel, *Z. Anorg. Allg. Chem.*, 1994, **620**, 117.
213. R. D. Gilardi and J. L. Flippen-Anderson, *Acta Crystallogr., Sect. C*, 1985, **41**, 72.
214. O. Foss and K. Maartmann-Moe, *Acta Chem. Scand., Ser. A*, 1986, **40**, 664.
215. R. Steudel, M. Pridöhl, J. Buschmann, and P. Luger, *Chem. Ber.*, 1995, **128**, 725.
216. Q. Shen, C. Wells, and K. Hagen, *Inorg. Chem.*, 1998, **37**, 3895.
217. J. Buschmann, P. Luger, T. Koritsanszky, H. Schmidt, and R. Steudel, *Z. Kristallogr., Suppl. Issue*, 1991, **3**, 40. unpublished results.
218. W. H. Watson, P. C. Jain, P. D. Bartlett, and T. Ghosh, *Acta Crystallogr., Sect. C*, 1986, **42**, 332.
219. M. Nishikawa, K. Kamiya, S. Kobayashi, K. Morita, and Y. Tomiie, *Chem. Pharm. Bull.*, 1967, **15**, 756.
220. J. Emsley, D. W. Griffiths, and R. Osborn, *Acta Crystallogr., Sect. B*, 1979, **35**, 2119.
221. F. Lemmer, F. Fehér, A. Gieren, S. Hechtfischer, and W. Hoppe, *Acta Crystallogr., Sect. B*, 1973, **29**, 2113.
222. M. Kamata, K. Murayama, T. Suzuki, and T. Miyashi, *J. Chem. Soc., Chem. Commun.*, 1990, 827.
223. B. R. Davis and I. Bernal, *Proc. Natl. Acad. Sci. USA*, 1973, **70**, 279.
224. F. R. Ahmed and M. Przybylska, *Acta Crystallogr., Sect. B*, 1977, **33**, 168.
225. F. Fehér, A. Klaeren, and K.-H. Linke, *Acta Crystallogr., Sect. B*, 1972, **28**, 534.
226. J. S. Ricci and I. Bernal, *J. Chem. Soc. B*, 1971, 1928.
227. F. Fehér and B. Engelen, *Z. Anorg. Allg. Chem.*, 1979, **452**, 37.
228. J. Pickardt, M. Kustos, and R. Steudel, *Acta Crystallogr., Sect. C*, 1992, **48**, 190.
229. J. D. Korp, I. Bernal, S. F. Watkins, and F. R. Fronczek, *J. Heterocycl. Chem.*, 1982, **19**, 459.
230. F. Fehér and J. Lex, *Z. Anorg. Allg. Chem.*, 1976, **423**, 103.
231. R. Steudel, V. Münchow, and J. Pickardt, *Z. Anorg. Allg. Chem.*, 1996, **622**, 1594.
232. L. K. Hansen and A. Hordvik, *J. Chem. Soc., Chem. Commun.*, 1974, 800.
233. R. Gleiter and R. Gygax, *Top. Curr. Chem.*, 1976, **63**, 49.
234. J. Hahn, *Z. Naturforsch., Part B*, 1985, **40**, 263.
235. D. Grant and J. R. Van Wazer, *J. Am. Chem. Soc.*, 1964, **86**, 3012.
236. J. D. Dorsey and K. A. Dill, *Chem. Rev.*, 1989, **89**, 331.
237. K. O. Hiller, B. Masloch, and H. J. Möckel, *Z. Anal. Chem.*, 1976, **280**, 293.
238. H. J. Möckel, F. Höfler, and H. Melzer, *J. Chromatogr.*, 1987, **388**, 267.
239. S. D. Thompson, D. G. Carroll, F. Watson, M. O’Donnell, and S. P. McGlynn, *J. Chem. Phys.*, 1966, **45**, 1367.
240. J. E. Baer and M. Carmack, *J. Am. Chem. Soc.*, 1949, **71**, 1215.
241. R. Steudel, E.-M. Strauss, and D. Jensen, *Z. Naturforsch., Part B*, 1990, **45**, 1282.

242. R. Steudel, D. Jensen, P. Göbel, and P. Hugo, *Ber. Bunsen. Phys. Chem.*, 1988, **92**, 118.

243. R. Steudel, H.-J. Mäusle, D. Rosenbauer, H. Möckel, and T. Freyholdt, *Angew. Chem.*, 1981, **93**, 402; *Angew. Chem., Int. Ed. Engl.*, 1981, **20**, 394.

244. R. Strauss and R. Steudel, *Fresenius' Z. Anal. Chem.*, 1987, **326**, 543.

245. R. Steudel and H.-J. Mäusle, *Z. Anorg. Allg. Chem.*, 1981, **478**, 156, 177.

246. N. Etzenbach, J. Hahn, and F. Rabet, *Bruker Rep.*, 1990, 44.

247. R. T. Honeyman, R. R. Schrieke, and G. Winter, *Anal. Chim. Acta*, 1980, **116**, 345.

248. R. Steudel, *Top. Curr. Chem.*, 1982, **102**, 149.

249. F. M. Bickelhaupt, M. Sola, P. von, and R. Schleyer, *J. Comput. Chem.*, 1995, **16**, 465.

250. Y. Steudel, R. Steudel, and M. W. Wong, *Chem. Eur. J.*, 2002, **8**, 217.

251. R. Steudel, Y. Steudel, and K. Miaskiewicz, *Chem. Eur. J.*, 2001, **7**, 3281.

252. R. A. Hayes, and J. C. Martin, in 'Organic Sulfur Chemistry: Theoretical and Experimental Advances', eds. I. G. Csizmadia, A. Mangini, and F. Bernardi, Elsevier, Amsterdam, 1985, p. 408.

253. S. Ogawa, Y. Matsunaga, S. Sato, I. Iida, and N. Furukawa, *J. Chem. Soc., Chem. Commun.*, 1992, 1141.

254. Y. Drozdova, R. Steudel, W. Koch, K. Miaskiewicz, and I. A. Topol, *Chem. Eur. J.*, 1999, **5**, 1936.

255. O. Foss, *Acta Chem. Scand.*, 1950, **4**, 404.

256. O. Foss and R. E. Davis, *Survey Progr. Chem.*, 1964, **2**, 189.

257. D. N. Harpp and R. A. Smith, *J. Am. Chem. Soc.*, 1982, **104**, 6045.

258. D. N. Harpp and R. A. Smith, *J. Org. Chem.*, 1979, **44**, 4140. references cited therein.

259. M. Arisawa, K. Tanaka, and M. Yamaguchi, *Tetrahedron Lett.*, 2005, **46**, 4797.

260. R. Steudel, *Phosphorus Sulfur*, 1985, **23**, 33.

261. R. Steudel, *Top. Curr. Chem.*, 2003, **231**, 203.

262. R. Steudel and J. Latte, *Chem. Ber.*, 1977, **110**, 423.

263. S. Satoh and R. Sato, *Bull. Chem. Soc. Jpn.*, 1992, **65**, 1188.

264. N. Yomoji, S. Takahashi, S. Chida, S. Ogawa, and R. Sato, *J. Chem. Soc., Perkin Trans. 1*, 1993, **17**, 1995.

265. G. Derbesy and D. N. Harpp, *J. Org. Chem.* 1995, **60**, 4468, 1996 and **61**, 991, 9471.

266. A. Ishii, H. Oshida, and J. Nakayama, *Bull. Chem. Soc. Jpn.*, 2002, **75**, 319.

267. A. Ishii, M. Suzuki, and R. Yamashita, *Tetrahedron*, 2006, **62**, 5441.

268. C. R. Williams, J. G. MacDonald, D. N. Harpp, R. Steudel, and S. Förster, *Sulfur Lett.*, 1992, **13**, 247.

269. D. N. Harpp, in 'Perspectives in the Organic Chemistry of Sulfur', eds. B. Zwanenburg, and A. J. H. Klunder, Elsevier, Amsterdam, 1987, p. 1.

270. D. N. Harpp, D. K. Ash, and R. A. Smith, *J. Org. Chem.*, 1979, **44**, 4135.

271. Y. H. Kim, in 'Organic Sulfur Chemistry: Biochemical Aspects', eds. S. Oae, and T. Okuyama, CRC Press, Tokyo, 1992, p. 137.

272. E. Strandberg, J. Koerdel, R. Lundin, T. Wehler, and G. Widmalm, *J. Peptide Res.*, 1997, **49**, 254.

273. L. Chen, I. Zoulikova, J. Slaninova, and G. Barany, *J. Med. Chem.*, 1997, **40**, 864. references cited therein.

274. C. Christophersen and U. Anthoni, *Sulfur Rep.*, 1986 **4**,, 365.

275. C.-C. Chen and C.-T. Ho, *J. Agric. Food Chem.*, 1986, **34**, 830.

276. C.-C. Chen, S.-D. Chen, J.-J. Chen, and C.-M. Wu, *J. Agric. Food Chem.*, 1984, **32**, 999.

277. B. Rajanikanth, B. Ravindranath, and M. L. Shankaranarayana, *Phytochemistry*, 1984, **23**, 899.

278. E. Block, *Angew. Chem.*, 1992, **104**, 1158.

279. E. Block, *Angew. Chem., Int. Ed. Engl.*, 1992, **31**, 1135.

280. J. C. Fletcher and A. Robson, *Biochem. J.*, 1963, **87**, 553.

281. R. E. Moore, *Chem. Commun.*, 1971, 1168.

282. C. Berger, J. A. Khan, P. Molimard, N. Martin, and H. E. Spinnler, *Appl. Environm. Microbiol.*, 1999, **65**, 5510.

283. R. Näf and A. Velluz, *Flavour Fragr. J.*, 1996, **11**, 295.

284. M. D. Lee, T. S. Dunne, C. C. Chang, G. A. Ellestad, M. M. Siegel, G. O. Morton, W. J. McGahren, and D. B. Borders, *J. Am. Chem. Soc.*, 1987, **109**, 3466.

285. U. Anthoni, C. Christophersen, J. O. Madsen, S. Wium-Andersen, and N. Jacobsen, *Phytochemistry*, 1980, **19**, 1228.

286. U. Anthoni, C. Christophersen, N. Jacobsen, and A. Svendsen, *Tetrahedron*, 1982, **38**, 2425.

287. S. J. Wratten and D. J. Faulkner, *J. Org. Chem.*, 1976, **41**, 2465.

288. R. Gmelin, R. Susilo, and G. R. Fenwick, *Phytochemistry*, 1981, **20**, 2521.

289. B. R. Copp, J. W. Blunt, and M. H. G. Munro, *Tetrahedron Lett.*, 1989, **30**, 3703.

290. R. L. De Vault and W. Rosenbrook, *J. Antibiot.*, 1973, **26**, 532.

291. M. Litaudon, F. Trigalo, M.-T. Martin, F. Frappier, and M. Guyot, *Tetrahedron*, 1994, **50**, 5323.

292. B. S. Davidson, T. F. Molinski, L. R. Barrows, and C. M. Ireland, *J. Am. Chem. Soc.*, 1991, **113**, 4709.

293. V. Behar and S. J. Danishefsky, *J. Am. Chem. Soc.*, 1993, **115**, 7017.

294. P. W. Ford and B. S. Davidson, *J. Org. Chem.*, 1993, **58**, 4522.

295. A. Kato and Y. Hashimoto, in ‘Natural Sulfur Compounds: Novel Biochemical and Structural Aspects’, eds. D. Cavallini, G. E. Gaull, and V. Zappia, Plenum, New York, 1980, p. 361.

296. G. M. Strunz, M. Kakushima, and M. A. Stillwell, *Can. J. Chem.*, 1975, **53**, 295.

297. K. H. Michel, M. O. Chaney, N. D. Jones, M. M. Hoehn, and R. Nagarajan, *J. Antibiot.*, 1974, **27**, 57.

298. D. Klamann, ‘’Schmierstoffe und verwandte Produkte’, VCH, Weinheim, Germany, 1982, p. 94.

299. A. Duda and S. Penczek, in ‘Encyclopedia of Polymer Science and Engineering’, 2nd edition., Wiley, New York, 1987, Vol. 16, p. 246.

300. A. V. Tobolsky, and W. J. MacKnight eds., in ‘Polymeric Sulfur and Related Polymers’, Interscience, New York, 1965.

301. S. M. Ellerstein and E. R. Bertozzi, ‘Kirk-Othmer Encyclopedia of Chemical Technology’, 3rd edition., Wiley, New York, 1982, Vol. 18, p. 814.

302. H. Lucke, ‘Aliphatische Polysulfide’, Hüthig & Wepf, Basel, 1992.

303. I. Fishbein, ‘Handbook of Environmental Chemistry’, Springer, Berlin, 1990, Vol. 3, Part E.

304. M. Porter, in ‘Organic Chemistry of Sulfur’, ed. S. Oae, Plenum, New York, 1977, p. 71.

305. M. Porter, in ‘Perspectives in the Organic Chemistry of Sulfur’, eds. B. Zwanenburg, and A. J. H. Klunder, Elsevier, Amsterdam, 1987, p. 267.

306. N. J. Morrison and M. Porter, *Rubber Chem. Technol.*, 1984, **57**, 63.

307. P. Versloot, J. G. Haasnoot, J. Reedijk, M. van Duin, E. F. J. Duynstee, and J. Put, *Rubber Chem. Technol.*, 1992, **65**, 343.

308. J. H. M. van den Berg, E. F. J. Duynstee, and P. J. D. Maas, *Rubber Chem. Technol.*, 1965, **58**, 58.

309. P. Nieuwenhuizen, J. Reedijk, M. van Duin, and W. J. McGill, *Rubber Rev.*, 1997, **70**, 368.

310. D. J. Bourne, ed., ‘New Uses of Sulfur II’, Advances in Chemistry Series 165, American Chemical Society, Washington, 1978.

311. L. Blight, B. R. Currell, B. J. Nash, R. A. M. Scott, and C. Stillo, in D. J. Bourne, ed., ‘New Uses of Sulfur II’, Advances in Chemistry Series 165, American Chemical Society, Washington, 1978, Chapt. 2.

312. L. B. Blight, B. R. Currell, B. J. Nash, R. T. M. Scott, and C. Stillo, ‘New Uses Sulfur II’, Advances in Chemistry Series 165, American Chemical Society, Washington, 1978, p. 13.

313. B. K. Bordoloi, E. M. Pearce, L. Blight, B. R. Currell, R. Merrall, R. A. M. Scott, and C. Stillo, *J. Polym. Sci., Polym. Chem. Ed.*, 1980, **18**, 383.

314. L. Field, G. T. Bowman, J. J. Clement, D. E. Davidson, Jr., V. Eswarakrishnan, L. Field, J. M. Hoch, H. A. Musallam, R. O. Pick, R. Ravichandran, and P. K. Srivastava *Chem. Biol. Interact.* 1986, **57**, 161.

315. W. O. Foye, in ‘Burger’s Medicinal Chemistry’, 4th edition., ed. M. E. Wolff, Wiley, New York, 1981, Part III, Chapt. 37.

Acknowledgment

The invaluable assistance with the graphics by Dr. Yana Steudel is gratefully appreciated.

Superconductivity

Charles P. Poole, Jr & Horacio A. Farach
University of South Carolina, Columbia, SC, USA

Based in part on the article Superconductivity by Jeremy K. Burdett which appeared in the Encyclopedia of Inorganic Chemistry, First Edition.

1	Introduction	1
2	Brief History	1
3	Persistent Currents below T_c	2
4	Isotope Effect	3
5	Magnetic Fields inside a Superconductor	3
6	Critical Magnetic Fields	4
7	Supercurrent	5
8	Elements and Alloys	6
9	Compounds	6
10	Carbon Containing Superconductors	8
11	The Cuprate High-temperature Superconductors	8
12	Hole Type Cooper Pairs	10
13	Ceramics and Perovskites	11
14	The Yttrium Compound	11
15	The Bismuth and Thallium Compounds	12
16	The Mercury Compounds	12
17	Summary of Properties of the Cuprates	13
18	References	13

1 INTRODUCTION

A perfect superconductor is a material that, when cooled below a characteristic temperature T_c called the critical temperature, conducts electricity without any losses or any heating, and expels magnetic fields from its interior. The former property is called zero resistance, and the latter is called perfect diamagnetism. At temperatures above T_c, it is a normal metal, and is ordinarily not a very good conductor. For example, lead and tin become superconductors while copper and silver, which are much better conductors, do not superconduct.

The second characteristic property called perfect diamagnetism means that the superconductor material does not permit an applied magnetic field B to penetrate into its interior. Those that totally exclude the applied magnetic field are known as Type I, and they are the superconducting elements such as tin, mercury, and lead, which have the respective transition temperatures 3.7, 4.1, and 7.2 K. Other superconductors called Type II are also perfect conductors of electricity, but their magnetic properties are more complex. They totally exclude magnetic fields when the applied field is low, but only partially exclude them when the applied field is larger. Thus, in the region of higher magnetic fields, their diamagnetism is not perfect.

2 BRIEF HISTORY

In 1908, H. Kamerlingh Onnes started the field of low-temperature physics by liquifying helium in his laboratory at Leiden in the Netherlands. Three years later when Onnes was measuring the electrical resistance R of mercury, he expected to find a gradual decrease in R as the temperature was lowered.[1] Instead, to his surprise, he found that below 4.2 K its value dropped abruptly to zero, as shown in Figure 1. The next year Onnes discovered that when he applied a sufficiently strong magnetic field the resistance was restored to its normal value. Soon thereafter he discovered that the element lead was a superconductor below 7.2 K. This was the highest known transition temperature for 17 years until the record was surpassed by the element niobium ($T_c = 9.2$ K), as shown in Table 1.

It was not until 1933 that scientists became aware of the second distinguishing feature of a superconductor, that

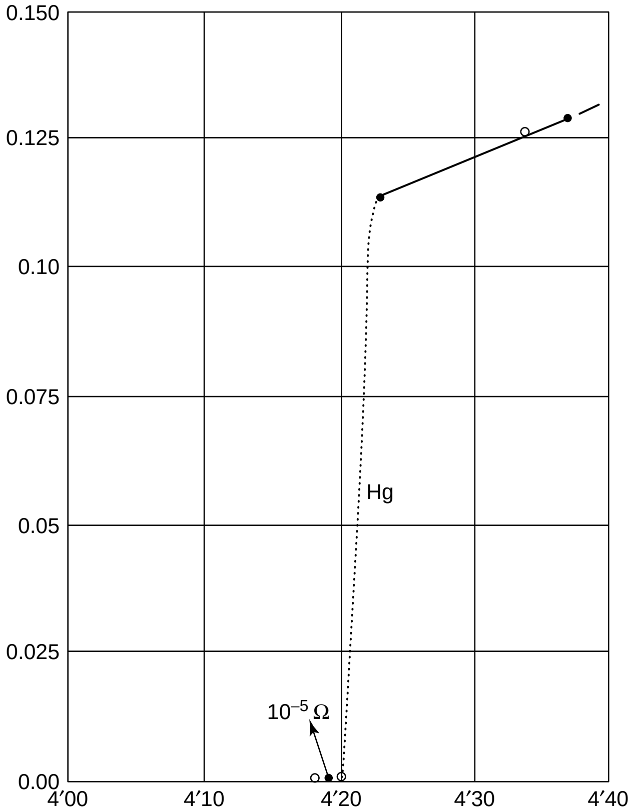

Figure 1 Resistivity versus temperature plot obtained by Kamerlingh Onnes when he discovered superconductivity in Leiden in 1911 (from Ref. 1)

Table 1 Superconducting transition temperature records through the years

Material	T_c (K)	Year
Hg	4.1	1911
Pb	7.2	1913
Nb	9.2	1930
$N_{0.96}Nb$	15.2	1950
Nb_3Sn	18.1	1954
$Nb_3(Al_{3/4}Ge_{1/4})$	20–21	1966
Nb_3 Ga	20.3	1971
Nb_3Ge	23.2	1973
$Ba_xLa_{5-x}Cu_5O_y$	30–35	1986
$(La_{0.9}Ba_{0.1})_2CuO_{4-\delta}$ at 1 Gpa	52	1986
$YBa_2Cu_3O_{7-\delta}$	95	1987
$Bi_2Sr_2Ca_2Cu_3O_{10}$	110	1988
$Tl_2Ba_2Ca_2Cu_3O_{10}$	125	1988
$Tl_2Ba_2Ca_2Cu_3O_{10}$ at 7 Gpa	131	1993
$HgBa_2Ca_2Cu_3O_{8+\delta}$	133	1993
$HgBa_2Ca_2Cu_3O_{8+\delta}$ at 25 Gpa	155	1993
$Hg_{0.8}Pb_{0.2}Ba_2Ca_2Cu_3O_x$	133	1994
$HgBa_2Ca_2Cu_3O_{8+\delta}$ at 30 Gpa	164	1994

is, its perfect diamagnetism. In that year, Meissner and Ochsenfeld[2] found that when they cooled a superconducting sphere below its transition temperature in a magnetic field it excluded the magnetic field, a phenomenon called the Meissner effect.

The report of the Meissner effect stimulated the London[3] brothers to develop the London equations, which explained this effect, and which also predicted how far a static external magnetic field can penetrate into a superconductor. The next theoretical advance came in 1950 with the theory of Ginzburg and Landau,[4] which described superconductivity in terms of an order parameter and provided a derivation for the London equations. Both of these theories are macroscopic or phenomenological in nature. In the same year, 1950, the isotope effect, whereby the transition temperature decreases when the average isotopic mass increases, was predicted theoretically by H. Fröhlich,[5] and observed experimentally by Maxwell and Reynolds *et al.*[6] This effect provided support for the then postulated electron–phonon interaction mechanism of superconductivity. Our present theoretical understanding of the nature of superconductivity is based on the BCS microscopic theory, which was proposed by J. Bardeen, L. Cooper, and J. R. Schrieffer in 1957.[7] This theory involves the coupling of conduction electrons as bound electron pairs called Cooper pairs that carry the supercurrent, and the presence of a gap between the normal and superconductive energy states. The earlier Ginzburg–Landau and London results fit well into the BCS formalism.

3 PERSISTENT CURRENTS BELOW T_C

The property of zero resistance is dramatically demonstrated by the phenomenon of persistent currents in superconducting loops. To establish an electrical current in a loop of superconducting wire, the ends of the wire can be connected to a battery in series with a resistor that limits the current,[8] as shown in Figure 2. When switch S_2 is closed, the current commences to flow in the loop, and then when switch S_1 is closed to bypass the battery and S_2 is opened to disconnect the battery, the loop resistance drops to zero and the current flow enters the persistent mode. The zero resistance property implies that the current will continue flowing indefinitely.

Many investigators have established currents in loops of superconducting wire and have monitored the strength of the associated magnetic field through the loop at later times using, for example, a magnetometer with a pickup coil, as shown in Figure 2. They find no detectable decay of the

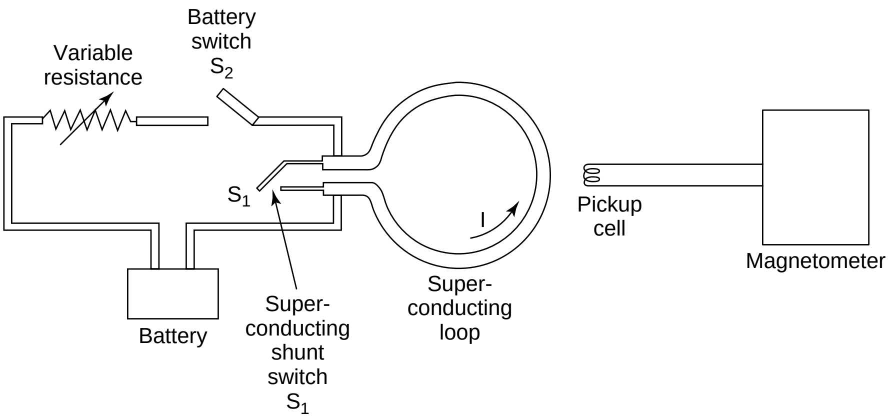

Figure 2 Experimental arrangement for establishing and measuring a persistent current. Switch S_2 is closed to send current through the loop, S_1 is closed to confine the current flow to the loop, and the magnetometer is employed to measure the magnetic field through the loop and thereby determine the current (from Ref. 8, p. 34)

current for times of the order of years. These experiments have established lower limits on the very long lifetime of the current and upper limits on the possible resistivity of superconducting materials. Several researchers have found that currents in superconductors persist for times far beyond a year, and resistivity limits as low as $\rho < 10^{-23}\,\Omega\,\mathrm{cm}$ have been reported.

The drop to zero resistance can be explained qualitatively in terms of a two fluid model in which some of the normal electrons transform to superelectrons that move through the material without resistance. The normal and superelectrons flow side by side, both carrying current. However, the current carried by the flow of superelectrons short circuits that arising from the flow of normal electrons, and the measured resistance vanishes.

4 ISOTOPE EFFECT

When an element has more than one isotope, the transition temperature often decreases with increasing isotopic mass M in accordance with the relation

$$M^{\alpha} T_{\mathrm{c}} = \text{constant} \tag{1}$$

where $\alpha = 1/2$ for the simplified BCS model. This is expected for a simple metal because the phonon frequency is proportional to the square root of the mass of the atom. For example, the electron–phonon coupling can also be mass dependent, and deviations from equation (1) are not unusual. Some elemental superconductors have isotope effect exponents α close to 1/2, such as Hg (0.50), Pb (0.489), Sn (0.47), and Zn (0.45). High-temperature superconductors ($T_{\mathrm{c}} > 77\,\mathrm{K}$) tend to have very low values of α.

5 MAGNETIC FIELDS INSIDE A SUPERCONDUCTOR

In free space, a magnetic field B, sometimes called magnetic induction, has associated with it an H-field given by the expression

$$B = \mu_{\mathrm{o}} H \tag{2}$$

where $\mu_{\mathrm{o}} = 4\pi \times 10^{-7}\,\mathrm{N/A^2}$ (newtons per square ampere) is the permeability of free space. It is the B-field that is experimentally measured because it enters into the Lorentz force equation $F = q(E + v \times B)$ for the force F on an electric charge q moving at a velocity v in the presence of an electric field E and a magnetic field B. The B-field inside a material with a permeability μ is given by

$$\begin{aligned} B &= \mu H && (3)\\ &= \mu_{\mathrm{o}} H(1+\chi) && (4)\\ &= \mu_{\mathrm{o}}(H+M) && (5) \end{aligned}$$

where $M = \chi H$ is the magnetization or magnetic moment per unit volume. The dimensionless susceptibility χ has a small positive value for a paramagnetic material, a large positive value ($\chi \gg 1$) for a ferromagnetic material, and a small negative value for a diamagnet ($\chi < 0$). The property of perfect diamagnetism corresponds to the susceptibility $\chi = -1$. This means that the B-field is zero inside a Type I superconductor, in accordance with the Meissner effect. The magnetization M is equal in magnitude and opposite in sign to the H-field: $M = -H$. When a Type I superconductor is placed between the pole pieces of a magnet, the B-field lines from the magnet go around it instead of entering it, and its own internal field remains zero, as shown in Figure 3.

There are two aspects to perfect diamagnetism in superconductors. The first is magnetic field exclusion: if a material in the normal state is zero field cooled (ZFC), that is, cooled below T_{c} to the superconducting state without any magnetic field present, and then it is placed in an external magnetic field, the field will be excluded from the superconductor. The second aspect is magnetic field expulsion. If the same material in its normal state is placed in a magnetic field, the field will penetrate and have almost the same value inside and outside because the permeability μ is so close to the free space value μ_{o}. If this material is then field cooled (FC), that is, cooled below T_{c} in the presence of this applied field, the field will be expelled from the material; this is the Meissner effect that was mentioned earlier.

When a Type I superconductor is in a magnetic field, the B-field is excluded from the interior, but there is a surface layer in which this field decays exponentially from its value B_0 outside to zero inside. This is expressed quantitatively by

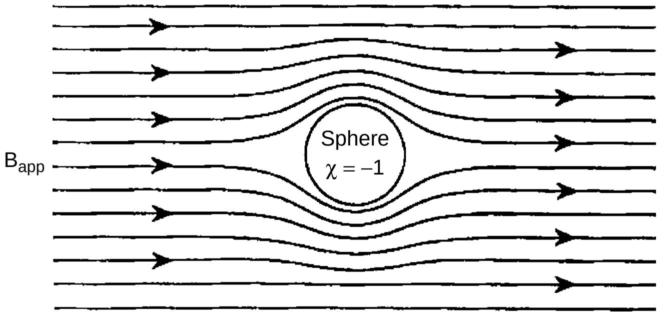

Figure 3 Curvature of magnetic field lines around a superconducting sphere in a constant applied field (from Ref. 8, p. 40)

the expression

$$B(x) \approx B_o \exp\left[\frac{-x}{\lambda}\right] \tag{6}$$

where in this equation we select $x = 0$ at the surface of the material, and the quantity λ is called the penetration depth. This is one of the two fundamental length parameters of a superconductor. The other, ξ, called the coherence length, will be introduced below. Values of λ and ξ for a number of superconductors are listed in Table 2. This exponential decay behavior is illustrated in Figure 4, where the origin of the coordinate x is now selected in the middle of the superconductor. It was mentioned above that a Type II superconductor partially excludes magnetic fields from its interior. For this case, there is an exponential falloff of the B-field from its value B_o outside to its value $B_\in$ inside, as shown in Figure 5.

Table 2 Coherence length ξ, penetration depth λ, and Ginzburg–Landau parameter $\kappa = \lambda/\xi$ for various superconductors

Material	T_c (K)	ξ (nm)	λ (nm)	κ
Cd	0.56	760	110	0.14
Al	1.2	550	40	0.03
Pb	7.2	82	39	0.48
Nb	9.25	39	50	1.28
NbTi	9.5	4	300	75
$PbMo_6S_8$ (Chevrel)	15.	2	200	100
Nb_3Ge (A-15)	23.2	3	90	30
K_3C_{60} (fullerene)	19	2.6	240	92
$La_{0.925}Ba_{0.075}CuO_4$	37	2.0	200	100
$YBa_2Cu_3O_7$	89	1.8	170	95
$HgBaCaCuO_x$	126	2.3		
$HgBa_2Ca_2Cu_3O_{8+\delta}$	131	100		

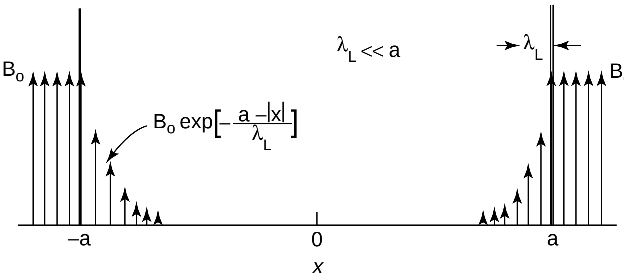

Figure 4 Exponential decay of magnetic field B in the surface layer of thickness λ of a Type I superconducting slab cylinder in an applied magnetic field B_{app} parallel to its surface (from Ref. 8, p. 135)

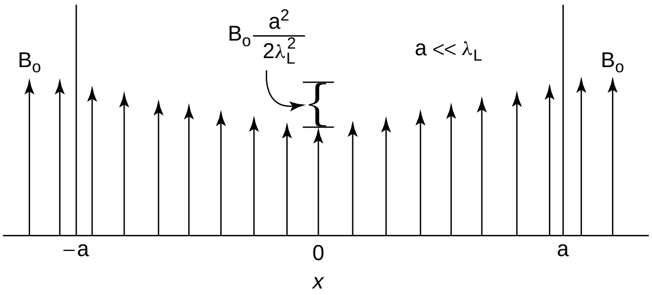

Figure 5 Magnetic field B outside and inside a Type II superconducting slab located in an applied magnetic field B_{app} oriented parallel to its surface (from Ref. 8, p. 135)

6 CRITICAL MAGNETIC FIELDS

If the external magnetic field applied to a Type I superconductor exceeds a certain value B_c, called the critical field, then the superconductor reverts to the normal state. The situation is more complicated in the case of a Type II superconductor. A Type II material becomes normal when the applied field exceeds a value B_{c2} called the upper critical field. There is also a lower critical field B_{c1} below which a Type II superconductor behaves like a Type I material and completely excludes all magnetic fields. In the intermediate range of applied fields

$$B_{c1} \le \mathrm{B}_{app} \le B_{c2} \tag{7}$$

the superconductor only partially excludes the applied field, in the manner illustrated in Figure 5. A Type II superconductor also has a characteristic magnetic field B_c called the thermodynamic critical field, which lies in the range $B_{c1} < B_c < B_{c2}$.

The values of these critical fields may be expressed in terms of the characteristic length parameters of a superconductor, that is, the penetration depth λ, the coherence length ξ, as well as in terms of the quantum of magnetic flux Φ_o. A constant magnetic field B passing through an area A perpendicular to the field direction has a quantity of magnetic flux Φ given by

$$\Phi = \mathrm{B\,A} \tag{8}$$

Since the SI unit for B is tesla (T), the units for magnetic flux are tesla meter squared. Magnetic flux is quantized, and a quantum of magnetic flux Φ_o. is a universal constant with the value

$$\Phi_{o\cdot} = \frac{\mathrm{h}}{2\mathrm{e}} = 2.068 \times 10^{-15}\ \mathrm{Tm}^2 \tag{9}$$

Expressed in terms of the flux quantum the critical fields have the values

$$B_c = \frac{\Phi_{o\cdot}}{2\sqrt{2}\pi\lambda\xi} \tag{10a}$$

$$B_{c1} = \frac{\Phi_{o\cdot}\ell n\kappa}{4\pi\lambda^2} \tag{10b}$$

$$B_{c2} = \frac{\Phi_{o\cdot}}{2\pi\xi^2} \tag{10c}$$

where $\kappa = \lambda/\xi$ is the Ginzburg–Landau parameter. A superconductor is Type I if $\kappa < 1/\sqrt{2}$, and Type II if $\kappa > 1/\sqrt{2}$

7 SUPERCURRENT

If Maxwell's inhomogeneous curl equation $\nabla \times H = J + \partial D/\partial t$ is invoked with the electric field term $D = 0$, then we obtain

$$\nabla \times B = \mu_o J_{sh} \tag{11}$$

where the quantity J_{sh} is called the shielding current. The presence of the curl operator $\nabla \times$ means that B and J_{sh} are everywhere mutually perpendicular to each other. The shielding current J_{sh} flows in the surface layer of a superconductor located in a magnetic field where B is decaying exponentially from its value B_0 outside to its final value inside. The presence of this current is the mechanism that shields the interior from the applied magnetic field B outside. Figure 6 shows the flow of this shielding current in the surface layer of a superconducting cylinder of thickness λ located in an external magnetic field directed along the axis of the cylinder.

When an applied current, called a transport current, is caused to flow through a superconductor it induces magnetic fields near it. For a Type I superconductor, this current flows in a surface layer of thickness λ, where λ is the penetration depth, corresponding to an area $A = 2\pi R\lambda$. The current $I = AJ$ is given by

$$I = 2\pi R\lambda J \tag{12}$$

where J is the current density, and this current produces a magnetic field at the surface of the conductor with the value

$$B_{surf} = \frac{\mu_o I}{2\pi R} \tag{13}$$

If the current is gradually increased in magnitude, then eventually B will reach the value of the critical field B_c and the superconductor will go normal. The current density J that is present when the superconductor goes normal is called the critical current density J_c, Its value is obtained by inserting equation (12) into equation (13) to give

$$B_c = \mu_o \lambda J_c \tag{14}$$

This expression depends on the temperature

$$B_c(T) = \mu_o \lambda(T) J_c(T) \tag{15}$$

At absolute zero, $T = 0$, we have $B_c(0) = \mu_o \lambda(0) J_c(0)$, and this is usually what is meant by equation (14). The existence of a critical current in a superconducting wire above which it goes normal is called the Silsbee effect.

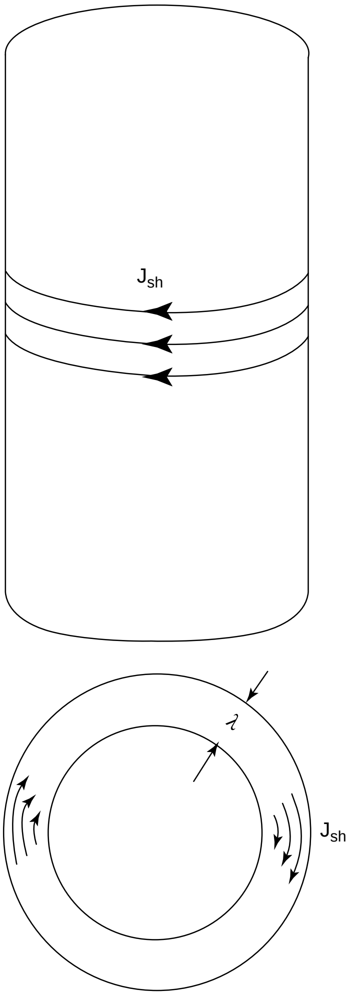

Figure 6 Shielding current flow J_{sh} in a surface layer of thickness λ around a Type I superconducting cylinder in an axial applied magnetic field B_{app} (from Ref. 8, p. 43)

These temperature dependencies often have the form

$$B_c(T) = B_c(0)\left[1 - \left(\frac{T}{T_c}\right)^2\right] \tag{16a}$$

$$\lambda(T) = \lambda(0)\left[1 - \left(\frac{T}{T_c}\right)^4\right]^{-1/2} \tag{16b}$$

$$J_c = J_c(0)\left[1 - \left(\frac{T}{T_c}\right)^2\right]\left[1 - \left(\frac{T}{T_c}\right)^4\right]^{1/2} \tag{16c}$$

We will also mention here the temperature dependencies of the energy gap E_g

$$E_g(T) \approx 3.52\, k_B T_c \left[1 - \left(\frac{T}{T_c}\right)\right]^{1/2} \tag{17}$$

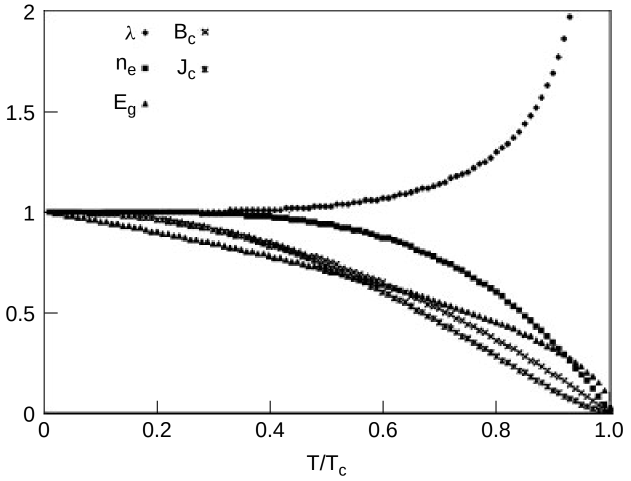

Figure 7 Temperature dependence of the relative values of the critical current density $J_c(T)$, critical field $B_c(T)$, energy gap Eg, density of superconducting electrons n_s, and penetration depth λ (T) in the Type II superconducting state below the transition temperature T_c

and the concentration n_s of superconducting electrons or Cooper pairs

$$n_s \approx n\left[1-\left(\frac{T}{T_c}\right)^4\right] \tag{18}$$

These temperature dependencies are sketched in Figure 7.

8 ELEMENTS AND ALLOYS

The earliest superconductors that were studied were elements and alloys (*see* ***Alloys***). All of the elements that superconduct except niobium are Type I superconductors, whereas niobium, alloys, and compounds are Type II. Elements with transition temperatures T_c above 2 K are: Tl (2.4 K), In (3.4 K), Sn (3.7 K), Hg (4.15 K), Ta (4.4 K), V (5.4 K), La (6.0 K), Pb (7.2 K), Tc (7.8 K), and Nb (9.25 K). Some elements become superconducting only as thin films, under pressure. The great majority of the superconductor elements have crystallographic structures of very high symmetry, either face-centered cubic (fcc), hexagonal close-packed (hcp), or body-centered cubic (bcc). Niobium, which has the highest transition temperature of an element, is also a constituent of many higher T_c compounds like Nb_3Ge ($T_c = 23.2$ K), but it has not appeared prominently in the newer cuprate high-temperature superconductors. Tables 1 and 2 list transition temperatures T_c for a number of elements, alloys, and compounds,

Random binary alloys in which two transition elements are mixed in all proportions have several possibilities: the transition temperature can be higher than that of both elements, between the T_c values of the constituents, or lower than either one alone The number of valence electrons N_e has a strong influence on the T_c values of transition elements and their alloys. Studies carried out with sequences of transition metals that are adjacent to each other in the periodic table show that T_c tends to have a maximum value near $N_e = 4.7$ and near $N_e = 6.5$. The elements Ta, V, and Nb with $N_e = 5$, and T_c with $N_e = 7$, have relatively high transition temperatures Other properties such as the electronic specific heat factor γ, the magnetic susceptibility χ, and the pressure derivative dT_c/dP have regular dependencies on the electron concentration.

9 COMPOUNDS

The phenomenon of superconductivity is common in several particular types of compounds. Thus more than two dozen binary compounds with the fcc sodium chloride (NaCl) structure are superconducting. The carbides AC and nitrides AN, such as NbN with $T_c = 17$ K, have the highest transition temperatures of this group, and the metallic A atoms with T_c values above 10 K were Nb, Mo, Ta, W, and Zr. The NaCl-type superconductors are compositionally stoichiometric but not structurally so. In other words, these compounds have a small to moderate concentration of vacancies in the lattice. For example, YS has 10% vacancies, which means that its chemical formula should properly be written $Y_{0.9}S_{0.9}$. Nonstoichiometric NaCl-type compounds such as $Ta_{1.0}C_{0.76}$ also exist. Ordinarily the vacancies are random, but sometimes they are ordered.

The highest transition temperatures of the older superconductors were obtained with intermetallic compounds A_3B, which have the cubic A-15 structure, and extensive data are available on them. Nb_3Sn can be considered the prototype of this class. These compounds have a cubic structure with the two B atoms at the body center and apical positions of the unit cell, and the six A atoms paired on each face in a configuration that amounts to the presence of chains of A atoms with spacings of one half of the lattice constant a. The A atom is one of the transition elements, and the B element is either a transition element or it is in row III, IV, V, or VI of the periodic table. High transition temperatures occur when B is either a metal (Al, Ga, Sn) or a nonmetal (Si, Ge), but not a transition element. Figure 8 shows T_c data for 8 A elements and 18 B elements for a total of 144 possibilities, and 43% of them superconduct.[9] The figure demonstrates the close correlation between the transition temperature and the valence electron concentration N_e that was mentioned above. High values of T_c occur for $N_e = 4.5$ (Nb_3Ga, $T_c = 20.3$ K), $N_e = 4.75$ (Nb_3Ge, $T_c = 23.2$ K), $N_e = 6.25$ (Nb_3Pt, $T_c = 9.9$ K) and $N_e = 6.5$ (Nb_3Au, $T_c = 11.5$ K).

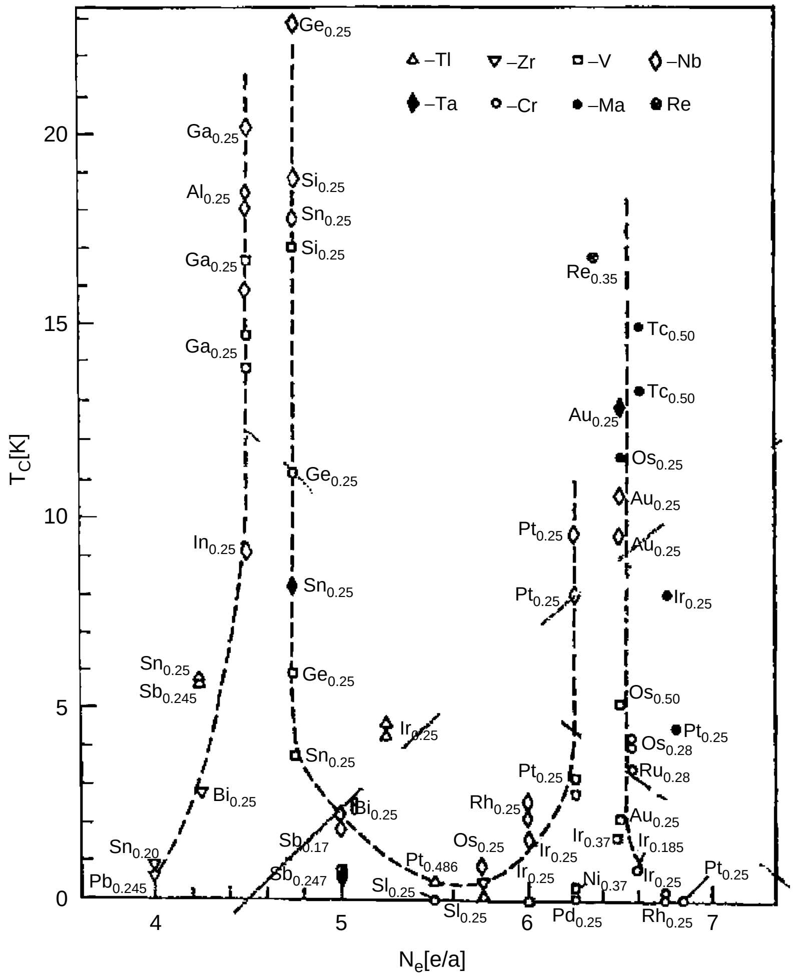

Figure 8 Dependence of the transition temperature T_c on the number of valence electrons Ne in $A_{0.75}B_{0.25}$ compounds of the A15 structure (from Ref. 9, p. 269)

There are several dozen metallic AB_2 compounds called Laves phases that are superconducting; they have either cubic or hexagonal crystal structures. Some have critical temperatures above 10 K and high upper critical magnetic fields B_{c2}. For example, $Zr_{1/2}Hf_{1/2}V_2$ has $T_c = 10.1$ K, $B_{c2} = 24$ T, and a compound with a different Zr/Hf ratio has similar T_c and B_{c2} values with the critical current density $J_c \approx 4 \times 10^5$ A/cm^2. These materials also have the advantage of not being as hard and brittle as some other intermetallics and alloys with comparable transition temperatures.

The Chevrel phases $A_xMo_6X_8$ are mostly ternary transition metal chalcogenides (*see* ***Chalcogenides: Solid-state Chemistry***) where X is S, Se, Te and A can be almost any element. These compounds have relatively high transition temperatures and critical fields B_{c2} of several tesla. However, the critical currents, typically 2 to 500 A/cm^2, are rather low. The trigonal structure sketched in Figure 9 is a simple cubic arrangement slightly distorted along the (111) axis of Mo_6X_8-group building blocks, each consisting of a deformed cube with large X atoms at the vertices and small Mo atoms at the centers of the faces. The Mo_6X_8 group may be considered as an Mo_6 octahedron inscribed in an X_8 cube. Mo_6X_{12} group building blocks are also found. The parameter x in the formula $A_xMo_6X_8$ assumes various values such as $x = 1$ (e.g. YMo_6S_8, $LaMo_6S_8$), $x = 1.2$ (e.g. $V_{1.2}Mo_6$ Se_8), $x = 1.6$ ($Pb_{1.6}Mo_6S_8$) and $x = 2$ (e.g. Cu_2Mo_6 Se_8). This parameter can vary because there are so many available sites between the cubes for the A cations. Most of the space is occupied by the large chalcogenide anions that have the radii S: 0.184, Se: 0.191, and Te: 0.211 nm. The electronic and superconducting properties depend mainly on the Mo_6X_8 group. Magnetic order and superconductivity are known to coexist in Chevrel phase compounds when A is a rare earth ion since its magnetic state does not influence the superconducting properties.

The compound $Ba_{1-x}K_xBiO_{3-y}$ with $T_c \approx 30$ K for $x \approx 0.4$ has the cubic perovskite structure. It is the first oxide superconductor without copper with a transition temperature above that of all of the A-15 compounds. The

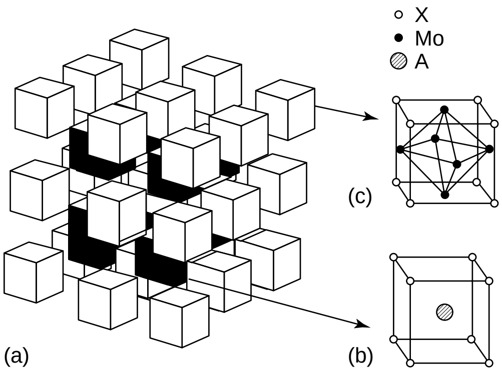

Figure 9 Structure of the Chevrel phase $A_xMo_6X_8$ (from Ref. 9, p. 431)

perovskite structure of this compound may be considered as a prototype of that of the high-temperature superconducting cuprates, which have a distorted perovskite type of atom arrangement.

10 CARBON CONTAINING SUPERCONDUCTORS

Organic compounds and polymers are ordinarily electrical insulators, but a few of them are good electrical conductors, such as organic compound 7,7,8,8-tetracyano-*p*-quinodimethane, called TCNQ for short, which forms highly conducting salts with a number of compounds. Several $(TMTSF)_2X$ charge transfer salts (tetramethyltetraselenafulvalene) superconduct under pressure, where TMTSF is an electron donor and the monovalent counterion X^- is, for example, $AsF_6{}^-$, $ClO_4{}^-$, $FSO_3{}^-$, $PF_6{}^-$, $ReO_4{}^-$, $SbF_6{}^-$, and $TaF_6{}^-$. The electrical properties of organic conductors are often highly anisotropic. TCNQ salts behave as quasi one-dimensional conductors, and salts of other organics such as bis(ethylenedithio)tetrathiafulvalene, called ET for short, exhibit low dimensional behavior, with T_c reported in excess of 13 K. In addition, the superconducting properties of the organics such as the critical fields and the coherence length are often anisotropic. For example, the triclinic compound ß-$(ET)_2I_3$ has the upper critical fields $B_{c2} = 1.78$, 1.70 and 0.08 T along the a, b and c crystallographic directions, respectively, The coherence lengths are $\xi_{\text{plane}} = 350\,\text{Å}$ in the conducting plane and $\xi_z = 23\,\text{Å}$ perpendicular to this plane, the latter being close to the longest lattice constant $c = 15.3\,\text{Å}$.

The fullerenes,[10] the third isotropic form of carbon, (*see **Carbon: Fullerenes***) have a basic C_{60} molecule, which consists of sixty carbon atoms at the apices or vertices of a regular truncated icosahedron (32 sided figure) 7.1 Å in diameter, as shown in Figure 10. This structure contains 12 regular pentagons and 20 hexagons, and all of the carbon atoms are equivalent to each other. It might be called the world's smallest soccer ball! Because of its resemblance to the geodesic dome of architect R. Buckminster Fuller, it has been referred to as Buckminsterfullerene, or fullerene for short. The dual resemblances have prompted the sobriquet Buckyball. There are other fullerenes C_n with, for example, $n = 70$, 76, 78, 84, ..., but none of these are superconductors.

The compound C_{60} is not itself a superconductor, but when alkali metals are added it becomes superconducting. The doped compound forms a face-centered cubic lattice with a lattice constant of 10.04 Å, and this structure has two tetrahedral holes and one octahedral hole per C_{60} molecule. If all of these holes are occupied by alkali metals A, the resulting compound is A_3C_{60}. An example of such a compound is K_2RbC_{60} with potassium in the smaller tetrahedral holes and rubidium in the larger octahedral holes. The transition temperatures of these doped fullerenes range from 19 to 47 K. The compound Rb_3C_{60} was found to have an isotope effect exponent $\alpha = 0.37$, somewhat less than the BCS value 0.5.

11 THE CUPRATE HIGH-TEMPERATURE SUPERCONDUCTORS

Until now we have been discussing the properties of superconductors in general, and the examples that we have given were usually classical types with transition temperatures T_c below 24 K, and which usually were studied with liquid helium (at 4.2 K) as the refrigerant. The discovery of the cuprate materials[11] that superconduct above 77 K raises the possibility of commercial applications using liquid nitrogen as the cooling fluid. This considerably reduces

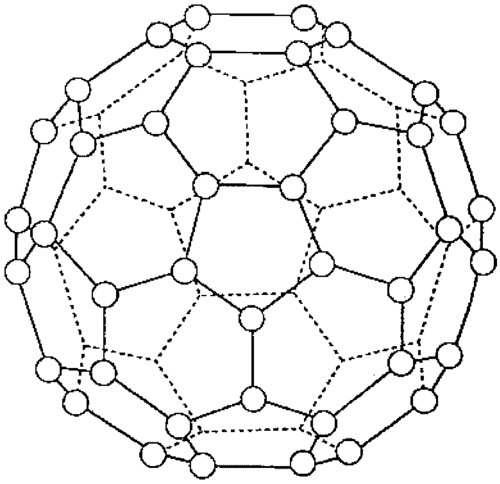

Figure 10 Structure of the Buckminsterfullerene molecule (from Ref. 8, p. 88)

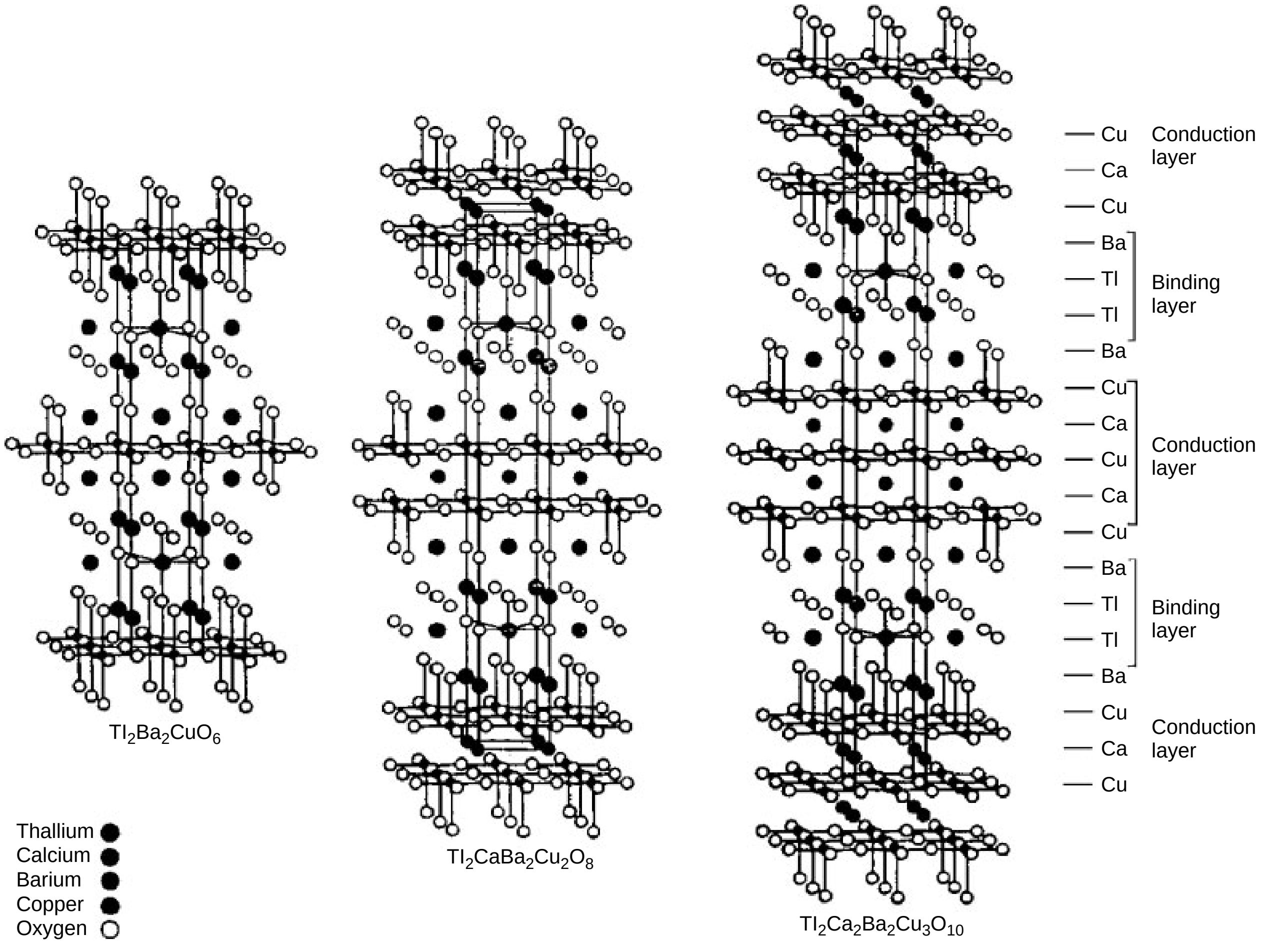

Figure 11 Layering schemes of three thallium compound superconductors $Tl_2Ba_2Ca_{n-1}Cu_nO_{2n+6}$, where there are $n = 1$, 2, 3 CuO_2 planes in the conduction layers, from left to right. (Reprinted with permission from C.C. Torardi, M.A. Subramanian, J.C. Calabrese, J. Gopalakrishnan, M.K. Morrissey, T.R. Askew, R.B. Flippen, U. Chowdhry and A.W. Sleight, *Science*, 1988, **240**, 631. © 1988 AAAS. Y-hotlink to www.sciencemag.org)

the high cost of operation since expensive liquid helium cryostats would no longer be needed. In addition, it is much more economical to use liquid nitrogen, which sells for 25¢ a liter, rather than liquid helium, which costs $4 a liter.

The cuprate superconductors all have the same layered structure**[12]** that is sketched in Figure 11 for three thallium cuprates, which have one, two, and three copper oxide planes, that is, $n = 1$, 2, and 3 in their chemical formula $Tl_2Ba_2Ca_{n-1}Cu_nO_{2n+4}$. There are alternating conduction layers where the flow of supercurrent takes place, and binding layers that support and hold together the conduction layers. The conduction layers contain copper oxide (CuO_2) layers of the type sketched in Figure 12, where each copper ion Cu^{2+} is surrounded by four oxygen ions O^{2-}.**[13]** These planes are held together in the structure by calcium Ca^{2+} ions located between them. An exception to this is the yttrium compound in which the intervening ions are yttrium Y^{3+} instead of calcium. These CuO_2 planes are very close to being flat. In the normal state above T_c the conduction electrons released by the copper atoms move about on these CuO_2 planes and carry the electric current. In the superconducting state below T_c these same electrons form the Cooper pairs that carry the supercurrent along the planes.

Each particular cuprate compound has its own specific binding layer consisting mainly of sublayers of metal oxides MO where M is a metal atom. Figure 11 shows the binding layers of the thallium compounds $Tl_2Ba_2Ca_{n-1}Cu_nO_{2n+4}$ that contain BaO and TlO. The analogous bismuth compounds contain BaO and BiO, while the mercury compounds have BaO and HgO. Planes of LaO and NdO, respectively, form the binding layers of the lanthanum and neodymium superconductors. These binding layers are sometimes called charge reservoir layers because they contain the source of charge that is called upon to bring about the hole doping of the conduction planes through the following interaction

$$Cu^{2+} \longrightarrow Cu^{3+} + e^- \qquad (19)$$

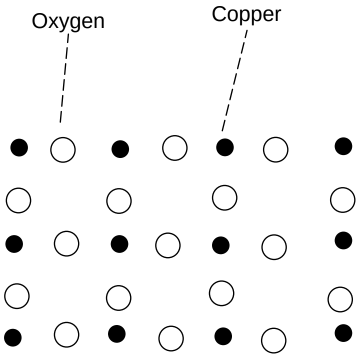

Figure 12 Arrangement of copper and oxygen atoms in a CuO_2 plane of the conduction layer (from Ref. 13, p. 99)

taking place in a copper oxide plane. Most cuprate compounds contain 1, 2, or 3 copper oxide planes, and Table 3 gives the transition temperatures of 11 of these compounds that superconduct. The dashes in the table designate compounds that either do not exist or do not superconduct. We see from this table that the mercury compounds are the best, with the thallium ones second, but the bismuth compounds seem to be more easily made into wire, and they may be preferable for applications. However, the yttrium compound, because of its ease of synthesis and interesting properties, has been the most widely studied of the group. We also see from this table that increasing the number n of CuO_2 planes in the conduction layers raises T_c, but unfortunately T_c begins to decrease for further increases in this number beyond 3.

12 HOLE TYPE COOPER PAIRS

In classical superconductors, the electric current is carried by paired electrons called Cooper pairs, with a charge of $-2e$. However, in most of the new cuprate materials the Cooper pairs have the positive charge $+2e$; in other words they are paired positive ‘holes’ designated by h. By holes we mean absent electrons in an energy level that is otherwise filled with electrons. A plus one hole would be formed in a level that is one electron short of being filled. The charge transfer process of equation (19) can be written in the equivalent way

$$Cu^{2+} + h^{+} \longrightarrow Cu^{3+} \qquad (20)$$

where hole notation is employed. The ion Cu^{3+} can be viewed as a Cu^{2+} ion containing a hole. Successive electron exchange interactions of the type

$$Cu^{2+} = Cu^{3+} + e^{-} \qquad (21a)$$

$$Cu^{3+} + e^{-} = Cu^{2+} \qquad (21b)$$

can cause the hole on Cu^{3+} to hop from Cu^{2+} ion to Cu^{3+} ion as it moves along a line of divalent copper ions in the conduction layer.

Table 3 Superconducting transition temperatures of the cuprates

		Number of Cu_2O planes		
Compound	Formula	$n = 1$	$n = 2$	$n = 3$
Lanthanum	$(La_{0.9}Sr_{0.1})_2CuO_4$	35	–	–
Neodymium	$(Nd_{0.9}Ce_{0.1})_2CuO_4$	35	–	–
Yttrium	$YBa_2Cu_3O_7$	–	92	–
Bismuth	$Bi_2Sr_2Ca_{n-1}Cu_nO_{2n+4}$	0	84	110
Thallium	$TlBa_2Ca_{n-1}Cu_nO_{2n+4}$	90	110	125
Thallium	$Tl_2Ba_2Ca_{n-1}Cu_nO_{2n+4}$	90	110	125
Mercury	$HgBa_2Ca_{n-1}Cu_nO_{2n+4}$	95	133	133

Another way to see that we are dealing with a hole conduction process is to consider the outermost electronic shell of the copper ions, which is called a 3d level in the notation of atomic spectroscopy. This level can hold a maximum of 10 electrons, and is filled for the ion Cu^{+}. The ion Cu^{2+} has only nine electrons in its 3d level, which corresponds to 10 electrons plus one hole, and Cu^{3+} has 8 electrons, or 10 electrons plus two holes. Electrical current in the normal state is carried by these holes, which are in the conduction band, via the hopping mechanism of equation (21). Electric current in the superconducting state is carried by Cooper pairs formed from these holes.

The number of holes in the copper oxide planes depends on the ratio of ions with Cu^{3+} to those with Cu^{2+} valence states. To see how this can be controlled by doping, consider La_2CuO_4 as a purely ionic compound composed of two La^{3+} ions, one Cu^{2+} ion and four O^{2-} ions. If 10% of the trivalent La^{3+} is replaced by divalent Sr^{2+} to form the compound $(La_{0.9},Sr_{0.1})_2CuO_{4-x}$, there are two ways to achieve electrical neutrality, that is, to make the positive charges balance the negative charges in the compound. One way is to let all of the copper remain as Cu^{2+} and reduce the amount of oxygen, and if we do this we obtain the compound $(La_{0.9},Sr_{0.1})_2CuO_{3.9}$. The copper oxide planes are not changed by this process since all of the copper is still in the Cu^{2+} state. The other way to keep the oxygen content the same corresponding to the formula $(La_{0.9},Sr_{0.1})_2CuO_4$ and to achieve charge neutrality is by converting 20% of the divalent Cu^{2+} ions to trivalent Cu^{3+}. This results in copper oxide planes with many holes arising from the presence of so many Cu^{3+} ions. The charge balance equation for achieving charge neutrality in this manner is

$$La^{3+} + Cu^{2+} \longrightarrow Sr^{2+} + Cu^{3+} \qquad (22)$$

In practice, both processes can occur; there can be some decrease of oxygen and some conversion to Cu^{3+} ions. The concentration of holes on the copper oxide planes can be calculated when the parameter x in the formula $(La_{0.9},Sr_{0.1})_2CuO_{4-x}$ is known. This superconductor is often called the lanthanum compound. The superconducting transition temperature depends on the hole concentration in

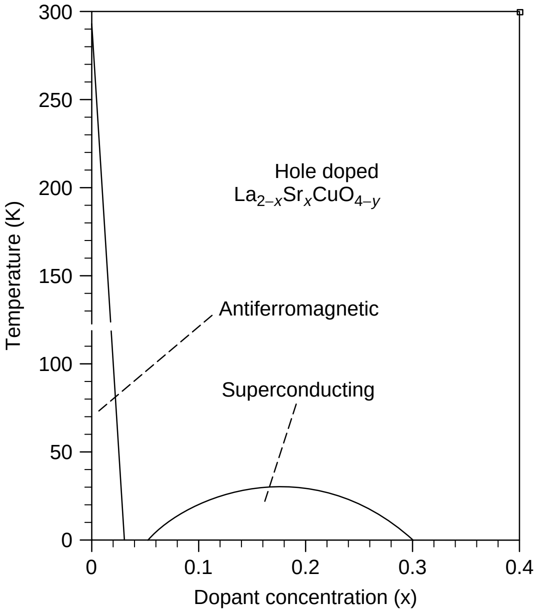

Figure 13 Plot providing the superconducting transition temperature versus the strontium content x of the compound $La_{2-x}Sr_xCu_{4-y}$. The region of antiferromagnetic behavior is also indicated. (Ref. 13, with kind permission of Springer Science & Business Media)

the manner indicated in Figure 13. The graph shows that superconductivity only occurs over a certain range of hole concentrations, and there is an optimum concentration for the highest T_c. The figure also shows that there is an ordered antiferromagnetic phase at low Sr contents.

One of the consequences of a hole hopping process involving a two dimensional array of copper ions is that the superconducting current is very directional dependent or anisotropic. The hopping tends to occur between the copper ions that have the smallest separation from each other, that is, those in the plane. The distance between copper ions in adjacent planes is much larger than within the planes, and hence charge hopping between planes is much less efficient. This means that the current flows much more easily within a plane than it does perpendicular to the planes. In a single crystal the measured current above T_c and the critical current density J_c below T_c will depend on the direction in which the determination is made. Many other properties of cuprate superconductors such as the critical fields B_{c1} and B_{c2}, the penetration depth λ and the coherence length ξ are also dependent on the direction.

13 CERAMICS AND PEROVSKITES

Although the new superconductors have been widely referred to as ceramics, they are more properly classified as perovskites since their structures resemble that of the mineral perovskite, or calcium titanate $CaTiO_3$. The atom positions in the upper (and lower) parts of the lanthanum compound unit cell of Figure 14 are similar to those in perovskite with Cu present in the titanium (Ti) sites of perovskite, La in the centrally located calcium positions, and oxygen at the same location in both structures.

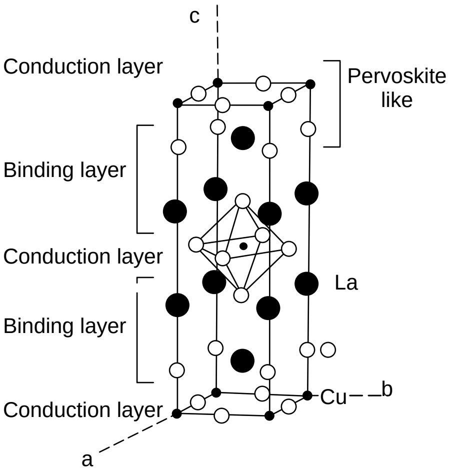

Figure 14 Atom positions in the tetragonal unit cell of the La_2CuO_4 compound. In the superconducting compound $La_{1-x}Sr_xCuO_4$ strontium replaces lanthanum in some of the La sites (from Ref. 13, p. 109)

In contrast to this, the ceramic designation was not based on structural grounds, but rather emerged from the similarity between the way the cuprate superconducting compounds and ceramics are made. For example, La–Sr–Cu–O is made by heating mixtures of lanthanum oxide, strontium carbonate, and copper oxide in air at 900 to 1000 °C for 20 h. The proportions of atoms in the initial mixture should be the same as in the end product, and for the compound $(La_{0.9}Sr_{0.1})_2CuO_4$ the ratio La:Sr:Cu is 1.8:0.2:1. The materials are usually ground to a fine mixture before heating. After the heating in air, they are cooled, pressed into pellets, and reheated from 900 to 1000 °C for several more hours.

14 THE YTTRIUM COMPOUND

The discoveries that generated the extensive news coverage in early 1987 were the initial report of superconductivity in the lanthanum compound by Bednorz and Müller,[11] and the observation of superconductivity in the compound $YBa_2Cu_3O_{7-x}$ at 92–94 K, well above the boiling point (77 K) of liquid nitrogen. The latter result was the outcome of a collaboration between the research groups of C. W. Chu[14] of the University of Houston and M. K. Wu[15] of the University of Alabama.

Like the lanthanum compound that we just described, the present material is deficient in oxygen, and the x in the chemical formula denotes the possibility of different amounts of oxygen in the crystal lattice. The parameter x is zero when all of the oxygen sites are full, and x is about 0.1 for the highest T_c. Many of the important electrical, magnetic, and other properties are also sensitive to the amount of oxygen in the crystal. As the oxygen content is varied, the relative amounts of Cu^{3+} to Cu^{2+} change to keep the crystal electrically neutral. The structure is orthorhombic with lattice constants a $\approx$ b, in the superconducting region, and tetragonal with a = b for $x < 0.4$ where it no longer superconducts. There are two copper oxide planes in the conduction layer, with yttrium ions between these two planes. The middle of the binding layer also has copper ions, and they form chains Cu–O–Cu–O–...... along the crystallographic b axis that may contribute to the superconducting properties.

The substitution of first transition series ions such as zinc or nickel for copper in $YBa_2Cu_3O_x$ generally causes a sharp reduction of the transition temperature, which underlines the important role that copper plays in the superconducting mechanism. The deterioration of the superconducting properties is greater when the nonmagnetic zinc ion is substituted for copper compared to the magnetic nickel ion, hinting at the importance of the magnetic nature of copper in the superconducting mechanism. Most of the rare earth elements can replace yttrium without a significant change in the superconducting properties.

15 THE BISMUTH AND THALLIUM COMPOUNDS

In this family of bismuth[16] and thallium[17] compounds, there are many compositional variations that give superconductivity, some of them involving, for example, the addition of lead. Table 3 lists transition temperatures for some members of these series of compounds

$$Bi_2Sr_2Ca_{n-1}Cu_nO_{2n+4} \quad \text{Bi22}(n-1)\text{n} \quad n = 1, 2, 3, 4 \qquad (23a)$$

$$Tl_2Ba_2Ca_{n-1}Cu_nO_{2n+4} \quad \text{Tl22}(n-1)\text{n} \quad n = 1, 2, 3, 4 \qquad (23b)$$

where n is the number of copper atoms that are present, which corresponds to the number of planes in the conduction layer. The binding layers for the thallium family are shown in Figure 11. The transition temperature rises as n increases from 1 to 3, and then decreases for $n = 4$, as indicated in Figure 15, with Tl 2223 or $Tl_2Ba_2Ca_2Cu_3O_{10}$ having the highest value $T_c = 125$ K. The similarity of all the structures having different n values has resulted in another problem. It is difficult to synthesize materials that are entirely of a single phase, having only one n value. Most of the fabrication processes result in a mixed phase product.

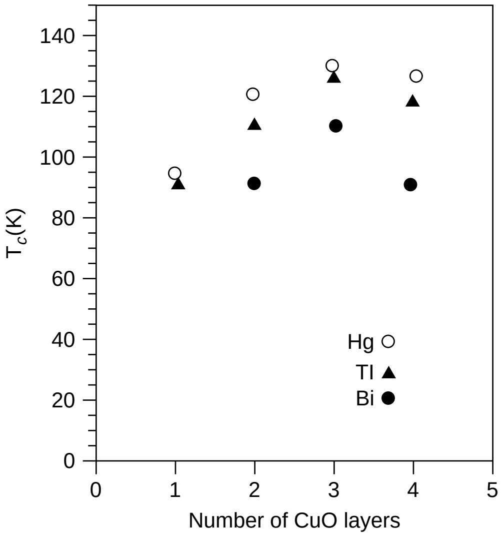

Figure 15 The superconducting transition temperature of the $Bi_2Sr_2Ca_{n-1}Cu_nO_{2n+4}$, $Tl_2Ba_2Ca_{n-1}Cu_nO_{2n+4}$ and $HgBa_2Ca_{n-1}$-Cu_nO_{2n+2} compounds versus the number n of copper oxide planes in the conduction layers. (Ref. 13, with kind permission of Springer Science & Business Media)

16 THE MERCURY COMPOUNDS

In the spring of 1994, a new superconductor was synthesized that had zero resistance at 133 K and some samples had an onset of superconductivity as high as 140 K. The material is $HgBa_2Ca_2Cu_3O_{8+x}$. The structure of this copper oxide superconductor is tetragonal. There is a small additional amount of oxygen in the mercury layer that is not strongly bonded in a particular site in this layer, but can diffuse between them. However, a more stable lead substituted version of this material $Hg_{0.7}Pb_{0.3}Ba_2Ca_2Cu_3O_{8+x}$ with about 1/3 of the mercury sites substituted by lead has been synthesized. This is because an oxygen at a site between lead and mercury is more strongly bonded than one between two mercury atoms. Table 3 and Figure 15 show the dependence of T_c on the number n of copper oxide planes.

There is much interest in this superconductor for two reasons. Measurements of the effect of pressure on the material indicate that the onset transition temperature increases to 147 K when the pressure is raised to 230 000 times atmospheric pressure (23.5 giga Pascal). The result excited many researchers because pressure on a material can be created chemically by replacing some fraction of an ion by a similar ion of smaller radius. The obvious choice in this case was to replace the larger barium with smaller strontium. This had worked with the lanthanum compound discussed earlier. Unfortunately nature is not always so predictable. Replacement of barium by strontium reduced T_c to 127 K instead of increasing it beyond 133 K. The other reason for the interest in this material seems much more important. Resistance measurements in dc magnetic fields have shown that fields up to 10 tesla do not increase the resistance at 77 K. This means that the flux is more strongly pinned in this superconductor than it is in the other cuprates at 77 K. This is good for applications because critical currents can reach higher values.

17 SUMMARY OF PROPERTIES OF THE CUPRATES

We have discussed the characteristics of a number of copper oxide superconductors, a group of materials that have many properties in common. These shared properties might well provide the key to the development of an explanation of the mechanism of high-temperature superconductivity. The most important common features are:

1. presence of magnetic copper ions
2. arrangement of copper and oxygen ions in two dimensional arrays
3. hole hopping conduction largely confined to copper oxide planes
4. presence of binding layers providing a source for hole doping of copper oxide planes
5. dependence of transition temperature and superconductivity of concentration of holes
6. evidence for short range antiferromagnetic ordering in copper oxide layers

18 REFERENCES

1. H. Kamerlingh Onnes, *Leiden Commun.*, 1911, 120b, 122b, 124c.
2. W. Meissner and R. Ochsenfeld, *Naturwissenschaften*, 1988, **21**, 787.
3. F. London and H. London, *Proc. Roy. Soc. (London)*, 1935, **A141**, 71.
4. V. L. Ginzburg and L. Landau, *Zh. Eksp. Teor. Fiz.*, 1950, **20**, 1064.
5. H. Fröhlich, *Phys. Rev.*, 1950, **79**, 845.
6. E. Maxwell, *Phys. Rev.* 1950, **78**, 477; C. A. Reynolds, B. Serin, W. H. Wright, and L. B. Nesbitt, *Phys. Rev.*, 1950, **78**, 487.
7. J. Bardeen, L. N. Cooper, and J. R. Schrieffer, *Phys. Rev.*, 1957, **108**, 1175.
8. C. P. Poole Jr, H. A. Farach, and R. J. Creswick, 'Superconductivity', Wiley, New York, 1995.
9. S. V. Vonsovsky, Yu. A. Izyumov, and E. Z. Kurmaev, 'Superconductivity in Transition Metals', Springer, Berlin, 1982.
10. M. S. Dresselhaus, G. Dresselhaus, and P. C. Eklund, 'Science of Fullerenes and Carbon Nanotubes', Academic Press, San Diego, CA, 1995.
11. J. G. Bednorz and K. Müller, *Z. Phys.*, 1986, **B64**, 189.
12. C. C. Torardi, M. A. Subramanian, J. C. Calabrese, J. Gopalakrishnan, M. K. Morrissey, T. R. Askew, R. B. Flippen, U. Chowdhry, and A. W. Sleight, *Science*, 1988, **240**, 631.
13. F. J. Owens and C. P. Poole Jr, 'The New Superconductors', Plenum, New York, 1996.
14. C. W. Chu, P. H. Hor, R. L. Meng, L. Gao, Z. J. Huang, and Y. Q. Wang, *Phys. Rev. Lett.*, 1987, **58**, 405; *Science*, 1987, **235**, 567.
15. M. K. Wu, J. R. Ashburn, C. J. Torng, P. H. Hor, R. L. Meng, L. Gao, Z. J. Huang, Y. O. Wang, and C. W. Chu, *Phys. Rev. Lett.*, 1987, **58**, 908.
16. C. W. Chu, P. H. Hor, R. L. Meng, L. Gao, Z. J. Huang, J. Bechtold, M. K. Wu, and Y. Q. Wang, *Mater. Res. Soc. Symp. Proc.*, 1987, **99**, 15.
17. Z. Z. Sheng and A. M. Hermann, *Nature*, 1988, **332**, 55.

Supported Organotransition Metal Compounds

Brian E. Hanson
Virginia Polytechnic Institute & State University, Blacksburg, VA, USA

1 Introduction 1
2 Solid Supports 1
3 Covalently Bound Organotransition Metal Compound 3
4 Physically Immobilized Organotransition Metal Complexes 6
5 Ionically Immobilized Organotransition Metal Complexes 7
6 Related Articles 8
7 References 8

Abbreviations

CP-MAS = cross-polarization magic angle spinning; HMDS = hexamethyldisilane; TPPTS = trisulfonated triphenylphosphine.

1 INTRODUCTION

Supported organotransition metal complexes have important applications in the design and modeling of new catalysts. They are of interest in the modification of surface properties of solids, including electrodes, and as stoichiometric reagents.

A catalyst may be defined as homogeneous or heterogeneous depending on the phase of matter that contains the catalytically active species. Heterogeneous catalysts comprise those systems in which the catalytically active species is in a separate phase from the substrate. For true heterogeneous catalysts, the catalytic reaction occurs at the interface between the two phases. Typically, the catalyst is a solid and substrates are liquids or gases, although it is possible to devise liquid/liquid and liquid/gas systems. A catalyst is defined as homogeneous when it is in the same phase as the substrate. Reactions catalyzed by organotransition metal complexes are generally homogeneous with all reactants, and the catalyst, dissolved in an appropriate solvent.

Heterogeneous catalysts are usually considered to have a technological advantage over homogeneous catalysts in that the products and the catalyst are easily separated. Homogeneous catalysts often have the advantage of milder reaction conditions and greater selectivity, but suffer in the ease of removal of the catalyst from products. In an effort to combine the relative merits of homogeneous and heterogeneous catalysts, organotransition metal complexes have been supported, that is, immobilized, on solids. The literature also refers to these complexes as ‘heterogenized.’ Immobilized organotransition metal complexes of this type comprise the largest class of supported complexes. Supported organotransition metal complexes can serve as models for heterogeneous catalysts or can be used synthetically as precursors for heterogeneous catalysts.

There are other instances when supporting an organotransition metal complex may have an advantage over its homogeneous counterpart. For example, when designing stoichiometric reagents for organic transformations, a solid reagent can be easily removed from a reaction by filtration.

Organometallic complexes are used as precursors for thin films generated by chemical vapor deposition techniques. Supported organotransition metal complexes can serve as both models for film growth and as precursors to films and other materials.

The literature of supported transition metal complexes has been thoroughly reviewed.[1–6] In this article, the chemistry of supported complexes is covered in general terms by class of solid support; these include metal oxides, clay minerals, zeolites, polymers, and ion-exchange resins.

2 SOLID SUPPORTS

2.1 Inorganic Metal Oxides

Many metal oxides, such as TiO_2 and Al_2O_3, can be prepared with relatively high surface areas. The exposed surfaces of metal oxides are typically terminated with oxo or hydroxy groups. A dehydroxylated surface is one from which most of the surface OH groups have been removed by heating (see below). Full or partial dehydroxylation may expose cation sites.

Several strategies have been employed in supporting metal complexes on oxide surfaces. For example, surface oxo and hydroxyl groups may be used as ligands; the surface may be modified by reaction of the hydroxyl groups to introduce ligands to the surface, and more recently amorphous metal oxides, such as silica, have been imprinted via sol-gel techniques to generate shape selective cavities.[7,8]

Identification of the types of oxo and hydroxyl groups, which can exist on a metal oxide surface, is important in developing strategies for the immobilization of organometallics. Models for the surface can be constructed by terminating the crystal lattice along a known face and determining the types of groups that can reasonably exist. Often the surface is not well defined as, for example, in gamma alumina, γ-Al_2O_3, and amorphous silica–alumina. In these cases, an empirical model for the surface is postulated from assumptions about the expected structure of the metal oxide. The viability of the surface model can be tested spectroscopically by titrating the surface with appropriate acids and bases and examining shifts in IR, Raman, or NMR parameters.

For example, five types of hydroxyl groups are predicted to occur on the (100), (111), and (110) surfaces of aluminas,[9] as depicted in Figure 1. The relative concentration and distribution of these groups depends on the exposed faces. Dehydroxylation of the surface, according to equation (1), yields surface oxo groups and exposes aluminum cations. The surface hydroxyl groups have Brønsted acidity, while exposed metal cations behave as Lewis acids.[9] Alumina surfaces with Lewis acidity can be prepared from aluminum alkoxides under mild conditions by protecting the incipient Lewis acid site with amines.[10]

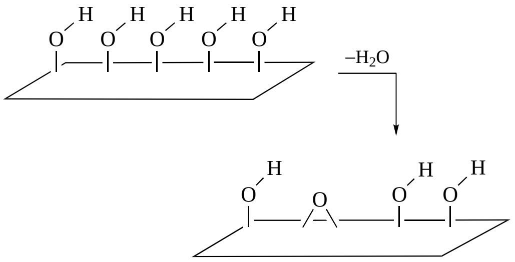

(1)

Surface hydroxyl groups on TiO_2 and SiO_2 are typically less acidic than those on alumina.[11] On silica surfaces, hydroxyl groups are associated with tetrahedrally coordinated silicon atoms. Functionalization of the surface silanols is readily achieved by reaction with chloro- or alkoxysilane reagents. Reactions such as those in equations (2) and (3) may be used to add phosphine, cyclopentadienyl, and other functionalities to the surface.[5,12,13]

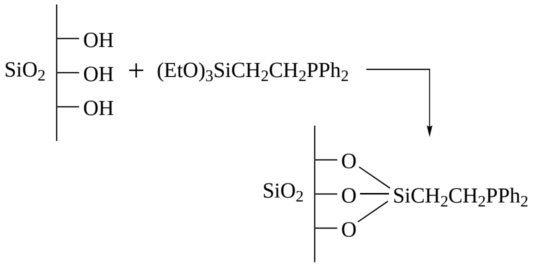

(2)

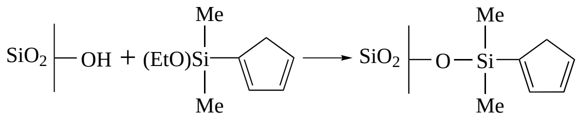

(3)

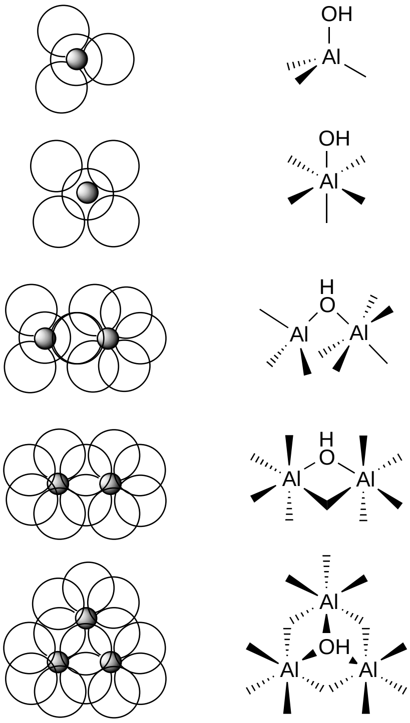

Figure 1 Representations of the five types of surface hydroxyl groups proposed to occur on γ-alumina. On the left is the view from directly above the surface with the open circles representing either O^{2-} or OH^- and the smaller filled circles representing aluminum

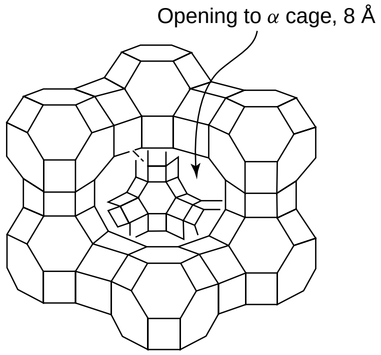

Figure 2 A portion of the faujasite framework. Each vertex represents either a silicon or an aluminum site, each line represents a bridging oxygen. The opening into the supercage is approximately 8 Å in diameter; it consists of 12 metal sites and 12 bridging oxygens

Zeolites, $(SiO_2)_x(AlO_2)_yNa_y{\cdot}nH_2O$, are use extensively as supports for organotransition metal complexes. The presence of framework AlO_2^- groups requires an extraframework cation to balance the negative charge; thus zeolites have cation-exchange capability. Faujasites are the most commonly used zeolite support for metal complexes and catalysts.[14,15] A schematic representation of the faujasitic framework is shown in Figure 2.

The pore opening in faujasites is estimated to be ca. 8 Å, while the large cavity, that is, the supercage or α-cage, is estimated to have a diameter of 13 Å.[14] Small molecules can readily enter the pores and large molecules can be synthesized within the supercage. Clusters such as $Rh_6(CO)_{16}$[16] and the Schiff base complex, VO(saloph),[17] can be prepared within the faujasite supercage. (Saloph =

N,*N′*-*o*-phenylenebis(salicylide naminato).) More commonly, zeolites are used to support small aggregates of metal atoms.[15]

The interlayer regions of clay minerals also have cation-exchange capability and can be modified by organotransition metal compounds.[18] Montmorillonite[19] is typical of these materials and is readily intercalated with transition metal complex ions. The layered structure of montmorillonite is shown in Figure 3.

2.2 Polymers as Supports

A wide variety of polymeric materials have been used for the immobilization of organotransition metal complexes, including ion-exchange resins[20] and linear and crosslinked polystyrene, polyethylene, and many other polymers.[21,22]

Polymers can be modified by methods similar to those described above for metal oxides.[23,24] For example, chloromethylated polystyrene reacts with diphenylphosphide to yield a phosphinated polystyrene (equation 4).[23] The modified polymer can then be used as a ligand for a variety of transition metal compounds.

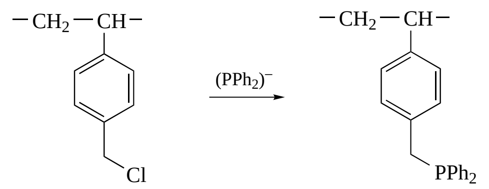

(4)

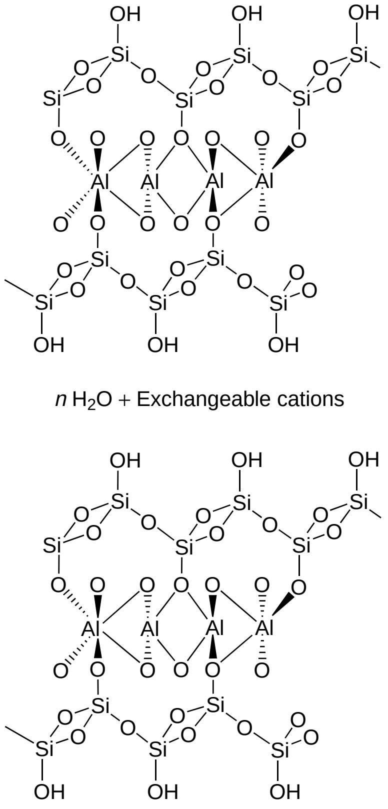

Figure 3 The layered structure of smectite clays such as montmorillonite or hectorite is represented. The aluminum sites are octahedral and the silicon sites are tetrahedral. The interlayer space is filled with water and metal cations

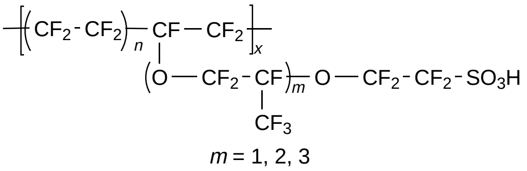
CF_2-CF_2 n CF — CF_2 x
O — CF_2-CF m O — CF_2-CF_2-SO_3H
CF_3
m = 1, 2, 3

Figure 4 The Nafion backbone and side chains. The sulfonic acid groups are hydrophilic and cluster together. This gives Nafion a relatively porous structure. Nafion swells in polar solvents, such as methanol and water

Cyclopentadienyl groups can be incorporated in a manner similar to that shown in equation (4) for phosphines.[19] Metallocene derivatives (*see Metallocene Complexes*), in turn, can be incorporated into these modified polymers. Also, chiral phosphines such as DIOP and BINAP have been immobilized on polymers to be used in asymmetric hydrogenation catalysis and related reactions.[25]

Nafion, a perfluorinated polymer with pendant sulfonic acid groups, has been used as a support for the immobilization of catalysts. The material phase separates into hydrophobic and hydrophilic regions comprising $-CF_2CF_2-$and $-SO_3H$ groups respectively;[26] the polymer morphology is thought to resemble a reverse micelle with the sulfonate groups aggregated inside the polymer matrix. The solid polymer is porous and, as such, the sodium salt acts as an ion conductor. The composition of nafion is shown in Figure 4.

Metal complexes bound to soluble polymers act as homogeneous catalysts; they can be selectively precipitated and separated from products, and thus behave as immobilized homogeneous catalysts because of the ease with which they can be separated from reaction products.[21] Alternatively, complexes can be physically trapped within the pores of swellable polymers. In this manner, they can be effectively immobilized without a direct bond to the support.[27] Polymers may be imprinted to give additional selectivity in the reactions of the supported metal catalysts and reagents.[28,29]

3 COVALENTLY BOUND ORGANOTRANSITION METAL COMPOUND

This comprises by far the largest class of supported organometallic reagents. Some of the earliest examples in the field can be classified as covalently bound. As described in Section 2.2, the bond to the transition metal complex can be from a ligand group that is inherently a part of the support or a ligand can be added to the surface by chemical modification of the support.

3.1 Unmodified Metal Oxide Supports

It was observed in the early 1960s that $Mo(CO)_6$ supported on aluminum oxide yields a catalyst for what is now known as the *Alkene Metathesis* reaction.**[30]** The reaction of molybdenum hexacarbonyl with the surface proceeds as in Scheme 1.**[31]**

Direct evidence for both the alumina-supported molybdenum pentacarbonyl and the molybdenum tricarbonyl species has been obtained by cross-polarization magic angle spinning (CP-MAS) ^{13}C NMR spectroscopy.**[32,33]** On other supports, the group 6 metal carbonyls do not appear to give well defined supported carbonyl fragments. For example, on TiO_2, molybdenum hexacarbonyl loses all of its CO ligands at 200 °C. Temperature-programmed desorption shows no evidence for stable metal subcarbonyl fragments.**[34]**

Ruthenium and rhenium tricarbonyl groups are formed on alumina surfaces from the decomposition of $Ru_3(CO)_{12}$ and $H_3Re_3(CO)_{12}$ respectively.**[35]** The supported carbonyl fragments serve as precursors to supported particles of the respective metals. $HRe(CO)_5$ decomposes on MgO to yield isolated rhenium tricarbonyl groups, while the cluster precursor, $H_3Re_3(CO)_{12}$, is thought to give ensembles of three rhenium tricarbonyl groups.**[36]** These are assigned as $Re(CO)_3\{OMg\}\{HOMg\}_2$ groups on the basis of gas evolution during adsorption.**[37]** The bracketed ligands, {OMg} and {HOMg}, represent surface oxo and hydroxy groups bonded to the rhenium carbonyl fragment.

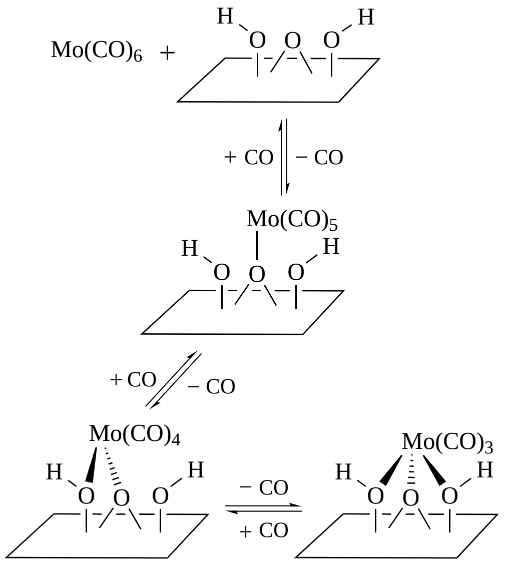

Scheme 1

The reaction of $Fe_3(CO)_{12}$ with hydroxylated metal oxide surfaces yields $HFe_3(CO)_{10}(ads)$**[38,39]** as determined by stoichiometry and CP-MAS ^{13}C NMR (equation 5).**[38,39]**

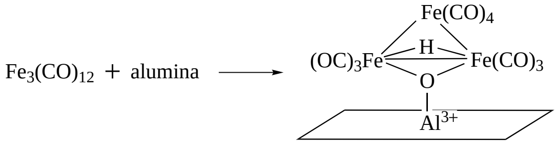

(5)

Ruthenium and osmium analogs of the μ-oxo bound cluster are known. For example, $(\mu\text{-H})Ru_3(CO)_{10}(\mu\text{-OSiEt}_3)$**[40]** and $(\mu\text{-H})Os_3(CO)_{10}(\mu\text{-OSiEt}_3)$**[41]** have been prepared, and the (μ-oxo)-bound triruthenium and the triosmium clusters can be selectively prepared on the surface of silica and alumina.**[40,42]**

Large metal clusters have been supported on many metal oxides. For example, the carbido-cluster anion $[Os_{10}C(CO)_{24}]^{2-}$ has been adsorbed directly onto MgO.**[43]** This cluster anion can also be prepared in situ on MgO by the *Reductive Carbonylation* of adsorbed H_2OsCl_6.**[43]** The adsorbed osmium cluster anion appears to be ionically bound to the surface.

In addition to the CO displacement reactions illustrated above for metal carbonyl derivatives, other reactive organometallic precursors have been used to yield supported organometallic complexes. For example, hydroxylated surfaces, such as silica, react with $Rh(C_3H_5)_3$ to yield propene and (surface)$Rh(C_3H_5)_2$.**[44]** Hydrolysis is suggested to generate a surface hydride. The reactions shown in Scheme 2 are illustrative of the surface complexes that can be formed from $Rh(C_3H_5)_3$. The supported rhodium hydrides are active for the hydrogenation of a variety of internal and terminal alkenes.**[44]** The trimethylphosphine complex shows reduced hydrogenation activity.

The imprinting of metal oxides is a relatively new method for the immobilization of metal complexes. The case of $Rh_2(CO)_4Cl_2$ on silica is illustrative.**[8]** The dimer is first adsorbed onto the surface of silica, most likely through a surface hydroxyl group, and then reacted with trimethylphosphite, $P(OMe)_3$. Amorphous silica is then

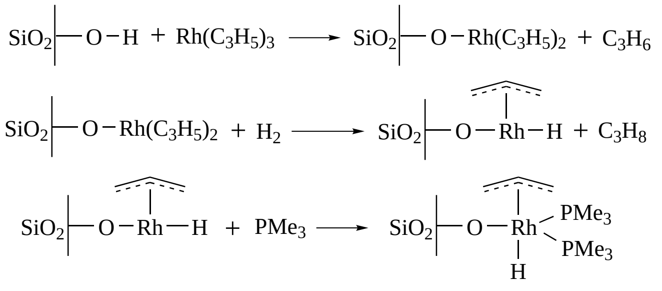

Scheme 2

formed around the supported metal by the reaction of $Si(OMe)_4$ and water under chemical vapor deposition conditions. The trimethylphosphite is then removed thermally to generate a templated void space in the amorphous oxide. Rhodium catalysts generated in this manner are active for the hydrogenation of olefins.[8]

3.2 Ligand-modified Metal Oxide Supports

Silica, SiO_2, has been modified with a variety of phosphines by methods similar to those discussed above. For example, chelating phosphines have been bound to hydroxylated silica surfaces using $(EtO)SiMe_2–C_6H_4–O–CH(PPh_2)CH_2PPh_2$ according to equation (6).[45] The use of chelating phosphines in immobilizing transition metal complexes has the advantage of reducing the likelihood of metal leaching from the support. The formation of rhodium complexes is represented in equation (7).

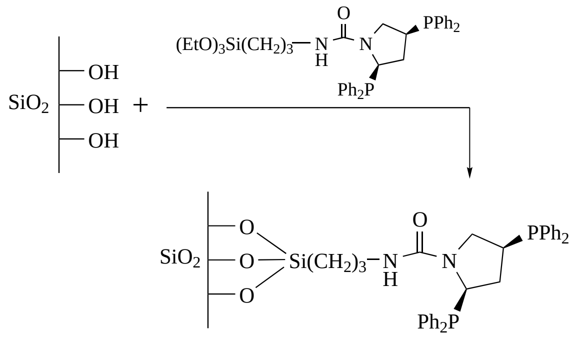

(6)

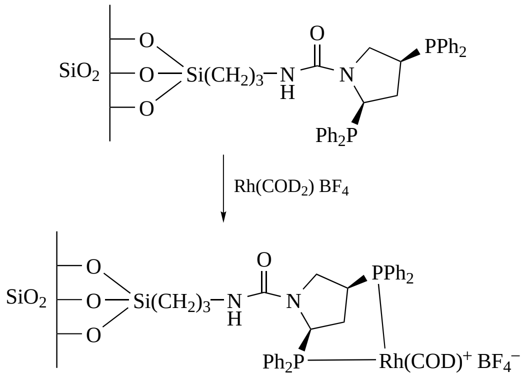

(7)

Rhodium catalysts supported via chelating phosphines as described above have been used as Asymmetric Hydrogenation catalysts.[45]

Cyclopentadienyl-modified silica reacts with $Co_2(CO)_8$ to yield cyclopentadienylcobalt dicarbonyl according to equation (8). The supported complex is characterized by IR spectroscopy by analogy with its homogeneous counterpart.[13]

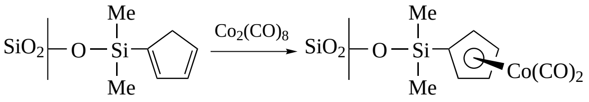

(8)

3.3 Polymer-supported Organotransition Metal Complexes

Metal–phosphine complexes can be immobilized on phosphinated polymers through simple ligand exchange reactions. *Wilkinson's Catalyst*, $Rh(PPh_3)_3Cl$, has been supported on phosphinated polystyrene as shown in equation (9).[24] The supported complex can be used as an alkene hydrogenation catalyst.

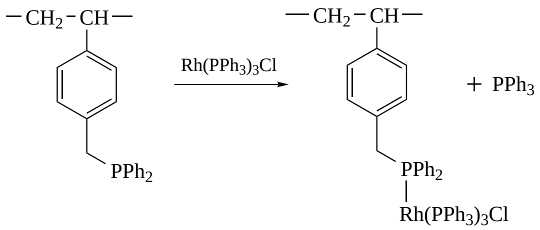

(9)

Bimetallic complexes, such as $RuPt(CO)_5(PPh_3)_3$, have been immobilized on phosphinated poly(styrene–divinylbenzene) by a similar ligand-substitution reaction (equation 10).[46] The resulting supported bimetallic complexes have been characterized by IR spectroscopy and are found to act as ethylene *Hydrogenation* catalysts.

$$\text{Polymer-PPh}_2 + \text{RuPt(CO)}_5(\text{PPh}_3)_3 \longrightarrow \text{RuPt(CO)}_5(\text{polymer-PPh}_2)_x(\text{PPh}_3)_{3-x} \qquad (10)$$

The preparation of silica- and polymer-supported cyclopentadienyl groups is discussed above. These modified solids can be used to generate a wide variety of immobilized metal complexes.[1,2,13,47] Reaction of a cyclopentadienyl-modified polystyrene with $(C_5H_5)TiCl_3$ yields supported titanocene dichloride (equation 11).

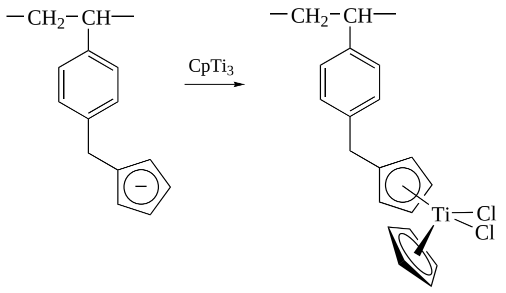

(11)

Direct reaction of soluble polymers that contain phenyl groups, for example, polystyrene, with chromium atoms leads to polymers crosslinked with bis(benzene)chromium.[48] Oxidation leads to aggregates of Cr_2O_3 imbedded with the polymer.

CP-MAS ^{31}P NMR can be used to characterize supported complexes, for example, the polypropylene-*p*-styryldiphenylphosphine-bound rhodium complex [(polymer)-PPh_2]Rh(acac)(CO) has been characterized in this manner.[49] Free and complexed phosphines are clearly distinguished. The bound complex is spectroscopically similar to its molecular analog, $(PPh_3)Rh(acac)(CO)$.

Anionic polymerization of ethylene has been used to prepare terminally functionalized ethylene oligomers. The reaction proceeds as shown in equation (12).[21] Phosphite as well as phosphine-functionalized ethylene oligomers have been prepared. Nickel(0) phosphine complexes can be bound to such a functionalized oligomer. The bound complexes have similar activity as their homogeneous counterparts for the cyclooligomerization of butadiene.[21]

$$H_2C{=}CH_2 \xrightarrow{RLi} R(CH_2CH_2)_nCH_2CH_2Li \xrightarrow[R(CH_2CH_2)_nCH_2CH_2PPh_2]{PPh_2Cl} \qquad (12)$$

The imprinting of polymer supports is an exciting development in the immobilization of transition metal complexes.[28,29] The process involves the copolymerization of an inorganic or an organic template into a crosslinked polymer network. In a subsequent step, the template is chemically removed leaving an imprint of molecular dimensions in the resin. Ideally, the imprint retains chemical information related to the size and shape of the template. This approach has been used to prepare chiral imprints in otherwise achiral polymer networks. The method is outlined in Scheme 3.[28,29]

4 PHYSICALLY IMMOBILIZED ORGANOTRANSITION METAL COMPLEXES

Organotransition metal complexes are physically immobilized on a solid when there is no direct covalent or ionic interaction between the complex and the solid. The complex may, for example, be dissolved in a stationary phase on a solid or entrapped with a solid matrix.

4.1 Immobilization in a Supported Liquid Phase

Adsorption of a high-boiling solvent onto a high-surface-area microporous solid yields a supported liquid phase that can be removed from the solid only by extraction with a second solvent or by distillation at high temperature under vacuum. Under typical reaction conditions, a solid that contains a supported liquid phase looks and behaves as a solid, yet it can dissolve small quantities of a metal complex into the supported phase. One of the first examples of this arrangement was achieved with the immobilization of $Rh(CO)(PPh_3)_2Cl$ in benzyl butyl phthalate on silica.[50] The supported complex was successfully used to effect the gas-phase hydroformylation of propene.

In a similar manner, the complexes $HRh(CO)(PR_3)_3$ have been dissolved in supported liquid phases, where the ligand, PR_3, forms the liquid phase. In one specific example,

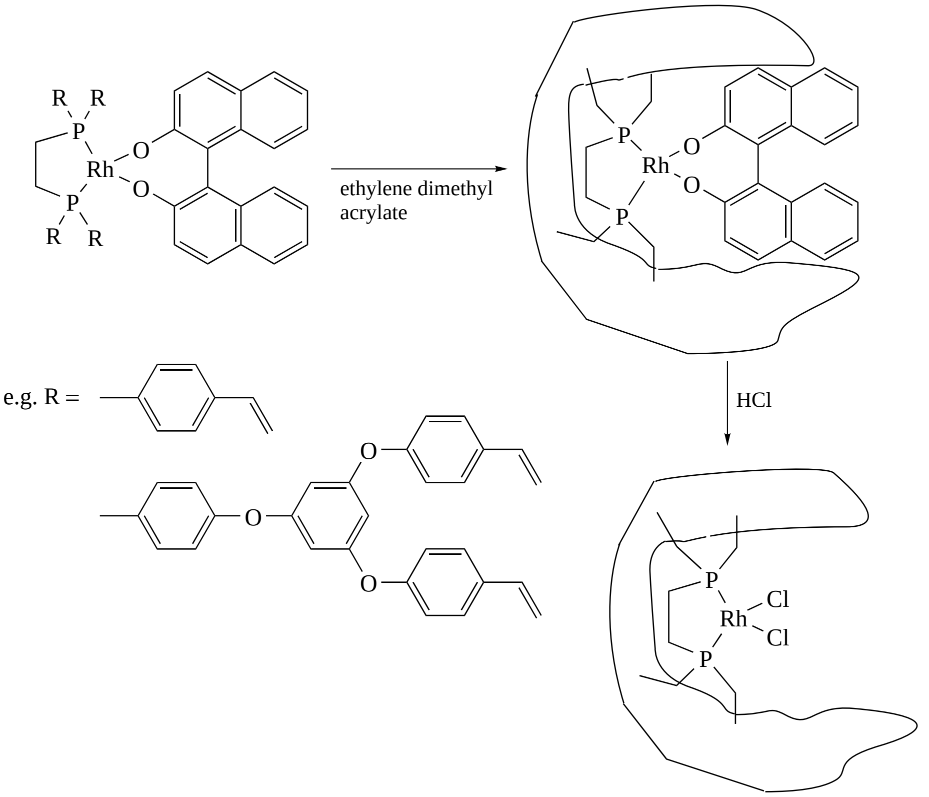

Scheme 3

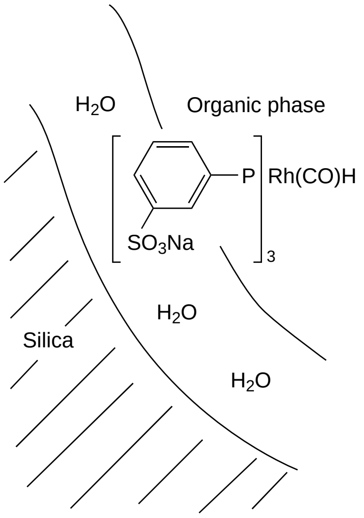

Figure 5 Rendering of the silica–water–substrate phase in the supported aqueous phase catalysts

$HRh(CO)(PPh_3)_3$ was supported in molten PPh_3 for use as a heterogeneous catalyst for the hydroformylation of propene.[51]

Recently a supported aqueous phase has been used in place of the high-boiling liquid phase for the immobilization of water-soluble metal complexes, such as $HRh(CO)(P(C_6H_4\text{-}m\text{-}SO_3Na)_3)_3$.[52,53] Catalytic applications proceed with water-soluble substrates by virtue of an increase in surface area between the catalytic-supported aqueous phase over that of a simple two-phase reaction, and by the inherent surface activity of water-soluble complexes based on sulfonated phosphines. The polar sulfonate groups are strongly bound to the supported aqueous phase, keeping the complex immobilized. The surface is schematically represented in Figure 5.

Alternatively, polar liquids other than water can be used to generate supported liquid-phase catalysts with sulfonated ligands. For example, supported liquid-phase Pd-TPPTS catalysts have been prepared on silica with ethylene glycol as the liquid phase.[54]

4.2 Entrapment of Metal Complexes within a Solid Matrix

Zeolites (molecular sieves) make ideal supports for the physical immobilization of organotransition metal complexes. The pores and cages of zeolites are of molecular dimensions, and several zeolites are available for which the cages have significantly larger dimensions than the pores or entrances to the cages. Under these circumstances, it is possible to envisage that a metal complex could be constructed to fill the cage of a zeolite, and thus be too large to leave via the smaller pore. Thus, a chemical bond to the zeolite is not required to keep the metal complex bound to the zeolite. This immobilization technique has been recently reviewed.[55]

For an organotransition metal complex, such an intrazeolitic synthesis was first accomplished with the preparation of $Rh_6(CO)_{16}$ within the faujasite framework.[14] Specifically, $[Rh(NH_3)_6]^{3+}$ was cation exchanged onto the zeolite, and the complex ion was reductively carbonylated to yield the rhodium cluster within the zeolite cages. The general technique has been referred to as ‘molecular ships in bottles’ in the context of forming $Ni(CO)_{4-x}L_x$ (L = phosphine) complexes with zeolites, such that the resulting substituted nickel complexes are too large to be removed from the zeolite.[56]

Long-range electron transfer is postulated to occur from ferrocene to tris(bipyridine)iron(III) constructed within the pores of a NaY zeolite.[57] The iron bipyridine complex is too large to move throughout the faujasite pores to the surface, thus requiring the long-range transfer. The asymmetric catalyst, titanium tartrate, has been prepared inside NaY and used as an immobilized catalyst for the epoxidation of cinnamyl alcohol.[58]

Discrimination between surface and intrazeolite sites is often difficult. The chemical reactivity of zeolite-bound complexes to reagents of different sizes is helpful in determining the location of an immobilized complex.[59] For example, in rhodium faujasites prepared from $Rh(allyl)_3$ and H–Na–X (i.e. the faujasite Na–X in which a fraction of the sodium ions have been replaced with protons), catalytic activity for hydrogenation can be limited to the intrazeolite sites only when $P(n\text{-}Bu)_3$ is used to poison the surface rhodium sites. Tri-*n*-butylphosphine is too large to penetrate the zeolite pores, thus the rhodium complexes within the zeolite remain catalytically active.

Polymers can also be used for the physical immobilization of metal complexes. For example, the degree of swelling observed for 1% crosslinked polystyrene varies with solvents; more swelling is observed in THF than in methanol. Thus, the cationic complex $[(diphos)Rh(NBD)]PF_6$ can be adsorbed onto polystyrene in THF. When dried and extracted with methanol, the complex is bound within the polystyrene matrix. The immobilized complex is a catalyst for the hydrogenation of 1-hexene in methanol.[21]

5 IONICALLY IMMOBILIZED ORGANOTRANSITION METAL COMPLEXES

Many inorganic and organic materials have an ion-exchange capacity. Zeolites and clay minerals, for example, contain exchangeable cations. These may be replaced with cationic transition metal complexes, which may be used directly as catalysts or used synthetically for the in situ preparation of a supported complex. Organic resins are available, which have either a cation or anion-exchange capacity. The cation-exchange resins typically have bound sulfonate groups, while anion-exchange resins are based on materials with bound quaternary ammonium anions.

5.1 Clay Minerals

The cationic ligand $[Ph_2P(CH_2)_2PPh_2(CH_2Ph)]^+$ ($P-P^+$) has been used to incorporate rhodium within the layers of hectorite, a layered clay mineral.**[18]** A 1:1:0.5 ratio of $P-P^+$:PPh_3:$[Rh(cod)Cl]_2$ is used to generate a hectorite-supported catalyst for the hydrogenation of 1-hexene. Similarly, prepared materials generated from $[Rh(cod)Cl]_2$, $P-P^+$, and hectorite yield catalysts suitable for the hydroformylation of 1-hexene.**[60]** The supported complex is thought to be $HRh(CO)_x(P-P^+)_2$.

A series of cluster complexes has been intercalated into hectorite, again with $P-P^+$ as the cationic ligand. Typical is the formation of $Ir_4(CO)_9(P-P^+)_3$ within the clay.**[51]** Intercalation of the clusters within the clay causes an increase in the interlayer spacing to as large as 17.5 Å.

5.2 Ion-Exchange Resins

Anionic metal complexes, for example $[Rh(CO)_2I_2]^-$, can be exchanged onto the anion-exchange resin Dowex 1-X8.**[61]** The supported rhodium carbonyl iodide complex functions as an immobilized methanol *Carbonylation* catalyst. Metal complexes of the water-soluble phosphine TPPTS and its monosulfonated analog have also been exchanged onto anion-exchange resins.**[62]** The pendant sulfonate groups provide the electrostatic attraction to the support.

Inherently cationic complexes of the type $[L_2Rh(cod)]^+$ can be directly exchanged onto sulfonated divinylbenzene–styrene resins, where L_2 is a chiral chelating phosphine; for example, $[(propraphos)Rh(cod)]^+$ can be cation exchanged according to Scheme 4.**[63]**

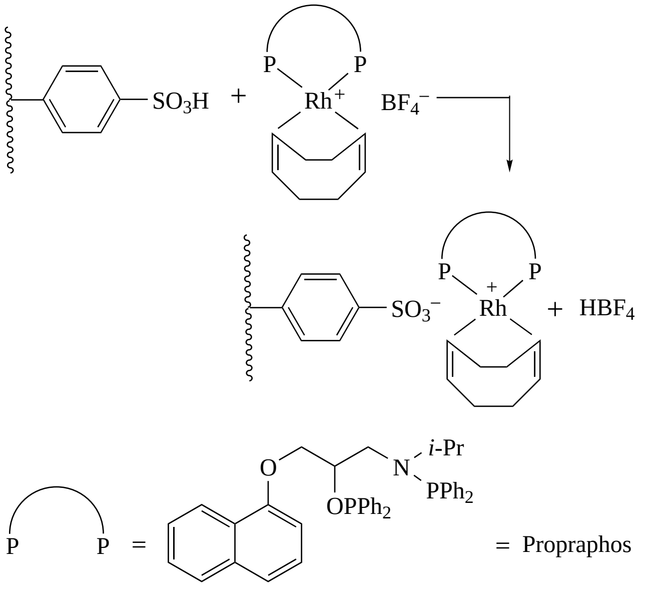

Scheme 4

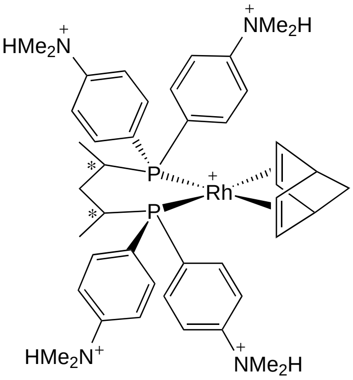

Figure 6 A cationic chiral rhodium complex with NMe_2 groups added to the BDPP ligand. The amine groups can be protonated to give a complex with a net charge of 5+. The protonated complex can be supported on the acid form of a cation-exchange resin

Additional cationic functionality can be added to this class of complexes via pendant quaternary amine groups on the phenyl groups of the phosphine. Typical is the BDPP(–$NMe_2H)_4$ ligand and its rhodium complex shown in Figure 6. This complex can be immobilized by reaction of the basic form of the compound with the acid form of a cation-exchange resin, for example, Nafion-H.**[64]** The net 5+ charge on the complex ensures strong binding to the resin. The immobilized chiral rhodium compounds are effective for the asymmetric hydrogenation of cinnamic acid derivatives.**[63,64]**

6 RELATED ARTICLES

Asymmetric Synthesis by Homogeneous Catalysis; Carbonyl Complexes of the Transition Metals; Carbonylation Processes by Homogeneous Catalysis; Heterogeneous Catalysis by Metals; Phosphides: Solid-state Chemistry; Polynuclear Organometallic Cluster Complexes; Zeolites.

7 REFERENCES

1. F. R. Hartley, ‘Supported Metal Complexes. A New Generation of Catalysts’, Reidel, Dordrecht, 1985.
2. C. U. Pittman, in ‘Comprehensive Organometallic Chemistry’, eds. E. W. Abel, F. G. A. Stone, and G. Wilkinson, Pergamon, Oxford, 1980.
3. D. Brunel, in ‘Supported Catalysts and Their Applications’, eds. D. Sherrington, and A. P. Kybet, Special Publication, 266, Royal Society of Chemistry, Cambridge, England, 2001, p. 38.
4. P. J. Dyson, *Transition Met. Chem.*, 2002, **27**, 353.

5. C. M. Crudden, D. P. Allen, I. Motorina, and M. Fairgreive, in 'Nanostructured Catalysts', eds. S. L. Scott, C. M. Crudden, and C. W. Jones, Kluwer Academic, New York, 2003, p. 113.
6. M. Tada and Y. Iwasawa, *J. Mol. Catal. A*, 2003, **199**, 115.
7. A. Katz and M. E. Davis, *Nature*, 2000, **403**, 286.
8. M. Tada, T. Sasaki, and Y. Iwasawa, *J. Catal.*, 2002, **211**, 496.
9. H. Knözinger and P. Ratnasamy, *Catal. Rev. Sci. Eng.*, 1978, **17**, 31.
10. A. I. Kozlov, M. C. Kung, W. M. Xue, and H. H. Kung, *Angew. Chem., Int. Ed. Engl.*, 2003, **42**, 2415.
11. T. Armaroli, F. Milella, B. Notari, R. J. Willey, and G. Busca, *Top. Catal.*, 2001, **15**, 63.
12. K. G. Allum, R. D. Hancock, I. V. Howell, S. McKenzie, R. C. Pitkethly, and P. J. Robinson, *J. Organomet. Chem.*, 1975, **87**, 203.
13. F. R. W. P. Wild, G. Gubitosa, and H. H. Brintzinger, *J. Organomet. Chem.*, 1978, **148**, 73.
14. D. W. Breck, 'Zeolite Molecular Sieves, Structure Chemistry and Use', Wiley, New York, 1973.
15. R. J. Davis, *J. Catal.*, 2003, **216**, 396.
16. E. Mantovani, N. Palladino, and Z. Zanobi, *J. Mol. Catal.*, 1977/78, **3**, 283.
17. T. Joseph, D. Srinivas, C. S. Gopinath, and S. B. Halligudi, *Catal. Lett.*, 2002, **83**, 209.
18. T. Sento, S. Shimazu, and N. Ichikuni, *Chem. Lett.*, 1998, 1191.
19. R. E. Grim, 'Clay Mineralogy', McGraw-Hill, New York, 1953.
20. W. O. Haag and D. D. Whitehurst, *Insoluble Resin-Metal Compound Complex Prepared by Contacting Weak Base Ion Exchange Resin with Solution of Metal-Ligand*, US Patent, 4 111 856, 1978.
21. D. E. Bergbreiter, *Chem. Tech.*, 1987, **17**, 686.
22. A. Kollehofer and H. Plenio, *Chem. – Eur. J.*, 2003, **9**, 1416.
23. R. H. Grubbs and L. C. Kroll, *J. Am. Chem. Soc.*, 1971, **93**, 3062.
24. J. P. Collman, L. S. Hegedus, M. P. Cooke, J. R. Norton, G. Dolcetti, and D. N. Marquardt, *J. Am. Chem. Soc.*, 1972, **94**, 1789.
25. D. J. Bayston and M. E. C. Polywka, in 'Chiral Catalyst Immobilization and Recycling', eds. D. E. DeVos, I. F. J. Vankelecom, and P. A. Jacobs, Oxford Asymmetry, Abington, 2000, p. 211.
26. D. E. Bryant and M. Kilner, *J. Mol. Catal. A*, 2002, **178**, 1.
27. A. Patchornik, Y. Ben-David, and D. Milstein, *J. Chem. Soc., Chem. Commun.*, 1990, 1090.
28. J. H. Koh, A. O. Larsen, P. S. White, and M. R. Gagne, *Organometallics*, 2002, **21**, 7.
29. J. J. Becker and M. R. Gagne, *Organometallics*, 2003, **22**, 4984.
30. R. L. Banks and G. C. Bailey, *Ind. Eng. Chem., Prod. Res. Dev.*, 1964, **3**, 170.
31. M. Kaltchev and W. T. Tysoe, *J. Catal.*, 2000, **193**, 29.
32. T. H. Walter, A. Thompson, M. Keniry, S. Shinoda, T. L. Brown, H. S. Gutowski, and E. Oldfield, *J. Am. Chem. Soc.*, 1988, **110**, 1065.
33. G. W. Wagner and B. E. Hanson, *J. Am. Chem. Soc.*, 1989, **111**, 5098.
34. P. N. Gonzalez, M. A. V. Garcia, and A. Brenner, *J. Catal.*, 1989, **118**, 360.
35. L. Guczi, A. Beck, and S. Dobos, *J. Mol. Catal.*, 1992, **74**, 317.
36. P. S. Kirlin, F. B. M. van Zon, D. C. Koningberger, and B. C. Gates, *J. Phys. Chem.*, 1990, **94**, 8439.
37. P. S. Kirlin, H. Knözinger, and B. C. Gates, *J. Phys. Chem*, 1990, **94**, 8451.
38. B. E. Hanson, J. J. Bergmeister, J. T. Petty, and M. C. Connaway, III *Inorg. Chem.*, 1986, **25**, 3089.
39. L. Reven and E. Oldfield, *Inorg. Chem.*, 1992, **31**, 243.
40. J. Puga, T. P. Fehlner, B. C. Gates, D. Braga, and F. Grepioni, *Inorg. Chem.*, 1990, **29**, 2376.
41. L. D'Ornelas, A. Choplin, J. M. Basset, L. Y. Hsu, and S. G. Shore, *Nouv. J. Chim.*, 1985, **9**, 155.
42. T. H. Walter, G. R. Frauenhoff, J. R. Shapley, and E. Oldfield, *Inorg. Chem.*, 1991, **30**, 4732.
43. H. H. Lamb and B. C. Gates, *J. Phys. Chem.*, 1992, **96**, 1099.
44. M. D. Ward and J. Schwarz, *J. Mol. Catal.*, 1981, **11**, 397; see also J. Schwarz, *J. Mol. Catal.*, 1992, **72**, 373; J. M. Basset, *J. Mol. Catal.*, 1992, **72**, 374.
45. K. J. Stanger, J. W. Wiench, M. Pruski, and R. J. Angelici, *J. Mol. Catal. A.*, 2003, **195**, 1381.
46. R. Pierantozzi, K. J. McQuade, B. C. Gates, M. Wolf, H. Knözinger, and W. Ruhman, *J. Am. Chem. Soc.*, 1979, **101**, 5438.
47. R. H. Grubbs, C. Gribbons, L. C. Kroll, W. D. Bonds, and C. H. Brubaker, *J. Am. Chem. Soc.*, 1973, **95**, 2373.
48. M. P. Andrews, M. E. Galvin, and S. A. Heffner, *Mater. Res. Soc. Symp. Proc.*, 1989, **131**, 21.
49. F. R. Hartley, S. G. Murray, and P. N. Nicholson, *J. Mol. Catal.*, 1982, **16**, 363.
50. P. R. Rony, *J. Catal.*, 1969, **14**, 142.
51. L. A. Gerritsen, J. M. Herman, W. Klut, and J. J. F. Scholten, *J. Mol. Catal.*, 1980, **9**, 157.
52. J. P. Arhancet, M. E. Davis, J. S. Merola, and B. E. Hanson, *Nature*, 1989, **339**, 454.
53. J. P. Arhancet, M. E. Davis, and B. E. Hanson, *J. Catal.*, 1991, **129**, 94.
54. S. Fujita, T. Yoshida, B. M. Bhanage, and M. Arai, *J. Mol. Catal. A*, 2002, **188**, 37.
55. A. Corma and H. Garcia, *Eur. J. Inorg. Chem.*, 2004, 1143.
56. N. Herron, G. D. Stucky, and C. A. Tolman, *Inorg. Chim. Acta*, 1985, **100**, 135.

57. S. Fukuzumi, Y. Yoshida, T. Urano, T. Suenobu, and H. Imahori, *J. Am. Chem. Soc.*, 2001, **123**, 11331.
58. A. X. Lu, Z. H. Fu, D. L. Yin, Y. Z. Xu, D. J. Ming, Q. Yang, and D. H. Yin, *Wuji Huaxue Xuebao*, 2004, **20**, 353.
59. T. N. Huang and J. Schwarz, *J. Am. Chem. Soc.*, 1982, **104**, 5244.
60. F. Farzaneh and T. J. Pinnavaia, *Inorg. Chem.*, 1983, **22**, 2216.
61. R. S. Drago, E. D. Nyberg, A. El A'mma, and A. Zombeck, *Inorg. Chem.*, 1981, **20**, 641.
62. F. Joo and M. T. Beck, *J. Mol. Catal.*, 1984, **24**, 135.
63. R. Selke, K. Haupke, and H. W. Krause, *J. Mol. Catal.*, 1989, **56**, 315.
64. I. Tóth and B. E. Hanson, *J. Mol. Catal.*, 1992, **71**, 365.

Surfaces

Scott S. Perry & Gabor A. Somorjai
University of California, Berkeley, CA, USA

1	Introduction	1
2	Techniques for Surface Studies	1
3	Surface Structure	2
4	Thermodynamic Properties of Surfaces	10
5	Electronic Properties of Surfaces	15
6	Optical Properties of Surfaces	18
7	Dynamic Properties of Surfaces	20
8	Surface Reactions	24
9	Related Articles	25
10	Further Reading	25
11	References	25

Glossary

Adsorbate: an atom, molecule, or molecular fragment held at a surface by attractive forces
Chemisorption: the process of adsorption on to a surface through the formation of a chemical bond; for molecules the process can be dissociative
Physisorption: the process of adsorption on to a surface induced by van der Waals or electrostatic forces between an adsorbate and the surface
Work function: the energy required to remove one electron from the highest filled energy level to a point of zero kinetic energy in a vacuum

1 INTRODUCTION

Surfaces can be broadly described as the boundary between a condensed phase (solid, liquid) of matter and another material (solid, gas, or liquid). Surfaces are encountered in most aspects of life, from the contact of a car's wheel with the pavement (solid–solid interface) to the evaporation of a water droplet (liquid–gas interface). Equally as important, surfaces play a fundamental role in many chemical processes including catalysis, thin film coatings, and electrochemical oxidation and reduction.

In the realm of chemical processes, surfaces are encountered in a number of forms and environments. Catalytic processes involve the reaction of liquids or gases at the surface of finely divided metal or metal oxide particles. Electrochemical reactions occur at the interface of a metal electrode and a solution. Many coating technologies involve the deposition of a compound from the gas phase on to a solid substrate. Zeolites are microporous aluminum silicates displaying enormous reactivity and selectivity based upon the structure and volume of their internal surfaces. The oxidation of metals involves diffusion and reaction of oxygen with a surface of changing composition.

In all of these systems, certain aspects of the reactions can be uniquely related to the properties of a surface. Surface properties may include those representative of the bulk material, ones unique to the interface because of the abrupt change in density of the material, or properties arising from the two-dimensional nature of the surface. In this article, the structural, thermodynamic, electrical, optical, and dynamic properties of solid surfaces are discussed in instances where properties are different from those of the bulk material. Predominantly, this discussion focuses on metal surfaces and their interaction with gas-phase atoms and molecules. The majority of fundamental knowledge of molecular-level surface properties has been derived from such low surface area systems. The solid–gas interface of high surface area materials has received much attention in the context of separation science, however, will not be discussed in detail here. The solid–liquid interface has primarily been treated from an electrochemical perspective and is discussed elsewhere (*see* ***Electrochemistry: Applications in Inorganic Chemistry***). The surface properties of liquids (liquid–gas interface) are largely unexplored on the molecular level; experimental techniques for their study have begun only recently to be developed. The information presented here is a summary of concepts; a more complete description can be found in one of several texts which discuss surface properties in more detail.[1–4]

2 TECHNIQUES FOR SURFACE STUDIES

The study of surfaces has led to the development of an entire class of experimental techniques capable of deriving information that is specific to the properties of the surface. Much of the effort in such experiments entails distinguishing surface signals from bulk phase signals or achieving the sensitivity to signals arising from the relatively few number of surface species (10^{15} atoms cm^{-2}) as compared to the bulk (10^{22} atoms cm^{-3}). The important parameters in doing so vary from one technique to another; however, several practices have been adopted in the effort to understand surface properties. One practice is the use of single crystal material in surface science studies.

2.1 Single Crystals

While 'real-world' surfaces can be far removed from that of an ideal single crystal, studying single crystal surfaces provides an ordered array of atoms of specific coordination and geometry, greatly reducing the number of possible interactions (see Section 3). The number of surface sites or atoms can be estimated from the bulk density. Most materials have densities on the order of one gram cm^{-3}. This value is equivalent to a molecular density (ρ) of 10^{22} atoms cm^{-3}. The concentration of atoms exposed to the surface is proportional to $\rho^{2/3}$, assuming a cube-like packing, and thus is on the order of 10^{15} atoms cm^{-3}. For the study of a surface or chemical reactions on a surface, this value establishes a limit to the number of species probed in an experiment. While much of the information discussed in this article focuses on information derived from single crystal studies, many of the techniques discussed here can also be applied to noncrystalline samples. This, however, complicates the interpretation of the findings and at times prevents a structurally specific understanding of the surface and its properties.

2.2 Vacuum Environment

Another practice common to many modern surface science studies is performing experiments in an ultrahigh vacuum ($<10^{-9}$ Torr) environment. The development of vacuum technology came largely as a result of space exploration research in the United States during the 1950s. From that time and initial knowledge base, the surface science community has developed a repertoire of techniques for preparing and handling samples in a vacuum environment. The advantages of working in a vacuum environment are mainly two-fold: (1) providing an appropriate environment for the use of electron- and ion-based spectroscopies; and (2) preparing and maintaining a clean surface. Many surface analytical techniques make use of electrons and ions incident on the surface which requires a mean free path of at least 10 cm. A vacuum of less than 10^{-3} Torr must be achieved to fulfill this condition.

Although a surface in an ambient environment may appear clean, in reality the surface is covered with a layer or layers of adsorbed species. These species may be either physically or chemically adsorbed to the surface, but in both instances prevent the study of a truly clean surface. Under a vacuum environment, such surface contaminants can be removed into the gas phase by sputtering the surface with energetic ions. Once the surface contaminants have been removed, ultrahigh vacuum conditions are required to keep the sample clean. For example, at a pressure of 1×10^{-6} Torr, a sample receives a flux of approximately 5×10^{14} molecules $\text{s}^{-1}\,\text{cm}^{-2}$. Assuming a surface density of 10^{15} atoms cm^{-2} and a sticking probability of 1 for the adsorption of the gas phase species, the sample would be covered by one monolayer of adsorbed species in seconds. Conversely, by working at pressures below 1×10^{-9} Torr, a sample can be easily maintained free of contaminants for times on the order of hours, the time frame required for most surface science experiments.

2.3 Overview of Techniques

A complete description of the numerous techniques that have been developed for the study of surfaces is beyond the scope of this article; however, several generalizations can be made about the approach of modern surface science techniques. The basic premise of studying surfaces involves probing species on a well-characterized surface with a species of known energy. Photons, electrons, atoms, or molecules can be scattered after undergoing collisions or reactions on the surface or producing secondary photons, electrons, atoms, or molecules. The outgoing product is then energy or mass analyzed for information regarding the interaction at the surface. The possible combinations of excitation sources and emitted ‘particles’ are numerous; however, the majority of these techniques provide some information concerning three fundamental properties of interfacial species: (1) the relative location of adsorbate and surface atoms, (2) the electronic character of both solid and adsorbate, and (3) the nature of the chemical bonding at the interface. Many techniques provide complementary information and it is rare when only one technique is capable of providing a complete picture of the interface. Thus these high vacuum techniques used together comprise modern surface chemical analysis. A listing of the majority of these techniques and the information gained from them is given in Table 1.[5] References to many of these techniques will be made in the description of surface properties that follow.

3 SURFACE STRUCTURE

3.1 Structure Determination

While many materials may appear flat or highly reflective, and thus ordered to the human eye, the surfaces of most ‘real’ materials are rough or disordered on the atomic scale. Therefore the determination of surface structure generally implies studying crystalline materials where the surface can be described in terms of the structure of the underlying solid. By definition, a surface represents the termination of the bulk structure. Therefore the simplest case of surface structure is where atoms exist in bulk-like positions, however with lower coordination. The picture of this model of a surface is represented by a perfectly flat plane of well ordered atoms. Any deviation of the surface plane from the crystallographic plane will induce the presence of steps or kinks where the atoms have even lower coordination (Figure 1). Surface structure is of great importance in understanding interfacial reactions with gases, liquids, and other solids. A complete description of surface structure on the atomic scale involves the determination of the relative location of surface atoms (distance from nearest neighbor), number of nearest neighbors, and the nature (directionality, charge distribution, strength) of the chemical bonds between atoms.[6]

Table 1 Surface science techniques that are used frequently

Name	Acronym	Description	Primary surface information
Adsorption or selective chemisorption	Adsorption	Atoms or molecules are physisorbed and their concentration measures total surface area. Chemisorption of atom or molecules on sites yield surface concentration of selected elements or atomic sites.	Surface area site concentration and composition
Atom or helium diffraction	AD	Monoenergetic beams of thermal energy neutral atoms are elastically scattered off ordered surfaces and detected as a function of scattering angle. This gives structural information on the outermost layer of the surface. Atom diffraction is extremely sensitive to surface ordering and defects.	Atomic structure
Auger electron appearance potential spectroscopy	AEAPS	The AEAPS cross-section is monitored by Auger electron intensity. Also known as APAES.	Electronic structure
Auger electron spectroscopy	AES	Core-hole excitations are created, usually by 1 – 10 keV incident electrons, and Auger electrons of characteristic energies are emitted through a two-electron process as excited atoms decay to their ground state. AES gives information on the near-surface chemical composition.	Composition
Atomic force microscopy	AFM	Similar to STM. An extremely delicate mechanical probe is used to scan the topography of a surface by measuring forces exerted by surface atoms. Light interference is used to measure the deflection of the mechanical surface probe. This is designed to provide STM-type images of insulating surfaces or to detect mechanical properties at the molecular level.	Atomic structure
Appearance potential Auger electron spectroscopy	APAES	See AEAPS.	
Appearance potential X-ray photoemission spectroscopy	APXPS	The EAPFS excitation cross-section is monitored by fluorescence from core-hole decay (also known as SXAPS).	Electronic structure
Angle-resolved Auger electron spectroscopy	ARAES	Auger electrons are detected as a function of angle to provide information on the spatial distribution or environment of the excited atoms (see AES).	Composition
Angle-resolved photoemission fine structure	ARPEFS	Electrons are detected at given angles after being photoemitted by polarized synchrotron radiation. The interference in the detected photoemission intensity as a function of electron energy ∼100 – 500 eV above the excitation threshold gives structural information.	Electronic structure
Angle-resolved photoemission spectroscopy	ARPES	A general term for structure-sensitive photoemission techniques, including ARPEFS, ARXPS, ARUPS, and ARXPD.	Electronic structure
Angle-resolved ultraviolet photoemission spectroscopy	ARUPS	Electrons photoemitted from the valence and conduction bands of a surface are detected as a function of angle. This gives information on the dispersion of these bands (which is related to surface structure) and also structural information from the diffraction of the emitted electrons.	Valence band structure
Angle-resolved X-ray photoemission diffraction	ARXPD	Similar to ARXPS and ARPEFS. The angular variation in the photoemission intensity is measured at a fixed energy above the excitation threshold to provide structural information.	Electronic structure
Angle-resolved X-ray photoemission spectroscopy	ARXPS	The diffraction of electrons photoemitted from core levels gives structural information on the surface.	Electronic structure
Conversion-electron Mössbauer spectroscopy	CEMS	A surface-sensitive version of Mössbauer spectroscopy. Like Mössbauer spectroscopy, this technique is limited to some isotopes of certain metals. After a nucleus is excited by γ-ray absorption, it can undergo inverse β-decay, creating a core hole. The decay of core holes by Auger processes within an electron mean free path of the surface produces a signal. Detecting emitted electrons as a function of energy gives some depth-profile information, because of the changing electron mean free path.	Oxidation state
Disappearance potential spectroscopy	DAPS	The EAPFS cross-section is monitored by variations in the intensity of electrons elastically backscattered from the surface.	Electronic structure

(cont’d overleaf)

Table 1 cont'd

Name	Acronym	Description	Primary surface information
Electron appearance potential fine structure	EAPFS	A fine-structure technique (see EXAFS). Core holes are excited by monoenergetic electrons at ∼1 eV. The modulation in the excitation cross-section may be monitored through adsorption, fluorescence or Auger emission.	Atomic structure
Electron energy-loss near-edge structure	ELNES	Similar to NEXAFS, except monoenergetic high-energy electrons of ∼60–300 keV excite core holes.	Atomic structure
Electron energy loss spectroscopy	ELS	Monoenergetic electrons of ∼5–50 eV are scattered off a surface and the energy losses are measured. This gives information on the electronic excitations of the surface and adsorbed molecules (see HREELS). Sometimes called EELS.	Electronic structure
Electron spectroscopy for chemical analysis	ESCA	Now generally called XPS.	Composition, cooxidation state
Electron-stimulated ion angular distribution	ESDIAD	Electrons break chemical bonds in adsorbed atoms or molecules, causing ionized atoms or radicals to be ejected from the surface along the axis of the broken bond by Coulomb repulsion. The angular distribution of these ions gives information on the bonding geometry of adsorbed molecules.	Molecular orientation
Extended X-ray adsorption fine structure	EXAFS	Monoenergetic photons excite a core hole. The modulation of the adsorption cross-section with energy 100–500 eV above the excitation threshold yields information on the radial distances to neighboring atoms. The cross-section can be monitored by fluorescence as core holes decay or by the attenuation of the transmitted photon beam. EXAFS is one of many 'fine-structure' techniques.	Local atomic structure coordination number
Extended X-ray energy-loss fine structure	EXELFS	A fine-structure technique similar to EXAFS, except that 60–300 eV electrons rather than photons excite core holes.	Atomic structure
Field ionization microscopy	FIM	A strong electric field (V Å^{-1}) is created at the tip of a sharp, single-crystal wire. Gas atoms, usually He, are polarized and attracted to the tip by the strong electrostatic field, and then ionized by electrons tunneling from the gas atoms into the tip. These ions, accelerated along radial trajectories by Coulomb repulsion, map out the variations in the electric field strength across the surface with atomic resolution, showing the surface topography.	Atomic structure and surface diffusion
Fourier-transform infrared spectroscopy	FTIR	Broad-band IRAS experiments are performed and the IR adsorption spectrum is deconvoluted by using a Doppler-shifted source and the Fourier analysis of the data. This technique is not restricted to surfaces.	Molecular structure
High-energy ion scattering	HEIS	High-energy ions, above ∼500 keV, are scattered off of a single-crystal surface. The 'channeling' and 'blocking' of scattered ions within the crystal can be used to triangulate deviations from the bulk structure. HEIS has been especially used to study surface reconstructions and the thermal vibrations of surface atoms. (See also MEIS and ISS.)	Atomic structure
High-resolution electron energy-loss spectroscopy	HREELS	A monoenergetic electron beam, usually ∼2–10 eV, is scattered off a surface, and energy losses below ∼0.5 eV to bulk and surface phonons and vibrational excitations of adsorbates are measured as a function of angle and energy (also called EELS).	Molecular structure
Ion neutralization spectroscopy	INS	Slow-ionized atoms, typically He$^+$, are incident on a surface where they are neutralized in a two-electron process that can eject a surface electron, a process similar to Auger emission from the valence band. The ejected electrons are detected as a function of energy, and the surface density of states can be determined from the energy distribution. The interpretation of the data is more complicated than for SPI or UPS.	Valence band
Infrared reflection adsorption spectroscopy	IRAS	Monoenergetic IR photons are reflected off a surface and the attenuation of the IR intensity is measured as a function of frequency. This yields a spectrum of the vibrational excitations of adsorbed molecules. Recent improvements in the sensitivity of this technique allow IRAS measurements to be made on single-crystal surfaces.	Molecular structure

Table 1 cont'd

Name	Acronym	Description	Primary surface information
Infrared emission spectroscopy	IRES	The vibrational modes of adsorbed molecules on a surface are studied by detecting the spontaneous emission of infrared radiation from thermally excited vibrational modes as a function of energy.	Molecular structure
Ion scattering spectroscopy	ISS	Ions are inelastically scattered from a surface and the chemical composition of the surface is determined from the momentum transfer to surface atoms. The energy range is ∼1 keV to 10 MeV, and the lower energies are more surface sensitive. At higher energies this technique is also known as Rutherford backscattering (RBS).	Composition
Low-energy electron diffraction	LEED	Monoenergetic electrons below ∼500 eV are elastically backscattered from a surface and detected as a function of energy and angle. This gives information on the structure of the near-surface region.	Atomic structure and molecular structure
Low-energy ion scattering	LEIS	Low-energy ions, below ∼5 eV, are scattered from a surface and the ion 'shadowing' gives information on surface structure. At these low energies the surface-atom ion scattering cross-section is very large, resulting in large surface sensitivity. Accuracy is limited because the low-energy ion scattering cross-sections are not well known.	Atomic structure
Low-energy positron diffraction	LEPD	Similar to LEED with positrons as the incident particles. The interaction potential for positrons is somewhat different than for electrons, so the form of the structural information is modified.	Atomic structure
Medium-energy electron diffraction	MEED	Similar to LEED, except the energy range is higher (∼300–1000 eV).	Atomic structure
Medium-energy ion scattering	MEIS	Similar to HEIS, except that incident ion energies are ∼50–500 keV.	Atomic structure
Neutron diffraction	ND	Neutron diffraction is not an explicitly surface-sensitive technique, but neutron diffraction experiments on large-surface-area samples have provided important structural information on adsorbed molecules and also on surface phase transitions.	Molecular structure
Near-edge X-ray adsorption fine structure	NEXAFS	A core hole is excited as in fine structure techniques (see EXAFS), except the fine structure within ∼30 eV of the excitation threshold is measured. Multiple scattering is much stronger at low electron energies, so this technique is sensitive to the local three-dimensional geometry, not just the radial separation between the source atom and its neighbors. The excitation cross-section may be monitored by detecting the photoemitted electrons or the Auger electrons emitted during the core-hole decay.	Atomic structure
Nuclear magnetic resonance	NMR	NMR is not an explicitly surface-sensitive technique, but NMR data on large-surface-area samples ($\geq 1\,\mathrm{m}^2$) have provided useful data on molecular adsorption geometries. The nucleus magnetic moment interacts with an externally applied magnetic field and provides spectra that are highly dependent on the nuclear environment of the sample. The signal intensity is directly proportional to the concentration of the active species. This method is limited to the analysis of magnetically active nuclei.	Molecular structure
Normal photoelectron diffraction	NPD	Similar to ARPEFS with a somewhat lower energy range.	Atomic structure
Rutherford backscattering	RBS	Similar to ISS, except the main focus is on depth profiling and composition. The momentum transfer in backscattering collisions between nuclei is used to identify the nuclear masses in the sample, and the smaller, gradual momentum loss of the incident nucleus through electron–nucleus interactions provides depth-profile information.	Composition
Reflection high-energy electron diffraction	RHEED	Monoenergetic electrons of ∼1–20 keV are elastically scattered from a surface at glancing incidence and detected as a function of angle and energy for small forward-scattering angles. Back-scattering is less important at high energies and glancing incidence is used to enhance surface sensitivity.	Atomic structure
Surface electron energy-loss fine structure	SELFS	A fine-structure technique similar to EXELFS, except the incident electron is more surface sensitive because of the lower excitation energy.	Atomic structure

(cont'd overleaf)

Table 1 cont'd

Name	Acronym	Description	Primary surface information
Surface-enhanced Raman spectroscopy	SERS	Some surface geometries (rough surfaces) concentrate the electric fields of Raman scattering cross-section so that it is surface sensitive. This gives information on surface vibrational modes and some information on geometry via selection rules.	Molecular structure
Surface-extended X-ray adsorption fine structure	SEXAFS	A more surface-sensitive version of EXAFS, where the excitation cross-section fine structure is monitored by detecting the photoemitted electrons (PE-SEXAFS), Auger electrons emitted during core-hole decay (Auger−SEXAFS) or ions excited by photoelectrons and desorbed from the surface (PSD−SEXAFS).	Atomic structure
Sum frequency generation	SFG	Similar to SHG. One of the lasers has a tuneable frequency that permits variation of the second-harmonic signal. In this way the vibrational excitation of adsorbed molecules is achieved.	Molecular structure
Second-harmonic generation	SHG	A surface is illuminated with a high-intensity laser and photons are generated at the second-harmonic frequency through a nonlinear optical process. For many materials, only the surface region has the appropriate symmetry to produce an SHG signal. The nonlinear polarizability tensor depends on the nature and geometry of adsorbed atoms and molecules.	Electronic structure and molecular orientation
Secondary ion mass spectroscopy	SIMS	Ions and ionized clusters ejected from a surface during ion bombardment are detected with a mass spectrometer. Surface chemical composition and some information on bonding can be extracted from SIMS ion fragment distributions.	Composition
Surface penning ionization	SPI	Neutral atoms, usually He, in excited states are incident on a surface at thermal energies. A surface electron may tunnel into the unoccupied electronic level, causing the incident atom to become ionized and eject an electron, which is then detected. This technique measures the density of states near the Fermi level and is highly surface sensitive.	Electronic structure
Spin-polarized low-energy electron diffraction	SPLEED	Similar to LEED, except the incident electron beam is spin-polarized. This is particularly useful for the study of surface magnetism and magnetic ordering.	Magnetic structure
Scanning tunneling microscopy	STM	The topography of a surface is measured by mechanically scanning a probe over a surface with angstrom resolution. The distance from the probe to the surface is measured by the probe-surface tunneling current. Also known as scanning electron tunneling microscopy (SETM).	Atomic structure
Soft X-ray appearance potential spectroscopy	SXAPS	Another name for APXPS.	
Transmission electron microscopy	TEM	TEM can provide surface information for carefully prepared and oriented bulk samples. Real images have been formed of the edges of crystals where surface planes and surface diffusions have been observed. Diffraction patterns of reconstructed surfaces, superimposed on the bulk diffraction pattern, have also provided surface structural information.	Atomic structure
Thermal desorption spectroscopy	TDS	An adsorbate-covered surface is heated, usually at a linear rate, and the desorbing atoms or molecules are detected with a mass spectrometer. This gives information on the nature of the adsorbate species and some information on adsorption energies and the surface structure.	Composition, heat of adsorption and surface structure
Temperature-programmed desorption	TPD	Similar to TDS, except the surface may be heated at a nonuniform rate to obtain more selective information on adsorption energies.	Composition and heat of adsorption
Ultraviolet photoemission spectroscopy	UPS	Electrons photoemitted from the valence and conduction bands are detected as a function of energy to measure the electronic density of states near the surface. This gives information on the bonding of adsorbates to the surface (see ARUPS).	Valence band structure
Work-function measurements	WF	Changes in the work function during the adsorption of atoms and molecules provide information on charge-transfer and chemical bonding.	Electronic structure
X-ray adsorption near-edge structure	XANES	Another name for NEXAFS.	

Table 1 cont'd

Name	Acronym	Description	Primary surface information
X-ray photoemission spectroscopy	XPS	Electrons photoemitted from atomic core levels are detected as a function of energy. The shifts of core-level energies give information on the chemical environment of the atoms (see ARXPS, ARXPD).	Composition and oxidation state
X-ray diffraction	XRD	X-ray diffraction has been carried out at extreme glancing angles of incidence where total reflection assures surface sensitivity. This provides structural information that can be interpreted by well-known methods. An extremely high X-ray flux is required to obtain useful data from single-crystal surfaces. Bulk X-ray diffraction is used to determine the structure of organometallic clusters, which provide comparisons to molecules adsorbed on surfaces. X-ray diffraction has also given structural information on large-surface-area samples.	Atomic structure

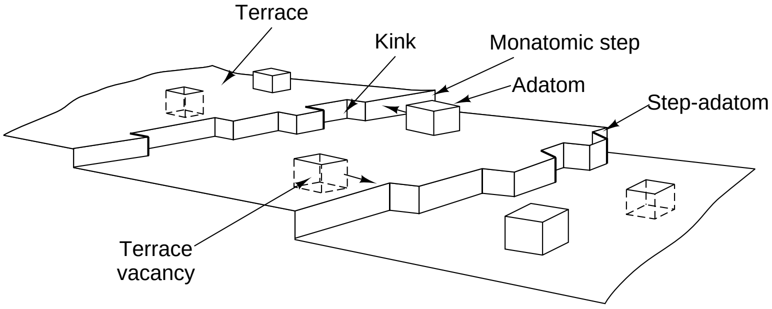

Figure 1 Model of a heterogeneous solid surface depicting different surface sites

The technique of low energy electron diffraction (LEED) has been the most widely used tool in the study of surface structure. LEED experiments involve the scattering of monoenergetic and collimated electrons from a crystal surface and detection of elastically diffracted electrons in a backscattering geometry (Figure 2). The characteristic diffraction pattern in LEED arises from constructive interference of electrons when scattered from ordered atomic positions. The diffraction pattern represents a reciprocal map of surface periodicities and allows access to surface unit cell size and orientation. Changes in the diffraction pattern from that of a clean surface can be indicative of surface reconstruction or adsorbed overlayers.

A LEED crystallography study to determine exact atomic geometries requires fitting spot intensities to theoretical calculations for a series of electron energies. Information about the internal structure of the unit cell may be gained by monitoring the intensity of diffraction spots as a function of incident energy. The analysis of such intensity versus voltage ($I-V$) curves can reveal the local structure of surface atoms or adsorbed molecules as well as the structure of subsurface layers. Analysis is carried out by comparison to curves generated by a theoretical treatment of the diffraction process. With the presence of multiple scattering events, this is a computationally complex task. The most recent advances in LEED theory include the use of automated search routines using linear expansions of structural parameters to solve for surface structures (tensor LEED).[7] An additional degree of complexity exists in both experiment and theory if a surface is disordered. In this case, intensity versus energy spectra are recorded by scanning the diffuse intensity at a constant reciprocal lattice position. Structural determination of a disordered layer involves the simulation of large unit cells and comparison to extensive experimental data sets.

Field ion microscopy (FIM) has also been used to study the surface structure of metals and metal–adsorbate systems. The experimental setup of FIM involves etching a very fine wire to a sharp tip with a radius of curvature of the order of nanometers. The tip is held in a vacuum at a high potential in the presence of a partial pressure of helium. As the helium atoms come into contact with the surface, they are ionized and then accelerated away from the tip by the large local electric field. The ions are detected on a phosphor screen creating a highly magnified real-space image of the tip. FIM has also been used to study the surface structure properties relating to thermal disordering, adsorbate overlayer structure, and atomic surface diffusion.

Recently, surface structure studies have been aided by the development of scanning tunneling microscopy (STM) and atomic force microscopy (AFM).[8] In STM, a very sharp metallic tip is brought into close proximity of a conducting sample through the use of piezoelectric scanners (Figure 3).

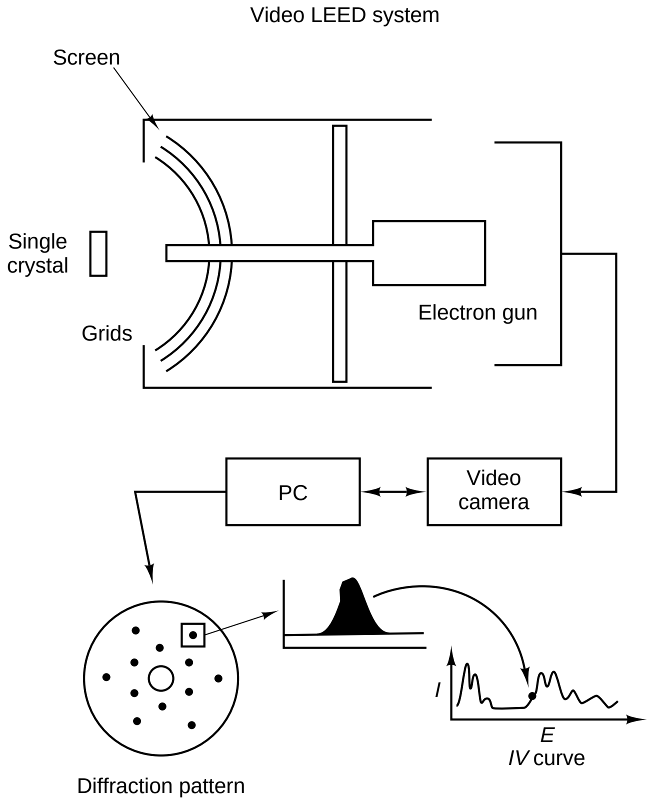

Figure 2 Schematic diagram of a video LEED system used to generate intensity versus voltage curves of electrons diffracted from ordered surfaces. The $I-V$ curves are compared to theory in solving a surface structure

Under certain biasing conditions, electrons are found to tunnel from the tip to the sample (or vice versa) across a potential barrier. By detecting the tunneling current as the tip is rastered across the surface, a real-space two-dimensional map of the surface is generated. Alternatively, the tunneling current can be held constant as the tip is rastered over the sample by fixing the tip to sample distance. In turn, variations in the voltage signal to the piezo scanner holding the tip sample distance constant is used to generate a topographic image of the surface. While such maps show symmetries and corrugations of atomic dimensions, the interpretation of regions of high and low tunneling current is dependent on the knowledge of the local density of states which is not fully understood at this time.

The AFM operates in an analogous fashion. A sharp tip mounted on a weak cantilever is rastered across the sample. Light interference or reflection is used to measure the deflection of the cantilever. The light signal measured as a function of sample location is used to generate a map of the surface topography. Because mechanical forces are responsible for the deflection of the probe arm, conductors as well as insulators can be studied.[9,10] STM and AFM provide local real space images of the surface and are thus complimentary to the information gained from LEED studies. In addition, both have the advantage of being able to work under a range of environmental conditions including liquid and ambient atmospheres.

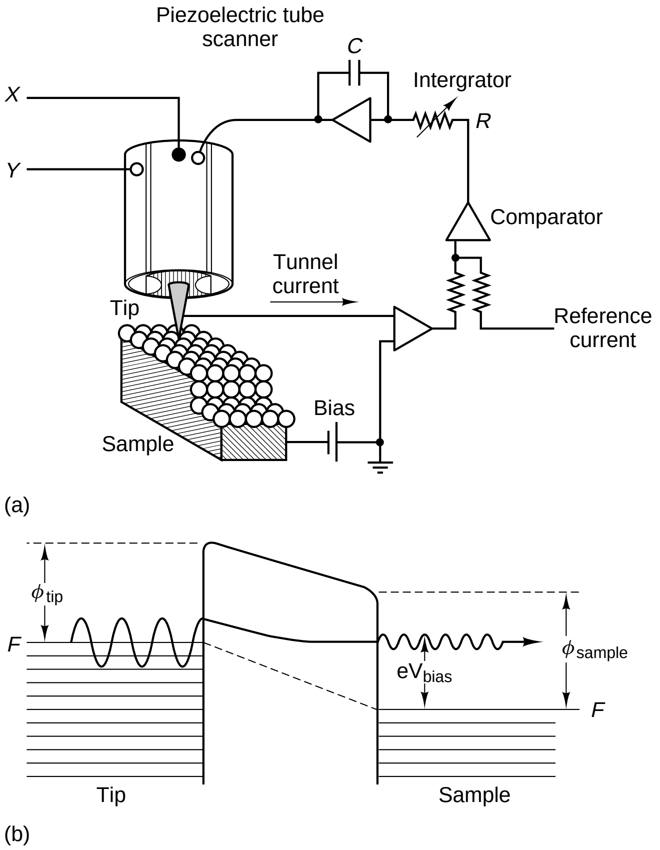

Figure 3 (a) Scanning tunneling microscope depicting tip and piezoelectric scanner. (b) With the tip in close proximity to the surface, tunneling between tip and surface electronic states can occur

Other techniques used in surface structure determination include extended X-ray absorption fine structure (EXAFS), ion scattering, electron forward focusing, and helium atom diffraction.

3.2 Surface Structure at the Solid–Vacuum Interface

A complete discussion of surface structure includes the use of a shorthand notation describing the location of surface atoms. This abbreviated representation of the surface is based upon a projection of the bulk structure on to the surface plane. From this projection the surface structure is described in terms of the unit cell vectors of the bulk material (***a, b***):

$$\boldsymbol{a}' = m_{11}\boldsymbol{a} + m_{12}\boldsymbol{b} \qquad (1)$$

$$\boldsymbol{b}' = m_{21}\boldsymbol{a} + m_{22}\boldsymbol{b} \qquad (2)$$

The surface and bulk unit cell vectors represent the periodicity which allows a translation operation to generate an infinite array of atoms in the surface or bulk structure. The coefficients m_{11}, m_{12}, m_{21}, and m_{22} define a matrix which describes the transformation of the bulk unit vectors into the surface unit vectors. For example, the simplest surface structure occurs when the surface maintains the same unit cell as the bulk. In this case the unit cell matrix would be

$$\begin{bmatrix} 1 & 0 \\ 0 & 1 \end{bmatrix} \tag{3}$$

and is abbreviated as (1 × 1). Thus the surface notation of a silver surface of (111) orientation [the surface plane is defined by the Miller indices (*hkl*)**[11]**] with a surface unit cell identical to that of the bulk would be written as Ag(111)-(1 × 1). This and other unit cells of a fcc (111) surface of larger periodicity are shown in Figure 4. When the surface unit cell is rotated with respect to that of the bulk, the notation includes the angle of rotation as in $(\sqrt{3} \times \sqrt{3})R30°$. Additional changes in the surface periodicity can arise from reconstructions of the surface and the presence of adsorbed gases, as will be discussed.

Complexities in describing the surface arise when the surface is not oriented along a principal crystallographic plane. These surface are referred to as high Miller index planes and can be described in terms of a collection of terraces separated by steps, which may also have kinks in them. This type of surface structure can be written in the general form

$$w(h_t k_t l_t) \times (h_s k_s l_s) \tag{4}$$

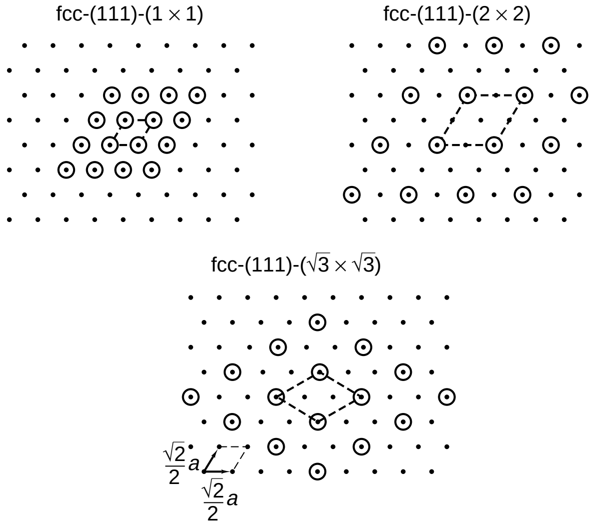

Figure 4 Commonly observed unit cells of adsorbate surface structure for a fcc (111) crystal face

where $(h_t k_t l_t)$ and $(h_s k_s l_s)$ are the respective Miller indices of the terrace and step planes and w is the width of the terrace in number of atoms. So a surface made up of terraces seven atoms wide oriented in the (111) direction separated by monoatomic steps of (310) orientation is written as 7(111) × 1(310) and abbreviated as (10,8,7). This surface of platinum as well as the (111) and (755) surfaces are shown with their corresponding LEED patterns in Figure 5.

Up to this point, only the structure of surfaces in terms of the terrace step kink model has been considered. LEED

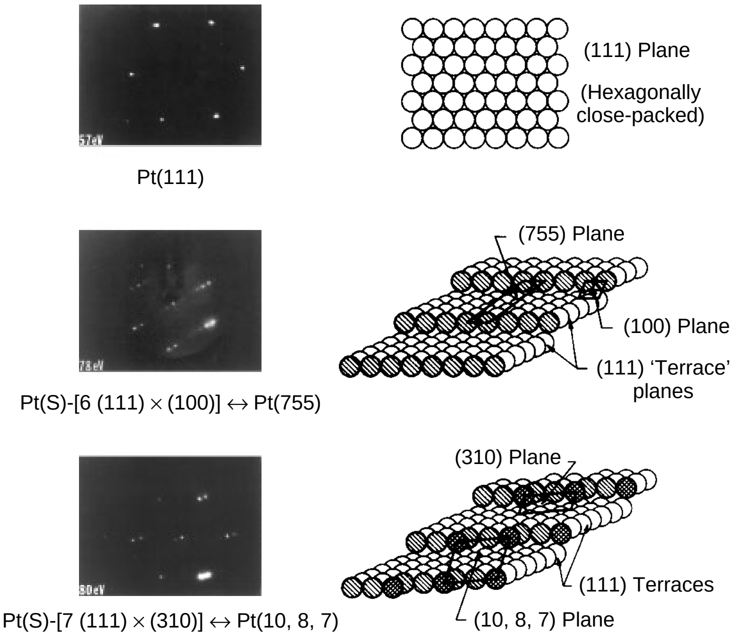

Figure 5 Surface structure of the (111), (755) and (10,8,7) crystal faces of platinum displayed with corresponding LEED images

crystallographic studies have shown that in fact surface atoms of most clean surfaces in a vacuum relax from their bulk positions.**[12]** These measurements typically depict the contraction of the two uppermost layers of the surface. In general, large inward contractions are observed for surfaces of lower atomic packing and density. Additional relaxations are seen to occur at steps on a surface as each atom attempts to optimize its coordination. This model of the surface represents nonrigid atom locations where motions are believed to play a significant role in much of surface chemistry.

An additional modification of the bulk structure occurs at many surfaces due to the lower coordination of surface atoms. The drastic rearrangement of surface atoms and bonding structures to compensate for the loss of nearest neighbors is referred to as surface reconstruction. While many metals display surface reconstructions, the phenomenon is most prevalent in covalently bound solids such as silicon, diamond, and gallium arsenide. At these surfaces the unsaturated dangling bonds drive a rearrangement of the surface atoms to maximize coordination, in turn affecting the bonding structure several layers into the bulk. Surface reconstruction is also observed for the polar faces of metal oxide crystals where long range electrostatic dipoles exist at the surface, terminated in only one ionic species.

3.3 Surface Structure at the Solid–Gas Interface

An additional aspect of surface structure determination involves the relationship between surface structure and reactivity. The study of adsorbates on well ordered solids constitutes much of the structural work being carried out today.**[13]** When an atom or molecule adsorbs on a clean substrate, its equilibrium position is determined by its interactions with the surface atoms, and its interactions with neighboring adsorbates. For physically adsorbed species, adsorbate–adsorbate interactions can equal the interaction between the adsorbate and substrate and affect the structure of the overlayer. However the adsorbate–adsorbate interactions are typically small when compared to the forces in chemical bonds formed upon adsorption and adsorbate–substrate interactions dominate in chemisorbed systems.

When considering adsorbate interactions, coverage is an important parameter affecting the structure of an adsorbed overlayer. Coverages are a measure of adsorbate surface concentration and are typically described in monolayers (ML), where one monolayer equals one adsorbed species per surface atom. Many adsorbate–metal systems exhibit a range of structures for different coverages of an adsorbate. For example, atomic oxygen forms ordered overlayers on Ni(100) at both quarter and half monolayer coverages.**[14]** Figure 6 presents the half monolayer structure where the appropriate surface structure notation is written as Ni(100)-$c(2 \times 2)$-O. The (2×2) unit cell refers to the location of the oxygen atoms with respect to the bulk unit cell of Ni (*c* refers to the unit cell being centered over a hollow site on the surface). For stepped surfaces where more than one adsorption site exists, coverages influence the local geometry of adsorbates as well as overlayer structure. The presence of coadsorbates and temperature can also affect the ordering and structure of adsorbed layers.

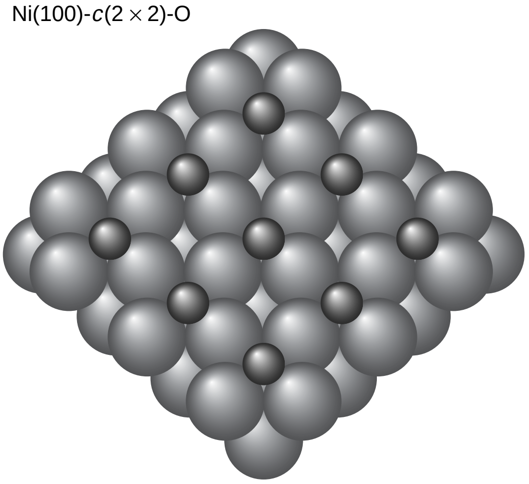

Figure 6 The half monolayer structure of atomic oxygen adsorbed on Ni(100)

The chemisorption of atoms and molecules can also induce the restructuring of the underlying substrate. As an example, the chemical reaction of ethylene on rhodium(111) produces the chemically adsorbed species ethylidyne (C_2H_3).**[15]** The ethylidyne species are bound in threefold hollow sites as depicted in Figure 7. LEED structure calculations have found that the three neighboring Rh atoms expand outward from the ethylidyne forcing the nearest neighbor Rh atoms into the surface. Thus the adsorption of ethylidyne induces a corrugation in the rhodium surface. Such adsorbate-induced reconstructions are believed to be closely related to the catalytic activity of many metal surfaces.

4 THERMODYNAMIC PROPERTIES OF SURFACES

4.1 Surface Thermodynamic Parameters

As revealed by structure studies, the environment of surface atoms differs markedly from atoms in the bulk. They have fewer nearest neighbors and consequently different bonding configurations. As a result, net forces beyond those found in the bulk are exerted on the surface atoms. The existence of these forces is the basis of the thermodynamic properties of a surface. These properties can be defined separately from bulk thermodynamic parameters in the following way. The energy specific to a surface, E^S, is related to the total energy of the

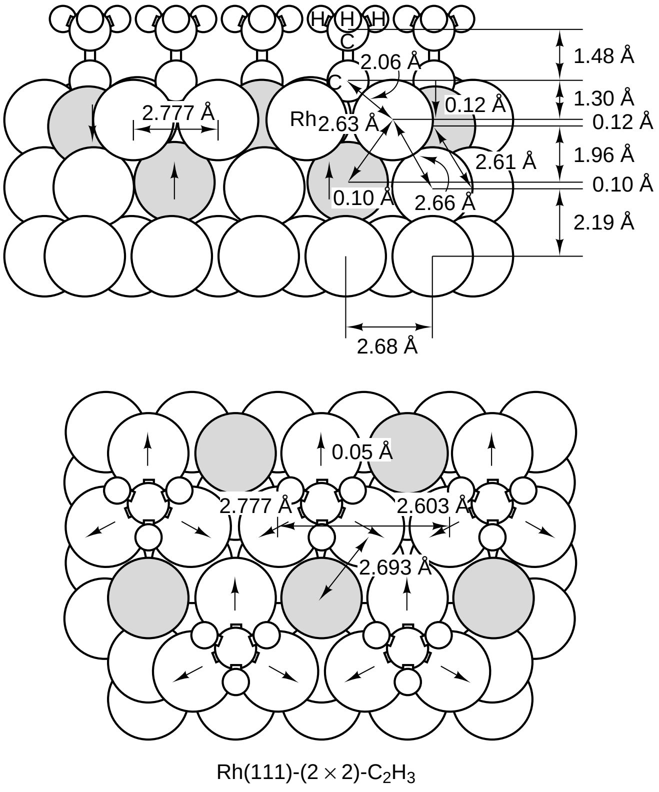

Figure 7 Surface structure of ethylidyne adsorbed on Rh(111) solved by LEED analysis. Arrows represent directions of surface reconstruction from bulk positions

system, E, by

$$E = NE^0 + AE^S \tag{5}$$

where A is the surface area of a solid of N atoms and E^0 is the bulk energy per atom. Thus the specific surface energy, E^S, can be viewed as the energy excess over that of the bulk energy.

Likewise, other thermodynamic properties of the surface can be defined separately from the bulk properties. The specific free energy of the surface, G^S, is given by

$$G^s = H^s + TS^s \tag{6}$$

where H^S and S^S are the respective surface enthalpies and entropies. The surface free energy is an important thermodynamic parameter related to the formation of a surface, which in turn describes many of the phenomena occurring at surfaces. The work required to create a surface arises from the energy involved in breaking bonds and removing nearest neighbors. The surface work, W^S, required to increase the surface area A by dA at constant temperature and pressure is given by

$$\partial W^S_{T,P} = G^S \, \mathrm{d}A \tag{7}$$

where G^S is assumed to be independent of surface area and dA is the change in surface area. In a one-component system, the surface free energy is equal to the surface tension, γ, and therefore

$$\gamma = G^s = \left(\frac{\partial G}{\partial A}\right)_{T,P} \tag{8}$$

The surface tension can be viewed as the two-dimensional analog of pressure opposing the creation of a fresh surface. Since work is required to increase the surface area and thus increase the total energy of the system, the free energy of formation of a surface is always positive. The reluctance of a solid to form a new surface defines many of the phenomena associated with surfaces.

4.2 Surface Phenomena Based on Thermodynamics

From equation (8) it can be seen that solids and liquids will form equilibrium shapes in an effort to minimize their surface area and thus the free energy of the system. Indeed, crystal faces with the closest packing of surface atoms have the lowest surface area and tend to be the most stable. When one considers a two-component system, with one material on top of the other, the interaction between the two will be defined by the surface tensions. The surface tensions of some selected solids and liquids are listed in Table 2.[16–18] From these values, it can be easily predicted which materials will be capable of wetting another. In general, most liquids have lower surface tensions than clean solids and will therefore spread to cover them.

In instances where complete wetting does not occur, there will be an interface between the solid, liquid, and gas phase at the point where the solid is not covered. This situation is represented in Figure 8. The contact angle θ, typically measured by visual inspection under low magnification, is used for a quantitative measurement of wetting ability.[4] For contact angles approaching zero, liquids readily wet and cover the surface. For higher contact angles, equilibrium shapes of

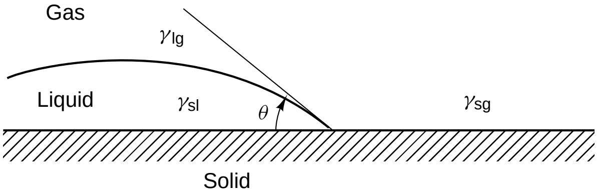

Figure 8 The contact angle between a solid and a liquid arises from differences in surface tensions and is used for a quantitative measurement of wetting ability

Table 2 Surface tension (γ) of selected solids and liquids

Material	γ (10^{-7} J cm^{-2})	Temp. (°C)
W (solid)	2900	1727
Nb (solid)	2100	2250
Au (solid)	1410	1027
Ag (solid)	1140	907
Ag (liquid)	879	1100
Fe (solid)	2150	1400
Fe (liquid)	1880	1535
Pt (solid)	2340	1311
Cu (solid)	1670	1047
Cu (liquid)	1300	1535
Ni (solid)	1850	1250
Hg (liquid)	487	16.5
LiF (solid)	340	−195
NaCl (solid)	227	25
KCl (solid)	110	25
MgO (solid)	1200	25
CaF_2 (solid)	450	−195
BaF_2 (solid)	280	−195
He (liquid)	0.308	−270.5
N_2 (liquid)	9.71	−195
Ethanol	22.75	20
Water	72.75	20
Benzene	28.88	20
n-Octane	21.80	20
Carbon tetrachloride	26.95	20
Bromine	41.5	20
Acetic acid	27.8	20
Benzaldehyde	15.5	20
Nitrobenzene	25.2	20

the liquid are formed on the surface. These shapes and the contact angle arise from the interaction of the surface tensions of the solid and liquid. Recalling that the surface tension is the two-dimensional pressure exerted along the surface, the surface free energy balance where solid and liquid are acting to minimize their surface respective surface areas, is given by

$$\cos\theta = \frac{(\gamma_{sg} - \gamma_{sl})}{\gamma_{lg}} \tag{9}$$

Here γ_{lg} is the interfacial tension at the liquid–gas interface and γ_{sg} and γ_{sl} are the interfacial tensions at the solid–gas and solid–liquid interfaces, respectively. Thus, by measuring the contact angle and liquid surface tension, γ_{lg}, the difference in the interfacial tensions ($\gamma_{sg}-\gamma_{sl}$) can be determined.

Knowledge of interfacial tensions is important in the practical problems of lubrication and adhesion. Successful lubrication occurs for a system where a lubricant completely wets a solid and maintains complete coverage under tribological conditions. The degree of adhesion of a lubricant to a solid or the strength of an adhesive can be determined by the extent to which the free energy of the system is lowered by the adsorption of the lubricant or adhesive. The energy necessary to separate the solid–liquid interface (in vacuum) is called the work of adhesion, W_A^S, and is given by

$$W_A^S = \gamma_{lo} - \gamma_{so} + \gamma_{sl} \tag{10}$$

where γ_{so} and γ_{lo} are the respective surface tension of the solid and liquid in vacuum.

A similar surface tension treatment can be made for the interface between metal oxides and metals. Native oxides typically have lower surface free energies than the bare metal, in turn driving the surface oxidation of most metals. However it is not true that all oxides have lower surface tensions than all metals or semiconductors. For the case of growth of a metal oxide film on a dissimilar metal, or a metal on a supporting metal oxide substrate, the initial phases of growth are determined by the respective surface tensions.[19] These are described by the Young–Dupré equation

$$\gamma_{MO} = \gamma_O - \gamma_M \cos\theta \tag{11}$$

where γ_{MO} is the interfacial tension between the metal and oxide, γ_O and γ_M are the respective surface tensions of the oxide and metal, and θ is the contact angle as described before. For the case of solid–solid interactions, registry, epitaxial orientation, and the possibility of interfacial reactions must be taken into account for a full treatment. The nucleation and growth properties of metals and metal oxides are critical parameters in many semiconductor and catalysis processing procedures. AES, SIMS, ISS, and various electron microscopies have been used extensively in the study of these problems.

Surface tensions can also be used to predict the behavior of multicomponent solid systems. Unlike single-component systems, the surface tension is no longer equal to the surface free energy G^S, but is related to the different component concentrations at the surface by the Gibbs equation:

$$d\gamma = -S^S\, dT - \sum \Gamma_i\, d\mu_i \tag{12}$$

Here Γ_i is the excess number of moles of compound i at the surface and μ_i is the chemical potential of the ith component. For an ideal binary solution at constant temperature, the surface composition of the solution can be estimated from the surface tensions of the two components by the equation

$$\frac{X_S^1}{X_S^2} = \frac{X_B^1}{X_B^2} \exp\left[\frac{(\gamma_2 - \gamma_1)a}{RT}\right] \tag{13}$$

In this formula, X_S^i and X_B^i refer to the respective atom fractions of the ith component at the surface and in the bulk, and a is the surface area occupied by the atoms. From this equation it can be seen that the component with the lowest surface tension will accumulate at the surface. Calculations of the segregation of silver to the surface of a Au–Ag alloy after those of William and Nason[20] are shown in Figure 9

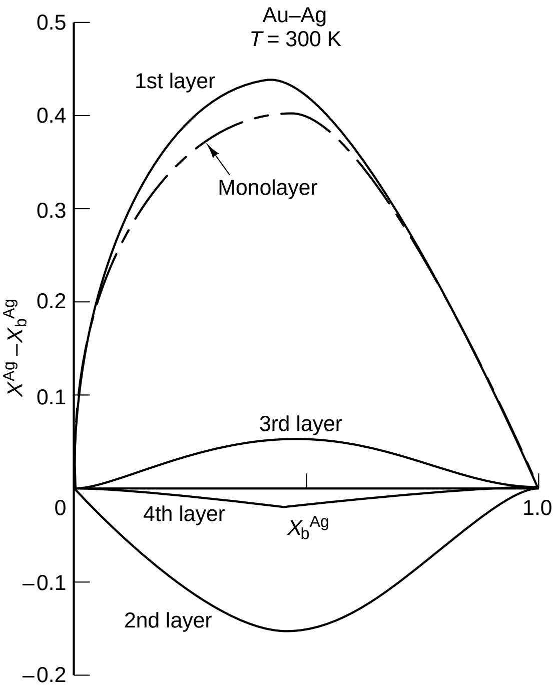

Figure 9 Preferential segregation of silver occurs at the surface of a Ag–Au alloy due to its lower surface tension

and readily demonstrate this phenomenon. The difference in surface and bulk concentrations of silver is plotted against the bulk concentration and shows a surface enrichment of silver for all compositions. A complete treatment of nonideal solutions such as the Au–Ag alloy must take into account differences in atomic diameters and the heat of mixing of the solution; however, equation (13) predicts quite well the behavior of most binary alloys. The temperature dependence of surface segregation is also predicted by equation (13), indicating a decrease in segregation with increasing temperature.

4.3 Physical and Chemical Adsorption

The thermodynamics of gas-phase species adsorbing on a surface can be separated into the classes of physical adsorption (physisorption) and chemical adsorption (chemisorption). The difference between the two classes of adsorption is related to the heat of adsorption, ΔH_{ads}. In physisorption, weak attractive forces (van der Waals) such as dipole–dipole and induced dipole interactions drive the adsorption of species from the gas phase. For chemisorbed systems, chemical bonds associated with electron transfer between adsorbate and substrate are formed upon adsorption. Each of these interactions can be described by a two-dimensional potential-energy diagram as in Figures 10 and 11.

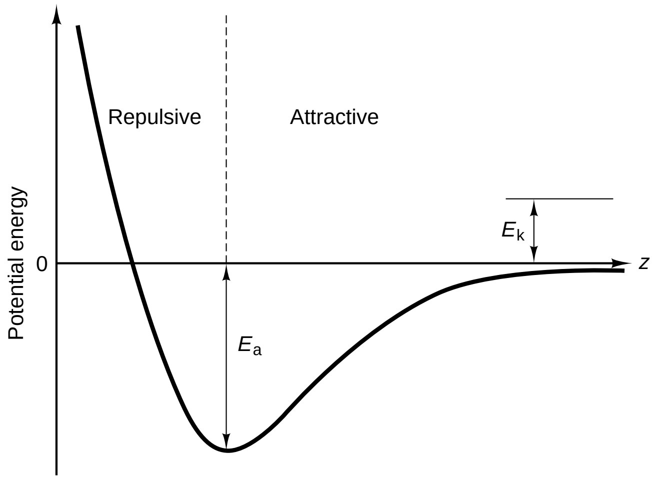

Figure 10 Potential energy diagram for the case of physisorption where adsorbates experience weak attractive forces near the surface

For the case of physisorption, an incoming molecule of kinetic energy E_k can lose energy by exciting lattice phonons of the substrate. The physisorbed molecule exists in a potential-energy well representative of an oscillating position of equilibrium near the surface (Figure 10). The depth of this well is equal to the binding energy E_a of the molecule to the surface. For physisorbed systems, the binding energy is equal to the heat of adsorption. For a molecule to leave the surface, it must overcome the potential-energy barrier E_a; the desorption energy E_d is, therefore, also equal to E_a.

For chemisorption, molecules similarly become bound in a weakly adsorbed state near the surface as, depicted in Figure 11(a). (For atomic species, adsorption directly into the chemisorbed state is possible.) While in this precursor state, internal vibrational or electronic excitations can provide the energy necessary to cross the potential-energy barrier to the chemisorbed state. The deep potential-energy well is associated with the strong chemical bond formed between adsorbate and substrate. Again the depth of the well is associated with the energy of adsorption and equal to the heat of adsorption. In the rare case of activated chemisorption (Figure 11(b)) the heat of adsorption is equal to the difference between the desorption energy, E_d, and the activation energy of adsorption.

Heats of adsorption can be experimentally measured by calorimetry, temperature programmed desorption (TPD), and adsorption isotherms taken at different temperatures. Calorimetry involves the direct measurement of temperature rise caused by the adsorption of a known amount of gas on to a well-characterized surface. TPD is the most common method of determining the heats of adsorption. In this procedure, molecules are adsorbed on to a clean well-characterized substrate at a fixed temperature. The sample is then heated in a linear fashion while the pressure of the desorbing species is monitored with a mass spectrometer. The desorption rate $F(t)$ is given by

$$F(t) = \nu f(\sigma) \exp\left(-\frac{E_d}{RT}\right) \tag{14}$$

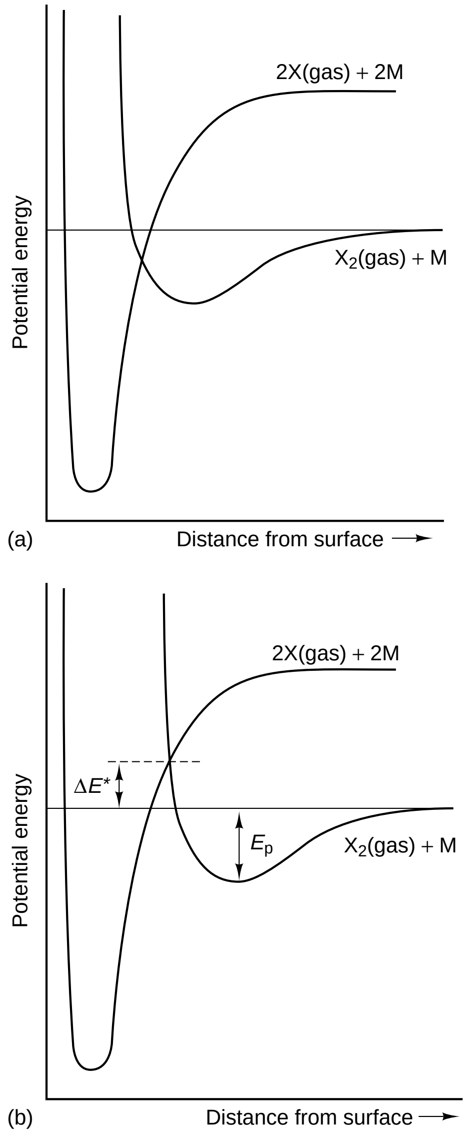

Figure 11 Potential energy diagrams for the chemisorption of a diatomic molecule: (a) the process results in the formation of a strong chemical bond and (b) in some cases may require a certain activation energy

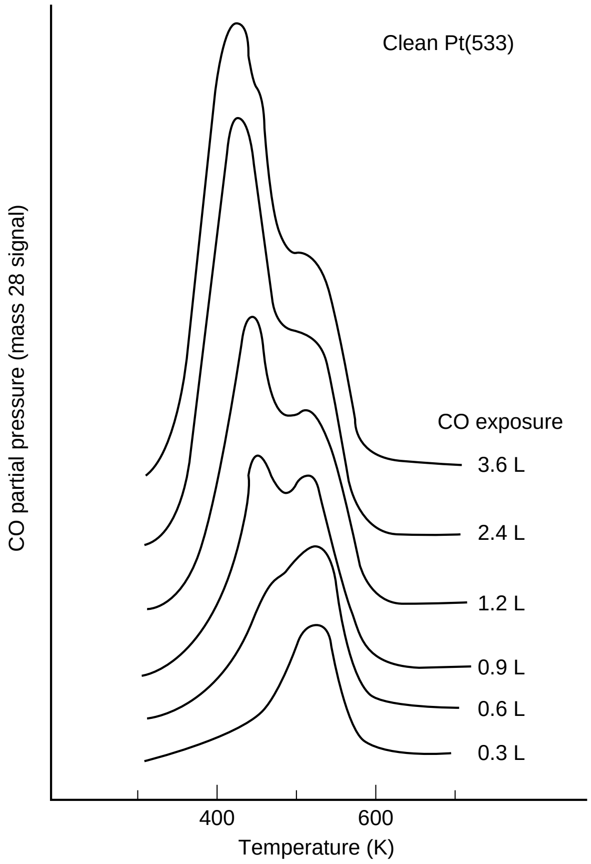

Figure 12 Temperature desorption spectrum of CO from a Pt(533) surface

where ν is the pre-exponential factor and $f(\sigma)$ is a coverage dependence factor. As an example, the plot of pressure versus temperature (desorption spectrum) for CO desorbing from a Pt(533) surface is shown in Figure 12.[21] The procedures for measuring the desorption energy and rate orders for desorption spectra are well described in the literature.[22]

The TPD spectra of CO on Pt(533) illustrate an important factor influencing the energy of desorption and hence the heat of adsorption, i.e. the local binding site. The spectra, measured as a function of coverage, depict two separate desorption peaks. The lower energy state occupied at high coverages has been associated with molecules adsorbed on the terraces of the surface, while the higher energy peak is associated with the desorption of molecules from step edges. Other factors affecting the heat of adsorption besides adsorbate–substrate interactions include coverage (as a result of adsorbate–adsorbate interactions) and temperature.

Adsorption isotherms are also used to determine heats of adsorption as well as entropy and heat capacity changes associated with adsorption. An adsorption isotherm is the relationship at constant temperature between the amount of a gas that is adsorbed on to a surface and the partial pressure of the gas. The two models most widely used to describe the adsorption process are the Langmuir isotherm[23] and the Brunauer–Emmett–Teller (BET) isotherm.[24] The Langmuir model assumes the presence of noninteracting adsorbates and a homogeneous surface, and that no adsorption occurs after the completion of a full monolayer. The possibility of multilayer formation is accounted for in the BET isotherm by introducing distinct heats of adsorption for the first and second molecular layers. The Langmuir isotherm most accurately describes systems of chemisorbed molecules, while the BET isotherm is more useful for systems involving physisorption. In practice, the heat of adsorption is obtained by measuring adsorption isotherms at two different temperatures and solving an integrated form of the Clausius–Clapeyron equation:

$$\ln\left(\frac{P_1}{P_2}\right)_\Theta = \frac{-\Delta H_{\text{ads}}}{R}\left(\frac{1}{T_1}-\frac{1}{T_2}\right) \qquad (15)$$

where $(P_1/P_2)_\Theta$ is the ratio of pressures required to produce identical coverages at different temperatures.

5 ELECTRONIC PROPERTIES OF SURFACES

5.1 Surface Potentials

Many physical and chemical properties of surfaces can be associated with the electronic nature of the surface. This electronic character is determined largely by the concentration of mobile charge carriers (electrons, holes, and diffusing ions). Their concentration is dependent on both the inherent electronic structure of the bulk and the unique environment of the surface. Band structure theory has been used successfully to describe many electronic properties of the bulk solid. Here the discussion of electronic properties is restricted to those associated with the presence of the surface.

Electrons of a solid, in the region of a surface, experience a potential (V_S) that may be divided into three parts:

$$V_\text{S}(x) = V_{\text{core}}(x) + V_{\text{exchange}}(x) + V_{\text{diploe}}(x) \qquad (16)$$

$V_{\text{core}}(x)$ is the potential associated with the interaction between valence and core electrons and $V_{\text{exchange}}(x)$ is the exchange potential between valence electrons. The exchange potential accounts for the repulsive interaction between electrons of like spin (Pauli exclusion principle) and electrons of either spin (correlation interaction). Both of these potentials are experienced in the bulk as well as at the surface. $V_{\text{dipole}}(x)$ is specific to the surface and arises from charge redistribution at the asymmetric surface.

As discussed earlier, a surface is characterized by the abrupt change in density of atoms in a given direction (boundary of the solid phase). A drastic change in electron density is associated with the change in atomic density. Electrons in a solid can be treated as electrostatically bound to a uniform density of positive charge (ion cores). This electronic picture of a solid is called the jellium model and has been used to describe many electronic properties of solids.[25] At a solid–vacuum interface, electrons are bound to the solid on only one side and can ‘spill out’ into the vacuum (Figure 13). The electrons which tunnel out of the solid at the surface leave behind a partial positive charge. This creates a space-charge region, often referred to as the electrical double layer, and leads to the associated space-charge potential $V_{\text{dipole}}(x)$.

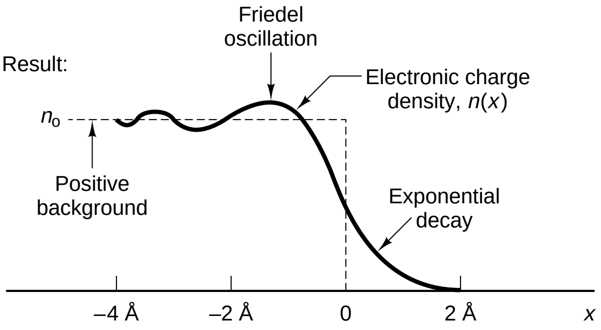

Figure 13 Plot of electronic charge density as a function of distance across a solid–vacuum interface as calculated from a jellium model

The magnitude of the space-charge potential is closely dependent on the local structure of the surface, as will be discussed in relation to work function measurements. In the region of the surface, the height of the surface potential $V_\text{S}(x)$ and the depth of penetration into the bulk is related to the number of free carriers in the solid. It can be shown that the depth of penetration d is given by

$$d = \left(\frac{2\varepsilon\varepsilon_0 V_\text{S}}{en_\text{e}(\text{bulk})}\right)^{1/2} \qquad (17)$$

where ε is the dielectric constant in the solid, ε_0 is the permittivity of free space, and n_e(bulk) is the concentration of charge carriers in the bulk. Thus the region of space charge will be much different for metals, semiconductors, and insulators; the higher the free concentration of carriers, the smaller the penetration depth of the surface potential. For metals where the range of free carriers is 10^{20}–$10^{23}\,\text{cm}^{-3}$, V_S is small and d is less than the thickness of one atomic layer. However, for semiconductors, where carrier concentrations are 10^{-10}–$10^{-16}\,\text{cm}^{-3}$, surface potentials can be large and penetration depths can extend over thousands of atomic layers into the bulk. The effect at insulating surfaces can be even more extreme.

The region of space charge and the height of the surface potential can be represented schematically by a change in the band structure of a material at the surface. By considering only the potential energy of electrons at the top of the valence band and the bottom of the conduction band, the bands can be plotted as straight lines as a function of distance through the crystal. In the region of the surface, the potential is altered by the space charge region and is represented by ‘band bending’. For the case of n-type and p-type semiconductors, the charge of the free carrier differs and thus the direction of band bending and the nature of charge accumulation at the surface differs (Figure 14). The surface region is depleted of electrons for n-type semiconductors, while the surface region becomes electron rich for p-type semiconductors.

As mentioned previously, the space-charge region can also be affected by the local structure at the surface. This is most often seen in measurements of the work function of a material. The work function (Φ) is defined as the energy required to remove an electron from the highest filled energy level to

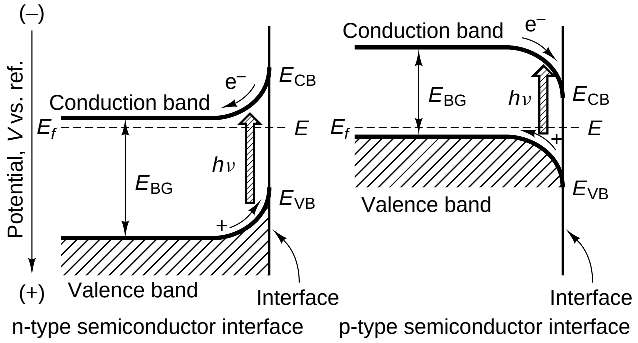
(–)
Potential, V vs. ref.
(+)
Conduction band
e⁻
E_{CB}
E_f
E
E_{BG}
hν
E_{VB}
+
Valence band
Interface
n-type semiconductor interface
Conduction band
e⁻
E_{BG}
hν
E_{CB}
E_f
E
+
Valence band
E_{VB}
Interface
p-type semiconductor interface

Figure 14 Electronic surface structure of n-type and p-type semiconductors depicting the effect of the space-charge region and band bending at the surface

the point of zero kinetic energy in vacuum, and is given by equation (18).

$$e\Phi = eV_{\text{exchange}} + eV_{\text{dipole}} - E_{\text{F}} \tag{18}$$

As before, V_{exchange} depends on the bulk electron density and V_{dipole} is due to the surface space charge potential that electrons must overcome in leaving the solid. The Fermi energy (E_{F}) is defined as the potential energy of an electron at the top of the valence band. Schematically, the relationship is represented in Figure 15. Equation (18) shows the direct relationship between the work function and the dipole potential. Experimentally, both the structure of the surface and the presence of adsorbates have been seen to affect work-function measurements. Table 3 lists the work function measured from several faces of tungsten, molybdenum, and tantalum crystals.[26,27] The more open and highly corrugated faces (or those containing a greater number of steps) yield a lower work function. Here, as the surface becomes more rough, the presence of ion cores of surface atoms protruding into vacuum effectively reduces the potential field at the surface (V_{dipole}) and lowers the work function.

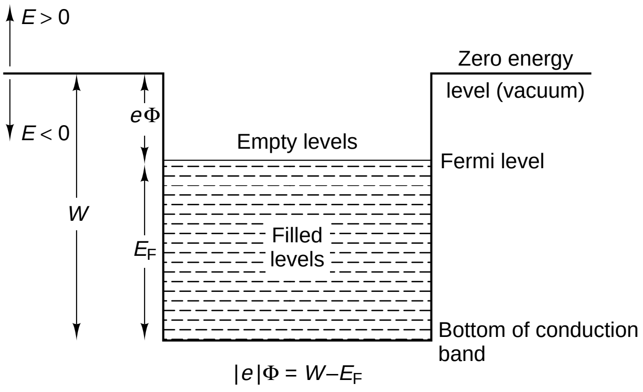
E > 0
E < 0
W
eΦ
E_F
Zero energy
level (vacuum)
Empty levels
Fermi level
Filled
levels
Bottom of conduction
band
$|e|\Phi = W - E_F$

Figure 15 The work function of a solid surface is defined as the energy required to remove an electron from the highest filled energy level to the point of zero kinetic energy in a vacuum

Table 3 Work function (eV) of different crystal faces of several metals

Crystal Face	Tungsten	Molybdenum	Tantalum
(110)	4.68	5.00	4.80
(112)	4.69	4.55	–
(111)	4.39	4.10	4.00
(001)	4.56	4.40	4.15
(116)	4.39	–	–

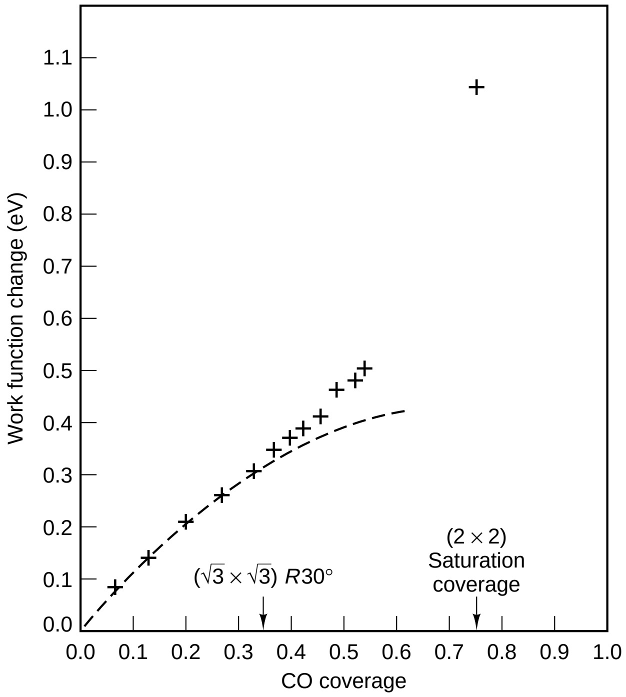

Figure 16 Work function changes induced by the adsorption of CO on Rh(111)

In a similar fashion, adsorption of atoms or molecules onto a surface can raise or lower the value of the work function. Figures 16 and 17 illustrate the affect of CO and Na adsorption on the work function of Rh(111). For the case of carbon monoxide, the presence of the double layer at the surface leads to the polarization of CO with the negative end of the induced dipole oriented away from the surface. The presence of this dipole reinforces the dipole potential and consequently increases the work function. For the case of sodium, charge transfer occurs upon adsorption leaving an electropositive element at the surface. This in turn decreases the effective magnitude of the dipole potential and lowers the work function. The data of Figure 17 also illustrate the role of adsorbate–adsorbate interactions as depolarization of the sodium occurs at near-monolayer coverage and reduces the effect. The adsorption of gas molecules on insulator

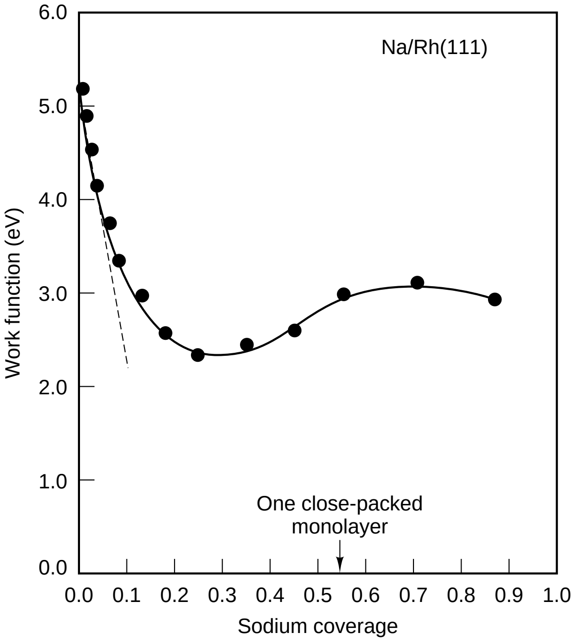

Figure 17 The work function of a Rh(111) surface is initially lowered by the adsorption of sodium atoms. The small increase at higher coverages arises from the depolarization of the sodium overlayer

and semiconductor surfaces can produce even more drastic changes in the magnitude of the dipole potential, markedly altering the electrical conductivity of these surfaces. As a result, many gas-sensor applications make use of thin films of insulators and semiconductors as detectors.

5.2 Electron Emission from Surfaces

Many of the surface characterization techniques listed in Table 1 are based on the analysis of electrons emitted from the surface region. The emission of these electrons can come as a result of temperature, applied electrical field, or the interaction of the surface species with incident photons or electrons.

As mentioned previously, the probability of emission (escape) of an electron from a solid surface is inversely proportional to the strength of interaction between the electron and the solid. In other terms, the higher the energy state of an electron in a solid, the lower the energy necessary for it to be removed from the surface. The population of these electronic energy states is proportional to temperature, and can be approximated by a Boltzmann distribution,

$$f(E) \approx \exp\left(-\frac{\Phi}{k_{\mathrm{B}}T}\right) \tag{19}$$

where Φ is the work function of the metal and k_{B} is the Boltzmann constant. Thus, the emission of electrons from a surface can be induced by raising the temperature to the point where energies of electrons at the surface are above the work function. This process is called thermionic emission and is often used to produce electron beams from metallic filaments. Refractory metals which can be heated to the high temperatures necessary to produce a large flux of electrons are typically used. In order to increase their lifetime, metals of a lower work function can be coated onto the filament, thereby reducing the temperature required to produce a given flux.

Electron emission can also be induced by the presence of large electric fields. When a potential V is applied between a sharp metal tip and a plate, a large electric field is generated at the tip (i.e. $E \approx 10^7\,\mathrm{V\,cm^{-1}}$ for a potential of 1000 V applied to a tip of $r = 10^{-4}\,\mathrm{cm}$). This electron emission process is known as field emission. In the field emission microscope (FEM), emitted electrons are detected at a phosphor plate as a function of potential and are used to measure the work function of different crystallographic planes of the metal tip.

Finally, electrons can be emitted from a surface as a result of photon–solid or electron–solid interactions. When high energy photons or electrons are incident upon solid samples, several electronic transitions can lead to the emission of electrons. First, if the energy ($h\nu$) of an incident photon exceeds that necessary to ionize an atom of the solid, electrons not suffering inelastic collisions will be emitted from the solid with a kinetic energy (*KE*) given by

$$KE \approx h\nu - BE - \Phi \tag{20}$$

where *BE* is the binding energy of the electron in the solid and Φ is the work function of the solid. The illumination of a solid with X-rays leads to the emission of electrons from core-level energy states and provides information about elemental composition. The use of lower energy UV photons in UV photoelectron spectroscopy (UPS) leads to emission of electrons from valence energy levels and probes the character of chemical bonding at the surface. A second electron emission process can occur as a result of the core level excitation process. When core level electrons are emitted, they leave behind an electron vacancy which can be filled by the de-excitation of electrons from higher energy states. The energy released by the resulting electronic transition can be transferred to still another electron which will be emitted from the solid if its energy exceeds its binding energy (Figure 18). Electrons emitted by this process

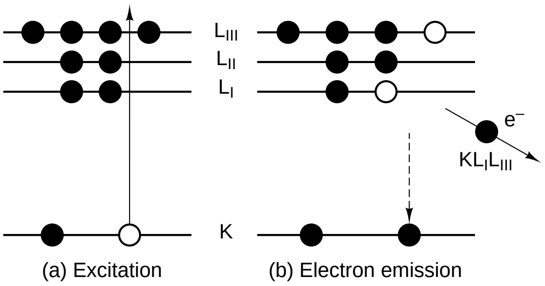

Figure 18 The Auger electron emission process is a three-electron process involving both core and valence-level electrons

are known as Auger electrons. Auger transitions are independent of the energy of the incident beam and therefore can be induced by both photon and electron excitation sources. Auger electron spectroscopy (AES) is widely used as a probe of composition and chemical state information.

The electronic transitions previously described can occur in both surface and bulk atoms of a solid. Electron spectroscopies such as XPS, UPS, and AES are capable of providing surface-specific information because of the relatively short mean free path of electrons in solids. In effect, only electrons emitted in a narrow region near the surface will escape before losing energy through inelastic scattering events. The mean free path of an electron in a solid is plotted versus electron kinetic energy in Figure 19. The data points for this plot are representative of the different kinetic energies of electrons photoemitted from a number of solids. The observed dependence of mean free path with kinetic energy is typically referred to as the ‘universal curve’.[28]

5.3 Electron Tunneling at Surfaces

In the discussion of the surface space-charge region, the idea of electrons spilling out or tunneling out of the solid into vacuum was presented. While the phenomenon has been understood within the solid state physics community for many years, it has recently received a much broader exposure in the context of scanning tunneling microscopy (STM). In STM, a very sharp tip is brought within close proximity (a few angstroms) of a surface such that tunneling can occur between the tip and the sample. The direction of tunneling (electrons traveling from tip to surface or from surface to tip) is dependent on the bias potential placed on either the tip or the sample. While much of the STM work has focused on generating topographic images of the surface, there is much information to be gained from the specifics of the tunneling current. The height of the local barrier to tunneling can be measured by modulating the tip and measuring current as a function of frequency. Barrier height measurements are similar to work-function measurements; however, they differ in magnitude because of the close proximity of the tip and sample. In addition, STM offers the possibility of spatially mapping the local density of electronic states. In both techniques, a comparison to theoretical calculations is necessary to understand the tunneling current data. To date, uncertainties in tip geometry and composition, and the presence of two different surfaces (tip and sample) have precluded an exact theoretical treatment of the problem and much work remains on this topic.

6 OPTICAL PROPERTIES OF SURFACES

6.1 Photon–Surface Interactions

The interactions between light and matter at a surface include absorption, reflection, phase shift, and diffraction. The

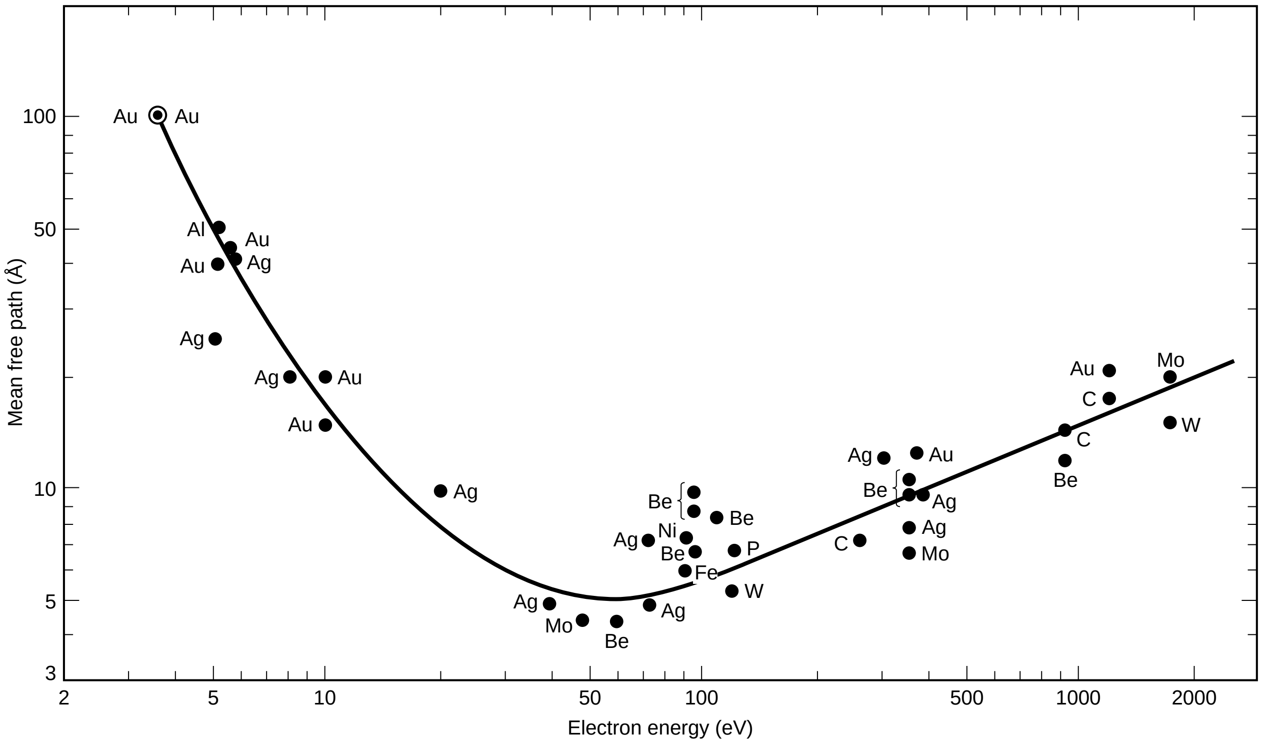

Figure 19 The ‘universal curve’ depicting the mean free path of different energy electrons measured in a number of materials

optical properties of surfaces, like those of the bulk, can be described in terms of two important parameters, the index of refraction η and the extinction coefficient k. The index of refraction is defined as the velocity of light propagating through a material relative to the velocity of light propagating through a vacuum. The extinction coefficient is related to the absorption or decay of radiation as it passes through matter. Often the two parameters are combined and quoted as a complex index of refraction N, given by the relation

$$N = \eta - ik \tag{21}$$

At this point it should be noted that both the index of refraction and the extinction coefficient are extremely frequency dependent. Consequently, the properties of absorption, reflection, and phase shift which depend on them will also show a frequency dependence. Value of η and k for most metals and semiconductors are tabulated in the *American Institute of Physics Handbook.*[29]

The absorption of visible light by many metals and semiconductors can be considered a surface phenomenon because much of the absorption takes place in a region very near the surface. The extent of absorption as a function of distance into a solid is given by the equation

$$I_t = I_0 \exp(-\alpha z) \tag{22}$$

where I_0 and I_t represent the incident and transmitted radiation, respectively, and α is the absorption coefficient (Figure 20). The absorption coefficient for a given wavelength λ is related to the extinction coefficient k by $\alpha = 4\pi k/\lambda$.

Another useful parameter in discussing the propagation of radiation into the surface region of a highly absorbing material is the optical skin depth. This is defined as the distance z into a material at which the ratio of transmitted intensity to incident intensity equals a value of $1/e$. Thus the optical skin depth can be defined as the reciprocal of the absorption coefficient and is useful in discussing relative penetration depths in different materials. For example, the optical skin depth of silver at an incident wavelength of 500 nm is ~150 Å while that of silicon is ~1000 Å at the same wavelength.

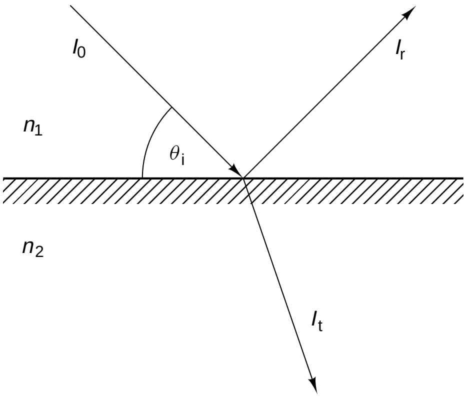

Figure 20 Schematic representation of the reflection and transmission of light at a solid surface

Closely related to the propagation of light into matter (refraction) is the reflection of light at a surface. Reflection is defined as the case of elastic scattering of radiation where the scattered angle is equal to the angle of incidence θ_i (Figure 20). For the case of normal incidence, the intensity of reflected light at the interface between two homogeneous media is given by

$$R = \frac{(\eta_0 - \eta_1)^2 + {k_1}^2}{(\eta_0 + \eta_1)^2 + {k_2}^2} \tag{23}$$

Here η_0 is the refractive index of the medium of incidence (approximately 1 for air and vacuum environments) and η_1 and k_1 are the index of refraction and extinction coefficients of the absorbing material. A complete treatment of the intensity of reflected light from a surface at angles other than normal incidence can made using Fresnel's equation.[30] Values of R at visible wavelengths for a transition metal surface typically fall within the range of 65–95%. Obviously, for many metal oxides which are transparent in the visible, the value of R will be very low.

A phase change ρ of the radiation will be associated with the reflection and is given by the equation

$$\rho = \tan^{-1} \frac{2\eta_0 k_1}{{\eta_0}^2 - {\eta_1}^2 - {k_1}^2} \tag{24}$$

It should be pointed out that the index of refraction and the extinction coefficient are quantities experimentally derived from reflectivity measurements. Variations in the chemical and mechanical properties of a surface are known to produce drastic changes in the values of these parameters. Therefore, the use of clean (by vacuum standards) and atomically flat surfaces is highly desirable for such measurements.

Finally, the incidence of radiation on to a surface can lead to diffraction. Diffraction arises from the interaction of a propagating wave, light in this case, with a periodic array of scattering sites. From the condition for diffraction,

$$n\lambda = 2d \sin\theta \tag{25}$$

where λ is the incident wavelength, n is the order of diffraction, d is the separation of scattering sites and θ is the angle of incidence, it is easily seen that the periodicity of scattering sites must be on the order of the incident wavelength. Thus, diffraction of visible light is only observed from surface structures with periodicity of hundreds of nanometers (i.e. gratings). Diffraction at an atomic scale is possible with the use of X-rays ($\lambda \approx \mathring{A}$'s); however, as most material is partially transparent at these wavelengths, X-ray diffraction typically arises from periodicity of the bulk lattice and surface symmetry is lost. Yet, with the high flux of X-rays available from synchrotron sources and the use of a glancing angle of incidence, X-ray diffraction has recently provided important structural information in studies of thin film growth.

6.2 Optical Measurements at Surfaces

The specific interactions of light and matter at a surface are an inherent part of optically based surface characterization techniques. While Fourier transform infrared (FTIR) spectroscopy and Raman spectroscopy are traditionally employed in analyzing bulk structural properties, careful consideration of surface properties has led to their development as surface techniques. Both of these spectroscopies have been used to measure the vibrational spectra of molecular adsorbates on a wide variety of surfaces.[31,32] Vibrational information is derived from the interaction of light with the dipole oscillation (IR) and polarizability (Raman) of the molecules. In both instances the intensity of the interaction is proportional to the electric field that the molecule experiences. This fact that is the basis of the widely studied phenomenon of surface-enhanced Raman scattering (SERS),[33] where a 10^4 enhancement of the electrical field strength is observed in the region of some roughened metal surfaces. Electric field strengths at the surfaces of conductors show a drastic dependence on angle of incidence and polarization as well as on the index of refraction and extinction coefficient of the solid. As a result, stringent requirements are placed on the experimental layout of the techniques. In addition, screening and the creation of image charges at the surface influence the selection rules of these spectroscopies.

The techniques of second-harmonic generation and sum-frequency generation derive their sensitivity to surfaces from the asymmetry of the surface region.[34] In second-harmonic generation (SHG), attention is focused on an induced-dipole component at twice the frequency of the incident radiation. The strength of this component is proportional to the nonlinear susceptibility of the material which is only active in regions that lack inversion symmetry. The physical origin of the surface nonlinearity can arise from both structural discontinuity, as in the dangling bonds of semiconductor surfaces and electric field discontinuities. SHG studies have addressed the processes of molecular adsorption and desorption as well as surface diffusion of molecular adsorbates. Sum-frequency generation (SFG) relies on the combination of two incident frequencies (one infrared) to produce a third frequency ($\omega_1 + \omega_2 = \omega_3$). Again, the process is dependent on nonlinear susceptibility and takes advantage of resonant enhancements of this effect at frequencies of molecular excitation or vibration. In this way, by tuning the infrared frequency, the vibrational spectrum of adsorbates can be obtained.

Alternatively, the technique of laser-induced desorption takes advantage of the adsorption properties of surfaces. As previously discussed, the optical skin depth of most metals is on the order of 50 Å for IR frequencies. As a result, local heating can occur (up to $10^{10}\,\mathrm{K\,s^{-1}}$) when incident radiation is focused to a small spot on a surface. By analogy to temperature programmed desorption (TPD), molecular species present in this region can be thermally desorbed and detected with a mass spectrometer. The rapid local heating of the surface induced by adsorption typically leads to the desorption of ‘intact’ species and thus allows the concentration of surface adsorbates to be probed as a function of time.

7 DYNAMIC PROPERTIES OF SURFACES

7.1 Surface Atomic Vibrations

Much of the previous discussion of surface properties has treated the surface as the termination of a rigid periodic lattice. In reality, at temperatures above 0 K, surface atoms are vibrating about their equilibrium position. A useful model of this process is the one-dimensional harmonic oscillator. In this model, atoms are treated as a mass attached through a spring to a fixed surface. As depicted in Figure 21, restoring forces are exerted on the atom as it moves from its equilibrium position r. This force is linearly proportional to the displacement x and a proportionality constant k, called the force constant. The force is given by the equation

$$f = m\frac{\mathrm{d}^2x}{\mathrm{d}t^2} = -kx \tag{26}$$

where m is the mass of the atoms and t is time. The potential energy change ($\mathrm{d}V$) of such a system with respect to displacement (vibration) of the atom is given by $\mathrm{d}V/\mathrm{d}x = kx$. Thus the potential energy of a vibrating surface atom can be

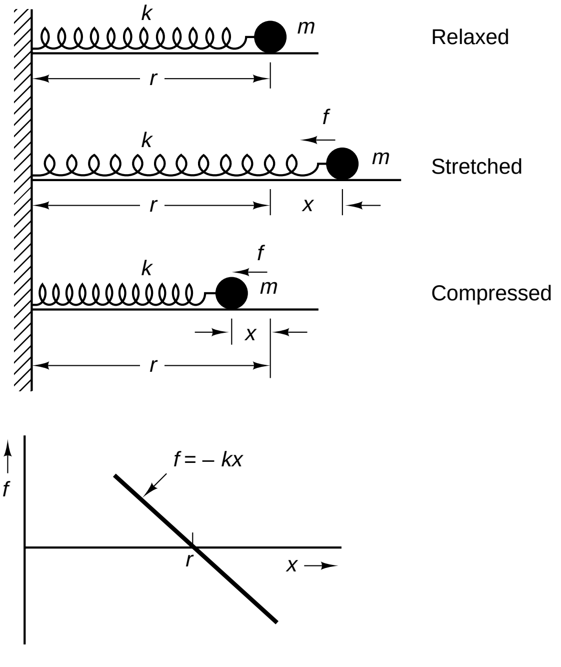

Figure 21 The model of a surface atom as a one-dimensional harmonic oscillator

modeled as

$$V = \frac{1}{2}kx^2 \tag{27}$$

Such a potential energy function gives rise to the familiar parabolic curve (Figure 22) where the curvature of the function is related to the force constant. The success of this simple harmonic model in treating surface atom vibrations lies in the relatively small displacement of surface atoms during a period of vibration. For some crystal properties, such as thermal expansion at elevated temperature, anharmonic contributions to the potential must be included for an accurate description.

The surface of a solid can be viewed as a collection of many harmonic oscillators, each coupled to its nearest neighbor. The surface vibrational modes of such a collection can be obtained by considering the propagation of waves in a semi-infinite isotropic elastic medium. For a stress-free surface, it is found that long wavelength modes of propagation exist parallel to the surface and decay exponentially into the bulk. The vibrational spectrum of atoms at solid surfaces has been measured by inelastic helium scattering and high resolution electron energy-loss spectroscopy (HREELS). Studies of this type have detected vibrational modes related to specific sites. They find that the inward relaxation of surface atoms at step sites is larger than that of terrace atoms and thus gives rise to a higher vibrational frequency. Surface vibrational modes (phonons) are typically low in energy (<70 meV) and are found in the 10–500 cm^{-1} region of the spectrum.

The effect of surface atom vibrations is seen clearly in low energy electron diffraction (LEED). Experimentally, an exponential decrease in the intensity of scattered beams and an increase in background intensity are observed with increasing temperature. This arises as a result of the increased vibrational amplitude of the surface atoms that occurs at elevated temperatures. Atoms displaced from their equilibrium position during the scattering process will scatter out of phase, reducing the number of electrons in the diffracted beam. A similar temperature dependence is observed in X-ray diffraction from bulk lattices. In both instances, the phenomenon can be described by the Debye–Waller factor which includes the material-dependent Debye temperature. By measuring the temperature dependence of diffracted beam intensities, the Debye temperature can be calculated and taken as a measure of surface vibrational amplitude perpendicular to the surface. For most metals, the rms vibrational amplitude of surface atoms normal to the surface is 1.4 to 2.5 times larger than the bulk atom displacements.

Atoms and molecules adsorbed on a surface will also have a characteristic vibrational spectrum. For the case of physisorbed molecules, ‘surface allowed’ vibrations will closely resemble those of the gas-phase molecule. However, new modes associated with local adsorption geometries and the formation of new chemical bonds arise for chemisorbed molecules. Reflection-absorption infrared spectroscopy (RAIRS), SFG, Raman, and HREELS are all useful techniques for studying the vibrational spectra of adsorbed species; however, there are limitations to each approach and careful consideration of the system to be analyzed must be made. As an example, the vibrational spectrum of CO adsorbed on Rh(111)[37] is shown as a function of coverage in Figure 23. At low coverages, CO occupies only atop sites and two bands characteristic of the carbon–oxygen stretch and the metal–carbon stretch are observed. At higher coverages, repulsive interactions between the adsorbates force CO to occupy sites of lower symmetry. As a result of the repulsion, the bonding of the molecules in bridging sites is weakened and additional bands lower in the vibrational spectrum are observed.

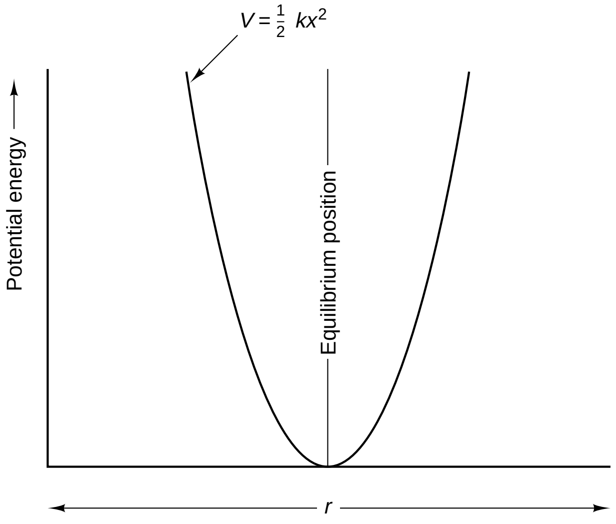

Figure 22 Potential energy of the one-dimensional harmonic oscillator as function of interatomic displacement *r*

7.2 Surface Diffusion

The motion of atoms both in and on the surface can also occur through surface diffusion. The concept of atom transport along the surface plane is important in equilibrium surface structure, nucleation and growth of thin films, and surface reactivity.

As discussed in relation to surface structure, surfaces can possess many defects on the atomic scale. The equilibrium distribution of these sites is reached through surface diffusion. This can be considered as a multistep process where atoms break away from their local position and migrate across the surface to a new equilibrium site. As each surface site (step, kink, terrace) will have a different binding energy, diffusion from lower binding energy defect sites is most common. The frequency ν with which an atom can escape from a site is exponentially proportional to the height of the potential energy barrier ΔE^* associated with leaving the site. The frequency is

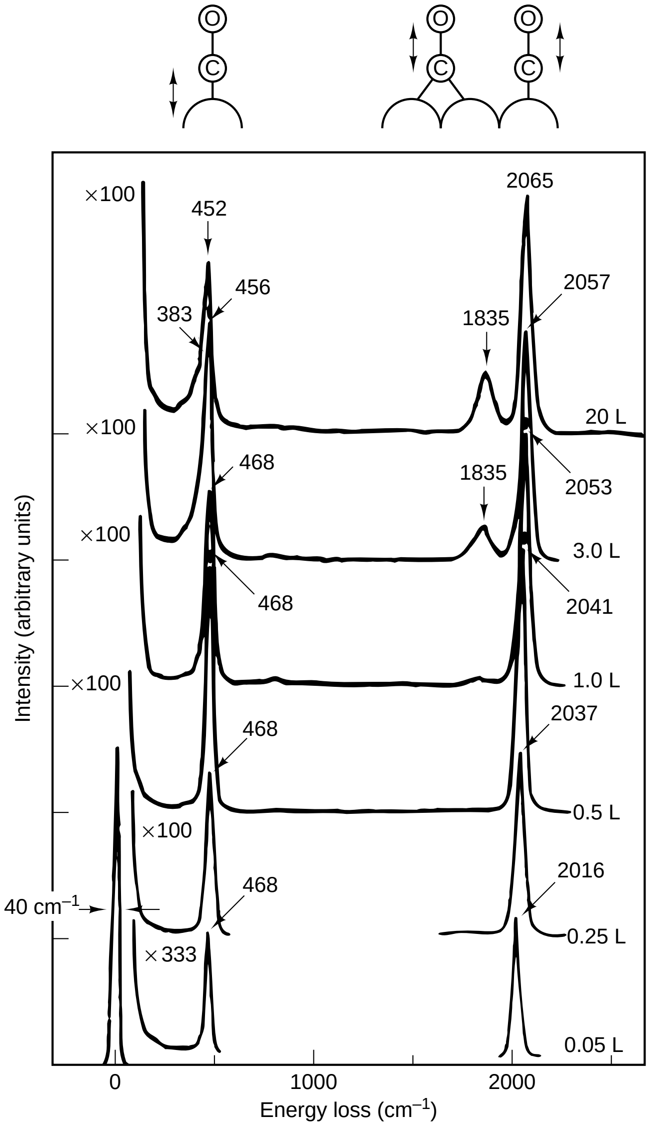

Figure 23 High-resolution electron energy-loss spectrum of CO adsorbed at different coverages on Rh(111)

given by the equation

$$\nu = z\nu_0 \exp\left(\frac{-\Delta E^*}{k_B T}\right) \tag{28}$$

where z is the number of nearest neighbors and ν_0 is the vibrational frequency of the escaping atom. Assuming a vibrational frequency of $10^{12}\,\mathrm{s}^{-1}$ and a barrier height of $20\,\mathrm{kcal\,mol}^{-1}$, surface atoms with six nearest neighbors are estimated to 'jump' once every 50 s at room temperature. However, the same atom at 1000 K is estimated to move from a site once in every 10^{-8} s!

While high diffusion *rates* can be induced by temperature, a more important parameter is the distance across the surface that the diffusing atom can travel. The rms diffusion distance is defined in terms of a diffusion coefficient which can be derived from experimental measurements. In most surface-diffusion experiments, a coverage gradient is evaluated by measuring the concentration of diffusing atoms as a function of distance along the surface. Optical reflection techniques, laser-induced desorption and scanning Auger electron spectroscopy have been used for such measurements. Field ion microscopy can also be used to monitor the diffusion of individual atoms at the surface of a very sharp metal tip.

7.3 Gas–Surface Interactions

The discussion to this point has only considered the dynamics of atoms of the surface plane and adsorbates at this plane. The dynamics of molecules arriving at the surface from the gas phase are important in determining the properties of physical and chemical adsorption (see also Section 4). The interaction of gas-phase atoms or molecules with a surface is a multistep process that begins with collision at the surface. The result of the collision can range from energetically elastic scattering back into the gas phase to chemical reaction and accommodation at the surface (sticking). The type of interaction is determined by the energy of the gaseous molecule, temperature, and the local structure of the surface.

Figure 24 represents the collision of a diatomic molecule with incident energy E_i with a surface of energy E'_i. The total energy of the incident molecule is the sum of its translational, vibrational, rotational, and electronic energies. During the collision process, the molecule can exchange energy with the

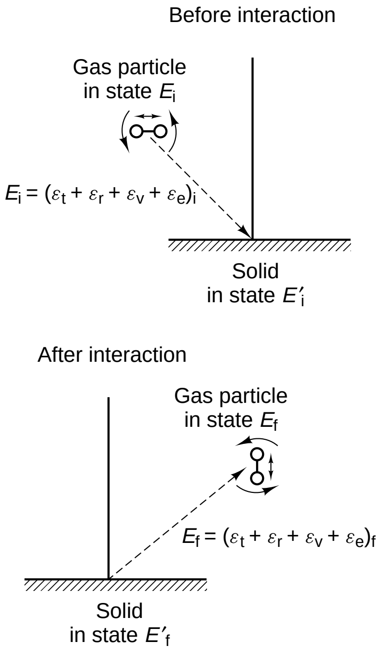
Before interaction
Gas particle
in state E_i
$E_\mathrm{i} = (\varepsilon_\mathrm{t} + \varepsilon_\mathrm{r} + \varepsilon_\mathrm{v} + \varepsilon_\mathrm{e})_\mathrm{i}$
Solid
in state E'_i
After interaction
Gas particle
in state E_f
$E_\mathrm{f} = (\varepsilon_\mathrm{t} + \varepsilon_\mathrm{r} + \varepsilon_\mathrm{v} + \varepsilon_\mathrm{e})_\mathrm{f}$
Solid
in state E'_f

Figure 24 Scheme of energy transfer in gas–surface interactions which involve translational, vibrational, rotational, and electronic energy states

surface through several channels. These include the transfer of energy between the translational, vibrational, and rotational states of the incident molecule and the vibrational energy states of the surface. Detection of the scattered molecule in a state-specific fashion provides a detailed picture of the dynamic collision process.

The most important technique for studying dynamic gas–surface interactions has been molecular beam surface scattering (MBS). In these experiments, a collimated beam of atoms or molecules of known energy (thermal, vibrational, and rotational) is impinged on a well-characterized, clean surface of known temperature. The scattered molecules are detected by a mass spectrometer with the angular spread in scattering measured by rotating the detector about the scattering plane. Velocity distributions are determined by chopping the incident beam and measuring the scattered molecules or atoms in a time-of-flight manner. Rotational and vibrational distributions have been measured by optically probing the scattered molecules (i.e. two-photon ionization).

The amount of incident energy of the molecule (E_{incident}) that is transferred to the surface can be represented by an energy accommodation coefficient γ^{E}:

$$\gamma^{\text{E}} = \frac{E_{\text{incident}} - E_{\text{scattered}}}{E_{\text{incident}} - E_{\text{surface}}} \tag{29}$$

Here E_{surface} is defined as the thermal energy of the solid. A plot of the component accommodation coefficients for NO molecules scattered from a Pt(111) surface as a function of crystal temperature is shown in Figure 25. Referring to equation (29), when the energy of the scattered molecule equals the thermal energy of the solid, the accommodation coefficient will be equal to 1. This can occur when incident molecules come to equilibrium with the surface atoms during the collision process. For the case of NO scattering from Pt(111), the thermal and vibrational energies are well accommodated at the surface over a wide range of temperature. The decrease in the rotation accommodation coefficient with temperature indicates that there is a barrier to free rotation of the molecule on the surface, most likely associated with the direction of the N–O bond.

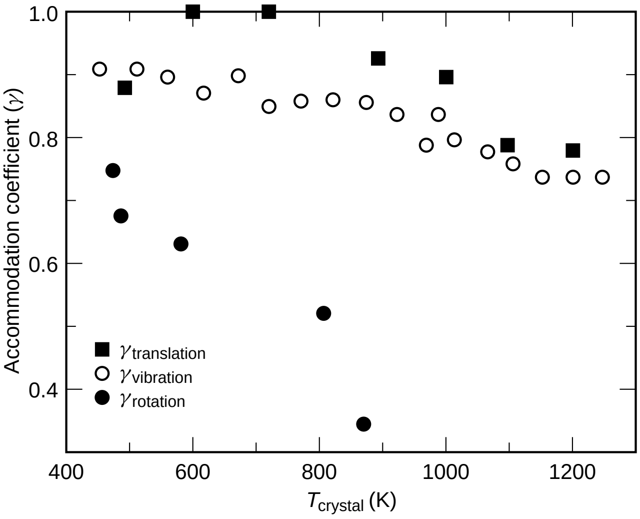

Figure 25 Translational, vibrational, and rotational accommodation coefficients for NO molecules scattered from a Pt(111) surface at different surface temperatures

The accommodation of energy at the surface suggests a finite residence time of the molecule or atom on the surface during the collision process. The residence of a molecule on the surface can arise from an attractive potential at the surface. The angular distribution of scattered species is representative of the strength of the attraction and thus the degree of interaction during the collision. The limiting cases of angular spread are shown in Figure 26. A peaked distribution in the specular direction (45° from surface normal in this case) is representative of short residence times and little interaction. Conversely, a cosine distribution is characteristic of long residence times where molecules have become strongly coupled to the energy states of the surface. This is the same angular distribution that is observed from physically adsorbed molecules desorbing with an energy equal to the surface energy (temperature).

Molecular beam scattering is also a powerful tool for probing the structure-sensitive nature of reactive (dissociative) scattering events.[35] In Figure 27 the production of HD from the surface reaction of a mixed H_2–D_2 molecular beam is plotted versus incident angle for two crystal faces of platinum. The close-packed Pt(111) surface shows a low reaction probability

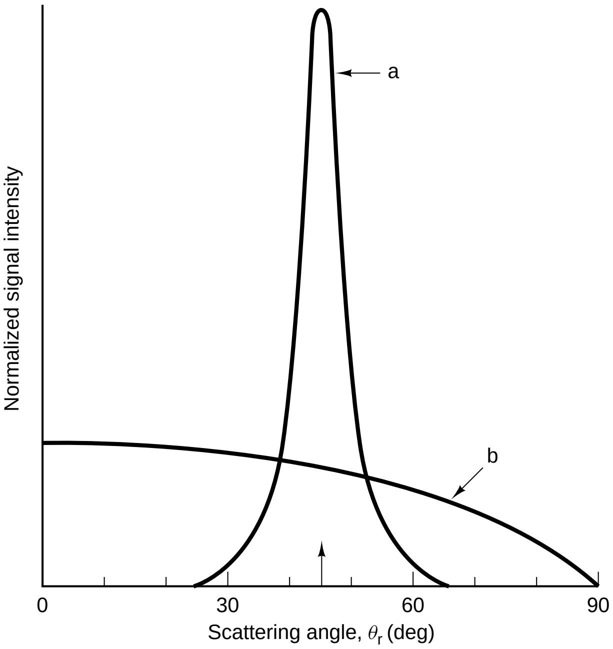

Figure 26 The limiting cases of angular distribution of species scattered from a solid surface: (a) specular scattering characteristics of short residence time, (b) cosine distribution characteristic of long residence times

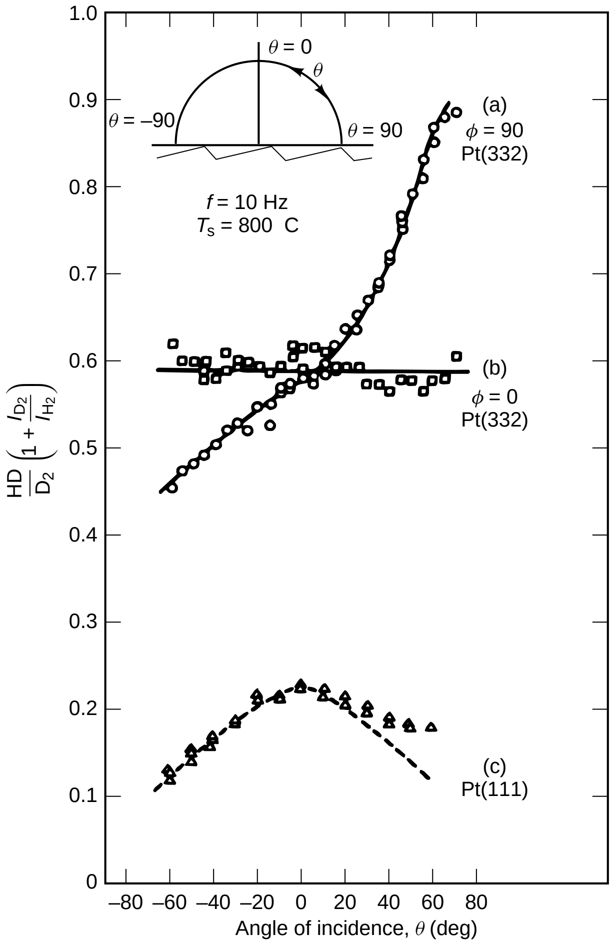

Figure 27 Reactive scattering cross-sections of the $H_2 + D_2$ reaction as a function of angle of incidence shown for three crystal faces of platinum

for the H_2–D_2 exchange. The Pt(332) surface contains a high concentration of steps (defects) and shows a much higher reactivity towards the dissociation of the incident H_2 and D_2 molecules. Furthermore, measurements as a function of azimuthal angle in the surface plane show that the greatest probability for reaction occurs for glancing angles of incidence normal to the step edge direction. This result illustrates the high reactivity of step sites for the dissociation of H_2 and D_2.

As mentioned earlier, the ultimate accommodation of incident energy occurs when the molecule becomes trapped by the attractive surface potential. The process can occur molecularly or dissociatively, leading to a new chemical species and is discussed in detail in Section 4.3.

8 SURFACE REACTIONS

The study of surface chemical reactions comprises much of the work being carried out on surfaces today and spans a number of disciplines (chemistry, materials science, and chemical and electrical engineering). A complete discussion of chemical reactions at surfaces is well beyond the scope of this discussion (*see* ***Heterogeneous Catalysis by Metals***). Here, only a classification of surface reactions will be presented. In general, surface reactions can be divided into four categories as follows.

8.1 Catalytic Reactions

A fundamental definition of a catalyst is a substance that increases the rate of a chemical reaction without being changed or consumed by the reaction. In surface-catalyzed reactions, the surface acts as a catalyst by providing a site for the reaction. During the course of the reaction, molecules adsorb from the gas or liquid phase, diffuse to the active site, undergo chemical reaction, and ultimately desorb, regenerating the active site. In addition to enhancing the rate of reaction, a surface can act as a catalyst by inducing selective channels of reactivity. Heterogeneous catalysis of this type is used in almost all chemical technologies and throughout many other industries. Understanding the role of surfaces as a catalyst on an atomic scale involves identifying active sites and potential poisons of the catalytic reaction and is one of the major focuses of fundamental surface science.

8.2 Crystal Growth Reactions

Alternatively, chemical reactions at a surface can lead to the deposition of material and the extension of the solid phase. Such reactions are involved in crystal growth, thin film deposition and the formation of novel heterostructures. In these reactions, the material being deposited can be the same as the substrate (crystal growth), or different as in the case of many coatings technologies. Atoms or molecules may be used as reactants and can be delivered by vaporization, molecular beam techniques, or diffusion through solution. Growth reactions are found in the common processes of chemical vapor deposition (CVD), molecular beam epitaxy (MBE) and electroplating.

8.3 Corrosion Reactions

Like growth reactions, corrosion at surfaces involves a change in surface composition: however, it is typically associated with a deleterious change. Corrosion reactions can be separated into two classes: those involving the removal of material from the solid and those involving the formation of a surface reaction layer. In the first type of reaction, gas- or solution-phase species react with the surface to produce volatile or soluble products as in the etching of silicon by hydrofluoric acid. The second type of reaction involves the reaction of surface atoms to form a new compound which remains on the surface. The oxidation of many metals is considered a corrosion reaction of this type.

8.4 Photochemical Surface Reactions

The illumination of solid surfaces can lead to unique photochemical reactions by one of two means. First, incident radiation can be absorbed directly by surface adsorbates thereby exciting certain electronic or vibrational modes of the adsorbate. This process allows these molecules to further react at the surface via energy pathways normally absent. Second, radiation can be absorbed by the solid, producing charge carriers in the surface region. These charge carriers, upon migrating to the surface, can drive the oxidation or reduction of adsorbates. The photoelectrochemical dissociation of water at the surface of TiO_2 is a classic example of this type of reaction. In both absorption processes, the wavelength of the incident radiation is directly related to the excitation probability and is thus an important parameter in these reactions.

9 RELATED ARTICLES

Electrochemistry: Applications in Inorganic Chemistry; Electronic Structure of Solids; Heterogeneous Catalysis by Metals; Photoelectron Spectroscopy of Transition Metal Systems; Semiconductor Interfaces; Thin Film Synthesis of Solids.

10 FURTHER READING

A. W. Adamson, ‘Physical Chemistry of Surfaces’, Wiley, New York, 1982.

L. H. Dubois and G. A. Somorjai, *ACS Symp. Ser.*, 1980, **137**, 263.

B. Lang, R. W. Joyner, and G. A. Somorjai, *Surf. Sci.*, 1972, **30**, 440.

11 REFERENCES

1. G. A. Somorjai, ‘Chemistry in Two Dimensions’, Cornell University Press, London, 1981.
2. G. A. Somorjai, ‘Introduction to Surface Chemistry and Catalysis’, Wiley, New York, 1993.
3. J. B. Hudson, ‘Surface Science: An Introduction’, Butterworth-Heinemann, Stoneham, MA, 1992.
4. A. W. Adamson, ‘Physical Chemistry of Surfaces’, Wiley, New York, 1982.
5. G. A. Somorjai, *Surf. Interface Anal.*, 1992, **19**, 493.
6. M. A. Van Hove, W. H. Weinberg, and C. M. Chan, ‘Low Energy Electron Diffraction: Experiment, Theory and Surface Structure Determination’, Springer Verlag, Berlin, 1986.
7. P. J. Rous, *Prog. Surf. Sci.*, 1992, **39**, 3.
8. F. Ogletree and M. Salmeron, *Prog. Solid State Chem.*, 1990, **20**, 235.
9. M. D. Antonik and R. J. Lad, *J. Vac. Sci. Technol.*, 1992, **A10**, 669.
10. A. Weisenhorn, P. N. Henrikson, H. T. Chu, R. D. Ramsier, and D. H. Reneker, *J. Vac. Sci. Technol.*, 1991, **B9**, 1333.
11. C. Kittel, ‘Introduction to Solid State Physics’, Wiley, New York, 1986.
12. M. A. Van Hove and S. Y. Tong, ‘Surface Crystallography by LEED; Theory, Computation and Structural Results’, Springer Verlag, Berlin, 1979.
13. G. A. Somorjai and U. Starke, *Pure Appl. Chem.*, 1992, **64**, 509.
14. J. M. MacLaren, J. B. Pendry, P. J. Rous, D. K. Saldin, G. A. Somorjai, M. A. Van Hove, and D. D. Vvedenshy, ‘Surface Crystallographic Information Service: A Handbook of Surface Structures’, Reidel, Dordrecht, 1987.
15. A. Wander, M. A. Van Hove, and G. A. Somorjai, *Phys. Rev. Lett.*, 1991, **67**, 626.
16. G. Korosi and E. Sz. Kovats, *J. Chem. Eng. Data*, 1981, **26**, 283.
17. J. Blakely and J. Shelton, in ‘Surface Physics of Materials’, ed. J. Blakeley, Academic Press, New York, 1975, Vol. 1.
18. P. Wynblatt and R. C. Ku, *Surf. Sci.*, 1977, **65**, 511.
19. L. C. Dufour and M. Perdereau, in ‘Surfaces and Interfaces of Ceramic Materials’, eds. L. C. Dufour *et al.*, Kluwer, Boston, MA, 1989, p. 419.
20. F. L. William and D. Nason, *Surf. Sci.*, 1974, **45**, 377.
21. R. C. Yeates and G. A. Somorjai, *Surf. Sci.*, 1983, **51**, 778.
22. J. L. Falconer and R. J. Madix, *Surf. Sci.*, 1975, **48**, 393.
23. I. Langmuir, *J. Am. Chem. Soc.*, 1918, **40**, 1361.
24. S. Brunauer, P. H. Emmett, and E. Teller, *J. Am. Chem. Soc.*, 1938, **60**, 309.
25. P. J. Feibelman, *Prog. Surf. Sci.*, 1982, **12**, 287.
26. M. Kaminsky, ‘Atomic and Ionic Impact Phenomena on Metal Surfaces’, Academic Press, New York, 1965.
27. O. D. Protopopov *et al.*, *Sov. Phys.-Solid State*, 1966, **8**, 909.
28. H. H. Farrell and G. A. Somorjai, *Adv. Chem. Phys.*, 1971, **20**, 215.
29. D. E. Gray ed., ‘American Institute of Physics Handbook’, McGraw-Hill, New York, 1972.
30. R. G. Greenler and T. L. Slager, *Spectrochim. Acta, Part A*, 1973, **29**, 193.
31. Y. L. Chabal, *Surf. Sci. Rep.*, 1988, **8**, 211.
32. A. Campion, *Annu. Rev. Phys. Chem.*, 1985, **36**, 1.
33. R. Chang and T. E. Furtak eds., ‘Surface Enhanced Raman Scattering’, Plenum Press, New York, 1982.
34. Y. R. Shen, *Nature*, 1989, **337**, 519.
35. T. H. Lin and G. A. Somorjai, *J. Chem. Phys.*, 1984, **81**, 704.

Symmetry Point Groups

R. Bruce King
University of Georgia, Athens, GA, USA

1 Introduction 1
2 Symmetry Operations 1
3 Mathematical Groups 1
4 Symmetry Point Groups 2
5 References 4

1 INTRODUCTION

The concept of symmetry is important in many structural and spectroscopic aspects of inorganic chemistry. The symmetry of a compound can be described by its point group, which is a mathematical group consisting of the symmetry operations of the molecule. This article summarizes some of the fundamental ideas of point group symmetry and the use of group theory to study various aspects of symmetry. For background information or further details the reader is referred to standard texts on chemical applications of group theory.[1]

2 SYMMETRY OPERATIONS

A symmetry operation is a movement of an object such that, after completion of the movement, every point of the body coincides with an equivalent point or the same point of the object in its original orientation. The position and orientation of an object before and after carrying out a symmetry operation are indistinguishable. Thus a symmetry operation takes an object into an equivalent configuration.

The symmetry operations for objects in ordinary three-dimensional space can be classified into four fundamental types, each of which is defined by a symmetry element around which the symmetry operation takes place. The four fundamental types of symmetry operations and their corresponding symmetry elements are listed in Table 1.

The identity operation, designated as E, leaves the object unchanged. Although this operation may seem trivial, it is mathematically necessary in order to convey the mathematical properties of a group on the set of all the symmetry operations applicable to a given object. This point will be clarified later in this article. The reflection operation, designated as σ, involves reflection of the object through a plane, known as a reflection plane. For example, in a reflection through the xy-plane (conveniently designated as σ_{xy}) the coordinates of a point (x, y, z) change to $(x, y, -z)$. A reflection operation thus can result in the change of only a single coordinate. A rotation operation, designated as C_n, consists of a $360°/n$ rotation around a line, known as a rotation axis. For example, a C_2 rotation around the z-axis changes the coordinates of a point (x, y, z) to $(-x, -y, z)$; a rotation operation thus can result in a change of only two coordinates. An improper rotation, designated as S_n, consists of a $360°/n$ rotation around a line followed by a reflection in a plane perpendicular to the rotation axis. An S_2 operation is called an inversion and is designated by i. The intersection of the C_2 axis and the perpendicular reflection plane is called an inversion center. Inversion through the origin changes the coordinates of a point (x, y, z) to $(-x, -y, -z)$. An S_n operation thus must change the signs of all three coordinates. An S_1 improper rotation in which the C_1 proper rotation component is equivalent to the identity E corresponds to a reflection operation σ. Thus the reflection operation σ is a special type of improper rotation, namely S_1.

3 MATHEMATICAL GROUPS

A set of elements forming a mathematical group (e.g. symmetry operations) must satisfy the following four conditions.

1. The product of any two elements in the group and the square of each element must be an element of the group. In order to apply this condition the concept of a product of elements must be defined. In this connection a product of two group elements is obtained by applying them successively. A square of a group element is obtained by applying the same operation twice. This definition can be extended to higher powers of group elements. Forming a product of two group elements is called multiplication by analogy to arithmetic. The multiplication of two group elements is said to be commutative if the order of multiplication is immaterial, i.e. if $AB = BA$. In such a case, A is said to commute with B. The multiplication of two group elements is not necessarily commutative.
2. One element in the group must commute with all others and leave them unchanged. This element is conventionally called the identity. In this case of symmetry point groups the identity element consists of 'doing nothing' and is conventionally designated as E (Table 1). This is why the 'trivial' identity operation E must be considered when treating symmetry point groups. This condition may be concisely stated as $EX = XE = X$.
3. The associative law of multiplication must hold. This condition may be expressed concisely as $A(BC) =$

Table 1 The four fundamental types of symmetry operations

Symmetry operation	Designation	Corresponding symmetry element	Dimensions
Identity (no change)	E	The entire object	3
Reflection	σ	Reflection plane	2
Rotation	C_n	Rotation axis	1
Improper rotation	S_n	Improper rotation axis (= point of intersection of a proper rotation axis and a perpendicular reflection plane)	0

$(AB)C$, i.e. the result must be the same if C is multiplied by B to give BC followed by multiplication of BC by A to give $A(BC)$ or if B is multiplied by A to give AB followed by multiplication of AB by C to give $(AB)C$.

4. Every element must have a reciprocal, which is also an element in the group. The element Z is the reciprocal of the operation A if $AZ = ZA = E$. The reciprocal of an element A is frequently designated by A^{-1}. Note that multiplication of an element by its reciprocal is always commutative.

These defining characteristics of a group have been summarized concisely[2] by defining a group as '... a mathematical system consisting of elements with inverses which can be combined in some operation without going outside the system'.

The elements in a group can be characterized by their periods. In this context the period of an element is the minimum number of times it must be multiplied by itself before the identity E is obtained. In the case of symmetry operations (Table 1) the period of the identity operation E is, of course, 1; the periods of the reflections σ are always 2; the periods of the proper rotations C_n are n; the periods of the even improper rotations S_{2n} are $2n$; and the periods of the odd improper rotations S_{2n+1} are $4n + 2$.

The number of elements in a group is sometimes called the order of the group. Within a given group it may be possible to select various smaller sets of elements, each set including the identity element E, which are themselves groups. Such smaller sets are called subgroups. A subgroup of a group G is thus defined as a subset H of the group G which is itself a group under the multiplication of G. The fact that H is a subgroup of G may be written $H \subset G$. The order of a subgroup must be an integral factor of the order of the group. Thus if H is a subgroup of G and $|H|$ and $|G|$ are the orders of H and G, respectively, then the quotient $|G|/|H|$ must be an integer; this quotient is called the index of the subgroup H in G.

Let A and X be two elements in a group. Then $X^{-1}AX = B$ will be equal to some element in the group. The element B is called the similarity transform of A by X and A and B may be said to be conjugate. Conjugate group elements have the following properties:

1. Every element is conjugate with itself. Thus for any particular group element A there must be at least one element X such that $A = X^{-1}AX$.
2. If A is conjugate with B, then B is conjugate with A. Thus if $A = X^{-1}BX$, then there must be some element, Y, in the group such that $B = Y^{-1}AY$.
3. If A is conjugate with B and C, then B and C are conjugate with each other.

A complete set of elements of a group which are conjugate to one another is called a class (or more specifically a conjugacy class) of the group. The number of elements in a conjugacy class is called its order; the orders of all conjugacy classes must be integral factors of the order of the group.

A group in which every element commutes with every other element is called a commutative group or an Abelian group after the famous Norwegian mathematician, Abel (1802–1829). In an Abelian group every element is in a conjugacy class by itself, i.e. all conjugacy classes are of order one. A normal subgroup N of G, written $N \lhd G$, is a subgroup which consists only of entire conjugacy classes of G.[3] A normal chain of a group G is a sequence of normal subgroups $C_1 \lhd N_{a_1} \lhd N_{a_2} \lhd N_{a_3} \lhd \cdots \lhd N_{as} \lhd G$, in which s is the number of normal subgroups (besides C_1 and G) in the normal chain. If such a chain starts with the identity group C_1 and leads to G and if all of the quotient groups $N_{a_1}/C_1 = C_{a_1}$, $N_{a_2}/N_{a_1} = C_{a_2}$, ..., $G/N_{a_s} = C_{a_{s+1}}$ are cyclic, then G is a composite or soluble group. Otherwise G is a simple group. Simple groups are particularly important in the theory of finite groups.[4] A soluble group can be expressed as a direct product of the factor groups $C_{a_1} \times C_{a_2} \times \cdots \times C_{a_{s+1}}$.

4 SYMMETRY POINT GROUPS

When any set of complete symmetry operations for an object satisfies the above four conditions for a mathematical group, such a group is called a symmetry point group. Such symmetry point groups have a standard designation, called the Schoenflies symbol, based on either a conspicuous operation in the point group (such as the highest order rotation axis) or a common case of occurrence of the symmetry point group (such as describing the symmetry of a well-known polyhedron like the tetrahedron, octahedron, or icosahedron).

There is a systematic way to classify objects by their symmetry point groups based on the following sequence of questions:

1. Is the object linear (i.e. only 'one-dimensional')?
   Linear objects are the only objects having infinite rather than finite symmetry point groups since the linear axis corresponds to an infinite order rotation axis, namely C_∞. If there is a reflection plane perpendicular to the infinite order rotation axis (dividing the object into two equivalent halves), then the symmetry point group is D_∞; if not, the symmetry point group is C_∞.
2. Does the object have multiple 'higher-order' rotation axes (i.e. $C_{>2}$ axes)?
   Multiple axes in this question refer to noncollinear $C_{>2}$ axes. Such nonlinear objects have the symmetries of well-known regular polyhedra and are generally readily recognizable in containing the regular polyhedra in some manner. Such groups are sometimes called the polyhedral point groups. Thus the tetrahedral groups T, T_h, and T_d with 12, 24, and 24 operations, respectively, have four non-collinear C_3 axes and are distinguished by the presence or absence of horizontal (σ_h) or diagonal (σ_d) reflection planes. The octahedral groups O and O_h with 24 and 48 operations, respectively, have not only four noncollinear C_3 axes but also six noncollinear C_4 axes and are distinguished by the presence or absence of reflection planes. The icosahedral groups I and I_h having 60 and 120 operations, respectively, require ten noncollinear C_3 axes and six noncollinear C_5 axes and are also distinguished by the presence or absence of reflection planes.
3. If the object does not belong to either a linear group or a polyhedral group, then does it have proper or improper axes of rotation (i.e. C_n or S_n)?
   If no axes of either type are found, the group is either C_s, C_i, or C_1 with 2, 2, and 1 operations, respectively, depending whether the object has a plane of symmetry (σ), an inversion center (i), or neither. The C_1 designation corresponds to an object with no symmetry at all and therefore to a symmetry point group containing only one element, namely the identity element E.
4. Does the object has an even-order improper rotation axis S_{2n} but no planes of symmetry or any proper rotation axis other than one collinear with the improper rotation axis?
   The presence of an improper rotation axis of even order S_{2n} without any noncollinear proper rotation axes or any reflection planes indicates the symmetry point group S_{2n} with $2n$ operations.
5. If the object does not belong to the linear point groups, the polyhedral point groups, or the point groups C_s, C_n, C_1 or S_{2n}, then look for the highest order rotation axis. Call the highest order rotation axis C_n.
6. Are there nC_2 axes lying in a plane perpendicular to the C_n axis? If there are nC_2 axes lying in a plane perpendicular to the C_n axis, then the object belongs to one of the symmetry point groups D_n, D_{nh}, or D_{nd} with $2n$, $4n$, and $4n$ operations, respectively, depending on whether there are no planes of symmetry, a horizontal plane of symmetry (σ_h), or n vertical planes of symmetry (σ_v), respectively. If there are no C_2 axes lying in a plane perpendicular to the C_n axis, then the object belongs to one of the symmetry point groups C_n, C_{nv}, C_{nh}, with n, $2n$, and $2n$ operations, respectively, depending upon whether there are no planes of symmetry, n vertical planes of symmetry (σ_v), or a horizontal plane of symmetry (σ_h), respectively. If there are only C_2 axes then a unique C_2 axis is chosen as the 'reference axis' if there is any ambiguity as to which C_2 axis to choose.

Some of these ideas are illustrated using the trigonal bipyramid depicted in Figure 1 with the locations of the C_3 and three C_2 axes indicated by a solid arrow and three dotted arrows, respectively.

The symmetry point group of the trigonal bipyramid is D_{3h} of order 12 with the conjugacy classes $E + 2C_3 + 3C_2 + \sigma_h + 2S_3 + 3\sigma_v$. Note the following concerning these conjugacy classes:

1. The identity operation E is in a class by itself.
2. The two operations in the C_3 class correspond to 120° (C_3) and 240° (C_3^2) rotations around the single C_3 axis. Note that the C_3^2 rotation is the inverse of the C_3 rotation, i.e. ${C_3}^{-1} = C_3^2$.
3. The C_2 rotations around each of the three C_2 axes form the class $3C_2$ of order 3.
4. Reflection in the plane of the equatorial vertices (σ_h) is in a class by itself.
5. The two operations in the S_3 class correspond to 120° and 240° rotations around the C_3 axis followed by reflection in the σ_h plane. Thus $S_3 = (\sigma_h)(C_3)$ and $S_3^2 = (\sigma_h)(C_3^2)$ are two examples of multiplication operations in the D_{3h} point group.
6. The three types of reflections in the planes containing both axial vertices and one of the three equatorial vertices (σ_v) form the class $3\sigma_v$ of order 3.

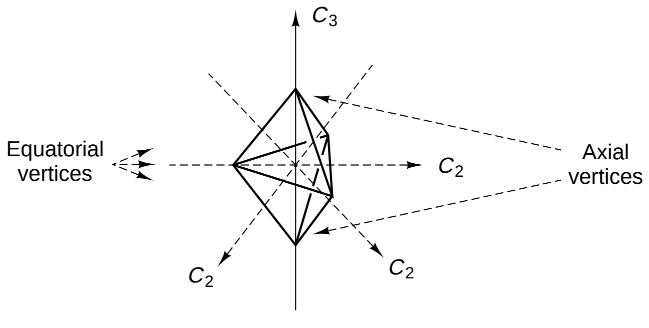

Figure 1 The rotation axes in a trigonal bipyramid

5 REFERENCES

1. F. A. Cotton, ‘Chemical Applications of Group Theory’, 3rd edn., Wiley, New York, 1990.
2. A. W. Bell and T. J. Fletcher, ‘Symmetry Groups’, Associated Teachers of Mathematics, 1964.
3. J. K. G. Watson, *Mol. Phys.*, 1971, **21**, 577.
4. D. Gorenstein, ‘Finite Groups’, Harper and Row, New York, 1968.

Technetium & Rhenium: Inorganic & Coordination Chemistry

Armando J. L. Pombeiro,[1] M. Fátima C. Guedes da Silva[1] & Robert H. Crabtree[2]
[1]Instituto Superior Técnico, Lisbon, Portugal
[2]Yale University, New Haven, CT, USA

1 Introduction – The Elements 1
2 Binary Compounds 2
3 Complexes 3
4 Radiopharmaceuticals 9
5 Catalysis 11
6 Related Articles 15
7 References 15

Abbreviations

$B(pz)_4$ = tetraquis(pyrazolyl)borate; Bp = H_2Bpz_2; Bp* = $H_2Bpz^*{}_2$; Bpy = 2,2′-bipyridine; Cyttp = $PhP(CH_2CH_2CH_2PCy_2)_2$; DDQ = 2,3-dichloro-5,6-dicyano-1,4-benzoquinone; dmb = 4,4′-dimethyl-2,2′-bipyridine; dmpm = bis(dimethylphosphino)methane = $Me_2PCH_2PMe_2$; $(DMG)_3$ 2MP = tris(dimethylglyoximate)(2-methylpropylborate); DMSA = 2,3-mercaptosuccinate; dppe = 1,2-bis(diphenylphosphino)ethane = $Ph_2PCH_2CH_2PPh_2$; dppee = 1,2-bis(diphenylphosphino)ethylene = $Ph_2PCH{=}CHPPh_2$; dppm = bis(diphenylphosphino)methane = $Ph_2PCH_2PPh_2$; ECD = *N*,*N*′-1,2-ethanediylbis(L-cysteine-ethylester); HEDP = 1-hydroxyethylidene diphosphonic acid = $O{=}P(OH)_2C(OH)MeP({=}O)(OH)_2$; HIDA = *N*-(2,6-dimethylphenylcarbamoylmethyl)iminodiacetate; HM-PAO = hexamethylpropyleneamine oxime; MAG_3 = mercaptoacetyltriglycine; mtp = 2-(mercaptomethyl)thiophenolate; noet = *N*-ethyl-*N*-ethoxydithiocarbamate; OAT = oxygen atom transfer; OTf = triflate = $OSO_2CF_3{}^-$; PhTp = $(Ph)B(pz)_3$; porph = porphyrinate; PyO = pyridine *N*-oxide; pz = pyrazolyl; pz* = 3,5-dimethylpyrazolyl; pzTp = $B(pz)_4$; tmeda = *N*,*N*,*N*′,*N*′-tetramethylethylenediamine = $Me_2NCH_2CH_2NMe_2$; Tp = $HB(pz)_3$ = tris(pyrazolyl) hydroborate; Tp* = $HB(pz^*)_3$ = tris(3,5-dimethylpyrazolyl)hydroborate.

1 INTRODUCTION – THE ELEMENTS

Tc and Re are Mendeleev's eka-manganese and dvi-manganese, which he recognized as blank spaces in his periodic table. Both elements are rare, and Tc is also radioactive. Selected properties: At. no. 43 (Tc), 75 (Re); At. wt. 98.906 (^{99}Tc), 186.207 (Re); Density (20 °C) 11.5 (Tc), 21.0 (Re); Mp (°C) 2200 (Tc), 3180 (Re); Bp (°C) 4567 (Tc); Electronegativity (Pauling) 1.9 (Tc, Re); Metallic radius (Å) 1.36 (Tc), 1.37 (Re); Covalent radius (Å) 1.31 (Tc); Tc for superconductivity (K) 7.7 (Tc); Principal isotopes (half-life, y) 97 (2.6×10^6) (Tc), 98 (1.5×10^6) (Tc), 99 (2.12×10^5) (Tc), 185 (37.4%, stable) (Re), 187 (62.6%, 5×10^{10}) (Re); Reduction potentials (V) for $M^{n+}(aq) + ne^- \rightarrow M(s)$ 0.4 ($n = 2$, Tc), 0.3 ($n = 3$, Re), for $MO_4{}^-(aq) + 5e^- \rightarrow M^{2+}(aq)$ 0.5 (Tc), 0.42 (Re); Common ox. states (geometries): +1 (oct.), +3 (sq. pyr., oct.), +5 (oct.), +7 (tet., oct.).

Rhenium was first detected (1925), from its X-ray emission, by Noddack, who later isolated it on a macroscopic scale from Mo ores. Re is not normally found alone in minerals but only in association with other metals, such as Mo, Cu, Pd, Zn, Pt, or Nb. Typical Re concentrations in molybdenite ores are $0.6–21\,g\,t^{-1}$, where Re can replace Mo in an isomorphous fashion. Re is often produced commercially as a by-product in Mo refining and so it is readily available even though its abundance in the Earth's crust is low (7 ppb). The element is usually isolated as the sparingly soluble potassium perrhenate, which is also a common synthetic precursor for Re chemistry. Re is extremely high melting (3180 °C). The extraction methods depend on the source.**[1]** It has relatively few uses but it forms part of several heterogeneous bimetallic catalysts, notably Pt–Re for petroleum reforming. Homogeneous catalysis constitutes a fruitful area in current expansion.

^{185}Re and ^{187}Re are the naturally occurring isotopes, the former being stable and the latter weakly radioactive (β-emission) with a very long half-life (5×10^{10} y). The ^{187}Re/^{187}Os isotope system is used in geology and cosmology to determine the age of minerals and meteorites. The radioactive ^{186}Re and ^{188}Re isotopes have nuclear properties suitable for therapeutic applications (Section 4.2); being β-emitting radionuclides (half-lives of 3.78 d and 17.0 h, 1.07 MeV β or 2.12 MeV β, respectively) and the beta particles having a large penetrability, with a low % of γ emission [137 keV γ (9%) or 155 keV γ (15%)]. ^{188}Re is readily obtained from a generator based on the decay of $[^{188}WO_4]^{2-}$ on a stationary phase where it disintegrates to form perrhenate or perrhenic acid. These can be eluted and provide the starting material for radiopharmaceutical preparations.

Tc was the first element to be synthesized artificially, hence its name. It was first detected in 1937 by Perrier and Segré in the products of deuteron bombardment of Mo. All the isotopes of Tc are radioactive but ^{99}Tc, with a half-life of 2.1×10^5 y, is a sufficiently long-lived β-emitter that it can be handled in standard laboratory equipment with appropriate precautions. It is recovered from fission reactors by solvent extraction and ion-exchange methods. It makes up ca. 6% of fission products from ^{235}U and so is available in kilogram amounts for macroscopic chemical study. Hot acid solutions of $[TcO_4]^-$ lose Tc_2O_7, which allows the element to be separated from Re, in which the oxide becomes volatile only on distillation from hot concentrated sulfuric acid. The ^{99m}Tc isotope required for nuclear medical applications (Section 4.1) is formed in 10^{-6}–10^{-9} M concentrations from $[^{99}MoO_4]^{2-}$ (66 h half-life) loaded in a generator column. The ^{99m}Tc nucleus ($t_{1/2} = 6.02$ h) is a nuclear excited state (hence the m for metastable) that decays by γ-ray emission at 141 keV; the detection of this emission allows imaging of organs. Tc is one of the most important elements in nuclear medicine, being used in the form of its ^{99m}Tc isotope. This has stimulated much work on the element. Ammonium pertechnetate is an effective corrosion inhibitor.

The elements are gray, chemically relatively unreactive powders both having an hcp lattice, and both can be obtained by hydrogen reduction of the ammonium permetallates or by heating $NH_4[MCl_6]$. As powders, both elements burn in oxygen at >400 °C to give the volatile heptaoxides. The metals are insoluble in nonoxidizing mineral acids but do dissolve in concentrated nitric or sulfuric acids or aqueous Br_2. Both elements form compounds with an unusually wide range of oxidation states from −3 to +7, although most M^I and lower compounds are organometallic (*see* ***Technetium: Organometallic Chemistry*** and ***Rhenium: Organometallic Chemistry***).

2 BINARY COMPOUNDS

2.1 Oxides and Sulfides[2]

The yellow heptaoxides (mps, 119.5 °C (Tc); 300 °C (Re)), formed by burning the metals in O_2, are O_3M–O–MO_3 (with tetrahedral metal coordinations) in the vapor but are polymeric in the solid with, in the case of Re, alternating corner-sharing ReO_4 and ReO_6. Both dissolve in water to give colorless perrhenic or pertechnetic acids, both strong acids with the structure O_3M–O–$MO_3(OH_2)_2$ in the crystalline form. Both the M_2O_7 oxides and these acids are relevant starting materials for coordination synthesis (see below).

Red ReO_3, which can be obtained by CO reduction of the heptaoxide at 175–280 °C, is a good electrical conductor with a metal-like temperature dependence; the d^1 electron is clearly delocalized. It has octahedral Re^{VI} and easily forms nonstoichiometric bronzes in which an alkali metal donates an electron to the metal–oxo lattice and enters the structure as a cation. Supported ReO_3 is important in alkene metathesis catalysis. No Tc analog is known. Blue Re_2O_5, brown ReO_2, and black Re_2O_3 are also known. For Tc, the only lower oxide is TcO_2.

The sulfides M_2S_7 and MS_2 are known, the first from the permetallate and either H_2S or thiosulfate and 2N HCl, and the latter by reducing the heptasulfide with sulfur or from the elements at 400 °C. The Re materials have catalytic activity for the hydrogenation of unsaturated species and are much less sensitive to poisons, especially S-based poisons, than the platinum group metal catalysts. Both diselenides and both ditellurides are formed from the elements on heating. Ternary chalcogenides, such as $M'_4M_6Q_{12}$ (M' = alkali metal; Q = S, Se), $M'_4M_6Q_{13}$, and $M'_{10}M_6S_{14}$, contain $[M_6Q_8]$ clusters with an octahedron of six metals.

2.2 Halides[2]

Re has the only heptavalent halide of these elements, ReF_7, a yellow, low-melting species, from fluorination of the element at high temperature and pressure. Fluorination at 120 °C and 1 atm gives the hexafluoride (mp 19 °C), which can be reduced with H_2 to the green-yellow, low-melting pentafluoride, or with Re to the blue ReF_4. For Tc, only the hexa- and pentafluorides are known. ReF_7 and ReX_6 have probably pentagonal bipyramidal and octahedral geometries respectively. Most of the penta- to hepta-halides can be obtained directly from the elements at appropriate temperatures and pressures.

$ReCl_6$ (mp 29 °C) is a greenish-red species. Chlorination of the element at ca. 600 °C gives dark red Re_2Cl_{10}, rhenium ‘pentachloride’, the dimer $[Cl_4Re(\mu\text{-}Cl)_2ReCl_4]$ with octahedral coordination that, after $KReO_4$, is the most common starting material for Re chemistry. The Re^{III} halides are obtained by thermal decomposition of higher halides, and heating Re_2Cl_{10} gives the important cluster halide Re_3Cl_9, which has a metal–metal double-bonded triangle of Re, with each Re–Re bond (d(Re–Re) = 2.48 Å) bridged by a Cl; no Tc analog is known. This unit persists in much of the chemistry of the compound, such as in the reaction with pyridine to give $[Re_3Cl_9(py)_3]$. Heating Re_3Cl_9 with Re_2Cl_{10} is a good route to $ReCl_4$, which is made of $ReCl_6$ octahedra with shared faces and corners, and has also metal–metal bonds, although not so extensive as in Re^{III} halides. Tc forms $TcCl_6$ and $TcCl_4$, the latter from chlorination of the element or from CCl_4 and the heptaoxide; unlike the Re analog, Tc–Tc bonding is not present.

The brown pentabromide is formed by bromination of Re at high temperature. The dark red tetrabromide is obtained from $HReO_4$ and HBr. Pyrolysis of the pentabromide gives reddish-brown Re_3Br_9, which resembles the analogous chloride. The highest iodide is black ReI_4, obtained from $HReO_4$ and HI; on heating it gives the black triiodide and diiodide. The latter probably contains Re–Re bonds.

Oxohalides are common: ReO_2F_3, $ReOF_5$, ReO_3X, $ReOX_4$, and $ReOX_3$ (X = F, Cl, Br), as well as TcO_3X, $TcOX_4$ (X = Cl, F), and $TcOCl_3$, are known. The oxohalides can be prepared by treatment of the halides with oxygen or of the oxides with halogens. Both the halides and the oxohalides with the oxidation states +5 and +6 readily hydrolyze with disproportionation to $[MO_4]^-$ and MO_2.

2.3 Other Binary Compounds

Several refractory borides, such as ReB_2 and $Re_{23}B_6$, can be prepared from heating the elements at ca. 1200 °C. $ReSi_2$ is a semiconductor. The nitride Re_3N is formed from ammonia and ammonium perrhenate, but Re does not form a nitride with N_2. MP_3, prepared from the elements in the presence of iodine, contain M^{III} and have both P–P and M–M bonds.[3] Re_2P, Re_3Q_7, and ReP are also known (Q = P or As).[4] Carbon dissolves in Re up to 5 mol%.

3 COMPLEXES

Several recent reviews on the coordination chemistry of Tc[5–7] and Re[8,9] are available.

3.1 Hydrides

Rhenium forms one of the most extensive series of polyhydrides.[8,10,11] The most remarkable is the homoleptic $K_2[ReH_9]$, with a tricapped trigonal prism (TTP) geometry. The Tc analog is also known. The Re compound may be substituted with a variety of phosphines (=L) to give $K[LReH_8]$. Treatment of $[ReOCl_3L_2]$ with hydride reducing agents under various conditions gives the polyhydrides $[ReH_7L_2]$ and $[ReH_5L_3]$. On heating, $[ReH_7(PPh_3)_2]$ converts to the unusual dimeric hydride $[H_2(PPh_3)_2Re(\mu\text{-}H)_4ReH_2(PPh_3)_2]$ with the $M(\mu\text{-}H)_4M$ system. Where L_2 is dppe, a neutron diffraction study of $[ReH_7L_2]$ shows a TTP structure, but where L is $P(p\text{-tolyl})_3$, a similar study shows the first example of a stretched dihydrogen complex, the H–H distance being 1.357 Å.[12] The coordination polyhedron is no longer TTP but dodecahedral, as appropriate for the formulation $[Re(H_2)H_5L_2]$.

Although a short ^1H NMR T_1 relaxation time (which can be related with the $H\cdots H$ distance) is usually diagnostic for a nonclassical $\eta^2\text{-}H_2$ ligand, T_1 measurements can be inconclusive for some Re polyhydrides. Nevertheless, in the series $[ReH_7\{P(C_6H_4X\text{-}4)_3\}_2]$ (X = OMe, Me, H, F, CF_3), with isosteric phosphines, T_1 decreases with the electron-withdrawing character of X as measured by the Hammett's σ_p constant, and the complexes are believed to display an elongated $\eta^2\text{-}H_2$ ligand with a $H\cdots H$ distance that shortens with the increase of that character.[13] In accord, the type of Re–H bond for $[ReH_2L_5]^+$ is dependent on the other ligands: a π-acid L, like CO or $CNBu^t$, favors the Re^I dihydrogen formulation, whereas a more basic L, for example, PMe_3, promotes the Re^{III} dihydride structure.[14] Neutral low oxidation state Re (or Tc)–H complexes are also known, as the dinitrogen complex *trans*-$[ReH(N_2)(dppe)_2]$ (obtained on treatment of $K_2[ReH_9]$ with dppe under N_2)[15] or the dihydrogen complexes $[ReCl(\eta^2\text{-}H_2)(PR_3)_4]$, which (e.g. $2PR_3$ = dppe, dppee) can display long H–H bonds,[16] and $[TcCl(\eta^2\text{-}H_2)(dppe)_2]$ derived from H_2 addition to $[TcCl(dppe)_2]$.[17]

Multinuclear Re hydrides, in particular CO/phosphine complexes, with the hydride bridging two or three metals and compounds with H atoms bridging Re and other metals, for example, obtained from the reactions of Re polyhydrides with metal salts,[8] have been reported. The coordination chemistry of hydrido/phosphine complexes has been extended, in a number of cases, to related phosphite, phosphonite, or arsine complexes.[8]

The H ligands can form interesting intermolecular $Re\text{–}H\cdots H\text{–}N$ 'dihydrogen bonds' with a suitable H-donor like the indole or imidazole of crystallization in $[ReH_5(PPh_3)_3]\cdot indole\cdot C_6H_6$ and $[ReH_5(PPh_3)_2(imidazole)]\cdot 0.5imidazole\cdot 1.5C_6H_6$, respectively, the latter obtained by treatment of $[ReH_7(PPh_3)_2]$ with imidazole in benzene.[18,19] The N–H moiety of the base is close to two of the Re hydrides forming a three-centre dihydrogen bond (**1**).

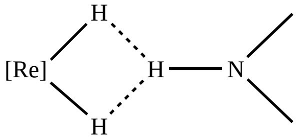

(**1**)

Protonation of a polyhydride can occur at the metal, increasing the number of hydride ligands or leading to a $\eta^2\text{-}H_2$ ligand, which can liberate as H_2. In spite of the low kinetic and thermodynamic ($pK_a = 25.5$ in acetonitrile) acidity of $[ReH_4(PMe_2Ph)_4]^+$, deprotonation occurs by a base like potassium phenolate.[20] Replacement of one phosphine by CO enhances the acidity of the complex by at least 7 orders of magnitude ($pK_a < 18.5$).[20]

Other common hydride reactions include its abstraction and replacement, for example, by a halide or a neutral ligand as in $[ReH_5L_3]$ [$L_3 = (PPh_3)_3$,[21] triphosphine, that is, Cyttp[22]] that, on treatment with the hydride abstractor $[C_7H_7]A$ (A = PF_6, BF_4) in the presence of a nitrile or an isocyanide (L′), lead to the corresponding $[ReH_4(L')L_3]A$. Insertion of an unsaturated molecule into a Re–H bond has also been reported, for example, in the reactions of $[ReH_5(Cyttp)]$ with heterocumulenes X=C=S [X = S, $p\text{-}O_2NC_6H_4N$, EtOC(O)N] to afford $[ReH_4(SCH{=}X)(Cyttp)]$.[22]

On heating in alkane in the presence of a hydrogen acceptor like $t\text{-}BuCH{=}CH_2$, $[ReH_7L_2]$ (L = PPh_3) gives dehydrogenation of alkanes, such as of cyclooctane to cyclooctene; enhanced reactivity is displayed by the chelating bis(silyl) complexes $[ReH_5(disil)(PPh_3)_2]$, with a stretched $\eta^2\text{-}H_2$ ligand, formed by reaction of $[ReH_7(PPh_3)_2]$ with 1,2-bis(dimethylsilyl)benzene or 1,2-bis(dimethylsilyl)ethane.[23] $[ReH_5(triphos)]$ also catalyzes alkane dehydrogenation driven by continuous removal of H_2 upon reflux of substrate or of cosolvent or by inert gas flow.

Scorpionate hydride complexes are also documented. [$TpReOCl_2$] reacts with $LiAlH_4$ to give [$TpReH_6$], which has a classical structure with all-terminal hydrides and was the first N-donor stabilized polyhydride; a related and classical species, [$\{CH_2(pz)_2\}ReH_7$], is also known.**[24]** The oxo-hydrides [$Tp^*ReO(H)Cl$], [Tp^*ReOH_2] and [$TpReO(H)Cl$] are obtained by reactions of [$Tp^*ReO(OMe)Cl$], [$Tp^*ReO(OMe)_2$], or [$TpReO(OEt)Cl$] with $BH_3{\cdot}THF$ at low temperature, whereas [Tp^*ReH_6] is formed upon prolonged reaction of [$Tp^*ReO(OR)_2$] with excess $BH_3{\cdot}THF$.**[25]** Insertion into a Re–H bond can occur and [$Tp^*ReO(X)(OTf)$] ($X = OEt$, Et, Pr) are formed by reacting [$Tp^*ReO(OH)(OTf)$] (derived from reaction of [$Tp^*ReO(H)Cl$] with AgOTf) with acetaldehyde, ethylene, or propylene, respectively.**[25]** The heteroscorpionate hydride complexes [$ReH_2\{\eta^3\text{-}B(OR)_2(pz)_2\}(PPh_3)_2$] and [$ReH_4\{\eta^3\text{-}BH(OR)(pz^*)_2\}(PPh_3)$] are prepared on reaction of [$ReOCl_3(PPh_3)_2$] with NaBp or NaBp*, respectively, in ROH as solvent.**[26]**

3.2 Metal–metal Bonded Species

[Re_2Cl_8]$^{2-}$ (**2**) was the first compound shown to contain a quadruple bond. It can be formed from [Bu_4N][ReO_4] and PhCOCl. Apart from a σ and two π bonds from overlap of d_{z^2} orbitals (σ) (z is the M–M axis) and of d_{xz} and d_{yz} (π) orbitals on each metal, the δ-bond comes from overlap of d_{xy} orbitals, implying that the two $ReCl_4$ units are eclipsed, the sterically least favorable arrangement.**[2,27]** The absorption in the visible (700 nm) assigned to a $\delta \rightarrow \delta^*$ transition is responsible for the royal blue color of the ion. One-electron oxidation and reduction of (**2**) and of its Tc analog is possible electrochemically.

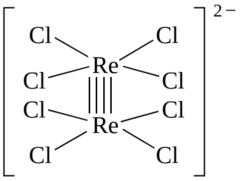

In the Cs salt:
Re–Re 2.237 Å
Re–Re–Cl 104°
Cl–Re–Cl 87°

(**2**)

[Re_2X_8]$^{2-}$ ($X = Cl$, Br) are usual starting materials for dirhenium(II) compounds. (**2**) reacts with carboxylic acids to give [$Re_2Cl_2(RCO_2)_4$], quadruply bonded species in which the carboxylates bridge the two metals and the halides bind along the M–M axis. Phosphine (=L) substitution occurs with reduction and gives [$Re_2Cl_4L_4$], a species in which the δ^* is filled and so the bond order drops to three. $NaBH_4$ reacts with (**2**) to give [$H_2L_2Re(\mu\text{-}H)_4ReH_2L_2$]. (**2**) reacts with dppm to give a triply M–M bonded species of the [$Re_2Cl_4L_4$] type. With the dppm (L_2) bridges to hold the dirhenium system together more tightly, it is possible to effect sequential oxidation and chloride addition ($-e^- + Cl^-$) two times, with concomitant M–M bond order decrease to 2.5 and 2.0. Other bridging groups have been used, such as Ph_2P(2-pyridyl) (=L), which gives [$Re_2Cl_4L_3$].

Dinuclear complexes with bridging both hydrides and diphosphines, prepared from multiply bonded Re species like [$Re_2Cl_4(\mu\text{-dppm})_2$] or [$Re_2Cl_4(\mu\text{-dmpm})_3$], exhibit a degree of Re–Re bonding that increases with the number (n) of the bridging hydrides,**[28]** for example, short Re–Re contacts of 2.5–2.6 Å occur for compounds with $n = 3$ or 4 like [$Re_2H_2(\mu\text{-}H)_3(\mu\text{-dppe})(dppe)_2$]$^+$, whereas no Re–Re bond is observed for $n = 1$, for example, in [$Re_2H_4(\mu\text{-}H)(\mu\text{-dmpm})_3$].

The Tc analogue of (**2**), [Tc_2Cl_8]$^{2-}$, is known but is less stable and has a longer M–M bond (2.147 Å) than expected; paramagnetic [Tc_2Cl_8]$^{3-}$ is easier to obtain by Zn reduction of [$TcCl_6$]$^{2-}$.

3.3 Complexes with Group 14 Elements

Re has an extensive organometallic chemistry, for example, the oxo-alkyls [$MeReO_3$], [Me_3ReO_2], and [Me_4ReO] (*see* ***Rhenium: Organometallic Chemistry***) but does not have many significant complexes with the other Group 14 elements. [ReH_7L_2] ($L = PPh_3$) reacts with R_3EH ($E = Si$ or Sn) to give adducts [$Re(ER_3)H_6L_2$] in which the TTP structure of [ReH_7L_2] is retained but in which neutron diffraction shows that two short $Si{\cdots}H$ distances are present. For a chelating disilane such as $(Me_2SiH)_2O$, the disilyl derivative [$Re\{(Me_2Si)_2O\}H_5L_2$] can be made (see Section 3.1 for other examples).

3.4 Complexes with Group 15 Elements

Re is one of the few elements in which series of N_2 complexes can be obtained,**[29,30]** normally from organohydrazines, which display a relevant role in the coordination chemistry of this metal, constituting also sources of a variety of other N-ligands like diazenides, hydrazides, and diazenes, whose formal bond description**[31]** can follow different conventions. The N_2 complexes, usually with a +1 metal oxidation state, can be formed by reaction of [$ReOCl_3(PPh_3)_2$] with benzoylhydrazine to give the cyclic hydrazide of Scheme 1, which is reduced with phosphine, phosphite, or phosphonite (=L) in refluxing MeOH to give *trans*-[$ReCl(N_2)L_4$] (**3**)**[32,33]** or related products. Mixed amine/phosphine and amine/phosphite N_2 complexes, which can be chiral,**[34]** can be prepared in similar ways, involving also ligand replacement by the appropriate amine.

The isolation of the hydrazide or derived diazenide species on the way to the N_2 complex is not always required and [$Re(N_2)_2L_4$][BPh_4] [$L = P(OMe)_3$, $P(OEt)_3$] can be prepared in a single-pot synthesis from reaction of [$ReOCl_3(AsPh_3)_2$] with L and Bu^tNHNH_2 in THF/ROH ($R = Me$, Et).**[35]**

The chloro-Re^I-N_2 complexes (**3**), typically (**3a**) (L_2 = dppe) and (**3b**) ($L = PMe_2Ph$), are particularly stable and the coordinated N_2 survives Cl^- replacement by NCS^-,

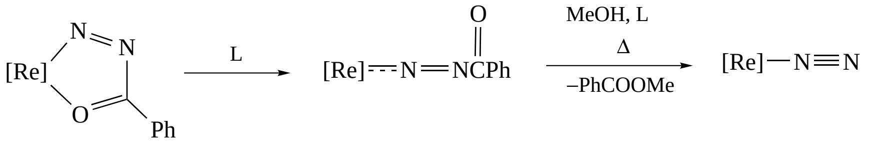

Scheme 1

NCO^-, or N_3^-,[36] phosphine or phosphite replacement by CNR[37] (which can compete with N_2 for the π-electron release from Re), or even one-electron oxidation of the complex. The ν (N≡N) stretching frequencies in the IR spectra are very low for terminally bound N_2, for example, 1923 cm^{-1} in (**3b**). The N–N distance at 1.06 Å is only slightly elongated relative to free N_2. The coordinated dinitrogen is very basic and linear Re–N–N–M′ adducts are formed with Lewis acids,[29,30] such as *trans*-$[ReCl(N{=}N{-}AlMe_3)L_4]$, *trans*-$[ClL_4Re{-}N{\equiv}N{-}Fe(porph)]^+$,[38] or $[\{ClL_4Re{=}N{=}N{=}\}_2MoCl_4]^+$. The N–N distance in the latter is long, 1.285 Å, and ν (N=N) stretching is low, 1660 cm^{-1}, showing that N_2 has been reduced toward the diimine level. Other N_2-bridged bimetallic complexes are known, for example, the pyrazolylborate $[\{Tp'M(CO)_2\}_2(\mu\text{-}N_2)]$ (M = Tc, Tp′ = Tp*;[39] M = Re, Tp′ = Tp[40]) with the strong CO competitor for π-electron backbonding. PhCOCl reacts with (**3b**) to give *trans*-$[ReCl_2(N{=}N{-}COPh)L_3]$,[30] an unusual case of C–N bond formation from an N_2 complex.

trans-$[ReCl(N_2)(dppe)_2]$ (**3a**) is a good precursor for a variety of other N- or P-ligated species, for example, *trans*- or *cis*-$[ReCl(NCR)(dppe)_2]$ (**4**) (R = alkyl, aryl); *trans*- or *cis*-$[Re(NCR)_2(dppe)_2]^+$ on reactions with NCR;[41–43] *trans*-$[Re(OH)(N{=}CR'_2)(dppe)_2]$ in which the azavinylidene (or methyleneamide) is derived from oxidative addition of an oxime, $HON{=}CR'_2$, with N–O bond cleavage;[44] *trans*-$[Re(NO)_2(dppe)_2]^+$ (a formal 20-electron Re^{-I} complex)[45] and *trans*-$[ReCl(NO)(dppe)_2][NO_3]_2$[46] on reaction with NO that in the latter case is oxidized to nitrate; and *trans*-$[ReCl(P{\equiv}CBu^t)(dppe)_2]$ in which the phosphaalkyne undergoes spontaneous hydrolysis to give the phosphinidine oxide *trans*-$[ReCl\{P(O)CH_2Bu^t\}(dppe)_2]$.[47] The mixed phosphirene-, cyanamide-, or cyanoguanidine-N_2 complexes *mer*-$[ReCl(N_2)L'L_3]$ [L′ = $\overline{PPhCPh{=}CPh}$,[48] $NCNR_2$ (R = Me, Et, H);[49] L = $PMePh_2$, PMe_2Ph] are obtained from reaction of the appropriate (**3**) and L′. The cyanamide complexes can also be obtained,[49] in a more direct way, by refluxing a methanol solution of $NCNR_2$ and the benzodiazenido complex $[ReCl_2(NNCOPh)L_3]$, which is a precursor for (**3**) (Scheme 1). The isocyanide[50,51] and alkyne-derived[47] vinylidene and allene complexes *trans*-$[ReCl(L')(dppe)_2]$ (**5**) (L′ = CNR, C=CHR, η^2-$CH_2{=}C{=}CHPh$), related to the nitrile compounds (**4**), are also obtained from (**3a**).

As a result of the strong π-electron-donating ability of the Re^I center in (**3a**) and (**5**), the nitrile and the other unsaturated L′ ligands are activated toward β-electrophilic attack (typically protonation) to afford the corresponding azavinylidene (reaction 1, E = H^+),[52] aminocarbyne,[50] carbyne,[47] or η^2-vinyl[47] products, that is, *trans*- or *cis*-$[ReCl(N{=}CHR)(dppe)_2]^+$ or *trans*-$[ReCl(L'H)(dppe)_2]^+$ (**6**) (L′H = CNHR, CCH_2R, η^2-CH_2CCH_2Ph), respectively. The azavinylidene ligand is essentially linear[52] thus acting as a 3e-donor, as the other L′H ligands.

However, when bound to a higher metal oxidation state center, with a limited π-electron donor ability, the nitriles display ν (N≡C) higher than in the free state and can be activated toward nucleophilic attack,[42,43] as observed for the reactions of *cis*-$[ReCl_4(NCMe)_2]$ (formed by spontaneous reduction of $ReCl_5$ in NCMe) with oximes, HON=CRR′, amino-alkylated adenines, or alcohols, which behave as protic nucleophiles (reaction 2) to yield, for example, in the first case, the imine complexes *cis*-$[ReCl_4\{NH{=}C(Me)ON{=}CRR'\}_2]$.

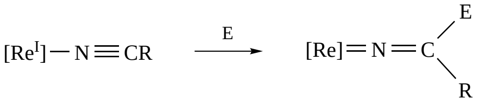

(1)

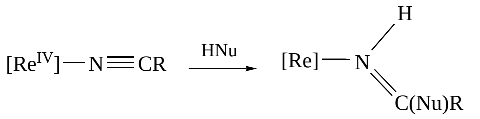

(2)

Isocyanides, when bound to weak π-donor metal centers, can also undergo addition of protic nucleophiles (HNu) to form aminocarbene M=C(Nu)NHR species.[53] Hence, a parallelism of behavior is observed for nitriles and isocyanides. In both ligands, either the electrophilic or the nucleophilic addition occurs at the unsaturated atom at the β-position that exhibits a higher reactivity than the metal coordinated terminal atom.

Nitriles are activated to hydrolysis by Re^{III} in di- and tri-nuclear cores with multiple metal–metal bonds like $[NBu^t_4]_2[Re_2Cl_8]$ and $[Re_3(\mu\text{-}Cl)_3Cl_6]$, to form amidate species as $[NBu^t_4][Re_2Cl_6(\mu\text{-}PhCONH)]$ and $[NBu^t_4][Re_2Cl_5(\mu\text{-}MeCONH)(\mu\text{-}MeC(OH)N)]$. The reactions are proposed to involve intramolecular nucleophilic attack of a hydroxide ligand to an NCR ligating an adjacent Re atom.[54]

Redox potential-electronic structure relationships in 18- and 17-electron mononitrile complexes of Re have been established.[55] It was possible to estimate, for the nitrile and related ligands, for example, in complexes (**3–6**), the values of the electrochemical P_L ligand parameter, a measure of the net electron donor minus π-acceptor character of a ligand. The order of this character is as follows: vinylidenes $>$ NCR $>$ CNR $>$ $N_2 \geq CO \geq$ aminocarbynes $>$ carbynes.[56]

The relative stability of the geometrical isomers of $[ReCl(NCR)(dppe)_2]$ (**4**) and $[Re(NCR)_2(dppe)_2]^+$ is markedly dependent on the metal oxidation state, oxidation promoting cis $\rightarrow$ trans isomerization.[57] The kinetics was investigated by digital simulation of cyclic voltammetry, according to double-square schemes. A high thermodynamic gain toward the trans isomer results from the first electron-transfer, but kinetic reasons hamper the isomerization, which, in order to readily occur, requires a second oxidation step to Re^{III}. The isomeric equilibrium constants and the rate constant for the isomerization respond to electronic and steric effects.[57] The related carbonyl complex *cis*-$[ReCl(CO)(dppe)_2]$ also undergoes an oxidative cis $\rightarrow$ trans isomeric conversion, which follows an electron-transfer chain (ETC) catalytic process.[57]

Nitrosyl complexes are rather numerous and $[Re(NO)X_5]^{2-}$ is known for all the halides (= X); addition of phen or bipy (= L–L) gives $[Re(NO)X_3(L\text{–}L)]$ or of pyridine, alcohols, DMSO, or MeCN (= solv) gives $[Re(NO)X_4(solv)]^-$; PPh_3 in EtOH followed by $NaBH_4$ gives the nitrosyl hydride $[ReH_2(NO)(PPh_3)_3]$.[58] Other nitrosyl complexes include $[Re(NO)Cl_2(OMe)(PPh_3)_2]$ and $[Tc(NO)Br_4]^-$ and the low-valent complexes indicated above.

Polypyridyl ligands can also stabilize low metal oxidation states since they can accept electron density from the metal. Among conventional N-donors, the $[M(bipy)_3]^+$ cations are known,[59] as are $[MOX_3(bipy)]$ (X = Cl or Br). Na/Hg reduction of $[ReCl_4(THF)_2]$ in the presence of phen or bipy (= L–L) give formally Re^0 species $[Re(L\text{–}L)_3]$, but the complex is probably better described as having reduced ligands. The coordination chemistry of Re (and, to a lesser extent, Tc) with pyrazolylborate ligands, that is, of scorpionate oxo-complexes, is being quite developed (Section 3.5).

Many tertiary phosphine complexes are known (see above), especially in oxidation states from +1 to +5: (**3–6**), $[MH(N_2)(dppe)_2]$, $[ReCl_3(PR_3)_3]$, $[TcBr_2(dppe)_2]^+$, and $[ReOCl_3(PR_3)_2]$ are typical. *cis*-$[ReCl_4(NCMe)_2]$, mentioned above, reacts with monodentate phosphines, L, to give *trans*-$[ReCl_4L_2]$; bidentate phosphines also react but the products are very dependent on conditions.[60]

Trigonal bipyramidal $[ReCl(dppe)_2]$, formed by photolytic displacement of N_2 from (**2a**),[61] is a rare example of 16-electron Re^I. It is also formed by cathodically induced Re–Cl bond cleavage in *trans*-$[ReCl_2(dppe)_2]^n$ ($n = 0, 1$).[62] The analogous $[TcCl(dppe)_2]$, obtained by reduction of $[TcCl_4(PPh_3)_2]$ with Zn in the presence of dppe, adds dinitrogen to form $[TcCl(N_2)(dppe)_2]$.[63] Both $[MCl(dppe)_2]$ add H_2 to give $[MCl(\eta^2\text{-}H_2)(dppe)_2]$.

Phosphites, in comparison with phosphines, tend to give lower oxidation state complexes: $[Re_2\{P(OR)_3\}_{10}]$, $[ReH\{P(OR)_3\}_5]$, and $[ReH_3\{P(OR)_3\}_4]$.[64] Much of the chemistry of Re^I involves carbonyl complexes (*see* ***Rhenium: Organometallic Chemistry***).

The multiple bonded π-electron donor nitride (N^{3-}) and imide (NR^{2-}) ligands are isoelectronic with the oxo (O^{2-}) ligand and also able to stabilize both Tc and Re (which can easily form multiple bonds to those electronegative elements) in the highest oxidation states (typically from +7 to +5). The +5 oxidation state provides the largest number of structurally characterized complexes and the strong trans influence of those ligands can lead to square-pyramidal five-coordinate compounds or to six-coordinate complexes with a pronounced tetragonal distortion.[58] The imido $\{M{=}NR\}^{3+}$ core is rarer, in particular for Tc. The nitride complexes $[ReNCl_4]^-$, $[ReNCl_2L_2]$ (L = PPh_3), and $[ReNCl_2L_3]$ (L = $PMePh_2$) are typical in having Re–N distances of 1.6–1.7 Å and, in the latter case, long M–X distances trans to ReN.[65] $[ReNCl_4]$ has Re≡N–Re chains in the structure.[66] $[ReNF_4]$ is also known from the reaction of Me_3SiN_3 with ReF_6. Since the first Tc≡N complex, $[TcN(dtc)_2]$ (1981; d(Tc–N) = 1.604(6) Å), a number have been made[5] and the corresponding ^{99m}Tc complexes can find radiopharmaceutical application (Section 4.1). These species are also basic at N and form adducts with Lewis acids, which can be applied to the synthesis of imido complexes.

Imido complexes are also readily formed from reactions of amines or isocyanates with oxides.[8] For example, $[Re({=}NR)Cl_3(PPh_3)_2]$ is obtained from primary amines and $[ReOCl_3(PPh_3)_2]$, and $[XRe({=}NR)_3]$ (**7**) (X = $OSiR'_3$, Cl; R = Bu^t), which are good starting materials for other Re^{VII} imido complexes, are prepared by reactions of amines or isocyanates with $[Me_3SiOReO_3]$ (X = $OSiR'_3$) or R_2O_7 (X = Cl).

Imido ligands are stronger electron-donors than the oxo ligand leading, for example, to Re^{VII} complexes harder to reduce (X in (**7**) can thus be a readily oxidizable species like H^- or $PR_2{}^-$) and reactive toward Lewis acids and proton. Hence, protonation of $[XRe({=}NR)_3]$ with HCl affords the di(imido) complexes $[ReCl_3({=}NR)_2]$. The tunable steric bulkiness of the =NR ligands can stabilize otherwise inaccessible low-coordination species like the trigonal-planar $[Re(NAr)_3]^-$.[67] Haloimido complexes may also have synthetic value.[68]

3.5 Complexes of Group 16 Elements

Perrhenates are important oxo-complexes and the perrhenate $[ReO_4]^-$ group can act as a ligand in metal complexes.[69] The Tl^+ and K^+ salts are sparingly soluble, the Ba^{2+} and $NH_4{}^+$ salts are moderately soluble, while the Na^+, Mg^{2+}, and Ca^{2+} salts are very soluble (1.6, ca. 10, 53.2, 62.3, 1000, 1679, and 1776 g L^{-1}, respectively, at 20 °C). The purple color of permanganate is a result of ligand-to-metal charge transfer (LMCT). The corresponding LMCT bands for the colorless pertechnetate and perrhenate ions are found in the UV because the central metals are more difficult to reduce. Salts of the rhenate ion, such as $Ba[ReO_4]$, are unstable to air and to water. Aqueous Re^V easily disproportionates into Re^{VII} and Re^{IV}, as shown by the hydrolysis of $ReCl_5$ to $HReO_4$ and ReO_2, driven in part by the insolubility of the dioxide.

Some of the early work in Re chemistry was in error because it was not realized how easily an oxo atom can be incorporated into a complex. The strong IR Re=O stretch at $950-1000\,cm^{-1}$ should always be searched. A problem with X-ray methods is the ease with which oxo-complexes can disorder and cocrystallize with halides.[70]

Oxo-complexes are very important for Re and Tc and dominate the aqueous chemistry. For both Re and Tc, the +5 oxidation state is the most studied one. This reflects the relevance of this oxidation state in ^{99m}Tc complexes applied in nuclear medicine and the use of Re complexes as nonradioactive models.[5,8] The complexes often exhibit the oxo $\{M{=}O\}^{3+}$ or the nitrido $\{M{\equiv}N\}^{2+}$ core (Section 3.4).

The coordination chemistries of these metals often are comparable, but the stronger oxidizing character of the Tc centers can result in considerable differences.

The permetallates $[MO_4]^-$ are the most common starting materials in this area, the Tc compound being somewhat more easily reduced. Air sensitive dianions are formed in aqueous solution by electrochemical reduction. Perrhenate reacts with phosphines in alcohol solutions containing HCl to give the very stable green oxo-complexes $[ReOCl_3L_2]$; the PPh_3 complex is a standard synthetic precursor in Re chemistry. In contrast, $[TcO_4]^-$ loses the oxo groups much more readily and is reduced by the phosphine to $[TcCl_4L_2]$ or $[TcCl_3L_3]$ under similar conditions. The Cl trans to the oxo group in $[ReOCl_3L_2]$ is labilized by the trans effect and is readily replaceable; for example, EtOH gives $[ReO(OEt)Cl_2L_2]$, which in turn reacts with acidic en (= L_2) or pyridine (=L) solutions to form the dioxo complexes *trans*-$[ReO_2L_4]^+$. The *trans*-Re^VO_2 group is a common one, as well as *trans*-O=Re–O–Re=O, for example, in $[Re_2O_3py_4Cl_4]$ formed from $[ReOCl_3(PPh_3)_2]$ with pyridine. Oxo groups can undergo protonation/deprotonation equilibria.

Tc^V oxo-complexes are often either of the square-pyramidal $[TcOL_4]$ type with a vacancy opposite the oxo group, or of the *trans*-$[TcO_2L_4]^+$ type. Examples used for organ imaging are given in Section 4.1. A number of THF complexes, such as $[Re_3Cl_9(THF)_3]$ and $[ReCl_4(THF)_2]$, are known. The homoleptic alkoxide $[Re(OMe)_6]$ is formed from ReF_6 and $Si(OMe)_4$.

Re^{VII} oxo-complexes are particularly interesting and their inorganic and organometallic chemistries, as well as those of related imido and amido complexes, have been reviewed.[71] The Re^{VII} trioxo complexes are much more common than the dioxo or monoxo ones, the latter being normally derived from Re^{VII} oxyfluorides or present catecholate ligands.[8]

Re_2O_7 is a key starting material. Its solid-state polymeric structure is broken by solvolysis, upon dissolution, to form the solvent adducts $Re_2O_7 \cdot L_2$ (**8**) (L = H_2O, NCMe, THF, DMF, etc., the Re–O–Re unit being essentially linear for L = H_2O but bent in other cases) with the octahedral center bearing both solvent ligands (Scheme 2). Similar structures are usually obtained by reacting Re_2O_7 in THF or NCMe with bidentate ligands (e.g. $L_2 = 2,2'$-bipyridine), but tridentate N or S donors (e.g. L'_3 = $HC(pz)_3$, 1,4,7-triazacyclononane or 1,4,7-trithiacyclononane) lead to the heterolytic cleavage of the μ-O bridge to give the ionic $[L'_3ReO_3][ReO_4]$ products (**9**).[71] Hence, Re_2O_7 can be regarded as a type $[XReO_3]$ (X = ReO_4) species with a $ReO_4{}^-$ leaving group that can be replaced by various nucleophiles like halides or pseudohalides to yield (Scheme 2) the trioxo complexes $[XReO_3]$ (**10**) (X = F, Cl, Br, CN, SCN), isolated as their bipy adducts.[71]

Alkoxide analogues like $[(R_3EO)ReO_3]$ (E = Si, Ge, Sn, Pb) can be obtained by related methods on reaction of Re_2O_7 with $(Me_3Si)_2O$ or Ph_3SiOH, Me_3Ge, Me_4Sn, or

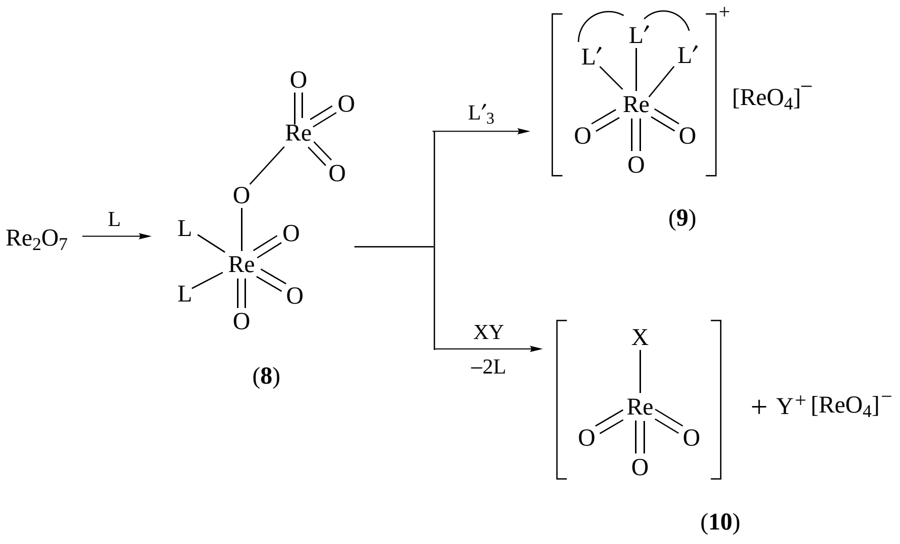

Scheme 2

Ph_4Pb respectively.[71] The siloxy derivative $[(Me_3SiO)ReO_3]$, known since long, can be used for the preparation of alkoxides $[(RO)ReO_3]$ on reaction with Me_3SiOR and as a starting material for organometallic Re oxides. The alkoxides can also be prepared by reaction of $[ClReO_3]$ with Me_3SiOR. They are unstable at room temperature, but are stabilized by adduct formation to give hexacoordinate species, for example *fac*-$[(RO)ReO_3(tmeda)]$ ($R = Me, Bu^t$); by dimerization, for example, in the case of $[\{ReO_3(MeOH)\}_2(\mu\text{-}OMe)_2]$ (**11**) (which, upon MeOH evolution, polymerizes to $[(MeO)ReO_3]_n$); or by intramolecular arrangements.[71]

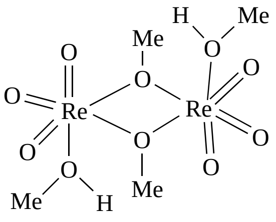

(**11**)

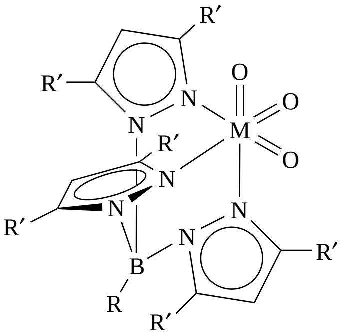

(**12**)

M = Re, Tc
R = H, pz, Ph
R′ = H, Me

Scorpionate Re^{VII} or Tc^{VII} trioxides $[Tp'MO_3]$ (**12**) (M = Re, Tc) with tridentate hydrotris- and tetrakis(pyrazolyl)-borates and related ligands [Tp′ = Tp, Tp*, $B(pz)_4$ (pzTp) or $(Ph)B(pz)_3$ (PhTp)] are obtained by reaction of M_2O_7 with the appropriate Na^+ or K^+ scorpionate salt (XY, Scheme 2); $Na[MO_4]$ or $K[MO_4]$ is the other product.[71–73] They exhibit a distorted octahedral coordination and their chemistry, as well as of the other (much less studied) Re or Tc oxidation state scorpionate complexes, has been reviewed.[72,73]

Like the related η^5-cyclopentadienyl $[C_pMO_3]$ species, $[TpMO_3]$ adds ethylene to give the glycolate $[TpMO(OCH_2CH_2O)]$, which is stable for Tc but reverts to the trioxide for Re. $[Tp'ReO_3]$ can undergo reductive deoxygenation with PPh_3 to give the Re^V dimers $[Tp'ReO(\mu\text{-}O)]_2$ (**13**) (Tp′ = Tp, pzTp) or, in the presence of L (pyridine, imidazole, 1/2 diphosphine), the dioxo complexes *trans*-$[(\kappa^2\text{-}Tp')ReO_2L_2]$ (Tp′ = Tp, pzTp, PhTp) with a bidentate pyrazolylborate and, in the presence of $ClSiMe_3$, the monoxo species $[Tp'ReOCl_2]$ (**14**) (Tp′ = Tp, pzTp, Tp*), which can be further deoxygenated to Re^{III} paramagnetic products.[72,73]

These oxo Re^V complexes can furnish various derivatives, for example, with N-, O-, S-, or C- ligands, that is, Re^V oxo-amido, -imido, -alkoxide, -phenoxide, -diolate, -thiolate, -alkyl, or – aryl complexes, on reactions of (**13**) or (**14**) with amines, alcohols, phenoxides, diols, thiols, organozinc, or Grignard reagents, respectively.[72,73]

The nucleophilicity of the oxo ligands at some of the alkoxide and diolate Re^V complexes was shown by addition of the strong Lewis acid $B(C_6F_5)_3$ to form the corresponding $OB(C_6F_5)_3$ complex adducts.[74] $[ClReO_3]$ also acts as a Lewis base, forming the adducts $[ClO_2ReO \rightarrow MX_n]$ with various Lewis acids MX_n, for example, $AlCl_3$, $NbCl_3$, $SbCl_5$, or $ReOCl_4$.[71]

In contrast, the cationic dioxo-phenyl Re^{VII} complex $[TpReO_2(Ph)]^+$, derived from the reaction of $[TpReO(Ph)(OTf)]$ (formed by phenylation of (**14**) (Tp′ = Tp) with PhLi followed by a reaction with I_2 and AgOTf) with O-atom donors, for example, PyO or Me_2SO, undergoes facile phenyl-to-oxo migration, at ambient temperature, to give a phenoxide product. This is the first well-established example of thermal migration of a ligand from a metal center to an oxo ligand, a step that is believed to be promoted by the high electrophilicity of the oxo ligand at the cationic Re^{VII} center.[75] A related, but photochemical, migration occurs in the photolysis of the Re^V complexes $[TpReO(R)Cl]$ (**15**) (R = aryl, ethyl) to form the Re^{III} alkoxides $[TpRe(OR)ClL]$ (L = py, NCMe, Me_3PO). Complexes (**15**) (R = aryl) were obtained by C-H activation of aromatic hydrocarbons (RH) on photolysis of solutions with $[TpReO(Cl)I]$. The photochemistry of the oxo-oxalate complex $[TpReO(C_2O_4)]$ was also investigated and shown to proceed via releasing of carbon dioxide and monoxide to form the transient {TpReO} that can be trapped with species like O_2 to give $[TpReO_3]$ as the final product, $CDCl_3$ to yield $[TpReOCl_2]$, or 9,10-phenanthrenequinone (L) to form $[TpReO(L)]$.[76]

Complexes with S donors are much less common. $[Et_4N][ReS_4]$, which is derived from heating $[ReO_4]^-$ in a methanolic ammonium polysulfide solution, can lead to sulfido-bridge polynuclear complexes, for example, with the tetrahedral $[ReS_4]^-$ ligand. $[ReO_4]^-$ and H_2S give $[ReO_3S]^-$, which is most conveniently isolated as the Tl^+ salt. $[ReS_4]^-$ is a useful synthon for S-rich Re complexes, yielding sulfido and thiolato Re^V, Re^{IV}, or Re^{III} complexes upon reactions with unsaturated species like alkenes, alkynes, or isocyanides.[8]

Other interesting all-sulfur examples are the square-pyramidal $[ReS(S_4)_2]^-$ (obtained from the reactions of polysulfides with Re_2O_7, $[ReO_4]^-$, $ReCl_5$, or $[Re_2Cl_8]^{2-}$) and $[ReS(SCH_2CH_2S)_2]$ (formed by a reaction of $[ReCl_6]^{2-}$ with 1,2-ethanedithiol), and the trigonal prismatic dithiolenes $[Re(S_2C_2R_2)_3]$.[8] The first complex with a Tc=S bond is $[TpTcSCl_2]$, obtained from $[TpTcOCl_2]$ and B_2S; the Re analog is similar.[77]

Oxo-complexes with S-donor ligands are well documented, mainly for Re,[8] for example, by the five-coordinate trigonal bipyramidal $[ReO(SR)_4]^-$ (SR = bulky thiolate) complexes (prepared by a ligand replacement from $[ReOCl_3(PPh_3)_2]$ or $[ReCl_6]^-$), the square-pyramidal dithiolate or dithiolene $[ReO(S^{\cap}S)_2]^-$ compounds, the tumor targeting $[ReO(DMSA)_2]^-$ mercaptosuccinate complex (Section 4.2), the thioether $[ReOX_3(RSC_6H_4SR)]$ (X =

halide) compounds, and the complexes [ReO(L)(SR)] with the tridentate $^{-}SCH_2CH_2YCH_2CH_2S^{-}$ (Y = S, O) ligands (prepared from a reaction of $[ReOCl_4]^-$ with H_2L and RSH). Chelating mixed-donor N,S ligands (e.g. aminothiolates, amidothiolates, *N*-heterocyclic thiolates (like pyridine-2-thiolate, pyrimidine-2-thiolate, thiazoline-2-thiolate), S-containing aminoacid derivatives) and P,O donors (e.g. $R_2PC_6H_4X$-2 ($X = O^-$, COO^-)) combining a harder (N or O) with a softer (S or P) coordinating atom can meet the electronic requirements of the $\{Re^VO\}^{3+}$ core (also of the related $\{ReN\}^{2+}$ or $\{Re(NR)\}^{3+}$ ones). Quite a good number of such types of oxo-complexes is known, also for Tc, in particular with possible medical use (Section 4). Those ligands are also adequate for Re^{III}, whose stabilization is favored by ligands that present good electron donor and π-acceptor character (PR_3 and CO are also favorable). Complexes with other chelating mixed ligands like P,S donors (e.g. phosphinothiolates) and P,N donors (as amino- and amido-phosphines) are also well represented.

3.6 Complexes with Group 17 Elements

Representative examples have been given in Sections 2.2 and 3.2. Others are as follows.[2,78] KF and ReF_6 give the square prismatic $K_2[ReF_8]$. The species $K_2[MX_6]$ are also known for both metals and all the halides. They are obtained by a mild reduction of the permetallate in HX solutions. The reaction of ReF_6 with $Re_2(CO)_{10}$ in HF gives $[Re(CO)_6][F_5Re(\mu\text{-}F)ReF_5]\cdot[Re_3Cl_{12}]^{3-}$ has the trirhenium cluster core of $[Re_3Cl_9]$ (Section 2.2). The phase changes in the hexahalogenorhenates have been rationalized on the basis of radius ratio effects. Reduction of acidic (HCl) perrhenate solutions with iodide gives the dimeric linear oxo-bridged species $[Cl_5ReOReCl_5]^{4-}$; spin pairing is almost complete and the ion is only weakly paramagnetic. In solution, the magnetism increases due to hydrolysis to give $[(HO)ReCl_5]^{2-}$. $[ReOX_4]^-$ is also known for Cl, Br, and I; these ions take up a variety of donors in the vacant site trans to the oxo group to give $[ReOX_4(L)]^-$ (L = py, MeCN, H_2O).

4 RADIOPHARMACEUTICALS

Tc and, in fewer cases, Re compounds have found applications in medicinal inorganic chemistry as radiopharmaceuticals for clinical diagnosis (^{99m}Tc for scintigraphic and emission tomographic imaging)[79–88] or even therapy (^{186}Re e.g. for the palliation of severe bone cancer pain).[79,83,88,89]

4.1 ^{99m}Tc

Most of the radiopharmaceuticals used in clinics are labeled with ^{99m}Tc, a γ-ray emitter with favorable nuclear properties toward an effective detection of the emitted γ-rays and a low radiation exposure of the patient, together with a relative ready availability and low cost (Section 1). $[^{99m}TcO_4]^-$ is available in very low concentration in the eluate from its generator column and thus the syntheses of the derived ^{99m}Tc radiopharmaceuticals take place in very dilute aqueous solutions and the common methods of characterization used for macroscopic amounts of compounds cannot be applied. Hence, in order to isolate and fully characterize technetium compounds, one has to work with the ^{99}Tc isotope that is a very long-lived weak β-emitter that can be handled safely under adequate precautions. Once characterized a ^{99}Tc compound, the confirmation of the identical ^{99m}Tc structure can be done by high performance liquid chromatography (HPLC) (UV and β-detection), electrophoresis, or mass spectrometry.

Although $Na[^{99m}TcO_4]$ can be applied as such for thyroid and brain imaging, most of the ^{99m}Tc radiopharmaceuticals are obtained upon the reduction of $[^{99m}TcO_4]^-$ (e.g. by Sn^{II}, $S_2O_6{}^{2-}$, H_3PO_4, $SO_3{}^{2-}$, or $S_2O_4{}^{2-}$) in the presence of a suitable coordinating species such as an amine oxime, a cysteine ester, an iminodiacetic acid derivative, a polyamino-polycarboxylic acid, a mercaptoacetyltriglycerine, a mercaptosuccinic acid, an alkyldiphosphonate, or an isocyanide.

The ^{99m}Tc complexes are conveniently prepared shortly before use, by addition of the ^{99m}Tc generator eluate to the contents of commercially available kits that contain the coordinating species to be labeled and often the reducing agent (usually Sn^{II}).

Examples of approved ^{99m}Tc radiopharmaceuticals are as follows: [TcO(D,L-HM-PAO)] (Ceretec) (**16**), [TcO(L,L-ECD)] (Neurolite) (**17**), and [TcCl{(DMG)$_3$2MP}] (**18**), which can penetrate the intact blood-brain barrier in view of their neutral and lipophilic character, used for cerebral imaging; $[TcO(MAG_3)]^-$ (TechneScan) (**19**) for renal function imaging; $[TcO_2(R_2PCH_2CH_2PR_2)_2]^+$ (Tc−tetrofosmin, Myoview) (**20**) ($R = CH_2CH_2OCH_2CH_2$), $[Tc(\text{Schiff base})(PR_3)_2]^+$ (Tc−furifosmin, TechneScan Q12) (**21**) (Schiff base = *trans*-(1,2-bis(dehydro-2,2,5,5-tetramethyl-3-furanone-4-methylene-amino)ethane), and $[Tc(CNR)_6]^+$ (Tc-sestamibi, Tc-hexamibi, Cardiolite) (**22**) ($R = CH_2CMe_2OMe$), for myocardial perfusion imaging (complex (**22**) also for breast cancer imaging); and $[Tc(HIDA)]^-$ (**23**) for liver and gall bladder imaging.[79,84,87,88]

Many of the Tc complexes (**16, 17, 19**) present the oxo $\{Tc^V{=}O\}^{3+}$ core and are pentacoordinate (square pyramid), but other metal oxidation states and coordination numbers are possible, for instance, in (**20**) (hexacoordinate with the dioxo $\{Tc^VO_2\}^+$ core), in (**18**) (heptacoordinate Tc^{III}), in (**21**) or (**23**) (hexacoordinate Tc^{III}), or in (**22**) (hexacoordinate Tc^I). In Tc-diphosphonate radiopharmaceuticals, used as bone imaging agents, the metal is believed to be in the +4 oxidation states.[81] The +1 oxidation state in the homoleptic isocyanide complex (**22**) is expected to be advantageous in terms of the kinetic inertness associated to its low-spin d^6 configuration, and the syntheses of various promising complexes with the organometallic $\{^{99m}Tc(CO)_3\}^+$ core has been achieved by displacement reactions of $[TcX_3(CO)_3]^{2-}$ ($X = Cl^-$, Br^-) or $[Tc(H_2O)_3(CO)_3]^+$ conveniently prepared from $[TcO_4]^-$ and CO (1 atm).**90** A similar $\{^{188}Re(CO)_3\}^+$-based chemistry has also been developed.**90**

The Tc-nitrido $\{Tc^V{\equiv}N\}^{2+}$ core, with the strong π-electron donor nitride ligand, which effectively stabilizes the Tc^V oxidation state, is isoelectronic with $\{Tc^V{=}O\}^{3+}$ and is known to form complexes with a variety of chelating ligands,**85** and $[^{99m}TcN(noet)_2]$ (**24**) constitutes a new myocardial imaging agent.**82** The preparation of the $^{99m}Tc{\equiv}N$ synthon can be conveniently achieved directly from $[^{99m}TcO_4]^-$ upon reaction with N-methyl, S-methyl dithiocarbazate, H_2N-NMeC(=S)SMe (which acts as the donor of the nitride N-atom), in the presence of reducing agents such as Sn^{2+} and tris(*m*-sulfophenyl)phosphine.**84**

The above ^{99m}Tc radiopharmaceuticals fall in the 'technetium essential' class of drugs (the Tc is an integral part without which the molecule would not be delivered to its target), but noticeable and rapid progresses are being achieved toward the development of 'technetium tagged' drugs, for which the targeting species (such as a peptide, an antibody, or a hormone) has been labeled with ^{99m}Tc (directly or by a bifunctional chelate) that is delivered to the target side as a passenger. Recent developments have been made in the field of ^{99m}Tc-based receptor (or target)-specific radiopharmaceuticals (whose ultimate distribution is determined by their receptor binding (or other biological) interactions.**81,82** In particular, the ^{99m}Tc-labeled P280 peptide (an oligopeptide with two identical 13 aminoacid monomers, each monomer containing a cysteine-glycine-cysteine sequence capable of S-binding to the $\{Tc{=}O\}^{3+}$ core) has been approved as a commercial product (Acutec) for thrombus imaging.**82**

4.2 ^{186}Re or ^{188}Re

The coordination chemistry of rhenium is better known and easier to handle than that of technetium and, in view of their expected analogies, the former metal can be used for nonradioactive model studies for technetium. In addition, ^{186}Re and ^{188}Re display attractive properties (Section 1) for nuclear medicine.**88,89** The biolocalizations of analogous Re and Tc compounds can also be similar. Hence, the ^{99m}Tc and the ^{186}Re (or ^{188}Re) radionuclides constitute a potential 'matched pair' for diagnosis and therapy.**85**

However, in spite of the similarity of the physical properties (like size, charge, and lipophilicity, which can determine the biodistribution) expected for analogous complexes of Re and Tc, on account of, for example, the 'lanthanide contraction', the former are usually easier to oxidize (harder to reduce) and less kinetically labile than the latter. The easier oxidation in vivo of the Re complexes to $[ReO_4]^-$ can be advantageous in terms of excretion from the body (via the kidneys) of the radionuclide.

The preparations of Re radiopharmaceuticals start from perrhenate with the radionuclide (Section 1) and involve metal reduction and complexation reactions, an overall procedure similar to that used for Tc.

As observed for diphosphonic acid derivatives (like HEDP) labeled with ^{99m}Tc that are used as bone imaging agents, related ^{186}Re-labeled diphosphonates, like ^{186}Re-HEDP formed on reaction of $[^{186}ReO_4]^-$ with HEDP in the presence of $SnCl_2$ as reductant, also accumulate at bone cancer sites and act as a 'rhenium essential' drug for palliation of metastatic bone cancer pain.**83,89** The Re-HEDP species appears to be polymeric (with a metal–metal multiple bond), as the analogous Tc agent. ^{99m}Tc complexes with dimercaptosuccinate (DMSA) have been applied for diagnoses of renal diseases and for imaging of medullary thyroid carcinoma. The related ^{186}Re complex, with a square-pyramidal structure and the apical Re^V-oxo group $[ReO(DMSA)_2]^-$ (**25**), which exists as a pH-dependent mixture of isomers (depending on the orientations of the carboxylic groups), also undergoes selective uptake in the carcinoma and is expected to be of a therapeutic value.**83,89**

The Re radionuclides have been applied not only in 'rhenium essential' drugs, as shown above, but also recently, and following strategies similar to those used for technetium, for labeling biomolecules like antibodies, steroids, and peptides, which thus become potential targeting agents for therapeutic uses of Re radionuclides. In particular, both Re and Tc square-pyramidal oxo-complexes with tetradentate bifunctional chelators (i.e. of the N_xS_{4-x} classes, see e.g. (**17**) and (**19**) for Tc) are adequate for such couplings.**81–83,89** The rhenium radiopharmaceutical chemistry for therapy, although yet little explored, is already a promising and developing field of research.

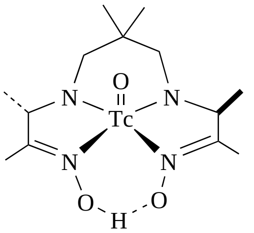

(**16**)

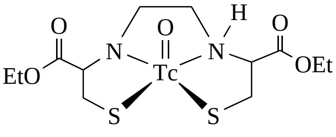

(**17**)

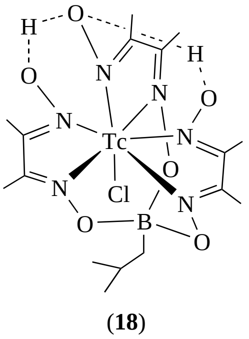

(**18**)

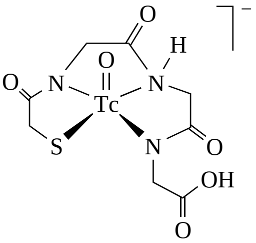

(**19**)

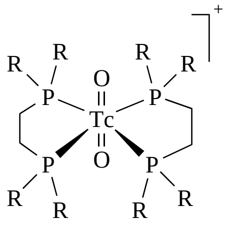

(20)

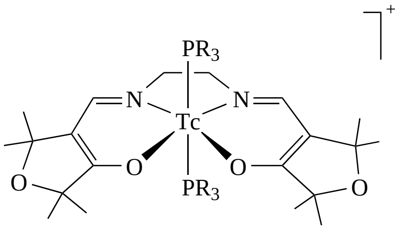

(21)

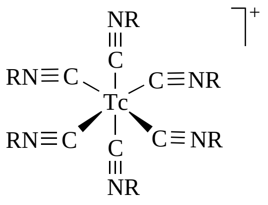

(22)

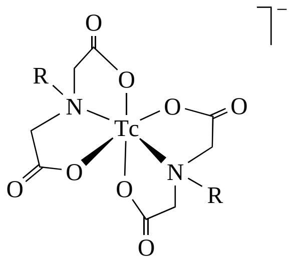

(23)

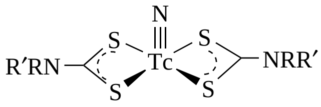

(24)

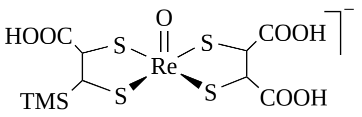

(25)

5 CATALYSIS

The use of rhenium complexes in catalysis has developed mainly during the last few years and constitutes a current and promising area of Re chemistry. Oxo-rhenium complexes can be active typically in oxidation catalysis, that is, OAT and related reactions. They can also catalyze other synthetically important reactions like isomerization or etherification of allylic or propargylic alcohols, the Beckmann rearrangement of oximes, the dehydration of primary amides and aldoximes, and, unconventionally, reduction of aldehydes and ketones. Other reactions like CO_2 reduction, dehydrogenation of alkanes, and H/D exchange have been catalyzed by some (nonoxo) rhenium catalysts. Examples are given below, but organometallic systems, mainly involving the extensively studied $[MeReO_3]$ and related organorhenium oxides, have been reviewed elsewhere.[91–93] (*see also* ***Rhenium: Organometallic Chemistry***)

5.1 Oxygen Atom Transfer (OAT) and Other Oxidation Reactions

Oxo-rhenium complexes can catalyze various OAT reactions between suitable oxo-donors (XO = sulfoxides (R_2SO); tertiary amine *N*-oxides (R_3NO); pyridine *N*-oxide (C_5H_5NO, PyO); triphenyl-phosphine, -arsine, or -stilbene oxide (R_3AO) (A = P, As, Sb); peroxides (Bu^tOOH, H_2O_2); perchlorate (ClO_4^-); epoxides 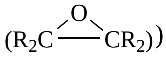 $(R_2C\overset{O}{\text{—}}CR_2)$) and oxo-acceptors (Y = sulfoxides (R_2SO); sulfides or thioethers (R_2S); disulfides (RS-SR); thiols (RSH); phosphines (PR_3); phosphites ($P(OR)_3$); and olefins ($R_2C{=}CR_2$)). The reactions comprise both oxidation of Y and reduction of XO but the oxidative viewpoint is that which is normally enhanced. Recent reviews focusing on rhenium oxazoline,[94] thiazoline,[94] and dithiolate[95] complexes are available.

Two overall mechanisms have been considered[94] for such reactions: one (Scheme 3) occurs via an electrophilically activated oxo-donor (XO) toward the oxo-acceptor (Y), upon coordination to a Lewis acid {ReO} center; and the other one (Scheme 4) involves a metal-centered oxygen transfer via a $\{Re^VO\}/\{Re^{VII}O_2\}$ couple that parallels that of Mo oxotransferases (via the isoelectronic Mo^{IV}/Mo^{VI} couple).

Examples of catalytic systems include the following ones. $[ReOCl_3(PPh_3)_2]$ catalyzes the oxidation (with sulfoxides) of thiols to disulfides,[96,97] of sulfides to sulfoxides,[98] of acyclic disulfides to thiosulfonates (RSO_2SR),[97] of cyclic disulfides to thiosulfites $[\overline{S{-}S(CH)_2)_3CH_2}$ to $O{=}\overline{S{-}S(CH)_2)_3CH_2}]$,[97]

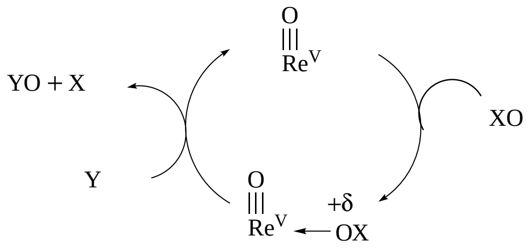

Scheme 3

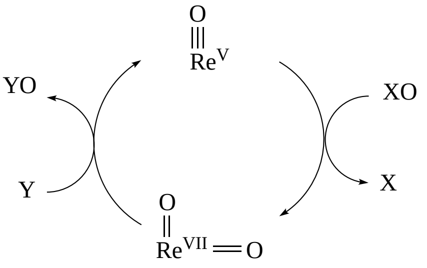

Scheme 4

and of PPh_3 to $OPPh_3$,[99] and some of the reactions are indicated to occur via the mechanism of Scheme 3. That of Scheme 4 is followed by the Re^V phenoxy-oxazoline and phenoxy-thiazoline (L) complexes $[ReOL_2(L')]OTf$ (**26**) and (**27**) ($L' = H_2O$, NCMe) obtained from the reaction of $[ReOCl_3(PPh_3)_2]$ or $[ReOCl_3(OPPh_3)(SMe_2)]$ with HL (**26**) or by using $[NBu_4][ReOCl_4]$ as the precursor (**27**), followed by chloride ligand replacement by L′ in the presence of AgOTf.[94] (**26**) and (**27**) are highly active in catalytic OAT from O-donors like perchlorate, sulfoxides, or pyridine *N*-oxide to O-acceptors like sulfoxides, thioethers, or $P(MeO)_2Ph$. The reduction of perchlorate by pure oxo-transfer is rather difficult to achieve and (**26**) and (**27**) catalyze the overall cycle more effectively than $[MeReO_3]$.[94]

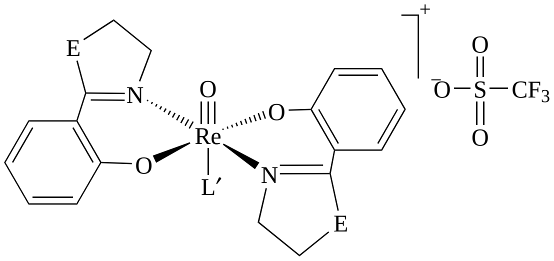

(**26**) E = O
(**27**) E = S; L′ = H_2O, NCMe

Re^V chloro oxo-complexes, with bi-, tri-, or tetra-dentate Schiff bases (L), like [ReOCl(L)] or $[ReOCl_2(L)]$, prepared from reaction of $[NBu_4][ReOCl_4]$ with the appropriate HL or H_2L, are also known catalysts for OAT reactions. Hence, (**28**) and (**29**) are catalysts for olefin epoxidation with Bu^tOOH (**28**, with two bidentate *N*,*O*-ligands, are better catalysts than (**29**) with a tetradentate *N*,*N*,*O*,*O*- one),[100,101] whereas (**30**) (with *N*,*N*,*S*-tridentate pyridylbenzothiazoline ligand) catalyzes the OAT from PyO to tris(*p*-methylphenyl)phosphine (however, the pentacoordinate oxo-methyl complexes (**31**) and (**32**), with the related *N*,*N*,*S*- or *O*,*N*,*S*-tiazoline derivatives, obtained from $[MeReO_3]$, are more active catalysts).[102]

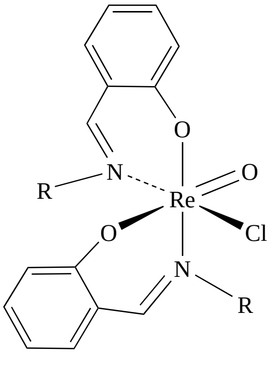

(**28**) (R = C_6H_5, C_6H_{11})

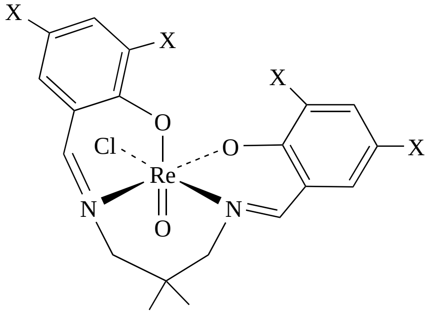

(**29**) (X = Cl, H, Bu^t)

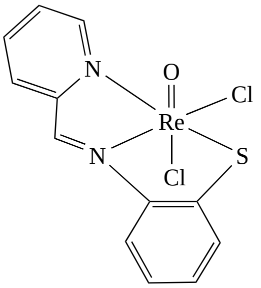

(**30**)

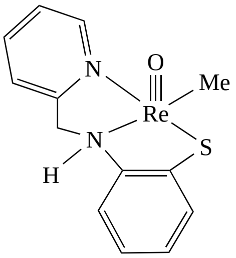

(**31**)

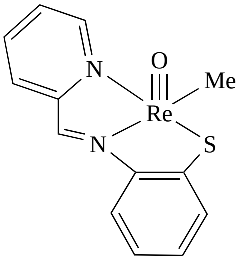

(**32**)

Other square-pyramid oxo-methyl Re^V complexes with dithiolate ligands like [MeReO(dithiolate)L] (e.g. (**33**) and (**34**), L = phosphine) or $[MeReO(dithiolate)]_2$ (derived from reaction of $[MeReO_3]$ with the appropriate dithiol, in the presence or in the absence of L, respectively) are also active, for example, for the OAT from PyO to PR_3, to R_2S, or to R_2SO; from R_2SO to R_2S; and from Bu^tOOH to PR_3, to R_2S, or to R_2SO.[95] Kinetic studies suggest a mechanism via a dioxorhenium(VII) intermediate (Scheme 4) for the PyO/PR_3/(**33**) system, or a mechanism according to Scheme 3 for the Bu^tOOH/PR_3/(**34**) case.[95] Interestingly, the dinuclear complex $[\{ReO\}_2(mtp)_3]$ (**35**), without any methyl ligand, prepared from the reaction of Re_2O_7 with H_2mtp, catalyzes the OAT from molecular oxygen to PR_3, via a postulated peroxo intermediate, apart from the more usual oxidation of PR_3 by Me_2SO and PyO.[95] The diimido complexes $[MeRe^V(NAr)_2(PR_3)_2]$ also catalyze the oxidation of phosphines by O_2, via the oxo-Re^{VII} intermediate

[$MeReO(NAr)_2$].[95] The dioxotris(pyrazolyl)borate Re^V complex [Tp^*ReO_2], obtained by in situ reduction of [Tp^*ReO_3] by PPh_3 or $P(OEt)_3$, catalyzes the OAT from epoxides to those P reductants, whose kinetics have also been studied.[103]

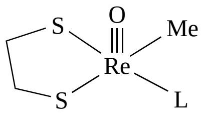

(**33**)

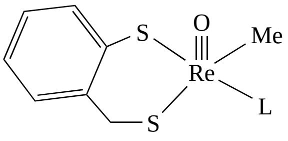

(**34**)

(L = phosphine)

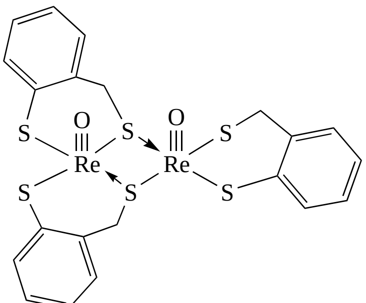

(**35**)

The ‘peroxo perhenic acid’ (**36**) (the molecular structures of the diglyme adduct was determined by X-rays) is believed to be the active species in the catalytic oxidation of olefins and aromatics by Re_2O_7/H_2O_2 or ReO_3/H_2O_2.[104] However, (**36**) is not so active a catalyst as the related peroxo methylrhenium(VII) [$MeReO(O_2)_2$]·H_2O (**37**) (the active species of the known [$MeReO_3$]/H_2O_2 system in a wide variety of oxidations) since the hydrolysis product (perhenic acid) of (**36**) is inactive whereas those from (**37**), that is, [$MeReO_3$] and [$MeReO(O_2)_2$]·H_2O, regenerate the catalyst (**37**) on reaction with H_2O_2.

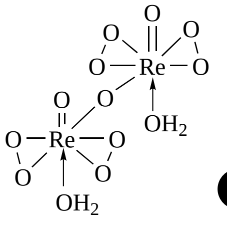

(**36**)

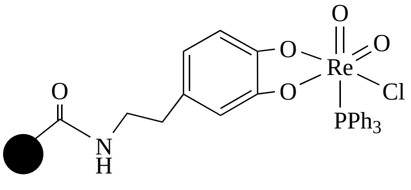

(**38**)

Supported oxo-rhenium catalysts in heterogeneous systems have also been reported, for example, the polystyrene-supported (catecholato)oxo-rhenium(VII) complexes (**38**), obtained from the reaction of polystyrene-supported catechol with [$ReOCl_3(PPh_3)_2$], which catalyze alcohol oxidation to ketones or aldehydes with dimethylsulfoxide and epoxide reductions to alkenes with PPh_3, following the proposed mechanism of Scheme 4.[105]

The use of technetium compounds in catalysis is a much less studied field. An example, investigated kinetically, is the oxidation of hydrazine (to NH_4^+, N_2 and other nitrogeneous products) by oxo-anions (nitrate or perchlorate) catalyzed by pertechnetate in aqueous acidic medium, which was proved to proceed via a chain process.[106] The hydrazine is oxidized by high oxidation state (+7, +6 or +5) Tc species and the reduced states of Tc are reoxidized by nitrate (or perchlorate) to regenerate the high Tc oxidation state. The reaction has significance in the technological reprocessing of nuclear fuel.

5.2 Isomerization or Etherification of Allylic or Propargylic Alcohols

The Re^{VII} trioxo compounds [ReO_3X] ($X = OSiMe_3$, $OSiPh_3$, $OReO_3$) act as catalysts, at room temperature, for the isomerization of allylic alcohols and allylic ethers (reactions 3 and 4), by 1,3-shift of a hydroxy or a trialkylsiloxy group, which is proposed to involve the initial replacement at Re of X by the allylic alkoxide (to form a perrhenic ester) followed by formation of a postulated allyl-dioxorhenium intermediate.[107] The isomerization of allylic and propargylic alcohols is also catalyzed by [NBu_4][ReO_4] and *p*-toluenesulfonic acid, via $HReO_4$.[108]

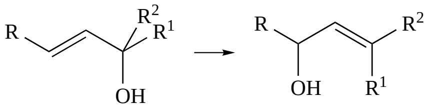

(3)

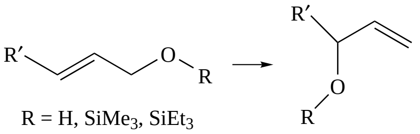

R = H, $SiMe_3$, $SiEt_3$

(4)

Single-pot etherification of propargyl alcohols by alcohols (reaction 5) has been achieved by the rhenium(V)-oxo complex [$ReOCl_3(dppm)$] bearing a diphosphine ligand, in NCMe, via a postulated allenolate intermediate $R^1CH=C=C(R^2)$-O-[Re]=O, which would undergo a nucleophilic addition of R^3OH at the R^1CH carbon.[109]

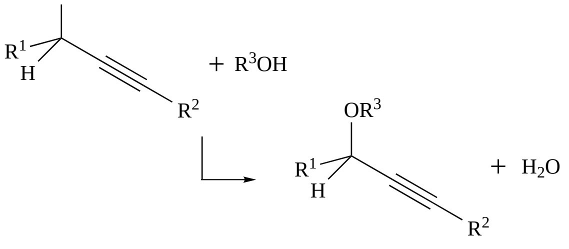

(5)

5.3 Beckman Rearrangement of Oximes to Amides and Lactams

The conversion of oximes into amides or lactams (reactions 6 or 7), in particular, ε-caprolactam from cyclohexanone oxime ($X = H$), is catalyzed by $[NBu_4][ReO_4]$ and CF_3SO_3H in refluxing nitromethane, via a postulated perrhenic ester of oxime $[RR'C{=}N\text{-}O\text{-}ReO_3]$.[110]

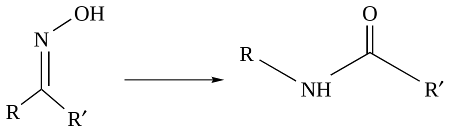

(6)

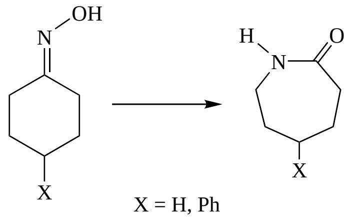

(7)

Since oximes are obtained from condensation reactions of ketones with hydroxylamine, the single-pot preparation of amides and lactams directly from ketones and $H_2NOH.HCl$ was achieved via in situ generated oximes, by using the above catalyst in nitromethane under azeotropic conditions.[110]

5.4 Dehydration of Primary Amides and Aldoximes to Nitriles

Nitriles can be prepared by dehydration of primary amides (reaction 8) or of aldoximes (reaction 9), catalyzed by the Re^{VII} trioxo compounds $[ReO_3X]$ ($X = OSiMe_3$, $OReO_3$, OH) in azeotropic (e.g. toluene/water or mesitylene/water) reflux.[111] Aqueous perrhenic acid ($X = OH$) is the most convenient catalyst in view of the moisture sensitivity of the others. The oxophilicity of the Re(VII) oxo-complexes is believed to play a determining role in the reactions, which are proposed to involve six-membered cyclic transition states formed upon preferential *O*-coordination, relative to *N*-coordination, of the amide or oxime.[111]

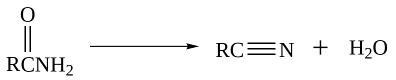

$$RC(=O)NH_2 \longrightarrow RC{\equiv}N + H_2O$$

(8)

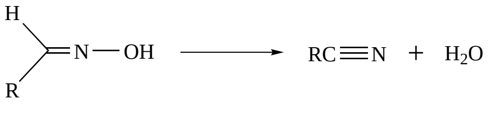

(9)

5.5 Reductive Hydrosilylation of Aldehydes and Ketones

In contrast with the common activity of oxo-rhenium compounds in oxidation catalysis (see above), the Re^V-dioxo-complex $[ReO_2I(PPh_3)_2]$ catalyzes the reductive hydrosilylation of aldehydes and ketones to give silyl ethers (reaction 10), which can provide a single-pot reduction-protection of carboxyl groups.[112] This silyl etherification conceivably proceeds via a $[2+2]$-type addition of the Si–H bond of the silane to the Re=O π-bond to yield a siloxy-substituted metal hydride that acts as a reductant of the aldehyde or ketone. The second oxo ligand appears to provide a spectator oxo effect favorable to the reaction.

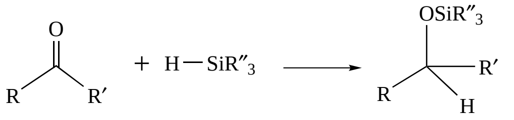

(10)

5.6 Photo- and Electrocatalysis

Re^I diimine complexes act as photocatalysts and/or electrocatalysts for CO_2 reduction to CO. Examples include the tricarbonyl complexes *fac*-$[Re(\alpha\text{-diimine})(CO)_3L]^n$ [$n = 0$, L = halide; $n = 1$, L = NCMe, $P(OR)_3$; α-diimine = 1,4-disubstituted 1,4-diazabuta-1,3-dienes or bpy and related chelating N-heterocycles],[113,114] for example, *fac*-$[Re(dmb)(CO)_3(NCMe)]^+$,[115] $[Re(dmb)(CO)_3]_2$[115] and *fac*-$[Re(bpy)(CO)_3\{P(OPr^i)_3\}]^+$.[116] Electron-transfer from an amine electron donor (e.g. triethanolamine or triethylamine) to the excited state complex is usually considered as the initiation of the photocatalysis, and metallocarboxylates and metallocarboxylic acids have been proposed as intermediates in the formation of CO.[115] The electrocatalytic process is triggered by a 1-electron or a 2-electron cathodically induced chloride (X) or L ligand dissociation to form the catalytic species.[117]

$[ReCl_6]^{2-}$ is photooxidized by electron acceptors, for example, 2,3,5,6-tetrachloro-1,4-benzoquinone (chloranil) and DDQ, to $[ReCl_6]^-$, which is an intermediate in the oxidation of Cl^- to Cl_2 and of toluene to benzaldehyde.[118]

5.7 Other Reactions

$[ReO_2I(PPh_3)_2]$, with an alkyl iodide as an initiator, in the presence of a metal alkoxide like $Al(OPr^i)_3$, catalyzes the living radical polymerization of styrene and para-substituted styrenes.[119]

In $[ReH(SH)_2(PMe_3)_4]$, unexpectedly obtained via S-atom transfer from $[ReS_4]^-$ to PMe_3 in a reaction with H_2S, the protic (SH) and hydridic (ReH) sites undergo intramolecular proton exchange and the SH proton exchanges with protic reagents like CH_3OD. The complex undergoes isotopic H/D exchange at both SH and ReH with D_2, and catalyzes the conversion of H_2 and D_2 into HD and the isotopic exchange between D_2 and H_2S to give HD and DHS.[120]

cis-$[ReH(N_2)L_4]$ ($L = PMe_2Ph$) catalyzes aldol-type reactions, for example, of ethyl cyanoacetate $NCCH_2CO_2Et$ or of $NCCH_2CN$ with benzaldehyde to yield the corresponding (*E*)-α-cyanocinnanamate derivatives, $NC(EtO_2C)C{=}CHPh$ or $NC(NC)C{=}CHPh$. The reaction proceeds via active Re^I enolate intermediates, $[Re(NCCRCO_2R')(NCCHRCO_2R')L_4]$ ($R = H$, Me; $R' =$ alkyl) and the derived $[Re(NCCHCO_2Et)\{NC(EtO_2C)C{=}CHPh\}L_4]$, which are also catalysts for olefin metathesis.[121]

Various polyhydride Re phosphine complexes catalyze alkane dehydrogenation, as described in Section 3.1.

Supported mono and bimetallic (M-Tc, with M = group 8–10 metal) technetium catalysts, in a number of cases similar to Re/supported (alumina, silica or MgO) ones, have shown activity in various reactions[122–124] like dehydrogenation of alkanes and hydrogenation of acetone (to isopropyl alcohol and propane), of aromatic hydrocarbons, of CO and of CO_2 (to methane). Re complexes with N,O-ligands catalyse (liquid biphasic catalysis) the peroxidative oxidation of alkanes under mild conditions.[125]

6 RELATED ARTICLES

Ammonia & N-donor Ligands; Dihydrogen Complexes & Related Sigma Complexes; Hydride Complexes of the Transition Metals; Hydrogen Bonding & Dihydrogen Bonding; Manganese: Inorganic & Coordination Chemistry; Manganese: Organometallic Chemistry; Metal-based Drugs; Metal-based Imaging Agents; Mixed Donor Ligands; Rhenium: Organometallic Chemistry; S-donor Ligands; Technetium: Organometallic Chemistry; Water & O-donor Ligands.

7 REFERENCES

1. K. B. Lebedev, ‘The Chemistry of Rhenium’, Butterworths, London, 1962.
2. N. N. Greenwood and A. Earnshaw, ‘Chemistry of the Elements’, 2nd edn., Butterworth-Heinemann, Oxford, 1998.
3. R. Ruhl and W. Jeitschko, *Acta Crystallogr., Sect. B*, 1982, **38**, 2784.
4. F. Hullinger, *Struct. Bonding (Berlin)*, 1968, **4**, 53.
5. R. Alberto, in ‘Comprehensive Coord. Chem. II’, J. A. McCleverty and T. J. Meyer (Eds.-in-Chief), eds. E. C. Constable and J. R. Dilworth, Elsevier, Amsterdam 2004, Vol. 5, Chap. 5.2, p. 127.
6. G. Bandoli, A. Dolmella, M. Porchia, F. Refosco, and F. Tisato, *Coord. Chem. Rev.*, 2001, **214**, 43.
7. C. E. Housecroft, *Coord. Chem. Rev.*, 1998, **169**, 187.
8. U. Abram, in ‘Comprehensive Coord. Chem. II’, J. A. McCleverty and T. J. Meyer (Eds.-in-Chief), eds. E. C. Constable and J. R. Dilworth, Elsevier, Amsterdam 2004, Vol. 5, Chap. 5.3, p. 271.
9. J. C. Vites and M. M. Lynam, *Coord. Chem. Rev.*, 1998, **172**, 357.
10. R. G. Teller and R. Bau, *Struct. Bonding (Berlin)*, 1981, **44**, 1.
11. R. H. Crabtree, *Acc. Chem. Res.*, 1990, **23**, 95.
12. L. Brammer, J. A. K. Howard, O. Johnson, T. F. Koetzle, J. L. Spencer, and A. M. Stringer, *J. Chem. Soc., Chem. Commun.*, 1991, 241.
13. D. Michos, X. -L. Luo, J. A. K. Howard, and R. H. Crabtree, *Inorg. Chem.*, 1992, **31**, 3914.
14. D. M. Heinekey, M. H. Voges, and D. M. Barnhart, *J. Am. Chem. Soc.*, 1996, **118**, 10792.
15. M. E. Tully and A. P. Ginsberg, *J. Am. Chem. Soc.*, 1973, **95**, 2042.
16. M. Kohli, D. J. Lewis, R. L. Luck, J. V. Silverton, and K. Sylla, *Inorg. Chem.*, 1994, **33**, 879.
17. A. K. Burrell, J. C. Bryan, and G. J. Kubas, *J. Am. Chem. Soc.*, 1994, **116**, 1575.
18. R. H. Crabtree, *Science*, 1998, **282**, 2000.
19. R. H. Crabtree, P. E. M. Siegbahn, O. Eisenstein, A. L. Rheingold, and T. F. Koetzle, *Acc. Chem. Res.*, 1996, **29**, 348.
20. S. S. Kristjánsdóttir, A. J. Loendorf, and J. R. Norton, *Inorg. Chem.*, 1991, **30**, 4470.
21. D. Michos, X.-L. Luo, J. A. K. Howard, and R. H. Crabtree, *Inorg. Chem.*, 1992, **31**, 3914.
22. Y. Kim, H. Deng, J. C. Gallucci, and A. Wojcicki, *Inorg. Chem.*, 1996, **35**, 7166.
23. M. L. Loza, S. R. de Gala, and R. H. Crabtree, *Inorg. Chem.*, 1994, **33**, 5073.
24. D. G. Hamilton, X.-L. Luo, and R. H. Crabtree, *Inorg. Chem.*, 1989, **28**, 3198.
25. Y. Matano, T. O. Northcutt, J. Brugman, B. K. Bennet, S. Lovell, and J. M. Mayer, *Organometallics*, 2000, **19**, 2781.
26. A. Paulo, J. Ascenso, A. Domingos, A. Galvão, and I. Santos, *J. Chem. Soc., Dalton Trans.*, 1999, 1293.
27. F. A. Cotton and R. A. Walton, ‘Multiple Bonds Between Metal Atoms’, 2nd edn., Oxford University Press, Oxford, 1993.
28. K. E. Meyer, D. R. Root, P. E. Fanwick, and R. A. Walton, *Inorg. Chem.*, 1992, **31**, 3067.
29. A. J. L. Pombeiro, in ‘New Trends in the Chemistry of Nitrogen Fixation’, eds. J. Chatt, L. M. C. Pina, and R. L. Richards Academic Press, London, 1980, Chap. 6.
30. J. R. Dilworth and R. L. Richards, in ‘Comprehensive Organometallic Chemistry’, eds. G. Wilkinson, F. A. G. Stone, and E. W. Abel, Pergamon, Oxford, 1982, Vol.8, p. 1073.
31. M. Hirsch-Kuchma, T. Nicholson, A. Davison, and A. G. Jones, *J. Chem. Soc., Dalton Trans.*, 1997, 3189.
32. J. Chatt, W. Hussain, G. J. Leigh, H. M. Ali, C. J. Pickett, and D. A. Rankin, *J. Chem. Soc., Dalton Trans.*, 1985, 1131.

33. M. F. N. N. Carvalho and A. J. L. Pombeiro, *J. Organomet. Chem.*, 1990, **384**, 121.
34. R. M. Chin, J. Barrera, R. H. Dubois, L. E. Helberg, M. Sabat, T. Y. Bartucz, A. J. Lough, R. H. Morris, and W. D. Harman, *Inorg. Chem.*, 1997, **36**, 3553.
35. G. Albertin, S. Antoniutti, E. Bordignon, and E. Visentin, *Inorg. Chem.*, 2001, **40**, 5465.
36. Y. Wang, J. J. R. Fraústo da Silva, A. J. L. Pombeiro, M. A. Pellinghelli, and A. Tiripicchio, *J. Organomet. Chem.*, 1993, **454**, 211.
37. M. F. N. N. Carvalho, A. J. L. Pombeiro, U. Schubert, O. Orama, C. J. Pickett, and R. L. Richards, *J. Chem. Soc, Dalton Trans.*, 1985, 2079.
38. Q. F. Zhang, J. L. C. Chim, W. Lai, W.-T. Wong, and W.-H. Leung, *Inorg. Chem.*, 2001, **40**, 2470.
39. J. E. Joachim, C. Apostolidis, B. Kanellakopulos, R. Maier, D. Meyer, J. Rebizant, and M. L. Ziegler, *J. Organomet. Chem.*, 1993, **455**, 137.
40. T. B. Gunnoe, M. Sabat, and W. D. Harman, *J. Am. Chem. Soc.*, 1998, **120**, 8747.
41. A. J. L. Pombeiro, *New J. Chem.*, 1994, **18**, 163.
42. V. Yu. Kukushkin and A. J. L. Pombeiro, *Chem. Rev.*, 2002, **102**, 1771.
43. A. J. L. Pombeiro and V. Yu. Kukushkin, in ‘Comprehensive Coordination Chemistry II’, J. A. McCleverty and T. J. Meyer (Eds.-in-chief), ed. A. B. P. Lever, Elsevier, Amsterdam 2004, Vol. 1, Chap. 1.34, p. 639.
44. C. M. P. Ferreira, M. F. C. Guedes da Silva, V. Yu. Kukushkin, J. J. R. Fraústo da Silva, and A. J. L. Pombeiro, *J. Chem. Soc., Dalton Trans.*, 1998, 325.
45. Y. Wang, J. J. R. Fraústo da Silva, A. J. L. Pombeiro, M. A. Pellinghelli, and A. Tiripicchio, *J. Organomet. Chem.*, 1994, **476**, C9.
46. Y. Wang, J. J. R. Fraústo da Silva, A. J. L. Pombeiro, M. A. Pellinghelli, and A. Tiripicchio, *J. Organomet. Chem.*, 1992, **430**, C56.
47. A. J. L. Pombeiro, *J. Organomet. Chem.*, 2001, **632**, 215.
48. A. J. L. Pombeiro, M. T. A. R. S. Costa, Y. Wang, and J. F. Nixon, *J. Chem. Soc., Dalton Trans.*, 1999, 3755.
49. M. T. A. R. S. Costa, J. J. R. Fraústo da Silva, A. J. L. Pombeiro, R. A. Michelin, G. Bombieri, and F. Benetollo, *Inorg. Chim. Acta*, 1998, **280**, 308.
50. A. J. L. Pombeiro, M. F. C. Guedes da Silva, and R. A. Michelin, *Coord. Chem. Rev.*, 2001, **218**, 43.
51. A. J. L. Pombeiro, *Inorg. Chem. Commun.*, 2001, **4**, 585.
52. M. F. C. Guedes da Silva, J. J. R. Fraústo da Silva, and A. J. L. Pombeiro, *Inorg. Chem.*, 2002, **41**, 219.
53. R. A. Michelin, A. J. L. Pombeiro, and M. F. C. Guedes da Silva, *Coord. Chem. Rev.*, 2001, **218**, 75.
54. J. L. Eglin, *Comments Inorg. Chem.*, 2002, **23**, 23.
55. M. F. C. Guedes da Silva, L. M. D. R. S. Martins, J. J. R. Fraústo da Silva, and A. J. L. Pombeiro, *Collect. Czech. Chem. Commun.*, 2001, **66**, 139.
56. A. J. L. Pombeiro, *New J. Chem.*, 1997, **21**, 649.
57. A. J. L. Pombeiro, M. F. C. Guedes da Silva, and M. A. N. D. A. Lemos, *Coord. Chem. Rev.*, 2001, **219–221**, 53.
58. G. Ciani, D. Giusto, M. Manassero, and A. Albinati, *J. Chem. Soc., Dalton Trans.*, 1976, 1943.
59. M. Stebler, A. Gutiérrez, A. Ludi, and H.-B. Bürgi, *Inorg. Chem.*, 1987, **26**, 1449.
60. R. E. Myers and R. A. Walton, *Inorg. Chem.*, 1976, **15**, 3065.
61. D. L. Hughes, A. J. L. Pombeiro, C. J. Pickett, and R. L. Richards, *J. Organomet. Chem.*, 1983, **248**, C26.
62. T. Al Salih, M. T. Duarte, J. J. R. Fraústo da Silva, A. M. Galvão, M. F. C. Guedes da Silva, P. B. Hitchcock, D. L. Hughes, C. J. Pickett, A. J. L. Pombeiro, and R. L. Richards, *J. Chem. Soc., Dalton Trans.*, 1993, 3015.
63. A. K. Burrell, J. C. Bryan, and G. J. Kubas, *J. Am. Chem. Soc.*, 1994, **116**, 1575.
64. H. W. Choi and E. L. Muetterties, *J. Am. Chem. Soc.*, 1982, **104**, 153.
65. P. J. Blower and J. R. Dilworth, *J. Chem. Soc., Dalton Trans.*, 1985, 2305.
66. W. Liese, K. Dehnicke, I. Walker, and J. Strähle, *Z. Naturforsch., Teil B*, 1979, **34**, 693.
67. C. C. Cummins, ‘Progress Inorganic Chemistry’, ed. K. D. Karlin John Wiley, New York, 1998, Vol. 47, p. 685.
68. K. Dehnicke and J. Strähle, *Chem. Rev.*, 1993, **93**, 981.
69. M. C. Chakravorti, *Coord. Chem. Rev.*, 1990, **106**, 205.
70. G. Parkin, *Chem. Rev.*, 1993, **93**, 887.
71. C. C. Romão, F. E. Kühn, and W. A. Herrmann, *Chem. Rev.*, 1997, **97**, 3197.
72. A. Paulo, J. D. G. Correia, and I. Santos, *Trends Inorg. Chem.*, 1998, **5**, 57.
73. A. Paulo, J. D. G. Correia, M. P. C. Campello, and I. Santos, *Polyhedron*, 2004, **23**, 331.
74. L. H. Doerrer, J. R. Galsworthy, M. L. H. Green, and M. A. Leech, *J. Chem. Soc., Dalton Trans.*, 1998, 2483.
75. Y. Matano, T. O. Northcutt, J. Brugman, B. K. Bennett, S. Lovell, and J. M. Mayer, *Organometallics*, 2000, **19**, 2781.
76. S. N. Brown and J. M. Mayer, *Inorg. Chem*, 1995, **34**, 3560.
77. A. Duatti, F. Tisato, F. Refosco, U. Mazzi, and M. Nicolini, *Inorg. Chem.*, 1989, **28**, 4564.
78. R. C. Colton and J. H. Canterford, ‘Halides of the 2nd and 3rd Row Transition Metals’, Wiley, New York, 1968.
79. Z. Guo and P. J. Sadler, *Angew. Chem., Int. Ed. Engl.*, 1999, **38**, 1512.
80. D. L. Nosco and J. A. Beaty-Nosco, *Coord. Chem. Rev.*, 1999, **184**, 91.
81. S. S. Jurisson and J. D. Lydon, *Chem. Rev.*, 1999, **99**, 2205.

82. S. Liu and D. S. Edwards, *Chem. Rev.*, 1999, **99**, 2235.
83. J. Dilworth and S. Parrot, *Chem. Soc. Rev.*, 1998, **27**, 43.
84. W. A. Volkert and S. Jurisson, Technetium-99m Chelates as Radiopharmaceuticals, in 'Technetium and Rhenium, Their Chemistry and its Applications' (Topics in Current Chemistry, Vol. 176), eds. K. Yoshihara and T. Omori, Springer-Verlag, Berlin, 1996, p. 123.
85. B. Johannsen and H. Spiess, Technetium(V) Chemistry as Relevant to Nuclear Medicine, in 'Technetium and Rhenium, Their Chemistry and its Applications' (Topics in Current Chemistry, Vol. 176), eds. K. Yoshihara and T. Omori, Springer-Verlag, Berlin, 1996, p. 77.
86. J. Baldas, The Chemistry of Technetium Nitrido Complexes, in 'Technetium and Rhenium, Their Chemistry and its Applications' (Topics in Current Chemistry, Vol. 176), eds. K. Yoshihara and T. Omori, Springer-Verlag, Berlin, 1996, p. 37.
87. K. Schwochau, *Angew. Chem., Int. Ed. Engl.*, 1994, **33**, 2258.
88. S. S. Jurisson, D. Berning, W. Jia, and D. Ma, *Chem. Rev.*, 1993, **93**, 1137.
89. K. Hashimoto and K. Yoshihara, Rhenium Complexes Labeled with 186/188Re for Nuclear Medicine, in 'Technetium and Rhenium, Their Chemistry and its Applications' (Topics in Current Chemistry, Vol. 176), eds. K. Yoshihara and T. Omori, Springer-Verlag, Berlin, 1996, p. 275.
90. R. Alberto, High and Low-Valency Organometallic Compounds of Technetium and Rhenium, in 'Technetium and Rhenium, Their Chemistry and its Applications' (Topics in Current Chemistry, Vol. 176), eds. K. Yoshihara and T. Omori, Springer-Verlag, Berlin, 1996, p. 149.
91. G. S. Owens, J. Arias, and M. M. Abu-Omar, *Catal. Today*, 2000, **55**, 317.
92. C. C. Romão, F. E. Kühn, and W. A. Herrmann, *Chem. Rev.*, 1997, **97**, 3197.
93. W. A. Herrmann and F. E. Kühn, *Acc. Chem. Res.*, 1997, **30**, 169.
94. M. M. Abu-Omar, *Chem. Commun.*, 2003, 2102.
95. J. H. Espenson, *Adv. Inorg. Chem.*, 2003, **54**, 157.
96. M. M. Abu-Omar and S. I. Khan, *Inorg. Chem.*, 1998, **37**, 4979.
97. J. B. Arterburn, M. C. Perry, S. L. Nelson, B. R. Dible, and M. S. Holguin, *J. Am. Chem. Soc.*, 1997, **119**, 9309.
98. J. B. Arterburn and S. L. Nelson, *J. Org. Chem.*, 1996, **61**, 2260.
99. J. B. Arterburn and M. C. Perry, *Tetrahedron Lett.*, 1996, **37**, 7941.
100. F. E. Kühn, M. U. Rauch, G. M. Lobmaier, G. R. J. Artus, and W. A. Herrmann, *Chem. Ber./Recueil*, 1997, **130**, 1427.
101. W. A. Herrmann, M. U. Rauch, and G. R. J. Artus, *Inorg. Chem.*, 1996, **35**, 1988.
102. C. Zhang, I. A. Guzei, and J. H. Espenson, *Inorg. Chem.*, 2001, **40**, 2437.
103. K. P. Gable and E. C. Brown, *J. Am. Chem. Soc.*, 2003, **125**, 11018.
104. W. A. Herrmann, J. D. G. Correia, F. E. Kühn, G. R. J. Artus, and C. C. Romão, *Chem. Eur. J.*, 1996, **2**, 168.
105. J. B. Arterburn, M. Liu, and M. C. Perry, *Helv. Chim. Acta*, 2002, **85**, 3225.
106. T. J. Kemp, A. M. Thyer, and P. D. Wilson, *J. Chem. Soc., Dalton Trans.*, 1993, 2601; 2607.
107. S. Bellemin-Laponnaz, J. P. Le Ny, and J. A. Osborn, *Tetrahedron Lett.*, 2000, **41**, 1549.
108. K. Narasaka, H. Kusama, and Y. Hayashi, *Tetrahedron*, 1992, **48**, 2059.
109. B. D. Sherry, A. T. Radosevich, and F. D. Toste, *J. Am. Chem. Soc.*, 2003, **125**, 6076.
110. H. Kusama, Y. Yamashita, and K. Narasaka, *Bull. Chem. Soc. Jpn.*, 1995, **68**, 373.
111. K. Ishihara, Y. Furuya, and H. Yamamoto, *Angew. Chem., Int. Ed. Engl.*, 2002, **41**, 2983.
112. J. J. Kennedy-Smith, K. A. Nolin, H. P. Gunterman, and F. D. Toste, *J. Am. Chem. Soc.*, 2003, **125**, 4056.
113. T. Scheiring, A. Klein, and W. Kaim, *J. Chem. Soc., Perkin Trans.*, 1997, **2**, 2569.
114. F. P. A. Johnson, M. W. George, F. Hartl, and J. J. Turner, *Organometallics*, 1996, **15**, 3374.
115. Y. Hayashi, S. Kita, B. S. Brunschwig, and E. Fujita, *J. Am. Chem. Soc.*, 2003, **125**, 11976.
116. H. Hori, K. Koike, Y. Suzuki, M. Ishizuka, J. Tanaka, K. Takeuchi, and Y. Sasaki, *J. Mol. Cat. A: Chem.*, 2002, **179**, 1.
117. A. Klein, C. Vogler, and W. Kaim, *Organometallics*, 1996, **15**, 236.
118. A. W. Maverick, Q. Yao, A. K. Mohammed, and L. J. Henderson Jr, *Adv. Chem. Series*, 1993, **238**, 131.
119. Y. Kotani, M. Kamigaito, and M. Sawamoto, *Macromolecules*, 2000, **33**, 6746.
120. D. E. Schwarz, J. A. Dopke, T. B. Rauchfuss, and S. R. Wilson, *Angew. Chem., Int. Ed. Engl.*, 2001, **40**, 2351.
121. M. Hirano, M. Hirai, Y. Ito, A. Fukuoka, and S. Komiya, *Chem. Lett.*, 1994, 165.
122. A. P. Barkova and D. B. Furman, *Kinet. Catal.*, 1999, **40**, 540.
123. G. N. Pirogova and N. N. Rimar, *Russ. Chem. Bull.*, 1994, **43**, 1475.
124. N. N. Rimar and G. N. Pirogova, *Russ. Chem. Bull.*, 1998, **47**, 398.
125. A. M. Kirillov, M. Haukka, M. F. C. Guedes da Silva and A. J. L. Pombeiro, *Eur. J. Inorg. Chem.*, 2005, in press.

Acknowledgment

We are grateful to Mr. Alexander Kirillov (Instituto Superior Técnico) for a literature survey.

Technetium: Organometallic Chemistry

Fernande D. Rochon
Université du Québec à Montréal, Montréal, QC, Canada

Based in part on the article Technetium: Organometallic Chemistry by Ronald J. Clark which appeared in the Encyclopedia of Inorganic Chemistry, First Edition.

1 Introduction 1
2 Hot-atom Chemistry 3
3 Starting Materials 3
4 Binary Carbonyl Compounds 4
5 Mixed-ligand Carbonyl Compounds 5
6 Cyclopentadienyl Complexes 7
7 Isonitrile Complexes 8
8 Cyanide Compounds 8
9 Arene Complexes 9
10 Miscellaneous Organometallic Compounds 9
11 Related Articles 9
12 References 9

Glossary

Diagnostic imaging: the use of an isotope which emits readily detectable radiation and which is present in a compound that is absorbed by a healthy target organ, in order to produce an image of soft tissue using a radiation source from within the organ; the procedure generally provides much better information than standard X-ray photographs
Nuclear medicine: the use of isotopes in any capacity to aid the practice of medicine

1 INTRODUCTION

Technetium belongs to group 7 of the second row transition metals and its chemistry is quite different from the two other elements of the same group, manganese and rhenium. The chemistry of technetium is not developed as much as the one of the relatively rare and expensive element rhenium and also much less than for the more common manganese. The reason for the difference is due to its natural absence in nature. Technetium is unique among the d-block elements since it has no stable isotope (*see Isotopes & Isotope Labeling*). As discussed elsewhere (*see* ***Technetium & Rhenium: Inorganic & Coordination Chemistry***), element 43 does not exist in nature in any significant quantity. All the isotopes are radioactive and among the approximately 20 known technetium isotopes (^{91}Tc–^{110}Tc), ^{99}Tc has the longest half-life (212 000 years, *see Radioactive Decay*). Since the earth is much older, most traces have already disintegrated since the 'big bang'. There might be ultratraces produced as the product of the natural fission of uranium, particularly in the natural reactor of Oklo in Gabon. However, technetium-99 constitutes about 5% of the fission by-products (*see Fission Product*) of nuclear reactors. It can be fairly readily isolated from these wastes and its abundance today has been estimated to exceed that of several naturally occurring elements. The price of solid $NH_4[^{99}TcO_4]$ is very low, but handling and packaging is expensive. It is available from Oak Ridge Laboratories (Batch No Tc-99-P-48 containing 51.6% Tc-99 by weight) for about 93.US$ per gram, but the technical services charges ($2765.) and radioisotope packing ($1200) are expensive. It has been said that rather large amounts are available in the former Soviet Union, so perhaps this supply will reach the commercial market in the near future.

The chemistry of technetium is quite complex especially because of its numerous oxidation states (+7 to −1). In the higher oxidations states (Tc(IV) to Tc(VII)), the metal behaves as a hard Lewis acid and its chemistry is dominated by multiple-bonded oxo ligands. The lower oxidation states ions can be classified as soft metals and will form stable compounds with ligands containing the following donor atoms: P, As, S, Se, X^- (except F^-), N, and π-acceptors such as CO, NO, and isonitriles.

The importance of the chemistry of technetium has greatly increased since the discovery that the element could be useful as a radiotracer in medicine. The ^{99m}Tc isotope which exists in a metastable nuclear excited state is now widely used in nuclear medicine as a diagnostic agent. It was first used in 1961 for diagnosis of thyroid disease. The compound $[^{99m}TcO_4]^-$ seemed to behave like the iodide ion, known to be taken up by the thyroid. Ten years later, a significant milestone was made with the development of a ^{99m}Tc-polyphosphonate preparation, since it provided the most sensitive method to study skeletal abnormality by imaging. Since the initial work in the field was performed by clinical diagnosticians, most of the earlier preparations were not fully characterized. But for the last 25 years, coordination chemists have clarified the structures and the chemistry of several of these radiopharmaceuticals, develop new methods and design many new imaging agents. Several of these are organometallic Tc compounds. Today, ^{99m}Tc is used in more than 85% of all the diagnostic scans done in hospitals. The nuclear properties of ^{99m}Tc are ideal for nuclear imaging. It emits a 140 KeV γ-ray with a half-life of 6 hours with negligible radiation dose to the patients.

No macroscopic chemistry, such as NMR or IR spectroscopy is possible with the ^{99m}Tc compounds. The decay product of ^{99m}Tc is the long-lived ^{99}Tc which emits weak β^- particles (292 KeV). This makes ^{99}Tc suitable for macroscopic studies. When present in significant quantity, a fair amount of bremsstrahlung radiation (fairly low energy) is produced from the absorption of the β particles in the glass or other container material, but it is possible to work fairly safely with small quantities of ^{99}Tc using normal glassware and prudent isolation conditions. Both Davidson[1] and the authors of Gmelin[2] give some helpful recommendations concerning the handling of this mildly radioactive material. Monitored hoods, gloves, aprons, and isolation are obvious precautions. The handling of ^{99}Tc on a small scale (<20 mg) does not present a danger to health provided some elementary precautions are taken. However, there are numerous examples of work, both in the current and in the older literature, in which the quantities far exceed these fairly conservative recommendations. This is particularly true when starting materials are prepared, or when the commercial source (usually bought in larger quantities) is handled.

The valuable tracer ^{99m}Tc used in nuclear medicine can be obtained as the pertechnetate ion using a ^{99}Mo–^{99m}Tc generator (*see Radioisotope Generators*), which takes advantage of the equilibrium between the parent radionuclide ^{99}Mo and the daughter radionuclide ^{99m}Tc. The separation between the two radionuclides is done on an alumina column by the selective elution of $[^{99m}TcO_4]^-$ with a saline solution.

$$^{99}\mathrm{Mo} \xrightarrow{66\ \mathrm{h}} {}^{99m}\mathrm{Tc} \xrightarrow{6\ \mathrm{h}} {}^{99}\mathrm{Tc} \xrightarrow{212\,000\ \mathrm{yrs}} {}^{99}\mathrm{Ru(stable)} \qquad (1)$$

Optimum isolation of ^{99m}Tc is achieved with minimal ^{99}Tc accumulation every 24 h, which is ideal for hospital use. A new generator is purchased every week and elution of $[^{99m}TcO_4]^-$ is done everyday for preparing the radiopharmaceuticals. The development of this generator has allowed the radionuclide to become routinely available in hospitals at a reasonably low price.

The radiopharmaceuticals are prepared by reacting the ^{99m}Tc(VII) starting material $[^{99m}TcO_4]^-$ with an excess of ligand usually in the presence of a reducing agent. The ^{99m}Tc radiopharmaceuticals can be roughly classified in two classes. The first class contains compounds which are called 'technetium essential'. They are small molecules in which the ^{99m}Tc core plays a very important role in the biodistribution, which depends on the geometry of the radioactive compound, the nature of the ligands, the oxidation state of Tc, and the charge on the complex. The product will be absorbed in different organs of the body. The radioactivity of ^{99m}Tc in the organ can be used to trace or map its functionality, using gamma cameras found in most hospitals. The second class of radiopharmaceuticals are larger molecules called 'technetium tagged'. These compounds are biomolecules like peptides, hormones, antibodies, which have been labeled with ^{99m}Tc in order to target more specifically a given organ. Sometimes, a chelating ligand (*see Chelating Ligands*) is attached to the molecule before the reaction with ^{99m}Tc. In this type of radiopharmaceuticals, the presence of Tc is hidden in a larger molecule in order to prevent a change in the biodistribution of the biomolecule.

Macroscopic chemistry with the long-lived ^{99}Tc isotope is usually conducted to determine the chemical nature of the species produced at the tracer level, especially for the 'technetium essential' molecules or models for the larger ones. These studies have revealed a considerable amount of technetium chemistry. In the past, many studies have been done on rhenium compounds instead of the ^{99}Tc complexes, especially since rhenium is not radioactive. But we believe that the chemistry of rhenium is too different from the one of technetium to be a good model. Rhenium is much more difficult to reduce than technetium. Many ligands (like phosphines) will easily reduce technetium in the absence of any other reducing agent, while it is much more difficult to change the oxidation state of rhenium. Therefore rhenium models for technetium chemistry should be used with caution.

Much of the technetium chemistry directed toward nuclear medicine deals with coordination compounds having oxygen, nitrogen, and other noncarbon atoms bonded to the metal, thereby removing them from the field of organometallic chemistry. This chemistry is discussed in considerable depth in the preceding article (*see* ***Technetium & Rhenium: Inorganic & Coordination Chemistry***). However, a number of recently prepared Tc compounds are classified as organometallic and are considered below. Classical organometallic compounds are very rare in biological systems. The vitamin B coenzyme adenosyl cobalamine is one of the rare natural organometallic compound known. But recently, bioorganometallic science has become an important emerging field and many new compounds containing Tc organometallic cores are under consideration for medical use. A good review was recently published on the current use and future potential of organometallic radiopharmaceuticals.[3]

Organometallic complexes of technetium-99 can be studied by the traditional physical tools used in chemistry. Techniques like infrared, multinuclear magnetic resonance, and mass spectroscopies, as well as magnetic susceptibility (to determine the number of unpaired electrons and thus the oxidation state) and X-ray crystallography are the main methods to study these complexes. X-ray diffraction methods are particularly important since only one small crystal is needed to determine the complete structure of the compound.

^{99}Tc NMR is a method that is worthy of special mention. Technetium is the fifth most sensitive nucleus for NMR work. The sensitivity per nucleus is less than that of hydrogen and fluorine but greater than that of phosphorus and particularly of carbon and other commonly studied nuclei. Its nuclear spin of 9/2 presents a potential problem owing to the possibility of quadrupolar broadening. Sharp NMR lines theoretically require highly symmetrical structures of the diamagnetic compounds. The pertechnetate ion (Tc(VII), d^0) can be detected with particular ease. The ^{99}Tc NMR signal of a dilute aqueous solution of ammonium pertechnetate can be seen with a good signal:noise ratio, with only a few pulses at concentrations so low that a typical survey meter will not detect the radioactivity of ^{99}Tc. A publication compiling a few NMR data was published by O'Connell *et al.*[4] Surprisingly, $Tc_2(CO)_{10}$ (Tc(0), d^7 with a metal–metal bond) gives also a sharp NMR spectrum. It is not yet clear whether the sharp line is fortuitious or has significance for other technetium organometallic complexes. When PF_3 is substituted for CO in $Tc_2(CO)_{10}$ to produce the monophosphine complex, the technetium signal broadens considerably, in spite of the fact that PF_3 is very similar to CO. More recently, a ^{99}Tc NMR investigation of complexes containing the moiety *fac*-$[Tc(CO)_3]^+$ with macrocyclic thioethers of various ring sizes has shown that this technique is becoming more common.**[5]**

The first phase of technetium organometallic chemistry concerns the hot-atom chemistry or recoil chemistry. A second phase deals with the early macroscopic chemistry, particularly the excellent, independent, pioneering work of Kaesz**[6]** and Fischer.**[7]** A third period concerns the work of more recent years, which were preceded by a number of years in which very little work on organometallic chemistry was published. The second and third phases are discussed together in the major part of this article.

2 HOT-ATOM CHEMISTRY

Technetium hot-atom chemistry can be considered almost as a by-product of other studies.**[8]** When a compound like $Mo(CO)_6$ or other organometallic compound is bombarded by thermal (low energy) neutrons, an (n, γ) nuclear reaction occurs on the ^{98}Mo isotope to produce the ^{99}Mo isotope (half-life of three days). The sum of the masses of the neutron and the ^{98}Mo atom exceeds the mass of the ^{99}Mo nuclide. The extra mass/energy is about 5 MeV and is rapidly lost. The bulk of this energy is carried off by γ-rays, but the ^{99}Mo still recoils with several hundred eV of energy. That energy is more than enough to break all the metal–carbonyl bonds in the hexacarbonyl. The bulk of such hot-atom studies have been designed to determine what happens to the molybdenum atom during the 98–99 transformation. A remarkable amount of the ^{99}Mo from such neutron bombardment ends up in the chemical form of an organometallic compound like the hexacarbonyl. The mechanism by which this process occurs is the subject of controversy.

Given a method of preparing ^{99}Mo organometallic compounds, the β decay transformation of ^{99}Mo to ^{99m}Tc could be studied. The β decay of ^{99}Mo to ^{99m}Tc yields a nuclide with much lower recoil energy than that formed in the molybdenum (n, γ) process. However, this decay produces a cascade of Auger electrons (*see Auger Spectroscopy*) which can cause bond disruption. These studies are difficult, because the technetium-99m product is produced at radiochemical tracer levels. Macroscopic quantities of products are not available for spectroscopic characterization.

It may be assumed that a Tc species that has undergone significant manipulations during various physical separations must be an 18-electron compound, since 17- or 19-electron species are not stable enough to survive such operations. Therefore ionic species such as $[Tc(CO)_6]^+$ or $[Tc(CO)_5]^-$ would be expected to form from the decay of $^{99}Mo(CO)_6$.

Two other examples of the preparation of organometallic compounds by a hot-atom route have been postulated. The β decay of the ^{99}Mo atoms in $Mo(CO)_6$ could yield the $\cdot Tc(CO)_5$ radical as an intermediate, which might be trapped as a stable compound using the $\cdot Mn(CO)_5$ radical, which could come from any of several manganese carbonyls. De Jong and Wiles**[9]** isolated a ^{99m}Tc material, which they assigned to a mixed manganese–technetium decacarbonyl. Another technetium compound is obtained during the ^{99}Mo decay in the dimer $[C_5H_5Mo(CO)_3]_2$. This compound could form a stable 18-electron species $C_5H_5Tc(CO)_3$ through the conversion of the dimer to a monomer, without breaking either carbonyl or cyclopentadienyl (*see Cyclopentadienyl*) bonds. The compound $C_5H_5Tc(CO)_3$ is known to be a stable species.

Many excellent and detailed radiochemical tracer experiments have been utilized to support these compound assignments. However, it should be emphasized that further confirmation by spectroscopic or other macroscopic means has not been possible, owing to the trace concentrations of these product species.

3 STARTING MATERIALS

The ultimate starting material for ^{99}Tc or ^{99m}Tc chemistry is always $NH_4[TcO_4]$. When the ^{99}Tc material is purchased, it must be purified by recrystallization from 30% hydrogen peroxide or from nitric acid (caution: $NH_4[TcO_4]$ in acid medium will produce some radioactive volatile compounds). All manipulations must be performed in a laboratory monitored for radioactive material according to the country's national regulations. For the ^{99m}Tc preparations, the ^{99}Mo–^{99m}Tc generator will be the source of the anion $[^{99m}TcO_4]^-$.

Several intermediate materials can be used for preparative work of Tc compounds in a lower oxidation state. The square-pyramidal complex $[TcOCl_4]^-$ has been commonly used as starting material for several potent $[Tc{=}O]^{3+}$ core radiopharmaceuticals. The oxo ligand is located in the apical position and these compounds exhibit relatively short Tc–O bond distances, indicating some partial triple bonding involving the dπ orbitals of Tc. Nitrido complexes containing the $Tc{\equiv}N$ core can be prepared by reduction of $[TcO_4]^-$ with hydrazine in the presence of dilute HCl. The strong π-accepting properties of the nitride ligand seems to promote the coordination of relatively soft ligands. Reaction of compounds like $TcCl_4$ with NaC_5H_5 in ether is a common synthetic method to synthesize cyclopentadienyl technetium complexes. Tc compounds with phosphine ligands are also interesting intermediates for preparing lower oxidation states compounds, especially those with phosphine and isonitrile ligands. The reaction of $[TcO_4]^-$ with phosphines in the presence of HCl will produce either $Tc^{IV}(PR_3)_2Cl_4$ or $Tc^{III}(PR_3)_3Cl_3$ depending on the conditions and the bulkiness of the phosphine. More recently, the ionic compounds $[Tc^{III}(PR_3)_4Cl_2]^+$ were reported with small phosphines, from the reaction of $[TcO_4]^-$ with the phosphine in methanol in the presence of a chloride salt. When using phosphine ligands, no other reducing agent is needed since phosphines are good reducing agents being oxidized to the phosphine oxide. The reactions of these phosphine complexes with another ligand like isonitrile will produce the mixed-ligand Tc complexes.**[10]**

The compound $Na[Tc_3(CO)_9(OMe)_4]$ prepared by the incomplete carbonylation of sodium pertechnetate in methanol shows promises as an important reagent for the future.**[11]** It has been used to prepare $LTc(CO)_3$, $Tc_2(CO)_{10}$, and various arene and cyclopentadienyl complexes (*see Arene Complexes* and *Cyclopentadienyl*). The reaction conditions for these syntheses are moderately mild.

More recently, the Tc(I) compound $[Tc(CO)_3(H_2O)_3]^+$ has become an important starting material for labeling organometallic pharmaceuticals. The compound can be prepared in water and at normal pressure. The use of the toxic gaseous CO was a problem, but a kit has recently been developed using solid nontoxic potassium boranocarbonate, which releases CO when hydrolyzed and which can reduce Tc(VII) to Tc(I).**[12]** Therefore this kit should increase drastically the use of the precursor $[Tc(CO)_3(H_2O)_3]^+$ for ^{99}Tc and ^{99m}Tc studies. The chemistry of this molecule will be discussed in more details in a later section.

4 BINARY CARBONYL COMPOUNDS

In organometallic chemistry, the most important π-accepting ligand (*see π-Acid Ligand*) is CO. The bond between the metal and CO is through the C atom. The nature of the linear terminal metal–CO bond is multiple. The σ bond is formed from the dative overlap of the filled CO σ orbital with an empty σ-type orbital on Tc. The back-donating (*see Back Bonding*) π bond is formed from the overlap of the filled dπ orbital of the metal with an empty π^* orbital on CO. This bonding mechanism is synergic (*see Synergic Bonding*) and the effects of σ-bond formation strengthen the π bonding and vice versa. Therefore the M–CO bond is quite strong. This type of π-accepting ligand is classified as a soft ligand and will interact with soft metal ions. Therefore in its compounds with technetium, the oxidation state of Tc is usually low (≤ 3).

The multiple nature of the M–CO bond increases the strength of the M–C bond and reduces the one of the C≡O bond, which can be observed in the vibrational spectrum of the metallic compound. The CO molecule has a stretching ν(C–O) frequency of 2143 cm^{-1}. When coordinated to a metal, the frequency is reduced to about 1900–2125 cm^{-1} for terminal CO groups, showing a reduction in the CO bond order. Moreover, when changes are made to increase the extent of back-bonding, the CO frequencies are shifted to even lower values. IR spectroscopy is also very useful to suggest the structure of metal carbonyl compounds. Bridging CO groups absorb between 1750 and 1850 cm^{-1}, while terminal groups absorb at higher frequencies (1850–2125 cm^{-1}).

For binary metal carbonyl compounds, the 18-electron rule is a very useful concept. Stable metal complexes will be formed when the metal has 18 electrons in its valence shell (metal valence electrons + 2 electrons from each CO ligand). Since Tc(0) has 7 valence electrons, the neutral monomeric species $Tc(CO)_x$ cannot be stable, but ions like $[Tc(CO)_6]^+$ or $[Tc(CO)_5]^-$ attain a total of 18 electrons. In the neutral molecule, it will dimerize to $Tc_2(CO)_{10}$ in order to obey the 18-electron rule. The formation of a Tc–Tc bond adds an electron on each Tc atom. This 18-electron rule is quite useful to predict the structures of the metal binary carbonyl compounds.

The initial synthesis of $Tc_2(CO)_{10}$ was quite difficult to perform and it became a significant barrier to future work. The high-pressure syntheses that were used for many years could not be performed in standard high-pressure equipment.**[13]** The synthetic situation has improved noticeably in the subsequent years. A preparation which is a refinement of the one reported earlier has been reported in 1991.**[14]** In this procedure, 0.5 g of $NH_4[TcO_4]$ is placed in a 450 mL autoclave with a small amount of THF as solvent and 2% sodium amalgam is added as reducing agent to produce $Na[TcO_4]$. Carbon monoxide at 70 atm at room temperature is introduced and the vessel is heated to 120 °C for 72 h. A 70% yield of $Tc_2(CO)_{10}$ was found. This procedure can be performed in standard readily accessible pressure equipment and is considerably less dangerous than the earlier reported work. In addition, the CO pressure can be provided directly by a tank of carbon monoxide. Another method published in 1991 involves also the conversion to sodium pertechnetate and then the transformation to $Tc_2(CO)_{10}$ by reaction with CO at 100 atm at 230 °C for 12 h in methanol. Four gram quantities have been prepared by this route.**[11]**

$$NH_4[TcO_4] \xrightarrow{N_2H_4} TcO_2 \xrightarrow{H_2O_2/NaOH} Na[TcO_4] \xrightarrow{CO} Tc_2(CO)_{10} \tag{2}$$

The decacarbonyl is moderately stable in air. It does not require special handling in glove boxes or Schlenk-tube apparatus. It must always be respected for its chemical toxicity, slight volatility, and mild radioactivity. The compound contains a metal–metal bond but no bridging carbonyl groups. The geometry around each Tc atom is octahedral with a Tc–Tc single bond distance is 3.036(6) Å. The four equatorial carbonyls on each metal atom are staggered relative to one another and are slightly bent back from the apical carbonyl. It has the approximately D_{4d} symmetry (Figure 1). The greater π-acceptor character of the axial CO ligands is shown by the shorter Tc–C distances (by 0.10 Å) than those of the equatorial ligands. The IR spectrum has been studied and the axial and equatorial CO stretching force constants have been evaluated

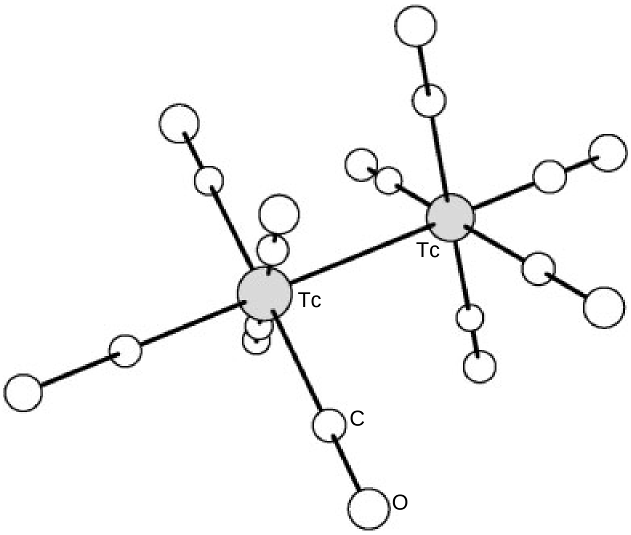

Figure 1 Structure of $Tc_2(CO)_{10}$. (Reproduced by permission of Springer-Verlag.[15])

at 16.316 and 16.642 mdyn Å^{-1} respectively, indicating a stronger equatorial CO bonds and therefore weaker Tc–C equatorial bonds. The ^{99}Tc NMR spectrum of $Tc_2(CO)_{10}$ have shown a single signal at −2777 ppm from $[TcO_4]^-$.

The mixed metal decacarbonyl complexes that have Mn–Tc and Tc–Re metal combinations have been prepared and the compounds have similar structures.

The most extensive substitution into $Tc_2(CO)_{10}$ has been with PF_3, and as many as 24 species have been clearly identified by gas chromatography/mass spectroscopy. Most of the $Tc_2(PF_3)_x(CO)_{10-x}$ species have had only tentative structural assignments.[16]

5 MIXED-LIGAND CARBONYL COMPOUNDS

There are numerous mixed-ligands Tc complexes where CO is present. A crystallographic structure data search of published structures containing the Tc–CO moiety produced 54 different mixed-ligands structures. These cannot be summarized here owing to the great variety of compounds. Only a few among the most simple molecules will be mentioned.

There are several examples of metal carbonyls containing a $Tc(CO)_5$ fragment.[15] The carbonyl halides $Tc(CO)_5X$ (X = Cl, Br, and I) may be prepared by the reaction of the halogen with $Tc_2(CO)_{10}$. The reaction with chlorine or bromine occurs readily at room temperature but the reaction with iodine is very slow. The IR spectra of these compounds have shown three ν(C–O) bands expected for C_{4v} symmetry, between 2153 and 1991 cm^{-1}. Several other technetium carbonyl halide species have been identified by mass spectroscopy (*see Mass Spectrometry*), which has been a primary tool in this gas phase chemistry.[17]

The structures of the halo-carbonyl compounds are usually oligomers. The dimers $\{Tc(CO)_4X\}_2$ where X = Cl, Br or I are formed from the reaction of the halogen with $Tc_2(CO)_{10}$ and the IR spectrum of the dimer has shown the absence of bridging CO vibrations and is consistent with a halo-bridged structure. The structure has been confirmed by crystallographic studies for the bromo compound and the iodo analogue $Tc(CO)_4(\mu\text{-}I)_2Tc(CO)_4$. The same authors have also published the structure of a tetramer $\{Tc(CO)_4Br\}_4$ consisting of a cube with four μ_3-Br bridges. An ionic dimer with three chloro bridges was reported for $NBu_4[Tc(CO)_3(\mu\text{-}Cl)_3Tc(CO)_3]$. A tetramer of formula $\{Tc(CO)_3\}_4(\mu\text{-}Cl)_4$ with a cubane-type structure was also reported. The same cubane structure was observed for the hydroxo analogue. When the halo ligand is replaced by hydride, a trimeric cluster with metal–metal bonds and hydrido bridges of formula $\{Tc(CO)_4\}_3(\mu\text{-}H)_3$ was characterized. Several other dimeric and polymeric complexes are also known.[18]

Several Tc compounds containing carbonyl, halo, and other ligands have been reported. Octahedral complexes of the type *trans*-$Tc(CO)_3Cl(PPh_3)_2$ and *trans*-$Tc(CO)Cl_3(PPh_3)_2$ are known. It is not possible to coordinate more than two PPh_3 ligands to Tc because of steric hindrance. Furthermore, they will always be located in trans position to each other. For less bulky phosphines, it is possible to bind three phosphines as in $Tc(CO)Cl_3(PPhMe_2)_3$ which is a seven-coordinate compound. Phosphite ligands are much less bulky and for example, the octahedral structure of *cis*-$Tc(CO)_2(PPh(OEt)_2)_4$ was reported.

Complexes of the type $Tc(CO)_4L$ have been prepared where L represents a series of anionic β-diketonate ligands (*see Diketones*). Several monomeric compounds can be prepared from dimers such as $[Tc(CO)_5(MeCN)]PF_6$, prepared from the reaction of $Tc_2(CO)_{10}$ with $NOPF_6$ and acetonitrile. The acetonitrile ligand is a good leaving group for the preparation of a variety of other mixed-ligand complexes that are cationic and water soluble. The compound $Na[Tc_3(CO)_9(OMe)_4]$ mentioned in the starting materials section has a cubane-type structure and it is a convenient precursor to carbonyl complexes in the $TcL(CO)_3$ family.

The reactions of the organometallic compound $[Tc(CO)_3X_3]^{2-}$ with three macrocyclic (*see Macrocycle*) thioethers were studied. A monomer $[Tc(CO)_3S_3]^+$ with a S_3 macrocyclic ring and dimers $[(CO)_3Tc(\mu\text{-}S_6)Tc(CO)_3]^{2+}$ with S_6 rings were characterized by X-ray diffraction methods. In the latters, the S_6 macrocyclic thioether forms a bridge between the two Tc atoms.[5] A series of dithiocarbamate and related complexes has been synthesized. These compounds include $Tc(CO)_4(S_2NEt_2)$, $Tc(CO)_2(PPh_3)_2(S_2NEt_2)$, $Tc(CO)_2(PPh_3)_2(S_2OEt)$ and $Tc(CO)_2(PPh_3)_2(S_2P(PMe)_2)$ and they have been characterized by IR and ^{1}H and ^{99}Tc NMR spectroscopies.

Tc in a low oxidation state can sometimes bind to very unusual ligands. Two examples of more complicated compounds are given below. These have been studied by crystallographic methods and have very interesting structures. The first one is a dimeric compound with a N_2 bridge. It can be formulated as $L(CO)_2Tc(\mu\text{-}N{\equiv}N)Tc(CO)_2L$ where L has the formula $BN_6C_{15}H_{22}$ and is a $N{\cap}N{\cap}N$ tridentate ligand. The second compound is an ionic carborane (*see Carborane*) compound $NEt_4[Tc(CO)_3(\eta^5\text{-}2,3\text{-}C_2B_9H_{11})]$ which was prepared from $[Tc(CO)_3Br_3]^{2-}$. The crystal structure of the compound is shown in Figure 2. Bifunctional carboranes have been used successfully as carriers of a variety of different metal radionuclides.

In the ion $[Tc(CO)_3(H_2O)_3]^+$, which has already been mentioned in the section on starting materials, the metal center is in the low oxidation state $+1$ (diamagnetic, d^6 configuration) and is quite inert to reduction or oxidation. The structure is octahedral and the aqua molecules should be replaced easily in solution by more strongly binding ligands. The development of a kit to prepare this compound should be extremely useful for the labeling of biomolecules. The use of sodium or potassium boranocarbonate $Na_2/K_2[H_3BCO_2]$ was a major breakthrough permitting broader application of organometallic Tc precursors to nuclear medicine. The reagent serves as a solid source of CO and reduces concomitantly Tc(VII) to Tc(I).

$$NH_4[TcO_4] \xrightarrow[H_2O]{Na_2/K_2\,[H_3BCO_2]} [Tc(CO)_3(H_2O)_3]^+ \tag{3}$$

The aqua complex can be easily prepared in 20 minutes at a temperature not higher than 100 °C. Subsequent substitution of the labile aqua ligands by a bifunctional group attached to a biomolecule enables the introduction of Tc–carbonyl complexes in life science in general and in nuclear medicine in particular. The molecule is remarkably stable in solution for long periods of time, a reflection of its low-spin d^6 electronic configuration. Although the compound is unreactive towards aliphatic amines and thioethers, it does react with the softer nitrogen atom of aromatic amines such as imidazole. As an example for the potential of the compound as an efficient label for derivatived biomolecules, Alberto *et al.* studied its reaction with the multifunctional ligand picolinamine-*N*,*N*-diacetic acid (PADA), which can be considered as a good model, since it provides three coordinating sites and one group for the covalent attachment to a biomolecule.**[20]**

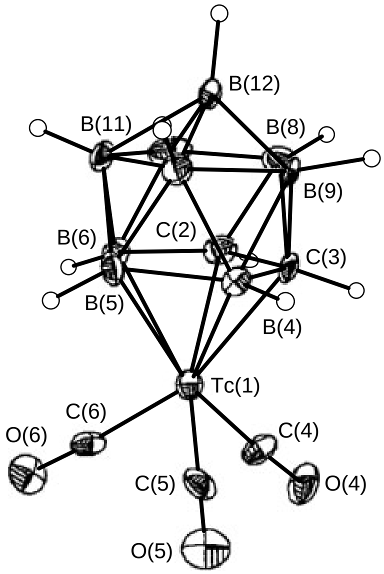

Figure 2 Structure of the anion $[Tc(CO)_3(\eta^5\text{-}2,3\text{-}C_2B_9H_{11})]^-$. (Reprinted with permission from Ref. 19. © 2002 American Chemical Society)

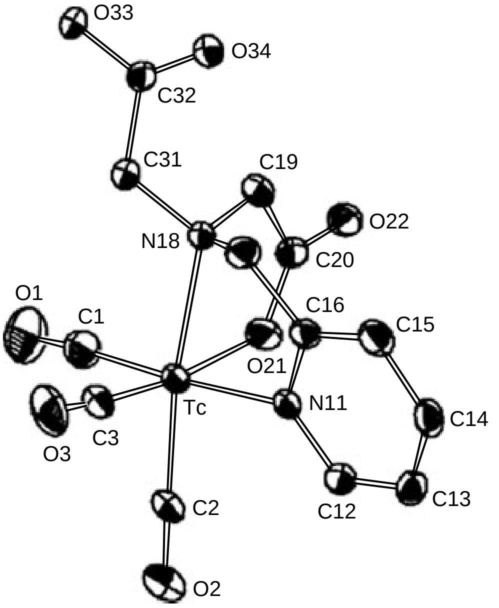

Figure 3 Structure of the compound $Tc(CO)_3$(PADA). (Reprinted with permission from Ref. 20. © 1998 American Chemical Society)

$$[^{99m}TcO_4]^- \longrightarrow [Tc(CO)_3(H_2O)_3]^+ \xrightarrow{PADA} Tc(CO)_3(PADA) \tag{4}$$

PADA :

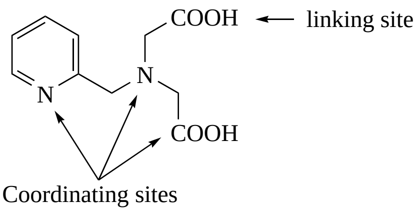

The structure of the neutral complex $Tc(CO)_3$(PADA) was determined and a drawing of the molecule is shown in Figure 3.

Although Tc(I) is a soft metal and amino and carboxylato ligands are rather expected to form stable compounds with harder metal centers, $Tc(CO)_3$(PADA) exhibits quite high stability. The second carboxylic group on the PADA ligand is accessible for covalent bonding to a biomolecule.

6 CYCLOPENTADIENYL COMPLEXES

Cyclopentadienyl (Cp) complexes (*see Cyclopentadienyl*) are known for almost all the metals of the periodic chart, including technetium. The compounds with transition metals usually possess covalent π Cp–M bonding. The nature of the metal–Cp bond is multiple. The σ-bond is formed from the overlap of an empty d orbital of Tc with one of the filled π bonding molecular orbital on Cp with good symmetry. Back-donation is usually also present from the filled d orbitals of Tc to one of the empty π molecular orbitals on Cp. These molecules are usually called sandwich compounds (*see Sandwich Compound*), when there are two Cp ligands bonded to the metal, or half-sandwich complexes (*see Half-sandwich Complexes*) when only one Cp ligand is present.

The earliest work with cyclopentadienyl was reported independently by Kaesz[6] and by Fischer.[7] They carried out reactions using $TcCl_4$ and sodium cyclopentadienyl in the presence of BH_4^- as a reducing agent. The species $Tc(Cp)_2H$ and $[Tc(Cp)_2H_2]^+$ have been prepared. These compounds are believed to have bent metallocene (*see Bent Metallocenes*) structures. The reaction of $TcCl_4$ and potassium cyclopentadienyl in THF gives the diamagnetic air-stable $Tc(Cp)_2Cl$, whose structure is shown in Figure 4.

Further reaction of the latter compound with KCp yields the red diamagnetic $Tc(\eta^5\text{-Cp})_2(\eta^1\text{-Cp})$, where one Cp ring is σ-bonded to Tc (Figure 5). Mass spectral evidence has been reported for a $Tc(Cp)_4$ compound, but it has not been characterized.

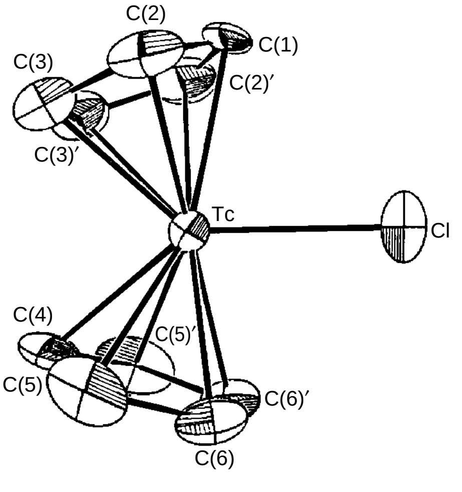

Figure 4 Structure of $Tc(Cp)_2Cl$. (Reprinted from Ref. 21. © 1990 Elsevier)

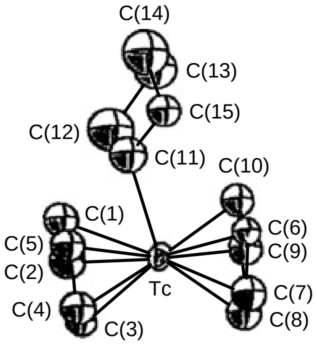

Figure 5 Structure of $Tc(\eta^5\text{-Cp})_2(\eta^1\text{-Cp})$. (Reprinted from Ref. 22. © 1991 Elsevier)

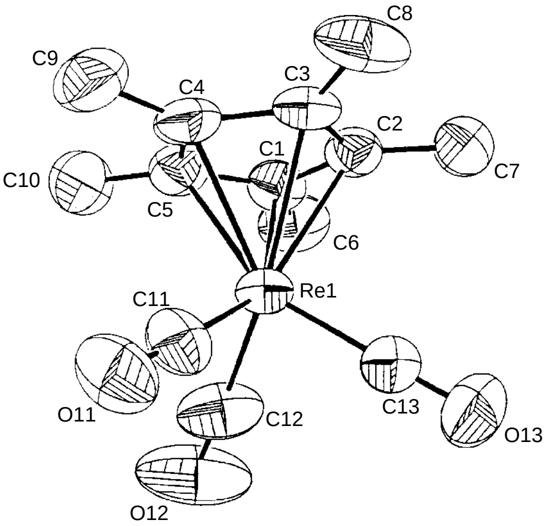

Figure 6 Structure of $Tc(CO)_3(\eta^5\text{-Cp}^*)$. (Reprinted from Ref. 23. © 1991 Elsevier)

The compound $Tc(\eta^5\text{-}C_5H_5)(CO)_3$ was prepared by the reaction of $Tc(CO)_5X$ with NaCp. Complexes with a number of cyclopentadienyl derivatives (Cp′) have been studied especially by the group of Ziegler. The crystal structures of several $Tc(CO)_3(Cp')$ compounds where $Cp' = C_5Me_5$ (Cp*), C_5Me_4Et, indenyl, and $Cp\text{–}COCH_2Ph$ were reported. All these compounds have the piano stool structure (*see Piano Stool Structure*) as shown in Figure 6.

Irradiation of $Tc(CO)_3(Cp^*)$ by a low pressure mercury lamp in dry cyclohexane in the absence of air produces two carbonyl-bridged dimers, $(Cp^*)Tc(\mu\text{-CO})_3Tc(Cp^*)$ which was characterized by crystallography and $(Cp^*)(CO)_2Tc(\mu\text{-CO})Tc(Cp^*)(CO)_2$ whose structure was suggested by spectroscopic comparison with the structurally characterized Re analogue. These two compounds can be separated by column chromatography. The IR spectrum of the former compound showed only one carbonyl stretching at 1785 cm^{-1} and its structure is shown in Figure 7.

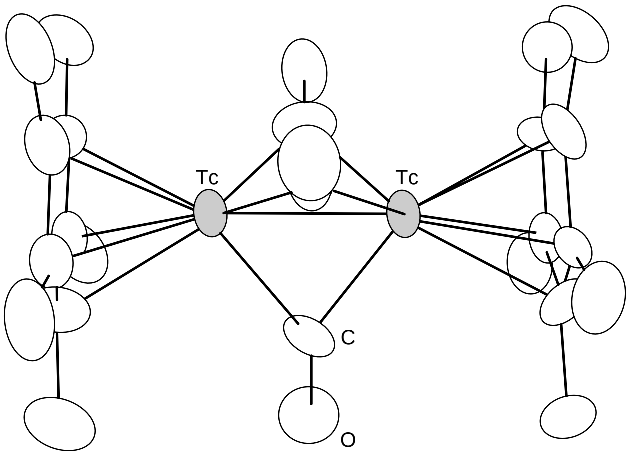

Figure 7 Structure of $(Cp^*)Tc(\mu\text{-}CO)_3Tc(Cp^*)$. (Reprinted from Ref. 24. © 1991 Elsevier)

The short Tc–Tc bond length 2.413(3) Å corresponds to a bond order of three. In the second molecule, a single Tc–Tc bond order has been proposed to satisfy the 18-electron rule (Cp is a 6 electron donor). The latter compound has shown several ν(C–O) bands between 1738 and 2012 cm^{-1}.

The oxidation of $Re^{I}(CO)_3(Cp^*)$ by H_2O_2 produces the trioxo compound $Re^{VII}O_3(Cp^*)$, but with $Tc^{I}(CO)_3(Cp^*)$, the product was reported as having a polymeric structure $\{Tc(\mu\text{-}O)_3Tc(Cp^*)\}_n$, with parallel Cp* planes and a very short Tc–Tc bond, 1.867(4) Å. But the crystal-structure determination has been questioned and it has been suggested that the product was in fact $Tc^{VII}O_3(Cp^*)$, which is probably more reasonable.

Attempts were made to use cyclopentadienyl technetium tricarbonyl derivatives for labeling estrogen receptor binding ligands as well as proteins and peptides.[25]

7 ISONITRILE COMPLEXES

A very important major class of organometallic compounds that will be discussed here are those containing isonitrile (or isocyanide) ligands (*see* ***Cyanide Complexes of the Transition Metals***). Isonitriles are bonded to the metal through the carbon atom, allowing them to be classified as organometallic compounds. They are electronically similar to carbon monoxide as a ligand. The isonitrile molecule donates σ electron density to the metal and has empty π-antibonding orbitals to accept back-donating electrons from the metal. These ligands will bind to soft metals like Tc in a low oxidation state.

Davison and coworkers[26] have extensively studied technetium compounds that have potential application in nuclear medicine. In this process, significant advances in the isonitrile chemistry of technetium have been achieved. The type of complex of greatest current interest has the basic formula $[Tc(CNR)_6]^+$. Monopositive cations of Tc in a low oxidation state are strongly absorbed by the myocardiac muscle, and technetium-99m complexes can therefore be used for diagnostic purposes in nuclear medicine. Group 1 cations have been known for a long time to accumulate in normal heart tissue. Later thallium(I) was thought to function as a K^+ analogue and ^{201}Tl has been used for many years as a heart agent in nuclear medicine. Later, it was suggested that +1 charged Tc complexes could mimic the Tl^+ compounds in a more effective way, since ^{201}Tl is a poor radionuclide relative to ^{99m}Tc. Studies on the changes in the R group on the isonitrile compound $[Tc(CNR)_6]^+$ have shown considerable property variations in the complexes and suggested the possibility to tailor a compound to meet specific needs. Extensive medical tests have been performed with these compounds. Several patents have been issued for the use of these complexes as imaging agents.

The most important compound is *cardiolite* which is a charged +1 cationic complex containing six isonitrile ligands, $[Tc(CNCH_2C(CH_3)_2OCH_3)_6]^+$ and has been used for myocardial perfusion imaging for several years now. More recently, it has been approved for breast cancer imaging. The synthesis of this complex is accomplished by the reaction of pertechnetate ion with an excess of the isonitrile ligand in the presence of a reducing agent $Na_2S_2O_4$. The complex is octahedral and is stable under aqueous aerobic conditions in the pH range of 5–7. A kit for the ^{99m}Tc preparation of the compound is commercially available for routine use in hospitals. *Cardiolite* is the first example of an organometallic complex routinely used in nuclear medicine.

Related Tc(I) octahedral complexes have been prepared containing mixed ligands. These include a few +1 ionic isonitrile-phosphine compounds such as $[Tc(PPhMe_2)(CN\mathit{t}Bu)_5]^+$ and *trans*-$[Tc(PPhMe_2)_2(CN\mathit{t}Bu)_4]^+$ which were prepared from $Tc(PPhMe_2)_{2or3}Cl^{10}_{4or3}$ and *trans*-$[Tc(dppe)_2(CNR)_2]^+$ synthesized from $Tc(N_2)H(dppe)_2$. These complexes were studied by crystallography. Other complexes of this type include $[Tc(CO)_3(CN\mathit{t}Bu)_3]^+$ and $[Tc(bpy)(CN\mathit{t}Bu)_4]^+$. In these structures, the segment Tc–C≡N–C is linear and the C≡N bonds are ~1.16 Å.

A few neutral mixed-ligands compounds were also reported. These are *cis* and *trans*-$Tc(CO)_3Cl(CN\mathit{t}Bu)_2$ and $Tc(NO)Br_2(CN\mathit{t}Bu)_3$. Two five-coordinate Tc(III) compounds Tc(*CNiPr*)(L) where L is a tetradentate ligand containing some P and S atoms have been studied. More recently, three five-coordinate neutral compounds with the formula $Tc(S_3NC_6H_{12})(CNR)$ where R=cyclohexyl, benzyl or CH_2COOEt were also reported.

8 CYANIDE COMPOUNDS

Technetium cyanide chemistry is more limited. A few Tc cyanide complexes (*see Cyanides*; ***Cyanide Complexes***

of the Transition Metals) are known, especially in the oxidations states of I, III, and V. The reduction of $[TcO_4]^-$ with KCN produces the Tc(I) compound $K_5[Tc(CN)_6]$, which is probably isostructural with the Mn and Re analogues. The cyanide ligand is a relatively strong π-acceptor. The only Tc(III) cyano compound is the seven-coordinate $K_4[Tc(CN)_7]\cdot 2H_2O$ which was prepared from the reaction of $(NH_4)_2Tc^{IV}I_6$ with KCN. IR and Raman spectroscopy suggest a pentagonal bipyramidal structure with C_{5h} symmetry. In aqueous solution, it decomposes in air to form the greenish Tc(V) compound $[TcO(CN)_5]^{2-}$. The IR spectrum of the latter compound seems to indicate C_{4v} symmetry. The lilac compound *trans*-$[TcO(OMe)(CN)_4]^{2-}$ was isolated from the reaction of $NBu_4[TcOCl_4]$ with CN^- in methanol. The compound NMe_4*trans*-$[TcO(H_2O)(CN)_4]\cdot 2H_2O$ was also isolated and its reaction with the thiocyanate ion produced *trans*-$[Tc^VO(NCS)(CN)_4]^{2-}$ which was studied by crystallographic methods. The thiocyanate ligand is coordinated through the N atom and the Tc=O bond is short (1.612(8) Å). Another interesting Tc(V) compound which was determined by X-ray diffraction methods is $(AsPh_4)_2$*trans*-$[TcN(H_2O)(CN)_4].5H_2O$. Tc-nitrido complexes have some importance in the radiopharmaceutical field.

9 ARENE COMPLEXES

No Tc-arene complexes (*see Arene Complexes*) seem to have been characterized by X-ray diffraction methods, but a few compounds have been reported. The reagent mentioned earlier, $Na[Tc_3(CO)_9(OMe)_4]$, can yield not only the decacarbonyl but also the $(C_5Me_5)Tc(CO)_3$ complex, as well as an arene complex, $[(C_6H_6)Tc(CO)_3]Cl$.

E. O. Fischer was the first to prepare arene complexes of technetium.**[27]** Arene ligands in these compound are typically six-electron donors. The nature of the Tc-arene bond is probably very similar to the one of the Tc–Cp bond. The $[Tc(arene)_2]^+$ complexes (arene = benzene or hexamethylbenzene) are prepared by the reaction of $TcCl_4$ with the appropriate arene in the presence of $AlCl_3/Al$. In a typical reaction, $TcCl_4$, $AlCl_3$, and aluminum were heated with benzene in a sealed tube to 135 °C for two days. The product is precipitated as a salt using the hexafluorophosphate ion. A variety of other 18-electron compounds can be prepared from this material, particularly through chemical reduction.

Recently, interest in the arene complexes has increased owing to their potential use as ^{99m}Tc imaging agents. Monopositive complexes are of particular interest because they may be suitable for myocardial uptake, and thus for use in heart imaging. Since one must use aqueous $[TcO_4]^-$ ion obtained from the ^{99}Mo generator as the source of ^{99m}Tc, the synthetic chemistry must be rather different from that used by Fischer. Among other things, anhydrous $AlCl_3$ would not be compatible with aqueous solutions. In addition, for such compounds to be of general use in nuclear medicine, it would be highly desirable to develop simplified synthetic procedures. An alternate preparation is cleverly initiated using ultrasound. Both ^{99}Tc and ^{99m}Tc complexes can be prepared and the identity of the two materials is verified by HPLC techniques. A series of arene complexes has been prepared, primarily containing various alkyl-substituted arenes, such as toluene or xylene.

10 MISCELLANEOUS ORGANOMETALLIC COMPOUNDS

Ziegler and coworkers**[28]** have synthesized a butadiene complex of technetium by the photolysis of $Tc_2(CO)_{10}$ in the presence of butadiene at −20 °C in pentane. The product $\{Tc(CO)_4\}_2(\mu\text{-}\eta^4\text{-}C_4H_6)$ has a butadiene ligand bridging two technetium atoms. A few crystal structures of dimers with metal–metal bonds and containing phenylimido ligands were characterized with the ligand – CH_3 and a similar monomer Tc(phenylimido)$_3$(CH_3) was reported. An interesting thiocarbonyl compound *trans*-$Tc(CS)(dppe)_2Cl$ was recently characterized by crystallography. In 1994, two unusual organometallic compounds of formula *trans*-$Tc(dppe)_2Cl(C{=}CH\text{–}Ph)$ and *trans*-$[Tc(dppe)_2Cl(C\text{–}CH_2\text{–}t\text{Bu})]^+$ were reported.

11 RELATED ARTICLES

Boron–Nitrogen Compounds; Rhenium: Organometallic Chemistry; Technetium & Rhenium: Inorganic & Coordination Chemistry.

12 REFERENCES

1. A. Davison, C. Orvig, H. S. Trop, M. Sohn, B. V. DePamphiles, and A. G. Jones, *Inorg. Chem.*, 1980, **19**, 1988.
2. ‘Gmelin Handbook of Inorganic Chemistry’, System. No. 69, Supplement Vol. 1, Springer-Verlag, Berlin, 1982.
3. R. Schibli and P. A. Schubiger, *Eur. J. Nucl. Med.*, 2002, **29**, 1529.
4. L. A. O’Connell, R. M. Pearlstein, A. Davison, J. R. Thornback, J. F. Kronauge, and A. G. Jones, *Inorg. Chim. Acta*, 1989, **161**, 39.
5. R. Schibli, R. Alberto, U. Abram, S. Abram, A. Egli, P. A. Schubiger, and T. A. Kaden, *Inorg. Chem.*, 1998, **37**, 3507.
6. M. M. Boog and H. D. Kaesz, in ‘Comprehensive Organometallic Chemistry’, eds. G. Wilkinson, F. G. A. Stone, and E. W. Abel, Pergamon, Oxford, 1982, Chap. 30.

7. C. Palm, E. O. Fischer, and F. Baumgartner, *Tetrahedron Lett.*, 1962, 253; E. O. Fischer and M. W. Schmidt, *Angew. Chem., Int. Ed. Engl.*, 1967, **6**, 93.
8. D. R. Wiles and F. Baumgartner, in 'Chemical Effects of Nuclear Transformation in Inorganic Systems', eds. G. Harbottle and A. G. Maddock, North-Holland, Amsterdam, NY, 1979.
9. I. G. de Jong and D. R. Wiles, *Inorg. Chem.*, 1973, **12**, 2519.
10. F. D. Rochon, R. Melanson, and P. C. Kong, *Inorg. Chim. Acta*, 1996, **245**, 251.
11. W. A. Herrmann, R. Alberto, J. C. Bryan, and A. P. Sattelberger, *Chem. Ber.*, 1991, **124**, 1107.
12. R. Alberto, K. Ortner, N. Wheatley, R. Schibli, and A. P. Schubiger, *J. Am. Chem. Soc.*, 2001, **123**, 3135.
13. R. J. Clark, 'Encyclopedia of Inorganic Chemistry', 1st edn., Wiley, 1994, p. 4099.
14. H. H. K. Castro, A. Meetsma, J. H. Teuben, W. Vaalburg, K. Pavel, and G. Ensing, *J. Organomet. Chem.*, 1991, **410**, 63.
15. 'Gmelin Handbook of Inorganic Chemistry', System No. 69, Supplement Vol. 2, Springer-Verlag, Berlin, 1983.
16. C. C. Grimm and R. J. Clark, *Organometallics*, 1990, **9**, 1123.
17. V. M. Adamov, A. E. Miroslavov, G. V. Sidorenko, and D. N. Suglobov, *Radiokhimiya*, 1991, **33**, 38, and related references.
18. J. Baldas, *Adv. Inorg. Chem.*, 1994, **41**, 1.
19. J. F. Valent, P. Morel, P. Schaffer, and J. H. Kaldis, *Inorg. Chem.*, 2002, **41**, 628.
20. R. Alberto, R. Schibli, A. Egli, and A. P. Schubiger, *J. Am. Chem. Soc.*, 1998, **120**, 7987.
21. C. Apostolidis, B. Kanellakopulos, R. Maier, J. Rebizant, and M. L. Ziegler, *J. Organomet. Chem.*, 1990, **396**, 315.
22. C. Apostolidis, B. Kanellakopulos, R. Maier, J. Rebizant, and M. L. Ziegler, *J. Organomet. Chem.*, 1991, **411**, 171.
23. K. Raptis, E. Domberger, B. Kanellakopulos, B. Nuber, and M. L. Ziegler, *J. Organomet. Chem.*, 1991, **408**, 61.
24. K. Raptis, B. Kanellakopulos, B. Nuber, and M. L. Ziegler, *J. Organomet. Chem.*, 1991, **405**, 323.
25. T. R. Spradau and J. A. Katzenellenbogen, *Bioconjugate Chem.*, 1998, **9**, 765.
26. J. F. Kronauge, A. Davison, A. M. Roseberry, C. E. Costello, S. Maleknia, and A. G. Jones, *Inorg. Chem.*, 1991, **30**, 4265, and numerous earlier papers.
27. E. O. Fischer and M. W. Manfred, *Chem. Ber.*, 1969, **102**, 1954.
28. B. Kanellakopulos, B. Nuber, K. Raplis, and M. L. Ziegler, *Z. Naturforsch., Teil B*, 1991, **46**, 55.

Tellurium: Inorganic Chemistry

Risto S. Laitinen & Raija Oilunkaniemi
University of Oulu, Oulu, Finland

Based in part on the article Tellurium: Inorganic Chemistry by William R. McWhinnie which appeared in the Encyclopedia of Inorganic Chemistry, First Edition.

1 Introduction 1
2 Elemental Tellurium and Related Mixed Chalcogen Systems 1
3 Tellurium-containing Ions 5
4 Tellurium–Halogen Compounds 9
5 Tellurium–Oxygen Compounds 13
6 Tellurium–Nitrogen Compounds 16
7 Outlook 19
8 Related Articles 20
9 References 20

1 INTRODUCTION

Tellurium was discovered in 1782 by Franz Josef Müller von Reichenstein from Transylvanian gold ore known as aurum album. Initially he believed he had isolated antimony but realized shortly that it was a previously unknown element. Since Müller von Reichenstein published his findings in an obscure journal,[1] the work was forgotten until 1798 when Martin Heinrich Klaproth, a German chemist, confirmed the discovery of the new metal and gave it the name tellurium, which derives from Latin tellus = Earth.[2]

The abundance of tellurium in earth's crust is ca. 0.01 ppm. Tellurium is found free in nature and over 100 tellurium-containing minerals are known (for some examples, see Table 1), but because of their low abundance, it is economically not viable to recover the element from its mineral ores. Since, like selenides, tellurides generally occur together with the sulfide ores, the element is commercially obtained from the anode sludge produced during the refining of copper from $CuSeF_2$.

The estimation of the world production of tellurium is difficult, since the two major producers do not publish production figures. The worldwide consumption in 2002 is estimated as 220 tonnes. It has slightly reduced over the recent years. Metallurgical uses dominate tellurium demand. In 2002, about 60% of tellurium was used as an alloying element to improve the properties of copper, iron, lead, and steel. Other uses include catalysts and chemicals (25%), photoreceptors and thermoelectric devices (8%), and miscellaneous minor uses (7%).[3]

Inorganic compounds of tellurium are considered moderately toxic and should be handled with care. The ingestion of even trace amounts of inorganic tellurium compounds results in the development of 'tellurium breath', caused by the garlic-like odor of dimethyltelluride, which is formed in vivo by slow biochemical methylation. The fatal doses of Na_2TeO_3 are estimated to be 2.25–2.50 mg Te kg^{-1}, and that of $Na_2Te_2O_4$ to be 20.0–30.0 mg Te kg^{-1}. The LD_{50} for tellurium aerosols is of the order of 10 mg m^{-3}. Tellurium is not considered to have carsinogenic, teratogenic, or mutagenic effects in humans.

2 ELEMENTAL TELLURIUM AND RELATED MIXED CHALCOGEN SYSTEMS

2.1 General

Crystalline tellurium is silvery-white and shows a metallic lustre when pure. It is rather brittle and is easily pulverized into dark grey powder. The Pauling electronegativity of tellurium is 2.1 and its absolute electronegativity is 5.49 eV. Some other useful physical properties are listed in Table 2.

Tellurium is a p-type semiconductor. The element shows anisotropy in electrical conductivity that is essentially independent of temperature in the range 78–200 K. It has been reported that single crystals grown in vapor show more strongly metallic conductivity parallel to the Te_n chains. The conductivity of tellurium is much less affected by illumination than that of selenium.

There are eight naturally occurring isotopes of tellurium (see Table 3). Of those, ^{123}Te and ^{125}Te have nuclear spin of $1/2$ and are convenient nuclei for NMR spectroscopy. ^{125}Te is also a suitable isotope for Mössbauer spectroscopy.

2.2 Allotropy of Tellurium

Hexagonal tellurium is the thermodynamically stable allotrope of the element. It is isostructural with hexagonal α-selenium[4] and is composed of a network of helical chains (see Figure 1). The Te–Te bond length is 2.831 Å and the closest interchain distance is 3.494 Å.[5] It can be seen from Figure 1 that the interchain contacts expand the coordination around each tellurium atom into a polyhedron. This kind of secondary bonding interactions has originally been proposed by Allcock[6] and discussed on several occasions in connection of a wide variety of tellurium compound (for some examples, see Ref. 7 and references therein). It is interesting to note that the corresponding interchain distances in hexagonal α-selenium are 3.463 Å[4] indicating that the secondary bonding interactions in selenium are weaker than in tellurium (the van der Waals' radii of selenium and tellurium are 1.80 and 2.20 Å, respectively).

The *TP* phase diagram of tellurium is complex[8] and indicates the presence of several high-pressure modifications. Five distinct phases have been isolated and structurally

Table 1 Tellurium-containing minerals

Element	tellurium	Te
Noble metal tellurides	stuzite	Ag_4Te
	empressite	AgTe
	hessite	Ag_2Te
	calaverite	$(Ag,Au)_2Te$
	petzite	Ag_3AuTe_2
	sylvanite	$(Ag,Au)_2Te_4$
	nigglite	$PtTe_3$
	krennerite	$AuTe_2$
Bismuth-containing tellurides	tetradymite	$Bi_2(Te,S)_3$
	wehrite	Bi_2Te_2
	tellurobismuthite	Bi_2Te_3
Other metal tellurides	weissite	Cu_5Te_3
	altaite	PbTe
	coloradoite	HgTe
	nagyagite	$Pb_5Au(Te,Sb)_4S_{5-8}$
Oxides	tellurite	TeO_2
	emmonsite	$TeO_2{\cdot}Fe_2O_3$
	magnolite	Hg_2TeO_4
	ferrotellurite	$FeTeO_4$

Table 2 Physical properties of elemental tellurium

Relative molar mass	127.60
Density ($kg\,m^{-3}$)	6240
Melting point (°C)	449.6
Boiling point (°C)	989.9
ΔH_{fus} ($kJ\,mol^{-1}$)	13.5
ΔH_{vap} ($kJ\,mol^{-1}$)	50.63
Specific heat ($J\,g^{-1}\,K^{-1}$)	0.20
Thermal conductivity ($W\,cm^{-1}\,K^{-1}$)	0.0235
Atomic radii (Å)	
r_{cov}	1.37
$r(Te^{6+})$	0.56
$r(Te^{4+})$	0.97
$r(Te^{2-})$	2.21
r_{VDW}	2.20
Ionization energies ($kJ\,mol^{-1}$)	
I_1	869.2
I_2	1795
I_3	2698
Electron affinities ($kJ\,mol^{-1}$)	
E_1	190.2

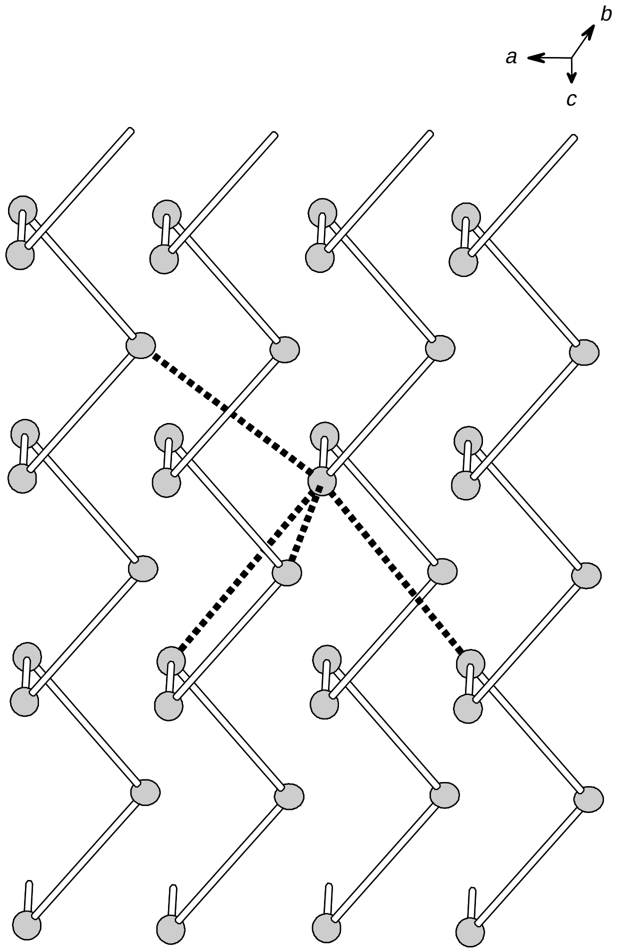

Figure 1 The crystal structure of hexagonal α-tellurium[5]

characterized.[9–13] The crystal structures are shown in Figure 2. It can be seen that as the pressure increases, the packing becomes more efficient and approaches the bcc structure. There is also a wide variety of studies concerning the superconductivity of high-pressure forms of tellurium.[14] The transition temperature seems to increase as a function of pressure and is in the range of 2.5–4.3 K up to 150 kbar and is ca. 6.5 K in the range 150–180 K.

Table 3 Naturally occurring isotopes of tellurium

Isotope	Atomic mass	Natural abundance	Half-life (y)	Nuclear spin	Nuclear magnetic moment	Receptivity in NMR ($^{13}C = 1$)	Magnetogyric ratio ($rad\,T^{-1}s^{-1}$)
^{120}Te	119.904048	0.09	stable	0			
^{122}Te	121.903050	2.57	stable	0			
^{123}Te	122.904271	0.89	$1.3{\cdot}10^{13}$	1/2	−0.73679	0.89	$-7.0006{\cdot}10^{7}$
^{124}Te	123.902818	4.76	stable	0			
^{125}Te	124.904428	7.10	stable	1/2	−0.88828	12.5	$-8.4398{\cdot}10^{7}$
^{126}Te	125.903309	18.89	stable	0			
^{128}Te	127.904463	31.73	stable	0			
^{130}Te	129.906229	33.97	$2.5{\cdot}10^{21}$	0			

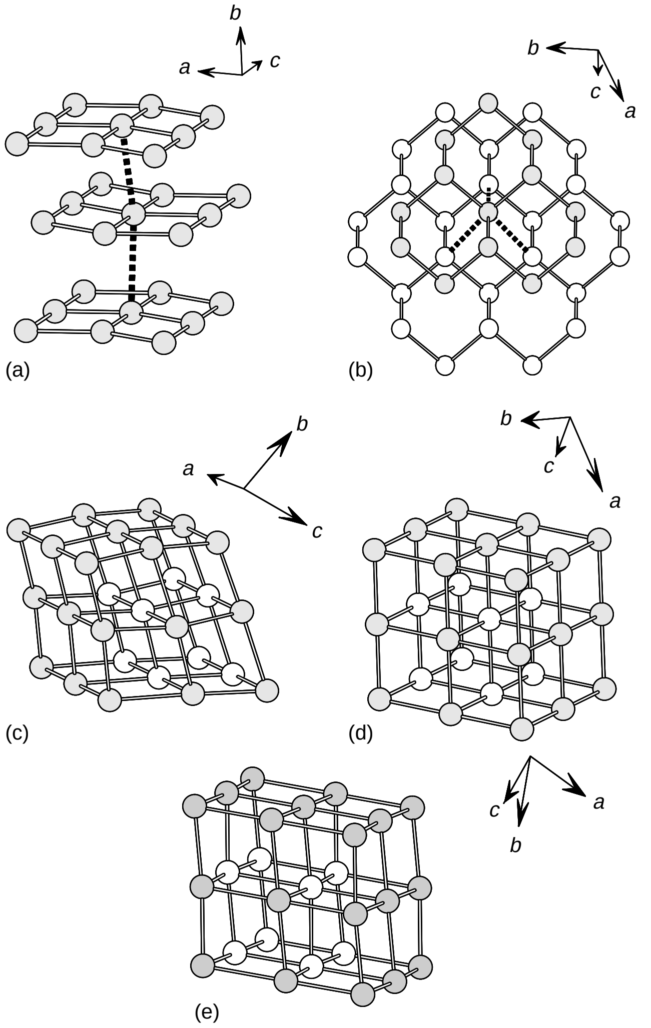

Figure 2 The high-pressure modifications of tellurium. (a) 40–70 kbar.[9] (b) 15–50 kbar.[10] (c) 45 kbar.[11] (d) > 70 kbar.[12] (e) 70–270 kbar[13]

Whereas sulfur and selenium exhibit a wide variety of cyclic molecular forms, the evidence of the existence of homocyclic tellurium rings is much hazier.[15] The existence of the Te_8 ring molecule in zeolites has been suggested on the basis of conductivity measurements and Raman spectroscopy.[16,17] The reaction of $[Ti(C_5H_5)_2(\mu\text{-}Te_2)_2Ti(C_5H_5)_2]$ and Te_2Cl_2 could also be expected to afford Te_8. Indeed, a single resonance at 869 ppm is observed in the ^{125}Te NMR spectrum of the reaction mixture.[18] This resonance is in the region that could be expected for Te_8 (c.f. 611.5 ppm for Se_8.[19]). The most direct evidence for the formation of the Te_8 ring comes from reaction of Cs_2CO_3 and As_2Te_3 in MeOH at 195 °C under an argon atmosphere.[20] The product has the composition Cs_3Te_{22} and contains crown-shaped puckered Te_8 rings between the $[Te_4Te_{4/2}]_{2\infty}{}^{3-}$ layer anions (see Figure 3). The Te–Te distances in the ring are 2.787–2.818 Å, the bond angles 99.32–101.12°, and the torsional angles 106.53–106.95°. Cs_4Te_{28} also contains a Te_8 ring in a related layered two-dimensional polytelluride lattice (see Figure 3).[21]

2.3 Tellurium-containing Chalcogen Chains and Rings

Tellurium is chemically similar to selenium and sulfur and though its allotropy is simpler than that of selenium and sulfur, it can form a number of acyclic and cyclic heteronuclear mixed chalcogen species. In the liquid state, tellurium and selenium can form miscible mixtures. The research activity has been boosted by the observation that mixed selenium–tellurium system shows enhanced conducting and photoconducting properties compared to those of selenium.[22] The indexing of X-ray powder diagrams in terms of a hexagonal unit cell indicates an almost linear variation in the lattice constants as a function of the elemental composition.[23] These results can be interpreted by the statistical distribution of tellurium and selenium atoms in the helical chain that is shown in Figure 1.

The formation of eight-membered tellurium sulfide rings in the molten mixtures has been deduced by mass spectrometry,[24] Mössbauer spectrometry,[25] and ^{125}Te NMR spectrometry.[26] The crystal structure of the phase prepared from H_2S and $TeCl_4$ was found to be disordered and was deduced to contain a mixture of the eight-membered crown-shaped ring molecules S_8, TeS_7, and Te_2S_6.[27] A similar eight-membered ring is also found in TeS_7X_2 (X = Cl, Br) with the two halogen atoms bound to tellurium.[28] Nagata *et al.*[29,30] have reported the structures of seven- and eight-membered selenium-rich selenium telluride heterocycles that have conformations similar to the analogous sulfur, selenium, and selenium sulfide ring molecules.[15]

Eight-membered $Te_nSe_mS_{8-(n+m)}$ rings have been detected in the ternary molten mixture containing 1.5 mol-% of both tellurium and selenium and 97 mol-% of sulfur.[31] The ^{125}Te NMR spectrum has been recorded at 145 °C for the melt containing selenium enriched in the ^{77}Se isotope and tellurium enriched in the ^{125}Te isotope (in both cases the enrichment is 92%) and is shown in Figure 4.

Tellurium-containing chalcogen rings are also formed by following the preparative routes known for other chalcogen rings (see Ref. 15 and references therein). The most important processes have been summarized below.

$$\left\{\begin{array}{c} [Ti(MeC_5H_4)_2(\mu\text{-}Te_2)_2(Ti(MeC_5H_4)_2] \\ (\boldsymbol{A}) \\ [Ti(MeC_5H_4)_2(\mu\text{-}Te_xS_{2-x})_2Ti(MeC_5H_4)_2] \\ (\boldsymbol{B}) \\ [Ti(MeC_5H_4)_2(\mu\text{-}Te_xSe_{2-x})_2Ti(MeC_5H_4)_2] \\ (\boldsymbol{C}) \end{array}\right\} + \left\{\begin{array}{c} 2S_2Cl_2 \\ 2S_2Cl_2/Se_2Cl_2 \end{array}\right\}$$

$$\longrightarrow \left\{\begin{array}{c} Te_xS_{8-x} \\ Te_xSe_yS_{8-(x+y)} \end{array}\right\} + 2[Ti(MeC_5H_4)_2Cl_2]$$

$$\underset{(\boldsymbol{D})}{(Me_3Si)_2Te} + ClSeS_5SeCl \longrightarrow 1,2,8\text{-}TeSe_2S_5 + 2Me_3SiCl$$

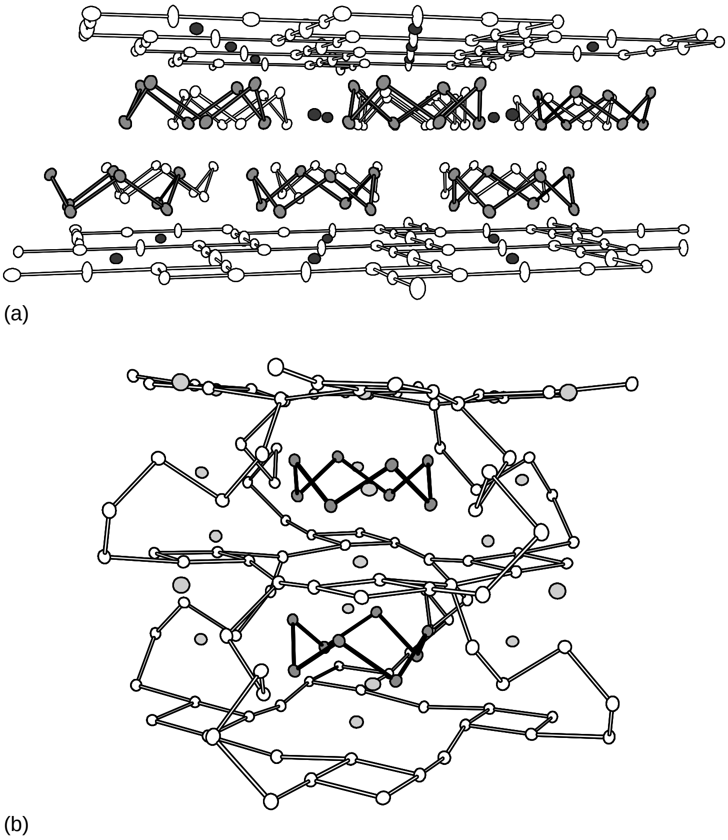

Figure 3 The Te_8 ring molecule in (a) Cs_3Te_{22} lattice[20] and (b) Cs_4Te_{28}[21]

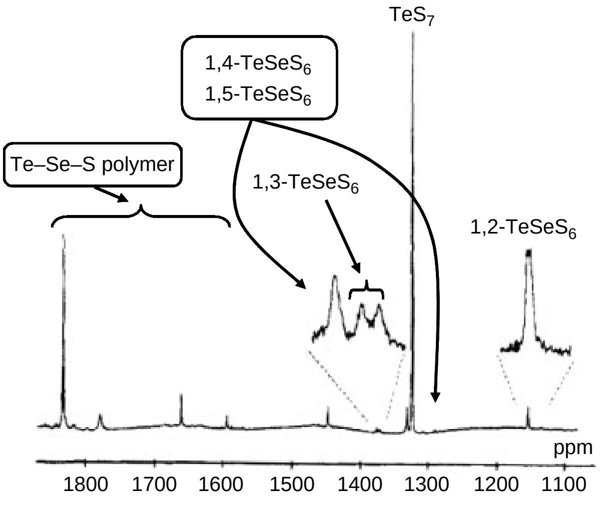

Figure 4 ^{125}Te NMR spectrum of the ternary sulfur–selenium–tellurium melt containing 1.5 mol% of both ^{77}Se-enriched selenium and ^{125}Te-enriched tellurium (enrichment 92%). The spectral assignments and the identification of the molecular species were made on the basis of combined information from the natural abundance and from the ^{77}Se- and ^{125}Te-enriched samples taking the known trends in the ^{77}Se and ^{125}Te chemical shifts into account. (Reprinted with permission from Ref. 26. © 1993 American Chemical Society)

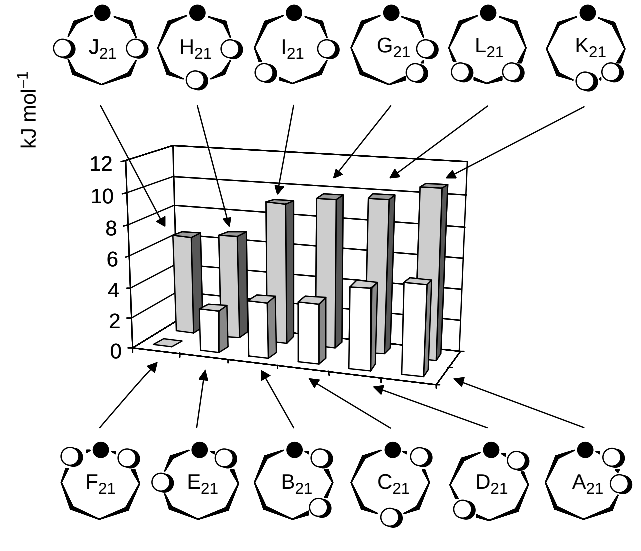

Figure 5 The relative stabilites of the isomers of $TeSe_2S_5$ calculated at MP2/3-21G*//HF/3-21G* level of theory. (Ref. 31. Reproduced by permission of Taylor & Francis (www.tandf.co.uk/journals))

An ab initio MO study of eight-membered sulfur-rich tellurium selenium sulfide rings has shown that the most stable species contain Se–Te bonds.[31] This is exemplified by the relative stabilities of the different isomers of $TeSe_2S_6$ that are shown in Figure 5. 1,2,8-$TeSe_2S_6$ is the most stable of the isomers. The formation of this species was observed in the reaction of $(Me_3Si)_2Te$ with $ClSeS_5SeCl$.[31]

3 TELLURIUM-CONTAINING IONS

3.1 General

Telluride anions have been known for a hundred years. Presently about 200 binary tellurides have been synthesized and there are ca. 50 species that have been structurally characterized. Their synthetic and structural chemistry as well as their ligand properties and applications have recently been reviewed several times.[32–39]

The propensity of tellurium to form intermolecular interactions distinguishes its chemical properties from those of sulfur and selenium for which such secondary bonding is virtually nonexistent (see Ref. 38 and references therein). By contrast to polysulfides and polyselenides, polytelluride anions can exhibit charges that deviate from -2.

The usual preparation of the materials involves direct high-temperature combination of the elements, solution reactions involving elemental tellurium and alkali metal carbonates, solventothermal reactions between the elements, or oxidation-reduction reactions with Lewis acids.[38] These methods have mostly been applied to alkali metal or alkaline earth metal tellurides that can then serve as precursors to other telluride species. The presence of a large organic cation or the encapsulating agent such as the crown ether complex of an alkali metal leads to the stabilisation of otherwise unstable polytellurides. Polytellurides have also been obtained as by-products in the electrochemical reduction processes involving tellurium and an organic cation.

Recently, low-temperature routes have been sought for by decomposition of organometallic complexes with tellurium-containing ligands. The optoelectronic devices normally require the material to be used as thin films. They are fabricated with special methods, such as molecular beam epitaxy, metal-organic chemical vapour deposition, or atomic layer deposition.

3.2 Monotellurides

Binary tellurides are generally solid crystalline substances at room temperature. The most common structural classes have been presented in Table 4. The telluride bulk materials are commonly prepared by the direct reaction between the elements. In recent years, low-temperature routes from transition metal complexes with tellurium-containing ligands are being sought for.

Most tellurides are semiconductors and find applications in the fabrication of electronic devises. Some tellurides, for example, HgTe, Ag_2Te, GeTe, and SnTe, are virtually metallic conductors.

Table 4 Structural classification of metal tellurides

Structure type	Example
Face center cubic lattice	
NaCl	CaTe, SrTe, BaTe, $Sc_{0.666}Te_{0.999}$, YTe, LuTe
Zinc blende	BeTe, ZnTe, CdTe, HgTe
Pyrite	$MgTe_2$, $MnTe_2$, $RuTe_2$, $OsTe_2$
Antifluorite	Li_2Te, Na_2Te, K_2Te, Rb_2Te
Hexagonal close packed lattice	
Wurzite	MgTe, ZnTe
CdI_2	$TiTe_2$, $PdTe_2$, $PtTe_2$, $CoTe_2$, $NiTe_2$, $IrTe_2$
NiS	MnTe, CrTe, PdTe, PtTe, CoTe, NiTe, IrTe

The chalcogenides of Be, Zn, Cd, and Hg are often referred to as II-VI semiconductors. They all have a zinc blende-type structure. The band gap decreases with increasing size of the metal from 3.0 eV in beryllium to 0.02 eV in mercury. The II-VI semiconductors find applications in solar cells, IR detectors, and optical communication devices.

One of the most important semiconductors in optoelectronic devices is cadmium mercury telluride (CMT), $Cd_xHg_{1-x}Te$ ($x = 0-1$). Its band gap can be tuned to any part of the spectral range 0.8–30 µm. Generally, the thermal imagining application requires the band gap to be tuned to the IR transmission windows of the atmosphere (3–5, $x = 0.3$ and 8–14 µm, $x = 0.2$).

3.3 Polytellurides

The homopolyatomic anions of tellurium exhibit a wide structural diversity. Simple polytelluride chains Te_x^{2-} ($x = 2-5$) have been isolated either as alkali metal salts or as salts containing crown ether or cryptate complexes of alkali metals or alkaline earth metals. Large organic cations like Et_4N^+, Ph_4P^+, and $[Ph_3PNPPh_3]^+$ have also been used for their stabilisation. Typical examples of the molecular structures are shown in Figure 6. While Li_2Te_6[40] and Na_2Te_6[41] have

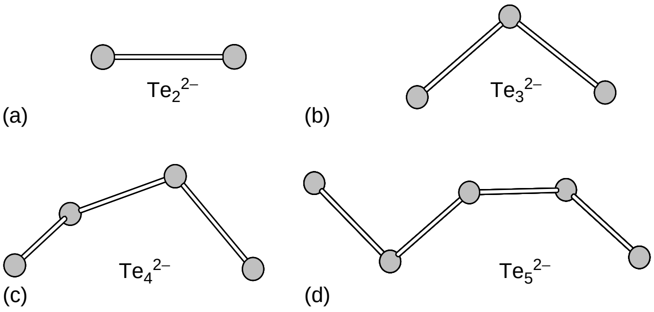

Figure 6 Polytelluride chains Te_x^{2-} ($x = 2-5$)[38]

been reported, they do not contain a discrete Te_6^{2-} ions. The structures rather consist of infinite helical $(Te_6^{2-})_n$ chains.

The Te–Te bond lengths in Te_2^{2-} anions have been tabulated by Smith and Ibers[38] and span a range 2.70(1)–2.86(1) Å. Tritelluride is a bent anion with the Te–Te distances and angles ranging 2.69–2.80 Å and 100–113°, respectively. The bond lengths and angles depend on the interionic interactions.[38] The terminal bond lengths in Te_4^{2-} and Te_5^{2-} chains vary more significantly [2.682(3)–2.964(3) Å and 2.704(1)–2.871(5) Å for Te_4^{2-} and Te_5^{2-}, respectively] than the internal bond lengths [2.686(1)–2.804(4) Å and 2.681(6)–2.793(6) Å for Te_4^{2-} and Te_5^{2-}, respectively]. The effects of the interionic interactions are more marked for Te_4^{2-} and Te_5^{2-} than for Te_2^{2-} and Te_3^{2-}.

The simple stoichiometry of the salts often obscures the complexity found in many polytellurides, the structures of which find few analogs in lighter chalcogen congeners sulfur and selenium. Spirocyclic Te_7^{2-}[42] and Te_8^{2-}[43] both show a square-planar tellurium atom (see Figure 7(a) and (b)). A similar motif is found in Rb_2Te_5 that exhibits a continuous

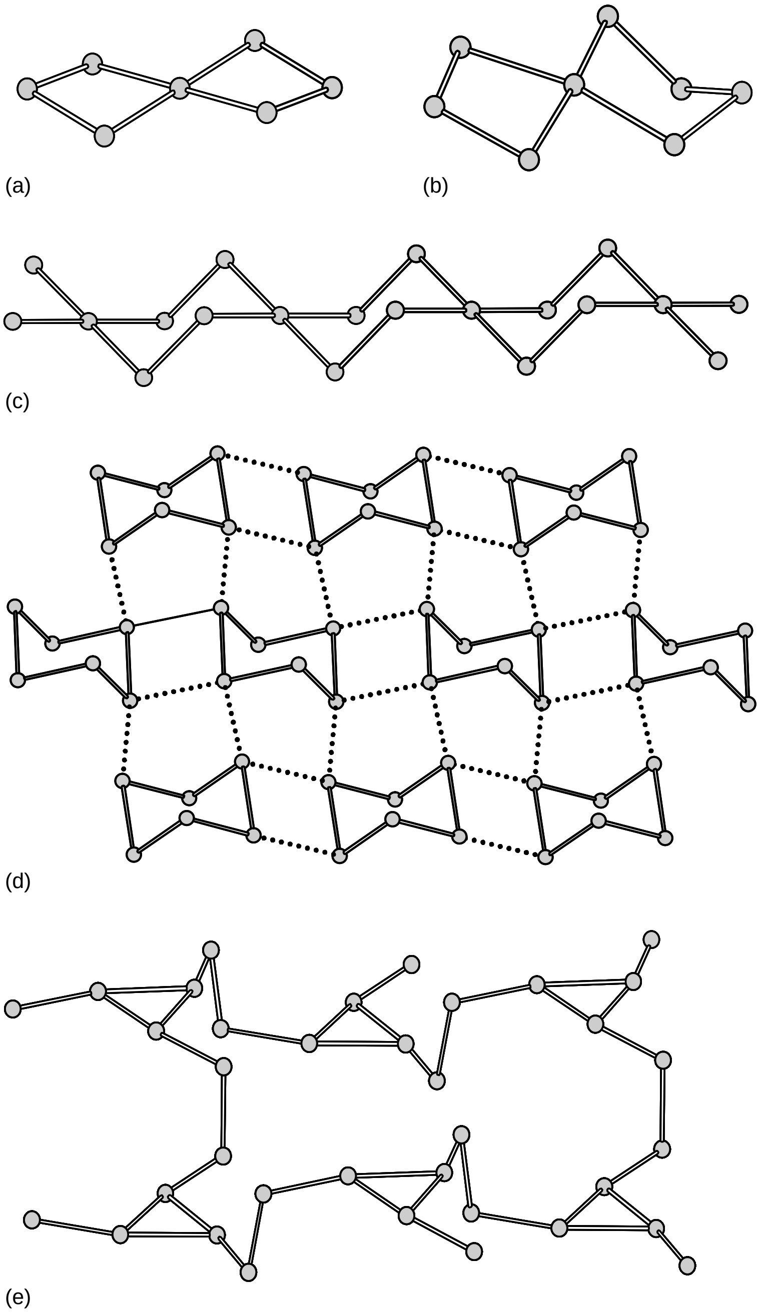

Figure 7 Cyclic and extended polytelluride networks. (a) Te_7^{2-},[42] (b) Te_8^{2-},[43] (c) $(Te_5)_n^{2-}$,[44] (d) $(Te_6)_n^{-}$,[45] (e) $(Te_6)_n^{3-}$[46]

spirocyclic chain $(\mathrm{Te}_5)_n{}^{2-}$.[44] This anion can also be thought as square-planar TeTe_4 units stacked together (see Figure 7(c)). Particularly interesting structures of $\mathrm{Cs_3Te_{22}}$[20] and $\mathrm{Cs_4Te_{28}}$[21] have been discussed above and have been shown in Figure 3.

Unlike sulfur and selenium, the charge of the polytellurides can vary from −2. This is exemplified by $\mathrm{RbTe_6}$,[45] which is shown in Figure 7(d). It consists of $\mathrm{Te_6}$ rings that show bond lengths of 2.777(3)–3.195(3) Å. They are linked together into a two-dimensional network by two pairs of Te···Te contacts of 3.214(3) and 3.449(3) Å. Another example is $[\mathrm{Cr(en)_3}]\mathrm{Te_6}$ containing a polymeric $\mathrm{Te_6}{}^{3-}$ anion (see Figure 7(e)).[46]

Tellurium forms a wide variety of tellurometallates that have recently attracted extensive attention.[47–50] They show a rich structural flexibility as exemplified in Figure 8. While no single general method can be assigned for the syntheses of $[\mathrm{M}_x\mathrm{Y}_y]^{n-}$ species, the most important routes involve the reaction of metal fragments with elemental tellurium, hydrogen telluride, polyatomic tellurium cations, and species, like $\mathrm{Te(SiR_3)_2}$ or $\mathrm{TePR_3}$.[47] Tellurometallates have also been prepared by the extraction of Zintl-anions.[51,52] and by reaction of metal salts with polytellurides in nonaqueous solvents.[53,54]

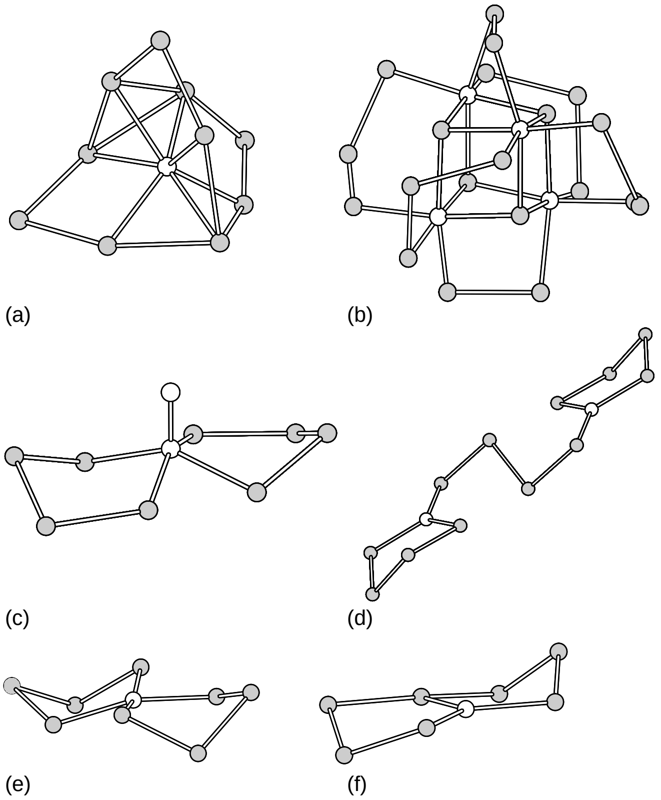

Figure 8 Illustrative examples of tellurometallates: (a) $[\mathrm{NbTe_{10}}]^{3-}$,[53] (b) $[\mathrm{Ni_4Te_{20}}]^{4-}$,[54] (c) $[\mathrm{MTe_8O}]^{-}$ (M = Pd, Pt),[55] (d) $[\mathrm{M_2Te_{12}}]^{3-}$ (M = Cu, Ag),[56] (e) $[\mathrm{MTe_8}]^{2-}$ (M = Pd, Pt),[57] (f) $[\mathrm{MTe_7}]^{2-}$ (M = Hg, Ag).[58] Tellurium atoms have been indicated in grey, transition metals and oxygen atoms are indicated in white

3.4 Polyatomic Tellurium-containing Cations

Like sulfur and selenium, tellurium forms homopolyatomic cations with weakly coordinating anions in strongly oxidizing media.[59–61] The synthetic routes involve super acids, acidic melts, or $\mathrm{SO_2}$ and related aprotic solvents. Suitable oxidizing agents comprise strong main group Lewis acids, like $\mathrm{AlCl_3}$, $\mathrm{AsF_5}$, $\mathrm{SbCl_5}$, and $\mathrm{BiCl_5}$ and transition metal halides such as $\mathrm{MF_6}$ (M = W, Re, Os, Ir, Pt), $\mathrm{MCl_6}$ (M = V, W, Zr, Hf, Nb, Ta, Re), $\mathrm{VOCl_3}$, $\mathrm{NbOCl_3}$, and $\mathrm{WOCl_4}$. Typical examples involving traditional oxidizing agents are the preparation of $\mathrm{Te_4}{}^{2+}$ from elemental tellurium in the melt containing tellurium tetrachloride and aluminium chloride, or the synthesis of $\mathrm{Te_6}{}^{4+}$ from elemental tellurium and arsenic pentafluoride in sulfur dioxide solution.

$$7\mathrm{Te} + \mathrm{TeCl_4} + 4\mathrm{AlCl_3} \longrightarrow 2(\mathrm{Te_4})[\mathrm{AlCl_4}]_2$$

$$6\mathrm{Te} + 6\mathrm{AsF_5} \xrightarrow{\mathrm{SO_2(l)}} (\mathrm{Te_6})[\mathrm{AsF_6}]_4 + 2\mathrm{AsF_3} \qquad (1)$$

In recent years, several novel cationic species have been prepared by utilizing chemical vapour transport. These cations exhibit unprecedented structural features that find no analogs in the lighter congeners.[59–61]

The $\mathrm{Te_4}{}^{2+}$ is a 6π electron square-planar dication. Numerous structures containing different counterions have been determined by X-ray crystallography.[60,61] The formal bond order is 1.25, but it has been noted that the bond length depends on the nature of the counterions spanning a range of 2.660–2.695 Å (see Figure 9).[60] In each salt there are close contacts between the cations and anions, in which the halogen

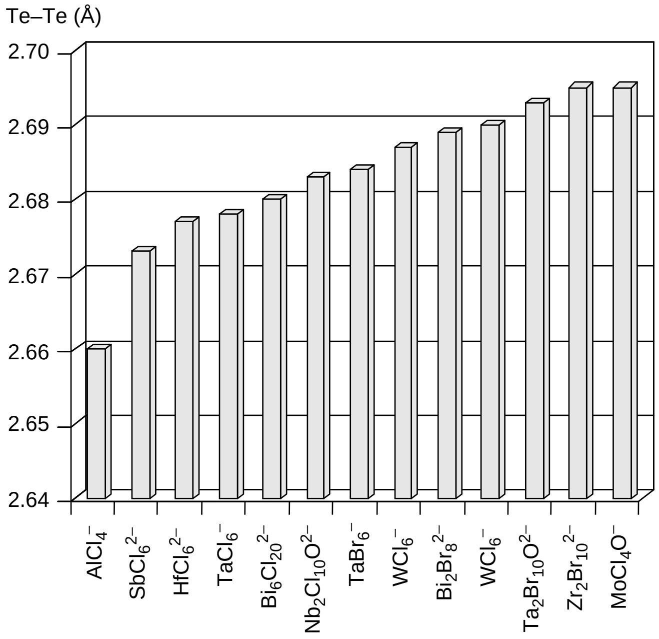

Figure 9 The dependence of the Te–Te bond length in $\mathrm{Te_4}{}^{2+}$ on the counterion[60]

atom bridges the Te–Te edges of the square-planar cation, as exemplified in Figure 10(a) by $(Te_4)[WCl_6]_2$.[62] It has been explained that the bond lengthening is caused by the transfer of electron density from the halogen into the σ^* orbital of the cation.[60] Therefore, the more basic anions give rise to longer bonds.[60]

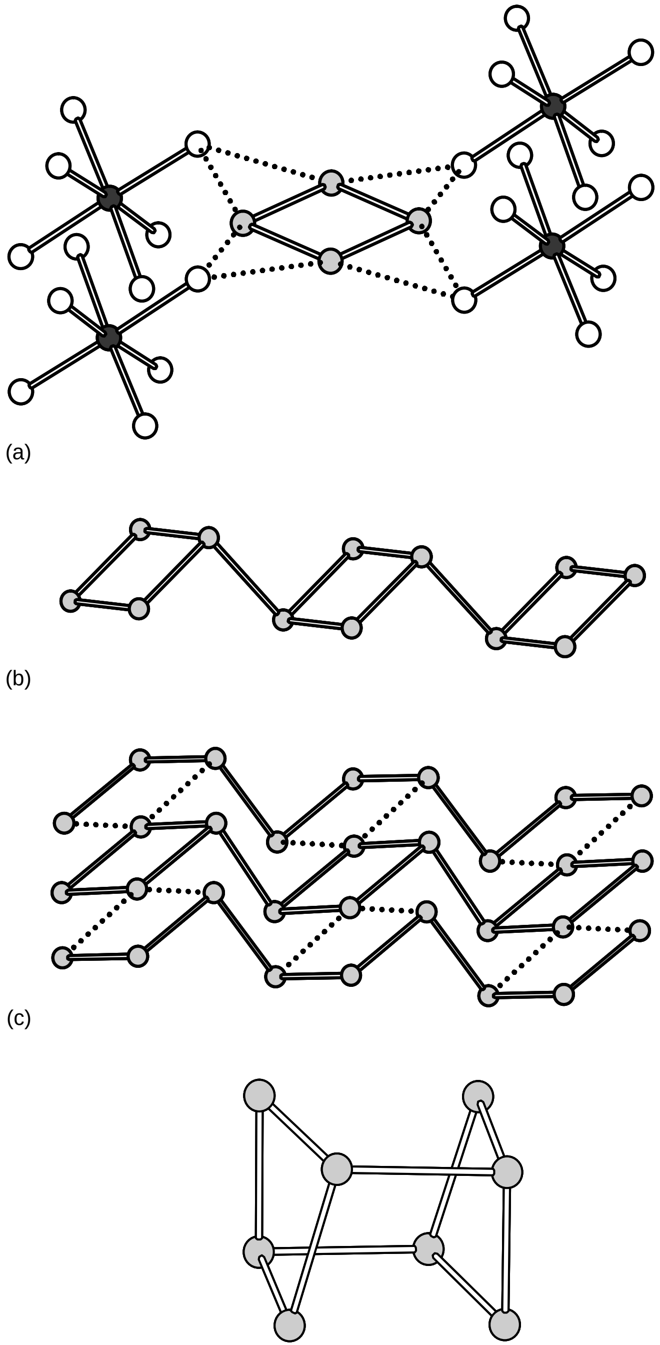

Figure 10 (a) The cation-anion interactions in $(Te_4)[WCl_6]_2$.[62] Tellurium atoms are indicated in grey, chlorine in white, and tungsten in dark grey. (b) The polymeric cation in $(Te_4)(Te_{10})[Bi_2Cl_8]_2$.[63] (c) The Te_8^{4+} cation in $(Te_8)[VOCl_4]_2$[64]

The Te_4^{2+} cation is a 22-electron species like S_4^{2+} and Se_4^{2+}. They should show a butterfly-shaped arachno-structure. The planar structure discussed above is explained by π-stabilisation. The classical bonding arrangement is observed in $(Te_4)(Te_{10})[Bi_2Cl_8]_2$,[63] which shows a polymeric arrangement of four-membered rings that are linked together in 1,3-positions (see Figure 10(b)). The Te_{10}^{2+} cation in the structure can be conceived to be formed of another stack of polymeric four-membered rings surrounded by two polymeric tellurium helical chains. The Te_4^{2+} cations have also been observed to dimerize into a Te_8^{4+} cation (Figure 10(c)).[64]

Te_6^{4+} is a trigonal prismatic cation (see Figure 11(a)) that has been known for a long time.[65,66] The bonds at the triangular face show approximately single bond lengths (2.662–2.702 Å) It is a 32 electron species, the structure of which can be rationalized according to the following resonance:

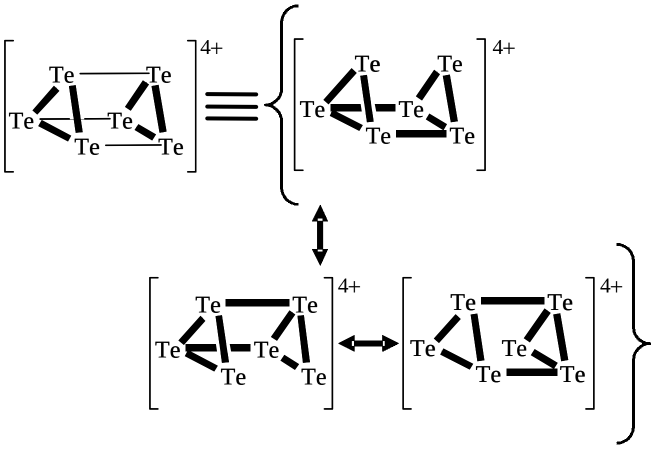

DFT calculations with local density approximation has indicated that the elongated D_{3h} structure is the ground state of the cation with the extra electron pair causing the simultaneous elongation of the three bonds parallel to the C_3 axis.[70] Recently, also Te_6^{2+} has been prepared and structurally characterized.[67,71] Compared to the classic Te_6^{6+} cage, two bonds should be broken because of two extra electron pairs.[72] However, one bond is delocalized between two positions in the triangular face (the Te–Te distance is 3.209–3,382 Å,[67,71] see Figure 11(b)) and only one bond is completely missing. It is only in the case of hybrid $Te_3S_3^{2+}$[68] and $Te_2Se_4^{2+}$[69] cations that the expected more open structure is seen, as shown in Figure 11(c) and 11(d).

Te_8^{2+} has several isomeric forms. The cation commonly shows the same structure as S_8^{2+} and Se_8^{2+} (see Figure 12(a)), but the transannular interaction seems to be stronger in tellurium than in sulfur or selenium.[60,61] An even more pronounced bicyclic nature is found in the Te_8^{2+} cation in $Te_8[WCl_6]$[73] (see Figure 12(b)). The transannular bond is only 2.993 Å. In addition, Te_8^{2+} has other isomers. It has been found to show a bicyclo[2,2,2]octane structure[60]

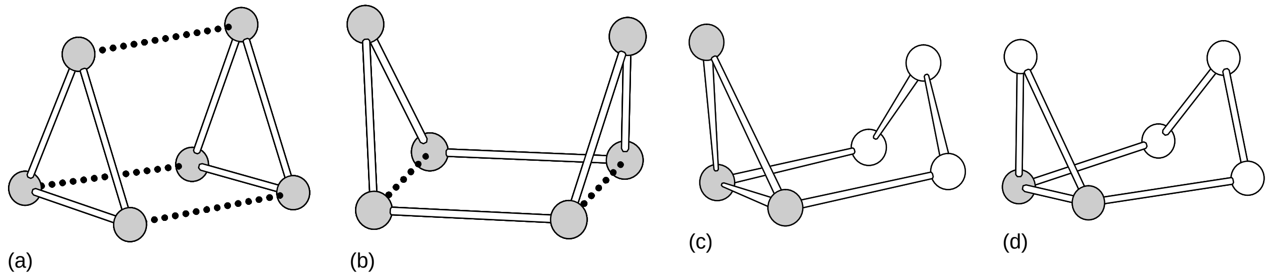

Figure 11 (a) The structure of the Te_6^{4+} cation.[65] (b) The structure of Te_6^{2+}.[67] (c) The structure of $Te_3S_3^{2+}$ cation.[68] Tellurium atoms are indicated in grey and sulfur atoms in white. (d) The structure of $Te_2Se_4^{2+}$ cation.[69] Tellurium atoms are indicated in grey and selenium in white

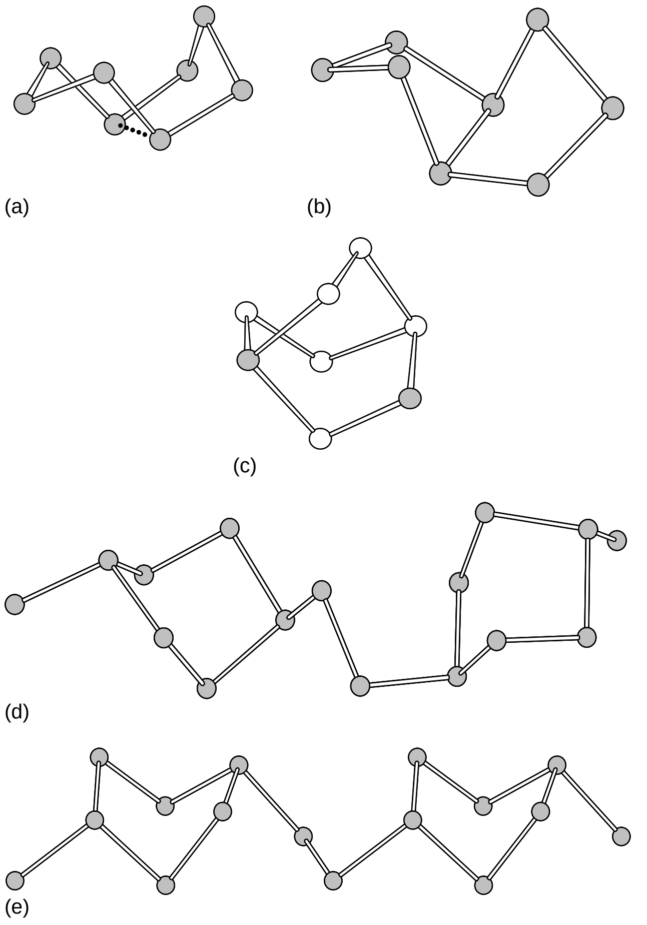

Figure 12 (a) The Te_8^{2+} cation in $(Te_8)[HfCl_6]$.[77] (b) The Te_8^{2+} cation in $(Te_8)[WCl_6]_2$.[73] (c) The $Te_2Se_6^{2+}$ cation in $(Te_2Se_6)(Te_2Se_8)[AsF_6]_4{\cdot}2SO_2$.[74] Tellurium atoms are indicated in grey and selenium in white. (d) The $(Te_8)_n{}^{2+}$ cation in $(Te_8)[Bi_4Cl_{14}]$.[75] (e) The $(Te_8)_n{}^{2+}$ cation in $(Te_8)[U_2Br_{10}]$[76]

similar to that observed in $Te_2S_6^{2+}$[74] (see Figure 12(c)). Two polymeric forms of $(Te_8)_n{}^{2+}$ both contain six-membered rings in boat conformation that are linked together by Te_2 fragments in 1,4-positions.[75,76] The main difference between the two isomers is the relative orientations of adjacent ring fragments (see Figures 12(d–e)). More extensive homonuclear tellurium cations have also been recently prepared, as shown in Figure 13. They are all based on repeating $(Te_7)_n{}^{2+}$ units.

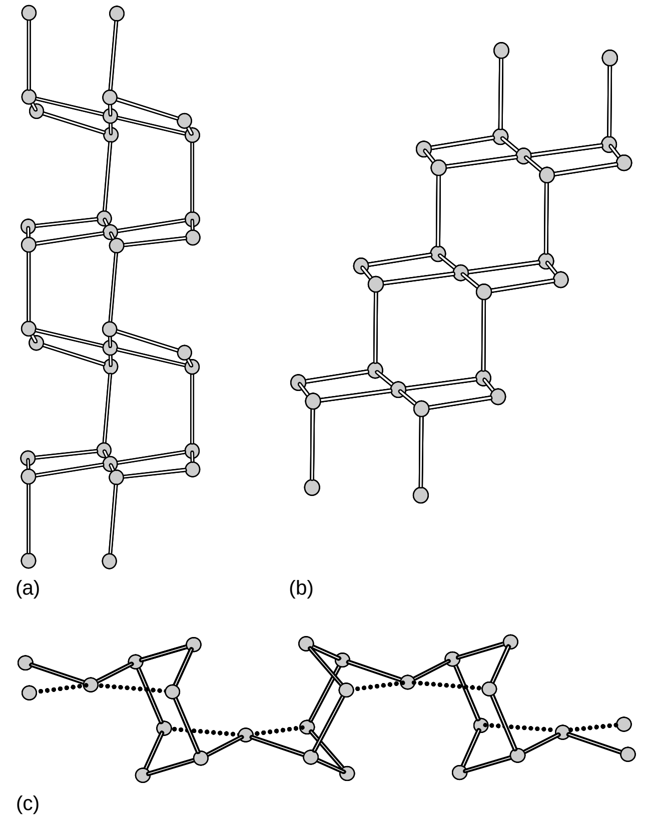

Figure 13 Examples of extended tellurium cations based on the Te_7 unit. (a) $(Te_7)[NbCl_4O]Cl$.[78] (b) $(Te_7)[Be_2Cl_6]$.[79] (c) $(Te_7)[AsF_6]_2$[80]

4 TELLURIUM–HALOGEN COMPOUNDS

4.1 General

Like lighter chalcogens, tellurium readily forms a number of compounds with halogen elements. Tellurium tetrahalides are the most stable species, but other binary compounds are also known, some of which do not find analogs with lighter chalcogen congeners. The bonding in these compounds eludes simple description and concepts, like hypervalence, multicenter bonding, charge-transfer interactions, and secondary bonding, have been evoked in the understanding of their structural and chemical properties (for a recent review of chalcogen halides, see Ref. 81).

4.2 Tellurium(IV) Halides

Tellurium tetrafluoride can be obtained by the reaction of SeF_4 with TeO_2 at 80 °C.[82] While it is considered to be monomeric in the gas phase, the low-temperature X-ray structure is a polymeric chain of *cis*-linked square-pyramidal TeF_5 groups (see Figure 14(a)).[82] Tellurium tetrafluoride is reactive giving mixtures of tellurides and fluorides with many metals such as copper and nickel. It also fluorinates silicon dioxide above the room temperature. Tellurium tetrafluoride decomposes at 190 °C to give octahedral TeF_6(g), the structure of which has been determined by electron diffraction.[83] The low-temperature crystal structure of the solid TeF_6 has also been recently determined.[84] In the solid state, the Te–F bonds span a range of 1.750–1.803 Å and the bond angles are 89.61–90.61°.

Gaseous $TeCl_4$ is also monomeric displaying a Ψ-tbp structure with a point group C_{2v}.[87] In the solid state, $TeCl_4$[85,88] and $TeBr_4$[89] have a tetrameric cubane-like structure (see Figure 14(b)). The terminal Te–X bonds are shorter than those involving the triply bridging halogen atoms and the structure can be rationalized either as covalently bound (Te_4X_{16}) molecules or as ionic $[(TeX_3{}^+X^-)_4]$.[85,90,91] The stereochemical activity of the tellurium lone-pairs are directed towards the center of the cubane cage.

TeI_4 has five different polymorphs (α-ε) that crystallize simultaneously from the methanol solution of TeI_4 containing HI.[90,91] The orthorhombic δ-TeI_4 is the thermodynamically stable polymorph at normal conditions.[81,92] It shows another tetrameric structure (Figure 14(c)) that can be formulated as $[(TeI_3{}^+\ I^-)_2(TeI_4)_2]$. The TeX_6-octahedra in TeI_4 are less distorted than those in $TeCl_4$ and $TeBr_4$. The different structure of TeI_4 is a consequence of a smaller electronegativity difference between tellurium and iodine compared to that between tellurium and chlorine or tellurium and bromine. The cubane structure is expected to favor larger charge separation and more polar bonds.[81] Orthorhombic β-TeI_4 and monoclinic γ-TeI_4 also exhibit the structure shown in Figure 14(c).[90,91] Trigonal α-TeI_4 shows a continuous 2H-CdI_2 structure that can also be understood in terms of a related repeating structural unit. Interestingly, only the thermodynamically least-stable tetragonal ε-TeI_4 shows the cubane structure.[90,91]

The tetrameric tellurium tetrachlorides, -bromides, and -iodides undergo a systematic stepwise degradation in the presence of stoichiometric amounts of halides in nonpolar solvents and form oligonuclear halogenotellurates(IV). There are numerous examples of the formation and equilibria between the different anions (for a detailed discussion, see Ref. 81).

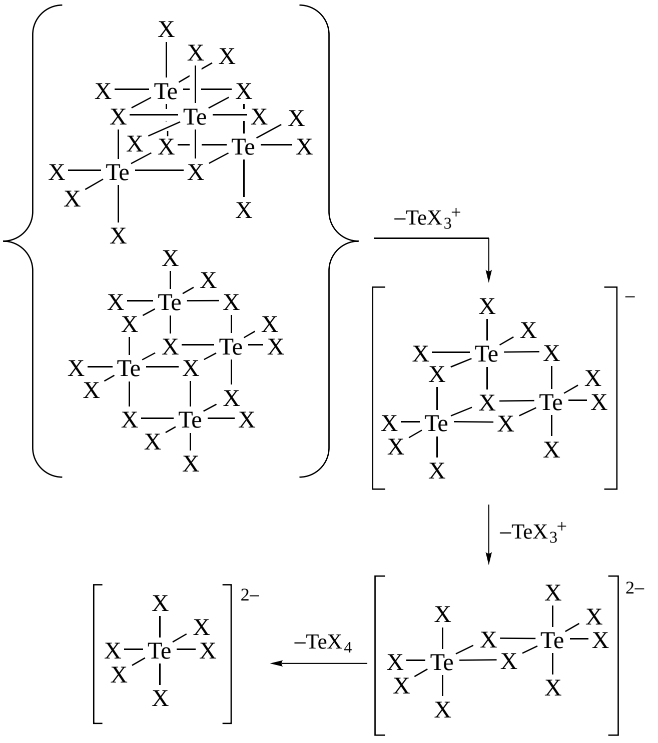

It is interesting to note that the coordination environment in the halidotellurate anions is an almost regular octahedron in apparent violation of the VSEPR rules for a 14 electron AX_6E system. It has been suggested that the lone electron pair of tellurium resides in the stereochemically inactive 6s orbital and the six Te–X bonds form three pairs of 3c–4e bonds involving the three 6p orbitals (for a more detailed discussion, see Ref. 81).

4.3 Tellurium(II) Halides

The existence of tellurium dichloride and dibromide has been shown in gaseous state[81] and their structures have been determined by electron diffraction.[92,93] Both molecules are expectedly bent with C_{2v} symmetry. The Te–Cl and Te–Br bonds are 2.329(3) Å and 2.51(2) Å, respectively, and the respective bond angles are 97.0(6) and 98(3)°.

The preparation of liquid or solid $TeCl_2$ or $TeBr_2$, on the other hand, is still controversial. It has been reported that the Te–TeX_4 (X = Cl, Br) phase diagrams give no evidence for the formation of TeX_2.[94] However, Paul *et al.*[95] have reported the preparation of $TeCl_2$ from $Me_3SiSiMe_3$ and $TeCl_4$. When the reaction was carried out in CS_2, polymeric $(MeTeCl_3)_n$ was obtained instead of $TeCl_2$.[96] It has also been reported

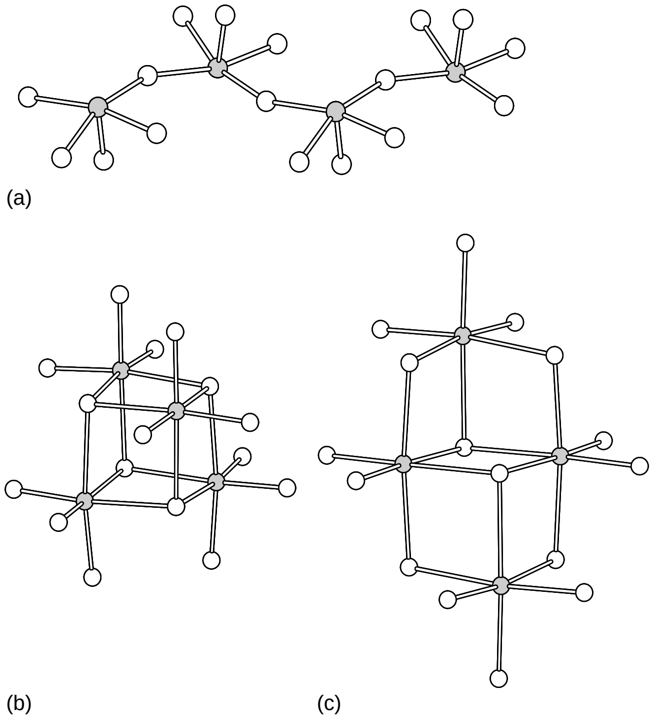

Figure 14 (a) The structure of TeF_4.[82] (b) The structure of $TeCl_4$.[85] $TeBr_4$ is isostructural with $TeCl_4$. (c) The structure of TeI_4.[86] Tellurium atoms are indicated in grey and halogens in white

that the reaction of liquid tellurium with CF_2Cl_2 affords black $TeCl_2$, which rapidly disproportionates to tellurium and $TeCl_4$.[97]

It was recently found that selenium dichloride can conveniently be prepared by the reaction of elemental selenium and SO_2Cl_2.[98] It is relatively stable in coordinating solvents and can be used as a reagent for synthetic applications. The attempt to prepare $TeCl_2$ in the analogous manner from elemental tellurium and SO_2Cl_2 resulted in the formation of various chloridotellurate anions with different counterions.[99] The solvent and the possible presence of a small amount of residual moisture probably determine the identity of the main product in each individual case.

The existence of TeI_2 is even more uncertain than that of $TeCl_2$ and $TeBr_2$.

Ditellurium dichloride and dibromide can be prepared in moderate yields by reducing elemental tellurium with $LiBHEt_3$ in thf followed by the treatment with TeX_4 ($X = Cl$, Br).[18] Both Te_2Cl_2 and Te_2Br_2 are dark brown liquids that decompose rapidly. In CS_2 solution, they turned out to be rather stable. The molecular species were identified by EI mass spectroscopy, as exemplified for Te_2Cl_2 in Figure 15. Furthermore, the reaction of Te_2Cl_2 and $[Ti(C_5H_5)_2S_5]$ or $[Ti(C_5H_5)_2Se_5]$ expectedly afforded 1,2-Te_2S_5 and 1,2-Te_2Se_5, respectively, that were identified by ^{77}Se and ^{125}Te NMR spectroscopy.

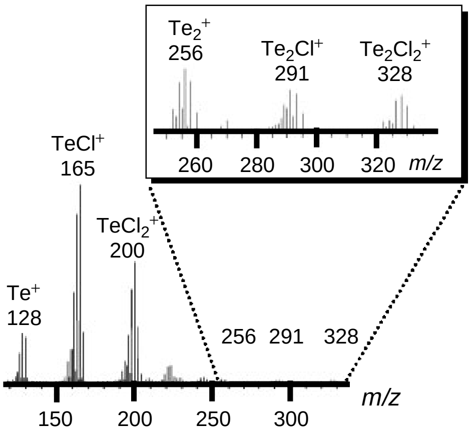

$Te_2Cl_2^+$		
m/z	I_{calc}	I_{obs}
316	0.84	-
317	1.23	-
318	3.97	-
319	3.31	-
320	12.42	4.7
321	10.10	-
322	28.14	25.4
323	18.86	9.2
324	54.04	28.9
325	22.03	19.1
326	87.53	85.5
327	9.55	-
328	100.00	100.0
329	1.32	-
330	74.33	70.5
332	-	9.8

Figure 15 The EI mass spectrum of Te_2Cl_2[18]

4.4 Tellurium Subhalides

Tellurium subhalides form an interesting class of solid phases.[81,100] The main characterized species comprise Te_3Cl_2, Te_2X ($X = Cl$, Br, I), and two polymorphs of TeI. They can be prepared by heating the elements at 200–300 °C followed by homogenization, annealing, quenching, and extraction to remove excess tellurium tetrahalide.[94,101–103] Single crystals of Te_2I, and α- and β-TeI have been grown by hydrothermal methods in concentrated aqueous hydroiodic acid.[102–104] Crystals of thermodynamically stable Te_3Cl_2, Te_2Br, and α-TeI can also be grown from the melt.[100] Tellurium subbromides and iodides have also been prepared by reducing tellurium tetrahalides with corresponding tin dihalides.[105,106]

Because of high tellurium content, the crystal structures of all subhalides show cumulated Te–Te bonds and bear a structural relationship with hexagonal tellurium. Te_3Cl_2 contains a continuous twisted tellurium chain with every third tellurium atom bonded to two chlorine atoms in axial positions of the trigonal bipyramidal coordination environment (see Figure 16(a)). The Te–Te bonds within the chain span a range of 2.670–2.861 Å. The axial Te–Cl bond lengths are 2.501 and 2.536 Å. The chains are connected by secondary Te$\cdots$Cl contacts of 3.363 and 3.400 Å.[103,104] Te_2Cl, Te_2Br, and Te_2I show mutually similar structures (see Figure 16(b)) containing fused Te_6 rings in boat conformation. The ring fragments are also connected together by two halogen bridges in 1- and 4-positions.[103,104] The Te–Te bonds within the cyclic arrangement range 2.808–2.919 Å and 2.861–2.917 Å for Te_2Br and Te_2I, respectively. The respective Te–X bond lengths are 2.904–3.017 Å and 3.084–3.179 Å. The polymeric units are linked together by very weak Te$\cdots$Br and Te$\cdots$I secondary contacts.

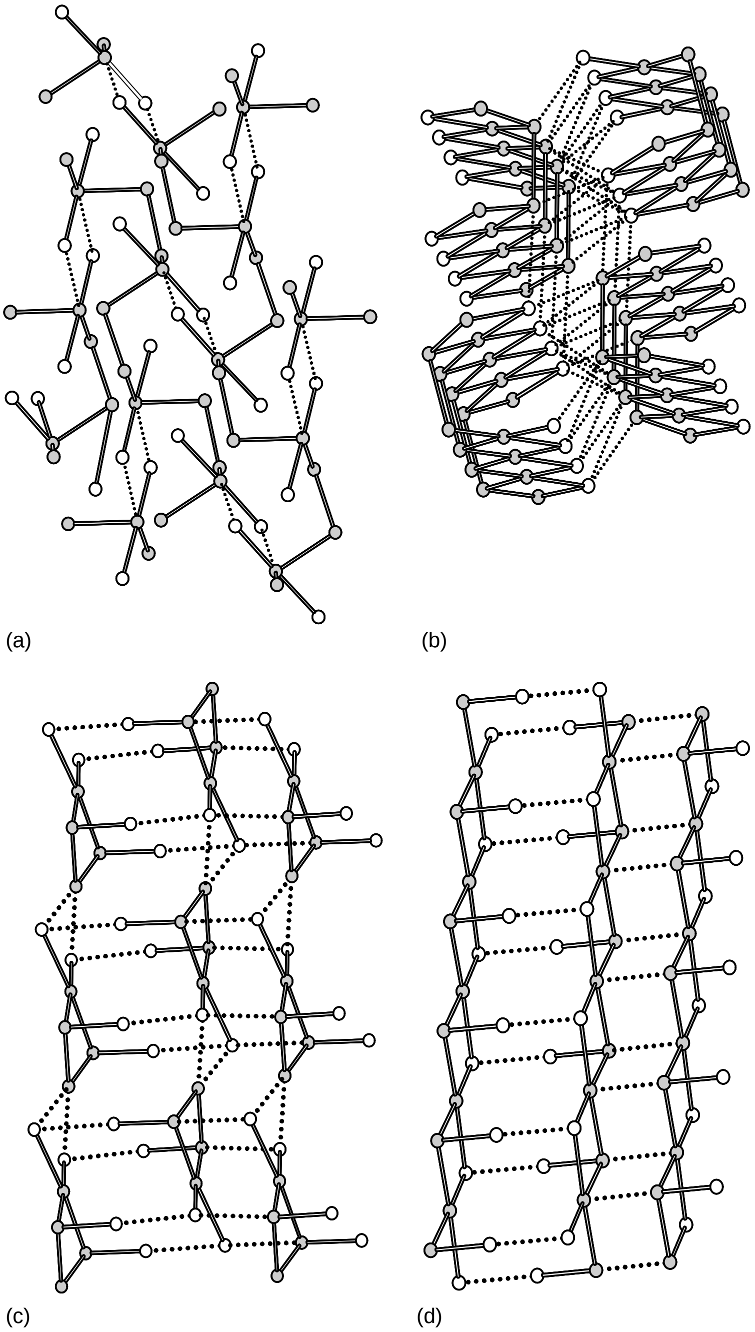

Figure 16 The structures of (a) Te_3Cl_2, (b) Te_2Br and Te_2I, (c) α-TeI, (d) β-TeI.[104] Tellurium atoms are indicated in grey and halogens in white

The two different polymorphs of TeI are shown in Figure 16(c–d). α-TeI is composed of infinite chains of $Te(TeI)_2(TeI_2)$ units containing a slightly puckered four-membered Te_4 ring with the Te–Te bond lengths of 2.786–2.928 Å.[104] There are two exocyclic Te–I bonds of 2.740 and 2.742 Å. One tellurium atom is bound to two iodine atoms (bond lengths of 3.042 and 3.110 Å) that also exhibit the Te···I close contacts of 3.349 and 3.404 Å to the adjacent unit (see Figure 16(c)). The Te···I and I···I secondary contacts of 3.551–3.601 Å and 3.627–3.690 Å, respectively, link the adjacent $[Te(TeI)_2(TeI_2)]_n$ chains together. β-TeI show a slightly different polymeric structure that is related to that in Te_2X (see Figure 16(d)).[104] The structure is composed of four-membered spirocyclic $(Te_3I_2)_n$ fragments with one exocyclic and one endocyclic iodine atoms. The Te–Te bond length is 2.909 Å. The exocyclic Te–I bonds are shorter (2.742 Å) than the endocyclic Te–I bonds (3.127 Å). The polymeric units are linked together by

Te···Te and I···I secondary contacts of 2.492 and 2.598 Å, respectively.

The optical, electrical, and thermodynamic properties of tellurium subhalides have attracted considerable research interest.[100] For instance, α-TeI has been suggested to find applications as solid electrolytes in galvanic cells.

4.5 Tellurium Oxohalides

One of the oldest tellurium oxofluorides is $(F_5Te)_2O$, which was originally thought to be Te_2F_{10}. It was prepared by fluorinating TeO_2 with a stream of N_2/F_2. Its structure was determined in the gas phase by electron diffraction[107,108] and was shown to contain two linked F_5Te fragments with an oxygen bridge resulting in the octahedral coordination environment around both tellurium atoms. The Te–O–Te bond angle of 145.5° and the two Te–O bonds of 1.83 Å have been rationalized in terms of pπ-dπ bonds.

The heating of equimolar amounts of TeO_2 and TeF_4 in a sealed platinum tube for 24 h at 250 °C or 140 °C affords $Te_2O_3F_2$[109] and $TeOF_2$,[110] respectively. The crystal structure of $Te_2O_3F_2$ is shown in Figure 17(a) and that of $TeOF_2$ in Figure 17(b). Both compounds show a continuous chain structure that bear similarities to α-TeO_2.

The teflate ion, $(OTeF_5)^-$, plays an important role in synthetic main group chemistry. Its effective electronegativity is similar to that of fluoride. A group of anions with a general formula of $[M(OTeF_5H)_6]^-$ (M = As, Sb, Bi, Ti, etc.) have recently been prepared.[111,112] They are only weakly coordinating and serve to stabilize otherwise unstable cations.

$Te(OTeF_5)_6$[113] can be prepared from tellurium tetrafluoride and $B(OTeF_5)_3$[114] upon treatment with $Xe(OTeF_5)_2$.[115]

$$TeF_4 + B(OTeF_5)_3 \longrightarrow Te(OTeF_5)_4 \xrightarrow{Xe(OTeF_5)_2} Te(OTeF_5)_6 \qquad (2)$$

When $Te(OTeF_5)_4$ is fluorinated with XeF_2, *cis*- and *trans*-$TeF_2(OTe_5)_4$ are obtained.[114] $Te(OTeF_5)_6$ crystallizes as two different polymorphs.[113] The molecule is an almost spherical molecule (see Figure 18(a)) with the central and outer Te–O distances of 1.903 Å and 1.893 Å, respectively. The structure of *trans*-$TeF_2(OTeF_5)_4$ (Figure 18(b)) is also based on octahedral Te(IV) with the bond lengths very near to the corresponding bonds in $Te(OTeF_5)_6$.[114]

The teflate anion has also been utilized in the preparation of a variety of species containing transition metals, as exemplified by $[Fe(OTeF_5)_3]$,[116] $[Nb(OTeF_5)_6]^-$,[117] and $[[\{(\eta^2\text{-tol})Ag\}_2(\mu\text{-}OTeF_5)_2]$.[118]

Though the structures of a tellurium oxochloride[119–121] and oxobromide[122] have also been reported, their chemistry is not as well-established as that of oxyfluorides. In addition, some organic species, like $(n\text{-}Pr_4N)[TeCl_4(OH)]$,[123] are known.

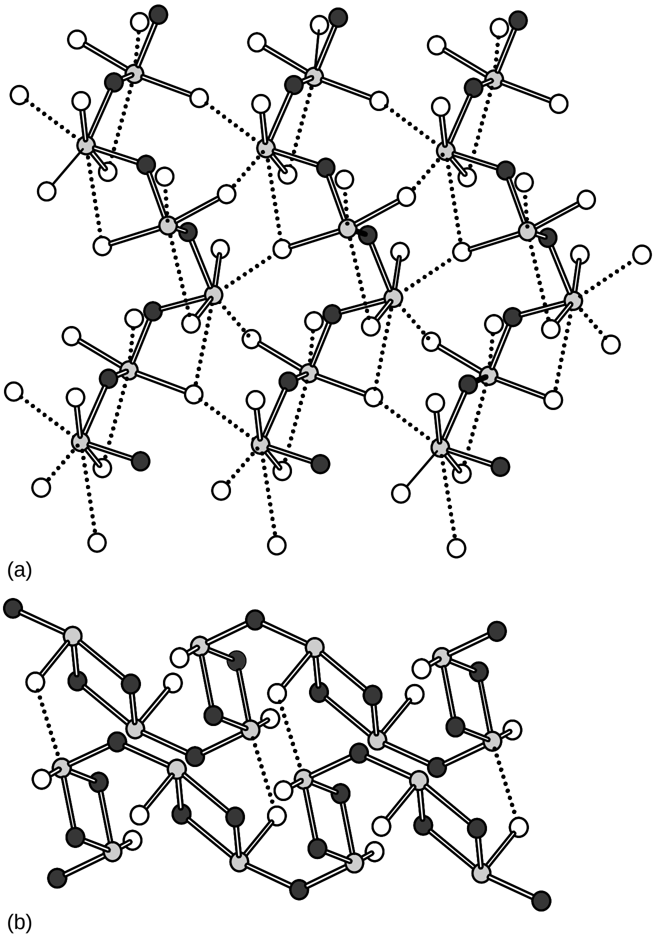

Figure 17 (a) The structure of $Te_2O_3F_2$.[100] (b) $TeOF_2$.[101] Tellurium atoms are indicated in grey, oxygen in white, and fluorine in dark grey

5 TELLURIUM–OXYGEN COMPOUNDS

5.1 Tellurium Oxides

Tellurium–oxygen system comprises a wide number of phases. Tellurium monoxide TeO probably exists only in the gas phase. No evidence of its existence in the solid state has been obtained. The He(I) photoelectron spectrum of the molecular beam that has been formed by heating TeO_2 in vacuo indicates that TeO is the dominant species in the vapor phase.[124] Studies of the absorption and emission spectra of TeO(g) have yielded the bond dissosiation energy of 263.2 kJ mol^{-1}.[125] The Te=O bond length of 1.828 Å.[126] is estimated from the rotational fine structure of the electronic absorption spectrum.

Tellurium dioxide exists as three crystallographic forms, the structures of which have been determined several times. Tetragonal, colorless α-TeO_2 is formed when elemental

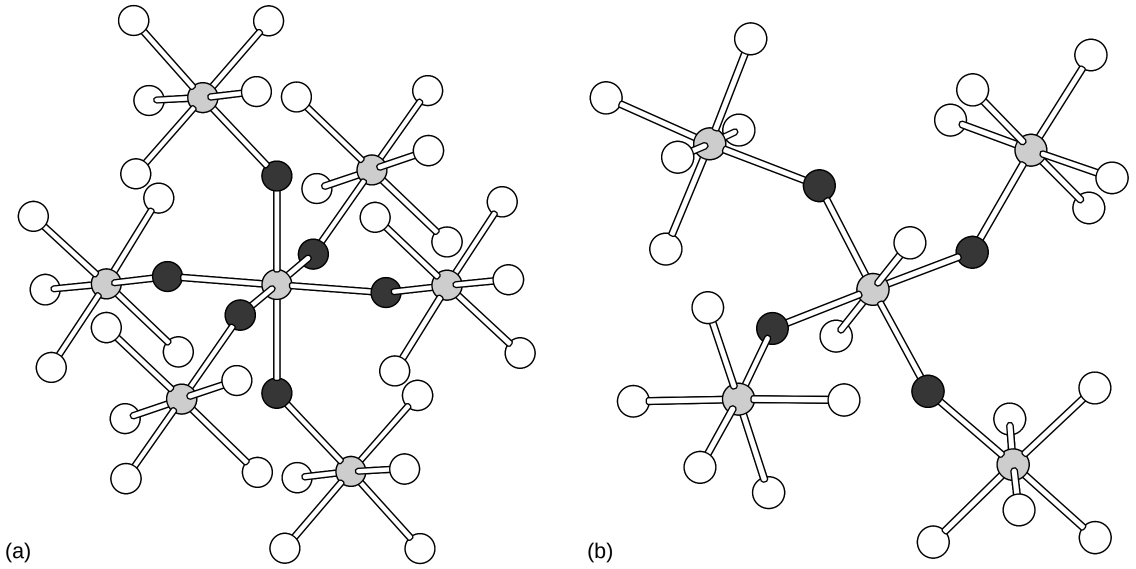

Figure 18 The structure of (a) $Te(OTeF_5)_6$[113] and (b) *trans*-$TeF_2(OTeF_5)_4$.[114] Tellurium atoms are indicated in grey, oxygen in dark grey, and fluorine in white

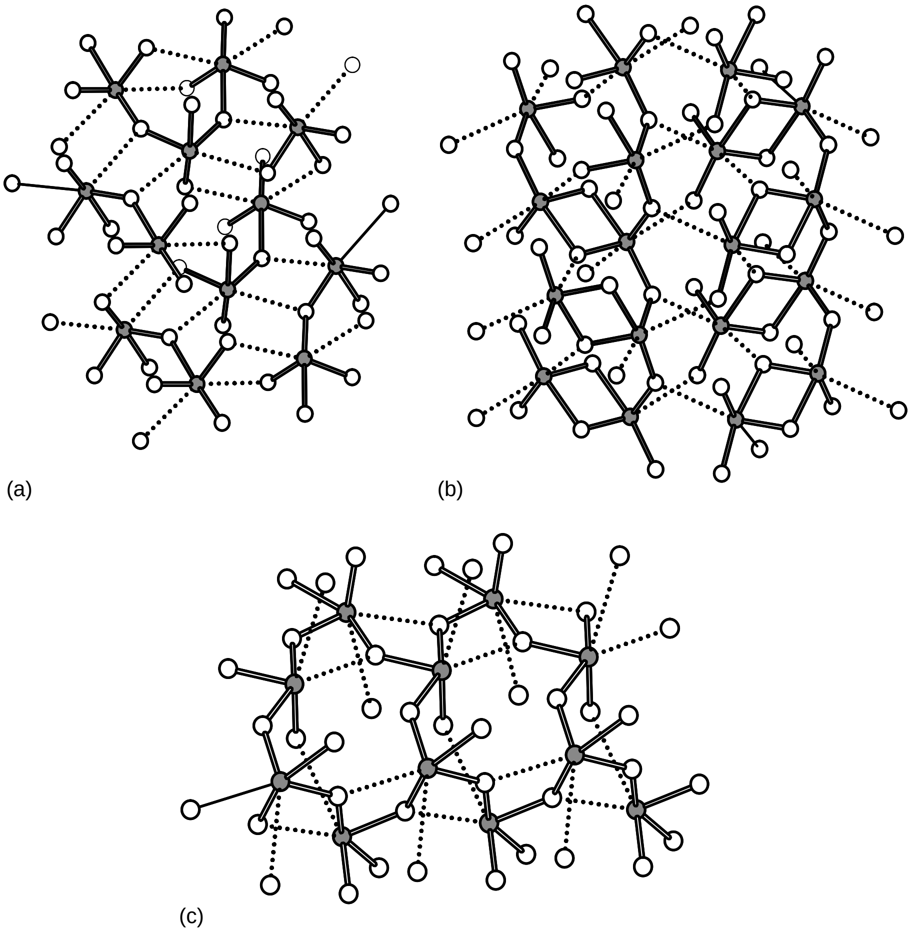

Figure 19 The crystal structures of (a) α-TeO_2,[127] (b)β-TeO_2,[128] and (c) γ-TeO_2.[129] Tellurium atoms are indicated in grey and oxygen in white

tellurium reacts with O_2,[127] yellow orthorhombic β-TeO_2 occurs naturally as the mineral tellurite,[128] and γ-TeO_2 has recently been isolated.[129] The coordination geometry around tellurium in all three oxides is a Ψ -trigonal bipyramid with the tellurium lone pair of electrons occupying one of the equatorial positions. The secondary bonding interactions, however, expand the coordination environments into distorted octahedra (see Figure 19). It is worth noting that there is a clear trend in the structures of sulfur dioxide, selenium dioxide, and tellurium dioxide: Sulfur dioxide is monomeric, solid selenium dioxide forms one-dimensional polymeric chains, and each crystallographic modification of tellurium dioxide is composed of a continuous three-dimensional network. At the same time, the bond order of the chalcogen-oxygen bond becomes smaller.

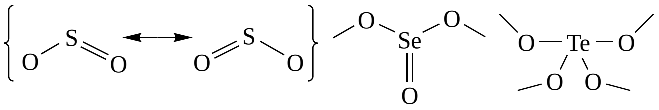

Tellurium dioxide is sparingly soluble in water but is a strong oxidizing agent for a number of elements. In hot alkaline solutions TeO_2 forms tellurates. With selenium halides it is readily halogenated:

$$\begin{aligned}\mathrm{TeO_2 + 4Se_2Cl_2} &\longrightarrow \mathrm{TeCl_4 + 2SeOCl_2 + 6Se}\\ \mathrm{TeO_2 + SeF_4} &\longrightarrow \mathrm{TeF_4 + SeO_2}\end{aligned} \tag{3}$$

Two crystallographic modifications have been reported for tellurium trioxide.[130] A definite structure determination has been carried out only for the more stable grey β-TeO_3 that is made by heating $Te(OH)_6$ in a sealed tube at 320 °C for 12 to 15 h in the presence of traces of H_2SO_4 and O_2.[131,132] α-TeO_3 is yellow. It is also made by dehydrating $Te(OH)_6$ at 300 °C. Further heating transforms it to β-TeO_3. Prolonged heating at 405 °C affords Te_2O_5, which is considered an intermediate product in the transformation of α-TeO_3 to TeO_2.[133] Its structure is based on a network in which $Te^{VI}O_6$ octahedra

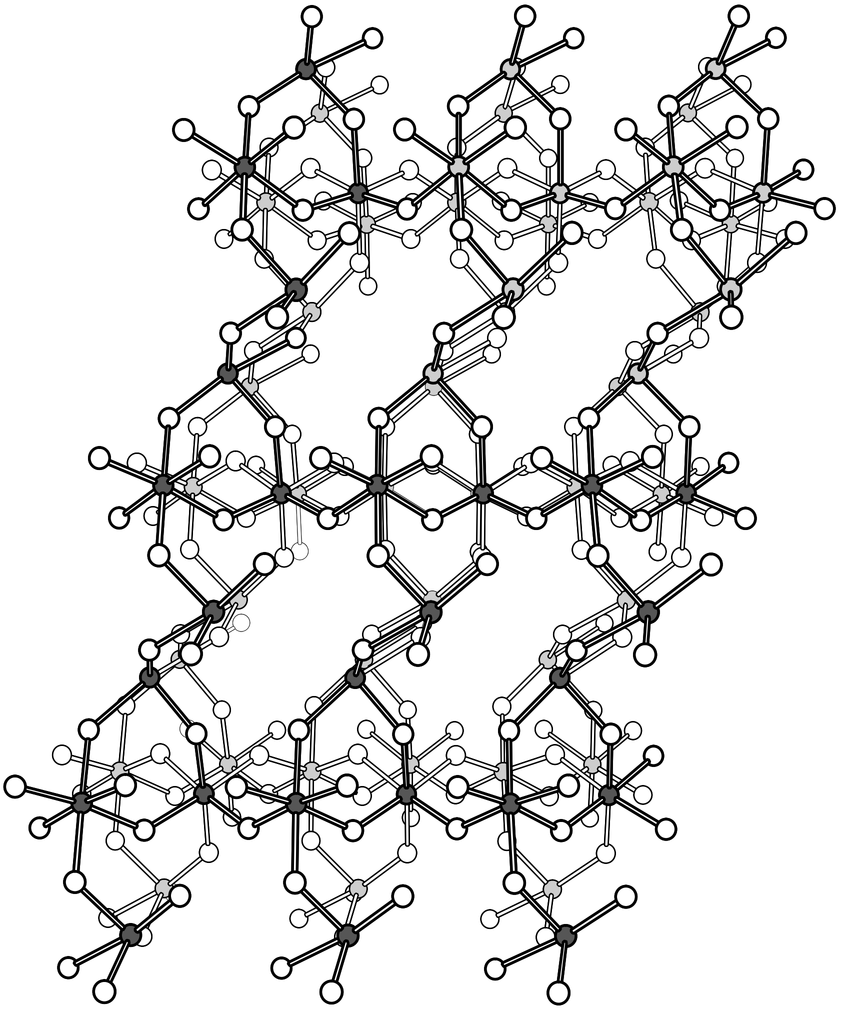

Figure 20 The crystal structure of Te_2O_5.[133] Tellurium is indicated in grey and oxygen in white

share oxygen vertices to form infinite sheets that are linked by four-coordinate Te^{IV} (see Figure 20).

5.2 Oxoacids of Tellurium

Telluric acid is a white solid the crystal structure of which is built up of discrete regular octahedral molecules of $Te(OH)_6$. It can conveniently be obtained by oxidizing TeO_2 in aqueous solution by, for example, $KMnO_4$. Anhydrous telluric acid can be crystallized in cubic, tetragonal, and monoclinic modifications. Structural data exist for the cubic and monoclinic forms. They both consist of discrete $Te(OH)_6$ molecules that are linked together by hydrogen bonds.[134–136]

In contrast to H_2SO_4 and H_2SeO_4, $Te(OH)_6$ is a weak three-basic acid. The acid constants are estimated to be $K_1 = 2 \times 10^{-8}$, $K_2 = 10^{-11}$, and $K_3 = 3 \times 10^{-15}$. It is a relatively strong oxidizing agent and is reduced to the element by SO_2 and to H_2TeO_3 by HCl:

$$\begin{aligned} &Te(OH)_6 + 3SO_2 \longrightarrow Te + 3H_2SO_4 \\ &Te(OH)_6 + 2HCl \longrightarrow H_2TeO_3 + Cl_2 + 3H_2O \end{aligned} \tag{4}$$

The crystal structure of H_2TeO_4 has also been determined. It has a slightly puckered planar structure in which the octahedral TeO_6 units share equatorial oxygen atoms (see Figure 21). Hydrogen atoms are bound to two exoplanar oxygen atoms that lie in trans- positions.[137] Another interesting oxoacid of tellurium is $H_2Te_2O_6$. It contains a network of alternating $Te^{VI}O_6$ and $Te^{IV}O_4$ fragments that share oxygen atoms (see Figure 22).

Tellurates are generally formed by solid-state reactions rather than by neutralization of aqueous $Te(OH)_6$ solutions. A typical example is the heating of the acid in the presence of copper carbonate:

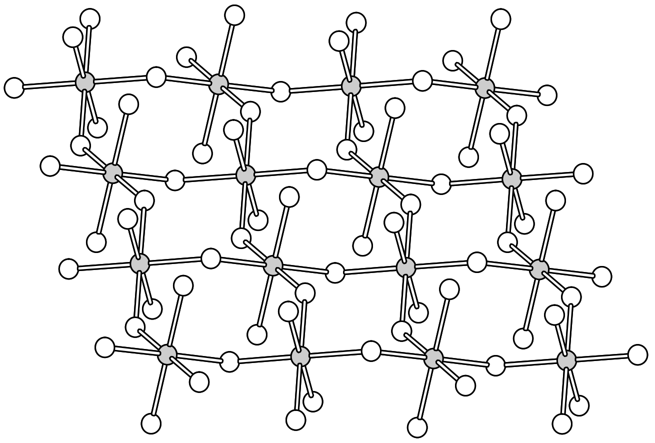

Figure 21 The crystal structure of H_2TeO_4.[137] Tellurium atoms are indicated in grey and oxygen in white

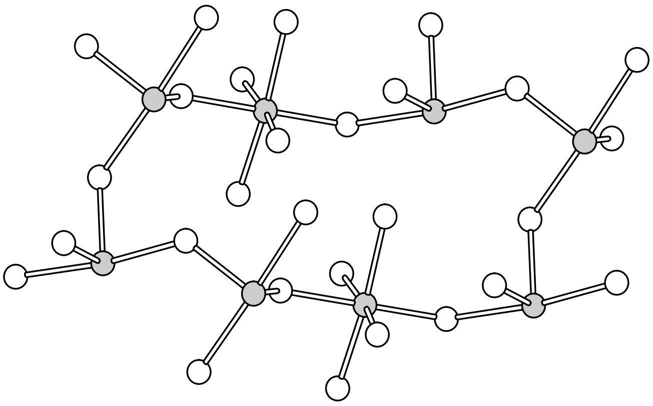

Figure 22 The crystal structure of $H_2Te_2O_6$.[138] Tellurium atoms are indicated in grey and oxygen in white

$$3CuCO_3(s) + Te(OH)_6(s) \xrightarrow{heat} Cu_3TeO_6(s) + 3CO_2(g) + 3H_2O(g) \tag{5}$$

Tellurium(VI) salts exhibit a large range of stoichiometries. Typical examples are Li_6TeO_6,[139] Na_2TeO_4,[140] Be_4TeO_7,[141] and Mg_3TeO_6.[142] As shown in Figure 23, all structures are based on TeO_6 octahedra and are generally more complex than what could be expected from the deceptively simple stoichiometry of the species. For example, the formula Na_2TeO_4 implies the presence of a $TeO_4{}^{2-}$ ion that could be analogous to $SO_4{}^{2-}$ and $SeO_4{}^{2-}$, but the structure is composed of chains of edge-shared TeO_6 octahedra (see Figure 23(a)) that are linked by NaO_6 polyhedra.

Tellurous acid H_2TeO_3 is also a weak acid with the acid dissociation constants of $K_1 = 2.7 \times 10^{-3}$ and $K_2 = 1.8 \times 10^{-8}$. By contrast to tellurates(VI), the tellurates(IV) can exist in solid state as discrete $TeO_3{}^{2-}$ anions as in $NaKTeO_3{\cdot}H_2O$[143] and $K_2TeO_3{\cdot}3H_2O$.[144] The anion in $K_2Te_2O_5{\cdot}3H_2O$ consists of Te_2O_5 units that are linked into infinite chains by sharing a terminal oxygen.[145] Tellurium shows a distorted trigonal bipyramidal coordination environment.

6 TELLURIUM–NITROGEN COMPOUNDS

While sulfur–nitrogen chemistry has a long and extensive history, selenium–nitrogen and tellurium–nitrogen chemistry has seen more extensive progress only during the recent decade.[59,146,147] One reason for the recent progress is the availability of versatile reagents, like $Te\{N(SiMe_3)_2\}_2$[148] and $\{Te(N^tBu)_2\}_2$.[149]

The existence of the tellurium analogue of S_4N_4 is unclear. It has long been known that explosive lemon-yellow nitride with the composition Te_3N_4 (**1**) can be prepared.[150–152] While the molecular structure is not known, it is conceivable that it has a tricyclic structure:[59]

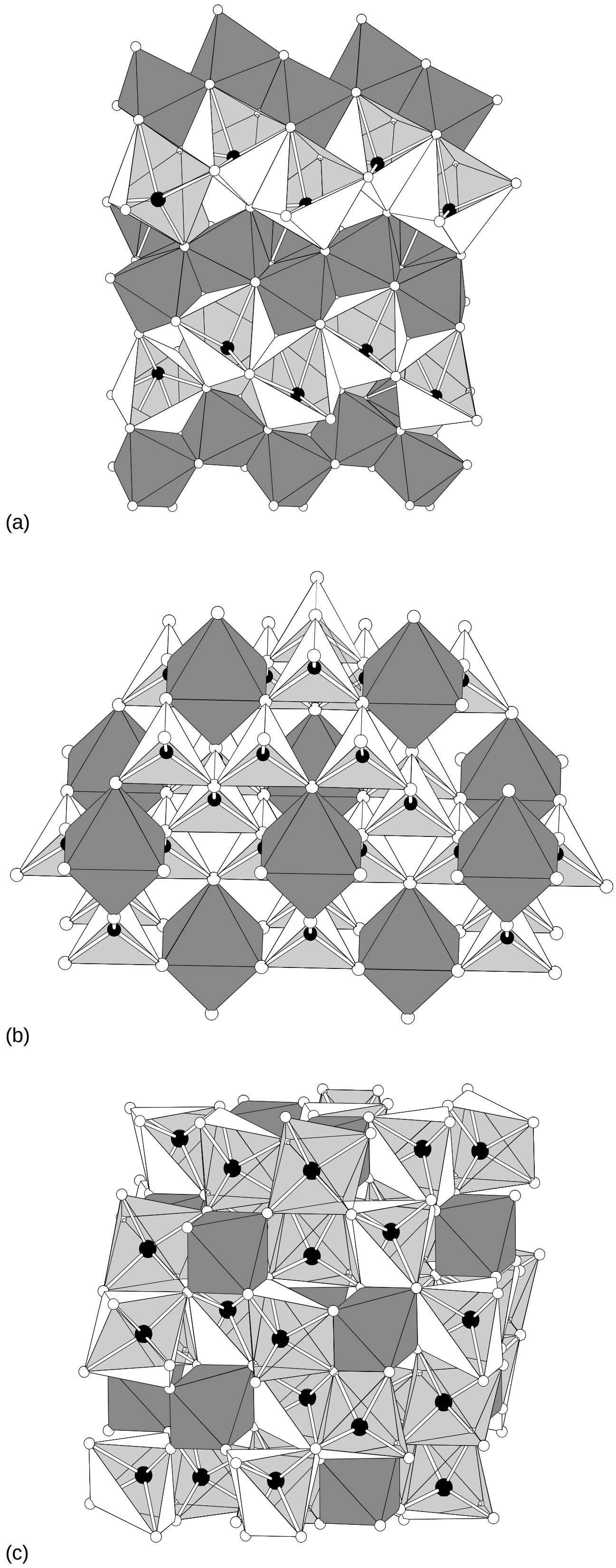

Figure 23 The crystal structures of (a) Na_2TeO_4,[140] (b) Be_4TeO_7,[141] and (c) Mg_3TeO_6[142]

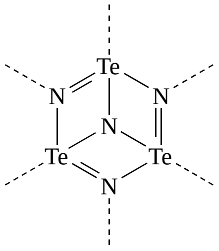

(**1**)

This is in contrast to the cage-like structures of S_4N_4 and Se_4N_4, which show weak transannular chalcogen–chalcogen interactions.[153–156] The very slight solubility of Te_3N_4 indicates that the molecules are strongly associated in the solid state as a result of intermolecular Te···N interactions. Support for the Te_3N_4 structure comes from $N(XTeNSN)_3$ (X = F (**2**), Cl (**3**)),[157,158] which also show a central nitrogen atom coordinated to three tellurium atoms.

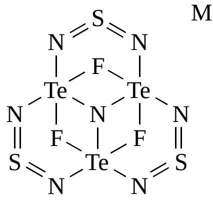

(**2**)

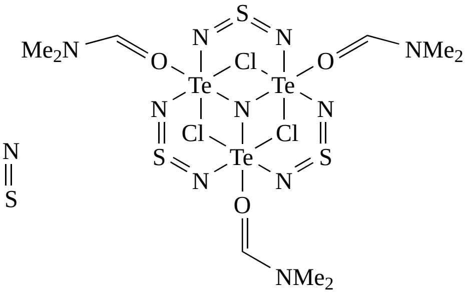

(**3**)

A core with similar features is also found in $[Te_6N_8(TeCl_4)_4{\cdot}(thf)_4]$ (see Figure 24).[159]

Tellurium imides comprise another class of tellurium–nitrogen compounds of recent interest.[59,147] Diorganotellurium imides $RR'TeNR''$ can formally be considered to contain a Te=N double bond, but the Te–N distance generally falls between the single and double bond lengths.[160,161] While the existence of monomeric tellurium diimides $(RN)_2Te$ have been suggested,[162] the recent structural characterization $RNTe(\mu\text{-}N^tBu)_2TeNR$ (R = ^{t}Bu[149] or PPh_2NSiMe_3[163]) shows them to be dimeric. Indeed, DFT calculations at different levels of theory[164,165] have shown that while the dimerization of $(MeN)_2S$ is clearly endothermic and that of $(MeN)_2Se$ is slightly endothermic, the dimerization of $(MeN)_2Te$ is clearly exothermic (see Figure 25). The exocyclic Te–N bonds show approximate double bond lengths[149,163] but the endocyclic bonds are longer exhibiting distance expected for a Te–N single bonds.[166] It has been deduced by ^1H, ^{31}P, and ^{125}Te NMR studies that both $RNTe(\mu\text{-}N^tBu)_2TeNR$ (R = ^{t}Bu[149] or PPh_2NSiMe_3[163]) species may exhibit isomerism in solution.[167] The main isomers have their exocyclic RNTe groups either in cis (**4**) or trans (**5**) positions with respect to the four-atomic Te_2N_2 ring:

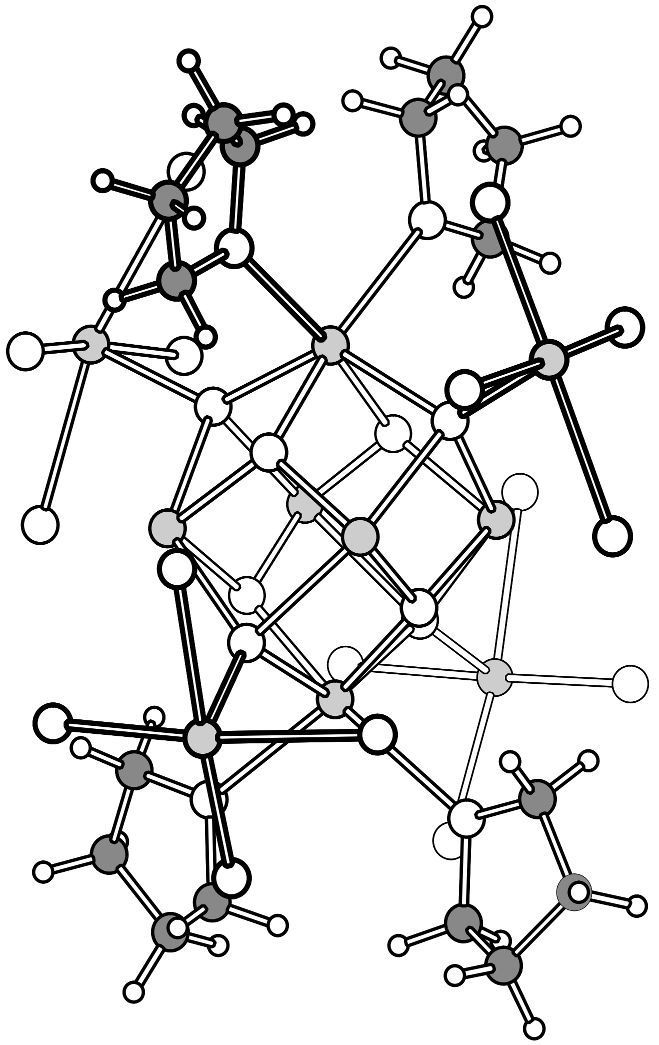

Figure 24 The structure of $[Te_6N_8(TeCl_4)_4 \cdot (thf)_4]$.[159] Tellurium atoms are indicated in grey, nitrogen, oxygen, and chlorine in white, and carbon atoms from the tetrahydrofuran rings in dark grey

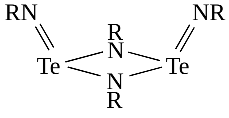

cis

(**4**)

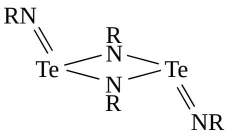

trans

(**5**)

It is interesting to note that the solid-state conformation of ^{t}BuNTe(μ-N^{t}Bu)$_2$TeN^{t}Bu is cis,[149] whereas that of Me$_3$SiN(Ph)$_2$PNTe(μ-N^{t}Bu)$_2$TeNP(Ph)$_2$NSiMe$_3$ is trans.[163]

Tellurium diimide dimers are thermally stable. For instance, ^{t}BuNTe(μ-N^{t}Bu)$_2$TeN^{t}Bu sublimes at 85 °C, 10^{-3} Torr and melts at 100–102 °C without decomposition.[149] This is a marked contrast to selenium diimides. $(RN)_2Se$ (R = ^{t}Bu[167,168] or adamantyl[169,170]) are monomeric species that are thermally unstable and decompose spontaneously in solution to a variety of selenium–nitrogen species.

The dimeric structure of tellurium diimides is retained upon complexation. The coordination with coinage metals leads to dinuclear complexes in which tellurium diimide can act either as a chelating or bridging ligand, as exemplified by [Ag$_2${^{t}BuNTe(μ-N^{t}Bu)$_2$TeN^{t}Bu}$_2$(CF$_3$SO$_3$)$_2$] and [Cu$_2${^{t}BuNTe(μ-N^{t}Bu)$_2$TeN^{t}Bu}$_3$](CF$_3$SO$_3$)$_2$·2CH$_2$Cl$_2$ (see Figure 26).[171] The two ligands in the silver complex retain the cis-conformation of the free ligand, but the exocyclic ^{t}Bu groups are both in exo positions to accommodate the coordination with Ag$^+$ ion. There is a Ag···Ag close contact of 2.888(2) Å in the structure that provides a contribution to controversy of the existence of metal–metal bonding in the d^{10}-d^{10} systems.[172–175] In the dinuclear copper complex cation, the two Cu$^+$ centers are coordinated to the exocyclic nitrogen atoms of two chelating and one bridging *tert*-butyl tellurium diimide dimer ligands. The chelating ligands show the exocyclic RN groups in cis positions while those of the bridging didentate ligand display them in trans positions.

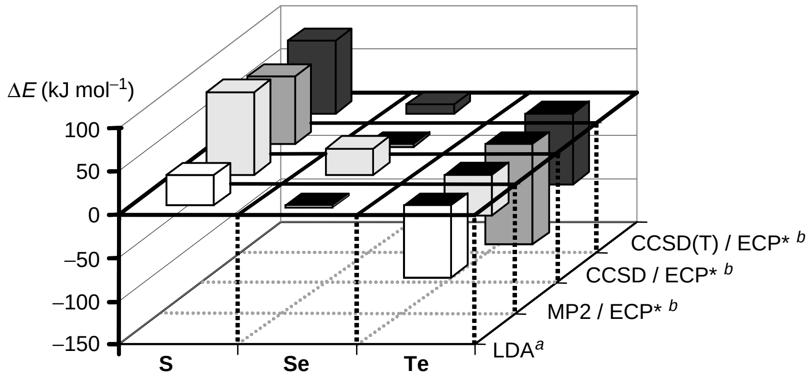

Figure 25 The calculated energy change in the [2 + 2] cyclodimerization of chalcogen diimides E(NMe)$_2$ (E = S, Se, Te). The calculations have been performed at ^{a}LDA[164] as well as at ^{b}MP2/ECP, CCSD/ECP, and CCSD(T)/ECP[165] levels of theory (© 2005 from Ref. 165 Reproduced by permission of Taylor & Francis, Inc. http://www.taylorandfrancis.com)

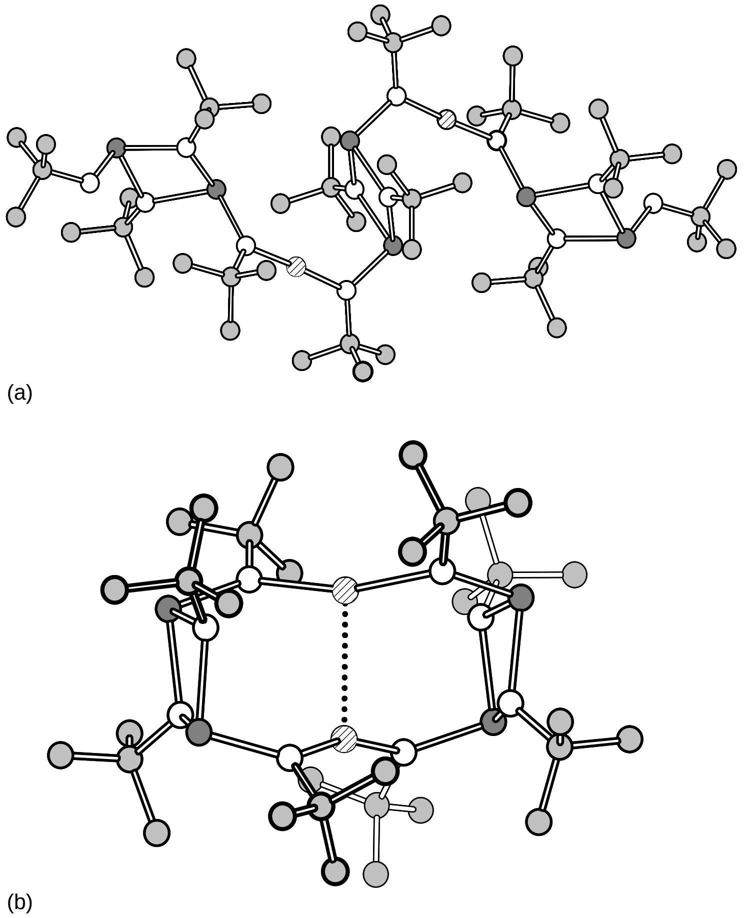

Figure 26 The structures of the complexes of $\{Te(N^tBu)_2\}_2$ with coinage metals: (a) $[Cu_2\{^tBuNTe(\mu\text{-}N^tBu)_2TeN^tBu\}_3](CF_3SO_3)_2\cdot 2CH_2Cl_2$, (b) $[Ag_2\{^tBuNTe(\mu\text{-}N^tBu)_2TeN^tBu\}_2(CF_3SO_3)_2]$.[171] Tellurium is indicated in dark grey, carbon in lighter grey, nitrogen in white, and transition metals as striped spheres

The tellurium diimide dimer readily reacts with nucleophiles. The treatment with potassium *tert*-butoxide generates the pyramidal *tert*-butoxybis(*tert*-butylimido)tellurite anion $[Te(N\text{-}^tBu)_2(O^tBu)]^-$.[176] In the solid state, the anion as its potassium salt adopts a dimeric arm-chair structure (see Figure 27(a)) The similar reaction with lithium *tert*-butylamide affords a centrosymmetric structure consisting of a distorted hexagonal prism involving two pyramidal tris(*tert*-butylimido)tellurite dianions linked by four lithium cations (see Figure 27(b)).[177,178]

7 OUTLOOK

While the chemistry of tellurium compounds is still in its infancy, the rapid recent progress has shown that tellurium has many unique properties compared to other chalcogen elements. The advent and development of modern instrumental structural methods of analysis have had a strong influence in the development of tellurium chemistry. Tellurium has two NMR-active $I = 1/2$ nucleii of which ^{125}Te (natural abundance 7.1%) is particularly useful for monitoring chemical reactions and identifying new species. X-ray crystallography has shown that the structural features of tellurium compounds often differ from those of sulfur and selenium.

Binary tellurides are convenient materials in many electronic devices. Active research interest is currently being directed into synthesis and characterization of novel nonmetallic tellurium compounds and transition metal compounds with tellurium-containing ligands, as well as into organic and organometallic tellurium chemistry. The goal is to use these compounds as single-source precursors for the generation of thin films for electronic applications. Many inorganic tellurium compounds also find utility in organic synthetic chemistry (*see* ***Tellurium: Organotellurium Chemistry***). Tellurium research is a prime example of the advances achieved by combining forces of fundamental and applied research.

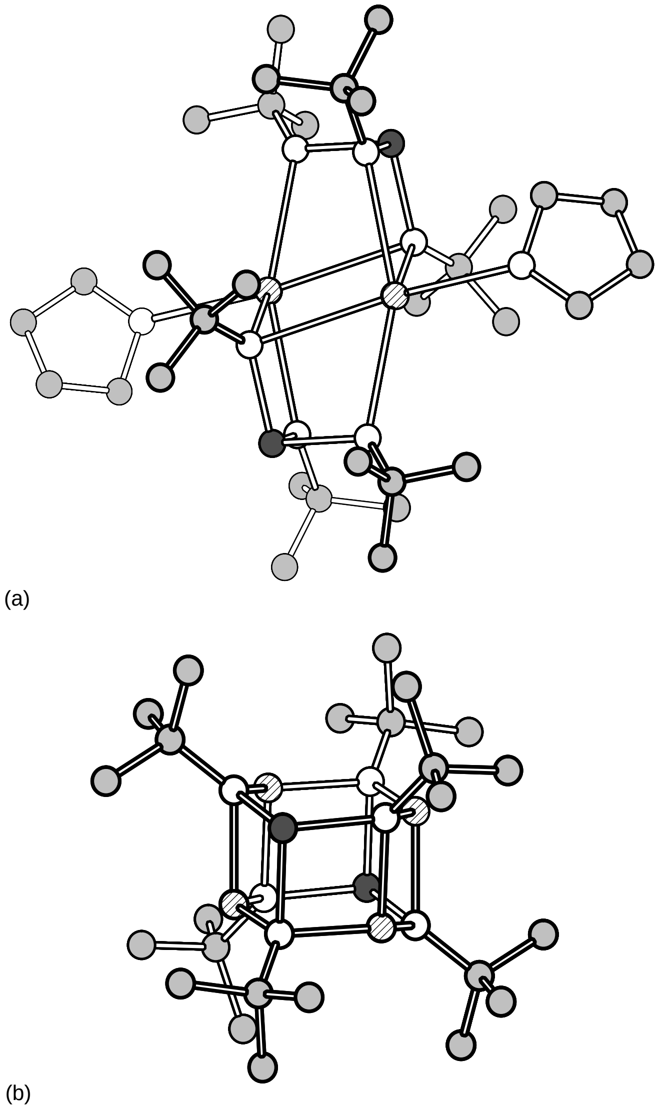

Figure 27 (a) The structure of $[\mathrm{Te(N^tBu)_2(O^tBu)}]^-$ ion in the potassium salt.[176] (b) The structure of the $[\mathrm{Te(N^tBu)_3}]^{2-}$ ion in $\mathrm{Li_4\{Te(N^tBu)_3\}_2}$.[178] Tellurium is indicated in dark grey, oxygen and nitrogen in white, carbon in light grey and the alkali metal as striped spheres

8 RELATED ARTICLES

Polonium: Inorganic Chemistry; Selenium: Inorganic Chemistry; Sulfur: Inorganic Chemistry; Sulfur–Nitrogen Compounds; Tellurium: Organotellurium Chemistry .

9 REFERENCES

1. F. J. Müller von Reichenstein, *Phys. Arb. Freunde Wien.*, 1785, **3**, 48.
2. M. H. Klaproth, *Mem. Akad. Berlin*, 1798, **50**, 17.
3. H. E. Hilliard, *Tellurium: U.S. Geol. Surv. Miner. Commodity Summ.*, 2003, 170.
4. R. Keller, W. B. Holzapfel, and H. Schulz, *Phys. Rev. B*, 1977, **16**, 4404.
5. C. Adenis, V. Langer, and O. Lindqvist, *Acta Crystallogr.*, 1989, **45**, 941.
6. N. W. Alcock, *Adv. Inorg. Chem. Radiochem.*, 1972, **15**, 1.
7. R. Oilunkaniemi, J. Pietikäinen, R. S. Laitinen, and M. Ahlgrén, *J. Organomet. Chem.*, 2001, **640**, 50.
8. D. M. Chizhikov, V. P. Shchastlivyi, in ‘Tellurium and tellurides’, ed. E. M. Elkin, Collet, Weilingborough, 1970.
9. G. C. Vezzoli, *Z. Kristallogr.*, 1974, **139**, 159.
10. S. S. Kabalkina, L. F. Vereshchagin, and B. M. Shulenin, *Zh. Eksp. Teor. Fiz.*, 1964, **45**, 2073.
11. K. Aoki, O. Shimomura, and S. Minomura, *J. Phys. Soc. Jpn.*, 1980, **48**, 551.
12. J. C. Jamieson and D. B. McWhan, *J. Chem. Phys.*, 1965, **43**, 1149.
13. M. Takumi, T. Masamitsu, and K. Nagata, *J. Phys.*, 2002, **14**, 10609.
14. E. Gregoryanz, V. V. Struzhkin, R. J. Hemley, M. I. Eremets, H.-K. Mao, and Yu. A. Timofeev, *Phys. Rev. B*, 2002, **65**, 064504.
15. R. S. Laitinen, P. Pekonen, and R. J. Suontamo, *Coord. Chem. Rev.*, 1994, **130**, 1.
16. V. N. Bogomolov, A. I. Zadorozhnii, V. P. Petranovskii, V. P. Podkhalyuzin, and A. L. Kholkin, *JETP Lett.*, 1979, **29**, 373.
17. V. N. Bogomolov, A. I. Zadorozhnii, T. M. Pavlova, V. P. Petranovskii, V. P. Podkhalyuzin, and A. L. Kholkin, *JETP Lett.*, 1980, **31**, 378.
18. J. Pietikäinen and R. S. Laitinen, *J. Chem. Soc., Chem. Commun.*, 1998, 2381.
19. R. S. Laitinen and T. A. Pakkanen, *Inorg. Chem.*, 1987, **26**, 2598.
20. W. S. Sheldrick and M. Wachhold, *Angew. Chem.*, 1995, **107**, 490.
21. W. S. Sheldrick and M. Wachhold, *J. Chem. Soc., Chem. Commun.*, 1996, **5**, 607.
22. R. Misra, S. Goel, S. K. Tripathi, A. K. Agnihotri, and A. Kumar, *Physica B*, 1990, **167**, 195.
23. K. W. Smith, S. D. Smith, and S. S. Badesha, *J. Am. Chem. Soc.*, 1994, **106**, 724.
24. R. Cooper and J. V. Culka, *J. Inorg. Nucl. Chem.*, 1967, **29**, 1877.
25. M. Binnewies, *Z. Anorg. Allg. Chem.*, 1976, **422**, 43.
26. T. Chivers, R. S. Laitinen, K. J. Schmidt, and J. Taavitsainen, *Inorg. Chem.*, 1993, **32**, 337.
27. M. Pupp and J. Weiss, *Z. Anorg. Allg. Chem.*, 1978, **440**, 31.

28. J. Weiss, M. Pupp, *Angew. Chem.*, 1970, **82**, 447; J. Weiss, M. Pupp, *Acta Crystallogr., Sect. B* 1972, **28**, 3653.
29. K. Nagata, H. Hayashi, and Y. Miyamato, *Fukuoka Univ. Sci. Rep.*, 1988, **18**, 23.
30. K. Nagata, H. Hayashi, and Y. Miyamato, *Fukuoka Univ. Sci. Rep.*, 1988, **18**, 35.
31. J. Taavitsainen and R. S. Laitinen, *Main Group Chem.*, 1999, **3**, 59.
32. J. W. Kolis, *Chem. Rev.*, 1990, **105**, 195.
33. M. G. Kanatzidis and S. P. Huang, *Coord. Chem. Rev.*, 1994, **130**, 509.
34. W. Tremel, H. Kleinke, V. Derstoff, and C. Reisner, *J. Alloys Compd.*, 1995, **219**, 73.
35. M. G. Kanatzidis, *Angew. Chem., Int. Ed. Engl.*, 1995, **34**, 2109.
36. M. G. Kanatzidis, *Nato ASI Series. Series B*, 1996, **354**, 83.
37. M. G. Kanatzidis and B. K. Das, *Comments Inorg. Chem.*, 1999, **21**, 29.
38. D. M. Smith and J. A. Ibers, *Coord. Chem. Rev.*, 2000, **200–202**, 187.
39. A. K. Singh and S. Sharma, *Coord. Chem. Rev.*, 2000, **209**, 49.
40. D. Y. Valentine, O. B. Cavin, and H. L. Yakel, *Acta Crystallogr., Sect. B*, 1977, **33**, 1389.
41. P. Böttcher and R. Keller, *Z. Anorg. Allg. Chem.*, 1986, **542**, 144.
42. B. Harbrecht and A. Selmer, *Z. Anorg. Allg. Chem.*, 1994, **620**, 1861.
43. B. Schreiner, K. Dehnicke, K. Maczek, and D. Fenske, *Z. Anorg. Allg. Chem.*, 1993, **619**, 1414.
44. P. Boettcher and U. Kretschmann, *J. Less-Common Met.*, 1983, **95**, 81.
45. W. S. Sheldrick and B. Schaaf, *Z. Naturforsch.*, 1994, **49**, 993.
46. C. Reisner and W. Tremel, *J. Chem. Soc., Chem. Commun.*, 1997, 387.
47. M. A. Ansari, J. M. McConnachie, and J. A. Ibers, *Acc. Chem. Res.*, 1993, **26**, 574.
48. L. C. Roof and J. W. Kolis, *Chem. Rev.*, 1993, **93**, 1037.
49. J. Beck, *Angew. Chem., Int. Ed. Engl.*, 1994, **33**, 163.
50. W. S. Sheldrick and M. Wachhold, *Angew. Chem., Int. Ed. Engl.*, 1997, **36**, 206.
51. R. Burns and J. D. Corbett, *Inorg. Chem.*, 1981, **20**, 4433.
52. R. C. Haushalter, *Angew. Chem., Int. Ed. Engl.*, 1985, **24**, 432.
53. W. A. Flomer and J. W. Kolis, *J. Am. Chem. Soc.*, 1988, **110**, 3682.
54. J. M. McConnachie, M. A. Ansari, and J. A. Ibers, *Inorg. Chim. Acta*, 1992, **198–200**, 85.
55. W. A. Flomer and J. W. Kolis, *Inorg. Chem.*, 1989, **28**, 2513.
56. M. A. Ansari, J. C. Bollinger, and J. A. Ibers, *Inorg. Chem.*, 1993, **32**, 1746.
57. R. D. Adams, T. A. Wolfe, B. W. Eichorn, and R. C. Haushalter, *Polyhedron*, 1989, **8**, 701.
58. J. M. McConnechie, M. A. Ansari, J. C. Bollinger, R. J. Salm, and J. A. Ibers, *Inorg. Chem.*, 1993, **32**, 3201.
59. T. Chivers, *J. Chem. Soc., Dalton Trans.*, 1996, 1185.
60. J. Beck, *Coord. Chem. Rev.*, 1997, **163**, 55.
61. S. Brownridge, I. Krossing, J. Passmore, H. D. B. Jenkins, and H. K. Roobottom, *Coord. Chem. Rev.*, 2000, **197**, 397.
62. J. Beck, *Z. Naturforsch.*, 1990, **45b**, 413.
63. J. Beck, A. Fischer, and A. Stankowski, *Z. Anorg. Allg. Chem.*, 2002, **628**, 2542.
64. J. Beck and G. Bock, *Angew. Chem., Int. Ed. Engl.*, 1995, **34**, 2559.
65. R. C. Burns, R. J. Gillespie, W. C. Luk, and D. R. Slim, *Inorg. Chem.*, 1979, **18**, 3086.
66. M. J. Collins, R. J. Gillespie, and J. F. Sawyer, *Acta Crystallogr.*, 1988, **44C**, 405.
67. J. Beck, *Chem. Ber.*, 1994, **128**, 23.
68. R. J. Gillespie, E. Maharajh, W. C. Luk, and D. R. Slim, *Inorg. Chem.*, 1977, **16**, 892.
69. R. C. Burns, M. J. Collins, S. M. Eicher, R. J. Gillespie, and J. F. Sawyer, *Inorg. Chem.*, 1988, **27**, 1807.
70. P. D. Lyne, D. M. P. Mingos, and T. Ziegler, *J. Chem. Soc., Dalton Trans.*, 1992, 2743.
71. J. Beck and G. Bock, *Z. Anorg. Allg. Chem.*, 1996, **622**, 823.
72. R. J. Gillespie, *Chem. Soc. Rev.*, 1979, **8**, 315.
73. J. Beck, *Angew. Chem., Int. Ed. Engl.*, 1990, **29**, 301.
74. M. J. Collins, R. J. Gillespie, and J. F. Sawyer, *Inorg. Chem.*, 1987, **26**, 1476.
75. J. Beck and A. Stankowski, *Z. Naturforsch.*, 2001, **56b**, 453.
76. J. Beck and A. Fischer, *Z. Anorg. Allg. Chem.*, 2002, **628**, 369.
77. A. Baumann, J. Beck, and T. Hilbert, *Z. Naturforsch.*, 1999, **54b**, 1253.
78. J. Beck and G. Bock, *Z. Anorg. Allg. Chem.*, 1994, **620**, 1971.
79. J. Beck, A. Fischer, and A. Stankowski, *Z. Anorg. Allg. Chem.*, 2002, **628**, 2542.
80. G. W. Drake, G. L. Schimek, and J. W. Kolis, *Inorg. Chem.*, 1996, **35**, 1740.
81. B. Krebs and F.-P. Ahlers, *Adv. Inorg. Chem.*, 1990, **35**, 235.
82. R. Kniep, K. Korte, R. Kryschi, and W. Poll, *Angew. Chem.*, 1984, **96**, 351.
83. H. M. Seip and R. Stölenik, *Acta Chem. Scand.*, 1966, **20**, 1535.
84. L. S. Bartell and B. M. Powell, *Mol. Phys.*, 1992, **75**, 689.
85. B. Buss and B. Krebs, *Inorg. Chem.*, 1971, **10**, 2795.
86. B. Krebs and V. Paulat, *Acta Crystallogr.*, 1976, **B32**, 1470.
87. D. J. Stevenson and V. Schomaker, *J. Am. Chem. Soc.*, 1940, **62**, 1267.
88. A. Alemi, E. Soleimani, and Z. A. Starikova, *Acta Chim. Sloven.*, 2000, **47**, 89.

89. B. Krebs, *Nova Acta Leopold.*, 1985, **59**, 131.
90. H. J. Beister, R. Kniep, and A. Schaefer, *Z. Kristallogr.*, 1986, **174**, 12.
91. R. Kniep, H. J. Beister, and D. Wald, *Z. Naturforsch.*, 1988, **43**, 966.
92. L. Fernholt, A. Haaland, and R. Seip, *Z. Naturforsch.*, 1983, **38b**, 1072.
93. L. Fernholt, A. Haaland, H. V. Volden, and R. Kniep, *J. Mol. Struct.*, 1985, **128**, 29.
94. A. Rabenau and H. Rau, *Z. Anorg. Allg. Chem.*, 1973, **395**, 273.
95. R. C. Paul, A. Arneja, and S. P. Narula, *Inorg. Nucl. Chem. Lett.*, 1969, **5**, 1013.
96. J. Pietikäinen, R. S. Laitinen, J. Konu, and J. Valkonen, *Z. Naturforsch., Teil B*, 2001, **56b**, 1369.
97. E. E. Aynsley, *J. Chem. Soc.*, 1953, 3016.
98. A. Maaninen, T. Chivers, M. Parvez, J. Pietikäinen, and R. S. Laitinen, *Inorg. Chem.*, 1999, **38**, 4093.
99. J. Pietikäinen, A. Maaninen, R. S. Laitinen, R. Oilunkaniemi, and J. Valkonen, *Polyhedron*, 2002, **21**, 1089.
100. R. Kniep and A. Rabenau, *Top. Curr. Chem.*, 1983, **111**, 145.
101. W. Bauhofer and R. Kniep, *Mater. Res. Bull.*, 1973, **8**, 989.
102. A. Rabenau, H. Rau, and P. Eckerlin, *Angew. Chem., Int. Ed. Engl.*, 1967, **6**, 706.
103. A. Rabenau, H. Rau, and G. Rosenstein, *Angew. Chem., Int. Ed. Engl.*, 1970, **9**, 802.
104. R. Kniep, D. Mootz, and A. Rabenau, *Z. Anorg. Allg. Chem.*, 1976, **422**, 17.
105. D. Katryniok and R. Kniep, *Angew. Chem., Int. Ed. Engl.*, 1980, **9**, 645.
106. D. Katryniok, R. Kniep, and D. Mootz, *Z. Anorg. Allg. Chem.*, 1980, **461**, 96.
107. H. Oberhammer and K. Seppelt, *Angew. Chem., Int. Ed. Engl.*, 1978, **17**, 69.
108. H. Oberhammer and K. Seppelt, *Inorg. Chem.*, 1978, **17**, 1435.
109. A. Ider, J. P. Laval, B. Frit, J. Carré, and J. P. Bastide, *J. Solid State Chem.*, 1996, **123**, 68.
110. L. Guillet, A. Ider, J. P. Laval, and B. Frit, *J. Fluorine Chem.*, 1999, **93**, 33.
111. H. P. A. Merciér, J. C. P. Sanders, and G. J. Schrobilgen, *J. Am. Chem. Soc.*, 1994, **116**, 2921.
112. D. M. Van Segge, P. K. Hurlburt, O. P. Anderson, and S. H. Strauss, *Inorg. Chem.*, 1995, **34**, 3453.
113. D. Lentz, H. Pritzkow, and K. Seppelt, *Inorg. Chem.*, 1978, **17**, 1926.
114. H. Pritzkow and K. Seppelt, *Inorg. Chem.*, 1977, **16**, 2685.
115. B. A. Fir, H. P. A. Merciér, J. C. P. Sanders, D. A. Dixon, and G. J. Schrobilgen, *J. Fluorine Chem.*, 2001, **110**, 89.
116. T. Drews and K. Seppelt, *Z. Anorg. Allg. Chem.*, 1991, **606**, 201.
117. K. Moock and K. Seppelt, *Z. Anorg. Allg. Chem.*, 1988, **561**, 132.
118. S. H. Strauss, N. D. Noirot, and O. O. Anderson, *Inorg. Chem.*, 1985, **24**, 4307.
119. W. Abriel, *Z. Naturforsch.*, 1981, **36b**, 405.
120. W. Abriel, *Z. Kristallogr.*, 1981, **156**, 8.
121. G. Giester, *Acta Crystallogr.*, 1994, **C50**, 3.
122. P. Khodadad and N. Rodier, *Bull. Chim. Soc. Fr.*, 1977, 251.
123. M. A. James, O. Knop, and T. S. Cameron, *Can. J. Chem.*, 1992, **70**, 1795.
124. A. W. Potts and T. A. Williams, *Chem. Phys. Lett.*, 1976, **42**, 550.
125. J. Drowart and P. Goldfinger, *Q. Rev.*, 1966, **20**, 545.
126. R. F. Barrow and H. J. Hurst, *Nature*, 1964, **201**, 699.
127. I. P. Kondratyuk, L. A. Muradyan, Yu. V. Pisarevskii, and V. I. Simonov, *Kristallografiya*, 1987, **32**, 609.
128. H. Beyer, *Z. Kristallogr.*, 1967, **124**, 228.
129. J. C. Champarnaud-Mesjard, S. Blanchadin, P. Thomas, A. Mirgorodsky, T. Merle-Mejean, and B. Frit, *J. Phys. Chem. Solids*, 2000, **61**, 1499.
130. M. A. K. Ahmed, H. Fjellvåg, and A. Kjekshus, *J. Chem. Soc., Dalton Trans.*, 2000, 4542 and references therein.
131. D. Dumora and P. Hagenmuller, *Compt. rend. Acad. Sci. (Paris)*, 1968, **266C**, 276.
132. M. Eudek and J. Loub, *Powder Diffr.*, 1988, **3**, 175.
133. O. Lindqvist and J. Moret, *Acta Crystallogr.*, 1973, **29B**, 643.
134. O. Lindqvist and M. S. Lehmann, *Acta Chem. Scand.*, 1973, **27**, 85.
135. C. Cohen-Addad, *Bull. Soc. Fr. Miner. Cristallogr.*, 1971, **94**, 172.
136. L. Falck and O. Lindqvist, *Acta Crystallogr.*, 1978, **34B**, 3145.
137. J. Moret, E. Philippot, M. Maurin, and O. Lindqvist, *Acta Crystallogr.*, 1974, **30B**, 1813.
138. O. Lindqvist and J. Moret, *Acta Crystallogr.*, 1973, **29B**, 956.
139. J. Hauck, *Z. Naturforsch.*, 1969, **24b**, 647.
140. B. Kratochvil and L. Jensovsky, *Acta Crystallogr.*, 1977, **33B**, 2596.
141. M. Troemel, J. Maetz, and M. Muellner, *Acta Crystallogr.*, 1977, **33B**, 3959.
142. H. Schulz and G. Beyer, *Acta Crystallogr.*, 1971, **27**, 815.
143. F. Daniel, J. Moret, M. Maurin, and E. Philippot, *Acta Crystallogr.*, 1982, **38B**, 703.
144. G. B. Johansson and O. Lindqvist, *Acta Crystallogr.*, 1978, **34B**, 2959.
145. L. Andersen and J. Moret, *Acta Crystallogr.*, 1983, **39C**, 143.
146. A. Haas, *J. Organomet. Chem.*, 2002, **646**, 80.
147. T. Chivers, *Can. J. Chem.*, 2001, **79**, 1841.
148. M. Björgvinsson, H. W. Roesky, F. Pauer, D. Stalke, and G. M. Sheldrick, *Inorg. Chem.*, 1990, **29**, 5140.

149. T. Chivers, X. Gao, and M. Parvez, *J. Am. Chem. Soc.*, 1995, **117**, 2359.

150. W. Strecker and W. Ebert, *Ber. Dtsch. Chem. Ges.*, 1925, **58**, 2527.

151. W. Strecker and C. A. Mahr, *Anorg. Chem.*, 1934, **221**, 199.

152. O. Schmitz-Dumont and B. Ross, *Angew. Chem., Int. Ed. Engl.*, 1967, **6**, 1071.

153. M. L. de Lucia and P. Coppens, *Inorg. Chem.*, 1978, **17**, 2336.

154. S. H. Irsen, P. Jacobs, and R. Dronskowski, *Z. Anorg. Allg. Chem.*, 2001, **627**, 321.

155. H. Baernighausen, T. von Volkmann, and J. Jander, *Acta Crystallogr.*, 1966, **21**, 571.

156. B. Jung, B. Neumüller, and K. Dehnicke, *Z. Anorg. Allg. Chem.*, 1994, **620**, 1011.

157. H. W. Roesky, J. Munzenberg, and M. Noltemeyer, *Angew. Chem., Int. Ed. Engl.*, 1990, **29**, 61.

158. J. Munzenberg, H. W. Roesky, S. Besser, R. Herbst-Irmer, and G. M. Sheldrick, *Inorg. Chem.*, 1992, **31**, 2986.

159. W. Massa, C. Lau, M. Mohlen, B. Neumüller, and K. Dehnicke, *Angew. Chem., Int. Ed. Engl.*, 1998, **37**, 2840.

160. V. I. Naddaka, I. D. Sadekov, A. A. Maksimenko, and V. I. Minkin, *Sulfur Rep.*, 1988, **8**, 61.

161. T. Shimizu, N. Kamigata, and S. Ikuta, *J. Chem. Soc., Perkin Trans. 2*, 1999, 1469.

162. L. N. Markovskii, E. A. Stukalo, and G. P. Kumitskayo, *J. Org. Chem. USSR (Engl. Transl.)*, 1977, **13**, 1911.

163. T. Chivers, X. Gao, and M. Parvez, *J. Chem. Soc., Chem. Commun.*, 1994, 2149.

164. N. Sandblom, T. Ziegler, and T. Chivers, *Inorg. Chem.*, 1998, **37**, 354.

165. R. S. Laitinen, *Phosphorus, Sulfur, Silicon Relat. Elem.*, in press.

166. A. Haas, J. Kasprowski, and M. Pryka, *Chem. Ber.*, 1992, **125**, 789.

167. T. Chivers, X. Gao, and M. Parvez, *Inorg. Chem.*, 1996, **35**, 9.

168. B. Wrackmeyer, B. Distler, S. Gerstmann, and M. Herberhold, *Z. Naturforsch.*, 1993, **48b**, 1307.

169. T. Maaninen, R. Laitinen, and T. Chivers, *Chem. Commun.*, 2002, 1812.

170. T. Maaninen, H. M. Tuononen, G. Schatte, R. Suontamo, J. Valkonen, R. S. Laitinen, and T. Chivers, *Inorg. Chem.*, 2004, **43**, 2097.

171. T. Chivers, M. Parvez, and G. Schatte, *Angew. Chem., Int. Ed. Engl.*, 1999, **38**, 2217.

172. K. M. Merz Jr and R. Hoffmann, *Inorg. Chem.*, 1988, **27**, 2120.

173. F. A. Cotton, X. Feng, M. Matusz, and R. Poli, *J. Am. Chem. Soc.*, 1988, **110**, 7077.

174. C. Kölmel and R. Ahlrichs, *J. Phys. Chem.*, 1990, **94**, 5536.

175. E. J. Fernández, J. M. López-de-Luzuriaga, M. Monge, M. A. Rodúguez, O. Gespo, M. C. Gimeno, A. Laguna, and P. G. Jones, *Inorg. Chem.*, 1998, **37**, 6090.

176. T. Chivers, X. Gao, and M. Parvez, *Inorg. Chem.*, 1996, **35**, 4633.

177. T. Chivers, X. Gao, and M. Parvez, *Angew. Chem., Int. Ed. Engl.*, 1995, **38**, 2549.

178. T. Chivers, X. Gao, and M. Parvez, *Inorg. Chem.*, 1996, **35**, 4336.

Tellurium: Organotellurium Chemistry

Risto S. Laitinen & Raija Oilunkaniemi
University of Oulu, Oulu, Finland

Based in part on the article Tellurium: Organotellurium Chemistry by William R. McWhinnie which appeared in the Encyclopedia of Inorganic Chemistry, First Edition.

1 Introduction 1
2 Diorganyl Tellurides 1
3 Organic Tellurium-Halogen Compounds 4
4 Triorganyltelluronium Salts 7
5 Organyltellurolates 8
6 Metal Complexes 10
7 Outlook 14
8 Related Articles 15
9 References 15

1 INTRODUCTION

The preparation of diethyl telluride in 1840 by F. Wöhler[1] marks the beginning of organic chemistry of tellurium. After the pioneering period during which several new organotellurium compounds were synthesized, the organic chemistry of tellurium saw only slow development for almost a century. However, during the recent decades the progress has been rapid and tellurium reagents have opened new vistas for the design of synthetic methodologies in organic chemistry. The utility of inorganic tellurium and organic tellurium reagents in synthetic chemistry are exemplified by the reduction of different functional groups and the reductive cleavage of carbon-heteroatom bonds. Tellurium reagents can be employed in mild conditions. The yields are generally high, the selectivity is good, and many reagents can be generated in situ leading to ‘one-pot’ syntheses. Organotellurium ligands have attracted interest in coordination chemistry with the goal of designing suitable precursors for chemical vapour deposition processes in order to fabricate thin-films that can be utilized in electronic materials such as II–VI semiconductors.

While organic tellurium derivatives are often thought to be malodorous, this reputation is deserved only by the light alkyl derivatives. With the exception of diphenyl telluride, the aromatic derivatives are solids at room temperature.

The research volume in organic and organometallic tellurium chemistry has grown very rapidly in recent years, as seen in Figure 1. A comprehensive review of the whole field is therefore beyond the scope of this article. The emphasis is on the preparation and structural characterization of some main classes of organic tellurium compounds and their organometallic complexes that are deemed of interest for inorganic chemists. Several books and monographs,[1–13] as well as review articles,[14–35] are available for more complete coverage of this vast subject.

2 DIORGANYL TELLURIDES

2.1 Preparation

Diorganyl mono- and ditellurides are the best-known classes of organic tellurium compounds comprising symmetric and unsymmetric alkyl, aryl, and alkyl–aryl tellurides. In addition to acyclic tellurides, heterocyclic aliphatic telluroethers as well as aromatic tellurophene-derivatives are known (for a review, see Ref. 36).

The original synthesis of diethyl telluride by Wöhler[1] was carried out by treating potassium telluride with ethyl sulfate. The preparation of potassium telluride was rather inconvenient and involved the reduction of elemental tellurium by heating the element at red heat with potassium–hydrogen *D*-tartrate.[37] An early report of Natta[38] demonstrated that the treatment of aluminium telluride by alcohols or ethers at 250–300 °C is also a promising route to diorganyl tellurides.

One common present day preparation of dialkyl mono- and ditellurides involves the reaction of alkyl halides with alkali metal tellurides that have been prepared in situ. The reactions are commonly carried out in aqueous or nonaqueous solutions.[39–41] Solutions of sodium in liquid ammonia also provide a useful media for the reduction of tellurium.[42]

$$\mathrm{M_2Te}_n + 2\mathrm{RX} \longrightarrow \mathrm{R_2Te}_n + 2\mathrm{MX} \quad \{\mathrm{M = Na, K; R = alkyl;}\ n = 1, 2\} \tag{1}$$

The telluride-anions are sufficiently nucleophilic to react also with aryl halides to afford aryl tellurides, but generally the aryl group must be activated either by an additional substituent, or the reaction must be carried out at higher temperatures.[8] For example, *para*-iodobenzene reacts at 110–120 °C with sodium telluride to form polymeric poly-*p*-phenylenetelluride.[43,44]

$$p\text{-}\mathrm{IC_6H_4I} + \mathrm{Na_2Te} \xrightarrow{\mathrm{DMF}} p\text{-}(\mathrm{C_6H_4Te})_n \tag{2}$$

Aryl tellurides can be prepared by utilization of Grignard or alkyl lithium reagents, since elemental tellurium can conveniently be inserted into Mg–C or Li–C bonds. The one-pot synthesis of tetratellurafulvalene illustrates the use of organolithium reagents.

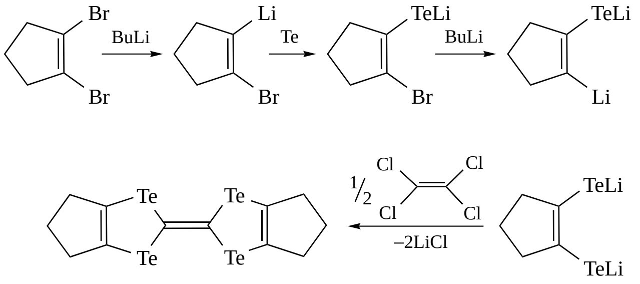

(3)

These reactions are commonly utilized in the preparation of ditellurides.[45,46]

$$\mathrm{Ar} + n\text{-}\mathrm{BuLi} \xrightarrow{\mathrm{THF},\ -78\,^{\circ}\mathrm{C}} \mathrm{ArLi} \xrightarrow{\mathrm{Te},\ 25\,^{\circ}\mathrm{C}} \mathrm{ArTeLi} \xrightarrow{\mathrm{K_3[Fe(CN)_6]\ (aq)}} \mathrm{Ar_2Te_2} \qquad (4)$$

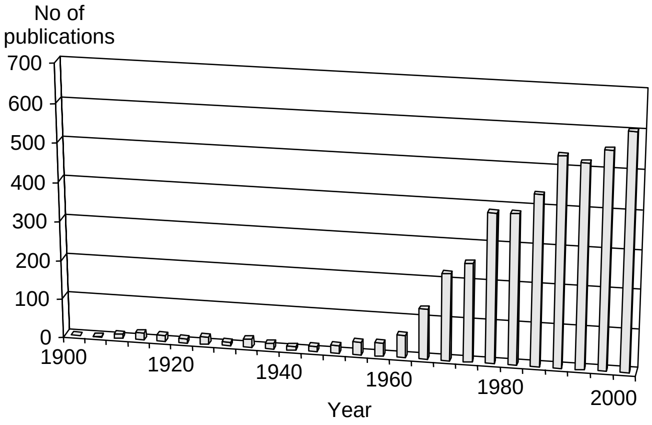

Figure 1 The growth of publication volume of organotellurium compounds

The final step in the reaction involves the oxidation of ArTeLi. Initially it has been carried out by oxygen in air, but it has been reported that $[\mathrm{Fe(CN)_6}]^{3-}$ (aq) is a superior choice of the oxidant.[46]

n-Butyllithium does not lithiate pyridine in the 2-position, because of the preferential ring alkylation to proton abstraction. 2-lithiopyridine can, however, be produced by treating 2-bromopyridine with *tert*-butyllithium.[45] Also pyrrole and indole can be regiospecifically lithiated in the 2-position when bearing a suitable nitrogen protecting group.

Treatment of alkali metal alkyl or aryltellurolates (Section 5) with alkyl halides, aryl halides, alkenes, or alkynes have been used to prepare unsymmetrical tellurides, as exemplified by the reaction of sodium phenyl tellurolate or paramethylphenyl tellurolate with $\mathrm{PhC{\equiv}CHCOPh}$.[47]

$$\mathrm{RTeNa} + \mathrm{PhC{\equiv}CHCOPh} \xrightarrow{\mathrm{EtOH}} \mathrm{RTeC(Ph)CHOPh}$$
$$(\mathrm{R} = \mathrm{Ph},\ p\text{-}\mathrm{MeC_6H_4}) \qquad (5)$$

One convenient method for the preparation of organyl tellurolates is the treatment of diorganyl ditellurides with $\mathrm{NaBH_4}$.

Diaryltellurium trichlorides and dichlorides (Section 3.2) can be converted to diorganyltellurides and ditellurides upon treating with reducing agents such as sodium sulfide,[48,49] potassium hydrogensulfite,[50] hydrazine,[51] or thiourea S,S-dioxide.[52] A typical example is shown in Eg. (6).[51]

$$2(4\text{-}\mathrm{CH_3OC_6H_4})_2\mathrm{TeCl_2} + \mathrm{N_2H_4} \longrightarrow 2(\mathrm{CH_3OC_6H_4})_2\mathrm{Te} + \mathrm{N_2} + 4\mathrm{HCl} \qquad (6)$$

Tellurium tetrachloride and Grignard reagents can also be used for the preparation of activated diaryl tellurides.

2.2 Molecular Structures

Various diaryl tellurides have been structurally characterized by single-crystal X-ray diffraction. Some illustrative

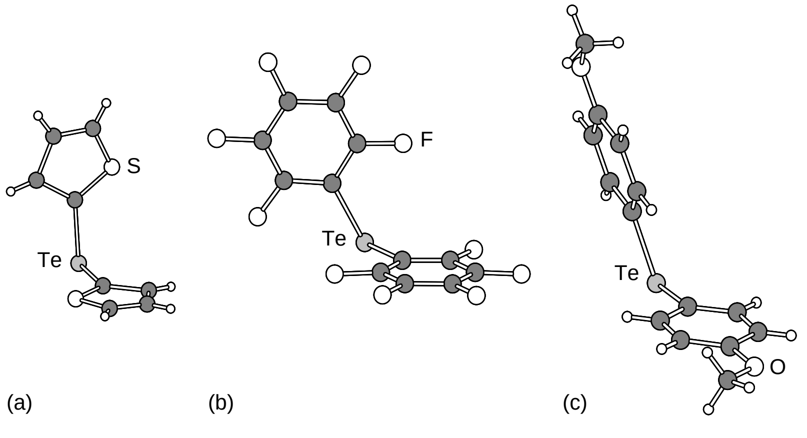

Figure 2 The crystal structures of (a) $\mathrm{Th_2Te}$ (Th = 2-thienyl, $\mathrm{C_4H_3S}$),[54] (b) $(\mathrm{F_5C_5})_2\mathrm{Te}$,[55] (c) $(\mathrm{MeOC_6H_4})_2\mathrm{Te}$[56]

structures are shown in Figure 2. The Te–C bond lengths are close to the single bond length of 2.10 Å (the sum of the covalent radii of carbon and tellurium is 2.14 Å[53]). The C–Te–C bond angle is close to 100°.

The Te–Te bond lengths in various diorganyl ditellurides are close to 2.70 Å defining an approximate single bond. The C–Te–Te bond angles span a range of 95–105°. In absence of steric effects, the C–Te–Te–C dihedral angles (τ) in ditellurides are close to 90° because of the minimized p lone-pair repulsion between the adjacent chalcogen atoms (see Figure 3).[57] For example, the dihedral angle of both $(C_6H_5)_2Te_2$[58] and $(C_8H_5S)_2Te_2$[59] is 88.5°; $(C_4H_3S)_2Te_2$ 86.5°,[57] and $(C_4H_3O)_2Te_2$ 91.6°.[57] It is well-established that the chalcogen–chalcogen bonds are lengthening, as the dihedral angle deviates from 90°. Like in the case of diselenides, bulky organic groups in ditellurides may lead to dihedral angles significantly above 90°, as exemplified by $\{2\text{-}(Re_2N)\text{-}4,6\text{-}(CF_3)_2C_6H_2\}_2Te_2$ ($\tau = 145.1°$)[60] and $(o\text{-}ClC_5H_3N)_2Te_2$ ($\tau = 180°$).[61] It has been suggested[62] that the steric strain is relieved by increasing the dihedral angle rather than by increasing the chalcogen–chalcogen and chalcogen-carbon bond lengths. Interactions between the p lone-pairs of tellurium and the π-electrons of the aromatic rings also explain why the Te–Te bonds are preferentially either perpendicular to the plane of the aromatic rings or lie on the same plane (see Figure 4).

The molecular structures of some diorganyltritellurides have been reported (see Figure 5). $\{(Me_3Si)_3C\}_2Te_3$ contains a bulky $(Me_3Si)_3C$ group.[63] The Te–Te bond shows a length of 2.710(1) Å and the Te–C bond is 2.213(7) Å. $\{2\text{-}(C_5H_4N)C_6H_4\}_2Te_3$[64] is probably stabilized by intramolecular Te···N interactions, as shown in Figure 5(b). The Te–Te bond shows a length of 2.776(1) Å and the Te–C bond shows a length of 2.130(9) Å. The Te–Te–Te bond angles are 103.8 and 100.4° for $\{(Me_3Si)_3C\}_2Te_3$ and $\{2\text{-}(C_5H_4N)C_6H_4\}_2Te_3$, respectively.

Tellurium has two NMR-active nucleii: ^{125}Te and ^{123}Te. Both have a nuclear spin of 1/2 (*see* ***Tellurium: Inorganic Chemistry***). ^{125}Te is more abundant and has a better receptivity than ^{123}Te. It has therefore found more general use in NMR spectroscopic characterization of tellurium-containing compounds. Some examples of the ^{125}Te chemical shifts of diorganyl tellurides and ditellurides are shown in Table 1. The lightest compound, Me_2Te, is the conventional reference for the ^{125}Te chemical shifts.

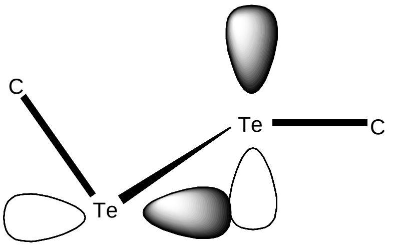

Figure 3 The observed torsional angle of ca. 90° is a consequence of minimized p lone-pair repulsion of adjacent tellurium atoms

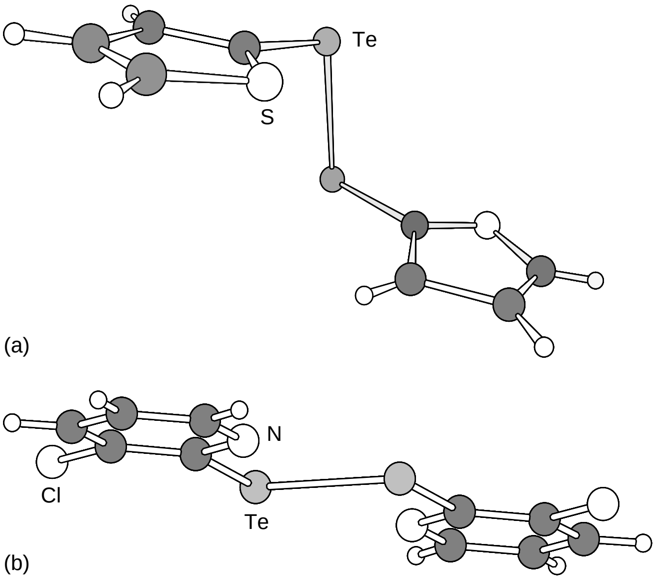

Figure 4 The crystal structures of (a) Th_2Te_2 (Th = 2-thienyl, C_4H_3S),[57] (b) $(o\text{-}ClC_5\ NH_3)_2Te_2$[61]

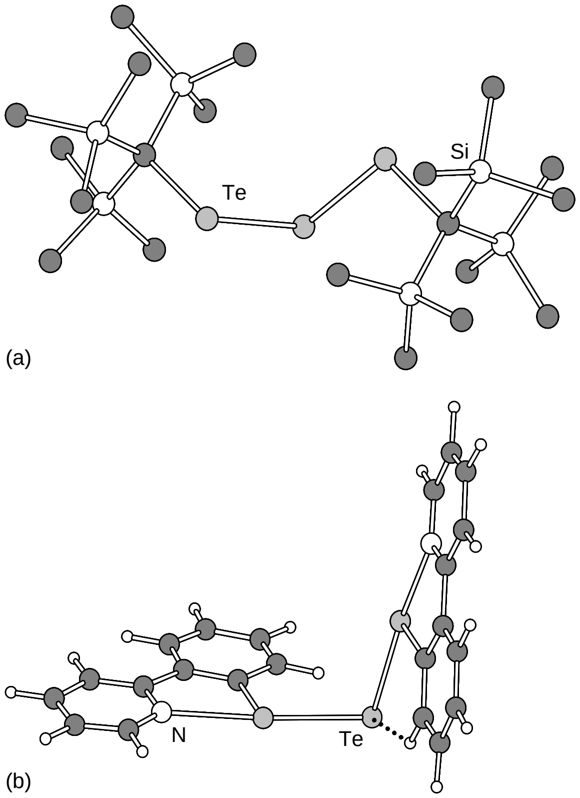

Figure 5 The crystal structures of (a) $\{(Me_3Si)_3C\}_2Te_3$,[64] (b) $\{2\text{-}(C_3H_4N)C_6H_4\}_2Te_3$[65]

Table 1 ^{125}Te chemical shifts of some diorganyl tellurides and ditellurides[a]

Compound	^{125}Te chemical shift (ppm)	Reference
MeTe(*n*-Pr)	95	65
MeTe(*n*-Bu)	103	65
MeTeEt	165	65
$(n\text{-Pr})_2$Te	213	65
$(n\text{-Bu})_2$Te	228	65
Et_2Te	356	65
MePh	329	65
(*n*-Pr)TePh	460	65
(*n*-Bu)TePh	468	65
Ph_2Te^b	688	66
MeTeTeEt	−48, 264	67
MeTeTe(*n*-Pr)	−31, 185	67
MeTeTe(*n*-Bu)	−31, 193	67
MeTeTeMe	49	67
EtTeTe(*n*-Pr)	88, 182	67
EtTeTe(*n*-Pr)	97, 183	67
(*n*-Pr)TeTe(*n*-Pr)	105	67
(*n*-Bu)TeTe(*n*-Bu)	113	67
EtTeTeEt	166	67
MeTeTePh	95, 384	67
(*n*-Pr)TeTePh	223, 305	67
(*n*-Bu)TeTePh	226, 304	67
EtTeTePh	295, 289	68
PhTeTePh	421	69

[a]The chemical shifts are reported relative to neat Me_2Te. The NMR spectra have been recorded in $CDCl_3$ unless otherwise indicated. [b]The NMR spectrum has been recorded in CH_2Cl_2.

Several cyclic telluroethers and their derivatives are known, as exemplified by some common examples below (for a more detailed discussion, see Ref. 36):

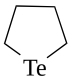

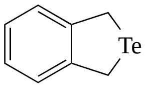

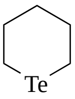

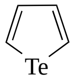

Tellurophene (C_4H_4Te; liquid; b.p. 151°; m.p. – 36°) was synthesized in 1972, disproving the suspected instability of the compound.[66]

It has been suggested that the ground-state aromaticity of furan and its heavier congeners follows the trend below (see Ref. 36 and references therein): thiophene > selenophene > tellurophene > furan.

Tellurophene reacts with Cl_2 to produce a stable 1,1-dichloro compound.[66] 2-Lithiotellurophene is obtained by α-metalation of the tellurophene. It can be used as starting product for the synthesis of some 2-substitued tellurophenes.

2.3 Uses

Diorganyl tellurides often serve as intermediates in organic reactions. An organic compound is first treated with an appropriate tellurium compound to give a diorganyl telluride. Subsequent reactions cleave at least one of the carbon–tellurium bonds and functionalize the group cleaved from the tellurium atom. This way alkenes can be converted to 4,5-dihydroxyoxazoles, cycloalkenes to acetals, and alkynes can be converted to vinyllithium compounds (see, for instance, Ref. 8).

Diorganyl tellurides are starting materials for the preparation of diorganyltellurium dihalides, pseudohalides, and carboxylates, of telluroxides, and of telluronium salts, and are used as ligands for the synthesis of transition metal complexes.

Diorganyl ditellurides can be used for the preparation of lithium and sodium tellurolates, which are frequently used for the introduction of the organyltelluro group into organic molecules, for the synthesis of organyltellurium chlorides or bromides, of organyltellurium trihalides, of symmetrical and unsymmetrical diorganyl tellurides, of telluroacetals, and of *Te*-organyl tellurocarboxylates (for recent reviews, see, for example, Refs. 5,6,8).

3 ORGANIC TELLURIUM-HALOGEN COMPOUNDS

3.1 Organotellurenyl Halides RTeX

While generally simple RTeX molecules are unstable, they can be stabilized by bulky organic group R or by secondary bonding interactions that were originally suggested by Allcock.[67] A recent example is illustrated in

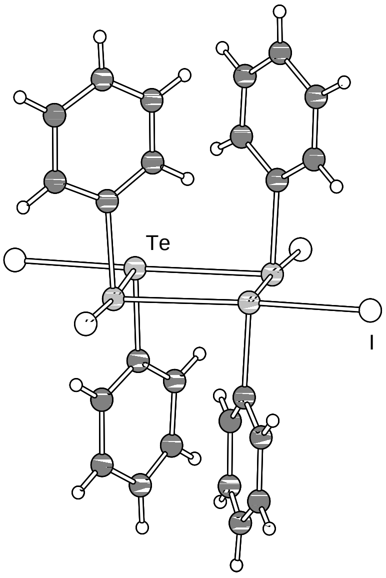

Figure 6 The crystal structure of $(PhTeI)_4$[68]

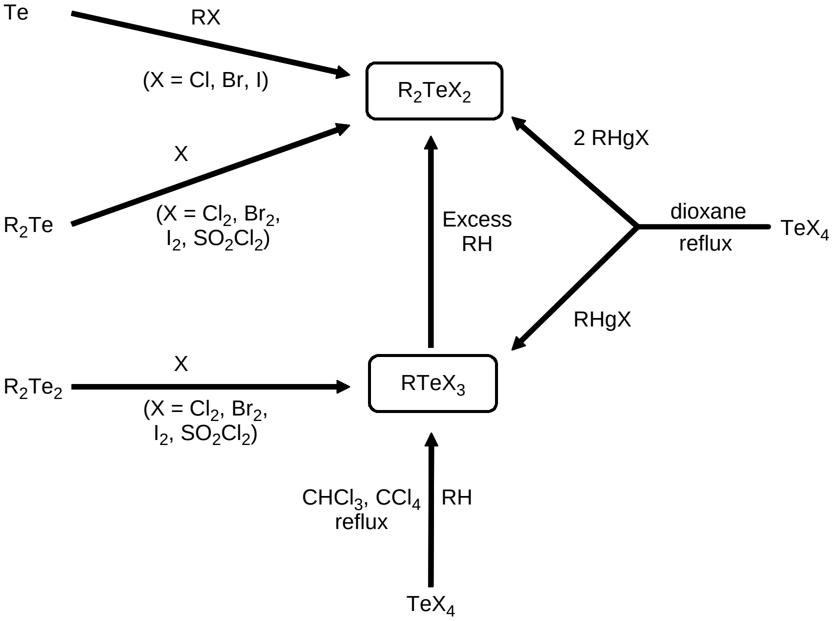

Figure 7 Common synthetic routes to organyltellurium halides

Figure 6 by $(PhTeI)_4$[68,69] that has been prepared by the reaction of Ph_2Te_2 and I_2. The molecules are arranged into tetramers by secondary bonding Te···Te interactions spanning 3.151–3.180 Å.

3.2 Diorganyltellurium Dihalides and Organyltellurium Trihalides

Dialkyl- and diaryltellurium dihalides are crystalline solids that can be easily purified by recrystallization. While a large number of chlorides, bromides, and iodides have been prepared,[4,5] only a few fluorides are known.

There are several convenient synthetic routes to organyltellurium halides. Some of the most common methods are summarized in Figure 7. Diorganyltellurium dihalides can be prepared in good yields from elemental tellurium and alkyl halides, or by halogenation of diorganyl tellurides with elemental halogens, sulfuryl, and thionyl halides. The latter reaction also affords organyltellurium trihalides, when the starting material is a ditelluride.

Tellurium tetrachloride is also a convenient synthon for diorganyltellurium dihalides and organyl trihalides (the most important preparative methods have been summarized by Irgolic;[13] see also Refs. 3, 4 and 8). The condensation reactions with aromatic compounds like alkoxybenzenes, hydroxybenzenes, and (diorganylamino)benzenes yield diaryltellurium dichlorides with the tellurium group in the para-position relative to the ring substituent. The reactions involving unsubstituted aromatic compounds require elevated temperatures and the presence of aluminium trichloride catalyst for the condensation to proceed at a reasonable rate. Tellurium tetrachloride also adds to carbon–carbon double bonds of alkenes and yields bis(2-chloroalkyl)tellurium dichlorides. The reaction with another molecule of the alkene affords 2-chloroalkyltellurium trichloride. Heterocyclic tellurium dichloride derivatives can be obtained, when $TeCl_4$ reacts with 1,5- or 1,6-dienes.

Unsymmetrical diorganyltellurium dihalides are formed upon condensation of aryltellurium trichlorides with activated aromatic compounds and with ketones. The addition of the trichloride across carbon–carbon double bonds in alkenes, as well as the reaction with aryl(trimethyl)silane, hexaphenyldilead, and arylmercury chlorides leads to the transfer of the aryl group to the tellurium atom.

It should also be noted that the chlorine atoms in diorganyltellurium dichlorides can be exchanged by other halogens or anionic groups.

Most diorganyltellurium dihalides are stable in air. This facilitates a convenient method to purify diorganyl tellurides that are liquid at room temperature. The raw product is converted to a dichloride or dibromide by direct chlorination or bromination, and the pure dihalides are easily be reduced back to the original telluride.[48–52]

Three representative diorganyltellurium dihalides are shown in Figure 8. It can be seen that in all cases the tellurium atom possesses the Ψ-trigonal bipyramidal coordination geometry with the halogen atoms occupying the axial positions and the tellurium lone-pair occupying the third equatorial position. The mean Te–Cl distance is 2.515 Å in Me_2TeCl_2,[70] 2.508 Å in $(PhOC_6H_4)_2TeCl_2$,[71] and 2.502 Å in the cyclic $\{(CH_2)_3TeCl_2\}_3$.[72] The mean Cl–Te–Cl bond angles

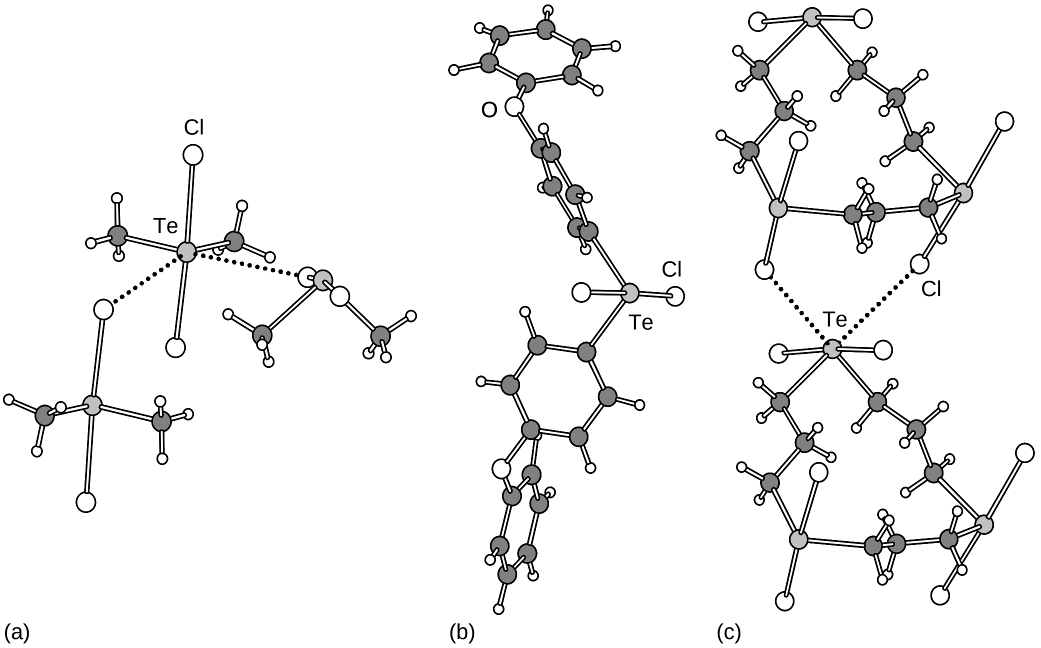

Figure 8 The crystal structures of (a) Me_2TeCl_2,[70] (b) {*p*-$(PhOC_6H_4)_2TeCl_2$,[71] (c) $\{(CH_2)_3TeCl_2\}_3$[72]

are 172.4, 177.2, and 175.8° for the three compounds, respectively, and the respective mean C–Te–C bond angles are 96.6, 98.7, and 102.4°.

However, tellurium commonly shows secondary bonding interactions that expand the coordination environment. It can be seen in Figure 8 that both Me_2TeCl_2 and $\{(CH_2)_3TeCl_2\}_3$ show two close Te···Cl close contacts of 3.412–3.478 Å[70] and 3.359–3.479 Å,[72] respectively. The coordination environment around tellurium can therefore be considered as AX_4Y_2E in which X represents the primary bonding interaction, Y the secondary bonding interaction, and E the tellurium lone-pair.

The secondary bonding interactions are particularly important in diorganyltellurium diiodides, since in addition to Te···I close contacts there can also be I···I close contacts. It has been reported that there is a qualitative correlation between the lengths of the Te–I bonds in R_2TeI_2 and the strength of the secondary bonding interactions,[73] though the bond lengths are naturally also affected by the organic group. McCullough *et al.*[74] have correlated the secondary bonds with the color of the crystalline material. In absence of I···I close contacts, the crystals appear orange. As the I···I interactions become stronger, the color becomes deeper red and tends towards purple and black. This is well illustrated by $(CH_2)_4TeI_2$. It had been reported already in the early 1930s that this compound crystallizes as two different polymorphs: one form is orange–red and the other deep red.[75] The crystal structures of both polymorphs were established recently[73] and show that the I···I contacts in the deeper red polymorphs are shorter than in the orange–red polymorph. The packing of molecules in both polymorphs is shown in Figure 9.

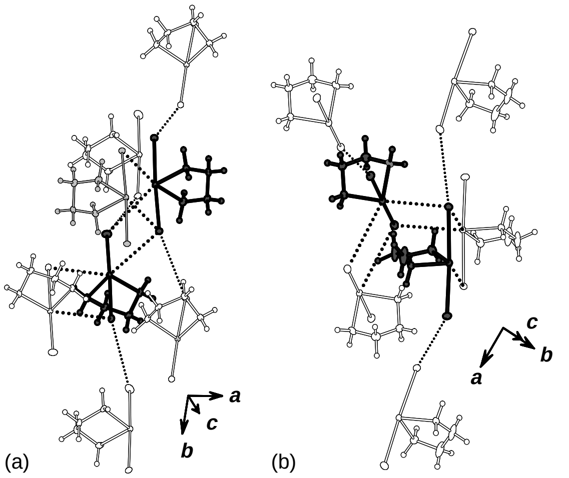

Figure 9 The packing in the two polymorphs of $(CH_2)_4TeI_2$. (Reprinted with permission from Ref. 73. © 2004 American Chemical Society)

Aryltellurium trihalides are generally more stable than alkyltellurium trihalides. They are relatively strong Lewis acids. Their most common coordination number is five based on the approximate square pyramidal coordination environment. As seen by some illustrative examples in Figure 10, these species can consequently exist as polymers (Figure 10(a)) or dimers (Figure 10(b)). In some cases there are also intramolecular interactions of variable strength. For instance, the Te–O distance of 2.441 Å[76] in Figure 10(c) and the Te···N distance of 2.402 Å[77] in Figure 10(d) imply

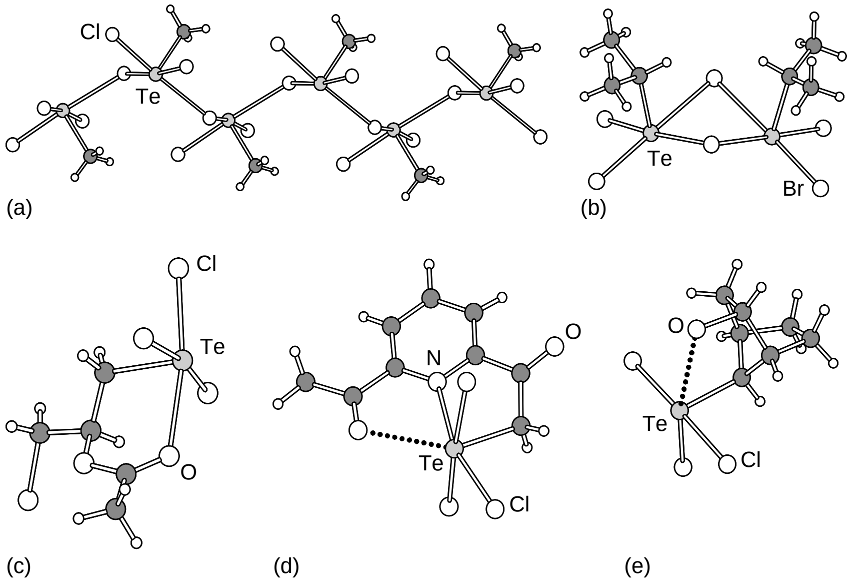

Figure 10 Organyl trihalides exist generally as (a) polymers[79] or (b) dimers.[80] Alternatively they may show intramolecular interactions of variable strength as an almost single Te–O bond in (c)[76] or weak secondary Te···Cl bonds in (d)[77] and (e)[78]

significantly stronger bonds than the clearly secondary Te···Cl interaction of 3.013 Å[78] in Figure 10(e). The trihalide in Figure 10(d) exceptionally shows an additional secondary bonding interaction of 2.878 Å, expanding the coordination sphere of tellurium to six.[77] The Te–Cl bonds cis to the Te–O, Te–N, or Te–Cl interactions span a narrow range of 2.462–2.500 Å, whereas the Te–Cl bond trans to them is strongly affected by the strength of the interaction. In case of strong Te–O and Te–N interactions, the Te–Cl bond is longer (2.354 and 2.438 Å, respectively), whereas the Te–Cl bond trans to the Te···Cl secondary bond is 2.298 Å. For comparison, the lengths of the terminal Te–Cl bonds in $(MeTeCl_3)_n$ are 2.352 and 2.366 Å, while the bridging Te–Cl distances are 2.759 and 2.814 Å.[79] The same trend is observed in the $\{(i\text{-Pr})TeBr_3\}_2$ dimer: the mean length of the terminal Te–Br terminal bonds is 2.545 Å while the bridging Te–Br bonds show the mean length of 2.922.[80]

4 TRIORGANYLTELLURONIUM SALTS

Triorganyltelluronium salts, R_3TeX, have been known for over a century.[81] In recent years, they have attracted considerable interest because of their role in organic synthetic chemistry.[8] For example, it has recently been reported that the telluronium salts are precursors for telluronium ylides that react with the carbonyl compounds, forming a variety of products like oxiranes and secondary alcohols.[82]

The X-ray structure determinations (see Ref. 83, and references therein) of several organotelluronium salts have established that in the solid state the structural features are governed by weak secondary tellurium-anion interactions[67] that expand the AX_3E (X = bonding pair, E = lone pair) trigonal pyramidal geometry around tellurium into a five- or six-coordinate entity. In the absence of these secondary interactions, simple ionic structures are expected.[84] Christian *et al.*[85] and Collins *et al.*[86] have discussed the nature of the secondary bonding and rationalized the structures in terms of the coordination geometry around tellurium. It has also been shown that solid-state ^{125}Te NMR spectroscopy is a sensitive tool to identify covalent secondary bonding interactions between the cations and anions.[40] Some illustrative examples are shown in Figure 11. The mean Te–C bond lengths are 2.131, 2.116, and 2.120 Å for $Ph_3TeCl{\cdot}1/2CHCl_3$,[86] $(Ph_3Te)[AuCl_4]$,[83] and $(Ph_3Te)_2[TeCl_6]$,[87] respectively, and are close to single bond lengths. The respective mean C–Te–C bond angles are 94.2, 97.9, and 97.8°.

It can also be seen from Figure 11 that in every case the trigonal pyramidal coordination around tellurium is expanded into an AX_3Y_3E octahedron by Te···Cl secondary contacts of 3.219–3.716 Å. In the case of Ph_3TeCl one of the three secondary contacts is to the center of a phenyl ring of the adjacent Ph_3Te^+ cation.[86]

In addition to the two polymorphs of $(CH_2)TeI_2$ discussed in Section 3.2, the reaction of TeI_4 and PPh_3 in THF affords also $\{(CH_2)_4TeI^+\}_2[Te_2I_{10}{}^{2-}]$ and $\{(CH_2)_4TeI^+\}_2(TeI_3{}^+)_2(I^-)_4$, both of which contain a related telluronium cation (see Figure 12).[73] The bond lengths and angles in the $[Te_2I_{10}]^{2-}$ anion are virtually identical to those found in $\{(C_7H_7)(C_2H_5)_3N^+\}_2[Te_2I_{10}{}^{2-}]$.[88] The Te–I bond in the $\{(CH_2)_4TeI\}^+$ cation is shorter than the axial Te–I bonds in $(CH_2)_4TeI_2$ with the Ψ-trigonal

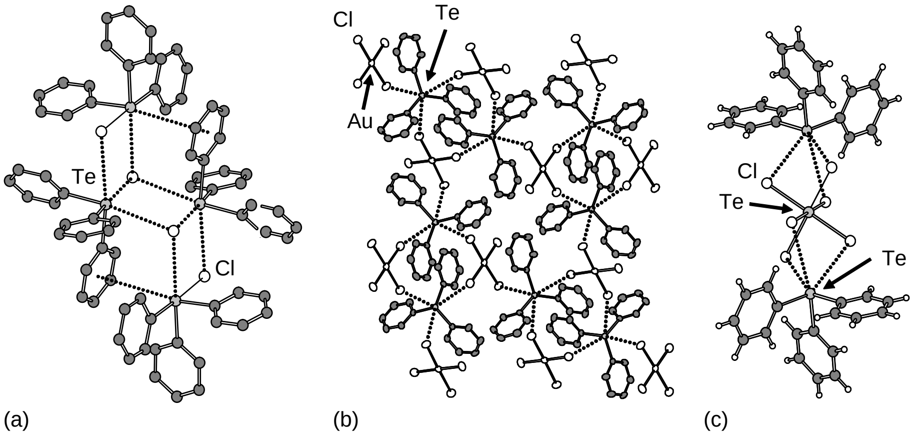

Figure 11 The crystal structures of (a) $(Ph_3Te)Cl$,[86] (b) $(Ph_3Te)_2[AuCl_4]$,[83] and (c) $(Ph_3Te)[TeCl_6]$.[87] Secondary bonds are indicated by dashed lines

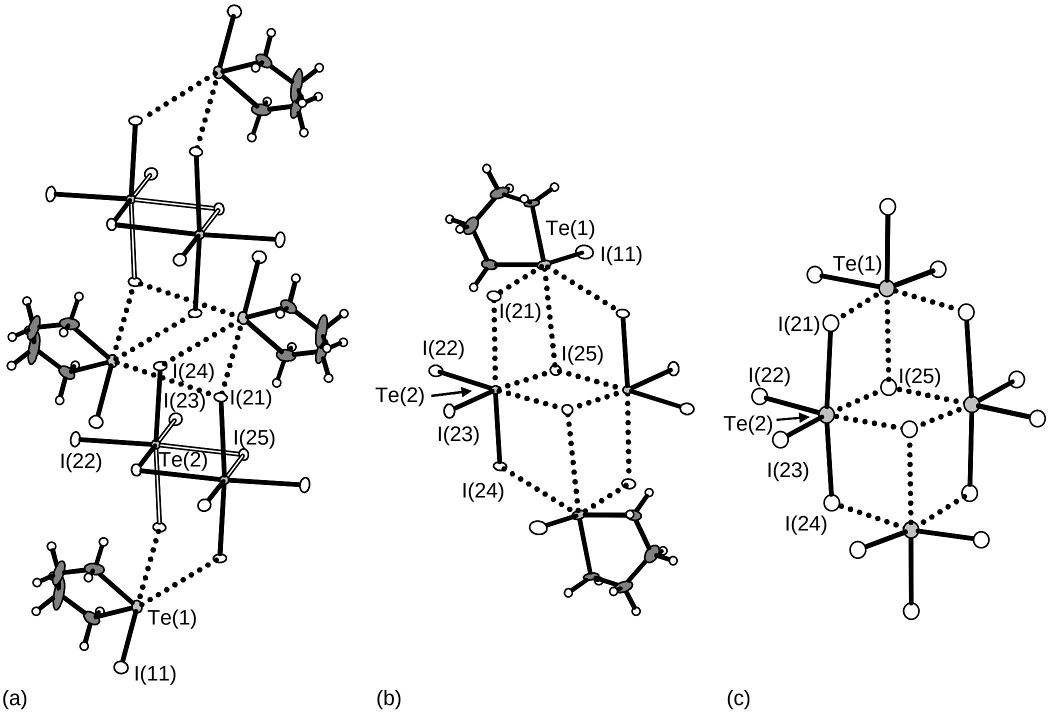

Figure 12 Comparison of the structures of (a) $\{(CH_2)_4Te^+\}_2[Te_2I_{10}{}^{2-}]$ and (b) $\{(CH_2)_4TeI^+\}_2(TeI_3{}^+)_2(I^-)_4$[73] with that of (c) $(TeI_3{}^+)_2(I^-)_2(TeI_4)_2$.[89] (Reprinted with permission from Ref. 73. © 2004 American Chemical Society)

bipyramidal coordination environment of tellurium, and is close to the single bond length, as expected for the eight-electron AX_3E cation. The I–Te–C bond angles of 93.3(2) and 96.8(2)° and the C–Te–C bond angle of 83.7(4)° are also consistent with the three-coordinate telluronium cation.[73]

$\{(CH_2)_4TeI^+\}_2(TeI_3{}^+)_2(I^-)_4$ (see Figure 12(b)) shows a structural framework that is similar to that of the tetramers in γ- and δ-TeI_4[90–93] and that have been formulated as $(TeI_3{}^+)_2(I^-)_2(TeI_4)_2$ based on the interatomic distances (see Figure 12(c)).[89]

5 ORGANYLTELLUROLATES

Organyl tellurolates are unstable, air-sensitive species and are normally used in situ without isolation. Some methods for their generation are described below. As discussed in Section 2.1, lithium tellurolates can be prepared by insertion of tellurium into the carbon–lithium bond by a direct reaction.

$$\mathrm{RLi} + \mathrm{Te} \longrightarrow \mathrm{RTeLi} \qquad (7)$$

The insertion tendency decreases in the order t-BuLi > s-BuLi > n-BuLi > PhLi > MeLi.[94] These insertions can be carried out by using lithium alkanides, alkenides, alkynides, and aromatic or heterocyclic lithium compounds. The lithiation should not be carried out by using alkyl halides, because the lithium tellurolates that are formed in the reaction may react with the alkyl halide reagent to produce organyl alkyl tellurides.[13]

Tellurolates can also be produced by reducing diorganyl ditelluride with sodium or lithium tetrahydridoborate:

$$\mathrm{RTeTeR} \xrightarrow{\mathrm{NaBH_4}} \mathrm{RTeNa} \qquad (8)$$

The reaction can be performed in different organic solvents. Currently ethanol seems to be the most common solvent. This method has been employed almost exclusively for the preparation of sodium alkyl-, alkenyl-, aryl-, and heteroaryl tellurolates. Metallic lithium and sodium can also be used for the reduction of diorganyl ditellurides.

Although the organotellurolates are normally used without isolation, some tellurolate salts have been isolated and structurally characterized. The structure of $(Ph_4P)[C_4H_3STe]$[95] (see Figure 13(a)), as well as $(Ph_4P)[5\text{-}CH_3\text{-}C_4H_3STe]$,[96] consists of well-separated organotelluride anions. The tellurolates with bulky aryl groups have also been isolated with alkali metals utilizing crown-ethers, as exemplified in Figure 13(b) by [K(18-crown-6)][Te{2,4,6-$(Me_2CH)_3C_6H_2$}].[97] Insertion of elemental Te into the C–Li bond of n-BuLi in the presence of TMEDA gave $[n\text{-BuTeLi}\cdot\text{TMEDA}]_2$, which was characterized in the solid and solution state resulting in the first crystal structure of a lithium alkyltellurolate.[98]

The reductive cleavage of diorganyl ditellurides with sodium borohydride is more complex than anticipated, as suggested by the isolation of a catenated organotelluride anion, $(C_6H_5Te)_3^-$ when molar ratio between diphenyl ditelluride and $NaBH_4$ was 3:2.[99] The tetraphenylphosphonium and tetraphenylarsonium tri(tellurophenolate) salts were isolated and structurally characterized, as shown in (Figure 14).[99] $(C_6H_5Te)_3^-$ has also been isolated as [Sm{hydrotris(3,5-dimethylpyrazolyl)borate}$_2$($TeC_6H_5Te)_3$] salt.[100]

Organyltellurolates are useful synthons in organic chemistry.[9,21,27,101] Tellurolates can be alkylated or arylated to afford diorganyl tellurides and they add to alkenes and alkynes. The latter reaction is both regioselective and trans-stereospecific. They can also be utilized in the generation of tellurium-containing heterocycles.

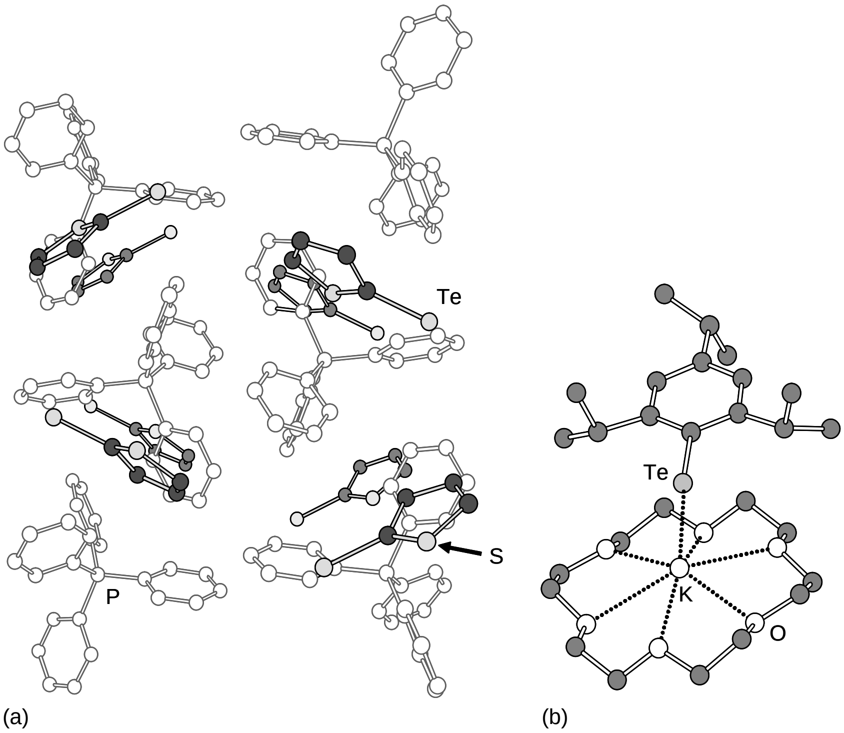

Figure 13 The discrete tellurolate anions in (a) $(Ph_4P)(TeTh)$ (Th = 2-thienyl, C_4H_3S)[95] and (b) [K(18-crown-6)][Te{2,4,6-$(Me_2CH)_3$ C_6H_2}][97]

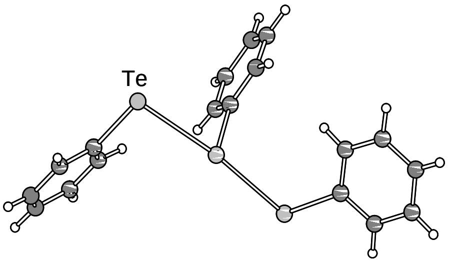

Figure 14 The structure of the $(Ph_3Te_3)^-$ anion[99]

6 METAL COMPLEXES

6.1 Organyltellurolato Complexes

Anionic organotellurolates can act both as terminal and bridging ligands. Their transition metal complexes can conveniently be prepared by the treatment of halogenated metal complexes with RTe^-, or by the oxidative addition of the R_2Te_2 to low-valent transition metal centers. The product distribution depends on the choice of the metal center, organic group, solvent, and the molar ratio of the reagents (for more detailed discussion, see, for instance, Refs. 15 and 27).

The examples of the structures of some typical mononuclear complexes are presented in Figure 15 and those for polynuclear complexes in Figure 16. It is conceivable that the more complicated polynuclear complexes are formed from mono- and dinuclear complexes by successive condensation reactions (see Figure 17).[102] This scheme follows the initial suggestion of Brennan *et al.*[102] They formulated a pathway for the formation on hexanuclear $[Pd_6Te_6(PEt_3)_8]$ with a dinuclear intermediate $[Pd_2Te_4(PEt_3)_4]$.[103,104] Because $[Pd_6Cl_2Te_4(TeR)_2(PPh_3)_6]$ contains the same framework as $[Pd_6Te_6(PEt_3)_8]$, their formation probably goes through similar stages. The suggested formation of $[Pd_2(TeTh)_4(PPh_3)_2]$ from Th_2Te_2 and $[Pd(PPh_3)_4]$ in benzene[105] and the formation of a trinuclear complex $[Pt_3Te_2(Th)(PPh_3)_5]Cl$ from Th_2Te_2 and $[Pt(PPh_3)_4]$[106] lends credibility to the reaction pathway in Figure 17.

Some main group metals also form mononuclear and dinuclear tellurolato complexes.[21,27,29] A few examples are shown in Figure 18.

6.2 Telluroether Complexes

Several types of telluroether (diorganyl telluride) ligands are known. They can be monodentate or polydentate, acyclic, cyclic, and macrocyclic as well as hybrid telluroether ligands containing other donor atoms in addition to tellurium. Complexes with telluroether ligands have seen extensive research activity in recent years (for two most recent reviews, see Refs. 27 and 35).

Though telluroether ligands have been known for almost a hundred years, the advent of their coordination chemistry dates back only to the 1970s. There are several reasons for this lack of interest: Telluroethers were considered weak donors with poor coordinating ability except to soft metals and they were thought to be only little different from the thioether analogs. Their reputation as toxic and malodorous compounds dates back to the original reports by Wöhler,[1] their commercial availability was very

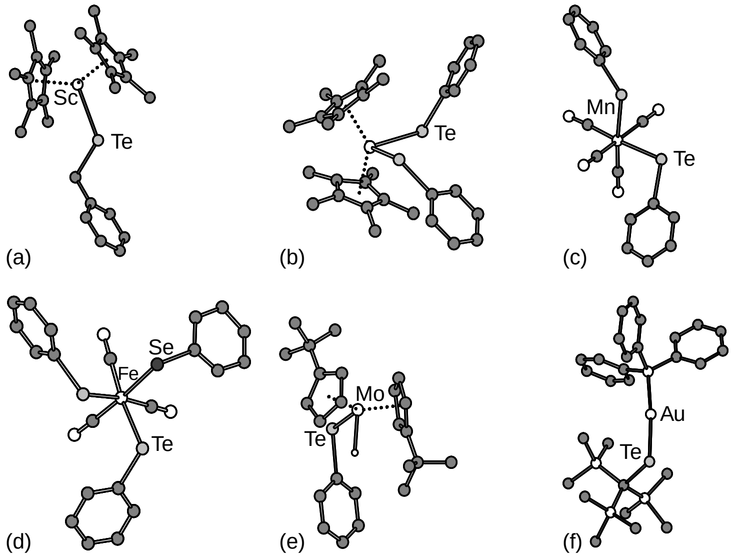

Figure 15 The crystal structures of (a) $[Sc(Me_5C_5)_2(TeCH_2Ph)]$,[107] (b) $[ZrCp^*_2(TePh)_2]$,[108] (c) $[Mn(CO)_4(TePh)_2]^-$,[109] (d) $[Fe(CO)_3(SePh)(TePh)_2]^-$,[110] (e) $[Mo(^tBuC_5H_4)_2(H)(TePh)]$,[111] and (f) $[Au(PPh_3)(TeSiMe_3)]$[112]

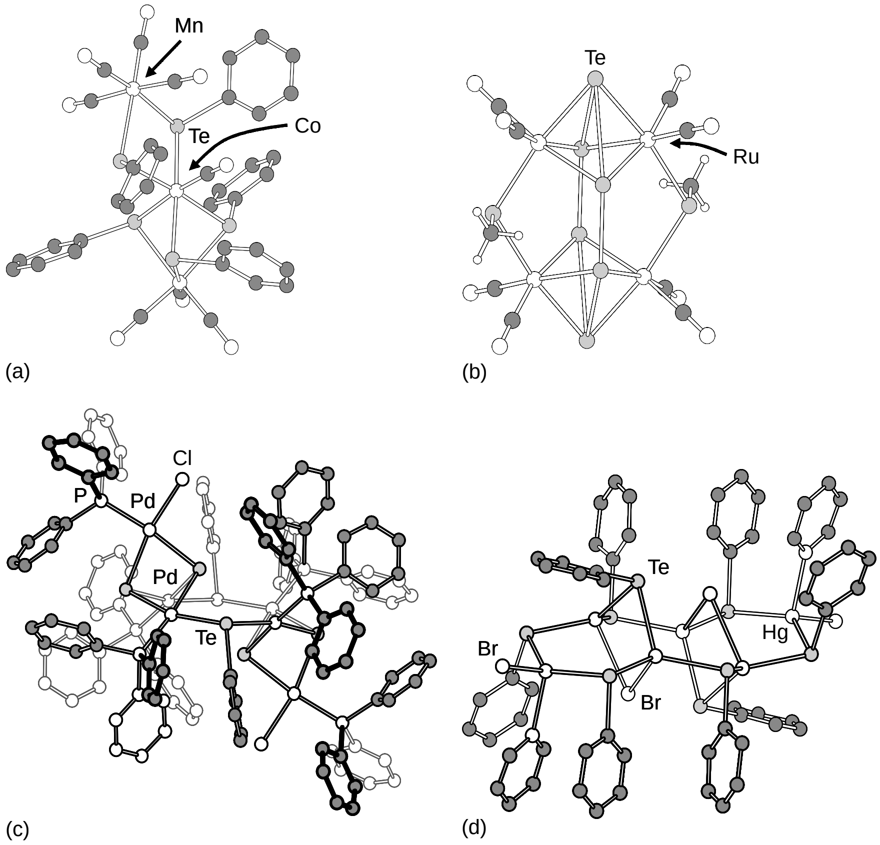

Figure 16 The crystal structures of (a) $[Mn_2Co(CO)_8(TePh)_5]$,[109] (b) $[Ru_4(CO)_8Te_6(TeMe)_2]^{2-}$,[113] (c) $[Pd_6Cl_2(SePh)_2(PPh_3)_6]$,[102] and (d) $[Hg_6Br_4(py)_2(TePh)_8]$[114]

limited, and the complexes were considered to have no applications.

Recent decades, however, have seen rapidly growing interest in this area. New synthetic approaches in the production of novel telluroether ligands have been designed. The advent of modern FT NMR techniques has enabled improved understanding of the tellurium-containing species in solution. The coordination chemistry of telluroether ligands has also proven to be much more varied than what was initially assumed.

Dialkyl as well as diaryl tellurides behave as monodentate ligands. Consistent with their soft character, their best explored group of complexes involves Pd(II) and Pt(II) centers. A variety of techniques have been applied to the characterization of their solid state and solution structures. In such square-planar complexes, $[MX_2(TeR_2)_2]$ (M = Pd, Pt; X = Cl, Br, I), cis – trans isomerization, intramolecular ligand exchange and tellurium inversion processes have all been observed by detailed far-infrared and variable-temperature NMR studies (see Refs. 14,15,17,35 for a more detailed review of the subject).

In the solid state, the characteristic feature in such mononuclear $[MX_2(TeR_2)_2]$ complexes is the formation of Te$\cdots$X secondary bonding contacts, as shown in Figure 19. They link individual complexes into dimeric units. The Te$\cdots$Cl distances in these complexes span a range of 3.393–3.523 Å, the Te$\cdots$Br distances 3.623–3.647 Å, and the Te$\cdots$I distances 3.679–3.862 Å.[119]

The ^{125}Te NMR chemical shifts of the complexes are found to high frequency of those of the free ligands, and vary with the metal, its oxidation state, the trans ligand, and the other (cis) ligands in the coordination sphere. Solvent effects appear to be considerably smaller for the complexes than for free ligands. Isomerism in solution can readily be detected for the square-planar $[ML_2TeR_2]$ (M = Pd, Pt; X = halide), since the chemical shifts of cis and trans isomers show a small difference of ca. 20 ppm.[17] In the case of NMR inactive metal, the chemical shift alone is an uncertain guide to the identification of the individual isomer. For the platinum complexes, the ^{195}Pt chemical shifts and the coupling constants are much better indicators. The $^1J(^{125}Te\text{-}^{195}Pt)$ coupling constants are larger for the cis-isomers than for the trans isomers and provide a better indicator of the structures when both forms are present in solution (see, for instance, Refs. 27,35 and references therein).

In almost all complexes, R_2Te acts as a terminal ligand. $[PtCl(Th)(TeMeTh)_2]_n$ (Th = 2-thienyl, C_4H_3S) is an exception (see Figure 20).[120] Two bridging ThTeMe ligands

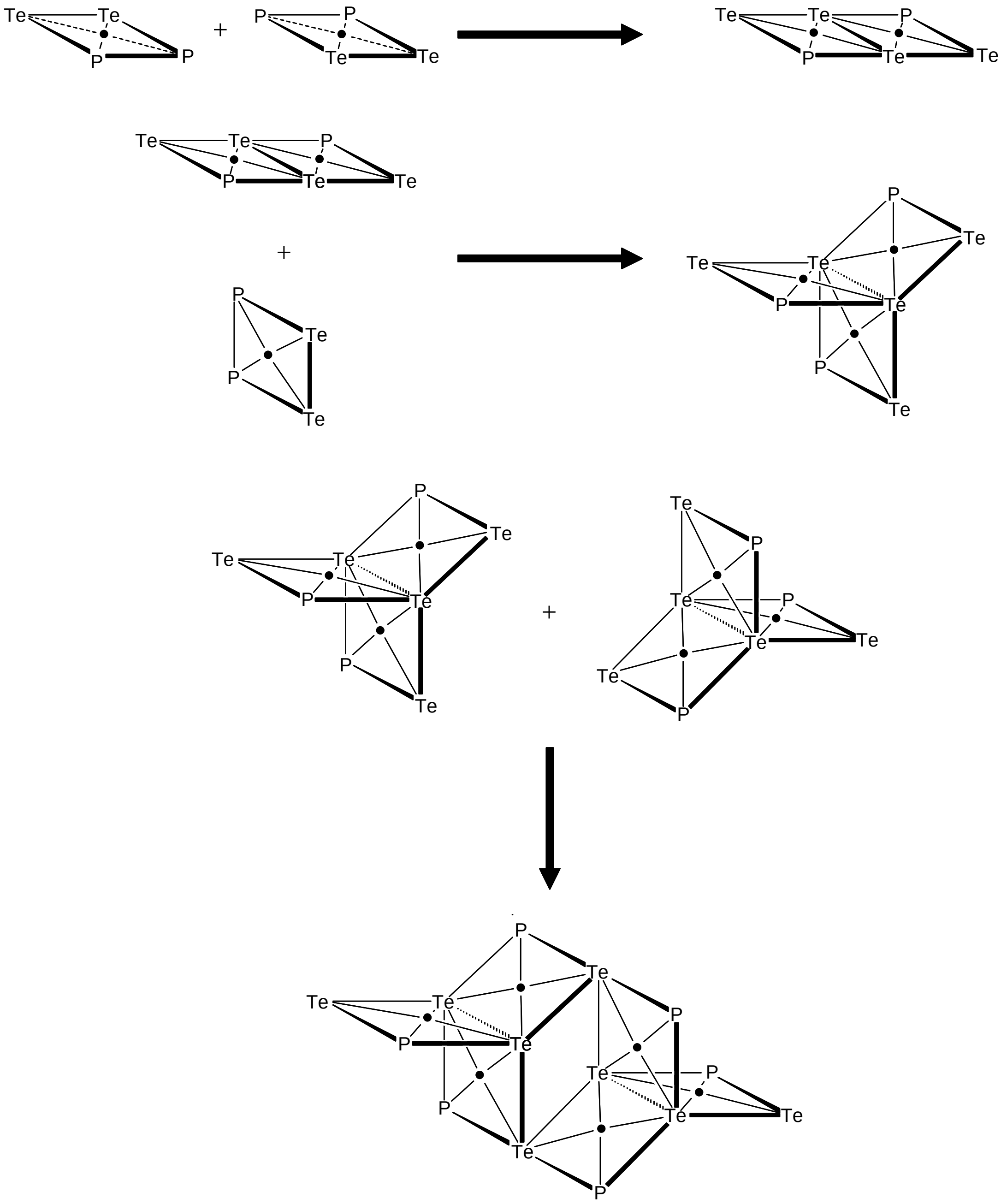

Figure 17 Structural relationships between the mono- and polynuclear frameworks of tellurolatopalladium complexes.[102] (Reprinted from Ref. 105. © 2000, with permission from Elsevier)

link the metal centers into polymeric chains and create a quasi-octahedral coordination environment around Pt(II) with two very long Pt–Te bonds of 2.898(1) and 3.419(1) Å.

$[PdCl_2(TeC_4H_8)_2]$ is an example of a complex with heterocyclic telluroether ligand (Figure 21). The molecules show Te· · ·Cl close contacts of 3.462 and 3.472 Å and consequently form dimeric units.[121] 1,3-dihydrobenzo[*c*]tellurophene (L) also behaves as a simple monodentate Te donor ligand with metals as exemplified by $[Mo(CO)_{6-n}L_n]$ ($n = 1-3$).[122] The reaction with $Fe_3(CO)_{12}$, however, results in the loss of tellurium and formation of tellurium-free organoiron complexes.[123,124] Similar loss of tellurium has reported on the reaction with tellurophenes and benzotellurophenes.[124]

6.3 Diorganyl Ditellurides Complexes

Although upon complex formation, ditellurides generally undergo cleavage of the Te–Te bond with formation of

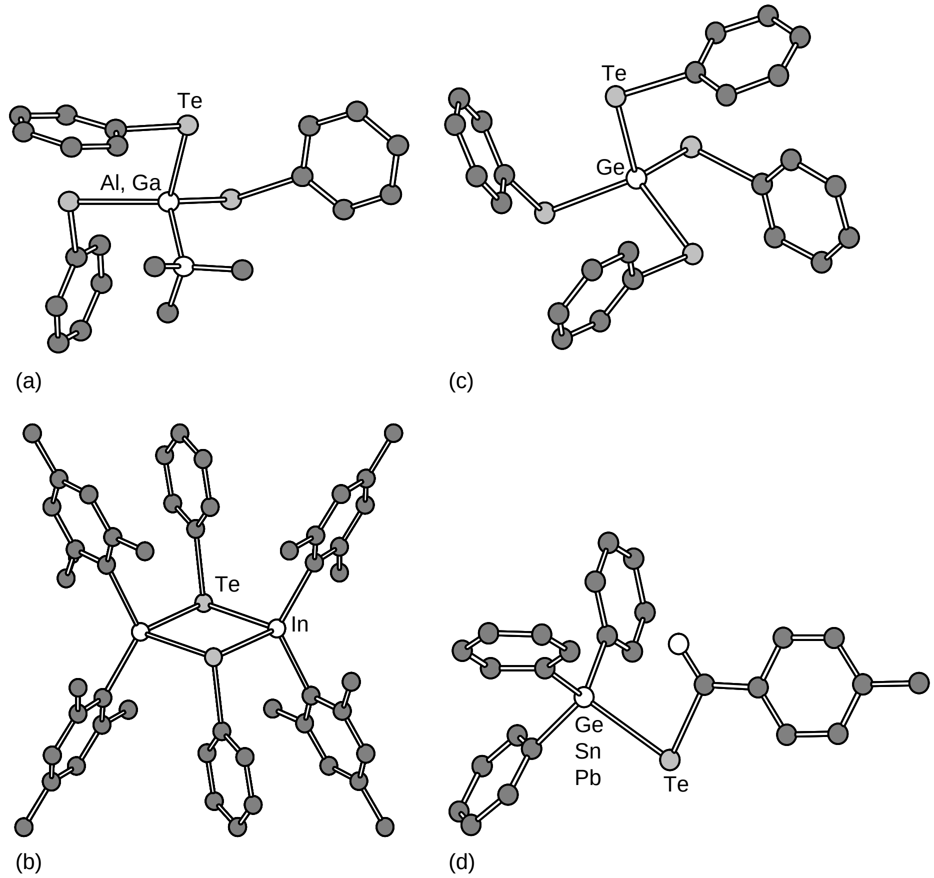

Figure 18 Examples of main group aryltellurolato complexes[115–118]

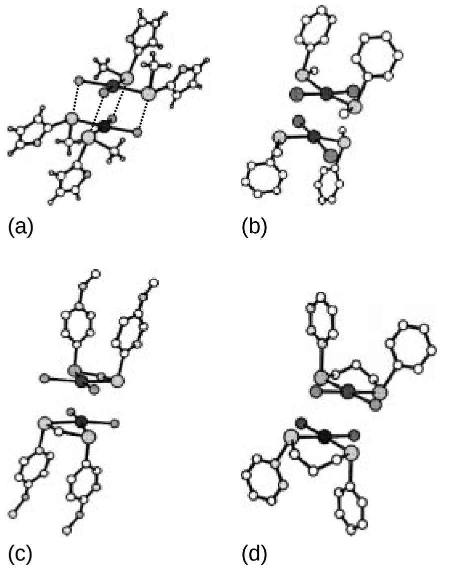

Figure 19 Secondary bonding interactions in (a) *cis*-$[PdCl_2\{(C_4H_3E)TeMe\}_2]$ (E = S, O), (b) *trans*-$[PtI_2(TePhMe)_2]$, (c) *cis*-$[PdCl_2\{$*meso*-$(4\text{-}MeOC_6H_4Te)_2CH_2\}_2]$, and (d) *cis*-$[PdBr_2\{$*meso*-$PhTe(CH_2)_3TePh\}_2]$.[119] (Reprinted from Ref. 119. © 1998, with permission from Elsevier)

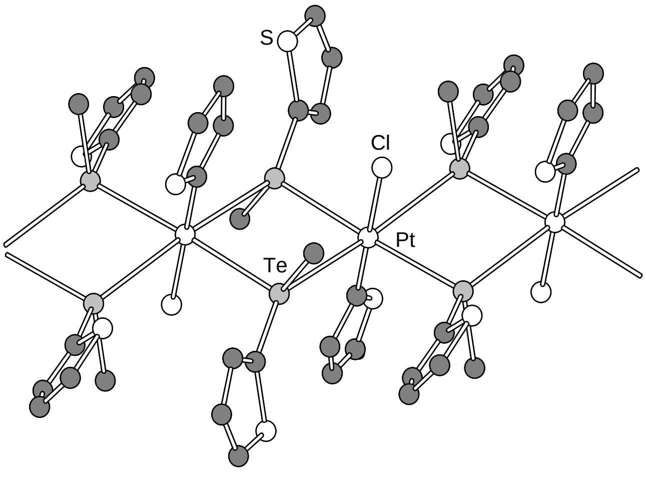

Figure 20 The crystal structure of $[PtCl(Th)(TeMeTh)_2]_n$ (Th = 2-thienyl, C_4H_3S)[120]

terminal or bridging TeR–ligands, in some cases they can also coordinate without Te–Te bond cleavage The ditelluride can act either as a monodentate terminal ligand or as a bridging bidentate ligand (see Figure 22).

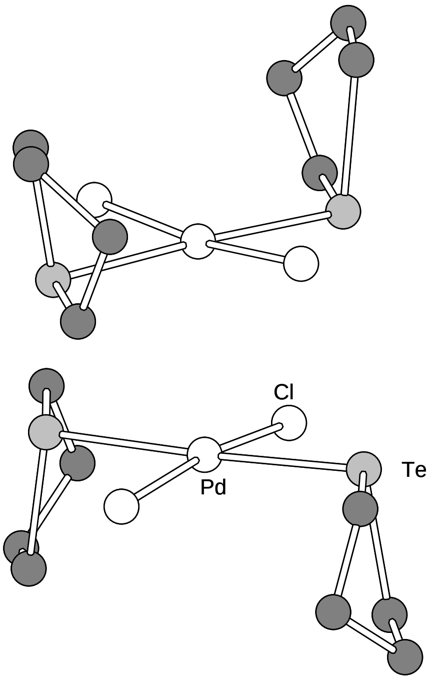

Figure 21 The crystal structure of $[PdCl_2(TeC_4H_8)_2]$[121]

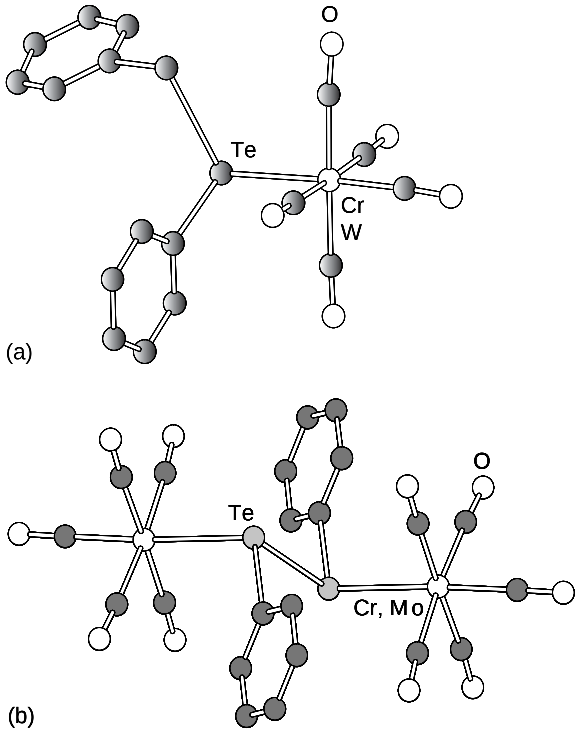

Figure 22 (a) The crystal structures of $[M(CO)_5(Te_2Ph_2)]$ ($M = Cr$, W) containing a monodentate terminal phenyldi telluride ligand.[127] (b) The crystal structures of $[\{M(CO)_5\}_2(\mu\text{-}Te_2Ph_2)]$ ($M = Cr$, Mo)[128,129] containing a bridging didentate phenyl ditelluride ligand[128]

The reaction of Me_3SiTeR ($R = 4\text{-}MeC_6H_4$, C_6H_5) with $[(\eta^5\text{-}C_5Me_5)RuCl_2]_2$ generates R_2Te_2 at the metal center resulting in $[Ru(\eta^5\text{-}C_5Me_5)(\mu_2\text{-}RTeTeR)(\mu_2\text{-}TeR)_2Ru(\eta^5\text{-}C_5Me_5)]$.[125] This metal complex contains both bridging ditelluride and tellurolate ligands (see Figure 23(a)). The Te–Te bond of 2.901 Å is very long. It is due to strong repulsion of the p lone-pairs of adjacent tellurium atoms that is a consequence of a very small torsional angle of 4.7° (for a discussion of the lone-pair interactions in chalcogen–chalcogen bonds, see Ref. 126).

The treatment of $(p\text{-}C_6H_4F)_2Te_2$ with an equimolar amount of $AgBF_4$ in acetonitrile at ambient temperature leads to the formation of a ditelluride bridged $[Ag_2(NCCH_3)_4\{\mu_2\text{-}(p\text{-}C_6H_4F)TeTe(p\text{-}C_6H_4F)\}_2][BF_4]_2$ in 96% isolated yield.[130] The interesting coordination mode can be seen in Figure 23(b). The two silver atoms are bridged by two ditellurides, resulting in a six-membered Ag_2Te_4 ring that adopts a chair configuration. The Te–Te bond of 2.752(1) Å is shorter than the Te–Te bond of 2.794(5) in $[(OC)_3Re(\mu\text{-}Br)_2(\mu\text{-}Te_2Ph_2)Re(CO)_3]$,[131] but can be compared to the Te–Te bond of 2.749(2) Å in $[(PtMe_3)_2(\mu\text{-}I)_2\{\mu\text{-}Te_2(p\text{-}MeOC_6H_4)\}_2]$.[132]

7 OUTLOOK

While organotellurium compounds have been known for a long time, it is only in recent decades that this area of chemistry has seen rapidly expanding interest. The thrust of research activity is being motivated by increasing number of applications of organic tellurium compounds in organic and inorganic syntheses, and by use of organometallic tellurium-containing complexes for catalytic and electronic applications.

The synthetic applications of organotellurium compounds can be divided into carbon–carbon bond forming reactions and various types of functional group interconversions. The tellurium reagents are primarily used in oxidation and reduction reactions. Indeed, new reactions are constantly being found that are entirely unique for tellurium reagents and cannot be executed by other means. The advantages of tellurium-mediated reduction reactions over conventional reagents include milder reaction conditions, better regioselectivity, in situ preparation of the reducing agent, and the ease of recovery of tellurium. Like selenium compounds, tellurium reagents can be used as mild oxidizing agents.

Other potential applications of novel organotellurium compounds include the conducting materials, nonlinear optical devices, polymer light emitting diodes (LEDs), and other materials for electronic devices. Major areas of current interest in organometallic complexes containing organic tellurium ligands is concerned with the fabrication of binary transition metal telluride thin films by MOCVD techniques.

While organotellurium chemistry has opened new avenues for applications, their structural chemistry is very varied. The

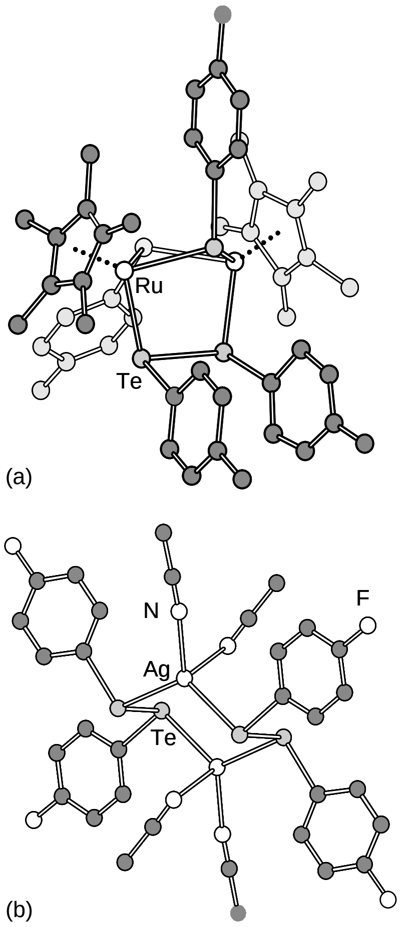

Figure 23 (a) A dinuclear ruthenium complex with a bridging $(CH_3C_6H_4)_2Te_2$ ligand and two bridging $CH_3C_6H_4Te$–ligands,[125] (b) A cyclic Ag complex with two bridging $(FC_6H_4)_2Te_2$ ligands[130]

field is still in its pioneering stage and rapid development both in terms of fundamental information of structures, bonding, and reactions, as well as in new applications can be expected in the coming years.

8 RELATED ARTICLES

Polonium: Inorganic Chemistry; Selenium: Organoselenium Chemistry; Tellurium: Inorganic Chemistry.

9 REFERENCES

1. F. Wohler, *Liebigs Ann. Chem.*, 1840, **35**, 111.
2. H. Rheinbold, 'Houben-Weyl Methoden der Organischen Chemie', Georg Thieme Verlag, Stuttgart, 1955, Vol. IX, p. 918.
3. K. J. Irgolic and R. A. Zingaro, Reactions of Organotellurium Compounds, in 'Organometallic Reactions', ed. E. I. Becker and M. Tsutsui, Wiley-Interscience, New York, 1971, Vol. 2, p. 117.
4. K. J. Irgolic, 'The Organic Chemistry of Tellurium', Gordon and Breach, New York, 1974.
5. S. Patai, Z. Rappoport ed., 'The Chemistry of Organic Selenium and Tellurium Compounds', John Wiley & Sons, New York, 1986, Vol. 1.
6. S. Patai ed., 'The Chemistry of Organic Selenium and Tellurium Compounds', John Wiley & Sons, New York, 1987, Vol 2.
7. W. R. McWhinnie, in 'Encyclopedia of Inorganic Chemistry', ed. R. B. King, John Wiley & Sons, Chichester, 1990, Vol. 8, p. 4117.
8. K. J. Irgolic, in 'Houben-Weyl Methods for Organic Chemistry', ed. D. Klamann, Organotellurium Compounds, Georg Thieme Verlag, Stuttgart, 1990, Vol 2.
9. P. A. W. Dean, J. Vittal, in 'Metallothioneins', eds. M. J. Stillman, F. C. Shaw II, and K. J. Suzuki, VCH, New York, 1992, p. 346.
10. N. Petragnani, 'Tellurium in Organic Synthesis', Academic Press, London, 1994.
11. M. R. Detty, M. B. O'Brien, 'Tellurium-Containing Heterocycles', Wiley, 1994, Vol. 53, p. 511.
12. N. Petragnani, in 'Comprehensive Organometallic Chemistry II', ed. A. McKillop, Elsevier, Exeter, 1995, Vol. 11, p. 571.
13. K. J. Irgolic, in 'Synthetic Methods of Organometallic and Inorganic Chemistry', ed. W. A. Herrmann, Sulfur, Selenium, and Tellurium, Georg Thieme Verlag, Stuttgart, 1997, Vol. 4, p. 176.
14. S. G. Murray and F. R. Hartley, *Chem. Rev.*, 1981, **81**, 365.
15. H. J. Gysling, *Coord. Chem. Rev.*, 1982, **42**, 133.
16. L. Engman, *Acc. Chem. Res.*, 1985, **18**, 274.
17. E. G. Hope and W. Levason, *Coord. Chem. Rev.*, 1993, **122**, 109.
18. I. D. Sadekov, B. B. Rivkin, and V. I. Minkin, *Surf. Rep.*, 1993, **159**, 103.
19. I. D. Sadekov and V. I. Minkin, *Adv. Heterocycl. Chem.*, 1993, **58**, 47.
20. I. Haiduc, R. B. King, and M. G. Newton, *Chem. Rev.*, 1994, **94**, 301.
21. J. Arnold, *Prog. Inorg. Chem.*, 1995, **43**, 353.
22. H. B. Singh and N. Sudha, *Polyhedron*, 1996, **15**, 745.
23. I. D. Sadekov and V. I. Minkin, *Surf Rep.*, 1997, **19**, 285.
24. N. Petragnani and W.-L. Lo, *J. Braz. Chem. Soc.*, 1999, **5**, 415.
25. I. D. Sadekov and A. V. Zakharov, *Russ. Chem. Rev.*, 1999, **68**, 909.
26. I. D. Sadekov, A. I. Uraev, and A. D. Garnovskii, *Russ. Chem. Rev.*, 1999, **68**, 415.

27. A. K. Singh and S. Sharma, *Coord. Chem. Rev.*, 2000, **209**, 49.
28. A. A. Maksimenko, A. V. Zakharov, and I. D. Sadekov, *Russ. Chem. Rev.*, 2000, **69**, 861.
29. U. Englich and K. Ruhlandt-Senge, *Coord. Chem. Rev.*, 2000, **210**, 135.
30. J. V. Comasseto and R. E. Barrientos-Astigarraga, *Aldrichimica Acta*, 2000, **33**, 66.
31. I. D. Sadekov and V. I. Minkin, *Adv. Heterocycl. Chem.*, 2001, **79**, 1.
32. I. D. Sadekov, *Russ. Chem. Rev.*, 2002, **71**, 99.
33. I. D. Sadekov, A. V. Zakharov, and A. A. Maksimenko, *Surf. Rep.*, 2002, **23**, 125.
34. I. D. Sadekov, *Russ. Chem. Rev.*, 2002, **71**, 929.
35. W. Levason, S. D. Orchard, and G. Reid, *Coord. Chem. Rev.*, 2002, **225**, 159.
36. M. Renson, in 'The Chemistry of Organic Selenium and Tellurium Compounds', ed. S. Patai and Z. Rappoport, Wiley, New York, 1986, Vol. 1, p. 399.
37. W. R. McWhinnie, in 'The Organic Chemistry of Selenium and Tellurium Compounds', ed. S. Patai, Wiley, Chichester, 1987, Vol. 2, p. 495.
38. G. Natta, *Giorn. Chim. Ind. Appl.*, 1926, **8**, 367.
39. L. Chugaev and W. Chopin, *Chem. Ber.*, 1914, **47**, 1269.
40. B. A. Trofimov, N. K. Gurasova, A. A. Tatarinova, S. V. Amosova, L. M. Sinegovskaya, V. V. Keiko, and V. A. Potapov, *Zh. Org. Khim.*, 1984, **20**, 1802.
41. B. A. Trofimov, S. V. Amosova, N. K. Gurasova, V. A. Potapov, and A. A. Tatarinova, *Surf. Lett.*, 1983, **1**, 151.
42. L. Brandsma and H. E. Wijers, *Recl. Trav. Chim. Pays-Bas*, 1963, **82**, 68.
43. D. J. Sandman, J. C. Stark, and B. M. Foxman, *Organometallics*, 1982, **1**, 739.
44. L. A. Acampora, D. L. Dugger, T. Emma, J. Mohammed, M. Rubner, L. A. Samuelson, D. J. Sandman, and S. Tripathy, in 'Polymers in Electronics', ed. T. Davidson, American Chemical Society, Washington, DC, 1983, p. 461.
45. L. Engman and M. P. Cava, *Organometallics*, 1982, **1**, 470.
46. L. Engman, M. P. Cava, J. Persson, *J. Organomet. Chem.*, 1990, **388**, 71.
47. N. Kondratenko, V. I. Popov, A. A. Kolomeitsev, I. D. Sadekov, V. I. Minkin, and L. M. Yagupol'skii, *Zh. Org. Khim.*, 1983, **15**, 1561.
48. L. Reichel and E. Kirschbaum, *Ber. Dtsch. Chem. Ges.*, 1943, **120**, 375.
49. N. Petragnani, *Tetrahedron*, 1960, **11**, 15.
50. L. Reichel and E. Kirschbaum, *Liebigs Ann. Chem.*, 1936, **523**, 211.
51. J. Bergman, *Tetrahedron*, 1972, **28**, 3323.
52. E. S. Lang and J. V. Comasseto, *Synth. Commun.*, 1988, **18**, 301.
53. J. Emsley, 'The elements', 3rd ed., Oxford University Press, 1998.
54. G. Bandoli, J. Bergman, K. J. Irgolic, A. Grassi, and G. C. Pappalardo, *Z. Naturforsch., Teil B*, 1985, **40**, 1157.
55. T. M. Klapötke, B. Krumm, P. Mayer, K. Polborn, and O. P. Ruscotti, *Inorg. Chem.*, 2001, **40**, 5169.
56. J. Farran, A. Alvarez-Larena, J. F. Piniella, M. V. Capparelli, and L. Torres-Castellanos, *Acta Crystallogr., Sect. C*, 1997, **53**, 342.
57. R. Oilunkaniemi, R. S. Laitinen, and M. Ahlgrén, *Z. Naturforsch., Teil B*, 2000, **55**, 361, and references there in.
58. G. Llabres, O. Dideberg, and L. Dupont, *Acta Crystallogr., Sect. B*, 1972, **28**, 2438.
59. S. K. Kumar, H. B. Singh, K. Das, and U. C. Sinha, *J. Organomet. Chem.*, 1990, **397**, 161.
60. A. Edelmann, S. Brooker, N. Bertel, M. Noltemeyer, H. W. Roesky, G. M. Sheldrick, and F. T. Edelmann, *Z. Naturforsch., Teil B*, 1992, **47**, 305.
61. T. Junk, K. Irgolic, and E. A. Meyers, *Acta Crystallogr., Sect. C*, 1993, **49**, 975.
62. T. G. Back and P. W. Codding, *Can. J. Chem.*, 1983, **61**, 2749.
63. F. Sladky, B. Bildstein, C. Rieker, A. Gieren, H. Betz, and T. Hubner, *J. Chem. Soc., Chem. Commun.*, 1985, 1800.
64. T. A. Hamor, N. I. Al-Salim, A. A. West, and W. R. McWhinnie, *J. Organomet. Chem.*, 1986, **310**, C5.
65. D. H. O'Brien, N. Dereu, C.-K. Huang, K. J. Irgolic, and F. F. Knapp, Jr, *Organometallics*, 1983, **2**, 305.
66. F. Fringuelli, A. Taticchi, *Ann. Chim. (Rome)*, 1972, **62**, 777; *J. Chem. Soc. Perkin Trans 1*, 1972, 199.
67. N. W. Alcock, *Adv. Inorg. Chem. Radiochem.*, 1972, **15**, 1.
68. E. S. Lang, R. M. Fernandez, E. T. Silveira, U. Abram, and E. M. Vazquez-Lopez, Jr, *Z. Anorg. Allg. Chem.*, 1999, **625**, 1401.
69. P. D. Boyle, W. I. Cross, S. M. Godfrey, C. A. McAuliffe, R. G. Pritchard, S. Sarwar, and J. M. Sheffeld, *Angew. Chem., Int. Ed. Engl.*, 2000, **39**, 1796.
70. R. F. Ziolo and J. M. Troup, *J. Am. Chem. Soc.*, 1983, **105**, 229.
71. M. de Matheus, L. Torres, J. F. Piniella, J. L. Brianso, and C. Miravittles, *Acta Crystallogr., Sect. C*, 1991, **47**, 703.
72. Y. Takaguchi, E. Horn, and N. Furukawa, *Organometallics*, 1996, **15**, 5112.
73. S. M. Närhi, R. Oilunkaniemi, R. S. Laitinen, and M. Ahlgrén, *Inorg. Chem.*, 2004, **43**, 3742.
74. J. D. McCullough, C. Knobler, and R. F. Ziolo, *Inorg. Chem.*, 1985, **24**, 1814.
75. G. T. Morgan and F. H. Burstall, *J. Chem. Soc.*, 1931, 180.
76. H. Fleischer, B. Mathiasch, and D. Schollmeyer, *Organometallics*, 2002, **21**, 526.
77. H. J. Gysling, H. R. Luss, and S. A. Gardner, *J. Organomet. Chem.*, 1980, **184**, 417.

78. D. Daternieks, J. O'Connell, and E. R. T. Tiekink, *J. Organomet. Chem.*, 2000, **598**, 49.
79. J. Pietikäinen, R. S. Laitinen, J. Konu, and J. Valkonen, *Z. Naturforsch., Teil B*, 2001, **56**, 1369.
80. T. M. Klapötke, B. Krumm, P. Mayer, H. Piotrowski, and D. P. Ruscotti, *Z. Anorg. Allg. Chem.*, 2002, **628**, 229.
81. A. Cahours, *Ann. Chem.*, 1865, **135**, 356.
82. Z.-L. Zhou, Y.-Z. Huang, Y. Tang, Z.-H. Chen, L.-P. Shi, X.-L. Jin, and Q.-C. Yang, *Organometallics*, 1994, **13**, 1575, and references therein.
83. R. Oilunkaniemi, J. Pietikäinen, R. S. Laitinen, and M. Ahlgrén, *J. Organomet. Chem.*, 2001, **640**, 50.
84. R. F. Ziolo and J. M. Troup, *Inorg. Chem.*, 1979, **18**, 2271.
85. B. H. Christian, M. J. Collins, R. J. Gillespie, and J. F. Sawyer, *Inorg. Chem.*, 1986, **25**, 777.
86. M. J. Collins, J. A. Ripmeester, and J. F. Sawyer, *J. Am. Chem. Soc.*, 1988, **110**, 8583.
87. S. Närhi, R. Oilunkaniemi, R. S. Laitinen, and M. Ahlgrén, *Acta Crystallogr., Sect. E*, 2004, **60**, 798.
88. B. Krebs, *Nova Acta Leopoldina*, 1985, **59**, 131.
89. B. Krebs and F.-P. Ahlers, *Adv. Inorg. Chem.*, 1990, **35**, 235.
90. H. J. Beister, R. Kniep, and A. Schaefer, *Z. Kristallogr.*, 1986, **174**, 12.
91. R. Kniep, H. J. Beister, and D. Wald, *Z. Naturforsch., Teil B*, 1988, **43**, 966.
92. B. Krebs and V. Paulat, *Acta Crystallogr., Sect. B.*, 1976, **32**, 1470.
93. V. Paulat and B. Krebs, *Angew. Chem.*, 1976, **88**, 28.
94. C. Köllemann, D. Obendorf, and F. Sladky, *Phosphorus Surf.*, 1988, **38**, 69.
95. J. Zhao, D. Adcock, W. T. Pennington, and J. W. Kolis, *Inorg. Chem.*, 1990, **29**, 4358.
96. J. Zhao, J. W. Kolis, and W. Pennington, *Acta Crystallogr., Sect. C*, 1993, **49**, 1753.
97. P. J. Bonasia and J. Arnold, *J. Chem. Soc., Chem. Commun.*, 1990, 1299.
98. W. Clegg, R. P. Davies, R. Snaith, and A. E. H. Wheatley, *Eur. J. Inorg. Chem.*, 2001, 1411.
99. D. Witthaut, K. Kirschbaum, O. Conrad, and D. M. Giolado, *Organometallics*, 2000, **19**, 5238.
100. A. C. Hillier, S.-Y.-. Liu, A. Sella, and M. R. J. Elsegood, *Angew. Chem. Int. Ed. Engl.*, 1999, **38**, 2745.
101. H. J. Gysling, in 'The Chemistry of Organic Selenium and Tellurium Compounds', ed. S. Patai and Z. Rappoport, Wiley, New York, 1986, Vol. 1, p. 679.
102. R. Oilunkaniemi, R. S. Laitinen, and M. Ahlgrén, *J. Organomet. Chem.*, 2001, **623**, 168.
103. J. G. Brennan, T. Siegrist, S. M. Stuczynski, and M. L. Steigerwald, *J. Am. Chem. Soc.*, 1990, **112**, 9233.
104. M. L. Steigerwald, S. M. Stuczynski, Y.-U. Kwon, D. A. Vennos, and J. G. Brennan, *Inorg. Chim. Acta*, 1993, **312**, 219.
105. R. Oilunkaniemi, R. S. Laitinen, and M. Ahlgrén, *J. Organomet. Chem.*, 2000, **595**, 232.
106. L.-Y. Chia and W. R. McWhinnie, *J. Organomet. Chem.*, 1978, **148**, 165.
107. W. E. Piers, D. J. Parks, L. R. MacGillivray, and M. J. Zaworotko, *Organometallics*, 1994, **13**, 4547.
108. W. A. Howard, T. M. Trnka, and G. Parkin, *Inorg. Chem.*, 1995, **34**, 5900.
109. W.-F.-. Liaw, D.-S. Ou, Y.-S. Li, W.-Z. Lee, C.-Y. Chuang, Y.-P. Lee, G.-H. Lee, and S.-M. Peng, *Inorg. Chem.*, 1995, **34**, 3747.
110. W.-F.-. Liaw, C.-H. Lai, M.-H. Chiang, C.-K. Hsieh, G.-H. Lee, and S.-M. Peng, *J. Chin. Chem. Soc. (Taipei)*, 1993, **40**, 437.
111. J. H. Shin, W. Savage, V. J. Murphy, J. B. Bonanno, D. G. Churchill, and G. Parkin, *J. Chem. Soc., Dalton Trans.*, 2001, 1732.
112. P. J. Bonasia, D. E. Gindelberger, and J. Arnold, *Inorg. Chem.*, 1993, **32**, 5126.
113. B. K. Das and M. G. Kanatzidis, *Inorg. Chem.*, 1995, **34**, 1011.
114. E. S. Lang, R. A. Zan, C. C. Gatto, R. A. Burrow, and E. M. Vazquez-Lopez, *Eur. J. Inorg. Chem.*, 2002, 331.
115. M. G. Gardiner, C. L. Raston, and V.-A. Tolhurst, *Chem. Commun.*, 1995, 1457.
116. S. Schlecht and K. Friese, *Eur. J. Inorg. Chem.*, 2003, 1411.
117. H. Rahbarnoohi, R. Kumar, M. J. Heeg, and J. P. Oliver, *Organometallics*, 1995, **14**, 502.
118. K. Tani, R. Yamada, T. Kanada, M. Suzuki, S. Kato, and T. Murai, *Organometallics*, 2002, **21**, 1482.
119. R. Oilunkaniemi, J. Komulainen, R. S. Laitinen, M. Ahlgrén, and J. Pursiainen, *J. Organomet. Chem.*, 1998, **571**, 129, and references therein.
120. R. Oilunkaniemi, R. S. Laitinen, and M. Ahlgrén, *Z. Naturforsch., Teil B*, 2004, **59**, 614.
121. T. Kemmitt, W. Levason, R. D. Oldroyd, and M. Webster, *Polyhedron*, 1992, **11**, 2165.
122. W. Levason, G. Reid, and V.-A. Tolhurst, *J. Chem. Soc., Dalton Trans.*, 1998, 3615.
123. K. Singh, W. R. McWhinnie, H. L. Chen, M. Sun, and T. A. Hamor, *J. Chem. Soc., Dalton Trans.*, 1996, 1545.
124. K. Badyal, W. R. McWhinnie, T. A. Hamor, and H. Chen, *Organometallics*, 1997, **16**, 3194.
125. H. Matsuzaka, T. Ogino, M. Nishio, M. Hidai, Y. Nishibayashi, and S. Uemura, *Chem. Commun.*, 1994, 223.
126. R. S. Laitinen, P. Pekonen, and R. Suontamo, *Coord. Chem. Rev.*, 1994, **130**, 1.
127. A. A. Pasynskii, Yu. V. Torubayev, A. G. Drukovsky, I. L. Eremenko, D. Veghini, E. V. Krasifnikova, V. I. Privalov,

A. I. Yanovsky, and Yu. T. Struchkov, *Zh. Neorg. Khim.*, 1997, **42**, 42.

128. A. A. Pasynskii, Yu. V. Torubayev, I. L. Eremenko, D. Veghini, S. E. Nefedov, Zh. V. Dobrokhotova, A. I. Yanovsky, and Yu. T. Struchkov, *Zh. Neorg. Khim.*, 1996, **41**, 2006.
129. A. A. Pasynskii, Yu. V. Torubayev, A. G. Drukovsky, I. L. Eremenko, D. Veghini, S. E. Nefedov, A. I. Yanovsky, and Yu. T. Struchkov, *Zh. Neorg. Khim.*, 1997, **42**, 957.
130. W.-F. Liaw, C.-H. Lai, S.-J.-. Chiou, Y.-C. Horng, C.-C. Chou, M.-C. Liaw, G.-H. Lee, and S.-M. Peng, *Inorg. Chem.*, 1995, **34**, 3755.
131. F. Calderazzo, D. Vitali, R. Poli, J. L. Atwood, R. D. Rogers, J. M. Cummins, and I. Bernal, *J. Chem. Soc., Dalton Trans.*, 1981, 1004.
132. H. B. Singh, A. Regini, J. P. Jasinski, E. S. Paight, and R. J. Butcher, *J. Organomet. Chem.*, 1997, **466**, 283.

Thallium: Inorganic Chemistry

Imre Tóth & Béla Győri
University of Debrecen, Debrecen, Hungary

1	Introduction	1
2	Properties of the Element	2
3	Thallium Compounds	4
4	Toxicity	10
5	Analytical Chemistry of Thallium	10
6	Related Articles	10
7	References	10

1 INTRODUCTION

The metallic element thallium, atomic number 81 (relative atomic mass 204.38), is the heaviest member of group 13 of the periodic table. The ground-state electron configuration is $[Xe]4f^{14}5d^{10}6s^26p^1$.

Thallium chemistry was divided into two independent fields nine years after the discovery of the element, with the first preparation of diethylthallium chloride. Organothallium chemistry thus became an independent and fruitful counterpart to the inorganic chemistry of this element (*see* ***Thallium: Organometallic Chemistry***).

The best-known property of this element to the layperson is its toxicity (*see* ***Metal Ion Toxicity***); indeed, the use of thallium as a 'rat poison' was the most important application for decades. Thallium appeared to be merely an exotic *Trace Element*, seeming to merit little attention from the scientific community. As a result, there are only a few books[1–7] specializing in the inorganic chemistry of thallium, and most of the recent papers have been published by a small group of research workers. However, subject areas such as coordination chemistry, redox reactions with inorganic and organic substrates (*see* ***Electron Transfer in Coordination Compounds***), solid structures and *High-Temperature Superconductivity*, metal–metal bonds (*see also* ***Polynuclear Organometallic Cluster Complexes***) should be mentioned as examples where the inorganic chemistry of thallium is ongoing (though, some of these fields are certainly related to the organometallic chemistry of thallium). NMR spectroscopy is the primary physical method used in studies of thallium chemistry. The thallium nuclei ^{205}Tl and ^{203}Tl both have spin $I = \frac{1}{2}$ and are suitable for NMR spectroscopy, the absolute sensitivities with respect to ^1H NMR being 0.13 and 0.055, respectively. Furthermore, the observation of large multibond coupling constants in many thallium compounds allows structural information to be obtained from ^1H or ^{13}C NMR spectra, which may be recorded routinely in most laboratories.

1.1 Discovery and History

The element thallium was discovered relatively recently. In 1861, the British chemist William Crookes attributed a bright green line in the emission spectrum of some residues from a sulfuric acid plant to a new element. However, the Frenchman C. A. Lamy was the first to obtain thallium in any quantity. Crookes named his discovery after the 'Latin *thallus*, a budding twig – a word that is frequently employed to express the beautiful green tint of young vegetation'.[8] However, his original idea that thallium was a member of the sulfur family was short lived, and on the basis of its chemical and physical properties Mendeleev rightly placed it in group 13.

1.2 Occurrence and Distribution[2]

Thallium is a relatively abundant element and is widely distributed in nature. Estimates for the abundance of thallium in the earth's crust range from 0.3 to 3 ppm, though about 1 ppm is the generally accepted value. The wide distribution is due to several factors, the most important being the isomorphous replacement of K^+ in potassium feldspars and micas (silicates) by Tl^+. Additionally, thallium sulfide is found in sphalerite, galena, pyrite, and other sulfide ores. Thallium also behaves as an accessory to manganese in geological processes; for example, manganese oxides and deep-sea manganese nodules may be enriched in thallium to levels of 0.01% and 0.1% respectively. The few existing thallium-based minerals such as lorandit ($TlAsS_2$), crookesite ($(Cu,Tl,Ag)_2Se$), and avicennite (Tl_2O_3) are very rare and have no commercial importance.

In the aquatic environment, thallium is present as Tl^I at a level of about 0.01 ppb in seawater. Tl^I is also strongly adsorbed by soils.

Of the total quantity of thallium mobilized by industry amounting to about 1600 tons in the United States during 1977, 70% was reemitted to the environment either in the form of air pollution (15%) or as solid waste (55%). Coal burning power plants account for the greater part of this air pollution, but the smelting of copper, zinc, and lead may also result in concentrated local emissions. The remaining 30% is incorporated in the final products, though usually at a lower level than in the raw materials.[2]

1.3 Production and Use

Thallium is manufactured commercially as a by-product from the roasting of pyrite ores, from sulfuric acid plants, and from the smelting of lead, zinc, and copper. The global production is estimated to be in the range of only 13–16 tons per annum during the last two decades.[9–12] Volatile compounds of thallium are gaseous at the temperature of these smelting operations and are collected in the flue dust in the form of oxides or sulfates. In a typical procedure for the recovery of thallium, the flue dust is first boiled in sulfuric acid, after which the dissolved thallium in the filtrate is precipitated by the addition of zinc. Impurities such as zinc, copper, lead, cadmium, and indium may be removed by dissolving the metal in dilute sulfuric acid and precipitating the trace elements with hydrogen sulfide. Thallium is recovered from saturated solutions of Tl_2SO_4 by electrolysis at low current density. The raw product is compressed into blocks and melted at 350–400 °C under a layer of oxalic acid or in a stream of H_2 gas. The metal obtained may be protected with a coating of paraffin or stored under glycerol or petroleum.

The commercial applications of thallium are limited, and at present there are no bulk consumers. Consumption of thallium in the United States has fallen steadily from 1.4 tons in 1987 to 0.3 tons in 1998.[11] Previously, though, over a period from 1920 to 1970, several tons of thallium were used each year in the form of insecticides and rodenticides. However, many countries have terminated its use because of accidental or secondary poisoning of wild animals and birds; even children have been known to be severely poisoned as a result of ingesting thallium-containing bait.

There are several uses of thallium in the optical industry. For example, mixed TlBr–TlI crystals may be used as optical elements for IR applications. Thallium is also added in small amounts to glass to increase the density and refractive index. For example, patents have been filed for thallium-containing glasses for use as sealants or coatings for semiconductor elements.

In the field of electronics, thallium oxysulfide is used in the so-called ‘Thalofide cell’, which has sensitivity for low-intensity, long-wavelength light better than that of the selenium cell, and thus has important military and research applications. Thallium-activated NaI or NaCl crystals are used in the photomultiplier tubes present in some scintillation counters. Future uses of thallium in this field can be expected because of its incorporation in thallium-based high-temperature superconductors.

Some of the alloys of thallium have found applications as a result of their unique properties. For example, the Tl–Hg alloy containing 8.7% thallium forms a eutectic mixture freezing at −59 °C, and has been considered for applications in low-temperature thermometers, switches, closures, and seals. Alloys of thallium are also used in good quality bearings, having a very high resistance to corrosion and low coefficients of friction. Thallium is also used in gold plating applications.

In spite of their known toxicity, compounds of thallium have been used in medicine and as cosmetics. Thallium has been used internally in the treatment of gonorrhea, syphilis, dysentery, and tuberculosis and externally as a depilatory. Serious cases of poisoning were recorded, some of which were even fatal. At present, the only medical application of thallium is its use in the form of intravenous injections of ^{201}Tl (half-life = 12.2 days) for myocardial imaging to diagnose the distribution of regional myocardial perfusion.

Most of the thallium in circulation today is probably present in research laboratories; in 1977 this share was estimated at 50% in the United States.[2] Thallium compounds are mainly used as intermediates or catalysts in organic synthesis and ‘must now be regarded as essential reagents for modern organic synthesis’.[12] Thallium-based superconducting materials are presently being prepared and characterized in material science laboratories.[13] The first large scale commercial application of $Ba_2CaCu_2Tl_2O_8$ thin films for a microwave device has recently been reported.[14] An X-ray laser using energized atoms of thallium has been developed.[15] Thallium has also found some applications in biological research;[16] for example, Tl^+ is able to mimic K^+ in certain biological reactions and can be easily detected using ^{205}Tl NMR or fluorescence methods. Metal activated enzymes such as pyruvate kinase, ATPase, and aldehyde dehydrogenase have been studied in this way. Tl^{III} has also been used as a probe to investigate the iron sites in human transferrin.

2 PROPERTIES OF THE ELEMENT

Thallium is a silver–gray, soft, heavy, and ductile metal having three forms. The normal close-packed hexagonal lattice transforms to a body-centered cubic structure above 230 °C and a face-centered cubic form is stable at high pressures. The triple point is at 110 °C and 30 kbar. Thallium vapor is essentially monatomic, but on heating to 2000 °C, the vapor emits a visible band due to Tl_2. Some properties are listed in Table 1.[9]

There are two stable isotopes of thallium, ^{203}Tl (29.5%) and ^{205}Tl (70.5%), and numerous radioactive isotopes; in the mass range 184–210, there are 41 isotopes including 16 with half-lives longer than 10 minutes.

Thallium has the stable oxidation states I and III; there are also several compounds in which thallium exists with the *Formal Oxidation State* II, though stable compounds of Tl^{II} are not known in aqueous solution. It has been proposed that Tl^{II} is present in reactions with one-electron reactants; half-lives of 0.5 ms have been measured for the Tl^{2+} intermediate by flash photolysis. It has been shown that the electron transfer in most Tl^{I}/Tl^{III} redox systems is a two-electron process[17] (*see* ***Electron Transfer Reactions: Theory***). However, thallium is present as Tl^{II} in the trinuclear $(NBu_4)_2[Tl\{Pt(C_6F_5)_4\}_2]$; an unpaired electron makes the solid compound paramagnetic.[18] Isolable molecular organothallium(II) compounds, $[(Me_3Si)_3Si]_2Tl{-}Tl[Si(SiMe_3)_3]_2$ and $(^tBu_3Si)_2Tl{-}Tl(Si^tBu_3)_2$ have been reported recently; the Tl–Tl contacts (resembling the well known $Hg_2{}^{2+}$) are 2.91 and 2.97 Å, respectively.[19]

Table 1 Some properties of thallium

Atomic number	81
Relative atomic mass	204.3833
Ground-state electron configuration	$[Xe]4f^{14}5d^{10}6s^{2}6p^{1}$
Radii (pm)	
atomic (α form)	170.4
Tl^{I}	149
Tl^{III}	105
covalent	155
Electronegativity (Pauling)	
Tl^{I}	1.62
Tl^{III}	2.04
Tl^{I}/Tl	-0.3363
Standard reduction potentials (V)	
Tl^{III}/Tl	0.72
Tl^{III}/Tl^{I}	1.25
$Tl \rightarrow Tl^{I}$	589.3
Ionization energies ($kJ\,mol^{-1}$)	
$Tl^{I} \rightarrow Tl^{II}$	1971.0
$Tl^{II} \rightarrow Tl^{III}$	2878
$Tl^{III} \rightarrow Tl^{IV}$	(4900)
Density ($g\,cm^{-3}$)	
at 293 K	11.850
liquid at mp	11.290
Melting point (K)	576.7
Boiling point (K)	1730
Electrical resistivity (Ωm) at 273 K	18.0×10^{-8}

The Tl^{I}–Tl^{III} relationship is therefore a dominant feature of thallium chemistry. The standard reduction potentials at 25 °C and unit activity of H^{+} are: $Tl^{I}/Tl = -0.336$ V, $Tl^{III}/Tl = +0.72$ V, and $Tl^{III}/Tl^{I} = +1.25$ V.**[9]** Estimates have also been made for the couples $Tl^{III}/Tl^{II} = +0.33$ V and $Tl^{II}/Tl^{I} = 2.22$ V. The generally valid limitations concerning the use of standard electrode potentials to predict the redox chemistry of 'real' systems are especially important in the case of thallium: factors such as complex formation in the presence of coordinating anions or neutral ligands and pH dependence due to hydrolysis do affect the actual or formal redox potentials. For example, redox potentials have been measured for $TlCl/TlCl_3 = +0.77$ V in 1 M HCl and $TlOH/Tl(OH)_3 = -0.05$ V in alkaline solution.**[1]** These formal potentials differ from the standard value for $Tl^{III}/Tl^{I} = +1.25$ V. The difference can be attributed to the substantial difference between the complex forming abilities of Tl^{I} and Tl^{III}, which will be discussed in detail later. The Tl^{III} is thermodynamically stable in the presence of strong complexing agents, even in acidic solutions, though in the absence of these ligands Tl^{+} can only be oxidized by strong oxidizing agents such as MnO_4^{-} or BrO_3^{-}. In contrast, Tl^{+} is a powerful reducing agent in alkaline media.

It is interesting to note that Tl^{I} is more stable than the monovalent oxidation states of the other three metallic elements of group 13, Al, Ga, and In. The occurrence of an oxidation state two units below the group valence is often known as the *Inert Pair Effect* (see, e.g. Hg, Sn, Pb, and Bi). This effect implies a resistance of a pair of s electrons (i.e. $6s^2$ for Tl) to be lost or to form covalent bonds. The reason for the stability of the lower oxidation state cannot be attributed to its unusually high ionization potential for this pair of s electrons. The sum of the second and third ionization enthalpies for Tl (4820 $kJ\,mol^{-1}$) is slightly higher than the same value for In (4501 $kJ\,mol^{-1}$), but lower when compared to Ga (4916 $kJ\,mol^{-1}$). On the other hand, the mean bond energies of the trichlorides are 242, 206, and 153 $kJ\,mol^{-1}$ for Ga, In, and Tl respectively. There is a substantial decrease in the bond strengths and this is the reason why the formation of $TlCl_3$ is less favored in comparison with $GaCl_3$ or $InCl_3$. The relativistic contribution of the inert pair effect has been appreciated in recent theoretical calculations. An s^2 pair is not stereochemically active because the s orbital is spherically distributed, unlike a 'lone pair' occupying a coordination site in a molecule (see, e.g. $SnCl_3^{-}$).**[17]**

The Pauling *Electronegativity* (EN) values of the stable oxidation states of thallium are 1.62 and 2.04 for Tl^{I} and Tl^{III} respectively.**[9]** The latter value is equal to that for boron, and thus Tl and B are the most electronegative elements of group 13. It should be noted that the trend in the electronegativities is not monotonic for this main group, and the values have limited importance in predicting trends even for compounds of elements having the III oxidation state. On the other hand, the concept of 'hard' or class 'a' and 'soft' or class 'b' metal ions and ligands (*see* ***Coordination & Organometallic Chemistry: Principles***) is a useful guideline in the classification of bond strengths and the ionic/covalent character of bonds in thallium compounds. Thallium(III) belongs to the group of 'soft' metal ions, in contrast to Al^{III}, Ga^{III}, and In^{III}, which are classified as 'hard' ions. The 'softness' of Tl^{III} is rationalized in terms of its strong interactions with 'soft' donor ligands such as sulfur or the halides, with the exception of F^{-}. One can find similarities in the chemistries of Au^{I}, Hg^{II}, and Tl^{III}. On the other hand, Tl^{I} is classified as a borderline ion, having similarities both with the alkali metal ions, which have comparable ionic radii, and also with Ag^{+}. Thallium(I) forms ionic crystals; however, the non-Coulombic interaction increases on moving from TlF to TlI. Furthermore, complexes of Tl^{I} are quite weak due to the s^2 electrons, which are σ-antibonding in all stereochemistries. The greater polarizability of Tl^{I} in comparison with the alkali metal ions may explain its pronounced similarity to Ag^{I}. The geochemical diversity of thallium might also be related to this character.

The TlX_3 compounds, like their Al, Ga, and In analogs, are found to behave as Lewis acids (*see Lewis Acids & Bases*) and accept ligands to form tetrahedral complexes. The position of Tl is uncertain in the $Al > Ga > In$ order. The polymerization of these compounds is extensive in order to achieve coordination saturation.**[17]**

Before discussing the compounds of thallium in detail, the chemical behavior of the metal will be illustrated by its reactions with some common reagents.

Freshly prepared thallium readily loses its bluish-gray tinge in air. The metal is slowly oxidized by dry air or oxygen at room temperature, forming Tl_2O, and reacts gradually with water or steam even in the absence of oxygen to form TlOH. Dissolution of thallium in hydrofluoric acid is fast. The decreased reactivity with other hydrogen halides is purely a result of the formation of a layer of insoluble thallium(I) halide. Thallium dissolves in oxidizing acids. Thallium is not soluble in sodium hydroxide, in contrast to the amphoteric metals Al and Ga. A remarkable reaction of the metal is with alcohols forming $Tl(OR)_3$ and H_2. The metal is fairly reactive with the halogens and also reacts with sulfur at elevated temperatures.

3 THALLIUM COMPOUNDS

3.1 Thallium Hydrides

The hydrides of thallium, like those of lead and bismuth, are unstable. However, the compound $LiTlH_4$ has claimed to be a relatively stable thallium hydride. Solid $LiTlH_4$ is easily prepared from $TlCl_3$ using lithium hydride[20] (equation 1):

$$\mathrm{TlCl_3 + 4LiH \xrightarrow[-15\,^\circ C]{Et_2O} LiTlH_4 + 3LiCl} \tag{1}$$

The compound readily decomposes to Tl, LiH, and H_2 above 30 °C, whereas in ether solutions a polymeric hydride is formed after a few hours at 0 °C (equation 2):

$$\mathrm{LiTlH_4 \xrightarrow[0\,^\circ C,\ -LiH]{Et_2O} TlH_3{\cdot}\mathit{n}Et_2O \longrightarrow (TlH_3)_\mathit{x}} \tag{2}$$

$(TlH_3)_x$ is thermally unstable and loses H_2 at 150 °C giving the stable polymeric Tl^I hydride $(TlH)_x$. This compound has also been prepared by the thermal decomposition of $TlBH_4$, or from TlOEt by addition of B_2H_6 in ether solution. The chemical properties of these compounds reported in the 1950s by Wiberg should be treated with some reservation; for example, the thermal stabilities of TlH_3 and $(TlH_3)_x$ published at that time are not in agreement with recent reports concerning other hydrides of the group 13 elements.[21] Wiberg's report on the stability of $(TlH_3)_x$ seems to be dubious on the basis of theoretical calculations also.[22] Recent ab initio calculations show the thermodynamic instability of Tl_2H_6 both in gas and solid phases, although kinetic stability has been predicted, that is, a local minimum has been found at the MP2 level. However, the isolation of $(TlH_3)_x$ still remains intricate.[23]

No experimental results appear to have been published since the late 1950s, except for the preparation of $TlHI_2$ (from TlI_3, Al, and H_2)[24] and also of HTl_2OH.[25] The latter species are hydrogen bonded and may be formed from Tl vapor with H_2O in an argon matrix by UV irradiation. TlH species have been detected and characterized by spectroscopy in the gas phase.[26] Moreover, a large body of theoretical calculations have been published dealing with the stability and bonding of the thallium hydrides.[23] It is worth mentioning a dimeric compound, Tl_2H_2, which is often used as a model in theoretical studies dealing with the stability of the Tl–Tl bond,[22] and the monohalide-thallanes (TlH_2X) as model systems for calculation of thermodynamic stability and the role of the π-back donation of the halogeno ligand.[27]

3.2 Halides and Pseudohalides

3.2.1 Halides and Halide Complexes

The series of compounds Tl^IX and $Tl^{III}X_3$, except for $Tl^{III}I_3$, are well characterized. The relative weakness of the Tl^{III}-halide bond has been previously discussed in connection with the 'inert pair effect' (see Section 2).

The Tl^I halides are similar to the silver halides in that they are sensitive to light. The yellow compound TlI has a curious orthorhombic layer structure, which is transformed to a red metastable cubic form (CsCl type) at 4.7 kbar or 175 °C, becoming a metallic conductor at about 160 kbar.[28] If a small quantity of a Tl^I halide is added to an aqueous solution of an alkali halide, a blue ***Luminescence*** is emitted; furthermore, TlCl doped KCl behaves as a thallium–alkali halide phosphor. In both cases, $TlCl_2^-$ is believed to be the active species.[1]

Thallium(I) halides are predominantly ionic, although there is a tendency toward increasing covalent character in the series of compounds TlCl (17%), TlBr (20%), and TlI (28%). This increased degree of covalency results in decreased solubility; for example, TlF is soluble in water whilst the other Tl^I halides are only sparingly soluble. The thallium(I) halides are classical examples of 'incompletely dissociated' 1:1 electrolytes. The stability of halide complexes of Tl^I is low and follows the order TlF < TlCl < TlBr < TlI, where for the series of halides, $K_1 = -$, 0.8, 2.1, 5.0 and $K_2 = -$, 0.2, 0.7, 1.5 respectively.[1] The fluoride ion F^- is preferred to perchlorate as a 'noncomplexing' counterion. Claims have been made for $TlX_n{}^{1-n}$ species with $n = 3$ and 4; however, the formation of complexes in aqueous solution with $n > 2$ seems unlikely.

The covalent trihalides of thallium(III) are less stable than the trihalides of the lighter metals of group 13. Aqueous solutions of these compounds are acidic because of their extensive hydrolysis. The compound $TlCl_3$ is an important starting material for the preparation of Tl^{III} organometallic compounds.

The white compound TlF_3 has been prepared by the direct fluorination of Tl_2O_3 with F_2, BrF_3, or SF_4 at 300 °C. TlF_3 decomposes at 500 °C before melting, it does not form hydrates, and it hydrolyzes in water; no complexes of type Tl^{III}–F^- have been detected. The solids $MTlF_4$, where M = Li or Na, are true double salts. The complexes M_3TlF_6 (M = Na, K, Rb, Cs) have been prepared by fluorination of a mixture of $TlCl_3$ and the appropriate alkali chloride. These compounds contain discrete octahedral $TlF_6{}^{3-}$ anions.[21]

Concentrated solutions of $TlCl_3$ and $TlBr_3$ can easily be prepared by oxidation of Tl^I halides with the appropriate halogen.[29] $TlCl_3{\cdot}4H_2O$ (mp = ca. 43 °C) and $TlBr_3{\cdot}4H_2O$ (decomposes at ca. 30 °C) may be crystallized from aqueous solutions; attempts at thermal dehydration lead to the formation of TlCl or TlBr. However, $SOCl_2$ may be used to dehydrate these compounds giving, for example, anhydrous $TlCl_3$ (mp = 115 °C). Solutions of anhydrous $TlCl_3$ or $TlBr_3$ in MeCN can be prepared by simply treating the solution of the monohalide with Cl_2 or Br_2. Solid $TlCl_3$ can be prepared as shown in equation (3):[17]

$$\text{Tl or TlCl or Tl}_2\text{CO}_3 \xrightarrow{\text{NOCl}} \text{TlCl}_3{\cdot}\text{NOCl} \xrightarrow{\text{heat}} \text{TlCl}_3 \qquad (3)$$

$TlCl_3$ is very hygroscopic and is soluble in water, acetonitrile, ether, and alcohols. In addition to $TlCl_3$, $TlCl_2^+$ and $TlCl_4^-$ species may coexist in solution. However, $TlCl_3$ reacts with ketones, yielding α-chloro ketones.[30]

As is to be expected from the 'soft' character of Tl^{III}, strong chloride and bromide complexes of type TlX_n^{3-n} are formed in solution, where n is less than or equal to 4. These species are more stable in aqueous solution than the analogous Al^{III}, Ga^{III}, and In^{III} halides. Some of these halides have been thoroughly characterized both in the solid state and in solution by means of X-ray crystallography, solution X-ray diffraction, and NMR. These complexes are among the most stable metal–halide complexes known, particular stability having been claimed for the TlX_2^+ complexes with chloride (see e.g. the overall stability constants, $\beta_n = 10^{7.16}$; $10^{12.60}$; $10^{16.15}$; $10^{18.32}$; and $\sim 10^{18.02}$; $n = 1$–5, respectively for X = Cl in 3 M $HClO_4$) and bromide ligands.[1,7] In addition, the formation of weaker species with $n > 4$ has been demonstrated.[31] In a detailed study of ligand exchange reactions between Tl^{III}–X^- complexes, where X = Cl, Br, and CN, the authors claim a preference for a bimolecular reaction between the lower complexes, as opposed to a direct reaction between the complexes and the free halide, which is present only at very low concentrations. The direct path becomes dominant only for the higher complexes.[32]

There is a systematic change in the coordination geometry of the Tl^{III} complexes TlX_n^{3-n} (X = Cl, Br). The $Tl(H_2O)_6^{3+}$ cation has a regular octahedral geometry, which appears to be retained in the first and second complexes, $TlX(H_2O)_5^{2+}$ and $TlX_2(H_2O)_4^+$, the TlX_2^+ unit being linear in aqueous solution. The solids $TlCl_3{\cdot}4H_2O$ and $TlBr_3{\cdot}4H_2O$ are isomorphous, having a trigonal bipyramidal coordination around Tl^{III}. X-ray diffraction studies indicate that the three halide ligands are coordinated in a trigonal arrangement with two water molecules completing the coordination sphere. In aqueous solution, the geometry is essentially the same for $TlBr_3(H_2O)_2$, but for the chloride complex the coordination is probably a distorted tetrahedral.[7,33] In the TlX_4^- complexes where X = Cl, Br, or I, the coordination sphere is tetrahedral with no water molecules in the inner sphere, either in solution or in the solid phase.[34] The complexes $TlX_5(H_2O)^{2-}$ (X = Cl, Br) occur in the crystal structures of $K_3TlCl_6{\cdot}\frac{13}{7}H_2O$ and $Rb_3TlBr_6{\cdot}\frac{13}{7}H_2O$ and also in solution for X = Cl; a distorted octahedral geometry has been found in the solids. The complexes of type TlX_6^{3-}, where X = Cl or Br, have a distorted octahedral geometry in the solid state. Numerous alkali, tetraalkyl, and arsonium salts of the tetra-, penta-, and hexahalides of thallium(III) have been prepared. $Cs_3Tl_2Cl_9$ is an example of an important structural type having the confacial bioctahedral structure.[3,21,28]

Our knowledge of the Tl^{III}–iodide complexes is relatively limited because redox reactions occur in solution. However, in the presence of a large excess of iodide, the redox reactions are avoided and a stable TlI_4^- complex has been observed; $\beta_4 =$ ca. 5×10^{35}. Derivatives of TlI_4^- with different cations have been prepared. The anion is clearly tetrahedral in the tetrabutylammonium salt[35] and probably also has the same structure in the other crystals.

Treatment of TlF with I_2, BrCl, ICl, or IBr yields $TlFI_2$, TlFClBr, TlFClI, and TlFBrI, respectively. These products may represent an intermediate between Tl^{III} compounds and molecular adducts of Tl^I.

No mixed Tl^I–Tl^{III} fluorides have been reported. The oxidation of TlCl and TlBr by halogens results, however, in a series of mixed-valence halides. Earlier these compounds were thought to be Tl^{II} salts, but neither magnetic susceptibility measurements nor crystal-structure determinations proved this hypothesis. For example, TlX_2 and Tl_4X_6 (X = Cl or Br) should be correctly formulated as Tl^+ $[TlX_4]^-$ and $(Tl^+)_3[TlX_6]^{3-}$. The mixed Tl^I–Tl^{III}–iodide Tl_3I_4 can be formulated with formulae $(Tl^+)_5[TlI_8]$, but another model involving $(Tl^+)_6I_5(I_3)$ with the triiodide ion cannot be ruled out.[1]

The black crystalline TlI_3 has been known since 1864 and is an intriguing compound. It is obtained by evaporating an equimolar solution of TlI and I_2 in concentrated HI. TlI_3 is isomorphous with CsI_3, and must therefore exist as $Tl^+I_3^-$ in the solid state. However, the absorption spectra of solutions of the compound in methanol do not indicate the presence of the I_3^- ion; indeed, the spectra are similar to those of $KTlI_4$, thus suggesting a tandem redox and complex formation equilibrium (equation 4):

$$4\text{TlI}_3 \rightleftharpoons \text{Tl[TlI}_4]_3 \qquad (4)$$

Solutions of TlI_3 yield Tl_2O_3 when shaken with sodium carbonate.[1] In order to understand these fairly complicated redox reactions in the chemistry of TlI_3, it is important to remember how the formal redox potentials vary with the experimental conditions such as solvent, pH, solubility, and complex formation (see Section 2).

The thallium(III) halides, TlX_3 (X = Cl, Br, I), form complexes with amines (L) with formulas $TlX_3{\cdot}L_n$, where $n = 1$–3. Among the most studied complexes with this ligand stoichiometry are the neutral monomeric species $TlX_3{\cdot}L_2$, where X = Cl or Br, the halide-bridged dimers

$L_2X_2TlX_2TlX_2L_2$, ionic monomers $[TlX_2L_2]X$, and dimer complexes of type $[TlX_2L_4][TlX_4]$.[3] Recently, $TlClBrI{\cdot}L_2$ complexes have also been prepared.

Our knowledge about the Lewis acid behavior of Tl^{III}-halides is scarce. A recent theoretical study claims that the π-donor ability of the halogens (X) increases with $F < Cl < Br < I$ both in TlX_3 and BX_3, and the $p(\pi)$ population at the central atom in TlX_3 is smaller than that is in BX_3. However, the hydride affinity of TlX_3 relative to TlH_3 is substantially higher compared to the hydride affinity of BX_3 relative to BH_3.[27]

3.2.2 Pseudohalides and Pseudohalide Complexes

Thallium(I) forms salts with cyanide (CN^-), cyanamide (NCN^{2-}), azide ($N_3{}^-$), cyanate (OCN^-), isocyanate (CNO^-), thiocyanate (SCN^-), and selenocyanate ($SeCN^-$); however, complexes with these ligands, like the Tl^I-halide complexes, are very weak. In contrast, the neutral $Tl^{III}X_3$ species are not well known, although the Tl^{III}-pseudohalide complexes are more or less stable.

Tl^I pseudohalides can be prepared from aqueous solutions of soluble Tl^I salts, usually the sulfate or nitrate, by adding the appropriate anion, thus precipitating the sparingly soluble Tl^I pseudohalide compounds. Thallium(I) azide has been prepared from Tl^I acetate, TlOAc, with NaN_3 in ethanol. TlN_3 is isomorphous with NaN_3 and RbN_3, but its physical properties suggest a somewhat more covalent Tl–N bond in the solid. The azide decomposes slowly at temperatures near the melting point (374 °C) and the liquid is explosive. Tl^I isocyanate, TlCNO, also explodes on heating to 105 °C.[3,21] K_1 has been determined as about 2.5 for TlN_3, but no cyano complexes of Tl^I, unlike Ag^+, have been detected. Weak complexes ($K_1 = 1.7$, $K_2 = 0.6$)[36] have been reported in the Tl^I–SCN^- system at high concentrations of the anion.

Tl^{III} azide complexes have been observed in solution, though the species are not well characterized. The solid complexes $[Ph_4As][Tl(N_3)_4Cl_2]$[1] and $H_3[Tl(N_3)_6]$ have been isolated, the latter being an explosive yellow compound.

The existence of Tl^{III} cyanide complexes has been mentioned previously; however, on the basis of the analogy with other Tl^{III}–pseudohalide redox reactions, and by analysis of the redox potentials, the existence of the $Tl(CN)_n{}^{3-n}$ complexes was not widely accepted for a time. However, a detailed investigation of this system using ^{205}Tl and ^{13}C NMR spectroscopy has indicated that Tl^{III} indeed forms very stable cyanide complexes (the overall formation constants, $\beta_n = 10^{13.2}$, $10^{26.5}$, $10^{35.2}$ and $10^{42.6}$ in 4 M ionic strength for $n = 1$, 2, 3 and 4 respectively).[37] These species are in fact the most stable complexes of Tl^{III} formed with monodentate ligands. The extra stability of the $Tl(CN)_2{}^+$ species is worth mentioning. It is certainly not a coincidence that the diorganothallium(III) compounds containing the linear C–Tl–C group (like doing the (N)C–Tl–C(N)) are also very stable. A number of mixed cyanide-halide complexes exist in aqueous solution.[7]

The lack of success encountered by attempts to prepare Tl^{III} pseudohalides might be related to the redox reaction between Tl^{III} and reducing ligands, as in the Tl^{III}–I^- system. In the case of the Tl^{III}–SCN^- system, the reaction stoichiometry appears to be as shown in equation (5):

$$4SCN^- + 3Tl^{3+} + 4H_2O \longrightarrow 3TlSCN + HCN + SO_4{}^{2-} + 7H^+ \qquad (5)$$

Recently, a quite stable $Tl(SCN)^{2+}$ complex was characterized by ^{205}Tl NMR, and may be the predominant intermediate in the course of the above redox reaction.[38] Stable complexes of $Tl(SCN)_3$ with 2,2′-bipyridyl and 1,10-phenanthroline have been prepared in the solid form.[1]

Mixed-valence Tl^I–Tl^{III} pseudohalides, such as $Tl(CN)_2$ and $Tl(N_3)_2$, were first prepared more than 100 years ago. Like the analogous halides, these compounds do not contain Tl^{II}, but instead can be formulated as $Tl[Tl(CN)_4]$ and $Tl[Tl(N_3)_4]$, respectively. The former compound can be isolated from both organic and aqueous solutions. As is expected, the Tl(III) is tetrahedrally coordinated.[39] The redox stability of the $TlX_4{}^-$ complex might be explained in a similar manner to that of $TlI_4{}^-$.

3.3 Oxides

3.3.1 Thallium(I) and Thallium(III) Oxides and Hydroxides

The two well-defined oxides of thallium are Tl_2O and Tl_2O_3. In addition, there are some poorly defined oxides such as the Tl^IO_2 (violet), a mixed oxide Tl_4O_3 or $Tl_2O{\cdot}Tl_2O_3$ (black), and some nonstoichiometric oxides with formulas $TlO_{1.5}$–$TlO_{1.75}$.

Black platelets of thallium(I) oxide are formed when thallium is oxidized in air at moderate temperatures, or from TlOH or Tl_2CO_3 by heating to 100 or 700 °C, respectively, in the absence of air. Tl_2O melts at 596 °C, indicating that the solid has an ionic nature; however, it is also rather volatile and very hygroscopic, forming the yellow solid TlOH on contact with water. Solutions of TlOH are basic, its dissociation constant is about $10^{-0.3}$ at 25 °C, and its basic strength is about 10^5 times greater than that of NH_3 and 10 times greater than for $Ca(OH)_2$.[36] Chemical shift of the ^{205}Tl NMR signal, affected by the equilibrium $Tl^+ + OH^- \rightleftharpoons TlOH$, can be used to monitor the alkalinity of concentrated aluminate solutions.[40] Tl_2O dissolves in ethanol to form TlOEt.

The brown–black thallium(III) oxide can be synthesized from elemental thallium by heating it to dull redness in the presence of oxygen, but is more conveniently prepared from Tl^I salts in alkaline solution by adding hydrogen peroxide or Cl_2. Tl_2O_3 is easily precipitated and can be dried at 500 °C. It is insoluble in water but can be dissolved in acids, giving the corresponding Tl^{III} salts (see Section 3.6). The oxide has a remarkably low electrical resistance at room temperature (about $7 \times 10^{-5} \Omega\,\mathrm{cm}$).[28] At elevated temperatures, Tl_2O_3 vaporizes and decomposes to Tl_2O and O_2.

The appearance of the brown color of Tl_2O_3 at higher pH is very common in solutions containing inorganic Tl^{III} species. Stepwise replacement of the L ligands in $Tl^{III}L_x$ may result in mixed hydroxo complexes, such as oxohalides. Previously the aqua ion, $[Tl(H_2O)_6]^{3+}$, has been claimed to have a distorted octahedral structure in which two of the water molecules are more strongly bound than the others. However, structural investigations, both in solution and in the solid state by X-ray diffraction, indicate a regular octahedral geometry for this cation.[41] The aqua ligands of the hexaaquathallium(III) ion are quite labile; the pseudo first-order rate constant for the exchange of water ligands has been estimated to $5 \times 10^7\ \mathrm{s}^{-1}$.[32] The $Tl^{III}\cdot$ aq ion is very acidic, the acid constants $K_{a,1}$ and $K_{a,2}$ having values of $10^{-0.5}$ and $10^{-1.2}$ in $1\,\mathrm{mol\,dm^{-3}}$ $NaClO_4$, respectively.[36] In other words, $Tl(OH)^{2+}$ and $Tl(OH)_2{}^{+}$ are among some of the most stable metal–hydroxo species. On the other hand, in contrast to Al^{III}, Ga^{III}, and In^{III}, no polynuclear species of type $M_x(OH)_y{}^{(+3x-y)}$ have been characterized for Tl^{III}. Even the formation of $Tl(OH)_3$ and its hydrates is not clearly proven.

3.3.2 *Ternary and More Complex Oxides*

Extensive studies of these compounds are in progress as a result of their potential applications in solid-state electronics. The electrical and magnetic properties of these compounds show a particular sensitivity to their composition and even to the often 'secret' methods used for their preparation. Selected topics will be briefly discussed here (*see also* ***Oxides: Solid-state Chemistry***).

In spite of the nonamphoteric character of thallium(I), the Tl–alkali metal oxides are often called oxythallates.[1] Red crystals, $KTl^{I}O$, and $RbTl^{I}O$ have been prepared by heating Tl_2O and an alkali oxide. Oxythallate(III) derivatives, $MTlO_2$ (formally metathallates), can be prepared in the same way as those of the alkali metals. The majority of these compounds have the α-$NaFeO_2$ structure: M^+ and Tl^{3+} cations lie in alternate layers in the octahedral interstices of the oxygen array. The solid-state electrolyte $Tl^{I}\beta$-alumina, $TlAl_{11}O_{17}$, can be prepared from sodium β-alumina by heating with a molten Tl^{I} salt (*see* ***Aluminum: Inorganic Chemistry***). The Tl^{I} based ferrites (*see Ferrite*) have the idealized formula $TlFe_{11}O_{17}$ and are structurally closely related to ionic conductors.[42]

The recently discovered thallium-based high-temperature superconductors[13,14] received extraordinary attention because their transition temperature is above that of liquid nitrogen, 100–120 K, and these materials seem to be both stable in air and resistant to moisture. Different thallium cuprates are prepared by melting (920–950 °C) appropriate amounts of mixed powders of Tl_2O_3, BaO/SrO, CaO, and CuO.[43] The oxides have the idealized formulas $TlA_2Ca_{m-1}Cu_mO_{2m+3}$ (A = Sr, Ba) and $Tl_2Ba_2Ca_{m-1}Cu_mO_{2m+4}$. No deviation from the ideal oxygen stoichiometry, 'O_{2m+3}' and 'O_{2m+4}', has been found, and the mixed oxidation state of Cu can be explained by the thallium deficiency in the lattice. The oxidation state of Cu and Tl in these materials has been investigated since this might be important for the superconducting properties: Cu^{II} and Cu^{III} have been proposed from X-ray absorption measurements, whilst Tl^{III} is clearly dominant. Both X-ray and ^{205}Tl NMR results show the existence of some Tl^{I},[44] but the 'issue of the competition between the systems Tl^{I}–Tl^{III} and Cu^{II}–Cu^{III} still remains open'.[45]

3.4 Chalcogenides

Chalcogenides of Tl, like those of Ga and In, are numerous and have been extensively studied since many of them are ***Semiconductors*** (*see* ***Semiconductor Interfaces***), semimetals (*see Semimetal*), photoconductors (*see Photoconductivity*), or light emitters. The compounds are covalent, and the formal oxidation states can be determined by checking the overall charge balance. However, this is somewhat arbitrary in such systems: Tl has two stable oxidation states and sulfur, especially, has a great propensity for *Catenation*. Existence of Tl^{III} sesquichalcogenides, Tl_2X_3, has been tentatively proposed; Tl^{III} may be reduced to Tl^{I} by chalcogenides. Well-characterized compounds include, for example, the black Tl_2S (distorted CdI_2 layer lattice), Tl_4S_3 ($Tl^{I}{}_3[Tl^{III}S_3]$), the black TlS ($Tl^{I}[Tl^{III}S_2]$), TlS_2, the red and black forms of Tl_2S_5 and Tl_2S_9 (Tl^{I} polysulfides), Tl_5X_3, TlX, and Tl_2X_3, where X = Se, Te.[28]

A large number of mixed chalcogenides and ternary or more complex thallium–chalcogenide complexes have been prepared and characterized (*see* ***Chalcogenides: Solid-state Chemistry***).

3.5 Thallium Salts with Oxoanions

Both Tl^{I} and Tl^{III} form salts with many oxoanions. Thallium(I) salts have no direct uses, except perhaps as starting materials for other reactions. Thallium(III) salts, however, especially thallium(III) nitrate, have been widely used in modern organic synthesis.

The following list gives some standard methods[1,3,29] for the preparation of Tl^{I} salts (examples shown in brackets):

1. dissolution of thallium metal in acid (Tl_2SO_4, $TlNO_3$)
2. neutralization of TlOH or Tl_2CO_3 with acid ($TlNO_3$, TlOAc, $TlClO_4$)
3. metathesis of Tl_2SO_4 with a barium salt ($TlNO_2$, $TlClO_3$, $TlBrO_3$, $TlIO_3$)
4. treatment of $TlNO_3$ with a nonvolatile acid ($TlClO_3$, Tl_3PO_4)
5. direct precipitation from aqueous solution ($TlIO_3$, Tl_2CrO_4).

Since TlOH and Tl_2CO_3 are commercially available, method 2 is a universal method for almost all salts. Thallium(I) salts of carbonic acids can be prepared in nonaqueous solvents (ethanol or ether) by the reaction of $Tl^{I}OEt$ with the appropriate acid.

Some weak interactions of Tl^{I} with certain oxoanions have been claimed and the following stability constants (K_1) measured: $TlCO_3^-$, 3.2; TlOAc, 0.8; $TlNO_3$, 0.3–0.7; $TlSO_4^-$, 0.3; $TlClO_4$, 0.3.[1]

Oxidation of Tl^{I} salts by bromine may yield stable mixed $Tl^{I}-Tl^{III}$ or Tl^{III} salts. $Tl_2Br_2SO_4$ has been prepared from Tl_2SO_4; it can be formulated as $Tl^{I}[Tl^{III}Br_2SO_4]$. The reaction of bromine with TlOAc gave $Tl(OAc)Br_2$.[1]

The preparation of Tl^{III} salts, including the nitrate, sulfate, phosphate, halogenates, acetate, and trifluoroacetate is based on the dissolution of Tl_2O_3 in the appropriate acid. Thallium(III) phosphate has also been prepared from $Tl(NO_3)_3$ by treatment with H_3PO_4. Solution of $Tl(ClO_4)_3$ can be prepared by the anodic oxidation of $TlClO_4$ in perchloric acid or by the reaction of $TlCl_3$ with $AgClO_4$.[7] Thallium(III) carboxylates are generated by the simple metathesis of $Tl(OAc)_3$ and a carboxylic acid.

Complexes of Tl^{III} with the oxoanions are much more stable than those of Tl^{I}. The coordination of perchlorate to Tl^{III} cannot be ruled out; however, ClO_4^- is considered to be the best noncoordinating counter anion for equilibrium studies. Related stability constant values (K_1) are: $Tl(NO_3)^{2+}$, $10^{0.9}$; $TlSO_4^+$, $10^{1.95}$; $TlHSO_4^{2+}$, $10^{1.2}$; $Tl(OAc)^{2+}$, $10^{6.2}$. The overall stability constant $\beta_3 = 10^{15.1}$ for $Tl(OAc)_3$. Some mixed hydroxo complexes have also been detected, including $Tl(OH)_2NO_3$ and $Tl(OH)(OAc)^+$. Numerous complexes have also been isolated in the solid state, such as $MTl(SO_4)_2$ (M = Li–Cs, NH_4), $K_2Tl(NO_3)_5 \cdot H_2O$, and $[NO]^+ [Tl(NO_3)_4]^-$; the last-named is produced by oxidizing $TlNO_3$ with N_2O_5. It is interesting that in the $Tl^{III}A_3 \cdot L_n$ complexes ($n = 2$, 3; L = bidentate N-donor ligands like 2,2′-bipyridyl or 1,10-phenanthroline), mentioned in Section 3.2.2 for A = SCN^-, A can also be NO_3^- or ClO_4^-, and the oxoanions might behave as inner-sphere ligands in the complexes.[3,21]

$Tl(OAc)_3$ is a strong Lewis acid and an effective Friedel–Crafts catalyst. The complex has been used in organic synthesis as the electrophilic agent for oxythallation reactions (*see* ***Thallium: Organometallic Chemistry***). In fact, $Tl(OAc)_3$ is only a weak electrophile, having mild oxidizing properties, because it is a stable complex. By contrast, thallium(III) nitrate (TTN) is highly ionic and thus a good electrophile. $Tl(NO_3)_3 \cdot 3H_2O$ now has a dominant role in oxythallation reactions.[46] It is soluble in a wide range of solvents, both organic and inorganic, and can be used as a solid supported catalyst. The water of crystallization cannot be removed by heating in vacuum or by treating with $SOCl_2$; indeed, Tl^{I} salts are formed. Dehydration has been achieved using methyl orthoformate[46] (equation 6):

$$Tl(NO_3)_3 \cdot 3H_2O + 3HC(OMe)_3 \longrightarrow Tl(NO_3)_3 + 6MeOH + 3HCO_2Me \qquad (6)$$

3.6 Complexes with Multidentate Organic Ligands

Thallium(I) acts as a weak Lewis acid and behaves similarly to the alkali metal ions, forming only weak complexes even with complexones such as edta and its analogs. The Macrocyclic Ligands (L), (*see* ***Macrocyclic Ligands***) and in particular the *Crown Ethers* containing 18-membered rings, such as 18-crown-6, do however form strong complexes. As is the case for other M^+ cations, the size of the macrocyclic cavity is critical for the formation of stable complexes. Unsymmetric benzo-type crown ethers possess high thallium(I) selectivity especially against potassium and rubidium ions.[47] Thallium can be immobilized as a thallium-rich mixed-valence solid, $[\{Tl(18\text{-crown-}6)Z\}_4CuCl_4][TlCl_4]_2 \cdot nH_2O$.[48] In addition to the $Tl^{I}LX$ compounds, $Tl^{I}L_2X$ sandwich complexes (*see Sandwich Compound*) are also known.[21]

Our knowledge of Tl^{III}–organic ligand systems is rather limited. Two important ‘side reactions’ must be mentioned: first, that $Tl(H_2O)_6{}^{3+}$ is easily hydrolyzed, leading to Tl_2O_3 even at pH = 2–3, and, secondly, that it is a strong oxidant. Both these effects prevent the formation and study of many such complexes. On the other hand, the interaction of Tl^{III} with multidentate ligands can stabilize the cation against both hydrolysis and reduction. These effects are exemplified by the $[Tl^{III}(edta)]^-$ complex, which is one of the most stable metal–edta species known ($K = 10^{37.8}$); only $[Co^{III}(edta)]^-$ is more stable.[49] The Tl^{III}–edta complex is stable up to pH = 12; $Tl(edta)(OH)^{2-}$ is formed in alkaline solutions. The structure of the Tl^{III}–edta complex in the solid phase is not known, but it could well be seven coordinate with one water molecule in the inner sphere since it readily forms $Tl(edta)X^{2-}$ mixed complexes with unidentate ligands, halides, and pseudohalides (including S-bonded SCN^-) without reduction of Tl^{III}. In solid $Na_2Tl(edta)CN \cdot 3H_2O$, the thallium(III) ion is hemispherically surrounded by the hexadentate edta, and there is also one strongly bound CN^- in the inner coordination sphere.[50]

However, the coordination number of thallium(III) is found to be eight in the bis(nitrilotriacetato) complex, $[Tl^{III}(nta)_2]^{3-}$ in solid by X-ray.[51] Stepwise formation of three $[Tl(en)_n]^{3+}$ complexes (en = ethylenediamine, $n = 1–3$) has been established by ^{205}Tl and ^{1}H NMR in a pyridine solvent. The $Tl^{III}$is octahedrally coordinated in the $[Tl(en)_3](ClO_4)_3$ solid.[52]

Porphyrin derivatives of Tl^{III} have been prepared; the metal ion lies 0.9 Å above the N_4 plane, with an anion coordinated as the fifth ligand.[21] A $Tl^{III}L_2$ species is formed with 1,4,7-triazacyclononane; two tridentate ligands are coordinated to a Tl^{III} ion in a distorted octahedron. It is an inert species with no additional labile coordination sites, and can therefore only be reduced via an outer-sphere electron-transfer process.[53] Crown ether complexes are known only for R_2Tl salts.[21]

3.7 Metal-metal bonded Tl-complexes

Recently the metallophilic interaction between heavy elements[54] has earned considerable interest (*see* ***Polynuclear***

Organometallic Cluster Complexes), and seems to be the most active research field of thallium coordination chemistry.

Although Tl(I) is often used as a large size counter cation in order to crystallize anionic metal complexes, its role might be more sophisticated as exemplified in the $Tl_2Pt(CN)_4$. This solid compound does not show the usual Pt–Pt 'linked' columnar structure of other $M_2Pt(CN)_4$ salts, but involves two Pt–Tl bonds with a weakly covalent character. The strong luminescence of the compound attributed to these bonds is not retained in solution.**[55,56]** On the contrary, the ligand supported metal–metal bond in the complex $[Tl^I(crown\text{-}P_2)Pt^{II}(CN)_2]NO_3$ ($P = -CH_2PPh_2$) is intact in solution.**[57]**

Recently, the formation,**[58]** structure,**[59–61]** equilibrium,**[62]** and kinetics**[63]** of a family of cyano compounds containing a direct and not supported by ligands platinum–thallium metal–metal bond have been reported. The complexes are synthesized according to the reaction:

$$mPt(CN)_4{}^{2-} + Tl^{3+} + nCN^- \rightleftharpoons [Pt_mTl(CN)_{4+n}]^{(n-1)-} \qquad (7)$$

Four binuclear species represented by a general formula $[(NC)_5Pt{-}Tl(CN)_{n-1}]^{(n-1)-}$ ($n = 1$–4) and a trinuclear complex $[(NC)_5Pt{-}Tl{-}Pt(CN)_5]^{3-}$ are formed in aqueous solution. The complexes exist in an equilibrium, which also includes the parent complexes $Pt(CN)_4{}^{2-}$ and $Tl(CN)_n{}^{3-n}$ ($n = 0$–4), and can be controlled by varying the cyanide concentration and/or pH of the solution.

Multinuclear NMR- (^{13}C, ^{195}Pt, ^{205}Tl), IR-, Raman-spectroscopy, Electron Spectroscopy for Chemical Analysis (ESCA), X-ray, and Extended X-ray Absorption Fine Structure (EXAFS) studies confirm direct, short (2.60–2.64 Å) Pt–Tl bonds. Figure 1. shows a typical ^{205}Tl NMR spectrum of $[(N^{13}C)_5Pt{-}Tl(^{13}CN)]^-$ together with the structure determined by EXAFS. The spin-spin coupling pattern is consistent with $4 + 1 + 1$ equivalent $^{13}CN^-$ ligands ($I = 1/2$), respectively and one ^{195}Pt nucleus (natural abundance 33.8%, $I = 1/2$). The spectrum has been selected to illustrate the usefulness of Tl NMR spectroscopy in studies of the inorganic chemistry of thallium. The compounds are diamagnetic, and

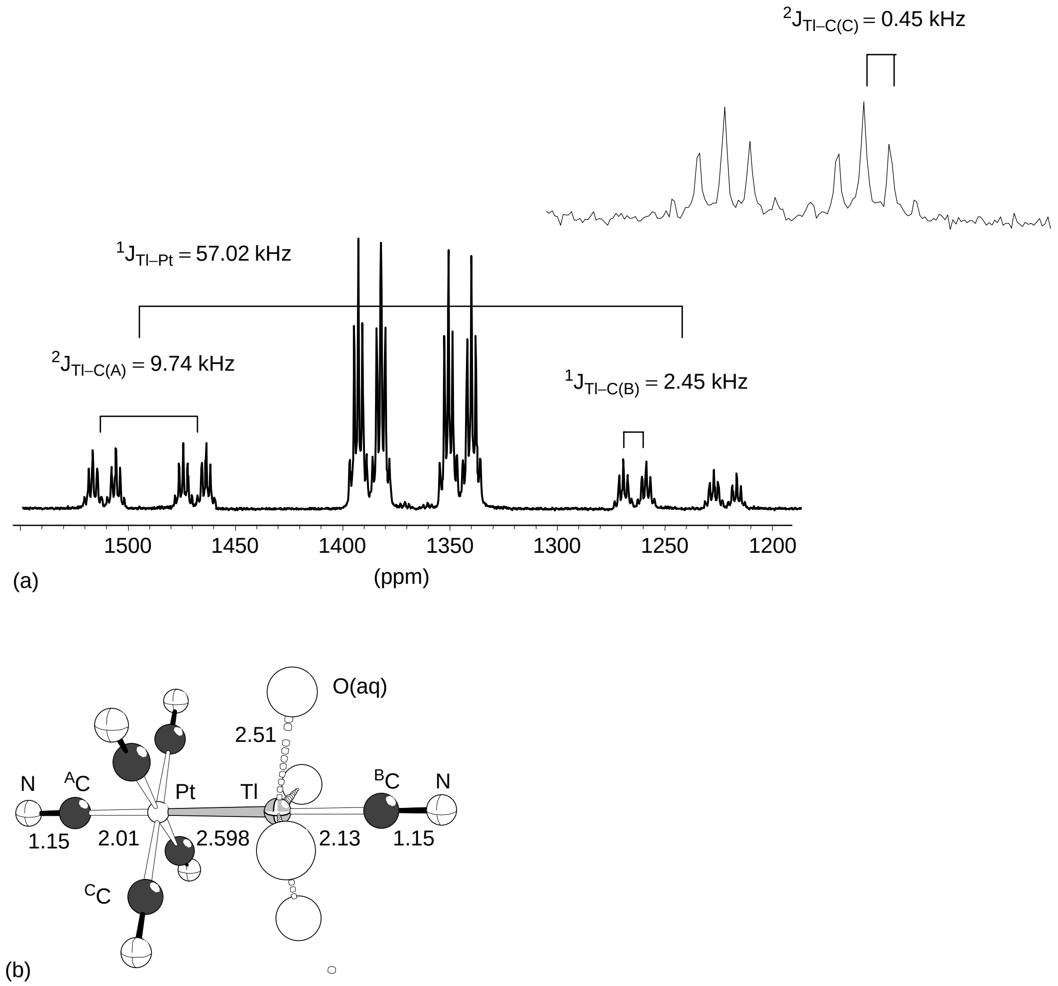

Figure 1 (a) 230.8 MHz ^{205}Tl NMR spectrum of the $[(^ACN)(^CCN)_4Pt{-}Tl(^BCN)]^-$-complex showing the spin-spin coupling schemes. The sample consists of 50 mM Tl^{3+}, 50 mM $Pt(^{13}CN)_4{}^{2-}$ and 150 mM $Na^{13}CN$, pH = 1.04. (b) Structural model based on Pt and Tl L_{III} EXAFS data

the electronic states and the nature of the Pt–Tl bonds have been elucidated by Density Function Theory (DFT) calculation.[64]

Selected crystal structures that contain platinum–thallium bonds can be divided into four groups depending on the formal oxidation states of the metal ions: Pt^0–Tl^I (2.86–3.05 Å),[65–67] Pt^{II}–Tl^I (2.88–3.15 Å),[54,57,68–73] Pt^{II}–Tl^{II} (2.70–2.71 Å),[18] and Pt^{II}–Tl^{III} (2.570–2.628 Å).[59–61,73]

4 TOXICITY[16]

The toxic effects of thallium are attributed to its ability to interfere with potassium-dependent biological reactions in a range of life forms extending from humans to plants and microorganisms.

The lethal dose of thallium is in the range of 10–50 mg kg^{-1}. In humans, 600 mg is often fatal. It should be noted that this dose is much larger than the lethal dose of many synthetic or naturally occurring organic poisons! The route of exposure and the chemical form seem to be insignificant for thallium's toxicity. Thallium is a cumulative poison that may be absorbed through the skin. Evidence of poisoning appears in 1–5 days. Acute thallium intoxication causes death by respiratory failure, preceded by paresthesia of the extremities, hypersecretion, loss of hair, uncontrolled muscle movements, convulsions, delirium, and coma. The most effective known antidote is colloidal Prussian Blue, $KFe^{III}[Fe^{II}(CN)_6]\cdot nH_2O$. Prussian Blue (prepared from $K_4[Fe^{II}(CN)_6]$) acts as an ion exchanger for Tl^+ in the intestines and accelerates the fecal elimination of Tl; 250 mg kg^{-1} body mass is administered daily. The use of activated charcoal or KCl as an antidote is recommended if Prussian Blue is not available.

5 ANALYTICAL CHEMISTRY OF THALLIUM

The qualitative detection of thallium is easily achieved by emission spectroscopy, thallium giving a green flame color. Thallium(I) iodide is a yellow precipitate that is insoluble in water, nonoxidizing acids, ammonia, and potassium cyanide, but that can be dissolved in sodium thiosulfate. Traces of thallium can be detected by dyes such as Brilliant Blue or Rhodamine B. Tl^I (or Tl^{III} after reduction by SO_2) can be determined by BrO_3^- or IO_3^- titrant. A gravimetric method uses Tl^I chromate.[3]

Instrumental analytical methods for thallium have been recently reviewed.[74] The low-detection limits of some methods allow the direct determination of thallium in environmental or biological samples, but preconcentration procedures may be necessary in order to achieve sufficient accuracy. A detection limit of 0.1 ppb (0.1 µg dm^{-3}) has been reported for electrothermal atomic absorption spectroscopy (ET-AAS) and for neutron activation analysis. Analytical methods including pulse voltammetry, isotope dilution and field desorption mass spectroscopy, X-ray fluorescence analysis, and some flame and plasma emission spectroscopic methods have been mentioned in a recent paper related to the environmental aspects of thallium chemistry.[10] Some photometric methods exist, though the detection limits are usually much higher than those of more sophisticated instrumental methods.

6 RELATED ARTICLES

Coordination & Organometallic Chemistry: Principles; Electron Transfer Reactions: Theory; Macrocyclic Ligands; Metal Ion Toxicity; Oxides: Solid-state Chemistry; Polynuclear Organometallic Cluster Complexes; Sulfur: Organic Polysulfanes; Thallium: Organometallic Chemistry.

7 REFERENCES

1. A. G. Lee, 'The Chemistry of Thallium', Elsevier, Amsterdam, NY, 1971.
2. I. C. Smith and B. L. Carson, 'Trace Metals in the Environment, V-1-Thallium', Ann Arbor Science, Ann Arbor, MI, 1977.
3. K. Wade and A. J. Banister, in 'Comprehensive Inorganic Chemistry', ed. J. C. Bailar, Pergamon, Oxford, 1973, Vol. 1, p. 1119.
4. P. I. Fedorov, M. V. Mokhosoyev, and F. P. Alexeyev, 'Khimiya Galliya, Indiya i Talliya', Nauka, Novosibirsk, 1977.
5. A. J. Downs ed., 'Chemistry of Aluminium, Gallium, Indium and Thallium', Chapman & Hall, London, 1993.
6. V. E. Plyutser, S. B. Stepina, and P. J. Fedorov, in 'Khimiya i Tekhnologhiya Redkikh i Rasseynnikh Elementov', ed. K. A. Bol'shakowa, Visshaya Shkola, Moscow, 1976.
7. J. Glaser, in 'Advances in Inorganic Chemistry' ed. G. Sykes, Academic Press: San Diego, CA, 1995, Vol. 43, pp. 1–78.
8. W. Crookes, *Chem. News*, 1861, **3**, 303.
9. J. Emsley, 'The Elements', 2nd edn., Clarendon Press, Oxford, 1991.
10. F. H. Kemper and H. P. Bertram, in 'Metals and Their Compounds in the Environment', ed. E. Merian, VCH, Weinheim, 1991, Chap. II.29.
11. C. A. DiFrancesco and G. R. Smith, Thallium Statistics, U.S. Geological Survey, Open-File Report 01-006, 2002.
12. A. McKillop and E. C. Taylor, *Chem. Br.*, 1973, **9**, 4.
13. J. G. Bednorz and K. A. Müller eds, 'Earlier and Recent Aspects of Superconductivity', Springer-Verlag, Berlin, 1991.

14. S. C. Speller, *Mater. Sci. Technol.*, 2003, **19**, 269.
15. T. O. Llewellyn, *Ceramic Bull.*, 1990, **69**, 885.
16. K. T. Douglas, M. A. Bunni, and S. R. Baindur, *Int. J. Biochem.*, 1990, **22**, 429.
17. F. A. Cotton and G. Wilkinson, 'Advanced Inorganic Chemistry', 5th edn., Wiley, New York, 1988.
18. R. Uson, J. Fornies, M. Tomas, R. Garde, and P. Alonso, *J. Am. Chem. Soc.*, 1995, **117**, 1837.
19. C. Janiak, *Coord. Chem. Rev.*, 1997, **163**, 107, references therein.
20. E. Wiberg and E. Amberger, 'Hydrides of the Elements of Main Groups I–IV', Elsevier, Amsterdam, NY, 1971.
21. D. G. Tuck, in 'Comprehensive Coordination Chemistry', ed. G. Wilkinson, Pergamon, Oxford, 1987, Vol. 3, Chap. 25.2.
22. M. J. Taylor and P. J. Brothers, in 'Chemistry of Aluminium, Gallium, Indium and Thallium', ed. A. J. Downs, Chapman & Hall, London, 1993, p. 111.
23. P. Schwerdtfeger, P. D. W. Boyd, G. A. Bowmaker, H. G. Mack, and H. Oberhammer, *J. Am. Chem. Soc.*, 1989, **111**, 15; P. Hunt and P. Schwerdtfeger, *Inorg. Chem.*, 1996, **35**, 2085.
24. T. H. Pearson, *Halogen-Substituted-Metal Hydrides and Hydrocarbons*, U.S. Patent, 2,992, 248; *Chem. Abstr.*, July 11, 1962, **56**, 167e.
25. R. H. Hauge, J. W. Kauffman, and J. L. Margrave, *J. Am. Chem. Soc.*, 1980, **102**, 6005.
26. K. P. Huber and G. Herzberg, 'Molecular Spectra and Molecular Structure Constants of Diatomic Molecules', Van Nostrand, New York, 1979.
27. G. Frenking, S. Fau, C. M. Marchand, and H. Grützmacher, *J. Am. Chem. Soc.*, 1997, **119**, 6648.
28. N. N. Greenwood and A. Earnshaw, 'Chemistry of the Elements', 2nd edn., Pergamon, Oxford, 1997.
29. G. Brauer, 'Handbook of Preparative Inorganic Chemistry', 2nd edn., Academic Press, New York, 1963, Vol. 1.
30. J. Glaser and I. Tóth, *J. Chem. Soc., Chem. Commun.*, 1986, 1337.
31. J. Glaser and U. Henrikson, *J. Am. Chem. Soc.*, 1981, **103**, 6642.
32. I. Bányai and J. Glaser, *J. Am. Chem. Soc.*, 1989, **111**, 3186; I. Bányai and J. Glaser, *J. Am. Chem. Soc.*, 1990, **112**, 4703; I. Bányai, J. Losonczy, and J. Glaser, *Inorg. Chem.*, 1997, **36**, 5900; I. Bányai, J. Glaser, and I. Tóth, *Eur. J. Inorg. Chem.*, 2001, 1709.
33. J. Glaser, *Acta Chem. Scand.*, 1979, **A33**, 789.
34. J. Glaser, *Acta Chem. Scand.*, 1980, **A34**, 75; J. Glaser, *Acta Chem. Scand.*, 1982, **A36**, 125; J. Glaser, *Acta Chem. Scand.*, 1982, **A36**, 451.
35. J. Glaser, P. L. Goggin, M. Sandström, and V. Lutsko, *Acta Chem. Scand.*, 1982, **A36**, 55.
36. E. Högfeldt, 'Stability Constants of Metal–Ion Complexes. Part A. Inorganic Ligands', Pergamon, Oxford, 1982.
37. J. Blixt, B. Győri, and J. Glaser, *J. Am. Chem. Soc.*, 1989, **111**, 7784.
38. J. Blixt, R. K. Dubey, and J. Glaser, *Inorg. Chem.*, 1991, **30**, 2824.
39. P. Nagy and M. Maliarik, Personal communication.
40. P. Sipos, S. G. Capewell, P. M. May, G. T. Hefter, G. Laurenczy, F. Lukács, and R. Roulet, *J. Solut. Chem.*, 1997, **26**, 419.
41. J. Glaser and G. Johansson, *Acta Chem. Scand.*, 1981, **A35**, 639.
42. S. Nariki, S. Ito, K. Uchinokura, and N. Yoneda, *Chem. Lett.*, 1989, 869.
43. S. E. Stupp and D. M. Ginsberg, in 'Physical Properties of High Temperature Superconductors', ed. D. M. Ginsberg, Word Scientific, Singapore, 1992, Vol. 3, Chap. 1.
44. M. Mehring, *Mater. Sci. Technol.*, 2003, **19**, 467.
45. B. Raveau, C. Michel, M. Hervieu, J. Provost, and F. Studer, *Mater. Sci. Technol.*, 2003, **19**, 66.
46. A. McKillop and A. Robert, *Welch Found. Conf. Chem. Res.*, 1973, 1974, **17**, 153; H. M. C. Ferraz, L. F. Silva Jr, and T. D. O. Vieira, *Synthesis*, 1999, **12**, 2001.
47. M. Ouchi and T. Hakushi, *Coord. Chem. Rev.*, 1996, **148**, 171.
48. I. A. Ishenkumba, D. Miller, M. Mitchel, F. R. Fronczek, R. G. Goodrich, D. J. Williams, C. A. O'Mahoney, A. M. Z. Slawin, S. V. Ley, and C. J. Groombridge, *Inorg. Chem.*, 1992, **31**, 3963.
49. G. Anderegg, 'Critical Survey of Stability Constants of EDTA Complexes', IUPAC Chemical Data Series 14, Pergamon, Oxford, 1977.
50. J. Blixt, J. Glaser, P. Solymosi, and I. Tóth, *Inorg. Chem.*, 1992, **31**, 5288.
51. M. A. Malyarik and A. B. Ilyukhin, *Russ. J. Inorg. Chem. (Int. Ed.)*, 1998, **43**, 865.
52. G. Ma, A. Ylyukhin, J. Glaser, I. Tóth, and L. Zékány, *Inorg. Chim. Acta*, 2001, **320**, 92.
53. K. Wieghardt, M. Kleine-Boymann, B. Nubert, and J. Weiss, *Inorg. Chem.*, 1986, **25**, 1309.
54. P. Pyykkö, *Chem. Rev.*, 1997, **97**, 5976.
55. J. K. Nagle, A. L. Balch, and M. M. Olmstead, *J. Am. Chem. Soc.*, 1988, **110**, 319.
56. T. Ziegler, J. K. Nagle, J. G. Snijders, and E. J. Baerends, *J. Am. Chem. Soc.*, 1989, **111**, 5631.
57. A. L. Balch and S. P. Rowley, *J. Am. Chem. Soc.*, 1990, **112**, 6139.
58. M. Maliarik, K. Berg, J. Glaser, M. Sandström, and I. Tóth, *Inorg. Chem.*, 1998, **37**, 2910.
59. F. Jalilehvand, M. Maliarik, M. Sandström, J. Mink, I. Persson, P. Persson, I. Tóth, and J. Glaser, *Inorg. Chem.*, 2001, **40**, 3889.
60. G. Ma, M. Kritikos, and J. Glaser, *Eur. J. Inorg. Chem.*, 2001, 1311.

61. F. Jalilehvand, L. Erikson, J. Glaser, M. Maliarik, J. Mink, M. Sandström, I. Tóth, and J. Tóth, *Chem. Eur. J.*, 2001, 2167.
62. M. Maliarik, J. Glaser, I. Tóth, M. W. da Silva, and L. Zékány, *Eur. J, Inorg. Chem.*, 1998, 565.
63. P. Nagy, I. Tóth, I. Fábián, M. Maliarik, and J. Glaser, *Inorg. Chem.*, 2003, **42**, 6907.
64. J. Autschbach and T. Ziegler, *J. Am. Chem. Soc.*, 2001, **123**, 5320.
65. O. J. Ezomo, M. P. Mingos, and I. D. Williams, *J. Chem. Soc., Chem. Commun.*, 1987, 924.
66. L. Hao, J. J. Vittal, and R. J. Puddephatt, *Inorg. Chem.*, 1996, **35**, 269.
67. V. J. Catalano, B. L. Bennett, R. L. Yson, and B. C. Noll, *J. Am. Chem. Soc.*, 2000, **122**, 10056.
68. O. Renn and B. Lippert, *Inorg. Chim. Acta*, 1993, **208**, 219.
69. R. Uson, J. Fornies, M. Tomas, R. Garde, and R. I. Merino, *Inorg. Chem.*, 1997, **36**, 1383.
70. I. Ara, J. R. Berenguer, J. Fornies, J. Gomez, E. Lalinde, and R. I. Merino, *Inorg. Chem.*, 1997, **36**, 6461.
71. W. Bronger and B. Bonsmann, *Z. Anorg. Allg. Chem.*, 1995, **621**, 2083.
72. K. O. Klepp, *J. Alloys Compd.*, 1993, **196**, 25.
73. K. Matsumoto, Personal communication.
74. M. Sager, ‘Trace Analytical Chemistry of Thallium’ (in German), Thieme, Stuttgart, 1986.

Acknowledgment

Dedicated to Prof. Ernő Brücher on his 70th birthday.

The authors are grateful to the Hungarian Science Research Foundation (OTKA, Project T 038296) for financial support and to Professor K. Matzumoto and M. Maliarik for data prior to publication.

Thallium: Organometallic Chemistry

Robert D. Pike
The College of William and Mary, Williamsburg, VA, USA

Based in part on the article Thallium: Organometallic Chemistry by William S. Rees, Jr. & Gertrud Kräuter which appeared in the Encyclopedia of Inorganic Chemistry, First Edition.

1 Introduction 1
2 Thallium(I) Compounds 1
3 Thallium(II) Compounds 4
4 Thallium(III) Compounds 4
5 The Toxicity of Organothallium Compounds 8
6 Organothallium Compounds as Precursors for Electronic Materials 8
7 Thallium in Organic Synthesis 9
8 Related Articles 10
9 References 10

Abbreviations

Cp = cyclopentadienyl; Cp′ = substituted cyclopentadienyl; Fc = ferrocenyl; Mesityl = 2,4,6-trimethylphenyl; PPN$^+$ = bis(triphenylphosphoranylidene)ammonium; TPP = 5,10,15,20-tetraphenylporphinato; OTs = *p*-toluenesulfonate.

1 INTRODUCTION

Although organothallium compounds were synthesized as early as 1870, only nine years after the discovery of the element thallium, for a long time organothallium chemistry received little attention compared to many other areas of organometallic chemistry. However, as the result of a discovery made in the late 1960s that certain thallium derivatives are remarkably efficient reagents or intermediates in organic syntheses, chemists have found an increasing interest in the organometallic chemistry of thallium. This interest has been stimulated further in recent years due to the discovery that certain thallium-containing superconducting metal oxides (SMO) possess among the highest critical temperatures identified so far (*see* ***Superconductivity***).

Organothallium compounds are now known in oxidation states +1, +2 (silyl ligands), and +3. Several review articles dealing with the organometallic chemistry of thallium are available.[1–8] This article is essentially limited to organothallium compounds that contain at least one Tl–C bond.

2 THALLIUM(I) COMPOUNDS

The calculated bond dissociation energy for Tl–C in the unknown MeTl is 59 kJ mol^{-1}, suggesting only limited stability for alkylthalliums (*see* ***Bonding Energetics of Organometallic Compounds***).[9] Known organothallium(I) compounds are almost strictly limited to π bonded species such as cyclopentadienylthallium, CpTl. The most likely reason for the dearth of RTl compounds stems from the combination of weak bonding and unsaturation. In fact, even the members of the Cp′Tl series show effects of coordinative unsaturation, as indicated by polymerization and Tl$\cdots$Tl interactions commonly observed in the solid state (see Section 2.1.1). The low-valent organometallic chemistry of thallium has been reviewed.[6]

2.1 Cyclopentadienylthallium(I) Complexes

2.1.1 Preparation and Properties

Cyclopentadienylthallium (**1**, X = H) first was described by Meister in 1957.[10] It can conveniently be prepared by the reaction of cyclopentadiene with thallium(I) salts in the presence of sodium hydroxide in aqueous solution (equation 1). Since this initial synthesis, a wide variety of Cp′Tl compounds have been prepared, largely for the purpose of acting as cyclopentadienide transfer reagents in transition metal organometallic chemistry (see Section *Reactions of Cyclopentadienylthallium with Transition Metal Compounds*). The range of ring-substituted Cp′Tl compounds known and the methods used to make them have been reviewed.[6,11] Although transmetallation reactions (equation 2) are often successful, the preferred preparation method is usually the acid–base reaction (equation 3), which sidesteps the need for premetallation and produces no salt by-products.

$$C_5H_6 + TlX \xrightarrow[-NaX]{NaOH/H_2O} C_5H_5Tl \qquad (1)$$

$$Cp'Li + TlX \xrightarrow{-LiX} Cp'Tl \qquad (2)$$

$$Cp'H + TlOEt \xrightarrow{-EtOH} Cp'Tl \qquad (3)$$

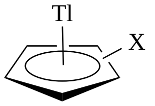

(**1**)

Neutral Cp′Tl species are usually polymeric in the solid state, showing a zigzag chain of alternating Tl(I) centers and bridging Cp′ units (e.g. see **2**, below).[6] However, several Cp′Tl monomers[12,13] and dimers[14,15] have been identified using X-ray diffraction (*see* ***Diffraction Methods in Inorganic Chemistry***). The compound 1,3-(SiMe$_3$)$_2$C$_5$H$_3$Tl[16] is a Cp′-bridged

Table 1 Thallium(I) cyclopentadienide compounds characterized by X-ray diffraction

Compound	Tl–Cp[a] (pm)	Cp–Tl–Cp (°)
C_5H_5Tl[20,21]	319	137
C_5HMe_4Tl[22]	268, 271	133.8
C_5Me_5Tl[23]	271	145[b]
C_5Bz_5Tl[d,24]	249, 488	175.7
C_5Bz_5Tl[d,14]	249	–
$C_5(CO_2Me)_5Tl$[13]	296[c]	–
$Me_3SiC_5H_4Tl$[16]	271, 284	149
$(NC)_2C{=}C(CN)C_5H_4Tl$[25]	301, 307	113.6
1,3-$(Me_3Si)_2C_5H_3Tl$[16]	274, 278	127, 133
1,3-$Ph_2C_5H_3Tl(THF)$[26]	283, 287	127.6, 118.7
$(Me_2PhSi)C_5Me_4Tl$[27]	263, 286	142.3
$(Me_2BzSi)C_5Me_4Tl$[27]	274	147
$Ph_2PC_5Me_4Tl$[27]	280, 288	122
8-quinolyl-C_5Me_4Tl[28]	263, 290	137.1[b]
(1,4,2-$P_2SbC_2Bu^t{}_2)Tl$[29]	289, 291	158.8
$(C_{60}Ph_5)Tl(THF)_{2.5}$[30]	260	–
$Au_2[(Ph_2PC_5H_4)_2Tl]_2(C_6H_6)_2$[31]	271, 275	–
$[CpMg(pmdeta)]^+ [Cp_2Tl]^-$[f,17]	272	156.7[c]
$[Li(12\text{-crown-}4)_2]^+ [Cp_3Tl_2]^- (THF)$[18]	263, 282	134.2
$[Cp_2Tl_3]^+ [CpMo(CO)_3]^-$[19]	258, 281, 285, 262, (320)[e]	114.9[b]

[a] Cp = cyclopentadienide centroid. [b] Tl···Tl···Tl. [c] Average value from different molecules in the asymmetric unit. [d] Two crystal modifications known. [e] Distance to Cp associated with anion unit. [f] pmdeta = pentamethyldiethylenetriamine.

hexamer. Also known are Cp-bridged ionic species, for example, Cp_2Tl^-, $Cp_3Tl_2{}^-$, and $Cp_2Tl_3{}^+$.[17–19] A list of structurally characterized Cp′Tl compounds is provided in Table 1.

Several oligomeric Cp′Tl species reveal weak metal–metal interactions, with Tl···Tl distances 363–400 pm.[14–16] Similar Tl···Tl interactions can be seen between chains in CpTl itself.[20,21] Theoretical calculations show that such short metal–metal contacts are on the borderline for weak bonding.[32–34] Homometallic interactions are expected to be weaker for thallium than for the other group 13 metals due to spin-orbit coupling and inert pair effects.[9,35]

The heteroatom cyclopentadienyl analog 1,4,2-$P_2SbC_2Bu^t{}_2$ has been coordinated to Tl(I) via equation (2), producing zigzag polymer (**2**).[29] Thallium coordination has played an important role in crystallographic characterization of metal–fullerene complexes, providing the first structurally characterized pentahapto metal complexes of C_{60} (**3**) and C_{70} (**4**).[30,36] The key to the formation of these monothallium(I) compounds was the arylation of the fullerenes. Methylated C_{60} forms a thallium complex as well.[37]

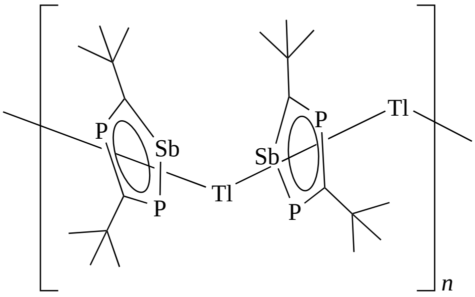

(**2**)

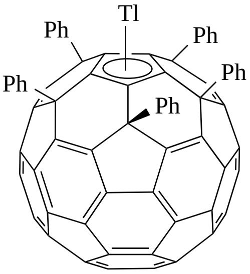

(**3**)

2.1.2 Reactions of Thallium Cyclopentadienides

Cyclopentadienylthallium compounds have demonstrated tremendous preparative potential as mild reagents for the synthesis of cyclopentadienyl derivatives of *Main Group Elements, Transition Metals*, and *Rare Earth Elements*. In fact, some alkyl-substituted cyclopentadienyl metal complexes can be obtained only from the analogous Tl(I) compounds. Reactions involving Cp′Tl compounds often are characterized by manipulative simplicity and high yields.

Reactions of Cyclopentadienylthallium with Transition Metal Compounds. Numerous *Metallocene Complexes* have been prepared using CpTl as a Cp-transfer reagent, including *Ferrocene, Cobaltocene*, and *Nickelocene*, as well

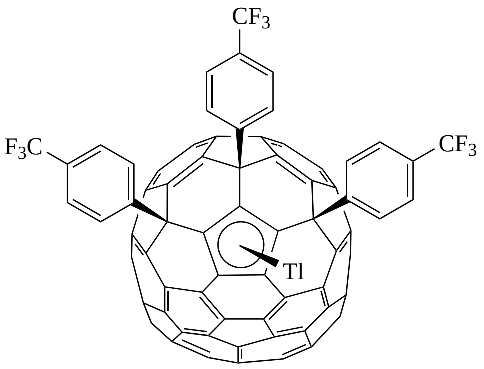

(**4**)

as dicyclopentadienylmercury.[1,38] The reaction of CpTl with transition metal–halide complexes containing carbonyl ligands gives the corresponding cyclopentadienyl metal carbonyls.[1,38,39] Ring-substituted cyclopentadienylthallium derivatives also have been used to prepare the corresponding Cp′ complexes of transition metals by substitution of a halide or Cp ligand.[40–46]

Reactions of Cyclopentadienylthallium with Main Group Compounds and Rare Earth Elements. Cyclopentadienylthallium has found great utility in the formation of cyclopentadienyl derivatives of main group elements. Germanium dibromide reacts with CpTl to give germanocene.[47] Cyclopentadienylphosphines, $CpPX_2$, and dicyclopentadienylphosphines, Cp_2PX, can be produced through the reaction of X_2PCl, and $XPCl_2$ with CpTl (X = R, F).[48,49] Cyclopentadienylthallium compounds react directly with rare earth metals to produce Cp_2M and Cp_3M complexes and elemental thallium.[50]

2.2 Alkylthallium(I) Complexes

Only two isolable σ-bound organothallium(I) compounds are known: $[(Me_3Si)_3C]Tl$[51] and $(2,6\text{-}Trip_2C_6H_3)Tl$ (Trip = 2,4,6-triisopropylphenyl).[52] Prepared by metathesis reaction (equation 4), $[(Me_3Si)_3C]Tl$ is of low thermal stability. X-ray diffraction analysis showed the compound to be tetrameric in the solid state (structure **5**) while cryoscopy indicated it to be monomeric in solution. The Tl···Tl distances in $\{[(Me_3Si)_3C]Tl\}_4$ range from 332 to 364 pm, suggesting relatively weak interactions, such as are found for Cp′Tl oligomers. Also thermally unstable, $(2,6\text{-}Trip_2C_6H_3)Tl$ is prepared by simple metathesis of TlCl and the aryllithium (equation 5). X-ray diffraction reveals it to be monomeric in the solid state. Other attempts to prepare Tl(I) σ-alkyls and -aryls via reactions of thallium(I) halides with lithium organyls or *Grignard Reagents* has lead to the formation of either organothallium(III) compounds or organic products.[1] Nevertheless, the proposed mechanism for these reactions involves the formation of organothallium(I) compounds as intermediates.[1,6]

$$CpTl + [(Me_3Si)_3]CLi{\cdot}2THF \xrightarrow{-CpLi,\ -2THF} [(Me_3Si)_3C]Tl \qquad (4)$$

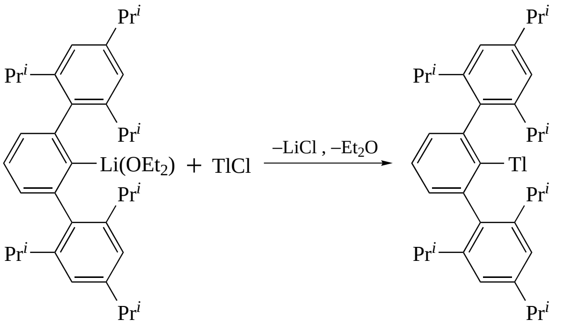

(5)

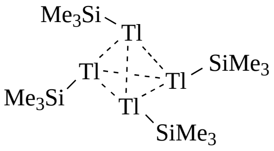

(**5**)

2.3 Complexes of Thallium(I) with Other Anionic Ligands

Several thallium(I) complexes with dicarbollide ligands (*see* ***Boron: Metallacarbaboranes***) have been prepared.[12,53] These compounds of the general formula $Tl_2C_2RR'B_9H_9$ usually are oxygen stable, and one of the thallium atoms can be readily replaced by a Ph_4As^+, Ph_3MeP^+, or PPN^+ cation.[54] The crystal structures of the resulting Ph_3MeP^+[54] and PPN^+ salts (Figure 1)[55] have been reported. Thallium dicarbollides react with aluminum alkyl derivatives and gallium trichloride, forming compounds of the general formula $Tl[M(C_2B_9H_{11})_2]$ (M = Al, Ga).[56] A complex between a cobalt-containing sandwich π-ligand and thallium(I) has been reported.[57] The resulting compound (**6**) is a monomer in the solid state and highly soluble in organic solvents. Thallium(I) also forms a complex (**7**) with the borabenzene anion.[58] (*see* ***Boron: Organoboranes***).

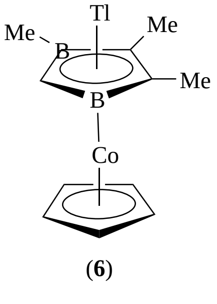

(**6**)

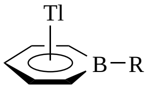

(**7**)

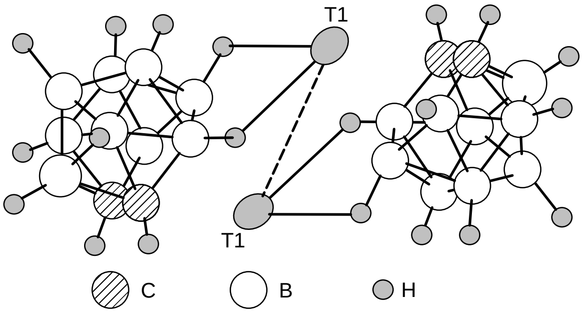

Figure 1 The structure of [*closo*-3,1,2-$\mathrm{TlC_2B_9H_{11}}]^-$. (Reprinted with permission from Ref. 55. © 1991 American Chemical Society)

2.4 Complexes of Thallium(I) with Neutral π-Ligands

Structurally uncharacterized π-arene Tl(I) compounds of the composition $\mathrm{C_6H_62{\cdot}TlAlCl_4}$, $\mathrm{C_6H_6{\cdot}TlAlCl_4}$,[59] and $[\mathrm{Tl{\cdot}2PhMe}]^+$ $[\mathrm{C_5Cl_5}]^-$[60] were described in the literature as early as 1968. Complexes of Tl(I) with toluene, 1,2,4- and 1,3,5-trimethylbenzene, and [2.2]paracyclophane have been isolated and structurally characterized.[60–64] These (η^6-arene)Tl complexes are little more than arene solvates, the Tl cations always being additionally coordinated to halide-bearing anions. Secondary π-interactions have been noted in the structures of the two crystal modifications of $[\mathrm{C_5H_4CMe_2}$(9-fluorenyl)]Tl[65] (Figure 2). Thallium coordination to the six-membered ring in these structures showed ring slippage to η^2- and η^3-arene. Very weak (η^6-phenyl)Tl interactions result in polymerization of (3,5-diphenylpyrazoyl)Tl[66] and tetramer formation for $[2,6\text{-}\mathrm{Pr}^i_2\mathrm{C_6H_3(Me_3Si)N]Tl}$ (**8**).[67] Olefin coordination of Tl(I) is virtually unknown. The complex $\mathrm{Tl_2[Pt(C_6F_5)_2(C{\equiv}CBu^t)_2](acetone)_2}$ (**9**) exhibits thallium–platinum bonds and Tl–η^2-alkyne interactions.[68]

3 THALLIUM(II) COMPOUNDS

True organothallium(II) compounds are unknown. Nevertheless, low-temperature disproportionation reactions (6) and (7) have produced a pair of silylthallium(II) dimers, (**10**), $\mathrm{R = Si(SiMe_3)_3}$[69] and $\mathrm{R = SiBu^t{}_3}$.[70] Both products were examined by X-ray crystallography, however, $\mathrm{(Bu^t{}_3Si)_4Tl_2}$ underwent decomposition in the X-ray beam, yielding only limited data. True Tl–Tl bonding distances of 291.4 and 296.6 pm were found for $\mathrm{[(Me_3Si)_3Si]_4Tl_2}$ and $\mathrm{(Bu^t{}_3Si)_4Tl_2}$ respectively.

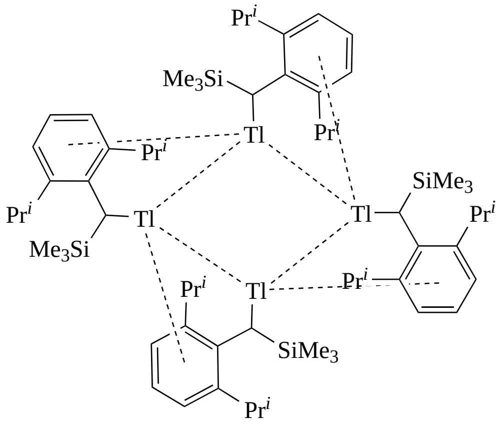

(**8**)

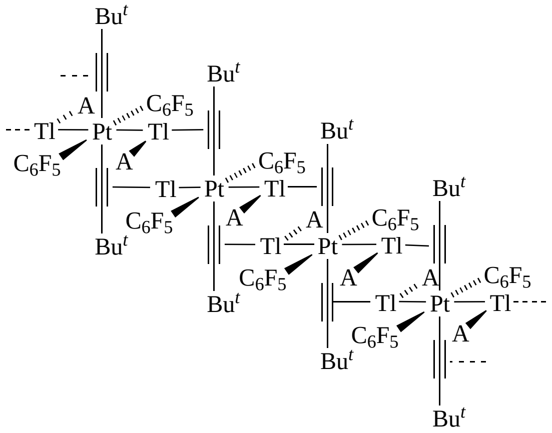

(**9**), A = acetone; Tl···F omitted for clarity

$$4(\mathrm{Me_3Si})_2\mathrm{NTl} + 4(\mathrm{Me_3Si})_3\mathrm{SiRb} \xrightarrow[-2\mathrm{Tl}]{-4\mathrm{RbN(SiMe_3)_2},} [(\mathrm{Me_3Si})_3\mathrm{Si}]_4\mathrm{Tl_2} \tag{6}$$

$$4\mathrm{TlBr} + 4\mathrm{NaSiBu^t{}_3} \xrightarrow{-4\mathrm{NaBr},\ -2\mathrm{Tl}} (\mathrm{Bu^t{}_3Si})_4\mathrm{Tl_2} \tag{7}$$

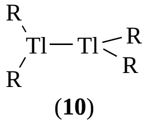

(**10**)

4 THALLIUM(III) COMPOUNDS

Thallium(III) compounds dominate the known organometallic chemistry of thallium. The structural chemistry organothallium(III) compounds has been reviewed.[7]

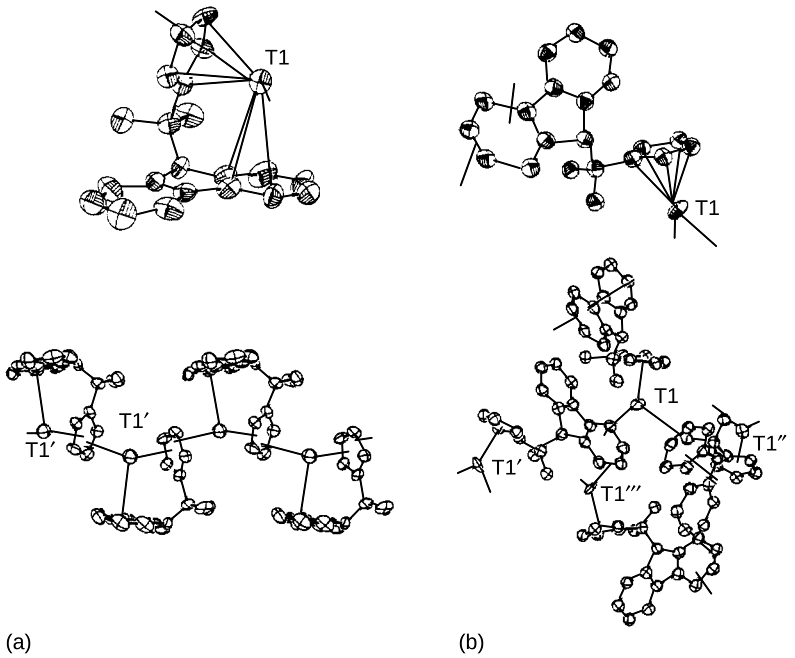

Figure 2 The structure of [$C_5H_4CMe_2$(9-fluorenyl)]Tl: (a) modification 1; (b) modification 2. (Ref. 65. Reproduced by permission of the John Wiley and Sons)

4.1 Triorgano-, tetraorgano-, and hexorganothallium Compounds

4.1.1 *Preparation and Properties*

Triorganothallium and the related compounds are usually prepared through the reaction of dialkyl- or diarylthallium(III) halides with organolithium compounds or, in some cases, Grignard reagents.[3] Aryllithium reagents have been used to effect conversion of $TlCl_3$, to Ar_3Tl.[71] Reactions involving excess carbanion source can produce peralkyl- or perarylthallium(III) anions, $[R_4Tl]^-$ and $[R_6Tl]^{3-}$.[71–74] To date, trimethylthallium and trimesitylthallium are the only structurally characterized R_3Tl species (see Table 2).[75–77] Trimethylthallium can be prepared conveniently by the reaction of methyllithium and thallium(I) iodide in the presence of methyl iodide (equation 8).[3] This reaction most likely involves the formation of methylthallium(I) as an intermediate. The reaction of dimethylthallium amide or trimethylthallium with R–C≡CH (R = H, Me, Ph) affords dimethyl(ethynyl)thallium compounds.[3]

$$2\text{MeLi} + \text{MeI} + \text{TlI} \xrightarrow{-2\text{LiI}} \text{Me}_3\text{Tl} \qquad (8)$$

Trimethylthallium is monomeric in the gas phase, in the melt, and in solution.[78] However, it forms a polymeric framework, with weakly bridging methyls, in the solid state.[75,77] Bonded Tl–C lengths are 219.6–221.6 pm and nonbonded Tl···C distances are 324.3–336.4 pm. The dissociation energy of the first Tl–C bond in trimethylthallium has been estimated as 152 kJ mol^{-1}.[79] The presence of this rather weak bond (compared to the corresponding values in Me_3Ga (249 kJ mol^{-1}) and Me_3In (197 kJ mol^{-1})) is the fundamental reason for the observed high reactivity of trimethylthallium and triorganothallium compounds in general. Triorganothallium compounds are oxygen and water sensitive. A word of caution is warranted about these compounds, as some have been known to decompose explosively upon heating.

Although triorganothallium compounds are much weaker electron-pair acceptors than the corresponding indium and gallium compounds, some adducts of R_3Tl with Lewis bases have been isolated.[3,71,74,80–86] Several such adducts have been examined using X-ray crystallography (Table 2). Two of these are chelates in which the bond lengths and angles are no doubt influenced by metallocycle formation. However, the simple Lewis base adducts $(Me_3SiCH_2)_3TlP(SiMe_3)_3$[84] and $(C_6F_5)_3TlOPPh_3$[74] show C-Tl-C bond angles of nearly 120°, suggesting fairly weak donor–acceptor bonding.

4.1.2 *Reactions of Triorganothallium Compounds*

Owing to the weakness of the Tl–C bonds, triorganothallium derivatives are highly reactive compounds. Trimethyl- and triphenylthallium react with mercury to form the corresponding diorganomercury derivatives and elemental thallium (equation 9).[2]

$$2\text{R}_3\text{Tl} + 3\text{Hg} \longrightarrow 3\text{R}_2\text{Hg} + 2\text{Tl} \qquad (9)$$

Table 2 Triorganothallium(III) compounds characterized by X-ray diffraction

Compound	Tl–C (pm)	C–Tl–C (°)	E, Tl–E (pm)
Me_3Tl[77]	219.6, 220.6, 221.6	115.1, 120.7, 124.1	–
$(Mesityl)_3Tl$[76]	222, 218, 216.9	116.9, 120.3, 122.8	–
$(Me_3SiCH_2)_3TlP(SiMe_3)_3$[84]	223, 224, 225	116.2, 116.5, 121.1	P, 292.2
$(C_6F_5)_3TlOPPh_3$[74]	218.0, 219.0, 219.2	116.9, 118.5, 122.2	O, 230.0
$(Me_2NFc)_3Tl$[85]	217.6, 218.1, 220.2	114.0, 118.5, 125.9	N, 252.3
$(2\text{-}Ph_2PCH_2C_6H_4)_3Tl$[86]	221.0, 221.4, 222.6	108.1, 122.5, 124.2	P, 279.5; P, 355.8

In the presence of acids, halogens, or pseudohalogens, one of the organic groups in R_3Tl is displaced and compounds of the general formula R_2TlX are formed (equations 10–12).[2] Insertion into the Tl–C bond occurs when trimethylthallium is reacted with either SO_2 or SO_3 (equation 13 and 14).[3]

$$2R_3Tl + ClN_3 \xrightarrow{-RCl} R_2TlN_3 \tag{10}$$

$$R_3Tl + HCl \xrightarrow{-RH} R_2TlCl \tag{11}$$

$$Ph_3Tl + Se(SeCN)_2 \xrightarrow{-PhSeCN,\ -Se} Ph_2TlSeCN \tag{12}$$

$$Me_3Tl + SO_2 \longrightarrow Me_2TlOS(O)Me \tag{13}$$

$$Me_3Tl + SO_3 \longrightarrow Me_2TlOS(O)_2Me \tag{14}$$

The reaction of trimethyl- or triethylthallium with Et_3MH (M = Si, Ge), $B_{10}H_{14}$, or $M'H(CO)_3Cp$ (M′ = Mo, W) leads to the formation of the thallium–metal bonded compounds $Tl(MEt_3)$, $[Me_2Tl][Me_2Tl(B_{10}H_{12})]$, and $Me_2Tl(M'(CO)_3Cp)$, respectively.[3]

4.2 Diorganothallium Compounds

4.2.1 Preparation and Properties

Diorganothallium compounds comprise the most stable class of organothallium(III) derivatives. They usually are prepared via the reaction of $TlCl_3$ with Grignard reagents (equation 15).[2] However, the yields are rather poor, due to the oxidation of the Grignard reagent by $TlCl_3$. Some di(*n*-alkyl)thallium bromides have been prepared in good yields by the reaction of TlBr with RMgBr in a 2:1 molar ratio. Diaryl- and divinylthallium halides can be conveniently synthesized by the reaction of thallium(III) halides with the appropriate organoboronic acid in aqueous solution (equation 16).[2] Arylsilver derivatives (R = mesityl, 2,4,6-$C_6F_3H_2$, C_6F_5) react with $TlCl_3$ to give the corresponding diarylthallium chloride.[87]

$$TlCl_3 + 2RMgX \xrightarrow{-2MgXCl} R_2TlCl \tag{15}$$

$$TlX_3 + 2RB(OH)_2 \xrightarrow[-2HX,\ -2B(OH)_3]{H_2O} R_2TlX \tag{16}$$

Other methods for the preparation of diorganothallium compounds are described in Section 4.1.2. Diorganothallium halides are solids and usually are unaffected by water and atmospheric oxygen. They have high melting and decomposition points and are only sparsely soluble in typical organic solvents. Most salt-type diorganothallium(III) compounds ionize in polar solvents. The dimethylthallium cation $[Me_2Tl^+]$, being isoelectronic with dimethylmercury, is one of the most stable methylated species in aqueous solution reported to date. Many diorganothallium compounds have been characterized by single crystal X-ray diffraction. Table 3 lists some representative diorganothallium compounds and their structural properties. A more complete list is available.[7] The thallium atom reaches coordination numbers between four and eight by both inter- and intramolecular coordination. For most dialkylthallium(III) compounds, an almost linear C–Tl–C arrangement is observed. However, significant deviations are sometimes encountered, usually owing to the steric demand of additional donor ligands and/or oligomerization. Complex (**11**) represents a particularly interesting combination of R_2Tl^+ and $RTlCl_3^-$ (R = mesityl).[87] The diarylthallium(III) cation and aryl(trichloro)thallium(III) anion in (**11**) are weakly associated through a series of long chloride bridges.

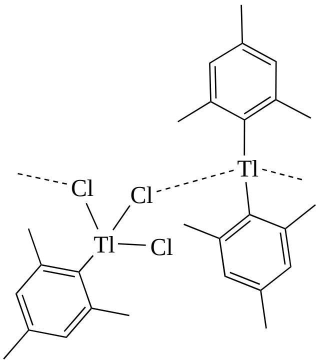

(**11**)

4.2.2 Reactions of Diorganothallium Compounds

Although the Tl–C bonds in diorganothallium compounds are considerably more stable than those in either triorgano- or monoorganothallium compounds, reactions that involve the

Table 3 Representative diorganothallium(III) compounds characterized by X-ray diffraction

Compound	Structure type	Tl–C (pm)	Angle C–Tl–C (°)
$[Me_2TlL][ClO_4]$[a,88]	monomeric ion	209.9	180
$Me_2Tl(acac)$[89]	polymer	205	171.8
$Me_2Tl(O_2CC{\equiv}CH)$[90]	polymer	216	174
$Me_2Tl(S_2PEt_2)$[91]	polymer	212.8	169.7
$Me_2Tl[S(O)CNEt_2]$[92]	polymer	213, 214	162.5
$Me_2Tl(HDaptsc)$[b,93]	polymer	213.1, 214.9	152.0
$Me_2Tl(FcEtsc)$[c,94]	monomer	211.4, 2.123	159.2
$Me_2Tl(FcDtsc)$[d,95]	dimer	214.8, 215.2	158.9
$Me_2Tl(4\text{-}CF_3PymS)$[e,95]	polymer	212, 215.2	161.2
$[Et_4N][Me_2Tl(S_2PPh_2)_2]$[96]	monomeric ion	212.4, 212.6	171.2
$[MePh_3P][Me_2Tl(B_{10}H_{12})]$[97]	monomeric ion	221, 223	134.1
$Ph_2Tl(S_2PEt_2)$[91]	polymer	214	165.6
$Ph_2TlS_2P(C_6H_{11})_2$[98]	polymer	210.7, 211.7	160.6
$Ph_2Tl(Cptsc)$[f,99]	monomer	214.6, 214.8	146.6
$Ph_2Tl(5\text{-}Ph\text{-}tetrazole)(MeOH)$[100]	polymer	213, 212	173.9
$[Et_4N][Ph_2Tl(S_2PPh_2)_2]$[101]	monomeric ion	214.3, 214.9	159.2
$[(Mesityl)_2Tl][(Mesityl)TlCl_3]$[87]	monomeric ion[g]	212.1, 213.1[g]	173.1[g]
$(C_6F_5)_2TlCl(OPPh_3)$[74]	dimer	215.6, 216.8	139.4
$(Me_3SiCH_2)_2TlCl$[102]	dimer	217, 221	168
$(Me_2NFc)_2TlCl$[103]	monomer	212.8	145.2

[a] L = tridecalino-18-crown-6{1,4,15,18,29,32-hexaoxaperhydro[4.4.4](4a,8a)naphthalenophane}. [b] HDaptsc = 2, 6-diacteylpyridine bis(thiosemicarbazone) anion. [c] FcEtsc = ferrocenyl-N-ethylthiosemicarbazone. [d] FcDtsc = ferrocenyl-dimethylthiosemicarbazone. [e] 4-CF_3PymS = 4-trifluoromethylpyrimidine-2-thionate. [f] Cptsc = cyclopentanone thiosemicarbazone. [g] Weakly polymeric through ion association, see (**11**); data for $[(Mesityl)_2Tl]^+$; see Table 4 for anion data.

cleavage of M–C bonds in diorganothallium compounds are known. Diorganothallium cations (R_2Tl^+) can be reduced electrochemically, presumably forming R_2Tl *Radicals* as intermediates (equation 17). The radicals then either form elemental Tl and R_3Tl via disproportionation (equation 18), or can be reduced further to afford the corresponding carbanion (equation 19).[3]

$$R_2Tl^+ + e^- \longrightarrow R_2Tl^\bullet \tag{17}$$

$$3R_2Tl^\bullet \longrightarrow 2R_3Tl + Tl \tag{18}$$

$$R_2Tl^\bullet + 2e^- \longrightarrow 2R^- + Tl \tag{19}$$

Diorganothallium compounds are known to undergo disproportionation and alkyl-exchange reactions, as shown in equations (20) and (21).[3] Dialkyl- and diarylthallium carboxylates react with mercury acetate to give monoorganothallium dicarboxylates (equation 22).[3]

$$3Me_2TlY \longrightarrow 2Me_3Tl + TlY_3 \tag{20}$$

$$Y = Co(CO)_4,\ Cr(CO)_3Cp,\ Fe(CO)_2Cp$$

$$Ph^*{}_2Tl^+ + Ph_2Hg \rightleftharpoons Ph_2Tl^+ + Ph^*{}_2Hg \tag{21}$$

$$* = {}^{14}C \text{ labeled}$$

$$R_2TlOAc + Hg(OAc)_2 \longrightarrow RTl(OAc)_2 + RHgOAc \tag{22}$$

4.3 Monoorganothallium Compounds

4.3.1 *Preparation and Properties*

Monoalkylthallium compounds are usually prepared either by the reaction of dialkylthallium carboxylates and mercury(II) carboxylates (equation 22), or by reacting dialkylthallium halides with Br_2 or I_2 (equation 23).[3,104,105] Aryl- and vinylthallium dichlorides are prepared conveniently by the reaction of aryl- and vinylboronic acid, respectively, with excess $TlCl_3$ in aqueous solution (equation 24).[2,3]

$$R_2TlX + Br_2 \xrightarrow{-RBr} RTlXBr \tag{23}$$

$$X = \text{halide},\ BF_4$$

$$RB(OH)_2 + TlCl_3 \xrightarrow[-HCl,\ -B(OH)_3]{H_2O} RTlCl_2 \tag{24}$$

$$R = Ar,\ Vi$$

Another synthetic route to monoorganothallium compounds is the reaction of aryl or vinyl derivatives of mercury(II) or tin(IV) with TlX_3 (X = halide, carboxylate). Monoalkylthallium derivatives are intermediates in the oxidation of alkenes and alkynes by thallium(III) salts (oxythallation) (see Section 7).

Several monoorganothallium(III) compounds have been characterized by single crystal X-ray diffraction. These

Table 4 Monoorganothallium(III) compounds characterized by X-ray diffraction

Compound	Tl Coordination sphere	Tl–C (pm)
$MeTl(BtaPy)_2$[a,106]	monomer, N_3S_2C	207.3
$(cyclo\text{-}C_3H_5)Tl(O_2CCHMe_2)_2$[107]	polymer, O_6C	216.0
MeTl(TPP)[108]	monomer, N_4C	214.7
RTl(TPP)[b,109]	monomer, N_4C	209
$(4\text{-}MeC_6H_4)Tl(S_2CNEt_2)_2$[110]	monomer, S_4C	215
$(Me_2NCH_2\text{-}2\text{-}C_6H_4)TlCl_2$[111]	dimer, NCl_3C	212.7
$PhTl[S_2CP(C_6H_{11})_2]_2$[98]	monomer, S_4C	213
$[(Mesityl)_2Tl][(Mesityl)TlCl_3]$[87]	monomeric ion, Cl_3C[c]	214.9[c]
PhTl(Daptsc)(acetone)[d,93]	monomer, N_3S_2C[e]	219.1
$[Me_4N][(PhN{=}N\text{-}2\text{-}C_6H_4)TlCl_3]$[111]	monomeric ion, NCl_3C	213.8

[a] BtaPy = 2,6-bis(2-methyl-2-benzothiazolinyl)pyridine. [b] R = 2-exo-bicyclo[2.2.1]hept-exo-3-acetato-5-enyl. [c] Weakly polymeric through ion association, see (**11**); see Table 4 for data on $[(Mesityl)TlCl_3]^-$; see Table 3 for data on $[(Mesityl)_2Tl]^+$. [d] Daptsc = 2,6-diacetylpyridine bis(thiosemicarbazone) dianion. [e] Polymer chain formed through interligand hydrogen-bonding.

are listed in Table 4. With macrocyclic ligands, such as porphyrins, the complexes are monomeric, but with smaller readily bridging ligands, such as halide or carboxylate, oligomers can form.

4.3.2 Reactions of Monoorganothallium Compounds

Monoorganothallium compounds readily undergo reductive cleavage of the thallium–carbon bond. Methylthallium diacetate decomposes slowly in various solvents (e.g. H_2O, methanol, THF, chloroform) at ambient temperature to give methyl acetate and thallium acetate (equation 25).[3] Phenylthallium dichloride is more stable, but the analogous dibromide, $PhTlBr_2$, decomposes rapidly into PhBr and TlBr when heated.[3] If $PhTlX_2$ ($X = Cl, O_2CCF_3$) is treated with KI, the formation of PhI and TlI is observed (equation 26).[3] Cleavage of the Tl–C bond also can be achieved electrochemically (equation 27).[3] Some electrophilic reactions at the Tl–C bond of monoarylthallium compounds are of synthetic interest, for example, the bromination of arylthallium compounds that gives aryl bromides.[3]

$$MeTl(OAc)_2 \xrightarrow{-MeOAc} TlOAc \qquad (25)$$

$$PhTlX_2 + 2KI \longrightarrow PhI + TlI + 2KX \qquad (26)$$

$$X = Cl, O_2CCF_3$$

$$2PhTl^{2+} + 4e^- \xrightarrow{Hg} Ph_2Hg + 2Tl \qquad (27)$$

5 THE TOXICITY OF ORGANOTHALLIUM COMPOUNDS

Elemental thallium and its compounds are extremely toxic and must be handled with care (*see* ***Metal Ion Toxicity***). The lethal dose is considered to be 10–12 mg kg^{-1} body weight. The organometallic chemistry of thallium shows similarity to that of Hg^{2+} and Pb^{2+}. Both Hg^{2+} and Pb^{2+} undergo *in vivo* biomethylation, with methylcobalamin ($MeCoB_{12}$) being the biological source of the methyl groups (*see* ***Cobalt: B$_{12}$ Enzymes & Coenzymes***).[112] It has been shown that $MeCoB_{12}$ can be demethylated by Tl^{3+}, but the resulting methylated Tl species has not been isolated.[113,114] Monovalent Tl is not able to demethylate $MeCoB_{12}$, however. Bacteria from an anaerobic lake sediment have been used to convert TlO_2CCH_3 into the water-stable Me_2Tl^+ cation in an atmosphere of N_2 and under the exclusion of light.[115] The formation of Me_2Tl^+ is unsurprising, considering that monomethylthallium(I) compounds are unstable and Me_3Tl decomposes in water. Unlike the organometallic derivatives of Pb^{2+} and Hg^{2+} generated by the biological system, Me_2Tl^+ appears to be less toxic than inorganic thallium compounds and elemental thallium itself. Dimethylthallium(I) has recently been detected in Atlantic Ocean water at levels up to 3.2 ng L^{-1} using isotope dilution mass spectrometry.[116]

Although detailed data about the biological effects of organothallium compounds remain sparse, they should be considered to be extremely toxic, taking into account their chemical similarity to organomercury and -lead compounds (*see* ***Mercury: Organometallic Chemistry*** and *Lead: Organometallic Chemistry*), combined with the known toxicity of inorganic thallium compounds and thallium metal.

6 ORGANOTHALLIUM COMPOUNDS AS PRECURSORS FOR ELECTRONIC MATERIALS

Thallium(III) oxide is a degenerate n-type semiconductor (*see* ***Semiconductors***) with a Band Gap of 1.4 eV, and it shows electronic and optical properties, which make it useful in applications such as solar cells and electrical contacts.[117] The interest in thallium oxide has been further stimulated by the discovery that the system Tl–Ca–Ba–Cu–O represents a class of superconducting materials with critical temperatures as high as 125 K, coupled with the presence of very high critical current densities.[118] Superconducting metal oxides (SMO) were originally studied as bulk materials;[119] however, it is as thin films that they attract the most interest (*see* ***Thin Film Synthesis of Solids***). One proven technique that provides high-quality films on large area substrates at mild conditions is Metal–Organic Chemical Vapor Deposition (MOCVD).[120,121] This method requires organometallic precursors that are chemically and thermally stable during their evaporation and transport to the substrate, and which decompose on the substrate to form the desired solid-state material and volatile by-products. Suitable organothallium MOCVD precursor compounds are relatively few in number, however, several have been used successfully in the preparation of thallium-containing superconductors and semiconductors by the MOCVD technique. Among them are thallium tris(β-diketonates)[122–124] and cyclopentadienylthallium.[123,125] The most promising precursors to date are CpTl and some of its derivatives. These compounds can be prepared relatively easily and come closest to possessing the necessary volatility.[126]

7 THALLIUM IN ORGANIC SYNTHESIS

7.1 Introduction

In contrast to the other elements of group 13, thallium is considered a soft acid in Pearson's soft/hard acid classification (*see* ***Hard & Soft Acids and Bases***).[127] This makes the element and its derivatives unique, and leads to its potentially most outstanding feature: the properties of thallium are a subtle blend of some of the most desirable properties of numerous other metals (e.g. heavy alkali metals, silver, mercury, and lead). Thallium compounds are stable in both oxidation states (+1 and +3). The trivalent cation is quite a strong oxidation reagent, since it is reduced to Tl^+ easily (standard redox potential $E°(Tl^{3+} \rightarrow Tl^+) = -1.25$ V). The ease of this reduction is utilized in certain organic reactions.

Numerous transformations in organic chemistry that occur in the presence of thallium reagents have been described. Many of these reactions are unique and are characterized by manipulative simplicity and high yields. Several review articles describe in detail the use of thallium reagents in organic synthesis.[1,127–131] Selected examples are discussed below.

7.2 Selected Examples[1,127–131]

The nonoxidative applications of thallium in organic synthesis are relatively few. Organothallium reagents act as mild nucleophiles. Thus, acid chlorides can be alkylated by R_3Tl, as can α-haloethers. Nucleophilicity is greater for R_4Tl^-. Alkyltrimethylthallate(III) is prepared from Me_3Tl and RLi, and may be used to alkylate α,β-unsaturated ketones.[130]

Symmetrical and unsymmetrical anhydrides can be prepared in quantitative yields by the reaction of Tl(I) carboxylates with carboxylic acid chlorides (equation 28).

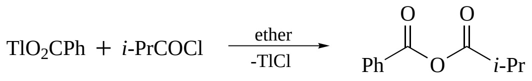

(28)

Thallium(III) reagents are useful for mediating electrophilic substitutions. The resulting arylthallium dications are converted into substituted aromatic compounds easily and in high yields. The new substituent enters the aromatic ring at the position in which the TlX_2 group was attached (equation 29).

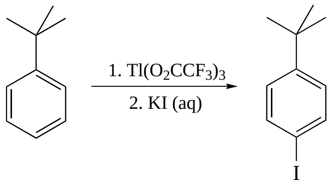

(29)

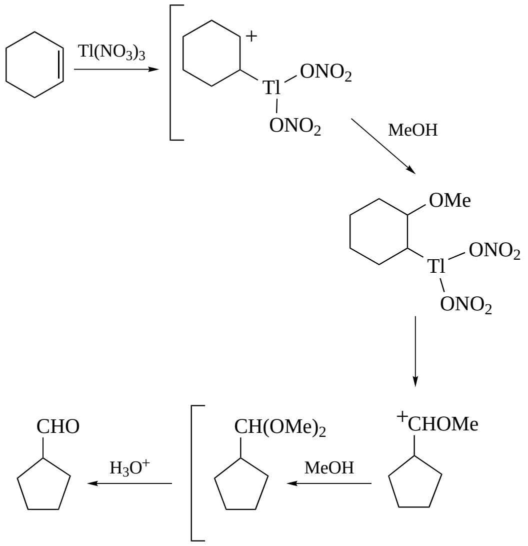

(30)

Thallium(III) salts, especially $Tl(NO_3)_3$, $Tl(O_2CCH_3)_3$, and $Tl(O_2CCF_3)_3$, are widely used as oxidizing reagents for nonaromatic unsaturated compounds.[11,130] This reaction is certainly the most important application of thallium in organic synthesis. The first step in the reaction of a thallium(III) salt with alkenes (oxythallation) takes place rapidly at ambient temperature and leads to the formation of monoalkylthallium(III) compounds. These intermediates are usually unstable under the reaction conditions, and undergo rapid decomposition to give the oxidation product of the organic substrate, while Tl^{3+} is reduced to Tl^+. Cyclic alkenes react with $Tl(NO_3)_3$ in methanol to give the ring-contracted products by oxidative rearrangement (equation 30). This reaction produces very high yields of ring-contracted products and has been used to great advantage in the conversion of flavanones to flavones, isoflavones, and benzofurans. Similar strategy can be used for ring closures and expansions (equations 31 and 32).[130] Enolizable ketones undergo oxidation at the α position in the presence of Tl(III) salts (equation 33).[130]

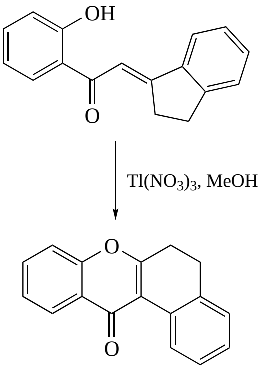

(31)

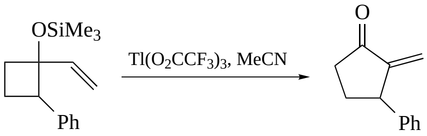

(32)

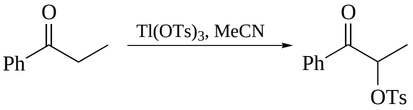

(33)

8 RELATED ARTICLES

Bonding Energetics of Organometallic Compounds; Diffraction Methods in Inorganic Chemistry; Gallium: Organometallic Chemistry; Indium: Organometallic Chemistry; Lead: Organometallic Chemistry; Mercury: Organometallic Chemistry; Metal Ion Toxicity; Semiconductors; Superconductivity; Thallium: Inorganic Chemistry; Thin Film Synthesis of Solids.

9 REFERENCES

1. A. McKillop and E. C. Taylor, *Adv. Organomet. Chem.*, 1973, **11**, 147.
2. A. G. Lee, in 'Organometallic Reactions', eds. E. I. Becker and M. Tsutui, Wiley, New York, 1975, Vol. 5, p. 1.
3. H. Kurosawa, in 'Comprehensive Organometallic Chemistry', eds. G. Wilkinson, F. G. A. Stone, and E. W. Abel, Pergamon, Oxford, 1982, Vol. 1, p. 725.
4. M. A. Paver, C. A. Russell, and D. S. Wright, in 'Comprehensive Organometallic Chemistry II', eds. E. W. Abel, F. G. A. Stone, and G. Wilkinson, Pergamon, Oxford, 1995, Vol. 1, p. 503.
5. A. McKillop and J. D. Smith, in 'Organometallic Compounds of Aluminum, Gallium, Indium, and Thallium', eds. A. McKillop, J. D. Smith, and I. J. Worall, Chapman and Hall, New York, 1985, p. 151.
6. C. Janiak, *Coord. Chem. Rev.*, 1997, **163**, 107.
7. J. S. Casas, M. S. García-Tasende, and J. Sordo, *Coord. Chem. Rev.*, 1999, **193–195**, 283.
8. B. Neumüller, *Coord. Chem. Rev.*, 1997, **158**, 69.
9. P. Schwerdtfeger, P. D. W. Boyd, G. A. Bowmaker, H. G. Mack, and H. Oberhammer, *J. Am. Chem. Soc.*, 1989, **111**, 15.
10. H. Meister, *Angew. Chem.*, 1957, **69**, 533.
11. P. Jutzi, *Adv. Organomet. Chem.*, 1986, **26**, 217.
12. H. Schumann, T. Ghodsi, L. Esser, and E. Hahn, *Chem. Ber.*, 1993, **126**, 591.
13. M. I. Bruce, J. K. Walton, M. L. Williams, S. R. Hall, B. W. Skelton, and A. H. White, *J. Chem. Soc., Dalton Trans.*, 1982, 2209.
14. H. Schumann, C. Janiak, J. Pickhardt, and U. Börner, *Angew. Chem., Int. Ed. Engl.*, 1987, **26**, 789.
15. P. Jutzi, J. Schnittger, and M. B. Hursthouse, *Chem. Ber.*, 1991, **124**, 1693.
16. S. Harvey, C. L. Raston, B. W. Skelton, A. H. White, M. L. Lappert, and G. Srivastsva, *J. Organomet. Chem.*, 1987, **328**, C1.
17. D. R. Armstrong, R. Herbst-Irmer, A. Kuhn, D. Moncrieff, M. A. Paver, C. A. Russell, D. Stalke, A. Steiner, and D. S. Wright, *Angew. Chem., Int. Ed. Engl.*, 1993, **32**, 1774.
18. D. R. Armstrong, A. J. Edwards, D. Moncrieff, M. A. Paver, P. R. Raithby, M.-A. Rennie, C. A. Russell, and D. S. Wright, *J. Chem. Soc., Chem. Commun.*, 1995, 927.
19. A. Dashti-Mommertz, B. Neumüller, S. Melle, D. Haase, and W. Uhl, *Z. Anorg. Allg. Chem.*, 1999, **625**, 1828.
20. E. Frasson, F. Menegus, and C. Panattoni, *Nature*, 1963, **199**, 1087.
21. J. F. Berar, G. Calvarin, C. Pommier, and D. Weigel, *J. Appl. Crystallogr.*, 1975, **8**, 386.
22. H. Schumann, H. Kucht, A. Kucht, F. H. Görlitz, and A. Dietrich, *Z. Naturforsch., Teil B*, 1992, **47B**, 1241.
23. H. Werner, H. Otto, and H. J. Kraus, *J. Organomet. Chem.*, 1986, **315**, C57.
24. H. Schumann, C. Janiak, M. A. Khan, and J. J. Zuckermann, *J. Organomet. Chem.*, 1988, **354**, 7.
25. M. B. Freeman, L. G. Sneddon, and J. C. Huffman, *J. Am. Chem. Soc.*, 1977, **99**, 5194.
26. H. Schumann, A. Lentz, and R. Weimann, *J. Organomet. Chem.*, 1995, **487**, 245.
27. H. Schumann, H. Kucht, A. Dietrich, and L. Esser, *Chem. Ber.*, 1990, **123**, 1811.
28. M. Enders, J. Fink, and H. Pritzkow, *Eur. J. Inorg. Chem.*, 2000, 1923.

29. M. D. Francis, C. Jones, G. B. Deacon, E. E. Delbridge, and P. C. Junk, *Organometallics*, 1998, **17**, 3826.
30. M. Sawamura, H. Iikura, and E. Nakamura, *J. Am. Chem. Soc.*, 1996, **118**, 12850.
31. G. K. Anderson and N. P. Rath, *J. Organomet. Chem.*, 1991, **414**, 129.
32. C. Janiak and R. Hoffmann, *J. Am. Chem. Soc.*, 1990, **112**, 5924.
33. P. Pyykkö, M. Straka, and T. Tamm, *Phys. Chem. Chem. Phys.*, 1999, **1**, 3441.
34. P. P. Power, *J. Chem. Soc., Dalton Trans.*, 1998, 2939.
35. P. Pyykkö, *Chem. Rev.*, 1988, **88**, 563.
36. M. Sawamura, H. Iikura, A. Hirai, and E. Nakamura, *J. Am. Chem. Soc.*, 1998, **120**, 8285.
37. M. Sawamura, M. Toganoh, Y. Kuninobu, S. Kato, and E. Nakamura, *Chem. Lett.*, 2000, 270.
38. A. F. Neto, A. D. L. Borges, J. Miller, and V. A. Darin, *Synth. React. Inorg. Met.-Org. Chem.*, 1997, **27**, 1299.
39. S. Top, C. Lescop, J.-S. Lehn, and G. Jaouen, *J. Organomet. Chem.*, 2000, **593–594**, 167.
40. G. Gassman and C. H. Winter, *J. Am. Chem. Soc.*, 1986, **108**, 4228.
41. B. G. Conway and M. D. Rausch, *Organometallics*, 1985, **4**, 688.
42. M. D. Rausch, W. C. Spink, B. G. Conway, R. D. Rogers, and J. L. Atwood, *J. Organomet. Chem.*, 1990, **383**, 227.
43. T. E. Bitterwolf, *J. Organomet. Chem.*, 1986, **312**, 197.
44. S. S. Jones, M. D. Rausch, and T. E. Bitterwolf, *J. Organomet. Chem.*, 1993, **450**, 27.
45. R. P. Hughes and J. R. Lomprey, *Inorg. Chim. Acta*, 1995, **240**, 653.
46. R. Wolgramm, C. Ramos, P. Royo, M. Lanfranchi, M. A. Pellinghelli, and A. Tiripicchio, *Inorg. Chim. Acta*, 2003, **347**, 114.
47. J. V. Scibelli and M. D. Curtis, *J. Am. Chem. Soc.*, 1973, **95**, 924.
48. T. Paine, R. W. Light, and D. E. Maier, *Inorg. Chem.*, 1979, **18**, 368.
49. F. Mathey and J.-P. Lampin, *Tetrahedron*, 1975, **31**, 2685.
50. G. B. Deacon, A. J. Koplik, and T. D. Tuong, *Aust. J. Chem.*, 1984, **37**, 517.
51. W. Uhl, S. U. Keimling, K. W. Klinkhammer, and W. Schwarz, *Angew. Chem., Int. Ed. Engl.*, 1997, **36**, 64.
52. M. Niemeyer and P. P. Power, *Angew. Chem., Int. Ed. Engl.*, 1998, **37**, 1277.
53. P. Jutzi, D. Wegener, and M. B. Hursthouse, *Chem. Ber.*, 1991, **124**, 295.
54. H. M. Colquhoum, T. J. Greenhough, and M. G. H. Wallbridge, *J. Chem. Soc., Chem. Commun.*, 1977, 737.
55. M. J. Manning, C. B. Knobler, and M. F. Hawthorne, *Inorg. Chem.*, 1991, **30**, 3589.
56. D. M. Schubert, M. A. Bandman, W. S. Rees, C. B. Knobler, P. Lu, W. Nam, and M. F. Hawthorne Jr, *Organometallics*, 1990, **9**, 2046.
57. K. Stumpf, H. Pritzkow, and W. Siebert, *Angew. Chem., Int. Ed. Engl.*, 1985, **25**, 71.
58. G. E. Herberich, H. J. Becker, and C. Engelke, *J. Organomet. Chem.*, 1978, **153**, 265.
59. T. Auel and E. L. Amma, *J. Am. Chem. Soc.*, 1968, **90**, 5941.
60. G. Wulfsberg and R. West, *J. Am. Chem. Soc.*, 1972, **94**, 6069.
61. R. S. Mathur, T. Drovetskaya, and C. A. Reed, *Acta Crystallogr., Sect. C*, 1997, **53**, 881.
62. W. Frank, G. Korrell, and G. J. Reiss, *J. Organomet. Chem.*, 1996, **506**, 293.
63. H. Schmidbaur, W. Bublak, J. Riede, and G. Müller, *Angew. Chem., Int. Ed. Engl.*, 1985, **24**, 414.
64. H. Schmidbaur, W. Bublak, B. Huber, J. Hofmann, and G. Müller, *Chem. Ber.*, 1989, **122**, 265.
65. W. Frank, D. Kuhn, S. Müller-Becker, and A. Razavi, *Angew. Chem., Int. Ed. Engl.*, 1993, **32**, 90.
66. G. B. Deacon, E. E. Delbridge, C. M. Forsyth, B. W. Skelton, and A. H. White, *J. Chem. Soc., Dalton Trans.*, 2000, 745.
67. S. D. Waezsada, T. Belgardt, M. Noltemeyer, and H. W. Roesky, *Angew. Chem., Int. Ed. Engl.*, 1994, **33**, 1351.
68. I. Ara, J. R. Berenguer, J. Forniés, J. Gómez, E. Lalinde, and R. I. Merino, *Inorg. Chem.*, 1997, **36**, 6461.
69. S. Henkel, K. W. Klinkhammer, and W. Schwarz, *Angew. Chem., Int. Ed. Engl.*, 1994, **33**, 681.
70. N. Wiberg, K. Amelunxen, H. Nöth, M. Schmidt, and H. Schwenk, *Angew. Chem., Int. Ed. Engl.*, 1996, **35**, 65.
71. R. Usón, A. Laguna, J. A. Abad, and E. de Jesús, *J. Chem Soc., Dalton Trans.*, 1983, 1127.
72. R. Usón, A. Laguna, and J. A. Abad, *J. Organomet. Chem.*, 1980, **194**, 265.
73. A. T. Weibel and J. P. Oliver, *J. Organomet. Chem.*, 1974, **74**, 155.
74. A. Mendía, E. Cerrada, E. J. Fernández, A. Laguna and M. Laguna, *J. Organomet. Chem.*, 2002, **663**, 289.
75. G. M. Sheldrick and W. S. Sheldrick, *J. Chem. Soc. (A)*, 1970, 28.
76. J. Blümel, B. Werner, T. Kräuter, and B. Neumüller, *Z. Anorg. Allg. Chem.*, 1997, **623**, 309.
77. R. Boese, A. J. Downs, T. M. Greene, A. W. Hall, C. A. Morrison, and S. Parsons, *Organometallics*, 2003, **22**, 2450.
78. A. P. Kurbakova, S. S. Bukalov, L. A. Leites, L. M. Golubinskaya, and V. I. Bregadze, *J. Organomet. Chem.*, 1997, **536–537**, 519.
79. S. J. Price, J. P. Richard, R. C. Rumfeldt, and M. G. Jacko, *Can. J. Chem.*, 1973, **51**, 1397.

80. S. Numata, H. Kurosawa, and R. Okawara, *J. Organomet. Chem.*, 1975, **102**, 259.
81. G. E. Coates and R. A. Whitcombe, *J. Chem. Soc.*, 1956, 3351.
82. J. P. Maher and D. F. Evans, *J. Chem. Soc.*, 1963, 5534.
83. G. B. Deacon and R. J. Phillips, *Aust. J. Chem.*, 1978, **31**, 1709.
84. R. A. Baldwin, R. L. Wells, and P. S. White, *Main Group Chem.*, 1997, **2**, 67.
85. K. Jacob, J. Scholz, C. Pietzsch, and F. T. Edelmann, *J. Organomet. Chem.*, 1995, **501**, 71.
86. G. Müller and J. Lachmann, *Z. Naturforsch.*, 1993, **B48**, 1544.
87. A. Laguna, E. J. Fernández, A. Mendía, M. E. Ruiz-Romero, and P. G. Jones, *J. Organomet. Chem.*, 1989, **365**, 201.
88. K. Kobiro, M. Takahashi, Y. Odaira, Y. Kawasaki, Y. Kai, and N. Kasai, *J. Chem. Soc., Dalton Trans.*, 1986, 2613.
89. Y. M. Chow and D. Britton, *Acta Crystallogr., Sect. B*, 1975, **31**, 1929.
90. M. J. Moloney and B. M. Foxman, *Inorg. Chim. Acta*, 1995, **229**, 323.
91. R. Carballo, J. S. Casas, E. E. Castellano, A. Sánchez, J. Sordo, E. M. Vázquez-López, and J. Zukerman-Schpector, *Polyhedron*, 1997, **16**, 3609.
92. J. S. Casas, A. Castiñeiras, A. Sánchez, J. Sordo, and E. M. Vázquez-López, *Main Group Met. Chem.*, 1996, **19**, 231.
93. J. S. Casas, E. E. Castellano, J. Ellena, M. S. García-Tasende, A. Sánchez, J. Sordo, E. M. Vázquez-López, and M. J. Vidarte, *Z. Anorg. Allg. Chem.*, 2003, **629**, 261.
94. J. S. Casas, M. V. Castaño, M. C. Cifuentes, A. Sánchez, and J. Sordo, *Polyhedron*, 2002, **21**, 1651.
95. A. Rodríguez, J. A. García-Vázquez, A. Sousa-Pedrares, J. Romero, and A. Sousa, *J. Organomet. Chem.*, 2004, **689**, 557.
96. G. B. Deacon, S. J. Faulks, B. M. Gatehouse, and A. J. Jozsa, *Inorg. Chim. Acta*, 1977, **21**, L1.
97. N. N. Greenwood and J. A. Howard, *J. Chem. Soc., Dalton Trans.*, 1976, 177.
98. J. S. Casas, E. E. Castellano, A. Castiñeiras, A. Sánchez, J. Sordo, E. M. Vázquez-López, and J. Zukerman-Schpector, *J. Chem. Soc., Dalton Trans.*, 1995, 1403.
99. T. S. Lobana, J. S. Casas, A. Castiñeiras, M. S. García-Tasende, A. Sánchez, and J. Sordo, *Inorg. Chim. Acta*, 2003, **347**, 23.
100. S. Bhandari, M. F. Mahon, K. C. Molloy, J. S. Palmer, and S. F. Sayers, *J. Chem. Soc., Dalton Trans.*, 2000, 1053.
101. J. S. Casas, A. Sánchez, J. Sordo, E. M. Vázquez-López, R. Carballo, and C. Maichle-Mössmer, *Polyhedron*, 1996, **15**, 861.
102. F. Brady, K. Henrick, R. W. Matthews, and D. G. Gilles, *J. Organomet. Chem.*, 1980, **193**, 21.
103. K. Jacob, J. Scholz, K. Merzweiler, and C. Pietzsch, *J. Organomet. Chem.*, 1997, **527**, 109.
104. I. F. Gun’kin and E. V. Finaevova, *Russ. Chem. Bull.*, 1997, **46**, 2130.
105. I. F. Gun’kin and K. P. Butin, *Russ. Chem. Bull.*, 1999, **48**, 448.
106. K. Henrick, R. W. Matthews, and P. A. Tasker, *Inorg. Chim. Acta*, 1977, **25**, L31.
107. F. Brady, K. Henrick, and R. W. Matthews, *J. Organomet. Chem.*, 1979, **165**, 21.
108. K. Henrick, R. W. Matthews, and P. A. Tasker, *Inorg. Chem.*, 1977, **16**, 3293.
109. F. Brady, K. Henrick, and R. W. Matthews, *J. Organomet. Chem.*, 1981, **210**, 281.
110. C. Burschka, *Z. Anorg. Allg. Chem.*, 1982, **485**, 217.
111. J. Vicente, J. A. Abad, J. F. Gutierrez-Jugo, and P. G.Jones, *J. Chem. Soc., Dalton Trans.*, 1989, 2241.
112. P. J. Craig, in ‘The Handbook of Environmental Chemistry’, ed. O. Hutzinger, Springer, New York, 1980, Vol. 1, p. 169.
113. G. Agnes, S. Bendle, H. A. O. Hill, F. R. Williams, and R. J. P. Williams, *J. Chem. Soc., Chem. Commun.*, 1971, 850.
114. G. Agnes, H. A. O. Hill, J. M. Pratt, S. C. Ridsdale, F. S. Kennedy, and R. J. P. Williams, *Biochim. Biophys. Acta*, 1971, **252**, 207.
115. F. Huber and H. Kirchmann, *Inorg. Chim. Acta*, 1978, **29**, L249.
116. O. F. Schedlbauer and K. G. Heumann, *Anal. Chem.*, 1999, **71**, 5459.
117. R. J. Phillips, M. J. Shane, and J. A. Switzer, *J. Mater. Res.*, 1989, **4**, 923.
118. Z. Z. Zheng and A. M. Herrmann, *Nature*, 1988, **332**, 138.
119. J. G. Bednorz and K. A. Müller, *Z. Phys. (B)*, 1986, **64**, 189.
120. B. Springfellow, ‘Organometallic Vapor-Phase Epitaxy: Theory and Practice’, Academic Press, New York, 1989.
121. T. Sugimoto, *Mater. Sci. Forum*, 1993, **137–139**, 395.
122. K. Zhang, E. P. Boyd, B. S. Kwak, A. C. Wright, and A. Erbil, *Appl. Phys. Lett.*, 1989, **55**, 1258.
123. A. D. Berry, R. T. Holm, R. L. Mowery, N. H. Turner, and M. Fatemi, *Chem. Mater.*, 1991, **3**, 72.
124. A. Ryohei and Y. Shiokawa, *Inorg. Chim. Acta*, 1993, **203**, 9.
125. D. S. Richeson, L. M. Tonge, J. Zhao, J. Zhang, H. O. Marcy, T. J. Marks, B. W. Wessels, and C. R. Kannewurf, *Appl. Phys. Lett.*, 1989, **54**, 2154.
126. P. Zanella, G. Rosetto, S. Sitran, and D. Ferro, *Eur. J. Sol. State Inorg. Chem.*, 1992, **29**, 181.
127. E. C. Taylor and A. McKillop, *Acc. Chem. Res.*, 1970, **3**, 338.
128. A. McKillop and E. C. Taylor, *Chem. Br.*, 1973, **9**, 4.

129. A. McKillop and E. C. Taylor, in ‘Comprehensive Organometallic Chemistry’, eds. G. Wilkinson, F. G. A. Stone, and E. W. Abel, Pergamon, Oxford, 1982, Vol. 7, p. 465.

130. H. M. C. Ferraz, L. F. Silva Jr, and T. de O. Vieira, *Synthesis*, 1999, 2001.

131. I. E. Marko and C. W. Leung, in ‘Comprehensive Organometallic Chemistry II’, eds. E. W. Abel, F. G. A. Stone, and G. Wilkinson, Pergamon, Oxford, 1995, Vol. 11, p. 437.

Thin Film Synthesis of Solids

Chunming Niu & Charles M. Lieber
Harvard University, Cambridge, MA, USA

1	Introduction	1
2	Fundamentals of PLD	2
3	Experimental Apparatus for PLD	3
4	Thin Film Synthesis Using PLD	4
5	Summary	7
6	Related Articles	7
7	References	7

Glossary

Laser ablation: light-driven nonequilibrium evaporation of a solid
Thin films: coatings that have thicknesses ranging from a single crystal unit-cell to several microns

Abbreviations

PLD = pulsed laser ablation and deposition; T_c = superconducting transition temperature; RBS = Rutherford backscattering spectrometry; RHEED = reflection high-energy electron diffraction.

1 INTRODUCTION

Inorganic thin films play a central role in many areas of technology and basic research.[1,2] Thin film coatings are essential to the function of numerous mechanical devices. Electronically active thin films have also been central to the discovery of new physical phenomena such as the quantum Hall effect. In general, it is possible to categorize the wide spectrum of inorganic thin films into two categories, passive or active, based simply on their function in a structure or device. Passive thin films are coatings that may be used for cosmetic purposes or to protect a surface from wear or deleterious chemical reactions; however, passive films do not serve a specific electronic or catalytic role. Examples of technologically important passive thin films include: (1) metal nitrides (e.g. TiN) and carbides, which are used as hard, wear-resistant coatings; (2) oxides such as Al_2O_3 and SiO_2, which are used as diffusion barriers and insulators; and (3) metal coatings (e.g. Au), which are used to provide chemically inert, decorative finishes.[1–3] In addition, electronically and chemically active thin films are of great importance to microelectronic devices, sensors, and other key technological areas. For example, alternating thin layers of GaAs and AlGaAs form the basis for optical detectors and semiconductor lasers. On the other hand, ZrO_2 thin films represent the key chemically selective component of oxygen sensors used in many automobile engines.

Central to thin film technology and research are the synthetic methods used to fabricate coatings and new thin film materials. These synthetic methods, which differ significantly from familiar inorganic preparative techniques, can be classified as either chemical or physical in nature. Chemical techniques include *Chemical Vapor Deposition* (CVD),[1] sol–gel techniques (*see* ***Sol–Gel Synthesis of Solids***),[2] and electrochemical plating. In general, chemical techniques rely on the decomposition of molecular precursors (*see* ***Metallic Materials Deposition: Metal-organic Precursors***), where the quality of a resulting thin film depends critically on excluding ligands and other contaminants. Inorganic chemists have made an impact in designing molecular precursors for film growth.

In contrast, physical techniques of thin film synthesis are based upon evaporation or sputtering of elemental or multicomponent sources and subsequent deposition of this material onto a substrate;[3–6] molecular precursors do not play a significant role in thin film synthesis via these techniques. Examples of physical techniques used to prepare thin films include: (1) *Molecular Beam Epitaxy* (MBE);[5] (2) sputtering,[4] and (3) pulsed laser ablation and deposition (PLD).[6] Physical techniques can be extremely powerful methods for fabricating new materials since they allow atomic level control of growth. For example, MBE has revolutionized the fabrication of complex semiconductor superlattices (e.g. GaAs/AlGaAs) that have abrupt variations in composition on an atomic scale. A major limitation of MBE is that it relies on thermal evaporation to generate the elemental components of a film. Equilibrium evaporation will yield films that have a stoichiometry which differs from the bulk starting material when the starting material melts incongruently. Because most chemically interesting complex inorganic materials, such as metal oxides and metal nitrides, melt incongruently, it is not clear whether MBE can contribute greatly to the synthesis of interesting inorganic oxides and nitrides.

On the other hand, we believe there is an emerging body of results which indicate that PLD may revolutionize the synthesis of complex inorganic thin film materials. A unique feature of PLD is that the source material is evaporated (ablated) in a nonequilibrium process such that material is evaporated at the stoichiometry of the bulk. Hence, it is possible to prepare thin films of incongruently melting solids that have a stoichiometry characteristic of the solid phase prior to melting. For example, PLD has been the most effective method for preparation of crystalline $YBa_2Cu_3O_7$

superconductor thin films for both research and commercial applications. Since $YBa_2Cu_3O_7$ melts incongruently, it is difficult to prepare films via conventional thermal evaporation. Furthermore, the PLD technique is a general one for thin film synthesis, and has been used to prepare materials with metallic, insulating, ferroelectric, piezoelectric, magnetic, and superconducting properties.[6] Because PLD can in principle be used to deposit widely varying types of materials and arbitrarily complex stoichiometries, we believe that it is a uniquely powerful approach to the synthesis of inorganic thin films. The remainder of this article will focus on the PLD technique of thin film synthesis, including the fundamental principles of laser ablation and applications of PLD to the synthesis of novel inorganic materials.

2 FUNDAMENTALS OF PLD

The utility of PLD for thin film synthesis is due in large part to the unique characteristics of the laser ablation process. As indicated above, laser ablation is a nonequilibrium process that enables stoichiometric evaporation of elements from a target source. In addition, it is also possible to control the energy of evaporated species in PLD, and thus control film growth on the substrate surface. The underlying basis for these features of laser ablation and their utility in thin film synthesis are described below.

2.1 Laser–Solid Interaction

The interaction of intense laser light with solid surfaces is a complex physical process. This section does not focus on the physics underlying this interaction, but rather reviews the factors that directly influence thin film growth. More detailed explanations of the laser–solid interaction can be found in several reviews of this subject.[7–9]

The interaction of pulsed laser light with a solid surface is shown schematically in Figure 1. Typically, lasers with pulse lengths <50 ns and energies on the order of $1\,\mathrm{J\,cm^{-2}}$ are used for thin film synthesis. Initially, laser light is absorbed by the solid and heats and melts the near-surface region of a target. The depth of the melted region depends upon the power density and rate of thermal diffusion.[7–9] At high power densities, the surface melts during the initial part of the laser pulse, and is then vaporized. In the intense electromagnetic field of the laser light, the vapor is ionized to form a plasma that contains ions, electrons, neutral atoms, and small clusters. The plasma, which is self-regulating,[7–9] is directed perpendicularly away from the target or source surface; this directional vaporization is termed laser ablation. The ions and neutral elements in the plasma can be readily deposited on a substrate located diametrically opposite to the target. During laser ablation it is important to recognize that temperatures in excess of 4000 K are readily achieved, and thus virtually any material can be evaporated. Furthermore, since the target material acts as its own crucible, contamination from a reaction crucible, which is common in conventional solid-state synthesis, is not a problem in PLD synthesis.

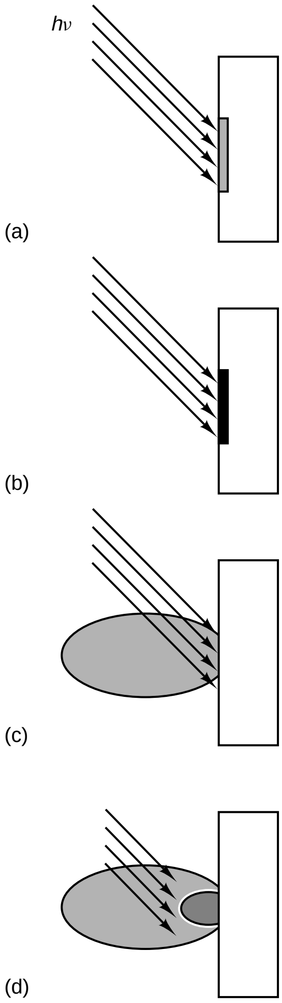

Figure 1 Schematic view of the interaction of laser light with a solid. Initial irradiation heats (a) and then melts (b) the surface. The liquid is then vaporized (c) and ionized (d) to form a plasma that is ejected away from the target surface. The time from (a) to (d) is approximately 30 ns

2.2 Important Laser Parameters

Central to the application of laser ablation in synthesis is the ability to control the rate, energies, and neutral:ion ratio of the evaporated elements through systematic variations in the wavelength, pulse-width, and power density of the laser light. The absorption depth of light by a solid is wavelength dependent, and thus the efficiency of target heating and evaporation will depend on the wavelength of irradiation. The target temperature increase during laser irradiation is inversely proportional to the optical penetration depth for a fixed energy input, where the penetration depth is directly proportional to wavelength.[10,11] Hence, the surface temperature of a target irradiated with short and long wavelength lasers of equal energy and pulse length will be higher for the former. In addition, the rate of energy input, which is governed by the laser pulse width, is directly related to the temperature increase of the target; i.e. for a shorter pulse length a smaller amount of heat will be transported into the bulk by thermal diffusion. Short wavelength and short pulse length lasers will thus ablate material from a small near-surface volume without segregation of elements from the bulk. That is, regardless of the nature of the equilibrium phase diagram, the evaporated species have the average stoichiometry of the bulk target. Therefore, laser sources that emit short UV pulses (e.g. the excimer laser) are ideal for complex thin film synthesis using PLD.

The laser power density also plays an important role in the evaporation process. First, at very low power densities (not employed typically for PLD) evaporation is nearly an equilibrium thermal process. As the power density increases, however, the process becomes nonequilibrium since heating and evaporation occur more rapidly than thermal and atomic diffusion. Furthermore, as the power density increases, the fraction of ionic to neutral species in the plasma and the kinetic energy of these species increases. Explicit measurement of these dependencies is possible using mass spectrometry.[12–18] Time of flight mass spectrometry measurements have shown that the energy of neutral species can be varied between 3 and 30 eV, while the ions produced in the plasma may have energies from 0.1 to $>$100 eV. These relatively high kinetic energies enhance the chemical reactivity and surface diffusion of the ablated species. Diffusion and reactivity are both important parameters for controlling film growth. Because it is straightforward to change the power density through simply focusing or defocusing of the laser, the synthetic chemist has a powerful variable for controlling thin film growth. Lastly, it is important to reiterate that high power density laser ablation in nearly all cases results in congruent (i.e. stoichiometric) evaporation of the source target. Congruent evaporation has been demonstrated in many important systems which cannot be prepared using conventional thermal evaporation, including ternary semiconductors such as HgCdTe and $Pb_{1-x}Cd_xSe$,[19,20] electronic ceramics,[21,22] and high-temperature copper oxide superconductors.[23] Of even greater importance to the synthesis of new inorganic thin films is the fact that congruent evaporation is also observed for multiphase targets.[24] That is, a thin film of virtually any stoichiometry can be prepared by laser ablation of a target that simply contains elements mixed in the desired stoichiometry.

3 EXPERIMENTAL APPARATUS FOR PLD

A general experimental apparatus for preparing thin films by PLD is shown in Figure 2. The PLD apparatus consists of a vacuum chamber containing a target holder, substrate heater positioned diametrically opposite to the target, optical window, and other components (Figure 2), together with a pulsed laser. Key features and considerations for the deposition apparatus are discussed below.

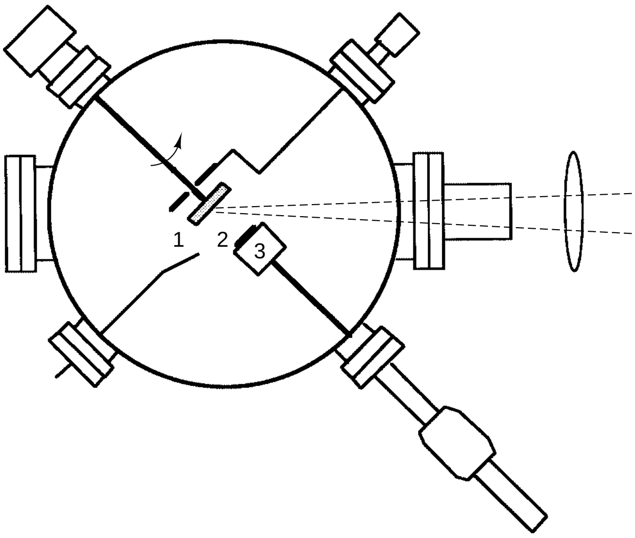

Figure 2 Schematic view of the PLD synthetic chamber. The target (1) is attached to a feedthrough that is rotated during laser irradiation. The growth substrate (2) is attached to a heater (3) that controls the growth temperature between 25 and 900 °C. The dashed lines represent the laser beam (laser not shown); the beam is focused onto the target

Deposition chambers are typically constructed of stainless steel in order to obtain a clean vacuum. Glass chambers can also be used for PLD, although they are generally less versatile than metal chambers. In either case, it is important to minimize the build-up of deposits on the optical window in the chamber since this effectively attenuates the laser power density at the target surface. The build-up of deposits on the optical window can be reduced by locating this window as far away from the target as is possible.

The synthesis of oxide and nitride materials is often carried out with a background pressure in the PLD chamber of 10 to 500 mTorr. This pressure regime can be readily achieved using inexpensive mechanical pumps. However, it is good synthetic procedure to use a turbomolecular pump to establish a high vacuum in the chamber initially, and then to increase the pressure using purified oxygen or nitrogen.

Another key element in the PLD apparatus is the substrate heater. Thin film synthesis of oxide materials may be carried out at temperatures as high as 800 °C in oxygen. These highly oxidizing conditions place severe demands on heating elements, although two general types of heaters, radiant and resistive, have been used successfully. Radiant heaters utilize lamps as a heat source. A simpler solution to this problem is to utilize simple resistance heaters. Resistance heaters are easily fabricated; however, the metal alloy utilized for the heater element must be chosen with care to ensure reliable heater operation at high temperature in oxygen.

Lastly, it is important to irradiate the target uniformly. If the laser is focused on a stationary target, the ablation process will create a localized depression in the surface. The formation of surface depressions or craters is deleterious to synthesis since it leads to incongruent target evaporation. One method to avoid the formation of localized craters is to rotate the target asynchronously with the laser pulses. Alternatively, when target rotation is not possible, the laser beam itself should be scanned over the surface of the target. Target rotation and beam scanning both lead to uniform (and stoichiometric) removal of material from the target.

4 THIN FILM SYNTHESIS USING PLD

In the remainder of this article specific examples of thin film synthesis using PLD are described. These examples are chosen to illustrate the unique characteristics of PLD that make it a powerful technique for the preparation of complex multicomponent solids and for exploratory synthesis of new materials.

4.1 Preparation of Known Materials

The discovery of high-temperature superconductivity in copper oxide based materials has been a remarkable triumph of inorganic solid-state chemistry (*see* ***Superconductivity*** and ***Oxides: Solid-state Chemistry***). A number of families of copper oxide superconductors are now known, and the transition temperatures (T_c) in many of these solids exceed the boiling point of liquid nitrogen (LN_2). The observation of T_c values above the boiling point of LN_2 has renewed interest in developing superconductor thin films for a variety of electronics devices. For the fabrication of thin film devices it is essential that the thin film material (1) is homogeneous and crystalline, (2) has a high critical current density, and (3) does not react with the substrate on which it is grown. PLD has been by far the most widely used technique for the preparation of these high-T_c thin films.[24–26] These films have been shown to preserve the structure and composition of bulk $YBa_2Cu_3O_7$. Thin films prepared by PLD also exhibit the high critical current densities required for technological applications. In addition, it is possible to grow crystalline, superconducting films of $YBa_2Cu_3O_7$ at temperatures significantly lower than those used to form the bulk phase (700 vs. >900 °C). Low-temperature growth minimizes, and in some cases eliminates, interdiffusion and reaction at the superconductor–substrate interface.

The successful preparation of high-quality $YBa_2Cu_3O_7$ films shows that PLD can readily deposit complex stoichiometry materials in crystalline form at temperatures significantly lower than those required in bulk syntheses. Furthermore, high-quality films have been routinely prepared in many laboratories worldwide. Hence, it is indeed reasonable to consider PLD as a general technique for the synthesis of complex inorganic films.

Another general class of solids that has been prepared as thin films using PLD is ferroelectric materials. A potentially useful characteristic of ferroelectric materials is that they can be polarized by an electric field and retain this polarization when the field is removed. In ferroelectric thin films it may be possible to exploit this polarization phenomenon to make sensors, displays, and memory devices.[27] A number of techniques have been used to prepare ferroelectric thin films. However, it has been difficult to control the stoichiometry (and correspondingly the properties) of these materials using thermal and sputtering techniques. In part, the difficulty in maintaining correct stoichiometry is due to the volatility of a component in the material (e.g. Pb in $PbTiO_3$).

The success of PLD in preparing high-quality superconductor thin films has led to considerable interest in applying this technique to the ferroelectrics. PLD is particularly attractive for the synthesis of ferroelectric materials since it can deposit stoichiometric and crystalline materials at low temperature. Deposition at low temperature (e.g. 300–500 °C) prevents the loss of volatile components from the film. However, simply preparing a film at low temperature using thermal sources would not yield a crystalline thin film since there is insufficient energy for elements to diffuse to the proper crystallographic sites. Laser ablation produces high kinetic energy particles (see Section 2) that can diffuse to the correct crystal sites after deposition and yield highly crystalline thin films at low growth temperatures.

PLD of crystalline and stoichiometric ferroelectric materials has been successful for a number of materials. For example, crystalline $PbTiO_3$ thin films have been deposited at only 350 °C using a KrF excimer laser ($\lambda = 248\,\mathrm{nm}$).[28] The low deposition temperature makes this a potentially attractive method for directly fabricating ferroelectric/semiconductor hybrid devices. A related solid that is more difficult to prepare in thin film form is $PbZr_{1-x}Ti_xO_3$. To maintain the Pb stoichiometry and ensure random mixing of Ti and Zr requires careful control of film synthesis conditions.[29,30]

Another recent application of PLD thin film synthesis has been in the area of magnetic ferrites. Thin film ferrites are of great technological interest since they could play a key role in high-density magnetic recording devices and in monolithic microwave integrated circuitry. It has been difficult to prepare thin films of ferrites due to their structural and compositional complexity. Attempts to prepare ferrites using sputtering and plasma spraying have not yet achieved high-quality thin films.

In contrast, synthetic investigations using PLD have been quite promising.[31,32] Recent studies of $Mn_xZn_{1-x}Fe_2O_4$ have shown that crystalline films can be prepared on $\langle 100\rangle$ oriented MgO substrates. Because the physical properties (e.g. resistivity and saturation magnetization) of this ferrite depend critically on the Mn:Zn:Fe ratio and the oxygen stoichiometry, PLD can be used to readily tune the properties of the films for specific applications. In addition, PLD has been used to grow high-quality epitaxial thin films of $BaFe_{12}O_{19}$ on ⟨0001⟩ sapphire and $Y_3Fe_5O_{12}$ on ⟨111⟩ garnet substrates. These results are quite promising and may lead to practical applications for thin film ferrites produced by PLD. More generally, however, they demonstrate the utility of PLD in the synthesis of complex inorganic thin films.

4.2 Synthesis of New Materials

Conventional synthetic methods for the preparation of inorganic materials involve reaction in the solid state. To facilitate diffusion and reaction in the solid state requires high temperature conditions. Hence, the products obtained from conventional solid-state reactions are typically limited to the ones thermodynamically stable at high temperature. In the past most solid-state synthetic studies have focused on high-temperature chemistry, although there is now a growing interest in the development of low-temperature approaches to inorganic solid-state synthesis.[33] Controlled low-temperature synthesis is a particularly attractive goal since it offers the possibility of obtaining new phases and materials with novel properties. PLD is an especially attractive method to explore the low-temperature synthesis of new materials since (1) stoichiometry can be readily controlled (i.e. laser evaporation is congruent irrespective of the equilibrium phase diagram) and (2) crystalline products can be grown at temperatures much lower than is possible with conventional solid-state reactions. Below, specific examples of the synthesis of several new materials by PLD are described.

The tetragonal infinite-layer phase of $SrCuO_2$, which consists of alternating Sr^{2+} and $CuO_2{}^{2-}$ sheets, represents the parent structure of the high-T_c copper oxide superconductors (Figure 3). In principle, this system is ideally suited for investigating high-T_c superconductivity since it contains only essential copper oxide layers and counterions. It has not been possible, however, to prepare and systematically dope this phase using conventional solid-state methods. Notably, recent studies in our laboratory have shown that it is possible to prepare this phase for a wide range of compositions, $Sr_{1-x}M_xCuO_2$ (M = Nd, Ca, Ba) using PLD.[33–35]

$Sr_{1-x}Ca_xCuO_2$ targets can be prepared using conventional solid-state methods at 900 °C. The $Sr_{1-x}Ca_xCuO_2$ targets are, however, multiphase, except for $SrCuO_2$ which has an orthorhombic structure. Laser ablation of these targets using a KrF laser and deposition onto ⟨100⟩ $SrTiO_3$ substrates at 500 °C yields single-phase materials for all values of x. The films can be structurally characterized using X-ray and electron diffraction. X-Ray diffraction scans ($\theta - 2\theta$) of $Sr_{1-x}Ca_xCuO_2$ films prepared by PLD are shown in Figure 4. These relatively simple diffraction patterns can be indexed as the infinite-layer phase (Figure 3), where the CuO_2 planes are all oriented parallel to the surface of the ⟨100⟩ $SrTiO_3$ substrate. A simulation of the diffraction pattern expected for a thin film with this orientation also agrees quite well with the experimental data.

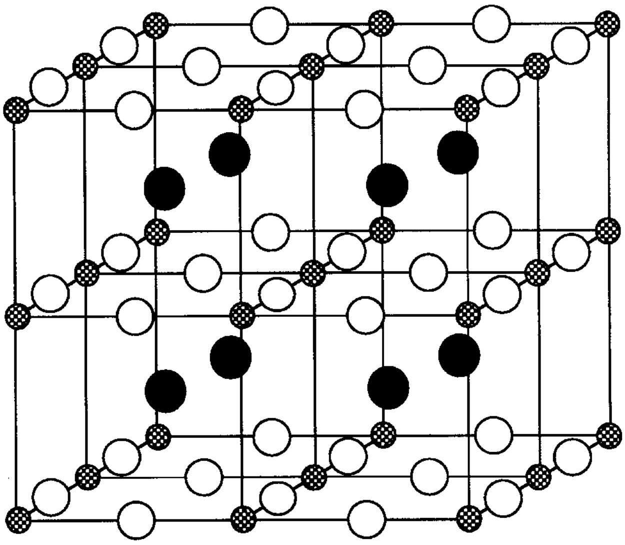
Figure 3 Structural model of the tetragonal infinite layer phase of $SrCuO_2$. The Sr^{2+} ions appear as isolated solid black spheres between the $CuO_2{}^{2-}$ layers. The copper ions are cross-hatched circles and the oxygen ions are open circles

The $\theta - 2\theta$ diffraction scans elucidate the layered structure of the $Sr_{1-x}Ca_xCuO_2$ materials. Electron diffraction can be used to complete the structural identification of these thin film materials. Electron diffraction patterns recorded along the [001] plane axis characterize the in-plane structure. An example of an electron diffraction pattern recorded on a $Sr_{0.7}Ca_{0.3}CuO_2$ sample is shown in Figure 5. The diffraction peaks exhibit a square symmetry, as expected for the in-plane structure of the tetragonal infinite-layer phase. Simulations have been used to confirm this in-plane structure. Thus, the X-ray and electron diffraction measurements provide an unambiguous identification of the structure of these thin film materials.

It is also possible to characterize accurately the composition of new thin film materials using RBS. RBS analysis of the $Sr_{1-x}Ca_xCuO_2$ materials demonstrates that the single-phase infinite-layer thin films have the same average composition as the multiphase targets from which they were prepared by laser ablation. These compositional analysis results demonstrate that PLD can be used to prepare readily a specific stoichiometry material even when the target is not single phase.

Since it was not possible to prepare the infinite-layer $Sr_{1-}Ca_xCuO_2$ materials previously using conventional solid-state methods, it is important to clarify what features of PLD enable the general synthesis of this new phase. Structural studies of the $Sr_{1-x}Ca_xCuO_2$ products obtained from PLD

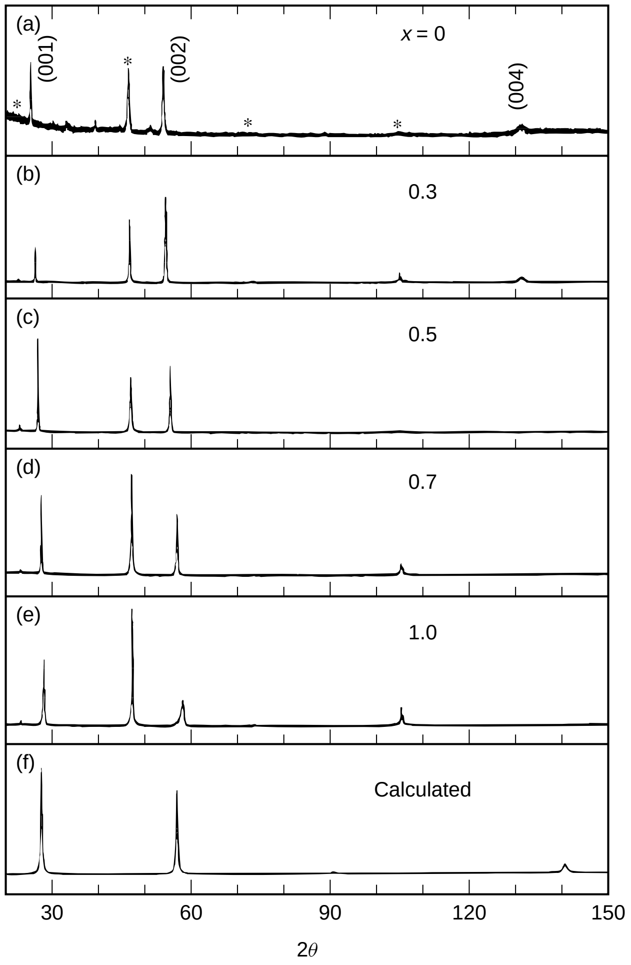

Figure 4 X-Ray diffraction patterns recorded on (a) $SrCuO_2$, (b) $Sr_{0.7}Ca_{0.3}CuO_2$, (c) $Sr_{0.5}Ca_{0.5}CuO_2$, (d) $Sr_{0.3}Ca_{0.7}CuO_2$, and (e) $CaCuO_2$. A simulation of the diffraction pattern for $SrCuO_2$ is shown in (f)

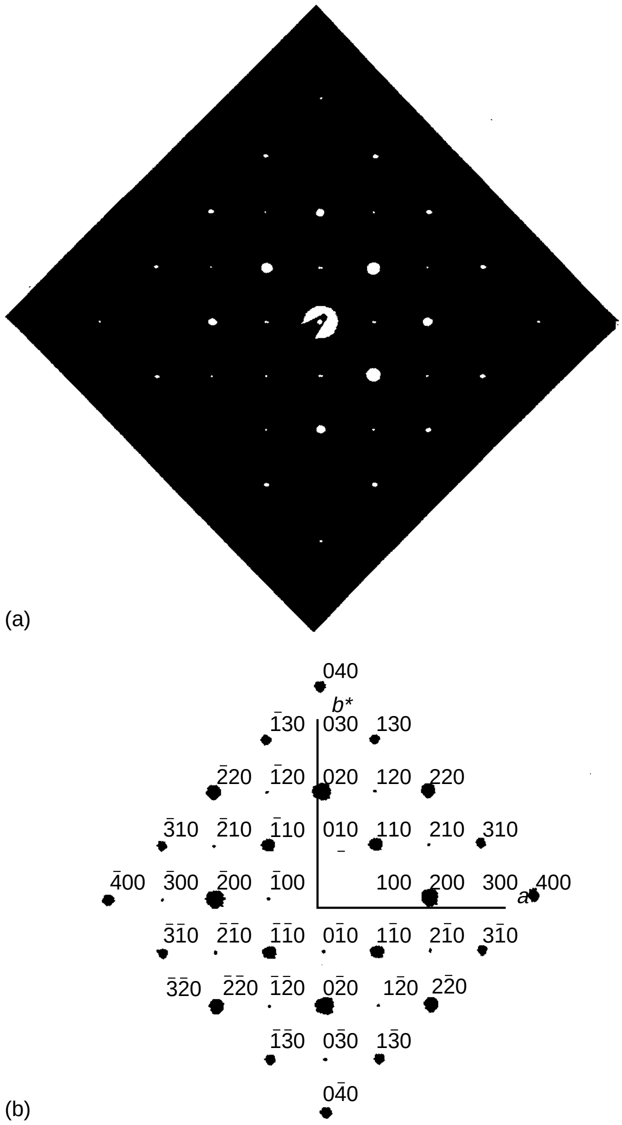

Figure 5 (a) Electron diffraction pattern recorded along the ⟨001⟩ zone axis of a $Sr_{0.7}Ca_{0.3}CuO_2$ sample. (b) Simulation of the diffraction pattern for the infinite-layer phase

growth at different temperatures provide key insight into this question. Temperature-dependent growth studies demonstrate that low-temperature growth is a key factor in stabilizing the infinite layer phase.[33–35] X-Ray diffraction patterns obtained from samples grown at temperatures from 500 to 700 °C (Figure 6) show that the concentration of the orthorhombic phase increases as the growth temperature increases. In the case of $SrCuO_2$, the orthorhombic phase, which is not a layered structure, is the single stable phase at high temperature. These results demonstrate that in the case of $Sr_{1-x}Ca_xCuO_2$, PLD can be used to trap a new metastable phase through low-temperature growth. This idea is expected to be generally useful for inorganic thin film synthesis in the future.

A second distinct example of PLD new materials synthesis involves substitutional doping of $YBa_2Cu_3O_7$.[36–38] It is well known that substitution of Y with other rare earth elements does not affect T_c significantly unless the rare earth is Pr. Indeed, $PrBa_2Cu_3O_7$ is not a superconducting material. To explain the disappearance of superconductivity in the Pr-substituted material it has been suggested that either Pr exists as Pr^{4+} (vs. Y^{3+}) or that the magnetic moment on Pr suppresses T_c. An experimental test of this hypothesis would be to prepare another M^{4+}-substituted compound and a M^{4+}/M^{2+} solid that would have the same average valence as Y^{3+}.

Substitution of Ce^{IV} for Y^{III} would be one possible choice, although it has not been possible to prepare single-phase Ce-doped solids. Nevertheless, PLD syntheses from multiphase $Ce_xY_{1-x}Ba_2Cu_3O_7$ targets yield high-quality single-phase materials. Since T_c is suppressed in the Ce-doped solids, these results indicate that M^{IV} cations may localize or trap

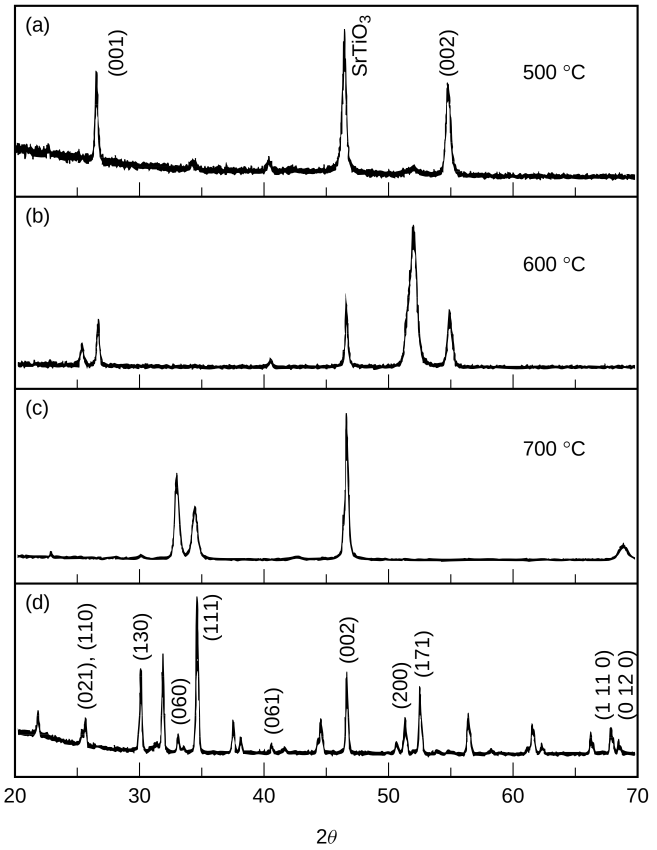

Figure 6 Series of X-ray diffraction patterns recorded on $SrCuO_2$ thin films that were deposited at (a) 500 °C, (b) 600 °C, and (c) 700 °C. The diffraction pattern for orthorhombic $SrCuO_2$ is shown in (d)

carriers in the solid. Similarly, PLD has also been used to synthesize $Pr_{0.5}Ca_{0.5}Ba_2Cu_3O_7$ materials from multiphase targets. Notably, the resulting thin films are single-phase crystalline Pr/Ca solids that exhibit superconductivity. On the basis of the studies of these new materials, which were prepared by PLD, it is apparent that it is the oxidation state of the substituted metal (and not magnetic moment) that is critical to T_c.

4.3 Novel Uses of PLD

As science and technology advances, it becomes increasingly important to integrate different materials with different physical properties into monolithic structures. From the perspective of thin film synthesis, integration requires precise control of the deposition, so that multiple layers can be studied.

One method of meeting this challenge is to use PLD to prepare materials a single layer at a time, so-called layer-by-layer growth.[39–42] To achieve layer-by-layer growth requires careful control of deposition. This can be done by calibrating the rate of thin film growth for ablation of specific targets with controlled laser power densities. Alternatively, growth can be monitored in situ using RHEED.

Kawai and co-workers have used in situ RHEED to synthesize $Bi_2Sr_2CuO_6/Bi_2Sr_2CaCu_2O_8$ superlattices and $Bi_2Sr_2Ca_{n-1}Cu_nO_x$ thin films where n can be as large as 8–10.[39–41] Similar ideas have also been used to carry out band-gap engineering in semiconductor materials. Band-gap engineering is a term coined to describe artificial structures that can be built up atomic layer by atomic layer. For example, Cheung and Shakur have reported the growth of $Hg_{1-x}Cd_xTe$ epitaxial layers with any predetermined composition.[43] The volatility of Hg is a problem in conventional film preparation; however, stoichiometric Hg–Cd–Te thin films can be prepared using low-temperature PLD. These examples of synthesis with atomic layer control represent a unique application of PLD, and suggests that it may be possible to build up very complex architectures in inorganic thin films with novel properties in the future.

5 SUMMARY

In conclusion, this article has introduced the importance of thin films in basic research and technology, and has reviewed thin film synthesis using PLD. From the standpoint of the synthesis of complex and new inorganic materials, PLD can be seen as a simple yet powerful synthetic tool. PLD has many unique features, including congruent target evaporation and low-temperature growth, that make it suitable for thin film preparation. We believe that this technique offers an exciting opportunity for inorganic synthesis in the future.

6 RELATED ARTICLES

Metallic Materials Deposition: Metal-organic Precursors; Oxides: Solid-state Chemistry; Superconductivity.

7 REFERENCES

1. W. Kern and V. S. Ban, ‘Thin Film Processes’, Academic Press, New York, 1978.
2. L. C. Klein, ‘Sol–Gel Technology for Thin Films, Preforms, Electronics and Specialty Shapes’, Noyes, New Jersey, 1989.
3. M. S. Hess and J. F. Milkosky, *J. Appl. Phys.*, 1972, **43**, 4680.
4. J. L. Vossen and W. Kern, ‘Thin Film Processes’, Academic Press, New York, 1978.
5. J. R. Auther, in ‘Critical Reviews of Solid State Science’, D. S. Schuele, and R. W. Hoffman, eds, CRC, Cleveland, OH, 1976.

6. J. Cheung and H. Sankur, *Crit. Rev. Solid State Mater. Sci.*, 1988, **15**, 63.
7. J. Cheung and J. Horwize, *MRS Bull.*, 1992, **2**, 30.
8. D. R. Olander, *High Temp. Sci.*, 1990, **27**, 411.
9. Y. I. Nissim, A. Lietoila, A. Gold, and J. F. Gibbons, *J. Appl. Phys.*, 1980, **51**, 274.
10. G. Koran, A. Gupta, R. J. Baserman, M. I. Lutythe, and R. B. Laibowitz, *Appl. Phys. Lett.*, 1989, **55**, 2450.
11. M. Lax, *J. Appl. Phys. Lett.*, 1977, **48**, 3919.
12. A. Inam, X. D. Wu, T. Venkatesan, S. B. Ogale, C. C. Chang, and D. Dijkkamp, *Appl. Phys. Lett.*, 1987, **51**, 1112.
13. S. R. Foltyn, R. E. Meunchausen, R. C. Estler, E. Peterson, W. B. Hutchinson, K. C. Ott, N. S. Nogar, K. M. Hubbard, in 'Laser Ablation of Materials Synthesis', D. C. Payne, and J. C. Bravman, eds, MRS, Pittsburgh, PA, 1990.
14. J. T. Cheung, *Appl. Phys. Lett.*, 1987, **51**, 1940.
15. A. Namiki, T. Kawai, Y. Yasuda, and T. Nakamura, *Jpn. J. Appl. Phys.*, 1985, **24**, 12, 270.
16. C. H. Chen, T. M. Murphy, and R. C. Phillips, *Appl. Phys. Lett.*, 1990, **57**, 937.
17. L. Weidman and H. Helvajian, *J. Appl. Phys.*, 1991, **70**, 233.
18. D. B. Geohegan and D. N. Mashburn, *Appl. Phys. Lett.*, 1989, **55**, 2345.
19. J. T. Cheung, *Proc. Mater. Res. Soc. Symp.*, 1983, **29**, 301.
20. M. I. Baleva, M. H. Maksimov, S. M. Metev, and M. S. Sendova, *J. Mater. Sci. Lett.*, 1986, **5**, 533.
21. H. Tabata, T. Kawai, S. Kawai, O. Murata, J. Fujioka, and S.-I. Minakata, *Appl. Phys. Lett.*, 1991, **59**, 2354.
22. H. Kidoh, T. Ogawa, A. Morimoto, and T. Shimizu, *Appl. Phys. Lett.*, 1991, **58**, 2910.
23. L. Weidman and H. Helvajian, *J. Appl. Phys.*, 1991, **70**, 253.
24. D. B. Chrisey and A. Inam, *MRS Bull.*, 1992, **2**, 37.
25. C. Zahopoulos, S. Sridhar, J. J. Bautista, G. Ortiz, and M. Lanagon, *Appl. Phys. Lett.*, 1991, **58**, 537.
26. K. Char, M. S. Colorough, S. M. Garrison, M. Newman, and G. Zaharchuk, *Appl. Phys. Lett.*, 1991, **59**, 733.
27. M. Sayer and K. Sreenivas, *Science*, 1990, **247**, 1056.
28. H. Tabata, T. Kawai, S. Kawai, O. Murata, J. Fujioka, and S.-I. Minakata, *Appl. Phys. Lett.*, 1991, **59**, 2354.
29. H. Kidoh, T. Ogawa, A. Morimoto, and T. Shimizu, *Appl. Phys. Lett.*, 1991, **58**, 2910.
30. A. M. Marsh, S. D. Harkness, F. Qian, and K. Singh, *Appl. Phys. Lett.*, 1993, **62**, 952.
31. P. Dorsey, R. Seed, C. Vittoria, D. B. Chrisey, C. Carosella, P. Lubitz, and J. S. Horwitz, *IEEE Trans. Magn.*, 1992, **28**, 3216.
32. C. A. Carosella, D. B. Chrissey, P. Lubitz, J. C. Horwitz, P. Dorsey, R. Seed, and C. Vittoria, *J. Appl. Phys.*, 1992, **71**, 5107.
33. C.-M. Niu and C. M. Lieber, *J. Am. Chem. Soc.*, 1993, **115**, 137.
34. C.-M. Niu and C. M. Lieber, *Appl. Phys. Lett.*, 1992, **61**, 1712.
35. C.-M. Niu and C. M. Lieber, *J. Am. Chem. Soc.*, 1992, **114**, 3570.
36. C. R. Fincher and G. B. Blanchet, *Phys. Rev. Lett.*, 1991, **67**, 2902.
37. D. P. Norton, D. H. Lowndes, B. C. Sales, J. D. Budai, B. C. Chakoumakos, and H. R. Kerchner, *Phys. Rev. Lett.*, 1991, **66**, 1, 537.
38. J. B. Barner, C. T. Rogers, A. Inam, R. Ramesh, and S. Barsey, *Appl. Phys. Lett.*, 1991, **59**, 792.
39. M. Kanai, T. Kawai, and S. Kawai, *Appl. Phys. Lett.*, 1991, **58**, 771.
40. T. Matsumoto, T. Kawai, M. Kanai, and S. Kawai, *Appl. Phys. Lett.*, 1991, **58**, 2039.
41. K. Horiuchi, T. Kawai, M. Kanai, and S. Kawai, *Jpn. J. Appl. Phys.*, 1991, **30**, L1381.
42. M. Y. Chern, A. Gupta, and B. W. Hussey, *Appl. Phys. Lett.*, 1992, **60**, 3045.
43. J. T. Cheung and H. Sankur, in 'Laser Ablation for Materials Synthesis', D. C. Paine and J. C. Bravman, eds, MRS, Pittsburgh, PA, p. 1990.

Tin: Inorganic Chemistry

James L. Wardell
University of Aberdeen, Aberdeen, UK

1 Tin Metal 1
2 Tin(II) Compounds 2
3 Tin(IV) Compounds 8
4 Mixed Tin(II)–Tin(IV) Compounds 10
5 Spectroscopic Studies of Tin Compounds 10
6 Industrial Uses of Tin and Tin Chemicals 12
7 Related Articles 14
8 Further Reading 14
9 References 14

1 TIN METAL[1]

Tin has been used by man for many centuries; it is mentioned in early books of the Old Testament. The alloying of copper with tin was discovered ca. 3500 BC, although the isolation of the pure metal probably dates much later, from 800 BC or so.

The abundance of tin is 2.1 parts per million and it is about the 48th most abundant element. Tin occurs mainly as cassiterite, SnO_2, with other, and minor, ores containing tin sulfides. Reduction of cassiterite is carried out using carbon in a reverberatory furnace at 1200–1300 °C. The major producers of tin are Malaysia, Indonesia, Thailand, Zaire, China, and Bolivia; Brazil, too, is developing its production of tin.

Tin has two allotropes: the stable modification above 13.2 °C is white, tetragonal, β-Sn. Below 13.2 °C, the thermodynamically stable form is gray α-Sn, which has a cubic diamond structure; however, the transformation is very slow and requires long exposure much below this temperature for extensive transformation. The transformation of β-Sn to α-Sn is also termed tin pest or tin disease and involves a structural distortion along the c-axis, with a density increase of 26%, i.e. the high temperature form is the more dense form.

Tin in the α-form, which has the diamond structure, has four nearest neighbours at 2.80 Å with six Sn–Sn–Sn valency angles of 109.5°. The β-form has a structure in which the Sn–Sn–Sn angles are two at 94° and four at 149.5°, with each tin having four neighbours at 3.02 Å and two at 3.18 Å. The transformation between the two allotropes is accompanied by a redistribution of the valency electrons: Mössbauer isomer shifts are 2.10 mm s^{-1} and 2.65 mm s^{-1} for the α- and β-forms, respectively.

Table 1 lists some properties of elemental tin.

Table 1 Properties of Tin

Atomic number	50
Electronic structure:	$[Kr]4d^{10}5s^25p^2$
Atomic weight	118.098
Stable isotope (%)	^{112}Sn (0.95), ^{114}Sn (0.65), ^{115}Sn (0.34) ^{116}Sn (14.24), ^{117}Sn (7.57), ^{118}Sn (24.0) ^{119}Sn (8.58), ^{120}Sn (32.97), ^{122}Sn (4.71) ^{124}Sn (5.98)
Ionization energies (kJ mol^{-1})	708.4, 1411.4, 2942.2, 3929.3
r^{IV} covalent	140.5 pm
r^{IV} (ionic, six-coordinate)	69 pm
r^{II} (ionic, six-coordinate)	118 pm
van der Waal's radii	217 pm
Electronegativity	1.8 (Pauling), 1.7 (Albert–Rochow)
Mp	232 °C
Bp	2623 °C (2270 °C)
Density (at 20 °C)	α-form 5.769 β-form 7.265
Structure	α: cubic, diamond-type [space group: $Fd3m$]: a_0: 649.1 pm nearest neighbors 4 at 2.80, 12 at 4.59 pm β: tetragonal [space group: $I4_1/amd$] a_0: 583.1 pm c_0: 318.1 pm nearest neighbors 4 at 3.02, 4 at 3.18, 4 at 3.77, 8 at 4.41 pm
ΔH_{fusion}	7.07 kJ mol^{-1}
ΔH_{vap}	296 kJ mol^{-1}
Electrical resistivity	α-tin at 20 °C: 12.6 μΩ cm β-tin at 0 °C: 300 μΩ cm
Band gap, E_g	α7.7 kJ mol^{-1} β0

1.1 Reactions of Tin

Tin forms compounds in the +II and +IV oxidation states; in the Sn^{IV} state tin uses all its $5s^25p^2$ valence electrons in bonding, while in the Sn^{II} state normally only the $5p^2$ valence electrons are used.

Potentials for $Sn^0 \rightarrow Sn^{II} \rightarrow Sn^{IV}$ are shown in equations (1) and (2).

$$\text{Acid solution:}\quad Sn \xrightarrow{0.136\,V} Sn^{II} \xrightarrow{-0.15\,V} Sn^{IV} \tag{1}$$

$$\text{Basic solution:}\quad Sn \xrightarrow{0.91\,V} Sn^{II}(OH)_3{}^- \xrightarrow{0.93\,V} [Sn^{IV}(OH)_6]^{2-} \tag{2}$$

The +IV state is more stable than the +II state, but the energy difference between the two states is low. Extensive chemistries for both oxidation states are known.

There are only a few known stable species in the +III oxidation state, e.g. the bulky $\cdot Sn[N(SiMe_3)_2]_3$ has a high kinetic stability; generally compounds in the +III oxidation state are unstable with respect to disproportionation.

Tin, although more reactive than germanium, is inert to water, air, hydrogen, and ammonia at ambient temperatures. However, tin does react with water vapor at temperatures above 700 °C, and reacts with air or oxygen at 200 °C to give SnO_2. Dilute hydrochloric acid and dilute sulfuric acid have little, if any, reaction with tin, but concentrated acids produce $SnCl_2$ and H_2 (from HCl) and $SnSO_4$ and SO_2 (from H_2SO_4). Dilute nitric acid is reported to give $Sn(NO_3)_2$ and NH_4NO_3. As noted by the above, Sn^{II} compounds are significant products in the reaction with these acids.

Tin metal reacts with chlorine and bromine in the cold and with fluorine and iodine on heating to give tin(IV) tetrahalides. Sulfur and selenium react vigorously with tin on heating to give tin(II) or tin(IV) chalcogenides, depending on the mole ratio of the elements used; reaction with tellurium only provides the tin(II) telluride.

Tin dissolves in hot aqueous alkali solutions to give hydroxystannates, $M_2[Sn^{IV}(OH)_6]$.

The reaction of $N(CH_2CH_2OCH_2CH_2OCH_2CH_2)_3N$ (crypt) with alkali metal–tin alloys in $H_2NCH_2CH_2NH_2$ produces[2] such polytin anionic species as $[K(crypt)]_2{}^+[Sn_4]^{2-}$ (tetrahedral tin), $[Na(crypt)]_2{}^+[Sn_5]^{2-}$ (trigonal bipyramidal tin), and $[Na(crypt)]_4{}^+[Sn_9]^{4-}$ (monocapped square antiprismatic tin) (Figure 1). Mixed zintl anions have also been characterized, including $[Sn_2Bi_2]^{2-}$, $[TlSn_9]^{3-}$, and $[TlSn_8]^{3-}$ (*see* ***Zintl Compounds***).

Some bond distances and energies of Sn–X bonds are given in Table 2.

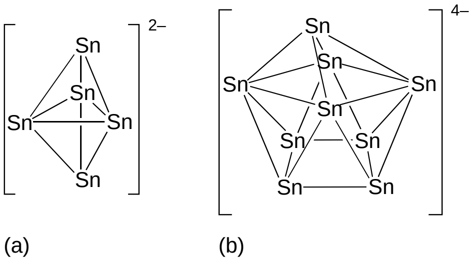

(a) (b)

Figure 1 Two types of metallic tin clusters (a) $[Sn_5]^{2-}$, (b) $[Sn_9]^{4-}$

Table 2 Bond distances and energies[1]

Bond	Bond distance, r(Sn–X) (Å)	Sum of van der Waal's radii (Å)	Bond energies (kJ mol^{-1})
Sn–F	1.97	3.52	–
Sn–H	2.15	3.37	251
Sn–O	2.15	3.57	300 ± 25
Sn–N	2.15	3.67	171
Sn–C	2.15	4.17	201
Sn–Cl	2.39	3.97	315
Sn–S	2.40	4.02	217
Sn–P	2.50	4.07	–
Sn–Br	2.55	4.12	255
Sn–Sn	2.75	4.34	160
Sn–I	2.69	4.32	188

2 TIN(II) COMPOUNDS[3,4]

2.1 General Considerations

Bivalent tin, in its compounds, is rarely found with a spherical symmetry. This is a consequence, in the condensed phases, of a ready distortion of the nonbonding pair of electrons (which are $5s^2$ in the free gaseous ion) due, for example, to the adoption of some p character. The lone pair therefore frequently has stereochemical activity. In addition, the nonbonding pair of electrons in tin(II) species can be used in coordination with acceptors or Lewis acids; furthermore, the empty 5p or d orbitals can be used to interact with donors or Lewis bases.

The simplest structural arrangement for tin(II) compounds is the angular geometric array (Figure 2). The ground state structure calculated for SnH_2 is the angular singlet state ($^1A_1$); the triplet ($^3B_1$) state has a higher energy. The tin(II) halides, SnX_2 (X = F, Cl, or Br), have also been shown to have the angular structure in both the vapor phase and in low-temperature inert matrices. Other SnX_2 compounds having an angular structure are those with extremely bulky ligands, X, e.g. X = $[2,6\text{-}t\text{-}Bu_2\text{-}4\text{-}MeC_6H_2O]$,[5] $(Me_3Si)_2N$,[6] and $2,4,6\text{-}t\text{-}Bu_3C_6H_2S$.[7] Table 3 lists some structural details of compounds having this basic angular geometry.

However, if longer contacts can also be taken into account, different geometries can be assigned, e.g. for $(Me_3Si)_2N$–Sn–NCS in the solid state,[8] as well as the two short Sn–N distances at 2.250(6) and 2.079(5) Å, there are two intermolecular Sn···S contacts at 3.047(2) and 3.316(2) Å. If both the Sn···S distances are considered to be significant,

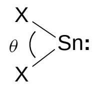

Figure 2 The angle (θ) formed between the substituents in divalent tin compounds

Table 3 Structural data for angular geometric Sn^{II} compounds[4]

Compound	M–X (Å)	X–M–X, θ (°)	Method
SnH_2 ($^1A_1$)	1.756	92.7	Calculation
SnH_2 ($^3B_1$)	1.707, 1.77	118.2, 93	Calculation
SnF_2	–	94(5)	ED
$SnCl_2$	2.347(7)	99(1)	ED
$SnBr_2$	2.55(2)	95	ED
$Sn[N(SiMe_3)_2]_2$	2.096(1), 2.088(6)	104.7(2)	X-ray
	2.09(1)	96	ED
$(SCN)SnN(SiMe_3)_2$	2.079(5), 2.250(6)	94.1(2)	X-ray
$Sn(OC_6H_2Me\text{-}4\text{-}t\text{-}Bu_2\text{-}2,6)_2$	1.995(4), 2.002(4)	88.8(2)	X-ray
$Sn(SC_6H_2\text{-}t\text{-}Bu_3\text{-}2,4,6)_2$	2.435(1)	85.4(1)	X-ray

then a pseudotrigonal bipyramidal geometry, with the tin nonbonding pair in an equatorial site, is realized.

It is generally found that bivalent tin compounds, wherever possible, adopt structures, by means such as bridging, chelation, and coordination, in which tin attains coordination numbers greater than two. Some basic structures found for tin(II) compounds having these higher coordination numbers are given in Table 4.[4] A frequently found tin(II) environment has a trigonal pyramidal arrangement of three short Sn–X distances coupled with three much longer Sn–X contacts, at or near the limits for bonding. The longer interactions can be considered to be a consequence of the hindrance by the nonbonding electron pair to the approach of ligands towards tin. If all six contacts are taken into account, the overall geometry can be deemed to be octahedral or, preferably, distorted octahedral.[3] An example of this structural arrangement is that shown by tin(II) sulfate,[9] in which there are three Sn–O bonds between 2.25 and 2.27 Å and three Sn–O contacts between 2.92 and 2.99 Å. Other compounds having this type of structure are $[NH_4]_2[Sn(O_2POH)_2]$[10] and $K[Sn(O_2CCH{=}CHCO_2)(O_2CCH{=}CHCO_2H)]$[11] (Figure 3).

Despite its bulky ligands, $[(Me_3Si)_3Si]_2(Sn(\mu\text{-}Cl)Li(THF)_3]$ (**1**), obtained from $SnCl_2$ and $LiSi(SiMe_3)_3$, has a three-coordinate tin atom with a bridging chloride ion.[12]

As stated earlier, and as shown in Table 3, very bulky tin(II) amides, $Sn(NR)_2$, alkoxides and aryloxides, $Sn(OR)_2$, and thiolates, $Sn(SR)_2$, can exist as monomeric angular-shaped species, even in the condensed phases. With less bulky groups, there is a strong tendency to form oligomers, e.g. dimers and trimers such as (**2**)–(**4**), and even polymeric species for compounds with small ligands, e.g. $[Sn(OR)_2]_n$ (R = Me or Et). Compounds (**2**)[13] and (**3**)[14] in the solid state have tin atoms with trigonal pyramidal geometries, while in (**4**)[4] the geometry of the terminal atoms is also trigonal (ignoring the lone pair). The geometry of the central tin atom in (**4**) can be considered to be pseudotrigonal bipyramidal with an equatorial lone pair.

Table 4 Basic structures of Tin(II) compounds having coordination numbers greater than two[4]

Three-coordinate Sn
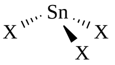
Pyramidal, e.g. SnS, SnO_4, orthorhombic SnSe
Four-coordinate Sn
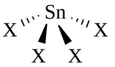
Pseudotrigonal pyramidal, e.g. $Sn(O_2CH_2)$, $[SnCl_4]^{2-}$, $Sn(S_2COMe)_2$
Five-coordinate Sn
tris(pyrazolyl)boratotin
Six-coordinate Sn
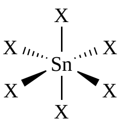
Octahedral, including distorted octahedral, e.g. cubic SnSe, SnTe
Nine-coordinate Sn
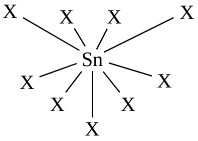
Facially-capped trigonal prismatic, e.g. $Sn(NCS)_2$, $[Sn(SbF_6)_2][AsF_3]_2$, $SnCl_2$ (solid state), $SnBr_2$ (solid state)

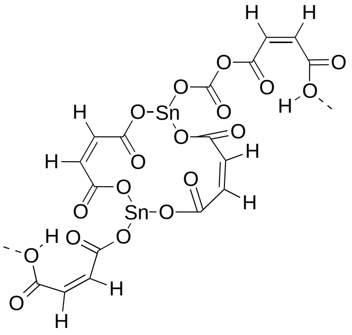

Figure 3 The trigonal pyramidal Sn environments with the three short Sn–O contacts shown

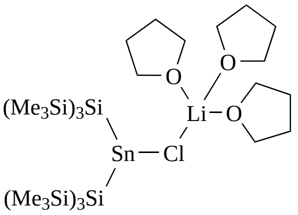

(**1**)

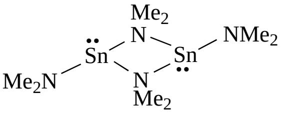

(**2**) d(Sn–N) = 2.07, 2.67, and 2.67 Å
next Sn..N = 2.98 Å

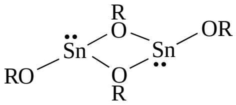

(**3**) R = t-Bu or Me_3Si

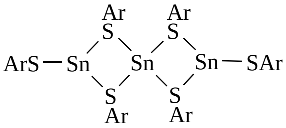

(**4**) Ar = 2,6-i-$Pr_2C_6H_3$

The compound $t\text{-Bu}\overline{\text{NSiMe}_2\text{N-}t\text{-BuSn}}$ (**5**) exists in the solid state both as a monomer (**5a**) and a dimer (**5b**); in the gas phase and in benzene solution (**5**) is monomeric.[15] The chloroamides (**6**) and (**7**) are dimeric in the solid state due to chloride bridging; of interest, (**6**) is a *trans* dimer in the

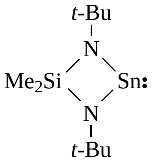

(**5a**)

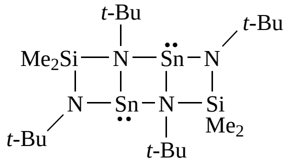

(**5b**)

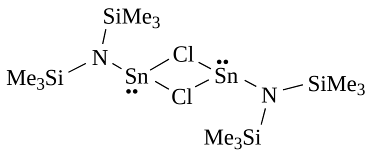

(**6**)

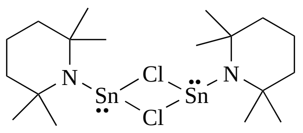

(**7**)

solid state, while (**7**) is a *cis* dimer.[16] In toluene solution, (**7**) undergoes *cis–trans* isomerization.

Also dimeric in the solid state is the series of compounds $[Sn(O\text{-}t\text{-}Bu)X]_2$ (X = Cl, O-*t*-Bu, and $N(SiMe_3)_2$); for this series of compounds, bridging is via the *t*-butoxy group.[17]

Bis(bis-*t*-butylphosphino)tin(II), obtained[18] from KP-*t*-Bu_2 and $SnCl_2$ (2:1 mole ratio), has been reported to be dimeric in benzene solution. The complexes $[LiSn(P\text{-}t\text{-}Bu_2)_3{\cdot}THF]$ (**8**), obtained[19] from LiP-*t*-Bu_2 and $SnCl_2$ (3:1 mole ratio), and $[Ph_4As][Sn(EPh)_3]$ (**9**; E = S or Se)[20] all have three-coordinate trigonal pyramidal tin atoms in the solid state.

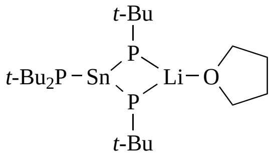

(**8**) *d*(Sn–P) = 2.671–2.814 Å
δ^{119}Sn = −1310 ppm

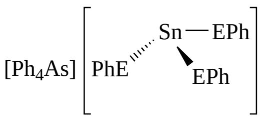

(**9**)
E = S, *d*(Sn–S) = 2.522–2.552 Å
δ^{119}Sn = 146 ppm
E = Se, *d*(Sn–Se) = 2.649–2.671 Å
angle Se–Sn–Se = 88.7–97.3°
δ^{119}Sn = 208 ppm

Monomeric, dimeric, and polymeric metal tin tris(*t*-butoxides) $[M(O\text{-}t\text{-}Bu)_3Sn]$ (**10**; M = In) and (**11**; M = Tl), $[M(O\text{-}t\text{-}Bu)_3Sn]_2$ (**12**; M = Li or Na), and $[M(O\text{-}t\text{-}Bu)_3Sn]_n$ (M = K, Rb, or Cl)[21,22] all contain three-coordinate trigonal bipyramidal tin, e.g. (**12**; M = Na). The indium (**10**) and thallium (**11**) complexes undergo[22] interesting regioselective complexations on reaction with $M(CO)_6$ (M = Cr or Mo); the favored site for coordination in the indium compound (**10**) is at indium, to give (**13**), in contrast to the tin site in the thallium complex (**11**). As shown in Scheme 1, additional complexation of (**13**) can occur at the Sn site; structural isomers of (**14**) have been obtained, e.g. (**14**; M = Mo, M′ = Cr) and (**14**; M = Cr; M′ = Mo). The four metals in (**14**) form a near linear arrangement.

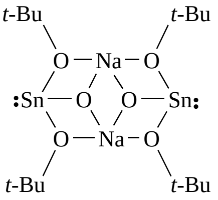

(**12**) M = Na

Tin(II) can act as a donor.[4] Complexation of various divalent tin compounds by Lewis acids has been realized, many in transition metal complexes, e.g. (**15**) and (**16**), but also with main group Lewis acids, e.g. (**16**).

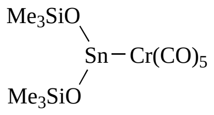

(**15**)

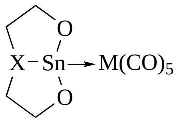

(**16**) M = Cr, Mo, or W;
X = *t*-BuN, PhO, O, or SO

Bivalent tin compounds can act both as donors and as acceptors in the same molecule, as in $F_3B \leftarrow SnX_2 \leftarrow NMe_3$ (X = Cl, Br).[23] The acceptor–donor complex (**17**) was obtained on treatment of the tin–nitrogen cage compound (**18**) with Al_2Cl_6; (**18**) was produced from (**5**) and *t*-Bu_2NH (equation 3). Various other tin–nitrogen cages have been characterized, e.g. (**19**)–(**22**).[24–26]

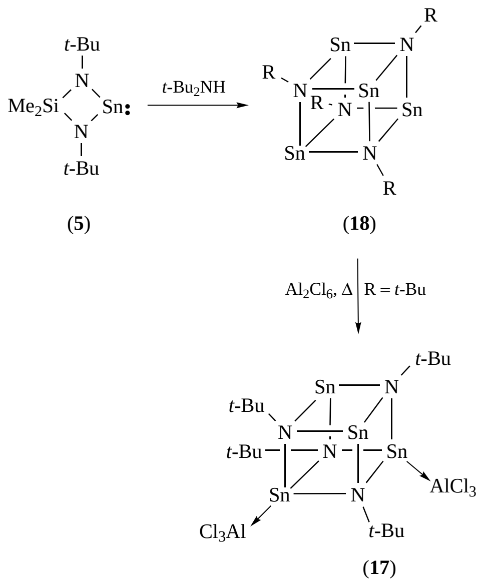

(3)

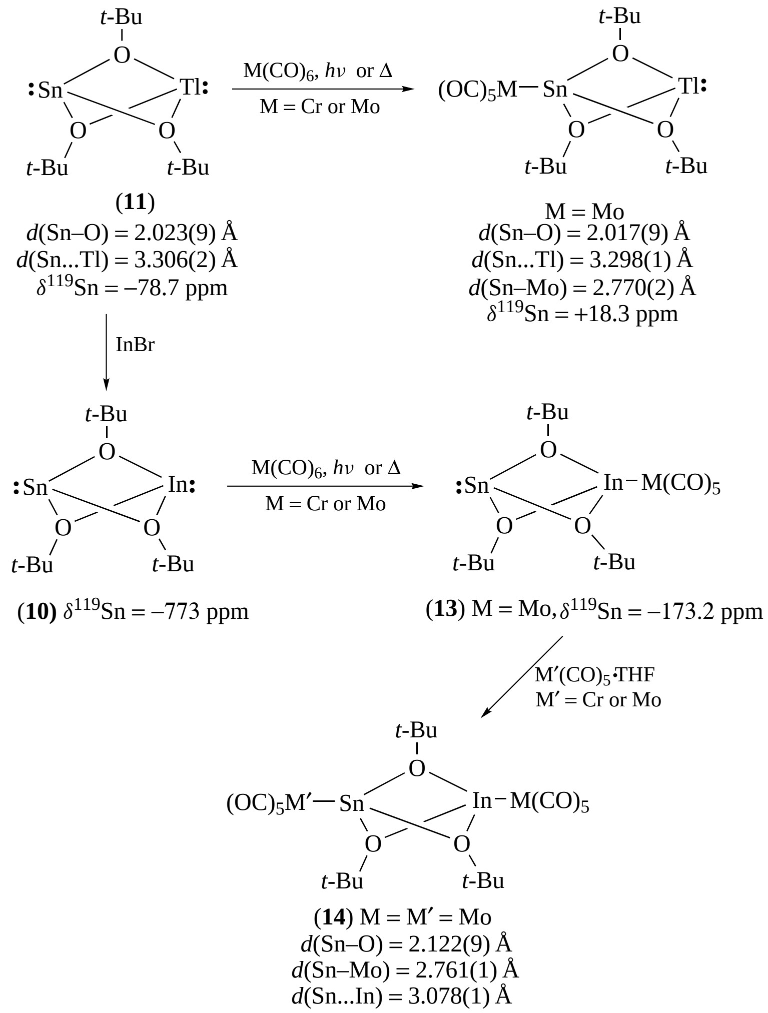
t-Bu
:Sn
Tl:
O
t-Bu
t-Bu
M(CO)6, hν or Δ
M = Cr or Mo
(OC)5M—Sn
(11)
d(Sn–O) = 2.023(9) Å
d(Sn...Tl) = 3.306(2) Å
δ119Sn = −78.7 ppm
M = Mo
d(Sn–O) = 2.017(9) Å
d(Sn...Tl) = 3.298(1) Å
d(Sn–Mo) = 2.770(2) Å
δ119Sn = +18.3 ppm
InBr
:Sn
In:
In−M(CO)5
(10) δ119Sn = −773 ppm
(13) M = Mo, δ119Sn = −173.2 ppm
M′(CO)5·THF
M′ = Cr or Mo
(OC)5M′—Sn
(14) M = M′ = Mo
d(Sn–O) = 2.122(9) Å
d(Sn–Mo) = 2.761(1) Å
d(Sn...In) = 3.078(1) Å

Scheme 1

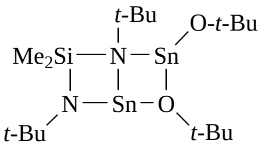
t-Bu
O-t-Bu
Me2Si
N
Sn
Sn
O
t-Bu
t-Bu

(**19**)

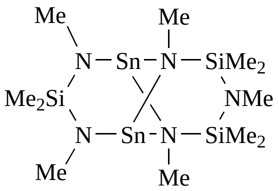
Me
Me
N
Sn
N
SiMe2
Me2Si
NMe
Sn
SiMe2
Me
Me

(**20**)

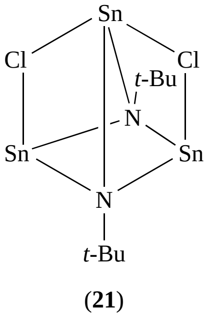
Sn
Cl
Cl
t-Bu
N
Sn
Sn
N
t-Bu

(**21**)

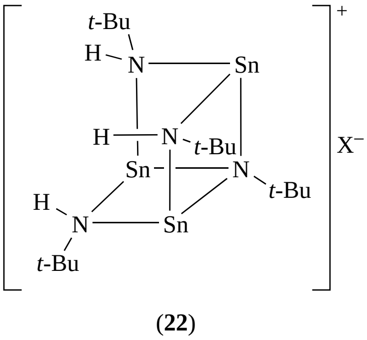
t-Bu
H
N
Sn
H
N
t-Bu
Sn
N
t-Bu
H
N
Sn
t-Bu
+
X−

(**22**)

The coordination number at tin can be expanded on chelation, as shown for example in $Sn(S_2COMe)_2$ (**23**),[27] in bis(ethyl cysteinato)tin(II) (**24**),[28] and in the β-diketonato complexes (**25**);[29] compounds (**23**)–(**25**) have pseudotrigonal pyramidal tin atoms, with equatorial lone pairs. Combinations of coordination and chelation, e.g. in (**26**)[30] and (**16**), and chelating and bridging, e.g. in (**27**),[31] further expand the coordination number.

Another common tin geometry in bivalent tin compounds is a distorted four-coordinate pyramidal arrangement; in this array there are two shorter and two longer bonds, e.g. as in sodium bisoxalatostannate(II) $Na_2Sn(C_2O_4)_2$ (**28**)[32] and in $Sn(O_2PH_2)_2$ (two Sn–O at 2.16 Å and two Sn–O at 2.35 Å, with next nearest neighbor at 3.36 Å; O–Sn–O from 79.0 to 151.4°).[3]

Although the majority of bivalent tin(II) compounds contain tin with a lone pair distorted geometry, some

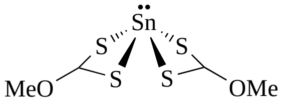

(**23**)

d(Sn–S) = 2.603(3), 2.644(3) Å
equatorial
2.813(3), 2.801(4) Å
axial

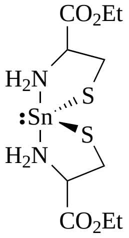

(**24**)

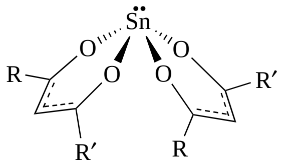

(**25**)

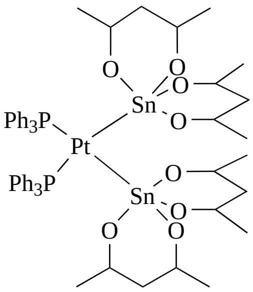

(**26**)

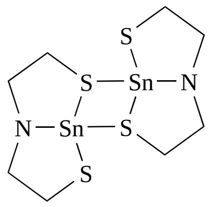

(**27**)

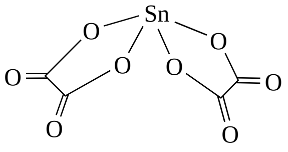

(**28**)

Sn−O = 2.357, 2.357, 2.246, 2.246 Å
angle O−Sn−O = 71.5–45.5°

highly symmetric octahedral tin(II) geometries have been found in some compounds, e.g. black $CsSnBr_3$, which has a perovskite lattice,[33] and in the high temperature form of $CsSnCl_3$.[34] In these compounds the high symmetry results from delocalization of the nonbonding electrons into solid-state bands. Tin(II) compounds having higher symmetry geometries have unusual optical and electrical solid-state properties, e.g. $CsSnBr_3$ is an electrical conductor and exhibits photoemission effects. Greatest distortion from symmetric tin(II) environments are realized for compounds with bonds to the lighter elements (e.g. N, O, and F).[3]

A rationale for the bonding in high symmetry bivalent tin(II) compounds is based on the energy levels of ligand (X) and Sn orbitals[3] (Figure 4). For $[SnX_3]^-$ (X = halide) it was argued that the stereochemical activity of the tin lone pair depends on the directional tin $5p_z$ orbital character in the nonbonding tin lone pair orbital. In order to form a strong a_1 bond, the tin 5s and $5p_z$ orbitals mix to give a hybrid orbital of a similar energy to that of the halogen np orbital. Thus for bonding to F the tin a_1 bonding orbital is rich in 5s character, but for I it is rich in $5p_z$ character. Hence the lone pair orbital in $[SnF_3]^-$ has a high $5p_z$ (i.e. directional) component and in $[SnI_3]^-$ it has a high 5s (i.e. nondirectional) component. The increase in the 5s character of the nonbonding pair on tin, from fluoride to iodide, results in more symmetric and less distorted structures. Further reduction in distortion can result from population of empty delocalized bonds in the solids by the nonbonding electron pair. For perovskite $CsSnBr_3$ a delocalized band system arises from the overlap of empty bromide t_2 4d-orbitals; on population of this solid-state band by the tin nonbonding electrons the distortive consequences of the nonbonding orbital are reduced.

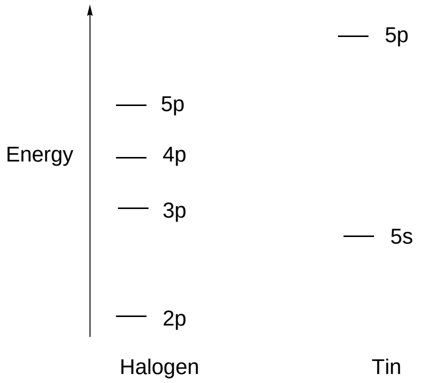

Figure 4 Relative binding energies of tin 5s and 5p and halogen np orbitals

Of interest, black $CsSn^{II}Br_3$ has a similar structure to white $Cs_2Sn^{IV}Br_6$, but $Cs_2Sn^{IV}Br_6$ has none of the optical/electric properties of $CsSnBr_3$. It has been argued that $Cs_2Sn^{IV}Br_6$ has a similar low-energy band to that of $CsSnBr_3$ but, unlike in $CsSnBr_3$, there are no high-energy nonbonding electrons present to populate the empty band.

The high symmetry Sn^{II} solid-state environment is only found in those compounds in which the distorting effect of the lone pair orbitals is reduced by allowing the electrons to populate a low-energy delocalized solid-state band in the structure. Tetragonal tin(II) oxide has short Sn–Sn contacts and in this compound the lone pair orbitals in tin can be used to populate the solid-state band, formed by overlap of the tin empty d-orbitals.

The nonbonding electrons on tin can also be delocalized into cluster molecules such as $K_3Sn_2(SO_4)_3Br$, which has a 3D network structure[35] of tin atoms and bridging sulfates, and also $Cs_2Sn_6Br_3F_{11}$, obtained from CsBr and SnF_2 (1:2 mole ratio).[36] There are three distinct tin sites in $Cs_2Sn_6Br_3F_{11}$, with strong tin bonding only to fluoride; each site has one short and one long Sn–F bond with additional bonding patterns being made up from Sn–F and cluster interactions involving Br atoms.

2.2 Solution Studies of Tin(II) Compounds

Bivalent tin species in acid solutions are frequently of the pyramidal $[SnX_3]^-$ type, (e.g. X = halide, pseudohalide, or carboxylate group). Increases in the coordination number beyond three are not normally realized. The $[SnF_3]^-$ ion is the stable and dominant ion in solutions containing excess F^-; however, when insufficient F^- is present, species such as $[F_2Sn(\mu\text{-}F)SnF_2]^-$ result.

The major species in alkaline solutions is $[Sn(OH)_3]^-$; however, $[(HO)_2Sn(\mu\text{-}O)Sn(OH)_2]^{2-}$ has also been detected. At high pH the dominant species is $[Sn_3(OH)_4]^-$.

Several bivalent tin compounds have appreciable water solubilities, e.g. the solubility of tin(II) chloride is 83.9 g in 100 mL at 0 °C, that of tin(II) fluoride is 4.1 g in 100 mL at 25 °C, and of tin(II) sulfate is 35.2 g in 100 mL at 10 °C. Aqueous solutions are susceptible to hydrolysis to hydrous tin(II) oxide and oxidation to Sn^{IV} species; the stability of aqueous solutions depends upon the anions present and the pH. The presence of anions that are able to form strong complexes with Sn^{II}, e.g. F^- or OAc^-, enhances resistance to hydrolysis and oxidation. Ease of hydrolysis increases with pH; at very high pH, disproportionation of Sn^{II} to Sn^0 and Sn^{IV} results.

Certain bivalent tin salts have solubilities in nonaqueous solvents, e.g. tin(II) chloride is soluble in many organic solvents, including alcohols, acetone, THF, and pyridine, probably to give rise to three-coordinate pyramidal $[SnCl_2{\cdot}L]$-type complexes. Other selected solubilities are $SnBr_2$ in methanol, pyridine, or THF and tin(II) formate in $HO(CH_2)_3OH$. Bivalent tin species are also soluble in acetonitrile solution, to give $[Sn(MeCN)_n]^{2+}$ (n = 2, 3, or 6), and in liquid ammonia, to give $[Sn(NH_2)_3]^-$.

2.3 Tin(II) Halide Species in the Solid State

In both the orthorhombic and monoclinic forms of tin(II) fluoride, the basic structural unit is the $[SnF_3]$ trigonal pyramid; additional fluoride bridging leads to pseudotrigonal, bipyramidal, and distorted octahedral tin geometries, respectively. Discrete $[SnF_3]^-$ anions are found in $[NH_4][SnF_3]$; however, in general the strong tendency for fluorine bridging is realized, e.g. in $Na[Sn_2F_5]$ (**29**), $Na_4[Sn_3F_{10}]$ (**30**) (both obtained from NaF and SnF_2 in aqueous solution), and $K[SnF_3]{\cdot}0.5H_2O$ (**31**).**4**

Various mixed halofluorotin(II) species, e.g. Sn_2F_3Cl, Sn_3F_5Br, Sn_2F_3I, and $[Sn_5F_9]BF_4$, contain pyramidal $[SnF_3]$ or distorted pyramidal $[SnF_4]$ units. Additional halide or BF_4 ions occupy holes in the network. Compounds [SnFCl] and [SnF(NCS)] have ribbon-like structures, with tin in pseudotrigonal bipyramidal sites (e.g. **32**).

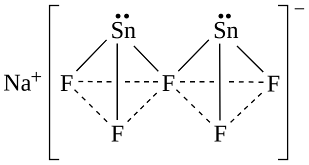

(**29**) Corner-sharing pyramids

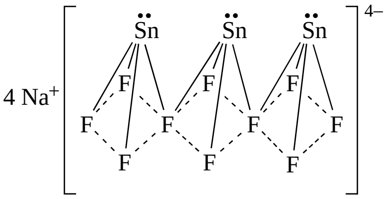

(**30**) Edge-sharing square pyramids

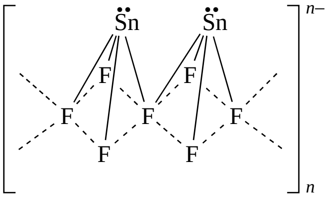

(**31**) Anionic arrangement in (**30**)

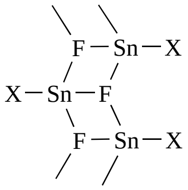

(**32**) X = Cl or NCS

Tin(II) chloride (mp 246 °C) and tin(II) bromide (mp 216 °C) have the $PbCl_2$-type lattice. In this, tin has nine halide neighbors from three different layers, six at the apexes of a trigonal prism and three in facially capped positions; only three of the tin halide interactions are weak.**37**

Tin(II) iodide (mp 316 °C) (from Sn and I_2 in 2 M hydrochloric acid) has a unique layered structure: tin(II) atoms are in two sites. Two-thirds of the tin atoms are in sites based on the $PbCl_2$-type structure, while the remainder are in $PdCl_2$-type chains, which interlock with the $PbCl_2$-type part of the structure to give almost perfect octahedral coordination.**38**

Many complexes of the types $SnX_2{\cdot}L$ and $SnX_2{\cdot}2L$ have been investigated.**4** The basic unit of crystalline $[SnCl_2{\cdot}2L]$ ($L = H_2O$ or $S{=}C(NH_2)_2$) is a pyramidal $[SnCl_2L]$ unit, which is tightly bound into 3D structures by hydrogen bonding and/or chloride and sulfur bridging. The structure of polymeric $[SnCl_2{\cdot}1,4\text{-dioxane}]_n$ consists of angular $[SnCl_2]$ units bridged by dioxane ligands to produce pseudotrigonal bipyramidal tin. Different structures arise with $SnCl_2 \cdot L$ (L = phen, bipy); in these chain complexes the tin atoms are chelated by the ligand, L, and have two strong and two weak interactions with chlorine.

The tin(II) bromide hydrates $[(SnBr_2)_2 \cdot H_2O]$, $[(SnBr_2)_3 \cdot H_2O]$, and $[(SnBr_2)_6 \cdot 5H_2O]$ all have structures based on trigonal prismatic geometry, in which the tin atom is surrounded by a trigonal prism of six bromine atoms and further bromines and water (or vacancies) at the facially capped sites.**[4]**

Discrete isolated $[SnCl_3]^-$ anions occur in $[Co(en)_3][SnCl_3][Cl]_2$. The $[SnCl_4]$ ion in $[Co(NH_3)_6][SnCl_4][Cl]$ has a pseudotrigonal bipyramidal geometry. No interaction occurs between $[SnCl_3]^-$ and $[Cl]^-$ in this complex, unlike the situation in $[NH_4]_2[SnCl_3][Cl] \cdot H_2O$, which has a highly distorted octahedral tin atom. A similar tin environment is found in the low-temperature form of $CsSnCl_3$, i.e. three long and three short Sn–Cl bonds; in contrast, the high-temperature form has a cubic perovskite structure, in which tin has an ideal cubic geometry. Tin also has a regular octahedral geometry in $[MeNH_3][SnBr_xI_{3-x}]$ ($x = 0$–3) and in $CsSnI_3$ compounds.

2.4 Tin(II) Chalcogenide Derivatives[4]

Tin(II) oxide exists in several modifications. The commonest is blue-black tetragonal tin(II) oxide, formed by alkaline hydrolysis of a tin(II) salt; it has a layer lattice with square pyramidal coordination at tin and equal Sn–O distances (Sn$\cdots$Sn distances between Sn atoms in adjacent layers are 3.70 Å, close to the values in β-Sn). Tin(II) oxide is amphoteric and dissolves in aqueous acid and alkalies. Tin(II) hydroxide, $Sn(OH)_2$, has been obtained from Me_3SnOH and $SnCl_2$. Tin(II) sulfide has a structure with parallel zig-zag – Sn–S– chains, which are connected by short interchain Sn$\cdots$S contacts; this gives a basic pyramidal $[SnS_3]$ unit. Tin(II) selenide (mp 861 °C) exhibits one phase which is isomorphous with SnS and a second cubic phase with the NaCl lattice; the latter is also taken up by tin(II) telluride.

$Sn_3(PO_4)_2$ and other phosphates, e.g. $Sn[O_2PO(OH)]$, $Sn[OPO(OH)_2]_2$, $Sn_2P_2O_7$, and $Sn(PO_3)_2$, have been reported. The structure of tin(II) sulfate, from tin and aqueous $CuSO_4$, consists of $[SO_4]$ groups linked into a framework of O–Sn–O bonds, and as pointed out in Section X.X, tin has three short oxygen contacts and three longer oxygen contacts.

Hydrolysis of tin(II) salts yields various oxotin ions; these species have similar structures, e.g. $Na_2[Sn_2O(OH)_4]$, which contains the $[Sn(OH)_3]^-$ unit, $Na_4[Sn_4O(OH)_{10}]$, which contains the oxo-bridged $[(HO)_2SnOSn(OH)_2]^{2-}$ anion, and $Ba[SnO(OH)]_2$, which contains the one-dimensional $[SnO(OH)]_\infty^{\infty-}$ polyanion.**[39]** These three oxotin species all have pyramidal coordination at tin.

The discrete cation in $[Sn_3O(OH)_2][SO_4]$ contains one tin atom with a pyramidal geometry and two in distorted square pyramidal (four-coordinate) geometry.**[40]** The hydrate $3SnO \cdot H_2O$ has an adamantane-like $[Sn_6O_8]$ structure, similar to that found in $[Sn_6O_4(OMe)_4]$; the latter compound was obtained by the controlled hydrolyses of $Sn(OMe)_2$. The tin atoms in $[Sn_6O_4(OMe)_4]$ have a distorted pseudotrigonal bipyramidal geometry.**[41]**

The basic salt $[Sn_3(OH)_4(NO_3)_2]$ has been obtained from hydrous SnO and aqueous HNO_3; anhydrous $Sn(NO_3)_2$ is unknown.

2.5 Other Reactions of Tin(II) Compounds

Inorganic tin(II) compounds can form tetravalent tin compounds on oxidative addition (equation 4).**[7]** UV irradiation of bivalent tin(II) can provide Sn ^{III} radical species (equation 5).**[7]** Other typical reactions of bivalent tin include substitutions. Examples are shown in Scheme 2.**[7]**

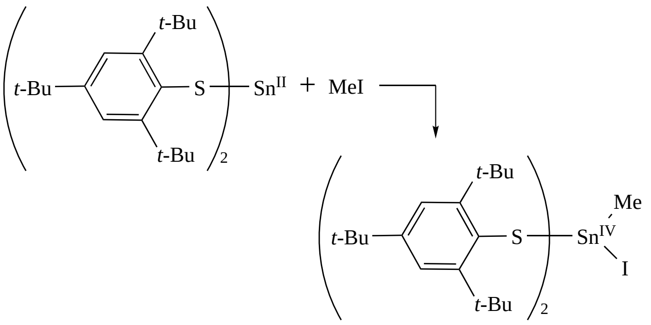

(4)

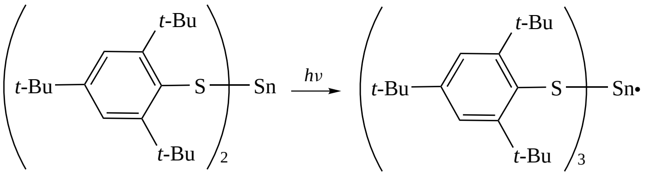

(5)

3 TIN(IV) COMPOUNDS[3]

Tin(IV) oxide is amphoteric and dissolves in aqueous acids or alkali solutions. The predominant tin species in appropriate acid solutions are of the type $[SnX_6]^{2-}$, where X = halide or pseudohalide, and also mixed anions $[SnX_nX'_{6-n}]^{2-}$ (e.g. X, X′ = halides or pseudohalides).

The main species in highly basic solutions is $[Sn(OH)_6]^{2-}$; in less basic solutions $[SnO_3]^{2-}$ is obtained. Tin(IV) sulfide is soluble in aqueous alkaline media, containing sulfide ion, to give $[SnS_3]^{2-}$. All tin(IV) species in aqueous solutions tend to undergo hydrolysis, e.g. to hydrous tin(IV) oxide.

Several tin(IV) compounds are soluble in organic solvents, e.g. $SnCl_4$ and $SnBr_4$ dissolve in acetone, pyridine, and benzene. Compounds such as $SnX_4 \cdot 2L$ can be obtained. Tin(IV) tetraiodide is soluble in chlorocarbon solvents,

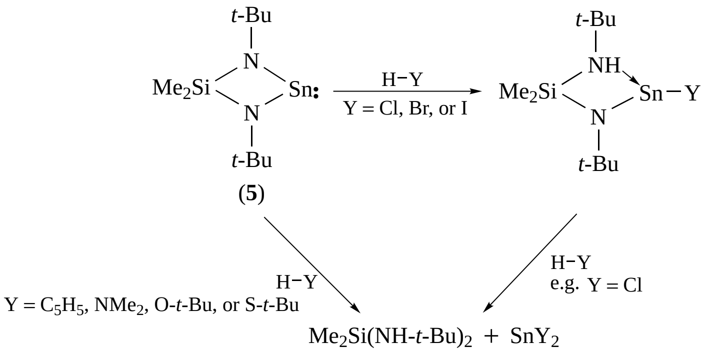

Scheme 2

hydrocarbons, and ethers. In liquid ammonia, $[Sn(NH_2)_6]^{2-}$ is obtained.

3.1 General Structures in Tin(IV) Chemistry

Basic structural types for inorganic tin(IV) compounds are given in Table 5; the most common higher coordination numbers are five and six. Thermally unstable, tin(IV) hydride (mp −146 °C), available from $SnCl_4$ and $LiAlH_4$, has tetrahedral geometry. Tin(IV) halides are also tetrahedral in the vapor and liquid phases. However, in the solid state, $SnBr_4$ (mp 31 °C) and SnI_4 (mp 144 °C) have hexagonally close-packed halogen atoms with tin occupying one-eighth of the tetrahedral holes; the tin atoms have distorted tetrahedral environments. Tin(IV) fluoride (which sublimes at 705 °C) forms a very strongly bridged, two-dimensional sheet polymer with octahedrally coordinated tin.

Tin(IV) tetrahalides are Lewis acids and readily form complexes with Lewis bases as well as halide ions (e.g. octahedral M_2SnX_6). The acceptor strength of SnX_4 decreases in the sequence F > Cl > Br > I.

Octahedral tin complexes, $SnX_4{\cdot}2L$, generally have a *cis* geometry; a few *trans* complexes are known for L = N-donors (amines, pyridines, or nitriles), P-donors (triorganophosphines), O-donors (carboxylic acids, carbonyl compounds, alcohols, esters, phosphine oxides, or sulfoxides), and S-donors (thiourea or alkyl sulfides), arsines, stibines, etc. Some five-coordinate tin complexes $SnX_4{\cdot}L$, e.g. $[SnF_4{\cdot}THF]$, $[SnBr_4{\cdot}NMe_3]$ or $[SnCl_4{\cdot}PPh_3]$, are known.

3.2 Chalcogenides[4]

Tin(IV) oxide has a rutile structure, i.e. tin has an almost perfect octahedral geometry.[42] Tin(IV) sulfide and selenide also contain six-coordinate tin, but have the hexagonal CdI_2 layer lattice.[43]

Octahedral coordinated tin is also found in $M_2Sn(OH)_6$ (M = Na or K) and in $MSn(OH)_6$ (M = Mg, Ca, Cu, Zn,

Table 5 Coordination Geometries for inorganic tin(IV) compounds

Coordination type	Coordination number	Examples
Trigonal[43]	3	$[SnE_3]^{2-}$ (E = Se or Te)
Tetrahedral[44]	4	K_4SnO_4 SnH_4
Trigonal bipyramid[45]	5	$[SnCl_5]^-$
Square pyramidal[46]	5	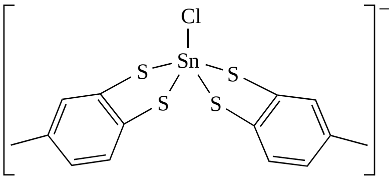
Octahedral[47–50]	6	SnO_2 $CaSnO_3$ $[SnX_6]^{2-}$ $SnCl_4{\cdot}2MeCN$
Dodecahedral[51,52]	8	$Sn(ONO_2)_4$ $Sn(O_2CMe)_4$

Cd, Fe, etc.); for M^{2+} having a radius less than 126 pm the structures are of the NaCl type; for M^{2+} having a radius greater than 126 pm the structures are hexagonal. Metal stannates, $MSnO_3$, produced by heating $MSn(OH)_6$ above 500 °C, have either an ilmenite-type structure (for M^{2+} radius $<$109 pm) or a perovskite structure (for M^{2+} radius $>$126 pm).[4]

In contrast to K_4SnO_4, which contains isolated $[SnO_4]$ tetrahedra, M_2SnO_4 (M = alkaline earth metal, Cd, Zn, Mn, or Co) contain $[SnO_6]$ octahedra, which share common edges to give chain or layer structures. The tin atom in $CaSnSiO_5$ has a tetragonally distorted geometry with two short axial and four long equatorial bonds. Compounds $M_2Sn_2O_7$ (M = Bi or lanthanide element) also contain octahedral tin. Potassium and rubidium metastannates (but not the lithium salt) contain square pyramidal five-coordinated tin atoms.[4]

The orthostannate anions $[SnX_4]^{4-}$ (X = S, Se, or Te) contain tetrahedral tin, while $[SnX_3]^{2-}$ contain trigonal planar tin. The salts $Na[Sn_2S_7]$ and $Na_4[Sn_2S_6]\cdot 14H_2O$ contain anions which are formed by vertex- and edge-sharing of $[SnS_4]$ tetrahedra; in $Eu_2Sn_2S_5$ there are two distinct tetrahedral tin sites. In contrast, $[Sn_2Te_6]^{6-}$ contains a Sn–Sn bond (Figure 5).

Complexed Sn–O-bonded compounds can have ladder,[44,45] e.g. $[SnCl_3(OH)\cdot H_2O]_2\cdot 4H_2O$ and $[Sn_3O_2Cl_4(ClO_4)_4]_2$, and cluster, e.g. $[Sn_2(O_2CC_6H_4NO_2\text{-}o)_4O\cdot THF]_2$, structures;[46] such compounds have Sn_2O_2 cores.

Tin tetracarboxylates, e.g. $Sn(O_2CCMe)_4$, are known;[47] $Sn(O_2CCMe)_4$ can be produced from SnI_4 and Ac_2O or from $(CH_2{=}CH)_4Sn$ and AcOH. Tin(IV) nitrate,[48] $Sn(ONO_2)_4$, prepared from N_2O_5 and $SnCl_4$, contains bidentate anions; it forms the adduct $Sn(ONO_2)_4\cdot 2py$, which has monodentate anions. Tin(IV) phosphates, e.g. SnP_2O_7 and $KSn_2(PO_4)_3$, are known, as is tin(IV) hypophosphite. Sulfates, $Sn(SO_4)_4\cdot 2H_2O$, $K_2Sn(SO_4)_3$, and $CaSn(SO_4)_3\cdot 3H_2O$, have also been prepared.

4 MIXED TIN(II)–TIN(IV) COMPOUNDS[3,4]

A number of mixed tin(II)–tin(IV) valency compounds are known. One example is the semiconductor Sn_2S_3, obtained from appropriate ratios of the elements at 720 °C. This compound has a polymeric lattice with octahedral Sn^{IV} [d(Sn–S) ranging from 2.46 to 2.60 Å] and trigonal bipyramidal Sn^{II} [d(Sn–S) from 2.65 to 2.77 Å].[49] Another mixed Sn^{II}/Sn^{IV} sulfide, $Sn_4^{II}\ Sn^{IV}Sb^{III}S_9$, has $[Sn^{IV}S_6]$ octahedral linked via $[(Sn^{II},Sb^{III})S_8]$ dodecahedra.[50]

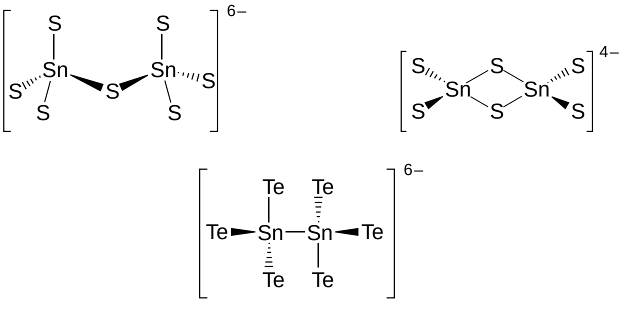

Figure 5 Examples of tin chalcogenides

The compound $[Sn_3F_8]$, i.e. $[(SnF)_2SnF_6]$, formed by oxidation in HF of SnF_2 by O_2, F_2, or even SO_2, has a structure consisting of *trans* fluorine-bridged $[Sn^{IV}F_6]$ octahedra linked to $[Sn^{II}{-}F]_\infty$ chains; the Sn^{II} sites are pyramidal (three nearest Sn–F contacts of 2.10–2.25 Å, with the next nearest F at 2.55 Å from tin).[51] Fluorides not only link Sn^{II} to Sn^{IV} but also Sn^{II} to Sn^{II} in zig-zag chains of $–(SnF)_n–$.

The structure of the ionic conductor $[NH_4]_3[F_2Sn^{II}(\mu\text{-}F)Sn^{II}F_2][Sn^{IV}F_6]$ contains octahedral $[SnF_6]^{2-}$ units.[52]

The compound $Sn_2^{II}Sn_2^{IV}\ F_4(CO_2CCF_3)_8]\cdot 2CF_3CO_2H$, produced from $Sn^{II}F_2/Sn^{IV}(O_2CCF_3)_4$ solutions, contains a $[Sn^{II}{-}F{-}Sn^{IV}{-}F]_2$ ring with bridging and unidentate CF_3CO_2 units: Sn^{IV} are in fluorine-bridged octahedral sites.[53]

Various mixed valency/mixed metal oxides of the general formula $[Sn^{II}_{2-x}(M^{V}_{2-y}Sn^{IV}_{y})O_{7-(x+y)}]$, (M = Nb or Ta), have been prepared: the Sn^{II} environments in these compounds are similar to those found in tin(II) sulfate.[54] The core of the mixed valence carboxylate $[Sn^{II}Sn^{IV}(O_2CC_6H_4NO_2\text{-}o)_4O\cdot THF]_2$ contains a [SnIV:2O$_2$] ring, with octahedral coordination at tin(IV). Carboxylate anions bridge Sn^{IV} and Sn^{II}; $d(Sn^{IV}{-}O)$ are between 2.047 and 2.067 Å, while pentagonal bipyramidal tin(II) are linked to four bridging carboxylate groups and to THF (apical Sn–O = 2.11 Å equatorial Sn–O = 2.41 and 2.66 Å).[46]

No evidence has been produced for intervalence hopping mechanisms in the mixed valency compounds.

5 SPECTROSCOPIC STUDIES OF TIN COMPOUNDS[3,4]

5.1 Mössbauer Spectroscopy

Mössbauer spectroscopy has proved to be of great value in inorganic tin chemistry (Table 6). Particularly useful have been isomer shift (δ) and quadrupole splitting (Δ) data. The recoil-free fraction and its temperature coefficient are other parameters that have found use in structural elucidations; variable temperature Mössbauer studies can be used, for example, in gaining information regarding the degree of aggregation in solid tin compounds.

5.1.1 Isomer Shift, δ

The largest contribution to the isomer shift value arises from the 5s electrons. Calculations have indicated that for tetrahedral and octahedral tin species the isomer shifts

Table 6 Mössbauer spectra[3,4]

Compound	δ (mm s^{-1})	ΔEq (mm s^{-1})	Comments
Tin(II) compounds			
Spherical tin(II) ion ($4d^{10}5s^2$)	4.84	–	Calculated
Distorted tin(II) ion (5sp hybridized)	2.26	–	Calculated
$[Sn(SbF_6)_2 \cdot (AsF_3)_2]$	4.66	0	–
$[Sn(ClO_4)_2$ (18-crown-6)]	4.445	0.88	–
α-SnF_2	3.472	1.520	$[SnF_3]$ and $[SnF_5]$ units
$CsSnF_3$	2.98	2.00	–
$Na_2Sn_2F_5$	3.32	1.86	–
Sn_2ClF_3	3.73	1.29	$[Sn_2F_3]_n{}^{n+}$ and Cl^- ions
$Cs_2Sn_6Br_3F_{11}$	3.50	1.50	See text
Sn_3BrF_5	3.69	1.18	Polymeric Sn–F anionic network free Br^-
$CsSnBr_3$	3.95	–	–
$SnBr_2$	3.98	0	–
$SnBr_2 \cdot$dioxane	3.71	–	–
$SnCl_2$	4.12	–	–
Sn_2OF_2	3.071	2.420	$SnOF_2$ units
	3.115	2.057	SnO_2F_2 units
SnO	2.708	1.308	Regular square pyramidal $[SnO_4]$
$[(Me_3Si)_2N]_2Sn$	2.88	3.52	Angular $[SnN_2]$ geometry
$[(Me_2N)_2Sn]_2$	2.72	2.07	$[SnN_3]$ geometry
Tin(IV) compounds			
SnF_4	−0.47	1.66	Four long Sn–F and two short Sn–F
$SnCl_4$	0.85	0	–
$SnBr_4$	1.15	0	–
SnI_4	1.55	0	–
K_2SnF_6	−0.59	0	–
K_2SnCl_6	0.45	0	–
$SnCl_4 \cdot 2NMe_3$	0.54	0	–
$SnCl_4 \cdot$2DMSO			
cis	0.40	0.41	–
trans	0.41	0.57	–
CN_2FeSnS_4	1.48	0	–
$Sn(O_2CCF_3)_4$	−0.04	1.56	–
Mixed valency compounds			
α-Sn_2F_6 Sn^{II}	−0.392	0.680	–
Sn^{IV}	4.103	0.493	–
Sn_3F_8 Sn^{IV}	−0.315	0.510	–
Sn^{II}	3.822	1.265	–
$[Sn_2(O_2CMe)_6]_2$ Sn^{II}	0.14	0.47	–
Sn^{IV}	3.48	1.83	–

correlate reasonably linearly with the 5s occupancy number and the 5s electron density at the tin nucleus: higher isomer shift values correspond to higher s electron density. Large differences in the isomer shifts between tin(II) and tin(IV) oxidation states arises from the lone pair orbital present in the tin(II) series. Thus the isomer shift values can be readily used to distinguish between tin(II) and tin(IV) states: the generally accepted ranges of δ for tin(II) compounds is $+2.5$ to 5.0 mm s^{-1} and for tin(IV) compounds -0.5 to $+2.1$ mm s^{-1} (relative to SnO_2). Values for α-Sn and β-Sn are 2.10 mm s^{-1} and 2.65 mm s^{-1} respectively.

For tin(IV) compounds, δ decreases as the total electronegativity of the groups attached to tin increases: the converse is found for tin(II) species, e.g. $[Sn^{II}(SbF_6)_2(AsF_3)_2]$ has one of the high δ values.

5.1.2 Quadrupole Splitting, Δ

The quadrupole splitting arises from the interaction of the nuclear quadrupole moment with an electric field gradient. Electric field gradients arise from three sources: (i) noncubic coordination geometries, (ii) imbalances in the σ framework of cubic (tetrahedral and octahedral) geometries, and (iii) distortions from regular cubic geometries. In tin(II) species the major contribution to the electric field gradient arises from the p_z electron density in the tin nonbonding orbitals.

Tin(IV) atoms in cubic environments, e.g. $SnCl_4$ and $[SnCl_6]^{2-}$, have no quadrupole splittings: in contrast, the tin(II) species $[SnCl_3]^-$ and SnO, as well as the tin(IV) anion $[SnCl_5]^-$, have splittings.

When the electronegativity difference of ligands on tetrahedral or octahedral tin are small, quadrupole splittings will be zero or at the most very small; large electronegativity differences lead to large Δ values.

The sign of the quadrupole splitting for many tin(II) compounds, e.g. SnO and SnS, is positive, which is consistent with the main contribution to the field gradient arising from the p-electron excess in the lone pair.

5.1.3 *Other Aspects for Tin(II) Compounds*

Isomer shift values are larger for SnX_2 than for $SnX_2{\cdot}L$ and $[SnX_3]^-$, e.g. δ for SnF_2 and $NaSnF_3$ are 3.62 and $3.12\,mm\,s^{-1}$, respectively; the value for $[F_2Sn(\mu\text{-}F)SnF_2]^-$ is intermediate ($\delta = 3.32\,mm\,s^{-1}$).[4] Values of the isomer shifts for tin compounds with bonds to lighter elements (N, O, or F) are usually lower than those corresponding to the heavier elements due to the high 5s electron character in the Sn–X bond and hence low 5s character in the lone pair. Consequently, quadrupole splitting values are greater for tin(II) compounds having bonds to the lighter elements. There is no correlation between δ and Δ values for tin(II) compounds.

For $[Sn^{II}X_3]$ species having a basic trigonal pyramidal geometry, δ values correlate with the Sn–X bond distance.

5.1.4 *Other Aspects for Tin(IV) Compounds*

Isomer shifts increase in tin(IV) compounds as the total electronegativities at tin decrease. An increase in coordination number from four to six also results in a decrease in δ values, e.g. δ values for $SnCl_4$, K_2SnCl_6, and $SnCl_4{\cdot}2MeOH$ are 0.85, 0.45, and $0.54\,mm\,s^{-1}$; δ values for $SnX_4{\cdot}2L$ are 0.22, 0.33, and 0.46 for L = Ph_3PO, Me_2SO, and pyridine, respectively.

Quadrupole splitting values, which generally indicate an imbalance in the p- or d-electron distribution around tin, only are found for tin(IV) compounds with quite different ligands or interactions, e.g. SnF_4 has two short and four long Sn–F bonds and a Δ value of $1.66\,mm\,s^{-1}$ while $SnCl_4{\cdot}2NMe_3$ has a Δ value of 0.

It has been found that *cis*-$SnX_4{\cdot}2L$ can have Δ values twice those for *trans*-$SnX_4{\cdot}2L$, e.g. values for *cis*- and *trans*-$SnBr_4{\cdot}(DMF)_2$ are 0.44 and $0.83\,mm\,s^{-1}$.

5.2 ^{119}Sn NMR Spectroscopy[4,55]

Tin NMR spectroscopy has been shown to be a useful and convenient analytical tool in inorganic tin chemistry. Of the three magnetically active tin isotopes (^{115}Sn, ^{117}Sn, and ^{119}Sn) with spin = 1/2, most use has been made of the ^{119}Sn nucleus. The usual reference standard for $\delta^{119}Sn$ values is Me_4Sn, a positive sign denoting lower shielding or a shift to lower frequency (lower field).

Major factors affecting $\delta^{119}Sn$ values are (i) the electronegativity of the groups attached to tin and (ii) the coordination number at tin. An illustration of the effect of ligand electronegativities is the change in $\delta^{119}Sn$ values for the group of $[SnX_6]^{2-}$ ions. Values of $\delta^{119}Sn$ shift to lower frequencies in passing from tetrahedral to trigonal bipyramidal to octahedral symmetries. Some representative solution values for $\delta^{119}Sn$ are given in Table 7. Solid-state $\delta^{119}Sn$ spectra are being increasingly reported. Comparison of solid-state and solution spectra can point out structural differences in the two phases.

5.3 IR Spectroscopy

Table 8 lists selected tin–element stretching frequencies. The mass effect is the dominant influence on the frequencies.

6 INDUSTRIAL USES OF TIN AND TIN CHEMICALS[56]

6.1 Tin

Tin is used as a coating and in alloys. Tin plate [ca. 0.4 to 25 µm thick] is used as a nontoxic corrosion-resistant cover for sheet steel, e.g. for drink cans. The main alloys of tin are (i) solder (mainly Sn/Pb), (ii) bronze (mainly Cu/Sn), (iii) babbitt (Sn/Pb/Cu or Pb/Sn/Sb/Cu), (iv) pewter (Sn/Sb/Cu) and (v) type metals (Pb/Sn/Sb).

6.2 Tin Compounds

Tin(IV) oxide is used as an opacifer in the ceramics industry in glazes and enamels. Various combinations of SnO_2/metal oxides are used as pigments, e.g. SnO_2/V_2O_5 is a yellow pigment, SnO_2/Sb_2O_5 is a blue-grey pigment, and SnO_2/Cr_2O_3 is a pink pigment.

A deposition of a thin film (<0.1 µm) of SnO_2 (produced from hydrolysis of $SnCl_4$ vapor or hydrolysis/thermolysis of organotin halides) on glass bottles increases the strength of the glass and the resistance to abrasion. At thicknesses from 0.1 to 1.0 µm a thin-film interference effect occurs, with the glass acquiring an attractive irridescense. At greater thicknesses, electrically conducting layers are obtained which, after doping with Sb or Fe ions, are used as electrodes, electroluminescent devices (for low intensity light panels and display signs, etc.), fluorescent lamps, antistatic cover-glasses, transparent tube furnaces, deiceable windscreens, etc. Another property of the thicker SnO_2 layers is their ability to reflect a high proportion of IR radiation whilst remaining transparent to visible radiation.

Tin(IV) oxide is used in various heterogeneous catalyst mixtures, e.g. SnO_2/V_2O_5 for oxidation of arenes to carboxylic acids and anhydrides, and SnO_2/Sb_2O_5 for selective oxidation and ammoxidation of propylene to acrolein, acrylic acid, and acrylonitrile.

Tin(IV) chloride is used as a homogeneous catalyst in Friedel–Craft alkylations and acylations.

Table 7 Some δ^{119}Sn NMR values for inorganic tin compounds (relative to Me_4Sn)

Compound	δ^{119}Sn	Solvent
SnF_2	−629.0	DMSO
$SnCl_2$	−358.2	DMSO
$SnBr_2$	−319.2	DMSO
SnI_2	−586.0	DMSO
$[SnCl_3]^-$	−30	CH_2Cl_2/C_6D_6
$SnCl_2{\cdot}PEt_3$	−47.3	C_6D_6
$(OC)_5W{\cdot}SnCl_2{\cdot}PEt_3$	−5.8	C_6D_6
$(OC)_5Cr{\cdot}SnCl_2{\cdot}PEt_3$	228.5	C_6D_6
$\{Sn[N(SiMe_3)_2]_2\}$	776	C_6D_6/C_6H_6 (100 °C)
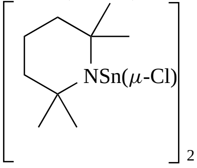	240	Toluene (32 °C)
$(t\text{-BuO})Sn(\mu\text{-O-}t\text{-Bu})_2Sn(\text{O-}t\text{-Bu})]$	−93	$Toluene/C_6D_6$
$Sn(OC\text{-}t\text{-Bu}_3)_2$	−162.9	Solid state
$[Sn(OSiPh_3)_2]$	−340	$Toluene/C_6D_6$
$[Tl(\mu\text{-O-}t\text{-Bu})_3Sn]$	−78.7	–
$[Tl(\mu\text{-O-}t\text{-Bu})_3Sn{\cdot}Mo(Co)_5]$	18.3	–
$[t\text{-BuSSn}(\mu\text{-S-}t\text{-Bu})_2SnS\text{-}t\text{-Bu}]$	77.7	$Toluene/C_6D_6$
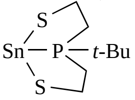	−238	C_6H_6
$[Sn(SPh)_3]^-$	140	CD_3OD
$[t\text{-Bu}_2PSn(\mu\text{-P-}t\text{-Bu}_2)_2P\text{-}t\text{-Bu}_2]$	328	–
$[Ph_4As][Sn(SePh)_3]^-$	208	CD_3OD
$[Ru(SnCl_3)_6]^{4-}$	−34.6	3 M aq HCl
$[Rh(SnCl_3)_5Cl]^{3-}$	−100.5	3 M aq HCl
$[Rh(SnCl_3)_4Cl_2]^{2-}$	−204.3	3 M aq HCl
$[Rh(SnCl_3)_3Cl_3]^{3-}$	−411.5	3 M aq HCl
$[Rh(SnCl_3)_2Cl_4]^{3-}$	−654.4	3 M aq HCl
$[Rh(SnCl_3)Cl_5]^{3-}$	−991.6	3 M aq HCl
cis-$[Pt(SnCl_3)_2Cl_2]^{2-}$	−142	CD_3COCD_3
$[SnF_6]^{2-}$	−888	H_2O
$[SnCl_6]^{2-}$	−732	CH_2Cl_2
$[SnBr_6]^{2-}$	−2064	CH_2Cl_2
$[Sn(OH)_6]^{2-}$	−590	H_2O
$SnCl_4$	−150	–
$SnBr_4$	−638	CS_2
SnI_4	1701	CS_2
$SnCl_4(PBu_3)_2$	−573	CH_2Cl_2
trans-$[SnCl_4{\cdot}(OPBu_3)_2]$	−622	CH_2Cl_2(−100 °C)
cis-$[SnCl_4{\cdot}(OPBu_3)_2]$	−632	CH_2Cl_2(−100 °C)
SnH_4	−500	–
$Sn(NMe_2)_4$	−121.8	CH_2Cl_2
$Sn(SePh)_4$	−135	CH_2Cl_2
$Sn(SPh)_4$	44	CH_2Cl_2
$Sn(SMe)_4$	160	CH_2Cl_2
$[SnTe_4]^{4-}$	−1828	en
$[Sn_4]^{2-}$	−1895	en
$[Sn_9]^{4-}$	−1230	en
$[Sn_8Tl]^{5-}$	−1167	en

Table 8 Selected Sn–X stretching frequencies[4]

Compound	ν(Sn–X) (cm^{-1})
SnH_4	1906
$Sn(NMe_2)_4$	535
$[SnF_6]^{2-}$	592
$SnCl_4$	407
$[SnCl_5]^-$	351
$[SnCl_6]^{2-}$	316
$SnBr_4$	280
$[SnBr_5]^-$	257
$[SnBr_6]^{2-}$	183
SnI_4	208
$[SnI_6]^{2-}$	156
$[Sn(OH)_6]^{2-}$	530
$[Sn(NMe_2)_2]_2$	440
$[Sn(OMe)_2]_n$	570
$[Sn(SMe)_2]_n$	361
$SnCl_2$ (matrix isolated)	353
$SnBr_2$ (matrix isolated)	244

Tin(II) salts (e.g. acetate, oxalate, oleate, stearate, and 2-ethylhexanoate) are catalysts for the curing of silicone elastomers and polyurethane foam.

7 RELATED ARTICLES

Lead: Inorganic Chemistry; Tin: Organometallic Chemistry.

8 FURTHER READING

W. E. Bennett, D. E. Broberg, and N. C. Baenziger, *Inorg. Chem.*, 1973, **12**, 930.

R. C. Burns, L. A. Devereux, P. Granger, and G. J. Schrobilgen, *Inorg. Chem.*, 1985, **24**, 2615.

K. B. Dillon, J. Halfpenny, and A. Marshall, *J. Chem. Soc., Dalton Trans.*, 1985, 1399.

B. Durand and H. Loiseleur, *J. Appl. Crystallogr.*, 1978, **11**, 289.

R. Marchand, Y. Piffard, and M. Tournoux, *Acta Crystallogr., Sect. B*, 1975, **31**, 511.

A. C. Sau, R. O. Day, and R. R. Holmes, *J. Am. Chem. Soc.*, 1981, **103**, 1264.

J. Shamir, S. Luski, A. Bino, S. Cohen, and D. Gibson, *Inorg. Chem.*, 1985, **24**, 2301.

M. Veith and W. Frank, *Angew. Chem., Int. Ed. Engl.*, 1985, **24**, 223.

M. Webster and H. E. Blayden, *J. Chem. Soc. (A)*, 1969, 2443.

9 REFERENCES

1. P. G. Harrison ed., ‘Chemistry of Tin’, Blackie, Glasgow, 1989.
2. P. A. Edwards and J. D. Corbett, *Inorg. Chem.*, 1977, **16**, 903; J. D. Corbett and P. A. Edwards, *J. Am. Chem. Soc.*, 1977, **99**, 3313.
3. J. D. Donaldson and S. M. Grimes, in ‘Chemistry of Tin’, ed. P. G. Harrison, Blackie, Glasgow, 1989, Chap. 4.
4. P. G. Harrison, in ‘Chemistry of Tin’, ed. P. G. Harrison, Blackie, Glasgow, 1989, Chap. 2.
5. T. Fjeldberg, H. Hope, M. F. Lappert, P. P. Power, and A. J. Thorne, *J. Chem. Soc., Chem. Commun.*, 1983, 639.
6. B. Cetinkaya, I. Gumruka, M. F. Lappert, J. L. Atwood, R. D. Rogers, and M. J. Zaworotko, *J. Am. Chem. Soc.*, 1980, **102**, 2088.
7. P. B. Hitchcock, M. F. Lappert, B. J. Samways, and E. L. Weinberg, *J. Chem. Soc., Chem. Commun.*, 1983, 1492.
8. R. W. Chorley, P. B. Hitchcock, and M. F. Lappert, *J. Chem. Soc., Dalton Trans.*, 1992, 1451.
9. J. D. Donaldson and D. C. Puxley, *Acta Crystallogr., Sect. B*, 1972, **28**, 864.
10. T. Yamaguchi and O. Lindquist, *Acta Crystallogr., Sect. B*, 1982, **38**, 1441.
11. J. D. Donaldson, S. M. Grimes, A. Nicolaides, and P. J. Smith, *Polyhedron*, 1985, **4**, 391.
12. A. M. Arif, A. H. Cowley, and T. M. Elkins, *J. Organomet. Chem.*, 1987, **325**, C11.
13. M. M. Olmstead and P. P. Power, *Inorg. Chem.*, 1984, **23**, 413.
14. W. W. Du Mont and M. Grenz, *Z. Naturforsch., Teil B*, 1983, **38**, 113.
15. M. Veith, *Z. Naturforsch., Teil B*, 1978, **33**, 7.
16. R. W. Chorley, P. B. Hitchcock, B. S. Jolly, M. F. Lappert, and G. A. Lawless, *J. Chem. Soc., Chem. Commun.*, 1991, 1302.
17. T. Fjeldberg, P. B. Hitchcock, M. F. Lappert, S. J. Smith, and A. J. Thorne, *J. Chem. Soc., Chem. Commun.*, 1985, 939.
18. W. W. du Mont and M. Grenz, *Chem. Ber.*, 1985, **118**, 1045.
19. A. M. Arif, A. H. Cowley, R. A. Jones, and J. M. Power, *J. Chem. Soc., Chem. Commun.*, 1986, 1446.
20. P. A. W. Dean, J. J. Vittal, and N. C. Payne, *Can. J. Chem.*, 1985, **63**, 394.
21. M. Veith and R. Rösler, *Z. Naturforsch., Teil B*, 1986, **41**, 1071.
22. M. Veith and K. Kunze, *Angew. Chem., Int. Ed. Engl.*, 1991, **30**, 95.
23. C. C. Hsu and R. A. Geanangel, *Inorg. Chem.*, 1980, **19**, 110.
24. M. Veith, *Angew. Chem., Int. Ed. Engl.*, 1987, **26**, 1.
25. H. Chen, R. A. Bartlett, H. V. R. Dias, M. M. Olmstead, and P. P. Power, *Inorg. Chem.*, 1991, **30**, 3390.
26. M. Veith, J. Fischer, T. R. Prout, M. Nötzel, P. Hobein, and V. Huch, *Inorg. Chem.*, 1991, **30**, 4130.
27. P. F. R. Ewings, P. G. Harrison, and T. J. King, *J. Chem. Soc., Dalton Trans.*, 1976, 1399.

28. J. E. Anderson, S. M. Sawtelle, J. S. Thompson, S. A. K. Nguyen, and J. Calabrese, *Inorg. Chem.*, 1992, **31**, 2778.
29. P. F. R. Ewings, P. G. Harrison, and T. J. King, *J. Chem. Soc., Dalton Trans.*, 1975, 1455.
30. G. W. Bushnell, D. T. Eadie, A. Pidcock, A. R. Sam, R. D. Holmes-Smith, S. R. Stobart, E. T. Brennan, and T. S. Cameron, *J. Am. Chem. Soc.*, 1982, **104**, 5837.
31. K. Jurkschat, M. Scheer, A. Tzschach, J. Meunier-Piret, and M. van Meerssche, *J. Organomet. Chem.*, 1985, **281**, 173.
32. J. D. Donaldson, M. T. Donoghue, and C. H. Smith, *Acta Crystallogr., Sect. B*, 1976, **32**, 2098.
33. J. D. Donaldson, J. Silver, S. Hadjiminolis, and S. D. Ross, *J. Chem. Soc., Dalton Trans.*, 1975, 1500.
34. J. D. Donaldson, D. R. Laughlin, S. D. Ross, and J. Silver, *J. Chem. Soc., Dalton Trans.*, 1973, 1985.
35. J. D. Donaldson and S. M. Grimes, *J. Chem. Soc., Dalton Trans.*, 1984, 1301.
36. I. Abrahams, J. D. Donaldson, and S. M. Grimes, *J. Chem. Soc., Dalton Trans.*, 1992, 669.
37. J. Andersson, *Acta Chem. Scand., Ser. A*, 1975, **29**, 956.
38. R. A. Howie, W. Moser, and I. C. Trevana, *Acta Crystallogr., Sect. B*, 1972, **28**, 2965.
39. H. G. von Schnering, R. Nesper, and H. Pelshenke, *Z. Anorg. Allg. Chem.*, 1983, **499**, 117; R. Nesper and H. G. von Schnering, *Z. Anorg. Allg. Chem.*, 1983, **499**, 109.
40. C. G. Davies, J. D. Donaldson, D. R. Laughlin, R. A. Howie, and R. Beddoes, *J. Chem. Soc., Dalton Trans.*, 1975, 2241.
41. P. G. Harrison, B. J. Haylett, and T. J. King, *J. Chem. Soc., Chem. Commun.*, 1978, 112.
42. J. Pannetier and G. Denes, *Acta Crystallogr., Sect. B*, 1980, **36**, 2763.
43. P. G. Harrison, T. J. King, and J. A. Richards, *J. Chem. Soc., Dalton Trans.*, 1974, 1723.
44. J. C. Barnes, H. A. Sampson, and T. J. R. Weakley, *J. Chem. Soc., Dalton Trans.*, 1980, 949.
45. C. Belin, M. Chaabouni, J. L. Pascal, J. Potier, and J. Roziere, *J. Chem. Soc., Chem. Commun.*, 1980, 105.
46. P. F. R. Ewings, P. G. Harrison, A. Morris, and T. J. King, *J. Chem. Soc., Dalton Trans.*, 1976, 1602.
47. N. W. Alcock and V. L. Tracy, *Acta Crystallogr., Sect. B*, 1979, **35**, 80.
48. C. D. Garner, D. Sutton, and S. C. Wallwork, *J. Chem. Soc. (A)*, 1967, 1949.
49. R. Kniep, D. Mootz, U. Severin, and H. Wunderlich, *Acta Crystallogr., Sect. B*, 1982, **38**, 2022.
50. J.-C. Jumas, J. Olivier-Fourcade, E. Philppot, and N. Maurin, *Rev. Chem. Miner.*, 1979, **16**, 48.
51. M. F. A. Dove, R. King, and T. J. King, *J. Chem. Soc., Chem. Commun.*, 1973, 944.
52. A. Soufiane and S. Vilminot, *Rev. Chem. Miner.*, 1985, **22**, 799.
53. T. Birchall and V. Manivannan, *J. Chem. Soc., Chem. Commun.*, 1986, 1441.
54. T. Birchall and A. W. Sleight, *J. Solid State Chem.*, 1975, **13**, 118.
55. B. Wrackmeyer, *Annu. Rep. NMR Spectrosc.*, 1985, **16**, 73.
56. C. J. Evans, in ‘Chemistry of Tin’, ed. P. G. Harrison, Blackie, Glasgow, 1989, Chap. 13.

Tin: Organometallic Chemistry

James L. Wardell & Gavin M. Spencer
University of Aberdeen, Aberdeen, UK

1	Introduction	1
2	Synthesis of Carbon–Tin(IV) Bonds	2
3	Spectroscopic Study of Organotin Compounds	6
4	Tetraorganotin Compounds	8
5	Cleavage of Carbon–Tin Bonds	8
6	Organotin(IV) Halides and Pseudohalides	11
7	Organotin(IV) Hydrides	14
8	Tin–Tin Bonded Compounds	15
9	Organostannyl Radicals	16
10	Tin–Nitrogen Bonded Compounds	17
11	Tin–Phosphorus, –Arsenic, and –Antimony Bonded Compounds	17
12	Tin–Oxygen Bonded Compounds	18
13	Tin–Sulfur, –Selenium, and –Tellurium Bonded Compounds	21
14	Industrial and Biological Applications	25
15	Environmental Aspects	26
16	Related Articles	27
17	Further Reading	27
18	References	27

1 INTRODUCTION[1–6]

The first organotin compound, Et_2SnI_2, was reported by Frankland in 1849. Interest in organotin chemistry developed steadily over the next decades, but it was not until the discovery of the industrial uses of organotin species (e.g. as PVC stabilizers and as biocidal species), a century or so later, that this area of chemistry expanded rapidly.

The bonding in organotin species is essentially covalent in the solid state, in nonpolar solvents, and in the gas phase. The bonds to tin are, however, readily polarizable, and some ionization can occur in polar solvents. The extent of dissociation is usually low, e.g. the specific conductance of Et_3SnCl is $1.8 \times 10^{-9}\ \Omega^{-1}\,cm^{-1}$ in 1 M solution in benzene and $1 \times 10^{-6}\ \Omega^{-1}\,cm^{-1}$ in nitrobenzene.

Compared to organosilicon and organogermanium compounds, organotin compounds show an increased reactivity and a lower thermal stability; this is linked to the longer C–Sn bonds (ca. 2.15 Å) (cf. C–Si 1.94 Å and C–Ge 1.99 Å) rather than to the electronegativity differences (electronegativities on the Allred–Rochow scale for Si, Ge, and Sn are 1.7, 2.0, and 1.7, respectively). The trend is continued with organolead compounds (C–Pb 2.29 Å).

Tin forms organic derivatives in both the Sn^{II} and Sn^{IV} oxidation states; by far the majority of known organic derivatives are tin(IV) compounds. The four electrons in the valence shell of the tin atom have the $5s^2p^2$ electronic configuration. The valence electrons can undergo sp^3 hybridization and so tetracoordinate tin atoms have tetrahedral geometries. For tin(IV) derivatives, compounds having one to four organic groups can be prepared, with the remaining bonds being to a variety of anionic groups (see Scheme 1 for selected transformations of organotin compounds). For organotin compounds, especially those having electronegative groups (e.g. halides or oxygen groups), coordination numbers greater than four (up to seven) frequently occur. Catenation in organotin chemistry is well developed, with R_3SnSnR_3, $R_3Sn(SnR_2)_nSnR_3$, and *cyclo*-$(R_2Sn)_n$ species known. Over the past few years, evidence has been gained for organotin compounds containing tin–element multiple bonds, e.g. Sn=C, Sn=N, Sn=P, Sn=Sn, etc. (see (**1**)–(**5**)), although ylidic forms may better describe some of these compounds.**[7]**

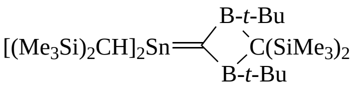

(**1**)

$Me_2Sn{=}NSi(t\text{-}Bu)_2Me$

(**2**)

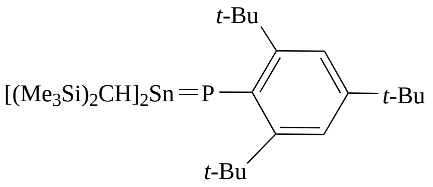

(**3**)

$[(Me_3Si)_2CH]_2Sn{=}Sn[CH(SiMe_3)_2]_2$

Sn—Sn = 2.768(1) Å

(**4**)

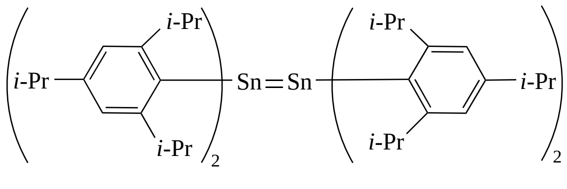

For organotin(II) compounds, there are six electrons in the valence shell and one electron pair is nonbonding. The most favorable electronic state is the singlet $(1\sigma^2)$ state, i.e. the electron pair resides in one orbital with antiparallel spins. From ^{13}C NMR data it appears that there is considerable s character in the orbitals between the tin atom and the carbon atom. Organotin(II) compounds (R_2Sn and RSnX) are

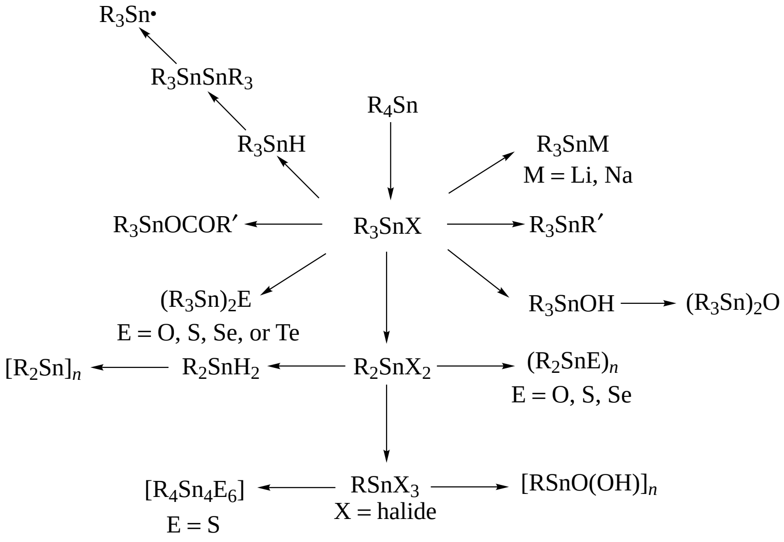

Scheme 1

known with both π-bonded, e.g. $(\eta^5\text{-}C_5H_5)_2Sn$, and σ-bonded organic groups. As anticipated, organotin(II) compounds are highly reactive and simple dialkyltin or diaryltin (diorganostannylenes) undergo rapid polymerization. Conditions that are found to stabilize divalent organotin compounds (i) have bulky organic groups, (ii) form adducts with Lewis bases, or (iii) coordinate the Sn lone pair to a suitable Lewis acid. Different coordination numbers and geometries are also possible for organotin(II) compounds on utilizing the 5d orbitals, e.g. trigonal planar (sp^2 hybridized), tetrahedral (sp^3), trigonal bipyramidal (sp^3d), and octahedral (sp^3d^2).

Triorganotin radicals, $R_3Sn\bullet$, having seven valence electrons, have been shown to have a large range of stabilities; radicals with bulky organic groups have appreciable lifetimes, e.g. $[(Me_3Si)_2CH]_3Sn\bullet$ has a half-life of 1 year at ambient temperature.

General books, reviews, and monographs cover the field of organotin chemistry.**[1–6]** Useful review articles on NMR spectroscopy,**[8]** Mössbauer spectroscopy,**[9]** and crystal structures**[10]** of tin compounds have also been published.

2 SYNTHESIS OF CARBON–TIN(IV) BONDS[2,5,6,11]

2.1 General Methods

2.1.1 Direct Synthesis[12]

The direct reaction of tin (as foil, powder, or alloy) with organic halides has been used to produce organotin halides. Catalysts and promoters are required for all but the most reactive organic halides; $MePh_3PBr$ and KI were used as catalyst and promoter, respectively, for the formation of Me_2SnCl_2 from MeCl and Sn at 180–190 °C. The dominant products from such direct syntheses are usually the diorganotin dihalides (equation 1).

$$2RX + Sn \longrightarrow R_2SnX_2 \qquad (1)$$

However, the use of stoichiometric amounts of molten quaternary halides R_4MBr (M = N, P, or Sb) at 120–140 °C leads**[13]** to excellent yields of trialkyltin bromides (R_3SnBr) from alkyl bromides, RBr, and tin powder; the alkylation of tin occurs in a stepwise manner and the process can be stopped at the mono- or diorganotin stages and the process can be modified to give mixed trialkyltin bromides ($R_2R'SnBr$).

Various allyl-, benzyl-, and alkyltin halides have been prepared by direct methods; compounds have included functionally substituted dialkyltin dihalides $X_2Sn[(CH_2)_nY]_2$ ($n = 1$ or 2, Y = R_2NCO, ROCO, RCO; $n = 2$, Y = NC; $n = 3$, Y = RO).

The reactivities of alkyl halides are in the sequence RI > RBr > RCl and MeX > EtX > PrX. Benzyl halide reactions with tin do not require catalysts (equation 2). For less reactive halides, the catalysts and promoters employed include metals (sodium, magnesium, zinc, or copper), Lewis bases (amines, triorganophosphines and -stibines, alcohols, or ethers), iodides, and onium salts (R_4MX). The use of tin–sodium alloys can result in tri- or tetraorganotin products. Electrochemical synthesis has also been reported, e.g. the formation of R_2SnX_2 from the oxidation of anodic tin by RX in benzene solution and the formation of R_4Sn from RI (R = Me or $NCCH_2CH_2$) and cathodic tin.

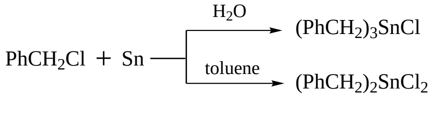

$$PhCH_2Cl + Sn \begin{cases} \xrightarrow{H_2O} (PhCH_2)_3SnCl \\ \xrightarrow[\text{toluene}]{} (PhCH_2)_2SnCl_2 \end{cases} \qquad (2)$$

The reaction between powdered tin, hydrogen chloride, and an α,β-unsaturated carbonyl or cyano compound produces diorganotin dichloride species (equation 3). Tin(II) halides react similarly to give $X_3SnCH_2CH_2Y$ (equation 4). Direct reactions of tin(II) halides with alkyl halides to give alkyltin trihalides require the same catalysts as used for tin/alkyl halide reactions: trialkylstibines are particularly effective catalysts (equation 5).

$$\mathrm{Sn + 2HCl + 2H_2C{=}CHY \longrightarrow Cl_2Sn(CH_2CH_2Y)_2}$$
$$\mathrm{Y = CO_2R,\ COR,\ CONR_2,\ or\ CN} \qquad (3)$$

$$\mathrm{SnCl_2 + HCl + H_2C{=}CHY \longrightarrow Cl_3SnCH_2CH_2Y} \qquad (4)$$

$$\mathrm{RBr + SnBr_2 \xrightarrow[\Delta]{Et_3Sb} RSnBr_3} \qquad (5)$$

2.1.2 Synthesis from Tin(IV) Halides

Reactions of tin(IV) halides or organotin halides with organic derivatives of more electropositive metals provide the most important general synthetic routes to carbon–tin bonds (equation 6). The most frequently used R′–M compounds are those of magnesium and lithium, with sodium, zinc, and aluminum having a more limited use. Some examples of these reactions are given in equations (7–9).

$$\mathrm{R_{4-n}SnX_n + nR'{-}M \longrightarrow R_{4-n}SnR'_n} \quad n = 1-4 \qquad (6)$$

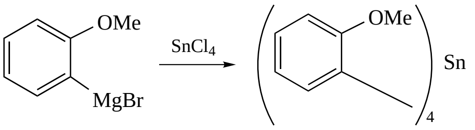

(7)

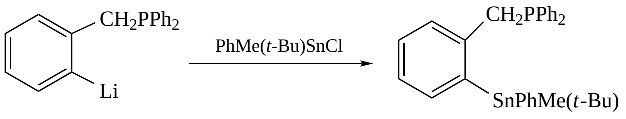

(8)

$$\mathrm{CH_2I_2 \xrightarrow{Zn/Cu} ICH_2ZnI \xrightarrow{Ph_2SnCl_2} Ph_2Sn(CH_2I)_2} \qquad (9)$$

The normal targeted products of reactions between tin(IV) halides and organomagnesium or organolithium reagents are the tetraorganotins, as it is difficult to control alkylation sufficiently well to a lower extent. However, controlled reactions can be achieved in certain cases, e.g. when bulky groups are present (such as cyclohexyl) or when an organotin halide product can be stabilized by chelation (equation 10).

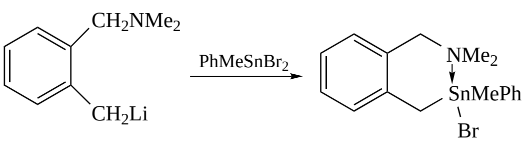

(10)

2.1.3 Synthesis from Triorganylstannyl Anionic Species, R_3SnM

Reactions of R_3SnM ($M = Li$, Na, MgX, or Cu) occur with various organic electrophiles, e.g. organic halides and tosylates, aldehydes and ketones, β-enones, and epoxides, to give new carbon–tin bonded compounds.

R_3SnM compounds can be obtained from (i) R_3SnX ($X =$ halide) and M or $ArH^- M^+$ ($ArH =$ an arene such as naphthalene; $M = Li$, Na, or K); (ii) R_3SnSnR_3 and M ($M = Li$, Na, or K) or R′Li in HMPA; or (iii) R_3SnH and MH ($M = Na$ or K), t-BuMgX, R'_2MLi, or R'_2 NM/LiO-t-Bu ($M = K$ or Cs). Addition of a copper(I) compound will provide the tin–copper or tin–cuprate.

Primary and secondary alkyl halides and tosylates react cleanly with R_3SnM (equation 11); however, with tertiary alkyl halides, some elimination reaction can also result. The mechanisms of the R_3SnM/alkyl halide or tosylate reactions can be (i) S_N2 type (with inversion of configuration); (ii) an electron transfer (or radical pair) mechanism (with possible predominant inversion of configuration); or (iii) an initial halogen–metal exchange, followed by substitution (with overall retention of configuration) (equation 12). Temperature, solvent, halide, and method of preparation of R_3SnM (and consequent presence of additional species, such as RM or M) affect the mechanism.

$$\mathrm{R_3SnM + R'X \longrightarrow R_3SnR'} \qquad (11)$$

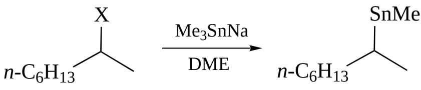

(12)

$X = OSO_2C_6H_4Me$-p,	100% inversion
Cl	78% inversion
Br	60% inversion

Mechanisms of triorganotin anionic reactions with haloarenes include $S_{RN}1$ and halogen–metal exchanges.**[14]** Further examples of the use of R_3SnM compounds are shown in equations (13–15). Various functional group substituents are clearly much less sensitive towards R_3SnM than to RM, e.g. CN, CO_2R, etc.

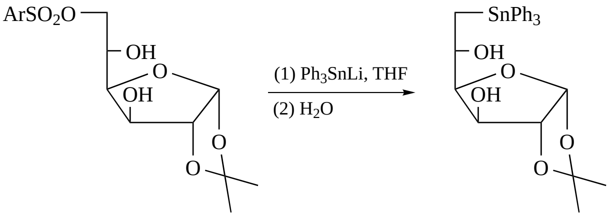

(13)

Ar = p-MeC$_6$H$_4$

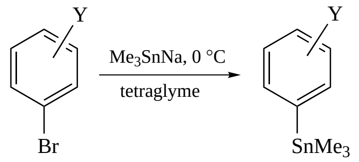
Y
Me3SnNa, 0 °C
tetraglyme
Br
SnMe3

(14)

Y = *p*-CN, *p*-NH$_2$, *o*-, *m*- or *p*-MeO

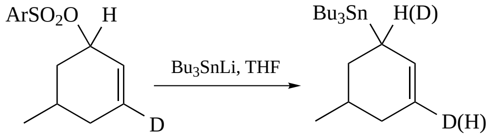
ArSO2O H
Bu3SnLi, THF
D
Bu3Sn H(D)
D(H)

(15)

cis:*trans* = 94:6 *cis*:*trans* = 8:92

Aldehydes and ketones react with R_3SnM ($M = Li$ or MgCl) to give α-hydroxyalkyltin compounds after hydrolysis (equation 16). 1,4-Additions occur with $RCH{=}CHCOR'$ and $Bu_3SnMgCl$ (in Et_2O), R_3SnLi, or $(R_3Sn)_2CuLi$ (equations 17 and 18). Ring-opened products result from reactions of epoxides, oxetanes, or thiiranes (equations 19–21).

$$Bu_3SnMgCl + RCHO \longrightarrow Bu_3SnCHROH \qquad (16)$$

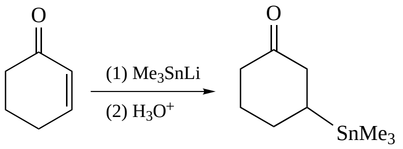
O
(1) Me3SnLi
(2) H3O+
O
SnMe3

(17)

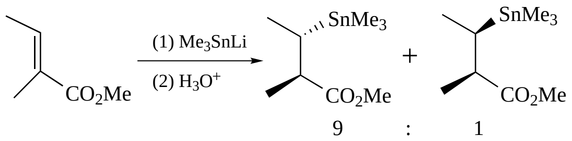
CO2Me
(1) Me3SnLi
(2) H3O+
SnMe3
CO2Me
+
SnMe3
CO2Me
9 : 1

(18)

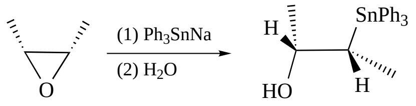
(1) Ph3SnNa
(2) H2O
O
H
SnPh3
HO
H

(19)

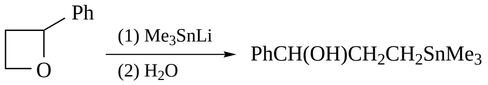
Ph
O
(1) Me3SnLi
(2) H2O
PhCH(OH)CH2CH2SnMe3

(20)

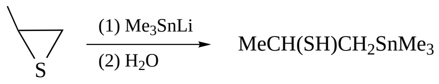
S
(1) Me3SnLi
(2) H2O
MeCH(SH)CH2SnMe3

(21)

2.1.4 Hydrostannation of Alkenes and Alkynes

Organotin hydrides add to alkenes and alkynes (equations 22 and 23). Unless strongly electron-withdrawing groups are present in the unsaturated species, the additions have radical-chain mechanisms (Scheme 2). For 1-alkenes, tin usually adds predominantly to the terminal carbon (equations 24 and 25).

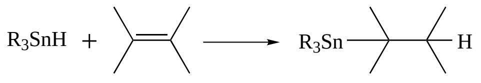
R3SnH +
R3Sn
H

(22)

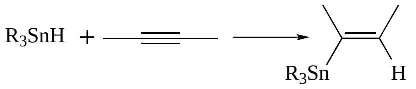
R3SnH +
R3Sn
H

(23)

$$H_2C{=}CHC_6H_{13} + Et_3SnH \longrightarrow Et_3SnCH_2CH_2C_6H_{13} \qquad (24)$$

$$Bu_2SnH_2 + 2H_2C{=}CHCH_2OH \longrightarrow Bu_2Sn(CH_2CH_2CH_2OH)_2 \qquad (25)$$

The regioselectivity of addition to $CH_2{=}CHCN$ depends on whether a nucleophilic (a) or a radical (b) mechanism operates (Scheme 3).

Various functional groups, X, can be tolerated in the alkenes $CH_2{=}CH(CH_2)_nX$, e.g. $X = SR$, SO_2R, OR, PR_2, $P(OR)_2$; however, amines and other basic groups, e.g. sulfoxides, catalyze decomposition of tin hydrides to tin–tin bonded compounds (equation 26).

$$Ph_3SnH + H_2C{=}CHSO_mC_6H_4Me\text{-}p \xrightarrow{\text{AIBN}} Ph_3SnCH_2CH_2SO_mC_6H_4Me\text{-}p \quad m = 0 \text{ or } 2 \qquad (26)$$

Hydrostannation of terminal alkynes containing a strongly electron-releasing group, e.g. CO_2R or CN, produces mainly the α-adduct via an ionic mechanism. Addition to alkynes bearing an electron-releasing group, such as an alkyl or alkoxyl group, or a weakly electron-withdrawing group, e.g. CH_2OH or Ph, yield mainly the *cis* and *trans* β-adduct (via a radical mechanism), as well as small amounts of the α-adduct. Initial additions occur in a *trans* manner (i.e. to form the *cis* adduct), with subsequent isomerism of the *cis*-$R_3SnCH{=}CHR'$ to give the thermodynamically more stable *trans* isomer. Hydrostannation of nonterminal alkynes by R_3SnH provides mainly the *trans* adducts.

2.2 Specific Types of Carbon–Tin Bonded Compounds

The general methods outlined above can be used to synthesize organotins having specific functionalities. Two important groups of organotin compounds are the vinyl- and allyltins; some further details of the synthesis of these compounds are

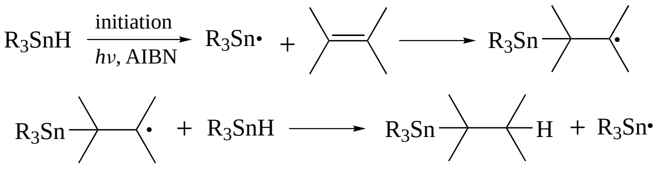
R3SnH
initiation
hν, AIBN
R3Sn•
+
R3Sn
R3Sn
+ R3SnH
R3Sn
H
+ R3Sn•

Scheme 2

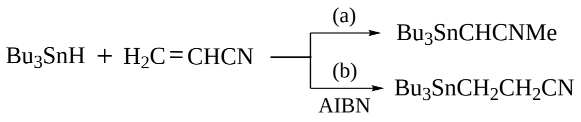
Bu3SnH + H2C=CHCN
(a)
Bu3SnCHCNMe
(b)
AIBN
Bu3SnCH2CH2CN

Scheme 3

given below. For functionally substituted alkyltins the general methods have proved to be useful; for example, (i) the use of reactions involving tin halides and YCR^1R^2Li compounds ($Y =$ nitrogen, phosphorus, sulfur, selenium containing group, halo, cyano, or carbonyl) can provide α-substituted derivatives; (ii) hydrostannation of alkenes $CH_2{=}CH(CH_2)_nY$ gives β, γ, and δ derivatives ($Y =$ oxygen, sulfur, phosphorus group, carbonyl); and (iii) reactions of R_3SnM with substituted halides or sulfonates $Y(CRR')_nX$ ($X =$ halide or sulfonate). The conversion of existing functionally substituted alkyltin groups to other groups may also be used, e.g. conversion of $\equiv Sn(CH_2)_nOH$ to $\equiv Sn(CH_2)_nX$ (halide), oxidation of $\equiv Sn(CH_2)_nSR$ to $\equiv Sn(CH_2)_nSO_mR$ ($m = 1$ or 2), and additions of electrophiles, radicals, and carbenes to alkenyl tin species (see also Scheme 4).

2.2.1 Vinyltins

Vinyltin compounds can be generated from the corresponding vinyl-Grignard reagents or vinyllithium compounds with a tin halide, with retention of configuration (equation 27). Reactions between triorganotin anionic species R_3SnM ($M =$ Li, Na, MgX) and vinyl halides or sulfonates provide vinyltin compounds; reactions of the sulfonates (but not iodides) are stereospecific (equation 28). Routes to vinylstannanes from ketones have also been devised (Scheme 5).

$$H_2C{=}CHMgBr + SnCl_4 \xrightarrow{THF} (H_2C{=}CH)_4Sn \tag{27}$$

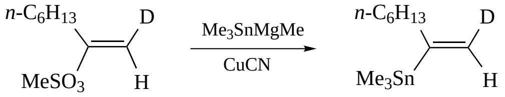
n-C6H13
D
MeSO3
H
Me3SnMgMe
CuCN
n-C6H13
D
Me3Sn
H

(28)

Hydrostannation of 1-alkynes does provide vinyltins (equation 29), but these reactions may not be stereospecific or give the desired regiospecificity. Other methods from alkynes are shown in equations 30 and 31 and Scheme 6. Stannyl cupration of allenes (using $(Bu_3Sn)_2CuLi$ or $(Bu_3Sn)BuCuLi$) also leads to allyl- and vinylstannanes.**[15]**

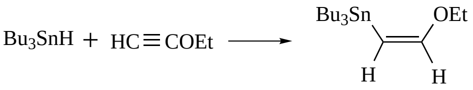
Bu3SnH + HC≡COEt
Bu3Sn
OEt
H
H

(29)

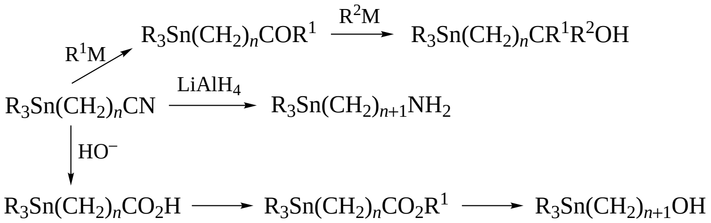
R3Sn(CH2)nCOR1
R2M
R3Sn(CH2)nCR1R2OH
R1M
R3Sn(CH2)nCN
LiAlH4
R3Sn(CH2)n+1NH2
HO−
R3Sn(CH2)nCO2H
R3Sn(CH2)nCO2R1
R3Sn(CH2)n+1OH

Scheme 4

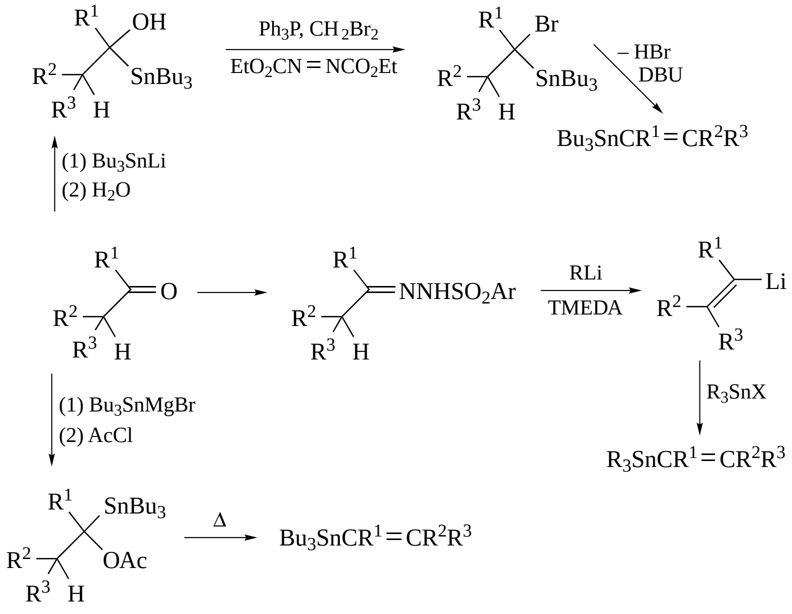
R1
OH
R2
SnBu3
R3
H
Ph3P, CH2Br2
EtO2CN=NCO2Et
R1
Br
R2
SnBu3
R3
H
− HBr
DBU
Bu3SnCR1=CR2R3
(1) Bu3SnLi
(2) H2O
R1
O
R2
R3
H
R1
NNHSO2Ar
R2
R3
H
RLi
TMEDA
R1
Li
R2
R3
R3SnX
R3SnCR1=CR2R3
(1) Bu3SnMgBr
(2) AcCl
R1
SnBu3
R2
OAc
R3
H
Δ
Bu3SnCR1=CR2R3

Scheme 5

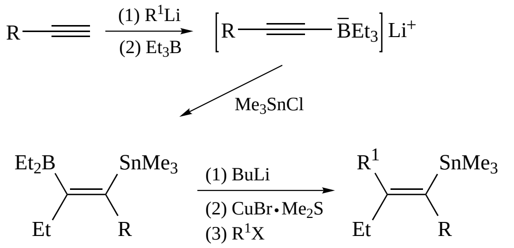
(1) R¹Li
(2) Et₃B
Li⁺
Me₃SnCl
Et₂B
SnMe₃
Et
R
(1) BuLi
(2) CuBr•Me₂S
(3) R¹X
R¹
SnMe₃
Et
R

(30)

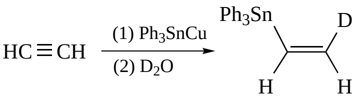
HC≡CH
(1) Ph₃SnCu
(2) D₂O
Ph₃Sn
D
H
H

(31)

2.2.2 *Allyltin Compounds*

Allylstannanes are available from reactions of allylmagnesium or allyllithium compounds with tin halides (equation 32). Other syntheses involve reactions of triorganotin anionic species with allylic halides or esters (equation 14), as well as reactions of allylic xanthates, tosylates, etc. with tin hydrides (equation 33).

$$H_2C{=}CHCH_2MgCl \xrightarrow{Ph_3SnCl} Ph_3SnCH_2CH{=}CH_2 \qquad (32)$$

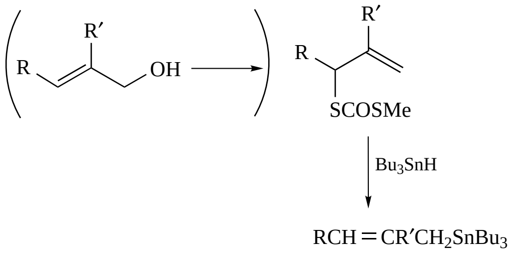
R′
R
OH
R′
R
SCOSMe
Bu₃SnH
RCH = CR′CH₂SnBu₃

(33)

Hydrostannation of 1,3-dienes produces allyltins. Specific modifications of certain functionally substituted alkyltin compounds have also been used (equation 34 and Scheme 7).

$$Me_3SnCH_2CH{=}PPh_3 \xrightarrow{R^1R^2C{=}O} Me_3SnCH_2CH{=}CR^1R^2 \qquad (34)$$

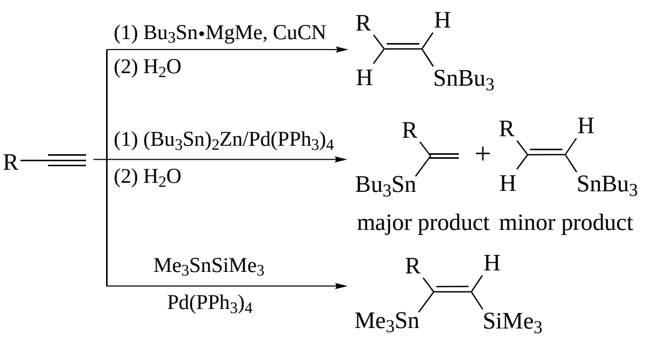
(1) Bu₃Sn•MgMe, CuCN
(2) H₂O
R
H
H
SnBu₃
(1) (Bu₃Sn)₂Zn/Pd(PPh₃)₄
(2) H₂O
R
Bu₃Sn
+
R
H
H
SnBu₃
major product
minor product
Me₃SnSiMe₃
Pd(PPh₃)₄
R
H
Me₃Sn
SiMe₃

Scheme 6

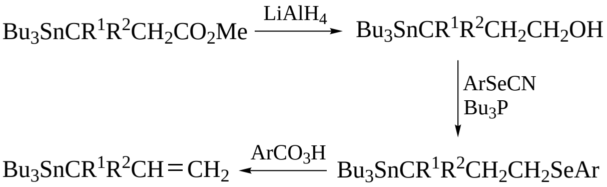
Bu₃SnCR¹R²CH₂CO₂Me
LiAlH₄
Bu₃SnCR¹R²CH₂CH₂OH
ArSeCN
Bu₃P
Bu₃SnCR¹R²CH=CH₂
ArCO₃H
Bu₃SnCR¹R²CH₂CH₂SeAr

Scheme 7

3 SPECTROSCOPIC STUDY OF ORGANOTIN COMPOUNDS[16]

Organotin compounds, as well as being open to study by general spectroscopic techniques, e.g. UV, IR, and ^1H and ^{13}C NMR spectroscopies as well as mass spectrometry, can also be investigated using such specific techniques as ^{119}Sn (or ^{117}Sn) NMR and ^{119m}Sn Mössbauer spectroscopies. The increasing availability of solid-state NMR spectroscopy provides further means of exploring structures.

Tin has 10 stable isotopes, the largest number of any element, and this can be used to advantage in spectroscopic study. The isotopes and their abundances are as follows: 112 (0.95%), 114 (0.65%), 115 (0.34%), 116 (14.24%), 117 (7.57%), 118 (24.01%), 119 (8.58%), 120 (32.97%), 122 (4.71%), and 124 (5.98%).

3.1 IR Spectroscopy

As a general rule, the positions of Sn–X stretching vibrations are dominated by the mass effect. As the mass of the bonding element increases, so the stretching vibration falls to lower frequencies. The stretching vibrations for Sn–H bonds occur in the region 1820–1920 cm^{-1}; those for bonds to first-row elements (C, N, O, or F) in the region 500–600 cm^{-1}; those for bonds to second-row elements (Si, P, S, or Cl), to third-row elements (Ge, As, Se, or Br), and to fourth-row elements (Sn, Sb, Te, or I) occur in the regions 300–380, 190–260, and 150–210 cm^{-1}, respectively.

These regions should only be used as guidelines for molecular complexes, since the positions of the bands are affected by the nature of the ligand, e.g. the values of ν(Sn–O) for Bu_3SnOR and Me_3SnONO_2 are ca. 500–525 and 220 cm^{-1}, respectively, and by other substituents at tin, as well as by any further coordination, e.g. monomeric R_3SnF have ν(Sn–F) in the region 555–590 cm^{-1}, but for fluoride-bridged $[R_3SnF]$ aggregates ν(Sn–F) occurs at 340–380 cm^{-1}.

3.2 NMR Spectroscopy

Three of the tin isotopes (^{115}Sn, ^{117}Sn, and ^{119}Sn) have spin values of 1/2, but, while in principle all are suitable for NMR study, only ^{117}Sn and, in particular, ^{119}Sn have found practical use.

3.2.1 ^{1}H and ^{13}C NMR Spectra in Solution

As with organic compounds, the ^{1}H and ^{13}C NMR spectra of organotins are used to assign protons and carbon atoms; in addition, values of coupling constants $^nJ(^{119}\mathrm{Sn}–^1\mathrm{H})$ and $^nJ(^{119}\mathrm{Sn}–^{13}\mathrm{C})$ are useful aids to bonding and to conformations.

Both the one-bond $^1J(^{119}\mathrm{Sn}–^{13}\mathrm{C})$ and the two-bond $^2J(^{119}\mathrm{Sn}–^1\mathrm{H})$ values have been used as guides to the s electron density in carbon–tin bonds. The changes in $^2J(^{119}\mathrm{Sn}–^1\mathrm{H})$ values for $\mathrm{Me}_n\mathrm{SnCl}_{4-n}$ (54.7, 58.2, 68.9, 96.9 Hz for $n = 4, 3, 2, 1$), indicate the increasing s electron density in the Me–Sn bond and hence the increasing p character of the Sn–Cl bond as n decreases.

The values of $^2J(^{119}\mathrm{Sn}–^1\mathrm{H})$ and $^1J(^{119}\mathrm{Sn}–^{13}\mathrm{C})$ also increase with the increasing coordination at tin, e.g. $^1J(^{119}\mathrm{Sn}–^{13}\mathrm{C})$ values for $\mathrm{Me_3SnCl}$ and $\mathrm{Me_3SnCl{\cdot}py}$ are 372 and 472 Hz, respectively. The usual ranges quoted for $^1J(^{119}\mathrm{Sn}–^{13}\mathrm{C})$ in four-coordinate $\mathrm{R_3SnX}$ are 330–400 Hz, in five-coordinate $\mathrm{R_3SnX}$ are 450–480 Hz, in four-coordinate $\mathrm{R_2SnX_2}$ are 370–480 Hz, and for octahedral $\mathrm{R_2SnX_2}$ are 900–970 Hz.

Correlations have been established between values of $^2J(^{119}\mathrm{Sn}–^1\mathrm{H})$ or $^1J(^{119}\mathrm{Sn}–^{13}\mathrm{C})$ and the C–Sn–C valency angles in series of diorganotin compounds. A Karplus-type relationship has been indicated between dihedral angle, ϕ, and the $^3J(^{119}\mathrm{Sn}–^{13}\mathrm{C})$ values in cyclic systems.

3.2.2 ^{119}Sn NMR Spectra in Solution

The usual reference standard used for ^{119}Sn values is $\mathrm{Me_4Sn}$; negative chemical shifts are upfield from $\delta^{119}\mathrm{Sn(Me_4Sn)} = 0$. Chemical shift values, δ^{119}Sn, are dominated by the paramagnetic contribution and span a range of greater than 4000 ppm.

The important factors which influence δ^{119}Sn are the electronegativities of substituents at tin and the geometry and coordination number at tin. The effect of different coordination numbers of tin on the δ^{119}Sn values can be seen in the following ranges: for four-coordinate organotin(IV), +200 to −150 ppm; for five-coordinate organotin(IV), −90 to −330 ppm; and for six-coordinate organotin(IV), −125 to −515 ppm.

π-Bonded organotin(II), e.g. $(\pi\text{-}\mathrm{C_5H_5})_2\mathrm{Sn}$, have δ^{119}Sn values of ca. −1630 to −2250 ppm; the reported value for the σ-bonded $\mathrm{Sn^{II}}$ species $[\mathrm{(Me_3Si)_2CH}]_2\mathrm{Sn}$ is 2315 ppm.

3.2.3 Solid-State NMR Spectra

Solid-state ^{13}C NMR and ^{119}Sn NMR spectra are being more frequently reported as the technique becomes more generally available. The combined use of X-ray crystallography, and solution and solid-state NMR spectra enables comparisons to be made between structures in the two phases. Changes in structures between the two phases are readily indicated by differences in δ^{119}Sn values, e.g. tricyclohexyltin hydroxide in the solid state is a linear polymer (δ^{119}Sn is −217 ppm) but the aggregation is broken down in solution (δ^{119}Sn is +11.66 ppm). Compounds having similar structures in both the solid state and in solution have $\Delta(\delta^{119}\mathrm{Sn})$ values differing by only a few ppm, e.g. for $t\text{-}\mathrm{Bu_2}\overline{\mathrm{SnSCH_2CH_2S}}$ the δ^{119}Sn values in solution and in the solid state are 171 and 173 ppm, respectively.

The one-bond coupling constant $^1J(^{119}\mathrm{Sn}–^{13}\mathrm{C})$ is also of interest; a linear relationship has been reported between these coupling constants in the solid state and the C–Sn–C valency angles in dimethyltin species.

3.3 ^{119}Sn Mössbauer Spectroscopy

Mössbauer spectroscopy is the study of recoilless resonant fluorescence; ^{119}Sn Mössbauer spectroscopy has been found to be a most useful method for studying the bonding and stereochemistry of tin compounds in the solid state. The two most important parameters are the isomer shift (δ, mm s^{-1}) and the quadrupole splitting (ΔE_Q, mm s^{-1}), although the recoil-free fractions and temperature coefficients can also supply useful structural indications.

3.3.1 Isomer Shifts (δ)

The isomer shift values (δ), usually quoted relative to $\mathrm{SnO_2}$, are dependent on the s electron density at the ^{119}Sn nucleus. A larger positive value of δ corresponds to an increase in the nuclear s electron density at tin; the range of δ observed for $\mathrm{Sn^{IV}}$ compounds is ca. −0.5 to 2.1 mm s^{-1}, and for $\mathrm{Sn^{II}}$ compounds, which contain a lone pair of 5 s electrons, the range is higher, being ca. +2.5 to +5 mm and especially about 3.6–3.9 mm s^{-1} for π-bonded organotin(II) species. For tin(II) species the isomer shift is increased as the total electronegativity of the groups at tin increase; however, for $\mathrm{Sn^{IV}}$ compounds the converse is found.

In such series of organotins as $\mathrm{R_4Sn}$ and $\mathrm{R_3SnOH}$, δ increases slightly with the electron-releasing ability of R, e.g. from 1.20 to 1.35 mm s^{-1} as R is varied from Me to Bu in $\mathrm{R_4Sn}$. Increases in the coordination number at Sn leads to a decreased δ value. *Cis* octahedral $\mathrm{R_2SnX_4}$ species have lower δ values than *trans* octahedral complexes, e.g. δ values for *cis*-$\mathrm{Ph_2Sn(NCS)_2{\cdot}bipy}$ and *trans*-$\mathrm{Ph_2SnCl_2{\cdot}bipy}$ are 0.82 and 1.22 mm s^{-1}, respectively.

3.3.2 Quadrupole Splitting Parameter (ΔE_Q)

If the tin atom has a perfectly spherical symmetry, e.g. as in $\mathrm{SnMe_4}$ and $[\mathrm{SnCl_6}]^{2-}$, only a single line is observed in the ^{119}Sn Mössbauer spectrum. However, a deviation from this symmetry (e.g. as in $SnCl_5^-$) will lead to a two-line quadrupole split spectrum, with ΔE_Q equal to the separation of the two lines. The main cause of asymmetry in the ^{119}Sn nuclear charge is an imbalance in the 5p valence electrons. For organotin compounds the spatial arrangement of the organic groups about tin has an effect on the ΔE_Q values; distinct ranges of ΔE_Q are found for different types of stereochemistry. Thus regular tetrahedral R_3SnY and R_2SnY_2 compounds have ΔE_Q values which fall into the range 1.00–2.40 mm s^{-1} (e.g. $(Ph_3Sn)_2S$ and $(Ph_2SnS)_3$ have ΔE_Q values of 1.46 and 1.60 mm s^{-1}, respectively) and ΔE_Q values for *cis* and *trans* trigonal bipyramidal R_3SnX_2 complexes are in the regions 1.20–2.40 and 3.00–4.00 mm s^{-1}, respectively (e.g. *cis*-$Ph_3SnONPhCOPh$ and *trans*-$Ph_3SnCl_2^-$ have ΔE_Q values of 1.94 and 2.89 mm s^{-1}).

For six-coordinate methyltin compounds the value of the C–Sn–C valency angle has been correlated with the value of ΔE_Q.

For *cis*- and *trans*-R_2SnX_4 species, values obtained for ΔE_Q are ca. 2.00 and 4.00 mm s^{-1}, respectively (e.g. *cis*-$Ph_2Sn(SCSNEt_2)_2$ and *trans*-$Ph_2SnCl_2 \cdot 2DMSO$ have ΔE_Q values of 1.72 and 3.86 mm s^{-1}, respectively). Other values obtained for diorganotin(IV) species are for seven-coordinate pentagonal bipyramidal *trans*-$Me_2Sn(NCS)_2 \cdot$terpy ($\Delta E_Q = 4.29$ mm s^{-1}) and *cis* five-coordinate trigonal bipyramidal R_2SnX_3 ($\Delta E_Q = 3.00–3.50$ mm s^{-1}) (e.g. $Me_2SnCl_3^-$, $\Delta E_Q = 3.30$ mm s^{-1}).

Monoorganotin complexes have similar ΔE_Q values irrespective of their geometry.

For π-bonded organotin(II) compounds, ΔE_Q values are in the region 0 to 1.0 mm s^{-1}; the complexes $(\pi\text{-}C_5H_5)_2SnM(CO)_5$ (M = Cr or Mo) have ΔE_Q values of ca. 2.6–2.7 mm s^{-1}, the ΔE_Q value for the σ-bonded $[(Me_3Si)_2CH]_2Sn$ is 2.31 mm s^{-1}; on complexation with $M(CO)_5$ (M = Cr or W), the ΔE_Q values increase to ca. 4.5 mm s^{-1}.

4 TETRAORGANOTIN COMPOUNDS

Tetraorganotin compounds are generally thermally stable, e.g. to 200 °C, and are stable towards air or water. Reactions occur with a variety of reagents, both heterolytic and homolytic (see also Section 5). In most cases tetraorganotin compounds contain tetrahedral, four-coordinate tin atoms; however, a few five- and six-coordinate tetraorganotin compounds have been characterized in the solid state and in solution. In these compounds, an internal nitrogen or oxygen atom is suitably sited to coordinate with the tin center (see (**6–10**)).

Compound (**10**) has an enhanced reactivity towards electrophilic reagents,[17] which has been ascribed to the ideal siting of the nitrogen atom to take part in nucleophilic assistance at the tin center during the cleavage reactions. Tetraorganotin compounds have in general very low Lewis acidity; only one adduct of a tetraorganotin species has been reported, i.e. $Me_3SnCF_3 \cdot O{=}P(NMe_2)_3$.

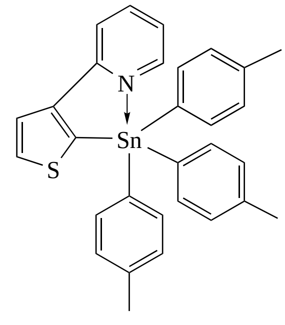

(**6**) Sn–N 2.841(7) Å

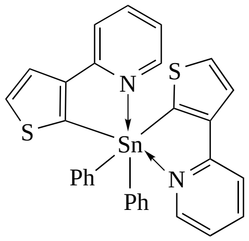

(**7**) Sn–N 2.560(2) Å

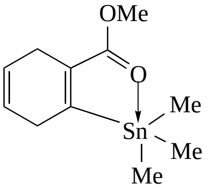

(**8**) Sn–O 2.781(3) Å

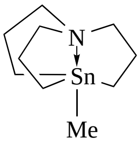

(**9**) Sn–N 2.624(8) Å

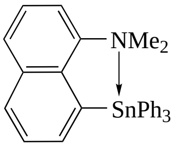

(**10**) Sn–N 2.884(3) Å

Resolution of chiral tetraorganotin compounds has been achieved, using chiral auxiliary groups (equation 35), as well as the use of chromatography on chiral stationary phases, e.g. cellulose triacetate for $Me(PhCMe_2CH_2)Ph(Ph_3C)Sn$.

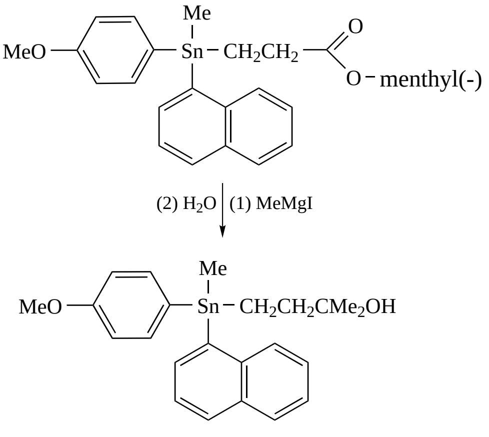

$[\alpha]_D^{20}$ +9°

(35)

5 CLEAVAGE OF CARBON–TIN BONDS

Tin–carbon bonds may be cleaved in either homolytic or heterolytic reactions.

5.1 Homolytic Cleavage[18]

Homolytic cleavage of a tin–carbon bond in a tetraorganotin compound is less frequently encountered than is heterolytic cleavage. Such radicals as Br•, I•, and the succinimidyl radical can take part in S_N2 displacement with tetraorganotins (Scheme 8). The reactivity of R_4Sn in Me_2CO towards the succinimidyl radical is in the sequence of $R = Me > Et > Pr > Bu$; this is the reverse of that for radical reactions of iodine and bromine.

Alkoxy radicals attack the α- and β-carbon atoms of tetraalkyltins; however, they react at the tin center in trialkyltin halides (equation 36).

$$t\text{-BuO}\bullet + \text{Bu}_2(t\text{-Bu})\text{SnCl} \longrightarrow \text{Bu}\bullet + (t\text{-BuO})\text{Bu}(t\text{-Bu})\text{SnCl} \quad (36)$$

5.2 Heterolytic Cleavages of Tin–Carbon Bonds[11]

In heterolytic cleavages of tin–carbon bonds, electrophilic attack (by E) at carbon is usually the more influential, although nucleophilic assistance (by Nu) at tin can also play a role, and in some cases can become dominant (equation 37).

$$\overset{\delta+\ \delta-}{\text{R}_3\text{Sn–R}} + \overset{\delta+\ \delta-}{\text{E–Nu}} \longrightarrow \text{R}_3\text{Sn–Nu} + \text{R–E} \quad (37)$$

5.2.1 Nucleophilic Cleavages

Nucleophilic cleavages have been reported by hydroxide and alkoxides with C_6F_5Sn, $PhCH_2Sn$, allyl-Sn, $RC{\equiv}CSn$, and, more generally, by organolithiums (equation 38). The transmetalation reaction (equation 38), which proceeds via an 'ate' complex, is an equilibrium. The position at equilibrium depends on the relative stabilities of the carbanion fragments, $(R^2)^-$ and $(R^1)^-$, with the more stable carbanionic fragment providing the greater amount of the organolithium product. Essentially quantitative exchanges occur between R^2Li = alkyl- or phenyl-Li with R^1SnR_3, where R^1 is allyl, vinyl, XCH_2 ($X = R^3O$, R^3S or R^3Se), etc (equation 39).

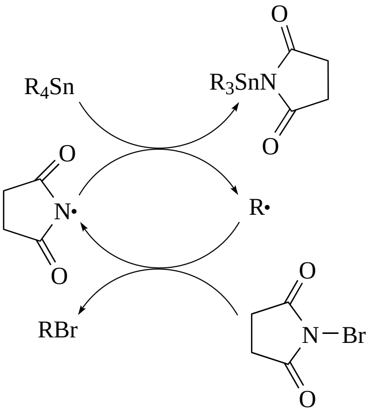

Scheme 8

$$\text{R}_3\text{SnR}^1 + \text{R}^2\text{Li} \rightleftharpoons \text{R}_3\text{SnR}^2 + \text{R}^1\text{Li} \quad (38)$$

$$\text{Bu}_3\text{SnCH}_2\text{OCH}_2\text{OMe} + \text{BuLi} \longrightarrow \text{Bu}_4\text{Sn} + \text{LiCH}_2\text{OCH}_2\text{OMe} \quad (39)$$

5.2.2 Electrophilic Cleavages

Electrophilic cleavages have been the most reported reactions with regard to both kinetics and synthetic utility (of either the organic or organometallic products). A great array of electrophilic reagents (E–Nu) have been employed, including halogens, proton acids (carboxylic and mineral acids), metal halides (e.g. SnX_4, HgX_2, BX_3, platinum halides), sulfur(II) halides, and sulfur oxides. With the more reactive reagents, more than one carbon–tin bond can be cleaved.

Transfer of organic groups from tin to carbon electrophiles, e.g. alkyl halides and acyl halides, can occur in the presence of a transition metal (e.g. Pd) catalyst (equation 40).[19] Reactivity sequences for electrophilic carbon–tin bond cleavages are generally allyl > phenyl > benzyl > vinyl > methyl > higher alkyl. The precise sequence is somewhat dependent on the solvent and electrophile.

$$\text{R}_3\text{SnR}^1 + \text{R}^2\text{X} \xrightarrow{\text{Pd}^0\text{or}\text{Pd}^{\text{II}}} \text{R}^1\text{R}^2 \quad (40)$$

Aryl–tin bond cleavages by electrophilic reagents are typical electrophilic aromatic substitutions,[2] with greater electron-releasing substituents in the aryl group leading to faster reaction (equations 41 and 42). The mechanism of cleavages of alkyl–tin bonds is usually S_E2; both retention and inversion of configuration have been realized for halogenations (equation 43). For protolysis of carbon–tin bonds, retention of configuration is frequently obtained, e.g. as found in reaction between CF_3CO_2H and cyclohexyl(triisopropyl)stannanes.

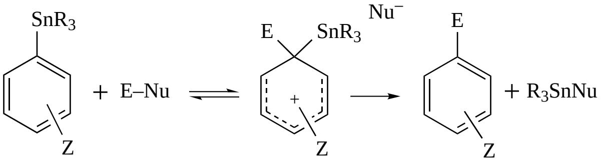

(41)

$$\text{Ph}_3\text{SnMe} + \text{I}_2 \longrightarrow \text{IPh}_2\text{SnMe} + \text{PhI} \quad (42)$$

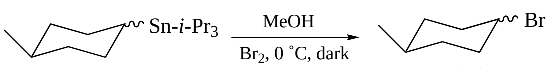

(11) **(12)** (43)

trans-(**11**) ⟶ (**12**) 56%, net inversion
cis-(**11**) ⟶ (**12**) 61%, net inversion

Enhanced reactivities for organotin bonds can be obtained on nucleophilic assistance by donor groups present within the organostannane (equations 44 and 45). In equation (44) the reactivity of the Me–Sn bond, normally inert to Me_3SnCl, is enhanced by the nucleophilic assistance provided by the ester group. In equation (45) the usual reactivity sequence of benzyltin > alkyltin is overturned by the nucleophilic assistance afforded by the NMe_2 group to cleavage of the Sn–Bu group.

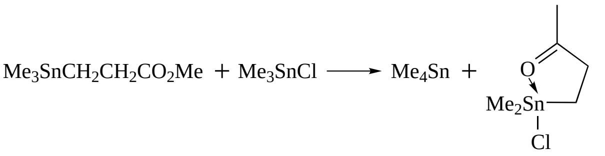

(44)

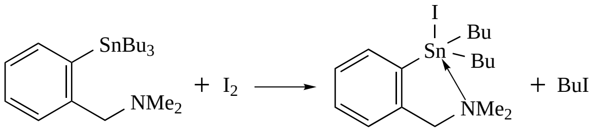

(45)

5.3 Specific Cleavages and Reactions

5.3.1 Vinyltin

Generally, cleavage of vinyltin compounds proceeds with retention of configuration during reaction with electrophilic reagents and organolithiums (equation 46). As well as the cleavage shown in equation (46), addition to the double bond has been found in some cases, as in heterolytic reactions, e.g. with ArS–Cl, in epoxidations, and in homolytic reactions, e.g. thiols and $Cl_3C{-}X$ ($X = Cl$ or Br).

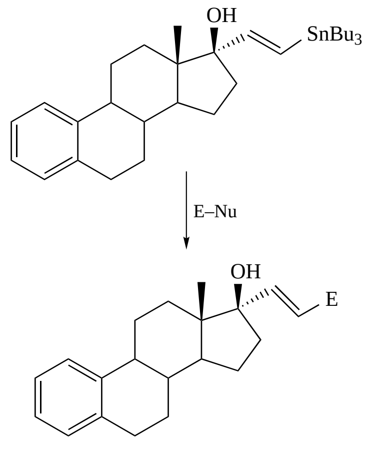

(46)

$E{-}Nu = H{-}O_2CCF_3$, I−I, PhSe−Br

5.3.2 Allyltin

Allyltin bonds are among the most reactive carbon−tin bonds and they undergo reactions with mild electrophiles, e.g. aldehydes (equation 47).[20] Protonolysis of allyltin bonds proceeds with γ-regioselectivity and *anti* stereoselectivity. Sulfur dioxide cleavages, however, occur with γ-regioselectivity and *syn* stereoselectivity (equation 48). Allyltin bonds are cleaved in homolytic reactions, e.g. by PhSSR, PhSePh, RCO_2Cl, and RX (QX) (equation 49).[21]

$$R_3SnCH_2CH{=}CHR^1 \xrightarrow[\Delta\ \text{or Lewis acid catalyst}]{R^2CHO} R_3SnOCHR^2CH_2CH{=}CHR^1 + R_3SnOCHR^2CHR^1CH{=}CH_2 \qquad (47)$$

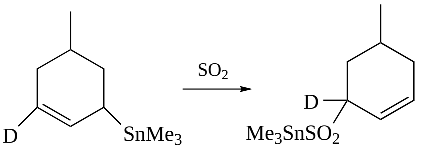

(48)

cis:*trans* = 29:71

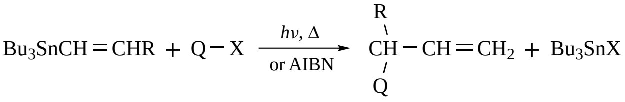

$$Bu_3SnCH{=}CHR + Q{-}X \xrightarrow[\text{or AIBN}]{h\nu,\ \Delta} \underset{Q}{\overset{R}{CH}}{-}CH{=}CH_2 + Bu_3SnX \qquad (49)$$

5.3.3 3-Butenyltin Compounds

γ-Eliminations have been reported in reactions of 3-butenyltin compounds (equation 50).

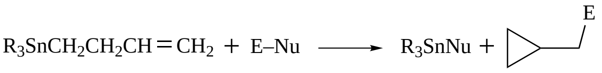

(50)

$E{-}Nu = Cl{-}Cl, I{-}I, Br{-}Br, ArS{-}Cl$

5.3.4 Propargyltin and Allenyltin Compounds

These compounds contain reactive carbon−tin bonds which are cleaved with complete rearrangement by electrophilic species (equations 51 and 52). Propargyltins also undergo S_H2' reactions with RSO_2Cl, Cl_3CCl, RBr, or RI (≡QX) (equation 53).

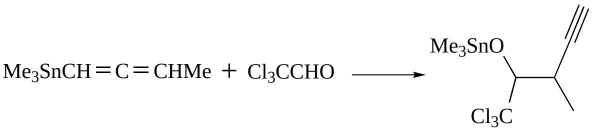

(51)

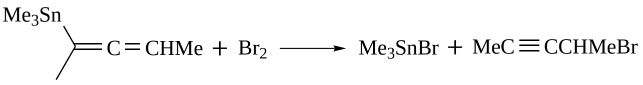

(52)

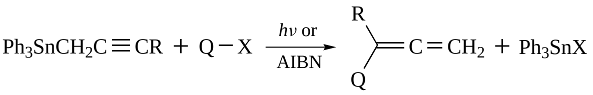

$$Ph_3SnCH_2C{\equiv}CR + Q{-}X \xrightarrow[\text{AIBN}]{h\nu\ \text{or}} \underset{Q}{\overset{R}{>}}C{=}C{=}CH_2 + Ph_3SnX \qquad (53)$$

5.3.5 Functionally Substituted Alkyltin Compounds

The presence of a functional group, Y, in an alkyl group in an organotin compound, e.g. $R_3Sn(CH_2)_nY$, can (i) affect the reactivity of the Sn–$(CH_2)_nY$ bond (by its electronic influence), (ii) affect the reactivity of the R–Sn bond (by nucleophilic assistance from Y at the tin center), or (iii) alter the type of reaction undergone (e.g. β- or γ-elimination). Depending on Y, other reactions, such as oxidation, reduction, salt formation, and substitution, can occur at Y without C–Sn bond cleavage.

Organotin compounds bearing such β-substituents as OH, OR, SR, NR_2, or PR_2 can undergo β-elimination, as shown in equations (54–56).[22] Alkene eliminations have been reported for alkyltins which have β-hydrogens when reacting with $Ph_3C^+\ BF_4^-$; the reaction proceeds via *trans* elimination (equation 57). An example of γ-elimination is shown in equation 58.

$$\mathrm{Ph_3SnCH_2CH_2OH} \xrightarrow{\mathrm{H_3O^+}} \mathrm{Ph_3SnOH} + \mathrm{H_2C{=}CH_2} \tag{54}$$

$$\mathrm{Ph_3SnCH_2CH_2NMe_2} \xrightarrow{\mathrm{ArSCl}} \mathrm{Ph_3SnCl} + \mathrm{H_2C{=}CH_2} + \mathrm{Me_2NSAr} \tag{55}$$

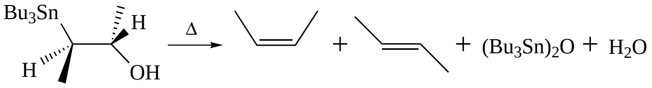

100 °C 9 : 89
160 °C 61 : 31

(56)

$$\mathrm{Me_3SnCHRCH_2R'} \xrightarrow{\mathrm{Ph_3C^+BF_4^-}} [\mathrm{Me_3SnBF_4}] + \mathrm{RCH{=}CHR'} + \mathrm{Ph_3CH} \tag{57}$$

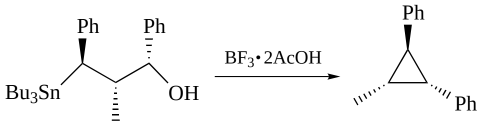

(58)

6 ORGANOTIN(IV) HALIDES AND PSEUDOHALIDES[5]

6.1 Synthesis

6.1.1 *Synthesis of Halides*

Organotin(IV) halides have been obtained directly from organic halides, RX and tin, or tin chlorides, as outlined in Section 2.1.1.

The Kocheshkov redistribution reaction between tetraorganotins and tin(IV) halides, in appropriate mole ratios, is a general method of synthesis of organotin halides (equations 59 and 60). It is a particularly useful reaction, since it is difficult to control the alkylation of SnX_4 by organolithium or Grignard reagents to the desired extent.

$$n\mathrm{R_4Sn} + (4-n)\mathrm{SnX}_n \longrightarrow 4\mathrm{R}_n\mathrm{SnX}_{4-n} \tag{59}$$

$$\mathrm{Ph_3SnMe} + 3\mathrm{SnCl_4} \longrightarrow 3\mathrm{PhSnCl_3} + \mathrm{MeSnCl_3} \tag{60}$$

Carbon–tin bonds are also readily cleaved by halogens (reactivity sequence $Cl_2 > Br_2 > I_2$), hydrogen halides, and metallic halides (including $TiCl_4$, $AlCl_3$, BCl_3, platinum chlorides, and $HgCl_2$) to give organotin halides. Scheme 9 shows products of monosubstitution; depending on the R groups and the halogenating agent, further substitution is possible. The reactivity of R–Sn bonds towards electrophiles such as halogen is usually in the sequence allyl > Ph > $PhCH_2$ > $CH_2{=}CH$ > Me > Et > Pr > Bu (see equation 42). For bromine reactions, tightly controlled conditions (i.e. temperature, solvent, and rate of addition) are necessary to minimize the formation of some diorganotin dibromides, even at a $R_4Sn{:}Br_2$ mole ratio of 1:1. Reactions of the less reactive iodine can be more easily limited to monosubstitutions, but disubstitution can arise with the more reactive organotins.

Organotin halides can also be obtained from oxides or hydroxides on reaction with hydrogen halides (or ammonium halides) (equation 61) and from tin–tin bonded species on reaction with halogens (equation 62).

$$[\mathrm{R_2SnO}]_n + 2n\mathrm{HX} \xrightarrow{-\mathrm{H_2O}} n\mathrm{R_2SnX_2} \tag{61}$$

$$\mathrm{R_3Sn{-}SnR_3} \xrightarrow{\mathrm{X_2}} 2\mathrm{R_3SnX} \tag{62}$$

6.1.2 *Synthesis of Pseudohalides*

Organotin halides can be converted to the corresponding pseudohalides on treatment with suitable metal salts (Scheme 10). Tin oxides or hydroxides have been used with NH_4Y, HY, or Me_3SiY and tin amides have been used with HY (Y = SCN (or NCS), NCO, N_3, CN, etc.)

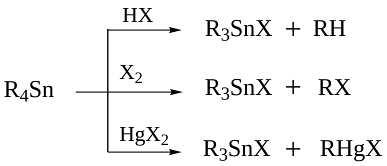

Scheme 9

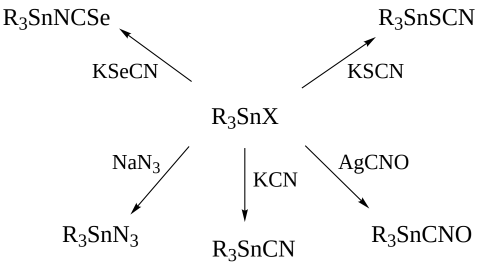

Scheme 10

6.2 Physical and Structural Properties

Triorganotin fluorides, except those with bulky organic groups, are highly associated, are very sparingly soluble in common organic solvents, and have high melting points. Me_3SnF, mp ca. 320 °C, has the asymmetrically fluoride-bridged structure (**13**). Ph_3SnF, $(PhCH_2)_3SnF$, and $(Me_3SiCH_2)_3SnF$ have symmetrically bridged structures[23] with linear Sn–F–Sn linkages (**14**).

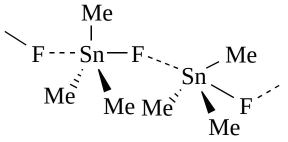
(**13**)

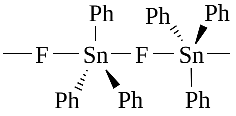
(**14**)

In contrast, bulky $(2,4,6\text{-}Me_3C_6H_2)_3SnF$, $[(Me_3Si)_3C]R_2SnF$ ($R = Me$ or Ph) and $(PhMe_2Si)_3CMe_2F$ are monomeric in the solid state and have appreciable solubility, e.g. in chloroform. The simple triorganotin chlorides, bromides, and iodides (along with the di- and monoorganotin derivatives) generally have lower melting points and are usually very much more soluble in chlorocarbon and alcohol solvents than their fluoride analogs; methyltin chlorides, bromides, and iodides have appreciable solubility in water.

The iodides are the least thermally stable in the series of related halides. Configurational stability of organotin halides is limited, e.g. chiral $MePh(PhCMe_2CH_2)SnCl$ can be obtained but, once formed in solution, it rapidly racemizes.

The organotin halides R_nSnX_{4-n} ($X = Cl$, Br, or I) are tetrahedral molecules in the vapor phase and as liquids. As a solid, Me_3SnCl has been shown to have a weakly chloride-bridged structure, but one which is broken up on dissolution. The geometry about tin in crystalline R_3SnCl becomes progressively more ideally tetrahedral in the sequence $R = \text{cyclohexyl} > Ph > (Me_3Si)_2CH$. Triorganotin bromides and iodides, due both to the reduced electronegativity and the larger size of the halides, more strongly favor monomeric tetrahedral structures, e.g. as shown by Ph_3SnBr.

Various triorganotin halides that have in-built donor groups have been found to be chelated in the solid state, with pentacoordinate trigonal bipyramidal tin atoms; the chelation can persist in solution too. Four-, five-, and six-membered chelate rings can be formed, e.g. (**15**)–(**17**).[24–26]

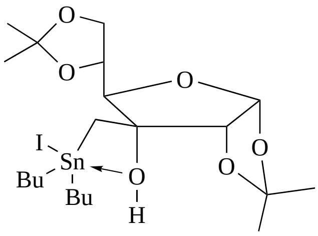
(**15**)

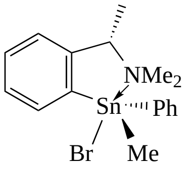
(**16**)

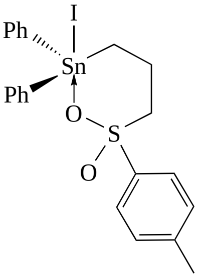
(**17**)

For pseudohalides, intermolecular bridging is usually a strong feature, e.g. in $Me_3SnC{\equiv}N$ (bridging N), $R_3SnN{=}C{=}S$ ($R = Me$ or Ph) (bridging S), $Ph_3Sn\text{–}N\text{–}C{=}O$ (bridging O), and $Me_3SnN{=}N{=}N$ (bridging α-N).

Ionization of tin–halogen bonds can occur in triorganotin halides containing two intramolecular donor groups, e.g. (**18**).[26] Diorganotin dihalides and bis-pseudohalides also exhibit strong tendencies to form aggregated species with hexacoordinate tin atoms, as in dimethyltin difluoride (**19**) and dimethyltin dicyanide.

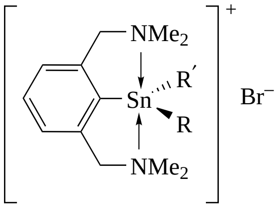
(**18**) R = R′ = Me or Ph; R = Me, R′ = Ph

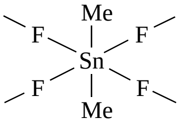
(**19**)

The halide bridging still persists in dialkyltin dichlorides[27] and dibromides, but is somewhat weaker and is of an asymmetric nature, either as in (**20**) or (**21**). Diphenyltin dichloride and methylphenyltin dichloride have weak tetrameric associated structures; the two terminal tin atoms are tetracoordinate, with the middle two tin atoms being hexacoordinate. Dicyclohexyltin dichloride has essentially a one-dimensional polymeric structure with a five-coordinate tin atom, but with an additional weak tin chlorine interaction (**22**). Both bis(2-biphenylyl)tin dichloride and 5,5-dichloro-10,11-dihydrodibenzo[*b*,*f*]stannepin (**23**) are monomeric in the solid state.[28]

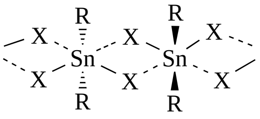
(**20**)
R = Me, Et or Bu; X = Cl;
R = Et, X = Br

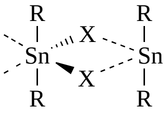
(**21**)
R = Et, X = I; R = Me, X = NCS

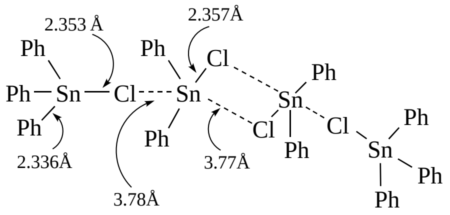

(**22**)

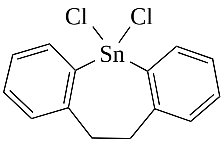

(**23**)

Diorganotin dihalides with in-built donor groups can form monomeric octahedral complexes (with two in-built donor centers) or trigonal bipyramidal complexes (with one in-built donor center), e.g. (**24**) and (**25**). Methyltin trihalides are assumed, from spectroscopic evidence, to have polymeric structures. For monoorganotin halides with in-built donor centers, chelate structures with trigonal bipyramidal tin atoms are possible, e.g. (**26**) and (**27**).

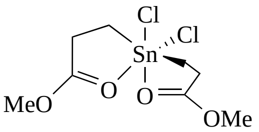

(**24**)

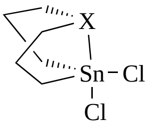

(**25**) X = NMe, O or S

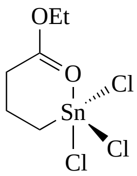

(**26**)

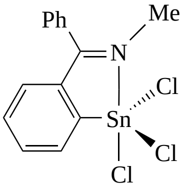

(**27**)

6.3 Reactions

Scheme 11 illustrates for R_3SnCl many of the transformations undertaken by organotin halides and pseudohalides. As already pointed out, trimethyltin halides dissolve to an appreciable extent in aqueous systems to give $[Me_3Sn(OH_2)_2]^+$; its $[BPh_4]^-$ salt has been isolated. A tetraaquadication $[Me_2Sn(OH_2)_4]^{2+}$ is similarly obtained from Me_2SnX_2. The general hydrolysis sequence for organotin halides is shown in Section 12.

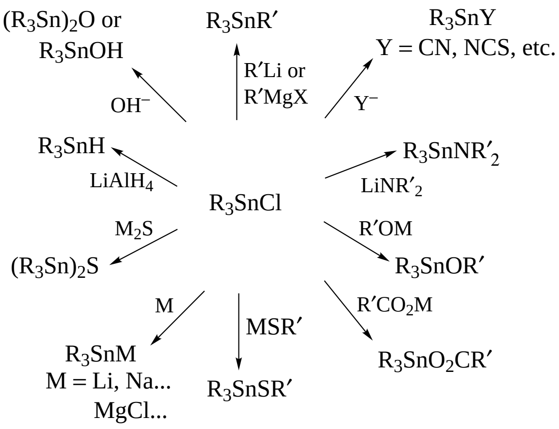

Scheme 11

6.4 Lewis Acidity

Organotin halides and pseudohalides are Lewis acids. As has already been indicated, they exhibit a strong tendency to expand their coordination number beyond four. This can be achieved by intermolecular associations or by forming complexes either with external ligands or via intramolecular complexation.

Sequences of acceptor strengths of organotin halides and pseudohalides for R_3SnX are $X = NCS > Cl > Br > I$ and for R_nSnX_{4-n} are $RSnX_3 > R_2SnX_2 > R_3SnX$. Stronger complexes are found for O and N ligands than for S and P ligands.

For $R_3SnX \cdot L$ complexes, trigonal bipyramidal geometry is obtained, e.g. for $Me_3SnCl \cdot py$ and $Ph_3SnCl \cdot OPPh_2CH{=}CHP(O)Ph_2$. Complexes of diorganotin dihalides and bis-pseudohalides can contain five-, six-, or seven-coordinate tin, e.g. $[Ph_2SnCl_2(2\text{-}H_2N\text{-benzothiazole})]$ (trigonal bipyramidal tin), $[Me_2SnBr_2(py)_2]$ (*trans* octahedral geometry), $[Ph_2Sn(NCS)_2(bipy)]$ (*cis* octahedral geometry), and $[Me_2Sn(NCS)_2(terpyridyl)]$ (pentagonal bipyramidal geometry with *trans* methyl groups).

A chloride-bridged dimeric complex $[Me_2SnCl_2 \cdot (2,3\text{-diphenylcyclopropanone})]$ (**28**) has been characterized. A seven-coordinate tin complex (**29**) has also been prepared.

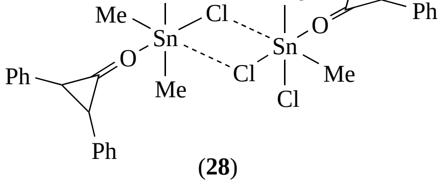

(**28**)

Both trigonal bipyramidal, e.g. as in $MeSnBr_3 \cdot DMF$, and octahedral complexes of organotin trihalides are known, e.g. *fac*- and *mer*-$[i\text{-}PrSnCl_3 \cdot (DMF)_2]$ (**30**) have been

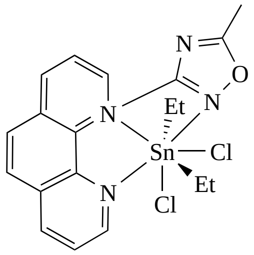

(**29**)

characterized.[29] Anionic complexes, $[R_3SnX_2]^-$, $[R_2SnX_3]^-$, $[RSnX_4]^-$, and $[RSnCl_5]^{2-}$, etc., can also be isolated, e.g. (**31**) and (**32**).[30]

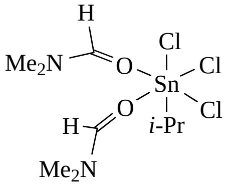

fac-(**30**)

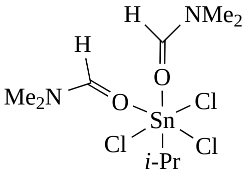

mer-(**30**)

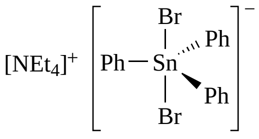

(**31**)

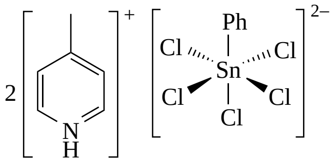

(**32**)

7 ORGANOTIN(IV) HYDRIDES

Reduction of organotin halides R_nSnX_{4-n} by $LiAlH_4$ or $NaBH_4$ in Et_2O at room temperature is the most frequently used route to R_nSnH_{4-n} (equation 63). Alternative routes include hydrolysis of tin–alkali metal or tin–alkaline earth metal bonded compounds. (equation 64). Deuterides may be similarly obtained using, for example, $LiAlD_4$ with organotin halides or D_2O with anionic Sn species.

$$\mathrm{Ph_3SnCl} \xrightarrow{\mathrm{LiAlH_4}} \mathrm{Ph_3SnH} \tag{63}$$

$$\mathrm{Bu_3SnNa} \xrightarrow{\mathrm{H_2O}} \mathrm{Bu_3SnH} \tag{64}$$

The thermal stability of R_nSnH_{4-n} falls in the sequence $n = 3 > 2 > 1$ and R = aryl > alkyl. They can normally be distilled under reduced pressure, but are sensitive towards oxygen. In their spectrum the Sn–H bond has a sharp absorption at 1800–1880 cm^{-1}. The hydrides are monomeric in both gas and solution phases. The crystal structure of the chiral tin hydride (−)-(*t*-Bu)(8-Me_2N-naphthyl)(menthyl)tin hydride (**33**) has been determined.[31]

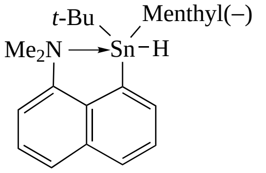

(**33**) Sn–N = 2.931 and 2.885 Å
Sn–H = 1.52(5) and 1.63(5) Å

Organotin hydrides can undergo either heterolytic or homolytic reactions. Reactions with carboxylic acids and with R'_3SnX (X = OR, NR_2, or other nucleophilic groups) are considered to be heterolytic reactions. Other heterolytic reactions of triorganotin hydrides are shown in Scheme 12.

Addition of tin hydrides to C=O and C=NR groups can proceed via a polar mechanism, or via a radical mechanism if azobis(isobutyronitrile) (AIBN) is added or UV irradiation is used. Alkenes with strongly electron-withdrawing groups, e.g. $CH_2{=}CHC{\equiv}N$, undergo nucleophilic addition reactions with R_3SnH to give the α-adduct; however, in the presence of a radical initiator, homolytic addition occurs to give the β-adduct (Scheme 3). Most additions of tin hydrides to alkenes (hydrostannations) proceed via homolytic chain mechanisms and usually a radical initiator (AIBN or UV light) is employed (Scheme 2).

Another important homolytic reaction of tin hydrides is the reduction of carbon–halogen bonds; the reaction is promoted by initiators and retarded by radical traps (Scheme 13). Reactivity decreases in the sequence X = I > Br > Cl and $Bu_3SnH > Bu_2SnH_2 \approx Ph_3SnH > BuSnH_3$. Other groups X in RX that can be reduced by tin hydrides include –OC(S)R, SR, SePh, TePh, NC, and NO_2. The intermediate radical, R′• in Scheme 13, can be trapped by additional substances, e.g. alkenes, or may undergo

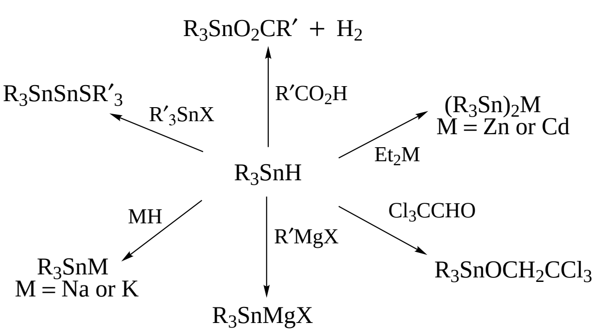

Scheme 12

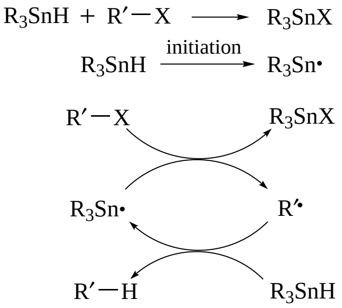
R3SnH + R′−X → R3SnX + R′−H
R3SnH → R3Sn•
initiation
R′−X
R3SnX
R3Sn•
R′•
R′−H
R3SnH

Scheme 13

cyclization or some other rearrangement before reaction with R_3SnH. Tin hydrides have found great use in organic synthesis.

8 TIN–TIN BONDED COMPOUNDS[2,32–34]

Various tin–tin bonded compounds are known. The simplest tin–tin bonded compounds, hexaorganoditins, R_3SnSnR_3, are available by several routes, including: (i) from triorganotin halides and alkali metals in ether or liquid ammonia (equation 65); (ii) from triorganotin halides and triorganotin lithium compounds (equation 66); and (iii) from triorganotin hydrides in the presence of a base (such as pyridine) or on reaction with Sn–O, Sn–N, or Sn–S species (Scheme 14).

$$2R_3SnCl + M \longrightarrow R_3SnSnR_3 \quad M = Na, Li, etc. \qquad (65)$$

$$R_3SnCl + R'_3SnLi \longrightarrow R_3SnSnR'_3 \qquad (66)$$

Extensions of these reactions lead to polytin species (equations 67 and 68). Oligomerization of diorganostannylenes provides cyclic species (Scheme 15). The resulting ring size is clearly dependent on conditions; various interesting cyclic species are available from hindered organostannylenes (equation 69 and Scheme 16).[35,36] The cyclic polystannanes have been reported to undergo disproportionations in solution, e.g. *cyclo*-$(Me_2Sn)_6$ in solution reorganizes to $(Me_2Sn)_n$ ($n = 7$, 8, and 9).

$$Ph_3SnSnPh_3 \xleftarrow[-H_2]{\text{pyridine}} 2Ph_3SnH \xrightarrow[-H_2O]{(Bu_3Sn)_2O} 2Ph_3SnSnBu_3$$

Scheme 14

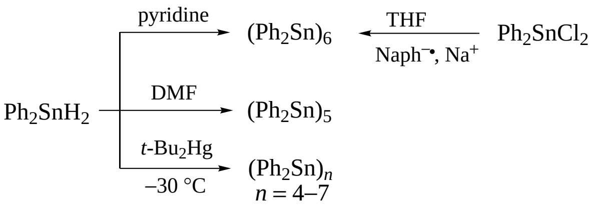
pyridine
(Ph2Sn)6
THF
Naph−•, Na+
Ph2SnCl2
Ph2SnH2
DMF
(Ph2Sn)5
t-Bu2Hg
−30 °C
(Ph2Sn)n
n = 4–7

Scheme 15

$$Ph_3SnH + (Me_2NCH_2CH_2CH_2)_2Sn(NEt_2)_2 \longrightarrow (Ph_3Sn)_2Sn(CH_2CH_2CH_2NMe_2)_2 \qquad (67)$$

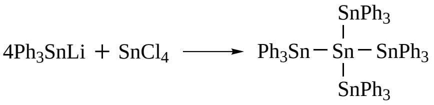

$$4Ph_3SnLi + SnCl_4 \longrightarrow Ph_3Sn-\overset{\displaystyle SnPh_3}{\underset{\displaystyle SnPh_3}{Sn}}-SnPh_3 \qquad (68)$$

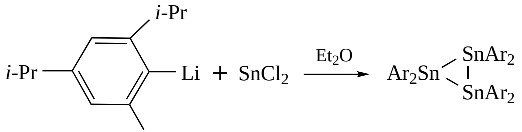
i-Pr
i-Pr
i-Pr
Li + SnCl2
Et2O
Ar2Sn
SnAr2
SnAr2

(34) (69)

An electron diffraction study of $Me_3SnSnMe_3$ has been carried out, as have crystal structure determinations of various R_3SnSnR_3 (e.g. R = Ph, p-MeC_6H_4, $PhCH_2$, and t-Bu), linear tri- and polytins (e.g. t-Bu_3SnSn-t-Bu_2Sn-t-Bu_3), $Ph_3SnSn(CH_2CH_2CH_2NMe_2)_2SnPh_3$, $Ph_3Sn(Sn$-t-$Bu_2)_nSnPh_3$ ($n = 3$ or 4), and cyclic polytin species, e.g. (**34**; Ar = 2,6-$Et_2C_6H_3$ or 2,4,6-i-$Pr_3C_6H_2$)[37] and (**35**)–(**41**).[38–40] The three-membered ring (Sn_2N) compound (**37**) was obtained from a stannylene and an acyl azide (equation 70).[41] The tin–tin bond lengths vary in the region 2.68–2.90 Å.[38–41] Compound (**40**), a dark-violet blue, air-sensitive compound, was produced on thermolysis of *cyclo*-$[(2,6\text{-}Et_2C_6H_3)_2Sn]_3$.[38]

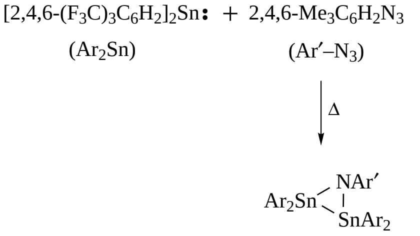
[2,4,6-(F3C)3C6H2]2Sn: + 2,4,6-Me3C6H2N3
(Ar2Sn)
(Ar′–N3)
Δ
Ar2Sn
NAr′
SnAr2

(70)

(**37**) d(Sn–Sn) 2.709Å

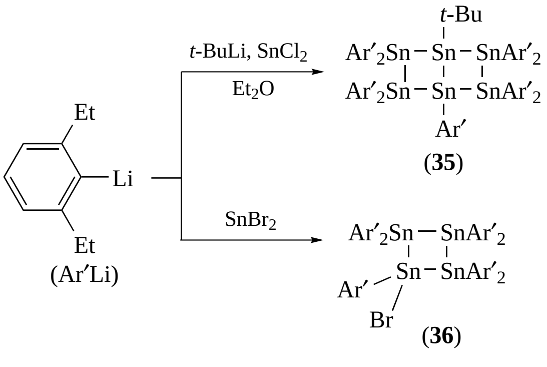
Et
Li
Et
(Ar′Li)
t-BuLi, SnCl2
Et2O
t-Bu
Ar′2Sn − Sn − SnAr′2
Ar′2Sn − Sn − SnAr′2
Ar′
(35)
SnBr2
Ar′2Sn − SnAr′2
Ar′ − Sn − SnAr′2
Br
(36)

Scheme 16

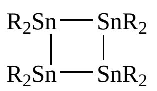

(**38**) R = Me_3SiCH_2, *t*-Bu or $EtCMe_2$

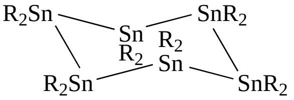

(**39**) R = Ph or $PhCH_2$

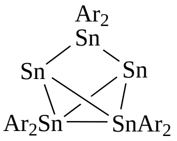

(**40**) Ar = 2,6-$Et_2C_6H_3$

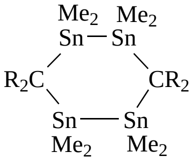

(**41a**) R = H or Me

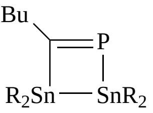

(**41b**) R = $(Me_3Si)_2CH$
d(Sn–Sn) 2.878(1) Å

The lower hexaalkylditins can be distilled in vacuo without decomposition. More elaborate ditins can suffer tin–tin homolytic cleavages on heating (equation 71). The dissociation energies for Me_6Sn_2, (**41a**), and (**41b**) are 225, 190, and 125 kJ mol^{-1}, respectively.

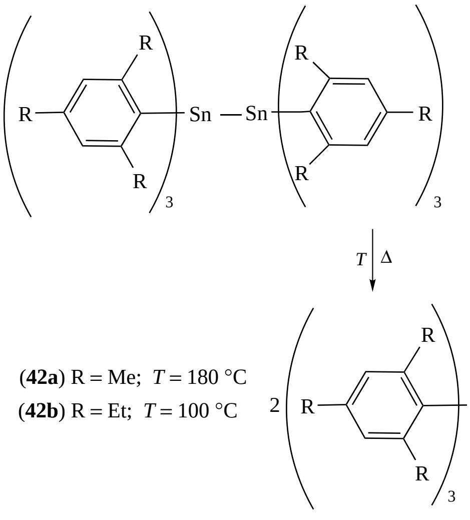

(71)

(**42a**) R = Me; *T* = 180 °C
(**42b**) R = Et; *T* = 100 °C

Tin–tin bonds also undergo photochemical cleavage (equations 72 and 73). The chemical reactions undergone by tin–tin compounds are illustrated in Scheme 17 and equation (74). Mixed Group 14 metal–metal compounds have also been studied, e.g. $(p\text{-}MeC_6H_4)_3SnPb(C_6H_4Me\text{-}p)_3$.[42]

$$R_3SnSnR_3 \xrightarrow{h\nu} 2R_3Sn\bullet \quad (72)$$

$$(R_2Sn)_n \xrightarrow{h\nu} R_2\dot{S}n(SnR_2)_{n-2}\dot{S}nR_2 \longrightarrow nR_2Sn\colon \quad (73)$$

$$cyclo\text{-}[t\text{-}Bu_2Sn]_4 \xrightarrow{I_2} I(t\text{-}Bu)_2Sn(Sn\text{-}t\text{-}Bu_2)_2Sn(t\text{-}Bu)_2I \quad (74)$$

9 ORGANOSTANNYL RADICALS[2]

Organostannyl radicals, $R_3Sn\bullet$, are generated as short-lived species in several reactions, e.g. of R_3SnH. Photolysis of hexaorganoditins, especially in the presence of *t*-BuOO-*t*-Bu, is a most convenient method of obtaining stannyl radicals for physical and ESR spectroscopic studies. Other routes to organostannyl radicals include (i) abstraction of hydrogen from R_3SnH using *t*-BuO• (generated from *t*-BuOO-*t*-Bu); (ii) photolysis of cyclopentadienyl-SnR_nX_{3-n} (X = chloro, alkyl, or C_5H_5) (which provides $R_nX_{3-n}Sn\bullet$); (iii) β-scission of a radical carrying a β-organotin substituent (equations 75 and 76); (iv) photolysis of solutions containing monomeric stannylenes, e.g. $[(Me_3Si)_2CH]_2Sn$ (equation 77); and (v) γ-irradiation of R_4Sn in hydrocarbon matrices at low temperatures (equation 78). Thermolysis of hindered $Ar_3SnSnAr_3$, e.g. Ar = 2,4,6-$R_3C_6H_2$ (R = Me, Et, or *i*-Pr), can also reversibly lead to triarylstannyl radicals (equation 71).

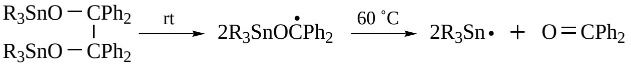

$$\begin{array}{l}R_3SnO-CPh_2\\ \quad\quad\ |\\ R_3SnO-CPh_2\end{array} \xrightarrow{rt} 2R_3SnO\dot{C}Ph_2 \xrightarrow{60\ ^\circ C} 2R_3Sn\bullet + O{=}CPh_2 \quad (75)$$

$$Me_3SnCH_2CHMe_2 \xrightarrow[-t\text{-}BuOH]{t\text{-}BuO\bullet} Me_3SnCH_2\dot{C}Me_2 \longrightarrow Me_3Sn\bullet + H_2C{=}CMe_2 \quad (76)$$

$$[(Me_3Si)_2CH]_2Sn\colon \xrightarrow{h\nu} [(Me_3Si)_2CH]_3Sn\bullet \quad (77)$$

$$Me_4Sn \xrightarrow[\text{adamantane } 77\,K]{\gamma\text{-irradiation}} Me_3Sn\bullet \quad (78)$$

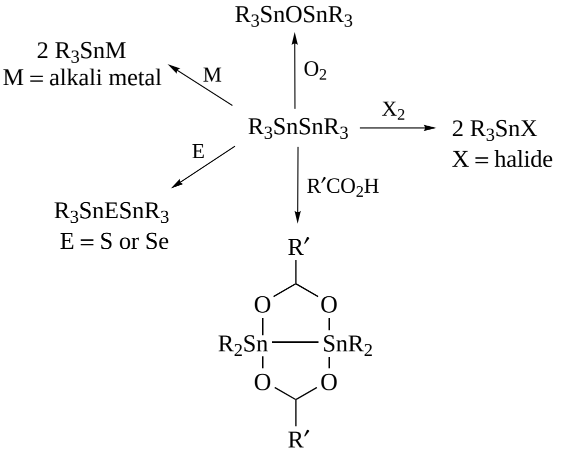

Scheme 17

The bulky stannyl radical $[(Me_3Si)_2CH]_3Sn\bullet$ has a half-life of ca. 1 year. The organostannyl radicals have pyramidal structures, with the unpaired electron in an orbital with a large degree of s character.

10 TIN–NITROGEN BONDED COMPOUNDS[2,43]

Tin–nitrogen bonded compounds are generally formed by reaction of an alkali or alkaline earth metal amide with an organotin halide; compounds of the types $R_nSn(NR'_2)_{4-n}$, ($n = 1-3$), $(R_3Sn)_nNR'_{3-n}$ ($n = 1-3$), and *cyclo*-$(R_2SnNR')_n$ ($n = 2$ or 3) can be prepared (equation 79). Other routes include transaminations (equations 80 and 81). Tin carboxamides and sulfonamides have been obtained by reaction of tin oxides or hydroxides with amides (equation 82).

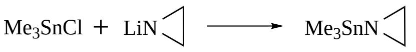

(**43**) (79)

$$2Me_3SnNMe_2 + EtNH_2 \longrightarrow (Me_3Sn)_2NEt + 2Me_2NH \quad (80)$$

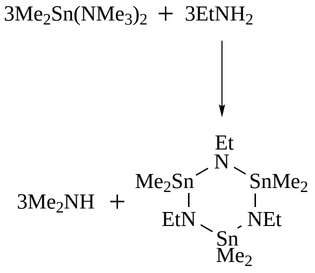

(81)

$$(Bu_3Sn)_2O + 2H_2NCOMe \longrightarrow 2Bu_3SnNHCOMe \quad (82)$$

10.1 Structures

Tetrahedral, four-coordinate tin is generally found in organotin amides. An electron diffraction structure revealed $(Me_3Sn)_3N$ to have a planar $[Sn_3N]$ core. The bulky aminohalides $[(Me_3Si)_2CH]_2Sn(X)NHC_6H_2$-*t*-$Bu_3$-2,4,6 (X = Cl or F) are monomeric compounds.[44] The $(SnN)_n$ rings in $[t$-$Bu_2SnNR]_2$ (R = *t*-Bu or SO_2Me) and $[t$-$Bu_2SnNH]_3$ were shown by X-ray crystallography to be planar.[45] An associated structure was indicated from Mössbauer data for the stannylaziridine compound (**43**). 1-Tricyclohexyltin-1,2,4-triazole is also associated in the solid state (via Sn–N(4) bridging); in contrast, the more bulky 1-$(PhCMe_2CH_2)_3Sn$-2,4-triazole is monomeric.

10.2 Reactions

Aminotin species are readily hydrolyzed and react with protic reagents (Scheme 18). Substitution reactions occur with reactive halides (equations 83 and 84), as do addition reactions with heterocumulenes, e.g. O=C=C=C=O (equation 85),[46] and with some simple carbonyl compounds (equation 86).

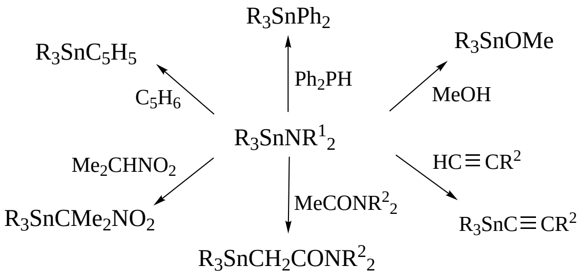

Scheme 18

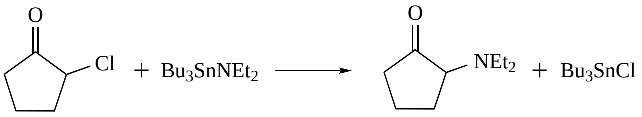

(83)

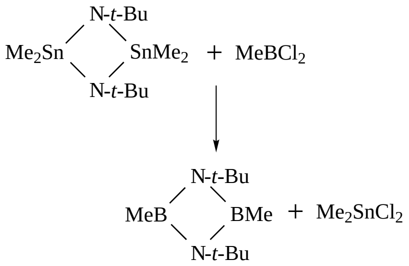

(84)

$$2Me_3SnNMe_2 + O{=}C{=}C{=}C{=}O \longrightarrow (Me_3Sn)_2C(CONMe_2)_2 \quad (85)$$

$$Me_2Sn(Cl)NEt_2 \xrightarrow{CS_2} ClMe_2SnSCSNEt_2 \quad (86)$$

11 TIN–PHOSPHORUS, –ARSENIC, AND –ANTIMONY BONDED COMPOUNDS

Synthesis of these compounds can be achieved by routes similar to those used for Sn–N bonded species (equation 87). Reactions of di- and trihalotins with R'_2PH_{3-n} ($n = 0$, 1) can lead to cages and rings (equations 88 and 89). The more bulky *t*-Bu_2SnCl_2 provides cyclic Sn_2P_2 compounds (**44**) on reaction with $NaPH_2$, $(Me_3Si)_2PMe$, or LiPH-*t*-Bu. Crystal structures have been determined for $[(Me_2Sn)_6P_2]$ and for $[(Me_2Sn)_5P_2]$ (**45**), which is obtained from $HMe_2SnSnMe_2H$ and phosphorus. Compounds with tin–phosphorus double bonds have also been reported,[47] e.g. $[(Me_3Si)_2CH]_2Sn{=}PC_6H_2$-*t*-$Bu_3$-2,4,6.

$$3Me_3SnCl + EH_3 \xrightarrow{NEt_3} 3(Me_3Sn)_3E \quad E = P \text{ or } As \quad (87)$$

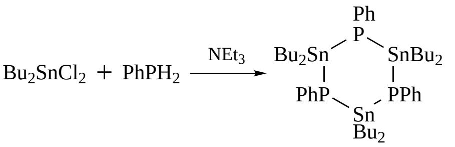
Bu2SnCl2 + PhPH2
NEt3
Ph
P
Bu2Sn
SnBu2
PhP
PPh
Sn
Bu2

(88)

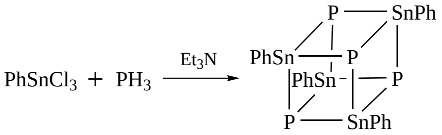
PhSnCl3 + PH3
Et3N
P
SnPh
PhSn
P
PhSn
P
P
SnPh

(89)

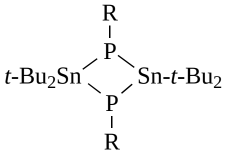
R
P
t-Bu2Sn
Sn-t-Bu2
P
R

(**44**) R = H, Me or *t*-Bu

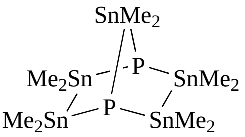
SnMe2
P
Me2Sn
SnMe2
Me2Sn
P
SnMe2

(**45**)

Examples of compounds with a Sn–Sb bond[48] are $(Me_3Sn)_2Sb–Sb(SnMe_3)_2$ (**46**) and $(Me_3Sn)_3Sb$ (**47**); photolysis of (**46**) provides (**47**). IR spectra of $(Me_3Sn)_3E$ (E = P, As, or Sb) indicate planar $[Sn_3E]$ cores. The Sn–P, Sn–As, and Sn–Sb bonds are thermally relatively stable, but are oxygen and water sensitive. Tin–phosphorus bonded compounds add[49] to heterocumulenes (as do Sn–N bonded compounds), and to alkenes, allenes, and alkynes such as $CH_2{=}CHCH_2Cl$, $CH_2{=}CHPh$ and $PhC{\equiv}CH$ (unlike Sn–N bonded species) (equation 90).

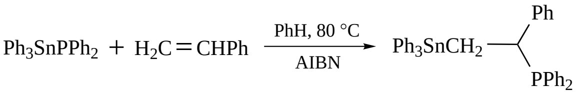
Ph3SnPPh2 + H2C=CHPh
PhH, 80 °C
AIBN
Ph3SnCH2
Ph
PPh2

(90)

12 TIN–OXYGEN BONDED COMPOUNDS[1,2]

A vast array of tin–oxygen bonded compounds is known. The majority of organotin–oxygen bonded compounds contain tin with a coordination number greater than four due to the high donor affinity of oxygen for tin and the relatively large nuclear charge at tin. Association results from oxygen bridging, which, however, can be prevented if bulky groups are present.

12.1 Organotin Oxides and Hydroxides

These compounds are most readily obtained by hydrolysis of organotin halides, especially under basic conditions, although hydrolysis of alkoxides and amides, etc., can also be used. Hydrolysis of di- and trihalides occurs in a stepwise fashion and various of the partial hydrolysis products have been characterized (Scheme 19).

Triorganotin hydroxides, R_3SnOH (R = Me, aryl, or bulky alkyl groups, e.g. $PhCMe_2CH_2$), are resistant to dehydration to the oxide, $(R_3Sn)_2O$; for other R_3SnOH, dehydration results relatively easily, e.g. on melting or on dissolution in nonaqueous media. Tris(2,4,6-trimethylphenyl)tin hydroxide is monomeric in the solid state (Sn–O = 1.999 Å).[50] Solid Me_3SnOH, which can be sublimed above 80 °C, has the associated structure (**48**) with OH groups bridging near planar Me_3Sn groups. Dehydration of Me_3SnOH, using sodium in benzene or CaH_2, provides the readily hydrated liquid $(Me_3Sn)_2O$, which in the gas phase has a Sn–O–Sn valency angle of 141° and a Sn–O bond length of 1.94 Å. The crystal structure of triphenyltin hydroxide consists of a zigzag chain of planar Ph_3Sn groups asymmetrically bridged by OH groups. Dehydration of Ph_3SnOH occurs at ca. 100 °C to give $(Ph_3Sn)_2O$, which has a four-coordinate tin atom and a Sn–O–Sn valency angle of 137°. Of interest, valency angles of 180° are found in solid $(PhCH_2)_3SnOSn(CH_2Ph)_3$ and t-Bu_3SnOSn-t-Bu_3.

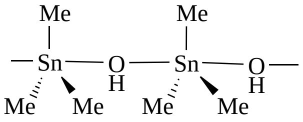
Me
Me
Sn
O
H
Sn
O
H
Me
Me
Me
Me

(**48**)

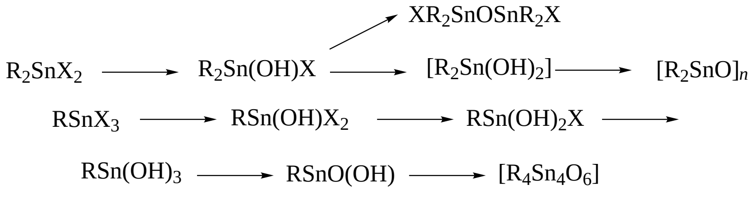
XR2SnOSnR2X
R2SnX2
R2Sn(OH)X
[R2Sn(OH)2]
[R2SnO]n
RSnX3
RSn(OH)X2
RSn(OH)2X
RSn(OH)3
RSnO(OH)
[R4Sn4O6]

Scheme 19

The hydroxides are characterized in the IR spectra by ν(O–H) bands at 3610–3630 cm^{-1} and δ(OH) at 890–920 cm^{-1}; oxides have a broad ν(Sn–O–Sn) band at 740–770 cm^{-1}.

12.2 Diorganotin Hydroxides and Oxides

Diorganotin oxides (R_2SnO) generally are polymeric species, which are insoluble in inert solvents; bulky compounds, e.g. (t-$Bu_2SnO)_3$ and $(EtCMe_2SnO)_3$, are trimeric in the solid state with planar Sn_3O_3 cores.

An interesting heterocycle (**49**) with a planar Sn_3O core was prepared by aerial oxidation**[51]** of the *cyclo*-tetratin, $Ar_2Sn–SnAr_2–SnAr_2–SnArBr$ (Ar = 2,6-$Et_2C_6H_3$). The crystal structure determination of the partial hydrolysis product of Me_2SnCl_2, viz. $ClMe_2SnOSnMe_2Cl$ (**50**), reveals a dimeric ladder-type structure with a central planar Sn_2O_2 core. This Sn_2O_2 feature is found in many structures.

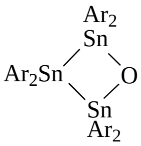

(**49**) Ar = 2,6-$Et_2C_6H_3$

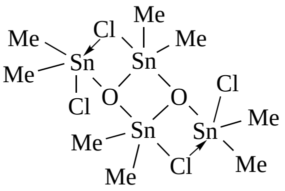

(**50**)

12.3 Monoalkyltin Hydroxides and Oxides

The fully hydrolyzed organotin trihalides are the aggregated alkane- or arenestannoic acids $[RSn(O)(OH)]_n$.

12.4 Alkoxides

Simple organotin alkoxides or phenoxides are available from the halides on reaction with MOR or MOAr, as well as from the oxides and the alcohol or phenol on azeotropic dehydration. These compounds are generally sensitive to H_2O and to CO_2. Cyclic alkoxides, e.g. (**51**) and (**52**),**[52]** and cyclic dialkoxides from diols, e.g. (**53**), can also be prepared. These complexes are usually oligomeric.

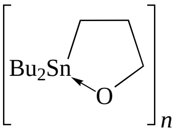

(**51**)

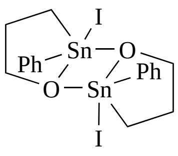

(**52**)

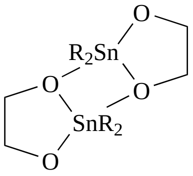

(**53**)

Stannoic acids react with triols, e.g. triethanolamine (equation 91). Triorganotin alkoxides R_3SnOR' (as well as oximes, etc.), similar to R_3SnOH, show a strong tendency to form one-dimensional polymers with oxygen bridging near planar R_3Sn units. Steric crowding at tin (but not at oxygen) reduces the tendency to associate; for example, as R in $R_3SnONC_6H_{11}$ changes in the sequence Me, Et, Pr, Ph, association becomes progressively weaker and the R_3Sn becomes more pyramidal in shape, and for R = Ph the geometry at tin is tetrahedral.

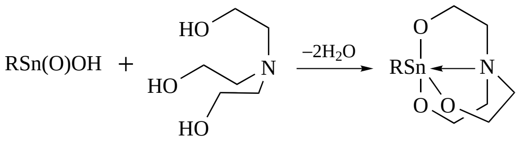

(91)

Derivatives of 1,3-diones can be prepared from the oxides with the dione (equation 92); as shown by (**54**) and (**55**), chelate complexes are formed.

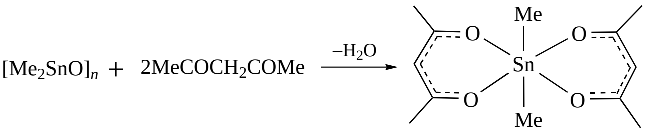

(**54**)

(92)

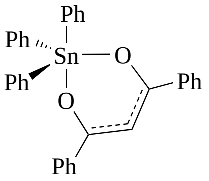

(**55**)

12.5 Reactions of the Sn–O Bond

The reactions of tin oxides and alkoxides fall into two categories: cleavage reactions and addition reactions. Cleavage or substitution reactions include reactions with acidic protic reagents, including amides (equation 93), thiols (equation 94), and acyl chlorides or anhydrides (equation 95). Addition reactions occur with heterocumulenes (equations 96 and 97).

$$(Bu_3Sn)_2O + HNPhCOMe \longrightarrow Bu_3SnNPhCOMe \tag{93}$$

$$(Bu_3Sn)_2O + HSR \longrightarrow Bu_3SnR + H_2O \tag{94}$$

$$Bu_3SnOR + MeCOCl \longrightarrow Bu_3SnCl + MeCO_2R \tag{95}$$

$$Me_3SnOMe + H_2C{=}C{=}O \longrightarrow Me_3SnCH_2CO_2Me \tag{96}$$

$$Bu_3SnOMe + PhNCO \longrightarrow Bu_3SnNPhCO_2Me \tag{97}$$

12.6 Organotin Carboxylates

Organotin carboxylates are generally available from the oxides (or hydroxides) on reaction with the carboxylic acid (equation 98), or from the organotin halides with sodium carboxylates (equation 99). Electrophilic cleavage of the more reactive carbon–tin bonds by RCO_2H also provides carboxylates (equation 100).

$$(R_3Sn)_3O + 2R'CO_2H \xrightarrow[-H_2O]{PhMe,\Delta} R_3SnO_2CR' \qquad (98)$$

$$R_nSnCl_{4-n} + (4-n)R'CO_2Na \longrightarrow R_nSn(O_2CR')_{4-n} \qquad (99)$$

$$R\text{–}Sn{=} + R'CO_2H \longrightarrow RH + R'CO_2Sn{\equiv} \qquad (100)$$

12.6.1 *Structures of Carboxylates*[53]

The crystal structures of triorganotin carboxylates, R_3SnO_2CR', fall into two groups: (i) the majority, including those with R = Me, $CH_2{=}CH$, Ph, and $PhCH_2$, which have a one-dimensional polymeric structure (**56**); and (ii) those with a monomeric five-coordinate trigonal bipyramidal tin atom, e.g. (**57**), with bulky R groups. For diorganotin dicarboxylates, structures such as *cis*-(**58**) and *trans*-(**59**) octahedral forms as well as skew-trapezoidal forms (**60**) are found.

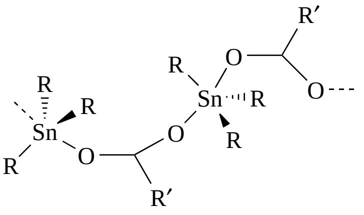

(**56**)

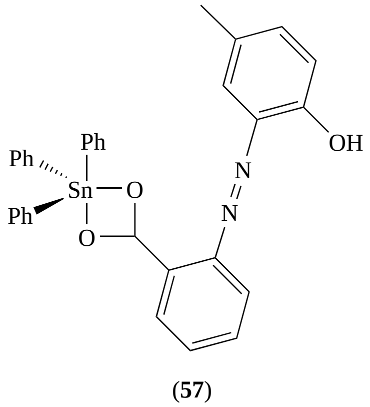

(**57**)

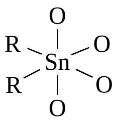

(**58**)

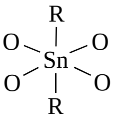

(**59**)

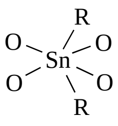

(**60**)

12.6.2 *Reactions of Carboxylates*

Most triorganotin carboxylates are stable to hydrolysis; however, $R_2Sn(O_2CR')_2$ and $RSn(O_2CR')_3$ show a progressive ease towards hydrolysis to form oxycarboxylates, e.g. $[R_2Sn(OCOR')OSnR_2OCOR']_2$ and $[RSn(O)O_2CR']_6$. The structure of the latter type of complex (e.g. R = Bu or Ph; R′ = cyclohexyl) is drum-like.

Certain carboxylates R_3SnO_2CR' (e.g. R′ = H, $C{\equiv}CR^2$, $CH_2{=}CH$, or C_6F_5) can be decarboxylated to R_3SnR' (equation 101). Other reactions include halide/carboxylate exchanges (equation 102).

$$Bu_3SnO_2C{\equiv}Ph \xrightarrow{60\,^{\circ}C} Bu_3Sn{\equiv}Ph \qquad (101)$$

$$R_2Sn(O_2CR')_2 + R_2SnX_2 \longrightarrow 2R_2Sn(X)O_2CR' \qquad (102)$$

12.7 Nitrates

Di- and triorganotin nitrates can be prepared from the corresponding oxides (or hydroxides) and nitric acid, or from treatment of the halides with $AgNO_3$ in acetone at 0 °C. Anhydrous $Me_2Sn(NO_3)_2$, which is explosive on heating, is available from Me_4Sn and N_2O_4 in dry EtOAc. Methyltin trinitrate has been produced from $MeSnCl_3$ and N_2O_5 in CCl_4.

The NO_3 groups are bidentate O,O ligands in $MeSn(NO_3)_3$ and in $Me_2Sn(NO_3)_2$, whereas in $[Me_3SnNO_3{\cdot}H_2O]$ the NO_3 group is monodentate: the three compounds have pentagonal bipyramidal, octahedral, and trigonal bipyramidal geometries, respectively.

The anionic species $[Ph_3Sn(NO_3)_2]^-$ also contain monodentate nitrate groups.[54] A different binding mode is found for NO_3 in anhydrous Me_3SnNO_3; it bridges Me_3Sn units to form a one-dimensional polymer.

12.8 Sulfates, Sulfinates, and Sulfonates

Preparative routes to these derivatives are shown in equations (103–108). The compounds $Me_3SnOSOR'$ (R′ = Me and $CH_2CH{\equiv}CH$) and $Me_3SnOSeOMe$ have polymeric chain structures with bridging O_2ER' (E = S or Se) groups, whereas $Me_2Sn(OSO_2F)_2$ has a polymeric sheet-type structure. A trigonal pyramidal tin atom is present in $(Me_3SnO)SO_2{\cdot}2H_2O$, with each H_2O acting as an axial ligand to each tin.[55]

$$2R_3SnX + Ag_2SO_4 \longrightarrow (R_3SnO)_2SO_2 \qquad (103)$$

$$(R_3Sn)_2O + H_2SO_4 \longrightarrow (R_3SnO)_2SO_2 \qquad (104)$$

$$R_4Sn + SO_2 \xrightarrow{<0\,^{\circ}C} R_3SnOSOR \qquad (105)$$

$$R_3SnCl + NaOSOR' \longrightarrow R_3SnOSOR' \qquad (106)$$

$$(R_3Sn)_2O + R'SO_3H \longrightarrow R_3SnO\text{–}S(O)OR' \qquad (107)$$

$$R_4Sn + SO_3 \xrightarrow{<0\,^{\circ}C} R_3Sn\text{–}O\text{–}S(O)OR \qquad (108)$$

13 TIN–SULFUR, –SELENIUM, AND –TELLURIUM BONDED COMPOUNDS

The best studied of these compounds are the tin–sulfur bonded species, with $(R_3Sn)_2S$, $(R_2SnS)_n$, $(R_4Sn_4S_6)$, and $R_nSn(SR')_{4-n}$ ($n = 1-3$) being particularly well investigated. The most frequently met Sn–Se and Sn–Te (Sn–E) bonded compounds are $(R_3Sn)_2E$, $(R_2SnE)_n$, and R_3SnER'. Their preparation usually involves reaction of the corresponding halide (or oxide) with H_2E or HER′ in the presence of a base or the use of sodium salts of the acids. Alternative methods include insertion of sulfur, selenium, or tellurium into tin–tin or tin–alkali metal bonds. The compounds R_3SnEH (E = S, Se, or Te) are generally unstable and decompose to $(R_3Sn)_2E$ and H_2E.

13.1 Structures

The tin atoms in these compounds have near tetrahedral geometry. Bis(triphenyltin) sulfide (Sn–S = 2.37 Å) and selenide (Sn–S = 2.525 Å) are monomeric molecules with nonlinear Sn–E–Sn valency angles; in the more bulky $(t\text{-}Bu_3Sn)_2E$, the valency angles decrease[56] in the sequence E = S, Se, Te, angle = 134.2, 127.2, 122.3°. In contrast to the polymeric diorganotin oxides, the diorganotin chalcogenides (R_2SnE) form ring structures, normally trimeric[57] with a twist-boat conformation (**61**) for the smaller R groups (e.g. R = Me or Ph); while dimers (**62**) with planar Sn_2E_2 cores are found for more bulky R groups (e.g. R = *t*-Bu).[58] In addition, a polymeric form of $[i\text{-}Pr_2SnS]_n$ has been reported. The sesquisulfides $R_4Sn_4S_6$ have an adamantane-type structure (**63**).

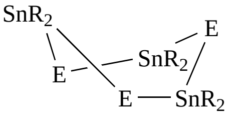

(**61**)

		d(Sn–E)Å
R = Me;	E = S	2.41
	E = Se	2.53
	E = Te	2.74

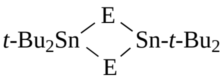

(**62**)

	d(Sn–E)Å
E = S	2.41–2.44
E = Se	2.55
E = Te	2.75–2.76

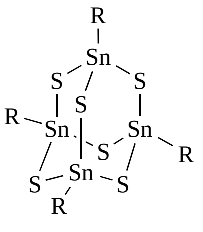

(**63**) R = Me, Ph or C_6F_5

Whereas R_3SnER' have essentially tetrahedral structures, dithiolates such as (**64**)–(**66**) have associated structures due to weak Sn–S interactions. Various other cyclic sulfido, seleno, and telluro derivatives are known, e.g. (**67**), including some with additional metal–metal bonds, e.g. (**68**)–(**70**).[32,59,60]

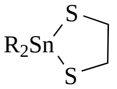

(**64**)

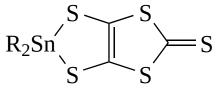

(**65**)

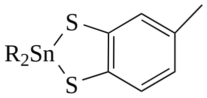

(**66**)

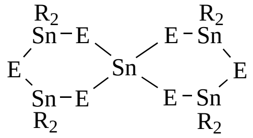

(**67**) e.g. R = *i*-Pr; E = S or Se

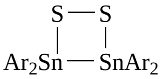

(**68**) Ar = 2,4,6-$i\text{-}Pr_3C_6H_2$

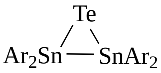

(**69**) Ar = 2,4,6-$i\text{-}Pr_3C_6H_2$

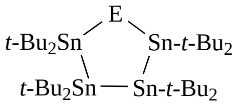

(**70**) E = S, Se or Te

13.2 Reactions

The Sn–S, Sn–Se, and Sn–Te bonded compounds are less reactive than Sn–O bonded species, e.g. towards water. Reactions proceed with a variety of electrophilic reagents (e.g. alkyl halides, halogens, and sulfur(II) halides).

13.3 Other Tin-Sulfur Bonded Compounds

Triorganotin dithiocarbamates, $R_3SnSCSNR'_2$, and dithiophosphates, $R_3SnSP(S)(OR')_2$, usually contain monodentate ligands. However for the di- and monoorganotin derivatives, these ligands normally act as chelating groups, for example as in $Ph_2Sn[S_2P(OEt)_2]_2$ and $Me_2Sn(S_2CSNMe_2)_2$ (skew trapezoidal tin), in $Ph_2Sn[S_2P(O\text{-}i\text{-}Pr)_2]_2$ (*trans* octahedral geometry), and in $MeSn(S_2CNEt_2)_3$ (distorted pentagonal bipyramidal tin).

13.4 Organotin(II) Compounds: Stannylenes[1,61,62]

Simple, unhindered, R_2Sn^{II} compounds (e.g. R = Me or Ph) have only a fleeting existence under normal conditions, and, in the absence of a trapping agent, rapidly oligomerize to $[R_2Sn]_n$ after formation. However, sufficient stability is realized[63] for study on isolation in argon matrices at low temperatures, e.g. 5 K for Me_2Sn. Conditions have been found to stabilize alkyl and aryl stannylenes at ambient temperatures. These conditions, each of which may be adequate on their own,[1,25] are (i) the use of bulky organic groups, e.g. (**71**); (ii) the formation of adducts with Lewis bases, especially intramolecular bases, e.g. (**72**), (**73**), and (**74**); and (iii) the coordination of the lone pair at Sn with suitable transition metal acceptors, e.g. (**75**). In addition, π-bonded organostannylenes, e.g. Cp_2Sn, have good thermal stabilities.

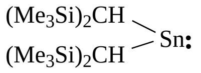

(**71**)

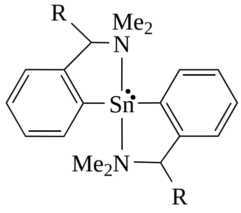

(**72**) R = H, Me, $SiMe_3$

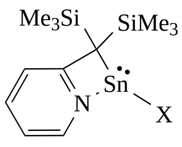

(**73**)

R′−SnX; X = Cl, $N(SiMe_3)_2$ or R′

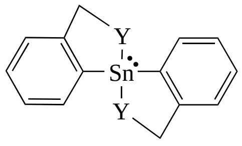

(**74**)

Y = PPh_2 or NMe_2

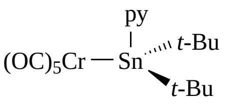

(**75**)

13.5 σ-Bonded Organotin(II) Compounds

Simple σ-bonded R_2Sn^{II} species have been generated (i) by thermolysis or photolysis of diorganotin oligomers $(R_2Sn)_n$; (ii) by controlled reaction of R_2SnCl_2 with $ArH^{-\bullet}$, M^+ (e.g. naphthalene$^{-\bullet}$, Na^+) or ArH^{2-}, $2M^+$ (e.g. anthracene^{2-}, $2Li^+$; Anth^{2-}, $2Li^+$); and (iii) by thermal elimination from 7-stannanorbornenes (Scheme 20).

Dimethylstannylene (either $(CH_3)_2Sn$ or $(CD_3)_2Sn$), when isolated in an argon matrix, was shown by IR spectroscopy to have a C_{2v} symmetry.[63] Conflicting predictions of bond lengths and dipole moments for Me_2Sn have been made from different theoretical treatments; however, a singlet ground state was suggested from such studies. From experimental studies, different spin states for R_2Sn have been indicated by the different reactivities of photochemically and thermally generated R_2Sn, e.g. towards MeCOCOMe.

The more hindered and stable $[(Me_3Si)_2CH]_2Sn$ has been obtained[64] by the routes shown in Scheme 21.

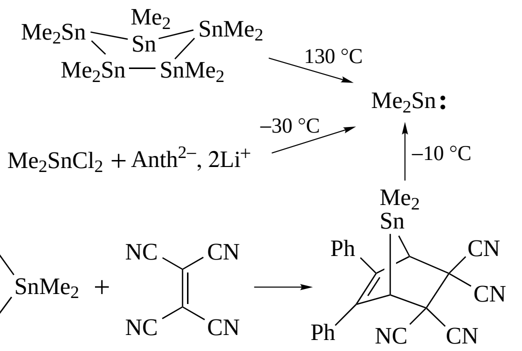

Scheme 20

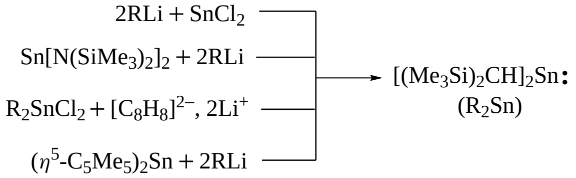

$[C_8H_8]$ = cyclooctatetraene

Scheme 21

In the solid state, red $[(Me_3Si)_2CH]_2Sn$ (**71**) was shown by X-ray crystallography to exist as a nonplanar, centrosymmetric, weakly datively bonded dimer (**76**) (Sn–Sn = 2.768(1) Å); in hydrocarbon solutions, NMR spectra indicated a monomer–dimer equilibrium with the energy of dissociation = 12.8 kcal mol^{-1} (equation 109). From an electron diffraction study, $[(Me_3Si)_2CH]_2Sn$ in the gas phase has a V-shaped monomeric structure, with C–Sn–C = 97(2)°. The related stannylene (**77**) is monomeric in the solid state, with the shortest Sn···Sn distance of 7.4 Å. The dark-red air- and moisture-sensitive compound (**77**) exists in a dimer–monomer equilibrium in solution.[65] Two crystal modifications of [2,4,6-$(F_3C)_3C_6H_2]_2Sn$ have been reported;[66] one is monomeric and the other is a weakly associated dimer with a Sn–Sn distance of 3.639(1) Å. There are Sn–F interactions (equation 110).

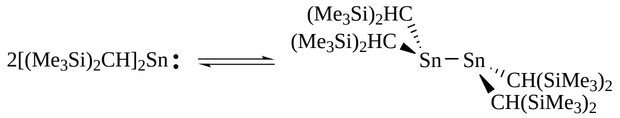

(**71**) (**76**)

(109)

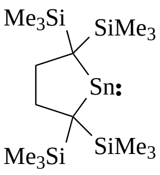

(**77**)

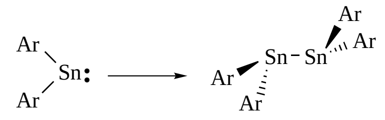
Ar
Sn:
Ar
Ar
Sn
Sn
Ar
Ar
Ar

(110)

yellow (**78**) red (**79**) Ar = 2,4,6–$(F_3C)_3C_6H_2$

d(Sn—Sn) = 3.64 Å

The distannene (**80**) is in equilibrium with a cyclic trimer (**81**) (equation 111).[67] Other chelated stannylenes include (**82**)–(**85**) (equations 112 and 113).[25,68] Compound (**82**) is a yellow, very oxygen-sensitive compound, stable to 180 °C and is soluble in organic solvents. In the solid the N–Sn–N and C–Sn–C valency angles are 165.2 and 93.8°, respectively, and it has a pseudotrigonal bipyramidal structure. It forms a white $W(CO)_5$ adduct (**83**).

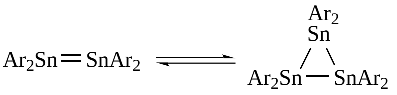
Ar2Sn=SnAr2
Ar2
Sn
Ar2Sn—SnAr2

(111)

(**80**) Ar = 2,4,6-i-$Pr_3C_6H_2$ (**81**)

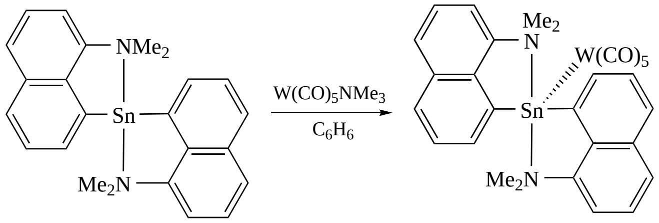
NMe2
Sn
Me2N
W(CO)5NMe3
C6H6
Me2
N
W(CO)5
Sn
Me2N

(**82**) (**83**)

(112)

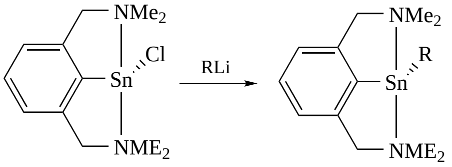
NMe2
Cl
Sn
NME2
RLi
NMe2
R
Sn
NME2

(113)

(**84**) (**85**)

R = p-MeC_6H_4, t-$BuCH_2$ or $PhCMe_2CH_2$

A novel dialkyl-Sn compound (**86**), stabilized by coordination to Zn, has been isolated and characterized. (equation 114).[25,69] The compound $[(Ph_2P)_2CH]_2Sn$ (**87**), obtained from $SnCl_2$ and $(Ph_2P)_2CHLi$, is a three-coordinate tin species with a pyramidal $[SnCP_2]$ core;[70] however, at a higher temperature (50 °C) ^{31}P NMR suggests a two-coordinate C–Sn–C bonded species. In contrast, $[(Me_2P)_2CH]_2Sn$ (**88**) contains a four-coordinate tin atom with four Sn–P contacts.

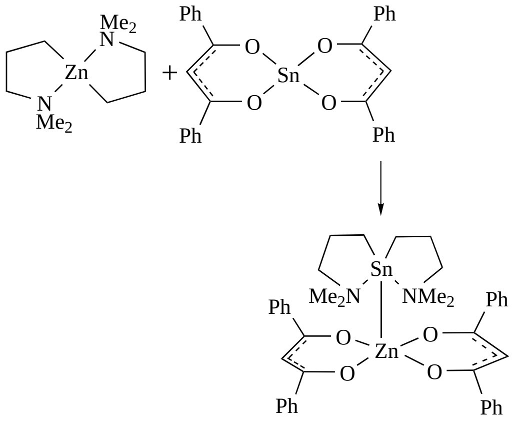
Me2
N
Zn
N
Me2
+
Ph
Ph
O
O
Sn
O
O
Ph
Ph
Sn
Me2N
NMe2
Ph
Ph
O
O
Zn
O
O
Ph
Ph

(114)

(**86**) d(Zn–Sn) = 2.634(6) Å

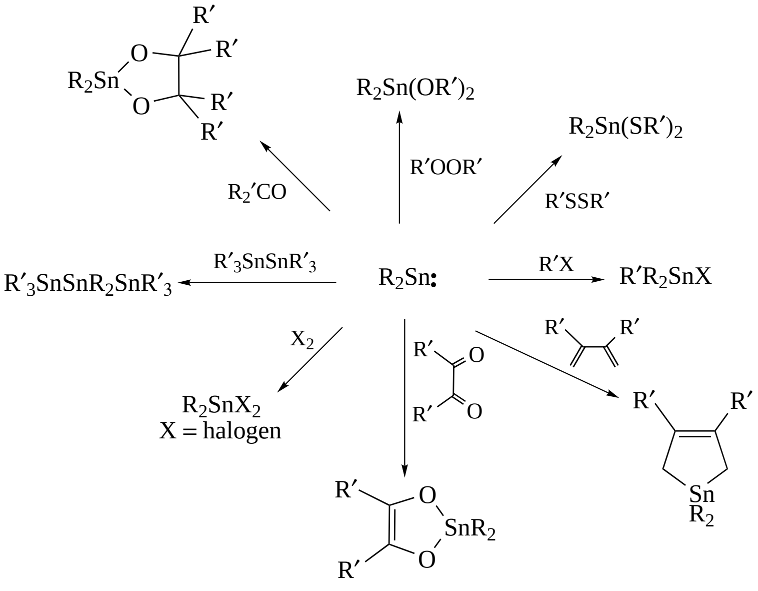
R′
O
R′
R2Sn
O
R′
R′
R2Sn(OR′)2
R2Sn(SR′)2
R2′CO
R′OOR′
R′SSR′
R′3SnSnR′3
R′3SnSnR2SnR′3
R2Sn:
R′X
R′R2SnX
X2
R2SnX2
X = halogen
R′
O
R′
O
R′
R′
R′
R′
Sn
R2
R′
O
SnR2
R′
O

Scheme 22

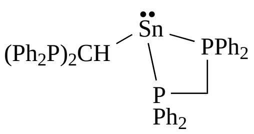

(87)

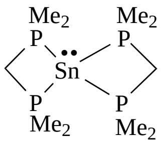

(88)

13.6 Reactions

σ-Bonded R_2Sn^{II} compounds, apart from oligomerizations, readily undergo oxidative addition and insertion reactions to give Sn^{IV} species, as shown in Scheme 22.

Cleavage of carbon–tin bonds has also been reported by protic species, e.g. in reactions of $[2,6\text{-}(F_3C)_2C_6H_3]_2Sn$ with MeOH and p-MeC_6H_4SH to give $2,6\text{-}(F_3C)_2C_6H_3SnOMe$ and $(p\text{-}MeC_6H_4S)_2Sn$, respectively.

Organotin(II) compounds also act as ligands in transition metal complexes. The stable stannylene $[(Me_3Si)_2CH]_2Sn$ has been widely studied and has been shown to replace a CO group in $M(CO)_6$ (M = Cr or Mo) on irradiation; the resulting Cr complex $[(Me_3Si)_2CH]_2SnCr(CO)_5$ (**89**) contains a planar $[C_2SnCr]$ arrangement. The bonding involves both σ-donation from tin to the transition metal and back donation from the transition metal to the p or d orbitals of tin. Bridging stannylene complexes are also known, e.g. (**90**); the latter has been obtained from $Na_2Fe(CO)_4$ and R_2SnCl_2, and from $Fe(CO)_5$ and $R_2Sn(CH{=}CH_2)_2$. As shown in equation (115), the bridging by the stannylene can be broken on treatment with donors such as THF or py. The bonding of the donor group, L, in (**91**) involves use of the empty p orbital on Sn.

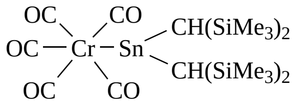

(**89**)

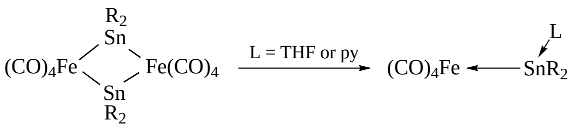

(**90**) R = Me, t-Bu or Ph (**91**)

(115)

13.7 π-Bonded Stannylenes[71]

π-Bonded stannylenes have also been studied extensively. Stannocene, $(\eta^5\text{-}C_5H_5)_2Sn$ (**92**), was first prepared in 1956 from $SnCl_2$ and C_5H_5Na. Subsequently, other bis(cyclopentadienyl)-stannanes have been prepared by similar means, e.g. $(\eta^5\text{-}RC_5H_4)_2Sn$ (R = t-Bu, $CH_2{=}CMe$–, or Me) and $(\eta^5\text{-}R_5C_5)_2Sn$ (R = $PhCH_2$, Ph, or Me). Ring lithiation of $(\eta^5\text{-}C_5H_5)_2Sn$ by BuLi is another method utilized in the preparation of substituted derivatives (Scheme 23).

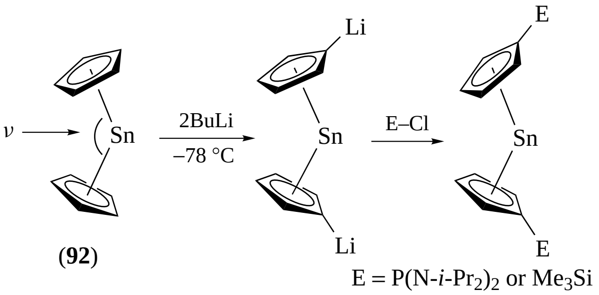

Scheme 23

Stannocene $(\eta^5\text{-}C_5H_5)_2Sn$ (**92**), is monomeric in the gas phase, and in the solid state X-ray crystallography revealed $(\eta^5\text{-}C_5H_5)_2Sn$ to have a bent sandwich structure, with a ring centroid–Sn–ring centroid angle (ν) of 148.0 and 143.7° in two independent molecules. Crystal structures of various substituted bis(cyclopentadienyl)stannanes have also been determined; generally it has been found that the larger the substituents on the rings, the nearer to parallel the rings become, e.g. the value of (ν) for $(\eta^5\text{-}Ph_5C_5)_2Sn$ is 180°.

The structure of most stannocenes is attributed to an sp^2 hybridized tin atom, with two of the three hybrid orbitals interacting with the π-systems of the rings and the third hybrid orbital containing the unshared electron pair. A tris(cyclopentadienyl)stannate complex (**93**) has been characterized; it has a trigonal planar paddle-wheel geometry.[72]

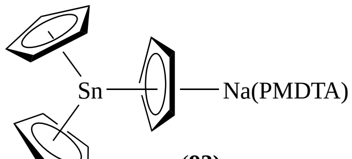

(93)

NMR spectra of $(\eta^5\text{-}MeC_5H_4)_2Sn$ in solution indicate rapid intermolecular exchanges at ambient temperature; ring substitution generally slows down these exchanges.

Crystal structures of monocyclopentadienyl–Sn^{II} derivatives have also been determined. The tin atom in $(\eta^5\text{-}Me_5C_5)Sn^+BF_4^-$ sits above the center of the ring; the tin–ring centroid distance is shorter than that found in $(\eta^5\text{-}Me_5C_5)_2Sn$. In both $(\eta^5\text{-}t\text{-}BuC_5H_4)Sn^+\ BF_4^-$ and $(\eta^5\text{-}C_5H_5)SnCl$ the atoms are not above the ring center: the ring centroid–Sn–Cl angle is 117.4° in the latter. The X-ray structures of $(Me_5C_5Sn{\cdot}L)^+OSO_2CF_3^-$ (L = py or bipy) have also been determined; the donor–ligand coordinations change the bonding mode of Sn to the cyclopentadienyl from η^5 toward η^2 or η^3.

Stannylenes have also been prepared with π-ligands related to the cyclopentadienyl group; these include 1,3-diborolenyl, 1,2-azaborolenyl, and diazastannocene species, e.g. (**94**)–(**96**).[73] Other π-complexes of Sn^{II} which have been obtained include carboranyl derivatives, e.g. (**97**), and the very air-sensitive arene derivatives $[(\eta^6\text{-}R_2C_6H_4)SnCl\cdot AlCl_4]$ (R = H or Me) and $[(\eta^6\text{-}C_6H_6)Sn(AlCl_4)_2]\cdot PhH$ (**98**).[74]

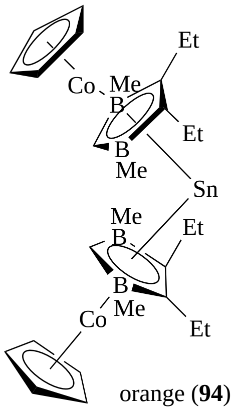

orange (**94**)
η^5-bonded
dec. 140 °C

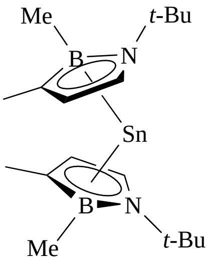

orange (**95**)
η^3-bonded
dec. −20 °C

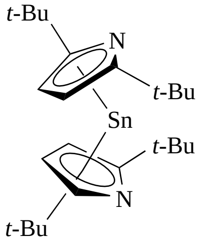

yellow (**96**)
η^5-bonded

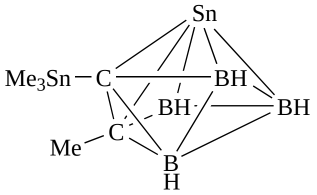

(**97**)

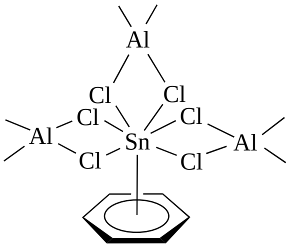

(**98**) η^6-bonded

13.8 Reactions of π-Bonded Stannylenes

Solid $(\eta^5\text{-}C_5H_5)_2Sn$ undergoes only a slow polymerization at room temperature; polymerization occurs much more readily in DMF. Rapid oxidation of $(\eta^5\text{-}C_5H_5)_2Sn$ occurs in air to $(C_5H_5)_2SnO$; oxidation proceeds more slowly for more substituted bis(cyclopentadienyl)stannylenes with, for example, $[\eta^5\text{-}(PhCH_2)_5C_5]_2Sn$ being reported to be air stable.

Oxidative additions to give Sn^{IV} species occur on reaction with a variety of reagents, including organic halides, disulfides, halogens, $Sn^{IV}Cl_4$, and $HgCl_2$.

Disproportionation reactions have been reported (equation 116), as have cleavage reactions which remove one group (equation 117) or both groups, e.g. by proton acids HA (HA = alcohols, phenols, thiols, $HONR_2$, $HON{=}CR_2$, HO_2CR, RSO_3H) to give inorganic SnA_2 species.

$$(\eta^5\text{-}C_5H_5)_2Sn + SnX_2 \longrightarrow 2\eta^5\text{-}C_5H_5SnX \qquad (116)$$

$$X = Cl,\ Br\ \text{or}\ N(SiMe_3)_2$$

$$(\eta^5\text{-}C_5Me_5)_2Sn + F_3CCO_2H \longrightarrow \eta^5\text{-}C_5Me_5SnO_2CCF_3 \qquad (117)$$

Ionic salts have been formed, e.g. $(\eta^5\text{-}Me_5C_5)Sn^+X^-$ ($X^- = CF_3SO_3{}^-$, $AlCl_4{}^-$, or $BF_4{}^-$) on reaction of $(\eta^5\text{-}Me_5C_5)_2Sn$ with CF_3SO_3H, $AlCl_3$, and HBF_4, respectively.

Bis(cyclopentadienyl)stannylenes can act as ligands in transition metal complexes, e.g. as in $(\eta^5\text{-}C_5H_5)_2Sn\text{–}M(CO)_5$ (M = Cr, Mo, or W).

14 INDUSTRIAL[75] AND BIOLOGICAL[76] APPLICATIONS

The use of organotins in industry rose especially markedly in the period from the mid 1960s to the mid 1980s. The largest use is as stabilizers for poly(vinyl chloride); the industrial applications of nontoxic organotin compounds, especially R_2SnX_2, account for a great proportion of the total consumption. The triorganotin compounds, R_3SnX, have found application as biocides and pesticides; however, a greater restriction has been placed on their use in the last few years.

14.1 Stabilizers for Poly(vinyl chloride), $[CH_2CHCl]_n$

Di- and triorganotin thiolates and carboxylates have been the most widely used organotin compounds in this area: typical compounds are $R_2Sn(SCH_2CO_2C_8H_{17})_2$ and $RSn(SCH_2CO_2C_8H_{17})_3$ (R = Me, Bu, C_8H_{17}, or $BuO_2CCH_2CH_2$), $R_2Sn(SC_{11}H_{25})_2$ (R = Me or Bu), $R_2Sn(OCOR')_2$ (R = Bu; R′ = $C_{11}H_{23}$, $CH{=}CHCO_2R''$; R = Me, Bu, or C_8H_{17}) and $[R_2Sn(OCOCH{=}CHCO_2)]$ (R = Me, Bu, or Oct). The Sn–S compounds are especially good as heat stabilizers, particularly during the processing of PVC at 180–200 °C, whereas the carboxylates provide good long-term UV/light stability. Frequently, monalkyltin and dialkyltin compounds are used together, as marked synergistic effects are produced.

Decomposition of PVC proceeds via loss of HCl and by autoxidation; these lead to embrittlement and to coloration, due at least in part to the formation of conjugated polyenes.

The modes of action of the organotin stabilizers added to the extent of ca. 1–5% are considered to be complex, but include (i) anionic exchanges at reactive chloride (i.e. allylic centers) within the polymer, which provides more stable species; and (ii) reaction with any free HCl.

14.2 Catalytic Applications

Dialkyltin dicarboxylates, e.g. $Bu_2Sn(O_2CC_{11}H_{23})_2$, are useful catalysts for polyurethane foam formation and as cross-linking agents for room-temperature vulcanization. Monobutyltins have been used as catalysts in transesterification and esterification reactions, e.g. in the reaction between phthalic anhydride and 2-ethylhexanol.

14.3 Biocidal Applications[76]

The biocidal activity of triorganotin compounds has been utilized in a number of applications, including as antifungal agents for crops, as acaricides, as antifouling agents in marine coatings of paints, and as wood preservatives. A more limited use has been made of the lower toxic effects of diorganotin species.

The biological activity of R_nSnX_{4-n} varies with R and n, the activity being maximum for $n = 3$. The sequence of activity is $R_3SnX > R_2SnX_2 > RSnX_3$; any activity of R_4Sn probably results from in vivo dealkylations to R_3SnX compounds. The nature of the X group in general has little affect on the biological activity, unless it possesses its own activity; in contrast, the nature of the organic group R is most important. In the trialkyltin species, trimethyltin compounds possess maximum toxicity to mammals and insects, triethyltins are most toxic to mammals, tripropyltins to Gram-negative bacteria, and tributyltins to Gram-negative bacteria and fungi. Further increases in the alkyl chain length results in a decrease in the biological toxicity, and, for example, triooctyltin compounds are essentially nontoxic to all living organisms. Triphenyltin compounds are highly active to fish, fungi, and mollusks, and tricyclohexyltins and trineophyltins are effective acaricides that possess low mammalian toxicity.

Both dialkyltins and trialkyltins inhibit oxidative metabolism, but in different ways. Triorganotin species act on the coupling ATPase, but the diorganotins act on substrate oxidation.

Examples of organotin compounds to have found applications as agrochemicals are Ph_3SnX (OH or OCOMe) (antifungicide for crops) and tricyclohexyltin hydroxide, $[(PhCMe_2CH_2)_3Sn]_2O$, and tricyclohexylstannyl-1,2,4-triazole (acaricides).

Tributyltin species, especially $(Bu_3Sn)_2O$ and tributyltin phosphate and naphthenate, have been used in wood preservation as fungicides and as biocides for destructive insects. Tributyltins (and to a lesser extent, triphenyltins) have been used in marine antifoulant paints due to their broad range activity. The use of organotin polymers in which the triorganotin groups are chemically bound to the polymer backbone, e.g. as in poly[tributyltin methacrylate–methyl methacylate], has been particularly useful (**99**). In contact with seawater, the organotin ester link is continuously hydrolyzed and the triorganotin moiety is released at a controlled rate. In addition, the depleted outer polymer layer is then eroded by the motion of the seawater past it, which not only exposes fresh surfaces but continually provides smooth surfaces. These 'self-polishing' paints can provide protection for up to five years.

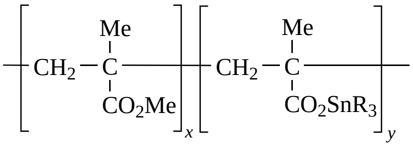

$$\left[\mathrm{CH_2-\overset{Me}{\underset{CO_2Me}{C}}}\right]_x\left[\mathrm{CH_2-\overset{Me}{\underset{CO_2SnR_3}{C}}}\right]_y$$

(99)

14.4 Diorganotin Biocidal Activity

Diorganotin species, e.g. $Bu_2Sn(O_2CC_{11}H_{23})_2$, have found use as anthelminthic agents in poultry, as insecticides for sheep and cattle, and as aparasitic agents for turkeys.

14.5 Anticancer Activity[77,78]

There have been various reports of the anticancer activities of organotin species, e.g. towards P388 lymphocytic leukemia in mice. Research work continues strongly in this area, but it appears that chemical use of organotin anticancer drugs is at the very best several years away.

15 ENVIRONMENTAL ASPECTS[79,80]

Because of the wide-ranging toxicity of the lower triorganotin species in particular, there is great interest in the distribution and extent of organotins in the environment, especially in estuarine and other aquatic systems. All industrial applications, in principle, will introduce organotins into the environment; however, it is the use of organotin marine antifoulants which has raised most concern. The liberal use of triorganotin antifouling paints has led to serious environmental pollution, particularly in areas where a large number of boats operate. The general toxicity of triorganotins, e.g. tributyltin compounds, means that nontargeted organisms, e.g. Pacific oysters, mussels, dog-whelks, and other shell-fish can (and have) become affected, and it is clear that greater care and restrictions have to be exercised in the use of these useful, but very toxic, materials.

While organotin species are stable in sterile environments (both aqueous as well as solid phases) and in the dark at usual environmental temperatures, the breakdown of triorganotin species occurs rapidly in sunlight and by biological action.

$$R_3Sn^+ \longrightarrow R_2Sn^{2+} \longrightarrow RSn^{3+} \longrightarrow Sn^{4+}$$

Scheme 24

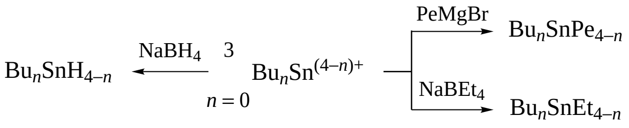

Scheme 25

These lead to the less toxic di- and monoorganotins, as well as inorganic tin species on successive dealkylation reactions (Scheme 24).

Triorganotin compounds, except Me_3SnX, have low solubility in water, but they have high affinities for soils and sediments and hence can concentrate there. Biomethylation of organotins is now well documented and so methylalkyltins, e.g. $MeBu_2Sn^+$, can be found in environmental samples. Environmental methylation of tin species can result from the interaction of such methylating agents as methylcorrinoids or betaines (from dead organisms) and methyl iodide or dimethyl sulfide (from living organisms).

Such is the difference in the toxicities of the tin species found in the environment, it is of utmost importance to carry out speciation studies rather than to simply determine the total tin content in any sample. Quantitative methods of determination are available for very low concentrations (at ppb and below).

One well-used speciation method involves the production of volatile tetraorganotins by treatment of environmental samples (suitably concentrated) using Grignard reagents (e.g. pentylmagnesium bromide) or sodium tetraethylborate, followed by separation and determination of the resulting products (e.g. by GC or GC/AAS techniques). An alternative method involves the generation of volatile organotin hydrides from treatment with $NaBH_4$ (Scheme 25).

16 RELATED ARTICLES

Lead: Organometallic Chemistry; Tin: Inorganic Chemistry.

17 FURTHER READING

D. E. Goldberg, P. B. Hitchcock, M. F. Lappert, K. M. Thomas, A. J. Thorne, T. Fjeldberg, A. Haaland, and B. E. R. Schilling, *J. Chem. Soc., Dalton Trans.*, 1986, 2387; M. F. Lappert, *Rev. Silicon Germanium Tin Lead Compd.*, 1986, **9**, 129; K. W. Zilm, G. A. Lawless, R. W. Merrill, J. M. Millar, and G. W. Webb, *J. Am. Chem. Soc.*, 1987, **109**, 7236.

18 REFERENCES

1. P. G. Harrison ed., ‘Chemistry of Tin’, Blackie, Glasgow, 1989.
2. A. G. Davies and P. J. Smith, in ‘Comprehensive Organometallic Chemistry’, eds. G. Wilkinson, F. G. A. Stone, and E. W. Abel, Pergamon, Oxford, 1982, Vol. 2, p. 519.
3. R. C. Poller, ‘The Chemistry of Organotin Compounds’, Logos, London, 1970; W. P. Neumann, ‘The Organic Chemistry of Tin’, Wiley, London, 1970.
4. A. K. Sawyer ed., ‘Organotin Compounds’, Dekker, New York, 1971, Vols. 1–3.
5. ‘Gmelin Handbuch der Anorganische Chemie, Tin’, Springer, Berlin, various parts, published since 1975.
6. M. Pereyre, J.-P. Quintard, and A. Rahm, ‘Tin in Organic Synthesis’, Butterworths, London, 1987.
7. T. Tsumuraya, S. A. Batcheller, and S. Masamune, *Angew. Chem., Int. Ed. Engl.*, 1991, **30**, 902; N. Wiberg and S. K. Vasisht, *Angew. Chem., Int. Ed. Engl.*, 1991, **30**, 93; G. A. Anselme, C. Couret, J. Escudie, S. Richelme, and J. Satgé, *J. Organomet. Chem.*, 1991, **418**, 321; A. Berndt, H. Meyer, G. Baum, W. Massa, and S. Berger, *Pure Appl. Chem.*, 1987, **59**, 1011; H. Ranaivonjatovo, J. Escudie, C. Couret, and J. Satgé, *J. Chem. Soc., Chem. Commun.*, 1992, 1047; G. Anselme, H. Ranaivonjatovo, J. Escudie, C. Couret, and J. Satgé, *Organometallics*, 1992, **11**, 2748.
8. B. Wrackmeyer, *Annu. Rep. NMR Spectrosc.*, 1985, **16**, 73; P. J. Smith and A. P. Tupciavska, *Annu. Rep. NMR Spectrosc.*, 1978, **8**, 291; V. S. Petrosyan, *Prog. Nucl. Magn. Reson. Spectrosc.*, 1977, **11**, 115; J. D. Kennedy and W. McFarlane, *Rev. Silicon, Germanium, Tin, Lead Compd.*, 1974, **1**, 235.
9. J. N. R. Ruddock, *Rev. Silicon Germanium Tin Lead Compd.*, 1976, **2**, 125; J. J. Zuckerman, *Adv. Organomet. Chem.*, 1970, **9**, 21.
10. J. A. Zubieta and J. J. Zuckerman, *Prog. Inorg. Chem.*, 1978, **24**, 251; P. A. Cusack, P. J. Smith, J. D. Donaldson, and S. M. Grimes, ‘A Bibliography of X-ray Crystal Structures of Tin Compounds’, International Tin Research Institute, London, 1980, Publication p. 588.
11. J. L. Wardell, in ‘Chemistry of Tin’, ed. P. G. Harrison, Blackie, Glasgow, 1989, Chap. 5.
12. J. Murphy and R. C. Poller, *J. Organomet. Chem. Libr.*, 1979, **9**, 189.
13. F. S. Holland, *Appl. Organomet. Chem.*, 1987, **1**, 185.
14. C. C. Yammal, J. C. Podesta, and R. A. Rossi, *J. Org. Chem.*, 1992, **57**, 5720.

15. A. Barbero, P. Cuadrado, I. Fleming, A. M. Gonzalez, and F. J. Pulido, *J. Chem. Soc., Perkin Trans. 1*, 1992, 327.
16. P. G. Harrison, in ‘Chemistry of Tin’, ed. P. G. Harrison, Blackie, Glasgow, 1989, Chap. 3.
17. J. T. B. H. Jastrzebski, J. Boersma, P. M. Esch, and G. van Koten, *Organometallics*, 1991, **10**, 930.
18. A. G. Davies, in ‘Chemistry of Tin’, ed. P. G. Harrison, Blackie, Glasgow, 1989, Chap. 9.
19. T. N. Mitchell, *Synthesis*, 1992, 803.
20. Y. Yamamoto, *Acc. Chem. Res.*, 1987, **20**, 243; G. Tagliavini, *Rev. Silicon, Germanium, Tin, Lead Compd.*, 1985, **8**, 237.
21. G. A. Russell and L. L. Herold, *J. Org. Chem.*, 1985, **50**, 1037.
22. B. Jousseaume, N. Noiret, M. Pereyre, and J. M. Frances, *J. Chem. Soc., Chem. Commun.*, 1992, 739.
23. D. Tudela, E. Gutierrez-Puebla, and A. Monge, *J. Chem. Soc., Dalton Trans.*, 1992, 1069.
24. P. J. Cox, S. M. S. V. Doidge-Harrison, R. A. Howie, I. W. Nowell, O. J. Taylor, and J. L. Wardell, *J. Chem. Soc., Perkins Trans. 1*, 1989, 2017.
25. J. T. B. H. Jastrzebski, Intramolecular Coordination in Organotin Chemistry, Ph.D. Thesis, University of Utrecht, Netherlands, 1991.
26. R. A. Howie and J. L. Wardell, unpublished results.
27. J. F. Sawyer, *Acta Crystallogr., Sect. C*, 1988, **44**, 633.
28. H. Preut, J. Koch, and F. Huber, *Acta Crystallogr., Sect. C*, 1990, **46**, 2088.
29. H. Reuter and H. Puff, *J. Organomet. Chem.*, 1992, **424**, 23.
30. I. Wharf and M. G. Simard, *Acta Crystallogr., Sect. C*, 1991, **47**, 1605; P. Storck and A. Weiss, *Acta Crystallogr., Sect. C*, 1990, **46**, 767.
31. H. Schumann, B. C. Wassermann, and F. E. Haln, *Organometallics*, 1992, **11**, 2803.
32. H. Puff, B. Breuer, G. Gehrke-Brinkmann, P. Kind, H. Reuter, W. Schuh, W. Wald, and G. Weidenbrück, *J. Organomet. Chem.*, 1989, **363**, 265.
33. T. Tsumuraya, S. A. Batcheller, and S. Masamune, *Angew. Chem., Int. Ed. Engl.*, 1991, **30**, 902.
34. F. Glocking, in ‘Chemistry of Tin’, ed. P. G. Harrison, Blackie, Glasgow, 1989, Chap. 8.
35. L. R. Sita and R. D. Bickerstaff, *J. Am. Chem. Soc.*, 1989, **111**, 3769.
36. C. J. Cardin, D. J. Cardin, M. A. Convery, M. M. Devereux, and N. B. Kelly, *J. Organomet. Chem.*, 1991, **414**, C9.
37. F. J. Brady, C. J. Cardin, D. J. Cardin, M. A. Convery, M. M. Devereux, and G. A. Lawless, *J. Organomet. Chem.*, 1991, **421**, 199.
38. L. R. Sita and R. D. Bickerstaff, *J. Am. Chem. Soc.*, 1989, **111**, 6454.
39. H. Preut and T. N. Mitchell, *Acta Crystallogr., Sect. C*, 1991, **47**, 951.
40. A. H. Cowley, S. W. Hall, C. M. Nunn, and J. M. Power, *Angew. Chem., Int. Ed. Engl.*, 1988, **27**, 838.
41. H. Grützmacher and H. Pritzkow, *Angew. Chem., Int. Ed. Engl.*, 1991, **30**, 1017.
42. C. Schneider and M. Dräger, *J. Organomet. Chem.*, 1991, **415**, 349.
43. M. F. Lappert, P. P. Power, A. R. Sanger, and R. C. Srivastava, ‘Metal and Metalloid Amides’, Ellis Horwood, Chichester, 1980, p. 235.
44. A. Raharinirina, R. Boese, and G. Schmid, *J. Organomet. Chem.*, 1990, **395**, 39.
45. H. Puff, D. Hänssgen, N. Beckermann, A. Roloff, and W. Schuh, *J. Organomet. Chem.*, 1990, **373**, 37.
46. P. Gamis, G. Paiaro, L. Pandolfo, and G. Vialla, *Organometallics*, 1988, **7**, 210.
47. C. Couret, J. Escudie, J. Satgé, A. Raharinirina, and J. D. Andriamizaka, *J. Am. Chem. Soc.*, 1985, **107**, 8280; H. Ranaivonjatovo, J. Escudie, C. Couret, and J. Satgé, *J. Chem. Soc., Chem. Commun.*, 1992, 1047.
48. D. Hänssgen, H. Aldenhoven, and M. Nieger, *J. Organomet. Chem.*, 1988, **367**, 47; *Chem. Ber.*, 1990, **123**, 1837; S. Roller, M. Dräger, H.-J. Breuning, M. Ates, and S. Gulec, *J. Organomet. Chem.*, 1987, **329**, 319.
49. T. N. Mitchell and H.-J. Belt, *J. Organomet. Chem.*, 1988, **345**, C28; 1990, **386**, 167.
50. H. Reuter and H. Puff, *J. Organomet. Chem.*, 1989, **379**, 223.
51. C. J. Cardin, D. J. Cardin, M. A. Convery, and M. M. Devereux, *J. Organomet. Chem.*, 1991, **411**, C3.
52. A. R. Forrester, S. J. Garden, R. A. Howie, and J. L. Wardell, *J. Chem. Soc., Dalton Trans.*, 1992, 2615.
53. E. Tiekink, *Appl. Organomet. Chem.*, 1991, **5**, 1.
54. D. Franzoni, G. Pelizzi, G. Predieri, P. Tarasconi, and C. Pelizzi, *Inorg. Chim. Acta*, 1988, **150**, 279.
55. K. C. Mollov, K. Quill, D. Cunningham, P. McArdle, and T. Higgins, *J. Chem. Soc., Dalton Trans.*, 1989, 267.
56. R. J. Batchelor, F. W. B. Einstein, C. H. W. Jones, and R. D. Sharma, *Inorg. Chem.*, 1988, **27**, 4636.
57. B. M. Schmidt and M. Dräger, *J. Organomet. Chem.*, 1990, **399**, 63; R. J. Batchelor, F. W. B. Einstein, and C. H. W. Jones, *Acta Crystallogr., Sect. C*, 1989, **45**, 1813.
58. H. Puff, G. Bertram, B. Ebeling, M. Franken, R. Gattermayer, R. Hundt, W. Schuh, and R. Zimmer, *J. Organomet. Chem.*, 1989, **379**, 235.
59. A. Schäfer, M. Wiedenbruch, W. Saak, S. Pohl, and H. Marsmann, *Angew. Chem., Int. Ed. Engl.*, 1991, **30**, 962.
60. A. Schäfer, M. Wiedenbruch, W. Sark, S. Pohl, and H. Marsmann, *Angew. Chem., Int. Ed. Engl.*, 1991, **30**, 834.
61. W. P. Neumann, *Chem. Rev.*, 1991, **91**, 314.
62. P. D. Lickiss, in ‘Chemistry of Tin’, ed. P. G. Harrison, Blackie, Glasgow, 1989, Chap. 7.
63. P. Bleckmann, M. Maly, R. Minkwitz, W. P. Neumann, and B. Watta, *Tetrahedron Lett.*, 1982, **23**, 4655.

64. T. Fjeldberg, A. Haaland, B. E. R. Schilling, M. F. Lappert, and A. J. Thorne, *J. Chem. Soc., Dalton Trans.*, 1986, 1551; P. J. Davidson, D. H. Harris, and M. F. Lappert, *J. Chem. Soc., Dalton Trans.*, 1976, 2268; P. Jutzi and B. Hielscher, *Organometallics*, 1986, **5**, 2511.
65. M. Kira, R. Yauchibara, R. Hirano, C. Kabuto, and H. Sakurai, *J. Am. Chem. Soc.*, 1991, **113**, 7785.
66. U. Lay, H. Pritzkow, and H. Grützmacher, *J. Chem. Soc., Chem. Commun.*, 1992, 260; H. Grützmacher, H. Pritzkow, and F. T. Edelmann, *Organometallics*, 1991, **10**, 23.
67. S. Masamune and L. R. Sita, *J. Am. Chem. Soc.*, 1985, **107**, 6390.
68. J. T. B. H. Jastrzebski, P. A. van der Schaaf, J. Boersma, G. van Koten, D. Heijdenrijk, K. Goubitz, and D. J. A. de Ridder, *J. Organomet. Chem.*, 1989, **367**, 55; J. T. B. H. Jastrzebski, P. A. van der Schaaf, J. Boersma, G. van Koten, M. C. Zoutberg, and D. Heijdenrijk, *Organometallics*, 1989, **8**, 1373.
69. J. T. B. H. Jastrzebski, H. A. J. Sypkens, F. J. A. des Tombe, P. A. van der Schaaf, J. Boersma, G. van Koten, A. L. Spek, and A. J. M. Duisenberg, *J. Organomet. Chem.*, 1990, **396**, 25.
70. H. H. Karsch, A. Appelt, and G. Müller, *Organometallics*, 1986, **5**, 1664; A. L. Balch and D. E. Oram, *Organometallics*, 1986, **5**, 2159.
71. P. Jutzi, *J. Organomet. Chem.*, 1990, **400**, 1; *Adv. Organomet. Chem.*, 1986, **26**, 217.
72. M. G. Davidson, D. Stalke, and D. S. Wright, *Angew. Chem., Int. Ed. Engl.*, 1992, **31**, 1226.
73. N. Kuhn, G. Henkel, and S. Stubenraulh, *J. Chem. Soc., Chem. Commun.*, 1992, 760.
74. H. Schmidbaur, T. Probst, B. Huber, G. Müller, and C. Krüger, *J. Organomet. Chem.*, 1989, **365**, 53.
75. C. J. Evans, in ‘Chemistry of Tin’, ed. P. G. Harrison, Blackie, Glasgow, 1989, Chap. 13.
76. M. J. Selwyn, in ‘Chemistry of Tin’, ed. P. G. Harrison, Blackie, Glasgow, 1989, Chap. 11.
77. A. J. Crowe, *Drugs Future*, 1987, **12**, 255.
78. N. F. Cardarelli ed., ‘Tin as a Nutrient: Implications in Cancer Prophylaxis and other Physiological Processes’, CRC Press, Boca Raton, FL, 1986.
79. S. J. Blunden and A. Chapman, in ‘Organometallic Compounds in the Environment: Principles and Reactions’, ed. P. J. Craig, Longman, Harlow, 1988.
80. A. J. Crowe, *Appl. Organomet. Chem.*, 1987, **1**, 143, 331.

Titanium: Inorganic & Coordination Chemistry

Ann M. Valentine
Yale University, New Haven, CT, USA

Based in part on the article Titanium: Inorganic & Coordination Chemistry by Charles A. McAuliffe & Neil Bricklebank which appeared in the Encyclopedia of Inorganic Chemistry, First Edition.

1 Introduction 1
2 Properties of the Metal 1
3 Titanium Compounds 2
4 Coordination Chemistry 5
5 Related Articles 9
6 References 9

Abbreviations

acac = acetylacetonate; Cp = cyclopentadienyl; bpy = 2,2′-bipyridyl; cat = catechol; diars = diarsine = *o*-phenylenebis(dimethylarsine); dppe = 1,2-bis(diphenylphosphino)ethane; dmpe = 1,2-bis(dimethylphosphino)ethane; en = ethylenediamine; *meso*-DME = *meso*-porphyrin dimethyl ester; mtc = methylthiocarbamate; OEP = octaethylporphyrin; ox = oxalate; por = porphyrin; pn = propylenediamine; py = pyridyl; Rdab = R–N=CH–CH=N–R; salen = *N*,*N*′-ethylenebis(salicylideneiminate); tacn = triazacyclononane.

1 INTRODUCTION

Titanium is a relatively common element comprising 0.63% of the earth's crust, making it the ninth most abundant element and the second most abundant transition element (after iron). Despite this abundance, it is only during the latter part of the twentieth century that the element has developed any industrial potential, which is due largely to the difficulties associated with its refinement.

1.1 Discovery

Titanium was discovered in 1791 by an English clergyman and amateur chemist, William Gregor. He identified it in a black sand (now known to be ilmenite, $FeTiO_3$, named after Russia's Ilmen lake and mountains) from the Menacchan Valley in Cornwall. Four years later, the German chemist M. H. Klaproth independently discovered the element in the TiO_2 form, as rutile. He gave it the name titanium after the Titans, who in Greek mythology were the sons of Earth.

1.2 Preparation of the Metal

Titanium is widely distributed in the earth's crust, the principal ores being ilmenite and rutile. It is not possible to obtain titanium metal by the usual method of reduction of the dioxide with carbon, because of the formation of a very stable carbide. Moreover, the metal is reactive toward both dioxygen and dinitrogen at elevated temperatures. Hydrogen reduction at 900 °C only reduces TiO_2 as far as Ti_2O_3, while reduction of TiO_2 with the common reducing metals, for example, Na, Al, Ca, or Mg, seldom yields pure products. Reduction of the tetrachloride is, therefore, the basis of the preferred methods.

Reduction to elemental titanium was first commercialized in the 1950s. A successful laboratory method is reduction of the dioxide with excess calcium hydride in a molybdenum boat. The reaction is carried out at 900 °C in a vacuum or an atmosphere of hydrogen (equation 1).[1] Extremely pure titanium can be prepared on a laboratory scale by the van Arkel–de Boer method;[2] in this method, pure TiI_4 is vaporized and decomposed on a hot wire in a vacuum.

$$TiO_2 + CaH_2 \longrightarrow Ti + 2CaO + 2H_2 \quad (1)$$

Industrially, titanium is prepared using the Kroll process;[3,4] in this process, ilmenite or rutile is treated at red heat with chlorine and carbon, producing $TiCl_4$ (equation 2). The $TiCl_4$ is fractionally distilled from $FeCl_3$ and other impurities and then reduced with molten magnesium at ca. 1000 °C in an atmosphere of argon (equation 3). The $MgCl_2$ and excess Mg are removed either by volatilization at 1000 °C or by leaching with dilute HCl. This leaves titanium as a spongy mass, which may be cast into ingots using an electric arc under an atmosphere of argon.

$$2FeTiO_3 + 7Cl_2 + 6C \xrightarrow{900\,^\circ C} 2TiCl_4 + 2FeCl_3 + 6CO \quad (2)$$

$$TiCl_4 + 2Mg \xrightarrow{1000\,^\circ C} Ti + 2MgCl_2 \quad (3)$$

2 PROPERTIES OF THE METAL

Table 1 summarizes some of the more important properties of titanium.

Titanium is a silvery ductile metal with important industrial uses because it is less dense than iron, much stronger than aluminum, and almost as corrosion resistant as platinum. This rare combination of properties makes it ideal for a variety of uses, particularly in engines, aircraft frames, marine equipment, and industrial plants. Titanium metal and alloys also replace bone and serve in dental implants. At normal temperatures, the metal is hexagonal ($D_{6h} - 6/mmc$, $Z = 2$);[5] however, the metal undergoes a phase change at 882 °C to give the β-form, which is cubic ($O_{h-}Im3m$, $Z = 2$).[5] At elevated temperatures, the metal has an enormous affinity for dioxygen, dinitrogen, and dihydrogen, however, it is only for H_2 that the absorption is reversible. Titanium dust is explosive in air, and even the fresh surface of the metal will spontaneously ignite in dioxygen at 25 atm. Traces of dioxygen and dinitrogen render the metal very brittle and hence of little utility.

Titanium is not attacked by mineral acids in the cold or by hot aqueous alkali, but it dissolves in HF, hot HCl, hot HNO_3, and hot concentrated H_3PO_4. It reacts with many metals and nonmetals, for example, Al, Sb, Be, Cr, Fe, and B, forming intermetallic or interstitial compounds.

2.1 General Properties of the Group 4 Elements

Titanium is the first member of the 3d transition series and has four valence electrons, $3d^24s^2$. The most stable and most common oxidation state is IV; however, compounds in a range of lower oxidation states, −I, 0, II, III, are also known, although they are readily oxidized to Ti^{IV} by air, water, or other reagents. The standard reduction potentials in volts versus NHE in acid solution are given in Scheme 1. The actual potentials of the titanium complexes are, of course, strongly dependent on the ligand environment and conditions.

Table 1 Some physical properties of titanium

Atomic number	22
Atomic weight	47.88 (±0.03)
Number of naturally occurring isotopes (all stable)	5
^{46}Ti (8.25% abundance, I = 0)	
^{47}Ti (7.44% abundance, I = 5/2)	
^{48}Ti (73.72% abundance, I = 0)	
^{49}Ti (5.41% abundance, I = 7/2)	
^{50}Ti (5.18% abundance, I = 0)	
Additional radioactive isotopes	>15
Electronic configuration	$[Ar]3d^24s^2$
Electronegativity (Ti^{IV}, Sanderson scale)	1.5
Mp (°C)	1667
Bp (°C)	3285
ΔH_{fus} (kJ mol^{-1})	18.8
ΔH_{vap} (kJ mol^{-1})	425
ΔH_f (monatomic gas) (kJ mol^{-1})	469
Density (25 °C) (g cm^{-3})	4.5
Electrical resistivity (20 °C) (μΩ cm)	42.0

The most common coordination number of titanium is six, although four-, five-, seven-, and eight-coordinate compounds are known (Table 2). Table 3 summarizes the common oxidation states of titanium with the associated coordination numbers and stereochemistries. Zirconium shows a similar range of oxidation states (*see* ***Zirconium & Hafnium: Inorganic & Coordination Chemistry***); however, Zr^{II} and Hf^{II} are much less stable, relative to Zr^{IV} and Hf^{IV}, than is the case for titanium.

The metal conducts heat and electricity, similar to iron or nickel. In the Ti^{IV} oxidation state, there are some similarities with the group 14 elements (Si, Ge, Sn, and Pb), particularly Sn. For example, the ionic radius of Ti^{4+} is 0.68 Å and of Sn^{4+}, 0.71 Å. Similarly, SnO_2 and TiO_2 are isomorphous, while the tetrachlorides of both elements are readily hydrolyzed liquids. However, the d electrons of the group 4 elements contribute more effectively to metal–metal bonding in the bulk materials than do the p electrons of the group 14 elements. A consequence of this is the increase in the difference between the melting points, boiling points, and enthalpies of atomization on passing from C and Si to Ti, Zr, and Hf, than from C and Si to Ge, Sn, and Pb.

3 TITANIUM COMPOUNDS

3.1 Oxides and Sulfides

The most important oxide of titanium is the dioxide, TiO_2, also known as titania. This importance arises predominantly from the use of TiO_2 as a white pigment in the manufacture of paint and paper and as a filler in rubber and plastics. Titanium

$$TiO^{2+} \xrightarrow{+0.10} Ti^{3+} \xrightarrow{-0.37} Ti^{2+} \xrightarrow{-1.63} Ti$$

Scheme 1

Table 2 Atomic radii of titanium[6]

Type of radius	Coordination	Radius (pm)	Crystal radius (pm)	Effective ionic radius (pm)
Metal radius		147		
Covalent		136		
Ionic: Ti^{II}	6-coordinate		100	86
Ti^{III}	6-coordinate		81	67
Ti^{IV}	4-coordinate		56	42
	5-coordinate		65	51
	6-coordinate		74.5	60.5
	8-coordinate		88	74

Table 3 Oxidation states and stereochemistry of titanium

Oxidation state	Configuration	Coordination	Stereochemistry	Example
Ti^{-I}	d^5	6	Octahedral	$[Ti(bpy)_3]^-$
Ti^0	d^4	6	Octahedral	$[Ti(bpy)_3]$
Ti^{II}	d^2	4	Distorted tetrahedral	$[Ti(Cp)_2(CO)_2]$
		6	Octahedral	$TiCl_2$
Ti^{III}	d^1	3	Planar	$[Ti\{N(SiMe_3)_2\}_3]$
		5	Trigonal bipyramidal	$[TiBr_3(NMe_3)_2]$
		6	Octahedral	$[Ti(urea)_6]^{3+}$
Ti^{IV}	d^0	4	Tetrahedral	$TiCl_4$
		5	Trigonal bipyramidal	$[TiOCl_2(NMe_3)_2]$
			Square pyramidal	$[TiOCl_4]^{2-}$
		6	Octahedral	$[TiF_6]^{2-}$
		7	Pentagonal bipyramidal	$[TiCl(S_2CNMe_2)_3]$
			Capped trigonal prismatic	$[TiF_5(O_2)]^{3-}$
		8	Dodecahedral	$[TiCl_4(diars)_2]$
		11	–	$[TiCp(S_2CNMe_2)_3]$

dioxide is also used in skin care and cosmetics products and in sunscreens. The use of TiO_2 as a pigment stems from its exceptionally high refractive index in the visible region of the electromagnetic spectrum, which is higher than the refractive index of diamond, as shown in Table 4. Thus, while large crystals of TiO_2 are transparent and do not refract, fine particles scatter light very strongly. Moreover, TiO_2 is chemically inert, so that it has displaced the pigment 'white lead' $(PbCO_3)_2{\cdot}Pb(OH)_2$. The photochemistry of TiO_2 has enabled important applications.[7]

Natural TiO_2 has three crystalline forms: rutile, the most common form, and anatase and brookite, both of which convert to rutile at elevated temperatures. All contain six-coordinate titanium atoms[8] though in anatase and brookite, the octahedra of oxygen atoms is distorted. Natural forms of TiO_2 are often colored due to the presence of impurities. Synthetic TiO_2 is manufactured either by oxidizing $TiCl_4$ with oxygen or by the hydrolysis of Ti^{IV} sulfate. Rutile can be reduced to give a wide range of nonstoichiometric oxide phases such as the Magneli-type phases Ti_nO_{2n-1} $(4 \le n \le 9)$, the broad nonstoichiometric phases TiO_x $(0.7 \le x \le 1.3)$, and the lower oxides Ti_3O_5 and Ti_2O_3.

A large number of complex oxides or 'titanates' are known. These are produced by fusing TiO_2 at high temperatures with stoichiometric amounts of the appropriate metal oxide. Orthotitanates, $M^{II}TiO_3$, in which the M^{II} is approximately the same size as Ti^{IV} (M = Mg, Mn, Fe, Co, Ni), all have the ilmenite structure, $FeTiO_3$. Recently, a single hanging crystal of ilmenite was discovered in each nest comb of the hornet *Vespa orientalis*.[9] The purpose and the origin of these crystals are still unclear, although they may indicate the downward direction and also help the hornets assess symmetry as they are building their nests. Metatitanates, $M^{II}TiO_3$, contain M^{II} ions that are larger than Ti^{IV} (M = Ca, Sr, Ba); in these compounds the preferred structure is that of perovskite, $CaTiO_3$. A third important structural type of titanate is the spinel structure, $MgAl_2O_4$, which is possessed by the compounds $M^{II}{}_2TiO_4$ (M = Mg, Zn, Mn, Fe, Co).

Table 4 Refractive index of various materials

Substance	Refractive index
NaCl	1.54
SiO_2	1.54–1.56
TiO_2 (rutile)	2.61–2.90
TiO_2 (anatase)	2.49–2.55
Diamond	2.42

An extensive series of phases of general formula $Ba_xTi_yO_{x+2y}$ are formed from the reaction of TiO_2 with barium oxide. The simplest, $BaTiO_3$, is known as barium titanate. These materials are of interest because of their ferroelectric properties, which result from the differences in the relative sizes of the Ba^{II} and Ti^{IV} ions. The Ti^{IV} ions are located between six Ba^{II} ions, which occupy octahedral positions. However, the Ti^{IV} ions are small compared to the Ba^{II} and so are free to move within their octahedral Ba^{II} 'holes'.

The sulfides have been studied much less than the oxides, but it is clear that many similarities exist. Like the oxides, a number of stable phases exist and nonstoichiometry is prevalent. The most important sulfide is TiS_2, which has the CdI_2 layer structure,[6] in which the Ti atoms occupy octahedral sites between alternate layers of close-packed sulfur atoms. The adjacent sulfur layers are able to intercalate Lewis bases such as aliphatic amines. Similar intercalation compounds can be made with MS_2 and MSe_2 compounds (M = Ti, Zr, Hf, V, Nb, Ta). Many of these compounds exhibit useful electrical properties including superconductivity (*see* ***Superconductivity***).

3.2 Halides

The most important halides are the tetrahalides.[10,11] TiF_4 is obtained either by the action of HF on $TiCl_4$ or by direct combination of the elements at 200 °C. It is a hygroscopic white solid. The structure was relatively recently solved,[12] to reveal columns of corner-linked TiF_6 octahedra. $TiCl_4$ is a pungent colorless liquid (mp −2.3 °C, bp 136 °C), which is the starting material for the formation of most Ti compounds. $TiCl_4$ itself is formed by heating Cl_2 and TiO_2 in the presence of a reducing agent. $TiCl_4$ fumes in moist air and is vigorously hydrolyzed by water (equation 4). Partial hydrolysis results in the formation of oxychlorides.

$$TiCl_4 + 2H_2O \longrightarrow TiO_2 + 4HCl \qquad (4)$$

$TiBr_4$ is formed in an analogous manner to $TiCl_4$, whereas TiI_4 is formed by reacting TiO_2 and AlI_3 at a temperature of 130–400 °C. They are orange and brown colored crystalline solids, respectively, which consist of molecular lattices isomorphous with EI_4 (E = Si, Ge, Sn). The interesting gradation in color shown by the titanium tetrahalides is due to a charge-transfer band, which moves toward lower energies as the anion becomes more easily oxidized by the small, highly polarizing titanium cation. All the tetrahalides behave as Lewis acids, dissolving in polar solvents to give a series of addition compounds and adducts.

One very important use of $TiCl_4$ is in Ziegler–Natta catalysis. (*see* ***Titanium: Organometallic Chemistry*** and ***Oligomerization & Polymerization by Homogeneous Catalysis***). The catalyst, a mixture of $TiCl_4$ and $AlEt_3$, induces the polymerization of ethylene under ambient conditions. Prior to this technology, ethylene could only be polymerized at high pressure and temperature. The mechanism is still not entirely understood; however, the most likely explanation is given in Scheme 2. This mechanism involves: (1) replacement of a coordinated chloride by an ethyl group derived from $AlEt_3$; (2) an ethylene molecule becoming bound to a vacant coordination site on the surface; (3) cis-insertion as the ethylene migrates to the ethyl group; and (4) another ethylene becoming bound at the vacant coordination site. The insertion is then repeated.

The trihalides of titanium can be prepared by reducing the tetrahalides with the metal. With the exception of the trifluoride, which has a magnetic moment of 1.75 BM, as expected for a d^1 ion, all the trihalides have low magnetic moments, indicative of metal–metal interaction. The structures consist of halogen-bridged polymers containing six-coordinate titanium.

The dihalides TiX_2 (X = Cl, Br, I) are black solids and have the CdI_2 structure. Magnetic susceptibility data provide evidence for extensive metal–metal bonding within the compounds. These compounds are sufficiently strongly reducing to reduce water.

Halides with the stoichiometry Ti_7X_{16} (X = Cl, Br) have also been prepared.[13] They are black crystalline solids sensitive to both oxidation and hydrolysis. They consist of octahedrally coordinated Ti^{IV} and Ti^{II} atoms in the ratio 1:6 (i.e. $TiCl_4 \cdot 6TiCl_2$).

3.3 Complex Halides

A large number of complex halides are known and have been reviewed.[14] The most common complex fluorides involve the TiF_5^- moiety. Complexes are conveniently prepared by adding $[N(n\text{-}Pr)_2H_2]F$ and a stoichiometric amount of the donor to a solution of TiF_4. Alternatively, an equimolar quantity of $[N(n\text{-}Pr)_2H_2]_2[TiF_6]$ is added to a solution of TiF_4L_2.[15] Solutions formed by the former method that do not form $[TiF_5L]^-$ were shown by ^{19}F NMR to contain the $[Ti_2F_{11}]^{3-}$ moiety.[15]

The $TiCl_6{}^{3-}$ anion is believed to form when Ti^{II} fused with chloride melts, but it can be isolated from the direct reaction of $TiCl_3$ with excess anhydrous pyHCl, or by the reaction of $TiCl_3(MeCN)_3$ with pyHCl. However, when Et_4NCl and Et_4NBr are reacted with $TiCl_3(MeCN)_3$, the expected hexahalo salts are not formed but $[TiCl_4(MeCN)_2]$ and (Et_4N) $[TiCl_3Br(MeCN)_2]$ are produced.[16] Reaction of $TiCl_4$ with t-butylamine in dichloroethane at −78 °C yields $[TiCl_2(NHBu\text{-}t)_2(NH_2Bu\text{-}t)_2]_n$, which loses the coordinated t-butylamine upon standing at room temperature.[17]

The $[Ti_2Cl_{10}]^{2-}$ species is also known.[18] For example, adducts of the type $(PCl_5)_n \cdot mTiCl_4$ (n, m = integer) have been known since 1867. Reaction of PCl_5 with $TiCl_4$ in $POCl_3$ and $SOCl_2$ gives $[PCl_4]_2[Ti_2Cl_{10}]$ and $[PCl_4][Ti_2Cl_9]$ respectively, which are unusual examples of face-shared bioctahedra containing transition metal ions in the +4 oxidation state.[19]

Reaction of $TiCl_4$ and $B_2[NMe_2]_4$ gives the unusual $\{[Me_2N]_2BCl\}_2[TiCl_4]_3$ species, as well as small quantities of Me_2NTiCl_3 and $Me_2NBu \cdot Ti_2Cl_6$.[20] The latter complex contains coordinated dimethylamino moieties, and a pentacoordinate structure has been proposed.[21] The $Ti_5Cl_{11}{}^-$ ion has been isolated in the salt $[(Ph_3P)_3PtCl]^+$ $[Ti_5Cl_{11}]^-$.[22]

Concomitant with the work on the chloride system, $\{[Me_2N]_2BBr\}_2\{TiBr_4\}_3$ has been prepared, and the following coordination has been proposed:[23]

$$Br_4Ti \leftarrow NMe_2B(Br)Me_2N \rightarrow TiBr_4 \leftarrow NMe_2B(Br)Me_2N \rightarrow TiBr_4$$

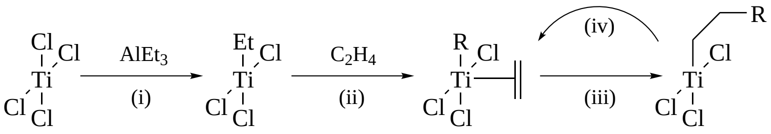

Scheme 2

Reaction of $TiBr_4$ with $B_2[NMe_2]_4$ gives dinuclear $B_2Br_2[NMe_2]_2{\cdot}TiBr_3$ (**1**).[24] Complexes $M_2[TiBr_5(H_2O)]$ (M = Cs, Rb, pyH) are also known.[25]

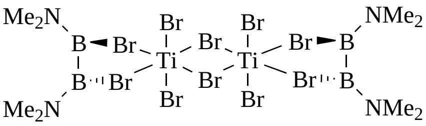

(**1**)

The species $TiI_6{}^{2-}$ is unknown. The only evidence for its formation comes from the treatment of $[Et_4N]_2TiCl_6$ with liquid HI, which yields a very unstable black solid. It has been predicted, by comparison with the electronic spectra of the $TiX_6{}^{2+}$ (X = Cl, Br) species, that $TiI_6{}^{2-}$ would be black.[26]

4 COORDINATION CHEMISTRY

A large number of titanium complexes are known and it is not possible to review the literature comprehensively in the space available. More comprehensive treatises have been published by Stephan,[27] McAuliffe,[26] and Clark.[14] Titanium in its common oxidation states is quite labile. Water exchange is used as a convenient benchmark. The rate constant for water exchange in the Ti^{III} species $[Ti(H_2O)_6]^{3+}$ is $1.8 \times 10^5\,s^{-1}$ at room temperature,[28] and a lower limit of $3.4 \times 10^3\,s^{-1}$ has been placed on the exchange of terminal water ligands in oligomeric hydrolyzed Ti^{IV} solutions.[29] These values can be compared to rate constants for exchange of $1.6 \times 10^2\,s^{-1}$ for $[Fe(H_2O)_6]^{3+}$ and 2.4×10^{-6} for the famously inert $[Cr(H_2O)_6]^{3+}$.[30]

4.1 Low-valent Titanium Complexes

Although the coordination chemistry of Ti^{IV} and, to a lesser extent, Ti^{III} has been relatively well investigated, few complexes are known in the lower oxidation states and are almost all unstable to oxidation.[10,14,26,27] Reduction of $TiCl_4$ with excess of dilithium 2,2′-bipyridyl in THF with excess bipyridyl gives $Li[Ti(bpy)_3]{\cdot}3THF$, as shown in equations (5) and (6). Further reduction to $Li_2[Ti(bpy)_3]{\cdot}3.7THF$ is possible.[26]

$$TiCl_4 + 2Li_2bpy + bpy \xrightarrow{THF} [Ti(bpy)_3] + LiCl \tag{5}$$

$$TiCl_4 + 2.5Li_2bpy + 0.5bpy \xrightarrow{THF} Li[Ti(bpy)_3]{\cdot}3.7THF + 4LiCl \tag{6}$$

Diazadiene or diimine ligands of the general type R–N=CH–CH=N–R (Rdab) are known to stabilize complexes in low oxidation states.[31] Cloke and coworkers have prepared titanium(0) complexes of Rdab (R = *i*-Pr, *i*-Bu) by cocondensation of titanium vapor with an excess of ligand in heptane.[32] $[Ti(\sigma,\sigma\text{-}N,N'\text{-}i\text{-Prdab})_3]$ (**2**) is an air-sensitive, blue colored crystalline solid. ^1H NMR data show the methyl groups of *i*-Pr substituents to be diastereotopic, confirming that the titanium center has octahedral coordination. $[Ti(\sigma,\sigma\text{-}N,N'\text{-}t\text{-Budab})_2]$ (**3**) forms as air-sensitive, red colored crystals. The latter complex is four-coordinate, and is presumed to be tetrahedral. Photoelectron spectroscopic data for both complexes confirm that coordination occurs through the N atoms of the ligands.

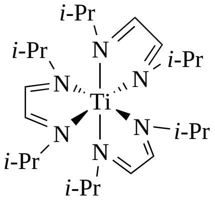

(**2**)

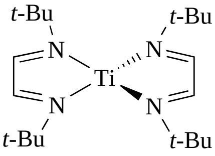

(**3**)

Titanium(II) complexes are better understood. Reaction of the deeply colored $TiX_2(MeCN)_2$ (X = Cl, Br) complexes with other ligands gives $TiCl_2L_2$ (L = C_4H_8O, $C_5H_{10}O$, py, 0.5bpy, 0.5phen) and $TiBr_2(bpy)$. The latter species react with water to liberate dihydrogen.[33] One example of an aquo-coordinated Ti^{II} complex was recently described, however. The UV/visible spectrum and structure from X-ray powder data of the aqueous Ti^{II} compound, $TiF_2(H_2O)_4$, were recorded after its formation from the dissolution of titanium metal in strong acid.[34]

Reaction of Na_2TiCl_4 with NMe_3 results in oxidation of the halide, leading to the formation of $TiCl_3(NMe_3)_2$.[35] Dialkylamides of Ti^{II} can be prepared by the volatility-controlled disproportionation of Ti^{III}.[36]

Gambarotta and coworkers have shown that reduction of $TiCl_3(THF)_3$ with lithium, in the presence of a large excess of TMEDA, allows the large-scale preparation of *trans*-$(TMEDA)_2TiCl_2$.[37] The TMEDA ligands are easily replaced by other amines, allowing the quantitative preparation of $TiCl_2L_4$ (L = 0.5*N*,*N*′,*N*′-trimethylethylenediamine, py, 0.5bpy).[37] Furthermore, reaction of *trans*-$(TMEDA)_2TiCl_2$ with $(Me_3Si)_2NLi$ leads to the formation of $\{[(Me_3Si)_2N]TiCl(TMEDA)\}_2[\mu\text{-}N_2]$ (**4**).[38] The complex consists of two identical $\{[(Me_3Si)_2N]TiCl(TMEDA)\}$ fragments, each bonded to one of the two nitrogen atoms of a bridging dinitrogen moiety. The Ti–(μ-N_2)–Ti moiety is almost linear. The Ti–N bonds are short, 1.762 Å, while the N–N distance is long, 1.289 Å, indicating considerable electronic delocalization over the $Ti_2(\mu\text{-}N_2)$ moiety. The titanium atom has a square pyramidal coordination geometry, but is elevated 0.466(3) Å above the plane. However, reaction with 2 equiv of $(Me_3Si)_2NLi$ in the presence of TMEDA yields the black crystalline solid

$\{[(Me_3Si)_2N]_2Ti\}_2(\mu\text{-}\eta^2\eta^2\text{:-}N_2)_2[(TMEDA)_2Li]$ (**5**), which is a mixed-valence Ti^I/Ti^{II} species.[38] The X-ray crystal structure of (**5**) shows it to consist of two separate $[Li(TMEDA)_2]$ and $[\{[(Me_3Si)_2N]_2Ti\}_2(\mu\text{-}\eta^2\text{:}\eta^2\text{-}N_2)_2]$ ionic fragments. The titanium-containing unit is dinuclear and is formed by two $[(Me_3Si)_2N]_2Ti$ groups that are symmetrically and perpendicularly arranged on the two sides of the two parallel dinitrogen molecules. Both titanium atoms are six coordinate, four of the coordination sites being occupied by the four nitrogen atoms of the two coplanar dinitrogen molecules. The N–N distance (1.379 Å) is significantly longer than that displayed in complex (**4**). The Ti–N distances are similarly elongated (Ti(1)–N(3) = 2.236 Å, Ti(1)–N(4) = 2.290 Å). These differences in the bond lengths are attributed to the different modes of bonding in the two complexes. The different bonding mode of the dinitrogen moiety in the two complexes (i.e. end-on versus side-on) could only be attributed to the different steric bulk of the two complexes.

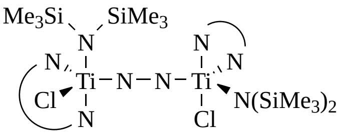

(**4**)

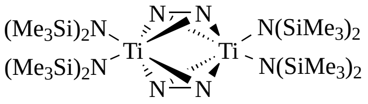

(**5**)

The cyclopentadienyl derivative of titanium(II), Cp_2Ti (*see* ***Titanium: Organometallic Chemistry***), has eluded isolation as a discrete compound.[26] However, $Cp_2Ti(PMe_3)_2$ (equation 7) provides a convenient route to the Cp_2Ti unit since the two phosphine ligands are easily displaced by a large number of substrates (e.g. CO, C_4H_4, C_4H_8, dmpe, MeCN) under very mild conditions.[39]

$$Cp_2TiCl_2 + Mg + 2PMe_3 \xrightarrow{\text{THF}} Cp_2Ti(PMe_3)_2 + MgCl_2 \qquad (7)$$

Phosphine complexes of the second and third row transition elements are common; in contrast, those of the early first-row transition elements are not.[40] Wilkinson and coworkers prepared a series of *trans*-$MCl_2(dmpe)_2$ complexes (M = Ti, V, Cr, Mn, Fe).[41] The red–black colored titanium complex *trans*-$TiCl_2(dmpe)_2$ was prepared in high yield by reacting $TiCl_4$, dmpe, and magnesium in THF. The complex was characterized using X-ray crystallography, which confirmed the trans geometry of the ligands. Attempts to prepare $TiMe_2(dmpe)_2$ by alkylating $TiCl_2(dmpe)_2$ with MeLi or Me_2Mg were unsuccessful, leading only to the isolation of a red–black material of stoichiometry *trans*-$TiMe_{1.3}Cl_{0.7}(dmpe)_2$, which was considered to be a mixture of $TiMeCl(dmpe)_2$ and $TiMe_2(dmpe)_2$. The reaction of $TiCl_3{\cdot}THF$ or $TiCl_4{\cdot}2THF$ with $LiPCy_2$ yields the dark brown adduct $Ti(PCy_2)_2$.[42] This complex is pyrophoric and reacts readily with iodine in benzene to give $TiI_2(PCy_2)_2$ and $TiI_3(PCy_2)_2$.[42]

4.2 Titanium(III) Complexes

The magnetic and electronic properties of Ti^{III} complexes have been well studied. Nearly all Ti^{III} complexes exhibit room temperature–magnetic moments close to the spin-only value of 1.73 BM.[10,14,26] However, rather than showing a great deal of temperature dependence, as would be expected for a d^1 ion in an electrostatic field of perfect O_h symmetry, the magnetic moments level off and in general vary from ~1.5 BM at 80 K to ~1.8 BM at about 300 K. These effects arise because of distortion and covalence, which cause a delocalization of the electron[10,14,26] (*see* ***Magnetism of Transition Metal Ions***).

The electronic spectra of Ti^{III} complexes can give a hint to quite subtle structural information. In a perfect octahedral field, the ^2D ground term of Ti^{III} is split into a $^2T_{2g}$ lower term and a ^2E_g upper term. The broad asymmetric band at ca. 20 100 cm^{-1} in the visible spectrum of $Ti(H_2O)_6{}^{3+}$ arises from a $^2T_{2g} \rightarrow {}^2E_g$ transition. The energy of this transition for a complex is a direct measure of the ligand field strength. The asymmetry comes from splitting of the ^2E_g term as a consequence of the Jahn–Teller effect.[26]

Most Ti^{III} complexes are octahedral and are produced by reacting $TiCl_3$ with an excess of ligands, giving rise to a range of stoichiometries, for example, $[TiL_6]^{3+}$, $[TiL_4X_3]$, $[TiL_3X_3]$, and $[TiL_2X_4]^-$. Fowles and coworkers isolated a range of Ti^{III} iodide complexes, TiI_3L_2, TiI_3L_3 (L = NMe_2, py, α-picoline), and $TiI_3(MeCN)_4$, the last being assigned the formula $[TiI_2(MeCN)_4]I$.[43] The X-ray crystal structure of $TiBr_3(NMe_3)_2$ shows it to be monomeric with a trigonal bipyramidal structure.[44] In contrast, reaction of $TiCl_3[N(SiMe_3)_2]_3$ with $LiN(SiMe_3)_2$ yields $Ti[N(SiMe_3)_3]_3$, which is a rare example of a three-coordinate Ti^{III} complex.[45]

Bi- and polydentate ligands also form Ti^{III} complexes with a variety of stoichiometries. For example, $[Ti(L)_3]^{3+}$ complexes are produced by the ligands en and pn,[14] whereas bpy and phen give $[TiCl_2(L)_2][TiCl_4(L)]$,[14] $[TiI_2(phen)_2]I$,[43] and $[TiI_2(bpy)_2][TiI_4(bpy)]$.[43]

A number of neutral and anionic complexes containing oxalato ligands have been prepared, for example, $Ti_2(ox)_3{\cdot}10H_2O$,[46] $Cs[Ti(ox)_2(H_2O)_3]{\cdot}2H_2O$,[47] and $K_3[Ti(ox)_3(H_2O)]{\cdot}6H_2O$.[48] All contain seven-coordinate pentagonal bipyramidal Ti atoms, though an eight-coordination sphere has been proposed for the $K[Ti(ox)_2]{\cdot}2H_2O$ complex.[26]

Bowden and Ferguson obtained an interesting range of Ti^{III} Schiff-base complexes starting from $TiCl_3(THF)_3$ and potentially quadridentate Schiff bases.[49] Species (**6**), initially green, slowly turns red (**7**) on stirring in THF. Reduction of $[TiCl_2(salen)]$ with zinc dust in THF gives $[\{Ti(salen)(THF)_2\}][ZnCl_4]$. Magnetic moments ($\mu_{\text{eff}}$ =

0.96 BM) suggest a strong Ti–Ti interaction. Treatment of the blue solution with pyridine leads to the isolation of monomeric [TiCl(salen)(py)]·THF.[49] Reaction of $TiCl_3$ with the macrocyclic ligand 1,4,7-trimethyl-1,4,7-triazacyclononane (tacn) at 20 °C affords blue [(tacn)$TiCl_3$], while at higher temperatures, this reaction leads to the formation of green colored crystals containing [(tacn)$Ti^{III}Cl_3$], with [(tacn)$Ti^{IV}(O)Cl_2$] as an impurity.[50]

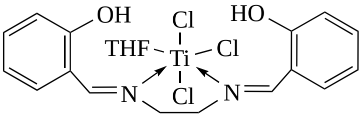

(**6**)

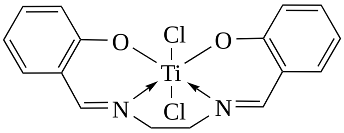

(**7**)

Titanium(III) phosphine complexes have received more attention than their titanium(II) analogs.[40] The first titanium(III) phosphine complex, $TiCl_3(PEt_3)\cdot C_2H_4$, was prepared by Chatt *et al.*[51] More recently, the monomeric complexes $TiCl_3(PR_3)_2$ (R_3 = MeH_2, Me_2H, Me_3, Et_3) have been prepared by the direct reaction of the components in toluene at 85 °C.[52] Weaker donors such as PPh_3 and PCl_3 do not complex with titanium(III). Recent work has also shown that $TiCl_3(THF)_3$ reacts with the diphosphine *i*-$Pr_2PCH_2CH_2P$-*i*-Pr_2 (dppe) to form the purple colored dimer $[TiCl_3(dppe)]_2$, which converts reversibly into the green monomeric complex $TiCl_3$(dppe) (THF). Most Ti^{III} complexes are susceptible to oxidation in air.

4.3 Titanium(IV) Complexes

As a result of the high ionic charge to radius ratio of titanium(IV), normal salts of titanium(IV) are difficult to prepare from aqueous solutions; these often yield basic, hydrolyzed species. A tris-catechol species, $[Ti(cat)_3]^{2-}$, prepared by Raymond *et al.* is one exception: it is stable in aqueous solution up to pH 12.[53] The catechol ligand is so stabilizing to Ti^{IV} that the Ti^{IV}/Ti^{III} reduction potential is shifted from the value of +0.1 V cited as the standard potential in acid in Scheme 1 to a value for $[Ti(cat)_3]^{2-}$ of −1.14 V vs. NHE, affording a powerful example of ligand tuning of metal redox potential.

Several oxotitanium(IV) compounds have been isolated, and were originally thought to contain TiO^{2+} ions. This notion, however, seems to be incorrect, the compounds actually being polymeric in the solid state. For example, $TiOSO_4\cdot H_2O$ consists of –Ti–O–Ti–O– chains, with each titanium being further coordinated to one water molecule and an oxygen from each of the three sulfates, giving a distorted octahedral geometry about the titanium. Similarly, $TiO(acac)_2$ is dimeric with a $Ti(\mu\text{-}O)_2Ti$ ring,[54] while the anion of $(NH_4)_2TiO(C_2O_4)_2\cdot H_2O$ is tetrameric with a central eight-membered $(–Ti–O–)_4$ ring.[55]

In contrast, studies on aqueous solutions of titanium(IV) in 2 M $HClO_4$ are consistent with the presence of doubly charged cationic species. However, it is not clear whether the predominant species is $[TiO]^{2+}$ or $[Ti(OH)_2]^{2+}$.[29]

Complexes containing Ti=O bonds are rare, although a few, mainly with porphyrins, have been characterized, for example, (*meso*-DME)Ti=O.[56] The Ti=O bonds appear to be short (∼1.62 Å), while IR bands are in the region 890–972 cm^{-1}, which is consistent with a Ti=O double bond.[57]

The Ti^{IV} halides readily give adducts of stoichiometry TiX_4L_2 and TiX_4(L–L) with donor molecules, where L and L–L are mono- and bidentate ligands, respectively. The potentially bidentate ligand *o*-allylaniline reacts with TiX_4 (X = Cl, Br) but only complexes via the nitrogen atom, forming the pentacoordinate monomeric complexes TiX_4L.[58] Titanium(IV) is predicted to be a 'hard' acid, whereas titanium(III) might be expected to show intermediate 'hard/soft' behavior. However, contrary to expectation, titanium(IV) has sometimes been shown to prefer sulfur to oxygen as a donor atom, as evidenced by the Ti–S bonds in the 1,4-thiozen complexes $TiX_4(C_4H_8OS)_2$.[35] Adducts of $TiOCl_2$ with MeCN and NMe_3 form $TiOCl_2L_2$; when L = NMe_3, the complexes are monomeric, the IR spectra indicating the presence of a terminal Ti=O moiety (978 cm^{-1}), whereas the MeCN adduct is probably polymeric, presumably having a Ti–O–Ti bridge (ν(Ti=O) ca. 890 cm^{-1}). Other complexes containing titanium in a trigonal bipyramidal geometry include the adduct formed from the reaction of $TiCl_4$ and $N(SiMe_3)_3$, which has planar four-membered $(Ti–N)_2$ rings with planar geometry at N, apparently with considerable π-bonding in the rings. These are linked by chlorine bridges to give the five-coordinate titanium atoms.[59] In contrast, the reaction of $TiCl_4$ with $Li[N(SiMe_3)_2]$ yields $[TiCl\{N(SiMe_3)_2\}_3]$.[60] Steric crowding prevents complete substitution of the chlorine atoms, and the complex has a distorted tetrahedral structure.

Some of the most useful and thus widely studied complexes of titanium(IV) are the alkoxides.[26,61] The materials range from solids to volatile liquids that can be distilled or sublimed and that are readily soluble in organic solvents. The complexes are easily hydrolyzed, even by traces of moisture. The ease of hydrolysis decreases with the increasing chain length of the alkyl group. Such reactions yield polymeric species, which contain either –OH or –O– bridges.

The complexes are prepared by reacting sodium alkoxide with titanium tetrachloride in the appropriate alcohol (equation 8). An alternative method is shown in equation (9). If a proton-accepting reagent, such as ammonia, is not employed, the reaction only proceeds as far as the $TiCl_2(OR)_2$ derivative. Compounds such as $Ti(OMe)_4$ are usually insoluble polymers, although a soluble tetramer, $[Ti(OMe)_4]_4$ (**8**), that has the same M_4O_{16} framework as $[Ti(OEt)_4]_4$ has been isolated. Both frameworks are centrosymmetric, containing six-coordinate titanium in a group of four edge-sharing octahedra.

$$TiCl_4 + 4NaOR \longrightarrow Ti(OR)_4 + 4NaCl \tag{8}$$

$$TiCl_4 + 4ROH + 4NH_3 \longrightarrow Ti(OR)_4 + 4NH_4Cl \tag{9}$$

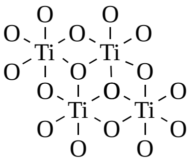

(**8**)

In solution, the degree and type of polymerization is dependent on both the –OR group and the solvent. For example, in benzene, primary –OR groups give trimers, whereas secondary and tertiary –OR groups form only monomers. Few adduct complexes of $Ti(OR)_4$ are known.**14** An example is $Ti_2(OR)_8{\cdot}en$ (R = Et, *i*-Pr), but the complexes almost completely dissociate in solution.**14** However, $Ti(OPh)_4$ readily forms 1:1 adducts with PhOH, NH_3, NH_2Me, $NHMe_2$, NMe_3, py, dioxin, $PhNH_2$, and Me_2CO.**62**

The ready hydrolysis, particularly of the lower titanium alkoxides, has led to a number of interesting applications. They can be used to apply a thin, transparent, adherent surface coating of TiO_2 to a variety of materials, including fabrics that require waterproofing, glass, and enamels, each of which become scratch resistant, and also in heat-resistant paints. The manufacture of paint provides the most important application of titanium alkoxides. When chelated with ligands such as β-diketonates, the resulting complexes $[Ti(OR)_2(L–L)_2]$ are resistant to hydrolysis. Furthermore, the complexes are water-soluble and when used in concentrations of less than 1% form gels with the cellulose ether colloids used to thicken latex paints. These gels impart the required characteristics for thixotropic, or nondrip paints. The area of titanium alkoxides has been extensively reviewed by Bradley.**61**

A large number of bidentate and chelated titanium(IV) complexes have been prepared. By far, the greatest number of reports concern the β-diketonate complexes, which provide an extensive series of types TiX_3L, $TiX_4(LH)$, TiX_2L_2, $[TiL_3]^+$, TiOXL, and $[TiOL]_2$ (L = β-diketonate, LH = β-diketone).**22**

One bis(β-diketonato)Ti^{IV} compound (budotitane) (**9**) has demonstrated anticancer activity and has been tested in the treatment of colon cancer.**63** It and the more extensively studied organometallic compound Cp_2TiCl_2 are thus potential anticancer therapeutics (*see also* ***Metal-based Drugs***).**63**

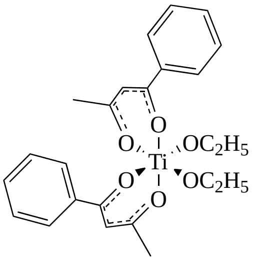

(**9**)

A number of titanium(IV) complexes have been characterized in which titanium shows coordination numbers greater than six. Investigations of the diars complexes of the Ti^{IV} halides resulted in the first example of eight coordination in the first-row transition series.**40** In $[TiCl_4(diars)_2]$ (**10**), the dodecahedron contains two diars forming an elongated tetrahedron, and four chlorine atoms in a flattened tetrahedron with respect to the fourfold inversion axis.**64** Despite numerous attempts to prepare similar complexes with a range of other bidentate ligands, only those with the *o*-phenylene or a similar backbone have proved successful. Other diars complexes include $[TiX_4(diars)]$ (X = Cl, Br), $[(TiF_4)_2(diars)]$, and $[TiI_4(diars)_2]$.**40**

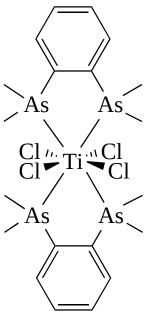

(**10**)

A large number of titanium(IV) phosphine complexes are known,**40** most being adducts of the tetrachloride $TiCl_4(PR_3)_2$, although $TiBr_4(PPh_3)$ and $TiBr_4(PPh_3)_2$ have also been reported.**65** The former has C_{3v} symmetry, whereas the latter has a cis octahedral structure. There is some evidence for the existence of the dinuclear species $Ti_2Cl_2(PR_3)$.**40** There is a paucity of well-characterized arsine and stilbine complexes. Thus, it seems quite surprising that a large number of patents have dealt with catalyst systems employing these compounds in the polymerization and oligomerization of alkenes.**26**

A further example of an eight-coordinate dodecahedral complex of titanium(IV) is the volatile, anhydrous $Ti(NO_3)_4$ in which the nitrate groups are bidentate, coordinating through two oxygen atoms (**11**). The nitrate groups are arranged symmetrically about the metal atom with D_{2d} symmetry in a flattened tetrahedral manner.**66**

There has been a great deal of interest in the complexes of 1,2-dithiolenes and 1,1-dithiolato complexes, which arises

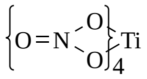

(**11**)

not only from their industrial applications but also from the bonding in the complexes.[26] The X-ray crystal structure of $Ti(S_2CNEt_2)_4$ shows it to contain discrete eight-coordinate molecules.[67] Furthermore, $TiCl(S_2CNMe_2)_3$ has been shown by X-ray crystallography to be seven coordinate (**12**).[68] The molecule has a pentagonal bipyramidal structure with the chlorine atom in the axial position. Prior to this structure elucidation, the existence of seven-coordinate titanium(IV) was uncertain.[68]

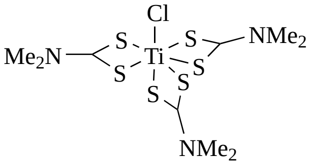

(**12**)

Fay and coworkers[68] have prepared a series of $Ti(S_2CNR_2)_nCl_{4-n}$ compounds ($n = 2$, 3, 4; R = Me, *i*-Pr, *i*-Bu; or $n = 3$, R = Et) by reacting $TiCl_4$ with anhydrous sodium *N*,*N*-dialkyldithiocarbamates in CH_2Cl_2 or benzene. The complexes are monomeric and nonelectrolytes. Thus when $n = 2$, 3, or 4, the titanium atom exhibits coordination numbers of six, seven, and eight respectively. These workers have also studied the monothiocarbamate complexes $Ti(R_2mtc)_4$.[69] The complexes are shown by ^1H NMR and X-ray diffraction to be eight-coordinate dodecahedra, which have an all-cis structure with four sulfur atoms on one side and four oxygen atoms on the other.

Reaction of aqueous solutions of titanium(IV) complexes with H_2O_2 results in an intense orange color. This color can be used analytically to determine titanium. It is due to the formation of the stable peroxo species $[Ti(O_2)(OH)]^+$.[70] There is a great deal of interest in peroxo complexes of titanium(IV) macrocycles and porphyrins.[26] Such complexes are readily oxidized to the corresponding peroxo complex by oxidizing the (por)TiO (por = porphyrin) complex to $(por)Ti(O_2)$ with H_2O_2 or benzoyl peroxide.[71] The crystal structure of the octaethylporphyrin-derived $(OEP)Ti(O_2)$ (**13**) is typical: $Ti–O(1) = 1.822\,Å$, $Ti–O(2) = 1.827\,Å$, and $O–O = 1.445\,Å$.

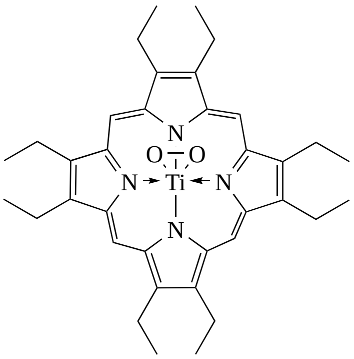

(**13**)

5 RELATED ARTICLES

Oligomerization & Polymerization by Homogeneous Catalysis; Titanium: Organometallic Chemistry; Zirconium & Hafnium: Inorganic & Coordination Chemistry.

6 REFERENCES

1. W. Freundlich and M. Bichara, *C. R. Hebd. Seances Acad. Sci.*, 1954, **238**, 1324.
2. A. E. Van Arkel and J. H. de Boer, *Z. Anorg. Allg. Chem.*, 1925, **148**, 345.
3. W. Kroll, *Trans. Electrochem. Soc.*, 1940, **78**, 35.
4. W. Kroll, *J. Less-Common Met.*, 1965, **8**, 361.
5. P. Pascal, 'Nouveau Traite de Chemie Minerale', Musson, Paris, 1963.
6. R. D. Shannon, *Acta Crystallogr.*, 1976, **A32**, 751.
7. K. Kalyanasundaram and M. Gratzel, *Coord. Chem. Rev.*, 1998, **177**, 347.
8. A. F. Wells, 'Structural Inorganic Chemistry', 5th edn., Clarendon Press, Oxford, 1984.
9. I. Stokroos, L. Litinetsky, J. J. van der Want, and J. S. Ishay, *Nature*, 2001, **411**, 654.
10. R. J. H. Clark, 'The Chemistry of Titanium and Vanadium', Elsevier, Amsterdam, 1968.
11. R. Colton and J. H. Canterford, 'Halides of the Transition Elements: Halides of the First Row Transition Metals', Wiley-Interscience, London, 1969.
12. H. Bialowons, M. Muller, and B. G. Muller, *Z. Anorg. Allg. Chem.*, 1995, **621**, 1227.
13. H. Schafer, R. Laumanns, B. Krebs, and G. Henkel, *Angew. Chem., Int. Ed. Engl.*, 1979, **18**, 325.
14. R. J. H. Clark, in 'Comprehensive Inorganic Chemistry', eds. J. C. Bailar, H. J. Emeleus, R. S. Nyholm, and A. F. Trotman-Dickenson, Pergamon Press, Oxford, 1973.
15. H. G. Lee, D. S. Dyer, and R. O. Ragsdale, *J. Chem. Soc., Dalton Trans.*, 1976, 1325.
16. B. J. Russ and G. W. A. Fowles, *Chem. Commun.*, 1966, 19.
17. C. H. Winter, P. H. Sheridan, T. S. Lewkebandara, M. J. Heeg, and J. W. Proscia, *J. Am. Chem. Soc.*, 1992, **114**, 1095.
18. C. S. Creaser and J. A. Creighton, *J. Chem. Soc., Dalton Trans.*, 1975, 1402.
19. T. J. Kistenmacher and G. D. Stucky, *Inorg. Chem.*, 1971, **10**, 122.

20. G. S. Kyker and E. P. Schram, *Inorg. Chem.*, 1969, **8**, 2306.
21. G. S. Kyker and E. P. Schram, *Inorg. Chem.*, 1969, **8**, 2313.
22. S. Wongnawa and E. P. Schram, *Inorg. Chim. Acta*, 1979, **36**, 45.
23. M. R. Suliman and E. P. Schram, *Inorg. Chem.*, 1973, **12**, 920.
24. M. R. Suliman and E. P. Schram, *Inorg. Chem.*, 1973, **12**, 923.
25. S. E. Adnitt, D. W. Barr, D. Nicholls, and K. R. Seddon, *J. Chem. Soc., Dalton Trans.*, 1974, 644.
26. C. A. McAuliffe and D. S. Barratt, Titanium, in ‘Comprehensive Coordination Chemistry’, eds. G. Wilkinson, R. D. Gillard, and J. A. McCleverty, Pergamon, Oxford, 1987, p. 323.
27. S. B. Smith and D. W. Stephan, Titanium, in ‘Comprehensive Coordination Chemistry II: From Biology to Nanotechnology’, vol. 4, eds. J. A. McCleverty and T. J. Meyer, Elsevier Pergamon, Oxford, 2004, p. 31.
28. A. D. Hugi, L. Helm, and A. E. Merbach, *Inorg. Chem.*, 1987, **26**, 1763.
29. P. Comba and A. Merbach, *Inorg. Chem.*, 1987, **26**, 1315.
30. F. A. Dunand, L. Helm, and A. Merbach, Solvent Exchange on Metal Ions, in ‘Advances in Inorganic Chemistry’, eds. R. van Eldik and C. D. Hubbard, Academic Press, Amsterdam, 2003, p. 1.
31. G. Van Koten and K. Vrieze, *Adv. Organomet. Chem.*, 1982, **21**, 151.
32. F. G. N. Cloke, H. C. Delemos, and A. A. Sameh, *J. Chem. Soc., Chem. Commun.*, 1986, 1344.
33. G. W. A. Fowles and T. E. Lester, *Chem. Commun.*, 1967, 47.
34. U. Kölle and P. Kölle, *Angew. Chem., Int. Ed. Engl.*, 2003, **42**, 4540.
35. G. W. A. Fowles, T. E. Lester, and R. A. Walton, *J. Chem. Soc. (A)*, 1968, 198.
36. M. F. Lappert and A. R. Sanger, *J. Chem. Soc. (A)*, 1971, 874.
37. J. J. H. Edema, R. Duchateau, S. Gambarotta, and C. Bensimon, *Inorg. Chem.*, 1991, **30**, 3585.
38. R. Duchateau, S. Gambarotta, N. Beydoun, and C. Bensimon, *J. Am. Chem. Soc.*, 1991, **113**, 8986.
39. L. B. Kool, M. D. Rausch, H. G. Alt, M. Herberhold, U. Thewalt, and B. Wolf, *Angew. Chem., Int. Ed. Engl.*, 1985, **24**, 394.
40. C. A. McAuliffe and W. Levason, ‘Phosphine, Arsine, and Stilbine Complexes of the Transition Elements’, Elsevier, Amsterdam, 1979.
41. G. S. Girolami, G. Wilkinson, A. M. R. Galas, M. Thorntonpett, and M. B. Hursthouse, *J. Chem. Soc., Dalton Trans.*, 1985, 1339.
42. K. Issleib and E. Wenschuh, *Chem. Ber.*, 1964, **97**, 715.
43. G. W. A. Fowles, T. E. Lester, and B. J. Russ, *J. Chem. Soc. (A)*, 1968, 805.
44. P. T. Greene, B. J. Russ, and J. S. Wood, *J. Chem. Soc. (A)*, 1971, 3636.
45. D. C. Bradley and R. G. Copperthwaite, *J. Chem. Soc., Chem. Commun.*, 1971, 764.
46. M. G. B. Drew, G. W. A. Fowles, and D. F. Lewis, *J. Chem. Soc., Chem. Commun.*, 1969, 876.
47. M. G. B. Drew and D. J. Eve, *Acta Crystallogr., Sect. B*, 1977, **33**, 2919.
48. D. J. Eve and M. L. Niven, *Inorg. Chim. Acta*, 1990, **174**, 205.
49. F. L. Bowden and D. Ferguson, *J. Chem. Soc., Dalton Trans.*, 1974, 460.
50. A. Bodner, P. Jeske, T. Weyhermuller, K. Wieghardt, E. Dubler, H. Schmalle, and B. Nuber, *Inorg. Chem.*, 1992, **31**, 3737.
51. J. Chatt and R. G. Hayter, *J. Chem. Soc.*, 1963, 1343.
52. C. D. Schmulbach, C. H. Kolich, and C. C. Hinckley, *Inorg. Chem.*, 1972, **11**, 2841.
53. B. A. Borgias, S. R. Cooper, Y. B. Koh, and K. N. Raymond, *Inorg. Chem.*, 1984, **23**, 1009.
54. G. D. Smith, J. A. Campbell, and C. N. Caughlan, *Inorg. Chem.*, 1972, **11**, 2989.
55. G. M. H. van de Velde, S. Harkema, and P. J. Gellings, *Inorg. Nucl. Chem. Lett.*, 1973, **9**, 1169.
56. M. Tsutsui, R. A. Velapold, K. Suzuki, and T. Koyano, *Angew. Chem., Int. Ed. Engl.*, 1968, **7**, 891.
57. R. Guilard and C. Lecomte, *Coord. Chem. Rev.*, 1985, **65**, 87.
58. D. A. Baldwin and R. J. H. Clark, *J. Chem. Soc. (A)*, 1971, 1725.
59. N. W. Alcock, M. Piercebutler, and G. R. Willey, *J. Chem. Soc., Dalton Trans.*, 1976, 707.
60. C. Airoldi, D. C. Bradley, H. Chudzynska, M. B. Hursthouse, K. M. Abdulmalik, and P. R. Raithby, *J. Chem. Soc., Dalton Trans.*, 1980, 2010.
61. D. C. Bradley, Metal Alkoxides and Dialkylamides, in ‘Advances in Inorganic Chemistry and Radiochemistry’, eds. H. J. Emeleus and A. G. Sharpe, Academic Press, New York, 1972, p. 259.
62. R. Masthoff, H. Kohler, H. Bohland, and F. Schmeil, *Z. Chem.*, 1965, **5**, 122.
63. Z. J. Guo and P. J. Sadler, *Angew. Chem., Int. Ed. Engl.*, 1999, **38**, 1513.
64. R. J. H. Clark, J. Lewis, R. S. Nyholm, P. Pauling, and G. B. Robertson, *Nature*, 1961, **192**, 222.
65. C. M. F. Rae and K. R. Seddon, *Inorg. Chim. Acta*, 1976, **17**, L35.
66. C. D. Garner and S. C. Wallwork, *J. Chem. Soc. (A)*, 1966, 1496.
67. M. Colapietro, A. Vaciago, D. C. Bradley, M. B. Hursthouse, and I. F. Rendall, *J. Chem. Soc., Chem. Commun.*, 1970, 743.
68. A. N. Bhat, R. C. Fay, D. F. Lewis, A. F. Lindmark, and S. H. Strauss, *Inorg. Chem.*, 1974, **13**, 886.

69. S. L. Hawthorne, A. H. Bruder, and R. C. Fay, *Inorg. Chem.*, 1983, **22**, 3368.
70. M. Inamo, S. Funahashi, and M. Tanaka, *Inorg. Chem.*, 1985, **24**, 2475.
71. R. Guilard, M. Fontesse, P. Fournari, C. Lecomte, and J. Protas, *J. Chem. Soc., Chem. Commun.*, 1976, 161.

Titanium: Organometallic Chemistry

Eric A. Mintz
Clark Atlanta University, Atlanta, GA, USA

1	Introduction	1
2	Carbonyl and Phosphine Complexes without π-Ligands	1
3	Carbonyl, Phosphine, Alkene, and Alkyne Complexes with π-Ligands	2
4	Alkyl and Aryl Complexes without π-Ligands	3
5	Alkylidene and Titanacyclobutane Complexes	3
6	Diene Complexes Lacking Other π-Ligands	5
7	Diene Complexes Containing Other π-Ligands	6
8	Arene Complexes	7
9	Cyclopentadienyl Complexes of Titanium(IV)	8
10	Cyclopentadienyl Complexes of Titanium(III)	15
11	Cyclopentadienyl Complexes of Titanium(II)	16
12	Constrained Geometry Titanium Complexes	18
13	Cycloheptatrienyl Complexes	21
14	Cyclopentadienyl–Cycloheptatrienyl Complexes	21
15	Cyclopentadienyl–Cyclooctatetraene Complexes	21
16	Cyclooctatetraene Complexes	22
17	Other η^5-Ligands	22
18	Alkoxides and Related Complexes	23
19	Related Articles	25
20	References	25

Abbreviations

Cryptand = 4,7,13,16,21,24-hexaoxa-1,10-diazabicyclo [8.8.8]hexacosane; Ind = η^5-indenyl; Trmpe = 1,1,1-tris (dimethylphosphinomethyl)ethane; tritox = $(t\text{-Bu}_3\text{C})_3\text{CO}^-$.

1 INTRODUCTION

The majority of titanium organometallic chemistry involves complexes in which the titanium is in its highest oxidation state (+4) and cyclopentadienyl (*see Cyclopentadienyl*) derivatives serve as ancillary ligands. However, considerable chemistry has also been developed in which the titanium is in the +3 and +2 oxidation state, with lesser amounts of chemistry known for titanium in lower oxidation states (+1, 0). Since the early 1980s, chemists have placed considerable emphasis on the fine-tuning of the structure and reactivity of titanium organometallic complexes. Particular emphasis has been devoted to tailoring the structure and reactivity of bis(cyclopentadienyl)titanium derivatives by incorporating electron-donating, electron-withdrawing, sterically demanding, bridging (constrained geometry), or chiral substituents on the cyclopentadienyl ring. Additional efforts at modifying the structure and reactivity have focused on varying the oxidation state or coordination geometry at the titanium center. Titanium organometallic chemistry through 1980 has been extensively reviewed by Bottrill, Gavens, Kelland, and McMeeking.**[1]** Several other articles in this encyclopedia are based on the application of titanium organometallic chemistry to catalysis and organic synthesis (*see* ***Asymmetric Synthesis by Homogeneous Catalysis***; ***Metathesis Polymerization Processes by Homogeneous Catalysis***; and ***Oligomerization & Polymerization by Homogeneous Catalysis***).

2 CARBONYL AND PHOSPHINE COMPLEXES WITHOUT π-LIGANDS

The hypothetical titanium heptacarbonyl Ti(CO)_7 is as yet unknown. However, Ti(CO)_6 has been prepared and characterized by matrix isolation techniques. Ti(CO)_6, thus prepared, is found to be unstable above −200 °C.**[2]** Titanium carbonyls Ti(CO)x (x = 1–6) are formed during deposition of laser-ablated titanium atoms with CO during condensation in excess Ne, or on annealing and photolysis of the matrix.**[3]** Titanium carbonyl complexes (*see* ***Carbonyl Complexes of the Transition Metals***) have also been observed spectroscopically (by IR) as intermediates in the low-temperature reaction of $\text{Ti(CH}_2\text{Ph)}_4$ and its dicyclohexylamine adduct with CO.**[4]**

Reduction of $\text{TiCl}_4\text{(THF)}_2$ with sodium naphthalenide in the presence of 2.1–2.3 equivalent of dmpe in THF at −70 to −80 °C followed by treatment with CO at 1 atm gives $\text{Ti(CO)}_3\text{(dmpe)}_2$ as shown in (equation 1). Treatment of $\text{Ti(CO)}_3\text{(dmpe)}_2$ with CO at room temperature gives $\text{Ti(CO)}_5\text{(dmpe)}$.**[5]** $\text{Ti(CO)}_3\text{(dmpe)}_2$ is monomeric in the solid state, possessing a monocapped octahedral structure. One of the carbonyls in $\text{Ti(CO)}_3\text{(dmpe)}_2$ can be replaced by treatment with PF_3 to give $\text{Ti(CO)}_2\text{(PF}_3\text{)(dmpe)}_2$.**[6]**

$$\text{TiCl}_4\text{(dmpe)}_2 + 2.1\text{–}2.3\text{NaC}_{10}\text{H}_8 + \text{CO(1 atm)} \longrightarrow \text{Ti(CO)}_3\text{(dmpe)}_2 \qquad (1)$$

Ellis and coworkers have found $\text{Ti(CO)}_5\text{(dmpe)}$ to be much more reactive than $\text{Ti(CO)}_3\text{(dmpe)}_2$, and have found that it can serve as a synthetic equivalent for Ti(CO)_7. Reaction of $\text{Ti(CO)}_5\text{(dmpe)}$ with NaCp, NaInd, or $\text{K[(HB(pz)}_3\text{)]}$ leads to loss of one carbonyl and dmpe to give the corresponding anionic complexes $[\text{CpTi(CO)}_4]^-$ (equation 2), $[\text{IndTi(CO)}_4]^-$, and $[\text{HB(pz)}_3\text{Ti(CO)}_4]^-$, respectively, in 70–80% yield. Treatment of $\text{Ti(CO)}_5\text{(dmpe)}$ with NaEPh_3

(E = Ge, Sn) results in loss of one CO to give the corresponding anionic complexes $[Ti(CO)_4(dmpe)(EPh_3)]^-$. Treatment of $Ti(CO)_5(dmpe)$ with the tridentate ligand trmpe gives $Ti(CO)_4(trmpe)$.[5] $Ti(CO)_4(trmpe)$ has also been prepared directly by the treatment of $TiCl_4(THF)_2$ with potassium naphthalenide in the presence of CO and trmpe.[7]

$$\mathrm{Ti(CO)_5(dmpe) + NaCp \longrightarrow Na[C_5H_5Ti(CO)_4]} \qquad (2)$$

Ellis and coworkers have extensively studied the chemistry of hexacarbonyltitanate(2−), $[Ti(CO)_6]^{2-}$. Reductive carbonylation (*see Reductive Carbonylation*) of $Ti(CO)_4(trmpe)$ with (cryptand 2,2,2)potassium naphthalenide at −70 °C followed by warming to room temperature gives the thermally robust $[K(cryptand\ 2.2.2)]_2[Ti(CO)_6]$ in quantitative yield.[8] Treatment of $Ti(CO)_6{}^{2-}$ with azobenzene gives $[Ti(PhN{=}NPh)(CO)_4]^{2-}$ (equation 3) in 40–65% yield. Hydrolysis of $[Ti(PhN{=}NPh)(CO)_4]^{2-}$ gives 1,2-diphenylhydrazine and the hydroxo-carbonyl titanium complex, $[Ti_2(\mu\text{-}OH)_2(CO)_8]^{2-}$ (equation 3), which was structurally characterized as the $[K(18\text{-crown-}6)]^+$ salt.[9]

$$\mathrm{Ti(CO)_6{}^{2-} + Ph\text{-}N{=}N\text{-}Ph \longrightarrow [Ti(PhN{=}NPh)(CO)_4]^{2-}} \qquad (3)$$

Reaction of $[Ti(CO)_6]^{2-}$ with MeOH and PhOH gives the metal-carbonyl dimers $[Ti(CO)_4(\mu\text{-}OR)]_2{}^{2-}$ (R = Me, Ph). The structure and reactivity of these complexes suggest that the bridging alkoxy ligands function as π-donors satisfying the electronic requirements of each titanium.[10] Reaction of $BH_3{\cdot}THF$ with $[K(15\text{-crown-}5)_2]_2[Ti(CO)_6]$ or $[K(18\text{-crown-}6)_2]_2[Ti(CO)_6]$ gives $[K(15\text{-crown-}5)_2]_2[Ti(CO)_4(\eta^3\text{-}BH_4)]$ and $[K(18\text{-crown-}6)][Ti(CO)_4(\eta^3\text{-}BH_4)]^-$ respectively. Treatment of $[K(15\text{-crown-}5)_2]_2[Ti(CO)_4(\eta^3\text{-}BH_4)]$ with KC_4H_4N gives $[K(15\text{-crown-}5)_2]_2[(\eta^5\text{-}C_4H_4N)Ti(CO)_4]$.[11]

Treatment of $Ti(CO)_6{}^{2-}$ with R_3SnCl (R = Me, Ph, cyclohexyl) in THF gives the thermally stable $R_3SnTi(CO)_6{}^-$ salts in 70–80% isolated yields.[12] In an analogous manner, reaction of $Ti(CO)_6{}^{2-}$ with $ClC(p\text{-}C_6H_4R)_3$ (R = H, OCH_3) in THF gives $Ti(CO)_4[\eta^5\text{-}C(p\text{-}C_6H_4R)_3]$ in 28–30% yields.[13]

The reduction of TiI_4 with 1 equivalent of Na/Hg amalgam in the presence of PMe_3 gives the bioctahedral complex $Ti_2I_6(PMe_3)_4$. The Ti–Ti distance of 4.30 Å in $Ti_2I_6(PMe_3)_4$ clearly indicates the absence of a Ti–Ti bond.[14]

Treatment of *trans*-$TiX_2(dmpe)_2$ (X = Cl, Br) with CO at low temperature gives the thermally unstable $TiX_2(CO)_2(dmpe)_2$. In an analogous manner, treatment of the mixed halide complex $TiClBr(dmpe)_2$ with CO gives the corresponding dicarbonyl complex $TiClBr(CO)_2(dmpe)_2$. NMR experiments suggest that these complexes adopt a bicapped octahedral structures, with the halide ligands in the capping sites and the carbonyl ligands mutually cis.[15]

Reaction of benzylbis(2-ethoxyethyl) phosphine ($PhCH_2P(CH_2CH_2OEt)_2$) with $TiCl_4$ gives $TiCl_4[PhCH_2P(CH_2CH_2OEt)_2]$ (**1**). The crystal structure of $TiCl_4[PhCH_2P(CH_2CH_2OEt)_2]$ shows the metal to have a distorted octahedral geometry, where the ligand acts as a P,O-bonding chelate ligand (*see Chelating Ligands*).[16] Treatment of TiI_4 with one equivalent of the bidentate ligands $o\text{-}(PMe_2)_2C_6H_4$ and $o\text{-}(AsMe_2)_2C_6H_4$ in anhydrous CH_2Cl_2 gives $TiI_4(o\text{-}(PMe_2)_2C_6H_4)$ and $TiI_4(o\text{-}(AsMe_2)_2C_6H_4)$ (**2**), respectively.[17]

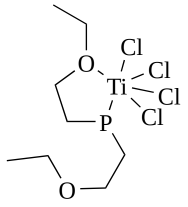

(**1**)

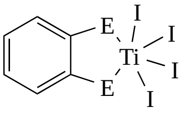

(**2**) E = PMe_2, $AsMe_2$

The reactions of 1,5,9-triethyl-1,5,9-triphosphacyclododecane, $[12]aneP_3Et_3$, with $TiCl_3$ THF gives $TiCl_3([12]aneP_3Et_3)$ (**3**).[18]

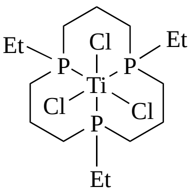

(**3**)

3 CARBONYL, PHOSPHINE, ALKENE, AND ALKYNE COMPLEXES WITH π-LIGANDS

The cyclopentadienyl titanium carbonyl anions $[CpTi(CO)_4]^-$ and $[Cp^*Ti(CO)_4]^-$ have been prepared and extensively studied by Ellis and coworkers.[19] Reduction of $CpTiCl_3$ or Cp^*TiCl_3 with alkali-metal naphthalenide at low temperature under a CO atmosphere followed by cation exchange gives $[Et_4N][CpTi(CO)_4]$ (equation 4) and $[Et_4N][Cp^*Ti(CO)_4]$, respectively, in moderate yield. X-ray crystallographic analysis of $[Ph_4As][CpTi(CO)_4]$ indicates that $[CpTi(CO)_4]^-$ is isostructural with the neutral isoelectronic vanadium complex $CpV(CO)_4$ (*see* ***Vanadium: Organometallic Chemistry***). The unsolvated $Na[(C_5H_5)Ti(CO)_4]$ was found to be explosive at room temperature. Treatment of $[CpTi(CO)_4]^-$ with Ph_3SnCl or Ph_3PAuCl gives the corresponding heterobimetallic titanium(II) complexes $CpTi(CO)_4E$ (E = Ph_3Sn, Ph_3PAu).[20–22]

$$\mathrm{CpTiCl_3 + 4NaC_{10}H_8 + CO \longrightarrow Na[CpTi(CO)_4]} \qquad (4)$$

The zerovalent cyclopentadienyl (*see Cymantrene*) titanium carbonyl phosphine complexes $[CpTi(CO)_3(PR_3)]^-$ and

$[\mathrm{Cp^*Ti(CO)_3(PR_3)}]^-$ ($\mathrm{R = Me, Ph}$) are prepared by the photo substitution reactions of $[\mathrm{CpTi(CO)_4}]^-$ and $[\mathrm{Cp^*Ti(CO)_4}]^-$, respectively, with phosphine ligands. The analogous dmpe complexes $[\mathrm{CpTi(CO)_2(dmpe)}]^-$ and $[\mathrm{Cp^*Ti(CO)_2(dmpe)}]^-$ are prepared by the reductive cleavage of $\mathrm{Cp_2Ti(CO)_2}$ and $\mathrm{Cp_2^*Ti(CO)_2}$ in the presence of dmpe. Protonation of the $[\mathrm{CpTi(CO)_3(PR_3)}]^-$ and $[\mathrm{Cp^*Ti(CO)_3(PR_3)}]^-$, gives the thermally unstable carbonyl hydrides $\mathrm{CpTi(CO)_3(PR_3)H}$ and $\mathrm{Cp^*Ti(CO)_3(PR_3)H}$, respectively. However, protonation of the analogous $[\mathrm{Cp^*Ti(CO)_2(dmpe)}]^-$ gives $\mathrm{Cp^*Ti(CO)_2(dmpe)H}$ which could be isolated at room temperature.[23]

Treatment of $(\mathrm{CpTiCl_2})_x$ with 1 equivalent or BuLi in the presence of dmpe in ether gives the diamagnetic $\mathrm{CpTiCl(dmpe)_2}$, which upon treatment with MeLi or BuLi gives $\mathrm{CpTiMe(dmpe)_2}$ and $\mathrm{CpTiH(dmpe)_2}$. respectively.[24]

Addition of $\mathrm{BH_3{\cdot}THF}$ to $[\mathrm{K(15\text{-}crown\text{-}5)_2}]_2[\mathrm{Ti(CO)_6}]$ and $[\mathrm{K(18\text{-}crown\text{-}6)}]_2[\mathrm{Ti(CO)_6}]$ gives $[\mathrm{K(15\text{-}crown\text{-}5)_2}]_2[\mathrm{Ti(CO)_4}(\eta^3\text{-}\mathrm{BH_4})]$ and $[\mathrm{K(18\text{-}crown\text{-}6)}][\mathrm{Ti(CO)_4}(\eta^3\text{-}\mathrm{BH_4})]^-$. Treatment of $[\mathrm{K(15\text{-}crown\text{-}5)_2}]_2[\mathrm{Ti(CO)_4}(\eta^3\text{-}\mathrm{BH_4})]$ with potassium-pyrrole gives $[\mathrm{K(15\text{-}crown\text{-}5)_2}]_2[(\eta^5\text{-}\mathrm{C_4H_4N})\mathrm{Ti(CO)_4}]$.[25]

Reduction of $(\eta^5\text{-}\mathrm{C_5Me_5})\mathrm{TiCl_3}$ with sodium naphthalenide at −60 °C in DME in the presence of dmpe, followed by carbonylation at one atm, gives the unstable olive-green complex $(\eta^5\text{-}\mathrm{C_5Me_5})\mathrm{Ti(CO)(dmpe)Cl}$ which has been characterized in solution by NMR and IR.[26]

4 ALKYL AND ARYL COMPLEXES WITHOUT π-LIGANDS

The synthesis and reactivity of σ-bonded alkyl (*see Alkyl Complexes*) and aryl titanium(IV) complexes has been extensively reviewed by Bottrill *et al.*[27]

Dialkyltitanium complexes have long been proposed as intermediates in the thermal and photochemical decomposition of tetraalkyltitanium complexes. Treatment of $\mathrm{TiCl_2(dempe)_2}$ with alkyllithium reagents gives mixed alkyl/halide products caused by incomplete exchange of the strongly held Cl.[28] However, treatment of $\mathrm{TiCl_2(dmpe)_2}$ with an excess of $\mathrm{LiBH_4}$ forms paramagnetic $\mathrm{Ti}(\eta^2\text{-}\mathrm{BH_4})_2\mathrm{(dmpe)_2}$, which upon treatment with MeLi gives $\mathrm{TiMe_2(dmpe)_2}$ (equations 5 and 6). Surprisingly, $\mathrm{TiMe_2(dmpe)_2}$ is found to be diamagnetic, and could be characterized by ^{1}H and ^{13}C NMR. Single-crystal X-ray and neutron diffraction studies have been carried out on $\mathrm{TiMe_2(dmpe)_2}$ at 173 and 30 K, respectively. The titanium center in $\mathrm{TiMe_2(dmpe)_2}$ adopts a regular octahedral structure with the methyl groups trans to each other. The Ti–C–H bond angles are all found to be 109 °C or greater, indicating no agostic bonding (*see Agostic Bonding*) in the solid state.[29]

$$\mathrm{TiCl_2(dmpe)_2} + 2\mathrm{LiBH_4} \longrightarrow \mathrm{Ti}(\eta^2\text{-}\mathrm{BH_4})_2\mathrm{(dmpe)_2} + 2\mathrm{LiCl} \qquad (5)$$

$$\mathrm{Ti}(\eta^2\text{-}\mathrm{BH_4})_2\mathrm{(dmpe)_2} + 2\mathrm{LiMe} \longrightarrow \mathrm{TiMe_2(dmpe)_2} \qquad (6)$$

Treatment of $\mathrm{TiCl_4}$ with one equivalent of dmpe gives $\mathrm{TiCl_4(dmpe)}$. This complex can be readily alkylated with 1 or 2 equivalent of $\mathrm{PhCH_2MgCl}$ to give $\mathrm{TiCl_3(PhCH_2)(dmpe)}$ and $\mathrm{TiCl_2(PhCH_2)_2(dmpe)}$, respectively. The corresponding thermally unstable mono t-butyl complex, '$\mathrm{TiCl_3}(t\text{-}\mathrm{Bu})\mathrm{(dmpe)}$', decomposes to give the dinuclear edge-sharing Ti(III) complex, $\mathrm{Ti_2Cl_4}(\mu\text{-}\mathrm{Cl})_2\mathrm{(dmpe)_2}$. The analogous, $\mathrm{Ti_2Cl_4}(\mu\text{-}\mathrm{Cl})_2\mathrm{(depe)_2}$ was prepared directly by the reaction of $\mathrm{TiCl_3(THF)_3}$ with the corresponding phosphine. Thermal decomposition of the thermally unstable di-t-butyl complex '$\mathrm{TiCl_2}(t\text{-}\mathrm{Bu})_2\mathrm{(dmpe)}$' gives $\mathrm{Ti_3Cl_6(dmpe)_3}$, which consists of an equilateral triangle of Ti(II) atoms with three coplanar μ-Cl atoms bridging the edges. Each Ti atom is further coordinated by a chelating dmpe ligand and a chloride ion, with Ti–Ti distances of 2.872(3) Å.[30]

Highly stericly hindered alkyl complexes $\mathrm{(Me_3CCH_2)_3TiSi(SiMe_3)_3}$ and $\mathrm{(Me_3SiCH_2)_3TiSi(SiMe_3)_3}$ were prepared by the reaction of $\mathrm{(Me_3CCH_2)_3TiCl}$ and $\mathrm{(Me_3SiCH_2)_3TiCl}$, respectively, with $\mathrm{LiSi(SiMe_3)_3(THF)_3}$. The structures of $\mathrm{(Me_3CCH_2)_3TiSi(SiMe_3)_3}$ and $\mathrm{(Me_3SiCH_2)_3TiSi(SiMe_3)_3}$ were determined by X-ray diffraction show that the three alkyl groups on the metal centers are staggered with respect to the trimethylsilyl groups on the central silicon atoms.[31]

Dialkyltitanium(IV) complexes $\mathrm{R_2TiX_2}$ ($\mathrm{R = Bu}$, iPr, $\mathrm{X = Cl}$, OiPr), react with olefins, acetylenes, azoarenes, aldehydes, ketones, amides, and imines, to undergo in high-yield epimetalation of the multiple bond with $\mathrm{TiX_2}$ giving transient 3-membered titanacycles. Treatment of alkynes with $\mathrm{R_2TiX_2}$ followed by hydrolytic work-up gave cis-alkenes with high selectivity. In a similar manner treatment of benzophenone with $\mathrm{R_2TiX_2}$ followed by hydrolytic work-up gave benzopinacol and benzhydrol.[32]

5 ALKYLIDENE AND TITANACYCLOBUTANE COMPLEXES

Tebbe's Reagent (*see Tebbe's Reagent*), a stable, soluble dimethylaluminum chloride−titanocene methylidene complex, is prepared from $\mathrm{Cp_2TiCl_2}$ and $\mathrm{(AlMe_3)_2}$, as shown in equation (7). Tebbe's reagent has been successfully utilized as an alkene metathesis (*see Metathesis*) catalyst and readily adds methylene to aldehydes, ketones, and esters. Treatment of Tebbe's reagent, in the presence of base, with alkenes or alkynes leads to titanacyclobutanes or titanacyclobutenes, as shown in Scheme 1. For monosubstituted titanacyclobutanes, the substituent prefers the β-position. Addition of a second β substituent to the metallacycles (*see Metallacycle*) results in significant destabilization of the metallacycles.[33] Bickelhapt and coworkers have developed an alternative preparation for $[\mathrm{Cp_2Ti{=}CH_2}]$. Thus, treatment of $\mathrm{Cp_2TiCl_2}$ with $\mathrm{(BrMg)_2CH_2}$ gives $[\mathrm{Cp_2Ti{=}CH_2}]$, which reacts with alkenes and alkynes to give titanacyclobutane and titanacyclobutene complexes in a manner similar to that of Tebbe's reagent.[34]

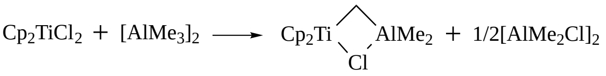
Cp2TiCl2 + [AlMe3]2
Cp2Ti
AlMe2 + 1/2[AlMe2Cl]2
Cl

(7)

Metal alkylidene complexes (*see Schrock-type Carbene Complexes*) have been proposed as intermediates in many catalytic reactions, including alkene metathesis (*see* ***Organic Synthesis Using Metal-mediated Metathesis Reactions***), alkene and alkyne polymerization, methylenation of carbonyl compounds, and cyclopropanation of alkenes.[35–39]

Titanacyclobutanes serve as ready sources of [$Cp_2Ti{=}CH_2$], reacting with alkenes and alkynes to give titanacyclobutane and titanacyclobutene complexes, as shown in Scheme 2, via slow formation of an alkene–methylidene intermediate which is rapidly trapped by the alkene or alkyne (equation 8). Titanacyclobutanes also transfer methylene groups to carbonyl groups, effect ring-opening polymerization of strained cyclic alkenes (*see Ring Opening Metathesis Polymerization Reactions*), and form dinuclear methylene complexes (Scheme 3).[35,36,39]

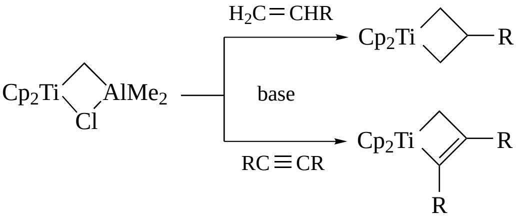
H2C=CHR
Cp2Ti
R
Cp2Ti
AlMe2
Cl
base
Cp2Ti
R
RC≡CR
R

Scheme 1

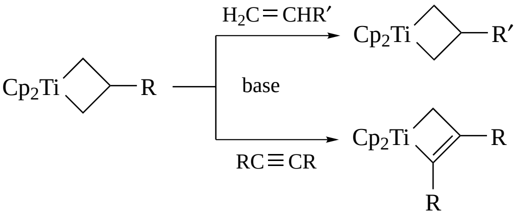
H2C=CHR′
Cp2Ti
R′
Cp2Ti
R
base
Cp2Ti
R
RC≡CR
R

Scheme 2

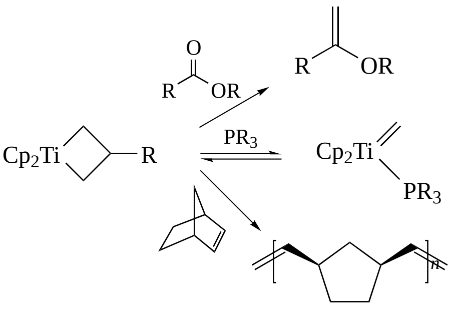
O
R
OR
R
OR
Cp2Ti
R
PR3
Cp2Ti
PR3
n

Scheme 3

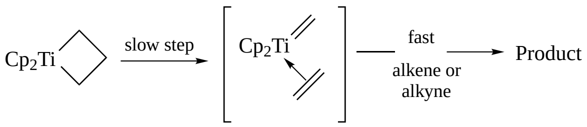
Cp2Ti
slow step
Cp2Ti
fast
alkene or alkyne
Product

(8)

Titanocene methylidene phosphine complexes $Cp_2Ti{=}CH_2L$ (L = PMe_3, PMe_2Ph, PEt_3) have been generated by the thermolysis of titanocene metallacyclobutanes in the presence of excess phosphine (equation 9). These titanocene methylidene phosphine complexes have been found to react with alkenes, alkynes, and CO to form metallacyclobutanes, metallacyclobutenes, and a ketene complex, respectively. The phosphine ligand is labile, and an equilibrium mixture is rapidly established if a second phosphine is added.[40]

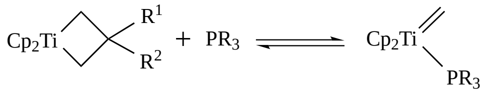
Cp2Ti
R1
R2
+ PR3
Cp2Ti
PR3

(9)

$R^1 = R^2 = Me$; $R^1 = Me$, $R^2 = Pr$; $PR_3 = PMe_3, PMe_2Ph, PEt$

Treatment of $Cp_2^*TiCl_2$ with 2 equivalents of vinyllithium gives the corresponding divinyl complex $Cp_2^*Ti(CH{=}CH_2)_2$ at low temperature. However, at room temperature, $Cp_2^*Ti(CH{=}CH_2)_2$ undergoes rearrangement quantitatively to give a titanacyclobutane with an exocyclic methylidene group (**4**) (equation 10).[41,42]

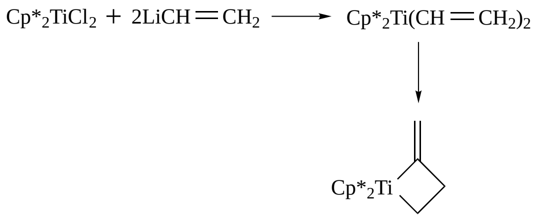
Cp*2TiCl2 + 2LiCH=CH2
Cp*2Ti(CH=CH2)2
Cp*2Ti

(10)

(**4**)

Migratory insertion (*see Migratory Insertion*) reaction of isonitriles, RN≡C, (R = C_6H_{11}, *t*-Bu) with 3-isoproplbis(pentamethylcyclopentadineyl)titanacyclobutane (**5**) gives the iminoacyl titanium complexes (**6**) (R = *t*-Bu, cyclohexyl) in 90–92%. Treatment of (**6**) (R = C_6H_{11}) with $CH_2{=}CH_2$ in tolune at 10 psi gave 94% cyclobutanimine (**7**). Treatment of (**6**) (R = C_6H_{11}, *t*-Bu) with 60 psi of CO at −78 °C gives the Cp_2^*Ticyclopentenamidolate complex in high yield.[43]

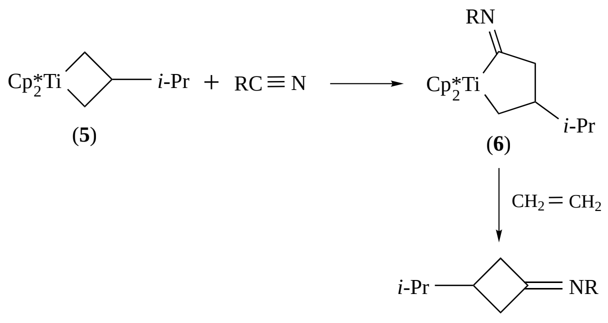

(5) (6) (7)

(11)

Addition of aryldiazoalkanes to $Cp_2^*Ti(C_2H_4)$ gives η^2-N_2-titanium aryldiazoalkane complexes $Cp_2^*Ti(N_2CHAr)$. Unlike most diazoalkane complexes, they release dinitrogen thermally to give transient carbene complexes which when trapped with styrene gives the titanacyclobutane complexes $Cp_2^*Ti(CHArCHPhCH_2)$. The addition of t-BuN≡C results in a coordination change of the diazoalkane fragment from η^2 to η^1 to give $Cp_2^*Ti(\eta^1$-$N^2CHPh)(t$-BuN≡C). The bound t-BuN≡C ligand exchanges with free t-BuN≡C in solution.[44]

Addition of (trimethylsilyl)diazomethane to $Cp_2^*Ti(\eta^2$-$C_2H_4)$ gives the η^2-N_2-diazoalkane complex $Cp_2^*Ti(N_2CH SiMe_3)$. $Cp_2^*Ti(N_2CHSiMe_3)$ loses N_2 in solution under mild conditions to give the fulvene complex $Cp^*(\eta^6$-$C_5Me_4CH_2)TiCH_2SiMe_3$. Thermolysis of $Cp_2^*Ti(N_2CH SiMe_3)$ in the presence of 1-alkenes yields the trans-α,β,-disubstituted titanacyclobutane complexes $Cp_2^*Ti(CH(SiMe_3)CH(R)CH_2)$.[45]

The titanocene vinylidene intermediate $Cp_2^*Ti(=C=CH_2)$ formed by ethane or methane elimination from titanacyclobutane (**4**) or $Cp_2^*Ti(CH=CH_2)Me$, respectively, reacts with isothiocyanates, RNCS (R = C_6H_{11}, Ph or t-Bu), by a [2 + 2] cycloaddition, to give the titanathietane complexes (**8**). In all cases, the regioisomer in which the S atom is bonded to Ti is found as the primary product. Upon heating in the presence of pyridine, a rearrangement of (**8**) to the regioisomeric titanacyclobutane derivative (**9**) was observed (equation 12).[46]

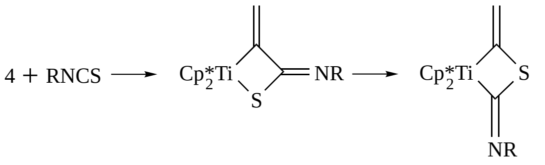

(**8**) (**9**)

(12)

Treatment of $Cp^*(C_5Me_4CH_2)TiCl$ with 2-methylallyl Gringard gives to $Cp^*(\eta^5$:η^2-$C_5Me_4CH_2CMe(CH_2)_2)Ti$ (**10**), with a titancyclobutane tethered to the Cp* ligand by a methylene bridge. Thermolysis of (**10**) gives a new fulvene complex $(C_5Me_4CH_2)(\eta^5$:η^1-$C_5Me_4CH_2CMe_2CH_2)Ti$.[47]

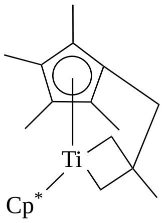

(**10**)

α-H elimination (*see α-Elimination*) from $(C_5Me_4CH_2 CH_2NMe_2)Cp^*Ti(CH=CH_2)(CH_3)$ gives $(C_5Me_4CH_2CH_2 NMe_2)Cp^*Ti=C=CH_2$, which further reacts to give the fulvene complexes $(C_5Me_3(CH_2CH_2NMe_2)CH_2)TiCH=CH_2$ and $(C_5Me_4CH_2CH_2NMe_2)(C_5Me_4CH_2)TiCH=CH_2$. The analogous α-H elimination from $(C_5Me_4CH_2CH_2NMe_2) Cp^*Ti(CH=CH_2)_2$ gives $(C_5Me_4CH_2CH_2NMe_2)Cp^*Ti =C=CH_2(\eta^2$-$CH_2=CH_2)$, which rearranges to a titanacyclobutane with an exocyclic methylidene group analogous to (**4**).[48]

6 DIENE COMPLEXES LACKING OTHER π-LIGANDS

The homoleptic (*see Homoleptic Compound*) titanium diene complex $(\eta^4$-t-BuCH=CHCH=CHBu-$t)_2Ti$ (**11**) has been prepared by the condensation of electron-beam vaporized titanium with an excess of 1,4-di-t-butylbuta-1,3-diene[49] (*see* ***Metal Vapor Synthesis of Transition Metal Compounds***). The bis-diene dmpe complex Ti(dmpe)$(\eta^4$-$C_4H_6)_2Ti$ (**12**) has been prepared by the reduction of $TiCl_4$(dmpe) with Na/Hg in the presence of butadiene, and by the reduction of $TiCl_4$ with $CH_2=CHLi$ in the presence of dmpe.[50–52]

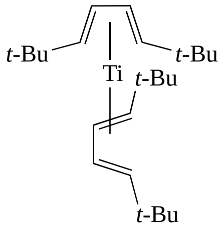

(**11**)

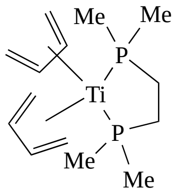

(**12**)

Reaction of *trans*-$TiMe_2(dmpe)_2$ with 1,3-butadiene and trans, trans-1,4-diphenyl-1,3-butadiene at −20 °C give the titanium(II) butadiene complexes $TiMe_2(\eta^4$-$C_4H_6)$(dmpe) and $TiMe_2(\eta^4$-$C_4H_4Ph_2)$(dmpe), respectively. The NMR of spectra $TiMe_2(\eta^4$-$C_4H_6)$(dmpe) and $TiMe_2(\eta^4$-$C_4H_4Ph_2)$(dmpe) are consistent with structures in which the Me groups are mutually cis, which was verified by X-ray crystallography for the $TiMe_2(\eta^4\text{-}C_4H_4Ph_2)(dmpe)$. These molecules are fluxional on the NMR timescale ($\Delta H^\ddagger = 9.1 \pm 0.2$ kcal/mol and $\Delta S^\ddagger = 3 \pm 1$ eu) for $TiMe_2(\eta^4\text{-}C_4H_4Ph_2)(dmpe)$. When the reaction of $TiMe_2(dmpe)_2$ and 1,3-butadiene was allowed to continue at $-20\,°C$ for more that 12 h, a second titanium complex is formed, which has been identified as (1-octa-1,6-diene-1,8-diyl) $(TiMe_2)_3$, (1-octa-1,6-diene-1,8-diyl)(dmpe). Both $Ti(\eta^4\text{-}C_4H_6)_2(dmpe)$ and $TiMe_2(\eta^4\text{-}C_4H_4Ph_2)(dmpe)$ exhibit the butadiene ligands bound as true dienes, unlike the structure observed for many other early transition metal butadiene complexes.**[53]**

7 DIENE COMPLEXES CONTAINING OTHER π-LIGANDS

Mixed cyclopentadienyl–diene titanium complexes, $Cp^*TiX(diene)$ (X = Cl, Br, I), have been prepared in 30–60% yield by the stoichiometric reaction of $CpTiX_3$ with (2-butene-1,4-diyl)magnesium derivatives or by the reduction of $CpTiX_3$ with RMgX (R = *i*-Pr, *t*-Bu, Et; X = Cl, Br, I) in the presence of conjugated dienes, as shown in Scheme 4. The butadiene, 1,3-pentadiene, and 1,4-diphenylbutadiene complexes of Cp^*TiX exhibit a unique prone (endo) conformation (**13**), while the isoprene, 2,3-dimethylbutadiene, and 2,3-diphenylbutadiene complexes prefer the supine (exo) conformation (**14**). Reduction of $Cp^*TiX(diene)$ with RMgX or Mg gives a low-valent species, which catalyzes a highly selective (>99%) tail-to-head linear dimerization of isoprene and 2,3-dimethylbutadiene.**[54,55]**

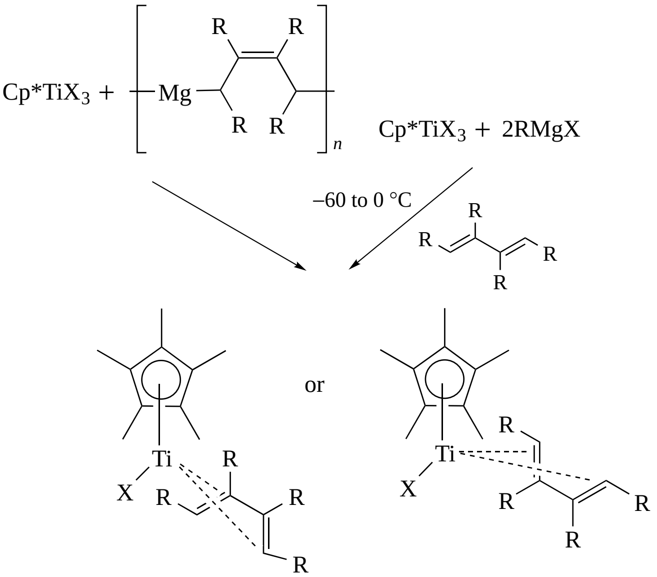

(**13**) prone *endo* (**14**) supine *exo*

Scheme 4

Addition of $[o\text{-}(CH_2)_2C_6H_4]Mg(THF)_2$ to Cp^*TiCl_3 in toluene gives the expected *o*-xylidene complex $Cp^*TiCl[o\text{-}(CH_2)_2C_6H_4]$. However, reaction of $[o\text{-}(CH_2)_2C_6H_4]Mg(THF)_2$ with Cp^*TiCl_3 in THF leads to the dinuclear bis(diene)titanium complex (**15**), in which two Cp^*TiCl fragments bond to *o*-xylidene through its exo- and endocyclic diene systems via σ^2 and η^4 bonding modes, respectively.**[56]**

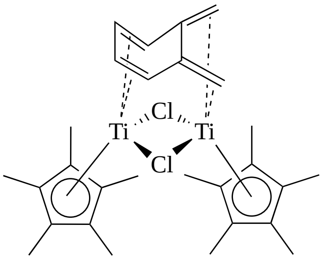

(**15**)

Diene–cyclopentadienyl titanium halide complexes react readily with unsaturated organic molecules. For example, reaction of $Cp^*TiCl(\eta^4\text{-}CH_2{=}CH(Me)CH(Me){=}CH_2)$ with symmetrical alkynes RC≡CR (R = Me, Ph) leads to reductive coupling (*see Reductive Coupling*) of the alkynes to give metallacyclo-2,4-pentadiene products $Cp^*Ti(C(Ph){=}C(Ph)C(Ph){=}C(Ph))Cl$ and the dinuclear metallacycle $[Cp^*TiCl]_2(C_4Me_4)$ (**16**).**[57]** In an analogous manner, treatment of $Cp^*Ti(CH_2{=}C(Me)C(Me){=}CH_2)Cl$ with 2,6-xylyl isocyanide at $-30\,°C$ gives the dimeric complex $(Cp^*TiCl)_2[\mu\text{-}N_2C_2(2,6\text{-xylyl})_2]$ (**17**) in 47% yield. Lesser amounts of (**18**) and (**19**) are also formed in this reaction, as shown in Scheme 5.**[58]**

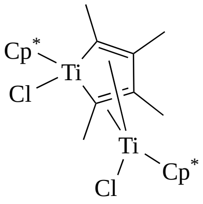

(**16**)

The cyclooctatetraene–diene complex $[(\eta^4\text{-}C_4H_6)cot]Ti$ has been reported and has been shown by ^1H NMR spectra to adopt an *s*-*cis*-η^4-butadiene conformation.**[59]**

Reduction of $TiCl_4(THF)_2$ with 2 equivalents of Mg in the presence of 2 equivalents of a sterically demanding 1-aza-1,3-diene, $ArN{=}CHC(CH_3){=}CAr$ (Ar = 1,5 $(i\text{-pr})_2C_6H_3$), gives the homoleptic early transition metal 1-aza-1,3-diene complex, $Ti(1\text{-aza-}1,3\text{-diene})_2$. X-ray diffraction analysis of this complex shows Ti–N distances of 1.949(2) and 1.939(2) Å and Ti–C distances of 2.317(3) and 2.132(3) Å. The subsequent addition of MeLi and elimination of methane

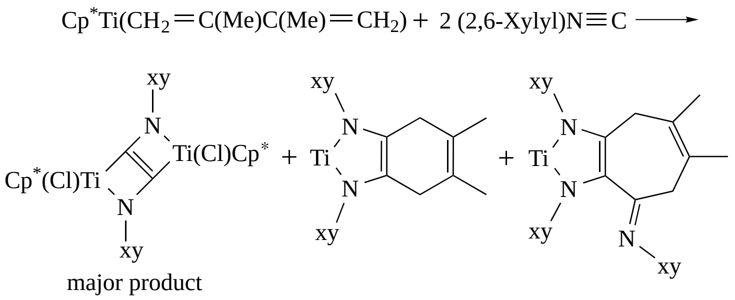

$Cp^*Ti(CH_2{=}C(Me)C(Me){=}CH_2) + 2\ (2,6\text{-Xylyl})N{\equiv}C \longrightarrow$
xy
N
Ti(Cl)Cp*
Cp*(Cl)Ti
N
xy
+
Ti
N
N
xy
xy
+
Ti
N
N
xy
xy
N
xy

major product

(17) **(18)** **(19)**

xy = Xylyl

Scheme 5

results in the formation of a novel metallacyclic titanium alkylidene complex, which affords the opportunity to compare of Ti–C σ- bond (2.163(3)) Å and Ti=C-bond (1.978(3) Å) distances within the same molecule.[60]

Reaction of $TiCl_4THF_2$ with $Na_2[MePhN{=}C{-}C{=}NPhMe]$ ($Ph = C_6H_5$, $4\text{-}MeC_6H_4$ and $2\text{-}MeC_6H_4$) or by reduction of $TiCl_4THF_2$ with Mg in presence of 2 equivalent of $MePhN{=}C{-}C{=}NPhMe$ give the corresponding homoleptic 1,4-diaza-1,3-diene complexes. The endiamide complexes are thermally stable and very sensitive to oxygen and water. An X-ray crystal structure reveals the Ti atom in theses complexes is in a strongly distorted tetrahedral environment. The two 5-membered metallacyclic rings are folded along the N,N' axis. Temperature-dependent ^1H NMR spectra indicate a rapid intramolecular inversion of this nonplanar ring system in solution even at room temperature. Reduction of $TiCl_4THF_2$ with Mg in presence of excess DAD [$PhRN{=}C{-}C{=}NRPh$ (DAD; $R = Ph$, $4\text{-}MeC_6H_4$, $4\text{-}MeOC_6H_4$)] gives the blue-violet complexes $(DAD)_3Ti$.[61]

8 ARENE COMPLEXES

8.1 Bis-arene Complexes

Bis-arene titanium complexes (*see Arene Complexes*) such as $(\eta^6\text{-}C_6H_6)_2Ti$ were first prepared by Green and coworkers by the reaction of titanium atoms with arenes on a liquid nitrogen cooled surface (equation 13).[62] A wide range of aromatic ligands have been incorporated in bis-arene titanium complexes by metal vapor synthesis, including highly sterically hindered arenes ($(\eta^6\text{-}t\text{-}Bu_3C_6H_3)_2Ti$) and heterocyclic arenes ($(\eta^6\text{-}2,6\text{-}Me_2C_5H_3N)_2Ti$).[63] Bis-arene titanium complexes are diamagnetic and exhibit sandwich structures (*see Sandwich Compound*) with essentially mutually parallel eclipsed planar arene ligands. However, $(\eta^6\text{-}2,6\text{-}Me_2C_5H_3N)_2Ti$ exhibits an unusual staggered configuration with a nitrogen center–titanium center'–nitrogen' torsional angle of 140.1°.[64,65]

$$C_6H_6 + \text{Ti vapor} \longrightarrow (\eta^6\text{-}C_6H_6)_2Ti \qquad (13)$$

Since bis-arene titanium complexes were initially prepared by metal-atom chemistry, 'conventional' chemical synthesis of bis-arene titanium complexes has been developed. Treatment of $TiCl_4(THF)_2$ with $K(Ph{-}Ph)_2$ and $K(4,4'\text{-}t\text{-}Bu_2Ph{-}Ph)_2$ gives $K[Ti(\eta^6\text{-}Ph{-}Ph)_2]$ (equation 14) and $K[Ti(\eta^6\text{-}4,4'\text{-}t\text{-}Bu_2Ph{-}Ph)_2]$, respectively, which are isolated as the corresponding K([2.2.2]cryptand) or K(15-crown-5)$_2$ bis(arene)titanates. Oxidation of these complexes with I_2 gives the corresponding bis-arene complexes (equation 15).[66] Ultrasound-mediated reduction of $TiCl_4(THF)_2$ or $TiCl_3(THF)_3$ with $K[BEt_3H]$ in benzene, toluene, *p*-xylene, or mesitylene gives the corresponding bis(η^6-arene)titanium complexes directly (equation 16).[67]

$$TiCl_4(THF)_2 + K(Ph{-}Ph)_2 \longrightarrow K[Ti(\eta^6\text{-}Ph{-}Ph)_2] \qquad (14)$$

$$K[Ti(\eta^6\text{-}Ph{-}Ph)_2] + I_2 \longrightarrow Ti(\eta^6\text{-}Ph{-}Ph)_2 \qquad (15)$$

$$TiCl_4(THF)_2 \text{ or } TiCl_3(THF)_3 \xrightarrow[C_6H_6\ )))]{K[BEt_3H]} (\eta^6\text{-}C_6H_6)_2Ti \qquad (16)$$

8.2 Monoarene complexes

Treatment of $[(Me_2PCH_2)_3Si\text{-}t\text{-}Bu]TiCl_3(THF)$ with sodium naphthalenide in THF gives $(\eta^6\text{-}C_{10}H_8)Ti[(Me_2PCH_2)_3Si\text{-}t\text{-}Bu]$ in 40% yield.[68]

Diamagnetic titanium(II) arene complexes $(\eta^6\text{-}C_6H_6)Ti[(\mu\text{-}X)_2(AlX_2)]_2$ (X = Cl, Br, I) (**20**) have been prepared by the reduction of TiX_4 (X = Cl, Br, I) with Al in the presence of $AlCl_3$ in C_6H_6 (equation 17). The arene ligands in these complexes are η^6 coordinated to the titanium, which exhibits square pyramidal coordination with four halides of two AlX_4 anions forming the basal square plane.

$$C_6H_6 + AlCl_3 + Al \longrightarrow (\eta^6\text{-}C_6H_6)Ti[(\mu\text{-}Cl)_2(AlCl_2)]_2 \qquad (17)$$

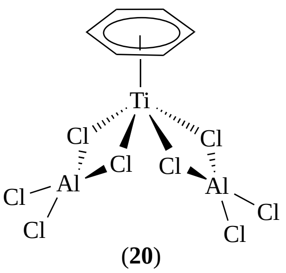

(20)

Treatment of $(\eta^6\text{-arene})Ti[(\mu\text{-}X)_2(AlX_2)]_2$ (X = Br, I) complexes with CO at low temperature gives the corresponding dicarbonyl derivatives $[(\eta^6\text{-arene})Ti(CO)_2[(\mu\text{-}X)(AlX_2)]]AlX_4$ (equation 18). Treatment of $(\eta^6\text{-arene})Ti(CO)_2[(\mu\text{-}X)_2(AlX_2)]_2$ (X = Cl, Br) with CpTl and 1 atm of CO at room temperature leads to the loss of the arene ligand and gives $Cp_2Ti(CO)_2$ in good yields (equation 19).[69]

$$(\eta^6\text{-arene})Ti[(\mu\text{-}Br)_2(AlBr_2)]_2 + CO \longrightarrow (\eta^6\text{-arene})Ti(CO)_2[(\mu\text{-}Br)(AlBr_2)] \qquad (18)$$

$$(\eta^6\text{-arene})Ti(CO)_2[(\mu\text{-}Br)(AlBr_2)] + CpTl \longrightarrow Cp_2Ti(CO)_2 \qquad (19)$$

Reaction of $Ti(\eta^6\text{-}MePh)[(\mu\text{-}X)_2(AlX_2)]_2$ (X = Cl, Br) with alkynes RC≡CR (R = Me, Ph) gives tetramethyl- and tetraphenylcyclobutadiene complexes, $Ti(\eta^4\text{-}C_4R_4)[(\mu\text{-}X)_2(AlX_2)]_2$ (R = Ph, X = Cl, Br; R = Me, X = Br), in good yield. The titanium atom in $Ti(\eta^4\text{-}C_4Ph_4)[(\mu\text{-}Br)_2(AlBr_2)]_2$ is found to have approximately square pyramidal coordination, with the apical position occupied by the symmetrically bonded tetraphenylcyclobutadiene ring with four bromines of two $AlBr_4$ anions forming the base of the pyramid. Treatment of $Ti(\eta^4\text{-}C_4Ph_4)[(\mu\text{-}Br)_2(AlBr_2)]_2$ with CpTl and K_2cot forms $Cp_2Ti[C(Ph)=C(Ph)C(Ph)=C(Ph)]$ and $(cot)Ti(\eta^4\text{-}C_4Ph_4)$, respectively, as shown in Scheme 6. $Ti(\eta^6\text{-}MePh)[(\mu\text{-}X)_2(AlX_2)]_2$ (X = Cl, Br) has been shown to cyclotrimerize (*see Cyclodimerization & -trimerization Reactions*) alkynes at 89 °C.[70]

Reduction of $TiCl_4(dmpe)$ or Cp^*TiCl_3 with K or Na anthracene in THF gave $[Ti(\eta^6\text{-}C_{14}H_{10})(\eta^4\text{-}C_{14}H_{10})(dmpe)]$ and $[Cp^*Ti(\eta^4\text{-}C_{14}H_{10})(\eta^2\text{-}C_{14}H_{10})]^-$, respectively. Treatment of $[Ti(\eta^6\text{-}C_{14}H_{10})(\eta\text{-}C_{14}H_{10})(dmpe)]$ and $[Cp^*Ti(\eta^4\text{-}C_{14}H_{10})(\eta^2\text{-}C_{14}H_{10})]^-$ with carbon monoxide in THF at −55 °C led to loss of the anthracene ligands to give $Ti(CO)_3(dmpe)_2$ and $Cp^*[Ti(CO)_4]^-$ in 57% and 62% yields, respectively.[71]

A small number of titanium complexes with heterocyclic ligands have been prepared. Reaction of $TiCl_4(THF)_2$ with 2,3,4,5-tetramethyl-1-trimethylstannyl phosphole in CH_2Cl_2/pentane followed by reduction with Mg in the presence of CO gives $(\eta^5\text{-}2,3,4,5\text{-}C_4Me_4P)Ti(CO)_2$ in 39% yield.[72] Reaction of $TiCl_4$ with $Li(C_5H_5BMe)$, 2-$(Me_3Si)C_5H_5BMe$, or 2-$(Me_3Sn)C_5H_5BMe$ gives $TiCl_3(\eta^6\text{-}C_5H_5BMe)$ in excellent yield. Cp $TiCl_2(\eta^6\text{-}C_5H_5BMe)$ was prepared in an analogous manner starting with $CpTiCl_3$ in place of $TiCl_4$.[73] The addition of potassium-pyrrole to $[K(15\text{-crown-}5)_2]_2[Ti(CO)_4(\eta^3\text{-}BH_4)]$ gives $[K(15\text{-crown-}5)_2]_2[(\eta^5\text{-}C_4H_4N)Ti(CO)_4)]$.[25]

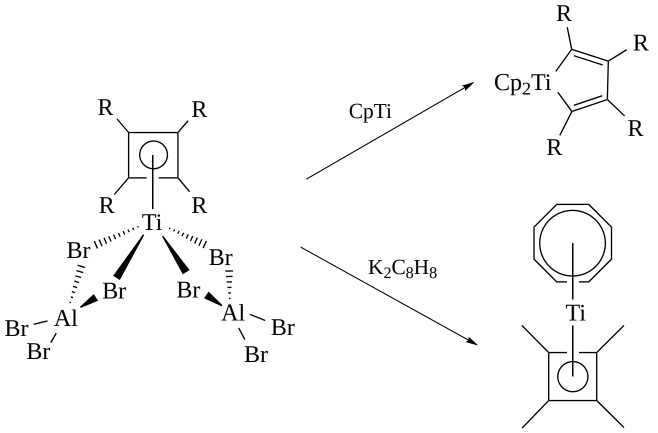

Scheme 6

9 CYCLOPENTADIENYL COMPLEXES OF TITANIUM(IV)

The vast majority of the organometallic chemistry of titanium is based upon complexes that incorporate one or two cyclopentadienyl or substituted cyclopentadienyl groups as ancillary ligands. Cyclopentadienyl (*see Cyclopentadienyl*) and substituted cyclopentadienyl ligands are ubiquitous in the organometallic chemistry of titanium. Bis(cyclopentadienyl)- and substituted bis(cyclopentadienyl)titanium dichloride complexes have been prepared by treatment of $TiCl_4$, or $TiCl_3$ followed by an oxidative work-up, with a wide range of cyclopentadienyl and substituted cyclopentadienyl salts of several metals, including Li^+, Na^+ (equation 20), MgX^+, Mg^{2+}, Tl^+, and Pb^{2+}. Bu_2TiCl_2, generated in hydrocarbon media at −78 °C by treating $TiCl_4$ with 2 equivalent of BuLi, functions a strong bases toward cyclopentadiene, substituted cyclopentadiene, and indene giving Cp_2TiCl_2 derivatives in high yield (equation 21).[74] Treatment of $Ti(NMe_2)$ and $Ti(NEt_2)_4$ the cyclopentadiene derivatives to give metallocenes (*see Metallocene Complexes*) (equation 22).[75] Modifications of this reaction have recently been widely used to prepare substituted Cp complexes including *ansa*-metallocenes and constrained geometry complexes.

$CpTiCl_3$ is conveniently prepared by treatment of $TiCl_4$ with $CpSiMe_3$ (equation 23).**[76]** The synthesis and reactivity bis(cyclopentadienyl)titanium through the mid- 90s has been extensively reviewed by Bechaus up.**[77]** The synthesis of chiral titanocene derivatives has been reviewed by Halterman.**[78]**

$$2RCpNa + TiCl_4 \longrightarrow RCp_2TiCl_2 \qquad (20)$$

$$Bu_2TiCl_2 + C_5H_6 \longrightarrow Cp_2TiCl_2 \qquad (21)$$

$$Ti(NMe_2)_4 + C_5H_6 \longrightarrow Cp_2Ti(NMe_2)_2 \qquad (22)$$

$$CpSiMe_2 + TiCl_4 \longrightarrow CpTiCl_3 \qquad (23)$$

$Cp^*_2TiCl_2$ is readily prepared by reaction of 2 equivalent of $Na[C_5Me_5]$ with $TiCl_3$, followed by oxidative work-up (equation 24).**[79]** The mono-ring complexes Cp^*TiX_3 ($X = Cl$, Br) are best prepared, in nearly quantitative yield, by the treatment of TiX_4 with $(C_5Me_5)SiMe_3$ (equation 25).**[80]**

$$2Na[C_5M_5] + TiCl_3 \longrightarrow Cp^*_2TiCl_2 \qquad (24)$$

$$TiCl_4 + (C_5Me_5)SiMe_3 \longrightarrow Cp^*TiCl_3 \qquad (25)$$

Treatment of Cp_2TiCl_2 with 1 equivalent of Grignard reagent (*see Grignard Reagents*) provides a convenient route for the preparation of the mono(σ-hydrocarbyl) complexes, Cp_2TiRCl ($R = Me$, Et, n-Pr, n-Bu, i-Bu, n-C_5H_{11}, CH_2Bu-t, CH_2Ph, CH_2SiMe_3, and Ph) (equation 26). Treatment of Cp_2TiCl_2 with 2 equivalent of MeLi or MeMgX leads to Cp_2TiMe_2 in good yield (equation 27). Cp_2TiMe_2 undergoes decomposition at room temperature rapidly in light and more slowly in the dark. Similar routes have been used to prepare other bis-alkyl and -aryl complexes; however, the stability of these complexes varies widely. $Cp_2Ti(Et)_2$ decomposes below 40 °C, while $Cp_2Ti(n\text{-}Bu)_2$ decomposes above −50 °C in solution. $Cp_2Ti(R)_2$ compounds not containing β-hydrogens exhibit considerably greater stability. Thus, $Cp_2Ti(CH_2SiMe_3)_2$ and Cp_2TiPh_2 exhibit good stability at room temperature; however, they undergo thermolysis in refluxing benzene, which has been well studied. Treatment of Cp_2TiCl_2 with 2 equivalent of the more sterically demanding $LiCHPh_2$ or $LiCH(SiMe_3)_2$ leads to reduction of the titanium center to give $Cp_2TiCHPh_2$ (equation 28) and $Cp_2TiCH(SiMe_3)_2$, respectively, while treatment of Cp_2TiCl_2 with 1 equivalent of $LiCH(SiMe_3)_2$ gives Cp_2TiCl (equation 29).**[81]**

$$Cp_2TiCl_2 + RMgX \longrightarrow Cp_2TiClR \qquad (26)$$

$$Cp_2TiCl_2 + 2MeMgX \longrightarrow Cp_2TiMe_2 \qquad (27)$$

$$Cp_2TiCl_2 + 2LiCH(SiMe_3)_2 \longrightarrow Cp_2TiCH(SiMe_3)_2 \qquad (28)$$

$$Cp_2TiCl_2 + LiCH(SiMe_3)_2 \longrightarrow Cp_2TiCl \qquad (29)$$

In contrast to the preparation of Cp_2TiClR (see above), treatment of $Cp^*_2TiCl_2$ with 1 equivalent of Me, Et, or Pr, Grignard or lithium reagents gives a mixture of Ti^{III} and Ti^{IV} complexes.**[42]**

The replacement of the cyclopentadienyl group with the strongly electron-donating and sterically more demanding pentamethylcyclopentadienyl group has been found to impart enhanced solubility and increased kinetic stability to many transition metal complexes. This enhanced stability is typified by the difference in stability of Cp_2TiMe_2 and $Cp^*_2TiMe_2$. While Cp_2TiMe_2 undergoes decomposition at room temperature rapidly in light and more slowly in the dark, $Cp^*_2TiMe_2$ is sufficiently stable to be stored at room temperature for an extended time. Cp_2TiMe_2 is thought to decompose via α-hydrogen elimination to give products which have not been fully characterized. Bercaw has established that upon heating to 110 °C, $Cp^*_2TiMe_2$ undergoes α-hydrogen abstraction or α-hydrogen elimination (*see α-Elimination*) followed by loss of methane to give the methylidene intermediate (**21**) (equation 30). This intermediate titanium methylidene complex undergoes hydrogen migration from a ring methyl group to the methylidene to give the turquoise fulvene complex $Cp^*(\eta^6\text{-}C_5Me_4CH_2)TiMe$ (**22**).**[82]** Thermolysis of $(\eta^5\text{-}C_5Me_4H)_2TiMe_2$ at 130 °C gives the analogous fulvene complex $(\eta^5\text{-}C_5Me_4H)(\eta^6\text{-}C_5Me_3HCH_2)TiMe$.**[83]**

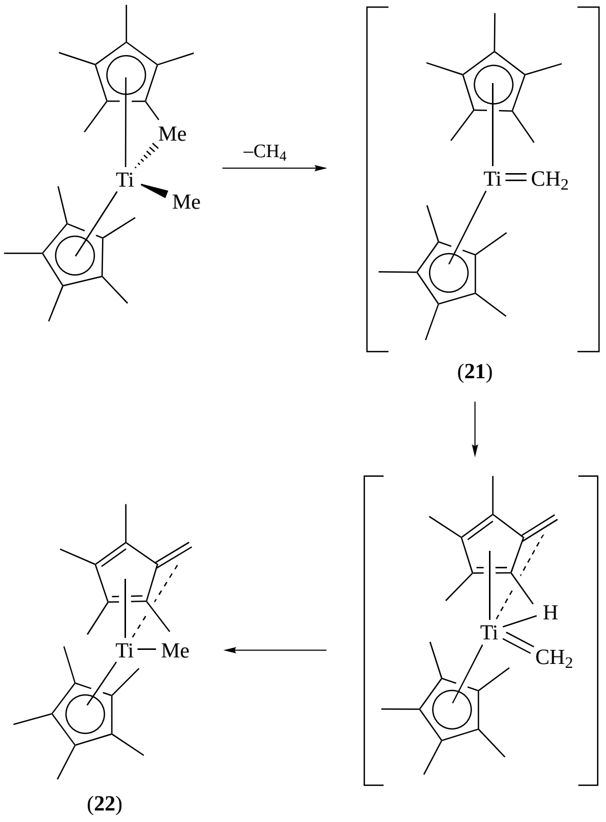

(30)

9.1 Bulky Ligands

Considerable work in recent years has been devoted to the synthesis of ring-substituted derivatives of bis(η^5-cyclopentadienyl)titanium dihalides. The ring orientation in the bis(η^5-alkylcyclopentadienyl)titanium dihalide derivatives that have been structurally characterized, to date, can be divided into two categories, which are illustrated schematically by (**23**) and (**24**) (Table 1).

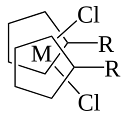

(**23**)

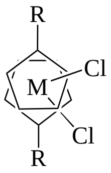

(**24**)

Several groups have investigated the incorporation of 1,3-di-*t*-butylcyclopentadienyl ligands in mono- and bis-cyclopentadienyltitanium complexes. The sterically congested compounds (η^5-1,3-*t*-$Bu_2C_5H_3)_2TiCl_2$ and (η^5-1,3-*t*-$Bu_2C_5H_3)TiCl_3$ are prepared in good yields by treating $TiCl_4$ or $TiCl_3$ with 2 or 1 equivalent of [1,3-*t*-$Bu_2C_5H_3$]Li, respectively.[85,86]

Reduction of (η^5-1,3-*t*-$Bu_2C_5H_3)_2TiCl_2$ with K metal in pentane gives the paramagnetic titanium(III) complex (η^5-1,3-*t*-$Bu_2C_5H_3)_2TiCl$ in high yield.[87] Treatment of (η^5-1,3-*t*-$Bu_2C_5H_3)_2TiCl_2$ with $LiBH_4$ in Et_2O leads to reduction of the titanium center to give (η^5-1,3-*t*-$Bu_2C_5H_3)_2TiBH_4$. The Ti$\cdots$B bond length is found to be 2.41 Å and the H–Ti–H bond angle is 58.2°.[88]

Bis- and tris(trimethylsilyl)cyclopentadienyl derivatives, $Ti[\eta^5\text{-1,3-}(SiMe_3)_2C_5H_3]_2Cl_2$ and $[\eta^5\text{-1,2,4-}(Me_3Si)_3C_5H_2]TiCl_3$, have been prepared in good yield by treating $TiCl_3$ with $Li[1,3\text{-}(SiMe_3)_2C_5H_3]$ or $Li[1,2,4\text{-}(Me_3Si)_3C_5H_2]$, respectively, followed by oxidative work-up.[89,90]

Reaction of $TiCl_3(THF)_3$ with 1 equivalent of the sterically demanding Li[*i*-PrC_5Me_4] in THF, followed by oxidation with HCl, affords (η^5-*i*-$PrC_5Me_4)TiCl_3$ in 66% yield. Treatment of (η^5-*i*-$PrC_5Me_4)TiCl_3$ with CpTl in refluxing benzene forms (Cp)(η^5-*i*-$PrC_5Me_4)TiCl_2$ in 95% yield. The highly sterically congested complex (η^5-*i*-$PrC_5Me_4)_2TiCl_2$ is prepared in 93% yield by reaction of $TiCl_3(THF)_3$ with 2 equivalent. of Li[*i*-PrC_5Me_4] in THF, followed by oxidation with HCl. The ring centroid–titanium–ring centroid angle of 137.4(1)° of (η^5-*i*-$PrC_5Me_4)_2TiCl_2$ is identical, within experimental error, to that found in $Cp^*_2TiCl_2$; however, the Cl–Ti–Cl bond angle of 88.81° is unusually acute (see Table 1).[84]

Table 1 Structural Parameters for RCp_2TiCl_2 Complexes[84]

	Structure type	Cp–M–Cp (°)	Cl–M–Cl (°)
$(\eta^5\text{-}C_5H_5)_2TiCl_2$	Staggered	131.0 (av.)	94.5 (av.)
$(\eta^5\text{-}C_5Me_5)_2TiCl_2$	Staggered	137.4	92.94(4)
$(\eta^5\text{-}MeC_5H_4)_2TiCl_2$	(**23**)	130.2	93.15(8)
(η^5-*i*-$PrC_5H_4)_2TiCl_2$	(**23**)	132.9	92.5(1)
(η^5-*t*-$BuC_5H_4)_2TiCl_2$	(**24**)	131.5	92.5(5)
$(\eta^5\text{-}Me_3SiC_5H_4)_2TiCl_2$		131.02	91.63
(η^5-*i*-$PrC_5Me_4)_2TiCl_2$	(**24**)	137.4	88.81
(η^5-isodiCp)$_2TiCl_2$		131.0	92.94

Treatment of $TiCl_3$ with $Li(Ph_4C_5H)$ or $K(Ph_4C_5H)$ gives $(Ph_4C_5H)_2TiCl$, which, upon treatment with HCl/THF or AgCl, affords the highly sterically hindered complex $(Ph_4C_5H)_2TiCl_2$.[91] In contrast to the less sterically hindered $[Cp_2TiCl]_2$, $(Ph_4C_5H)_2TiCl$ crystallizes as well-separated monomeric units with the tetraphenylcyclopentadienyl rings staggered, with a ring centroid–metal–ring centroid angle of 136.4°, and a short Ti–Cl bond length of 2.312(2) Å. Solution EPR (*see Electron Paramagnetic Resonance*) studies show evidence for free $(C_5Ph_4H)_2TiCl$ ($g = 1.957$) and a THF adduct ($g = 1.979$). Reduction of a THF solution of $(Ph_4C_5H)_2TiCl$ with sodium naphthalenide under argon and CO yields a species with IR absorptions at 1966 and 1892 cm^{-1}, which suggests the formation of $(C_5Ph_4H)_2Ti(CO)_2$.[92]

Reaction of $CpTiCl_3$ with $K(C_5Ph_5)$ or $K(C_5Ph_4H)$ in THF gives $Cp(\eta^5\text{-}Ph_5C_5)TiCl_2$ and $Cp(\eta^5\text{-}Ph_4C_5H)TiCl_2$, respectively. The Ti–C bond lengths for the C_5Ph_5 group in $Cp(\eta^5\text{-}Ph_5C_5)TiCl_2$ are found to be considerably longer than those for the C_5H_5 group; average bond lengths are 2.53(3) and 2.39(4) Å, respectively.[93]

9.2 Functionalized Ligands

Cyclopentadienyl ligands incorporating potentially chemically reactive functional groups have also been used in the preparation of bis(cyclopentadienyl)titanium dihalides. For example, reaction of (methoxycarbonylcyclopentadienyl)thallium with $CpTiCl_3$ or $TiCl_4$ gives $Cp(\eta^5\text{-}MeOC(O)C_5H_4)TiCl_2$ and $(\eta^5\text{-}MeOC(O)C_5H_4)_2TiCl_2$, respectively, in good yield. Reductive carbonylation of these complexes affords $Cp(\eta^5\text{-}MeOC(O)C_5H_4)Ti(CO)_2$ and $(\eta^5\text{-}MeOC(O)C_5H_4)_2Ti(CO)_2$, respectively, in good yield.[94]

Treatment of $TiCl_4$ with 2 equivalent of $Li[ClC_5H_4]$ or $Tl[ClC_5H_4]$ forms $(\eta^5\text{-}ClC_5H_4)_2TiCl_2$, while treatment of $CpTiCl_3$ with $Tl[ClC_5H_4]$ gives $Cp(\eta^5\text{-}ClC_5H_4)TiCl_2$ in good yields. Reductive carbonylation of $(\eta^5\text{-}ClC_5H_4)_2TiCl_2$ and $Cp(\eta^5\text{-}ClC_5H_4)TiCl_2$ leads to the corresponding dicarbonyl derivatives.[94,95]

Several groups have prepared titanium-based metalloligands incorporating phosphine-substituted cyclopentadienyl ligands as the first step in the synthesis of new bimetallic complexes. Treatment of $CpTiCl_3$ with $Tl(Ph_2PC_5H_4)$ affords $Cp(\eta^5\text{-}(Ph_2P)C_5H_4)TiCl_2$ in 95% yield. Reductive carbonylation of $Cp(\eta^5\text{-}Ph_2PC_5H_4)TiCl_2$ gives $Cp(\eta^5\text{-}Ph_2PC_5H_4)Ti(CO)_2$. Both of these phosphine-substituted titanocene complexes react with $Cp(CO)_2(THF)Mn$ to give the corresponding bimetallic complexes $CpMn(CO)_2\{(Cp)(\eta^5\text{-}Ph_2PC_5H_4)TiCl_2\}$ and $CpMn(CO)_2\{Cp(\eta^5\text{-}Ph_2PC_5H_4)Ti(CO)_2\}$ in good yield.[96]

Reaction of $Li[Ph_2PC_5Me_4]$ with $CpTiCl_3$ and $TiCl_3$ followed by treatment with CCl_4 leads to the formation of $Cp(\eta^5\text{-}Ph_2PC_5Me_4)TiCl_2$ and $(\eta^5\text{-}Ph_2PC_5Me_4)_2TiCl_2$, respectively, in good yield.[97] In an analogous manner, reaction of Tl[$Ph_2PC_5Me_4$] and Tl[$Me_2PC_5Me_4$] with Cp*$TiCl_3$ forms [η^5-$Ph_2PC_5Me_4$]$_2$$TiCl_2$ and [η^5-$Me_2PC_5Me_4$]$_2$$TiCl_2$, respectively, in good yield.[98] The metalloligand [η^5-(Ph_2P)C_5Me_4]$_2$$TiCl_2$ reacts readily with $Mo(CO)_4$cod, $Mo(CO)_5$THF, and $Mo(CO)_6$ to give in each case [cyclic][(η^5-$Ph_2PC_5Me_4$)$_2$$TiCl_2$]$Mo(CO)_4$ as the sole product. The long Mo–Ti distance of 5.194(1) Å in this complex rules out any metal–metal interaction.[96]

The reaction of ($CpTiCl_2$)$_n$ and Cp*$TiCl_2$(THF) with Li($C_5Me_4CH_2CH_2NMe_2$) gives ($C_5Me_4CH_2CH_2NMe_2$)CpTiCl and ($C_5Me_4CH_2CH_2NMe_2$)Cp*TiCl, respectively, which are oxidized by $PbCl_2$ to give ($C_5Me_4CH_2CH_2NMe_2$)$CpTiCl_2$ and ($C_5Me_4CH_2CH_2NMe_2$)Cp*$TiCl_2$, respectively. The nitrogen of the NMe_2 group in ($C_5Me_4CH_2CH_2NMe_2$)CpTiCl was found to bond with the Ti (Ti–N, 2.437(3) Å), while the NMe_2 group in ($C_5Me_4CH_2CH_2NMe_2$)Cp*$TiCl_2$ was found not be coordinated to the titanium in the solid state by single-crystal X-ray diffraction.[48]

Chlorosilyl-cyclopentadienyl titanium complexes have been prepared, as starting materials allowing further modification. Treatment of MCl_4 with two equivalents of $C_5H_5(SiClMe_2)$ in toluene under reflux and in the presence of two equivalents of NEt_3 gives (η^5-$C_5H_4SiClMe_2$)$_2$$TiCl_2$.[99] [Ti($\eta^5$-$C_5Me_4SiMeCl_2$)$Cl_3$] and [Ti($\eta^5$-$C_5Me_4SiMeHCl$)$Cl_3$], are prepared by the treatment of $TiCl_4$ with the trimethylsilyl derivatives of the corresponding cyclopentadienes. Methylation of these complexes with MeMgCl gives the corresponding Me complexes [Ti(η^5-$C_5Me_4SiMe_2R$)XMe_2] (R = H, Cl; Me; R = X = Me).[100]

K[C_5Me_4-P-*t*-Bu(NEt_2)] and K[*t*-BuC_5H_3-P-*t*-Bu(NEt_2)] are efficiently transmetalated by Me_3SnCl, subsequent reaction with $TiCl_4(L)_2$ (L = THF, tetrahydrothiophene, Me_3P) gives the half-sandwich complexes (*see Half-sandwich Complexes*) [Me_4Cp-P-*t*-Bu(NEt_2)]$TiCl_3$ and [*t*- BuC_5H_3-P-*t*-Bu(NEt_2)]$TiCl_3$, respectively in moderate yields. Treatment of [*t*- BuC_5H_3-P-*t*-Bu(Cl)] with $TiCl_4$ in the presence of Et_3N at low temperature gives the half-sandwich complex [*t*-BuC_5H_3-P-*t*-Bu(Cl)]$TiCl_3$ quantitative yield.[101]

9.3 Annulated Cyclopentadienyl Ligands

Considerable effort has been directed to the stereoselective synthesis of annulated cyclopentadienyl complexes of the group 4 transition metals. C_1 asymmetric and C_2 symmetric annulated cyclopentadienyl ligands have been used to prepare chiral organotitanium complexes, which are now being actively studied as catalysts for asymmetric synthesis and olefin polymerization (*see* ***Asymmetric Synthesis by Homogeneous Catalysis***).

Halterman and Vollhardt[102] and Paquette and coworkers[103] have prepared bis(annulated cyclopentadienyl)titanium complexes, and have separated (**25**) and (**26**) when starting from the chiral natural product camphor. They have shown that use of complex (**25**) as a catalyst precursor for asymmetric hydrogenation of 2-phenylbutene forms 2-phenylbutane quantitatively at up to 34% *ee*.

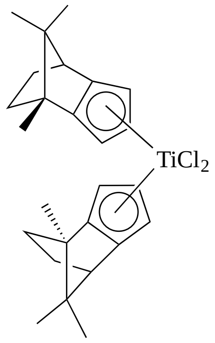

(**25**)

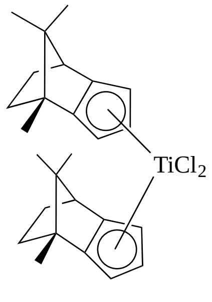

(**26**)

The C_2 symmetric chiral cyclopentadienes (+)-(1*R*, 7*R*, 8*R*, 10*R*)-8,10-diisopropyltricyclo[5.2.2.0^{2,6}]undeca-2,5-diene (Me_2-BCO-CpH) and (−)-(1*S*, 7*S*, 8*R*,10*R*)-8,10-dimethyltricyclo[5.2.2.0^{2,6}]undeca-2,5-diene (BCO-CpH) have been metalated and treated with $TiCl_3$, followed by oxidative work-up, to give enantiomerically pure (Me_2-BCO-Cp)$_2$$TiCl_2$ and (BCO-Cp)$_2$$TiCl_2$ in 45 and 55% yield, respectively (equations 31 and 32).[104]

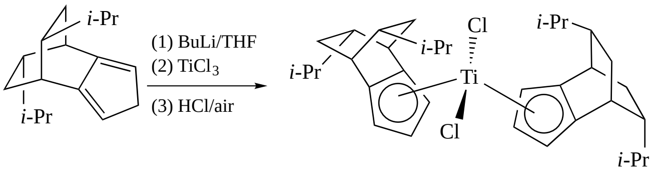

(31)

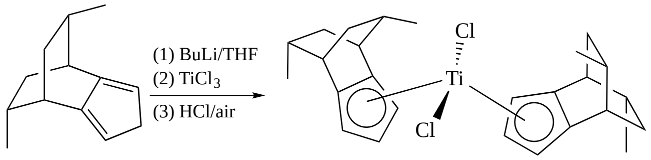

(32)

Paquette and coworkers have extensively studied the complexation of C_1 symmetric annulated cyclopentadienides with $TiCl_3$, $TiCl_4$, $CpTiCl_3$, and Cp*$TiCl_3$ to give the corresponding complexes. Reaction of lithium isodicyclopentadienide (isodiCpLi) with $CpTiCl_3$, $MeCpTiCl_3$, or Cp*$TiCl_3$ proceeds under conditions which are kinetically controlled and take place with complete bifacial stereoselectivity depending upon temperature (with endo complexation occurring at −78 °C and exo complexation occurring at room temperature and above).[105] For example, treatment of $CpTiCl_3$ with isodiCpLi at −78 °C gives (**27**), while the same reaction at room temperature gives (**28**). Paquette and coworkers have prepared each of the three possible diisodicyclopentadienyltitanium dichlorides with a high degree of selectivity. The pronounced influence of reaction temperature on stereoselectivity is further demonstrated by reacting $TiCl_3$ with the isodiCpLi at 25 °C, followed by oxidative work-up, to obtain the exo,exo isomer, or reacting at −64 °C for the endo,endo isomer. In the exo,exo isomer, the cyclopentadienyl rings are almost eclipsed and the norbornane substituents on the rings are oriented away from each other. The Cl–Ti–Cl and ring centroid−Ti−ring centroid angles of 92.94 and 131.0°, respectively, are within the normal range for Cp_2TiCl_2 complexes (see Table 1). *Exo*-isodiCp$TiCl_3$ was synthesized specifically by treatment of $TiCl_4$ with isodiCp$SiMe_3$. Reaction of *exo*-isodiCp$TiCl_3$ with isodiCpLi at −78 °C leads to the endo,exo isomer selectively.[106,107] The three diastereomeric $(isodiCp)_2TiCl_2$ complexes were prepared. Treatment of the exo,exo $(isodiCp)_2TiCl_2$ with MeLi gives $(isodiCp)_2TiClMe_2$. However, treatment of the endo,endo and endo,exo $(isodiCp)_2TiCl_2$ does not lead to stable products under analogous conditions. Treatment of all three $(isodiCp)_2TiCl_2$ isomers with C_6F_5Li gives the corresponding air stable, $(isodiCp)_2Ti(C_6F_5)Cl$.[108] Reduction of exo,exo $(isodiCp)_2TiCl_2$ gives exo,exo $(isodiCp)_2TiCl$, or in the presence of BMTA $(isodiCp)_2TiCl(Me_3SiC{\equiv}CSiMe_3)$.[109]

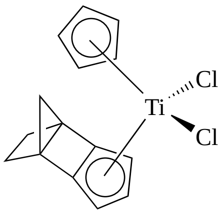

(**27**)

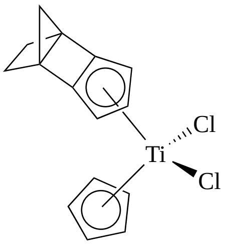

(**28**)

Paquette has shown that lithium salts of annulated cyclopentadienides coordinate to a metal atom predominantly or exclusively from a single π surface. Paquette has proposed that this facial selectivity is controlled by the locus of the lithium counterion and the state of aggregation of the reactive organometallic species. Recently, Paquette and Sivik have shown that it is possible to take advantage of the high stereoselectivity of *C*-silylation of annulated cyclopentadienides and the strict inversion of configuration that occurs during electrophilic condensation of these silanes with titanium chloride reagents, as shown in Scheme 7.[110]

9.4 *ansa*-Metallocenes

There has been considerable interest in the synthesis of *ansa*-metallocenes of the group 4 transition metals because of their potential use as reagents or catalysts in organic synthesis. The bridging of the two rings in an *ansa*-metallocene can, if the bridge is short enough, cause significant changes in the ring centroid−Ti−ring centroid angle and give a more open coordination geometry. In addition, the bridging of the two rings can 'lock' substituents on the two rings relative to each other.

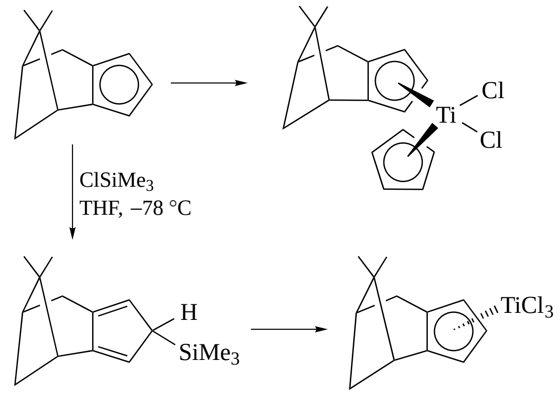

Scheme 7

Many *ansa*-metallocene complexes of titanium are best prepared by treatment of $TiCl_3$ or $TiCl_3THF_3$ with the dianion of a bridged dicyclopentadienyl ligand, followed by an oxidative work-up. Simple *ansa*-metallocenes (**29**) have been prepared with hydrocarbon bridges ($CH_2CH_2CH_2$,[111] CMe_2CMe_2,[112] CMe_2[113]) rigid hydrocarbon bridges, $C({=}CH_2)C{=}CNR_2$,[114] and hetero atom containing bridges, $SiMe_2$,[115] $Me_2Si(CH_2)_3SiMe_2$,[116] $Me_2SiN(R)SiMe_2$,[117] $Me_2SiOSiMe_2$.[99] *ansa*-metallocenes incorporating permethylated cyclopentadienyl rings (**30**) have been prepared with CMe_2[118] $GeMe_2$,[119,120] PPh[121] bridges and a smaller number of *ansa*-metallocene have been prepared the incorporate one Cp and one Cp* bridged by $SiMe_2$,[122] $GeMe_2$[122,123] Treatment of the lithium slats 1,2-bis(1-indenyl)benzenes with $TiCl_3$ followed by oxidation gives the phenyl-bridged *ansa*-bis(indenyl)titanium dichloride in good yield.[124] Several *ansa*-metallocenes bridged at the 7,7′-positions of the indenyl moiety have been prepared.[125]

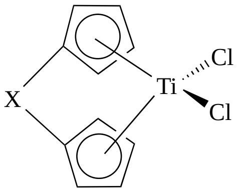

(**29**)

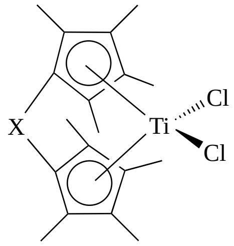

(**30**)

A small number of alkene-linked *ansa*-metallocenes are known for titanium. Thus reaction of $Na_2(C_5H_4)C(R){=}C(R)(C_5H_4)$ with $TiCl_4$ or $TiCl_3THF_3$ affords the corresponding alkene-bridged *ansa*-titanocene dichlorides. There is no indication of interaction between the alkene π-system and the titanium center.[126]

ansa-Metallocenes of titanium dichloride undergo many of the same reactions as the unbridged analogs. For example, reduction of $(Me_2SiCp_2)TiCl_2$ with Na/Hg gives the corresponding dimeric titanium(III) *ansa*-metallocene $[(Me_2SiCp_2)TiCl]_2$. Treatment of $[(Me_2SiCp_2)TiCl]_2$ with PMe_2Ph or reduction of $(Me_2SiCp_2)TiCl_2$ with Na/Hg in the presence of PMe_2Ph forms $(Me_2SiCp_2)TiCl(PMe_2Ph)$. Alkylation of $(Me_2SiCp_2)TiCl(PMe_2Ph)$ leads to the titanium(III) alkyls $[(Me_2SiCp_2)TiR(PMe_2Ph)]$.[127]

ansa-Metallocenes have been prepared in which the two cyclopentadienyl rings are differently substituted. For example, treatment of $TiCl_4$ with the unsymmetrical dianions $(C_5H_4)CHR(Cp')^{2-}$ ($R = Me$, CMe_3; $Cp' = Cp$, indenyl, fluorenyl) affords the corresponding *ansa*-metallocenes $[(C_5H_4)CHR(Cp')]TiCl_2$.[128]

ansa-Metallocenes and, in particular, chiral *ansa*-metallocenes have generated considerable interest because of their use as reagents and catalysts to carry out stereoselective polymerization, hydrogenation, alkylation of ketones, and aminoalkylation of alkynes.

Addition of a substituent, such as an alkyl group or a fused ring, to the cyclopentadienyl group in *ansa*-metallocenes leads to the possibility of racemic and meso complexes. For example, ethylenebis(1-indenyl) and ethylenebis(tetrahydro-1-indenyl) complexes prepared by Brintzinger and coworkers have been isolated in both the racemic form (**31**) and meso form (**32**).[129–131]

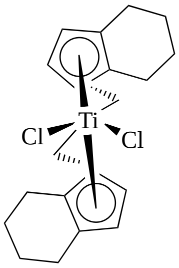

(**31**) racemic

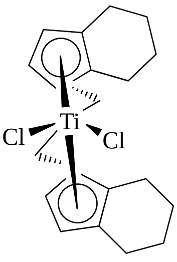

(**32**) *meso*

Titanium *ansa*-metallocenes incorporating a $SiMe_2$ or CMe_2CMe_2 bridge and a Ph or 1-naphthyl substituent in one β-position of each Cp ring have been prepared as a mixture of racemic and meso complexes.[132] Synthesis of the racemic and meso diastereomers of disubstituted tetramethylethanediyl-bridged titanocene derivatives $Me_4C_2(1\text{-}C_5H_3\text{-}3\text{-}R)_2TiCl_2$ ($R = t$-Bu, $SiMe_3$, i-Pr, α,α-dimethylbenzyl, or 1-phenylcyclohexyl) is accomplished by reductive coupling of the appropriately substituted 6,6-dimethylfulvenes with Mg/CCl_4 and reaction of the resulting di-Grignard reagents with $TiCl_3{\cdot}3THF$, followed by oxidative work-up.[133]

Several titanium *ansa*-metallocenes have been prepared which incorporate chiral centers in the backbone as a way of influencing the stereoselectivity of *ansa*-metallocene formation. Chiral backbones that have been prepared and used in this fashion include $(1R,2R)$-*trans*-1,2-bis(1-indenylmethyl)cyclopentane,[134] (S,S)-2,3-butylene-1,1′-bis(indenyl),[135] and 2,3-bis[3-(1,1-dimethylethyl)-1,3-cyclopentadien-5-yl]-2,3-dimethylbutane.[136] Chiral *ansa*-metallocene such as $(\eta^5{:}\eta^5\text{-}C_5Me_4SiMe_2C_5H_3R^*)TiCl_2$ ($R^* =$ menthyl, neomenthyl) incorporating a chiral group on one of the Cp rings have been prepared.[137] Chiral *ansa* complexes utilizing annulated cyclopentadienyl ligands have also been prepared.[138] Chiral *ansa*-metallocene complexes based upon biphenyl and binaphthyl bridges have been prepared.[139–144] The chiral annulated *ansa*-metallocenes such as (+)-[ethylene-1,2-bis[η^5-$(1R,7R,8R,10R)$-8,10-dimethyltricyclo[5.2.2.02,6]-2,5-undecadien-4-yl]]titanium dichloride (**33**) has been prepared.[145]

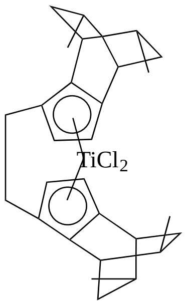

(**33**)

Collins and coworkers have developed two synthetic routes for the preparation of chiral [1,2-ethylenebis(η^5-3-alkylcyclopentadienyl)]titanium dichlorides ($R = Me$, Et, i-Pr, t-Bu) in 80–85% yields as a mixture of racemic and meso-titanocene dichlorides.[146] In more recent work, the addition of a methyl group to the cyclopentadienyl rings has allowed Collins and coworkers to prepare a series of [1,2-ethylene-1,1′-bis(4-R-2-methylcyclopentadienyl)] titanium dichlorides ($R = Me$, i-Pr, t-Bu) stereoselectively to give the racemic isomers.[147]

Biscyclopentadienly incorporating reactive functional groups on each Cp ring have been utilized to prepare *ansa*-metallocenes. Thus, treatment of $(\eta^5\text{-}C_5H_4SiClMe_2)_2TiCl_2$ with a stoichiometric amount of water with selective hydrolysis of the Si–Cl bonds to gives the tetramethyldisiloxane-bridged dicyclopentadienyl complexes $[(\eta^5\text{-}C_5H_4)SiMe_2OSiMe_2(\eta^5\text{-}C_5H_4)]TiCl_2$.[99] In an analogous manner, treatment of $(Cp\text{-}P\text{-}t\text{-}BuCl)_2CMe_2$ with one equivalent of $TiCl_4$ in the presence of Et_3N gives complex $[(Cp\text{-}P\text{-}t\text{-}BuCl)_2CMe_2]TiCl_2$.[101]

Cationic *ansa*-(η^5-cyclopentadienyl)(η^6-arene) titanium derivatives have been prepared with both Cp and Cp* derivatives. Treatment of $TiCl_4$ with $C_5H_4(R)SiMe_3$ ($R = CMe_2Ph$, CMe_2CH_2Ph, $CHPh_2$) gives the corresponding half-sandwich complexes $(\eta^5\text{-}C_5H_4R)TiCl_3$ Alkylation of $(\eta^5\text{-}C_5H_4R)TiCl_3$ gives $(\eta^5\text{-}C_5H_4R)TiMe_3$ which upon treatment with $[Ph_3C]^+$ $[B(C_6F_5)_4]^-$ in dichloromethane at low temperature gives the cationic $[(\eta^5\text{-}C_5H_4R)TiMe_2]^+$ *ansa* complexes; with π-coordination of the Ph ring with one-

and two-carbon bridges.[148] An analogous permethyl complex $[(\eta^5,\eta^6\text{-}C_5H_4CMe_2Ar)TiMe_2][MeB(C_6F_5)_3]$ is prepared by treatment of $(\eta^5\text{-}C_5H_4CMe_2Ar)TiMe_3$ (Ar = 3, 5-$Me_2C_6H_3$) with $B(C_6F_5)_3$. Treatment of $(\eta^5\text{-}C_5H_4CMe_2Ar)TiMe_3$ with $B(C_6F_5)_3$ in bromobenzene give the unusual dimeric Ti(III) dicationic *ansa*-metallocene, $\{[(\eta^5,\eta^6\text{-}C_5H_4CMe_2Ar)Ti(\mu\text{-}Br)]_2\}[B(C_6F_5)_4]_2$.[149]

9.5 Cationic Bis(cyclopentadienyl)titanium Complexes

Since cationic titanium complexes have been proposed as intermediates in alkene polymerization by soluble Cp_2TiCl_2/AlR_3-based Ziegler–Natta catalysts (*see Ziegler–Natta Catalysts*), there has been considerable interest in the synthesis and reactivity of cationic titanium complexes (*see* ***Oligomerization & Polymerization by Homogeneous Catalysis***).

The reaction of Cp_2TiCl_2 with $AgAsF_6$ or the reaction of Cp_2TiF_2 with AsF_5, in SO_2, gives $Cp_2Ti(AsF_6)_2$ in quantitative yields.[150] The reaction of $Cp_2Ti(AsF_6)_2$ in SO_2 with HCN, ICN, $AsMe_3$, or As_2Me_4 affords the new cationic titanocene complexes $[Cp_2Ti(HCN)_2][AsF_6]_2$, $[Cp_2Ti(ICN)_2][AsF_6]_2$, $[Cp_2Ti(AsMe_3)_2][AsF_6]_2$, and $[Cp_2Ti(As_2Me_4)]_2[AsF_6]_4$.[151] Treatment of Cp_2TiCl_2 with 2 equivalent of $AgSbF_6$ in SO_2 gives $Cp_2Ti(SbF_6)_2$ and AgCl quantitatively.[152]

Treatment of $Cp_2Ti(O_2CPh)_2$ with H_2SO_4 or H_2SeO_4 in Ac_2O forms $[Cp_2Ti(H_2O)_2]SO_4$ and Cp_2TiSeO_4 in 85 and 78% yield, respectively. Reaction of Cp_2TiCl_2 with 4 M H_2SO_4 and $K_2Cr_2O_7$ gives $[Cp_2Ti(H_2O)_2]Cr_2O_7$ in 50% yield. Cp_2TiSeO_4 and $[Cp_2Ti(H_2O)_2]Cr_2O_7$ are found to be explosive when heated or mechanically agitated.[153]

$[Cp^*_2Ti(DMF)Cl]CF_3SO_3$ and $[Cp^*_2Ti(DMF)_2](CF_3SO_3)_2$ have been prepared by reaction of $Cp^*_2TiCl_2$ with CF_3SO_3Ag in DMF. The structures of $[Cp^*_2Ti(DMF)Cl]CF_3SO_3$ and $[Cp^*_2Ti(DMF)_2](CF_3SO_3)_2$ have been determined by X-ray diffraction, and the titanium atom in each of these complexes was found to have the expected, approximately tetrahedral, coordination geometry typical for $Cp^*_2Ti^{IV}$ complexes.[154]

The reaction of $Cp_2Ti(CF_3SO_3)_2$ with bipy or phen forms $[Cp_2Ti(bipy)](CF_3SO_3)_2$ and $[Cp_2Ti(phen)](CF_3SO_3)_2$, respectively. An X-ray structure determination indicates that the Ti atoms are to a first approximation tetrahedrally coordinated, and the atoms of the bipy or phen chelate ligands are nearly coplanar.[155]

Reaction of Cp_2TiCl_2 with Zn in the presence of MeCN gives $[Cp_2Ti(MeCN)_2]_2[ZnCl_4]$. Treatment of $[Cp_2Ti(MeCN)_2][BPh_4]$ with PMe_3 in a stepwise fashion forms $[Cp_2Ti(MeCN)(PMe_3)][BPh_4]$ initially, and then $[Cp_2Ti(PMe_3)_2][BPh_4]$ upon addition of excess PMe_3. Similar reaction of $[Cp_2Ti(MeCN)_2][BPh_4]$ with excess PEt_3 gives only the monosubstitution product $[Cp_2Ti(MeCN)(PEt_3)][BPh_4]$. PCy_3 and PPh_3 fail to react with $[Cp_2Ti(MeCN)_2][BPh_4]$.[156]

Nitrile complexes of the type $[Cp_2TiMe(N{\equiv}CR)]BPh_4$ (R = Me, Pr, *t*-Bu, Ph) react with excess nitrile in CH_2Cl_2 at room temperature to give azaalkenylidine complexes, $[Cp_2Ti(N{=}CMeR)(N{\equiv}CR)]BPh_4$, in quantitative yield by migratory insertion (*see Migratory Insertion*) of nitrile into the Ti–Me bond (equation 33). The indenyl complexes $[Ind_2Me(N{\equiv}CR)]BPh_4$ are more reactive with nitriles than are the corresponding cyclopentadienyl complexes $[Cp_2TiMe(RCN)]BPh_4$. The structure of $[(C_9H_7)_2Ti(NCMePh)(NCPh)]BPh_4$ has been determined by X-ray crystallography. The Ti–azavinylidene arrangement is linear, with a short Ti–N double bond; the Me and Ph substituents adopt a Me-outside conformation in the plane bisecting the indenyl–Ti–indenyl angle. The indenyl ring centroid–titanium–indenyl ring centroid angle is 135.8(6)°.[157]

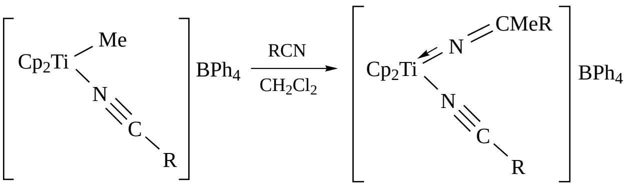

R = Me, Ph, *t*-Bu, *n*-Pr

(33)

$[Cp_2TiMe(L)]BPh_4$ (L = MeCN, PrCN, *t*-BuCN, PhCN, Me_3P, Me_2PPh, $MePPh_2$, Bu_3P, py) have been prepared in high yields by treating $Cp_2TiMeCl$ with L and $NaBPh_4$ in polar solvents (equation 34). In a similar manner, treatment of $Ind_2TiMeCl$ with L (L = MeCN, PrCN, *t*-BuCN, PhCN, Me_3P, Me_2PPh) and $NaBPh_4$ gives the corresponding complexes $[Ind_2TiMe(L)]BPh_4$. The nitrile complexes readily undergo substitution with pyridine or PMe_3, but fail to react with $PhC{\equiv}CR$ (R = $SiMe_3$, Me, Ph). Treatment of $[Cp_2TiMe(MeCN)]BPh_4$ with 1 atm of CO forms the η^2-acyl complex $[Cp_2Ti(\eta^2\text{-}COMe)(MeCN)]BPh_4$ in which the nitrile ligand has been retained. Addition of *t*-BuNC to $[Cp_2TiMe(MeCN)]BPh_4$ in acetonitrile gives $[Cp_2Ti(\eta^2\text{-}C(Me){=}N\text{-}t\text{-}Bu)(C{\equiv}N\text{-}t\text{-}Bu)(MeCN)]BPh_4$.[158]

$$Cp_2TiMeCl + L + NaBPh_4 \longrightarrow [Cp_2TiMe(L)]BPh_4 + NaCl \quad (34)$$

$$L = MeCN, PrCN, t\text{-}BuCN, Me_3P, Me_2PPh, MePPh_2, Bu_3P, Py$$

Reaction of Cp_2TiMe_2 and Ind_2TiMe_2 with $(PhNMe_2H)BPh_4$ or $(Bu_3NH)BPh_4$ in CD_2Cl_2 forms the corresponding base-free cationic 14-electron alkyltitanium complexes $[Cp_2TiMe]BPh_4$ and $[Ind_2TiMe]BPh_4$. Treatment of $[Ind_2TiMe]BPh_4$ with Et_2O forms black crystals of $[Ind_2TiMe(OEt_2)]BPh_4$, whereas reaction of $[Cp_2TiMe]BPh_4$ with MeCN yields $[Cp_2TiMe(NCMe)]BPh_4$. $[Cp_2TiMe]BPh_4$ and $[Ind_2TiMe]BPh_4$ catalytically polymerize ethylene.[159] The oxidation of Cp^*_2TiMe with $AgBPh_4$ in THF gives $[Cp^*_2TiMe(THF)]BPh_4$.[160]

The reaction of $CpTiCl_3$ with $AgAsF_6$ and $AgSbF_6$ in SO_2 at −50 °C forms $CpTi(AsF_6)_3{\cdot}SO_2$ and $CpTi(SbF_6)_3{\cdot}SO_2$.

$CpTi(AsF_6)_3{\cdot}SO_2$ and $CpTi(SbF_6)_3{\cdot}SO_2$ are Lewis acid adducts of $CpTiF_3$. $CpTi(AsF_6)_3{\cdot}SO_2$ and $CpTi(SbF_6)_3{\cdot}SO_2$ decompose in solution at room temperature and slowly at −50 °C, but are nonexistent in the solid state.**161**

10 CYCLOPENTADIENYL COMPLEXES OF TITANIUM(III)

Dang and Geise have reviewed the reduction of Cp_2TiCl_2 to $[Cp_2Ti(\mu\text{-}Cl)]_2$. This reduction has been carried out using Al, K, Na, Zn, or lithium and sodium amalgams.**162** Alternatively, treatment of Cp_2TiCl_2 with $LiAlH_4$, $NaBH_4$, MgH_2, bulky Grignard reagents (*see Grignard Reagents*), and organoaluminum and organolithium reagents also leads to Ti^{III} species. Electrochemical and photochemical procedures to produce Ti^{III} have also been investigated.**163** In the reduction of Cp_2TiCl_2 with Zn the intermediate $(Cp_2Ti(\mu\text{-}Cl)_2)_2Zn$ has been isolated and characterized (equation 35).**164** The reduction of Cp_2TiCl_2 with Mg in THF in the presence of P_4 leads to $(Cp_2Ti(\mu\text{-}Cl)_2)_2Mg(THF)_2$ and $(Cp_2Ti(\mu\text{-}Cl)_2Mg(THF)_2(\mu\text{-}Cl)_2)_2$, which have been characterized also. Reaction of $(Cp_2Ti(\mu\text{-}Cl)_2)_2Mg(THF)_2$ and $(Cp_2Ti(\mu\text{-}Cl)_2Mg(THF)_2(\mu\text{-}Cl)_2)_2$ with PMe_3 forms $Cp_2Ti(PMe_3)Cl$, which upon reduction with Mg in the presence of PMe_3 gives $Cp_2Ti(PMe_3)_2$.**165**

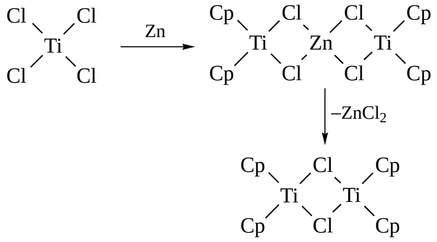

(**35**)

(35)

Treatment of Cp_2TiCl_2 and $CpTiCl_3$ with $[Li[\mu\text{-}P(SiMe_3)_2](THF)_2]_2$ in THF at room temperature leads to the reduced species $Cp_2TiCl(THF)$ and $CpTiCl_2(THF)$, respectively, in high yields.**166**

Reaction of $Cp_2Ti(CO)_2$ with Cp_2TiBr_2 or Cp_2TiCl_2 in C_6H_6 forms $[Cp_2TiBr]_2$ and $[Cp_2TiCl]_2$, respectively, in 90% yield.**167** An ESR study of the reaction solution of the reaction of $Cp_2Ti(CO)_2$ with Cp_2TiBr_2 indicates the presence of $[Cp_2TiBr]$ in equilibrium with the dimer, as well as the presence of the unstable intermediate $[Cp_2Ti(CO)Br]$.**168**

Reduction of Cp_2TiCl_2 with 1.5 equivalent of Na(Hg) gives a mixture of the dinuclear fulvalene complexes $[CpTi(\mu\text{-}Cl)]_2(\mu\text{-}\eta^5{:}\eta^5\text{-}C_{10}H_8)$ (**34**) and $[CpTi(\mu\text{-}H)]_2(\mu\text{-}\eta^5{:}\eta^5\text{-}C_{10}H_8)$ ('titanocene') (**35**) in 40% yield each (equation 36). Both compounds contain Ti^{III} species, which undergo quick oxidation upon exposure to air, yielding $[CpTiCl]_2(\mu\text{-}O)(\mu\text{-}\eta^5{:}\eta^5\text{-}C_{10}H_8)$. Reduction of $[CpTi(\mu\text{-}Cl)]_2(\mu\text{-}\eta^5{:}\eta^5\text{-}C_{10}H_8)$ with $LiBHEt_3$ gives $[CpTi(\mu\text{-}H)]_2(\mu\text{-}\eta^5{:}\eta^5\text{-}C_{10}H_8)$.**169**

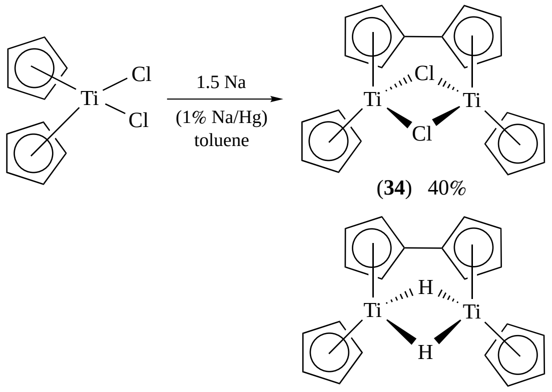

(**34**) 40%

(**35**) 40%

(36)

The chemistry of the Ti–C bond in Cp_2TiR has been reviewed.**170** The paramagnetic, 15-electron, d^1 titanium complexes Cp_2^*TiR (R = Me, Et, Pr, $CH_2\text{-}t\text{-}Bu$, CH_2Ph, $\eta^3\text{-}C_3H_5$, $\eta^3\text{-}C_4H_7$, $CH{=}CH_2$, $C{\equiv}CMe$, Ph) have been prepared by the reaction of Cp_2^*TiCl with the corresponding anion (equation 37). The ethyl and *n*-propyl complexes, Cp_2^*TiEt and Cp_2^*TiPr, have also been prepared by the addition of ethylene or propylene, respectively, to Cp_2^*TiH (equation 38). Treatment of Cp_2^*TiR with CO at approx. −70 °C in pentane or toluene leads to the formation of the corresponding η^2-acyl complexes, which are thermally stable up to 0 °C (equation 39). Above 0 °C, these acyl complexes are unstable, leading to $Cp_2^*Ti(CO)_2$ and unidentified paramagnetic products. Treatment of Cp_2^*TiMe with $t\text{-}BuN{\equiv}C$ gives the corresponding η^2-iminoacyl complex $Cp_2^*Ti(CMe{=}N\text{-}t\text{-}Bu)$. Reaction of CO_2 with Cp_2^*TiR, in which the R group does not contain a β-hydrogen, gives the corresponding carboxylate complexes $Cp_2^*Ti(\eta^2\text{-}O_2CR)$. However, treatment of alkyl complexes Cp_2^*TiR, in which the R group bears a β-hydrogen, with CO_2 forms the formate complex $Cp_2^*Ti(\eta^2\text{-}O_2CH)$ as the dominant product (equation 40). This formate complex is produced by β-H transfer to the incoming CO_2 and extrusion of an alkene. These Cp_2^*TiR complexes are surprisingly unreactive toward $CH_2{=}CH_2$, with Cp_2^*TiMe recovered unchanged even after treatment with 10 atm of $CH_2{=}CH_2$ at 50 °C for 100 h.**171**

$$Cp_2^*TiCl + MR \longrightarrow Cp_2^*TiR + MCl \qquad (37)$$

$$Cp_2^*TiH + H_2C{=}CHR \longrightarrow Cp_2^*TiCH_2CH_2RR = H, Me \qquad (38)$$

$$Cp_2^*TiR + CO \longrightarrow Cp_2^*Ti(\eta^2\text{-}COR) \qquad (39)$$

$$Cp_2^*TiR + CO_2 \longrightarrow Cp_2^*Ti(\eta^2\text{-}O_2CR)$$

$$\text{or } Cp_2^*Ti(\eta^2\text{-}O_2CH) \text{ if R contains a } \beta\text{-H} \qquad (40)$$

Further studies have been carried out on Cp_2^*TiMe and Cp_2^*TiEt. Reaction of Cp_2^*TiMe and Cp_2^*TiEt with $HO_2C\text{-}i\text{-}Pr$, HOEt, or $HC{\equiv}CMe$ forms $Cp_2^*TiO_2C\text{-}i\text{-}Pr$, Cp_2^*TiOEt, and $Cp_2^*TiC{\equiv}CMe$, respectively, and RH. Reaction of Cp_2^*TiMe

with neat MeC≡CMe gives $Cp^*_2TiC(Me){=}CMe_2$ via migratory insertion (*see Migratory Insertion*); however, PhC≡CPh and $Me_3SiC{\equiv}CSiMe_3$ are unreactive toward Cp^*_2TiMe.

The β-H atom of the ethyl group in Cp^*_2TiEt exhibits agostic bonding (*see Agostic Bonding*) with the titanium. Cp^*_2TiEt reacts with t-BuC≡N, $Me_2C{=}O$, and alkynes via a Cp^*_2TiH intermediate to give products of migratory insertion into the Ti–H bond of Cp^*_2TiH.[172]

Oxidative alkylation of Cp^*_2TiX (X = OMe, Cl, N=CH-t-Bu) and Cp^*_2TiMe by $CdMe_2$ or $ZnMe_2$ forms the diamagnetic complexes $Cp^*_2Ti(Me)X$ and $Cp^*_2TiMe_2$, respectively, and cadmium or zinc metal (equation 41). Oxidative alkylation of Cp^*_2TiR (R = Et, $CH{=}CH_2$, Ph) with $CdMe_2$ or $ZnMe_2$ forms a statistical mixture of $Cp^*_2Ti(Me)R$, $Cp^*_2TiMe_2$, and $Cp^*_2TiR_2$.[173] Oxidation of Cp^*_2TiR with $PbCl_2$ gives $Cp^*_2Ti(R)Cl$ (R = Me, Et, Pr, $CH{=}CH_2$, Ph, OPr) in good yield (equation 42).

$$Cp^*_2TiX + CdMe_2 \text{ or } ZnMe_2 \longrightarrow Cp^*_2TiXMe \qquad (41)$$

$$Cp^*_2TiR + PbCl_2 \longrightarrow Cp^*_2Ti(R)Cl \qquad (42)$$

Thermolysis of $Cp^*_2Ti(Me)CH{=}CH_2$, prepared by the reaction of $Cp^*_2Ti(CH{=}CH_2)Cl$ with MeLi, gives $Cp^*(\eta^6\text{-}C_6Me_4CH_2)TiCH{=}CH_2$ via a vinylidene intermediate, $Cp^*_2Ti{=}C{=}CH_2$, formed by a rate-limiting vinylic α-hydrogen abstraction. $Cp^*_2Ti(Me)Ph$ undergoes thermally induced decomposition to give $Cp^*(\eta^6\text{-}C_6Me_4CH_2)TiPh$ and methane. This thermolysis occurs via *ortho*-hydrogen abstraction from the phenyl ligand, giving an o-phenylene intermediate, which can be trapped by CO_2 to yield the titanacycle, as shown in Scheme 8.[18]

Thermolysis of Cp^*_2TiR (R = Me, Et, n-Pr, C_2H_3, CH_2-t-Bu, Ph) forms $Cp^*(\eta^6\text{-}C_5Me_4CH_2)Ti$ in high yield as the exclusive organometallic product, along with RH (equation 43). Kinetic measurements and deuterium-labeling studies show that this decomposition is catalyzed by Cp^*_2TiH, which is formed either by β-hydrogen elimination (*see β-Hydride Elimination*) from a titanium alkyl $Cp^*_2TiCH_2CH_2R$ at low temperature or by hydrogenolysis of Cp^*_2TiR or $Cp^*(\eta^6\text{-}C_5Me_4CH_2)Ti$, deriving dihydrogen by elimination from $Cp^*(\eta^6\text{-}C_5Me_4CH_2)Ti$ at elevated temperatures. Permethyltitanocene, Cp^*_2Ti, is found not to be an intermediate in these thermolysis reactions.[174]

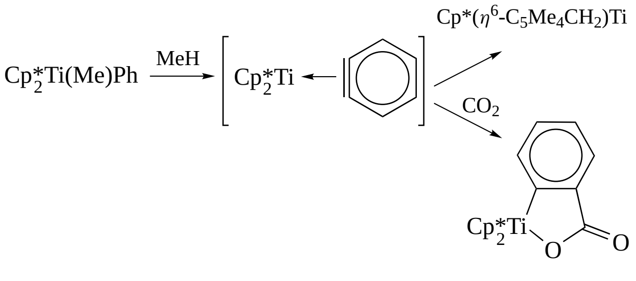

Scheme 8

$$Cp^*_2TiR \xrightarrow[\Delta]{} Cp^*(\eta^6\text{-}C_5Me_4CH_2)Ti + RH \qquad (43)$$

Treatment of $Cp^*(\eta^6\text{-}C_5Me_4CH_2)Ti$ with $PbCl_2$ gives $Cp^*(\eta^6\text{-}C_5Me_4CH_2)TiCl$, which reacts with C≡N(2,6-$Me_2C_6H_3$) to give the η^1-iminoacyl complex (**36**). Reaction of iminoacyl (**28**) with a second equivalent of isonitrile gives (**37**).[175]

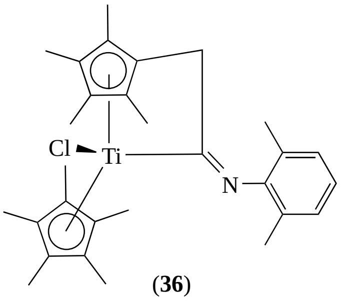

(**36**)

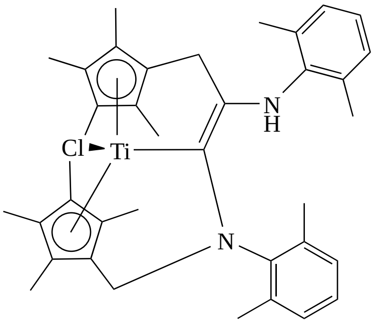

(**37**)

The titanocene(III) complexes $Cp_2TiX(PMe_3)$ (X = F, Cl, Br, I, Me, SMe) are readily prepared by *comproportionation* reactions of $Cp_2Ti(PMe_3)_2$ and Cp_2TiX_2. The products are characterized by EPR spectroscopy.[176]

11 CYCLOPENTADIENYL COMPLEXES OF TITANIUM(II)

Bis-cyclopentadienyltitanium(II) species are unstable 14-electron d^2 species, with one lone-electron pair and two vacant valence orbitals. The reactivity of 'Cp_2Ti' has been compared to carbenes. The interactions between the occupied and unoccupied orbitals can explain why 'Cp_2Ti' reacts with unsaturated compounds to give metallacycles (*see Metallacycle*).

Murry first prepared $Cp_2Ti(CO)_2$ via the high-pressure carbonylation of $Cp_2Ti(\eta^1\text{-}C_5H_5)_2$ (equation 44).[177] The reduction and carbonylation of Cp_2TiCl_2 to give $Cp_2Ti(CO)_2$

was first achieved with Mg in the presence of CO. *Reductive carbonylation* (*see Reductive Carbonylation*) of Cp_2TiCl_2 or $Cp^*_2TiCl_2$ with Mg, activated with $HgCl_2$, and CO in THF affords $Cp_2Ti(CO)_2$ (equation 45) and $Cp^*_2Ti(CO)_2$, respectively, in good yield.**178** In recent years a wide range of ring-substituted biscyclopentadienyl derivatives have been reductively carbonylated. This work has recently been reviewed by Sikora *et al.***179**

$$Cp_2Ti(\eta^1\text{-}C_5H_5)_2 + CO(\text{high pressure}) \longrightarrow Cp_2Ti(CO)_2 \quad (44)$$

$$Cp_2TiCl_2 + CO \xrightarrow{Mg/HgCl_2} Cp_2Ti(CO)_2 \quad (45)$$

Rausch and coworkers have shown that $Cp_2Ti(CO)_2$ reacts reversibly with PF_3, under irradiation, to give $Cp_2Ti(PF_3)_2$ (equation 46). In contrast, treatment of $Cp_2Ti(CO)_2$ with PEt_3 or PPh_3 gives $Cp_2Ti(CO)PEt_3$ and $Cp_2Ti(CO)PPh_3$, respectively, in good yield (equation 47). $Cp_2Ti(CO)PEt_3$ can serve as a convenient source of $[Cp_2Ti(CO)]$. Thus, treatment of $Cp_2Ti(CO)PEt_3$ with alkynes, $RC{\equiv}CR$ ($R = Ph$, C_6F_5), or alkenes, $RO_2CCH{=}CHCO_2R$ ($R = Me$, Et), leads to the corresponding alkyne and alkene complexes, $Cp_2Ti(CO)(\eta^2\text{-}RC{\equiv}CR)$ and $Cp_2Ti(CO)(\eta^2\text{-}RO_2CCH{=}CHCO_2R)$, respectively, in good yields (equation 48).**180**

$$Cp_2Ti(CO)_2 \xrightleftharpoons[\text{Hexane}]{h\nu,\ PF_3} Cp_2Ti(CO)PF_3 \xrightleftharpoons[\text{Hexane}]{h\nu,\ PF_3} Cp_2Ti(PF_3)_2 \quad (46)$$

$$Cp_2Ti(CO)_2 + PEt_3 \xrightarrow[\text{hexane}]{h\nu \text{ or } \Delta} Cp_2Ti(CO)PEt_3 \quad (47)$$

$$Cp_2Ti(CO)PEt_3 + PhC{\equiv}CPh \longrightarrow Cp_2Ti(CO)(\eta^2\text{-}PhC{\equiv}CR) \quad (48)$$

Rausch and coworkers have also developed a convenient, high-yield synthesis for $Cp_2Ti(PMe_3)_2$, which has often been referred to as stabilized 'titanocene' (*see Titanocene*), by utilizing Mg to reduce Cp_2TiCl_2 in the presence of PMe_3 (equation 49).**181**

$$Cp_2TiCl_2 + Mg + PMe_3 \longrightarrow Cp_2Ti(PMe_3)_2 \quad (49)$$

The unique phosphine–carbon dioxide complex $Cp_2Ti(CO_2)PMe_3$ is prepared by treatment of $Cp_2Ti(PMe_3)_2$ with dry CO_2 at −180 °C (equation 50). Slow thermal decomposition of $Cp_2Ti(CO_2)PMe_3$ at room temperature leads principally to $Cp_2Ti(CO)_2$.**182**

$$Cp_2Ti(PMe_3)_2 \xrightarrow[-180\,^\circ C]{CO_2} Cp_2Ti(CO_2)PMe_3 \quad (50)$$

The titanium alkene complex $Cp^*_2Ti(\eta^2\text{-}CH_2{=}CH_2)$ can be prepared in greater than 80% yield by the Na/Hg reduction of $Cp^*_2TiCl_2$ in toluene under 700 torr of ethylene (equation 51), or in nearly quantitative yield by the addition of ethylene to $[Cp^*_2Ti]_2(\mu\text{-}N_2)$ (equation 52).**183** Alternatively, treatment of $Cp^*_2TiEtCl$ with MeLi, KCH_2Ph, or $LiCH{=}CH_2$ leads to $Cp^*_2Ti(\eta^2\text{-}C_2H_4)$ in quantitative yield and the formation of RH via β-hydride elimination (*see β-Hydride Elimination*).**39** This titanium ethylene complex undergoes facile displacement of the ethylene by two-electron donors. For example, reaction of $Cp^*_2Ti(\eta^2\text{-}CH_2{=}CH_2)$ with CO or MeNC leads to quantitative displacement of alkene to give $Cp^*_2Ti(CO)_2$ (equation 53) or the thermally unstable $Cp^*_2Ti(CNMe)_2$, respectively.**183**

$$Cp^*_2TiCl_2 + C_2H_4(700\text{ torr}) \xrightarrow{Na/Hg} Cp^*_2Ti(\eta^2\text{-}CH_2{=}CH_2) \quad (51)$$

$$[Cp^*_2Ti](\mu\text{-}N_2) + 2C_2H_4 \longrightarrow Cp^*_2Ti(\eta^2\text{-}CH_2{=}CH_2) \quad (52)$$

$$Cp^*_2Ti(\eta^2\text{-}CH_2{=}CH_2) + 2CO \longrightarrow Cp^*_2Ti(CO)_2 \quad (53)$$

$Cp^*_2Ti(\eta^2\text{-}CH_2{=}CH_2)$ undergoes a reversible reaction with $CH_2{=}CH_2$ to give the corresponding unstable titanacyclopentane complex (equation 54). Addition of $MeC{\equiv}CH$ to $Cp^*_2Ti(\eta^2\text{-}CH_2{=}CH_2)$ at −50 °C gives a mixture of metallacycle (*see Metallacycle*) (**38**) and the propynyl ethyl tautomer (**39**) (equation 55), which over several days rearranges to (**38**). Treatment of $Cp^*_2Ti(\eta^2\text{-}CH_2{=}CH_2)$ with *t*-BuC≡CH affords rapidly and quantitatively the *t*-butylacetylide ethyl complex $Cp_2Ti(Et)(C{\equiv}C\text{-}t\text{-}Bu)$ (**40**). In contrast to this result, reaction of $Cp^*_2Ti(\eta^2\text{-}CH_2{=}CH_2)$ with 2-butyne over 8 h at 25 °C gives quantitatively the metallacycle $Cp^*_2Ti(C(Me){=}C(Me)CH_2CH_2)$ (equation 56). However, reaction of $Cp^*_2Ti(\eta^2\text{-}CH_2{=}CH_2)$ with diphenylacetylene yields the alkyne complex $Cp^*_2Ti(\eta^2\text{-}PhC{\equiv}CPh)$ (equation 57). Reaction of $Cp^*_2Ti(\eta^2\text{-}CH_2{=}CH_2)$ with 1 equivalent of acetonitrile at −50 °C results in quantitative formation of the metallacycloimine complex $Cp^*_2Ti(N{=}C(Me)CH_2CH_2)$, which above −10 °C establishes an equilibrium with its metallacycloenamine tautomer (equation 58). Addition of CO_2 to $Cp^*_2Ti(\eta^2\text{-}CH_2{=}CH_2)$ at −78 °C gives $Cp^*_2Ti(OC(O)CH_2CH_2)$ (equation 59).**184**

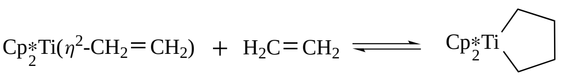

(54)

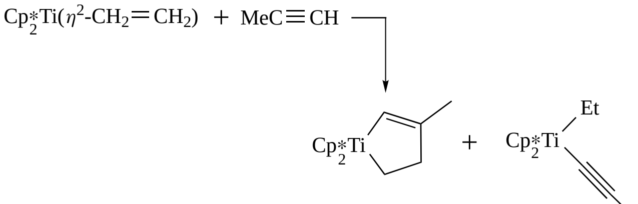

(**38**) (**39**)

(55)

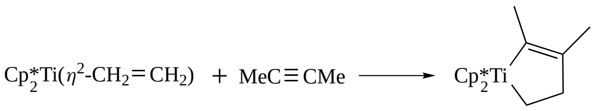

(56)

$$Cp^*_2Ti(\eta^2\text{-}CH_2{=}CH_2) + PhC{\equiv}CPh \longrightarrow Cp^*_2Ti(\eta^2\text{-}PhC{\equiv}CPh) \quad (57)$$

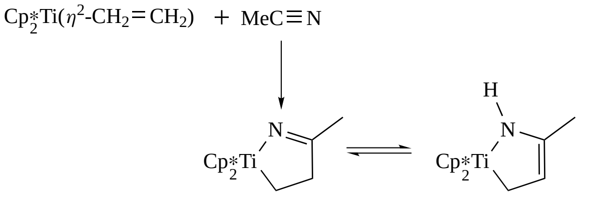

(58)

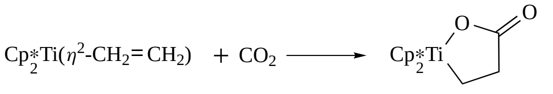

(59)

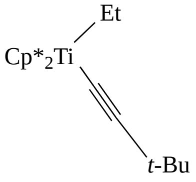

(**40**)

$Cp_2Ti(\eta^2\text{-}Me_3SiC{\equiv}CSiMe_3)$, which is readily prepared in large quantities by the reduction of Cp_2TiCl_2 with magnesium in the presence of $Me_3SiC{\equiv}CSiMe_3$, serves as ready sources of The chemistry of $Cp_2Ti(\eta^2\text{-}Me_3SiC{\equiv}CSiMe_3)$ has been extensively reviewed by Rosenthal and coworkers.**[185,186]**

$Cp_2Ti(\eta^2\text{-}Me_3SiC{\equiv}CSiMe_3)$ can release $Me_3SiC{\equiv}CSi\,Me_3$ quantitatively under mild conditions to give the unstable highly reactive 'Cp_2Ti', which can then react with a wide range of unsaturated molecules. Treatment of $Cp_2Ti(\eta^2\text{-}Me_3SiC{\equiv}CSiMe_3)$ with one equivalent of $PhC{\equiv}CPh$ leeds to exchange of the acetylene to give $Cp_2Ti(\eta^2\text{-}PhC{\equiv}CPh)$, which on treatment with additional $PhC{\equiv}CPh$ gives the corresponding metallocycle $Cp_2Ti[C(Ph){=}C(Ph)C(Ph){=}C(Ph)]$. This reaction is very general, working with a wide range of substituted Cp derivatives and a wide range of substituted and disubstituted acetylenes including α,ω-diynes, $RC{\equiv}C(CH_2)_nC{\equiv}CR$ to give bicyclic titanacyclopentadienies.

Thermolysis of $Cp_2Ti(\eta^2\text{-}Me_3SiC{\equiv}CSiMe_3)$ in the absence of substrate gives $[CpTi(\mu\text{-}H)]_2(\mu\text{-}\eta^5{:}\eta^5\text{-}C_{10}H_8)$ (**35**), while thermolysis of $[C_5Me_4(SiMe_3)]_2Ti(\eta^2\text{-}Me_3SiC{\equiv}CSiMe_3)$ gives on dissociation of $Me_3SiC{\equiv}CSiMe_3$ in the absence of other ligands, stable, free $[C_5Me_4(SiMe_3)]_2Ti$, which cannot be prepared directly by the reduction of $[C_5Me_4(SiMe_3)]_2\,TiCl_2$.

Reaction of $Cp_2Ti(\eta^2\text{-}Me_3SiC{\equiv}CSiMe_3)$ with $B(C_6F_5)_3$ in toluene leads via electrophilic substitution on one of the Cp rings to the zwitterionic titanium(III) complex $CpTi[\eta^5\text{-}C_5H_4B(C_6F_5)_3]$. Treatment of $Cp_2Ti(\eta^2\text{-}Me_3SiC{\equiv}CSiMe_3)$ with fullerene gives the unique fullerene complex $Cp_2Ti(\eta^2\text{-}C_{60})$.

$Cp_2Ti(CO)_2$ and $Cp^*_2Ti(CO)_2$ react instantaneously with TCNE (tetracyanoethene) and TCNQ (7,7,8,8-tetracyano-*p*-quinodimethane) to give the corresponding highly air-sensitive monocarbonyl TCNE (**41**) and TCNQ complexes. The $Cp^*_2Ti(CO)(TCNE)$ and $Cp^*_2Ti(CO)(TCNQ)$ complexes were characterized in the oxidized and reduced forms through cyclic voltammetry, EPR, IR, and UV-visible spectroelectrochemistry. While oxidation at rather low potentials yields labile carbonyltitanium(IV) species of the TCNE and TCNQ ligands, the reduction occurs stepwise at unusually negative potentials, first on the ligand (to yield coordinated $TCNE^{2-}$ and $TCNQ^{2-}$) and then on the metal, to form Ti(II).**[187]**

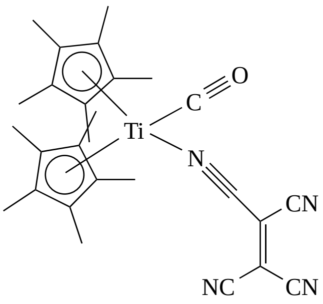

(**41**)

12 CONSTRAINED GEOMETRY TITANIUM COMPLEXES

Constrained geometry titanium complexes (**42**), also know as *ansa* half-sandwich complexes, are currently of great scientific and technological interest as precursors to a new generation of high activity, high selectively Ziegler–Natta (*see Ziegler–Natta Catalysts*) type α-olefin polymerization catalysts. A wide range of constrained geometry titanium complexes incorporating a η^5-cyclopentadienly derivative with a remote η^1-hetero atom tethered via a wide range of bridging groups have been prepared. These complexes incorporate rigid bridges such as phenolates and carboranes and flexible hydrocarbon chains, or a single intervening C, Si, B, or P attached to a N, O, or P. The vast majority of these complexes have been evaluated for their potential for upon activation with MAO, and so on, for Ziegler–Natta type α-olefin polymerization (*see* ***Oligomerization & Polymerization by Homogeneous Catalysis***).

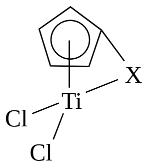

(**42**)

A verity of synthetic methods have been developed for the preparation cyclopentadienyl-phenoxytitanium

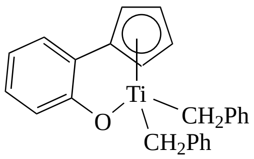

(**43**)

derivatives. Reaction of $\mathrm{TiCl_4}$ with the corresponding dilithio salts 2-(3,4-diphenylcyclopentadienyl)-6-phenylphenol derivatives gives the corresponding constrained geometry complexes.**188** Treatment of $\mathrm{TiCl_4}$ with one equivalent of a 2-tetramethylcyclopentadienyl phenol derivative to give a coordination intermediates, followed by treatment with 2 equivalent of n-BuLi at low temperature gives tetramethylcyclopentadienyl-phenoxytitanium dichlorides in moderate yields.**189** Treatment of $\mathrm{Ti(CH_2Ph)_4}$ with 2-(tetramethylcyclopentadienyl)-4-methylphenol at 60° in toluene cleanly gives $(\eta^1\text{-}\mathrm{OC_6H_3(CH_3)}\text{-}\eta^5\text{-}\mathrm{C_5Me_4})\mathrm{Ti(CH_2Ph)_2}$ (**43**). In solution at room temperature, the two benzyl groups of (**37**) are magnetically equivalent; however, in the solid state, X-ray diffraction reveals that one benzyl group is coordinated in a normal η^1-fashion and the other in an η^2 mode. Low-temperature NMR-scale reactions of (**37**) with $\mathrm{B(C_6F_5)_3}$ and $\mathrm{Ph_3C^+\,B(C_6F_5)_4^-}$ indicate the formation of the corresponding cationic complexes.**190** Several of the cyclopentadienyl-phenoxytitanium datives have been structurally characterized by single-crystal X-ray diffraction and the Cp(cent)-Ti-O angle in all cases was found to be approximately 107°.**188–190**

The analogous indenyl-phenoxytitanium complexes have recently been reported, and structurally characterized, with the Ind(cent)-Ti-O angle of approximately 105°. Treatment of $\mathrm{Ti(NMe_2)_4}$ with one equivalent 2-(inden-3-yl)-4,6-di-*tert*-butylphenol and its 1,2-di-Me, 2,4,7-tri-Me, and 1,2,4,7-tetra-Me derivatives gives the corresponding bis(dialkylamido) complexes such as, $[\mathrm{Ti}(\eta^1\text{-}\mathrm{OC_6H_2}\{\eta^5\text{-Ind}\}\text{-2-Bu}^t{}_2\text{-4,6})(\mathrm{NMe_2})_2]$.**191** Thermolysis of $[\eta^5\text{-}\mathrm{C_5H_4CMe_2}\text{-2-}\mathrm{C_6H_4OCH_3}]\mathrm{TiCl_3}$ gives $[\eta^5{:}\eta^1\text{-}\mathrm{C_5H_4CMe_2}\text{-2-}\mathrm{C_6H_4O}]\mathrm{TiCl_2}$ which is analogous to 37 with a $\mathrm{CMe_2}$ group between the Cp ring and the phenoxide.**192**

A verity of carborane (*see Carborane*)-appended cyclopentadienyl constrained geometry complexes have been prepared. $[\eta^5{:}\eta^1\text{-}\mathrm{Me_2Si(C_5Me_4)(C_2B_{10}H_{10})}]\mathrm{TiCl_2}$ was prepared via salt metathesis and amine elimination reactions utilizing the linked o-carboranyl ligand, $\mathrm{Me_2Si(C_5Me_4H)(C_2B_{10}H_{11})}$.**193** $\mathrm{Me_2C(C_5H_4)(C_2B_{10}H_{10})]Ti(NR_2)_2}$ $\mathrm{Me_2Si(C_5H_4)(C_2B_{10}H_{10})]}$ $\mathrm{Ti(NR_2)_2}$ (R = Me, Et), were prepared in good yield via amine elimination reactions of $\mathrm{Ti(NMe_2)_4}$ and the corresponding neutral ligands in toluene. Treatment of $[\eta^5{:}\sigma\text{-}\mathrm{Me_2C(C_5H_4)(C_2B_{10}H_{10})}]\mathrm{Ti(NMe_2)_2}$ with excess $\mathrm{Me_3SiCl}$ gives $[\eta^5{:}\sigma\text{-}\mathrm{Me_2C(C_5H_4)(C_2B_{10}H_{10})}]\mathrm{TiCl(NMe_2)}$.**194** Treatment of $\mathrm{Ti(NMe_2)_4}$ with carboranyl-thiol-appended cyclopentadiene ligand, 1-SH-2-[HCpCH(Ph)]-closo-1,2-$\mathrm{C_2B_{10}H_{10}}$, gives the corresponding Ti complex $[1\text{-}(\sigma\text{-S})\text{-2-}(\eta^5\text{-}\mathrm{C_5H_4CH(Ph)}\text{-1,2-}\mathrm{C_2B_{10}H_{10}})]\mathrm{Ti(NMe_2)_2}$, which undergoes exclusively monohalogenation at titanium with $\mathrm{Me_3SiCl}$ or $\mathrm{Me_3NHCl}$, giving $[1\text{-}(\sigma\text{-S})\text{-2-}(\eta^5\text{-}\mathrm{C_5H_4CH(Ph)}\text{-1,2-}\mathrm{C_2B_{10}H_{10}})]\mathrm{TiCl(NMe_2)}$ in 71% yield.**195** Treatment of $\mathrm{Ti(NMe_2)_4}$ with 1 equivalent of i-$\mathrm{Pr_2NB(C_9H_7)(C_2B_{10}H_{11})}$, gives deborated product $(\eta^5\text{-}\mathrm{C_2B_9H_{11}})\mathrm{Ti(NMe_2)_2(HNMe_2)}$. Salt metathesis reaction between $\mathrm{TiCl_4(THF)_2}$ and $\mathrm{Li_2}[i\mathrm{Pr_2NB(C_9H_6)(C_2B_{10}H_{10})}]$ $\mathrm{(Et_2O)_2}$ afforded $[\eta^5{:}\sigma\text{-}i\text{-}\mathrm{Pr_2NB(C_9H_6)(C_2B_{10}H_{10})}]\mathrm{TiCl_2}$. Alternatively, $[\eta^5{:}\sigma\text{-}i\text{-}\mathrm{Pr_2NB(C_9H_6)(C_2B_{10}H_{10})}]\mathrm{TiCl_2}$ was also prepared by the treatment of $\mathrm{TiCl_3(THF)_3}$ with one equivalent of $\mathrm{Li_2}[i\text{-}\mathrm{Pr_2NB(C_9H_6)(C_2B_{10}H_{10})}]\mathrm{(Et_2O)_2}$ followed by addition of 0.5 equivalent of $\mathrm{PbCl_2}$ in THF.**196** In an analogous manner, treatment of $\mathrm{Ti(NMe_2)_4}$ with a series of nido-7,8-$\mathrm{(NMe_2CH_2)_2}$-7,8-$\mathrm{C_2B_9H_{11}}$ dicarbollide ligands gives mono- and trimetallic titanium complexes $[\eta^5{:}\eta^1\text{-}\mathrm{(NMe_2CH_2)C_2B_9H_9CH_2NMe_2}]\mathrm{Ti(NMe_2)_2}$ and $[\eta^5{:}\eta^1\text{-}[\mathrm{(NMe_2CH_2)C_2B_9H_9CH_2NMe_2}]\mathrm{Ti(NMe_2)}]_2(\mu_3\text{-O})[\mathrm{Ti(NMe_2)_2}]$.**197**

Constrained geometry titanium complexes with cyclopentadienyl derivatives bridged to the Ti via a Si–N linkage have been prepared and extensively studied as precursors to Ziegler–Natta type polymerization catalysts. Treatment of $(\eta^5\text{-}\mathrm{C_5H_4SiMe_2Cl})\mathrm{TiCl_3}$ with primary aryl amines $\mathrm{H_2NR}$ (R = $\mathrm{C_6H_5}$, 2,6-$\mathrm{Me_2C_6H_3}$, 2-Me-6-i-Pr-$\mathrm{C_6H_3}$) gives the constrained geometry derivatives $(\eta^5{:}\eta^1\text{-}\mathrm{C_5H_4SiMe_2NR})\mathrm{TiCl_2}$. $(\eta^5{:}\eta^1\text{-}\mathrm{C_5H_4SiMe_2N}\text{-2,6-}\mathrm{Me_2C_6H_3})\mathrm{TiCl_2}$ is converted to $(\eta^5{:}\eta^1\text{-}\mathrm{C_5H_4SiMe_2N}\text{-2,6-}\mathrm{Me_2C_6H_3})\mathrm{TiR_2}$ (R = Me, $\mathrm{CH_2Ph}$, $\mathrm{CH_2SiMe_3}$, $\mathrm{NMe_2}$), by treatment with the appropriate Grignard or organolithium reagents.**198** Marks and coworkers have reported that the treatment of constrained geometry precursors such as $\mathrm{C_5H_5Si(Me_2)NHCMe_3}$ with n-BuLi to give the dianion followed treatment with $\mathrm{TiCl_3THF_3}$, oxidation with $\mathrm{PbCl_2}$ and alkylation with MeLi to give $\mathrm{Me_2Si}(\eta^5\text{-}\mathrm{Me_4C_5})(t\text{-BuN})\mathrm{TiMe_2}$, is time consuming and leads to only poor yields. However, they found that treatment of $\mathrm{C_5H_5Si(Me_2)NHCMe_3}$ with $\mathrm{Ti(CH_2Ph)_4}$ in aromatic or saturated hydrocarbon solvents at 60° gives $\mathrm{Me_2Si}(\eta^5\text{-}\mathrm{Me_4C_5})(t\text{-BuN})\mathrm{Ti(CH_2Ph)_2}$, in 90% isolated yield in 12 h.**199** Treatment of $(\eta^5{:}\eta^1\text{-}\mathrm{C_5Me_4SiMe_2NR'})\mathrm{Ti(CH_2Ph)_2}$ (R′ = Me, i-Pr, t-Bu) with $\mathrm{B(C_6F_5)_3}$ or $\mathrm{[Ph_3C][B(C_6F_5)_4]}$ in bromobenzene gives the corresponding cationic monbenzyl complex $[(\eta^5{:}\eta^1\text{-}\mathrm{C_5Me_4SiMe_2NR'})\mathrm{Ti(CH_2Ph)}]^+$. Solution NMR studies suggest that the benzyl titanium cations contain a fluxional η^2-coordinated benzyl ligand.**200**

A series of heteroatom substituted indenyl constrained geometry complexes $[(\eta^5\text{-}\mathrm{C_9H_5X})(\mathrm{SiMe_2}\text{-}t\text{-Bu})\mathrm{TiR_2}]$ (X = 2-OEt, 2-$\mathrm{NMe_2}$, 3-OMe, 3-$\mathrm{NC_4H_4}$; R = Cl, Me) were prepared in moderate yield by treatment of the dilithium salt of the ligand with $\mathrm{TICl_3THF_3}$ in THF followed by treatment with $\mathrm{PbCl_2}$.**201**

Reactions of $[\mathrm{Ti}(\eta^5\text{-}\mathrm{C_5Me_4SiMeXCl})\mathrm{Cl_3}]$ with two equiv. of LiNH-t-Bu afforded the *ansa*-silyl-η-amido compounds $(\eta^5{:}\eta^1\text{-}\mathrm{C_5Me_4SiMeX}\text{-N-}t\text{-Bu})\mathrm{TiCl_2}$ (X = H, Cl). Methylation of $(\eta^5{:}\eta^1\text{-}\mathrm{C_5Me_4SiMeX}\text{-N-}t\text{-Bu})\mathrm{TiCl_2}$ with MgClMe gives

$(\eta^5{:}\eta^1\text{-}C_5Me_4SiMeX\text{-}N\text{-}t\text{-}Bu)TiMe_2$.[100] Treatment of $(\eta^5\text{-}1,3\text{-}t\text{-}Bu_2C_5H_3)(\eta^5\text{-}C_5H_4SiClMe_2)TiCl_2$, with two equiv. of LiNH-t-Bu in toluene at 50–60° gives $(\eta^5\text{-}1,3\text{-}t\text{-}Bu_2C_5H_3)(\eta^5{:}\eta^1\text{-}C_5H_4SiMe_2N\text{-}t\text{-}Bu)TiCl$.[99]

Treatment of $\{\eta^5{:}\eta^1\text{-}C_5R_4SiMe_2N\text{-}t\text{-}Bu\}TiMe_2$ ($R = H$, Me) with $HOCMe_2CH_2CH_2CH{=}CH_2$ gives a mixture of $\{\eta^5\text{-}C_5R_4SiMe_2NH\text{-}t\text{-}Bu\}TiMe_2(OCMe_2CH_2CH_2CH{=}CH_2)$ and $\{\eta^5{:}\eta^1\text{-}C_5R_4SiMe_2N\text{-}t\text{-}Bu\}TiMe(OCMe_2CH_2CH_2CH{=}CH_2)$. Treatment of a mixture of $\{\eta^5\text{-}C_5R_4SiMe_2NH\text{-}t\text{-}Bu\}TiMe_2(OCMe_2CH_2CH_2CH{=}CH_2)$ and $\{\eta^5{:}\eta^1\text{-}C_5R_4SiMe_2N\text{-}t\text{-}Bu\}TiMe(OCMe_2CH_2CH_2CH{=}CH_2)$ with $B(C_6F_5)_3$ gives the chelated olefin complexes $[\{\eta^5{:}\eta^1\text{-}C_5R_4SiMe_2N\text{-}t\text{-}Bu\}Ti(OCMe_2CH_2CH_2CH{=}CH_2)][MeB(C_6F_5)_3]$ which serves as a model for the Ti-olefin interaction in the putative $[\{\eta^5{:}\eta^1\text{-}C_5R_4SiMe_2N\text{-}t\text{-}Bu\}Ti(R')(olefin)]^+$ intermediates in constrained geometry Ti-catalyzed olefin polymerization. A similar reaction with $[Ph_3C][B(C_6F_5)_4]$ yields $[\{\eta^5{:}\eta^1\text{-}C_5Me_4SiMe_2N\text{-}t\text{-}Bu\}Ti(OCMe_2CH_2CH_2CH{=}CH_2)][B(C_6F_5)_4]$.[202]

Treatment of $TiCl_4$ with $Li[(C_5H_4)CMe_2NMe_2]$ followed by treatment with CH_3Li gives $[CpCMe_2NMe_2]Ti(CH_3)_2$. The reaction of $[CpCMe_2NMe_2]Ti(CH_3)_2$ with $B(C_6F_5)_3$ gives a reactive metallocene cation complex that instantaneously undergoes CH activation at a N-CH_3 group to yield the metallacyclic constrained geometry complex (**44**).[203]

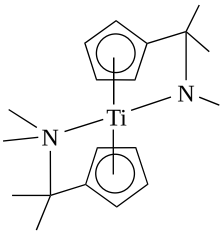

(**44**)

Treatment of $Ti(NMe_2)_4$ with $(C_5H_5)CH_2(2\text{-}C_4H_3NH)$ gives $[(\eta^5{:}\eta^1\text{-}C_5H_4)CH_2(2\text{-}C_4H_3N)]Ti(NMe_2)_2$ via amine elimination. In an analogous manner treatment of $Ti(NMe_2)_4$ with 1,3- and 1,4-$\{CH_2(2\text{-}C_4H_3NH)\}_2C_5H_4$ gives $[(\eta^5{:}\eta^1{:}\eta^1)\text{-}1,3\text{-}\{CH_2(2\text{-}C_4H_3N)\}_2(\eta^5\text{-}C_5H_3)]TiNMe_2$.[204]

Reduction of $(\eta^5{:}\eta^1\text{-}C_5Me_4SiMe_2NR)TiCl_2$ ($R = t$-Bu, Ph) with BuLi in the presence of various 1,3-dienes gives the unique constrained geometry diene complexes, $(\eta^5{:}\eta^1\text{-}C_5Me_4SiMe_2NR)Ti(diene)$ complexes (**45**). The diene coordination mode (π, formally Ti(II), or metallacyclic, formally Ti(IV)) and the activity for olefin polymerization are highly sensitive to the identity of R.[205] Treatment of $(\eta^5{:}\eta^1\text{-}C_5Me_4SiMe_2NR)TiCl_2$ ($R = t$-Bu, $CHMe(1\text{-}C_{10}H_7)$) with butadienemagnesium gives butadiene complexes analogous to (**39**) in good yield. The isomer which has the s-cis-butadiene ligand oriented with its open side toward the amido group (prone) is favored.[206]

Treatment of $Ti(NMe_2)_4$ with $C_5H_5B(NR_2)NHPh$ ($R = i$-Pr, $SiMe_3$) and $C_9H_2B(N\text{-}i\text{-}Pr_2)NHPh$ gives the boron–nitrogen bridged constrained geometry titanium complexes $(\eta^5{:}\eta^1\text{-}C_5H_4B(NR_2)NPh)Ti(NMe_2)_2$ and $(\eta^5{:}\eta^1\text{-}C_9H_6B(N\text{-}i\text{-}Pr_2)NPh)Ti(NMe_2)_2$ in good yields via the amine elimination reaction. Subsequent deamination-chlorination with excess Me_3SiCl gives the corresponding dichloro complexes $(\eta^5{:}\eta^1\text{-}C_5H_4B(NR_2)NPh)TiCl_2$ and $(\eta^5{:}\eta^1\text{-}C_9H_6B(N\text{-}i\text{-}Pr_2)NPh)TiCl_2$, respectively. Reaction of the analogous ligand precursors containing more bulky R groups at nitrogen $C_5H_5B(N\text{-}i\text{-}Pr_2)N(H)R$ ($R = Cy$, t-Bu) with $Ti(NMe_2)_4$ gives the half-sandwich complexes (*see Half-sandwich Complexes*) $(\eta^5\text{-}C_5H_4B(N\text{-}i\text{-}Pr_2)N(H)R)Ti(NMe_2)_3$ ($R = Cy$, t-Bu) rather than the corresponding bridged complexes.[207]

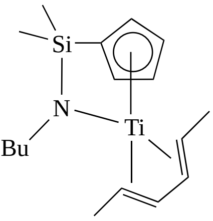

(**45**)

Treatment of $Li_2[C_5H_4C(Me_2)PR]$ and $Li_2[C_5H_4CH(t\text{-}Bu)PR]$ ($R = Cy$ and Ph) with $Cl_2Ti(NR'_2)_2$ ($R' =$ Me, Et) gives the corresponding constrained geometry complexes $(\eta^5{:}\eta^1\text{-}C_5H_4C(Me_2)PR)Ti(NR'_2)_2$ and $(\eta^5{:}\eta^1\text{-}C_5H_4CH(t\text{-}Bu)PR)Ti(NR'_2)_2$ with a C–P bridge as red oils in good yield.[208] The analogous Si–P bridged complex, $(\eta^5{:}\eta^1\text{-}C_5Me_4SiMe_2Pcy)Ti(NMe_2)_2$, was prepared moderate yield by treatment of $Li_2[C_5Me_4SiMe_2P(cyclohexyl)]$ with $Cl_2Ti(NMe_2)_2$.[209] Treatment of $(t\text{-}BuCpP(\text{-}t\text{-}Bu)Cl)TiCl_3$ with LiN(H)-t-Bu in the presence of Et_3N leads to the formation of the constrained geometry complex $(\eta^5{:}\eta^1\text{-}t\text{-}BuCpP(\text{-}t\text{-}Bu)N\text{-}t\text{-}Bu)TiCl_2$ in high yield.[101]

Constrained geometry complexes with other π ligands have also been prepared. Treatment of (4-Dimethylsilyl-*tert*-butylamido)-N,N-diisopropyl-1-aminoboratabenzene with two equivalents of t-BuLi followed by treatment with $TiCl_4$ gives (4-Dimethylsilyl-*tert*-butylamido)-N,N-diisopropyl-1-aminoboratabenzene titanium dichloride complexes (**46**).[210] Treatment of $TiCl_3THF_3$ with dianions (**47**) at low temperature followed by $PbCl_2$ gives the corresponding constrained geometry complexes (**48**) based on the dimethylcyclohexadienyl and dimethylsilacyclohexadienyl ligands.[211]

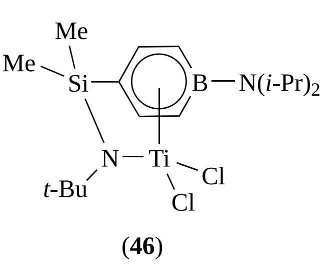

(**46**)

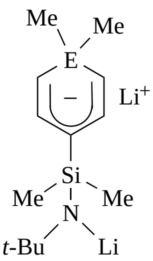

(**47**)

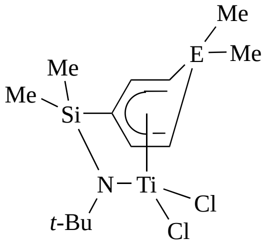

(**48**)

E = $SiMe_2$, CMe_2

13 CYCLOHEPTATRIENYL COMPLEXES

Reduction of $TiCl_4$ in the presence of PMe_3, $Me_2PCH_2PMe_2$, and $Me_2NCH_2CH_2NMe_2$ with an excess of cycloheptatriene gives $(\eta^7\text{-}C_7H_7)Ti(PMe_3)_2Cl$, $(\eta^7\text{-}C_7H_7)Ti(Me_2PCH_2PMe_2)Cl$, and $(\eta^7\text{-}C_7H_7)Ti(Me_2NCH_2CH_2NMe_2)Cl$, respectively.[212,213]

14 CYCLOPENTADIENYL–CYCLOHEPTATRIENYL COMPLEXES

The mixed cyclopentadienyl–cycloheptatrienyl (‘5–7’) titanium complex $Cp(\eta^7\text{-}C_7H_7)Ti$ has been prepared in 33–40% yield by the reduction of $CpTiCl_3$ with isopropylmagnesium bromide or Mg in the presence of cycloheptatriene.[1] Reduction of Cp^*TiCl_3 in THF with Mg in the presence of cycloheptatriene gives $Cp^*(\eta^7\text{-}C_7H_7)Ti$ in 68% yield.[214] Titanium ‘5–7’ complexes exhibit sandwich structures (*see Sandwich Compound*) with the five-membered and seven-membered rings nearly parallel to each other.

Metalation of $Cp(\eta^7\text{-}C_7H_7)Ti$ with *n*-butyllithium occurs predominantly at the seven-membered ring (equation 60). Dimetalation of $Cp(\eta^7\text{-}C_7H_7)Ti$ to give $(\eta^5\text{-}C_5H_4Li)(\eta^7\text{-}C_7H_6Li)Ti(TMEDA)_2$ has been achieved in 61% yield by treatment with 2 equiv. of BuLi/TMEDA. The dimetalated complex $(\eta^5\text{-}C_5H_4Li)(\eta^7\text{-}C_7H_6Li)Ti(TMEDA)_2$ reacts with a wide range of electrophilies, including MeI, Me_3SiCl, CO_2, and R_2PCl, to give the corresponding disubstituted complexes $(\eta^5\text{-}C_5H_4X)(\eta^7\text{-}C_7H_6X)Ti$ (X = Me, Me_3Si, CO_2^-, Me_2P, Ph_2P) in good yield (equation 61).[215]

$$Cp(\eta^7\text{-}C_7H_7)Ti \xrightarrow[\text{2. MeI}]{\text{1.}n\text{-BuLi}} \underset{95\%}{Cp(\eta^7\text{-}MeC_7H_6)Ti} + \underset{5\%}{MeCp(\eta^7\text{-}C_7H_7)Ti} \quad (60)$$

$$Cp(\eta^7\text{-}C_7H_7)Ti \xrightarrow[\text{2. 2 MeI}]{\text{1.}n\text{-BuLi/TMEDA}} (\eta^5\text{-}MeC_5H_4)(\eta^7\text{-}MeC_7H_6)Ti \quad (61)$$

Rausch and coworkers have extensively studied the use of $(\eta^5\text{-}C_5H_4PR_2)(\eta^7\text{-}C_7H_6PR_2)$ (R = Me, Ph) complexes as metalloligands. Reactions between $(\eta^5\text{-}C_5H_4PMe_2)(\eta^7\text{-}C_7H_6PMe_2)Ti$ and $M(CO)_6$ (M = Cr, Mo) in refluxing xylene result in the formation of chelated heterobimetallic complexes, $[(\eta^5\text{-}C_5H_4PMe_2)(\eta^7\text{-}C_7H_6PMe_2)Ti]M(CO)_4$ (M = Cr, Mo) in high yields, whereas a reaction between $(\eta^5\text{-}C_5H_4PMe_2)(\eta^7\text{-}C_7H_6PMe_2)Ti$ and $Fe_2(CO)_9$ under similar conditions gives the nonchelated product $[(\eta^5\text{-}C_5H_4PMe_2)(\eta^7\text{-}C_7H_6PMe_2)Ti][Fe(CO)_4]_2$. Treatment of bis(1,5-cod) nickel with 2 equiv. of $(\eta^5\text{-}C_5H_4PMe_2)(\eta^7\text{-}C_7H_6PMe_2)Ti$ in toluene at room temperature leads to displacement of the cod ligands and formation of $[(\eta^5\text{-}C_5H_4PMe_2)(\eta^7\text{-}C_7H_6PMe_2)Ti]_2Ni$ in 78% yield.[215]

The metalloligand $(\eta^5\text{-}C_5H_4PPh_2)(\eta^7\text{-}C_7H_6PPh_2)Ti$ reacts with a variety of metal carbonyls in refluxing toluene to produce a series of chelated heterobimetallic compounds, including $[(\eta^5\text{-}C_5H_4PPh_2)(\eta^7\text{-}C_7H_6PPh_2)Ti]M(CO)_4$ (M = Cr, Mo), $[(\eta^5\text{-}C_5H_4PPh_2)(\eta^7\text{-}C_7H_6PPh_2)Ti](CpCo)$, and $[(\eta^5\text{-}C_5H_4PPh_2)(\eta^7\text{-}C_7H_6PPh_2)Ti]Fe(CO)_3$. The crystal structure of the hemitoluene solvate of $[(\eta^5\text{-}C_5H_4PPh_2)(\eta^7\text{-}C_7H_6PPh_2)Ti]Cr(CO)_4$ has been determined. The phosphino groups are both on the same side of the molecule and coordinated to the Cr atom (Cr–P(av.) = 2.43(2) Å). The Ti–C(η^7) and Ti–C(η^5) distances average 2.19(1) and 2.31(2) Å, respectively, with an observed centroid(C5)–Ti–centroid(C7) angle of 173.5°, compared to a centroid(C5)–Ti–centroid(C7) angle of 175.8° in the parent bisphosphine.[216]

Treatment of $Mn_2(CO)_{10}$ with 2 equiv. of $(\eta^5\text{-}C_5H_4PPh_2)(\eta^7\text{-}C_7H_6PPh_2)Ti$ in refluxing toluene results in carbonyl group displacement, metal–metal bond cleavage, and hydrogen abstraction to give $HMn(CO)_3[(\eta^5\text{-}C_5H_4PPh_2)(\eta^7\text{-}C_7H_6PPh_2)Ti]$ in 57% yield. The Mn atom exhibits a distorted octahedral geometry with *cis* phosphines. The coordination geometry in the titanium complex backbone is relatively unaffected by the coordination of manganese.[217]

Treatment of $(\eta^5\text{-}C_5H_4Li)(\eta^7\text{-}C_7H_6Li)Ti\cdot 2TMEDA$ with two equivalents of dimethyldisulfide, diphenyldisulfide, and diphenyldiselenide and gives $(\eta^5\text{-}C_5H_4SCH_3)(\eta^7\text{-}C_7H_6SCH_3)Ti$, $(\eta^5\text{-}C_5H_4SPh)(\eta^7\text{-}C_7H_6SPh)Ti$, and $(\eta^5\text{-}C_5H_4SePh)(\eta^7\text{-}C_7H_6SePh)Ti$, respectively in low yield. The crystal structure of $(\eta^5\text{-}C_5H_4SPh)(\eta^7\text{-}C_7H_6SPh)Ti$, indicates that the five and seven-membered rings are essentially coplanar, and the two phenylthio substituents are in a trans-orientation.[218]

Treatment of $(\eta^7\text{-}C_7H_7)Ti(\eta^5\text{-}C_5H_5)$ with dithioacetic acid, CH_3CS_2H, leads to loss of the cycloheptatrienyl to give $(\eta^5\text{-}C_5H_5)Ti(S_2CCH_3)_3$.[219]

15 CYCLOPENTADIENYL–CYCLOOCTATETRAENE COMPLEXES

Mixed ‘5–8’ titanium complexes have been prepared by reduction of Cp^*TiCl_3 and $CpTiCl_3$ with Mg in THF in the presence of cyclooctatetraene to give $Cp^*(\eta^8\text{-}C_8H_8)Ti$

and Cp(η^8-C_8H_8)Ti in 31 and 38% yield, respectively. Alternatively, reaction of Cp*$TiCl_3$ with $K_2C_8H_8$ in THF gives Cp*(η^8-C_8H_8)Ti in 34% yield.[214]

16 CYCLOOCTATETRAENE COMPLEXES

Treatment of $TiCl_4(THF)_2$ with 2 equiv. of $Li_2[C_8H_6(SiMe_3)_2]$ and in THF gives $[Ti\{C_8H_6(SiMe_3)_2\}_2]$. The X-ray structure of $[Ti\{C_8H_6(SiMe_3)_2\}_2]$ indicates one ring is η^8 bound while the other is less readily classified, being intermediate between the η^3 structure found for $[Zr\{C_8H_6(SiMe_3)_2\}_2]$ and the η^4 structure found in $Ti(C_8H_8)_2$. In a variable-temperature solution NMR study on $[Ti\{C_8H_6(SiMe_3)_2\}_2]$, the two rings only become equivalent on the NMR timescale above 328 K.[220] In contrast, treatment of $TiCl_3(THF)_3$ with one equivalent of 1,4-bis(trimethylsilyl)cyclooctatetraene dianion (COT″) gives a mixture of (COT″)$_2$Ti, [(COT″)Ti]$_2$(μ-Cl)$_3$ and $\{[\eta^8\text{-}1,4\text{-}(SiMe_3)_2C_8H_6]Ti(\mu\text{-}Cl)\}_2(THF)$.[221]

The reduction of $[(\eta^8\text{-}C_8H_8)Ti(THF)(\mu\text{-}Cl)]_2$ with magnesium in the presence of bis(trimethylsilyl)acetylene (BTMSA) gives $[(\eta^8\text{-}C_8H_8)Ti]_2[\mu\text{-}\eta^2{:}\eta^2\text{-}Me_3SiC{\equiv}CSiMe_3]$ in high yield. The crystal structure of $[(\eta^8\text{-}C_8H_8)Ti]_2[\mu\text{-}\eta^2{:}\eta^2\text{-}Me_3SiC{\equiv}CSiMe_3]$ revealed that BTMSA serves as a four-electron ligand to two equivalent (η^8-C_8H_8)Ti units. The average C–C distance of 1.51 Å in the acetylene ligand is close to that of a sp^3 carbon–carbon single bond, however, the high thermal stability and a large down-field chemical shift of the acetylenic carbon atoms (δ292.8 ppm) suggests unusually high π-back-bonding in the Ti–acetylene bond. In contrast, the reduction of $[(\eta^8\text{-}C_8H_8)Ti(THF)(\mu\text{-}Cl)]_2$ by magnesium in the presence of diphenylacetylene gave (η^8-C_8H_8)Ti(η^4-C_4Ph_4) and hexaphenylbenzene.[222]

17 OTHER η^5-LIGANDS

Seminal work by Ernst and coworkers has shown that the pentadienyl ligand η^5-C_5H_7 and its alkylated congeners are versatile ligands, possessing features of both Cp and allyl ligands. Treatment of $TiCl_2$, prepared in situ by the reduction of $TiCl_4$ with Mg, with potassium 2,4-dimethylpentadienide gives (η^5-2,4-$Me_2C_5H_5$)$_2$Ti (equation 62). Complexes (η^5-2,4-t-$Bu_2C_5H_5$)$_2$Ti and (η^5-2,4-$(SiMe_3)_2C_5H_5$)$_2$Ti have been prepared in a similar manner. Somewhat surprisingly, these 14-electron open-sandwich compounds have been found to be low-spin (diamagnetic), whereas Cp^*_2Ti possesses two unpaired electrons.[223] The three bis(pentadienyl) complexes have staggered pentadienyl groups. Addition of CO or phosphines leads to the diamagnetic 16-electron complexes (η^5-2,4-$Me_2C_5H_5$)$_2$TiL (L = CO (ν_{CO} = 1942 cm^{-1}), PMe_3, PEt_3, $P(OMe)_3$, PMe_2Ph) (equation 63) in which the pentadienyl ligands are syn eclipsed. (η^5-C_5H_7)$_2$TiPEt$_3$ can be prepared directly by treatment of '$TiCl_2$' with 2 equiv. of $[C_5H_7]^-$ and 1 equiv. of PEt_3.[224]

$$2K(2,4\text{-}Me_2C_5H_3) + TiCl_2 \longrightarrow (\eta^5\text{-}2,4\text{-}Me_2C_5H_3)_2Ti \quad (62)$$

$$(\eta^5\text{-}2,4\text{-}Me_2C_5H_3)_2Ti + L \longrightarrow (\eta^5\text{-}2,4\text{-}Me_2C_5H_3)_2TiL \quad (63)$$

The bis(6,6-dimethylcyclohexadienyl)titanium bent-sandwich complex (η^5-6,6-$Me_2C_6H_5$)$_2$Ti has been prepared in 50% yield by treatment of $TiCl_3(THF)_3$ or $TiCl_4(THF)_2$ with 6,6-dimethylcyclohexadienylpotassium (K(dmCh)). Carbonylation of (dmCh)$_2$Ti at 1 atm and 25 °C gives the thermally sensitive cherry-red carbonyl adduct (dmCh)$_2$TiCO (ν_{CO} = 1904 cm^{-1}) in 95% yield. The carbonyl complex (dmCh)$_2$TiCO has C_{2v} symmetry, with a dmCh–Ti–dmCh angle of 155°. Treatment of (dmCh)$_2$Ti with PF_3, PMe_3, or $P(OMe)_3$ at low temperature in solution leads to adducts; however, the lability of these adducts does not allow direct characterization.[225]

Bis(η^5-cyclooctadienyl)Ti complexes form monoadducts with both CO and the cage phosphite $P(OCH_2)_3CEt$. The 16 electron titanium complexes are diamagnetic, exhibiting broad ^{1}H NMR spectra indicating that the phosphite complex undergoes rapid, reversible ligand dissociation. Structural data reveal a high degree of steric crowding in these complexes, while the IR data for the bis(η^5-cyclooctadienyl)Ti carbonyl complex indicates that the edge-bridged dienyl ligands are substantially stronger electron donors than typical pentadienyl ligands, comparable to the Cp ligand.[226]

The reactions of $CpTiCl_2(PR_3)_2$ (R = Me, Et) with 2 equiv. of KC_5H_7 or K(2,4-C_7H_{11}) (C_7H_{11} = dimethylpentadienyl) gives the corresponding diamagnetic 16 electron Cp(pendadienyl)TiPR$_3$ complexes. A single-crystal X-ray diffraction study of Cp (η^5-2,4-C_7H_{11})TiPEt$_3$ revealed that the Ti–C bond lengths for the open dienyl ligand are much shorter than those for the Cp ligand, 2.240(3) versus 2.346(4) Å, indicative of stronger Ti–C_7H_{11} bonding. Reaction of Cp(η^5-2,4-C_7H_{11})TiPEt$_3$ with MeCN leads to loss of the PEt_3 ligand and coupling to the 2,4-C_7H_{11} ligand. Thus, the C_7H_{11} ligand is bound more strongly than the Cp ligand (*see Ligand*), yet more reactive. The phosphine ligands in these complexes are readily replaced by treatment with $P(OMe)_3$ or $P(OEt)_3$. Treatment of CpTi(η^5-2,4-C_7H_{11})(PEt_3) with CO leads to thermally unstable monocarbonyl and dicarbonyl complexes.[227]

Pentadienyl complexes $[\eta^5\text{-}1,3\text{-}C_5H_3(t\text{-}Bu)_2]Ti(\eta^5\text{-}2,4\text{-}C_7H_{11})(PMe_3)$, $Ti[\eta^5\text{-}1,3\text{-}C_5H_3(t\text{-}Bu)_2](\eta^5\text{-}C_5H_7)(PR_3)$ (R = Me or Et) and $[\eta^5\text{-}1,3\text{-}C_5H_3(SiMe_3)_2]Ti(\eta^5\text{-}2,4\text{-}C_7H_{11})(PMe_3)$ (C_7H_{11} = dimethylpentadienyl) containing bulky Cp ligands have been prepared. The X-ray structure of $[\eta^5\text{-}1,3\text{-}C_5H_3(t\text{-}Bu)_2]Ti$ (η^5-C_5H_7)PMe$_3$ revealed a markedly shorter Ti–C bonds for the open dienyl ligand as compared to the cyclic one.[228] Structural data have been obtained for these complexes, and for Ti(η^5-2,4-C_7H_{11})$_2$(PEt_3). The presence of the coordinated phosphines in all cases led to the adoption of the expected syn-eclipsed geometries, with the phosphines positioned by the open dienyl edges. These phosphine ligands cause substantial alterations of the bonding patterns in these species, relative to ligand-free complexes. Most notably, the shortest M–C distances involve the central dienyl carbon atoms.[229]

18 ALKOXIDES AND RELATED COMPLEXES

Rothwell and Wolczanski have developed considerable titanium organometallic chemistry utilizing sterically hindered alkoxides as ancillary ligands.

Wolczanski and coworkers have shown that the tritox ligand t-$\mathrm{Bu_3CO}$, with a cone angle (*see Cone Angle*) of 125 °C, which is slightly smaller than the 136° cone angle for Cp, can serve to sterically ‘saturate’ titanium and allow the development of considerable organometallic chemistry. Reaction of 2 equiv. of Li(tritox) with $\mathrm{TiCl_3}$ gives ‘$\mathrm{(tritox)_2TiCl}$’, which appears to be monomeric, in contrast to the Cp analog $\mathrm{[Cp_2TiCl]_2}$ (equation 64). Treatment of ‘$\mathrm{(tritox)_2TiCl}$’ with excess $\mathrm{CCl_4}$ gives $\mathrm{(tritox)_2TiCl_2}$, which can also be prepared directly, in 51% yield, by reaction of $\mathrm{TiCl_4}$ with 2 equiv. of Li(tritox) (equation 65). Similarly, $\mathrm{(tritox)TiCl_3}$ is prepared in 57% yield by treatment of $\mathrm{TiCl_4}$ with 1 equiv. of Li (tritox) (equation 66).

$$2\mathrm{Li(tritox)} + \mathrm{TiCl_3} \xrightarrow[\text{hexane}]{\mathrm{Et_2O}} \text{‘}\mathrm{(tritox)_2TiCl}\text{’} + 2\mathrm{LiCl} \tag{64}$$

$$\text{‘}\mathrm{(tritox)_2TiCl}\text{’} + \mathrm{CCl_4} \longrightarrow \mathrm{(tritox)_2TiCl2} \tag{65}$$

$$\mathrm{Li(tritox)} + \mathrm{TiCl_4} \xrightarrow{\mathrm{Et_2O}} \mathrm{(triox)TiCl_3} + \mathrm{LiCl} \tag{66}$$

In a manner analogous to the reactivity of $\mathrm{Cp_2TiCl_2}$, treatment of $\mathrm{(tritox)_2TiCl_2}$ with 2 equiv. of MeLi gives $\mathrm{(tritox)_2TiMe_2}$ in 76% yield (equation 67). In an analogous manner, treatment of $\mathrm{(tritox)TiCl_3}$ with 3 equiv. of MeLi gives $\mathrm{(tritox)TiMe_3}$ in 60% yield (equation 68). $\mathrm{(Tritox)_2TiMe_2}$ exhibits high thermal stability, with less than 10% decomposition observed over 2 weeks in a benzene solution at 100 °C.[230]

$$\mathrm{(triox)_2TiCl_2} + 2\mathrm{LiMe} \xrightarrow{\mathrm{Et_2O}} \mathrm{(triox)_2TiMe_2} + 2\mathrm{LiCl} \tag{67}$$

$$\mathrm{(triox)TiCl_3} + 3\mathrm{LiMe} \xrightarrow{\mathrm{Et_2O}} \mathrm{(triox)TiMe_3} + 3\mathrm{LiCl} \tag{68}$$

Reaction of $\mathrm{(tritox)_2TiMe_2}$ with dry $\mathrm{O_2}$ for 8–30 h gives $\mathrm{(tritox)_2Ti(OMe)_2}$ in 87% yield. Reaction of $\mathrm{(tritox)TiMe_3}$ with $\mathrm{O_2}$ gives three different methoxide complexes, depending upon the stoichiometry of the reagents (equations 69–71).[231]

$$\mathrm{(triox)TiMe_3} + \frac{1}{2}\mathrm{O_2} \longrightarrow \frac{1}{n}[\mathrm{(triox)TiMe_2(OMe)}]_n \tag{69}$$

$n = 1$ in solution, 2 in solid state

$$\mathrm{(triox)TiMe_3} + \mathrm{O_2} \longrightarrow \mathrm{(triox)TiMe(OMe)_2} \tag{70}$$

$$\mathrm{(triox)TiMe_3} + \frac{3}{2}\mathrm{O_2} \longrightarrow \mathrm{(triox)Ti(OMe)_3} \tag{71}$$

Rothwell and coworkers have shown that treatment of $\mathrm{Ti(CH_2Ph)_4}$ with 2 equiv. of 2,6-di-t-butylphenol gives the deep-red complex $\mathrm{Ti(2,6\text{-}}t\mathrm{\text{-}Bu_2C_6H_3O)_2(CH_2Ph)_2}$ in 25–40% yield (equation 72). Thermolysis of $\mathrm{Ti(2,6\text{-}}t\mathrm{\text{-}Bu_2C_6H_3O)_2(CH_2Ph)_2}$ at 120 °C in hydrocarbon solvents leads to cyclometalation (*see Cyclometalation*) to give $\mathrm{Ti[2,6\text{-}(}t\mathrm{\text{-}Bu)(CMe_2CH_2)C_6H_3O](2,6\text{-}}t\mathrm{\text{-}Bu_2C_6H_3O)(CH_2Ph)}$ (**47**) (equation 73). Reaction of $\mathrm{Ti(CH_2SiMe_3)_4}$ with 2,6-t-$\mathrm{Bu_2C_6H_3OH}$ at 25 °C for several days gives no observable reaction; however, warming the reaction mixture to 80 °C affords $\mathrm{Ti[2,6\text{-}(}t\mathrm{\text{-}Bu)(CMe_2CH_2)C_6H_3O](2,6\text{-}}t\mathrm{\text{-}Bu_2C_6H_3O)(CH_2SiMe_3)}$.[232] Complexes $\mathrm{Ti(2,6\text{-}Ph_2C_6H_3O)_2R_2}$ (R = Me, $\mathrm{CH_2SiMe_3}$, $\mathrm{CH_2Ph}$, Ph) and $\mathrm{Ti(2,6\text{-}Ph_2C_6H_3O)_3R}$ (R = Me, $\mathrm{CH_2SiMe_3}$) are obtained by treating the corresponding homoleptic (*see Homoleptic Compound*) alkyl $\mathrm{TiR_4}$ with 2,6-diphenylphenol in the proper stoichiometry. X-ray crystallographic analysis of $\mathrm{Ti(2,6\text{-}Ph_2C_6H_3O)_2(Ph)_2}$ and $\mathrm{Ti(2,6\text{-}Ph_2C_6H_3O)_3(CH_2SiMe_3)}$ demonstrates that the Ti atoms in these complexes are in a pseudotetrahedral environment with short Ti–O distances (1.794(3)–1.806(2) Å) and large Ti–O–C angles (153–179°).[233]

$$\mathrm{Ti(CH_2Ph)_4} + 2(2,6\text{-}t\text{-}\mathrm{Bu_2C_6H_3OH}) \longrightarrow \mathrm{Ti(2,6\text{-}}t\mathrm{\text{-}Bu_2C_6H_3O)(CH_2Ph)_2} \tag{72}$$

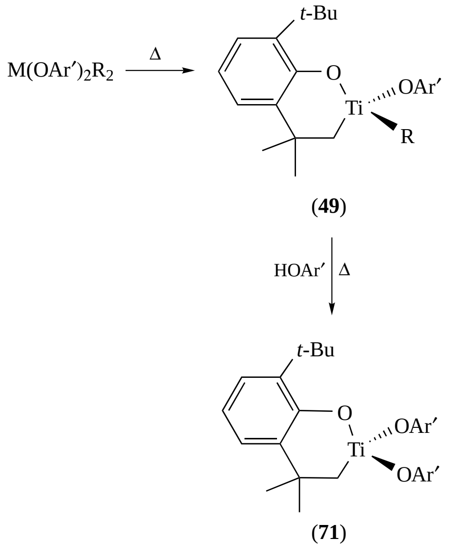

(**49**)

(**71**)

(73)

Mixed (alkyl)(aryl oxide) complexes of $\mathrm{(ArO)_2Ti(CH_2Ph)_2}$ (Ar = $\mathrm{2,6\text{-}Ph_2C_6H_3}$, 2,6-$i$-$\mathrm{Pr_2C_6H_3}$) have been found to undergo migratory insertion (*see Migratory Insertion*) with organic isocyanides to give η^2-iminoacyl derivatives (equation 74). Reaction of $\mathrm{(ArO)_2Ti(CH_2Ph)_2}$ with 2,6-dimethylphenyl isocyanide leads initially to the monoiminoacyl derivative $\mathrm{(ArO)_2Ti(}\eta^2\mathrm{\text{-}2,6\text{-}Me_2C_6H_3N{=}CCH_2Ph)(CH_2}$

Ph) and finally to the bis-insertion product $(ArO)_2Ti(\eta^2\text{-}2,6\text{-}Me_2C_6H_3N{=}CCH_2Ph)_2$ (equation 75).[234] Mild thermolysis of $(ArO)_2Ti(\eta^2\text{-}2,6\text{-}Me_2C_6H_3N{=}CCH_2Ph)_2$ in hydrocarbon solvents gives the corresponding enediamido complexes (equation 76). Treatment of the alkyl–iminoacyl–aryl oxide complexes with 200–1000 psi of CO forms enamidolate complexes (equation 77).[235]

$$(ArO)_2Ti(CH_2Ph)_2 \xrightarrow{RN\equiv C} (ArO)_2Ti(\eta^2\text{-}2,6\text{-}Me_2C_6H_3N{=}CCH_2Ph)(CH_2Ph) \quad (74)$$

$$(ArO)_2Ti(\eta^2\text{-}RN{=}CCH_2Ph)(CH_2Ph) \xrightarrow{RN\equiv C} (ArO)_2Ti(\eta^2\text{-}RN{=}CCH_2Ph)_2$$

$Ar = 2,6\text{-}Ph_2C_6H_3,\ 2,6\text{-}i\text{-}Pr_2C_6H_3;\ RN{\equiv}C = 2,6\text{-}Me_2C_6H_3N{\equiv}C$

(75)

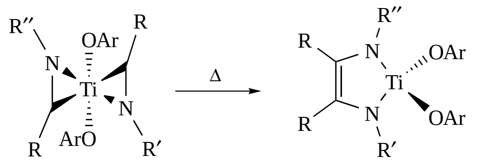

(76)

$Ar = 2,6\text{-}i\text{-}Pr_2C_6H_3$; $R = CH_2Ph$, $R' = Ph$, $2,6\text{-}Me_2C_6H_3$, t-Bu; $R'' = 2,6\text{-}Me_2C_6H_3$, t-Bu

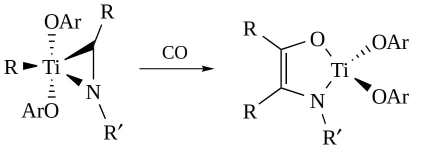

(77)

$Ar = 2,6\text{-}i\text{-}Pr_2C_6H_3$; $R = CH_2Ph$, $R' = t$-Bu;

Reduction of $Ti(2,6\text{-}Ph_2C_6H_3O)_2Cl_2$ (which can be prepared by the reaction of $TiCl_4$ with $2,6\text{-}Ph_2C_6H_3OH$)[236] with sodium amalgam at room temperature in the presence of EtC≡CEt gives a new titanacyclopentadiene complex in 89–90% yield. Titanocycles supported by aryl oxide ligation undergo fragmentation and isomerization and are more reactive than the corresponding bis(cyclopentadienyl)titanacyclopentadiene complexes, as shown in Scheme 9. Treatment of $(2,6\text{-}Ph_2C_6H_3O)Ti(EtC{=}CEtCEt{=}CEt)$ with 3-hexyne at 110 °C gives hexaethylbenzene catalytically. $(2,6\text{-}Ph_2C_6H_3O)Ti(EtC{=}CEtCEt{=}CEt)$ reacts rapidly with MeCN to produce the corresponding pyridine. Addition of PhN=CMeCMe=NPh or azobenzene to $(2,6\text{-}Ph_2C_6H_3O)Ti(EtC{=}CEtCEt{=}CEt)$ gives the corresponding enediamido complexes $(RO)_2Ti(PhNCMe{=}CMeNPh)$ and $(RO)_2Ti(PhNCEt{=}CEtNPh)$, respectively.[237] Exposure of $(2,6\text{-}Ph_2C_6H_3O)Ti(EtC{=}CEtCEt{=}CEt)$ to ethylene in solution leads rapidly to the formation of the saturated titanacyclopentane $(2,6\text{-}Ph_2C_6H_3O)_2Ti(CH_2CH_2CH_2CH_2)$ and 1,2,5,6-tetraethyl-1,3-cyclohexadiene, as shown in Scheme 10.[238]

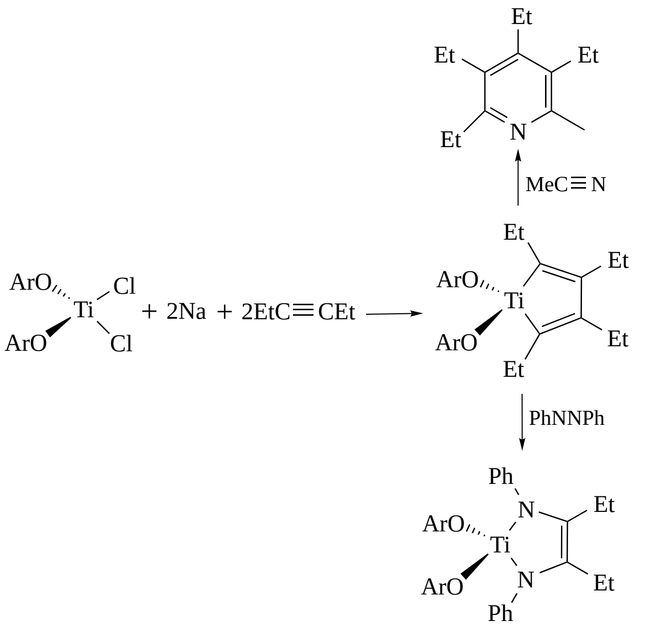

Scheme 9

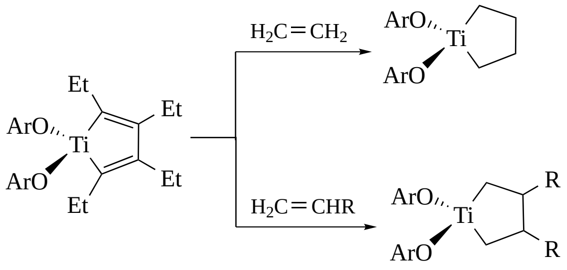

R = Me, Et

Scheme 10

Treatment $(2,6\text{-}Ph_2C_6H_3O)Ti(EtC{=}CEtCEt{=}CEt)$ with olefins gives a variety of stable titanacyclopentane derivatives and one equivalent of substituted 1,3-cyclohexadiene. Reduction of the $(O\text{-}2,6\text{-}Ph_2C_6H_3)_2TiCl_2$ or $(O\text{-}2,3,5,6\text{-}Ph_4C_6H)_2TiCl_2$ with Na amalgam (2 Na per Ti) or 2 equiv. of BuLi in the presence of an olefin give the corresponding titanacyclopentane derivatives. These titanacyclopentane complexes undergo facile fragmentation. Addition of phosphine donor ligands gives $(O\text{-}2,6\text{-}Ph_2C_6H_3)_2Ti(\eta^2\text{-}CHR{=}CH_2)(L)$ (R = H, Me, Et, Ph,) along with 1 equiv. of free olefin. Addition of $Ph_2C{=}O$ or PhCH=NR (R = Ph, CH_2Ph) to the titanacyclopentane and leads to different products depending upon the reagent and reaction conditions.[239]

Treatment of a hydrocarbon solution of $(2,6\text{-}Ph_2C_6H_3O)_2Ti(CH_2)_4$ with PMe_3 leads to the formation of the deep-purple η^2-ethylene complex $(2,6\text{-}Ph_2C_6H_3O)_2Ti(\eta^2\text{-}C_2H_2)(PMe_3)$. A single-crystal X-ray diffraction analysis of $(2,6\text{-}Ph_2C_6H_3O)_2Ti(\eta^2\text{-}C_2H_2)(PMe_3)$ shows a pseudotetrahedral environment about the titanium center with the ethylene aligned perpendicular to the O–Ti–O plane. The Ti–C (ethylene) distances of 2.110 (2) and 2.148 (2) Å, as well as a C–C distance of 1.425 (3) Å, are consistent with a titanacyclopropane bonding description. Addition of Ph_2CO to $(2,6\text{-}Ph_2C_6H_3O)_2Ti(\eta^2\text{-}C_2H_2)(PMe_3)$ gives initially the oxatitanacyclopentane complex $(2,6\text{-}Ph_2C_6H_3O)_2Ti(OCPh_2CH_2CH_2)$, which upon addition of a second equivalent of Ph_2CO gives the dioxametallacyclic complex $(2,6\text{-}Ph_2C_6H_3O)_2Ti(OCPh_2CH_2CH_2CPh_2O)$, as shown in Scheme 11.[240]

$CpTiCl_2X$ complexes where X is a OAr, SAr, or carbazole have been prepared. Treatment of $CpTi(OAr)Cl_2$ and $Cp^*Ti(OAr)Cl_2$ where OAr is a bulky phenol derivative, with 2 equiv. of LiMe gives $CpTi(OAr)Me_2$ and $Cp^*Ti(OAr)Me_2$, respectively. Alternatively, treatment of $CpTiMe_3$ in a cold ether solution of a bulky phenol gives $CpTi(OAr)Me_2$. Reaction of $CpTiMe_3$ with 2 equiv. of less bulky phenol derivatives, $HOAr'$ ($Ar' = 2, 6$-dimethyl-phenyl, 2,6-dimethyl-4-Br-phenyl), gives $[CpTi(OAr')_2Me]$. Reaction of the $CpTi(OAr)Me_2$ with $[B(C_6F_5)_3]$ generates the corresponding cationic complex, $[CpTi(OAr)Me][MeB(C_6F_5)_3]$. The thermally unstable cationic readily eliminates methane at room temperature giving $CpTi(OAr)(C_6F_5)(CH_2B(C_6F_5)_2)$. The solid-state structure of $CpTi(OC_6H\text{-}2,6\text{-}Ph_2\text{-}3,5\text{-}Me_2)(C_6F_5)(CH_2B(C_6F_5)_2)$ confirms the transfer on one C_6F_5 to titanium and no interaction of the trigonal-planar boron atom with the adjacent Ti–C_6F_5 group.[241]

Treatment of $CpTiCl_3$ with 1 equiv. of substituted arylsulfide ligands ($SAr = 4\text{-}Me\text{-}SC_6H_4$, $2,4,6,\text{-}Me_3\text{-}SC_6H_2$, $2,4,6\text{-}i\text{-}Pr_3\text{-}SC_6H_2$, $2,4,6\text{-}Ph_3\text{-}SC_6H_2$) in benzene gives $CpTi(SAr)Cl_2$. One electron reduction of $CpTi(SAr)Cl_2$ with Na/Hg gives the sulfur-bridged dimmers, $[CpTiCl(\mu\text{-}SAr)]_2$ ($SAr = 2, 4, 6,\text{-}Me_3\text{-}SC_6H_2$, $2,4,6\text{-}i\text{-}Pr_3\text{-}SC_6H_2$, $2,4,6\text{-}Ph_3\text{-}SC_6H_2$). The solid-state structures of these dimers show that the cyclopentadienyl rings are arranged in a transoid fashion about the $Ti(\mu\text{-}SAr)_2Ti$ core.[242] The reaction of $CpTiCl_3$ with K carbazolate (Kcb) gives $CpTi(cb)Cl_2$ which can readily be converted $CpTi(cb)Me_2$.[243]

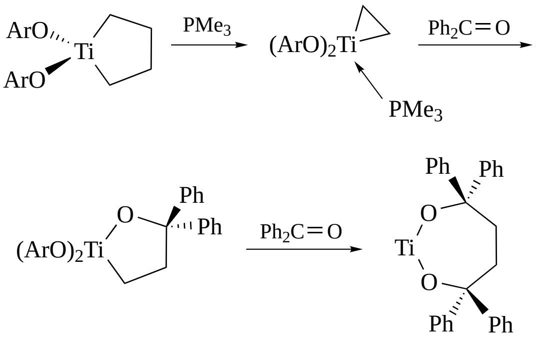

Scheme 11

Reduction of $CpTi(OAr)Cl_2$ ($OAr = 2,3,5,6$-tetraphenylphenoxide) with 2 equivalent of sodium amalgam at room temperature in the presence of $Me_3C{\equiv}CH$ gives the 2,5-di(t-butyl)titanacyclopentadiene complex, $Cp(ArO)Ti(2,5\text{-}t\text{-}Bu_2\text{-}C_4H_2)$. When $Cp(ArO)Ti(2,5\text{-}t\text{-}Bu_2\text{-}C_4H_2)$ is heated at 100 °C for a few days in C_6D_6 it isomerizes to the more stable 2,4-di(t-butyl) regioisomer.[244]

Treatment of $[Ti(CH_2Ph)_4]$ with carbazole gives $Ti(cb)_2(CH_2Ph)_2$. $Ti(cb)_2(CH_2Ph)_2$ reacts with 2,6-dimethylphenyl isocyanide to generate the corresponding bis(iminoacyl) derivative, in which the iminoacyl is η^2-C,N binding. The reaction of the more bulky $[Ti(CH_2SiMe_3)_4]$ with cbH at 100 °C gives the alkylidene bridged dimer $[(cb)_2Ti(\mu\text{-}CHSiMe_3)_2Ti(cb)_2]$ which was structurally characterized. The reaction of $CpTiCl_3$ with K carbazolate (Kcb) gives $CpTi(cb)Cl_2$ which can readily be converted $CpTi(cb)Me_2$.[243]

Treatment o $(2,6\text{-}Ph_2\text{-}3,5\text{-}Me_2C_6HO)_2Ti(CH_2Ph)_2$ with $[B(C_6F_5)_3]$ gives the corresponding zwitterionic species $(2,6\text{-}Ph_2\text{-}3,5Me_2\text{-}C_6HO)_2Ti(CH_2Ph)[\eta^6\text{-}C_6H_5CH_2B(C_6F_5)_3]$[245]

19 RELATED ARTICLES

Asymmetric Synthesis by Homogeneous Catalysis; Metal Vapor Synthesis of Transition Metal Compounds; Metathesis Polymerization Processes by Homogeneous Catalysis; Oligomerization & Polymerization by Homogeneous Catalysis; Organic Synthesis Using Metal-mediated Metathesis Reactions; Titanium: Inorganic & Coordination Chemistry.

20 REFERENCES

1. M. Bottrill, P. D. Gavens, J. W. Kelland, and K. McMeeking, in ‘Comprehensive Organometallic Chemistry’, eds. G. Wilkinson, F. G. A. Stone, and E. W. Abel, Pergamon, Oxford, 1982, Vol. 3, Chap. 22.1, p. 271; Chap. 22.2, p. 281; Chap. 22.3, p. 331; Chap. 22.4, p. 433.
2. R. Busby, W. Klotzbücher, and G. A. Ozin, *Inorg. Chem.*, 1977, **16**, 822.
3. M. Zhou and L. Andrews, *J. Phys. Chem. A*, 1999, **103**, 5259.
4. A. Röder, K. Thiele, G. Palyi, and L. Marko, *J. Organomet. Chem.*, 1980, **199**, C31.
5. K. M. Chi, S. R. Frerichs, B. K. Stein, D. W. Blackburn, and J. E. Ellis, *J. Am. Chem. Soc.*, 1988, **110**, 163.
6. P. J. Domaille, R. L. Harlow, and S. S. Wreford, *Organometallics*, 1982, **1**, 935.
7. D. W. Blackburn, K. M. Chi, S. R. Frerichs, M. L. Tinkham, and J. E. Ellis, *Angew. Chem.*, 1988, **100**, 408.
8. J. E. Ellis and K. M. Chi, *J. Am. Chem. Soc.*, 1990, **112**, 6022.
9. G. Tripepi, V. G. Young Jr, and J. E. Ellis, *J. Organomet. Chem.*, 2000, **593–594**, 354.

10. P. J. Fischer, P. Yuen, Y. Pong; V. G. Young, G. Victor Jr, and J. E. Ellis, *J. Am. Chem. Soc.*, 1997, **119**, 5980.
11. P. J. Fischer, V. G. Young, G. Victor Jr, and J. E. Ellis, *Angew. Chem., Int. Ed. Engl.*, 2000, **39**, 189.
12. J. E. Ellis and P. Yuen, *Inorg. Chem.*, 1993, **32**, 4998.
13. P. L. Fischer, K. A. Ahrendt, A. Kateri, V. G. Young Jr, and J. E. Ellis, *Organometallics*, 1998, **17**, 13.
14. S. I. Troyanov, A. Meetsma, and J. H. Teuben, *Inorg. Chim. Acta*, 1998, **271**(1,2), 180.
15. M. D. Spencer and G. S. Girolami, *J. Organomet. Chem.*, 1994, **483**, 99.
16. S. J. Chadwell, S. J. Coles, P. G. Edwards, and M. B. Hursthouse, *J. Chem. Soc., Dalton Trans.: Inorg. Chem.*, 1996, **6**, 1105.
17. W. Levason, M. L. Matthews, B. Patel, G. Reid, and M. Webster, *Polyhedron*, 2004, **23**, 605.
18. R. J. Baker, P. C. Davies, P. G. Edwards, R. D. Farley, S. S. Liyanage, D. M. Murphy, and B. Yong, *Eur. J. Inorg. Chem.*, 2002, 1975.
19. J. E. Ellis, *Organometallics*, 2003, **22**, 3322.
20. B. A. Kelsey and J. E. Ellis, *J. Chem. Soc., Chem. Commun.*, 1986, 331.
21. B. A. Kelsey and J. E. Ellis, *J. Am. Chem. Soc.*, 1986, **108**, 1344.
22. J. E. Ellis, S. R. Frerichs, and B. K. Stein, *Organometallics*, 1993, **12**, 1048.
23. J. E. Ellis, B. K. Stein, and S. R. Frerichs, *J. Am. Chem. Soc.*, 1993, **115**, 4066.
24. Y. You, S. R. Wilson, and G. S. Girolami, *Organometallics*, 1994, **13**, 4655.
25. P. J. Fischer, V. G. Young Jr, and J. E. Ellis, *Angew. Chem., Int. Ed. Engl.*, 2000, **39**, 189.
26. B. K. Stein, S. R. Frerichs, and J. E. Ellis, *Organometallics*, 1987, **6**, 2017.
27. M. Bottrill, P. D. Gavens, J. W. Kelland, and K. McMeeking, in ‘Comprehensive Organometallic Chemistry’, eds. G. Wilkinson, F. G. A. Stone, and E. W. Abel, Pergamon, Oxford, 1982, Vol. 3, Chap. 22.4, p. 433.
28. G. S. Girolami, G. Wilkinson, A. M. R. Galas, M. Thornton-Pett, and M. B. Hursthouse, *J. Chem. Soc., Dalton Trans.*, 1985, 1339.
29. J. A. Jensen, S. R. Wilson, A. J. Schultz, and G. S. Girolami, *J. Am. Chem. Soc.*, 1987, **109**, 8094.
30. F. A. Cotton, C. A. Murillo, and M. A. Petrukhina, *J. Organomet. Chem.*, 1999, **573**, 78.
31. L. H. McAlexander, M. Hung, L. Li, J. B. Diminnie, Z. Xue, G. P. A. Yap, and A. L. Rheingold, *Organometallics*, 1996, **15**, 5231.
32. J. J. Eisch and J. N. Gitua, *Organometallics*, 2003, **22**, 24.
33. D. A. Straus and R. H. Grubbs, *Organometallics*, 1982, **1**, 1658.
34. J. W. Bruin, G. Schat, O. S. Akkerman, and F. Bickelhaupt, *Tetrahedron Lett.*, 1983, **24**, 3935.
35. P. B. Mackenzie, R. J. Coots, and R. H. Grubbs, *Organometallics*, 1989, **8**, 8.
36. L. R. Gilliom and R. H. Grubbs, *J. Am. Chem. Soc.*, 1986, **108**, 733.
37. T. J. Katz and S. J. Lee, *J. Am. Chem. Soc.*, 1980, **102**, 422.
38. M. Brookhart, J. R. Tucker, and G. R. Husk, *J. Am. Chem. Soc.*, 1983, **105**, 258.
39. L. F. Cannizzo and R. H. Grubbs, *J. Org. Chem.*, 1985, **50**, 2316.
40. J. D. Meinhart, E. V. Anslyn, and R. H. Grubbs, *Organometallics*, 1989, **8**, 583.
41. R. Beckhaus, K. H. Thiele, and D. Ströhl, *J. Organomet. Chem.*, 1989, **369**, 43.
42. G. A. Luinstra and J. H. Teuben, *Organometallics*, 1992, **11**, 1793.
43. G. Greidanus-Strom, C. A. G. Carter, and J. M. Stryker, *Organometallics*, 2002, **21**(6), 1011.
44. A. W. Kaplan, J. L. Polse, G. E. Ball, R. A. Andersen, and R. G. Bergman, *J. Am. Chem. Soc.*, 1998, **120**, 11649.
45. J. L. Polse, A. W. Kaplan, R. A. Andersen, and R. G. Bergman, *J. Am. Chem. Soc.*, 1998, **120**, 6316.
46. R. Beckhaus, J. Sang, T. Wagner, and U. Bohme, *J. Chem. Soc., Dalton Trans.: Inorg. Chem.*, 1997, 2249.
47. P. H. P. Brinkmann, M.-H. Prosenc, and G. A. Luinstra, *Organometallics*, 1995, **14**, 5481.
48. R. Beckhaus, J. Oster, B. Ganter, and U. Englert, *Organometallics*, 1997, **16**, 3902.
49. F. G. N. Cloke and A. McCamley, *J. Chem. Soc., Chem. Commun.*, 1991, 1470.
50. S. Datta, M. B. Fischer, and S. S. Wreford, *J. Organomet. Chem.*, 1980, **188**, 353.
51. S. S. Wreford, M. B. Fisher, L.-S. Lee, E. J. James, and S. C. Nyburg, *J. Chem. Soc., Chem. Commun.*, 1981, 458.
52. R. Beckhaus and K. H. Thiele, *J. Organomet. Chem.*, 1986, **317**, 23.
53. M. D. Spencer, S. R. Wilson, and G. S. Girolami, *Organometallics*, 1997, **16**, 3055.
54. H. Yamamoto, H. Yasuda, K. Tatsumi, K. Lee, A. Nakamura, J. Chen, Y. Kai, and N. Kasai, *Organometallics*, 1989, **8**, 105.
55. J. Blenkers, B. Hessen, F. Van Bolhuis, A. J. Wagner, and J. H. Teuben, *Organometallics*, 1987, **6**, 459.
56. M. Mena, P. Royo, R. Serrano, M. A. Pellinghelli, and A. Tiripicchio, *Organometallics*, 1988, **7**, 258.
57. B. Hessen and J. H. Teuben, *Recl. Trav. Chim. Pays-Bas*, 1988, **107**, 208.
58. B. Hessen, J. Blenkers, J. H. Teuben, G. Helgesson, and S. Jagner, *Organometallics*, 1989, **8**, 830.
59. R. Benn and G. Schroth, *J. Organomet. Chem.*, 1982, **228**, 71.
60. J. Scholz and H. Görls, *Organometallics*, 2004, **23**, 320.

61. R. Goddard, C. Krueger, H. G. Abdul, K. H. Thiele, and J. Scholz, *Z. Naturforsch., B: Chem. Sci.*, 1994, **49**, 519.
62. M. T. Anthony, M. L. H. Green, and D. Young, *J. Chem. Soc., Dalton Trans.*, 1975, 1419.
63. F. G. N. Cloke, K. A. E. Courtney, A. A. Sameh, and A. C. Swain, *Polyhedron*, 1989, **8**, 1641.
64. E. J. Wucherer and E. L. Muetterties, *Organometallics*, 1987, **6**, 1696.
65. E. J. Wucherer and E. L. Muetterties, *Organometallics*, 1987, **6**, 1691.
66. D. W. Blackburn, D. Britton, and J. E. Ellis, *Angew. Chem., Int. Ed. Engl.*, 1992, **31**, 1495.
67. H. Bsoennemann and B. Korall, *Angew. Chem., Int. Ed. Engl.*, 1992, **31**, 1490.
68. T. G. Gardner and G. S. Girolami, *Angew. Chem.*, 1988, **100**, 1755.
69. P. Biagini, F. Calderazzo, and G. Pampaloni, *J. Organomet. Chem.*, 1988, **355**, 99.
70. F. Calderazzo, F. Marchetti, G. Pampaloni, W. Hiller, H. Antropiusova, M. Helena, and K. Mach, *Chem. Ber.*, 1989, **122**, 2229.
71. J. K. Seaburg, P. J. Fischer, V. G. Young Jr, and J. E. Ellis, *Angew. Chem., Int. Ed. Engl.*, 1998, **37**, 155.
72. T. K. Hollis, Y. J. Ahn, and F. S. Tham, *Organometallics*, 2003, **22**, 1432.
73. G. E. Herberich, U. Englert, and A. Schmitz, *Organometallics*, 1997, **16**, 3751.
74. J. J. Eisch, F. A. Owuor, and P. O. Otieno, *Organometallics*, 2001, **20**, 4132.
75. G. Chandra and M. F. Lappert, *J. Chem. Soc. A*, 1968, 1940.
76. A. M. Cardoso, R. J. H. Clark, and S. Moorhouse, *J. Chem. Soc., Dalton Trans.*, 1980, 1156.
77. R. Beckhus, Titanocenes, in ‘Metallocenes Synthesis Reactivity Applications’, eds. A. Togni and R. L. Halterman, Wiley-VCH, Weinheim, 1998, p. 153.
78. R. L. Halterman, in ‘Metallocenes Synthesis Reactivity Applications’, eds. A. Togni and R. L. Halterman, Wiley-VCH, Weinheim, 1998, p. 355.
79. J. E. Bercaw, R. H. Marvich, L. G. Bell, and H. H. Brintzinger, *J. Am. Chem. Soc.*, 1972, **94**, 1219.
80. L. G. Hidalgo, M. Mena, F. Palacios, P. Royo, and R. Serrano, *J. Organomet. Chem.*, 1988, **340**, 37.
81. M. Bottrill, P. D. Gavens, J. W. Kelland, and K. McMeeking, in ‘Comprehensive Organometallic Chemistry’, eds. G. Wilkinson, F. G. A. Stone, and E. W. Abel, Pergamon, Oxford, 1982, Vol. 3, Chap. 22.3, p. 396.
82. C. McDade, J. C. Green, and J. E. Bercaw, *Organometallics*, 1982, **1**, 1629.
83. K. Mach, V. Varga, V. Hanus, and P. Sedmera, *J. Organomet. Chem.*, 1991, **415**, 87.
84. D. T. Mallin, M. D. Rausch, E. A. Mintz, and A. R. Rheingold, *J. Organomet. Chem.*, 1990, **381**, 35.
85. I. Jibril, S. Abu-Orabi, S. A. Klaib, W. Imhof, and G. Huttner, *J. Organomet. Chem.*, 1992, **433**, 253.
86. J. Okuda, *J. Organomet. Chem.*, 1990, **385**, C39.
87. I. F. Urazowski, V. I. Ponomaryov, O. G. Ellert, I. E. Nifant’ev, and D. A. Lemenovskii, *J. Organomet. Chem.*, 1988, **356**, 181.
88. A. I. Sizov, G. L. Soloveichik, I. F. Urazowskii, V. K. Bel’skii, and B. M. Bulychev, *Metalloorg. Khim.*, 1988, **1**, 793.
89. J. Okuda, *J. Organomet. Chem.*, 1988, **356**, C43.
90. J. Okuda, *Chem. Ber.*, 1990, **123**, 87.
91. K. H. Thiele, F. Rehbaum, H. Baumann, H. Schumann, F. H. Goerlitz, and R. Weimann, *Z. Anorg. Allg. Chem.*, 1992, **613**, 76.
92. M. P. Castellani, S. J. Geib, A. L. Rheingold, and W. C. Trogler, *Organometallics*, 1987, **6**, 2524.
93. U. Thewalt and G. Schmid, *J. Organomet. Chem.*, 1991, **412**, 343.
94. M. D. Rausch, J. F. Lewison, and W. P. Hart, *J. Organomet. Chem.*, 1988, **358**, 161.
95. E. A. Anslyn, R. H. Grubbs, C. Felten, and D. Rehder, *Inorg. Synth.*, 1992, **29**, 198.
96. M. D. Rausch, B. H. Edwards, R. D. Rogers, and J. L. Atwood, *J. Am. Chem. Soc.*, 1983, **105**, 3882.
97. J. Szymoniak, M. M. Kubicki, J. Besancon, and C. Moise, *Inorg. Chim. Acta*, 1991, **180**, 153.
98. M. D. Rausch and W. C. Spink, *Synth. React. Inorg. Met.-Org. Chem.*, 1989, **19**, 1093.
99. S. Ciruelos, A. Sebastian, T. Cuenca, P. Gomez-Sal, A. Manzanero, and P. Royo, *J. Organomet. Chem.*, 2000, **604**, 103.
100. A. B. Vazquez, P. Royo, and E. Herdtweck, *J. Organomet. Chem.*, 2003, **683**, 155.
101. V. V. Kotov, E. V. Avtomonov, J. Sundermeyer, K. Harms, and D. A. Lemenovskii, *Eur. J. Inorg. Chem.*, 2002, 678.
102. R. L. Halterman and K. P. C. Vollhardt, *Organometallics*, 1988, **7**, 883.
103. L. A. Paquette, K. J. Moriarty, J. A. McKinney, and R. D. Rogers, *Organometallics*, 1989, **8**, 1707.
104. Z. Chen, K. Eriks, and R. L. Halterman, *Organometallics*, 1991, **10**, 3449.
105. L. A. Paquette, K. J. Moriarty, P. Meunier, B. Gautheron, C. Sornay, R. D. Rogers, and A. L. Rheingold, *Organometallics*, 1989, **8**, 2159.
106. J. C. Gallucci, B. Gautheron, M. Gugelchuk, P. Meunier, and L. A. Paquette, *Organometallics*, 1987, **6**, 15.
107. C. Sornay, P. Meunier, B. Gautheron, G. A. O’Doherty, and L. A. Paquette, *Organometallics*, 1991, **10**, 2082.
108. F. Zaegel, J. C. Gallucci, P. Meunier, B. Gautheron, E. I. Bzowej, and L. A. Paquette, *Organometallics*, 1995, **14**, 4576.

109. M. Horacek, P. Stepnicka, S. Gentil, K. Fejfarova, J. Kubista, N. Pirio, P. Meunier, F. Gallou, L. A. Paquette, and K. Mach, *J. Organomet. Chem.*, 2002, **656**, 81.
110. L. A. Paquette and M. R. Sivik, *Organometallics*, 1992, **11**, 3503.
111. M. Hillman and A. Weiss, *J. Organomet. Chem.*, 1972, **42**, 123.
112. J. J. Eisch, X. Shi, and F. A. Owuor, *Organometallics*, 1998, **17**, 5219.
113. I. F. Urazowski, L. O. Atovmyan, S. G. Mkoyan, R. Broussier, G. Perron, B. Gautheron, and F. Robert, *J. Organomet. Chem.*, 1997, **536/537**, 531.
114. S. Knuppel, G. Erker, and R. Frohlich, *Angew. Chem. Int. Ed. Engl.*, 1999, **38**, 1923.
115. P. Jutzi and G. Dickbreder, *Chem. Ber.*, 1986, **119**, 1750.
116. H. Lang and D. Seyferth, *Organometallics*, 1991, **10**, 347.
117. H. G. Alt, K. Fottinger, and W. Milius, *J. Organomet. Chem.*, 1998, **564**, 109.
118. F. Wochner, L. Zsolnai, G. Huttner, and H. H. Brintzinger, *J. Organomet. Chem.*, 1985, **288**, 69.
119. C. Alonso-Moreno, A. Antinolo, I. Lopez-Solera, A. Otero, S. Prashar, A. M. Rodriguez, and E. Villasenor, *J. Organomet. Chem.*, 2002, **656**, 129.
120. G. Tian, B. Wang, X. Dai, S. Xu, X. Zhou, and J. Sun, *J. Organomet. Chem.*, 2001, **634**, 145.
121. J. H. Shin, T. Hascall, and G. Parkin, *Organometallics*, 1999, **18**, 6.
122. G. Tian, B. Wang, X. Dai, S. Xu, X. Zhou, and J. Sun, *J. Organomet. Chem.*, 2001, **634**, 145.
123. C. Alonso-Moreno, A. Antinolo, I. Lopez-Solera, A. Otero, S. Prashar, A. M. Rodriguez, and E. Villasenor, *J. Organomet. Chem.*, 2002, **656**, 129.
124. R. L. Halterman, A. Tretyakov, and M. A. Khan, *J. Organomet. Chem.*, 1998, **568**, 41.
125. R. L. Halterman, D. Combs, and M. A. Khan, *Organometallics*, 1998, **17**, 3900.
126. P. Burger and H. H. Brintzinger, *J. Organomet. Chem.*, 1991, **407**, 207.
127. R. Gomez, T. Cuenca, P. Royo, M. A. Pellinghelli, and A. Tiripicchio, *Organometallics*, 1991, **10**, 1505.
128. G. S. Herrmann, H. G. Alt, and M. D. Rausch, *J. Organomet. Chem.*, 1991, **401**, C5.
129. F. R. W. P. Wild, L. Zsolnai, G. Huttner, and H. H. Brintzinger, *J. Organomet. Chem.*, 1982, **232**, 233.
130. F. R. W. P. Wild, M. Wasiucionek, G. Huttner, and H. H. Brintzinger, *J. Organomet. Chem.*, 1985, **288**, 63.
131. A. K. Schäfer, L. Zsolnai, G. Huttner, and H. H. Brintzinger, *J. Organomet. Chem.*, 1987, **328**, 87.
132. P. Burger, K. Hortmann, J. Diebold, and H. H. Brintzinger, *J. Organomet. Chem.*, 1991, **417**, 9.
133. S. Gutmann, P. Burger, H. U. Hund, J. Hofmann, and H. H. Brintzinger, *J. Organomet. Chem.*, 1989, **369**, 343.
134. T. K. Hollis, A. L. Rheingold, N. P. Robinson, J. Whelan, and B. Bosnich, *Organometallics*, 1992, **11**, 2812.
135. A. L. Rheingold, N. P. Robinson, J. Whelan, and B. Bosnich, *Organometallics*, 1992, **11**, 1869.
136. M. S. Erickson, F. R. Fronczek, and M. L. McLaughlin, *J. Organomet. Chem.*, 1991, **415**, 75.
137. P. Beagley, P. Davies, H. Adams, and C. White, *Can. J. Chem.*, 2001, **79**, 731.
138. R. L. Halterman, Z. Chen, and M. A. Khan, *Organometallics*, 1996, **15**, 3957.
139. M. J. Burk, S. L. Colletti, and R. L. Halterman, *Organometallics*, 1991, **10**, 2998.
140. M. E. Huttenloch, J. Diebold, U. Rief, H. H. Brintzinger, A. M. Gilbert, and T. J. Katz, *Organometallics*, 1992, **11**, 3600.
141. M. Ringwald, R. Stuermer, and H. H. Brintzinger, *J. Am. Chem. Soc.*, 1999, **121**, 1524.
142. R. L. Halterman and T. M. Ramsey, *J. Organomet. Chem.*, 1997, **530**, 225.
143. R. L. Halterman and T. M. Ramsey, *J. Organomet. Chem.*, 1997, **530**, 225.
144. R. L. Halterman, D. Combs, J. Kihega, and M. A. Khan, *J. Organomet. Chem.*, 1996, **520**, 163.
145. R. L. Halterman, Z. Chen, and M. A. Khan, *Organometallics*, 1996, **15**, 3957.
146. S. Collins, Y. Hong, and N. J. Taylor, *Organometallics*, 1990, **9**, 2695.
147. S. Collins, Y. Hong, R. Ramachandran, and N. J. Taylor, *Organometallics*, 1991, **10**, 2349.
148. J. Sassmannshausen, A. K. Powell, C. E. Anson, S. Wocadlo, and M. Bochmann, *J. Organomet. Chem.*, 1999, **592**, 84.
149. P. J. W. Deckers, A. J. Van der Linden, A. Meetsma, and B. Hessen, *Eur. J. Inorg. Chem.*, 2000, 929.
150. T. Klapoetke and U. Thewalt, *J. Organomet. Chem.*, 1988, **356**, 173.
151. P. Gowik and T. Klapötke, *J. Organomet. Chem.*, 1991, **402**, 349.
152. T. Klapötke, *Polyhedron*, 1988, **7**, 1221.
153. J. Malek, T. Jelinek, J. Holecek, and K. Handlir, *Z. Chem.*, 1993, **23**, 189.
154. B. Honold and U. Thewalt, *J. Organomet. Chem.*, 1986, **316**, 291.
155. U. Thewalt and K. Berhalter, *J. Organomet. Chem.*, 1986, **302**, 193.
156. P. A. Seewald, G. S. White, and D. W. Stephan, *Can. J. Chem.*, 1988, **66**, 1147.
157. M. Bochmann, L. M. Wilson, M. B. Hursthouse, and M. Motevalli, *Organometallics*, 1988, **7**, 1148.
158. M. Bochmann, L. M. Wilson, M. B. Hursthouse, and R. L. Short, *Organometallics*, 1987, **6**, 2556.

159. M. Bochmann, A. J. Jaggar, and J. C. Nicholls, *Angew. Chem.*, 1990, **102**, 830.
160. M. Bochmann, A. J. Jaggar, L. M. Wilson, M. B. Hursthouse, and M. Motevalli, *Polyhedron*, 1989, **8**, 1838.
161. T. Klapoetke, *Inorg. Chim. Acta*, 1988, **150**, 165.
162. Y. Dang and H. J. Geise, *J. Organomet. Chem.*, 1991, **405**, 1.
163. E. Samuel and J. Vedel, *Organometallics*, 1989, **8**, 237.
164. R. Jungst, D. Sekutowski, and G. Stucky, *J. Am. Chem. Soc.*, 1974, **96**, 8108.
165. D. W. Stephan, *Organometallics*, 1992, **11**, 996.
166. P. C. Blake, E. Hey, M. F. Lappert, J. L. Atwood, and H. Zhang, *J. Organomet. Chem.*, 1988, **353**, 307.
167. J. Wang, F. Liu, and L. Bai, *Chem. Res. Chin. Univ.*, 1991, **7**, 47.
168. J. Wang, F. Liu, and L. Bai, *Org. React. Mech.*, 1989, 47.
169. T. Cuenca, W. A. Herrmann, and T. W. Ashworth, *Organometallics*, 1986, **5**, 2514.
170. H. H. Teubenn, in 'Fundamental and Technological Aspects of Organo-f-Element Chemistry', eds. T. J. Marks and I. L. Fragala, Reidel, Dordrect, 1986, p. 195.
171. G. A. Luinstra, L. C. Ten Cate, H. J. Heeres, J. W. Pattiasina, A. Meetsma, and J. H. Teuben, *Organometallics*, 1991, **10**, 3227.
172. G. A. Luinstra, J. Vogelzang, and J. H. Teuben, *Organometallics*, 1992, **11**, 2273.
173. G. A. Luinstra and J. H. Teuben, *J. Organomet. Chem.*, 1992, **420**, 337.
174. G. A. Luinstra and J. H. Teuben, *J. Am. Chem. Soc.*, 1992, **114**, 3361.
175. R. Fandos, A. Meetsma, and J. H. Teuben, *Organometallics*, 1991, **10**, 2665.
176. L. Hao and J. F. Harrod, *Inorg. Chem. Commun.*, 1999, **2**, 191.
177. J. G. Murry, *J. Am. Chem. Soc.*, 1959, **81**, 752.
178. D. J. Sikora, K. L. Moriarty, and M. D. Rausch, *Inorg. Synth.*, 1990, **28**, 248.
179. D. J. Sikora, D. W. Macomber, and M. D. Rausch, *Adv. Organomet. Chem.*, 1986, **25**, 317.
180. B. H. Edwards, R. D. Rogers, D. J. Sikora, J. L. Atwood, and M. D. Rausch, *J. Am. Chem. Soc.*, 1983, **105**, 416.
181. L. B. Kool, M. D. Rausch, H. G. Alt, M. Hererhold, U. Thewalt, and B. Wolf, *Angew. Chem., Int. Ed. Engl.*, 1985, **24**, 394.
182. C. Jegat, M. Fouassier, M. Tranquille, and J. Mascetti, *Inorg. Chem.*, 1991, **30**, 1529.
183. S. A. Cohen, P. R. Auburn, and J. E. Bercaw, *J. Am. Chem. Soc.*, 1983, **105**, 1136.
184. S. A. Cohen and J. E. Bercaw, *Organometallics*, 1985, **4**, 1006.
185. U. Rosenthal, V. V. Burlakov, P. Arndt, W. Baumann, and A. Spannenberg, *Organometallics*, 2003, **22**, 884.
186. A. Ohff, S. Pulst, C. Lefeber, N. Peulecke, P. Arndt, V. V. Burkalov, and U. Rosenthal, *Synlett*, 1996, 111.
187. H. Hartmann, B. Sarkar, W. Kaim, and J. Fiedler, *J. Organomet. Chem.*, 2003, **687**, 100.
188. Y. Zhang, Y. Mu, Z. Shi, C. Lue, J. Wang, Y. Zhang, L. Qiao, and S. Feng, *Organometallics*, 2003, **22**, 3877.
189. Y. M. Zhang, L. C. Ying, G. Li, J. Xu, Y. Zhang, D. Zhu, and S. Feng, *Organometallics*, 2004, **23**, 540.
190. Y.-X. Chen, P.-F. Fu, C. L. Stern, and T. J. Marks, *Organometallics*, 1997, **16**, 5958.
191. L. E. Turner, M. G. Thorn, P. E. Fanwick, I. P. Rothwell, and P. Ian, *Organometallics*, 2004, **23**, 1576.
192. A. Rau, S. Schmitz, and G. Luft, *J. Organomet. Chem.*, 2000, **608**, 71.
193. M. H. Lee, J.-W. Hwang, Y. Kim, Y. Han, and Y. Do, *Organometallics*, 2000, **19**, 5514.
194. H. Wang, Y. Wang, H.-W. Li, and Z. Xie, *Organometallics*, 2001, **20**, 5110.
195. J. Wang, C. Zheng, J. A. Maguire, and N. S. Hosmane, *Organometallics*, 2003, **22**, 4839.
196. G. Zi, H.-W. Li, and Z. Xie, *Organometallics*, 2002, **21**, 3850.
197. Y.-L. Lee, J.-D. Lee, J. Ko, S.-H. Kim, and S. O. Kang, *Chem. Commun.*, 2003, 1364.
198. R. Gomez, P. Gomez-Sal, A. Martin, A. Nunez, P. A. del Real, and P. Royo, *J. Organomet. Chem.*, 1998, **564**, 93.
199. Y.-X. Chen and T. J. Marks, *Organometallics*, 1997, **16**, 3649.
200. J. Okuda, K. Musikabhumma, and P.-J. Sinnema, *Isr. J. Chem.*, 2003, **42**, 383.
201. J. Klosin, W. J. Kruper Jr, P. N. Nickias, G. R. Roof, P. De Waele, and K. A. Abboud, *Organometallics*, 2001, **20**, 2663.
202. J.-F. Carpentier, V. P. Maryin, J. Luci, and R. F. Jordan, *J. Am. Chem. Soc.*, 2001, **123**, 898.
203. A. Bertuleit, M. Konemann, L. Duda, G. Erker, and R. Frohlich, *Top. Catal.*, 1999, **7**, 37.
204. W. S. Seo, Y. J. Cho, S. C. Yoon, J. T. Park, and Y. Park, *J. Organomet. Chem.*, 2001, **640**, 79.
205. D. D. Devore, F. J. Timmers, D. L. Hasha, R. K. Rosen, T. J. Marks, P. A. Deck, and C. L. Stern, *Organometallics*, 1995, **14**, 3132.
206. M. Dahlmann, J. Schottek, R. Frohlich, D. Kunz, M. Nissinen, G. Erker, G. Fink, and R. Kleinschmidt, *Dalton*, (12), 2000, 1881.
207. H. Braunschweig, F. M. Breitling, C. von Koblinski, A. J. P. White, and D. J. Williams, *Dalton Trans.*, 2004, **6**, 938.
208. S. Bredeau, G. Altenhoff, K. Kunz, S. Döring, S. Grimme, G. Kehr, and G. Erker, *Organometallics*, 2004, **23**, 1836.
209. G. Altenhoff, S. Bredeau, G. Erker, G. Kehr, O. Kataeva, and R. Froehlich, *Organometallics*, 2002, **21**, 4084.
210. A. J. Ashe III, X. Fang, and J. W. Kampf, *Organometallics*, 1999, **18**, 1363.

211. S. Feng, J. Klosin, W. J. Kruper Jr, M. H. McAdon, D. R. Neithamer, P. N. Nickias, J. T. Patton, D. R. Wilson, K. A. Abboud, and C. L. Stern, *Organometallics*, 1999, **18**, 1159.

212. G. M. Diamond, M. L. H. Green, and N. M. Walker, *J. Organomet. Chem.*, 1991, **413**, C1.

213. G. M. Diamond, M. L. H. Green, P. Mountford, and N. M. Walker, *J. Chem. Soc., Dalton Trans.*, 1992, 2259.

214. L. B. Kool, M. D. Rausch, and R. D. Rogers, *J. Organomet. Chem.*, 1985, **297**, 289.

215. M. Ogasa, M. D. Rausch, and R. D. Rogers, *J. Organomet. Chem.*, 1991, **403**, 279.

216. L. B. Kool, M. Ogasa, M. D. Rausch, and R. D. Rogers, *Organometallics*, 1989, **8**, 1785.

217. M. D. Rausch, M. Ogasa, M. A. Ayers, R. D. Rogers, and A. N. Rollins, *Organometallics*, 1991, **10**, 2481.

218. R. Fierro, M. D. Rausch, R. D. Rogers, and M. Herberhold, *J. Organomet. Chem.*, 1994, **472**, 87.

219. M. T. Andras and S. A. Duraj, *Inorg. Chem.*, 1993, **32**, 2874.

220. F. G. N. Cloke, J. C. Green, P. B. Hitchcock, S. C. P. Joseph, P. Mountford, N. Kaltsoyannis, and A. McCamley, *J. Chem. Soc., Dalton Trans.: Inorg. Chem.*, 1994, 2867.

221. M. Horacek, V. Kupfer, U. Thewalt, M. Polasek, and K. Mach, *J. Organomet. Chem.*, 1999, **579**, 126.

222. M. Horacek, J. Hiller, U. Thewalt, P. Stepnicka, and K. Mach, *J. Organomet. Chem.*, 1998, **571**, 77.

223. R. D. Ernst, *Chem. Rev.*, 1988, **88**, 1255.

224. R. D. Ernst, *Chem. Rev.*, 1988, **88**, 1255.

225. P. T. DiMauro and P. Wolczanski, *Organometallics*, 1987, **6**, 1947.

226. V. Kulsomphob, R. Tomaszewski, A. L. Rheingold, A. M. Arif, R. D. Ernst, and D. Richard *J. Organomet. Chem.*, 2002, **655**, 158.

227. I. Hyla-Kryspin, T. E. Waldman, E. Melendez, W. Trakarnpruk, A. M. Arif, M. L. Ziegler, R. D. Ernst, and R. Gleiter, *Organometallics*, 1995, **14**, 5030.

228. R. Tomaszewski, K.-C. Lam, A. L. Rheingold, and R. D. Ernst, *Organometallics*, 1999, **18**, 4174.

229. B. G. Harvey, R. Basta, A. M. Arif, and R. D. Ernst, *Dalton Trans.*, 2004, 1221.

230. T. V. Lubben, P. T. Wolczanski, and G. D. Van Duyne, *Organometallics*, 1984, **3**, 977.

231. V. Lubben and P. T. Wolczanski, *J. Am. Chem. Soc.*, 1987, **109**, 424.

232. S. L. Latesky, A. K. McMullen, I. P. Rothwell, and J. C. Huffman, *J. Am. Chem. Soc.*, 1985, **107**, 5981.

233. R. W. Chesnut, L. D. Durfee, P. E. Fanwick, I. P. Rothwell, K. Folting, and J. C. Huffman, *Polyhedron*, 1987, **6**, 2019.

234. L. R. Chamberlain, L. D. Durfee, P. E. Fanwick, L. Kobriger, S. L. Latesky, A. K. McMullen, I. P. Rothwell, K. Folting, J. C. Huffman, W. E. Streib, and R. Wang, *J. Am. Chem. Soc.*, 1987, **109**, 390.

235. L. R. Chamberlain, L. D. Durfee, P. E. Fanwick, L. M. Kobriger, S. L. Latesky, A. K. McMullen, B. D. Steffey, I. P. Rothwell, K. Folting, and J. C. Huffman, *J. Am. Chem. Soc.*, 1987, **109**, 6068.

236. J. R. Dilworth, J. Hanich, M. Krestel, J. Beck, and J. Strähle, *J. Organomet. Chem.*, 1986, **315**, C9.

237. J. E. Hill, P. E. Fanwick, and I. P. Rothwell, *Organometallics*, 1990, **9**, 2211.

238. J. E. Hill, P. E. Fanwick, and I. P. Rothwell, *Organometallics*, 1991, **10**, 15.

239. M. G. Thorn, J. E. Hill, S. A. Waratuke, E. S. Johnson, P. E. Fanwick, and I. P. Rothwell, *J. Am. Chem. Soc.*, 1997, **119**, 8630.

240. J. E. Hill, P. E. Fanwick, and I. P. Rothwell, *Organometallics*, 1992, **11**, 1771.

241. A. E. Fenwick, K. Phomphrai, M. G. Thorn, J. S. Vilardo, C. A. Trefun, B. Hanna, P. E. Fanwick, and I. P. Rothwell, *Organometallics*, 2004, **23**, 2146.

242. A. E. Fenwick, P. E. Fanwick, and I. P. Rothwell, *Organometallics*, 2003, **22**, 535.

243. P. N. Riley, P. E. Fanwick, and I. P. Rothwell, *J. Chem. Soc., Dalton Trans.*, 2001, 181.

244. J. Lee, P. E. Fanwick, and I. P. Rothwell, *Organometallics*, 2003, **22**, 1546.

245. M. G. Thorn, Z. C. Etheridge, P. E. Fanwick, I. P. Rothwell, *Organometallics*, 1998, **17**, 3636.

Transition Metal Carbonyls: Infrared Spectra

John A. Timney
Newcastle Church High School, Newcastle upon Tyne, UK

1 Introduction 1
2 Principles of Molecular Force Fields 1
3 Energy Factored Force Fields 3
4 CO–CO Interaction Constants 5
5 Calculating Force Constants from ν(CO) Spectra 6
6 Applications of CO Force Constants 11
7 Polynuclear Carbonyl Complexes 13
8 Intensities 13
9 Recent Developments 13
10 Related Articles 14
11 Further Reading 14
12 References 14

1 INTRODUCTION

Metal carbonyl compounds are, with very few exceptions, polyatomic molecules with, as might be expected, rich and interesting infrared spectra. For a molecule $M(CO)_x(L)_y$, there will be absorptions due to the motions of the CO groups and, of course, any other ligands attached to the metal. It might seem a little myopic then to concentrate by far the greatest proportion of spectroscopic effort to the region around 2000 cm^{-1}. Around this 2000 cm^{-1} region of the IR (and Raman) spectrum, we find the 'CO-stretching' bands, ν(CO), of metal carbonyl complexes. The number, pattern, and position of these absorptions give an enormous amount of information about molecular structure, symmetry, and bonding. The 'ν(CO)' region has, since the early 1960s, been the scene of some exciting work and the arena for many arguments.

In the mid-1970s, Braterman[1] published a complete text devoted to metal carbonyl spectra and, although out of date in several areas, it remains a valuable resource, particularly in its advice on sample preparation and handling where the generally high toxicity and ready decomposition of metal carbonyl complexes causes more problems than might be usually found. Another helpful source of information, although even older, by Adams[2] contains ν(CO) information on a large number of transition metal carbonyl complexes.

Paradoxically, gaseous carbon monoxide itself is not a strong IR absorber. Yet the IR spectrum of any transition metal carbonyl complex with terminal CO groups is dominated by the very high intensity of some of the CO-stretching absorptions. Since IR intensities are proportional to the square of the dipole change associated with the vibration, the implication is that there is a large dipole change when a carbonyl group vibrates. This effect derives from the π-bonding in the M–C–O unit.[3] The stretching of a CO group bonded to a metal atom leads to a lowering of the energy of the 2π orbital, since the antibonding interaction is weakened and the orbital becomes a better acceptor. At the same time, the overlap of the carbon and the metal orbitals is increased as the M–C distance lessens. There is, therefore, a great deal of electronic flow and ebb within each vibration and, consequently, a high dipole change.

2 PRINCIPLES OF MOLECULAR FORCE FIELDS

The bonds that hold molecules together obey Hooke's law (for small distortions at least). That is, the restoring force F is proportional to the extension x

$$F = -kx \tag{1}$$

The potential energy, V, of such a system is given by

$$V = \frac{(kx^2)}{2} \tag{2}$$

The constant of proportionality (k) in both cases is the stretching force constant and, in the same way that a force constant can measure the strength of a mechanical spring, k gives a measure of the strength of a chemical bond. Indeed, the force constant measures bond strength when the atoms are near their equilibrium positions, a far more subtle measure than the dissociation energy.

The vibration of a molecule does not affect its center of mass. The vibration is equivalent to that of a single particle of reduced mass μ moving in a field of force constant k. A diatomic molecule AB (such as CO) will vibrate with a frequency ν_{AB} given by the equation

$$\nu_{AB} = \frac{1}{2\pi}\sqrt{\frac{k_{AB}}{\mu_{AB}}} \tag{3}$$

where μ_{AB} is the reduced mass of the molecule, given by

$$\mu_{AB} = \frac{(m_A \times m_B)}{(m_A + m_B)} \tag{4}$$

Rearranging equations (3) and (4), and gathering constants so that ν_{AB} is in cm^{-1} and the masses of the atoms are in atomic mass units, gives k_{AB} in SI units of newtons per meter ($\mathrm{N\,m^{-1}}$):

$$k_{AB} = 5.8915 \times 10^{-5} \nu_{AB}^2 \mu_{AB} \tag{5}$$

If the atoms concerned are ^{12}C and ^{16}O, then

$$k_{CO} = 4.0393 \times 10^{-4} \nu_{CO}^2 \tag{6}$$

Clearly, calculating the force constant of a diatomic molecule is simple if we know its vibrational frequency.

Unfortunately, the finding of a set of force constants for a polyatomic molecule is greatly complicated by the fact that distorting one bond will affect all the other bonds in the molecule to some extent. A rigorous description of the problem of finding force constants from frequencies (and *vice versa*) in polyatomic molecules has been given by Wilson, Decius, and Cross.[4] Here a simpler, almost qualitative approach, is presented.

Equation (5) could have been written as

$$k_{AB}\mu_{AB}^{-1} - 5.8915 \times 10^{-5} \nu_{AB}^2 = 0$$

or, more conveniently,

$$k_{AB}\mu_{AB}^{-1} - \lambda_{AB} = 0 \tag{7}$$

If the bonds in a polyatomic molecule were to vibrate in total isolation (i.e., without affecting any other bonds in the molecule), there would be a series of equations similar to equation (7):

$$\begin{aligned} k_1\mu_1^{-1} - \lambda_1 &= 0 \\ k_2\mu_2^{-1} - \lambda_2 &= 0 \\ k_3\mu_3^{-1} - \lambda_3 &= 0 \end{aligned} \tag{8}$$

and so on.

Unfortunately, in real molecules the situation is not that simple. Stretching a bond in a polyatomic molecule has consequences for every other bond in the molecule, both in terms of the alteration of orbital energies (and by implication, the strength of the bonds) and the mechanical movement of neighbor atoms. The effects on the orbital energies can be thought of as a matrix containing all the force constants (called the F matrix). The F matrix contains **stretching force constants** along the diagonal (e.g., k_1, k_2, k_3, etc.) and off-diagonal terms, which are called **interaction constants** (k_{12}, k_{13}, k_{23}, etc.). Similarly, the matrix with inverse reduced masses (called the G matrix) contains off-diagonal terms for atoms, which are common between two bonds, although the G matrix elements linking distortions with no atom in common are zero. Short-circuiting some involved mathematics then, this reduces our overall problem to a single secular equation:

$$|FG - \lambda E| = 0 \tag{9}$$

The off-diagonal terms in λ have been removed (simply because they do not exist), while the diagonal elements occur with coefficients of unity.

Theoretically then, given the complete structure of a molecule (from which the G matrix can be constructed) and all the force constants (the force field from which the F matrix can be constructed), we can calculate the vibrational frequencies. Unfortunately, the problem is nearly always the other way round. We invariably have the observed vibrations and need to calculate force constants. The basic problem with calculating force fields is that a nonlinear molecule of N atoms has $3N - 6$ fundamental vibrations and there are $(N^2 + N)/2$ independent force constants. Clearly then, for substantial transition metal carbonyl molecules, such as *cis*-$Cr(CO)_4(PF_3)_2$ for example, there are (even allowing for symmetry) many more force constants than observable fundamental frequencies. So, even in the most sophisticated force fields, approximations will appear in some form or the other. A 'general quadratic valence force field' (GQVFF)[5] seeks to use harmonic frequencies and to take account of all terms in the F and G matrices. In truth, the GQVFF is the only way to find a 'real' solution to equation (9). A general procedure for a GQVFF study is as follows: high-resolution IR and Raman spectra are taken; intensity data are collected; fundamental, combination, and overtone bands are analyzed; and related species are compared to establish trends and aid the assignment of fundamental vibrations. Isotopic substitution is routinely used to give a chemically identical molecule with atoms of different masses (i.e., the F matrix is unchanged but the G matrix has different elements). This, hopefully, provides sufficient additional data to ensure that the number of observed frequencies equals or is greater than the number of force constants. After all accessible information has been gathered, it is processed to give a force field. This has, for many years now, been accomplished by computer programs that can optimize a solution to a 'best fit' situation and provide some feel for the errors that are present in the measurements. This list of prerequisites for a GQVFF study limits the enthusiasm for undertaking such work. In his study of the group 6 hexacarbonyls ($Cr(CO)_6$, $Mo(CO)_6$, $W(CO)_6$), Jones[6] collected and analyzed IR and Raman spectra of the $M(^{12}C^{16}O)_6$ species in the gas phase, cyclohexane or CCl_4 solution, and as solids. He then repeated the entire process for the $M(^{12}C^{18}O)_6$ and $M(^{13}C^{16}O)_6$ species. Even then, for $Cr(CO)_6$, a 'unique solution' depended on some minor, but still fairly arbitrary, approximations.

Clearly, a method that requires such devotion will only ever attract a small number of protagonists. A different approach has been adopted for metal carbonyls, which arises from an interesting situation.

3 ENERGY FACTORED FORCE FIELDS

The vibrational spectra of metal carbonyls have absorptions that involve the M–C–O unit in the regions given in Table 1.

Notice that the ν(CO) vibrations are much higher in frequency than all other involving the M–C–O unit. Thus, it is not unreasonable to think of the ν(CO) modes as completely C–O stretching. Taking this thought one stage further, we might argue that, while coupling between different ν(CO) modes occurs (via off-diagonal terms in the F matrix), coupling between ν(CO) and any other vibration can be neglected. By this process, usually described as energy factoring, we radically reduce the sizes of the F and G matrices. In effect, we are blinkered so that we totally ignore every vibration except those assigned as 'C–O stretching' modes. In the F matrix, all terms which link the displacement of a C–O bond to the change in any other bonds (apart from another CO group) are neglected. This means that only two types of force constant remain in the F matrix: C–O stretching force constants (k_{CO}) along the diagonal, and CO–CO interaction constants ($k_{\mathrm{CO,CO}}$) as off-diagonal terms. The G matrix is reduced to an array containing the reciprocal mass of the CO group as the only elements (along the diagonal) since no two CO groups have a common atom. For the spectroscopist, a carbonyl such as $\mathrm{Ni(CO)_3PF_3}$ might have a rich and interesting spectrum, but in trying to glean some information about the bonding within the molecule, we here would only be interested in the two sharp, intense bands in the ν(CO) region.

This approach was first described in detail by Cotton and Kraihanzel in 1962.**[7]** The *Cotton–Kraihanzel Force Field* (CKFF) was very quickly taken up by workers in the field and extensively used as a tool for analyzing ν(CO) frequencies to produce force constants that made chemical sense and were readily accessible. Now, with its application in metal nitrosyl**[8]** and dinitrogen spectroscopy**[9]** the CKFF often appears under the more general name of the *Energy Factored Force Field* (EFFF) or *Frequency Factored Force Field* ($\mathrm{F^4}$). An equally important paper, by Haas and Sheline,**[10]** followed Cotton's pioneering work and investigated the mathematics rather more fully, and facilitated work on isotopic species.

However, the Cotton–Kraihanzel force field and the entire philosophy of energy factoring was sharply criticized by Jones who contended that the CKFF yielded CO force constants, which showed some consistency of pattern but which had no theoretical foundation except in 'gross approximation'.**[5]** The validity of the EFFF was further called into question following the GQVFF study of the group 6 hexacarbonyls.**[6]** The GQVFF force constants (especially the CO–CO interaction constants) calculated were *very* different from those obtained by using anharmonic frequencies in an EFFF. This meant that the proposal that (in octahedral complexes) the *cis* and *trans* CO–CO interaction constants should be related by:

$$k_{trans} = 2k_{cis} \tag{10}$$

was extremely dubious. It remained, however, a useful approximation when there were more EFFF force constants than observable frequencies and, for anharmonic frequencies at least, it seemed to work. For example, the monosubstituted octahedral complexes $\mathrm{M(CO)_5L}$ (C_{4v} point group) have four fundamental ν(CO) modes ($2a_1 + b_2 + e$). Unfortunately, there are five force constants, which means that the problem is underdetermined with one degree of freedom. However, this can be removed by using equation (10) and a 'solution' can be obtained. If the b_2 mode is not observed (it is, strictly, IR-inactive), Cotton approximated further and reduced all the CO–CO interactions to a single parameter, k_i:

$$k_{cis} = \tfrac{1}{2}k_{trans} = k_i \tag{11}$$

Confusingly, in the light of Jones' work,**[11]** a number of studies by Bor**[12]** showed that the EFFF was capable of accurately analyzing complicated isotopic spectra. Elsewhere, Turner and coworkers were producing transition metal carbonyl fragments (e.g., $\mathrm{Mo(CO)_5}$, $\mathrm{Fe(CO)_3}$) in low-temperature matrices and using the EFFF to fit observed frequencies very closely to a set of force constants.**[13]** Like Bor, they were not using completely substituted species, but the whole range of isotopomers (e.g., $\mathrm{Mo(^{12}C^{16}O)_{5-\mathit{x}}(^{13}C^{16}O)_{\mathit{x}}}\,x = 0-5$). Remarkably, in view of Jones' comments, an entire spectrum was regularly being fitted with an average error of less than 1 $\mathrm{cm^{-1}}$ with a unique set of EFFF force constants.

Obviously, there is a dilemma here. Without doubt, the EFFF can be used to fit complicated isotopic spectra with remarkable accuracy, and yet the force constants it uses appear to be at variance with the 'true' force constants. If the F matrix of the EFFF is only a gross approximation of the 'true' (viz. GQVFF) F matrix, then why does the EFFF work so well?

Isotopic substitution in metal carbonyl complexes does not alter the force constant matrix, but changes the elements along the diagonal of the simplified EFFF G matrix from the inverse reduced mass of $\mathrm{^{12}C^{16}O}$ to the inverse reduced mass of the isotopic group (most frequently $\mathrm{^{13}C^{16}O}$, although $\mathrm{^{12}C^{18}O}$ was commonly used for earlier studies**[14]**). Relevant data for the commonly used isotopes in CO is given in Table 2.

When the molecule is completely substituted by isotopically different CO, the ν(CO) frequencies of the fully

Table 1 Vibrations associated with $\mathrm{M(CO)_\mathit{n}}$ complexes

Approximate description	Range ($\mathrm{cm^{-1}}$)
C–O stretching ν(CO)	2150–1750
M–C–O bending δ(MCO)	700–500
M–C stretching ν(MC)	500–300
C–M–C bending δ(CMC)	150–50

Table 2 Mass data for ${}^{x}C^{y}O$ ($x = 12,13$; $y = 16,18$)

	${}^{12}C^{16}O$	${}^{13}C^{16}O$	${}^{12}C^{18}O$	${}^{13}C^{18}O$
Reduced mass	6.85621	7.17241	7.19987	7.54937
Reduced mass ratio	1.00000	0.97771	0.97586	0.95300

substituted molecule should be related to those of the parent (all ${}^{12}C^{16}O$) molecule by

$$\nu' = \left(\frac{\mu}{\mu'}\right)^{\frac{1}{2}} \nu = R\nu \qquad (12)$$

where ν and ν' are the frequencies of the parent and the fully substituted molecule, respectively, and μ and μ' are the reduced masses of the ${}^{12}C^{16}O$ and the isotopic CO. The constant R has been called (somewhat incorrectly) the reduced mass ratio. Unfortunately, equation (12) is not found to be absolutely accurate in practice. When ${}^{12}C^{16}O$ is replaced by ${}^{13}C^{16}O$ ($R = 0.977709$), the differences between observed and calculated frequencies are generally low. However, when ${}^{12}C^{18}O$ ($R = 0.975855$) replaces ${}^{12}C^{16}O$, errors of up to 5 cm^{-1} are commonplace. Bor**[15,16]** used the idea of an 'effective reduced mass ratio', which reduces the error, but this is clearly hiding problems within the EFFF. The double assumptions that anharmonicity (up to 40 cm^{-1} in some cases) can be neglected and that M–C/C–O coupling is negligible are breaking down.

Burdett *et al.***[17]** showed that, to fit isotopic spectra accurately, the EFFF needed two corrections: a factor that takes into account the particular isotope of CO used and a further correction to ameliorate the effects of using anharmonic frequencies. The effect of the neglect of M–C/C–O coupling was originally explained by Miller**[18]** in terms of an x-factor, which depended on the particular CO isotope being used. Anharmonicity is accounted for by another correction that could be determined from the all-${}^{12}C^{16}O$ molecule and the reduced mass ratio.

The effect of these two corrections is best shown (in Table 3) by the close examination of the t_{1u} mode of various isotopomers of $Cr(CO)_6$ in methane matrices at 20 K.

The convincing fit is a considerable improvement on the simplest equation. For other carbonyls and other modes, the dramatic reduction in error is similar. However, it is not possible to apply the x-shift and the anharmonicity correction unless the GQVFF force field and the anharmonicity corrections are known. That said, some useful generalizations can be outlined:

1. the shift due to anharmonicity is always positive for ${}^{13}C^{16}O$, ${}^{12}C^{18}O$, and ${}^{13}C^{18}O$;
2. the x-factor shift is negative for ${}^{13}C^{16}O$, but positive for ${}^{12}C^{18}O$ and ${}^{13}C^{18}O$.

Table 3 Observed and calculated wavenumbers for the $t_{1u}\nu(CO)$ mode of $Cr({}^{a}C^{b}O)_6$ (a = 12, 13; b = 16, 18)

	${}^{12}C^{16}O$	${}^{13}C^{16}O$	${}^{12}C^{18}O$	${}^{13}C^{18}O$
Equation (12) only	1985.4[a]	1941.1	1937.5	1892.1
Anharmonicity correction	0.0	0.9	1.0	1.9
C–O/M–C shift	0.0	−0.3	0.6	0.2
ν_{calc}	1985.4	1941.7	1939.1	1894.2
ν_{obs}	1985.4	1941.7	1939.4	1894.0
$\Delta\nu$ (cm^{-1})	0.0	0.0	0.3	−0.2

[a] Used to calculate other frequencies (in methane matrices at 20 K).

The general conclusion from these observations is that ${}^{13}C^{16}O$ will follow the restrictions of the EFFF best because the shifts caused by anharmonicity and M–C/C–O coupling are of similar magnitude and opposite in sign. We can also see that Bor's effective reduced mass arises through combining the corrections for M–C/C–O coupling and anharmonicity into a single parameter.

The vibrational frequencies of a fully isotopically substituted carbonyl are more or less related to those of the parent molecule in such a way that no new information about the force field can be learned. The situation is different when molecules are partially substituted; $Cr(CO)_6$ is used to illustrate the point. $Cr({}^{12}C^{16}O)_6$ has three fundamental C–O stretches: a_{1g} (Raman), e_g (Raman), and t_{1u} (IR). The force constants that are required are a single stretching force constant (k_{CO}), an interaction constant for mutually *cis* CO groups (k_{cis}), and another interaction constant for mutually *trans* CO groups (k_{trans}). There are three absorptions and three fundamentals, so the force field is fully determined. If, instead of the parent molecule, we had $Cr({}^{12}C^{16}O)_5({}^{13}C^{16}O)$ we would have a molecule with C_{4v} symmetry and five fundamental $\nu(CO)$ bands ($3a_1 + b_2 + e$). With five observed frequencies and only three force constants the force field can be optimized to give a best fit. Access to the entire range of isotopomers in the $Cr({}^{12}C^{16}O)_{6-x}({}^{13}C^{16}O)_x$ series would provide many more observable absorptions than force constants. The best fit force field can be defined as that which reproduces a set of frequencies closest to those observed. From the discussion above, a ${}^{12}C^{16}O/{}^{13}C^{16}O$ mixture would be expected to give low mean errors for ${}^{12}C^{16}O/{}^{12}C^{18}O$, with ${}^{12}C^{16}O/{}^{13}C^{18}O$ giving substantially higher mean errors; this is indeed the case. When Bor's effective reduced mass is introduced as an additional variable, the errors in ${}^{12}C^{16}O/{}^{12}C^{18}O$ and ${}^{12}C^{16}O/{}^{13}C^{18}O$ spectra become comparable with those for ${}^{12}C^{16}O/{}^{13}C^{16}O$.

A point to be made here, most forcibly, is that, although the EFFF is an *approximate* force field, it readily produces force constants that are *valid* (in the sense that they provide crucial information about chemical bonding) and *reliable*.

4 CO–CO INTERACTION CONSTANTS

Without a large number of GQVFF studies on carbonyl complexes the actual relationship between EFFF and GQVFF interaction constants will not be resolved. This does not mean, however, that the CO–CO interaction constants are of no value. Indeed, the magnitude of the interaction constant had long been thought of as a strong indicator of π-bonding within M-C-O units;**[19]** for a large number of tetrahedral $Ni(CO)_3(L)$, $Ni(CO)_2(L)_2$, and $Co(CO)_2(NO)(L)$ complexes there is an excellent linear correlation**[20]** between the CO-stretching force constant, k_{CO}, and the associated CO–CO interaction constant, k_i:

$$k_i = 203 - 0.983k_{CO} \tag{13}$$

So, while remaining as an unknown and complex mixture of GQVFF force constants, k_i must reflect systematic changes in these ‘true’ force constants. Similar straight lines are found for CO groups at 90°, 120°, and 180°. In summary, if two CO groups (with force constants k_1 and k_2) are bonded to a metal atom M, the EFFF interaction constant (k_{12}) is given by

$$k_{12} = A - B\left[\frac{(k_1 + k_2)}{2}\right] \tag{14}$$

where A and B are empirical constants (given in Table 4) for a given C–M–C bond angle. The importance of these relationships is that it removes the need for the arbitrary constraints such as those proposed by Cotton**[7]** and, later, by van der Kelen**[21]** and it provides an excellent way of removing various degrees of freedom from force fields.

Let us take the simple case of $Ni(CO)_4$ to demonstrate the usefulness of equation (14).

A dilute solution of $Ni(CO)_4$ in heptane shows a single band at $2045.7\,cm^{-1}$ in the ν(CO) region.**[22]** This is the t_2 asymmetric stretch. The symmetric stretch (a_1) is Raman-active only. The EFFF force constants required for $Ni(CO)_4$ are k_{CO} and k_i (the CO-stretching force constant and the CO,CO interaction constant respectively) and it would appear impossible to calculate two force constants from one ν(CO) absorption. However, the symmetry force constant for the t_2 mode is

$$K(t_2) = k_{CO} - k_i \tag{15}$$

which, using equation (15), can be rewritten as

$$K(t_2) = k_{CO} - (A - Bk_{CO}) \tag{16}$$

This can be rearranged to give

$$k_{CO} = \frac{(K(t_2) + A)}{(1 + B)} \tag{17}$$

from which it can be calculated that $k_{CO} = 1723.9\,Nm^{-1}$ and $k_i = 33.6\,Nm^{-1}$, and coincidentally, predicting that the a_1 stretch would occur at $2125.3\,cm^{-1}$ (observed in the Raman spectrum at $2125.0\,cm^{-1}$).

Table 4 Values of A and B for common C–M–C bond angles

Bond angle	A ($N\,m^{-1}$)	B (dimensionless)
90	180	0.0929
109	203	0.0983
120	221	0.1115
180	241	0.1134

It is a simple enough matter to extend this to complexes which, even if all the ν(CO) absorptions were observed, would still have more force constants than observed frequencies (i.e., underdetermined force fields). As an example, consider the force field (Table 5) of $HMn(CO)_5$ isolated in a methane matrix at 20 K which has three IR absorptions and five force constants. The close correspondence between the force constants calculated by different means is quite striking.

Carbonyl anions and cations are found not to obey equation (14) in its most simple form. They can be included in the scheme, however, if the charge is taken into account via a parameter C (the charge factor) to give the more complete relationship

$$k_{a,b} = A - B\left[\frac{(k_a + k_b)}{2} - C\right] \tag{18}$$

It is found that C ($120\,N\,m^{-1}$) is independent of the structure of the molecule. If a molecule is doubly charged, the correction is $2C$. The effect of charges on the force constants of the three d^6 hexacarbonyl species $V(CO)_6{}^-$, $Cr(CO)_6$ and $Re(CO)_6{}^+$ is illustrated in Table 6.

Table 5 Energy factored force field for $HMn(CO)_5$

	Approx.[a]	Exact[b]
k_2	1656	1652.42
k_1	1692	1690.61
k_{12}	28	32.60
$k_{11(cis)}$	23	24.72
$k_{11(trans)}$	49	48.27

[a]Using equation (14). [b]Best fit values from isotopic spectra. All force constants in Nm^{-1}.

Table 6 Force constants of d^6 hexacarbonyls**[1]**

	k_{CO}	k_{cis}	k_{trans}
$V(CO)_6{}^-$	1454.9	33.2	60.4
$Cr(CO)_6$	1644.2	26.1	53.6
$Re(CO)_6{}^+$	1809.2	21.8	53.2

In the light of the k_{CO}/k_i relationships of table 4. Cotton's durable approximation (equation 10) has been reevaluated and the empirical relationship

$$k_{trans} = 21.3 + 1.22k_{cis} \tag{19}$$

has been proposed.**[23]** This equation agrees very well with Cotton's approximation when k_{CO} is in the region of $1650\,\text{N m}^{-1}$. Coincidentally, this is almost the same as the force constants for the group 6 hexacarbonyls.

5 CALCULATING FORCE CONSTANTS FROM ν(CO) SPECTRA

5.1 Force Constant Nomenclature and Symmetry Considerations

Before describing how force fields may be calculated, let us clarify the nomenclature used. The stretching force constants of a metal carbonyl will be numbered sequentially as k_1, k_2, k_3 and so on. The CO groups denoted by k_1 will be the most common. The CO,CO interaction constants will refer to the CO groups interacting. Thus, k_{11} arises in the F matrix where two k_1 CO groups interact. So, for a molecule such as Fe(CO)_5 there will be five EFFF force constants: k_1 (for the equatorial CO groups), k_2 (for the axial CO groups) and three interaction constants, k_{11}, k_{12}, k_{22}. Even where there is only one type of carbonyl group in the molecule, we will adhere to this convention for the sake of consistency.

We will, throughout this section, refer to 'symmetry force constants' (K(Γ) where Γ is the symmetry of the vibrational mode) derived directly from observed frequencies. Since we will be dealing with all-$^{12}\text{C}^{16}\text{O}$ molecules as a matter of course, these are simply found *via* a relationship analogous to equation (6):

$$K(\Gamma) = 4.0393 \times 10^{-4}\nu(\Gamma)^2_{\text{CO}} \tag{20}$$

The number of force constants required for the force fields of carbonyls depends, of course, on the number of CO groups and the point group of the complex. For example, Mo(CO)_5 PF_3 is treated as a C_{4v} structure based on an octahedron. This is not strictly true since the PF_3 ligand has a threefold rather than a fourfold axis of symmetry and Mo(CO)_5 PF_3 is, at best, C_s. However, most ligands behave more or less as single spherical entities and it is more convenient to regard them as such. However, a note of caution must be registered in that some ligands, for example the phosphites, such as P(OMe)_3, distort the CO framework significantly and reduce the symmetry away from the idealized situation.

Extending the example of $\text{Mo(CO)}_5\text{PF}_3$ further, this complex has four equivalent CO groups *cis* to the PF_3 ligand and a chemically distinct CO group *trans* to the PF_3. Therefore the EFFF of this complex needs two CO-stretching force constants, k_1 for the more numerous CO groups *cis* to PF_3 and k_2 for the CO group *trans* to PF_3. In the F matrix of the molecular force field these constants would occupy the positions along the diagonal. Furthermore, we need off-diagonal terms in the F matrix, that is, the interaction constants. There are three interaction constants: $k_{11(cis)}$ linking mutually cis equatorial CO groups, $k_{11(trans)}$ for mutually trans CO groups and k_{12} linking the axial CO group with the equatorial CO groups. The EFFF F matrix for this molecule is shown below:

$$F : \begin{vmatrix} k_1 & k_{11(cis)} & k_{11(trans)} & k_{11(cis)} & k_{12} \\ k_{11(cis)} & k_1 & k_{11(cis)} & k_{11(trans)} & k_{12} \\ k_{11(trans)} & k_{11(cis)} & k_1 & k_{11(cis)} & k_{12} \\ k_{11(cis)} & k_{11(trans)} & k_{11(cis)} & k_1 & k_{12} \\ k_{12} & k_{12} & k_{12} & k_{12} & k_2 \end{vmatrix} \tag{21}$$

The text below describes the force fields and possible ν(CO) absorptions of the various types of mononuclear transition metal carbonyl complex. Although it is not an exhaustive survey, most of the important groups are covered. A summary of the structures covered is given in Table 7. Where a ligand is denoted as L it is a two-electron donor (e.g., PF_3) and where it is X it is a one-electron donor (e.g., Br).

Before attempting to calculate a force field, it is best to ensure that the wavenumbers of the ν(CO) bands are accurately known and the relative intensities are also known. A very useful quantity to have at hand at the start of the process that changes frequencies into force constants is $\sum K$, the sum of all the symmetry force constants (allowing for degeneracy). For example, $\sum K$ for Cr(CO)_6 would be found by:

$$\sum K = K(a_{1g}) + 2K(e_g) + 3K(t_{1u}) \tag{22}$$

For any carbonyl complex $\text{M(CO)}_x\text{(L)}_y$, the mean CO-stretching force constant ($\bar{k}_{\text{CO}}$) is

$$\bar{k}_{\text{CO}} = \frac{\sum K}{x} \tag{23}$$

where x is the number of CO groups. In any iterative procedure for calculating force constants, $\bar{k}_{\text{CO}}$ is a very good starting point.

5.2 Monocarbonyls

The case of a monocarbonyl is the most simple. The force constant is given simply by

$$k_1 = 4.0393 \times 10^{-4}\nu^2_{\text{CO}} \tag{24}$$

There will be a weak feature to lower frequency due to $^{13}\text{C}^{16}\text{O}$ in natural abundance. Check that this band is in

Table 7 Energy factored force fields of mononuclear carbonyl complexes

			Force constants	
Point group	Example	ν(CO) modes	Stretching	Interaction
Monocarbonyls				
C_{nv}	$Mo(L)_5CO$	a_1	k_1	
Dicarbonyls				
D_{4h}	*trans*-$Mo(CO)_2(L)_4$	$a_{1g} + b_{2u}$	k_1	k_{11}
D_{3h}	*trans*-$Fe(CO)_2(L)_3$	$a_1' + a_2''$	k_1	k_{11}
C_{2v}	$Ni(CO)_2(L)_2$	$a_1 + b_2$	k_1	k_{11}
C_s	$Co(CO)_2(NO)(L)$	$a' + a''$	k_1	k_{11}
Tricarbonyls				
D_{3h}	*trans*-$Fe(CO)_3(L)_2$	$a_1' + e'$	k_1	k_{11}
C_{3v}	$Ni(CO)_3(L)$	$a_1 + e$	k_1	k_{11}
C_{2v}	*mer*-$Mo(CO)_3(L)_3$	$2a_1 + b_2$	k_1, k_2	k_{11}, k_{12}
C_s	*fac*-$Re(CO)_3(L)_2X$	$2a' + a''$	k_1, k_2	k_{11}, k_{12}
Tetracarbonyls				
T_d	$Ni(CO)_4$	$a_1 + t_2$	k_1	k_{11}
D_{4h}	*trans*-$Cr(CO)_4(L)_2$	$a_{1g} + b_{2g} + e_u$	k_1	$k_{11(cis)}, k_{11(trans)}$
C_{3v}	$HCo(CO)_4$	$2a_1 + e$	k_1, k_2	k_{11}, k_{12}
C_{2v}	$Fe(CO)_4(PF_3)$	$2a_1 + b_1 + b_2$	k_1, k_2	k_{11}, k_{22}, k_{12}
C_s	$Cr(CO)_4(CS)(L)$	$3a' + a''$	k_1, k_2, k_3	$k_{11}, k_{12}, k_{13}, k_{23}$
Pentacarbonyls				
D_{3h}	$Fe(CO)_5$	$2a_1' + a_2'' + e'$	k_1, k_2	k_{11}, k_{22}, k_{12}
C_{4v}	$Mn(CO)_5X$	$2a_1 + b_2 + e$	k_1, k_2	$k_{11(cis)}, k_{11(trans)}, k_{12}$
Hexacarbonyls				
O_h	$W(CO)_6$	$a_{1g} + e_g + t_{1u}$	k_1	$k_{11(cis)}, k_{11(trans)}$

the correct place by multiplying the $\nu(^{12}C^{16}O)$ frequency by 0.977709 to give that for $\nu(^{13}C^{16}O)$.

5.3 Dicarbonyls

The force field for dicarbonyls with equivalent CO groups (e.g., $Ni(CO)_2(L)_2$ complexes[24]) is straightforward, since there are as many absorptions as there are force constants. The secular equations and force constants for a C_{nv} dicarbonyl are shown in Table 8, but for different point groups the only difference is the convention of labeling the symmetric and asymmetric modes:

In general, the lower frequency (b_2) mode will be considerably stronger than the a_1 mode. The C–M–C bond angle, θ, can be estimated from the relative intensities of the a_1 and b_2 bands:

$$\theta = 2\tan^{-1}\sqrt{\frac{I(b_2)}{I(a_1)}} \tag{25}$$

where $I(b_2)$ and $I(a_1)$ are the intensities of the absorptions.

Table 8 $M(CO)_2$ dicarbonyl with C_{nv} or higher symmetry

K(Γ)	$K(a_1) = k_1 + k_{11}$
	$K(b_2) = k_1 - k_{11}$
	$\sum K = K(a_1) + K(b_2)$
Force field	$k_1 = \sum K \Big/ 2$
	$k_{11} = k_1 - K(b_2)$

An identical treatment to that above can be carried out for dicarbonyls of point group C_s (e.g., $Co(CO)_2(NO)(L)$ complexes[25]). The only difference is that the a_1 mode is now of symmetry a' and the b_2 mode is reclassified as a''. In octahedral species of the type *trans*-$M(CO)_2(L)_4$ (point group D_{4h}) and trigonal-bipyramidal structures of the type *trans*-$M(CO)_2(L)_3$ (point group D_{3h}) there are two ν(CO) vibrations, a symmetric and an asymmetric stretch.[26] The symmetric stretch is at higher frequency (by virtue of the fact that CO–CO interaction constants are always positive) and is Raman-active only. If both frequencies are known, the procedure is identical to complexes of the C_{2v} type. If Raman spectra are not available, the force constants can be estimated by using equation (18) and the asymmetric stretch.

In dicarbonyls where the CO groups are chemically different the force field is underdetermined with three force constants (k_1, k_2, and k_{12}) and only two absorptions which have the same symmetry (a′ for C_s, a for C_1). Without any further information, only equation (18) can be invoked, since

$$k_{12} = A - B\left\{\frac{[K(a)_1 + K(a)_2]}{2}\right\} \tag{26}$$

This would, assuming a particular C–M–C bond angle to provide appropriate values of A and B, enable an approximate force field to be calculated. That said, accurate force constants can only be obtained from the isotopic spectrum.

5.4 Tricarbonyls

Tricarbonyls with D_{3h} symmetry (see Table 9) occur commonly in complexes of the type $Fe(CO)_3(L)_2$**[27]** (and their ruthenium and osmium analogs). There are two ν(CO) modes, an a_1' symmetric stretch, which is inactive in the IR, and an e' stretch. These two absorptions are sufficient to determine the two force constants.

The a_1' band is IR-inactive but is often present as a very weak feature. If Raman spectra are not available to confirm the location of this absorption, the force field can be determined from the isotopic spectrum. Naturally abundant $^{13}C^{16}O$ would provide for 3.3% of the molecules being isotopically substituted and this would give rise to the usual satellite bands.

Examples of tricarbonyl molecules with C_{3v} symmetry are not difficult to find (see Table 10). A multitude of $Ni(CO)_3L$**[24]** and *fac*-$M(CO)_3(L)_3$ (M = Cr, Mo, W)**[28]** complexes fall into this category. The treatment is very similar to that for the D_{3h} tricarbonyls above but, if anything, simpler since both absorptions ($a_1 + e$) are active in both the IR and Raman.

The force field is, therefore, fully determined. Since both absorptions are present in the infrared, it is unlikely that isotopic data would be required for C_{3v} tricarbonyl complexes.

Tricarbonyl complexes of C_{2v} symmetry are represented by the octahedral *mer*-$M(CO)_3(L)_3$ species**[29]** and equatorially substituted trigonal-bipyramid $M(CO)_3(L)_2$ complexes (see Table 11). There are three ν(CO) modes ($2a_1 + b_2$) and four force constants (k_1, k_2, k_{11}, k_{12}) in the force field. The higher frequency a_1 mode tends to be sharp and of quite low relative intensity. The b_2 mode is much stronger than the low-frequency a_1 mode, but the two may overlap. The problem is, in any case, underdetermined with one degree of freedom. If k_1 is defined as the force constant for the two equivalent CO groups and k_2 as the force constant for the single, chemically different CO group, two interaction constants (k_{11} and k_{12}) are required to complete the force field. Although a full solution of the force field is always possible using isotopic CO, a simpler solution will be found *via* equation (18).

Table 9 $M(CO)_3$ tricarbonyl with D_{3h} symmetry

K(Γ)	$K(a_1') = k_1 + 2k_{11}$ $K(e') = k_1 - k_{11}$ $\sum K = K(a_1') + 2K(e')$
Force field	$k_1 = \sum K \big/ 3$ $k_{11} = k_1 - K(e')$

Table 10 $M(CO)_3$ tricarbonyl with C_{3v} symmetry

K(Γ)	$K(a_1) = k_1 + 2k_{11}$ $K(e) = k_1 - k_{11}$ $\sum K = K(a_1) + 2K(e)$
Force field	$k_1 = \sum K \big/ 3$ $k_{11} = k_1 - K(e)$

Table 11 $M(CO)_3$ tricarbonyl with C_{2v} symmetry

K(Γ)	$a_1\colon \begin{vmatrix} k_1 + k_{11} - K & \sqrt{2}k_{12} \\ \sqrt{2}k_{12} & k_2 - K \end{vmatrix} = 0$ $K(b_2) = k_1 - k_{11}$ $\sum K = K(a_1)_1 + K(a_1)_2 + K(b_2)$
Force field	$k_1 = (K(b_2) + A)/(1 + B)$ $k_{11} = k_1 - K(b_2)$ $k_2 = \sum K - 2k_1$ $k_{12} = A - B[k_1 + k_2]/2$

This method of calculating the force field introduces two constraints where only one is strictly necessary. An iterative balancing of the force constants may be more illuminating. A better solution would be found using isotopic data. Given reasonable spectra showing enough satellite bands, the force field can be manipulated to give a best fit.

An important class of tricarbonyls are of C_s symmetry (see Table 12). These include such species as *fac*-$Re(CO)_3(L-L)X$ where L−L is a bidentate ligand (for example, 2,2′-bipyridyl) and X is a halogen or pseudohalogen.**[30]** There has been considerable interest in these species recently as they have interesting catalytic**[31]** and photochemical**[32]** properties. The EFFF treatment for these complexes is very similar to that for the C_{2v} tricarbonyls.

The infrared spectrum of these complexes is like the *fac*-substituted $M(CO)_3(L)_3$ complexes where the e mode is split. The higher frequency a' mode is often relatively quite intense and the lower a' and a'' are usually quite close in frequency and, although the latter is usually more intense, overlap may make it difficult to assign them unambiguously from the IR spectrum alone. Judicious use of equation (18) usually solves assignment problems.

Table 12 $M(CO)_3$ tricarbonyls with *Cs* symmetry akin to *fac*-$Re(CO)_3(L\text{-}L)X$ complexes

K(Γ)	$a'\colon \begin{vmatrix} k_1 + k_{11} - K & \sqrt{2}k_{12} \\ \sqrt{2}k_{12} & k_2 - K \end{vmatrix} = 0$ $K(a'') = k_1 - k_{11}$ $\sum K = K(a')_1 + K(a')_2 + K(a'')$
Force field	$k_1 = (K(a'') + A)/(1 + B)$ $k_{11} = k_1 - K(a'')$ $k_2 = \sum K - 2k_1$ $k_{12} = A - B[k_1 + k_2]/2$

5.5 Tetracarbonyls

The force field of tetrahedral $M(CO)_4$ (e.g., $Ni(CO)_4$, $[Co(CO)_4]^-$) is fully determined if the a_1 (Raman) and t_2 (IR and Raman) are both observed (see Table 13).

If the Raman spectrum is not available, the force field can be determined from the naturally occurring isotopic species (≈4.4% abundance), which belongs to the point group C_{3v}, or by using equation (18).

Most octahedral disubstituted $M(CO)_4(L)_2$ complexes have a cis isomer of C_{2v} symmetry (discussed below) and a trans isomer, which has D_{4h} symmetry if the ligand has fourfold symmetry or is a single atom (see Table 14). D_{4h} tetracarbonyl molecules have a center of symmetry and none of the vibrations appear in both IR and Raman spectra. In the CO region there are three vibrations: a_{1g} (Raman), b_{2g} (Raman), and e_u (IR). Given all three ν(CO) frequencies, the force field (k_1, $k_{11(cis)}$, and $k_{11(trans)}$) is fully determined.

The IR spectrum of complexes such as these will therefore show a single band (the e_u mode). If Raman data are unavailable, and the supposedly IR-inactive bands are not observed as weak features,[33] reasonably accurate force constants can be obtained from equation (18). More usually, asymmetry in the ligand or distortion of the force field due to solvent–CO interactions makes both the Raman-active bands very slightly allowed in the IR. Indeed, *trans*-$[(i\text{-}PrO)_3P]_2Mo(CO)_4$ shows pronounced effects due to the irregular packing of the phosphite ligands. Not only are the a_{1g} and b_{2g} bands readily observable, but the e_u band is rather broader than is usually found. In the absence of such data, isotopic spectra will provide enough information to resolve the problem. The monosubstituted molecule is present at 4.4% (natural abundance). The force fields of this type of molecule invariably support Cotton's approximation (equation 10) in that:

$$K(b_{2g}) \approx k_1 \tag{27}$$

Table 13 $M(CO)_4$ tetracarbonyls with T_d symmetry

K(Γ)	$K(a_1) = k_1 + 3k_{11}$
	$K(t_2) = k_1 - k_{11}$
	$\sum K = K(a_1) + 3K(t_2)$
Force field	$k_1 = \sum K \big/ 4$
	$k_{11} = k_1 - K(t_2)$

Table 14 $M(CO)_4$ tetracarbonyls with D_{4h} symmetry

K(Γ)	$K(a_{1g}) = k_1 + 2k_{11(cis)} + k_{11(trans)}$
	$K(b_{2g}) = k_1 - 2k_{11(cis)} + k_{11(trans)}$
	$K(e_u) = k_1 - k_{11(trans)}$
	$\sum K = K(a_{1g}) + K(b_{2g}) + 2K(e_u)$
Force field	$k_1 = \sum K \big/ 4$
	$k_{11(trans)} = k_1 - K(e_u)$
	$k_{11(cis)} = [K(a_{1g}) - k_1 - k_{11(trans)}]/2$

Table 15 $M(CO)_4$ tetracarbonyls with C_{3v} symmetry

K(Γ)	$a_1\colon \begin{vmatrix} k_1 + 2k_{11} - K & \sqrt{3}k_{12} \\ \sqrt{3}k_{12} & k_2 - K \end{vmatrix} = 0$
	$K(e) = k_1 - k_{11}$
	$\sum K = K(a_1)_1 + K(a_1)_2 + 2K(e)$
Force field	$k_1 = (K(e) + A)/(1 + B)$
	$k_{11} = k_1 - K(e)$
	$k_2 = \sum K - 2k_1$
	$k_{12} = A - B[k_1 + k_2]/2$

If a species $M(CO)_4$ is intermediate between tetrahedral and square planar, it belongs to the point group D_{2d}. The a_{1g}, b_{2g}, and e_u modes of the D_{4h} structure are relabeled a_1, b_2, and e, respectively. All three modes are Raman-active, although the intensity of the e mode in the Raman spectrum is likely to be low if the distortion from square planar is small. The a_1 mode remains, formally, IR-inactive. The force field can be determined by using the equations for the D_{4h} tetracarbonyl above. It has been suggested that octahedral species of the D_{4h} type show some distortion toward D_{2d}, as the 'b_{2g}' mode of these complexes is often observed in their IR spectrum. This does not explain the appearance of the 'a_{1g}' mode in the IR and it is likely that some ligands (e.g., $P(OR)_3$) cause a considerable overall reduction in symmetry.

Many $Fe(CO)_4L$, $Ru(CO)_4L$, and $Os(CO)_4L$ complexes[34] have C_{3v} symmetry, along with a large number of $Co(CO)_4L$ compounds (see Table 15).[35] On the basis of the trigonal-bipyramidal structure, these complexes have a single ligand, occupying an axial site. Typically their IR spectra show a weak, sharp absorption at high frequency (the a_1 mode that is primarily due to the symmetric breathing mode of the equatorial CO groups), a moderately strong absorption (of a_1 symmetry, due to the motion of the axial CO group), and a very strong absorption at lower frequency (the asymmetric e mode). Unfortunately, the force field is underdetermined and it is necessary to resort to equation (18) for approximate force constants or to utilize isotopic spectra for an exact solution. At natural abundance, 1.1% of the molecules will have a $^{13}C^{16}O$ group in an axial position and 3.3% will be substituted in an equatorial position. The axially substituted molecule retains the symmetry of the parent. The equatorially substituted molecule belongs to the point group C_s and has four ($3a' + a''$) ν(CO) modes. If all the parent and naturally occurring isotope bands were observed, there would be eight frequencies with which to fix four force constants. It is unlikely, however, that this would be the case as all but two of the isotope bands are likely to be very weak. The use of equation (18) to fix at least one of the interaction constants makes the calculation of an approximate force field for these molecules quite simple.

Table 16 M(CO)$_4$ tetracarbonyls with C_{2v} symmetry

K(Γ)	$a_1{:}\begin{vmatrix} k_1+k_{11}-K & 2k_{12} \\ 2k_{12} & k_2+k_{22}-K \end{vmatrix} = 0$
	$K(b_1) = k_1 - k_{11}$
	$K(b_2) = k_2 - k_{22}$
	$\sum K = K(a_1)_1 + K(a_1)_2 + K(b_1) + K(b_2)$
Force field	$k_1 = (K(b_1) + A)/(1 + B)$
	$k_{11} = k_1 - K(b_1)$
	$k_2 = \left(\sum K - 2k_1\right)\Big/2$
	$k_{22} = k_2 - K(b_2)$
	$k_{12} = A - B[k_1 + k_2]/2$

Tetracarbonyls with C_{2v} symmetry (see Table 16), such as *cis*-M(CO)$_4$(L)$_2$ (M = Cr, Mo, W) and M(CO)$_4$L (M = Fe, Ru, Os; L in an equatorial position in a trigonal bipyramid) are common.[33,36,37] There are four ν(CO) absorptions ($2a_1 + b_1 + b_2$) and five force constants (k_1, k_2, k_{11}, k_{22}, k_{12}), which means that the force field is underdetermined with one degree of freedom. One of the a_1 modes is at higher frequency and of lower intensity than the other three modes and the lower frequency a_1 mode is always higher in frequency than the b_2 mode. The ordering of the low-frequency a_1 and the b_1 mode is not easily predicted. Indeed, the IR spectrum of Mn(CO)$_4$NO, which is of this class, was initially confusing since the b_1 and low-frequency a_1 are accidentally degenerate.[38]

Using equation (18) to determine the force fields of octahedral *cis*-M(CO)$_4$(L)$_2$ complexes can be done in two ways. Either the b_1 or the b_2 modes can be used to obtain a set of force constants and the others can then be calculated. For equatorially substituted M(CO)$_4$(L) complexes based on a trigonal bipyramid, the only variation is in changing the values of A and B in equation (18). While the force fields that this method produces are not exact, they are usually good enough to predict the a_1 modes with reasonable accuracy and enable the $^{13}C^{16}O$ satellite bands to be assigned. At natural abundance, 2.2% of the molecules will be substituted in an axial position and 2.2% in an equatorial position. All together, there are six possible absorptions because of the naturally occurring $^{13}C^{16}O$ in addition to the four modes of the all-$^{12}C^{16}O$ molecule.

Of even lower symmetry are the C_s, octahedral *cis*-M(CO)$_4$(L$_1$)(L$_2$) complexes. The power of the EFFF in fitting isotopic spectra is, perhaps, best illustrated with a complex of this type: Poliakoff's matrix-isolated fragment *cis*-Cr(CO)$_4$CS.[39] The spectrum of a C_s tetracarbonyl complex shows three reasonably strong bands (all a' symmetry) and a very strong band (a'' symmetry), although overlap may reduce this number. The force field is badly underdetermined, with three degrees of freedom. Even so, using equation (18) gives surprisingly accurate results.

5.6 Pentacarbonyls

Pentacarbonyliron(0) is the best known example of a pentacarbonyl complex. Others in this category include [Mn(CO)$_5$]$^-$, [Cr(CO)$_5$]$^{2-}$, Ru(CO)$_5$, and Os(CO)$_5$. As they have D_{3h} symmetry (see Table 17), the energy factored force field requires five force constants but there are only four ν(CO) frequencies (only two of which appear in the infrared) so the force field is underdetermined. Two of the ν(CO) modes are fully symmetrical (a_1') and are IR-inactive. The asymmetric stretches are labeled a_2'' (due to the stretching of the axial CO groups) and e' (due to stretching of the equatorial CO groups). The e' mode is IR and Raman-active; the a_2'' mode is active in the IR only.

With the force field, we must use equation (18) or isotopic data to solve the force field. At natural abundance, isotopic labeling will occur in axial and equatorial positions, in 2.2% and 3.3% of the molecules, respectively. The axially substituted species belongs to the point group C_{3v}. The equatorially substituted species belongs to the point group C_{2v}. The a_2'' and one of the e' modes of the parent are relabeled b_1 and b_2, but are otherwise unchanged. The remaining modes belong to the representation a_1. Thus, there will be a total of six isotope bands in the IR spectrum of trigonal-bipyramidal M($^{12}C^{16}O$)$_4$($^{13}C^{16}O$). Two will be readily apparent as satellites of the two IR absorptions, but the others will be much weaker. However, the observation of two isotope bands in the IR still leaves the problem underdetermined and isotopic enrichment by CO exchange is the only realistic answer to solving the force field and providing accurate force constants.

Complexes of the type M(CO)$_5$L (e.g., Mo(CO)$_5$PF$_3$, Cr(CO)$_5$CS, HMn(CO)$_5$, BrMn(CO)$_5$) are among the most common and widely studied of carbonyl compounds.[40] There are, given both IR and Raman spectra, four ν(CO) absorptions ($2a_1 + b_2 + e$). At highest frequency is a generally sharp, often weak, feature that is (mainly) due to the in-phase (hence a_1 symmetry) motion of the four equatorial CO groups (see Table 18). To lower frequency is the b_2 mode which is, strictly, Raman-active only. However, this band very often appears as a weak feature in the IR spectrum, arising from asymmetric effects from either the ligand or the solvent.

Table 17 M(CO)$_5$ pentacarbonyls with D_{3h} symmetry

K(Γ)	$a_1'{:}\begin{vmatrix} k_1+k_{11}-K & \sqrt{6}k_{12} \\ \sqrt{6}k_{12} & k_2+2k_{22}-K \end{vmatrix} = 0$
	$K(a_2'') = k_1 - k_{11}$
	$K(e') = k_2 - k_{22}$
	$\sum K = K(a_1')_1 + K(a_1')_2 + K(a_2'') + 2K(e')$
Force field	$k_1 = (K(b_1) + A)/(1 + B)$
	$k_{11} = k_1 - K(b_1)$
	$k_2 = \left(\sum K - 2k_1\right)\Big/3$
	$k_{22} = k_2 - K(b_2)$
	$k_{12} = A - B[k_1 + k_2]/2$

Table 18 $M(CO)_5$ pentacarbonyls with C_{4v} symmetry

K(Γ)	$a_1\colon \begin{vmatrix} k_1 + 2k_{11(cis)} + k_{11(trans)} - K & 2k_{12} \\ 2k_{12} & k_2 - K \end{vmatrix} = 0$
	$K(b_2) = k_1 - 2k_{11(cis)} + k_{11(trans)}$
	$K(e) = k_1 - k_{11(trans)}$
	$\sum K = K(a_1)_1 + K(a_1)_2 + K(b_2) + 2K(e)$
Force field	$k_1 = (K(e) + A)/(1 + B)$
	$k_{11(trans)} = k_1 - K(e)$
	$k_2 = \sum K - 4k_1$
	$k_{11(cis)} = (k_1 - K(b_2) + k_{11(trans)})/2$
	$k_{12} = A - B[k_1 + k_2]/2$

Ligand asymmetry cannot be the whole story, as $Mn(CO)_5Br$ has a weak IR absorption corresponding to the b_2 mode. The remaining bands, as seen in the IR spectrum, are a very strong e mode (weak in the Raman) and a fairly strong a_1 mode that is mainly due to the stretching of the CO group trans to the ligand L. The order of the e and low-frequency a_1 modes is largely determined by the ligand. For strong π-acceptors (e.g., CS, PF_3), the a_1 mode is at higher frequency than the e mode. The situation is reversed for weaker π-acceptors (e.g., PPh_3, PMe_3). The number of force constants exceeds the ν(CO) absorptions by one and, so, the EFFF is underdetermined.

For more accurate force constants, we must use isotopic data. At natural abundance, 1.1% of the molecules will have a $^{13}C^{16}O$ group in an axial position and 4.4% will be isotopically substituted in an equatorial position. The axially substituted molecule retains the symmetry of the parent and only the a_1 modes are affected by the isotopic CO group. The high frequency a_1 mode of the axially substituted molecule is (for $^{13}C^{16}O$ in natural abundance) almost certainly too weak to be detected. The lower frequency a_1 mode will be very weak. The equatorially substituted molecule is of symmetry C_s and responsible for the stronger satellite bands. The a'' mode of *cis*-$M(^{12}C^{16}O)_4(^{13}C^{16}O)L$ is identical to the e mode of the parent and gives no new information. However, if one or more of the a' modes can be located they can be used to remove the degree(s) of freedom in the force field. The observation of the b_2 mode in the IR spectrum has been taken to indicate ligand asymmetry reducing the nominal symmetry of $M(CO)_5L$ complexes to C_s or lower. Additional to this, the e mode is usually broader than the other absorptions, which suggests a lifting of the twofold degeneracy.

5.7 Hexacarbonyls

Octahedral $M(CO)_6$[1,6] is a straightforward case. There are three ν(CO) absorptions (a_{1g} (Raman) + e_g (Raman) + t_{1u} (IR)) and three force constants in the force field (k_1, $k_{11(cis)}$, and $k_{11(trans)}$) (see Table 19).

The ordering $K(a_{1g}) > K(e_g) > K(t_{1u})$ is unambiguous since the interaction constants are always positive.

Table 19 $M(CO)_6$ hexacarbonyls with O_h symmetry

K(Γ)	$K(a_{1g}) = k_1 + 4k_{11(cis)} + k_{11(trans)}$
	$K(e_g) = k_1 - 2k_{11(cis)} + k_{11(trans)}$
	$K(t_{1u}) = k_1 - k_{11(trans)}$
	$\sum K = K(a_{1g})_1 + 2K(e_u) + 3K(t_{1u})$
Force field	$k_1 = \sum K \big/ 6$
	$k_{11(trans)} = k_1 - K(t_{1u})$
	$k_{11(cis)} = (K(a_{1g}) - k_1 - k_{11(trans)})/4$

The monosubstituted species $M(^{12}C^{16}O)_5(^{13}C^{16}O)$ occurs at natural abundance to the extent of nearly 7%. The species belongs to the point group C_{4v} and the b_2 and e modes correlate with the e_g and t_{1u} modes, respectively, of $M(^{12}C^{16}O)_6$. The remaining modes are of symmetry a_1. Thus, the monosubstituted species should, in principle, give rise to three isotope bands. In the IR spectrum, one of these will be a lower frequency satellite of the strong t_{1u} mode, while the other two will be at a higher energy and much weaker.

6 APPLICATIONS OF CO FORCE CONSTANTS

There have been several attempts to use energy factored force constants, calculated from transition metal ν(CO) spectra, as probes into the nature of metal–ligand bonding[41] or reactivity,[42] as indicators of bond order.[43] A comprehensive study of the success (or otherwise) of these various studies has been published.[44]

One of the most successful systems[20] uses ligand effect constants and the k_{CO} for the triatomic metal monocarbonyl M–C–O. Assuming that ligand effect constants are additive, this model uses the simple equation

$$k_{CO} = k_d + \sum e_L^{\theta} \tag{28}$$

The parameter k_d is the force constant for the isolated monocarbonyl M(CO). The subscript 'd' draws attention to the fact that this parameter is more concerned with the number of d-electrons than the specific metal at the center. This means that $Cr(CO)_6$, $HMn(CO)_5$, and $[V(CO)_5PBu_3]^-$ will share a common value for k_d (*viz.* $k_6 = 1387\,N\,m^{-1}$). The terms contained in the summation are the ligand effect constants, which are transferable between metal centers. The values of k_d used are given in Table 20. In Table 21 are ligand effect constants for a variety of ligands. For ligands in an octahedral setting, two ligand effects constants (${e_L}^{cis}$ and ${e_L}^{trans}$) are required. In tetrahedra only one (${e_L}^{td}$) is needed and it is very easily calculated. For trigonal-bipyramidal species, three (${e_L}^{ax,ax}$, ${e_L}^{ax,eq}$ and ${e_L}^{eq,eq}$) are needed although ${e_L}^{eq,eq}$ is not always necessary since a large number of ligands only occupy an axial position in these systems.

Table 20 k_d Parameters

Period	k_5	k_6	k_7	k_8	k_9	k_{10}
1st	1373	1387	1444	1498	1554	1610
2nd	$-^{a}$	1389	$-^{a}$	1506	$-^{a}$	1636
3rd	1353	1381	1445	1498	$-^{a}$	1613

[a] Not determined, but probably close to the other group members.

It is quite a simple task to calculate ligand effect constants from force constants and *vice versa*. For example, the force constants for a M(CO)$_5$L complex are given (in terms of equation 27) by:

$$\begin{aligned} k_1 &= k_d + 3e^{cis}_{CO} + e^{trans}_{CO} + e^{cis}_{L} \\ k_2 &= k_d + 4e^{cis}_{CO} + e^{trans}_{L} \\ k_{11(cis)} &= 180 - 0.0929k_1 \\ k_{11(trans)} &= 241 - 0.1134k_1 \\ k_{12} &= 180 - 0.0929(k_1 + k_2)/2 \end{aligned} \tag{29}$$

Using these equations, we can calculate ligand effect constants for some new ligand or, alternatively, calculate ν(CO) frequencies for a M(CO)$_5$L complex with a known ligand.

The method has enjoyed considerable success in predicting ν(CO) frequencies for assumed structures[45] and assigning spectra. Much of the utility of the method stems from the ability to generate a force field for a supposed structure and then test this against experimental findings. For example, the ν(CO) frequencies for the whole series of unsaturated Mo(CO)$_{5-x}$(PF$_3$)$_x$ complexes isolated in CH$_4$ matrices at 20 K were predicted with a mean accuracy of 3 cm^{-1}.

The link between the matrix-isolation technique and metal carbonyl chemistry has had a relatively long and certainly fruitful history. The pairing began in the early 1960s with a series of experiments by Sheline and coworkers[46] using a variety of glassy matrices held at 77 K by liquid nitrogen. In 1969, Turner and Rest[47] began the study of carbonyls in less reactive matrices (e.g., argon) at lower temperatures (commonly 20 K). Comprehensive reviews of the matrix-isolation studies involving carbonyls exist.[48] Suffice it to say here that this work has produced some extremely interesting results and without using an energy factoring approach to the ν(CO) modes it is difficult to see how the many structural determinations could have been carried out.

Table 21 Ligand effect constants

Ligand	e^{cis}_{L}	e^{trans}_{L}	e^{td}_{L}	$e^{ax,eq}_{L}$	$e^{eq,eq}_{L}$	$e^{ax,ax}_{L}$
(Cl$_2$PCH$_2$)$_2$	15	105				
(F$_2$PCH$_2$)$_2$	17	112				
PCl$_2$OEt	19	97				
PCl$_3$	31	109	35			
PF$_3$	33	142	45	16	48	130
PCl$_2$Ph	14	82	13			
PClPh$_2$	−5	55	−11			
PCy$_3$	−35	28	−51			
PPhCy$_2$	−34	13				
PMe$_3$	−28	30	−39	−65		48
PEt$_3$	−32	26	−40	−65		41
PBu$_3$	−32	14	−40	−59		
P(OMe)$_3$	−15	66	−11	−31	1	72
PMe(OMe)$_2$	−19	60				
P(OCH$_2$)$_3$CEt	4	67	−5		9	71
P(OPh)$_3$	1	64	0			
PPh$_3$	−21	29	−32	−52		44
PPhMe$_2$	−28	25	−60			69
PPh$_2$Me	−26	24	−60			69
P(NMe$_2$)$_3$	−21	38				
AsH$_3$	−22	42				
CS	56	160	65			
N$_2$	14	52	6	13		102
NO	42	232	30	45	22	
CO	34	126	37	26	51	126
C$_2$H$_4$	1	80	4	6		
CN-Me	−14	30	−24	−30		61
CN-Et	−10	30	−23	−22		53
CN-Bu	−9	31	−24	−25		50
CN-Ph	−14	−17				43
H$_2$O	−33	−27				
NH$_3$	−55	−70				

Technological advances have allowed the development of time-resolved infrared (TRIR) techniques in recent years and they too have exploited the intense, sharp spectra of the transition metal carbonyls. Some TRIR work has now been carried out, which confirms earlier matrix work;[49] and a review was published[50] some time ago. TRIR involving metal carbonyl species is now a maturing technique, with a considerable number of publications logged over the past 10 years.

The understanding of metal carbonyl reactions at electrode surfaces is also being tackled via the IR spectra of the participating complexes,[51] as are the chemical changes occurring on zeolites.[52]

7 POLYNUCLEAR CARBONYL COMPLEXES

Although the IR spectra of mononuclear carbonyl complexes are well understood, difficulties arise when dealing with the spectra of dinuclear complexes (e.g., $Mn_2(CO)_{10}$ and its substitution products), trinuclear species (e.g., $Os_3(CO)_{12}$), and larger carbonyls. In principle, the methodology for calculating energy factored force constants from observed ν(CO) bands (using either all-^{12}CO or isotopically enriched spectra) is identical with that employed so successfully for mononuclear complexes. The problems spring from the very large numbers of force constants required in the F matrix. Consider the $Mn(CO)_5$ fragment. This has (given IR and Raman spectra) four ν(CO) modes ($2a_1 + b_2 + e$) and five force constants. The problem has one degree of freedom but, with a little data from isotopes, is relatively easily solved. Dimanganese decacarbonyl has seven ν(CO) modes:[53] two a_1 modes (Raman only), two b_1 modes (IR only), and three doubly degenerate e modes ($e_1 + e_2 + e_3$) of which only the e_3 mode is IR-active. In addition to the five force constants for the $Mn(CO)_5$ fragments, there are another four interaction constants linking CO groups on different metals. This makes available seven ν(CO) fundamentals with which to calculate nine force constants, that is, two degrees of freedom. These ‘through-space’ interaction constants are generally smaller than those linking CO groups on the same metal but are certainly significant. There are few studies dealing with the force fields of polynuclear carbonyl complexes.[54]

For larger numbers of metal atoms surrounded by CO groups, the situation becomes quite perplexing. Instead of gradually increasing in complexity as the number of metal atoms increases, the IR spectra become extremely sparse with very few ν(CO) bands. One interpretation is that there is an ‘F matrix collapse’, with all the small through-space interactions tending to zero and the F matrix becoming quasi-diagonal. Supporting this view is the observation that partial ^{13}CO enrichment creates very few new absorptions and not the forest that might be expected.

There is much work still to be done on the force fields of polynuclear species and, with that area of carbonyl chemistry forming a sizable percentage of all carbonyl research, the work is overdue.

8 INTENSITIES

Apart from a fleeting mention earlier, the numerical analysis of the relative intensities of ν(CO) bands has not been elaborated on in this article. The topic of ν(CO) intensities has been authoritatively reviewed by Burdett.[55] In general, the use of intensity data depends on the nature of the carbonyl complex. If all the CO groups are chemically equivalent and the force field is fully determined (e.g., *cis*-$Cr(CO)_2(PMe_3)_4$, $Ni(CO)_3PMe_3$), there are few problems and the geometry of the molecule can be calculated from the relative intensities of the ν(CO) bands. Indeed, for all such cases the geometry of the $M(CO)_n$ unit can be determined without reference to the force constants. The situation becomes far more complex when there are chemically inequivalent CO groups (e.g., $HMn(CO)_5$, $Fe(CO)_4PMe_3$). Regardless of the symmetry, there will be as many symmetric stretches as there are different types of CO group. Since these modes will mix through the off-diagonal terms in the F matrix, the intensities associated with these vibrations will be redistributed. This generates two problems. Firstly, to ascertain the degree of mixing, the force field must be accurately known. Secondly, the dipole change caused by the vibration of one group may well be different to that caused by a chemically different group in the same molecule. In the case of C_{4v} pentacarbonyl complexes, the problem has been thoroughly investigated and, on the whole, bond angles calculated from intensities are in good agreement, where they can be checked, with observed bond angles (from X-ray data). This general confidence in the method tends to suggest that the calculation of bond angles from intensity considerations for matrix-isolated species is likely to be valid.

However, there is a caveat to add at this point. The fluctuating dipoles responsible for the infrared intensities may not, in fact, lie along the lines described by the atoms. So, while we can calculate ‘geometries’ we may not, in truth, be describing angles between bonds but angles between dipoles. The contribution of other ligands into this complex problem has yet to be quantified and our present level of understanding only allows us to offer general conclusions about bond angles. The curious ν(CO) intensities of $Cr(CO)_5CS$, where all the C–M–C bond angles are virtually 90° is a case in point. From the intensity data, we would conclude that the angle between the axial CO group and the equatorial groups was 82°.

9 RECENT DEVELOPMENTS

Studies involving the close scrutiny of the CO-stretching region of the spectrum have continued to be published. Indeed, studies using TRIR (noted earlier) and the newer technique of carbonyl chemistry in supercritical fluids are highly dependent on the ν(CO) region. Fewer publications have followed the first studies of metal carbonyl photochemistry in supercritical fluids (such as scXe and $scCO_2$) but the work that has been done (e.g., by Poliakoff[56] and coworkers) makes considerable use of the ν(CO) bands around 2000 cm^{-1}.

Carbonyl spectra continue to be used to analyze σ/π bonding effects[57] and to monitor the processes taking place where CO groups are involved. Throughout the 1990s and into the new century, the number of studies dealing with $Re(CO)_3$(N-N)X complexes assumed plague proportions and each carried with it a more or less detailed description of the ν(CO) bands.

The combination of matrix-isolation and infrared spectroscopy has, since 1969, been used to identify carbonyl fragments (e.g., $Cr(CO)_5$), radicals (e.g., $Mn(CO)_5$) or unstable species (e.g., $Pd(CO)_4$). This type of work continues[58] and the understanding of what is actually going on in the ν(CO) region is crucial to the success or otherwise of the study. Recent work in this field includes the reactions of zirconium and hafnium atoms with CO, manganese carbonyl nitrosyl complexes in solid argon, reactions of iron atoms with nitric oxide and carbon monoxide in excess argon and reactions of laser-ablated ruthenium atoms with CO and H_2 mixtures. It would not be overstating the value of the ν(CO) spectra to say that, without this information the characterization of these matrix-isolated molecules would be impossible. The same is certainly true of species observed in TRIR studies where, in addition to structural information, we can also determine kinetic behavior.

There is no doubt that there remains much to be done and seen between 2100 to 1850 cm^{-1}.

10 RELATED ARTICLES

Carbonyl Complexes of the Transition Metals.

11 FURTHER READING

(a) M. F. Zhou and L. Andrews, *J. Am. Chem. Soc.*, 2000, **122**, 1531; (b) X. F. Wang, M. Zhou and L. Andrews, *J. Phys. Chem. A*, 2000, **104**, 7964; (c) X. F. Wang, M. Zhou and L. Andrews, *J. Phys. Chem. A*, 2000, **104**, 10104; (d) X. F. Wang and L. Andrews, *J. Phys. Chem. A*, 2000, **104**, 9892.

12 REFERENCES

1. P. S. Braterman, ‘Metal Carbonyl Spectra’, Academic Press, London, 1975.
2. D. M. Adams, ‘Metal-ligand and Related Vibrations’, Arnold, London, 1967.
3. P. S. Braterman, *Struct. Bonding*, 1972, **10**, 57.
4. E. B. Wilson, J. C. Decius, and P. R. Cross, ‘Molecular Vibrations’, McGraw-Hill, New York, 1955.
5. L. H. Jones, ‘Inorganic Vibrational Spectroscopy’, Dekker, New York, 1971.
6. L. H. Jones, R. S. McDowell, and M. Goldblatt, *Inorg. Chem.*, 1969, **8**, 2349.
7. (a) F. A. Cotton and C. S. Kraihanzel, *J. Am. Chem. Soc.*, 1962, **84**, 4432; (b) F. A. Cotton and C. S. Kraihanzel, *Inorg. Chem.*, 1963, **2**, 533; (c) F. A. Cotton, *Inorg. Chem.*, 1964, **3**, 702.
8. O. Crichton, A. J. Rest, M. Poliakoff, and J. J. Turner, *J. Chem. Soc., Dalton Trans.*, 1973, 1321.
9. E. P. Kundig, M. Moskovits, and G. A. Ozin, *Can. J. Chem.*, 1973, **51**, 2737.
10. H. Haas and R. K. Sheline, *J. Chem. Phys.*, 1967, **47**, 2996.
11. (a) L. H. Jones, R. S. McDowell, and M. Goldblatt, *J. Chem. Phys.*, 1968, **48**, 2663; (b) L. H. Jones, R. S. McDowell, M. Goldblatt, and B. I. Swanson, *J. Chem. Phys.*, 1972, **57**, 2050; (c) L. H. Jones, R. S. McDowell, and B. I. Swanson, *J. Chem. Phys.*, 1973, **58**, 3757; (d) D. K. Ottensen, H. B. Gray, L. H. Jones, and M. Goldblatt, *Inorg. Chem.*, 1973, **12**, 1051.
12. G. Bor, *Inorg. Chim. Acta*, 1969, **3**, 191.
13. (a) A. J. Rest, *J. Organomet. Chem.*, 1972, **40**, C76; (b) M. A. Graham, M. Poliakoff, and J. J. Turner, *J. Chem. Soc. (A)*, 1971, 2939; (c) R. N. Perutz and J. J. Turner, *Inorg. Chem.*, 1975, **14**, 262; (d) R. N. Perutz and J. J. Turner, *J. Am. Chem. Soc.*, 1975, **97**, 4800; (e) S. P. Church, M. Poliakoff, J. A. Timney, and J. J. Turner, *Inorg. Chem.*, 1983, **22**, 3259; (f) S. P. Church, M. Poliakoff, J. A. Timney, and J. J. Turner, *J. Am. Chem. Soc.*, 1981, **103**, 7515.
14. J. H. Darling and J. S. Ogden, *J. Chem. Soc., Dalton Trans.*, 1972, 2496.
15. G. Bor, B. F. G. Johnson, J. Lewis, and P. W. Robinson, *J. Chem. Soc. (A)*, 1971, 696.
16. G. Bor and G. Jung, *Inorg. Chim. Acta*, 1969, **3**, 69.
17. J. K. Burdett, M. Poliakoff, J. A. Timney, and J. J. Turner, *Inorg. Chem.*, 1978, **17**, 948.
18. J. R. Miller, *J. Chem. Soc. (A)*, 1971, 1885.
19. R. Poilblanc and M. Bigorgne, *Bull. Soc. Chim. Fr.*, 1962, 1301.
20. J. A. Timney, *Inorg. Chem.*, 1979, **18**, 2502.
21. F. T. Delbeke, E. G. Claeys, G. P. van der Kelen, and R. M. de Caluwe, *J. Organomet. Chem.*, 1970, **23**, 497.
22. G. Bor, *J. Organomet. Chem.*, 1967, **10**, 343.
23. J. A. Timney and W. C. Heslop, *Spectrochim. Acta*, 1992, **48A**, 1189.
24. (a) A. Loutellier and M. Bigorgne, *Bull. Soc. Chim. Fr.*, 1965, 3186; (b) M. Bigorgne, in ‘Advances in the Chemistry of Coordination Compounds’, ed. S. Kirschner, Macmillan, New York, 1961, p. 199; (c) A. Loutellier and M. Bigorgne, *J. Chim. Phys. Phys. Chim. Biol.*, 1970, **67**, 99.

25. (a) W. Beck and K. Lottes, *Chem. Ber.*,1965, **98**, 2657; (b) W. D. Horrocks and R. C. Taylor, *Inorg. Chem.*, 1963, **2**, 723; (c) M. Foa and L. Cassar, *J. Organomet. Chem.*, 1971, **30**, 123.

26. (a) E. W. Abel, R. A. N. McLean, M. G. Norton, and S. P. Tyfield, *J. Chem. Soc., Chem. Commun.*, 1968, 900; (b) B. E. Cavit, K. R. Grundy, and W. R. Roper, *J. Chem. Soc., Chem. Commun.*, 1972, 60.

27. (a) F. A. Cotton and R. V. Parish, *J. Chem. Soc.*, 1960, 1440; (b) M. Bigorgne, *J. Organomet. Chem.*, 1970, **24**, 211.

28. E. W. Abel, M. A. Bennett, and G. Wilkinson, *J. Chem. Soc.*, 1959, 2323.

29. R. Poilblanc and M. Bigorgne, *J. Organomet. Chem.*, 1966, **5**, 93.

30. (a) A. G. Osborne and M. H. B. Stiddard, *J. Chem. Soc.*, 1962, 4715; (b) E. W. Abel and G. Wilkinson, *J. Chem. Soc.*, 1959, 1501.

31. (a) J. Hawacker, J.-M. Lehn, and R. Zeissel, *Helv. Chim. Acta*, 1986, **69**, 1990; (b) P. Christensen, A. Hamnett, A. V. G. Muir, and J. A. Timney, *J. Chem. Soc., Dalton Trans.*, 1992, 1455.

32. P. Glyn, F. P. A. Johnson, M. W. George, A. J. Lees, and J. J. Turner, *Inorg. Chem.*, 1991, **30**, 3543.

33. C. E. Jones and K. J. Coskran, *Inorg. Chem.*, 1971, **10**, 55.

34. D. Seyferth, *J. Am. Chem. Soc.*, 1960, **82**, 1080.

35. J. K. Ruff, *Inorg. Chem.*, 1968, **7**, 1499.

36. M. H. B. Stiddard, *J. Chem. Soc.*, 1963, 4712.

37. G. Bouquet and M. Bigorgne, *Bull. Soc. Chim. Fr.*, 1962, 433.

38. A. J. Rest, *J. Chem. Soc., Chem. Commun.*, 1970, 345.

39. M. Poliakoff, *Inorg. Chem.*, 1976, **15**, 2022.

40. (a) H. D. Kaesz, R. Bau, D. Hendrickson, and M. J. Smith, *J. Am. Chem. Soc.*, 1967, **89**, 2844; (b) W. Jetz, P. B. Simons, J. A. J. Thompson, and W. A. G. Graham, *Inorg. Chem.*, 1966, **5**, 2217.

41. C. A. Tolman, *J. Am. Chem. Soc.*, 1970, **92**, 2953.

42. E. C. Alyea, in ‘Catalytic Aspects of Metal Phosphine Complexes’, Advances in Chemistry Series, ed. D. W. Meek, American Chemical Society, Washington, 1982.

43. C. De La Cruz and N. Sheppard, *J. Mol. Struct.*, 1990, **224**, 141.

44. (a) Md. M. Rahman, H.-Y. Liu, A. Prock, and W. P. Giering, *Organometallics*, 1987, **6**, 650; (b) M. N. Golovin, Md. M. Rahman, J. E. Belmonte, and W. P. Giering, *Organometallics*, 1985, **4**, 1981; (c) Md. M. Rahman, H.-Y. Liu, K. Eriks, A. Prock, and W. P. Giering, *Organometallics*, 1989, **8**, 1.

45. J. A. Timney, *J. Mol. Struct.*, 1991, **263**, 229.

46. (a) I. W. Stolz, G. R. Dobson, and R. K. Sheline, *J. Am. Chem. Soc.*, 1962, **84**, 3589; (b) I. W. Stolz, G. R. Dobson, and R. K. Sheline, *J. Am. Chem. Soc.*, 1963, **85**, 1013.

47. A. J. Rest and J. J. Turner, *J. Chem. Soc., Chem. Commun.*, 1969, 375.

48. G. A. Ozin, in ‘Cryochemistry’, eds. G. A. Ozin and M. Moskovits, Wiley, New York, 1977.

49. P. L. Bogdan and E. Weitz, *J. Am. Chem. Soc.*, 1990, **112**, 639.

50. J. J. Turner and M. Poliakoff, *Polyhedron*, 1989, **8**, 1611.

51. (a) E. F. Dalton, S. Ching, and R. W. Murray, *Inorg. Chem.*, 1991, **30**, 2642; (b) J. E. Cyr and P. H. Reiger, *Organometallics*, 1991, **10**, 2153; (c) G. V. Burmakina, S. P. Gubin, V. A. Maksakov, and V. A. Trukhacheva, *Koord. Khim.*, 1990, **16**, 1393.

52. S. Ozkar, G. A. Ozin, K. Moller, and T. Bein, *J. Am. Chem. Soc.*, 1990, **112**, 9575.

53. (a) W. F. Edgell and M. P. Dunkle, *J. Phys. Chem.*, 1964, **68**, 452; (b) G. Bor, *J. Chem. Soc., Chem. Commun.*, 1969, 641.

54. (a) E. R. Corey, L. F. Dahl, and W. J. Beck, *J. Am. Chem. Soc.*, 1963, **85**, 1202; (b) V. Albano, P. L. Bellon, P. Chini, and V. Scatturin, *J. Organomet. Chem.*, 1969, **16**, 461; (c) F. Cariati, P. Romiti, and V. Valenti, *Gazz. Chim. Ital.*, 1968, **98**, 615; (d) A. R. Manning and J. R. Miller, *J. Chem. Soc. (A)*, 1970, 3352; (e) A. Ceriotti, R. Della Pergola, L. Garlaschelli, M. Mannassero, and M. Sansoni, *J. Chem. Soc., Dalton Trans.*, 1991, 2357.

55. J. K. Burdett, in ‘Advances in Infrared and Raman Spectroscopy’, eds. R. J. H. Clark and R. E. Hester, Heyden, London, 1976.

56. (a) J. A. Banister, A. I. Copper, S. M. Howdle, M. Jobling and M. Poliakoff, *Organometallics*, 1996, **15**, 1804; (b) X.-Z. Sun, M. W. George, S. G. Kazarian, S. M. Nikiforov and M. Poliakoff, *J. Am. Chem. Soc.*, 1996, **118**, 10525.

57. S. A. McGregor and D. MacQueen, *Inorg. Chem.*, 1999, **38**, 4868.

58. L. Perrin, E. Clot, O. Eisenstein, J. Loch, and R. H. Crabtree, *Inorg. Chem.*, 2001, **40**, 5806.

Tungsten: Inorganic & Coordination Chemistry

Jon A. McCleverty
University of Bristol, Bristol, UK

1 Introduction 1
2 Halide and Cyanide Complexes 1
3 Cyanide and Other Group IV Donor Atom Complexes 2
4 Complexes with O-donor Atoms 2
5 Complexes with Sulfur, Selenium, and Tellurium Donor Atoms 5
6 Complexes with N-donor Atoms 8
7 Complexes with P-, As-, Sb-, and Bi-donor Atoms 15
8 Hydrido and Borohydrido Complexes 16
9 Metal–Metal Bonded Complexes and Cluster Compounds 17
10 Related Articles 25
11 References 25

Abbreviations

abt = 1-iminobenzene-2-thiolate (2−); acac = pentane-2,5-dionate (2−); bdt = benzene-1,2-dithiolate (2−); cat = catecholate (2−); benzene-1,2-diolate (2−); cyclam = 1,4,8,11-tetraazacyclotetradecane; depe = bis(diethylphosphino)ethane; dme = 1,2-dimethoxyethane; dppe = bis(diphenylphosphino)ethane; diphos = chelating bis(dialkyl)- or (diaryl)- phosphine; dme = 1,2-dimethoxyethane; en = 1,2-diaminoethane; mnt = maleonitriledithiolate (2−); *cis*-1,2-dicyanoethene-1,2-dithiolate (2−); OTf = trifluoromethanesulfonate (1−) (triflate (1−)); pz = pyrazine; py = pyridine; tdt = toluene-3,4-dithiolate (2−); tht = tetrahydrothiophene; tos = tosyl.

1 INTRODUCTION

Unlike its congener element molybdenum, tungsten does not play a significant industrial catalytic role. The element is encountered in a number of enzymes,[1,2] and following from earlier developments in the understanding and modeling of nitrogen fixation, the coordination chemistry of tungsten with simple nitrogen-based ligands was extensively developed.

During the last decade of the twentieth century, the inorganic and coordination chemistry of tungsten has expanded. Among the major developments in this period have been (1) the introduction of a versatile range of polydentate ligands, including the tripodal tris(amido, triamidoamine, and tris(pyrazolyl)borato species, which have enabled the stabilization of novel species and chemistry; (2) continuing development of the chemistry of a range of complexes containing oxo and imido ligands; (3) increased activity and substantial sophistication in the chemical modeling of tungsto-enzymes structure, function and spectroscopy (*see* ***Tungsten Proteins***) and (4) the development and rationalization of major areas of cluster chemistry (*see* ***Cluster Compounds: Inorganometallic Compounds Containing Transition Metal & Main Group Elements***), including the assembly of polyoxoanions (*see* ***Polyoxometalates***) and rational construction of chalcogenide-containing clusters.

Tungsten coordination has recently been comprehensively reviewed in *Comprehensive Coordination Chemistry*, particularly in the areas of mononuclear complexes,[3] dinuclear species containing single and multiple W–W bonds,[4] polyoxometallate synthesis, structure, and reactivity,[5,6] and chalcogen-containing cluster complexes.[7]

2 HALIDE AND CYANIDE COMPLEXES

Addition of one equivalent of anhydrous Et_4NF in thf to $[W(CO)_5(thf)]$ afforded $[Et_4N]_3[W_2(CO)_6(\mu\text{-F})_3]$. Reaction of this species, whose structure was confirmed crystallographically, with CO afforded the unstable $[W(CO)_5F]^-$, which containing labile CO ligands. In the absence of CO, this anion reverted to the dinuclear species or to $[W(CO)_6]$ on prolonged exposure to CO. Reaction of $[W(CO)_6]$ with $LiI\cdot OEt_2$ afforded $[W(CO)_5I]^-$.

Reaction of $[W(CO)_6]$ with SbF_5 in the superacid mixture HF/SbF_5 afforded $[W^{II}(CO)_6(FSbF_5)][Sb_2F_{11}]$, without loss of CO.

The tungsten(III) fluoride, $K_3[WF_6]$ was obtained, as a mixture with $K_2[WF_7]$, when $K_3[WF_8]$ was reduced by tungsten metal. Treatment of WCl_4 with one equivalent of a reducing agent, usually Na/Hg or $NaBHEt_3$ in toluene in the presence of PMe_2Ph, afforded $[(PMe_2Ph)_2Cl_2W(\mu\text{-Cl})_2WCl_2(PMe_2Ph)_2]$. By slight alteration of the stoichiometry, $[(PMe_2Ph)_2ClW(\mu\text{-Cl})_3WCl_2(PMe_2Ph)]$ was obtained, and the analogous bromide was prepared from WBr_5. Monomeric $[WCl_3(PMe_2Ph)_3]$ was synthesized in the comproportionation reaction between $[WCl_4(PMe_2Ph)_2]$ and *trans*-$[WCl_2(PMe_2Ph)_4]$. The stable mer-isomer was obtained as the major product, but low yields of the fac-isomer were isolated.

The dinuclear mixed-valence W^{II}/W^{III} species $[(Me_2S)Cl_2W(\mu\text{-Cl})(\mu\text{-SPh})_2WCl_2(SMe_2)]$ was obtained in the reaction between $[WCl_4(SMe_2)_2]$ with exactly one equivalent of Me_3SiSPh. Treatment of this air-sensitive species with $[Ph_4As]Cl$ afforded $[Cl_3W(\mu\text{-Cl})(\mu\text{-SPh})_2WCl_2]^{2-}$, and analogous species $[Cl_3W(\mu\text{-Cl})(\mu\text{-SePh})_2WCl_3]^{2-}$ and the W^{IV}/W^{IV} species $[Cl_3W(\mu\text{-Se})(\mu\text{-SePh})_2WCl_3]^{2-}$ were also isolated.

The seven-coordinate W^V fluoride K_2WF_7 was prepared by reaction of KWF_6 with LiF at high temperatures and under vacuum.

3 CYANIDE AND OTHER GROUP IV DONOR ATOM COMPLEXES

Reaction of $[W(CO)_5(CN)]^-$ with $[Cu(NCMe)_4]^+$ and PPh_3 afforded $[(OC)_5W(CN)Cu(PPh_3)_3]$ and the analogous isocyanide-bridged species $[(OC)_5W(NC)Cu(PPh_3)_3]$ was obtained by addition of $[Cu(PPh_3)_3CN)]$ to $[W(CO)_5(thf)]$ at low temperature. The latter slowly rearranged to the former.

Treatment of $[W_2(CO)_{10}]^{2-}$ with $Pb(NO_3)_2$ afforded $[\{W(CO)_5\}_4Pb_2]^{2-}$ (**1**), where the Pb–Pb distance was short (2.82 Å).

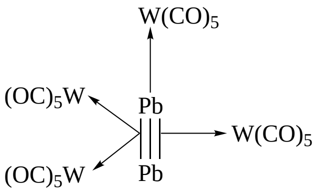

(**1**)

Polymeric $[W^{IV}(CN)_8(SnMe_3)_4]_n$ was obtained by reaction of $K_4[W(CN)_8]$ with four equivalents of Me_3SnCl, whereas the hexanuclear $[\{Mn(bipy)_2\}_2(\mu\text{-NC})_2\{W^{IV}(CN)_4\}_2(\mu\text{-CN})_2\{Mn(bipy)_2\}_2]$ was obtained by reaction of $[Mn(bipy)_2Cl_2]\cdot 2H_2O\cdot EtOH$ with $[W(CN)_8]^{4-}$ in aqueous media.

The W^V octacyanide $[W(CN)_8]^{3-}$ formed adducts or clusters with other metals, an example being $[Pt(en)_2]_3[W(CN)_8]_2$, in which there was electronic coupling between the metal centers in solution and in the solid state. Magnetically interesting materials were obtained in reactions between $[W(CN)_8]^{3-}$ and Mn^{2+}, namely $[Mn^{II}{}_6(H_2O)_9\{W^V(CN)_8\}_4 \cdot 13H_2O)]_n$ and $[Mn_9(W(CN)_8\}_6\cdot 24EtOH]\cdot 2EtOH$, the latter being high spin ($S = 39/2$).

4 COMPLEXES WITH O-DONOR ATOMS

4.1 Tungstates and Oxo–tungsten Complexes

$[W^{IV}O(dppe)_2F]^+$ was prepared by reaction of *trans*-$[W(PPh_3)_2Cl_4]$ with $BF_4{}^-$ and reacted with $[Et_4N]OH$ giving *trans*-$[WO_2(dppe)_2]$. On treatment of *trans*-$[WO_2(dppe)_2]$ with halide ions, NCS^- and MeI, the complexes *trans*-$[W^{IV}O(dppe)_2X]$ ($X =$ halide, NCS, NCS, OMe) were formed.

Tungstate ion $[WO_4]^{2-}$ reacted readily with the Lewis acid $B(C_6F_5)_3$, giving tetrahedral $[WO\{OB(C_6F_5)_3\}_3]^-$.

Treatment of $WOCl_4$ with hexamethyldisiloxane in oxygenated solvents effected extraction of the chloride ion giving solvated species such as $[WO_2Cl_2(MeOCH_2CH_2OMe)]$, via elimination of Me_3SiCl. Polymeric $[\{WO_2Cl_2\}_n]$ reacted with 1,3-dimethylalloxazine (L^1) and bis(1-methylimidazol-2-yl)ketone (L_2) afforded the monomeric six-coordinated species $[WO_2Cl_2L^1]$ (**2**), and $[WO_2Cl_2L^2]$ (**3**).

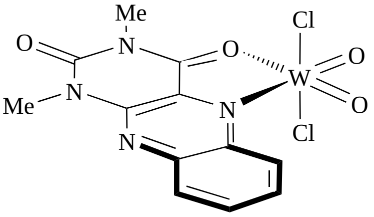

(**2**)

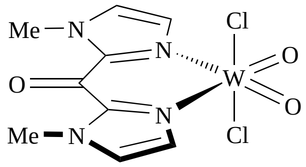

(**3**)

4.2 Alkoxide, Aryloxide, and Catecholate Complexes

4.2.1 *Alkoxide Complexes*

Reaction of $[W_2(NMe_2)_6]$ with an excess of cyclopentanol in hexane afforded first the dimethylamine adduct $[W^{III}{}_2(O\text{-}c\text{-}C_5H_9)_6(NHMe_2)_2]$ but over a prolonged period in contact with cyclopentanol and $NHMe_2$, the green diamagnetic mixed-valence $W^{III}W^V$species $[W_2(\mu\text{-H})(\mu\text{-O-}c\text{-}C_5H_9)_2(O\text{-}c\text{-}C_5H_9)_5(NHMe_2)]$ (**4**) ($R = c\text{-}C_5H_9$) was formed. The W–W distance (2.44 Å) is consistent with a double bond.

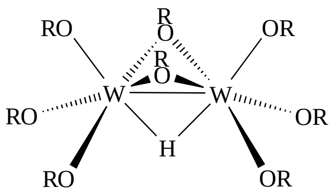

(**4**)

Reaction of $[W_2(OCH_2Bu^t)_6(NHMe_2)_2]$ with P_4 in hydrocarbon solvents afforded the phosphido-capped $W_3{}^{IV}$

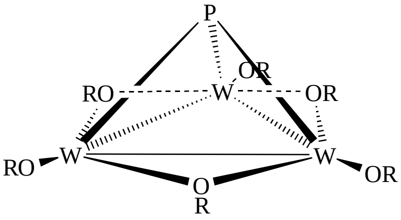

(**5**)

alkoxide $[W_3(\mu^3\text{-P})(\mu\text{-OCH}_2\text{Bu}^t)_3(\text{OCH}_2\text{Bu}^t)_3]$ (**5**), together with the previously known $[W(\eta^3\text{-P}_3)(\text{OCH}_2\text{Bu}^t)(\text{NHMe}_2)]$.

Treatment of $[W(\text{PMe}_2\text{Ph})_2\text{Cl}_4]$ with two equivalents of $\text{TlOCH}_2\text{CF}_3$ afforded $[W^{IV}\text{Cl}_2(\text{OCH}_2\text{CF}_3)_2(\text{PMe}_2\text{Ph})_2]$. Reaction of $[\text{WO}_{2-n}\text{S}_n]^{2-}$ with SiClPh_3 and Me_4phen (3,4,7,8-tetramethyl-1,10-phenanthroline) gave $[\text{WO}_{2-n}\text{S}_n(\text{OSiPh}_3)_2(\text{Me}_4\text{phen})]$ (**6**).

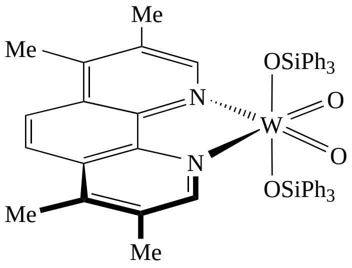

(**6**)

Reaction of $[W_2(\text{OCH}_2\text{Bu}^t)_8]$ with pyridine-*N*-oxide, elemental sulfur, selenium, and $\text{Bu}^t{}_3\text{PTe}$ afforded $[W^V{}_2(\mu\text{-E})(\mu\text{-OCH}_2\text{Bu}^t)_2(\text{OCH}_2\text{Bu}^t)_6]$ (E = O, S, Se, or Te).

Anodic oxidation of metallic tungsten in methanol afforded a mixture of $[W(\text{OMe})_6]$ and $[\text{WO}(\text{OMe})_4]$, and reaction of $[W(\text{NMe}_2)_6]$ with pinacol afforded the tris-pinacolate (2−) $[W(\text{OCMe}_2\text{CMe}_2\text{O})_3]$. Treatment of WCl_6 with one or two equivalents of the silsesquinoxane $R_7\text{Si}_7\text{O}_9(\text{OH})_3$ afforded the bis(silsesquinoxanato) complexes (**7**).

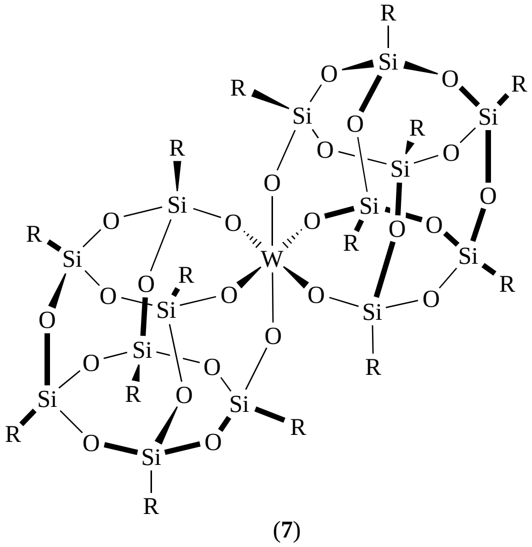

(**7**)

4.2.2 *Aryloxide Complexes*

Reaction of $[\text{WCl}_4(\text{SEt}_2)_2]$ with $(\text{OC}_6\text{H}_3\text{R}_2)^-$ (R = Me, Pr^i) afforded the nearly square-planar species $[W^{IV}(\text{OC}_6\text{H}_3\text{R}_2)_4]$. Reaction of substituted pyridines (L), dipyridyls, and phenanthrolines (L_2) with *trans*-$[W(\text{OC}_6\text{H}_3\text{Ph-C}_6\text{H}_4\text{-}O,C)(\text{PMePh}_2)_2]$, itself generated by sodium amalgam reduction of $[W(\text{OC}_6\text{H}_3\text{-2,6-Ph}_2)_2\text{Cl}_4]$ in the presence of PMePh_2, gave $[W(\text{OC}_6\text{H}_3\text{Ph-C}_6\text{H}_4\text{-}O,C)\text{L}_2]$ (**7**), in which the diphenylphenoxide ligands are cyclometallated, the complex having mutually trans O atoms and cis pyridine ligands. The complexes (**8**) exhibited sharp contact-shifted ^{1}H NMR spectra, the amount of contact shifting being strongly dependent on the nature of the N-donor ligand L. Assignment of the signals in the ^{1}H NMR spectra, as well as their temperature dependence, indicated that there was a thermal equilibrium between a single ground state for the d^2 W^{IV} center and a triplet excited state, which underwent through-bond coupling to the ligand protons. The relative singlet-triplet energy gap for several ligand systems was calculated from the spectral data.

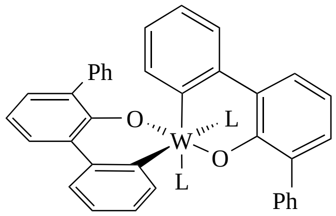

(**8**)

Reduction of $[\text{WCl}_2(\text{OAr})_4]$ (Ar = $\text{C}_6\text{H}_3\text{Cl}_2$-2,6) by sodium amalgam afforded $[W^V\text{Cl}(\text{OAr})_4(\text{OEt}_2)]$, in which the ether is trans to Cl. Reaction of $[\text{WCl}_4(\text{OAr})_2]$ (Ar = $\text{C}_6\text{H}_3\text{Ph}_2$-2,6) with an excess of LiBH_4 or an equivalent of sodium amalgam in the presence of PMe_2Ph afforded $[\text{WCl}_3(\text{OAr})_2(\text{PMe}_2\text{Ph})]$, and $\text{WCl}_2(\text{OAr})_2(\text{thf})]$ was isolated following reduction by $\text{Mg}(\text{C}_4\text{H}_6)_2$ in thf.

Reaction of WOCl_4 with phenols (ArOH) afforded $[W^{VI}\text{OCl}_2(\text{OAr})_2]$. With aromatic diols, species such as $[\text{WO}(\text{OArOCl}_2(\text{thf})_2]$ or $[\text{WOCl}_3(\text{OArOH})\cdot\text{OEt}_2]$ were formed, depending on solvents used. Reaction of WOCl_4 with 1,3-dialkyl-*p*-Bu^tcalix[4]arene (R_2calH_2; R = Me, Et) afforded $[\text{WOCl}_2(\text{R}_2\text{cal})]$ (**9**), whereas use of the unalkylated calixarene (R = H) gave $[\text{WO(cal)}]\cdot n$(solvent) and $[\text{WO(cal)L}]$ (L = H_2O, MeCO_2H). Reaction of $[W(\text{OCH}_2\text{CH}_2\text{O})_2(\text{OAr})_2]$ with HCl afforded *trans*-$[\text{WCl}_2(\text{OCH}_2\text{CH}_2\text{O})(\text{OAr})_2]$ (Ar = $\text{C}_6\text{H}_2\text{Me}_2$-2,6, $\text{C}_6\text{H}_2\text{Pr}^i{}_2$-2,6 and $\text{C}_6\text{H}_2\text{Me}_2$-2,6. The first structurally characterized complex containing W^{VI}–I bonds, $[\text{WI}_2(\text{OBu}^t)_4]$, was also reported.

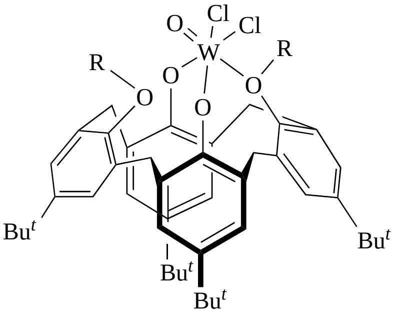

(**9**)

4.2.3 Catecholate Complexes

Treatment of $[W(CO)_5(thf)]$ with two equivalents of $[Et_4N][OC_6H_4OH]$ afforded the orange catecholato (2−) species $[Et_4N]_2[W(CO)_4(O_2C_6H_4)]\cdot HOC_6H_4OH$, in which the catechol hydrogen-bonded to adjacent O atoms of the catecholato (2−) ligands, thereby forming a chain-like structure in the solid state. Treatment of this species with an excess of NaOMe afforded $[Et_4N]_2[W(CO)_4(O_2C_6H_4)]$, and similar complexes containing $[O_2C_6H_2Bu^t{}_2]^{2-}$ (di-*t*-butylcatecholate) were also isolated. The tetracarbonyl species reversibly decarbonylated, affording $[W(CO)_3(O_2C_6H_2R_2]_2-(R = H$ or But), and crystallographic studies showed the geometry of these five-coordinate species as intermediate between trigonal bipyramidal and square planar. A related amido-phenolato species $[W(CO)_3\{O(NH)C_6H_4\}]^{2-}$ was also reported.

4.2.4 Peroxide Complexes

Reaction of $WO_3\cdot H_2O$ with hydrogen peroxide (30%) followed by addition of $SiPh_2(OH)_2$ or $[\{Ph_2Si(OH)\}_2O]$ afforded dimeric species $[Ph_2SiO_2\{W_2O_2(\mu\text{-}O_2)_2(O_2)_2\}]_2-$(**10**), and $[\{Ph_2SiOW(O)(O_2)_2\}_2\mu\text{-}O]_2-$(**11**).

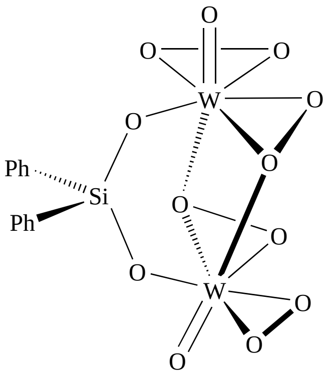

(**10**)

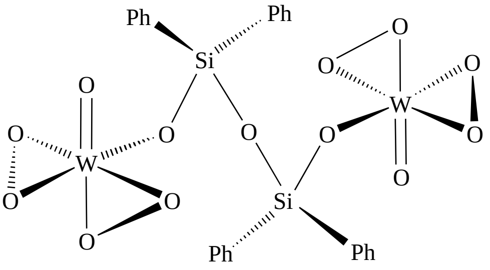

(**11**)

4.2.5 Carboxylato, Carbonato, and Related Complexes

Glycinato derivatives $[W(CO)_4\{\kappa^2\text{-}O_2CCH_2NRR'\text{-}N,O)]^-$ ($RR' = H_2$, HMe, Me_2) were prepared by reaction of $[W(CO)_5(thf)]$ with the corresponding glycine derivatives. Reaction of $[W(CO)_5(NCMe)]$ with one equivalent of oxalate ion afforded $[W(CO)_4(\kappa^2\text{-}O_2CO_2)]^{2-}$. With two equivalents of oxalate, $[W_2(CO)_{10}(\mu\text{-}\kappa^1\text{-}O_2C_2O_2)]^-$ was formed initially, and following loss of CO, $[W_2(CO)_8(\mu\text{-}\kappa^2\text{-}O_2C_2O_2)]^{2-}$ was generated.

Reaction of bicarbonate ion with $[W(CO)_5(acetone)]$ or of $[W(CO)_5(OH)]^-$ with CO_2 afforded $[W(CO)_5\{\kappa^1\text{-}OCO(OH)\}]^-$. Insertion of COS into the W–O bond in $[W(CO)_5(OC_6H_3Ph_2\text{-}2,6)]^-$ afforded $[W(CO)_5\{SC(O)OC_6H_3Ph_2\}]^-$ (**12**).

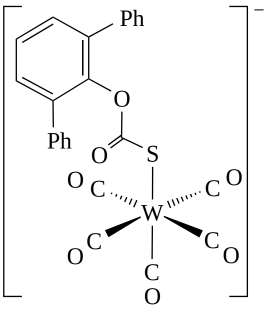

(**12**)

Reaction of *trans*-$[W(CO)(N_2)(dppe)_2]$ with an excess of methanol of secondary amine under CO_2 afforded $[W^{II}H(\kappa^1\text{-}OCO_2Me)(CO)(dppe)_2]$ or the carbamato species $[W^{II}H(\kappa^2\text{-}O_2CNR_2(CO)(\kappa^1\text{-}dppe)(\kappa^2\text{-}dppe)]$. Treatment of the latter with $AlEt_3$ in thf under CO_2 afforded *trans*-$[W(CO)(\kappa^2\text{-}OCO\text{-}C,O)(dppe)_2]$.

Reaction of WCl_6 or $WOCl_4$ with salicylic acid (H_2sal) followed by crystallization of the product from thf afforded $[W^{VI}OCl(Hsal\cdot thf)(sal)]$. However, treatment of $WOCl_4$ with three equivalents of salicylic acid gave $[\{WO(Hsal)(sal)\}_2O]$.

4.2.6 Schiff Base Complexes

The dinuclear species $[W_2(CO)_8(salen)]^{2-}$ was obtained by reaction of two equivalents of $[W(CO)_5(thf)]$ with $(salen)^{2-}$.

Reaction of $[W(CN)_3O_2]^{4-}$ with salicylaldehyde and 1,2-diaminoethane (precursors of the Schiff base salenH_2) afforded $[W^{IV}O(CN)(salen)]^{2-}$.

5 COMPLEXES WITH SULFUR, SELENIUM, AND TELLURIUM DONOR ATOMS

5.1 Dithiolene Complexes

Reaction of $[W(CO)_5(thf)]$ with $[HXYC_6H_4]^-$ (X = Y = S, X = O, Y = S, X = NH, Y = S) initially afforded $[W(CO)_4(HXYC_6H_4]^-$, but further treatment with OMe^- gave the dithiolate species $[W(CO)_4(XYC_6H_4)]^{2-}$. These tetracarbonyl complexes gradually converted to tricarbonyl species on bubbling argon into acetonitrile solutions at 40 °C. Trigonal bipyramidal structures were determined for $[PPN][W(CO)_3\{S(NH)C_6H_4\}]$ and $[PPN][W(CO)_3\{SOC_6H_4\}]$, but $[PPN]_2[W(CO)_4(S_2C_6H_4)]$ was octahedral.

Reaction of $[W(CO)_3L_2I_2]$ (L = PEt_3, PPh_3, L_2 = dppe) with mnt^{2-} or bdt^{2-} afforded $[W^{II}(CO)_2L_2(mnt)]$ and $[W^{II}(CO)_2L_2(bdt)]$. The related complexes $[W^{II}(CO)_2L_2(S_2C_2S_2CS)]$ ($S_2C_2S_2CS$ = (**13**)) were prepared similarly.

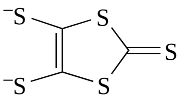

(**13**)

Reduction of $[W(S_2C_2Me_2)_3]$ by Et_4NBH_4 afforded $[W(S_2C_2Me_2)_3]^{2-}$ while $[WSe_9]^{2-}$ or $[WSe(Se_4)_2]^{2-}$ reacted with dimethylacetylenedicarboxylate, giving the tris(diselenolene) complex $[W(Se_2C_2R_2)_3]^{2-}$ (R = CO_2Me). Reaction of tetrathiapentalenedione, $C_2S_4(CO)_2$, with $[WS_4]^-$ afforded $[W\{S_2C_2S_2CO\}_3]^{2-}$. These 'noninnocent' species formally contain W(IV).

Treatment of $[W(CO)_2(S_2C_2R_2)_2]$ (R = Me, Ph) with OH^-, S^{2-}, or Se^{2-} afforded $[W^{IV}E(S_2C_2R_2)_2]^{2-}$ (E = O, S, Se).

Bis(dithiolene) tungsten(IV) complexes have been synthesized for comparison with the active sites in tungsto-enzymes. $[WO(bdt)_2]^{2-}$ was prepared by borohydride reduction of $[WO(bdt)_2]^-$, and the analogous $[WO(mnt)_2]^{2-}$ was prepared by reduction of $[W^{VI}O(\kappa^2\text{-}S_2)(mnt)_2]^{2-}$. Reaction of $[WO_2(CN)_4]^{4-}$ with $[SC(H){=}C(Ar)S]^{2-}$ (Ar = Ph, 2-, 3- or 4-pyridyl, quinoxalinyl) has afforded mixtures of cis (**14a**) and trans (**14b**) isomers of $[WO\{SC(H)C(Ar)S\}_2]^{2-}$, established by ^{1}H NMR spectroscopy, but only cis-isomers were crystallized and characterized crystallographically.

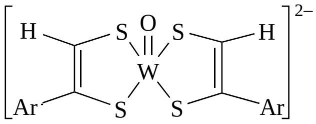

(**14a**)

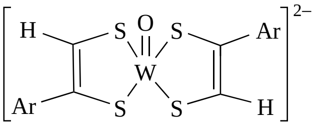

(**14b**)

Reaction of $[WO(bdt)_2]^{2-}$ with one equivalent of $SiBu^tR_2Cl$ (R = Me, Ph) afforded the 'desoxo' complexes $[W(OSiR_2Bu^t)(bdt)_2]^-$. Addition of OR'^- (R′ = Pr^i or Ph) to $[W(CO)_2(S_2C_2Me_2)_2]$ afforded $[W(OR'(S_2C_2Me_2)_2]^-$ and reaction of these species with Me_3NO afforded $[WOOR'(S_2C_2Me_2)_2]^-$. With EAr^-, $[W(CO)(EAr)(S_2C_2Me_2)_2]^-$ (E = S, Se; Ar = 2-adamantyl, Ph, C_6H_2-2,4,6-Pr^i_3) was formed. Similar reactions with alkoxides and phenolates afforded $[WO(ER)(S_2C_2Me_2)_2]^{3-}$ (E = O, R = Pr^i, 2-adamantyl, *p*-C_6H_4X, where X = CN, Br, Me, OMe, NH_2; E = S, Se, R = 2-adamantyl). Treatment of $[W(CO)_2(S_2C_2Me_2)_2]$ with O_2CPh^- gave $[W(O_2CPh)(S_2C_2Me_2)_2]^-$. The structure of $[WO(OPh)(S_2C_2Me_2)_2]^-$ and the catalytic center of one DMSO reductase isoenzyme have similar overall stereochemistry and comparable bond lengths. The W^{IV} complex $[W(OPh)(S_2C_2Me_2)_2]^-$ reacted quantitatively with various substrates XO to afford $[W^{VI}O(OPh)(S_2C_2Me_2)_2]^-$ and X in second order reactions with associative transition states.

Sodium naphthalenide reduction of $[W^{V}O(bdt)_2]^-$ afforded a mixture of $[W(bdt)_3]^{2-}$ and $[W^{IV}O(bdt)_2]^{2-}$ which, with Me_3NO, under O-atom transfer afforded $[W^{VI}(O)_2(bdt)_2]^{2-}$. Reaction of this dioxo species with Me_3SiCl afforded $[W^{VI}OCl(bdt)_2]^-$. Reaction of the oxo-chloro complex with $P(OEt)_3$) in the absence and presence of Bu^{t}NC afforded $[W^{IV}\{(P(OEt)_3\}_2(bdt)_2]$ and $[W^{IV}CNBu^t)_2(bdt)_2]$, both reduction processes, but with OBu^{t-} and SPh^- $[W^{VI}(O)(OBu^t)(bdt)_2]^-$ and $[W^{VI}(O)(SPh)(bdt)_2]^-$ were formed. Reaction of $[W^{IV}O(bdt)_2]^{2-}$ with Me_3SiCl afforded $[W^{IV}(OSiMe_3)(bdt)_2]^-$.

Treatment of $[W(CO)_3(NCMe)_3]$ with $[Ni(S_2C_2R_2)_2]$ gave the dithiolene complexes $[W(CO)_2(S_2C_2R_2)_2]$ (R = Me, Ph). Reaction of $[W(CO)_2(S_2C_2Me_2)_2]^{2-}$ with $[W(CO)_2(S_2C_2Me_2)_2]$ afforded the paramagnetic $[W(CO)_2(S_2C_2Me_2)_2]^-$. The dicarbonyl species $[W(CO)_2(S_2C_2Me_2)_2]^z$ and the related tris(dithiolene) complexes $[W(S_2C_2Me_2)_3]^z$ exist as a three-membered electron transfer chain, $z = 0$, -1, and -2, which were interconnected by reversible redox reactions. Members of both series have similar distorted trigonal prismatic structures. As the most oxidized species ($z = 0$) were reduced, the M–S, S–C, and C–O distances increased, and the M–C, chelate ring C–C, and ν_{CO} values decreased. Whereas the most oxidized species $[W(CO)_2(S_2C_2Me_2)_2]$ and $[W(S_2C_2Me_2)_3]$ formally contain W^{IV} and W^{VI}, respectively, the trends in bond lengths and vibrational frequencies, coupled to density functional calculations, established that the redox orbital in these 'noninnocent' complexes was predominantly sulfur ligand based, that is, that the electron transfer behavior is largely ligand based.

Crystallographic studies of $[WO(bdt)_2]^-$ and $[WO(S_2C_2Me_2)_2]^-$ established that they had square pyramidal structures. Reaction of $[W^{IV}(OPh)(S_2C_2Me_2)_2]^-$ with two equivalents of benzenethiol or benzene selenol afforded $[W^{V}(EPh)_2(S_2C_2Me_2)_2]^-$ (E = S or Se), but when one equivalent of Ph_3CSH was employed, dinuclear $[W_2(\mu\text{-}S_2(S_2C_2Me_2)_4]^{2-}$ was formed. This complex could also be generated by reaction of $[W(CO)_2(S_2C_2Me_2)_2]$ with $S_2{}^{2-}$ or the oxidation of $[W^{IV}S(S_2C_2Me_2)_2]^{2-}$ by iodine. The corresponding dinuclear species $[W_2(\mu\text{-}S_2(S_2C_2Ph_2)_4]^{2-}$ was obtained by tropylium cation oxidation of $[WS(S_2C_2Ph_2)_2]^{2-}$.

Recent crystallographic studies of the active sites in tungsto-enzymes has suggested the possibility of desoxo-tungsten(IV) and mono-oxo-tungsten (VI) bis(dithiolato) centers to which serine molecules might be additionally coordinated. Attempts to mimic the coordination environment around the tungsten atom led to the generation of $[W^{VI}O(OSiBu^tPh_2)(bdt)_2]^-$ and $[WO(OPh)(S_2C_2Me_2)_2]^-$ (**15**) by treatment of $[W(OR)(dithiolate)_2]^-$ precursors with an excess of Me_3NO, as described above.

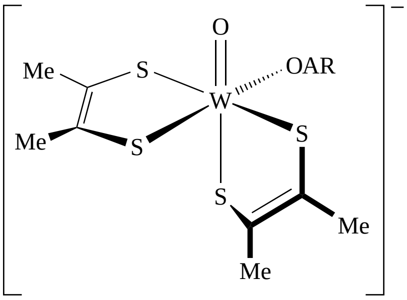

(**15**)

Treatment of $WOCl_4$ with Li_2bdt or of $[WO(bdt)_2(OSiBu^tPh_2)]^-$ with $SiMe_3Cl$ afforded $[W^{VI}O(bdt)_2Cl]^-$. Reaction of $[W(OR)(S_2C_2Me_2)_2]^-$ (R = Ph or $SiBu^tPh_2$), which formally contains W(IV), with dibenzyltrisulfide or $(Me_3Si)_2S$ afforded the sulfido complexes $[W^{VI}S(bdt)(OR)]^-$, an oxidative addition formally generating W(VI) species.

Addition of trimethylamine *N*-oxide to $[W^{IV}O(bdt)_2]^-$ and to $[WO(S_2C_2Me_2)_2]^-$ afforded the W(VI) complexes $[WO_2(bdt)_2]^{2-}$ and $[WO_2(S_2C_2Me_2)_2]^{2-}$, in which the oxo groups were mutually cis. Because of trans influences, the W–S bonds trans to the oxo groups in $[WO_2(bdt)_2]^{2-}$ (as the Et_4N^+ salt) were longer (2.60 Å) than those which were cis (2.43 Å). Reaction of aqueous $WO_4{}^{2-}$ with mnt^{2-} in the presence of an excess of $HSO_3{}^-$ (*pH* 5.5) followed by addition of acetic acid afforded the structurally similar $[WO_2(mnt)_2]^{2-}$.

5.2 Thiolato Complexes

Addition of RSH (R = Bu^t, Ph) to $[W(CO)_3(phen)(NCEt)]$ afforded $[W(CO)_3(phen)(Bu^tSH)]$ or $[W(CO)_3H(phen)(SPh)]$. $[W(CO)_5(SPh)]^-$, obtained by reaction of $[W(CO)_5(thf)]$ with $(SPh]^-$, converted slowly to $[W(\mu\text{-}S)_2(CO)_8]^{2-}$ on gentle heating.

Addition of PhSSPh to $[W(CO)_3(PPr^i{}_3)_2]$ afforded the paramagnetic W^I complex $[W(CO)_3(PPr^i{}_3)_2(SPh)]$.

Reaction of $[W^{IV}H(tipt)_3(PMe_2Ph)_2]$ with CNMe in thf afforded *cis*-$[W^{II}(CNMe)_4(tipt)_2]$ (tipt = $SC_6H_2Pr^i{}_3$-2.4.6). Similarly, reaction of $[WH(tipt)_3(PMe_2Ph)_2]$ with CO led to loss of thiol and formation of $[W(CO)_2(PMe_2Ph)_2](tipt)_2]$. The dicarbonyl was isolated as two isomers (green 90%; red 10%), and variable-temperature ^1H NMR spectroscopy indicated that they were fluxional and interconverted in solution. The structure of the green isomer of the analogous $[W(CO)_2(PMe_2Ph)_2(SC_6H_2Me_3\text{-}2,4,6)_2]$ revealed that it had a twisted trigonal prismatic geometry. The selenolate $[W(CO)_2(PMe_2Ph)_2(SeC_6H_3Pr^i{}_2)_2]$ was obtained similarly and had a slightly distorted trigonal prismatic geometry.

Reaction of $[W(CO)_3(PEt_3)_2I_2]$ with SPh^- or $[S(CH_2)_nS]^{2-}$ (n = 2, 3) afforded the octahedral species $[W^{II}(CO)_2(PEt_3)_2(SPh)_2]$ and $[W^{II}(CO)_2(PEt_3)_2\{S(CH_2)_nS\}]$. The W(0) complex$[W(CO)_3(phen)(NCEt)]$ underwent oxidative addition with dialkyl and diaryl disulfides forming $[W^{II}CO)_2(phen)(SR)_2]$ (R = Ph, CH_2Ph, Me, Bu^t). $[W(CO)_2(phen)(SPh)_2]$ reacted with $P(OMe)_3$ giving $[W(CO)\{P(OMe)_3\}(phen)(SPh)_2]$ and the X-ray structures of $[W(CO)_2(phen)(SPh)_2]$ and $[W(CO)\{P(OMe)_3\}(phen)(SPh)_2]$ showed that they were both octahedral, with the phenylthiolato ligands in trans positions. Both molecules reacted with SO_2 giving $[W(CO)(phen)(SPh)_2)(\kappa^2\text{-}SO_2)]$. The coordinated S–O bond was long (1.58 Å) and could be cleaved to give $[WO_2(phen)(SPh)_2]$ (cis dioxo groups, trans thiolato groups), with loss of CO and sulfur.

The tetrathiolate $[W^{IV}(SBu^t)_4]$ was obtained by reaction of $[WCl_4(SEt_2)_2]$ with SBu^{t-}. Reaction of *cis*-$W(N_2)_2(PMe_2Ph)_4]$ with Bu^tSH in thf afforded the dinuclear species $[\{W(SBu^t)_2(PMe_2Ph)\}_2(\mu\text{-}S)_2]$ (**16**). Reaction of $[W(CO)_3I_2(NCMe)]$ with the potential NS_3-podand ligand $N(CH_2CH_2SH)_3$ afforded, in the presence of NEt_3, the dinuclear species $[\{W^{IV}(SCH_2CH_2)_3N\}_2\{\mu\text{-}SCH_2CH_2N(CH_2CH_2SH)_2\}_2]$.

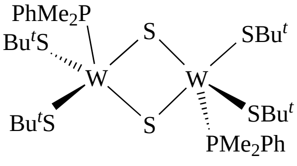

(**16**)

The square-planar ethanedithiolato complexes $[W^{V}O(SCH_2CH_2S)_2]^-$ were obtained by a ligand exchange reaction involving $[WO(SPh)_4]^-$. The X-ray crystallographic examination of $[W^{V}O(SC_6H\text{-}2,3,5,6\text{-}Me_4)_4]^-$ revealed that it too was nearly square planar.

5.3 Thioether Complexes

The cyclic polythioether complex [W(CO)$_4$L] (L = 2,5,8,11-tetrathia[12](2,5)thiophenophane was prepared by UV irradiation of [W(CO)$_6$] in the presence of the ligand in thf. Variable-temperature ^{1}H NMR studies showed that this species was fluxional, and the derived molecular structure indicated κ^2-L-S^5S^8 coordination (**17**). The thioether-bridged complexes [{W(CO)$_4$}$_2$L] (**18**), where L is the hexakis(alkylsulfanylmethyl)benzene, C$_6$(CH$_2$SR)$_6$ (R = C$_5$H$_{11}$, Pr^n) were obtained by reaction of [W(CO)$_4$(NCMe)$_2$] with the appropriate thioether. Reaction of [W(CO)$_4$(tmpa)] (tmpa = N,N,N',N'-tetramethyl-1,3-propanediamine) with 1,5-diselenacyclooctane ([8]aneSe$_2$) gave the cis-disubstituted produce [W(CO)$_4${[8]aneSe$_2$}].

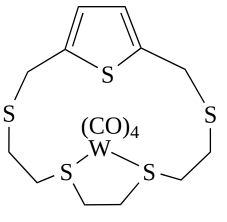

(**17**)

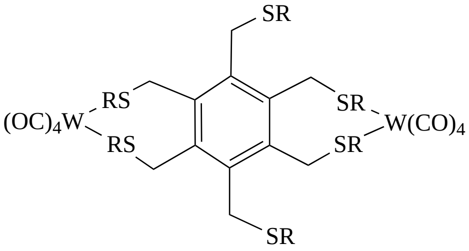

(**18**)

5.4 Sulfides, Selenides and, Tellurides

Reaction of Se$_4$(AsF$_6$)$_2$ or Se$_8$(AsF$_6$)$_2$ with [W(CO)$_6$] in liquid SO$_2$ afforded the diamagnetic [W$_2$(CO)$_{10}$Se$_4$][AsF$_6$]$_2$ (**19**), which contained a μ-Se$_4{}^+$ moiety. The short Se···Se bond lengths (2.29 Å) are close to those found in gaseous Se$_2$ (2.19 Å), while the longer Se–Se bonds suggested that the complex should be formulated as containing two {W(CO)$_5$(κ^2-Se$_2$)}$^+$ groups.

Treatment of [W(CO)$_6$] with Te$_4$(SbF$_6$)$_2$ in SO$_2$/AsF$_3$ afforded [W(CO)$_4$(η^3-Te$_3$)][SbF$_6$]$_2$ (**20**). The molecular structure of this species confirmed the 'piano-stool' geometry, and the triangular Te$_3{}^{2+}$ group. Reaction of [W(CO)$_6$] with K$_2$Te$_4$ afforded [W(CO)$_4$(κ^2-Te$_4$)], which contained a five-membered WTe$_4$ chelate ring.

Reaction of [W(CO)$_5$(thf)] with [Fe(CO)$_3$I$_2$(TePh$_2$)] and with Bu$^t{}_3$P=Te caused replacement of the thf and formation of the tellurium adducts [W(CO)$_5$(TePh$_2$)] and [W(CO)$_5$(Te=PBu$^t{}_3$)], respectively.

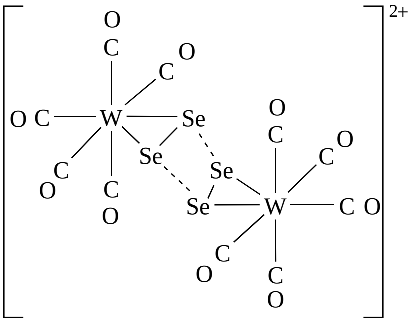

(**19**)

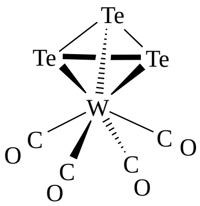

(**20**)

The monomeric tetraselenide ion [W^{IV}(E)(Se$_4$)$_2$]$^{2-}$ (E = O, S, Se) was prepared by reaction of [WSe$_4$]$^{2-}$ with Se$_8$, SeS$_2$, or Se$_4$(NC$_5$H$_{10}$)$_2$ in dmf, respectively. Tungsten hexachloride, WCl$_4$, or WOCl$_4$ reacted with polytelluride ions Te$_3{}^{2-}$, Te$_4{}^{2-}$, and Te$_5{}^{2-}$ in dmf giving W^{IV}O(κ^2-Te$_4$)$_2$]$^{2-}$.

Reaction of [WSe$_4$]$^{2-}$ with phosphorus selenide glass, 'P$_2$Se$_4$', afforded [W^{IV}Se(PSe$_2$)(PSe$_4$)]$^{2-}$ (**21**), which contained PSe$_4{}^{3-}$ and the trihapto hetero-allylic PSe$_2{}^{2-}$ group. Treatment of [W(CO)$_6$] or W(CO)$_2$(As$_2$Se$_3$)$_2$]$^{2-}$ with As$_4$Se$_4$ and K$_2$Se$_3$ afforded [W(AsSe$_5$)$_2$]$^{2-}$ (**22**). [W(CO)$_2$(As$_3$Se$_3$)$_2$]$^{2-}$ (**23**) was generated by reaction of [W(CO)$_6$] with As$_4$Se$_6{}^{2-}$, and its reaction with red selenium converted it into [W(AsSe$_5$)$_2$]$^{2-}$.

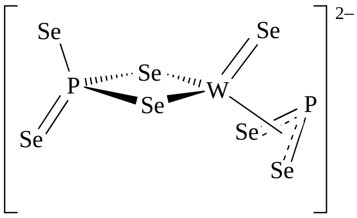

(**21**)

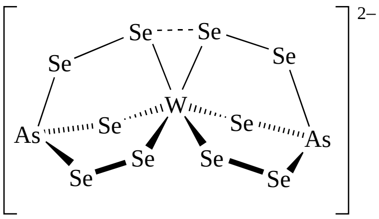

(**22**)

Treatment of [W(PMe$_3$)$_6$], better formulated as [W(κ^2-CH$_2$PMe$_2$)$_2$H$_2$(PMe$_3$)$_4$], with H$_2$E (E = S or Se) or elemental tellurium afforded *trans*-[W(E)$_2$(PMe$_3$)$_4$] (E = S, Se or Te). These reactions proceeded through the intermediate [W(E)(H$_2$)(PMe$_3$)$_4$], the species containing E = Se being characterized crystallographically. The species

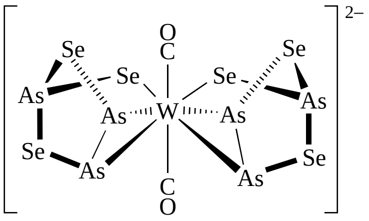

(**23**)

$[W(PMe_3)_4(H)_2(SH)_2]$ could also be detected. Reaction of the dihydride $[WH_2(PMe_3)_4]$ with elemental tellurium afforded $[WH_2(PMe_3)_4(\kappa^2\text{-}Te_2)_2]$, from which $[W(Te)_2(PMe_3)_4]$ could be obtained by oxidative cleavage of the Te–Te bonds.

Reaction of *trans*-$W(E)_2(PMe_3)_4]$ (E = S or Se) with isonitriles, CNR (R = alkyl, aryl), afforded all-*trans*-$[W(E)_2(CNR)_2(PMe_2)_2]$ whereas reaction of $[W(Te)_2(PMe_3)_4]$ with $CNBu^t$ afforded $[W(CNBu^t)_4(PMe_3)(\kappa^2\text{-}Te_2)]$ (**24**).

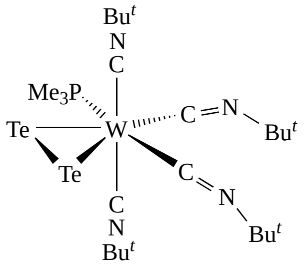

(**24**)

Treatment of $[WO_4]^{2-}$ with NH_4SCN in aqueous HCl gave oxotungsten(V) species, and reaction of this solution with polysulfide ion afforded $[(S_4)(O)W(\mu\text{-}S)_2W(O)(S_2)]^{2-}$ and the symmetrical species $[\{WO(S_4)\}_2)\mu\text{-}S)_2]^{2-}$.

Relatively few tungsten(VI) selenide or telluride species are known. Treatment of *trans*-$[W^{IV}E_2(PMe_3)_4]$ (E = S, Se, Te) with aldehydes afforded the metalla-oxirane derivative $[W^{VI}E_2(PMe_3)_2(\kappa^2\text{-}OCHR)]$ (**25**). Reaction of species containing $\{WO\}^{3+}$ with $(NH_4)_2S_x$ in the presence of 2,2′-dipyridyl (bipy) afforded the mononuclear species $[WO(\kappa^2\text{-}S_2)_2(bipy)]$ and reaction of $[WO_2S_2]^{2-}$ with elemental sulfur and hydrazinium hydrochloride afforded $[\{WO(\kappa^2\text{-}S_2)_2\}_2(\mu_2\text{-}S_7)(\mu_2\text{-}NH_2NH_2)]$ (**26**).

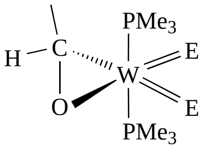

(**25**)

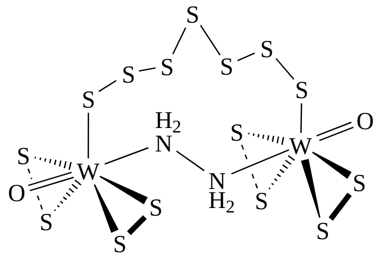

(**26**)

5.5 Dithioacid, Dithiocarbamate, Dithiophosphate, and Related Complexes

Elimination of HCl from $[W(CO)_2(H)Cl(PMe_3)_2]$ upon treatment with CS_2 and PMe_3 afforded $[W(CO)_2(PMe_3)_2](\kappa^3\text{-}S,S',C\text{-}S_2CPMe_3]$. Treatment of this complex with HBF_4 generated a dithioformato species $[W(CO)_2(PMe_3)_2\{\kappa^2\text{-}S_2C(H)PMe_3\}]^+$ and addition of MeI gave the analogous $[W(CO)_2(PMe_3)_2\{\kappa^2\text{-}S_2C(SMe)PMe_3\}]^+$

The tungsten carbyne complex $[W(\equiv CPh)(CO)_2(py)_2Cl]$ reacted with $(S_2CNEt_2)^-$ giving $[W^{II}(CO)(\eta^2\text{-}SCHPh)(\kappa^2 = C,S\text{-}SCNEt)_2]$, which was regarded as containing a neutral dihapto thiobenzaldehyde group. The complex could equally well be regarded as a metallacyclic W^{IV} complex binding $(SCHPh)^{2-}$.

Reaction of $[WOCl_2(PMe_3)_2]$ with potassium *O*-alkyl xanthates, KS_2COR (R = Me, Et, Pr^i) in thf afforded two isomers of $[W^{IV}O\{S_2C(PMe_3)(OR)\text{-}S,S'\}(S_2COR\text{-}S,S'C]$ (**27a**) and (**27b**). These two isomers were identified in solution, and the structure of (**27a**) was confirmed for a molybdenum analog (R = Pr^i). It was suggested that the zwitterionic ligand $^-S_2C^-(^+PMe_3)OR$ was generated by nucleophilic attack of trimethylphosphine on the C atom of the CS_2 moiety.

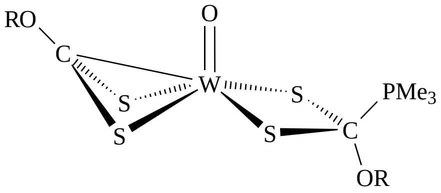

(**27a**)

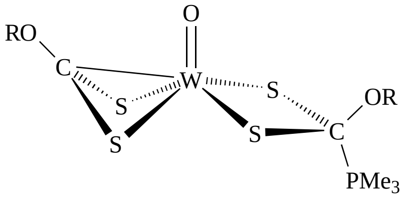

(**27b**)

Reductive desulfurization of $[WS(S_2)(S_2CNEt_2)_2]$ using $SiMe_3I$ afforded $W^V(\mu\text{-}S_2)_2(S_2CNEt_2)_4]I(I_3)$. Reaction of $[W(S_2CNR_2)_4]^+$ with LiTCNQ gave $[W(S_2CNEt_2)_4][TCNQ]$.

6 COMPLEXES WITH N-DONOR ATOMS

6.1 Nitrido Complexes

Reaction of WCl_6 with $Me_3SiNPMePh$ afforded the mixed-valence $W^V{}_2W^{VI}{}_2$ species $[PClMePh_2]_2[W_4N_2Cl_{18}]$ (**28**). This species contains two W^{VI} components $[WNCl_4]^-$ and

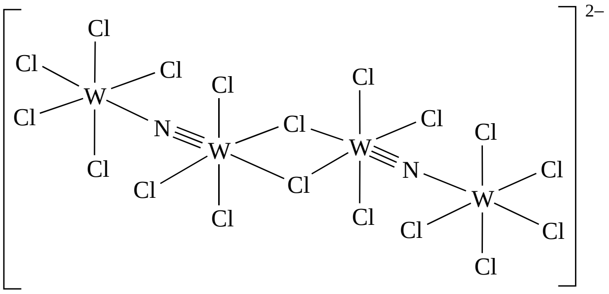

(**28**)

two neutral WCl_5 fragments. Two distinct W–N bonds were detected in the crystal structure, one a triple bond (1.69 Å) and the other a single bond (2.06 Å), with an almost linear W–N–W bond angle (178°).

Reaction of $[W^{III}_2(OBu^t)_6]$ with acetonitrile or benzonitrile afforded alkylidyne and nitrido complexes: $[\{W^{VI}(N)(OBu^t)_3\}_n]$ was polymeric, the terminal nitrido group interacting with neighboring W atoms via a weak donor bond. While $[W_2(OCH_2CH_2CF_3)_6]$ did not react with acetonitrile, with benzonitrile the trinuclear triangular species $[\{W(N)(OCH_2CH_2CF_3)\}_3]$, having μ-nitrido bridges, was formed. The W–N bond lengths alternate from 1.72 Å to 2.14 Å.

6.2 Imido Complexes

Reaction of the zwitterionic $[W(CO)_5\{NPhNPhC(OMe)Ph\}]$ with PCl_5, Br_2, or I_2 gave the imido complex $[\{W^{IV}(NPh)_2(CO)_2X(\mu\text{-}X)\}_2]$. This dinuclear species reacted with donor ligands (L = pyridine, PR_3, or NCMe) giving $[WNPh)_2(CO)_2(LX_2]$.

The dinuclear complex containing a bridging diimido ligand $[\{W^{IV}(CO)(PMePh_2)_2Cl_2\}_2(\mu\text{-}NHC_6H_4NH\text{-}p)]$ was obtained by the reaction of $[WCl_2(PMePh_2)_4]$ with the diisocyanate 1,4-$C_6H_4(NCO)_2$. A range of analogous complexes $[\{W(CO)(\{PMePh_2)_2Cl_2)_2(\mu\text{-}N\text{–}X\text{–}N)]$, where

N–X–N = p-N-o-MeC_6H_3N, p-N(o-$MeOC_6H_3C_6H_3$ OMe-o)N, 1,5-$NC_{10}H_6N$, or m-NC_6H_4N, were prepared similarly and several complexes were investigated crystallographically. In all of these species, the $PMePh_2$ groups are mutually trans and the chloride ions cis. Electrochemical studies established that all complexes underwent two oxidation processes at low temperatures, indicating weak electronic communication between the metal centers. Only the species containing p-NC_6H_4N and p-N-o-MeC_6H_3N exhibited well-defined reduction behavior, undergoing two one-electron reduction processes, the remainder of the complexes exhibiting irreversible reduction behavior.

The silylimido complex $[W(NSiMe_3)Cl_2(PMe_3)_3]$ was prepared by reaction of $WCl_2(PMe_3)_4]$ with Me_3SiN_3.

Treatment of $[WCl_4(SEt_2)_2]$ with the tetradentate triamidoamine ligand $N(CH_2CH_2NHC_6F_5)_3$ afforded $[W^{IV}\{[N(C_6F_5)CH_2CH_2]_3N\}Cl]$, which had a distorted trigonal bipyramidal structure.

Reaction of $[W(NPh)(\eta^4\text{-}C_6H_5Pr^n)\{(o\text{-}C_6H_4(NSiMe_3)_2\}]$ with pyridine, 4-picoline, or quinoline (L) or reduction of $[W(NPh)\{o\text{-}C_6H_4(NSiMe_3)_2\}Cl_2]$ with sodium in the presence of L afforded $[W^{IV}(NPh)\{o\text{-}C_6H_4(NSiMe_3)_2\}L_2]$ (**29**). This complex reacted with CO or PMe_3 (L′) in toluene to form the 6-coordinate *trans*-$[W(NPh)\{o\text{-}C_6H_4(NSiMe_3)_2\}L_2L']$.

Addition of $LiOC_6H_2(CH_2NMe_2)_2$-2,6-Me-4 to $[W(NPh)Cl_4((OEt_2)]$ resulted in displacement of the ether and formation of $[W^{VI}(NPh)Cl_3\{OC_6H_2(CH_2NMe_2)_2Me\}]$ (**30**), in which one of the two NMe_2 groups is coordinated trans to the phenylimido ligand. Oxidation of $[W(NPR_3)Cl_5]$ (R = Me or Ph), or addition of R_3PO to $[\{W(NCl)Cl_4\}_2]$, afforded $[W(NCl)Cl_4(OPR_3)]$.

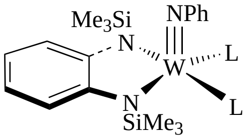

(**29**)

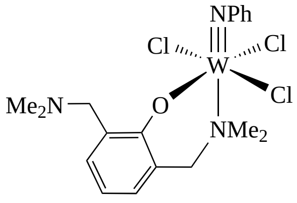

(**30**)

Treatment of $[W(NAr)Cl_4(thf)]$ (Ar = 2,6-$Pr^i{}_2C_6H_3$) with two equivalents of $Me_3SiNHAr$ in thf gave $[W(NAr)_2Cl_2(thf)_2]$ and this dichloride reacted with LiNHAr giving tetrahedral $[W(NAr)_3Cl]^-$.

Deprotonation of $[W(NBu^t)_2(NHBu^t)_2]$ by LiMe afforded dimeric $Li_2[W(NBu^t)_4]$, whose crystal-structure determination revealed that it should be formulated as $[Li_4W_2(NBu^t)_8]$ (**31**). The bridging NBu^t groups are coordinated as amido rather than imido ligands, and the terminal NBu^t group exhibits a reasonably short W=N bond (1.72 Å). This species reacted with the Lewis acids $AlCl_3$, $GaCl_3$, and $AlMe_3$ giving $[\{W(\mu\text{-}NBu^t)_2M'X_2\}_2]$ (M′ = Al or Ga, X = Cl or Me, e.g. (**32**)).

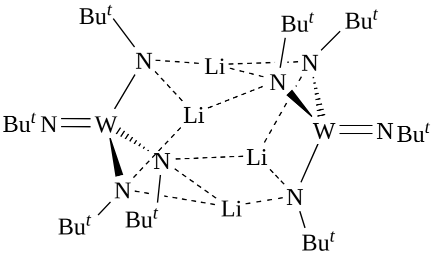

(**31**)

Protonation of $Li_2[W(NBu^t)_4]$ in ether gave initially $[W(NBu^t)_2(NHBu^t)_2]$, but further acid (CF_3SO_3H, CF_3CO_2H)

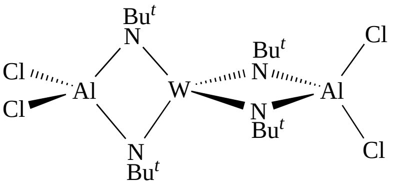

(**32**)

gave octahedral species such as $[W(NBu^t)_2(NH_2Bu^t)_2X_2]$ ($X = OSO_2CF_3$, $OC(O)CF_3$). With HBF_4, two species, $[W(NBu^t)_2(NHBu^t)(NH_2Bu^t)][BF_4]$ and $[W(NBu^t)_2(NHBu^t)(NH_2Bu^t)(F_2BF_2)]$, were isolated, whereas with HCl, only $[\{W(NBu^t)_2(NH_2Bu^t)Cl\}_2(\mu\text{-}Cl)_2]$ was formed. Treatment of $[W(NR)Cl_4L]$ (R = Et, L = nothing; R = C_6H_4Me-4, L = OEt_2) with $N(SiMe_3)_3$ in a 2:1 ratio afforded the hexanuclear species $[\{W_2(\mu_2\text{-}N)(NR)_2Cl_5\}_3]$ (**33**). Within each $(RN)W(\mu\text{-}N)W(NR)$ group, the two imido groups have nearly orthogonal orientations that maximize W–N π-bonding.

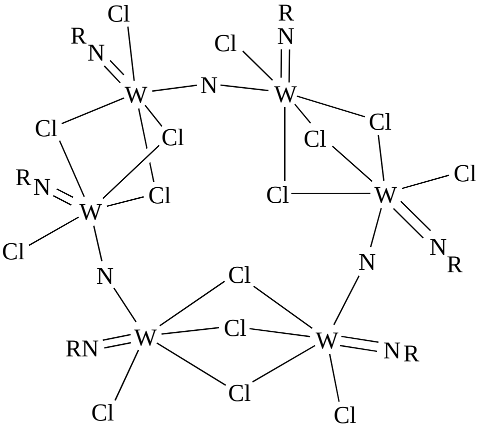

(**33**)

Reaction of $[W^{II}Cl_2L_4]$ (L = PMe_3 or $PMePh_2$) with one equivalent of Me_3SiN_3 gave the bis(silylimido) complex $[W^{VI}(NSiMe_3)_2Cl_2L_3]$. When two equivalents of Me_3SiN_3 were used, oxidative replacement afforded the five-coordinate mono(silylimido) complex $[W(NSiMe_3)Cl_2(PMePh_2)_2]$, which has a trigonal bipyramidal geometry, with cis equatorial imido ligands and short W–N bonds (1.70 Å).

Treatment of $[W(NAr)_2(PMe_2Ph)_2]$ (Ar = 2,6-$Pr^i{}_2C_6H_3$) with acetone in pentane afforded $[W(NAr)_2(PMe_2Ph)(\kappa^2\text{-}OCMe_2)]$. The long C–O bond (1.39 Å) in, and spectroscopic properties of, this complex were thought to be consistent with an oxo-metallopropane W^{VI} arrangement (**34**). Tetradentate Schiff bases derived by condensation of 1-hydroxy-2-benzaldehydes with alkane diamines reacted with $[W(NBu^t)_2(NHBu^t)_2]$ giving six-coordinate species such as (**35**), which contained *cis*-butylimido groups. Reaction of $[W(NBu^t)_2(NHBu^t)_2]$ with $\{HOSiPh_2\}_2O$ afforded an imido metallosiloxane $[W(NBu^t)(NH_2Bu^t)(OSiPh_2OSiPh_2O)_2]$, in which the two N atoms were trans to each other, and the two Bu^t groups were distinguishable by ^1H NMR spectroscopy.

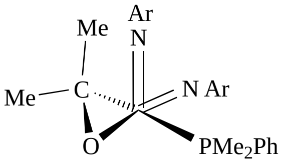

(**34**)

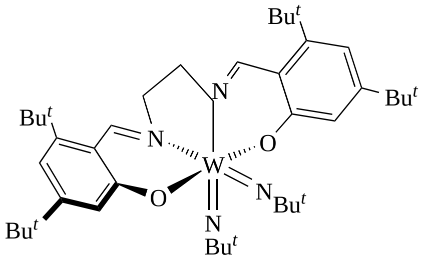

(**35**)

Treatment of $[W(NBu^t)_2(NHBu^t)_2]$ with a Me_2NP-modified calix[5]arene afforded (**36**), in which the W···P bond was relatively weak. The amido ligand was displaced by triflic acid, the W–P bond in the resulting triflate species becoming stronger.

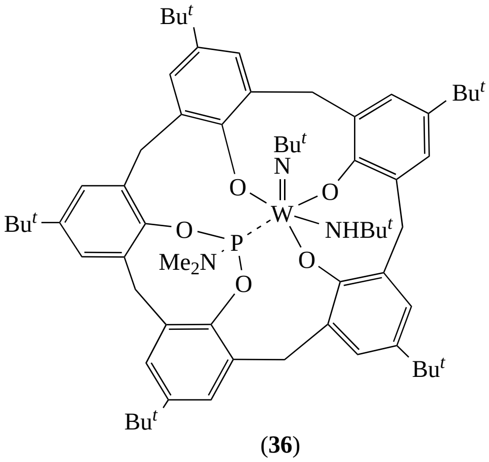

(**36**)

6.3 Amido Complexes

Treatment of $W(CO)_5(thf)]$ with $o\text{-}[OC_6H_4NH_2]^-$ and $o\text{-}C_6H_4(NH_2)_2$ in the presence of deprotonating agents afforded $[W(CO)_3\{o\text{-}O(NH)C_6H_4\}]^-$ and $[W(CO)_3\{o\text{-}(NH_2)C_6H_4\}]^-$, which had trigonal bipyramidal structures. Reaction of 2-aminopyridine (2-ampH) with $[W(CO)_5(thf)]$ gave

$[\mathrm{W(CO)_5(2\text{-}ampH)}]$, which was deprotonated by NAH giving dinuclear $[\{\mathrm{W(CO)_4}(\mu\text{-}2\text{-}\mathrm{amp})\}_2]$ and mononuclear $[\mathrm{W(CO)_5}(\kappa^1\text{-}2\text{-}\mathrm{amp})]^-$, the latter stabilized by a $\{\mathrm{Na^+}$-crown ether$\}$ counter-cation.

Reaction of $[\mathrm{W(NSiMe_3)Cl_2(PMe_3)_3}]$ with $\mathrm{PCl_2RR'_2}$ ($\mathrm{R = R' = Me}$ or $\mathrm{R = Me,\ R' = Ph}$) afforded the diamagnetic phospho-aminato species $[\mathrm{W^{IV}N{=}PR_3)Cl_2(PMe_3)_3]Cl}$. Treatment of $\mathrm{WSCl_4}$ with $\mathrm{NR_2(SiMe_3)}$ afforded *fac*-$[\mathrm{WCl_3(NR_2)_3}]$ R = Me, Et, or pyrrolidine). Reaction of $[\mathrm{W(NSiMe_3)Cl_2(PMe_3)_3}]$ with $\mathrm{Cl_2}$ at −196 °C, followed by warming to room temperature, caused elimination of $\mathrm{Me_3SiCl}$ and $\mathrm{Me_3PCl_2}$, the speed of the warm-up procedure determining the product. By these procedures, the phosphoraminato complexes $[\mathrm{W(N{=}PMe_3)Cl_5}]$ and $[\mathrm{W(N{=}PMe_3)Cl_4(PMe_3)}]$ were formed. Stoichiometric reaction of $\mathrm{WCl_6}$ with one or two equivalents of $\mathrm{Cl_3P{=}NSiMe_3}$ afforded $[\mathrm{W(NPCl_3)Cl_5}]$ and $[\{\mathrm{W(N{=}PCl_3)Cl_4}\}_2]$. Reaction of $[\mathrm{W(N{=}PCl_3)Cl_5}]$ with $\mathrm{GaCl_3}$ gave $[\mathrm{W(N{=}PCl_3)WCl_4][GaCl_4]}$, in which a chlorine atom of the $[\mathrm{GaCl_4}]^-$ ion is weakly coordinated to the tungsten trans to in aminato group, making W six-coordinate.

Reaction of lithium salts of pyridino-amido ligands $\mathrm{LiN(SiMe_3)(2\text{-}C_5H_3N\text{-}6\text{-}Me)}$ and $\mathrm{LiN(SiBu^{\mathit{t}}Me_2)(2\text{-}C_5H_3N\text{-}6\text{-}Me)}$ with $[\mathrm{WO_2Cl_2(dme)}]$ (dme = 1,2-dimethoxyethane) gave *cis*-$\mathrm{W^{VI}O_2\{N(SiR_3)C_5H_3MeN\}_2}]$ (**37**).

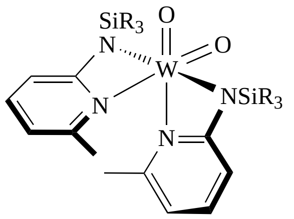

(**37**)

Reaction of the tungsten(IV) complex $[\mathrm{W(NPh)}\{o\text{-}\mathrm{(Me_3SiN)_2C_6H_4}\}\mathrm{(py)_2}]$ with two equivalents of thiophene gave the *S*,*C*-chelated species $[\mathrm{W^{VI}(NPh)}\{o\text{-}\mathrm{(Me_3SiN)_2C_6H_4}\}\mathrm{(SC_4H_4)}]$ (**38**).

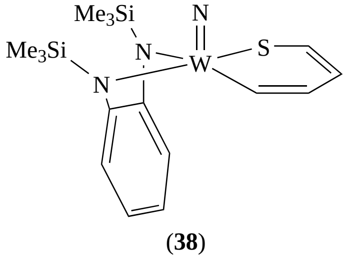

(**38**)

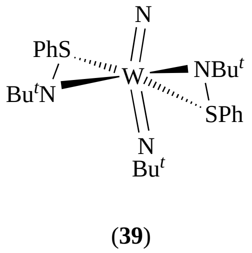

(**39**)

Treatment of $\mathrm{Li_2[W(NBu^{\mathit{t}})_4]}$ with PhSCl gave the sulfenamido complex $[\mathrm{W(NBu^{\mathit{t}})_2}(\kappa^2\text{-}\mathrm{PhSNBu^{\mathit{t}}})_2]$ (**39**), which has a distorted bicapped tetrahedral geometry.

Treatment of $[\mathrm{W(NPh)Cl_4}]$ with one equivalent of methanol afforded $[\mathrm{W(NPh)Cl_3OMe)}]$, which reacted further with $\mathrm{LiNMe_2}$ to give $[\mathrm{W(NPh)(NMe_2)_4}]$.

6.4 Hydrazido Complexes

Reaction of lithium trimethylsilyldiazomethanide with $[\mathrm{W(CO)_5(PPh_3)}]$ in the presence of $\mathrm{Me_3SiCl}$ afforded $[\mathrm{W(CO)_4(PPh_3)}\{\kappa^1\text{-}\mathrm{NNC(SiMe_3)_2}\}]$ (**40**). The W–N bond is long (2.16 Å) and the N=N (1.17 Å) and N–C (1.343 Å) distances are intermediate between double and triple, and single and double bonds, respectively. Treatment of $[\mathrm{W(CO)_5({=}NNMe_2)}]$ with dppe afforded $[\mathrm{W(CO)_3(dppe)({=}NNMe_2)}]$, in which the W=N–N group is bent.

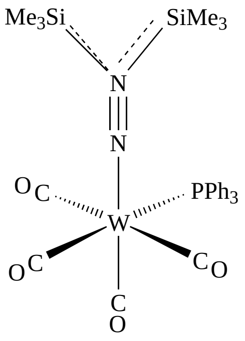

(**40**)

The arylation of $[\mathrm{WCl_4(dme)}]$ with mesityl magnesium bromide under nitrogen afforded the dinuclear $\mathrm{W^{III}}$ species $[\{\mathrm{W_2(mes)_3Cl}\}_2(\mu\text{-}\mathrm{N_2})]$ (mes = 2,4,6-$\mathrm{Me_3C_6H_2}$), a species which could be regarded as containing the bridging $\mathrm{N_2}^{4-}$ group. Further addition of magnesium under nitrogen and under thf or mixtures of thf and dioxane afforded tri and tetranuclear species, $[\mathrm{Cl(mes)_3W(N{=}N)W(mes)_3(N{=}N)W(mes)_3Cl}]^-$ and $[\mathrm{Cl(mes)_3W(N{=}N)W(mes)_3(N{=}N)W(mes)_3(N{=}N)W(mes)_3Cl}]^{2-}$.

Reaction of $\mathrm{WCl_6}$ with $\mathrm{Ph_2NNH_2{\cdot}HCl}$ afforded $[\mathrm{W^{VI}(NNPh_2)Cl_4}]$, which on Na/Hg reduction in the presence of $\mathrm{PMe_2Ph}$, afforded $[\mathrm{W^{IV}(NNPh_2)(PMe_2Ph)_2Cl_2}]$. This complex reacted with HCl or water to generate ammonia and diphenylamine.

Reaction of $[\mathrm{W(NNH_2)(dppe)_2F}]^+$ (dppe = bis(diphenylphosphine)ethane) with 2,5-dimethoxotetrahydrofuran under acid-catalyzed conditions afforded the pyrrolylimido complex (**41**). However, when the same reaction was carried out with the corresponding 2,5-dihydrofuran, the kinetic product formed initially (**42**), slowly isomerizing to the thermodynamically more stable (**43**).

In related reactions, *cis,mer*-$[\mathrm{W(NHNH_2)(PMe_2Ph_2)_3X_2}]$ (X = Cl or Br) with phthalaldehyde afforded (**44**).

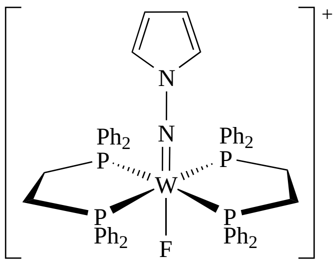

(**41**)

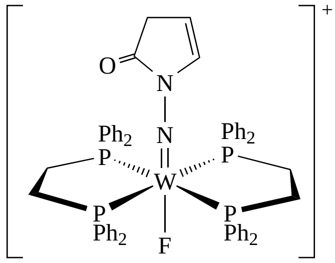

(**42**)

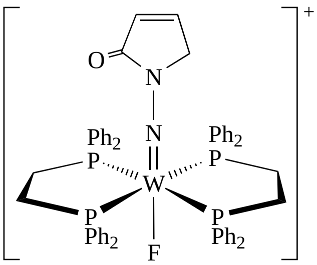

(**43**)

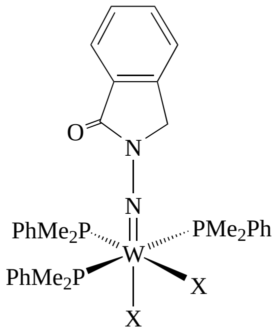

(**44**)

Treatment of $[W(N_2)_2(PMe_2Ph)_4]$ with HCl under CO afforded $[W^{IV}(NNH_2)(CO)(PMe_2Ph_2)Cl_2]$, which reacted with 2,4,6-trimethylpyrylium tetrafluoroborate in the presence of HCl giving the (1-pyridino)imino complex $[W^{IV}(NNC_5H_2Me_3)(CO)(PMe_2Ph)_2]^+$.

Reaction of *cis*-$[W(N_2)_2(dppe)_2]$ with triflic acid afforded *trans*-$[W^{IV}(NNH_2)(dppe)_2(OTf)]^+$, which could also be generated by reaction with two equivalents of *trans*-$[Ru(\eta^2\text{-}H_2)(dppe)_2Cl][OTf]$ under hydrogen.

Treatment of $[WCl_4(PR_3)_2]$ with two equivalents of $Me_3SiNHNMe_2$ gave the bis(hydrazido(2−) complex $[W^{VI}(NNMe_2)_2(PR_3)_2Cl]^+$. Reaction of $[W(NNPh_2)Cl_4]$ with Me_3SiCH_2MgCl and C_6F_5OH in thf afforded $[W(NNPh_2)(CH_2SiMe_3)_3(OC_6F_5)]$ whereas with $PhCH_2MgCl$, $[W(NNPh_2)Cl_2(OC_6F_5)_2(thf)]$ was formed.

Reaction of $[W(NAr)Cl_4]$ ($Ar = 2,6\text{-}Pr^i{}_2C_6H_3$) with AgOTf followed by the tridentate pyridyl ligand L (**45**) afforded $[W^{VI}(NAr)L(OTf)Cl]$, which reacted with two equivalents of hydrazine giving the hydrazido(1−) complex $[W(NAr)(\kappa^2\text{-}NHNH_2)LCl]$ (**46**).

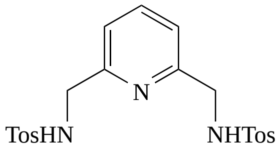

(**45**)

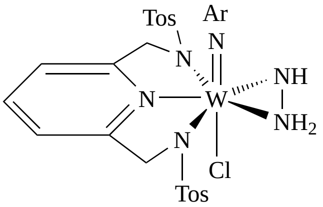

(**46**)

Ligand exchange reactions involving $[W(NNPh_2)(OBu^t)_4]$ with calixarenes afforded $[W(NNPh_2)(cal)]$. The W–N–bond angle was nearly linear, and the W–N was short (1.74–1.75 Å) whereas the N–N distance was long (1.32–1.33 Å), consistent with a $W{=}N\text{-}NPh_2$ bonding arrangement.

6.5 Tris(pyrazolyl)borato and Related Triaza Ligand Complexes

6.5.1 Nitrosyl Complexes

Treatment of $[W(NO)Tp^*Cl_2]$ [for Tp* and related ligands see (**47**)] with 1,3:5,6-di-*O*-isopropylidene-D-glucofuranase, HG_f, afforded diastereoisomers of $[W(NO)Tp^*Cl(OG_f)]$, a crystallographic study of the thermodynamically stable isomer establishing *S* absolute configuration at the metal atom.

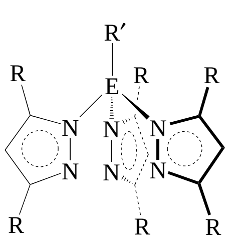

(**47**)

Tp^{*-}, E = B, R′ = H, R = Me

A series of complexes $[Fe(C_5H_5)\{C_5H_4QNHW(NO)Tp^*Cl\}]$, where Q = nothing, C_6H_4, $CH{=}CHC_6H_4$, or

$N{=}NC_6H_4$, were prepared by reaction of the appropriate amino or anilino ferrocene with $[W(NO)Tp^*Cl_2]$. Some of these complexes exhibited nonlinear optical properties, in particular, second order harmonic generation, although the response was significantly lower than that of their molybdenum counterparts.

6.5.2 *Carbonyl Complexes*

Treatment of $[W(CO)_3Tp^*]$ with bromine or iodine in acetonitrile afforded $[W^{II}(CO)_3Tp^*X]$ ($X = Br$, I). Under certain circumstance, addition of Br_2 also caused bromination of the Tp^* ligand at the 4-position on the pyrazole rings. These complexes were monodecarbonylated by heating in acetonitrile, the products being, for example, $[W(CO)_2\{HB(3,4\text{-}Me_2\text{-}4\text{-}BrC_3N_2)_3\}]$ and $[W(CO)(\eta^2\text{-}NCMe)\{HB(3,4\text{-}Me_2\text{-}4\text{-}BrC_3N_2)_3\}]$, the precise product being determined by the heating time. The structures of the sideways-bonded acetonitrile adduct (C–N 1.10 Å) and that of the seven-coordinate $[W(CO)_3\{HB(3\text{-}Pr^iC_3H_2)_3\}I]$ were determined crystallographically.

The dinuclear species $[\{W^{II}(CO)_2Tp^*\}_2(\mu\text{-}S)]$ was obtained by refluxing $[W(CO)_2Tp^*Br]$ or $[W(CO)_3Tp^*H]$ with propylene sulfide in 1,2-dichloroethane. The W–S–W chain is nearly linear, suggesting multiple bond character within the group, consistent with relatively short W–S bonds (2,17–2.18 Å).

Treatment of $[W^{II}(CO)_2Tp^*I]$, obtained by prolonged refluxing of $[W(CO)_3Tp^*I]$ in thf, with alkyl and aryl thiolates afforded $[W(CO)_2Tp^*(SR)]$ ($R = Me, Et, Pr^i, CH_2Ph$ or $p\text{-}C_6H_4NO_2$). However, reaction of $[W(CO)_3Tp^*Br]$ with $NaSPr^i$ in acetonitrile afforded $[\{W(CO)_2Tp^*\}_2\{\mu\text{-}NC(Me)C(Me)N\text{-}N,N'\}]$, which contains a bridging *anti*-butane-2,3-diimino-(2−) -$N{:}N'$ ligand formed by the coupling of two acetonitrile molecules.

Reaction of $[W^{II}(CO)(\eta^2\text{-}NCMe)Tp^*Br]$ with $(S_2PR'_2)^-$ ($R' = (-)$-mentholate) afforded $[W(CO)(\eta^2\text{-}NCMe)Tp^*(\kappa^1\text{-}S_2PR'_2)]$, the structure of the (*R*)-isomer being determined crystallographically. Oxidative decarbonylation of $[W(CO)_3Tp^*]^-$ by tetraethylthiuramdisulfide, $Et_2NC(S)SSC(S)NEt_2$, afforded the seven-coordinate W^{II} species $[W(CO)_2Tp^*(\kappa^1\text{-}S_2CNEt_2)_2]$, which had distorted pentagonal bipyramidal structure with a CO group and one N-donor atom of the Tp^* occupying the axial positions.

The seven-coordinate phosphine complexes $[W^{II}(CO)_3Tp^*L]^+$ were prepared by oxidation of the radical species $[W(CO)_3Tp^*]$ by ferrocenium cation, followed by addition of L (PMe_3, PEt_3, PPh_3, PMe_2Ph). These species exhibited capped octahedral geometries.

Reaction of $[W(CO)_2Tp^*I]$ with ammonia in dichloromethane at low temperatures afforded the amido species $[W^{II}(CO)_2Tp^*(NH_2)]$ which, on treatment with LDA or $LiBu^t$ followed by MeI, could be converted to $[W(CO)_2Tp^*(NMe_2)]$. Hydride ion abstraction from $[W(CO)_2Tp^*(NH_2)]$ using $CPh_3{}^+$ afforded the 'nitrene' species $[W(CO)_2Tp^*(NR)]^+$ ($R = H$, CPh_3). Treatment of $[W(CO)_2Tp^*(NH)]^+$ with base (KH, LDA, or NEt_3) afforded the nitrido W^{IV} species $[W(CO)_2Tp^*(\equiv N)]$ and reaction of this with MeOTf and MeCOCl afforded $[W(CO)_2Tp^*(NMe)]^+$ and $[WTp^*Cl\{NC(O)Me)]$, respectively. Heating $[W(CO)_3Tp^*H]$ with tosyl azide in thf gave the amido species $[W^{II}(CO)_2Tp^*(NHtos)]$.

Irradiation of $[W(CO)_3Tp^*H]$ in the presence of benzonitrile caused insertion of the nitrile into the W–H bond, giving $[W^{II}(CO)_2Tp^*(N{=}CHPh)]$, and related complexes $[W(CO)_2Tp^*(NCHR)]$ ($R = Me$, Et) were prepared similarly. Protonation of $[W(CO)_2Tp^*(NCHR)]$ by HBF_4 at low temperature afforded the cationic imido complexes $[W^{IV}(CO)_2Tp^*({=}NCH_2R)]^+$ ($R = Me$, Et, CH_2Ph), but when Ph_3CBF_4 was used instead of HBF_4, $[W^{IV}CO)_2Tp^*\{{=}NCH(R)CPh_3\}]^+$ was formed.

Oxidative decarbonylation of $[W(CO)_3Tp^*]^-$ by tetraethylthiuram disulfide afforded a mixture of $[\{W(S_2CNEt_2)_2\}_2(\mu\text{-}S)]$ and $[W^{IV}(S)Tp^*(S_2CNEt_2)]$. $[W(S)_2Tp^*(OPh)]$ reacted with $MeO_2CC{\equiv}CCO_2Me$ giving the dithiolato species $[W^{IV}Tp^*(OPh)\{S_2C_2(CO_2Me)_2\}]$.

Air oxidation of $[W(CO)_3Tp^*I]$ in refluxing toluene afforded $W^{IV}(O)(CO)Tp^*I]$. Reaction of $[W(CO)Tp^*I(\kappa^2\text{-}C,N\text{-}NCMe)]$ with pyridine-*N*-oxide afforded the acylimino complex $[W^{IV}(CO)Tp^*\{{=}NC(O)Me\}I]$, whereas reaction with propylene sulfide afforded $[W^{IV}(S)(CO)Tp^*I]$. Reaction of $[W(CO)Tp^*I\{NC(O)Me\}]$ with SPh^- and with $\{S_2PPh_2)^-$ afforded $[W^{IV}(CO)Tp^*\{NC(O)Me\}(SPh)]$ and $[W^{IV}(CO)Tp^*\{NC(O)Me\}(\kappa^1\text{-}S_2PPh_2)]$. Propylene sulfide reacted with this last complex, affording the sulfido derivative $[W^{IV}(S)(CO)Tp^*(\kappa^1\text{-}S_2PPh_2)]$, and the analogous oxo species $[W^{IV}(O)(CO)Tp^*(\kappa^1\text{-}S_2PPh_2)]$ was prepared by reaction of $[W(CO)_2Tp^*(\kappa^1\text{-}S_2PPh_2)]$.

Treatment of the amido W^{II} complex $[W(CO)_2Tp^*(NHtos)]$ (tos = tosyl) with AgOTf or I_2 afforded the 'nitrene' (or imido complex) $[W(CO)_2Tp^*(Ntos)]^+$, and iodine or trityl cation oxidation of $[W(CO)_2Tp^*(NHR)]$ ($R = Bu^t$, Ph) similarly afforded $[W(CO)_2(NR)Tp^*]^+$. The W–N–C bond angles and W–N distances were 172° ($R = Bu^t$ and Ph), and 1.72 Å ($R = Bu^t$ and 1.76 Å ($R = Ph$), respectively. A related carbene complex $[W(CO)_2\{{=}C(Ph)Me\}Tp^*]$ was also reported, in which there was an agostic interaction between a methyl hydrogen atom of the carbene and the metal. Reaction of $[W(CO)_2Tp^*(Ntos)]^+$ with PMe_3 afforded the phosphinimine $Me_3P{=}Ntos$, $[W(CO)_2Tp^*(PMe_3)_2]^+$, and $[W(CO)_2Tp^*(PMe_3(Ntos)]^+$. $[W(CO)_2Tp^*(PMe_3(Ntos)]I_3$ slowly decomposes to form $[W(CO)Tp^*(Ntos)I]$.

Reaction of WCl_6 with $Me_3SiCH{=}CH_2$ in ether and thf afforded $[WCl_3(thf)_2]$, which reacted with Tp^{*-} giving low yields of $[W^V(O)Tp^*Cl_2]$. This complex reacted with mono and difunctional phenolates, affording $[W^V(O)Tp^*Cl(OAr)]$ ($Ar = Ph$, $2,5\text{-}Cl_2C_6H_3$, C_6Cl_5, $C_6H_4R\text{-}p$ where $R =$ OMe, OH, C_6H_4OH, $N_2C_6H_4OH$) and the dinuclear $[\{W^V(O)Tp^*Cl\}_2(OC_6H_4O)]$, $[\{W^V(O)Tp^*Cl\}_2(OC_6H_4QC_6$

$H_4O)]$, and $[\{W^{V}(O)Tp^{*}Cl\}_2(OC_6H_2Cl_2O)]$. The tungsten atom in each of these species has pseudo-octahedral geometry. The mononuclear species could be electrochemically oxidized and reduced in reversible one-electron steps to W^{VI} and W^{IV} species, but none of these was isolated. The dinuclear complexes exhibited more complex redox behavior, oxidation occurring in discrete one-electron steps, generating mono and dications. Reduction occurred, at least for the species containing OC_6H_4O, in two clearly separate one-electron processes, but for the other species reduction appeared to occur in two nearly or actually coincident one-electron steps. From simple molecular orbital calculations, supported by detailed spectroelectrochemical and EPR spectral measurements, it was clear that for most of the complexes, the first one-electron oxidation resulted in the formation first of mixed-valence species ($W^{V}W^{VI}$) and the second process resulted in formation of the $W^{VI}W^{VI}$ dication. Reduction resulted in generation of $W^{IV}W^{V}$ and $W^{IV}W^{IV}$ species, the interaction between the two oxidized species being significantly greater than that between the reduced species. The antiferromagnetic magnetic exchange interactions in the dinuclear species, apparent in the EPR spectra and quantified by the determination of J by solid-state susceptibility measurements, depended on the length and planarity of the bridging ligand and hence was strongest for $[\{W(O)Tp^{*}Cl\}_2(OC_6H_4O)]$ and weakest for $[\{W(O)Tp^{*}Cl\}_2OC_6H_4C_6H_4O]$. The EPR spectra of the mono-oxidized dinuclear species indicated that these monocations were valence-trapped, at least on the EPR timescale. These dinuclear tungsten complexes exhibited weaker electronic and magnetic interactions than their molybdenum analogs probably because of poorer W–OAr $d_\pi - p_\pi$ orbital overlap.

Oxidative hydrolysis of $[W(CO)_3Tp^{*}]^{-}$ afforded the mixed-valence species $[Tp^{*}(O)_2W(\mu\text{-}O)W(CO)(O)Tp^{*}]$, which is believed to contain W^{VI} and W^{IV} centers.

6.5.3 Other Complexes

Reaction of $[W(CO)_3Tp^{*}I]$ with DMSO in the presence of water afforded $[W^{VI}Tp^{*}(O)_2(OH)]$, which, on treatment with OH^{-}, afforded the octahedral species $[WTp^{*}(O)_3]^{-}$. Oxidation of $[WTp^{*}(O)_2(\mu\text{-}O)W(O)(CO)Tp^{*}]$ by $Bu^{t}OOH$ gave the dinuclear $[\{WTp^{*}(O)_2\}_2(\mu\text{-}O)]$.

Treatment of $[W(CO)_3Tp^{*}]^{-}$ with one equivalent of elemental sulfur in dmf afforded the mononuclear species $[WTp^{*}(S)_3]^{-}$, analogous to $[WTp^{*}(O)_3]^{-}$. A similar reaction using $[W(CO)_3Tp]^{-}$ afforded the trisulfide and $[\{WTp^{*}(O)(S_2)_2\}_2(\mu\text{-}S)]^{2-}$. Reaction of $[WTp^{*}(O)_2Cl]$ with B_2S_3 or P_4S_{10} afforded $[WTp^{*}(O)(S)Cl]$ and $[WTp^{*}(S)_2Cl]$, which reacted with OPh^{-}, SPh^{-}, $SePh^{-}$, or (−)-mentholate (X) giving $[WTp^{*}(O)(S)X]$ and $[WTp^{*}(S)_2X]$, the crystal structures of $[W(S)_2Tp^{*}(OPh)]$ and (R,S)-$[W(O)(S)Tp^{*}\{(-)\text{-mentholate}\}]$ confirming their octahedral geometries.

Reaction of $[WTp^{*}(S)_2X]$ (X = monoanion) with alkynes afforded dithiolato complexes $[W^{VI}Tp^{*}(S_2C_2R_2)X]$ (R = CO_2Me or Ph; X = SePh or 2-quinoxalinyl). Treatment of $[W(CO)Tp^{*}(S)(S_2PR_2)]$ (R = OEt or Ph) with pyridine-N-oxide in toluene afforded $[W^{VI}Tp^{*}(O)(S)(\kappa^1\text{-}S_2PR_2)]$, and when $[WTp^{*}(O)(S)Cl]$ reacted with $[Spy]^{-}$red $[W^{VI}Tp^{*}(O)(S)(Spy)]$ was formed. In this last species, the pyridine thiolato ligand was monodentate and S-bonded. Reaction of $[W^{VI}Tp^{*}(O)(S)(Spy)]$ with NO^{+} afforded green paramagnetic $[W^{V}Tp^{*}(O)(S_2py)]^{+}$ (**48**).

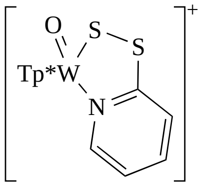

(**48**)

6.6 Complexes of Cyclic Triaza and Related Ligands

Photolysis of $[W(CO)_6]$ in the presence of $Bu^{t}{}_3tacn$ (**49**, R = Bu^{t}), afforded $[W(CO)_3(Bu^{t}{}_3tacn)]$, which has a piano-stool conformation similar to that of $WO_3(Bu^{t}{}_3tacn)]$. Reaction of $[W(CO)_3(tdcn)]$ (tdcn = (**50**)) with NO^{+} (prepared directly from $NaNO_2$/HCl) gave $[W(CO)_2(NO)(tdcn)]^{+}$, which, on prolonged exposure to NO^{+}, was converted to $[W(NO)_2(tdcn)Cl]^{+}$.

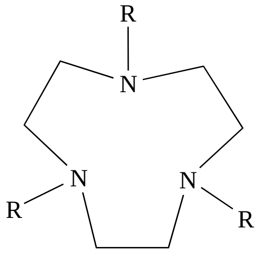

(**49**)

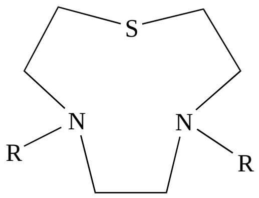

(**50**)

Oxidation of $[W(CO)_3(R_3tacn)]$ (R = benzyl (**49**, R = CH_2Ph) by ferrocenium cation afforded the air- and light-sensitive $[W^{I}(CO)_3(R_3tacn)]^{+}$. Oxidation of $[W(CO)_3(R_3\ tacn)]$ (R = H (**49**, R = H), itself obtained by reaction of $[W(CO)_6]$ with R_3tacn) by iodine afforded $[W^{II}CO)_3(R_3tacn)I]^{+}$.

Oxidation of $[W(CO)_3(Bu^{t}{}_3tacn)]$ $[Bu^{t}{}_3tacn$ = (**49**, R = Bu^{t})] by hydrogen peroxide afforded $[W^{VI}(Bu^{t}{}_3tacn)(O)_3]$, which also has octahedral symmetry.

6.7 Nitrosyl Complexes

Reaction of NO with $[W(CO)_2(phen)(SPh)_2]$ gave $[W(CO)_2(NO)(phen)(SPh)]$, formally containing W^0, together with PhSNO. The NO group is trans to the thiophenolate ligand. Similar treatment of *cis*-$W(CO)_2$(phen)(tdt)] (tdt = toluene-3,4-dithiolate), the dinitrosyl *cis*-$[W(NO)_2$(phen)(tdt)] was formed. $[W(CO)_3H$(phen)(SPh)], the latter reacting with NO to give $[W(CO)_2(NO)$(phen)(SPh)], N_2O and HNO_2 (the last two by decomposition of eliminated HNO).

The hydrido complex *trans,trans*-$[WH(CO)_2(NO)(PR_3)_2$ (R = Me, Et, Ph, OPr^i) reacted with $BH_3{\cdot}L$ (L = thf, SMe_2) to give *trans*-$[W(\kappa^2\text{-}BH_4)(CO)(NO)(PR_3)_2]$, which has octahedral geometry (R = Me confirmed crystallographically). $[WH(CO)_2(NO)(PMe_3)_2]$ reduced β-diketones to β-hydroxyketones with concomitant formation of *trans*-[W(diketonate)(CO)(NO)$(PMe_3)_2$].

Treatment of $[W_2H(CO)_9(NO)]$ with tertiary phosphines or pyridine afforded mono and disubstituted complexes, two isomers existing for each compound, although only one was isolated successfully by column chromatography. The species $[(OC)_5W(\mu\text{-}H)W(CO)_3L(NO)]$ [L = $P(p\text{-}C_6H_4F)_3$] and $[(OC)_5W(\mu\text{-}H)W(CO)_2L_2(NO)]$ (L = py or $P(p\text{-}C_6H_4F)_3$; L_2 = bipy) were characterized crystallographically. Treatment of $[W_2H(CO)_7(thf)_2(NO)]$ with the sterically bulky $PBu^t{}_3$ caused monosubstitution, giving $[W_2H(CO)_8(PBu^t{}_3)(NO)]$, and also abstraction of the hydride with formation of $[HPBu^t{}_3]^+$ as well as $[W_2(\mu\text{-}H)(CO)_{10}]^-$ and $[W_3(\mu\text{-}H)_2(CO)_{13})(NO)]^-$. The trinuclear tungsten nitrosyl dihydride was also formed by reaction of $[W_2H(CO)_9(NO)]$ with $[W(CO)_5H]^-$, and reacted with PMe_3 giving $[W_3(\mu\text{-}H)_2(CO)_{12}(PMe_3)(NO)]^-$ (**51**).

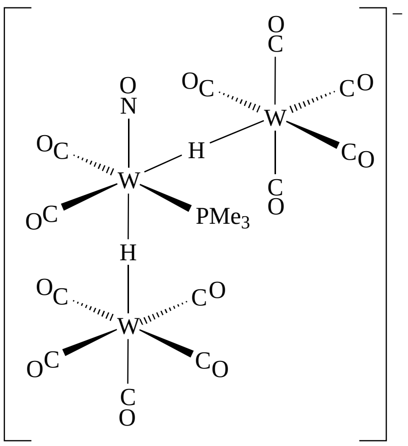

(**51**)

$[W(NO)(SBu^t)_3(py)]$ was prepared by reaction of $[W(NO)(OBu^t)_3(py)]$ with an excess of Bu^tSH in toluene. The structure of this molecule was trigonal bipyramidal, in which the py and NO ligands were in axial positions. The W–N–O bond was linear.

7 COMPLEXES WITH P-, As-, Sb-, AND Bi-DONOR ATOMS

When *trans*-$[W(N_2)_2(dppe)_2]$ was irradiated in the presence of 1,4-diisocyanobenzzene and 4-isocyanobenzonitrile, *cis*-$[W(CNC_6H_4NC)_2(dppe)_2]$ and *cis*-$[W(CNC_6H_4CN)_2(dppe)_2]$ were formed. The isocyanide ligands exhibited bent W–C–NAr bonds.

Reduction of WCl_6 by an excess of Mg powder in the presence of 4,4′,5,5′-tetramethyl-2,2′-diphosphinine, tmbp (**52**) (E = P), a fully phosphinated analog of 2,2′-dipyridyl, afforded the trigonal $[W(tmbp)_3]$. A regular octahedral complex would have a twist angle $\theta = 60°$ and in this complex the twist angle θ is $15 \pm 0.6°$ indicating that the ligand may be partially reduced, a situation reminiscent of the behavior of tris(dithiolene) complexes. UV irradiation of $[W(CO)_6]$ with (**52**) (E = N), another analog of 2,2′-dipyridyl, afforded $[W(CO)_4(\kappa^2\text{-}C_{12}H_{12}NP\text{-}N,P)]$.

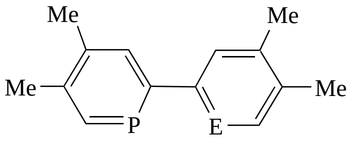

(**52**)

Reaction of $[W(CO)_5(thf)]$ with the phosphorus-antimony cage $P_4Sb_2C_4Bu^t{}_4$ afforded the dinuclear $[\{W(CO)_5\}\{\kappa^1\text{-}P_4Sb_2C_4Bu^t{}_4\text{-}P,Sb\}]$ (**53**).

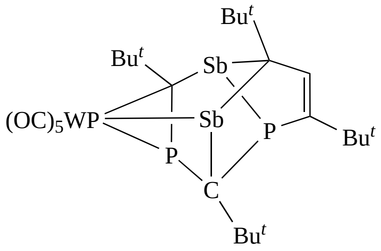

(**53**)

Reaction of $[W(CO)_5Br]^-$ and *fac*-$W(CO)_3(NCMe)_3]$ with $Me_2SbCH_2SbMe_2$ afforded $[W(CO)_5(\kappa^1\text{-}Me_2SbCH_2SbMe_2)]$ and *fac*-$[W(CO)_3(\kappa^1\text{-}Me_2SbCH_2SbMe_2)_3]$ whereas $W(CO)_5$(thf)], $[W(CO)_6]$, and $[W(CO)_4(Me_2NCH_2CH_2CH_2NMe_2)]$ reacted with $Ph_2SbCH_2SbPh_2$ affording $[(OC)_5W(\mu\text{-}Ph_2SbCH_2SbPh_2)W(CO)_5]$ and *cis*-$[W(CO)_4(\kappa^1\text{-}Ph_2SbCH_2SbPh_2)_2]$, respectively.

Treatment of the cyclic $[As(PBu^t)_3]^-$ with water afforded $[Bu^tP(PHBu^t)_2$, which subsequently reacted with $[W(CO)_5(thf)]$ giving $[W(CO)_4\{\kappa^2\text{-}(Bu^tP)_2PBu^t\text{-}P,P'\}]$. Reaction of $[W_2(CO)_{10}]^{2-}$ with PCl_3 afforded a mixture of $[W(CO)_5(PCl_3)]$, $[\{W(CO)_5)_2(\mu\text{-}PCl)]$, and $[W(CO)_5\{\mu,\eta^2{:}\kappa^1{:}\kappa^1\text{-}P_2Cl_2[W(CO)_5]\}]$.

The phosphole complex (**54**) reacted with $MeO_2CC{\equiv}CCO_2Me$ giving phosphanornadiene complexes (**55**). This reacted in turn with PEt_3 giving a phosphoranylidenephosphine complex $[W(CO)_5\{EtO_2CPPEt_3\}]$, in which the P–P bond length (2.16 Å) was closer to a single bond than to a double bond, consistent with zwitterionic character in the diphosphorus ligand, viz. $\{EtO_2CP^{-}-^{+}PEt_3\}$. A similar zwitterionic situation appears to have occurred in the diphosphate derivative (**56**) (R = $SiMe_3$), which reacted with F^- affording (**56**) (R = H).

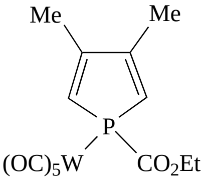

(**54**)

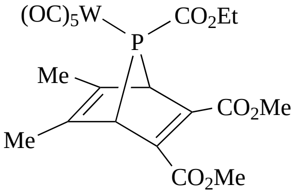

(**55**)

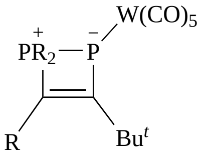

(**56**)

Reaction of *trans*-$W(N_2)_2(dppe)_2]$ with aromatic isocyanides afforded *cis*- and *trans*-$[W(CNAr)_2(dppe)_2]$ (Ar = p-RC_6H_4 where R = CF_3, NO_2, CN, NC, F, and Me).

Treatment of $[W(CO)_3(\eta^6\text{-}C_6H_3Me_3)]$ with K_3P_7 (**57**) and 2,2,2-crypt in 1,2-diaminoethane afforded $[W(CO)_3(P_7)]^{3-}$ (**58**), which could be alkylated and protonated giving $[W(CO)_3(P_7Et)]^{2-}$ (**59**) and $[W(CO)_4(P_7H)]^{2-}$ (**60**). Under CO at atmospheric pressure, (**58**) was converted to $[W(CO)_4(\kappa^2\text{-}P_7)]^{3-}$.

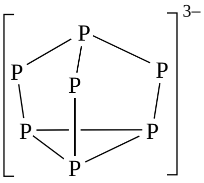

(**57**)

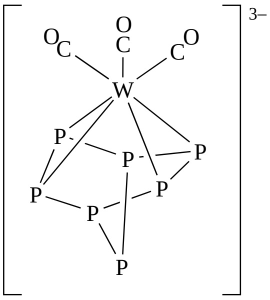

(**58**)

Reaction of $[W(CO)_5]^{2-}$ with $(Me_3Si)_2CHBiCl_2$ afforded $[\{W(CO)_5\}_2(\mu_3\text{-}\kappa^2\text{-}Bi_2)]$ (**61**) and $[W_2(CO)_8(\mu\text{-}\kappa^2\text{-}Bi_2)(\mu\text{-}BiMe)W(CO)_5]$ (**62**). The species (**62**) contains a Bi_2 group bridging two W atoms and if the Bi–Bi bond order is regarded as one, then the formal oxidation state of the transition metal is II. However, the Bi–Bi bond is quite short (2.80 Å) and corresponds approximately to a bond order of 2, and so the formal oxidation state of the tungsten atoms is between I and II.

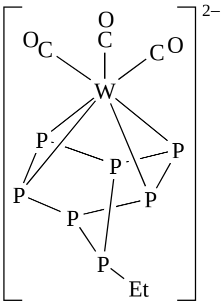

(**59**)

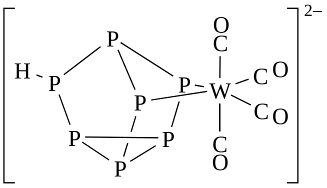

(**60**)

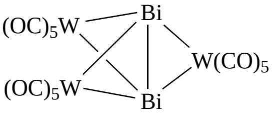

(**61**)

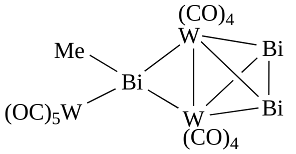

(**62**)

Reaction of $[W(CO)_5]^{2-}$ with $Br_2BN(SiMe_3)_2$ afforded the terminal borylene complex $[\{(Me_3Si)_2NB{=}\}W(CO)_5]$, which is octahedral, with a linear W–B–N group and short B–N bonds (1.34 Å).

Reaction of $[WCl_2(PMe_3)_4]$ with ArP=C=O (Ar = 2,4,6-$Bu^t{}_3C_6H_2$) afforded the W^{IV} complex $[W({=}PAr)(CO)(PMe_3)Cl_2]$, in which the W–P–C group was essentially linear (168°).

Treatment of $[WCl\{(Me_3SiNCH_2CH_2)_3N\}]$ with LiPHPh afforded the phosphido tungsten (VI) species $[W({\equiv}P)\{(Me_3SiNCH_2CH_2)_3N\}]$ (**63**, R = $SiMe_3$), and the corresponding arsenido complex, $[W({\equiv}As)\{(Me_3SiNCH_2CH_2)_3N\}]$ (very low yield), together with $[WPh\{(Me_3SiNCH_2CH_2)_3N\}]$, was obtained using LiAsHPh. The arsenide was obtained in more substantial yields in the reaction between $[WPh\{(Me_3SiNCH_2CH_2)_3N\}]$ and a small excess of AsH_2Ph.

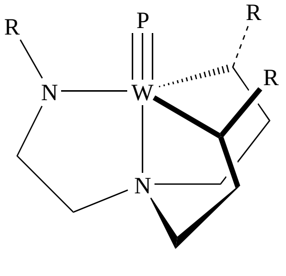

(**63**)

8 HYDRIDO AND BOROHYDRIDO COMPLEXES

Photolysis of $[W(CO)_6]$ in the presence of $B_2H_4(PMe_3)_2$ afforded $[W(CO)_5\{\kappa^1\text{-}HB_2H_3(PMe_3)_2\}]$ (**64**) and $[W(CO)_4$

$\{(\kappa^2\text{-}H_2B_2H_2(PMe_3)_2\}]$ (**65**). Analogous reactions involving $BH_3(PR_3)$ (R = Me, Ph) or $BH_3(NMe_3)$ afforded $[W(CO)_5(\kappa^1\text{-}HBH_2L)]$ (L = PR_3 or NMe_3) (**66**).

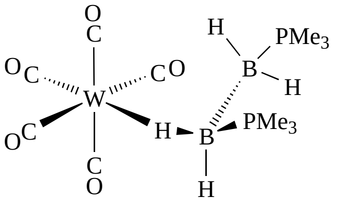

(**64**)

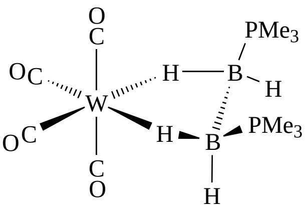

(**65**)

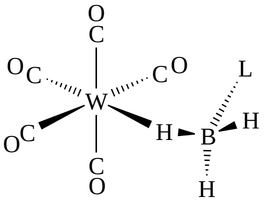

(**66**)

The species previously formulated as $[W(PMe_3)_4H_2(H_2O)F]F$ was reformulated as $[W^{IV}(PMe_3)_4H_2F_2(H_2O)]$ or $[W(PMe_3)_4H_2F_2(FHF)]$. Treatment of $[W(PMe_3)_4(\kappa^2\text{-}CH_2PMe_2)H]$ with aqueous HCl afforded $[W^{IV}(PMe_3)_4H_2Cl_2]$ and anion exchange with bromide and iodide gave $[W(PMe_3)_4H_2X_2]$ (X = Br or I). The structure of these species is represented as (**67**) (X = Y = F, Cl, Br, I; X = F, Y = F···H–F).

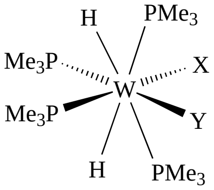

(**67**)

Controlled potential electrolysis of $[WH_2(\kappa^2\text{-}O_2CMe)(dppe)_2]^+$ containing one equivalent of $MeCO_2H$ afforded $[W^{IV}H_3(\kappa^1\text{-}OCOMe)(dppe)_2]$ in high yields.

9 METAL–METAL BONDED COMPLEXES AND CLUSTER COMPOUNDS

9.1 Dinuclear Complexes

Several reviews of ditungsten compounds having multiple bonds have described this area.[4,8] In very general terms, the formal bond order for ditungsten compounds ranges from four to less than unity. The range of bond lengths varies from ca. 2.30 Å, formally representing a quadruple bond, to ca. 2.83 Å, formally representing a single bond, although variations occur depending on the nature of the terminal and bridging ligands. Quadruply bonded species are normally encountered in $W^{II}W^{II}$ complexes, triply bonded species in $W^{III}W^{III}$ compounds, and doubly bonded species in $W^{IV}W^{IV}$ complexes. Dinuclear complexes containing the W^VW^V core usually have W–W single bonds. A significant number of multiply bonded ditungsten complexes carry the $\eta^5\text{-}C_5H_5$ or related ligands but these are not discussed here.

Probably the most dominant species amongst the dinuclear species are those containing W^{III}, lower oxidation state species being highly susceptible to oxidation.

9.1.1 Complexes Containing $W^{II}W^{II}$

The dominant structural feature of complexes containing $W_2{}^{4+}$ is the presence of a quadruple bond. However, the ditungsten core is extremely sensitive to oxidative addition and consequently the chemistry of $W^{II}W^{II}$ species is less well developed than that of molybdenum. However, $[(Me_3P)_2(MeCC)_2WWCl_2(PMe_3)_2]$ ($d_{W\text{–}W}$ 2.27 Å) was obtained by reaction of $[W_2Cl_4(PMe_3)_4]$ with LiC≡CMe. A range of complexes containing carboxylates, amines, N-based chelating ligands, tertiary phosphines, and halides has also been described. Addition of $PhICl_2$ to $[W_2Cl_4(PMe_3)_4]$ afforded the mixed-valent $W^{III}W^{II}$ species $[W_2Cl_5(PMe_3)_3]$ ($d_{W\text{–}W}$ 2.43 Å).

9.1.2 Complexes Containing $W^{III}W^{III}$

The simplest dinuclear tungsten (III) species are of the type $[W_2X_6]$ have an ethane-like structure and have W–W bonds in the range 2.26–2.29 Å. A smaller but significant group also contain the $\{W_2X_6\}$ core but carry two or three additional neutral ligands and in some species, although the ditungsten core can be defined as carrying a +6 charge, the two W atoms may have different formal oxidation states. In general, in these latter species, the W–W bond distances are slightly larger than in $[W_2X_6]$, within the range 2.31–2.50 Å, depending on the coligands.

Reduction of WCl_4 by one equivalent of $NaBHEt_3$ in the presence of Lihpp (hppH = (**68**)) afforded $[W_2(hpp)_4Cl_2]$ (W–W 2.25 Å).

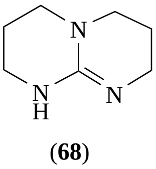

(**68**)

However, reduction of WCl_4 using sodium amalgam in the presence of an excess of tertiary phosphine L afforded $[W_2(\mu\text{-}Cl)_2Cl_4L_4]$ [L = PMe_2Ph (d_{W-W} 2.70 Å); L = PEt_3 (d_{W-W} 2.74 Å), PMe_3 (d_{W-W} 2.71 Å)]. These complexes have edge-sharing dioctahedral geometries, but their face-sharing analogs $[W_2(\mu\text{-}X)_3X_3L_3]$ were obtained by restricting the amount of L used in the reaction. Species characterized crystallographically included $[W_2(\mu\text{-}Cl)_3Cl_3(PMe_2Ph)_3]$ (d_{W-W} 2.44 Å), $[W_2(\mu\text{-}Cl)_3Cl_3(PEt_3)_3]$ (d_{W-W} 2.47 Å), and $[W_2(\mu\text{-}Br)_3Br_3(PMe_2Ph)_3]$ (obtained from WBr_5) (d_{W-W} 2.48 Å). Addition of water to $[W_2(\mu\text{-}Cl)_3Cl_3(PEt_3)_3]$ afforded $[W_2(\mu\text{-}Cl)_3Cl_4(PEt_3)_3]^-$ (d_{W-W} 2.44 Å).

When WCl_4 was reduced by sodium amalgam in the presence of thioethers such as SEt_2, 1,4-dithiane, 1,4-dithioxane, or pentamethylene sulfide, the sulfur rather than Cl ligand frequently acted as the bridging ligand, viz. $[W_2(\mu\text{-}SR_2)_3Cl_6]$ (**69**) (L = SEt_2, d_{W-W} 2.50 Å, L = 1,4-dithiane, d_{W-W} 2.48 Å, L = 1,4-dithioxane, d_{W-W} 2.50 Å, L = pentamethylene sulfide, d_{W-W} 2.51 Å). However, reaction with SMe_2 invariably afforded $[W_2(\mu\text{-}Cl)(\mu\text{-}SMe_2)_2Cl_6]^-$ and the precise nature of these bridged species (i.e. exclusively bridging SR_2 or mixtures of halide and SR_2) was dependent on reaction conditions. The bridging sulfur centers in the anionic species were susceptible to attack by anions X^- (X = SR, SeR, Cl, Br or H), resulting in loss of an alkyl group, as in conversion of $[W_2(\mu\text{-}SEt_2)_3Cl_6]$ to $[W_2(\mu\text{-}Cl)(\mu\text{-}SEt)(\mu\text{-}SEt_2)Cl_6]^-$ (d_{W-W} 2.44 Å) by treatment of the former with $[SC_6H_4Me]^-$. Further, cyclic species, such as those containing μ-tetrahydrothiophene, underwent ring opening on addition of Cl^- giving $[W_2(\mu\text{-}SC_4H_8)_2(\mu\text{-}SCH_2CH_2CH_2CH_2Cl\}Cl_6]^-$ (d_{W-W} 2.49 Å).

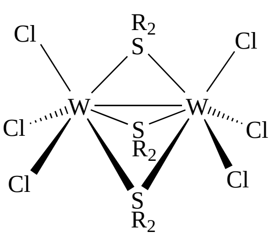

(**69**)

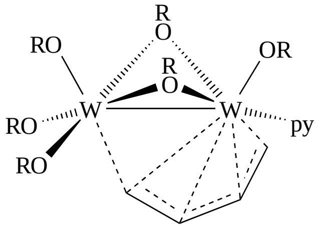

(**70**)

9.1.3 Complexes Containing $W^{IV}W^{IV}$

Reaction of $[W_2(OR)_6(py)_2$ (R = CH_2Bu^t) with 1,3-butadiene and with isoprene afforded blue–black $[W_2(\mu\text{-}\kappa^1{:}\eta^4\text{-}C_4H_6)(\mu\text{-}OR)_2(OR)_4(py)]$ (**70**) (d_{W-W} 2.49 Å) and $[W(\mu\text{-}\kappa^1{:}\eta^4\text{-}C_5H_8)(\mu\text{-}OR)_2(OR)_4(py)]$ (d_{W-W} 2.46 Å). The metal–metal separations were indicative of double bonds.

In the reaction between $[W_2(OR'')_6]$ (R″ = $SiMe_2Bu^t$) and NO in hydrocarbon solvents containing pyridine, $[W(NO)(OR'')_3(py)_2]$, $[WO(OR'')_4(py)]$, and $[W_2O_4(OR'')_4(py)_2]$ were formed. An intermediate $[W_2(\mu\text{-}O)(\mu\text{-}OR'')(OR'')_5(py)_2]$ was apparently formed along with N_2O after the coupling of two nitrosyl ligands during this reaction. This subsequently decomposed with loss of W–W bonding and the generation of the tungsten oxo complexes, which were also thought to arise from reactions involving N_2O. Both $[W^{VI}{}_2O_4(OR'')_4(py)_2]$ (d_{W-W} 3.04 Å) and $[W_2(\mu\text{-}O)(\mu\text{-}OR'')(OR'')_6(py)_2]$ (d_{W-W} 2.49 Å) were characterized crystallographically.

The species $[W_2(OBu^t)_7]^-$, which existed in an equilibrium with $[W_2(OBu^t)_6]$ and $[OBu^t]^-$, decomposed forming red $[W_2(\mu\text{-}O)(\mu\text{-}H)(OR)_6]^-$ with concurrent loss of $Me_2C{=}CH_2$. The structure of the oxo-hydride was confirmed crystallographically, the metal–metal distance (d_{W-W} 2.44 Å), being consistent with a double bond in a $W_2{}^{8+}$ core. $[W_2(OR')_6(NHMe_2)_2]$ (R = *cyclo*-C_5H_9) also decomposed over four days in the presence of cyclopentanol, affording a bridging hydride species $[W_2(\mu\text{-}H)(\mu\text{-}OR')(OR')_5(NHMe_2)]$ (d_{W-W} 2.44 Å). This molecule was fluxional in solution, and the dimethylamine could be replaced by PMe_3.

Treatment of $[W_2Cl_2(NMe_2)_4]$ with $Li_2C_8H_8$ afforded $[W^{IV}{}_2(\mu\text{-}\eta^5,\eta^5\text{-}C_8H_8)(NMe_2)_4]$ (**71**) (d_{W-W} 2.43 Å), in which the hydrocarbon ligand, regarded formally as $C_8H_8{}^{4-}$, functioned as a four electron bridging group.

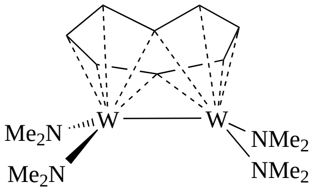

(**71**)

9.1.4 Complexes Containing W^VW^V

Treatment of *cis*-$[WF_2(OMe)_4]$ in thf with lithium powder, followed by an excess of NaOMe, afforded $[W_2(OMe)_{10}]$, which has an edge-sharing dioctahedral structure (d_{W-W} 2.79 Å). Aldehydes RCHO (R = cyclopropyl, tolyl, anisyl) reacted with $[W^{III}{}_2(ONp)_6(py)_2]$ (Np = CH_2Bu^t) giving alkylidene complexes $[W_2(\mu\text{-}ONp)_2(ONp)_4(\mu\text{-}CHR)(O)(py)]$ (**72**) (R = cyclopropyl or tolyl, d_{W-W} 2.66 Å). These complexes reacted with an excess of pyridine giving $[W_2(\mu\text{-}CR)(\mu\text{-}O)(ONp)_5(py)_2]$, (**73**) (R = cyclopropyl or anisyl, d_{W-W} 2.45 Å). Reaction of $[W^{III}{}_2(OR)_6(py)_2]$ with cyclohexenone afforded $[W_2(\mu\text{-}O)((\mu\text{-}OC_{12}H_{16})(OR)_6]$ (d_{W-W} 2.82 Å) and other dinuclear species containing W^V centers were obtained from reaction with acrolein (d_{W-W} 2.65 Å), methyl vinyl ketone (d_{W-W} 2.79 Å), and crotonaldehyde (d_{W-W} 2.62 Å).

Reaction of cooled solutions of $[W^{IV}{}_2(\mu\text{-}H)(\mu\text{-}OR')_2(OR')_5(NHMe_2)]$ (R′ = *cyclo*-C_5H_9) with four equivalents of ethane afforded the diamagnetic $[W_2(\mu\text{-}OR')_3(OR')_4Et(\eta^2\text{-}C_2H_4)]$ (**74**) (d_{W-W} 2.67 Å). $[W_4(\mu\text{-}H)_2(\mu\text{-}OPr^i)_6(OPr^i)_8]$ reacted similarly but no crystalline product was obtained.

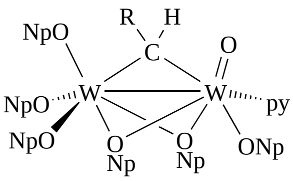

(72)

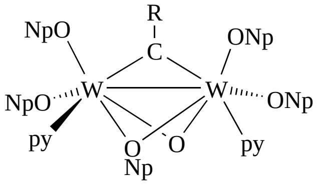

(73)

When two equivalents of cyclopentanone in hexane were added to the same hydrido precursor, diamagnetic $[W_2(\mu\text{-OR}')_3(OR')_5(\eta^2\text{-OC}_5H_8)]$ (**75**) ($d_{W\text{–}W}$ 2.67 Å) was formed. Treatment of $[W_4H_2(OPr^i)_{14}]$ with benzophenone in pentane afforded the analogous $[W_2(H)(\mu\text{-OPr}^i)_3(OPr^i)_4(\eta^2\text{-OCPh}_2)]$ ($d_{W\text{–}W}$ 2.65 Å), in which one terminal alkoxide group was replaced by hydride. Reaction of the tetranuclear dihydride with nitriles led to coupling of the nitrile molecules and formation of a dinuclear species $[W_2(\mu\text{-OPr}^i)_2(OPr^i)_5\{NC(Ph)C(Ph)NH\}]$ (**76**) ($R' = Ph$, $d_{W\text{–}W}$ 2.59 Å).

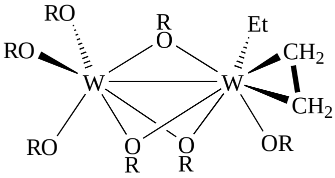

(74)

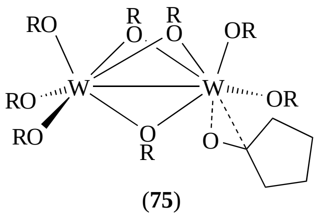

(75)

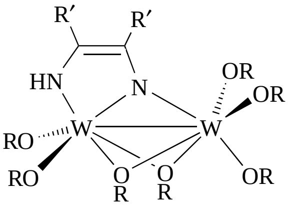

(76)

Addition of t-butanol to hydrocarbon solutions of $[W_2(\kappa^1\text{-SC}_4H_3)_2(NMe_2)_4]$ afforded $[W_2(\mu\text{-SC}_4H_4(\kappa^1\text{-SC}_4H_3)(OBu^t)_5]$ ($d_{W\text{–}W}$ 2.63 Å). Treatment of $[W_2(OR)_8]$ ($R = CH_2Bu^t$) with pyridine-N-oxide and elemental sulfur, elemental selenium, and tellurium afforded $[W_2(\mu\text{-E})(\mu\text{-OR})_2(OR)_6]$ (**77**) ($E = O$, Se or Te), in which the metal–metal bond was in the range 2.55–2.66 Å.

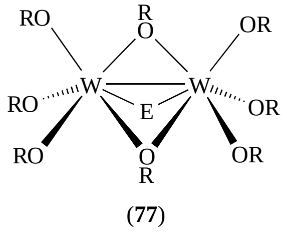

(77)

Treatment of $[W_2S_4Br_4]^{2-}$ with PPh_3 afforded $[W_2(\mu\text{-S})_2S_2Br_2(PPh_3)_2]$, which contains the *syn*-$\{(S)W)\mu\text{-})_2W(S)\}^{2+}$ fragment ($d_{W\text{–}W}$ 2.81 Å). When $[WSe_4]^{2-}$ was stirred in an $MeCN/CH_2Cl_2$ solution with PPh_3, $[W_2Se_6]^{2-}$ ($d_{W\text{–}W}$ 2.85 Å) was formed. Further reaction of this species with $P(c\text{-}C_6H_{11})_3$ in the presence of copper (I) chloride afforded the cluster species $[Cu\{P(C_6H_{11})_3\}_2(\mu\text{-Se}_2WSe_2)Cu\{P(C_6H_{11}\}_3\}]$ and the cubane-like $[W_2(\mu_3\text{-Se})_4(\kappa^2\text{-Se}_2CH_2)_2Cu\{P(C_6H_{11})_3\}_2]$.

The diamagnetic $[W_2(\mu\text{-CNEt}_2)(\mu\text{-S})(\mu\text{-S}_2CNEt_2)(\mu\text{-S}_2SnCHSiMe_3)(S_2CNEt_2)_2]$ ($d_{W\text{–}W}$ 2.61 Å) was formed by refluxing the mononuclear $[W(CO)_2(S_2CNEt_2)(SnCHSiMe_3)]$ in benzene. Addition of N-bromophthalimide to a chloroform solution of $[\{W_2(Ntol)\{S_2P(OEt)_2\}S\}_4]$ containing $[Et_4N][OAc]$ afforded the sulfur-bridged species $[W_2(Ntol)_2\{S_2P(OEt)_2)_2\}(\mu\text{-OAc})(\mu\text{-S})(\mu\text{-SBr})]$ (**78**) ($d_{W\text{–}W}$ 2.83 Å).

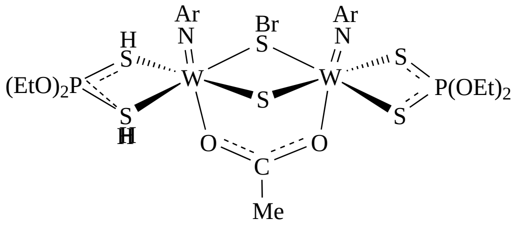

(**78**)

Pyridine reacted at 60 °C with $[W_2Cl_2(NHSiBu^t{}_3)_4]$ to give $[WHCl(NSiBu^t)_2(py)]$, $[WCl_2(NBu^t{}_3)_2(py)]$, and $[W_2(\mu\text{-H})_2(\mu\text{-Cl})HCl_2(NHSiBu^t{}_3)_3(py)_2]$ (**79**) ($d_{W\text{–}W}$ 2.79 Å).

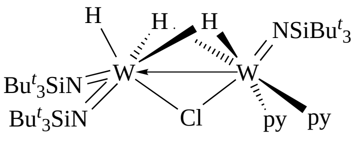

(**79**)

9.2 Polyoxoanions

Polyoxometallate ions containing tungsten form an enormous range of compounds, which have been reviewed extensively.[5,6] They may be subdivided into (1) isopolyanions containing W as the dominant and frequently the only metal component, and (2) heteropolyanions where other metals and/or nonmetal atoms may be present in the core structure.

9.2.1 Isopolyanions

NMR studies have demonstrated that above pH 6 the major polytungstate species are $[W_7O_{24}]^{6-}$ (known also as paratungstate-A) and $[H_2W_{12}O_{42}]^{10-}$ (known as paratungstate-B). These species have been isolated as several different types of salt, and have been characterized crystallographically and by their ^{183}W chemical shifts. Below pH 5.5, equilibria are slowly established and most polytungstate species, excepting the Keggin ion α-$[(H_2)W_{12}O_{40}]^{6-}$ (known as metatungstate and in which the protons are in the center of the cage) are normally metastable. Acidification of solutions containing paratungstates ultimately afforded α-$[H_2W_{12}O_{40}]^{6-}$, but intermediates appear to include the partially characterized $[H_7W_{11}O_{40}]^{7-}$, which may be a lacunary species derived from $[H_2W_{12}O_{42}]^{10-}$, $[W_{10}O_{32}]^{4-}$ (sometimes known as tungstate-Y), and small amounts of β-$[(H_2)W_{12}O_{40}]^{6-}$ (known previously as tungstate-X), α- and β-$[(H)W_{12}O_{40}]^{7-}$, in which the protons are in the center of the cage. Other isopolytungstates have been reported, including $[(H_4)W_{12}O_{40}]^{4-}$, in which the protons are thought to be in the center of the cage, $[H_3W_6O_{22}]^{5-}$, and $[HW_5O_{19}]^{7-}$.

In nonaqueous media, $[W_6O_{19}]^{2-}$ and $[W_{10}O_{32}]^{4-}$ are stable and have been characterized spectroscopically (particularly by ^{183}W nmr), and $[H_6W_{18}O_{60}]^{6-}$ exhibited reversible voltammetric behavior in acetonitrile.

Mixed metal isopolyanions incorporating vanadium, $[V_xW_{6-x}O_{19}]^{(2+x)-}$ ($x = 1–3$), the Keggin ions $[(V)V_x W_{12-x}O_{40}]^{(3+x)-}$ ($x = 1–4$), and $[H_2W_{11}VO_{40}]^{7-}$ have been described. ^{51}V NMR spectral investigations of vanadate-tungstate mixtures revealed that $[WV_9O_{28}]^{5-}$ existed at pH 5 and an isomer of $[V_3W_3O_{19}]^{5-}$ at pH 6.5. From ^{183}W and ^{95}Mo NMR spectral studies, it was established that all possible mixtures of $[(Mo,W)_7O_{24}]^{6-}$ existed but that only one molybdenum center could be substituted into $[H_2W_{12}O_{42}]^{10-}$ and α-$[H_2W_{12}O_{40}]^{6-}$.

9.2.2 Heteropolyanions

The Keggin-structure anion α-$[XW_{12}O_{40}]^{n-}$, particularly the tungstophosphates and tungstosilicates, are the most frequently investigated because of the potential and real catalytic applications. The central heteroatoms, X, in the Keggin and isomeric anions $[XW_{12}O_{40}]^{n-}$ include, in the α-form $(H)_2$, Be, B, Al, Ga, Si, Ge, P^V, As^V, V, Cr^{3+}, Fe^{3+}, $Co^{2+,3+}$, $Co^{1+,2+}$, and Zn, and in the β form $(H)_2$, Al, Ga, Si, Ge, and P^V. Unlike the situation in heteropolymolybdate chemistry, no capped heteropolytungstates have yet been reported.

Four of the possible six possible skeletal isomers having the Wells–Dawson structure, as exemplified by $[E_2W_{18}O_{62}]^{6-}$ (E = P or As), have been structurally identified. The so-called ‘Preyssler’ anion was structurally identified as $[\{Na(H_2O)\}P_5W_{30}O_{110}]^{14-}$, it being shown that the $Na(H_2O)^+$ group was tightly bound in the center of the cluster. However, under forcing conditions, the aqua-sodium cation could be replaced by Ca^{2+}, trivalent lanthanide cations and some tetravalent actinide cations, all of which have similar ionic radii (ca. 1/Å). All of these anions exhibited reversible tungsten-based reduction behavior.

Lacunary version of the Keggin- and Dawson-type structures have been isolated and crystallographically characterized. In these species, up to three ‘octahedral W’ units may be extracted, generating species such as $[EW_{11}O_{39}]^{n-}$, $[EW_{10}O_{36}]^{n-}$, $[EW_9O_{34}]^{n-}$, $[E_2W_{17}O_{61}]^n$, and $[E_2W_{15}O_{56}]^{12-}$. In an exceptional case, α-$[P_2W_{12}O_{48}]^{14-}$, which has six W units extracted from the Wells–Dawson core, has been characterized. All of these lacunary anions have structures, in which no WO_6 octahedral has more than two (cis) terminal oxygen atoms. As such, these species are particularly useful synthetic precursors for the incorporation of other metal ions, thereby reconstituting the idealized Keggin or Wells–Dawson structure. Species having one mixing W unit, such as $[EW_{11}O_{39}]^{n-}$ or $[E_2W_{17}O_{61}]^{n-}$, have generated a very large number of species, in which the inserted atom is a metal cation carrying a variety of terminal ligands, or in some case, no addition ligands. Such cluster complexes could be regarded as coordination compounds with the polyoxometallate group functioning as a tetra or pentadentate ligand. In such species, the polyoxometallate ligand appears to act as a π-acceptor species. Corresponding heteropolytungstates with two missing W units may be reconverted to Keggin structures, as in the conversion of $[SiW_{10}O_{36}]^{8-}$ to $[SiW_{10}M_2O_{40}]^{n-}$ where M = Mo, Mn^{III}, Fe^{III}, $Ti(\eta\text{-}C_5H_5)_2$, and a similar situation occurred with the trivacant lacunary anions, $[EW_9O_{34}]^{n-}$ and $[P_2W_{15}O_{56}]^{12-}$. The magnetic properties of a number of metal complexes containing $M^{II}O_6$ octahedra, such as $[PW_9O_{34}Ni_4(OH)_3(H_2O)_6]^{4-}$ and $[Co_7(H_2O)_2(OH)_2\{PW_9O_{34}\}_2(W_7O_{26})]^{16-}$, have been measured.

A large number and variety of polytungstate complexes incorporate pairs of trivacant lacunary anions, which effectively sandwich three of four metal atoms. Typical examples include $[\{EW_9O_{34}\}_2(RQ)_3]^{n-}$ (E = P or Si; Q = Si or Sn), $[\{EW_9O_{34}\}_2(UO_2)_2]^n$–(E = P or Si),$[\{PW_9O_{34}\}_2Fe^{III}{}_4(H_2O)_2]^{n-}$, $[\{P_2W_{15}O_{56}\}_2Fe^{III}{}_4(H_2O)_2]^{12-}$, and $[\{BiW_9O_{33}\}_2Cu_3]^{n-}$.

Polyoxo(thio)metallates have been prepared by incorporating thio-metal groups into lacunary anions, giving, for example, $[PW_{11}O_{39}(MX)]^{4-}$ (M = Nb, Ta; X = S, Se)$[SiW_{10}O_{38}M_2S_2]^{6-}$(M = Mo or W), $[\{PW_{11}O_{39}\}_2\{Mo_2S_2(OH)_2O_2]^{10-}$, $[\{PW_9O_{234}\}_2\{Mo_2S_2(OH)_2O_2\}_3]^{10-}$, and $[\{SiW_{11}O_{39}\}_2\{Mo_3S_4(H_2O)_3(OH)\}_2]^{10-}$.

9.2.3 Very Large Polyoxotungsten Anions

Composite anions have been constructed from assemblies of relatively simple, usually lacunary, polytungstate anions. Examples include $[Ln_2(H_2O)_2\{SbW_9O_{33}\}(W_5O_{18})_2]^{15-}$ (molar mass 5056; Ln = Y, Sm, Er), $[Ce_4(OH)_2(H_2O)_9\{P_2W_{16}O_{59}\}_2]^{4-}$ (molar mass 8652), $[Ln(Ln_2(OH)(H_2O)_{11}(WO_4)_4\{AsW_9O_{33}\}_4]^{20-}$ (molar mass 10 529; Ln = Ce, Nd, Sm, Gd), and $[Ln_{16}(H_2O)_{36}(WO_4)_4(W_2O_6)_8\{AsW_9O_{33}\}_{12}(W_5O_{18})_4]^{76-}$ (molar mass 39 383).

9.3 Cluster Compounds Containing Chalcogenide Atoms

There are three main cluster types encountered in this group of important compounds: the incomplete cuboid $\{W_3(\mu_3\text{-}E)(\mu\text{-}E)_3\}^{4+}$, the sulfur-rich incomplete cuboid $\{W_3(\mu_3\text{-}E)(\mu,\mu'\text{-}E)_3\}^{4+}$, and the cuboid $\{W_4(\mu_3\text{-}E_4)\}^{5+}$.[7] These species are described as 'cuboidal' since this illustrates the best approximation in what are usually somewhat distorted structures.

9.3.1 Trinuclear Clusters, $[W_3E_4]^{4+}$

The parent species $[W_3S_4(H_2O)_9]^{4+}$ is well established and characterized (**80**) but an efficient synthesis was devised by heating $[W_3S_4(S_4)_3(NH_3)_3]^{2-}$ with concentrated HCl, or by treatment of polymer $[\{W_3S_7Br_4\}_n]$ with H_3PO_2 in hot concentrated HCl. The core cluster $[W_3S_4(H_2O)_9]^{4+}$ was structurally characterized in two salts, establishing the W–W bond length as 2.72 Å, identical to that in the analogous molybdenum cluster $[Mo_3S_4(H_2O)_9]^{4+}$. All three mixed O/S clusters were prepared by comproportionation of $[[NH_4]_2[WS_4]$ with $K_3[W_2Cl_9]$ in aqueous media. $[W(CO)_6]$ reacted with Na_2S in acetic anhydride, affording the $\{W_3O_3S\}^{4+}$ core as the sole isolable product, and it was extracted by NCS^-, giving $[W_3O_3S(NCS)_9]^{5-}$ (W–W 2.61 Å).

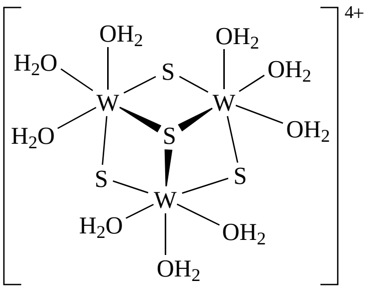

(**80**)

While no fully chlorinated species $[W_3E_4Cl_9]^{5-}$ (E = S or Se) have been detected, some Cl^- coordination can occur giving, for example, $[W_3E_4Cl(H_2O)_8]^{3+}$, $[W_3S_4Cl_2(H_2O)_7]^{2+}$, and $[W_3S_4Cl_3(H_2O)_6]^+$. Apparently no complexes containing F^-, Br^- or, I^- have been described. In $[W_3S_4(O_2CH)_9]^{5-}$ it was established crystallographically that the formato ligand was monodentate, whereas in $[W_3S_4(O_2C_2O_2)_3(H_2O)_3]^{2-}$ the oxalato ligand was bidentate. The pentanedionato species $[W_3E_4(acac)(py)_3]^+$ (E = S or Se) were obtained by reaction of $[W_3E_4(H_2O)_9]^{4+}$ in dilute HCl with Hacac, followed by addition of pyridine and a precipitating anion (usually PF_{6-}). ^1H NMR spectral studies established the stereochemical rigidity of these species in solution, and cyclic voltammetric studies established that the clusters underwent two quasi-reversible reductions corresponding to the generation of species containing $W^{IV}{}_2W^{III}$ and $W^{IV}W^{III}{}_2$. The species $[W_3S_4(acac)(NH_3)_3]^+$ has also been reported. Nitrilotriacetic acid (H_3nta) reacted with mixed O/S clusters, affording species including $[W_3O_3S(Hnta)_3]^{2-}$, $[WO_2S_2(Hnta)_3[^{2-}$, and $[WOS_3(Hnta)_3]^{2-}$, and mixed metal clusters $[Mo_2WS_4(Hnta)_3]^{2-}$ and $[MoW_2S_4(Hnta)_3]^{2-}$ have also been characterized. These clusters undergo three consecutive one-electron reductions corresponding to the stepwise reduction of each metal center. Polyaminoplycarboxylic acids also formed complexes containing the $\{W_4S_{4-n}O_n\}^{4+}$ cores. These included $[\{W_3S_4\}_2(egta)_3]^{4-}$ (H_4egta = ethyleneglycol-bis(2-aminoethyl)tetraacetic acid), $[\{W_3O_3S\}_2(egta)_3]^{4-}$, $[W_3S_4(ttha)]^{2-}$ (H_6ttha = triethylenetetraminehexaacetic acid), $[\{W_3S_4\}_2(ttha)_2]^{4-}$, and $[\{W_3S_4\}_2(ttha)_3]^{10-}$. The crystal-structure determination of a salt of $[\{W_3S_4\}_2(ttha)_2{}^{4-}$ revealed that the ttha ligands were decadentate, being alternately hexadentate with respect to one $\{W_3S_4\}$ cluster and tetradentate with respect to the other. Anionic clusters of similar complexity containing the $\{W_3O_3S\}^{4+}$ core included $[W_3O_3S(obeta)_3]^{4-}$ (H_4obeta = oxybis(ethylamine)tetraacetic acid), $[\{W_3O_3S\}_2(obeta)_3]^{4-}$, $[\{W_3O_3S\}_2(bdta)_3]^{4-}$ (H_4bdta = 1, 4-butylenediaminetetraacetic acid), and $[\{W_3O_3S\}_2(pdta)_3]^{4-}$ (H_4pdta = 1, 3-propylenediaminetetraacetic acid). In studies of the reactions of $[W_3E_4(H_2O)_9]^{4+}$ (E = S or Se) with NCS^-, it was concluded that the first product formed involved an S-bonded thiocyanate isomer, but this later isomerized to a more stable N-bonded form, $[W_3E_4(NCS)_9]^{5-}$. $[W_3S_4(NCS)_9]^{5-}$ was obtained either by heating polymeric $[\{W_3S_7Br_4\}_n]$ in a melt of KNCS or by reaction of NCS^- with $[W_3S_7Br_6]^{2-}$ in refluxing acetonitrile. Reaction of $[\{W_3Se_7Br_4\}_n]$ with KNCS afforded a mixture of all possible $[W_3S_nSe_{4-n}(NCS)_9]^{5-}$, but these were eventually converted into $[W_3S_4(NCS)_9]^{5-}$.

Polymeric $[\{W_3S_7Br_4\}_n]$ reacted slowly with $(NH_4)_2S_x$ at room temperature giving black needles of $[NH_4]_2[W_3S_4(S_4)_3(NH_3)_3]\cdot H_2O$. The tetrasulfido ligand was bidentate and the W–S bond distances were rather long (2.5 Å), explaining why this species reacted with concentrated HCl easily giving $[W_3S_4(H_2O)_9]^{4+}$.

Treatment of $[\{W_3S_7Cl_4\}_n]$ with PPh_3 in thf afforded $[W_3S_4Cl_4(PPh_3)_3(H_2O)_2]\cdot 3thf$. However, reaction of PEt_3 with $[\{W_3S_7Br_4\}_n]$ in thf afforded $[W_3S_4Br_4(PEt_3)_3\{P(O)HEt_2\}(H_2O)]$, in which partial P–C bond fission and phosphine oxidation had occurred. With bidentate phosphines (dmpe, dppe), $[\{W_3S_7X_4\}_n]$ (X = Cl or Br) was converted to $[W_3S_4X_3(dmpe)_3]^+$ and $[W_3S_4X_3(dppe)_3]^+$. In the course of these reactions, mixed halide clusters $[W_3S_4Cl_2Br(dmpe)_3]^+$ and $[W_3S_4ClBr_2)dmpe)_3]^+$ could be detected. The mixed sulfido/selenido cluster $[W_3S_xSe_{4-x}(NCS)_9]^{5-}$ reacted with dppe giving $[W_3S_xSe_{4-x}(NCS)_3(dppe)_3]^+$, and $[W_3Se_4Br_3(dppe)_3]^+$ was obtained directly from $[\{W_3Se_7Br_4\}_n]$.

Reaction of $[W_3S_4Cl_3(dmpe)_3]^+$ with BH_4^- gave the pink air-stable trihydrido complex $[W_3S_4H_3(dmpe)_3]^+$.

Treatment of polymeric $[\{W_3Se_7Br_4\}_x]$ with hot aqueous KCN afforded $[W_3Se_4(CN)_9]^{5-}$, which could be electrochemically reduced in a one-electron step, affording $[W_3Se_4(CN)_9]^{6-}$, containing the $W^{IV}{}_2W^{III}$ core.

9.3.2 Trinuclear Complexes, $[W_3E_7]^{4+}$

The polymeric clusters $[\{W_3E_7X_4\}_x]$ (E = S or Se; X = Cl or Br) were prepared by heating the elements in a sealed tube at ca. 350 °C. The structure of $[\{W_3S_4Br_4\}_x]$ consists of $W_3(\mu_3\text{-}S)(\mu\text{-}S_2)_3{}^{4+}$ units bridge by four Br atoms forming an extended zigzag structure. The corresponding selenides are thought to have the same basic structure. The bridging S_2 groups are asymmetrically coordinated and since the metal atoms are formally in oxidation state IV, there are six electrons available to form three single metal–metal bonds in the triangle. Under certain conditions, the halide ion can cleave the bridges giving $[W_3E_7X_6]^{2-}$ (**81**) (X = Cl or Br) and the clusters can be aquated to form relatively stable ions $[W_3E_7(H_2O)_6]^{4+}$. The structural dimensions of the $\{W_3S_7\}^{4+}$ core are very similar to those of its molybdenum analog.

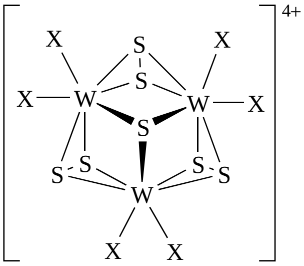

(**81**)

Treatment of $[\{W_3Se_7X_4\}_x]$ with PPh_4X (in melts) or Et_4NX (in vibration mills) afforded $[W_3Se_7X_6]^{2-}$. Treatment of the hexahalides with NaS_2CNR_2 afforded $[W_3Se_4(S_2CNR_2)_3]^+$, in which there are strong interactions between the axial Se atom and an S atom of the dithiocarbamate ligand. When $[W(CO)_6]$ was refluxed with selenium and tetraethylthiuram disulfide in 1,2-dichlorobenzene, red $[\{W_3Se_7(S_2CNEt_2)_3\}_2Se]$ was formed. Treatment of $[W_3Se_7Br_6]^{2-}$ with $[S_2P(OEt)_2]^-$ in acetonitrile afforded the dithiophosphato cluster $[W_3Se_7\{S_2P(OEt)_2\}_3]^-$ and the 1,10-phenanthroline (phen) cluster $[W_3Se_7(phen)_3]^{4+}$ was obtained by melting $[\{W_3Se_7X_4\}_x]$ with the bidentate heterocycle. Treatment of $[W_3S_7X_6]^{2-}$ (X = Cl or Br) with PPh_3Se afforded $[W_3S(SSe)_3X_6]^{2-}$ and reaction of this with KNCSe, in the presence of an excess of KNCS, gave $[W_3S(SSe)_3(NCS)_6]^{2-}$. The aqua cluster $[W_3Se_4(H_2O)_9]^{4+}$ reacted with P_4S_{10} in ethanolic HCl to give $[W_3Se(SSe)_3\{S_2P(OEt)_2\}^3]^+$.

9.3.3 Tetranuclear cubic $\{W_4E_4\}^{5+}$ Clusters

Brown–red $[W_4S_4(H_2O)_{12}]^{6+}$ was prepared by the reaction of $[W_3S_4(H_2O)_6]^{4+}$ with $[W(CO)_6]$ in aqueous HCl under hydrothermal conditions. This species is presumed to have a structure very similar to its molybdenum analog, viz. consisting of two interpenetrating W_4 and S_4 tetrahedra of different sizes, leading to a distorted pseudo-cubic geometry. The hexa-cation was electrochemically reduced to $[W_4S_4(H_2O)_{12}]^{5+}$, the potentials indicating its oxidative instability.

Mixed metal clusters were obtained by reaction of $[W_3S_4(H_2O)_9]^{4+}$, $[W_3Se_4(H_2O)_9]^{4+}$, $[MoW_2S_4(H_2O)_9]^{4+}$, and $[Mo_2WS_4(H_2O)_9]^{4+}$ with $[Mo_2Cl_8]^{4-}$, giving $[MoW_3S_4(H_2O)_{12}]^{5+}$, $[MoW_3Se_4(H_2O)_{12}]^{5+}$, $[Mo_2W_2S_4(H_2O)_{12}]^{5+}$, and $[Mo_3WS_4(H_2O)_{12}]^{5+}$. Oxidation of these pentacationic species by $[Fe(H_2O)_6]^{3+}$ initially afforded the hexacations but these decomposed by loss of one W atom, for example, in the process $[MoW_3S_4(H_2O)_{12}]^{5+} \rightarrow [MoW_3S_4(H_2O)_{12}]^{6+} \rightarrow [MoW_2S_4(H_2O)_9]^{4+}$. Electrochemical studies of these pentacationic mixed metal cubic clusters revealed two reversible redox processes corresponding to a one-electron reduction and a one-electron oxidation.

When WTe_2 was heated with KCN, $[W_4Te_4(CN)_{12}]^{6-}$ was formed, while in a KNCS melt, chalcogen exchange occurred, leading to $[W_4S_4(CN)_{12}]^{6-}$. These species have been structurally characterized and it was established that the symmetry of the cluster core was sensitive to the nature of the counter ion. The core clusters in the $NH_6{}^+$ salts had ideal T_d symmetry ($d_{W\text{–}W}$ 2.85 Å) in the $[KCs_5]^{6+}$ salt C_1 symmetry ($d_{W\text{–}W}$ 2.80–90 Å), and in the K^+ salt C_2 symmetry ($d_{W\text{–}W}$ 2.83–2.91 Å). $K_6[W_4Se_4(CN)_{12}]\cdot 6H_2O$ exhibited a cuboidal core with C_{2v} symmetry ($d_{W\text{–}W}$ 2.88 Å). The complexes were electrochemically active, showing two reversible or quasi-reversible reduction processes, one corresponding to the formation of 7(−) and 8(−) species. Despite the distortions observed in the solid state, the ^{77}Se, ^{125}Te and ^{183}W NMR studies on $[W_4E_4(CN)_{12}]^{6-}$ indicated the equivalence of metal and chalcogen atoms in solution.

In a solvento-thermal reaction involving $[W(CO)_6]$, K_2S_4, and 1,2-diaminoethane (en) at 300 °C, the slightly electron-deficient (54-valence electron) black–red cluster $[W_4S_4(en)_4(S)_4]S$ was formed. This species contains a W_4S_4 cuboidal skeleton ($d_{W\text{–}W}$ 2.80–2.88 Å) and S^{2-} as a counter-anion. While the W–S bonds involving the μ_3-bridges is 2.36–2.41 Å, the formal W=S bond lengths are 2.54 Å, rather longer than expected. This suggested that the species might be better formulated as the 58-electron $[W_4S_4(en)_4(SH)_4]S$, which was more consistent with the geometry of the cluster but no S–H vibrational bands were detected by IR spectroscopy. The species was paramagnetic, obeying the Curie–Weiss law, with $\mu = 2.67$ BM at 400 K.

9.3.4 *Raft-like Clusters* $[W_4(\mu_3 - S)_2)\ (\mu\text{-}S)_4]^{2+}$

Treatment of *cis*-$W(N_2)_2(PMe_2Ph)_4]$ with two equivalents of $(Me_3Si)_2S$ in methanol afforded $[W_4(\mu_3\text{-}S)_2(\mu\text{-}S)_4(SH)_2(PMe_2Ph)_6]$. This 58-electron cluster has sufficient electrons (10) to form five W–W bonds, including one between the hinge atoms (see (**82**)) ($d_{W\text{–}W}$ 2.81–2.84 Å), and the presence of S–H groups was confirmed crystallographically. Reaction of this complex with $SnCl_2$ in thf effected Cl/SH group exchange, giving $[W_4(\mu_3\text{-}S)_2(\mu\text{-}S)_4Cl_2(PMe_2Ph)_6]$. Oxidation of this species by Ag^+ afforded $[W_4(\mu_3\text{-}S)_2(\mu\text{-}S)_4Cl_2(PMe_2Ph)_6]^{2+}$, a 56-electron cluster that retained its raft-like connectivity, although the core no longer retained C_{2h} symmetry but was distorted, with a pair of opposing W–W bonds elongated to 2.94 Å, another pair shortened to 2.74 Å, and only the W–W hinge remaining relatively unperturbed at 2.83 Å. Reduction of $[W_4(\mu_3\text{-}S)_2(\mu\text{-}S)_4Cl_2(PMe_2Ph)_6]$ by sodium amalgam afforded $[W_4(\mu\text{-}S)_6(PMe_2Ph)_4]$, which contains an adamantane-like core. There are 12 electrons in this W^{III} species ($d_{W\text{–}W}$ 2.63 Å), the basic coordination geometry around each metal atom (neglecting the formal W–W bond) being essentially tetrahedral.

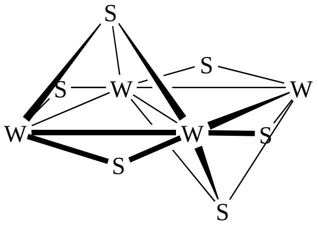

(**82**)

9.3.5 *Heterometallic Derivatives of* $[W_3E_4(H_2O)_9]^{4+}$

The incomplete cubes $[W_3E_4(H_2O)_9]^{4+}$ (E = S, Se) reacted with metal ions to generate cuboidal species. These are generally of three types, shown in (**83**), (**84**), and (**85**). The cluster (**83**) utilizes a heterometal atom with variable coordination preferences (usually octahedral or tetrahedral), constituting a cuboidal species. However when M′ prefers tetrahedral geometry, the edge-linked double cube (**84**) can be formed. The incomplete cube can also function as a pair of tridentate 'ligands', generating a corner-shared cube (**85**).

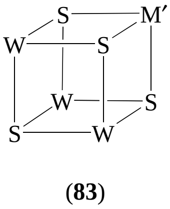

(**83**)

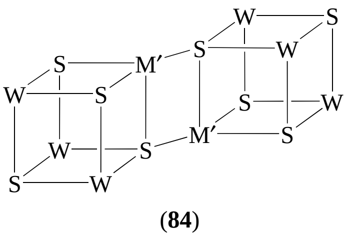

(**84**)

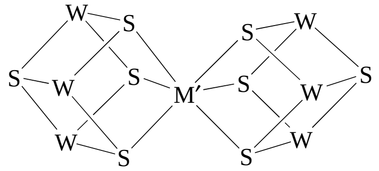

(**85**)

The conversion of (**83**) to (**84**) occurred when the anions accompanying the reaction were normally noncoordinating, such as $ClO_4{}^-$ or p-$MeC_6H_4SO_3{}^-$, and regeneration of (**83**) would occur when ligands such as CO, PR_3, Cl^-, or NCS^- were added and attached to M′. In general, the W–W distances in these species were relatively short (2.5–2.8 Å) and while relatively short W–M′ bonds (ca. 2.7 Å) were characteristic when M′ was a transition metal in (**84**) and (**85**), long nonbonding interactions (>3.5 Å) were typical features of (**83**) and (**84**) when M′ was a metal from groups 12 or 13.

While the mixed metal clusters $[Mo_3WS_4(H_2O)_9]^{4+}$ and $[WMo_3S_4(H_2O)_9]^{4+}$ were described earlier, there are no reported examples of $[CrW_3S_4(H_2O)_9]^{4+}$. A similar situation exists with Mn and Re. No clusters containing Fe, Ru, Os, or Co have been reported but there is evidence that $[W_3S_4(H_2O)_9]^{4+}$ reacted with $RhCl_3$ in 4M HCl, although the product was not characterized. Reaction of metallic Ni with $W_3S_4(H_2O)_9]^{4+}$ afforded green $[W_3NiS_4(H_2O)_{10}]^{4+}$ [(**83**, M′ = Ni(H_2O)], and the mixed Mo/W clusters $[MoW_2NiS_4(H_2O)_{10}]^{4+}$ and $[Mo_2WNiS_4(H_2O)_{10}]^{4+}$ were also isolated. In these three species, the Ni^{II} center adopted tetrahedral geometry. Crystallization of the tungsten-rich clusters resulted in edge-linked double cubes $[\{W_3NiS_4(H_2O)_9\}_2]^{8+}$ ($d_{Ni\text{–}Ni}$ 2.56 Å) and $[\{MoW_2NiS_4(H_2O)_9\}_2]^{8+}$ ($d_{Ni\text{–}N}$i 2.55 Å), (**84**). $[W_3NiS_4(H_2O)_{10}]^{4+}$ reacted with CO giving $[W_3Ni(CO)S_4(H_2O)_9]^{4+}$. While no clusters containing Pd have been described, $[W_3S_4(H_2O)_9]^{4+}$ reacted with $[PtCl_4]^{2-}$ giving the edge-linked double cube $[\{W_3PtS_4(H_2O)_9\}_2]^{8+}$.

Reaction of $[W_3S_4(H_2O)_9]^{4+}$ with copper metal afforded the green air-sensitive $[W_3CuS_4(H_2O)_{10}]^{5+}$, but no evidence for $[W_3CuS_4(H_2O)_{10}]^{4+}$ could be found. $[W_3S_4X_3(dmpe)_3]^+$ (X = Cl or Br) reacted with Cu^I halides or with $[Cu(NCMe)_4]^+$ in the presence of X^- to give $[W_3(CuX)S_4X_3(dmpe)_3]^+$ ($d_{W\text{–}W}$ 2.78 Å; $d_{Cu\text{–}W}$ 2.88 Å). Dithiophosphato derivatives such as $[W_3(CuI)S_4(\mu\text{-}O_2CCCl_3)\{S_2P(OEt)_2\}_3(NCMe)]$ and $[W_3(CuI)S_4(\mu\text{-}O_2CMe)\{S_2P(OEt)_2\}_3(py)]$ were also prepared. Reaction of $[Mo_2WS_4(\mu\text{-}S_2PR_2)(S_2PR_2)_3]$ with CuI in the presence of pyridine afforded $[Mo_2W(CuI)(\mu\text{-}S_2PR_2)(S_2PR_3)_3(py)]$ (R = Et, Pr^n).

Treatment of $[W_3S_4(H_2O)_9]^{4+}$ with mercury afforded the purple corner-shared double cube $W_6Hg_2S_8(H_2O)_{18}]^{8+}$ (**85**). However, no reaction was observed between the trinuclear tungsten species and metallic Ga or $GaCl_3$ reduced by $NaBH_4$. However, when metallic In was added to $[W_3E_4(H_2O)_9]^{4+}$, $[W_3InE_4(H_2O)_{12}]^{5+}$ was formed (**83**; E = S, dark blue, E = Se, blue–green). When equimolar amounts of $[W_3InS_4(H_2O)_{12}]^{5+}$ and $[Mo_3S_4(H_2O)_9]^{4+}$ were mixed, rapid and quantitative In^+ transfer took place, giving $[W_3S_4(H_2O)_9]^{4+}$ and $[Mo_3InS_4(H_2O)_{12}]^{5+}$. Treatment of $[W_3E_4(H_2O)_9]^{4+}$ (E = S or Se) with GeO or GeO_2/H_3PO_2, the single cubes $[W_3GeE_4(H_2O)_{12}]^{6+}$ (**83**), only were formed. However, the double cubes $[W_6GeE_8(H_2O)_{18}]^{8+}$, (**85**), were obtained by reduction of $[W_3GeE_4(H_2O)_{12}]^{6+}$ ($d_{W–W}$ 2.67 Å when E = S) by BH_4^- in the presence of a further equivalent of $[W_3E_4(H_2O)_9]^{4+}$. Solution studies of $[W_3GeS_4(H_2O)_{12}]^{6+}$ indicated that the Ge center was coordinated by three H_2O ligands, which could be replaced by Cl^- giving $[W_3(GeCl_3)S_4(H_2O)_{12}]^{3+}$. Reaction of metallic tin (as shot) with $[W_3S_4(H_2O)_9]^{4+}$ gave only the single cube $[W_3SnS_4(H_2O)_{12}]^{6+}$. However, BH_4^- reduction of $[W_3(SnCl_3)S_4(H_2O)_9]^{3+}$ in the presence of $[W_3S_4(H_2O)_9]^{4+}$ afforded the double cube $[\{W_6SnS_8(H_2O)_{18}]^{8+}$ (**85**, M′ = Sn). This method of reductive coupling was also employed to make $[Mo_3W_3SnS_8(H_2O)_{18}]^{8+}$ and $[Mo_3W_3SnS_4Se_4(H_2O)_{18}]^{8+}$, the latter being obtained in a reaction involving BH_4^- reduction of $[Mo_3(SnCl_3)S_4(H_2O)_9]^{3+}$ in the presence of $[W_3Se_4(H_2O)_9]^{4+}$. These double cubes could be oxidized by O_2 or $[Fe(H_2O)_6]^{3+}$ to $[W_3SnE_4(H_2O)_{12}]^{6+}$ and then, with an excess of oxidant, to $[W_3E_4(H_2O)_9]^{4+}$ and Sn^{IV}. Treatment of $[W_3Se_4(H_2O)_9]^{4+}$ with Pb shot afforded the air-sensitive wine-red $[W_6PbSe_8(H_2O)_{18}]^{8+}$ (**85**, M′ = Pb), but no reaction occurred with $[W_3S_4(H_2O)_9]^{4+}$. No single cubes of the type $[W_3PbE_4(H_2O)_{12}]^{6+}$ have been reported but treatment of $[W_3S_4(H_2O)_9]^{4+}$ with PbI_3^- in the presence of $[S_2P(OEt)_2]^-$ in pyridine-based media afforded $[W_3(PbI_3)S_4\{S_2P(OEt)_2\}_3(py)_3]$.

Gray arsenic did not react with $[W_3E_4(H_2O)_9]^{4+}$ (E = S or Se) but with $NaAsO_2$ in the presence of H_3PO_2, red $[W_6AsSe_8(H_2O)_{18}]^{8+}$ (**85**, M′ = As^0) was formed. No single cubes containing As were detected, but oxidation of the double cube afforded As^{III} and $[W_3Se_4(H_2O)_9]^{4+}$. Treatment of $[W_3Se_4(H_2O)_9]^{4+}$ with $SbCl_3$ or with Sb shot in the presence of HCl afforded yellow–brown $[W_3(SbCl_3)Se_4(H_2O)_9]^{4+}$ (**83**, M′ = $SbCl_3$). The dithiophosphate complex $[W_3(SbI_3)S_4(OAc)\{S_2P(OEt)_2\}_3](dmf)]$ was also prepared, and the $SbCl_3$ group in $[W_3(SbCl_3)Se_4(H_2O)_9]^{4+}$ could be readily exchanged with $SnCl_3^-$. Reaction of $[W_3Se_4(H_2O)_9]^{4+}$ with $SbCl_3$ and H_3PO_2 gave the green–blue double cube $[W_6SbSe_8(H_2O)_{18}]^{8+}$ (**85**, M′ = Sb^0). Like its arsenic analog, this species could be oxidized with degradation to Sb^{III} and the precursor cluster. Reduction of Bi^{III} citrate by H_3PO_2 in the presence of $[W_3Se_4(H_2O)_9]^{4+}$ afforded the green–blue $[W_6BiSe_8(H_2O)_{18}]^{8+}$ (**85**, M′ = Bi^0), which was oxidized to regenerate Bi^{III} and $[W_3Se_4(H_2O)_9]^{4+}$. The dithiophosphato cluster $[W_3(BiI_3)S_4(OAc)\{S_2P(OEt)_2\}_3(H_2O)]$ has also been characterized.

9.3.6 Octahedral Clusters, W_6E_8

Clusters of this type are found, with Mo, in the Chevrel phases Mo_6E_8 (E = S, Se or Te) and in the ternary phases $M'Mo_6E_8$, but no such solid-state analogs containing tungsten have been confirmed. However, reaction of $[\{W_6Cl_{12}\}_n]$ with NaSH and OBu^{n-} in pyridine afforded the dark red 20-electron cluster $[W_6S_8(py)_6]$ if the molar ratio of W:S was at least 1:12. This species was diamagnetic and insoluble, although single crystals could be obtained under special conditions. The cluster has an octahedral core of W atoms, each triangular face being bridged by S, the pyridine ligands binding terminally to the metal centers. If the W:S molar ratios were set at 1:8 and the reaction took longer, the insoluble red 22-electron cluster $[W_6S_6Cl_2(py)_6]$ was produced and if the molar ratio was maintained between 1:6 and 1:8, and using shorter reactions times, the red soluble 24-electron cluster $[\{W_6Cl_6S_2\}Cl_2(py)_6]\cdot 5py$ was generated. However, if pyridine was replaced by its 4-butyl analog, Bu^tpy, and if $[Bu_4N]_2[W_6Cl_{14}]$ was used in place of $[\{W_6Cl_{12}\}_n]$, the orange soluble $[W_6S_8(Bu^tpy)_6]$ was formed. The pyridine could be substituted by piperidine or PEt_3, and $[W_6S_8(PEt_3)_6]$ could also be generated by reductive dimerization of $[W_3S_4Cl_4(PEt_3)_n]$ ($n = 3$ or 4) using Mg in thf.

The clusters $[W_6S_8L_6]$ (L = PEt_3, Bu^tpy) could be oxidized by ferrocenium cation to give the green paramagnetic 19-electron species $[W_6S_8L_6]^+$ (L = PEt_3, $\mu = 1.71$ BM; L = Bu^tpy, $\mu = 1.60$ BM). The structures of the neutral and cationic $[W_6S_8(PEt_3)_6]^z$ ($z = 0$ or $+1$) showed that oxidation only marginally increased the W–W distances in the cluster (ca. 2.68 Å in both species). Treatment of $[W_6S_8(Bu^tpy)_6]$ with CN^-afforded $[W6S_8(CN)_6]^6{}_-$ but with $P(C_6H_{11})_3$, only partial substitution could occur, affording *cis*-$[W_6S_8(Bu^tpy)_2\{P(C_6H_{11})_3\}_4]$. $[W_6S_8\{P(C_6H_{11})_3\}_6]$ could be obtained from $[W_6S_8(NH_2Bu^n)_6]$. Prolonged heating of *cis*-$[W_6S_8(Bu^tpy)_2\{P(C_6H_{11})_3\}_4]$ in benzene afforded a mixture of redistribution products, *fac*- and *mer*-$[W_6S_8(Bu^tpy)_3\{P(C_6H_{11})_3\}_3]$, *cis*- and *trans*-$[W_6S_8(Bu^tpy)_2\{P(C_6H_{11})_3\}_4]$, and $[W_6S_8(Bu^tpy)\{P(C_6H_{11})_3\}_5]$.

Red $[W_6Se_8L_6]$ (L = piperidine or pyridine) were obtained by reaction of $[\{W_6Cl_{12}\}_n]$, Na_2Se and L over several days. However, reaction with PEt_3 (W:Se ratio 1:8) afforded the red–brown 20-electron species $[W_6Se_7Cl(PEt_3)_6]^+$ (counter-anion Cl^-). The Se and Cl atoms were randomly distributed over the eight possible positions ($d_{W–W}$ 2.70 Å). If K_2Se replaced Na_2Se, the W:Se ratio being 1:10, $[W_6Se_{6.4}Cl_{1.6}(PEt_3)_6]^+$ (as Cl^-) was formed, this cation being shown to be a mixture of diamagnetic 20-electron $[W_6Se_7Cl(PEt_3)_6]^+$ and paramagnetic 21-electron $[W_6Se_6Cl_2(PEt_3)_6]^+$ in the ratio 2:3.

Reaction of $[\{W_6Cl_{12}\}_n]$ with Na_2Te in refluxing piperidine or pyridine afforded the dark blue 20-electron $[W_6Te_8(pip)_6]\cdot 6pip$ (W–W 2.74 Å) and the 21-electron $[Na(py)_6][W_6Te_8(py)_6]\cdot py$ ($d_{W–W}$ 2.72–2.75 Å). Treatment of the piperidine cluster with pyridine afforded black $[W_6Te_8(py)_6]$ and of this with PEt_3 dark purple $[W_6Te_8(PEt_3)_6]$ ($d_{W–W}$ 2.77 Å).

10 RELATED ARTICLES

Cluster Compounds: Inorganometallic Compounds Containing Transition Metal & Main Group Elements; Heterogeneous Catalysis by Metals; Oxidation Catalysis by Transition Metal Complexes; Polyoxometalates; Tungsten: Organometallic Chemistry.; Tungsten Proteins.

11 REFERENCES

1. R. S. Pilato and E. I. Stiefel, Molybdenum and Tungsten Enzymes, in ‘Bioinorganic Catalysis’, 2nd edn., eds. J. Reedijk and E. Bouwman, Marcel Dekker, New York, 1999, p. 81.
2. A. Sigel and H. Sigel eds, ‘Molybdenum and Tungsten: Their Roles in Biological processes’, Marcel Dekker, New York, 2002, Vol. 39.
3. T. Okamura and N. Ueyama, Tungsten, in ‘Comprehensive Coordination Chemistry II’, eds. J. A. McCleverty and T. J. Meyer, Elsevier, Amsterdam, 2004, Vol. 4, p. 529.
4. J. L. Eglin, Dinuclear Metal-metal Bonded Systems, in ‘Comprehensive Coordination Chemistry II’, eds. J. A. McCleverty and T. J. Meyer, Elsevier, Amsterdam, 2004, Vol. 4, p. 575.
5. M. T. Pope, Polyoxo Anions: Synthesis and Structure, in ‘Comprehensive Coordination Chemistry II’, eds. J. A. McCleverty and T. J. Meyer, Elsevier, Amsterdam, 2004, Vol. 4, p. 635.
6. C. L. Hill, Polyoxometallates: Reactivity, in ‘Comprehensive Coordination Chemistry II’, eds. J. A. McCleverty and T. J. Meyer, Elsevier, Amsterdam, 2004, Vol. 4, p. 679.
7. M. N. Sokolov, V. P. Fedin, and A. G. Sykes, Chalcogenide-containing Metal Clusters, in ‘Comprehensive Coordination Chemistry II’, eds. J. A. McCleverty and T. J. Meyer, Elsevier, Amsterdam, 2004, Vol. 4, p. 761.
8. M. H. Chisholm, *Acc. Chem. Res.*, 1990, **23**, 419.

Tungsten: Organometallic Chemistry

Craig B. Pamplin, Trevor W. Hayton & Peter Legzdins
The University of British Columbia, Vancouver, BC, Canada

Based in part on the article Tungsten: Organometallic Chemistry by Andreas Mayr which appeared in the Encyclopedia of Inorganic Chemistry, First Edition.

1	Introduction	1
2	Tungsten Complexes Containing Carbonyl, Isocyanide, and Cyanide Ligands	1
3	Tungsten Complexes Containing Hydrocarbon Ligands	3
4	Related Articles	17
5	References	17

Abbreviations

bipy = 2,2′-bipyridyl; $Cp^* = \eta^5$-pentamethylcyclopentadienyl; dmpm = bis(dimethylphosphino)methane; dmpe = 1,2-bis(dimethylphosphino)ethane; dppe = 1,2-bis(diphenylphosphino)ethane; $[N_3N]$ = tris[2-(trimethylsilylamido)ethyl]amine; tmeda = *N*,*N*,*N*′,*N*′-tetramethylethylenediamine; Tp^* = hydrotris(3,5-dimethyl-1-pyrazolyl) borate.

1 INTRODUCTION

This article surveys the organometallic chemistry of tungsten in a systematic manner according to the various types of complexes known to contain tungsten–carbon bonds. Within each category of complex, the material is generally presented in the following order: common methods of synthesis of these complexes, their characteristic physical properties, and their representative chemical properties. The latter are usually illustrated by examples taken from the literature published since 1992, the final year of coverage by the first edition of the Encyclopedia of Inorganic Chemistry. Other articles in the current encyclopedia also cover some aspects of this chemistry, most notably alkene and alkyne metathesis reactions mediated by organotungsten complexes (*see* ***Organic Synthesis Using Metal-mediated Metathesis Reactions***), the organometallic chemistry of di- and polynuclear tungsten complexes (*see* ***Dinuclear Organometallic Cluster Complexes***), and tungsten compounds containing main group element ligands (*see* ***Cluster Compounds: Inorganometallic Compounds Containing Transition Metal & Main Group Elements***). Consequently, these topics are not specifically discussed in this article, which focuses primarily on the chemistry of mononuclear tungsten complexes containing organic ligands.

2 TUNGSTEN COMPLEXES CONTAINING CARBONYL, ISOCYANIDE, AND CYANIDE LIGANDS

2.1 Tungsten–Carbonyl Complexes

$W(CO)_6$ continues to be the most ubiquitous and readily available low-valent organometallic complex of tungsten (*see* ***Carbonyl Complexes of the Transition Metals***), and it serves as a convenient entry point into much of the organometallic chemistry described in this chapter. One or more of its CO ligands may be replaced with neutral donors to form carbonyl compounds (*see Carbonyl Compound*) of the type $W(CO)_{6-n}(L)_n$ (L = Lewis base). The homoleptic (*see Homoleptic Compound*) carbonyl anions $[W(CO)_5]^{2-}$ and $[W(CO)_4]^{4-}$ have been prepared by chemical reduction of suitable carbonyl compounds,**[1]** and the di- and tritungsten carbonyls, $[W_2(CO)_{10}]^{2-}$ (**1**) and $[W_3(CO)_{14}]^{2-}$, containing W–W bonds have also been described.**[2,3]** The photochemistry of (**1**), which results in the formation of the highly reducing 19e radical $[W(CO)_5(S)]^-$ upon irradiation in donor solvents, S (e.g. S = MeCN, THF), has been the topic of a recent review.**[2]** Treatment of $W(CO)_6$ with HF/SbF_5 in the presence of CO results in a remarkable 2e oxidation process and leads to the isolation of the cationic, seven-coordinate carbonyl complex $[W(CO)_6(\eta^1\text{-}FSbF_5)][Sb_2F_{11}]$, that is, $[(\mathbf{2})][Sb_2F_{11}]$.**[4]**

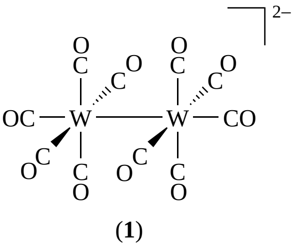
(**1**)

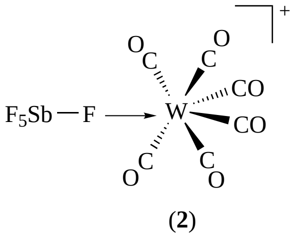
(**2**)

The substitution of carbonyl ligands in $W(CO)_6$ may be effected either thermally or photochemically. Among the more important reactions from a synthetic standpoint are those of $W(CO)_6$ with nitriles (RCN) to generate *fac*-$W(CO)_3(RCN)_3$ (**3**) (equation 1), the nitrile ligands of which may be displaced by other Lewis bases (*see Lewis Acids & Bases*) under mild conditions.**[5]** The reactions of $W(CO)_6$ with the cyclopentadienyl (*see Cyclopentadienyl*) reagents MCp′ (M = Li, Na, K; Cp′ = Cp, Cp*, etc.) afford anionic $[\mathrm{Cp'W(CO)_3}]^-$ derivatives (**4**)[6,7] (equation 2) that have been used to prepare complexes such as $\mathrm{Cp'W(CO)_2(NO)}$ (**5**),[6,7] $\mathrm{Cp'W(CO)_3(X)}$ (X = H, halide, alkyl) (**6**),[8] and $[\mathrm{Cp'W(CO)_3}]_2$ (**7**).[9] Seven-coordinate halocarbonyl complexes of the type $\mathrm{W(CO)_{5-\mathit{n}}(L)_\mathit{n}(X)_2}$ ($n = 1$, 2; X = halide) are obtained upon addition of L to $[\mathrm{W(CO)_4(X)(\mu\text{-}X)}]_2$ or from the reactions of halogens with $\mathrm{W(CO)_{6-\mathit{n}}(L)_\mathit{n}}$.[10,11]

$$\mathrm{W(CO)_6} \xrightarrow[\mathrm{RCN}]{\Delta} \underset{(\mathbf{3})}{\mathrm{W(CO)_3(RCN)_3}} + 3\mathrm{CO} \qquad (1)$$

$$\mathrm{W(CO)_6} + \mathrm{MCp'} \xrightarrow[\mathrm{THF}]{\Delta} \underset{(\mathbf{4})}{\mathrm{M[Cp'W(CO)_3]}} + 3\mathrm{CO} \qquad (2)$$

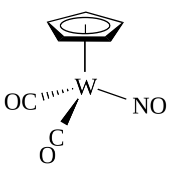

(**5**)

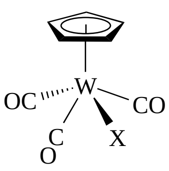

(**6**)

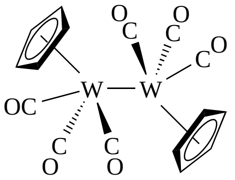

(**7**)

The Lewis-acidic (*see Lewis Acids & Bases*) $\mathrm{W(CO)_5}$ fragment binds a variety of weakly coordinating ligands. As a result, there are a great many $\mathrm{W(CO)_5(L)}$ complexes known, some of which have found applications in catalysis (*see* ***Organic Synthesis using Transition Metal Carbonyl Complexes***). For example, the thiirane complex $\mathrm{W(CO)_5(SCH_2CH_2)}$ catalyzes the conversion of thioethers to cyclic disulfides.[12] Of particular interest are transient $\mathrm{W(CO)_5}$(alkane) complexes detected by IR spectroscopy at low temperature upon irradiation of $\mathrm{W(CO)_6}$ in hydrocarbon solvents; in these σ-alkane adducts, the tungsten atom interacts with a single C–H bond of the alkane ligand.[13] The $\mathrm{W(CO)_5}$(alkane) derivatives react rapidly with Lewis bases (*see Lewis Acids & Bases*) to form $\mathrm{W(CO)_5(L)}$, which may also be generated directly by photolysis of $\mathrm{W(CO)_6}$ in the presence of L. In related $\mathrm{W(CO)_5(\eta^1\text{-}BH_3{\cdot}L)}$ complexes (L = py, $\mathrm{NMe_3}$, $\mathrm{PMe_3}$), the borane-Lewis base adduct coordinates with the tungsten center via a B–H bond in a three-center, 2e interaction (*see* ***Dihydrogen Complexes & Related Sigma Complexes***).[14]

The most common mode of reactivity involving carbonyl ligands in organometallic complexes of tungsten is CO insertion into a W–R bond (R = alkyl, aryl) to form tungsten–acyl complexes. For example, the reaction of *cis*-$\mathrm{Cp^*W(CO)_2(MeCN)(Me)}$ with CNBu^t affords a mixture of ligand-substitution products, *cis*- and *trans*-$\mathrm{Cp^*W(CO)_2(CNBu^\mathit{t})(Me)}$, and the CO insertion products, *cis*- and *trans*-$\mathrm{Cp^*W(CO)(CNBu^\mathit{t})_2(COMe)}$.[15] A remarkable 6e reductive cleavage of a CO ligand occurs upon thermolysis of $[\mathrm{WCl(CO)(OR)_2}]_2$ (**8**, $\mathrm{R = SiBu^\mathit{t}_3}$) at 120 °C in toluene to give the oxo-μ-carbido complex $\mathrm{(RO)_2(O)W{=}C{=}WCl_2(OR)_2}$ (**9**) (equation 3). An analogous imido-μ-carbido complex $\mathrm{(RO)_2(ArN)W{=}C{=}WCl_2(OR)_2}$ is formed when the related aryl isocyanide species, $\mathrm{(RO)_4W_2Cl_2(CNAr)}$ (Ar = 2,6-$\mathrm{Me_2C_6H_3}$), is heated at 60 °C in the same solvent.[16]

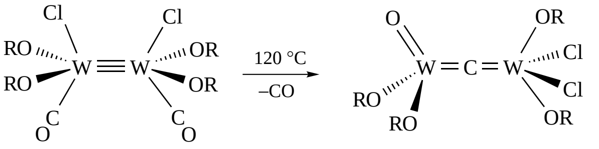

(**8**) (**9**) (3)

2.2 Tungsten–Isocyanide and – Cyanide Complexes

Neutral and cationic homoleptic (*see Homoleptic Compound*) tungsten–isocyanide complexes $\mathrm{W(CNR)_6}$ and $[\mathrm{W(CNR)_7}]^{2+}$ (R = alkyl, aryl) are known,[17] and $\mathrm{W(CO)_{6-\mathit{n}}(CNR)_\mathit{n}}$ ($n = 1$–3) complexes may be prepared from $\mathrm{W(CO)_6}$ and excess isocyanide in the presence of catalytic amounts of $\mathrm{CoCl_2}$ or PdO.[18,19] Isocyanides are isoelectronic with CO and also insert into the W–R bonds of alkyl complexes (*see Alkyl Complexes*). For instance, the alkyl–nitrosyl complexes $\mathrm{Cp^*W(NO)(X)(CH_2Bu^\mathit{t})}$ ($\mathrm{X = NHBu^\mathit{t}}$, $\mathrm{OBu^\mathit{t}}$) react with CNBu^t to afford η^2-iminoacyl complexes,[20] and the isocyanide complexes, $\mathrm{Cp^*W(CO)_2(Me)(CNR)}$ (**10**, R = alkyl), rearrange to afford either η^2-iminoacyl $\mathrm{Cp^*W(CO)_2(\eta^2\text{-}MeCNR)}$ (**11**) or η^3-1-azaallyl $\mathrm{Cp^*W(CO)_2(\eta^3\text{-}CH_2CHNR)}$ (**12**) derivatives, depending upon the reaction conditions (equation 4).[21]

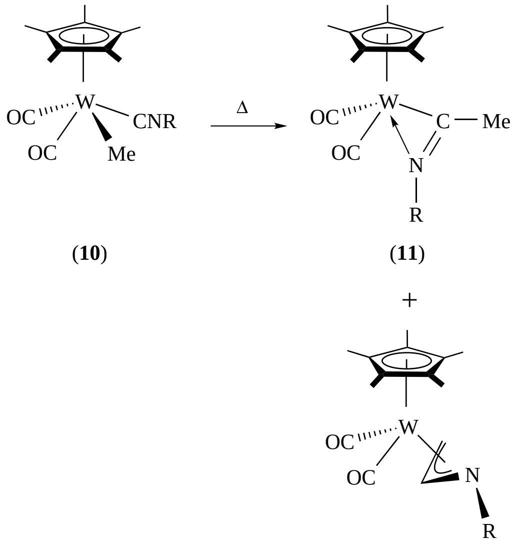

(**10**) (**11**) (**12**) (4)

The coupling of isocyanide ligands (*see Isocyanide Ligands*) via C–C bond formation has also been observed. Thus, $[\mathrm{(Me_3SiN)_2C_6H_4}]\mathrm{(NPh)WMe_2}$ reacts with CNBu^t to form the octahedral adduct $[\mathrm{(Me_3SiN)_2C_6H_4}]\mathrm{(NPh)WMe_2(CNBu^\mathit{t})}$ (**13**), which in the presence of CNBu^t is converted to a trigonal–bipyramidal bis(η^2-iminoacyl) species (**14**) that thermally isomerizes to the square–pyramidal metallacyclic complex (**15**) (equation 5, R = $SiMe_3$).[22]

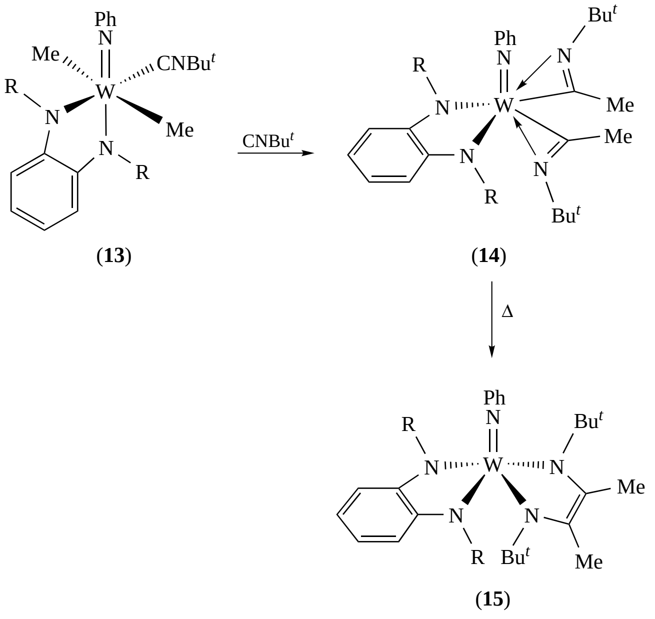

(5)

Research involving the octacyanotungstate anions, $[W(CN)_8]^{n-}$ ($n = 3, 4$), is experiencing a renaissance since these complexes exhibit unusual photochemical behavior and have been used as molecular components for the construction of multidimensional polymeric materials;[23,24] for instance, the reaction of $K_4[W(CN)_8]$ with Me_3SnCl affords the three-dimensional coordination polymer $\{(Me_3Sn)_4[W(CN)_8]\}_n$.[25] The octacyanotungstate anions may possess dodecahedral or square–antiprismatic coordination geometries in the solid state (*see* ***Cyanide Complexes of the Transition Metals***), and the addition of labile (*see Labile*) coordination complexes to solutions of $[W(CN)_8]^{n-}$ often affords compounds that possess potentially useful magnetic properties. Specifically, the reaction of $[HNBu_3]_3[W(CN)_8]$ with $Mn(ClO_4)_2$ in EtOH provides $Mn_9[W(CN)_8]_6 \cdot 24EtOH$ that consists of cyanide-bridged $Mn^{II}{}_9W^{V}{}_6$ units with a capped-cubane geometry and exhibits the largest known spin-value $S = 39/2$ ground state.[26]

3 TUNGSTEN COMPLEXES CONTAINING HYDROCARBON LIGANDS

3.1 η^1-Hydrocarbyl Complexes

3.1.1 Alkyl and Aryl Complexes

Hexamethyltungsten, WMe_6 (**16**), was first isolated by Wilkinson and coworkers, and it may be prepared by the reactions of WCl_6 with methylating reagents such as MeLi, $AlMe_3$, or $ZnMe_2$. Recent structural analyses have shown that (**16**) has a distorted trigonal–prismatic structure of C_{3v} symmetry with three long and three short W–C bonds,[27] an unusual structural motif found primarily in d^0 (*see d^n Configuration*) complexes containing σ-only donor ligands.[28] The reactions of (**16**) with O_2 or MeOH afford $W(OMe)_6$ (**17**), and treatment with CO forms $W(CO)_6$ and Me_2CO.[29] In contrast, the reaction of (**16**) with NO affords $WMe_4(MeN_2O_2)_2$ (**18**),[30] and the seven- and eight-coordinate alkyl anions $[WMe_7]^-$ (**19**), $[WMe_6(CH_2SiMe_3)]^-$, or $[WMe_8]^{2-}$ are formed when (**16**) is treated with RLi (R = Me, CH_2SiMe_3) reagents (Scheme 1).[31,32] Photolysis of (**16**) in the presence of PMe_3 produces $W(Me)(\equiv CMe)(PMe_3)_4$ (**20**) and CH_4,[33] and an unusual five-coordinate W^{VI} imido complex (**21**) is formed when (**16**) is treated with excess $CNBu^t$.[29] Mixed complexes WX_nMe_{6-n} are predicted to exhibit a gradual increase in the preference for octahedral geometry as n increases;[34] for instance, WMe_5X (X = Cl, F) species possess a distorted trigonal–prismatic geometry, while $WMe_3(OMe)_2Cl$ and WF_6 are octahedral molecules.[35] Few other homoleptic (*see Homoleptic Compound*) alkyl complexes of tungsten are known, but $W(CH_2Ph)_4$,[36] along with ditungsten complexes $W_2(CH_2R)_6$ (R = Ph, $SiMe_2Ph$) containing a W≡W

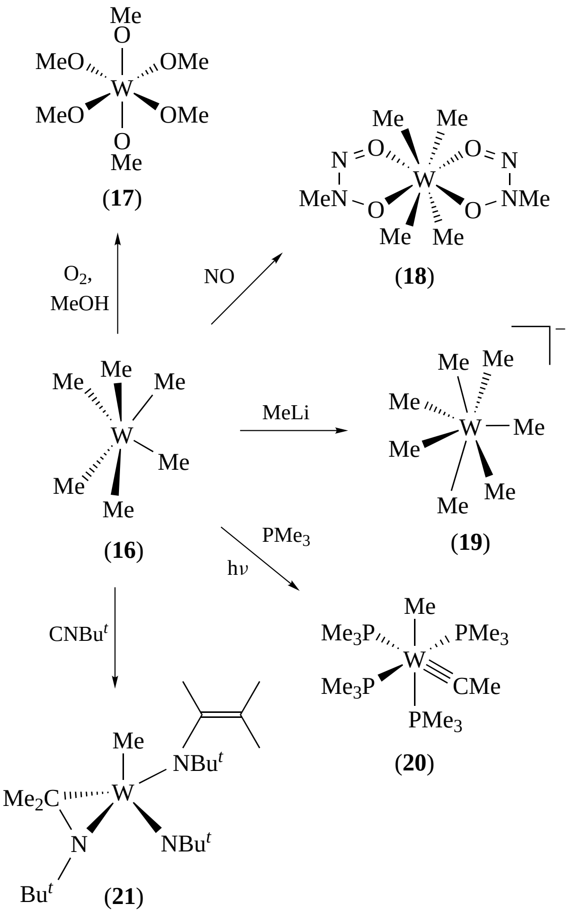

Scheme 1

triple bond[37] have been reported. Homoleptic (*see Homoleptic Compound*) aryl complexes $W(aryl)_4$ (aryl = $2\text{-}MeC_6H_4$ (**22**), $2,5\text{-}Me_2C_6H_3$) may be prepared by treating $W(OPh)_6$ with appropriate Grignard reagents (*see Grignard Reagents*), and they react with PMe_3 to give the η^2-aryne complexes $W(\eta^2\text{-}C_6H_3MeR)(aryl)_2(PMe_3)_2$ (R = H (**23**), Me) (equation 6).[38]

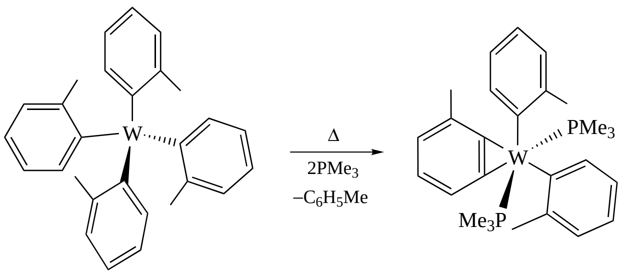

(**22**) (**23**)

(6)

In general, alkyl and aryl complexes of tungsten are prepared by metathesis of suitable halide precursors using various alkylating or arylating reagents. Thus, $Tp^*W(O)_2R$ derivatives (R = Me, CH_2SiMe_3, CH_2Bu^t, CH_2CMePh_2, etc.) are obtained from $Tp^*W(O)_2Cl$ and Grignard reagents (*see Grignard Reagents*),[39] and the 16e dialkyl–nitrosyl complexes $Cp'W(NO)R_2$ are accessed by treating $[Cp'W(NO)Cl_2]_n$ (Cp' = Cp, Cp*; $n = 1$, 2) with dialkylmagnesium reagents, $R_2Mg{\cdot}x(\text{dioxane})$.[40] For instance, the reaction of $Cp^*W(NO)Cl_2$ with MeLi affords the monomeric dimethyl complex, $Cp^*W(NO)Me_2$, which reacts with PMe_3 to form an isolable $Cp^*W(NO)Me_2(PMe_3)$ adduct. In the absence of a supporting donor interaction, the dimethyl compound undergoes spontaneous isomerization via nitrosyl N–O bond cleavage to its oxo(imido) form, $Cp^*W(NMe)(O)Me$.[41]

Electron-deficient tungsten–alkyl complexes exhibit some unusual bonding interactions. Specifically, the benzyl complexes $Cp^*W(NO)(\eta^2\text{-}CH_2Ph)(R)$ possess W-η^2-benzyl linkages,[42] and the bis(neopentyl) compound, $Cp^*W(NO)(CH_2Bu^t)_2$ (**24**), contains one strongly agostic and one weakly agostic methylene hydrogen atom in the solid state, and these α-agostic (*see Agostic Bonding*) interactions persist in solutions.[43] In addition, these alkyl complexes undergo thermal or photochemical reactions to give alkene (*see Alkene Complexes*), alkylidene (*see Alkylidene*), or alkylidyne (*see Alkylidyne*) complexes that are discussed further in the appropriate sections (vide infra). Thermolysis of (**24**) in methyl-substituted arenes such as p-xylene results in the α-elimination (*see α-Elimination*) of neopentane and formation of a mixture containing the aryl and the η^2-benzyl complexes, that is, $Cp^*W(NO)(CH_2Bu^t)(2,5\text{-}Me_2C_6H_3)$ (**25**) and $Cp^*W(NO)(CH_2Bu^t)(\eta^2\text{-}CH_2C_6H_4\text{-}4\text{-}Me)$ (**26**), derived from aromatic sp^2 or benzylic sp^3 C–H bond activations of the solvent molecule, respectively (equation 7) (*see* ***Alkane Carbon–Hydrogen Bond Activation***). These and related mixed alkyl-aryl species may also be produced by metatheses from $Cp^*W(NO)(CH_2Bu^t)(Cl)$ and appropriate aryl Grignard reagents (*see Grignard Reagents*).

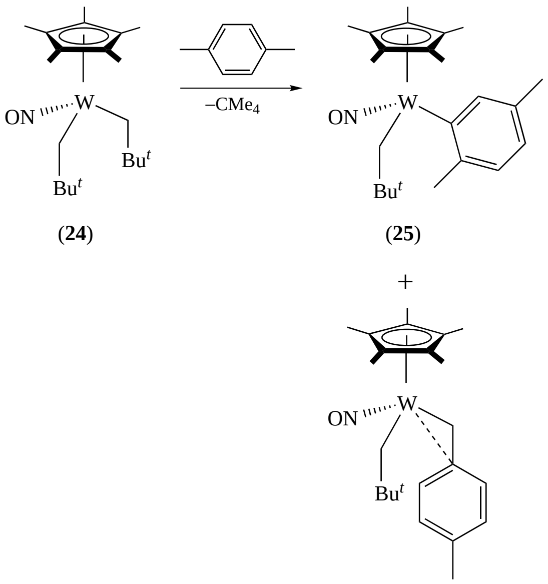

(**24**) (**25**) (**26**)

(7)

Treatment of $Cp^*W(NO)Cl_2$ with $(aryl)_2Mg$ (aryl = Ph, o- and p-tolyl) affords 16e $Cp^*W(NO)(aryl)_2$ complexes that react with CO, CO_2, CS_2, or aryl isocyanates to produce η^2-acyl, η^2-carboxylate, η^2-thiocarboxylate, and η^2-amide-containing complexes, respectively.[40,44] In a related system, the water-induced isomerization of $CpW(NO)(o\text{-tolyl})_2$ affords the isomeric oxo(imido) complex $CpW(O)(N\text{-}o\text{-tolyl})(o\text{-tolyl})$.[45] Furthermore, the ortho-metalated phosphine complex, $Cp^*W(NO)(H)(\eta^2\text{-}PPh_2C_6H_4)$ (**27**), undergoes intramolecular reductive elimination (*see Reductive Elimination*) of the aryl and hydrido ligands to afford the strong π-donor fragment $Cp^*W(NO)(PPh_3)$, which subsequently reacts with unsaturated molecules L = CNR (R = Bu^t, Cy), Me_2CO, and EtOAc to afford $Cp^*W(NO)(PPh_3)(\eta^2\text{-}L)$ adducts, including the η^2-ester complex (**28**, equation 8).[46]

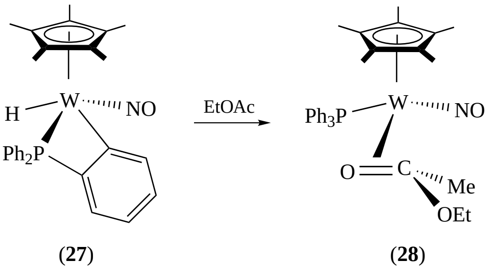

(**27**) (**28**)

(8)

3.1.2 Vinyl and Alkynyl Complexes

Vinyl (or alkenyl) ligands may adopt either η^1- (**A**) or η^2- (**B**) limiting coordination modes depending on the electronic saturation of the tungsten center. In η^2-vinyl complexes, both alkenyl carbon atoms are bound to the metal, and the resulting metallacyclopropene ligand increases the formal electron count at the metal by two relative to an η^1-vinyl ligand.[47] Typical synthetic routes to vinyl complexes involve transmetallation using vinylmagnesium reagents, deprotonation of η^2-alkene ligands, and nucleophilic addition (e.g. protonation) of η^2-alkyne ligands. The insertion of an alkyne into a W–H bond also affords a vinyl complex, as in the reaction of $Cp^*W(NO)(CH_2SiMe_3)(H)$ with $PhC{\equiv}CH$ to form $Cp^*W(NO)(CH_2SiMe_3)(\eta^2\text{-}CPh{=}CH_2)$.[48] η^1-Vinyl complexes can isomerize via a formal [1,2]-*H* shift to generate alkylidyne complexes; these reactions generally proceed via formation of intermediate metallacyclopropene species (**B**) and therefore require a vacant coordination site at the tungsten center. The isomerization of η^2-vinyl complexes to η^3-allyl complexes via intermediate η^2-allene hydride species has also been documented.[47]

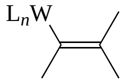

η^1-vinyl
A

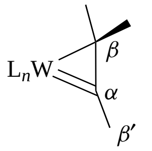

η^2-vinyl
(1-metallacyclopropene)
B

Deprotonation of $Tp^*W(CO)_2(\eta^2\text{-}H_2C{=}C(CH_2R))$ (R = H, Pr, Ph) at the β'-site results in the formation of anionic η^2-allene species $[Tp^*W(CO)_2(\eta^2\text{-}H_2C{=}C{=}CHR)]^-$, which react in turn with MeI to form $Tp^*W(CO)_2(\eta^2\text{-}H_2C{=}C(CHRMe))$.[49] Furthermore, the characteristic chemistry of dioxotungsten–vinyl complexes has been described,[50] and sequential C–F oxidative addition (*see Oxidative Addition*) and migratory insertion of electron-deficient alkynes at a tungsten center gives rise to novel η^2-vinyl complexes (**29**) in which an aromatic C–F bond has been replaced by a C–C bond (equation 9).[51]

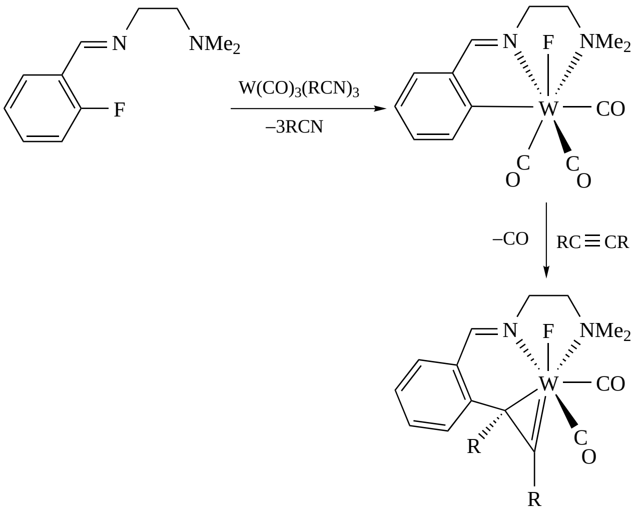

(**29**)

(9)

The solid-state molecular structure of $Cp^*W(NO)(CH_2SiMe_3)(CPh{=}CH_2)$ (**30**) reveals that its vinyl ligand exists in a distorted form that cannot readily be described by either of the classic η^1-vinyl (**A**) or 1-metallacyclopropene (**B**) limiting structures. However, the NMR spectroscopic parameters for the $CPhCH_2$ fragment of (**30**) in solutions are characteristic of those of structure **B**, a feature reflecting the metal center's attainment of the favored 18e configuration (*see Eighteen Electron Compounds*). Thermolysis of (**30**) in neat hydrocarbon solutions transiently generates $Cp^*W(NO)(\eta^2\text{-}PhC{\equiv}CH)$, which subsequently activates solvent C–H bonds to afford either 18e $Cp^*W(NO)(R)(\eta^2\text{-}CPh{=}CH_2)$ complexes (e.g. R = phenyl) or 18e η^1,η^3-metallacyclic species (**31**) (R = OEt, Pr^n, Bu^n, Bu^t) (*see* ***Alkane Carbon–Hydrogen Bond Activation***). In the absence of alkyl groups with β-C–H bonds, a different mode of reactivity occurs; for instance, the activation of 2,3-dimethyl-2-butene results in fusion of the olefinic fragment to the vinyl ligand at the α-C of the vinyl moiety, and two C–H bond activations occur at the trans-γ positions of the olefinic substrate to afford (**32**).

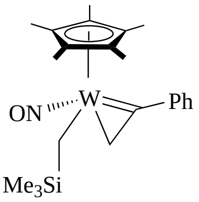

(**30**)

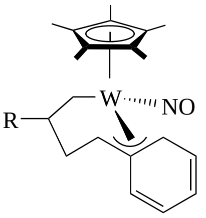

(**31**)

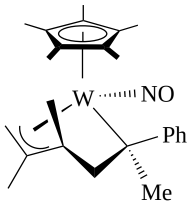

(**32**)

Alkynyl complexes are typically prepared by the reactions of appropriate tungsten precursors with acetylide reagents, for example $LiC{\equiv}CR$, or by deprotonation of η^2-alkyne or vinylidene complexes. The characteristic reactivity of alkynyl complexes most commonly involves electrophilic attack at the β-carbon, a fact rationalized by invoking resonance forms **C** and **D** shown below. Form **D** becomes dominant as the electron density on the complex increases, and therefore anionic complexes of the type $[W(CO)_5(C{\equiv}CR)]^-$, $[W(CO)_4(PPh_3)(C{\equiv}CR)]^-$ or *fac*-$[W(C{\equiv}CR)(CO)_3(dppe)]^-$ react with electrophiles exclusively at the β-carbon atom to yield vinylidene complexes.[52,53] Likewise, the negative charge in $[CpW(CO)_2]_2(\mu\text{-}\sigma{:}C{\equiv}CPh)^-$ is delocalized between the tungsten atom and the β-carbon atom of the bridging alkynyl ligand.[54] Neutral $W(CO)_2(NO)(dppe)(C{\equiv}CR)$ (R = H, Bu^t, Pr^n) compounds have also been described, but these nitrosyl complexes (*see Nitrosyl Complexes*) do not react with electrophiles to afford vinylidene complexes.[55]

$$L_nW-\underset{\alpha}{C}{\equiv}\underset{\beta}{C}-R \longleftrightarrow L_n\overset{+}{W}{=}\underset{\alpha}{C}{=}\underset{\beta}{\overset{-}{C}}-R$$

C **D**

In rare cases, electrophilic attack may occur directly at the metal center of an alkynyl complex, as when anionic $[CpW(NO)(CO)(C{\equiv}CR)]^-$ (R = $SiMe_3$, Bu^t, Ph) is treated with allylic iodides to obtain $CpW(NO)(\eta^3\text{-allyl})(C{\equiv}CR)$ via a sequence involving electrophilic attack at the tungsten, CO elimination, and $\eta^1 \rightarrow \eta^3$ isomerization of the allyl ligand.[56] Isolable *trans*-$W(C{\equiv}CR)(CO)_2(\eta^3\text{-allyl})(dmpm)$ complexes (**33**) are prepared from *cis*-$WCl(CO)_2(\eta^3\text{-allyl})(dmpm)$ and $LiC{\equiv}CR$, and the alkynyl ligand of (**33**) can undergo an intramolecular (*see Intramolecular*) metal-to-allyl migration to produce free eneynes derived from alkynyl–allyl coupling (equation 10).[57]

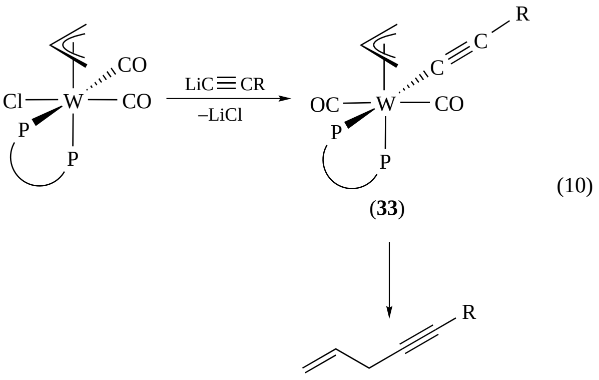

(**33**)

(10)

Photolysis of *trans*-$W(N_2)_2(dppe)_2$ in the presence of $RC{\equiv}CH$ (R = Ph, CO_2Me, CO_2Et) gives a mixture of the alkynyl complexes, *trans*-$[M(C{\equiv}CR)_2(dppe)_2]$, and eight-coordinate *trans*-$[W(H)_2(C{\equiv}CR)_2(dppe)_2]$. The latter compounds react with HBF_4 to give either neutral $WF({\equiv}CCH_2R)(dppe)_2$ (R = CO_2Me) or cationic $[WF({=}CHCH_2R)(dppe)_2]^+$ (R = Ph).[58] Reactions of $LiC{\equiv}CR$ with $W_2Cl_4(PMe_3)_4$ afford $W_2(C{\equiv}CR)_4(PMe_3)_4$ complexes of D_{2d} symmetry; however, the alkynyl ligands in these complexes are not oriented parallel to one another due to a combination of steric and electronic effects. The existence of π-δ-π conjugation (involving the π/π^* and δ/δ^* orbitals of the alkynyl and metal–metal quadruple bond, respectively) in these and related complexes has been demonstrated using a variety of spectroscopic techniques, and the IR $\nu(C{\equiv}C)$ frequencies have been shown to be a sensitive probe of orbital mixing.[59] Finally, the unusual methylidyne complexes, $W(C{\equiv}CR)({\equiv}CH)(dmpe)_2$ (R = H, Ph, $SiMe_3$), contain linear metallabutadiyne units that exhibit considerable π-$HC{\equiv}W{-}C{\equiv}CR$ conjugation.[60]

The alkynyl complexes $CpW(CO)_3(C{\equiv}CR)$ are versatile reagents for the preparation of organometallic cluster compounds[61] (*see* ***Cluster Compounds: Inorganometallic Compounds Containing Transition Metal & Main Group Elements***), and they and propargyl complexes of the type $CpW(CO)_3(CH_2C{\equiv}CR)$ (**34**) have found use as templates during the synthesis of heterocyclic and carbocyclic compounds, especially lactones (e.g. equation 11).[62] Treatment of $CpW(CO)_3(CH_2C{\equiv}CH)$ with $[Ph_3C]PF_6$ generates cationic $[CpW(CO)_3(\eta^2\text{-}H_2C{=}C{=}CHCPh_3)]^+$, which eliminates tritylallene, $H_2C{=}C{=}CHCPh_3$, upon treatment with excess Me_3NO.[63] The reaction of $CpW(CO)_3Cl$ with buta-1,3-diyne in the presence of $CuI/NHEt_2$ affords $CpW(CO)_3(C{\equiv}CC{\equiv}CH)$, from which a series of functionalized diynyl derivatives $CpW(CO)_3(C{\equiv}CC{\equiv}CR)$ (R = Ph, $SiMe_3$, $P(O)Ph_2$) may be obtained.[64] Furthermore, the alkynyl ligand in $Cp^*W(CO)(C{\equiv}CR)(\eta^2\text{-}HC{\equiv}CR)$ reacts with $[Me_3O]BF_4$ to form the cationic vinylidene complex (**35**) that when deprotonated in the presence of CO affords the coupled product $Cp^*W(CO)_2(\eta^3\text{-}RC{\equiv}CC{=}CMeR)$ (**36**, R = Bu^t, equation 12).[65]

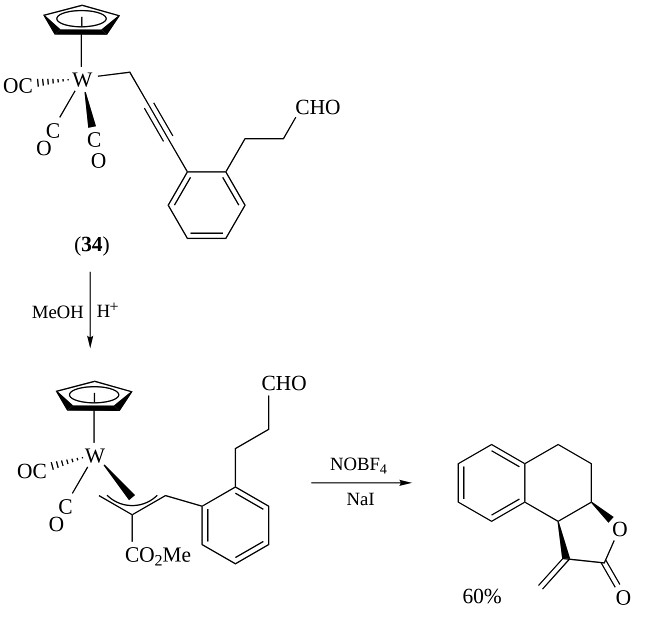

(**34**)

(11)

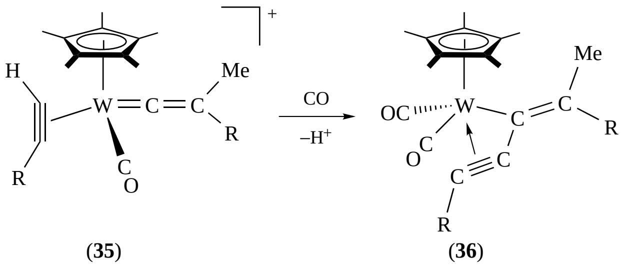

(**35**)

(**36**)

(12)

Finally, the reaction of $[CpW(CO)_3]^-$ with CH_2I_2 in MeCN produces the dinuclear acetylide complex $[CpW(CO)_3]_2(\mu\text{-}C{\equiv}C)$ (**37**) along with $CpW(CO)_3Me$ and $CpW(CO)_3I$, but when the same reaction is carried out in MeOH, the dinuclear ketene complex $Cp_2\,W_2(CO)_5(\mu,\eta^1,\,\eta^2\text{-}CH_2CO)$ (**38**) is obtained.[66]

3.1.3 Carbene Complexes

Tungsten–carbene complexes contain W=C linkages, and if they also contain alkyl substituents on the carbene carbon,

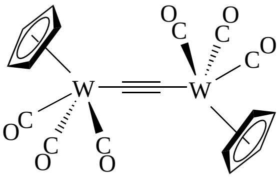

(**37**)

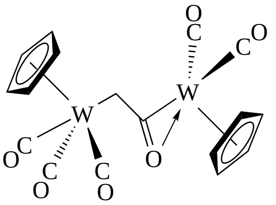

(**38**)

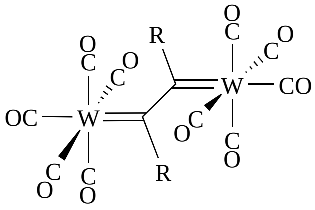

(**42**)

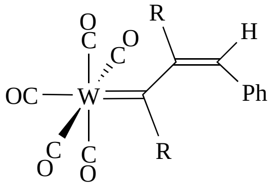

(**43**)

they are frequently referred to as alkylidene complexes (*see* ***Carbene Complexes***). The two extreme types of carbene complexes are the Schrock type (**39**) with at least one alkyl substituent on the α-carbon atom, and the Fischer type (**40**), which possess a π-donor heteroatom substituent on the α-carbon atom. However, many carbene complexes lie between these extremes. Fischer carbenes (*see Fischer-type Carbene Complexes*) contain the metal in a low oxidation state and have π-donor substituents on C_α, which exhibits electrophilic behavior that is generally ascribed to the combined effect of π-acceptor ligands on the metal and inductive effects of the electronegative heteroatom substituent.

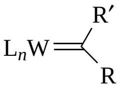

(**39**)

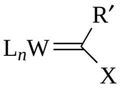

(**40**)

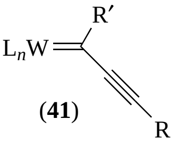

(**41**)

X = OR, SR, NR_2

The first tungsten–carbene complexes were generated by Fischer in 1964 by the addition of alkyllithium reagents to $W(CO)_6$ followed by quenching with an electrophile (*see Electrophile*). Derivatives of these species exhibit a multitude of carbene-centered ligand reactions and interligand coupling reactions,[67,68] and they have been used for the polymerization of alkynes and as a carbene source for the cyclopropanation of alkenes. Related (1-alkynyl)carbene complexes (**41**) have found use in various cyclization reactions,[69] and 1-metalla-1,3,5-hexatriene complexes are key intermediates during the synthesis of heterocyclic compounds (e.g. equation 13); they have also been used as stoichiometric reagents in organic synthesis.[70] Related allenylidene complexes $W(CO)_5({=}C{=}C{=}CR_2)$ react with amines, imines, and hydrazines via addition of the nitrogen nucleophile (*see Nucleophile*) to the C_α allenylidene atom.[71] Interestingly, the reaction of $W(CO)_5({=}CHPh)$ with $RC{\equiv}CR$ affords both the dinuclear complex (**42**) and the alkyne insertion product (**43**, R = NMe_2).[72]

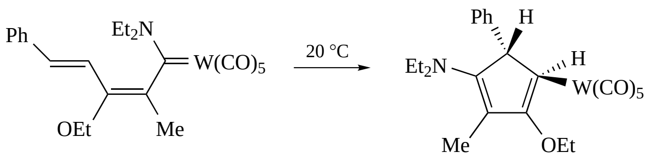

(13)

In Schrock-type carbene complexes (*see Schrock-type Carbene Complexes*), the tungsten is typically in a high oxidation state and the C_α substituents are devoid of π-donor character, and the resulting strong $W{\rightarrow}C_\alpha \pi$-backbonding interaction (*see Back Bonding*) imparts nucleophilic behavior on the complexes. The alkylidene ligands in these complexes are most commonly formed by α-deprotonation of an alkyl group. Such transformations may occur upon coordinative saturation of the metal center, as in the reaction of $W({\equiv}CBu^t)(CH_2Bu^t)_3$ (**44**) with PMe_3 to afford $W({\equiv}CBu^t)({=}CHBu^t)(CH_2Bu^t)(PMe_3)_2$ (**45**) (equation (14), R = Bu^t),[73] or during intramolecular α-H elimination (*see α-Elimination*) reactions induced by thermal or photochemical means. Finally, it should be noted that tungsten–carbene complexes may be prepared by direct carbene transfer, as in the synthesis of $W({=}CHR)Cl_2(NPh)(PMePh_2)_2$ from the reactions of $WCl_2(NPh)(PMePh_2)_3$ and $Ph_3P{=}CHR$ (R = aryl, vinyl).[74]

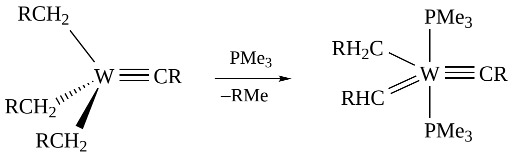

(14)

(**44**) (**45**)

Thermolysis of $Cp^*W(NO)(CH_2Bu^t)_2$ in neat hydrocarbon solutions transiently generates the neopentylidene complex, $Cp^*W(NO)({=}CHBu^t)$, which subsequently activates solvent C–H bonds.[75] The trialkyl complexes $Cp'W(NBu^t)(CH_2R)_3$ (R = Me, Et) undergo a similar thermal decomposition to afford the isolable alkylidene derivatives, $Cp'W(NBu^t)({=}CHR)(CH_2R)$.[76] Photolysis of the metallacyclopentane complex, $\{p\text{-}Bu^t\text{-calix}[4]\text{-}(O)_4\}W(CH_2)_4$ (**46**), affords the alkylidene complex, $\{p\text{-}Bu^t\text{-calix}[4]\text{-}(O)_4\}W({=}CHPr)$ (**47**, equation 15).[77] The related W^{VI} alkylidene complex, $(NPh)W({=}CHSiMe_3)(CH_2SiMe_3)(OR)$ (R = $C(py)Ph_2$), is formed via intramolecular α-H abstraction from the trialkyl complex $(NPh)W(CH_2SiMe_3)_3(OR)$,[78] and the unusual square–pyramidal compound, $[(Me_3SiN)_2C_6H_4](NPh)W({=}CHBu^t)(PMe_3)$, reacts with ethene to afford the metallacyclopentane complex, $[(Me_3SiN)_2C_6H_4](NPh)W(CH_2)_4$

and neohexene.[79]

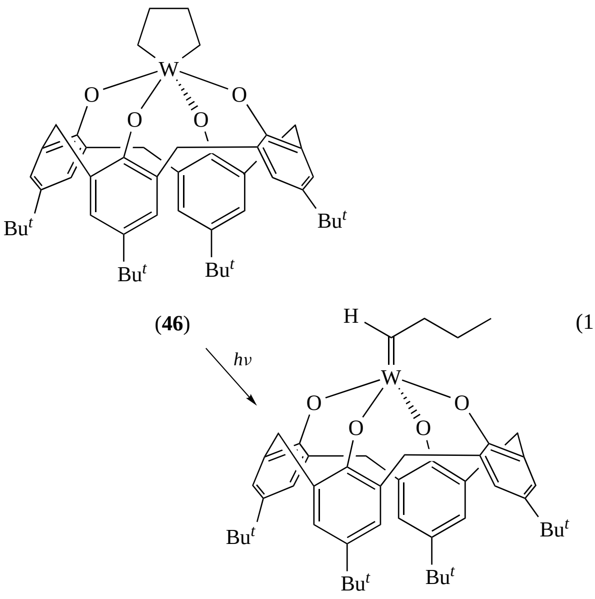

(**46**)

(15)

(**47**)

Protonation of the η^2-vinyl complex, Tp*W(CO)$_2$(η^2-CPh=CHMe), with HBF$_4$ affords the cationic alkylidene complex, [Tp*W(CO)$_2$(=CPhCH$_2$Me)]$^+$,[47] and this and related Tp*W(CO)$_2$(=CMePh) complexes contain β-agostic (*see Agostic Bonding*) C–H bonds.[80] In a similar manner, protonation of W(≡CR)(Cl)(CO)(L)(PMe$_3$)$_2$ (L = PMe$_3$, py) with HCl affords an alkylidene complex, W(=CHR)(Cl)$_2$(CO)(PMe$_3$)$_2$ (R = Me, Et, Ph, *p*-Tol), that contains α-agostic C–H interactions.[81] The related η^3-allylidene complex W(=CPhCH=CHMe)(Br)$_2$(CO)$_2$(L) (**48**) contains an alkylidene ligand that coordinates with the metal via a second intraligand donor site involving the β- and γ-carbon atoms.[82] Alternatively, the deprotonation of Tp*W(CO)(Me)(η^2-PhC≡CMe) with trityl cation yields the cationic methylene complex [Tp*W(CO)(=CH$_2$)(η^2-PhC≡CMe)]$^+$.[83] Finally, treatment of the anionic alkylidene complex, [CpW(CO)$_2$(=CHPh)]$^-$, with MeI affords *trans*-CpW(Me)(CO)$_2$(=CHPh) that isomerizes via an intramolecular (*see Intramolecular*) methyl-to-carbene migration to form the η^3-benzyl complex, CpW(CO)$_2$(η^3-CH(Me)C$_6$H$_5$) (**49**).[84]

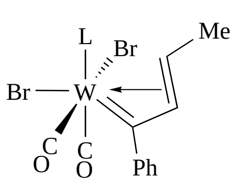

(**48**)

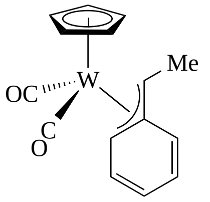

(**49**)

Complexes incorporating a W$^{\mathrm{VI}}$ center with supporting alkoxide ligands and an imido ligand, for example W(NAr)(=CHBu^t)(OR)$_2$ (R = CMe(CF$_3$)$_2$, **50**) are highly active catalysts for the metathesis of internal alkenes (equation 16),[85] and also effect the stereoselective olefination of hydroxy ketones (equation 17).[86] The reactivity of these catalysts can be tuned by varying the alkoxide ligands; for example, when R = Bu^t, the complex acts only upon strained cyclic alkenes and is a highly effective ring-opening metathesis polymerization (ROMP) catalyst (*see* ***Metathesis Polymerization Processes by Homogeneous Catalysis***).

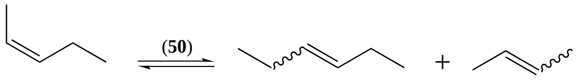

(16)

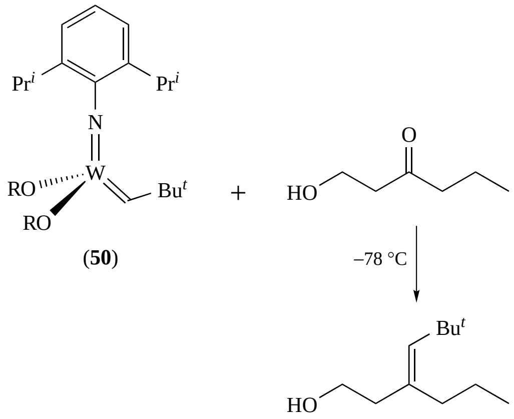

(**50**)

(17)

3.1.4 Carbyne Complexes

Tungsten–carbyne (or alkylidyne) complexes (*see Carbyne Complexes*) contain W≡C–R linkages that are often slightly bent. This bending has been attributed to electronic rather than steric effects,[87] and spectroscopic investigations have revealed carbon p orbital character in these bonds greater than that expected for formal sp-hybridization.[88] The first tungsten–carbyne complexes, *trans*-W(CO)$_4$(≡CR)(X) (R = alkyl, X = halide), were obtained by Fischer who treated his carbene complexes with BX$_3$. Using related methodology, alkynylcarbyne complexes W(CO)$_2$(≡CC≡CR)(CF$_3$CO$_2$)(bipy) (R = SiMe$_3$, Ph, *p*-Tol, Bu^t) may be prepared by treating W(CO)$_6$ with LiC≡CR, trifluoroacetic anhydride, and bipy in a sequential manner.[89]

High-valent alkylidyne complexes (*see Schrock-type Carbyne Complexes*) of tungsten are most commonly prepared from alkylidene precursors by α-deprotonation or α-H elimination (*see α-Elimination*). These reactions are often facile, as illustrated by the reaction of WCl$_6$ with LiCH$_2$Bu^t to give dimeric [W(CH$_2$Bu^t)$_3$(μ-CBu^t)]$_2$ with bridging neopentylidyne ligands. This dimeric compound readily dissociates into monomers that react with PMe$_3$ to produce neopentane and W(CH$_2$Bu^t)(=CHBu^t)(≡CBu^t)(PMe$_3$)$_2$.[73] In a related manner, treatment of W(≡CBu^t)(CH$_2$Bu^t)$_2$Cl with Li(THF)$_3$SiPh$_2$Bu^t affords an equilibrium mixture of W(≡CBu^t)(CH$_2$Bu^t)$_2$(SiPh$_2$Bu^t) (**51**) and W(=CHBu^t)$_2$(CH$_2$Bu^t)(SiPh$_2$Bu^t) (**52**), thereby permitting the study of direct α-H exchange between alkylidene and alkylidyne species (equation 18).[90]

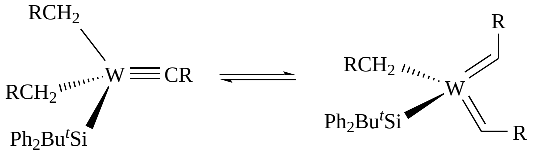

(18)

(**51**) (**52**)

Spontaneous loss of H_2 from the W^{IV} methyl complex, $[N_3N]WMe$ affords $[N_3N]W{\equiv}CH$ (**53**, Scheme 2),[91] and higher alkyl complexes $[N_3N]WR$ (R = Et, Bu) undergo a similar α,α-dehydrogenation to afford $[N_3N]W{\equiv}CR$ and H_2. The related hydride complex $[N_3N]WH$ reacts with ethene or propene to yield $[N_3N]W{\equiv}CR$ (R = Me, Et),[92] or with alkynes $RC{\equiv}CPh$ (R = H, Ph) to afford diamagnetic 1-tungstenacyclopropene complexes $[N_3N]W(\eta^2\text{-}PhCCHR)$ (**54**, Scheme 2) in which the phenyl ring resides on the alkylidene carbon atom.[92] Among cycloalkyl derivatives, $[N_3N]W(cyclopropyl)$ evolves ethene to give $[N_3N]W{\equiv}CH$, and $[N_3N]W(cyclobutyl)$ is converted to $[N_3N]W{\equiv}CPr^n$ via an intermediate 1-tungstenacyclopentene complex, $[N_3N]W(CH{=}CH_2CH_2CH_2)$. In contrast, the cyclopentyl complex $[N_3N]W(C_5H_9)$ is more stable, and in solution it exists in equilibrium with its cyclopentylidene hydride isomer, $[N_3N]W({=}C_5H_8)(H)$.[93]

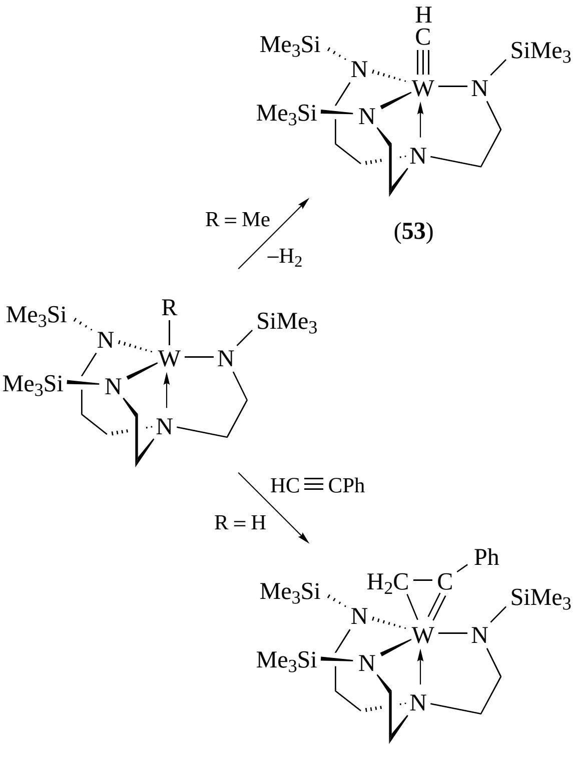

(**53**)

(**54**)

Scheme 2

Monomeric alkylidyne complexes, $(Bu^tO)_3W{\equiv}CR$ (**56**), have been prepared from $W_2(OBu^t)_6$ (**55**) and $RC{\equiv}CR$ (R = Me, Et, Pr^n) via the metathesis reaction shown in equation (19), and a related reductive cleavage of acetonitrile provides the alkylidyne complex (**56**) and a terminal nitrido complex, $(Bu^tO)_3W{\equiv}N$.[94] Generation of $W_2(OR)_4$ (R = $SiBu^t{}_3$) in the presence of ethene at low temperature results in cleavage of the ethene C=C bond to give the bridging alkylidyne complex, $W_2(OR)_4(\mu\text{-}CH)(\mu\text{-}CH_2)(\mu\text{-}H)$, which upon warming converts to $W_2(OR)_4(\mu\text{-}CH)_2$ and H_2.[95] The specific alkylidyne complex, $(Bu^tO)_3W{\equiv}CBu^t$, is an important catalyst for the ring-closing metathesis of alkynes.[96] The structure of $W_2(\mu\text{-}C_2)(OBu^t)_6$ exhibits diyne-like connectivity (i.e. W≡C–C≡W) with a short internal C–C bond length (*see Bond Length*) of 1.38(2) Å.[97] Interestingly, $WX_2(PMe_3)_4$ (X = Cl, Br) compounds react with vinylsilanes, $H_2C{=}CHSiR_3$ (R = Me_3, OMe), to yield R_3SiX and $W({\equiv}CMe)(X)(PMe_3)_4$,[98] and these alkylidyne complexes react further with alkynes to form $W({\equiv}CMe)(X)(PMe_3)_2(\eta^2\text{-alkyne})$ derivatives.[99] The unusual silyl complex, $W(CH_2Bu^t)_2({\equiv}CBu^t)[Si(SiMe_3)_3]$, is synthesized by the reaction of $W(CH_2Bu^t)_2({\equiv}CBu^t)Cl$ with $LiSi(SiMe_3)_3(THF)_3$.[100]

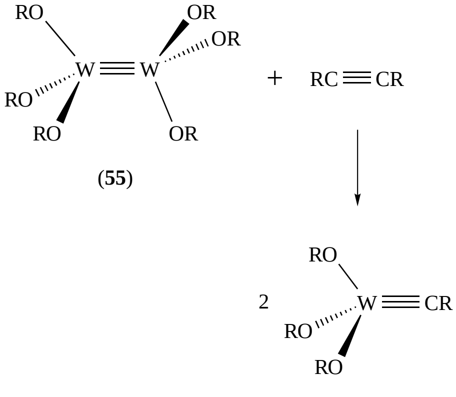

(**55**)

(19)

(**56**)

Treatment of $[Tp^*W(CO)_2({\equiv}CPPh_3)]^+$ with $Na[HBEt_3]$ in THF affords the amphoteric methylidyne complex, $Tp^*W(CO)_2({\equiv}CH)$, via the intermediate formyl and carbene complexes, $Tp^*W(CO)(C(O)H)({\equiv}CPPh_3)$ and $Tp^*W(CO)_2({=}CH(PPh_3))$, respectively. Protonation of $Tp^*W(CO)_2({\equiv}CH)$ yields the cationic α-agostic (*see Agostic Bonding*) methylidene complex $[Tp^*W(CO)_2({=}CH_2)]^+$, while deprotonation with alkyllithium reagents provides the terminal carbido complex, $Tp^*W(CO)_2({\equiv}CLi)$, which reacts with electrophiles to generate $Tp^*W(CO)_2({\equiv}CR)$ derivatives (R = Me, $SiMe_3$, I, $C(OH)Ph_2$, $CH(OH)Ph$, and $C(O)Ph$).[101] Deprotonation of $Tp^*W(CO)_2({\equiv}CMe)$ forms the nucleophilic vinylidene anion, $[Tp^*W(CO)_2({=}C{=}CH_2)]^-$, that reacts with MeI or $PhC(O)R$ (R = H, Me) to afford $Tp^*W(CO)_2({\equiv}CCH_2Me)$

or $Tp^{*}W(CO)_2(\equiv CCH_2CR(OH)Ph)$, respectively,[102] and protonation of $CpW(CO)_2(\equiv CC\equiv CR)$ with HI produces the alkylidene complexes, $CpW(CO)_2(=CHC\equiv CR)(I)$ ($R = Bu^t$, p-Tol).[103] Similarly, protonation of the $[\{p\text{-}Bu^t\text{-calix[4]-}(O)_4\}W(\equiv CR)]^-$ anion ($R = Ph, Pr^n, SiMe_3$) leads to the corresponding neutral alkylidene complexes, $\{p\text{-}Bu^t\text{-calix[4]-}(O)_4\}W(=CHR)$, which may be reversibly deprotonated back to the starting alkylidyne anions by using BuLi.[77] Zwitterionic (*see Zwitterion*) alkylidene complexes, $Tp^{*}W(CO)_2(=C(CH_2R)(PPhMe_2))$ ($R = Ph, CH{=}CH_2$), readily lose $PPhMe_2$ to form neutral $Tp^{*}W(CO)_2(\equiv CCH_2R)$, and deprotonation of these complexes with a strong base occurs at C_β to form the reactive vinylidene anions, $[Tp^{*}W(CO)_2(=C{=}CHR)]^-$.[104]

The photooxidation of tungsten–alkylidyne complexes results in the formation of organic products derived from the carbyne substituent (e.g. equation 20). These reactions involve a 1e oxidation of the alkylidyne reactant to form a 17e radical cation species, followed by H atom abstraction from the solvent, to yield a cationic alkylidene complex that may undergo a [1,2]-H shift to afford an η^2-alkene compound. Photooxidation of the cyclohexenyl alkylidyne complex, $CpW(CO)(PR_3)(\equiv CC_6H_{10})$ ($R = OMe$) (**57**), in $CHCl_3$ affords the stable η^3-vinylcarbene complex, $CpWCl(PR_3)(=CHC_6H_{10})$ (**58**) (equation 21), thereby providing the first direct evidence for alkylidene intermediates in the single-electron oxidation reactions of alkylidyne complexes.[105,106]

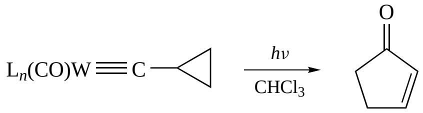

(20)

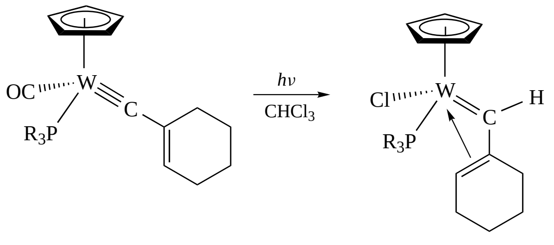

(21)

(**57**) (**58**)

3.2 η^2-Hydrocarbon Complexes

3.2.1 Alkene Complexes

Tungsten-alkene bonding is best described by the Dewar–Chatt–Duncanson model (*see Dewar–Chatt–Duncanson Bonding Model*) in which σ-type electron donation from the alkene π orbital occurs along with π-backbonding (*see Back Bonding*) from a metal $d\pi$ orbital into the empty π^* orbital of the alkene. According to this synergistic bonding model, η^2-coordination results in a decrease in the alkene C–C bond order (*see Bond Order*). For this reason, complexes containing η^2-alkene ligands may be viewed in the limit as either planar alkene adducts (**E**) or metallacyclopropane (**F**) complexes.

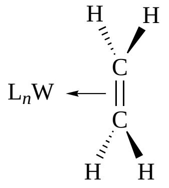

η^2-alkene
E

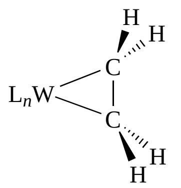

metallacyclopropane
F

Tungsten–alkene complexes (*see Alkene Complexes*) are typically prepared by ligand-substitution reactions under thermal or photolytic conditions. For example, photolysis of $W(CO)_6$ in the presence of an alkene provides simple $W(CO)_{6-n}(\eta^2\text{-alkene})_n$ ($n = 1, 2$) complexes, and irradiation of these species gives rise to two competitive primary photoprocesses, that is, alkene and CO dissociation.[107] The labile (*see Labile*) ethene complexes, $W(CO)_5(\eta^2\text{-}C_2H_4)$ and *cis*-$W(CO)_4(\eta^2\text{-}C_2H_4)_2$, have been characterized only at low temperatures in ethene-saturated hydrocarbon solutions. However, *trans*-$W(CO)_4(\eta^2\text{-}C_2H_4)_2$ (**59**, $L = CO$) is thermally stable and possesses D_{2d} symmetry, with the ethene ligands in a trans, orthogonal conformation that maximizes the efficiency of tungsten to alkene (π^*) back donation.[108] Photolysis of (**59**) ($L = CO$) in the presence of H_2 at −90 °C results in the formation of the dihydrogen complexes, *mer*-$W(CO)_3(\eta^2\text{-}H_2)(\eta^2\text{-}C_2H_4)_2$ and *cis*-$W(CO)_4(\eta^2\text{-}H_2)(\eta^2\text{-}C_2H_4)$.[109]

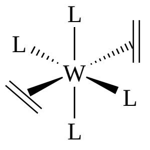

(**59**)

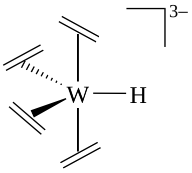

(**60**)

The alkene derivatives, *cis*-$W(CO)_4(PR_3)(\eta^2\text{-alkene})$ (R = alkyl or aryl), are typically prepared by ligand substitution (*see Ligand Substitution*) from $W(CO)_4(L)(PR_3)$ (L = Lewis base), whereas the related compounds, $W(CO)_3(PR_3)_2(\eta^2\text{-alkene})$, are readily accessed via photolysis of $W(CO)_4(PR_3)_2$ in the presence of an alkene. The bis(ethene) complex, *trans*-$W(PMe_3)_4(\eta^2\text{-}C_2H_4)_2$ (**59**, $L = PMe_3$), reversibly eliminates PMe_3 in solution,[110] and the coordinatively unsaturated $W(PMe_3)_3(\eta^2\text{-}C_2H_4)_2$ fragment reacts with Lewis bases, L, to yield complexes of the type *mer,trans*-$W(L)(PMe_3)_3(\eta^2\text{-}C_2H_4)_2$ or *trans*-$W(L)_2(PMe_3)_2(\eta^2\text{-}C_2H_4)_2$ (L = CNR, CO). More interesting are the reactions of (**59**) ($L = PMe_3$) and related complexes containing bidentate (*see Bidentate*

Ligand) phosphine ligands with CS_2 or CO_2, which lead to coupled products containing η^3-C_2S_4 or acrylate ligands, respectively.**[111,112]** The reactions of $WCl_2(PR_3)_4$ with alkenes provide the bis(alkene) complexes, *cis,trans*-$WCl_2(PR_3)_2(\eta^2$-alkene$)_2$, in which the *cis*-alkene ligands are oriented parallel to one another. The oxo, sulfido, and imido complexes, $WCl_2(E)(PR_3)_2(\eta^2$-alkene) (E = O, S, NPh) possess alkene ligands that are cis to the π-ligand E and are oriented perpendicular to the W=E linkage.

Alkene complexes (*see Alkene Complexes*) can also be formed from tungsten–alkyl complexes via β-H migration. Thus, photolysis of $CpW(CO)_3(Et)$ results in the elimination of CO and the transient formation of $CpW(CO)_2(H)(\eta^2$-$C_2H_4)$, and time-resolved infrared spectroscopic (*see Infrared Reflection Adsorption Spectroscopy*) studies indicate that this species undergoes cis to trans isomerization prior to the elimination of ethene and uptake of CO to yield $CpW(CO)_3(H)$.**[113]** Although a vacant coordination site is usually required for such transformations to occur, examples of ligand-induced β-H transfer have been reported for a series of W^{VI} dialkyl complexes.**[114]** Finally, the reaction of $W(OMe)_3Cl_3$ with excess EtLi followed by the addition of tmeda yields $[Li(tmeda)]_3[WH(\eta^2$-$C_2H_4)_4]$ (i.e. $[Li(tmeda)]_3[(\mathbf{60})]$), presumably via thermal decomposition of an undetected ethyl complex. The anion $[(\mathbf{60})]^{3-}$ is trigonal–bipyramidal in the solid state, with two mutually perpendicular ethene ligands in the axial sites and two coplanar ethene ligands and a hydride ligand constituting the equatorial plane.**[115]**

Protonation of *trans*-$W(dppe)_2(\eta^2$-$C_2H_4)_2$ with HX (X = Cl, Br) results in the formation of the cationic hydrido complexes, $[trans\text{-}WH(dppe)_2(\eta^2\text{-}C_2H_4)_2]X$, and stopped-flow kinetic studies have shown that these reactions proceed via two parallel pathways involving either slow protonation at tungsten or rapid protonation of the ethene ligand followed by slow β-H elimination (*see β-Elimination*) from an intermediate ethyl complex.**[116]** The interesting reaction of $Cp_2W(\eta^2$-$C_2H_4)$ with perfluoro-*tert*-butyl iodide results in fluoroalkylation of the ethene ligand and formation of $Cp_2W[CH_2CH_2C(CF_3)_3]I$.**[117]**

Metallacyclopentane complexes are obtained similarly by reductive coupling (*see Reductive Coupling*) of alkene ligands,**[77,79]** by reduction of the ester functionalities in $CpW(\eta^2$-$C_2H_2R_2)$ (R = CO_2Me),**[118]** or via intramolecular (*see Intramolecular*) hydrogen transfer in an alkyl–vinyl complex.**[119]** Formal addition of an alkene across a W=C bond gives rise to metallacyclobutane complexes that are intermediates in catalytic alkene metathesis (*see Alkene Metathesis*) reactions.**[85,120,121]** Cycloalkene adducts are believed to be intermediates in ROMP reactions (*see Ring Opening Metathesis Polymerization Reactions*), and the solid-state molecular structure of the cycloheptene adduct (**61**) (X = $GaBr_4$) provides convincing evidence for the existence of intermediate alkene complexes in ROMP catalysis (equation 22).**[122]**

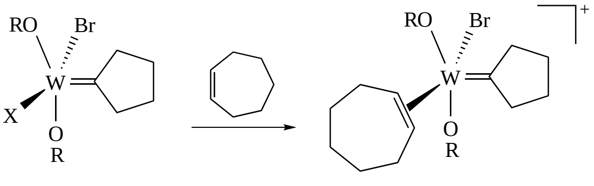

(22)

(**61**)

The ditungsten–hexakis(alkoxide) complexes, $W_2(OR)_6$, react with ethene to give initially the bis(ethene) adduct (**62**) when R = CH_2Bu^t or the metallacylopentane complex (**63**) when R = Pr^i. These isolable intermediates are eventually converted to the 1-metallacyclopentene complex (**64**), which is formed by α-H transfer from the metallacyclopentane ring of (**63**) to the coordinated ethene ligand.**[94]** A variety of alkene rearrangements also occur in tungsten complexes containing calixarene (*see Calixarenes*) ligands, including deprotonation of an η^2-alkene ligand to give 1-metallacyclopropene or alkylidyne derivatives, and reductive coupling (*see Reductive Coupling*) to form metallacyclopentanes.**[77]**

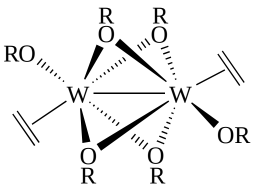

(**62**)

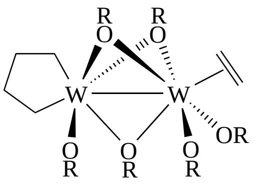

(**63**)

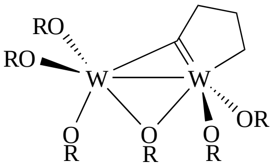

(**64**)

Other types of tungsten–alkene complexes that merit mention include the first group six η^2-benzene complex, $TpW(NO)(PMe_3)(\eta^2$-$C_6H_6)$, that contains a π-bound benzene ligand activated toward Diels–Alder cycloaddition.**[123]** Also, the η^2-fullerene complexes, *mer*-$W(CO)_3(L\text{-}L)(\eta^2$-$C_{60})$ (**65**), have been prepared from $W(CO)_4(L\text{-}L)$ (L-L = a bidentate N- or P-donor ligand) in the presence of C_{60}.**[124,125]** In some cases, a bimetallic complex in which two metal centers are attached to a single fullerene (*see Buckminsterfullerene*) moiety, that is, $[mer\text{-}W(CO)_3(L\text{-}L)]_2(\eta^2,\eta^2\text{-}C_{60})$, (**66**) is also formed, and analogous complexes containing C_{70} have also been prepared.**[125]** The dumbbell-shaped complex, $W(\eta^2$-$C_{60})_2(CO)_2(L\text{-}L)$ (**67**, L-L = 4,4′-di(butylcarboxyl)-2,2′-bipyridine), contains two C_{60} ligands, each of which is coordinated to the metal center in an η^2-fashion.**[126]**

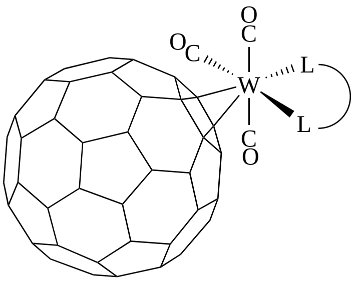

(**65**)

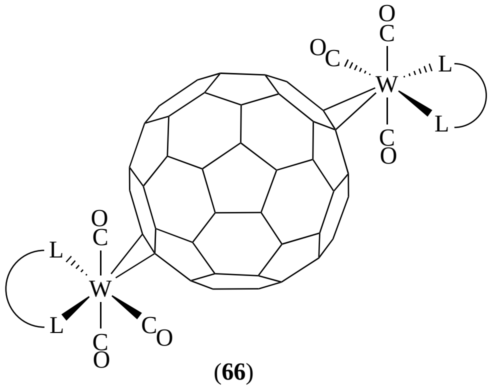

(**66**)

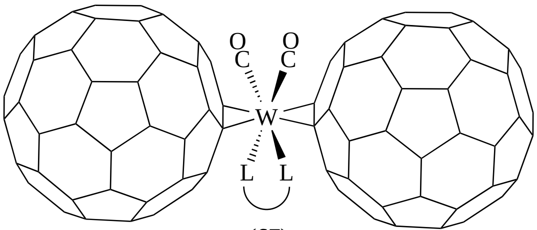

(**67**)

3.2.2 *Alkyne Complexes*

Alkynes may function as 2e alkene analogues or as formal 4e donor ligands. This situation arises because an alkyne can engage a metal center using not only the π and π^* orbitals involved in σ-donor and π-acceptor bonding, but also by employing a second π orbital oriented perpendicular to the tungsten-alkyne bond axis; these are known as $\pi_{\parallel}$ and $\pi_{\perp}$ interactions, respectively. In low-valent, d^6 (*see d^n Configuration*) tungsten complexes, alkyne ligands generally act as 2e donors since repulsive interactions between the alkyne $\pi_{\perp}$ orbital and filled metal dπ orbitals dictate the geometry and reactivity of the complexes. In d^4 and d^2 tungsten complexes, the $\pi_{\perp}$ orbital may interact with an empty metal d orbital to form an additional π-donor bond, and the alkyne then acts as a formal 4e donor ligand.**[127]** In complexes containing more than one alkyne ligand, the $\pi_{\perp}$ orbitals may donate electron density into the same metal dπ orbital, thus giving rise to formal electron donor counts between two and four. The unique ability of an ancillary alkyne ligand to function as a variable (i.e. three or four) electron donor in the presence of competing π-ligands can lead to very interesting reaction chemistry, for example, in the stepwise oxidation of a benzylamine ligand to a benzonitrile ligand via isolable amido, imine, and azavinylidene intermediate complexes on the $[Tp^*W(CO)(\eta^2\text{-HC}{\equiv}CPh)]^+$ fragment (Scheme 3).**[128]** Regio- and stereoselective reactions of η^2-alkyne ligands, followed by their removal from the metal fragment, have provided synthetic routes to chiral alkynes that are difficult to prepare by conventional means.**[129]** The subsequent material in this section is divided into W^0, W^{II}, and $W^{IV/VI}$ subsections.

Zero-valent tungsten complexes containing one, two, or three alkyne ligands are known. Photochemical and thermal reactions of $W(CO)_6$ with alkynes lead to thermally unstable $W(CO)_{6-n}(\eta^2\text{-alkyne})_n$ ($n = 1, 2$) species, and those containing terminal alkyne ligands (**G**) often undergo a formal [1,2]-*H* shift to afford vinylidene complexes $W(CO)_5({=}C{=}CHR)$ (**H**).**[130]** This mode of reactivity also occurs during the isomerization of *fac*-$[W(CO)_3(dppe)(\eta^2\text{-HC}{\equiv}CR)]$ (R = H, Ph, *n*-Bu) to *mer*-$[W({=}C{=}CHR)(CO)_3(dppe)]$, and it is attributed to unfavorable repulsion between the alkyne $\pi_{\perp}$ orbital and a filled metal dπ orbital.**[131]** Theoretical studies of the mechanism of acetylene–vinylidene rearrangement have shown that model tungsten complexes containing these ligands are best formulated as metallacyclopropene (**I**) and metallaallene species, respectively,**[132]** and it should be noted that vinylidene complexes may also be prepared by the addition of electrophiles to tungsten–alkynyl complexes or by deprotonation of alkylidyne complexes.**[133]** Vinylidene ligands are among the

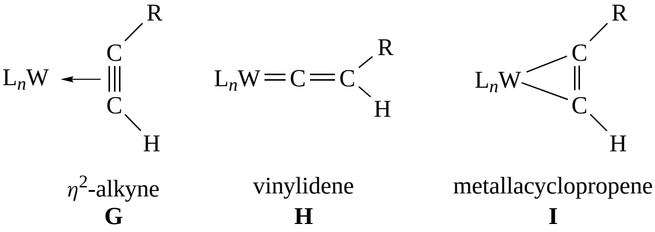

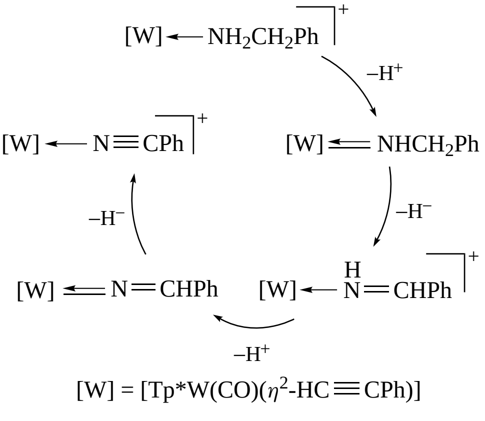

Scheme 3

strongest π-acceptor ligands known, and they have found use as catalysts in $[2 + 2]$ cycloaddition and alkyne dimerization reactions.**[134]**

Bis(alkyne) complexes of W^0 generally have the compositions $W(CO)_2(L\text{-}L)(\eta^2\text{-}RC{\equiv}CR)_2$ (L-L = a bidentate N- or P-donor ligand) and invariably contain cis CO ligands and mutually trans, orthogonal alkyne ligands.**[135]** The crucial presence of electron-withdrawing alkyne substituents (i.e. $R = CO_2Me$, CO_2Et) is thought to enhance tungsten $d\pi$ to alkyne $\pi_{||}{}^*$ backbonding (*see Back Bonding*) and delocalize alkyne $\pi_\perp$ electron density. Consequently, the alkyne ligands in these complexes function as formal 2e donors.

Thermally stable $W(CO)(\eta^2\text{-alkyne})_3$ complexes, in which the three alkyne ligands contribute a total of 10 electrons to the metal center, may be prepared from suitable tricarbonyl precursors,**[136]** and the apical CO ligand can be replaced with other neutral Lewis bases (*see Lewis Acids & Bases*).**[137]** $W(PMe_3)(\eta^2\text{-}HC{\equiv}CPh)_3$ may be prepared via this method or by the reduction of $WCl_4(PMe_3)_2$ in the presence of $HC{\equiv}CPh$.**[138]** Alkyne–alkyne coupling occurs when $W(L)(\eta^2\text{-}PhC{\equiv}CPh)_3$ (L = CO, MeCN) is treated with excess $PhC{\equiv}CPh$, resulting in the formation of $(\eta^4\text{-}C_4Ph_4)W(L)(\eta^2\text{-}PhC{\equiv}CPh)_2$ and related carbocyclic derivatives.**[137]** The labile (*see Labile*) acetonitrile complex, $W(MeCN)(\eta^2\text{-}PhC{\equiv}CPh)_3$ (**68**), undergoes rearrangement upon reaction with $o\text{-}Ph_2PC_6H_4CH{=}CH_2$ via cleavage of both C=C and C≡C bonds to yield $(\eta^5\text{-}C_5Ph_4H)W({\equiv}CPh)(Ph_2PC_6H_4CH{=}CHPh)$ (**69**) (equation 23).**[139]**

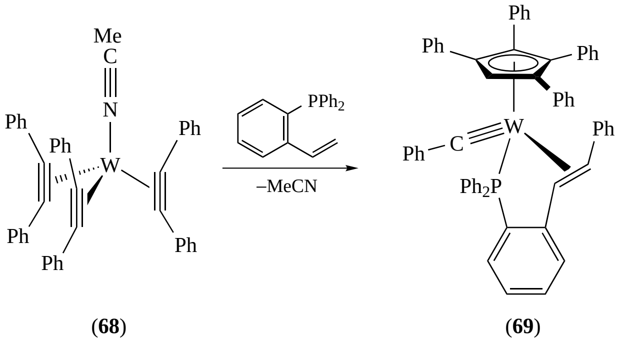

(**68**) (**69**)

(23)

Numerous W^{II} complexes of the type $W(CO)_{3-n}(L)_n(X)_2(\eta^2\text{-alkyne})$ ($n = 1, 2$) are known, most of which have been prepared from reactions of appropriate W^{II} or W^{III} precursors with an alkyne.**[127]** Thus, reduction of $WCl_3(PMe_3)_2(\eta^2\text{-alkyne})$ in the presence of a Lewis base (*see Lewis Acids & Bases*) generates $WCl_2(PMe_3)_2(L)(\eta^2\text{-alkyne})$. Alkyne ligands may also be prepared via intramolecular (*see Intramolecular*) coupling of alkylidyne, isocyanide, and carbonyl ligands, or by treating the alkynyl anions, $[CpW(NO)(CO)(C{\equiv}CR)]^-$, with an electrophile (*see Electrophile*).**[140]** Simple alkyne complexes such as $CpW(CO)(X)(\eta^2\text{-alkyne})$ or $W(S_2CNR_2)_2(L)(\eta^2\text{-alkyne})$ react with excess alkyne under forcing conditions to yield bis(alkyne) derivatives, $CpW(X)(\eta^2\text{-alkyne})_2$ and $W(S_2CNR_2)_2(\eta^2\text{-alkyne})_2$, in which the alkyne ligands are oriented parallel to one another in order to facilitate π donation from both alkynes into the same $d\pi$ orbital (i.e. each alkyne ligand acts as a formal 3e donor). Related W^{II} bis(alkyne) complexes, $W(CO)(X)_2(L)(\eta^2\text{-}RC{\equiv}CR)_2$, are prepared by the reactions of $W(CO)_3(X)_2(L)_2$ with alkynes, and ligand substitution generates cationic $[W(CO)(X)(L\text{-}L)(\eta^2\text{-}RC{\equiv}CR)_2]^+$ derivatives. Alternatively, reduction of Cp^*WX_4 in the presence of two equivalents of an alkyne affords $Cp^*WX(\eta^2\text{-alkyne})_2$.**[141]**

Alkyne ligands are susceptible to attack by nucleophiles, which typically leads to the formation of η^2-vinyl complexes;**[47]** this is particularly true in the case of electron-deficient alkynes. Noteworthy in this regard are the reactions of $[Tp^*W(CO)_2(\eta^2\text{-}RC{\equiv}CR')]^+$ cations with hydride reagents that yield η^2-vinyl, η^2-allene, or η^3-allyl complexes depending upon the nature of the alkyne substituents.**[49]**

Interestingly, the properties of some high oxidation state tungsten–alkyne complexes indicate that there has been considerable transfer of electron density to the alkyne ligands. For instance, the $W(4f_{7/2})$ binding energy (determined by X-ray photoelectron spectroscopy) of $[WCl_4(\eta^2\text{-}PhC{\equiv}CPh)]_2$ is similar to that measured for the d^0 (*see d^n Configuration*) imido complex, $[WCl_4(NPh)]_2$, and is in agreement with a W^{VI} oxidation state.**[142]** Similarly, computational investigations support the experimental evidence that $WCl_3(\eta^2\text{-}PhC{\equiv}CPh)(PMe_3)_2$ and $WCl_2(\eta^2\text{-}PhC{\equiv}CPh)(PMe_3)_3$ are appropriately formulated as complexes of W^V and W^{IV}, respectively. Given these observations, the description of the related $[WCl_2(\eta^2\text{-}HC{\equiv}CH)(MeCN)_3]^+$ as a monomeric W^{III} complex is by no means certain.**[143]** Consistent with their anionic character, the alkyne ligands in $[WCl_4(\eta^2\text{-}PhC{\equiv}CPh)]_2$ undergo ready hydrolysis to form free *cis*-stilbene. A great many W^{IV} alkyne complexes containing alkylidene, imido, oxo, and sulfido ligands are also known, and the alkyne ligands in these complexes, like the alkene ligands in related complexes described in a previous section (vide supra), are generally coordinated cis to the π-donor ligand and perpendicular to its multiple bond with tungsten.

The ditungsten–hexakis(alkoxide) complexes, $W_2(OR)_6$, exhibit a wide range of reactivity toward alkynes. Thus, when $R = Bu^t$, reaction with $PhC{\equiv}CPh$ yields a mixture of $W_2(OR)_4(\mu\text{-}PhC{\equiv}CPh)_2$ and $W_2(OR)_4(\mu\text{-}CPh)_2$, but the analogous reaction with ethyne produces $W_2(OR)_6(\mu\text{-}HC{\equiv}CH)(L)$ (**70**) in the presence of L = pyridine. When $R = OSiMe_2Bu^t$, the elimination of ROH from complex (**70**) affords the μ-η:η^2-ethynyl complex, $W_2(OR)_5(\mu\text{-}C_2H)$ (**71**), and the liberated alcohol converts any remaining (**70**) to a mixture of the vinyl and ethylidyne isomers, $W_2(OR_7)(\mu\text{-}CHCH_2)$ (**72**) and $W_2(OR)_7(\mu\text{-}CMe)$ (**73**), which are related by a [1,2]-*H* shift but do not interconvert in solution

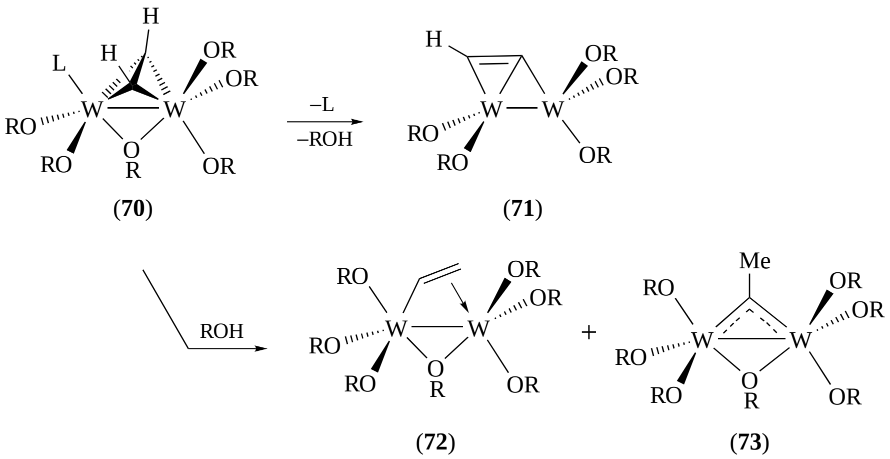

Scheme 4

(Scheme 4).[94] In contrast, the addition of ethyne to $W_2(OR)_8$ ($R = CH_2Bu^t$) yields an unusual 1:1 adduct in which the bridging μ,η^2-HC≡CH ligand is neither parallel nor perpendicular to the W–W bond.[144]

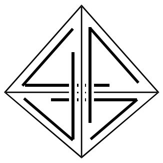

(74)

3.3 η^3-Hydrocarbon Complexes

Tungsten–allyl complexes may be prepared by metathesis from suitable halide precursors using allyl Grignard reagents (*see Grignard Reagents*) or from the reactions of $[CpW(NO)(CO)(C{\equiv}CR)]^-$ ($R = Ph, Bu^t, SiMe_3$) with allylic halides.[56] The homoleptic (*see Homoleptic Compound*) allyl complex, $W(\eta^3\text{-}C_3H_5)_4$, has been known for many years, but questions as to its exact structure have remained unanswered until recently. A thorough analysis by Casey and coworkers has shown that the molecular structure that best agrees with the NMR spectroscopic data is one in which the complex has S_4 symmetry (**74**).[145] The tris(allyl) dimer, $[(\eta^3\text{-}C_3H_5)_3WCl]_2$, reacts with methyl-substituted allylmagnesium halides to form $(\eta^3\text{-}C_3H_5)_3\ W(\eta^3\text{-}MeC_3H_4)$ and $(\eta^3\text{-}C_3H_5)_3\ W(\eta^3\text{-}1,3\text{-}Me_2C_3H_3)$ as a mixture of isomers and with alkylmagnesium halides to give β-agostic (*see Agostic Bonding*) alkyl complexes, $(\eta^3\text{-}C_3H_5)_3W(R)$. The reaction of $(\eta^3\text{-}C_3H_5)_3\ W(Et)$ with PMe_3 initiates an intramolecular (*see Intramolecular*) protonation of an allyl group to give $(\eta^3\text{-}C_3H_5)_2\ W(\eta^2\text{-}CH_2{=}CH_2)(PMe_3)_2$ and propene, and the ethyl complex also readily inserts $CNBu^t$ into its W–C link to form $(\eta^3\text{-}C_3H_5)_3\ W(\eta^2\text{-}EtC{=}NBu^t)$.[146] Finally, the reaction of $WCl_2(PMe_3)_4$ with $Me_3SiOCH_2CH{=}CH_2$ affords Me_3SiCl and the oxo allyl complex, $WCl(O)(\eta^3\text{-}C_3H_5)(PMe_3)_2$.[147]

Thermal α-elimination (*see α-Elimination*) of neopentane from the dimethylallyl complex, $Cp^*W(NO)(CH_2Bu^t)(\eta^3\text{-}Me_2C_3H_3)$, generates a reactive 16e η^2-allene intermediate that activates hydrocarbon solvent C–H bonds to yield $Cp^*W(NO)(R)(\eta^3\text{-}Me_2C_3H_3)$ ($R = Ph, CH_2SiMe_3$).[75] In cyclohexane, three C–H bonds of the solvent are activated to give the η^3-cyclohexenyl complex, $Cp^*W(NO)(\eta^3\text{-}C_6H_9)(H)$ (**75**),[148] and related η^3-allyl hydrido complexes, $Cp^*W(NO)(\eta^3\text{-}C_7H_{11})(H)$ (**76**) and $Cp^*W(NO)(\eta^3\text{-}C_8H_{13})(H)$ (**77**), are formed from $Cp^*W(NO)(CH_2Bu^t)_2$ upon thermolysis in methylcyclohexane or ethylcyclohexane, respectively.[75] Irradiation of $Tp^*W(CO)_3(H)$ in the presence of unconjugated dienes or alkynes generates η^3-allyl complexes, that is, $Tp^*W(CO)_2(\eta^3\text{-}CHRCHCHR')$, via insertion into the W–H bond.[149] The reactions of *cis*-$Cp^*W(CO)_2(Me)(MeCN)$ with $HSiMe_2(CH{=}CR_2)$ ($R = H$, Me) afford novel η^3-1-silaallyl complexes, $Cp^*W(CO)_2(\eta^3\text{-}Me_2SiCHCR_2)$, via thermal Si–H bond activation.[150] Reaction of $[Tp^*W({=}CH_2)(CO)(L)]^+$ with excess base yields the unusual allyl-bridged dimer, $[Tp^*W(CO)(L)]_2(\mu\text{-}C_3H_5)^+$ (**78**, $L = \eta^2\text{-}PhC{\equiv}CMe$), which is inert toward a variety of nucleophiles.[151]

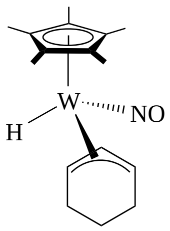

(75)

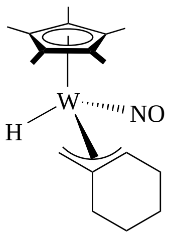

(76)

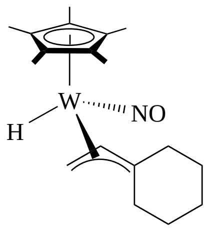

(77)

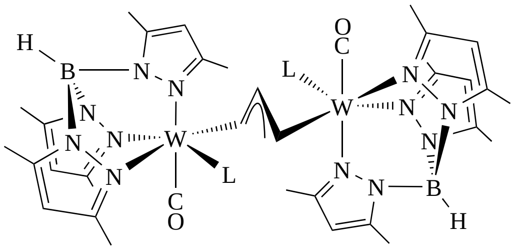

(**78**)

The ditungsten complex, $W_2(C_3H_5)_2(NMe_2)_4$ (**79**), has C_2 symmetry in the solid state with bridging allyl ligands that exhibit an unusual μ-η^1:η^2-2-propenyl coordination mode,[152] and the reaction of $W_2(OR)_8$ with allene generates the $W_2(OR)_8(\mu\text{-}\eta^1,\eta^3\text{-}C_3H_4)$ adduct (**80**, R = CH_2Bu^t).[153]

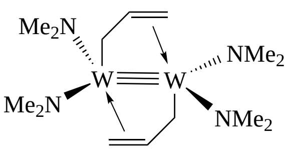

(**79**)

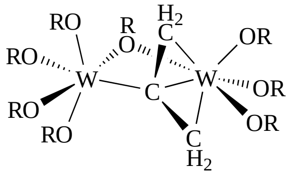

(**80**)

Substituted allyl complexes of the type $Cp'W(CO)_2(\eta^3$-allyl) are useful synthetic reagents, and their organic chemistry has been reviewed.[62] The reaction of $CpW(CO)_3(\eta^1$-*trans*-$CH_2CH{=}CHC{\equiv}CMe)$ (**81**) with ROH (R = H, Me) over SiO_2 affords $CpW(CO)_2(\eta^3$-3-*syn*-CO_2R-3-*anti*-Me-1-vinylallyl) compounds (**82**), thereby providing the only direct evidence available for tandem 1,3-metal shifts across conjugated allyl and alkyne bonds (equation 24).[154]

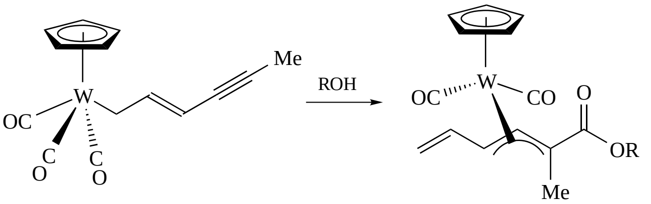

(**81**) (**82**)

(24)

3.4 η^4-Hydrocarbon Complexes

The complexes $W(\eta^4\text{-diene})_n(CO)_{6-2n}$ ($n = 2$, diene = 1,3-butadiene, (**83**); $n = 3$, diene = 2,3-dimethylbutadiene, **84**) have been prepared, and their solid-state molecular structures have been determined. Interestingly, the two diene ligands in (**83**) are twisted relative to one another, imparting C_2 symmetry to the complex.[155] Homoleptic (**84**) has been the subject of a detailed theoretical investigation[156] in an attempt to explain its rare trigonal–prismatic coordination geometry.[157] The related carbonyl species, $W(CO)_4(\eta^4$-1,3-butadiene), can be generated transiently in solution, but it has not yet been isolated.[158]

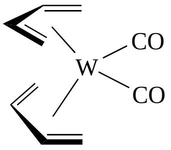

(**83**)

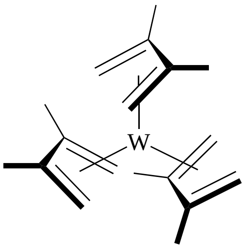

(**84**)

Many diene complexes (*see Diene Complexes*) having the general composition $W(\eta^4\text{-diene})(CO)_{4-n}(L)_n$ (e.g. $n = 2$, **85**) are known, as are $CpW(\eta^4\text{-diene})(CO)(R)$ species (**86**, L = Lewis base, R = alkyl, acyl). Hydrogenation of $Cp^*W(NO)(CH_2SiMe_3)_2$ in the presence of acyclic, conjugated dienes leads to the formation of a variety of $Cp^*W(NO)(\eta^4$-*trans*-diene) complexes, and when 1,3-cyclooctadiene is employed as the diene substrate, it undergoes an unprecedented coupling to afford the triene complex (**87**).

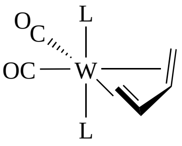

(**85**)

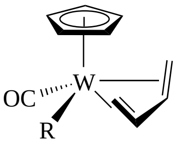

(**86**)

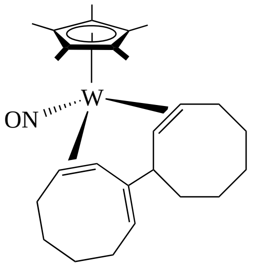

(**87**)

Several η^4-norbornadiene (nbd) complexes containing the $W(CO)_x$ fragment are also known, among them $W(CO)_4(\eta^4$-nbd) and complexes of the type $W(CO)_2(X)_2(\eta^4$-nbd).[159] Finally, several tungsten–cyclobutadiene complexes have been described, and they are generally formed by the coupling of two alkyne ligands, as in the case of $(\eta^4\text{-}C_4Ph_4)W(\eta^2\text{-}PhC{\equiv}CPh)_2(CO)$ (**88**).[160]

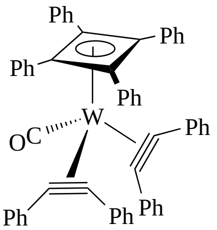

(**88**)

3.5 η^5-Hydrocarbon Complexes

3.5.1 Tungstenocene-derived Complexes

Tungstenocene (Cp_2W) is very reactive once generated by photolysis of Cp_2WH_2 or by thermolysis of $Cp_2W(Me)H$,**[161]** and it inserts readily into C–H, O–H or B–B**[162]** bonds. The dihydride, Cp_2WH_2, is a strong Lewis base (*see Lewis Acids & Bases*), and it reacts with Lewis acids including $AgBF_4$ to form adducts, for example $[(Cp_2WH_2)_2Ag]BF_4$, bridged by the hydrido ligands.**[163]** Chlorination of Cp_2WH_2 with $CHCl_3$ (or the reaction of $WCl_4(DME)$ with LiCp) affords Cp_2WCl_2, which can be oxidized to $[Cp_2WCl_2]^{2+}$.**[164]** The dichloro complex serves as an excellent entry point into related tungstenocene chemistry;**[165]** for example, alkyl derivatives are prepared by halide metathesis, and the electronic structures of Cp_2WR_2 species have recently been described in detail.**[166]** The related oxo complex, $Cp_2W(O)$, has been the subject of a detailed thermochemical and theoretical investigation in order to understand its [2 + 2] cycloaddition reactions.**[167]** The intramolecular (*see Intramolecular*) thermal rearrangement of $W(\eta^2\text{-PhC}{\equiv}\text{CPh})(\eta^8\text{-}C_8Ph_8)$ (**89**) results in the formation of the isolable perphenylated tungstenocene, $(\eta^5\text{-}C_5Ph_5)_2W$ (**90**) (equation 25),**[137]** and the tungstenocenium cations, $[(\eta^5\text{-}C_5Ph_5)_2W]^+$ and $[(\eta^5\text{-}C_5Ph_5)_2W]^{2+}$, may be generated by oxidation of the neutral compound.**[168]**

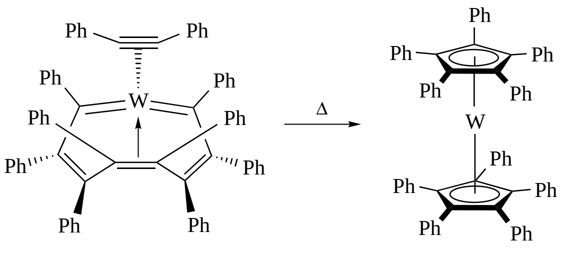

(25)

(**89**) (**90**)

The *ansa*-tungstenocene complex, $[Me_2Si(\eta^5\text{-}C_5Me_4)_2]W(Me)H$, also eliminates methane upon thermolysis in benzene and forms the phenyl complex $[Me_2Si(\eta^5\text{-}C_5Me_4)_2]W(Ph)H$. Careful experimental work by Parkin and coworkers has established the existence of an inverse equilibrium isotope effect (*see Isotope Effect*) during this reaction.**[169]** This work follows a related study by Norton and coworkers on $Cp_2W(Me)H$ that revealed similar results.**[170]** This C–H activation chemistry has also attracted the interest of theoretical chemists.**[166]** The intramolecular (*see Intramolecular*) H/D exchange observed in $[Me_2C(\eta^5\text{-}C_5H_4)_2]W(R)H$ complexes containing adjacent alkyl and hydrido ligands has provided compelling evidence for the existence of intermediate σ-alkane complexes of tungsten.**[171]**

3.5.2 Non-tungstenocene-derived Complexes

As amply illustrated throughout this article, the pentamethylcyclopentadienyl ligand (Cp^*) effectively stabilizes many types of organometallic complexes of tungsten. However, on occasion, it can undergo intramolecular (*see Intramolecular*) C–H activation to afford so-called 'tuck-in' complexes. For instance, upon reaction of $Cp^*W(NR)_2Cl$ with LiNHR, the initially formed amido complex, $Cp^*W(NR)_2(NHR)$ (**91**), eliminates amine to afford the $\eta^1,\eta^5\text{-}CH_2C_5Me_4$ complex (**92**) (equation 26, $R = 2,6\text{-}Pr^i{}_2C_6H_3$).**[172]**

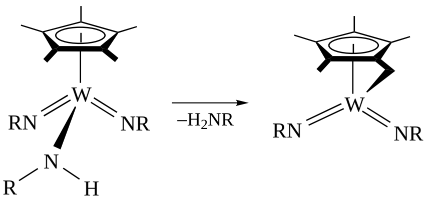

(26)

(**91**) (**92**)

The cyclopentadienyl tungsten–chloro complexes, $[Cp^*W]_2(\mu\text{-Cl})_4$ (**93**) and $Cp'Cl_2W{\equiv}WCl_2Cp'$ (**94**, $Cp' = \eta^5\text{-}C_5H_4R$),**[173]** are important precursors for the synthesis of other organometallic compounds.**[174]** High-yield syntheses of $Cp'WCl_4$ and related imido complexes, including $Cp'WCl_3(NBu^t)$ and 17e $Cp'WCl_2(NBu^t)$, have also been reported ($Cp' = Cp$, Cp^*).**[161,175]** The tetrachloro complex, Cp^*WCl_4 (**95**), has been used to prepare the organometallic fluoride complex, Cp^*WF_5 (**96**),**[176]** and the square–pyramidal tetramethyl complex, Cp^*WMe_4 (**97**),**[177]** that rearranges upon oxidation to give the trigonal–bipyramidal cation, $[Cp^*WMe_4]^+$.**[178]** Terminal chalcogenide derivatives $[Cp^*WE_3]^-$ (E = O, S, Se) are known, and chiral $[Cp^*W(O)(S)(Se)]^-$ can be prepared by treating $Cp^*W(S)_2Cl$ sequentially with H_2O and diselenide reagents.**[179]** Finally, related oxo and sulfido derivatives including $Cp^*W(O)_2Cl$ and $[Cp^*WS_3]^-$ have been used as reagents for the synthesis of cluster complexes**[180–182]** (*see* ***Cluster Compounds: Inorganometallic Compounds Containing Transition Metal & Main Group Elements***).

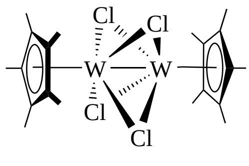

(**93**)

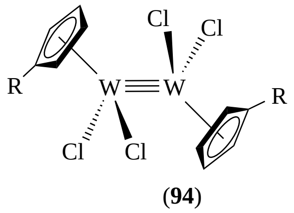

(**94**)

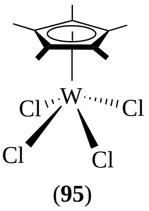

(**95**)

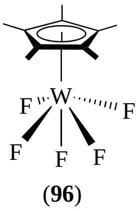

(**96**)

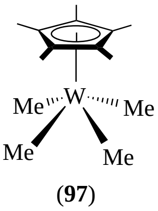

(**97**)

Important advances in the field of C–H bond activation have involved the photochemical reactions of boryl complexes such as Cp*W(CO)$_3$(Bcat) (**98**, cat = 1,2-O$_2$-3,5-Me$_2$C$_6$H$_2$). Transient species derived from these complexes efficiently activate the C–H bonds of alkanes and arenes (*see* ***Alkane Carbon–Hydrogen Bond Activation***), and they can convert hydrocarbon solvents into alkylboronate esters (equation 27).[183,184] Experimental and theoretical studies have shown that these reactions proceed via a boron-assisted, σ-bond metathesis (*see σ-Bond Metathesis*) pathway involving back donation of electron density from the tungsten atom to a formally unoccupied p orbital centered on the boryl ligand.[185]

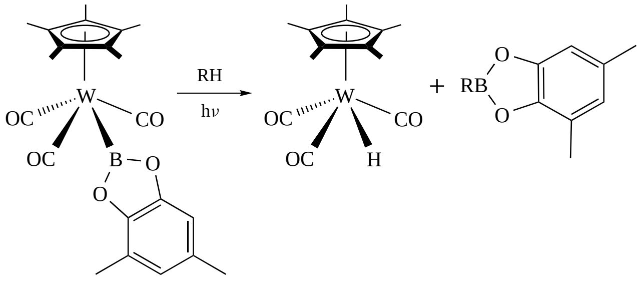

(**98**)

(27)

Photolysis of Cp*W(CO)$_3$Me in the presence of excess HSiMe$_2$SiMeR$_2$ affords dimeric [Cp*W(CO)$_2$(=SiR$_2$)(SiMe$_3$)]$_2$ (**99**) when R = Me. However, the novel silylene complex, Cp*W(CO)$_2$(=SiR$_2$)(SiMe$_3$) (**100**), is obtained when R = Mes.[186] Kinetic analyses (*see Kinetic Methods*) of hydride abstraction from Cp′W(CO)$_3$H using [Ph$_3$C]BF$_4$ have revealed that when Cp′ = Cp*, a normal kinetic isotope effect (*see Isotope Effect*) is observed, but when Cp′ = η^5-C$_5$H$_4$CO$_2$Me, an inverse isotope effect results.[187]

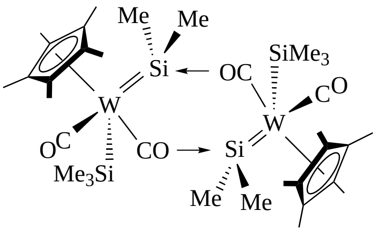

(**99**)

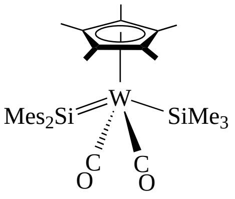

(**100**)

3.6 η^6-Hydrocarbon Complexes

Surprisingly, little new research on the prototypal tungsten–arene complex (*see Arene Complexes*), (η^6-C$_6$H$_6$)$_2$W, has appeared, possibly because of the low-yielding and elaborate experimental procedures required for its synthesis.[188,189] Photolysis of W(CO)$_6$ in the presence of ethyne leads to the formation of benzene and (η^6-C$_6$H$_6$)W(CO)$_3$ (**101**),[130] and the solid-state molecular structure of this complex was only recently reported.[190] Related (η^6-arene)W(CO)$_3$ complexes catalyze the cyclotrimerization and polymerization of alkynes.[191] Intramolecular (*see Intramolecular*) capture of aryl-containing ligands by an unsaturated metal center also leads to the formation of η^6-arene complexes; for instance, hydrogenolysis of [(Me$_3$SiN)$_2$C$_6$H$_4$](NPh)WR$_2$ (R = CH$_2$CH$_2$Ph, CH$_2$CH$_2$CH$_2$Ph) in toluene affords [(Me$_3$SiN)$_2$C$_6$H$_4$](NPh)W(η^6-C$_6$H$_5$R) (R = Et, Pr^n), and the arene ligands adopt an unusual η^4-coordination mode in the solid state.[192] Furthermore, Na reduction of W(OAr)$_2$Cl$_4$ (Ar = 2,3,5,6-C$_6$HPh$_4$) in the presence of a Lewis base generates W(OC$_6$HPh$_3$-η^6-C$_6$H$_5$)(OAr)(L) (**102**, L = NC$_5$H$_4$Bu^t),[193] and a closely related complex (L = PMe$_2$Ph) effects an unprecedented 4e reduction of azobenzene at a single metal center.[194]

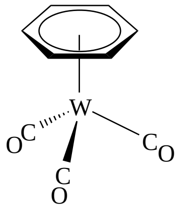

(**101**)

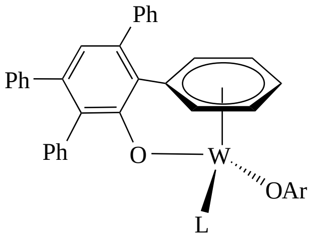

(**102**)

4 RELATED ARTICLES

Bonding Energetics of Organometallic Compounds; Coordination & Organometallic Chemistry: Principles; Electronic Structure of Organometallic Compounds; Mechanisms of Reaction of Organometallic Complexes; Stability Constants & their Determination; Tungsten: Inorganic & Coordination Chemistry.

5 REFERENCES

1. J. E. Ellis, *Organometallics*, 2003, **22**, 3322.
2. I. S. Zavarine and C. P. Kubiak, *Coord. Chem. Rev.*, 1998, **171**, 419.
3. I. P. Beletskaya, A. Z. Voskoboynikov, E. B. Chuklanova, A. I. Gusev, and A. V. Kisin, *J. Organomet. Chem.*, 1993, **454**, 1.
4. H. Willner and F. Aubke, *Organometallics*, 2003, **22**, 3612.
5. G. J. Kubas, *Inorg. Synth.*, 1990, **27**, 1.
6. J. E. Veltheer and P. Legzdins, in ‘Synthetic Methods of Organometallic and Inorganic Chemistry’, ed. W. A. Herrmann, Thieme, Stuttgart, 1997, Vol. 8, p. 79.

7. T. T. Chin, J. K. Hoyano, P. Legzdins, and J. T. Malito, *Inorg. Synth.*, 1991, **28**, 196.
8. E. O. Fischer, *Inorg. Synth.*, 1963, **7**, 136.
9. A. R. Manning, P. Hackett, R. Birdwhistell, and P. Soye, *Inorg. Synth.*, 1991, **28**, 148.
10. P. K. Baker, *Adv. Organomet. Chem.*, 1996, **40**, 45.
11. P. K. Baker, *Chem. Soc. Rev.*, 1998, 125.
12. R. D. Adams, *Acc. Chem. Res.*, 2000, **33**, 171.
13. R. Paur-Afshari, J. Lin, and R. H. Schultz, *Organometallics*, 2000, **19**, 1682.
14. M. Shimoi, S.-I. Nagai, M. Ichikawa, Y. Kawano, K. Katoh, M. Uruichi, and H. Ogino, *J. Am. Chem. Soc.*, 1999, **121**, 11704.
15. H. Sakaba, M. Tsukamoto, C. Kabuto, and H. Horino, *Chem. Lett.*, 2000, 1404.
16. R. L. Miller, P. T. Wolczanski, and A. L. Rheingold, *J. Am. Chem. Soc.*, 1993, **115**, 10422.
17. L. Weber, *Angew. Chem., Int. Ed. Engl.*, 1998, **37**, 1515.
18. M. O. Albers, E. Singleton, and N. J. Coville, *J. Chem. Ed.*, 1986, **63**, 444.
19. M. O. Albers and N. J. Colville, *Inorg. Synth.*, 1990, **28**, 140.
20. P. Legzdins, S. J. Rettig, and K. J. Ross, *Organometallics*, 1994, **13**, 569.
21. P. J. Daff, A. Monge, P. Palma, M. L. Poveda, C. Ruiz, P. Valerga, and E. Carmona, *Organometallics*, 1997, **16**, 2263.
22. R. L. Huff, S.-Y. S. Wang, K. A. Abboud, and J. M. Boncella, *Organometallics*, 1997, **16**, 1779.
23. A. Samotus and J. Szklarzewicz, *Coord. Chem. Rev.*, 1993, **125**, 63.
24. B. Sieklucka, R. Podgajny, T. Korzeniak, P. Przychodzen, and R. Kania, *C. R. Chimie*, 2002, **5**, 639.
25. J. Lu, W. T. A. Harrison, and A. J. Jacobson, *Angew. Chem., Int. Ed. Engl.*, 1995, **34**, 2557.
26. Z. J. Zhong, H. Seino, Y. Mizobe, M. Hidai, A. Fujishima, S.-I. Ohkoshi, and K. Hashimoto, *J. Am. Chem. Soc.*, 2000, **122**, 2952.
27. V. Pfennig and K. Seppelt, *Science*, 1996, **271**, 626.
28. K. Seppelt, *Acc. Chem. Res.*, 2003, **36**, 147.
29. K. W. Chiu, R. A. Jones, G. Wilkinson, A. M. R. Galas, and M. B. Hursthouse, *J. Am. Chem. Soc.*, 1980, **102**, 7978.
30. A. J. Shortland and G. Wilkinson, *J. Chem. Soc., Dalton Trans.*, 1973, 872.
31. V. Pfennig, N. Robertson, and K. Seppelt, *Angew. Chem., Int. Ed. Engl.*, 1997, **36**, 1350.
32. A. L. Galyer and G. Wilkinson, *J. Chem. Soc., Dalton Trans.*, 1976, 2235.
33. K. W. Chiu, R. A. Jones, G. Wilkinson, A. M. R. Galas, M. B. Hursthouse, and K. M. A. Malik, *J. Chem. Soc., Dalton Trans.*, 1981, 1204.
34. M. Kaupp, *Chem. – Eur. J.*, 1998, **4**, 1678.
35. B. Roessler, V. Pfennig, and K. Seppelt, *Chem. – Eur. J.*, 2001, **7**, 3652.
36. K. H. Thiele, A. Russek, R. Opitz, B. Mohai, and W. Brueser, *Z. Anorg. Allg. Chem.*, 1975, **412**, 11.
37. T. M. Gilbert, C. B. Bauer, and R. D. Rogers, *Polyhedron*, 1999, **18**, 1303.
38. S. U. Koschmieder, B. S. McGilligan, G. McDermott, J. Arnold, G. Wilkinson, B. Hussain-Bates, and M. B. Hursthouse, *J. Chem. Soc., Dalton Trans.*, 1990, 3427.
39. J. Sundermeyer, J. Putterlik, and H. Pritzkow, *Chem. Ber.*, 1993, **126**, 289.
40. P. Legzdins and J. E. Veltheer, *Acc. Chem. Res.*, 1993, **26**, 41.
41. W. B. Sharp, P. J. Daff, W. S. McNeil, and P. Legzdins, *J. Am. Chem. Soc.*, 2001, **123**, 6272.
42. N. H. Dryden, P. Legzdins, J. Trotter, and V. C. Yee, *Organometallics*, 1991, **10**, 2857.
43. R. Bau, S. A. Mason, B. O. Patrick, C. S. Adams, W. B. Sharp, and P. Legzdins, *Organometallics*, 2001, **20**, 4492.
44. E. B. Brouwer, P. Legzdins, S. J. Rettig, and K. J. Ross, *Organometallics*, 1993, **12**, 4234.
45. P. Legzdins, S. J. Rettig, K. J. Ross, R. J. Batchelor, and F. W. B. Einstein, *Organometallics*, 1995, **14**, 5579.
46. D. J. Burkey, J. D. Debad, and P. Legzdins, *J. Am. Chem. Soc.*, 1997, **119**, 1139.
47. D. S. Frohnapfel and J. L. Templeton, *Coord. Chem. Rev.*, 2000, **206–207**, 199.
48. J. D. Debad, P. Legzdins, S. A. Lumb, R. J. Batchelor, and F. W. B. Einstein, *Organometallics*, 1995, **14**, 2543.
49. D. S. Frohnapfel, A. E. Enriquez, and J. L. Templeton, *Organometallics*, 2000, **19**, 221.
50. T. W. Crane, P. S. White, and J. L. Templeton, *Inorg. Chem.*, 2000, **39**, 1081.
51. J. L. Kiplinger, M. A. King, A. Fechtenkoetter, A. M. Arif, and T. G. Richmond, *Organometallics*, 1996, **15**, 5292.
52. K. R. Birdwhistell and J. L. Templeton, *Organometallics*, 1985, **4**, 2062.
53. J. Milke, K. Sunkel, and W. Beck, *J. Organomet. Chem.*, 1997, **543**, 39.
54. S. F. T. Froom, M. Green, R. J. Mercer, K. R. Nagle, A. G. Orpen, and R. A. Rodrigues, *J. Chem. Soc., Dalton Trans.*, 1991, 3171.
55. M. P. Gamasa, J. Gimeno, L. Zhang, M. Lanfranchi, and A. Tiripicchio, *J. Organomet. Chem.*, 1996, **514**, 287.
56. J. Ipaktschi, F. Mirzaei, G. J. Demuth-Eberle, J. Beck, and M. Serafin, *Organometallics*, 1997, **16**, 3965.
57. J. Perez, V. Riera, A. Rodriguez, and S. Garcia-Granda, *Angew. Chem., Int. Ed. Engl.*, 2002, **41**, 1427.
58. A. Hills, D. L. Hughes, N. Kashef, M. A. N. D. A. Lemos, A. J. L. Pombeiro, and R. L. Richards, *J. Chem. Soc., Dalton Trans.*, 1992, 1775.
59. S. K. Hurst and T. Ren, *J. Organomet. Chem.*, 2003, **670**, 188.

60. J. Manna, S. J. Geib, and M. D. Hopkins, *J. Am. Chem. Soc.*, 1992, **114**, 9199.
61. P. Mathur, A. K. Bhunia, A. Kumar, S. Chatterjee, and S. M. Mobin, *Organometallics*, 2002, **21**, 2215.
62. C.-L. Li and R.-S. Liu, *Chem. Rev.*, 2000, **100**, 3127.
63. I. Y. Wu, J. H. Tsai, B. C. Huang, S. C. Chen, and Y. C. Lin, *Organometallics*, 1993, **12**, 3971.
64. M. I. Bruce, M. Ke, P. J. Low, B. W. Skelton, and A. H. White, *Organometallics*, 1998, **17**, 3539.
65. A. K. McMullen, J. P. Selegue, and J. G. Wang, *Organometallics*, 1991, **10**, 3421.
66. Y.-L. Yang, L. J.-J. Wang, Y.-C. Lin, S.-L. Huang, M.-C. Chen, G.-H. Lee, and Y. Wang, *Organometallics*, 1997, **16**, 1573.
67. K. H. Dotz and J. Pfeiffer, *Transit. Met. Org. Synth.*, 1998, **1**, 335.
68. C. F. Bernasconi, *Chem. Soc. Rev.*, 1997, **26**, 299.
69. R. Aumann and H. Nienaber, *Adv. Organomet. Chem.*, 1997, **41**, 163.
70. R. Aumann, *Eur. J. Org. Chem.*, 2000, 17.
71. H. Fischer, G. Roth, D. Reindl, and C. Troll, *J. Organomet. Chem.*, 1993, **454**, 133.
72. C. Hartbaum, E. Mauz, G. Roth, K. Weissenbach, and H. Fischer, *Organometallics*, 1999, **18**, 2619.
73. D. N. Clark and R. R. Schrock, *J. Am. Chem. Soc.*, 1978, **100**, 6774.
74. L. K. Johnson, M. Frey, T. A. Ulibarri, S. C. Virgil, R. H. Grubbs, and J. W. Ziller, *J. Am. Chem. Soc.*, 1993, **115**, 8167.
75. C. B. Pamplin and P. Legzdins, *Acc. Chem. Res.*, 2003, **36**, 223.
76. S. Acebron, M. V. Galakhov, P. Gomez-Sal, A. Martin, P. Royo, and A. Vazquez de Miguel, *J. Organomet. Chem.*, 1999, **580**, 110.
77. C. Floriani and R. Floriani-Moro, *Adv. Organomet. Chem.*, 2001, **47**, 167.
78. P. A. van der Schaaf, R. A. T. M. Abbenhuis, W. P. A. van der Noort, R. de Graaf, D. M. Grove, W. J. J. Smeets, A. L. Spek, and G. van Koten, *Organometallics*, 1994, **13**, 1433.
79. S.-Y. S. Wang, D. D. VanderLende, K. A. Abboud, and J. M. Boncella, *Organometallics*, 1998, **17**, 2628.
80. S. G. Feng, P. S. White, and J. L. Templeton, *J. Am. Chem. Soc.*, 1992, **114**, 2951.
81. C. M. Bastos, K. S. Lee, M. A. Kjelsberg, A. Mayr, D. Van Engen, S. A. Koch, J. D. Franolic, W. T. Klooster, and T. F. Koetzle, *Inorg. Chim. Acta*, 1998, **279**, 7.
82. A. Mayr, M. F. Asaro, T. J. Glines, D. Van Engen, and G. M. Tripp, *J. Am. Chem. Soc.*, 1993, **115**, 8187.
83. T. B. Gunnoe, P. S. White, J. L. Templeton, and L. Casarrubios, *J. Am. Chem. Soc.*, 1997, **119**, 3171.
84. J. E. Muir, A. Haynes, and M. J. Winter, *J. Chem. Soc., Chem. Commun.*, 1996, 1765.
85. R. R. Schrock and A. H. Hoveyda, *Angew. Chem., Int. Ed. Engl.*, 2003, **42**, 4592.
86. O. Fujimura, G. C. Fu, P. W. K. Rothemund, and R. H. Grubbs, *J. Am. Chem. Soc.*, 1995, **117**, 2355.
87. K. A. Jorgensen, *J. Organomet. Chem.*, 1994, **478**, 9.
88. J. Manna, R. J. Kuk, R. F. Dallinger, and M. D. Hopkins, *J. Am. Chem. Soc.*, 1994, **116**, 9793.
89. B. Schwenzer and H. Fischer, *J. Organomet. Chem.*, 2003, **667**, 16.
90. T. Chen, Z. Wu, L. Li, K. R. Sorasaenee, J. B. Diminnie, H. Pan, I. A. Guzei, A. L. Rheingold, and Z. Xue, *J. Am. Chem. Soc.*, 1998, **120**, 13519.
91. K.-Y. Shih, K. Totland, S. W. Seidel, and R. R. Schrock, *J. Am. Chem. Soc.*, 1994, **116**, 12103.
92. D. A. Dobbs, R. R. Schrock, and W. M. Davis, *Inorg. Chim. Acta*, 1997, **263**, 171.
93. R. R. Schrock, S. W. Seidel, N. C. Moesch-Zanetti, D. A. Dobbs, K.-Y. Shih, and W. M. Davis, *Organometallics*, 1997, **16**, 5195.
94. M. H. Chisholm, *J. Chem. Soc., Dalton Trans.*, 1996, 1781.
95. R. L. M. Chamberlin, D. C. Rosenfeld, P. T. Wolczanski, and E. B. Lobkovsky, *Organometallics*, 2002, **21**, 2724.
96. A. Furstner and G. Seidel, *Angew. Chem., Int. Ed. Engl.*, 1998, **37**, 1734.
97. T. M. Gilbert and R. D. Rogers, *Acta Crystallogr., Sect. C*, 1993, **C49**, 677.
98. L. M. Atagi and J. M. Mayer, *Polyhedron*, 1995, **14**, 113.
99. L. M. Atagi and J. M. Mayer, *Organometallics*, 1994, **13**, 4794.
100. Z. Xue, L. Li, L. K. Hoyt, J. B. Diminnie, and J. L. Pollitte, *J. Am. Chem. Soc.*, 1994, **116**, 2169.
101. A. E. Enriquez, P. S. White, and J. L. Templeton, *J. Am. Chem. Soc.*, 2001, **123**, 4992.
102. B. E. Woodworth, D. S. Frohnapfel, P. S. White, and J. L. Templeton, *Organometallics*, 1998, **17**, 1655.
103. G. C. Bruce and F. G. A. Stone, *Polyhedron*, 1992, **11**, 1607.
104. A. E. Enriquez and J. L. Templeton, *Organometallics*, 2002, **21**, 852.
105. A. D. Main and L. McElwee-White, *J. Am. Chem. Soc.*, 1997, **119**, 4551.
106. K. E. Torraca and L. McElwee-White, *Coord. Chem. Rev.*, 2000, **206–207**, 469.
107. T. Szymanska-Buzar, K. Kern, and D. J. Stufkens, *New J. Chem.*, 1998, **22**, 1539.
108. T. Szymanska-Buzar, K. Kern, A. J. Downs, T. M. Greene, L. J. Morris, and S. Parsons, *New J. Chem.*, 1999, **23**, 407.
109. S. A. Jackson, P. M. Hodges, M. Poliakoff, J. J. Turner, and F. W. Grevels, *J. Am. Chem. Soc.*, 1990, **112**, 1221.
110. D. Del Rio, G. Schubert, I. Papai, and A. Galindo, *J. Organomet. Chem.*, 2002, **663**, 83.

111. E. Carmona, A. Galindo, A. Monge, M. A. Munoz, M. L. Poveda, and C. Ruiz, *Inorg. Chem.*, 1990, **29**, 5074.

112. A. Galindo, A. Pastor, P. J. Perez, and E. Carmona, *Organometallics*, 1993, **12**, 4443.

113. F. P. A. Johnson, C. M. Gordon, P. M. Hodges, M. Poliakoff, and J. J. Turner, *J. Chem. Soc., Dalton Trans.*, 1991, 833.

114. S.-Y. S. Wang, K. A. Abboud, and J. M. Boncella, *J. Am. Chem. Soc.*, 1997, **119**, 11990.

115. Q. D. Shelby and G. S. Girolami, *Organometallics*, 1999, **18**, 2297.

116. R. A. Henderson and K. E. Oglieve, *J. Chem. Soc., Chem. Commun.*, 1991, 584.

117. R. P. Hughes, S. M. Maddock, I. A. Guzei, L. M. Liable-Sands, and A. L. Rheingold, *J. Am. Chem. Soc.*, 2001, **123**, 3279.

118. G. E. Herberich and K. Linn, *J. Organomet. Chem.*, 1992, **425**, C4.

119. J. D. Debad, P. Legzdins, S. A. Lumb, S. J. Rettig, R. J. Batchelor, and F. W. B. Einstein, *Organometallics*, 1999, **18**, 3414.

120. K. J. Ivin and J. Kress, *C. R. Chimie*, 2002, **5**, 345.

121. W. C. P. Tsang, K. C. Hultzsch, J. B. Alexander, P. J. Bonitatebus Jr, R. R. Schrock, and A. H. Hoveyda, *J. Am. Chem. Soc.*, 2003, **125**, 2652.

122. J. Kress and J. A. Osborn, *Angew. Chem., Int. Ed. Engl.*, 1992, **31**, 1585.

123. P. M. Graham, S. H. Meiere, M. Sabat, and W. D. Harman, *Organometallics*, 2003, **22**, 4364.

124. H.-F. Hsu, Y. Du, T. E. Albrecht-Schmitt, S. R. Wilson, and J. R. Shapley, *Organometallics*, 1998, **17**, 1756.

125. L.-C. Song, J.-T. Liu, Q.-M. Hu, G.-F. Wang, P. Zanello, and M. Fontani, *Organometallics*, 2000, **19**, 5342.

126. X. Jin, X. Xie, and K. Tang, *Chem. Commun.*, 2002, 750.

127. J. L. Templeton, *Adv. Organomet. Chem.*, 1989, **29**, 1.

128. T. B. Gunnoe, P. S. White, and J. L. Templeton, *J. Am. Chem. Soc.*, 1996, **118**, 6916.

129. M. B. Wells, J. E. McConathy, P. S. White, and J. L. Templeton, *Organometallics*, 2002, **21**, 5007.

130. T. Szymanska-Buzar and K. Kern, *J. Organomet. Chem.*, 2001, **622**, 74.

131. K. R. Birdwhistell, T. L. Tonker, and J. L. Templeton, *J. Am. Chem. Soc.*, 1987, **109**, 1401.

132. R. Stegmann and G. Frenking, *Organometallics*, 1998, **17**, 2089.

133. M. I. Bruce, *Chem. Rev.*, 1991, **91**, 197.

134. C. Bruneau and P. H. Dixneuf, *Acc. Chem. Res.*, 1999, **32**, 311.

135. T. Y. Hsiao, P. L. Kuo, C. H. Lai, C. H. Cheng, C. Y. Cheng, and S. L. Wang, *Organometallics*, 1993, **12**, 1094.

136. M. V. Baker and M. R. North, *J. Organomet. Chem.*, 1998, **565**, 225.

137. W.-Y. Yeh, C.-L. Ho, M. Y. Chiang, and I. T. Chen, *Organometallics*, 1997, **16**, 2698.

138. K. W. Chiu, D. Lyons, G. Wilkinson, M. Thornton-Pett, and M. B. Hursthouse, *Polyhedron*, 1983, **2**, 803.

139. G. A. Cairns, N. Carr, M. Green, and M. F. Mahon, *Chem. Commun.*, 1996, 2431.

140. J. Ipaktschi, G. J. Demuth-Eberle, F. Mirzaei, B. G. Mueller, J. Beck, and M. Serafin, *Organometallics*, 1995, **14**, 3335.

141. M. B. O'Regan, M. G. Vale, J. F. Payack, and R. R. Schrock, *Inorg. Chem.*, 1992, **31**, 1112.

142. A. J. Nielson, P. D. W. Boyd, G. R. Clark, P. A. Hunt, M. B. Hursthouse, J. B. Metson, C. E. F. Rickard, and P. A. Schwerdtfeger, *J. Chem. Soc., Dalton Trans.*, 1995, 1153.

143. M. Kersting, A. El-Kholi, U. Mueller, and K. Dehnicke, *Chem. Ber.*, 1989, **122**, 279.

144. M. H. Chisholm, W. E. Streib, D. B. Tiedtke, and D.-D. Wu, *Chem. – Eur. J.*, 1998, **4**, 1470.

145. C. R. Landis, T. Cleveland, and C. P. Casey, *Inorg. Chem.*, 1995, **34**, 1285.

146. R. Benn, T. H. Brock, P. W. Jolly, A. Rufinska, and G. Schroth, *Polyhedron*, 1990, **9**, 23.

147. L. M. Atagi, S. C. Critchlow, and J. M. Mayer, *J. Am. Chem. Soc.*, 1992, **114**, 1483.

148. S. H. K. Ng, C. S. Adams, and P. Legzdins, *J. Am. Chem. Soc.*, 2002, **124**, 9380.

149. D. S. Frohnapfel, P. S. White, and J. L. Templeton, *Organometallics*, 2000, **19**, 1497.

150. H. Sakaba, S. Watanabe, C. Kabuto, and K. Kabuto, *J. Am. Chem. Soc.*, 2003, **125**, 2842.

151. T. B. Gunnoe, P. S. White, and J. L. Templeton, *Organometallics*, 1997, **16**, 3794.

152. R. H. Cayton, M. H. Chisholm, M. J. Hampden-Smith, J. C. Huffman, and K. G. Moodley, *Polyhedron*, 1992, **11**, 3197.

153. M. H. Chisholm, K. Folting, M. A. Lynn, W. E. Streib, and D. B. Tiedtke, *Angew. Chem., Int. Ed. Engl.*, 1997, **36**, 52.

154. K.-W. Liang, G.-H. Lee, S.-M. Peng, and R.-S. Liu, *J. Chem. Soc., Chem. Commun.*, 1994, 2705.

155. S. Özkar, C. G. Kreiter, and M. Kotzian, *J. Organomet. Chem.*, 1995, **494**, 115.

156. M. Kaupp, T. Kopf, A. Murso, D. Stalke, C. Strohmann, J. R. Hanks, F. G. N. Cloke, and P. B. Hitchcock, *Organometallics*, 2002, **21**, 5021.

157. B. Bogdanovic, H. Bönneman, R. Goddard, A. Startsev, and J. M. Wallis, *J. Organomet. Chem.*, 1986, **299**, 347.

158. I. A. Morkan and A. Uztetik-Morkan, *Z. Naturforsch.*, 2000, **55b**, 1153.

159. P. K. Baker, M. G. B. Drew, M. M. Meehan, and J. Mueller, *Z. Anorg. Allg. Chem.*, 2002, **628**, 1727.

160. W.-Y. Yeh and L.-K. Liu, *J. Am. Chem. Soc.*, 1992, **114**, 2267.

161. M. L. H. Green, *Pure Appl. Chem.*, 1995, **67**, 249.

162. J. F. Hartwig and X. He, *Angew. Chem., Int. Ed. Engl.*, 1996, **35**, 315.

163. H. Brunner, M. Muschiol, T. Neuhierl, and B. Nuber, *Chem. – Eur. J.*, 1998, **4**, 168.

164. A. Schulz and T. M. Klapötke, *J. Organomet. Chem.*, 1994, **480**, 195.

165. C. Persson and C. Andersson, *Organometallics*, 1993, **12**, 2370.

166. J. C. Green and C. N. Jardine, *J. Chem. Soc., Dalton Trans.*, 1998, 1057.

167. L. Luo, G. Lanza, I. L. Fragala, C. L. Stern, and T. J. Marks, *J. Am. Chem. Soc.*, 1998, **120**, 3111.

168. C.-I. Li, W.-Y. Yeh, S.-M. Peng, and G.-H. Lee, *J. Organomet. Chem.*, 2001, **620**, 106.

169. D. G. Churchill, K. E. Janak, J. S. Wittenberg, and G. Parkin, *J. Am. Chem. Soc.*, 2002, **125**, 1403.

170. R. M. Bullock, C. E. L. Headford, K. M. Hennessy, S. E. Kegley, and J. R. Norton, *J. Am. Chem. Soc.*, 1989, **111**, 3897.

171. A. Chernega, J. Cook, M. L. H. Green, L. Labella, S. J. Simpson, J. Souter, and A. H. H. Stephens, *J. Chem. Soc., Dalton Trans.*, 1997, 3225.

172. S. R. Huber, T. C. Baldwin, and D. E. Wigley, *Organometallics*, 1993, **12**, 91.

173. Q. Feng, M. L. H. Green, and P. Mountford, *J. Chem. Soc., Dalton Trans.*, 1992, 2171.

174. M. L. H. Green and P. Mountford, *Chem. Soc. Rev.*, 1992, **21**, 29.

175. P. Gomez Sal, I. Jimenez, A. Martin, T. Pedraz, P. Royo, A. Selles, and A. Vazquez de Miguel, *Inorg. Chim. Acta*, 1998, **273**, 270.

176. K. Köhler, A. Herzog, A. Steiner, and H. W. Roesky, *Angew. Chem., Int. Ed. Engl.*, 1996, **35**, 295.

177. K. Köhler, A. Steiner, and H. W. Roesky, *Z. Naturforsch., B: Chem. Sci.*, 1995, **50**, 1207.

178. S. A. Lerke and D. H. Evans, *J. Am. Chem. Soc.*, 1995, **117**, 11768.

179. H. Kawaguchi and K. Tatsumi, *Angew. Chem., Int. Ed. Engl.*, 2001, **40**, 1266.

180. M. S. Rau, C. M. Kretz, G. L. Geoffroy, and A. L. Rheingold, *Organometallics*, 1993, **12**, 3447.

181. M. S. Rau, C. M. Kretz, G. L. Geoffroy, A. L. Rheingold, and B. S. Haggerty, *Organometallics*, 1994, **13**, 1624.

182. J.-P. Lang, S.-J. Ji, Q.-F. Xu, Q. Shen, and K. Tatsumi, *Coord. Chem. Rev.*, 2003, **241**, 47.

183. K. M. Waltz and J. F. Hartwig, *Science*, 1997, **277**, 211.

184. K. M. Waltz and J. F. Hartwig, *J. Am. Chem. Soc.*, 2000, **122**, 11358.

185. C. E. Webster, Y. Fan, M. B. Hall, D. Kunz, and J. F. Hartwig, *J. Am. Chem. Soc.*, 2003, **125**, 858.

186. K. Ueno, S. Asami, N. Watanabe, and H. Ogino, *Organometallics*, 2002, **21**, 1326.

187. T.-Y. Cheng and R. M. Bullock, *J. Am. Chem. Soc.*, 1999, **121**, 3150.

188. E. O. Fischer, F. Scherer, and H. O. Stahl, *Chem. Ber.*, 1960, **93**, 2065.

189. F. G. N. Cloke and M. L. H. Green, *J. Chem. Soc., Dalton Trans.*, 1981, 1938.

190. J. M. Oh, S. J. Geib, and N. J. Cooper, *Acta Crystallogr., Sect. C*, 1998, **54**, 581.

191. T. A. Vijayaraj and G. Sundararajan, *Organometallics*, 1997, **16**, 4940.

192. R. C. Mills, K. A. Abboud, and J. M. Boncella, *Organometallics*, 2000, **19**, 2953.

193. M. R. Lentz, P. E. Fanwick, and I. P. Rothwell, *Organometallics*, 2003, **22**, 2259.

194. F. Maseras, M. A. Lockwood, O. Eisenstein, and I. P. Rothwell, *J. Am. Chem. Soc.*, 1998, **120**, 6598.

Tungsten Proteins

Michael W. W. Adams[1] & Roopali Roy[2]
[1] *University of Georgia, Athens, GA, USA*
[2] *Harvard Medical School, Boston, MA, USA*

1 Introduction 5743
2 Molecular and Catalytic Properties of Tungstoenzymes 5744
3 Physiological Roles 5746
4 Structural Properties of Tungstoenzymes 5747
5 Spectroscopic Properties 5748
6 Evolutionary Considerations 5749
7 Related Articles 5750
8 Further Reading 5750
9 References 5750

Glossary

Acetogen: a strictly anaerobic bacterium that produces acetate as the sole fermentation product
Methanogen: a strictly anaerobic bacterium that produces methane
Hyperthermophile: a microorganism that grows at or above 90 °C

Abbreviations

FDH = Formate dehydrogenase; CAR = Carboxylic acid reductase; FMDH = Formylmethanofuran dehydrogenase; MFR = Methanofuran; AOR = Aldehyde ferredoxin oxidoreductase; MPT = Molybdopterin; Fd_{ox} = Oxidized ferredoxin; Fd_{red} = Reduced ferredoxin; FOR = Formaldehyde ferredoxin oxidoreductase; EXAFS = X-ray absorption edge fine structure; kDa = Kilodaltons; EPR = Electron paramagnetic resonance.

1 INTRODUCTION

The element Tungsten (W, atomic number 74) has long been prized for its high melting point, good conductivity, and strength. It is used in the manufacture of a wide variety of industrial and household products including light bulb filaments. W is relatively scarce in natural environments, the usual source for this metal being oxo-rich mineral ores such as wolframite ($[Fe/Mn]WO_4$, scheelite ($CaWO_4$) or the more reduced form tungstenite (WS_2)). The concentration of W in soil and freshwater is very low (less than 0.5 nM). In contrast, significantly higher amounts (>50 nM) can be found in alkaline brine lakes, hot springs, and marine hydrothermal vents.[1,2]

Tungsten is a 5d series element and its ionic electronic configuration is $[Xe]4f^{14}5d^{4}6s^{2}$ (*see* ***Tungsten: Inorganic & Coordination Chemistry***). The 4d series element Molybdenum (Mo), situated above W in the periodic table, shares similar chemical properties. The atomic and ionic radii of W and Mo, as well as their electron affinity, are identical. In aqueous solution, both elements are more stable at higher oxidation states and the reduction potentials of their (V/VI) and (IV/V) couples are in the same range, being slightly more negative for W. However, these two analogous elements differ considerably with regard to their role in biology. Molybdoenzymes are ubiquitous in nature and are found in virtually all life forms from microorganisms to eukaryotes (*see* ***Molybdenum: MPT-containing Enzymes***). They play intrinsic roles in the global cycles of nitrogen, carbon, and sulfur metabolism, and their biochemical, structural, and spectroscopic properties have been extensively analyzed.[3,4] In contrast, a functional role for tungsten in biological systems was not realized until the 1970s. Traditionally W had been regarded as an antagonist of the biological function of Mo. Thus microorganisms grown in the presence of W typically try to incorporate W into their molybdoenzymes. This results in the production of either inactive molybdoenzymes lacking any metal or tungsten-substituted molybdoenzymes that have little or no catalytic activity.[5–7] The one notable exception is an enzyme (DMSO reductase) from a photosynthetic bacterium (*Rhodobacter capsulatus*). In this case, the substitution of Mo, the metal that occurs naturally at the active site, by W resulted in an enzyme that retained its three-dimensional structure as well as enzymatic properties.[8] However, this still remains very much an exception and in spite of the high degree of chemical similarity between these two elements, nature is highly selective. Even if tungsten does become incorporated into a molybdoenzyme, its properties are different enough from those of molybdenum to preclude significant catalytic activity.

The first indications that W has a positive role in biology came from reports in the early 1970s when the growth of certain acetate- and methane-producing microorganisms was shown to be stimulated by the addition of tungstate to their growth media.[9] Subsequently, the first naturally occurring tungsten-containing protein was isolated from an acetogen.[10] Since then this field has grown and at present more than a dozen, naturally occurring tungsten-containing enzymes are known. Tungstoenzymes can be found in a variety of microorganisms including those that grow at extreme (hyperthermophiles) as well as conventional temperatures (mesophiles), in archaea and bacteria, and in organisms that reduce sulfur or sulfate, produce methane or acetate, or use acetylene during growth. However, a functional role for W has not been recognized in any eukaryote.

So, what types of organisms have evolved to use tungsten-dependent rather than molybdenum-dependent enzymes, what reactions do these enzymes catalyze, and why is tungsten utilized rather than molybdenum? In the following we address these questions, the answers to which are only just beginning to emerge.

All known tungstoenzymes can be classified into three functionally, phylogenetically, and evolutionarily distinct families. These are: (1) the FMDH family that has two members; formate dehydrogenase (FDH), found in methanogens and acetogens, and N-formylmethanofuran dehydrogenase (FMDH), from methanogenic species; (2) the Aldehyde ferredoxin oxidoreductase (AOR) family, which is represented by the prototypical member, aldehyde ferredoxin oxidoreductase (AOR), and also includes formaldehyde ferredoxin oxidoreductase (FOR), glyceraldehyde-3-phosphate ferredoxin oxidoreductase (GAPOR), the recently identified WOR4 from hyperthermophilic archaea, carboxylic acid reductase (CAR) from acetogens, and aldehyde dehydrogenase (ADH) from sulfate-reducing bacteria; and (3) the acetylene hydratase (AH) family, which has a single member from an acetylene-utilizing bacterium.

2 MOLECULAR AND CATALYTIC PROPERTIES OF TUNGSTOENZYMES

2.1 F(M)DH Family

It was shown in the mid-1970s that tungstate stimulated the growth of certain acetogenic *Clostridia*, such as *C. thermoaceticum*[11] and *C. formicoaceticum*.[11] These organisms grow by the fermentation of sugars to produce acetate as the sole product. The addition of tungstate to their growth media resulted in a substantial increase in the NADP-dependent formate dehydrogenase activity of cell-free extracts. In addition, the metabolism of formate by the methane-producing organism, *Methanococcus vannielii*, appeared to be tungsten-dependent.[12] Its growth was stimulated by tungstate when formate was used as the carbon and energy source, but not when the organism was grown on H_2 and CO_2. Partial purification of the formate dehydrogenase activity of *M. vannielii* in the early 1980s showed that it contained two types of formate dehydrogenase:[12] one contained molybdenum, while the other seemed to utilize tungsten. The first highly purified form of a tungsten-containing enzyme was reported in 1983 from *C. thermoaceticum.* Its formate dehydrogenase (FDH) contained tungsten, iron and the unusual amino acid selenocysteine, as well as acid-labile sulfur,[10] see Table 1. The tungsten-containing FDHs of methanogens are similarly complex enzymes that contain W, iron−sulfur centers and selenium. Recently two tungsten- and selenium-containing FDHs were isolated from another type of anaerobic bacterium (*Eubacterium acidacminophilum*).[13] FDHs catalyze the reversible reduction of CO_2 to formate (Table 2), with the concomitant transfer of two electrons from the appropriate electron carrier. This reaction has a very negative reduction potential (−420 mV, SHE). The syntrophic bacterium *Syntrophobacter fumaroxidans* constitutively expressed two W-containing FDH's (FDH-1 and FDH-2) when grown on fumarate or propionate.[14] The purified enzymes exhibit high formate-oxidation and CO_2-reduction rates and very low K_m values for formate.

In 1984, a newly isolated methanogen, *Methanobacterium wolfei*, was also shown to require tungsten for growth,[29] although in contrast to *M. vannielii*, *M. wolfei* grew only on H_2 and $CO_2{}^-$ it did not utilize formate. A subsequent and extensive survey[30] of the incorporation of radiolabeled tungstate (^{185}W) into methanogenic species showed that several accumulated significant amounts of the element into their protein fractions. An additional role for tungsten in some methanogens, however, remained unknown until the discovery of the enzyme FMDH. FMDH is found only in the methanogens where it catalyzes the reduction and addition of CO_2 to the organic, methanogenic cofactor, methanofuran (Table 2). The physiological electron donor for this reaction is not known. Methanogens grow on H_2 and CO_2 and generate methane. FMDH catalyzes the first step in the conversion of CO_2 to methane. FMDHs are complex multisubunit enzymes (Table 1) that are intrinsically labile and extremely oxygen sensitive. Usually these enzymes have a Mo cofactor, however, in several thermophilic and hyperthermophilic methanogens, the enzyme contains W.

2.2 AOR Family

The AOR family has been the most extensively studied and the majority of tungstoenzymes known at present belong to this family.[2,31] AOR was first isolated from the hyperthermophilic archaeon *Pyrococcus furiosus*.[15,16] Subsequently, three other members of this family FOR, GAPOR, and WOR4 were purified and characterized from *P. furious*.[17,19,21] All four enzymes consist of a single type of subunit of ∼70 Kilodaltons (kDa) in size, but they differ in their quaternary structures (Table 1). Whereas GAPOR is monomeric, AOR and WOR4 are dimeric and FOR is a tetramer. Each of their subunits contains a mononuclear W site and one iron−sulfur cluster (*see* ***Iron–Sulfur Proteins***). A comparison of their complete amino acid sequences show that AOR, FOR, and WOR4 are most closely related (40% sequence identity with each other) while GAPOR is more distant (23% identity).[21] AOR, FOR, and GAPOR catalyze the conversion of various types of aldehyde to the corresponding acid (Table 2). The reaction involves two-electron oxidation and *in vivo* ferredoxin serves as the electron acceptor. In contrast to other members of the family *P. furiosus* WOR4 does not appear to oxidize

Table 1 Molecular properties of tungsten-containing enzymes

Organism/enzyme[a]	Holoenzyme M_r (kDa)	Subunits/M_r(kDa)	W content[b]	FeS or cluster content[c]	Pterin cofactor[d]
AOR-type					
Pf AOR	136	α_2(67)	2	$2[Fe_4S_4] + 1Fe$	Nonnuc
Pf FOR	280	α_4(69)	4	$4[Fe_4S_4]$	Nonnuc
Pf GAPOR	73	α(73)	1	$1[Fe_4S_4]$	Nonnuc
Pf WOR4	138	α_2(69)	2	$2[Fe_4S_4]$	Nonnuc
Ct CAR (form I)	86	$\alpha\beta$(64,14)	1	∼29 Fe, ∼25 S	Nonnuc
Ct CAR (form II)	300	$\alpha_3\beta_3\gamma$(64,14,43)	3	∼82 Fe, ∼54 S	Nonnuc
Cf CAR	134	α_2(67)	2	∼11 Fe, ∼16 S	Nonnuc
Dg ADH	132	α_2(62)	2	$2[Fe_4S_4]$	NR
F(M)DH-type					
Ct FDH	340	$\alpha_2\beta_2$(96,76)	2	20–40 Fe, 2 Se	NR
Mw FMDH	130	$\alpha\beta\gamma$(64,51,35)	1	2–5 Fe	Nuc[e]
AH-type					
Pa AH	73	α(73)	1	$1[Fe_4S_4]$	Nuc[e]

[a] The abbreviations and sources of data are: Pf (*P. furiosus*) AOR;[15,16] Pf FOR;[17,18] Pf GAPOR;[19,20] Pf WOR4;[21] Ct (*C. thermoaceticum*) CAR;[22,23] Cf (*C. formicoaceticum*) CAR;[22] Dg (*D. gigas*) ADH;[24] Ct FDH;[11,25] Mw (*M. wolfei*) FMDH;[26] Pa (*P. acetylenicus*) AH.[27,28] Modified from Adams and Kletzin.[2] [b] Expressed as integer value per mole of holoenzyme. [c] Cluster content expressed per mole of holoenzyme. [d] Indicates whether the pterin is with (Nuc) or without (Nonnuc) an appended nucleotide. NR, not reported. [e] Appended nucleotide is GMP.

Table 2 Catalytic properties of tungstoenzymes

Enzyme/source[a]	Reaction catalyzed	K_m (mM)	V_{max}[b]
AOR (*P. furiosus*)	$RCHO^c + H_2O + 2Fd^d(ox) \longrightarrow RCOOH + 2H^+ + 2Fd(red)$	0.04^e	67 (80 °C)
FOR (*P. furiosus*)	$HCHO^f + H_2O + 2Fd(ox) \longrightarrow HCOOH + 2H^+ + 2Fd(red)$	25.00^g	62 (80 °C)
GAPOR (*P. furiosus*)	$R'CHO^h + H_2O + 2Fd(ox) \longrightarrow R'COOH + 2H^+ + 2Fd(red)$	0.03	350 (70 °C)
CAR (*C. formicoaceticum*)	$RCHO + MV^{++i} + OH^- \longleftrightarrow RCOO^- + 2H^+ + MV^+$	0.14^j	500 (40 °C)
ADH (*D. gigas*)	$RCHO + BV^{++k} + H_2O \longrightarrow RCOOH + 2H^+ + BV^+$	0.01^l	38 (30 °C)
FDH (*C. thermoaceticum*)	$CO_2 + NADPH + H^+ \longrightarrow HCOOH + NADP^+$	0.11	880 (55 °C)
FMDH (*M. wolfei*)	$CO_2 + MFR^m + 2H^+ \longrightarrow CHO\text{–}MFR + H_2O$	0.01	11 (65 °C)
AH (*P. acetylenicus*)	$C_2H_2 + H_2O \longrightarrow CH_3CHO$	0.01	69 (30 °C)

[a] The sources of data are given in Table 1. [b] μ mole of substrate utilized min^{-1} mg^{-1} of protein at the indicated temperature. [c] R = H, C1–C4, Ar. [d] Fd, ferredoxin. [e] The K_m value was obtained using crotonaldehyde as the substrate for AOR. [f] R = H, C1–C3, C4–C6 di/semialdehydes. [g] The K_m value was obtained using formaldehyde as the substrate for FOR. [h] $R' = CHOHCH_2OPO_3{}^{2-}$. [i] Methyl viologen. [j] The K_m value was obtained using butyraldehyde as the substrate for CAR. [k] Benzyl viologen. [l] The K_m value was obtained using acetaldehyde as the substrate for ADH. [m] N-formylmethanofuran.

aldehydes or 2-hydroxyacids or catalyze the reverse reaction of acid reduction.[21]

CAR was discovered in acetate-producing bacteria based on its ability to catalyze the reverse reaction, the reductive activation of carboxylic acids, though it can also catalyze aldehyde oxidation (Table 2). The acid/aldehyde couple has an extremely low reduction potential, for example, E_0' value for acetaldehyde/acetate is −580 mV (SHE) and therefore, aldehyde oxidation is much more thermodynamically favorable than acid reduction. The electron carrier for the enzyme inside the cell is not known. CAR isolated from *C. formicoaceticum* has molecular properties very similar to that of *P. furiosus* AOR whereas CAR from *C. thermoaceticum* has a more complex organization[22] (Table 1). The final member of this family is ADH from sulfate-reducing bacteria.[24] Its molecular properties closely resemble those of AOR (Table 1).

2.3 Acetylene Hydratase

This family is represented by just one member, AH from the acetylene-utilizing anaerobic bacterium, *Pelobacter acetylenicus*.[27] It comprises a single type of subunit that contains one W and a single iron–sulfur cluster (Table 1).

In contrast to reactions catalyzed by other tungstoenzymes, this enzyme does not appear to catalyze an overall oxidation or reduction. AH catalyzed the hydration of acetylene to acetaldehyde (Table 2). However, AH was found to be active only in the presence of a strong reducting agent, therefore, acetylene hydration might involve consecutive reduction, hydration, and oxidation steps, wherein the W site and the FeS center are required to carry out the redox chemistry. When *P. acetylenicus* was grown in the presence of Mo a fully functional Mo-containing AH was obtained, suggesting that W is not essential for the catalysis of acetylene hydration.[27]

3 PHYSIOLOGICAL ROLES

Most tungstoenzymes isolated so far have been from obligate anaerobes that are also thermophilic to a greater or lesser extent. Moreover, the enzymes have similar catalytic properties. They all catalyze a redox reaction involving conversions at the level of carboxylic acids and aldehydes (with the exception of AH). However, their physiological roles are distinctly different.

FMDH is found only in methane-producing organisms and catalyzes the first step in the conversion of CO_2 to methane. Using methanofuran as the C–1 carrier, FMDH catalyzes the reduction of CO_2 to N-formylmethanofuran. The formyl group is then reduced by a complex series of enzymes and novel cofactors to methane. FMDH is a molybdoenzyme in almost all methanogens so far examined. The notable exception is the moderate thermophile, *M. wolfei*, which grows optimally at 65 °C, in which the enzyme contains tungsten.[26] In fact, this organism contains two FMDHs: one (FMDH II) contains tungsten while the other (FMDH I) contains molybdenum.[32] The latter has also been purified as a catalytically active, 'tungsten-substituted molybdoenzyme' from cells grown in the absence of molybdenum and presence of tungsten.

Like methanogens, the acetogenic clostridia also grow on H_2 and CO_2 (as well as on sugars) but in these organisms CO_2 is ultimately reduced to acetate rather than methane. The first step in the conversion of CO_2 to the methyl group of acetate is catalyzed by FDH. This generates formate, which is subsequently activated and reduced by a series of enzymes using tetrahydrofolate as the C–1 carrier.[33] Acetogens vary in their responses to the addition of tungsten and molybdenum to their growth media, and in some species FDH appears to contain molybdenum while in others FDH seems to be dependent upon tungsten.[34,35] Tungsten-containing FDHs have been purified from the moderate thermophile *C. thermoaceticum*, which grows optimally near 60 °C, and from the mesophile *C. formicoaceticum*.[35] The effects of these two elements on the growth of acetogens is complicated by the finding, in at least some of these organisms, of a second tungstoenzyme, CAR, which reduces carboxylic acids. So far CAR has been purified from the same two acetogens as FDH, *C. thermoaceticum* and *C. formicoaceticum*.[22,36] In fact, *C. formicoaceticum* has been shown to produce two distinct CARs, one containing molybdenum and one containing tungsten.[23] Neither the role of CAR nor its physiological electron carrier are known.[37] This is in spite of the fact that CAR represents about 4% of the total cytoplasmic protein in *C. formicoaceticum*.

It is now evident that tungsten has as at least four different physiological roles in hyperthermophilic microorganisms. In the saccharolytic fermenters such as *P. furiosus*, tungsten-containing GAPOR is known to catalyze a key step in the unusual glycolytic pathway that this microorganism uses to convert glucose to pyruvate.[19,20] GAPOR is absolutely specific for glyceraldehyde-3-phosphate, which is oxidized to 3-phosphoglycerate. Under proteolytic growth conditions of *P. furiosus* or *T. litoralis*, AOR is thought to play a role in the degradation of amino acids.[38] The enzyme shows the highest catalytic efficiencies (and low K_m values) with acetaldehyde (from alanine), isovaleraldehyde (from valine), indoleacetaldehyde (from tryptophan), and phenylacetaldehyde (from phenylalanine). These aldehydes are derived by the transamination (conversion of an amino acid to a keto acid) and decarboxylation (conversion of a keto acid to an aldehyde) of the common amino acids alanine, valine, tyrptophan, and phenylalanine, respectively. A third role for tungstoenzymes comes in the form of FOR, which also appears to be involved in the breakdown of amino acids by *P. furiosus*.[17] Originally isolated based on its ability to oxidize formaldehyde, FOR can also use other short-chain (C_1–C_4) aldehydes as substrates. However, the K_m values for such substrates are very high (>10 mM), especially for formaldehyde (25 mM), indicating that these are unlikely to be physiological substrates (Table 2). The lack of significant activity with longer chain aldehydes (≥C–5) or with aromatic aldehydes indicates that the catalytic site of FOR is probably accessible to only short-chain aldehydes. Interestingly, this tungstoenzyme shows high activity (and low K_m values) with C4–C6 di- and semialdehydes. Such compounds are intermediates in the metabolic pathways of amino acids such as arginine, lysine, and proline. Since the organisms in which FOR has been found, such as *P. furiosus* and *T. litoralis*, grow using proteins as a primary carbon source, FOR may well have a role in amino acid metabolism, although this has yet to be established.[17] Neither GAPOR, FOR, nor AOR can utilize the nicotinamide nucleotides, NAD and NADP, as electron carriers. Instead, these enzymes couple substrate oxidation to the reduction of the extremely thermostable redox protein, ferredoxin. Excess reductant generated from the fermentative metabolism is then disposed of as H_2 by a thermostable hydrogenase which uses reduced ferredoxin as the electron donor.[39] Despite sharing high homology with AOR the fourth tungstoenzyme isolated from *P. furiosus* WOR4[21] does not appear to catalyze aldehyde oxidation or acid reduction. In fact, the reaction catalyzed by this novel enzyme, the fourth for a

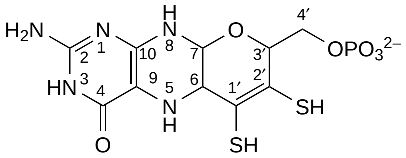

Figure 1 Structure of pterin cofactor found in tungstoenzymes such as *P. furiosus* AOR

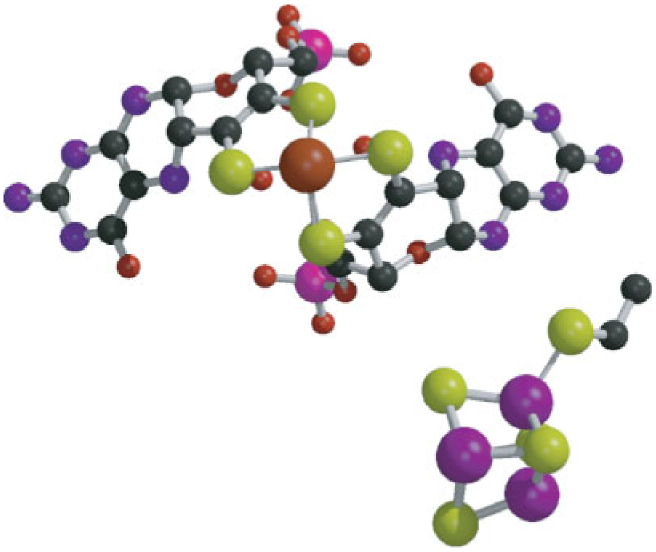

Figure 2 Ball-and-stick representation of the pterin cofactor and the adjacent [4Fe–4S] cluster in *P. furiosus* AOR. The side chain of a Cys residue that coordinates the cluster and hydrogen bonds with an N atom of the pterin cofactor is indicated[40]

tungstoenzyme in this organism, and thereby its physiological role, remains unknown.

4 STRUCTURAL PROPERTIES OF TUNGSTOENZYMES

The W atom in tungstoenzymes is coordinated by the same cofactor that coordinates the Mo in molydbdoenzymes: An organic moiety known as the pterin cofactor that is based on the two-ring pteridine nucleus that is present in the vitamin folic acid (Figure 1; *see* ***Molybdenum: MPT-containing Enzymes***). The crystal structure of *P. furiosus* AOR was the first for a tungsten-containing protein and for a pterin-containing protein (and the first for an enzyme from an organism that can grow at 100 °C).[16] Interestingly, the structure revealed that the cofactor in the W-enzymes is a *three*-ring system. The third ring contains a dithiolene group, where the two sulfur atoms coordinate the W atom (Figure 2). Subsequent structural analyses of molybdoenzymes have shown that the pterin cofactor in the two types of enzyme are the same. Analyses of the cofactor from the protein indicated that in molybdoenzymes from bacteria the pterin is usually modified with a mononucleotide (AMP, GMP, CMP, or IMP) attached to a terminal phosphate, which is typically lacking in Mo-enzymes from higher organisms. Such an appended nucleotide is also absent in the members of the AOR family of tungstoenzymes (Table 1) but the dinucleotide form of the cofactor is present in FMDH and FDH.

P. furiosus AOR is a homodimer in which each subunit contains an iron–sulfur cluster and coordinates a single mononuclear Fe site at the dimer interface. The W atom in AOR was found to be coordinated not by two S atoms from one pterin cofactor, but by four S of the dithiolene side chains from two pterins (Figure 2). The geometry of the W site in the enzyme displays a distorted square pyramidal arrangement, with an angle of 97° between the planes of the pterin ligands. The pterins are linked to each other through their phosphate groups, which coordinate the same Mg^{2+} ion. The W atom is buried deep inside the protein approximately 10 Å away from the iron–sulfur cluster (Figure 2). A hydrophobic channel leads from the W site to the surface of the protein. This channel is lined with apolar residues and is large enough to accommodate even aromatic substrates, consistent with the ability of AOR to oxidize a broad range of substrates. The iron–sulfur cluster is located close to the protein surface consistent with its role as an intermediary electron carrier between the W atom and the redox protein ferredoxin. The cluster is coordinated by the protein via four cysteine ligands. One of these Cys is positioned to accept a hydrogen bond from a pterin ring nitrogen, hinting at pterin's role as an active participant in the redox chemistry of the enzyme (Figure 2).

The crystal structure of FOR from *P. furiosus* has been solved at 1.8 Å resolution.[18] The overall folding of the FOR subunit is very similar to that of AOR, consistent with their high sequence similarity. However, FOR is a homotetramer with the four subunits arranged around a central cavity approximately 27 Å in diameter. Like AOR, each subunit of FOR comprises an iron–sulfur cluster and one W atom coordinated to a bis-pterin cofactor. FOR does have an additional metal site, a Ca ion situated close to one of the pterin cofactors, but it appears to play a purely structural role (*see* ***Calcium-binding Proteins***). The active site cavity in FOR has two distinctive parts: a large chamber at the bottom and a much narrower channel leading toward the protein surface. The bottom chamber that contains the tungstopterin site is lined with amino acids with bulky side chains. Consequently, the active site cavity in FOR is much smaller than that in AOR, and these variations contribute to the differences in substrate specificity between these two enzymes. Although the structures of the other tungstoenzymes from *P. furiosus*, GAPOR and WOR4, is not known, their amino acid sequence, size, and W and Fe contents suggest that these enzymes are probably closely related in structure to AOR and FOR. The molecular properties of *C. formicoaceticum* CAR are similar to those of *P. furiosus* AOR, although its larger counterpart isolated from *C. thermoaceticum* contains additional subunits, FAD and a much higher Fe content (Table 1). The same is probably true for ADH, whose quaternary structure, subunit size, and W and Fe contents also match those of *P. furiosus* AOR (Table 1).

Structures have yet to be reported for the FDH and FMDH class of tungstoenzyme. However, the structure of the Mo-containing FDH_H from *E. coli*,[25] which shows 20% similarity in its amino acid sequence to that of the catalytic subunit of *Methanopyrus kandeleri* FMDH, has recently been elucidated. FDH_H is a component of the anaerobic formate hydrogen lyase complex and is a monomer of 79 kDa. It contains an iron–sulfur cluster and one Mo atom coordinated by a bis-pterin-MGD cofactor and the selenium atom of a selenocysteine residue (*see* ***Selenium Proteins Containing Selenocysteine***). The coordination geometry of Mo in the reduced enzyme is square pyramidal where the four sulfur atoms form the equilateral ligands and the Se site is at the axial position. Sequence comparisons suggest that W-containing FMDH may have a similar active site, especially since FMDHs of some methanogens also appear to contain selenium.

5 SPECTROSCOPIC PROPERTIES

By analogy with the redox behavior of molybdenum in molybdoenzymes (*see* ***Molybdenum: MPT-containing Enzymes***), a monomeric tungsten site in a tungstoenzyme could be reasonably expected to exist in oxidized (W(VI)), intermediate (W(V)), and reduced (W(IV)) states, where only the intermediate state is paramagnetic and thus Electron paramagnetic resonance (EPR) active. In recent years, the tungstoenzymes listed in Table 1 have been subjected to detailed studies using electron paramagnetic resonance (EPR), X-ray absorption (XAS), resonance Raman, and variable temperature magnetic circular dichroism (MCD) spectroscopies, in an effort to investigate their structure and mechanism. The reduced form of *P. furiosus* AOR is red in color and exhibits broad visible absorption peaks near 400 and 540 nm. When oxidized either by exposure to air or by treatment with ferricyanide, the protein turns a greenish-brown color and the absorption at 400 nm increases by about two-fold. This increase in visible absorption is characteristic of the Fe–S chromophore (*see* ***Iron–Sulfur Proteins***). FOR, GAPOR, ADH, and CAR all exhibit similar absorption spectra in their oxidized and reduced forms. Any contribution of the tungstopterin cofactor to the visible spectrum in these enzymes is probably masked by the broad peak from their Fe–S cluster.

During catalysis the W center is thought to undergo a two-electron cycle between the (IV)/(V)/(VI) oxidation states. W(V) has a d^1-configuration, is paramagnetic and exhibits electron paramagnetic resonance (EPR) signals with g-values less than 2. These signals are typically slow-relaxing and observable at temperatures above 100 K. W(IV) and W(VI), on the other hand, are diamagnetic and do not display EPR signals. Enzymes from all three classes of tungstoenzyme, AOR, FM(D)H, and AH, show resonances attributed to W(V) species.[31] The spectra are assigned to W(V) based on their relaxation properties and g-values. Unambiguous identification of the resonances come from hyperfine interactions arising from ^{183}W, which has a nuclear spin $I = 1/2$. The enriched enzymes are obtained from cells grown in the presence of ^{183}W-tungstate.[31]

Extensive EPR studies of AOR and FOR from *P. furiosus* show that the W site in these enzymes is not homogeneous. As many as four distinct W species are present and each has a distinctive W(V) EPR signal.[41,42] For example, the catalytically active form of the W site is thought to represent less than 50% of the total, and this gives rise to a 'low-potential' magnetically isolated W(V) species, that cycles between the W(IV)/W(V)/W(VI) states at physiologically relevant potentials (-450 mV to -250 mV at 25 °C). The signal has a rhombic lineshape with g-values, which are directly related to the electronic properties of the W atom, of 1.98, 1.90, 1.85. This low-potential signal is observed in all active AOR and FOR samples. A further 30% of the total W gives rise to a 'high-potential' W(V) signal at potentials (>0 mV) that are considered not to be physiologically relevant. The presence of up to four different W species in the same sample, representing active and inactive forms of these enzyme, explains the ambiguity observed in conclusively identifying the ligands to the W atom by crystallographic analyses.[16,18] The W centers of ADH and CAR also give rise to multiple EPR signals.[11] The source of the heterogeneity at the active center of members of the AOR group of tungstoenzymes is not clear.

The [4Fe–4S] cluster in AOR and FOR is paramagnetic in its reduced form and displays characteristic EPR resonances, although the spin relaxation rate is very fast and the spectra are observed only at very low temperatures (*see* ***Iron–Sulfur Proteins***). Hence, at 4K, the EPR spectrum of AOR is dominated by resonances from its reduced Fe–S cluster. However, this gives rise to a rhombic signal from a $S = 3/2$ ground state, while reduced 4Fe-clusters typically have an $S = 1/2$ ground state. In fact, while mixed spin, $S = 3/2$ and $S = 1/2$ reduced [4Fe–4S] clusters are sometimes observed in some iron–sulfur proteins (*see* ***Iron–Sulfur Proteins***), clusters that have exclusively $S = 3/2$ ground states are so far unique to AOR.[41] Indeed, the reduced 4Fe-cluster of FOR has a mixed spin state with $S = 3/2$ (80%) and $S = 1/2$ (20%) components. The factors that determine the spin state of a [4Fe–4S] center have yet to be elucidated.

FDH provided the first example of W(V) EPR resonances from a biological system.[43] At lower temperatures, resonances are seen from reduced iron–sulfur centers (both [2Fe–2S] and [4Fe–4S]), whereas at higher temperatures the reduced enzyme exhibits a slow-relaxing signal with unusually high g-values ($g = 2.1$, 1.98, 1.95). These anomalous EPR properties have been attributed to the S-rich environment of the W comprising four S from two dithiolene side chains, a coordinated selenocysteine and the lack of an oxo ligand in the W(V) state.[31] On the other hand, simple rhombic-type EPR spectra from a W(V) site were reported in the mid 70s from catalytically inactive, tungsten-substituted sulfite oxidase,[44] and more recently from the catalytically active, tungsten-substituted form of *M wolfei* FMDH I. The latter enzyme in its air-oxidized form exhibited a rhombic EPR signal ($g_z = 2.049$, $g_y = 2.012$, $g_x = 1.963$) from the W(V) site and this had the expected isotope splitting (^{183}W, 14.4%, $I = 1/2$). Since this enzyme is rapidly inactivated in air, the catalytic significance of the air-oxidized form is not known, although the results suggest that the active enzyme as isolated under reducing conditions contains a reduced W(IV) center. The EPR properties of FMDH have not been reported but the sole member of the third class of tungstoenzyme, AH, also gives rise to a slow-relaxing EPR signal with relatively high g-values ($g = 2.04$, 2.02, 2.00) that is assigned to W(V).[28] These properties suggest that the enzyme contains a W site coordinated by the S atoms of two pterins and possibly a cysteine ligand. Unfortunately the latter cannot be substantiated by sequence comparisons with F(M)DH and the FDH family of molybdoenzymes. Tungstoenzymes can therefore be classified into two distinct groups based on their EPR properties. In the AOR class, the active site W is coordinated by the dithiolene side chains from two nonnucleotide pterin cofactors and an oxo (or possibly an hydroxyl) ligand in the W(V) state, but there is no direct interaction with any protein side chain. AOR, FOR, GAPOR, ADH, and CAR all appear to fit in this group, despite considerable heterogeneity of their active sites by EPR analyses. In contrast, it appears that the FM(D)H class contain a W center coordinated by the nucleotide form of pterin cofactor with an additional cysteine or selenocysteine ligand from the protein. The latter property leads to an increase in the g_{av} value of the W(V) EPR signal. This second category may also include AH.

6 EVOLUTIONARY CONSIDERATIONS

The tungstoenzymes known so far (Table 1) all catalyze reactions of very low potential (≤ -420 mV) and have been found only in strictly anaerobic organisms, the majority of which grow at moderate or extreme temperatures. The moderately thermophilic organisms appear not to be obligately dependent upon tungsten for growth as analogous molybdoenzymes seem to be synthesized if tungsten is omitted and molybdenum is added to the culture medium. Whether the hyperthermophiles are the first organisms to absolutely require tungsten for growth remains to be established. Nevertheless, tungstoenzymes appear to play key roles in the primary metabolic pathways for the catabolism of both carbohydrates and peptides in the hyperthermophiles. If one compares the properties of the mononuclear W and Mo synthetic complexes,[6,45] it is evident that the relevant W complexes are much more oxygen sensitive than the equivalent Mo compounds, indicating that such a W site within an enzyme would be active only under anaerobic conditions. Similarly, the W complexes display enhanced thermal stability compared to Mo complexes, suggesting that the former rather than the latter would be preferred at temperatures near the normal boiling point. This enhanced bond strength of W complexes may also account for the observation that such complexes are generally kinetically slower than the equivalent Mo complexes. In addition, the much lower redox potentials (typically by more than 300 mV) for the W complexes compared to the Mo ones indicate W is better suited to catalyze lower potential redox processes.[6] Lastly, availability of these metals may play a major role in which of these metals is utilized in different ecosystems. For example, in freshwater and marine environments the concentration of W is typically several orders of magnitude lower than Mo, although in deep-sea hydrothermal vent systems W is much more prevalent than Mo.[2] Hence, it might be expected that W would only be utilized in biological systems to catalyze low-potential reactions under anaerobic conditions, and that significant catalytic rates would be observed only at high temperatures. Conversely, Mo complexes would be unstable at high temperatures but at lower temperatures they would be catalytically competent over the whole biological range of potentials under both aerobic and anaerobic conditions.[6] In fact, most of the W-utilizing microorganisms produce functional Mo-containing isoforms of their tungstoenzymes when they are grown in the presence of Mo rather than W. For example, functional Mo-containing isoenzymes exist for W-containing FMDH, CAR, FDH, and AH in their respective mesophilic or thermophilic organism.[31] The notable exception is the AOR family of tungstoenzymes found in hyperthermophiles such as *P. furiosus*.[2,31] So far they are the only known organisms that obligately require W for growth. They do not contain Mo-analogs of the AOR family, and they appear not to utilize Mo. Such organisms carry out chemical reactions near the limits of biology, at extremely low potentials and at high temperatures. It is possible that catalysis under such extreme conditions is a feat that can be accomplished by W but not by Mo. As yet, a Mo-containing enzyme has not been isolated from an organism that can grow at the normal boiling point.

7 RELATED ARTICLES

Iron–Sulfur Proteins; Molybdenum: Inorganic & Coordination Chemistry; Molybdenum: MPT-containing Enzymes; Tungsten: Inorganic & Coordination Chemistry.

8 FURTHER READING

J. B. Jones and T. C. Stadtman, *J. Bacteriol.*, 1977, **130**, 1404.

9 REFERENCES

1. K. B. Krauspof, Tungsten, in 'Handbook of Geochemistry', ed. K. H. Wedepohl, Springer-Verlag, New York, 1972, Vol. II, chap. 42.
2. A. Kletzin and M. W. W. Adams, *FEMS Microbiol. Rev.*, 1996, **18**, 5.
3. E. I. Stiefel, *Met. Ions Biol. Syst.*, 2002, **39**, 1.
4. R. Hille, *Met. Ions Biol. Syst.*, 2002, **39**, 187.
5. T. G. Spiro, ed., in 'Molybdenum Enzymes', Wiley Interscience, New York, 1985, p. 611.
6. B. J. Hales and E. E. Case, *J. Biol. Chem.*, 1987, **262**, 16205.
7. S. Siemann, K. Schneider, M. Oley, and A. Muller, *Biochemistry*, 2003, **42**, 3846.
8. P. L. Hagedoorn, W. R. Hagen, L. J. Stewart, A. Docrat, S. Bailey, and C. D. Garner, *FEBS Lett.*, 2003, **555**, 606.
9. L. G. Ljungdahl, *Trends Biochem. Sci.*, 1976, **3**, 63.
10. I. Yamamoto, T. Saiki, S.-M. Liu, and L. G. Ljungdahl, *J. Biol. Chem.*, 1983, **258**, 1826.
11. J. R. Andreesen, E. El Ghazzawi, and G. Gottschalk, *Arch. Microbiol.*, 1974, **96**, 103.
12. J. B. Jones and T. C. Stadtman, *J. Biol. Chem.*, 1981, **256**, 656.
13. A. Graentzdoerffer, D. Rauh, A. Pich, and J. R. Andreesen, *Arch. Microbiol.*, 2003, **179**, 116.
14. F. A. de Bok, P. L. Hagedoorn, P. J. Silva, W. R. Hagen, E. Schiltz, K. Frirsche, and A. J. Stams, *Eur. J. Biochem.*, 2003, **270**, 2476.
15. S. Mukund and M. W. W. Adams, *J. Biol. Chem.*, 1993, **268**, 13592.
16. M. K. Chan, S. Mukund, A. Kletzin, M. W. W. Adams, and D. C. Rees, *Science*, 1995, **267**, 1463.
17. R. Roy, S. Mukund, G. J. Schut, D. M. Dunn, R. Weiss, and M. W. W. Adams, *J. Bacteriol.*, 1999, **181**, 1171.
18. Y. Hu, S. Faham, R. Roy, M. W. W. Adams, and D. C. Rees, *J. Mol. Biol.*, 1999, **286**, 899.
19. S. Mukund and M. W. W. Adams, *J. Biol. Chem.*, 1995, **270**, 8389.
20. J. van der Oost, G. J. Schut, S. W. M. Kengen, W. R. Hagen, M. Thomm, and W. M. de Vos, *J. Biol. Chem.*, 1998, **273**, 28149.
21. R. Roy and M. W. W. Adams, *J. Bacteriol.*, 2002, **184**, 6952.
22. H. White, R. Feicht, C. Huber, F. Lottspeich, and H. Simon, *Biol. Chem. Hoppe-Seyler*, 1991, **372**, 999.
23. H. White, C. Huber, R. Feicht, and H. Simon, *Arch. Microbiol.*, 1993, **159**, 244.
24. C. M. H. Hensgens, W. R. Hagen, and T. H. Hansen, *J. Bacteriol.*, 1995, **177**, 6195.
25. J. C. Boyington, V. N. Gladyshev, S. V. Khangulov, T. C. Stadtman, and P. D. Sun, *Science*, 1997, **275**, 1305.
26. R. A. Schmitz, M. Richter, D. Linder, and R. K. Thauer, *Eur. J. Biochem.*, 1992, **207**, 559.
27. B. Rosner and B. Schink, *J. Bacteriol*, 1995, **177**, 5767.
28. R. U. Meckenstock, R. Kreiger, S. Ensign, P. M. H. Kroneck, and B. Schink, *Eur. J. Biochem.*, 1999, **264**, 176.
29. J. Winter, C. Lerp, H.-P. Zabel, F. X. Wildenauer, H. König, and F. Schindler, *Syst. Appl. Microbiol.*, 1984, **5**, 457.
30. G. Zellner and J. Winter, *FEMS Microbiol. Lett.*, 1987, **40**, 81.
31. M. K. Johnson, D. C. Rees, and M. W. W. Adams, *Chem. Rev.*, 1996, **96**, 2817.
32. R. A. Schmitz, S. P. J. Albracht, and R. K. Thauer, *Eur. J. Biochem.*, 1992, **209**, 1013.
33. L. G. Ljungdahl, *Annu. Rev. Microbiol.*, 1986, **40**, 415.
34. L. G. Ljungdahl, in 'Molybdenum and Molybdenum-Containing Enzymes', ed. M. P. Coughlan, Pergamon Press, Oxford, 1979, p. 463.
35. S. P. Cramer, C. L. Liu, L. E. Mortenson, J. T. Spence, S. Liu, I. Yamamoto, and L. G. Ljungdahl, *J. Inorg. Biochem.*, 1989, **23**, 119.
36. G. Strobl, R. Feicht, H. White, F. Lottspeich, and H. Simon., *Biol. Chem. Hoppe-Seyler*, 1992, **373**, 123.
37. H. White and H. Simon, *Arch. Microbiol.*, 1992, **158**, 81.
38. J. Heider, K. Ma, and M. W. W. Adams, *J. Bacteriol*, 1995, **177**, 4757.
39. F. O. Bryant and M. W. W. Adams, *J. Biol. Chem.*, 1989, **264**, 5070.
40. R. Roy, I. K. Dhawan, M. K. Johnson, D. C. Rees, and M. W. W. Adams, Aldehyde ferredoxin oxidoreductase, in 'Handbook of Metalloproteins', eds. A. Messerschmidt, R. Huber, T. Poulos, and K. Wieghardt, John Wiley, New York, 2001, p. 1097.
41. B. P. Koehler, S. Mukund, R. C. Conover, I. K. Dhawan, R. Roy, M. W. W. Adams, and M. K. Johnson, *J. Am. Chem. Soc.*, 1996, **118**, 12391.
42. I. K. Dhawan, R. Roy, B. P. Koehler, S. Mukund, M. W. W. Adams, and M. K. Johnson, *JBIC*, 2000, **5**, 313.
43. J. C. Deaton, E. I. Solomon, G. D. Watt, P. J. Weatherbee, and C. N. Durfor, *Biochem. Biophys. Res. Commun.*, 1997, **149**, 424.
44. J. L. Johnson, R. V. Rajagopalan, S. Mukund, and M. W. W. Adams, *J. Biol. Chem.*, 1993, **268**, 4848.
45. R. Hille, *Trends Biochem. Sci.*, 2002, **27**, 360.

Vanadium in Biology

Ron Wever, Rokus Renirie & Zulfiqar Hasan
University of Amsterdam, Amsterdam, The Netherlands

1 Introduction 1
2 Vanadium Bromoperoxidases 1
3 Vanadium Chloroperoxidases 4
4 Vanadium in Tunicate Vanadocytes 8
5 Amavadin 10
6 Related Articles 10
7 References 10

Abbreviations

EPR = Electron paramagnetic resonance; EXAFS = Extended X-ray fine structure analysis; ESEEM = Electron spin echo envelope spectroscopy; XANES = X-ray absorption near edge structure analysis; NMR = Nuclear magnetic resonance.

1 INTRODUCTION

It is now well established that the element vanadium, which is universally distributed in the soil,[1] plays a role in biological systems. This metal is essential for the functioning of the bacterial nitrogen fixation system (*see* ***Nitrogenase Catalysis & Assembly***) and vanadate is the prosthetic group in the vanadium haloperoxidases from seaweeds and dematiaceous hyphomycetes. As a result, the chemistry of model compounds[2,3] for these biomolecules has been investigated in detail. Furthermore, some vanadium compounds mimic most of the metabolic effects of insulin and the number of publications dealing with the subject has increased exponentially. Four books[4–7] and a large number of reviews[8–10] have appeared which cover several aspects such as the role of the metal in the biosphere, the inorganic and redox chemistry of vanadium, and the insulin mimetic effect of vanadate. An international symposium on chemistry and biological chemistry of vanadium is also organized regularly. In this chapter, the role of the metal in vanadium haloperoxidases will be discussed and the status of the high concentration of vanadium in fan worms and its possible role in the blood cells of Ascidians will be reviewed. It is clear that the field of vanadium biochemistry has rapidly developed and further discoveries and surprises are expected.

Vanadium has 4 oxidation states of which only vanadium$^{\mathrm{III,IV}}$ and V occur in biological systems. Vanadium$^{\mathrm{V}}$ and IV are the most common and vanadium$^{\mathrm{III}}$ has been detected only in tunicates and fan worms.[11] At neutral pH, vanadium is mostly found as vanadate and depending upon pH and concentration, vanadate oligomers including the dimer, tetramer, and decamer forms are found. At low concentrations such as in seawater,[12] only the monomeric species will be present, probably in the diprotonated state. Vanadate, by virtue of being a structural analogue of phosphate, has inhibitory, stimulatory, and regulatory effects on biochemical processes that in a number of cases are due to the formation of enzyme-vanadate intermediates.[9] Vanadate is easily reduced to the IV state by common reducing agents under physiological conditions. In aqueous solutions, most of the reduced vanadium species found exists as vanadyl (VO^{2+}), which forms strong complexes with a great variety of ligands including proteins (*see* ***Vanadium: Inorganic & Coordination Chemistry***). At neutral pH values the vanadyl species are easily oxidized by air to vanadium$^{\mathrm{V}}$. As a d^1 metal ion, vanadium$^{\mathrm{IV}}$ has one unpaired electron which is strongly coupled to the ^{51}V nucleus ($I = 7/2$) giving rise to either 8 or 2 sets of 8 overlapping lines in axial symmetric complexes. This typical signal is easily detectable and it is possible by the EPR technique (*see Electron Paramagnetic Resonance*) to observe relatively low concentrations of the metal.

2 VANADIUM BROMOPEROXIDASES

2.1 Occurrence

A striking array of halogenated products produced by natural sources is found in the biosphere. The majority are probably formed by the enzymatic activity of haloperoxidases.[13] The detailed mechanism by which haloperoxidases catalyze the insertions of a halogen into organic molecules is still a point of debate. However, for most of these enzymes a simple reaction mechanism has been observed that consists of a two-electron oxidation of the electron donor (Cl^-, Br^-, I^-) by H_2O_2 to hypohalous acids (equation 1):

$$H_2O_2 + X^- + H^+ \longrightarrow HOX + H_2O \qquad (1)$$

By definition enzymes that are able to oxidize chloride, bromide, and iodide are called chloroperoxidases and those able to oxidize bromide and iodide, bromoperoxidases. If a nucleophilic acceptor (RH) is present, a reaction will occur with HOX and halogenated compounds (*see Halocarbons & Halocarbon Complexes*) are produced (equation 2).

$$HOX + RH \longrightarrow RX + H_2O \qquad (2)$$

HOX will react with a broad range of acceptors (RH) to form a diversity of halogenated reaction products (RX). As we know now, most of the marine haloperoxidases contain vanadate in the active site.[14,15] These enzymes, which have been detected in a great variety of brown and red seaweed samples, are widespread in the marine environment and have been found in seaweeds from the Great Barrier Reef in Australia, the Sea of Japan, the East Pacific, and the North Atlantic Ocean. Vanadium iodoperoxidases have also been identified in some brown seaweeds but they have hardly been studied. Also diatoms have been reported to contain haloperoxidases. The vanadium peroxidases are probably also responsible for the formation of huge amounts of bromoform by seaweeds and phytoplankton. Some oceans are even saturated with this compound with the result that ventilation to the atmosphere occurs and this volatile organohalogen participates in chemical processes in the atmosphere.[13] The biological function of the formation of bromoform by these algae is not clear. Some of the organohalogens formed and also HOBr have biocidal effects and prevent biofilm formation by bacteria on the surface of seaweeds. It is likely that formation of these compounds is part of a host defense system.[13]

2.2 Catalytic Properties

The vanadium peroxidases differ from the heme-containing peroxidases (*see* ***Iron: Heme Proteins, Peroxidases, Catalases & Catalase-peroxidases***) in their specificity for halides. The vanadium enzymes do not oxidize classical organic electron donors such as guaiacol, *o*-dianisidine, and benzidine. Thus assay systems used are those that detect the formation of HOCl, HOBr, or HOI. Routinely, the halogenating activity of these enzymes is determined by measuring the bromination or chlorination of the cyclic diketone monochlorodimedon to the dihalogenated compound. At more alkaline pH values and in particular at high concentrations of H_2O_2, a competing reaction (equation 3) between H_2O_2 and HOX occurs. This results in singlet oxygen formation and an apparent decrease in the rate of bromination or chlorination of monochlorodimedon.

$$\mathrm{H_2O_2 + HOX \longrightarrow {}^1O_2 + H_2O + HX} \tag{3}$$

Therefore it is also possible to measure enzyme activity without a HOX scavenger by monitoring the rate of dioxygen formation directly using an oxygen electrode.[16] This is at high pH a more accurate measure of bromoperoxidase activity. $^1O_2$ production can also be measured at 1268 nm (*see* ***Dioxygen & Related Ligands***).[17] A convenient qualitative method to assay the haloperoxidase activity is following the bromination of phenol red to bromophenol blue; this results in a marked color change taking place which allows screening of haloperoxidase activity of large numbers of samples by simple visual inspection.[18] The turnover values of the bromoperoxidases vary considerably among the various seaweed species. Extensive steady-state kinetic studies have been carried out that show that hydrogen peroxide and bromide (as a substrate) react with the enzyme in a sequential order and the kinetic mechanisms for the bromoperoxidases from various sources are all very similar.[10] Slight inhibition of bromoperoxidase by high concentrations of H_2O_2 (120–400 mM) with stronger inhibition at higher pH has been observed. Interestingly, the K_M value for H_2O_2 increases with increasing proton concentration. This appears to be due to protonation of a group with a pK_a of 5.7–6.7 that upon protonation prevents binding of peroxide. In contrast the K_M for bromide is hardly affected by pH.

On the basis of kinetic studies the presence of a peroxo-intermediate was postulated and spectroscopic evidence for such an intermediate has been obtained.[10,19] Br_3^-, Br_2, or HOBr appear to be the primary reaction products of the enzyme-mediated peroxidation of bromide.[19] The vanadium enzyme also uses phenylperacetic acid, *m*-chloroperoxybenzoic acid, and *p*-nitroperoxybenzoic acid as oxidants, but alkyl peroxides such as ethylhydroperoxide, tert-butyl hydroperoxide, and cuminyl hydroperoxide are not substrates for the enzyme in the oxidation of bromide.[20] The enzyme from the brown seaweed *Ascophyllum nodosum* does not display any specificity with regard to bromination of various organic nucleophilic acceptors which suggests a mechanism in which the oxidized bromine species are released into solution by the enzyme.[21] Figure 1 gives a simple model for the reaction mechanism of the enzyme.

However, it is clear that during catalysis an enzyme-bound bromonium intermediate is formed which binds specifically indoles and catalyzes a regio-selective bromoperoxidative oxidation.[22] This brown seaweed produces highly volatile and simple halohydrocarbons such as CH_2Br_2 and CH_3Br. These halohydrocarbons are formed by reaction of enzymatically generated HOBr with organic matter that slowly decays to form these halohydrocarbons.[13,23] Thus the reported oxidation of indoles[22] is most probably not related to the known physiological role of the enzyme.

2.3 Nature of the Active Site

Vanadium bromoperoxidases lose their enzymic activity at low pH in buffers containing phosphate and EDTA. Also during purification procedures, the enzyme slowly

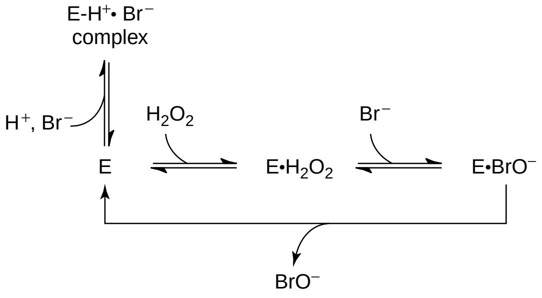

Figure 1 Simplified model for the reaction mechanism of the vanadium bromoperoxidases. As we will see later this mechanism may be slightly different for the vanadium chloroperoxidases

inactivates if phosphate buffers are used.[10] However, in the absence of phosphate-containing buffers, the enzyme retains its activity for months.[10] To inactivate the enzyme completely the presence of phosphate in the procedure is essential.[14] Incubation of the apoenzyme at neutral pH with orthovanadate (VO_4^{3-}, which is the vanadium^V oxy-anion) results in recovery of the enzymatic activity as discovered originally by Vilter.[14] Reconstitution is inhibited competitively by structural analogs such as phosphate (PO_4^{3-}), arsenate (AsO_4^{3-}), molybdate (MoO_4^{2-}), fluoroberyllate, and fluoroaluminate.[10] The reconstitution of the apoenzyme by vanadate suggests that vanadate is present in the active site. The X-ray structures show that vanadate is indeed the prosthetic group in these enzymes.[24] The affinity of the apobromoperoxidase for vanadate is quite high. Values of 35–55 nM have been reported[10,14] that are close to the concentration of vanadate in seawater of 35 nM[12] suggesting that for incorporation of vanadate into the apoenzyme, in vivo, no additional enzyme system is required.

Since the enzyme is nearly colorless and displays only a weak band around 315 nm in the optical absorption spectrum,[10] it is difficult to gain information by optical spectroscopy. EPR, Electron Spin Echo Envelope Modulation Spectroscopy (ESEEM), X-ray spectroscopy, and ^{51}V NMR have been used to probe the nature of the active site in these peroxidases. EPR studies on the bromoperoxidase from the brown seaweed *A. nodosum* have shown that the oxidation state of the metal in the native form is vanadium^V and that its redox state does not change during turnover.[25,26] The role of the vanadium^V in the enzyme is probably to coordinate and to activate hydrogen peroxide resulting in reaction of the halide with this activated peroxide to yield hypohalous acid. Owing to its low radius/charge ratio vanadium may act as a Lewis acid in which the metal effectively withdraws electron density from the bound peroxide in such a way that the halide is able to react with this activated peroxide intermediate of the enzyme to yield hypohalous acid. In this mechanism, no redox changes occur in the vanadium metal center. These spectroscopic methods have not only yielded insight into the mechanism but structural data have also been obtained. For example, based on the results of EXAFS studies the conclusion was reached that the geometry of the metal oxide bound in the active site was five-coordinate.[27] EPR and ESEEM studies on the reduced enzyme demonstrated clearly that water is in the direct coordination sphere of the metal oxide.[25,26] The EXAFS data showed the presence of multiple scattering effects from outer atoms of a group corresponding to a histidine ligated to vanadium. Also the ESEEM experiments[26] clearly indicated the presence of a histidine residue in the active site as confirmed now by the X-ray structure of the vanadium bromoperoxidase from *Ascophyllum nodosum.*[24]

2.4 X-ray Structures of Vanadium Bromoperoxidases

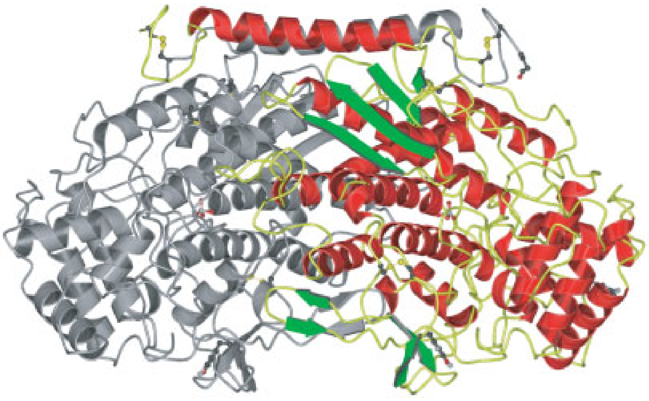

Figure 2 Ribbon type representation of the vanadium bromoperoxidase dimer from *A. nodosum*. The α helices on the top are linked together by two disulfide bridges. (Reprinted from Ref. 24, © 1999, with permission from Elsevier)

The homo-dimeric structure of the enzyme from *A. nodosum* consists of 1111 amino acids with a calculated molecular mass of 120 kDa.[24] The primary sequence was determined by combining the results of DNA sequencing, protein sequencing, and electron density interpretation. The dimeric enzyme is a compact ellipsoid of approximately 90 Å in length and with a diameter of about 76 Å (Figure 2). The monomer of the enzyme consists of a predominantly helical secondary structure, being composed of 18 α-helices and eight short β-strands. Two four-helix bundles and six long helices (each monomer donating a four-helix bundle and three long helices) form the highly rigid and compact core of the dimeric structure. This includes the two vanadium active sites, which reside at the N-terminal end of one of the four helices of each monomer. The monomers are linked covalently in the N-terminal region by two disulfide bridges, four well-defined salt bridges and a large number of hydrogen bonds involving both side-chain and main-chain residues. The two long helices at the N-terminus in each monomer are aligned antiparallel with respect to each other. Additionally, each monomer has three intramolecular disulfide bridges. Thus each dimer contains eight disulfide bridges in line with previous estimates.[10]

Vanadate is bound on the N-terminal side of a four-helix bundle and the vanadium metal is the center of a trigonal bipyramid with three oxygen atoms coordinated in the equatorial plane, one oxygen in the axial position (Figure 3), and a covalent linkage to the $N^{\varepsilon 2}$ of His486. The negative charge of the oxygen atoms in the equatorial plane is compensated by hydrogen bonds donated by several hydrophilic and positively charged amino acids in the vicinity, including Lys341, Arg349, Ser416, and Arg480. The axial oxygen atom forms a hydrogen bond with the $N^{\delta 1}$ of distal His418, which is the proposed conserved catalytic residue in vanadium peroxidases.[10]

Both hydrophilic and hydrophobic residues cover the entrance channel with hydrophobic residues dominating the lower part near the vanadate-binding site. Interestingly, amino acid residues from both monomers contribute to the substrate

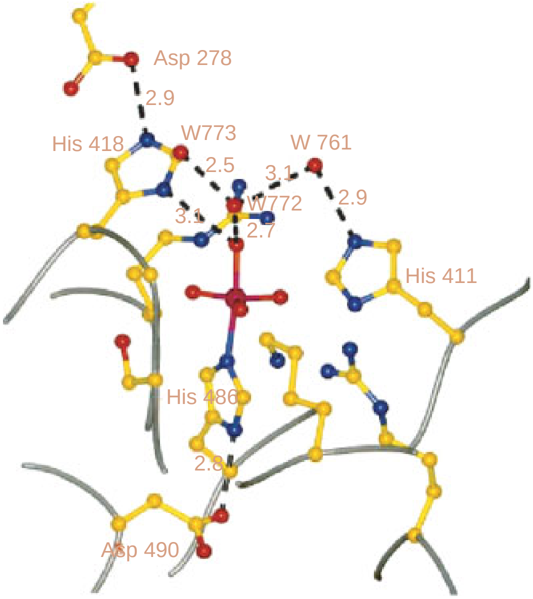

Figure 3 The active site residues around the vanadate center of vanadium bromoperoxidase from *A. nodosum*. There are also three water molecules (W772, W773 and W761) in the active site. (Reprinted from Ref. 24, © 1999, with permission from Elsevier)

access channel of each active center. The channel to the active site of each monomer is 15 Å deep with a diameter of 12 Å at the entrance, decreasing to 8 Å near the axial oxygen of the vanadate prosthetic group, where the channel exhibits a more hydrophobic character.[27]

The X-ray structures of vanadium bromoperoxidases from the red seaweeds *Corallina pilulifera* and *C. officinalis* have also been determined and their structures are almost identical.[28,29] The native structure of these enzymes is dodecameric and the structure is made up of 6 homo-dimers. The secondary structure of the chloroperoxidase from the fungus *Curvularia inaequalis* that will be discussed later can be superimposed with the *Corallina* bromoperoxidase dimer. Many of the α helices of each chloroperoxidase domain are structurally equivalent to the α helices in the *Corallina* bromoperoxidase dimer. This is in line with the evolutionary relationship between the haloperoxidases that will be discussed later. The disulfide bridges in the enzyme from *A. nodosum* are not found in the enzyme from *Corallina* and the two remaining cysteine residues are not involved in disulfide bonds. Additionally, in this enzyme binding sites are present for divalent cations that seem to be necessary to maintain the structure of the active site cleft. All the residues directly involved in the binding of vanadate are conserved in the algal bromoperoxidases.[30]

An extraordinary feature of these enzymes is their remarkable stability.[18] The bromoperoxidase from the brown seaweed *A. nodosum* remains completely functional upon storage in up to 60% methanol, ethanol, and isopropanol for up to a month, and remains fully active when exposed to temperatures up to 70 °C. The enzyme was observed to be unaffected by detergents and reagents such as guanidine-HCl and to withstand oxidative inactivation in the presence of high concentrations of highly reactive oxidants, including hydrogen peroxide and hypohalous acid.[10] The high stability of this enzyme can be attributed to the highly rigid core of the dimeric enzyme and to the fact that more than 46% of the surface of each monomer is part of the dimer interface. In addition, 2 intermolecular salt bridges contribute to the stability of the homo-dimeric enzyme structure. The stability of the enzyme from *Corallina* appears to be the result of the dodecameric structure that shields the solvent accessible area. These fascinating features are of considerable interest for the potential application of the vanadium peroxidase as (industrial) biocatalyst in organic synthesis.

3 VANADIUM CHLOROPEROXIDASES

3.1 Discovery and Physiological Function

During the course of screening for haloperoxidases with tolerance to high pH environments and high temperatures, it was observed that dematiaceous hyphomycetes isolated from plant material and soils collected in Death Valley possessed haloperoxidase activity.[31] In 1993, it was shown[32] that the nonheme chloroperoxidase produced by one such hyphomycete, the fungus *Curvularia inaequalis* also contains vanadate as the prosthetic group in the enzyme. These peroxidases escape detection if classical peroxidase assay systems (e.g. guaiacol) are used and consequently it took a long time to identify the peroxidases in hyphomycetes. Furthermore, when the fungus is grown in vanadate-deficient media, the enzyme is secreted in an inactive apoform.[10] Expression studies showed that the vanadium enzyme is produced in the secondary growth phase, when nutrients become limiting and the expression appears to be mainly regulated at transcription level.[33] Several species in the group of the dematiaceous hyphomycetes produce haloperoxidases (e.g. *Drechslera biseptata*, *D. subpapendorfii*, *Embellisia didymospora*, and *Ulocladium chartarum*), which are vanadium chloroperoxidases.[10] Thus, vanadium chloroperoxidases occur widely in nature. Many of these hyphomycetes are phytopathogenic and/or saprophytes and this raises the question of the physiological function of the vanadium chloroperoxidases. It has been proposed that the generated HOCl is used by the fungus as an attack mechanism to oxidize the lignocellulose in the cell walls of the plant in order to facilitate penetration of the fungal hyphae into the host.[33] It may well be that HOCl which is generated by fungi in soils also reacts with organic matter resulting in the formation of these organohalogens in plants and soil. This may explain the presence of chlorinated compounds in soils that are of nonanthropogenic origin.

3.2 Kinetic and Other Properties of Chloroperoxidases

Research on the vanadium chloroperoxidase obtained a large impetus by cloning of the gene encoding vanadium chloroperoxidase[31] and successful expression of the recombinant enzyme.[33,34] The gene encodes a protein of 609 amino acids with a calculated molecular mass of 67 488 Da. The apoform of the enzyme, either secreted by the fungus or produced as recombinant enzyme, can easily be activated upon addition of vanadate to the growth medium.[10,32] Thus, these enzymes do not require an additional enzyme system for the incorporation of vanadate. In most soils, a high concentration (100 ppm) of vanadium is present and considering the reported affinity of the apochloroperoxidase for vanadate (K_d 140 nM), the amount of vanadium is not a limiting factor in the conversion of the apoenzyme into the holo-enzyme. Additionally, in the presence of H_2O_2 the affinity of the apoenzyme for vanadate increases at least 200-fold. This appears to be due to the formation of pervanadate that binds much more strongly to the active site than vanadate.[35]

Steady-state kinetic studies[36,37] showed that the kinetics of the enzyme resemble those of the vanadium bromoperoxidases.[16,19] The chloroperoxidase exhibits a pH profile similar to vanadium bromoperoxidases although the optimal pH of 4.5–5.0 is at a lower value. At low pH the enzyme is inhibited by chloride in a competitive way whereas at higher pH values the activity displays normal Michaelis-Menten type of behavior (*see Michaelis Constant*). The log K_M for chloride increases linearly with pH whereas that for hydrogen peroxide decreases with pH demonstrating that in the catalytic mechanism protons are involved. These observations have led to a simplified ping-pong type of mechanism for the chloroperoxidase similar to that shown in (Figure 1).

The enzyme will first react with peroxide to form a peroxointermediate, after which a chloride ion and a proton react resulting in the formation of an enzyme-HOCl, which decays in a rate-determining step to enzyme and free HOCl.[35] The linear dependency of the logK_M for hydrogen peroxide on pH suggests that an ionizable group is involved in the binding of hydrogen peroxide. When this group is protonated hydrogen peroxide is unable to bind. The linear dependence of the logK_M for chloride on pH shows that for binding of chloride to occur, protonation of a group is essential.[10]

The binding of substrates to the chloroperoxidase has also been studied using substrate-induced spectral changes. Figure 4 illustrates the UV–VIS absorption spectra of the vanadium chloroperoxidase. A band is present at 315 nm ($\Delta\varepsilon = 2.8\,\text{mM}^{-1}\,\text{cm}^{-1}$) in the native enzyme which is not found in the apoenzyme. The absorption of this band decreases upon addition of hydrogen peroxide.[35] When chloride is added, the original intensity of the band is reformed as a result of halide oxidation. Stopped-flow studies were also carried out confirming the catalytic sequence of events and evaluation of the first-order rate constant for the binding of hydrogen peroxide to the enzyme ($0.8 \times 10^5\,\text{M}^{-1}\,\text{s}^{-1}$ at pH 5). Sequential mix studies show the first direct monitoring of the decay of the peroxo intermediate to the native enzyme during chloride oxidation, which consists of at least two steps.

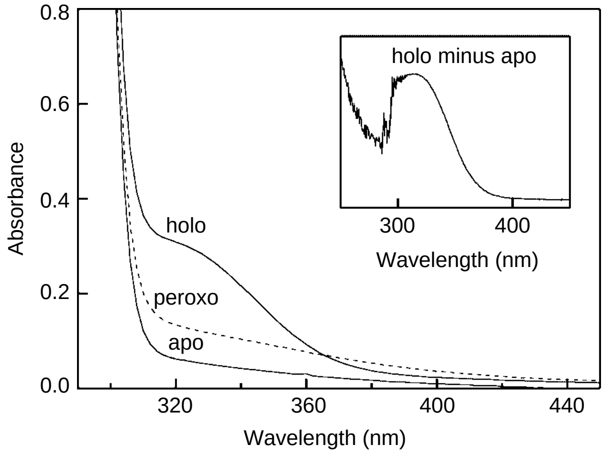

Figure 4 UV-VIS absorption spectra of 100 μM chloroperoxidase at pH 8.3. Holo-enzyme was obtained by addition of 100 μM vanadate to the apoenzyme and the peroxo form by addition of 100 μM H_2O_2 to the holo-enzyme. (Reprinted with permission from Ref. 35. © 2000 American Chemical Society)

The chloroperoxidase also has bromoperoxidase activity.[34,37] Compared to the vanadium bromoperoxidases the chloroperoxidase has a very high affinity for bromide (K_M about 5 μM). The enzyme is strongly inhibited by excess bromide and hardly any activity is observed at 100 mM bromide. An interesting difference is also observed between the bromo- and chloroperoxidase activity of this enzyme. As discussed before, the K_M for chloride is strongly pH dependent, whereas the K_M for bromide is hardly affected by pH as is also observed for the bromoperoxidase from *Ascophyllum nodosum*. An X-ray study proved that during turnover a peroxo intermediate is formed.[38] The peroxide is bound side-on and it has been proposed[37,39] that protonation of one of the oxygen atoms of the peroxide is required to allow the more difficult oxidation of the chloride. Protonation of the bound peroxide is not required for bromide oxidation since bromide is more easily oxidized. Based upon the effects of mutations of the active site residues, the following mechanism has been proposed.[34] By the Lewis acid properties of vanadium and the two positively charged arginine residues (Arg490 and Arg360), electron density is withdrawn from the bound peroxide. The bound peroxide is further polarized and activated by a conserved lysine residue (Lys353) that forms a hydrogen bond to one of the oxygen atoms. The kinetic studies suggest that protonation of the bound peroxide occurs thereby increasing its reactivity. The model to explain the difference in reactivity between a bromo- and a chloroperoxidase is shown in Figure 5.

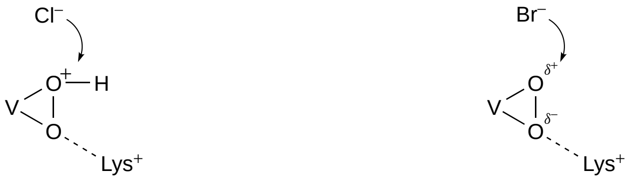

Strongly oxidizing protonated form of the side-on bound peroxide oxygen that faces the active site entrance channel.

Less oxidizing unprotonated form of the side-on bound peroxide oxygen that faces the active site entrance channel.

Figure 5 A possible explanation for the difference in reactivity between vanadium chloroperoxidase and bromoperoxidase[39]

After formation of the peroxide intermediate, the next step in catalysis is the nucleophilic attack by the halide breaking the oxygen–oxygen bond, resulting in formation of HOX or XO^-.

All mutations of the active site residues result in enzymes that are dead or kinetically crippled. Most or all of the chloroperoxidase activity is lost; however, some mutants retain bromoperoxidase activity.[10] A similar effect has been observed in the bromoperoxidase from *Fucus distichus*. Mutation of a phenylalanine in the active site of the bromoperoxidase to an alanine yielded a mutant that only showed iodoperoxidase activity.[40] Satisfactory explanations have not been offered for these observations and neither the question regarding the factors important in tuning the reactivity of the haloperoxidases has been answered. Mutagenesis studies on both bromoperoxidase and chloroperoxidase of the only residue that differs in the two enzymes (Phe in chloroperoxidase versus His in bromoperoxidase) have not clarified this either.[37,41] It can only be concluded that the difference in oxidative ability between VBPO and VCPO as modeled in Figure 5 is not simply due to a single residue. This protonation of the bound peroxide may only occur when a specific hydrogen-bonding network is present that involves bound water molecules and that plays an important role in tuning the reactivity of these enzymes and thus many factors are involved.

3.3 Sulfoxidation Reactions

The haloperoxidases in the absence of halides but in the presence of hydrogen peroxide are also capable of catalyzing the sulfoxidation of organic sulfides with a very high enantioselectivity.[41,42] The bromoperoxidase from the brown seaweed *A. nodosum* produces the R-enantiomer of methyl phenyl sulfoxide (96% e.e.) under slightly acidic conditions, while the bromoperoxidase from the red seaweed *C. pilulifera* produces the S-enantiomer of this sulfoxide (55% e.e.). The bromoperoxidase from the seaweed *C. officinalis* was also observed to convert organic sulfides that structurally resemble indenes to the S-enantiomer of the corresponding sulfoxides showing high selectivities. Also, small sulfides, possessing a *cis*- positioned carboxyl group with respect to the sulfur atom, are rapidly converted to the corresponding sulfoxides with selectivities exceeding 95% e.e. The vanadium bromoperoxidase from *A. nodosum* catalyzes the sulfoxidation of racemic nonaromatic cyclic thioethers with kinetic resolution.[43] By using ^{18}O-labeled hydrogen peroxide, it was shown that the vanadium bromoperoxidases mediates the direct transfer of the peroxide oxygen to the sulfide in a selective manner, strongly suggesting that the aromatic sulfide binds near or at the active site with a relatively low affinity.[43] The k_{cat} for the sulfoxidation reactions is low ($1\,\text{min}^{-1}$) compared to the brominating activity of the bromoperoxidase from *A. nodosum* ($166\,\text{sec}^{-1}$). Vanadium chloroperoxidase in contrast to vanadium bromoperoxidase appears not to be capable of mediating the direct and selective transfer of peroxide oxygen to methyl phenyl sulfide. This may be due to the high reactivity of the chloroperoxidase resulting in electron abstraction from the substrate and formation of a positively charged sulfur radical. This radical migrates from the enzyme and is subsequently converted to the sulfoxide via reaction with water.

3.4 Stability of Chloroperoxidase

The vanadium chloroperoxidases are highly resistant towards elevated temperatures; the midpoint temperatures determined from thermal denaturation curves range from 82 to 90 °C. It is also possible to store the enzyme at elevated temperatures and it has even been reported that incubation at 75 °C for 8 hours resulted in only a 20% loss of activity.[40] The factors contributing to the thermostability are the compactness of the molecule and the large amounts of α helical structure found in the chloroperoxidase.[30] Pronounced chemostability and resistance towards oxidative agents such as H_2O_2, HOCl, and singlet oxygen have been reported.[17,36] Heme-containing peroxidases with their electron-rich aromatic ring system are much more easily oxidized and inactivated by oxidative agents (*see* ***Iron: Heme Proteins, Peroxidases, Catalases & Catalase-peroxidases***). In this respect, the vanadium haloperoxidases are unique and the ability of the

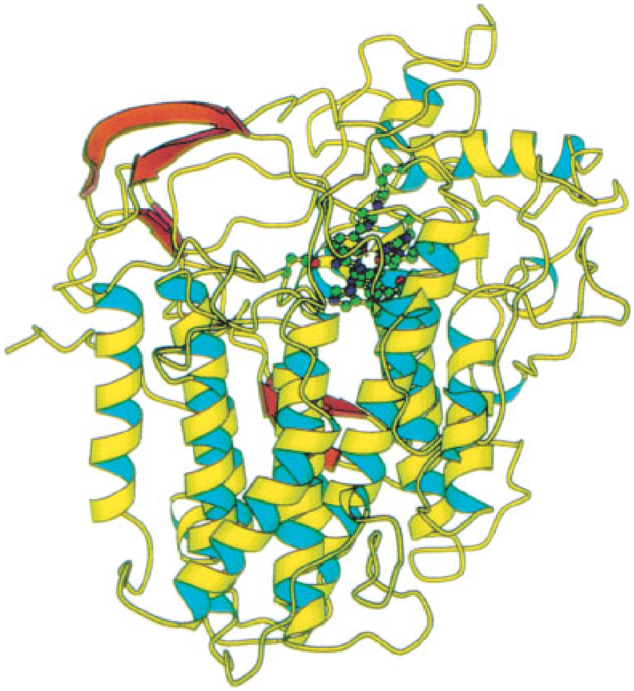

Figure 6 Ribbon type representation of the vanadium chloroperoxidase from *C. inaequalis*. (Reproduced from A. Messerschmidt and R. Wever, *Proc. Natl. Acad. Sci USA*, 1999, **93**, 392. © 1996 National Academy of Sciences, U.S.A.)

enzymes to handle the oxidative substrate and product are the consequences of the nature of the active site.

3.5 X-ray Structure of the Vanadium Chloroperoxidase and Details of the Active Site

Both the 2.1 Å crystal structure of the native chloroperoxidase and recombinant chloroperoxidase at 1.66 Å resolution have been reported.[30,44] The enzyme molecule has an overall cylindrical shape (Figure 6) with a length of about 80 Å and a diameter of 55 Å. The protein fold is mainly α helical with two four-helix bundles as the main structural motifs. The structure also contains some antiparallel β sheets. The very compact packing of the helical structure is different from other known protein structures. There are no disulfide bridges which is in contrast to the vanadium bromoperoxidase from *A. nodosum.*[28] The vanadium-binding center is located on top of the second four-helix bundle and the residues binding the prosthetic group span a length of approximately 150 residues in the primary structure.

The X-ray structure analysis of the active site (Figure 7a) shows that vanadium is bound as orthovanadate$^{\mathrm{V}}$ in the same way as in the bromoperoxidases in which three oxygen atoms form a plane (bond length about 1.65 Å), the fourth oxygen is found at the apex (bond length 1.93 Å) which is in the range of a vanadium$^{\mathrm{V}}$ hydroxyl bond. It is hydrogen bonded to the nitrogen $\mathrm{N}^{\delta 1}$ of His404.

The $\mathrm{N}^{\varepsilon 2}$ atom from a histidine (His496) ligating directly to the metal completes the trigonal bipyrimidal coordination. The negative charge of the vanadate group is compensated by hydrogen bonds to three positively charged residues (Arg360, Arg490, Lys353). Further, the vanadate forms hydrogen bonds with a glycine (Gly403) and a serine residue (Ser402). There is also a histidine residue (His404) close to the apical hydroxyl moiety of the vanadate which may act as an acid/base group in catalysis. These residues are in fact the same as in bromoperoxidase and the active sites are structurally nearly superimposable.[10] The pocket where vanadate is bound is at the end of a channel which supplies access and release of the small substrates and products of the reaction. Part of the surface of the channel is mainly hydrophobic with Pro47, Pro221, Trp350, Phe393, Pro395 as contributing side chains. The other half of the channels is predominantly polar with several carbonyl oxygens and the ion pair Arg490-Asp292. It is interesting to note that the Arg490 is also directly bound to the orthovanadate. A prominent difference in the active site architecture of the bromo- and chloroperoxidase is the presence of a second histidine in the bromoperoxidase, a residue substituted by a phenylalanine in chloroperoxidase.[24] Site-directed mutagenesis of this residue into a histidine partially abolished the chlorinating activity and surprisingly the mutant showed a higher k_{cat} in the bromination reaction at high pH values than the native enzyme.[37]

3.6 Homology Between Haloperoxidases and Acid Phosphatases

The vanadate-binding residues in the active site of the vanadium chloroperoxidase were shown to be conserved in two bromoperoxidases from seaweeds and a large group of phosphatases including glucose-6-phosphatase.[45] Based on the sequence similarity, it was concluded that the architecture of the active sites in the two classes of enzymes is very similar.[45] The X-ray structure of the acid phosphatase from *Escherichia blattae* (Figure 7b) confirmed the remarkable similarity of the residues binding the oxyanions.[46] Sulfate cocrystallizes with the acid phosphatase and its binding site is comparable to that of vanadate in the chloroperoxidase. Remarkably, the apochloroperoxidase has some phosphatase activity though the turnover with *para*-nitrophenyl phosphate as a substrate is about 10 000 times slower than that of the various acid phosphatases. However, the K_M for the substrate is of the same order of magnitude as various acid phosphatases. The data show that the active site of the haloperoxidase has a good affinity for the substrate but is not optimized for phosphatase activity.

Similarly, when vanadate is introduced in the active site of the acid phosphatases, these artificial enzymes are able to oxidize bromide in the presence of H_2O_2 and to sulfoxidize sulfides in an enantioselective manner. The turnover frequency

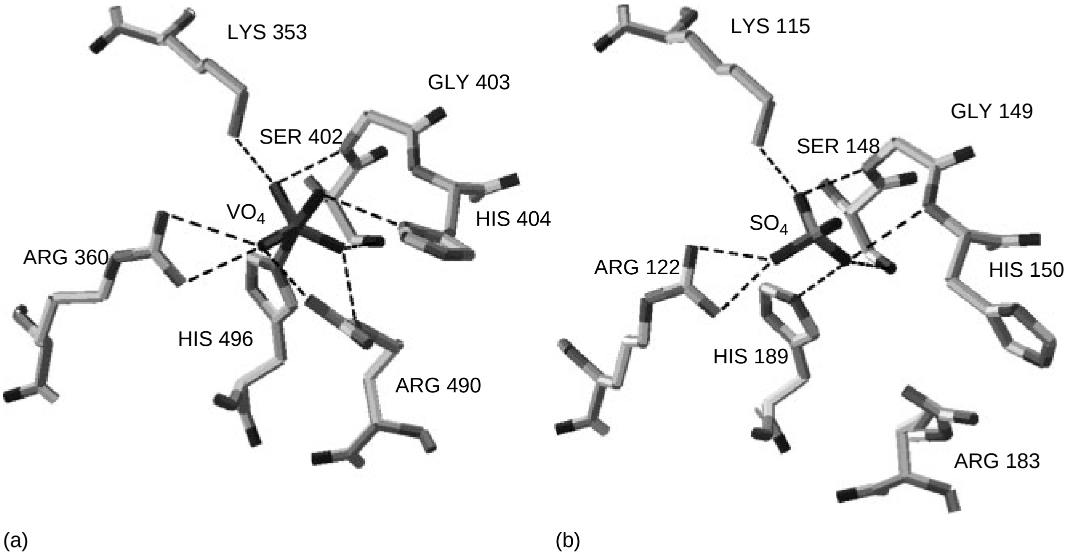

Figure 7 The active site of vanadium chloroperoxidase from *C. inaequalis* (a) and the acid phosphatase from *E. blattea* (b)

of the bromide oxidation and the specificity constant are however very low. The family of acid phosphatases that contains this active site is very large. These include glucose-6-phosphatase, lipid phosphatases from bacteria and yeast, and lipid phosphatases from higher eukaryotes that are involved in signal transduction and secreted bacterial acid phosphatases. Proteins from this superfamily have different physiological functions and are found in species varying from *E.coli* to humans. However, vanadium-containing haloperoxidases have thus far only been isolated from eukaryotes and are not detected yet in prokaryotes. Since phosphate and phosphate-metabolizing enzymes have entered evolution in an early stage it seems likely that vanadate was coined by nature to become the prosthetic group in the vanadium-containing haloperoxidases at a more recent stage and thus that these enzymes have evolved from the phosphatases.

4 VANADIUM IN TUNICATE VANADOCYTES

4.1 Introduction

Ascidians or tunicates (Phylum Chordata) belong to the class of Ascidiacea and are common marine animals whose body is enclosed in a jacket or tunic. The animals are attached to rocks and are either solitary or colonial. They continuously filter seawater to obtain minute organisms and particulate organics. As was originally discovered by Henze[47] the animals concentrate vanadium from seawater to levels about 10^6 times that present in seawater (35 nM), a phenomenon that has attracted considerable interest. The transition metal is present in very high concentrations (up to 150 mM) in certain blood cells of the animal.

4.2 Cell Types

There is considerable confusion concerning the cells that contain vanadium. Tunicates possess several types of blood cells: lymphocytes, leucocytes, pigment cells, and cells containing vacuoles, that is, signet ring cells, morula cells, and compartment cells. The bulk of the vanadium is contained within the signet ring cells and compartment cells. Morula cells were originally thought to be involved in the accumulation of vanadium and thus were named vanadocytes. However, from a comparison of vanadium distribution over the 4 bands of blood cells from *Ascidia gemmata* and *A. ahodori* with the main population of the various cells in these bands, it was concluded that the morula cell contains little or no vanadium.[11] This was confirmed recently by scanning X-ray microscopy at the European Synchrotron Radiation Facility.[11] The data also clearly show that vanadium is present in the vacuoles in the signet ring cells of *P. mammallita* blood cells. In contrast, in *A. ceratodes* and *A. mentula* a significant amount of vanadium is also found in the morula cells. Clearly the presence of vanadium in a cell type depends on the species investigated and there is not a specific vanadocyte in the various *Ascidia*. Thus care should be taken not to extrapolate results from one species to another even if they are closely related.

4.3 Valence State and Intracellular pH

A number of biophysical techniques have been used to probe the valence state of vanadium in blood cells and their intracellular pH. Most data suggest a predominance of vanadium^{III}; the vanadium^{IV} state which can be detected by EPR, is probably due to oxidation by oxygen.[48] Similarly, Magnetic Susceptibility Measurements show that vanadium^{III} is the predominant species in the blood sample of *A. nigra*.

pH measurements showed that for signet ring cells of *A. gemmata*, *A. ahodori*, and *A. sydneinsis*, which contain the highest concentration of vanadium, pH values of 2.4, 2.7, and 4.2, respectively, were found. These low pH values support the X-ray absorption spectroscopy (XAS) measurements,[11,49] which indicate that nearly all the vanadium is present in the form of unchelated vanadium^{III} coordinated only to water. Whole blood cells also contain large amounts of intracellular sulfate as is evident from sulfur X-ray Absorption Near Edge Structure (XANES), suggesting that the vanadium^{III} is present as a sulfato complex ion.[11] An aliphatic sulfonic acid analogous to cysteic acid was also identified, the overall concentration of which is unprecedented in marine organisms and is comparable to that of sulfate in the blood cells and further, is approximately equal to that of vanadium. There are no clues as to the role of the high levels of the sulfate in vanadocytes.

The acidity of the blood cells is due to the low pH within the vacuole and a clear correlation between the acidity of the vacuoles and the concentration of vanadium in the vacuole has been shown.[11] An ATPase appears to be involved in generation and maintenance of the low pH. Addition of an ATPase inhibitor neutralizes the vacuole content. If one accepts that there is a link between the low pH in the blood cells and accumulation of vanadium, there is no need to invoke a mechanism stabilizing the vanadium^{III} state since oxidation at low pH will not occur. Obviously there should be a mechanism to accumulate vanadium and to reduce the vanadate from seawater to the vanadium^{III} state. A vanadium-binding protein vanabin has been identified that has a very high content of cysteine residues, its role may be trapping vanadium^{V} and subsequent reduction to the IV state.[50] These vanadium-binding proteins bind up to 20 vanadium^{IV} ions per mol of vanabin; however, the affinity for vanadium^{IV} is not very high (K_d 21 µM) in view of the concentration of vanadium in seawater. The affinity of the vanabins for vanadium^{V} has not yet been reported and may be much higher. The suggestion has been made that NADPH generated by the pentose phosphate pathway is involved in the reduction step. However, vanadium^{V} is easily reduced to the IV state by most biological reductants. The reductant involved to reduce the IV state to the III state, however, remains a mystery.

Tunicates not only contain a considerable amount of vanadium but also contain the biomolecule tunichrome which is mainly present in morula cells. Tunichrome makes up 50% of the dry weight of these cells. This blood pigment consists of a class of tripeptides containing di- and trihydroxybenzene substituents with strong chelating and reducing properties towards transition metals such as iron and vanadium.[11] These compounds coordinate and reduce vanadium^{V} and also vanadium^{IV} to the III oxidation state. However, the signet ring cells from the tunicates (*A. ahodori*) do not seem to contain tunichrome and its role in the reduction of vanadate remains doubtful.[11]

The physiological role of the vanadium accumulation is still a mystery. Several proposals have been made in the last 5 decades. One proposal suggests that vanadium acts as an electron sink.[51] This sink for electrons may be used by the animals to regenerate NADP$^+$ when they are exposed to anaerobic conditions. It should be noted that there is apparently no oxygen transport system in the circulation of these animals and oxygen may often be limiting. Under aerobic conditions, the vanadium^{III} may reoxidize to a higher oxidation state. It is clear that still many pieces of the puzzle relating vanadium uptake, redox reactions and low pH in the vacuoles are missing. However, the approach[11] to elucidate the functions of genes and proteins obtained from ascidian blood cells may well lead to clarification of the entire mechanism involved in accumulation and reduction of vanadium in ascidian vanadocytes.

4.4 Vanadium in Fan Worms

Fan worms belonging to the genus *Pseudopotamilla* also contain a high concentration of vanadium.[52] Most of the vanadium in this worm is located in the branchial crown and more specifically in the vacuoles of the epidermal cells. Sulfur seems to be colocalized with vanadium. EXAFS spectral data on living *P. occelata* indicate that most of the vanadium *in vivo* exists in the vanadium^{III} state. Analysis of the XANES data indicates that the vanadium is present in solution in the form of an aqua complex with symmetrical octahedral coordination. Vanabin may also be present since the animal possesses antigens recognized by a monoclonal antibody raised against vanabin from *Ascidia sydneinsis*. The physiological role of vanadium in the animal is not known.

4.5 Vanadium as a Terminal Electron Acceptor in Bacteria

Microbial reduction of metals of variable valence is a universal method by which microorganisms are able to regenerate NADH and this process is in general coupled to ATP synthesis. Vanadium has all the properties necessary for utilization by microorganisms in respiratory processes. The metal occurs in different oxidation states and it occurs extensively in the earth's crust. A search for bacteria in habitats rich in vanadium, like wastewater from a plant processing vanadium-containing slags, resulted in the finding that *Pseudomonas* strains under anaerobic conditions reduce vanadate to the tetra and trivalent states with organic electron donor as well as with molecular hydrogen and carbon monoxide.[53] Clearly, under anaerobic conditions, vanadate may act as the terminal electron acceptor in these bacteria. These observations give some weight to the hypothesis that vanadate in tunicates is also used as an electron sink under anaerobic conditions.

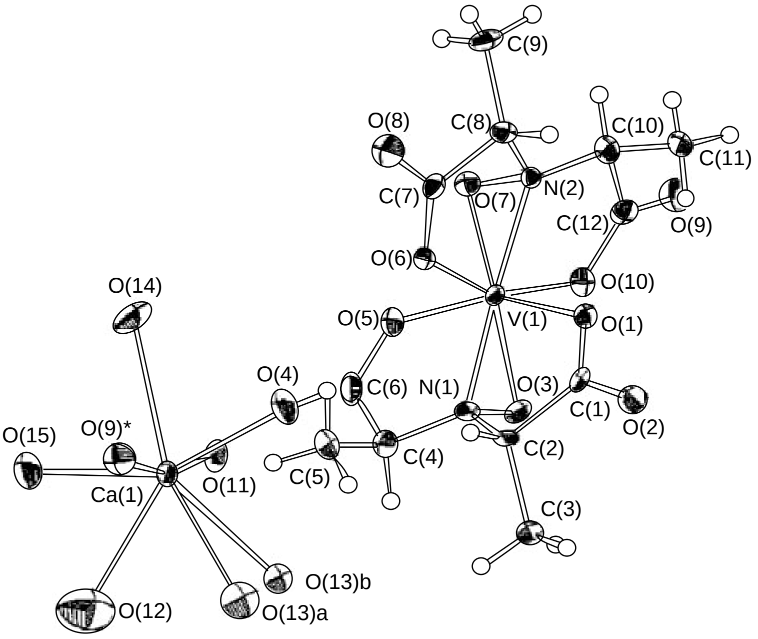

Figure 8 X-ray structure of amavadine. (Reproduced by permission of Wiley-VCH)

5 AMAVADIN

The first report that vanadium occurs in fungal species dates back to 1931 when it was reported[54] that the fly agaric *Amanita muscaria* contains a high concentration of this element. Also in other *Amanita* species, such as *A. regalis* and *A. velatripes*, high amounts (up to 400 ppm) were found. Most other mushroom species have much lower vanadate concentrations. Apparently, vanadium is present in the IV state. The first EPR spectrum reported of an extract of the cap of the mushroom showed clearly an EPR signal characteristic of vanadium^{IV}. The pale blue vanadium-containing compound from *A. muscaria* which was isolated later was named amavadine.[55] Structural elucidation has been controversial and many model complexes analogous to amavadine were reported.[9] Crystallization of the amavadine and structure determination gave the final clue to the peculiar structure of amavadin (Figure 8).[56]

The vanadium^{IV} is eightfold coordinated to nitrogen in an unusual geometry and a V=O group is lacking. Amavadine possesses five chiral centers: four chiral centers all have the S configuration and the fifth chiral center is generated by the manner in which the ligands to the vanadium wrap around the vanadium atom.[56] The electrochemistry of amavadine is such that the compound may have a role in electron transfer reactions involving the vanadium$^{V/IV}$ redox couple. Studies have shown that amavadine can catalyze thiol oxidation.[57] Amavadine also has some peroxidase-like activity. In the presence of hydrogen peroxide it is able to oxidize halides and catalyze the hydroxylation and oxygenation of alkyl and aromatic substrates.[9] Interestingly, it was reported recently by the Portuguese group that amavadine could convert methane into acetic acid in the presence of peroxodisulfate and trifluoroacetic acid. Other vanadium complexes could replace amavadine.[58] Despite all these studies, the physiological function of amavadine in mushrooms is still elusive.

6 RELATED ARTICLES

Dioxygen & Related Ligands; Iron: Heme Proteins, Peroxidases, Catalases & Catalase-peroxidases; Nitrogenase Catalysis & Assembly; Vanadium: Inorganic & Coordination Chemistry; Vanadium: Organometallic Chemistry.

7 REFERENCES

1. D. Bertrand, *Bull. Am. Mus. Nat. Hist.*, 1950, **94**, 403.
2. Y. Shechter, I. Goldwasser, M. Mironchik, M. Fridkin, and D. Gefel, *Coord. Chem. Rev.*, 2003, **237**, 3.
3. D. Rehder, G. Santonin, G. M. Licini, C. Schulzke, and B. Meier, *Coord. Chem. Rev.*, 2003, **237**, 53.
4. N. D. Chasteen ed., ‘Vanadium in Biological Systems’, Kluwer Academic Publishers, Amsterdam, 1990.
5. J. O. Nriagu ed., ‘Vanadium in the Environment’, John Wiley & Sons, New York, 1998.

6. A. C. Tracey and D. C. Crans eds, ‘Vanadium Compounds, Chemistry, Biochemistry and Therapeutic Applications’, American Chemical Society Serie, Washington, DC, 1998.
7. H. Sigel and A. Sigel eds, Vanadium and its Role in Life, ‘Metal Ions in Biological Systems’, Marcel Dekker, New York, 1995.
8. A. Butler, *Coord. Chem. Rev.*, 1999, **187**, 17.
9. D. C. Crans, J. J. Smee, E. Gaidamauskas, and L. Q. Yang, *Chem. Rev.*, 2004, **104**, 849.
10. R. Wever and W. Hemrika, in ‘Handbook of Metalloproteins’, eds. A. Messerschmidt, R. Huber, T. Poulos, and K. Wieghardt, John Wiley & Sons, Chichester, 2001, p. 1417.
11. H. Michibata, N. Yamaguchi, T. Uyama, and T. Ueki, *Coord. Chem. Rev.*, 2003, **237**, 41.
12. P. Mira and S. W. Fowler, *Adv. Environ. Sci. Technol.*, 1998, **30**, 167.
13. R. Wever, M. G. M. Tromp, B. E. Krenn, A. Marjani, and M. van Tol, *Environ. Sci. Technol.*, 1990, **25**, 446.
14. H. Vilter, *Phytochemistry*, 1984, **23**, 1387.
15. E. De Boer, Y. Van Kooyk, M. G. M. Tromp, H. Plat, and R. Wever, *Biochim. Biophys. Acta*, 1986, **869**, 48.
16. H. S. Soedjak and A. Butler, *Biochim. Biophys. Acta*, 1991, **1079**, 1.
17. R. Renirie, C. Pierlot, J.-M. Aubry, A. F. Hartog, H. E. Schoemaker, P. L. Alsters, and R. Wever, *Adv. Synth. Catal.*, 2003, **345**, 1.
18. E. De Boer, H. Plat, M. G. M. Tromp, M. C. R. Franssen, H. C. Van der Plas, E. M. Meijer, H. E. Schoemaker, and R. Wever, *Biotechnol. Bioeng.*, 1987, **30**, 607.
19. E. De Boer and R. Wever, *J. Biol. Chem.*, 1988, **263**, 12326.
20. H. S. Soedjak and A. Butler, *Biochemistry*, 1990, **29**, 7974.
21. M. C. R. Franssen, J. D. Jansma, H. C. Van der Plas, E. de Boer, and R. Wever, *Bioorg. Chem.*, 1988, **16**, 352.
22. J. S. Martinez, G. L. Caroll, R. A. Tschirret-Guth, G. Altenhoff, R. Daniel Little, and A. Butler, *J. Am. Chem. Soc.*, 2001, **123**, 3289.
23. K. Ballschmiter, *Chemosphere*, 2003, **52**, 313.
24. M. Weyand, H.-J. Hecht, M. Kiess, M.-F. Liaud, H. Vilter, and D. Schomburg, *J. Mol. Biol.*, 1999, **293**, 864.
25. R. Wever and W. Hemrika, *Adv. Environ. Sci. Technol.*, 1998, **30**, 285.
26. E. De Boer, C. P. Keijzers, A. A. K. Klaassen, E. J. Reijerse, D. Collison, C. D. Garner, and R. Wever, *FEBS Lett.*, 1988, **235**, 93.
27. C. J. Carrano, M. Mohan, S. M. Holmes, R. De la Rosa, A. Butler, A. J. M. Charnock, and C. D. Garner, *Inorg. Chem.*, 1994, **33**, 64.
28. M. N. Isupov, A. R. Dalby, A. A. Brindley, Y. Izumi, T. Tanabe, G. N. Murshudov, and J. Littlechild, *J. Mol. Biol.*, 2000, **299**, 1035.
29. J. Littlechild and E. Garcia-Rodriquez, *Coord. Chem. Rev.*, 2003, **237**, 65.
30. A. Messerschmidt and R. Wever, *Proc. Natl. Acad. Sci U.S.A.*, 1999, **93**, 392.
31. J. C. Hunter Cevera and L. S. Sotos, *Microbiol. Ecol.*, 1986, **12**, 121.
32. J. W. P. M. Van Schijndel, E. G. M. Vollenbroek, and R. Wever, *Biochim. Biophys. Acta*, 1993, **1161**, 249.
33. P. Barnett, D. L. Kruitbosch, W. Hemrika, H. L. Dekker, and R. Wever, *Biochim. Biophys. Acta*, 1997, **1352**, 73.
34. W. Hemrika, R. Renirie, S. Macedo-Ribeiro, A. Messerschmidt, and R. Wever, *J. Biol. Chem.*, 1999, **274**, 23820.
35. R. Renirie, W. Hemrika, S. R. Piersma, and R. Wever, *Biochemistry*, 2000, **39**, 1133.
36. J. W. P. M. Van Schijndel, P. Barnett, J. Roelse, E. G. M. Vollenbroek, and R. Wever, *Eur. J. Biochem.*, 1994, **225**, 151.
37. N. Tanaka, Z. Hasan, and R. Wever, *Inorg. Chim. Acta*, 2003, **356**, 288.
38. A. Messerschmidt, L. Prade, and R. Wever, *Biol. Che.*, 1997, **378**, 309.
39. R. Renirie, W. Hemrika, and R. Wever, *J. Biol. Chem.*, 2000, **275**, 11650.
40. N. J. Carter, K. E. Beatty, M. T. Simpson, and A. Butler, *J. Inorg. Biochem.*, 2003, **91**, 59.
41. M. Andersson, A. Willet, and S. Allenmark, *J. Org. Chem.*, 1997, **62**, 8455.
42. H. B. Ten Brink, A. Tuynman, H. L. Dekker, W. Hemrika, Y. Izumi, T. Oshiro, H. E. Schoemaker, and R. Wever, *Inorg Chem.*, 1998, **37**, 6780.
43. H. B. Ten Brink, H. E. Schoemaker, and R. Wever, *Eur. J. Biochem.*, 2001, **268**, 132.
44. S. Macedo-Ribeiro, W. Hemrika, R. Renirie, R. Wever, and A. Messerschmidt, *J. Biol. Inorg. Chem.*, 1999, **4**, 209.
45. W. Hemrika, R. Renirie, H. L. Dekker, P. Barnett, and R. Wever, *Proc. Natl. Acad. Sci. U.S.A.*, 1997, **94**, 2145.
46. K. Ishikawa, Y. Mihara, K. Gondoh, E.-I. Suzuki, and Y. Asano, *EMBO J.*, 2000, **19**, 2412.
47. M. Henze, *Hoppe-Seyler’s Z. Physiol. Chem.*, 1911, **72**, 494.
48. P. Frank, R. M. K. Carlson, and K. O. Hodgson, *Inorg. Chem.*, 1988, **27**, 118.
49. T. D. Tillius, W. O. Gillum, R. M. K. Carlson, and K. O. Hodgson, *J. Am. Chem. Soc.*, 1980, **102**, 5670.
50. S. Trivedi, T. Ueki, N. Yamaguchi, and H. Michibata, *Biochim. Biophys. Acta*, 2003, **163**, 67.
51. M. J. Smith, *Experientia*, 1989, **45**, 452.

52. T. Ishii, *Adv. Environ. Sci. Technol.*, 1998, **30**, 199.
53. N. A. Yurkova, N. D. Sval'eva, and N. N. Lyalikova, *Microbiology*, 1993, **62**, 367.
54. H. Ter Meulen, *Recl. Trav. Chim. Pays-Bas*, 1931, **50**, 491.
55. E. Bayer and H. Kneifel, *Z. Naturforsch.*, 1972, **39b**, 207.
56. R. E. Berry, E. M. Amstrong, R. L. Bedddoes, D. Collison, S. N. Ertok, M. Helliwell, and C. D. Garner, *Angew. Chem., Int. Ed. Engl.*, 1999, **38**, 795.
57. M. F. C. Guedes da Silva, J. A. L. da Silva, J. J. R. Frausto da Silva, A. J. L. Pombeiro, C. Amatore, and J.-N. Verpeaux, *J. Am. Chem. Soc.*, 1996, **118**, 7568.
58. P. M. Reis, J. A. L. Silva, A. F. Palavre, J. J. R. Frausto Da Silva, T. Kitamoura, Y. Fujiwara and A. J. L. Pombeiro, *Angew. Chem., Int. Ed. Engl.*, 2003, **42**, 821.

Acknowledgment

Dr. Michael Weyand and Dr. Naoko Tanaka are kindly thanked for providing Figure 2 and Figure 7 respectively.

Vanadium: Inorganic & Coordination Chemistry

Raymond L. Richards
University of Sussex, Brighton, UK

Based in part on the article Vanadium: Inorganic & Coordination Chemistry by Elizabeth M. Page & Sherilyn A. Wass which appeared in the Encyclopedia of Inorganic Chemistry, First Edition.

1	Introduction	1
2	The Element	1
3	Binary Compounds	2
4	Coordination Chemistry of Vanadium	6
5	Related Articles	14
6	References	15

Abbreviations

Haacda = 2-aminocyclopent-1-ene-1-carbodithioic acid; H_2 acen = N,N'-ethylenebis(acetylacetonoylideneamine); big = biguanidine; H_2Cl_4cat = tetrachlorocatechol; H_2-coll = pyridine-2,4,6-tricarboxylic acid (collidinic acid); dpot = potassium 1,3-diamino-2-propanol-N,N,N',N'-tetraacetate (−); DIPP = 2,6-diisopropylphenolate; diphos = ethylenebis (diphenylphosphine); hedtra = N'-(2-hydroxyethyl)ethylenediamine-N,N,N'-triacetate(3−); Hgly = glycine; H_2lut = pyridine-2,6-dicarboxylic acid (lutidinic acid); mal = malonate(2−); MNT = maleonitrile dithiolate; pcH_2 = phthalocyanine; picH = picolinic acid; pinH = pinacol; pmida = pyridylmethyliminodiacetate; pycH = pyridine-2-carboxylic acid; SAL = salicylaldehyde(−); SALIMH = 4-(2-(salicylideneamino)ethyl)imidazole; salser = N-salicylideneserinate; S-peida = (S)-[1-(-2-pyridylethyl)iminodiacetate]; saled-5-Me = slan(5-Me)$_2$; TMTP = tetra-m-tolylporphyrinate(2−); TPTP = tetra-p-tolylporphyrinate(2−); trdta = 1, 3-diaminopropane-N,N, N',N'-tetraacetate(−).

1 INTRODUCTION

This article is essentially an update of the article of the same name published in the first volume of this Encyclopedia.[1] The present article includes a survey of the literature from the years 1992 to 2002 inclusive, but a number of references from the prior literature are included for continuity and completion. For ease of cross-reference, the format of the first article has also been retained as far as possible, with additions and deletions to reflect the advances in the chemistry of vanadium that have occurred since the period surveyed by the first article.

2 THE ELEMENT

2.1 Occurrence, Uses, and Properties

2.1.1 Occurrence and Properties

Although the existence of vanadium was first claimed in 1801 by del Rio, it was identified independently in 1831 by Sefstrom who named the element vanadium after the Scandinavian goddess Vanadis. In 1869, Roscoe succeeded in isolating pure metallic vanadium by the reduction of VCl_2 with H_2 under conditions that required rigorous exclusion of air and moisture.

Vanadium is widely distributed in nature, it forms up to 0.05% of the earth's crust and there are over 60 vanadium ores. Vanadium occurs widely in coal and certain petroleums, especially those from Venezuela (up to 1%), in the form of oxovanadium(IV) porphyrins.[1,2] The major world producers of vanadium in recent years have been the United States, South Africa, and Finland.

The major industrial use of vanadium is in alloy steels and cast iron, to which it lends ductility and shock resistance. Commercial production is mainly as the iron alloy ferrovanadium, a tough, high-speed steel containing around 4−5% V. In ferrovanadium manufacture, vanadium pentoxide is reduced in an airtight electric furnace by ferrosilicon.[1,3]

The pure metal is much more difficult to obtain because of its reactivity with C, N_2, H_2, and O_2. There are four different routes to its production; reduction of chlorides, reduction of the oxide, thermal dissociation of the iodide, and an electrochemical process.[1,4,5]

Vanadium has atomic number 23, atomic mass 50.94, and a density of $6.0\,\mathrm{g\,cm^{-3}}$. Bulk samples are inert to air, moisture, alkalis, and other nonoxidizing acids other than HF at 25 °C. However, the metal is attacked by conc. H_2SO_4, HNO_3, and aqua regia. At elevated temperatures, vanadium combines with most nonmetals including N_2, C, Si, and B to give a variety of products such as VC, VSi_2, V_3Si, VB, and VB_2. Most of these compounds are nonstoichiometric and interstitial. In air, V_2O_5 is formed along with lower oxides.[1,6]

Vanadium metal forms definite compounds with several other metals and forms a solid solution in all proportions with titanium. It shows catalytic activity in a wide number of applications.[1,6]

Vanadium is an essential element[7,8] and the biochemistry of vanadium is dealt with elsewhere (*see* ***Vanadium in Biology***). Here it is worth pointing out that the importance of vanadium in several biological systems has led to an upsurge in the extent and breadth of the coordination chemistry of the element.

The toxicity of vanadium is well known. No matter by which route the metal is absorbed, it acts by depressing the respiratory center, constricting the peripheral arteries of the viscera, and causing hyperperistalsis and enteritis. It has also been shown to be one of the few metals that can modify amino acid secretion. The effects of the vanadate(V) ion on the cardiovascular system have been studied. Numerous enzymes are inhibited by vanadium ions or their complexes.[1]

2.1.2 *Analytical Chemistry*[1,9,10]

Analytical methods for the quantitative determination of vanadium by volumetric, colorimetric, or gravimetric techniques are all available.

Chemical Methods. In general, vanadium is reduced to the +II oxidation state by zinc amalgam, the vanadium can then be determined volumetrically by oxidation with a standard oxidizing agent (e.g. $KMnO_4$) to the +V state. The formation of the reddish-brown peroxo-complex is used as the basis of a colorimetric technique for the determination of vanadium. Gravimetric techniques are not as useful for the determination of vanadium as the volumetric and colorimetric techniques.

Spectroscopic Techniques. In absorption spectroscopy, Vanadium(V), a d^0 system, shows no transitions in the visible region. The yellow color of some V^V complexes can be ascribed to the tail of an intense absorption in the ultraviolet. Absorption spectroscopy is more useful for V^{IV} systems ($3d^1$), where electronic energies of transitions generally correlate well with ligand type and with electron spin resonance (ESR) parameters.

^{51}Vanadium NMR is a useful diagnostic tool for the detailed investigation of V^V coordination environments. The large magnetic moment of the ^{51}V nucleus, its high natural abundance (99.76%), and favorable relaxation properties make it a useful probe for the investigation of vanadium in its isolated complexes and in biological systems. This area has been reviewed recently.[11–13]

ESR spectroscopy is often used to study the VO^{2+} ion and its complexes. The unpaired electron is strongly coupled to the ^{51}V nucleus to give ESR spectra consisting of eight-line manifolds in frozen solution. The hyperfine coupling constants and g-factors are sensitive to the ligand field of the vanadium atom.[1,7]

Superhyperfine interactions are rarely observed in the ESR spectrum of the VO^{2+} ion because the unpaired electron interacts only weakly with the ligand nuclei, so that often the size of the coupling is less than the ESR bandwidth. This problem has been surmounted through the use of ENDOR spectroscopy.[1,7] In ENDOR spectroscopy, molecules with their $V{=}O$ axes either parallel or perpendicular to the direction of the static magnetic field are selectively irradiated. In this way, the anisotropic superhyperfine coupling constants of ^1H and ^{14}N and the ^{14}N quadrupolar coupling constants can be obtained.

EXAFS has recently become more extensively used in the study of vanadium in complexes and in biology to investigate the nature of the local environment around the vanadium atom.[14,15]

3 BINARY COMPOUNDS

3.1 Hydrides

Vanadium can absorb hydrogen reversibly up to the final composition $VH_{0.94}$ when heated at 300 °C in a 48.4% hydrogen atmosphere at 1 atm pressure.[1] The product is a gray metallic material whose brittleness increases with increasing hydrogen content. The structure is of a single phase having a tetragonal unit cell and lattice parameters $a = 3.02$, $c = 3.36$.[2] A recent review on vanadium hydrides is available.[16] Stoichiometric vanadium hydrides such as VH_4 have been observed spectroscopically[17] in an H_2 matrix at 2–4 °K and coordination compounds containing V–H bonds are described later in this article (see Sections 4.3.2 and 4.4.2).

3.2 Halides

The halides are extremely important compounds providing convenient starting materials for other species. Their preparations and properties have been comprehensively reviewed elsewhere[1,4,18] and references to individual synthetic methods can be found in these works. The halides are discussed here in order of decreasing oxidation state.

3.2.1 *Pentavalent State*

Vanadium Pentafluoride, VF_5. Vanadium pentafluoride is the only pentahalide so far reported. It is best prepared by direct reaction between metallic vanadium and fluorine in a flow system at 300 °C under moisture free conditions. It is an extremely reactive white solid at room temperature and an extremely powerful oxidizing and fluorinating agent.

Crystalline VF_5 is isomorphous with $MoOCl_4$ and the pentafluorides of Cr, Tc, and Re. The structure consists of infinite chains of octahedrally coordinated vanadium atoms linked by shared fluorine atoms.[19] In the gas phase, electron diffraction has shown VF_5 to exist as a monomeric molecule having D_{3h} symmetry.[20]

3.2.2 *Tetravalent State*

VF_4, VCl_4, and VBr_4 are all well documented, but VI_4 has been detected only in equilibrium mixtures and to date has not been isolated.

Vanadium Tetrafluoride. VF_4 is formed along with VF_5 and VF_3 in the fluorination of metallic vanadium and the difference in volatilities of the three fluorides allows their separation by fractional sublimation. It can also be prepared by treatment of VCl_4 with anhydrous HF in an inert solvent such as CCl_3F at −78 °C. Pure VF_4 is a bright green hygroscopic solid, which disproportionates at 100 °C to VF_5 and VF_3. Its structure consists of octahedrally coordinated VF_6 units linked by shared F atoms into polymeric strings.[1,21] VF_4 reacts with BF_3 or F_2 to give VF_5, but is a weaker fluorinating agent than the latter.

Vanadium Tetrachloride. VCl_4 is produced in the reaction between dry chlorine and vanadium or by the action of chlorinating agents such as $COCl_2$, $SOCl_2$, S_2Cl_2, or CCl_4 on V_2O_5 or the metal itself.[1] It is a reddish-brown, viscous liquid, mp = −26 °C, bp = 153 °C, which is hydrolyzed readily in moist air. It is soluble in nonpolar solvents such as CCl_4 and reacts violently with electron donor solvents to form adducts. VCl_4 is monomeric in the vapor phase having a regular tetrahedral structure.[1] Decomposition of the tetrachloride to VCl_3 and Cl_2 occurs slowly at room temperature, even under a positive pressure of chlorine.

Vanadium Tetrabromide. VBr_4 has been isolated by quenching (−78 °C) the vapor obtained from heating the solid tribromide to 325 °C. Although it is stable only up to −45 °C, decomposing to VBr_3 and Br_2, its absorption spectrum in the range 200–600 nm has been obtained.[22]

Vanadium Tetraiodide. VI_4 is unstable and has not been isolated, but its absorption spectrum has been observed in the range 230–500 nm in the vapor, and thermodynamic data for its dissociation into VI_3 and I_2 have been determined[23] ($\Delta H^\circ = 104.8\,\text{kcal m}^{-1}$, $\Delta S^\circ = 98.4\,\text{kJ m}^{-1}$).

3.2.3 Trivalent State

Vanadium Trifluoride. VF_3 is prepared by passing anhydrous HF in N_2 over VCl_3 or VCl_2 at 600 °C in a platinum crucible. The structure is rhombohedral, each vanadium atom having an almost regular octahedron of fluorine atoms with the octahedra joined by shared corners.[1] Pure anhydrous VF_3 is yellowish-green in color. It is slightly soluble in water, giving acidic solutions, and is virtually insoluble in organic solvents. It sublimes without decomposition at 800 °C.

Vanadium Trichloride. VCl_3 can be prepared by decomposition of vanadium tetrachloride under reflux or by heating the trioxide, V_2O_3, with thionyl chloride.[1] Its structure is similar to that of α-$TiCl_3$ and is composed of hexagonally close-packed chloride ions, with vanadium atoms occupying 2/3 of the octahedral interstices in alternate layers. Within a layer, each VCl_6 octahedron has three neighboring VCl_6 octahedra with which it shares edges.[1] VCl_3 disproportionates above 600 °C, to VCl_4 and VCl_2 and therefore cannot be sublimed. It is also extremely sensitive to traces of oxygen, which results in the formation of oxochlorides.

Vanadium Tribromide. VBr_3 is formed directly from the reactions of bromine with vanadium or its nitride or carbide at elevated temperatures.[1] More recently, it has been prepared from the reaction between V_2O_5 and CBr_4 and by treatment of VCl_4 with dry HBr.[24] It is purified by sublimation at 350 °C in a bromine atmosphere, which reverses the dissociation to VBr_2 and Br_2. Anhydrous VBr_3 is a grayish-black crystalline powder with a structure analogous to that of VCl_3.[1]

Vanadium Triiodide. VI_3 can be prepared by reaction of vanadium metal with iodine at elevated temperatures. It is a brownish-black, hygroscopic crystalline powder, soluble in most nonpolar solvents, that begins to dissociate into VI_2 and I_2 at 270 °C.[1]

Vanadium Iodo-Chlorides. The reaction of VCl_4 with dry HBr has been reported to give the mixed halides $VClI_2$ and VCl_2I.[24]

3.2.4 Divalent State

The preparations, structures, and properties of V^{II} halides have been reviewed.[1,25]

VF_2 forms deep blue crystalline needles having the rutile type structure with two VF_2 units per unit cell. VCl_2 and VBr_2 can be prepared from the appropriate trihalide by their reduction by dihydrogen or by their disproportionation at an elevated temperature. VI_2 can also be prepared by direct reaction of the elements.

VBr_2 has a layered triangular lattice in the range 1.5–35 °K and is a Heisenberg antiferromagnet.[26] Two forms of VI_2 are produced, depending upon the reaction temperature. The red form has the CdI_2 structure; the black form is closely related but with mixed hexagonal and cubic close-packing of iodide ions.[1] VCl_2 sublimes without decomposition in an inert or HCl atmosphere above 900 °C. Similarly, VBr_2 and VI_2 sublime without loss of halogen in the range 800–900 °C. The dihalides are hygroscopic and dissolve in water to yield blue–purple solutions of $[V(H_2O)_6]^{2+}$. Acidic solutions of the dihalides are strongly reducing.[1]

3.3 Oxohalides

The oxohalides form an important set of compounds, closely related to the halides. Their preparations and properties are well-documented[1,4,27,28] and therefore only a summary is given here.

3.3.1 Pentavalent Oxohalides

The following oxohalides are known for vanadium(V): $[VOX_3]$ (X = F, Cl, Br) and VO_2X (X = F, Cl); preparative routes are available for all.[1,4]

$[VOCl_3]$ is a pale yellow liquid with physical properties similar to VCl_4. $VOBr_3$ slowly decomposes at 25 °C to $VOBr_2$

and Br_2. Both compounds are extremely unstable toward moist air. The gas-phase structures of $[VOCl_3]$ and $[VOBr_3]$ consist of trigonally distorted tetrahedra as predicted for $[VOF_3]$.[1,4]

3.3.2 *Tetravalent Oxohalides*

All the oxohalides of vanadium(IV), $[VOX_2]$ ($X = F$, Cl, Br), are known. In general, the complexes are green and monomeric and their chemistry is dominated by the strong vanadium–oxygen bond of the VO^{2+} group. The hydrates $[VOF_2]\cdot 4H_2O$ and $[VOF_2]\cdot 2H_2O$ are known and several hydrates of $[VOCl_2]$ have been reported, of which the best known is $[VOCl_2]\cdot 2.5H_2O$, but many of their stoichiometries are uncertain.

3.3.3 *Trivalent Oxohalides*

Crystalline VOCl, prepared by reaction between V_2O_5 and VCl_3, has a layered structure. Each oxygen atom is surrounded by a tetrahedron of vanadium atoms. Each vanadium atom is surrounded by four oxygen and two chlorine atoms in a distorted octahedral arrangement.[1]

3.4 Oxides (*See Oxides: Solid-state Chemistry*)

These have been described in a number of general texts.[1,28] In addition, a number of phases of intermediate composition have been identified, and the lower oxides, in particular, have wide ranges of homogeneity. There is a vast chemistry of polyoxovanadates, which are of interest with regard to their structural and catalytic properties,[29,30] but discussion of their chemistry is outside the scope of this article.

3.4.1 *Pentavalent State*

V_2O_5 is well known and has a structure that essentially comprises distorted trigonal bipyramids of VO_5 sharing edges to form zigzag double chains.[1,31,32] V_2O_5 loses dioxygen reversibly on heating, and this may partly explain its function as a catalyst in a wide variety of both organic and inorganic reactions, an important example being the oxidation of SO_2 to SO_3 in the contact process for the manufacture of sulfuric acid. It is reduced by a number of reagents, such as H_2, C, CO, SO_2, alkali metals, Al, and Ca. The products include the lower oxides, VO_2, V_2O_3, and VO, as well as many other distinct oxide phases. With chlorine it forms oxotrichloride and dioxygen, and with metal oxides it forms vanadates.[1]

V_2O_5 is slightly soluble in water, producing a pale yellow, acidic solution that readily becomes colloidal. In alkalis, it dissolves to form colorless solutions, the nature of the species present depending upon the pH. At high pH, the orthovanadate ion $[VO_4]^{3-}$ is formed, and at intermediate pH a series of hydrolysis–polymerization reactions occur, forming isopolyvanadates.[1,32]

3.4.2 *Tetravalent State*

VO_2 may be prepared by the mild reduction of V_2O_5 with reducing agents such as CO, SO_2, oxalic acid, or hydroxylamine hydrochloride.[1,28,33] At room temperature, it has a distorted rutile structure but above 341 K, an undistorted rutile structure is adopted. Both phases consist of edge-sharing VO_6 octahedra with similar O frameworks.[34] On passing from the low-temperature to the high-temperature form, the V^{4+}-V^{4+} distance changes[34] from 2.7695 Å to 3.0794 Å. VO_2 is amphoteric, dissolving in nonoxidizing acids to give solutions containing the blue oxovanadium(IV) (vanadyl) ion $[VO]^{2+}$, and in alkalis to give the yellow–brown vanadate(IV) (hypovanadate) ion $[V_4O_9]^{2-}$. $[VO_4]^{4-}$ is formed at high pH.[1]

3.4.3 *Tervalent State*

V_2O_3 may be prepared by reduction of V_2O_5 by reducing agents such as C, CO, or H_2. It crystallizes with the corundum structure.[1,28] It is believed to possess only a narrow range of homogeneity. V_2O_3 is antiferromagnetic, having a transition temperature of approximately 160 K. It is readily oxidized in air to VO_2, and may be reduced to the metal by calcium hydride. It reacts with thionyl chloride to give VCl_3. V_2O_3 is basic, dissolving in aqueous acids to give blue or green V^{III} solutions that are strongly reducing.[1]

3.4.4 *Divalent State*

VO is formed as a gray metallic powder by the reduction of higher oxides with a variety of reducing agents such as vanadium or potassium. It has a defect NaCl structure with a wide range of homogeneity, $VO_{1.20}$–$VO_{0.75}$. Above 950 °C, in a vacuum, it decomposes into vanadium metal and V_2O_3. It is an electrical conductor and is paramagnetic between 77 and 300 K. VO is basic and dissolves in mineral acids to give a violet solution of vanadium(II).[1]

3.4.5 *Other Oxides*

In addition to the phases already mentioned, many others in the composition range V_2O_5–VO have been investigated.[1,28,35] Between V_2O_5 and VO_2, there is a succession of phases of general formula V_nO_{2n+1}, of which V_3O_7, V_4O_9, and V_6O_{13} have been characterized. V_6O_{13} is obtained as a blue–black crystalline powder, and is formed by loss of oxygen from one-third of the V_2O_5 [010] planes on heating. Between VO_2 and V_2O_3, there is a series of shear phases, Magneli phases, of general formula V_nO_{2n-1}, based on a rutile structure with periodic defects. Examples are V_8O_{15}, V_7O_{13}, V_6O_{11}, V_5O_9, and V_4O_7. V_3O_5, which is also known, and V_2O_3 and VO also conform to this general equation, but their structures are not related by chemical shear to those of the Magneli phases. On further reduction of the system, the corundum structure of V_2O_3 is retained down to compositions as low as $VO_{1.35}$, after which VO is formed. This is also nonstoichiometric, with a composition range of $VO_{0.75}$ to $VO_{1.20}$.

3.5 Sulfides

A number of vanadium sulfide phases, ranging from VS_4 to V_3S, have been reported, although few have been well characterized and some may not exist at all. The structures, where known, are often complicated and difficult to describe.[1,28,36]

3.5.1 VS_4

VS_4 may be prepared by the reaction of V_2S_3 with an excess of sulfur at 400 °C. It is a diamagnetic black powder, with a fibrous structure similar to SiS_2, but with S_2^{2-} ions replacing S^{2-} ions. It is a semiconductor. VS_4 is thermally unstable above 500 °C and dissolves readily in alkalis but not in acids.[1,28]

3.5.2 V_2S_5

This compound is obtained by thermal decomposition of ammonium thiovanadate, $(NH_4)_3[VS_4]$. It is readily decomposed to V_2S_3 and free sulfur, and this may be the reason for doubts about its existence.[1,28]

3.5.3 VS_2

Little is known about this sulfide, which is believed to have the CdI_2 structure.[1,28]

3.5.4 V_2S_3

V_2S_3 has a range of homogeneity extending from $VS_{1.17}$ to $VS_{1.53}$. It is obtained as a black paramagnetic solid from the reaction of H_2S on V_2O_3, VO_2, or V_2O_5, or by treating V_2O_5 with carbon disulfide at 700 °C. On heating to 850–950 °C in a vacuum, it dissociates into VS and sulfur. It is oxidized by air and nitric acid, but is insoluble in dilute alkali.[1,28]

3.5.5 VS

This sulfide has a range of homogeneity extending from $VS_{1.00}$ to $VS_{1.16}$. It is obtained as an air-sensitive brownish-black solid by dihydrogen reduction of V_2S_3 at 1000 °C or by reaction between the metal and sulfur in a sealed silica tube at 1000 °C. VS has the NiAs structure and is metallic with essentially temperature-independent paramagnetism.[1,28]

3.5.6 V_3S_4

A high-temperature and a low-temperature form are known. The low-temperature form is hexagonal, isotopic with Nb_3S_4 and transforms above 825 °C to the monoclinic form, which is stable above 950 °C. This form is isostructural with Cr_3S_4.[37,38]

3.5.7 V_5S_4

This sulfide is tetragonal and isostructural with Ti_5Te_4.[1,28]

3.6 Sulfates

The only simple sulfates of vanadium are formed in the oxidation states +3 and +2. Vanadium(III) sulfate can be crystallized as a hydrate from aqueous solution, and is strongly reducing. It gives rise to a series of alums of the type $M^IV(SO_4)_2\cdot 12H_2O$, which have been shown to contain the $[V(H_2O_6)]^{3+}$ ion. The ammonium alum, $(NH_4)V(SO_4)_2\cdot 12H_2O$, is obtained as air-stable blue–violet crystals by electrolytic reduction of $NH_4[VO_3]$ in sulfuric acid.[1,28]

The violet divalent sulfate $VSO_4\cdot 7H_2O$ may be prepared by electrolytic sodium amalgam, or by zinc reduction of a solution of vanadium pentoxide in sulfuric acid, followed by evaporation of the resulting solution in a vacuum over phosphorous pentoxide. It is also strongly reducing, and evolves dihydrogen in water, but not in acid solution. The hexahydrate, $VSO_4\cdot 6H_2O$, is obtained by electrolytic reduction of vanadyl(IV) sulfate solution.[21,28]

Both the hepta- and hexahydrate give rise to the reddish-violet Tutton's salts, $M_2[V(H_2O)_6]\cdot(SO_4)_2$ ($M = NH_4$, K, Rb, or Cs), on treatment of an aqueous solution of the salt with the appropriate alkali metal sulfate. These salts have the schonite, $K_2Mg(SO_4)_2\cdot 6H_2O$, structure. They are more stable than the simple sulfate, especially in the presence of excess acid.[1,28]

3.7 Selenides and Tellurides

Several studies have been carried out on the vanadium–selenium and vanadium–tellurium systems,[1] and some of the components of these systems are described below. Vanadium diselenide, $V_{1+x}Se_2$ $(0.02 < x < 0.18)$ has a structure of the $Cd(OH)_2$–NiAs type. Several other phases, such as V_5Se_8, V_3Se_4, and V_7Se_8, have ordered superstructures of this type. VSe has the hexagonal NiAs structure. The vanadium-rich phase V_5Se_4 has a tetragonal structure. The magnetic susceptibility of V_5Se_8 increases significantly with temperature, but VSe_2, V_3Se_4, and the selenides richer in vanadium are metallic, with essentially temperature-independent paramagnetism.[1,39]

Vanadium ditelluride, $V_{1+x}Te_2$ ($0.03 < x < 0.14$), has a monoclinic structure related to that of $Cd(OH)_2$. The nonstoichiometric phases V_5Te_8 and Ve_3Te_4 have superstructures intermediate between the $Cd(OH)_2$ and NiAs types. The vanadium-rich phase, V_5Te_4, is monoclinic. The vanadium tellurides are metallic, with essentially temperature-independent paramagnetism.[1,39]

3.8 Nitrides

Vanadium nitride, VN, with a range of homogeneity from $VN_{1.00}$ to $VN_{0.71}$, may be prepared as a grayish-violet powder by the action of dinitrogen on a mixture of V_2O_3 and carbon at 1250 °C, or by the reaction of vanadium and dinitrogen or ammonia at 900–1300 °C. It is also formed by the thermal decomposition of $(NH_4)_3[VF_6]$ at 600 °C. It has the sodium chloride structure. It reacts with alkalis to give ammonia, and it is also attacked by boiling nitric acid. Another phase, V_2N, with a range of homogeneity from $VN_{0.5}$ to $VN_{0.37}$ is also known.[1]

3.9 Phosphides, Carbides, Silicides, and Borides

The V/P, V/C, V/Si, and V/N systems have been studied over various composition ranges and the main phases correspond to the stoichiometries V_3P, VP, VC, V_3Si, V_5Si_3, VSi_2, V_3B_2, VB, V_3B_4, and VB_2.[1]

3.10 Phosphates

The binary phosphate $V(PO_3)_3$ can be prepared by heating $V_2O_5/H_3PO_4/H_2SO_4$ mixtures at 300 °C. The structure is monoclinic consisting of a mixed network of VO_6 octahedra and PO_4 tetrahedra bonded at the apices into chains.[1,28]

4 COORDINATION CHEMISTRY OF VANADIUM

4.1 Introduction

The coordination chemistry of vanadium is dominated by its variable oxidation numbers, which range over the −I, 0, +I, +II, +III, +IV, and +V states. A very large number of compounds have been prepared, particularly for the higher oxidation states, since the previous edition of this Encyclopedia and reviews have appeared on general coordination chemistry,[40–43] structural advances,[44] aqueous vanadate chemistry,[45] and biologically related topics, including vanadium as a phosphate analogue, haloperoxidases, amavadin, and other biological systems,[46–48] and modeling of vanadium nitrogenase.[46,49]

Much of the recent coordination chemistry of vanadium has been stimulated by interest in the biological significance of the element. Vanadium is important in both reductive[49] and oxidative catalytic transformations[46–48] in biological chemistry (*see* ***Vanadium in Biology***).

Vanadium is known to exist in petroleum and shale deposits as a porphyrin complex.[50] Many catalytic processes that take place in oil production or advanced coal conversion may be critically affected by the presence of trace amounts of vanadium. Also it is known that vanadium, in combination with S compounds, can cause problems in oil hydroprocessing. Investigation of the manner in which V is present in coal, oil, and bitumen has resulted in many studies on porphyrin complexes of V^{IV} and V^{II}.[50,51]

The types of coordination complexes known for vanadium in its various oxidation states are discussed in the following sections.

4.2 Coordination Complexes in Low Oxidation States (<2) (*See also Vanadium: Organometallic Chemistry*)

Complexes containing vanadium in low oxidation states, apart from organometallic compounds, are known with ligands such as bipy, phen, nitric oxide, and tertiary phosphines, which stabilize such oxidation states.[1] Depending on their electronic structure, V^I and V^{-I} complexes may be diamagnetic, which permits study by NMR spectroscopy, and EPR spectroscopy has been used to study paramagnetic V^0 complexes.

4.2.1 Vanadium(-I)

Reduction of $[V(bipy)_3]I_2$ with the metals Mg or Zn yields the complex $[V(bipy)_3]$, which will undergo further reduction by lithium aluminum hydride to $Li[V(bipy)_3]\cdot 4THF$, which formally contains V^{-I}. Similarly, reduction of $[V(phen)_3]$ with dilithium naphthalenide or dilithium benzophenone in THF yields $[V(phen)_3]I_2$. Further reduction with dilithium benzophenone gives the V^{-I} complex $Li[V(phen)_3]\cdot 3.5THF$. The terpyridyl complex $[V(terpy)_2]$ can be obtained as black crystals by reduction of DMF solutions of $[V(terpy)_2]I_2$ with Mg or LiAlH. Such low oxidation state complexes are highly air sensitive and decompose if heated to 100–200 °C in a vacuum. In these systems, the ligands may have an anion radical character.[1]

Tertiary phosphines, together with dinitrogen ligands, stabilize the V(-I) state in complex anions such as *trans*-$[V(N_2)_2(Ph_2PCH_2CH_2PPh_2)_2]^-$, whose X-ray structure is known, and *cis*-$[V(N_2)_2\{(Ph_2P)(CH_2CH_2PPh_2)_3\}]^-$.[52] Monodinitrogen compounds as well as complexes with monodentate phosphines have also been obtained, however, most complexes are unstable in the solid state even under a dinitrogen atmosphere.[52]

Nitrosyl ligands also stabilize V^{-I} complexes because, like dinitrogen, they are good π-acceptors that serve to remove electron density from electron-rich metals. Thus, addition of bpy or phen to an aqueous solution of $[V(CN)_5(NO)]^{3-}$ gives the complexes $[V(NO)_2L_2][CN]$ (L = bipy or phen), and similar products were obtained from mixtures of $H_2VO_4^-$, hydroxylamine hydrochloride and pseudo-halides, such as NCS^- or N^{3-}.[53]

4.2.2 *Vanadium(0)*

EPR spectroscopy has been used to study the $[V(bpy)_3]$ complex and demonstrate that the single unpaired electron is extensively delocalized on the bipyridyl ligands.[54] The V^0 complex $[V(PF_3)_6]$ has been prepared by the oxidation of $[Na(diglyme)_2][V(PF_3)_6]$ with benzenediazonium tetrafluorborate.[55]

4.2.3 *Vanadium(1)*

Some nitrosyl complex compounds have been prepared in which the vanadium center is formally V(I). They carry the triethanolamine (tea) coligand and the vanadium in a structurally characterized example, $[V(NO)(tea)]^-$, is in a distorted, trigonal-bipyramidal environment with the amine and nitrosyl nitrogen donors in the axial positions.[56]

4.3 Vanadium(II) Coordination Complexes

The preparation of complexes of V^{II} was hampered in the past by their easy oxidation.[1,43,57] However, as techniques for the handling of air- and moisture-sensitive compounds have become more routine, the number of synthetic routes to such complexes and the types of complexes formed have increased.

Until recently, the majority of V^{II} coordination complexes contained the hydrated V^{2+} ion, obtained by reduction of acidic solutions of V^V, V^{IV}, or V^{III}. The solutions are strongly reducing, and are oxidized by water with the evolution of dihydrogen. Several crystalline salts containing the $[V(H_2O)_6]^{2+}$ ion are known. The most important of these is the sulfate, $VSO_4{\cdot}6H_2O$, formed by reduction of V_2O_5 solutions in H_2SO_4, and the double sulfates (Tutton's salts), $M_2[V(H_2O)_6](SO_4)_2$ (M = NH_4, K, Rb, or Cs).[1,43,57] The solid-state structures of several vanadium(II) hydrates have been obtained by X-ray structural or neutron diffraction methods.[58]

Most V(II) complexes have predominantly N-, O-, S-, P-, and halide donor ligands. They are presented below in terms of the predominant ligand in the coordination sphere.

4.3.1 *Oxygen Ligands*

Mononuclear octahedral complexes have been obtained for carbonyl-bound acetic acid,[59] and five-coordinate complexes of sterically hindered phenoxides of the type $[V(py)_3(C_6H_3Ph_2\text{-}2,6)_2]$.[60] A more hindered phenol gave a four-coordinate complex, $[V(C_6H_3Pr^i_2\text{-}2,6)_4\{Li(thf)\}_2]$ in which two pairs of *cis*-phenolates were linked by a single $Li(thf)^+$ unit.[61] A binuclear complex of a substituted acetylacetone[62] has the structure shown in (**1**).

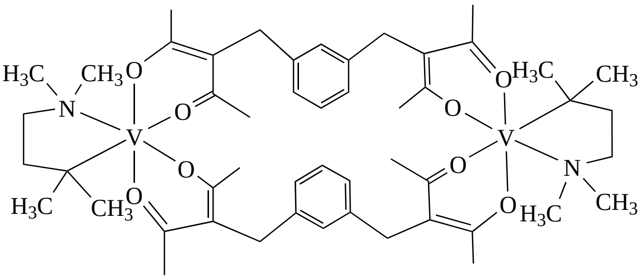

(**1**)

4.3.2 *Nitrogen and Phosphorus Ligands*

A general synthetic route to a range of V^{II} complexes has involved well-characterized precursor complexes in this oxidation state.[1,43] Thus, the anion $[V_2(\mu\text{-}Cl_3)(thf)_6]^-$ has been used[43] to give complexes with diamino, pyridyl, and pyrrolidyl ligands and *trans*-$[VCl_2(Me_2NCH_2CH_2NMe_2)_2]$ has been used as a starting material for complexes of organic amidates $[RNC(R^1)NR^-]$ and acetanilide $[PhNC(Me)O^-]$ ligands.[63] Amidinate and amide ligands have been used to prepare dinitrogen complexes such as $[V\{(SiMe_3)NC(Ph)N(SiMe_3)_2\}_2(\mu\text{-}N_2)]$, which reacts reversibly with thf to give $[V\{(SiMe_3)NC(Ph)N(SiMe_3)\}_2(thf)_2]$.[64] Complexes of tertiary phosphine ligands include $[VX_2(R_2PCH_2CH_2PR_2)_2]$ (X = halide or BH_4^-, R = Me or Et)[1,43] and the hydride-bridged complex cation $[\{V(PMe_3)_3\}_2(\mu\text{-}H)_3]^+$.[65]

Vanadium(II) heterocyclic amine complexes of the type $[VX_2L_4]$ and $[VL_6]X_2$ (L = heterocyclic amine, e.g. pyrazole, imidazole, 2-methylimidazole, benzimidazole, isoquinoline; X = anionic ligand) have been known for some time and more recent examples of such complexes include polypyridyl V^{II} complexes of the type $[V(terpy)(bipy)L]^{n+}$. Such complexes are obtained as a result of the disproportionation reaction of $[V^{III}(terpy)Cl_3]$, which yields $[V^{II}(terpy)_2]^{2+}$ and $[V^{IV}O]^{2+}$ in CH_2Cl_2 suspensions.[1]

Low-valent metal porphyrins have been extensively studied, and show some promise in the understanding of the reactions of hemes with dioxygen. Until recently, there have been few examples of low-valent V porphyrins, presumably due to the stability of the oxovanadium(IV) species. The first V^{II} porphyrins to be isolated have been obtained by reduction of nonoxo V^{IV} complexes of the type $[V^{IV}X_2L]$ (X = Cl, Br; L = porphyrinate(2−), OEP, TPP, TMTP, TPTP) by Zn amalgam to give $[V^{II}Y_2L]$ (Y = thf, $PPhMe_2$). The structures of both complexes $[V^{II}Y_2L]$ showed that the two nonporphyrin ligands assume a trans configuration with the octahedrally coordinated V atom in the plane of the four porphyrin N atoms.[1] An octaethylporphyrinogen V^{II} complex was found to form a μ-N dinuclear V^{III} complex.[66]

4.3.3 *Other Ligands*

With halide ligands, complex cations of the type $[L_3V(\mu\text{-}Cl)_3VL_3]$ (L = thf or 3-Me-thf) have been extensively studied and give a wide range of halide and other complexes by breaking up the dimer with ligands to give monomeric compounds, or by substitution into the dimer to give complexes such as $[L_3V(\mu\text{-}Cl)_3VL_2(PPh_3)]$.[1,43] Halide complexes of the type *trans*-$[VX_2L_4]$ (X = Cl, Br, I, SCN, N_3, PhS, EtS or BH_4; L = py) have been prepared.[1,43] Oligonuclear complexes have been prepared in addition to the dinuclear cations, these include the series of complexes having a very stable $\{V_3Cl_3\}$ core, *triangulo*-$[V_3(\mu\text{-}Cl)_3(\mu_3\text{-}Cl)L_3]^+$ (L = MeOH, EtOH, etc.),[43] and a tetranuclear species $[V_4(\mu_3\text{-}Cl)_2(\mu\text{-}Cl)_2(\mu\text{-}CF_3CO_2)_2(thf)_6]$.[67]

Vanadium(II) complexes with sulfur-donor ligands are relatively rare. Those reported are prepared from the usual V^{II} precursors noted above. Thus *trans*-$[VCl_2(Me_2NCH_2CH_2NMe_2)_2]$ reacted with 1,2-bis(2-sulfido-phenylsulfanyl)ethane(2-) to give the mixed N,S ligated complex $[V(2\text{-}SC_6H_4SCH_2CH_2SCH_2CH_2C_6H_4S\text{-}2)(Me_2NCH_2CH_2NMe_2)]$. With the tridentate ligand, 1,4,7-trithiocyclononane, (9[ane]S_3), $[V_2(\mu\text{-}Cl)_3(thf)_6]Cl$ gives $[\{V(9[ane]S_3)\}_2(\mu\text{-}Cl)_3]Cl$ and $[VI_2(thf)_4]$ gives the monomer $[VI_2(thf)(9[ane]S_3)]$.[14]

4.4 Vanadium(III) Coordination Complexes

Vanadium(III) complexes are most commonly prepared from V^{III} halides, principally VCl_3, or by electrolytic reduction of V^{IV} or V^V solutions. Most are readily oxidized or hydrolyzed in the presence of air or moisture.

Complexes with monodentate ligands are generally six-coordinate cationic or neutral species having octahedral stereochemistry with trigonal distortion. The electronic spectra and magnetic properties of many six-coordinate V^{III} complexes have been studied and are in accordance with those expected for a d^2 ion in an octahedral field with trigonal distortion.[1]

More recent work has involved the preparation and characterization of vanadium(III) complexes with bidentate and multidentate ligands, especially those with nitrogen- and oxygen-donor atoms, because of their biological significance. Hydride derivatives are of interest in connection with the catalytic properties of vanadium, for example, in alkene dehydrogenation or polymerization. Complexes with sulfur-donor and possibly also nitrogen-donor atoms are relevant to the role played by vanadium in the poisoning of the Co–Mo catalyst used for the hydrodesulfurization of crude oil.[1]

4.4.1 *Oxygen Ligands*

The chemistry of the blue hexahydrate ion $[V(H_2O)_6]^{3+}$ has been reviewed.[1] Complexes of alkoxides are of interest with regard to biological systems, particularly tunicates,[46] and to polymerization catalysis of alkenes.[68] Alkoxide and phenoxide complexes are often oligomeric and insoluble,[1] unless the O-donor carries bulky substituents, when soluble, mononuclear complexes can be isolated. Five-coordination is then common, for example, in $[VCl(OC_6H_3Pr^i_2\text{-}2,6)_2(thf)_2]$.[69] Binuclear complexes with phenoxides bridging six-coordinate vanadiums are also known, such as $[\{V(OPh)_2(thf)\}_2(\mu\text{-}OPh)_2]$, and a binuclear complex with terminal esters, $[\{VCl_2[CH_3C(O)OC_2H_5]_2\}_2(\mu\text{-}Cl)_2]$, has also been prepared.[70]

With bidentate ligands, both mononuclear and complexes of higher nuclearities may be obtained. The acetylacetonate complex $[V(acac)_3]$ has a monomeric, octahedral structure as do tris(oxalate) complexes and the oxalate anion $[V(oxalate)_2(H_2O)_2]^-$, but catecholate ligands form dinuclear complexes containing a linear oxide-bridged unit, $[\{V(catecholate)_2(L)\}_2(\mu\text{-}O)]$, which are interesting as polymerization procatalysts.[1,68,71] Carboxylate ligands also support oxo-bridged structures, which include complexes having the $\{(\mu\text{-oxo})\text{-bis}(\mu\text{-carboxylate})\}$ core, in which the two V^{III} (d^2) ions show antiferromagnetic coupling, and also the trinuclear oxo-bridged cations illustrated in (**2**).[1,72]

The tetranuclear compounds $[V_4O_2(O_2CEt)_7(bpy)2]$-$[ClO_4]$ (bpy = 2,2-bipyridine), and the related complex $[NEt_4][V_4O_2(O_2CEt)_7(pic)_2]$ (pic = 2-picolinate) have a $[V_4O_2]^{8+}$ 'butterfly' core (**3**) and a $S = 3$ ground state.[73]

Because of their biological relevance, complexes of bidentate amino acids and related ligands have been widely studied[46] (*see* ***Vanadium in Biology***) and are merely mentioned here. Six-coordinated complexes of proline, phenyl analine, tryptophan, histidine, and valine have been prepared and structures are known.[46,74]

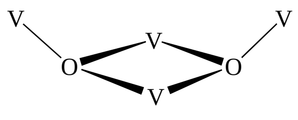

(**3**)

Some V^{III} complexes involving the ONO donor ligand pyridine-2,6-dicarboxylic acid, (DPA), include the seven-coordinated mononuclear complex, $[V(DPA)(PA)(H_2O)_2]$

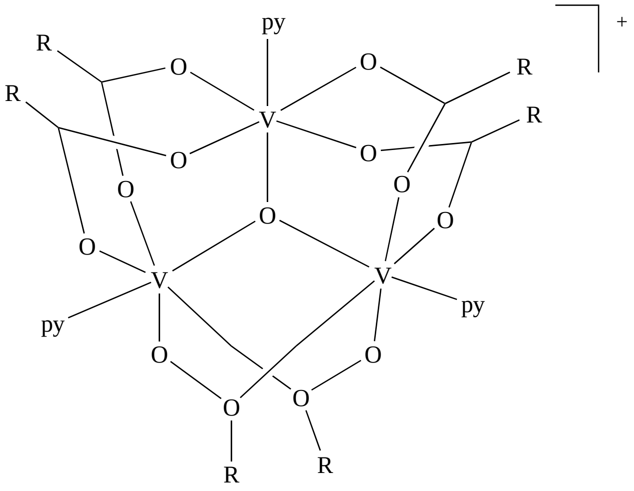

(**2**)

(PA = picolinate anion). This complex has a pentagonal bipyramidal structure with the equatorial plane accommodating the ONO and NO donor points, while the two water molecules occupy the axial positions.[75] Seven-coordination is more often seen with polydentate ligands, in particular, tetradentate EDTA and its analogues,[1] for example [V(EDTA)(H_2O)], which is converted to a six-coordinated complex by protonation of an oxygen atom of the EDTA. Nitrilotriacetate (NTA) and related ligands are tridentate O-donors that give six-coordinated complexes of the type [V(NTA)$(H_2O)_3$].[76]

4.4.2 *Nitrogen Ligands*

A number of acetonitrile, pyridine, and related complexes are known. Examples are $[VX_3(RCN)_3]$ (X = halide; R = Me, Et, or Pr) and $[VCl_3L_3]$ (L = pyridine and γ-picoline).[1] $[VCl_3(MeCN)_3]$ shows *fac*- and *mer*-isomers in solution and $[VCl_3py_3]$ has the *mer*-structure in the solid state, with the pyridines twisted out of the metal–ligand planes.[77]

Polydentate N-donor ligands have been developed with the aim of stabilizing vanadium complexes with low-coordination numbers or with relatively rare ligands, such as hydride or dinitrogen, at vanadium in a higher oxidation state than those previously used (see Sections 4.2 and 4.3) Thus, tris(amide) ligands are used to obtain complexes with hydrides or dinitrogen as bridging ligands in $[\{V[Me_3SiN(CH_2CH_2NSiMe_3)_2]\}_2(\mu\text{-}H)_2]$ and $[\{V[CH_3C(CH_2NPr^i)_3]\}_2(\mu\text{-}N_2)]$,[78] and the tridentate ligand $N\{CH_2CH_2N(C_6F_5)\}_3$ gives the five-coordinated, monopyramidal complex shown in (**4**).[79]

There have been extensive studies of V^{III} complexes of polydentate N- and N,O-donor ligands. These include porphyrins and phthalocyanins.[1,46] X-ray structures have recently been obtained as exemplified in (**5**).[80]

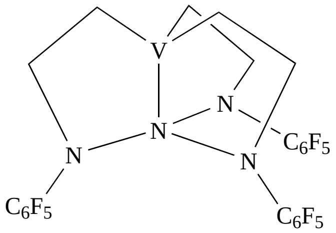

(**4**)

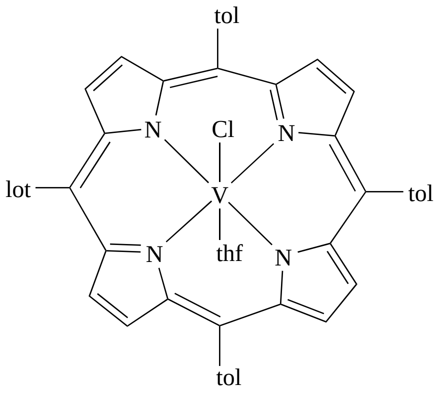

(**5**), tol = tolyl

Many complexes have been prepared using Schiff-base-type ligands,[1,46] which can be heptadentate and octadentate and give mononuclear or dinuclear complexes.[1,46,81]

4.4.3 *Sulfur Ligands*

Compounds in this area have been studied with regard to biological systems and polymerization catalysis; multidentate ligands are generally used. L-cysteine gives[46] the anion $[V(\text{L-cysteine})]^-$ and other mononuclear complexes are: $[VCl_3(1,4,7\text{-trithiacyclononane})]$,[14] the trigonal bipyramidal hydrazine complex $[V\{N(CH_2CH_2S)_3\}(N_2H_4)]$,[82] and a series of complexes of the ligand $[O(CH_2CH_2S)_2]^{2-}$, such as $[V\{O(CH_2CH_2S)_2\}(OC_6H_3Pr^i_2\text{-}2,6)(\text{pyridine})]$, which are catalyst precursors for olefin polymerization.[83]

Bidentate ligands can be used to generate both homo-metallic and hetero-metallic species. Thus, ethanethiolate (ent) gives[84] the anions $[\{V(\text{ent})\}_2(\mu\text{-ent})2]^-$ and $[\{VCl_3\}_2(\mu\text{-ent})_3]^{3-}$ and 2-aminoethanethiolate gives a series of linear-type, S-bridged, trinuclear complexes[85] incorporating V^{III} together with Rh^{III} or Ir^{III}. Cubane-type cluster complexes of iron, sulfur, and vanadium, such as the anion $[VFe_3S_4X_3(\text{dimethylformamide})_3]^-$ (X = halide), have been developed to mimic the behavior of the active center in vanadium nitrogenase and are discussed elsewhere (*see* ***Vanadium in Biology***).[46]

4.4.4 Halide and Other Ligands

Many examples of [MX_3L_3] complexes with N and P-donor ligands are known and recent X-ray structures generally confirm the proposed geometries for these octahedral compounds.[1] Halide bridges feature in polynuclear complexes of V^{III}, such as the structurally characterized anions [$\{VCl_3\}_2(\mu\text{-}Cl)_3]^{3-}$ and [$V_3OCl_4\{O_2C(C_6H_4SO_2\text{-}2)\}_5]^-$. The terminal and bridging halides of the former complex can be exchanged and the latter compound contains the triangular $[V_3(\mu\text{-}O)_3]^{7+}$ core structure seen in (**2**).[72] Linear oxo-bridged complexes of V^{III} with the $\{V\text{-}O\text{-}V\}^{4+}$ core and such terminal ligands such as PMe_3, BH_4^-, and 1,4,7-triazacylononane have been structurally characterized.[1]

4.5 Vanadium(IV) Coordination Complexes

4.5.1 Introduction

This is the most stable and important oxidation state for vanadium. Aqueous solutions of V^{III} are air oxidized to V^{IV}, and V^V reacts with mild reducing agents to give V^{IV}. The blue oxovanadium(IV) cation $[VO(H_2O)_5]^{2+}$ is prevalent in aqueous solution and in many salts and is used as a starting material for a wide number of complexes. The vanadyl ion $[VO]^{2+}$ dominates the aqueous chemistry of vanadium(IV) and this aspect of vanadium chemistry is effectively summarized in reviews that have already appeared.[1,46,57] The vanadyl ion is still ubiquitous in the more recent chemistry of vanadium(IV), but there has been a considerable expansion in the range of coordination compounds that do not contain the terminal oxo-group. We will discuss vanadyl complexes as a separate group, concentrating on examples from the recent past and outline the chemistry of nonvanadyl complexes according to the predominant donor atom in the coordination sphere of vanadium.

4.5.2 Coordination Complexes of Vanadium(IV) Halides

The earlier coordination chemistry of vanadium(IV) was based upon complexes of VX_4 formed generally by direct interaction with ligands in nonaqueous solvents. The majority of the complexes are of the type [VX_4L_2] (X = halide; L = O-, S-, Se-, N-, P or As-donor ligand), or are anionic complexes such as the hexachlorovanadate(IV), $[VCl_6]^{2-}$, with largely octahedral stereochemistries, showing some tetragonal distortion. The types of complexes formed, along with their methods of preparation, have been reviewed.[1] Simple oxohalide complexes [VOX_2L_2] and oxo-anions such as $[VOF_4]^{2-}$ are also well known and are often used as precursors to the vanadyl complexes discussed in the following section.[1,57]

4.5.3 Complexes of Oxovanadium(IV)

The VO^{2+} (vanadyl) ion is one of the most stable oxo-metal species known, and probably the most stable diatomic ion. Most of these properties stem from the ground-state electronic configuration of the vanadium atom, [Ar]$3d^1$, which shows similarities to the Cu^{2+} d^9 system. The ion also lends itself to study by ESR because of the isotopic purity of the ^{51}V isotope, its high nuclear spin, $I = 7/2$, and the single unpaired outer electron.

Examples of some of the main types of complexes formed by the VO^{2+} ion are shown in Table 1, which is a revised version of that found in Reference 1 in that it includes some recent examples, although most of the original entries are retained for continuity and because the structural pattern is largely unchanged. The complexes formed are classified according to the generalized formula.[1] Monodentate ligands are represented by lower case letters and multidentate ones by LL, LL′, LL′L″ and so on.[1,46,86–90,90]

The VO^{2+} ion bonds most effectively to electronegative donor atoms, that is, F, Cl, O, or N, but complexes having S-donor atoms are known. The vanadyl complexes formed are generally green or blue–green and can be neutral, anionic, or cationic. A commonly used starting reagent for the formation of VO^{2+} complexes is the sulfate, $VOSO_4{\cdot}5H_2O$, prepared by reduction of vanadium(V) in sulfuric acid. Probably, the most extensively studied complex of oxovanadium(IV) is [$VO(acac)_2$], which is also often used as a starting reagent for VO^{2+} compounds.[1,46] This stable complex has been used as a starting material for the preparation of mixed-ligand complexes by displacement reactions of one or both acac groups,[1,86] and has also been much used in physical studies of the nature of the V=O bond by spectroscopic and crystallographic techniques. The latter investigations indicate that the bond has a partial triple bond character with a predominant axial interaction and an equatorial component involving σ-bonding between the oxygen lone pairs and the V $3d_{xy}$ orbital.[87] This bonding system gives rise to a characteristic strong, sharp IR stretching frequency at around $985 \pm 50\,\text{cm}^{-1}$. The position of the V=O stretching frequency is insensitive to molecular changes in the coordination sphere of the V atom.

The vast majority of oxovanadium(IV) complexes have magnetic moments that lie within $0.03\,\mu_B$ of the spin-only value for one electron, that is, $1.73\,\mu_B$. These are magnetically dilute complexes in which the metal ion is not involved in a magnetic exchange with the neighboring metal ions through exchange forces and the orbital contribution to the magnetic moment is quenched. Two complexes that show this behavior are [VO(salicylaldimine)] and VO(phthalocyanine).[1]

The X-ray crystal structures of many oxovanadium(IV) complexes have been determined. In general, the V=O bond is shorter than most other V–O bond lengths, ranging between 1.57 and 1.68 Å, which is in keeping with the above view of the multiple characters of this bond.[1] The most common

Table 1 Examples of types of VO^{2+} complexes[1,7,14,46,88–94]

General formula[a]	Ligands
$[VOa_{4\,or\,5}]$	a = H_2O, F^-, Cl^-, NCS^-, CN^-, HCO_2^- DMSO, Ph_3PO, pyNO
$[VOa_4b]$	b = H_2O, ROH,
$[VOa_3b_2]$	a = py, DMSO, THF, Ph_3PO, ROH, H_2O
$[VOa_2b_2]$	b = Cl^-, F^-, SO_4^{2-}, Br^-
$[VOa_{2\,or\,3}\cdot LL]$	LL = ox^{2-}, phen, bipy, SO_4^{2-}, diphos, catecholates
	a = F^-, Cl^-, Br^-, NCS^-, H_2O
$[VOa_2LLL]$	a = Cl, LLL = 1,4,7-trithiacyclononane
$[VO(LL)_2]$	LL = $acac^-$, phen, ox^{2-}, MNT, bipy, (HOOCR) (R = H,
$[VO(LL)_2a]$	Me, Et, $ClCH_2$, Cl_2CH, etc.), other β -diketones, maltolates, thiocatecholate, 1-oxy-2-pyridinethiolate
	a = H_2O, X^-, NCS^-, py, Ph_3PO, pyNO, DMSO, N-bases, MeOH
$[VO(LL')_2]$	LL' = $oxine^-$, unsym. β-diketones, sal^{2-}, benzohydroxamate,
$[VO(LL')_2a]$	quinaldinate, N-1- and N-3-substituted hydroxytriazenes, big^-, pyc^-
	a = solvent molecule, aromatic amine, heterocyclic base
$[VO(LL')(L''L''')]$	LL' = X-salen-N(R)(R'), R and R' alkyl or aryl
	$L''L'''$ = X-sal^- (X = H, 5,6-benzo-, 5-halido-, alkoxy-; R, R' = alkyl or aryl)
$[VO(LL'L)a_{4\,or\,2}]$	$LL'L$ = lut^{2-}, $coll^{2-}$, iminodiacetate
	a = H_2O, aromatic amine or heterocyclic base
$[VO(LL'L)(LL)]$	$LL'L$, $LL'L$ = lut^{2-}, $coll^{2-}$, iminodiacetate
$[VO(LL'L'')(LL)]$	LL = phen, bipy, $acac^-$
$[VO(LL'L)(LL')]$	LL' = gly, oxine, $benzohydroxamate^-$, pic^-
$[VO(LL'L'')(LL')]$	
$[VO(LLLL)]$	LLLL = TPP^{2-}, pc^{2-}
$[VO(LL'L'L)]$	$LL'L'L$ and $LL'L'L''$ = various Schiff bases
$[VO(LL'L'L')]$	$N(CH_2CH_2S)_3^{3-}$
$[VOY]\cdot xH_2O$	Y = EDTA
$(VO)_2(\mu\text{-}Y)\cdot$	Y = tartrate, citrate
$[(VO)_2(LL)_2]$	dba, $danaH_2$, salen-5-Me

[a]The general charge has been omitted from outside the square brackets.

stereochemistry for five-coordinate complexes of VO^{2+} is square pyramidal, as in $[VO(acac)_2]$, although some trigonal bipyramidal structures are known. In complexes such as $[VO(acac)_2]$, the O–V=O angle is greater than 90°; and the V atom lies above the plane formed by the four basal singly bonded oxygen atoms. Similar structural features occur in six-coordinate oxovanadium(IV) complexes, although the sixth ligand is often found to be only weakly coordinated and trans to the V=O bond in such structures.[1]

A great number of Schiff-base complexes of oxovanadium(IV) have been studied by X-ray diffraction. Many of these bases contain O,O,N,N-donor atoms in ligands formed from reaction between substituted salicylaldehyde and aliphatic or aromatic amines,[1,46,88,89,91] but examples with S-donor ligands have also been reported.[92] The distorted square pyramidal geometry found for most of these complexes is analogous to that found with simpler ligands. In some cases, the structure of the Schiff-base complexes is polymeric with the sixth, vacant, position of the square pyramid being occupied by the oxygen atom of the vanadyl group of the adjacent molecule,[1,46,91] or a hydrogen-bonding interaction can occur, as shown in (**6**), where the formation of the binuclear complex makes this system more stable toward reduction to V^{III} than related complexes.[88]

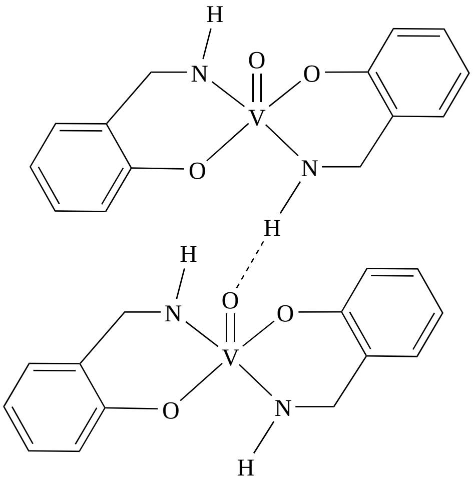

(**6**)

Attempts to model the structure of the V-dependent bromoperoxidase enzyme have resulted in the characterization by X-ray crystallography of a great number of VO^{2+} complexes having N,N,N,N-donor atoms. The imidazole group is thought to mimic the protein environment and complexes such as [VO(SALIMH)(acac)(MeOH)], [VO(SALIMH)SAL], and $[VO(SALIMH)_2(EtOH)]$, have been prepared[1,46] (*see* ***Vanadium in Biology***).

The mixed valence $[V^{IV}–O–V^{V}]^{3+}$ bridge is a fairly common unit. It is found in complexes such as $Na[V_2O_3(\text{DL-salser})_2]\cdot 5H_2O$, $[V_2O_3(S\text{-peida})_2]^-$, $[V_2O_3(NTA)_2]^{3-}$, $[V_2O_3(pmida)_2]^-$,[1] and $[VO\{salen(5\text{-}Me)_2\}_2][ClO_4]$.[1,88] Multinuclear complexes can also be obtained using Schiff-base ligands carrying pendant donor groups that can bind other metallic centers, such as in the Gd^{3+} adduct shown in (**7**), which shows a ferromagnetic interaction between the metals.[90] Similar complexes have also been obtained with catecholate ligands.[93]

Dinuclear complexes of vanadyl ions have been obtained where two such units are bridged by a tetradentate ligand, such as tartrate, citrate or N,N-bis(2-hydroxybenzyl)aminoacetate.[95] Dinuclear complexes with bridging alkoxide and carboxylate coligands are also known, structurally characterized examples include $[PPh_4]_2[(VO)_2Cl_4(OR)_2]$ (R = CH_3 or CH_2CH_2Cl) and $[(VO)_2Cl_2\{MeC(CH_2OH)(CH_2O)_2\}_2]$.[96]

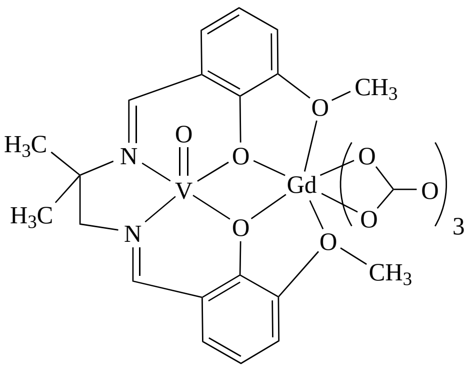

(**7**)

Because of the interest in the nature of vanadium porphyrins occurring in petroleum and coal, there have been many studies on the syntheses of these complexes, their magnetic properties, and ESR spectra and structures.**[1,46,51]**

4.5.4 Nonoxo Vanadium Complexes

A range of coordination complexes of V^{IV} has been prepared in which the vanadyl group is absent, a number of these compounds being synthesized as part of an effort to understand the nature of biological vanadium sites, such as amavadin,**[46]** which contains an octadentate, hydroxyiminodipropionate ligand bound to vanadium^{IV} A number of model complexes of this type have been prepared and discussion of this area can be found in the article ***Vanadium in Biology*** Further discussion in this section follows the main ligand donor atom to vanadium.

Nitrogen Ligands. Amide ligands have been used to give four and five-coordinate complexes, such as $[V(NMe_2)_4]$**[97]** and $[V\{N(CH_2CH_2NR)_3\}X]$ (R = bulky substituent; X = Cl or N_3^-)**[98]** [see also (**4**)]. Treatment of $[V(NMe_2)_4]$ with aniline gives the V^{IV} imido-complex $[V(NMe_2)_2(NHMe_2)_2(=NAr)]$, which with an excess of Me_3SiCl gives $[V(NMe_2)_2Cl_2(=NAr)]$.**[97]**

Vanadyl porphyrins, VOP, mentioned above [see (**5**)] have been used as precursors for nonoxo vanadium(IV) porphyrins, $[VPX_2]$ (P = OEP, TPP, TMTP, TPTP; X = Cl or Br).**[1]** EXAFS at the Br K-edge has been used to confirm the trans configuration of X atoms in the complexes. The 'bare' V^{IV} atom renders the compounds extremely reactive and one theory is that they could act as precursors in the synthesis of complexes formed during coal conversion.**[1]**

N-donor macrocyclic ligands, based on 1,4,7-trithiacyclononane and carrying three pendant arms bearing alkoxides give nonoxo vanadium(IV) complexes.**[99]**

Sulfur and Selenium Ligands. Complexes containing the $V{=}S^{2+}$ (thiovanadyl) moiety are known. The V=S bond length, 2.061(**1**) Å, is longer than would be expected from comparison with analogous vanadyl complexes. This finding agrees with molecular orbital calculations, which predict a relatively weaker V=S bond.**[1]** Recently, the thiovanadyl, dithiocarbamate complexes $[VS(S_2CNR_2)_2]$**[100]** and also the nonthiovanadyl derivatives $[VX_2(S_2CNR_2)_2]$ (X = halide; R = alkyl) have been prepared.**[101]**

The tridentate, dithiolate ligand $O(CH_2CH_2S)_2$ (odt) gives the six-coordinate compounds $[V(odt)_2]$ and $[V(NCMe)_6][VCl_2(odt)]_2$, whose structures have been determined.**[83]** The tris-dithiolene complex $[V(SCHCHS)_3]$ has D_{3h} symmetry and the compound has a delocalized electronic structure involving a spread of charge over the dithiolene ligands.**[102]**

A number of ligands having NSSN- and SNO-donor sets have been developed to bind nonoxo V^{IV}, using Schiff-base-type ligands or the tetradentate disulfide ligand 1,6-bis(*o*-pyridyl)-2,4, dithiahexane (NSSN) which forms the octahedral complex $[VCl_2(NSSN)]$.**[103]**

4.6 Vanadium(V) Coordination Complexes

4.6.1 Introduction

Many of the complexes of vanadium in their highest oxidation states contain oxygen and fluorine, and most contain at least one terminal oxygen atom. The d^0 electronic configuration means that the complexes are diamagnetic, and their color is the result of charge-transfer transitions. Their diamagnetism has allowed extensive study by ^{51}V NMR spectroscopy.**[13]** In aqueous solution, vanadium(V) forms a range of oxometalates, whose structures vary with concentration, temperature, and other conditions. Their study is well established and is beyond the scope of this survey, except to note the increasing use of NMR spectroscopy to examine the species that are present in solution.**[1,46]**

4.6.2 Halide Complexes

The structure of VF_5 has been studied theoretically.**[104]** A number of hexafluorovanadates(V) such as $K[VF_6]$ are well known.**[1]**

4.6.3 Oxo Complexes

Neutral and Cationic Species Containing the VO^{3+} Unit. This unit is found in the oxohalides VOX_3 (X = F, Cl, Br) and the nitrate, $[VO(NO_3)_3]$, that has a distorted pentagonal bipyramidal structure with overall Cs symmetry in the gas phase.**[105]** The oxochloride, $VOCl_3$, forms a number of addition complexes of the type $[VOCl_3L_n]$ with monodentate ($n = 1$) or bidentate ($n = 2$) O-, S-, or N-donor ligands.**[1]**

$VOCl_3$ also undergoes a number of solvolysis reactions, mainly with alcohols, phenols, and carboxylic acids. Substitution products of the general type $[VOCl_2(OR)]$, $[VOCl(OR)_2]$, and $[VO(OR)_3]$ are obtained. The nature of the product depends on the conditions used, especially the nature of the solvent and the stoichiometry of the reactants.[1] With bulky substituents, mononuclear complexes of this type can be crystallized and structurally characterized, for example $[VO(OC_6H_3Pr^i_2\text{-}2,6)_3]$, has a trigonal pyramidal structure.[69] A related compound is $[VO\{N(CH_2CH_2O)_3\}]$, which has a trigonal pyramidal structure in the solid and in the organic solution, but a different structure in water.[106]

A large group of mononuclear complex cations of the type $[VO(L)]^+$ is known where L is commonly a Schiff-base,[46,107] or a hydroxamate. For example, the series $[VO\{salen(5\text{-}X)\}]^+$ (X = OMe, Me, or Br),[88] and $[VOClL_2]$ (L = benzohydroxamate or N-phenylbenzohydroxamate).[46] They have the essentially square pyramidal geometry of their V^{IV} uncharged analogues (see Section 4.5.3). Dinuclear Schiff-base complexes of the type $[(VOL)_2]$ (L = Schiff base particularly with alkoxysubstituents), have been obtained and have bis(alkoxy) bridging units.[107] Other examples of this type of complex use hydrazone ligands and include, as well as mononuclear complexes, binuclear, ligand-bridged compounds such as shown in (**8**).[108]

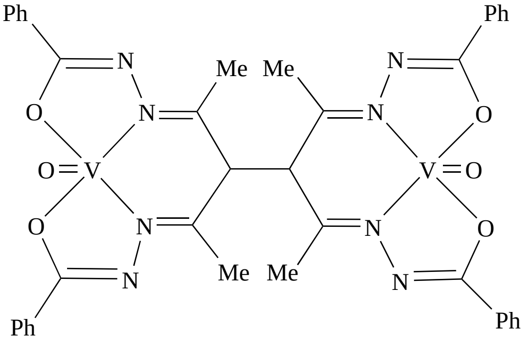

(**8**)

Other dinuclear complexes use bridging oxide[109] or fluoride[88] groups. Examples of this type with Schiff bases can be symmetric, as in the cation[88] $[\{VOL\}_2(\mu\text{-F})]^+$ or asymmetric as in $[(VOLL')(\mu\text{-O})(VOLL'')]$[109] (L Schiff-base or similar ligand; L′ and L″ = monodentate ligands).With certain polydentate Schiff-base ligands, dimeric complexes are formed that contain a μ-oxo or μ-OR ligand together with a bridge formed by a pendant phenolate group from the ligand. The V^{IV}–V^{V} $[V_2O_3]^+$ core in these compounds has the unpaired electron delocalized over the two vanadiums.[109,110]

Anionic Species Containing the VO^{3+} Unit[1]. Complex oxofluorides are well established, as are salts of $[VOCl_4]^-$ and $[VOCl_5]^{2-}$. Anionic complexes with other ligands are rare, but a structurally characterized example is known, as shown in (**9**), and other examples with different ligands have been observed.[92,111]

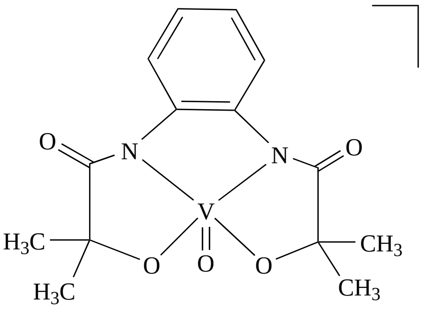

(**9**)

Species Containing the VO_2^+ Unit. Among the first examples of complexes shown to contain the *cis*-dioxo unit were $[VO_2(NO_3)]$, and $[PPh_3Me][VCl_2O_2]$. The oxo-groups were found to be cis to each other and to give rise to the expected two V=O IR bands found in the region of 960 and 970 cm^{-1}.[1] Since that time, a range of mononuclear five-coordinated complexes showing these features has been prepared, most often with Schiff-base coligands, of general formula $[VO_2L]$ (L = Schiff base with NNO- or NO_2-atom ligation).[107,112] Anionic monomeric complexes that have a six-coordinate vanadium such as ammonium dioxo(2-hydroxynaphthaldehyde semicarbazonato)vanadate(V) has been prepared[1] and the species $[VO_2L]^-$ (L = maltolate or triethanolamine) have been observed in solution.[46]

Dimeric complexes of the VO_2^+ group have single oxo-bridges giving a $[O_2V\text{–}O\text{–}VO_2]$ core such as in $[L_2V_2O_4(\mu\text{-}O)]$ (L = 1,4,7-trimethyl-1,4,7-triazacyclononane),[1] or a rare type of dioxo bridge as seen in the compound shown in (**10**).[113] In this compound, the μ-O distances are asymmetric, as indicated, the shorter being about 1.675 Å and the other around 2.27 Å.

A further type of dinuclear VO_2^+ complex has terminal V=O groups but a pendant alkoxy group from a coligand on each vanadium gives rise to a bis(μ-alkoxy) system, as in $[\{VO_2Ad\}2]^{2-}$ (Ad = adenosine).[46,114]

Perox- Species. Addition of aqueous H_2O_2 to aqueous V^V results in the formation of various peroxo-complexes. In neutral or alkaline solutions, the yellow diperoxoorthovanadate ion, $[VO_2(O_2)_2]^{3-}$, is formed, whereas in acid solutions the red–brown peroxovanadium ion, $[V(O_2)]^{3+}$, is the main species present. Acidic salts such as $KH_2[VO_2(O_2)_2]\cdot H_2O$ and $(NH_4)_2H[VO_2(O_2)_2]\cdot nH_2O$ have been prepared and their IR spectra are characterized by the presence of a strong band at about 850 cm^{-1}, probably associated with the O–O stretching vibration of the peroxo-group, which is coordinated

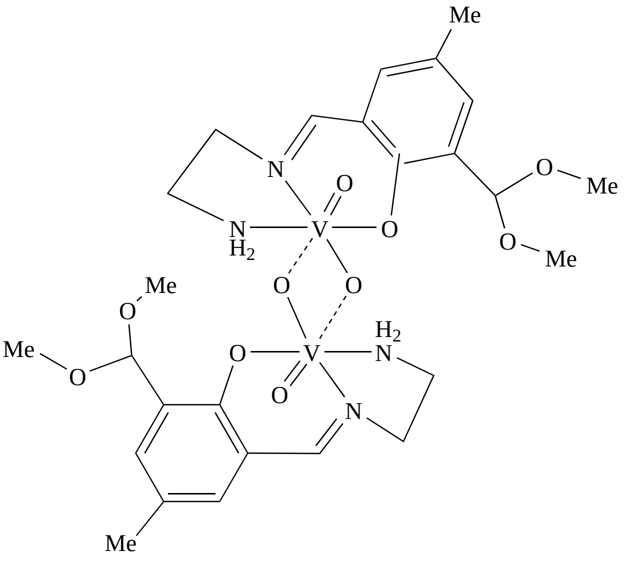

(**10**)

side-on to the metal (**11a**).[1,46] The peroxo-ligand can act as a terminal, side-on ligand, or in a (μ-peroxy) mode (**11b, 11c**).

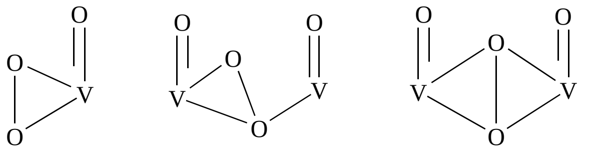

(a) (b) (c)

(**11**)

Recent investigations of peroxo-complexes, especially those containing amino and carboxylate ligands, have been stimulated by interest in the vanadium bromoperoxidases and a wide range of peroxo-complexes has been prepared. Several reviews have been devoted to their chemistry and structures[46,115] and only a very brief outline is therefore given here. Types of complexes include those with: one peroxo-ligand $[VO(O_2)(L)]^-$ [L = tridentate, tetradentate or (bidentate)$_2$ ligand], two peroxo-ligands such as $[VO(O_2)_2(L)]^{\tilde{n}-}$ [L = monodentate or 1/2(bidentate ligand)], three peroxo-ligands, $[V(O_2)_3(L)]^{2-}$, or four peroxo-ligands, $[V(O_2)_4]^{3-}$. Binuclear complexes are also known with $VO(O_2)$ units bridged by one peroxo-group, or one or two such groups together with bridges formed by other ligands.[46,115]

4.6.4 *Nonoxo Complexes*

There are few well-characterized examples of this type. Neutral tris(bidentate) V^V complexes of the type $[V(N_3S_2)L(L')]$ (L′ = bipy or phen; L = cat or dtbc) have been synthesized.[1] Complexes of the general type $[V(dtbc)_2L'][SbF_6]$, prepared by oxidation $[V(dtbc)_2L']$ with $Ag[SbF_6]$, have also been investigated.[1]

4.6.5 *Nitrogen Ligands*

Nitrido- and imido-complexes of V^V have drawn attention because of the interest in nitrogen fixation intermediates and in complexes that might provide catalyst precursors for polymerization of alkynes. Recent examples of such compounds are the six-coordinated cation[116] $[VN(acac)(1,4,7\text{-triazacyclononane})]^+$ and the six-coordinated complexes $[V(NR)(L)]$ [R = alkyl or aryl; L = $N(CH_2CH_2S)_3{}^{3-}$ or $N(CH_2CH_2NR')_3{}^{3-}$].[82,98] The related hydazido(2-) complexes $[V\{N(CH_2CH_2S)_3\}(NNR_2)]$ (R_2 = CPh_2 or C_5H_{10})[117] and the doubly nitrido-bridged dimer $[\{V[Me_3SiN(CH_2CH_2NSiMe_3)_2]\}_2(\mu\text{-}N)_2]$[118] have also been structurally characterized.

4.6.6 *Sulfur and Selenium Ligands*

A number of V^V complexes of the various types described in previous sections have S-donor ligands and a study has been made of vanadium complexes with cysteine and other biologically relevant S-donors[46] (*see* ***Vanadium in Biology***). In this section, we draw attention to the known terminal sulfide and persulfide complexes. The complex anion $[VS_2(S_2)SPh]^{2-}$ (**12**) has both sulfide and persulfide groups and two persulfide groups are found in $[NEt_4][VO(S_2)_2(bpy)]$.[119] The terminal chalcogenide complexes $[V(=Y)\{N(CH_2CH_2NR')_3\}]$ (Y = S or Se, R′ = $SiMe_3$) have been prepared by reaction of $[V\{N(CH_2CH_2NR')_3\}]$ with S_8 or gray selenium,[120] and the four-coordinate V=Se complex $[V(Se)\{Se(SiMe_3)_3\}N(SiMe_3)_2]$ has been prepared.[121]

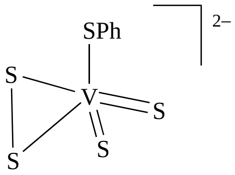

(**12**)

5 RELATED ARTICLES

Vanadium in Biology; Vanadium: Organometallic Chemistry.

6 REFERENCES

1. E. M. Page and S. A. Wass, 'Encyclopedia of Inorganic Chemistry', 1st edn., Wiley, 1994.
2. R. Bonnett and P. Brewer, *Tetrahedron Lett.*, 1970, **30**, 2579.
3. S. J. Briggs, *Met. Technol.*, 1983, **10**, 150.
4. R. J. H. Clarke, 'The Chemistry of Titanium and Vanadium', Elsevier, Amsterdam, NY, 1968.
5. R. K. McKechnie and A. U. Seybolt, *J. Electrochem. Soc.*, 1950, **97**, 311.
6. D. R. Lide ed., 'CRC Handbook of Chemistry and Physics', 74th edn., CRC Press, Boca Raton, FL, 1994.
7. N. D. Chasteen, *Struct. Bonding*, 1983, **53**, 105.
8. D. Rehder, *Angew. Chem., Int. Ed. Engl.*, 1991, **30**, 148.
9. R. J. H. Clarke, in 'Comprehensive Inorganic Chemistry', ed. A. F. Trotman-Dickenson, Pergamon Press, Oxford, 1973, Vol. 3.
10. R. S. Young, *CHEMSA*, 1980, **6**, 141; (*Chem. Abstr.*, 1981, **94**, 10601).
11. D. C. Crans and I. Boukhoba, *J. Am. Chem. Soc.*, 1998, **120**, 8069.
12. C. Slebodnick and V. L. Pecoraro, *Inorg. Chim. Acta*, 1998, **283**, 37.
13. D. Rehder, in 'Multinuclear N.M.R.', ed. J. Mason, Plenum, New York, 1987, Chap. 19.
14. S. C. Davies, M. C. Durrant, D. L. Hughes, C. Le Floc'h, G. Reid, R. L. Richards, and J. R. Sanders, *J. Chem. Soc., Dalton Trans.*, 1998, 2191.
15. R. R. Eady, *Chem. Rev.*, 1996, **96**, 3013.
16. A. Y. Esayed and D. O. Northwood, *Int. J. Hydrogen Energy*, 1992, **17**, 41.
17. J. T. Graham, L. Li, and W. Weltner, *J. Phys. Chem.*, 2000, **104**, 9302.
18. E. M. Page, in 'Inorganic Reactions and Methods', ed. J. J. Zuckerman and A. Hagen, VCH, New York, 1991, Vol. 4.
19. A. J. Edwards and G. R. Jones, *J. Chem. Soc. (A)*, 1969, 1651.
20. K. Hagen, M. M. Gilbert, L. Hedberg, and K. Hedberg, *Inorg. Chem.*, 1982, **21**, 2690.
21. S. Becker and B. G. Mueller, *Angew. Chem., Int. Ed. Engl.*, 1990, **29**, 406.
22. N. W. Gregory, *Inorg. Chem.*, 1994, **33**, 3014.
23. N. W. Gregory, *J. Chem. Eng. Data*, 1994, **39**, 922.
24. F. Calderazzo, C. Maichle-Mossmer, G. Pamploni, and J. Straehle, *J. Chem. Soc., Dalton Trans.*, 1993, 655.
25. C. Cros, *Rev. Inorg. Chem.*, 1979, **1**, 163.
26. J. Wosniza, R. Deutschmann, H. von Lehneysen, and R. K. Kremer, *J. Phys.: Condens. Matter*, 1994, **6**, 8045.
27. E. M. Page and D. A. Rice, in 'Inorganic Reactions and Methods', ed. J. J. Zuckerman and A. Hagen, VCH, New York, 1991, Vol. 4.
28. N. N. Greenwood and A. Earnshaw, 'Chemistry of the Elements', Pergamon Press, Oxford, 1984, Chap. 22.
29. M. I. Khan and J. Zubieta, *Prog. Inorg. Chem.*, 1995, **43**, 1.
30. A. Müller, H. Reuter, and S. Dillinger, *Angew. Chem., Int. Ed. Engl.*, 1995, **34**, 2329.
31. A. Brystrom, K. A. Wilhelmi, and O. Brotzen, *Acta Chem. Scand.*, 1950, **4**, 1119.
32. H. G. Bachmann, F. R. Ahmed, and W. H. Barnes, *Z. Kristallogr.*, 1961, **115**, 110.
33. V. Manivannan and J. B. Goodenough, *Inorg. Chem.*, 1998, **37**, 3448.
34. Y. Oka, S. Sato, T. Yao, and N. Yamamoto, *J. Solid State Chem.*, 1998, **141**, 594.
35. A. Müller, F. Peters, M. T. Pope, and D. Gatteschi, *Chem. Rev.*, 1998, **98**, 239.
36. A. F. Wells, 'Structural Inorganic Chemistry', 5th edn., Clarendon Press, Oxford, 1984.
37. C. Mujica, J. Llanos, and O. Wittke, *J. Alloys Compd.*, 1995, **236**, 136.
38. W. Bensch and J. Koy, *Acta Crystallogr. Sect. C*, 1993, **C49**, 1133.
39. F. Jellinek, 'MTP International Review of Science, Inorganic Chemistry Series One', Butterworths, London, 1972, Vol. 5.
40. F. A. Cotton, G. Wilkinson, C. A. Murillo, and M. Bockmann, 'Advanced Inorganic Chemistry', 6th edn., Wiley Interscience, New York, 1999.
41. E. M. Page and S. A. Wass, *Coord. Chem. Rev.*, 1997, **164**, 203.
42. E. M. Page, *Coord. Chem. Rev.*, 1998, **172**, 111.
43. G. J. Leigh and J. S. de Souza, *Coord. Chem. Rev.*, 1996, **154**, 71.
44. Q. Chen and J. Zubieta, *Coord. Chem. Rev.*, 1992, **114**, 107.
45. D. C. Crans, *Comments Inorg. Chem.*, 1994, **16**, 1.
46. D. C. Crans, J. J. Smee, E. Gaidamuskas, and L. Yang, *Chem. Rev.*, 2004, **104**, 849.
47. A. Butler and A. H. Baldwin, *Struct. Bonding*, 1997, **89**, 109.
48. D. Rehder, *Coord. Chem. Rev.*, 1999, **181**, 297.
49. D. Coucouvanis, *JBIC*, 1996, **1**, 594.
50. B. R. James, in 'The Porphyrins', ed. D. Dolphin, Academic Press, New York, 1979, Vol. 5, Chap. 6.
51. H. Duval, V. Bulach, J. Fischer, and R. Weiss, *Acta Crystallogr.*, 1998, **C54**, 1781.
52. H. Gailus, C. Woitha, and D. Rehder, *J. Chem. Soc., Dalton Trans.*, 1994, 3471.

53. M. Mallik, P. N. Ghosh, and R. Battacharyya, *J. Chem. Soc., Dalton Trans.*, 1993, 1731.
54. A. L. Rieger, J. B. Scott, and P. H. Rieger, *Inorg. Chem.*, 1984, **33**, 621.
55. W. Collong and T. Kruck, *Chem. Ber.*, 1990, **123**, 1655.
56. S. Kitagawa, M. Munakata, and M. Ueda, *Inorg. Chim. Acta*, 1989, **164**, 49.
57. L. V. Vilas Boas and J. Costa Pessoa, in 'Comprehensive Coordination Chemistry', eds. G. Wilkinson, R. D. Gillard, and J. A. Mcleverty, Pergamon, New York, 1987, Vol. 3, p. 453.
58. F. A. Cotton, L. R. Favello, C. A. Murillo, I. Pascual, A. J. Schultz, and M. Tomas, *Inorg. Chem.*, 1994, **33**, 5391.
59. D. G. L. Holt, L. F. Larkworthy, D. C. Povey, D. C. Smith, and G. J. Leigh, *J. Chem. Soc., Dalton Trans.*, 1990, 3229.
60. R. K. Minas, J. J. H. Edema, S. Gambarotta, and A. Meetsma, *J. Am. Chem. Soc.*, 1993, **115**, 6710.
61. M. J. Scott, W. C. A. Wilisch, and W. H. Armstrong, *J. Am. Chem. Soc.*, 1990, **112**, 2429.
62. P. J. Bonitatebus, S. K. Mandal, and W. H. Armstrong, *J. Chem. Soc., Chem. Commun.*, 1998, 939.
63. J.-I. Song and S. Gambarotta, *J. Am. Chem. Soc.*, 1994, **116**, 6927.
64. S. Hao, P. Berno, R. Minhas, and S. Gambarotta, *Inorg. Chim. Acta*, 1996, **244**, 37.
65. P. Berno and S. Gambarotta, *Angew. Chem., Int. Ed. Engl.*, 1995, **34**, 822.
66. J. Jubb, L. Scoles, H. Jenkins, and S. Gambarotta, *Chem. Eur. J.*, 1996, **2**, 767.
67. P. J. Bonitatebus, S. K. Mandal, and W. H. Armstrong, *J. Chem. Soc., Chem. Commun.*, 1999, 55.
68. P. Sobota and S. Szafert, *J. Chem. Soc., Dalton Trans.*, 2001, 1379.
69. R. A. Henderson, D. L. Hughes, Z. Janas, R. L. Richards, P. Sobota, and S. Szafert, *J. Organomet. Chem.*, 1998, **554**, 195.
70. P. Sobota, J. Ejfler, S. Szafert, T. Glowiak, I. O. Fitzky, and K. Szczgot, *J. Chem. Soc., Dalton Trans.*, 1995, 1727.
71. E. Solari, S. de Angelis, C. Floriani, A. Chiesi-Villa, and C. Guastini, *Inorg. Chem.*, 1992, **31**, 141.
72. G. B. Karet, S. L. Castro, K. Folting, J. C. Bollinger, R. A. Heintz, and G. Christou, *J. Chem. Soc., Dalton Trans.*, 1998, 67.
73. Z. Sun, D. N. Hendrickson, C. M. Grant, S. L. Castro, and G. Christou, *J. Chem. Soc., Chem. Commun.*, 1998, 721.
74. C. P. Magill, C. Floriani, A. Chiesi-Villa, and C. Rizzoli, *Inorg. Chem.*, 1993, **32**, 2729.
75. M. Chatterjee, M. Maji, S. Ghosh, and T. C. W. Mak, *J. Chem. Soc., Dalton Trans.*, 1998, 3641.
76. K. Miyoshi, J. Wang, and T. Mizuta, *Inorg. Chim. Acta*, 1995, **228**, 165.
77. K. L. Sorenson, J. W. Ziller, and N. M. Doherty, *Acta Crystallogr.*, 1998, **C50**, 407.
78. G. P. Clancy, H. C. S. Clark, G. K. B. Klentsmith, F. G. N. Cloke, and P. B. Hitchcock, *J. Chem. Soc., Dalton Trans.*, 1999, 3345.
79. C. Rosenberger, R. R. Schrock, and W. M. Davis, *Inorg. Chem.*, 1997, **36**, 123.
80. L. Berreau, J. A. Hays, V. G. Young, and L. K. Woo, *Inorg. Chem.*, 1994, **33**, 105.
81. P. E. Kruger, B. Moubaraki, and K. S. Murray, *J. Chem. Soc., Dalton Trans.*, 1996, 1223.
82. S. C. Davies, D. L. Hughes, Z. Janas, L. B. Jerzykiewicz, R. L. Richards, J. R. Sanders, J. E. Silverston, and P. Sobota, *Inorg. Chem.*, 2000, **39**, 3485.
83. Z. Janas, L. B. Jerzykiewicz, S. Przybylak, R. L. Richards, and P. Sobota, *Organometallics*, 2000, **19**, 4252.
84. J. R. Rambo, S. L. Castro, K. Folting, S. A. Bartley, R. Heintz, and G. Christou, *Inorg. Chem.*, 1996, **35**, 6844.
85. Y. Myashita, M. Hamajima, Y. Yamada, K. Fujisawa, and K. Okamoto, *J. Chem. Soc., Dalton Trans.*, 2001, 2089.
86. M. R. Maurya, S. Khurana, W. Zhang, and D. Rehder, *J. Chem. Soc., Dalton Trans.*, 2002, 3015.
87. S. Di Bella, G. Lanza, A. Guilino, and I. Fragala, *Inorg. Chem.*, 1996, **35**, 3885.
88. N. Choudhary, N. G. Connelly, P. B. Hitchcock, and G. J. Leigh, *J. Chem. Soc., Dalton Trans.*, 1999, 4437.
89. M. Tsuchimoto, G. Hoshina, N. Yoshioka, H. Inoue, K. Nakajima, M. Kamishima, M. Kojima, and S. Ohba, *J. Solid State Chem.*, 2000, **153**, 9.
90. J.-P. Costes, A. Dupuis, and J.-P. Laurent, *J. Chem. Soc., Dalton Trans.*, 1998, 735.
91. C. Slebodnick, B. J. Hamstra, and V. L. Pecoraro, *Struct. Bonding*, 1997, **89**, 51.
92. A. D. Kermidas, A. B. Papaioannu, A. Vlahos, T. A. Kabanos, G. Bonas, A. Makriannis, C. P. Rapropoulou, and A. Terzis, *Inorg. Chem.*, 1996, **35**, 357.
93. R. Cortes, M. K. Urtiaga, L. Lezama, M. I. Arriortua, and T. Rojo, *Inorg. Chem.*, 1994, **33**, 829.
94. K. K. Nanda, E. Sinn, and A. W. Addison, *Inorg. Chem.*, 1996, **35**, 1.
95. A. S. Ceccato, A. Neves, M. A. De Brito, S. M. Dreschel, A. S. Mangrich, R. Werner, W. Haase, and A. J. Bortoluzzi, *J. Chem. Soc., Dalton Trans.*, 2000, 1573.
96. J. Salta and J. Zubieta, *Inorg. Chim. Acta*, 1996, **257**, 83.
97. S. R. Dubberly, B. R. Tyrrell, and P. Mountford, *Acta Crystallogr.*, 2001, **C57**, 902.
98. R. R. Schrock, *Acc. Chem. Res.*, 1997, **30**, 9.
99. I. Fallis, L. J. Farrugia, N. M. McDonald, and R. D. Peacock, *Inorg. Chem.*, 1993, **32**, 779.

100. H. Sakurai, H. Watanabe, H. Tamura, H. Yasui, R. Matsushita, and J. Takada, *Inorg. Chim. Acta*, 1998, **283**, 175.

101. E. L. Jones, J. G. Reynolds, J. C. Huffman, and G. Christou, *Polyhedron*, 1991, **10**, 1817.

102. M. Kondo, S. Minakoshi, K. Iwata, T. Shimizu, H. Matsuzaka, N. Kamigata, and S. Kitagawa, *Chem. Lett.*, 1996, **25**, 489.

103. M. Farahbaksh, H. Nekola, H. Schmidt, and D. Rehder, *Chem. Ber.*, 1997, **130**, 1129.

104. R. J. Gillespie, I. Bytheway, T.-H. Tang, and R. F. W. Bader, *Inorg. Chem.*, 1996, **35**, 3954.

105. B. A. Smart, H. E. Robertson, D. W. H. Rankin, E. G. Hope, and C. J. Marsden, *J. Chem. Soc., Dalton Trans.*, 1999, 473.

106. D. C. Crans and P. K. Shin, *J. Am. Chem. Soc.*, 1994, **116**, 1305.

107. G. Asgedom, A. Sreedhara, J. Kivikoski, J. Valkonen, E. Kolemainen, and C. P. Rao, *Inorg. Chem.*, 1996, **35**, 5674.

108. X.-M. Zhang and X.-Z. You, *Polyhedron*, 1996, **15**, 1793.

109. C. Gruning, H. Schmidt, and D. Rehder, *Inorg. Chem. Commun.*, 1999, **2**, 57.

110. E. P. Copeland, I. A. Kahwa, and J. T. Mague, *J. Chem. Soc., Dalton Trans.*, 1997, 2849.

111. C. R. Cornman, K. M. Geiser-Bush, and P. Singh, *Inorg. Chem.*, 1994, **33**, 4621.

112. A. G. J. Ligtenbarg, A. L. Spek, R. Hage, and B. L. Feringa, *J. Chem. Soc., Dalton Trans.*, 1999, 659.

113. C. A. Duncan, E. R. Copeland, I. A. Kahwa, A. Quick, and D. J. Williams, *J. Chem. Soc., Dalton Trans.*, 1997, 917.

114. S. J. Angus-Dunne, R. J. Batchelor, A. S. Tracey, and F. W. Eisenstein, *J. Am. Chem. Soc.*, 1995, **117**, 6015.

115. A. Butler, M. J. Clague, and G. E. Meister, *Chem. Rev.*, 1994, **94**, 625.

116. A. Niemann, U. Bossek, G. Haselhorst, K. Wieghardt, and B. Nuber, *Inorg. Chem.*, 1996, **35**, 906.

117. S. C. Davies, D. L. Hughes, M. Konkol, R. L. Richards, J. R. Sanders, and P. Sobota, *J. Chem. Soc., Dalton Trans.*, 2002, 2811.

118. G. K. B. Clentsmith, V. M. E. Bates, P. B. Hitchcock, and F. G. N. Cloke, *J. Am. Chem. Soc.*, 1999, **121**, 10444.

119. S. L. Castro, J. D. Martin, and G. Christou, *Inorg. Chem.*, 1993, **32**, 2978.

120. C. C. Cummins, R. R. Schrock, and W. M. Davies, *Inorg. Chem.*, 1994, **33**, 1448.

121. C. P. Gerlach and J. Arnold, *Inorg. Chem.*, 1996, **35**, 5770.

Vanadium: Organometallic Chemistry

Toshikazu Hirao
Osaka University, Yamadaoka, Japan

Based in part on the article Vanadium: Organometallic Chemistry by Dieter Rehder which appeared in the Encyclopedia of Inorganic Chemistry, First Edition.

1	Introduction	1
2	η^6- to η^8-Arene and Related Complexes	1
3	η^5-Cyclopentadienyl and Related Complexes	3
4	η^3-Allyl and Related Complexes	7
5	η^2-Alkyne or Alkene Complexes	9
6	Carbene Complexes	11
7	σ-Bonded Organo- or Hydridovanadium Complexes	13
8	Conclusion	17
9	Related Articles	17
10	References	17

1 INTRODUCTION

Vanadium compounds exist in a variety of formal oxidation states from -3 to $+5$. Their coordination number varies from 3 to 8. The stereochemistry depends on their oxidation state; V(II): 6-coordinate octahedral, V(III): 3–7-coordinate ($V[CH(SiMe_3)_2]_3$: 3-coordinate planar), V(IV): 4–6 or 8-coordinate ($V(CH_2SiMe_3)_4$: 4-coordinate tetrahedral, $VO(acac)_2$: 5-coordinate tetragonal), V(V): 4–7-coordinate ($VOCl_3$: 4-coordinate tetrahedral). Standard electrode potential in acidic aqueous solution is as follows: $V^{2+} + 2e^- = V - 1.19\,V$, $V^{3+} + e^- = V^{2+} - 0.26\,V$, $VO^{2+} + 2H^+ + e^- = V^{3+} + H_2O + 0.36\,V$, $VO^{2+} + 4H^+ + 5e^- = V + 2H_2O - 0.25\,V$. Generally speaking, vanadium compounds in a high oxidation state serve as oxidants. On the contrary, low-valent vanadium compounds are considered to be reductants. Paramagnetism is another interesting feature of some vanadium compounds.

The first organovanadium compound, which was discovered in 1953, is Cp_2VCl_2. Most organovanadium compounds are highly air and moisture sensitive, but not especially toxic except for the volatile carbonyl compounds. The organovanadium compounds are mostly subjected to interconversion via one-electron redox. Although vanadium compounds including vanadium(II), vanadium(III), vanadium(IV), oxovanadium(IV), and oxovanadium(V) are utilized in organic synthesis as reagents, catalysts, and polymerization catalysts (Ziegler–Natta catalysts, *see Ziegler–Natta Catalysts*), the application of organovanadium compounds to synthetic reactions is rather limited.**[1–5]** The transformations are characterized by organometallic and/or redox-based reactions. This chapter describes the chemistry of organovanadium compounds mostly from synthetic viewpoints, which are classified depending on the coordination-binding mode.

2 η^6- TO η^8-ARENE AND RELATED COMPLEXES

(η^6-Arene)vanadium(0) and related complexes bearing the corresponding aromatic hydrocarbons are one of the important classes of organovanadium compounds. Bis(η^6-arene)vanadiums are synthesized by reductive aromatization of vanadium(III) or vanadium(IV) chloride with arenes in the presence of aluminum and aluminum trichloride, followed by hydrolysis of the generated cationic sandwich complexes.**[6,7]** Bis(η^6-arene)vanadium(0) is a thermally stable 17-electron neutral sandwich complex. Thus obtained Mes_2V (**1**) undergoes further transformations as shown in Scheme 1; (**1**) is reduced with alkali metal to give the 18-electron complex (**2**).**[6]** The oxidation with silver tetraphenylborate leads to the vanadium(+1) cation (**3**).**[8]** A similar transformation is also achieved by treatment with bromo- or iodotriphenylmethane.**[9,10]** Generally, the six-membered rings are planar with the eclipsed conformation. On the contrary, almost staggered conformation is observed in the case of $[Mes_2V]^-$,**[8]** in which the distance of V to the ring centroid is around 1.67 Å.

Hexacarbonylvanadium(0), $V(CO)_6$, which is a 17-electron, low-spin d^5, and paramagnetic complex, is reduced to the closed-shell 18-electron species, $V(CO)_6{}^-$, via one-electron reduction (*see **Carbonyl Complexes of the Transition Metals***). This redox process is applied to the disproportionation reaction (*see Disproportionation*) in the presence of arene to give $[V(\eta^6\text{-arene})(CO)_4][V(CO)_6]$ (**4**) (Scheme 2).**[11]**

Another route to bis(η^6-arene)vanadium(0) compounds is the cocondensation of arenes with vaporized vanadium metal (*see **Metal Vapor Synthesis of Transition Metal Compounds***).**[12,13]** On treatment with 1,3-cyclohexadiene and butyllithium, 15-electron vanadocene (**5**) is converted to 16-electron (η^6-benzene)(η^5-cyclopentadienyl)vanadium(I) (**6**) (Scheme 3).**[14]** Use of potassium naphthalenide affords the corresponding naphthalene complex.

Various bis(η^6-arene)vanadium(0) derivatives are prepared through substitution on the arene ring. Bis(η^6-benzene)vanadium(0) (**7**) undergoes lithiation and coupling with electrophiles to give the substituted bis(η^6-arene)vanadium compounds, like the silyl-bridged derivative (**8**) (Scheme 4).**[15]**

Triple-decker complexes (**9** and **10**, *see Triple-decker Sandwich*) are also accessible from $CpV(\eta^3\text{-}C_3H_5)_2$ and 1,3-cyclohexadiene, or vanadocene and (naphthalene)$Yb(THF)_3$, respectively.**[16]** The middle-deck

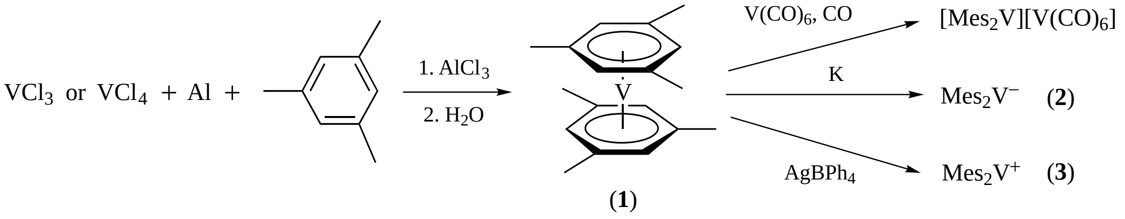
VCl3 or VCl4 + Al +
1. AlCl3
2. H2O
V
(1)
V(CO)6, CO
[Mes2V][V(CO)6]
K
Mes2V− (2)
AgBPh4
Mes2V+ (3)

Scheme 1

$$2V(CO)_6 + \text{arene} \longrightarrow [V(\eta^6\text{-arene})(CO)_4][V(CO)_6]$$

(**4**)

Scheme 2

benzene can be replaced by mesitylene or toluene in the boiling aromatic.**17,18**

As η^7-complex analogs, η^7-Tp or tropylium vanadium complexes (**11**) and (**12**) are obtained from cycloheptatriene by treatment with VCl_4 in the presence of *i*-PrMgBr (Scheme 5) or $CpV(CO)_4$, respectively (Scheme 6).**19–21**

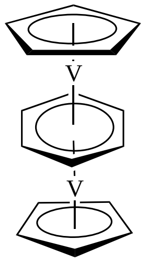

(**9**)

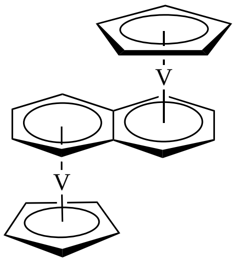

(**10**)

[7-7]Bitrovacene, μ-η^7:η^7-$C_{14}H_{12}[(\eta^5\text{-}C_5H_5)V_2]$ (**13**), is synthesized from $CpV(CO)_4$ and dicycloheptatriene. Intervanadium electro- and magneto-communication depends on

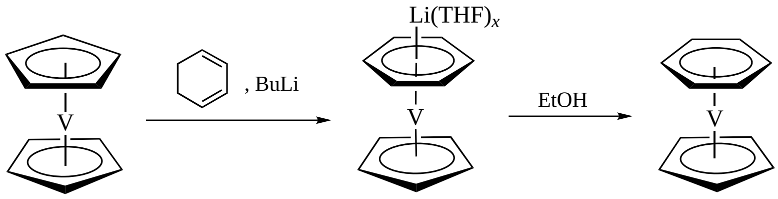
V
, BuLi
Li(THF)x
V
EtOH
V

(**5**) (**6**)

Scheme 3

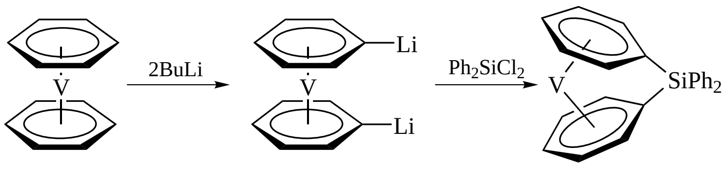
V
2BuLi
Li
V
Li
Ph2SiCl2
V
SiPh2

(**7**) (**8**)

Scheme 4

$$VCl_4 + C_7H_8 \xrightarrow{i\text{-PrMgBr}} V(C_7H_8)_2 \xrightarrow{Ph_3C^+} TpVC_7H_8^+ \xrightarrow{Ph_3C^+} Tp_2V^{2+}$$

(**11**)

Scheme 5

the isomer (**14**) possessing the μ-η^5:η^5-fulvalenediyl unit (Scheme 7).[22]

The complexation with the dianion of cyclooctatetraene leads to the formation of the mixed or half-sandwich complexes (*see Half-sandwich Complexes*) as shown in Scheme 8.[23–25] The coordination of the planar η^8-cyclooctatetraene$^{(2-)}$ ligand is observed with $V(cot)_2$. Generally, the distance between vanadium and ring centroid decreases with the increase of the ring size, Cp < C_6H_6 < Tp < cot.

$$CpV(CO)_4 + C_7H_8 \longrightarrow CpVTp + 1/2\,H_2 + CO$$

(**12**)

Scheme 6

3 η^5-CYCLOPENTADIENYL AND RELATED COMPLEXES

This section describes the organovanadium compounds containing η^5-cyclopentadienyl (Cp) or substituted (Cp′) ligands, which are classified into half-sandwich (*see Half-sandwich Complexes*), sandwich (*see Sandwich Compound*), bent sandwich (*see Bent Metallocenes*), and pseudo-triple decker derivatives. Cyclopentadienyl vanadium compounds are used for the synthesis of various vanadium compounds as mentioned above. Generally, the oxidation state of the cyclopentadienyl vanadium complexes is from −1 to +5.

Bis(η^5-cyclopentadienyl)vanadium (vanadocene, **5**, *see Metallocene Complexes*), which is the key derivative of this series, is characterized by a 15-electron species. Vanadocene is thermally stable under nitrogen but air sensitive. The

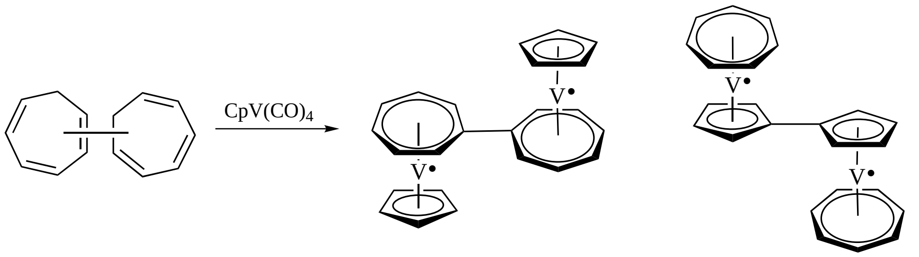

(**13**) (**14**)

Scheme 7

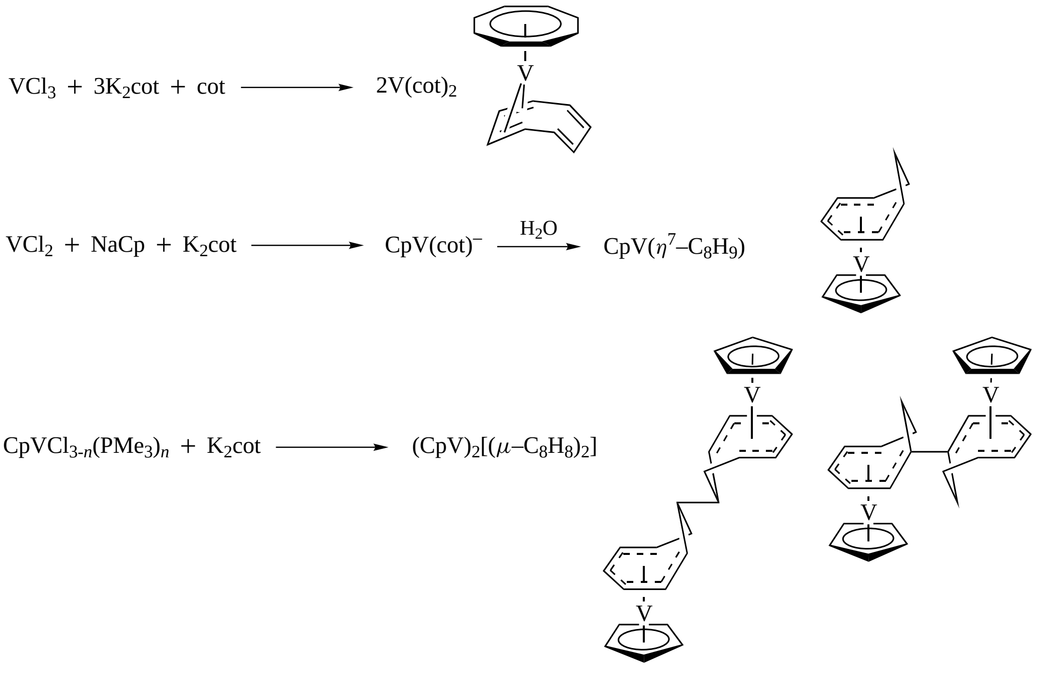
VCl3 + 3K2cot + cot → 2V(cot)2
V
VCl2 + NaCp + K2cot → CpV(cot)⁻ →(H2O) CpV(η7–C8H9)
V
CpVCl3-n(PMe3)n + K2cot → (CpV)2[(μ–C8H8)2]
V
V
V
V

Scheme 8

$$VCl_3 \xrightarrow{Zn} VCl_2(THF)_3 \xrightarrow{NaCp} \underset{(\mathbf{5})}{Cp_2V}$$

$$VCl_3 \xrightarrow{NaCp^*} \underset{(\mathbf{15})}{Cp^*{}_2V} \; (Cp^* = \eta^5\text{-}C_5Me_5)$$

Scheme 9

vanadocenes are synthesized from VCl_3 or VCl_2 and alkali metal cyclopentadienide directly or after reduction (Scheme 9).[26–35] For example, the parent vanadocene (**5**) is obtained by reduction of vanadium(III) chloride with zinc and subsequent treatment with the cyclopentadienyl anion. Vanadium(III) chloride is directly converted to a similar complex (**15**) in the presence of sodium or lithium cyclopentadienide even in the absence of a reductant. VCl_4 is also reduced to give vanadocene.[36]

The Cp rings of vanadocenes are usually in the staggered conformation.[37] Electrochemical properties in THF depend on the reversible one-electron reduction to $[Cp_2V]^-$. The oxidation process of Cp_2V involves reversible one-electron oxidation and successive irreversible one-electron oxidation.[38]

Sterically bulky vanadocene $[C_5(i\text{-Pr})_nH_{5-n}]_2V$ is prepared by treatment of VCl_3 or $[V_2Cl_3]_2[Zn_2Cl_6]$ with the corresponding $K[C_5(i\text{-Pr})_nH_{5-n}]$.[39] The dinuclear cyclopentadienyl complex is also accessible. The fulvalenediyl complex (**16**) is obtained from $VCl_2(THF)_2$ and $C_{10}H_6Li_2$ as shown in Scheme 10.[40–42]

Bis(alkylcyclopentadienyl)vanadium (**17**), which is synthesized as shown in Scheme 11, undergoes chlorination with PCl_3 to give the corresponding blue monochloride (**18**) and green dichloride (**19**).[43]

Heteroatom ring substituted vanadocenes are rare except $(C_5H_4EMe_3)_2V$ (E = Si, Ge, Sn).[44] $(\eta^5\text{-}C_5H_4CH_2CH_2NMe_2)_2V$ is obtained by treatment with $Li(C_5H_4CH_2CH_2NMe_2)$.[45] The amino-functionalized vanadocene derivative (**20**) is also known.[46]

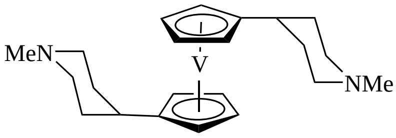

(**20**)

The bimetallic pentalene-bridged complex $[Cp_2V]_2Pn$ (**21**, Pn = C_8H_6) containing a V–V triple bond, in which the vanadium centers adopt a *syn*-coordination, is synthesized from $Li_2Pn{\cdot}xDME$ (DME = 1,2-dimethoxyethane) with 2 equiv of $[CpVCl{\cdot}THF]_n$.[47] The complex shows a high-spin/low-spin (*see High-spin & Low-spin Compounds*) equilibrium in both solution and solid states.

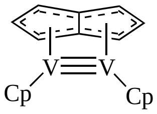

(**21**)

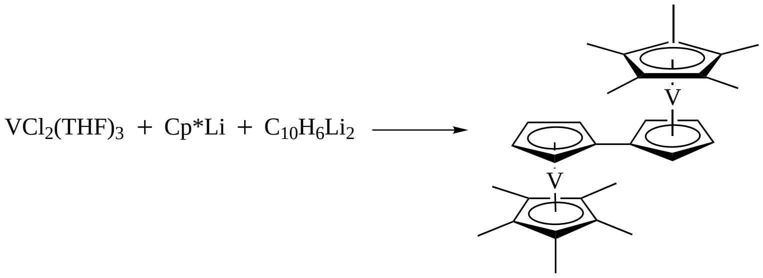

(**16**)

Scheme 10

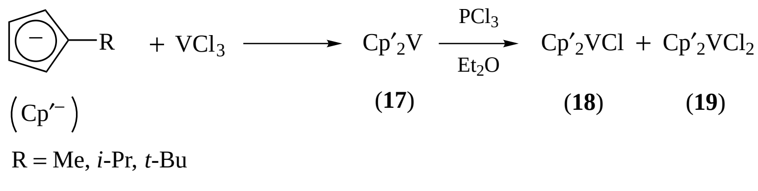

Scheme 11

Since the vanadium center of vanadocenes is electron-deficient, various vanadium derivatives are formed by the attack with PR_3, CO, or unsaturated π-donating ligands.**[48]** This reaction provides a useful synthetic method for the synthesis of η^2-alkene complexes as described later. Thus formed $Cp^*{}_2V(CO)$ (**22**) is converted to the cyano derivative (**23**, *see* ***Cyanide Complexes of the Transition Metals***) on treatment with the isocyanide (Scheme 12). $(\eta^5\text{-}C_5Me_5)_2V$ is incubated with O_2 at −78 °C to yield $[(\mu\text{-}\eta^3\text{-}C_5Me_5O_3)V(O)]_2$ via oxygen insertion into the carbon–vanadium bond.**[49]**

Various halides (VCl_4, VCl_3, and VBr_2) react with the 6-Me-*nido*-5,6,9-$C_3B_7H_9{}^-$ to give the paramagnetic air- and moisture-sensitive product, $V(Me\text{-}C_3B_7H_9)_2$, which is considered a tricarbadecaboranyl (*see Carborane*) analog of vanadocene. The complex is not oxidized with Br_2 or Ag^+, indicating that the tricarbadecaboranyl anion stabilizes the metal in a low oxidation state.**[50]**

1,10-Phenanthroline-5,6-dione reacts with Cp_2V to form the O,O′-coordinated complex (**24**), which is subjected to further complexation with $M'Cl_4$ ($M' = Ti$ or Hf) to give the bimetallic complex (**25**) (Scheme 13).**[51]** The opposite complexation process is also possible, affording a similar bimetallic complex (**26**) (Scheme 14).

Vanadocene halide is another important analog that is transformed to various vanadocene derivatives. Vanadocene chloride is prepared from vanadium(III) chloride and thallium cyclopentadienide**[52]** or vanadocene and hydrogen chloride.**[53]** Vanadocene dihalide is similarly synthesized from vanadium(IV) halide via nucleophilic substitution.**[54]** Displacement of the chloro group results in functionalization as shown in Scheme 15.

Ring-bridged vanadocene halide and dihalide, (**28**) and (**29**) are obtained from bis(cyclopentadienyl)-substituted dianion (**27**) as shown in Scheme 16.**[55]** Furthermore,

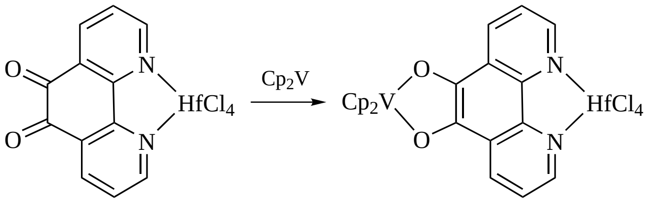

(**26**)

Scheme 14

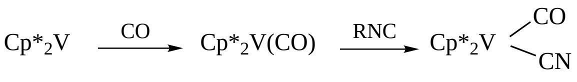

(**22**) (**23**)

Scheme 12

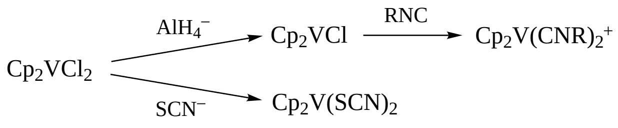

Scheme 15

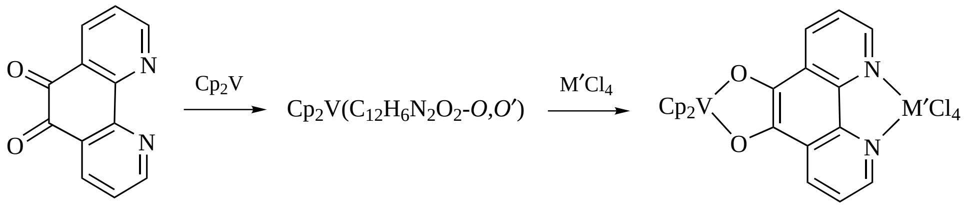

(**24**) (**25**)

M′ = Ti, Hf

Scheme 13

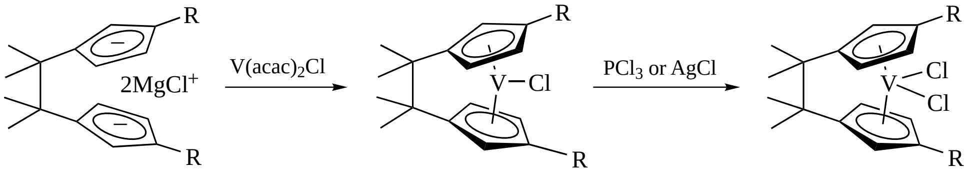

(**27**) (**28**) (**29**)

Scheme 16

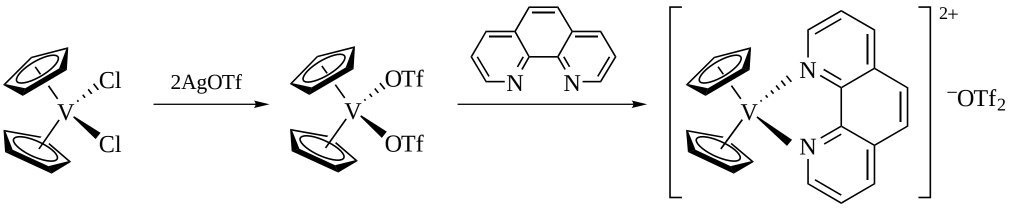

(**30**) (**31**)

Scheme 17

bis(cyclopenta-2,4-dienyl)dimethylsilanes or -germanes can be used as starting ligands.**[56]**

$Cp_2V(OTf)_2$ (**30**), which is derived from vanadocene dichloride, forms the d^1 vanadocene complex (**31**) with 1,10-phenanthroline or 2,2′-bipyridine (Scheme 17).**[57]** The two nitrogen atoms and centroids of the two cyclopentadienyl rings occupy a distorted tetrahedral geometry around V(IV) center. Relatively low V(IV)–V(III) reduction potential is observed.

A series of soluble vanadocene porphyrazines (**32**) and (**33**) are prepared.**[58]** The porphyrazine macrocycle mediates magnetic exchange interactions between metal ions bound to the periphery, separated by 14.5 Å.

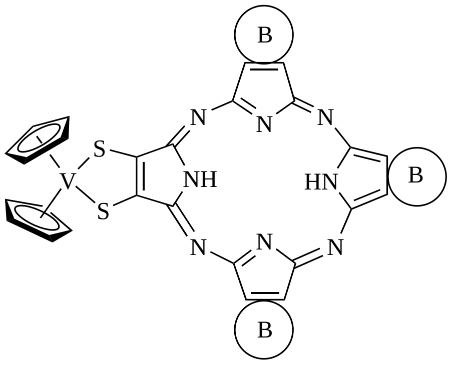

(**32**)
B = (4-*t*-butylphenyl)$_2$

The 14-electron $[Cp_2V]^+$ cation (**34**) is isolated as an unsolvated species by one-electron oxidation of Cp_2V with $[Cp_2Fe]^+$ (Scheme 18).**[59]** Cp_2VCl is prepared by treatment of the cation with [PPN]Cl (PPN = bis(triphenylphosphine)nitrogen(+1)). The reaction of vanadium hexacarbonyl with Cp_2V results in the formation of the μ-isocarbonyl (*see Isocarbonyl Complexes*) derivative (**35**) as a transient species, which is converted to $[Cp_2V(CO)_2][V(CO)_6]$ (**36**) on treatment with CO. Use of $Co_2(CO)_8$ instead of $V(CO)_6$ leads to $Cp_2VCo(CO)_4$ (**37**), which slowly decomposes to $[Cp_2V\ (CO)_2][Co(CO)_4]$ (**38**). Ground-state electron transfer between TCNE and 16-electron $V(C_5R_5)_2Br$ (R = H, Me) is investigated.**[60]**

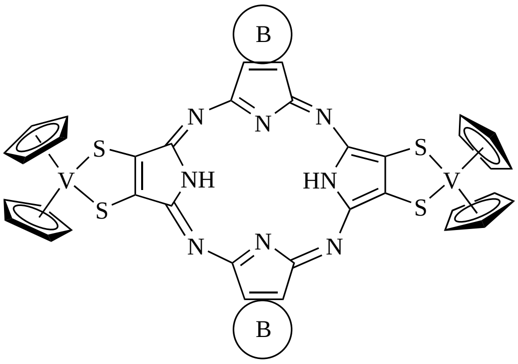

(**33**)
B = 3,6-butyloxybenzene
B = (4-*t*-butylphenyl)$_2$

Methyl substitution on the cyclopentadienyl rings of $Cp'VCl_2$ on the spermicidal activity is investigated.**[61]** The corresponding oxo compound, $Cp'V(O)Cl_2$, does not show the activity. $V(\eta^5\text{-}C_5H_5)_2((C_2H_5)_2NCS_2)(BF_4)$ is reported to be a potential and stable spermicidal compound.**[62]** $[Cp_2V(acac)](CF_3SO_3)$ is known as a dual-function anticancer agent with antiangiogenic and antimitotic properties.**[63]**

$CpV(CO)_4$, which is a typical half-sandwich complex, is prepared by reduction of vanadocene with sodium or potassium under carbon monoxide. Another route to $CpV(CO)_4$ involves the direct reaction of hexacarbonylvanadium(0) with cyclopentadiene. The Cp ring is disordered between staggered and eclipsed conformations.**[64]** The distance between the centroid and vanadium is 1.9–2.0 Å.

Replacement of the carbonyl ligand affords the corresponding vanadium derivatives.**[65–67]** The partially phosphine-substituted complex (**39**) is obtained by treatment of phosphine-stabilized VCl_3 with cyclopentadienide, followed by reductive carbonylation (Scheme 19).**[68]** A variety of cyclopentadienylvanadium halides in the oxidation state 2–5 are synthesized from Cp_2V or $CpV(CO)_4$.**[69–75]** For example, the reaction of $CpV(CO)_4$ with halogen or oxygen provides the corresponding oxidized complexes as shown in Scheme 20. Use of thiols or chalcogens results in the formation of the corresponding substituted complexes (**40**)**[76]** and (**41**)**[77]** (Scheme 21).

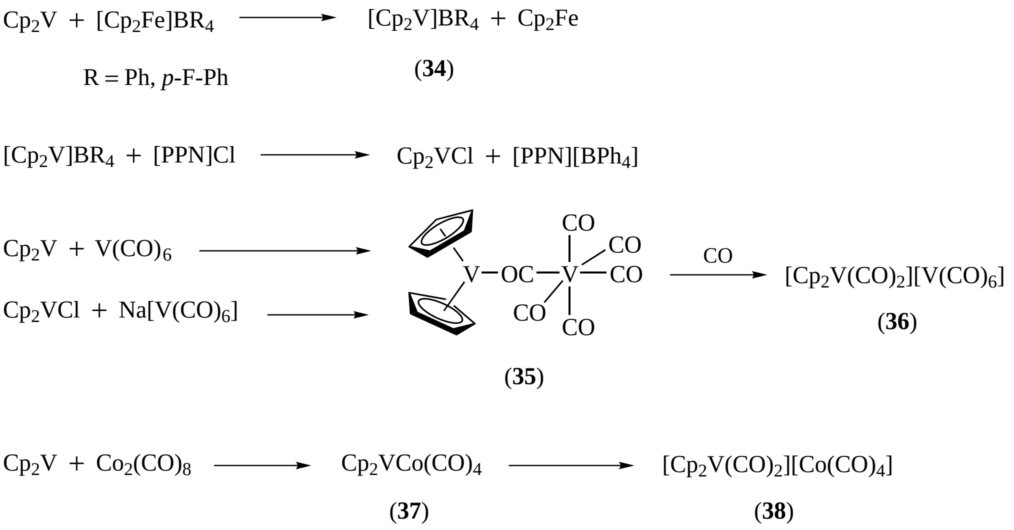
Cp2V + [Cp2Fe]BR4 → [Cp2V]BR4 + Cp2Fe
R = Ph, p-F-Ph
(34)
[Cp2V]BR4 + [PPN]Cl → Cp2VCl + [PPN][BPh4]
Cp2V + V(CO)6 →
Cp2VCl + Na[V(CO)6] →
V–OC–V
CO
CO
(35)
[Cp2V(CO)2][V(CO)6]
(36)
Cp2V + Co2(CO)8 → Cp2VCo(CO)4 → [Cp2V(CO)2][Co(CO)4]
(37)
(38)

Scheme 18

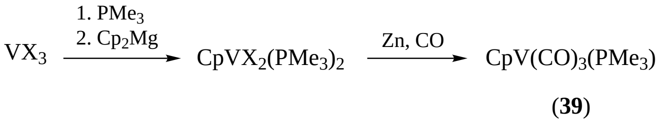

$$VX_3 \xrightarrow[\text{2. Cp}_2\text{Mg}]{\text{1. PMe}_3} CpVX_2(PMe_3)_2 \xrightarrow{\text{Zn, CO}} CpV(CO)_3(PMe_3)$$

(**39**)

Scheme 19

$$CpV(CO)_4 + X_2 \longrightarrow CpVX_3$$

$$CpV(CO)_4 + Cl_2 + O_2 \longrightarrow CpV(O)Cl_2$$

Scheme 20

A fulvene is used for the preparation of the substituted η^5-cyclopentadienylvanadium(I) complexes (**42**) and (**43**) (Scheme 22).[78,79]

Dimerization or cyclotrimerization is performed by reduction of $(C_5Me_4R)VX_3$ (**44**, R = Me, Et) with Na or treatment of VX_3L_3 (L = THF, THT) with $(C_5Me_4R)SnBu_3$ to give the vanadium(III) halides, $(\eta^5\text{-}C_5Me_4R)_2V_2(\mu\text{-}Br)_4$ (**45**, paramagnetic, V–V distance, 2.565 Å) and $(\eta^5\text{-}C_5Me_4R)_3V_3(\mu\text{-}Cl)_6$ (**46**, spin-frustrated antiferromagnetic (*see Antiferromagnetism*), V–V distance, 3.373 Å) (Scheme 23).[80] Unusual difference in V–V distance and magnetochemistry is observed. Halogenation leads to the reformation of (**44**).

Reduction of $[(\eta\text{-}C_5Me_5)VCl(\mu\text{-}N)]_2$ (**47**) with sodium amalgam in toluene, or with lithium nitride or magnesium in tetrahydrofuran, gives diamagnetic $[(\eta^5\text{-}C_5Me_5)V(\mu_3\text{-}N)]_4$ (**48**) (Scheme 24).[81]

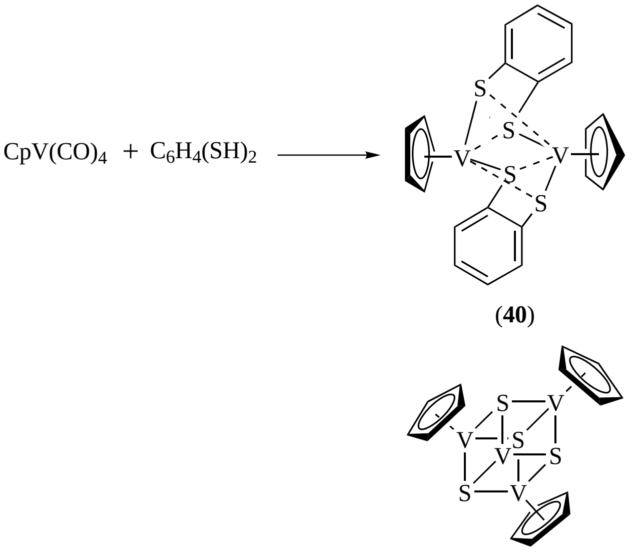
CpV(CO)4 + C6H4(SH)2 →
S
V
(41)

(**40**)

(**41**)

Scheme 21

4 η^3-ALLYL AND RELATED COMPLEXES

η^3-Allylvanadium complexes (*see Allyl Complexes*) are synthesized by allylation with Grignard reagents as shown in Scheme 25.[82] Another synthetic route lies in the allylation of a vanadium anionic species with allylic chloride.[83] Codimerization of vanadium-coordinated diphenylacetylene (tolane) and 1,3-butadiene affords the allyl complex (**49**) (Scheme 26).[84]

The η^3-1-azaallyl complex (**51**) is formed by [2 + 2] cycloaddition of (**50**) with alkyne. The metallacycle intermediate is considered to be involved in this transformation (Scheme 27).[85]

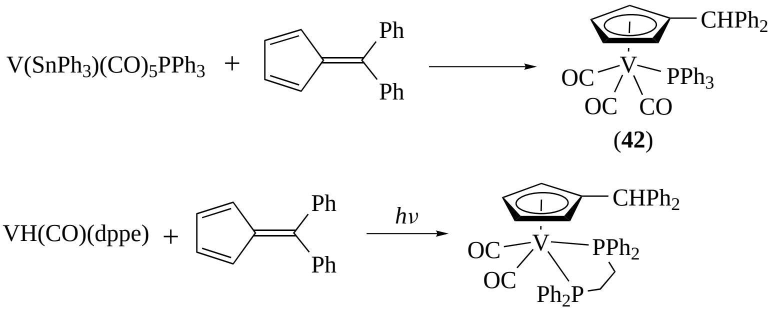
V(SnPh3)(CO)5PPh3 +
Ph
Ph
CHPh2
OC
V
PPh3
OC CO
VH(CO)(dppe) +
Ph
Ph
hν
CHPh2
OC
V
PPh2
OC
Ph2P

(**42**)

(**43**)

dppe = 1,2-bis(dipenylphosphino)ethane

Scheme 22

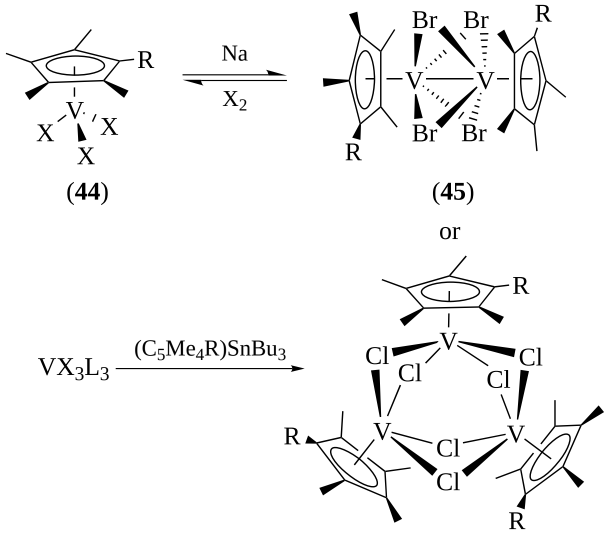
R
V
X
X
X
Na
X2
Br
Br
R
V
V
Br
Br
R
or
R
VX3L3
(C5Me4R)SnBu3
Cl
V
Cl
Cl
Cl
R
V
Cl
V
Cl
R

(**44**)

(**45**)

(**46**)

Scheme 23

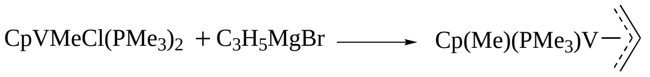
CpVMeCl(PMe3)2 + C3H5MgBr
Cp(Me)(PMe3)V

Scheme 25

Three-electron donor ligands like η^2-acyl ones are also described here. The η^2-CH_2O complex (**52**) is formed by treatment of Cp_2V with paraformaldehyde. Various vanadium compounds are available from (**52**) as shown in Scheme 28.[86]

Use of an acyl chloride permits the transformation from the V(0) compound (**53**) to the η^2-acyl complex (**54**) (Scheme 29).[87–89] The iminoacyl group of (**55**) is also coordinated in the η^2-mode (Scheme 30).[90]

A variety of vanadium carbonyl compounds are obtained from $[V(CO)_6]^-$. Use of 1-chloropenta-2,4-diene under photoirradiation leads to $V(\eta^5\text{-}C_5H_7)(CO)_4$. The η^2-bonded acyl complex is formed similarly by photoinduced substitution with benzoyl chloride.[91] The η^2-C,O coordination mode is

$$2[(\eta\text{-}C_5Me_5)VCl(\mu\text{-}N)]_2 \ + \ 4Na \longrightarrow [(\eta\text{-}C_5Me_5)V(\mu_3\text{-}N)]_4 \ + \ 4NaCl$$

(**47**) (**48**)

Scheme 24

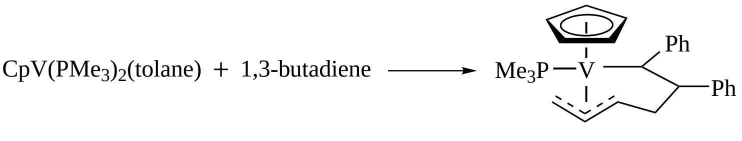
CpV(PMe3)2(tolane) + 1,3-butadiene
Ph
Me3P
V
Ph

(**49**)

Scheme 26

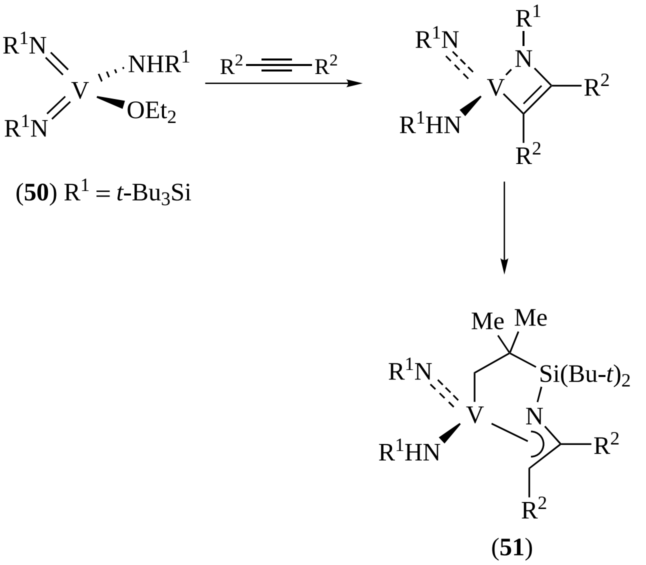
R¹N
NHR¹
V
OEt₂
R¹N
R²—≡—R²
R¹
N
R²
R¹HN
R²
Me Me
Si(Bu-t)₂
R¹N
V
N
R¹HN
R²
R²

(**50**) R^1 = t-Bu_3Si

(**51**)

Scheme 27

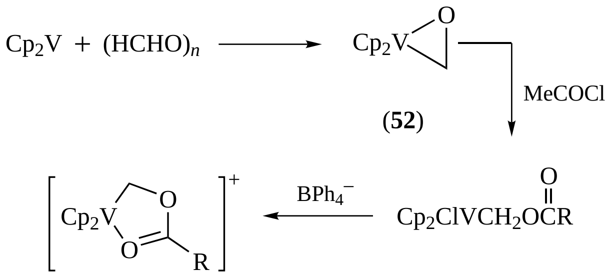
Cp₂V + (HCHO)ₙ
Cp₂V
O
MeCOCl
Cp₂ClVCH₂OCR
O
BPh₄⁻
Cp₂V
O
O
R
+

(**52**)

Scheme 28

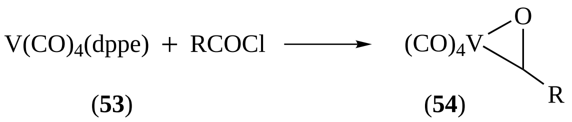
V(CO)₄(dppe) + RCOCl
(CO)₄V
O
R

(**53**) (**54**)

Scheme 29

observed with the ketene complex (**56**), which undergoes the attack of butyllithium and silylation to give the silyl enol ether (**57**) (Scheme 31).[92]

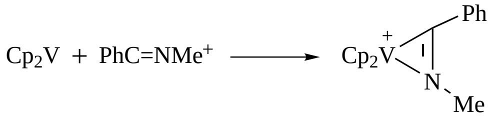
Cp₂V + PhC=NMe⁺
Cp₂V
+
Ph
N
Me

(**55**)

Scheme 30

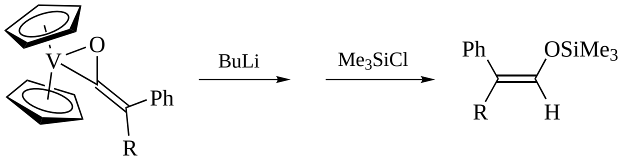
V
O
Ph
R
BuLi
Me₃SiCl
Ph
OSiMe₃
R
H

(**56**) (**57**)

Scheme 31

5 η^2-ALKYNE OR ALKENE COMPLEXES

Side-on coordination of an unsaturated ligand, alkyne or alkene, provides the corresponding complexes in the η^2-mode. Vanadium-alkyne complexes like $Cp_2V(RC{\equiv}CR)$ ($R = COOMe, CF_3$) are formed by treatment of vanadocene with alkynes as shown in Scheme 32.[93–96] (η^2-Alkyne)(η^5-cyclopentadienyl)bis(trimethylphosphine)vanadium(I) (**59**) is obtained by reductive coordination of $CpVCl_2(PMe_3)_2$ (**58**) with alkyne (Scheme 33).[84,97]

Use of $CpV(CO)_4$ under photoirradiation affords $CpV(\eta^2\text{-}C_6F_5C{\equiv}CC_6F_5)(CO)_2$ (Scheme 34).[98] Cyclooligomerization of diphenylacetylene with $Cp_2V_2(CO)_5$ affords the η^4-cyclobutadiene complex (**60**), $V(C_4Ph_4)Cp(CO)_2$ (Scheme 35).[99] The above-mentioned side-on monomeric complex is obtained with the more basic alkyne like dimethylacetylene.

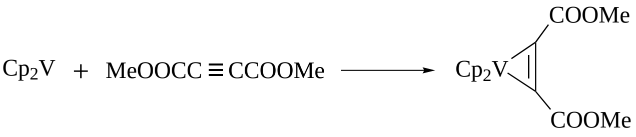
Cp₂V + MeOOCC≡CCOOMe
Cp₂V
COOMe
COOMe

Scheme 32

$$\mathrm{CpVCl_2(PMe_3)_2 + RC{\equiv}CR' \xrightarrow{Mg} CpV(RC{\equiv}CR')(PMe_3)_2}$$

(**58**) (**59**)

Scheme 33

$$\mathrm{CpV(CO)_4 + C_6F_5C{\equiv}CC_6F_5 \xrightarrow{h\nu} CpV(CO)_2(C_6F_5C{\equiv}CC_6F_5)}$$

Scheme 34

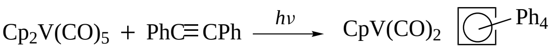
Cp₂V(CO)₅ + PhC≡CPh
hν
CpV(CO)₂
Ph₄

(**60**)

Scheme 35

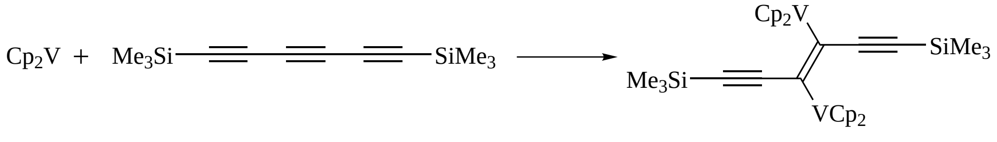

(**61**) (**62**)

Scheme 36

The homobimetallic vanadium d^1-d^1 complex (*see* ***Dinuclear Organometallic Cluster Complexes***), $(Cp_2V)_2(1-2\eta:3-4\eta\text{-}RC{=}C\text{–}C{=}CR)$ is formed by treatment of Cp_2V with $Me_3SiC{\equiv}C\text{–}C{\equiv}CSiMe_3$ or $Ph_2PC{\equiv}C\text{–}C{\equiv}CPPh_2$.[100] Antiferromagnetic moments depend on the bridging spacer. The d^2-d^2 homobimetallic complex (**62**) is derived from $Me_3SiC{\equiv}C\text{–}C{\equiv}C\text{–}C{\equiv}CSiMe_3$ (**61**) as shown in Scheme 36.[101] Cp_2V migration is observed with further complexation of $Cp_2V(3-4\eta\text{-}t\text{-}BuC{\equiv}C\text{–}C_2\text{–}C{\equiv}CC{\equiv}CBu\text{-}t)$ to give the dimetallic complex $(Cp_2V)_2(1-2\eta:7-8\eta\text{-}t\text{-}BuC{\equiv}C\text{–}C_2\text{–}C{\equiv}CC{\equiv}CBu\text{-}t)$.[102]

Bis(alkynyl)phosphane (**63**) similarly reacts with Cp_2V to give the vanadacyclopropene phosphane (**64**), which is converted to the alkenyl–alkynyl phosphane (**65**) on treatment with HCl in toluene (Scheme 37).[103]

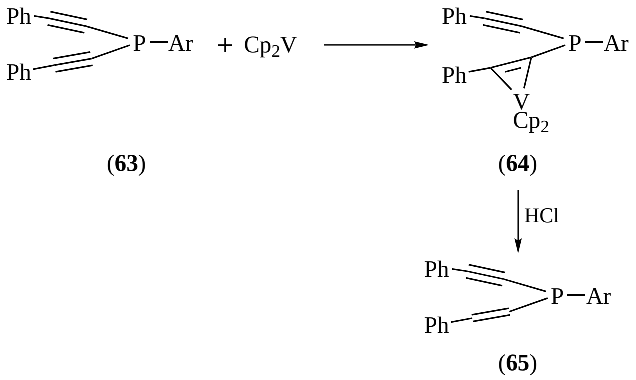

(**63**) (**64**) (**65**)

Scheme 37

$(C_5H_4R)_2Zr(C{\equiv}CPh)_2$ (**66**, R = Me, t-Bu) is transformed to $Cp_2V(\mu\text{-}\eta^2:\eta^4\text{-butadiyne})ZrCp'_2$ (**67**) in the presence of Cp_2V via the zirconacyclocumulene intermediate as shown in Scheme 38.[104]

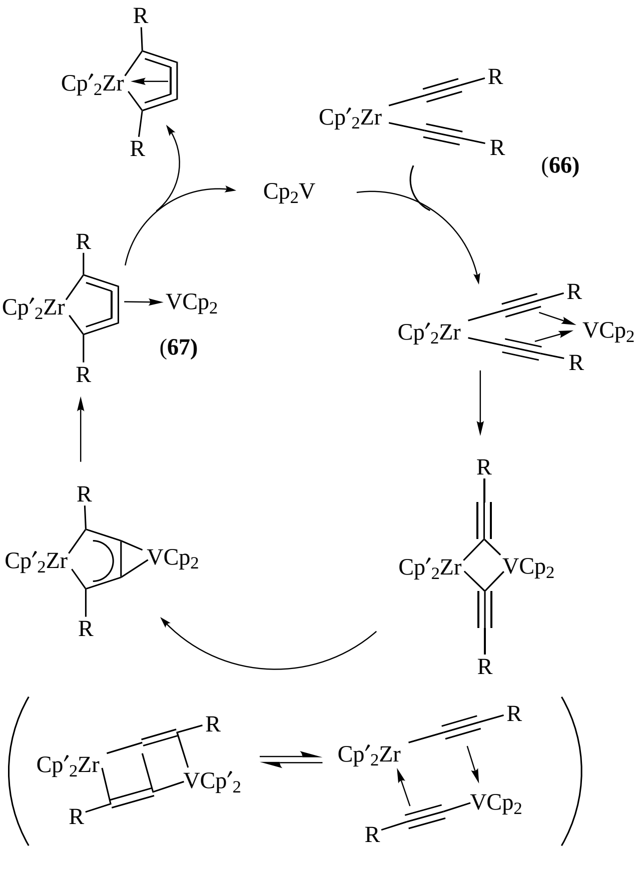

(**66**) (**67**)

Scheme 38

The alkyne complex (**68**) reacts with two equivalents of ethene to give the *s-cis*-3,4-(E)-diphenyl-1,3-hexadiene complex (**69**) as shown in Scheme 39. Use of 2-butyne leads to the metallacycle (**70**) via bis(alkyne) complex.[84] The bicyclic vanadacyclopentatriene complex (**71**) is formed from 1,7-nonadiyne.

$Cp_2V(\eta^2\text{-alkene})$ is synthesized by treatment of vanadocene with alkene bearing an electron-withdrawing group.[93,105,106] The reaction of vanadocene with dimethyl fumarate or dimethyl maleate leads to the formation of the same complex, bis(η^5-cyclopentadienyl)(η^2-dimethyl fumarate)vanadium (**72**), via isomerization (Scheme 40).

$CpV(\eta^2\text{-ethene})(PMe_3)_2$ (**74**) is obtained as a green paramagnetic complex via the carbon–carbon bond cleavage of the 1,4-divanabutane intermediate, $Cp(PMe_3)_2V(CH_2)_4\text{-}V(PMe_3)_2Cp$, which is produced by reduction of dichloro(η^5-cyclopentadienyl)bis(trimethylphosphine)vanadium(II) (**73**) with Na/Hg and successive treatment with 1,4-di-Grignard compound (Scheme 41).[84,107] Reaction of (**74**) with carbon monoxide or diphenylacetylene provides the ligand exchange complexes (**75**) and (**76**), respectively. The vanadolactone (**77**) is formed on treatment with carbon dioxide.

The η^4-vinylketene complex is obtained by photoirradiation of $CpV(CO)_4$ with triphenylcyclopropene via CO insertion.[99]

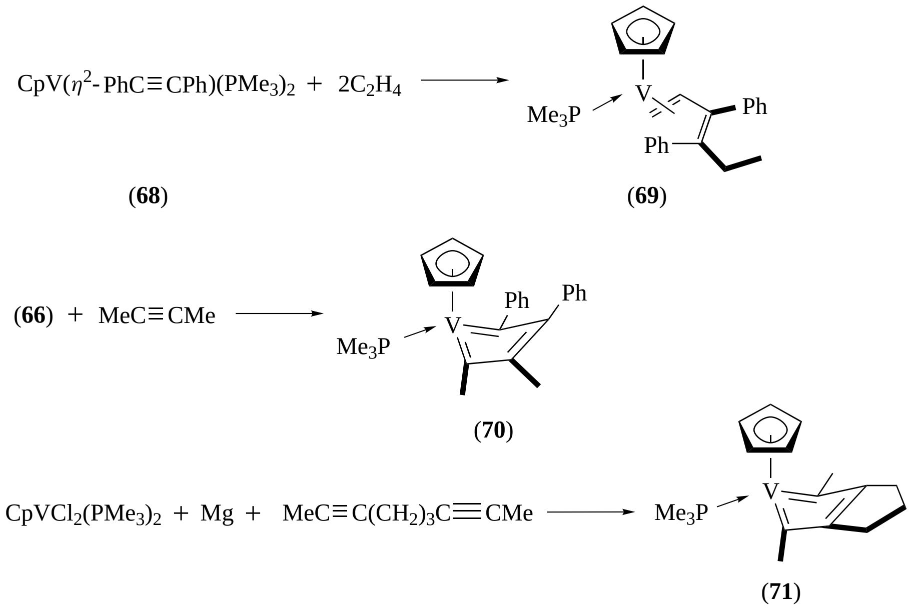
CpV(η2- PhC≡CPh)(PMe3)2 + 2C2H4
(68)
Me3P
V
Ph
Ph
(69)
(66) + MeC≡CMe
Me3P
V
Ph
Ph
(70)
CpVCl2(PMe3)2 + Mg + MeC≡C(CH2)3C≡CMe
Me3P
V
(71)

Scheme 39

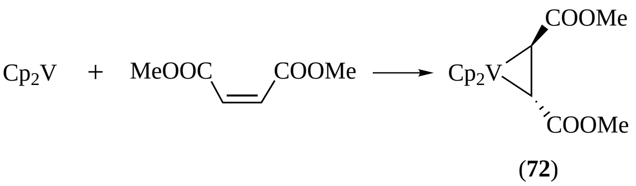
Cp2V + MeOOC COOMe
Cp2V
COOMe
COOMe
(72)

Scheme 40

6 CARBENE COMPLEXES

Carbene complexes, in which the carbenes generally bind end-on to the metals through σ donor bond and π bond, are recognized as one of the key organometallics and used especially as catalysts for metathesis polymerization. Although vanadium complexes are of importance in the field of polymer chemistry, only few carbene complexes have been isolated so far.

The acylvanadium complex (**78**) is converted to the Fischer type (*see Fischer-type Carbene Complexes*) vanadium complex (**79**) on treatment with $Me_3{}^+BF_4{}^-$ (Scheme 42).**108**

The N-substituted carbene analog is formed from $Na_2[VCp(CO)_3]$ and iminium chloride (**80**) as shown in

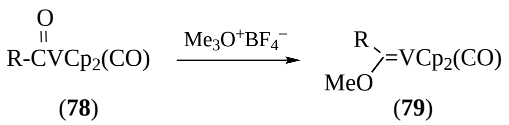
O
R-CVCp2(CO)
(78)
Me3O+BF4−
R
MeO
=VCp2(CO)
(79)

Scheme 42

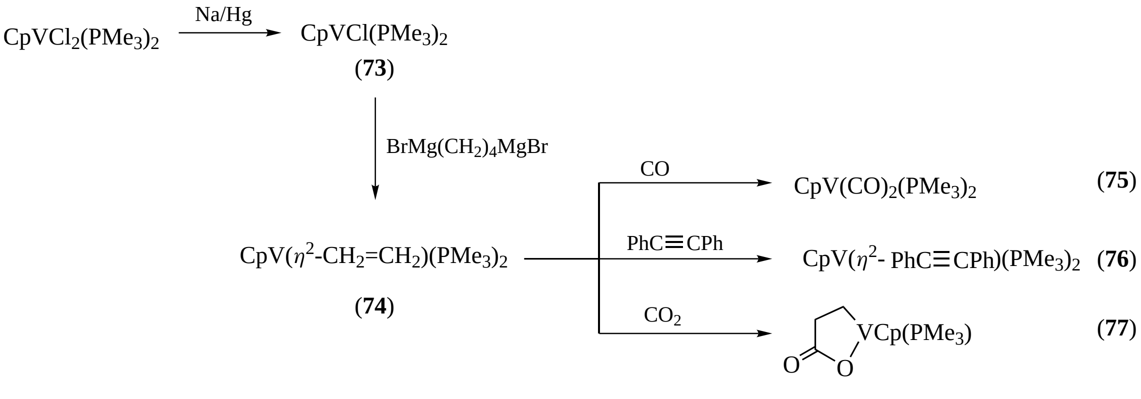
CpVCl2(PMe3)2
Na/Hg
CpVCl(PMe3)2
(73)
BrMg(CH2)4MgBr
CpV(η2-CH2=CH2)(PMe3)2
(74)
CO
CpV(CO)2(PMe3)2
(75)
PhC≡CPh
CpV(η2- PhC≡CPh)(PMe3)2
(76)
CO2
VCp(PMe3)
O
O
(77)

Scheme 41

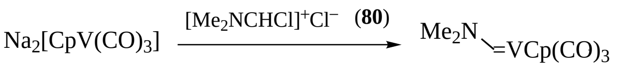

Scheme 43

Scheme 43.[109] The Fischer-type (*see Fischer-type Carbene Complexes*) vanadium complexes are prepared by treatment of (butadiene)hafnocene (**81**) or (butadiene)zirconocene with $CpV(CO)_4$ (Scheme 44). The equilibrium mixture reacts with cyclopentanone to give the adduct complex (**82**).[110–112]

Thermolysis of (η^5-cyclopentadienyl)bis(neopentyl)(trimethylphosphine)vanadium(I) (**82**) in the presence of 1,2-bis(dimethylphosphino)ethane leads to the formation of the Schrock-type (*see Schrock-type Carbene Complexes*) alkylidene vanadium complex (**83**), which is supported by X-ray crystallographic analysis (Scheme 45).[113,114] The imido vanadium complex (**84**) is converted to the corresponding alkylidene complex (**86**) on treatment with benzylidene(triphenyl)phosphorane (**85**) via substitution of the phosphine ligand (Scheme 46).[115]

Silylation of $Na[V(CO)_2(Me_2PCH_2CH_2PMe_2)_2]$ affords the vanadium carbyne complex (*see Carbyne Complexes*), $V(COSiPh_3)(CO)(Me_2PCH_2CH_2PMe_2)_2$, which is supposed to be a precursor complex for the formation of a η^2-acetylene complex via reductive C–C coupling (*see Reductive C–C Coupling*).[116]

Isocyanide ligands (*see Isocyanide Ligands*) are comparable to carbon monoxide in their σ-donor and π-acceptor ability. Isocyanide complexes (**87**) are formed by ligand exchange of $CpV(CO)_4$ with an isocyanide, which is facilitated by palladium(II) catalyst (Scheme 47).[117] The ligand substitution reaction is also observed with $[V(CO)_6]^-$ to give the corresponding vanadium isocyanide complex (**88**) with the oxidation state −1 (Scheme 48).[118–121] The ligand exchange reaction proceeds via oxidation to give the homoleptic (*see Homoleptic Compound*) vanadium(II) complex (**89**) as shown in Scheme 49.[122,123]

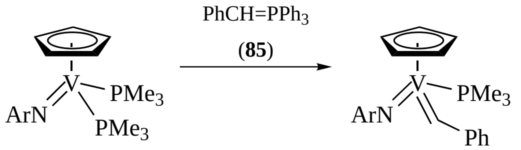

(**84**) (**86**)

Scheme 46

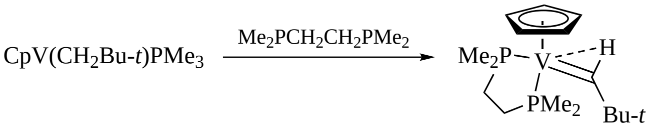

(**82**) (**83**)

Scheme 45

$$VCp(CO)_4 + nRNC \xrightarrow{\text{Pd(II) cat.}} VCp(CO)_4(CNR)_n$$

(**87**)

$n = 1$; R = Me, Bn, *i*-Pr, C_6H_{11}, *t*-Bu, 2,6-$Me_2C_6H_3$
$n = 2, 3$; R = *t*-Bu, 2,6-$Me_2C_6H_3$

Scheme 47

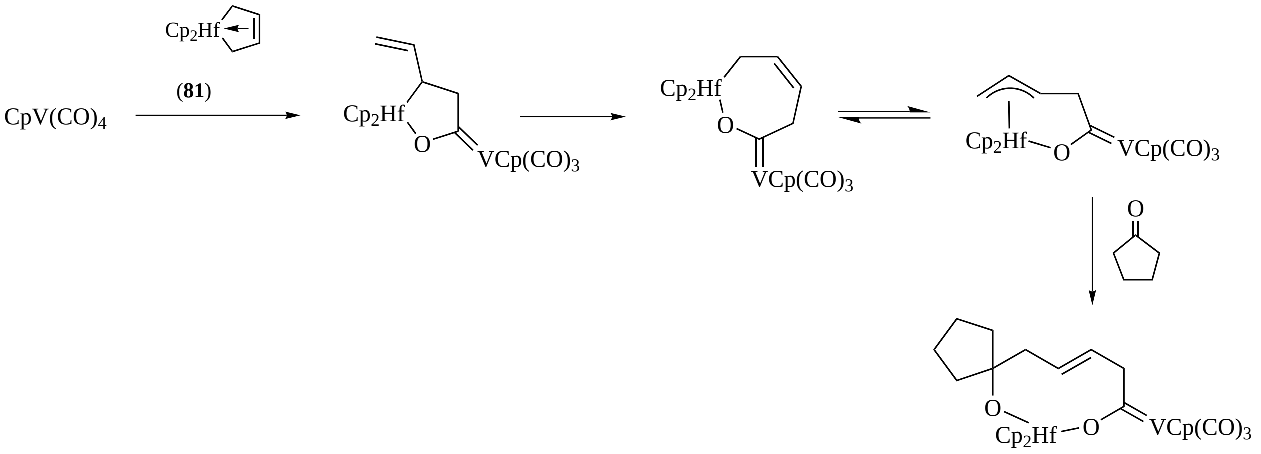

(**82**)

Scheme 44

$$[Et_4N]^+[V(CO)_5(NH_3)]^- + RNC \longrightarrow \underset{(\mathbf{88})}{[Et_4N]^+[V(CO)_5(CNR)]^-}$$

R = Me, C_6H_{11}, *t*-Bu, Ph

Scheme 48

$$[Et_4N]^+[V(CO)_6]^- + t\text{-BuNC} \xrightarrow{PhICl_2} \underset{(\mathbf{89})}{[V(CNBu\text{-}t)_6][V(CO)_6]_2}$$

Scheme 49

7 σ-BONDED ORGANO- OR HYDRIDOVANADIUM COMPLEXES

The σ-bonded organovanadium compounds are generally unstable, but a wide variety of usage has been developed in organic reaction. The synthetic routes to organovanadium compounds depend on the oxidation state of vanadium. For medium- and high-valent compounds, V–X is replaced by an organic group. Alkyl or aryl vanadium(III) or (IV) compounds (**90**) are synthesized by the reaction of VCl_3 or VCl_4, respectively, with organolithium compounds or Grignard reagents, in which 2,4,6-$Me_3C_6H_2$-, Me_3SiCH_2-, and C_6F_5-substituted derivatives are used (Scheme 50).[124–130] The nitrogen-bridged organovanadium(III) complex (**91**) is obtained when the reaction is carried out under nitrogen (Scheme 51).[131] Thus formed complex (**91**) undergoes oxidation with styrene oxide to the corresponding oxo complex (**92**).

Cyclopentadienyl-substituted vanadium(III) compound (**93**) is also allowed to undergo the substitution reaction to give the σ-alkyl, σ-alkynyl, or σ-aryl complexes (**94**, Scheme 52).[82,132–137] $[NBu_4][V(C_6Cl_5)_4]$, which is prepared from $VCl_3(THF)_3$ and C_6Cl_5Li, is isolated and characterized as a homoleptic, tetrahedral, and paramagnetic d^2 complex.[138]

$$VCl_3(THF)_3 + RM \longrightarrow \underset{(\mathbf{90})}{VR_3}$$

RM = Me_3SiCH_2MgCl, C_6F_5Li,

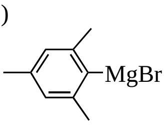

Scheme 50

In the case of low-valent vanadium compounds, metathesis or hydrovanadation is used for the synthesis of organovanadium compounds. Treatment of vanadocene with halomethane results in the formation of the methyl-substituted halovanadocene (**95**) (Scheme 53).[139] The dianion species (**96**) is similarly used for this purpose (Scheme 54).[140]

Coordination numbers of organovanadium compounds are 3 to 6 as exemplified by pseudotetrahedral ($Cp_2V(C{\equiv}CBu\text{-}t)$,[136] $OVMes_3$[126]), square pyramidal (VPh_4),[141] and octahedral ($[(LiOEt_2)_4VPh_6]$).[142] The V(II) and V(III) compounds in a high-spin configuration (*see High-spin & Low-spin Compounds*) exhibit normal Curie–Weiss behavior.[143] Reaction modes vary disproportionation, symproportionation, ligand coupling, and insertion as shown in Scheme 55.

$$\underset{(\mathbf{93})}{CpVCl_2(PMe_3)_2} + RM \longrightarrow \underset{(\mathbf{94})}{CpVR_2(PMe_3)_2}$$

RM = MeLi, PhMgBr

Scheme 52

$$Cp_2V + MeX \longrightarrow \underset{(\mathbf{95})}{Cp_2VMeX}$$

Scheme 53

$$\underset{(\mathbf{96})}{CpV(CO)_3^{2-}} + MeI \longrightarrow CpV(CO)_3Me^- + I^-$$

Scheme 54

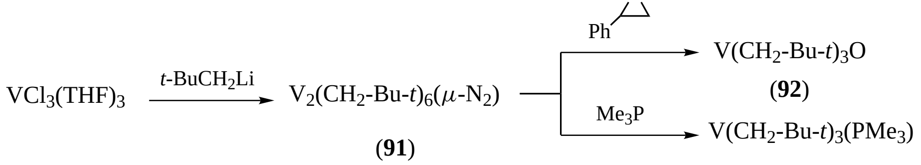

(**91**) (**92**)

Scheme 51

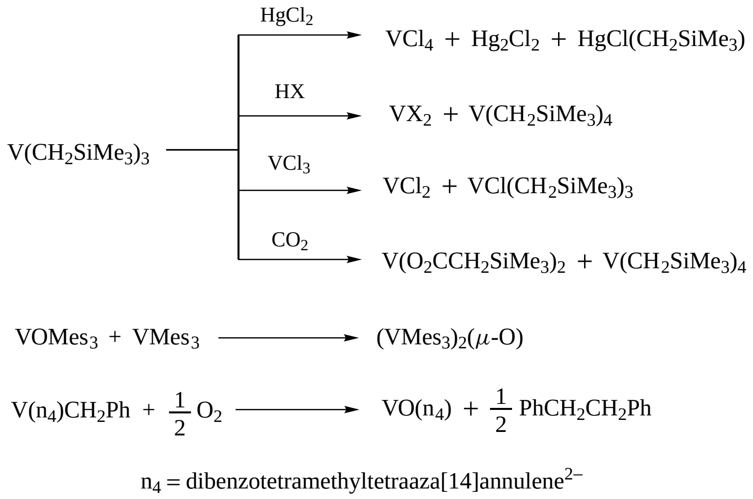
$V(CH_2SiMe_3)_3$
$HgCl_2$
$VCl_4 + Hg_2Cl_2 + HgCl(CH_2SiMe_3)$
HX
$VX_2 + V(CH_2SiMe_3)_4$
VCl_3
$VCl_2 + VCl(CH_2SiMe_3)_3$
CO_2
$V(O_2CCH_2SiMe_3)_2 + V(CH_2SiMe_3)_4$
$VOMes_3 + VMes_3 \longrightarrow (VMes_3)_2(\mu\text{-O})$
$V(n_4)CH_2Ph + \frac{1}{2}O_2 \longrightarrow VO(n_4) + \frac{1}{2}PhCH_2CH_2Ph$
n_4 = dibenzotetramethyltetraaza[14]annulene^{2-}

Scheme 55

A variety of synthetic transformations have been developed by using vanadium compounds or intermediates. Cp-substituted vanadiums are used in catalytic polymerization, which involves organovanadium intermediates.[144]

Isomerization of alkenes is catalyzed by bis(η^3-allyl)(η^5-cyclopentadienyl)vanadium(IV).[145] Cyclohexene undergoes catalytic stereoselective aerobic oxidation with $CpV(CO)_4$.[146] Reductive coupling (*see Reductive Coupling*) of aldehydes and aldimines is catalyzed by a Cp-substituted vanadium compound in the presence of a chlorosilane and zinc or aluminum.[147–151] Vanadocene or bis(η^5-cyclopentadienyl)dimethylvanadium(IV) catalyzes the synthesis of 1,2-diphenyldisilane and 1,2,3-triphenyltrisilane from phenylsilane.[152]

Organovanadium compounds exhibit unique reactivity on the basis of the redox characteristics of the vanadium. For example, treatment of VCl_3 in THF with a stoichiometric amount of *n*- or *s*-alkylmagnesium halides affords alkanes, alkenes, and dimers.[153] The organovanadium compounds generated in situ couple chemoselectively with acid chlorides or allyl halides.[154] A related reaction with aldehydes yields coupled ketones via oxidative nucleophilic addition (Scheme 56).[155,156]

Direct geminal allylation of propiophenone with allyl bromide proceeds in the presence of $VCl_3(THF)_3$/Zn or $VCl_2(TMEDA)_2$/Zn.[157] This deoxygenative transformation is performed by the oxophilicity of low-valent vanadium (Scheme 57). Successive treatment of propiophenone with a Grignard reagent, $VCl_2(TMEDA)_2$, and allylic bromide results in geminal carbon–carbon bond formation at the carbonyl carbon (Scheme 58). Homocoupling, rather than allylation, of the alkoxyvanadium intermediate (**97**) occurs in the presence of a catalytic amount of molecular oxygen.[158] Allylic vanadium and oxovanadium compounds are characterized.[159]

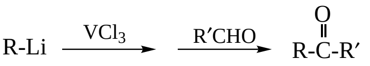

$$\text{R-Li} \xrightarrow{VCl_3} \xrightarrow{R'CHO} \text{R-}\overset{\overset{\displaystyle O}{\|}}{C}\text{-R}'$$

Scheme 56

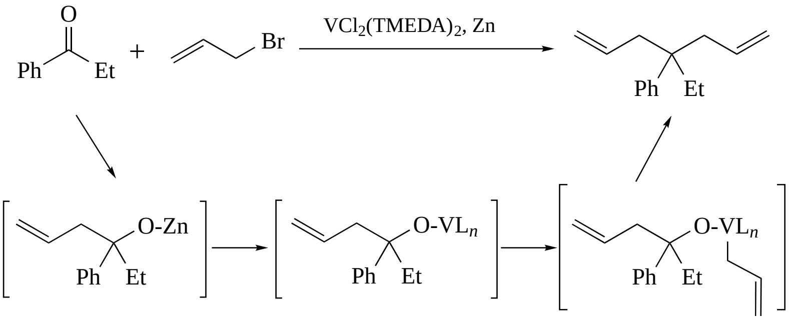
O
Ph
Et
+
Br
$VCl_2(TMEDA)_2$, Zn
Ph
Et
O-Zn
Ph
Et
O-VL$_n$
Ph
Et
O-VL$_n$
Ph
Et

Scheme 57

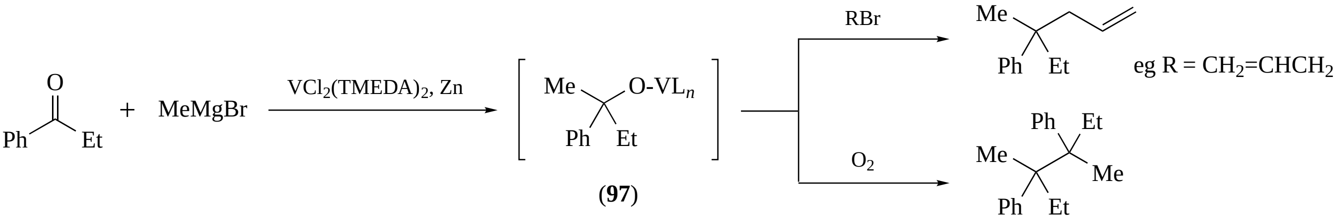

Scheme 58

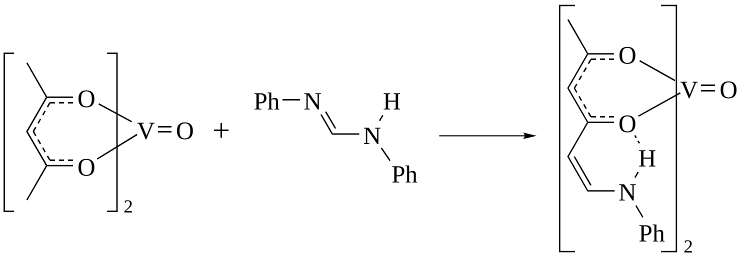

(98) **(99)**

Scheme 59

VO(acac)$_2$ reacts with N,N'-diphenylformamidine (**98**) to give oxobis[6-(phenylamino)hexane-2,4-dionato-O,O′]vanadium(IV) (**99**) via substitution onto methyl group of the acetylacetonate ligand (Scheme 59).[160]

Insertion into a carbon–vanadium bond provides a variety of useful synthetic strategies. For example, the methylvanadium complex (**100**), obtained from CpVCl$_2$(PMe$_3$)$_2$ and MeLi, rapidly inserts carbon monoxide (*see CO Insertion*) to give acetone and CpV(CO)$_2$(PMe$_3$)$_2$ (Scheme 60).[161]

t-Butyl isocyanide likewise inserts into three carbon–vanadium bonds of [V(Mes)$_3$(THF)] to give the tris(η^2-iminoacyl) complex (**101**). When the complex (**101**) is exposed to air, (**101**) is converted to the corresponding amide (**102**), while its exposure to water produces the imine (**103**) through hydrolysis (Scheme 61).[162]

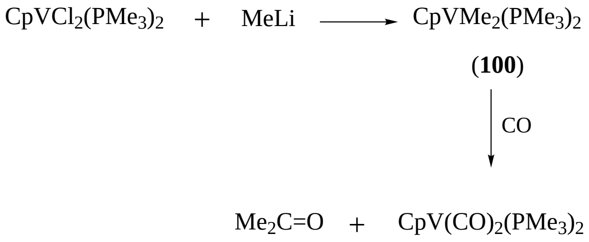

Scheme 60

The reaction of VCl$_3$(THF)$_3$ with (Me$_3$Si)$_2$NLi leads to the dimeric complex (**104**) via C–H σ-bond metathesis (*see σ-Bond Metathesis*) of a trimethylsilyl group (Scheme 62). The dinuclear enolate complex (**105**) is then formed by treatment of (**104**) with carbon monoxide, which inserts into the vanadium–carbon bonds.[163]

Hydrovanadation is an effective route to the organovanadium compounds as shown in Scheme 63.[164–166] Hexacarbonylhydridovanadium, VH(CO)$_6$, is a thermally unstable,

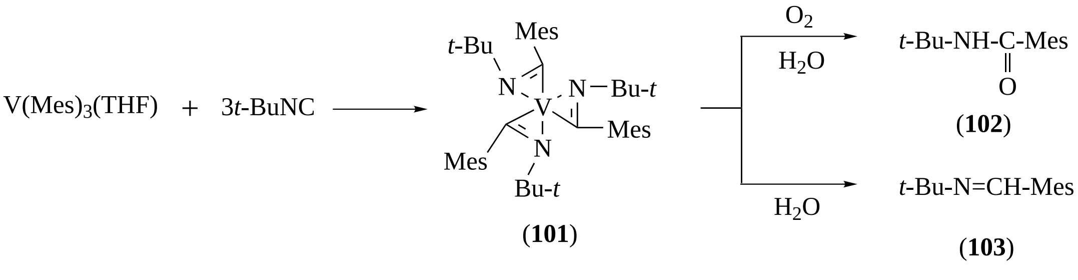

Scheme 61

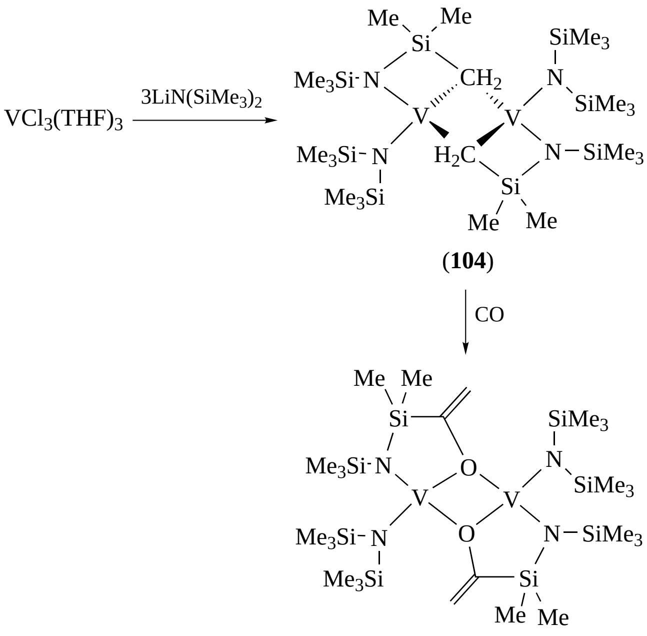

(**104**)

(**105**)

Scheme 62

neutral complex with 18-electron configuration. Ligand exchange with the phosphine ligand provides a more stable complex.[167] Treatment of $V(CO)_6^-$ with silica gel leads to a similar hydridovanadium complex (*see Hydrides*).[168–170]

The air-sensitive Cp-substituted hydridovanadium complex is obtained by hydrogenolysis of the corresponding methyl derivative.[53] The corresponding anionic compound is obtained by reduction of $CpV(CO)_4$ with sodium and protonation with water (Scheme 64).[140] Thus obtained $[CpVH(CO)_3]^-$ (**106**) is a useful one-electron reductant to reduce bromo- and iodoalkanes, bromoalkenes, and arylbromides in THF. Furthermore, acid chlorides are reduced to the aldehydes. A similar reduction with (**106**) is performed by using phase-transfer conditions in the presence of tetrabutylammonium hydrogen sulfate. Nitro compounds and organic halides are reduced under these conditions.

Complexation of the oxo group of $VO(CH_2SiMe_3)_n(OSiPh_3)_{3-n}$ ($n = 0-3$) with $Al(CH_2SiMe_3)_3$ facilitates the insertion of ethylene into the carbon–vanadium bond by reducing the degree of π-donation from the oxo ligand. This type of interaction is important in olefin polymerization.[171] The oxovanadium(V)-catalyzed oxidation of benzyltin compounds occurs under oxygen atmosphere to afford the aromatic aldehydes (ketones) and/or carboxylic acids. Oxidative ligand coupling of organoaluminums, organoborons, organozincs, and their -ate complexes is achieved by treatment with oxovanadium(V) compound, leading to the formation of the C,C-coupled adducts.[172] The reaction is considered to proceed via electron-transfer process or transmetalation (*see Transmetalation*) to generate organovanadium species.

The 1,2,4-azaphosphavanada(V)cyclobutane (**108**), which is obtained by cyclization of the imidovanadium(V) compound (**107**) with phosphaalkyne, reacts with alkyne to give

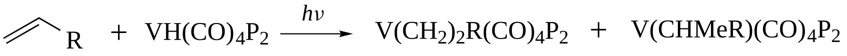

P = tris(3-diethylphophinopropyl)phosphine

Scheme 63

$$CpV(CO)_4 \xrightarrow{\text{Na or Na/Hg}} [Na_2[CpV(CO)_3]^{2-} \xrightarrow[\text{2. }[(Ph_3P)_2N]^+Cl^-]{\text{1. }H_2O} [(Ph_3P)_2N]^+[CpVH(CO)_3]^-$$

(**106**)

Scheme 64

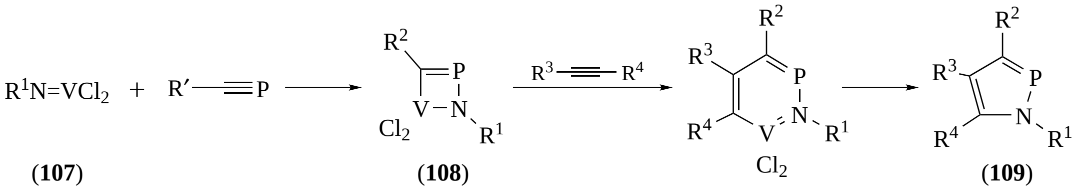

(**107**) (**108**) (**109**)

Scheme 65

the 1*H*-1,2-azaphosphole (**109**) via reductive elimination, (*see Reductive Elimination*), (Scheme 65).[173,174]

8 CONCLUSION

The investigation on the chemistry of organovanadium compounds is rather limited probably because of the difficulty in the characterization and isolation, but their properties and reactivities appear to be of potential as materials, medicine, reagents, and catalysts. Functionalization or design of organic moieties and redox properties will provide a variety of organovanadium compounds, which may open the door of new vanadium chemistry.

9 RELATED ARTICLES

Carbonyl Complexes of the Transition Metals; Mechanisms of Reaction of Organometallic Complexes; Niobium & Tantalum: Organometallic Chemistry.

10 REFERENCES

1. D. Rehder, ‘Encyclopedia of Inorganic Chemistry’, John Wiley & Sons, Chichester, UK, 1994, Vol. 8, p. 4321.
2. T. Imamoto and I. D. Gridnev, in ‘Science of Synthesis, Houben-Weyl Methods of Molecular Transformations’, eds. B. M. Trost and M. Lautens, Thieme, Stuttgart, New York, 2001, Vol. 2, p. 385.
3. N. G. Connelly, in ‘Comprehensive Organometallic Chemistry’, eds. G. Wilkinson, F. G. A. Stones, and E. W. Abel, Pergamon, Oxford, 1982, Vol. 3, p. 647.
4. P. Berno, S. Gambarotta, and D. Richeson, in ‘Comprehensive Organometallic Chemistry II’, eds. E. W. Abel, F. G. A. Stones, G. Wilkinson, D. F. Shriver, and M. I. Bruce, Elsevier, Oxford, 1995, Vol. 4, p. 1.
5. T. Hirao, *Chem. Rev.*, 1997, **97**, 2707.
6. D. C. Gordon, L. Deakin, A. M. Arif, and J. S. Miller, *J. Am. Chem. Soc.*, 2000, **122**, 290.
7. F. Calderazzo, G. Pampaloni, L. Rocchi, and F. Marchetti, *J. Organomet. Chem.*, 1991, **417**, C16.
8. G. Fochi, D. Braga, and P. Sabatino, *Organometallics*, 1988, **7**, 565.
9. F. Calderazzo, G. E. De Benedetto, and G. Pampaloni, *J. Organomet. Chem.*, 1993, **451**, 73.
10. C. Elschenbroich, J. Hurley, B. Metz, W. Massa, and G. Baum, *Organometallics*, 1990, **9**, 889.
11. F. Calderazzo, G. Pampaloni, D. Vitali, and P. F. Zanazzi, *J. Chem. Soc., Dalton Trans.*, 1982, 1993.
12. E. J. Wucherer and E. L. Muetterties, *Organometallics*, 1987, **6**, 1691.
13. E. J. Wucherer and E. L. Muetterties, *Organometallics*, 1987, **6**, 1696.
14. K. Jonas, W. Rüsseler, K. Angermund, and C. Krüger, *Angew. Chem.*, 1986, **98**, 904; *Angew. Chem., Int. Ed. Engl.*, 1986, **25**, 927.
15. C. Elschenbroich, A. Bretschneider-Hurley, J. Hurley, A. Behrendt, W. Massa, S. Wocadlo, and E. Reijerse, *Inorg. Chem.*, 1995, **34**, 743.
16. M. N. Bochkarev, I. L. Fedushkin, H. Schumann, and J. Loebel, *J. Organomet. Chem.*, 1991, **410**, 321.
17. A. W. Duff, K. Jonas, R. Goddard, H.-J. Kraus, and C. Krüger, *J. Am. Chem. Soc.*, 1983, **105**, 5479.
18. K. Jonas, W. Rüsseler, K. Angermund, and C. Krüger, *Angew. Chem.*, 1986, **98**, 904.
19. G. Herberich and H. Ohst, *Adv. Organomet. Chem.*, 1986, **25**, 199.
20. J. Müller and B. Mertshenk, *J. Organomet. Chem.*, 1972, **34**, C41.
21. J. Müller and B. Mertshenk, *Chem. Ber.*, 1972, **105**, 3346.
22. C. Elschenbroich, J. Plackmeyer, K. Harms, O. Burghaus, and J. Pebler, *Organometallics*, 2003, **22**, 3367.
23. D. Gourier, E. Samuel, B. Bachmann, F. Hahn, and J. Hech, *Inorg. Chem.*, 1992, **31**, 86.
24. B. Bachmann and J. Heck, *Organometallics*, 1991, **10**, 1373.
25. B. Bachmann, J. Heck, G. Meyer, J. Pebler, and T. Schleid, *Inorg. Chem.*, 1992, **31**, 607.
26. R. B. King, ‘Organometallic Syntheses’, Academic, New York, 1965, Vol. 1, p. 64.
27. F. H. Köhler and W. Prössdorf, *Z. Naturforsch B*, 1977, **32B**, 1026.
28. F. H. Köhler, K. H. Doll, and W. Prössdorf, *J. Organomet. Chem.*, 1982, **224**, 341.
29. S. Gambarotta, C. Floriani, A. Chiesi-Villa, and C. Guastini, *Inorg. Chem.*, 1984, **23**, 1739.
30. M. P. Castellani, S. J. Geib, A. L. Rheingold, and W. C. Trogler, *Organometallics*, 1987, **6**, 1703.
31. F. H. Köhler and W. A. Geike, *J. Organomet. Chem.*, 1987, **328**, 35.
32. R. M. Kowaleski, F. Basolo, W. C. Trogler, R. W. Gedridge, T. D. Newbound, and R. D. Ernst, *J. Am. Chem. Soc.*, 1987, **109**, 4860.
33. F. H. Köhler, ‘Organometallic Syntheses’, Academic Press, New York, 1988, Vol. 4, p. 15.
34. P. Hudeczek and F. H. Köhler, *Organometallics*, 1992, **11**, 1773.
35. B. Dorer, J. Diebold, O. Weyand, and H.-B. Brintzinger, *J. Organomet. Chem.*, 1992, **427**, 245.
36. J. M. Birmingham, A. K. Fischer, and G. Wilkinson, *Naturwissenscaften*, 1955, **42**, 96.

37. C. E. Holloway and M. Melnik, *J. Organomet. Chem.*, 1986, **304**, 41.
38. J. D. Holloway, W. L. Bowden, and W. E. Geiger Jr, *J. Am. Chem. Soc.*, 1977, **99**, 7089.
39. J. S. Overby, K. C. Jayaratne, N. J. Schoell, and T. P. Hanusa, *Organometallics*, 1999, **18**, 1663.
40. J. C. Smart and B. L. Pinsky, *J. Am. Chem. Soc.*, 1980, **102**, 1009.
41. J. C. Smart and B. L. Pinsky, *J. Am. Chem. Soc.*, 1980, **102**, 3663.
42. P. Hudeczek and F. H. Köhler, *Organometallics*, 1992, **11**, 1773.
43. J. A. Belot, R. D. McCullough, A. L. Rheingold, and G. P. A. Yap, *Organometallics*, 1996, **15**, 5062.
44. F. H. Köhler and W. A. Geike, *J. Organomet. Chem.*, 1987, **328**, 35.
45. M. Enders, K. Köhler, W. Frosch, H. Pritzkow, and H. Lang, *J. Organomet. Chem.*, 1997, **538**, 163.
46. S. Bradley, P. C. McGowan, K. A. Oughton, M. Thornton-Pett, and M. E. Walsh, *Chem. Commun.*, 1999, 77.
47. S. C. Jones and D. O'Hare, *Chem. Commun.*, 2003, 2208.
48. S. Gambarotta, C. Floriani, A. Chiesi-Villa, and C. Guastini, *Inorg. Chem.*, 1984, **24**, 1739.
49. F. Bottomley, C. P. Magill, and P. S. White, *J. Am. Chem. Soc.*, 1989, **111**, 3070.
50. M. D. Wasczcak, Y. Wang, A. Garg, W. E. Geiger, S. O. Kang, P. J. Carroll, and L. G. Sneddon, *J. Am. Chem. Soc*, 2001, **123**, 2783.
51. F. Calderazzo, F. Marchetti, G. Pampaloni, and V. Passarelli, *J. Chem. Soc., Dalton Trans.*, 1999, 4389.
52. L. E. Manzer, *Inorg. Synth.*, 1982, **21**, 84.
53. C. J. Curtis, J. C. Smart, and J. L. Robbins, *Organometallics*, 1985, **4**, 1283.
54. G. Wilkinson and J. M. Birmingham, *J. Am. Chem. Soc.*, 1954, **76**, 4281.
55. B. Dorer, M.-H. Prosenc, U. Riff, and H.-H. Brintzinger, *Collect. Czech. Chem. Commun.*, 1997, **62**, 265.
56. N. Klouras, *Z. Naturforsch.*, 1991, **46B**, 650.
57. P. Ghosh, A. T. Kotchevar, D. D. DuMez, S. Ghosh, J. Peiterson, and F. M. Uckun, *Inorg. Chem.*, 1999, **38**, 3730.
58. S. L. J. Michel, D. P. Goldberg, C. Stern, A. G. M. Barrett, and B. M. Hoffmann, *J. Am. Chem. Soc.*, 2001, **123**, 4741.
59. F. Calderazzo, I. Ferri, and G. Pampaloni, *Organometallics*, 1999, **18**, 2452.
60. F. Baumann, M. Heilmann, W. Matheis, A. Schulz, W. Kaim, and J. Jordanov, *Inorg. Chim. Acta*, 1996, **251**, 239.
61. P. Ghosh, O. J. D'Cruz, D. D. DuMez, J. Peitersen, and F. M. Uckun, *J. Inorg. Biochem.*, 1999, **75**, 135.
62. P. Ghosh, S. Ghosh, O. J. D'Cruz, and F. M. Uckun, *J. Inorg. Biochem.*, 1998, **72**, 89.
63. P. Ghosh, S. Ghosh, C. Navara, R. K. Narla, and F. M. Uckun, *J. Inorg. Biochem.*, 2001, **84**, 241.
64. M. Hoch and D. Rehder, *Chem. Ber.*, 1988, **121**, 1541.
65. W. A. Herrmann and W. Kalcher, *Chem. Ber.*, 1982, **115**, 3886.
66. M. Hoch, A. Duch, and D. Rehder, *Inorg. Chem.*, 1986, **25**, 2907.
67. M. Herberhold, W. Kremnitz, M. Kuhnlein, M. L. Ziegler, and K. Brunn, *Z. Naturforsch.*, 1987, **42B**, 1520.
68. J. Nieman, J. H. Teuben, J. C. Huffman, and K. G. Caulton, *J. Organomet. Chem*, 1983, **255**, 193.
69. K. Jonas, W. Rüsseler, C. Krüger, and E. Raabe, *Angew. Chem.*, 1986, **98**, 902; *Angew. Chem., Int. Ed. Engl.*, 1986, **25**, 925.
70. R. B. King and C. D. Hoff, *J. Organomet. Chem.*, 1982, **225**, 245.
71. E. O. Fischer, S. Vigoureux, and P. Kuzel, *Chem. Ber.*, 1960, **93**, 701.
72. D. B. Morse, D. N. Hendrickson, T. B. Rauchfuss, and S. R. Wilson, *Organometallics*, 1988, **7**, 496.
73. M. S. Hammer and L. Messerle, *Inorg. Chem.*, 1990, **29**, 1780.
74. D. B. Morse, T. B. Rauchfuss, and S. R. Wilson, *Inorg. Chem.*, 1991, **30**, 775.
75. W. A. Herrmann, G. Weichselbaumer, and H. J. Kneuper, *J. Organomet. Chem.*, 1987, **319**, C21.
76. D. W. Stephan, *Inorg. Chem.*, 1992, **31**, 4218.
77. J. Darkwa, J. R. Lockemeyer, P. D. W. Boyd, T. B. Rauchfuss, and A. L. Rheingold, *J. Am. Chem. Soc.*, 1988, **110**, 141.
78. D. Rehder and D. Wenke, *J. Organomet. Chem.*, 1988, **348**, 205.
79. D. Wenke and D. Rehder, *J. Organomet. Chem.*, 1984, **273**, C43.
80. C. Ting, M. S. Hammer, N. C. Baenziger, and L. Messerle, *Organometallics*, 1997, **16**, 1816.
81. C. D. Abernethy, F. Bottomley, A. Decken, and T. S. Cameron, *Organometallics*, 1996, **15**, 1758.
82. B. Hessen, T. H. Lemmen, H. J. G. Luttikhedde, J. H. Teuben, J. L. Petersen, J. C. Huffman, S. Janger, and K. G. Caulton, *Organometallics*, 1987, **6**, 2354.
83. U. Franke and E. Weiss, *J. Organomet. Chem.*, 1979, **168**, 311.
84. B. Hessen, A. Meetsma, F. van Bolhujs, J. H. Teuben, G. Helgesson, and S. Jagner, *Organometallics*, 1990, **9**, 1925.
85. J. de With and A. D. Horton, *Organometallics*, 1993, **12**, 1493.
86. S. Gambarotta, C. Floriani, A. Chiesi-Villa, and C. Guastini, *Organometallics*, 1986, **5**, 2425.
87. M. Schneider and E. Weiss, *J. Organomet. Chem.*, 1976, **121**, 189.
88. U. Francke and E. Weiss, *J. Organomet. Chem.*, 1979, **165**, 329.

89. J. Schiemann and E. Weiss, *J. Organomet. Chem.*, 1983, **255**, 179.
90. A. M. Carrier, J. G. Davidson, K. E. Barefield, and D. G. Van Derveer, *Organometallics*, 1987, **6**, 454.
91. W.-J. Lin, G.-H. Lee, S.-M. Peng, and R.-S. Liu, *Organometallics*, 1991, **10**, 2519.
92. J. M. Galante, J. W. Bruno, and P. N. Hazin, *Organometallics*, 1988, **7**, 1066.
93. G. Fachinetti, C. Floriani, A. Chiesi-Villa, and C. Guastini, *Inorg. Chem.*, 1979, **18**, 2282.
94. R. Tsumura and N. Hagihara, *Bull. Chem. Soc. Jpn.*, 1965, **38**, 861.
95. H. J. de Liede Maijer and F. Jellinek, *Inorg. Chim. Acta*, 1970, **4**, 651.
96. J. L. Petersen and L. Griffith, *Inorg. Chem.*, 1980, **19**, 1852.
97. N. Hessen and J. H. Teuben, *J. Organomet. Chem.*, 1989, **367**, C18.
98. D. F. Foust and M. D. Rausch, *J. Organomet. Chem.*, 1982, **239**, 321.
99. L. N. Lewis and K. G. Caulton, *J. Organomet. Chem.*, 1983, **252**, 57.
100. R. Choukroun, B. Donnadieu, I. Malfant, S. Haubrich, R. Frantz, C. Guerin, and B. Henner, *Chem. Commun.*, 1997, 2315.
101. R. Choukroun, C. Lorber, B. Donnadieu, B. Henner, R. Frantz, and C. Guerin, *Chem. Commun.*, 1999, 1099.
102. R. Choukroun, B. Donnadieu, C. Lorber, P.-M. Pellny, W. Baumann, and U. Rosenthal, *Chem. Eur. J.*, 2000, **6**, 4505.
103. R. Choukroun, Y. Miquel, B. Donnadieu, A. Igau, C. Blandy, and J. P. Majoral, *Organometallics*, 1999, **18**, 1795.
104. R. Choukroun, B. Donnadieu, J.-S. Zhao, P. Cassoux, C. Lepetit, and B. Silvi, *Organometallics*, 2000, **19**, 1901.
105. M. Morán, J. J. Santos-Garcia, J. R. Maságuer, and V. Fernandez, *J. Organomet. Chem.*, 1985, **295**, 327.
106. G. Fachinetti, S. Del Nero, and C. Floriani, *J. Chem. Soc., Dalton Trans.*, 1976, 1046.
107. N. Hessen, A. Meetsma, and J. H. Teuben, *J. Am. Chem. Soc.*, 1988, **110**, 4860.
108. J. Martin, C. Moise, and J. Tirouflet, *C. R. Hebd. Séances Acad. Sci. Ser.*, 1981, **2**, 292.
109. A. J. Hartshorn, M. F. Lappert, and K. Turner, *J. Chem. Soc., Dalton Trans.*, 1978, 348.
110. G. Erker, R. Lecht, R. Schlund, K. Angermund, and C. Krüger, *Angew. Chem.*, 1987, **99**, 708; *Angew. Chem., Int. Ed. Engl.*, 1987, **26**, 666.
111. G. Erker, R. Pfaff, C. Krüger, and S. Werner, *Organometallics*, 1991, **10**, 3559.
112. M. Berlekamp, G. Erker, and J. L. Petersen, *J. Organomet. Chem.*, 1993, **458**, 97.
113. B. Hessen, A. Meetsma, and J. H. Teuben, *J. Am. Chem. Soc.*, 1989, **111**, 5977.
114. B. Hessen, J.-K. F. Buijink, A. Meetsma, J. H. Teuben, G. Helgesson, M. Hakansson, S. Jagnen, and A. L. Spek, *Organometallics*, 1993, **12**, 2268.
115. J.-K. F. Buijink, J. H. Teuben, H. Kooijman, and A. L. Spek, *Organometallics*, 1994, **13**, 2922.
116. J. D. Protasiewicz and S. Lippard, *J. Am. Chem. Soc.*, 1991, **113**, 6564.
117. N. J. Coville, G. W. Harris, and D. Rehder, *J. Organomet. Chem.*, 1985, **293**, 365.
118. J. E. Ellis and K. L. Fjare, *J. Organomet. Chem.*, 1981, **214**, C33.
119. J. E. Ellis and K. L. Frare, *Organometallics*, 1982, **1**, 898.
120. M. Y. Darenbourg and J. M. Hanckel, *J. Organomet. Chem.*, 1981, **217**, C9.
121. M. Y. Darenbourg and J. M. Hanckel, *Organometallics*, 1982, **1**, 82.
122. L. D. Silverman, J. C. Dewan, C. M. Giandomenico, and S. J. Lippard, *Inorg. Chem.*, 1980, **19**, 3379.
123. L. D. Silverman, P. W. R. Corfield, and S. J. Lippard, *Inorg. Chem.*, 1981, **20**, 3106.
124. G. A. Razuvaev, V. N. Latyaeva, L. I. Vyshinskaya, and V. V. Drobotenko, *J. Organomet. Chem.*, 1981, **208**, 169.
125. S. Gambarotta, C. Floriani, A. Chiesi-Villa, and C. Guastini, *J. Chem. Soc., Chem. Commun.*, 1984, 886.
126. J. Ruiz, M. Vivanco, C. Floriani, A. Chiesi-Villa, and C. Guastini, *J. Chem. Soc., Chem. Commun.*, 1991, 762.
127. B. K. Bower and H. G. Tennent, *J. Am. Chem. Soc.*, 1972, **94**, 2512.
128. W. Mowat, A. Shortland, G. Yagupsky, N. J. Hill, M. Yagupsky, and G. Willkinson, *J. Chem. Soc., Dalton Trans.*, 1972, 533.
129. W. Seidel and G. Kreisel, *Z. Chem.*, 1976, **16**, 115.
130. T. Glowiak, G. Grobelny, B. Jezowka-Trzebiatowska, G. Kreisel, W. Seidel, and E. Uhlig, *J. Organomet. Chem.*, 1978, **155**, 39.
131. J.-K. F. Buijink, A. Meetsma, and J. H. Teuben, *Organometallics*, 1993, **12**, 2004.
132. G. S. Girolami, G. Wilkinson, A. M. R. Galas, M. Thornton-Pett, and M. B. Hursthouse, *J. Chem. Soc., Dalton Trans.*, 1985, 1339.
133. J. J. H. Edema, W. Stauthamer, F. van Bolhuis, S. Gambarotta, W. J. J. Smeets, and A. L. Spek, *Inorg. Chem.*, 1990, **29**, 1302.
134. V. C. Gibson, C. Redshaw, L. Sequeira, K. B. Dillon, W. Clegg, and M. R. J. Elsegood, *Chem. Commun.*, 1996, 2151.
135. F. H. Köhler, W. Prössdorf, U. Schubert, and D. Neugebauer, *Angew. Chem.*, 1978, **90**, 912; *Angew. Chem., Int. Ed. Engl.*, 1978, **17**, 850.
136. W. J. Evans, I. Bloom, and R. J. Doedens, *J. Organomet. Chem.*, 1984, **265**, 249.

137. J. K. F. Buijink, K. R. Kloetstra, A. Meetsma, J. H. Teuben, W. J. J. Smeets, and A. L. Spek, *Organometallics*, 1996, **15**, 2523.

138. P. J. Alonso, J. Forniés, M. A. García-Monforte, A. Martín, and B. Menjón, *Chem. Commun.*, 2001, 2138.

139. R. Sustmann and G. Kopp, *J. Organomet. Chem.*, 1988, **347**, 325.

140. R. J. Kinney, W. D. Jones, and R. C. Bergman, *J. Am. Chem. Soc.*, 1978, **100**, 7902.

141. E. Solari, S. De Angelis, C. Floriani, A. Chiesi-Villa, and C. Rizzoli, *Inorg. Chem.*, 1992, **31**, 96.

142. M. M. Olmstaed, P. P. Power, and S. C. Shoner, *Organometallics*, 1988, **7**, 1380.

143. C. J. Curtis, J. C. Smart, and J. L. Robbins, *Organometallics*, 1985, **4**, 1283.

144. L. Wang, P. Y. Zhang, L. F. Feng, B. Ji, Y. L. Yuan, J. Pan, C. Y. Ye, S. Jiang, and L. X. Feng, *J. Appl. Poly. Sci.*, 2001, **79**, 1188.

145. J. Nieman, J. W. Pattiasima, and T. H. Teuben, *J. Organomet. Chem.*, 1984, **262**, 157.

146. J. E. Lyons, *Tetrahedron Lett.*, 1974, 2737.

147. T. Hirao, T. Hasegawa, Y. Muguruma, and I. Ikeda, *J. Org. Chem.*, 1996, **61**, 366.

148. T. Hirao, M. Asahara, Y. Muguruma, and A. Ogawa, *J. Org. Chem.*, 1998, **63**, 2812.

149. T. Hirao, B. Hatano, M. Asahara, Y. Muguruma, and A. Ogawa, *Tetrahedron Lett.*, 1998, **39**, 5247.

150. B. Hatano, A. Ogawa, and T. Hirao, *J. Org. Chem.*, 1998, **63**, 9421.

151. T. Hirao, B. Hatano, Y. Imamoto, and A. Ogawa, *J. Org. Chem.*, 1999, **64**, 7665.

152. C. Aitken, J.-P. Barry, F. Gauvin, J. F. Herold, A. Malek, and D. Rousseau, *Organometallics*, 1989, **8**, 1732.

153. R. P. A. Sneeden and H. H. Zeiss, *J. Organomet. Chem.*, 1970, **22**, 713.

154. T. Hirao, D. Misu, and T. Agawa, *Tetrahedron Lett.*, 1986, **27**, 929.

155. T. Hirao, D. Misu, and T. Agawa, *J. Am. Chem. Soc.*, 1985, **107**, 7179.

156. T. Hirao, D. Misu, and T. Agawa, *Tetrahedron Lett.*, 1986, **27**, 933.

157. Y. Kataoka, I. Makihira, H. Akiyama, and K. Tani, *Tetrahedron Lett.*, 1995, **36**, 6495.

158. Y. Kataoka, H. Akiyama, I. Makihira, and K. Tani, *J. Org. Chem.*, 1996, **61**, 6094.

159. T. Kauffmann, W. Bonrath, C. Beirich, W. Li, C. Pahde, S. Raedeker, B. Wichmann, and D. Wingbermühle, *Chem. Ber.*, 1993, **126**, 2093.

160. D. Arnold, F. A. Cotton, J. H. Matonic, and C. A. Murillo, *J. Chem. Soc., Chem. Commun.*, 1996, 2113.

161. B. Hessen, J. H. Teuben, T. H. Lemmen, J. C. Huffman, and K. G. Caulton, *Organometallics*, 1985, **4**, 946.

162. M. Vivanco, J. Ruiz, C. Floriani, A. Chiesi-Villa, and C. Guastini, *Organometallics*, 1990, **9**, 2185.

163. P. Berno, M. Minhas, S. Hao, and S. Gambarotta, *Organometallics*, 1994, **13**, 1052.

164. D. Rehder, F. Süßmilch, W. Priebsch, and M. Fornalczyk, *J. Organomet. Chem.*, 1991, **411**, 357.

165. F. Süßmilch, F. Olbrich, H. Gailus, D. Rodewald, and D. Rehder, *J. Organomet. Chem.*, 1994, **472**, 119.

166. F. Süßmilch, F. Olbrich, and D. Rehder, *J. Organomet. Chem.*, 1994, **481**, 125.

167. W. Hieber, E. Winter, and E. Schubert, *Chem. Ber.*, 1961, **94**, 2572.

168. U. Puttfarcken and D. Rehder, *J. Organomet. Chem.*, 1978, **157**, 321.

169. U. Puttfarcken and D. Rehder, *J. Organomet. Chem.*, 1980, **185**, 219.

170. F. Süßmilch, W. Glockner, W. Rehder, and D. Rehder, *J. Organomet. Chem*, 1990, **388**, 95.

171. F. J. Feher and R. L. Blanski, *Organometallics*, 1993, **12**, 958.

172. T. Hirao, *Coord. Chem. Rev.*, 2003, **237**, 271.

173. C. Peters, F. Tabellion, M. Schroder, U. Bergstraßer, F. Preuss, and M. Regitz, *Synthesis*, 2000, 417.

174. F. Tabellion, C. Peters, U. Fischbeck, M. Regitz, and F. Preuss, *Chem. Eur. J.*, 2000, **6**, 4558.

Acknowledgment

I thank Prof. T. Imamoto at Chiba University for his valuable information.

Water & O-donor Ligands

Mark I. Ogden[1] **& Paul D. Beer**[2]

[1] *Curtin University of Technology, Perth, Australia*
[2] *University of Oxford, Oxford, UK*

1 Introduction 1
2 Water, Hydroxide, and Oxide 1
3 Alkoxides and Aryloxides 3
4 β-Diketones and Related Ligands 5
5 Oxoanions 7
6 Carboxylate and Related Species 9
7 Macrocyclic O-donor Ligands 11
8 Miscellaneous η^1O-donor Ligands 16
9 Related Articles 17
10 References 17

Abbreviations

bzacH = 1-phenyl-1,3-butanedione; dikeH = β-diketone; dpmH = 2,2,6,6-tetramethylheptanedione (dipivaloylmethane); HIm = imidazole; Hpz = pyrazole; pico = 2-picolylamine.

1 INTRODUCTION

There are a vast number of O-donor ligands, ranging from simple naturally occurring ligands such as water, which have been studied for many decades, to artificial systems such as the crown ethers and calixarenes, which are a relatively recent development. Exhaustive coverage of all these ligands is not possible here, and hence the discussion is divided into categories of the most widely studied systems. The aim of the article is to demonstrate the nature of the complexes formed by the ligands and some of the chemistry involved in obtaining them.

2 WATER, HYDROXIDE, AND OXIDE

2.1 Introduction

A large proportion of inorganic chemistry takes place in aqueous solution, and hence the nature of the species formed when a metal ion is dissolved in water is of great importance, and has been the subject of study for many years. This leads to consideration of water, hydroxide, and oxide as ligands. These are discussed individually below, but it is appropriate to briefly consider the relationship between the three species.

Deprotonation of the parent aqua ions, $[M(OH_2)_x]^{n+}$, gives rise to hydroxo and then oxo complexes, and consequently the nature of the species present in solution is strongly dependant on pH. The acidity of the aqua ions varies enormously with the metal ion, with an approximate correlation with electrostatic considerations. Thus, higher charge density of the metal ion is often associated with greater acidity of the aqua ion. Such trends are not reliable, however, since properties such as high oxidizing power and ‘softness’ (*see* ***Hard & Soft Acids and Bases***) are generally associated with strongly acidic aqua ions. It follows that hydroxo and oxo ligands tend to be associated with highly charged metal ions, while only oxo ligands, which are very difficult to oxidize, are found with the highest oxidation states, in species such as MnO_4^- and CrO_4^{2-}. Exceptions to this can be found in the larger actinide cations, where water molecules are found coordinated to metal ions in oxidation states of 5+ and 6+, although the complexes also include oxo ligands; one example is the complex ion $[UO_2(OH_2)_5]^{2+}$. Various combinations of aqua, hydroxo, and oxo ligands can be found, including species containing all three (most commonly with the vanadyl (*see* ***Vanadium: Inorganic & Coordination Chemistry***), and uranyl (*see* ***Actinides: Inorganic & Coordination Chemistry***) cations).

Finally, it is important to note that, while H_2O is a relatively poor bridging ligand, both hydroxo and oxo ligands readily act as bridges between metal atoms, giving rise to polynuclear species, which are not discussed in detail here (*see* ***Polyoxometalates***).

2.2 Aqua Complexes

Discrete $[M(OH_2)_x]^{n+}$ species are found in the hydrates of many metal salts where the anion is a poor ligand, such as ClO_4^-, PF_6^-, BF_4^-, and so on. In many cases, particularly for the first-row transition metals but also other cations such as Mg^{2+}, Al^{3+}, and In^{3+}, hexaaqua ions are formed with an octahedral arrangement of water O atoms about the metal atom. The larger lanthanide and actinide ions generally form octa- or nonaaqua ions, although octahedral hexaaqua ions have been found in $Ln(ClO_4)_3{\cdot}6H_2O$.**[1]** Water is a relatively poor bridging ligand, although a search of the Cambridge Structural Database reveals ~500 examples including main group and transition metal complexes.**[2]**

The nature of ions in aqueous solution has been studied using a wide variety of techniques, including X ray and neutron diffraction, and quasielastic neutron scattering, NMR, IR, and UV spectroscopies. The ions are generally considered to have primary and secondary hydration spheres, although there is relatively little quantitative information available concerning the second sphere in solution.**[3]** The rate of exchange of the

H_2O molecules in the hydration spheres with the bulk H_2O solvent varies by many orders of magnitude depending on the metal ion.[3] This, combined with the use of many different experimental techniques, has resulted in discrepancies in the literature, particularly for metal ions with a weakly bound, rapidly exchanging hydration sphere. The Na^+ cation, for example, has had quoted values for the primary solvation number ranging from 2 to 13, although a value close to six is generally accepted.[4]

Metals that form relatively stable aqua ions in solution have generally been well characterized. The hydration numbers of the transition metals, for example, have commonly been found to be six, consistent with the results of solid-state studies of crystalline hydrates. Exceptions include Ag^+, which has a hydration number of four, and Cu^{2+}, which has been found to have four short M–O interactions and two longer ones, consistent with a Jahn–Teller distortion (*see Jahn–Teller Effect*) of the complex. The hydration numbers of the lanthanide ions in solution have been the subject of many investigations and some controversy; recent results suggest a decrease from nine to eight across the series from La^{3+} to Lu^{3+}.[4]

2.3 Hydroxo Complexes

The hydroxide ion assumes bridging coordination modes more often than water. Double μ_2-hydroxide bridges (**2**) are the most common, although single hydroxide bridges (**1**) have been known for some time in complexes such as $[(H_3N)_5Co(\mu\text{-}OH)Co(NH_3)_5]^{5+}$. Both double and single hydroxide bridges may be supported by another bridging ligand. Triple hydroxide bridges are relatively rare and quadruple hydroxide bridges (**3**) have only been observed to date linking zirconium porphyrin moieties.[5] μ_3-Hydroxide (**4**) is also relatively rare, occurring most frequently in cubane type structures (**5**), in species such as $[Cr_4(OH)_4]^{8+}$ and $[Ni_4(OH)_4]^{4+}$.[6]

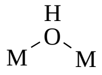

(**1**)

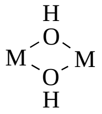

(**2**)

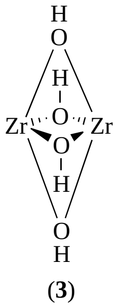

(**3**)

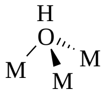

(**4**)

Hydrated hydroxide metal complexes can also form a hydrogen-bonded $H_3O_2^-$ bridging moiety, which has been structurally characterized in single bridged[7] and double bridged species; $[(pico)_2Cr(H_3O_2)_2Cr(pico)_2]$ (**6**),[8] is an example of the latter. These bridges have been formulated as discrete $H_3O_2^-$ and alternatively as H_2O/OH^- bridges; theoretical studies suggest the bridging H atom should be increasingly asymmetrically positioned as the O···O distance increases.[9]

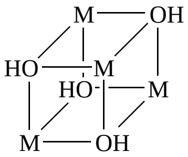

(**5**)

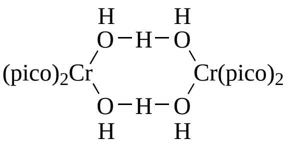

(**6**)

2.4 Oxo Complexes

The multiply bonded oxo group, found in transition metal complexes such as UO_2^{2+}, MnO_4^-, and OsO_4, is usually terminal, although very asymmetric μ_2-oxide bridges have been observed, suggesting an $M=O \rightarrow M$ bridge.

Single, double, and triple μ_2-oxo bridges are known, although single bridges are the most common. The M–O–M angle about a single oxo bridge can vary from 140 to 180°, depending mainly on steric and electronic factors. Double and triple bridges are most commonly found in ***Polyoxometalates***.

μ_3-Oxo bridges are well known and can form planar or pyramidal M_3–O units, usually with equal M–O distances. Molybdenum(IV) in aqueous solutions forms $Mo_3O_4^{4+}$ (**7**), for example, which has three μ_2-oxo bridges and a pyramidal μ_3-oxo bridge.[10] Trimetallic, triangular metal carboxylates contain a triangular μ_3-oxo ligand and are known for a number of transition metals (see Section 6.1). μ_4-Oxide is less common, but is found in a number of carboxylates where the oxo ligand is surrounded by a tetrahedral arrangement of M atoms, which are also linked by the carboxylate ligands (**8**). The $Zn_4O(carboxylate)_6$ unit, for example, has been used as a building block in constructing impressive metal-organic frameworks with highly porous structures.[11] (*See also* ***Oxides: Solid-state Chemistry***).

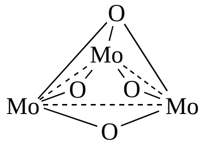

(**7**)

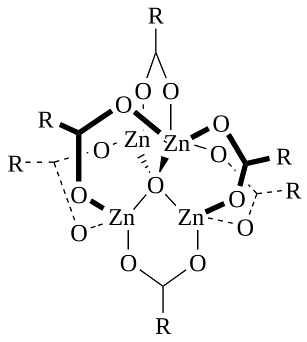

(**8**)

3 ALKOXIDES AND ARYLOXIDES

Metal alkoxides and aryloxides, of the general formula $M(OR)_x$, can be considered as derived from the alcohol ROH by replacement of the hydroxylic hydrogen atom by the metal.[12] These complexes have been known for many years; $Ti(OEt_4)$ was prepared in 1924 by Bischoff and Adkins,[13] and the synthesis was attempted as early as 1875 by Demarçay[14] although pure product was apparently not obtained. Potential technological applications have resulted in increased activity in this area in recent years (*see* ***Sol–Gel Synthesis of Solids***).[15,16]

3.1 Structure and Bonding

Although usually considered to be a one-electron ligand, alkoxide and aryloxide groups can assume a number of modes of coordination (Figure 1), with the M–O distances decreasing in the order M–OR (μ_3) > (μ_2) > terminal. Shorter terminal M–O distances are found to be associated with larger M–O–C angles; for example, the Zr–O–C angle in $[ZrCl_4(OMe)(MeOH)]$ is 171.4°, compatible with a Zr–O triple bond, with the alkoxide ligand acting as a three-electron donor. Shorter M–O bonds and larger M–O–C angles appear to be associated with increasing electron deficiency of the metal.[17]

Most alkoxides with simple R groups are polymeric or oligomeric to an extent that satisfies the coordination of the metal.[18] Some common types of small oligomeric structures are shown in Figure 2. Although a large body of data has been collected on these systems, it is still difficult to predict which structure will be formed by a certain combination of M and RO. Factors that appear to influence the structure include the size and oxidation state of the metal atom, the steric bulk of the alkyl or aryl group, and the d^n configuration (for the transition elements). The introduction of very bulky alkyl or aryl groups favors the formation of lower oligomers or monomeric species, often with unusually low coordination numbers. A decrease in the extent of oligomerization usually results in an increase in the volatility of the metal alkoxide.

3.2 Synthesis

In some cases, metal alkoxides and aryloxides can be obtained simply by direct reaction of the appropriate alcohol or phenol with the bulk metal (equation 1). The method is limited by the low pK_a of alcohols and most phenols to the more electropositive elements. Group 1 metals react readily in this way, while group 2, 3, and the lanthanide metals require the presence of a catalyst, such as iodine or a mercury(II) salt, for the reaction to take place. Electrochemical synthesis using a sacrificial anode of the required metal is applicable to a greater range of metals, but this method has not been widely exploited.

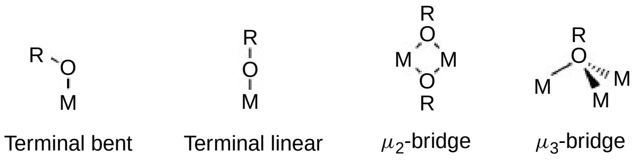

Terminal bent   Terminal linear μ_2-bridge μ_3-bridge

Figure 1 Coordination modes of alkoxide and aryloxide ligands

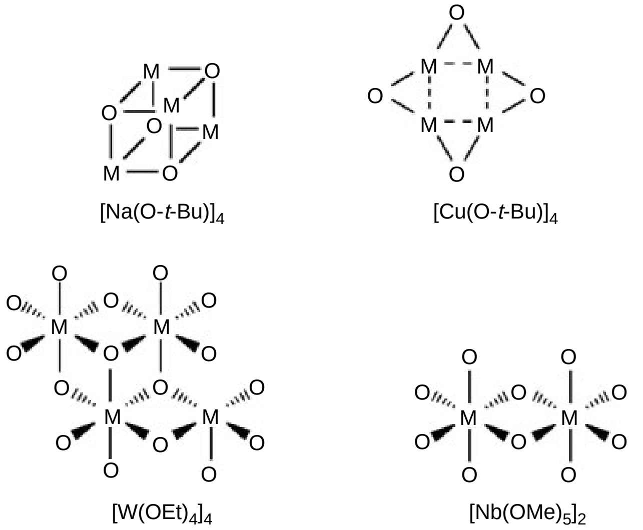

$[Na(O\text{-}t\text{-}Bu)]_4$ $[Cu(O\text{-}t\text{-}Bu)]_4$

$[W(OEt)_4]_4$ $[Nb(OMe)_5]_2$

Figure 2 Some structural types for small oligomeric metal alkoxides

$$M + nROH \longrightarrow M(OR)_n + \frac{n}{2}H_2 \tag{1}$$

A more common approach to the synthesis of metal alkoxides and aryloxides is to make use of a metal halide. This method is particularly effective for the less electropositive elements such as B, Si, and P, where the reaction readily goes to completion (equation 2). Analogous reactions of the halide derivatives of more electropositive elements, such as the transition metals, often give products containing both halide and alkoxide ligands, as shown in equation (3). The acidity of the alcohol also influences the course of the reaction; phenols, for example, are more acidic than alcohols and are more likely to effect complete substitution of the halide ligands (compare equations 3 and 4). The problem of incomplete substitution can be overcome by carrying out the reaction of the metal halide and alcohol in the presence of a base. Anhydrous ammonia is often employed as the proton acceptor, with the precipitation of ammonium chloride forcing the reaction to completion (equation 5). This is probably the most widely used method of synthesizing homoleptic alkoxides and aryloxides.

$$SiCl_4 + 4EtOH \longrightarrow Si(OEt)_4 + 4HCl \tag{2}$$

$$WCl_6 + 3EtOH \longrightarrow WCl_3(OEt)_3 + 3HCl \tag{3}$$

$$WCl_6 + 6PhOH \longrightarrow W(OPh)_6 + 6HCl \tag{4}$$

$$TiCl_4 + 4ROH + 4RNH_3 \longrightarrow Ti(OR)_4 + 4NH_4Cl \tag{5}$$

The reaction of metal halides with an alkoxide or aryloxide (most commonly an alkali metal alkoxide), can result in metathetic exchange to give the required complex (equation 6). Such reactions can also result in the formation of heterometallic species (such as $NaZr_2(OR)_4$); this can be a problem when homometallic alkoxides are desired, but it is an important route to heterometallic alkoxides and aryloxides. The nature of the product can be influenced by the alkali metal, the alkoxide ligand, and the relative amounts of the reactants.[19]

$$CuCl_2 + 2LiOR \longrightarrow Cu(OR)_2 + 2LiCl \tag{6}$$

Metal diamides are useful starting materials in the synthesis of these compounds, particularly for the early transition metals where available routes to the metal alkoxides are limited (equation 7). R in equation (7) is often the bulky $SiMe_3$ group; $N(SiMe_3)_2$ is known to be a good leaving group, and the by-product $HN(SiMe_3)_2$ is reasonably volatile. The use of less bulky dialkylamides such as $M(NMe_2)_n$ can lead to complications such as adduct formation where the dimethylamine formed is coordinated to the metal center. Other convenient starting materials include metal hydrides and alkyls, which react similarly, to give volatile by-products (hydrogen or an alkane) and the metal alkoxide. Finally, alcohol interchange reactions make use of metal alkoxides to produce new alkoxides as shown in equation (8). The order of reactivity of the attacking alcohol tends to be primary > secondary > tertiary. Interchange reactions are particularly useful in the synthesis of phenoxides owing to the higher acidity and lower volatility of phenols relative to alcohols.

$$M(NR_2)_n + nR'OH \longrightarrow M(OR')_n + nHNR_2 \tag{7}$$

$$M(OR)_n + nR'OH \longrightarrow M(OR')_n + nROH \tag{8}$$

It is important to note that efforts to synthesize metal alkoxides and aryloxides (particularly lanthanide and actinide complexes) have sometimes produced unexpected products, incorporating halide or oxide ligands, for example. As a result, some early literature may contain incorrect formulations.[12,15,17]

3.3 Reactions of Alkoxides and Aryloxides

Protonolysis reactions of alkoxides and aryloxides are common; one example is hydrolysis of the metal alkoxide, giving metal oxide with elimination of the alcohol. Although the aim is often to avoid such a reaction, it is of great interest in the deposition of high-purity metal oxides, which are used in areas such as optoelectronics, high T_c superconductors, and advanced ceramics.[15]

Other protonolysis reactions include reactions with carboxylic acids to give metal carboxylates (see Section 6) and with β-diketones to give the metal β-diketonates (see Section 4), as shown in equations (9) and (10), respectively.

$$M(OR)_n + nR'CO_2H \longrightarrow M(O_2CR')_n + nROH \tag{9}$$

$$M(OR)_n + n(\text{dikeH}) \longrightarrow M(\text{dike}')_n + nROH \tag{10}$$

Hydrogenolysis can provide a route to metal hydrides; one example is shown in equation (11) (*see* ***Hydride Complexes of the Transition Metals***).

$$(CuO\text{-}t\text{-}Bu)_4 \xrightarrow[PR_3]{H_2} [HCu(PR_3)_2]_2 + t\text{-}BuOH \tag{11}$$

Insertion reactions involving metal alkoxides are also known. For example, carbon dioxide is known to react with some metal alkoxides as shown in equation (12). The formation of a bidentate ligand is a significant thermodynamic driving force for some of these reactions. The isoelectronic aryl and alkyl isocyanates and carbodiimides can react similarly. Insertion reactions involving alkenes and carbon monoxide are known for platinum alkoxides.

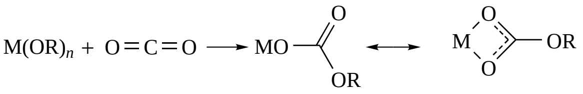

(12)

3.4 Catecholates, *o*-Quinone, and *o*-Semiquinone Ligands

These three ligands are related by the addition or removal of electrons as shown in equation (13). A metal–quinone chelate ring can be considered to have three potential isoelectronic forms, depending on the distribution of formal charge between the metal and ligand. The form that predominates can depend, for example, on the other ligands attached to the metal, as shown for the copper complexes (**9**) and (**10**).[19]

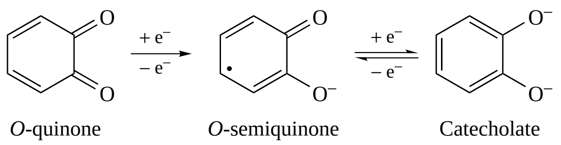

(13)

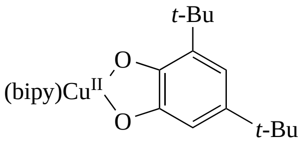

(**9**)

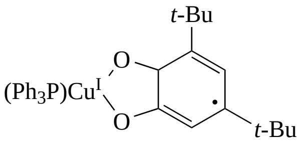

(**10**)

Just as the free ligand can be interconverted by redox processes, so can the corresponding metal complexes. For example, tris(semiquinone)chromium(III) can undergo a stepwise three-electron oxidation to the tris(benzoquinone) complex, or a stepwise three-electron reduction to the tris(catecholato)chromium(III) trianion. Intermediate, mixed-ligand species have also been characterized.[20]

o-Quinone and semiquinone complexes are generally prepared under anhydrous conditions, either directly by combination of the ligand and a metal salt or complex (such as a metal carbonyl complex), or by electrochemical procedures from catecholate complexes. Catecholate complexes are more readily synthesized, and are known for a wide range of metal ions. Characterization of these complexes as quinone, semiquinone, or catecholate, using X-ray diffraction, EPR (*see Electron Paramagnetic Resonance*), NMR, and magnetic methods (*see Magnetochemistry*), is generally straightforward, but complications can arise in systems where there is a small separation between the energies of the metal and quinone electronic levels. This can result in an equilibrium between redox isomers with differing charge distributions as shown in equation (14). The term valence tautomerism has been applied to this phenomenon.[19] Changes in the charge distribution can be induced by changes in temperature, light irradiation or altering the structure of the coligands. These systems have potential applications as sensors and switches.[21]

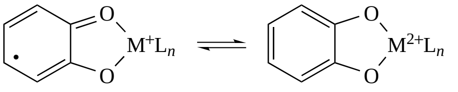

(14)

Much of the interest in these complexes arises from their relevance to biological systems. For example, the binding site for iron in some siderophores is found to include three catecholate groups (*see* ***Iron Transport: Siderophores***). This has led to a great deal of work using catecholate-based systems as sequestering agents for metals of biological and environmental importance.[22,23] Quinone–iron interactions are also important in photosynthesis and respiration processes (*see* ***Photosynthesis***). Finally, it should be noted that *p*-quinones and the related mon*o*- and dianions, by nature of the geometry of the molecule, often form a bridge between metal atoms.

4 β-DIKETONES AND RELATED LIGANDS

2,4-Pentanedione (acac) and related β-dicarbonyl compounds are an extremely important class of ligands that have been studied widely for many years. In general, β-dicarbonyl compounds exist as mixtures of tautomeric keto and enol forms (equation 15). These compounds are usually easily deprotonated to form monoanions, which form the basis for a large class of coordination compounds, encompassing virtually every element. In addition, coordination compounds of the dianions and trianions of β-diketones have been observed, as well as complexes of the neutral molecules.[24,25]

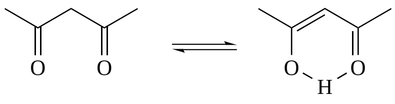

(15)

4.1 Structure and Bonding

The β-diketones are a versatile class of ligand with many known modes of coordination, some of which are shown in Figure 3. O,O′-chelation (**11**) of the monoanion is by far the most common mode, being found for almost all of the metallic and metalloid elements. Compounds of the stoichiometry M(dike)$_3$ and M(dike)$_2$ are the most common. The former generally have an almost octahedral distribution of the six oxygen atoms when M is a main group or transition metal. These compounds have been used extensively in studies of the mechanism of the racemization of trischelate complexes.

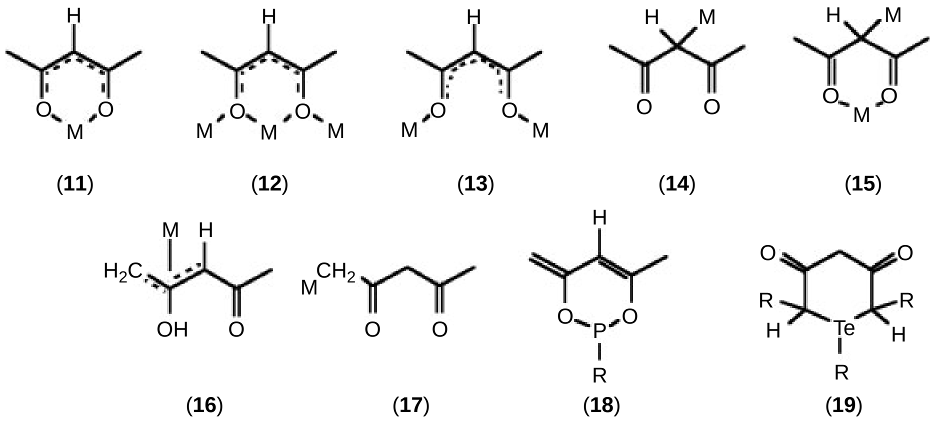

Figure 3 Examples of some of the coordination modes known for β-diketonate anions

β-Diketone complexes of the lanthanides tend to adopt higher coordination numbers, often crystallizing as hydrates.

Complexes with the composition M(dike)$_2$ usually exist as oligomers, so that the metal atoms are coordinatively saturated. For example, the acetylacetonate complexes of Ni, Zn, and Mn^{II} exist in the solid state as trimers of varying structure, with bridging β-diketonate groups (**20**).[26] The extent of oligomerization varies with the metal cation: Cu^{II} forms a monomer, while Co^{II} forms a tetrameric structure. Substituting the terminal methyl groups with larger substituents favors the formation of the monomer, although these are often solvated to give five- or six-coordinate complexes. O-O′-chelation in combination with bridging (**12**) is thus quite common, whereas the purely bridging mode of coordination (**13**) is rare, but was first observed in lanthanide complexes such as $Er_8O(OH)_{12}(dpm)_{10}$, which has a complex structure where eight of the dpm ligands are bidentate chelate, and the remaining two are purely bridging.

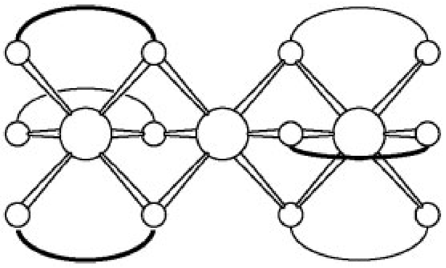

(**20**) [Mn(acac)$_2$]$_3$

The monoanions of β-dicarbonyl compounds also form organometallic species, usually involving the central carbon atom in the M–C bond (**14**). Such species are known for a number of metals, particularly those of the platinum group. This mode of binding leaves the two carbonyl oxygen atoms free, allowing the formation of bimetallic species (**15**). η^3-Allylic (**16**) and terminal (**17**) carbon bonding have also been observed.

Dianions of β-diketones are also known to form metal complexes, but are much less common than systems containing the monoanion. Such complexes usually involve main group elements or members of the platinum group, and may be coordinated to the O atoms (**18**) or terminal C-atoms (**19**).[25,27]

4.2 Synthesis

Metal β-diketonates are generally synthesized from the neutral β-diketones and the appropriate bulk metal or metal salt are synthesized in solvents such as water, dioxane, ethanol, or neat diketone. The use of the bulk metal is limited to the more electropositive elements such as the group 1 and 2 metals, although the method is more widely applicable with more acidic β-diketones, such as those with perfluoroalkyl substituents. Electrochemical syntheses of some acac complexes have been described, using the appropriate metal anode.

More common is the use of a metal salt, such as halide, hydroxide, oxide, sulfate, carboxylate, and so on. A base can also be added, to convert the β-diketone to the β-ketoenolate anion, which usually has greater solubility in aqueous media.

Metal alkoxides and alkyls are useful starting materials, particularly for the preparation of some unsolvated β-diketones that require anhydrous conditions (see Section 3.3). Addition of β-diketonate ligands to metal alkoxides has also been used to produce heteroleptic metal complexes that are less reactive than the homoleptic metal alkoxides; this simplifies the use of such complexes in chemical vapor deposition applications.[16]

4.3 Reactions of β-diketonates

Metal β-diketonates, particularly acetylacetonates, will undergo electrophilic substitution at the central methine carbon atom in a similar way to aromatic compounds. Known reactions of this sort include bromination, nitration, acylation, and the Mannich reaction.

Hydrolysis (the reverse of the preparative reaction) and other exchange reactions of the metal β-diketonates have been studied in some detail in order to probe the mechanisms of inorganic substitution reactions. As mentioned in Section 4.1, there has been intense study of the intramolecular rearrangements of M(dike)$_3$ complexes. Decomposition of metal β-diketonate complexes to give high-purity metals or metal oxides is of technological importance.

Metal β-diketonates are often coordinatively unsaturated (*see Coordinative Saturation & Unsaturation*) and will therefore react with Lewis bases to form complexes. For example, the trimer [Ni(acac)$_2$]$_3$ will react with Lewis bases such as water or pyridine to form monomeric *trans*-[Ni(acac)$_2$L$_2$]. The formation of weak complexes with lanthanide β-diketonates is critical in their use as NMR shift reagents.

4.4 Complexes of Neutral β-diketones

A number of complexes of neutral β-diketones are known, although such complexes are generally not very stable. They can be synthesized by addition of the β-diketone to a simple metal salt or coordinatively unsaturated metal complex, by controlled hydrolysis of a metal β-diketonate, or by displacement of a weakly bound neutral ligand by the β-diketone.

O,O′-chelation (**21**) of acacH has been found in $NiBr_2(acacH)_2$ and $[Ni(acacH)_2(H_2O)_2](ClO_4)_2$. O-unidentate coordination of the enol form (**22**) has been structurally characterized in $MnBr_2(acacH)_2$ and $[ReCl(CO)_3(bzacH)]_2$. η^2(C,C′) coordination of the enol (**23**) has been implicated by NMR and IR studies of the platinum complex [PtCl(acac)(acacH)].[28]

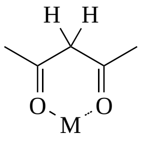

(**21**)

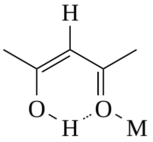

(**22**)

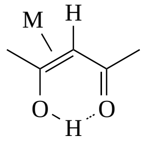

(**23**)

4.5 Polyketonate and Bis-β-diketonate Complexes

1,3,5-Triketones and similar polyketones exhibit keto–enol tautomerism and have been found to coordinate to one or more metal atoms (**24**). Such complexes can bring metal atoms in close proximity, resulting in interesting magnetic properties (*see* ***Magnetism of Transition Metal Ions***).

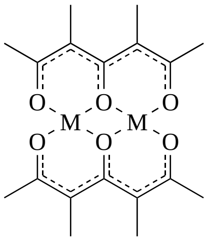

(**24**)

A series of bis-β-diketones, linked by the methine carbon atoms, have been found to form ‘cofacial’ dicopper(II) species (**25**) which have cavities of varying sizes, depending on the nature of the linking group.**29** The inclusion of various small molecules within the cavity has been investigated. Another interesting system involves bis-β-diketones linked at the terminal carbon atoms by glycol ether linkages of varying lengths, which will transport alkali metal atoms through a membrane only when complexed to a copper(II) cation (**26**).**30**

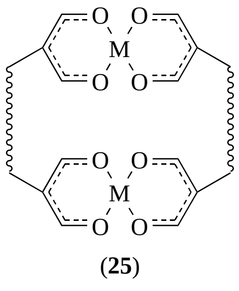

(**25**)

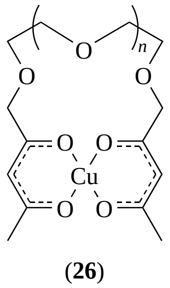

(**26**)

4.6 Tropolonates

Although formally an α-diketone, tropolone gives rise to a monoanion (equation 16) with coordination chemistry similar to that of the β-diketonate anions. The tropolonate ion forms a five-membered chelate ring, which has a smaller Bite Angle (*see Bite Angle*) than β-diketonate anions. This feature, in combination with its rigid planar nature, makes the tropolonate ion suitable for the formation of complexes with high coordination numbers at the central metal ion. For example, the thorium(IV) and uranium(IV) complex anions $M(trop)_5^-$ are 10 coordinate. Another result of the small bite angle of this ligand is that tristropolonato metal complexes are considerably distorted from octahedral geometry.**31**

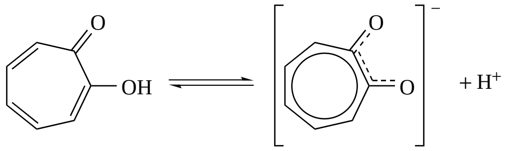

(16)

5 OXOANIONS

Oxoanions (*see Oxoanion*) include species such as SO_4^{2-}, CrO_4^{2-}, and so on. They consist of a central element, which is often nonmetallic but can also be metallic, to which is bound a number of terminal oxygen atoms.**32** Oxoanions where the central element is carbon, such as CO_3^{2-}, and related substituted species such as carboxylates, RCO_2^-, exhibit somewhat different coordination chemistry to other oxoanions and are discussed in Section 6.

5.1 Structure and Bonding

The terminal oxygen atom in an oxoanion has three lone pairs, and can therefore, in principle, coordinate to up to three metal atoms. The maximum coordination number (i.e. the number of metals to which the oxoanion is bound) for an oxoanion $[XO_n]^{m-}$ is therefore $3n$. In practice, the great majority of mononuclear oxoanions have n in the range 2 to 6, and m in the range 1 to 6, with coordination numbers of four or less.

There are a large number of possible coordination modes for the various oxoanions, in association with varying numbers of metal atoms. It should be noted that a significant problem in defining coordination modes is the length of an M–O bond. It has been suggested that, where the M–O distances differ by less than 0.7 Å, there is a significant interaction between the M atom and both O atoms.**32** Longer bond distances are indicated by dashed lines in the following diagrams. Consideration of the bond lengths within the oxoanion can be useful in describing the bonding, since most X–O bonds in oxoanions have some double bond character and therefore the X–O distances for the coordinated O atoms are expected to increase, while the noncoordinated X–O distances decrease, relative to the free oxoanion. Unfortunately, the changes in the geometry of oxoanions upon coordination are usually small and are difficult to determine accurately.

5.1.1 Coordination Modes of Triangular Oxoanions

The most widely studied of these oxoanions is the nitrate anion, NO_3^-. Some of the known coordination modes of this anion are shown in Figure 4(a). The most common is the symmetrical bidentate mode (**27**). Examples of unidentate (**28**) and asymmetrical bidentate (**29**) coordination modes are also quite plentiful. The most common bridging coordination mode for these and all oxoanions is the symmetrical *syn–syn* mode involving two oxygen atoms of the oxoanion (**30**). The other modes (**31–33**) shown in Figure 4 are relatively rare. The η^1:μ_3 mode with a single oxygen bridging three metal atoms (**32**) has been observed in a tetranuclear manganese complex.[33] The η^3:μ_3 mode (**33**) has been found in $[Cu_3(OH)(pz)_3(Hpz)_2(O_3N)(ONO_2)]\cdot H_2O$[34] and more recently in a bis-β-diketonate complex, where the nitrate anion links octanuclear copper clusters.[31]

5.1.2 Coordination Modes of Bent Oxoanions

Examples of this group of oxoanions include NO_2^-, ClO_2^-, and $H_2PO_2^-$, although most of the available data concern the nitrite anion and hence the discussion will center on complexes of this anion.[35] Some of the known coordination modes are shown in Figure 4(b) (**34–39**). Monodentate coordination predominates, through the terminal O atoms to give nitrito complexes (**34**), and through the central N atom to give nitro complexes (**35**). The most common bridging mode is the N–O mode (**36**), although others are known, combining bidentate O chelate plus monodentate O or N coordination (**37** and **38**, respectively).

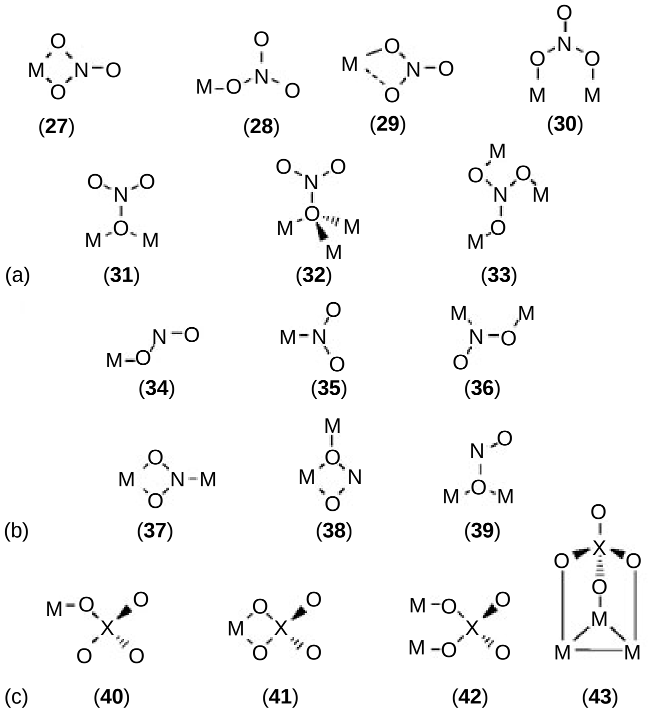

Figure 4 Some coordination modes of the (a) nitrate anion, (b) nitrite anion, and (c) tetrahedral anions

5.1.3 Coordination Modes of Tetrahedral Oxoanions

Examples of oxoanions of this geometry are numerous, and include SO_4^{2-}, SeO_4^{2-}, AsO_4^{3-}, PO_4^{3-}, SiO_4^{4-}, VO_4^{3-}, CrO_4^{2-}, and ReO_4^-. Tetrahedral oxoanions are found to coordinate to up to 12 metal atoms, although simple unidentate (**40**), bidentate chelate (**41**), and bidentate (and higher) bridging (**42**) coordination modes are more common.[32] The tridentate triply-bridging mode (**43**) is an interesting example of coordination to a metal cluster.[36] The number of examples known decreases rapidly for coordination numbers above three.

5.1.4 Coordination Modes of Pyramidal Oxoanions

The most widely studied of these oxoanions is SO_3^-; others include HPO_3^{2-} and IO_3^-. The coordination modes known are similar to those of the tetrahedral oxoanions (Figure 4c), with additional modes involving bonding to the central heteroatom.

5.2 Spectroscopy

The IR spectra of the free oxoanions are well characterized, with the modes of vibration being determined by the number of atoms and the symmetry of the ion. The changes in symmetry and bond order that take place upon coordination can result in significant changes in the IR spectrum, allowing differentiation of the free and complexed species.[28] For example, the IR spectrum of free NO_3^- ion has absorptions at $\sim$1390, 830, and 720 cm^{-1}, whereas coordinated nitrate groups, which have lower symmetry, exhibit six absorptions. While it is usually relatively easy to distinguish between free and complexed oxoanions, it is often much more difficult to determine the mode of coordination (e.g. distinguishing between mono- and bidentate coordination or between bidentate chelate and bridging modes), and hence it is often necessary to obtain crystallographic structure determinations to determine the coordination modes of these anions with certainty. Other spectroscopic techniques that have been employed include EXAFS (*see Extended X-ray Absorption Fine Structure*), ^{17}O NMR, and X-ray powder diffraction.[37]

5.3 Synthesis

Oxoanions usually have weak donor properties relative to water and nitrogen donors, and thus the properties of coordination complexes of these anions are extremely solvent dependent. For example, the ClO_4^- ion is generally considered to be a weakly coordinating anion in aqueous solution, and yet in nonaqueous solvents such as $HClO_4$ or Cl_2O_6, ClO_4^- forms complexes with a variety of metals clearly involving anion coordination to the metal ions. Stronger ligands, such as the NO_3^- anion, are known to form complexes even in aqueous solution. The octahedral periodate and tellurate anions readily form stable complexes in aqueous solutions.[38] Hence, synthesis of oxoanion complexes is generally straightforward, provided water or other strong ligands are excluded.

6 CARBOXYLATE AND RELATED SPECIES

6.1 Monocarboxylates

Monocarboxylates are an attractive class of ligand for the coordination chemist; they bind to metal atoms in a variety of ways giving, in many instances, complexes with interesting properties, and they are readily available.[37] Figure 5(a) shows some of the known modes of coordination (**44**–**51**). Unidentate (**44**) and symmetrical chelate coordination (**45**) modes are well established, with the unidentate mode being more commonly observed. The presence of unidentate carboxylate can be established by IR spectroscopy, by virtue of the inequivalence of the two C–O bonds in the coordinated anion,[28] although care must be exercised since the environment of the free carboxylate O atom, and even sample preparation, can influence the IR spectrum.

The most common bridging mode of coordination is *syn*–*syn* (**47**). The nature of the metal–metal interactions in such systems has been the subject of much study, with interaction varying from the relatively weak in dimeric Cu^{II} complexes, to strongly M–M bonded species such as $Mo_2(O_2CR)_4$, which contains a formal quadruple bond. The two systems that have been most studied are the bimetallic (**52**) and trimetallic (**53**) complexes, often referred to as 'paddle-wheel' and 'triangular' complexes respectively.[39] These structural motifs have been widely utilized in the construction of coordination polymers and metal-organic frameworks.[11,40]

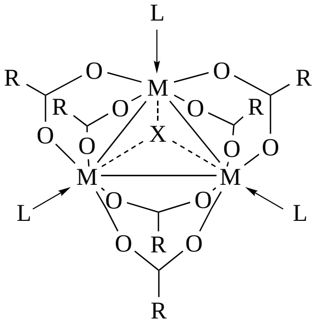

(**52**)

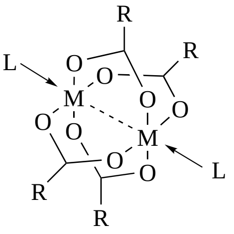

(**53**)

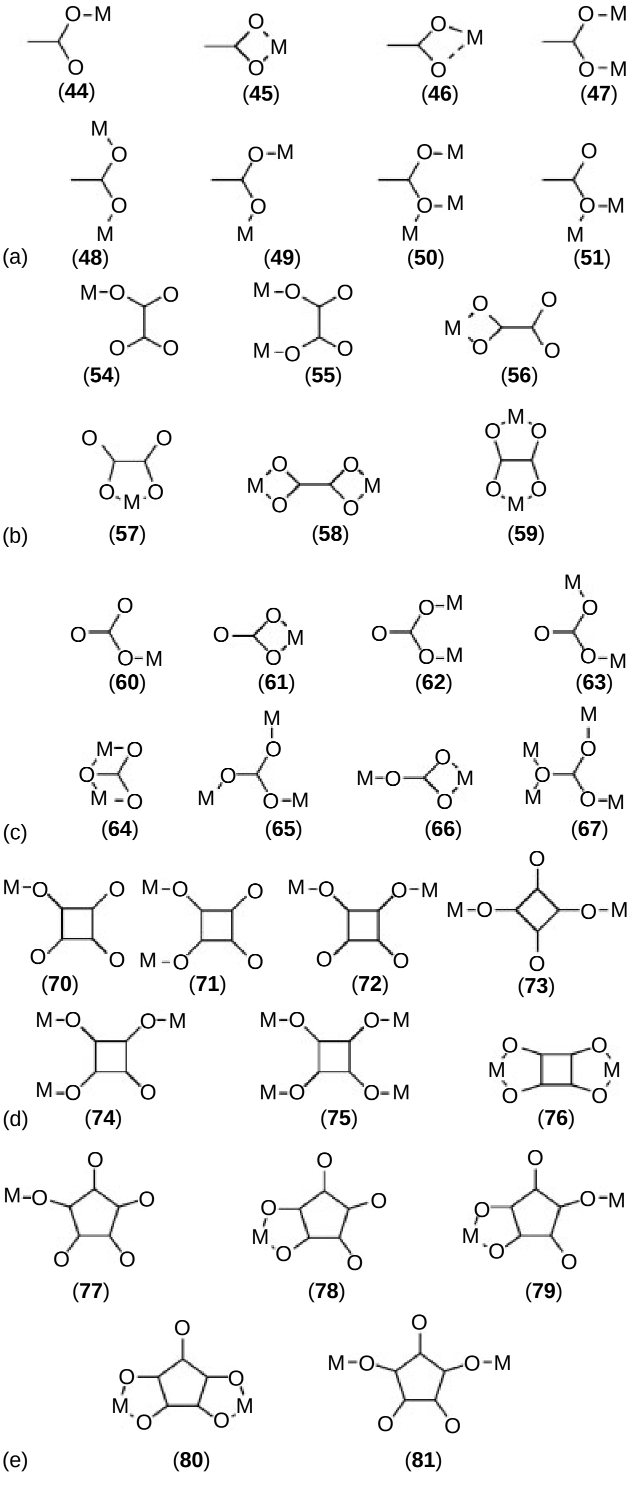

Figure 5 Some coordination modes of (a) monocarboxylate anions, (b) dicarboxylate anions, (c) the carbonate anion, (d) the dianion of squaric acid, and (e) the dianion of croconic acid

Distinguishing the various bridging modes of the carboxylates has been carried out using IR and NMR spectroscopies and magnetic measurements, although support from X-ray structure determinations has been vital in obtaining definitive information on these complexes.

Carboxylate complexes are often synthesized by refluxing the acid with the metal salts (such as carbonate, sulfate, oxide, etc.), or by reaction of the sodium or silver salt of the acid with the metal halide. Insertion of CO_2 into σ-bonded organotransition metal species has also been used to generate carboxylate complexes, as has exchange reactions with metal alkoxides (see Section 3.3).

6.2 Dicarboxylates

The coordination chemistry of the dicarboxylates is somewhat different to that of the monocarboxylates, since the close proximity of the carboxylate groups allows coordination involving one O atom of each. The simplest and most intensively studied of these compounds is oxalic acid (ethanedioic acid), complexes of which are found in nature (e.g. in the mineral humboltine). Some coordination modes for this acid are shown in Figure 5(b). Unlike monocarboxylates, chelate coordination is favored over the unidentate mode (**54**). Of the two modes of chelate coordination, the formation of the larger chelate ring (**57**) is generally formed in preference to the four-membered chelate ring (**56**), with the latter becoming more common in higher members of the dicarboxylate series, where the two carboxylate groups are further apart.

There are many possible bridging modes (**55**,**58**,**59**) for the dicarboxylic acids with the bis-bidentate bridging mode (**59**) being the most common. The bridging mode (**58**) is very rare for the shorter dicarboxylates,[35] but is widely observed with the longer more rigid dicarboxylates used in some metal-organic frameworks.[11,40] X-ray diffraction is the most reliable method of determining the coordination mode of the dicarboxylates, although chemical methods have been useful; for example, protonation reactions can reveal the presence of uncoordinated carboxylate groups, since these are easily protonated unlike the coordinated groups. Metal interactions in dicarboxylate complexes, particularly oxalate complexes, have been of interest, with copper complexes being the most studied. The magnetic properties of oxalate-bridged Cu^{II} dimers $[LCu(ox)CuL']^{2+}$ has been found to be highly variable, and strongly influenced by the nature of the terminal ligands L and L′.[41] Dicarboxylate complexes are usually synthesized by reaction of an aqueous solution of the alkali metal salt of the dicarboxylate with a metal halide, or by reduction of a metal salt by the dicarboxylic acid. For example, oxalic acid readily reduces iron oxides to form the iron(II) complex.

6.3 Carbonates

The carbonate ion is a component of many naturally occurring minerals and is important in biological systems and thus it has been widely studied. The coordination chemistry of this anion is well developed and the common unidentate (**60**) and bidentate chelate (**61**) coordination modes have been observed, as well as a wide variety of quite complex bridging modes (**62–67**). Vibrational spectroscopy is quite useful in distinguishing free carbonate from the nonbridging coordination modes, since coordination results in a change in the symmetry of the ion.[28] The bridging modes can usually only be determined via structure determination studies.

Carbonate complexes are usually synthesized from carbonate or bicarbonate anions in alkaline aqueous solution. The reaction of metal hydroxides with carbon dioxide is another route to carbonate complexes. Other methods include the oxidation of metal carbonyl complexes (equation 17), and the oxidation of metal salts in the presence of carbon dioxide.

$$[CpMo(CO)_3]^- \xrightarrow{O_2} CpMo(CO)_2(\eta^2\text{-}O_2CO) \qquad (17)$$

6.4 Cyclic Oxocarbon Acids

Of the known cyclic oxocarbon acids, the systems based on squaric (**68**) and croconic (**69**) acids have been most widely studied.[42] The loss of two protons from these acids gives rise to aromatic dianions as shown in equations (18) and (19), and these can coordinate to metal anions in a variety of ways. Unidentate coordination (**70**,**77**) is known for both systems but is not common. Simple bidentate chelate coordination (**78**) is also relatively uncommon but is observed in a number of croconate complexes. The squarate anion adopts this mode only with larger cations, such as the group 2 and lanthanide metals, and then only in association with additional bridging interactions. Bridging coordination modes dominate the chemistry of these anions, some of which are shown here (**71–76**), (**79–81**). The various modes of coordination can usually be distinguished by IR spectroscopy, and the use of ^{13}C NMR spectroscopy has also been investigated.

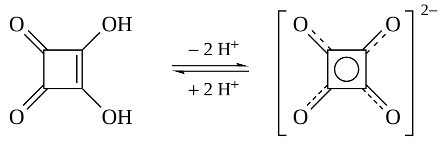

(18)

(**68**) Squaric acid

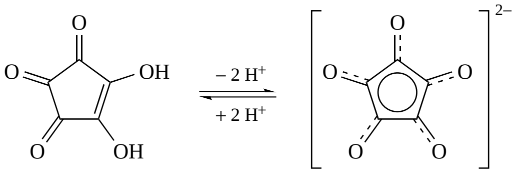

(19)

(**69**) Croconic acid

The magnetic properties of complexes of these anions have been studied, particularly copper(II) complexes, and have been compared with the results obtained with analogous oxalato complexes;[41] the squarato and croconato bridges are able to transmit magnetic effects between metal atoms, but are not as efficient as the oxalato bridge.[42]

Squarato and croconato metal complexes are usually synthesized by mixing an aqueous solution of the dipotassium salt of the acid with a metal ion, although nonaqueous solvents have also been employed.

6.5 Carbamates

Carbamate ($R_2NCO_2{}^-$) complexes are similar electronically and structurally to monocarboxylate complexes, although they are not as accessible synthetically and are generally less stable.[43] Unidentate, chelate, and bridging coordination modes have been observed, although the number of bridging modes found to date is less than that known for carboxylates. *Syn–syn* bridging is the most common, and bimetallic ‘paddlewheel’ type structures (**53**) are known.

Carbamate complexes are synthesized by carbonation of metal dialkylamides (equation 20), or by reaction of the appropriate amine, carbon dioxide, and a metal halide (equation 21). In both cases, it has been suggested that the reaction involves combination of the amine and carbon dioxide to form the carbamate anion, followed by anion exchange.[43]

$$M(NMe_2)_n + nCO_2 \longrightarrow M(O_2CNMe_2)_n \qquad (20)$$

$$MCl_n + 2n\ NHR_2 + nCO_2 \longrightarrow M(O_2CNR_2)_n + nNH_2R_2Cl \qquad (21)$$

6.6 Hydroxycarboxylic Acids

Many hydroxycarboxylic acids are naturally occurring, and their coordination chemistry is of importance in biological processes.[44] These complexes also have uses in many other areas such as analytical chemistry, electroplating processes, and pharmacology. The most widely studied aliphatic hydroxy acids are the lower members of the 2-hydroxyalkanoic acids, while studies of aromatic hydroxy acids have often centered on salicylic acid. A number of these acids contain one or more chiral carbon centers, and hence complexes of these acids have been useful in studying chiroptical properties such as the Cotton Effect (*see Cotton Effect*).

A common feature of the coordination chemistry is the formation of a five-membered chelate ring involving one O atom of the carboxylate group, and the O atom of the hydroxyl group, which may or may not retain the hydroxylic H atom (**82**). The O atoms may also bridge to other metal atoms.

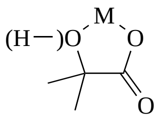

(**82**)

6.7 Hydroxamates

Hydroxamic acid[45] exists in two tautomeric forms (**83**) and (**84**). Spectroscopic evidence suggests that metal complexes are generally best described by the structure (**85**), as a hydroxamide group rather than a hydroxyoxime. Hydroxamic acids are of importance in analytical chemistry, having been widely used as metal precipitants and as colorimetric reagents. Another interesting aspect is the presence of hydroxamate binding groups in siderophores (*see* ***Iron Transport: Siderophores***).[23]

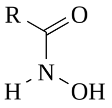

(**83**)

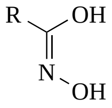

(**84**)

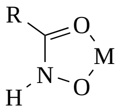

(**85**)

7 MACROCYCLIC O-DONOR LIGANDS

7.1 Introduction

Unlike most of the O-donor ligands discussed in this article, the study of synthetic macrocycles (*see* ***Macrocyclic Ligands***) such as Crown Ethers (*see Crown Ethers*), Cryptands & Cryptates (*see Cryptands & Cryptates*), and the calixarenes (*see Calixarenes*) is a relatively recent development. The beginnings of this area are perhaps best marked by the paper by C. J. Pedersen published in 1967, describing the synthesis of a number of crown ethers, and most importantly, the ability of these macrocycles to form stable complexes with simple inorganic cations.[46] The development of the macropolycyclic cryptands, by J. M. Lehn, followed soon after.[47] The pioneering work of C. D. Gutsche in the mid-1970s initiated study of the macrocycles now known as calixarenes.[48] The rapid expansion of this field forces us to limit the discussion here to some representative aspects of metal complexes of these O-donor macrocycles.

7.2 Crown Ethers and Cryptands

7.2.1 *Complexation*

The crown ethers form stable complexes with many cations, both inorganic and organic, as well as neutral species.[49] As would be expected, the Macrocyclic Effect (*see Macrocycle*) provides a significant contribution to this stability. For example, the stability constant of the K^+ complex of 18-crown-6 in anhydrous methanol is $10^{6.1}$, whereas the complex of the open chain analog has a stability constant of $10^{2.3}$. The tricyclic cryptands are even more preorganized, and generally form more stable complexes than the corresponding crown ethers (this is sometimes called the 'cryptate effect').[49] The preorganization concept is taken to its logical conclusion in the class of receptors termed *spherands*, which are fully preorganized for the target guest producing extremely stable complexes.[50]

The crown ethers and cryptands generally form more stable complexes with 'hard' metal ions, such as the group 1, 2, and lanthanide ions. The introduction of softer heteroatoms into the macrocycle can change the selectivity dramatically. There is much interest in 'tuning' macrocycles in this way to favor complexation of certain metal atoms, but O-donor macrocycles will dominate the discussion here.

There has been a great deal of work on group 1 metal ion complexes of crown ethers and cryptands, producing many estimates of stability constants and other thermodynamic data. The importance of factors such as relative sizes of the cation and the macrocycle cavity has been widely discussed (the 'hole-size' effect). This concept is of most use in relatively rigid systems such as the cryptands, where the receptor molecule cannot easily distort to accommodate cations of the 'wrong' size. Thus, [2.2.2]cryptand has a cavity size close to the ionic radius of K^+, and it complexes this cation selectively over the smaller Na^+ and larger Cs^+. In more flexible systems, other factors such as ligand conformations, chelate ring size and solvation enthalpy become relatively more important, so that a simple match of cation and macrocycle hole size is generally not sufficient to predict selectivity.[51] Changing solvents, for example, can reverse the trends in stability constants in some systems. The thermodynamics and kinetics of cation/macrocycle interaction is an important area of study, and a great deal of the available data has been compiled by R. Izatt and coworkers, along with useful discussion of the factors influencing the stability of the complexes.[52,53]

7.2.2 Structural Aspects

The solid-state structures of crown ether complexes can be broadly categorized on the basis of relative sizes of the cation radius and the macrocycle cavity. The simplest case is where there is a close fit between the cation and macrocycle; a beautiful example of this is the potassium complex of 18-crown-6 (**86**). The K^+ ion is bound to all six O atoms of the crown, and sits in the plane of the macrocycle. The structural chemistry of this seemingly complementary pairing is far from simple, however, and a range of different structural types has been found for these complexes.[51] For example, additional ligands are often found coordinated to the potassium cation in 18-crown-6 complexes, as shown for (**87**) where two thf molecules are bound to the potassium cation, above and below the plane of the macrocycle. Remarkably, structures (**86**) and (**87**) are found in a single crystal structure,[54] illustrating that subtle changes can induce different crown ether complex structures.

If the cation is large relative to the cavity size of the macrocycle, the cation can still interact with the crown ether, by 'perching' out of the average plane of the crown. There are a number of structural types that can occur in such complexes. One case is the formation of a complex with the metal ion situated above the crown, and the coordination sphere saturated by other ligands; an example of this is the $[Sm(15\text{-crown-}5)(H_2O)_4]^{3+}$ cation (**88**).[55] Alternatively, a 1:2 complex may be formed, with the metal ion sandwiched between two crown ethers. The K^+ complex of 15-crown-5 (**89**) exhibits such a structure, with the ten-coordinate K^+ ion bound to all the O-donor atoms of the two crowns.[56] A sandwich-type structure is also possible in 1:1 crown ether complexes, as shown for the CsSCN complex of 18-crown-6 (**90**).[57] In this case, the SCN^- ligands act as bridges to give the Cs^+ ion a coordination number of eight. A triple layer 'club sandwich' structure with a 2:3 metal to crown ratio has also been observed in a Cs^+ complex of 18-crown-6.[58]

Examples where the metal cation is small compared to the size of the macrocycle fall into two categories. The most common result is a constriction of the crown ether cavity, so that the macrocycle shrinks to match the cation radius. An example is the Na^+ complex of 18-crown-6 (**91**);[59] the conformation of the crown is quite distorted compared to that observed in (**86**), with five of the O-donor atoms lying in a plane about the metal ion, and the sixth folded out of the plane.

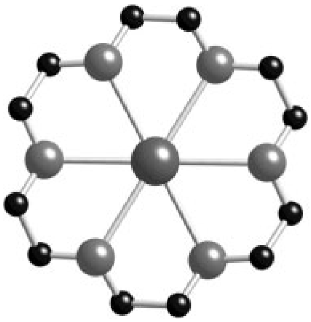

(**86**)

$[K^+(18\text{-crown-}6)]$[54]

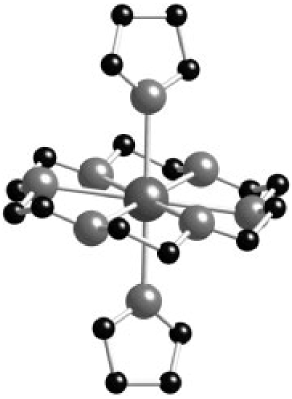

(**87**)

$[K^+(18\text{-crown-}6)(thf)^2]$[54]

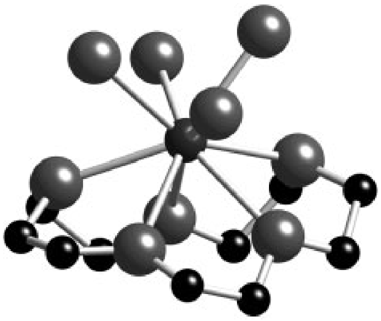

(**88**)

$[Sm(H_2O)_4(15\text{-crown-5})]^{3+}$[55]

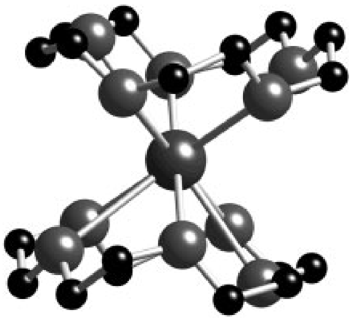

(**89**)

$[K(15\text{-crown-5})_2]^{+}$[56]

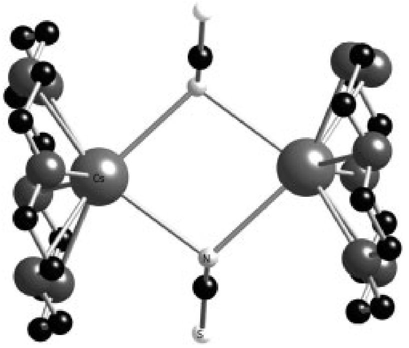

(**90**)

$[Cs(SCN)(18\text{-crown-6})]_2$[57]

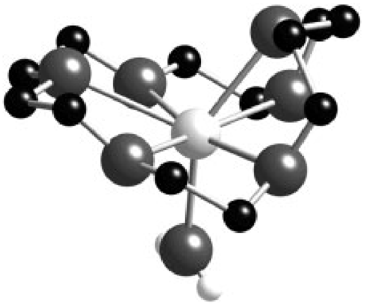

(**91**)

$[Na(18\text{-crown-6})OH_2)]^{+}$[59]

Distortion such as this may result in the exclusion of one or more of the crown O atoms from the coordination sphere of the metal. This situation is found in another Na^+ complex of 18-crown-6 (**92**), again showing that subtle structural differences can occur for the same cation-crown combination.[60] Extremely large and flexible crown ethers can completely encapsulate metal ions, as is found in the K^+ complex of a 30-crown-10 ligand, and the Na^+ complex of a 24-crown-8 derivative, for example.[51] This 'wrapping' of the cation bears structural resemblance to the complexes formed by natural ionophores such as valinomycin.

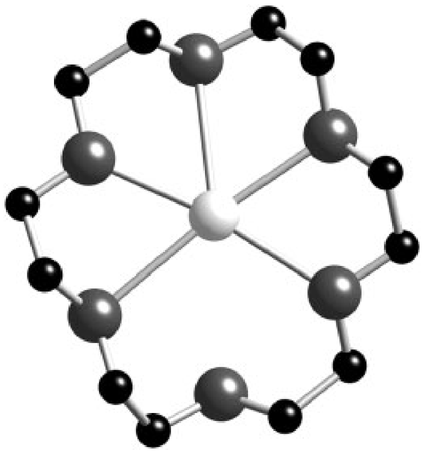

(**92**)

$[Na(18\text{-crown-6})]^{+}$[60]

The second structural type that can be formed where the cation is small relative to the macrocycle is a bimetallic complex where the crown contains two metal ions. One example is the disodium complex of dibenzo[24]crown-8 (**93**), where each sodium ion is bound to three O atoms of the crown.[61] Such complexes are relatively rare, and usually limited to singly charged cations, presumably for electrostatic reasons.

The complexes discussed so far all involve direct interaction between the metal ion and the crown ether. Another important class of crown ether derivatives is that involving second sphere coordination.[62] These compounds involve interaction between the ligands in the primary coordination sphere (such as H_2O in $M(H_2O)_6{}^{n+}$ cations), and the second sphere ligand, the crown ether, often by means of hydrogen bonds. Such a structure is found in the $[Mn(OH_2)_6](ClO_4)_2$ adduct of 18-crown-6 (**94**).[63] It is not surprising that transition metal/crown ether chemistry often involves adducts, since

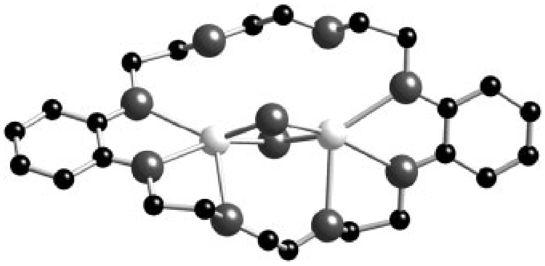

(**93**)

$[Na_2(\text{benzo-24-crown-8})(\text{2-nitrophenolato})_2]$ –
only O-atoms of bridging phenolates shown for clarity[61]

ligands such as H_2O and NH_3 tend to bond to transition metal ions more strongly than the crown ethers. Aqua and ammine complexes dominate this area, although interaction between acidic methyl group C–H bonds and crown ethers has been observed. It is interesting to note the formation of complexes where the crown ether is simultaneously involved in both the primary and secondary coordination spheres. This is often observed where the cation is small relative to the crown ether. An example is the lithium complex of 18-crown-6 (**95**), where water molecules coordinated to the lithium cation also form hydrogen bonds with the crown ether O atoms.[64]

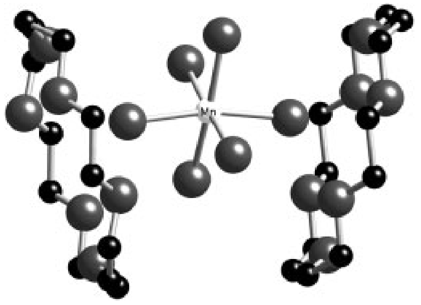

(**94**)

$Mn(H_2O)_6{}^{2+}\cdot 2(\text{18-crown-6})$[63]

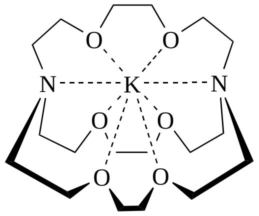

(**96**)

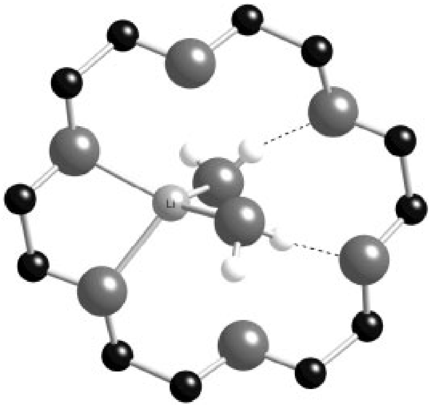

(**95**)

$[Li(\text{18-crown-6})(OH_2)_2]^+$[64]

Crystal structure determinations of various cryptates have shown that the metal atom is usually held within the three-dimensional cavity, as shown for the K^+ complex of [2.2.2]-cryptate (**96**). The cavity can expand to accommodate larger cations, and this is often accompanied by coordination of solvent or anionic ligands; for example, the $[Eu(ClO_4)([2.2.2]\text{-cryptand})]^{2+}$ cation is 10 coordinate with bidentate coordination of the $ClO_4{}^-$ anion.[65] As mentioned above, the cryptands are less flexible than the crown ether, and this is reflected in the less variable structures of the metal complexes.

7.3 Calixarenes

7.3.1 Introduction

An interesting group of aryloxides are the macrocyclic polyphenols known as calix[*n*]arenes (**97**), where *n* indicates the number of aryl units comprising the macrocycle.[48,66] More recently, the term calixarene has been extended to include macrocycles comprising of other aromatic units (such as resorcinols, napthols, pyrroles, furan, etc.);[66] here, the discussion will be limited to the calixarenes produced from the base catalyzed condensation of para-substituted phenols and formaldehyde. The most common ring sizes are $n = 4$, 6, or 8, although ring sizes up to $n = 20$ have been isolated.[66] The phenolic calixarenes act as effective ligands, particularly for hard metal cations. The parent macrocycles can also be functionalized in a wide variety of ways to give macrocycles with desired properties. A brief overview of the phenolic calixarenes, and then derivatized calixarenes, as ligands is given below.

7.3.2 Phenoxide Calixarene Complexes

The cyclic tetramer is the smallest readily available calixarene; it can assume a number of conformations, but is most commonly found in the conelike conformation (**98**)

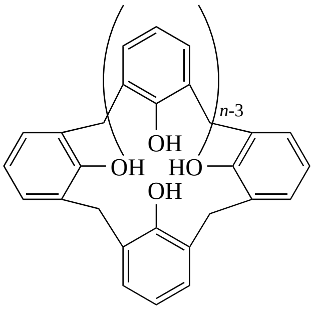

(**97**)

that gave rise to the name calixarene (from the Greek *calix* meaning ‘vase’). Metal cations typically interact with the phenol O-donor atoms at the lower rim of the calixarene forming mono or binuclear complexes;[48] the 2:2 europium complex of *p*-*t*-butylcalix[4]arene (**99**) is a typical example.[67] Conversely, the cation Cs^+ has been shown to occupy the cavity defined by the aromatic rings (**100**).[68]

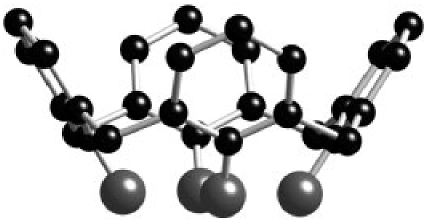

(**98**)

Cone conformer of calix[4]arene

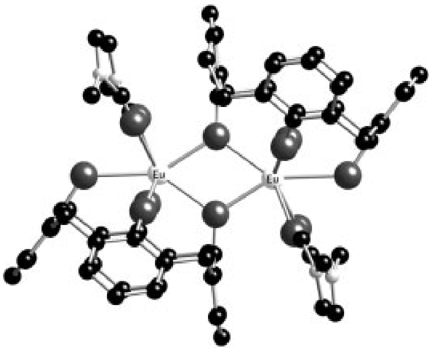

(**99**)

Europium complex of *p*-*t*-butylcalix[4]arene [$Eu_2(dmf)_4$(t-butylcalix[4]arene-3H)$_2$] (butyl groups omitted for clarity)[66]

The quasi-planar array of oxygen atoms at the lower rim of the calix[4]arene has inspired studies of calix[4]arene-metal complexes as models for metal-oxo surfaces of heterogeneous catalysts.[69]

Structurally characterized complexes of larger calixarenes are less common than those of calix[4]arenes, but the number is rapidly increasing.[70] Calix[6]arenes have been found to act as a ditopic ligand for a number of alkali metals and transition elements, although a Eu^{III} complex of *p*-*t*-butylcalix[6]arene was found to have a 1:2 metal:calixarene ratio, where one calixarene was bound to the metal atom by only one phenolic O atom, and the other was free in the crystal lattice.[71]

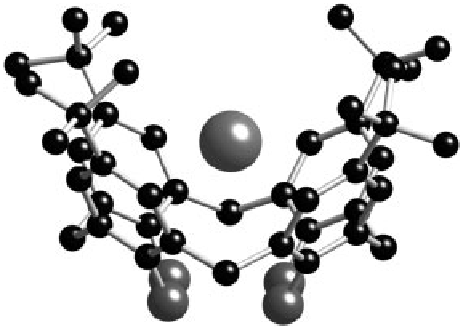

(**100**)

Cesium complex of *p*-*t*-butylcalix[4]arene[67]

Calix[8]arenes are also found to act as a ditopic receptor in most cases.[66,70] The calixarenes assume various ‘pinched’ conformations in these complexes, resembling two calix[4]arene cone units linked together. Two 1:1 complexes, of Ca^{II} and Eu^{III}, have been characterized where a roughly planar circular conformation is observed, with only two of the phenolic O atoms interacting with the metal atom.[70] It is interesting to note that the free *p*-*t*-butylcalix[8]arene has been found to crystallize as a pyridine solvate with a planar, circular conformation in one case, and a pinched conformation in a subsequent report.[48]

7.3.3 Derivatized Calixarene Complexes

Both the lower (phenolic) rim and the upper rim of the calixarene can be functionalized. A huge range of calixarene derivatives have been synthesized in this way, and only a few can be mentioned here. In addition, the linking methylene groups can be modified to give another group of useful ligands.[48]

Alkylation of the lower rim substitution with carbonyl-containing groups (**101**) has produced probably the most widely studied of the calixarene-based ionophores.[72] These derivatives have been studied predominantly as ionophores for hard metal cations, and can form complexes of comparable stability to those of the cryptands in some cases. Such calixarenes have found applications as ionophores in ion selective electrodes.[73]

Lower rim substitution can also be used to link calixarene molecules. An elegant example was produced by linking two calix[4]arenes with four ethylene bridges to produce what was termed as a calix[4]tube (**102**).[74] The synthesis was templated by the potassium ion, and the product was found to bind this cation selectively.

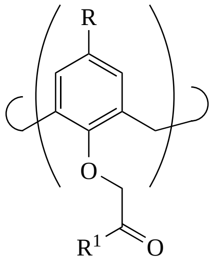

R^1 = O-alkyl
= alkyl
= N-(alkyl)$_2$
= OH

(**101**)

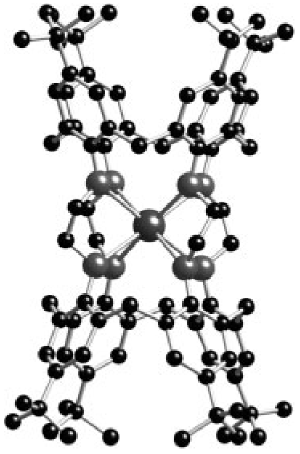

(**102**)

‘‘Calix[4]tube’’ potassium complex[73]

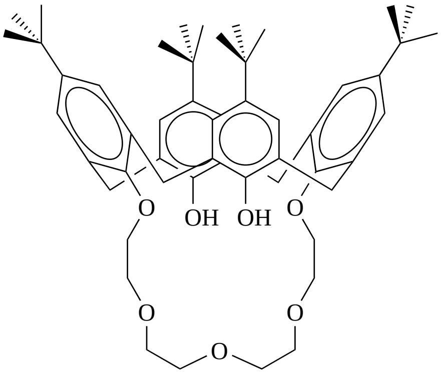

(**103**)

Upper rim substitution is typically more synthetically challenging than the lower rim, but can confer very useful properties on the macrocycle. For example, water soluble *p*-sulfonatocalixarenes have been synthesized and found to be highly water soluble, unlike the hydrophobic *p*-*t*-butyl derivatives.[75] The sulfonated calixarenes form a variety of metal complexes where the metal is usually bound to the sulfonato groups of the calixarene.

Finally, both upper and lower rim substitution have been used to produce a class of macrocycles referred to as *calixarene-crown ethers*, or *calixcrowns*. One simple example is shown here (**103**). These receptors combine characteristics of the crown ethers and calixarenes, and have been intensively studied for metal ion extraction, in particular, for the removal of cesium from nuclear waste.[76]

8 MISCELLANEOUS η^1O-DONOR LIGANDS[77]

8.1 Dialkyl Sulfoxides

The most widely studied is dimethyl sulfoxide (DMSO), with the number of studies increasing sharply in the mid-1960s, when DMSO became commercially available. DMSO can form O-bonded and S-bonded complexes, with hard metal ions generally forming O-bonded complexes and softer metal ions S-bonded complexes as expected.[78] Complexes such as $[RhCl_3(OSMe_2)(SMe_2O)_2]$, containing both O- and S-bonded DMSO, have been described, however.

DMSO complexes can often be prepared simply by dissolving the appropriate metal salt in DMSO, and then precipitating the complex by adding a less polar solvent such as benzene. The hydrated metal salt can often be used in this process, although in the preparation of other dialkyl sulfoxide solvates it has been found that removal of water is necessary.

8.2 Carboxylic Acid Amides

The carboxylic acid amides most commonly studied as ligands are formamide, acetamide, and the *N*-substituted derivatives, particularly *N*,*N*-dimethylformamide (DMF). These compounds are often used as solvents and have high dielectric constants, particularly when they contain an N–H bond, and such uses helped to stimulate interest in the amides as ligands. There are two possible donor atoms, N or O, but all complexes of the simple amide ligands, characterized by X-ray structure determination at least, have M–O bonds. The amides are usually terminal ligands but can bridge between metal atoms in some instances.

The carbonate acid amides are not generally as strongly bound as the dialkyl sulfoxides and water competes for coordination sites, giving products containing coordinated amide and water. Anhydrous reagents, or dehydration procedures using triethyl orthoformate or 2,2′-dimethoxypropane, are generally required in the preparation of such complexes. In addition, complexes containing the amide and an anionic ligand are often obtained when the anion has some coordinating ability (e.g. Cl^-, NO_3^-), to give molecular rather than ionic species.

8.3 Amine *N*-oxides

The majority of studies involve aromatic N–O ligands, some common examples being pyridine *N*-oxide and methyl substituted derivatives (**104–106**). They are versatile ligands, forming complexes with almost every element. The *N*-oxide ligands can often be displaced by water, and hence the complexes are generally prepared under anhydrous conditions.

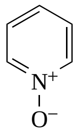
(**104**) pyNO

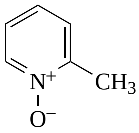
(**105**) 2-MepyNO

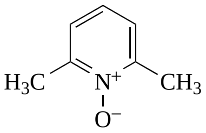
(**106**) 2,6-diMepyNO

The first-row transition metals generally form octahedral complexes $[M(pyNO)_6]^{n+}$ with pyridine *N*-oxide in the absence of other competing coordinating agents. An interesting example is $[Cu(pyNO)_6](ClO_4)_2$, which has a regular octahedron of O atoms about the Cu atoms, rather than the expected Jahn–Teller distortion. Ligands with substituents ortho to the nitrogen atom can tend to form complexes with lower coordination numbers, such as four-coordinate Co^{II} in $[Co(2,6\text{-diMepyNO})_4](ClO_4)_2$.

8.4 Phosphine Oxides and Arsine Oxides

These ligands have the general formulae OPX_3 where X = alkyl or aryl (R), OR, NR_2 or halide, and $OAsR_3$. The most widely studied of these is $OPPh_3$. Complexes are prepared by direct reactions of the ligand and a metal salt in an organic solvent. The ligands form M–O bonds, and can form bridges between metal atoms. In almost all cases, no more than four of the bulky triphenylphosphine oxide ligands are found coordinated to a metal center, with the remainder of the coordination sphere comprising of smaller ligands.

IR spectroscopy has been useful in detecting interactions between these ligands and metal ions, by virtue of the lowering of the P–O and As–O stretching frequencies upon complexation. ^{31}P NMR has also been investigated but is of limited use, since most systems exhibit fast ligand exchange on the NMR timescale.

9 RELATED ARTICLES

Dioxygen & Related Ligands; Iron Transport: Siderophores; Macrocyclic Ligands; Oxides: Solid-state Chemistry; Oxygen: Inorganic Chemistry; Polyoxometalates; Sol–Gel Synthesis of Solids.

10 REFERENCES

1. M. S. Wickleder, *Chem. Rev.*, 2002, **102**, 2011.
2. F. H. Allen, *Acta Crystallogr.*, 2002, **B58**, 380.
3. L. Helm and A. E. Merbach, *Coord. Chem. Rev.*, 1999, **187**, 151.
4. A. E. Martell and R. D. Hancock, in ‘Metal Complexes in Aqueous Solutions’, ed. J. P. Frackler, Plenum Press, New York, 1996.
5. A. Tutass, M. Klopfer, H. Huckstadt, and U. Cornelissen, *Z. Anorg. Allg. Chem.*, 2002, **628**, 1027.
6. J. Burgess, in ‘Comprehensive Coordination Chemistry’, eds. G. Wilkinson and R. D. Gillard, Pergamon, Oxford, 1987, Vol. 2, p. 295.
7. M. J. Drewitt, M. Niedermann, and M. C. Baird, *Inorg. Chim. Acta*, 2002, **340**, 207.
8. M. Ardon, A. Bino, and K. Michelsen, *J. Am. Chem. Soc.*, 1987, **109**, 1986.
9. D. Wei, E. I. Proynov, A. Milet, and D. R. Salahub, *J. Phys. Chem. A*, 2000, **104**, 2384.
10. M. T. Pope, *Prog. Inorg. Chem.*, 1991, **39**, 181.
11. O. M. Yaghi, M. O’Keefe, N. W. Ockwig, H. K. Chae, M. Eddaoudi, and J. Kim, *Nature*, 2003, **423**, 705.
12. N. Y. Turova, E. P. Turevskaya, V. G. Kessler, and M. I. Yanovskaya, ‘The Chemistry of Metal Alkoxides’, Kluwer, Amsterdam, 2002.
13. F. Bischoff and H. Adkins, *J. Am. Chem. Soc.*, 1924, **46**, 256.
14. E. Demarcay, *C. R. Hebd. Seances Acad. Sci.*, 1875, **80**, 51.
15. L. G. Hubert-Pfalzgraf, *Inorg. Chem. Commun.*, 2003, **6**, 102.
16. A. C. Jones, *J. Mater. Chem.*, 2002, **12**, 2576.
17. R. C. Mehrotra, A. Singh, and U. M. Tripathi, *Chem. Rev.*, 1991, **91**, 1287.
18. R. C. Mehrotra and A. Singh, *Prog. Inorg. Chem.*, 1997, **46**, 239.
19. C. G. Pierpont, *Coord. Chem. Rev.*, 2001, **216–217**, 99.
20. C. G. Pierpont, *Coord. Chem. Rev.*, 2001, **219–221**, 415.
21. P. Gütlich and A. Dei, *Angew. Chem., Int. Ed. Engl.*, 1997, **36**, 2734.
22. A. E. V. Gorden, J. Xu, and K. N. Raymond, *Chem. Rev.*, 2003, **103**, 4207.
23. Z. D. Liu and R. C. Hider, *Coord. Chem. Rev.*, 2002, **232**, 151.
24. R. C. Mehrotra, R. Bohra, and D. P. Gaur, ‘Metal β-Diketonates and Allied Derivatives’, Academic Press, London, 1978.
25. A. D. Garnovskii, A. P. Sadimenko, M. I. Sadimenko, and D. A. Garnovskii, *Coord. Chem. Rev.*, 1998, **173**, 31.
26. S. Shibata, S. Onuma, and H. Inoue, *Inorg. Chem.*, 1985, **24**, 1723.
27. S. Kawaguchi, ‘Variety in Coordination Modes of Ligands in Metal Complexes’, Springer Verlag, Berlin, 1988.
28. K. Nakamoto, ‘Infrared and Raman Spectra of Inorganic and Coordination Compounds. Part B: Applications in Coordination, Organometallic, and Bioinorganic Chemistry’, John Wiley & Sons, New York, 1997.
29. A. W. Maverick, D. R. Billodeaux, D. R. Ivie, F. R. Fronczek, and E. F. Maverick, *J. Incl. Phenom. Macrocycl. Chem.*, 2001, **39**, 19.

30. Y. Kobuke and Y. Satoh, *J. Am. Chem. Soc.*, 1992, **114**, 789.
31. G. Aromi, P. Gamez, O. Roubeau, H. Koojiman, A. L. Spek, W. L. Driessen, and J. Reedijk, *Angew. Chem., Int. Ed. Engl.*, 2002, **41**, 1168.
32. B. J. Hathaway, in ‘Comprehensive Coordination Chemistry’, eds. G. Wilkinson and R. D. Gillard, Pergamon, Oxford, 1987, Vol. 2, p. 413.
33. G. Aromi, S. Bhaduri, P. Artus, K. Folting, and G. Christou, *Inorg. Chem.*, 2002, **41**, 805.
34. F. B. Hulsbergen, R. W. M. ten Hoedt, G. C. Verschoor, J. Reedijk, and A. L. Spek, *J. Chem. Soc., Dalton Trans.*, 1983, 539.
35. C. Ruiz-Perez, Y. Rodriguez-Martin, M. Hernandez-Molina, F. S. Delgado, J. Pasan, J. Sanchiz, F. Lloret, and M. Julve, *Polyhedron*, 2003, **22**, 2111.
36. G. R. Frauenhoff, *Coord. Chem. Rev.*, 1992, **121**, 131.
37. C. Oldham, in ‘Comprehensive Coordination Chemistry’, eds. G. Wilkinson and R. D. Gillard, Pergamon, Oxford, 1987, Vol. 2, p. 435.
38. W. Levason, *Coord. Chem. Rev.*, 1997, **161**, 33.
39. R. D. Cannon and R. P. White, *Prog. Inorg. Chem.*, 1988, **36**, 195.
40. S. L. James, *Chem. Soc. Rev.*, 2003, **32**, 276.
41. J. Carranza, C. Brennan, J. Sletten, B. Vangdal, P. Rillema, F. Lloret, and M. Julve, *New J. Chem*, 2003, **27**, 1775.
42. L. A. Hall and D. J. Williams, *Adv. Inorg. Chem.*, 2001, **52**, 249.
43. D. B. Dell’Amico, F. Calderazzo, L. Labella, F. Marchetti, and G. Pampaloni, *Chem. Rev.*, 2003, **103**, 3857.
44. J. D. Pedrosa de Jesus, in ‘Comprehensive Coordination Chemistry’, eds. G. Wilkinson and R. D. Gillard, Pergamon, Oxford, 1987, Vol. 2, p. 461.
45. R. C. Mehrotra, in ‘Comprehensive Coordination Chemistry’, eds. G. Wilkinson and R. D. Gillard, Pergamon, Oxford, 1987, Vol. 2, p. 505.
46. C. J. Pedersen, *J. Am. Chem. Soc.*, 1967, **89**, 2495.
47. J.-M. Lehn, *Angew. Chem., Int. Ed. Engl.*, 1988, **27**, 89.
48. C. D. Gutsche, in ‘Calixarenes Revisited’, ed. J. F. Stoddart, The Royal Society of Chemistry, Cambridge, 1998.
49. G. W. Gokel, in ‘Crown Ethers and Cryptands’, ed. J. F. Stoddart, The Royal Society of Chemistry, 1991.
50. D. J. Cram, *Angew. Chem., Int. Ed. Engl.*, 1986, **25**, 1039.
51. J. W. Steed, *Coord. Chem. Rev.*, 2001, **215**, 171.
52. J. S. Bradshaw and R. M. Izatt, *Acc. Chem. Res.*, 1997, **30**, 338.
53. R. M. Izatt, K. Pawlak, J. S. Bradshaw, and R. L. Bruening, *Chem. Rev.*, 1991, **91**, 1721.
54. W. W. Brennessel, V. G. Young, and J. E. Ellis, Jr, *Angew. Chem., Int. Ed. Engl.*, 2002, **41**, 1211.
55. T. J. Lee, H.-R. Sheu, T. I. Chiu, and C. T. Chang, *Acta Crystallogr.*, 1983, **C39**, 1357.
56. M. L. Cole, C. Jones, and P. C. Junk, *Dalton Trans.*, 2002, 896.
57. M. Dobler and R. P. Phizackerley, *Acta Crystallogr.*, 1974, **B30**, 2748.
58. K. V. Domasevitch, V. V. Ponomareva, and E. B. Rusanov, *J. Chem. Soc., Dalton Trans.*, 1997, 1177.
59. M. Dobler, J. D. Dunitz, and P. Seiler, *Acta Crystallogr.*, 1974, **B30**, 2741.
60. L. Ventelon, C. Lescop, T. Arliguie, P. C. Leverd, M. Lance, M. Nierlich, and M. Ephritikhine, *Chem. Commun.*, 1999, 659.
61. D. L. Hughes, *J. Chem. Soc., Dalton Trans.*, 1975, 2374.
62. R. D. Rogers and C. B. Bauer, in ‘Comprehensive Supramolecular Chemistry’, eds. J. L. Atwood, J. E. D. Davies, D. D. MacNicol, and F. Vögtle, Pergamon, Oxford, 1996, Vol. 1, p. 315.
63. T. B. Vance, E. M. Holt, D. L. Varie, and S. L. Holt, Jr, *Acta Crystallogr.*, 1980, **B36**, 153.
64. P. Groth, *Acta Chem. Scand. Ser. A*, 1982, **36**, 109.
65. J.-C. G. Bünzli and D. Wessner, *Coord. Chem. Rev.*, 1984, **60**, 191.
66. Z. Asfari, V. Böhmer, J. Harrowfield, and J. Vicens eds, ‘Calixarenes 2001’, Kluwer, Dordrecht, 2001.
67. B. M. Furphy, J. M. Harrowfield, M. I. Ogden, B. W. Skelton, A. H. White, and F. R. Wilner, *J. Chem. Soc., Dalton Trans.*, 1989, 2217.
68. J. M. Harrowfield, M. I. Ogden, W. R. Richmond, and A. H. White, *Chem. Commun.*, 1991, 1159.
69. C. Floriani and R. Floriani-Moro, in ‘Calixarenes 2001’, ed. J. Vicens, Kluwer, Dordrecht, 2001, p. 536.
70. C. Redshaw, *Coord. Chem. Rev.*, 2003, **244**, 45.
71. P. Thuéry, M. Nierlich, J. Harrowfield, and M. Ogden, in ‘Calixarenes 2001’, ed. J. Vicens, Kluwer, Dordrecht, 2001, p. 561.
72. F. Arnaud-Neu, M. A. McKervey, and M.-J. Schwing-Weill, in ‘Calixarenes 2001’, ed. J. Vicens, Kluwer, Dordrecht, 2001, p. 385.
73. F. Cadogan, K. Nolan, and D. Diamond, in ‘Calixarenes 2001’, ed. J. Vicens, Kluwer, Dordrecht, 2001, p. 627.
74. S. E. Matthews, P. Schmitt, V. Felix, M. G. B. Drew, and P. D. Beer, *J. Am. Chem. Soc.*, 2002, **124**, 1341.
75. A. Casnati, D. Sciotto, and G. Arena, in ‘Calixarenes 2001’, eds. Z. Asfari, V. Böhmer, J. Harrowfield, and J. Vicens, Kluwer, Dordrecht, 2001, p. 440.
76. F. Arnaud-Neu, M.-J. Schwing-Weill, and J.-F. Dozol, in ‘Calixarenes 2001’, eds. Z. Asfari, V. Böhmer, J. Harrowfield, and J. Vicens, Kluwer, Dordrecht, 2001, p. 642.
77. P. L. Goggin, in ‘Comprehensive Coordination Chemistry’, eds. G. Wilkinson and R. D. Gillard, Pergamon, Oxford, 1987, Vol. 2, p. 487.
78. M. Calligaris and O. Carugo, *Coord. Chem. Rev.*, 1996, **153**, 83.

Zeolites

Craig D. Williams
University of Wolverhampton, Wolverhampton, UK

Based in part on the article Zeolites by Alan Dyer which appeared in the Encyclopedia of Inorganic Chemistry, First Edition.

1 Introduction 2
2 Zeolite Structures 3
3 Zeolite Compositions 10
4 Zeolite Genesis 19
5 Zeolite Properties 26
6 Commercially Useful Zeolites and their Well Known Uses 31
7 Related Articles 35
8 References 35

Glossary

Atlas: ch. Baerlocher, W. M. Meier and D. H. Olson, 'Atlas of Zeolite Structure Types', Elsevier, 2001

Basalt: fine-grained rock of volcanic origin

Biogenic: produced from living organisms

Borolanite: coarse-grained volcanic rock with high feldspar and felspathoid content

Boronation: reaction of borane (BH_3) with OH groups

Carboniogenic: production of carbon cations from hydrocarbons

Clathrate: a three-dimensional assemblage of molecular units, held together by weak van der Waals type forces, forming cavities of molecular dimensions in which can be located 'guest' molecules

Cracking: splitting of the long hydrocarbon chains in crude oil to small molecular units

Crown ether: complex synthetic organic molecule containing ether 'rings'

Crystal system: classification of crystals by the symmetry of their external or internal geometries

Cubic close packing: arrangement of atoms in a crystal in their closest possible way having cubic symmetry

Diagenesis: process that affects a sediment while it is at, or near, the Earth's surface (caused by temperature and pressure)

Dyke: a vertical sheet of igneous rock extruded into an existing rock

Fault plane: layers in a crystal structure at which defect(s) arrangements in the normal stacking of the layer can occur

Feldspar: alkali aluminosilicate rocks with dense framework structures

Felspathic: containing feldspar minerals

Felspathoid: natural aluminosilicate minerals with framework structures containing water and salt molecules in their cavities

Gas–solid chromatography: analytical separation of gases on a solid, porous, substrate

Granodiorite: coarse-grained acid rock of volcanic origin

Guest: molecule trapped inside a clathrate

Hexagonal close packing: as for cubic close packing but with adoption of hexagonal symmetry

Hydrolysis: splitting of water molecules to give H^+ and OH^- species

Ignimbrite: tuffs welded by their high-temperature deposition caused by the emission of an incandescent cloud of gas and ash from a volcano (a 'nuée ardente')

Intergrowth: simultaneous crystallization of two minerals

Intumescence: visible loss of water with heating

Isotypic: having the same structure

Magma: molten fluid formed within the Earth's crust or mantle containing molten silicates, water, and gases; magma that is extruded on to the surface of the Earth is called lava

Metamorphism: change created in rocks by heat, pressure, and chemically active fluids within the Earth's crust

Meteoric (water): water that percolates rocks from above (e.g. from rivers, rain, snow, etc.)

Microporous: solid material containing pores of less than about 20 Å in diameter

Molecular sieve: a structure that can separate molecules on the basis of size

Mepheline: a sodium felspathoid

Pegmatite: coarse-grained mineral vein with well formed crystals

Plagioclase: sodium/calcium aluminosilicate mineral of the feldspar group

Pyroclastic: ejected by volcanic eruption

Radiolarians: a protozoon having a silica skeleton

Sedimentary: processes whereby rocks (minerals) are formed from materials derived from other rocks by weathering, erosion, and transportation

Silanation: reaction of silane (SiH_4) with OH groups

Sorption: uptake of liquid or gas by a microporous material

Space-filling: spatial arrangement of polyhedra such that each polyhedron shares all its faces with other polyhedra

Stacking fault: misalignment of layer(s) arising from a fault plane

Stoichiometry: the relative numbers of atomic constituents making up a chemical compound

Truncated octahedron: a polyhedron composed of eight hexagonal and six square faces

Tuff: ash and dust blown out of a volcano during eruption and subsequently consolidated

Unit cell: the smallest repeating structural unit in a solid structure at the atomic scale

Zeolites: natural and synthetic hydrated aluminosilicates with open framework structures enclosing cavities and channels in which reside mobile cations and water molecules

Zeotypes: zeolite-like framework structures with atoms other than Si, Al in the tetrahedral positions in the framework

---

Abbreviations

$AlPO_4$ = Aluminophosphate; BP = British Petroleum; BET = Brunauer, Emmett, and Teller; DABCO = 1,4-diazabicyclo[2,2,2]octane; FCAPO = Framework constituent aluminophosphate; FCC = Fluidized bed cracking catalyst; LPG = Liquid petroleum gas; MAS NMR = Magic angle spinning nuclear magnetic resonance; MeAPO = Metal aluminophosphate; MeAPSO = Metal silicoaluminophosphate; PSA = Pressure swing application; REY = Rare earth exchanged synthetic zeolite Y; SAPO = Silicoaluminophosphate; SBU = Secondary building unit; T = tetrahedrally coordinated atom; TEA = Triethanolamine; TMA = Tetramethylammonium; TPA = Tetrapropylammonium; UOP = Union Oil Products, USA; USY = Ultrastable synthetic zeolite Y; VEB = VEB Leuna Werke, Bitterfeld, Germany; XAPO = Aluminophosphate containing Fe, Ti, as T atoms; ZSM = Zeolite Socony Mobil.

---

1 INTRODUCTION

In 1756, Cronstedt,[1] a Swedish mineralogist, discovered a new mineral that visibly lost water when heated. Because of this easily observed intumescence, he coined the word ‘zeolite’ from two Greek words ‘zein’ and ‘lithos’, meaning ‘boiling stone’, to name the new species. Cronstedt’s mineral was later named stilbite.

This facile loss of water was shown to be reversible by Damour[2] (1840) and, in 1858, Eichorn[3] showed that the zeolite chabazite contained alkali and alkaline earth metals, which were capable of being reversibly replaced, that is, the zeolite exhibited cation-exchange properties. Analysis of zeolite minerals showed them to be aluminosilicates and their easy loss of water and cation exchange was evidence for the open nature of their structures, often likened to a sponge. The description ‘zeolitic water’ has been widely used to describe loosely held water in any solid.

The need for commercial water softeners prompted attempts to synthesize zeolites. These were not successful, although St Claire Deville[4] (1862) claimed to be able to make levyne. The early attempts at zeolite synthesis have been extensively reviewed by Morely and Ingersoll[5] (1937). Lack of available, definitive, characterization methods makes it difficult to confirm their work.

Progress to 1925 was largely through mineralogical identification of new zeolite species but in this year Weigel and Steinhoff[6] reported that chabazite sorbed water, methanol and ethanol, and methanoic (formic) acid but excluded acetone, ether, and benzene. The significance of this observation was realized by McBain,[7] who described it as a ‘molecular sieving’ effect (1932). In 1930, Taylor[8] solved the structure of analcime and Pauling[9] published a series of seminal papers based upon single-crystal X-ray studies, which showed how silicates and aluminosilicates were constructed from tetrahedral building blocks, that is, the $[SiO_4]^{4-}$ and $[AlO_4]^{5-}$ units of structure. His work included the zeolite natrolite and the felspathoids sodalite and cancrinite, which are now known to have structures closely related to the zeolite minerals. Figure 1 shows the Si/Al coordination tetrahedra and their linking to create the chain-like element of structure identified in natrolite. The importance of Pauling’s work was that it illustrated the way in which the tetrahedral units linked by sharing all corners to produce the three-dimensional framework structures associated with the zeolite and felspathoid minerals. It is this regular and reproducible molecular architecture that confers on the zeolites their uniquely useful properties.

This was evident to R. M. Barrer[10] who from the mid-1930s to 1996 provided the scientific base upon which the current widespread industrial use of zeolites has been founded. His pioneering work on zeolite synthesis, ion exchange, gas sorption, and structures, from both theoretical and practical standpoints, has spawned the continuing growth of zeolite science and technology encouraged by the discovery of their catalytic properties in the early 1960s. The world’s zeolite literature continues to grow at a rate of close to 100 publications per week. This is almost entirely devoted to synthetic materials of zeolite structure type, and has caused a reassessment of the strict mineralogical concept of zeolites as aluminosilicates containing mobile cations and water molecules that promote the properties of cation exchange and reversible water uptake.

This will be considered in detail later in this article but it is convenient first to consider the assemblages of (Si,Al)

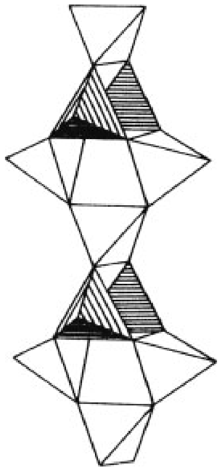

Figure 1 Si,AlO_4 tetrahedra linked as in the zeolite natrolite

tetrahedra, which can be recognized as forming part of zeolitic frameworks.

2 ZEOLITE STRUCTURES

2.1 Introduction to Zeolite Structures

The picture of a zeolite structure can now be refined as closer to a honeycomb of channels and cavities created by rigidly (at room temperature) linked tetrahedra. The three-dimensional structures are constructed from pores of molecular dimensions, that is, zeolites are microporous solids. The *Atlas of Zeolite Structure Types* 5th Edition edited by Baerlocher, Meier, and Olson.[11] defines the framework density in terms of the number of tetrahedrally coordinated atoms (T) per unit of 1000 Å^3, and sets 20–21 T per 1000 Å^3 as the lower limit of micro-porosity. The current upper limit is about 11 T per 1000 Å^3 in a synthetic framework structure known as cloverite. The *Atlas* will be used as a major source throughout this section. The *Atlas* lists all known zeolite-type frameworks and encompasses materials not previously included in the restricted definition of zeolites as being only continuous aluminosilicate structures. This extension will be expanded on later but it is important to appreciate that the major bases for definition are the recognition of micro-porosity, as mentioned above, and the identification of structural subunits constraining the pores and cavities within the frameworks. These are called secondary building units (SBUs) and can be simple arrangements of tetrahedra to construct obvious arrangements such as four-, six-, or eight-membered rings or more complex structures (Figure 2). They contain up to 16 tetrahedral (T) atoms and are identified as being the only SBU linking to produce an entire and unique zeolite framework. The more simple SBUs are often described as oxygen rings or windows (clearly linkage of, say, six tetrahedra by two of their corners to create an hexagonal ring will also produce a ring of six oxygens).

Table 1 lists their shorthand notation often found in zeolite texts.

Table 1 Simple zeolite SBUs and their shorthand notation

Number of linked tetrahedra	SBU created	Shorthand description^a
4	4 oxygen ring	S4R
5	5 oxygen ring	S5R
6	6 oxygen ring	S6R
8	8 oxygen ring	S8R
8	4–4 oxygen rings	D4R
12	6–6 oxygen rings	D6R
16	8–8 oxygen rings	D8R

^{a}S = single, D = double.

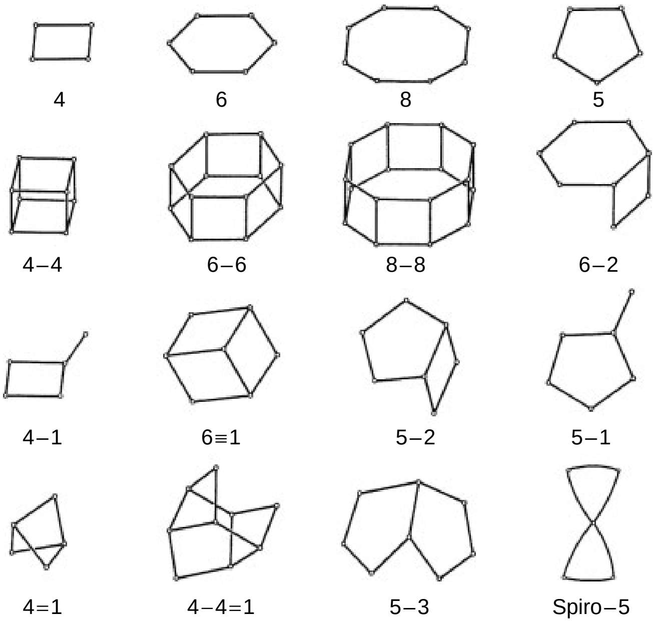

Figure 2 Secondary building units (SBUs) of zeolite structures. (Reproduced by permission of Butterworth-Heinemann from Baerlocher, Meier, and Olson[11])

2.2 Oxygen Windows

In some zeolite-type structures, the spatial linkages between these SBUs produce oxygen windows that define the useful pore diameters within the zeolite structures. These provide another way of classifying zeolite frameworks but it must be realized that these oxygen windows arise from the geometric arrangements of SBUs and are not necessarily the SBUs themselves.

Tables 2–5[11] lists all known zeolite-type frameworks on the basis of their major pore dimensions, and Table 6 illustrates the shorthand notation used. The pore diameter dimensions are based upon crystallographic measurements assuming that the oxygen radius is 1.35 Å. Note that not all pores are circular, or planar, so maximum and minimum diameters are given in these cases and even these may be

Table 2 Zeolite frameworks by channel geometries of largest pores in structures containing 14, 18, and 20-membered oxygen rings[11]

IUPAC code	Name	Ring	Channel geometries and ring size (Å)
–CLO	Cloverite	20	⟨100⟩ *20* 13.2 × 4.0***|⟨100⟩ *8* 3.8***
VFI	VPI-5	18	[100] *18* 12.1*
AET	AlPO$_4$-8	14	[001] *14* 7.9 × 8.7*
CFI	CIT-5	14	[010] *14* 7.2 × 7.5*
DON	UTD-1F	14	[010] *14* 8.1 × 8.2*
OSO	OSB-1	14	[001] *14* 5.4 × 7.3*↔ ⊥ [001] *8* 2.8 × 3.3**

Table 3 Listing of zeolite frameworks containing 12-membered rings (12SR) in their main channels[11]

IUPAC code	Name	Channel geometries
AFI	$AlPO_4$-5	[100] *12* 7.3*
AFR	SAPO-40	[100] *12* 6.7 × 6.9* ↔ [010] *8* 3.7*
AFS	MAPSO-46	[101] *12* 6.3* ↔ ⊥[001] *8* 4.0 × 4.0**
AFY	CoAPO-50	[001] *12* 6.1* ↔ ⊥[001] *8* 4.0 × 4.3**
ASV	ASV-7	[001] *12* 4.1 × 4.1*
ATO	$AlPO_4$-31	[001] *12* 5.4*
ATS	MAPO-36	[001] *12* 6.5 × 7.5*
*BEA	Beta	[001] *12* 7.6 × 6.4 ↔ ⟨100⟩ *12* 5.5 × 5.5**
BOG	Boggsite	[001] *12* 7.0 × 7.0* ↔ [101] *10* 5.2 × 5.8*
BPH	Beryllophosphate-H	[001] *12* 6.2 × 6.7* ↔ ⊥[001] *8* 3.0 × 3.2**
CAN	Cancrinite	[001] *12* 5.9*
CON	CIT-1	[001] *12* 6.4 × 7.0* ↔ [100] *12* 7.0 × 5.9* ↔ [010] *10* 5.1 × 4.5*
CZP	Chiral Zincophosphate	[001] *12* 3.8 × 7.2*
DFO	DAF-1	{[001] *12* 7.3 × 7.3 ↔ ⊥ [001] 83.4 × 5.6}*** ↔ {[001] 126.2 × 6.2 ↔ ⊥ [001] 105.4 × 6.4}***
EMT	EMC-2	[001] *12* 7.4 × 7.6* ↔ ⊥ [001] *12* 6.6 × 6.7**
FAU	Faujasite	⟨111⟩ *12* 7.4***
GME	Gmelinite	[001] *12* 7.0** ↔ ⊥ [001] *8* 3.6 × 3.9**
GON	GUS-1	[001] *12* 5.4 × 6.6*
IFR	ITQ-4	[001] *12* 6.2 × 7.2*
ISV	ITQ-7	⟨100⟩ *12* 6.1 × 6.5** ↔ [001] 125.9 × 6.6*
LTL	Linde Type L	[001] *12* 7.1*
MAZ	Mazzite	[001] *12* 7.4⊥ [001] 83.4 × 5.6*
MEI	ZSM-18	[001] *12* 6.9* ↔ ⊥ [001] 73.2 × 3.5**
MOR	Mordenite	[001] *12* 6.5 × 7.0* ↔ [010] *8* 2.6 × 5.7*
MTW	ZSM-12	[101] *12* 5.5 × 5.9*
OFF	Offretite	[001] *12* 6.7* ↔ ⊥ [001] *8* 3.6 × 4.9**
OSI	UiO-6	[001] *12* 5.2 × 6.0*
–RON	Roggianite	[001] *12* 4.3 × 4.3*
SAO	STA-1	⟨100⟩ *12* 6.5 × 7.2** ↔ [001] *12* 7.0 × 7.0*
SBE	UCSB-8Co	⟨100⟩ *12* 7.2 × 7.4** ↔ [001] *8* 4.0 × 4.0*
SBS	UCSB-6GaCo	[001] *12* 6.8 × 6.8 ↔ ⊥ [001] *12* 6.9 × 7.0**
SBT	UCSB-10GaZn	[001] *12* 6.4 × 7.4* ↔ ⊥ [001] *12* 7.3 × 7.8**
SFE	SSZ-48	[010] *12* 5.4 × 7.6*
VET	VPI-8	[001] *12* 5.9 × 5.9*

altered by the state of hydration of the framework and also are temperature dependent. The maximum flexibility of the oxygen windows is roughly 0.3 Å over their useful temperature range. Included in Tables 2–5 are the structure-type codes allocated by the IZA Structure Commission following the rules set up by an International Union of Pure and Applied Chemistry (IUPAC) Commission on Zeolite Nomenclature. These tables include:

1. natural aluminosilicate zeolites;
2. natural minerals with zeolite frameworks but with tetrahedrally coordinated atom (T) atoms *other* than Si or Al (zeotypes).
3. structures basically of zeolite framework type but not strictly three-dimensional in that a proportion of the subunits are not linked by all tetrahedral corners; in these cases, terminal OH groups are included in the incomplete 'frameworks' and this is signified by a hyphen that precedes the IUPAC code, as in '–PAR' for partheite;
4. synthetic aluminosilicate zeolites;
5. synthetic zeotypes;
6. synthetic and natural phases of silica constructed from SBUs;
7. felspathoids, for example, cancrinite; this arises because the cancrinite cage structure can be identified as a structural subunit of zeolites, that is, as a zeolitic cavity, and the *Atlas* includes several felspathoid frameworks because of their close relationship to zeolites;

These subheadings will be used later to furnish a more detailed description of zeolite structure types.

2.3 Zeolite Channels

Each channel system is defined as being one-, two-, or three-dimensional with respect to the zeolite framework and a simple notation describes whether or not the channel

Table 4 Listing of zeolite frameworks containing 10 and nine-membered rings (10SR, 9SR) in their main channels[11]

IUPAC code	Name	Channel geometries
AEL	$AlPO_4$-11	[100] *10* 3.9 × 6.3*
AFO	$AlPO_4$-41	[001] *10* 4.3 × 7.0*
AHT	AlPO-H2	[001] *10* 3.3 × 6.8*
CGF	Co-Ga-Phosphate-5	{[100] *10* 2.5 × 9.2* + *8* 2.1 × 6.7*} ↔ [001] *8* 2.4 × 4.8*
CGS	Co-Ga-Phosphate-6	{[001] *10* 3.5 × 8.1 ↔ [100] *8* 2.5 × 4.6}***
DAC	Dachiardite	[010] *10* 3.4 × 5.3* ↔ [001] *8* 3.7 × 4.8*
EPI	Epistilbite	[100] *10* 3.4 × 5.6* ↔ [001] *8* 3.7 × 5.2*
EUO	EU-1	[100] *10* 4.1 × 5.7* with large side pockets
FER	Ferrierite	[001] *10* 4.2 × 5.4* ↔ [010] *8* 3.5 × 4.8*
HEU	Heulandite	{[001] *10* 3.0 × 7.6 + 83.3 × 4.6*} ↔ [100] *8* 2.6 × 4.7*
LAU	Laumontite	[100] *10* 4.0 × 5.3*
MEL	ZSM-11	⟨100⟩ *10* 5.3 × 5.4***
MFI	ZSM-5	{[010] *10* 5.3 × 5.6 ↔ [100] *10* 5.1 × 5.5}***
MFS	ZSM-57	[100] *10* 5.1 × 5.4* ↔ [010] *8* 3.3 × 4.8*
MTT	ZSM-23	[001] *10* 4.5 × 5.2*
MWW	MCM-22	⊥ [001] *10* 4.0 × 5.5** |⊥ [001] 4.1 × 5.1**
NES	NU-87	[100] *10* 4.7 × 6.0**
–PAR	Partheite	[001] *10* 3.5 × 6.9*
SFF	SSZ-44	[001] *10* 5.4 × 5.7*
STF	SSZ-35	[001] *10* 5.4 × 5.7*
STI	Stilbite	[100] *10* 4.9 × 6.1 ↔ [101] *8* 2.7 × 5.6*
TER	Terranovaite	[100] *10* 5.0 × 5.0* ↔ [001] *10* 4.1 × 7.0*
TON	Theta-1	[001] *10* 4.4 × 5.5*
WEI	Weinebeneite	[001] *10* 3.1 × 5.4* ↔ [100] *8* 3.3 × 5.0*
–WEN	Wenkite	⟨100⟩ *10* 2.6 × 4.9** ↔ [001] *8* 2.2 × 2.7*
–CHI	Chiavennite	[001] *9* 3.9 × 4.3*
LOV	Lovdarite	[010] *9* 3.2 × 4.4* ↔ [100] *8* 3.6 × 3.7*
NAT	Natrolite	⟨100⟩ *8* 2.6 × 3.9** ↔ [001] *9* 2.5 × 4.1*
RSN	RUB-17	[100] *9* 3.3 × 4.4* ↔ [001] *9* 3.1 × 4.3* ↔ [010] *8* 3.4 × 4.1*
STT	SSZ-23	[101] *9* 3.7 × 5.3* ↔ [001] *7* 2.4 × 3.5*
VSV	VPI-7	[01-1] *9* 3.3 × 4.3* ↔ [011] *9* 2.9 × 4.2* ↔ [011] *8* 2.1 × 2.7*

systems interconnect and their spatial relationships to the crystallographic axes of the zeolite unit cell (see Table 6).

Three examples will suffice to demonstrate this information: Figure 3 shows the polyhedral units in the synthetic zeolite Linde Type A, which link to provide a three-dimensional interconnecting array of channels, Figure 4 illustrates the essentially two-dimensional system of channels in the mordenite framework, and Figure 5 shows the major channels in synthetic zeolite Linde Type L arranged as parallel one-dimensional channels and shown as a stereo pair. Table 6 lists the *Atlas* notations for these structures with explanations, including the symbols used in Tables 2–5.

2.4 Zeolite Structural Families

As has been discussed already, the primary building unit of all zeolite and zeotype frameworks is the tetrahedral unit, which can be linked to produce the SBUs seen in Figure 2. In some cases, it is convenient to describe zeolite structure-type frameworks by the recognition of larger assemblages of tetrahedra. Examples of this approach will now be discussed to emphasize how it can be used to simplify complex frameworks.

2.4.1 Structures Based upon Linkages of the Double Hexagonal Ring SBU, (D6R)

The chabazite framework is a sequence of D6R units joined, via S4Rs, into the same sequence as that in cubic close packing, that is, ABCABCABC (see Figure 6, also Figure 2 and Table 1). This means that an easy way to describe the chabazite structure is that of a NaCl-type arrangement with a D6R unit at each corner of a simple cubic assemblage.

This produces a large cavity, created by the D6R constructional elements, and access to it is governed by passage through an eight-oxygen aperture (S8R) as listed in Table 5. Eleven specific cation and water locations have been identified by single-crystal X-ray studies within the chabazite framework. In the natural mineral, some calcium ions reside in the D6Rs in the dehydrated state, but in the fully hydrated mineral, the cations have near complete coordination spheres of water and ‘float’ inside the larger cavities.

The movement from relatively loosely bound sites within the larger cavities to smaller cages with little associated water is common behaviour for cations in zeolites. Their presence in the large cavities, in what has been described as a brine is, of course, the source of facile cation-exchange properties. It

Table 5 Listings of zeolite frameworks containing eight-membered rings (S8R) in their main channels[11]

IUPAC code	Name	Channel geometries
ABW	Li-A	[001] 8 3.4 × 3.4*
ACO	ACP-1	⟨100⟩ 8 2.8 × 3.5** ↔ [001] 8 3.5 × 3.5*
AEI	AlPO$_4$	[001] 8 ≈ 3.8 × 3.8* ↔ ⊥ [001] 8 ≈ 3.8 × 3.8**
AEN	AlPO-EN3	[100] 8 3.1 × 4.3 ↔ [010] 8 2.7 × 5.0*
AFN	AlPO-14	[100] 8 1.9 × 4.6* ↔ [010] 8 2.1 × 4.9* ↔ [001] 8 3.3 × 4.0*
AFT	AlPO$_4$-52	⊥ [001] 8 2.8 × 4.4***
AFX	SAPO-56	⊥ [001] 8 3.4 × 3.6***
ANA	Analcime	Irregular distorted 8-rings
APC	AlPO$_4$-C	[001] 8 3.4 × 3.7* ↔ [100] 8 2.9 × 5.7*
APD	AlPO$_4$-D	[010] 8 2.1 × 6.3* ↔ [001] 8 1.3 × 5.8*
ATN	MAPO-39	[001] 8 4.0*
ATT	AlPO$_4$-12-TAMU	[100] 8 4.2 × 4.6* ↔ [010] 8 3.8 × 3.8*
ATV	AlPO$_4$-25	[001] 8 3.0 × 4.9*
AWO	AlPO-21	[100] 8 2.7 × 5.5*
AWW	AlPO$_4$-22	[001] 8 3.9*
BIK	Bikitaite	[001] 8 2.8 × 3.7*
BRE	Brewsterite	[100] 8 2.3 × 5.0* ↔ [001] 8 2.8 × 4.1*
CAS	Cesium aluminosilicate	[100] 8 4.7 × 2.2*
CHA	Chabazite	⊥ [001] 8 3.8 × 3.8***
DDR	Deca-dodecasil	⊥ [001] 8 3.6 × 4.4**
DFT	DAF-2	[001] 8 4.1 × 4.1* ↔ [100] 8 1.8 × 4.7* ↔ [010] 8 1.8 × 4.7*
EAB	TMA-E	⊥ [001] 8 3.7 × 5.1**
EDI	Edingtonite	[110] 8 2.8 × 3.8** ↔ [001] 8 variable*
ERI	Erionite	⊥ [001] 8 3.6 × 5.1***
ESV	ERS-7	[010] 8 3.5 × 4.7*
GIS	Gismondine	{[100] 8 3.1 × 4.5 ↔ [010] 8 2.8 × 4.8}***
GOO	Goosecreekite	[100] 8 2.8 × 4.0* ↔ [010] 8 2.7 × 4.1* ↔ [001] 8 2.9 × 4.7*
ITE	ITQ-3	[010] 8 3.8 × 4.3* ↔ [001] 8 2.7 × 5.8*
JBW	NaJ	[100] 8 3.7 × 4.8*
KFI	ZK-5	⟨100⟩ 8 3.9***|⟨100⟩ 8 3.9***
LEV	Levyne	⊥ [001] 8 3.6 × 4.8**
LTA	Linde Type A	⟨100⟩ 8 4.1***
MER	Merlinoite	[100] 8 3.1 × 3.5 ↔ [010] 8 2.7 × 3.6* ↔ [001] {8 3.4 × 5.1* + 8 3.3 × 3.3*}
MON	Montesommaite	[100] 8 3.2 × 4.4* ↔ [001] 8 3.4 × 3.6*
MTF	MCM-35	[001] 8 3.6 × 3.9*
PAU	Paulingite	⟨100⟩ 8 3.8*** |⟨100⟩ 8 3.8***
PHI	Phillipsite	[100] 8 3.6* ↔ [010] 8 3.0 × 4.3* ↔ 8 3.2 × 3.3*
RHO	Rho	⟨100⟩ 8 3.6*** |⟨100⟩ 8 3.6***
RTE	RUB-3	[001] 8 3.7 × 4.4*
RTH	RUB-13	[100] 8 3.8 × 4.1* ↔ [001] 8 2.5 × 5.6*
SAS	STA-6	[001] 8 4.2 × 4.2*
SAT	STA-2	⊥ [001] 3.0 × 5.5***
SAV	Mg-STA-7	⟨100⟩ 8 3.8 × 3.8** ↔ [001] 8 3.9 × 3.9*
THO	Thomsonite	[010] 8 2.3 × 3.9* ↔ [010] 8 2.2 × 4.0* ↔ [001] 8 2.2 × 3.0*
TSC	Tschörtnerite	⟨100⟩ 8 4.2 × 4.2*** ↔ ⟨110⟩ 8 3.1 × 5.6***
VNI	VPI-9	{⟨110⟩ 8 3.1 × 4.0 ↔ [001] 8 3.5 × 3.6}***
YUA	Yugawaralite	[100] 8 2.8 × 3.6* ↔ 8 3.1 × 5.0*
ZON	ZAPO-M1	[100] 8 2.5 × 5.1* ↔ [010] 8 3.7 × 4.4*

has been estimated that the hydrated cation concentration in zeolite cavities is around 5 M.

Gmelinite also has a framework, which can be described as a linkage of D6R units. In this case, they are arranged in the sequence ABABAB, that is, that of a hexagonal close-packed array. This architecture also produces a large cavity containing sites for four divalent hydrated cations.

An extension of this approach can be to consider stackings of S6R SBUs in the zeolite structure so that chabazite would be described as AABBCCAABBCC and gmelinite as AABBAABB. On this basis, erionite has the stacking arrangement of AABAAC and offretite AABAAB (Figure 7). These zeolites often occur naturally as intergrowths, and from the same syntheses, as might be anticipated from their framework similarities.

2.4.2 *Structures Based upon Linkages Between Chains of Tetrahedra*

In phillipsite, S4R are linked to form chains resembling a double crankshaft (Figure 8). Gismondine has a related

Table 6 Examples of the notation used in Baerlocher, Meier, and Olson[11] to describe the major channels in zeolitic frameworks

Zeolite framework	IUPAC code	Notation[a]	Description of notation
Linde type A	LTA	⟨100⟩ *8* 4.1***	⟨100⟩: channels parallel to all crystallographic equivalent axes in the cubic system, viz. x, y, z; *8*: channel constricted by an S8R; 4.1: the crystallographic dimension of the S8R in Å
Ferrierite	FER	[001] *10* 4.2 × 5.4* ↔ [010] *8* 3.5 × 4.8*	Channels parallel to the 001 crystallographic axis constricted by a 10SR with dimensions 4.2 × 5.4 Å intersecting (↔ or ↔) with channels parallel to the 010 axis constricted by an S8R with dimensions 3.5 × 4.8 Å
Linde type L	LTL	[001] *12* 7.1*	Channels parallel to the 001 axis constricted by 12SR of 7.1 Å diameter

[a] Number of asterisks denotes dimensionality of the channel. Other symbols used in Tables 2–5: | no direct access from one channel system to another; ⊥ channels interconnect at right angles; + two constrictions to the same channel.

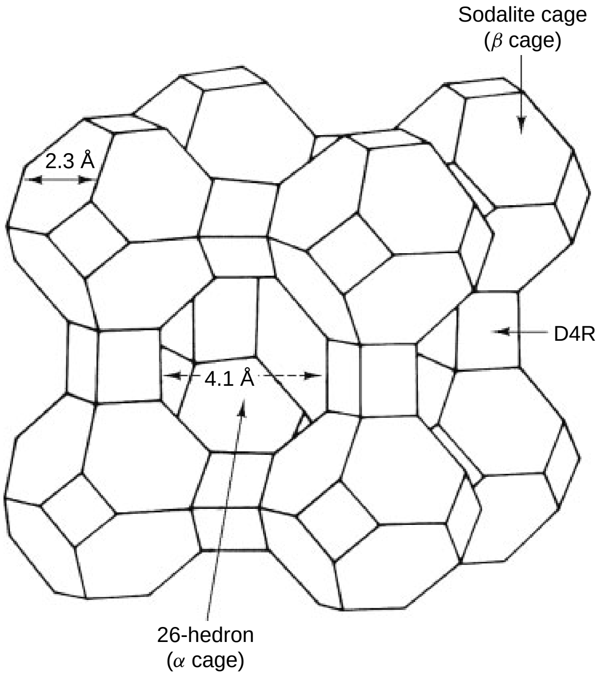

Figure 3 Framework of synthetic zeolite A (LTA) showing constituent cage structures and their dimensions

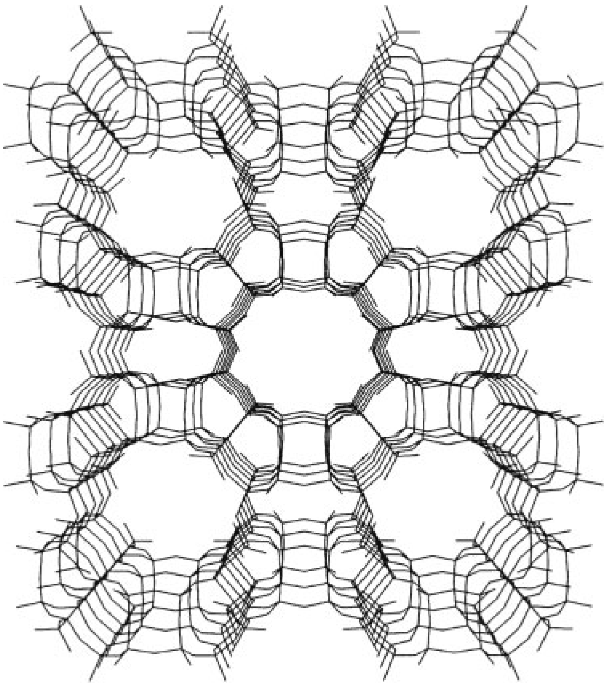

Figure 4 Framework of mordenite (MOR) showing channels

structure but with chains joined together in a different way, as shown in Figure 9. The differences can be seen to be variations in the relative spatial orientations of the linked tetrahedra described as up (U) and down (D), and adjacent tetrahedra are arranged as two pointing up and two down (UUDD). Note that, again, restricting S8R units have been created (Table 5), but of different diameters to those seen in chabazite. The cations reside close to the S8R positions.

It must be emphasized that both phillipsite and gismondine have unique frameworks. Mineralogically speaking they both are members of different families (see Tables 11 and 13).

Figure 1 illustrated the chain of tetrahedra identified in the natrolite framework. These are of UDUD alignments derived from the 4–1 SBU (Figure 2) whereby the ‘1’ links adjacent chains. Other zeolites in this family are mesolite, gonnardite, and scolecite (see Table 12). The natrolite family of structures also has S8Rs as restricting dimensions. The cations sit in sites close to four oxygens, two each from adjacent 4–1 chains. They are relatively unhydrated at these sites and are difficult to replace by ion exchange.

2.4.3 *Structures Based upon Assemblages of Cages*

In some cases, it is easiest to describe a zeolite by relating the framework to a series of component polyhedra, each polyhedral cage being a clustering of linked tetrahedra. The

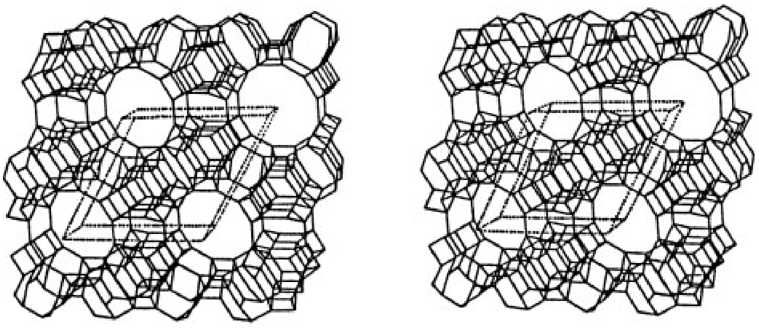

Figure 5 Stereopair of zeolite L (LTL) structure viewed along [001]

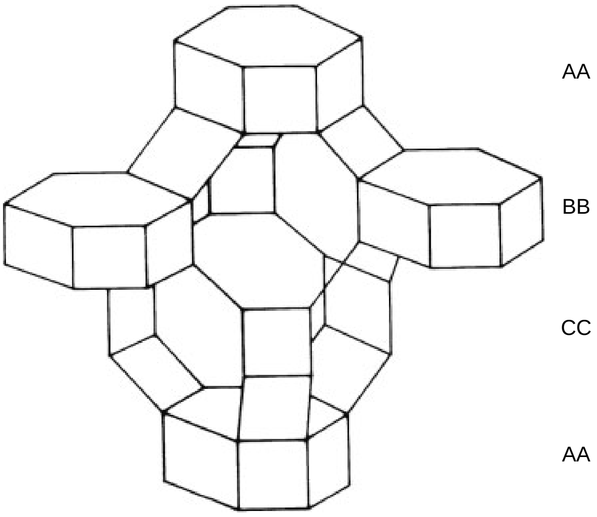

Figure 6 Structure of chabazite showing AABBCC sequence of S6Rs

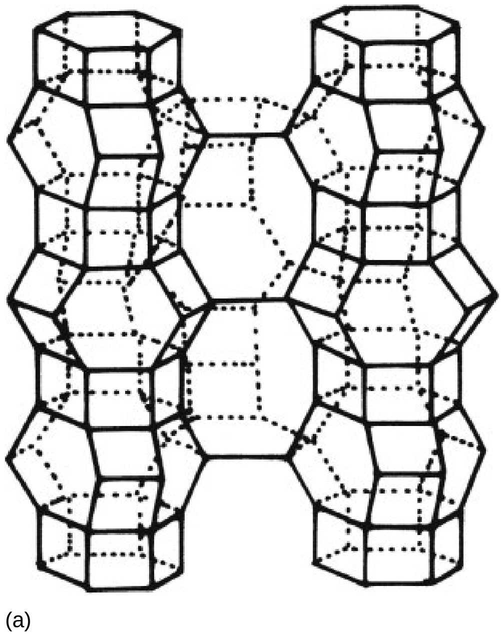

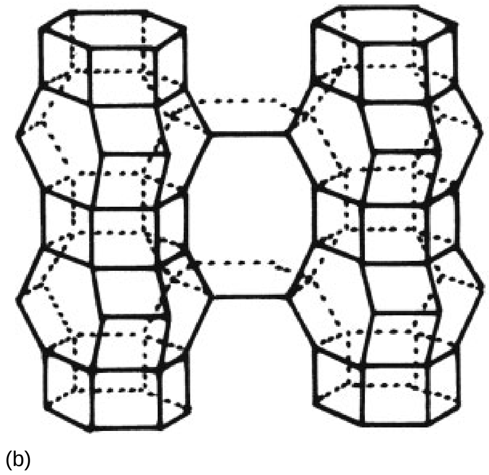

Figure 7 Structure of (a) erionite (AABAAC, S6R sequence) and (b) offretite (AABAAB, S6R sequence)

best-known example of this approach is for the synthetic zeolites A, X, and Y.

The polyhedra making up the A framework can be seen in Figure 10. The smallest unit is the D4R SBU, which joins truncated octahedral units to surround a large central cavity. The truncated octahedra are the structural unit of the felspathoid sodalite (discussed later). These sodalite cages are also often described as β-cages while the large cavity, which has 48 sides, is known as an α-cage or a ‘Type I’ 26-hedron. Note that the LTA framework is composed entirely of these three polyhedra, which share all their faces with each other. This is therefore a space-filling structure. An alternative view of the LTA-type structure is as a series of β-cages jointed by cubes (D4R) to propagate cubic symmetry in which each β-cage occupies a position analogous to that of the atoms in an NaCl array, that is, a similar approach to that described in chabazite.

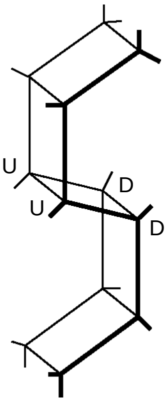

Figure 8 The ‘double crankshaft’ chain element of structure in gismondine (GIS) and related zeolites (U = up, D = down describes the configuration of linked pairs of Si,AlO$_4$ tetrahedra)

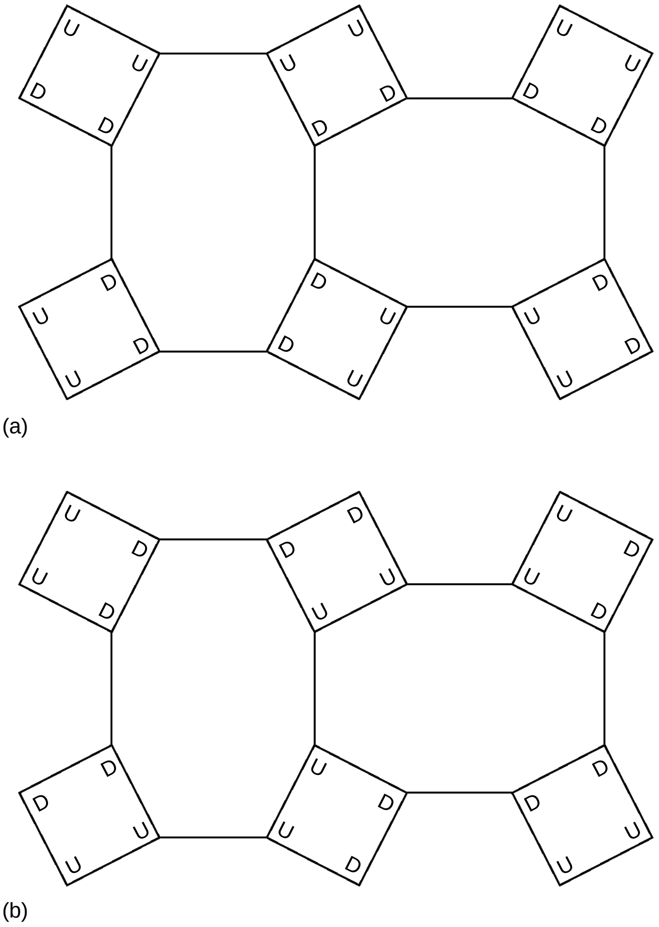

Figure 9 Linkage of chains in (a) phillipsite (PHI) and (b) gismondine (GIS)

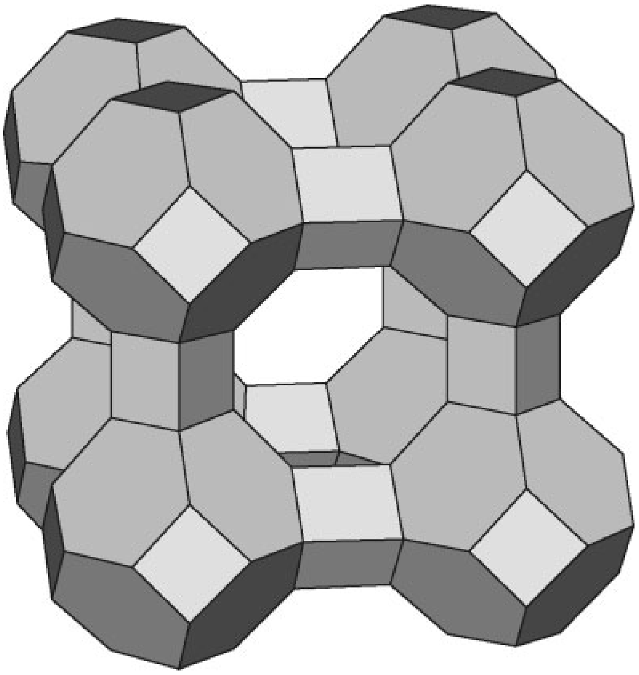

Figure 10 LTA structure emphasizing the linkage of truncated octahedra (β-cages) via D4R units (compare with Figure 3)

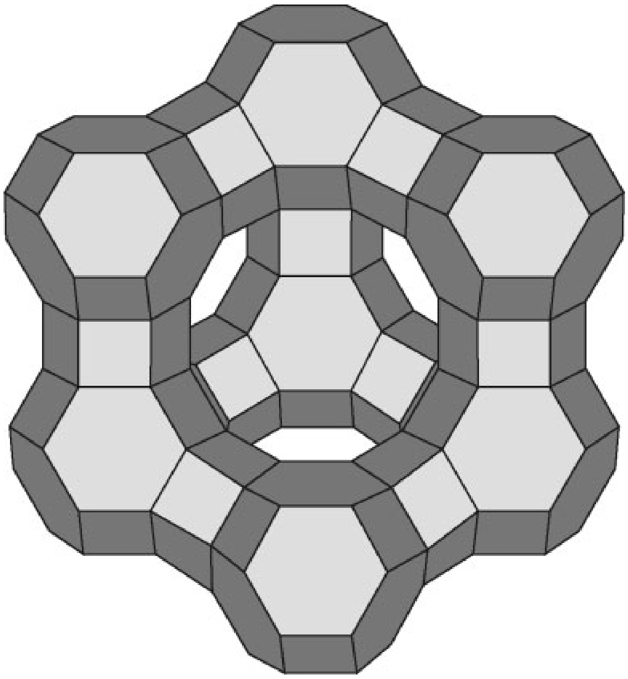

Figure 11 Faujasite (FAU) structure emphasizing the linkage of truncated octahedra (β-cages) via D6R units

This way of imagining polyhedral linkages can be extended to consider the FAU framework shared by the synthetic zeolites X and Y and the natural zeolite faujasite. Here (Figure 11) the composite polyhedra are the 6DR, which link β-cages to create a large internal cavity, the 'Type II' 26-hedron. Again this is a space-filling arrangement that can be alternatively viewed as an assemblage of β-cages joined by one half of their available S6R faces to produce another framework of cubic symmetry in which the sodalite units have the same spatial arrangement to each other, as do the carbon atoms in a diamond lattice. Zeolite X and Y are synthetic faujasites with the FAU framework, and differ only in the relative amounts of Si and Al isomorphously substituted in tetrahedral interstices. Their cation sites will be considered later.

2.4.4 Summary

This section has attempted to give an appreciation of the ways in which zeolite structures arise. It has not been intended to be all-encompassing and other types of framework will arise in further sections. It will also be appropriate to introduce additional information on zeolite cation and water locations on various industrially significant zeolites. Not all zeolites will be described and full details of known cation and water sites were collated by Mortier to 1982.[12] No further compilation has yet been made.

3 ZEOLITE COMPOSITIONS

3.1 Natural Aluminosilicate Zeolites

Table 7 lists the currently known aluminosilicate zeolites based upon definition by their unique frameworks following Baerlocker, Baerlocher, Meier, and Olson.[11] It also contains typical unit cell compositions, the IUPAC code, and type localities, but is restrictive in the sense that it does not consider the mineralogical aspects of the study of zeolites. The authoritative body for these is the Subcommittee for Zeolite Nomenclature of the Commission on New Minerals and Mineral Names of the International Mineralogical Association. Their guidelines have been cited in a recent book on natural zeolites by Tschernich,[13] as follows.

1. A new zeolite must have a unique framework. Evidence of a framework different from existing species must be demonstrated as a condition for approval of a new species. Zeolites that have the same framework and are separated by a well-established gap in chemical composition that is controlled by the structure are acceptable as separate species.
2. A new mineral cannot be defined solely on the basis of exchangeable cations. Because cations in zeolites are largely exchangeable, the dominance of one over all the others should not be the basis for a mineral species. End members, or intermediate members, of a zeolite composition cannot be considered new species. Existing species with the same frameworks that are defined only by the exchangeable cations should be redefined.
3. A new zeolite cannot be defined solely on the basis of Si/Al ratio.
4. A new zeolite cannot be defined solely by the symmetry difference from order or disorder of the aluminum and silicon in the framework.

Following these guidelines extends the list of accepted naturally occurring zeolite species because, as seen in Section. 2.4.2, there are families of zeolites with the same framework but of different cation content. In some cases, the guidelines have become blurred with inconsistencies arising whereby end members of cation composition are accepted as distinct zeolite species in one family but not in another.

Before going on to list these families, one further point needs to be made. This arises because there are several instances where a unique zeolite framework has been first characterized from a laboratory preparation and later identified as a natural species. The first of these was mazzite, prepared first as synthetic zeolite ZSM-4 (or omega) but known in nature prior to the allocation of the IUPAC code; hence its inclusion in Table 7. The other species have been discovered in nature after an IUPAC code had been allocated to their synthetic analogs. The details for these materials are given in Table 8.

3.1.1 Natural Aluminosilicate Zeolite Families

Analcime Family. Table 9 lists all known aluminosilicate minerals with the ANA structure, with their compositions and type localities. It does not include all compositional variations, only those that have been given different mineral names.

Chabazite Family. Table 10 records details of the chabazite family.

Gismondine Family. Four minerals are accepted with the gismondine framework, again based upon variation of cation content and Si/Al disorder. These are listed in Table 11.

Natrolite Family. This family also contains four members distinguished by different Si/Al framework ordering and cation content, as shown in Table 12.

Phillipsite Family. Family details are in Table 13.

Stilbite Family. Details are in Table 14.

Other Zeolites with Isotypic Frameworks (Listed in Table 15). Heulandite and clinoptilolite share the same anionic framework and the differences between them have been the subject of much discussion, best summarized by Gottardi and Galli.[14] These authors suggest heulandite has

Table 7 Aluminosilicate zeolites with unique frameworks

IUPAC code	Name	Idealized unit cell composition	Type locality(ies)
ANA	Analcime	$Na_{16}[Al_{16}Si_{32}O_{96}]\cdot 16H_2O$	Island of Cyclopes (Sicily), Mount Etna (Sicily), Dumbarton (Scotland)
BIK	Bikitaite	$Li_2[Al_2Si_4O_{12}]\cdot 2H_2O$	Bikita (Zimbabwe)
BOG	Boggsite	$Na_4Ca_7[Al_{18}Si_{78}O_{192}]\cdot 74H_2O$	Neer Rd. Pit (Columbia County, Oregon, USA)
BRE	Brewsterite	$(Sr,Ba)_2[Al_4Si_{12}O_{32}]\cdot 10H_2O$	Strontian (Scotland)
CHA	Chabazite	$Ca_6[Al_{12}Si_{24}O_{72}]\cdot 40H_2O$	Oberstein (Germany)
DAC	Dachiardite	$Na_5[Al_5Si_{19}O_{48}]\cdot 12H_2O$	San Pieri di Campo (Elba, Italy)
EDI	Edingtonite	$Ba_2[Al_4Si_6O_{20}]\cdot 8H_2O$	Old Kilpatrick (Dumbarton, Scotland)
EPI	Epistilbite	$Ca_3[Al_6Si_{18}O_{48}]\cdot 16H_2O$	Iceland, Faroes
ERI	Erionite	$(Na_2,Ca_{3.5})K_2[Al_9Si_{27}O_{72}]\cdot 27H_2O$	Durkee Opal Mine (Swayze Creek, Baker County, Oregon, USA)
FAU	Faujasite	$(Na_2,Ca,Mg)_{29}[Al_{58}Si_{134}O_{384}]\cdot 240H_2O$	Sasbach (Kaiserstuhl, Baden, Germany)
FER	Ferrierite	$Na_2Mg_2[Al_6Si_{30}O_{72}]\cdot 18H_2O$	Kamloops Lake (British Columbia, Canada)
FRA	Franzinite	$(Na,K)^{+}{}_{30}Ca^{2+}{}_{10}(SO_4)^{2-}{}_{10}(H_2O)_2$ $[Al_{30}Si_{30}O_{120}]$	Italy
GIS	Gismondine	$Ca_4[Al_8Si_8O_{32}]\cdot 16H_2O$	Capo di Bova (Rome, Italy)
GME	Gmelinite	$(Na_2,Ca)_3[Al_8Si_{16}O_{48}]\cdot 24H_2O$	Glenarm (Co. Antrim, N. Ireland), Montecchio Maggiore (Vicenza, Italy)
GOO	Goosecreekite	$Ca_2[Al_4Si_{12}O_{32}]\cdot 10H_2O$	Goose Creek Quarry (Leesburg, Loudoun County, Virginia, USA)
HEU	Heulandite	$Ca_4[Al_8Si_{24}O_{72}]\cdot 24H_2O$	None
LAU	Laumontite	$Ca_4[Al_8Si_{16}O_{48}]\cdot 16H_2O$	Bleigrube Lead Mine (Huelgoat, Brittany, France)
LEV	Levyne	$Ca_9[Al_{18}Si_{36}O_{108}]\cdot 50H_2O$	Dalsnipa (Sandoy, Faroes)
MAZ	Mazzite	$(Na_2,K_2,Ca,Mg)_5[Al_{10}Si_{26}O_{72}]\cdot 28H_2O$	Mont Semiol (Montbrison, Loire, France)
MER	Merlinoite	$K_5Ca_2[Al_9Si_{23}O_{64}]\cdot 24H_2O$	Cupaello Quarry (Santa Rufina, Rieti, Latium, Italy)
MON	Montesommaite	$(K,Na)_9[Al_9Si_{23}O_{64}]\cdot 24H_2O$	Pollena (Monte Somma, Vesuvius, Italy)
MOR	Mordenite	$Na_8[Al_8Si_{40}O_{96}]\cdot 24H_2O$	Morden (King’s County, Nova Scotia, Canada)
NAT	Natrolite	$Na_{16}[Al_{16}Si_{24}O_{80}]\cdot 16H_2O$	Hohentwiel (Hegau, Baden-Württemberg, Germany)
OFF	Offretite	$(Ca,Mg)_{1.5}K[Al_4Si_{14}O_{36}]\cdot 14H_2O$	Mont Semiol (Montbrison, Loire, France)
PAU	Paulingite	$(K_2,Ca,Na_2)_{76}[Al_{152}Si_{520}O1344]\cdot \approx 700H_2O$	Rock Island Dam (Douglas County, Washington, USA)
PHI	Phillipsite	$K_2(Ca,Na_2)_2[Al_6Si_{10}O_{32}]\cdot 12H_2O$	Aci Castello (Sicily)
STI	Stilbite	$Na_4Ca_8[Al_{20}Si_{52}O_{144}]\cdot 56H_2O$	Helgusta Iceland Spar Mine (Reydarfjordur, Iceland)
TER	Terranoviate	$Na^{+}{}_{4.2}K^{+}{}_{0.2}\ Mg^{2+}{}_{0.2}Ca^{2+}{}_{3.7}(H_2O)_{29}$ $[Al_{12.3}Si_{67.7}O_{160}]$	Terranova Bay, Antarctica
THO	Thomsonite	$Na_4Ca_8[Al_{20}Si_{20}O_{80}]\cdot 24H_2O$	Old Kilpatrick (Dumbarton, Scotland)
TSC	Tschörtnerite	$Ca^{2+}{}_{64}(K^{+}{}_2,Ca^{2+},Sr^{2+},Ba^{2+})_{48}$ $Cu^{2+}{}_{48}(OH)^{-}{}_{128}(H_2O)_x\ [Al_{192}Si_{192}O_{768}]$	USA
YUG	Yugawaralite	$Ca_2[Al_4Si_{12}O_{32}]\cdot 8H_2O$	Yugawara Hot Springs (Kanagawa Prefecture, Honshu, Japan)

the cation composition $(Ca + Sr + Ba) > (Na + K)$ with clinoptilolite being rich in monovalent cations.

An unusual variation is that seen in leonhardite, which is merely a water-deficient laumontite and should now be discontinued as a named mineral. This also applies to the name ‘svetlozarite’, which has been used for a Ca-rich dachiardite containing stacking faults.

Cowlesite. Cowlesite is the name given by Wise and Tschernich (see page 121 in Tschernich**[13]**) to a mineral found at the Neer Road, Goble, Oregon location. It has the composition $Ca[Al_2Si_3O_{10}]\cdot 6H_2O$ and has now been found at many locations worldwide. It is listed by the IMA as a zeolite but its framework has not yet been characterized.

3.2 Naturally Occurring Zeotypes

Table 16 lists minerals that have zeolite frameworks but have atoms other than just Si and Al in their

Table 8 Natural zeolites identified after characterization of their laboratory-made analogs

IUPAC code	Synthetic analog	Natural species	Idealized unit cell composition of natural species	Type locality
*BEA[a]	Beta	Tschernichite	$Ca[Al_2Si_6O_{16}]\cdot 8H_2O$	Neer Rd. Pit (Goble, Columbia County, Oregon, USA)
EAB	TMA-E(AB)	Bellbergite	$(K,Ba,Sr)_2Sr_2Ca_2(Ca,Na)_4Al_{18}Si_{18}O_{72}.30H_2O$	Bellerberg (also Bellberg) volcano, 2 km north of Mayen, Eifel, Germany
MFI	ZSM-5	Mutinaite	$Na_3Ca_4Si_{85}Al_{11}O_{192}.\ 60H_2O$	Mount Adamson Antartica
LOS	Losod	Bystrite	$Ca(Na,K)_7Si_6Al_6O_{24}S_{4.5}\cdot H_2O$	Malo-Bystrinskoe deposit, Russia
LTL	Linde type L	Perlialite	$K_9Na(Ca,Sr)[Al_{12}Si_{24}O_{72}]\cdot 15H_2O$	Mounts Evelochorr and Yukspor (Khibina Massif, Kola Peninsula, Russia)
NES	NU-87	Gottardiite	$Na_3Mg_3Ca_5Si_{117}Al_{19}O_{272}\cdot 93H_2O$	Mount Adamson Antartica

[a]The asterisk denotes a well-defined framework subunit for which the pure end members have not been synthesized.[11]

Table 9 The analcime family

Mineral name	Idealized unit cell composition	Type locality	Comment
Analcime varieties	$Na_{16}[Al_{16}Si_{32}O_{96}]\cdot 16H_2O$	Isle of Cyclops (Catania, Sicily)	Ca,Mg-rich;[a] identified but not confirmed as distinct species (see also wairakite below)
Leucite[b]	$K_{16}[Al_{16}Si_{32}O_{96}]\cdot H_2O$		
Pollucite	$(Cs,Na)_{16}[Al_{16}Si_{32}O_{98}]\cdot nH_2O$	San Piero in Campo (Sicily)	Cs must be present in excess of 50% to be defined as pollucite
Wairakite	$(Ca,Na_2)_8[Al_{16}Si_{32}O_{98}]\cdot 16H_2O$	Wairakei (New Zealand)	Ca should be in excess of 50% to be defined as wairakite

[a]Mg-rich analcime has been described as doranite. [b]Also ammonioleucite, $(NH_4,K_{16})[Al_{16}Si_{32}O_{96}]$.

Table 10 The chabazite family

Mineral name	Idealized unit cell composition	Type locality
Chabazite	$Ca_6[Al_{12}Si_{24}O_{72}]\cdot 40H_2O$	Oberstein (Germany)
Willhendersonite	$Ca_2K_2[Al_6Si_6O_{24}]\cdot 10H_2O$	San Venanzo Quarry (Terni, Italy)
Herschelite	$Na_6K_2Ca_2[Al_{12}Si_{24}O_{72}]\cdot 36H_2O$	Aci Castello (Sicily)

Table 11 The gismondine family

Mineral name	Idealized unit cell composition	Type locality
Amicite	$K_4Na_4[Al_8Si_8O_{32}]\cdot 10H_2O$	Höwenegg (Hegau, Germany)
Garronite	$NaCa_{2.5}[Al_6Si_{10}O_{32}]\cdot 14H_2O$	Garron Plateau (Co. Antrim, N. Ireland)
Gismondine	$Ca_4[Al_8Si_8O_{32}]\cdot 16H_2O$	Capo di Bova (Rome, Italy)
Gobbinsite	$Na_5[Al_5Si_{10}O_{32}]\cdot 11H_2O$	Gobbins Escarpment (Co. Antrim, N. Ireland)

tetrahedral interstices. Kehoeite has the apparent composition $(Zn,Ca)Al_2(PO_4)_2(OH)_2\cdot 5H_2O$ and has formerly been included in this category, but is now known to be a mixture of different minerals.

Lovdardite has a particular significance as it contains three-membered rings of linked tetrahedra, which also have been identified in synthetic zeolite-like substances.

3.3 Natural Zeolite-like Minerals with Incomplete Frameworks

Baerlocher, Meier, and Olson[11] have included materials in their listing in which the Si/Al tetrahedra do not share all four corners to complete a framework. These minerals have an appreciable content of hydroxyl groups located at

Table 12 The natrolite family

Mineral name	Idealized unit cell composition	Type locality
Gonnardite	$(Na_{10}Ca_4)[Al_{18}Si_{22}O_{80}]\cdot\approx 20H_2O$	Chaux de Bergonne (Gignat, Puy de Dome, France)
Natrolite	$Na_{16}[Al_{16}Si_{24}O_{80}]\cdot 16H_2O$	Hohentwiel (Hegau, Baden-Württemberg, Germany)
Mesolite	$Na_6Ca_5[Al_{16}Si_{24}O_{80}]\cdot 22H_2O$	Nova Scotia (Canada)
Scolecite	$Ca_8[Al_{16}Si_{24}O_{80}]\cdot 24H_2O$	None
Paranatrolite	$(Na,Ca)_{16}[Al_{16}Si_{24}O_{80}]\cdot 24H_2O$	Mont Saint-Hilaire (Montreal, Canada)
Tetranatrolite	$(Na,Ca)_{16}[Al_{16}Si_{24}O_{80}]\cdot 16H_2O$	None

Table 13 The phillipsite family

Mineral name	Idealized unit cell composition	Type locality
Harmotome	$Ba_2(Ca_{0.5}Na)\ [Al_5Si_{11}O_{32}]\cdot 12H_2O$	Andreasburg (Germany)
Phillipsite	$K_2(Ca,Na_2)_2\ [Al_6Si_{10}O_{32}]\cdot 12H_2O$	Aci Castello (Sicily)
Wellsite	$Ca_{1.6}Ba_{0.4}(Na,K)\ [Al_5Si_{11}O_{32}]\cdot 13H_2O$	None

Table 14 The stilbite family

Mineral name	Idealized unit cell composition	Type locality
Barrerite	$Na_{16}[Al_{16}Si_{56}O_{144}]\cdot 52H_2O$	Capo Pula (Sardinia)
Stellerite	$Ca_8[Al_{16}Si_{56}O_{144}]\cdot 56H_2O$	Komandar Islands (Bering Sea)
Stilbite	$Na_4Ca_8[Al_{20}Si_{52}O_{144}]\cdot 56H_2O$	Helgusta Iceland Spar Mine (Reydarfjordur, Iceland)

tetrahedral corners. The justification for their inclusion as zeolite-like minerals arises from the recognition of the openness of their incomplete frameworks in which are recognizable zeolitic cavities and channels. Three minerals of these are aluminosilicates (partheite, roggianite, and wenkite) and the other is a beryllosilicate, chiavennite. Further details of these minerals are in Table 17.

Table 15 Other isotypic zeolites

Mineral name	Idealized unit cell composition
Heulandite	$Ca_4[Al_8Si_{28}O_{72}]\cdot 24H_2O$
Clinoptilolite	$(Na, K)_6[Al_6Si_{30}O_{72}]\cdot 20H_2O$
Laumontite	$Ca_4[Al_8Si_{16}O_{48}]\cdot 16H_2O$
Leonhardite	$Ca_4[Al_8Si_{16}O_{48}]\cdot 14H_2O$
Dachiardite	$Na_5[Al_5Si_{19}O_{48}]\cdot 12H_2O$
Svetlozarite	$Na_5[Al_5Si_{19}O_{48}]\cdot 12H_2O$

3.4 Further Information on Natural Zeolites and Related Species

It can be seen from earlier sections that some anomalies have arisen between the recognition of zeolite species by mineralogists and the characterization of their frameworks by crystallographers. Many mineralogists (amateur and professional) collect natural zeolite specimens because of their beauty and novel crystal habits. Both Tschernich**[13]** and Gottardi and Galli**[14]** have provided excellent texts covering the mineralogical properties of zeolites. These authors provide line drawings of zeolite crystal habit and details of their geological occurrences and genesis. Tschernich lists classical mineralogical physical and optical properties, as do Gottardi and Galli, who also provide details of cation sites and framework configuration. These authors also discuss, in detail, the interrelationships between the zeolite families as well as their chemistries and syntheses.

Table 16 Naturally occurring zeotypes

IUPAC framework code	Mineral name	Idealized unit cell composition	Type locality
ANA	Hsianghualite	$Li_{16}Ca_{24}[Be_{24}Si_{24}O_{96}]$	Hunan (China)
	Viseite	$Na_2Ca_{10}[Al_{20}Si_6P_{10}O_{60}\ (OH)_{36}]\cdot 16H_2O$	Visé (Belgium)
LOV	Lovdarite	$K_4Na_{12}[Be_8Si_{28}O_{72}]\cdot 18H_2O$	Lovozero (Russia)
RHO	Pahasapaite	$(Ca,Li,K,Na)_{11}Li_8[Be_{24}(PO_4)_{24}]\cdot 38H_2O$	None
WEI	Weinebenite	$Ca^{2+}{}_4(H_2O)_{16}\ [Be_{12}P_8O_{32}(OH)_8]$	Weinebene, Austria

Table 17 Zeolite-type minerals with incomplete frameworks

IUPAC framework code	Mineral name	Idealized unit cell composition	Type locality
–CHI	Chiavennite	$Ca_4Mn_4[Be_8Si_{20}O_{52}(OH)_8]\cdot 8H_2O$	None
–CLO	Cloverite	$(C_7H_{14}N+)_{24}$ $[F_{24}$ $Ga_{96}P_{96}O_{372}(OH)_{24}]$	None
–PAR	Partheite	$Ca_8[Al_{16}Si_{16}O_{60}(OH)_8]\cdot 16H_2O$	Taurus Mts (Turkey)
–ROG	Roggianite	$Ca_{16}[Al_{16}Si_{32}O_{88}(OH)_{16}](OH)_{16}\cdot 26H_2O$	Alpe Rosso (Val Vigezzo, Novara, Italy)
–WEN	Wenkite	$Ba_4(Ca,Na_2)_3[Al_8Si_{12}O_{39}(OH)_2(SO_4)]\cdot 3H_2O$	None

Tschernich provides a comprehensive list of outmoded zeolite mineral names. Table 18 gives examples of some of the more well known.

3.5 Synthetic Species

3.5.1 Synthetic Aluminosilicate Zeolites

As mentioned earlier, pioneering work by Barrer showed that some natural zeolite species could be synthesized in the laboratory. This has led to many synthetic routes and to a proliferation of other species with novel structures not known in nature.

Table 19 lists all synthetic zeolites (included those analogous to naturally occurring ones) whose structures are confirmed in Baerlocher, Meier, and Olson.[11] Note that many are still described by acronyms related to their original source. In some cases, this is to the discoverer, for example, those synthesized for the first time by George Kerr from the Mobil Corporation have been given the code ZK. In other cases, the code relates to the company in whose laboratory the discovery was first made. Examples of this are ZSM, which comes from Zeolite Socony Mobil, and LZ, which relates to the Linde Company. Full explanations of these codes are available.[15] Table 19 also reflects the earlier confusion in the zeolite literature whereby claims to have discovered new materials were later discredited. It should also be remarked that often the isotypic structures reflect synthetic success in preparing analogs with differing Si/Al ratios, that is, with various amounts of Al isomorphously substituting Si tetrahedral positions. The best-known examples of this can be seen in the synthetic faujasites Linde X and Linde Y and the high-silica zeolites exemplified by the BETA, EMC-2, EU-1, MAZ, MEI, MEL, MFI, MFS, MTT, MTW, NES, and TON frameworks. Their production reflects the high catalytic activity noted for silica-based structures containing very small proportions of isomorphously substituted Al. By the same token, synthetic analogs of natural species can be high-silica materials (e.g. as seen in CHA, ERI, FAU, FER, MAZ, and OFF variants).

Table 18 Some well known zeolites and their outmoded names

Zeolite	Outmoded name
Analcime	Analcite
Chabazite	Acadialite, haydenite, phacolite, seebachite, herschelite
Epistilbite	Orizite, parastilbite, reissite
Gismondine	Gismondite, zeogonite (with phillipsite)
Gmelinite	Sarcolite
Laumontite	Laumonite, scheiderite, sloanite, leonhardite
Levyne	Levynite, mesoline
Mesolite	Mesotype
Mordenite	Arduinite, flokite, pseudonatrolite, ptilolite, steelite
Natrolite	Galaktite, mesotype, fargite, laubanite
Phillipsite	Christianite, wellsite
Stilbite	Desmine, epidesmine, foresite
Thomsonite	Comptonite, faroelite, mesole, mesotype

3.5.2 Synthetic Zeotypes

In 1983, workers at the Union Carbide (formerly Linde, now Union Oil Products (UOP)) laboratories in Tonawanda near New York reported a new class of microporous inorganic solids. Some materials were layered but, of the 20 new phases reported,[16] no less than 14 were framework compounds based upon three-dimensional arrays of linked $[AlO_4]^{5-}$ and $[PO_4]^{3-}$ coordination polyhedra. These novel zeotypes were designated by the acronym $AlPO_4$. As would be expected, the linkage of the Al/P tetrahedra created an uncharged framework and so no charge-balancing cations are present and the materials have water in the voids of the framework. Clearly these do not have the property of ion exchange expected from a zeolitic type material. Subsequent work demonstrated that many other closely related microporous materials could be synthesized with a wide variety of cations in the tetrahedral interstices, including those requiring a charge-balancing cation. Furthermore, a high proportion of these novel zeotypes have structures isotypic with some 15 natural and synthetic aluminosilicate zeolites. Table 20 lists synthetic zeotypes with unique frameworks and Table 21 classifies further examples according to isotypic aluminosilicate frameworks.

The acronyms used in these tables require further explanation. The known Aluminophosphate ($AlPO_4$) structures also have a number (e.g. $AlPO_4$-5), or a further letter code (e.g. $AlPO_4$-D), appended. They are the labels given by the first literature report and have no scientific significance. Note that the ATT framework, coded as $AlPO_4$-12 TAMU, marks that the material was first synthesized at Texas A&M University. Similarly, those encoded as MCM are Mobil products. Apart from those that are self explanatory, such as gallosilicate ABW or beryllosilicate gismondine, the remaining acronyms

Table 19 Synthetic aluminosilicate zeolites[a]

IUPAC code	Name or acronym	Idealized composition	Other isotypic synthetic aluminosilicates
ABW	Li-A(BW)	$Li_4[Al_4Si_4O_{16}]\cdot 4H_2O$	$CsAlSiO_4$, $RbAlSiO_4$, $TlAlSiO_4$
ANA	Analcime	$Na_{16}[Al_{16}Si_{32}O_{96}]\cdot 16H_2O$	Ca-D, Na-B, pollucite
*BEA[b]	BETA	$Na_n[Al_nSi_{64-n}O_{128}]$, $n < 7$	–
BIK	Cs-aluminosilicate bikitaite	$Cs_{0.35}[Al_{0.35}Si_{2.65}O_6]$	–
BRE	CIT-4	$Ba^{2+}{}_2\ (H_2O)_{10}\ [Al_4Si_{12}O_{32}]$	Synthetic Brewsterite
CAS	Cesium aluminosilicate (Araki)	$Cs_4[Al_4Si_{20}O_{48}]$	–
CHA	Chabazite	$Ca_6[Al_{12}Si_{24}O_{72}]\cdot 40H_2O$	LZ-218, Linde D, Linde R, ZK-14, ZYT-6, SSZ-13
EAB	TMA-E(AB)	$(Me_4N)_2Na_7[Al_9Si_{27}O_{72}]\cdot 26H_2O$	Bellbergite
EDI	Edingtonite	$Ba_2[Al_4Si_6O_{20}]\cdot 8H_2O$	KF, Linde F
EMT[c]	EMC-2 (hexagonal faujasite)	$Na_{21}(18\text{-crown-6})_n[Al_{21}Si_{75}O_{192}]$	ECR-30, SZM-20 ZSM-3, CSZ-1
EPI	Synthetic Epistilbite	$Ca^{2+}{}_3\ (H_2O)_{16}\ [Al_6Si_{18}O_{48}]$	
ERI[d]	Erionite	$(Na_2,Ca)_{3.5}K_2[Al_9Si_{27}O_{72}]\cdot 27H_2O$	LZ-220, Linde T
ESV	ERS-7	$H^+{}_{5.06}Na^+{}_{0.07}\ [Al_{5.13}Si_{42.87}O_{96}]$	
EUO	EU-1	$Na_n[Al_nSi_{112-n}O_{224}]\cdot\approx 26H_2O$, $n < 19$, typically $n = 3.6$	TPZ-3, ZSM-50
FAU[c]	Synthetic faujasites	$(Na_2,Ca,Mg)_{29}[Al_{58}Si_{134}O_{384}]\cdot 240H_2O$	Linde X, Linde Y, LZ-210
FER	Ferrierite	$Na_2,Mg_2[Al_6Si_{30}O_{72}]\cdot 18H_2O$	FU-9, ISI-6, NU-23, Sr-D, ZSM-35
GIS	Gismondine	$Ca_4[Al_8Si_8O_{32}]\cdot 16H_2O$	Na-P1, Na-P2, TMA-gismondine
GME	Gmelinite	$(Na_2,Ca)_4[Al_8Si_{16}O_{48}]\cdot 24H_2O$	Synthetic fault-free gmelinite
HEU	Heulandite	$Ca_4[Al_8Si_{28}O_{72}]\cdot 24H_2O$	LZ-219
JBW	NaJ (Barrer and White)	$Na_3[Al_3Si_3O_6]\cdot 1.5H_2O$	–
KFI	ZK-5	$Na_{30}[Al_{30}Si_{66}O_{192}]\cdot 98H_2O$	P, Q, (Cs,K)-ZK-5
LEV	Levyne	$Ca_9[Al_{18}Si_{36}O_{108}]\cdot 50H_2O$	ZK-20, LZ132, SSZ-17
LOS	Losod	$Na_{12}[Al_{12}Si_{12}O_{48}]\cdot 18H_2O$	Bystrite
LTA	Linde Type A	$Na_{12}[Al_{12}Si_{12}O_{48}]\cdot 27H_2O$	Alpha, LZ-215, N-A, ZK-4
LTL	Linde Type L	$K_6Na_3[Al_9Si_{27}O_{72}]\cdot 21H_2O$	LZ-212
LTN	Linde Type N	$Na_{384}[Al_{384}Si_{384}O_{1536}]\cdot 518H_2O$	NaZ-21
MAZ	Mazzite	$(Na_2,K_2,Ca,Mg)_5[Al_{10}Si_{26}O_{72}]\cdot 28H_2O$	LZ-202, Omega, ZSM-4
MEI	ZSM-18	$Na_n[Al_nSi_{34-n}O_{68}]\cdot 28H_2O$, $n = 2.1-5.7$	–
MEL	ZSM-11	$Na_n[Al_nSi_{96-n}O_{192}]\cdot\approx 16H_2O$, $n < 16$	–
MER	Merlinoite	$K_5Ca_2[Al_9Si_{23}O_{64}]\cdot 24H_2O$	K-M, Linde W, barium silicate merlinoite
MFI	ZSM-5	$Na_n[Al_nSi_{96-n}O_{192}]\cdot\approx 16H_2O$, $n < 27$	AZ-1, FZ-1, LZ-105, NU-4, NU-5, TSZ, TSZ-111, TZ-01, US1-108, ZKQ-1B, ZMQ-TB, ZBM-30
MFS	ZSM-57	$H_{1.5}[Al_{1.5}Si_{34.5}O_{72}]$	–
MOR	Mordenite	$Na_8[Al_8Si_{40}O_{96}]\cdot 24H_2O$	Na-D, Ca-Q, Zeolon, LZ-211
MSO	MCM-61	$K^+{}_{2.1}\ C_{12}H_{24}O_6\ [Si_{27.9}Al_{2.1}O_{60}]$	MESOPOROUS
MTT	ZSM-28	$Na_n[Al_nSi_{24-n}O_{48}]\cdot\approx 4H_2O$, $n < 2$	EU-13, KZ-1, ISI-4
MTW	ZSM-12	$Na_n[Al_nSi_{28-n}O_{56}]\cdot\approx 4H_2O$, $n < 2.5$	NU-13, Theta-3, CZH-5, TPZ-12
NES	NU-87	$H_4[Al_4Si_{64}O_{136}]\cdot nH_2O$	Gottardiite
OFF[d]	Offretite	$(Ca,Mg)_{1.5}K[Al_4Si_{14}O_{36}]\cdot 14H_2O$	Linde T, LZ-217, TMA-O
PHI	Phillipsite	$K_2(Ca,Na_2)_2[Al_6Si_{10}O_{32}]\cdot 12H_2O$	ZK-19
RHO	Rho	$(Na,Cs)_{12}[Al_{12}Si_{36}O_{96}]\cdot 44H_2O$	LZ-214
TON	Theta-1	$Na_n[Al_nSi_{24-n}O_{48}]\cdot\approx 4H_2O$	NU-10, ISI-1, KZ-2, ZSM-22

[a] When synthetic analogs of naturally occurring aluminosilicate zeolites have been synthesized they are listed by the natural mineral names and their idealized compositions. [b] For *BEA the asterisk denotes a well-defined structural subunit for which the pure end members have not been obtained. [c] The structures EMT and FAU also crystallize as a series of structural intermediates. [d] ERI and OFF also form as a series of structural intermediates.

in both Tables 20 and 21 denote zeotypes prepared by Union Carbide workers who have developed the following shorthand notation for framework materials in which tetrahedral positions accommodate atoms other than Si and Al.

1. Silicoaluminophosphates are described as SAPO, for example, the AFR structure assigned to SAPO-40 (see Table 20).
2. Metal aluminophosphates have the generic acronym MeAPO and metal aluminosilicophosphates are MeAPSO. More specific descriptions come by inserting the appropriate chemical symbol(s) into the code. There are many examples of this in Table 21, for example, AsPO-34, AsVBeAPO-34, CoAPO-34, MnAPSO-34, FeAPSO-44, and so on The letters C, M, and Z are sometimes used

Table 20 Synthetic zeotypes with unique frameworks

IUPAC code	Name or acronym	Idealized composition	Other isotypic synthetic zeotypes[a]
ACO	ACP-1	$(C_2H_{10}N_2^{2+})4\ (H_2O)_2\ [Al_{0.88}Co_{7.12}P_8O_{32}]$	
AEI	$AlPO_4$-18	$[Al_{24}P_{24}O_{96}]$	MCM-7
AEL	$AlPO_4$-11	$[Al_{20}P_{20}O_{80}]$	
AET	$AlPO_4$-8	$[Al_{36}P_{36}O_{144}]$	MCM-37
AFI	$AlPO_4$-5	$[Al_{12}P_{12}O_{48}]\cdot R\cdot qH_2O$, R = Pr_4NOH	MCM-6[b]
AFO	$AlPO_4$-41	$[Al_{20}P_{20}O_{80}]$	–
AFR	SAPO-40	$[(Si,Al,P)_{32}O_{64}]\cdot 2TPA\cdot OH$	–
AFS	MAPSO-46	$(PrNH_2)_8[Mg_6Al_{22}P_{26}Si_2O_{112}]$	–
AFT	$AlPO_4$-52	$(Et_4N\cdot H_2PO_4)_{3.6}[Al_{36}P_{36}O_{144}]\cdot 76H_2O$	–
AFY	CoAPO-50	$(Pr_2\ NH_2)_3[Co_3Al_5P_8O_{32}]\cdot 7H_2O$	–
AHT	AlPO-H2	$(H_2O)_8\ [Al_6P_6O_{24}]$	
APC	$AlPO_4$-C	$[Al_6P_{16}O_{64}]$	$AlPO_4$-H3 (anhyd), MCM-1
APD	$AlPO_4$-D	$[Al_{16}P_{16}O_{64}]$	$AlAsO_4$-1
AST	$AlPO_4$-16	$[Al_{20}P_{20}O_{80}]\cdot 4R\cdot 16H_2O$, R = quinuclidinium	–
ASU	ASU-7	$(C_2H_7N)_2\ (H2O)_2\ [Ge_{20}O_{40}]$	
ATN	MAPO-39	$H_n[Mg_nAl_{8-n}P_8O_{32}]$	–
ATO	$AlPO_4$-31	$[Al_{18}P_{18}O_{72}]$	SAPO-31
ATS	MAPO-36	$[MgAl_{11}P_{12}O_{48}]$	–
ATT	$AlPO_4$-12-TAMU	$[Al_{12}P_{12}O_{48}]\cdot 4R$, R = Me_4NOH	$AlPO_4$-33
ATV	$AlPO_4$-25	$[Al_{12}P_{12}O_{48}]$	[Ga-P-O]-ATV
AWO	AlPO-21	$H^+4\ (C_2H_7N)_{10.66}\ (C_3H_8)_{5.33}\ (OH)^-{}_4\ [Al_{12}P_{12}O_{48}]$	–
AWW	$AlPO_4$-22	$(C_7H_{14}N)_4(HPO_4)_2[Al_{24}P_{24}O_{96}]$	–
BPH	Beryllophosphate-H	$Na_7K_7[Be_{14}P_{14}O_{56}]\cdot 20H_2O$	– [c]
CGF	Co-Ga-Phosphate-5	$(C_6H_{14}N_2^{2+})_2\ [Co_4\ Ga_5P_9O_{36}]$	–
CGS	Co-Ga-Phosphate-6	$(C_7H_{14}N_2^{+})_4\ [Co_4\ Ga_{12}P_{16}O_{64}]$	TNU-1, TsG-1
CLO	Cloverite	$\{[Ga_{96}P_{96}O_{360}(OH)_{24}]\cdot 24RF\}_8$, R = quinuclidinium	–
CON	CIT-1	$H^+{}_2\ [B_2Si_{54}O_{112}]$	SSZ-26, SSZ-33
CZP	Chiral Zincophosphate	$Na^+{}_{12}\ (H_2O)_{12}\ [Zn_{12}P_{12}O_{48}]$	
DFO	DAF-1	$(C_{16}H_{38}N_2^{2+})_7\ (H_2O)_{40}\ [Mg_{14}Al_{52}P_{66}O_{264}]$	
DFT	DAF-2	$(C_2H_{10}N_2^{2+})_2\ [Co_4P_4O_{16}]$	ACP-3, UCSB-3GaGe, UCSB-3ZnAs,UiO-20
LOV	Lovdarite (synthetic)	$K_4Na_{12}[Be_8Si_{28}O_{72}]\cdot 18H_2O$	–
MWW	MCM-22	$H^+{}_{2.4}Na^+{}_{3.1}\ [Al_{0.5}B_{5.}1Si_{66.5}O_{144}]$	ERB-1, ITQ-1, PSH-3, SSZ-25
OSI	UiO-6	$[Al_{16}P_{16}O_{64}]$	
OSO	OSB-1	$K^+{}_6(H_2O)_9\ [Be_3Si_6O_{18}]$	
RSN	RUB-17	$K^+{}_4Na^+{}_{12}(H_2O)_{18}\ [Zn_8Si_{28}O_{72}]$	
RTH	RUB-13	$(C_{10}H_{21}N^+)_2\ [B_2Si_{30}O_{64}]$	
RUT	RUB-10	$(C_4H_{12}N+)_4\ [B_4Si_{32}O_{72}]$	NU-1
SAO	STA-1	$(C_{21}H_{40}N_2^{2+})_{2.6}(H_2O)_6\ [Mg_5Al_{23}P_{28}O_{112}]$	
SAS	STA-6	$(C_{14}H_{34}N_4^{2+})_{1.5}(H_2O)_{2.5}\ [Mg_3Al_{13}P_{16}O_{64}]$	
SAT	STA-2	$(C_{18}H_{34}N_2^{2+})_3(H_2O)_{22.5}\ [Mg_{5.4}Al_{30.6}P_{36}O_{144}]$	
SAV	STA-7	$(C_{18}H_{42}N_6)_{1.96}(H_2O)_7\ [Mg_{4.8}Al_{19.2}P_{28}O_{96}]$	
SBE	UCSB-8	$(C_9H_{24}N_2^{2+})_{16}\ [M_{32}Al_{32}P_{64}O_{256}]$	M = Co, Mg, Mn, or Zn
SBS	UCSB-6	$(C_9H_{24}N_2^{2+})_{12}\ [M_{24}M'_{24}P_{48}O_{192}]$	M = Ga, Co, Mg, Mn, or Zn M′ = Co, Mg, or Zn
SBT	UCSB-10	$(C_{10}H_{26}N_2O_3^{2+})_{18}\ [Ga_{36}Zn_{36}P_{72}O_{288}]$	
VFI	VPI-5	$[Al_{18}P_{18}O_{72}]\cdot 42H_2O$	$AlPO_4$-54, MCM-9
VNI	VPI-9	$Rb^+{}_{44}K^+{}_4(H_2O)_{48}\ [Zn_{24}Si_{96}O_{240}]$	
VSV	VPI-7	$Na^+{}_{26}H^+{}_6(H_2O)_{44}\ [Zn_{16}Si_{56}O_{144}]$	Gaulite
ZON	ZAPO-11	$(C_4H_{12}N+)_8\ [Zn_8Al_{24}P_{32}O_{128}]$	

[a] See also Tables 21 and 22 and note[d] below.[11] [b] The synthetic aluminosilicate zeolite SSZ-24 has the AFI framework. [c] The synthetic aluminosilicate zeolite Linde Q has the BPH framework (Linde Q is not the same as Q, which has the KFI structure). [d] $AlPO_4$-52, of composition $0.2(TEA)(H_2PO_4)[Al_{0.5}P_{0.5}]\cdot O_2$ has an idealized CHA-like D6R sequence AABBCCAACCBB.[16] $AlPO_4$-EN3, of composition $[Al_6(PO_4)_6]\cdot 4H_2O\cdot en$, where en = ethylenediamine, has a partially derived structure.[16] Note: (TPA), Tetrapropylammonium.

Table 21 Synthetic zeotypes with frameworks common to known aluminosilicate zeolites[a]

IUPAC code	Zeotype name or acronym
ABW	Gallosilicate ABW, berylloarsenate ABW, beryllophosphate ABW, zincophosphate ABW
ANA	$AlPO_4$-24, $AlPO_4$- pollucite, aluminosilicophosphate analcime, Cs beryllosilicate pollucite, Cs, Fe silicate pollucite, gallosilicate analcime, $Cs_2CuSi_5O_{12}$
*BEA	Boron-beta
CHA	AsAPO-34, AsAPO-44, AsVBe APO-34, BeAPSO-34, BeAPSO-44, CAPSO-34, CAPSO-44, Co APO-34, CoAPO-44, CoAPO-47, CoSAPO-34, FCAPO-34, FCAPO-44, FCAPO-47, FeAPSO-34, FeAPSO-44, FeMnAPO-44, FeTiCoAPO-34, GaAPO-44, GeAPO-34, GeBAPO-44, MAPO-34, MAPO-44, MAPO-47, MgAPSO-34, MgAPSO-44, Mg APSO-47, MnAPO-34, MnAPO-44, Mn APO-47, MnAPSO-34, MnAPSO-44, MnAPSO-47, SAPO-34, SAPO-44, SAPO-47, XAPO-34, XAPO-44, XAPO-47, ZAPO-34, ZAPO-44, ZAPO-47, Zn APSO-34, Zn APSO-44, Zn APSO-47, MCM-2
ERI	$AlPO_4$-17, As APO-17, BeAPO-17, BeAPSO-17, CAPO-17, CAPSO-17, CrGaAPO-17, FCAPO-17, FeCoMgAPO-17, MAPO-17, SAPO-17, XAPO-17
FAU	FCAPO-37, SAPO-37, XAPO-37, beryllophosphate X, zincophosphate X
GIS	Beryllosilicate gismondine, MAPSO-43
LEV	CoAPO-35, FCAPO-35, FeAPSO-35, MAPO-35, Mg PSO-35, MnAPO-35, MnAPSO-35, SAPO-35, XAPO-35, ZAPO-35, ZnAPO-35
LTA	Gallogermanate A, gallophosphate A, ZK-21, FCAPO-42, SAPO-42, XAPO-42
LTL	Gallosilicate L
MAZ	Gallosilicate mazzite
MEL	Boralite D, TS-2 (titanosilicate)
MFI	AMS-IB, BOR-C, Encilite, ZBM-30(B), ZBH (all borosilicates), TS-I (titanosilicate)[b]
NAT	Gallosilicate natrolite, Rb gallogermanate natrolite
RHO	Berylloarsenate rho, synthetic pahasapaite
–ROG[c]	–

[a]Names as listed in Table 19.[11,16] See text for explanation of acronyms. [b]Recent evidence is that the Ti may well be hexacoordinate in this and related materials. [c]A recent report suggests that roggianite has some Be in framework sites.[11] Note: Frameworkconstituent luminophosphate, (FCAPO).

as shorthand for the elements chromium, magnesium, and zinc, respectively.

3. When wide compositional ranges can be prepared as isomorphous substitutions into aluminophosphates, two generalized acronyms are used: (a) FCAPO, where FC means framework constituents, and encompasses structures containing proportions of As, Be, B, Cr, Ga, Li, and V; (b) Aluminophosphate containing Fe, Ti, as T atoms (XAPO), where Fe or Ti are in combination with Co, Mg, Mn, or Zn. Further examples of compositional variations in the unique zeotype frameworks listed in Table 20 are given in Table 22. It should be noted that not all these compounds have been fully structurally characterized at the time of writing.

The material designated $AlAsO_4$-1 comprises linked $[AlO_4]^{5-}$ and $[AsO_4]^{3-}$ tetrahedra.

Finally, it must be mentioned that catalytic interest has promoted the preparation of many high-silica zeolitic-like phases modified to include other T atoms such as B, Ti, Fe, or Ga. This modification can be at synthesis, or by postsynthesis treatment to replace Si and/or Al from existing high-silica frameworks. Not all these are recorded here because these modified materials again may not be fully characterized; however, Table 21 lists well-characterized examples, for example, analogs of the MFI (ZSM-5) framework.

3.5.3 Phases of Silica with Open Zeolite-like Frameworks

Synthetic studies on high-silica zeolites showed that silicon end members of structural groups could be prepared. Clearly these are pure silica phases and to date several have been prepared including a synthetic analog of the natural silica phase melanophlogite. These are listed in Table 23. They have sometimes been described as clathrasils, in deference to their strong structural links to clathrates as can be seen from their soap-bubble like frameworks (illustrated in Figure 12).

3.5.4 Felspathoid Frameworks

Earlier discussion introduced the concept of using the characteristic truncated octahedral elements of the sodalite framework to explain the molecular architecture of the synthetic zeolites X and Y (see Section. 2.4.3). There are other structural correlations that can be drawn between felspathoids and zeolites, for example, that the cancrinite cage (11-hedron) is a face-sharing element seen in the LTL, ERI, OFF, and LOS frameworks. Furthermore, in nature, salt ion pairs are contained in felspathoid minerals and when these are removed the residual framework exhibits the zeolitic properties of ion exchange and reversible water loss. Other similarities arise in that zeolites can imbibe salt ion pairs, and isotypic structures

Table 22 Compositional variations in unique zeotype frameworks[a]

IUPAC code	Zeotype name or acronym
AEL	AsAPO-11, BAPO-11, BeAPSO-11, BeGeAPO-11, CAPO-11, CAPSO-11, CoAPO-11, FCAPO-11, FeMnAPO-11, LiAPO-11, MAPO-11, MgAPSO-11, MnAPSO-11, SAPO-11, VAPO-11, XAPO-11, ZAPO-11, ZnAPSO-11, MCM-7
AEN	AlPO-EN3, AiPO-53(A), AlPO-53(B), CFSAPO-1A, JDF-2, MSC-1, UiO-12-500, UiO-12-as
AET	SAPO-8, MCM-37
AFI	AsPO-5, As GaAPO-5, BAPO-5, BeAPO-5, BeAPSO-5, CAPO-5, CAPSO-5, CoAPO-5, FCAPO-5, FCAPSO-5, FeMgAPO-5, GaAPO-5, GeAPO-5, Li PO-5, MAPO-5, Mg PSO-5, MnAPO-5, MnAPSO-5, SAPO-5, SnAPO-5, VAPO-5, XAPO-5, ZAPO-5, ZnAPSO-5
AFN	AlPO-14, GaPO-14
AFO	CAPO-41, FCAPO-41, SAPO-41, XAPO-41
AFR	FCAPO-40, SAPO-40, XAPO-40
AFS	FCAPO-46, FeAPSO-46, Mg PSO-46, XAPO-46, ZnAPSO-46
AFX	SAPO-56, SSZ-16
AFY	CoAPO-50, MAPO-50, ZAPO-50
APD	$AlAsO_4-$. 1, AlPO-D
AST	AsAPO-16, CAPSO-16, CoAPO-16, FCAPO-16, FeAPSO-16, MAPO-16, Mg APSO-16, MnAPO-16, MnAPSO-16, SAPO-16, XAPO-16
ATN	CoAPO-39, FCAPO-39, MAPO-39, MgAPSO-39, MnAPSO-39, XAPO-39, ZnAPSO-39
ATO	AsAPO-31, AsBeAPO-31, BeAPSO-31, CAPO-31, CAPSO-31, FCAP-31, Fe APSO-31, Mg APSO-31, MnAPSO-31, SAPO-31, Ti,ZnAPO-31, XAPO-31, Zn APSO-31
ATS	CoXAPO-31, FCAPO-36, MAPO-36, MgAPSO-36, MnAPO-36, XAPO-36, ZAPO-36, ZnAPSO-36
ATT	FCAPO-33, XAPO-33
ATV	$GaPO_4$-25

[a] Compare with Table 20. See text for explanations of the acronyms.

Table 23 Phases of silica with open zeolite-like frameworks

IUPAC code	Name or acronym	Idealized composition	Isotypic framework
AST	Octadecasil	$[Si_{20}O_{40}]\cdot 2(RF)$, R = quinuclidinium or TMA	$AlPO_4$-16?
CFI	CIT-5	$[Si_{32}O_{64}]$	
DDR	Deca-dodecasil 3R	$[Si_{120}O_{240}]\cdot qR$, R = 1-aminoadamantane	Sigma-1 ($SiO_2/Al_2O_3 \approx 60$)
DOH	Dodecasil 1H	$[Si_{34}O_{68}]\cdot qR$, R = N_2 or piperidine	
DON	UTD-1F	$((Cp^*)_2Co)^+{}_2F^-{}_{1.5}(OH)\text{-}_{0.5}\ [Si_{64}O_{128}]$ Cp* = pentamethylcyclopentadiene	UTD-1
GON	GUS-1	$[Si_{32}O_{64}]$	
IFR	SSZ-42	$[Si_{16}O_{32}]$	ITQ-4, MCM-42
ISV	ITQ-7	$[Si_{64}O_{128}]$	
ITE	ITQ-3	$[Si_{64}O_{128}]$	
MEL	Silicalite-2		ZSM-11[a], SSZ-46
MEP	Melanophlogite (natural)	$[Si_{46}O_{92}]\cdot qR$, R = N_2, CO_2, CH_4	Synthetic melanophlogite
MFI	Silicalite (silicalite-1)	$TMA_2OSi_{48}O_{96}\cdot H_2O$	USC-4[a]
MTF	MCM-35	$[Si_{44}O_{88}]$	MESOPOROUS
MTN	ZSM-39 (dodecasil-3C)	$[Si_{136}O_{272}]\cdot qR$, R = tetraethylammonium hydroxide	Holdstite, CF-3 (ZSM-39 contains 0.2% Al)
NON	Nonasil (nonasil-$[4^15^8]$)	$[Si_{88}O_{176}]\cdot 4R$, R = 2-aminopentane	ZSM-51 (SiO_2/Al_2O_3 13 → ∞)
RTE	RUB-3	$(C_8H_{15}N)_2\ [Si_{24}O_{48}]$	
SFE	SSZ-48	$[Si_{14}O_{28}]$	
SFF	SSZ-44	$[Si_{16}O_{32}]$	
SGT	Sigma-2	$[Si_{64}O_{128}]\cdot 4R$, R = $C_{10}H_{15}\ NH_2$	ZSM-58 (SiO_2/Al_2O_3 50 → 1000), B-SGT (B-analog)
STF	SSZ-35	$[Si_{16}O_{32}]$	ITQ-9
STT	SSZ-23	$(C_{13}H_{24}N^+)_{4.1}\ F^-{}_{3.3}(OH)^-{}_{0.8}\ [Si_{64}O_{128}]$	
VET	VPI-8	$[Si_{17}O_{34}]$	

[a] See also Tables 19 and 21.

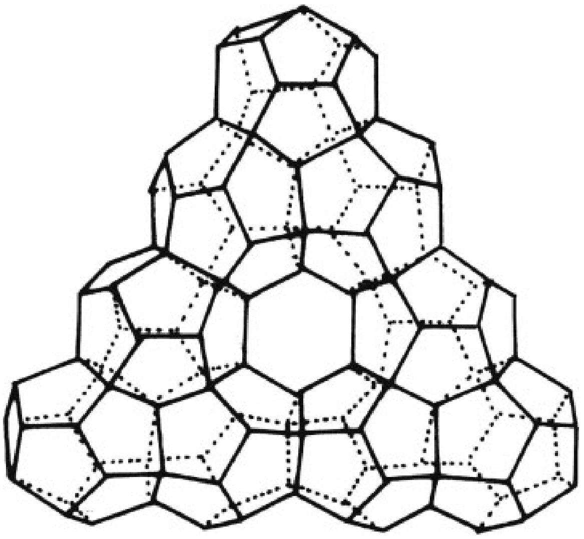

Figure 12 The clathrate-type structure of dodecasil-3C (MTN) (see Table 23)

with T atoms other than Si and Al are known in both natural and synthetic felspathoid analogs.

Table 24 lists felspathoid frameworks included in Baerlocher, Meier, and Olson.[11]

4 ZEOLITE GENESIS

4.1 Natural Species

4.1.1 Introduction

Most mineralogical displays in museums contain zeolite specimens because of their large attractive crystals and regular crystalline habit. These are of volcanic origin, which, until comparatively recent times, was regarded as their predominant mode of genesis. This view changed dramatically in the early 1960s when several of the major oil companies sent out survey teams into the western United States. These teams were hopeful of finding zeolites of sedimentary origin that might be of sufficient purity to be of commercial value. In fact, reports as early as 1891, from the first ever oceanographic survey (1873–1876) made by *HMS Challenger*, had described zeolites in 'red mud' recovered from the bed of the Pacific Ocean, and in 1914 Johannsen had reported fine-grained zeolites in beds of volcanic tuffs in Colorado, Wyoming, and Utah in the USA.

The survey teams subsequently identified many large-scale sedimentary zeolite deposits and today these are known to occur worldwide in vast quantities. The occurrences vary from those of high zeolite purity (>90%), such as those located in California, to tuffaceous materials of around 50–60% zeolite content (as in Italy). Commercial mining operations are known in USA, Japan, Cuba, Italy, Hungary, Bulgaria, Czechoslovakia, Indonesia, Korea, Russia, and South Africa. Workable deposits also exist in Mexico, Greece, and other Balkan states.

It has been reported by F.A. Mumpton[17] (1978) that more than 1000 occurrences of zeolite minerals in over 40 countries have been discovered since 1950. In addition to the hydrated aluminosilicate species, new minerals related to zeolites have been discovered, including the porous clathrasils such as Melonophlogite (a silica only framework). Species in which the aluminum or silicon has been replaced by other elements (such as phosphorus, iron, and beryllium) have also been discovered as exemplified by viscite, a silicoaluminophosphate related to analcime. At the present there are 38 different natural framework topologies, as shown in Table 25.

It is now recognized that natural zeolites arise from a wide variety of geological events and these will now be briefly discussed. Gottardi[18] and Tschernich[13] have reviewed these in more detail.

Table 24 Felspathoid frameworks listed in Baerlocher, Meier, and Olson[11]

IUPAC code	Name	Idealized unit cell formula	Isotypic materials (examples)
AFG	Afghanite	$(Na_2,Ca,K_2)_{12}\ [Al_{24}Si_{24}O_{96}] \sim (Na_2,Ca,K_2)_6(Cl_2,SO_4,CO_3)_6{\cdot}2H_2O$	–
CAN	Cancrinite	$Na_6[Al_6Si_6O_{24}]{\cdot}CaCO_3{\cdot}2H_2O$	Tiptopite[a], basic cancrinite, cancrinite hydrate, gallosilicate cancrinite, alumino-germanate, cancrinite
LIO	Liottite	$(Ca,Na_2,K_2)_9\ [Al_{18}Si_{18}O_{72}] \sim (Ca,Na_2,K_2)_9(SO_4,CO_3)_6Cl_3(OH)_3{\cdot}2H_2O$	
SOD	Sodalite	$Na_6[Al_6Si_6O_{24}]{\cdot}2NaCl$	G, $AlPO_4$-20, Tugtupite[b], Danalite[b], Genthelvite[b], Helvite[c], Hydroxysodalite (HS), beryllophosphate sodalite, zincophosphate sodalite

[a]Natural beryllophosphate. [b]Natural alumino beryllosilicate. [c]Natural beryllosilicate.

Table 25 The 38 naturally occuring zeolite topologies

IZA Code	Mineral Name	Typical Composition
AFG	Afghanite	$(Na_2,Ca,K_2)_{12}[Al_{24}Si_{24}O_{96}]n(Na_2,Ca,K_2)_6 (Cl_2,SO_4,CO_3)_6\ 2H_2O$
ANA	Analcime	$Na_{16}[Al_{16}Si_{32}O_{96}]\ 16H_2O$
BIK	Bikitaite	$Li_2[Al_2Si_4O_{12}]\ 2H_2O$
BRE	Brewsterite	$(Sr,Ba)_2[Al_4Si_{12}O_{32}]\ 10H_2O$
CAN	Cancrinite	$Na_6[Al_6Si_6O_{24}]\ CaCO_3\ 2H_2O$
CHA	Chabazite	$Ca_6[Al_{12}Si_{24}O_{72}]\ 40H_2O$
CHI	Chiavennite	$Ca_4Mn_4[Be_8Si_{20}O_{52}(OH)_8]\ 8H_2O$
DAC	Dachiardite	$Na_5[Al_5Si_{19}O_{48}]\ 12H_2O$
EDI	Edingtonite	$Ba_2[Al_4Si_6O_{20}]\ 8H_2O$
EPI	Epistilbite	$Ca_3[Al_6Si_{18}O_{48}]\ 16H_2O$
ERI	Erionite	$(Na_2,Ca)_35K_2[Al_9Si_{27}O_{72}]\ 27\ H_2O$
FAU	Faujasite	$(Na_2,Ca,Mg)_{29}[Al_{58}Si_{134}O_{384}]\ 240\ H_2O$
FER	Ferrierite	$Na_2\ Mg_2[Al_6Si_{30}O_{72}]\ 18\ H_2O$
GIS	Gismondine	$Ca_4[Al_8Si_8O_{32}]\ 16H_2O$
GME	Gmelinite	$(Na_2,Ca)_4[Al_8Si_{16}O_{48}]\ 24\ H_2O$
GOO	Goosecreekite	$Ca_2[Al_4Si_{12}O_{32}]\ 10\ H_2O$
HEU	Heulandite	$Ca_4[Al_8Si_{28}O_{72}]\ 24H_2O$
LTL	Perliate	
LAU	Laumontite	$Ca_4[Al_8Si_{16}O_{48}]\ 16\ H_2O$
LEV	Levyne	$Ca_9[Al_{18}Si_{36}O_{108}]\ 50H_2O$
LIO	Liottite	$(Ca,Na_2,K_2)_9[Al_{18}Si_{18}O_{72}]n(Ca,Na_2,K_2)_9 (SO_4,CO_3)_6Cl_3(OH)_3\ 2H_2O$
LOV	Lovdarite	$K_4Na_{12}[Be_8Si_{28}O_{72}]\ 18\ H_2O$
MAZ	Mazzite	$(Na_2,K_2,Ca,Mg)_5[Al_{10}Si_{26}O_{72}]\ 28\ H_2O$
MEP	Melanophlogite	$[Si_{46}O_{92}]\ 9R\ (R = N_2,\ CO_2,\ CH_4)$
MER	Merlinoite	$K_2Ca_2[Al_9Si_{23}O_{64}]\ 24H_2O$
MOR	Mordenite	$Na_8[Al_{18}Si_{40}O_{96}]\ 24H_2O$
NAT	Natralite	$Na_{16}[Al_{16}Si_{24}O_{80}]\ 16H_2O$
OFF	Offretite	$(Ca,Mg)_{1.5}K[Al_4Si_{14}O_{36}]\ 14H_2O$
PAR	Partheite	$Ca_8[Al_{16}Si_{16}O_{60}(OH)_8]\ 16H_2O$
PHI	Phillipsite	$K_2(Ca,Na_2)_2[Al_6Si_{10}O_{32}]\ 12H_2O$
RHO	Pahasapite	
ROG	Roggianite	$Ca_{16}[Al_{16}Si_{32}O_{88}(OH)_{16}]\ (OH)_{16}26H_2O$
SOD	Sodalite	$Na_6[Al_6Si_6O_{24}]\ 2NaCl$
STI	Stilbite	$Na_4Ca_8[Al_{20}Si_{52}O_{144}]\ 56H_2O$
THO	Thomsonite	$Na_4Ca_8[Al_{20}Si_{20}O_{80}]\ 24H_2O$
WEN	Wenkite	$Ba_4[Ca,Na_2]_3[Al_8Si_{12}O_{39}(OH)_2](SO_4)_3\ H_2O$
YUG	Yugawaralite	$Ca_2[Al_4Si_{12}O_{32}]\ 8H_2O$

4.1.2 Formation of Zeolites in Nature

Zeolites arise naturally by broadly two routes, one predominantly at low temperatures (below 40 °C) and associated with sedimentary processes, with the second being at higher temperatures and linked to volcanic and associated thermal processes.

Low-Temperature Diagenic Routes to Zeolite Formation.

1. Land processes. Strictly, the majority of diagenic routes are also associated with vulcanism because they are a consequence of alteration processes to wind-blown glassy volcanic ashes or layers of pyroclastic tuffs.

   Alteration can be in a hydrologically open system when percolation of meteoric water through tuff layers creates a series of zeolitized zones. The deeper zones contain, successively, zeolites such as clinoptilolite, mordenite, chabazite, phillipsite, and analcime. (The name clinoptilolite will be used throughout the rest of this article to signify silica-rich, alkali metal forms of heulandite as this is the preferred designation in most literature references to this material.) Typical examples of this are in the John Day Formation (Oregon, USA) and at Oahu (Hawaii). At some locations (e.g. in Japan), similar zeolite zoning is linked to burial diagenesis where pressure and temperature effects have contributed to the formation of zeolites in underlying zones, with the lowest zones containing the most dense zeolite (e.g. analcime).

   Hydrologically closed systems also create zeolites when glassy volcanic ash falls into a saline lake under arid, or semiarid, conditions. Conditions of high pH and salt concentration arise from evaporation, producing ideal conditions for zeolites to form. Lake Tecopa, California, and Lake Magadi in Kenya contain zeolites formed in this way. The silica source in this route is not confined to glassy ash and can be clays, plagioclases, or even biogenic silica.

   Finally, some soils contain relatively high proportions of zeolites ($\approx$15%). These result again from arid or semiarid environments where evaporation produces a high concentration of sodium carbonate, which can alter clay minerals to produce zeolites. Examples of this are the heulandite found in the Harwell soil series in Southern England and the analcime in the San Joaquin Valley (California).

2. Marine processes. Sea water reacts with ocean-bed sediments containing volcanic ash, or biogenic silica from Radiolarians, to form zeolites. This process is common in deep-sea sediments and phillipsite makes up 80% of the sediment in the Indian and Pacific Oceans. Clinoptilolite is abundant in Atlantic sediments and both phillipsite and clinoptilolite are found in manganese nodules on the ocean beds.

   Zeolites created in shallow sea sediments are also widespread. Other marine zeolites include analcime, merlinoite, chabazite, stilbite, and more rarely, erionite, mordenite, and laumontite. Figure 13 shows a schematic of the zoning patterns of autogenic zeolites and feldspars in tuffs of saline alkaline lakes, saline alkaline soils, deep-sea sediments, open hydrologic systems and burial diagenesis

Hydrothermal Routes at Higher Temperatures. Zeolites are commonly found in veins or cavities in volcanic rock as a result of the alteration of cooling lava flows coming into contact with surface water. Hot thermal salt solutions are created that circulate through the flow, dissolving out glass to form zeolites. Examples of this mode of occurrence occur in basalts and are common at many locations throughout the world. Zeolites arise in pegmatites from late-stage

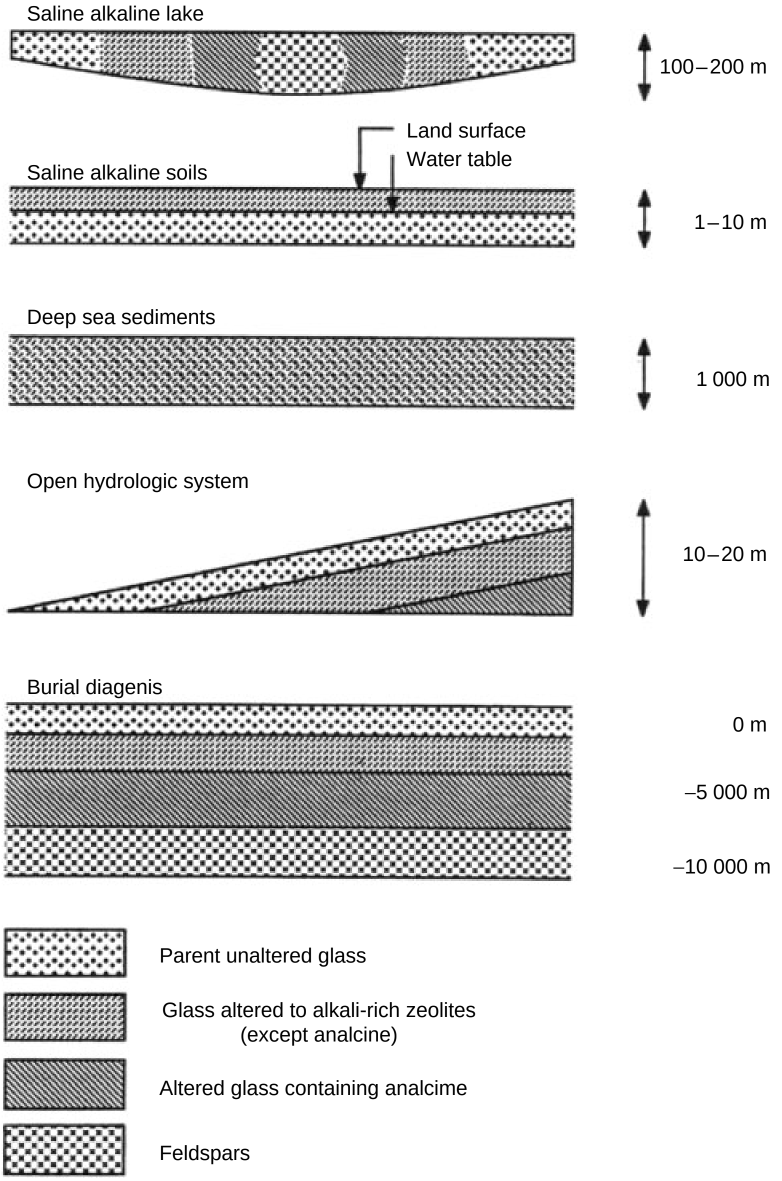
Saline alkaline lake
100–200 m
Land surface
Water table
Saline alkaline soils
1–10 m
Deep sea sediments
1 000 m
Open hydrologic system
10–20 m
Burial diagenis
0 m
–5 000 m
–10 000 m
Parent unaltered glass
Glass altered to alkali-rich zeolites (except analcine)
Altered glass containing analcime
Feldspars

Figure 13 Schematic representation of zoning patterns of autogenic zeolites and feldspars. (Reprinted from Ref. 17. © 1978, with permission from Elsevier)

crystallization involving alteration of pegmatic minerals, and also ultimately when silica-rich hot water is expelled, which then alters surrounding rocks to zeolite phases. Examples of this can be seen in the Elba granodiorites (Italy) and in the borolanite found near Altnahara (Scotland).

Hydrothermal ore deposits can contain local zeolites (e.g. the Andreasburg sulfide deposit in Germany) arising from circulating hot fluids. Similarly, zeolites arise in hydrothermal veins and cavities in felspathic rocks like the Adamello granite in Italy.

Geothermal fluids are a common agency for zeolite formation and this has been well documented in Iceland, at Wairakei (New Zealand), and in Yellowstone Park (USA). Often, well-defined zones (illustrated for Iceland in Figure 14) can be identified with, say, clinoptilolite and mordenite at shallow (cooler) depths with deeper (hotter) environs containing heulandite, laumontite, and then wairakite and analcime. These assemblages feature a continuous transition to burial diagenesis.

Other Routes. When heat from a magma chamber, or an intrusive dyke, bakes surrounding rocks, zeolites can be part of the suite of minerals produced in zones via this process of contact metamorphism. This sequence has been identified in the Rhodope Mountains of Bulgaria. Bulgaria also has been cited as the location of proposed geoautoclaves, where enclosed conditions of high temperature and vapor pressure

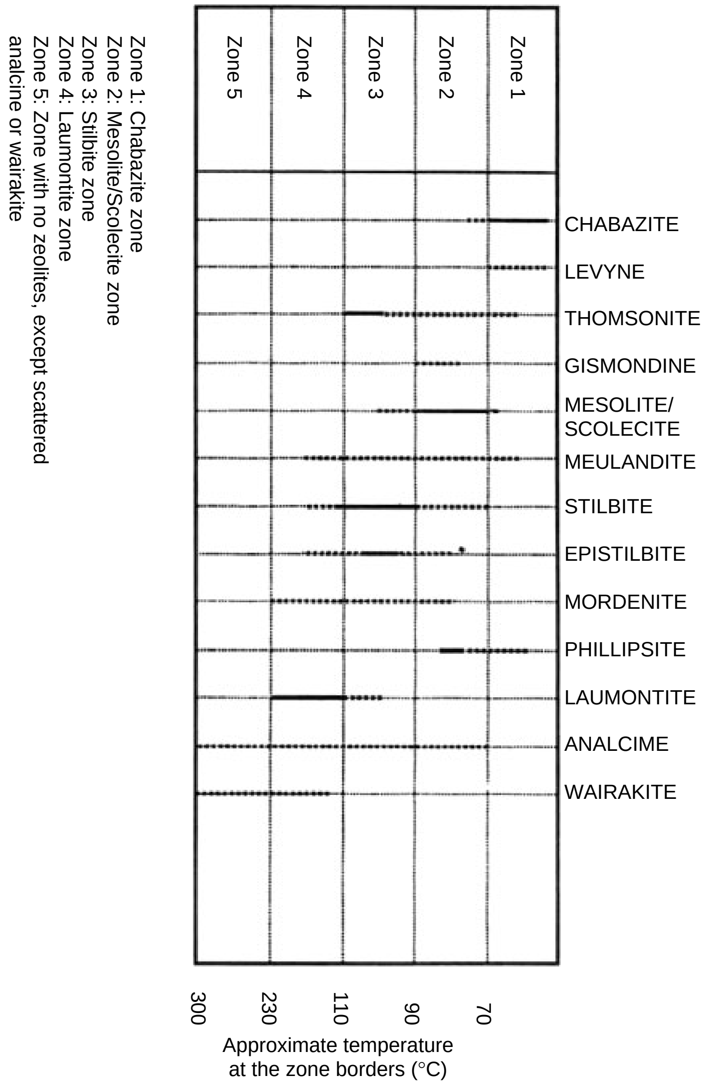

Figure 14 Temperature zoning of zeolites occurring in geothermal areas of Iceland. (Reprinted from Ref. 17. © 1978, with permission from Elsevier)

exist in an ignimbrite immediately after the deposition and zeolites are formed as a consequence.

In all the modes of formation discussed, zeolites are clearly secondary minerals, that is, created by alteration of existing rocks. Only analcime and natrolite have been suggested as primary minerals, that is, ones created by direct magmatic crystallization. This issue is still in doubt but may be true for analcimes from the Crowsnest Formation, Alberta, Canada, and the Colima lavas of Mexico.

4.2 Synthetic Species

4.2.1 Introduction

The progress of laboratory synthesis of zeolites first followed the high temperature and pressure experiments conceived by Barrer to mimic the then perceived geological genesis. With the wider realization of the sedimentary route to the formation of zeolites came studies at lower temperature, hydrothermal, conditions (e.g. by R. M. Barrer in the UK and R.M. Milton and D.W. Breck of the then Union Carbide laboratories in New York State). In 1948, Barrer[19] reported the first confirmed synthesis of a zeolite, in which he had produced a synthetic zeolite with no known natural counterpart, Zeolite P. In this first paper, Barrer documented the fundamental methodology that is still used today in exploratory zeolite synthesis:

- The effect of the reaction gel composition on crystallization product
- The effect of pH on crystallization
- The effect of temperature and time
- The nature of the starting materials

Early work concentrated on the use of inorganic cation-based formulations but both Barrer and Kerr (Mobil) pioneered the use of organic cations as ingredients for zeolite synthesis. This approach later produced the industrially significant high-silica zeolites, such as ZSM-5, and the explosion of zeotypes listed in the previous section. Some of these materials can even be best made at subambient temperatures. Another significant change of recent origin is that of the substitution of the F^- ion for OH^- as the so-called mineralizer in zeolite synthesis.

The facile way by which zeolitic frameworks can be formed is further confirmed by their production under acid and nonaqueous conditions, from the gas phase, and with organic additives as diverse as simple alcohols[20] and amines, polymers, crown ethers, and dye molecules.

4.2.2 Outline of Zeolite Synthesis

Figure 15 presents a general view of the elements of zeolite synthesis. There are a number of factors, which affect zeolite crystallization:

- Silica/alumina sources
- Hydroxide and/or fluoride concentration
- Cations (both organic and/or inorganic)
- Anions (other than OH^- or F^-)
- Water content of gel
- Time
- Reaction temperature (ambient ~40 °C, low ~110 °C, moderate 150 °C and high >200 °C)
- Reaction gel ageing
- Stirring
- Nature of mixture (gel, sol, or solution)
- Order of reagent mixing

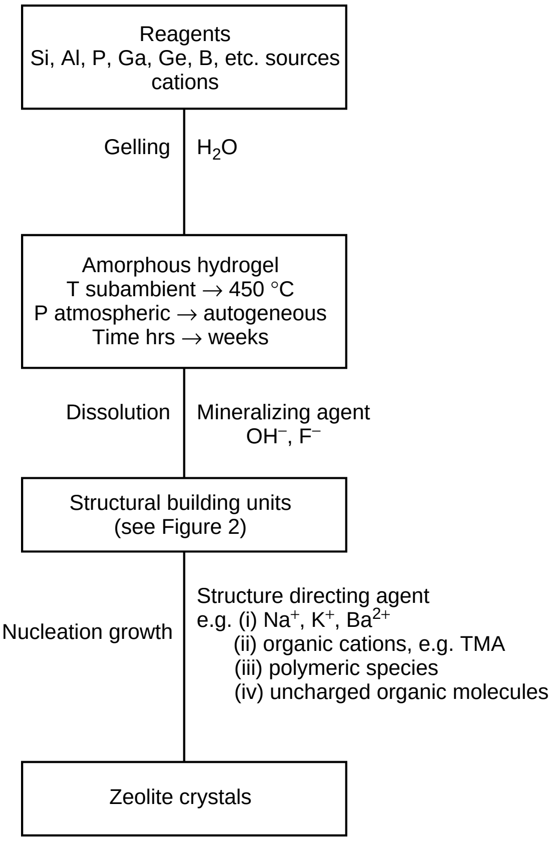

Figure 15 Schematic of the steps typical in zeolite (zeotype) syntheses

Several zeolites crystallize with a fairly narrow range of Si/Al ratios, for example, Zeolites A, X and Y. However other materials like the pentasil (ZSM-5 or ZSM-11) can be produced over a wide range from ratios of 7.5 to infinity and sodalite from ratios of 1 to infinity. Attempts to change the Si/Al ratio of the final product by changing the ratio in the reaction gel often leads to cocrystallization of different zeolite types. The source of the silica and/or alumina can also affect the final product. A very wide range of silica sources have been used including natural materials such as kaolinite, volcanic glasses, rice husks, and nepheline, but most laboratory and industrial preparations use an ‘active silica’. This is either a silicate, hydrated silicate, or a dispersion of high surface area silica (i.e. a silica sol.).

Aluminium sources have also been very varied and include aluminium wire, metal aluminates, aluminium alkoxide, and aluminium oxides and hydroxides. For zeotype synthesis, boehmite, a reactive aluminium oxide/hydroxide, is the preferred source with phosphoric acid providing the phosphorus content. In zeolite synthesis, if the hydroxide content is increased there is generally an increase in crystallization rate, which can be beneficial. However it must be remembered that if a number of different zeolites can crystallize from one reaction mixture with only time being the separating variable then the use of increased hydroxide can lead to cocrystallization and impure final products. The cation source can be one or more alkali metal cations, less frequently an alkaline earth cation, or an organic cation (e.g. Tetramethylammonium (TMA)). The main role of inorganic cations is to balance the negative charge created on the zeolite framework with the incorporation of Al^{3+}. As space is limited, if a monovalent cation replaces a divalent cation then we tend to see a reduction in the aluminium content of the zeolite framework. In addition to charge balancing, inorganic cations can also influence the framework structure formed, as seen in Table. 26.

It has been found that organic agents present in the gel can have a profound influence on syntheses, especially for zeotypes and high-silica species. Organic cations can interact with the reaction gel in a number of ways. They can

- act as templating of structure-directing agents
- act as gel modifiers, allowing higher silica/alumina ratios to be achieved for particular zeolite structures than could otherwise be obtained.
- interact with the gel affecting alkalinity

Table 26 Some zeolite syntheses in relation to inorganic cation content

Zeolite	Cations in Reaction Mixture	Preferred
Faujasite types	Na, Na + NMe_4, Na + Li, Na + Ba	Na
Zeolite A types	Na, Na + NMe_4, Na + K, Na + Ba, Na + Ba + NMe_4, Li + Cs + NMe_4	Na
Mordenites	Na, Ca, Sr	Na, alkaline earth ions
Zeolite L	K + Na, K, Ba, Ba + K, Na + Ba	K, Ba
XK-5 types	Ba, Na + Ba, K + Ba, Li + Cs + NMe_4	Ba
ZSM-2 type	Li + Cs + NMe_4	Li

- interact physically affecting the gelling process
- act as void filler, similar to water and indeed replacing water as the main void filler in nonaqueous systems.

Examples of their structure-directing influence can be seen in Table 27. This is a restricted list and Szostak has provided a comprehensive survey.[15]

The primary reagents are combined in an OH^- medium and the gel, so-formed, held at defined temperatures and pressures for the crystallization period (Figure 16). Gel ageing prior to this crystallization time can be needed. More recent syntheses have shown that high-silica zeolites prepared with a F^- mineralizer are almost fault-free, unlike those prepared in OH^- media.[22]

Comprehensive texts exist covering all aspects of zeolite synthesis methodology, and those by Barrer,[23] Jacobs and Martens,[24] and Szostak[25] are especially useful and for a recent historical survey the reader is directed to the review by Cundy and Cox.[26]

Table 27 Organic agents directing the production of framework structures[21]

MFI	MAZZ	FER	AFI
TPA	TMA	Choline	TEAOH
TEA	Choline chloride	Ethylenediamine	TPAOH
Ethanolamine	Pyrrolidine	Piperidine	Choline hydroxide
Glycerol	DABCO	1,3-Diaminopropane	Cyclohexylamine
Propylamine			2-Picoline
1,6-Diaminohexane			3-Picoline
Pentaerythritol			4-Picoline
Hexanediol			DABCO
Morpholine			Dicyclohexylamine

Note: Triethanolamine (TEA).

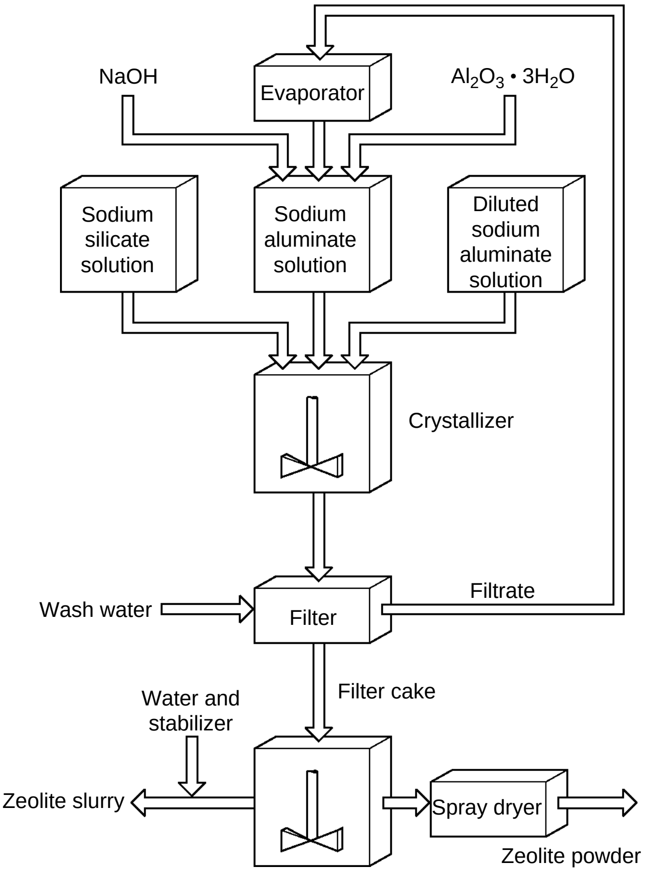

Figure 16 Process for the production of NaA zeolite. (Reproduced from E. Roland, 'Zeolites as Catalysts, Sorbents and Detergent Builders', eds. H.G. Karge and J. Weitkamp, 1989, p. 650 by permission of E. Roland)

4.2.3 *Mechanism of Zeolite Synthesis*

Researchers have attempted to elucidate the mechanism for zeolite formation for over 50 years. Two directions of experimental work have been examined:

Identification of species during the crystallization process;

Monitoring of the crystallization kinetics.

There are a number of different factors that can operate in a crystallizing gel and these have been summarized by Sand:[27]

- Precipitation of the gel
- Gel dissolution
- Zeolite nucleation
- Crystal growth of the zeolite nuclei
- Dissolution/recrystallization of metastable phases (Oswald's Law of successive transformations)
- Formation of more stable phases
- Successive nucleation, crystal growth, and further nucleation
- Formation of the equilibrium phase.

A number of analytical techniques have been used to identify the species present in the reaction gels. These include chemical analysis of the various phases, powder X-ray diffraction analysis to identify the crystal structure, IR spectroscopy to help identify substructural species early in the nucleation phase. Thermal analysis to yield information on the degree of hydration and thermal stability, and electron microscopy to give information on crystal shape and size. Other techniques are now also being used such as NMR, which with the advent of Magic angle spinning nuclear magnetic resonance (MAS-NMR) can now analyze both the reaction gel/solution and the final solid zeolite product. The combination of X-ray methods providing data on the long-range order and NMR providing short range order of the crystal-structure data ensures that these two methods are very powerful complementary techniques.

It is anticipated that the continued application of sophisticated NMR spectroscopy to solution and solid phases with the development of diffraction techniques to study the early stages of zeolite crystallization may ultimately clarify the problems of the mechanisms whereby zeolites are formed.

There have been two main schools of thought regarding synthetic zeolite formation: on the one hand it was considered that the crystallization process only occurred in the solution phase, with the gel just acting as a nutrient source. On the other it was proposed that there was direct hydrogel transformation. Different experimental work has supported both ideas.[28,29] Recently work on ZSM-5 has thoroughly investigated its formation,[30] and two processes have been proposed type 'A' and type 'B'. Type 'A' occurs in highly alkaline media with a polymeric silica source depolymerizing to yield negatively charged monomers that condense aluminate species around organic cations; this is a solution process. In type 'B', we start with monomeric silica in the reaction gel and the fast nucleation rate leads to direct hydrogel transformation, with any dissolved silica species being incorporated into the solid product last. Subotic[31] has proposed a kinetic model to discriminate between the two mechanisms. Formation of zeolite material has been shown to occur from pH values of 2.6 (for fluoride based media) to 14 (for hydroxide based media), over a wide range of Si/Al ratios. In many instances the same zeolite product can be produced from clear solutions, gels, and solid phases, while some zeolites can only be formed with difficulty over narrow compositions, temperatures, and times. This leads one to believe that no single mechanism exists to explain zeolite formation.

The stages shown above in Figure 15 are meant to imply that zeolite crystallization proceeds via a cooperative equilibrium interaction between the gel and species in solution rather than that whereby the gel reorganizes itself without influence from the liquid phase. This emphasizes two important concepts: firstly, that water plays a critical role in the zeolite framework genesis and, secondly, the function fulfilled by OH^- (or F^-) in providing control of pH, and gel chemistry, to facilitate the production of precursors germane to the building of frameworks via SBUs (Figure 2).

The role of the cations and organic agents can now be imagined as that of organizing water structures around which the subunits of structure assemble themselves. Earlier concepts described this as a templating effect, which envisaged close correlation between the sizes of hydrated cations, or organic entities, and the production of specific sizes or shapes in the microporous frameworks obtained. Experience has shown that specific templating is rare, such as that of TPA-OH in directing ZSM-5 synthesis and the use of 1,4-diazabicyclo[2,2,2]octane (DABCO) polymers in preparing gmelinite and mordenite structures. In the latter case the size of the polymeric unit controls the zeolite produced. The modern view tends to that of a guest agency (organic or inorganic) encouraging the formation of a water clathrate as a former for zeolite or zeotype structures. This simplistic approach needs to be extended to include the role of the cation species in pH control and the ability of all agencies to stabilize the various zeolite-like frameworks in the gel crystallization stage.

4.3 Industrial-scale Synthesis of Zeolites

Industrial production of synthetic zeolites gives fine powders ($<10\,\mu m$) in their sodium exchanged form. These materials can be used 'as synthesized', such as for use as detergents, and Figure 16 is a schematic diagram of the production of zeolite LTA (Na form) for this purpose. The manufacture of the synthetic faujasite (FAU) zeolite Y for catalytic uses follows a similar route.

Today there are three processes used industrially: hydrogel, clay conversion, and 'other' such as volcanic glass conversion. The first commercial process for preparing zeolites on a large scale was based on the hydrogel procedures developed in the laboratory. Here reagents included sodium silicate, sodium aluminate, and sodium hydroxide solutions. The hydrogel process is further classified into processes that use homogeneous gels, processes based on heterogeneous gels (here one reagent is a solid while the rest are usually liquids) and finally the gel-preform process, in which the aluminosilicate is formed into a pellet prior to crystallization to a zeolite. This produces 'binderless' zeolite aggregate. If possible, reaction temperatures are kept just below 100 °C and the crystallization is monitored by in situ XRD and/or spectroscopic methods. The mother liquor left over after crystallization is recycled but the number of cycles is limited owing to the increased chances of cocrystallization of unwanted side products. To use zeolites as desiccants and specialized sorbents, the fine powders need to be modified, prior to use, by agglomeration (and often ion exchange). The crystallites are invariably bound together with clay minerals, such as sepiolite, attapulgite, or kaolinite (as beads or extrudates), that make up 10–20% of the final composite. The major clay-type material used in the manufacture of zeolites is kaolin. For Zeolites A and X, in the clay conversion process manufacture the kaolin is generally dehydroxylated to form metakaolin by calcining in air at 550 °C. For Zeolite Y, the kaolin is heated to 925 °C to form a defect spinel. These intermediate products are subsequently treated with sodium hydroxide, which creates the required zeolite, so linking the existing crystallites into an aggregate suitable for industrial use. If the zeolite is to be used as an Fluidized bed cracking catalyst (FCC) catalyst, then it is spray dried to yield particles of around 60 μm. For other applications, a larger particle size maybe required and here oil-drop or extrusion techniques are used.[32]

4.4 Mesoporous Silicas

In 1992, Mobil workers[33] reported that they had prepared two mesoporous silicas, MCM-41 and MCM-48. These phases are related to the mineral silica species imogolite and marine diatoms. MCM-41 is a hexagonal structure while MCM-48 is a cubic one, and these two names actually represent families of materials. The pore sizes of these materials can be affected by which surfactant is used as the structure-directing agent during synthesis. To indicate pore sizes, the materials are usual labelled as MCM-41 (38), with the 38 representing the pore size of 38 Å. The MCM-41 family is composed of large diameter tubes, organised into an hexagonal array. It is interesting to note that the actual tube walls are amorphous silica (and/or alumino/silica) and can vary in thickness making them very different to zeolitic materials. These materials are normally prepared by cohydrolysis of tetraethylorthosilicate and a surfactant molecule like cetyltrimethylammonium hydroxide, an organo-aluminium or other organo-metal salt can also be introduced at this stage. Varying the amount and size of surfactant in the gel will change the nature of the pore structure in the crystallized product.

5 ZEOLITE PROPERTIES

5.1 Stability

Thermal and hydrothermal stability varies widely with both zeolite species and cation content, larger cations tending to make the zeolite structure less stable. It should be noted that, geologically speaking, zeolites are metastable species and interconversions in both natural and synthetic species are common, for example, synthetic gismondine (NaP) crystallizes as a cubic form but on standing at room temperature changes to the tetragonal form. Despite this variation, it should be commented that the zeolites used for catalytic purposes are very stable under the conditions of the industrial processes used. Similarly, zeolites used as sorbents and desiccants have very long useful lives. In a static application, the lifetime, to all intents and purposes, are indefinite and in a dynamic circumstance; where a regeneration process is carried out, the lifetime period should still be about five years.

Zeolites are generally very chemically stable and well able to withstand poisoning by nitrogen and sulfur compounds. Their acid stability, however, is dependent on their Si/Al ratio, with those zeolites having Si/Al ~ 1 being unable to withstand pH < 4 and those with Si/Al > 5 being usefully acid resistant in mineral acids. The loss of intracrystalline water may result in structure collapse to an amorphous phase, for example, BaA loses water between 100–180 °C then collapses above 180 °C. Alkaline stability is good up to around pH 11 and zeolite frameworks are stable to β-, α-, and γ-radiation, with only minor damage arising from prolonged exposure to neutron beams.

5.2 Zeolite Surfaces

It is important to realize that useful zeolites have large internal surfaces, that is, a reminder of the ‘sponge’ analogy, and it is *these* surfaces that control their observable surface properties. Normally, surface areas of inorganic materials are quantified by standard gas sorption techniques, for example, N_2 uptake analyzed by Brunauer, Emmett, and Teller (BET) isotherm plots, and zeolites have nitrogen surface areas in the approximate region 100–1000 $m^2\,g^{-1}$. These estimates should be considered with caution because:

1. the precalcination step, required before N_2 uptake, can cause structural change,
2. the probe molecule may not have access to all the channels and cavities in the zeolite structure and, most importantly,
3. the value for the surface area obtained depends upon the assumption of monolayer coverage as required by BET theory.

A better view of the extent of the void volume available within a zeolite comes from simple measurements of water content as listed in Table 28. Zeolites with high voidage (e.g. LTA, CHA, FAU) can be assumed to have only 1% of their useful surface on the exterior of the crystal.

One final generalization about zeolite surfaces is to mark the presence of OH groups on internal and external surfaces despite the presumption of the three-dimensional nature of zeolite architecture arising from full corner sharing of Si/Al tetrahedra. The concentration of these OH groups in synthetic species is usually low (about 2 $nmol\,g^{-1}$), but note the inclusion of incomplete framework structures in Baerlocher,

Table 28 Void fractions of some zeolites assessed from their water content[34]

Natural species	Void fraction	Synthetic species	Void fraction
Analcime	0.18	ZSM-5	0.10
Mordenite	0.28	L	0.32
Clinoptilolite	0.34	A	0.47
Gmelinite	0.44	Y	0.48
Chabazite	0.47	X	0.50

Meier, and Olson's compilation[11] (see Tables 16, 17, and 20). The OH groups are in highest concentration in synthetic high-silica zeolites and, in ZSM-5 for instance, have been identified as terminal and bridging entities. The presence of these OH groups has great significance in zeolite catalysis and modification, as will be briefly reviewed later.

5.3 Ion Exchange

5.3.1 Background

The identification of charge-balancing cations in crystallographically well-defined structures that change very little during cation-exchange processes has attracted the use of zeolites as models for the testing of the theory of ion exchange. This is true for both the equilibrium and kinetic aspects of the phenomenon.

Zeolites can have very high selectivities for specific cations but a full understanding of all the factors involved in delineating these selectivities has not yet been reached. Detailed consideration of this topic, and ion-exchange kinetics, are not appropriate here and has been reviewed elsewhere.[35]

Nevertheless, it is useful to point out that zeolites with higher framework Si content generally prefer larger, less hydrated cations (e.g. Cs with its smaller hydrodynamic radii), while those with Si/Al ~ 1 take up hydrated polyvalent cations selectively. The role of water is apparent here and also with the growing realization that water in immediate contact with an aluminous zeolite surface is hydrolyzed with two foreseeable consequences:

1. the production of OH^-, which can lead to precipitation of metal oxides/hydroxides on the surface (e.g. Zn on LTA[36])
2. immediate cation exchange, with H_3O^+ entering the zeolite phase.

The latter process seems to be very selective against alkali metal cations in the initial stages of exchange and is critically dependent on alkali metal solution phase concentration.[37] Sometimes ion-exchange processes can be described as ion sieving when a particular cation (hydrated or unhydrated) is too large to enter all, or part of, the zeolite internal structure.

5.3.2 Ion-exchange Applications

Detergency. The largest-scale industrial production of zeolites is that devoted to the production of the sodium form of zeolite A (LTA) for use in the detergent industry. This uses currently in excess of 0.5 million metric tonnes per annum worldwide. Zeolite A (NaA) is added to washing powders and other household detergents or cleansing powders as a water softener (described by the detergent industry as a builder). It has a high selectivity for Ca^{2+} (less so for Mg^{2+}) following the simple theory outlined in Section. 5.3.1.

The advantage of zeolite builders comes in their use as a replacement (sometimes only partial) for sodium tripolyphosphate, hence reducing the release of phosphates to the environment. An earlier Section. (4.3) showed the schematics of a production process for detergent grade A. It is interesting to record that the technology includes the 'design' of NaA crystals without sharp edges or corners to encourage their early removal from fabrics in the washing cycle. The release of NaA to the environment has been shown to be acceptable (Dyer[38] discusses the hazard assessment of this and other zeolites). The natural zeolites clinoptilolite and chabazite also are used as detergent builders.

Radioisotope Scavenging. Clinoptilolite has a relatively high Si/Al ratio and has the ability to scavenge cesium radioisotopes from aqueous nuclear wastes. An example of its industrial-scale use is in the development of the site ion-exchange effluent plant (SIXEP) by British Nuclear Fuels at their Sellafield site.[39] This uses a clinoptilolite, from Mud Hills, California, and meets the stringent performance requirements. The Cs selectivity of clinoptilolite has led to its possible use to reduce Cs radioisotope body burdens in sheep, and mordenite has been studied for the same use in reindeer. Mordenite also has been used to treat aqueous nuclear waste, as has an acid washed chabazite (AW500).

Clinoptilolite amendments to soil have greatly reduced cesium uptake by plants (e.g. on Bikini Atoll) and clinoptilolite from the Belli Plest deposit in Bulgaria was dropped by air to help control the Chernobyl accident. Finally, both zeolite A and a chabazite played key roles in the Three Mile Island clean-up program, again to scavenge Cs radioisotopes.

Waste-Water Treatment. There is a requirement in waste-water treatment to remove the ammonium ion and clinoptilolite has an appropriate selectivity for this ion. This zeolite is used in municipal sewage treatment in the USA and Hungary, and in Japan for cleaning up water from fish farms. The Italians have used chabazite-rich tuffs for a variety of water treatments.

These and other uses of natural zeolites have been reviewed.[40]

Agriculture and Horticulture.[40] There is a considerable literature relating how natural zeolites, and occasionally synthetic species, can be fed to various animal species (sheep, pigs, beef cattle, horses, and so on) with advantage. The benefits probably arise from a pH control effect in the animal gut (i.e. an ion-exchange phenomenon), and produce improved weight gains and disease reduction.

Other publications describe how the quality of soil can be improved by a 5–10% zeolite addition, followed by an increase in crop yield. This can be related to the zeolite acting as a controlled release fertilizer based upon an ammonium selectivity.

The zeolite most studied in both these areas is, again, clinoptilolite.

5.4 Sorption and Separations on Zeolites

5.4.1 Background

When the inherent water has been removed from a zeolite, the remaining voidage often has a useful capacity to take in guest molecules. Removal of water is described as activation and can be achieved by heating to about 350 °C. Industrially this is usually in combination with an applied vacuum or an inert gas purge. The guest molecules enter the internal regions of the zeolite host crystal through restricted dimensions prescribed by the oxygen atoms of the zeolite framework. Zeolite A (LTA; Figure 3) provides an example of this in that entry to the large cavity is via an S8R (crystallographic diameter 4.1 Å) and to the smaller sodalite unit through a S6R (crystallographic diameter 2.3 Å).

5.4.2 Uses of Zeolites as Molecular Sieves

Dimensions are comparable to molecular sizes and so zeolites can behave as molecular sieves. Indeed, this term is widely used to describe commercially available zeolites as typified by the well known Linde Molecular Sieves whose manufacture was pioneered by the Linde Corporation (latterly Union Carbide and now UOP) in New York State. These are sold as 3A, 4A, and 5A and are, respectively, the potassium, sodium, and calcium exchanged form of zeolite A, where the numbers represent their effective pore sizes in angstroms. Table 29 shows examples of the oxygen rings (windows) governing access into zeolites, with an indication of their sizes and the types of molecules able to pass through them. Note that the crystallographically measured ring sizes are not the same as their effective pore sizes. This arises principally from the thermal flexing of the aluminosilicate framework (±0.3 Å) and the inherent polarizability of organic molecules (i.e. their ability to be ‘squeezed’ through the window). Again zeolites have been popular models for sorbent theory, as described comprehensively in books by Barrer**[41]** and Ruthven.**[42]**

The separation of molecules on the basis of size has high potential at research and commercial levels. Many separations have been described**[34,40]** and the most well known are described in the following sections. It should also be pointed out that the technology exists whereby pore dimensions of zeolites can be modified by silanation or boranation. This can be done to achieve highly specific separations and/or gas encapsulation. Details are in the monograph written by Vansant.**[43]**

Table 29 Zeolite molecular sieving, correlation between oxygen ring diameter and molecules admitted[a]

Crystallographic dimension (Å)	No. of oxygens	Zeolite	Examples of molecules admitted
2.3	6	A, X	H_2O, NH_3
3.8[b]	8	Chabazite	He, Ne, Ar, CO_2
4.1	8	A	C_2H_2, $MeNH_2$
4.2 and 5.4	10	Ferrierite	As through S8R
7.4	12	X, Y	Cyclohexane, benzene, CCl_4, B_5H_9

[a] Two zeotypes have larger rings, VPI (18SR, 12.1 Å) and cloverite (20 SR, 13 × 4.0 Å); see Table 2 for other details. [b] Distorted.

Desiccants. The ion-exchanged forms of zeolite A are well known as general laboratory and industrial drying agents in the form of extrudates or beads. The success of these materials as desiccants arises from several possible reasons, viz.:

1. their ability to exclude other molecules on the basis of size;
2. the strong affinity of water for the internal zeolite surfaces;
3. accommodation of water molecules in voids containing cations;
4. ease of regeneration;
5. long useful life (natural gas drying towers have a five-year lifetime).

Gas Purification. There are many and varied examples using both natural and synthetic zeolites. The natural zeolites are likely to be chabazite, clinoptilolite, or mordenite. The latter two are useful for dealing with acid gas streams.

A common purification is the use of 4A to remove CO_2 from natural gas as well as sweetening the gas, that is, removing H_2S and nitrogen products. Zeolite 13X (synthetic faujasite containing only Na cations) also is used to remove undesirable larger molecules that contain S and N atoms from natural gas. In 2002, Engelhard introduced ‘Molecular Gate’ for the separation of both CO_2 and N_2 from natural gas using pressure swing applications (PSA). This material is one of the recently discovered titanium silicates (ETS-4). Already two plants in the USA are using this technology to removed unwanted gases from natural gas. Clearly, natural gas treatment plants link purification with drying and regeneration processes.

Gas Separation. The best-known process is the use of 5A to separate *n*- from *i*-alkanes. This is the basis of several commercial processes (e.g. Union Carbide Isosiv, and Exxon Ensorb). Their purpose is to provide feedstocks for the detergent and chemical industry. Currently there is considerable interest in using zeolites in PSA, especially in the enrichment of gases from the air. Oxygen production to hospitals is an example of this, both in the provision of oxygen lines and in portable units for individual use or in field hospitals as in the Gulf War. Again, zeolite A is widely used but clinoptilolite, mordenite, and chabazite are important PSA substrates, for example, the separation of methane and nitrogen mixtures using clinoptilolite.[44] Earlier separations of this sort on zeolites were cryogenic in nature.

Finally, synthetic zeolites have long been used in gas–solid chromatography for permanent gas and hydrocarbon analyses. Some modern GC capillaries are coated with zeolites.

Liquid Phase Separation. UOP have pioneered several small-scale processes to fractionate mixtures of liquids. The Parex process was introduced in 1971 and by 2001 71 units were running commercially. The MX-Sorbex process was introduced in 1998 and so far 5 units have been commercialized. Very recently,[45] in 2001, UOP introduced a new Sorbex process, MaxEne, to increase the ethlene yield from Naphtha Crackers. Examples of these are listed in Table 30.

Only the Molex process depends upon molecular size, whereas the others function on the basis of a liquid chromatographic fractionation. Quite recent work[46] shows that high-silica zeolites (synthetic) make good high performance liquid chromatographic (HPLC) media. The mechanisms whereby these chromatographic separations are achieved await elucidation but it seems that both internal and external surface attractions are important, as are zeolite structures and the nature of the cation present. Silica analogs of zeolite structures are hydrophobic and so offer the possibility to separate organic molecules from aqueous environments.

Carriers. The encapsulation of molecules into zeolite voids has been used to handle unpleasant chemicals, such as vulcanizing agents, and to carry CO_2 in carbonated drinks. Other prospective uses are to store and transport methane and hydrogen.

5.5 Zeolites as Catalysts

5.5.1 Background

Some 40 years ago it was discovered that synthetic faujasites could act as effective isomerization and cracking catalysts. The latter advance, based on the pioneering work of Plank and Rosinski, produced the current situation whereby essentially all the world's motor vehicle and aviation fuels are derived from crude oil by use of a zeolite catalyst. Zeolites have replaced the earlier silica/alumina and silica/clay catalysts in this area with a resulting annual savings estimated in billions of dollars.

The success has prompted an explosion of patents, journal publications, and conference proceedings, devoted to the study of the theory, mechanism, and utility of zeolites in promoting virtually any organic (and some inorganic) reaction. Rabo[47] has compiled a comprehensive treatise on the earlier work on zeolite catalysts, and Jacobs[48] has discussed their carboniogenic activity. Amongst the copious literature the reviews by Dwyer[49] on the evaluation of zeolites and the tailoring of the acid–base properties of zeolites, and by John *et al*.[50] describing the range of reactions catalyzed and their industrial relevance are recommended. This section provides an overview of current commercial use of zeolite catalysts with some indications of their mode of action and ease of modification (see also Section. 6).

5.5.2 Commercial Processes Using Zeolite Catalysts

Table 31 provides some details of zeolite catalyst usage. The best known is that of zeolite Y as a fluidized bed catalyst (FCC) to crack crude oil for gasoline production. The zeolite is used as a promoter and comprises up to 50% of a small composite with a clay or silica binder. As such it can remain stable throughout many cycles in the catalyst riser (at 480–520 °C), where it meets the downstream of crude oil followed by a steam blast to release the cracking products, and then a stream of air in a regenerator (590–730 °C). This regeneration process cleans the catalyst of coke and the residual oil products.

Clearly the success of the catalyst depends upon its ability to withstand these extreme conditions and this is one of the advantages of the ultrastable synthetic faujasite (USY) and ZSM-5 materials and is always a consideration in the other applications listed in Table 31. It is, however, only one of the known advantages acquired when zeolites are considered as industrial catalysts. Other benefits come from the zeolite

Table 30 UOP sorbex processes for liquid phase separations[38,42]

Process	Separation	Zeolite	Desorbent
Parex	*p*-Xylene from its isomers	KBaY, SrBaX KbaX	Toluene *p*-Diethylbenzene *p*-Diethylbenzene
Ebex	Ethylbenzene from its isomers	NaY, SrKX	Toluene
Molex	n-Alkanes/i-alkanes, naphthalenes, aromatics	5A	Light paraffins
Olex	Linear long-chain alkanes from other alkanes	CaX SrX	
Sorbutene	1-Butene from C_4 alkanes and alkenes	–	–
MaxEne	Separates C_5-C_{11} from full range Naphtha	–	–
MX-Sorbex	High purity meta-xylene from its isomers	–	–
Sarex	Fructose from sucrose and other sugars (corn syrup feed)	CaY	Aqueous systems

properties of high internal surface area and variable pore sizes, which lead to both reactant and product selectivity via molecular sieving. This is described as shape-selectivity and is controlled by configurational diffusion, the phrase used to describe a diffusion-controlled regime in which useful catalytic reactions are encouraged by a matching of size, shape, and orientation of the product and reactant molecules to the molecular architecture of the zeolite.[51] An additional bonus comes from the ease with which zeolites can be modified; examples of this have been mentioned earlier, for example, ion exchange and the introduction of heteroatoms (other than Si and Al) into the zeolite framework. This latter change can be achieved by a postsynthetic modification and an interesting prospect is that of inducing ion exchange and catalytic properties into the uncharged frameworks of aluminophosphates ($AlPO_4$) by inserting Si atoms into existing $AlPO_4$ structures. A further modification is that of salt occlusion, that is, the introduction of a salt ion pair into a zeolite cavity to attain improved thermal stability and to reduce the deleterious effects of trace elements such as Ni, Fe, and V, which occur in some crude oils.

5.5.3 Source of Zeolite Catalytic Activity

Broadly, zeolites have high catalytic activity because their structures can produce a higher proportion of the so-called active sites per unit surface area than competing catalysts. These sites are the traditional Brønsted sites that arise from the creation of hydroxyl groups and this can be via one of the three routes illustrated below.

1. Ammonium ion exchange (e.g. as in production of USY)

$$\mathrm{NaZ(s) + NH_4{}^+(aq) \longrightarrow NH_4Z(s) + Na^+(aq)} \tag{1}$$

$$\mathrm{NH_4Z(s) \xrightarrow{calcine} HZ(s) + NH_3(g)} \tag{2}$$

2. Polyvalent ion exchange (e.g. as in rare earth exchanged Y, ReY)

$$\mathrm{NaZ(s) + M(H_2O)^{n+}(aq) \longrightarrow M(H_2O)^{n+}Z(s) + \mathit{n}Na^+(aq)} \tag{3}$$

$$\mathrm{M(H_2O)^{n+}Z(s) \xrightarrow{calcine} MOH^{(n-1)}(s) + HZ(s)} \tag{4}$$

3. Direct ion exchange with mineral acid (e.g. with ZSM-5).

In all three cases the protonated zeolite, HZ, is created containing Brønsted sites, which, when heated above 550 °C, lose water to produce Lewis sites, viz.

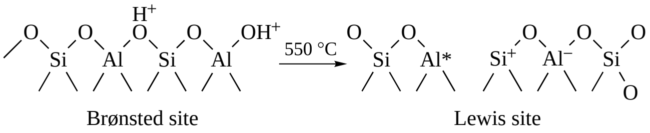

(5)

The Lewis sites are unstable, especially in the presence of water vapor, and an annealing process stabilizes the structure. This is thought to create true Lewis sites by ejecting Al

Table 31 Commercial processes using zeolitic materials

Process	Catalyst	Advantages in using zeolite-based catalysts
Catalytic cracking	Ultrastable Y[a] (USY), ZSM-5, rare earth exchanged Y (REY)	Selectivity and high rates
Hydrocracking	Y, erionite, mordenite	High conversion rates
Selectoreforming	Ni erionite, Ni erionite/clinoptilolite	Increase in octane number via LPG[b] production
Hydroisomerism	Pt mordenite	Converts low octane, pentane, and hexane to higher yields
Dewaxing	ZSM-5, ZSM-23, mordenite	Improved pour points for heavy oils and fuels (e.g. diesel)
Benzene alkylation	ZSM-5, REY	Ethylbenzene and styrene production with low by-product yield
Xylene isomerization	ZSM-5	Increase in *p*-xylene yield with low by-product yield
Methanol to gasoline conversion	ZSM-5	High gasoline yield with high-octane rating
NO_x reduction	H mordenite	Effluent clean-up in nitric acid and nuclear reprocessing plants
Aromatic hydroxylation/alkene epoxidation	Titanium silicate	Styrene to phenylacetaldehyde, ethylene to ethylene oxide and other reactions
LPG to aromatics	Ga ZSM-5	Benzene, toluene, xylene production
Methanol amination by ammonia → dimethylamine	Mordenite	–

[a] (USY), Ultrastable synthetic zeolite Y treated to reduce aluminum content and improve thermal and hydrothermal stability (see Section. 6.1).
[b] LPG = liquid propane gas.

oxide/hydroxide species from the framework, viz.

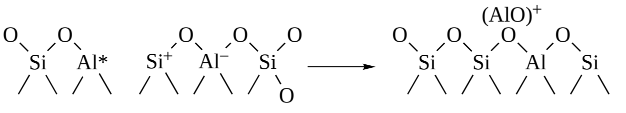

(6)

This extra framework Al can be identified by MAS-NMR but is in at least two forms. It is these Al species that are thought to be the 'super acid' sites inducing the high zeolite surface reactivity.

Another aspect to zeolite catalytic activity, briefly mentioned earlier, is the use of ion-exchange modification to introduce elements of known catalytic propensity into the zeolite promoter. Examples of this are in Table 31. There has been a considerable amount of work devoted to the investigation of the dispersion of metal particles (e.g. Ni and Fe) on zeolite substrates to enhance specific organic reactions.

5.5.4 The Future

The SAPO materials seem likely to provide novel catalysts, especially as the emphasis of zeolite usage turns to chemical intermediates and fine chemical production,[50,52] and processes using the B analog of ZSM-5 (boralite) and SAPO-34 have been commercialized.

Another advance seems likely through the use of zeolites as enzyme mimics.[53] This centers on the reactions of organometallics with zeolite internal surfaces. The best-known example is the production of a $[\mathrm{Co^{II}(bipyridyl)(terpyridyl)}]^{2+}$ complex inside the main cavity of zeolite Y that can selectively and reversibly absorb oxygen from the air. The catalytic potential of a Co phthalocyanine moiety prepared in the Y cavity has also been demonstrated.

6 COMMERCIALLY USEFUL ZEOLITES AND THEIR WELL KNOWN USES

6.1 Synthetic Zeolite A (LTA)

6.1.1 Cation Positions

The element of structure of this zeolite, illustrated in Figure 3, represents a convenient segment of the full unit cell of the LTA structure and should be described as its pseudounit cell (puc). Each puc has 12 sodium cations and, in the hydrated zeolite, eight occupy sites close to each of the S6R openings to the component β-cages (Site I), three are in sites near the centers of some of the S8R openings to the larger α-cage (Site II), and the final sodium is in the center of the puc (Site III). Each pseudo unit cell contains 27 water molecules, and 20 of these form a pentagonal dodecahedron that lines the α-cage (Figure 17). This water structure is found in some water clathrates and in LTA surrounds the central Na ion with its attendant three water molecules. It is cation–water assemblages like this that are likely to be the precursors for the formation of zeolite frameworks in synthesis gels (see Section. 4.2.3).

The remaining four water molecules are in the β-cages. If the zeolite is dehydrated, the cations adopt other convenient crystallographic sites of minimum potential energy. This, of course, is common to all zeolites and ultimate sitings depend upon the Si/Al ratios and geometries of their frameworks, as well as the nature of the cation (size, charge, bonding properties); more details are available.[12]

In the commercial sorbents Linde Molecular Sieves 3A, 4A, and 5A, the resiting of cations on calcination tailors their effective pore sizes. In dehydrated 3A and 4A, the K and Na ions, respectively, occupy positions obstructing entry to the α-cage (i.e. across the 8SR), and the cation size difference (K > Na) changes the pore size from 3 to 4 Å. When the divalent Ca^{2+} is introduced into the large cage, there are, of course, fewer cations present ($2Na^+ \rightleftharpoons Ca^{2+}$) and, upon dehydration, these occupy Site I positions, away from the S8R windows, so opening up the effective pore size to 5 Å (note that 3A and 5A are both partially exchanged forms of NaA).

One final comment is that an increase in the Si/Al ratio in the LTA synthesis encourages the production of the crystallites with chamfered edges and corners, appropriate to their detergent use.

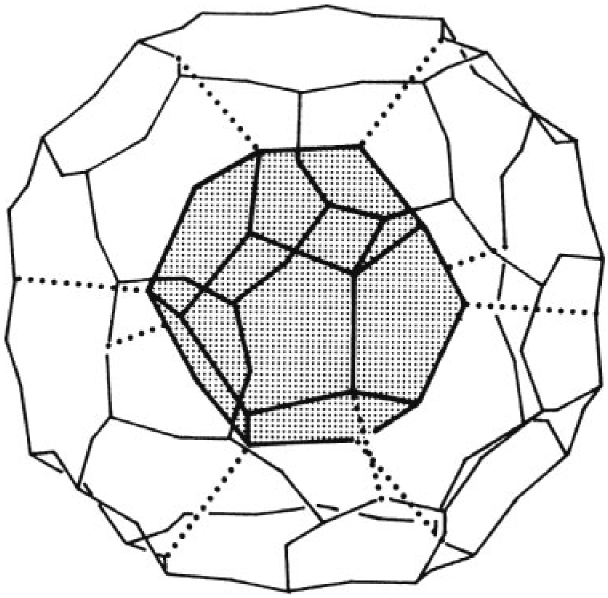

Figure 17 The water clathrate in the large cage of hydrated zeolite A. It is composed of 20 H_2O molecules arranged in a pentagonal dodecahedron

6.1.2 Commercial Uses of Zeolite A

Detergency. NaA is now a common builder, added to solid and liquid detergents and to other household and laundry products.

Desiccant. The forms 3A, 4A, and 5A are in general laboratory use as drying agents for air and nitrogen lines and organic liquids. Both 3A and 4A are used worldwide to dynamically dry liquid halocarbons and hydrocarbons, especially Liquid petroleum gas LPG and natural gas. 3A is preferred for drying refinery streams containing alkenes (cracked gas), ethene, proplene, and methanol, and 4A is used to dry other alcohols, benzene, and natural gas. Other industrial gas streams commonly dried by zeolite beads are oxygen, nitrogen, air, and CO_2 in nuclear power installations. Examples of static drying using 3A and 4A in sealed systems are widespread, for example, in sealed double-glazing units, refrigeration circuits (domestic and industrial), vehicle braking, air conditioning systems, and in heavy duty transformers filled with hydrocarbon liquids.

Gas Separation. 5A efficiently separates n- from i-alkanes. This is used to provide feedstocks to the detergent and chemical industries and is the basis of several commercial processes, that is, those developed by Union Carbide (Isosiv), British Petroleum BP, Shell, Texaco (TSF), Exxon (Ensorb), and VEB Leuna Werke, Bitterfeld, Germany (VEB) Germany. The latter process is called the Parex process. This should not be confused with the process of the same name developed by UOP to separate *liquid* C_8 hydrocarbons (see Table 30 and elsewhere), and note that UOP use 5A to separate n-alkanes from i-alkanes, naphthalenes, and aromatics in the liquid phase via their Molex process. Ambient pressure swing processes, using 5A, have been developed to produce both O_2 and N_2 from air. The nitrogen generators are used in steel-making while oxygen generators principally are used for medical purposes (for hospital oxygen lines, individual patients units, and in field hospitals), in welding, in water-oxygenating kits, and as emergency oxygen supplies in aircraft.

Gas Purification. The best-known purification process using 4A is that of natural gas; this involves two benefits, namely, peak-shaving whereby the calorific value of the gas is adjusted by CO_2 (and water) removal, and sweetening by H_2S removal. The latter purification also is used in LPG treatment. Another example is the trapping of hydrocarbons in gas and vacuum circuits.

Other Uses. The form 5A is a traditional gas–solid chromatographic substrate for permanent gas analysis, the butane isomers, and cryogenic analyses of hydrogen isotopes. It is an additive to powders to improve flow properties and to dry them (including food products) and an encapsulant for CO_2 in carbonated drinks.

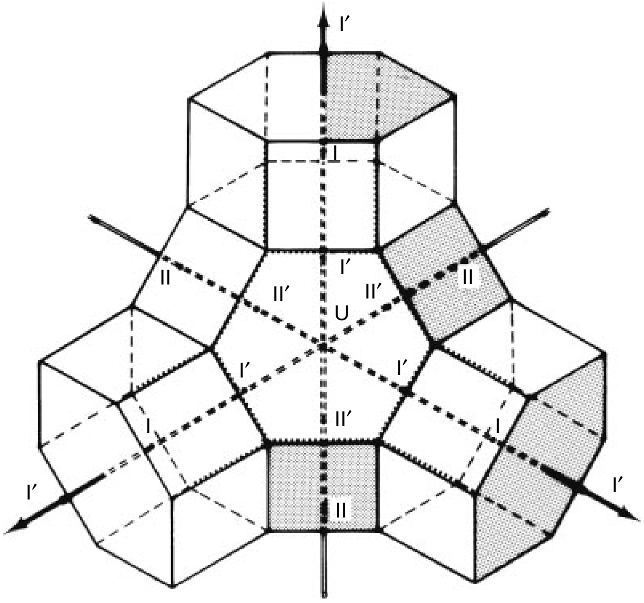

Figure 18 The cation sites of the faujasite (FAU) framework (see text for explanation of symbols). (Reprinted with permission from J.V. Smith, 'Molecular Sieve Zeolites-1', eds. E.M. Flanigen and L.B. Sand, *ACS Symp. Ser.*, 1971, **101**, 173. © 1971 American Chemical Society)

6.2 Synthetic Faujasites: Zeolites X and Y (FAU)

6.2.1 Cation Positions

Zeolites X and Y are isostructural with the natural mineral faujasite. They differ in the amount of Al occupying tetrahedral sites such that the Si/Al ratio of X is in the range 1–1.4 (but commonly 1) whilst that of Y can vary, according to synthesis conditions, up to Si/Al = 3. The cation sites available are shown in Figure 18, which represents an element of the full structure illustrated in Figure 11. The as-synthesized cation form is sodium. The cation sites can be listed as Site I in a D6R (hexagonal prism), Site I′ close to the D6R in the sodalite (β) cages, Site II′ in the sodalite cage near the S6R entrances to the large α-cage, II is in the large cages near the S6R entrances. U is at the centre of the sodalite cages and other sites (e.g. IV and V) are in less well-defined sites in the large cage.

The sites adopted by cations in these structures are complex and will not be considered here but, broadly, an increase in Si/Al (decrease in framework charge) depopulates Sites I and I′ in the hydrated zeolites in favor of positions in the large cage. Removal of water causes an increase in population of the Sites I and I′ regardless of framework charge. Details of individual cation sitings in ion-exchanged forms of X and Y are available,[12] with water molecule positions, where known.

Early references describe the Na and Ca exchanged forms of X as 13X and 10X, respectively. The figures were meant to imply their respective pore sizes, over assessments of the restriction offered by the 12SR window entry to the main cavity, which has the crystallographic dimension of 7.4 Å.

The Y framework is more stable than the X, to both thermal and hydrothermal treatments, so methods were developed to dealuminate the FAU framework to attain the improved stabilities needed for catalytic use, especially under the extreme fluidized bed conditions applied in cracking crude oil (see Section. 5.5.2). The end product is known as ultrastable Y (USY) and can be made by one of four ways: (a) acid treatment, (b) high-temperature steam treatment of the ammonium exchanged form of Y (NH_4Y), perhaps followed by acid treatment, (c) reaction of NH_4Y with an aqueous solution of $(NH_4)_2SiF_6$, and (d) reaction of NaY with gaseous $SiCl_4$.

The last treatment is the best method of retaining the excellent crystallinity and high hydrophobicity (Si/Al $>$ 25) synonymous with a good fluidized cracking catalyst (FCC).

6.2.2 Commercial Uses of Zeolites X and Y

Detergency. Zeolite X has been included in some builder compositions because it has a better selectivity for Mg^{2+} than does zeolite A.

Gas Separation and Purification. Zeolite X has been used for many hydrocarbon separations and to trap molecules containing S and N from industrial gases. It is used to dry and purify SF_6 in high-voltage switching apparatus and in oxygen-generating emergency supplies in fighter aircraft. It finds use in double-glazing units to scavenge residual solvents from the sealants used and to pick up iodine species from gaseous effluents from nuclear installations (as AgX).

Liquid Separation. Zeolites X and Y, in various ion-exchanged forms, are the substrates used in the processes developed by UOP for separating liquid mixtures (see Table 30). The hydrophobic nature of Y and its modified forms are used to scavenge organic molecules from aqueous environments (e.g. halohydrocarbons).

Catalysis. Various forms of zeolite Y find uses in industrial catalytic processes. These have already been listed in Table 31 and account for the second highest annual tonnage use of synthetic zeolites (approx 60 000 metric tonnes). This continues to increase as zeolite catalysts aid the shift to unleaded gasoline and to the use of cheaper feedstocks.

6.3 Synthetic Zeolite ZSM-5 (MFI)

6.3.1 Structure and Cation Positions

The structure of this high-silica species can be regarded as an arrangement of layers created by linking the 5–1 SBU (see Figure 2), as shown in Figure 19. The full three-dimensional framework can be regarded as a series of channels circumscribed by the 10SR seen in Figure 19. The spatial arrangement of these channels is shown in Figure 20 together with those in ZSM-11 (MEL). The cation positions have not yet been defined except that they behave as if they are occupying two distinct crystallographic sites.

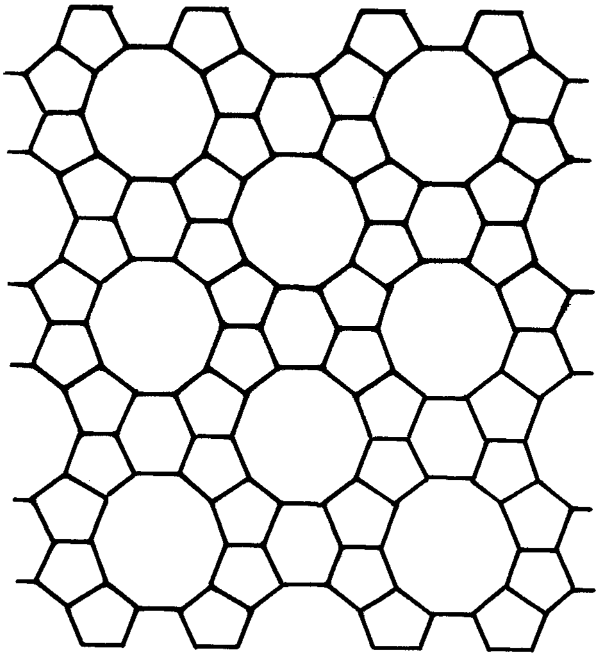

Figure 19 Sheet projection for ZSM-5 (MFI) structure showing 12SR and 8SR openings

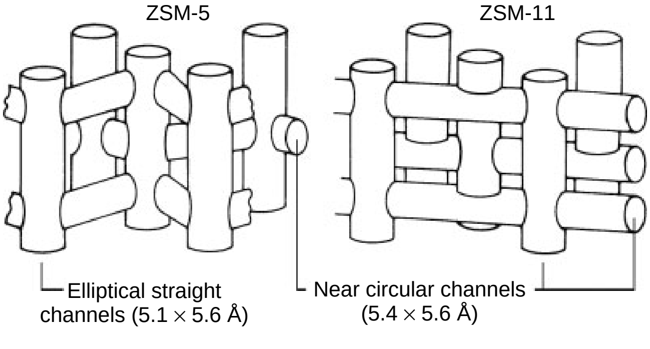
ZSM-5
ZSM-11
Elliptical straight channels (5.1 × 5.6 Å)
Near circular channels (5.4 × 5.6 Å)

Figure 20 Channel arrangements in ZSM-5 (MFI) and ZSM-11 (MEL). (Ref. 40. Reproduced by permission of Society of the Chemical Industry)

6.3.2 Commercial Uses of ZSM-5

The hydrophobic character of the high-silica MFI framework lends itself to the separation of polar and nonpolar molecules. There are many patents claiming this use but no details of commercial processes have appeared in the literature. ZSM-5 is used as a cocatalyst in FCC compositions. This makes use of its shape-selective properties to improve the octane quality of gasoline. It has been used with both Rare-earth exchanged synthetic zeolite Y (REY) and USY. It is also an effective catalyst for the conversion of methanol to higher carbon-number molecules. This is the basis of the methanol to alkenes (MTO) and methanol to gasoline (MTG) processes developed by Mobil. This discovery offers the prospect of conversion of the methane component of natural gas to synthesis gas (carbon monoxide and hydrogen) and then to methanol and gasoline. Dimethyl ether, an important industrial intermediate, can also be obtained from these reactions.

Gallium loaded ZSM-5 is the catalyst used in the Cyclar process (UOP/BP) whereby LPG (largely propane and butane) is converted to high-octane fuels and benzene/toluene/xylene (BTX) as petrochemicals.

ZSM-5 catalyzes alkene oligomerization, using its shape-selective ability, and both Mobil and Shell (methanol to gasoline and distillates (MOGD) and polygasoline and kerosene (SPGK)) use a ZSM-5 catalyst for this purpose. The production of ethylbenzene from benzene and ethylene is catalyzed by ZSM-5 in the Mobil/Badger process. Mobil also have improved the production of benzene and xylene from toluene disproportionation using ZSM-5.

Finally, ZSM-5 is used to dewax gas oils and lubricating base oils, and to produce low-temperature diesel fuel. In all these cases, the processes catalytically remove long-chain waxy n-alkanes, which otherwise crystallize out at low temperatures and cause increased viscosity.

6.4 Mordenite (MOR)

6.4.1 Structure and Cation Positions

The structure of mordenite contains two channels (Figure 4), one restricted by a 12SR and one by an 8SR. Eight cations and water sites have been located, with the most occupied being at the centers of the 8SRs, adjacent to the 5SR units, which link the 12SR channels, and near to S4Rs, which link adjacent five-membered rings around the smaller channel.

Divalent ions (Ca^{2+}, Ba^{2+}) occupy sites in the larger channels so that, on dehydration, molecular sieving is controlled by the dimensions of the smaller channel (2.6×5.7 Å); when monovalent ions are introduced they lie in the small channels so that molecular sieving is controlled by the 12SR (dimension 6.5×7.0 Å).

Early sorption experiments were carried out on natural mordenites, which behaved as small-port sorbents (i.e. had effective pore sizes of <4 Å). Synthetic mordenite behaves as a large-port material, displaying an effective pore size closer to that expected from a 12SR opening. Later work was able to synthesize both large (LP) and small (SP) ported mordenites, and discussion has taken place over a number of years concerning the reasons for the differences between these materials. The apparent channel restrictions in SP mordenite can be ascribed to the presence of extraneous material or to the presence of stacking faults. The fact that the channels in mordenite can be enlarged by acid leaching favours the channel blockage concept. Synthetic LP mordenites have been marketed by the Norton company as Zeolon 100, 200, and 900, and the product that is available as AW300 (AW = acid washed) is also likely to be a mordenite.

6.4.2 Commercial Uses of Mordenite

The relatively high Si/Al content of mordenite confers on it a certain acid stability that enables it to be used to remove water from acid gas streams such as reformer recycle hydrogen, reformer catalyst regeneration gas, HCl, Cl_2, and chlorinated hydrocarbons. It can also be used to treat off-gas for removal of oxides of sulfur and nitrogen (SO_x and NO_x). Mordenite's ion-exchange selectivity for Cs has been used to remove Cs radioisotopes from nuclear waste (Zeolon 900) and it is used in Japan on a plant scale to separate gases from the air.

LP mordenite doped with platinum is the catalyst used in the Shell Hysomer process for alkane hydroisomerization; this can be linked to the Isosiv separation process whereby i-/n-alkanes are separated on LTA zeolite. This link is the basis of the joint Shell/UOP Total Isomerization Process (TIP). Similar catalysts have been employed to hydrocrack (i.e. dewax) diesel fuels. There have also been reports of commercial use of mordenite to catalyze methanol amination with ammonia, to produce dimethylamine.

6.5 Chabazite (CHA)

6.5.1 Cation Positions

11 cation/water sites have been identified in the chabazite framework. In the hydrated mineral, the bulk of the cations are present as fully hydrated species in the large cavity with less than one Ca^{2+} puc being in the D6R sites. On dehydration, the cation population of the D6R site increases (≈ 2) and the other ions adopt two other sites, one just outside the six-ring entrance to the D6R and the other near four rings that connect adjacent D6Rs (see framework in Figure 6). The natural mineral (with erionite) has been marketed by Norton as Zeolon 500 and by other suppliers as AW500. Synthetic chabazite can be obtained from custom synthesis.

6.5.2 Commercial Uses of Chabazite

Chabazite has found a wide variety of occasional uses as a cheap desiccant and molecular sieve and as a selective ion exchanger in the nuclear industry. Current interest is in its use as a selective sorbent (in Li form for instance) in PSA and related applications.

6.6 Clinoptilolite (HEU)

6.6.1 Structure and Cation Positions

The clinoptilolite (heulandite) structure is that of an assemblage of 4-4-1 SBUs to create a layer-like array. The layers are joined to create two channels, both composed of 10SRs parallel to the crystallographic *c*-axis, and one 8SR limited channel parallel to the *a*-axis.

In clinoptilolites rich in alkali metal ions (Na/K), and in the hydrated state, two cations have specific sites in the main channels, one is in the smaller channels, and the final one lies near the center at an S8R.

6.6.2 Commercial Uses of Clinoptilolite

Like chabazite, clinoptilolite has been used as a cheap desiccant and molecular sieve. As noted earlier, its selectivity for Cs has led to its use in aqueous nuclear waste treatment and its ability to remove NH_4^+ from water has been used on a plant scale (see Section. 5.3.2). An extensive literature describes its use in horticulture and agriculture as an amendment to soils and composts. Similarly, the benefits of its addition to animal feeds is well documented. These uses have been reviewed[40] and three conference reports also can be recommended for further details.[54–56]

7 RELATED ARTICLES

Aluminum: Inorganic Chemistry; Oxides: Solid-state Chemistry; Silicon: Inorganic Chemistry; Solids: Characterization by Powder Diffraction.

8 REFERENCES

1. A. F. Cronstedt, *Akad. Handl. Stockholm*, 1756, **18**, 120.
2. A. Damour, *Ann. Mines*, 1840, **17**, 191.
3. H. Eichhorn, *Poggendorf Ann. Phys. Chem.*, 1858, **105**, 126.
4. H. C. R. St. Claire Deville, *Seances Acad. Sci.*, 1862, **54**, 324.
5. G. W. Morely and E. Ingersoll, *Econ. Geol.*, 1937, **32**, 607.
6. O. Weigel and E. Steinhoff, *Z. Kristallogr.*, 1925, **61**, 125.
7. J. W. Mc Bain, ‘The Sorption of Gases and Vapours by Solids’, Rutledge and Sons, London, 1932, Chap. 5.
8. W. H. Taylor, *Z. Kristallogr.*, 1930, **74**, 1.
9. L. Pauling, *Proc. Natl. Acad. Sci. U.S.A.*, 1930, **16**, 453.
10. C. D. Williams ed., ‘R.M. Barrer 1910–1996, Founding Father of Zeolite Science’, British Zeolite Association, University of Wolverhampton, 1999.
11. Ch. Baerlocher, W. M. Meier and D. H. Olson, ‘Atlas of Zeolite Structure Types’, 5th edn., Elsevier, 2001.
12. W. J. Mortier, ‘Compilation of Extra Framework Sites in Zeolites’, Butterworth, Guildford, 1982.
13. R. W. Tschernich, ‘Zeolites of the World’, Geoscience Press, Phoenix, AZ, 1992.
14. G. Gottardi and E. Galli, ‘Natural Zeolites’, Springer, Berlin, 1985.
15. R. Szostak, ‘Handbook of Molecular Sieves’, Van Nostrand Reinhold, New York, 1992.
16. S. T. Wilson, B. M. Lok, C. A. Messina, T. C. Cannan, and E. M. Flanigen, in ‘Intrazeolite Chemistry’, ACS Symposium Series, eds. G. D. Stuckey, and F. G. Dwyer, American Chemical Society, Washington, DC, 1983, Vol. 218, p. 79.
17. F. A. Mumpton, in ‘Natural Zeolites, Occurrence, Properties and Use’, eds. L. B. Sand and F. A. Mumpton, Pergamon Press, Oxford, 1978, p. p3.
18. G. Gottardi, *Eur. J. Mineral.*, 1989, **1**, 479.
19. R. M. Barrer, *J. Chem. Soc.*, 1948, 217.
20. M. P. W. Edmunds, S. J. Hill, K. Latham, and C. D. Williams, *Zeolites*, 1994, **14**, 529.
21. B. M. Lok, T. R. Cannan, and C. A. Messina, *Zeolites*, 1983, **3**, 282.
22. M. A. Camblor, L. A. Villaescusa, and M. J. Diaz-Cabanas, *Topics Catal.*, 1999, **9**, 77.
23. R. M. Barrer, ‘Hydrothermal Chemistry of Zeolites’, Academic Press, New York, 1982.
24. P. A. Jacobs and J. A. Martens, ‘Synthesis of High-Silica Aluminosilicate Zeolites’, Elsevier, Amsterdam, 1987.
25. R. Szostak, ‘Molecular Sieves, Principles of Synthesis and Identification’, Van Nostrand Reinhold, New York, 1989.
26. C. S. Cundy and P. A. Cox, *Chem. Rev.*, 2003, **103**, 663.
27. L. B. Sand, *Pure Appl. Chem.*, 1980, **52**, 2105.
28. G. T. Kerr, *J. Phys. Chem.*, 1968, **72**, 1385.
29. P. A. Jacobs, E. G. Derouane, and J. Weitkamp, *J. Chem. Soc., Chem. Commun.*, 1981, 591.

30. J. B. Nagy, Ph. Bodart, H. Collette, Ch. Frenandez, Z. Gabelica, A. Nastro, and R. Aiello, *J. Chem. Soc., Faraday Trans. 1*, 1989, **85**, 2749.
31. B. Subotic and A. Graval, *Stud. Surf. Sci. Catal.*, 1985, **24**, 199.
32. T. G. Roberie, D. Hildebrant, and J. Creighton in ‘Zeolites for Greener Technologies’ eds. M. Guisnet and J.-P. Gilson, Imperial College Press, 2002, Chap. 3.
33. C. T. Kresge, M. E. Leonowicz, R. W. J. Roth, J. C. Vartuli, and J. S. Beck, *Nature*, 1992, **359**, 710.
34. D. W. Breck, ‘Zeolite Molecular Sieves’, Krieger, 1984.
35. A. Dyer, in ‘Inorganic Ion Exchangers in Chemical Analysis’, eds. M. Qureshi and K. G. Varshney, CRC Press, 1991, p. 33.
36. W. Lutz, H. Fichtner-Schmittler, M. Bülow, E. Schierhorn, N. Van Phat, E. Sonntag, I. Kosche, S. Amin, and A. Dyer, *J. Chem. Soc., Faraday Trans.*, 1990, **86**, 1989.
37. R. Harjula, J. Lehto, J. H. Pothuis, A. Dyer, and R. P. Townsend, *J. Chem. Soc., Faraday Trans.*, 1993, **89**, 971.
38. A. Dyer, ‘An Introduction to Zeolite Molecular Sieves’, Wiley, Chichester, 1988.
39. M. Howden and J. Pilot, in ‘Ion Exchange Technology’, eds. D. Naden and M. Streat, Ellis Horwood, Chichester, 1984, p. 66.
40. A. Dyer, *Chem. Ind. (London)*, 1984, 241.
41. R. M. Barrer, ‘Zeolites and Clay Minerals as Sorbents and Molecular Sieves’, Academic Press, London, 1978.
42. D. M. Ruthven, ‘Principles of Adsorption and Adsorption Processes’, Wiley, New York, 1984.
43. E. F. Vansant, ‘Pore Size Engineering in Zeolites’, Wiley, Chichester, 1990.
44. J. Guest and C. D. Williams, *J. Chem. Soc., Chem. Commun.*, 2002, (23), 2870.
45. T. D. Foley, D. W. Green, and P. R. Pujado, MaxEne Process: Increased Ethylene Yield in Naphtha Crackers, AIChE Spring National Meeting, Houston, TX, 2001.
46. A. Dyer and T. I. Emms, PhD thesis, Salford University Library, unpublished work.
47. J. A. Rabo ed., ‘Zeolite Chemistry and Catalysis’, ACS Monograph No. 171, American Chemistry Society, Washington, DC, 1976.
48. P. A. Jacobs, ‘Carboniogenic Activity of Zeolites’, Elsevier, Amsterdam, 1977.
49. J. Dwyer, in ‘Zeolite Microporous Solids: Synthesis, Structure and Reactivity’, eds. E. G. E. Derouane, F. Lemos, C. Naccache, and F. Ramôa Riberio, Kluwer, Dordrecht, 1992, p. 303, p. 321.
50. S. John, D. M. Clark, and I. E. Maxwell, in ‘Perspectives in Catalysis’, eds. J. M. Thomas, and K. I. Zamarov, Blackwell, Oxford, 1992, p. 387.
51. C. D. Williams, *Chimica Oggi*, 2002, **20**, 74.
52. W. F. Hoelderich, in ‘Zeolites, Facts, Figures, Future’, eds. P. A. Jacobs and R. A. van Santen, Elsevier, Amsterdam, 1989, p. 69.
53. R. Parton, D. De Vos, and P. A. Jacobs, in ‘Zeolite Microporous Solids: Synthesis, Structure and Reactivity’, eds. E. G. Derouane, F. Lamos, C. Naccache, and F. Ramôa Riberio, Kluwer, Dordrecht, 1992, p. 555.
54. W. G. Pond and F. A. Mumpton eds, ‘Zeo-Agriculture’, Westview Press, Boulder, CO, 1985.
55. D. Kalló and H. S. Sherry eds, ‘Occurrence, Properties and Utilization of Natural Zeolites’, Akadémiai Kaidó, Budapest, 1988.
56. ZEOLITE ′026th International Conference on the Occurrence, Properties and Utilisation of Natural Zeolites (Thessaloniki, Greece) 2003, abstract available at www.supersorb.com.au/PDF/Conference%20Zeolite%20′02.pdf.

Zinc: DNA-binding Proteins

Mario A. Pennella & David P. Giedroc
Texas A&M University,College Station, TX, USA

1 Introduction 1
2 Zinc-containing Transcription Factors: Structural Zinc Sites 2
3 Regulatory Zinc in Metalloregulatory Proteins 8
4 Perspectives/Conclusions 15
5 Related Articles 16
6 References 16

Glossary

Chimeric (hybrid) protein: a nonnatural protein created when homologous regions of two homologous proteins are exchanged
Gag knuckle: this fold is composed of short (∼20 amino acids) Cys_2His_2 zinc fingers from retroviral gag proteins
Motif: a primary, secondary, or tertiary structural domain
Palindromic DNA-binding site: a DNA sequence that contains one inverted repeat composed of two half-sites of nucleotides
Zinc Knuckle: this fold group is composed of two short β-strands connected by a turn followed by a short helix or a loop, and it also may possess a unique turn with the consensus sequence CPXCG at either termini

Abbreviations

DBD = DNA-binding domain; HRE = Hormone response element; LIM = **L**in11, **I**sl1, and **M**ec3 (abbreviations for the genes in which the LIM domain was originally discovered); MT = Metallothionein; NCP = Nucleocapsid protein; PHD = Plant homeodomain; RING = Really interesting new gene; TFIIIA = Transcription factor IIIA; activator of transcription by RNA polymerase III; zf = Zinc finger.

1 INTRODUCTION

The local folding of small globular domains within gene regulatory proteins is required for sequence-specific DNA binding, an event that underlies gene expression in all kingdoms of life.[1] The formation of zinc-ligand coordination bonds provides the major driving force for the folding of these mini domains that lack an appreciable hydrophobic core.[2] Over the last two decades, an explosion in our knowledge of the diverse roles that the essential trace element zinc plays in DNA metabolism, chromatin remodeling, transcriptional regulation, nucleic acid packaging, and ribosome biogenesis has taken place.[3–7] Fueling this explosion is the structural characterization of zinc-containing nucleic acid-binding proteins at atomic resolution by X-ray crystallography and NMR spectroscopy. This chapter will survey these structural findings and develop unifying concepts that have emerged from these studies.

Zinc is found in all human body tissues with 30 to 40% found in the nucleus, 50% in the cytosol, and the remainder found in organelles, vesicles, and the cell membrane.[8] Zinc plays critical roles in the reduction of common infections, helps in the prevention of stunting growth, and supports neurobehavioral development among other attributes (*see* ***Nutritional Aspects of Metals & Trace Elements***).[9] Zinc is an essential trace element in all organisms, and the unique combination of structural and thermodynamic properties of zinc make it ideally suited for a diverse array of biological roles. These properties include its ready availability, Lewis acidity, high concentration of charge (atomic radius of 0.65 Å), lack of redox reactivity and stable oxidation state (2+). Zn(II) is a d^{10} transition metal ion that forms metal complexes of high thermodynamic stability that are often characterized by facile ligand exchange (*see* ***Zinc: Inorganic & Coordination Chemistry***).[5]

Zinc binds nearly exclusively to three types of amino acid side chains in proteins. These are cysteines, histidines, and carboxylates (Asp and Glu) with thiolate sulfurs and imidazole nitrogens by far the most common donor atoms. Zinc sites in proteins adopt a variety of coordination structures that differ in the number of ligands bound (coordination number), the type of ligands, metal-ligand bond lengths, dihedral ligand-metal-ligand bond angles, and, in some cases, second-shell interactions.[5] The Metalloprotein Database and Browser hosted by The Scripps Research Institute (http://metallo.scripps.edu/) reveals that among the approximately 3100 structurally characterized zinc coordination sites deposited in the Protein Data Bank (http://www.rcsb.org/pdb), the most prominent coordination number is four (1726), and the most common liganding pattern tetrathiolate (484), with tetrahedral or distorted tetrahedral coordination geometries by far the most prevalent for zinc sites classified as of April 2004.[10]

Zinc complexes in proteins perform structural, catalytic, and regulatory functions. Structural zinc sites typically adopt tetrahedral or distorted tetrahedral coordination geometries formed by four protein-derived ligands with no bound water molecules. Cysteines and histidines are by far the preferred ligands in such sites (e.g. zinc fingers; see Section 2).[11]

Catalytic and regulatory Zn(II) sites utilize the same amino acid ligands as structural sites, but include a greater percentage of carboxylate ligands derived from aspartate and glutamate, as well as solvent molecules (H_2O), which are almost always found in catalytic sites in enzymes (e.g. carbonic anhydrase) (*see* ***Zinc Enzymes***).**[11]** Cocatalytic sites, defined as catalytic metal sites that coordinate two metal ions via a bridging ligand(s) (e.g. phosphotriesterase), are formed by ligand sets similar to those found in catalytic sites, except that cysteine residues that typify structural zinc cluster sites (e.g. metallothioneins) (*see* ***Metallothioneins***) are never found as a bridging ligand in metalloenzymes (*see* ***Zinc Enzymes***).**[11]**

Structural zinc ions stabilize protein tertiary structure, protein–protein, and protein-nucleic acid interfaces. The zinc coordination bonds induce thermal stability and conformational rigidity to these important domains of proteins much like disulfide bonds do in oxidizing environments. In the absence of zinc, these protein domains are unfolded, exist in a predominantly random coil conformation, and are presumably subjected to rapid degradation and clearance by the cell. The most striking and seminal illustration of how ‘structural zinc’ stabilizes tertiary structure formation in DNA-binding proteins is in zinc finger (zf) proteins.**[12]** Classical C_2H_2 (Cys_2His_2) zinc finger domains, which mainly include DNA-binding proteins (they also mediate protein-RNA, protein–protein, and protein-lipid interactions) are small (∼30 amino acid residues) domains that fold around one or more zinc ions, and are nearly exclusively found in eukaryotic organisms (see Sections 2.1–2.2).**[13,14]**

The number and complexity of structurally characterized zinc fingers has increased dramatically over the last ten years. In order to understand the seemingly endless collection of known zinc finger structures, a classification scheme was devised that combines all structures of functionally diverse proteins into well-defined fold groups, each of which is discussed here (see Section 2). Recent findings reveal that canonical C_2H_2 zinc finger domains in transcriptional regulatory proteins in eukaryotes are not exclusively involved in structural stability but have also been implicated in regulating the concentration of bioavailable zinc in cells (see Section 3.5).**[15,16]**

Suboptimal or toxic (above normal physiological levels) concentrations of intracellular zinc have adverse affects on many aspects of cellular metabolism (*see* ***Metalloregulation***; ***Metal Ion Toxicity***). Zinc is now known to function at the level of transcription by binding directly to regulatory proteins, that is, metal sensor proteins that repress, derepress, or activate the transcription of genes that encode metal transporters (importers/exporters) and/or metal chelators. This helps cells maintain homeostasis (*see* ***Metallochaperones & Metal Ion Homeostasis***), or an optimal steady-state concentration of zinc within the cytosol and other intracellular organelles.**[3,17]** Zinc sensor proteins and the determinants of their coordination chelates (number of ligands, types of ligands, and coordination geometry) are discussed as important factors that determine metal selectivity (zinc vs. other metal ions) in these families of related sensor proteins (see Section 3).

2 ZINC-CONTAINING TRANSCRIPTION FACTORS: STRUCTURAL ZINC SITES

2.1 The Zinc Finger Story

Structurally distinct ‘zinc finger’ (zf) protein classes have emerged over the past two decades where the sole common feature is that each employs multiple cysteine and/or histidine residues to coordinate tetrahedrally a Zn(II) ion in order to stabilize their folds.**[13,18]** Zinc finger proteins thus defined comprise ≈3% of the proteins encoded by the human genome making them, by far, the most common proteins in eukaryotes.**[13]** A recent analysis of the mouse transcriptome identifies 46 distinct conserved zf protein families that constitute 7.5% of the nonredundant full-length protein sequences in that organism.**[19]** The structure and properties of DNA-binding zinc fingers, particularly the classical C_2H_2 zfs (see Section 2.2 below) have been studied extensively and recently reviewed as to their structural properties and efforts at design, and myriad of biological functions including transcriptional activation and repression, DNA replication and repair, translation, programmed cell death, and metalloregulation.**[14,18,20–23]**

Zinc finger proteins have recently been classified into eight distinct structural groups distinguished by their tertiary structural folds around the zinc coordination complex and the spatial arrangement of secondary structural elements that contribute zinc ligands.**[12]** Table 1 lists representative members from each of six of these eight structural classes that are known to interact directly with nucleic acids. These are discussed in turn.

The first zinc finger domain discovered contained C_2H_2 motifs found originally in nine tandemly arranged ∼30 amino acid residue repeats in the *Xenopus laevis* RNA polymerase III basal transcription factor IIIA (TFIIIIA).**[24]** In 1985, it was proposed that in the presence of zinc each of these repeats defined an independently folded mini-domain where the zinc ion was ligated tetrahedrally by two S^- (Cys) and two N^ε (His) side chains and the amino acids between the second and third ligands comprised the ‘fingertip’, which would interact directly with DNA.**[24,25]** All essential features of this seminal hypothesis have since proved to be correct. Figure 1 shows the crystal structure of the six N-terminal zinc fingers of *X. laevis* TFIIIA bound with 31 bp of the 5S rRNA gene promoter.**[26]** It is now known that much of the evolutionary and functional diversity of these canonical or classical C_2H_2 zinc finger proteins (Section 2.2) derives from the appendage of additional conserved domains to the zf domain to create modular proteins with new functionalities. An excellent illustration of this is the ubiquitous family

Table 1 Classes of zinc fingers

Classification	Fold/Motif[a]	Example(s)	Binding domain(s)	Structure
C_2H_2	$\beta\beta\alpha/C_2H_2$ 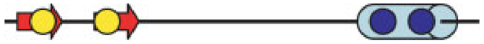	TFIIIA, MTF-1, WT1, & Zap1	DNA, RNA, protein	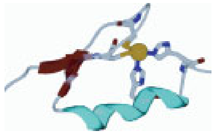
Treble clef	$\beta\beta\beta\beta\alpha/C_4$[b] 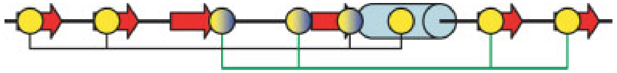	GATA-1 Nuclear Hormone Receptors (ER and GR) RING, FYVE, PHD	DNA DNA DNA, protein	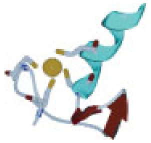
	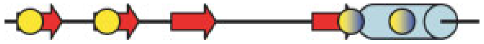 (x2)	LIM domains	Protein	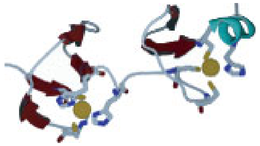
Zinc Ribbon	$\beta\beta\beta\beta\beta/C_4$ 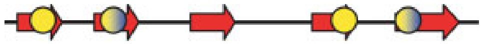	TFIIB, DNA Primase Ribosomal protein L31e	DNA, RNA	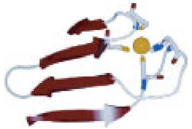
Gag knuckle	Truncated $\beta\beta\alpha/C_2HC$ 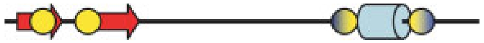	Retroviral nucleocapsid	RNA	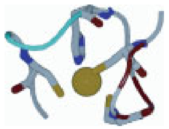
TAZ2-like domain	$\alpha\alpha/C_4$ 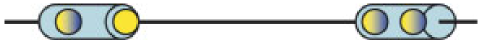	DNA Polymerase III γ subunit TAZ1/TAZ2 domains of Protein CBP/p300	DNA	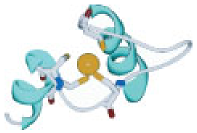
Zn2/Cys6-like	$\alpha\alpha/C_6$[b] 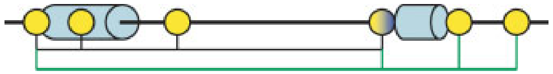	Gal4, Hap1, PUT3	DNA	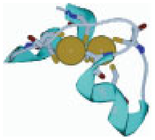

[a] *Yellow* spheres represent the positions of cysteine residues, and *blue* spheres represent positions of histidine residues; spheres showing gradients from *yellow to blue* represent positions predominantly occupied by cysteines and less frequently by histidines; spheres showing gradients from *blue to yellow* represent positions predominantly occupied by histidines and less frequently by cysteines. *Red* arrows represent β-strands, *blue* cylinders represent α-helices. [b] Interleaved zinc-binding sites in treble-clef motifs and Zn2/Cys6-like motifs are represented by *green* lines connecting the ligands that coordinate one zinc ion and *black* lines connecting ligands that ligate another zinc ion.

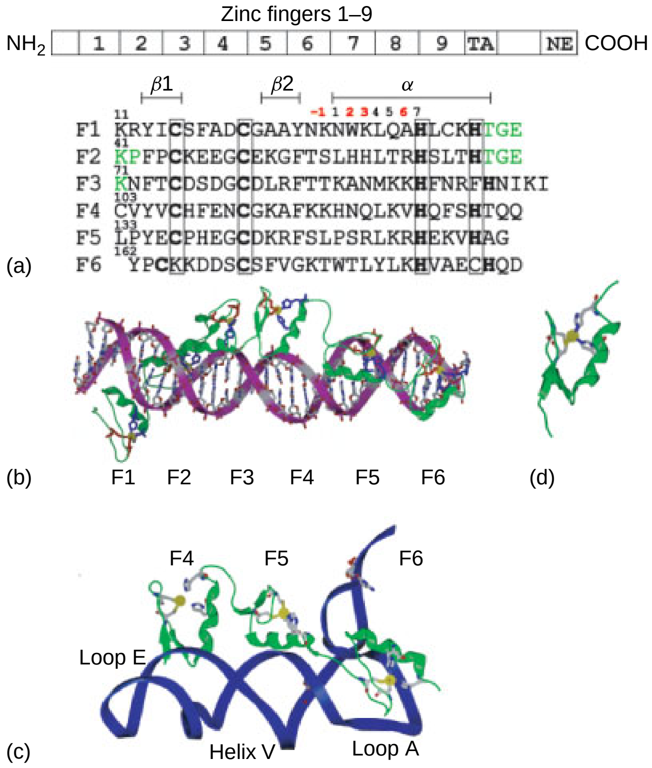
Zinc fingers 1–9
NH2
1
2
3
4
5
6
7
8
9
TA
NE
COOH
β1
β2
α
−1 1 2 3 4 5 6 7
11
F1 KRYICSFADCGAAYNKNWKLQAHLCKHTGE
41
F2 KPFPCKEEGCEKGFTSLHHLTRHSLTHTGE
71
F3 KNFTCDSDGCDLRFTTKANMKKHFNRFHNIKI
103
F4 CVYVCHFENCGKAFKKHNQLKVHQFSHTQQ
133
F5 LPYECPHEGCDKRFSLPSRLKRHEKVHAG
162
F6 YPCKKDDSCSFVGKTWTLYLKHVAECHQD
(a)
(b)
F1
F2
F3
F4
F5
F6
(d)
F4
F5
F6
Loop E
Helix V
Loop A
(c)

Figure 1 (a) A schematic domain structural representation of transcription factor IIIA (TFIIIA) from *Xenopus laevis* (top) and the primary structure of the N-terminal zinc fingers 1 to 6 with secondary structure assignments shown above the sequence (bottom). The metal-binding amino acids are in bold. Residues that possess a burgundy-shaded number above them (−1, +2, +3, and +6, corresponding to amino acid positions relative to the start of the α-helix in each $\beta\beta\alpha$ structure) are commonly involved in making base-specific contacts with the major groove of the DNA; (b) The X-ray crystallographic structure of the six N-terminal zinc fingers of *X. laevis* TFIIIA bound to 31 bp of the 5 S rRNA gene promoter determined at a resolution of 3.1 Å, with the zinc finger region represented in green and the DNA represented in blue;[26] (c) The X-ray crystallographic structure of the complex of fingers 4 to 6 of TFIIIA from *X. laevis* and 61 bases of 5S RNA derived from the central region of the complete nine-finger TFIIIA-5S RNA complex. Finger 4 interacts with the 'loop E' motif, finger 5 with helix V, and finger 6 with loop A.[29] (d) A ribbon diagram of a single $\beta\beta\alpha$ C_2H_2 zinc finger from the structure of TFIIIA. Conserved Cys and His residues donate coordination bonds to the zinc ion (*yellow* sphere)[26]

of Krüppel-associated box (KRAB) zf proteins, where the appended KRAB domain functions as a potent repressor of transcription.[27,28]

2.2 Classical Zinc Fingers (C_2H_2)

Each zinc finger forms a compact $\beta\beta\alpha$ structure (see Figure 1(d)) and basic and hydrophobic amino acids on the surface of the α-helix make specific contacts with the edges of the nucleotide bases in the major groove of the DNA.[13,14,18] Two or more C_2H_2 zinc fingers arranged in tandem are required to bind DNA with sequence specificity, and each finger is often separated by a conserved TGEKP linker.[13,21] One of the known functions of the linker is to cap the C-terminus of the preceding helix, but only in the DNA-bound conformation; in the unbound protein the linker is unstructured.[21,30] The classical C_2H_2 motif actually conforms to the consensus sequence (F/Y)-X-C-X_{2-5}-C-X_3-(F/Y)-X_5-ψ-X_2-H-X_{3-5}-H, where X represents any amino acid and ψ is a hydrophobic residue.[18] A single zinc ion is tetrahedrally coordinated between two cysteines at one end of a two-stranded antiparallel β-sheet (a β-hairpin) and two histidines found along one face of a C-terminal α-helix (Figure 1d).[18,21] The conserved hydrophobic amino acids form a mini-hydrophobic core stacked on top of the zinc coordination complex. Despite this, these fingers are essentially fully unfolded when zinc is not bound.[31] Therefore, the stability of these domains is largely derived from zinc coordination, which induces the proper architecture of this $\beta\beta\alpha$ structure. The structural paradigm of zf protein recognition of DNA is exemplified by the mouse transcription factor Zif268.[18] The primary site-specific contacts are made in the DNA major groove by the α-helix through primary hydrogen-bond interactions from helical positions −1, +3, and +6 to one strand of the DNA (Figure 1b). This is considered the sequence-specific recognition motif of DNA binding by C_2H_2 zinc fingers.[18,21]

Although the C_2H_2 zfs interact nearly exclusively with duplex DNA, there are also examples of classical C_2H_2 zfs that have been shown to interact with complex RNA and DNA/RNA heteroduplexes and mediate protein–protein interactions. One example is the Wilms' tumor suppressor protein (WT1), which binds both DNA and RNA and is thought to be involved in mRNA maturation.[21,32–34] The Ikaros family of transcription factors, which are essential regulators of lymphocyte development in vertebrates, is another example of zf proteins that interact with both proteins as well as nucleic acids.[13,21,35] Ikaros proteins contain two clusters of zf domains, with the N-terminal four-finger domain involved in DNA binding while the C-terminal two-finger cluster facilitates protein dimerization.[35] Interestingly, it has recently been shown that phosphorylation of Thr residues within the **T**GEKP linkers in Ikaros is inhibitory to DNA binding, potentially providing another level of regulatory control.[36]

The crystal structure of the central three-finger domain of TFIIIA (zf4-zf5-zf6), shown previously to provide major determinants for 5S RNA recognition,[37] complexed with 61 nucleotides of a truncated 5S RNA molecule, provides an opportunity to compare the determinants of specific DNA versus RNA recognition (Figure 1c).[29] In *Xenopus* oocytes, TFIIIA and 5S RNA form a 7S ribonucleoprotein (RNP) particle that constitutes the major storage form of this important ribosomal RNA. As stated above, the mode of DNA binding is quite well elucidated for TFIIIA, but the molecular basis of recognition of RNA was not. RNA molecules possess a more irregular structure than duplex DNA with a major groove that is too deep and narrow in a standard A-form helical conformation to be accessible to the ‘reading’ helices of zf proteins. The structure reveals that zf4 and zf5 interact with the major groove sides of the ‘loop E’ motif and helix V, respectively, with zf6 bound to the conserved ‘loop A’ motif. Strikingly, zinc fingers 4 and 5 bind to 5S RNA in a manner that is superficially similar to that of the DNA complex; this is accomplished by a significantly widened major groove in these regions of the RNA. In contrast, the spatial relationship of fingers 5 and 6 in the RNA complex differs radically from that of DNA complex (compare Figure 1b vs. Figure 1c).[29]

2.3 Zinc Fingers: Treble-clef Fingers

The treble-clef motif is the underlying structural architecture of many zinc finger protein families and constitutes the second-most abundant zinc finger domain encoded by mammalian genomes, behind classical C_2H_2 zfs. Treble-clef zinc fingers include FYVE fingers, typically found in proteins that mediate the recruitment of proteins involved in membrane trafficking and cell signaling to phosphatidylinositol 3-phosphate-containing membranes; LIM domains, often found in adaptor proteins that interact with other proteins that enable integrin signaling within focal adhesions; nuclear hormone receptor-like fingers, hormone-dependent transcriptional activators; PHD fingers, found predominantly in chromatin regulatory proteins; and RING fingers, most commonly associated with ubiquitin protein ligases (Table 1). They are characterized by undetectable amino acid sequence similarity and an enormous diversity of biological function. Besides DNA binding, treble-clef finger proteins therefore mediate protein-RNA and protein–protein interactions in biological processes related to apoptosis, cell-cycle control and protein ubiquination, leading to protein degradation and turnover. In most instances, treble-clef motifs are derived from large, multidomain proteins.[12]

Coordination of each of the zinc ions in treble-clef fingers is either via four thiolate ligands (C_4), a Cys_3His, or a $Cys_2HisCys$ structure. The designation of this large family of proteins derives from the fact that when the Cα trace of a member of this class is viewed in a specific orientation, the polypeptide chain resembles a treble-clef sign found in musical notation.[38] The treble-clef finger consists of a β-hairpin (see Figure 2; containing the ‘*a*’ and ‘*b*’ β-strands) that incorporates a zinc-ligating C-X_2-C sequence, designated as a zinc knuckle, followed by a loop, and a second orthogonally positioned β-hairpin (containing the ‘*c*’ and ‘*d*’ β-strands) connected to a C-terminal α-helix (see Table 1 and Figure 2). A zinc knuckle is defined here as composed of two short β-strands connected by a turn followed by a short helix or a loop (it may also possess a unique turn with the consensus sequence CPXCG at either termini).[12] The last two zinc ligands (from a C-X_n-C sequence) are derived from the C-terminus of β-strand ‘*d*’ and a residue from the immediately adjacent α-helix.[12,13,38,39] This domain is stabilized by the bound zinc ion and does not have a pronounced hydrophobic core.[38] Although the basic treble-clef motif contains a single zinc-binding site (corresponding to ion 1, Figure 2), many treble-clef finger proteins incorporate a second interleaved zinc-binding site within the same basic fold (e.g. RING, PHD, and FYVE finger domains, corresponding approximately to metal ions labeled 2, 3, and 8 in Figure 2), while others (e.g. LIM proteins) contain tandemly duplicated treble-clef motifs (Table 1). Strikingly, at least four additional distinct Zn(II) chelates can be accommodated by the basic treble-clef architecture (ions labeled 4, 5, 6, and 7 in Figure 2), suggesting considerable evolutionary pressure to maintain the functionality of this biologically important fold.

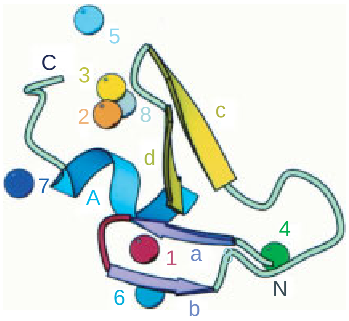

Figure 2 Ribbon representation of treble-clef zinc finger.[38] The protein ribbon corresponds to the structure of the Cys2 activator-binding domain of protein kinase C.[40] Examination of the structures of 42 treble-clef zinc fingers reveals that structural zinc ions are bound at up to eight distinct sites (displayed as spheres numbered from 1 to 8) in this fold. β-Strands and α-helices are labeled in lower and upper case letters, respectively. The short β-strands in the zinc knuckle region are shown in purple (a and b) with the zinc knuckle turn shaded red. The other two β-strands are colored yellow (c and d) and the α-helix is colored light blue (A). Metal ion 1 occupies the canonical treble-clef zinc site, with ions roughly corresponding to 2, 3, 5 and 8 corresponding to the second ‘interleaved’ zinc site found in RING, PHD, and FYFE zinc fingers (see Table 1). Metal ions labeled 4, 6, and 7 represent three additional sites accommodated by this basic fold. (Ref. 38. Reproduced by permssion of Oxford University Press)

2.3.1 Nuclear Hormone Receptor-like Zinc Fingers

This subfamily within the treble-clef class is comprised of a large group of evolutionarily related nucleic acid proteins involved in transcriptional or translational regulation. This class of proteins include ribosomal proteins (S14, L24e, and L31e), the zinc-binding domain of the DNA repair factor XPA, and recombination endonucleases (VIII and I-TevI).[12,38] Nuclear receptor-like fingers also include GATA-1 and nuclear hormone receptor DNA-binding domain proteins.

Mammalian nuclear receptors regulate the expression or activation of target genes from promoter sequences that contain either a palindromic or a direct repeat DNA sequence collectively termed hormone response elements (HREs). Most nuclear receptors bind to HREs as either a homodimer of steroid hormone receptors or heterodimers containing one retinoid X receptor (RXR) subunit and one nonsteroid hormone receptor subunit. Two highly conserved 66-residue core zf DNA-binding domains (DBDs) from two hormone receptor protomers make up the dimer.[41] Specific ligands recognized by these receptor proteins bind to C-terminal regulatory domains, known as the ligand binding-domain (LBD), which is connected to the N-terminal DBD by a hinge region.[41] Known ligands include sex steroids, for example, estrogen, progesterone, and testosterone, glucocorticoids, mineralocorticoids, bile acids, vitamin D_3, thyroid hormone, and retinoids.

The DBD of nuclear hormone receptors bind two zinc ions tetrahedrally through two conserved C_4 motifs. The N-terminal zinc site is a prototypical treble-clef zinc finger (Table 1) where the α-helix is positioned in the major groove of the conserved DNA half-sites.[13,38,41] The C-terminal zinc domain stabilizes the DBD dimerization interface. The structures of the glucocorticoid receptor (GR) and estrogen receptor (ER) homodimers on their cognate HREs were the first ones reported.[42,43] In the last ten years, structural studies together with biochemical and genetic data, on the DBD of RXR in combination with various nuclear receptor partners, as well as studies on the monomeric complex of NGFI-B, have helped decipher the mechanisms by which members of this class of zf proteins selectively bind their cognate DNA targets.[41,44–46]

2.4 Zinc Fingers: Zinc-Ribbon Motif

The zinc-ribbon motif consists of two structurally similar CPXCG zinc knuckles derived from two β-hairpins within a three-stranded antiparallel β-sheet (Table 1). The tertiary structural organization of the zinc-binding site bears a striking resemblance to the Fe-binding site in the electron transfer protein rubredoxin.[47] Some zinc-ribbon proteins are characterized by a long C-terminal β-hairpin that donates the third and fourth zinc ligands, thus the name ribbon.[12] The zinc ribbon is unique among zf proteins in that it completely lacks α-helical structure with all zinc-ligating residues derived from β-hairpins. The zinc ligation pattern is predominantly C_4 but some members contain C_3H coordination complexes.

The zinc-ribbon motif is found in a diverse group of proteins with limited sequence similarity and includes proteins involved in transcription (e.g. Transcription Factor IIB[47]) and translation (the G domain of the γ-subunit of the heterotrimeric translation initiation factor eIF2).[12,47,48] In TFIIB, the surface of the ribbon domain is conserved and is essential for the recruitment of RNA polymerase II (Pol II) to the Preinitiation Complex (PIC).[49] The GCM (glia cell missing) transcriptional regulators make novel use of a ribbon-like zinc complex to bind to DNA in an unusual way. Here, one edge of a five-stranded antiparallel β-sheet inserts into the major groove. The middle three antiparallel β-strands of the five-stranded sheet coordinate a zinc ion via two His and two Cys residues; this complex tethers the DNA-binding domain to a secondary distal domain that also contains a C_2H_2-like mixed α/β zinc finger.

In addition, three enzymes involved in DNA replication, including DNA primases, prokaryotic DNA topoisomerase I and some hexameric DNA helicases, are also classic zinc-ribbon proteins.[50] In bacteriophage DNA primases, mutations of the zinc-binding residues abrogate the synthesis of RNA primers for lagging strand DNA synthesis.[50] Strikingly, each subunit of the mini-chromosomal maintenance (MCM) protein, a heterohexameric helicase that initiates DNA replication in *S. cerevisiae*, contains an independently folded zinc-ribbon domain that appears to stabilize the dodecameric structure (a dimer of hexamers) of this replication complex.[51]

2.5 Zinc Fingers: Gag Knuckle

Gag knuckles are comprised of a zinc knuckle (two short β-strands connected by a turn) connected to a short α- or 3_{10}-helix or a loop (Table 1). They conform to the consensus sequence, Cys-X_2-Cys-X_{4-16}-His-X_4-Cys, originally discovered in retroviral *gag*-gene encoded nucleocapsid proteins.[52] Gag knuckles are more broadly defined by Grishin as ≈15 to 25 amino acid C_2H_2 or C_2HC modules that incorporate the zinc knuckle found in retroviral gag proteins.[12] The β-hairpin and α-helix of the gag knuckle is truncated relative to classical C_2H_2 zinc fingers, thus their designation as knuckles rather than fingers.[53] There are three subfamilies of gag knuckle proteins that carry out different biological functions and include retroviral nucleocapsid proteins, eukaryotic transcription factor IIA (TFIIA), and the reovirus outer capsid protein $\sigma 3$.

2.5.1 *Retroviral Gag Knuckle*

Retroviral nucleocapsid proteins (NCPs) are the major RNA-packaging proteins of animal retroviruses. The retroviral gag knuckle appends an N-terminal β-hairpin to one turn of a 3_{10}- or α-helix.[12] These are small (∼50–100 residues), extremely basic proteins that usually possess two conserved knuckle domains that conform to a Cys-X_2-Cys-X_{4-16}-His-X_4-Cys sequence separated by a short (5–15 amino acid) linker. Retroviral gag knuckles recognize and bind to specific sequences of single-stranded RNA (ssRNA), which then allows for RNA encapsidation and replication of these viruses;[12,52] they also possess potent nucleic acid chaperone activity.[54] Gag knuckles are mostly found as two conserved domains separated by a linker of variable length and amino acid composition. This differs from the classical C_2H_2 zf proteins, where tandem zf domains are typically repeated more than twice and contain high sequence conservation in a large subset of linkers.[12]

2.6 Zinc Fingers: TAZ2 Domain-like

Transcriptional adaptor zinc finger (TAZ) domain proteins function by mediating protein–protein interactions between the basal transcriptional machinery and transcription factors.[12,21] This domain folds around three tetrahedrally coordinated zinc ions and adopts a novel triangular domain structure. The TAZ2 family is one of three distinct subfamilies of TAZ domain proteins, and includes the TAZ1 and TAZ2 domains found in the ubiquitous transcriptional coactivator CREB-binding transcriptional adaptor protein (CBP).[55] The ligation pattern contains three duplicated HCCC-type zinc-binding sites, and each site is formed by the C-terminus of an α-helix, a short loop, and the N-terminus of the next α-helix (Table 1).[12] Other members of this class include the zinc-binding domain of DNA polymerase III γ subunit from *E. coli* and the N-terminal domain of HIV-1 integrase. The ligation pattern for these proteins are C_4 and C_2H_2, respectively.[12]

It was recently shown that the catalytic core of *E. coli* RecQ, a helicase-primase and homolog of the human BLM protein, contains a single TAZ2 domain-like helix-loop-helix zinc-binding motif.[56] Mutations of the human gene, BLM, cause Bloom's syndrome in humans. The ligation pattern in RecQ is C_4, and the zinc-binding motif is formed by the N-terminus of an α-helix, a short loop, and the N-terminus of the next α-helix. The product of the potent SV40-tumor promoting oncogene, large T-antigen (LTg) also possesses a RecQ-like C_2H_2 TAZ2 zinc domain where the first two cysteines are derived from the N-terminus of an α-helix with the two histidines from the N-terminus of the next α-helix.[57] It has been suggested that the TAZ2-like zinc domain stabilizes the biologically active, hexameric form of this replicative LTg helicase.

2.7 Zn2/Cys6-like Finger

These DNA-binding proteins are unique among zf proteins, in that two tetrahedrally coordinated zinc ions are ligated by six conserved cysteines, with two bridging thiolates shared between the metal ions. This motif has been dubbed a binuclear cluster, reminiscent of metallothioneins, Cys-rich intracellular zinc chelators (*see* ***Metallothioneins***). The zinc-binding domains possess two ligands from a helix and two ligands from a loop (see Table 1).[12] These transcriptional regulators function as homodimers and are ubiquitous in fungi and notably absent in higher eukaryotes.[58] Structurally characterized binuclear cluster zf proteins include the *S. cerevisiae* transcriptional regulators Gal4, Hap1, and PUT3.[58]

2.8 Other zf Domains

A comprehensive compilation of zinc finger domains encoded by mammalian genomes (http://www.ebi.ac.uk/InterPro) contains 46 conserved zinc finger domains.[19] As mentioned above, the combinatorial diversity of these protein families arises from the modularity of the zf domain itself, which has been repeatedly fused to other conserved domains to create new proteins with new biological functions during evolution. Of particular note are two new motifs that have been recently identified in *enzymes* involved in chromatin remodeling and gene silencing. These are histone lysine (K) methyltransferases (HKMTs; e.g. *N. crassa* DIM-5 and human SET7/9) and sirtuins, NAD^+-dependent Sir2 (silent information regulator protein 2) protein (histone) deacetylases. Many HKMTs incorporate *in toto*, a Zn_3-Cys_9 triangular zinc cluster structurally superimposable on the β-domain of mammalian metallothioneins (*see* ***Metallothioneins***). Although relatively far from the active site and of unknown function, removal of zinc from this domain greatly inhibits histone methylase activity. Recent experiments suggest that a fourth C_4-Zn(II) binding site is assembled near the active site upon binding of the methyl donor substrate AdoMet; formation of this chelate appears absolutely essential for catalytic activity. Sirtuins contain a structural C_4 zinc ribbon-like motif, where the zinc ion is coordinated via two ligands derived from a β-hairpin and two derived from a loop between a β-strand and an α-helix rather than a second β-hairpin as in the classical zinc-ribbon motif (Section 2.4). Although far from the active site, in at least one sirtuin, *S. cerevisiae* Hst2, this zinc-binding module may well negatively regulate deacetylase activity by stabilizing assembly of a catalytically inactive homotrimeric enzyme.[59]

Additional proteins with novel zinc-binding domains include the SQUAMOSA promoter binding proteins (SBPs), which are plant-specific transcription factors that possess two zinc finger domains within a $\approx$65 residue globular domain. The N-terminal zinc finger somewhat resembles the classical $\beta\beta\alpha$ zinc finger (Section 2.2) and is followed by a C-terminal zinc ribbon-like DNA-binding domain (Section 2.4).[60] The N-terminal zinc finger consists predominantly of a C_3H ligation pattern while the C-terminal domain possesses an invariant C_2HC ligation pattern. These novel structures also suggest new modes of DNA recognition by zinc finger proteins.[60] Another zf protein characterized by an unclassified fold is the $\approx$70 amino acid tandem zinc finger (TZF) domain of the TIS11d protein, which regulates posttranscriptional control of mRNA stability by binding to class-II AU-rich elements (AREs) in the 3′ UTR of target mRNAs.[61] TIS11d contains two highly conserved CCCH zinc finger motifs with an invariant 18-residue linker. Although largely devoid of regular secondary structure, each CCCH zinc finger superficially resembles the retroviral Gag knuckle (Section 2.5), and contains a short α-helix after the first ligating cysteine, a turn of 3_{10}-helix between the second and third cysteine and another 3_{10}-helix located at the interface between finger 1 and the linker.[61]

3 REGULATORY ZINC IN METALLOREGULATORY PROTEINS

Transition metal ions, including Zn(II) are essential for survival, but become toxic at high intracellular concentrations (*see* ***Metal Ion Toxicity***). In all kingdoms of life, cells must therefore be capable of regulating the steady-state concentration or available pool of individual metal ions via the coordinate regulation of specific metal import and metal efflux or chelation systems. This metal homeostasis (*see* ***Metallochaperones & Metal Ion Homeostasis***) is established by metalloregulatory proteins that 'sense' when the concentration or pool of a particular transition metal ion in the cytosol or an intracellular compartment becomes either deficient or exceeds critical levels required for normal cellular metabolism (*see* ***Metalloregulation***). Through extensive biochemical, molecular genetic and more recently, whole genome sequencing efforts, a large number of known or putative metal-responsive regulator proteins have been identified, especially in eubacteria and archeabacteria. Four distinct subfamilies of prokaryotic metal-sensing transcriptional regulators have emerged from these studies and include the MerR, ArsR (or SmtB/ArsR), DtxR and Fur families of metalloregulators. Zinc-specific metalloregulators in each family have been discovered, and in some cases extensively characterized as to the structure of the coordination chelate, how individual family members recognize or detect a specific metal ion, and how metal binding positively or negatively allosterically regulates DNA binding and transcription of the resistance or uptake operons. These aspects of metal regulation in prokaryotes, and to a lesser degree, in eukaryotes, are discussed in turn.

3.1 MerR Family

The MerR family of regulators activate gene expression by distorting the operator DNA sequence and causing RNA polymerase to initiate transcription at an otherwise suboptimal promoter.[62] Members of this family are characterized by N-terminal winged-helix DNA-binding domains, followed by a long coiled-coil region. The C-terminal helical domain is the effector binding domain.[62] MerR orthologs that bind a wide range of inducers including metal ions, lipophilic drugs, nitric oxide and superoxide (induced by oxidative stress) are known. The paradigm of this family and hence where the name derives comes from the seminal studies of *merR* genes of transposons Tn*501* from *P. aeruginosa* and Tn*21* from *Shigella flexneri* R100 plasmid. In gram-negative systems, MerR regulates expression of the mercury resistance divergon (*merTP(C/F)AD(E)* and *merR*) from the major regulated promoter.[63] MerR has been shown to bind to the operator/promoter region of the *mer* operon that contains a 7-4-7 inverted repeat. MerR activates the transcription of the operon in the presence of Hg(II) and acts as a weak repressor in the absence of Hg(II).[62] A unifying feature of the family of MerR is that repression and activation requires the regulator to be bound on the −35 and −10 regions of the promoter. The −35 and −10 regions are separated by a longer spacer than normal (19 bp versus 17 bp). This suggested that the promoter structure was important to the regulatory mechanism. Activation distorts the DNA at the center of the operator to realign the −35 and −10 sequence, allowing RNA polymerase to transcribe the genes upon activation.[64] Insertions or deletions (1 to 2 bp) in the 19-bp spacer have been shown to abolish promoter activity or increase constitutive promoter activity, respectively, indicating the 19-bp spacer is essential for regulation.[62]

Although the structure of MerR has not yet been solved, the X-ray crystallographic structures of BmrR and MtaN, two MerR orthologs that regulate multidrug resistance in pathogenic bacteria have been determined.[65,66] More recently, the crystal structures of two *E. coli*-derived metal regulators from the MerR family have been reported. These include the zinc-specific regulator ZntR (to 1.9 Å resolution) (Section 3.2.1), and CueR, a Cu(I) sensor (to 2.2 Å resolution), which regulates the expression of the efflux pump CopA and periplasmic copper oxidase CueO in response to moderate copper stress (*see* ***Metal Ion Toxicity***; ***Metallochaperones & Metal Ion Homeostasis***). Au(I)- and Ag(I)-liganded complexes of CueR (to 2.5 and 2.1 Å resolution, respectively) have also been determined.[67] The metal coordination environment of these proteins is likely essential for determining metal specificity of MerR proteins.

3.1.1 *E. Coli ZntR: A Zn(II)-dependent MerR Family Regulator*

E. coli ZntR is mainly zinc inducible and regulates the expression of *zntA*, which encodes a Zn(II)/Cd(II)/Pb(II) ATPase. The ZntR operator is uniquely defined by a 20-bp sequence spacer between the canonical −35 and −10 regions of the promoter. ZntR exists as a dimer, binds two zinc ions per monomer (as determined by X-ray crystallography), and utilizes a MerR-like DNA distortion mechanism to activate the expression of *zntA*.[67,68] Strikingly, X-ray crystallography reveals a binuclear zinc site with each zinc ion bound in a tetrahedral coordination environment and an internuclear Zn–Zn distance of 3.6 Å.[67] One zinc ion (designated as A) is ligated by Cys114 and Cys124 of the metal-binding loop while the other zinc ion (designated as B) is ligated by Cys115 and His119 of the same metal-binding loop (Figure 3).[67] The two zinc ions are bridged by the oxygen atoms of a phosphate (or sulfate) anion and by Cys79′ from the other protomer.

This binuclear Zn(II) coordination complex in ZntR, coupled with the bound anion, was totally unexpected since Hg-MerR requires just one trigonally coordinated Hg(II) ion that bridges the MerR dimer to effect metalloregulation of the *mer* operon.[62] The extent to which occupancy of one or both metal sites in each of two symmetry-related metal-binding loops in ZntR regulates transcriptional activation has yet to

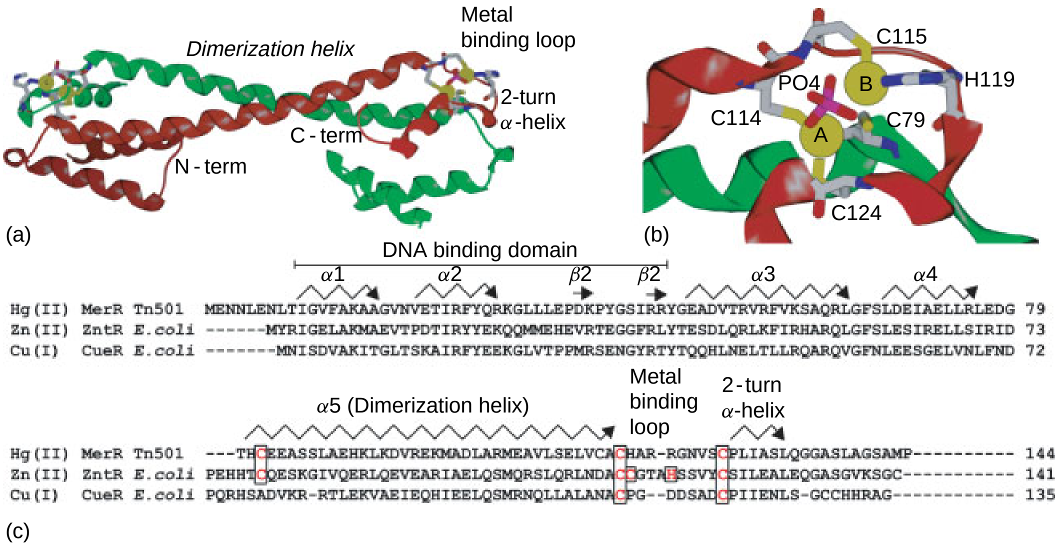

```
Hg(II) MerR Tn501   MENNLENLTIGVFAKAAGVNVETIRFYQRKGLLLEPDKPYGSIRRYGEADVTRVRFVKSAQRLGFSLDEIAELLRLEDG 79
Zn(II) ZntR E.coli ------MYRIGELAKMAEVTPDTIRYYEKQQMMEHEVRTEGGFRLYTESDLQRLKFIRHARQLGFSLESIRELLSIRID 73
Cu(I)  CueR E.coli -------MNISDVAKITGLTSKAIRFYEEKGLVTPPMRSENGYRTYTQQHLNELTLLRQARQVGFNLEESGELVNLFND 72

Hg(II) MerR Tn501   ---THCEEASSLAEHKLKDVREKMADLARMEAVLSELVCACHAR-RGNVSCPLIASLQGGASLAGSAMP---------- 144
Zn(II) ZntR E.coli PEHHTCQESKGIVQERLQEVEARIAELQSMQRSLQRLNDACCGTAHSSVYCSILEALEQGASGVKSGC----------- 141
Cu(I)  CueR E.coli PQRHSADVKR-RTLEKVAEIEQHIEELQSMRNQLLALANACPG--DDSADCPIIENLS-GCCHHRAG------------ 135
```

Figure 3 (a) Structure of the Zn_4ZntR dimer. The ribbon diagram shows one protomer in red and the other in green. The N-terminal ∼50-residue DNA-binding domains are not present in this structure.[67] The long α-helix is the dimerization helix while the metal-binding domain is formed by a metal-binding loop that connects the dimerization helix and two short C-terminal α-helices. (b) Close-up of the metal-binding domain of ZntR with two bound zinc ions shown as yellow spheres. Four zinc-ligating residues are derived from the red protomer (C114, C115, H119, and C124), while a phosphate (or sulfate) anion and the side chain of C79′ from the green protomer bridge the two zinc ions. (c) Sequence alignment of Hg(II)-specific Tn501 MerR, Zn(II)-specific *E. coli* ZntR, and Cu(I)-specific *E. coli* CueR.[67] Known metal-binding residues are colored red and are boxed. Secondary structure elements are represented above the sequence: β strands, horizontal arrows; α-helices, zig-zag arrows

be firmly established, although substitution of all five protein-derived zinc ligands reduces or abrogates the Zn(II) response in vivo.[69] Interestingly, inspection of the ZntR structure and sequence alignment of known ZntRs suggests that a $C_3H(D)$ mononuclear, tetrahedral Zn(II) complex involving Cys114, His(Asp)119, Cys124 and Cys79′ could also be readily accommodated by ZntR. Interestingly, His29 and His53 are also required for metalloregulation, although these additional residues likely play a role in mediating DNA distortion by Zn(II)-ZntR.[69] Three of the four metal-binding cysteines in ZntR (Cys79′, Cys114, and Cys124) are conserved in Hg-sensing MerRs, and likely constitute the donor atoms to the subunit-bridging *tris*-thiolato Hg(II) complex. In Cu(I)-CueR, cysteines analogous to Cys114 and Cys124 form a linear S-Cu-S regulatory complex. Only in known zinc-sensing ZntRs are His29, His53 and His119 invariant or conserved. Hence, the metal selectivity of MerR family members appears to derive from differences in coordination number and type of metal ligands utilized by different proteins (see Figure 3), a finding exactly analogous to that previously demonstrated for two members of the ArsR/SmtB family, a zinc-sensing *S. aureus* CzrA versus the nickel-sensing NmtR (Section 3.2).[70]

As a further test of the inducer specificity of the metal-binding domains in MerR proteins, a chimeric protein has been characterized in which the N-terminal winged-helix DNA-binding domain (44 residues) of *Tn501* MerR was fused to the C-terminal 103 amino acids of ZntR and transcriptional activation measured from a *mer* operator/promoter that contained a 20-bp −10/−35 spacer uniquely characteristic of the *zntA* promoter rather than the wild-type 19-bp spacer in the *mer* operon.[71] This hybrid protein responded to Zn(II), but not Hg(II), consistent with the hypothesis that the C-terminal metal-binding domain of MerR proteins plays a major role in metal selectivity and adjustment of the appropriate degree of DNA distortion required by various operator-promoters.[62]

3.2 SmtB/ArsR Family: *S. Aureus* CzrA and *Synechococcus* SmtB

The SmtB/ArsR family consists of homodimeric ‘winged’ helix-turn-helix (HTH) transcriptional repressors that are specifically bound to their operator/promoter (O/P) DNA-binding sites in the metal-free apo state. Metal binding allosterically negatively regulates DNA binding and de-represses transcription.[72] Most of the O/P sequences of this family contain one or two imperfect 12-2-12 inverted repeats but little is known at the molecular level of how apo-repressor binds to these sites. The name of this family is derived from its two founding members, ArsR from *E. coli* and *Synechococcus* PCC 7942 SmtB. ArsR is an arsenic/antimony-responsive repressor of the *ars* operon that encodes an arsenate reductase, as well as proteins required for metal export.[72–74] SmtB functions as a zinc-responsive repressor that represses transcription of a divergently transcribed operon containing both the *smtA* gene (encodes a class-II metallothionein) and the *smtB* gene (Figure 4).[72,75,76]

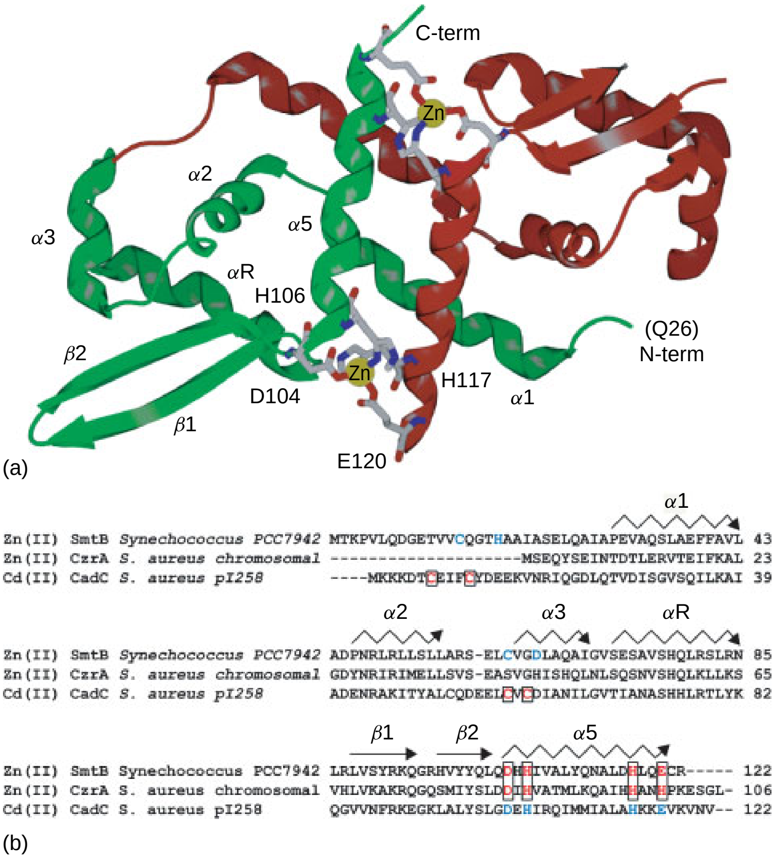

```
Zn(II) SmtB Synechococcus PCC7942 MTKPVLQDGETVVCQGTHAAIASELQAIAPEVAQSLAEFFAVL 43
Zn(II) CzrA S. aureus chromosomal --------------------MSEQYSEINTDTLERVTEIFKAL 23
Cd(II) CadC S. aureus pI258       ----MKKKDTCEIFCYDEEKVNRIQGDLQTVDISGVSQILKAI 39

Zn(II) SmtB Synechococcus PCC7942 ADPNRLRLLSLLARS-ELCVGDLAQAIGVSESAVSHQLRSLRN 85
Zn(II) CzrA S. aureus chromosomal GDYNRIRIMELLSVS-EASVGHISHQLNLSQSNVSHQLKLLKS 65
Cd(II) CadC S. aureus pI258       ADENRAKITYALCQDEELCVCDIANILGVTIANASHHLRTLYK 82

Zn(II) SmtB Synechococcus PCC7942 LRLVSYRKQGRHVYYQLQDHHIVALYQNALDHLQECR----- 122
Zn(II) CzrA S. aureus chromosomal VHLVKAKRQGQSMIYSLDDIHVATMLKQAIHHANHPKESGL- 106
Cd(II) CadC S. aureus pI258       QGVVNFRKEGKLALYSLGDEHIRQIMMIALAHKKEVKVNV-- 122
```

Figure 4 (a) A ribbon representation of the X-ray crystallographic structure of Zn_2 SmtB is shown with one protomer in green and the other in red.[77] Residues known to ligate the $\alpha5$ Zn(II) ions are shown. (b) Multiple sequence alignment of *Synechococcus* SmtB, *S. aureus* CzrA, and *S. aureus* pI258 CadC. Known metal-binding residues are boxed.[72] Residues shown to be involved in negatively allosterically regulating DNA binding are colored red. Blue residues are ligands to a second Zn(II) or Cd(II) but are *not* involved in metal sensing. $\alpha3N$ amino acids are the boxed and red cysteines in CadC. Secondary structure elements are as defined in Figure 3

Ten years of molecular genetic, biochemical, biophysical, and structural studies reveal that this family of metal-sensing transcriptional repressors generally possesses two well-characterized metal-binding sites (for a recent review see Busenlehner *et al*.[68]). They are termed the $\alpha3N$ site and the $\alpha5$ site. The $\alpha3N$ site is composed of cysteine residues from the N-terminal portion of the protein and a highly conserved ELCVCD motif in $\alpha3$ (Figure 4), initially termed the 'metal-binding box'.[72] The $\alpha5$ site is composed of histidines and carboxylate residues, and is found in the C-terminal portion of the protein. Not all members of this family contain both metal-binding sites. Some possess $\alpha3N$ only and others $\alpha5$ only, some have both sites, and a few have neither site (these proteins appear to possess a new, as yet to be characterized site).[72,78] The $\alpha5$ site interacts preferably with smaller divalent metal ions, for example, Zn(II), Co(II), and Ni(II), while the $\alpha3N$ site preferentially binds larger thiophilic metal ions such as Cd(II), Pb(II), and Bi(III). SmtB/ArsR proteins that possess both metal-binding sites have been shown to utilize only one site for regulation, not both sites. What factors determine which site is functional in a protein that possesses both sites is still unclear, but it is known that this selectivity of the allosteric response requires determinants outside of the primary metal ligands.[70,77,79]

3.2.1 SmtB/CzrA

Staphylococcus aureus CzrA is a Zn(II)/Co(II) sensing repressor. Like SmtB, CzrA metalloregulates DNA-binding through zinc binding to the $\alpha5$ site, which results in a quaternary structural conformational change that stabilizes a low affinity DNA-binding conformation.[70,77] Structural studies performed on apo- and Zn(II)-forms of CzrA and SmtB reveal that the $\alpha5$ metal-binding site is formed by a pair of ligands derived from the $\alpha5$ helix of one protomer, D84 (D104 in SmtB) and H86 (H106), and two derived from the $\alpha5$ helix of the other protomer, H97 (H117) and H100 (E120) (Figure 4).[77] The crystal structure of the Zn(II)-bound form of SmtB reveals an intersubunit hydrogen-bonding network that appears to link the metal-binding site ($\alpha5$) to the putative DNA-binding helix (αR). The Nε2 atom of His117 (the nonliganding nitrogen of this histidine) is within hydrogen-bonding distance to the backbone carbonyl of R87 in the Zn(II)-ligated state (2.67 Å N-O), while in the apo-protein it is not (3.6 Å N-O distance). The residue adjacent to R87 is a conserved L88 that then donates a backbone hydrogen bond via its amide proton to the backbone carbonyl of a conserved L83 in the DNA recognition helix (αR) (Figure 4). Detailed hydrogen-deuterium exchange studies carried out with *S. aureus* CzrA by NMR methods are consistent with the formation of this hydrogen-bonding network in solution as well, with zinc binding to the α5 sites dramatically dampening internal motion throughout the dimer.[77] This work provides the first clear evidence of how metal binding allosterically regulates DNA binding in a prokaryotic metalloregulator at the atomic level.

3.3 DtxR Family: TroR

The DtxR family of regulators is named after its founding member DtxR from *Cornybacterium diphtheria*. DtxR and a homolog found in *M. tuberculosis*, IdeR, function as Fe(II)-dependent repressors that bind to a hyphenated palindromic sequence as a dimer.[80] DtxR negatively regulates genes required for iron acquisition, and expression of a major virulence factor, diphtheria toxin, in response to its corepressor iron. DtxR contains an N-terminal winged-helix ($\alpha\alpha\alpha\beta\beta\alpha$) DNA-binding domain followed by a helical dimerization domain; some DtxRs also contain a C-terminal Src homology 3 (SH3)-like domain that is rare in bacterial proteins.[81] At least 18 crystallographic structures of *C. diphtheria* DtxR and *M. tuberculosis* IdeR have been reported with a variety of divalent metal ions bound, in the presence and absence of DNA. While the coordination structures and functional importance of these bound metal ions is controversial, two distinct metal sites in DtxR/IdeR, termed site 1 and site 2, emerge from these studies. Metal site 1 adopts a distorted octahedral coordination geometry and is coordinated by three residues derived from the α4 (H79, E83) and α5 (H98) helices (Figure 5c), and two residues contributed by the C-terminal SH3 domain (E170 and Q173). Metal site 2 is the putative metalloregulatory site, and adopts a distorted pentacoordinate geometry formed by three closely spaced and invariant residues in the α5 helix (C102, E105, and H106) as well as M10 from helix α1 (Figure 5c).[81]

DtxR (IdeR) orthologs have recently been discovered that are involved in the regulation of genes that encode metal transporters apparently specific for other divalent metal ions, including Mn(II) and perhaps Zn(II). These include *Bacillus subtilis* MntR, highly specific for Mn(II), and *Treponema pallidum* TroR. *B. subtilis* MntR regulates the expression of two manganese transporters, the Nramp-type transporter MntH under high Mn(II) and the ABC-type transporter MntABCD under low Mn(II) conditions.[82,83] In high manganese, Mn(II)-MntR functions as a repressor by binding to operators upstream of the coding regions of both *mntH* and *mntABCD* operons. MntR is selective for manganese while DtxR is activated to bind DNA by various divalent metals including manganese in vitro.

Strikingly, the high-resolution crystallographic structure of Mn(II)-bound MntR (to 1.75 Å resolution) reveals a binuclear Mn(II) center, with the two Mn(II) ions bridged by two glutamates, E102 and E11, the latter unique to MntR, and a solvent molecule (Figure 5a).[83] The other ligands to the site A Mn(II) ion are H77 and E99 (C102 in DtxR) and two water molecules, creating a distorted octahedral coordination geometry.[83] $\mathrm{Mn_B}$ also adopts an octahedral geometry and is ligated by D8, which is M10 in Fe(II)-sensing DtxR, H103, and two solvent molecules, in addition to the bridging ligands E11 and E102.[83] $\mathrm{Mn_B}$ is roughly positioned in the same place as a Co(II) ion bound to metal site 1 in IdeR. In an effort to understand the molecular basis of metal ion discrimination between DtxR/IdeR and MntR, a D8M substitution mutant of MntR was functionally and structurally characterized. D8M MntR shows relaxed specificity for Mn(II) and is activated by both Fe(II) and Mn(II) in vivo.[84] The high-resolution crystallographic structure of D8M MntR (to 1.6 Å resolution) reveals why (Figure 5b): D8M MntR retains just one of the two Mn(II) ions and is coordinated by E11, H77, E102, and a solvent molecule (the introduced M8 is *not* ligated to the metal) in a distorted trigonal bipyramidal geometry, closer to the position of $\mathrm{Mn_A}$ in wild-type MntR.[83] These findings suggest that metal selectivity in the DtxR family is governed by the number and type of ligands bound to the metal, exactly analogous to findings in the MerR- and SmtB/ArsR-family regulators. Interestingly, the amino acid sequence of the putative Zn(II) regulator *T. pallidum* TroR lacks all N-terminal α1-derived metal-binding residues that play critical roles in DtxR/IdeR and MntR (Figure 5c); this might explain its reported ability to respond to Zn(II) versus other divalent transition metal ions (Section 3.3.1).

3.3.1 TroR

In 1997, Hardham *et al*. discovered a six-gene cluster termed the transport-related operon (*tro*) from *Treponema pallidum*.[85] Two genes of the operon include TroA, which encodes the solute-binding protein (SBP) component of an ATP-binding cassette transporter, and TroR, a DtxR-like metalloregulator.[85,86] TroR is similar to MntR in sequence (Figure 5c), and has been characterized as both a Mn(II)-specific,[87,88] and a Zn(II)-specific[85,89] regulator in vivo. Only limited metal-binding experiments have been reported for TroR, and there is currently no available structure. However, the crystallographic structure of Zn(II)-bound TroA,[86,90] the SBP whose expression is metalloregulated by TroR, may provide some insight as to the natural metal ligand(s) for TroR.

TroA coordinates a single Zn(II) ion in a pentavalent coordination geometry formed by H68, H133, H199 and D279(Oδ1 and Oδ2).[86] This coordination structure differs

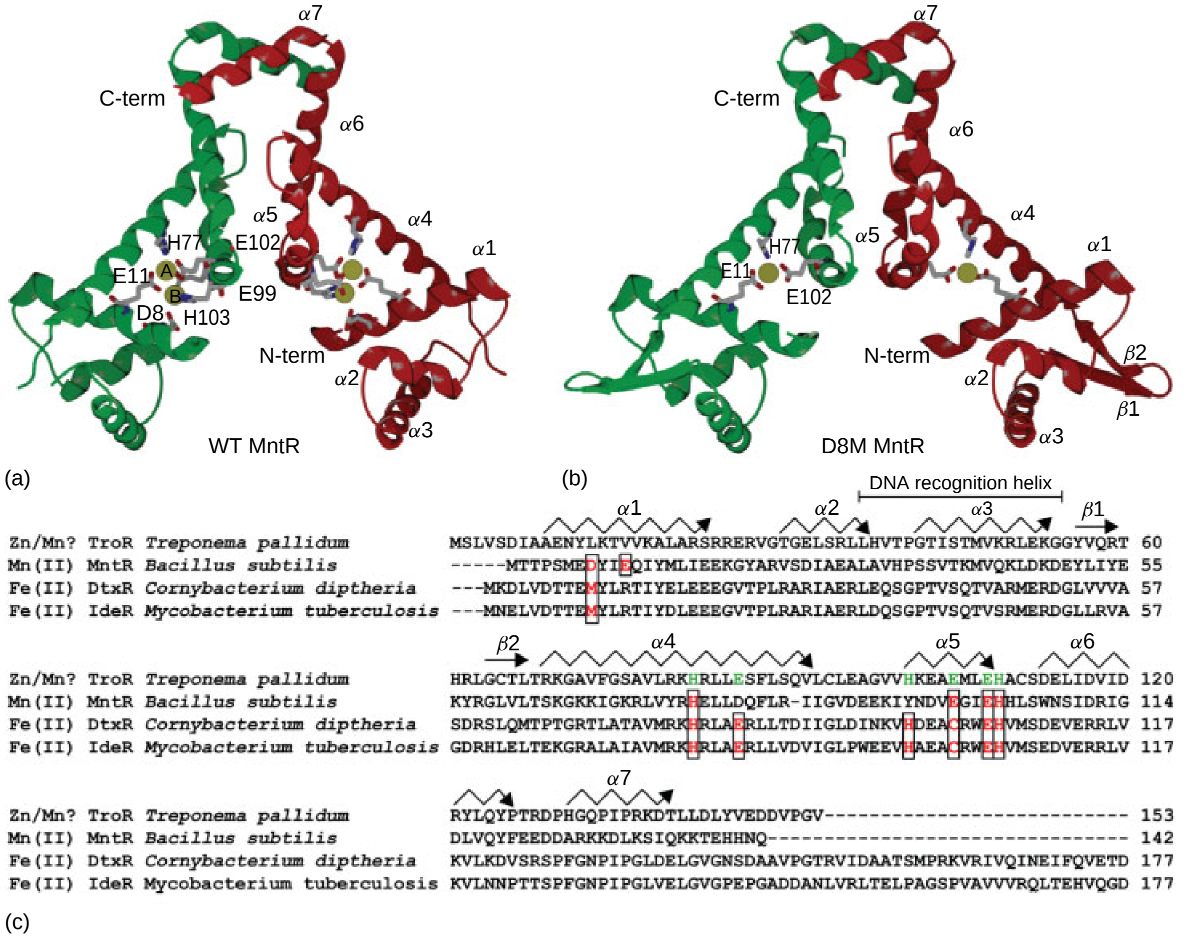
α7
C-term
α6
α5
α4
α1
H77
E102
E11
A
B
E99
D8
H103
N-term
α2
α3
WT MntR
(a)
α7
C-term
α6
α5
α4
α1
H77
E11
E102
N-term
β2
α2
β1
α3
D8M MntR
(b)
DNA recognition helix
α1
α2
α3
β1
Zn/Mn? TroR Treponema pallidum MSLVSDIAAENYLKTVVKALARSRRERVGTGELSRLLHVTPGTISTMVKRLEKGGYVQRT 60
Mn(II) MntR Bacillus subtilis -----MTTPSMEDYIEQIYMLIEEKGYARVSDIAEALAVHPSSVTKMVQKLDKDEYLIYE 55
Fe(II) DtxR Cornybacterium diptheria ---MKDLVDTTEMYLRTIYELEEEGVTPLRARIAERLEQSGPTVSQTVARMERDGLVVVA 57
Fe(II) IdeR Mycobacterium tuberculosis ---MNELVDTTEMYLRTIYDLEEEGVTPLRARIAERLDQSGPTVSQTVSRMERDGLLRVA 57
β2
α4
α5
α6
Zn/Mn? TroR Treponema pallidum HRLGCTLTRKGAVFGSAVLRKHRLLESFLSQVLCLEAGVVHKEAEMLEHACSDELIDVID 120
Mn(II) MntR Bacillus subtilis KYRGLVLTSKGKKIGKRLVYRHELLDQFLR-IIGVDEEKIYNDVEGIEHHLSWNSIDRIG 114
Fe(II) DtxR Cornybacterium diptheria SDRSLQMTPTGRTLATAVMRKHRLAERLLTDIIGLDINKVHDEACRWEHVMSDEVERRLV 117
Fe(II) IdeR Mycobacterium tuberculosis GDRHLELTEKGRALAIAVMRKHRLAERLLVDVIGLPWEEVHAEACRWEHVMSEDVERRLV 117
α7
Zn/Mn? TroR Treponema pallidum RYLQYPTRDPHGQPIPRKDTLLDLYVEDDVPGV--------------------------- 153
Mn(II) MntR Bacillus subtilis DLVQYFEEDDARKKDLKSIQKKTEHHNQ-------------------------------- 142
Fe(II) DtxR Cornybacterium diptheria KVLKDVSRSPFGNPIPGLDELGVGNSDAAVPGTRVIDAATSMPRKVRIVQINEIFQVETD 177
Fe(II) IdeR Mycobacterium tuberculosis KVLNNPTTSPFGNPIPGLVELGVGPEPGADDANLVRLTELPAGSPVAVVVRQLTEHVQGD 177
(c)

Figure 5 (a) Ribbon representation of the structure of wild-type *B. subtilus* MntR with two Mn(II) ions bound per protomer in a binuclear cluster. One subunit is shaded green and one in red. Residues E11, H77, E99, and E102 coordinate the Mn(II) ion designated as $\mathrm{Mn_A}$ while D8, E11, E102, and H103 coordinate the Mn(II) ion designated as $\mathrm{Mn_B}$. The Mn(II) ions are bridged by bidentate interactions of E11, E102, and a solvent molecule; (b) structure of D8M MntR with one Mn(II) bound per protomer. One subunit is shown in green and the other in red. Residues E11, H77, and E102 coordinate the Mn(II) ion along with a solvent molecule (not shown); (c) sequence alignment of *T. pallidum* TroR, *B. subtilis* MntR, C. *diphtheria* DtxR, and *M. tuberculosis* IdeR with the secondary structure regions (based upon crystal structure of MntR) shown as above. Known metal-binding residues are colored red and boxed. Proposed metal-binding residues of TroR are shaded green. Note that the metal specificity of TroR (Zn vs. Mn) has not yet been firmly established (see text for details)

from that recently reported for Zn(II)-bound *Synechocystis* 6803 ZnuA, the SBP of the ZnuABC metal transporter, which is highly selective for Zn(II). In ZnuA, Zn(II) is bound in a distorted tetrahedral coordination geometry with just three protein-derived histidines, exactly analogous to H68, H133 and H199 in TroA, and a solvent molecule; the bidentate ligand D279 in TroA is conserved in ZnuAs. Although both ZnuA and TroA belong to the same cluster 9 family of ABC transporters, it has been argued that ZnuA preferentially binds Zn(II) over Mn(II) by providing just three protein-derived ligands, since Mn(II) complexes with low-coordination numbers are essentially inaccessible owing to ligand-field destabilization arguments and the well understood Irving–Williams series; Zn(II) with its full *d*-shell readily adopts four-coordinate complexes.[91] Since TroA apparently binds Zn(II) in a five-coordinate geometry, Mn(II) should bind to TroA with high affinity as well; this will effectively relax the metal selectivity of this transporter system. This is in fact the case since the measured metal-binding affinities of Zn(II) and Mn(II) ($K_\mathrm{d} = 1.3\pm0.4\,\mu\mathrm{M}$ and $K_\mathrm{d} = 1.0\pm0.2\,\mu\mathrm{M}$, respectively) are identical within experimental error.[89] One would expect that the metalloregulator TroR would have evolved to sense both Zn(II) and Mn(II) as well.

3.4 Fur Family: Zur

E. coli Fur and homologs in other prokaryotes regulate the transcription of genes required for iron acquisition, including a host of distinct iron scavenging systems as well as the enzymes for siderophore biosynthesis (*see* ***Iron Transport: Siderophores***; ***Metalloregulation***).[80] In addition,

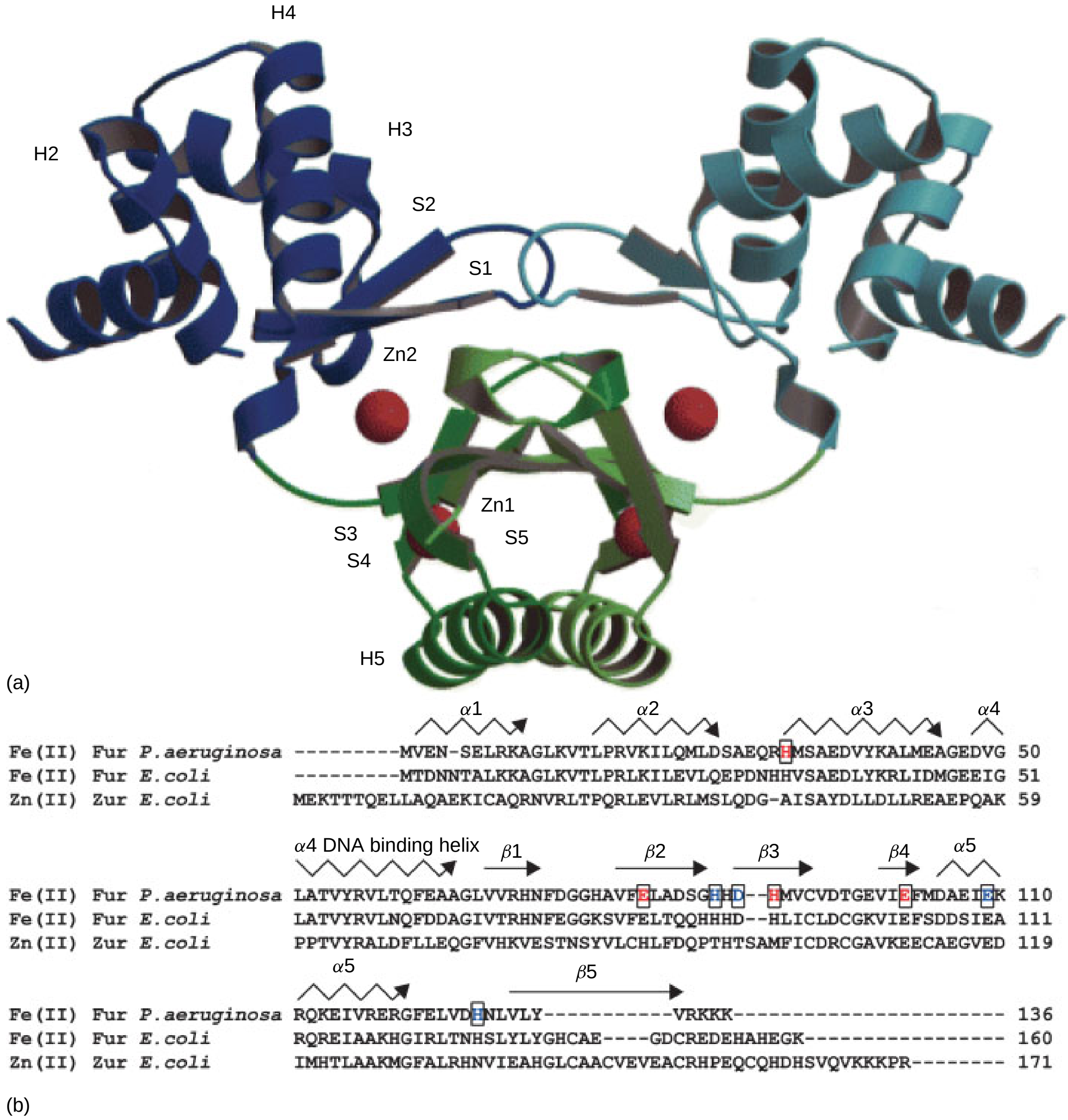

```
Fe(II) Fur P.aeruginosa ---------MVEN-SELRKAGLKVTLPRVKILQMLDSAEQRHMSAEDVYKALMEAGEDVG 50
Fe(II) Fur E.coli       ---------MTDNNTALKKAGLKVTLPRLKILEVLQEPDNHHVSAEDLYKRLIDMGEEIG 51
Zn(II) Zur E.coli       MEKTTTQELLAQAEKICAQRNVRLTPQRLEVLRLMSLQDG-AISAYDLLDLLREAEPQAK 59

Fe(II) Fur P.aeruginosa LATVYRVLTQFEAAGLVVRHNFDGGHAVFELADSGHHD--HMVCVDTGEVIEFMDAEIEK 110
Fe(II) Fur E.coli       LATVYRVLNQFDDAGIVTRHNFEGGKSVFELTQQHHHD--HLICLDCGKVIEFSDDSIEA 111
Zn(II) Zur E.coli       PPTVYRALDFLLEQGFVHKVESTNSYVLCHLFDQPTHTSAMFICDRCGAVKEECAEGVED 119

Fe(II) Fur P.aeruginosa RQKEIVRERGFELVDHNLVLY-----------VRKKK----------------------- 136
Fe(II) Fur E.coli       RQREIAAKHGIRLTNHSLYLYGHCAE----GDCREDEHAHEGK----------------- 160
Zn(II) Zur E.coli       IMHTLAAKMGFALRHNVIEAHGLCAACVEVEACRHPEQCQHDHSVQVKKKPR-------- 171
```

Figure 6 (a) A ribbon representation of the crystallographic structure of the Zn_4 *Pa* Fur dimer. Blue, DNA-binding domains; green, C-terminal dimerization domain (see text for details). Zinc ions are shown as dark magenta spheres. (Ref. 92. Reproduced by permission of Blackwell); (b) Sequence alignment of *Pseudomonas aeruginosa* Fur, *E. coli* Fur, and *E. coli* Zur using ClustalW (http://www.ebi.ac.uk/clustalw).[93] Known metal-binding ligands are boxed and the secondary structural elements are as above. Blue residues in *P. aeruginosa* Fur represent the proposed regulatory Fe-binding site; red residues in *P. aeruginosa* represent the proposed structural Zn binding site

the expression of key virulence factors in pathogenic bacteria are also regulated by Fur. The working model is that the iron-bound form of Fur binds to specific target sequences in the promoter of iron-regulated genes, collectively known as 'iron boxes', blocking access by RNA polymerase. Like the DtxR family regulators, iron functions as a corepressor of the expression of those genes linked to iron acquisition; in iron-starved conditions, these genes are constitutively expressed. The high-resolution crystallographic structure of *Pseudomonas aeruginosa* Fur complexed with Zn(II) (rather than iron) has recently been reported to 1.8 Å resolution, with a ribbon representation of the structure shown in Figure 6.[92] The global structure of the Fur homodimer is superficially similar to that of DtxR; in fact the winged-helix DNA-binding domains superimpose with a backbone rmsd of 1.8 Å from helix α2-α4 through the β1-β2 hairpin. The dimerization domain of each protomer is an α/β domain consisting of a 3-stranded β-sheet topped by the C-terminal α5 helix. Dimerization results in a six-stranded β-barrel capped by an antiparallel coiled-coil formed by the α5 helices.

Two metal ions are bound per protomer for a total of four metal ions per dimer, designated Zn1 and Zn2. Zn1 is coordinated by residues located exclusively in the dimerization domain and adopts a distorted octahedral geometry with four protein-derived ligands (H86, D88, E107 and H124), and includes one bidentate carboxylate (D88) and a well-ordered water molecule. Zn2 bridges the DNA-binding and dimerization domains and adopts distorted tetrahedral coordination geometry (H32, E80, H89 and E100).[92] Fe(II) exchange experiments and characterization of the resulting Zn/Fe hybrid protein by X-ray absorption spectroscopy reveals that Zn1 is readily exchanged with Fe(II) and adopts a coordination complex that is isostructural with Zn1, with coordination of Zn2 unchanged. Therefore, Pohl *et al.* argue that in *Pa* Fur, the regulatory metal site corresponds to Zn1 located exclusively in the dimerization domain, while Zn2 is an unusual structural Zn(II) site, which forms part of the long-range allosteric pathway of communication between the regulatory sites and the DNA-binding domains of PA Fur. It seems plausible that metal binding to site 1 might globally alter the orientation of one subunit relative to the other, stabilizing a high-affinity binding conformation. All Fur homologs contain the full complement of metal sites structurally characterized in *Pa* Fur.

Interestingly, many Fur homologs, including *E. coli* Fur, contain two pairs of cysteine residues not present in *Pa* Fur. One pair is C92 and C95, just C-terminal to H86 and D88 of the Zn1(Fe) site and H89 of the Zn2 site, and N-terminal to E100 of Zn2 site in *Pa* Fur; *Pa* Fur contains a residue analogous to C92 only, which does not participate in metal binding (see Figure 6b). In addition, most Fur homologs contain a short C-terminal extension that contains a C-X_4-C sequence that is not present in *Pa* Fur (Figure 6(b)). X-ray absorption studies of *E. coli* Fur suggest at least one sulfur-containing Zn(II) coordination complex; spectroscopic studies of mutants suggest that C92 and C95 ligate this Zn(II) ion in the formation of a structural $S_2(N/O)_2$ complex, although this remains to be definitely determined.[93,95]

3.4.1 E. Coli Zur

Zur is a recently discovered Fur ortholog (27% sequence identity) that regulates the expression of a divergently transcribed operon that encodes the high-affinity zinc uptake system, *znuBC* and *znuA*, in a highly Zn(II)-specific fashion.[96,97] The high-resolution structure of Zur is not yet available and the molecular basis for metal ion discrimination by *E. coli* Zur remains unclear. However, it is possible to speculate on metal selectivity on the basis of an amino acid sequence alignment and limited spectroscopic findings reported for the Zn(II) and Co(II) metalloderivatives of *E. coli* Zur. Zur binds two metal ions per subunit and four per dimer in two spectroscopically distinguishable tetrahedral sites.[98] One Zn(II) ion, ZnA, is tightly bound in an $S_3(N/O)$ coordination environment and is refractory to metal exchange with Co(II). This site is likely analogous to the structural Zn2 site in Fur homologs that contain the C92-X_2-C95 cysteine pair. The other site, ZnB, is readily exchanged with Co(II) and is characterized by tetrahedral $S(N/O)_3$ coordination geometry, in striking contrast to the octahedral, putative Fe(II)-sensing Zn1(Fe) site of Fur.[98] Although the four donor atoms to this putative Zn(II)-sensing site remain unknown, at least two cysteine residues just C-terminal to the $\alpha 5$ helix in *Pa* Fur appear to be uniquely conserved in all functionally characterized Zur proteins (Figure 6b); one of these may well correspond to the thiolate donor in the ZnB site. Regardless of the details, these comparative structural studies of Fur and Zur emphasize the recurring theme that the primary determinant for metal selectivity in metal sensor proteins is coordination number and geometry, with a lesser role played by the nature of the donor atoms. This is exactly in accord with the conclusions reached by the Fierke group from a careful investigation of the metal affinities and structural studies of an extensive panel of carbonic anhydrase mutants (*see* ***Zinc Enzymes***).[99]

3.5 MTF-1 and *S. Cerevisiae* Zap1

Eukaryotic cells, like prokaryotes, have evolved efficient mechanisms to govern metal ion homeostasis, except that the regulatory logic is far more complex than simple regulation of DNA binding. In eukaryotes, metalloregulation of intracellular (cytoplasmic-nuclear) trafficking, posttranslational modification, protein–protein interactions and DNA binding are all possible and have been documented to occur in some cases. Two zinc finger proteins are known to play major roles in regulating zinc homeostasis in eukaryotes. They are *S. cerevisiae* Zap1, which controls the expression of a number of genes (>40) involved in zinc accumulation and storage, and vertebrate metal-response element (MRE)-binding Transcription Factor 1 (MTF-1). MTF-1 up-regulates the transcription of genes encoding metallothioneins, small cysteine-rich metal-sequestering proteins, ZnT-1, a cytoplasmic efflux pump, and other genes in response to heavy-metal (Zn/Cd) and oxidative stress in mammals. Both proteins possess multiple tandem C_2H_2 zinc fingers (7 zf's in Zap1 and 6 zf's in MTF-1), a subset of which appears to metalloregulate DNA-binding upon zinc binding (Figure 7).[15,100–102] A cluster of five zinc fingers near the C-terminus of Zap1 mediates high-affinity binding to an 11-bp zinc-response element (ZRE), while fingers 1 to 4 of MTF-1 play this role on the 12-bp MRE.[101–103]

A popular metalloregulatory model proposes that these or other remaining zinc fingers might regulate gene expression in response to fluctuations in bioavailable zinc concentration. In Zap1, zinc fingers zf1 and zf2 appear to play a direct role in zinc sensing by negatively regulating activation domain 2 function as the intracellular zinc concentration rises (see Figure 7).[16] In MTF-1, the precise mechanism of Zn(II)-activation of MRE-binding has been far more elusive, although recent experiments suggest that zinc fingers zf1, zf5, and zf6 stabilize the interaction of MTF-1 with chromatin-embedded

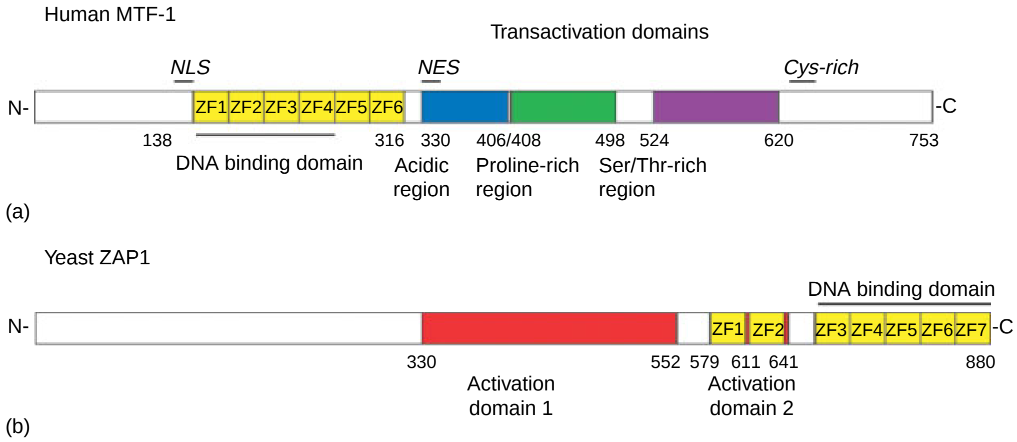

Figure 7 (a) Domain organization of human MTF-1 in which zinc finger domains are colored yellow and denoted by ZF (zinc finger). The acidic, proline-rich, and Ser/Thr-rich transactivation domains are indicated. *NLS*, nuclear localization signal; *NES*, nuclear export signal; *Cys-rich*, a cysteine cluster that functions in metal-inducible transcriptional activation;[104] (b) Domain organization of *S. cerevisiae* Zap1. Transactivation domains are indicated as is the DNA-binding domain (zf3-zf7)[16]

MREs.[100,105] Interestingly, all six zinc fingers of hMTF-1 bind Co(II) with equilibrium affinities that are more similar than different ($K_{\mathrm{Co}} \approx 2 \times 10^6 - 5 \times 10^7\ \mathrm{M}^{-1}$ at pH 7.0),[106] despite the vastly different reactivities of the cysteine thiolates of C-terminal fingers zf5 and zf6 toward an exogenous alkylating reagent, that is, these fingers exhibit an enhanced kinetic lability relative to primary MRE-binding fingers. Likewise, a peptide corresponding to the regulatory fingers (zf1-zf2) of Zap1 binds Zn(II) with the same apparent affinities as a DNA-binding finger pair (zf3-zf4) ($K_{\mathrm{Zn}} \approx 10^9\ \mathrm{M}^{-1}$) despite more rapid metal dissociation rates for the zf1-zf2 pair.[16] These findings suggest that zinc metalloregulation of gene expression in eukaryotic cells might be under kinetic, rather than thermodynamic control (see Section 4). Recently, it has been shown that a conserved cluster of four cysteines (^{632}**C**Q**C**Q**C**A**C**^{638}) located just C-terminal to the Ser/Thr-rich transcription activation domain of hMTF-1 (see Figure 7) is required for activation of transcription in the presence of zinc and cadmium in vivo.[104] These findings suggest that other domains outside of the zinc fingers themselves in MTF-1 play a role in metal inducibility. MTF-1 and Zap1 utilize their zinc fingers to bind DNA with high affinity and help regulate the expression of genes involved in metal sequestration and/or transport. Exactly how these domains regulate transcription in response to changes in intracellular zinc concentration still requires clarification.

4 PERSPECTIVES/CONCLUSIONS

As summarized in this chapter, zinc-containing nucleic acid-binding proteins are ubiquitous in nature and play integral roles in all aspects of nucleic acid metabolism, including DNA replication, recombination and repair, transcriptional activation/repression and chromatin remodeling, translational regulation, mRNA stability, ribosome dynamics and biogenesis. Although the molecular structures of these zinc coordination complexes are remarkably diverse and encompass all α-, all β- and mixed α/β-domains (Table 1), the common feature is a tetrahedral coordination geometry formed by four protein-derived ligands, two or more of which must be cysteine thiolates. Formation of the zinc coordination complex directs the folding of what are often mini domains that typically lack a hydrophobic core, thereby functionally stabilizing protein–protein and protein-nucleic acid interfaces. The classification of these zinc finger proteins into distinct fold groups begs the question of how many additional novel structures of zinc finger proteins might exist. Section 2.8 lists several proteins that do not precisely adhere to the structural classification scheme summarized in this chapter. However, global examination of their structures seems to suggest that as new zinc finger or zinc fingerlike domains are characterized, they will likely have some similarity to existing fold groups already described.

Is there additional functional currency that comes with the specific utilization of thiolate-rich Zn(II) coordination complexes to fulfill these myriad of important roles? One possibility may lie in the distinctive features of Zn-thiolate chemistry itself.[107] There is emerging evidence in support of the idea that zinc sites in nucleic acid-binding proteins are susceptible to rapid, and in some cases, reversible inactivation via formation of disulfide bonds between metal-ligating cysteines, with concomitant expulsion of the Zn(II) and local unfolding, under conditions of oxidative stress. For example, cysteine thiolates are readily *S*-nitrosylated when intracellular NO concentrations in mammalian cells rise; in at least one case, increasing NO gives rise to transient increases in intracellular zinc levels that is detectable by zinc-selective intracellular dyes.[108] In addition, *S*-nitrosylation of the RING finger domain

(Section 2.3) of a ubiquitin E3 ligase *parkin* is positively linked to neurodegenerative loss of dopamine neurons in Parkinson's disease.[109] A similar perturbation of zinc pools by heavy-metal xenobiotics, for example, Cd, in mammalian cells has also been proposed.[40] These and other findings suggest a strong link between intracellular zinc levels and various stress responses and the progression of human disease perhaps mediated in part by zinc release from metallothioneins, with Zn-thiolate coordination bonds a 'composite' redox sensor, rather than the metal ion itself, which obviously does not change oxidation state.[107] Such a redox sensor might also transiently disable fundamental processes devoted to DNA replication, DNA recombination, transcription initiation and regulation, and ribosome biogenesis until a full-scale redox stress response could be mounted by the cell.

Interestingly, metalloregulatory zinc sites in prokaryotic and mammalian metal sensor proteins, like structural zinc finger complexes, often contain thiolate ligands as well; in fact, homologous SmtB/ArsR sensors *Synechococcus* SmtB and *S. aureus* CzrA are currently the lone exceptions to this trend (Section 3.2.1) In these systems, zinc coordination number, rather than ligand type, appears to dictate metal selectivity among closely related orthologs from different metal sensor families (Section 3). The common structural feature is that metalloregulatory zinc sites, like structural zinc finger sites, are rigorously four-coordinate, but may be characterized by perhaps one weakly bound metal ligand that would enable ligand exchange and zinc transfer to acceptor proteins in establishing metal resistance.[94] This may be particularly important for zinc sensors since the thermodynamic stabilities of these zinc regulatory proteins are high (pM and fM zinc dissociation equilibrium constants for SmtB and ZntR/Zur, respectively).[110,111] This makes it unlikely that zinc will move from donor to acceptor, be it protein, metallothionein or small molecule (reduced glutathione), via the solvent and may instead be directly transferred from donor to acceptor in a process characterized by an equilibrium constant near one that might be kinetically facilitated by transient docking and rapid ligand exchange. This would have the effect of maintaining zinc homeostasis even upon challenge with toxic concentrations of the metal in the absence of large thermodynamic gradients of 'free' zinc inside the cell or within other intracellular compartments. Obtaining a mechanistic understanding of zinc homeostasis and trafficking within living cells in normal versus stressed states will surely prove to be an exciting area of future work in the general area of zinc and nucleic acid-binding proteins.

5 RELATED ARTICLES

Iron Transport: Siderophores; Metal Ion Toxicity; Metal-related Diseases of Genetic Origin; Metallochaperones & Metal Ion Homeostasis; Metalloregulation; Metallothioneins; Nucleic Acid–Metal Ion Interactions; Nutritional Aspects of Metals & Trace Elements; Peptide–Metal Interactions; Zinc Enzymes; Zinc: Inorganic & Coordination Chemistry.

6 REFERENCES

1. R. S. Spolar and M. T. Record Jr, *Science*, 1994, **263**, 777.
2. J. M. Berg and H. A. Godwin, *Annu. Rev. Biophys. Biomol. Struct.*, 1997, **26**, 357.
3. D. K. Blencowe and A. P. Morby, *FEMS Microbiol. Rev.*, 2003, **27**, 291.
4. W. Maret, *Biometals*, 2001, **14**, 187.
5. J. Frausto da Silva and R. Williams, 'The Biological Chemistry of Elements: The Inorganic Chemistry of Life', 2nd edn., Oxford University Press, Oxford, 2001, p. 575.
6. R. A. Katz and J. E. Jentoft, *Bioessays*, 1989, **11**, 176.
7. I. Fingerman, V. Nagaraj, D. Norris, and A. K. Vershon, *Eukaryotic Cell*, 2003, **2**, 1061.
8. H. Tapiero and K. D. Tew, *Biomed. Pharmacother.*, 2003, **57**, 399.
9. C. Hotz, N. M. Lowe, M. Araya, and K. H. Brown, *J. Nutr.*, 2003, **133**, 1563S.
10. J. M. Castagnetto, S. W. Hennessy, V. A. Roberts, E. D. Getzoff, J. A. Tainer, and M. E. Pique, *Nucleic Acids Res.*, 2002, **30**, 379.
11. D. S. Auld, *Biometals*, 2001, **14**, 271.
12. S. S. Krishna, I. Majumdar, and N. V. Grishin, *Nucleic Acids Res.*, 2003, **31**, 532.
13. J. M. Matthews and M. Sunde, *IUBMB Life*, 2002, **54**, 351.
14. D. Jantz, B. T. Amann, G. J. Gatto Jr, and J. M. Berg, *Chem. Rev.*, 2004, **104**, 789.
15. D. P. Giedroc, X. Chen, and J. L. Apuy, *Antioxid. Redox Signal.*, 2001, **3**, 577.
16. A. J. Bird, K. McCall, M. Kramer, E. Blankman, D. R. Winge, and D. J. Eide, *EMBO J.*, 2003, **22**, 5137.
17. D. J. Eide, *J. Nutr.*, 2003, **133**, 1532S.
18. S. A. Wolfe, L. Nekludova, and C. O. Pabo, *Annu. Rev. Biophys. Biomol. Struct.*, 2000, **29**, 183.
19. T. Ravasi, T. Huber, M. Zavolan, A. Forrest, T. Gaasterland, S. Grimmond, and D. A. Hume, *Genome Res.*, 2003, **13**, 1430.
20. C. O. Pabo, E. Peisach, and R. A. Grant, *Annu. Rev. Biochem.*, 2001, **70**, 313.
21. J. H. Laity, B. M. Lee, and P. E. Wright, *Curr. Opin. Struct. Biol.*, 2001, **11**, 39.
22. A. Klug, *J. Mol. Biol.*, 1999, **293**, 215.
23. D. J. Segal and C. F. Barbas, *Curr. Opin. Biotechnol.*, 2001, **12**, 632.
24. J. Miller, A. D. McLachlan, and A. Klug, *EMBO J.*, 1985, **4**, 1609.

25. J. M. Berg, *Proc. Natl. Acad. Sci. U.S.A.*, 1988, **85**, 99.
26. R. T. Nolte, R. M. Conlin, S. C. Harrison, and R. S. Brown, *Proc. Natl. Acad. Sci. U.S.A.*, 1998, **95**, 2938.
27. J. F. Margolin, J. R. Friedman, W. K. Meyer, H. Vissing, H. J. Thiesen, and F. J. Rauscher, *Proc. Natl. Acad. Sci. U.S.A.*, 1994, **91**, 4509.
28. R. Witzgall, E. O'Leary, A. Leaf, D. Onaldi, and J. V. Bonventre, *Proc. Natl. Acad. Sci. U.S.A.*, 1994, **91**, 4514.
29. D. Lu, M. A. Searles, and A. Klug, *Nature*, 2003, **426**, 96.
30. J. H. Laity, H. J. Dyson, and P. E. Wright, *J. Mol. Biol.*, 2000, **295**, 719.
31. A. D. Frankel, J. M. Berg, and C. O. Pabo, *Proc. Natl. Acad. Sci. U.S.A.*, 1987, **84**, 4841.
32. J. H. Laity, J. Chung, H. J. Dyson, and P. E. Wright, *Biochemistry*, 2000, **39**, 5341.
33. M. Little, G. Holmes, and P. Walsh, *Bioessays*, 1999, **21**, 191.
34. J. H. Laity, H. J. Dyson, and P. E. Wright, *Proc. Natl. Acad. Sci. U.S.A.*, 2000, **97**, 11932.
35. K. Georgopoulos, *Nat. Rev. Immunol.*, 2002, **2**, 162.
36. D. Jantz and J. M. Berg, *Proc. Natl. Acad. Sci. U.S.A.*, 2004, **101**, 7589.
37. M. A. Searles, D. Lu, and A. Klug, *J. Mol. Biol.*, 2000, **301**, 47.
38. N. V. Grishin, *Nucleic Acids Res.*, 2001, **29**, 1703.
39. C. Scazzocchio, *Curr. Opin. Microbiol.*, 2000, **3**, 126.
40. B. Zhang, O. Georgiev, M. Hagmann, C. Gunes, M. Cramer, P. Faller, M. Vasak, and W. Schaffner, *Mol. Cell. Biol.*, 2003, **23**, 8471.
41. S. Khorasanizadeh and F. Rastinejad, *Trends Biochem. Sci.*, 2001, **26**, 384.
42. B. F. Luisi, W. X. Xu, Z. Otwinowski, L. P. Freedman, K. R. Yamamoto, and P. B. Sigler, *Nature*, 1991, **352**, 497.
43. J. W. Schwabe, L. Chapman, J. T. Finch, and D. Rhodes, *Cell*, 1993, **75**, 567.
44. F. Rastinejad, T. Wagner, Q. Zhao, and S. Khorasanizadeh, *EMBO J.*, 2000, **19**, 1045.
45. G. Meinke and P. B. Sigler, *Nat. Struct. Biol.*, 1999, **6**, 471.
46. Q. Zhao, S. A. Chasse, S. Devarakonda, M. L. Sierk, B. Ahvazi, and F. Rastinejad, *J. Mol. Biol.*, 2000, **296**, 509.
47. H. T. Chen, P. Legault, J. Glushka, J. G. Omichinski, and R. A. Scott, *Protein Sci.*, 2000, **9**, 1743.
48. A. Roll-Mecak, P. Alone, C. Cao, T. E. Dever, and S. K. Burley, *J. Biol. Chem.*, 2004, **279**, 10634.
49. S. Hahn, *Nat. Struct. Mol. Biol.*, 2004, **11**, 394.
50. D. N. Frick and C. C. Richardson, *Annu. Rev. Biochem.*, 2001, **70**, 39.
51. R. J. Fletcher, B. E. Bishop, R. P. Leon, R. A. Sclafani, C. M. Ogata, and X. S. Chen, *Nat. Struct. Biol.*, 2003, **10**, 160.
52. M. F. Summers, L. E. Henderson, M. R. Chance, J. W. Bess Jr, T. L. South, P. R. Blake, I. Sagi, G. Perez-Alvarado, R. C. Sowder III, D. R. Hare, and L. O. Arthur, *Protein Sci.*, 1992, **1**, 563.
53. R. N. De Guzman, Z. R. Wu, C. C. Stalling, L. Pappalardo, P. N. Borer, and M. F. Summers, *Science*, 1998, **279**, 384.
54. A. Rein, L. E. Henderson, and J. G. Levin, *Trends Biochem. Sci.*, 1998, **23**, 297.
55. R. N. De Guzman, H. Y. Liu, M. Martinez-Yamout, H. J. Dyson, and P. E. Wright, *J. Mol. Biol.*, 2000, **303**, 243.
56. D. A. Bernstein, M. C. Zittel, and J. L. Keck, *EMBO J.*, 2003, **22**, 4910.
57. D. Li, R. Zhao, W. Lilyestrom, D. Gai, R. Zhang, J. A. DeCaprio, E. Fanning, A. Jochimiak, G. Szakonyi, and X. S. Chen, *Nature*, 2003, **423**, 512.
58. R. B. Todd and A. Andrianopoulos, *Fungal Genet. Biol.*, 1997, **21**, 388.
59. K. Zhao, X. Chai, A. Clements, and R. Marmorstein, *Nat. Struct. Biol.*, 2003, **10**, 864.
60. K. Yamasaki, T. Kigawa, M. Inoue, M. Tateno, T. Yamasaki, T. Yabuki, M. Aoki, E. Seki, T. Matsuda, E. Nunokawa, Y. Ishizuka, T. Terada, M. Shirouzu, T. Osanai, A. Tanaka, M. Seki, K. Shinozaki, and S. Yokoyama, *J. Mol. Biol.*, 2004, **337**, 49.
61. B. P. Hudson, M. A. Martinez-Yamout, H. J. Dyson, and P. E. Wright, *Nat. Struct. Mol. Biol.*, 2004, **11**, 257.
62. N. L. Brown, J. V. Stoyanov, S. P. Kidd, and J. L. Hobman, *FEMS Microbiol. Rev.*, 2003, **27**, 145.
63. T. Barkay, S. M. Miller, and A. O. Summers, *FEMS Microbiol. Rev.*, 2003, **27**, 355.
64. A. Z. Ansari, M. L. Chael, and T. V. O'Halloran, *Nature*, 1992, **355**, 87.
65. M. H. Godsey, N. N. Baranova, A. A. Neyfakh, and R. G. Brennan, *J. Biol. Chem.*, 2001, **276**, 47178.
66. E. E. Heldwein and R. G. Brennan, *Nature*, 2001, **409**, 378.
67. A. Changela, K. Chen, Y. Xue, J. Holschen, C. E. Outten, T. V. O'Halloran, and A. Mondragon, *Science*, 2003, **301**, 1383.
68. C. E. Outten, F. W. Outten, and T. V. O'Halloran, *J. Biol. Chem.*, 1999, **274**, 37517.
69. S. Khan, K. R. Brocklehurst, G. W. Jones, and A. P. Morby, *Biochem. Biophys. Res. Commun.*, 2002, **299**, 438.
70. M. A. Pennella, J. E. Shokes, N. J. Cosper, R. A. Scott, and D. P. Giedroc, *Proc. Natl. Acad. Sci. U.S.A.*, 2003, **100**, 3713.
71. K. R. Brocklehurst, J. L. Hobman, B. Lawley, L. Blank, S. J. Marshall, N. L. Brown, and A. P. Morby, *Mol. Microbiol.*, 1999, **31**, 893.
72. L. S. Busenlehner, M. A. Pennella, and D. P. Giedroc, *FEMS Microbiol. Rev.*, 2003, **27**, 131.
73. J. Wu and B. P. Rosen, *J. Biol. Chem.*, 1993, **268**, 52.
74. W. Shi, J. Wu, and B. P. Rosen, *J. Biol. Chem.*, 1994, **269**, 19826.

75. J. W. Huckle, A. P. Morby, J. S. Turner, and N. J. Robinson, *Mol. Microbiol.*, 1993, **7**, 177.
76. A. P. Morby, J. S. Turner, J. W. Huckle, and N. J. Robinson, *Nucleic Acids Res.*, 1993, **21**, 921.
77. C. Eicken, M. A. Pennella, X. Chen, K. M. Koshlap, M. L. VanZile, J. C. Sacchettini, and D. P. Giedroc, *J. Mol. Biol.*, 2003, **333**, 683.
78. J. S. Cavet, A. I. Graham, W. Meng, and N. J. Robinson, *J. Biol. Chem.*, 2003, **278**, 44560.
79. L. S. Busenlehner, T. C. Weng, J. E. Penner-Hahn, and D. P. Giedroc, *J. Mol. Biol.*, 2002, **319**, 685.
80. S. C. Andrews, A. K. Robinson, and F. Rodriguez-Quinones, *FEMS Microbiol. Rev.*, 2003, **27**, 215.
81. A. White, X. Ding, J. C. vanderSpek, J. R. Murphy, and D. Ringe, *Nature*, 1998, **394**, 502.
82. D. G. Kehres and M. E. Maguire, *FEMS Microbiol. Rev.*, 2003, **27**, 263.
83. A. Glasfeld, E. Guedon, J. D. Helmann, and R. G. Brennan, *Nat. Struct. Biol.*, 2003, **10**, 652.
84. E. Guedon and J. D. Helmann, *Mol. Microbiol.*, 2003, **48**, 495.
85. J. M. Hardham, L. V. Stamm, S. F. Porcella, J. G. Frye, N. Y. Barnes, J. K. Howell, S. L. Mueller, J. D. Radolf, G. M. Weinstock, and S. J. Norris, *Gene*, 1997, **197**, 47.
86. Y. H. Lee, R. K. Deka, M. V. Norgard, J. D. Radolf, and C. A. Hasemann, *Nat. Struct. Biol.*, 1999, **6**, 628.
87. J. E. Posey, J. M. Hardham, S. J. Norris, and F. C. Gherardini, *Proc. Natl. Acad. Sci. U.S.A.*, 1999, **96**, 10887.
88. S. Benoit, J. E. Posey, M. R. Chenoweth, and F. C. Gherardini, *J. Bacteriol.*, 2001, **183**, 4702.
89. K. R. Hazlett, F. Rusnak, D. G. Kehres, S. W. Bearden, C. J. La Vake, M. E. La Vake, M. E. Maguire, R. D. Perry, and J. D. Radolf, *J. Biol. Chem.*, 2003, **278**, 20687.
90. Y. H. Lee, M. R. Dorwart, K. R. Hazlett, R. K. Deka, M. V. Norgard, J. D. Radolf, and C. A. Hasemann, *J. Bacteriol.*, 2002, **184**, 2300.
91. S. Banerjee, B. Wei, M. Bhattacharyya-Pakrasi, H. B. Pakrasi, and T. J. Smith, *J. Mol. Biol.*, 2003, **333**, 1061.
92. E. Pohl, J. C. Haller, A. Mijovilovich, W. Meyer-Klaucke, E. Garman, and M. L. Vasil, *Mol. Microbiol.*, 2003, **47**, 903.
93. J. L. Apuy, L. S. Busenlehner, D. H. Russell, and D. P. Giedroc, *Biochemistry*, 2004, **43**, 3824.
94. L. Jacquamet, D. Aberdam, A. Adrait, J. L. Hazemann, J. M. Latour, and I. Michaud-Soret, *Biochemistry*, 1998, **37**, 2564.
95. A. Gonzalez de Peredo, C. Saint-Pierre, A. Adrait, L. Jacquamet, J. M. Latour, I. Michaud-Soret, and E. Forest, *Biochemistry*, 1999, **38**, 8582.
96. S. I. Patzer and K. Hantke, *Mol. Microbiol.*, 1998, **28**, 1199.
97. S. I. Patzer and K. Hantke, *J. Biol. Chem.*, 2000, **275**, 24321.
98. C. E. Outten, D. A. Tobin, J. E. Penner-Hahn, and T. V. O'Halloran, *Biochemistry*, 2001, **40**, 10417.
99. K. A. McCall and C. A. Fierke, *Biochemistry*, 2004, **43**, 3979.
100. D. C. Bittel, I. V. Smirnova, and G. K. Andrews, *J. Biol. Chem.*, 2000, **275**, 37194.
101. M. V. Evans-Galea, E. Blankman, D. G. Myszka, A. J. Bird, D. J. Eide, and D. R. Winge, *Biochemistry*, 2003, **42**, 1053.
102. A. Bird, M. V. Evans-Galea, E. Blankman, H. Zhao, H. Luo, D. R. Winge, and D. J. Eide, *J. Biol. Chem.*, 2000, **275**, 16160.
103. X. Chen, A. Agarwal, and D. P. Giedroc, *Biochemistry*, 1998, **37**, 11152.
104. X. Chen, B. Zhang, P. M. Harmon, W. Schaffner, D. O. Peterson, and D. P. Giedroc, *J. Biol. Chem.*, 2003, **279**, 4515.
105. X. Chen, M. Chu, and D. P. Giedroc, *Biochemistry*, 1999, **38**, 12915.
106. A. L. Guerrerio and J. M. Berg, *Biochemistry*, 2004, **43**, 5437.
107. W. Maret, *Biochemistry*, 2004, **43**, 3301.
108. C. J. Chang, J. Jaworski, E. M. Nolan, M. Sheng, and S. J. Lippard, *Proc. Natl. Acad. Sci. U.S.A.*, 2004, **101**, 1129.
109. K. K. Chung, B. Thomas, X. Li, O. Pletnikova, J. C. Troncoso, L. Marsh, V. L. Dawson, and T. M. Dawson, *Science*, 2004, **304**, 1328.
110. M. L. VanZile, N. J. Cosper, R. A. Scott, and D. P. Giedroc, *Biochemistry*, 2000, **39**, 11818.
111. C. E. Outten and T. V. O'Halloran, *Science*, 2001, **292**, 2488.

Acknowledgments

The authors wish to acknowledge the generous support from the National Institutes of Health (GM042569) and the Robert A. Welch Foundation (A-1295).

Zinc Enzymes

David S. Auld
Boston College, Chestnut Hill, MA, USA

1 Introduction 1
2 Some General Features of Zinc-binding Sites 2
3 Catalytic Zinc Sites 2
4 Cocatalytic Zinc Sites 22
5 Structural Zinc Sites 23
6 Protein Interface Zinc Sites 29
7 Zinc-binding Proteins 36
8 Related Articles 38
9 Further Reading 38
10 References 39

Abbreviations

ABC = ATP-binding cassette; ADA = Adenosine deaminase; ADAM = A distintegrin and metalloprotease domain; ADH = Alcohol dehydrogenase; Apo2L or TRAIL = Apoptosis-inducing ligand 2; BIR = Baculovirus Inhibitor of apoptosis repeat; BHMT = Betaine-homocysteine methyltransferase; BRCT = Breast cancer tumor suppressor protein C-terminous; CA = Carbonic anhydrase; CAM = γ-carbonic anhydrase; C1 = Cysteine-rich domain; CH1 = Cysteine/histidine rich domain; CPD A = Carboxypeptidase A; CDA = Cytidine deaminase; CTAD = C-terminal transactivating domain; CRP = Cysteine-rich protein; CRIP = Cysteine-rich intestinal protein; DBD = DNA-binding domain; e/aIf2 = Eukaryotic/archaeal Initiation Factor; EDTA = Ethylenediaminetetraacetic acid; eNOS or NOS-3 = Endothelial nitric oxide synthase; H_4B = Tetrahydrobiopterin; HIF = Hypoxia-inducible factor; HIV = Human immunodeficiency virus; HMTase = Histone methyltransferase; HLA-DR = Class II major histocompatibility molecule; huIFN = Human interferon; KSR = Kinase suppressor of Ras; IAP = Inhibitor of apoptosis; iNOS or NOS-2 = Inducible nitric oxide synthase; IUB = International Union of Biochemistry; MEROPS = System for classification of peptidase sequences; *mt* = *Methanobacterium thermautotrophicum*; MCM = Minichromosome maintenance; MHC = Major histocompatibility complex; Mip = Macrophage infectivity potentiator protein; MMP = Matrix metalloproteinase; MPD = 2-methyl-2,4-pentanediol; NAD = Nicotinamide adenine dinucleotide; NADH = Reduced nicotinamide adenine dinucleotide; NADP = Nicotinamide adenine dinucleotide phosphate; NGF = Nerve growth factor; nNOS, NOS-1 = Neuronal nitric oxide synthase; PDE = Phosphodiesterase; Peptidase = Enzyme acting on peptides; PINCH = Particularly interesting new Cys-His protein; PLBP = Periplasmic ligand-binding protein; PMI = Phosphomannose isomerase; PTS = Signal transducing protein; PsaA = Pneumococcal surface antigen; Proteinase = Enzyme acting on proteins; RS = tRNA synthetase; SAM = S-adensoyl-L-methionine; SEA, B etc. = Staphylococcal enterotoxins type A, B etc; SPEA, C etc. = Streptococcal pyrogenic exotoxins type A, C etc; SET = Su(var), Enhancer of zeste, Trithorax; SHBG = Sex hormone binding-globulin; SMEZ = streptococcal mitogenic exotoxin; Sir2 = Silencing information regulator 2; SOD = Superoxide dismutase; TCR = T-cell receptor; TNF = Tumor necrosis factor; TACE = Tumor necrosis factor-α-converting enzyme; TSST = Toxic shock syndrome toxin; VanX = Dipeptidase of vancomycin-resistant pathogenic *Enterococci*; VDR = Vitamin D-Receptor; XAFS = X-ray absorption fine structure; XIAP = X-linked inhibitor of apoptosis protein.

1 INTRODUCTION

The importance of zinc to growth and development in all forms of life was first established through zinc deficiency studies of microorganisms followed by those in plants and animals (*see* ***Nutritional Aspects of Metals & Trace Elements***).[1] The involvement of zinc in a wide variety of metabolic processes including carbohydrate, lipid, protein, and nucleic acid synthesis and degradation paralleled the technical advances in analytical methods that could detect the presence of zinc in minute amounts coupled with advances in the methodology for protein isolation and purification.

The molecular characterization of zinc sites in biological systems came first through replacing the spectroscopically silent zinc with the chromophoric metal cobalt. These studies in conjunction with kinetic studies gave information on the importance of the metal site to protein function. Structural studies of the entire protein obtained by X-ray diffraction and NMR now give detailed information of the metal ligands and the coordination geometry of the metal site. X-ray absorption fine structure, XAFS, permits visualization of the zinc site directly in the solution and crystal states and enhances the ability to identify the manner in which zinc is involved in the function of the protein.[2] The combination of all of these approaches allows formulation of how the zinc influences protein function that can be tested by a combined approach including mutagenesis and rapid kinetics. Finally, the ability to determine primary protein structure through translation of DNA sequences in combination with our increasing knowledge of zinc-binding sites permits prediction of new zinc-binding sites and thereby protein function without even having an expressed protein.[3,4]

Zinc is the only metal to have representatives in all six of the International Union of Biochemistry, IUB, classes of enzymes. The function of these enzymes is therefore related to the chemistry of zinc, which is quite versatile. It has a remarkably adaptable coordination sphere that allows it to accommodate a broad range of coordination numbers and geometries. If zinc retains a positive charge after ligating to protein side chains, it can act as a Lewis acid in catalysis. If a zinc-bound water is converted to hydroxide, the zinc site can act as a base or nucleophile in catalysis. In this sense, the zinc sites are amphoteric. The oxidation/reduction properties of its neighboring transition metals is a major cause of their ligand exchange rates, amphoteric properties, and coordination geometries. Since zinc has a filled d-shell, it does not have oxidation/reduction properties, thus providing a stable metal ion species in a biological medium whose redox potential is in constant flux.

Our first attempts at classifying the manner in which zinc binds to enzymes was made on the basis of the zinc ligands and coordination geometries of from one to three dozen zinc enzymes during the period 1988 to 1993 (Figure 1). This led to the recognition of three types of zinc-binding sites: *catalytic*, *cocatalytic*, and *structural*.[5,6] As of 2003, the structural characteristics of more than thirty dozen zinc sites have been reported, the great majority of which still fit into the original classification (see below). A new type of zinc-binding site, *protein interface*, has become apparent during the past few years.[3,4] In this case, zinc-binding sites are formed through ligands supplied from amino acid residues residing in the binding surface of two protein molecules.

2 SOME GENERAL FEATURES OF ZINC-BINDING SITES

The secondary support and scaffolding in combination with the direct ligands of the zinc allows fine tuning of the role of the zinc and its neighboring amino acids in the protein function. The following general observations pertain to the structural properties of zinc-binding sites found in enzymes and other zinc-binding proteins.[4] (1) Nearly all the zinc sites contain at least one secondary structural element. (2) β-sheets supply ligands to a wide variety of zinc-binding sites. (3) Ligands frequently come from the first, last, or 1 or 2 amino acids before or after a β-sheet or α-helix. (4) Small loop regions (6 amino acids) between two types of secondary structure can also supply the ligands. This may allow more freedom in the coordination properties of the zinc site. (5) Short spacers of one generally use a β-sheet to supply the ligands while a spacer of three uses an α-helix. (6) An α-helix is used to supply the short spacer ligands most frequently in hydrolytic enzymes (in particular, the metalloproteases). (7) His ligands are often H-bonded to carboxyl groups of Asp or Glu or carbonyl groups of a variety of amino acids. (8) Hydrophobic amino acids likely are involved in stabilizing the zinc-binding site through orientation of the ligands.

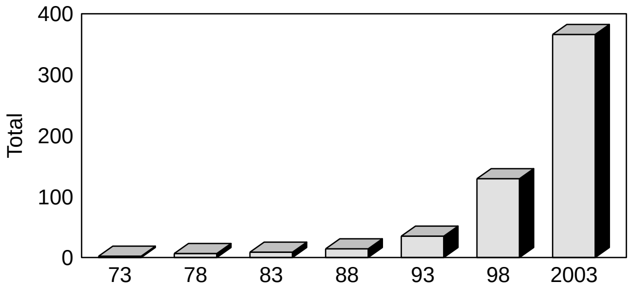

Figure 1 Time course of structural determination of zinc-binding sites in enzymes

3 CATALYTIC ZINC SITES

There are today about 12 dozen 3-dimensional structural references of *catalytic* zinc sites encompassing all six classes of enzymes (Table 1). The hydrolase enzyme class (III) has the greatest number of representatives. A catalytic zinc generally forms complexes with any three nitrogen, oxygen, and sulfur donors of His, Glu, Asp, and Cys with His being the predominant amino acid chosen. Histidine (usually the NE2 nitrogen) may be chosen because of its capacity to disperse charge through H-bonding of its nonliganding nitrogen. The overall sequence length of such sites can be as small as 11 amino acids as is observed in the zinc endoprotease families with the zinc site signature HExxHxxGxxH/D and the 5-aminolevulinic acid dehydratase enzymes (Table 1). The zinc ligands are separated by comparatively short and long amino acid spacers. While in principle the third ligand could be supplied from either the C- or N-terminal side of the first two ligands, the C-terminus is preferred by a ratio of about 5 to 1. The great majority of the short spacers contain one to three amino acids (Table 1). The length of the short spacer is often dictated by the ligand support structure: 3 for an α-helix and 1 for a β-sheet. In the case of the oxidoreductases, the involvement of H-bonding interactions between residues in the short spacer (for example, His47 and/or His51 in ADH) and the cofactor reduced nicotinamide adenine dinucleotide (NADH) may have led to the extension of the ‘short’ spacer to 17 to 29 (versus a long spacer of 82 to 106).

The coordination number for such sites is usually 4 or 5 and the geometry in the free state is frequently distorted-tetrahedral or trigonal-bipyramidal. Water is always a ligand to the catalytic zinc. The zinc-bound water can be directly involved in catalysis by its ionization or it can be activated through polarization by a neighboring amino acid residue acting as a general acid/base (Figure 2). The zinc can function as a Lewis acid by a substrate ligand displacement by the water or expansion of the coordination shell. The chemical nature of the three protein ligands, their spacing and secondary

Table 1 Catalytic zinc sites[a]

Enzyme	PDB#	L$_1$	X	L$_2$	Y	L$_3$	Z	L$_4$	L$_5$
Class I: Oxidoreductases									
Alcohol Dehydrogenase family									
Horse EE	8ADH, 3BTO	Cys$_L$	20	His$_{b\beta}$	106	Cys$_L$		H_2O	
Cod	1CDO	Cys$_L$	21	His$_{b\beta}$	106	Cys$_L$		H_2O	
Human Class I									
$\alpha\alpha$	1HSO	Cys$_L$	20	His$_{b\beta}$	106	Cys$_L$		H_2O	
$\beta_1\beta_1$	1HDZ	Cys$_L$	20	His$_{b\beta}$	106	Cys$_L$		H_2O	
$\beta_2\beta_2$	1HDY	Cys$_L$	20	His$_{b\beta}$	106	Cys$_L$		H_2O	
$\beta_3\beta_3$	1DEH	Cys$_L$	20	His$_{b\beta}$	106	Cys$_L$		H_2O	
$\gamma\gamma$	1HTO	Cys$_L$	20	His$_{b\beta}$	106	Cys$_L$		H_2O	
Mouse Class II	1E3E	Cys$_L$	20	His$_{b\beta}$	110	Cys$_L$		H_2O	
Human Class III									
$\chi\chi$	1TEH	Cys$_L$	20	His$_{b\beta}$	106	Cys$_{b\alpha}$		H_2O	Glu$_\beta$
or glutathione- dependent									
formaldehyde dehydrogenase	1M6H	Cys$_L$	21	His$_{b\beta}$	106	Cys$_\alpha$		H_2O	
Pseudomonas putida									
formaldehyde dehydrogenase	1KOL	Cys$_L$	20	His$_{b\beta}$	101	Asp$_{2b\alpha}$		H_2O	
Human Class IV									
$\sigma\sigma$	1AGN	Cys$_L$	20	His$_{b\beta}$	106	Cys$_L$		H_2O	
Amphibian (ADH8)	1P0F	Cys$_L$	20	His$_{b\beta}$	105	Cys$_L$		H_2O	
Sulfolobus solfataricus	1JVB,1NTO	Cys$_L$	29	His$_{b\beta}$	85	Cys$_L$		Glu$_\beta$	H_2O?
Aeropyrum pernix	1H2B	Cys$_L$	24	His$_{b\beta}$	88	Asp$_L$		H_2O	
Clostridium beijerinckii	1KEV,IJQB	Cys$_L$	21	His$_{b\beta}$	90	Asp$_L$		H_2O	
Thermoanaerobacter brockii	1YKF	Cys$_L$	21	His$_{b\beta}$	90	Asp$_L$		H_2O	
Sorbitol dehydrogenase family									
Silverleaf Whitefly ketose reductase	1E3J	Cys$_L$	24	His$_{b\beta}$	0	Glu$_\beta$		H_2O	
Human SDH	1PL8	Cys$_L$	24	His$_{b\beta}$	0	Glu$_\beta$		H_2O	
Rat SDH		Cys	24	His$_{b\beta}$	85	Glu		H_2O	Glu
Bacillus stearothermophilus									
Glycerol dehydrogenase	1JQ5	His$_\alpha$	17	His$_\alpha$	82	Asp$_\alpha$ (N)		H_2O	
Thermotoga maritima glycerol dehydrogenase	1KQ3	His$_\alpha$	16	His$_\alpha$	82	Asp$_\alpha$ (N)		Tris(OH,NH$_2$)	
Class II: Transferase									
Rat farnesyl transferase	1 FT1	Asp	1	Cys	62	His$_\alpha$		H_2O	
human farnesyl transferase	1MZC	Asp	1	Cys	62	His$_\alpha$		Inhib N	
Rat Rab geranylgeranyltransferase	1DCE	Asp$_{b\alpha}$	1	Cys$_\alpha$	49	His$_\alpha$		H_2O	
Human BHMT	1LT8	Cys$_{a\beta}$	0	Cys$_\beta$	81	Cys$_\beta$ (N)		H_2O	
Escherichia coli DNA relaxase Trwc	1QX0	His$_\beta$	1	His$_\beta$	10	His$_\beta$ (N)		H_2O	
Class III: Hydrolase									
Carboxypeptidase (CPD) family									
Bovine A	3CPA, 1CPX	His	2	Glu$_{2b\alpha}$	123	His$_\beta$		H_2O	
Bovine B	1CPB	His	2	Glu	123	His		H_2O	
Rat A$_2$		His	2	Glu	123	His		H_2O	
Human A$_2$	1DTD	His	2	Glu$_{2b\alpha}$	124	His$_\beta$		H_2O	
Avian D	1QMU	His	2	Glu$_{2b\alpha}$	103	His$_\beta$		H_2O	
Thermoactinomyces vulgaris T	1OBR	His	2	Glu$_{2b\alpha}$	131	His$_\beta$		H_2O	
Porcine PCPD A	1PCA	His	2	Glu$_{2b\alpha}$	123	His$_\beta$		H_2O	
Bovine PCPD A	1PYT	His	2	Glu$_{2b\alpha}$	123	His$_\beta$		H_2O	
Porcine PCPD B	1NSA	His	2	Glu$_{2b\alpha}$	123	His$_\beta$		H_2O	
Human PCPD B	1KWM	His	2	Glu$_{2b\alpha}$	123	His$_\beta$		H_2O	
Human PCPD A2	1AYE	His	2	Glu	123	His$_\beta$		H_2O	
Mycobacterium tuberculosis									
D-glucopyranoside deacetylase (Msbb)	1Q74	His$_L$	2	Asp$_\alpha$	130	His$_\alpha$		H_2O	

(cont'd overleaf)

Table 1 cont'd

Enzyme	PDB#	L$_1$	X	L$_2$	Y	L$_3$	Z	L$_4$	L$_5$
Thermolysin family									
Bacillus thermoproteolyticus	1LND	His$_\alpha$	3	His$_\alpha$	19	Glu$_\alpha$		H_2O	
Bacillus cereus	1ESP	His$_\alpha$	3	His$_\alpha$	19	Glu$_\alpha$		H_2O	
Pseudomonas aeruginosa	1EZM	His$_\alpha$	3	His$_\alpha$	19	Glu$_\alpha$		H_2O	
Staphylococcus aureus	1BQB	His$_\alpha$	3	His$_\alpha$	19	Glu$_\alpha$		H_2O	
Human leukotriene A$_4$ hydrolase	1HS6	His$_\alpha$	3	His$_\alpha$	18	Glu$_\alpha$		H_2O	
Rat neurolysin	1I1I	His$_\alpha$	3	His$_\alpha$	24	Glu$_\alpha$		H_2O	
Pyrococcus furiosus CPD	1 KA4	His$_\alpha$	3	His$_\alpha$	25	Glu$_\alpha$		H_2O	
Human angiotensin-converting enzyme	1O8A,1R42	His$_\alpha$	3	His$_\alpha$	23	Glu$_\alpha$		H_2O	
Clostridium botulinum neurotoxin A	3BTA	His$_\alpha$	3	His$_\alpha$	34	Glu$_L$		H_2O	
Clostridium botulinum neurotoxin B	1EPW	His$_\alpha$	3	His$_\alpha$	33	Glu$_\alpha$		H_2O	
Bacillus anthracis anthrax toxin lethal factor	1J7N,1PWP	His$_\alpha$	3	His$_\alpha$	44	Glu$_\alpha$		H_2O	
Human neutral endoprotease (Neprilysin)	1DMT	His$_\alpha$	3	His$_\alpha$	58	Glu$_\alpha$		H_2O	
Leishmania major surface proteinase	1LML	His$_\alpha$	3	His$_\alpha$	65	His$_\beta$		H_2O	
Yeast mitochondrial processing protease	1HR6	His$_\alpha$	3	His$_\alpha$	75	Glu$_\alpha$		H_2O	
Streptomyces albus G DD-CPD	1LBU	His	6	Asp$_\beta$	35	His$_\beta$		H_2O	
VanX D-Ala-D-Ala carboxypeptidase		His$_\alpha$	6	Asp$_\beta$	60	His$_\beta$		H_2O	
Mouse sonic hedgehog	1VHH	His	6	Asp$_\beta$	34	His$_\beta$		H_2O	
Streptomyces caespitosus endopeptidase	1KUH	His$_\alpha$	3	His$_\alpha$	5	Asp		H_2O	
Grifola frondosa aspzincin	1G12	His$_\alpha$	3	His$_{a\alpha}$	8	Asp		H_2O	
Aspergillus oryzae Deuterolysin	1EB6	His$_\alpha$	3	His$_{a\alpha}$	10	Asp		H_2O	
Astacin	1AST	His$_\alpha$	3	His$_\alpha$	5	His$_{a\beta}$		H_2O	Tyr
Serratia Family									
Pseudomonas aeruginosa alkaline protease	1KAP	His$_\alpha$	3	His$_\alpha$	5	His		H_2O	Tyr
Pseudomonas sp. TAC II 18 protease	1G9K	His$_\alpha$	3	His$_\alpha$	5	His		H_2O	
Serratia marcescens metalloprotease	1SAT	His$_\alpha$	3	His$_\alpha$	5	His		H_2O	Tyr
Serratia sp. E-15 metalloprotease	1SRP	His$_\alpha$	3	His$_\alpha$	5	His		H_2O	Tyr
Snake Venom Protease Family									
Crotalus adamanteus, Adamalysin II	1IAG	His$_\alpha$	3	His$_\alpha$	5	His		H_2O	
Crotalus atrox, Atrolysin C	1ATL	His$_\alpha$	3	His$_\alpha$	5	His		H_2O	
Trimeresurus flavoviridis H$_2$-Proteinase		His$_\alpha$	3	His$_\alpha$	5	His		H_2O	
Agkistrodon acutus, Acutolysin A	1BSW	His$_\alpha$	3	His$_\alpha$	5	His		H_2O	
Agkistrodon acutus, Acutolysin C	1QUA	His$_\alpha$	3	His$_\alpha$	5	His		H_2O	
Trimeresurus mucrosquamatus, Habu	1KUF	His$_\alpha$	3	His$_\alpha$	5	His		H_2O	
Bothrops Asper, Bap1	1ND1	His$_\alpha$	3	His$_\alpha$	5	His		H_2O	
Human TNF-α-converting enzyme, TACE	1BKC	His$_\alpha$	3	His$_\alpha$	5	His		H_2O	

Table 1 cont'd

Enzyme	PDB#	L_1	X	L_2	Y	L_3	Z	L_4	L_5
Matrix Metalloproteinase family									
Human fibroblast collagenase (MMP-1)	1CGL	His$_{\alpha}$	3	His$_{\alpha}$	5	His		H_2O	
Human fibroblast collagenase (MMP-1)	1AYK	His$_{\alpha}$	3	His$_{\alpha}$	5	His		H_2O	
Human Progelatinase 72 kDa (MMP-2)	1CK7	His$_{\alpha}$	3	His$_{\alpha}$	5	His	200	Cys$_{\beta}$ (N)	
Human stromelysin-1 (MMP-3)	2SRT, 1BM6	His$_{\alpha}$	3	His$_{\alpha}$	5	His		H_2O	
Human stromelysin-1 (MMP-3)	1B3D	His$_{\alpha}$	3	His$_{\alpha}$	5	His		H_2O	
Human prostromelysin-1 (MMP-3)	1SLM	His$_{\alpha}$	3	His$_{\alpha}$	5	His	125	Cys$_{\beta}$ (N)	
Human matrilysin (MMP-7)	1MMP	His$_{\alpha}$	3	His$_{\alpha}$	5	His		H_2O	
Human neutrophil collagenase (MMP-8)	1KBC	His$_{\alpha}$	3	His$_{\alpha}$	5	His$_{a\beta}$		H_2O	
Human gelatinase 92 kDa (MMP-9)	1GKC	His$_{\alpha}$	3	His$_{\alpha}$	5	His		H_2O	
Human macrophage elastase (MMP-12)	1JIZ	His$_{\alpha}$	3	His$_{\alpha}$	5	His$_{a\beta}$		H_2O	
Human collagenase-3 (MMP-13)	830C	His$_{\alpha}$	3	His$_{\alpha}$	5	His		H_2O	
Mouse collagenase-3 (MMP-13)	1CXV	His$_{\alpha}$	3	His$_{\alpha}$	5	His		H_2O	
Human Membrane Mt1 (MMP-14)	1BQQ	His$_{\alpha}$	3	His$_{\alpha}$	5	His		H_2O	
Archaeoglobus fulgidus Jabi/Mpn	1OI0	His$_{\beta}$	1	His$_{\beta}$	10	His$_{\alpha}$		H_2O	
Archaeoglobus fulgidus JAMM	1R5X	His$_{\beta}$	1	His$_{\beta}$	10	His$_{\alpha}$		H_2O	
Deaminases									
Murine adenosine deaminase	2ADA, 1A4L	His	1	His	196	His$_{\beta}$	80	Asp$_{L}$	H_2O
Bovine adenosine deaminase	1KRM	His	1	His	196	His$_{\beta}$	80	Asp$_{L}$	H_2O
Escherichia coli cytidine deaminase	1CTT	Cys$_{\alpha}$	2	Cys$_{b\alpha}$	26	His$_{b\alpha}$ (N)		H_2O	
S. cerevisiae cytidine deaminase	1OX7	Cys$_{\alpha}$	2	Cys$_{b\alpha}$	28	His$_{b\alpha}$ (N)		H_2O	
Bacillus subtilis cytidine deaminase	1JTK	Cys$_{\alpha}$	2	Cys$_{b\alpha}$	32	Cys$_{b\alpha}$ (N)		H_2O	
Drosophilia melanogaster α-mannosidase II	1 PS3	His$_{\beta}$	1	Asp$_{2a\beta}$	111	Asp$_{2a\beta}$	266	His	Inh.
Bovine α-mannosidase	1O7D	His	1	Asp	121	Asp$_{2a\beta}$	249	His$_{L}$	Inh.
Peptide deformylase Family									
Escherichia coli	1BS4	His$_{\alpha}$	3	His$_{\alpha}$	41	Cys(N)		H_2O	
Staphylococcus aureus	1LMH	His$_{\alpha}$	3	His$_{\alpha}$	41	Cys(N)		H_2O	
Pseudomonas aeruginosa	1LRY,1N5N	His$_{\alpha}$	3	His$_{\alpha}$	41	Cys$_{2a\beta}$ (N)		H_2O	
Bacillus stearothermophilus	1LQY	His$_{\alpha}$	3	His$_{\alpha}$	42	Cys(N)		H_2O	
Streptococcus pneumoniae	1LM6	His$_{\alpha}$	3	His$_{\alpha}$	42	Cys(N)		H_2O	
E. coli colicin E7 (ColE7) DNase	7CEI,1MZ8	His$_{\alpha}$	3	His$_{\alpha}$	24	His$_{\beta}$ (N)		H_2O	
E. coli colicin E9 (ColE9) DNase	1FSJ	His$_{a\alpha}$	3	His$_{\alpha}$	24	His$_{\beta}$ (N)		H_2O	
Pyrococcus woesei α-amylase	1MWO	His$_{\beta}$	4	His	13	Cys$_{\beta}$		H_2O	
Human GTP cyclohydrolase I	1FB1	Cys$_{\beta}$	2	His$_{L}$	67	Cys$_{a\beta}$		H_2O	
E. coli GTP cyclohydrolase I	1FBX	Cys$_{\beta}$	2	His$_{L}$	67	Cys$_{a\beta}$		H_2O	
Rat GTP cyclohydrolase I	1IS8	Cys$_{\beta}$	2	His$_{L}$	67	Cys$_{a\beta}$		H_2O	
S. cerevisiae π-Scei endonuclease	1EF0	Cys$_{\beta}$	1	His$_{\beta}$	372	Glu$_{\beta}$ (N)		H_2O	
Bacteriophage T7 lysozyme	1LBA	Cys$_{2b\beta}$	7	His$_{\beta}$	104	His$_{\beta}$ (N)		H_2O	
Aquifex aeolicus LpxC deacetylase	1P42,1NZT	Asp$_{\alpha}$	3	His$_{\alpha}$	158	His$_{\alpha}$ (N)		H_2O	

(cont'd overleaf)

Table 1 cont'd

Enzyme	PDB#	L_1	X	L_2	Y	L_3	Z	L_4	L_5
β-Lactamase Family									
Bacillus cereus	1BMC	His$_{2a\beta}$	1	His	60	His		H_2O	
Bacteroides fraglis	1ZNB	His	1	His	60	His		H_2O	
Pseudomonas aeruginosa	1DD6	His$_{2a\beta}$	1	His	59	His		H_2O	
Chryseobacterium meningosepticum	1M2X	His$_{2a\beta}$	1	His	77	His		Solv	
Stenotrophomonas maltophilia	1SML	His	1	His	73	His$_L$		H_2O	
Fluoribacter gormanii	1K07	His	1	His	73	His$_L$		Solv	
Hepatitis C virus proteinase	1A1Q, 1JXP	Cys	1	Cys	45	Cys$_\beta$		H_2O	
Hepatitis C virus NS3 proteinase	1BT7	Cys	1	Cys	45	Cys$_{2a\beta}$		H_2O	
Class IV: Lyase									
Carbonic Anhydrase Family									
Homo Sapiens CA I	2CAB	His$_\beta$	1	His$_\beta$	22	His$_\beta$		H_2O	
Homo Sapiens CA II	1CA2	His$_\beta$	1	His$_\beta$	22	His$_\beta$		H_2O	
Bovine CA III		His$_\beta$	1	His$_\beta$	22	His$_\beta$		H_2O	
Rattus Norvegius CA III	1FLJ	His$_\beta$	1	His$_\beta$	22	His$_\beta$		H_2O	
Homo Sapiens membrane CA IV	1ZNC	His$_\beta$	1	His$_\beta$	22	His$_\beta$		H_2O	
Murine CA IV	2ZNC	His$_\beta$	1	His$_\beta$	22	His$_\beta$		H_2O	
Murine mitochrondrial CA V	1DMX	His$_\beta$	1	His$_\beta$	22	His$_\beta$		H_2O	
Neisseria gonorrhoeae CA	1KOP	His$_\beta$	1	His$_\beta$	16	His$_\beta$		H_2O	
Pisum sativum β-CA	1EKJ	Cys$_L$	2	His$_\beta$	59	Cys$_\beta$ (N)		Acetate	
Porphyridium purpureum β-CA	1DDZ	Cys$_L$	2	His$_\beta$	55	Cys$_\beta$ (N)		Asp$_{a\beta}$	
Methanobacterium thermoautotrophicum β-CA	1G5C	Cys$_{2a\beta}$	2	His$_\beta$	54	Cys$_\beta$ (N)		H_2O	
E. coli β-CA	1I6P	Cys$_{b\alpha}$	2	His$_\beta$	55	Cys$_\beta$ (N)		Asp$_{a\beta}$	
Methanosarcina thermophila γ-CA	1THJ	His$_\beta$	4	His$_{a\beta}$	35	His$_\beta$ (N)		H_2O See Table 5	
Rat 6-pyruvoyl-tetrahydropterin synthase	1B6Z	His$_\beta$	1	His$_\beta$	24	His$_\beta$ (N)		H_2O	
E. coli 2C-methyl-D-erythritol 2,4-cyclodiphosphate synthase	1GX1,1JY8	Asp$_\beta$	1	His$_\beta$	31	His$_\alpha$		H_2O	
S. cerevisiae 5-aminolaevulinate dehydratase	1AW5,1QNV	Cys$_{a\beta}$	1	Cys	7	Cys$_{2b\beta}$		H_2O	
E. coli 5-aminolaevulinate dehydratase	1B4E,1L6S	Cys$_{a\beta}$	1	Cys	7	Cys		H_2O	
E. coli fuculose 1-phosphate aldolase	4FUA,1DZU	His$_\beta$	1	His$_{a\beta}$	60	His$_{b\beta}$		H_2O	Glu$_L$
E. coli L-rhamnulose-1-phosphate aldolase	1OJR	His$_\beta$	1	His$_L$	68	His$_L$		H_2O	
Class V: Isomerase									
E. coli L-ribulose-5-phosphate-4-epimerase	1JDI	His$_\beta$	1	His$_L$	73	His$_{b\beta}$		H_2O	
Orysa sativa D-ribulose-5-phosphate-3-epimerase	1H1Z	His$_\beta$	1	Asp$_\beta$	30	His$_\beta$	108	Asp$_\beta$	H_2O
Candida albicans phosphomannose isomerase	1PMI	Gln$_\beta$	1	His$_{a\beta}$	24	Glu$_\beta$	146	His$_\beta$	H_2O
Class VI: Ligase									
E. coli CysRS	1LI5, 1LI7	Glu$_\alpha$	3	His$_\alpha$	24	Cys$_\alpha$	180	Cys$_{a\beta}$ (N)	Cys (SH)
Staphylococcus aureus ThrRS	1NYQ	Cys$_\alpha$	50	His$_\beta$	129	His$_\beta$			Thr(OH,NH_2)

[a] The amino acid spacer between ligands L_1 and L_2 is X, that between L_3 and nearest ligand L_1 or L_2 is Y, and that between L_3 and L_4 is Z. The symbol N indicates that L_3 is located on the amino (N) side of L_2. If no letter is present, L_3 is located on the carboxy-terminal side of L_2. The subscripts α, β refer to the α-or 3_{10} helix and β-sheet structure that supplies the ligand. The subscript L denotes an amino acid sequence of $\leq$ 6 residues between two structural elements. The subscripts a and b indicate the ligand is either one (or two) residues after or before the secondary structural element.

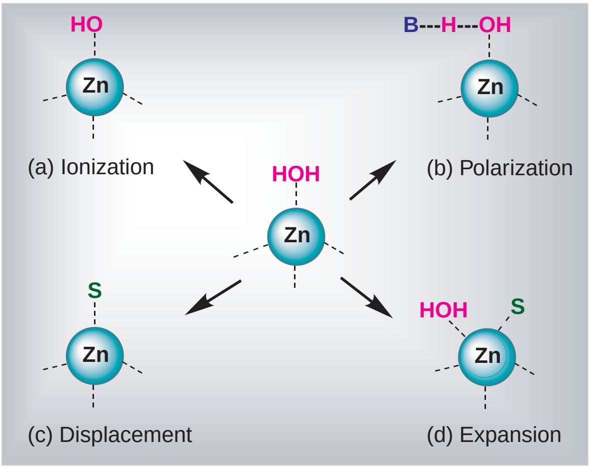

Figure 2 The role of the zinc and its bound water in catalysis. The water can ionize either (a) without or (b) with the help of an adjacent base, B, supplied by an amino acid residue. The zinc-bound water can also (c) be displaced by substrate, S or (d) the coordination sphere be expanded upon interaction with substrate

interactions with neighboring amino acids in conjunction with the vicinal properties of the active center created by protein folding are all critical for the various mechanisms through which zinc can be involved in catalysis.

3.1 Scaffolding of the Catalytic Zinc Sites

In considering how tightly the zinc will bind to the protein site, how readily it can be released from the protein, and its effect on protein function one must not only take into account the first shell ligands but the scaffolding of these sites. The scaffolding encompasses not only the type of secondary structure supplying the ligands, but also the effects of amino acid residues on the metal ligands. These amino acids are sometimes thought of as the ‘outer or second’ shell of ligands. Indeed comparative structural studies of the metal sites in four of the first known zinc enzymes, carbonic anhydrase, carboxypeptidase A, alcohol dehydrogenase, and thermolysin led to the identification of carbonyl and carboxyl ‘orienters’, or amino acids that formed H-bonds to the ligands to the metal.[7]

Many of the catalytic and structural zinc-binding sites contain His imidazole and Glu or Asp carboxyl groups as ligands to the zinc. The tight binding and often slow off rates for zinc from such sites is not expected based on the binding constants for imidazole and acetate binding to zinc. The pK_1 values for acetate and imidazole of ~ 1.5 are not particularly strong.[2] Binding three imidazole groups and an acetate to a zinc would then be expected to have an overall binding constant of $10^5 - 10^7$. However, the binding constant for zinc to the Thr199Glu mutant carbonic anhydrase II[8] that contains 3 His and 1 Glu as ligands is 5×10^{13}. The fact that so many catalytic zinc sites bind zinc with picomole binding constants, yet have imidazole and acetate as their ligands likely reflects their proximity and restricted mobility in the protein. A regular form of secondary structure can supply some of the correct orientation needed for good ligand binding to zinc. However, the stability and the function of the metal site is also likely influenced by the outer shell of residues in the vicinity of the metal-binding site. The secondary interactions of the ligands with ionic groups of the side-chain groups of the outer shell amino acid residues or the carbonyl oxygen of the backbone peptide chain may be critical to the formation and stabilization of the zinc sites containing oxygen, nitrogen, and sulfur ligands.

3.1.1 *Carbonic Anhydrases: Hydrophilic Orienters*

Examination of the effect of the orienters or indirect ligands on stability of the zinc-binding site and catalysis has been most thoroughly examined in the carbonic anhydrase α-class of enzymes.[9,10] There are currently X-ray crystal structures for catalytic zinc-binding sites of 5 of the mammalian α-carbonic anhydrases (Figure 3). The zinc ion is coordinated by the imidazole side chain of His94, His96 and His119 in all of these mammalian carbonic anhydrases. The three His ligands

		94		96			119	
Consensus	FQF	H	F	H	WGS	AAEL	H	LVHW
CAH1_human	FQF	H	F	H	WGS	SAEL	H	VAHW
CAH1_macne	FQF	H	F	H	WGS	SSEL	H	IVHW
CAH1_macum	FQF	H	F	H	WGS	SSEL	H	IVHW
CAH1_horse	FQF	H	F	H	WGS	SAEL	H	LVHW
CAH1_mouse	FQF	H	F	H	WGS	SGEL	H	LVHW
CAH1_sheep	RQF	H	F	H	WGS	SAEL	H	LVHW
CAH1_rabbit	SQF	H	F	H	WGK	SAEL	H	LVHW
CAH2_mouse	FQF	H	F	H	WGS	AAEL	H	LVHW
CAH2_human	IQF	H	F	H	WGS	AAEL	H	LVHW
CAH2_rabbit	IQF	H	F	H	WGS	AAEL	H	LVHW
CAH2_bovine	FQF	H	F	H	WGS	AAEL	H	LVHW
CAH2_sheep	VQF	H	F	H	WGS	AAEL	H	LVHW
CAH2_rat	IQF	H	F	H	WGS	AAEL	H	LVHW
CAH2_chick	VQF	H	I	H	WGS	DAEL	H	IVHW
CAH3_mouse	FQF	H	F	H	WGS	AAEL	H	LVHW
CAH3_rat	RQF	H	L	H	WGS	AAEL	H	LVHW
CAH3_horse	RQF	H	L	H	WGS	AAEL	H	LVHW
CAH3_human	RQF	H	L	H	WGS	AAEL	H	LVHW
CAH4_rat	IQL	H	L	H	WSE	AMEM	H	VVHK
CAH4_rabbit	TQL	H	L	H	WSQ	AMEM	H	IVHQ
CAH4_mouse	VQL	H	L	H	WSN	AMEM	H	IVHK
CAH4_human	KQL	H	L	H	WSD	AMEM	H	IVHE
CAH4_bovin	TQL	H	L	H	WSR	AMEM	H	IVHE
CAH5_human	KQF	H	F	H	WGA	PAEL	H	LVHW
CAH5_rat	KQF	H	F	H	WGA	PAEL	H	LVHW
CAH5_mouse	KQF	H	F	H	WGA	PAEL	H	LVHW

Figure 3 Zinc ligands of mammalian carbonic anhydrases, CA I-V. Names denote type and species of CA. Data obtained using the sequence of human CA I and the resources of the EMBL computer center[3]

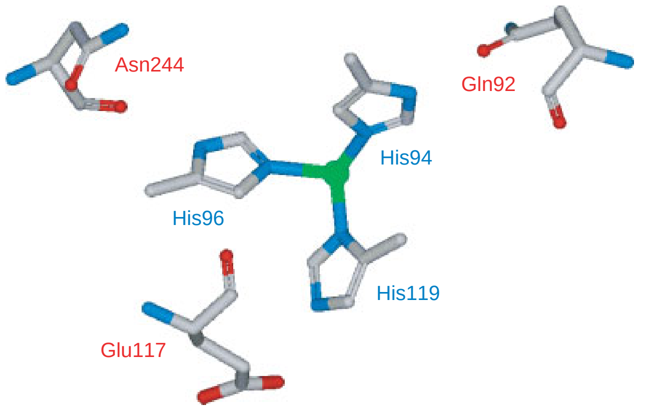

Figure 4 Catalytic zinc-binding site of human carbonic anhydrase II (pdb# 1CA2[12]) showing the zinc ligands NE2 of His94 and His96 and ND1 of His119 and their oxygen atom 'orienters' from Gln92, Ans244, and Glu117 respectively. Structure prepared using DS ViewerPro 5.0 Accelrys Inc. San Diego, CA

of these enzymes readily allow formation of zinc hydroxide, which can then add OH^- to CO_2 to form $HCO_3{}^-$. The amino acids adjacent to these zinc ligands are also highly conserved compared to the rest of the protein.[3] Thus, while the similarity scores for this set of proteins is between 60 to 99% the metal-binding site ligand sequence (9 amino acids used for each region) is above 90% for the majority of the sequences. In terms of identity of amino acids the overall structures are 35 to 95% identical while the metal-binding site sequences are 60 to 100% conserved. One of the reasons for this is that H-bonds are formed between Gln92 amide nitrogen and His94 and between the Glu117 carboxyl group and His119 (Figure 4). These interactions likely stabilize zinc binding and influence the function of the zinc in catalysis. In addition, the backbone carbonyl of Asn 244 accepts a H-bond from His96 and the hydroxyl group of Thr199 accepts a hydrogen bond from the zinc-bound water.[11] These residues are also conserved in all the carbonic anhydrase I-V enzymes.

Secondary ligand interactions are postulated to be involved in strengthening the metal complexation and/or modulating the nucleophilicity of the zinc-bound water.[13] Both interactions occur in the case of carbonic anhydrase based on the examination of functional and structural consequences of mutating the orientating residues Gln92, Glu117, Asn244 and Thr199.[11,14,15] The results indicate the zinc affinity is reduced by about a factor of five- to ten-fold when a native H-bond is eliminated. The effects also appear to be additive. Thus, the combined mutations of Gln92Ala and Glu117Ala leads to a 40-fold increase in the dissociation constant for zinc while the individual mutations lead to 4- and 10-fold increases, respectively.[11] The weakened binding of zinc is largely accounted for by an increased off-rate constant for zinc dissociation.

These secondary protein interactions would also be expected to affect the charge on the zinc. The interaction of hydrogen donating or accepting groups to the zinc ligands might therefore modulate the pK_a of the catalytic zinc-bound water resulting in changes in the nucleophilicity of the water and the ease at which it can expand its coordination shell or allow the zinc-bound water or hydroxide to be displaced. The pH dependence of the carbonic anhydrase II catalyzed hydrolysis of *p*-nitrophenylacetate was used to examine this postulate. In the wild type enzyme, it is characterized by a pK_a of 6.8, which is believed to reflect the ionization of the zinc-bound water molecule.[11] In the case of the Gln92Glu mutation in carbonic anhydrase II, a neutral hydrogen bond acceptor is replaced by a negatively charged acceptor. The positive charge on the zinc should therefore be reduced, which in turn should make the ionization of the water more difficult. The results of the functional studies confirm this relationship since the kinetically determined pK_a for the water increases by 0.7 units for this mutation.[11]

The reverse effect is expected for a mutation that removes this negative charge since this should increase the charge on the zinc leading to a lower pK_a for ester hydrolysis. Replacing Glu117 with Asp led to a slight decrease of 0.2 units consistent with a less favorable interaction of the Asp117 carboxylate with the His119 imidazole group. However, the results with Glu117Ala did not agree with the expectations. The pK_a values for the native and Glu117Ala mutant are 6.8 and 6.9 respectively. The value for the Ala mutant was expected to be lowered by as much as 1 unit owing to the loss of the anionic interaction with the His ligand. The X-ray studies found a chloride ion binding in the crystalline Glu117Ala mutant in the region of the Glu-117 carboxylate-His-119 interaction of the native enzyme.[15] The kinetic assays didn't contain any chloride ions but did use 0.1 M sulfate for controlling ionic strength.[11] If sulfate can bind in the same region as chloride, His119 may still have an interaction with an anionic species.

However, inspection of the X-ray structure of the native enzyme suggests another explanation (Figure 5). There are

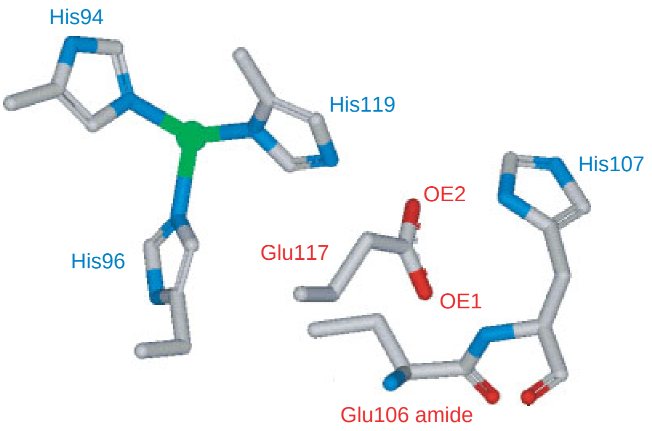

Figure 5 H-bonds to the side-chain carboxyl group of Glu117 of human carbonic anhydrase II (pdb# 1CA2[12]). Structure prepared using DS ViewerPro 5.0 Accelrys Inc. San Diego, CA

several potential H-bonds for the carboxyl group of Glu117 with other amino acids in its vicinity in the native enzyme. Thus, the OE2 of Glu117 is 2.57 Å and 2.93 Å from the NE2 of His119 and ND1 of His107, respectively (pdb # 1CA2[12]). In addition, the OE1 of Glu117 is 2.83 Å and 2.87 Å from the amide NHs of both His107 and Glu106. This intricate pattern of H-bonds would be expected to reduce the effect of relaying negative charge to the zinc ligand His119. Removal of this carboxyl group would therefore not be expected to change the charge on the His ligand in agreement with the results. The loss of the extensive H-bonding network to this ligand might be expected to be reflected in a relaxing of the conformation of this ligand, which could in turn lead to an increased off-rate for zinc dissociation. This is in fact what occurs for mutations of this ligand in contrast to the same mutations for His94 that does not have as extensive H-bonding network. Thus, the conversion of His94Ala leads to a 2-fold increase in the off-rate constant for zinc dissociation, while that for His119Ala leads to a 300-fold increase.[11] It is also of interest to note that a new H-bond is gained in the mutation of Gln92Glu. In this case, the OE1 oxygen of the carboxyl group of Glu92 is 2.94 Å from ND1 of His94 and is 3.01 Å from the amide NH of Phe93. This would tend to reduce the effect of relaying negative charge to the zinc and might place more constraint on the zinc ligand, His94, in the mutant enzyme. The fact that the zinc off-rate constant is now 6-fold slower than that of the native enzyme[11] is consistent with the increased H-bonding network found in the mutant enzyme.

3.1.2 Carbonic Anhydrase: Hydrophobic Orienters

The hydrophobic residues at positions 93, 95 and 97 are also highly conserved for this family of enzymes (Figure 3).[3] These residues are generally Phe for positions 93 and 95 and Trp for 97. The aromatic residues would be expected to restrict the motion of the His ligands and/or provide an environment of low dielectric constant that would enhance electrostatic interactions.[16] A cassette mutagenesis technique was used to select CA II enzymes mutated at positions 93, 95 and 97 that retained high zinc affinity.[17] The best variant enzymes contained Ile, Phe, Leu, and Met at position 93; Ile, Leu, and Met at position 95 and Trp or Val at position 97 in general agreement with what is found for this class of enzymes. When small hydrophilic residues are introduced at these positions, the zinc affinity decreases. Thus, the Thr-**His**-Ser-**His**-Val mutant compared to the native Phe-**His**-Phe-**His**-Trp enzyme has a 110-fold increased K_D for zinc essentially owing to an increase in the off-rate constant of 400-fold. The k_{cat}/K_m for the CO_2 hydrase and esterase activity is decreased 90- and 30-fold, respectively, but the pK_a for esterase activity doesn't change. The better zinc-binding and higher catalytic efficiency correlate with the combined volume of the residues at positions 93, 95, and 97.[17]

The effect of these amino acids on the zinc dissociation rate constant was also examined. Replacement of the hydrophobic amino acid by Ser at any position increased the zinc off-rate constant. The results suggested replacing the large aromatic residues at positions 93, 95, and 97 with smaller residues may increase the conformational mobility of the β-strand, permitting the adjacent histidines that coordinate zinc (His94 and His96) additional flexibility.[18] The variants with the slowest dissociation rate constant retain Trp at position 97. Comparison of the properties of the variants Ile 93 Met 95 Trp 97 and Ile 93 Met 95 Val 97 shows the affinity constant values for zinc are comparable, whereas the zinc dissociation rate constant increases 10-fold for substitution of Trp 97 with Val in agreement with the postulate of the aromatic residues anchoring the β-strand to reduce the conformational flexibility of His94 and His96 metal ligands.[18] The reason Trp97 is able to do this better than a Phe residue may be due to its indole NH. Inspection of the X-ray structure of the native enzyme (pdb # 1CA2[12]) indicates this NH is within H-bonding distance (2.75 Å) from the backbone amide carbonyl oxygen of Met241 (Figure 6). This amino acid is the last residue of a short (3-residue) β-strand and two amino acids removed from Asn244 that H-bonds His96 through its side-chain amide group. Disruption of this H-bond may therefore have an added effect on the increased zinc off-rate constants whenever Trp97 is replaced by other amino acids.

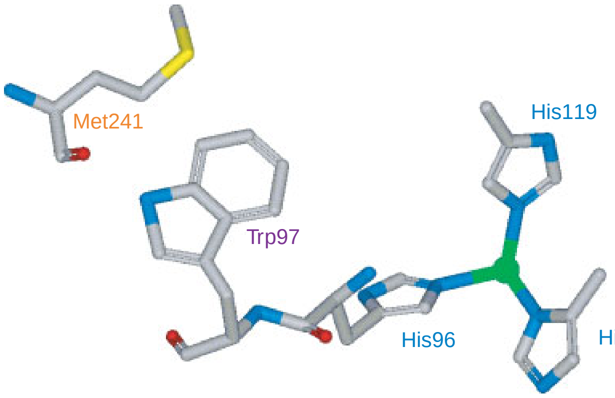

Figure 6 Amide of Met241 of human carbonic anhydrase II H-bonds to the indole NH of Trp100 (pdb# 1CA2[12]). Structure prepared using DS ViewerPro 5.0 Accelrys Inc. San Diego, CA

The results of studies of the cobalt- and copper-substituted mutants have indicated these hydrophobic residues may be important to retaining a tetrahedral geometry for the zinc site.[18] The correlation of the additive hydrophobicity of the amino acids bordering the metal ligands to copper binding strength is the reverse of that observed for zinc and cobalt. The lower their collective hydrophobicity the better the copper binding. The mutant enzyme Thr93Ser95Val97 binds copper 8×10^5 times more tightly than zinc. The inactive copper-substituted native enzyme has a bipyramidal geometry.[19] The results suggest the hydrophobic cluster of amino acids orients the His ligands to stabilize a distorted-tetrahedral geometry and to destabilize the bipyramidal geometry observed when copper binds.[18]

Although copper binds tighter than zinc to all forms of the enzyme tested, zinc stabilizes the protein fold better as judged by solvent-induced denaturation experiments. In addition the dissociation rate constant for zinc is about 100 times slower than copper suggesting the zinc is kinetically trapped once folding has occurred. This may thus be a physiological means by which metal ion specificity is achieved.[18]

3.1.3 Metalloproteases

The closely linked family of carboxypeptidases, CPD, and large group of proteases sharing an HExxH zinc signature serve to illustrate the variation in the level of scaffolding even in such closely related enzymes.[20] The CPD A family includes the A1-A5, B, B3, and U (R) enzymes (MEROPS M14A family)[21] while the CPD E family contains the D, E, X1, X2, and Z enzymes (MEROPS M14B family).[21] Both carboxypeptidase subfamilies show strong conservation of the ligands to the zinc (Table 1) and have an Asp residue from the C-terminal side of the first His ligand that H-bonds to its nonmetal bound NH (Table 2). This residue is conserved in 90 of the 92 sequences reported. This interaction will likely stabilize the zinc-binding site and make the ionization of the zinc-bound water more difficult since the negative charge on the carboxylate oxygen will be transmitted to the metal through the aromatic imidazole ring. The M14 subclasses of carboxypeptidases differ in some likely important aspects in their secondary ligand shell. The residues on each side of the second ligand, L_2, of the short spacer for the CPD A class are Arg71 and Trp73. The Arg residue is invariant in 56/56 sequences and the Trp residue in 53/56 (3 are His) sequences. In the case of the CPD E class, the L_2 minus one residue is Asn or Asp in 34/36 sequences while the residue equivalent to Trp73 varies considerable and is generally much smaller (15Val, 9Ala, 5Thr, 5 Pro, 1E, and 1 W). Trp residues can often stabilize the zinc binding to its ligands (see above) so its replacement by relatively small amino acids could destabilize zinc binding and/or increase the off-rate constant for zinc. The replacement of the positive Arg residue by a negatively charged Asp or neutral Asn residue would also effect the charge in the active site, which in turn could effect specificity and function of the enzyme.

A large number of the catalytic zinc sites in metalloproteases have either two His and a Glu or an Asp or three His ligands (Table 1). It is therefore generally assumed these sites behave the same with respect to the stability and catalytic function of the metal. However, the scaffolding differs even in relatively closely related family groups (Table 2). Thermolysin, neprilysin, mono-zinc aminopeptidases (represented by leukotriene hydrolase), matrix metalloproteinases, snake venoms (ADAMS), astacin and serriatia all have an HExxH metal-binding sequence containing the catalytic group Glu. Nevertheless, they all differ in the type of H-bonding interactions that occur with the His ligands of the short spacer (Figure 7).

The catalytic zinc site of thermolysin contains His142 and His146 from the short spacer and Glu166 from the long spacer arm. In this case two other conserved amino acids from the long spacer arm make interactions with the ligands from the short spacer arm. Thus, the carboxamide group of Asn165

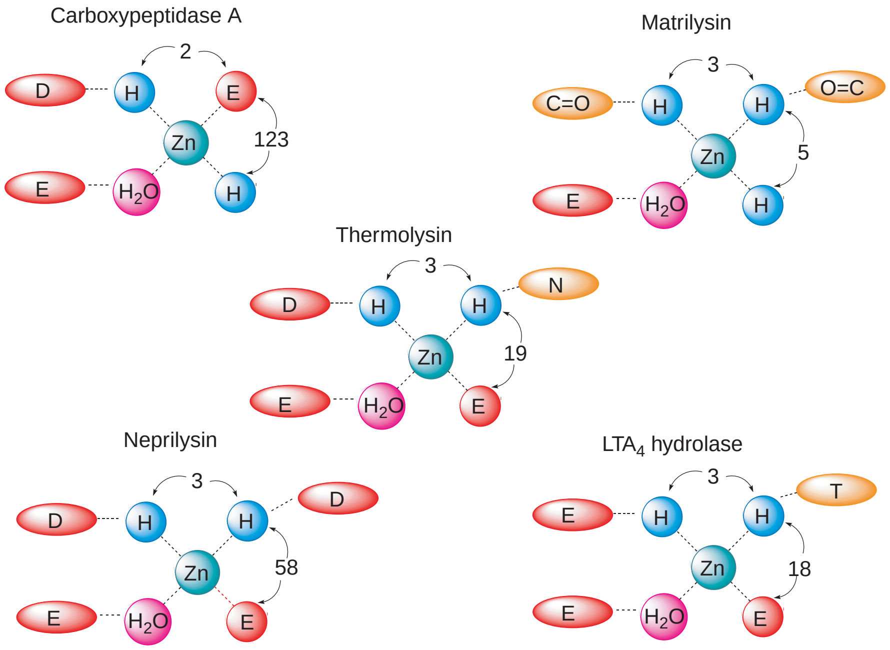

Figure 7 Scaffolding in catalytic sites of the metalloproteases, carboxypeptidase A (M14A), thermolysin (M4), matrilysin (M10A), neutral endoprotease (M13), NEP, Leukotreine Hydrolase,LTA_4 (M1)

Table 2 Scaffolding of catalytic and cocatalytic zinc sites in metalloproteases[a]

Enzyme family	MEROPS family	L_1	H-bond to L_1	Spacer	Residue conserved	L_2	H-bond to L_2	Spacer	Residue conserved
Carboxypeptidase A	M14A	His69	Asp COO	+72	55/56				
Carboxypeptidase E	M14B	His72	Asp COO^-	+71	35/36				
Thermolysin	M4	His142	Asp COO^-	+27	49/49	His146	Asn amideCO	+18	48/49
Neprilysin	M13	His583	Asp COO^-	+66	69/72	His587	Asp COO^-	+2	72/72
Leukotriene Hydrolase	M1	His295	Glu COO^-	+29	11/11	His299	ThrOH	+21	11/11
Matrix Metalloproteinases	M10A	His197	Leu/Ile/Val amideCO	+16	133/138	His201	Leu amideCO	+3	135/138
Serriatia	M10B	His176	Ile/Val/Leu amide CO	+36	21/22	His180	Leu amideCO	+3	22/22
Astacin	M12A	His92	Ile/Val amideCO	+53	64/70	His96	Phe amideCO	+3	57/70
Snake Venom Proteases	M12B	His142	Ile/Val/Leu amideCO	+22	132/137	His146	Ile/Met amideCO	+3	118/137
Aeromonas AP	M28A	His97	Asp COO^-	+1	9/9	Asp179	SerOH	+48	9/9
S. grieus AP	M28B	His85	Asp COO^-	+1	23/23	Asp160	SerOH	+42	19/23
E. coli AP	M24A	His171	Gly amideCO	+0	81/100	Glu204	Gln/His	+28	100/100

[a] X-ray structures (Table 1) and the sequence information in the MEPORS 1.7 database[21] are source of information.

H-bonds His146 and the carboxylate of Glu170 H-bonds the NH of His142. Both residues are highly conserved (Table 2). In the neprilysin family, two acidic (Asp) amino acids that are supplied by the short and long spacer arms serve this function. The replacement of the Asn amide H-bonding group observed in thermolysin by an Asp carboxylate group in neprilysin should change the charge on the zinc.

A bifunctional zinc metalloenzyme, Leukotriene A4 hydrolase, catalyzes the rate-limiting step in the biosynthesis of leukotriene B4, a classical chemoattractant and immune-modulating lipid mediator.[22] It also acts as an aminopeptidase and is inhibited by aminopeptidase inhibitors. It has been placed in the aminopeptidase M1 class[21] based on it sequence similarities to aminopeptidases. It uses the carboxylate of Glu235 and the OH of Thr321, residing in the C-terminal arm of the third ligand, to H-bond to the first two His ligands (Table 2). The Thr likely H-bonds through the oxygen to the NH of the His ligand, which should remove charge from the zinc but not as much as a carboxylate. Thr321 is conserved in all 11 of the identified leukotriene enzymes but in the greater M1 class this residue is not highly conserved being Ala in several. The Glu325 residue in LTA4 hydrolase is also conserved in 11/11 sequences while in the greater aminopeptidase class this residues is Glu in several, replaced by Asp for the Ala aminopeptidases and varies greatly for 30 members of the141 sequence-postulated aminopeptidases.

A superfamily of metalloproteases, encompassing the protease classes[21] M10A&B and M12A&B use backbone amide carbonyls to H-bond the first two His ligands (Table 2). The amide carbonyl of the residue 3 amino acids away from the second His ligand on its C-terminal side H-bonds this His in all the subclasses. It is a highly conserved Leu for members of M10A&B and either a Phe/Ile or Met for the majority of the members of the M12A&B (Table 2). The first His is also H-bonded by an amide carbonyl of a hydrophobic aliphatic amino acid with spacers characteristic of each subclass of protease, varying from 16 to 53 amino acids away. The use of amide carbonyls to H-bond the His ligands would increase the positive charge on the zinc compared to the use of one or two carboxylates for the thermolysin and neprilysin families (Table 2). This in turn could favor the ionization of the zinc-bound water and the use of hydroxide as a nucleophile.

Similar scaffolding interactions occur in the cocatalytic sites of aminopeptidases as well (Table 2). A second type of interaction occurs in many of these sites. When only one of the oxygens of an Asp or Glu ligand binds the metal the other oxygen forms a H-bond with a Ser or Gln or its isosteric amino acid His. The particular type of interactions are again highly conserved and characteristic of the class of peptidase.

These secondary ligand interactions will likely effect the stability of the zinc site, the dissociation rate constant for zinc and the manner in which zinc participates in catalysis. Thus disruption of these interactions could lead to weakened metal binding and inactivation of the enzyme. If the secondary ligand changes the charge on the catalytic metal, it will change the capacity of the metal to act as a Lewis acid catalyst as well as effect its ability to influence the ionization of the metal-bound water.

3.2 Inhibition of Zinc Enzyme Catalysis

Since the zinc-bound water is one of the most critical components of the catalytic zinc site, there are three ways that one can envision inhibiting the metalloenzyme. Thus inhibition should occur if a potential inhibitor can displace the water by binding directly to the zinc, or remove the zinc ion from the protein or bind a second zinc ion to the catalytic zinc-bound water and/or another catalytic group (Figure 8).

3.2.1 *Inhibition of Catalysis by Removing the Zinc-bound Water or the Zinc*

The importance of zinc enzymes in both normal and pathological processes makes them targets for drug design. The active-site zinc in these enzymes is a particularly attractive target because the strength of a chelator-metal interaction increases the potency and specificity of an inhibitor. Zinc metalloprotease inhibitors are usually designed to inactivate the enzyme by displacing the zinc-bound water and forming a stable ternary complex with the enzyme and active-site zinc. The success of this approach with the angiotensin-converting enzyme (ACE) inhibitor Captopril ([2S]-N-L-3-mercapto-2-methyl-propionyl-L-proline) on the treatment of hypertension[23] led to the design of many types of metal-binding agents that displace the metal-bound water and in addition are designed to mimic the transition state of the enzyme. Popular groups are hydroxamates and thiolates for the C-terminal side, phosphoryl goups for the N-terminal side

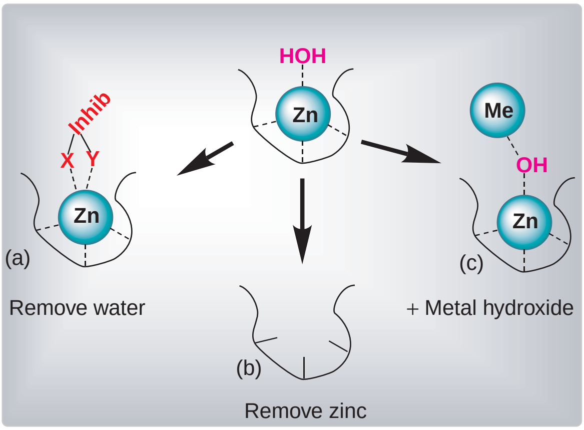

Figure 8 Inhibition of zinc metalloenzymes is accomplished by: (a) an Inhibitor displacing the zinc-bound water, (b) removing the metal, or (c) bridging an inhibitory zinc to the catalytic zinc

and carboxyalkyl and phosphinic acids as transition state or tetrahedral intermediate mimics.[24] Specificity can be built into the inhibitor on either side of the metal-binding ligand. Many of the crystal structures of zinc enzymes reported in the literature are in fact ternary complexes where the zinc-bound water has been displaced by the inhibitor. An excellent source of information on natural metalloprotease inhibitors is the MEROPS protease database.[21]

While there has been extensive research on inhibitors that bind by displacing the catalytic zinc-bound water, relatively little is known about the molecular mechanisms of how a metal-binding agent or chelator removes zinc.[25,26] In most cases, the zinc dissociation rate constant for the metalloenzyme is the controlling factor for such inhibition. D-penicillamine (D-PEN), a drug used for many years in the treatment of rheumatoid arthritis and Wilson's disease (*see* ***Metal-related Diseases of Genetic Origin***), was recently shown to be capable of catalyzing the removal of the metal from zinc proteases.[27] It is a member of the Cys family of amino acids. It differs from D-Cys by the presence of two methyl groups on the β-carbon. D-Cys inhibits carboxypeptidase A by displacing the zinc-bound water as might be expected since it contains a sulfhydryl binding group.[28] D-PEN in marked contrast inhibits by increasing the zinc dissociation rate constant for CPD by 420-fold and then acting as the receptor of the freed zinc ion.[27]

Complete removal of zinc and thus inactivation of the enzyme can be accomplished in these systems at low D-PEN concentrations if a secondary scavenger chelator is added to the system. Such chelators bind metal that has been released from the enzyme but do not participate in the release.[25,26] In the case of carboxypeptidase A, μM thionein (apo-metallothionen; *see* ***Metallothioneins***) inhibits catalysis by only about 10% over a 15-min period consistent with its action as a secondary chelator.[3] However, in the presence of 250 μM D-PEN and μM thionein total inhibition is achieved in less than 15 min. D-PEN accelerates zinc equilibration between carboxypeptidase A and thionein (Scheme 1). This is accomplished by D-PEN catalyzing the release of Zn from the enzyme. Since D-PEN is in vast excess over both the enzyme and thionein, the enzyme-released zinc would be expected to bind to D-PEN first. However, since thionein binds zinc more tightly than D-penicillamine and can accept 7 moles of zinc per mole of thionein, it should be the ultimate acceptor of the released zinc.

Consequently, the *in vivo* potency of D-PEN as a zinc enzyme inhibitor can be augmented by coadministration of secondary chelators or through the presence of natural chelators such as thionein or other metal-binding species. From a physiological perspective, such a mechanism of inhibition would be essentially irreversible, given the minuscule levels of *free* zinc believed present in the body.[29]

$$\text{EZn} + \text{D-PEN} \rightleftharpoons \text{D-PEN}{\bullet}\text{E}{\sim}\text{Zn} \qquad [1]$$

$$\text{D-PEN}{\bullet}\text{E}{\sim}\text{Zn} \rightleftharpoons \text{Zn}^{2+} + \text{D-PEN}{\bullet}\text{E} \qquad [2]$$

$$\text{Zn}^{2+} + \text{D-PEN} \rightleftharpoons \text{Zn(D-PEN)}_2 \qquad [3]$$

$$\text{T} + \text{Zn(D-PEN)}_2 \rightleftharpoons \text{Zn}_7\text{T} + \text{D-PEN} \qquad [4]$$

Scheme 1

3.2.2 *Inhibition of Enzyme Catalysis by Zinc*

Investigations into the metalloenzyme nature of an enzyme frequently involves an attempt to inhibit it with a chelator, followed by reversal of any inhibition by adding excess metal.[26] If excess zinc doesn't reverse the inhibition, it may be due to the fact that zinc can inhibit the zinc enzyme. A considerable amount of anecdotal information exists that zinc inhibits zinc enzymes but how it accomplishes it is not well established. The most thorough study of its mechanism of inhibition is on CPD A.[30,31]

A combination of steady-state and presteady sate kinetic and spectral and chemical modification studies led to a mechanistic scheme in which inhibition occurs through the binding of the zinc-monohydroxide species to the active EH species of the enzyme (Scheme 2).[2] The pH independent constant for the inhibition by zinc is 0.71 μM. The derived pK_a of 6 for the inhibition studies agrees with the corresponding value obtained in peptide hydrolysis experiments for the group, EH_2, whose ionization leads to formation of the catalytically active form of the enzyme.

The ionizable ligand, EH_2, is assigned to Glu270, since chemical modification of this residue with CMC (1-cyclohexyl-3-(2-morpholinoethyl) carbodiimide) decreases the binding affinity of carboxypeptidase A for zinc and lead by more than 60- and 200-fold, respectively.[31] A bridging interaction between the Glu270-coordinated zinc hydroxide is implicated by the ability of Zn and Pb to induce a marked increase in the visible absorption spectrum of the cobalt enzyme within 20 ms of mixing 10^{-4} M Zn or Pb with 10^{-4} M cobalt enzyme.[31]

Based on the spectro-kinetic and chemical modification studies, a binding mode for the inhibitory zinc ion was proposed to account for its inhibition (Figure 9).[30] The zinc-monohydroxide ion binds to the ionized carboxylate of Glu270 and displaces the zinc-bound water. The inhibitory zinc bridging interaction explains both the loss of metal binding upon chemical modification of Glu270 or lowering pH as well as the increase in absorbance in the cobalt enzyme upon binding lead or a zinc ion. Removal of the Glu270 carboxylate through protonation or chemical modification should decrease inhibitory metal binding. Replacement of the catalytic cobalt-bound water molecule with the hydroxide anion should lead to an increase in visible absorbance (as is observed when azide binds to the metal). A water molecule and a chloride anion complete the zinc inhibitory site since chloride enhances the inhibition by zinc and lead. The K_i values for the charge-neutral Zn(OH)Cl and Pb(OH)Cl are both about 5×10^{-7} M.[30] If the inhibitory

$$Zn^{2+} \overset{K_1}{\rightleftharpoons} ZnOH^{+} \overset{K_2}{\rightleftharpoons} Zn(OH)_2 \overset{K_3}{\rightleftharpoons} Zn(OH)_3^{-} \overset{K_4}{\rightleftharpoons} Zn(OH)_4^{2-} \qquad [5]$$

$$EH{\cdot}ZnOH^{+} \overset{K_{I,\,lim}}{\rightleftharpoons} EH + ZnOH^{+} \qquad [6]$$

$$EH_2 \overset{K_{EH_2}}{\rightleftharpoons} EH + H^{+} \qquad [7]$$

Scheme 2

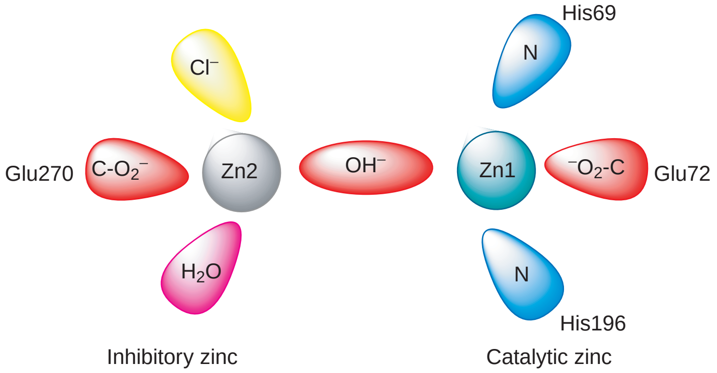

Figure 9 Schematic of inhibitory zinc-binding site in carboxypeptidase A

metal-monohydroxide complex is charge-neutralized by a multidentate ligand that can bind to other active-site residues, an even lower inhibition constant can be anticipated. Such inhibitory complexes could be very important to regulatory processes and/or toxicological processes involving Pb or other heavy metals with zinc enzymes.

This mode of zinc inhibition is confirmed in its entirety by two different crystallography studies of carboxypeptidase A.[32,33] A 1.7 Å structure of the crystalline carboxypeptidase A that was dialyzed versus 0.33 mM $ZnCl_2$ reveals a second zinc bound in a distorted tetrahedron composed of the carboxylate of Glu270, a water molecule, a chloride ion and a hydroxide ion.[32] The hydroxide forms a 114° angular bridge between the inhibitory and the catalytic zinc ions. The inhibitory zinc holds the hydroxide at the same location as the catalytic zinc-bound water molecule in the uninhibited enzyme. Superposition of the benzylsuccinate inhibitory complex on the $ZnOH^+$ inhibited complex demonstrates that the carbonyl group of the inhibitor and the inhibitory zinc ion are almost the same indicating the second zinc ion should interfere with proper positioning of the substrate.[32] This is consistent with the competitive inhibition observed with both zinc and lead.[30]

A similar type inhibitory zinc-binding site is observed in crystals of thermolysin.[34] The features have been compared to those for carboxypeptidase A.[32] The inhibitory zinc to catalytic zinc distance is 3.2 Å for thermolysin and 3.3 Å for carboxypeptidase A. A water/hydroxide bridges the two sites with a similar geometry, 116° in thermolysin and 114° in carboxypeptidase A. In thermolysin, the coordination sphere is completed by Tyr157, His231 and one of the carboxylate oxygens of Glu166. The latter is particularly interesting since it is the third ligand to the catalytic zinc as well. This inhibitor site therefore resembles the cocatalytic sites seen in many hydrolytic enzymes (Table 3). It therefore means the structural detection of multiple metal-binding sites should always be accompanied with functional studies to discern whether the metal site is active or inhibitory.

This type of inhibitory zinc binding is also observed in other zinc enzymes. The zinc-dependent UDP-3-O-acyl-N-acetylglucosamine deacetylase (LpxC) catalyzes the first committed step in the biosynthesis of lipid A, the hydrophobic anchor of lipopolysaccharide (LPS) that constitutes the outermost monolayer of gram-negative bacteria.[35,36] The catalytic zinc is bound to the NE2 nitrogens of His79 and His242, and an oxygen of the carboxyl group of Asp238 (Table 1).[35,36] (Note the spacing of the first amino acids differs in these studies owing to the numbers given). Mutation of Glu78 to Ala removes zinc inhibition of the enzyme.[36] Based on this finding and the earlier studies of carboxypeptidase A,[30–32] the authors proposed the inhibitory zinc bridges to the catalytic zinc by a water/hydroxide ion. Addition of excess zinc to the crystalline enzyme leads to the observation of two

Table 3 Cocatalytic zinc sites^a

Enzyme	PDB#	Metal	R, Å	L$_1$	X	L$_2$	Y	L$_3$	Z	L$_4$	L$_5$
Class I: Oxidoreductases											
Superoxide Dismutase Family											
Bovine	2SOD	Cu(II)	6.2	His$_{\beta}$	1	His$_{\beta}$	14	***His***$_{\beta}$	56	His$_{\beta}$	Solv
		Zn		***His***$_{\beta}$	7	His	8	His$_{2b\beta}$	2	Asp$_{\beta}$	
Human	1SPD	Cu(II)	5.5	His$_{\beta}$	1	His$_{\beta}$	14	***His***$_{\beta}$	56	His$_{\beta}$	
		Zn		***His***$_{\beta}$	7	His	8	His$_{2b\beta}$	2	Asp$_{\beta}$	
Frog (*Xenopus laevis*)	1XSO	Cu(II)	6.0	His$_{\beta}$	1	His$_{\beta}$	14	***His***$_{\beta}$	56	His$_{\beta}$	Solv
		Zn		***His***$_{\beta}$	7	His	8	His$_{2b\beta}$	2	Asp$_{\beta}$	
Spinach (*Spinacia oleracea*)	1SRD	Cu(II)	6.0	His$_{\beta}$	1	His$_{\beta}$	14	***His***$_{\beta}$	56	His$_{\beta}$	
		Zn		***His***$_{\beta}$	7	His	8	His$_{2b\beta}$	2	Asp$_{\beta}$	
Yeast (*S. cerevisiae*)	1SDY	Cu(II)	6.1	His$_{\beta}$	1	His$_{\beta}$	14	***His***$_{\beta}$	56	His$_{\beta}$	Solv
		Zn		***His***$_{\beta}$	7	His	8	His$_{2b\beta}$	2	Asp$_{\beta}$	
Escherichia coli	1ESO	Cu(II)	6.5	His$_{\beta}$	1	His$_{\beta}$	14	***His***$_{\beta}$	56	His$_{\beta}$	
		Zn		***His***$_{\beta}$	7	His	8	His$_{2b\beta}$	2	Asp$_{\beta}$	
Salmonella tryphimurium	1EQW	Cu(II)	6.2	His$_{\beta}$	1	His$_{\beta}$	14	***His***$_{\beta}$	56	His$_{\beta}$	
		Zn		***His***$_{\beta}$	7	His	8	His$_{2b\beta}$	2	Asp$_{\beta}$	
Photobacterium leiognathi	1YAI	Cu(II)	6.2	His$_{\beta}$	1	His$_{\beta}$	22	***His***$_{\beta}$	54	His$_{\beta}$	
		Zn		***His***$_{\beta}$	8	His	8	His$_{2b\beta}$	2	Asp$_{\beta}$	
Brucella abortus		Cu(II)		His	1	His	22	***His***	54	His	
		Zn		***His***	8	His	7	His		?	
Actinobacillus pleuropneumoniae	2APS	Cu(II)	6.4	His$_{\beta}$	1	His$_{\beta}$	22	***His***$_{\beta}$	55	His$_{\beta}$	
		Zn		***His***$_{\beta}$	8	His	8	His$_{2b\beta}$	2	Asp$_{\beta}$	
Yeast (*Candida albicans*)	1YSO	Cu(I)	6.5	His$_{\beta}$	1	His$_{\beta}$	71	–		His$_{\beta}$	
		Zn		His$_{\beta}$	7	His	8	His$_{2b\beta}$	2	Asp$_{\beta}$	
Yeast (*S. cerevisiae*)	2JCW	Cu(I)	6.7	His$_{\beta}$	1	His$_{\beta}$	71	–		His$_{\beta}$	
		Zn		His$_{\beta}$	7	His	8	His$_{2b\beta}$	2	Asp$_{\beta}$	
Bovine	1Q0E	Cu(I)	6.9	His$_{\beta}$	1	His$_{\beta}$	71	–		His$_{\beta}$	
		Zn		His$_{\beta}$	7	His	8	His	2	Asp$_{2b\beta}$	
Class III: Hydrolase											
Phosphatase Family											
E. coli	1ALK	Zn1	4.0	Asp$_{\alpha}$	3	His$_{a\alpha}$	80	His		H_2O	
		Zn2	4.6	His	0	Asp$_{2a\beta}$	266	Ser$_{b\alpha}$	50	***Asp***$_{\beta}$ (N)	
		Mg		***Asp***$_{\beta}$	103	Thr$_{\alpha}$	166	Glu$_{\beta}$		H_2O	

(cont'd overleaf)

Table 3 cont'd

Enzyme	PDB#	metal	R, Å	L_1	X	L_2	Y	L_3	Z	L_4	L_5
Human	1EW2	Zn1	4.0	Asp$_{\alpha}$	3	His$_{\alpha}$	111	His		H_2O	
		Zn2	4.8	His$_{L}$	0	Asp$_{L}$	264	Ser$_{b\alpha}$	49	***Asp***$_{\beta}$ (N)	
		Mg		***Asp***$_{\beta}$	112	Ser$_{\alpha}$	155	Glu$_{\beta}$		H_2O	
Shrimp	1 KH7	Zn1	4.5	Asp$_{\alpha}$	3	His$_{a\alpha}$	112	His		H_2O	
		Zn2	4.5	His$_{L}$	0	Asp$_{L}$	269	Ser$_{b\alpha}$	48	***Asp***$_{\beta}$ (N)	
		Zn3		***Asp***$_{\beta}$	111	His$_{b\alpha}$	1	Thr$_{\alpha}$	158	Glu$_{\beta}$	H_2O
E. coli D153H	2ANH	Zn1	4.1	Asp$_{\alpha}$	3	His$_{a\alpha}$	80	His		H_2O	
		Zn2	4.7	His	0	Asp$_{2a\beta}$	266	Ser$_{b\alpha}$	50	***Asp***$_{\beta}$ (N)	
		Zn3		***Asp***$_{\beta}$	101	His$_{b\alpha}$	1	Thr$_{\alpha}$	166	Glu$_{\beta}$	
E. coli D153H,D330N	1KHK	Zn1	4.4	Asp$_{\alpha}$	3	His$_{a\alpha}$	80	His		H_2O	
		Zn2	4.7	His$_{L}$	0	Asp$_{L}$	266	Ser$_{b\alpha}$	50	***Asp***$_{\beta}$ (N)	
		Mg		***Asp***$_{\beta}$	103	Thr$_{\alpha}$	166	Glu$_{\beta}$		H_2O	
B. cereus phospholipase C1	1 AH7	Zn1	6.1	Glu$_{\alpha}$	3	His$_{\alpha}$	13	His$_{\alpha}$ (N)		H_2O	
		Zn2	3.6	***Asp***$_{a\alpha}$	3	His$_{\alpha}$	48	His	13	Asp$_{a\alpha}$ (N)	$\boldsymbol{H_2O}$
		Zn3		Trp$_{b\beta}$	12	His$_{\alpha}$	107	***Asp***$_{a\alpha}$		$\boldsymbol{H_2O}$	
Clostridium absonum PLC	1OLP	Zn1	6.1	Glu$_{\alpha}$	3	His$_{\alpha}$	11	His$_{\alpha}$ (N)		H_2O	
		Zn2	3.4	***Asp***$_{\alpha}$	3	His$_{\alpha}$	57	His	11	Asp$_{a\alpha}$ (N)	$\boldsymbol{H_2O}$
		Zn3		Trp	9	His$_{\alpha}$	118	***Asp***$_{\alpha}$		$\boldsymbol{H_2O}$	
Clostridium perfringens α-toxin avian strain (SWCP)	1KHO	Zn1	6.3	Glu$_{\alpha}$	3	His$_{\alpha}$	11	His$_{\alpha}$ (N)		H_2O	
		Zn2	3.3	***Asp***$_{\alpha}$	3	His$_{\alpha}$	57	His	11	Asp (N)	
		Zn3		Trp	9	His$_{\alpha}$	118	***Asp***$_{\alpha}$			
bovine strain CER89L43, open	1CA1	Cd1	5.5	Glu$_{\alpha}$	3	His$_{\alpha}$	11	His$_{\alpha}$ (N)		H_2O	
		Cd2	3.5	***Asp***$_{\alpha}$	3	His$_{\alpha}$	57	His	11	Asp$_{a\alpha}$ (N)	H_2O
		Zn3		Trp	9	His$_{\alpha}$	118	***Asp***$_{\alpha}$			
bovine strain CER89L43, closed	1GYG	Zn2	3.4	***Asp***$_{\alpha}$	3	His$_{\alpha}$	57	His	11	Asp$_{a\alpha}$ (N)	
		Zn3		Trp	9	His$_{\alpha}$	118	***Asp***$_{\alpha}$			
P. citrinium P1 nuclease	1AK0	Zn1	5.9	Asp$_{a\alpha}$	3	His$_{\alpha}$	12	His (N)		H_2O	
		Zn2	3.7	***Asp***$_{\alpha}$	3	His$_{\alpha}$	55	His$_{a\alpha}$	14	Asp$_{\alpha}$ (N)	
		Zn3		Trp$_{2b\alpha}$	4	His$_{\alpha}$	113	***Asp***$_{\alpha}$		H_2O	
E. coli Endonuclease IV	1QTW	Zn1	4.7	His$_{\beta}$	1	Asp$_{b\beta}$	46	His$_{\alpha}$ (N)		H_2O	
		Zn2	3.4	***Glu***$_{\beta}$	33	Asp$_{\beta}$	36	His$_{\beta}$	44	Glu$_{a\beta}$	$\boldsymbol{H_2O}$
		Zn3		***Glu***$_{\beta}$	35	His$_{a\beta}$	39	His$_{\beta}$ (N)		$\boldsymbol{H_2O}$	
E. coli YcdX	1M68	Zn1	4.9	His	24	His$_{a\beta}$	153	His		H_2O	
		Zn2	3.4	His$_{2a\beta}$	1	His	63	***Glu***$_{\beta}$	118	Asp$_{2a\beta}$	$\boldsymbol{H_2O}$
		Zn3		***Glu***$_{\beta}$	27	His$_{2a\beta}$	29	His$_{2a\beta}$		$\boldsymbol{H_2O}$	

Phosphotriesterase Family										
Pseudomonas diminuta	1EYW	Zn1	3.5	His$_{a\beta}$	1	His	111	***Lys***$_{\beta}$ ***CO***$_{2}^{-}$	131	Asp$_{2a\beta}$	***OH***
		Zn2		***Lys***$_{\beta}$ ***CO***$_{2}^{-}$	31	His$_{\beta}$	28	His$_{a\beta}$		***OH***	
Escherichia coli	1BF6	Zn1	3.4	His$_{2a\beta}$	1	His	110	***Glu***$_{b\beta}$	117	Asp$_{2a\beta}$	***Unk***
		Zn2		***Glu***$_{b\beta}$	32	His$_{\beta}$	27	His$_{a\beta}$		***Unk***	
Purple acid phosphatase Family											
Kidney bean	1KBP	Fe(III)	3.3	Asp$_{\beta}$	28	***Asp***$_{\beta}$	2	Tyr$_{2a\beta}$	157	His$_{2b\beta}$	
		Zn		***Asp***$_{\beta}$	36	Asn$_{b\alpha}$	84	His$_{a\beta}$	36	His$_{2a\beta}$	H_2O
Rat	1QFC	Fe(III)	3.1	Asp$_{2a\beta}$	37	***Asp***$_{2a\beta}$	2	Tyr	167	His$_{b\beta}$	H_2O
		Fe(II)		***Asp***$_{2a\beta}$	38	Asn$_{b\alpha}$	94	His$_{a\beta}$	34	His$_{2a\beta}$	H_2O
Porcine (uteroferrin)	1UTE	Fe(III)	3.3	Asp$_{2a\beta}$	37	***Asp***$_{2a\beta}$	2	Tyr	167	His$_{b\beta}$	***OH***
		Fe(II)		***Asp***$_{2a\beta}$	38	Asn$_{\alpha}$	94	His$_{a\beta}$	34	His$_{2a\beta}$	***OH***
Human protein phosphatase I		Fe(III)	3.5–4.0	Asp	1	His	25	***Asp***	179	Tyr	***H$_2$O***
		Mn		***Asp***	31	Asn	48	His	74	His	***H$_2$O***
Human brain calcineurin	1AUI	Fe(III)	3.1	Asp$_{2a\beta}$	1	His$_{L}$	25	***Asp***$_{2a\beta}$	H_2O	***H$_2$O***	
		Zn		***Asp***$_{2a\beta}$	31	Asn$_{L}$	48	His$_{a\beta}$	81	His$_{2a\beta}$	***H$_2$O***
E. coli UDP-sugar hydrolase	1USH,1HP1	Zn1	3.3	Asp$_{2a\beta}$	1	His	40	***Asp***$_{2a\beta}$	169	Gln$_{b\beta}$	***H$_2$O***
		Zn2		***Asp***$_{2a\beta}$	31	Asn$_{2a\beta}$	100	His$_{\beta}$	34	His$_{a\beta}$	***H$_2$O***
Amidohydrolase Family											
Escherichia coli dihydroortase	1J79	Zn1	3.5	His	1	His	83	***Lys***$_{\beta}$ ***CO***$_{2}^{-}$	147	Asp	***OH***
		Zn2		***Lys***$_{\beta}$ ***CO***$_{2}^{-}$	36	His$_{\beta}$	37	His$_{\beta}$		***OH***	
Arthobacter aurescens	1GKR	Zn1	3.6	His	1	His	84	***Lys***$_{\beta}$ ***CO***$_{2}^{-}$	164	Asp$_{2a\beta}$	***OH***
L-hydantoise		Zn2		***Lys***$_{\beta}$ ***CO***$_{2}^{-}$	35	His$_{\beta}$	55	His$_{a\beta}$		***OH***	
Thermus sp. D-hydantoise	1GKP	Zn1	3.6	His	1	His	88	***Lys***$_{\beta}$ ***CO***$_{2}^{-}$	164	Asp$_{2a\beta}$	***OH***
		Zn2		***Lys***$_{\beta}$ ***CO***$_{2}^{-}$	32	His$_{\beta}$	55	His$_{a\beta}$		***OH***	
Bacillus stearothermophilus	1K1D	Zn1	3.0	His$_{2a\beta}$	1	His$_{L}$	89	***Lys***$_{\beta}$ ***CO***$_{2}^{-}$	164	Asp	***OH***
D-hydantoinase		Zn2		***Lys***$_{\beta}$ ***CO***$_{2}^{-}$	32	His$_{\beta}$	55	His$_{a\beta}$		***OH***	
Burkholderia picketti	1NFG	Zn1	3.2	His$_{2a\beta}$	1	His$_{L}$	88	***Lys***$_{\beta}$ ***CO***$_{2}^{-}$	164	Asp	***OH***
D-hydantoinase		Zn2		***Lys***$_{\beta}$ ***CO***$_{2}^{-}$	32	His$_{\beta}$	55	His$_{\beta}$		***OH***	
Escherichia coli	1ONW	Zn1	3.4	His$_{2a\beta}$	1	His$_{L}$	91	***Lys***$_{\beta}$ ***CO***$_{2}^{-}$	122	Asp$_{2a\beta}$	***H$_2$O***
isoaspartyl dipeptidase		Zn2		***Lys***$_{\beta}$ ***CO***$_{2}^{-}$	38	His$_{\beta}$	28	His$_{a\beta}$		***H$_2$O***	

(cont'd overleaf)

Table 3 cont'd

Enzyme	PDB#	metal	R, Å	L_1	X	L_2	Y	L_3	Z	L_4	L_5
Alcaligenes faecalis D-aminocyclase	1M7J	Zn1	3.2	His	1	His$_{2b\alpha}$	26	***Cys***		***Acetate***	
		Zn2		His$_{\beta}$	29	His$_{\beta}$	123	***Cys*** (N)		***Acetate***	
Pseudomonas putida creatininase	1Q3K	Zn1	3.5	His	8	***Asp***$_{\alpha}$	137	Glu$_{\alpha}$		***H_2O***	
		Zn2		Glu	10	***Asp***$_{\alpha}$	74	His$_{a\beta}$		***H_2O***	H_2O
Aminopeptidase Family											
bovine lens	1BLL	Zn1	2.9	***Glu***$_{b\alpha}$	1	Asp$_{L}$	76	***Asp***$_{2a\beta}$ (N)		***H_2O***	
		Zn2		Lys$_{\beta}$	4	***Asp***$_{2a\beta}$	17	Asp$_{2b\alpha}$	60	***Glu***$_{b\alpha}$	H_2O
Escherichia coli PepA	1GYT	Zn1	3.0	***Glu***$_{b\alpha}$	1	Asp	76	Asp$_{b\beta}$ (N)		***H_2O***	
		Zn2		Lys$_{\beta}$	22	Asp$_{2a\beta}$	60	***Glu***$_{b\alpha}$		***H_2O***	
Aeromonas proteolytica	1AMP, 1LOK	Zn1	3.5	***Asp***$_{2b\alpha}$	34	Glu	103	His		***H_2O***	
		Zn2		His$_{\beta}$	19	***Asp***$_{2b\alpha}$	61	Asp$_{a\beta}$		***H_2O***	
Streptomyces griseus	1XJO, 1QQ9	Zn1	3.6	***Asp***$_{2b\alpha}$	34	Glu	114	His		***H_2O***	
		Zn2		His$_{\beta}$	11	***Asp***$_{2b\alpha}$	62	Asp$_{a\beta}$		***H_2O***	
Saccharomyces kluyveri Ala Synthase	1R3N	Zn1	3.3	***Asp***	34	Glu	260	His		***H_2O***	
		Zn2		His$_{a\beta}$	10	***Asp***	100	His$_{\beta}$		***H_2O***	H_2O
Methionine aminopeptidases											
Escherichia coli methionine-1	1MAT	Co1	2.9	Asp$_{\beta}$	10	***Asp***$_{\beta}$	126	***Glu***$_{b\beta}$			
		Co2		***Asp***$_{\beta}$	62	His$_{\beta}$	32	Glu$_{a\beta}$	30	***Glu***$_{b\beta}$	
Pyrococcus furiosus methionine-2	1XGM	Co1	2.8	Asp$_{\beta}$	10	***Asp***$_{\beta}$	186	***Glu***$_{\beta}$		***H_2O***	
		Co2		***Asp***$_{\beta}$	59	His$_{\beta}$	33	Glu$_{a\beta}$	92	***Glu***$_{\beta}$	***H_2O***
Human methionine-2	1B59	Co1	3.1	Asp$_{\beta}$	10	***Asp***$_{a\beta}$	196	***Glu***$_{\beta}$		***H_2O***	
		Co2		***Asp***$_{a\beta}$	68	His$_{\beta}$	32	Glu$_{\beta}$	94	***Glu***$_{\beta}$	***H_2O***
Escherichia coli proline	1AZ9	Mn1	3.3	Asp$_{\beta}$	10	***Asp***$_{\beta}$	134	***Glu***$_{\beta}$		***H_2O***	H_2O
		Mn2		***Asp***$_{\beta}$	82	His$_{\beta}$	28	Glu$_{\beta}$	22	***Glu***$_{\beta}$	***H_2O***
Other peptidases											
Pseudomonas sp. CPD G_2	1CG2	Zn1	3.3	***Asp***$_{2b\alpha}$	34	Glu	208	His		***H_2O***	
		Zn2		His$_{\beta}$	28	***Asp***$_{2b\alpha}$	58	Glu$_{\beta}$		***H_2O***	
Lactobacillus delbrueckii PepV	1LFW	Zn1	3.8	***Asp***$_{2b\alpha}$	34	Glu	284	His -		***H_2O***	
		Zn2		His$_{\beta}$	31	***Asp***$_{2b\alpha}$	57	Asp$_{b\beta}$		***H_2O***	
S. tryphimurium Peptidase T	1FNO	Zn1	3.4	***Asp***$_{2b\alpha}$	33	Glu	204	His			
		Zn2		His$_{\beta}$	61	***Asp***$_{2b\alpha}$	55	Asp$_{a\beta}$			

Bacillus subtilis Dppa	1HI9	Zn1	3.2	***Asp***$_{\beta}$	1	Glu$_{2a\beta}$	49	His$_{a\beta}$		$\boldsymbol{H_2O}$	
		Zn2		***Asp***$_{\beta}$	95	His$_{2a\beta}$	28	Glu$_{\alpha}$		$\boldsymbol{H_2O}$	
Human renal dipeptidase	1ITU	Zn1	3.3	His$_{2a\beta}$	1	Asp$_{2b\alpha}$	102	***Glu***$_{\beta}$		H_2O	
		Zn2		***Glu***$_{\beta}$	72	His$_{L}$	20	His$_{2a\beta}$		H_2O	
Human Glyoxalase II	1QH3,1QH5	Zn1	3.3	His$_{2a\beta}$	1	His	53	His$_{L}$	23	***Asp***$_{L}$	$\boldsymbol{H_2O}$
		Zn2		Asp	0	His	74	***Asp***$_{L}$	38	His$_{\beta}$	$\boldsymbol{H_2O}$
***β*-lactamase Family**											
Bacillus cereus	1BMC	Zn1		His$_{2a\beta}$	1	His	60	His		H_2O	
Bacillus cereus	1BC2	Zn1	3.8–4.4	His$_{2a\beta}$	1	His	60	His		H_2O	
		Zn2		Asp	77	Cys$_{2a\beta}$	41	His		H_2O	H_2O
Bacteroides fragilis	1ZNB	Zn1	3.5	His	1	His	60	His		$\boldsymbol{H_2O}$	H_2O
		Zn2		Asp	77	Cys$_{2a\beta}$	41	His		$\boldsymbol{H_2O}$	H_2O
Pseudomonas aeruginosa	1DD6	Zn1	3.6	His$_{2a\beta}$	1	His	59	His			
		Zn2		Asp	76	Cys$_{2a\beta}$	38	His		H_2O	
Chryseobacterium meningosepticum	1M2X	Zn1	3.7	His$_{2a\beta}$	1	His	77	His		***Inh***	
		Zn2		Asp	100	Cys$_{2a\beta}$	41	His$_{\beta}$		***Inh***	
Stenotrophomonas maltophilia	1SML	Zn1	3.5	His	1	His	73	His$_{L}$		$\boldsymbol{H_2O}$	
		Zn2		Asp	0	His	135	His		$\boldsymbol{H_2O}$	H_2O
Fluoribacter gormanii	1K07	Zn1	3.7	His	1	His	73	His$_{L}$		***Glycerol***	
		Zn2		Asp	0	His	141	His$_{\beta}$		***Glycerol***	

---

[a] The amino acid residue that bridges the two-metal sites is shown in ***italic bold face***. When the symbol H_2O is given this may represent from one to three metal-bound water molecules. R is the distance between the metal atoms. When Trp is listed as a ligand, the α-amino and a amide carbonyl are the ligands. See footnote of Table 1 for the definitions of other terms.

zinc ions bound in the active site in much the same fashion as is observed in the metalloproteases discussed above.[35] The postulated inhibitory zinc ion binds 3.4 Å from the catalytic zinc (pdb 1P42). The second zinc binds in a tetrahedral coordination geometry to a solvent molecule, the NE2 nitrogen of His265, and an oxygen from the carboxyl groups of Glu78 and the fatty acid inhibitor, myristic acid.[36] The binding of the inhibitory zinc to the carboxylate of the myristic acid is reminiscent of the binding of similar inhibitory complexes in carboxypeptidase A.[31] The invariant residues, Glu 78 and His265, of the enzyme LpxC are believed to play the same roles in catalysis as Glu166 and His231 do in thermolysin on the basis of the structure of the inhibitory zinc site.

Examination of the crystals of yeast cytosine deaminase shows a second zinc ion coordinated to the active site by a bridging water/hydroxide ion to the catalytic zinc ion. This zinc ion has three other water molecules bound to it some of which have very short (∼1.8 Å) bonds to the second zinc.[37] This may represent an inhibitory zinc ion that has bound to the protein with more than one hydroxide ion coordinated to the zinc.

Zinc also inhibits a variety of nonmetalloenzymes.[3] Inhibition constants in the nM range are observed in some cases. In these situations it is possible that the zinc could be involved in regulating the activity of the enzyme. Thionein has been demonstrated to reverse the inhibition glyceraldehyde-3-phosphate dehydrogenase by zinc ions, suggesting the possibility that thionein (apo-metallothionien; *see* ***Metallothioneins***) can be involved in a regulatory capacity with zinc as its partner.[38]

The fact that zinc inhibits enzymes has also been used to design new serine protease inhibitors.[39,40] The type of zinc ligand is important to the inhibition. Thus the zinc-bound bis(5-amidino-2-benzimidazolyl)methane, BABIM, and derivatives of it inhibit several human serine proteases with an inhibition constant of 1 to 25 nM. Zinc increases the inhibition by the agent up to 10 000 times. For example, the K_i for BABIM inhibition of trypsin decreases from 19 µM to 5 nM in the presence of 100 nM zinc ions at pH 8.2.[39] The crystal structure of trypsin cocrystallized with BABIM and zinc shows zinc tetrahedrally coordinated to two nitrogens of BABIM and two of the catalytic triad residues, His57 and Ser195. This type of zinc-binding site is quite similar to that observed for the inhibition of zinc proteases by zinc ions. Thus, the inhibitory zinc is bridging two catalytic components His57 and Ser195 for trypsin and Glu270 and a zinc-bound hydroxide for carboxypeptidase A. In these enzymes, the zinc hydroxide and serine oxide are the nucleophiles and the glutamate carboxyl group and His imidazole are the general acid/base catalysts. Prostrate specific antigen, PSA, or prostrate kallikrein is a serine protease that is inhibited by zinc and mercury ions.[41] One of the three zinc-binding sites in the crystalline enzyme is to Asp91, His101 and His234 and a water molecule. It has been postulated that zinc binding could distort the catalytic triad through minor movements of His101 since it is next to catalytic triad residue Asp102.

3.3 Specific Zinc Enzymes

The large number of this class of enzymes makes it difficult to cover the properties of each specific member in any detail. Many have been commented on in other general reviews on this class of enzymes.[3,4] However, some brief comments will be made on some newer members.

3.3.1 Alcohol Dehydrogenases

The ligand nature of the catalytic zinc site varies considerably for the overall grouping of the dehydrogenases but is quite constant for the subfamilies (Table 1). The dimeric mammalian ADHs are NADH-dependent and have two Cys and one His as ligands to a catalytic zinc site (Table 1). The crystal structures of several tetrameric bacterial ADHs have been reported recently. The medium chain alcohol dehydrogenases from thermostable *Thermoanaerobacter brockii*, TBADH,[42,43] originally isolated from a Yellowstone Park hot spring, its mesophilic counterpart *Clostridium beijerinckii*, CBADH,[44] and the archaeon ADH from *Aeropyrum pernix*[45] are all NADP(H) dependent while the archaeon SsADH from *Sulfolobus solfataricus*[46] is NADH-dependent. The catalytic zinc sites of the former NADP(H)-dependent enzymes all have the Cys and His ligands separated by a spacer of 21 to 24 amino acids similar to other ADHs (Table 1). They differ in that the third ligand is now an Asp residue rather than a Cys. All have water as the fourth ligand.

The catalytic zinc site of the NADH-dependent archaeon SsADH is closer to the dimeric ADHs in that it has a Cys as its third ligand. The presumed fourth ligand water is not found, however. The Glu residue next to the second His ligand is now bound to the zinc.[46] The carboxylate oxygens of the equivalent Glu residue in the other tetrameric ADHs are 4 to 7 Å removed form the zinc (pdb files 1KEV, 1H2B, 1YKF). In CBADH this Glu residue is a zinc ligand in the Nicotinamide adenine dinucleotide phosphate (NADP)-free form of the enzyme.[42] However, the distance between the carboxylate oxygen and the zinc increases from 2.35 to 3.94 Å upon binding the coenzyme. In the human $\chi\chi$ alcohol dehydrogenase, ADH, the equivalent residue, Glu68 is observed 2.9 Å and 2.0 Å from the catalytic zinc in the A and B subunits respectively.[47] In other human and horse ADHs, the carboxylate oxygens are at least 4.7 Å from the catalytic zinc atom. The binding of the Glu to the zinc in this case may be a reflection of the involvement of Glu68 in the displacement of water in a late step-in catalysis as predicted by molecular dynamics calculations.[47,48]

3.3.2 Sorbitol Dehydrogenases

The Glu residue that is sometimes seen as a ligand in the ADHs is also a ligand in some of the structures of the sorbitol dehydrogenases (SDH) (Table 1). This enzyme and aldose reductase form the polyol pathway that interconverts glucose and fructose. Overproduction of the coenzyme NADH by SDH may play a role in diabetes-induced dysfunction in sensitive tissues.[49] Human SDH is a tetramer that has a catalytic zinc coordinated by Cys44, His69, Glu70 and a water molecule in both the apo and NAD^+ complex.[49] The inhibitor CP-162,572 coordinates the zinc through the N1 nitrogen of its pyrimidine ring and an oxygen of its hydroxymethyl substitutent causing the dissociation of Glu70. The inhibitor forms hydrophobic interactions to NADH and likely sterically occludes substrate binding.

The silverleaf whitefly, *Bemisia argentifolii* ketose reductase (BaKR), is tetrameric, with the monomer having a very similar fold to the alcohol dehydrogenases (ADHs).[50] The catalytic zinc ion is tetrahedrally coordinated to Cys41, His66, Glu67, and a water molecule in the enzyme form lacking its coenzyme NADP(H) as is seen in the hSDH. The residue equivalent to the third Asp ligand in the tetrameric ADHs is Glu152 in BaKR. The carboxylate of this residue hydrogen bonds the zinc-bound water. Glu152 has been reported to be the third ligand in rat SDH in place of the Glu67 observed in hSDH and BaKR.[51]

The sequence of *Bacillus stearothermophilus* glycerol dehydrogenase (GlyDH) indicates that it is a member of the third grouping of ADHs, the so-called iron-containing alcohol dehydrogenase family. However it has a strict dependence on zinc for activity.[52] It catalyzes the oxidation of glycerol to dihydroxyacetone (1,3-dihydroxypropanone) with concomitant reduction of NAD^+ to NADH. The catalytic zinc is bound to the NE2 nitrogens of His274 and His256, an oxygen of the carboxylate of Asp173 and a water molecule.[52] The ligand nature of the catalytic zinc site is similar to the tetrameric ADHs but the first cysteine ligand is now replaced by a histidine (Table 1).

3.3.3 Hydrolases

This is the largest class of zinc enzymes. The detailed description of the properties of just the metalloprotease group is a major section of a new handbook of proteases.[53] This perspective will therefore only highlight the results of a few novel findings in recent 3-dimensional structures.

Angiotensin-converting enzyme (ACE) plays a critical role in cardiovascular function by catalyzing the cleavage of the carboxy-terminal His-Leu dipeptide from angiotensin I to produce a potent vasopressor octapeptide, angiotensin II. Inhibitors of hypertension were designed in the 1970s on the basis of an assumed mechanistic homology with carboxypeptidase A. Such inhibitors are a first line of therapy for hypertension, heart failure, myocardial infarction, and diabetic nephropathy.[54] Much effort has been put into obtaining a crystalline structure of the enzyme. However, this was not accomplished until very recently when the X-ray structure of human testicular ACE and its complex with one of the most widely used inhibitors, lisinopril (N2-[(S)-1-carboxy-3-phenylpropyl]-L-lysyl-L-proline; also known as Prinivil or Zestril) was reported at 2.0 Å resolution.[54] Analysis of the three-dimensional structure of ACE shows that it bears little similarity to that of carboxypeptidase A, but instead resembles neurolysin[55] and *Pyrococcus furiosus* carboxypeptidase[56] zinc metallopeptidases that have little sequence similarity to ACE. The active site of testicular ACE corresponds to the C-terminal domain of somatic ACE.[57] The somatic ACE contains active sites in its C-and N-terminal domains, which presents new opportunities in drug design.[58]

Mycothiol (1-D-myo-inosityl 2-(N-acetyl-L-cysteinyl) amido-2-deoxy-alpha-D-glucopyranoside, MSH or AcCys-GlcN-inositol (Ins)) is the major reducing agent in actinomycetes, including *Mycobacterium tuberculosis*.[59] The biosynthesis of MSH involves a zinc-dependent deacetylase, MshB, that removes the acetyl group from the precursor GlcNAc-Ins to yield GlcN-Ins. The 3-dimensional structure reveals a protein that folds in a manner resembling lactate dehydrogenase in the N-terminal domain. The catalytic zinc-binding site is in the N-terminal domain occupying a position equivalent to that of the NAD^+ coenzyme of lactate dehydrogenase. The zinc ion binds to the ND1 nitrogen of His13, the NE2 nitrogen of His147, a carboxylate oxygen of Asp16 and two water molecules. One of the waters is hydrogen-bonded to Asp15. This residue would therefore be in the position of the Glu residues believed to be the general acid/base catalyst in many metalloproteases. This would be the first instance in a metallohydrolase where an Asp residue would be the acid/base catalyst. In addition to the zinc providing electrophilic assistance by allowing substrate to displace the second water molecule, the imidazole of His144 is in a position to form a hydrogen bond to the oxyanion of the tetrahedral intermediate.[59]

The deamination mechanism of *E. coli* cytidine deaminase (CDA) is believed to be similar to that of *E. coli* adenosine deaminase (ADA).[60,61] However, the zinc-binding site of the ADA contains 3 His residues while that of CDA contains two Cys and one His residue (Table 1). Examination of the structures of transition state analogs show that the inhibitor complex is stabilized by a zinc hydroxide and an adjacent carboxyl group of an Asp or Glu residue in the active site. The differences in zinc ligands and tertiary structures of the dimeric ADA and CDA have led to the proposal that the common features in the transition state stabilization have arisen from convergent evolution.[60] The variation in the zinc-binding site in this functional class of enzymes is also evident in the tetrameric *Bacillus subtilis* cytidine deaminase that has three Cys ligands, Cys89, Cys86, and Cys53[62] in agreement with sequence alignment that led to the proposal of the three Cys ligands.[63]

3.3.4 β-Carbonic Anhydrases

The β-class of carbonic anhydrases includes CAs from plants, algae, bacteria, and archea.[64,65] The higher plant and unicellular green algae use the β-CAs for photosynthetic CO_2 fixation. The three-dimensional structures *Pisum sativum* β-CA,[66] *Porphyridium purpureum* β-CA,[67] and *Methanosarcina thermophila* β-CA[68] show that this group of carbonic anhydrases has a strikingly different catalytic zinc coordination site from the mammalian class (Table 1). In all cases, the catalytic zinc is coordinated by two Cys and a His as was anticipated by XAFS studies of the spinach CA.[69,70] Two of the ligands, His87 (NE2) and Cys90, are supplied by a loop region and a β-sheet, respectively and are separated by a short spacer of two (Table 1). The third ligand, Cys32 (*M. thermophila* β-CA numbering), is supplied by a β-sheet from the N-terminal side. The structure reported for the *P. purpureum* β-CA[67] has an additional Asp coordinated to the zinc and no bound water molecules. On the basis of this structure, it was proposed that this β-CA and possibly the γ-class of CAs do not use a zinc hydroxide mechanism in their function.[67] However, in the other two reported structures the fourth ligand is a solvent molecule (acetate) for *P. sativum* β-CA[66] and a water molecule for *M. thermophila* β-CA.[68] The putative Asp ligand exists in all three enzymes in a highly conserved loop region C-terminal to the third Cys ligand (CysXAspSerArg). In the enzymes in which the Asp is not a ligand, the Arg guanidinium group is hydrogen-bonded to the Asp carboxyl group preventing it from coordinating the zinc.[68] The zinc-coordinated water molecule in the *M. thermophila* β-CA has therefore been displaced by either an acetate carboxylate in the *P. sativum* β-CA or the carboxylate of Asp151 in the *P. purpureum* β-CA. Further studies will be needed to determine what is the function of the Asp residue in question. However, comparison of the α- and β-CA catalytic zinc sites is of interest in this regard. The positive charge on the zinc in the β-CAs should be reduced by the replacement of two His imidazole ligands by Cys sulfur ligands. The ionization of the zinc-bound water molecule might therefore need the assistance of a neighboring carboxyl group as is postulated in metalloproteases.[2,20,71] A role for Asp151 in catalysis rather than zinc binding could be inferred from the results of a mutation of this residue to an Asn in spinach β-CA.[72] The resulting enzyme still binds zinc but retains little CO_2 hydratase activity.

The γ-class of CAs has one structural representative from *Methanosarcina thermophila*.[73,74] While it retains three His ligands as in the α-class, the spacing characteristics change (Table 1). The resulting trimeric enzyme forms a zinc site from the interface of its subunits (*see* 6.1.2 and Table 5).

3.4 Mechanisms of Zinc Enzymes Containing Catalytic Zinc Sites

A number of representatives from the enzymes containing catalytic zinc sites have been extensively studied by both functional and structural means. This group of zinc sites is too large for this perspective to do justice to this voluminous body of work on so many enzymes. However, there are several recent sources of information on the properties of these enzymes and their mechanism of action. The Handbooks on Metalloproteins[75,76] are particularly good sources for a number of the zinc enzymes having catalytic zinc sites. The large class of metalloproteases is extensively covered in the Handbook of Proteolytic Enzymes,[53] including a separate chapter on their mechanism of action.[20]

4 COCATALYTIC ZINC SITES

Cocatalytic zinc sites occur in metalloenzymes where two or three metals are closely spaced to bring about catalysis. There are over five dozen representatives of this type of zinc site with the great majority belonging to the Class III hydrolases (Table 3). The fact that many zinc enzymes required more that one metal for full activity was known for many years. However, the location of these metals relative to one another was often in debate. Prior to structural analyses these metal atoms were often referred to as a combination of a catalytic zinc site and a ‘modulating’ or ‘regulatory’ zinc.[77] The metal can usually be removed from a catalytic zinc site without a major effect on the structure of the protein. However, cocatalytic metal sites are often formed from ligands that extend over a large portion of the protein structure. It is therefore not unreasonable that enzymes containing two or more metals in the absence of a structure have been described as having one catalytic metal and a second metal that has structural and/or regulatory effects on activity. Thus far, three-dimensional structures of these enzymes show the metals are always in close proximity.

The alkaline phosphatase family contains three metals in the active site while the rest of the cocatalytic zinc sites contain two metals (Figure 10) (Table 3). Some of these sites contain metals such as copper, iron, and magnesium in combination with zinc. Combinations of Cu(II)/Zn are seen in the superoxide dismutase (SOD) family (*see* ***Copper Proteins with Type 2 Sites***), Zn/Mg are seen in alkaline phosphatase family and lens aminopeptidase, and Fe(III)/Zn in the purple acid phosphatase family.

The bridging of two of the metal sites by a side-chain moiety of a single amino acid residue, usually Asp, and sometimes a water molecule is a novel characteristic of these sites.[6] In principle, any sp^2 center containing two nucleophilic atoms should have a bridging potential. Thus, the carboxylate oxygens of Asp or Glu, or of a carboxylated lysine, LysCO-2, or the ring nitrogens of the imidazole group of His are found to bridge such sites. This bridging interaction of the amino acid requires the metals to be in close proximity to each other. The distance between the metals in these sites depends on the bridging amino acid. In the case of an Asp, Glu, or LysCO-2 carboxylate, it is generally between 3 and 4 Å (Table 3). In the case of a His imidazole group the distance increases to about 6 Å.

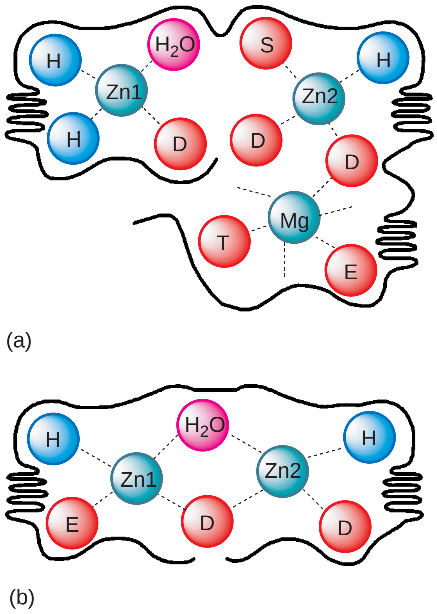

Figure 10 Schematics of three-metal cocatalytic sites (a) represented by *E. coli* alkaline phosphatase,[78] and two-metal cocatalytic sites (b) represented by *Aeromonas proteolytic* amino peptidase.[79] The one-letter codes D, E, and H are given for the amino acids Asp, Glu, and His respectively

Asp and His predominate as ligands in cocatalytic zinc sites where the frequency is Asp $\simeq$ His $>$ Glu. These sites also occasionally contain unusual zinc ligands such as amide carbonyls provided by Asn, Gln, and the peptide backbone; hydroxyl groups from Ser, Thr, and Tyr and the amine nitrogen of Lys or the N-terminal amino group of the protein. Perhaps remarkable is the low utilization Cys ligands in these metal sites. Since the ligands to cocatalytic zinc sites often come from nearly the entire length of the protein, the metals may be also important to the overall fold of the protein as well as catalytic function. The secondary structure of the protein plays a major role in providing the ligands to these sites. Some of the families use almost exclusively β-sheets to provide the ligands while other families use all α-helices (Table 3). In many cases ligands are provided by amino acids residing 1 or 2 residues before or after a β-sheet or an α-helix. The zinc ions are often pentacoordinate and arranged in a trigonal-bipyramidal geometry.

4.1 Mechanism of Cocatalytic Enzymes

The bridging amino acids and H_2O likely have critical roles in catalysis. Thus, their dissociation from either metal atom during catalysis will change the charge on the metal promoting its action as a Lewis acid or allowing interaction with an electronegative atom of the substrate. In addition, a released bridging ligand can participate transiently in the reaction as a nucleophile or general acid/base catalyst. The flexibility of the arm supplying the bridging ligands (e.g. one carbon, C, for Asp and His, 2 C for Glu or 5 C/N for LysCO-2) would be expected to influence the stability and reactivity of the two-metal sites. Thus, it can be envisioned for cocatalytic sites in hydrolytic enzymes that substrate binding involves one zinc site acting as a template for substrate binding while the other zinc provides hydroxide for nucleophilic attack on the sp^2 center of the ester or amide bond of the substrate. In the next step the roles of the metals can be reversed. In this manner, the metal atoms and their associated ligands play specific roles in each step of the reaction that works to bring about catalysis. The ligands in these sites, in particular, the histidines, are often involved in further hydrogen-bonding interactions with other amino acids. These interactions should effect the charge on the metal and the stability of the metal complex thus fine tuning catalysis and the stability of the metal sites.[3,20]

The reader is referred to the following sources of further information on the specific cocatalytic enzymes: superoxide dismutase,[80] and the reduced form,[81] alkaline phosphatases,[78,82] nuclease P1,[83] purple acid phosphatase,[84,85] amidohydrolase,[86,87] leucine aminopeptidase,[88] general comments on the mechanisms of the phosphatases[89] and aminopeptidases,[89,90] and other cocatalytic zinc enzymes.[76]

5 STRUCTURAL ZINC SITES

The early structural studies of metalloenzymes led to the suggestion that metal atoms that have a catalytic role would be composed of ligands from different parts of the polypeptide chain whereas ligands to metal atoms in structural sites would be close together. We now know that both types of zinc sites generally contain at least two ligands that are separated by a short spacer.[4,91] In addition, while many structural zinc sites are composed of ligands from a relatively short sequence in the protein, this is not always the case as might be anticipated from inspection of disulfide structural elements that often come from vastly separated regions of the protein primary structure.

The role of structural zinc sites is likely two-fold. They maintain the structure of the protein in the immediate vicinity of the metal site. In this manner it may influence enzymatic activity by providing active-site residues involved in catalysis and/or effecting the chemical environment of catalytic groups through interaction with amino acids originating from within its metal-binding spacers. However, in many cases, these metal sites also effect the overall stability of the protein as judged by temperature and pH criteria.

While zinc can readily form four-, five-, and six-coordinate complexes, structural zinc sites in proteins have 4 protein ligands and no bound water molecule. This type of coordination is also observed in many of the *Protein Interface* zinc sites.[3,4] The first zinc enzymes recognized to have a

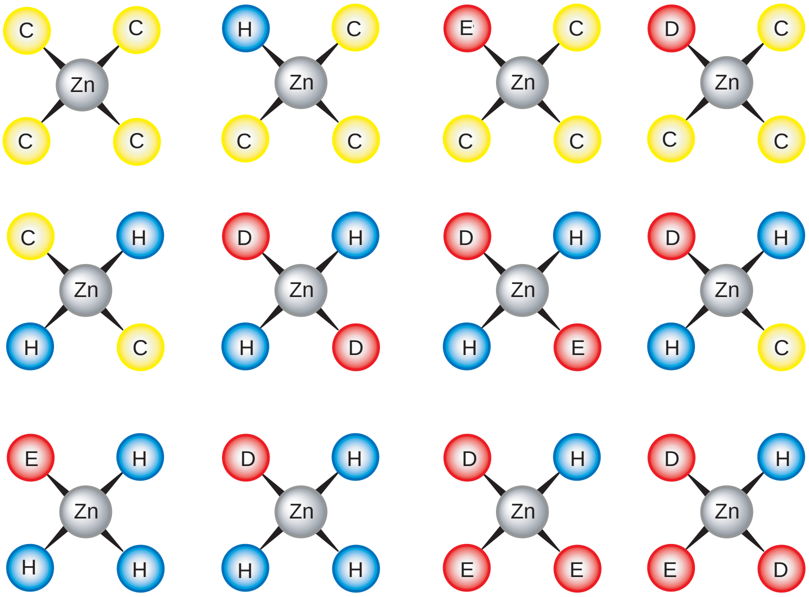

Figure 11 Schematic of the four-coordinate zinc sites observed thus far in terms of the type of bound ligands. The one-letter codes C, D, E and H are given for the amino acids Cys, Asp, Glu, and His, respectively

structural zinc site were horse liver alcohol dehydrogenase, ADH,[92] and the regulatory subunit of *E. coli* aspartate carbamoyltransferase.[93] In both cases the zinc is bound to four cysteines in a relatively short linear sequence of 15 to 33 amino acids, respectively. There are today more than eleven dozen structural zinc sites with representatives in all six enzyme classes defined by the International Union of Biochemists. The ligands to these metal sites are provided by protein sequences as small as 10 amino acids and as large as 212 amino acids but the majority fall within the range of 15 to 40 amino acids (Table 4). There is nearly always one short spacer separating two amino acids in these sites. The ligands are frequently supplied from within or just before or after a β-sheet secondary structure. Several ligands are supplied by a short amino acid sequence of 3 to 6 amino acids (loop) between two peptide regions of regular (β-sheet or α-helical) secondary structure. The majority of these loop regions are composed of two β-sheets. While the sulfur of a Cys is by far the preferred ligand for such sites, it is also found in combination with an imidazole nitrogen of His, and/or a carboxylate oxygen from Asp or Glu. The second most prevalent ligand is histidine.

The presence of His and/or Cys in the same zinc-binding site frequently gets some form of a 'zinc-finger' nomenclature (*see* ***Technetium: Organometallic Chemistry***). Based on only 'loose' criteria, some of the sites listed here are still referred to as zinc-finger domains,[94] even if they do not fit the criteria of having DNA-binding properties and/or the ligand nature (2His/2Cys), sequence length (~30 amino acids) and presence of both α-helix and β-sheets in the zinc-binding site associated with a classical zinc finger.[95] Several reviews exist on the expansion of this nomenclature in the area of zinc protein sites interacting with nucleic acids (*see* ***Zinc: DNA-binding Proteins***).[96–100]

The expansion of this nomenclature thus far deals mainly with the type of secondary structure present in combination with Cys and His ligands. However, even if one considers only the four main amino acid ligand donors, Cys, His, Asp and Glu, there are 22 permutations of a zinc bound to these four ligands, 12 of which have been observed in zinc enzymes and zinc proteins (Figure 11, Tables 4–6). Several other features of the site can also be important to the resulting influence of the zinc ion. These include the type of secondary structure, outer shell interactions, how many short spacers occur and the order of the ligand donors. This is likely the reason for the frequent use of the word novel in describing new zinc-binding sites owing to the difficulty in classifying the site in terms of the relatively small number of proposed names such as zinc-box, -bundle, -cluster, -finger, -knuckle, ribbon, -ring, etc. The one feature they have in common is the presence of four protein ligands and no coordinated water molecule.[4,5,91]

5.1 Structural Sites Involved in Function

Some of these sites can effect function in zinc proteins as well as stabilizing structure. The hydrolase class of zinc enzymes are good examples of this action.[91] In this case, one or more amino acid residues within the active site may be provided by the amino acid spacers between zinc ligands (Figure 12). The side chain of these amino acids may be involved in substrate binding, bond cleavage or modulating the chemical environment of the active site. In addition, other active-site residues are often provided by

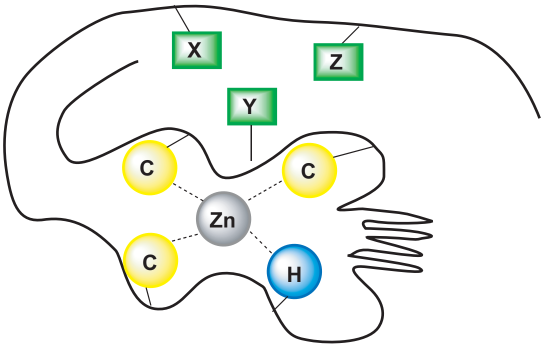

Figure 12 Schematic of a structural zinc-binding site that provides active-site residues from amino acids located within the metal-coordination spacers. Other active-site residues are often provided by the peptide sequence N-terminal to the structural zinc site. The symbol Y can represent more than one amino acid. (Table 4)

the peptide sequence N-terminal to the structural zinc site. Some structural zinc sites that exert influence on function are given below.

5.1.1 *Formamidopyrimidine-DNA Glycosylase Family*

The bacterial formamidopyrimidine-DNA glycosylase (alias Fpg or MutM) is a bifunctional base-repair enzyme (DNA glycosylase/AP lyase) that removes a wide range of oxidized purines from oxidatively damaged DNA.[101] The crystal structures of the Fpg (MutM) enzymes from *Thermus thermophilus*,[102] *Lactococcus lactis*,[101] *Escherichia coli*,[103] *Bacillus stearothermophilus*[104] and the sequence similar endonuclease VIII (Nei) from *E. coli*,[105] all share the same type of structural zinc-binding site at the end of the C-terminus of the proteins. This zinc site is composed of four cysteine sulfur ligands (Table 4). The first three cysteines are supplied by two β-sheets. The zinc site influences the function of the enzyme through an amino acid located within its metal-binding spacer. The guanidinium group of an Arg residue from within the large central coordination spacer makes two H-bonds with the p^{-1} and p^{0} phosphates of the pyrimidine cleavage site of the substrate. In addition, several other binding interactions come from the N-terminal side of the zinc-binding site.

5.1.2 *Rhinovirus-2 Proteinase*

The human 2A proteinase from the common cold (rhinovirus) is structurally related to the cysteine proteases.[106] Its active site contains a characteristic catalytic AspHisCys triad. This proteinase also contains a structural zinc-binding site in the N-terminus of the protein composed of Cys52, Cys54, Cys112 and His114 as ligand donors (Table 4). Two β-sheets supply the last three amino acids. The site is believed to be structural since it is not accessible to other ligands and is unlikely to have any functional role in RNA binding. Chelation and site-directed mutagenesis studies indicate the zinc is essential for formation of an enzymatically active form of the enzyme.[107,108] The zinc-depleted enzyme shows mostly unchanged secondary structure as determined by CD spectroscopy, but not a fully denatured random coil as obtained by the presence of guanidinium hydrochloride.[109] The zinc may therefore be stabilizing a local conformation of the protein that is critical for activity.

This zinc site likely influences enzymatic function through its effect on local conformation. In this case, the crucial catalytic residue Cys106 is supplied from within the large central coordination spacer and the other members of the triad, His14 and Asp35, come from the N-terminal side of the zinc-binding site.

5.1.3 *Endonucleases*

The enzyme from *Physarum polycephalum* is a homodimer containing two zinc sites per monomer of 324 amino acids.[110] The two zinc sites originate in the N-terminus of the protein spanning residues 41 to 138. The first zinc site is formed from Cys41, Cys100, Cys105 and His110 supplied by three β-sheets while the second zinc uses Cys125, Cys132, His134 and Cys138 as ligands that are supplied from a largely unstructured region of the protein except for one short α-helix (Table 4). The two zinc ions are separated by 15.3 Å. Both sites contain 3 Cys and 1 His ligand although the order of ligand coordination is different. The second zinc site may play a role in stabilizing the dimer interface since the indole rings of Trp 125 from each monomer are stacked against each other.[110] Neither site is involved in DNA-binding since both are 15 to 17 Å from the substrate complex. However, the active-site His98 amino acid is one residue away from the second Cys ligand in the first zinc site.

5.1.4 *Matrix Metalloproteinases*

The matrix metalloproteinase (MMP) class of enzymes contain a non-Cys zinc-binding site that has the characteristics of a structural zinc site, that is, four ligands, and no metal-bound water (Table 4). This site contains three His and an Asp residue in a linear sequence spanning 28 amino acids (Table 4).[111,112] The site is highly conserved in the MMPs, occurring in the great majority of sequence-identified MMPs (125/138 sequences in MEROPS 1.7 data set)[113] and has a signature of $HX_1DX_{12}HX_{12}H$. As is likely the case for many structural metal sites, this site may be indirectly effecting the activity of the enzyme. Although this zinc is separated by 12 Å from the catalytic zinc site, the amino acids adjacent to the third and fourth ligands (His) to the ‘structural’ zinc site provide a number of hydrophobic residues that border the catalytic Glu residue. These regions contain LeuAla and AlaPhe/Tyr sequences on the two sides of one His and an Ala and Phe adjacent to the other His. These residues could provide a hydrophobic environment for the catalytic Glu carboxylate

Table 4 Structural zinc sites[a]

Enzyme	PDB#	L_1	X	L_2	Y	L_3	Z	L_4
Class I: Oxidoreductase								
Alcohol Dehydrogenase family								
Horse EE	8ADH 3BTO	Cys	2	Cys$_{b\alpha}$	2	Cys$_{\alpha}$	7	Cys
Cod	1CDO	Cys	2	Cys$_{b\alpha}$	2	Cys$_{\alpha}$	7	Cys
Human Class I								
$\alpha\alpha$	1HSO	Cys	2	Cys$_{b\alpha}$	2	Cys$_{\alpha}$	7	Cys
$\beta_1\beta_1$	1HDZ	Cys	2	Cys$_{b\alpha}$	2	Cys$_{\alpha}$	7	Cys
$\beta_2\beta_2$	1HDY	Cys	2	Cys$_{b\alpha}$	2	Cys$_{\alpha}$	7	Cys
$\beta_3\beta_3$	1DEH	Cys	2	Cys$_{b\alpha}$	2	Cys$_{\alpha}$	7	Cys
$\gamma\gamma$	1HT0	Cys	2	Cys$_{b\alpha}$	2	Cys$_{\alpha}$	7	Cys
Mouse Class II	1E3E	Cys	2	Cys$_{b\alpha}$	2	Cys$_{\alpha}$	7	Cys
Human Class III								
$\chi\chi$	1TEH	Cys	2	Cys$_{b\alpha}$	2	Cys$_{\alpha}$	7	Cys
or glutathione- dependent formaldehyde dehydrogenase	1M6H	Cys	2	Cys$_{b\alpha}$	2	Cys$_{\alpha}$	7	Cys
Pseudomonas putida formaldehyde dehydrogenase	1KOL	Cys	2	Cys$_{b\alpha}$	2	Cys$_{\alpha}$	7	Cys
Human Class IV								
$\sigma\sigma$	1AGN	Cys	2	Cys$_{b\alpha}$	2	Cys$_{\alpha}$	7	Cys
Amphibian (ADH8)	1P0F	Cys	2	Cys$_{b\alpha}$	2	Cys$_{\alpha}$	7	Cys$_{L}$
Sulfolobus solfataricus ADH	1JVB, 1NTO	Glu$_{L}$	2	Cys$_{b\alpha}$	2	Cys$_{\alpha}$	7	Cys
Aeropyrum pernix ADH	1H2B	Asp	2	Cys$_{b\alpha}$	2	Cys$_{\alpha}$	7	Cys
Silverleaf whitefly ketose reductase	1E3J	Cys$_{L}$	2	Cys$_{b\alpha}$	2	Cys$_{\alpha}$	7	Cys
Thermoplasma acidophilum glucose dehydrogenase		Cys	2	Cys	7	Cys	5	Asp$_{b\beta}$
Bovine heart cytochrome *c*-oxidase	1OCC	Cys$_{\beta}$	1	Cys$_{2a\beta}$	19	Cys$_{\beta}$	2	Cys$_{L}$
Bacteriophage T4 ribonucleotide reductase	1HK8	Cys$_{\beta}$	2	Cys$_{2a\beta}$	14	Cys$_{a\beta}$	2	Cys
Class II: Transferase								
Aspartate carbamoyltransferase	1AT1	Cys$_{L}$	2	Cys$_{\beta}$	23	Cys$_{2b\alpha}$	4	Cys (N)
Human Bruton's tyrosine kinase	1BTK	His$_{a\beta}$	10	Cys$_{a\beta}$	0	Cys$_{2a\beta}$	9	Cys$_{b\beta}$
Bacillus stearothermophilus adenylate kinase	1ZIP	Cys$_{\beta}$	2	Cys$_{L}$	16	Cys$_{\beta}$	2	Cys$_{L}$
Protein kinase family								
Rat protein kinase C-α	1TBN	Cys$_{\beta}$	2	Cys$_{L}$	21	His$_{a\beta}$	2	Cys$_{b\alpha}$
		His$_{b\beta}$	29	Cys$_{\beta}$	2	Cys$_{L}$	15	Cys
Rabbit C-α Cys-rich domain		Cys$_{\beta}$	2	Cys$_{L}$	21	His$_{\beta}$	2	Cys$_{\alpha}$
		His$_{b\beta}$	29	Cys$_{\beta}$	2	Cys$_{b\beta}$	15	Cys
Mouse C-δ activator-binding domain	1PTQ	Cys$_{\beta}$	2	Cys$_{L}$	21	His$_{a\beta}$	2	Cys$_{\alpha}$
		His$_{b\beta}$	29	Cys$_{\beta}$	2	Cys$_{L}$	15	Cys
Human Raf-1	1FAR	Cys$_{\beta}$	2	Cys$_{L}$	17	His$_{a\beta}$	2	Cys
		His	25	Cys$_{\beta}$	2	Cys$_{L}$	15	Cys
Mouse KSR C1 domain	1KBE	Cys	2	Cys	17	His$_{a\beta}$	2	Cys
		His	24	Cys$_{\beta}$	2	Cys$_{L}$	14	Cys
Human casein kinase, truncated dimerCK2β	1QF8	Cys$_{L}$	2	Cys$_{\beta}$	22	Cys$_{L}$	4	Cys$_{\beta}$ (N)
		Cys$_{L}$	2	Cys$_{\beta}$	22	Cys$_{L}$	4	Cys$_{\beta}$ (N)
Human casein kinase, holoenzyme CK2	1JWH	Cys$_{L}$	2	Cys$_{\beta}$	22	Cys	4	Cys$_{\beta}$ (N)
		Cys	2	Cys$_{a\beta}$	22	Cys$_{L}$	4	Cys$_{\beta}$ (N)
Human Sirt2 histone deacetylase	1J8F	Cys$_{L}$	2	Cys$_{\beta}$	20	Cys$_{\beta}$	4	Cys$_{\beta}$ (N)
Archaeoglobus fulgidus Sir2 protein deacetylase	1ICI,1M2G	Cys$_{\beta}$	2	Cys$_{L}$	17	Cys$_{\beta}$	4	Cys$_{L}$
Saccharomyces cerevisiae Hst2 protein deacetylase	1Q14	Cys$_{\beta}$	2	Cys$_{L}$	23	Cys$_{\beta}$	2	Cys$_{L}$
Polymerase Family								
Yeast RNA polymerase II subunit A	1K83	Cys	2	Cys	6	Cys	2	His$_{2b\beta}$
		Cys	2	Cys	37	Cys$_{\beta}$	18	Cys$_{L}$
Yeast RNA polymerase II subunit A	1NIK	Cys	2	Cys	6	Cys?[b]	2	His$_{2b\beta}$
		Cys$_{2a\alpha}$?[b]	2	Cys	37	Cys$_{2b\beta}$?[b]	18	Cys
Yeast RNA polymerase II subunit B	1K83	Cys$_{\beta}$	2	Cys$_{2a\beta}$	15	Cys$_{a\beta}$	2	Cys
Yeast RNA polymerase II subunit B	1NIK	Cys$_{\beta}$	2	Cys$_{2a\beta}$	15	Cys	2	Cys

Table 4 cont'd

Enzyme	PDB#	L$_1$	X	L$_2$	Y	L$_3$	Z	L$_4$
Yeast RNA polymerase II subunit C	1K83	Cys	1	Cys	3	Cys	2	Cys$_{2b\beta}$
Yeast RNA polymerase II subunit C	1NIK	Cys	1	Cys	3	Cys	2	Cys$_{2b\beta}$
Yeast RNA polymerase II subunit I	1K83	Cys	2	Cys	18	Cys$_{\beta}$	2	Cys$_{L}$
		Cys	2	Cys	24	Cys$_{\beta}$	2	Cys$_{L}$
Yeast RNA polymerase II subunit I	1NIK	Cys$_{\beta}$	2	Cys$_{L}$	18	Cys$_{\beta}$	2	Cys$_{L}$
		Cys	2	Cys	24	Cys$_{\beta}$	2	Cys$_{L}$
Yeast RNA polymerase II subunit J	1K83	Cys$_{\alpha}$	0	Cys$_{\alpha}$	34	Cys$_{L}$	2	Cys$_{\beta}$ (N)
Yeast RNA polymerase II subunit J	1NIK	Cys$_{2b\alpha}$	0	Cys	34	Cys	2	Cys (N)
Yeast RNA polymerase II subunit L	1K83	Cys	2	Cys	13	Cys	2	Cys (CO)
Yeast RNA polymerase II subunit L	1R5U	Cys$_{\beta}$	2	Cys$_{L}$	13	Cys	2	Cys
Thermococcus celer RNA polymerase II RPB9	1QYP	Cys$_{\beta}$	2	Cys$_{L}$	24	Cys$_{\beta}$	2	Cys$_{L}$
Methanobacterium thermautotrophicum								
RNA polymerase subunit RPB10	1EF4	Cys$_{\alpha}$	0	Cys$_{\alpha}$	33	Cys	2	Cys (N)
Thermus aquaticus RNA polymerase	1HQM	Cys	2	Cys	6	Cys	81	Cys (N)
E. coli DNA polymerase III δ' subunit	1A5T	Cys$_{\alpha}$	2	Cys$_{b\alpha}$	2	Cys	8	Cys$_{a\alpha}$ (N)
E. coli DNA polymerase III γ subunit	1JR3,1NJF	Cys$_{\alpha}$	2	Cys$_{b\alpha}$	2	Cys	8	Cys$_{2s\alpha}$ (N)
Human E1 enzyme for NEDD8	1NGV	Cys	2	Cys	140	Cys	2	Cys
DNA Primases								
Bacillus stearothermophilus	1D0Q	Cys$_{2a\beta}$	2	His	17	Cys$_{\beta}$	2	Cys$_{L}$
Pyrococcus furisosus	1G71	Cys	1	His	5	Cys$_{b\alpha}$	2	Cys$_{\alpha}$
Bacteriophage T7	1NUI	Cys$_{2a\beta}$	2	Cys	15	Cys$_{\beta}$	2	Cys$_{L}$
Sulfolobus islandicus	1RO0	Cys	4	Cys	2	His$_{\beta}$	46	His$_{L}$ (N)
Transferases								
Human O-6-Alkylguanine-DNA alkyltransferase	1EH6	Cys	18	Cys$_{\beta}$	4	His$_{\beta}$	55	His
E. coli galactose-1-phosphate uridylyltransferase	1GUP	Cys	2	Cys	59	His	48	His$_{b\beta}$
Pyrococcus horikoshii tRNA guanine transglycosylase	1IT7, 1J2B	Cys	1	Cys$_{b\alpha}$	2	Cys$_{\alpha}$	22	His$_{\alpha}$
Zymomonas mobilis tRNA guanine transglycosylase	1P0B	Cys	1	Cys$_{b\alpha}$	2	Cys$_{\alpha}$	25	His$_{\alpha}$
Neurospora crassa								
Histone H3-Lys-N-methyltransferase Dim-5	1PEG	Cys	4	Cys	1	Cys	63	Cys (N)
Class III: Hydrolase								
Matrix Metalloproteinase Family								
Human fibroblast collagenase (MMP-1)	1CGL	His	1	Asp	12	His$_{\beta}$	12	His$_{\beta}$
Human fibroblast collagenase (MMP-1)	3AYK	His	1	Asp	12	His$_{\beta}$	12	His$_{\beta}$
Human progelatinase 72 kDa (MMP-2)	1CK7	His	1	Asp	12	His$_{\beta}$	12	His$_{\beta}$
Human stromelysin-1 (MMP-3)	2SRT, 1BM6	His	1	Asp	12	His$_{\beta}$	12	His$_{\beta}$
Human stromelysin-1 (MMP-3)	1B3D	His	1	Asp	12	His$_{\beta}$	12	His$_{\beta}$
Human prostromelysin-1 (MMP-3)	1SLM	His	1	Asp	12	His$_{\beta}$	12	His$_{\beta}$
Human matrilysin (MMP-7)	1MMP	His	1	Asp	12	His$_{\beta}$	12	His$_{\beta}$
Human neutrophil collagenase (MMP-8)	1KBC	His	1	Asp	12	His$_{\beta}$	12	His$_{\beta}$
Human gelatinase 92 kDa (MMP-9)	1GKC	His	1	Asp	12	His$_{\beta}$	12	His$_{\beta}$
Human macrophage elastase (MMP-12)	1JIZ	His	1	Asp	12	His$_{\beta}$	12	His$_{\beta}$
Human collagenase-3 (MMP-13)	830C	His	1	Asp	12	His$_{\beta}$	12	His$_{\beta}$
Mouse collagenase-3 (MMP-13)	1CXV	His	1	Asp	12	His$_{\beta}$	12	His$_{\beta}$
Human Membrane Mt1 (MMP-14)	1BQQ	His	1	Asp	12	His$_{\beta}$	12	His$_{\beta}$
Bacillus stearothermophilus lipase	1JI3	Asp$_{\alpha}$	19	His$_{\alpha}$	5	His$_{L}$	150	Asp$_{2b\alpha}$
Bacillus stearothermophilus lipase L1	1KU0	Asp$_{\alpha}$	19	His$_{\alpha}$	5	His$_{L}$	150	Asp$_{2b\alpha}$
Thermus thermophilus A4β-galactosidase	1KWG	Cys$_{\alpha}$	2	Cys$_{b\alpha}$	1	Cys	43	Cys (N)
E. coli DNA mismatch endonuclease	1VSR, 1ODG	Cys$_{\alpha}$	4	His$_{2a\alpha}$	1	Cys	43	Cys$_{\alpha}$

(cont'd overleaf)

Table 4 cont'd

Enzyme	PDB#	L$_1$	X	L$_2$	Y	L$_3$	Z	L$_4$
P. polycephalum endonuclease I-PpoI	1A73,1EVX	His$_{\beta}$	4	Cys$_{\beta}$	4	Cys$_{a\beta}$	58	Cys$_{\beta}$ (N)
		Cys	3	His	1	Cys	6	Cys$_{2a\alpha}$ (N)
Bacteriophage T4 endonuclease VII	1EN7, 1E7D	Cys$_{\beta}$	2	Cys$_{L}$	31	Cys$_{L}$	2	Cys$_{\alpha}$
E. coli Recq helicase catalytic core	1OYW	Cys$_{\alpha}$	2	Cys$_{b\alpha}$	2	Cys	16	Cys$_{b\alpha}$ (N)
E. coli 3-methyladenine DNA glycosylase I	1NKU	Cys	3	His$_{a\beta}$	157	His$_{\alpha}$	12	Cys (N)
Human 3′, 5′ cyclic-nucleotide PDE	1OYN	His$_{\alpha}$	35	His$_{a\alpha}$	0	Asp$_{2a\alpha}$	116	Asp$_{a\alpha}$
Clostridium cellulolyticum cellulase Cel9M	1IA6	Cys$_{\alpha}$	15	Cys	0	His	15	His$_{\beta}$
Formamidopyridimine-DNA glycosylase MutM (Fpg) Family								
Thermus thermophilus HB8 MutM	1EE8	Cys$_{\beta}$	2	Cys$_{L}$	16	Cys$_{a\beta}$	2	Cys
Lactoccus lactis Fpg	1KFV	Cys$_{\beta}$	2	Cys$_{L}$	16	Cys$_{a\beta}$	2	Cys
Escherichia coli Fpg	1K82	Cys$_{\beta}$	2	Cys$_{L}$	16	Cys$_{a\beta}$	2	Cys
Bacillus stearothermophilus MutM	1L1T	Cys$_{\beta}$	2	Cys$_{L}$	16	Cys$_{a\beta}$	2	Cys
E. coli Endonuclease VIII (Nei)	1K3W	Cys$_{\beta}$	2	Cys$_{L}$	16	Cys$_{a\beta}$	2	Cys
Human picornavirus endoprotease 2A	2HRV	Cys	1	Cys$_{b\beta}$	57	Cys$_{\beta}$	1	His$_{L}$
Class IV: Lyase								
E. coli Fructose Bisphosphate Aldolase	1DOS	His	37	His	51	Glu$_{\beta}$	63	His$_{a\beta}$ (N)
Class V: Isomerase								
E. coli Rhamnose Isomerase	1DE5	Glu$_{\beta}$	32	Asp$_{\beta}$	26	His$_{\beta}$	39	Asp$_{\beta}$
Class VI: Ligase								
tRNA synthetase Family								
Escherichia coli MetRS	1QQT,1F4L	Cys$_{\beta}$	2	Cys$_{L}$	9	Cys$_{\beta}$	2	Cys$_{L}$
Thermus thermophilus HB8 MetRS	1A8H	Cys$_{\beta}$	2	Cys$_{L}$	13	Cys	2	His
Thermus thermophilus HB8 ProRS	1HC7	Cys$_{L}$	2	Cys$_{\beta}$	25	Cys$_{\alpha}$	4	Cys$_{L}$ (N)
Methanothermobacter thermautotrophic ProRS	1NJ1	Cys$_{L}$	2	Cys$_{\beta}$	22	Cys$_{\alpha}$	4	Cys$_{L}$ (N)
Thermus thermophilus IleRS	1ILE	Cys$_{L}$	1	Cys$_{\beta}$	37	Cys$_{L}$	2	Cys$_{\beta}$ (N)
		Cys$_{\beta}$	2	Cys$_{L}$	204	Cys$_{\beta}$	2	Cys$_{L}$
Thermus thermophilus ValRS	1GAX	Cys$_{\beta}$	2	Cys$_{L}$	17	Cys	2	Cys
		Cys$_{\beta}$	2	Cys$_{L}$	164	Cys$_{\beta}$	2	Cys$_{L}$
Thermus thermophilus LeuRS	1OBC	Cys$_{\beta}$	2	Cys$_{L}$	13	Cys$_{\beta}$	2	His$_{L}$
		Cys$_{\beta}$	2	Cys$_{L}$	41	Cys$_{\beta}$	2	Cys$_{L}$
Escherichia coli IlelRS	1QU2	Cys$_{\beta}$	2	Cys$_{L}$	16	Cys$_{b\alpha}$	2	Cys$_{\alpha}$
Staphylococcus aureus IleRS	1FFY	Cys$_{\beta}$	2	Cys$_{L}$	16	Cys$_{b\alpha}$	2	Cys$_{\alpha}$
Pyrococcus horikoshii LysRS	1IRX	Cys$_{a\beta}$	2	His$_{L}$	18	Cys$_{a\beta}$	3	His$_{2b\beta}$
		Asp	4	Cys	0	His	5	His$_{\alpha}$
HIV-1 Integrase	1WJA	Cys$_{\alpha}$	2	Cys$_{L}$	23	His$_{\alpha}$	3	His$_{L}$ (N)
HIV-2 Integrase	1E0E	Cys$_{\alpha}$	2	Cys$_{L}$	23	His$_{L}$	3	His$_{\alpha}$ (N)
Thermus filiformis DNA ligase	1DGS	Cys$_{\beta}$	2	Cys$_{L}$	12	Cys$_{\beta}$	4	Cys
Mouse Siah ubiquitin ligase	1K2F	Cys$_{L}$	3	His$_{\alpha}$	11	Cys	6	Cys (N)
		His$_{L}$	3	His$_{\alpha}$	11	Cys	6	Cys (N)

[a] See footnote of Table 1 for the definitions of terms. [b] A ? means the ligand is in question.

group of the MMPs and thus raise its pK_a, allowing it to play a role in stabilizing the transition state in catalysis.[2] The properties of the structural zinc site in the MMPs and in other similar sites may therefore influence function indirectly through effects on local conformation or local environment.

5.2 Zinc Clusters Class II: Histone Lysine Methyl Transferases

Histones undergo extensive posttranslational modifications such as acetylation, phosphorylation, and methylation on their N-terminal peptides that extend out of the nucleosome. Such modifications have been proposed to be part of a histone code that is recognized by cellular factors that influence gene expression.[114] Some of the SET (Su(var), Enhancer of zeste, Trithorax) domain proteins,[115] in combination with a cofactor S-adensoyl-L-methionine (SAM), are enzymes that methylate lysine 9 of histone H3. These enzymes contain minimally a histone methyltransferase (HMTase) catalytic domain that includes the conserved SET domain flanked by cysteine-rich pre- and post-SET motifs.[116,117] A zinc cluster-type binding site, Zn_3Cys_9, is believed to be important to the structural stability of the pre-SET domains of the histone lysine methyl transferases, DIM-5[116] (the gene product of *Neurospora crassa* defective in methylation gene, *dim-5*),[118] and the *Schizosaccharomyces pombe* cryptic loci regulator 4, Clr4.[117] A fourth zinc site has been found in the *Neurospora* *crassa* Dim-5 enzyme bound to four Cys residues (Table 4).[119] This zinc is 39 to 43 Å from the zinc cluster.

The zinc cluster sites have several features in common with the β-domain three-metal clusters of eukaryotic metallothioneins (*see* ***Metallothioneins***). All of these clusters can be viewed as simple hexagons in two dimensions (Figure 13). The hexagon is composed of alternating zinc ions and bridging Cys ligands. Each zinc has two other nonbridging Cys sulfurs ligated to it. In each case there is a short spacer of 7 amino acids between two of the bridging Cys ligands. However, the spacers to the third bridging Cys are much larger for the histone methyltransferases. This is due to large inserts of 28 and 46 amino acids between the fifth and sixth cysteines in the Clr4 and DIM-5 HMTases, respectively, compared to 1- and 3-amino acid spacers for the human,[120] mouse,[121] and sea urchin[122] metallothioneins, respectively. The spacing characteristics of the last four cysteine ligands in the HMTases is highly conserved compared to that of the first five cysteine ligands. A search using the motif [YFIK]ECX$_3$CXCX$_3$CX$_2$R leads to only 46 proteins, many of which are suspected to be HMTases.[91] The majority of the putative large spacers between the fifth and sixth Cys ligands are between 24 and 29 amino acids while two are 46 and 66 amino acids. The resulting variation in the putative spacing of the first five Cys residues is given by the subscripts in the sequence: CX$_{1-2}$CX$_{2-6,8}$CX$_{3-7}$CX$_{0-1}$C.

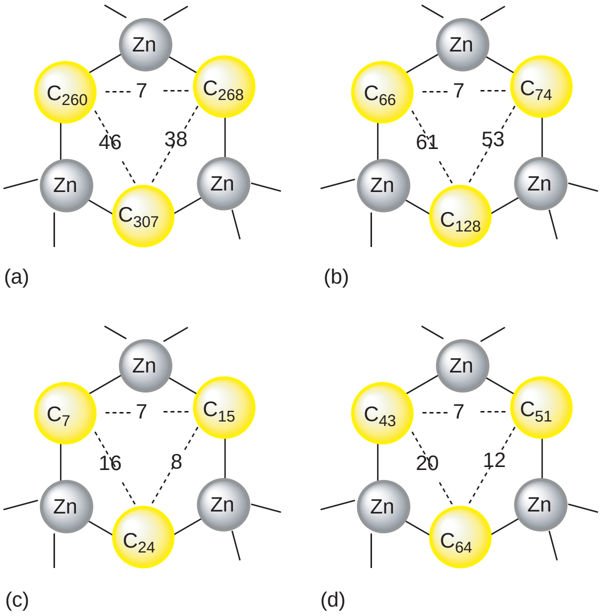

Figure 13 Properties of some zinc cluster sites observed in zinc enzymes and metallothionein. The bridging Cys residues as well as their spacing are identified for (a) *Schizosaccharomyces pombe* Lysine methyltransferase Clr4,[117] (b) *Neurospora crassa* Histone H3 methyltransferase DIM-5,[116] (c) β-domain of human metallothionein-2,[120] and (d) β-domain of sea urchin metallothionein MTA.[122] The PDB numbers are respectively: 1MVH, 1 ML9, 1MHU, and 1QJL

6 PROTEIN INTERFACE ZINC SITES

Thus far, we have considered how zinc can directly influence enzyme structure and function through its action in catalytic, cocatalytic, and structural zinc-binding sites formed from intramolecular ligands in monomeric proteins or in a subunit of a multi-subunit protein. However, zinc can also bind to the interface of protein molecules and form all of the zinc-binding sites mentioned above. In this capacity, it may also influence the quaternary structure of proteins. Zinc binding to ligands supplied from protein molecules at their interface contact surface has been observed in increasing numbers in the last few years.[3,4,123] These interactions can lead to dimers or trimers of the same protein or link two different proteins through the intermolecular ligands. The amino acid residues His, Glu, and Asp primarily supply the ligands to these sites but Cys-containing sites are also found (Table 5). The ligands are generally contributed by some form of secondary structure with β-sheets predominating. The most common types of these sites are formed from either each protein molecule providing two zinc ligands or one protein moiety providing three ligands and the second providing one as in the case of the nitric oxide synthase family and superantigens, respectively (Figure 14).

The resulting zinc-binding sites can function as catalytic zinc sites as in γ-carbonic anhydrase[74] or structural-like sites as in the proposed superantigen-MHC class II complexes[124] or cocatalytic-like sites as in the zinc-sensing transcriptional regulator ZntR.[125]

6.1 Protein Interface Catalytic Zinc Sites

While one might anticipate the binding of zinc between protein molecules to indirectly effect protein function by a number of means, it is perhaps most remarkable that these interactions can lead to catalytic zinc sites. This can occur even when all of the elements are in each monomer of the enzyme. In other cases, the intermolecular zinc site may be involved in placing the enzyme in the proper physiological place to exercise its function.

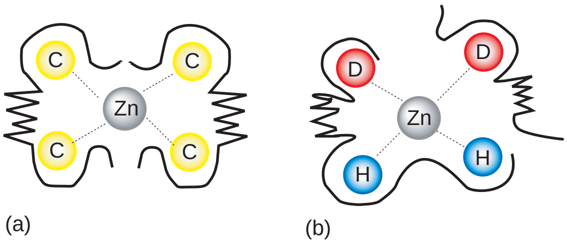

Figure 14 Protein interface zinc sites are formed at the interface of two proteins with generally four amino acid ligands binding to the zinc ion. The most common forms supply (a) two amino acid ligands from both protein moieties or (b) three amino acids ligands from one protein moiety and one ligand from another

6.1.1 γ-Carbonic Anhydrase: Trigonal-Bipyramidal Zinc Site

The carbonic anhyrases are classified broadly as α, β and γ enzymes. X-ray structures exist for all three forms (Tables 1 and 5). The catalytic zinc sites are highly conserved for each class of enzymes but differ markedly when the classes are compared. The α-class of enzymes contain two His ligands separated by a short spacer of one, a third His ligand supplied from the C-terminal side of the protein and one water molecule to complete the tetrahedrally bound zinc (Table 1). The β-class of enzymes contain a zinc site formed from a Cys and His ligand separated by 2 amino acids and another Cys ligand supplied from the N-terminal side of the protein (Table 1). The first member of the γ-class of carbonic anhydrases, CAM, was isolated and characterized from the methanogenic archaeon *Methanosarcina thermophila*.**[126]** Both the α and γ classes of enzymes have three histidine ligands supplied by β-sheet secondary structures in the catalytic zinc site (Tables 1 and 5). However they differ in the length of their short spacers (one versus four). This in turn allows the second His of the trimeric CAM enzyme to become part of the zinc-binding site in an adjacent monomer rather than bind to its own active-site zinc. The crystal structures of the native zinc enzyme and the cobalt-substituted enzyme show the metal-binding site is formed from His81 (ND1) and His122 (NE2) of one monomer and His117 (NE2) of another monomer.**[73,74]** In contrast to the tetrahedral zinc site observed in the α-class of enzymes that have only one zinc-bound water molecule (Table 1), the zinc CAM contains two water molecules in a trigonal-bipyramidal coordination geometry while the cobalt CAM contains three bound waters in an octahedral geometry. Both of these crystalline geometries are consistent with results obtained from XAFS studies performed in the solution state.**[127]**

6.1.2 Human Glyoxalase I: Square Pyramidal and Octahedral Zinc Sites

Another remarkable catalytic zinc site is found in human glyoxalase I where the C-terminal domain of one monomer interacts with the N-terminal domain of a second monomer to form two zinc-binding sites at the interface of the subunits.**[128]** The active-site zinc is coordinated by four protein residues and one water molecule in a square pyramidal coordination geometry. The base of the pyramid is formed from Gln33 and Glu99 of one subunit, Glu172 from the second subunit and a water molecule. The apex of the pyramid uses His126 from the second subunit. Such a geometry could be viewed as octahedral with one axial ligand missing. The results of EPR (cobalt enzyme)**[129]** and XAFS (zinc enzyme)**[130]** studies suggest a distorted octahedral coordination in solution. The sixth ligand site may be a water molecule. Another remarkable feature of this metalloenzyme is that while zinc binds tighter than Mg (3×10^{-11} vs 1×10^{-6} M) the Mg enzyme is fully active.**[131]** The octahedral metal-coordination geometry and the functional replacement of Zn by Mg is unusual for catalytic zinc sites. These results raise the possibility that Mg is the functional metal *in vivo*.

Mutagenic studies of the zinc ligands of the human enzyme suggest that the metal ligand Glu172 may be directly involved in catalysis.**[132]** Thus, both the E172Q and Q33E/E172Q double mutant still bind zinc but the catalytic activity is decreased by 10^5 and 10^8 fold, respectively. Crystallographic results of the enzyme complexed with a transition state analog S-(N-hydroxy-N-p-iodophenylcarbamoyl)glutathione, HIPC-GSH, that mimics the enediolate intermediate that should form along the reaction pathway are consistent with this hypothesis.**[133]** In this structure, the two oxygen atoms of the hydroxycarbamoyl moiety displace two zinc-bound water molecules that are observed in a possible product-like complex of S-p-nitrobenzyloxycarbonylglutathione, NBC-GSH. In addition the Glu172 carboxylate oxygen-Zn distance has increased from 2.0 Å to 3.3 Å in the HIPC-GSH complex indicating it is no longer a ligand to the zinc. The resulting coordination of the zinc thus changes from square pyramidal in the transition state-like complex to distorted octahedral in the product-like complex. The zinc ion is envisioned to play a Lewis acid role in catalysis by directly coordinating the enediol intermediate and the freed zinc ligand Glu172 is proposed to facilitate proton transfer between the adjacent carbon atoms of the substrate.**[133]**

6.1.3 E. Coli Glyoxalase I: Trigonal-Bipyramidal Zinc Site

While the human and *E. coli* enzymes have similar amino acid sequences and three-dimensional structures, they do not have the identical protein ligands. Nickel is believed to be the native metal in the *E. coli* glyoxalase I enzyme (*see* ***Nickel Enzymes & Cofactors***).**[134]** The nickel is bound octahedrally to His5 (NE2) and Glu56 (OE1) from one monomer, His74 (NE2) and Glu122 (OE1) from the other, and two water molecules.**[135]** Structure and function studies of *E. coli* glyoxalase I have shown the active nickel, cobalt, and cadmium enzymes have octahedral geometry while the zinc enzyme has trigonal-bipyramidal coordination and is inactive.**[135]** The zinc coordination site contains four protein ligands plus a single water molecule. In contrast, the metal-coordination sites in the active forms of the enzyme includes two water molecules bound to the metal ion, suggesting that this may be a key feature of the catalytic mechanism.

6.1.4 E. Coli Pdxa: Octahedral Zinc Site

Pyridoxal 5′-phosphate is an essential cofactor for many enzymes responsible for the metabolic conversions of amino acids. The fourth step in its synthetic pathway in *Escherichia coli* is catalyzed by the divalent metal ion-dependent enzyme 4-hydroxythreonine-4-phosphate dehydrogenase (PdxA), which converts 4-hydroxy-l-threonine phosphate (HTP) to 3-amino-2-oxopropyl phosphate.**[136]** The enzyme active site is located at its dimer interface, within a cleft between two subdomains and involves residues from both monomers and two zinc ions. Each zinc ion is bound to NE2 nitrogens of His166 and His266 from one monomer and the NE2 nitrogen of His211 of a second monomer and 3 water molecules in an octahedral coordination geometry (Table 5). These histidines are strictly conserved in 74 members of this family of enzymes. The amino and hydroxyl groups of the substrate, HTP, bind to the zinc ion in a pentacoordinate manner by replacing the three water molecules.[136]

6.1.5 *E. Coli L-histidinol Dehydrogenase: Octahedral Zinc Site*

L-histidinol dehydrogenase (HisD) catalyzes the last two steps in the biosynthesis of L-histidine: sequential NAD-dependent oxidations of L-histidinol to L-histidinaldehyde and then to L-histidine.[137] HisD functions as a homodimer and requires the presence of one zinc ion per monomer. The x-ray structure of *E. coli* HisD in the presence of zinc, NAD^+ and the substrate, L-histidinol, shows the zinc bound to the side-chain amide carbonyl of Gln259, the NE2 nitrogen of His262 and Asp360(OD2) of one monomer and the NE2 nitrogen of His419 of the other monomer and the substrate ND1 nitrogen and its amino group in a octahedral coordination geometry.[137] The role of zinc in this case is to position the substrate for catalysis. Since the NE2 nitrogen of His237 is within H-bonding distance of the histidinol OH, it likely participates in acid-base catalysis.

6.2 Protein Interface Structural-like Zinc Sites

There are a number of protein interface sites that have the properties of an enzyme structural zinc-binding site in that they are composed of four protein ligands and no water molecules. These sites may be involved in local protein conformation or be involved in stabilizing quaternary structure. The metal ion acting in this manner is not directly involved in the function of the protein but may still play an indirect role in aligning critical components of the protein for its intended function.

6.2.1 *Zinc-binding Sites in Superantigens*

Streptococcus pyogenes and *Staphylococcus aureus* secrete a number of enterotoxins and pyrogenic exotoxins, respectively. These toxins are known as superantigens, since they simultaneously form complexes with the major histocompatibility class II (MHC-II) molecules and T-cell receptors (TCRs) enabling them to activate a number of T-cell lymphocytes.[124,138,139] Thus, superantigens stimulate up to 20% of the T cells while only 0.0001% to 0.001% T cells are stimulated upon normal antigen presentation. The massive T-cell activation leads to cytokine release and systemic shock. The staphylococcal enterotoxins (SE) A, B, C1-C3, D and E, toxic shock syndrome toxin (TSST-1), the streptococcal pyrogenic exotoxins (SPE) A, B, Cs, G, and H, the streptococcal mitogenic exotoxins, SMEZ and SMEZ-2 are the best structurally studied superantigens thus far (Tables 5 and 6).

Zinc is believed to be an important factor in the mechanism of T-cell activation. Thus binding of staphylococcal enterotoxin A and enterotoxin E to HLA-DR1 is completely abolished by low concentrations of Ethylenediaminetetraacetic acid (EDTA).[140] This binding is completely restored by the addition of a 2 μM excess of Zn^{2+} but not by Ca^{2+}, Mg^{2+} or other metal ions. Studies using EDTA ± $ZnCl_2$ show zinc-dependent binding of *Streptococcus pyogenes* exotoxin (SPE-C), SPE-G, SPE-H and SMEZ and SMEZ-2 to the MHC class II molecule HLA-DR1 (affinities of 15 to 36 nM).[138] On the basis of these criteria, the superantigens SEB and the toxic shock syndrome toxin TSST do not show zinc-dependent binding to the MHC class II molecule.

Two distinct zinc-binding sites are apparent from the reported structures of the superantigens (Tables 5 and 6). These zinc sites contain at least three protein ligands with each site having short and long spacers. The third ligand comes from the N-terminal side of the second ligand. In one case the short spacer is one (Asp (OD1)-X-His (NE2)) with both ligands coming from a β-sheet, located in the C-terminal side of the protein. The third ligand is either an Asp or His residue located 33 to 39 amino acids away: SEA,[141,142] SEC3,[143] SED,[144] and SEH[145] (partial) and SPE-C,[146] SPE-H, and SMEZ-2[147] all contain this type of zinc-binding site (Tables 5 and 6). The second type of zinc-binding site has a short spacer of 3 and contains two His ligands in the N-terminal side of the superantigen with the third ligand located 27 to 34 amino acids away: SEC2,[148] SEA[149] (2nd Zn site) and SPEA and SPEA1[150,151] contain this type of site. The fourth ligand in these sites is quite variable. It may come from a neighboring protein molecule, from within the same molecule or be a bound water molecule. The variability in the fourth ligand could be due to the fact that this ligand should come from the MHC class II molecule. His81 of the β chain of the DR1 molecule has been proposed to be this ligand based on the fact that mutation of this ligand disrupts HLA-DR1 binding to SEA but not SEB or TSST-1 that do not bind zinc strongly.[152]

A somewhat similar zinc-binding site was observed in crystals of rat submaxillary gland tonin that had been grown in a zinc-containing mother liquor.[153] The zinc binds to the NE2 nitrogens of His97, His99, and the catalytic His57 of one molecule and Glu148 of an adjacent one. The presence of zinc was reported to inhibit the enzyme at pH 6.5. The structure of the zinc-binding sites in the dimeric form of psoriasin (S100A7) also contains three His and one Asp ligand.[154] This 22.7 kDa homodimeric protein belongs to the S100 class of calcium-binding EF-hand proteins (*see* ***Calcium-binding Proteins***). Two zinc-binding sites occur per dimer through the formation of a tetrahedral site consisting of the N-terminal

Table 5 Protein interface zinc sites[a]

Enzyme/Protein		PDB#	Class	L_1	X	L_2	Y	L_3	L'_1	Z	L'_2
Nitric Oxide SynthaseFamily			I								
Bovine endothelial		1NSE		Cys$_{\beta}$	4	Cys			Cys$_{\beta}$	4	Cys
Human endothelial		3NOS		Cys$_{\beta}$	4	Cys			Cys$_{\beta}$	4	Cys
Human inducible		1NSI		Cys	4	Cys			Cys	4	Cys
Mouse inducible		1DWV		Cys	4	Cys			Cys	4	Cys
Rat neuronal		1P6H		Cys	4	Cys			Cys	4	Cys
Sulfolobus solfactaricus Cytochrome P450		1F4T	I	Glu$_{2b\alpha}$	38	His$_{a\alpha}$			Glu$_{2b\alpha}$	38	His$_{a\alpha}$
Desulfovibrio desulfuricans											
Cytochrome C nitrite reductase		1OAH	I	His$_{L}$	62	Asp$_{L}$			His		Cl^-
E. coli Pdxa		1 PS6	I	His	99	His			His		$3H_2O$
E. coli L-histidinol dehydrogenase		1KAE	I	Gln$_{\alpha}$	2	His$_{a\alpha}$	97	Asp$_{\alpha}$	His$_{\alpha}$		free His
E. coli signal transducing protein, PTS IIA^{Glc}		1F3Z	II	His$_{\beta}$	14	His$_{\beta}$			Glu$_{\beta}$		H_2O
E. coli PTS IIA^{Glc}/glycerol kinase		1GLC	II	His$_{\beta}$	14	His$_{\beta}$			Glu$_{\alpha}$		H_2O
E. coli Histidine protein kinase domain of ArcB		1A0B	II	Glu$_{\alpha}$	3	Glu$_{\alpha}$	25	His$_{\alpha}$ (N)	Asp$_{\alpha}$		
Human Tyr kinase Lck$_{(7-35)}$-CD4$_{(396-433)}$		1Q68	II	Cys$_{\beta}$	2	Cys$_{L}$			Cys	1	Cys
Human Tyr kinase Lck$_{(7-35)}$-CD8$_{(189-207)}$		1Q69	II	Cys$_{\beta}$	2	Cys$_{L}$			Cys	1	Cys
Rat tonin		1TON	III	His	1	His	39	His (N)	Glu		
Mouse 7S nerve growth factor		1SGF	III	Glu	6	His$_{\beta}$			His$_{a\beta}$	4	Glu
Human glyoxalase I		1FRO	IV	Gln$_{\beta}$	65	Glu$_{\beta}$	–	H_2O	His$_{\beta}$	45	Glu$_{\beta}$
E. coli glyoxalase I		1F9Z	IV	His$_{\beta}$	50	Glu$_{\beta}$	–	H_2O	His$_{\beta}$	47	Glu$_{\beta}$
Methanosarcina thermophila γ-CA		1THJ	IV	His$_{\beta}$	–	H_2O	–	H_2O	His$_{\beta}$	40	His$_{\beta}$
Legionella pneumophila Mip		1FD9	V	Glu$_{\beta}$	74	His$_{\beta}$			Glu$_{\alpha}$		
Superantigen Family											
Staphylococcus aureus enterotoxin (SEC2)		1STE		His	3	His$_{\beta}$	34	Asp$_{\beta}$ (N)	Asp		
Staphylococcus aureus enterotoxin (SEC3)		1CK1		His	3	His$_{\beta}$	34	Asp$_{\beta}$ (N)	Asp		
Staphylococcus aureus enterotoxin (SEA)		1ESF		H_2O		His$_{\beta}$	27	Asp$_{\beta}$ (N)	Glu$_{a\beta}$		
Staphylococcus aureus enterotoxin (SEA)		1SXT		Asp$_{\beta}$	1	His$_{\beta}$	37	His$_{\beta}$ (N)	His or H_2O		
Staphylococcus aureus enterotoxin (SED)				Asp$_{\beta}$	1	His$_{\beta}$	37	Asp$_{\beta}$ (N)	His$_{\beta}$		
Staphylococcus aureus enterotoxin (SED)				His$_{\beta}$	3	Glu$_{\beta}$			His	3	Lys
Staphylococcus aureus enterotoxin (SEH)		1EWC		Asp$_{\beta}$	1	His$_{\beta}$			H_2O		H_2O
Streptococcus pyogenes exotoxin (SPE-C)		1AN8		Asp$_{\beta}$	1	His$_{\beta}$	33	His$_{\beta}$ (N)	His$_{b\beta}$		
Staphylococcus aureus TSST-1		4TSS		His	60	His$_{\beta}$			His	60	His$_{\beta}$
Human psoriasin (S100A7)		3PSR		His$_{\alpha}$	3	His$_{2a\alpha}$			Asp	6	His$_{\alpha}$
Human interferon-$\alpha_{2\beta}$ dimer				Glu$_{\alpha}$	0	Glu$_{\alpha}$			Glu$_{\alpha}$	0	Glu$_{\alpha}$
Human interferon β dimer		1AU1		His$_{\alpha}$	3	His$_{\alpha}$			His$_{b\alpha}$		H_2O
Human prolactin receptor/growth hormone		1BP3		Asp$_{\beta}$	0	His$_{a\beta}$			His$_{\alpha}$	155	Glu$_{\alpha}$
Mouse survivin		1M4M		Glu$_{\beta}$	3	His$_{a\beta}$			Glu$_{\beta}$	3	His$_{a\beta}$
Chicken E-tropomudulin		1IO0		Asp$_{L}$	1	Asp$_{L}$			Asp$_{\beta}$	29	His$_{L}$
Urtica dioica agglutinin isolectin I		1IQB		His$_{\beta}$ Asp					His$_{L}$ His$_{\beta}$		
bacteriophage T4 gp12 trimer		1OCY		(His	1	His)$_3$					
Shaw T1 tetramer KV3		3KVT		Cys$_{2b\alpha}$	0	Cys$_{b\alpha}$	26	His (N)	Cys$_{b\alpha}$		
Shaw T1 tetramer KV4		1NN7		Cys$_{2b\alpha}$	0	Cys$_{b\alpha}$	26	His (N)	Cys$_{b\alpha}$		
Human Apo21L/TRAIL		1DG6		(Cys$_{a\beta}$)$_3$		Solv					
Squash trypsin inhibitor		1LU0		(Glu$_{2b\beta}$)$_4$							
E. coli colicin 3 Immunity Protein		3EIP		Cys$_{b\beta}$					Cys$_{b\beta}$		
E. coli ZntRSensor	Zn1	1Q08		Cys$_{L}$	9	Cys$_{L}$			***Cys***$_{\beta}$		***Pi***
	Zn2			Cys$_{L}$	3	His$_{\beta}$			***Cys***$_{\beta}$		***Pi***

[a] L'_1 and L'_2 are the second subunit or protein zinc ligands and Z is the spacer for these ligands. See footnote in Table 1 for other definitions.

Table 6 Zinc-binding proteins[a]

Protein	Classification	PDB#	L_1	X	L_2	Y	L_3	Z	L_4
Human endostatin	Angiogenesis Inhibitor	1BNL	His	1	His	7	His$_{\beta}$	64	Asp$_{b\beta}$
Mouse endostatin	Angiogenesis Inhibitor	1DY0	His	1	His	7	His$_{\beta}$	64	Asp$_{b\beta}$
			His	3	Asp	5	His$_{\beta}$	64	Asp$_{b\beta}$
Toxin Family									
Staphylococcus aureus A (SEA)	Enterotoxin	1ESF	Asp$_{\beta}$	1	His$_{\beta}$	37	His$_{\beta}$	185	Ser (N)
Streptococcus pyogenes (SPE-H)	Exotoxin	1 EU3	Asp$_{\beta}$	1	His$_{\beta}$	39	His$_{\beta}$ (N)		H_2O
Streptococcus pyogenes (SMEZ-2)	Exotoxin	1 EU4	Asp$_{\beta}$	1	His$_{\beta}$	37	Asp$_{\beta}$ (N)		H_2O
Streptococcus pyogenes A(SPE-A1)	Exotoxin	1B1Z	His$_{\beta}$	3	His$_{\beta}$	28	Asp$_{\beta}$ (N)		H_2O
Streptococcus pyogenes A(SPE-A)	Exotoxin	1FNU	His$_{\beta}$	3	His$_{\beta}$	28	Asp$_{\beta}$	43	Glu$_{\beta}$ (N)
Sulfolobus Sp. Ferredoxin	Electron transport	1XER	His$_{\beta}$	2	His$_{\beta}$	14	His$_{\beta}$	41	Asp$_{\beta}$
Saccharomyces cerevisiae Actin interacting protein, Aip1p	Protein binding	1PGU	His$_{2a\beta}$	1	Glu$_{L}$	37	His$_{\beta}$	1	Asp$_{L}$
ABC Transporters									
Treponema pallidum Troa A	Zn binding protein	1TOA	His	64	His$_{2a\beta}$	65	His$_{L}$	79	Asp
S. Pneumoniae Surface antigen PsaA	Zn binding protein	1PSZ	His	71	His$_{2a\beta}$	65	Glu$_{L}$	74	Asp
Synechocystis sp. 6803 ZnuA	Zn binding protein	1PQ4	His	95	His$_{2a\beta}$	63	His$_{L}$		H_2O, Solv
Neisseria meningitidis Opca	membrane protein	1K24	His$_{\beta}$	1	Asp$_{\beta}$	19	His$_{\beta}$	H_2O	
			Glu$_{1b\beta}$	1	His				
			Asp	58	His$_{\beta}$	47	Thr(CO)		
Escherichia coli ZntA	Zn transport	1MWZ	Asp$_{2b\alpha}$	0	Cys$_{b\alpha}$	2	Cys$_{\alpha}$		
Human oncoprotein Ski	Signaling Protein	1MR1	His	1	His	11	Cys$_{L}$	2	Cys$_{\beta}$ (N)
Protector protein $\sigma 3$	Viral	1JMU	Cys	1	His	16	Cys$_{L}$	2	Cys$_{\beta}$ (N)
Haemophilus influenzae SecA	Chaperone	1OZB	Cys$_{\beta}$	1	Cys$_{\beta}$	8	Cys	0	His
Bir Domain Family									
Human Survivin	Apoptosis	1F3H	Cys$_{\beta}$	2	Cys$_{L}$	16	His$_{\alpha}$	6	Cys$_{L}$
Mouse Survivin	Apoptosis	1M4M	Cys$_{\beta}$	2	Cys$_{2a\beta}$	16	His$_{\alpha}$	6	Cys$_{L}$
Human Xiap-Bir3	Apoptosis	1G73,1NW9	Cys$_{\beta}$	2	Cys$_{L}$	16	His$_{\alpha}$	6	Cys$_{b\alpha}$
Drosophila melanogaster Diap1-Bir2	Apoptosis	1Q4Q, 1JD4	Cys$_{\beta}$	2	Cys$_{L}$	16	His$_{\alpha}$	6	Cys$_{b\alpha}$
Human Xiap-Bir2	Apoptosis	1I3O	Cys$_{\beta}$	2	Cys$_{L}$	16	His$_{\alpha}$	6	Cys$_{b\alpha}$
Human melanoma inhibitor	Apoptosis	1OXN	Cys$_{\beta}$	2	Cys$_{L}$	16	His$_{\alpha}$	6	Cys$_{b\alpha}$
Methanothermobacter thermautotrophic									
ARF-GAP domain PYK2-associated protein β		1DCQ	Cys$_{\beta}$	2	Cys$_{L}$	16	Cys$_{b\alpha}$	2	Cys$_{\alpha}$
Xenopus laevis Xnf7 Bbox	Developmental protein	1FRE	Cys$_{\beta}$	2	His	18	Cys	5	His
Thermus thermophilus chain D	30 SRibosomal protein	1N32	Cys$_{2b\alpha}$	2	Cys$_{\alpha}$	13	Cys	4	Cys
Thermus thermophilus chain N			Cys$_{\alpha}$	2	Cys$_{b\alpha}$	12	Cys	2	Cys (N)
Human replication protein A	Replication	1L1O	Cys$_{L}$	2	Cys$_{\beta}$	13	Cys$_{\beta}$	4	Cys$_{\beta}$ (N)
Saccharomyces cerevisiae Sec23	Signaling Protein	1M2O	Cys$_{L}$	2	Cys$_{\beta}$	18	Cys$_{\beta}$	4	Cys$_{\beta}$ (N)
mt MCM	Replication	1LTL	Cys$_{\beta}$	2	Cys$_{L}$	18	Cys	2	Cys
Pyrococcus abyssi γ subunit of initiation factor, e/aIf2	Translation	1KJZ	Cys$_{\beta}$	2	Cys$_{L}$	8	Cys$_{\beta}$	2	Cys$_{L}$
Human VDR DBD	Transcription	1 KB2	Cys$_{\beta}$	2	Cys$_{L}$	13	Cys$_{L}$	2	Cys$_{\alpha}$
			Cys$_{\alpha}$	2	Cys$_{b\alpha}$	9	Cys	5	Cys (N)
Human CH1 domain of p300 bound to HIF-1α (CTAD)	Transactivation	1L3E	His$_{\alpha}$	3	Cys$_{\alpha}$	12	Cys	4	Cys$_{\alpha}$
			His$_{\alpha}$	3	Cys	5	Cys	4	Cys$_{\alpha}$
			His$_{\alpha}$	3	Cys$_{a\alpha}$	4	Cys$_{b\alpha}$	2	Cys$_{\alpha}$
Human CH1 domain of p300 bound to CITED2-TAD	Regulation	1P4Q	His$_{\alpha}$	3	Cys$_{\alpha}$	12	Cys	4	Cys$_{\alpha}$
			His$_{\alpha}$	3	Cys$_{a\alpha}$	5	Cys	4	Cys$_{\alpha}$
			His$_{\alpha}$	3	Cys$_{a\alpha}$	4	Cys	2	Cys$_{\alpha}$
Human 53BP1 BRCT	Gene regulation	1GZH	Cys$_{b\alpha}$	2	His$_{\alpha}$	58	Cys$_{a\beta}$	3	Cys
LIM Domain Family									
Mouse N-term LMO4 LIM1	Gene regulation	1M3V	Cys	2	Cys	17	His$_{a\beta}$	2	Cys
			Cys	2	Cys	19	Cys$_{a\beta}$	2	Asp$_{\alpha}$
Mouse Flin2 N-term LMO2	Gene regulation	1J20	Cys	2	Cys	17	His	2	Cys
			Cys	2	Cys	19	Cys$_{b\alpha}$	2	Asp$_{\alpha}$
Chicken CRP2 LIM2	Contractile protein	1CTL	Cys$_{\beta}$	2	Cys$_{L}$	17	His$_{\beta}$	2	Cys$_{b\beta}$
			Cys$_{\beta}$	2	Cys$_{L}$	17	Cys$_{\beta}$	2	Cys$_{2a\beta}$

(cont’d overleaf)

Table 6 cont'd

Protein	Classification	PDB#	L_1	X	L_2	Y	L_3	Z	L_4
Chicken CRP1 LIM2	Contractile protein	1B8T	Cys$_{\beta}$	2	Cys$_{L}$	17	His$_{a\beta}$	2	Cys$_{b\beta}$
			Cys$_{\beta}$	2	Cys$_{L}$	17	Cys$_{\beta}$	2	Cys$_{\alpha}$
Chicken CRP1 LIM1	Contractile protein	1B8T	Cys$_{\beta}$	2	Cys$_{L}$	17	His$_{a\beta}$	2	Cys$_{b\beta}$
			Cys$_{\beta}$	2	Cys$_{L}$	17	Cys$_{\beta}$	2	Cys$_{\alpha}$
Quail CRP2 LIM2	Contractile protein	1QLI	Cys$_{\beta}$	2	Cys$_{L}$	17	His$_{a\beta}$	2	Cys
			Cys	2	Cys	17	Cys$_{a\beta}$	2	Cys
Quail CRP2 LIM2	Contractile protein	1IBI	Cys$_{\beta}$	2	Cys$_{L}$	17	His	2	Cys
			Cys	2	Cys	17	Cys$_{b\alpha}$	2	Cys$_{\alpha}$
Quail CRP2 LIM1	Contractile protein	1A7I	Cys	2	Cys	17	His	2	Cys
			Cys	2	Cys	17	Cys$_{2b\alpha}$	2	Cys$_{\alpha}$
Rat CRIP	Contractile protein	1IML	Cys$_{\beta}$	2	Cys$_{L}$	17	His$_{\beta}$	2	Cys$_{b\beta}$
			Cys$_{\beta}$	2	Cys$_{L}$	17	Cys$_{\beta}$	3	Cys$_{\alpha}$
Human Pinch protein LIM1	Cell adhesion	1G47	Cys$_{\beta}$	2	Cys$_{L}$	17	His$_{a\beta}$	2	Cys$_{b\beta}$
			Cys$_{\beta}$	2	Cys$_{L}$	17	Cys$_{a\beta}$	1	His$_{\alpha}$
Human Pinch protein LIM4	Cell adhesion	1NYP	Cys$_{\beta}$	2	Cys$_{L}$	16	His$_{a\beta}$	2	His$_{b\beta}$
			Cys$_{\beta}$	2	Cys$_{L}$	17	His$_{a\beta}$	2	Cys$_{\alpha}$
Sv40 T antigen helicase domain	Viral Protein	1N25	Cys$_{b\alpha}$	2	Cys$_{\alpha}$	7	His	3	His$_{\alpha}$
Human Mob1	Cell cycle	1PI1	Cys	4	Cys	76	His$_{\alpha}$	4	His$_{L}$
Thermus thermophilus L36	Ribosomal protein	1DGZ	Cys	2	Cys$_{b\beta}$	12	Cys$_{a\beta}$	4	His$_{2b\beta}$
Methanococcus jannashii Eif-2β	Translation	1K81	Cys	2	Cys	17	Cys$_{\beta}$	4	Cys$_{L}$
E. coli DnaJ protein	Chaperone	1EXK	Cys$_{\beta}$	2	Cys$_{L}$	49	Cys$_{\beta}$	2	Cys
			Cys$_{\beta}$	2	Cys$_{L}$	18	Cys$_{\beta}$	2	Cys
Saccharomyces cerevisiae Hsp Ydj1	Protein transport	1NLT	Cys$_{\beta}$	2	Cys	54	Cys	2	Cys
			Cys$_{\beta}$	2	Cys$_{2a\beta}$	22	Cys	2	Cys
Vibrio cholerae EpsE	Protein transport	1P9R	Cys$_{\beta}$	2	Cys$_{L}$	29	Cys	2	Cys
E. coli ADA	Repair	1EYF	Cys	2	Cys$_{\beta}$	26	Cys	3	Cys$_{\beta}$ (N)
E. coli Thr-tRNA synthetase	Discriminating	1EVK	Cys$_{\alpha}$	50	His$_{\beta}$	125	His$_{\beta}$		H_2O
Human SHBG	Signaling protein	1F5F	Asp$_{\beta}$	17	His$_{s\beta}$	52	His$_{b\beta}$		?
Auxin Binding Protein	Receptor	1LR5	His$_{\beta}$	1	His$_{a\beta}$	3	Glu$_{\beta}$	42	His$_{\beta}$$H_2O$

[a] See footnote of Table 1 for the definitions of terms.

His17 (NE2) and Asp24 (OD1) of one monomer and His86 (NE2) and His90 (NE2) of the other. This binding site is apparently weak since it is reported to have a dissociation constant of 100 μM.

The finding of zinc binding at the interface of two enterotoxin molecules in several of the superantigens (Table 5) could mean that zinc influences the function by forming dimers of the superantigen. SED crystallizes as a Zn^{2+}-dependent dimer with two high affinity zinc sites located between the C-terminal β-sheets of the two monomers.[144] Each zinc is tetrahedrally coordinated by His118 from one SED molecule and Asp182, His220 and Asp222 from the other. Thus, in the case of SED it has been suggested that zinc binding could induce dimer formation and each monomer could bind to the MHC class II molecule.[144] This type of zinc ligation and zinc-mediated dimerization occurs in several SECs, but not in most staphylococcal enterotoxins. The potential importance of zinc in SEC-mediated pathogenesis was investigated by site-directed mutagenesis by replacing the SEC zinc-binding ligands with alanine.[143] The SEC mutants were unable to bind zinc and failed to form dimers. However, it was concluded that zinc binding was not essential for T-cell stimulation, emesis, or lethality although in general the mutants were less pyrogenic.

6.2.2 *Nitric Oxide Synthase*

Although His, Glu, and Asp residues are frequently used in forming these protein interface sites, Cys-containing sites are also observed. A zinc ion is tetrahedrally coordinated to a pair of symmetry-related Cys residues near the bottom of dimer interface of the bovine endothelial nitric oxide synthase, eNOS or NOS-3 (Table 5) (*see* ***Nitrogen Monoxide (Nitric Oxide): Bioinorganic Chemistry***).[155] The Cys ligands, Cys96 and Cys101, are part of a small three-stranded antiparallel β-sheet that orientates the Cys ligands in the same direction directly across the antiparallel strands. The zinc site is further stabilized by H-bonds between the Cys ligands and the backbone amide NH of Leu102 and Gly103 as well as a H-bond of the amide NH of Cys101 to the carbonyl of Asn468. The zinc is positioned equidistant from each heme (21.6 Å) and each tetrahydrobiopterin, H_4B (12 Å). Ser104, 2 amino acids removed from one of the Cys ligands, H-bonds directly to the pterin side-chain hydroxyl group. The metal center is believed to act in a structural capacity to maintain the integrity of the pterin-binding site. It is also centered in the most electropositive region of eNOS. It could therefore provide a binding site for the electronegative reductase domain. In addition, if one of the Cys ligands has nucleophilic capacity it could undergo S-nitrosylation.[156] A precedent for this is the DNA repair protein *Escherichia coli* Ada in which a zinc-bound Cys can be methylated irreversibly in the DNA complex.[157] The nitrosylated Cys might then release zinc, which may be controlled by the redox status in situ.[158]

These Cys residues are conserved in 20 mammalian e, i, and n-NOS enzymes, suggesting that the site may occur in all forms of NOS.[155] The crystal structures of the *E. coli* expressed human endothethial, eNOS,[159] the human inducible form iNOS or NOS-2,[159,160] mouse iNOS[161] and the rat neuronal nNOS or NOS-3[162] all have this same zinc-binding site in agreement with the sequence analysis.

6.2.3 Shaw T1

A highly conserved zinc protein interface Cys/His site occurs in the N-terminal, cytoplasmic tetramerization domain (T1) of voltage-gated K^+ channels.[163] The crystal structure of the *Shaw* T1 tetramers reveals a four-layered protein scaffolding. Within layer 4 on the proposed membrane side of the tetramer, there are 4 zinc ions coordinated by a His and two Cys from one monomer and one Cys from another. The zinc is tetrahedrally coordinated by Cys102 and Cys103 from layer 4 and His75 (ND1) from layer 3 of one monomer and Cys81 from layer 3 of another monomer. This site (CysCysX_{20}CysX_5His of one monomer) is conserved for 62 members of the *Shaw*, *Shab*, and *Shal* T1 domain sequences but not for the *Shaker* T1 domain.[163] The physiological function of this zinc site is unknown.

6.2.4 Human Tyrosine Kinase Lck complexes with CD4 and CD8

The Sarc family tyrosine kinase Lck transduces signals that are required for normal T-cell lymphocyte development and antigen-dependent activation of mature T cells.[164] It does this by associating its N-terminus with the cytoplasmic tails of T-cell coreceptors CD4 and CD8α in a zinc-dependent manner. The solution structures of ternary zinc-CD4-Lck and zinc-CD8α-Lck complexes were determined by using peptides of the appropriate regions of the proteins.[164] In each case, zinc binds to Cys23 and Cys29 of Lck and completes its tetrahedral coordination by binding to two Cys residues of CD4 (Cys420 and Cys422) or CD8α (Cys194 and Cys196). The zinc is thus used to clasp the T-cell receptors to Lck. Other similar structural elements also are observed in this binding process.

6.2.5 Zinc-his/Glu Sites at Protein Interfaces

There are several His/Glu combinations that lead to zinc binding at the interface of proteins (Table 5). A number of these zinc sites are symmetry related. Thus zinc binds between Glu139 (OE1) and His178 (NE2) in one molecule of the asymmetric crystal unit of the 4 phenylimidazole-bound *Sulfolobus solfataricus* cytochrome P450 and their symmetry residues in another molecule.[165] The functional importance of a dimer and zinc's contribution to its stability is not known. However, no zinc was added in the crystalline procedure. A His/Glu site with a short spacer of 3 is observed in the dimer interface of mouse survivin (Table 5).[166] The human survivin does not form a similar intermolecular zinc site.[167]

In crystals of the high molecular weight form of nerve growth factor 7S NGF, a zinc is tetrahedrally bound between His82 (NE2) and Glu75 (OE1) of the α-subunit and His217 (NE2) and Glu222 (OE1) of the γ-subunit.[168] The binding of zinc to this interface is consistent with the observation that zinc enhances the stability of the 7S complex.

6.3 Zinc Sites Induced by High Zinc Concentrations in Crystallization Solutions

Zinc is often used in crystallization buffers because it appears to aid in formation of high quality crystals. Since the zinc concentrations used to obtain the crystals is in the range of a few mM to over 100 mM these sites often may not be of physiological significance. The effect of zinc on protein function and/or structure should be correlated to the concentration needed to observe zinc binding to the crystalline enzyme. However, the fact that zinc has the property of making better protein crystals may reflect its ability to perform inter-protein interactions under physiological conditions where the concentration of water may not be 55 M and the amount of zinc needed for the binding maybe much less. The great majority of these zinc sites use His, Asp, and Glu as ligands.

The human pathogen *Legionella pneumophila*, the etiological agent of the severe and often fatal Legionnaires' disease, produces a major virulence factor, termed macrophage infectivity potentiator protein (Mip), that is necessary for optimal multiplication of the bacteria within human alveolar macrophage.[169] The interaction of the C-terminal FKBP (binds drug FK506) domains of adjacent Mip dimers in the crystal lattice is mediated by two zinc ions, which were added for crystallization and enabled the solving of the structure. The NE2 nitrogen of His205 from one Mip C-terminal domain and Glu164(OE1) from a neighboring molecule and two water molecules one of which bridges to a second zinc ion that binds to Glu130(OE1) of the first Mip molecule and two water molecules complete the tetrahedral coordination of each zinc ion. Zinc is not an intrinsic part of the Mip protein and does not influence the enzyme's peptidylprolyl isomerase activity.[169] The authors reason its sole function is to form the observed crystal contact.

The crystals of the human interferon-α_{2B} dimers, huIFN-α_{2B}, obtained in the presence of 40 mM zinc acetate[170] show the most extensive interactions occur in the vicinity of the zinc-binding site. This site is formed from adjacent Glu residues 41 and 42 located on a 3_{10} helix. A distorted-tetrahedral zinc coordination sphere is completed by the identical glutamates from a two-fold symmetry-related molecule. However, gel permeation studies indicate huIFN-α_{2B} is a monomer up to 50 μM and the presence of 1 mM Zn does not shift the equilibrium toward a dimer.[170]

A tetrahedral zinc-binding site between symmetry-related monomers in the cytochrome C reductase is composed of a His and an Asp ligand in one monomer, a His ligand from the second monomer and a chloride ion.[171] Since there is no known effect of zinc in this system, the site is considered to be an artifact. Five tetrahedral zinc-binding sites are observed in symmetry-related molecules of granzyme B in complex with a peptide analog, AC-IEPD-CHO.[172] These zinc coordination sites are believed to be artifacts of using zinc in the crystallization buffer since zinc is not required for substrate binding.

Zinc (6–10 mM) is used to aid in crystallization of chicken tropomodulin.[173] The resulting crystals contain a zinc-binding site at the interface of two protein molecules in the crystal lattice (Table 5). It is not known what effect zinc has on the protein function in solution. When the crystals of *Urtica dioica* agglutinin isolectin I are grown in 100 mM zinc acetate, the C-terminal domains binds two zinc ions at the sugar binding site.[174] Thus, His47 of one protein molecule and His67 of a second one bind the first zinc while Asp 75 of molecule one and His47 of molecule two bind the second zinc ion. The effect of zinc under more physiological conditions is not known.

7 ZINC-BINDING PROTEINS

Structural studies in recent years have revealed a number of zinc-binding sites in proteins of diverse function. In compiling Table 6, a number of DNA-binding proteins have been left out since there are several good sources of information on these zinc sites, which usually contain Cys and His ligands (*see* ***Zinc: DNA-binding Proteins***).[96–100,175,176]

The great majority of these zinc sites are formed from four protein side-chain ligands to yield a tetrahedral binding site. Their function may therefore be related to the local and/or overall structure since the sites span from 22 to 227 amino acids. As in the case of structural zinc sites in enzymes (Table 4), the vast majority of the sites contain at least one short spacer. The residues generally are supplied from β-sheets or reside within one or two residues of such a secondary structure (Table 6). The amino acids, His and Cys, are the predominate suppliers of ligands but several sites are made up of combinations of His, Asp, and Glu residues. Some examples of the group will be highlighted herein since the properties of a number of the listed proteins have been detailed elsewhere.[4]

7.1 LIM Domain Proteins

Two consecutive zinc-binding sites spanning 50 to 54 amino acids with the zinc ions located between 16.5 Å and 18.0 Å occurs in a number of proteins of diverse physiological function (Table 6). The zinc-binding sites are often referred to as zinc fingers but they are not involved in DNA-binding and their purpose appears to be a structural one. The name LIM comes from the identification of tandem copies of a Cys-rich motif that was present amino-terminal to the homeodomains in the proteins encoded by the *Caenorhabditis elegans* genes lin-11, isl-1 and mec-3 (*see* ***Zinc: DNA-binding Proteins***).[177] NMR studies have determined the structural properties of several of the LIM domains (Table 6). These tetrahedral zinc sites contain four protein ligands that are mainly Cys residues in combination with His and Asp residues. The N-terminal zinc site is highly conserved having a zinc signature of CCHC. The C-terminal site is more variable with the last two ligands being various combinations of Cys with His or Asp. No bound water molecules are found in these sites. The first and third ligands usually are supplied from a β-sheet structure. The second ligand resides in a loop region between two β-sheets while the fourth ligand may come from an α-helix, or β-sheet region of the protein (Table 6).

These domains are often found as repeats in proteins that are involved in diverse biochemical processes. The LIM domains are thought to function as protein interaction modules, mediating specific contacts between members of functional complexes and modulating the activity of some of the constituent proteins.[178] Group 1 of the LIM proteins contain the LIM homeodomain (LHX), LIMK (LIM kinases) and LMO (rhombotin) subfamilies.

LMO2 and LMO4 are members of a small family of nuclear transcriptional regulators that are important for both normal development and disease processes. LMO2 is essential for hemopoiesis and angiogenesis, and inappropriate overexpression of this protein leads to T-cell leukemias.[179] LMO4 is developmentally regulated in the mammary gland and has been implicated in breast oncogenesis.

Group 2 of the LIM domains contains the Cys-rich Proteins (CRP) and Cys-rich Intestinal Protein (CRIP) subfamilies that have tandem repeats of zinc-binding sites containing the ligands CCHC and CCCC (Table 6). The structures of the chicken,[180] quail,[181,182] and rat[183,184] proteins are determined by NMR. These proteins have a role in the contractile machinery of muscle. Three vertebrate CRPs (CRP1-3) are associated with the actin cytoskeleton, and one has been shown to be required for striated muscle structure and function in muscle differentiation and function.[180]

The PINCH (Particularly Interesting New Cys/His rich protein) is a widely expressed adapter protein that contains five LIM domains that belong to group 3 of the LIM domain subfamilies.[185] PINCH is found in focal adhesions, large cellular complexes that link extracellular matrix to the actin cytoskeleton and has been implicated as a platform for multiple protein–protein interactions that mediate integrin signaling within focal adhesions.[186]

7.2 BIR Domain Proteins

Another repeating zinc-binding site defines a domain in a protein that is an inhibitor of apoptosis, IAP. Apoptosis is a physiological cell suicide program that is essential to the development and maintenance of healthy tissues.[187] Thus, malfunctioning cells are targeted for destruction. Disruption of this process is implicated in cancer, auto immune, and immunodeficiency diseases. The IAP family members contain a protein segment of about 80 amino acids, named the baculovirus IAP repeat (BIR), domain since it was first observed in apoptosis suppressors in the genome of baculoviruses. BIR domains have been found in mammalian, fly, nematode, yeast and virus proteins.[187] One of the first described members of the family was Survivin, a relatively small 16 kDa protein. Both the human and mouse proteins contain a zinc-binding site in the N-terminal, BIR-like domain.[166,167] The zinc binds to Cys57, Cys60, His77 (NE2) and Cys84 in both human and mouse proteins (Table 6).

The X-ray structures of several of these proteins shows a highly conserved zinc-binding site spanning 28 amino acids with the spacing characteristics of $Cx_2Cx_{16}Hx_2C$ (Table 6). The first two Cys ligands are supplied by a β-sheet and loop region between two β-sheets, while the third His ligand resides in an α-helix and the last Cys ligand is in a loop between two α-helices.

Proteins containing these domains have been shown to inhibit caspases.[187] At least 8 members of the mammalian family of IAP proteins containing two to three copies of the BIR domain have been identified.[188] These BIR domains may function differently in the inhibition of the caspases. The third BIR repeat, BIR3, of the X-linked protein, X-linked inhibitor of apoptosis protein (XIAP) binds to monomeric initiator caspase-9 to form a heterodimer and thus prevents caspase-9 from forming its functional dimer, resulting in loss of enzymatic activity.[188]

The crystal structure of the BIR2 domain of XIAP in complex with caspase-3 reveals the inhibitor makes limited contacts through its BIR domain to the surface of the enzyme, and most contacts to caspase-3 originate from the N-terminal extension.[189] The mechanism of inhibition is likely due to blocking substrate binding.

The mitochondrial protein Smac/DIABLO promotes apoptosis by eliminating the inhibitory effect of IAPs through physical interactions.[190] The crystal structure of Smac/DIABLO complexed with the BIR3 domain of XIAP indicate the relief of inhibition by the IAP protein occurs mainly through the N-terminal four residues (Ala-Val-Pro-Ile) in Smac/DIABLO. The N-terminal Ala binds in a hydrophobic pocket of BIR3, that makes five hydrogen bonds to neighboring residues on BIR3.

The inhibitor of apoptosis protein DIAP1 suppresses Dronc-dependent cell death in *Drosophila melangaster*, with the second BIR domain (BIR2) playing an important role.[191] DIAP1 is an E3 ubiquitin ligase. The BIR2 domain of DIAP1 recognizes a 12-amino acid residue sequence in Dronc that is essential for DIAP1 binding to Dronc, and for targeting Dronc for ubiquitination. Three proteins, Reaper, Hid and Grim, (RHG proteins) promote apoptosis in *Drosophilia melangaster* in part by binding to the BIR2 of DIAP1 through their conserved N-terminal sequences in a manner similar to that observed for the Smac and XIAP complex.[192]

Five very similar BIR repeats are observed in the melanoma inhibitor of apoptosis (ML-IAP).[193] The zinc sites in these domains lie in a trapezoid-like geometry (pdb# 1OXN) with the distances between zinc in domains A and D and B and C being 13.5 Å while all other distances between neighboring zinc sites varies between 26 and 35 Å (Figure 15). Peptides based on the processed N-terminus of Smac/DIABLO can negate the ability of overexpressed ML-IAP or XIAP to suppress drug-induced apoptosis.[193] These peptides have been demonstrated to bind to a single BIR of ML-IAP (protomer E) and the BIR3 of XIAP with similar high affinities ($\sim$0.5 μM).[193] Protomers A-D form a tetramer with the N-terminus peptide of a neighboring domain binding to the Smac binding site.

A somewhat similar zinc site is seen in one of the ADP ribosylation factors (ARFs), which are members of the Ras superfamily of GTP-binding proteins. Sequences of ARF-GAP domains show no recognizable similarity to those of

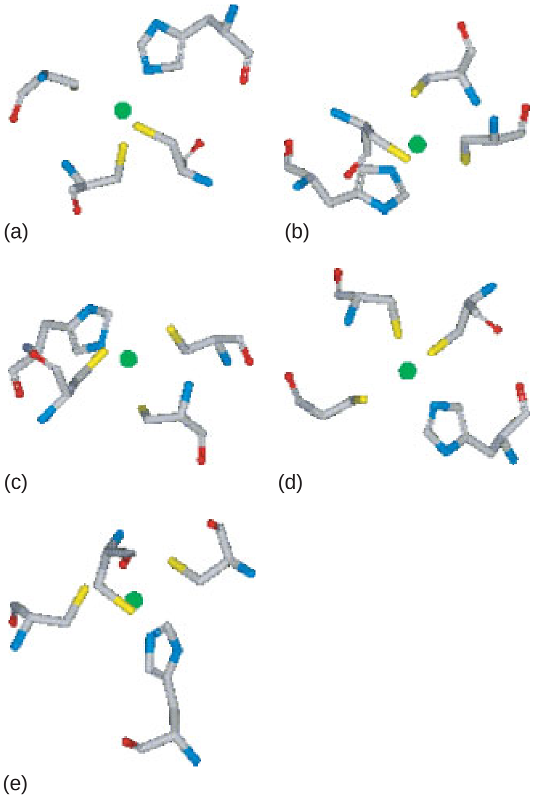

Figure 15 The zinc sites in the five BIR domains of the melanoma inhibitor of apoptosis are arranged in a trapezoid-like geometry (pdb# 1OXN). Structure prepared using DS ViewerPro 5.0 Accelrys Inc. San Diego, CA

other GAPs, and contain a characteristic $Cx_2Cx_{16-17}Cx_2C$ motif[194] similar to that found for the zinc sites in inhibitor of apoptosis proteins (Table 6). The crystal structure of the ARF-GAP domain comprises a central three-stranded β-sheet flanked by five α-helices, with a zinc ion coordinated by four cysteines with spacing and secondary structure similar to that found in the zinc sites of the BIR-containing proteins (Table 6).

7.3 CH1 Domain

Three zinc ions bound in a triangular relationship are found in the transcriptional coactivators CBP and p300.[195] Adaptation to hypoxia is mediated by transactivation of hypoxia-responsive genes by hypoxia-inducible factor-1 (HIF-1) in complex with the CBP and p300. The domain the zinc ions bind to is referred to as a Cys/His region, CH1. The three zinc ions bind to Cys and His ligands covering 66 amino acids, with no overlaps in the sequence (Table 6). Each binding site contains three Cys and one His ligand. The first two ligands are always a His and Cys with a spacer of 3 and supplied by α-helices. The spacing varies for the last two Cys ligands. The three zinc sites are at the vertices of a nearly perfect equilateral triangle with 21 to 22 Å distances between zinc ions on the sides of the triangle (pdb# 1P4Q). The zinc ions are critical to the structural stability of this domain since their removal by EDTA yields an NMR spectrum characteristic of an unfolded protein.[195] CH1 serves as a scaffold for folding of the HIF-1α C-terminal transactivation domain (TAD), which forms a vise-like clamp on the CH1 domain that is stabilized by extensive hydrophobic and polar interactions.

The protein CITED2, which binds p300/CBP, is thought to be a negative regulator of HIF-1 transactivation.[196] The CITED2-TAD binds a more extensive surface of CH1 than does the HIF-1α C-TAD. However, a conserved amino acid sequence motif, LPxL, in CITED2 and HIF-1α interacts with an overlapping binding site on CH1 likely accounting for the negative regulation effect.

7.4 Zinc Transporters

A number of bacterial metal transporters belong to the family of ATP-binding cassette (ABC) transporter system (*see* ***Metallochaperones & Metal Ion Homeostasis***).[197] These systems constitute one of the most abundant superfamilies of proteins. They are involved in the transport of a wide variety of substances and in many cellular processes. The zinc transporter ZnuA from *E. Coli* and *Synechocystis* sp. 6803, the proposed zinc transporter TroA from *Treponema pallidum,* and the proposed manganese transporter *Streptococcus pneumoniae* surface antigen, PsaA, are placed in cluster 9 of the ABC transporters.[198]

These zinc-binding sites mainly use His ligands and span a relatively great distance in the protein (Table 6). The periplasmic zinc-binding protein TroA from the human parasite *Treponema pallidum*[199] and pneumococcal surface antigen PsaA[200] are very similar. The bound zinc ion is coordinated by the NE2 nitrogens of His68, His133, His199 and both oxygens of Asp279 in TroA and His67 (NE2), His139 (NE2), and one oxygen of the carboxylates of Glu205 (OE1) and Asp280 (OD1) in PsaA. The latter two His residues of TroA are also further stabilized by H-bonding interactions with the carboxylates of Asp131 and Glu248 (pdb# 1TOA). In the case of PsaA only His139 is observed H-bonding the carboxylate of Asp137 (pdb# 1PsZ). The coordination geometries are described as tetrahedral for PsaA and distorted square pyramidal in TroA owing to the interaction of both oxygens of Asp279. The apex of the pyramid is occupied by the nitrogen of His199 while the other His ligands and the two oxygens of Asp279 make up the square plane.

A similar zinc-binding site is predicted by sequence alignment for Znu.[201] The bound zinc ion is coordinated by the NE2 nitrogens of His83, His179, His243 in a manner quite similar to TroaA (Table 6). The latter two His residues are also further stabilized by H-bonding interactions with the carboxylates of Asp177 and Glu261 (pdb# 1PQ4) as in TroA and PsaA. However, the proposed fourth Asp ligand does not bind and is replaced by a water molecule in a large hydrophobic cavity.[201]

The function of the proteins is presumed to be similar to that of members of the periplasmic ligand-binding protein (PLBP) family that function as ligand-binding receptors for active transport and chemotaxis. However, these proteins do not have the flexible interdomain β-strands of the PLBPs. An argument has been proposed for a more rigid hinge (in this case a backbone α-helix) if the purpose of these proteins is ‘small’ metal ion transport.[199] Thus, since the free energy difference of zinc in solution and bound to a protein is considered to be small,[202] the binding of zinc to a protein cannot incur the large entropy changes that would be associated with the ordering of a very mobile hinge region.

8 RELATED ARTICLES

Zinc: DNA-binding Proteins.

9 FURTHER READING

L. Claudio, ‘Zinc Enzymes, in the Encyclopedia of Inorganic Chemistry’, 1st edn., ed. R. B. King, John Wiley & Sons, Vol. 10, p. 4406.

10 REFERENCES

1. B. L. Vallee and K. H. Falchuk, *Physiol. Rev.*, 1993, **73**, 79.
2. D. S. Auld, *Struct. Bonding*, 1997, **89**, 29.
3. D. S. Auld, Zinc Sites In Metalloenzymes And Related Proteins, in ‘Handbook on Metalloproteins’, eds. I. Bertini, A. Sigel, and H. Sigel, Marcel Dekker, New York, 2001, p. 881.
4. D. S. Auld, *BioMetals*, 2001, **14**, 271.
5. B. L. Vallee and D. S. Auld, *Biochemistry*, 1990, **29**, 5647.
6. B. L. Vallee and D. S. Auld, *Biochemistry*, 1993, **32**, 6493.
7. P. Argos, R. M. Garavito, W. Eventoff, M. G. Rossmann, and C. I. Branden, *J. Mol. Biol.*, 1978, **126**, 141.
8. J. A. Ippolito, T. T. Baird Jr, S. A. McGee, D. W. Christianson, and C. A. Fierke, *Proc. Natl. Acad. Sci. U.S.A.*, 1995, **92**, 5017.
9. D. W. Christianson and C. A. Fierke, *Acc. Chem. Res.*, 1996, **29**, 331.
10. D. W. Christianson and J. D. Cox, *Annu. Rev. Biochem.*, 1999, **68**, 33.
11. L. L. Kiefer, S. A. Paterno, and C. A. Fierke, *J. Am. Chem. Soc.*, 1995, **117**, 6831.
12. A. E. Eriksson, T. A. Jones, and A. Liljas, *Proteins*, 1988, **4**, 274.
13. D. W. Christianson and R. S. Alexander, *J. Am. Chem. Soc.*, 1989, **111**, 6412.
14. J. F. Krebs, J. A. Ippolito, D. W. Christianson, and C. A. Fierke, *J. Biol. Chem.*, 1993, **268**, 27458.
15. C. A. Lesburg and D. W. Christianson, *J. Am. Chem. Soc.*, 1995, **117**, 6838.
16. M. M. Yamashita, L. Wesson, G. Eisenman, and D. Eisenberg, *Proc. Natl. Acad. Sci. U.S.A.*, 1990, **87**, 5648.
17. J. A. Hunt and C. A. Fierke, *J. Biol. Chem.*, 1997, **272**, 20364.
18. J. A. Hunt, M. Ahmed, and C. A. Fierke, *Biochemistry*, 1999, **38**, 9054.
19. K. Hakansson, A. Wehnert, and A. Liljas, *Acta Crystallogr., Sect. D*, 1994, **D50**, 93.
20. D. S. Auld, Catalytic Mechanisms For Metallopeptidases, in ‘Handbook of Proteolytic Enzymes’, eds. A. J. Barrett, N. D. Rawlings, and J. F. Woessner, Academic Press, London, 2004, p. 268.
21. A. J. Barrett and N. D. Rawlings, in MEROPS the Peptidase Database, 2004.
22. M. Andberg, A. Wetterholm, J. F. Medina, and J. Z. Haeggstrom, *Biochem. J.*, 2000, **345**(Pt 3), 621.
23. M. A. Ondetti, B. Rubin, and D. W. Cushman, *Science*, 1977, **196**, 441.
24. W. H. Johnson, N. A. Roberts, and N. Borkakoti, *J. Enzyme. Inhib.*, 1987, **2**, 1.
25. D. S. Auld, *Methods Enzymol.*, 1988, **158**, 110.
26. D. S. Auld, *Methods Enzymol.*, 1995, **248**, 228.
27. C. R. Chong and D. S. Auld, *Biochemistry*, 2000, **39**, 7580.
28. D. M. van Aalten, C. R. Chong, and L. Joshua-Tor, *Biochemistry*, 2000, **39**, 10082.
29. L. M. Canzoniero, D. M. Turetsky, and D. W. Choi, *J. Neurosci.*, 1999, **19**, RC31.
30. K. S. Larsen and D. S. Auld, *Biochemistry*, 1989, **28**, 9620.
31. K. S. Larsen and D. S. Auld, *Biochemistry*, 1991, **30**, 2613.
32. M. Gomez-Ortiz, F. X. Gomis-Ruth, R. Huber, and F. X. Aviles, *FEBS Lett.*, 1997, **400**, 336.
33. J. T. Bukrinsky, M. J. Bjerrum, and A. Kadziola, *Biochemistry*, 1998, **37**, 16555.
34. D. R. Holland, A. C. Hausrath, D. Juers, and B. W. Matthews, *Protein Sci.*, 1995, **4**, 1955.
35. B. E. Coggins, X. Li, A. L. McClerren, O. Hindsgaul, C. R. Raetz, and P. Zhou, *Nat. Struct. Biol.*, 2003, **10**, 645.
36. D. A. Whittington, K. M. Rusche, H. Shin, C. A. Fierke, and D. W. Christianson, *Proc. Natl. Acad. Sci. U.S.A.*, 2003, **100**, 8146.
37. G. C. Ireton, M. E. Black, and B. L. Stoddard, *Structure (Camb.)*, 2003, **11**, 961.
38. W. Maret, C. Jacob, B. L. Vallee, and E. H. Fischer, *Proc. Natl. Acad. Sci. U.S.A.*, 1999, **96**, 1936.
39. B. A. Katz, J. M. Clark, J. S. Finer-Moore, T. E. Jenkins, C. R. Johnson, M. J. Ross, C. Luong, W. R. Moore, and R. M. Stroud, *Nature*, 1998, **391**, 608.
40. B. A. Katz and C. Luong, *J. Mol. Biol.*, 1999, **292**, 669.
41. A. L. Carvalho, L. Sanz, D. Barettino, A. Romero, J. J. Calvete, and M. J. Romao, *J. Mol. Biol.*, 2002, **322**, 325.
42. Y. Korkhin, A. J. Kalb, M. Peretz, O. Bogin, Y. Burstein, and F. Frolow, *J. Mol. Biol.*, 1998, **278**, 967.
43. C. Li, J. Heatwole, S. Soelaiman, and M. Shoham, *Proteins*, 1999, **37**, 619.
44. O. Bogin, I. Levin, Y. Hacham, S. Tel-Or, M. Peretz, F. Frolow, and Y. Burstein, *Protein Sci.*, 2002, **11**, 2561.
45. J. E. Guy, M. N. Isupov, and J. A. Littlechild, *J. Mol. Biol.*, 2003, **331**, 1041.
46. L. Esposito, F. Sica, C. A. Raia, A. Giordano, M. Rossi, L. Mazzarella, and A. Zagari, *J. Mol. Biol.*, 2002, **318**, 463.
47. Z. N. Yang, W. F. Bosron, and T. D. Hurley, *J. Mol. Biol.*, 1997, **265**, 330.
48. U. Ryde, *Protein Sci.*, 1995, **4**, 1124.
49. T. A. Pauly, J. L. Ekstrom, D. A. Beebe, B. Chrunyk, D. Cunningham, M. Griffor, A. Kamath, S. E. Lee, R. Madura, D. McGuire, T. Subashi, D. Wasilko, P. Watts,

B. L. Mylari, P. J. Oates, P. D. Adams, and V. L. Rath, *Structure (Camb.)*, 2003, **11**, 1071.

50. M. J. Banfield, M. E. Salvucci, E. N. Baker, and C. A. Smith, *J. Mol. Biol.*, 2001, **306**, 239.
51. K. Johansson, M. El-Ahmad, C. Kaiser, H. Jornvall, H. Eklund, J. Hoog, and S. Ramaswamy, *Chem.-Biol. Interact.*, 2001, **130–132**, 351.
52. S. N. Ruzheinikov, J. Burke, S. Sedelnikova, P. J. Baker, R. Taylor, P. A. Bullough, N. M. Muir, M. G. Gore, and D. W. Rice, *Structure (Camb.)*, 2001, **9**, 789.
53. A. J. Barrett, N. D. Rawlings, and J. F. Woessner, 'Handbook of Proteolytic Enzymes', London, 2004.
54. R. Natesh, S. L. Schwager, E. D. Sturrock, and K. R. Acharya, *Nature*, 2003, **421**, 551.
55. C. K. Brown, K. Madauss, W. Lian, M. R. Beck, W. D. Tolbert, and D. W. Rodgers, *Proc. Natl. Acad. Sci. U.S.A.*, 2001, **98**, 3127.
56. J. W. Arndt, B. Hao, V. Ramakrishnan, T. Cheng, S. I. Chan, and M. K. Chan, *Structure (Camb.)*, 2002, **10**, 215.
57. M. R. Ehlers, E. A. Fox, D. J. Strydom, and J. F. Riordan, *Proc. Natl. Acad. Sci. U.S.A.*, 1989, **86**, 7741.
58. K. R. Acharya, E. D. Sturrock, J. F. Riordan, and M. R. Ehlers, *Nat. Rev. Drug Discov.*, 2003, **2**, 891.
59. J. T. Maynes, C. Garen, M. M. Cherney, G. Newton, D. Arad, Y. Av-Gay, R. C. Fahey, and M. N. James, *J. Biol. Chem.*, 2003, **278**, 47166.
60. L. Betts, S. Xiang, S. A. Short, R. Wolfenden, and C. W. Carter Jr, *J. Mol. Biol.*, 1994, **235**, 635.
61. Z. Wang and F. A. Quiocho, *Biochemistry*, 1998, **37**, 8314.
62. E. Johansson, N. Mejlhede, J. Neuhard, and S. Larsen, *Biochemistry*, 2002, **41**, 2563.
63. D. C. Carlow, C. W. Carter Jr, N. Mejlhede, J. Neuhard, and R. Wolfenden, *Biochemistry*, 1999, **38**, 12258.
64. D. Hewett-Emmett and R. E. Tashian, *Mol. Phylogenet. Evol.*, 1996, **5**, 50.
65. K. S. Smith and J. G. Ferry, *FEMS Microbiol. Rev.*, 2000, **24**, 335.
66. M. S. Kimber and E. F. Pai, *EMBO J.*, 2000, **19**, 1407.
67. S. Mitsuhashi, T. Mizushima, E. Yamashita, M. Yamamoto, T. Kumasaka, H. Moriyama, T. Ueki, S. Miyachi, and T. Tsukihara, *J. Biol. Chem.*, 2000, **275**, 5521.
68. P. Strop, K. S. Smith, T. M. Iverson, J. G. Ferry, and D. C. Rees, *J. Biol. Chem.*, 2001, **276**, 10299.
69. M. H. Bracey, J. Christiansen, P. Tovar, S. P. Cramer, and S. G. Bartlett, *Biochemistry*, 1994, **33**, 13126.
70. R. S. Rowlett, M. R. Chance, M. D. Wirt, D. E. Sidelinger, J. R. Royal, M. Woodroffe, Y. F. Wang, R. P. Saha, and M. G. Lam, *Biochemistry*, 1994, **33**, 13967.
71. D. S. Auld, Acyl Group Transfer- Metalloproteinases, in 'Enzyme Mechanisms', eds. M. I. Page and A. Williams, Royal Society of Chemistry Burlington House, London, 1987, p. 241.
72. M. Yamamoto, T. Kumasaka, T. Fujisawa, and T. Ueki, *J. Synchrotron Radiat.*, 1998, **5**, 222.
73. C. Kisker, H. Schindelin, B. E. Alber, J. G. Ferry, and D. C. Rees, *EMBO J.*, 1996, **15**, 2323.
74. T. M. Iverson, B. E. Alber, C. Kisker, J. G. Ferry, and D. C. Rees, *Biochemistry*, 2000, **39**, 9222.
75. I. Bertini, A. Sigel, and H. Sigel, 'Handbook on Metalloproteins', New York, 2001.
76. A. Messerschmidt, W. Bode, and M. Cygler, 'The Handbook of Metalloproteins', Chichester, 2004.
77. B. L. Vallee and D. S. Auld, *Matrix Suppl.*, 1992, **1**, 5.
78. E. E. Kim and H. W. Wyckoff, *J. Mol. Biol.*, 1991, **218**, 449.
79. B. Chevrier, C. Schalk, H. D'Orchymont, J. M. Rondeau, D. Moras, and C. Tarnus, *Structure*, 1994, **2**, 283.
80. J. S. Valentine, in 'Metal ions in Biological Systems', eds. A. Sigel and A. Sigel, New York, 1998.
81. M. A. Hough and S. S. Hasnain, *Structure (Camb.)*, 2003, **11**, 937.
82. E. R. Kantrowitz, E. Coli alkaline Phosphatase, in 'The Handbook of Metalloproteins', eds. A. Messerschmidt, W. Bode, and M. Cygler, John Wiley & Sons, Chichester, 2004.
83. A. Volbeda, C. Romier, and D. Suck, Nuclease P1, in 'The Handbook of Metalloproteins', eds. A. Messerschmidt, W. Bode, and M. Cygler, John Wiley & Sons, Chichester, 2004, p. 51.
84. T. Klabunde and B. Krebs, *Struct. Bonding*, 1997, **89**, 177.
85. A. Vogel, F. Spener, and B. Krebs, Purple Acid Phophatase, in 'Handbook of Metalloproteins', eds. A. Messerschmidt, R. Huber, K. Poulos, and K. Wieghardt, Wiley, Chichester, 2001, p. 1284.
86. J. Abendroth, K. Niefind, O. May, M. Siemann, C. Syldatk, and D. Schomburg, *Biochemistry*, 2002, **41**, 8589.
87. J. B. Thoden, R. Marti-Arbona, F. M. Raushel, and H. M. Holden, *Biochemistry*, 2003, **42**, 4874.
88. N. Strater and W. N. Lipscomb, Leucine Aminopeptidase, in 'The Handbook of Metalloproteins', eds. A. Messerschmidt, W. Bode, and M. Cygler, John Wiley & Sons, Chichester, 2004, p. 199.
89. D. S. Auld, Cocatalytic Zinc Sites, in 'The Handbook of Metalloproteins', eds. A. Messerschmidt, W. Bode, and M. Cygler, John Wiley & Sons, Chichester, 2004, p. 416.
90. R. C. Holz, K. P. Bzymek, and S. I. Swierczek, *Curr. Opin. Chem. Biol.*, 2003, **7**, 197.
91. D. S. Auld, Structural Zinc Sites, in 'The Handbook of Metalloproteins', eds. A. Messerschmidt, W. Bode, and M. Cygler, John Wiley & Sons, Chichester, 2004, p. 403.

92. H. Eklund, B. Nordstrom, E. Zeppezauer, G. Soderlund, I. Ohlsson, T. Boiwe, and C. I. Branden, *FEBS Lett.*, 1974, **44**, 200.

93. R. B. Honzatko, J. L. Crawford, H. L. Monaco, J. E. Ladner, B. F. Ewards, D. R. Evans, S. G. Warren, D. C. Wiley, R. C. Ladner, and W. N. Lipscomb, *J. Mol. Biol.*, 1982, **160**, 219.

94. A. Klug and D. Rhodes, *Trends Biochem. Sci.*, 1987, **12**, 464.

95. J. M. Berg, *Science*, 1986, **232**, 485.

96. A. Klug and J. W. Schwabe, *FASEB J.*, 1995, **9**, 597.

97. J. M. Berg and Y. Shi, *Science*, 1996, **271**, 1081.

98. J. P. Mackay and M. Crossley, *Trends Biochem. Sci.*, 1998, **23**, 1.

99. S. S. Krishna, I. Majumdar, and N. V. Grishin, *Nucleic Acids Res.*, 2003, **31**, 532.

100. G. E. Folkers, H. Hanzawa, and R. Boelens, Zinc Finger Protein*s*, in 'Handbook on Metalloproteins', eds. I. Bertini, A. Sigel, and H. Sigel, Marcel Dekker, New York, 2001, p. 961.

101. L. Serre, K. Pereira de Jesus, S. Boiteux, C. Zelwer, and B. Castaing, *EMBO J.*, 2002, **21**, 2854.

102. M. Sugahara, T. Mikawa, T. Kumasaka, M. Yamamoto, R. Kato, K. Fukuyama, Y. Inoue, and S. Kuramitsu, *EMBO J.*, 2000, **19**, 3857.

103. R. Gilboa, D. O. Zharkov, G. Golan, A. S. Fernandes, S. E. Gerchman, E. Matz, J. H. Kycia, A. P. Grollman, and G. Shoham, *J. Biol. Chem.*, 2002, **277**, 19811.

104. J. C. Fromme and G. L. Verdine, *Nat. Struct. Biol.*, 2002, **9**, 544.

105. D. O. Zharkov, G. Golan, R. Gilboa, A. S. Fernandes, S. E. Gerchman, J. H. Kycia, R. A. Rieger, A. P. Grollman, and G. Shoham, *EMBO J.*, 2002, **21**, 789.

106. J. F. Petersen, M. M. Cherney, H. D. Liebig, T. Skern, E. Kuechler, and M. N. James, *EMBO J.*, 1999, **18**, 5463.

107. W. Sommergruber, G. Casari, F. Fessl, J. Seipelt, and T. Skern, *Virology*, 1994, **204**, 815.

108. W. Sommergruber, J. Seipelt, F. Fessl, T. Skern, H. D. Liebig, and G. Casari, *Virology*, 1997, **234**, 203.

109. T. Voss, R. Meyer, and W. Sommergruber, *Protein Sci.*, 1995, **4**, 2526.

110. K. E. Flick, M. S. Jurica, R. J. Monnat Jr, and B. L. Stoddard, *Nature*, 1998, **394**, 96.

111. D. Soler, T. Nomizu, W. E. Brown, Y. Shibata, and D. S. Auld, *J. Protein Chem.*, 1995, **14**, 511.

112. Q. A. Sang and D. A. Douglas, *J. Protein Chem.*, 1996, **15**, 137.

113. A. J. Barrett and N. D. Rawlings, in MEROPS the Peptidase Database, 2001.

114. T. Jenuwein and C. D. Allis, *Science*, 2001, **293**, 1074.

115. T. O. Yeates, *Cell*, 2002, **111**, 5.

116. X. Zhang, H. Tamaru, S. Khan, J. Horton, L. Keefe, E. Selker, and X. Cheng, *Cell*, 2002, **111**, 117.

117. J. Min, X. Zhang, X. Cheng, S. I. Grewal, and R. M. Xu, *Nat. Struct. Biol.*, 2002, **9**, 828.

118. H. Tamaru and E. U. Selker, *Nature*, 2001, **414**, 277.

119. X. Zhang, Z. Yang, S. I. Khan, J. R. Horton, H. Tamaru, E. U. Selker, and X. Cheng, *Mol. Cells*, 2003, **12**, 177.

120. B. A. Messerle, A. Schaffer, M. Vasak, J. H. Kagi, and K. Wuthrich, *J. Mol. Biol.*, 1990, **214**, 765.

121. K. Zangger, G. Oz, J. D. Otvos, and I. M. Armitage, *Protein Sci.*, 1999, **8**, 2630.

122. R. Riek, B. Precheur, Y. Wang, E. A. Mackay, G. Wider, P. Guntert, A. Liu, J. H. Kagi, and K. Wuthrich, *J. Mol. Biol.*, 1999, **291**, 417.

123. W. Maret, Protein Interface Zinc Sites: The Role of Zinc in The Supramolecular Assembly of Proteins and in Transient Protein-Protein Interactions, in 'The Handbook of Metalloproteins', eds. A. Messerschmidt, W. Bode, and M. Cygler, John Wiley & Sons, Chichester, 2004, p. 432.

124. A. C. Papageorgiou and K. R. Acharya, *Structure*, 1997, **5**, 991.

125. A. Changela, K. Chen, Y. Xue, J. Holschen, C. E. Outten, T. V. O'Halloran, and A. Mondragon, *Science*, 2003, **301**, 1383.

126. B. E. Alber and J. G. Ferry, *Proc. Natl. Acad. Sci. U.S.A.*, 1994, **91**, 6909.

127. B. E. Alber, C. M. Colangelo, J. Dong, C. M. Stalhandske, T. T. Baird, C. Tu, C. A. Fierke, D. N. Silverman, R. A. Scott, and J. G. Ferry, *Biochemistry*, 1999, **38**, 13119.

128. A. D. Cameron, B. Olin, M. Ridderstrom, B. Mannervik, and T. A. Jones, *EMBO J.*, 1997, **16**, 3386.

129. S. Sellin, L. E. Eriksson, A. C. Aronsson, and B. Mannervik, *J. Biol. Chem.*, 1983, **258**, 2091.

130. L. Garcia-Iniguez, L. Powers, B. Chance, S. Sellin, B. Mannervik, and A. S. Mildvan, *Biochemistry*, 1984, **23**, 685.

131. S. Sellin and B. Mannervik, *J. Biol. Chem.*, 1984, **259**, 11426.

132. M. Ridderstrom, A. D. Cameron, T. A. Jones, and B. Mannervik, *J. Biol. Chem.*, 1998, **273**, 21623.

133. A. D. Cameron, M. Ridderstrom, B. Olin, M. J. Kavarana, D. J. Creighton, and B. Mannervik, *Biochemistry*, 1999, **38**, 13480.

134. S. L. Clugston, J. F. Barnard, R. Kinach, D. Miedema, R. Ruman, E. Daub, and J. F. Honek, *Biochemistry*, 1998, **37**, 8754.

135. M. M. He, S. L. Clugston, J. F. Honek, and B. W. Matthews, *Biochemistry*, 2000, **39**, 8719.

136. J. Sivaraman, Y. Li, J. Banks, D. E. Cane, A. Matte, and M. Cygler, *J. Biol. Chem.*, 2003, **278**, 43682.

137. J. A. Barbosa, J. Sivaraman, Y. Li, R. Larocque, A. Matte, J. D. Schrag, and M. Cygler, *Proc. Natl. Acad. Sci. U.S.A.*, 2002, **99**, 1859.

138. T. Proft, S. L. Moffatt, C. J. Berkahn, and J. D. Fraser, *J. Exp. Med.*, 1999, **189**, 89.

139. J. Fraser, V. Arcus, P. Kong, E. Baker, and T. Proft, *Mol. Med. Today*, 2000, **6**, 125.

140. J. D. Fraser, R. G. Urban, J. L. Strominger, and H. Robinson, *Proc. Natl. Acad. Sci. U.S.A.*, 1992, **89**, 5507.

141. E. M. Schad, I. Zaitseva, V. N. Zaitsev, M. Dohlsten, T. Kalland, P. M. Schlievert, D. H. Ohlendorf, and L. A. Svensson, *EMBO J.*, 1995, **14**, 3292.

142. M. Sundstrom, D. Hallen, A. Svensson, E. Schad, M. Dohlsten, and L. Abrahmsen, *J. Biol. Chem.*, 1996, **271**, 32212.

143. Y. I. Chi, I. Sadler, L. M. Jablonski, S. D. Callantine, C. F. Deobald, C. V. Stauffacher, and G. A. Bohach, *J. Biol. Chem.*, 2002, **277**, 22839.

144. M. Sundstrom, L. Abrahmsen, P. Antonsson, K. Mehindate, W. Mourad, and M. Dohlsten, *EMBO J.*, 1996, **15**, 6832.

145. M. Hakansson, K. Petersson, H. Nilsson, G. Forsberg, P. Bjork, P. Antonsson, and L. A. Svensson, *J. Mol. Biol.*, 2000, **302**, 527.

146. A. Roussel, B. F. Anderson, H. M. Baker, J. D. Fraser, and E. N. Baker, *Nat. Struct. Biol.*, 1997, **4**, 635.

147. V. L. Arcus, T. Proft, J. A. Sigrell, H. M. Baker, J. D. Fraser, and E. N. Baker, *J. Mol. Biol.*, 2000, **299**, 157.

148. A. C. Papageorgiou, K. R. Acharya, R. Shapiro, E. F. Passalacqua, R. D. Brehm, and H. S. Tranter, *Structure*, 1995, **3**, 769.

149. E. M. Schad, A. C. Papageorgiou, L. A. Svensson, and K. R. Acharya, *J. Mol. Biol.*, 1997, **269**, 270.

150. A. C. Papageorgiou, C. M. Collins, D. M. Gutman, J. B. Kline, S. M. O'Brien, H. S. Tranter, and K. R. Acharya, *EMBO J.*, 1999, **18**, 9.

151. C. A. Earhart, G. M. Vath, M. Roggiani, P. M. Schlievert, and D. H. Ohlendorf, *Protein Sci.*, 2000, **9**, 1847.

152. D. R. Karp and E. O. Long, *J. Exp. Med.*, 1992, **175**, 415.

153. M. Fujinaga and M. N. James, *J. Mol. Biol.*, 1987, **195**, 373.

154. D. E. Brodersen, J. Nyborg, and M. Kjeldgaard, *Biochemistry*, 1999, **38**, 1695.

155. C. S. Raman, H. Li, P. Martasek, V. Kral, B. S. Masters, and T. L. Poulos, *Cell*, 1998, **95**, 939.

156. J. S. Stamler, *Cell*, 1994, **78**, 931.

157. L. C. Myers, T. D. Cushing, G. Wagner, and G. L. Verdine, *Chem. Biol.*, 1994, **1**, 91.

158. W. Maret and B. L. Vallee, *Proc. Natl. Acad. Sci. U.S.A.*, 1998, **95**, 3478.

159. T. O. Fischmann, A. Hruza, X. D. Niu, J. D. Fossetta, C. A. Lunn, E. Dolphin, A. J. Prongay, P. Reichert, D. J. Lundell, S. K. Narula, and P. C. Weber, *Nat. Struct. Biol.*, 1999, **6**, 233.

160. H. Li, C. S. Raman, C. B. Glaser, E. Blasko, T. A. Young, J. F. Parkinson, M. Whitlow, and T. L. Poulos, *J. Biol. Chem.*, 1999, **274**, 21276.

161. D. K. Ghosh, B. R. Crane, S. Ghosh, D. Wolan, R. Gachhui, C. Crooks, A. Presta, J. A. Tainer, E. D. Getzoff, and D. J. Stuehr, *EMBO J.*, 1999, **18**, 6260.

162. M. L. Flinspach, H. Li, J. Jamal, W. Yang, H. Huang, J. M. Hah, J. A. Gomez-Vidal, E. A. Litzinger, R. B. Silverman, and T. L. Poulos, *Nat. Struct. Mol. Biol.*, 2004, **11**, 54.

163. K. A. Bixby, M. H. Nanao, N. V. Shen, A. Kreusch, H. Bellamy, P. J. Pfaffinger, and S. Choe, *Nat. Struct. Biol.*, 1999, **6**, 38.

164. P. W. Kim, Z. Y. Sun, S. C. Blacklow, G. Wagner, and M. J. Eck, *Science*, 2003, **301**, 1725.

165. J. K. Yano, L. S. Koo, D. J. Schuller, H. Li, P. R. Ortiz De Montellano, and T. L. Poulos, *J. Biol. Chem.*, 2000, **275**, 31086.

166. S. W. Muchmore, J. Chen, C. Jakob, D. Zakula, E. D. Matayoshi, W. Wu, H. Zhang, F. Li, S. C. Ng, and D. C. Altieri, *Mol. Cells*, 2000, **6**, 173.

167. M. A. Verdecia, H. Huang, E. Dutil, D. A. Kaiser, T. Hunter, and J. P. Noel, *Nat. Struct. Biol.*, 2000, **7**, 602.

168. B. Bax, T. L. Blundell, J. Murray-Rust, and N. Q. McDonald, *Structure*, 1997, **5**, 1275.

169. A. Riboldi-Tunnicliffe, B. Konig, S. Jessen, M. S. Weiss, J. Rahfeld, J. Hacker, G. Fischer, and R. Hilgenfeld, *Nat. Struct. Biol.*, 2001, **8**, 779.

170. R. Radhakrishnan, L. J. Walter, A. Hruza, P. Reichert, P. P. Trotta, T. L. Nagabhushan, and M. R. Walter, *Structure*, 1996, **4**, 1453.

171. C. A. Cunha, S. Macieira, J. M. Dias, G. Almeida, L. L. Goncalves, C. Costa, J. Lampreia, R. Huber, J. J. Moura, I. Moura, and M. J. Romao, *J. Biol. Chem.*, 2003, **278**, 17455.

172. J. Rotonda, M. Garcia-Calvo, H. G. Bull, W. M. Geissler, B. M. McKeever, C. A. Willoughby, N. A. Thornberry, and J. W. Becker, *Chem. Biol.*, 2001, **8**, 357.

173. I. Krieger, A. Kostyukova, A. Yamashita, Y. Nitanai, and Y. Maeda, *Biophys. J.*, 2002, **83**, 2716.

174. K. Harata, W. D. Schubert, and M. Muraki, *Acta Crystallogr., D Biol. Crystallogr.*, 2001, **57**, 1513.

175. A. Klug, *J. Mol. Biol.*, 1999, **293**, 215.

176. J. H. Laity, B. M. Lee, and P. E. Wright, *Curr. Opin. Struct. Biol.*, 2001, **11**, 39.

177. G. Freyd, S. K. Kim, and H. R. Horvitz, *Nature*, 1990, **344**, 876.

178. I. B. Dawid, J. J. Breen, and R. Toyama, *Trends Genet.*, 1998, **14**, 156.

179. J. E. Deane, J. P. Mackay, A. H. Kwan, E. Y. Sum, J. E. Visvader, and J. M. Matthews, *EMBO J.*, 2003, **22**, 2224.

180. X. Yao, G. C. Perez-Alvarado, H. A. Louis, P. Pomies, C. Hatt, M. F. Summers, and M. C. Beckerle, *Biochemistry*, 1999, **38**, 5701.

181. R. Konrat, R. Weiskirchen, B. Krautler, and K. Bister, *J. Biol. Chem.*, 1997, **272**, 12001.

182. G. Kontaxis, R. Konrat, B. Krautler, R. Weiskirchen, and K. Bister, *Biochemistry*, 1998, **37**, 7127.

183. G. C. Perez-Alvarado, C. Miles, J. W. Michelsen, H. A. Louis, D. R. Winge, M. C. Beckerle, and M. F. Summers, *Nat. Struct. Biol.*, 1994, **1**, 388.

184. G. C. Perez-Alvarado, J. L. Kosa, H. A. Louis, M. C. Beckerle, D. R. Winge, and M. F. Summers, *J. Mol. Biol.*, 1996, **257**, 153.

185. A. Velyvis, Y. Yang, C. Wu, and J. Qin, *J. Biol. Chem.*, 2001, **1976**, 4932.

186. A. Velyvis, J. Vaynberg, Y. Yang, O. Vinogradova, Y. Zhang, C. Wu, and J. Qin, *Nat. Struct. Biol.*, 2003, **10**, 558.

187. Q. L. Deveraux and J. C. Reed, *Genes Dev.*, 1999, **13**, 239.

188. E. N. Shiozaki, J. Chai, D. J. Rigotti, S. J. Riedl, P. Li, S. M. Srinivasula, E. S. Alnemri, R. Fairman, and Y. Shi, *Mol. Cells*, 2003, **11**, 519.

189. S. J. Riedl, M. Renatus, R. Schwarzenbacher, Q. Zhou, C. Sun, S. W. Fesik, R. C. Liddington, and G. S. Salvesen, *Cell*, 2001, **104**, 791.

190. G. Wu, J. Chai, T. L. Suber, J. W. Wu, C. Du, X. Wang, and Y. Shi, *Nature*, 2000, **408**, 1008.

191. J. Chai, N. Yan, J. R. Huh, J. W. Wu, W. Li, B. A. Hay, and Y. Shi, *Nat. Struct. Biol.*, 2003, **10**, 892.

192. J. W. Wu, A. E. Cocina, J. Chai, B. A. Hay, and Y. Shi, *Mol. Cells*, 2001, **8**, 95.

193. M. C. Franklin, S. Kadkhodayan, H. Ackerly, D. Alexandru, M. D. Distefano, L. O. Elliott, J. A. Flygare, G. Mausisa, D. C. Okawa, D. Ong, D. Vucic, K. Deshayes, and W. J. Fairbrother, *Biochemistry*, 2003, **42**, 8223.

194. V. Mandiyan, J. Andreev, J. Schlessinger, and S. R. Hubbard, *EMBO J.*, 1999, **18**, 6890.

195. S. J. Freedman, Z. Y. Sun, F. Poy, A. L. Kung, D. M. Livingston, G. Wagner, and M. J. Eck, *Proc. Natl. Acad. Sci. U.S.A.*, 2002, **99**, 5367.

196. S. J. Freedman, Z. Y. Sun, A. L. Kung, D. S. France, G. Wagner, and M. J. Eck, *Nat. Struct. Biol.*, 2003, **10**, 504.

197. P. Bouige, D. Laurent, L. Piloyan, and E. Dassa, *Curr. Protein Pept. Sci.*, 2002, **3**, 541.

198. J. P. Claverys, *Res. Microbiol.*, 2001, **152**, 231.

199. Y. H. Lee, R. K. Deka, M. V. Norgard, J. D. Radolf, and C. A. Hasemann, *Nat. Struct. Biol.*, 1999, **6**, 628.

200. M. C. Lawrence, P. A. Pilling, V. C. Epa, A. M. Berry, A. D. Ogunniyi, and J. C. Paton, *Structure*, 1998, **6**, 1553.

201. S. Banerjee, B. Wei, M. Bhattacharyya-Pakrasi, H. B. Pakrasi, and T. J. Smith, *J. Mol. Biol.*, 2003, **333**, 1061.

202. W. N. Lipscomb and N. Strater, *Chem. Rev.*, 1996, **96**, 2375.

Zinc: Inorganic & Coordination Chemistry

John Burgess[1] **& Reg H. Prince**[2]
[1]*University of Leicester, Leicester, UK*
[2]*St. John's College, Cambridge University, Cambridge, UK*

Based in part on the article Zinc: Inorganic & Coordination Chemistry by Reg H. Prince which appeared in the Encyclopedia of Inorganic Chemistry, First Edition.

1	Introduction	1
2	Production of the Element	3
3	Uses	3
4	Properties of the Element	5
5	Oxidation State and Stereochemistry	7
6	Binary Compounds	8
7	Salts	12
8	Coordination Chemistry	13
9	Aqueous Solution Chemistry	19
10	Related Articles	22
11	References	22

1 INTRODUCTION

1.1 Historical Background

Zinc is a relatively recent arrival among the common metals, having been produced commercially in Europe only since the middle of the eighteenth century – in fact in Bristol in 1738. However, its history begins in prehistoric times. The oldest known piece is a Dacian idol discovered in a ruined prehistoric settlement at Dordosch, Transylvania, consisting of zinc of 87% purity. Bracelets in the form of hollow silver rings filled with zinc were made by the early Greeks and were found at Cameiros on the island of Rhodes. In fact, zinc was known in the brasses, alloys of zinc and copper, long before its isolation in a pure state. Brasses were known at least a thousand years before the Christian era; the Romans smelted mixtures of calamine (zinc carbonate) with copper ores to obtain brass.

Knowledge of zinc smelting appears to have come originally from India (13th century) and spread to Sumatra and China, where it was produced commercially by the middle of the eighteenth century: such a sample dated 1745 contained 99% of zinc with tin and iron as impurities. There is evidence that zinc was being imported into Europe from these countries as early as 1611, but zinc smelting in Europe and America really started on a large scale in the nineteenth century in centers such as Liege, Bristol, and Swansea in Europe and at the Washington arsenal in America.

Zinc compounds were known to the alchemists; several have been in therapeutic use (calamine for skin problems, zinc sulphate for eye treatments) for over a thousand years.

1.2 Occurrence and Abundance

Estimates of the abundance of zinc in the sun, in meteorites, in the Earth's core and crust, and in the oceans are very difficult to make,**[1]** but its abundance in the Earth's crustal rocks and soils is of the order of 100 ppm, about 1000 times as abundant as its congeners cadmium and mercury. All three elements are *Chalcophiles* so that, in the reducing atmosphere that prevailed when the earth's crust solidified, they were deposited in the sulfide phase giving rise to the sulfide ores, their most important source. Later, as weathering took place, zinc became soluble only to be precipitated as the carbonate, silicate, or phosphate.

The main zinc ores are the sulfide ZnS, known as zinc blende in Europe and sphalerite in the United States, and the carbonate $ZnCO_3$ (calamine in Europe, smithsonite in the United States). Major deposits are found in Canada, Australia, Mexico, Peru, Russia, and the United States. Minor ores include the silicates willemite, Zn_2SiO_4 and hemimorphite, $Zn_4Si_2O_7(OH)_2 \cdot H_2O$. Franklinite, $(Zn, Fe)O \cdot Fe_2O_3$, is mainly a zinc ferrite (see below), but is also important for its manganese content. Zinc also occurs in a number of other minerals, for example, goslarite, $ZnSO_4 \cdot 7H_2O$, wurtzite, ZnS, zincite, ZnO, and a number of secondary arsenate and phosphate minerals, such as hopeite, $Zn_3(PO_4)_2 \cdot 4H_2O$.**[2]**

Zinc occurs to the extent of between 5 and $10 \times 10^{-3}\,\mathrm{mg\,L^{-1}}$ in seawater, with a residence time of about 2×10^4 years; there are significant amounts of zinc in the manganese nodules on the ocean floor. In river waters, there is between $100\,\mathrm{mg\,L^{-1}}$ (in the Nile) and $900\,\mathrm{mg\,L^{-1}}$ (in the Garonne),**[3]** mainly in particulate form rather than dissolved. The principal species present in natural waters**[4]** are Zn^{2+}aq, $[ZnOH]^+$, $ZnCO_3$, and, in the oceans, $[ZnCl]^+$. Kinetic processes in natural waters have been reviewed,**[5]** as have methods for analysing for zinc in natural, potable, and effluent waters.**[6]**

1.3 Biological Importance

Zinc was demonstrated to be an essential trace element for eukaryotes in 1869; it has subsequently been shown to be essential for all life forms.**[7–9]** It generally plays either a catalytic or a structural role; in some metalloproteins that interact with DNA, zinc appears to play both roles. It is an essential constituent of many enzyme systems, as first demonstrated, for carbonic anhydrase, in 1940. Several hundred zinc metalloenzymes and metalloproteins have now been recognized, in a wide range of organisms. It generally functions at or near the active site, particularly in catalysis of nucleophilic substitutions. In the early years of bioinorganic chemistry, analytical difficulties and spectroscopic restrictions hampered the investigation of zinc centers in biological systems, but increasingly powerful diffraction, spectroscopic, and other techniques have in recent decades enormously increased understanding of their structure and function. The development during the past decade of fluorescent probes for zinc has also helped in studying the nature and function of zinc-containing species in biological systems. Such probes generally contain an anthracene or fluorescein moiety substituted into a cyclic, acyclic, or tripodal polyamine that can bind firmly to the zinc. Photoinduced electron transfer (PET) sensors operate by the Zn^{2+} interrupting the PET of the ligand and restoring or enhancing its fluorescence.[10–12]

The long history and slow early development of the subject has been briefly reviewed (*see also* ***Zinc Enzymes*** and ***Zinc: DNA-binding Proteins***).[13,14] More recent general reviews of the biological role of zinc, including its regulatory role and the intriguing question of the localization of zinc in particular organs (e.g. parts of the male reproductive system of both plants and animals have high concentrations of zinc, as has the hippocampus in the brain), are available.[15,16] The manifold important zinc-containing biological systems have spawned a multitude of model complexes,[17] thereby greatly enriching knowledge of the coordination chemistry of zinc (see Sections 8 and 9). Types of model complexes include those with amino acid ligands to model zinc-peptide interactions, NNN-donor ligands to model the active site of carbonic anhydrase or carboxypeptidases, NO-donor Schiff bases to model Zn_2 sites, and μ-O^{2-} and μ-$CO_3{}^{2-}$ polynuclear complexes to model Zn_3 and Zn_2Mg active sites. The biological inorganic chemistry, particularly the coordination chemistry of Zn^{2+} in biological systems, has been well covered in a number of books[18–20] and several aspects are mentioned elsewhere in this encyclopedia.

1.4 Zinc in the Human Body

There is a somewhat more than 2 g of zinc in the average adult; its plasma concentration is about 20 μM. There are believed to be some 200 zinc-requiring enzymes in the human body. Zinc is essential for healthy skin and proper wound healing, for a strong immune system, for bone metabolism, and for normal taste and smell. To maintain the required levels of zinc in the human body, a daily intake of several milligrams is required. Recommended Dietary Allowances (RDA; USA; 1989) are 12 and 15 mg per day for adult females and males respectively; Reference Nutrient Intakes (RNI; UK; 1991) are 9.5 and 7.0 mg per day.[21] Zinc contents of foods are 3 to 4 mg per serving for meat, 1 to 2 mg, for, for example, grains, nuts, cheese (there is very little zinc in fruit), giving a daily intake of the order of 20 mg.[22] But there can be problems of absorption, with the phytates present in many cereals significantly reducing zinc uptake by forming a stable complex that is very poorly absorbed from the gastrointestinal tract. A low-zinc diet, especially a plant-based diet with high phytate levels, results in slow growth, as first convincingly demonstrated in Iran in the late 1960s. Zinc deficiency reduces testosterone production in men, and delays puberty for male adolescents. Some 30 clinical disorders may be attributed to zinc deficiency; correcting this may be the key to delaying macular degeneration of vision, and to curing anorexia, acne, alcoholism, postnatal depression, and even the common cold.[23] There is a continuing controversy as to whether a large number of people suffer from a modest zinc deficiency in their daily diet; zinc supplements are popular. However, it is important not to exceed daily requirements, as a modest excess of zinc leads to reduced copper absorption and a large excess of zinc is toxic. One gram of zinc sulfate may induce nausea, vomiting, abdominal cramps, and diarrhea; higher doses have proved fatal. Rice polluted with zinc sulfide was implicated in an outbreak of severe skeleto-muscular disorders in Japan. Zinc inhalation can give rise to ‘metal fume fever’, whose symptoms are similar to those of influenza. The nutritional role[24,25] and the toxicity[26,27] of zinc have been considered in detail, its diverse function in the particular context of inorganic microbiology has been explored,[28] and the biological monitoring of zinc has been reviewed.[29]

A number of zinc compounds and complexes have been developed for therapeutic purposes.[30] Several zinc complexes of cyclam-based ligands have proved potent inhibitors of HIV, while hydroxypyridinone complexes are being assessed as insulin mimics for the treatment of diabetes. There is some evidence that the administration of certain zinc chelates may help to ward off strokes, while a suberoylanilide hydroxamate complex has been in clinical trials as an anticancer agent since 2000.

1.5 Zinc in Supramolecular Chemistry

A wide range of zinc-based coordination polymers[31] has been developed in recent years, ranging from simple chains to layers, clusters, and a variety of three-dimensional frameworks. Molecular architectures generated include helicates, rotaxanes, catenanes, knots,[32] grids, cylinders, capsules, and various structures containing tailored holes and channels. Such supramolecular assemblies can be valuable in molecular recognition, in catalysis, in separation, and in modeling of biological systems, for example, the ‘biological motors’ that operate flagella and muscles – where zinc is almost certainly involved in association with adenosine phosphates.

Supramolecular entities are prepared either by designed or self-assembly, or by the breakdown of larger species – the so-called ‘bottom-up’ and ‘top-down’ approaches respectively. Most supramolecular zinc compounds have been obtained by self-assembly methods, often operating in a rather hit-and-miss way. However, controlled cleavage of coordination polymers should prove a useful route to predesigned supramolecular assemblies. An example of this approach is provided by the generation of a supramolecular hexanuclear zinc species from the three-dimensional coordination polymer prepared from zinc acetate and di-2-pyridyl ketone.[33]

1.6 General

There are good overviews of zinc chemistry in several inorganic textbooks, especially those by Greenwood and Earnshaw[34] and by Cotton, Wilkinson, and their recent collaborators.[35] Much detailed information, especially on the preparation and properties of binary compounds and salts, can be found in the elderly multivolume treatises of Mellor[36] and Pascal,[37] while Sidgwick's more modest pair of volumes[38] also contains much useful information of this type. The organometallic chemistry of zinc is considered in detail elsewhere (*see* ***Zinc: Organometallic Chemistry***).

2 PRODUCTION OF THE ELEMENT

World production of zinc rose from about 300000 tons per annum towards the end of the nineteenth century to about 7 million tons in 1996. Zinc blende is the most important ore of zinc and is usually found in association with galena, PbS, and some mineral detritus from which it is separated by differential flotation. The concentrate is then heated in air to give SO_2, which is used in sulfuric acid manufacture, and zinc oxide. The latter is then used in either an electrolytic isolation step or in a smelting process. In the former, extensively used in North America and in Tasmania, the oxide is leached out with dilute sulfuric acid and the solution electrolyzed with aluminum cathodes and, usually, lead anodes, the deposited zinc (99.95% pure) being stripped off the cathodes from time to time. Various smelting processes, based on the reduction of ZnO with coke, rely on the low boiling point of zinc (907 °C). Early batchwise procedures using horizontal retorts were superseded by continuous processes using vertical retorts made of silicon carbide. The zinc produced by such procedures was fairly pure but required to be further purified, by fractional distillation or electrolytic refining, to 99.99% for use in die-casting alloys and in high quality brass. The retort processes do not have the thermal efficiency of a blast furnace in which the combustion of the fuel for heating takes place in the same space as the reduction of the oxide. Early attempts at adapting the blast furnace for zinc smelting were unsuccessful, for which there are sound thermodynamic reasons.[39] There are two main difficulties: firstly, ZnO reduction by carbon is not spontaneous below the boiling point of zinc and, secondly, the zinc vapor is a good reducing agent for CO_2 so that, during subsequent cooling of the vapor to condense it, the zinc is liable to be reoxidized to ZnO, with concomitant formation of CO. A solution to the problem is found in the Imperial Smelting Process in which hot Zn and CO from the blast furnace are passed through a chamber drenched by a spray of molten lead at 550 °C. Zinc dissolves appreciably in lead at this temperature so that it is collected in the lead droplets and passes down with them, too quickly to be oxidized, into a molten lead bath below. The solution of zinc in lead passes to a separate cooler chamber at 440 °C, when the lower solubility of zinc at this temperature causes it to separate from the lead. The molten zinc is run off and the lead returned to the spray chamber. The process can be operated continuously and mixed zinc and lead ores may be used so that both metals can be produced simultaneously.

For small deposits, the ZnS may be converted into $ZnCl_2$ and thence into the metal. Zinc can also be solubilized from sphalerite by bacterial oxidation.[40]

Technical aspects of the production and of the uses (cf. following section) of the element have been detailed at length.[41]

3 USES

The most important of the many uses of zinc is as an anticorrosion agent for iron and steel,[42] in the form of a coating that may be applied by immersion in molten zinc ('hot-dip galvanizing'), electrolytic deposition, spraying with liquid metal, or heating with powdered zinc ('sherardizing' after its inventor Sherard Cowper-Coles). Zinc is also used to prevent corrosion in the form of sacrificial anodes (*see Sacrificial Anode*), particularly in marine applications. Zinc sheeting is used in roof cladding, zinc plates are used in lithography (zinc has a low contact angle with respect to printing inks), and zinc dust is used as a reductant.

A major use is in the manufacture of brasses, alloys of copper and zinc containing about 20–50% zinc, the ductility and tensile strength of which are controlled by the zinc content. The *Phase Rule* diagram of the zinc-copper system is complex: of the six solid solutions that may be formed as the zinc concentration increases over the whole composition range, the practically useful alloys are confined mainly to two, the α and β (the latter being much harder than the former) and their mixtures. The topic is interesting both from a practical and structural point of view and has been dealt with in detail elsewhere.[43] Small percentages of aluminum, iron, manganese, tin, and nickel are frequently added to 60–40 copper–zinc alloy to increase tensile strength without markedly affecting ductility: these are referred to as 'high tensile brasses' (*see* ***Alloys***).

As a casting metal for pressure die casting into permanent, steel casting dies, zinc is one of the cheapest metals and is widely used to produce small parts of complex shape such as automobile parts (door handles, locks, carburettors, petrol (gasoline) pumps) and is readily chromium plated. The zinc used for such castings must be highly pure to avoid corrosion and disintegration along impurity grain boundaries.

It is alloyed with about 4% Al and 0.02% Mg. The aluminum strengthens the zinc and also prevents the molten alloy from attacking the steel pressure casting dies. Zinc readily reacts with mercury or will displace mercury from a mercury(II) salt to form an amalgam that is useful for reductions, as in the preparation of compounds of the lower oxidation states of transition metals and lanthanides (e.g. Cr^{II}, V^{II}, Eu^{II}, dimeric Mo^{III}) and in analytical chemistry (e.g. in the Jones reductor; *see* ***Analytical Chemistry of the Transition Elements***).

The long-familiar Daniell cell used a zinc electrode; zinc sheeting is still much used in battery manufacture. Useful background material for this aspect of zinc chemistry is to be found in the article ***Electrochemistry: Applications in Inorganic Chemistry***, further details elsewhere.[44,45] The original Leclanché battery (1866), based on the cell

$$Zn(s)|ZnCl_2(aq), NH_4Cl(aq)|MnO_2(s), C(s)$$

was a wet cell. Some two decades later, Geissner patented the idea of manufacturing the zinc anode in the form of a cup that would act as a container for the electrolyte, which was immobilized with plaster of Paris. This development was combined with the use of the manganese dioxide/carbon cathode and an electrolyte immobilized using a cereal paste to form the basis of modern dry cell technology. The discharge mechanism of the Leclanché cell is not as simple as it is sometimes represented. In outline, oxidation of zinc to Zn^{2+}aq occurs at the anode, while at the cathode reduction of Mn^{IV} to Mn^{III}, either as MnO(OH) (s) or $Mn_2O_3{\cdot}H_2O$, takes place. The initial products of the electrode reactions then undergo further reactions in solution, mainly forming $[Zn(NH_3)_2]^{2+}$, then slightly soluble $Zn(NH_3)_2Cl_2$. For light discharges, an alternative reaction between $Zn^{2+}(aq)$ and a Mn^{III} hydroxyoxide can give $ZnO{\cdot}Mn_2O_3$. At lower NH_4^+ concentrations, chloride and hydroxide or hydroxide alone are preferred ligands to NH_3, and a variety of solid complexes are formed, such as $ZnCl_2{\cdot}4Zn(OH)_2$ or simply $Zn(OH)_2$. The main cell reactions can be summarized as

$$Zn\ (s) + 2MnO_2\ (s) + 2NH_4^+\ (aq) + 2Cl^-\ (aq) \longrightarrow 2MnO{\cdot}OH\ (s) + Zn(NH_3)_2Cl_2\ (s) \tag{1}$$

and

$$Zn\ (s) + 2MnO_2\ (s) \longrightarrow ZnO{\cdot}Mn_2O_3\ (s) \tag{2}$$

However, if the initial ammonium chloride concentration is depleted, the reaction, as indicated above, becomes more complex and formation of hydroxochloro complexes plays an increasingly important role. The zinc alloy sheet used for the anode manufacture contains small quantities of lead and cadmium, and various corrosion inhibitors, such as a soluble mercury salt, are added to improve shelf life.

A variation of the Leclanché cell is the zinc chloride cell in which the ammonium chloride is completely replaced with zinc chloride. Such cells have a better service capacity at high current drain, at low temperatures, and on continuous discharge.

A further variation of the Leclanché cell is the so-called alkaline manganese cell. The negative pole is a hollow cylinder of powdered amalgamated zinc set in carboxymethylcellulose gel. The current collector is usually made of brass and the interior space is filled with immobilized KOH electrolyte solution. The positive pole consists of a mixture of electrolytic MnO_2 and graphite in a ratio of 4–5:1 wetted with electrolyte solution. The cell reaction is given approximately by the equation

$$2Zn\ (s) + 2MnO_2\ (s) + H_2O\ (l) \longrightarrow 2MnO{\cdot}OH\ (s) + 2ZnO\ (s) \tag{3}$$

but in practice is considerably more complicated. The main advantage of alkaline manganese cells over Leclanché cells is their relatively constant capacity over a wide range of current drainage conditions. An interesting feature of these cells is that provided the discharge is limited when the cell voltage reaches about 0.9 V, the cell reaction can be reversed and the system can function as a secondary cell.

The Ruben-Mallory zinc–mercury(II) oxide battery, which revolutionized the battery industry, uses the cell

$$Zn(s)|ZnO(s)|KOH(aq)|HgO(s),C(s)$$

The anode reaction is

$$Zn\ (s) + 2OH^-\ (aq) \longrightarrow ZnO\ (s) + H_2O\ (l) + 2e^- \tag{4}$$

and the cathode reaction may be represented as

$$HgO\ (s) + H_2O\ (l) + 2e^- \longrightarrow Hg\ (l) + 2OH^-\ (aq) \tag{5}$$

The overall cell reaction is then

$$Zn\ (s) + HgO\ (s) \longrightarrow ZnO\ (s) + Hg\ (l) \tag{6}$$

Important features here are (i) the invariance of the electrolyte solution and (ii) the constancy of the chemical potentials of the reactants and products as the cell is discharged. The former fact means that only a very small quantity of electrolyte is required, giving the cell an almost constant internal resistance and therefore a flat discharge curve; the latter means that, during discharge, the open circuit voltage remains constant, both desirable features in a battery. (The standard free energies of formation of Hg(s) and Zn(s) are respectively $-58.4\,kJ\,mol^{-1}$ and $-318.2\,kJ\,mol^{-1}$, giving a free energy change for the cell reaction of $-259.8\,kJ\,mol^{-1}$ and a cell emf of 1.347 V, close to the open circuit voltage of 1.357 V of commercially produced cells.)

The zinc–silver oxide cell, widely used in miniature applications and larger ones in military applications, is closely related to the zinc–mercury(II) oxide system and has the configuration

$$Zn(s)|ZnO(s)|KOH(aq)|Ag_2O(s), C(s)$$

The main features of the zinc–silver oxide cell are similar to those of the zinc–mercury(II) oxide system. The principal difference apart from cost is the higher open circuit voltage: the emf calculated from the standard free energies of formation of ZnO and Ag_2O is 1.593 V, in close agreement with the open circuit voltage of commercial cells of 1.60 V.

Zinc has found application in several other types of battery, including industrially important zinc-air cells in which the oxygen of the air is used as the cathodic reactant in a cell such as

$$Zn(s)|NaOH(aq)|C(s), O_2(g)$$

The zinc-air cell has marginally the highest theoretical voltage (1.65 V) of all these zinc-based cells.

All the zinc-based cells, except for the alkaline manganese cell under certain conditions, are primary cells. Secondary (rechargeable) cells are generally based on cadmium rather than zinc, especially in the form of nickel–cadmium cells.

4 PROPERTIES OF THE ELEMENT

4.1 Physical Properties

Some physical properties of zinc are shown in Table 1. The naturally occurring isotopes, with their abundances, are ^{64}Zn(48.89%), ^{66}Zn(27.81%), ^{67}Zn(4.11%), ^{68}Zn(18.57%), and ^{70}Zn(0.62%). Man-made isotopes include ^{63}Zn ($\tau_{1/2} = 38.1$ min; $E_{\beta^+} = 2.32$ MeV), ^{65}Zn ($\tau_{1/2} = 243.6$ days; $E_{\beta^+} = 1.353$ MeV, EC, γ), and ^{69m}Zn ($\tau_{1/2} = 13.9$ h; $E_{IT} = 0.4389$ MeV, γ). All three have been used for tracer studies, for example, of zinc absorption; ^{65}Zn has been used to monitor the performance of diesel engines and to trace the movement of underwater silts and sediments (^{65}Zn is incorporated into powdered glass mixed with natural sand); ^{63}Zn can be used for PET (Positron Emission Tomography); ^{67}Zn is suitable for Mössbauer and nuclear magnetic resonance (NMR) spectroscopy (see below).

The electron configuration of zinc, [Ar]3d^{10}4s^{2}, might have been expected to lead to a structure based on close packing of spheres (see Figure 1); such is not the case and the experimental hexagonal close-packed structure is markedly distorted, the axial ratio being nearly 1.9 instead of 1.63 as in perfect hexagonal closest packing. Each Zn atom has six nearest neighbors in its own plane at a distance of 2.659 Å; the other six, three above and three below, in the adjacent planes, are at a greater distance, 2.906 Å. It is not satisfactory simply to regard the atoms in this structure as packing like prolate spheroids, for in the close-packed ε-phase of the Cu–Zn system the axial ratio is less than 1.63 and one would then have to assume that the atoms are behaving at some compositions as prolate and at others as oblate spheroids. It has been suggested that there is some tendency to form covalent bonds, with dp^2 hybrids playing a part in the basal planes, leading to a smaller interatomic distance in the close-packed planes.

Table 1 Selected physical properties of zinc

Atomic number	30
Relative atomic mass	65.38
Electron configuration	[Ar]3d^{10}4s^{2}
Ionization energies (kJ mol^{-1})	906.1 (1st); 173.3 (2nd); 3831 (3rd)
Density (g cm^{-3})	7.14 (at 298 K)
Mp (°C)	419.5
Bp (°C)	907
Lattice type	Hexagonal close-packed
ΔH°_{fus} (kJ mol^{-1})	7.28
ΔH°_{vap} (kJ mol^{-1})	114.2
S° (J K^{-1} mol^{-1})	41.6
C°_p (J K^{-1} mol^{-1})	25.1
Electrical conductivity (S m^{-1})	0.167 (at 298 K)

4.1.1 Zinc Mössbauer Spectroscopy

Zinc is one of the few elements with an isotope useful for Mössbauer spectroscopy.[46,47] ^{67}Zn has a long-lived isomer state, which leads to potentially narrow line widths (as narrow as 3.2×10^{-4} mm s^{-1}) in the Mössbauer spectrum. Disadvantages are a smaller cross section than, for example, ^{57}Fe and a much higher recoil energy, decreasing the rate of recoil-free events. The ^{67}Zn isomer may be produced using a ^{67}Ga source.

4.1.2 NMR Spectroscopy in Zinc Systems

The only NMR-active isotope of zinc is ^{67}Zn, whose resonance is at 6.254 MHz at 2.344 T. Sensitivity with respect to ^{1}H is only 2.85×10^{-3}, and the natural abundance of ^{67}Zn is only 4.1%. The nucleus ($I = 5/2$) has a quadrupole moment and because of line broadening this causes difficulties in the study of binding with large ligands, especially in metalloproteins (*see* ***Zinc Enzymes***). Given the low abundance of ^{67}Zn, Fourier Transform NMR methods are used. For example, in such an NMR study[48] of zinc halide solutions the dependence of the chemical shift on concentration is strongly nonlinear, higher frequencies being observed with increasing concentration, an effect partly ascribed to the change of stereochemistry from octahedral to tetrahedral on passing along the series from $[Zn(H_2O)_6]^{2+}$ to $[ZnX_4]^{2-}$ (cf. Section 9.2). In contrast, no shifts were observed for perchlorate, nitrate, or sulfate salts, where presumably the zinc-containing species is $[Zn(H_2O)_6]^{2+}$ throughout.

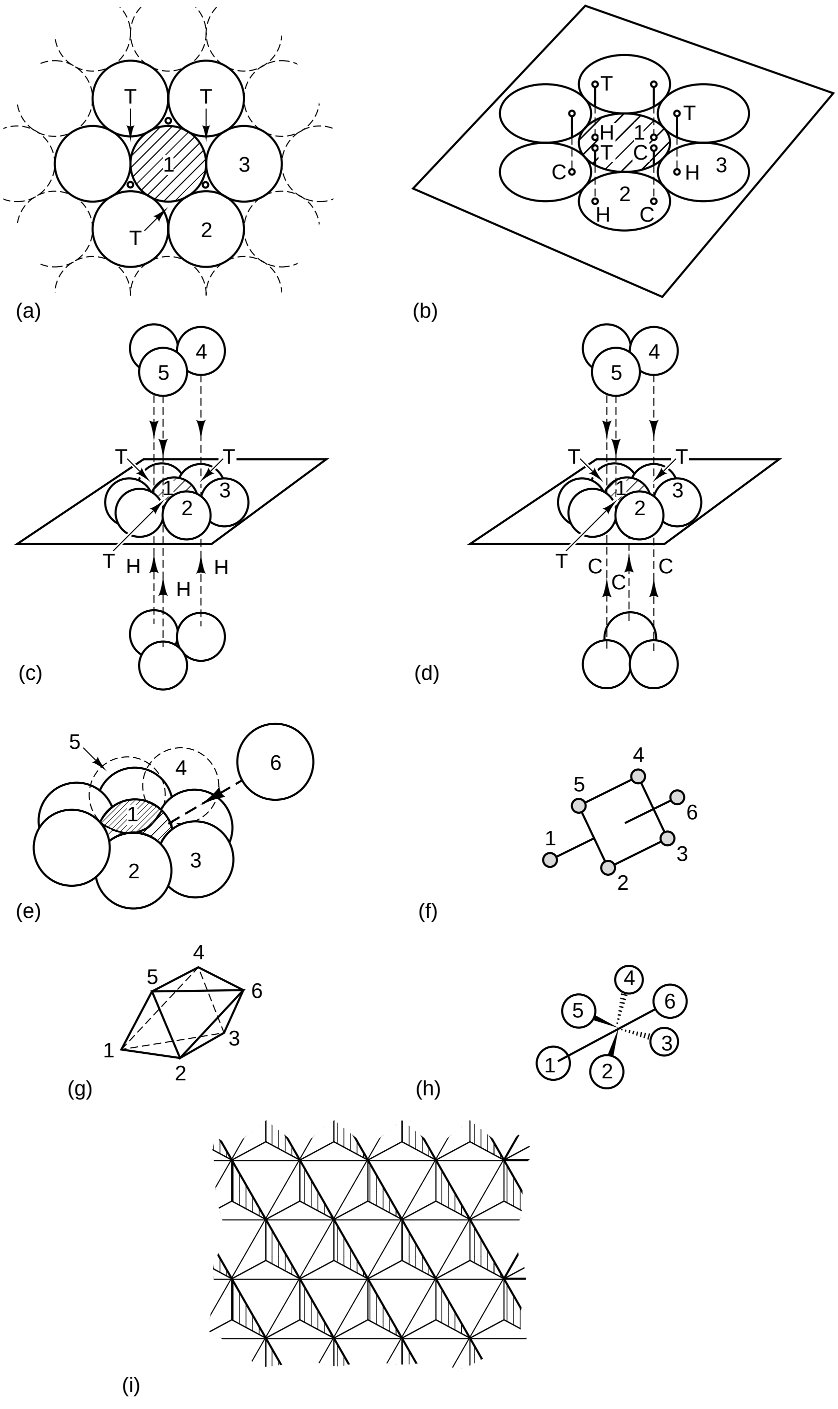

Figure 1 The relation of close packing to the structural chemistry of zinc and its compounds. (a) Close-packed identical spheres in a plane surrounding a central sphere (shaded, 1). (b) An equatorial plane through the spheres in (a) showing the location of the centers of holes above and below the equatorial plane. Only three spheres from above the plane may be placed in the positions corresponding to alternate holes, such as those marked T, so as to achieve close packing; the centers of these spheres lie directly over the hole centers. An atom at the center of the T holes is coordinated to the four contact spheres in regular tetrahedral coordination. (c), (d) The two ways of adding three spheres from below the equatorial plane to achieve close packing; in (c) the centers of the upper and lower spheres lie above each other so that the lower ones are located at H in (b). This is hexagonal close packing and is found in the structure of metallic zinc (albeit distorted, see text). In (d) the three lower spheres alternate with respect to the upper ones (i.e. three upper spheres at T, three lower spheres at C, in b). This is cubic close packing and is the foundation of the structures of many zinc compounds (e.g. ZnS, ZnO, see text). (e) Two of the three spheres, 4 and 5, added above the plane form an octahedral hole when sphere 6 is added. Spheres 1–6 surround this hole in an octahedral arrangement that may be represented as shown in (f), (g), or (h). If a zinc atom lies at the center of the octahedral holes and the spheres are, for instance, halogen atoms linked in layers of MX_6 octahedra sharing edges, this is the so-called cadmium iodide structure adopted by the zinc halides as in (i)

Ligand nuclei have been the subject of many studies; for example, ^{35}Cl NMR has been used to examine the environment of chelated zinc(II). Molar relaxivity can be used to characterize the zinc environment in terms of the quadrupolar relaxation of ^{35}Cl that it can produce in 0.5 M NaCl. Bidentate chelation (as with glycinate, glutamate, succinate) increases its effectiveness in producing ^{35}Cl relaxation. Terdentate chelation (iminodiacetate, aspartate) can either increase or decrease the amount of relaxation caused by zinc; the least relaxation is produced when the ligand atoms have a formal negative charge and a large acidity constant. In some cases, zinc chelated by four ligand atoms (nitrilotriacetate) is effective for ^{35}Cl relaxation, a good indication that such chelation does not constitute a coordinatively saturated environment. This point is significant in connection with the function of zinc in the active site of zinc metalloenzymes (*see* ***Zinc Enzymes***). Molar relaxivities for 1:1 and 2:1 chelates usually differ and it is possible to derive formation constants that are consistent with literature values determined by other methods. Carbon-13 NMR studies have been widely used to investigate complexing of a variety of organic ligands with zinc. A more exotic example of the use of ligand nuclei to evaluate the properties of zinc-containing species is afforded by the ^{119}Sn NMR study of a zinc complex derived from a tripodal triamidostannate(II) ligand, viz. $Zn[Sn\{SiMe_2N(p\text{-tolyl})\}_3SiMe]_2$. The NMR results establish the metal–metal bond polarity, X-ray diffraction having shown the Sn–Zn–Sn unit to be linear.**[49]**

4.2 Chemical Properties

Freshly cut zinc is a shiny metal with a bluish lustre but it tarnishes rapidly in moist air, to give a protective coating of ZnO, $Zn(OH)_2$, and $ZnCO_3$. It combines readily with oxygen, sulfur, phosphorus, or the halogens on heating. Nonoxidizing acids dissolve zinc with evolution of hydrogen to give zinc(II) salts that, in aqueous acids, contain the hydrated Zn^{2+} ion and often a range of its complexes with the acid anion. With oxidizing acids, the reactions are more complicated: nitric acid, for example, gives a variety of nitrogen oxides (and frequently some of their reduction products) depending on the concentration and temperature. Zinc is the only element of the Zn, Cd, Hg triad to dissolve in aqueous alkali to give ions such as aquated $[Zn(OH)]_4{}^{2-}$, the zincate ion. Such solutions are technically important in the electrolytic deposition of zinc on aluminum.

Since zinc has a filled d shell, few characteristic transition metal properties are shown and zinc(II) compounds are colorless and diamagnetic. Indeed, zinc shows similarities to magnesium, many of their compounds being isomorphous and, like magnesium, it displays class a (hard) behavior in complexing readily with O-donor ligands (*see Class A & Class B Behavior*). In contrast to magnesium, however, zinc has a much greater tendency to form covalent compounds (e.g. ZnO has a tetrahedral wurtzite structure whereas MgO has the normal NaCl structure). Zinc does share one feature in common with transition elements and that is its tendency to form a large number of stable complexes not only with O-donor ligands but also with N- and S-donor ligands and with halides, pseudohalides, and cyanide (Section 8). Its versatile complexing behavior places zinc on the class a/b (hard/soft) borderline (*see Class A & Class B Behavior*) and this feature of zinc chemistry is doubtless important in the catalytically active and structural sites of zinc enzymes in which complexation with O-, N-, and S-containing groups from amino acid side chains readily occurs (*see also* ***Zinc Enzymes*** and ***Zinc: DNA-binding Proteins***). In a more specific resemblance to a transition metal, zinc(II) complexes resemble those of high-spin cobalt(II) in terms of *Kinetic Lability* and *Stereochemistry*; for each element in the +II state it is generally true that four-, five-, and six-coordinated complexes readily interconvert. This is reasonable since, in terms of electron density, high-spin $3d^54s^2$ would be expected to behave similarly to $3d^{10}4s^2$, and the ionic radii are almost identical. Use is made of this in the substitution of cobalt for zinc in zinc metalloenzymes, with minimal structural perturbation, thereby providing a spectroscopically active probe for the active site environment of the metal ion.

5 OXIDATION STATE AND STEREOCHEMISTRY

5.1 Oxidation State

The Raman spectrum of the glassy solid obtained from a melt of Zn in $ZnCl_2$ indicates the presence of the $(Zn–Zn)^{2+}$ ion, but the chemistry of zinc is dominated by the +II state and, except possibly in the *Pulse Radiolysis* of complexes of Zn^{2+}, for example, those of cyclic ligands (L) such [14]ane-1,4,8,11-N_4 where species of the type LZn^+ have been detected, and the radical ligand complex of the same stoichiometry where L = the radical anion of glyoxal bis(*N*-*t*-butylamine) generated in the cavity of an electron spin resonance (ESR) spectrometer, the role of zinc(I), real or apparent, is minimal so far as the general chemistry of zinc is concerned. It is interesting, however, that the Zn^+ ion is formed, albeit slowly ($k < 10^5\,M^{-1}\,s^{-1}$), by the reaction of the *Hydrated Electron* with Zn^{2+}. The Zn^+ species is a powerful reductant and from the *Marcus Treatment* of the reduction of $[Ru(NH_3)_6]^{3+}$ it is estimated that $E°(Zn^{2+/+})$ is approximately -1.0 V; other estimates are even more negative.

5.2 Coordination Numbers and Stereochemistry

The key one-volume source of information on inorganic structures remains the overview by Wells,**[50]** the source of most unattributed structural information in this article. It is necessary to trace specific zinc compounds through

Table 2 Stereochemistry of Some Zinc(II) Compounds

Coordination number	Stereochemistry	Example
2	Linear	$ZnCl_2$ (g), $ZnEt_2$
3	Planar	$[ZnMe(NPh_3)]_2$, bis(ethylxanthato) (py)Zn
4	Tetrahedral	$[ZnCl_4]^{2-}$, $[Zn(NH_3)_4]^{2+}$
	Planar	$[Zn(TPP)]^{2+}$
5	Trigonal bipyramidal	$[Zn(tren)NCS]^+$
	'Square' pyramidal	$[Zn(S_2CNEt_2)_2]_2$, $[Zn(acac)_2OH_2]$
6	Octahedral	$[Zn(en)_3]^{2+}$
7	Pentagonal bipyramidal	$[Zn(H_2dapp)(H_2O)_2]^{2+}$
8	Distorted dodecahedral	$[Zn(NO_3)_4]^{2-}$

Wells's formula index as well as consulting his general discussion of zinc compounds. Coordination numbers of Zn^{2+} in its compounds and complexes range from 2 to 8 (Table 2). The filled d shell confers no crystal field stabilization on Zn^{2+} (*see Crystal Field Stabilization Energy*) and coordination number and stereochemistry are determined by the size of the Zn^{2+} cation and the *Steric requirements* of the ligands. Both tetrahedral and octahedral geometry are commonly found in complexes, though essentially all Zn^{2+} ions in biological systems are in tetrahedral coordination. Several zinc complexes are mentioned in a recent review of seven-coordinate complexes.[51] Where ligands bind by chelation (*see Chelating Ligands*), and quite often even where ligands are monodentate, distortions from regular geometries are widespread.

Six-coordinate complexes may be octahedral or trigonal prismatic. The synthesis of a number of six- and five-coordinate complexes with amino acids and pyrazole throws light on the factors involved both in the determination of the geometry of six coordination and on possible mechanisms of interconversion through a five-coordinate intermediate or transition state.[52] Zn^{2+} can exhibit two coordination numbers in the same compound – indeed the unit cell of the maltol complex $[Zn(malt)_2]\cdot 1.5H_2O$ contains both five- and six-coordinate Zn^{2+} ions.[53] Both five- and six-coordinate cations have been found in a binuclear complex of an unsymmetrical compartmental ligand,[54] in a tetrazinc metallacrown species,[55] and in the bis-Zn^{2+} complex of a ligand containing both a bipy and a terpy unit. Zn^{2+} occupies both octahedral and trigonal bipyramidal sites in $Zn_3V_4(PO_4)_6$, and square pyramidal sites in $Zn_2(VO)(PO_4)_2$,[56] while Zn is found in trigonal planar, tetrahedral, and trigonal bipyramidal sites in $[Zn_4(thf)_4(MeZn)_4(O_3SiR)_4]$, where $R = -N(SiMe_3)(2,6\text{-}^iPr_2C_6H_3)$.[57] Such metallasiloxanes can act as models for zinc-containing zeolite catalysts, which have recently been reported to facilitate a range of organic reactions.

6 BINARY COMPOUNDS

6.1 Zinc Hydride, Carbide, and Related Compounds

Zinc hydride, a moderately stable solid slowly decomposed by water, may be prepared by the reaction of LiH, NaH, or $LiAlH_4$ on a zinc halide such as the bromide or iodide. If organometallic derivatives of zinc of the type Li_nZnR_{n+2} are treated with $LiAlH_4$, complex hydrides such as $LiZnH_3$, Li_2ZnH_4, and Li_3ZnH_5 may be prepared.

The carbide ZnC_2 may be regarded as an acetylide containing the $C_2{}^{2-}$ ion. A zinc carbene, $ZnCH_2$, can be prepared by the *Matrix Isolation* technique; it undergoes a carbene-carbyne change to HZnCH on UV irradiation. The carbene may possibly be regarded as a radical ion pair formed by transfer of an electron from Zn to CH_2 to give an anionic carbene.[58,59]

Zinc alkyls and aryls are reactive to air and water and their reactions are similar to, but less vigorous than, those of Grignard reagents, from which they differ in the important respect that they do not react with CO_2 and are usually prepared in an atmosphere of this gas. Zinc may be used to generate, in effect, the nucleophile $^-CH_2CO_2R$ from α-halo esters that can then react with carbonyl compounds as in the well-known Reformatsky reaction:

$$RCOR' + BrCH_2CO_2Et \longrightarrow RR'C(OH)CH_2CO_2Et \qquad (7)$$

Metal–hydrogen and metal–carbon bond strengths, including some values for zinc, have been reviewed.[60]

6.2 Compounds with Group 15 Elements

Zinc nitride, Zn_3N_2, may be prepared by heating zinc amide, $Zn(NH_2)_2$, to 330 °C or by heating zinc dust to 600 °C in a stream of ammonia. It is regarded as an ionic nitride containing the N^{3-} ions in an α-Mn_2O_3 structure in which the zinc ions have four tetrahedral neighbors and N has two types of distorted octahedral coordination groups. The radius of the nitride ion in this and similar nitrides is close to 1.5 Å, larger than that of most metal ions.

Zinc phosphides, which include Zn_3P_2, Zn_7P_{10}, ZnP_2 (α- and β-forms), and ZnP_4, may be prepared from the elements. The structure of Zn_3P_2 is closely related to that of Zn_3N_2: the zinc atoms are surrounded tetrahedrally by four P but each P is surrounded by six Zn at six of the vertices of a distorted cube. The compound is used as a lubrication additive and as a pesticide and rodenticide. It works as a poison by releasing phosphine in the rat's stomach. Phosphidozincates $M[ZnP]_2$ are known for M = Ca, Sr, Ba, Cd; the Sr^{2+} salt has been shown to have the calcium aluminum silicide structure, consisting of layers of edge-shared ZnP_4 tetrahedra alternating with Sr^{2+} layers.[61]

Zinc antimonides (Zn_3Sb_2, Zn_4Sb_3, and ZnSb) are semiconductors.

6.3 Compounds with Group 16 Elements

Tetrahedral coordination is again a dominant theme. All the monochalcogenides adopt either a wurtzite or zinc blende structure, described below, in which the metal is tetrahedrally coordinated. Various aspects of close packing in relation to the structures of ZnO, ZnS, and other zinc compounds are depicted in Figure 1.

6.3.1 Zinc Oxide, Zinc Hydroxide, and Zincates

ZnO is the most important manufactured zinc compound; it was known long before the metal itself. The technical product is made by burning in air the zinc vapor obtained on smelting the ore but this can contain a few tenths of a per cent of lead as an impurity. A purer product is made from the vapor of refined zinc. It is a finely divided white solid with the wurtzite structure (cf. Figure 1 and zinc sulfide below). On heating, it changes to a yellow colored solid: this is associated with the evaporation of oxygen from the lattice to give a nonstoichiometric phase ZnO_{1-x} ($x \leq 70\,\text{ppm}$).[62] The excess zinc atoms produce lattice defects that can be excited by absorption of visible light, and by 'doping' zinc oxide with an excess of 0.02–0.03% zinc metal a range of colors – yellow, green, brown, or red – can be obtained. The photophysics of zinc oxide and its functioning as an archetypal binary compound semiconductor have been reviewed,[63] and the self-assembly of zinc oxide into nanorods reported.[64]

The major use of zinc oxide is in rubber production, where it lowers the vulcanization temperature and shortens vulcanization time. It is also used as a pigment in paints, 'zinc white' in oils and 'chinese white' in water colors, having the twin advantages compared with 'white lead' (the 'flake white' or Cremnitz white of the artist), a basic lead carbonate, that it is nontoxic. Also, since zinc sulfide is white, it is not discolored by sulfur compounds. It has the disadvantages compared with TiO_2 (*see* ***Titanium: Inorganic & Coordination Chemistry***) of a lower refractive index and therefore a lower covering power, sometimes used to advantage by the artist. In some paint vehicles, it is inclined to give a brittle paint film and consequent durability problems. However, it improves the chemical durability of glass and for this reason is used in the production of special glasses, both opaque and transparent, and in enamels and glazes. It is used as the starting material for a range of other zinc chemicals such as zinc soaps (zinc salts of the longer chain fatty acids) that are used as paint driers, fungicides, and stabilizers in plastics. It is used in the production of zinc silicate, Zn_2SiO_4, for television screen manufacture. A minor but important use is in the manufacture of 'zinc ferrites' (*see Ferrite*). These are *Spinels*, $Zn^{II}_{x}M^{II}_{1-x}Fe^{III}_{2}O_4$, having the second metal, M, in oxidation state two (M is frequently Mn or Ni). When $x = 0$ the structure is that of an inverse spinel (i.e. half the Fe^{III} ions occupy tetrahedral sites in the close-packed array of oxide ions, the other half of the Fe^{III} ions occupying octahedral sites), and when $x = 1$ it is that of a normal spinel in which all the Fe^{III} ions occupy octahedral sites because Zn^{II} displaces Fe^{III} at the tetrahedral sites. Lowering the fraction of Fe^{III} ions in the tetrahedral sites lowers the *Curie Temperature*. The magnetic properties of the ferrite are therefore controllable by adjustment of the zinc content. Thin films of zinc oxide have excellent piezoelectric properties and high transmittance and are used in transducers, gas sensors, surface acoustic wave devices, solar cell windows, and transparent conducting films;[65] spectra of transparent colloidal suspensions of very small zinc oxide particles have been reported.[66] Zinc oxide is also used for desulphurization of, inter alios, carbon dioxide, and feedstocks for catalytic processes, and in ZnO/Cr_2O_3 catalysts for high-pressure synthesis of methanol.[67] There are also a number of medicinal and cosmetic uses for zinc oxide – it is used in various dermatological treatments, alone or mixed with Bi_2O_3 or bismuth subgallate in the treatment of hemorrhoids, in dental cements, in sun screens, and to give 'body' to cosmetic formulations.

ZnO is amphoteric, dissolving in acids to form salts containing the hydrated zinc(II) cation (cf. Section 9.1), which may be more or less complexed with the acid anion depending upon its affinity for zinc and on concentration. Zinc oxide dissolves in alkalis to form zincates such as $[Zn(OH)_3]^-$ and $[Zn(OH)_4]^{2-}$. Various salts of these hydroxy-ions have been structurally characterized. Zinc also forms zincates of the type $M^{II}ZnO_2$, where M = Sr or Ba, and $M^{I}M^{I'}ZnO$, where M^{I}, $M^{I'}$ = Li, Na, K variously. These are prepared from the respective component oxides. In $SrZnO_2$, layers of ZnO_4 tetrahedra, sharing all vertices, provide sites for Sr^{2+} ions in seven coordination between the layers, whereas in $BaZnO_2$ the ZnO_4 tetrahedra form a quartz-like framework containing Ba^{2+} ions in positions of irregular eight coordination.

An important structure in the chemistry of hydroxy (and carbonate) derivatives of zinc is the so-called CdI_2 (or brucite, $Mg(OH)_2$) structure. This structure may be represented in various ways – Figure 1(a) shows one representation. From this close-packed description, it follows that because different layer sequences are possible there is a very large number of closely related structures (more than 80 such structures have been characterized). Zinc hydroxide, for example, exists in a number of forms based on this structure but with differing layer sequences; one of them has the simple CdI_2 structure, others have more complex layer sequences and one, the γ-form, has an entirely different structure consisting of rings of three tetrahedral $Zn(OH)_4$ units that are linked through their remaining vertices into infinite columns (Figure 2). The upper vertices (x) of the tetrahedra of one ring are the lower vertices (y) of the ring above, thus sharing all the vertices within the column and giving the composition $Zn(OH)_2$. Each column is linked to neighboring ones by hydrogen bonds.

A number of zinc hydroxy compounds are based on the CdI_2 layer structure but with zinc ions attached to the outside of the layer. Since the I atoms are close packed in a CdI_2 layer, there are two kinds of site on either side of such a layer for

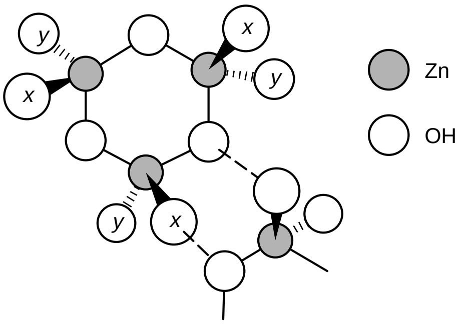

Figure 2 The coordination of zinc in γ-Zn(OH)$_2$

additional metal ions: above an occupied octahedral interstice or above an empty tetrahedral site. On electrostatic grounds, neither type of site is suitable for a straightforward addition of the metal ion to the layer because of the proximity to either one or three cations of the layer. This difficulty is overcome in the first case by removing the metal ion from within the layer (Figure 3). The mineral chalcophanite, $ZnMn_3O_7 \cdot 3H_2O$, has layers of the simplest cadmium iodide type (cf. Figure 1) derived from Mn^{4+} and O^{2-} ions from which one-seventh of the metal ions have been removed, giving the composition Mn_3O_7 instead of MnO_2. Bound to each side of this layer directly above and below the unoccupied Mn^{4+} positions are Zn^{2+} ions and between the uncharged layers are layers of water molecules, three of which complete the octahedral coordination of the Zn^{2+}.

In the hydroxy chloride $Zn_5(OH)_8Cl_2 \cdot H_2O$, the structure is based on charged layers with chloride ions and water molecules in between. One-quarter of the zinc ions are missing from a $Zn(OH)_2$ layer, and for each absent Zn^{2+} two such ions are added beyond the surfaces of the layer so that the composition is $Zn_5(OH)_8{}^{2+}$. The charge is balanced by the chloride ions between the layers. The Zn^{2+} ions are tetrahedrally coordinated on the outer surfaces of the layers, in contrast to octahedrally coordinated Zn^{2+} within the layers. A similar structure is found in the hydroxy nitrate, $Zn_5(OH)_8(NO_3)_2 \cdot 2H_2O$. Closely related to these structures is one in which the layers are linked by bonds to the Zn^{2+} ions on the surface: the compound in question is hydrozincite, $Zn_5(OH)_6(CO_3)_2$, formed during the corrosion of zinc and in the weathering of zinc ores. Again one-quarter of the Zn^{2+} are absent from a $Zn(OH)_2$ layer and replaced by twice their number of zincs, equally distributed on either side of the layer. In addition, there is replacement of one-quarter of the OH^- ions in the layer by O atoms of $CO_3{}^{2-}$ ions, giving the composition $Zn_2[Zn_3(OH)_6](CO_3)_2$ instead of $Zn_4(OH)_8$ of the parent compound. A second O atom of each $CO_3{}^{2-}$ is bonded to the surface Zn atoms, which are tetrahedrally coordinated as in the hydroxy chloride (see Figure 3). Since there is bonding between the Zn and O throughout the structure in its entirety, this is not a layer structure although its relation to one is clear. The close-packed layers of O atoms around octahedrally coordinated Zn atoms are again a prominent feature of the structure. All these structures illustrate the ease with which zinc is able to enter into tetrahedral and octahedral coordination.

In addition to the normal oxide, ZnO, a peroxide MO_2 is also known. This decomposes slowly at ambient temperature, but nonetheless has been used as an astringent, a deodorant, and a vulcanizing agent.

6.3.2 *Zinc Sulfide*

ZnS, zinc blende or sphalerite, is the most common ore of zinc, but it is also found in a rarer mineral, wurtzite, which is the more stable at high temperatures. These minerals are important archetypal structures found in many other AB compounds that are essentially nonionic and these structures bear the names of the respective minerals. In both, each Zn is tetrahedrally coordinated by four S and each S is coordinated tetrahedrally by four Zn. The structures differ only in the type

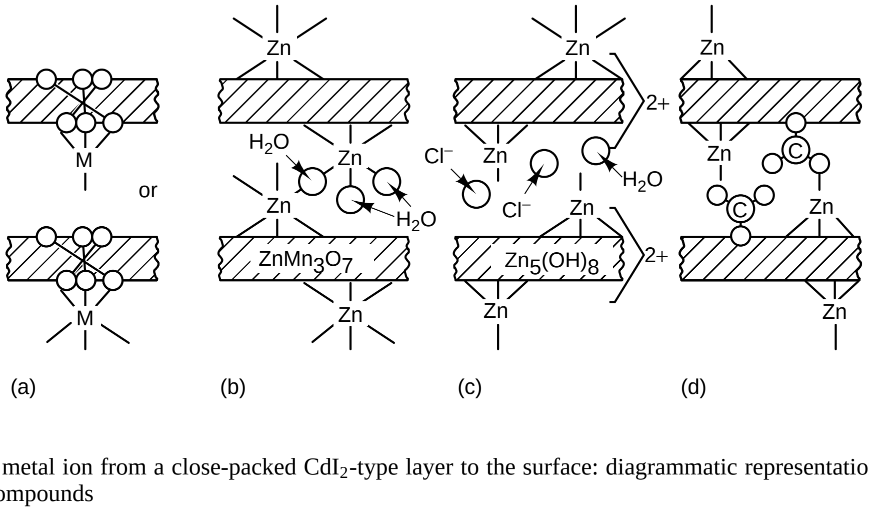

Figure 3 Removal of a metal ion from a close-packed CdI$_2$-type layer to the surface: diagrammatic representation of its occurrence in the structures of some zinc compounds

of close packing: it is cubic in zinc blende and hexagonal in wurtzite (see Figure 1).

When pure, ZnS is white and is used as a pigment that, when coprecipitated with barium sulphate, gives the white pigment 'lithopone'. Various grades are produced containing 26–60% ZnS; it is more opaque than zinc white and when suspended in water or oil has thixotropic properties. Its commercial importance has greatly decreased, however, since the introduction of titanium pigments. Zinc sulfide when freshly precipitated dissolves easily in mineral acids with evolution of H_2S, but roasting renders it far less reactive and it is then used as a harmless nontoxic pigment.

Zinc sulfide turns gray on exposure to UV light, probably due to some dissociation into the elements, a process that is inhibited by trace addition of cobalt salts. X-rays, radioactivity, and cathode rays produce fluorescence or luminescence in a variety of colors (e.g. traces of copper give a greenish phosphorescence after exposure to light or in the presence of a trace of a radioactive compound). The range of colors can be extended by changing the trace metal added or by the replacement of zinc by Cd and of S by Se. It is widely used in the manufacture of cathode-ray tubes and of luminous dials. Zinc sulfide is a semiconductor; Mn-doped zinc sulfide nanoparticles have promising optical properties.[68]

6.3.3 Zinc Selenide and Telluride

Zinc selenide (yellow) and telluride (brown) have similar structures to those of the sulfide, both existing in both wurtzite and zinc blende modifications. The selenide is used with zinc sulfide as a phosphor. It has the interesting property that it can act as a blue–green solid state laser: blue–green laser action in solids is rare (most solid-state lasers function towards the red end, 635 nm or more, of the spectrum). At room temperature, laser action with the selenide at a wavelength of 525 nm (green) is observed and at −196 °C at 495 nm (blue). Unfortunately the laser is relatively short-lived. Zinc telluride is a wide band gap semiconductor whose electron transport properties in the form of thin films of stoichiometric and nonstoichiometric forms have been much studied.[69,70] Its applications in optoelectronics, for example, as an optical recording material, have been reviewed.[71]

6.4 Zinc Halides and Pseudohalides

All four halides are known. In the gas phase, they consist of linear X–Zn–X molecules with internuclear distances (in Å) as a function of X as follows: F, 1.81; Cl, 2.05; Br, 2.21; I, 2.38. The difluoride has the highest melting point (872 °C), the melting points rising thereafter from chloride to bromide to iodide (275, 394, and 446 °C, respectively). ZnF_2 may be prepared by the action of HF on the metal or by the action of heat on the tetrafluoroborate $Zn(BF_4)_2$. It has the typically ionic 6:3 rutile structure in which zinc is six coordinated by F^- ions. This stereochemistry persists in the complex fluoride $KZnF_3$, which has the ideal perovskite structure. Although its solubility is low, ZnF_2 may be crystallized as a tetrahydrate from aqueous solutions. The nearly anhydrous compound has been used in the fluorination of organic compounds and has been used in the manufacture of phosphors for fluorescent lights, glazes, and enamels for porcelain, for preserving wood, and in electroplating.

$ZnCl_2$, $ZnBr_2$, and ZnI_2 are hygroscopic with extremely high solubilities in water, which is able to dissolve about four times its mass of ZnX_2. Aqueous methods of preparation give hydrates, of which a number are known. The halides are best prepared anhydrous by the usual dry methods such as treating the heated metals with HCl, Br_2, or I_2, as required. Water-free solutions of ZnX_2 may also be prepared by treating a suspension of finely divided zinc in an inert solvent with the appropriate halogen.

The chloride, bromide, and iodide show properties characteristic of covalent compounds such as solubility in ethanol, acetone, methyl cyanide, and other organic solvents. They also have comparatively low-melting points, and crystal structures based on a two-dimensional array that may be regarded as derived from a close-packed lattice of halide ions in which the zinc ions occupy the tetrahedral sites. The crystal chemistry of $ZnCl_2$ is more complex than at first appeared. Three polymorphs were originally described that, although they can be regarded as having approximately close-packed chloride ions, had different layer sequences. It has been found, however, that the structure is extremely sensitive to the presence of water and if crystallization is carried out with rigorous exclusion of water, an orthorhombic hexagonal close-packed structure is formed that changes into one of the other structures on exposure to the atmosphere. The presence of OH^- ions formed on exposure to moisture may facilitate the rearrangement of the layers. The hcp structure is the only stable one for $ZnCl_2$. All four structures consist of tetrahedral $ZnCl_4$ groups, each sharing vertices with four others. The bromide is also based on tetrahedral MX_4 units. The iodide has a unique structure: one-quarter of the tetrahedral interstices in a ccp array of I atoms are occupied in groups of four to form supertetrahedral Zn_4I_{10} groups, which are joined by sharing four vertices to form a three-dimensional structure. The structures of all three halides contrast strikingly with those of the typically ionic MX_2 halides. Molten $ZnCl_2$ has a remarkably high viscosity at its melting point and an X-ray diffraction study indicates that the liquid consists of Zn^{2+} and $[ZnCl_4]^{2-}$ ions, rather than molecular $ZnCl_2$. On the other hand, the temperature dependence of the viscosity and the electrical conductance of the liquid has been interpreted in terms of polymeric species $[ZnCl_2]_x$ and free Zn^{2+} and Cl^- ions arising from dissociation of the salt.

Zinc chloride has a large number of uses. It has been used as a deodorant, disinfecting, and embalming material; alone or with phenols or other fungicides in the preservation of railway sleepers (ties); for fireproofing timber; with ammonium chloride as a flux for soldering (it readily dissolves other oxides); for etching metals; in the manufacture of parchment paper, artificial silk, dyes, activated carbon, cold-water glues, and vulcanized fiber; for browning steel, galvanizing iron, copper plating iron; in magnesia cements, and with zinc oxide in dental cements; in petroleum oil refining; in cements for metals and for facing stone; as a mordant in printing and dyeing textiles; for carbonizing woollen goods; in producing crepe and crimping fabrics; for mercerizing cotton, sizing and weighting fabrics, and vulcanizing rubber; as a solvent for cellulose; for preserving anatomical specimens; in microscopy for separating silk, wool, and plant fibers; as a dehydrating agent and catalyst in some organic syntheses. Its astringent properties make it useful in dentistry as a dentine desensitizer and in veterinary practice in the treatment of ulcers and similar conditions.

Zinc bromide is used in making silver bromide collodion emulsions for photography and in the shielding of viewing windows for nuclear reactions.

Zinc cyanide has a three-dimensional structure with tetrahedral zinc and coordination to both C and N of the cyanide, the latter lying along the line joining the zincs in the tetrahedral array of zincs in its anticuprite structure. $Zn[C(CN)_3]_2$ has a rutile-related infinite framework in which trigonal carbon centers are linked via –C≡N– units to half as many octahedral zinc(II) centers; the structure resembles knitting and exhibits a twofold penetration.[72] Zinc thiocyanate in the solid consists of thiocyanate-bridged tetrahedral ZnN_4 and ZnS_4 centers; it decomposes on heating to give ZnS.

7 SALTS

7.1 Oxoanion Salts: Preparation, Properties, and Structures

The salts are prepared by the usual neutralization methods. They are generally isomorphous with the corresponding salts of magnesium but are not thermally as stable. The nitrate, sulfate, and carbonate all decompose ultimately to the oxide on heating. Many of the salts, such as the nitrate, perchlorate, and sulfate, are very soluble in water and often form more than one hydrate; octahedral $Zn(H_2O)_6{}^{2+}$ units are usually present when there is sufficient water of crystallization. Attempts to prepare anhydrous salts by heating give hydroxy salts. The volatile anhydrous nitrate may be prepared by the action of N_2O_4 in ethyl acetate or methyl cyanide on the metal. The zinc phosphates provide a range of structures–α-$Zn_3(PO_4)_2$ contains ribbons of ZnO_4 tetrahedra, β-$Zn_3(PO_4)_2$ contains ZnO_4 and ZnO_5 polyhedra, while $Zn(HPO_4)\cdot H_2O$ consists of H-bonded sheets of linked ZnO_3 and ZnO_6 polyhedra. Templated hydrothermal syntheses in the presence of organic bases, for example, triethylenetetramine or piperazine (whose protonated forms provide the necessary cations), gives a variety of zincophosphate (and zincoarsenate[73]) anions,[74] all of which contain zinc in ZnO_4 tetrahedra. Such compounds generally have infinite structures, such as 3D frameworks ($[Zn_2P_2O_8]^{2-}$ and $[Zn_3(PO_4)_2(HPO_4)]^{2-}$ consist of ZnO_4 and PO_4 tetrahedra, the latter ion with 1D channels), 2D layers (e.g. $[Zn_2(HPO_4)_3]^{2-}$ and $[Zn_4P_4O_{16}]^{2-}$), and 1D ladders (e.g. $[Zn(HPO_4)_2]^{2-}$).[75] The use of creatinine as template permitted the synthesis of the first uncharged cluster, $C_4H_7N_3O\cdot Zn(H_2O)(HPO_4)$.[76] It is fairly easy to transform low dimensional structures, such as 1D ladders, into 2D and 3D structures. Zinc phosphonates appear in intercalated layer, pillared, and porous forms;[77] the complex prepared hydrothermally from *N*-methyliminobis(methylenephosphonic acid) is monoclinic, comprising a 3D network of phosphonate-bridged ZnO_4 tetrahedra.[78] Zinc 2-aminoethylphosphate has a phosphate-bridged infinite chain structure; it provides a useful model for metal–phosphate interactions.[79]

Anhydrous zinc acetate may be prepared from zinc nitrate and acetic anhydride; the dihydrate may be crystallized from dilute acetic acid. The zinc in the dihydrate is in an octahedral environment with *trans* diaxial water ligands and bidentate chelating (*see Chelating Ligands*) acetate groups. In the anhydrous salt, the zinc is in a distorted tetrahedral environment with bridging acetate groups. Distillation of zinc acetate gives a crystalline basic acetate $[Zn_4O(OCOMe)_6]$, the structure of which (**1**) is analogous to that of basic beryllium acetate. The two compounds are isomorphous; in each the metal is coordinated by four oxygens, three from bridging acetate groups and the fourth lying at the center of the tetrahedron of zinc ions. The two compounds differ in that the zinc complex is hydrolyzed rapidly in water. Absorption and emission spectra of $[Zn_4O(OCOMe)_6]$ have been investigated[80] as well as the X-ray PES (Photoelectron Spectroscopy), and a theoretical treatment shows how well this complex throws light on the electronic structure of zinc oxide itself.[81] The complex is photoluminescent and has a *Ligand-to-Metal Charge Transfer* band, a feature not shown by simple $[ZnX_4]^{2-}$ complexes. Other basic carboxylates $[Zn_4O(RCO_2)_6]$ with R = for example, Et, or *n*-Pr, or NEt_2 are known.

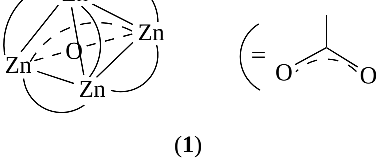

(**1**)

The crystal structures of a wide range of carboxylates have been described, the main features being that octahedral and tetrahedral coordination, sometimes distorted, are commonly observed and polymeric structures, especially with polyfunctional ligands, are frequently found.

7.2 Oxoanion Salts: Uses

Zinc sulfate has been used in rayon manufacture, as a mordant in calico printing, for preserving wood and skins, for clarifying glue, in electrodeposition processes, and in the manufacture of other zinc salts. Thus, for example, zinc nitrite cannot be prepared from aqueous solutions because of rapid hydrolysis but it can be prepared by treating sodium nitrite with zinc sulfate in alcohol. Zinc sulfate also has medicinal uses, in eye lotions and drops, in postoperative tissue healing, and as an emetic. It is also used as a zinc supplement, as also are zinc gluconate, zinc citrate, and zinc picolinate. Zinc phosphate is used in dental cements and temporary fillings. Zinc carbonate and basic zinc carbonate have, alongside zinc oxide, been used since the time of Ancient Egypt to treat a variety of skin conditions (Calamine Lotion, and a variety of ointments and dusting powders).

Several zinc salts act as, or can be doped to give, pigments.[82] Zinc germanate doped with V^{4+} (cf. zircon purple, V^{4+} doped into $ZrGeO_4$) and Fe^{3+} doped into $ZnGa_2O_4$ give brown pigments; the brown color of the latter can be varied by varying the Fe^{3+} content. Zinc chromate(VI) is a useful yellow pigment widely used in metal priming paints. Zinc in a silicate matrix is used as a gray pigment in primers; a zincosilicate has been synthesized that acts as a molecular sieve containing three-membered rings.[83]

Zinc acetate is used in wood preservation, as a mordant in dyeing, and in the manufacture of glazes for painting on porcelain. Zinc citrate is used in toothpastes and mouthwashes – it inhibits plaque growth.[84] The sulfanilate and several carboxylates, for example, propionate, caprylate, and undecenoate, find use in skin dusting powders and as fungicides. Zinc *p*-phenolsulfonate has been used in insecticide formulations and in veterinary practice for the treatment of ulcers. Polymerization of metal-containing monomers in the matrix of a different polymer or compound can lead to dramatic modification of properties; for example, of the tensile strength of materials such as polyethylene, where zinc acrylates and acrylamide complexes are useful in this context in giving rise to cross-linking that is controllable by adjusting the concentration of the zinc compound.

7.3 Other Salts

Zinc thiocyanate forms colorless deliquescent crystals, but zinc cyanide is insoluble in water. The salts $Zn_3[Co(CN)_6]_2$ and $Zn_3[Fe(CN)_5(NO)]_2$ can act as molecular sieves. The former can separate hexane isomers, thanks to the large holes arising from anion vacancies.[85] The latter has no large holes, but can separate methane from carbon dioxide. $Zn[Au(CN)_2]_2$ has a quartz-like structure with –NCAuCN– units bridging tetrahedral zinc centers.[86] Zinc cyanamide, $ZnCN_2$, a nonpolluting white pigment, has a structure in which ZnN_4 tetrahedra form Zn_4N_4 rings that in turn form twisted chains.[87] Zinc also forms a number of stable fluoroanion salts, such as $Zn(BF_4)_2$ (see Section 6.4) and water-soluble $ZnSiF_6 \cdot H_2O$.

8 COORDINATION CHEMISTRY

Zinc has an extensive coordination chemistry, though less extensive than that of some of the preceding 3d elements. Tetrahedral complexes are particularly readily formed with halides and with a variety of O-donors. Numerous stable complexes are formed with N-donors such as NH_3, amines, and azaheterocycles, but complexing to phosphines is limited. Complexes with S-donors are common; several have unusual structural features. Zinc complexes have in recent years assumed considerable importance in the generation and self-assembly of a great range of 1-, 2-, and 3-D infinite structures and frameworks, of which a few examples are cited below. Zn^{2+} has also recently proved useful as a templating cation for the preparation of a variety of macrocycles, rotaxanes, catenanes, and molecular knots, though it must be admitted that its importance in this area, though increasing, is much less than that of Cu^+.[88]

Zinc(II) complexes of amino acid, peptide, nucleotide, and nucleoside ligands are of obvious biological significance. We mention them here as they illustrate well the variety of coordination modes exhibited by tetrahedral Zn^{2+}. Individual amino acids can bind through one or more N, O, or S-donor atoms. In metalloenzymes (*see* ***Zinc Enzymes*** and ***Zinc: DNA-binding Proteins***) and metalloenzyme models, the overall coordination environment of the Zn^{2+} is usually NNN, NNO, or NNS, with water in the fourth position. The most common ligating residues are histidine, glutamate, aspartate, and cysteine – the Zn^{2+} is, for example, bonded to cysteine and histidine in zinc finger proteins. The area is well covered in the introductory chapters of several standard bioinorganic chemistry textbooks; the amino acid moieties bonded to the zinc in 21 zinc enzymes have been detailed.[89] Many zinc metalloproteins contain Zn^{2+} bound to one or more imidazole ligands of the amino acid residue histidine (**2a**). Purely in terms of mode of coordination of the ligand, it is interesting to note that, where more than one histidine coordinates to the metal ion, coordination is not always through the same N atom of the imidazole ring. Thus, in carbonic anhydrase, in which the zinc is bound to three histidines and a water molecule, two of the histidines, which are on the same strand of β-pleated sheet separated by one amino acid residue, bind through the N(3′) atom of the imidazole ring whereas the imidazole of the third histidine, lying in an adjacent strand of β-pleated sheet, binds through the N(1′) atom (**2b**). A distorted tetrahedral coordination results that has some unusual features: one of the N(3′)-zinc distances is the same as the N(1′)-zinc distances. Furthermore, the two N(3′) atoms are not bound equivalently: one of them is 0.4 Å further from the zinc atom than the other one and the imidazole bearing it is also the most exposed. The latter may well be concerned with the hydration mechanism of the enzyme[90,91] (*see also* ***Zinc Enzymes***). The role of the coordination chemistry of Zn^{2+} in the mechanisms of action of carbonic anhydrase, carboxypeptidase, and alcohol dehydrogenase has been reviewed.[92]

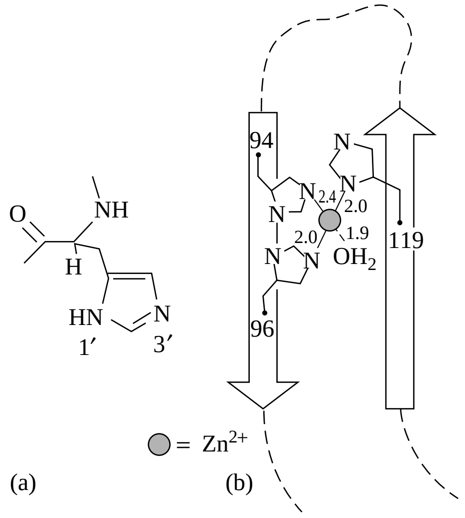

(a) (b)

(**2**)

Very thorough and comprehensively referenced surveys of the coordination chemistry of zinc are available. In each of these multivolume compendia, there is an article devoted to zinc complexes,[93] but there are also numerous mentions of zinc complexes in the introductory volumes and in the volumes on applications and uses.[94] Thermodynamic data (ΔH_f°, ΔS_f°, ΔG_f°; also some ΔX° values for e.g. $ZnX_2 + 2L$) are available for about 100 zinc complexes.[95] In this present encyclopedia, we are only able to mention a very small selection of the more important and interesting complexes. Preparations, structures, properties, and uses are dealt with in this section, the solution chemistry of zinc complexes in later sections (Sections 9.2 and 9.3).

8.1 N-Donors

In salts of $[Zn(NCS)_4]^{2-}$, the thiocyanate ligand is N-bonded, whereas it is S-bonded to cadmium in $[Cd(SCN)_4]^{2-}$ salts, reflecting the respective hard and soft characters of the respective metal ions. Zinc complexes with the azide ion are well known; crystallographic determinations of the structures of the compounds $M_2Zn(N_3)_4$ ($M = K$ or Cs) show the presence of discrete $[Zn(N_3)_4]^{2-}$ tetrahedra with linear azide groups. Some of the complexes in this category, such as those with hydrazine and azide, for example $[Zn(N_2H_4)_2(N_3)_2]$, are of interest as primary explosives and care is needed in their manipulation. The 2,2′-dipyridylamine-azide complexes $[Zn(dpa)(N_3)_2]$ and $[Zn(dpa)(N_3)(NO_3)]$, which have infinite 2D and 3D structures respectively, display fluorescence and phosphorescence.[96]

The complexes $[M(NH_3)_4]^{2+}$ and $[M(NH_3)_6]^{2+}$ ($M = Zn$ or Cd) have long been known. They have tetrahedral and octahedral coordination, respectively. Interestingly, the Zn–N distance in the tetrammine complex is shorter than that in the analogous N_4 bis-1,2-ethanediamine chelate, $[Zn(en)_2]^{2+}$. Raman and IR studies, including ^{15}N labelling, have been used in the calculation of the force constants for the M–N bond in these complexes. The force constant increases with decreasing coordination number and also decreases from zinc to cadmium. Zinc ammine complexes can function as host lattices. For example, the compounds $[M(NH_3)_2Ni(CN)_4]$, where $M = Zn$ (or Cd), which consist of two-dimensional polymeric sheets of tetracyanonickelate ions bridged by coordinating diamminezinc(II) cations, function as host lattices for the clathration (*see Clathrate*) of small aromatic molecules such as thiophen, furan, pyrrole, or pyridine; IR studies indicate hydrogen-bonding between the host lattice ammonia ligands and the aromatic guest molecules.

Less work has been done on the complexes of amines, RNH_2, than on those with polyfunctional amines such as 1,2-diaminoethane, and to a lesser extent its N-alkylated derivatives, for which a large body of data exists. Tetrahedral and octahedral coordination again feature prominently in the structures of these compounds, though with some interesting variations. For example, the hydrido complex $[ZnH(MeNCH_2CH_2NMe_2)]$ (**3**) is dimeric; each zinc atom has a terminal hydride bonded to it and is also bonded to three nitrogen atoms to give a distorted tetrahedral N_3H environment.

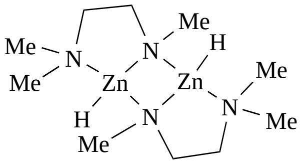

(**3**)

In relation to polyfunctional amines, it is interesting to observe the way in which the chelating properties of a ligand (*see Chelating Ligands*) vary with the metal: in studies on the chelating behavior of the triamine $H_2N(CH_2)_2NH(CH_2)_4NH_2$ (L) towards copper, nickel, and zinc, the five complexes ML^{2+}, $ML_2{}^{2+}$, MHL^{3+}, $M(HL)_2{}^{4+}$, and $MHL_2{}^{3+}$ are common to all three metals. In addition, Cu^{2+} and Zn^{2+} form the hydroxo complexes $[Cu(OH)L]^+$, $[Zn(OH)L]^+$, and $[Zn(OH)_2L]$. With regard to the complex ML^{2+}, the amine acts as a *Bidentate Ligand* towards Ni^{2+} and Zn^{2+} and in a terdentate manner towards Cu^{2+}, the latter containing both five- and seven-membered rings. On the other hand, the $ML_2{}^{2+}$ complexes contain only five-membered rings, with both amine ligands acting in a bidentate manner.

The catalytic properties of polyazamacrocyclic complexes of the transition metals and zinc[97] represent an active area of investigation that began on a large scale in the 1960s. Macrocyclic ligands that can bind two different metal ions (Zn,Co; Zn,Mn) in six- and four-coordination sites within the same ligand are interesting both from the catalytic and the structural point of view.[98] The cation of $[Zn_3(triscyclam)](NO_3)_6$ is trinuclear, with a Zn^{2+} in each of the macrocyclic rings of the triscyclam ligand, which consists of three cyclam units linked by a pair of $–CH_2–p–C_6H_4–CH_2–$ bridges.[99]

Complexes of pyridine, substituted pyridines, and ligands containing fused pyridine rings (bipyridyls and 1,10-phenanthrolines) have been widely studied. Many of these complexes have interesting photophysical properties (*see* ***Photochemistry of Transition Metal Complexes***). The suberate ($^-O_2C(CH_2)_6CO_2{}^-$) hydrate of $[Zn(phen)_3]^{2+}$ has a three-dimensional hydrogen-bonded network with the cations in tunnels in the structure; suberate, glutarate, and succinate can all bridge pairs of $[Zn(phen)_2]$ units to give binuclear complexes.[100] Early studies of bipyridyl complexes concentrated on the 2,2′-isomer,[101] but in recent years there has been increasing interest in the 4,4′-isomer, arising from the numerous structural possibilities inherent in its bridging properties. The compound $Zn(4,4'\text{-bipy})SiF_6{\cdot}2H_2O$ has a structure consisting of interpenetrating perpendicular square grid sheets, each sheet stretching to infinity. Each zinc is octahedrally coordinated to four pyridine nitrogens with two water molecules in *trans* positions; the four pyridine rings about each zinc are arranged in propeller fashion and the 4,4′-ligand bridges the zinc centers.[102] 4,4′-Bipyridyl, and analogs containing units such as –C≡C– linking the pyridine rings, can be used to build a range of coordination frameworks consisting of penetrating and noninterpenetrating ladders.[103] In fact, ligands containing the 2,2′-diimine chelating group of 2,2′-bipyridyl can also be used to generate clusters and supramolecular species, though to achieve this it is necessary to have two such units in the potential linking ligand, as, for example, in Schiff bases of the type $RN{=}CHCH{=}N(p\text{-}C_6H_4)_2N{=}CH–CH{=}NR$. Three-coordinate zinc complexes of the extremely sterically demanding diazabutadiene ligand $RN{=}CMe–CMe{=}NR$ with $R = 2,6\text{-}{}^iPr_2C_6H_3$ (the third ligand is alkyl or $N(SiMe_3)_2$) are catalysts for ring-opening polymerization of propene oxide and ε-caprolactone, thanks to the relatively high Lewis acidity of the zinc and its accessibility in this low-coordination number environment.[104] Both Zn^{2+} ions are five coordinate in a dimeric rotaxane containing phen and terpy units in each monomeric component. Addition of an excess of Cu^+ to this doubly threaded molecular assembly displaces the zinc, and decreases the length of the molecule from 83 to 65 Å as the threads slide along each other so that the Cu^+ ions are both coordinated by two phen moieties.[105]

Pyrazine, piperazine, and pyrazole[106] are, like 4,4′-bipyridyl, suitable ligands for bridging pairs of Zn^{2+} ions to give a variety of polynuclear species, while multifunctional (bi)pyridine-pyrazine ligands give scope for the assembly of various supramolecular assemblies. Using pyrazine with two 2,2′-bipyridinyl substituents as bridging ligands leads to chiral molecular squares, which can be considered to be circular helicates,[107] while diffusion of a methanolic solution of zinc iodide into a nitrobenzene/methanol solution of 2,4,6-tris(4-pyridyl)triazine, tptz, gives a complex with a doubly interpenetrated 3D network structure. This latter species crystallizes with guest nitrobenzene molecules, whose reversible release from the complex gives rise to contraction and expansion without disturbing the overall structure – behavior described as ‘springlike’ by its discoverers.[108]

Pyrazole rings are also important as constituents of the tripodal ligands colloquially known as scorpionates (polypyrazolylborates and polypyrazolylmethane), which family includes ligands with NNN-, NNO-, and NNS-donor sets.[109,110] Zinc complexes of hydrotris(pyrazolyl)borate ligands have been used to elucidate drug-metalloprotein interactions[111] and to model carbonic anhydrase and several hydrolysis enzymes.[112] Imidazole can also act as a component of similar tripodal ligands. Thus, reaction of zinc acetate with the ligand consisting of three imidazol-1-ylmethyl groups attached at the 2,4,6-positions benzene gives a complex whose structure is described as one-dimensional tubelike.[113]

Porphyrin and phthalocyanine complexes show many interesting features, including their photochemical and photophysical properties. Zinc phthalocyanine complexes have good photosensitizing properties for photodynamic therapy, PDT. In a polymetallic system containing a zinc porphyrin and silver, a photoinduced charge separation occurs giving rise to a long-lived ($\tau = 1.4\,\text{ms}$) charge-separated state of the complex.[114] The limit of charge separation is redox reaction, which in the case of zinc complexes generally involves redox at the ligand. Both porphyrins and phthalocyanines can act as π-electron acceptors or donors, to give radical ligands bonded to Zn^{2+}.[115] Much effort has been devoted to varying the electronic properties of ligand substituents to tune redox potentials.[116] There is currently considerable interest in assembly and self-assembly of zinc porphyrins,[117] for example the generation of a nonameric porphyrin array.[118] A phosphine-substituted porphyrin zinc complex has been found to be a useful building block for supramolecular assemblies thanks to the high affinity of phosphines for ruthenium(II) centers.[119] Several groups have demonstrated that porphyrin dimers have a high affinity for [60]fullerene; a high affinity for [60]fullerene has now been found for a dendritic hexa-zinc-porphyrin receptor.[120]

8.2 O-Donors

Water is a good O-donor ligand, both in the solid state, where many crystal hydrates, for example, of the sulphate, bromate, and perchlorate, contain octahedral $[Zn(H_2O_6)]^{2+}$, with Zn–O 2.08–2.14 Å, and in solution (Zn^{2+}aq is discussed in Section 9.1 below).

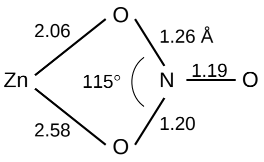

Figure 4 Bond distances in the coordination of nitrate ligands in the $[Zn(NO_3)_4]^{2-}$ ion

$[Zn(NO_3)_4]^{2-}$, which can be isolated as its tetraphenylarsonium salt, has a distorted dodecahedral structure,[121] each nitrate functioning as a bidentate chelating ligand (*see Bidentate Ligand* and *Chelating Ligands*) through two oxygen atoms to give eight-coordinated zinc. The nitrate coordination is not symmetrical (Figure 4), the longer bond to zinc corresponding to the shorter N–O bond and vice versa, the asymmetry tending towards tetrahedral coordination for the zinc.

Monodentate perchlorate complexes of zinc have been identified.[122] The NO_2^- ion can, like NO_3^-, function either as a monodentate or as a chelating ligand[123] depending upon the steric requirements of other ligands present in the complex. Interestingly, nitrobenzene can also function as a mono-O- or bidentate O,O′-donor, which it does in ternary complexes also containing the $–OTeF_5^-$ ligand.[124] Carbonate can act as a monodentate or bidentate ligand – in the binuclear complex $[(bipy)_2(H_2O)Zn(\mu\text{-}CO_3)Zn(bipy)_2]^{2+}$, isolated as its nitrate heptahydrate, the bridging carbonate acts in both capacities.[125] Indeed, tetrahedral, trigonal bipyramidal, and octahedral sites have been identified in various carbonate-bridged polynuclear zinc complexes;[126] carbonate is able to act in a μ_1, μ_2, μ_3, or even μ_4 fashion in this type of complex. Zinc complexes of benzoates and related carboxylates have long been studied as catalysts for the coupling of epoxides with carbon dioxide to afford polycarbonates. Dissolution of the 2,6-difluoro- or 2,6-dichloro-benzoates – the former complex is heptanuclear with μ-benzoate and μ_4-oxo ligands – in pyridine gives mononuclear ternary complexes.[127] Dicarboxylates as bridging ligands for $[Zn(phen)_2]$ moieties are mentioned in Section 8.1.

Phosphate and vanadate complexes of zinc show a diversity of coordination behavior. Zn^{2+} accelerates polyphosphate hydrolysis (Section 9.3); appropriate zinc-organic phosphate complexes provide models for ATP transport and biological phosphate transfer, and are of possible relevance to DNA and RNA polymerases (*see* ***Zinc: DNA-binding Proteins***).

As with oxoanion salts, a number of interesting structures are found with simple organic species as ligands, for example, a crystal-structure determination of the tetrameric methylzinc(II) methoxide, $\{MeZn(OMe)\}_4$, reveals the structure (**4**) in which zinc and oxygen are each tetrahedrally coordinated. Closely related to this structure is that of the polymerization catalyst $Zn(OMe)_2(EtZnOMe)_6$ (**5**). The complex is centrosymmetric and consists of two enantiomorphic cubes sharing a corner at which a zinc atom is situated; the zincs occupy the corners of a tetrahedron and the oxygens the corners of an interpenetrating, but smaller, tetrahedron. The structure illustrates the occurrence of both four- and six-coordinated zinc in the same structure. It is interesting that mass spectroscopic investigations of the complexes MeZnOR (R = Me, Et, or *t*-Bu) show that all form oligomers in the gaseous state having either six or seven monomer units. So far as solution reactions are concerned, depending on the molar ratio of reactants, the reaction of NaOMe with $ZnCl_2$ in MeOH produces the complex ions: $[Zn(OMe)_4]^{2-}$, $[Zn(OMe)_3(MeOH)]^-$, $[ZnCl(OMe)_2]^-$, and $[Zn_2Cl_4(OMe)]_2{}^{2-}$. The last complex is postulated to have methoxide bridges rather than bridging chlorides; analogous reactions occur with sodium isopropoxide. The synthesis, properties, structures, and uses (e.g. as precursors for ceramics) of alkoxides have been reviewed.[128]

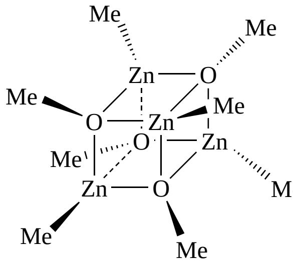

(**4**)

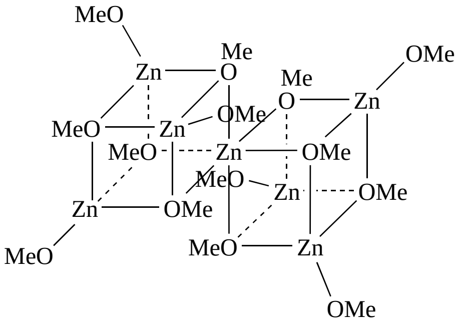

(**5**)

Complexes of Zn^{2+} with carbohydrates such as D-fructose and D-galactose have been isolated. Complexes with ethers, simple or crown, are rare, though it is possible to prepare zinc salts of several crown ethers from ethylene oxide and zinc fluoroanions in the presence of BF_3. An interesting template synthesis of ether-containing ligands with metal-ether bonds has been described in which zinc (and cadmium) are used to template the condensation; this contrasts with their usual inactivity in analogous aza systems.[129] Complexes with aldehydes and simple carbonyl compounds coordinated through oxygen in η^1 mode are also rare but bonding of an aromatic aldehyde, as well as acetone, in this way to zinc in the compounds $[Zn(EC_6H_4\text{-}t\text{-}Bu_3)_2(p\text{-}O{=}CHOCHOMe)]_2$ (E = S, Se) has been reported.[130] On the other hand, β-diketones have long been studied as ligands for zinc. With acetylacetone, zinc achieves both five and six coordination in the trimer $[Zn(acac)_2]_3$ (**6**). The complex $[Zn(acac)_2(H_2O)]$ has a distorted bipyramidal structure. Complexes of the β-diketone itself, as opposed to those of the β-diketonate anion, are rare but such complexes have been described in the cases of $[Zn(acacH)_3][InCl_4]$ and $[Zn(MeCOCH_2CO_2Et)_3][InCl_4]$. Five coordination at zinc is also found in $[ZnL_2][ClO_4]_2$ [L = o-phenylenebis(dimethylarsine oxide)], which consists of dimeric cations, $[ZnL_2]_2{}^{4+}$, with approximately trigonal bipyramidal coordination about each zinc.

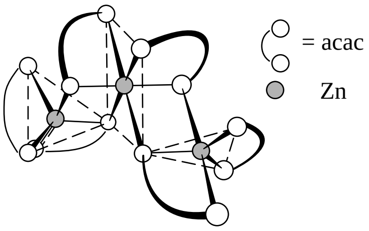

(**6**)

Zinc complexes with hydroxypyranones, for example, maltol or kojic acid, have been known for many years.[131,132] These, and analogous complexes with hydroxypyridinones, have been assessed as zinc supplements in cases of severe zinc deficiency, and more recently as potential insulin mimics.

8.3 N/O Donors

There are several series of important complexes in which zinc is coordinated by O,N-donor ligands, in particular, amino acid and aminocarboxylate anions. Both types of ligand frequently chelate metal ions through $>NCH_2CH_2CO_2{}^-$– units. The aminocarboxylate group contains not only such familiar ligands as ethylenediaminetetraacetate (EDTA) and nitrilotriacetate (nta), but also a number of polyazamacrocyclic ligands bearing pendant methylene carboxylate groups. Complexes of such high-denticity ligands are stabilized by both the chelate effect and the macrocyclic effect (*see* ***Macrocyclic Ligands***), and can be extremely inert to substitution, that is, dissociate extremely slowly. Zn^{2+} forms complexes with a variety of cryptands, for example, $N[(CH_2)_nNHCH_2\text{–}o\text{-}C_6H_4O(CH_2)_2]_3N$, with $n = 1, 2$, or 3. Anthracene derivatives of these ligands can act as fluorescent Zn^{2+} sensors (cf. Section 1.3 above).[133] Cryptands incorporating longer chains, for example $N[(CH_2)_2\,NH(CH_2)_2O(CH_2)_2NH(CH_2)_2]_3N$, can form stable binuclear complexes, in which the two Zn^{2+} ions are 4 to 5 Å apart. There is little metal–metal interaction at such separations, indeed it is possible to bridge the two metal centers by adding an appropriate small anion or molecule. A chiral hexaazatriphenolic macrocycle has been synthesized in efforts to model the active site of P1 nuclease. This macrocycle forms Zn_3 and Zn_2Cu trinuclear complexes. The Zn^{2+} ions in the Zn_3 complex have N_2O_2 and N_2O_3 coordination shells; the two N_2O_3 coordinated ions are bridged by acetate in the active site model.[134] Zinc complexes of calixarene-imidazole ligands mimic the active sites of other zinc enzymes.

NO-Donor Schiff bases (*see Schiff Base*), particularly multidentate ones, are powerful ligands and many examples of their zinc complexes are known. Zinc(II) often promotes formation of such Schiff bases, for example, those from salicaldehyde and 1,2-diaminoethane or 1,3-diaminopropane.[135] An interesting feature here is that these ligands readily exert a stereochemical control over the complex and thereby provide many examples of unusual geometry about the central ion, illustrating once more the coordination flexibility of zinc. An example is provided by the complex (**7**), $[ZnLCl_2]{\cdot}H_2O$ (L = 2, 6-diacetylpyridine dioxime), in which the metal is in a distorted trigonal bipyramidal environment. Schiff bases incorporating aliphatic or phenolic hydroxy groups as well as tertiary or pyridine nitrogens can give binuclear (Zn_2 or e.g. ZnCu) complexes. Such Schiff bases may be linear, tri- or tetrapodal,[136] or macrocyclic.[137]

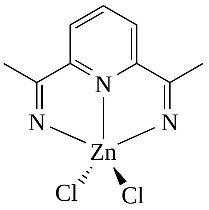

(**7**)

Zinc will dissolve in a solution of oxine (8-hydroxyquinoline). The anhydrous complex $Zn(oxinate)_2$ is a linear tetramer with bridging oxygens; the two central zinc atoms are six-coordinated octahedral and the two terminal zincs are five-coordinated trigonal bipyramidal units (Zn–O between 1.97 and 2.18 Å). This structure is reminiscent of that of the $Zn(acac)_2$ trimer.[138] Zinc complexes of oxines with a $p\text{-}NC_6H_4NMe_2$ group linked to the 5-position are luminescent, and potentially of interest in relation to OELDs (Organic Light Emitting Devices).[139]

In hydroxylamine complexes of the type ZnX_2L_2 (X = Cl, Br, or $0.5SO_4$), coordination to zinc can be through either N or O depending on the method of preparation (with Cd, coordination is exclusively to N). In the corresponding O-methyl derivative, $ZnCl_2(MeONH_2)_2$, bonding is through nitrogen. A substantial number of hydrazide complexes using $RCONHNH_2$ as a ligand are known and the ligand usually binds through the carbonyl oxygen and the NH_2 nitrogen atom when R is unbranched, but through N only when R is branched, for example, when $R = {}^i Pr$. Much of the interest in amides as ligands has been directed towards the factors that control the alternative O- or N-binding modes adopted in these compounds. With simple amides, L, such as acetamide or N,N-dimethylacetamide, in complexes of the type L_2ZnX_2 (X = halide or SCN), the coordination is tetrahedral to oxygen. On the other hand, binding of Zn^{II} enhances amide deprotonation of N,N-bis(2′-pyridinecarboxamide)-1,2-benzene (**8**), LH_2, to give planar $[ZnL·H_2O]$, having maximum electron delocalization; here coordination of the amide oxygens is hindered by the resulting decrease in the chelating ability of the ligand.

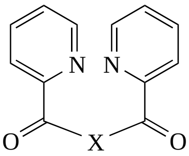

(**8**) X = –NH(o-C_6H_4)NH–

An interesting case in which the stereochemistry of zinc coordination is controlled by the local environment is provided by the heteronuclear chelate complex (**9**) in which planar Ni^{II} selects the N_2O_2 sites and the Zn^{II} the O_2O_2 sites. Coordinated pyridine completes five coordination for the zinc. The Zn–O distances average 1.95 Å to the terminal oxygens and 2.09 Å to the bridging oxygens. The zinc is displaced from the basal plane by 0.32 Å towards the pyridine.[140]

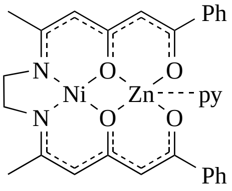

(**9**)

8.4 S, S/N, and S/O Donors

Complexes of dithiolene anions, such as maleonitriledithiolate and toluene dithiolate, where the delocalized S–C–C–S unit chelates the metal ion (*see Chelating Ligands*), are interesting from several points of view.[141] These include the frequent occurrence of square-planar and trigonal prismatic coordination geometries, the often extensive charge transfer, which can lead to unusual formal oxidation states (spectra of $[Zn^{II}(mnt)_2]^{2-}$ in dichloromethane, suggest a Zn^{III} complex containing an mnt^{3-} radical ligand), and their potentially valuable conductivity, optical, and magnetic properties. The recently reported first molecular magnetic semiconductors are based on 1,3-dithiol-2-thione-4,5-dithiolate ligands. Zn^{2+}-dithiolene centers occur in several essential enzymes.

Sulfur- and selenium-donor ligands stabilize several polynuclear zinc complexes, for example, the $[E_4Zn_4(SPh)_{16}]^{4-}$ (E = S or Se) anions, prepared as their Me_4N^+ salts.[142] The complex $[Zn_4(SPh)_{10}]^{2-}$ forms a ground-state charge transfer complex with methyl viologen.[143] These zinc–sulfur anions, and also $[Zn_4(SPh)_4]^{2-}$, all contain tetrahedral ZnS_4 units. They may be regarded as fragments of the cubic ZnS lattice. The benzylthiolate complex $[Zn_4(SBz)_{10}]^{2-}$ has an adamantane framework; $[Zn_8(S)(SBz)_{16}]^{2-}$ incorporates a cuboctahedral framework.[144] Self-assembly of a zinc-cyclen complex with thiocyanuric acid gives a Zn_{12} supramolecular capsule consisting of a cuboctahedral framework enclosing a tetrahedral cavity in which lipophilic organic molecules of appropriate size, for example, adamantane or 2,4-dinitrophenol, can be accommodated as guests.[145] $[Zn_8(SPh)_{16}Cl]^-$ consists of a tetracapped tetrahedron of zincs with the Cl^- at the center; 12 thiolate ligands act as bridging edge groups, four are terminal. The thiophosphate $Zn_3(PS_4)_2$ contains ZnS_4 and PS_4 tetrahedra; the former form corner-shared two-dimensional layers.[146] Reaction of zinc perchlorate with bis(2-aminoethanethiolato)zinc in aqueous acetonitrile gives polynuclear complexes with Zn_3S_3 and Zn_4S_4 cores; all zincs also bear N-donor ligands.[147] Zinc diethyldithiocarbamate is a rubber preservative; zinc halide thiosemicarbazone complexes show promising second-order nonlinear optical properties.

Complexes with the thio-oxamate ligands $NH_2(CO)CSO^-$ and $NH_2(CS)CO_2{}^-$, which bind through O and S, exhibit trigonal bipyramidal geometry around the zinc.[148] The zinc complex of the O,S-donor ligand 2-pyridinethiolate 1-oxide, known as zinc pyrithione, is a fungicide and bacteriocide much used in hair shampoos.

Thiolate-thioether complexes with $S_2S'_2N$ donor sets provide useful models for such bioinorganic systems as alcohol dehydrogenase and zinc fingers[149] (cf. start of this Section). The affinity of Zn^{2+} for nitrogen/sulfur donor ligands means that there are a few zinc complexes of thioazacryptands, as well as complexes of standard (aza)cryptands. Nitrogen- and sulfur-containing macrocyclic ligands are important in the modeling of enzymes and transmembrane metal ion carriers.[150]

8.5 Halide, Cyanide, and Thiocyanate Complexes

Complex anions $[ZnX_4]^{2-}$ are readily obtained for X = Cl, Br, or I, though not for X = F. They may be isolated as solids using the standard technique of precipitation using a large cation such as $[Ph_4As]^+$ or $[Co(NH_3)_6]^{3+}$. Zinc chloride readily accepts chloride ions to form tetrahedral $[ZnCl_4]^{2-}$ complexes, and a large number of structural studies on these and related complexes have been carried out. For example, the crystal structure of Cs_2ZnCl_4 contains this ion with very little distortion from tetrahedral,[151] but it is interesting that in the complex $[Co(NH_3)_6][ZnCl_4][Cl]$ the same anion shows marked distortion (Zn–Cl = 2.22 to 2.36 Å; ∠Cl–Zn–Cl = 101.6 to 115.4°). Calculations indicate that the major cause of the bond length distortion is anisotropy in the applied electrostatic crystal forces.[152] Other cases of deviation from tetrahedral geometry caused by packing forces are known, for example, the $[ZnI_4]^{2-}$ ion in its salt with the 2,4-dimethyl-1H-1,5-benzodiazepinium cation has strict C_2 symmetry. These findings suggest that care should be exercised in other cases when seeking explanations for stereochemical distortions in a complex in the solid state in terms of electronic and bonding effects within the complex itself. The $[Zn(NCS)_4]^{2-}$ anion is tetrahedral; Zn–NCS–Zn bridging has been demonstrated in molten KNCS at 200 °C.

9 AQUEOUS SOLUTION CHEMISTRY

9.1 The Zn^{2+} Aqua Cation

The Zn^{2+} cation appears to be six coordinate in water, from NMR (^1H peak areas), EXAFS (Extended X-ray Absorption Fine Structure), and Raman evidence, and six in methanol. X-ray and neutron diffraction studies indicate a Zn–O distance between 2.08 and 2.17 Å (cf. 2.08–2.14 Å in crystal hydrates). There is EXAFS evidence for a secondary hydration shell, containing about 12 water molecules at an average Zn–O distance of 4.1 Å.[153] Hydration numbers determined by methods other than NMR peak areas indicate values substantially larger than six, generally because both primary and secondary hydration shells are being monitored. The single-ion hydration enthalpy, ΔH_{hydr}, of Zn^{2+} is $-2044\ \mathrm{kJ\,mol^{-1}}$ (relative to $\Delta H_{\mathrm{hydr}}(H^+) = -1091\ \mathrm{kJ\,mol^{-1}}$). Full discussions of hydration of metal ions are available.[154–157] The Zn^{2+}aq ion is labile to water exchange ($k > 5 \times 10^7\ \mathrm{s^{-1}}$ at 298 K). There is some evidence that Zn^{2+} is only five coordinated in some mixed aqua ligand complexes.

Zn^{2+}aq has very weak acidic properties – the most favored value for its pK_a is 8.96, though values ranging from 8 to over 10 have been reported from determinations by various physical techniques in a variety of media of different ionic strengths and containing different counterions. $ZnOH^+$aq is, like all hydroxo-metal ions, prone to polymerize; species such as $[Zn_2(OH)]^{3+}$, $[Zn_2(OH)_6]^{2-}$, and $[Zn_4(OH)_4]^{4+}$ (cf. the well-established $[Pb_4(OH)_4]^{4+}$ and $[Ni_4(OH)_4]^{4+}$) have been postulated.

9.2 Stoichiometry, Structure, and Stability of Complexes in Solution

Table 3 collects together a number of stability constants (*see* ***Stability Constants & their Determination***) for formation of monoligand complexes of Zn^{2+} in aqueous solution ($\log_{10}K_1$), culled from several sources. Stability constants for no fewer than 81 bis-ligand complexes ($\log_{10}\beta_2$) were conveniently collected together as long ago as 1959.[158] Much additional information on zinc complexes with ligands of biological importance is available.[159] Figures mapping the predominant species in solution over a range of pHs are available for 21 Zn^{2+}-ligand systems.[160]

Table 3 Stability constants ($\log_{10}K_1$) for formation of a range of Zn^{2+} complexes, in aqueous solution at 298.2 K

Group 15		*Group 16*	
Azide	0.8	Acetate	1.6
Thiocyanate	0.9	Thiosulphate	2.3
Pyridine	1.0	Phosphate	2.4
Ammonia	2.3	Oxalate	4.3
Imidazole	2.6	Citrate	5.0
2,2′-bipyridyl	5.1	Acetylacetonate	5.1
Ethanediamine	5.9	ATP	5.2
1,10-phenanthroline	6.4	Maltolate	5.6
Group 15/16		*Group 17*	
Glycine	5.0	Fluoride	1.1
Cysteine	9.2	Chloride	0.5
Penicillamine	9.5	Bromide	−0.6
nta	10.7	Iodide	−1.5
EDTA	16.4		

Stability constant comparisons should be made with some caution, since the accuracies of some values may be no better than ±1, and experimental conditions (ionic strengths and the salts used to maintain them) are not identical for all systems. Nonetheless, the Table 3 values give some idea of relative stabilities for a range of ligands. The order of $\log_{10}K_1$ values for the halide ions should be noted, for comparison of this set of values for Zn^{2+} with analogous values for Cd^{2+} and Hg^{2+} (Table 4) positions these cations according to the ***Hard & Soft Acids and Bases*** principle, with Zn^{2+} just on the hard side, Cd^{2+} just on the soft side, of the hard/soft border, and Hg^{2+} definitely soft.

Zn^{2+} forms stable complexes with the group 14 donor ligand cyanide (mean $\log_{10}K_1 = 5.1$). The cyanide ion is a good σ-donor (e.g. the pK_a of HCN is 9.4) and this may be the main factor in complex stabilization here. Interestingly, the Zn^{2+} ion does not form π-complexes (*see* ***Coordination & Organometallic Chemistry: Principles***) with CO, NO, or alkenes although it is isoelectronic with Ni^0, archetypal in forming such species; possibly the 2+ charge on the Zn^{2+} ion is able to contract the d orbitals on the metal and reduce back donation (*see Back Bonding*) to the π-orbitals of the ligand.

Comparison of the stability constants for Zn^{2+} complexes with those for the preceding transition metal M^{2+} cations shows conformance to the Irving-Williams stability order (*see Irving–Williams Series*) ($Mn^{2+} < Fe^{2+} < Co^{2+} < Ni^{2+} < Cu^{2+} \gg Zn^{2+}$) for essentially all ligands. As an example,

Table 4 Comparison of stability constants ($\log_{10}K_1$) for complex formation between Zn^{2+}, Cd^{2+} and Hg^{2+} and halide ligands

	Zn^{2+}	Cd^{2+}	Hg^{2+}
Fluoride	1.1	0.5	1.6
Chloride	0.5	1.8	6.7
Bromide	−0.6	1.9	9.4
Iodide	−1.5	2.0	12.9

Table 5 Stepwise stability constants ($\log_{10}K_n$) for formation of a selection of Zn^{2+} complexes, in aqueous solution at 298.2 K

Monodentate ligands					Bidentate ligands				
	Imidazole	Ammonia	Thiocyanate	Azide		Oxalate	Glycinate	Kojate	ethanediamine
$\log_{10}K_1$	2.6	2.3	0.9	0.8					
$\log_{10}K_2$	2.4	2.5	0.7	0.5	$\log_{10}K_1$	4.3	5.0	5.0	5.9
$\log_{10}K_3$	2.2	2.3	0.6	1.0					
$\log_{10}K_4$	2.0	2.2	0.3	0.6	$\log_{10}K_2$	2.5	4.2	4.2	5.2
					$\log_{10}K_3$	1.0	2.5	2.6	1.9

the values of $\log_{10}K_1$ for 1,2-ethanediamine complexes are 2.7, 4.3, 5.9, 7.6, 10.7, and 5.9 respectively. Differences between stability constants for Zn^{2+} complexes and of their respective Mg^{2+} analogs are much larger for N-donor than for O-donor ligands. Indeed, a formula relating to the difference and the number of N- and O-donor sites on various ligands has been developed and used to determine the nature of the coordination sphere of the Zn^{2+} in cases where this is not clear-cut.[161,162]

Stability constants for Zn^{2+} complexes of the homologous dicarboxylate ligand series $^{-}O_2C(CH_2)_nCO_2{}^{-}$ provide a good illustration of the decrease in stability as chelate ring size increases. $\mathrm{Log}_{10}K_1$ values for the oxalate ($n = 0$), malonate ($n = 1$), succinate ($n = 2$), and glutarate ($n = 3$) complexes are 5.0, 3.7, 2.5, and 2.0, quantifying the decrease in stability as the chelate ring increases in size from a five-membered to an eight-membered ring. The ligand series NH_3 to en to dien to tren gives rise to modest chelate effects – $\log_{10}\beta_2$ for $[Zn(NH_3)_2]^{2+}$ is 4.8, $\log_{10}K_1$ for $[Zn(en)_2]^{2+}$5.9, while $\log_{10}\beta_3$ for $[Zn(NH_3)_3]^{2+}$ is 7.1, $\log_{10}K_1$ for $[Zn(dien)]^{2+}$8.9,[163] and $\log_{10}\beta_4$ for $[Zn(NH_3)_4]^{2+}$ is 9.3, $\log_{10}K_1$ for $[Zn(tren)]^{2+}$14.5.

Zn^{2+} forms stable complexes with the standard tetraaza-macrocyclic ligands, though the variation of stability constants with ring size is unusually small – $\log_{10}K_1$ values decrease from 16.2 for the 12-membered ring through 15.6 and 15.5 to 15.0 for the 15-membered ring ligand.[164] Studies on the complexing of zinc with 1,3,5-*cis,cis*-triaminocyclohexane (L) show that the $[ZnL]^{2+}$ complex formed is less stable than that formed with analogous linear triamines such as 3,3′-diaminodipropylamine (in the presence of excess of ligand only the hydroxo-ion $[ZnL(OH)]^{+}$ is formed in both cases). However, a significant macrocyclic effect is evident in the large stability constant observed for the $[ZnL]^{2+}$ complex of the cyclic triamine 1,4,7-triazacyclononane. Chelate and macrocyclic effects (K, ΔH, and ΔS), effects of ligand N-alkylation, and stability comparisons with selected M^{2+} ions, have been conveniently documented, for edta and for some tetra-aza macrocyclic ligands.[165] A comprehensive survey of thermodynamic, and kinetic, data for macrocyclic ligand interaction with cations, including extensive data on zinc, is available[166] (*see also* ***Macrocyclic Ligands***). Macrocyclic complexes sometimes have unexpected properties; for example, zinc complexes with the tetraazacycloalkanes [14]aneN_4 and [15]aneN_4 reversibly take up CO_2 in basic alcoholic solutions to form monoalkyl carbonates.[167]

Trends in stepwise stability constants (successive formation constants); (*see* ***Stability Constants & their Determination***) for Zn^{2+} complexes (Table 5) are often irregular, differing markedly from the normal trend of K_n decreasing as n increases. This has been known for at least sixty years – Jannik Bjerrum, in his seminal study of metal-ammine complexes carried out in about 1940, documented an irregular variation of K_n with n for this classic series. Table 5 documents this behavior for the ammines, and shows irregular behavior also for azide and for 1,2-ethanediamine. Only the imidazole, thiocyanate, and oxalate data in Table 5 show normal trends. Irregularities are all ascribed to changes between octahedral and tetrahedral geometries, as for example, for the unexpectedly large drop from K_2 to K_3 for 1,2-ethanediamine, and calculations have been made of the proportions of tetrahedral and octahedral species in several systems.[168] For penicillamine, $K_2 > K_1$, which unusual behavior has been ascribed to a change from tridentate to bidentate coordination.

In order to probe the immediate coordination sphere of the metal in zinc complexes in solution, especially to attempt to solve the tetrahedral versus octahedral uncertainties outlined above, it is possible to have recourse to a number of physical techniques, including Raman spectroscopy, NMR, X-ray and neutron diffraction,[169] and X-ray scattering (EXAFS). However, the complex equilibria present in electrolytically produced supersaturated solutions of zinc(II) in aqueous KOH show how different techniques can lead to different results in identifying the species present in what appears at first sight to be a simple system. Light scattering and NMR techniques[170] indicate the excess of zinc to be present as a solute, rather than a colloid, and the predominant species appears to be $[Zn(OH)_4]^{2-}$. However, Raman and potentiometric studies[171] indicate that initially quasicolloidal particles, based on $Zn(OH)_2$ and hydrating water molecules, are present. These undergo a first-order decay to yield a solution containing the species $[Zn(OH)_2(H_2O)_2]$, $[Zn(OH)_3(H_2O)]^{-}$, and $[Zn(OH)_4]^{2-}$, the actual composition depending on the concentration. The noncolloidal species in this system appear to be tetrahedral rather than octahedral.

X-ray scattering measurements, Raman, and IR spectroscopy on aqueous solutions containing Zn^{2+} and Br^{-} ions show that the highest complex formed is tetrahedral

$[ZnBr_4]^{2-}$; pyramidal $[ZnBr_3]^-$ is also formed but there is no evidence of Zn–Br–Zn bridges.[172] Studies of Zn^{2+}/Cl^- solutions have provided conflicting results, with X-ray studies indicating $[ZnCl_4]^{2-}$, other techniques indicating octahedral geometry, that is, $[ZnCl_4(H_2O)_2]^{2-}$. The apparent disagreement is almost certainly due to the different concentration ranges pertaining to the techniques used – the X-ray methods require concentrated solutions, the other techniques less concentrated media. Indeed neutron diffraction suggests $[ZnCl_4(H_2O)_2]^{2-}$ in 1 or 2 M $ZnCl_2$, $[ZnCl_4]^{2-}$ in more concentrated solutions. Diffraction results are consistent with tetrahedral $[Zn(NH_3)_4]^{2+}$ (Zn–N = 2.03 Å) and with both tetrahedral $[Zn(en)_2]^{2+}$ (Zn–N = 2.13 Å) and octahedral $[Zn(en)_3]^{2+}$ (Zn–N = 2.28 Å), depending on conditions.[173]

Complexes of the Group 12 metal cations with thiocyanate provide data on the relative affinities of these ions for N- or S-donors. X-ray scattering studies indicate the existence in solution of $[Zn(NCS)_4]^{2-}$, $[Cd(NCS)_2(SCN)_2]^{2-}$, and $[Hg(SCN)_4]^{2-}$, all tetrahedral, consistent with the 'hard' to 'soft' trend of the respective M^{2+} cations. A Raman study of zinc(II) coordination in aqueous thiocyanate solutions[174] showed that bonding to the zinc is totally in the Zn–NCS mode and the results were consistent with the presence of all four $[Zn(NCS)_{1-4}]^{n\pm}$ species. The two lower species are probably octahedrally coordinated, the remaining coordination sites being occupied by water molecules; higher species are probably tetrahedrally coordinated. No bridging thiocyanate is observed. This contrasts with evidence from the Raman spectrum of coordinated zinc in KSCN at 200 °C, which shows the presence of tetrahedral $[Zn(NCS)_4]^{2-}$ species, somewhat distorted by polymerization, and bands owing to Zn–NCS–Zn bridges are also observed. *Linkage Isomerism* is also present owing to both Zn–NCS and Zn–SCN bonding modes.

Sometimes coordination can affect the behavior of another ligand in the coordination shell of the metal and this is well illustrated by acidities of ternary aqua-ligand-Zn^{2+} complexes. Quadridentate 1,5-diazocyclooctane-N,N'-diacetic acid, H_2L, forms $[Zn(L)(H_2O)]$, the pK_a of whose coordinated H_2O (8.6) is slightly lower than that of Zn^{2+}aq (9.0), and considerably lower than that of the coordinated H_2O (10.5) in the octahedral complex formed by ethylenediaminediacetate. Increased acidity of coordinated H_2O with decreasing coordination number has also been observed in other complexes such as $[Zn(Me_6tren)(H_2O)]^{2+}$, $[Zn([12]aneN_3)(H_2O)]^{2+}$ ($pK_a = 7.3$) and $[Zn(cyclen)(H_2O)]$ ($pK_a = 7.9$).[175] This has been attributed, at least in part, to the hydrophobic environment provided by the methyl and methylene groups. This finding has some implications for the role of the $Zn–OH_2/OH$ species in the zinc metalloenzyme carbonic anhydrase (*see* ***Zinc Enzymes***), where this unit is contained in a site of low-coordination number and a small movement can place it in an environment of decreased polarity. Such marked increase in the acidity of coordinated water has important implications, especially for biological systems: essentially the metal ion-hydroxy complex provides an efficient nucleophile at neutral pH[176] (*see also* ***Zinc Enzymes***). Model studies with metal ions, mainly zinc(II), as Lewis acid catalysts have been reviewed.[177]

Binding constants determined for ternary complex formation between capped and uncapped zinc porphyrins and small molecules such as imidazole and (substituted) pyridine[178] contribute to the understanding of capped zinc porphyrins in molecular recognition,[179] to which topic ternary zinc-cyclen complexes are also relevant.[180]

9.3 Kinetics and Mechanisms

Complex formation between Zn^{2+} and most monodentate and simple chelating ligands is rapid, with $k_f \sim 10^7\ M^{-1}\ s^{-1}$ at 298 K.[181] However, there are exceptions where the steric requirements of the ligand are particularly stringent. Reactions of Zn^{2+}aq with tetraazamacrocycles are slow – rate laws are complicated, but half-lives are of the order of a second. Formation of the Zn^{2+} complex of the *Quadridentate Ligand* 1,4,8,11-tetramethyl-1,4,8,11-tetraazacyclotetradecane (L), which is a five-coordinated species $[ZnL(H_2O)]^{2+}$, is probably slow owing to the requirement for conformational change on complexation. Dissociation of this complex is acid catalyzed (*see Acid Catalyzed Reaction*), with this five-coordinate species more labile than four- or six-coordinated complexes, a feature that could be relevant to the biological function of zinc.[182] Other cases of slow complex formation are provided by several porphyrins and by the catenand ligand (**10**). Half-lives for incorporation of zinc into porphyrins are typically of the order of a second. Reaction with the catenand is biphasic (*see Biphasic Process*); the first step (overall second order) probably represents binding of the ligand to one of the chelating subunits of (**10**). The second step, which is first order, is very slow ($k \ll 1\ s^{-1}$) and could well correspond to the sliding motion of one ring within the other while the second phenanthroline unit attempts to seek out and bind the zinc center.[183] Metal-for-metal replacement in porphyrin complexes can, however, be quite rapid, as in the case of Zn^{2+} with Hg(tpp) in pyridine, where no less than seven isosbestic points are observed.[184] There is rapid equilibration between Zn^{2+} and Pb^{2+} at the metal-binding site of zinc fingers despite steric constraints;[185] the rate constant for reaction of a typical *Zinc Finger* peptide with Zn^{2+}aq has been estimated as $2.8 \times 10^7\ M^{-1}\ s^{-1}$.[186]

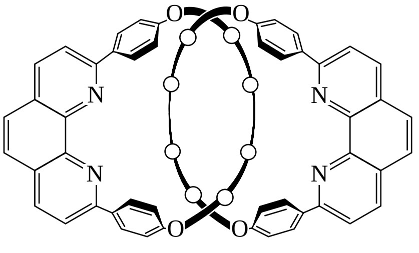

(**10**)

There is a marked contrast between zinc and cadmium in the context of complexing of the 2+ ions with bipy, studied by high-pressure stopped-flow. There is a striking difference between the two elements, with Zn^{2+} reacting progressively more slowly with bipy as pressure increases, Cd^{2+} more rapidly. The *Activation Volume* ($\Delta V^{\ddagger}$) for the zinc reaction is $+7.1\,cm^3\ mol^{-1}$ whereas for cadmium the value is $-5.5\,cm^3\ mol^{-1}$. These values suggest that the substitutions are I_d and I_a in character respectively.[187] $\Delta V^{\ddagger}$ values for the reverse, dissociation, reaction and $\Delta S^{\ddagger}$ values for formation and for dissociation, are all consistent with this assignment of mechanism. Positive activation volumes for a few other substitution reactions at $Zn^{2+}aq$[188] also indicate I_d mechanisms, as proposed many years ago in discussions of ultrasonic data on complex formation from $Zn^{2+}aq$.

Metal ion promoted reactions are important – Zn^{2+}-catalyses of hydrolysis of a range of organic substrates, for example, phosphate and carboxylate esters and Schiff bases, have recently been reviewed,[189] as has their relevance to biological catalysis, particularly of reactions of phosphates.[190]

Kinetic patterns and parameters, and mechanisms, of these and other reactions involving zinc complexes have been detailed and reviewed.[191,192]

10 RELATED ARTICLES

Alloys; Coordination & Organometallic Chemistry: Principles; Nutritional Aspects of Metals & Trace Elements; Peptide–Metal Interactions; Solids: Computer Modeling; Stability Constants & their Determination; Water & O-donor Ligands; Zinc: DNA-binding Proteins; Zinc Enzymes; Zinc: Organometallic Chemistry.

11 REFERENCES

1. P. A. Cox, ‘The Elements’, Oxford University Press, 1989, see Appendix A.
2. P. A. Williams, ‘Oxide Zone Geochemistry’, Ellis Horwood, Chichester, 1990.
3. J.-M. Martin and M. Maybeck, *Mar. Chem.*, 1979, **7**, 173.
4. W. Stumm and J. J. Morgan, ‘Aquatic Chemistry’, Wiley-Interscience, New York, 1970; J. F. Pankow, ‘Aquatic Chemical Concepts’, Lewis Publishers, Michigan, MI, 1991, Parts III and IV.
5. J. G. Hering and F. M. M. Morel, in ‘Aquatic Chemical Kinetics’, ed. W. Stumm, Wiley-Interscience, New York, 1990.
6. T. R. Crompton, ‘Determination of Metals in Natural and Treated Waters’, Spon, London, 2002.
7. J. E. Coleman, *Annu. Rev. Biochem.*, 1992, **61**, 897.
8. J. E. Coleman, *Annu. Rev. Biophys. Biomol. Struct.*, 1992, **21**, 441.
9. I. Bertini, C. Luchinat, W. Maret, and M. Zeppezauer eds, ‘Zinc Enzymes’, Birkhauser, Boston, 1986.
10. P. Jiang and Z. Guo, *Coord. Chem. Rev.*, 2004, **248**, 205.
11. L. Fabbrizzi, M. Licchelli, F. Mancin, M. Pizzeghello, G. Rabaioli, A. Taglietti, P. Tecilla, and U. Tonellato, *Chem. – Eur. J.*, 2002, **8**, 94.
12. S. C. Burdette and S. J. Lippard, *Inorg. Chem.*, 2002, **41**, 6816.
13. J. R. Wright, W. A. Hendrickson, S. Osaki, and G. T. James, in ‘Physical Methods for Inorganic Biochemistry’, *Biochemistry of the Elements* Vol. 5, ed. E. Frieden, Plenum, New York, 1986.
14. R. J. P. Williams, *Polyhedron*, 1987, **6**, 61.
15. J. M. Berg, *Annu. Rev. Biophys. Biophys. Chem.*, 1990, **19**, 405.
16. J. J. R. F. da Silva and R. J. P. Williams, ‘The Biological Chemistry of the Elements’, Oxford University Press, Oxford, 1991.
17. G. Parkin, *Chem. Rev.*, 2004, **104**, 699.
18. J. A. Cowan, ‘Inorganic Biochemistry’, Wiley-VCH, New York, 1997.
19. W. Kaim and B. Schwederski, ‘Bioinorganic Chemistry: Inorganic Elements in the Chemistry of Life’, Wiley, Chichester, 1994, Chap. 12.
20. A. S. Prasad, ‘Biochemistry of Zinc’, Plenum, New York, 1994.
21. J. E. F. Reynolds ed., ‘Martindale, The Extra Pharmacopoeia’, 31st edn., Royal Pharmaceutical Society of Great Britain, London, 1996.
22. C. C. Pfeiffer, ‘Mental and Elemental Nutrients’, Keats Publishing, New Canaan, CT, 1975, Chap. 16.
23. D. Bryce-Smith and L. Hodgkinson, ‘The Zinc Solution’, Arrow Books, London, 1986.
24. M. H. Stipanuk and W. B. Saunders eds, ‘Biochemical and Physiological Aspects of Human Nutrition’, Philadelphia, PA, 2000, Chap. 32.
25. R. Wildman, ‘The Nutritionist – Food, Nutrition, and Optimal Health’, The Haworth Press, Binghamton, 2002.
26. H. G. Seiler, H. Sigel, and A. Sigel, ‘Handbook of Toxicity of Inorganic Compounds’, Marcel Dekker, New York, 1988.
27. S. S. Brown and Y. Kodama eds, ‘Toxicology of Metals’, Ellis Horwood, Chichester, 1987.
28. M. N. Hughes and R. K. Poole, ‘Metals and Micro-organisms’, Chapman and Hall, London, 1989.
29. H. K. Dillon and M. H. Ho, ‘Biological Monitoring of Exposure to Chemicals’, Wiley, New York, 1991.
30. Z. Guo and P. J. Sadler, *Angew. Chem., Int. Ed. Engl.*, 1999, **38**, 1512.
31. A. Erxleben, *Coord. Chem. Rev.*, 2003, **246**, 203.
32. L. Carlucci, G. Ciani, and D. M. Proserpio, *Coord. Chem. Rev.*, 2003, **246**, 247.

33. N. Lalioti, C. P. Raptopoulou, A. Terzis, A. E. Aliev, I. P. Gerothanassis, E. Manessi-Zoupa, and S. P. Perlepes, *Angew. Chem., Int. Ed. Engl.*, 2001, **40**, 3211.
34. N. N. Greenwood and A. Earnshaw, 'Chemistry of the Elements', 2nd edn., Butterworth-Heinemann, Oxford, 1997, Chap. 29.
35. F. A. Cotton, G. Wilkinson, C. A. Murillo, and M. Bochmann, 'Advanced Inorganic Chemistry', 6th edn., Wiley-Interscience, New York, 1999, Chap. 15.
36. J. W. Mellor, 'A Comprehensive Treatise on Inorganic and Theoretical Chemistry', Longman, Green, London, 1946, Vol. 4, Chap. 30.
37. P. Pascal ed., 'Nouveau Traité de Chimie Minérale', Masson, Paris, 1962, Vol. 5.
38. N. V. Sidgwick, 'The Chemical Elements and Their Compounds', Clarendon Press, Oxford, 1950, Vol. 1, p. 262.
39. A. Cottrell, 'An Introduction to Metallurgy', Arnold, London, 1975.
40. J. Barrett, M. N. Hughes, G. I. Karavaiko, and P. A. Spencer, 'Metal Extraction by Bacterial Oxidation of Minerals', Ellis Horwood, Chichester, 1993.
41. F. E. Goodwin, 'Kirk-Othmer Encyclopedia of Chemical Technology', 4th edn., Wiley-Interscience, New York, 1998, Vol. 25, p. 789.
42. U. R. Evans, 'An Introduction to Metallic Corrosion', Arnold, London, 1982.
43. E. C. Rollason, 'Metallurgy for Engineers', Arnold, London, 1973.
44. C. A. Vincent, 'Modern Batteries', Arnold, London, 1984.
45. R. Brodd, 'Kirk-Othmer Encyclopedia of Chemical Technology', 4th edn., Wiley-Interscience, New York, 1992, Vol. 3, p. 963.
46. G. J. Long ed., 'Mössbauer Spectroscopy Applied to Inorganic Chemistry', Plenum, New York, 1984.
47. A. G. Maddock, 'Mössbauer Spectroscopy: Principles and Applications', Ellis Horwood, Chichester, 1997.
48. B. W. Epperlein, H. Krüger, O. Lutz, and A. Schwenk, *Z. Naturforsch., Teil. A.*, 1974, **29**, 1553.
49. M. Lutz, B. Findeis, M. Haukka, R. Graff, T. A. Pakkanen, and L. H. Gade, *Chem. – Eur. J.*, 2002, **8**, 3269.
50. A. F. Wells, 'Structural Inorganic Chemistry', 5th edn., Oxford University Press, Oxford, 1984.
51. I. Ivanović-Burmazović and K. Andjelković, *Adv. Inorg. Chem.*, 2004, **55**, 315.
52. N. Niklas, O. Walter, F. Hampel, and R. Alsfasser, *J. Chem. Soc., Dalton Trans.*, 2002, 3367.
53. S. I. Ahmed, J. Burgess, J. Fawcett, S. A. Parsons, D. R. Russell, and S. H. Laurie, *Polyhedron*, 2000, **19**, 129.
54. H. Adams, D. Bradshaw, and D. E. Fenton, *Polyhedron*, 2002, **21**, 1957.
55. M. Alexiou, C. Dendrinou-Samara, C. P. Raptopoulou, A. Terzis, and D. P. Kessissoglou, *Inorg. Chem.*, 2002, **41**, 4732.
56. R. C. Finn, J. Zubieta, and R. C. Haushalter, *Prog. Inorg. Chem.*, 2003, **51**, 421.
57. G. Anantharaman, H. W. Roesky, and J. Magull, *Angew. Chem., Int. Ed. Engl.*, 2002, **41**, 1226.
58. S.-C. Chang, R. H. Hauge, Z. H. Kafafi, J. L. Margrave, and W. E. Billups, *J. Chem. Soc., Chem. Commun.*, 1987, 1682.
59. T. P. Hamilton and H. F. Schaefer, *J. Chem. Soc., Chem. Commun.*, 1991, 621.
60. J. A. Martinho Simões and J. L. Beauchamp, *Chem. Rev.*, 1990, **90**, 629.
61. P. Klüfers and A. Mewis, *Z. Krystallogr.*, 1984, **169**, 135.
62. N. N. Greenwood, 'Ionic Crystals, Lattice Defects, and Non-stoichiometry', Butterworth, London, 1968.
63. W. H. Hirschwald, *Acc. Chem. Res.*, 1985, **18**, 228.
64. C. Pacholski, A. Kornowski, and H. Weller, *Angew. Chem., Int. Ed. Engl.*, 2002, **41**, 1188.
65. K. Omichi, N. Takahashi, T. Nakamura, M. Yoshioka, S. Okamoto, and H. Yamamoto, *J. Mater. Chem.*, 2001, **11**, 3158.
66. D. W. Bahnemann, C. Kormann, and M. R. Hoffmann, *J. Phys. Chem.*, 1987, **91**, 3789.
67. M. V. Twigg ed., 'Catalyst Handbook', 2nd edn.,, Wolfe Publishing, London, 1989.
68. M. A. Malik, P. O'Brien, and N. Revaprasadu, *J. Mater. Chem.*, 2001, **11**, 2382.
69. I. S. Athwal and R. K. Bedi, *J. Appl. Phys.*, 1988, **64**, 6345.
70. I. S. Athwal and R. K. Bedi, *J. Mater. Sci.*, 1989, **24**, 110.
71. R. H. Miles, J. O. McCaldin, and T. C. McGill, *J. Cryst. Growth*, 1987, **85**, 188.
72. S. R. Batten, B. F. Hoskins, and R. Robson, *J. Chem. Soc., Chem. Commun.*, 1991, 445.
73. S. Chakrabarti and S. Natarajan, *J. Chem. Soc., Dalton Trans.*, 2002, 4156.
74. S. Natarajan, *Inorg. Chem.*, 2002, **41**, 5530.
75. A. Choudhury, S. Natarajan, and C. N. R. Rao, *Inorg. Chem.*, 2000, **39**, 4295.
76. I. Macdonald and W. T. A. Harrison, *Inorg. Chem.*, 2002, **41**, 6184.
77. A. Clearfield, *Prog. Inorg. Chem.*, 1998, **47**, 371.
78. J.-G. Mao, Z. Wang, and A. Clearfield, *Inorg. Chem.*, 2002, **41**, 2334.
79. P. Bissinger, O. Kumberger, and A. Schier, *Chem. Ber.*, 1991, **124**, 509.
80. H. Kunkely and A. Vogler, *J. Chem. Soc., Chem. Commun.*, 1990, 1204.
81. R. Bertoncello, M. Bettinelli, M. Casarin, A. Gulino, E. Tondello, and A. Vittadini, *Inorg. Chem.*, 1992, **31**, 1558.

82. A. Bartecki and J. Burgess, 'The Colour of Metal Compounds', Gordon and Breach, Reading, UK, 2000.
83. M. J. Annen, M. E. Davis, J. B. Higgins, and J. L. Schlenker, *J. Chem. Soc., Chem. Commun.*, 1991, 1175.
84. R. J. Gilbert and G. S. Ingram, *J. Pharm. Pharmacol.*, 1988, **40**, 399.
85. G. Boxhoorn, J. Moolhuysen, J. G. F. Coolegem, and R. A. van Santen, *J. Chem. Soc., Chem. Commun.*, 1985, 1305.
86. B. F. Hoskins, R. Robson, and N. V. Y. Scarlett, *Angew. Chem., Int. Ed. Engl.*, 1995, **34**, 1203.
87. M. Becker and M. Jansen, *Acta Crystallogr.*, 2001, **C57**, 347.
88. N. V. Gerbeleu, V. B. Arion, and J. Burgess, 'Template Synthesis of Macrocyclic Compounds', Wiley-VCH, Weinheim, 1999.
89. W. N. Lipscomb and N. Strater, *Chem. Rev.*, 1996, **96**, 2375.
90. B. W. Matthews, *Acc. Chem. Res.*, 1988, **21**, 333.
91. D. W. Christianson and W. N. Lipscomb, *Acc. Chem. Res.*, 1989, **22**, 62.
92. R. H. Prince, *Adv. Inorg. Chem. Radiochem.*, 1979, **22**, 349.
93. R. H. Prince, 'Comprehensive Coordination Chemistry', eds. G. Wilkinson, R. D. Gillard, and J. A. McCleverty, Pergamon, Oxford, 1987, Vol. 5, Chap. 56; S. J. Archibald, 'Comprehensive Coordination Chemistry', 2nd edn., ed. J. A. McCleverty and T. J. Meyer, Elsevier-Pergamon, Oxford, 2004, Vol. 6; D. E. Fenton ed., Chap. 6.9.
94. G. Wilkinson, R. D. Gillard, and J. A. McCleverty eds, 'Comprehensive Coordination Chemistry', Pergamon, Oxford, 1987, Vols. 1, 2, and 6; J. A. McCleverty and T. J. Meyer eds, 'Comprehensive Coordination Chemistry', 2nd edn., Elsevier-Pergamon, Oxford, 2004, Vols. 1, 2, and 7–9.
95. S. J. Ashcroft and C. T. Mortimer, 'Thermochemistry of Transition Metal Complexes', Academic Press, London, 1970.
96. D. Bose, S. H. Rahaman, G. Mostafa, R. D. B. Walsh, M. J. Zaworotko, and B. K. Ghosh, *Polyhedron*, 2004, **23**, 545.
97. L. F. Lindoy, 'The Chemistry of Macrocyclic Ligand Complexes', CUP, Cambridge, 1989.
98. C. Fraser, L. Johnston, A. L. Rheingold, B. S. Haggerty, G. K. Williams, J. Whelan, and B. Bosnich, *Inorg. Chem.*, 1992, **31**, 1835.
99. Y. Dong and L. F. Lindoy, *Coord. Chem. Rev.*, 2003, **245**, 11.
100. D.-Y. Wei, Y.-Q. Zheng, and J.-L. Lin, *Z. Anorg. Allg. Chem.*, 2002, **628**, 2005.
101. E. C. Constable, *Adv. Inorg. Chem.*, 1989, **34**, 1.
102. R. W. Gable, B. F. Hoskins, and R. Robson, *J. Chem. Soc., Chem. Commun.*, 1990, 1677.
103. S. A. Barnett and N. R. Champness, *Coord. Chem. Rev.*, 2003, **246**, 145.
104. M. D. Hannant, M. Schormann, and M. Bochmann, *J. Chem. Soc., Dalton Trans.*, 2002, 4071.
105. M. C. Jimenez-Molero, C. Dietrich-Buchecker, and J.-P. Sauvage, *Chem. – Eur. J.*, 2002, **8**, 1456.
106. G. La Monica and G. A. Ardizzoia, *Prog. Inorg. Chem.*, 1997, **46**, 151.
107. T. Bark, M. Düggeli, H. Stoeckli-Evans, and A. von Zelewsky, *Angew. Chem., Int. Ed. Engl.*, 2001, **40**, 2848.
108. K. Biradha and M. Fujita, *Angew. Chem., Int. Ed. Engl.*, 2002, **41**, 3392.
109. S. Trofimenko, *Chem. Rev.*, 1993, **93**, 943.
110. H. Vahrenkamp, *Acc. Chem. Res.*, 1999, **32**, 589.
111. D. T. Puerta and S. M. Cohen, *Inorg. Chem.*, 2002, **41**, 5075.
112. N. Kitajima and W. B. Tolman, *Prog. Inorg. Chem.*, 1995, **43**, 419.
113. J. Fan, H.-F. Zhu, T.-A. Okamura, W.-Y. Sun, W.-X. Tang, and N. Ueyama, *Inorg. Chem.*, 2003, **42**, 158.
114. M. Gubelmann, A. Harriman, J. M. Lehn, and J. L. Sessler, *J. Chem. Soc., Chem. Commun.*, 1988, 77.
115. S. P. Keiser, W. Han, and M. J. Stillman, *Inorg. Chem.*, 2002, **41**, 353.
116. Y. Terazono, B. O. Patrick, and D. H. Dolphin, *Inorg. Chem.*, 2002, **41**, 6703.
117. L. Baldini and C. A. Hunter, *Adv. Inorg. Chem.*, 2002, **53**, 213.
118. T. N. Milic, N. Chi, D. G. Yablon, G. W. Flynn, J. D. Batteas, and C. M. Drain, *Angew. Chem., Int. Ed. Engl.*, 2002, **41**, 2117.
119. S. L. Darling, E. Stulz, N. Feeder, N. Bampos, and J. K. M. Sanders, *New J. Chem.*, 2000, **24**, 261.
120. M. Ayabe, A. Ikeda, Y. Kubo, M. Takeuchi, and S. Shinkai, *Angew. Chem., Int. Ed. Engl.*, 2002, **41**, 2790.
121. C. Bellitto, L. Gastaldi, and A. A. G. Tomlinson, *J. Chem. Soc., Dalton Trans.*, 1976, 989.
122. N. M. N. Gowda, S. B. Naikar, and G. K. N. Reddy, *Adv. Inorg. Chem. Radiochem.*, 1984, **28**, 255.
123. A. J. Finney, M. A. Hitchman, C. L. Raston, G. L. Rowbottom, and A. H. White, *Aust. J. Chem.*, 1981, **34**, 2061.
124. P. K. Hurlburt, P. J. Kellett, O. P. Anderson, and S. H. Strauss, *J. Chem. Soc., Chem. Commun.*, 1990, 576.
125. Z. W. Mao, F. W. Heinemann, G. Liehr, and R. van Eldik, *J. Chem. Soc., Dalton Trans.*, 2001, 3652.
126. A. N. Acharya, A. Das, and A. C. Dash, *Adv. Inorg. Chem.*, 2004, **55**, 127.
127. D. J. Darensbourg, J. R. Wildeson, and J. C. Yarbrough, *Inorg. Chem.*, 2002, **41**, 973.
128. R. C. Mehrotra and A. Singh, *Prog. Inorg. Chem.*, 1997, **46**, 239.
129. M. L. Tulchinsky, L. I. Demina, S. V. Lindemann, A. Yu. Tsivadze, and Y. T. Struchkov, *J. Chem. Soc., Chem. Commun.*, 1990, 785.
130. M. Bochmann, K. J. Webb, M. B. Hursthouse, and M. Mazid, *J. Chem. Soc., Chem. Commun.*, 1991, 1735.
131. G. Choux and R. L. Benoit, *Bull. Soc. Chim. Fr.*, 1967, 2920.
132. C. Gérard, *Bull. Soc. Chim. Fr.*, 1979, I–451.

133. P. K. Bharadwaj, *Prog. Inorg. Chem.*, 2003, **51**, 251.
134. S. R. Korupoju, N. Mangayarkarasi, P. S. Zacharias, J. Mizuthani, and H. Nishihara, *Inorg. Chem.*, 2002, **41**, 4099.
135. R. S. McQuate and D. L. Leussing, *J. Am. Chem. Soc.*, 1975, **97**, 5117.
136. H. Adams, D. Bradshaw, and D. E. Fenton, *J. Chem. Soc., Dalton Trans.*, 2002, 925.
137. M. Yonemura, K. Arimura, K. Inoue, N. Usuki, M. Ohba, and H. Okawa, *Inorg. Chem.*, 2002, **41**, 582.
138. Y. Kai, M. Morita, N. Yasuoka, and N. Kasai, *Bull. Chem. Soc. Jpn.*, 1985, **58**, 1631.
139. M. Ghedini, M. La Deda, I. Aiello, and A. Grisolia, *J. Chem. Soc., Dalton Trans.*, 2002, 3406.
140. M. D. Glick, R. L. Lindvedt, D. P. Gavel, and B. Tomlonovic, *Inorg. Chem.*, 1976, **15**, 1654.
141. E. I. Stiefel ed., ‘Dithiolene Chemistry – Synthesis, Properties, and Applications’ *Progress in Inorganic Chemistry*, Wiley, 2004, Vol. 52.
142. I. G. Dance, A. Choy, and M. L. Scudder, *J. Am. Chem. Soc.*, 1984, **106**, 6285.
143. T. Türk, U. Resch, M. A. Fox, and A. Vogler, *Inorg. Chem.*, 1992, **31**, 1854.
144. M. Gelinsky and H. Vahrenkamp, *Z. Anorg. Allg. Chem.*, 2002, **628**, 1017.
145. S. Aoki, M. Shiro, and E. Kimura, *Chem. – Eur. J.*, 2002, **8**, 929.
146. S. Jörgens, D. Johrendt, and A. Mewis, *Z. Anorg. Allg. Chem.*, 2002, **628**, 1765.
147. Y. Yamada, Y. Miyashita, K. Fujisawa, and K. Okamoto, *Bull. Chem. Soc. Jpn.*, 2001, **74**, 97.
148. J. Bertels and R. Mattes, *Z. Naturforsch., Teil. B*, 1985, **40b**, 1068.
149. H. Nekola and D. Rehder, *Inorg. Chim. Acta.*, 2002, **337**, 467.
150. A. J. Blake and M. Schröder, *Adv. Inorg. Chem.*, 1990, **35**, 1.
151. J. A. McGinnety, *Inorg. Chem.*, 1974, **13**, 1057.
152. D. W. Meek and J. A. Ibers, *Inorg. Chem.*, 1960, **9**, 465.
153. A. Muñoz-Páez, R. R. Pappalardo, and E. S. Marcos, *J. Am. Chem. Soc.*, 1995, **117**, 11710.
154. J. Burgess, ‘Metal Ions in Solution’, Ellis Horwood, Chichester, 1978.
155. G. W. Neilson and J. E. Enderby, *Adv. Inorg. Chem.*, 1989, **34**, 195.
156. H. Ohtaki and T. Radnai, *Chem. Rev.*, 1993, **93**, 1157.
157. D. T. Richens, ‘The Chemistry of Aqua Ions’, Wiley, Chichester, 1997.
158. H. Freiser, Q. Fernando, and G. E. Cheney, *J. Phys. Chem.*, 1959, **63**, 250.
159. K. Burger ed., ‘Biocoordination Chemistry’, Ellis Horwood, Chichester, 1990, Chap. III, V, and VII.
160. J. Kragten, ‘Atlas of Metal-Ligand Equilibria in Aqueous Solution’, Ellis Horwood, Chichester, 1978, Chap. 45.
161. K. B. Yatsimirskii, *Russ. J. Inorg. Chem.*, 1960, **5**, 128.
162. M. T. Beck, ‘Chemistry of Complex Equilibria’, Ellis Horwood, Chichester, 1970, p. 253.
163. D. Kroczewska, B. Kurzak, and E. Matczak-Jon, *Polyhedron*, 2002, **21**, 2183.
164. M. Kodama and E. Kimura, *J. Chem. Soc., Dalton Trans.*, 1977, 2269.
165. A. E. Martell and R. D. Hancock, *ACS Symp. Ser.*, 1994, **565**, 240.
166. R. M. Izatt, K. Pawlak, J. S. Bradshaw, and R. L. Bruening, *Chem. Rev.*, 1991, **91**, 1721.
167. H. Ito and T. Ito, *Bull. Chem. Soc. Jpn.*, 1985, **58**, 1755.
168. H. Sigel and R. B. Martin, *Chem. Soc. Rev.*, 1994, **23**, 83.
169. G. W. Nielson and R. H. Tromp, *Annu. Rep. Chem., Sect. C.*, 1991, **88**, 45.
170. W. Van Doorne and T. P. Dirkse, *J. Electrochem. Soc.*, 1975, **122**, 1.
171. A. G. Briggs, N. A. Hampson, and A. Marshall, *J. Chem. Soc., Faraday Trans. 2*, 1974, **70**, 1978.
172. P. L. Goggin, G. Johansson, M. Maeda, and H. Wakita, *Acta Chem. Scand.*, 1984, **38A**, 625.
173. S.-I. Ishiguro and H. Ohtaki, *J. Coord. Chem.*, 1987, **15**, 237.
174. D. P. Strommen and R. A. Plane, *J. Chem. Phys.*, 1974, **60**, 2643.
175. S. Aoki and E. Kimura, *Chem. Rev.*, 2004, **104**, 769.
176. D. A. Buckingham and C. A. Clark, *Aust. J. Chem.*, 1982, **35**, 431.
177. J. Suh, *Acc. Chem. Res.*, 1992, **25**, 273.
178. R. P. Bonar-Law and J. K. M. Sanders, *J. Chem. Soc., Chem. Commun.*, 1991, 574.
179. R. P. Bonar-Law, L. G. Mackay, C. J. Walter, V. Marvaud, and J. K. M. Sanders, *Pure Appl. Chem.*, 1994, **66**, 803.
180. R. P. Bonar-Law and J. K. M. Sanders, *J. Am. Chem. Soc.*, 1995, **117**, 259.
181. D. T. Richens, ‘The Chemistry of Aqua Ions’, Wiley, Chichester, 1997, p. 547.
182. L. Hertli and T. A. Kaden, *Helv. Chim. Acta*, 1974, **57**, 1328.
183. A.-M. Albrecht-Gary, C. Dietrich-Buchecker, Z. Saad, and J.-P. Sauvage, *J. Am. Chem. Soc.*, 1988, **110**, 1467.
184. C. Grant and P. Hambright, *J. Am. Chem. Soc.*, 1969, **91**, 4195.
185. J. C. Payne, M. A. ter Horst, and H. A. Godwin, *J. Am. Chem. Soc.*, 1999, **121**, 6850.
186. J. C. Buchsbaum and J. M. Berg, *Inorg. Chim. Acta.*, 2000, **297**, 217.
187. Y. Ducommun, G. Laurenczy, and A. E. Merbach, *Inorg. Chem.*, 1988, **27**, 1148.

188. A. Drljaca, C. D. Hubbard, R. van Eldik, T. Asano, M. V. Basilevsky, and W. J. le Noble, *Chem. Rev.*, 1998, **98**, 2167.

189. J. Burgess and C. D. Hubbard, *Adv. Inorg. Chem.*, 2003, **54**, 71. (see 130).

190. P. Hendry and A. M. Sargeson, *Prog. Inorg. Chem.*, 1990, **38**, 201.

191. R. G. Wilkins, ‘Kinetics and Mechanism of Reactions of Transition Metal Complexes’, 2nd edn., VCH, Weinheim, 1991.

192. M. L. Tobe and J. Burgess, ‘Inorganic Reaction Mechanisms’, Addison Wesley Longman, Harlow, 1999.

Zinc: Organometallic Chemistry

Jean-Michel Grévy
Universidad Autónoma del Estado de Morelos, Cuernavaca, México

Based in part on the article Zinc: Organometallic Chemistry by Gerard Parkin which appeared in the Encyclopedia of Inorganic Chemistry, First Edition.

1 Introduction 1
2 Diorganozinc Compounds 1
3 Organozinc Compounds of the Type RZnX 12
4 Alkylzinc Anions and Cations 26
5 Geminate Organodimetallic Species Containing Zinc 29
6 Reactivity of Organozinc Compounds 32
7 Related Articles 47
8 References 47

Abbreviations

9-BBN = 9-Borabicyclo-3,3,1-non-9-yl; acac = Acethylacetonate; Ar* = 2,4,6-tri(*tert*-butyl)phenyl; *azol* = 1-aziridineethanolate; BDI = β-diketiminate; Bz = Benzyl; Cp = Cyclopentadienyl; Cp* = Pentamethylcyclopentadienyl; Cp$'$ = Methylcyclopentadienyl; Cy = Cyclohexyl; DABCO = 1,4-diazabicyclo[2,2,2]octane; DAIB = 3-exo-dimethylamino-isoborneol; DBNE = N,N-dibutylnorephedrine; dippp = 1,3-bis(diisopropylphosphino)propane; DMA = Dimethylacetamide; DME = 1,2-dimethoxyethane; DPMPM = diphenyl(1-methylpyrrolidin-2-yl)methanol; ebpe = Ethylene-bis(1-phenylethylamine); ET = Electron Transfer; EWG = Electron-Withdrawing Group; FG = Functional Group; Imz = imidazolyl; Mes = 2,4,6-(Trimethyl)phenyl; MIB = 3-exo-morpholineisoborneol; MOCVD = Metal Organic Chemical Vapor Deposition; MOM = Methoxy-methyl-ether; N_4-aza crown = 1,4,8,11-tetramethyl-1,4,8,11-tetra-azacyclotetradecane; N_6-aza crown = 1,4,7,10,13,16-hexa-methyl-1,4,7,10,13,16-hexaazacyclooctadecane; Pyr* = 2,5-di(tert-butyl)pyrrolide; TAC = Triazacyclohexane; TADDOL = $\alpha,\alpha,\alpha',\alpha'$-tetraaryl-1,3-dioxolane-4,5-dimethanolate; THF = Tetrahydrofuran; TMEDA = Tetramethylendiamine; TImz = mercaptoimidazolyl; TMS = Trimethylsilyl.

1 INTRODUCTION

The first organometallic compounds of zinc, namely, ethylzinc iodide (EtZnI) and diethylzinc (Et_2Zn), were prepared by Sir Edward Frankland in 1849[1–3] when he attempted the preparation of 'ethyl radical'. Even if these two species were not the first organometallic derivatives to be prepared (cacodyl compounds and Zeise's salt (*see Zeise's Salt*) were discovered in 1760 and 1827, respectively), the work of Frankland is now recognized as the beginning of modern organometallic chemistry. He recognized very early the synthetic utility of EtZnI and Et_2Zn, and devoted his career to studying their properties and to preparing other organic compounds of tin, mercury, and arsenic. Owing to their low reactivity, a result of the high covalent character of the zinc−carbon bond and the low Lewis acidity (*see Lewis Acids & Bases*) of Zn^{II}, the organozinc reagents were replaced at the beginning of the twentieth century by the more reactive Grignard and organolithium reagents. For more than half a century, their application to organic synthesis was limited to specific reactions, mostly cyclopropanation and aldol reactions. However, in recent years it was found that the low reactivity of organozinc species makes them highly tolerant to a wide range of functional groups and allows good regio- and enantioselectivities in their transformations.

Furthermore, organozinc derivatives readily form complexes with electron-donating ligands as a result of the electron-deficient character of zinc. In spite of the early knowledge of this property, it was only after the 1960s that this subject became the source of extensive investigations and led to the development of an extremely rich coordination chemistry.

In the past few decades, these features have stimulated a growing interest for this area of organometallic chemistry and nowadays the organozinc compounds play a very important role in organic, organometallic, and inorganic chemistry. Their low toxicity, excellent functional group tolerance, chemoselectivity, and stereoselectivity make them ideal reagents for the building of complex molecules bearing polyfunctional groups.

Over the years, several reviews dealing with different aspects of the organometallic chemistry of zinc have been published.[4,5]

2 DIORGANOZINC COMPOUNDS

2.1 Preparation

The different routes for the preparation of organozinc compounds are summarized in Scheme 1. Detailed experimental protocols including important tips can be found in references 6 and 7. In the last decade, this subject was included in several reviews dealing with the applications of polyfunctional organozinc compounds in organic synthesis.[8–10]

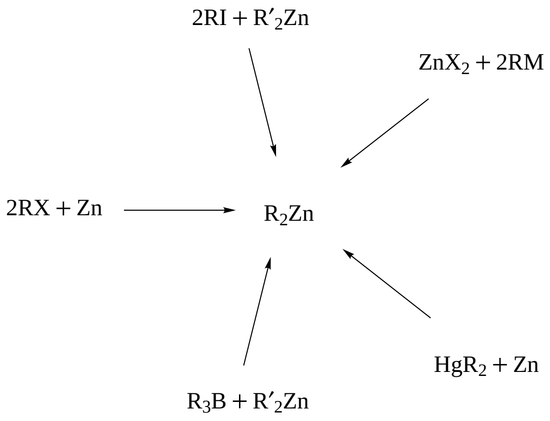

Scheme 1

2.1.1 *Direct Reaction of Zn with Alkyl Halides*

This method was originally used by Frankland to prepare diethylzinc. It is described as an oxidative insertion (*see Insertion*) of zinc metal inside the carbon-halogen bond of an organic halide. The initial product of the reaction is an alkylzinc halide derivative (RZnX), from which the dialkylzinc compound (R_2Zn) is formed as the Schlenk-type equilibrium establishes (equations 1 and 2).

$$\mathrm{Zn} + \mathrm{RX} \longrightarrow \mathrm{RZnX} \tag{1}$$

$$2\mathrm{RZnX} \rightleftharpoons \mathrm{ZnR_2} + \mathrm{ZnX_2} \tag{2}$$

The ideal alkyl halide substrates are the alkyl iodides and usually the reaction requires the zinc to be activated by forming an alloy (*see* ***Alloys***) with a metal such as copper, sodium, or mercury. Finely divided forms of zinc (powder or dust), alone or previously treated with copper or sodium acetate, are also very effective.

Another procedure for the preparation of very active zinc uses the ‘metal atom’ approach in which zinc-metal vapor is coprecipitated with an ethereal solvent.[11] The unstable bis(trifluorosilyl)zinc and bis(trifluoromethyl)zinc have been prepared by cocondensing Zn atoms with $\cdot SiF_3$ radicals (*see Radicals*) and $\cdot CF_3$ radicals, respectively (generated by low-temperature radio-frequency glow discharge or plasma of hexafluoroethane or hexafluorodisilane).[12]

The Riecke zinc,[13] obtained by reduction of a zinc halide with sodium or potassium in THF, is commonly used for the preparation of simple or functionalized organozinc compounds and allows the use of less reactive alkyl halide reagents like alkyl bromides. The reaction of this very active form of zinc with organic bromides was shown to be strongly dependent on the structure of the organic moiety.[14] The results also support the presence of radicals (*see Radicals*) in the reaction and suggest a mechanism in which electron transfer (*see* ***Electron Transfer Reactions: Theory***) (ET) is the rate-determining step. In the reaction with alkyl bromides, the ET has an important component of inner sphere, whereas in the reaction with aryl halides there is a participation of aryl halide radical anions as intermediates. A classification of the organic bromides, depending on the nature of the organic group and attending to their relative reactivity, can be summarized by the diagram presented in Figure 1. The less reactive vinyl bromides are found in one extreme and the most reactive benzylic bromides in the other.

In the past years, numerous modifications for zinc activation have been developed, not only to increase the reaction efficiency, but also to allow the use of less reactive and inexpensive organic halides such as organic chlorides.

2.1.2 *Iodine–Zinc Exchange*

Diorganozinc reagents can be prepared efficiently by an iodine–zinc exchange reaction[15] between the appropriate alkyl halide and an excess of Et_2Zn or i-Pr_2Zn (equation 3). This method is suitable for primary and secondary alkyl iodides and requires catalytic amounts of a Cu^I salt. The reaction conditions with i-Pr_2Zn (25 °C, 1 h) are considerably milder than those used with Et_2Zn (50 °C) and allow the preparation of complex diorganozinc species in good yields. A possible mechanism for the catalyzed reaction with Cu^I is given in Scheme 2.[8]

$$2\mathrm{FG{-}RCH_2{-}I} + \mathrm{ZnR'_2} \longrightarrow \mathrm{Zn(CH_2R{-}FG)_2} + 2\mathrm{R'I} \tag{3}$$

$$\mathrm{R'} = \mathrm{Et}, i\mathrm{Pr} \qquad \mathrm{FG} = \text{Functional Group}$$

Other transition metals (*see Transition Metals*) such as $PdCl_2(dppf)$ and $Ni(acac)_2$[16,17] catalyze the reaction but lead to alkylzinc iodides instead of dialkylzinc compounds.

Recently, it was shown that the exchange reaction can be photochemically (*see Photochemistry*) induced by irradiating at $\lambda \geq 280\,\mathrm{nm}$ the reaction mixture of an alkyl iodide and 0.5 equiv of R_2Zn (R = Et or i-Pr) (equation 4).[18]

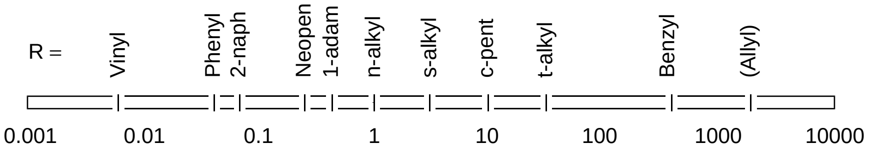

Figure 1 Relative dimensionless rates for $\mathrm{RBr} + \mathrm{Zn}^* \longrightarrow \mathrm{RZnBr}$

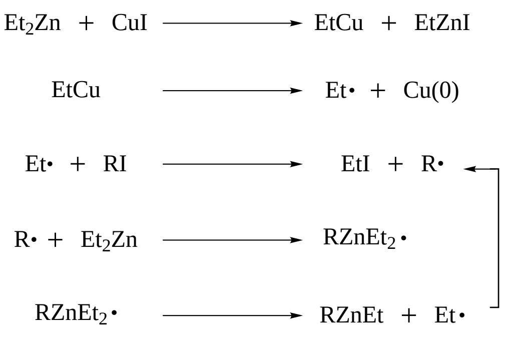

Scheme 2

In these conditions, excess of R_2Zn and the catalyst (transition metal) are not required. In addition, when a solution of an alkyl iodide is mixed with 1 equiv of R_2Zn the mixed diorganozinc compounds (R–Zn–R′) are obtained (equation 5). This reaction takes place only between dialkylzincs and alkyl iodides; however, in comparison with the few other methods described for the preparation of mixed diorganozincs, this procedure represents a fantastic enhancement for alkyl group exchange (R–Zn–R′).[19,20]

$$2RI + ZnR'_2 \xrightarrow[h\upsilon]{CD_2Cl_2} ZnR_2 + 2R'I \qquad (4)$$

$$RI + ZnR'_2 \xrightarrow[h\upsilon]{CD_2Cl_2} RZnR' + R'I \qquad (5)$$

2.1.3 *Alkylation of Zinc Salts*

This method, presented in equation (6), involves the alkylation of zinc salts, usually zinc halides or zinc acetate. The alkylating agents are typically Grignard reagents or organolithium (*see* ***Alkali Metals: Organometallic Chemistry***) reagents in an ethereal solvent, but trialkylaluminum or zirconocene reagents can also be used. For example the preparation of dimethyl- and diethylzinc is described by the reaction of trimethyl- and triethylaluminum with zinc acetate[21] (equation 7). This procedure is useful for the preparation of simple dialkylzinc but the high reactivity of organolithium or magnesium (*see* ***Beryllium & Magnesium: Organometallic Chemistry***) reagents precludes the synthesis of zinc derivatives containing functional groups, although the use of low temperature can in some cases overcome this problem.[22]

$$2R[M] + ZnX_2 \longrightarrow ZnR_2 + 2[M]X \qquad (6)$$

$$[M] = Li, MgX \qquad X = Cl, Br, I$$

$$2AlMe_3 + Zn(OAc)_2 \longrightarrow 2Me_2Al(OAc) + Me_2Zn \qquad (7)$$

It is worth mentioning here that disupersilylmetals $(t\text{-}Bu_3Si)_2M$, supersilylmetal halides $(t\text{-}Bu_3Si)MX$ and bis(disupersilyl)silylmetals $[(t\text{-}Bu_3Si)_2SiH]_2M$ (M = Zn, Cd, Hg; X = Cl, Br) have been recently prepared by reaction of the corresponding silyl-sodium salts with metal dihalides in 1:1 or 2:1 ratio, and could be fully characterized[23,24] (Scheme 3). The disupersilylzinc compound was found to react with $BiCl_3$ or BBr_3 to give the corresponding supersilylzinc halide $(t\text{-}Bu_3Si)ZnX$.

2.1.4 *Boron–Zinc Exchange*

The first boron–zinc exchange reported in the literature was the reaction of dimethylzinc with triethylborane to produce diethyl zinc[25] (equation 8). The driving force of the reaction is the formation of stable dialkylzinc compounds, and in some cases the formation of volatile organoboranes such as BMe_3 (bp = −22 °C). Primary dialkyl and benzylic organozinc compounds are successfully prepared when Me_2Zn or Et_2Zn are used as reagents,[26] but the B–Zn exchange is usually slow with hindered secondary alkylboranes. However, $i\text{-}Pr_2Zn$ has been found to undergo rapid exchange with both primary and secondary substrates, leading to the preparation of secondary dialkylzincs. An important feature of the exchange reaction is that retention of configuration was observed with several

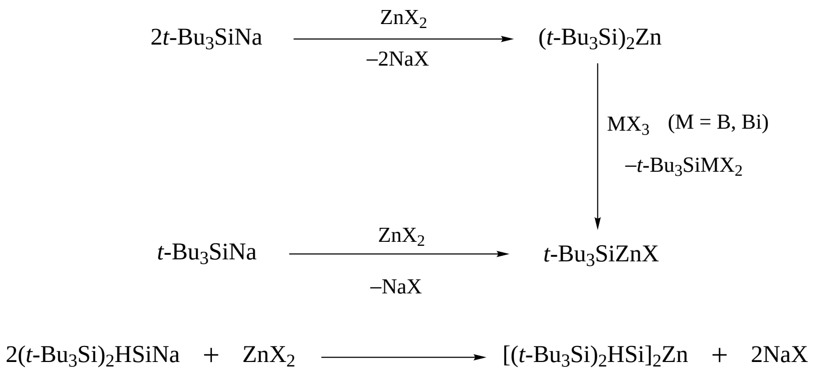

Scheme 3

systems at low temperature[27] ($-10\,^\circ$C).

$$3\mathrm{BEt_3} + 2\mathrm{ZnMe_2} \longrightarrow 3\mathrm{ZnEt_2} + 2\mathrm{BMe_3} \qquad (8)$$

The reaction conditions are significantly mild (0 °C) and allow the presence of a number of sensitive functional groups. Although this procedure presented limited applications when it was discovered, during the last years it became one of the most versatile preparations of polyfunctional diorganozinc species; a consequence of both its high tolerance towards functional groups and its high stereoselectivity.[8]

A recent theoretical study has shown that the B–Zn exchange proceeds with a low activation energy and could involve two intermediates (Figure 2), the particularly unusual bonding structures of which would be responsible for the retention of configuration.[28]

2.1.5 *Transmetallation with Mercury*

In 1864, Frankland discovered the transmetallation reaction between diorganomercurials and zinc metal[29] (equation 9). It is generally applicable when the organomercury compounds are available and when it is necessary to prepare absolute salt free diorganozinc compounds.

$$\mathrm{Zn\,(excess)} + \mathrm{HgR_2} \longrightarrow \mathrm{ZnR_2} + \mathrm{Zn/Hg} \qquad (9)$$

Usually the reaction requires an excess of zinc metal, a few hours in refluxing toluene, and can eventually be catalyzed with small amounts of zinc salts. A modification of this method, employing dimethyl zinc instead of zinc metal, has been used to prepare a stable complex of bis(trifluoromethyl)zinc with pyridine[30,31] (equation 10).

$$\mathrm{Hg(CF_3)_2} + \mathrm{ZnMe_2} \xrightarrow{\text{Pyridine}} \mathrm{Zn(CF_3)_2(pyridine)} + \mathrm{HgMe_2} \qquad (10)$$

2.2 Properties of Diorganozinc Compounds

Depending on the nature of the alkyl group, simple dialkylzinc compounds can be mobile liquids or low-melting solids (Table 1). They are all colorless and completely miscible with common nonprotic solvents. With polar (*see Polar Compounds*) organic solvents containing electron-donating atoms, they form soluble complexes. However, in pure form or in hydrocarbon solvents, they exist as monomers, since association via alkyl bridges doesn't occur with zinc. Dialkylzinc compounds are all very susceptible to oxygen and moisture attack; in consequence all manipulations must be performed in an inert atmosphere. The derivatives of low-molecular weight are spontaneously flammable on contact with air, producing a fume of ZnO, while higher molecular weight derivatives are less sensitive. It is worth noting that both $[(\mathrm{Me_3Si})_3\mathrm{C}]_2\mathrm{Zn}$ and the closely related cyclic derivative $[\text{–}\mathrm{C(SiMe_3)_2SiMe_2CH_2CH_2Me_2Si(Me_3Si)_2C}\text{–}]$ Zn are remarkably resistant towards water or electrophilic (*see Electrophile*) reagents.[32,33] The thermal stability of dialkylzinc compounds also varies with the nature of the alkyl group; it decreases with the increase of the chain length and the substitution degree on the α-carbon atom. Dimethylzinc is stable at room temperature, whereas di-*iso*-propyl- and di-*tert*-butylzinc decompose at 0 °C and should be stored at dry ice temperature. The mean Zn–C bond dissociation energies ($\bar{D}$) (*see Bond Dissociation Energy*) have been determined by calorimetric studies for some of the compounds listed in Table 1.[34] In the particular case of $\mathrm{Me_2Zn}$, the first- and second-bond dissociation energies have also been calculated[35] ($D_1 = 266 \pm 6\,\mathrm{kJ\,mol^{-1}}$; $D_2 = 102 \pm 17\,\mathrm{kJ\,mol^{-1}}$).

Table 1 Physical properties and mean bond dissociation energies of some diorganozinc compounds

	M.P. (°C)[4]	B.P. (°C/mmHg)[4]	$\overline{D}$ (Zn–R) ($\mathrm{kJ\,mol^{-1}}$)
$\mathrm{Me_2Zn}$	−29	46	183 ± 7
$\mathrm{Et_2Zn}$	−28	118	133 ± 10
n-$\mathrm{Pr_2Zn}$	−81 to −84	139	145 ± 25
i-$\mathrm{Pr_2Zn}$	–	40/12	–
n-$\mathrm{Bu_2Zn}$	−57	61/4	157 ± 25
t-$\mathrm{Bu_2Zn}$	28.8	34/12	–
$\mathrm{Ph_2Zn}$	107	280–285 (dec)	–
$\mathrm{(Me_3CCH_2)_2Zn}$	–	–	157
$\mathrm{(Me_3SiCH_2)_2Zn}$	–	–	195

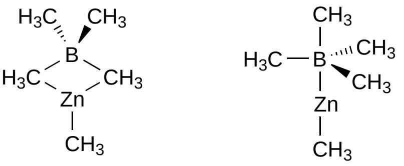

Figure 2 Calculated intermediates in the methyl exchange between $\mathrm{BMe_3}$ and $\mathrm{ZnMe_2}$

2.3 Structure of Diorganozinc Compounds

2.3.1 *Dialkylzinc Compounds*

Two-coordinate organozinc compounds, containing saturated alkyl or aryl groups (with the exception of $\mathrm{Ph_2Zn}$), are invariably monomeric with linear geometries at the Zn atom. Therefore they are nonpolar, and most of those whose structures have been determined bear this out[36] (Table 2). Several studies of the vibrational spectrum of $\mathrm{Me_2Zn}$ showed unequivocally that the valence angle C–Zn–C is 180° and that the methyl groups undergo virtually free internal rotation. The

Table 2 C–Zn–C angle and C–Zn bond length of some dialkylzinc compounds

	C–Zn–C (°)	C–Zn (Å)
Me_2Zn[a]	180	1.93
Et_2Zn[a]	180	1.95
n-Pr_2Zn[a]	180	1.95
$[2,4\text{-}(t\text{-}Bu)_2C_6H_3]_2Zn$[b]	180	1.97
$[(MeOMe_2Si)(Me_3Si)_2C]_2Zn$[b]	180	1.98
$(Me_3Si)_2CHZnC^*(SiMe_3)_3$[b]	176.2	C^H–Zn 1.97/ C^* –Zn 1.95
$PhZnC^*(SiMe_3)_3$[b]	177.6	C^{Ph}–Zn 1.92/ C^* –Zn 1.96

[a]Data determined by gas-phase electron diffraction.[38] [b]Data determined by X-ray crystallography.[36,39]

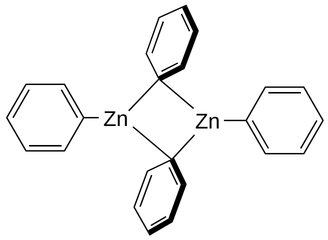

Figure 3 Structure of $PhZn(\mu\text{-}Ph)_2ZnPh$

molecular structures of dimethyl-, diethyl- and dipropylzinc, determined by gas-phase electron diffraction,[37] display the Zn–C bond distances listed in Table 2.

This observation contrasts dramatically with the property of the pretransition metals, magnesium and beryllium (*see* ***Beryllium & Magnesium: Organometallic Chemistry***), to adopt polymeric structures with bridging alkyl groups and four-coordinate metal centers. The low electronegativity (*see Electronegativity*) difference between zinc and carbon ($\chi Zn = 1.7$; $\chi C = 2.5$) leads to a low polarity (*see Polar Bonds*) of the Zn–C bond which associated with the large size of the zinc atom are thought to be responsible for the monomeric nature of diorganozinc compounds. However, an NMR study of methyl group exchange between dimethylzinc and dimethylcadmium shows that bridging alkyl groups between zinc and cadmium may be possible at least in transition states.[40,41]

The only exception to linear monomeric structure is diphenylzinc, which presents a dimeric structure in solid state by virtue of an interaction between the ipso carbon of one σ-bound phenyl group and the zinc center of another Ph_2Zn unit.[38] The bond lengths between zinc and the terminal phenyl groups are as expected [1.941(4) and 1.951(5) Å]. Nevertheless, the two phenyl groups bridge the two metal centers in an asymmetric fashion, with two short [2.006(5) and 2.016(3) Å] and two long [2.442(4) and 2.364(5) Å] Zn–C bonds (Figure 3). Thus, this interaction was best pictured as an electrophilic attack on the zinc phenyl group by an adjacent Lewis acidic (*see Lewis Acids & Bases*) center than as an association via three-center, two-electron (*see Three-center Bond*) alkyl bridges. The fact that diphenyl zinc is monomeric in hexane solution supports this suggestion.

In contrast to $(Ph_2Zn)_2$, both bis(pentafluorophenyl)zinc[42] and bis[2,4,6-tris(trifluoromethyl)phenyl]zinc[43] have a two-coordinate monomeric solid-state structure approaching linearity, which is certainly a result of electronic and steric (*see Steric Effect*) properties of the *ortho* substituents (Figure 4). In the crystal structure of both compounds, the aromatic rings are almost orthogonal to one another. This special situation alleviates intramolecular (*see Intramolecular*) steric interactions and allows intramolecular stacking interactions between rings on adjacent molecules.

It is worth mentioning that the molecular structures of different bis(disupersilyl)silylmetals $[(t\text{-}Bu_3Si)_2HSi]_2M$, determined by X-ray analysis,[24] show nonlinear frameworks Si–M–Si (M = Zn, Cd, Hg) (Figure 5). This feature, which is unprecedented for homoleptic (*see Homoleptic Compound*) dicoordinate zinc compounds, is believed to arise from van der Waals-attractions between methyl groups of the supersilyl substituents. In contrast, supersilylmetal derivatives of general formula $(t\text{-}Bu_3Si)_2M$ (M = Zn, Cd, Hg), present a common linear geometry at the metal center with a Si–M–Si angle of 180°.[23] The Si–Zn bond lengths vary from 2.384 Å in $(t\text{-}Bu_3Si)_2Zn$ to 2.449 Å in $[(t\text{-}Bu_3Si)_2HSi]_2Zn$.

2.3.2 *Unsaturated Dialkylzinc Compounds*

The situation is different when diorganozinc species bear unsaturated moieties. Although dialkenylzinc compounds such as divinylzinc are monomeric in benzene solution, they have higher melting and boiling points than their saturated analogues, indicating larger intermolecular interactions in

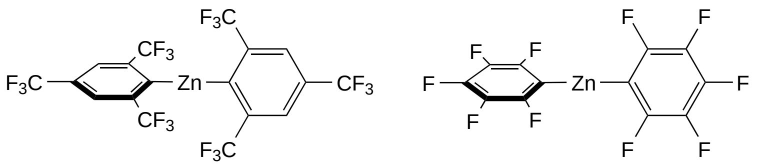

Figure 4 Structure of $[2,4,6\text{-}(CF_3)_3C_6H_2]_2Zn$ and $(C_6F_5)_2Zn$

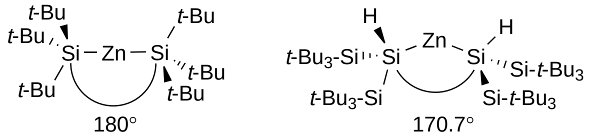

Figure 5 Structure of supersilylzinc $(t\text{-Bu}_3\text{Si})_2\text{Zn}$ and bis(disupersilyl)silylzinc compounds $[(t\text{-Bu}_3\text{Si})_2\text{HSi}]_2\text{Zn}$

solid and liquid phases. Directly bounded alkynyl groups are believed to be the only ones that can form stable bridges between zinc atoms (Figure 6). So far there is no structural determination of this type of compounds, but their associative nature is reflected by their high melting points and low solubility in nonpolar solvents.**[44]**

From ^{1}H NMR studies, it was shown that diallylzinc compounds undergo fluxional processes between all possible isomeric σ-bonded (*see σ-Bond*) allylic forms[45] (Scheme 4).

2.3.3 Cyclopentadienylzinc Compounds (See Cyclopentadienyl)

While dicyclopentadienyl compounds of transition metals (*see Transition Metals*) typically have a ferrocene-like (*see Ferrocene*) sandwich structure, the electron-deficient cyclopentadienides of the main group metals tend to form polymers with bridging cyclopentadienyl (Cp) groups.**[46]** Although exceptions are known, the tendency is rather consistent. The element zinc, owing to its borderline position between transition metals and main group metals, presents a variety of coordination (*see* ***Coordination Numbers & Geometries***) modes with the Cp anion.

The structure of CpZnCH_3 has been determined in both solid state and gas phase.**[47,48]** In the gas phase, the compound is monomeric with $C_{5\text{v}}$ symmetry. The Cp ligand features η^5-coordination to zinc, thereby creating an 18-electron (*see Eighteen Electron Compounds*) shell for the zinc atom (Figure 7). However, in crystalline state, the compound exists as a polymer with Cp ligands bridging zinc centers. The hapticity (*see Hapticity*) of the Cp groups varies from two to three (Figure 8).

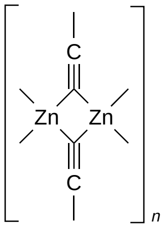

Figure 6 Bridging alkynyl groups between zinc atoms

A related polymeric structure, somewhat more complex, occurs in the solid state of Cp_2Zn.**[49]** This structure consists of infinite chains of zinc atoms with bridging Cp groups and, in addition, each zinc atom carries a terminal Cp group (Figure 9). Neither the terminal nor the bridging Cp groups are bounded to zinc in a purely η^1-faschion; the bonding situation is best described as '$\eta^{2.5}$'. Owing to its low thermal stability, this compound could not be studied in the gas phase.

Zinconocenes possessing Cp ligands of different electronic and steric properties (*see Steric Effect*) have been synthesized and structurally characterized. Whereas Cp_2Zn is polymeric in the solid state, replacement of hydrogen atoms by methyl or isopropyl groups lead to compounds which exhibit a 'slipped-sandwich' (*see Slip Processes in Ligands*) motif with both η^1- and η^5-Cp ligands. For example, the structure of bis(pentamethylcyclopentadienyl)Zn (Cp_2^*Zn) determined in gas phase**[50,51]** and in crystalline state**[52]** is presented in Figure 10. The ^{1}H NMR spectra at room temperature of this derivative shows only one set of resonances, indicating a rapid haptotropic exchange, or 'ring-slippage', between η^1- and η^5-coordination (Figure 11). Comparable situations, showing different degree of 'ring-slippage', have been observed in gas phase for $(\text{C}_5\text{H}_4\text{SiMe}_3)_2\text{Zn}$, and by X-Ray diffraction

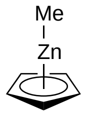

Figure 7 Structure of monomeric CpZnMe in the gas phase

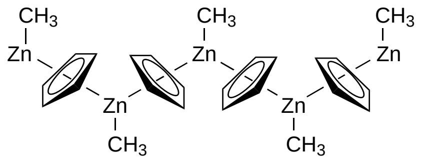

Figure 8 Part of the polymeric structure of CpZnMe in the solid state

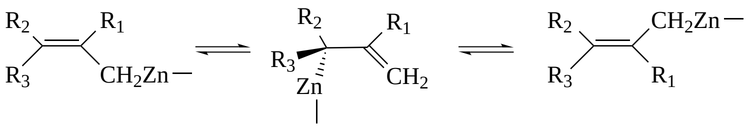

Scheme 4

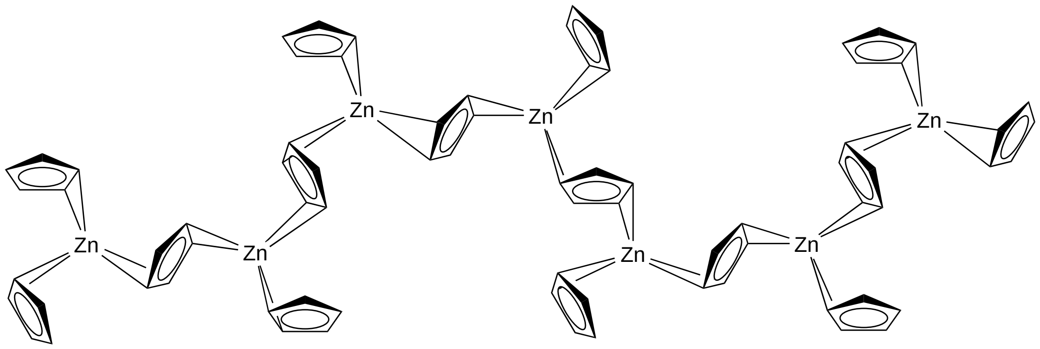

Figure 9 Schematic representation of the chain structure of Cp_2Zn

for $(C_5Me_4Ph)_2Zn$ and $(C_5H\text{-}i\text{-}Pr_4)_2Zn$.[52,53] Compared to the magnesium (*see* ***Beryllium & Magnesium: Organometallic Chemistry***) derivatives η^5-Cp_2Mg or η^5-Cp^*_2Mg of regular sandwich (*see Sandwich Compound*) structures, zinc metallocenes are highly sensitive on contact with air. This sensitivity of slipped-sandwich compounds can be explained by a less effective encapsulation of the metal center.

A new bonding mode between the Cp ring and Zn has been observed for $[CpZn(\mu\text{-}Cp)\{\mu\text{-}N(TMS)_2\}ZnCp]$.[54] This compound is the first example of a Cp group that bridges between nonbonded metal atoms located on the same side of the ring plane (Figure 12).

The nature of the binding mode between zinc and three different (dialkylamino)ethylcyclopentadienyl ligands has been studied.[55] X-ray structural determinations of such derivatives show that the Cp rings are bound to the zinc centers in a η^1 fashion and via their amine groups, thus forming stable six-membered metallacycle (Figure 13). Similarly, the acyclic pentadienyl ligands in $(2,4\text{-}t\text{-}Bu_2C_5H_5)_2Zn$ and in the complex $(C_5H_7)ZnCl\cdot TMEDA$ only exhibit η^1 coordination.[56,57]

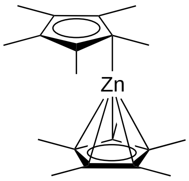

Figure 10 Molecular structure of $(Me_5C_5)_2Zn$ in the gas phase

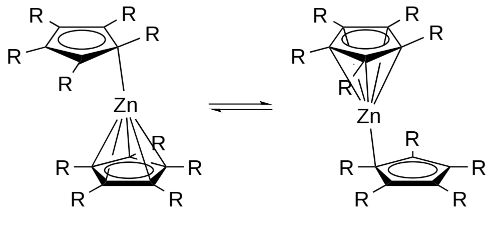

Figure 11 ‘‘Ring-slippage’’ in zinconocene compounds

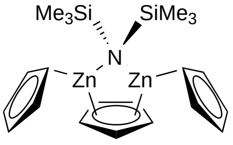

Figure 12 Structure of $Cp_3Zn_2N(SiMe_3)_2$

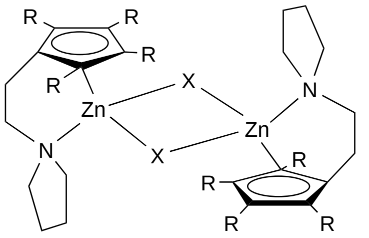

R = Me, *i*-Pr, H. X = Cl, OAc

Figure 13 Structure of (dialkylamino)ethylcyclopentadienylzinc derivatives

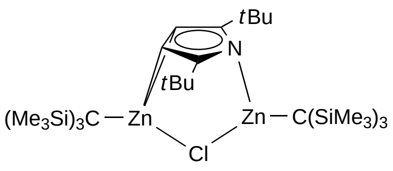

Figure 14 Structure of $[(Me_3Si)_3C\text{–}Zn]_2(\mu\text{-}Cl)(\mu\text{-}Pyr^*)$

Interestingly, the anion 2,5-di(*tert*-butyl)pyrrolide $[2,5\text{-}(t\text{-}Bu)_2C_4H_2N]^-$ (Pyr^*), which is isoelectronic (*see Isoelectronic*) with the Cp anion, reacts with tris(trimethylsilyl)methylzinc chloride to give the very stable bis[tris(trimethylsilyl)methylzinc] chloride 2,5-di(*tert*-butyl)pyrrolide dimer (equation 11). The solid-state structure of the compound, shown in Figure 14, shows an unusual binding mode for Pyr^* with high steric shielding (*see Steric*

Effect) of the central Zn–Cl–Zn moiety. The Pyr* ligand and the chlorine atom bridge the zinc atoms that are found on the same side of the ligand. One zinc atom is bound to the N of the Pyr* ligand, while the other is bound in a η^2 fashion to the opposite C atoms.**[58]**

$$2(\mathrm{Me_3Si})_3\mathrm{C–ZnCl} + \mathrm{Li–Pyr^*} \longrightarrow [(\mathrm{Me_3Si})_3\mathrm{C–Zn}]_2(\mu\text{-Cl})(\mu\text{-Pyr}^*) + \mathrm{LiCl} \qquad (11)$$

In the different examples presented above, the coordination at zinc suggests that both σ- (*see σ-Bond*) and π-type interactions (*see π-Bond*) contribute to the cyclopentadiene-zinc bonding.

2.4 Coordination of Diorganozinc Compounds (*See Coordination Theory*)

In its ground state (*see Ground State*), the zinc atom has the electronic configuration [Ar] $3d^{10}4s^2$ (*see* ***Electronic Structure of Main-group Compounds***) and so, the low-lying 3*d* shell is completely filled. Therefore the coordination chemistry (*see* ***Coordination Numbers & Geometries***) of zinc is mainly determined by electrostatic factors with no ligand field effects. In terms of simple valence theory (*see Valence Bond Theory*), the zinc atom in diorganozinc compounds is *sp*-hybridized (*see Hybridization*) with a linear geometry and two low-energy orbitals remain available for coordination with electron-donating ligands. Additionally, this capacity to form complexes is enhanced by the low electronegativity (*see Electronegativity*) of zinc ($\chi\mathrm{Zn} = 1.7$), making it a rather electropositive element when bound to carbon ($\chi\mathrm{C} = 2.5$).

If only one coordinate bond is formed between the diorganozinc and a ligand, the zinc atom becomes sp^2-hybridized (*see Hybridization*) with the typical trigonal planar geometry and it still has an unoccupied valence orbital (*see Valence Orbitals*). This case is quite rare and usually favored with sterically hindered ligands that can avoid the approach of a fourth ligand. When two-coordinate bonds are formed, the zinc atom becomes approximately sp^3-hybridized (*see Hybridization*) with the typical tetrahedral or pseudotetrahedral geometry. This is the most common situation, encountered in the majority of complexes with diorganozinc species. Despite five- and six-coordinated zinc atoms being common in inorganic zinc chemistry (*see* ***Zinc: Inorganic & Coordination Chemistry***), this situation is rare for organozinc compounds. Finally, intramolecular (*see Intramolecular*) coordination may occur when the alkyl groups of R_2Zn include donor atoms (*see Donor Atom*) or insaturations.**[59]**

2.4.1 *Coordination with Oxygen-containing Ligands*

When diorganozinc compounds dissolve in ethereal solvents, they readily form complexes with either one or two molecules of the solvent. Complexes with straight chain dialkyl ethers as Me_2O or Et_2O, have been known for a long time but they are generally not stable enough to be isolated.**[60]** Nevertheless, with cyclic ethers such as THF, and also with bifunctional ethers like 1,4-dioxane or 1,2-dimethoxyethane, the resulting complexes are more stable and some of them could be characterized. Several examples of ether complexes with diorganozinc compounds are presented in Table 3; all of them possess a tetracoordinated zinc center.**[61]**

The coordination of few diorganozinc species with crown ethers (*see Crown Ethers*) has been studied. The reaction of Ph_2Zn**[64]** or Et_2Zn**[65]** with 18-crown-6-ether leads to the formation of the corresponding rotoxane (Figure 15). The average Zn–C bond length found in the Et_2Zn rotoxane [1.957(5) Å] is almost identical with that found in gaseous Et_2Zn [1.950(2) Å], whereas it is somewhat longer in the Ph_2Zn rotoxane [1.984(3) Å]. The Zn–O distances are extremely long [average >2.8 Å] indicating only weak Zn–O bonding. Therefore these rotoxanes might be best regarded as clathrates (*see Clathrate*), having nearly linear R_2Zn encapsulated within the crown ether (*see Crown Ethers*) but only weakly bonded to its oxygens. The mechanism of formation of threaded $Ar_2Zn\cdot$(18-crown-6) species has been studied.**[66]** The observations indicate that R_2Zn and 18-crown-6 rapidly form a 1:1 peripheral complex and more slowly form a rotoxane. The formation and dethreading of the rotoxane require free R_2Zn. Thus pure rotoxane is stable indefinitely in a benzene solution unless some R_2Zn compound is added.

A different coordination mode has been found with 1,3-xylyl 15-crown-4 and 1,3-xylyl 18-crown-5 ethers.**[67]** The crystal structure of three adducts with Ph_2Zn shows that bonding takes place only with two oxygens of the cryptand (*see*

Table 3 Physical properties of ether complexes with diorganozinc compounds

	M.P. (°C)	B.P. (°C)
$Me_2Zn\cdot$1,4-dioxane**[61]**	65	–
$Me_2Zn\cdot$1,4-thioxane**[61]**	23	–
$Me_2Zn\cdot$Dimethoxyethane**[61]**	5.5	–
$Me_2Zn\cdot$(Dimethoxyethane)$_2$**[61]**	–	90.5
$Me_2Zn\cdot$(Dimethoxypropane)$_2$**[61]**	–	100.5
$Ph_2Zn\cdot$Dimethoxyethane**[62]**		
$(C_6F_5)Zn\cdot(THF)_2$**[63]**	91–93	

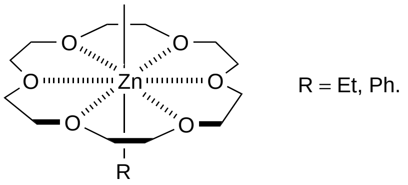

Figure 15 Structure of rotoxane $R_2Zn\cdot$18-crown-6

Cryptands & Cryptates) (Figure 16), leading to a tetrahedrally surrounded zinc atom which remains outside the cavity of the crown ether (*see Crown Ethers*).

To date, the only five-coordinated Zn adduct structurally characterized is formed between Ph_2Zn and diglyme[62] (Figure 17) and has been shown to persist in solution.

Finally, an unusual planar-trigonal geometry of the zinc atom has been observed in the molecular structure of $(i\text{-PrOSiMe}_2\text{CH}_2)_2\text{Zn}$.[68] This situation results from intermolecular (*see Intermolecular*) coordination of one oxygen atom belonging to a neighboring molecule (Figure 18). Table 4 outlines important bond lengths and bond angles found in some adducts of dialkylzinc compounds with oxygen-containing ligands.

2.4.2 Coordination with Nitrogen-containing Ligands

The coordination chemistry of diorganozinc compounds with nitrogen-containing ligands has been known for many years, but until recently only little structural information was accessible. Zinc–nitrogen coordinate bonds are stronger than zinc–oxygen coordinate bonds because of the relatively soft character (*see* ***Hard & Soft Acids and Bases***) of zinc (*b*-type) in diorganozinc compounds. But, even though tertiary amines form very stable complexes, primary and secondary amine-complexes are usually unstable as a result of the protonolysis of the zinc–carbon bonds by the nitrogen-bound hydrogen(s) (equation 12). When bidentate ligands (*see Bidentate Ligand*) such as TMEDA are used, chelate complexes (*see Chelate Effect*) are formed[71] (Figure 19). This property has been successfully used to synthesize and isolate heteroleptic (*see Heteroleptic Compound*) diorganozinc compounds (RZnR′) which are otherwise unstable.[72,73] In fact, the occupation of the coordination sites at the zinc atom prevents dismutation to the homoleptic (*see Homoleptic Compound*) derivatives (R_2Zn and R'_2Zn). It is also worth mentioning that the complex between Me_2Zn and the chelate ligand (*S*,*S*)-*NN*′-ethylenebis(1-phenylethylamine) [(S,S)-ebpe] is the sole example of a complex between a dialkylzinc compound and a secondary amine to be isolated

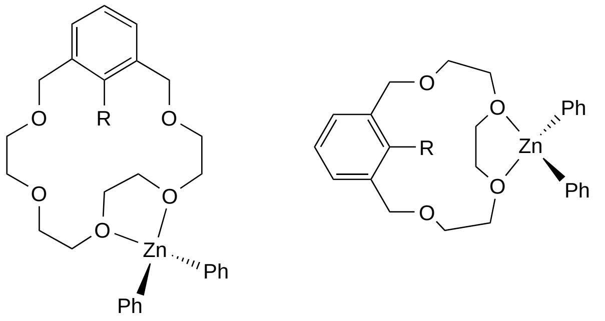

Figure 16 Coordination of Ph_2Zn with 1,3-xylyl crown ethers. R = H, Br

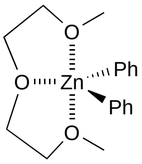

Figure 17 Structure of $Ph_2Zn{\cdot}$diglyme

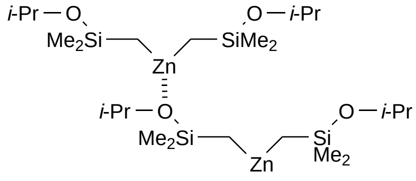

Figure 18 Intermolecular coordination in the solid state of bis[(dimethylisopropoxysilyl)methyl]zinc

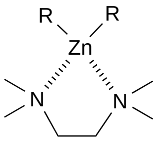

Figure 19 Chelate complexes between dialkylzinc compounds and TMEDA

Table 4 Average bond lengths and bond angles for some structurally characterized adducts between dialkylzinc and oxygen-containing ligands

Compound	Zn–C(Å)	Zn–O(Å)	C–Zn–C(°)	O–Zn–O(°)
$Ph_2Zn{\cdot}$DME[62]	1.963	2.273	146.65	72.16
$Ph_2Zn{\cdot}$Diglyme[62]	1.969	2.496/2.330	149.69	69.01
$(C_6F_5)_2Zn{\cdot}(THF)_2$[63]	2.005	2.103	132.12	92.39
$(Fluorenyl)_2Zn$[69]	2.047	2.104	117.57	89.29
$(ICH_2)_2Zn{\cdot}$(dimethoxynorbormane)[70]	1.981	2.181	137.76	72.24
$Ph_2Zn{\cdot}$2-bromo-1,3-xylyl 15-crown-4[67]	1.960	2.269	139.60	71.60
$Ph_2Zn{\cdot}$1,3-xylyl 18-crown-5[67]	1.958	2.307	147.70	73.04
$Ph_2Zn{\cdot}$2-bromo-1,3-xylyl 18-crown-5[67]	1.963	2.284	146.70	72.47

and characterized by X-ray crystallography.[74]

$$R_2Zn + R'_2NH \rightleftharpoons R_2Zn{\cdot}HNR'_2 \rightleftharpoons RZnNR'_2 + RH \quad (12)$$

In the 1960s, Thiele[54,75,76] reported the preparation of complexes with both monodentate (e.g. triethylamine, pyridine) and bidentate ligands (*see Bidentate Ligand*) (e.g. 2,2-bipyridyl, 1,10-phenanthroline). While low-boiling liquid adducts were obtained with monodentate ligands, both in the 1:1 and 2:1 ligand to diorganozinc ratio, volatile solid adducts were obtained with bidentate ligands. As shown by cryoscopic molecular weight measurements in nonpolar solvents, extensive dissociation occurred for the 2:1 species giving equilibrium mixtures of the 1:1 adduct, the free amine and the 2:1 species. Eventually, on repeated distillation, these liquids of 2:1 stoichiometry reach a stable 1:1 stoichiometry. The adducts with N-heterocyclic ligands such as pyridine, 2,2′-bipyridine and 1,10-phenanthroline, are brightly colored owing to metal-to-ligand charge-transfer transitions.[77] A series of complexes between dialkylzinc compounds and bipyridine has been studied. The variation of the dissociation constants indicates that the metal-nitrogen bond strength increases with the size of the alkyl group; bigger alkyl groups provide more electron density, reducing the Lewis acidity (*see Lewis Acids & Bases*) of the metal but increasing back bonding (*see Back Bonding*) to the ligand.[4]

Recently there has been revived interest for adducts of dimethylzinc and diethylzinc with nitrogen-containing ligands owing to their useful application as precursors in metal organic chemical vapor deposition[78] (*see Metal–Organic Chemical Vapor Deposition*) (MOCVD) and in the purification of metal alkyls for subsequent use in MOCVD.[79] Less volatile adducts such as $[R_2Zn\{(C_5H_4N)(CH_2)_3(C_5H_4N)\}]_n$ have been used for the production of electronic grade R_2Zn by mild thermal dissociation.[80]

A number of relevant structures have been published. Table 5 summarizes some of the important bond lengths and bond angles found in complexes between diorganozinc compounds and amines. As a result of amine coordination, the geometry around the zinc center changes from linear to distorted tetrahedral (*see* ***Coordination Numbers & Geometries***).

It is noteworthy that the potentially tridentate triazine ligand coordinates only via one of its nitrogen atoms to form the $[Me_2Zn(CH_2NMe)_3]_2$.[81] In contrast, the reaction of Et_2Zn with 1,4-diazabiciclo[2,2,2]octane (DABCO) results in the formation of molecular chains in which the metal atom exhibits a distorted tetrahedral geometry through coordination to one nitrogen atom of two different DABCO molecules[82] (Figure 20).

The coordination of Me_2Zn with macrocyclic amines (*see* ***Macrocyclic Ligands***) such as 1,4,8,11-tetramethyl-1,4,8,11-tetraazacyclotetradecane (N_4-aza crown) and 1,4,7,10,13,16-hexamethyl-1,4,7,10,13,16-hexaazacyclooctadecane (N_6-aza crown) has been studied.[85] As shown by X-ray diffraction analysis, the structure of the complexes consists of molecular units with distorted tetrahedral coordination at zinc (Figure 21, Table 5). In $(Me_2Zn)_2[N_4$-aza crown], the

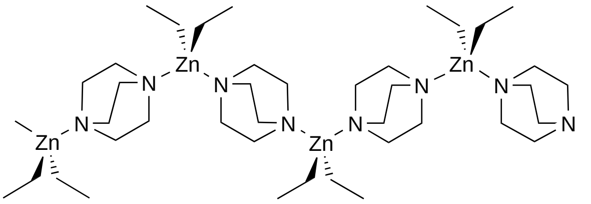

Figure 20 Polymeric structure of $(Et_2Zn{\cdot}DABCO)_n$

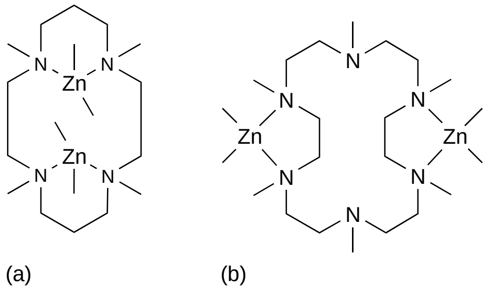

Figure 21 Structure of $(Me_2Zn)_2[N_4$-aza crown] (a) and $(Me_2Zn)_2{\cdot}[N_6$-aza crown] (b)

Table 5 Average bond lengths and bond angles for some structurally characterized adducts between dialkylzinc and nitrogen-containing ligands

Compound	Zn–C(Å)	Zn–N(Å)	C–Zn–C(°)	N–Zn–N(°)
$Me_2Zn{\cdot}TMEDA$[83]	1.982	2.269	135.8	79.8
$Et_2Zn{\cdot}TMEDA$[84]	2.173	2.293	118.08	80.68
$(Me_3CCH_2)_2Zn{\cdot}TMEDA$[83]	2.000	2.411	148.3	77.3
$(PhCH_2)_2Zn{\cdot}TMEDA$[73]	2.036	2.206	122.22	82.72
$Me_2Zn{\cdot}[(CH_2NMe)_3]_2$[81]	1.987	2.410	145.1	105.6
$Me_2Zn{\cdot}[N_4$-aza crown][85]	2.012	2.282	125.5	87.18
$Me_2Zn{\cdot}[N_6$-aza crown][85]	2.000	2.331	138.1	80.35
$Me_2Zn{\cdot}[(C_5H_4N)(CH_2)_3(C_5H_4N)]$[79]	2.000	2.241	145.5	98.4
$Et_2Zn{\cdot}DABCO$[82]	1.975	2.285	135.3	102.2
$Me_2Zn{\cdot}(S,S)$-ebpe[74]	2.006	2.231	134.75	80.29
$(CF_3)_2Zn{\cdot}(C_6H_5N)_2$[86]	2.062	2.078	121.72	99.39

Me_2Zn forms two six-membered chelate rings, clearly favored over the more sterically strained five-membered configuration, whereas in $(Me_2Zn)_2[N_6\text{-aza crown}]$, the Me_2Zn forms two five-membered chelate rings. While the N_4-aza crown adduct has the predictable Me_2Zn:ligand stoichiometry of 2:1, steric constraints (*see Steric Effect*) in the N_6-aza crown adduct limit the stoichiometry to 2:1. These adducts thermally dissociate at relatively low temperatures, making them suitable for Me_2Zn purification and its further use in MOCVD (*see Metal–Organic Chemical Vapor Deposition*).

The structures of some complexes with perfluoroalkylzinc derivatives have also been determined by X-ray diffraction. The first fully characterized compound of this type was the pyridine adduct $[(CF_3)_2Zn(C_5H_5N)_2]$, which presents the typical four-coordinated zinc center with a distorted tetrahedral geometry[86,87] (Table 5). The tetramethyltetrazene ligand forms a four-membered chelate ring via a 1,3-coordination with $(C_6F_5)_2Zn$[88] (Figure 22).

2.4.3 Coordination with other Ligands

The synthesis and characterization of Et_2Zn adducts with nucleophilic carbenes (*see* ***Carbene Complexes***) have been described.[89] They are directly available and in good yields from a smooth reaction between Et_2Zn and stable carbenes (*see* ***Carbene Complexes***) such as 1,3-dimesitylimidazol-2-ylidene or 1,3-di(1-adamantyl)imidazol-2-ylidene (equation 13). The solid-state structure of $[Et_2Zn\{1,3\text{-di(1-adamantyl)imidazol-2-ylidene}\}]$ shows a zinc atom in a rather unusual trigonal planar arrangement, certainly due to a steric protection of the zinc center by the adamantyl substituents.

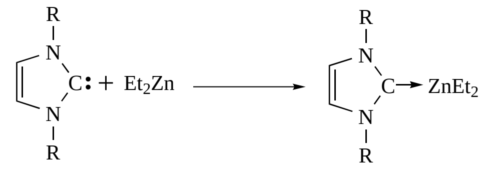

R = mesityl or 1-adamantyl

(13)

The recent preparation of $[Ph_2Zn\{S(CH_2)_n\}_2]$ ($n = 3$, 4) represent the first examples of complexes between a diorganozinc compound and a sulfur donor ligand.[90] The molecular structure of $[Ph_2Zn\{S(CH_2)_4\}_2]$, determined by X-ray crystallography, reveals a dimeric association with carbon-bridging groups (Figure 23).

2.4.4 Intramolecular Coordination

Diorganozinc compounds containing potential coordinating substituents beyond the α position generally exhibit intramolecular (*see Intramolecular*) coordinative interactions between the substituent groups and the central zinc atom.[52] This is the case for all the compounds containing carbon–carbon multiple bonds and those containing oxygen, nitrogen, sulfur, and phosphorus (Figure 24). In a study involving bis[3-(dimethylamino)propyl]zinc, both electron diffraction in gas phase and X-ray diffraction in solid state show a weak contact, around 0.23 nm, between the nitrogen and the zinc atom.[91] Analogous intramolecular coordination of the heterocyclic-*N* is found in the sterically hindered complex $[(2\text{-}C_5H_4N)(Me_3Si)_2C]_2Zn$[92] or with the amine-*N* in 2-[(dimethylamino)methyl]phenyl- and 2-(dimethylamino)benzyl derivatives.[93,94]

The monomeric zinc complex $[Zn(2\text{-}C_6H_4PPh_2NSiMe_3)_2]$, which was recently obtained by reaction of the *ortho*-metallated species $[Li(2\text{-}C_6H_4PPh_2NSiMe_3)]_2\cdot Et_2O$ with $ZnCl_2$ in THF, represents a good example of side-arm intramolecular coordination.[95] Its molecular structure determined by X-ray crystallography shows a tetrahedrally

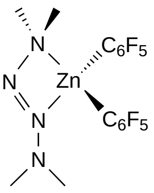

Figure 22 Coordination of tetramethyltetrazene to $(C_6F_5)_2Zn$

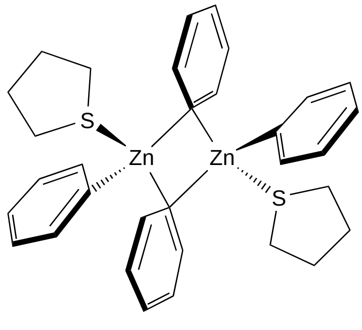

Selected bond length(Å): Zn–S 2.502, Z–$C_{\text{bridg.}}$ 2.114/2.261, Zn–$C_{\text{term.}}$ 1.983
Selected angles(°):Zn–$C_{\text{bridg.}}$–Zn 69.27, $C_{\text{bridg.}}$–Zn–$C_{\text{bridg.}}$ 110.73, $C_{\text{bridg.}}$–Zn–$C_{\text{term.}}$ 121.98, S–Zn–$C_{\text{bridg.}}$ 100.40, S–Zn–$C_{\text{term.}}$ 111.59.

Figure 23 Molecular structure for $Ph_2Zn\cdot[S(CH_2)_4]$

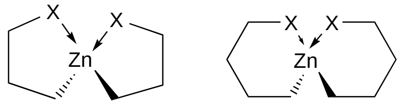

X = OR, SR, NR_2, PR_2, C=CR_2, CCR.

Figure 24 Intramolecular adducts

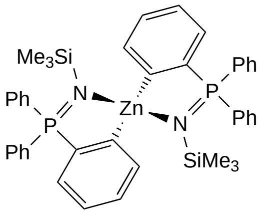

Figure 25 Structure of [Zn(2-$C_6H_4PPh_2NSiMe_3)_2$]

coordinated zinc atom with a Zn–C distance (2.008 Å) comparable to those found in diarylzinc compounds and a Zn–N distance (2.158 Å) typical for Zn–N dative bonds (Figure 25).

In compounds containing multiple carbon–carbon bonds, such as $[CH_2{=}CH(CH_2)_3]_2Zn$ and $[MeC{\equiv}C(CH_2)_3]_2Zn$, interactions between the multiple bond and the zinc center are also proposed on the basis of NMR spectra (^1H and ^{13}C) and Raman spectroscopy.[96,97] An electron diffraction study of the linear di-3-butenylzinc and the molecular structure of (2,4-t-$Bu_2C_5H_5)_2Zn$ determined by X-ray diffraction have been published.[52,98]

Interestingly, the intramolecular coordination of the carbon–carbon double bond in $[CH_2{=}CH(CH_2)_4]_2Zn$ is thought to be responsible for the formation of di(cyclopentylmethyl)zinc in 90% yield when the compound is kept several days at 120 °C (equation 14).[99]

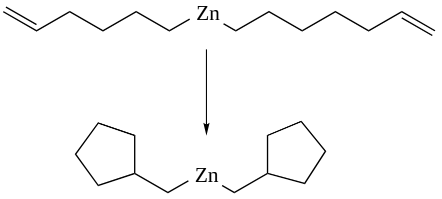

(14)

3 ORGANOZINC COMPOUNDS OF THE TYPE RZnX

3.1 Organozinc Halides

3.1.1 Preparation

The procedures used for the preparation of diorganozinc compounds must be modified in order to obtain organozinc halide derivatives. The aim of these modifications is to avoid the Schlenk-type equilibrium which leads to diorganozinc derivatives (equations 1 and 2) although the positions of the equilibria are such that the R–Zn–X compounds are favored. In the last decade, this subject has been included in different reviews concerning the applications of polyfunctional organozinc compounds.[8–10]

Direct Reaction of Zn with Alkyl Halides. The direct insertion (*see Insertion*) reaction of Zn metal into alkyl halides – alkyl iodides being the ideal substrates – is a useful reaction to prepare simple or polyfunctional organozinc halide compounds (equation 1). With primary alkyl iodides, the reaction requires an excess of Zn dust (ca. 3 equiv), previously treated with few mol % of 1,2-dibromoethane and TMSCl, and a temperature of 40 °C in THF. In these conditions, secondary alkyl iodides react at room temperature and benzylic and allylic bromides at 0 °C. The insertion (*see Insertion*) into less activated C–X bonds may require more reactive forms of zinc (Riecke zinc), higher temperatures, or the use of polar (*see Polar Compounds*) solvent or cosolvent.

A novel and simple modification uses the catalysis with iodine in dimethylacetamide[100] (DMA) (equation 15). In these conditions, any form of metallic zinc can be used (dust, powder, granule, shot), a variety of functional groups is tolerated, and the use of less reactive alkyl chlorides is possible, although in this special case the reaction requires stoichiometric amounts of bromide salts. Electrochemical procedures, using a sacrificial zinc anode (*see Sacrificial Anode*), have been successfully employed to prepare organozinc halides from aryl bromides and chlorides in high yields, even those that are unreactive in the Riecke process.[101,102] Recently it was found that reducing agents can advantageously replace electricity and the group of Périchon developed a purely chemical reaction based on the activation of aryl bromides by low-valent cobalt species arising from the reduction of cobalt halide by zinc dust.[103] A possible catalytic cycle is shown in Scheme 5.

$$\text{R–X} + 1.5\text{Zn} \xrightarrow[\text{DMA } 80\,^\circ\text{C},\ 3-12\,\text{h}]{\text{I}_2(1-5\,\text{mol\%})} \text{R–Zn–X} \qquad (15)$$
$$\text{X} = \text{Cl, Br}$$

Numerous modifications of the direct zinc insertion procedure can be found in the literature. For example, simple dialkylzincs can be used as reagents instead of metallic Zn, but in this case the reaction is accelerated by catalytic quantities of zinc salts or transition metal (*see Transition Metals*) salts. Whereas the Cu^I-catalyzed iodine–zinc exchange reaction provides diorganozincs, the Pd^{II}, Mn^{II} and Ni^{II} catalyzed iodine- or bromine–zinc exchange leads to organozinc halides.

Lithium–Zinc Transmetallation. The transmetallation reaction of organolithium reagents with zinc salts is a more

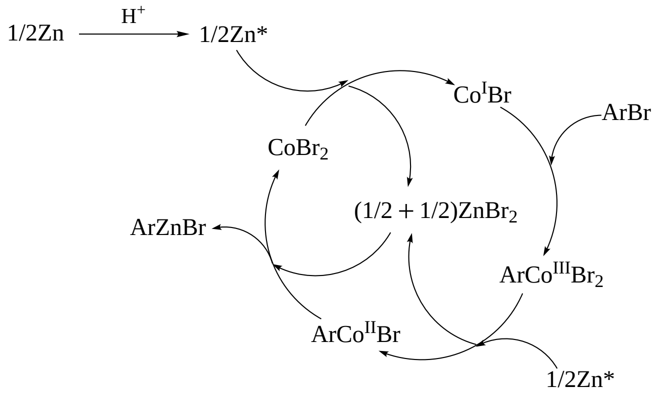

Scheme 5

straightforward approach to organozinc halide derivatives, but the high reactivity and instability of these very polar (*see Polar Compounds*) reagents limit the applicability of this reaction. However, alkenyl- and aryllitiums are known to be less reactive than their alkyl counterparts. Thus, at low temperature (−100 °C), they tolerate a range of functional groups and readily undergo transmetallation reaction with zinc halides, leading to the corresponding organozinc halides**[21,104]** (equation 16).

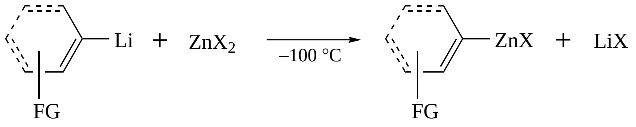

X = Br, I. FG = functional group.

(16)

Other Preparations. A less general procedure involves the reaction of diorganomercurials with zinc dust in the presence of zinc bromide.

Allyliczinc halides reagents have been prepared from sterically hindered homoallylic alcohols, using a novel fragmentation reaction of the corresponding zinc alkoxide**[105]** (Scheme 6). The interest of this reaction resides in the absence of the Wurtz homocoupling product, usually present in high proportion when the direct reaction of zinc with allylic halides is used.

An *in situ* (*see In Situ Reaction*) generation of zinc acetylides has been performed in very mild conditions by the combination of a terminal alkyne with $Zn(OTf)_2$ and a tertiary amine base**[106]** (equation 17). The zinc acetylides were not isolated but they could be unequivocally identified by the large, characteristic shifts of the ^{13}C NMR corresponding to the *sp*-hybridized (*see Hybridization*) carbons.

$$\text{R–C≡C–H} + \text{Zn(OTf)}_2 \xrightarrow{\text{R}_3\text{N}} \text{R–C≡C–Zn(OTf)} + \text{R}_3\text{N·HOTf} \quad (17)$$

3.1.2 Structure of Organozinc Halides

As a result of the Schlenk-type equilibrium (equation 2), alkylzinc halide solutions are believed to contain some amounts of the corresponding dialkylzinc compound and zinc halide salt. The equilibrium usually lies on the left side in such a way that the alkylzinc halide compound is favored. Nevertheless, as already mentioned in Section 2, the equilibrium can be shifted to the right by distillation of the more volatile dialkylzinc derivative or by addition of complexing agents to remove the zinc dihalides from the solution.

Although organozinc halides have been extensively used in organic synthesis for many years, comparatively little information is available concerning their structure and coordination behavior. The crystalline ethylzinc iodide is a coordination polymer, with the iodine−zinc linkages giving rise to a layer structure as shown in the Figure 26. Each iodine atom forms one short (2.64 Å) and two long (2.91 Å) bonds to zinc.**[107]**

Ethylzinc chloride and ethylzinc bromide are tetrameric in benzene solutions and are believed to have the cubane-type structure**[108]** shown in Figure 27. In the Zn_4X_4 core, the zinc-halogen coordination is relatively weak; consequently when these compounds dissolve in coordinating solvents or when

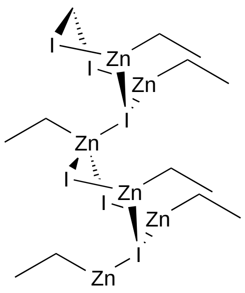

Selected bond lengthsÅ: Zn–C 1.94, Zn–I 2.64/2.91
Selected bond angle (°): I–Zn–C 143.9

Figure 26 Part of the ethylzinc iodide polymer in the solid state

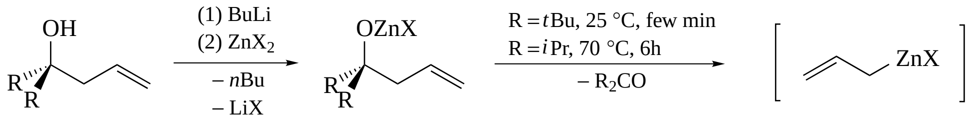

Scheme 6

they are reacted with ligands like TMEDA or bipyridine, they exist as monomeric complexes.[84] The highly sterically demanding $(PhMe_2Si)_3CZnCl$ exist as a dimer in solid state, with tricoordinate zinc atoms and bridging chlorine atoms.[109] As shown in Figure 27, the solid-state structure of the complex consists of a planar arrangement of zinc and chlorine atoms forming a parallelogram.

The reaction between lithiated bidentate ligands (*see Bidentate Ligand*), such as lithium (dialkylaminoethyl)cyclopentadienide or $[2\text{-}C_5H_4N(Me)_2Si(Me_3Si)_2C]Li$, with zinc dihalide ($ZnX_2$) also leads to dimeric derivatives containing bridging chlorine atoms but with tetracoordinate zinc centers as a result of intramolecular (*see Intramolecular*) coordination[55,110] (Figure 13 and 28 respectively). A cryoscopic study of $Et_2N(CH_2)_3ZnCl$ in benzene solution has shown a related dimeric structure with bridging chlorines independent of the concentration[111] (Figure 28). Selected bond lengths and bond angles for dimeric alkylzinc halide compounds characterized by X-ray crystallography are reported in Table 6.

A number of monomeric adducts between alkylzinc halide compounds and chelating ligands (*see Chelating Ligands*) have been isolated and structurally characterized (Table 7). For example, the reaction between the TMEDA adduct of lithium-phenyl(trimethylsilyl)methanide and $ZnCl_2$[63] directly led to the formation of the TMEDA complex of phenyl(trimethylsilyl)methanidezinc chloride. Its molecular structure determined by X-ray diffraction crystallography, and that of $EtZnCl{\cdot}TMEDA$, are presented in Figure 29.

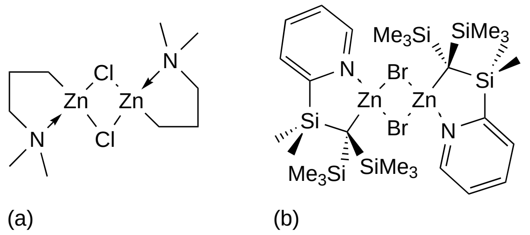

Figure 28 Dimeric structure of $Me_2NCH_2CH_2CH_2ZnCl$ (a) and $[(C_5H_4N)(Me)_2Si(Me_3Si)_2C]ZnBr$ (b)

Even if alkylzinc halides in the absence of chelating ligands (*see Chelating Ligands*) or coordinating solvents generally form dimeric or polymeric species with bridging halogen atoms, a different situation has been found with the Reformatsky reagents derived from the ethyl- and *tert*-butyl esters of bromoacetic acid.[113] In the crystalline state, $(Br\text{–}Zn\text{–}CH_2COO^tBu)_2$ exists as a dimeric unit consisting of a nonplanar 8-membered $(ZnCCO)_2$ ring in which the THF coordination is preferred over the Zn–Br–Zn bridging (Figure 30). A rather short C–C bond length (1.41 Å)

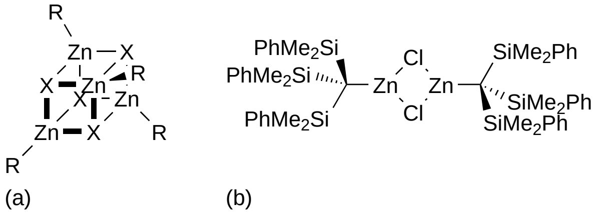

Figure 27 Structure of polymeric EtZnX (X = Br, Cl) (a) and dimeric $(PhMe_2Si)_3CZnCl$ (b)

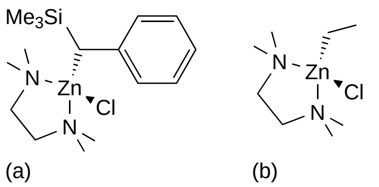

Figure 29 Monomeric structures of the TMEDA complexes with $Ph(Me_3Si)CHZnCl$ (a) and EtZnCl (b)

Table 6 Selected average bond lengths and bond angles for some dimeric alkylzinc compounds

Compound	Zn–C (Å)	Zn–X (Å)	Zn–N (Å)	C–Zn–X (°)	C–Zn–N (°)	Zn–X–Zn (°)
$[(PhMe_2Si)_3C\text{-}Zn(\mu\text{-}Cl)]_2$[109]	1.98	2.30		133.4		91.5
		2.35		138.2		92.3
$[(\eta^1\text{-}Me_2NC_2H_4C_5H\text{-}i Pr_3)Zn(\mu\text{-}Cl)]_2$[55]	2.06	2.35	2.12	123.9	108.7	86.9
$[(C_5H_4N)(Me)_2Si(Me_3Si)_2C\text{-}Zn(\mu\text{-}Br)]_2$[110]	2.04	2.5	2.08	128.1	98.9	88.2

Table 7 Selected bond lengths and bond angles for some alkylzinc halide complexes with TMEDA

Compound	Zn–C (Å)	Zn–X (Å)	Zn–N (Å)	C–Zn–X (°)	N–Zn–N (°)
$EtZnCl{\cdot}TMEDA$[84]	1.94	2.27	2.14	124.9	80.7
$(Me_2SiCH_2SiMe_2)CHZnCl{\cdot}TMEDA$[112]	1.98	2.25	2.16	127.0	84.0
$Ph(Me_3Si)CHZnCl{\cdot}TMEDA$[72]	2.01	2.25	2.15	122.2	84.4
$(CH_2{=}CHCH{=}CHCH_2)ZnCl{\cdot}TMEDA$[57]	2.03	2.26	2.15	118.7	84.4

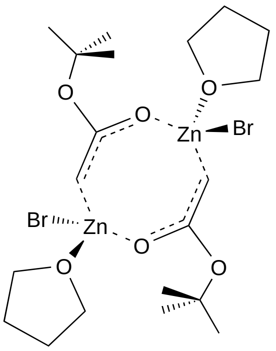

Figure 30 Structure of $(t\text{BuOCOCH}_2\text{ZnBr})_2$

associated to a quite long carbonyl C–O bond distance (1.31 Å) suggest that the Reformatsky reagent exists neither as a strictly *C*-metalated species nor as a strictly *O*-metalated form, but rather as a combination of the two. Association measurements and NMR spectroscopy studies show that the reagents are dimeric in all but the most polar (*see Polar Compounds*) solvents like dimethylsulfoxide.

Among the alkylzinc halide compounds, iodomethylzinc iodide deserves a special attention owing to its important applications in organic synthesis. This highly reactive reagent can be stabilized by chelation to ethers or even more efficiently to bipyridine.[114] In the later case, the resulting adducts are stable enough to be stored several months in the freezer with almost no decomposition. The complexes of ICH_2ZnI with 18-crown-6 and benzo-18-crown-6 ethers have been prepared and structurally characterized by X-ray diffraction crystallography.[115] The two structures are very similar; they reveal a coordination of three oxygen atoms from the crown ether (*see Crown Ethers*) to the zinc atom (Figure 31). Interestingly, this is one of the few crown ether-derived complex in which the metal atom is not centrosymmetric. Selected bond lengths and bond angles for alkylzinc halides coordinated to oxygen-containing ligands are found in Table 8.

3.2 Alkylzinc Compounds Containing a Zinc–Oxygen Bond

There are two principal classes of alkylzinc compounds containing a zinc−oxygen bond, that is, those derived from aliphatic and aromatic alcohols (commonly called alkylzinc alkoxides and aryloxides) and those derived from other oxygen-containing compounds like water, carboxylic acids, silanol, boronic acids, and so on. Recently, Zn^{II} alkoxide or phenoxide derivatives have attracted much interest for their ability to catalyze numerous reactions, such as enantioselective (*see Enantioselectivity*) alkylation of aldehydes, asymmetric epoxidation of α,β unsaturated ketones, decarboxylation of carboxylic acids, copolymerization (*see* ***Oligomerization & Polymerization by Homogeneous Catalysis***) of carbon dioxide with epoxides.

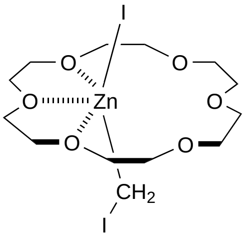

Figure 31 Structure of $\text{ICH}_2\text{ZnI}\cdot$18-crown-6 complex

3.2.1 Alkylzinc Alkoxides and Aryloxides

Preparation. The synthesis of alkylzinc alkoxides and aryloxides is achieved by an alkane elimination process in the simple reaction of a dialkylzinc compound, R_2Zn, with one equivalent of an alcohol, R′OH (equation 18). This reaction proceeds either in hydrocarbon solvents or neat solution, to give essentially quantitative yields of the desired products. The volatility of the RH side product helps to drive the equilibrium to the right. The formation of relatively strong Zn–O and C–H bonds, at the expense of breaking the O–H and a relatively weak Zn–C bond also guarantee favorable reaction energetics.

$$\text{R}'\text{EH} + \text{ZnR}_2 \longrightarrow \text{RZnER}' + \text{RH} \qquad (18)$$

$$\text{R} = \text{Alkyl, Me}_3\text{SiCH}_2\cdot\text{E} = \text{O, S, Se}$$

Structure. The presence of an oxygen atom directly bound to zinc increases both the electron deficiency of the zinc and the donor character of the oxygen atom. This condition will inevitably result in intermolecular (*see Intermolecular*) association increasing the coordinative saturation of zinc and leading to high thermal stability and low sensitivity towards oxygen and moisture. Organozinc alkoxides and aryloxides

Table 8 Selected bond lengths and bond angles for some alkylzinc halide complexes with oxygen-containing ligands

Compound	Zn–C(Å)	Zn–X(Å)	Zn–O(Å)	C–Zn–X(°)	O–Zn–O(°)
$\text{ICH}_2\text{ZnI}\cdot$18-crown-6[115]	1.99	3.49	2.34/2.55/2.60	156.8	67.8/68.4
$\text{ICH}_2\text{ZnI}\cdot$benzo-18-crown-6[115]	2.04	3.47	2.39/2.56/2.24	124.9	69.8/70.9
$\text{ICH}_2\text{ZnI}\cdot$benzo-15-crown-4[116]	1.98	2.56	2.17/2.24	126.09	70.6
$\text{CF}_3\text{CCl}_2\text{ZnCl}\cdot\text{DMA}$[117]	2.02	2.21	1.99	122.1	94.0

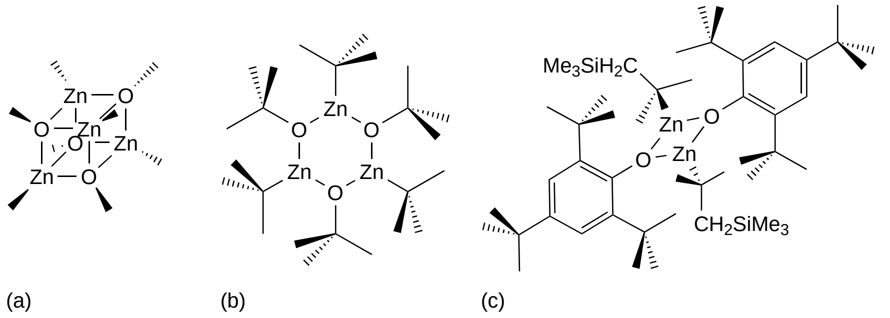

(a) (b) (c)

Figure 32 Tetrameric MeZn–OMe (a), trimeric t-BuZnO-t-Bu (b) and dimeric $Me_3Si(Me_2)CZn2,4,6$-t-$Bu_3C_6H_2$ (c)

are usually colorless or light-yellow solids. Depending on the nature of the alkyl and alkoxide groups and on the degree of association, they can be either highly soluble or virtually insoluble in both apolar and polar organic solvents.

The coordination chemistry (*see* ***Coordination Numbers & Geometries***) of organozinc alkoxides and aryloxides is very diverse but follow fairly well established patterns that can be rationalized mainly on the basis of steric considerations (*see Steric Effect*). As shown in Figure 32, the solid-state structure of methylzinc methoxide is tetrameric.**[118]** Although this tetrameric association with distorted cubic Zn_4O_4 core is observed as a common feature, the degree of association decreases with increasing bulk of the alkyl and alkoxide groups, resulting in trimeric**[119]** or dimeric species,**[120]** for example, [t-BuZn-(O-t-Bu)]$_3$ and [$(Me_3SiCH_2)(Me)_2CZnO$-2,4,6-t-$Bu_3C_6H_2$]$_2$ (Figure 32). The structure of these complexes also depends on the presence of potentially intramolecular coordinating donor atoms in either the organic or the alkoxide group. Such donor atoms are often involved in intramolecular coordination and may give rise to a very complex coordination behavior.

A number of alkylzinc complexes derived from phenoxide ligands, containing one or two potentially coordinating NMe_2 groups, have been studied by cryoscopic molecular weight determination.**[121]** When the potentially chelating groups (*see Chelating Ligands*) are in positions that result in the formation of six-membered chelate rings upon intramolecular coordination, the complexes are dimers or dimer–monomer equilibria, and when the potential chelate ring size is decreased from six- to five-membered, trimeric aggregation is observed (Figure 33). The introduction of bulky substituents in a potential five-membered chelate ring leads to further dissociation, and dimer formation becomes favorable. The dimer formation can also be favored when a strongly electron-withdrawing group is bound to the oxygen, leading to a weaker zinc–oxygen coordinate bond. Therefore, when ethylzinc phenoxide is a tetramer the related ethylzinc pentafluorophenoxide is a dimer.**[119]**

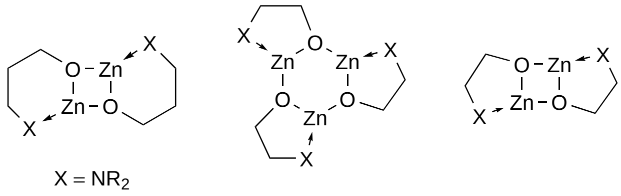

Figure 33 Intramolecular coordination in alkylzinc alkoxides

Multinuclear aggregates of alkylzinc derivatives have been prepared and structurally characterized by the reaction between tris(3,5-dialkyl-2-hydroxyphenyl)methanes with dimethyl- or diethylzinc.**[122]** Depending on both the steric requirements (*see Steric Effect*) of the dialkylzinc reagent/trisphenol precursors and on the solvent used, hexa-, penta-, tetra-, and trinuclear aggregates are isolated. The reactions of polyalcoholic compounds (diphenol and triphenol derivatives) have also been studied, they lead to a variety of products depending on the conditions used.**[123,124]**

When the zinc atom is coordinatively unsaturated or when the oxygen atoms bound to zinc have a low electron density rising from mesomeric or inductive effects, the compounds can easily form complexes with coordinative reagents like pyridine and TMEDA.

In some cases, alkylzinc compounds containing oxygen are subject to redistribution equilibria.**[125,126]** This is shown in solution by the presence of different species. For example, compounds of general formula $R_6Zn_7(OMe)_8$ can be isolated from solutions of $[RZn(OMe)]_4$ ($R = Et, Me$). The structure of these aggregates, as shown in Figure 34, consists of two Zn_4O_4 cubic

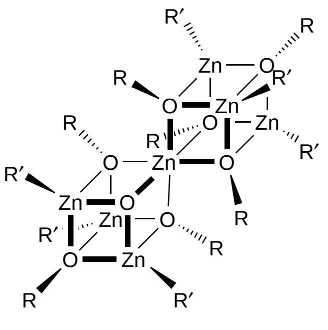

Figure 34 Structure of $(RO)_8Zn_7R'_6$

cores sharing a zinc atom. Interestingly, it has been found that the related compound $(ICH_2)_6Zn_7(MeO)_8$ is cleanly formed when a solution of ethylzinc methoxide and diiodomethane is photochemically (*see Photochemistry*) irradiated.[127]

In the last years, a large number of alkylzinc alkoxide or aryloxide derivatives have been prepared and structurally characterized. They have gained interest for their valuable catalytic activity for various reactions including enantioselective alkylation of aldehydes, asymmetric epoxidation of α,β-unsaturated ketones, and the copolymerization of carbon dioxide with epoxides (Section 6). Some selected averaged bond lengths found in organozinc compounds containing a zinc–oxygen bond are summarized in Table 9.

3.2.2 *Other Organozinc Compounds Containing Oxygen*

The dialkylzinc compounds are extremely moisture sensitive and even react explosively with bulk water. Nevertheless, cryoscopic studies carried out on the controlled hydrolysis of diethylzinc show the formation of organozinc hydroxide EtZnOH as intermediate.[130,131] This intermediate, which is thought to have the dimeric structure $(EtZnOH)_2$, is very unstable and reacts further to give polymers of the form $Et(ZnO)_n$ (equation 19). Some of these products exhibit a good catalytic activity for the polymerization of lactones and cyclic ethers.

$$nR_2Zn + nH_2O \longrightarrow [nRZnOH] \longrightarrow R(ZnO)_nH + (n-1)RH \tag{19}$$

The stabilization approach with bulky ligands allowed the isolation of the stable alkylzinc hydroxide dimer, that is, $[\{Zn(\mu\text{-}OH)C(SiMe_2Ph)_3\}_2]$ (Figure 35), obtained by reaction of $(Me_2PhSi)_3CZnCl$ with NaOH.[132] The hydroxy group is characterized by a sharp ν(OH) IR absorption at 3680 cm^{-1}.

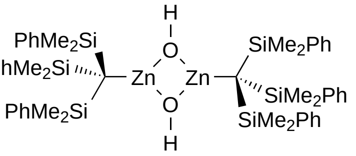

Figure 35 Structure of dimeric $[\{Zn(\mu\text{-}OH)C(SiMe_2Ph)_3\}_2]$

Table 9 Average bond lengths for some structurally characterized organozinc compounds containing a zinc–oxygen bond

Compound	Zn–C (Å)	Zn–O (Å)	E–O/[E] (Å)
$(MeZnOMe)_4$	1.95	2.08	1.43/[C]
$(MeZnO\text{-}t\text{-}Bu)_4$	1.96	2.07	1.46/[C]
$(MeZnOCHPhCH_2NHMe)_3$	1.97	2.00	1.41/[C]
$[Me_3SiCH_2ZnO(\text{-}2,4,6\text{-}t\text{-}Bu_3C_6H_2)]_2$	1.95	1.99	1.39/[C]
$[(PhMe_2Si)_3CZnOH]_2$	1.95	1.90	–
$(MeZnOSiEt_3)_4$	1.96	2.08	1.67/[Si]
$(EtZnOBMes_2)_2$	1.94	1.97	1.34/[B]
$[EtZnO(9\text{-}BBN)]_4$	1.94	2.11	1.37/[B]

Data taken from *The CSD System*[128] using *ConQuest*.[129]

Zinc siloxides derived from Si–OH species have received considerable attention in recent years, since they can be used as precursors for metal silicates and mixed-metal oxide systems as well as for models for heterogeneous silica-supported catalytic systems and complex zeolite systems. A polyhedral zinc siloxane compound, which was obtained in the reaction between dimethylzinc and trimethylsilanol, has been reported in 1965.[133] More recently, di-, tri-, and tetranuclear compounds of this kind have been prepared; the nature of the product being dependent on the molar ratio of the monosilanol to the alkylzinc compounds and on the steric demand (*see Steric Effect*) of the substituents at both the oxygen and zinc atoms.[134,135] The structures for the di- and tetranuclear species are similar to those found with alkoxide derivatives (Figure 32). In contrast, the trinuclear alkylzinc siloxides show a specific type of association, that is, two four-membered rings sharing a zinc atom (Figure 36). Recently, larger aggregates which remain soluble in organic solvents, have been prepared using the silanetriol $RSi(OH)_3$ [$R = 2,6\text{-}i\text{-}Pr_2C_6H_3N(SiMe_3)$]. Its reaction with an excess of Me_2Zn in THF/hexane at room temperature led to the neutral compound $[Zn_4(THF)_4(MeZn)_4(O_3SiR)_4]$,[136] while the ionic zinc siloxane $(LZnLiO_3SiR)_4$ was obtained when MeLi and N,N,N',N'-tetramethyl-1,-4-phenylenediamine (L) were present in the reaction mixture.[137] The molecular structure of the neutral aggregate exhibits a $Zn_8Si_4O_{12}$ core in which the zinc atoms are in a variety of geometries and coordination environments (Figure 36).

Recently, some interest in the chemistry of metal diorganoboryloxides $[M(OBR_2)]$ has emerged from their potential catalytic activity. Some alkylzinc diorganoboryloxides $[RZn(OBR'_2)]$ have been prepared with the expectation that the $p_\pi - p_\pi$ interaction between boron and oxygen may reduce π-donor properties of the latter, and consequently decrease the tendency for autoassociation to afford a coordinatively unsaturated boron atom.[138] Unfortunately, the diverse results obtained so far show no significant difference between diorganoboryloxides and typical alkoxides in their reactivity with dialkylzinc. Typical Zn_4O_4 heterocubane cores were obtained when $(9\text{-}BBN)_2O$ (9-BBN = 9-Borabicyclo-3,3,1-non-9-yl) or $(Et_2B)_2O$ was treated with Et_2Zn in toluene at room temperature (Figure 32). A less classic discrete dimer $[(Mes_2BO)ZnEt]_2$, comparable to the dimeric alkoxides $[(2,6\text{-}i\text{-}Pr_2C_6H_3O)\text{-}ZnCH_2SiMe_3]_2$ and $[(2,4,6\text{-}t\text{-}Bu_3C_6H_2O)ZnCH_2SiMe_3]_2$ (Figure 32), has been obtained in the reaction of dimesitylboronic acid (Mes_2BOH) with diethylzinc in toluene at 0 °C.[139]

The preparation and reactions of alkylzinc enolates have been studied. The main methods for their synthesis are metal exchange between lithium enolates and zinc chloride,[140] deprotonations of carbonyl compounds with

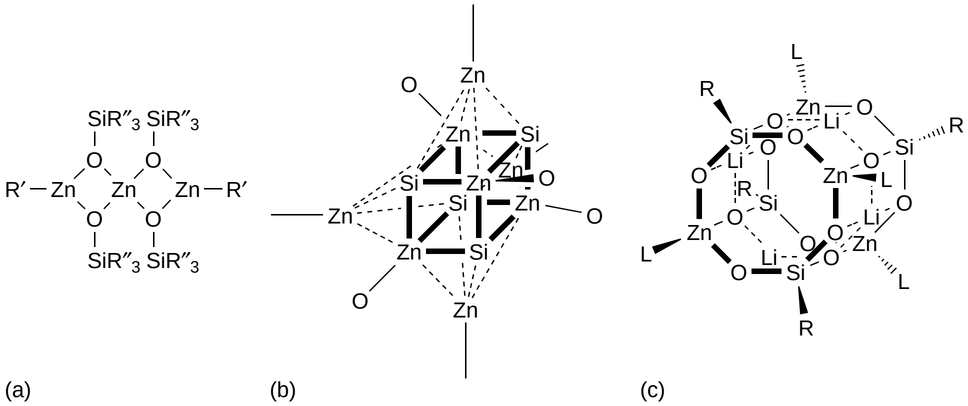

Figure 36 Structures of the trinuclear aggregate $[Zn(R'Zn)_2(OSiR''_3)_4]$ (a), the core of the neutral $[Zn_4(THF)_4(MeZn)_4(O_3SiR'')_4]$ (b) and the ionic $(LZnLiO_3SiR)_4$ (c) (R = 2,6-i-$Pr_2C_6H_3N(SiMe_3)$)

basic alkylzinc amides,[141] reduction of α-bromo carbonyl compounds[142] (Reformatsky reaction) and addition reactions of dialkylzincs to α,β-unsaturated carbonyl and heterocarbonyl compounds[143–145] (Scheme 7). Spectroscopic studies of the resulting alkylzinc ketone enolates suggest the presence of oxygen- rather than carbon-bound metal species. Oxygen-metalated compounds have also been found in N-protected α-amino-substituted zinc ester enolates.[146] In this case, the zinc atom is fixed via N,O-chelation, and intramolecular aggregates of various composition are formed. The same N,O-chelation occurs in ethyl zinc derivatives of β-carbonyl sulfoximines with formation of dimeric aggregates through dative Zn–O interactions in the case of β-ketosulfoximine, and through Zn–C interactions in the case of β-amidosulfoximine.[147]

Organozinc carboxylates formally derived from carboxylic acids are prepared *via* protonolysis of diorganozinc compounds by carboxylic acids (equation 20). Although dimeric carbamate complexes of the general formula $[RM(E_2CNR'_2)]_2$ (E = S or Se, R = Me or Et, R′ = alkyl, M = Zn or Cd) are readily formed by reaction of CE_2 with $RM(NR'_2)$[148,149] (equation 21), insertion (*see Insertion*) of CO_2 into methylzinc diethylamide leads to unusual species such as the tetramers $[Me_2Zn_4(O_2CNEt_2)_6]$ and $[Me_4Zn_4(O_2CNEt_2)_4]$[150,151] (Figure 37). Diorganozinc compounds are typically unreactive towards insertion of carbon dioxide into the zinc–carbon bond with one exception, that is, the specific activation of diethylzinc by N-methylimidazole.[152]

$$ZnR_2 + R'COOH \longrightarrow RZnO_2CR' + RH \qquad (20)$$

$$RZnNR'_2 + CE_2 \longrightarrow RZnE_2CNR'_2 \qquad (21)$$

$$E = O, S, Se$$

3.3 Alkylzinc Compounds Containing a Zinc–Sulfur or Zinc–Selenium Bond

Heteroleptic (*see Heteroleptic Compound*) alkylzinc thiolate and selenolate compounds present two major interests; they can be used as models for metalloenzyme activity[153] and as precursors for the formation of binary metal sulfides and selenides.[154] Furthermore, these compounds tend to

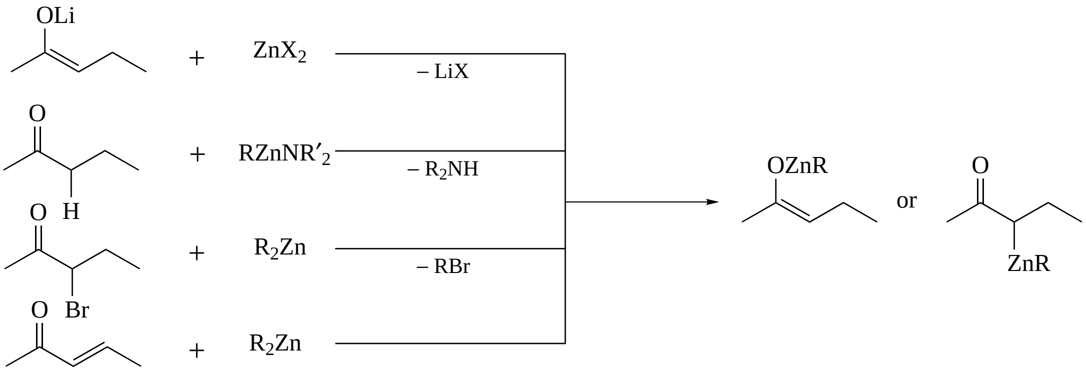

Scheme 7

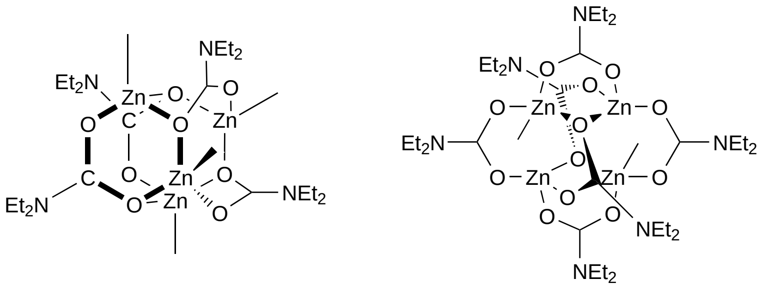

Figure 37 Structures of $[Me_4Zn_4(O_2CNEt_2)_4]$ and $[Me_2Zn_4(O_2CNEt_2)_6]$

oligomerize leading to a variety of inorganic rings (*see* ***Inorganic Ring Systems***) or larger aggregates with interesting optical and electronic properties.

3.3.1 Preparation

The title compounds are usually obtain in a straightforward manner and in almost quantitative yields by alkane elimination process between a dialkylzinc compound ZnR_2 and the desired thiol R′SH or selenol R′SeH species[155,156] (equation 18). This reaction works equally well in hydrocarbon solvent or neat solution. If thiocyanogen $(SCN)_2$ is used as the reagent, then alkylzinc thiocyanate derivatives (RZnSCN) are obtained.[157]

A different strategy, involving chlorotrimethylsilane elimination from the reaction of a Zn^{II} or Cu^{I} halide with (trimethylsilyl)arenethiolates $RSSiMe_3$, has been described for the preparation of zinc- and copper arenethiolates[158] (equation 22).

$$ArSSiMe_3 + RZn\text{–}Cl \longrightarrow ArS\text{–}Zn\text{–}R + ClSiMe_3 \qquad (22)$$

Although insertion (*see Insertion*) of elemental sulfur into the zinc–carbon bond of dialkylzinc has not been studied extensively, it has been described in the special case of diethylzinc for the preparation of EtZn(SEt)[159] (equation 23).

$$Et_2Zn + \frac{1}{8}S_8 \longrightarrow EtS\text{–}Zn\text{–}Et \qquad (23)$$

Mixed alkylzinc dithio- or diselenocarbamates of general formula $RZnE_2CNEt_2$ ($R = Me_3SiCH_2, Me_3C$; $E = S, Se$) are prepared by two different ways, namely, ligand redistribution between the corresponding dialkylzinc (R_2Zn) and bis(ditio- or bis(diseleno- carbamato)zinc compounds[160] (equation 24), and insertion of CE_2 into the zinc–nitrogen bond of a mixed alkylzinc amide $RZnNR'_2$ which was first reported by Noltes (Section 3.2.2 equation 21).[161]

$$(R'_2NCE_2)_2Zn + R_2Zn \longrightarrow 2R\text{–}ZnE_2CNR'_2 \qquad (24)$$
$$E = O, S, Se$$

3.3.2 Structure

Alkylzinc thiolate compounds are insoluble or poorly soluble in hydrocarbon solvents, indicating their tendency to form aggregates. Indeed, all the compounds that have been structurally characterized obey the empirical formula $(RZnSR')_n$ with values of n varying from 2 to 10. As shown in Figure 38, these species reveal a remarkable structural chemistry.[158] The dimeric complex $(Me_3SiCH_2ZnSCPh_3)_2$ possesses a planar Zn_2S_2 array with trigonal planar zinc atoms and trigonal pyramidal sulfur centers. The core of the trimers $[Me_3SiCH_2ZnS\text{-}i\text{-}Pr_3C_6H_2]_3$ and $[Me_3SiCH_2ZnS\text{-}t\text{-}Bu_3C_6H_2]_3$ consists of an almost planar six-membered Zn_3S_3 ring, suggesting that the six nonbonded electron pairs of the sulfur atoms tend to delocalize (*see Delocalized Bonding*). More complicated arrays are found in the solid-state structure of the pentamer $[MeZn(S\text{-}t\text{-}Bu)]_5$[162] and the octamer $[MeZn(S\text{-}i\text{-}Pr)]_8$.[163] Interestingly, the octameric aggregation of the last compound is not retained in benzene solution where hexamers are observed. Finally, a wurtzite-like structure has been found for the decamer $[EtZn(SEt)]_{10}$.[159] The pentamer $[MeZn(S\text{-}t\text{-}Bu)]_5$ readily reacts with nitrogenous bases like pyridine and 1,3,5-trimethylhexahydro-1,3,5-triazine to form stable adducts of the dimeric species,[164] which, in contrast to the parent oligomers, present a good solubility in organic solvents. A selection of average bond lengths in organozinc compounds containing a zinc–sulfur bond can be found in Table 10.

Recently, some mononuclear alkylzinc complexes containing a zinc–sulfur bond could be prepared and structurally

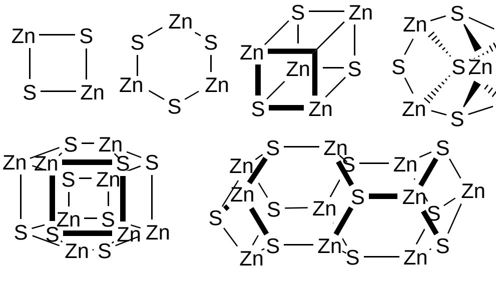

Figure 38 Structure of the $[RZn(SR')]_n$ cores that have been structurally characterized

Table 10 Average bond lengths for some structurally characterized organozinc compounds containing a zinc–sulfur bond

Compound	Zn–C (Å)	Zn–S (Å)	C–S (Å)
$(Me_3SiCH_2ZnCPh_3)_2$	1.97	2.40	1.88
$(MeZnS\text{-}t\text{-}Bu)_5$	2.01	2.43	1.87
$(EtZnSEt)_{10}$	2.09	2.40	2.02
$MeZnS\text{-}t\text{-}Bu\cdot [(MeNCH_2)_3]_2$	1.97	2.39	1.86
$MeZn\text{-}t\text{-}Bu\cdot (C_6H_5N)_2$	1.98	2.41	1.85
MeZn[(TImz)$_2$(Imz)BH]^a	1.99	2.40	1.71
MeZn[(TImz)$_2$BH$_2$]^a	1.97	2.36	1.71

^{a}TImz = mercaptoimidazolyl; Imz = imidazolyl. Data taken from *The CSD System*[128] using *ConQuest*.[129]

characterized using the monoanionic bis- and tris (mercaptoimidazolyl)hydroborate ligands[165,166] (Figure 39). Their preparation follows the metathesis reaction between the corresponding thallium complexes and dimethylzinc (equation 25). The complexes with tridentate ligands show a classic pseudotetrahedral coordination geometry around the zinc atom, but an interesting feature is found in the solid-state structure of the bis(mercaptoimidazolyl)hydroborate derivative, that is, the presence of a 'boat like' eight-membered ring that allows for intramolecular (*see Intramolecular*) interaction between the zinc atom and one BH ligand (d $Zn\cdots B = 2.88$ Å; d $Zn\cdots H = 1.77$ Å). The compounds are strictly monomeric in the solid state but undergo redistribution reactions in solution to give the homoleptic (*see Homoleptic Compound*) species L_2Zn. In contrast, a monomeric solid-state structure which subsists in solution has been found for [MeZn(PATH)] (PATH = 2-methyl-1-[methyl-(2-pyridin-2-ylethyl)amino]propane-2-thiolate) (Figure 40). This complex is a valuable synthetic precursor to other complexes that are good models for the catalytic site of metalloenzymes.[153]

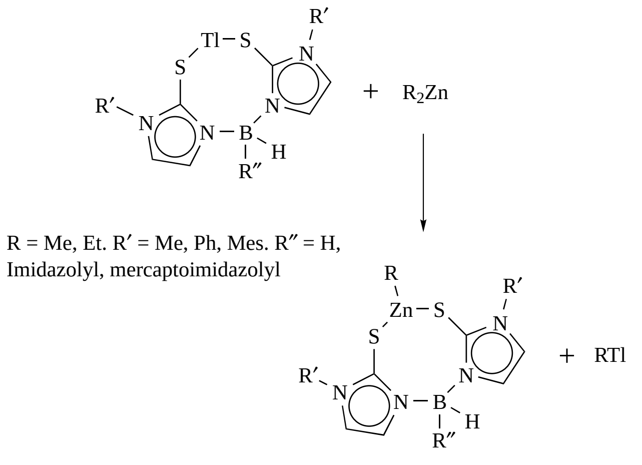

R = Me, Et. R′ = Me, Ph, Mes. R″ = H, Imidazolyl, mercaptoimidazolyl

(25)

So far, the only alkylzinc selenolate compound to be structurally characterized is the trimeric $[Me_3SiCH_2ZnSe\text{-}2,4,6\text{-}t\text{-}Bu_3C_6H_2]_3$. In contrast with the parent compound $[Me_3SiCH_2ZnS\text{-}2,4,6\text{-}t\text{-}Bu_3C_6H_2]_3$, the central Zn_3Se_3 possesses a twist structure with more pyramidal geometries at selenium.[167] However, it is worth mentioning that various diselenolato- and ditellurolatozinc compounds have been prepared and their adducts with nitrogenous bases such as TMEDA and pyridine could be structurally characterized.[168–170] Furthermore, the reaction of sterically hindered chalcogenolato compounds $[Zn(EAr^*)_2]_2$ ($E = S$, Se; $Ar^* = 2,4,6\text{-}t\text{-}Bu_3C_6H_2$) with excess tert-butylisocyanide gave the first examples of well-characterized isocyanide complexes of zinc $Zn(EAr^*)_2(CN\text{-}t\text{-}Bu)_2$.[171]

Alkylzinc thio- and selenocarbamate derivatives are commonly air-sensitive white crystalline solids, with the thiocarbamate derivatives being more soluble in organic solvents than the selenocarbamate derivatives. They have been found to be dimers of general formula $[RZnE_2CNR'_2]_2$, in which each carbamate chelates one metal atom and bridges to the next one (Figure 41). The zinc atoms are four-coordinate with a distorted tetrahedral geometry.

Two new bonding modes have been found for the monothiocarbamato ligand in the novel tetrameric complex $[Et_4Zn_4(OSCNEt_2)_2(NEt_2)_2]$, which was prepared by reaction of $EtZnNEt_2$ with carbonyl sulfide.[172] The cage compound contains two six-membered Zn_2CNOS cycles and both the oxygen and sulfur are binucleating (Figure 42).

3.4 Organozinc Compounds Containing a Zinc–Nitrogen Bond

In recent years, the interest for the preparation of alkylzinc amides has been motivated by their potential application as catalyst for polymerization of propylene oxide, and also as precursors for the MOCVD (*see Metal–Organic Chemical Vapor Deposition*) process.

3.4.1 *Preparation*

Even though zincation of secondary amines was already studied by Frankland in 1856 and 1867, it is only in the past few decades that some efforts were made to isolate and characterize the products. Numerous compounds of the type $RZnNR'_2$ or $Zn(NR'_2)_2$ can now be prepared using two principal procedures, namely the zincation of amines with simple dialkylzinc compounds[173–175] (equation 26) and the metathesis reaction of alkali metal amides with anhydrous zinc dihalide (equation 27).

$$R'_2NH + R_2Zn \longrightarrow R'_2N\text{–}Zn\text{–}R + RH \qquad (26)$$

$$R'_2NLi + RZnX \longrightarrow R'_2N\text{–}Zn\text{–}R + LiX \qquad (27)$$

The first step of the zincation route is the formation of an adduct between the amine and the dialkylzinc compound. Such a complex can rarely be isolated since one of the Zn–C bonds readily suffers protonolysis. Mechanistic studies of the

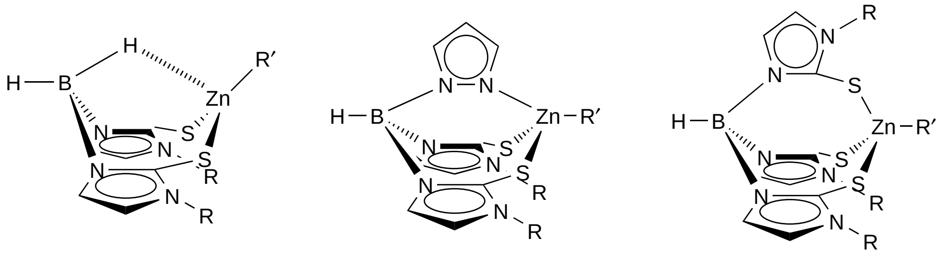
H
H
B
R′
Zn
N
S
N
S
R
N
N
R
H
B
N
N
Zn
R′
N
S
N
S
R
N
N
R
R
N
N
S
H
B
Zn
R′
N
S
N
S
R
N
N
R

Figure 39 Zinc alkyls stabilized by (mercaptoimidazolyl)hydroborato ligands

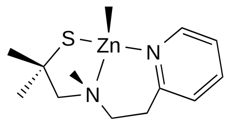

Figure 40 Structure of MeZn(PATH)

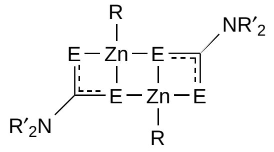
R
NR′2
E
Zn
E
E
Zn
E
R′2N
R

Figure 41 Dimeric organozinc thio- and selenocarbamates. E = S, Se

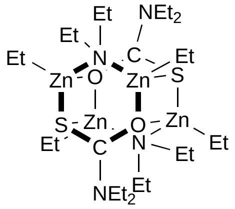
Et
NEt2
Et
N
C
Et
Et
Zn
O
Zn
S
S
Zn
O
Zn
Et
C
N
Et
Et
NEt2
Et

Figure 42 Structure of $Et_4Zn_4(OSCNEt_2)_2(NEt_2)_2$

protonolysis step in the reaction of various dialkylzinc compounds with cyclohexylamine and *p*-toluidine, have shown an S_E1 mechanism.[176] The reaction can easily be stopped at the mono substitution product because the remaining C–Zn bond is far less reactive than in the parent dialkylzinc compounds.

A very fast reaction occurs between dialkylzinc compounds and the more acidic amide and thioamide derivatives of the type HNPhCXR′ (X = O or S), leading to RZnNPhCXR′ complexes. An alternative route for the preparation of such compounds is the insertion reaction (*see Insertion*) of iso- and isothio-cyanates into the Zn–O and Zn–N bond of monosubstituted organozinc derivatives[161] (equations 28 and 29).

$$\text{R–Zn–OR}' + \text{R}''\text{NCX} \longrightarrow \text{R–Zn–NR}''\text{C(X)OR}' \qquad (28)$$

$$\text{R–Zn–NR}'_2 + \text{R}''\text{NCX} \longrightarrow \text{R–Zn–NR}''\text{C(X)NR}'_2 \qquad (29)$$

Some heteroleptic (*see Heteroleptic Compound*) alkylzinc amides have been prepared by addition reaction of dialkylzinc compounds (ZnR_2) on 1,4-di-*tert*-butyl-1,4-diaza-1,3-butadiene (*t*-BuN=CHCH=N-*t*-Bu). Extensive studies[177,178]

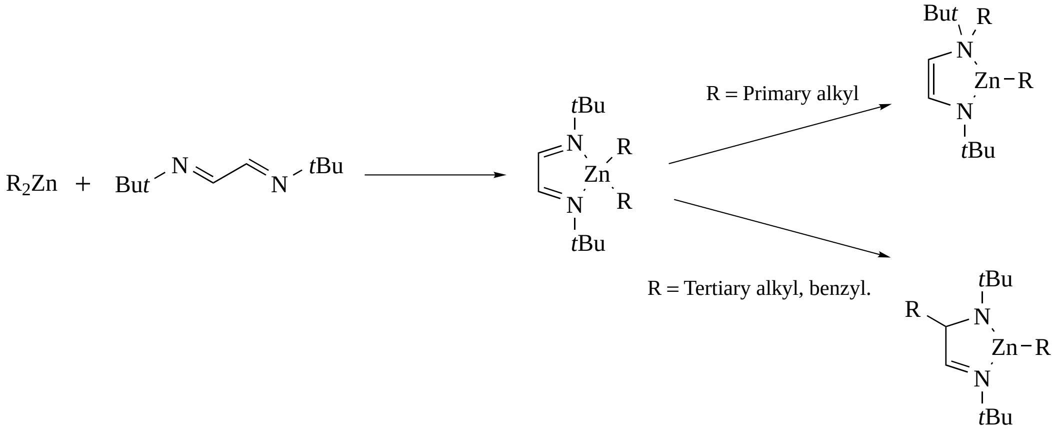
R2Zn + But N N tBu
tBu
N
R
Zn
N
R
tBu
R = Primary alkyl
But R
N
Zn−R
N
tBu
R = Tertiary alkyl, benzyl.
tBu
R
N
Zn−R
N
tBu

Scheme 8

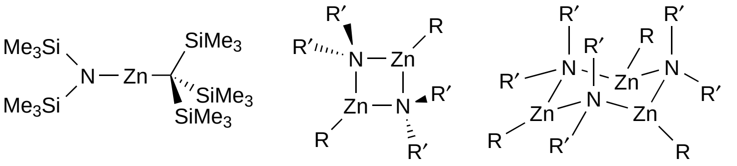

Figure 43 Structure of $(R'_2NZnR)_n$

have shown that the addition is regioselective (*see Regioselectivity*) to the *N*-alkylated product RZn(*t*-BuN(R)CH=CHN-*t*-Bu) when R is a primary alkyl group, and to the *C*-alkylated product RZn(*t*-BuNCH(R)CH=N-*t*-Bu) when R is a tertiary or benzylic alkyl group (Scheme 8). The reaction probably follows a radical mechanism subsequent to the initial formation of the coordination complex $R_2Zn\cdot(t\text{-BuN=CHCH=N-}t\text{-Bu})$.

Very recently, the preparation of zinc β-diiminate derivatives became the subject of interest due to their catalytic activity in the copolymerization of CO_2 with epoxides.[179–181] They can be prepared in high yields by direct reaction of the corresponding β-diimines with dialkylzinc compounds or by treatment of the β-diimine-lithium salts with zinc halide followed by an alkylation reaction (Scheme 9).

3.4.2 Structure

Nitrogen has only one nonbonding electron pair (*see Lone Pair*); consequently, alkylzinc amide compounds generally do not form the typical cubic structure found with alkylzinc alkoxide derivatives. Various alkylzinc amides derived from secondary amines and few derived from primary amines have been structurally characterized. Depending on the steric demand (*see Steric Effect*) of the substituents at both the zinc and the nitrogen atom different degrees of association are observed in solid state. For example, the highly sterically hindered $(Me_3Si)_3CZn\text{–}N(H)Si\text{-}i\text{-}Pr_3$ and $(Me_3Si)_3CZn\text{–}N(SiMe_3)_2$ exist as monomers[182] with an almost linear C–Zn–N center for the latter. Dimers with a central planar four-membered ring are formed with less bulky primary amines such as 2,4,6-trimethylaniline, 2,6-diisopropylaniline or triisopropylsilylamine[174] (Figure 43). This coordination mode is also typical for alkylzinc dialkylamide compounds. Trimers with a chair-shaped Zn_3N_3 ring are obtained in the reaction of dimethyl- or diethylzinc with *tert*-butylamine and naphtylamine.[175] The unusual structure observed in the dimeric compound $\{(\eta^1\text{-Cp})Zn\}_2(\mu\text{-Cp})\{\mu\text{-N}(SiMe_3)_2\}$, readily prepared by combining Cp_2Zn and $Zn[N(SiMe_3)_2]_2$ in hot benzene, has already been mentioned in Section 2.3.3[54] (Figure 12). Table 11 lists some selected bond lengths found in organozinc compounds containing a Zn–N bond.

Finally, as a result of intra- or intermolecular (*see Intermolecular*) coordination, a large variety of association modes is observed when the amine residue contains electron-donating atoms in appropriate position. Two extremely rare examples of monomeric three-coordinate zinc complexes have been obtained by the reaction of R_2Zn ($R = Me$, Et) with *N*-(2-diphenylphosphinophenyl)-2,6-diisopropylaniline in Et_2O at – 35 °C.[183] As shown in Figure 44, the molecular

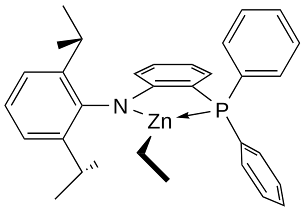

Figure 44 Structure of EtZn{*N*-(2-diphenylphosphinophenyl)-2,6-diisopropylanilide}

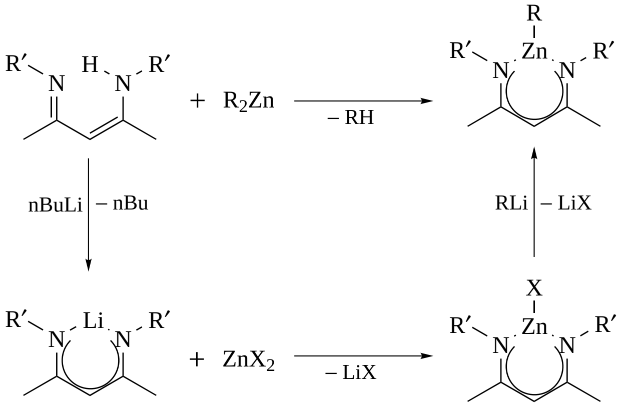

Scheme 9

Table 11 Average bond lengths for some structurally characterized organozinc compounds containing a zinc–nitrogen bond

Compound	Zn–C (Å)	Zn–N (Å)	E–N(Å)/E
$(Me_3Si)_3CZnN(SiMe_3)_2$	1.94	1.84	1.73/Si
$(MeZnNPh_2)_2$	1.95	2.07	1.44/C
$(MeZnNHSi\text{-}i\text{-}Pr_3)_2$	1.94	2.03	1.73/Si
$(EtZnNHSi\text{-}i\text{-}Pr_3)_2$	1.96	2.03	1.74/Si
$[Me_3SiCH_2ZnNH(2,6\text{-}i\text{-}Pr_2C_6H_3)]_2$	1.98	2.04	1.42/C
$(EtZnNH\text{-}t\text{-}Bu)_3$	1.98	2.02	1.48/C

Data taken from *The CSD System*[128] using *ConQuest*.[129]

structure of the ethyl derivative, determined by X-ray analysis, indicates a trigonal planar geometry at zinc (sum of the bond angles = 359.81°) and typical distances for the three different bonds Zn–C (1.956 Å), Zn–P (2.445 Å), and Zn–N (1.911 Å). The compounds were found to be highly sensitive towards hydrolysis, but thermally very stable under inert atmosphere as they do not show decomposition after three days at 100 °C in toluene.

The reaction of N,N,N'-trimethylethylene- or propylenediamine ($HNMe(CH_2)_nNMe_2$; $n = 2$ or 3) with dimethyl- or diethylzinc gives dimeric molecular units of general formula $[RZnNMe(CH_2)_nNMe_2]_2$ (Figure 45). A central four-membered ring is formed with bridging nitrogen atoms and two five- or six-membered side rings are respectively produced by intramolecular (*see Intramolecular*) coordination of the amino group.**[184]**

Bis- and tris(pyrazolyl)borato ligands have been widely used to stabilize a variety of alkylmetal complexes among which several alkylzinc derivatives.**[185]** Stable monomeric three-coordinate alkylzinc complexes, $\{\eta^2\text{-}H_2B(3\text{-}t\text{-}Bupz)_2\}ZnR$, could be prepared by reaction of R_2Zn with the thallium derivative $Tl\{\eta^2\text{-}H_2B(3\text{-}t\text{-}Bupz)_2\}$ (equation 30). In these complexes, both the B–H and the Zn–C bonds are potential reactive sites; while ketones and aldehydes react at the former, protic reagents react at the subsequent.**[186]** The tris(pyrazolyl)hydroborato ligand allowed the formation of monomeric four-coordinate zinc alkyl derivatives.**[187]** A comparison with analogous magnesium (*see* ***Beryllium & Magnesium: Organometallic Chemistry***) complexes has shown that the Mg–C bond in these systems is more reactive than the related Zn–C bond, especially with respect to CO_2 insertion (*see Insertion*).

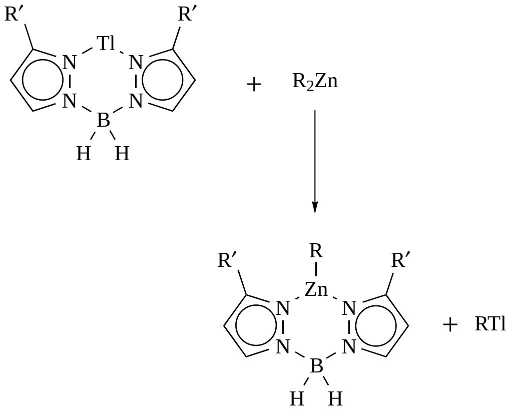

(30)

Although the cubic structure with a Zn_4N_4 core is not as common as with alkoxy-zinc derivatives, it was recurrently found in tetrameric organozinc phosphoraneiminato complexes $[RZn(NPR'_3)]_4$. Several compounds with different R and R′ groups (R′ = Me, Et; R = Me, n-Bu, C≡CR″) were prepared in good yields by the reaction of $[BrZn(NPR'_3)]_4$ with the corresponding organolithium reagent in hexane**[188,189]** (equation 31). All the complexes that have been characterized by X-ray crystallography present a heterocubane Zn_4N_4 structure – only slightly distorted from the cube – where the zinc atoms are linked via μ^3-N bridges of the phosphoraneiminato groups. In the Zn_4N_4 frame, all the bond angles are close to 90° and the Zn–N bond distances have an average value of 2.07 Å (Figure 46).

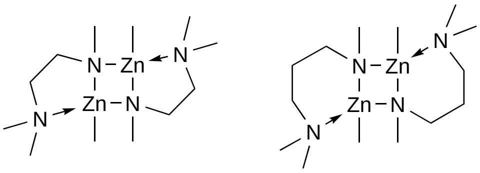

Figure 45 Intramolecular coordination in $[RZnNMe(CH_2)_nNMe_2]_2$ ($n = 2, 3$)

$$[BrZn(NPR'_3)]_4 + 4RLi \xrightarrow{\text{hexane}} [RZn(NPR'_3)]_4 + 4LiCl \qquad (31)$$

R′ = Me, Et

R = Me, n-Bu, CCPh, $CCSiMe_3$, $CCCCSiMe_3$

3.5 Alkylzinc Compounds Containing a Zinc–Phosphorus or Zinc–Arsenic Bond

3.5.1 Preparation

Some interest in group 12 phosphide and arsenide complexes has come from their possible applications as precursors for II/V semiconductors (*see* ***Semiconductors***). They can be prepared by two different ways, namely, by metallation reaction of phosphines and arsines with diorganozinc compounds (equation 32), and by transmetallation reaction between organozinc halides and lithium salt of the corresponding phosphines and arsines (equation 33).

$$R'_2E\text{–}H + R_2Zn \longrightarrow R'_2E\text{–}Zn\text{–}R + RH \qquad (32)$$

E = P, As

$$R'_2E\text{–}Li + RZnX \longrightarrow R'_2E\text{–}Zn\text{–}R + LiX \qquad (33)$$

E = P, As

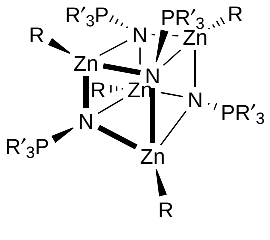

Figure 46 Structure of organozinc phosphoraneiminato complexes $[RZn(NPR'_3)]_4$

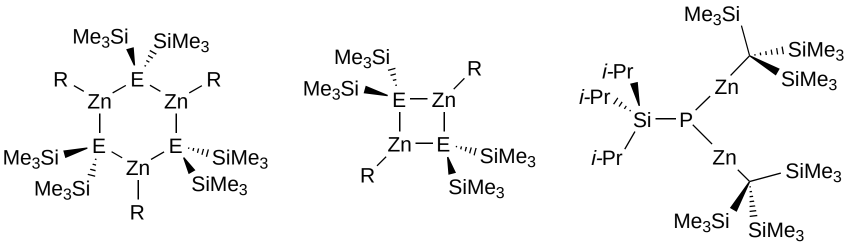

Figure 47 Structure of $(RZnER'_2)_n$ (E = P, As) and $[(Me_3Si)_3CZn]_2$ PSi-*i*-Pr$_3$

3.5.2 Structure

So far only few compounds of this family have been structurally characterized. The nonbonding electron pair present on the group 15 atom leads to intermolecular (*see Intermolecular*) associations similar to those observed in organozinc amides. The degree of association is controlled by the steric demand of the substituents at the zinc atom. For example, in solid state the general compound $RZn[E(SiMe_3)_2]$ (E = P or As) can form trimers[190,191] with a central cyclic Zn_3E_3 core in a twist-boat conformation (E = P, R = Me, Et, n-Butyl; E = As, R = Me, Et) or dimers[192,193] with a central planar Zn_2E_2 ring (E = P, R = CH_2SiMe_3) (Figure 47). An intermediate position is found with *i*-PrZnP$(SiMe_3)_2$ which shows in solution a temperature-dependent equilibrium of dimeric and trimeric species, and gives a 1:1 mixture of these two oligomers in crystalline state.[194] So far, the only compound found to be monomeric both in crystalline state and in solution, is the binuclear bis[tris(trimethylsylil)methylzinc]triisopropylsilylphosphandiide $\{[(Me_3Si)_3CZn]_2PSi\text{-}i\text{-}Pr_3\}$ obtain in the reaction of tris(trimethylsilyl)methylzinc chloride with lithium triisopropylsilylphospanide (equation 34). The crystalline structure of this compound shows a very short zinc–phosphorus bond of 2.23 Å, owing to the low-coordination state of the phosphorus and zinc atoms.[195]

$$2(Me_3Si)_3CZn\text{–}Cl + 2Li\text{–}P(H)Si\text{-}i\text{-}Pr_3 \longrightarrow i\text{-}Pr_3SiP[ZnC(SiMe_3)_3]_2 + 2LiCl + H_2PSi\text{-}i\text{-}Pr_3 \quad (34)$$

A series of compounds with general formula $[RMAs(t\text{-}Bu)_2]_n$ (R = Me, *t*-Bu; M = Zn, Cd, Hg) has been studied and it was found that their stability decreases in the order Zn > Cd ≫ Hg. Table 12 summarizes some representative average bond distances and bond angles found in organozinc compounds containing a phosphorus–or arsenic–zinc bond.

3.6 Alkylzinc Compounds Containing a Zinc-metal Bond

A number of compounds having a direct zinc transition metal bond are known for long time, that is, zinc-bis(transition metal) such as $Zn[Co(CO_4)]_2$[196] and transition metal zinc halides such as $(CO)_4Fe(ZnCl)_2$.[197] However, organozinc-transition metal compounds RZn–TM are comparatively more recent. They can be prepared by hydrocarbon elimination between a diorganozinc derivative and a transition metal hydride[198] (*see Hydrides*) (equation 35), but dialkyl- and diarylzinc compounds usually fail to react or react very slowly. Furthermore, when they do react they give unstable products that show a very strong tendency to disproportionate and cannot be isolated[199] (equation 36).

$$L_xMH + R_2Zn \longrightarrow L_xM\text{–}ZnR + RH \quad (35)$$

$$L_xM\text{–}ZnR \longrightarrow \tfrac{1}{2}R_2Zn + \tfrac{1}{2}[L_xM]_2Zn \quad (36)$$

Table 12 Average bond lengths and bond angles for some structurally characterized organozinc compounds containing a zinc–phosphorus or zinc–arsenic bond

Compound	E	Zn–C(Å)	Zn–E(Å)	Zn–E–Zn(°)	E–Zn–E(°)
$[(Me_3Si)_3CZn]_2PSi\text{-}i\text{-}Pr_3$	P	1.97	2.23	105.1	–
$[i\text{-}PrZnP(SiMe_3)_2]_2$		2.00	2.41	89.1	90.9
$[Me_3SiCH_2ZnP(SiMe_3)_2]_2$		1.97	2.41	89.2	90.8
$[i\text{-}PrZnP(SiMe_3)_2]_3$		1.99	2.41	115.8	111.7
$[EtZnP(C_6H_{11})_2]_3\cdot THF$		2.00	2.40	118.6	108.2
$[MeZnP(SiMe_3)_2]_3$		1.97	2.23	121.9	111.2
$[n\text{-}BuZnP(SiMe_3)_2]_3$		2.03	2.39	122.7	111.9
$[(Me_3Si)_3CZn]_2AsSi\text{-}i\text{-}Pr_3$	As	1.97	2.32		
$[tBuZnAs(t\text{-}Bu)_2]_2$		1.99	2.51	92.5	87.5
$[MeZnAs(SiMe_3)_2]_3$		1.96	2.46	123.8	109.3
$[EtZnAs(SiMe_3)_2]_3$		1.98	2.48	125.4	109.1

Data taken from The *CSD System*[128] using *ConQuest*.[129]

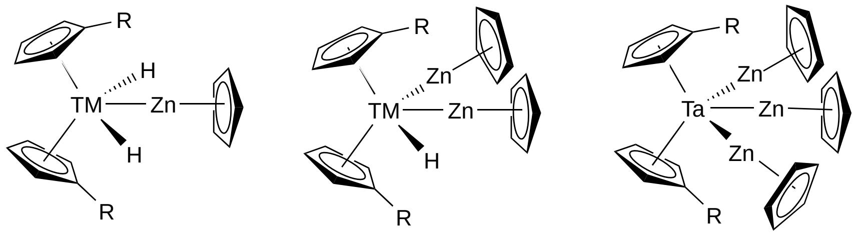

TM = Ta, Nb. R = H, Me.

Figure 48 Structure $Cp_2TMH_{3-n}(ZnCp)_n$ ($n = 1, 2, 3$)

However, it has been shown that Cp_2Zn is more reactive with transition metal hydrides (*see Hydrides*) and leads to more stable compounds. A number of complexes with different transition metals have been isolated by this route; these include derivatives of nickel (e.g. $Cp_6Ni_2Zn_4$),[200] manganese (e.g. $CpZnMn(CO)_5$),[201] rhodium (e.g. $[(dippp)Rh]_2(\mu\text{-}H)_2(\mu\text{-}ZnCp)_2$),[202] tantalum (e.g. $Cp'_2TaH_{3-n}(ZnCp)_n$, $n = 1, 2, 3$)[203] and niobium $Cp_2NbH_{3-n}(ZnCp)_n$, ($n = 1, 2$).[204] The greater reactivity of Cp_2Zn can be appreciated in its stoichiometric reaction with Cp_2NbH_3, which gives the disubstituted $Cp_2NbH(ZnCp)_2$ as the only product. The isolation of Cp_2NbH_2ZnCp requires the use of a coordinating solvent like THF to decrease the reactivity of Cp_2Zn. This last compound and the related $Cp'_2TaH(ZnCp)_2$ (Cp' = methylcyclopentadienyl) have been structurally characterized, they resemble the parent molecule Cp_2NbH_3 and Cp'_2TaH_3 with one or two hydrogens replaced by one or two ZnCp groups, respectively (Figure 48).

Stable organozinc transition metal compounds can also be obtained when the alkyl group bound to zinc is a chelating ligand (*see Chelating Ligands*) such as the (dimethylamino)propyl group $[Me_2N(CH_2)_3]$ or the 2-[(dimethylamino)methyl]penyl group ($2\text{-}C_6H_4CH_2NMe_2$) (Figure 49). A number of complexes with different transition metals have been isolated; that is, manganese, cobalt, molybdenum, and tungsten.[59] The crystal structure of $Me_2N(CH_2)_3ZnW(Cp)(CO)_3$, determined by X-ray crystallography, shows a tricoordinate zinc atom with a zinc–tungsten bond distance of 2.685 Å.

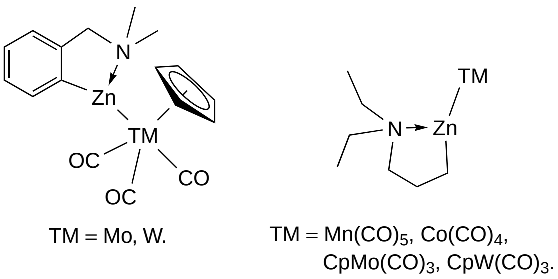

TM = Mo, W.

TM = $Mn(CO)_5$, $Co(CO)_4$, $CpMo(CO)_3$, $CpW(CO)_3$.

Figure 49 Intramolecular coordination in organozinc transition metal compounds

Organozinc compounds containing a zinc main-group metal bond are extremely rare. With the exception of compounds containing zinc–zinc and zinc–nickel bonds such as the clusters (*see Cluster*) $Cp'_6Ni_2Zn_4$ ($Cp'_6 = Cp_6$;[200] $Cp^*_2Cp_4$;[205] $(Me_3SiC_5H_3)_6$[206]), only few zincate derivatives (see Section 4.1) containing weak contacts between zinc and different metals such as Ba,[207] Li,[208] or Na have been structurally characterized (Figure 50).

It is also worth mentioning here that two compounds containing a Zn–Sn coordinate bond have been reported. The first of these is the sole example of a dialkyltin^{II} species (*see* ***Tin: Organometallic Chemistry***) stabilized by coordination to zinc-β-diketonate. It was obtained by reaction of bis[3-dimethylamino)propyl]zinc with bis(dibenzoylmethanato)tin (equation 37) and its molecular structure shows a Zn–Sn bond length of 2.634 Å.[209] The second compound is

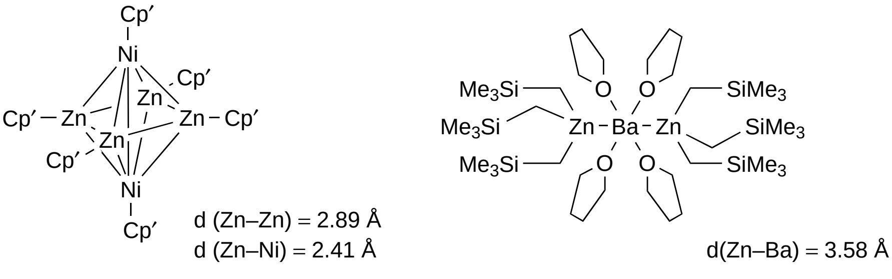

d (Zn–Zn) = 2.89 Å
d (Zn–Ni) = 2.41 Å

d(Zn–Ba) = 3.58 Å

Figure 50 Organozinc compounds containing Zn main-group metal bond

the heterodimetallic complex [MeSi{SiMe$_2$N(Tol)}$_3$Sn]$_2$Zn (Tol = p-toluyl), which was recently prepared together with the Cd and Hg derivatives, by reaction of [MeSi{SiMe$_2$N(p-Tol)}$_3$SnLi(OEt$_2$)] with the corresponding MCl$_2$ (M = Zn, Cd, Hg).[210] As shown in Figure 51, its molecular structure is unsymmetrical with only one stannate unit bound to zinc (d(Zn–Sn) = 2.578 Å).

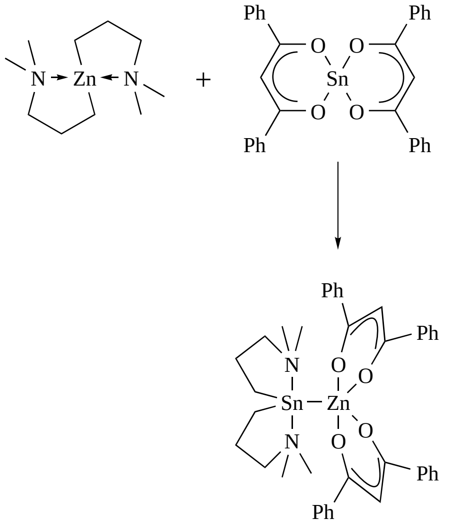

(37)

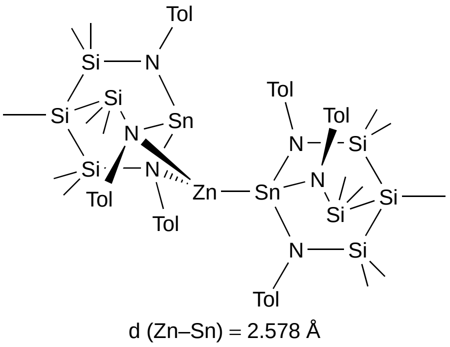

Figure 51 Structure [MeSi{SiMe$_2$N(Tol)}$_3$Sn]$_2$Zn

4 ALKYLZINC ANIONS AND CATIONS

4.1 Alkylzinc anions (*See Anion*)

The alkylzinc anions, defined as ate complexes (*see Ate Complexes*), are heterodimetallic systems which can be divided in two different classes, namely, the trialkylzincates of general formula $M^+R_3Zn^-$ and the tetraalkylzincates of general formula $M^{2+}R_4Zn^{2-}$. The first zincate derivatives, that is, NaZnEt$_3$ and KZnEt$_3$, were prepared by Wanklyn in 1858 from the reaction of metallic sodium or potassium with diethylzinc[211] (equation 38). In spite of this early discovery, many of the efforts to study this class of compounds are very recent. Today these heterodimetallic compounds are of great interest for inorganic and organic chemists because they show a unique reactivity and selectivity, different from those of either parent single-metal species. For example, they are known to achieve 1,4-conjugate addition to α,β-unsaturated ketones,[212] to metalate aromatic halide or vinyl halides,[213–215] and to reduce various carbonyl compounds.[216–218]

$$R_2Zn + \frac{2}{3}M \longrightarrow \frac{2}{3}R_3ZnM + \frac{1}{3}Zn \qquad (38)$$

M = Alkali metal

4.1.1 *Preparation*

Homoleptic (*see Homoleptic Compound*) triorganylzincates are readily prepared via the route originally used by Wanklyn, that is, the reaction of a metal with a dialkylzinc compound (equation 38). This reaction presents the advantage to avoid the incorporation of halide or pseudohalide (*see Pseudohalide*) in the products. When alkali metals (*see **Alkali Metals: Organometallic Chemistry***) are used without solvent or in hydrocarbon solvent, the homoleptic MZnR$_3$ species (R = CH$_2$CMe$_3$, CH$_2$SiMe$_3$; M = Na, K) are obtained in good yield.[219] In contrast, the reaction in benzene solution produces the heteroleptic (*see Heteroleptic Compound*) MZnPhR$_2$ resulting from the metallation of benzene[220] (equation 39).

$$R_3ZnM + C_6H_6 \longrightarrow R_2PhZnM + RH \qquad (39)$$

M = Alkali metal

Early studies of the reaction between diorganozinc compounds and alkaline earth metals (*see **Alkaline Earth Metals: Organometallic Chemistry***) (Ca, Sr, Ba) were reported to give complexes with general formula $R_2M{\cdot}R_2Zn$.[221] Subsequent investigations of these complexes in solution using NMR, cryoscopy and UV techniques, have shown the existence of a complex equilibrium (Scheme 10) and also suggested a tetrahedral structure for the $ZnR_4{}^{2-}$ ion.[222] While ionic species are favored in donor solvents, the free alkyl compounds and the contact ion pair $M^{2+}ZnR_4{}^{2-}$ are favored in nonpolar (*see Polar Compounds*) solvents. Recently, barium and strontium bis{tris[(trimethylsilyl)methyl]zincates}have been prepared by this route.[207]

A different approach was used to prepare the magnesium derivative [Mg^{2+} (THF)$_6$][(PhCH$_2$)$_3$Zn$^-$]$_2$, that is the addition of (PhCH$_2$)$_2$Mg to a THF solution of (PhCH$_2$)$_2$Zn in a 1:2 molar ratio (equation 40). It is interesting to note that the 1:1 molar ratio reaction produces the same compound with an equimolar amount of (PhCH$_2$)$_2$Mg that remains in solution.[223]

$$1(PhCH_2)_2Mg{\cdot}(THF)_2 + 2(PhCH_2)_2Zn \longrightarrow Mg(THF)_6[Zn(CH_2Ph)_3]_2 \qquad (40)$$

Homo- and heteroleptic (*see Heteroleptic Compound*) triorganozincates can also be prepared by reacting an

$$\begin{array}{ccccccccc} MR_2 + R_2Zn & \rightleftharpoons & MZnR_4 & \rightleftharpoons & M^{2+}ZnR_4{}^{2-} & \rightleftharpoons & M^{2+}(S)ZnR_4{}^{2-}(S) & \rightleftharpoons & M^{2+} + Zn\,R_4{}^{2-} \\ \mathrm{I} & & \mathrm{II} & & \mathrm{III} & & \mathrm{IV} & & \mathrm{V} \end{array}$$

M = Akaline earth metal, I = Free alkyl compounds, II = ate complex, III = contact ion pair, IV = solvated contact ion pair, V = free ions.

Scheme 10

organometallic reagent RM (M = Li, Na; R = alkyl, dialkylamide) with a diorganozinc compound ZnR'_2 (R′ = alkyl, dialkylamide) (equation 41). When the substituents are bulky, then potentially intramolecular coordinating groups (2-$C_6H_4CH_2NMe_2$) or the presence of a strong coordinating agent (TMEDA or crown ethers) appear necessary to isolate the trialkylzincate and prevent its dissociation into dialkylzinc and the organometallic reagent.[224–226] On the other hand, it was shown that addition of TMEDA to a solution of the zincate $[(THF)_6Mg][Zn(CH_2Ph)_3]$ leads to its decomposition in the corresponding dialkylzinc and dialkylmagnesium (*see* ***Beryllium & Magnesium: Organometallic Chemistry***) species.[227] Dialkyl(hydro)zincates ($MZnHR_2$; M = Li, Na) have been obtained in situ (*see In Situ Reaction*) when lithium hydride (*see Hydrides*) LiH or sodium hydride NaH was reacted with a diorganozinc compound in a 1:1 molar ratio.[216]

$$RM + R'_2Zn \longrightarrow MZnR'_2R \qquad (41)$$

R, R′ = H, alkyl, dialkylamide; M = Li, Na

Trialkylzincate compounds exhibit an sp^2 hybridized (*see Hybridization*) zinc atom having 16 electrons in his outer shell; consequently, an empty valence orbital (*see Valence Orbitals*) remains available at the zinc atom for coordination of a fourth ligand to reach the 18-electron state (*see Eighteen Electron Compounds*). Thus, tetraalkylzincates ($M_2{}^{2+}R_4Zn^{2-}$) are usually obtained directly when organometallic reagents (MR; M = Li, Na, MgX) are reacted with dialkylzinc (R_2Zn) compounds in a 2:1 molar ratio (equation 42), as well as in direct reaction of four equivalents of an organometallic reagent with zinc dihalides (ZnX_2) (equation 43).[228] The first reaction allows the synthesis of heteroleptic tetraalkylorganozincates of general formula $M_2{}^{2+}\ (ZnR_nR'_{4-n})^{2-}$ ($n = 1$ to 3; R and R′ = alkyl, R′ ≠R; $M_2{}^{2+} = 2Li^+$, $2Na^+$, Mg^{2+}) by conveniently choosing the diorganozinc and organometallic species.

$$2RM + R'_2Zn \longrightarrow M_2ZnR'_2R_2 \qquad (42)$$

R, R′ = alkyl, dialkylamide; M = Li, Na

$$4RM + ZnX_2 \longrightarrow M_2ZnR_4 + 2MX \qquad (43)$$

R, R′ = alkyl, dialkylamide; M = Li, Na

It is interesting to note that the readily available dilithium teramethylzincate was found to react with trimethylsilyl cyanide (Me_3SiCN) or trimethylsilylisothiocyanate (Me_3SiSCN) to give the corresponding modified zincates $Me_3Zn(CN)Li_2$ and $Me_3Zn(SCN)Li_2$[229] (equation 44).

$$Li_2ZnMe_4 + Me_3SiR' \longrightarrow Li_2ZnMe_3R' + Me_4Si \qquad (44)$$

R′ = CN, SCN

Finally, zincate complexes of general formula $M_nZn_mR_{2m+n}$ react with $LiAlH_4$ or $NaAlH_4$ in ethereal solvents to give complex metal hydrides of zinc with composition $M_nZn_mH_{2m+n}$[230,231] (M = Li, Na, K; $n = 1$ to 3; $m = 1$ or 2).

4.1.2 Structure

Zincate complexes are colorless, air- and moisture-sensitive solids; indeed the low-molecular species are pyrophoric on contact with air and react explosively with water. However, they are usually stable at room temperature when stored under a nitrogen atmosphere.

On the basis of conductivity studies, it was shown that $NaZnEt_3$ possesses a salt-like character, $Na^+\ [Et_3Zn]^-$. The X-ray structure determinations of higher molecular weight compounds $MZnR_3$ (R = CH_2Ph, M = Mg; R = CH_2SiMe_3, M = K; R = CH_2-t-Bu, M = Na, K; R = C≡CPh, M = Na) revealed that the metal cation is separated from the zinc center of the counterion.[219,220,223,232] All the trialkylzincates cited before have in common a ZnC_3 core in which the zinc atom is three-coordinate with an almost trigonal planar geometry (Figure 52).

A rather different situation was found in the solid-state structure of the heavier metal group 2 (*see* ***Alkaline Earth Metals: Organometallic Chemistry***) complexes[225,233] $[M{\cdot}(THF)_n]\{Zn[(CH_2SiMe_3)_3]\}_2$ (M = Sr, $n = 2$; M = Ba, $n = 4$). As shown in Figure 52, the trialkylzincate anions coordinate the metal cation like bidentate ligands (*see Bidentate Ligand*), via M–C–Zn three-center, two-electron bonds (*see Three-center Bond*), forming two four- membered MC_2Zn rings. Under application of ultrasound (*see Sonication*) in heptane, the barium derivative further reacts with additional barium metal to form a dimeric alkyldibariumtriszincate with a tetraanionic triszincate ligand and a unique $Ba_4Zn_2C_6$ core shown in Figure 53.

When the trialkylzincate contains suitably placed donor atoms, then intramolecular (*see Intramolecular*) coordination occurs. For example, the molecular structure of the complex

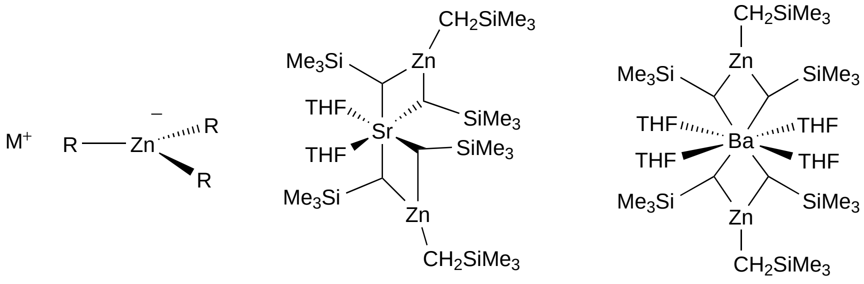

Figure 52 Structure of some triorganozincate compounds

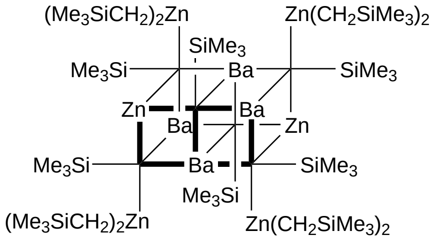

Figure 53 Structure of the $Ba_4Zn_2C_6$ in the dimeric alkyldibarium-triszincate

$(2\text{-}Me_2NCH_2C_6H_4)_3ZnLi{\cdot}THF$ exhibits a four-coordinated zinc center with a distorted tetrahedral geometry, resulting from intramolecular coordination of an amino group.[224]

Comparatively few tetraalkylzincates have been structurally characterized. The crystal structure of Me_4ZnLi_2 and Me_4ZnK_2, determined from X-ray powder diffraction studies, shows isolated $[Me_4Zn]^{2-}$ units with a four-coordinate zinc center in a tetrahedral arrangement.[234] A series of metallacyclopentane compounds of the type $[LiL_x]_2Zn[\text{-}(CHR)_4\text{-}]_2$ ($R = H$, Me; $L =$ TMEDA, THF; $x = 1, 2$) have been prepared by treating $ZnCl_2$ with the corresponding dilithium compounds $Li(CHR)_4Li$ in diethyl ether.[208] These compounds were found to be thermally very stable. As shown in Figure 54, the structure of $[Li(TMEDA)]_2Zn[(CH_2)_4]_2$ determined by X-ray crystallography, contains a central ZnC_4 core with distorted tetrahedral geometry, which is connected to each of the two Li·TMEDA rests via two bridging carbon atoms. It is worth mentioning that the average distance Zn–Li (2.42 Å) in this complex is comparable with the sum of their covalence radii (2.48 Å). A similar structure has been found for the related $[Li(TMEDA)]_2Zn[(CH_2SiMe_2)_2]_2$ containing silicon atoms in the metallacyclopentane rings.[235]

Even if the solid-state structures known so far exhibit separated ions, the nature of the different species in solution is not yet certain. The ^1H and ^7Li NMR studies of methyllithium mixed with dimethylzinc (and dimethylmagnesium) in ether solutions have shown that complex species such as $Li_2Zn(CH_3)_4$ and $Li_3Zn(CH_3)_5$ are formed, and no 1:1 complex was observed.[236] Furthermore, other studies (conductivity, cryoscopy, NMR and UV spectroscopy) of ethyllithium solutions in diethylzinc and $MZnEt_4$ solutions ($M =$ Ca, Ba, Sr) have shown the existence of complicated exchange equilibria between various species.

Finally, mixing toluene solutions of potassium *tert*-butoxide (*t*-BuOK) and diethylzinc results in the formation of the zincate $[Et_2Zn(O\text{-}t\text{-}Bu)]^-K^+$ (equation 45). An X-ray diffraction study of the compound reveals a dimeric structure, $(2K^+)$ $[Et_2Zn(\mu\text{-}O\text{-}t\text{-}Bu)_2ZnEt_2]^{2-}$, containing a four-membered Zn_2O_4 ring[237] (Figure 55). This Zn_4O_4 core is somewhat similar to that found for the neutral alkylzinc alkoxide $[EtZn(O\text{-}2,4,6\text{-}t\text{-}Bu_3\text{–}C_6H_2)]_2$, but with longer zinc–carbon bonds ($d(Zn\text{–}C)_{\text{neutral complex}} = 1.99$ and 1,95 Å, $d(Zn\text{–}C)_{\text{zincate complex}} = 2.07$ Å).

$$Et_2Zn + t\text{-}BuOK \longrightarrow [Et_2Zn(\mu\text{-}t\text{-}BuO)_2ZnEt_2]^{2-}2K^+ \qquad (45)$$

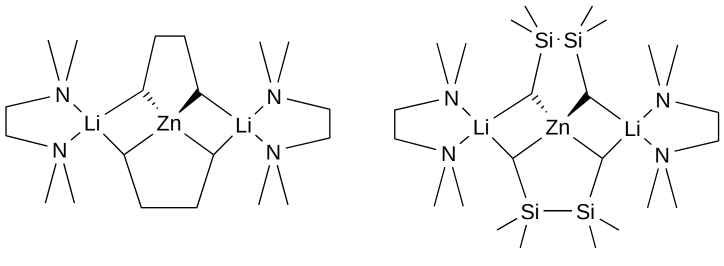

Figure 54 Structure of $[Li(TMEDA)]_2Zn[(CH_2)_4]_2$ and $[Li(TMEDA)]_2Zn[(CH_2SiMe_2)_2]_2$

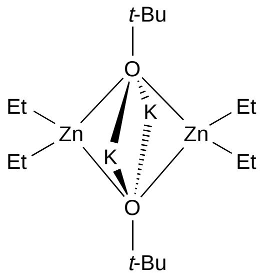

Figure 55 Structure of $[Et_2Zn(\mu\text{-}O\text{-}t\text{-}Bu)_2ZnEt_2]^{2-}$ $2K^+$

4.2 Alkylzinc Cations (*See Cation*)

4.2.1 Preparation

In contrast to organomagnesium (*see* ***Beryllium & Magnesium: Organometallic Chemistry***) compounds, dialkylzinc derivatives do not disproportionate in coordinated zincate anions and organozinc cations under addition of cryptand (*see Cryptands & Cryptates*) or crown ether (*see Crown Ethers*). However, it was shown by NMR spectroscopy that both organozinc anion and cation are formed in benzene solution when equimolar amounts of diethylzinc, diphenylzinc and a cryptand (*see Cryptands & Cryptates*) N_4-aza crown (N_4-aza crown = 1,4,8,11-terамethyl-1,4,8,11-teraazacyclotetradecane) were mixed**[238]** (equation 46). Furthermore, if triethylaluminum (a more effective R^- acceptor than R_2Zn) was used instead of diphenyl zinc, then the complex $[EtZn(C)]^+$ $(Et_4Al)^-$ (C = crown ether, N_4-aza crown) separated as a dense liquid phase (equation 47). Some recent studies have extended this reaction to organozinc halide and alkoxide derivatives, and also verified that the formation of ionic species is favored by nitrogen-containing macrocycles**[239–241]** (*see* ***Macrocyclic Ligands***). A series of ethylzinc cationic complexes has been prepared by protonolysis of diethylzinc with acidic tertiary ammonium salts of N-alkylated 1,3,5-triazacyclohexanes (R_3TAC)(R = Me, Bz, *i*-Pr, 4-fluorobenzyl). The products were found to have the general formula $[(R_3TAC)Zn(Et)]X$ ($X = ClO_4^-$, BF_4^-, $[B(C_6F_5)_4]^-$, PF_6^-) and to be sensitive to protic reagents.**[242,243]**

$$Et_2Zn + Ph_2Zn + C \rightleftharpoons EtZnC^+ + Ph_2ZnEt^- \quad (46)$$

C = cryptand

$$R_2Zn + R_3Al + C \rightleftharpoons RZnC^+ + R_4Al^- \quad (47)$$

C = cryptand

Actually, the presence of crown ether (*see Crown Ethers*) is not necessary to prepare a cationic zinc species. It was found that the reaction between diorganozinc compounds R_2Zn (R = Me, Et, *t*-Bu) and $[H(OEt_2)_2]^+$ $[B(C_6F_5)_4]^-$ in ether, led via alkane elimination to the salts $[RZn(OEt_2)_3]^+$ $[B(C_6F_5)_4]^-$ in quantitative yields**[244]** (equation 48). The compounds were isolated as colorless crystalline solids that are soluble in ether and dichloromethane.

$$R_2Zn + [H(Et_2O)_2]^+[B(C_6F_5)_4]^- \xrightarrow[-RH]{} [RZn(Et_2O)_3]^+[B(C_6F_5)_4]^- \quad (48)$$

4.2.2 Structure

The structure of the derivative $[EtZn(OEt_2)_3]^+$ $[B(C_6F_5)_4]^-$ could be determined by X-ray crystallography**[244]** (Figure 56). The zinc atom is tetracoordinated with a slightly distorted tetrahedral geometry, and the zinc–carbon bond length of 1.964 Å is comparable with that observed in the methylzinc alkoxide species $[MeZn(O\text{-}t\text{-}Bu)]_4$ (1.955 Å).

A similar zinc–carbon bond length (1.93 Å) is found in the solid-state structure of the compound $[(Bz_3TAC)Zn(Et)](PF_6)$, in which the ethylzinc cation coordinates to three nitrogen atoms of the 1,3,5-triazacyclohexane ligand**[242]** (Figure 56). It is worth noting that the benzyl substituents occupy two different positions, and that the two short Zn–F distances (2.85 Å) indicate anion–cation contacts. These observations confirm the previous NMR spectroscopy studies in solution of the related series $[(R_3TAC)Zn(Et)](X)$**[243]** (R = Me, Bz, *i*Pr, 4-fluorobenzyl; $X = ClO_4^-$, BF_4^-, $[B(C_6F_5)_4]^-$).

5 GEMINATE ORGANODIMETALLIC SPECIES CONTAINING ZINC

The synthesis and reactivity of geminate organodimetallic compounds is a useful approach for the building of complex architectural molecules by combining multiple reactions in a single operation. These reagents, which possess two nucleophilic (*see Nucleophile*) sites on a single carbon atom, are valuable tools for organic chemists since they can form two C–C bonds in a one-pot reaction. The synthesis and reactivity of geminate organodimetallic derivatives have been recently reviewed.**[245,246]**

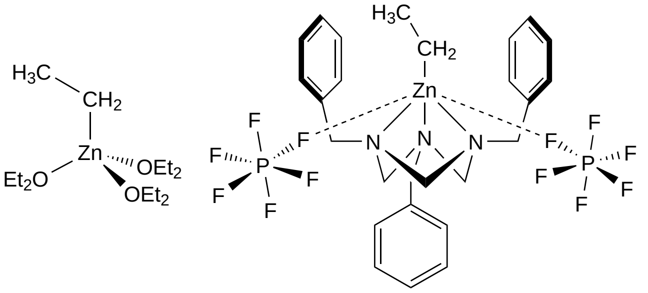

Figure 56 Structure of $[EtZn(OEt_2)_3]^+$ and $[EtZn(Bz_3TAC)]^+$ $(PF_6)^-$ cations

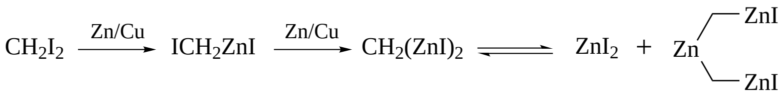

Scheme 11

5.1 Synthesis

Whereas a stoichiometric reaction of Zn/Cu couple with CH_2I_2 leads to the well-known Simmons–Smith reagent (ICH_2ZnI) (Section 6.6), the same reaction in presence of a large excess of zinc leads to an organo-*gem*-dizincio alkane (Scheme 11). The Zn/Cu couple can be efficiently replaced by a mixture of zinc dust and cuprous chloride, a mixture of zinc and Me_3Al, or a Zn/Pb couple. For example, the methylenating reagent ($XZnCH_2ZnCH_2ZnX \cdot THF$), also known as the Nysted reagent, can be obtained by reaction of CH_2X_2 ($X = Br$, I) with Zn/Pb couple in THF (equation 49). It has been shown that the catalytic effect of Hg in the formation of geminal dizincio alkanes follows the mechanism presented in Scheme 12. It is worth mentioning here that Charette and coworkers reported in 2002 the first evidence for the formation of a geminate dizinc carbenoid upon mixing iodoform (CHI_3) with diethylzinc (Et_2Zn) or ethylzinc iodide (EtZnI) at 0 °C. The novel compound was found very efficient to undergo cyclopropanation reactions with olefins (Section 6.7).

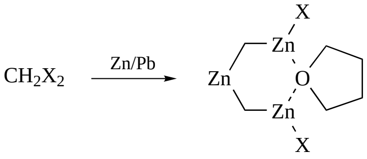

(49)

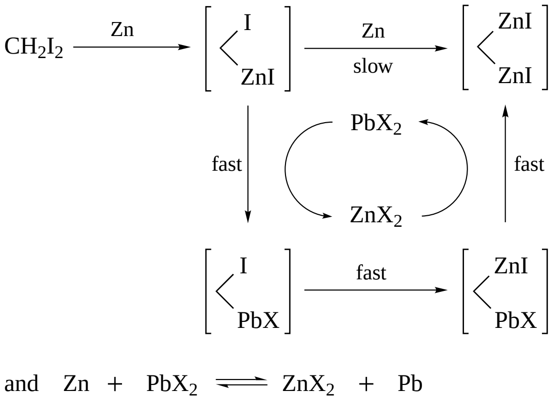

Scheme 12

The allylmetalation reaction, reported by Gaudemar, is an elegant alternative route for the synthesis of *gem*-dimetallic compounds. The addition of allylzinc bromide on substituted vinyl Grignard reagents gives the organo-*gem*-dimetallic derivative in moderate yields (equation 50). Even if the exact mechanism of the reaction remains uncertain, three hypotheses deserve consideration: a suprafacial addition of the allylic zinc bromide to the vinyl metal with further dimerization, especially when $MX_n = Li$ (path A); an anti-allylzincation of the vinyl metal (path B); formation of a mixed vinyl–allyl zinc species which undergoes a rearrangement similar to the

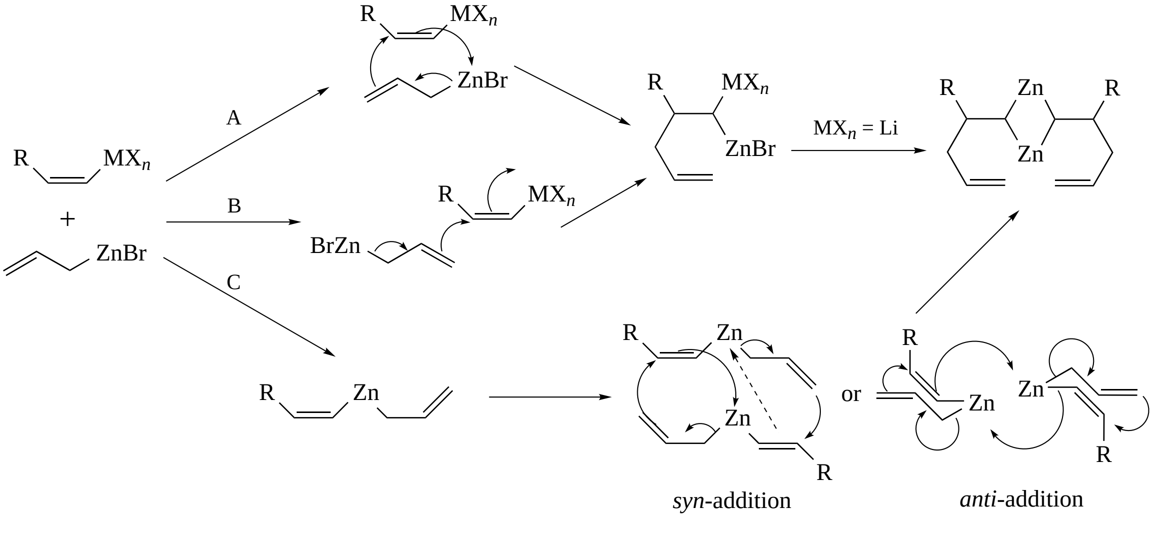

Scheme 13

Claisen rearrangement where zinc would act as the oxygen (path C) (Scheme 13). It has been found that the diastereoselectivity of allylmetalation is highly dependent on the temperature and on the nature of the solvent. Changing the solvent from THF to Et$_2$O considerably improves the diastereoselectivity since the poorer Lewis basicity (*see Lewis Acids & Bases*) of Et$_2$O accelerates the reaction and consequently allows lower temperature conditions. The different diastereomers can be independently obtained only by changing the stereochemistry of the starting vinyl Grignard reagent (Scheme 14).

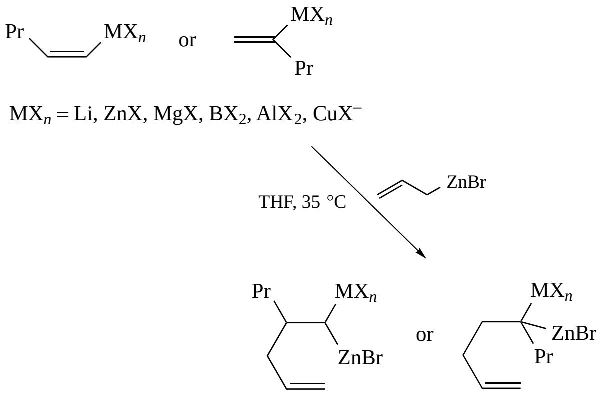

MX$_n$ = Li, ZnX, MgX, BX$_2$, AlX$_2$, CuX$^-$

(50)

The related addition reaction of allylzinc bromide to alkynil zinc reagents in refluxing THF leads to a mixture of vinylic 1,1-organo-*gem*-dimetallic species and *gem*-trimetallic species, which respectively result from single and double additions (equation 51). The presence of a Lewis basic (*see Lewis Acids & Bases*) group suitably placed for intramolecular (*see Intramolecular*) chelation, and bearing a secondary substituent, avoids the formation of double addition products and allows the reaction to take place in mild conditions (equation 52).

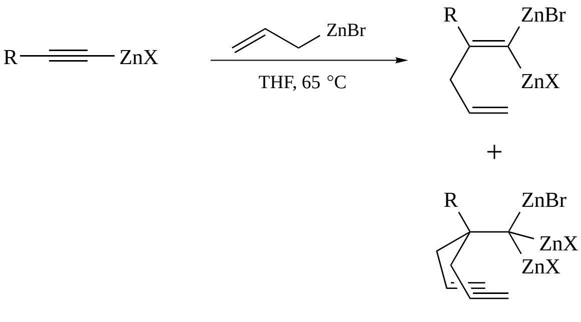

(51)

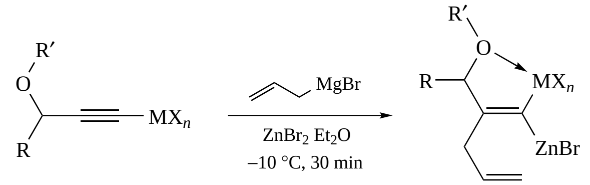

(52)

R′ = secondary substituent
MX$_n$ = Li, ZnX, MgX

1,1-Boro zincioalkane and 1,1-boro zincioalkene can be prepared by a different route, that is, the reaction of α-haloboronic esters with zinc dust in *N*,*N*-dimethylacetamide (DMA). The zinc insertion (*see Insertion*) into α-haloalkenylboronic esters is not stereospecific, so a pure Z reagent will be converted to an E/Z mixture of the corresponding alkenylzinc iodide (equation 53).

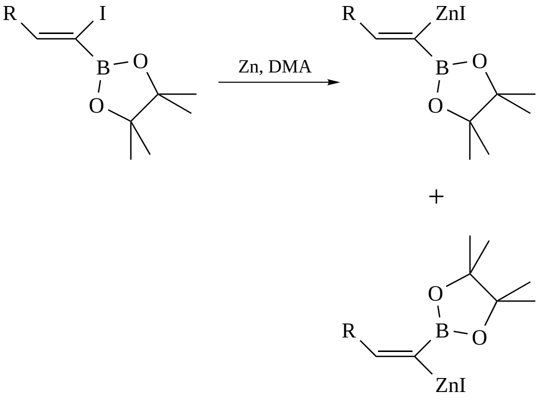

(53)

Other mixed *gem*-dimetallic compounds containing zinc and either zirconium, aluminum, or titanium have been successfully prepared from alkynylzinc halide compounds via hydrozirconation by H(Cl)ZrCp$_2$ (the Schwartz's reagent) or carbometalation by a combination of Me$_3$Al/Cp$_2$TiCl$_2$ (Scheme 15).

5.2 Structure

Compared with organo-*gem*-dilithio and dimagnesio compounds, the corresponding organo-*gem*-dizincio derivatives are relatively more stable and less reactive. However, they are usually prepared in situ (*see In Situ Reaction*) and directly

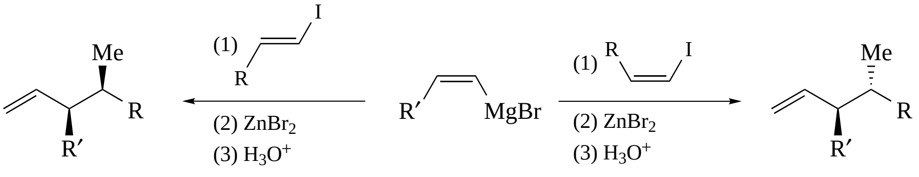

Scheme 14

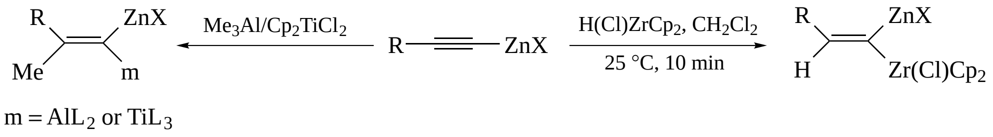
R
ZnX
Me
m
m = AlL2 or TiL3
Me3Al/Cp2TiCl2
R—≡—ZnX
H(Cl)ZrCp2, CH2Cl2
25 °C, 10 min
R
ZnX
H
Zr(Cl)Cp2

Scheme 15

reacted with electrophiles (*see Electrophile*); so, despite their great synthetic value, very little is known about their structure. The first structurally characterized organo-*gem*-dizincio species, namely, the $[Zn\{C(SiMe_3)(2\text{-pyridyl})\}]_4$ tetrameric cage, has been reported only a few years ago.**[84]** This novel compound was obtained in low yield (20%) by reacting a distibine polymer $[\{(2\text{-pyridyl})(SiMe_3)C\}SbCl]_\infty$ with Et_2Zn (equation 54). As shown in Figure 57, the compound contains a tetrameric array of $\{(2\text{-pyridyl})(Me_3Si)C\}Zn$ in which each ligand bridges two zinc atoms via the *gem*-C centers and bridges to a third zinc atom through the pyridyl nitrogen atom. The three-coordinate metal centers present a distorted trigonal planar geometry with a C–Zn distance of 2.032 Å. The *gem*-C centers are distorted from the tetrahedral environment with a Zn–C–Zn angle of 82.2(2)°.

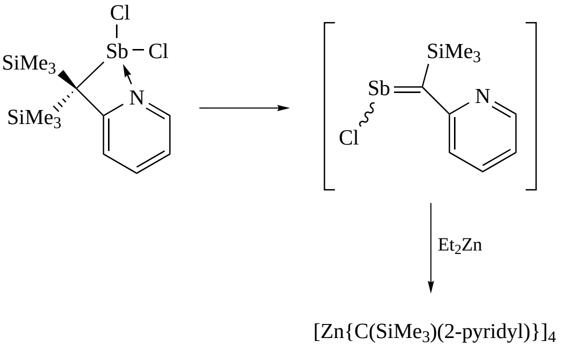
Cl
Sb
Cl
SiMe3
SiMe3
N
SiMe3
Sb
Cl
N
Et2Zn
[Zn{C(SiMe3)(2-pyridyl)}]4

(54)

The only other geminal dizincated alkane reported so far is the dimeric alkyldibarium triszincate, $(4Ba^{2+})\cdot\{[(Me_3SiCH_2)_2ZnCH(SiMe_3)]_2ZnCH(SiMe_3)\}_2{}^{4-}$, the synthesis and structure of which have already been mentioned in Section 4.1.2.**[233]** So as to make it clear, Figure 58 shows only the structure of one tetraanionic tris(zincate) ligand of the dimeric complex. Owing to the special coordination situation and the presence of anionic charges, the Zn–C bond distances of the *gem*-dizincated carbons are rather long (2.15 Å) compared to the Zn–C bond distances found in dialkylzinc compounds (1.95 Å) or in the structure described before (2.03 Å). A comparable elongation of the Zn–C bond was found in the solid-state structure of different geminal organodimetallic compounds containing zinc and other metal. For example, the tantalum−zinc akylidine complexes presented in Figure 59 show bridging Zn–C bond lengths ranging from 1.11 to 1.15 Å, reflecting weak Zn–C interactions.**[247,248]**

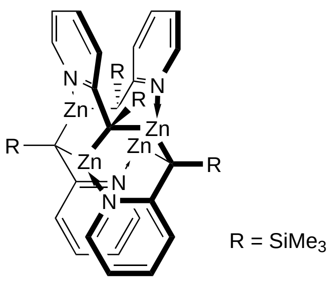
N
Zn
R
R
N
Zn
R
Zn
Zn
R
N
N
R = SiMe3

Figure 57 Schematic structure of $[Zn\{C(SiMe_3)(2\text{-pyridyl})\}]_4$

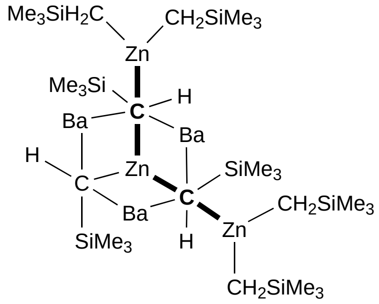
Me3SiH2C
CH2SiMe3
Zn
Me3Si
H
Ba
C
Ba
H
C
Zn
SiMe3
Ba
C
CH2SiMe3
Zn
SiMe3
H
CH2SiMe3

Figure 58 Structure of the tetraanionic tris(zincate) ligand of $\{[(Me_3SiCH_2)_2ZnCH(SiMe_3)]_2ZnCH(SiMe_3)\}_2{}^{4-}\cdot 4Ba^{2+}$

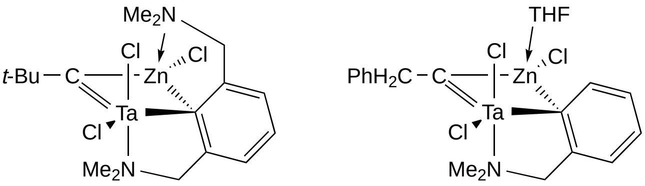
Me2N
Cl
Cl
t-Bu
C
Zn
Ta
Cl
Me2N
THF
Cl
Cl
PhH2C
C
Zn
Ta
Cl
Me2N

Figure 59 Structure of tantalum−zinc alkylydine complexes

6 REACTIVITY OF ORGANOZINC COMPOUNDS (*See Organic Synthesis Using Metal-mediated Coupling Reactions*)

The reactivity of organozinc compounds with various reagents such as water, amines, alcohols, and CO_2 has already been mentioned in the preceding sections and will not be considered here.

6.1 Reactivity with CO

In contrast to Grignard reagents, dialkylzinc compounds are inert to carbon monoxide at atmospheric pressure either in the absence of solvents or in solution in THF, diglyme, ether, or benzene. Although Rathke and Yu reported in 1972 that the addition of potassium *tert*-butoxide in stoichiometric amounts promoted the absorption of carbon monoxide, it is now known that the actual reactive species was the corresponding zincate compound $(R_2ZnO\text{-}t\text{-}Bu)^-K^+$. The only zinc carbonyl species reported so far has been observed by ^{13}C NMR studies of ^{13}CO on zeolite ZnY and polycrystalline ZnO, at low temperature.[249] Before this report, such species were only suggested from infrared and photoelectron studies of CO weakly bound to ZnO.

6.2 Reactivity with O_2

The high reactivity of organozinc compounds towards oxygen was already noted by Frankland, who reported some 150 years ago the formation of $Zn(OEt)_2$ by the controlled oxidation of Et_2Zn.[250] Even if this reaction was successfully used to prepare alcohols and hydroperoxides (*see Peroxide*) in relatively good yields[251] (Scheme 16), the exact composition of the products and the reaction mechanism remain rather uncertain. In 1864, Lissenko proposed the formation of EtZnOEt,[252] whereas Demuth and Meyer claimed some years later the isolation of the peroxide (*see Peroxide*) EtZnOOEt, a white powder resulting from the oxidation of Et_2Zn in ligroine.[253] However, subsequent studies agreed with rapid oxidation of both Zn–C bonds and formation of compounds with general formula $(ROO)_2Zn$, ROZnOOR and $(RO)_2Zn$.[254]

Even if the free radical chain process shown in Scheme 17[255] was a commonly accepted mechanism, some very recent work published by Lewinski and coworkers strongly questions it. They initially reported the first zinc alkylperoxide structurally characterized by X-ray diffraction, the dimeric $[EtOOZn(BDI)]_2$ (BDI = β-diketiminate ligand) obtained in high yield and in a few minutes by reaction of EtZn(BDI) complex with O_2 at O °C.[256]

$$\mathrm{ROH} \xleftarrow[\substack{(2)\ \mathrm{O_2,\ C_6F_{14},\ -78\ °C}\\(3)\ \mathrm{Zn,\ HCl}}]{(1)\ \mathrm{ZnBr_2}} \mathrm{R_2Zn} \xrightarrow[(2)\ \mathrm{O_2,\ C_6F_{14},\ -78\ °C}]{(1)\ \mathrm{ZnBr_2}} \mathrm{ROOH}$$

Scheme 16

$$\begin{aligned} \mathrm{R\cdot} + \mathrm{O_2} &\longrightarrow \mathrm{ROO\cdot} \\ \mathrm{ROO\cdot} + \mathrm{Et_2Zn} &\longrightarrow \mathrm{ROOZnEt} + \mathrm{Et\cdot} \\ \mathrm{Et\cdot} + \mathrm{O_2} &\longrightarrow \mathrm{EtOO\cdot}\quad \text{etc.} \end{aligned}$$

Scheme 17

In 2003, the same group published a study of the reaction of O_2 with the chelate complex $[EtZn(\mathit{azol})]_n$ (*azol* = 1-aziridineethanolate) and isolated the zinc ethylperoxide complex $[EtOOZn(azol)]_2[EtZn(azol)]_2$ in 92% yield from the reaction in benzene[257] (Figure 60). The compound was found resistant to further oxidation with O_2 and the reaction was significantly inhibited in THF solution. They also studied the controlled oxidation of Et_2Zn by O_2, which led to the compound $Me_6Zn_7(OMe)_8$ in high yield. This compound is analogous to the product of methanolysis of Et_2Zn (Section 'Structure' and Figure 34), showing that selective oxidation of dialkylzinc compounds may be a route for the preparation of zinc alkoxides.

Various modes of oxygen-capture by lithiated organozinc reagents have been described in the sequential reaction of Me_2Zn with a 2-pyridylamine $[HN(2\text{-}C_5H_4N)R$, R = Ph, 3,5-xylyl, 2,6-xylyl, benzyl, Me], *t*-BuLi and afterward O_2.[258] The nature of the products was found to be dependent on R and suggested a competition between the oxophilicity of lithium and zinc (Scheme 18). When N,N'-diphenylbenzamidine (HAm) is used instead of 2-pyridylamine, and depending on the solvent conditions, the sequential reaction leads to various triorganozincate species.[259] While the product isolated from THF solutions is the dimer $[THF{\cdot}Li(Me)OZnAm_2]_2$ corresponding to a formal insertion (*see Insertion*) of oxygen into the Zn–C bond, without donor solvent the polymer $[(LiO\text{-}t\text{-}Bu)(MeZnO\text{-}t\text{-}Bu)_3]_n$ and the oxide-encapsulation complex $(\mu_6\text{-}O)(Li_2ZnAm_3)_2$ were obtained.

6.3 Substitution Reactions

6.3.1 *With Inorganic Halides*

As a result of their low basicity and low reducing power, organozinc reagents are more suitable than the corresponding magnesium (*see* ***Beryllium & Magnesium: Organometallic Chemistry***) or lithium (*see* ***Alkali Metals: Organometallic Chemistry***) derivatives for the alkylation of some transition metal halides. For example, bis(trimethylsilylmethyl)zinc

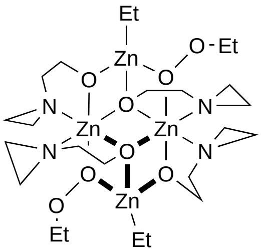

Figure 60 Structure of the zinc ethylperoxide $[EtOOZn(\mathit{azol})]_2[EtZn(\mathit{azol})]_2$

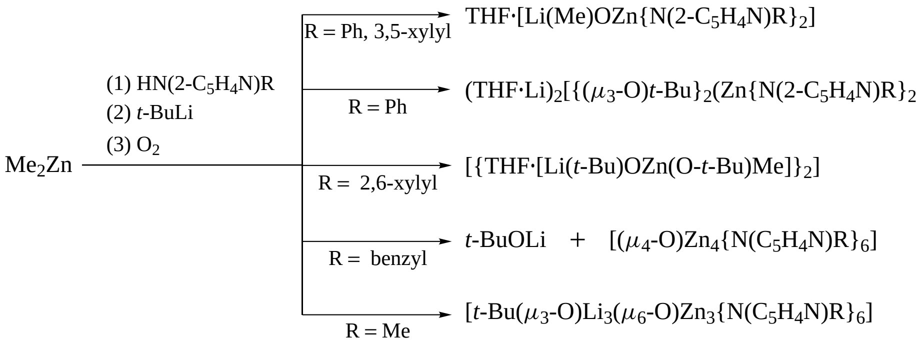
Me2Zn
(1) HN(2-C5H4N)R
(2) t-BuLi
(3) O2
R = Ph, 3,5-xylyl
THF·[Li(Me)OZn{N(2-C5H4N)R}2]
R = Ph
(THF·Li)2[{(μ3-O)t-Bu}2(Zn{N(2-C5H4N)R}2
R = 2,6-xylyl
[{THF·[Li(t-Bu)OZn(O-t-Bu)Me]}2]
R = benzyl
t-BuOLi + [(μ4-O)Zn4{N(C5H4N)R}6]
R = Me
[t-Bu(μ3-O)Li3(μ6-O)Zn3{N(C5H4N)R}6]

Scheme 18

$[(Me_3SiCH_2)_2Zn]$ and bis(neopentyl)zinc $[(Me_3CCH_2)_2Zn]$ react with tantalum chloride ($TaCl_5$) and niobium chloride ($NbCl_5$) to give the corresponding alkyl metal chlorides of general formula R_nMCl_{5-n} ($M = Ta$, $n = 1$–3; $M = Nb$, $n = 2$; $R = Me_3SiCH_2$, Me_3CCH_2)[260] (equation 55).

$$\frac{n}{2}(Me_3SiCH_2)_2Zn + MCl_5 \longrightarrow (Me_3SiCH_2)_nMCl_{5\text{-}n} + \frac{n}{2}ZnCl_2$$
$$M = Ta, n = 1\text{–}3; \quad M = Nb, n = 3 \qquad (55)$$

The oxidative alkylation of titanium compounds (Cp^*_2TiX; $Cp^* = \eta^5\text{-}C_5Me_5$, $X = Me$, OMe, Cl, N=CH-*t*-Bu) by dimethylzinc and dimethylcadmium has been reported to afford diamagnetic (*see Diamagnetism*) compounds of general formula $Cp^*_2TiMe(X)$ and metallic zinc and cadmium, respectively.[261]

Organozinc halides and diorganozinc compounds smoothly alkylate chlorophosphane derivatives in THF at 0 °C in good to excellent yields[262] (equation 56).

$$RZnX \xrightarrow[0\,^\circ C,\ 1h]{Cl_nPR'_{3\text{-}n},\ THF} R_n\text{-}PR'_{3\text{-}n} \qquad (56)$$
$$X = \text{Halide, R.}$$
$$R' = Ph, NR''_2$$

Addition of catalytic or stoichiometric quantities of $CuCN{\cdot}(LiCl)_2$ radically increases the reactivity of diorganozinc (R_2Zn) and organozinc halide (RZnX) compounds. The resulting copper–zinc species (RCu(CN)ZnR or RCu(CN)ZnX) react with stannyl chlorides (R'_3SnCl) to give the corresponding alkylated stannyl derivatives (R'_3SnR) in high yields[8] (Scheme 19). It is worth mentioning that Me_3SiCl generally fails to react with either organozinc or zinc–copper compounds.

6.3.2 *With Organic Halides*

When diorganozinc and organozinc halide compounds react with allylic halides in the presence of Cu^I salts, the S_N2' (*see Nucleophilic Addition: Rules for Predicting Direction*) products are selectively obtained. In contrast, the reactions catalyzed by Ni^0 or Pd^0 lead to the S_N2 products (Scheme 20).

The cross-coupling reaction between organozinc halides and alkenyl or aromatic halides is efficiently catalyzed by Pd^{II} or Ni^{II} salts. Organo-copper reagents derived from organozinc halide compounds react similarly with alkenyl halides but in harsh conditions (refluxing DME several days) to give the coupling products in a stereocontrolled way (Scheme 21). It has been found that the presence of an electron-withdrawing group (NO_2, COOR, COR) in the *β*-position facilitates the substitution reaction via an addition-elimination mechanism. In contrast, the coupling reaction with 1-iodo- and 1-bromoalkynes takes

$$RZnX \xrightarrow{Cu(CN){\cdot}2LiCl} RCu(CN)X \xrightarrow{R'_3SnCl} R'_3SnR$$
$$X = \text{Halide, R.}$$

Scheme 19

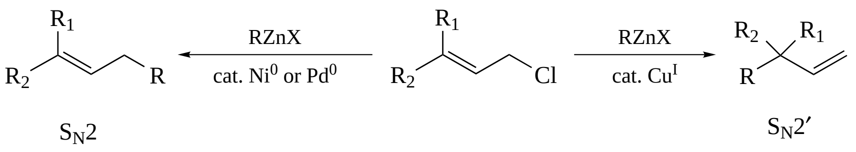

Scheme 20

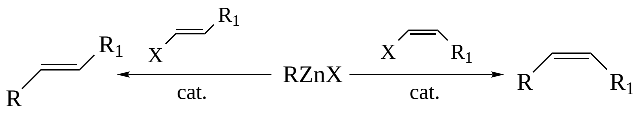

Cat. = Cu^{I}, Pd^{II}, Ni^{II} salts.

Scheme 21

place in mild conditions (−80 to 0 °C, few hours) (equation 57).

$$\text{R}_1\text{–C}\equiv\text{C–X} \xrightarrow{\text{RCu(CN)ZnX}} \text{R}_1\text{–C}\equiv\text{C–R} \tag{57}$$

While the reaction of acid chlorides with organozinc halide compounds is relatively inefficient, the reaction with the corresponding copper−zinc reagents or the catalysis with Pd^{II} salts represents a smooth route for the preparation of ketones in very good yields (equation 58).

$$\text{R}_1\text{COCl} \xrightarrow{\text{RCu(CN)ZnX}} \text{R}_1\text{COR} \tag{58}$$

The more difficult cross-coupling reaction between Csp^3-Csp^3 can be accomplished by mixed zincate compounds, prepared by the reaction of diorganozinc derivatives with $\text{Me}_2\text{CuMgCl}\cdot\text{MgCl(CN)}$ (equation 59). Substitution reaction at Csp^3 centers are also efficiently catalyzed by Ni^{II} salts when the alkyl halide contains a double bond in remote position (Scheme 22). Changing the double bond for a triple bond leads to an intramolecular carbozincation reaction (equation 60).

$$\text{R–X} \xrightarrow[\text{3) R}'\text{X, }-78\,^{\circ}\text{C}]{\substack{\text{1) Et}_2\text{Zn, CuCN(0.3 mol\%)} \\ \text{2) Me}_2\text{Cu(CN)(MgCl)}_2\text{, DMPU, }-50\,^{\circ}\text{C}}} \text{R–R}' \tag{59}$$

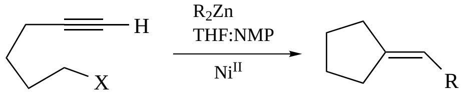

(60)

6.4 Addition to Carbonyl Compounds

In contrast to organomagnesium (*see* ***Beryllium & Magnesium: Organometallic Chemistry***) and organolithium (*see* ***Alkali Metals: Organometallic Chemistry***) reagents, dialkylzinc compounds react only slowly with aldehydes to give addition products. Moreover, when the zinc compounds bear hydrogens in β-position a competitive reduction reaction can take place. Reduction is also the main reaction with ketones. Thus, the addition of organozinc derivatives with carbonyl compounds usually requires the presence of metal salts, Lewis acids (*see Lewis Acids & Bases*) $[\text{Ti(O-}i\text{-Pr)}_n\text{Cl}_{4-n}$, Me_3SiCl, $\text{BF}_3\cdot\text{OEt}_2]$, donor ligands or auxiliaries. However, it has been shown that aryl-, vinyl-, and alkynylzinc reagents are more reactive than the saturated organozinc reagents. They react smoothly with carbonyl derivatives in the absence of catalysts. For example, alkenylzinc chlorides add to α-amino aldehydes to give unsaturated 1,2-amino alcohols with acceptable yields and good stereoselectivity (equation 61). More generally, highly reactive allylic zinc reagents add to a wide range of carbonyl functionalities. In contrast, the reaction of propargylic zinc derivatives with aldehydes or ketones always give mixtures of rearranged products.

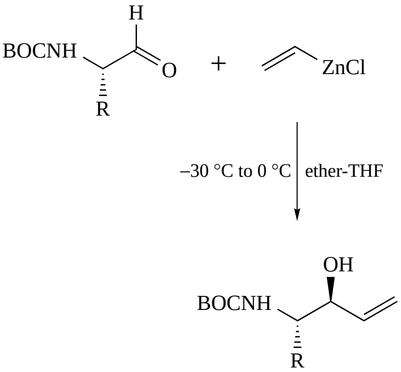

(61)

The research on asymmetric organozinc additions to carbonyl compounds started in 1984 when Oguni and Omi obtained 49% e.e. in the reaction of diethylzinc with benzaldehyde catalyzed by (*S*)-leucinol. Since then, a huge number of chiral (*see Chiral*) catalysts, mostly derived from amino alcohols, have been developed and the subject has been extensively reviewed.**[263,264]** The first highly enantioselective (*see Electrophile*) ligand (−)-3-exo-dimethylaminoisoborneol [(−)-DAIB] developed by Noyori and coworkers in 1986 is still used even if its application is mostly limited to aromatic and heteroaromatic aldehydes (equation 62). As shown by previous studies, chiral (*see Chiral*) ligands have a dual

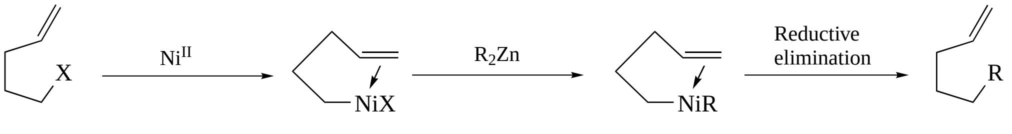

Scheme 22

function: they control the stereochemistry of the organozinc addition and increase the nucleophilicity (*see Lewis Acids & Bases*) of the alkyl groups bound to zinc through their coordination to the zinc center.

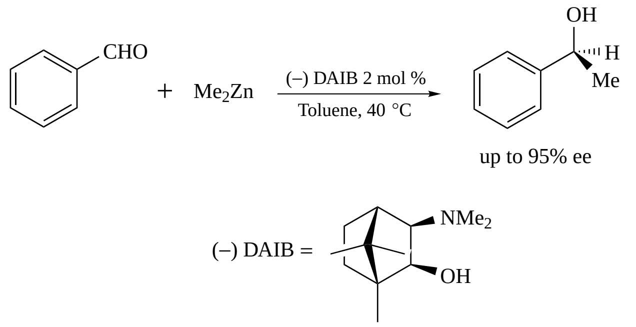

(62)

The amino-alcohol promoted addition of dialkylzinc to aldehydes has been extensively studied and several types of transition states have been proposed (Figure 61 and 62). Some years ago, Yamakawa and Noyori characterized two tricyclic transition states (syn- and anti-orientation) and suggested the mechanism shown in Scheme 23.**265** In the first step, a complex between Me_2Zn and (−)-DAIB is formed. This complex, which has no alkylating properties, further coordinates a second Me_2Zn molecule trough the oxygen atom. After that, a benzaldehyde molecule coordinates to the former zinc atom in *anti* position with respect to the chiral (*see Chiral*) ligand. A following methyl migration to the *si* face of the aldehyde produces the asymmetric center. Finally further reaction with Me_2Zn can regenerate the bis(dimethylzinc)·(−) DAIB complex and liberate (S)-(1-phenyl)ethoxy–ZnMe which gives (S)-1-phenylethanol under aqueous workup.

Theoretical investigations have shown that the most favored tricyclic transition state has the *anti*-configuration, which is 12–13 $kJmol^{-1}$ more stable than the *syn*-configuration and 29 $kJmol^{-1}$ more stable than the bicyclic transition state (Figure 61). However, few years later Rasmussen and Norrby**266** could characterized two new six-membered transition states, *env* and *chai*r (Figure 62), which are lower in energy (respectively by 19 and 50 $kJmol^{-1}$) than the more stable *anti* form characterized by Yamakawa and Noyori.

Interestingly, it was found that this reaction shows a large positive nonlinear effect with the enantiomeric purity of the DAIB ligand. In other words, higher enantioselectivity is obtained with lower enantiomeric purity of the ligand. For example, when diethylzinc was added to benzaldehyde in presence of DAIB with 100% e.e., the addition product was obtained in 98% e.e., whereas DAIB with only 15% e.e. led to the addition product with 95% e.e. In addition, if a racemic DAIB mixture was used instead of an enantiomerically pure ligand, the reaction rate was reduced by 13 times. This behavior can be explained by the formation of two different dimeric species, in the first step of the reaction, when DAIB is not enantiomerically pure, that is, the homodimer $[RZn\{(-)\text{-DAIB}\}]_2$ with C_2 symmetry and the heterodimer with C_i symmetry, which was found to be the more stable and less reactive one (Figure 63). Thus, the observed nonlinear effect comes from the consumption of the minor enantiomer through formation of the stable and faintly reactive heterodimer.

In 1995, Soai and coworkers reported a highly enantioselective asymmetric autocatalysis of pyrimidyl alkanol in the enantioselective addition reaction of i-Pr_2Zn to pyrimidine-5-carboxaldehyde**267** (equation 63). When a 5-pyrimidyl alkanol with a small enantiomeric excess such as $5\text{x}10^{-5}$% is added to i-Pr_2Zn and pyrimidine-5-carboxaldehyde, then the reaction

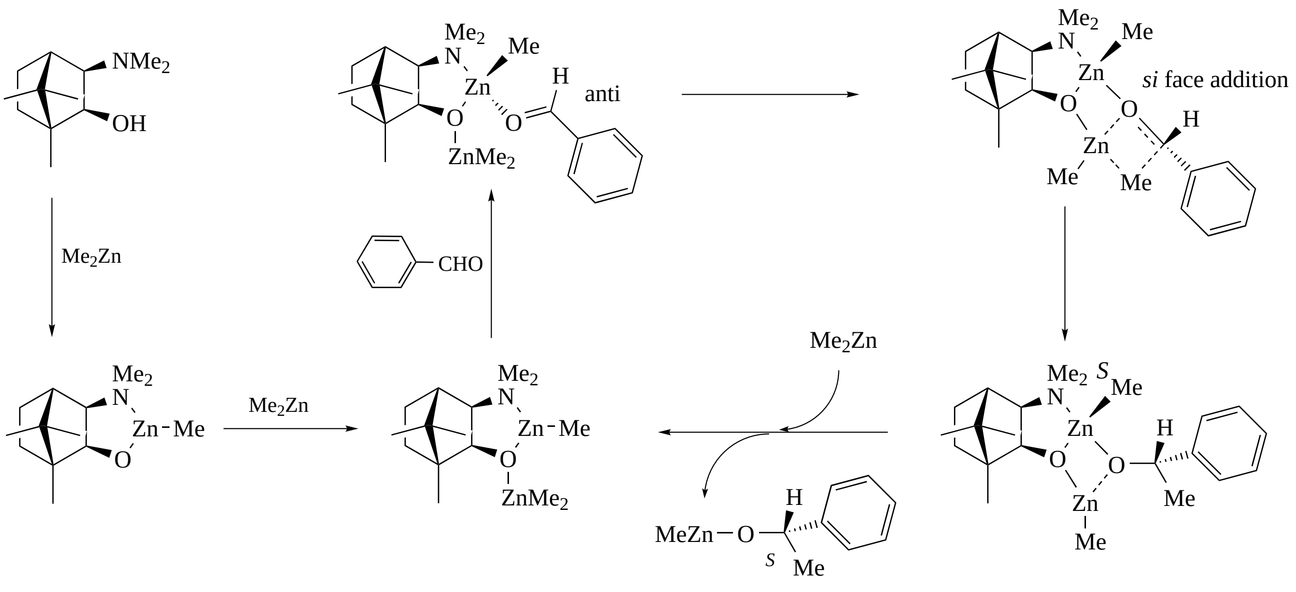

Scheme 23

gives the alkanol of the same absolute configuration with up to 99.5% e.e. The autocatalytic feature of the reaction has been proven by recent kinetic analysis[268] (*see Kinetic Methods*).

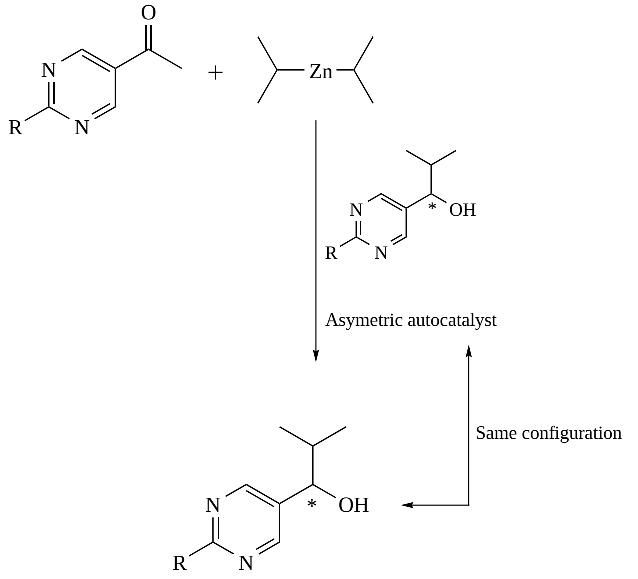
O
N
R
N
+
Zn
*
OH
Asymetric autocatalyst
Same configuration

(63)

Recently, it has been found that shifting the NMe_2 moiety in (−)-DAIB to a morpholine group (MIB) gives a much more stable derivative, which also displays a wider reactivity[269] (equation 64).

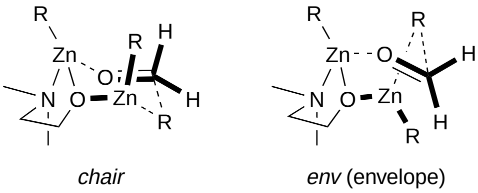
R
Zn
O
N
Zn
H
R
chair
env (envelope)

Figure 62 New transition states characterized by Rasmussen and Norrby

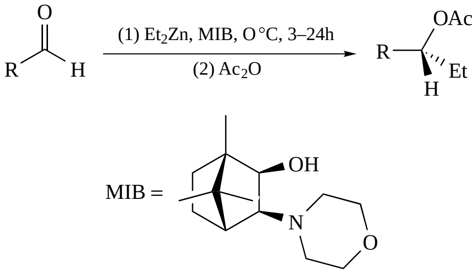
O
R
H
(1) Et₂Zn, MIB, O °C, 3–24h
(2) Ac₂O
OAc
R
Et
H
MIB =
OH
N
O

(64)

In addition to amino alcohols, numerous other ligands such as amines, amino thiols, diols, disulfides, and diselenides have been developed and tested. Several have shown a very good enantioselectivity for dialkylzinc additions to a variety of aldehydes. In contrast, the addition of aryl-, vinyl-, and alkynylzinc compounds was not so extensively studied and more work is still needed in

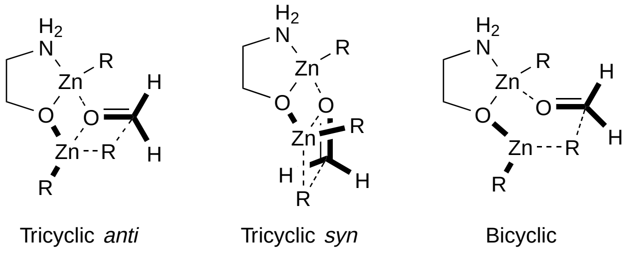
H₂
N
Zn
R
O
H
Tricyclic anti
Tricyclic syn
Bicyclic

Figure 61 Transition states characterized by Yamakawa and Noyori

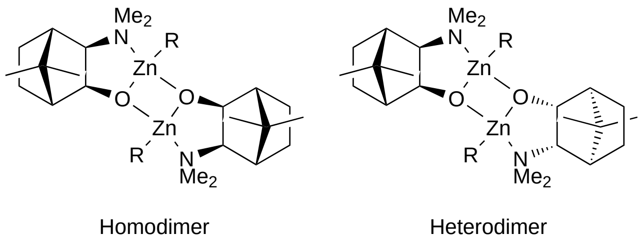
Me₂
N
R
Zn
O
Homodimer
Heterodimer

Figure 63 Structure of the homo- and heterodimer $[RZn(DAIB)]_2$

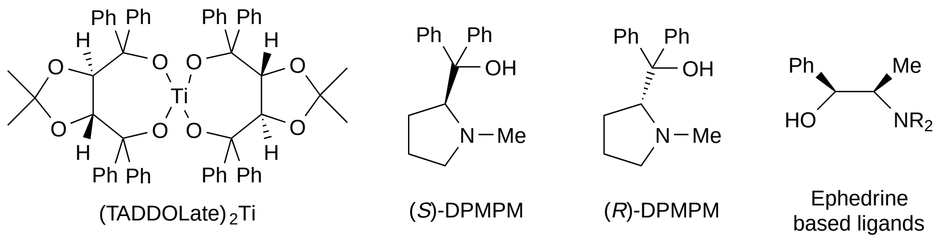
Ph Ph
H
O
Ti
(TADDOLate)₂Ti
OH
N−Me
(S)-DPMPM
(R)-DPMPM
Ph
Me
HO
NR₂
Ephedrine based ligands

Figure 64 Structure of some enantioselective ligands for vinyl- and alkynylzinc additions to aldehyde

this area. Nevertheless, some highly enantioselective catalysts have been recently obtained.[264] For example, Ph_2Zn reacts with propionaldehyde in the presence of 10 mol % of the chiral (*see Chiral*) binaphtyl ligand (*R*)-3,3′-bis(2″,5″-dihexyloxyphenyl)-1,1′-binaphthol to give (S)-1-phenylpropanol with 87% e.e. (equation 65). The spirotitanate complex $(TADDOLate)_2Ti$ (TADDOLate = α,α,α', α'-tetraaryl-1,3-dioxolane-4,5-dimethanolate) was reported to give 84% e.e. in the reaction of divinylzinc with benzaldehyde. Even higher e.e., up to 92%, have been obtained for the addition of diisopropenylzinc to aromatic aldehydes catalyzed by proline based ligands such as DPMPM [diphenyl(1-methylpyrrolidin-2-yl)methanol] and ephedrine based ligands (Figure 64). Addition of stoichiometric amounts of *N*-methylephedrine to the reaction of terminal alkynes with different aromatic and aliphatic aldehydes containing α-substituents led to very high enantioselectivity.

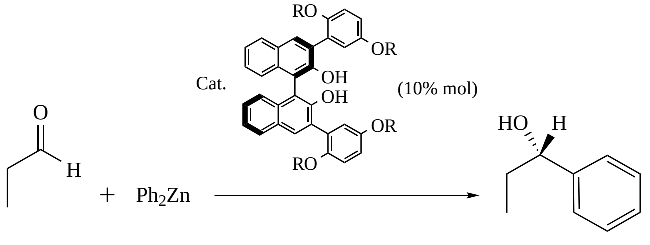

(65)

Compared to the well-developed organozinc addition to aldehydes, the related addition to ketones has been far less studied. However, the first catalytic addition of dialkylzinc to ketones has been achieved few years ago using camphorsulfonamide alcohols ligands and Ti(O-i-Pr)$_4$ salt (equation 66). In the same year, it was also discovered that 15 mol % of (+)-DAIB catalyze the diphenylzinc addition to ketones to generate chiral (*see Chiral*) tertiary alcohols with up to 91% e.e. (equation 67).

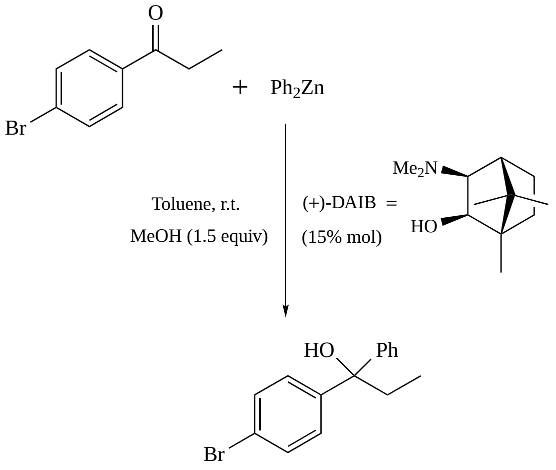

(66)

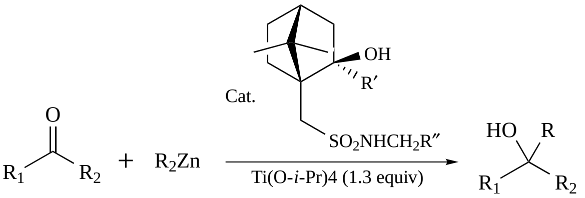

(67)

6.5 Addition to C=N bonds

The development of organozinc addition reactions to imines and imine derivatives has been somewhat limited by both the poor electrophilicity of the azomethine carbon and the low reactivity of organozinc reagents.

Even the very efficient enantioselective catalysts used in organozinc addition reactions to carbonyl compounds failed to catalyze the corresponding addition reactions to nonactivated imines such as *N*-silyl-, *N*-phenyl-, or *N*-benzyl-imines. However, enantioselective additions of dialkylzinc compounds to more activated imines, like *N*-acyl- or *N*-phosphinoyl-imines, in the presence of catalytic or stoichiometric amounts of chiral (*see Chiral*) aminoalcohols, have been recently reported. For example, in presence of 1 equiv of (*N*,*N*-dibutylnorephedrine) (DBNE) diethylzinc reacts with masked *N*-acyl imines like *N*-(amidobenzyl)benzotriazoles, to give chiral *N*-(1-phenylpropyl)amides with up to 76% e.e.[270] (equation 68).

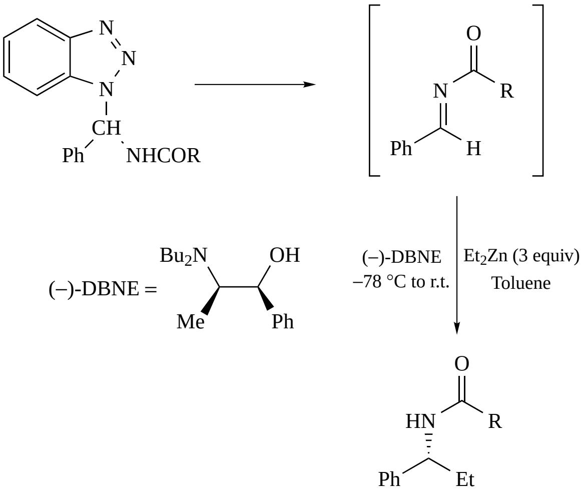

(68)

N-diphenylphosphinoyl imines also react with dialkylzinc in the presence of stoichiometric or catalytic amounts of different chiral (*see Chiral*) ligands[271] (Scheme 24). Acid hydrolysis of the resulting phosphinamides occurs without racemization and gives enantiomerically enriched primary amines. The allylation of various cyclic imines was obtained with high enantioselectivity (*see Electrophile*), 77 to 99% e.e., in the presence of lithiated bis-oxazoline ligands (Scheme 25).

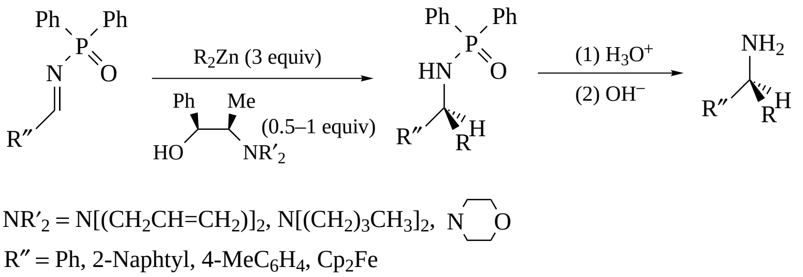

NR′$_2$ = N[(CH$_2$CH=CH$_2$)]$_2$, N[(CH$_2$)$_3$CH$_3$]$_2$,

R″ = Ph, 2-Naphtyl, 4-MeC$_6$H$_4$, Cp$_2$Fe

Scheme 24

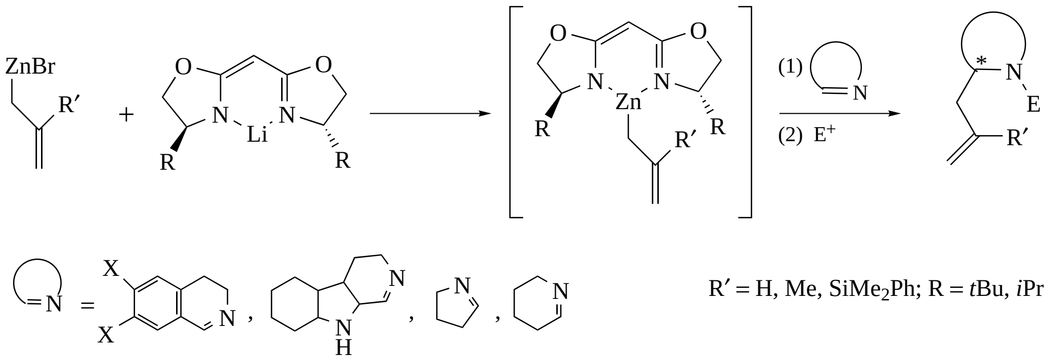

R′ = H, Me, SiMe$_2$Ph; R = *t*Bu, *i*Pr

Scheme 25

6.6 Reactions with Carbon–Carbon Multiple Bonds

Saturated organozinc halides are usually unreactive towards alkenes and nonterminal alkynes, but as already mentioned in previous reactions, allylic zinc derivatives were found to be more reactive towards such functionalities. Furthermore, the reactivity of diorganozinc derivatives can be enhanced by the use of polar (*see Polar Compounds*) solvents, or the addition of diverse Lewis acids**[8,9,262]** (*see Lewis Acids & Bases*). For example, conjugate addition reactions (or 1,4-additions) involving a variety of double bonds in conjugation with an electron-withdrawing group (EWG) work well in *N*-methylpyrrolidine (NMP) and in the presence of Me$_3$SiX (equation 69). A 1,4-addition pathway is also observed in the reaction of diorganozinc compounds with cyclic enones (equation 70). Even if only one of the two R groups is transferred to the substrate, mixed organozinc compounds bearing a nontransferable group such as R–Zn–CH$_2$SiMe$_3$ are usually preferred in order to avoid the waste of an R group.

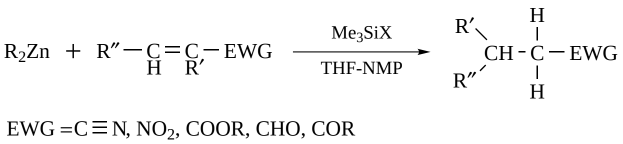

$$R_2Zn + R''-\underset{H}{C}=\underset{R'}{C}-EWG \xrightarrow[\text{THF-NMP}]{Me_3SiX} \overset{R'}{\underset{R''}{}}CH-\overset{H}{\underset{H}{C}}-EWG$$

EWG =C≡N, NO$_2$, COOR, CHO, COR
X = Cl, Br

(69)

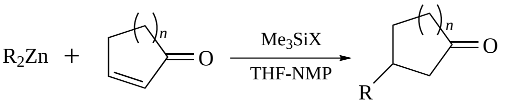

n = 1, 2

(70)

Cyclic enones were also found to react with alkynylzinc halides in the presence of *tert*-butyldimethylsilyl triflate (equation 71).

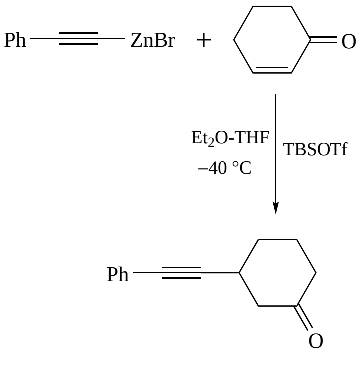

(71)

The addition of diorganozinc compounds to alkynes can be promoted by different metallic species such as Cp$_2$ZrI$_2$ and Ni(acac)$_2$ to give the corresponding vinylic zinc compounds (equation 72). A subsequent hydrolysis leads to the alkene, whereas iodinolysis provides the vinyl iodide derivative. Copper–zinc species, readily obtained by the reaction of organozinc compounds with the THF soluble copper salt $CuCN{\cdot}2LiCl$, add to a variety of conjugated alkenes and alkynes with 1,4-regioselectivity (*see Regioselectivity*) (Scheme 26). Addition to conjugated unsaturated aldehydes usually needs the presence of a Lewis acid catalyst, which nature also determines the regioselectivity (*see Regioselectivity*) of the reaction. While Me_3SiCl promotes 1,4-additions, reactions with $BF_3{\cdot}Et_2O$ lead only to 1,2-addition products. It is worth mentioning that the 1,2-addition pathway was also observed in the reaction of diallylzinc with both linear and cyclic enones (Scheme 27). The peculiar dynamic properties of allylic zinc compounds (see Section 2.3.2) may be the origin of this behavior.

$$R_2Zn + R'{-}{\equiv}{-}H \xrightarrow{\text{Cat.}} R'RC{=}C(H)ZnR \qquad (72)$$

$$\text{Cat.} = Ni(acac)_2,\ Cp_2ZrI_2$$

Organozinc addition reactions to unsaturated systems lead to an intermediate zinc compound which is in most cases further hydrolyzed to give the corresponding protonated organic compound. This intermediate can also be trapped by reaction with electrophiles (*see Electrophile*) (E^+) such as aldehydes, acyl chlorides, organic halides, silyl halides, and so on. Depending on the nature of the electrophile (*see Electrophile*) used, zinc enolate intermediates obtained in organozinc addition to enones can be either O-trapped or C-trapped (Scheme 28).

6.7 The Simmons–Smith Reaction

The original Simmons–Smith reaction is a cyclopropanation reaction of olefins, achieved by an ethereal solution of a zinc–copper couple and diiodomethane[272] (equation 73). It is without doubt one of the most important applications of organozinc reagents in organic synthesis. Its synthetic value emerges from the following features: mild conditions; broad generality with regard to the olefin structure; stereospecificity with respect to the olefin geometry; stereoselectivity with allylic alcohols, acetals, and enol ethers (equation 74). Furthermore, although some insertion (*see Insertion*) of methylene groups into the α-C–H bond of the ethereal solvent occurs, insertion into vinylic C–H bond has never been observed.

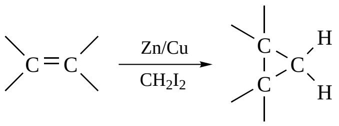

(73)

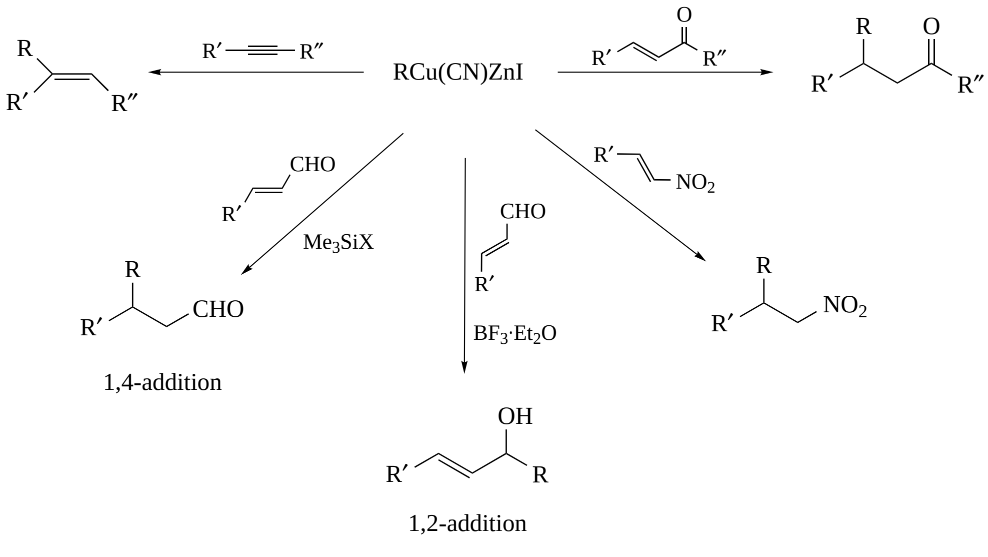

Scheme 26

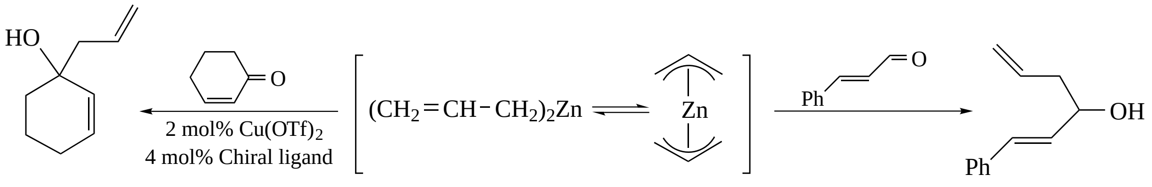

Scheme 27

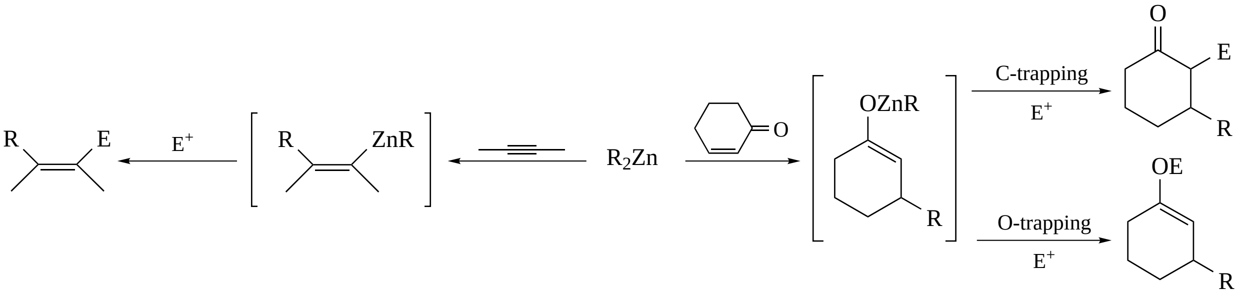

Scheme 28

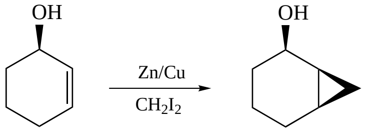

(74)

Over the past 40 years, several modifications of the original procedure have been reported. Wittig and coworkers first reported that carbenoid reagents of the type XCH_2ZnX or $(XCH_2)_2Zn$ could also be prepared by the reaction of Zn^{II} salts with diazoalkane.[273] Later, a significant improvement was made by Furukawa when he found out that diethylzinc could advantageously replaced activated zinc in the reaction with diiodomethane.[274] This procedure, in contrast to the original one, allows the preparation of substituted carbenoid reagents (equation 75). More recently, it was shown that (chloromethyl)zinc reagents are generally more reactive than the (iodomethyl)zinc analogues when 1,2-dichloroethane was used as the solvent.[275]

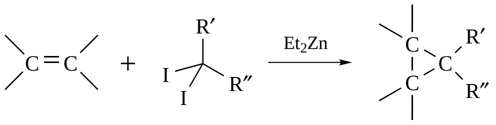

(75)

A detailed comprehension of the mechanism and the exact structure of the species responsible for the cyclopropanation are still the subject of controversies. Since the participation of free carbenes (*see* ***Carbene Complexes***) is unlikely, the reagents are frequently referred to as carbenoids. Simmons and Rickborn first proposed that $(ICH_2)_2Zn{\cdot}ZnI_2$, resulting from the Schlenk equilibrium of ICH_2ZnI, was the reactive species, whereas Dauben concluded from his studies that ICH_2ZnI should be responsible for the cyclopropanation. Relating to the system Et_2Zn/CH_2I_2, Furukawa took an intermediate position when he stipulated that 'the active species may include $EtZnCH_2I$, ICH_2ZnI and/or $Zn(CH_2I)_2$ or associated complexes containing these molecules'.[276] In fact, during the past decade the solid-state structure of both $ICH_2ZnI{\cdot}L$ and $Zn(CH_2I)_2{\cdot}L$ ($L =$ crown ether, glycol bis-ether) has been unambiguously characterized by X-ray crystallography (see Section 2.4.1 Table 4 and Section 3.1.2 Table 7). Moreover, Charette and Marcoux could differentiate the three reagents $EtZnCH_2I$, ICH_2ZnI and $(ICH_2)_2Zn$ by low-temperature ^{13}C spectroscopy in CD_2Cl_2 and in the presence of a chiral (*see Chiral*) complexing agent.[277] In these conditions, they found that ICH_2ZnI did not rearrange in ZnI_2 and $(ICH_2)_2Zn$, and also that the Furukawa's reagent $EtZnCH_2I$ was in equilibrium with Et_2Zn and $(ICH_2)_2Zn$. Finally, it is interesting to note that Charette reported few years ago a storable complex, bipyridine$\cdot Zn(CH_2I)_2$, which could efficiently cyclopropanate olefins upon addition of ZnI_2.

An investigation of the potential energy surface for the model reaction between ethylene and $ClCH_2ZnCl$ reveals the existence of two reaction pathways:[278] the addition process (leading to the cyclopropane product) and the insertion (*see Insertion*) process (leading to the cyclopropene product). However, the energy barrier for the addition process (24.75 kcal mol^{-1}) is found to be smaller than for the insertion process (36.01 kcal mol^{-1}). Thus, at this point both computational and experimental results agree in that the addition pathway is favored and the insertion (*see Insertion*) negligible. This theoretical study also validates the three-centered transition state first suggested by Simmons to account for the stereochemical features of the reaction (Figure 65).

The last few years have seen some development in the preparation of carbenoid reagents. In 1998, Shi and coworkers reported that a new class of (iodomethyl)zinc compounds ($RXZnCH_2I$), readily obtained by the reaction of RXH (ROH, RCO_2H) with $RZnCH_2I$, can efficiently cyclopropanate olefins.[279] The carbenoid reactivity was found to increase with the acidity of RXH. For example, $CF_3CO_2ZnCH_2I$

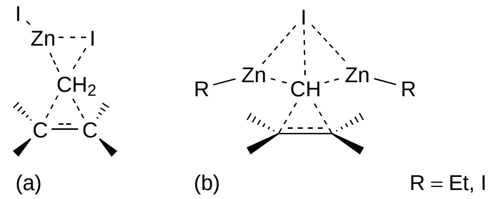

Figure 65 Transition states in the cyclopropanation of ethylene with mono zinc carbenoids (a) and with *gem*-dizinc carbenoids (b)

could cyclopropanate *trans*-β-methylstyrene at room temperature within 30 min[280] (equation 76). Two years later, Charette showed that ethylzincmethyl perfluoropentanoate ($C_4F_9CO_2CH_2ZnEt$), obtained quantitatively by the reaction of diethylzinc with iodomethyl perfluoropentanoate is a highly reactive carbenoid reagent owing to internal Lewis acid (*see Lewis Acids & Bases*) activation[281] (equation 77). This acyloxymethylzinc compound can cyclopropanate poorly reactive alkenes, such as *trans*-stilbene, in moderate yield. In addition, from ^1H NMR and GC analysis he attributed the improved reactivity of Shi's reagent ($CF_3CO_2ZnCH_2I$) to the in situ (*see In Situ Reaction*) formation of the corresponding acyloxymethylzinc ($CF_3CO_2CH_2ZnI$) (Scheme 29).

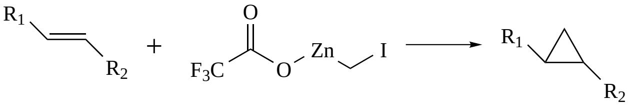

(76)

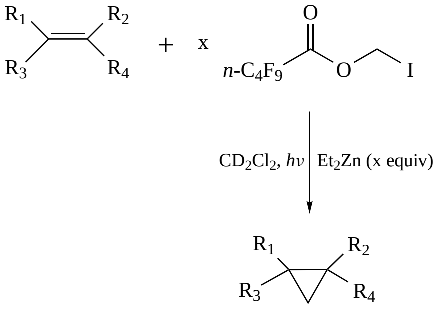

(77)

Alkylbenzenes undergo a remarkable ring expansion reaction with zinc carbenoid reagents derived from CHI_3, which results in the formation of cycloheptatrienyl derivatives (Scheme 30). In 2002, the group of Charette reported that CHI_3 reacts with Et_2Zn or EtZnI at 0 °C to form *gem*-dizinc carbenoids with general formula $ICH(ZnR)_2$ (R = Et, I) which are very reactive and provide access to substituted cyclopropanes in excellent yields.[282] A density functional theory investigation for the cyclopropanation of ethylene has shown that these *gem*-dizinc carbenoids, compared to their corresponding mono zinc carbenoids, react with lower barriers to reaction (about 15 kcal mol^{-1}) which can further be lowered upon addition of ZnI_2 as a Lewis acid.[283] The authors also identified transition states on the way to cyclopropanation products for the reaction of *gem*-dizinc carbenoids with C_2H_2 which present the general schematic structure shown in Figure 65.

A novel application of Simmons–Smith reagents designed for the epoxidation of carbonyl compounds has been reported a few years ago[284] (Scheme 31). The zinc reagents react with sulfides to give the corresponding sulfur ylides, which are then used to generate epoxides from aldehydes. The reaction takes place in mild conditions and works well with aromatic or aliphatic aldehydes. It is interesting to note that unsaturated aldehydes also give the epoxidation compound without undergoing cyclopropanation.

6.8 The Reformatsky Reaction

In its original version the so called Reformatsky reaction was the preparation of β-hydroxy esters, or their deshydratation products, by reacting a mixture of activated zinc, an α-bromo ester and a carbonyl compound in ethereal

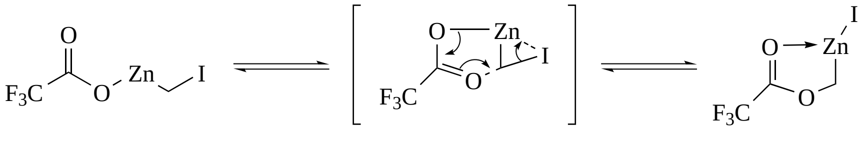

Scheme 29

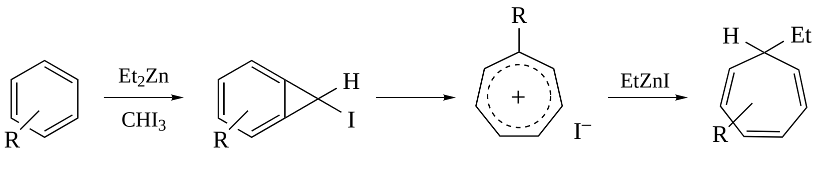

Scheme 30

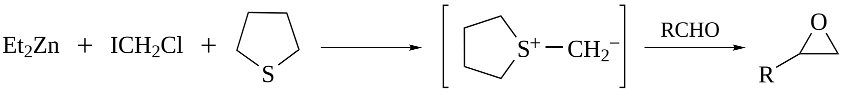

Scheme 31

solvent with subsequent hydrolysis (equation 78). The reaction between zinc and the α-halo ester generates in situ (*see In Situ Reaction*) an organozinc species which further reacts with the aldehydes or ketones to give the corresponding β-hydroxy ester. However, the actual synthesis is typically carried out in two stages with the previous formation of a zinc enolate derivative followed by the addition of a carbonyl compound. The reaction has been extended to other α-halogeno compounds, such as α-halo-nitriles and -amides, and to a large variety of substrates.

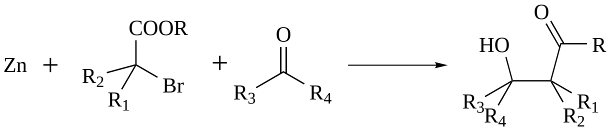

(78)

There has been considerable discussion concerning the nature of the Reformatsky reagent with suggestions for an *O*-metalated species or alternatively a *C*-metalated species. However, as shown by the solid-state structure of $[BrZnCH_2CO_2\text{-}t\text{-}Bu(THF)]_2$ the real situation is best described as a combination of both species (see Section 3.1.2 Figure 30 and Section 3.2.2).

An underlying problem associated with the traditional procedure, which uses zinc dust, is the low reactivity of this metal towards α-halo esters; consequently initiation of the reaction requires an activation of zinc such as Riecke zinc, Zn–Cu couple, Zn/Ag−graphite or Zn/Hg amalgam. It has been shown recently that high-intensity ultrasound (*see Sonication*) irradiation of the reaction mixture in presence of I_2 leads to very high yields in short reaction time, without activation of zinc and even using undistilled reagent-grade dioxane.[285] A variety of other low-valent metals (Ba,[286] Mg, Cd, Ni, In, Ce, Li, $FeCO_5$) or metal derivatives such as Cp_2TiCl,[287] $Li[Bu_2SnI_3]$,[288] SmI_2,[289,290] can efficiently substitute zinc dust. However, because of their susceptibility to oxidation and hydrolysis these reagents need to be freshly prepared. Therefore, efforts are now focused on developing catalytic versions of the Reformatsky reaction. For example, it was found that a number of metal salts such as $RhCl(PPh_3)_3$,[291] $CeCl_3$,[292] Cp_2TiCl_2[293] allow inter- and intramolecular Reformatsky reactions to be achieved under mild condition and with better yields.

In most cases, the Reformatsky reaction is not very stereospecific and mixtures of *erythro*- and *threo*-β-hydroxyesters are obtained when asymmetric α-haloesters are used as reagents (equation 79). The erythro:threo ratio appears to depend on the solvent polarity and the reaction time. However, it is of current interest to develop highly stereocontrolled asymmetric Reformatsky reactions. To date, high diastereoselectivities could be achieved only in a few cases either by substitution of zinc with other metal salts[288,289,290] or by addition of chiral (*see Chiral*) ligands.[294]

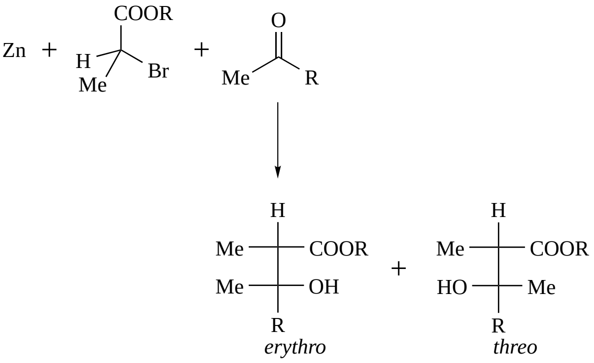

(79)

6.9 Oligomerization and Polymerization (*See Oligomerization & Polymerization by Homogeneous Catalysis*)

Organozinc compounds are efficient catalysts in the polymerization of vinylic monomers, but they have found more applications as catalysts/initiators for ring opening polymerization of heterocyclic monomers[295] such as lactides,[296] lactones, and epoxides[297] (Scheme 32). The organozinc derivatives are usually combined in various stoichiometries with cocatalysts like water, alcohols, carboxylic acid, or amines. The active catalysts are proposed to be complexes with general formula L_nZnX, where X is an active initiating group such as OR, NR_2, or alkyl, and L_n is a ligand that coordinates the Zn^{II} center. As shown in Scheme 32 for the copolymerization of CO_2 and epoxides and in Scheme 33 for the polymerization of lactides, it is generally accepted that the reaction occurs via coordination of a monomer to the coordinatively unsaturated zinc center of the catalyst, followed by insertion (*see Insertion*) into the Zn–X bond.

During the last decade, the design and synthesis of new ligands for specific polymerization reactions has been the focus of much interest. Among the different ligands tested so far, β-diiminates (see Section 3.4.1) have shown the highest activity reported for the copolymerization of CO_2 and epoxides.[179]

When chiral (*see Chiral*) complexes are used as catalysts, they can exhibit some diastereoselectivity. For example, optically active polycarbonates have been prepared by asymmetric copolymerization of cyclohexene oxide and carbon dioxide in the presence of a mixture of Et_2Zn and a chiral amino alcohol[298] (Scheme 34). Even achiral complexes have been found to exhibit some diastereoselectivity in polymerization reactions. For instance, monomeric Zn^{II} complexes with tris(pyrazolyl- and indazolyl-)hydroborate ligands (see Section 3.4.2) polymerize preferentially *meso*-lactide over D-lactide and L-lactide in CH_2Cl_2 at 22 °C.[299] The compound EtZnN(*t*-Bu)ZnEt, which is easily prepared by reaction of Et_2Zn with *t*-$BuNH_2$, was found to be an excellent catalyst for the stereospecific polymerization of propylene oxide.[300]

The construction of chiral (*see Chiral*) zinc complexes in order to perform stereoselective polymerizations has

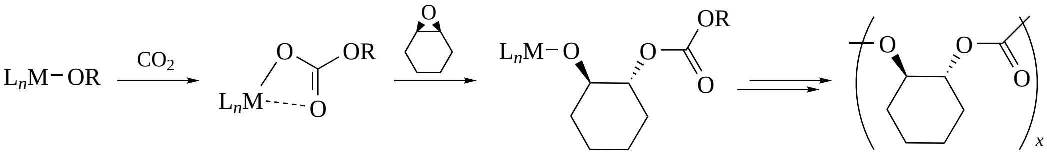

Scheme 32

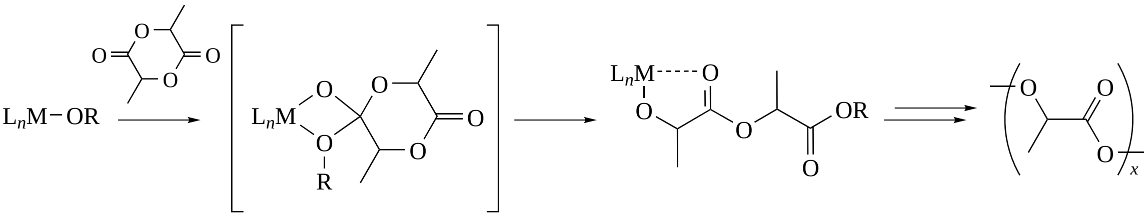

Scheme 33

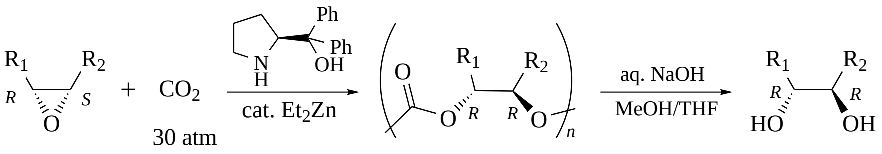

Scheme 34

been recently undertaken by Chakraborty and Chen.[301] They have found that the tetranuclear complex {(±)-*trans*-Cy($NSiMe_3$)$_2$}$_2$$Zn_4Et_4$ and the dinuclear complex {(±)-*trans*-Cy($NHSiMe_3$)($NSiMe_3$)}$_2$$Zn_2Et_2$ are obtained in good yields from the reaction of racemic (±)-*trans*-1,2-($NHSiMe_3$)$_2$-cyclohexane ((±)-trans-cy($NHSiMe_3$)$_2$) with two equiv of Et_2Zn and one equiv of Et_2Zn, respectively. In both cases, only one diastereomer was formed and its molecular structure determined by X-ray crystallography (Figure 66). Whereas the two complexes were shown to be efficient initiators for polymerization of ϵ-caprolactone and L-lactide, only the tetranuclear complex was efficient for the polymerization of methyl methacrylate upon activation with $Al(C_6F_5)_3$.

Cationic organozinc compounds are expected to be good catalysts for ring opening polymerization reactions of epoxides and lactones because the enhanced Lewis acidity (*see Lewis Acids & Bases*) of the zinc center favors its coordination to the monomer. For example, Walker and coworkers have found that the cationic zinc substituted cyclopentadienyl complex [3,5-$Me_2C_6H_3CH_2CMe_2C_5H_4Zn$(TMEDA)]$^+$ [EtB(C_6F_5)$_3$]$^-$ is an active initiator species for the polymerization of cyclohexene oxide and ϵ-caprolactone.[302]

6.10 Reactivity of *Gem*-Dimetallic Species

Organo-*gem*-dimetallic compounds that possess two nucleophilic (*see Lewis Acids & Bases*) sites on one carbon atom

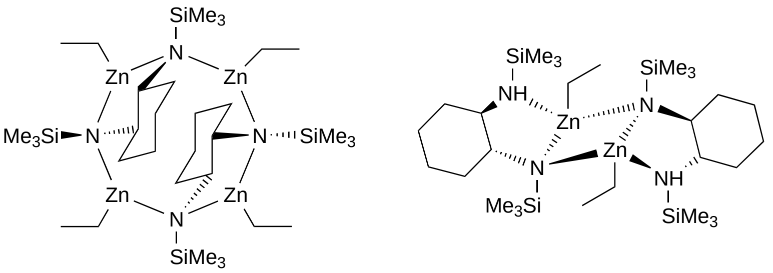

Figure 66 Structures of {(±)-*trans*-Cy($NSiMe_3$)$_2$}$_2$$Zn_4Et_4$ and {(±)-*trans*-Cy($NHSiMe_3$)($NSiMe_3$)}$_2$$Zn_2Et_2$

can undergo multiple transformations in one-pot reactions and form two new C–C bonds. This is particularly attractive for organic chemists who need new strategies with a minimum of chemical steps for the building of complex molecules. In recent years, *gem*-dizincio reagents in particular have been the focus of much interest because their relative stability and moderate reactivity, compared to the related *gem*-dilithio and -dimagnesio derivatives, permit the control of both chemoselectivity and stereoselectivity during the transformations. The synthesis and synthetic applications of 1,1-sp^3 and 1,1-sp^2 organodimetallic derivatives have been specifically covered in two different reviews.[245,246]

The simplest *gem*-dizincio alkane bis(iodozincio)methane [$CH_2(ZnI)_2$] reacts with aldehydes, and with ketones in presence of a suitable activator or catalyst, to produce the corresponding olefinated compounds in good yields (equation 80). It has been shown that the nucleophilicity of the zinc atom in $CH_2(ZnI)_2$ can be enhanced by coordination of a heteroatom from a ligand or a solvent. Substrates which contain a suitably placed donor atom also lead to activation. For example, 1,2-diketones (*see Diketones*) such as benzil (PhCOCOPh) undergo efficient [2+1] cycloaddition reactions with $CH_2(ZnI)_2$[303] (equation 81). The reaction is stereoselective, leading only to *cis*-diol derivatives.

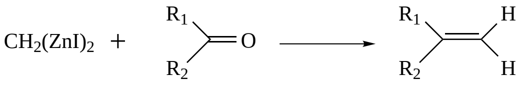

(80)

$R_1 = R_2 =$ Alkyl or $R_1 =$ H, $R_2 =$ Alkyl

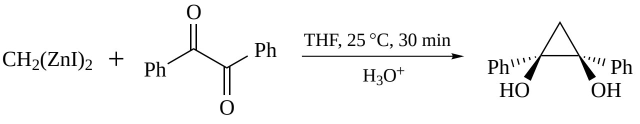

(81)

Substituted *gem*-dimetallic compounds, readily obtained via allylation of alkenyl organometallics, react with aldehydes in the presence of $BF_3{\cdot}Et_2O$ but do not react with ketones. When alkylidenemalonates are used instead of aldehydes, the Z-olefins (*see (E) & (Z) Isomers*) are obtained with a very high stereoselectivity (Scheme 35). A transmetallation reaction with copper cyanide significantly increases the reactivity of *gem*-dimetallic derivatives via formation of 1,1-zinca cyanocuprates. Indeed, when these compounds react with alkylating or allylating reagents, they give products of double alkylation or allylation (equation 82).

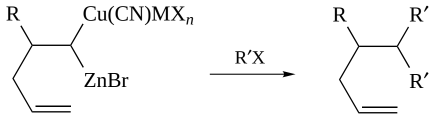

(82)

$MX_n =$ ZnBr, Li, MgBr
$R'X = Me_3SnCl$, MeI, $CH_2{=}CHCH_2Br$

When *gem*-dimetallic reagents contain zinc and a metal of different nature MX_n (MX_n = MgBr, Li), they can react successively with two different electrophiles (*see Electrophile*) $E_1{}^+$ and $E_2{}^+$, with the more reactive C–M bond reacting first (Scheme 36). Consequently, the vinylation of 1,1-borio zincioalkanes, catalyzed by Pd^{II} salts, is an excellent procedure for the preparation of reactive allylboranes (equation 83).

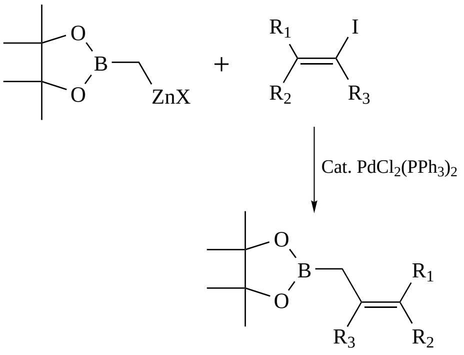

(83)

A strong intramolecular chelation (*see Chelate Effect*) of a donor group to one of the zinc atoms leads to a good selectivity between the two metallic centers in sequential addition reactions, and also leads to a good diastereoselective reactivity of the organo-*gem*-dimetallics. As seen in Section 5.1 concerning allylmetalation of vinyl organometallic compounds, the intramolecular coordination of a basic atom (sulfur < oxygen < nitrogen) to the metal of the starting vinyl reagent allows the creation of two stereogenic centers in the resulting *gem*-dimetallic derivatives. Thus, a third stereogenic center can be produced by diastereoselective reactivity of the two metals (Scheme 37). Nevertheless, it was shown that the stereoselectivity depends strongly on the nature of the first electrophile (*see Electrophile*) used.

When the intramolecular chelating group (*see Chelating Ligands*) is a methoxy-methyl-ether (MOM) in γ-position, an

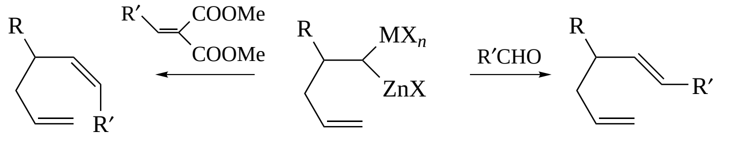

Z = 100% MX_n = MgBr, ZnBr E/Z = 92/8 to 99/1

Scheme 35

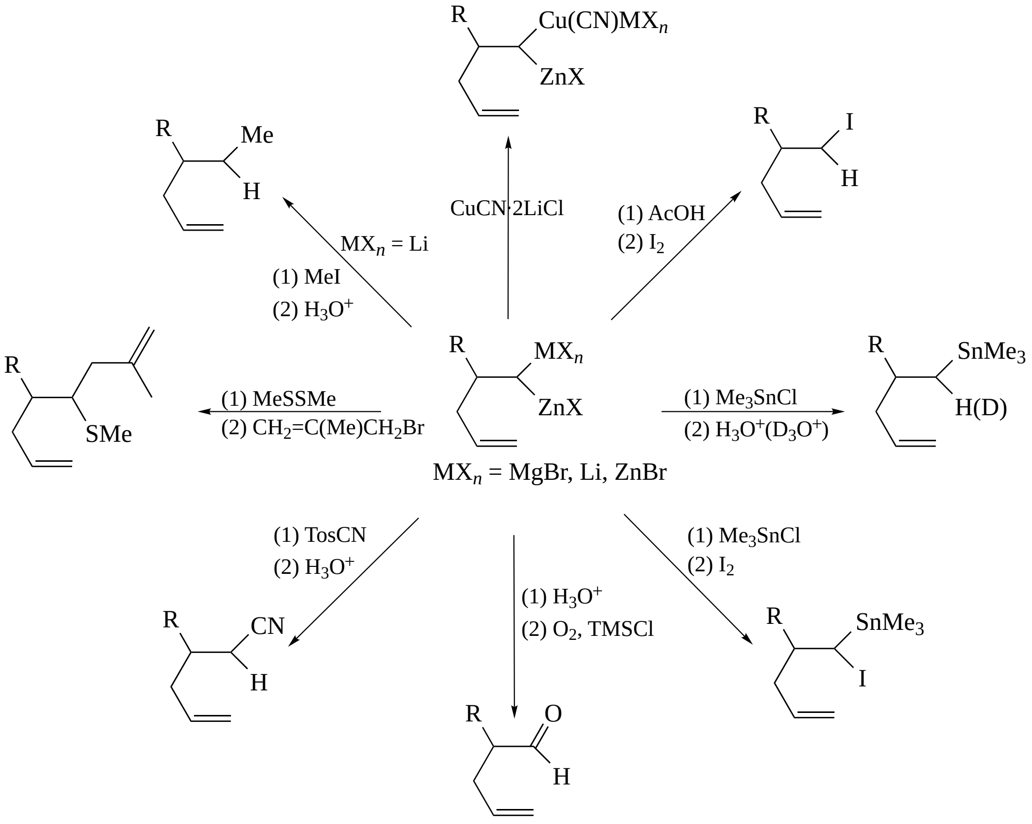
R
Cu(CN)MX$_n$
ZnX
CuCN·2LiCl
R
Me
H
MX$_n$ = Li
(1) MeI
(2) H$_3$O$^+$
R
I
H
(1) AcOH
(2) I$_2$
R
SMe
(1) MeSSMe
(2) CH$_2$=C(Me)CH$_2$Br
R
MX$_n$
ZnX
MX$_n$ = MgBr, Li, ZnBr
(1) Me$_3$SnCl
(2) H$_3$O$^+$(D$_3$O$^+$)
R
SnMe$_3$
H(D)
(1) TosCN
(2) H$_3$O$^+$
R
CN
H
(1) H$_3$O$^+$
(2) O$_2$, TMSCl
R
O
H
(1) Me$_3$SnCl
(2) I$_2$
R
SnMe$_3$
I

Scheme 36

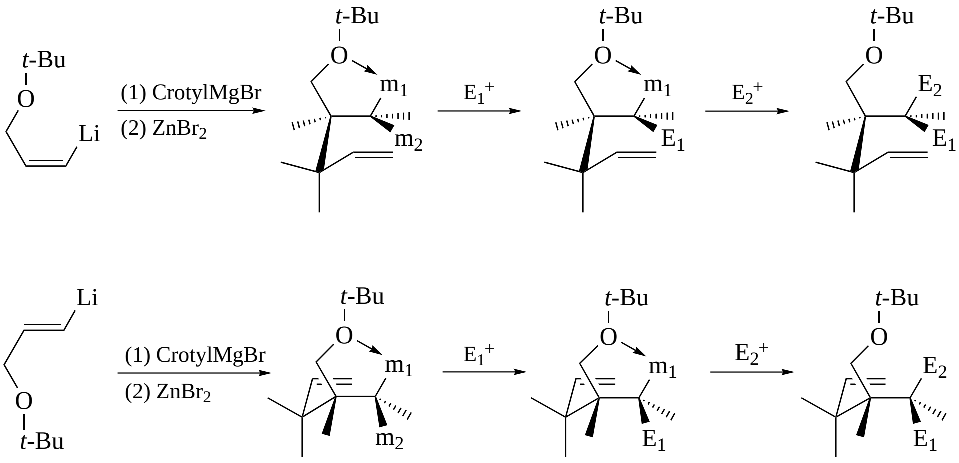
t-Bu
O
Li
(1) CrotylMgBr
(2) ZnBr$_2$
m$_1$
m$_2$
E$_1^+$
E$_1$
E$_2^+$
E$_2$

Scheme 37

internal nucleophilic substitution occurs at room temperature and products of cyclopropanation are obtained in good yields (equation 84).

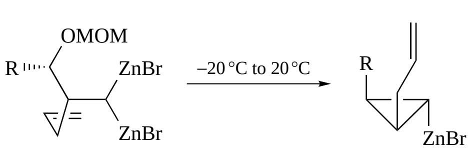
OMOM
R
ZnBr
ZnBr
−20 °C to 20 °C
R
ZnBr

(84)

The reactivity of *gem*-dizincioalkenes (prepared by metal allylation of alkynyl metals (see Section 5.1)) with aldehydes leads to the corresponding allene derivatives in moderate yields (Scheme 38). As already seen for *gem*-dizincioalkanes, an internal chelation of the 1,1-dimetalloalkene with a Lewis functional group allows differentiation of the reactivity of the two metal centers towards electrophile (*see Electrophile*) reagents. Scheme 39 summarizes the reactivity

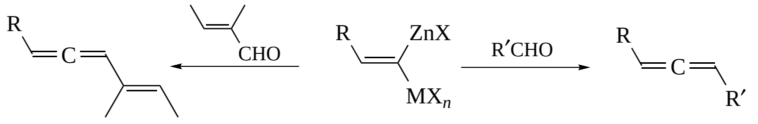

R
C
CHO
R
ZnX
MX$_n$
R′CHO
R
C
R′

Scheme 38

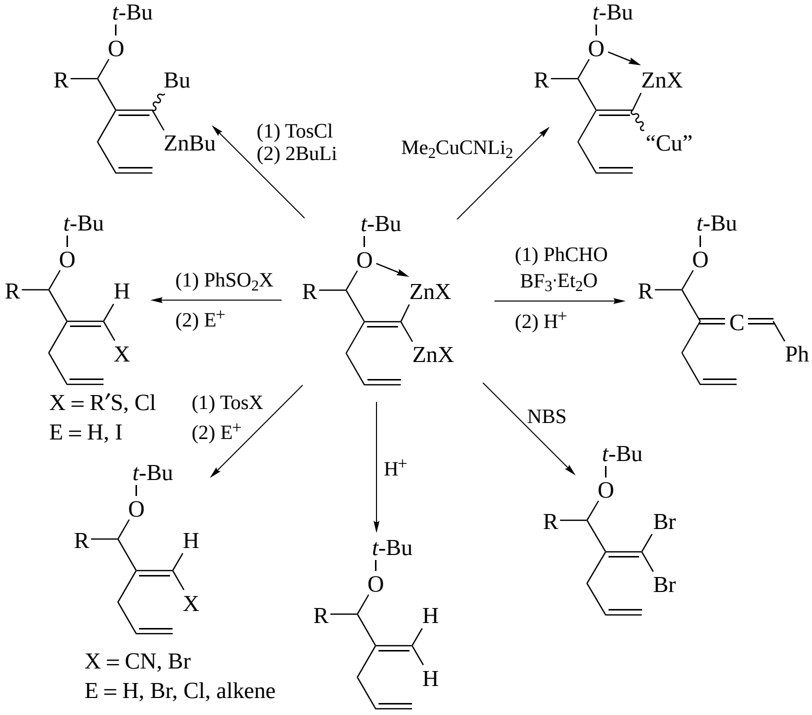

t-Bu
O
R
Bu
ZnBu
(1) TosCl
(2) 2BuLi
Me$_2$CuCNLi$_2$
ZnX
"Cu"
(1) PhSO$_2$X
(2) E$^+$
H
X
X = R′S, Cl
E = H, I
ZnX
(1) PhCHO
BF$_3$·Et$_2$O
(2) H$^+$
C
Ph
(1) TosX
(2) E$^+$
H$^+$
NBS
Br
X = CN, Br
E = H, Br, Cl, alkene

Scheme 39

of 1,1-dizincioalkene compounds containing a *tert*-butylether group in γ-position.

gem-Dizincioalkenes derivatives containing a suitably placed alkyl halide group can also be used for the synthesis of cyclobutene and cyclopentene compounds via intramolecular (*see Intramolecular*) nucleophilic substitution reactions (equation 85).

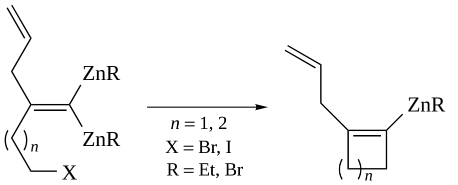

ZnR
ZnR
( )$_n$
X
n = 1, 2
X = Br, I
R = Et, Br
ZnR
( )$_n$

(85)

7 RELATED ARTICLES

Alkali Metals: Organometallic Chemistry; Alkaline Earth Metals: Organometallic Chemistry; Asymmetric Synthesis by Homogeneous Catalysis; Beryllium & Magnesium: Organometallic Chemistry; Cadmium: Organometallic Chemistry; Coordination & Organometallic Chemistry: Principles; Mechanisms of Reaction of Organometallic Complexes; Mercury: Organometallic Chemistry; Organic Synthesis Using Metal-mediated Coupling Reactions.

8 REFERENCES

1. E. Frankland, *Ann.*, 1849, **71**, 171.
2. E. Frankland, *J. Chem. Soc.*, 1850, **2**, 263.
3. D. Seyferth, *Organometallics*, 2001, **20**, 2940.
4. J. Boersma, in 'Comprehensive Organometallic Chemistry I', eds. G. Wilkinson, F. G. A. Stone, and E. W. Abel, Pergamon Press, Oxford, 1982, Vol. 2, Chap. 16, p. 824.
5. P. O'Brien, in 'Comprehensive Organometallic Chemistry II', eds. G. Wilkinson, F. G. A. Stone, and E. W. Abel, Pergamon Press, Oxford, 1995Vol., 3, Chap. 4, p. 175.
6. P. Knochel and P. Jones, 'Organozinc Reagents – A Practical Approach', Oxford University Press, Oxford, 1999.

7. W. A. Herrmann, ‘Synthetic Methods of Organometallic and Inorganic Chemistry Volume 5’, Georg Thieme Verlag, 1998.
8. P. Knochel and R. D. Singer, *Chem. Rev.*, 1993, **93**, 2117.
9. P. Knochel, J. J. Almena Perea, and P. Jones, *Tetrahedron*, 1998, **54**, 8275.
10. A. Boudier, L. O. Bromm, M. Lotz, and P. Knochel, *Angew. Chem., Int. Ed. Engl.*, 2000, **39**, 4414.
11. K. J. Klabunde and T. O. Murdock, *J. Org. Chem.*, 1976, **41**, 1076.
12. M. A. Guerra, T. R. Bierschenk, and R. J. Lagow, *J. Am. Chem. Soc.*, 1986, **108**, 4103.
13. R. D. Riecke, *Acc. Chem. Res.*, 1977, **10**, 301.
14. A. Guijarro, D. M. Rosenberg, and R. D. Riecke, *J. Am. Chem. Soc.*, 1999, **121**, 4155.
15. M. J. Rozema, S. Achyutha Rao, and P. Knochel, *J. Org. Chem.*, 1992, **57**, 1956.
16. S. Vettel, A. Vaupel, and P. Knochel, *J. Org. Chem.*, 1996, **61**, 7473.
17. T. Hayashi, M. Konishi, Y. Kobori, M. Kumada, T. Higuchi, and K. Hirotsu, *J. Am. Chem. Soc.*, 1984, **106**, 158.
18. A. B. Charette, A. Beauchemin, and J.-F. Marcoux, *J. Am. Chem. Soc.*, 1998, **120**, 5114.
19. S. Berger, F. Langer, C. Lutz, P. Knochel, T. A. Mobley, and C. K. Reddy, *Angew. Chem., Int. Ed. Enl.*, 1997, **36**, 1496.
20. C. Lutz and P. Knochel, *J. Org. Chem.*, 1997, **62**, 7895.
21. A. L. Galyer and G. Wilkinson, *Inorg. Synth.*, 1979, **19**, 253.
22. I. Klement, M. Rottländer, C. E. Tucker, T. N. Majid, P. Knochel, P. Venegas, and G. Cahiez, *Tetrahedron*, 1996, **52**, 7201.
23. N. Wiberg, K. Amelunxen, H.-W. Lerner, H. Nöth, A. Appel, J. Knizek, and K. Polborn, *Z. Anorg. Allg. Chem.*, 1997, **623**, 1861.
24. N. Wiberg, W. Niedermayer, H.-W. Lerner, and M. Bolte, *Z. Anorg. Allg. Chem.*, 2001, **627**, 1043.
25. L. I. Zakharkin and O. Y. Okhlobystin, *Z. Obshch. Khim.*, 1960, **30**, 2134.
26. K. H. Thiele, G. Engelhardt, J. Köhler, and M. Arnstedt, *J. Organomet. Chem.*, 1967, **9**, 385.
27. R. Duddu, M. Eckhardt, M. Furlong, H. P. Knoess, S. Berger, and P. Knochel, *Tetrahedron*, 1994, **50**, 2415.
28. E. Hupe, P. Knochel, and K. J. Szabó, *Organometallics*, 2002, **21**, 2203.
29. E. Frankland and D. F. Duppa, *Justus Liebigs Ann. Chem.*, 1864, **130**, 117.
30. E. K. S. Liu, *Inorg. Chem.*, 1980, **19**, 266.
31. E. K. S. Liu and L. B. Asprey, *J. Organomet. Chem.*, 1979, **169**, 249.
32. M. Westerhausen, B. Rademacher, and W. Poll, *J. Organomet. Chem.*, 1991, **421**, 175.
33. C. Eaborn, M. S. Hill, P. B. Hitchcock, J. D. Smith, and S. Zhang, *Organometallics*, 1999, **18**, 2342.
34. I. E. Gümrükcüoglü, J. Jeffery, M. F. Lappert, J. B. Pedley, and A. K. Rai, *J. Organomet. Chem.*, 1988, **341**, 53.
35. R. L. Jackson, *Chem. Phys. Lett.*, 1989, **163**, 315.
36. M. Melnik, J. Skorsepa, K. Györyová, and C. E. Holloway, *J. Organomet. Chem.*, 1995, **503**, 1.
37. A. Almenningen, T. U. Helgaker, A. Haaland, and S. Samdal, *Acta Chem. Scand.*, 1982, **A36**, 159.
38. P. R. Markies, G. Schat, O. S. Akkerman, F. Bickelhaupt, W. J. J. Smeets, and A. L. Spek, *Organometallics*, 1990, **9**, 2243.
39. M. Westerhausen, B. Rademacher, W. Schwarz, and J. Weidlein, *J. Organomet. Chem.*, 1994, **469**, 135.
40. J. Soulati, K. L. Henold, and J. P. Oliver, *J. Am. Chem. Soc.*, 1971, **93**, 5694.
41. K. L. Henold, J. Soulati, and J. P. Oliver, *J. Am. Chem. Soc.*, 1969, **91**, 3171.
42. Y. Sun, W. E. Piers, and M. Parvez, *Can. J. Chem*, 1998, **76**, 513.
43. S. Brooker, N. Bertel, D. Stalke, M. Noltemeyer, H. W. Roesky, G. M. Sheldrick, and F. T. Edelmann, *Organometallics*, 1992, **11**, 192.
44. E. A. Jeffery, T. Mole, and J. K. Saunders, *Aust. J. Chem.*, 1968, **21**, 137.
45. R. Benn, E. G. Hoffmann, H. Lehmkuhl, and H. Nehl, *J. Organomet. Chem.*, 1978, **146**, 103.
46. P. H. M. Budzelaar, J. J. Engelberts, and J. H. van Lenthe, *Organometallics*, 2003, **22**, 1562.
47. T. Aoyagi, H. M. M. Shearer, K. Wade, and G. Whitehead, *J. Organomet. Chem.*, 1978, **146**, C29.
48. A. Haaland, S. Samdal, and R. Seip, *J. Organomet. Chem.*, 1978, **153**, 187.
49. P. H. M. Budzelaar, J. Boersma, G. J. M. van der Kerk, A. L. Spek, and A. J. M. Duisenberg, *J. Organomet. Chem.*, 1985, **281**, 123.
50. R. Blom, A. Haaland, and J. Weidlein, *J. Chem. Soc., Chem. Commun.*, 1985, **5**, 266.
51. R. Blom, J. Boersma, P. H. M. Budzelaar, B. Fischer, A. Haaland, H. V. Volden, and J. Weidlein, *Acta Chem. Scand.*, 1986, **A40**, 113.
52. B. Fischer, P. Wijkens, J. Boersma, G. van Koten, W. J. J. Smeets, A. L. Spek, and P. H. M. Budzelaar, *J. Organomet. Chem.*, 1989, **376**, 223.
53. D. J. Burkey and T. P. Hanusa, *J. Organomet. Chem.*, 1996, **512**, 165.
54. P. H. M. Budzelaar, J. Boersma, G. J. M. Van der Kerk, and A. L. Spek, *Organometallics*, 1984, **3**, 1187.
55. D. J. Darensbourg, J. R. Wildeson, and J. C. Yarbrough, *Organometallics*, 2001, **20**, 4413.
56. R. D. Ernst, J. W. Freeman, P. N. Swepston, and D. R. Wilson, *J. Organomet. Chem.*, 1991, **402**, 17.
57. H. Yasuda, Y. Ohnuma, A. Nakamura, Y. Kai, N. Yasuoka, and N. Kasai, *Bull. Chem. Soc. Jpn.*, 1980, **53**, 1101.

58. M. Westerhausen, M. Wieneke, H. Nöth, T. Seifert, A. Pfitzner, W. Schwarz, O. Schwarz, and J. Weidlein, *Eur. J. Inorg. Chem.*, 1998, 1175.
59. G.-J. M. Gruter, G. P. M. van Klink, O. S. Akkerman, and F. Bickelhaupt, *Chem. Rev.*, 1995, **95**, 2405.
60. K.-H. Thiele, *Z. Anorg. Allg. Chem.*, 1962, **319**, 183.
61. K.-H. Thiele, *Z. Anorg. Allg. Chem.*, 1963, **322**, 71.
62. P. R. Markies, G. Schat, O. S. Akkerman, F. Bickelhaupt, and A. L. Spek, *J. Organomet. Chem.*, 1992, **430**, 1.
63. M. Weidenbruch, M. Herrndorf, A. Schäfer, S. Pohl, and W. Saak, *J. Organomet. Chem.*, 1989, **361**, 139.
64. R. M. Fabicon, M. Parvez, and H. G. Richey Jr, *Organometallics*, 1999, **18**, 5163.
65. A. D. Pajerski, G. L. BergStresser, M. Parvez, and H. G. Richey, *J. Am. Chem. Soc.*, 1988, **110**, 4844.
66. J. E. Chubb and H. G. Richey Jr, *Organometallics*, 1998, **17**, 3204.
67. P. R. Markies, G. Schat, O. S. Akkerman, and F. Bickelhaupt, *Organometallics*, 1991, **10**, 3538.
68. H.-J. Gais, G. Bülow, and G. Raabe, *J. Am. Chem. Soc.*, 1993, **115**, 7215.
69. B. Fischer, J. Boersma, G. Van Koten, W. J. J. Smeets, and A. L. Spek, *Organometallics*, 1989, **8**, 667.
70. S. E. Denmark, J. P. Edwards, and S. R. Wilson, *J. Am. Chem. Soc*, 1992, **114**, 2592.
71. P. O'Brien, M. B. Hursthouse, M. Motevalli, J. R. Walsh, and A. C. Jones, *J. Organomet. Chem.*, 1993, **449**, 1.
72. M. Westerhausen, M. Wieneke, and W. Schwarz, *J. Organomet. Chem.*, 1996, **522**, 137.
73. M. Westerhausen, M. Wieneke, B. B. Rademacher, and W. Schwarz, *Chem. Ber. Recl.*, 1997, **130**, 1499.
74. H. Mimoun, J. Y. de Saint Laumer, L. Giannini, R. Scopelliti, and C. Floriani, *J. Am. Chem. Soc.*, 1999, **121**, 6158.
75. K.-H. Thiele, *Z. Anorg. Allg. Chem.*, 1963, **325**, 156.
76. K.-H. Thiele, *Z. Anorg. Allg. Chem.*, 1964, **330**, 8.
77. J. G. Notes and J. Boersma, *J. Organomet. Chem.*, 1967, **9**, 1.
78. A. C. Jones, S. A. Rushworth, P. O'Brien, J. R. Walsh, and C. Meaton, *Adv. Mater. Opt. Electron.*, 1994, **4**, 343.
79. N. L. Pickett, P. Lightfoot, and D. J. Cole-Hamilton, *Adv. Mater. Opt. Electron.*, 1997, **7**, 23.
80. D. F. Foster and D. J. Cole-Hamilton, *Inorg. Synth.*, 1996, **31**, 29.
81. M. B. Hursthouse, M. Motevalli, P. O'Brien, J. R. Walsh, and A. C. Jones, *Organometallics*, 1991, **10**, 3196.
82. X. Huang, H. Sun, X. Wang, Y. J. Liu, X. You, and X. Sun, *Main Group Met. Chem.*, 1996, **19**, 161.
83. P. O'Brien, M. B. Hursthouse, M. Motevalli, J. R. Walsh, and A. C. Jones, *J. Organomet. Chem.*, 1993, **449**, 1.
84. P. C. Andrews, C. L. Raston, B. W. Skelton, and A. H. White, *Organometallics*, 1998, **17**, 779.
85. K. M. Coward, A. C. Jones, A. Steiner, J. F. Bickley, L. M. Smith, and M. E. Pemble, *J. Chem. Soc., Dalton Trans.*, 2000, **19**, 3480.
86. J. Behm, S. D. Lotz, and W. A. Hermann, *Z. Anorg. Allg. Chem.*, 1993, **619**, 849.
87. E. K. S. Liu, *Inorg. Chem.*, 1980, **19**, 266.
88. V. W. Day, D. H. Campbell, and C. J. Michejda, *J. Chem. Soc., Chem. Commun.*, 1975, **4**, 118.
89. A. J. Arduengo III, H. V. Rasika Dias, F. Davidson, and R. L. Harlow, *J. Organomet. Chem.*, 1993, **462**, 13.
90. R. S. Dickson, G. D. Fallon, and Q.-Q. Zhang, *J. Chem. Soc., Dalton Trans.*, 2000, **13**, 1973.
91. J. Dekker, J. Boersma, L. Fernholt, A. Haaland, and A. L. Spek, *Organometallics*, 1987, **6**, 1202.
92. M. J. Henderson, R. I. Papasergio, C. L. Raston, A. H. White, and M. F. Lappert, *J. Chem. Soc., Chem. Commun.*, 1986, **9**, 672.
93. J. L. Atwood, D. E. Berry, S. R. Stobart, and M. J. Zaworotko, *Inorg. Chem.*, 1983, **22**, 3480.
94. H. Schumann, S. freitag, F. Girgsdies, H. Hemling, and G. Kociok-Köhn, *Eur. J. Inorg. Chem.*, 1998, 245.
95. S. Wingerter, H. Gornitzka, G. Bertrand, and D. Stalke, *Eur. J. Inorg. Chem.*, 1999, 173.
96. E. Okninska and K. B. Starowieyski, *J. Organomet. Chem.*, 1988, **347**, 1.
97. E. Okninska and K. B. Starowieyski, *J. Organomet. Chem.*, 1989, **376**, 7.
98. A. Haaland, H. Lehmkuhl, and H. Nehl, *Acta. Chem. Scand., Ser. A*, 1984, **A38**, 547.
99. J. St. Denis, J. P. Oliver, T. W. Dolzine, and J. B. Smart, *J. Organomet. Chem.*, 1974, **71**, 315.
100. S. Huo, *Org. Lett.*, 2003, **5**, 423.
101. S. Sibille, V. Ratovelomanana, and J. Périchon, *J. Chem. Soc., Chem. Commun.*, 1992, 283.
102. C. Gosmini, Y. Rollin, J. Y. Nédélec, and J. Périchon, *J. Org. Chem.*, 2000, **65**, 6024.
103. H. Fillon, C. Gosmini, and J. Périchon, *J. Am. Chem. Soc.*, 2003, **125**, 3867.
104. S. Norsikian, I. Marek, S. Klein, J. F. Poisson, and J. F. Normant, *Chem. Eur. J.*, 1999, **5**, 2055.
105. P. Jones and P. Knochel, *J. Org. Chem.*, 1999, **64**, 186.
106. D. E. Frantz, R. Fässler, C. S. Tomooka, and E. M. Carreira, *Acc. Chem. Res.*, 2000, **33**, 373.
107. B. T. Moseley and H. M. M. Shearer, *Chem. Commun.*, 1966, **23**, 876.
108. J. Boersma and J. G. Noltes, *Tetrahedron Lett.*, 1966, **7**, 1521.
109. S. S. Al-Juaid, C. Eaborn, A. Habtemariam, P. B. Hitchcock, J. D. Smith, K. Tavakkoli, and A. D. Webb, *J. Organomet. Chem.*, 1993, **462**, 45.
110. C. Eaborn, M. S. Hill, P. B. Hitchcock, and J. D. Smith, *J. Chem. Soc., Dalton Trans.*, 2002, **12**, 2467.

111. K.-H. Thiele, E. Langguth, and G. E. Müller, *Z. Anorg. Allg. Chem.*, 1980, **462**, 152.
112. B. Rademacher, W. Schwarz, and M. Westerhausen, *Z. Annorg. Allg. Chem.*, 1995, **621**, 1395.
113. J. Dekker, P. H. M. Budzelaar, J. Boersma, and G. J. M. van der Kerk, *Organometallics*, 1984, **3**, 1403.
114. A. B. Charette, J. F. Marcoux, C. Molinaro, A. Beauchemin, C. Brochu, and E. Isabel, *J. Am. Chem. Soc.*, 2000, **122**, 4508.
115. A. B. Charette, J.-F. Marcoux, and F. Bélanger-Gariépy, *J. Am. Chem. Soc.*, 1996, **118**, 6792.
116. G.-J. M. Gruter, O. S. Akkerman, F. Bickelhaupt, W. J. J. Smeets, and A. L. Spek, *Recl. Trav. Chim. Pays-Bas*, 1993, **112**, 425.
117. D. Bellus, B. Klingert, R. W. Lang, and G. Rihs, *J. Organomet. Chem.*, 1988, **339**, 17.
118. H. M. M. Shearer and C. B. Spencer, *Acta Crystallogr.*, 1980, **B36**, 2046.
119. J. G. Noltes and J. Boersma, *J. Organomet. Chem.*, 1968, **12**, 425.
120. G. E. Coates and D. Ridley, *J. Chem. Soc. A*, 1966, 1064.
121. P. A. van der Schaaf, E. Wissing, J. Boersma, W. J. J. Smeets, A. L. Spek, and G. van Koten, *Organometallics*, 1993, **12**, 3624.
122. M. B. Dinger and M. J. Scott, *Inorg. Chem.*, 2001, **40**, 1029.
123. P. Górecki and W. Kuran, *J. Organomet. Chem.*, 1986, **312**, 1.
124. W. Kuran and E. Mazanek, *J. Organomet. Chem.*, 1990, **384**, 13.
125. M. L. Ziegler and J. Weiss, *Angew. Chem., Int. Ed. Engl.*, 1970, **9**, 905.
126. M. Ishimori, T. Hagiwara, T. Tsuruta, Y. Kai, N. Yasuoka, and N. Kasai, *Bull. Chem. Soc. Jpn.*, 1976, **49**, 1165.
127. A. Charette, A. Beauchemin, S. Francoeur, F. Bélanger-Gariépy, and G. D. Enright, *Chem. Commun.*, 2002, **5**, 466.
128. F. H. Allen, *Acta Crystallogr.*, 2002, **B58**, 380.
129. I. J. Bruno, J. C. Cole, P. R. Edington, M. Kessler, C. F. Macrae, P. McCabe, J. Pearson, and R. Taylor, *Acta Crystallogr.*, 2002, **B58**, 389.
130. R. J. Herold, S. L. Aggarwal, and V. Neff, *Can. J. Chem.*, 1963, **41**, 1368.
131. W. Kuran and M. Czernecka, *J. Organomet. Chem.*, 1984, **263**, 1.
132. S. S. Al-Juaid, N. H. Buttrus, C. Eaborn, P. B. Hitchcock, A. T. L. Roberts, J. D. Smith, and A. C. Sullivan, *J. Chem. Soc., Chem. Commun.*, 1986, **12**, 908.
133. F. Schindler, H. Schimbaur, and U. Krüger, *Angew. Chem., Int. Ed. Engl.*, 1965, **4**, 876.
134. K. Su, T. Don Tilley, and M. J. Sailor, *J. Am. Chem. Soc.*, 1996, **118**, 3459.
135. M. Driess, K. Merz, and S. Rell, *Eur. J. Inorg. Chem.*, 2000, 2517.
136. G. Anantharaman, H. W. Roesky, and J. Magull, *Angew. Chem., Int. Ed. Engl.*, 2002, **41**, 1126.
137. G. Anantharaman, N. D. Reddy, H. W. Roesky, and J. Magull, *Organometallics*, 2001, **20**, 5777.
138. S. Luli, I. Madura, J. Serwatowski, and J. Zachara, *Inorg. Chem.*, 1999, **38**, 4937.
139. R. Anulewicz-Ostrowska, S. Luli, E. Pindelska, and J. Serwatowski, *Inorg. Chem.*, 2002, **41**, 2525.
140. J. Dekker, A. Schouten, P. H. M. Budzelaar, J. Boersma, G. J. M. van Der Kerk, A. L. Spek, and A. J. M. Duisenberg, *J. Organomet. Chem.*, 1987, **320**, 1.
141. F. H. Van der Steen, J. Boersma, A. L. Spek, and G. Van Koten, *Organometallics*, 1991, **10**, 2467.
142. R. L. Shiner, *Org. React. (N.Y.)*, 1942, **1**, 1.
143. M. M. Hansen, P. A. Bartlett, and C. H. Heathcock, *Organometallics*, 1987, **6**, 2069.
144. R. Tsushima and T. Tsuruta, *Makromol. Chem.*, 1973, **166**, 325.
145. J. Boersma and J. G. Noltes, *Recl. Trav. Chim. Pays-Bas*, 1973, **92**, 229.
146. F. H. van der Steen, J. Boersma, A. L. Spek, and G. van Koten, *Organometallics*, 1991, **10**, 2467.
147. C. Bolm, J. Müller, M. Zehnder, and M. A. Neuburger, *Chem. Eur. J.*, 1995, **5**, 312.
148. M. B. Hursthouse, M. A. Malik, M. Motevalli, and P. O'Brien, *Organometallics*, 1991, **10**, 730.
149. M. A. Malik and P. O'Brien, *Inorg. Chem. Acta*, 1998, **274**, 239.
150. M. B. Hursthouse, M. A. Malik, M. Motevalli, and P. O'Brien, *J. Chem. Soc., Chem. Commun.*, 1991, 1690.
151. I. Abrahams, M. A. Malik, M. Motevalli, and P. O'Brien, *J. Chem. Soc., Dalton Trans.*, 1995, 1043.
152. S. Inoue and Y. Yokoo, *J. Organomet. Chem.*, 1972, **39**, 11.
153. S. Chang, R. D. Sommer, A. L. Rheingold, and D. P. Goldberg, *Chem. Commun.*, 2001, **22**, 2396.
154. P. O'Brien, in 'Inorganic Materials', eds. D. W. Bruce and D. O'Hare, John Wiley & Sons, 1992, p. 491.
155. G. E. Coates and D. Ridley, *J. Chem. Soc.*, 1965, 1870.
156. P. P. Power, *J. Organomet. Chem.*, 1990, **400**, 49.
157. J.-E. Förster, M. Vargas, and H. Müller, *J. Organomet. Chem.*, 1973, **59**, 97.
158. M. M. Olmstead, P. P. Power, and S. Shoner, *J. Am. Chem. Soc.*, 1991, **113**, 3379.
159. D. Zeng, M. J. Hampden-Smith, and E. N. Duesler, *Inorg. Chem.*, 1994, **33**, 5376.
160. M. A. Malik, M. Motevalli, J. R. Walsh, and P. O'Brien, *Organometallics*, 1992, **11**, 3136.
161. J. G. Noltes, *Recl. Trav. Chim. Pays-Bas*, 1965, **84**, 126.

162. G. W. Adamson, N. A. Bell, and H. M. M. Shearer, *Acta Crystallogr.*, 1982, **B38**, 462.
163. G. W. Adamson and H. M. M. Shearer, *Chem. Commun.*, 1969, **16**, 897.
164. M. A. Malik, M. Motevalli, J. R. Walsh, P. O'Brien, and A. C. Jones, *J. Mater. Chem.*, 1995, **5**, 731.
165. C. Kimblin, B. M. Bridgewater, T. Hascall, and G. Parkin, *J. Chem. Soc., Dalton Trans.*, 2000, **8**, 1267.
166. C. Kimblin, B. M. Bridgewater, T. Hascall, and G. Parkin, *J. Chem. Soc., Dalton Trans.*, 2000, **6**, 891.
167. K. Ruhlandt-Senge and P. P. Power, *Inorg. Chem.*, 1993, **32**, 4505.
168. Y.-W. Jun, C.-S. Choi, and J. Cheon, *Chem. Commun.*, 2001, **1**, 101.
169. Y.-W. Jun, J.-E. Koo, and J. Cheon, *Chem. Commun.*, 2000, **14**, 1243.
170. M. A. Malik, M. Motevalli, and P. O'Brien, *Polyhedron*, 1999, **18**, 1259.
171. M. Bochmann, G. C. Bwembya, and A. K. Powell, *Polyhedron*, 1993, **12**, 2929.
172. M. Chunggaze, M. A. Malik, P. O'Brien, A. J. P. White, and D. J. Williams, *J. Chem. Soc., Dalton Trans.*, 1998, **22**, 3839.
173. M. Westerhausen, T. Bollwein, A. Pfitzner, T. Nilges, and H.-J. Deiseroth, *Inorg. Chem. Acta*, 2001, **312**, 239.
174. M. M. Olmstead, W. J. Grigsby, D. R. Chacon, T. Hascall, and P. P. Power, *Inorg. Chem. Acta*, 1996, **251**, 273.
175. M. G. Davidson, D. Elilio, S. L. Less, A. Martin, P. R. Raithby, R. Snaith, and D. S. Wright, *Organometallics*, 1993, **12**, 1.
176. M. H. Abraham and J. A. Hill, *J. Organomet. Chem.*, 1967, **7**, 23.
177. E. Rijnberg, B. Richter, K.-H. Thiele, J. Boersma, N. Veldman, A. L. Spek, and G. van Koten, *Inorg. Chem.*, 1998, **37**, 56.
178. E. Rijnberg, J. Boersma, J. T. B. H. Jastrzebski, M. T. Lakin, A. L. Spek, and G. van Koten, *Organometallics*, 1997, **16**, 3158.
179. M. Cheng, D. R. Moore, J. J. Reczek, B. M. Chamberlain, E. B. Lobkovsky, and Ge. W. Coates, *J. Am. Chem. Soc.*, 2001, **123**, 8738.
180. J. Prust, A. Stasch, W. Zheng, H. W. Roesky, E. Alexopoulos, I. Usón, D. Böhler, and T. Schuchardt, *Organometallics*, 2001, **20**, 3825.
181. A. Kasani, R. McDonald, and R. G. Cavell, *Organometallics*, 1999, **18**, 3775.
182. M. Westerhausen, M. Wieneke, and W. Schwarz, *J. Organomet. Chem.*, 1999, **572**, 249.
183. L.-C. Liang, W.-Y. Lee, and C.-H. Hung, *Inorg. Chem.*, 2003, **42**, 5471.
184. M. A. Malik, P. O'Brien, M. Motevalli, and A. C. Jones, *Inorg. Chem.*, 1997, **36**, 5076.
185. R. Alsfasser, A. K. Powell, S. Trofimenko, and H. Vahrenkamp, *Chem. Ber.*, 1993, **126**, 685.
186. A. Looney, R. Han, I. B. Gorrell, M. Cornebise, K. Yoon, G. Parkin, and A. L. Rheingold, *Organometallics*, 1995, **14**, 274.
187. J. L. Kisko, T. Fillebeen, T. Hascall, and G. Parkin, *J. Organomet. Chem.*, 2000, **596**, 22.
188. M. Krieger, R. O. Gould, B. Neumüller, K. Harms, and K. Dehnicke, *Z. Anorg. Allg. Chem.*, 1998, **624**, 1434.
189. M. Krieger, R. O. Gould, K. Harms, S. Parsons, and K. Dehnicke, *Chem. Ber.*, 1996, **129**, 1621.
190. A. J. Edwards, M. A. Paver, P. R. Raithby, C. A. Russel, and D. S. Wright, *Organometallics*, 1993, **12**, 4687.
191. M. G. Davidson, A. J. Edwards, M. A. Paver, P. R. Raithby, C. A. Russell, A. Steiner, K. L. Verhorevoort, and D. S. Wright, *J. Chem. Soc., Chem. Commun.*, 1995, **19**, 1989.
192. T. J. Groshens, K. T. Higa, and R. J. Butcher, *J. Organomet. Chem.*, 1993, **463**, 97.
193. B. Rademacher, W. Schwarz, and M. Westerhausen, *Z. Anorg. Allg. Chem.*, 1995, **621**, 1439.
194. B. Rademacher, W. Schwarz, and M. Westerhausen, *Z. Anorg. Allg. Chem.*, 1995, **621**, 287.
195. M. Westerhausen, M. Wieneke, K. Doderer, and W. Schwarz, *Z. Naturforsch.*, 1996, **51b**, 1439.
196. W. Hieber and U. Teller, *Z. Anorg. Allg. Chem.*, 1942, **249**, 43.
197. J. M. Burlitch and R. C. Winterton, *Inorg. Chem.*, 1979, **18**, 2309.
198. J. N. St Denis, W. Butler, M. D. Glick, and J. P. Oliver, *J. Organomet. Chem.*, 1977, **129**, 1.
199. P. H. M. Budzelaar, H. J. Alberts-Jansen, K. Mollema, J. Boersma, G. J. M. van der Kerk, A. L. Spek, and A. J. M. Duisenberg, *J. Organomet. Chem.*, 1983, **243**, 137.
200. P. H. M. Budzelaar, J. Boersma, and G. J. M. van der Kerk, *Angew. Chem., Int. Ed. Engl.*, 1983, **22**, 329.
201. P. H. M. Budzelaar, J. Boersma, and G. J. M. Van Der Kerk, *J. Organomet. Chem.*, 1980, **202**, C71.
202. M. D. Fryzuk, D. H. McConville, and S. J. Rettig, *Organometallics*, 1993, **12**, 2152.
203. P. H. M. Budzelaar, A. A. H. Van der Zeijden, J. Boersma, G. J. M. Van der Kerk, A. L. Spek, and A. J. M. Duisenberg, *Organometallics*, 1984, **3**, 159.
204. P. H. M. Budzelaar, K. H. Den Haan, J. Boersma, G. J. M. Van der Kerk, and A. L. Spek, *Organometallics*, 1984, **3**, 156.
205. B. Fischer, H. Kleijn, J. Boersma, G. Van Koten, and A. L. Spek, *Organometallics*, 1989, **8**, 920.
206. B. Fischer, J. Boersma, G. van Koten, and A. L. Spek, *New. J. Chem.*, 1988, **12**, 613.
207. M. Westerhausen, C. Gückel, T. Habereder, M. Vogt, M. Warchhold, and H. Nöth, *Organometallics*, 2001, **20**, 893.

208. H.-O. Fröhlich, B. Kosan, B. Undeutsch, and H. Görls, *J. Organomet. Chem.*, 1994, **472**, 1.
209. J. T. B. H. Jastrzebski, H. A. J. Sypkens, F. J. A. des Tombe, P. A. van der Schaaf, J. Boersma, and G. van Koten, *J. Organomet. Chem.*, 1990, **396**, 25.
210. M. Lutz, B. Findeis, M. Haukka, R. Graff, T. A. Pakkanen, and L. H. Gade, *Chem.-Eur. J.*, 2002, **8**, 3269.
211. J. A. Wanklyn, *Ann.*, 1858, **108**, 67.
212. R. A. N. C. Crump, I. Fleming, and C. J. Urch, *J. Chem. Soc., Perkin Trans. 1*, 1994, **6**, 701.
213. Y. Kondo, N. Takazawa, C. Yamazaki, and T. Sakamoto, *J. Org. Chem.*, 1994, **59**, 4717.
214. T. Harada, T. Katsuhira, D. Hara, Y. Kotani, K. Maejima, R. Kaji, and A. Oku, *J. Org. Chem.*, 1993, **58**, 4897.
215. Y. Kondo, M. Fujinami, M. Uchiyama, and T. Sakamoto, *J. Chem. Soc., Perkin Trans. 1*, 1997, **6**, 799.
216. M. Uchiyama, S. Furumoto, M. Saito, Y. Kondo, and T. Sakamoto, *J. Am. Chem. Soc.*, 1997, **119**, 11425.
217. M. Uchiyama, M. Kameda, O. Mishima, N. Yokoyama, M. Koike, Y. Kondo, and T. Sakamoto, *J. Am. Chem. Soc.*, 1998, **120**, 4934.
218. K. M. Maclin and H. G. Richey Jr, *J. Org. Chem.*, 2002, **67**, 4602.
219. M. Westerhausen, B. Rademacher, and W. Schwarz, *Z. Annorg. Allg. Chem.*, 1993, **619**, 675.
220. A. P. Purdy and C. F. George, *Organometallics*, 1992, **11**, 1955.
221. H. Gilman and L. A. Woods, *J. Am. Chem. Soc.*, 1945, **67**, 922.
222. F. Kaufmann, A. Geraudelle, B. Kaempf, F. Schué, A. Deluzarche, and A. Maillard, *J. Organomet. Chem.*, 1970, **24**, 13.
223. M. Krieger, G. Geiseler, K. Harms, J. Merle, W. Massa, and K. Dehnicke, *Z. Annorg. Allg. Chem.*, 1998, **624**, 1387.
224. E. Rijnberg, J. T. B. H. Jastrzebski, J. Boersma, H. Kooijman, N. Veldman, A. L. Spek, and G. van Koten, *Organometallics*, 1997, **16**, 2239.
225. M. Westerhausen, M. Wieneke, W. Ponikwar, H. Nöth, and W. Schwarz, *Organometallics*, 1998, **17**, 1438.
226. M. Westerhausen, B. Rademacher, W. Schwarz, and S. Henkel, *Z. Naturforsch.*, 1994, **49b**, 199.
227. E. Rijnberg, J. T. B. H. Jastrzebski, J. Boersma, H. Kooijman, A. L. Spek, and G. van Koten, *J. Organomet. Chem.*, 1997, **541**, 181.
228. D. T. Hurd, *J. Org. Chem.*, 1948, **13**, 711.
229. M. Uchiyama, M. Koike, M. Kameda, Y. Kondo, and T. Sakamoto, *J. Am. Chem. Soc.*, 1996, **118**, 8733.
230. A. B. Goel, S. Goel, and E. C. Ashby, *Inorg. Chem.*, 1979, **18**, 1433.
231. E. C. Ashby and J. J. Watkins, *Inorg. Chem.*, 1973, **12**, 2493.
232. M. A. Putzer, B. Neumüller, and K. Dehnicke, *Z. Annorg. Allg. Chem.*, 1997, **623**, 539.
233. M. Westerhausen, C. Gückel, and P. Mayer, *Angew. Chem., Int. Ed. Engl.*, 2001, **40**, 2666.
234. E. Weiss and R. Wolfrum, *Chem. Ber.*, 1968, **101**, 35.
235. R. Wyrwa, H.-O. Fröhlich, and H. Görls, *Organometallics*, 1996, **15**, 2833.
236. L. M. Seitz and T. L. Brown, *J. Am. Chem. Soc.*, 1966, **88**, 4140.
237. R. M. Fabicon, M. Parvez, and H. G. Richey, *J. Am. Chem. Soc.*, 1991, **113**, 1412.
238. R. M. Fabicon, A. D. Pajerski, and H. G. Richey Jr, *J. Am. Chem. Soc.*, 1991, **113**, 6680.
239. R. M. Fabicon and H. G. Richey Jr, *Organometallics*, 2001, **20**, 4018.
240. H. Tang, M. Parvez, and H. G. Richey Jr, *Organometallics*, 2000, **19**, 4810.
241. H. Tang and H. G. Richey Jr, *Organometallics*, 1996, **15**, 4891.
242. M. Haufe, R. D. Köhn, G. Kociok-Köhn, and A. Filippou, *Inorg. Chem. Commun.*, 1998, **1**, 263.
243. M. Haufe, R. D. Köhn, R. Weimann, G. Seifert, and D. Zeigan, *J. Organomet. Chem.*, 1996, **520**, 121.
244. D. A. Walker, T. J. Woodman, D. L. Hughes, and M. Bochmann, *Organometallics*, 2001, **20**, 3772.
245. I. Marek and J.-F. Normant, *Chem. Rev.*, 1996, **96**, 3241.
246. I. Marek, *Chem. Rev.*, 2000, **100**, 2887.
247. M. H. P. Rietveld, P. Lohner, M. G. Nijkamp, D. M. Grove, N. Veldman, A. L. Spek, M. Pfeffer, and G. van Koten, *Chem. Eur. J.*, 1997, **3**, 817.
248. H. C. L. Abbenhuis, N. Feiken, H. F. Haarman, D. M. Grove, E. Horn, H. Kooijman, A. L. Spek, and G. van Koten, *Angew. Chem., Int. Ed. Engl.*, 1991, **30**, 996.
249. T. R. Krawietz, D. H. Barich, L. W. Beck, T. Howard, T. Xu, and J. F. Haw, *J. Am. Chem. Soc.*, 1995, **117**, 10407.
250. E. Frankland, *J. Chem. Soc.*, 1862, **15**, 363.
251. I. Klement and P. Knochel, *Synlett*, 1995, 113.
252. A. Lissenko, *Jahresber Schweiz Akad Med Wiss*, 1864, 470.
253. R. Demuth and V. Meyer, *Ber. Bunsen-Ges. Phys. Chem.*, 1890, **23**, 394.
254. M. H. Abraham, *J. Chem. Soc.*, 1960, 4130.
255. A. G. Davies and B. P. Roberts, *J. Chem. Soc. B*, 1968, 1074.
256. J. Lewinski, Z. Ochal, E. Bojarski, E. Tratkiewicz, I. Justyniak, and J. Lipkowski, *Angew. Chem., Int. Ed. Engl.*, 1996, **35**, 1725.
257. J. Lewinski, W. Marciniak, J. Lipkowski, and I. Justyniak, *J. Am. Chem. Soc.*, 2003, **125**, 12698.
258. R. P. Davies, D. J. Linton, P. Scooler, R. Snaith, and A. E. H. Wheatley, *Chem. Eur. J.*, 2001, **7**, 3696.
259. A. D. Bond, D. J. Linton, P. Schooler, and A. E. H. Wheatley, *J. Chem. Soc., Dalton Trans*, 2001, 3173.
260. S. Moorhouse and G. Wilkinson, *J. Chem. Soc., Dalton Trans.*, 1974, **20**, 2187.

261. G. A. Luinstra and J. H. Teuben, *J. Organomet. Chem.*, 1991, **420**, 337.
262. P. Knochel, F. Langer, A. Langneau, M. Rottländer, and T. Studemann, *Chem. Ber. Recl.*, 1997, **130**, 1021.
263. K. Soai and S. Niwa, *Chem. Rev.*, 1992, **92**, 833.
264. L. Pu and H.-B. Yu, *Chem. Rev.*, 2001, **101**, 757.
265. M. Yamakawa and R. Noyori, *J. Am. Chem. Soc.*, 1995, **117**, 6327.
266. T. Rasmussen and P.-O. Norrby, *J. Am. Chem. Soc.*, 2001, **123**, 2464.
267. K. Soai, T. Shibata, H. Morioka, and K. Choji, *Nature*, 1995, **378**, 767.
268. I. Sato, D. Omiya, K. Tsukiyama, Y. Ogi, and K. Soai, *Tetrahedron: Asymmetry*, 2001, **12**, 1965.
269. W. A. Nugent, *Chem. Commun.*, 1999, **15**, 1369.
270. A. R. Katritzky and P. A. Harris, *Tetrahedron: Asymmetry*, 1992, **3**, 437.
271. R. Bloch, *Chem. Rev.*, 1998, **98**, 1407.
272. H. E. Simmons and R. D. Smith, *J. Am. Chem. Soc.*, 1958, **80**, 5323.
273. G. Wittig and K. Schwarzenbach, *Angew. Chem.*, 1959, **71**, 652.
274. J. Furukawa, N. Kawabata, and J. Nishimura, *Tetrahedron Lett.*, 1966, **7**, 3353.
275. S. E. Denmark and J. P. Edwards, *J. Org. Chem.*, 1991, **56**, 6974.
276. J. Furukawa and N. Kawabata, *Adv. Organomet. Chem.*, 1974, **12**, 83.
277. A. B. Charette and J.-F. Marcoux, *J. Am. Chem. Soc.*, 1996, **118**, 4539.
278. F. Bernardi, A. Bottoni, and G. P. Miscione, *J. Am. Chem. Soc.*, 1997, **119**, 12300.
279. Z. Q. Yang, J. C. Lorenz, and Y. Shi, *Tetrahedron Lett.*, 1998, **39**, 8621.
280. J. C. Lorenz, J. Long, Z. Yang, S. Xue, Y. Xie, and Y. Shi, *J. Org. Chem.*, 2004, **69**, 327.
281. A. B. Charette, A. Beauchemin, and S. Francoeur, *J. Am. Chem. Soc.*, 2001, **123**, 8139.
282. A. B. Charette, A. Gagnon, and J.-F. Fournier, *J. Am. Chem. Soc.*, 2002, **124**, 386.
283. C. Zhao, D. Wang, and D. L. Phillips, *J. Am. Chem. Soc.*, 2002, **124**, 12903.
284. V. K. Aggarwal, A. Ali, and M. P. Coogan, *J. Org. Chem.*, 1997, **62**, 8628.
285. N. A. Ross and R. A. Bartsch, *J. Org. Chem.*, 2003, **68**, 360.
286. A. Yanagisawa, H. Takahashi, and T. Arai, *Chem. Commun.*, 2004, **5**, 580.
287. J. D. Parrish, D. R. Shelton, and R. D. Little, *Org. Lett.*, 2003, **5**, 3615.
288. I. Shibata, T. Suwa, H. Sakakibara, and A. Baba, *Org. Lett.*, 2002, **4**, 301.
289. S.-I. Fukusawa, H. Matsuzawa, and S.-I. Yoshimitsu, *J. Org. Chem.*, 2000, **65**, 1702.
290. M. Obringer, F. Colobert, B. Neugnot, and G. Solladié, *Org. Lett.*, 2003, **5**, 629.
291. K. Kanai, H. Wakabayaschi, and T. Honda, *Org. Lett.*, 2000, **2**, 2549.
292. R. Ocampo, W. R. Dolbier Jr, K. A. Abboud, and F. Zuluaga, *J. Org. Chem.*, 2002, **67**, 72.
293. Y. Ding and G. Zhao, *Chem. Commun.*, 1992, **13**, 941.
294. K. Soai and Y. Kawase, *Tetrahedron: Asymmetry*, 1991, **2**, 781.
295. W. Kuran, *Prog. Polym. Sci.*, 1998, **23**, 919.
296. B. J. O'Keefe, M. A. Hillmyer, and W. B. Tolman, *J. Chem. Soc., Dalton Trans.*, 2001, 2215.
297. M. H. Chisholm, J. Gallucci, and K. Phomphrai, *Inorg. Chem.*, 2002, **41**, 2785.
298. K. Nozaki, K. Nakano, and T. Hiyama, *J. Am. Chem. Soc.*, 1999, **121**, 11008.
299. M. H. Chisholm, N. W. Eilerts, J. C. Huffman, S. S. Iyer, M. Pacold, and K. Phomphrai, *J. Am. Chem. Soc.*, 2000, **122**, 11845.
300. N. Oguni and H. Tani, *J. Polym. Sci., Polym. Chem. Ed.*, 1973, **11**, 573.
301. D. Chakraborty and E. Y.-X. Chen, *Organometallics*, 2003, **22**, 769.
302. D. A. Walker, T. J. Woodman, M. Schormann, D. L. Hughes, and M. Bochmann, *Organometallics*, 2003, **22**, 797.
303. K. Ukai, K. Oshima, and S. Matsubara, *J. Am. Chem. Soc.*, 2000, **122**, 12047.

Zintl Compounds

Susan M. Kauzlarich
University of California, Davis, CA, USA

1 Introduction 1
2 Background 1
3 Structure and Bonding 2
4 Characterization 7
5 Related Articles 7
6 References 7

Glossary

Homoatomic: same element
Pnictide: group 15 anion
Pnicogen: group 15 element

Abbreviations

A^I = Alkali metal; A^{II} = alkaline earth metal; en = Ethylenediamine; crypt = 4,7,13,16,21,24-hexaoxa-1,10-diazatricyclo[8.8.8]hexacosane; Pn = Group 15 element (pnicogen).

1 INTRODUCTION

Zintl phases make up a class of compounds which are electronically positioned between the class of intermetallic compounds and insulating valence compounds.[1] These compounds are made up of electropositive elements from groups 1, 2 that, in a formal sense, donate their electrons to the electronegative elements from groups 13, 14, and 15, which use them to form the correct number of bonds such that each element has a filled shell. A more succinct definition of Zintl compounds is that they are normal valence compounds in which there is both ionic and covalent bonding. If the anionic units have enough electrons, they will form isolated anionic atoms. If there are not enough electrons to provide a closed shell of electrons (eight total for a main group element), then the main group element forms two-center–two-electron bonds. Zintl compounds are normally considered to be semiconductors, although the class also includes compounds whose structures can be described by the Zintl concept and are metallic. Pearson[2] classifies these as a subset of intermetallics that obey the rules of valence; however, they are better classified as Zintl phases.[3] Because of the ionic nature of bonding between the cations and anions in Zintl compounds, they are soluble in polar, basic solvents. Anionic clusters of the heavier main group elements isolated from reactions of Zintl phases are known as Zintl anions.[4,5] The reactivity of these anions has been explored and this work has produced new cluster compounds[6–12] as well as novel materials.[13–18]

The description of bonding within these compounds has been treated by several different approaches that come to the same conclusion. The $(8 - N)$ rule that is generalized by Mooser and Pearson[19–21] uses a covalent model with collective counting of electrons. The generalized $8 - N$ rule can be easily defined for simple binary compounds of the general formula, M_mX_x as $8x$ electrons are required in order to achieve the octet shells for the x X atoms. The valence electron count, VEC(X) can be defined as the total number of all valence electrons in relation to the number of the anionic atoms: $\mathrm{VEC(X)} = [m\cdot e(M) + x\cdot e(X)]/x$, where an M atom has e(M) valence electrons. If covalent bonds exist between M atoms, the M atoms cannot donate all of their electrons and if covalent bonds exist between X atoms, the X atoms require fewer electrons. Typically, there are no bonds between M for a Zintl phase, and bonds are formed between X. The number of bonds, b(XX), can be accounted for in the equation and results in the equation: $b(XX) = 8 - \mathrm{VEC(X)}$.[22] Zintl[23] and Klemm[24] examine local configurations in a setting of formal ions. Once the formal charges are assigned, the anionic lattice can be described as a pseudoelement that exhibits structural chemistry closely related to the isoelectronic element. The definition of a Zintl phase has undergone several revisions and has been expanded to include ternary[25–27] and transition metal compounds.[27–32] Although the bonding description originally proposed by Zintl has been augmented and is sometimes referred to as the Zintl-Klemm concept,[33] or Zintl-Klemm-Busmann concept,[25] the term Zintl concept is generally considered to be inclusive of those revisions. For transition metals, an estimation of the number of electrons which are localized on the metal and do not take part in the bonding must be considered, as described by Pauling.[34] Since bonding descriptions are effective only to the extent that they adequately relate structure and properties, only those transition metal compounds that are understood according to the Zintl model will be described herein. The reactivity and uses of Zintl phases for the synthesis of Zintl ions, new compounds, and novel materials by means of solution chemistry will also be presented.

2 BACKGROUND

Compounds of alkali and alkaline earth metals with elements of groups 16 and 17 are usually described as ionic compounds or salts with respect to their physical and chemical properties, as well as their structures. The compounds with elements of groups 14 and 15 become increasingly metallic with increasing atomic number of the electronegative element and occur in stoichiometries not readily described by valence rules.[20] Many of these compounds were thought to be best classified as intermetallics. Hume-Rothery phases are certain alloys with the structures of different types of brass. Hume-Rothery found that valence electron concentration (number of valence electrons)/(number of atoms) dictated the structure. Shortly after the presentation of the Hume-Rothery rules concerning the relationship of electron concentration to crystal structure in intermetallic phases,[35] Eduard Zintl proposed that a subgroup of the intermetallic compounds were, in fact, not well represented within the descriptions of intermetallic phases. Zintl had prepared a number of alkali and alkaline earth metal groups 13, 14, and 15 binaries and investigated their structures.[23] The majority of these phases adopt the β-brass structure, while some crystallize in the NaTl structure type, both derivatives of the W structure. Hume-Rothery rules predicted an optimal electron concentration of $3/2e^-$ per atom for compounds crystallizing in this structure type, but most of these compounds show electron concentrations of $(1-5/2)e^-$ per atom. In addition, for these phases, significant contraction of the volume compared to the volume of the elements occurs; this is attributed to the ionic interactions between the electropositive and electronegative element that forms the correct number of homoatomic bonds, such that each element has a complete octet. The prototype Zintl compound, NaTl, could be described by Na^+Tl^-, where the polyanion or Zintl anion ${}^3_\infty[Tl^-]$ forms a diamond framework. ${}^3_\infty[Tl^-]$ can be thought of as a pseudoelement of group 14, recognizing that the diamond structure is a preferred structure type for this element. Laves listed all the intermetallic compounds whose structures were known in 1941 that obeyed the rules of valence under the heading ‘Zintl phases’, in recognition of Zintl’s contribution to the study of these compounds.[36]

The ability of Zintl compounds to dissolve in coordinating solvents such as ammonia and ethylenediamine (en) is another property that sets these compounds apart from intermetallics. At the same time that much of this investigation of the solid state was occurring, several scientists, including Zintl, also were studying the solution chemistry of alkali metals in liquid ammonia with a variety of the heavy main group metals.[4,5] Electrochemical investigations indicated that there existed discrete anion clusters in these solutions and provided the first evidence for the so-called Zintl ions. The isolation of a solid derivative of a Zintl anion was first accomplished by Kummer and Diehl[37] with the compound, $Na_4Sn_9\cdot 7en$. A large advance was made in this area by the use of crypt to sequester the cation and this allowed the isolation of a number of salts containing Zintl anions. Many of these solvated Zintl anions have been isolated and their structures determined. In addition, many have been used as precursors for the synthesis of new organometallic compounds, in the metallization of polymer substrates, and in the synthesis of novel magnetic colloids. The classification of Zintl ions is normally limited to polyatomic anions of the metals of groups 14 and 15.[4,38]

3 STRUCTURE AND BONDING

3.1 Solid-state Binary Compounds

Laves proposed that all intermetallic compounds that obeyed valence or the $(8-N)$ rule should be classified as Zintl compounds. These alkali and alkaline earth main group compounds typically crystallize in salt-like structures such as antifluorite, *anti*-Mn_2O_3, and *anti*-La_2O_3. For example, the compounds $A^I{}_3Pn$ or $A^{II}{}_3Pn_2$ can be formed; they consist of isolated A cations and Pn anions. The corresponding situation occurs for group 14 only with some of the alkaline earth cations. The term ‘isolated’ is used to describe atoms that do not form part of a polyatomic unit; the distance to another atom of the same type is too large to be considered a bond. Although these structures can be described as salt-like, the atoms have high coordination numbers typical of metals and the heavier groups 14 and 15 compounds are metallic. Many of the $A^I{}_3Pn$ compounds have the hexagonal Na_3As (*anti*-LaF_3) structure in which equal numbers of Na and As form hexagonal nets (as in boron nitride) and the remaining Na atoms are arranged in layers on either side of these nets. Each As has five neighbors at the corners of a trigonal bipyramid and six other Na atoms tin a trigonal prismatic arrangement, making the total coordination number of As to be 11. The Na atoms have two types of environment. The Na in the NaAs net has three As atoms and six Na atoms, whereas the Na in between the nets has four As and six Na nearest neighbors. Binary compounds with lithium have been excluded because in many cases they show unique behavior with respect to their structure and stoichiometries.[33] Table 1 gives some examples of binary Zintl compounds with salt-like structures.

The prototype Zintl compounds are those with the NaTl structure type. As more X-ray structure analyses were performed, the number of structure types that could be interpreted in such as manner increased. Klemm and Busmann[39] formalized this interpretation: the electropositive element transfers electrons to the electronegative element, which then uses these electrons to form an anion partial lattice that resembles the elemental lattice with the same number of valence electrons. The coordination in the anion partial lattice analogy conforms to the $(8-N)$ rule. In many of these structures, an analogy to the corresponding elemental lattices can be made. By obtaining one electron from an alkali metal, the group 13 elements can form a diamond lattice and are isostructural (and isoelectronic) with the corresponding group 14 elements. There has been a significant amount of research on the composition and properties of compounds that crystallize in the NaTl structure type.[40] These compounds show properties that are characteristic of covalently bonded

Table 1 Structure types of binary solids with salt-like structures[a]

	P	As	Sb	Bi
Li	Na_3As	Na_3As	Na_3As, Li_3Bi	Li_3Bi
Na	Na_3As	Na_3As	Na_3As	Na_3As
K	Na_3As	Na_3As	Na_3As	Na_3As
Rb	–	Na_3As	Na_3As	Li_3Bi
Cs	–	Na_3As	Li_3Bi	Li_3Bi
Mg	*anti*-Mn_2O_3	*anti*-Mn_2O_3, *anti*-La_2O_3	*anti*-La_2O_3	*anti*-La_2O_3
Ca	?	?		–
Sr	*anti*-Ce_2S_3	?		?
Ba	*anti*-Ce_2S_3	?		?
	Si	**Ge**	**Sn**	**Pb**
Be	–	–	–	–
Mg	*anti*-CaF_2	*anti*-CaF_2	*anti*-CaF_2	*anti*-CaF_2
Ca	*anti*-$PbCl_2$	*anti*-$PbCl_2$	*anti*-$PbCl_2$	*anti*-$PbCl_2$
Sr	*anti*-$PbCl_2$	*anti*-$PbCl_2$	–	*anti*-$PbCl_2$
Ba	*anti*-$PbCl_2$	*anti*-$PbCl_2$	*anti*-$PbCl_2$	*anti*-$PbCl_2$

[a] – , compound unknown; ?, structure unknown.

compounds, although it has been shown that there are deviations in stoichiometry that give rise to metallic behavior. In addition to the example given above, further comparisons between polyatomic anions found in Zintl compounds and the isoelectronic elements can be made. For example, in the case of NaSi,[41] the Si is given a formal charge of -1. The structure contains isolated $(Si_4)^{4-}$ tetrahedra that are isoelectronic and isostructural with P_4. Figure 1 shows a view of the unit cell. In addition, there are compounds whose anion lattices are not isosteric with elemental lattices having the same number of valence electrons. However, the coordination of the anion partial lattice conforms to the $(8-N)$ rule and thus can be described by normal valence rules. Table 2 gives a partial listing of some compounds obeying this rule.

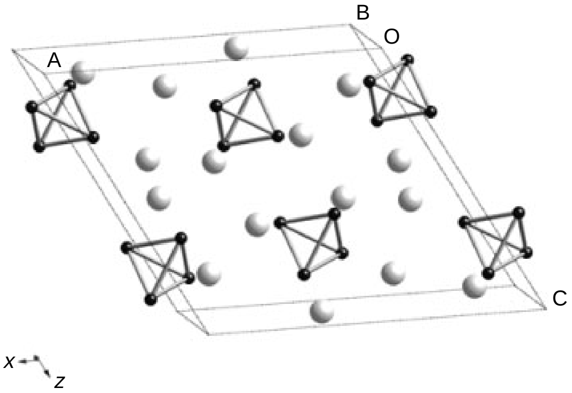

Figure 1 A view of the unit cell for NaSi showing the $Si_4{}^{4-}$ tetrahedral

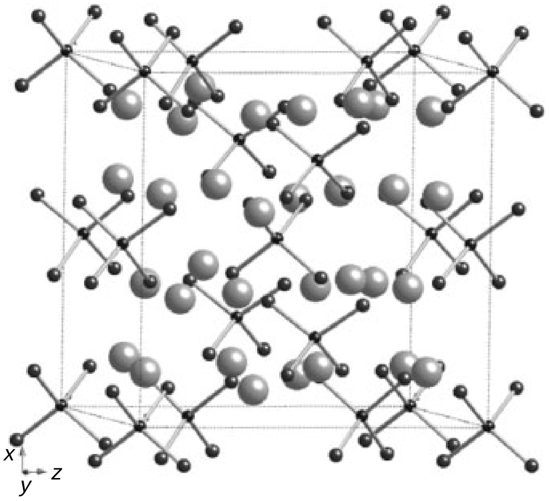

Figure 2 The structure of Ba_4SiAs_4

3.2 Solid-state Ternary Compounds

The structure and bonding of ternary compounds can also be described within the Zintl concept. Some ternary Zintl compounds have structures that can be described as complex salts. For example, Ba_4SiAs_4,[42] whose structure is shown in Figure 2, is composed of $SiAs_4{}^{8-}$ tetrahedra whose charge is balanced by the alkaline earth cation. Such isolated tetrahedra are also formed with group 13 atoms in combination with group 14 or group 15 atoms. There are discrete $GeAs_4{}^{8-}$, $GeP_4{}^{8-}$, and $SiP_4{}^{8-}$ tetrahedra in this structure type whose charges are balanced by the alkaline earth cations. The term orthophosphido- or orthoarsenidosilicates or -germanates has been used to describe these anions because they are isoelectronic with the ordinary silicate $(SiO_4{}^{4-})$, with the O^{2-} ions being replaced by As^{3-} or P^{3-} ions.[27] According to the $(8-N)$ rule, Ge or Si is given a formal charge of zero and the As or P is assigned a formal charge of -2, giving rise to the overall charge of -8 on the polyatomic unit. The compound $A^{I}{}_2SiAs_2$ (A^{I} = K, Rb, Cs)[43–45] can be prepared and is composed of anionic chains of $^{1}{}_{8}[SiAs_{4/2}{}^{2-}]$ (edge-sharing tetrahedral) (Figure 3). The anionic lattice is isoelectronic and isostructural with SiS_2.

Synthesis with cations of different sizes provides two new structures in the system A^{II}–Si–As: $Sr_3Si_2As_4$ and $Ca_3Si_2As_4$, Figures 4 and 5[46,47] These two structures contain Si_2As_6 units that are linked in different ways. The Si_2As_6 anions found in $Sr_3Si_2As_4$ are connected by a common edge as shown in Figure 4 and can be described by the notation $^{1}{}_{\infty}[(SiAsAs_{2/2})_2{}^{6-}]$. In the case of $Ca_3Si_2As_4$, one of the Si has all three of the As bonded to another Si_2As_4 unit, whereas the Si in the other half has only one As bonded to another Si_2As_4 unit (Figure 5). The anionic unit can be described as consisting of $^{1}{}_{\infty}[As_2As_{1/2}SiSiAs_{3/2}{}^{6-}]$ chains. Many of these ternary compounds are classified as Zintl compounds. However, few transport properties have

Table 2 Examples of binary compounds obeying the Zintl concept

N	Compound	Formal charge	Coordination	Structure of anion lattice	Structure type
4	LiAl	−1	4	Diamond	NaTl
	LiIn				NaTl
	NaIn				NaTl
	$CaIn_2$			3D network of distorted tetrahedrally coordinated atoms	$CaIn_2$
	$SrTl_2$				$CaIn_2$
	$SrAl_2$				KHg_2
5	NaSi	−1	3	P_4 (isolated X_4 tetrahedra)	NaSi
	KSi				KGe
	RbGe				KGe
	CsSn				NaPb
	CsPb				NaPb
	$SrGe_2$				$BaSi_2$
	$CaSi_2$			As (layers of infinite puckered hexagonal networks)	$CaSi_2$
	$SrSi_2$			3D network of 3-coordination Si atoms	$SrSi_2$
6	CaSi	−2	2	Planar zigzag chains	CrB
	BaSn				CrB
	LiP			Se (spiraled chains)	LiAs
	KSb				LiAs

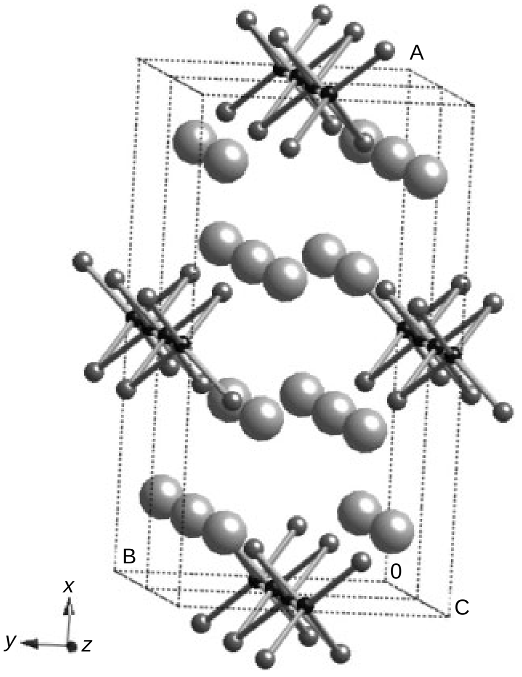

Figure 3 A view of the structure of $A^{I}_2SiAs_2$ showing the $^{1}_{\infty}[SiAs_{4/2}{}^{2-}]$ chains

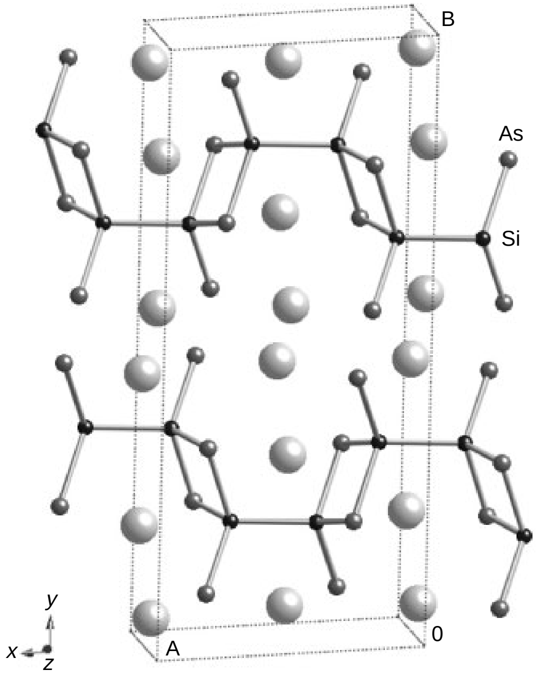

Figure 4 A view of the structure of $Sr_3Si_2As_4$ showing the $^{1}_{\infty}[(SiAsAs_{2/2})_2{}^{6-}]$ chains

been measured, because their structures can be interpreted according to the (8 − N) rule. Table 3 gives a partial listing of ternary Zintl phases with complex anions.[25–27,48,49] In addition, exploring the Zintl boundary has led to the discovery of novel cluster solid-state compounds.[5,50]

3.3 Transition Metal Zintl Compounds

The Zintl concept has been extended to include transition metal compounds, with some success.[1,18,28,31,32,51,52] Although many main group metal Zintl compounds are known,[25–27,33] there are relatively few examples of isostructural transition

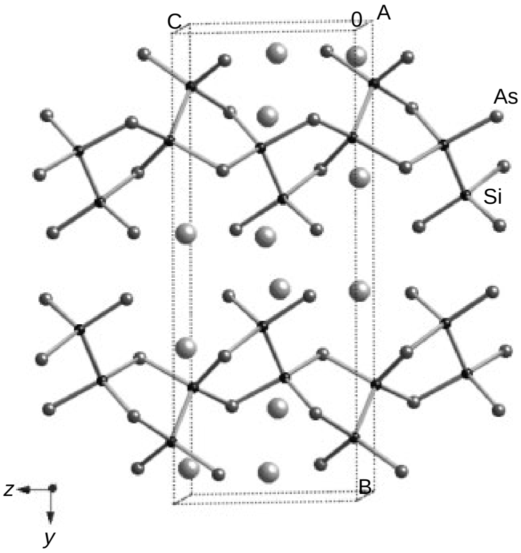

Figure 5 A view of the structure of $Ca_3Si_2As_4$ showing the ${}^{1}_{\infty}[(As_2As_{1/2}SiSiAs_{3/2})^{6-}]$ chains

Table 3 Examples of ternary compounds obeying the Zintl concept

Compound	Structure of anion lattice	Structure type
Ba_4SiAs_4	$SiAs_4{}^{8-}$ isolated tetrahedra	Ba_4SiAs_4
Ba_4GeAs_4		
$Ca_3Si_2As_4$	${}^{1}_{\infty}[As_2As_{1/2}SiSiAs_{3/2}{}^{6-}]$ chains	$Ca_3Ge_2As_4$
$Sr_3Ge_2As_4$		
$Sr_3Si_2As_4$	${}^{1}_{\infty}[((SiAsAs_{2/2})_2)^{6-}]$ chains	$Sr_3Si_2As_4$
$BaGe_2As_2$	${}^{3}_{\infty}[(Ge_2As_2)^{2-}]$ 3D network	$BaGe_2As_2$
Ca_3AlAs_3	${}^{1}_{\infty}[(AlAs_2As_{2/2})^{6-}]$ chains	Ca_3AlAs_3
Sr_3GaSb_3		
$Ca_3Al_2As_4$	${}^{2}_{\infty}[(AlAs_{4/2})_2{}^{6-}]$ layers	$Ca_3Al_2As_4$
$Ca_5Al_2Sb_6$	${}^{1}_{\infty}[(AlSbSb_{2/2}(Sb_2)_{1/2})_2{}^{10-}]$ chains	$Ca_5Al_2Sb_6$
$Ca_5In_2Sb_6$		
$Sr_5In_2Sb_6$		
$Ca_{14}AlSb_{11}$	$AlSb_4{}^{9-}+Sb_3{}^{7-}+$ isolated Sb^{3-} anions	$Ca_{14}AlSb_{11}$
$Sr_{14}GaAs_{11}$		
$Ca_{11}InSb_9$	$InSb_4{}^{9-}+Sb_2{}^{4-}+$ isolated Sb^{3-} anions	$Ca_{11}InSb_9$
$Ca_{11}AlSb_9$		

metal analogs. Some transition metal sulfides have been described by the Zintl rules.[28] Binary and ternary transition metal complexes with metals having filled d orbitals can also be described according to the Zintl concept, although inclusion of the d orbitals complicates the bonding description.[28] The Zintl concept has also been used to explain the structure and properties of ternary transition metal pnictides crystallizing in the $ThCr_2Si_2$ structure type.[51,52] Two structure types that appear to be amenable to having a transition metal replacing the main group metalloid are the $A^{II}{}_{14}MPn_{11}$ (M = Al,[53,54] Ga,[55,56] In,[57] Mn,[30–32] Zn,[58] Nb,[59] and Pn = P, As, Sb, Bi) compounds and the $A^{I}{}_{5}MPn_3$ (M = Si, Ge,[60] Sn, Hf[61]) compounds. There have also been a number of new transition metal Zintl phases prepared which have no structure type equivalent to the main group elements, but appear to be valence precise and semiconducting.[62–67]

The structure and bonding in the $A^{I}{}_{5}HfPn_3$ can be easily understood in terms of the Zintl rules, since the Hf is formally a +4 ion. In this structure, two $HfAs_4$ tetrahedra are connected by a common edge to form $(Hf_2As_6)^{10-}$ anions. The structure and bonding in the $A_{14}MPn_{11}$ series of compounds is more complicated. In the framework of the Zintl rules, the structure of these compounds, $A_{14}MPn_{11}$ can be understood as consisting of 14 A^{2+} cations, four Pn^{3-} anions, a $MPn_4{}^{9-}$ tetrahedron, and a linear $Pn_3{}^{7-}$ unit. Figure 6 shows a perspective view of the unit cell. The $Pn_3{}^{7-}$ unit is well described as a three-center-two-electron bond and is isoelectronic with $X_3{}^{-}$ (X = halogen)[68] (*see* ***Hypervalent Compounds***). These compounds are isostructural with the main group Zintl compounds, and so the transition metal Mn has been proposed to be Mn^{3+}.[30–32] A more recent understanding of the bonding has recently lead to a different picture with the Mn better considered to be formally Mn^{2+}.[69,70] In this view, the charge counting of the tetrahedron can be explicitly stated as $[Mn^{2+}\ (Sb_4)^{11-}]$ rather than $[Mn^{3+}\ (Sb_4)^{12-}]$. In either description, the paramagnetic temperature-dependent magnetic susceptibility data is consistent with four unpaired electrons. However, this electronic structure leads to unusual magnetic and electronic transport properties (*see* ***Magnetism of Transition Metal Ions***).[32]

Recent publications on other transition metal Zintl phases[62–67] suggest that this is a rich area for study with applications for magnetic and electronic devices.

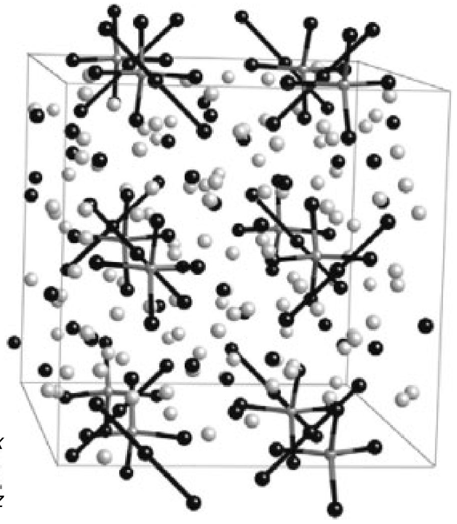

Figure 6 A perspective view of the structure of $A_{14}MPn_{11}$

3.3.1 *Zintl Ions*

This subtopic of Zintl compounds relates to those homo- and heteropolyanions that have been isolated and characterized. Although clusters containing the heavier group 16 chalcogenides, such as Se and Te, are sometimes considered to be Zintl anions, those compounds are not considered here. Chalcogenides have extensive cluster chemistry and are traditional anions. It has been known for some time that sodium and lead or their alloys dissolve in liquid ammonia to yield an intensely colored green solute.[71] Electrochemical investigations of these solutions led to the hypothesis that the Pb exists as $Pb_9{}^{4-}$ in solution.[72] Zintl and coworkers extensively studied these types of solutions and were able to identify $Sn_9{}^{4-}$, $Pb_7{}^{4-}$, $Pb_9{}^{4-}$, $Sb_5{}^{3-}$, $Sb_7{}^{3-}$, $Bi_3{}^{3-}$, $Bi_5{}^{3-}$, and $Bi_7{}^{3-}$.[73] However, structural studies were not possible owing to decomposition of the solids isolated by solvent evaporation. There was little work in this area again until 1970, when several Zintl anions were isolated from ethylenediamine (en) solutions.[4,38] A structural study of one of these compounds, $Na_4Sn_9{\cdot}7en$, showed a Sb_9 polyhedron.[37] Two other compounds, $Na_3Sb_7{\cdot}4en$ and $Na_4Ge_9{\cdot}5en$, were prepared by this method.[74] A significant number of Zintl anions were discovered by the use of a *Macrocycle*, crypt, to stabilize the polyatomic anions, which allowed for their isolations and structural characterization. In addition, heteropolyatomic anions are also possible and have been synthesized and characterized. Table 4 gives some examples of Zintl anions that have been structurally characterized.

3.3.2 *Reactivity*

Incorporation of transition metals into the Zintl anions described above has been somewhat successful, although in many cases, the emphasis has been on the solution chemistry of the metal chalcogenides. The heavier group 14/15 anion clusters, such as $Sn_9{}^{4-}$, $Sb_7{}^{3-}$, and $As_{11}{}^{3-}$, have received much less attention but have proved to be equally interesting.[38,50] More recently, there has been renewed interest in exploring Zintl ions prepared from dissolving Zintl phases with an aim towards understanding cluster growth and the solution chemistry of these phases.[10,11,38,75–77]

Table 4 Examples of Zintl anions

Anion	Symmetry	Isoelectronic analog
$Ge_9{}^{2-}$	C_{2v}	$B_9H_9{}^{2-}$
$Ge_9{}^{4-}$	C_{4v}	$Bi_9{}^{5+}$ (D_{3h})
$Sn_9{}^{4-}$	C_{4v}	$Bi_9{}^{5+}$ (D_{3h})
$Sn_9{}^{3-}$	D_{3h}	
$Sn_5{}^{2-}$	D_{3h}	$Pb_5{}^{2-}$, $Bi_5{}^{3-}$
$Sb_4{}^{2-}$	D_{4h}	$Bi_4{}^{2-}$, $Pb_2Sb_2{}^{2-}$, $Te_4{}^{2+}$, $Se_4{}^{2+}$
$As_{11}{}^{3-}$	$\sim D_3$	$P_{11}{}^{3-}$
$Sb_7{}^{3-}$	C_{3v}	$As_7{}^{3-}$
$Sn_2Bi_2{}^{2-}$	$\sim T_d$	
$Tl_2Te_2{}^{2-}$	C_{2v}	
$TlSn_8{}^{3-}$	C_{2v}	$Ge_9{}^{2-}$
$TlSn_9{}^{3-}$	C_{4v}	$B_{10}H_{10}{}^{2-}$

The reactivities of the binary Zintl compounds have been explored for the synthesis of new compounds.[78] There have been new compounds prepared by the reaction of Zintl phases with a metal or metal carbonyl to produce new compounds such as $[Rb(NbAs_8)]^{2-}$.[6] The compounds contains chains of alternating Rb^+ cations and $[NbAs_8]^{3-}$ units that each consist of a monocyclic crown shaped polyanion $As_8{}^{8-}$ with a Nb^V ion in the center. More recently, the series of compounds with $ME_8{}^{n-}$ anions (M = Cr, Mo; E = As, Sb) have been crystallized and their properties explored.[79] $Sn_9Cr(CO)_3{}^{4-}$ was prepared by reacting $Cr(CO)_3(Mes)$ with a deep red en extract of K_4Sn_9. The crystals were isolated by the use of the crypt complexing agent to give $[K(crypt)_4][Sn_9Cr(CO)_3]$.[8] The structure consists of a *nido*-$Sn_9{}^{3-}$ cluster (isoelectronic and isostructural with $B_{10}H_{10}{}^{2-}$) which is bonded in an η^4 fashion to the $Cr(CO)_3$ fragment. $As_7Cr(CO)_3{}^{3-}$ can be prepared in an analogous manner as described above from a Zintl phase dissolved in en and a metal carbonyl.[9] The structure consists of an open As_7 cage that is bound in an η^4 fashion to the $Cr(CO)_3$ fragment.

Reactions of metal carbonyls with Zintl phases do not always yield the desired result. An example is the reaction of KSi with the metal carbonyls $M(CO)_6$ (M = Cr, Mo, W) and the chromium complex $Cr(CO)_5NMe_3$.[80] Instead of forming a structure with a Si_4 anion, KSi reduces these transition metal compounds to form the anions, $[M_2(CO)_{10}]^{2-}$. In addition, certain organometallic transition metal clusters have been synthesized that contain Zintl anions coordinated to the metal,[81–84] but Zintl compounds are not used as the reagents.

The salt-like description of bonding between the cations and polyatomic anions of Zintl compounds adequately accounts for their solubility in polar solvents. As mentioned above, a large number of binary Zintl compounds will dissolve in ammonia or amine solvents. Some Zintl phases will even dissolve in methanol (e.g. K_4SnTe_4).[15] These Zintl anions have been studied in solution and can react with transition metal cations to give new intermetallic phases. The reaction consists of electron transfer from the Zintl polyanion to the transition metal cations, resulting in the rapid precipitation of the neutral solid product. The intermetallic solids formed by this route are often amorphous and metastable. Using this simple metathesis reaction with, for example, K_4SnTe_4, a series of ternary transition metal chalcogenides of the formula M_2SnTe_4 (M = Cr, Mn, Fe, Co, Ni, and Cu) have been synthesized and characterized.[15,17] In addition, the compounds $M_5(InTe_4)_2$ (M = Cr, Mn, Fe, Co, and Ni) have been synthesized and characterized.[85–87] These materials exhibit remarkable properties, including a spin glass transition at temperature ranging from 5 to 18 K.

Zintl ion solutions have been explored for the metallization of polymers.[14] Oxidizing polymers such as polyimide can be topochemically metallized by reaction with Zintl ion solutions.

In addition, the reactivity of Zintl ion solutions with layered materials have been reported. Solutions of K_4Sn_9 in en reduce graphite and HfTe; the potassium is intercalated into the structure and tin metal is deposited on the edges of the layered substrate.[13]

More recently Zintl phases have been used to prepare novel semiconducting phases such as nanocrystals.[7,88–90] Group IV nanoparticles have been prepared either by metathesis route or an oxidation of a binary Zintl phase.

4 CHARACTERIZATION

The results of X-ray crystal-structure determinations have assumed great significance in discussions of the bonding in these phases. Relatively speaking, this is the field with the greatest amount of experimental material. In addition, in recent years the requirement of additional characterization by most Journals has resulted in more property measurements and theoretical calculations on Zintl phases published.

Theoretical calculations on compounds crystallizing in the NaTl structure type have been performed and their properties reviewed.[40] In addition to the crystal structure, the thermodynamic behavior, electrical conductivity, magnetic susceptibility, nuclear magnetic resonance (NMR) data, elastic constants, and optical properties have been studied. Based upon experimental data, the bonding in Zintl phases is considered to be a mixture of covalent, ionic, and metallic contributions. In many cases, the transport properties indicated metallic behavior arising from deviations from ideal stoichiometry. However, the thermal and elastic behavior of these phases indicates strong covalent bonding. Most theoretical studies have focused on compounds in which the Zintl concept does not appear to hold, such as $Ba_7Ga_4Sb_9$[91] or $A_{14}MPn_{11}$.[68,69] Theoretical calculations have also been performed on Zintl anions such as X_2Y_2 type clusters,[92,93] as well as the more classic structures that are considered to be Zintl ions.[4,38]

A few IR and Raman spectroscopic investigations on Zintl ions have been reported. The assignment of the observed frequencies is determined by normal coordinate analysis and force constants for such compounds as $Cs_6M_2Pn_4$ ($M = Al, Ga; Pn = P, As$),[94] Cs_6MPn_3 ($M = In, Al; Pn = As, Sb$),[95] and M_3Pn_{11} ($M = Na, K, Rb, Cs; Pn = P, As$).[96] Some properties of the homoatomic nine-atom Zintl ions of group 14 (Si–Pb) have been reviewed.[38]

Nearly all information on the solution chemistry of the Zintl ions has come from NMR studies.[97–101] The majority of these were carried out in en without the addition of crypt. Clusters that have been identified by ^{119}Sn, ^{205}Tl, or ^{207}Pb NMR include $Sn_{9-x}Pb_x{}^{4-}$ ($x = 0 - 9$), $Sn_{9-x}Ge_x{}^{4-}$ ($x = 0 - 9$), Sn_8Tl^{5-}, $Sn_4{}^{2-}$, $SnTe_4{}^{4-}$, $Sn_{8-x}Pb_xTl^{\hat{n}-}$ ($x = 1 - 4, n$ probably 5), and $Sn_2Bi_2{}^{2-}$.

5 RELATED ARTICLES

Alloys; Chalcogenides: Solid-state Chemistry; Hypervalent Compounds; Magnetism of Extended Arrays in Inorganic Solids; Magnetism of Transition Metal Ions; Semiconductors.

6 REFERENCES

1. S. M. Kauzlarich ed., ‘Chemistry, Structure, and Bonding of Zintl Phases and Ions’, VCH Publishers, New York, 1996.
2. W. B. Pearson, *J. Less-Common Met.*, 1985, **109**, L3.
3. R. Nesper, *Angew. Chem., Int. Ed. Engl.*, 1991, **30**, 789.
4. J. D. Corbett, *Chem. Rev.*, 1985, **85**, 383.
5. J. D. Corbett, *Angew. Chem., Int. Ed. Engl.*, 2000, **39**, 671.
6. H.-G. von Schnering, J. Wolf, D. Weber, R. Ramirez, and T. Meyer, *Angew. Chem., Int. Ed. Engl.*, 1986, **23**, 169.
7. R. A. Bley and S. M. Kauzlarich, *J. Am. Chem. Soc.*, 1996, **118**, 12461.
8. B. W. Eichhorn, R. C. Haushalter, and W. T. Pennington, *J. Am. Chem. Soc.*, 1988, **110**, 8704.
9. B. W. Eichhorn, R. C. Haushalter, and J. C. Huffman, *Angew. Chem., Int. Ed. Engl.*, 1989, **28**, 1032.
10. R. Hauptmann and T. F. Fässler, *Z. Anorg. Allg. Chem.*, 2003, **629**, 2266.
11. A. Ugrinov and S. C. Sevov, *J. Am. Chem. Soc.*, 2003, **125**, 14059.
12. A. Schnepf, *Angew. Chem., Int. Ed. Engl.*, 2003, **42**, 2624.
13. R. C. Haushalter, *Angew. Chem., Int. Ed. Engl.*, 1983, **22**, 558.
14. R. C. Haushalter and L. J. Krause, *Thin Solid Films*, 1983, **102**, 2312.
15. R. C. Haushalter, C. J. O’Conner, A. M. Umarji, G. K. Shenoy, and C. K. Saw, *Solid State Commun.*, 1984, **49**, 929.
16. R. C. Haushalter, C. J. O’Connor, J. P. Haushalter, A. M. Umarji, and G. K. Shenoy, *Angew. Chem., Int. Ed. Eng.*, 1984, **23**, 169.
17. R. C. Haushalter, D. P. Goshorn, M. G. Sewchok, and C. B. Roxlo, *Mater. Res. Bull.*, 1987, **22**, 761.
18. S. M. Kauzlarich, J. Y. Chan, and B. R. Taylor, in ‘Inorganic Materials Synthesis’, ACS Symposium Series Vol. 727, eds. C. H. Winter and D. M. Hoffman, American Chemical Society, Washington, DC, 1999, p. 15.
19. E. Mooser and W. B. Pearson, *Physiol. Rev.*, 1956, **101**, 1608.
20. W. B. Pearson, *Acta Crystallogr.*, 1964, **17**, 1.
21. A. Kjekshus and T. Rakke, in ‘Structure and Bonding’, Springer-Verlag, 1974, Vol. 19, p. 45.
22. U. Müller, ‘Inorganic Structural Chemistry’, John Wiley & Sons, West Sussex, 1993.
23. E. Zintl, *Angew. Chem.*, 1939, **52**, 1.
24. W. Klemm, *Proc. Chem. Soc., London*, 1958, 329.

25. H. Schäfer, B. Eisenmann, and W. Müller, *Angew. Chem., Int. Ed. Engl.*, 1973, **12**, 694.
26. B. Eisenmann and H. Schäfer, *Rev. Inorg. Chem.*, 1981, **3**, 29.
27. H. Schäfer, *Annu. Rev. Mater. Sci.*, 1985, **15**, 1.
28. W. Bronger, *Pure Appl. Chem.*, 1985, **57**, 1363.
29. S. M. Kauzlarich, T. Y. Kuromoto, and M. M. Olmstead, *J. Am. Chem. Soc.*, 1989, **111**, 8041.
30. S. M. Kauzlarich, in 'Chemistry, Structure, and Bonding of Zintl Phases and Ions', ed. S. M. Kauzlarich, VCH Publishers, New York, 1996, p. 245.
31. S. M. Kauzlarich, *Comments Inorg. Chem.*, 1990, **10**, 75.
32. S. M. Kauzlarich, A. C. Payne, and D. J. Webb, in 'Magnetism: Molecules to Materials III', eds. J. S. Miller and M. Drillon, Wiley-VCH, Weinham, 2002, p. 37.
33. R. Nesper, *Prog. Solid State Chem.*, 1990, **20**, 1.
34. L. Pauling, 'The Nature of the Chemical Bond', Cornell University Press, Ithaca, NY, 1960.
35. W. Hume-Rothery, *J. Inst. Met.*, 1926, **35**, 295.
36. F. Laves, *Naturwissenschaften*, 1941, **29**, 244.
37. D. Kummer and L. Diehl, *Angew. Chem., Int. Ed. Engl.*, 1970, **9**, 895.
38. T. F. Fässler, *Coord. Chem. Rev.*, 2001, **215**, 347.
39. W. Klemm and E. Busmann, *Z. Anorg. Allg. Chem.*, 1963, **319**, 297.
40. P. C. Schmidt, 'Structure and Bonding', Springer-Verlag, Berlin, 1987, Vol. 65, p. 91.
41. J. Witte and H. G. von Schnering, *Z. Anorg. Allg. Chem.*, 1964, **327**, 260.
42. B. Eisenmann, H. Jordan, and H. Schäfer, *Z. Anorg. Allg. Chem.*, 1981, **475**, 74.
43. J. Wolfe, D. Weber, and H.-G. von Schnering, *Z. Naturforsch.*, 1986, **41B**, 731.
44. W.-M. Hurng, E. S. Peterson, and J. D. Corbett, *J. Am. Chem. Soc.*, 1989, **28**, 4177.
45. B. Eisenmann and J. Klein, *J. Less-Common Met.*, 1991, **175**, 109.
46. B. Eisenmann and H. Schäfer, *Angew. Chem., Int. Ed. Engl.*, 1980, **19**, 490.
47. B. Eisenmann and H. Schäfer, *Z. Anorg. Allg. Chem.*, 1982, **484**, 142.
48. H. Schäfer and B. Eisenmann, *Rev. Inorg. Chem.*, 1981, **3**, 29.
49. D. M. Young and S. M. Kauzlarich, *Chem. Mater.*, 1995, **7**, 206.
50. T. F. Fässler, *Angew. Chem., Int. Ed. Engl.*, 2001, **40**, 4161.
51. W. Jeitschko and M. Reehuis, *J. Phys. Chem. Solids*, 1987, **48**, 667.
52. W. K. Hofmann and W. Jeitschko, *J. Less-Common Met.*, 1988, **138**, 313.
53. G. Cordier, H. Schäfer, and M. Stelter, *Z. Anorg. Allg. Chem.*, 1984, **519**, 183.
54. S. L. Brock, L. J. Weston, M. M. Olmstead, and S. M. Kauzlarich, *J. Solid State Chem.*, 1993, **107**, 513.
55. S. M. Kauzlarich and T. Y. Kuromoto, *Croat. Chem. Acta*, 1991, **64**, 343.
56. J. T. Vaughey and J. D. Corbett, *Chem. Mater.*, 1996, **8**, 671.
57. W. Carrillo-Cabrera, M. Somer, K. Peters, and H. G. von Schnering, *Chem. Ber.*, 1996, **129**, 1015.
58. I. R. Fisher, S. L. Bud'ko, C. Song, P. C. Canfield, T. C. Ozawa, and S. M. Kauzlarich, *Phys. Rev. Lett.*, 2000, **85**, 1120.
59. K. Vidyasagar, W. Honle, and H. G. von Schnering, *Z. Anorg. Allg. Chem.*, 1996, **622**, 518.
60. B. Eisenmann and M. Somer, *Z. Naturforsch.*, 1985, **40b**, 886.
61. A. Adam and H.-U. Schuster, *Z. Naturforsch.*, 1990, **45b**, 559.
62. H. Kim, C. L. Condron, A. P. Holm, and S. M. Kauzlarich, *J. Am. Chem. Soc.*, 2000, **122**, 10720.
63. F. Gascoin and S. C. Sevov, *Inorg. Chem.*, 2002, **41**, 5920.
64. A. P. Holm, M. M. Olmstead, and S. M. Kauzlarich, *Inorg. Chem.*, 2003, **42**, 1973.
65. F. Gascoin and S. C. Sevov, *Inorg. Chem.*, 2003, **42**, 904.
66. F. Gascoin and S. C. Sevov, *Inorg. Chem.*, 2003, **42**, 8567.
67. A. S. Sefat and J. E. Greedan, *Inorg. Chem.*, 2004, **43**, 142.
68. R. F. Gallup, C. Y. Fong, and S. M. Kauzlarich, *Inorg. Chem.*, 1992, **31**, 115.
69. D. Sánchez-Portal, R. M. Martin, S. M. Kauzlarich, and W. E. Pickett, *Phys. Rev. B*, 2002, **65**, 144414.
70. A. P. Holm, S. M. Kauzlarich, S. A. Morton, G. D. Waddill, W. E. Pickett, and J. G. Tobin, *J. Am. Chem. Soc.*, 2002, **124**, 9894.
71. A. Johannis, *Ann. Chim. Phys.*, 1906, **7**, 75.
72. C. A. Kraus, *J. Am. Chem. Soc.*, 1907, **29**, 1571.
73. E. Zintl and H. Kaiser, *Z. Anorg. Allg. Chem.*, 1933, **211**, 113.
74. L. Diehl, K. Khodadedeh, D. Kummer, and J. Strähle, *Chem. Ber.*, 1976, **109**, 3404.
75. L. Xu and S. C. Sevov, *J. Am. Chem. Soc.*, 1999, **121**, 9245.
76. C. Downie, Z. Tang, and A. M. Guloy, *Angew. Chem., Int. Ed. Engl.*, 2000, **39**, 338.
77. A. Ugrinov and S. C. Sevov, *J. Am. Chem. Soc.*, 2002, **124**, 10990.
78. H. G. von Schnering, *Angew. Chem., Int. Ed. Engl.*, 1981, **20**, 33.
79. B. Kesanli, J. Fettinger, and B. Eichhorn, *J. Am. Chem. Soc.*, 2003, **125**, 7367.
80. E. Hey-Hawkins and H. G. von Schnering, *Chem. Ber.*, 1990, **124**, 1167.
81. K. H. Whitmire, M. R. Churchill, and J. C. Fettinger, *J. Am. Chem. Soc.*, 1985, **107**, 1056.
82. A.-J. Dimaio and A. L. Rheingold, *Chem. Rev.*, 1990, **90**, 169.

83. W. J. Evans, S. L. Gonzales, and J. W. Ziller, *J. Chem. Soc., Chem. Commun.*, 1992, 1138.

84. B. Kesanli, J. Fettinger, D. R. Gardner, and B. W. Eichhorn, *J. Am. Chem. Soc.*, 2002, **124**, 4779.

85. J. H. Zhang, A. J. van Duyneveldt, J. A. Mydosh, and C. J. O'Conner, *Chem. Mater.*, 1989, **1**, 404.

86. J. H. Zhang, B. Wu, and C. J. O'Conner, *Chem. Mater.*, 1993, **5**, 17.

87. C. J. O'Connor, J.-S. Jung, and J. H. Zhang, in 'Chemistry, Structure, and Bonding of Zintl Phases and Ions', ed. S. M. Kauzlarich, VCH Publishers, New York, 1996, p. 275.

88. C. S. Yang, Q. Liu, S. M. Kauzlarich, and B. Phillips, *Chem. Mater.*, 2000, **12**, 983.

89. B. R. Taylor, S. M. Kauzlarich, G. R. Delgado, and H. W. H. Lee, *Chem. Mater.*, 1999, **11**, 2493.

90. K. A. Pettigrew, Q. Liu, P. P. Power, and S. M. Kauzlarich, *Chem. Mater.*, 2003, **15**, 4005.

91. P. Alemany, S. Alvarez, and R. Hoffmann, *Inorg. Chem.*, 1990, **29**, 3070.

92. F. U. Axe and D. S. Marynick, *Inorg. Chem.*, 1988, **27**, 1426.

93. R. J. Cave, E. R. Davidson, P. Sautet, E. Canadell, and O. Eisenstein, *J. Am. Chem. Soc.*, 1989, **111**, 8105.

94. M. Somer, D. Thiery, K. Peter, L. Walz, M. Hartweg, T. Popp, and H. G. von Schnering, *Z. Naturforsch.*, 1991, **46b**, 789.

95. W. Blase, G. Cordier, K. Peters, M. Somer, and H. G. von Schnering, *Angew. Chem., Int. Ed. Engl.*, 1991, **30**, 326.

96. H. G. von Schnering, M. Somer, G. Kliche, W. Hönle, T. Meyer, J. Wolf, L. Ohse, and P. B. Kempa, *A. Anorg. Allg. Chem.*, 1991, **601**, 13.

97. R. W. Rudolph, W. L. Wilson, F. Parker, R. C. Taylor, and D. C. Young, *J. Am. Chem. Soc.*, 1978, **100**, 4629.

98. R. W. Rudolph, W. L. Wilson, and R. C. Taylor, *J. Am. Chem. Soc.*, 1981, **103**, 2480.

99. W. L. Wilson, R. W. Rudolph, L. L. Lohr, R. C. Taylor, and P. Pyykkö, *Inorg. Chem.*, 1986, **25**, 1535.

100. H. Borrmann, J. Campbell, D. A. Dixon, H. P. A. Mercier, A. M. Pirani, and G. J. Schrobilgen, *Inorg. Chem.*, 1998, **37**, 1929.

101. B. Kesanli, S. Charles, Y. F. Lam, S. G. Bott, J. Fettinger, and B. Eichhorn, *J. Am. Chem. Soc.*, 2000, **122**, 11101.

Zirconium & Hafnium: Inorganic & Coordination Chemistry

Christopher M. Kozak & Philip Mountford
University of Oxford, Oxford, UK

Based in part on the article Zirconium & Hafnium: Inorganic & Coordination Chemistry by Grigorii L. Soloveichik which appeared in the Encyclopedia of Inorganic Chemistry, First Edition.

---

1 Introduction 1
2 Properties of the Elements 2
3 Natural Abundance and Production 2
4 Oxidation States, Coordination Numbers, and Stereochemistry 4
5 Binary and Mixed Compounds 4
6 Salts of Oxoacids 7
7 Aqueous Chemistry 8
8 Coordination Compounds 9
9 Lower Oxidation States 21
10 Related Articles 22
11 References 22

Abbreviations

Ar′O = 2,6-di-*t*-butylphenoxide; acac = acetylacetonate; bppy = 4-(1-butylpentyl)pyridine; cup = cupferron; dippe = 1,2-bis(diisopropylphosphino)ethane; dppe = 1,2-bis(diphenylphosphino)ethane; fcc = face-centered cubic; $^{f}R = CH(CF_3)_2$; hcp = hexagonal close-packed; hexone = methyl isobutyl ketone; OEP = octaethylporphyrinogen; phen = phenanthroline; py′ = 4-pyrrolidinopyridine; tritox = $(t\text{-Bu})_3CO^-$; tbp = Bu_3PO_4; TPP = tetraphenyl-porphyrinogen; trmpe = tris(dimethylphosphinomethyl)ethane.

---

1 INTRODUCTION

Zirconium (atomic number 40) and hafnium (atomic number 72) are members of group 4 of the *periodic table* (*see Periodic Table*), below titanium (atomic number 22) and above Rutherfordium, (element 104). Zirconium (named from the Arabic *zargun*, meaning gold-colored) was discovered in 1789 by the German chemist Martin Heinrich Klaproth (1743–1817), who prepared zirconium oxide from the mineral zircon, $ZrSiO_4$. Gems that contain zirconium were known in the ancient world and were known by such names as hyacinth, jacinth, jargon, and zircon. It was such a specimen of zircon from Ceylon (Sri Lanka) that Klaproth heated with alkali to produce a new oxide, which he called *zirconia*. The Swedish chemist Jöns Jacob Berzelius isolated zirconium in the free state by reduction of potassium hexafluorozirconate (K_2ZrF_6) with potassium in a sealed iron tube to obtain a black powder.

Dimitri Mendeleev predicted the existence and the main properties of the 72nd element in 1870, and George Urbain in 1911 mistakenly thought he had discovered it, calling it celtium. Henry Moseley deduced the presence of element 72 (among the other undiscovered elements 43, 61, and 75) from X-ray spectra, but was misled thinking that it was the recently announced celtium. Celtium was discredited, but in 1923 Dirk Coster of the Netherlands and George Charles de Hevesy of Hungary used Moseley's method of X-ray analysis on a sample of Norwegian zircon and observed the spectrum for the element, which proved to be hafnium. It was named after Hafnia, the Latin name for Copenhagen where the discovery was made. Pure metallic hafnium was first obtained in 1925 by decomposing hafnium tetraiodide (HfI_4) over a hot tungsten wire.[1]

In most of their compounds, zirconium and hafnium exist in the oxidation state IV (*see Oxidation Number*). Compared with titanium, their M^{III} chemistry is limited,[2] but they show much greater ability to form M–M bonds in oxidation states $\leq$ III (for example, in dimers, layered compounds, and M_6Cl_{12} clusters). The basicities of the group 4 elements increase in the order Ti $<$ Zr $<$ Hf. Therefore the MX_4 compounds with d^0 configuration (*see d^n Configuration*) readily produce high CN neutral or anionic coordination complexes (*see Coordination Complexes*) with Lewis bases. Zirconium and hafnium compounds are rather hard Lewis acids and yield stable complexes with hard bases, such as O- and N-donor ligands (*see Ligand*). The coordination and organometallic complexes of zirconium and to a lesser extent, hafnium, have found use in both hetero- and homogeneous catalysis. In aqueous solutions, Zr and Hf ions are extensively hydrolyzed, and their cations form polynuclear species. In contrast to niobium and tantalum, their neighbors in the periodic table, and titanium, their lighter congener, zirconium and hafnium do not form $M{=}O^{2+}$ species (*see* ***Periodic Table: Trends in the Properties of the Elements***). The chemistry of zirconium and hafnium is characterized by their remarkable resemblance, which is due to their almost identical atomic sizes owing to the lanthanide contraction and their analogous electronic structures.[3,4]

The development of nuclear power opened a new chapter in the inorganic chemistry of these two elements. They show useful but diametrically opposite abilities to transmit thermal neutrons, a fact that stimulated the development of methods for their isolation, careful separation, and metal analysis (*see Metal Analysis*).

2 PROPERTIES OF THE ELEMENTS

2.1 Physical Properties

Table 1 summarizes some of the properties of zirconium and hafnium. Each element has several naturally occurring isotopes. The least abundant of these are ^{96}Zr (2.76% natural abundance) and ^{174}Hf (0.162% n. a.), which are radioactive with half-lives of 3.6×10^{17} y and 2.0×10^{15} y, respectively. The man-made isotopes ^{95}Zr ($t_{1/2} = 65.3$ d), ^{175}Hf ($t_{1/2} = 70$ d), and ^{181}Hf ($t_{1/2} = 70$ d) are used as tracers in scientific research.

In appearance, the metals are lustrous, silvery, and ductile and have high melting points. Their structures are typically hcp, which transform to bcc at high temperatures (870 °C for Zr and 1760 °C for Hf). Owing to the lanthanide contraction (*see Lanthanide Contraction*), the metallic and ionic radii of the two elements are almost identical. As a result, the properties of the metals are very similar.

2.2 Chemical Properties

Zirconium and hafnium possess nearly identical chemistry. No other pair of congeners has chemical properties so similar to each other. This is mostly a result of the metals possessing nearly identical atomic and ionic radii (1.45 and 1.44 Å for Zr and Hf, and 0.86 and 0.85 Å for Zr^{4+} and Hf^{4+}) as a result of the lanthanide contraction. They are relatively electropositive, but less so than the group 3 metals. The metals themselves are highly pyrophoric when finely divided. However, in the bulk form at room temperature they are resistant to corrosion, which is due to the formation of a dense protective oxide film. At high temperature, they react directly with most nonmetals, especially oxygen, hydrogen, and the halogens. For example, the metals burn in oxygen and chlorine gas to yield MO_2 and MCl_4, respectively. Mineral acids (with the exception of hydrofluoric acid) have little effect on the metals unless hot. Oxidizing agents such as nitric acid frequently reduce the activity of the metals by stabilizing the adherent oxide film. Aqueous alkalis have no effect, even at elevated temperatures.

Table 1 The main properties of zirconium and hafnium

Property	Zirconium	Hafnium
Atomic number	40	72
Mass numbers of natural isotopes (%)	90 (51.5)	174 (0.2)
	91 (11.2)	176 (5.2)
	92 (17.1)	177 (18.6)
	94 (17.4)	178 (27.1)
	96 (2.8)	179 (13.7)
		180 (35.2)
Relative atomic mass	91.22	178.49 (3)
Electronic configuration	$[Kr]4d^2 5s^2$	$[Xe]4f^{14} 5d^2 6s^2$
Electronegativity	1.4	1.3
Metal radius (pm)	160	159
Covalent radius (pm)	148	147
Ionic radius (M^{4+}) (pm)	72 (6)	71 (6)
Melting point (°C)	1857	2222
Boiling point (°C)	4377	4602
Density ($g\,cm^{-3}$)	6.51	13.28
ΔH_{fus} ($kJ\,mol^{-1}$)	19.2	(25)
ΔH_{vap} ($kJ\,mol^{-1}$)	567	571 (25)
ΔH_f (monoatomic gas) ($kJ\,mol^{-1}$)	612 (11)	611 (17)
Ionization potential (V)	6.835	7.003
Electrical resistivity (20 °C) (μΩ cm)	40.0	35.1

3 NATURAL ABUNDANCE AND PRODUCTION

3.1 Natural Abundance

Zirconium comprises 0.016% (162 ppm) of the Earth's crust and, as a transition element, is only less abundant than Fe, Ti, and Mn. Hafnium is much less abundant at 2.8 ppm, but is still comparable in quantity to Cs and Br. The most important minerals of zirconium are zircon ($ZrSiO_4$), which is mostly mined in Australia, South Africa, the USA, and Sri Lanka, and baddeleyite (ZrO_2), found mostly in Brazil. The estimated reserves exceed a billion tonnes. Australia and South Africa account for about 80% of zircon mining. All zirconium minerals are contaminated by small quantities of hafnium (0.5–2% of Zr content), but in a few (such as alvite, $MSiO_4 \cdot xH_2O$, M = Hf, Zr, Th) the content of Hf is comparable with that of Zr. The above-mentioned similarities in the chemical behavior of these metals explain their close association in Nature and the similarity of their isolation procedures.

3.2 Industrial Isolation and Production

There are three industrial routes used for the extraction of zirconium and hafnium from ores: (1) caking of zircon with K_2SiF_6, alkaline extraction of the cake, separation of K_2HfF_6 from K_2ZrF_6 by fractional crystallization, and reduction of the complex fluorides to the metal; (2) chlorination of zircon in the presence of coke, purification of MCl_4 (for example, by distillation of adducts with $POCl_3$), and their reduction by metallothermy; (3) caking of zircon with lime, soda, or NaOH, acid extraction of the cake, extractional separation by hexone as the thiocyanates or by tributyl phosphate as the nitrates, and precipitation of the tetrafluorides by HF and their reduction to the metal.

The most important commercial methods of production of metallic zirconium and hafnium are based on furnace reduction, either of MCl_4 with magnesium or a Na–Mg mixture (the Kroll process), yielding a metal sponge, or of metal fluorides with Ca at 2000 °C to give an ingot. The elimination of oxygen and nitrogen impurities is achieved by the van Arkel–de Boer process, which involves the heating of a crude sponge metal *in vacuo* with iodine to give volatile MI_4, and the decomposition of the iodide at a filament heated above 1300 °C. The annual world production of zircon exceeds 900 000 tonnes and that of zirconium metal is about 7000 tonnes. Industrial production of hafnium metal is about 50 tonnes a year.

3.3 Separation

Despite zirconium and hafnium being among the most difficult elements to separate, some highly effective methods have been developed to purify the metals.[5] The most effective method is a liquid extraction. Fractional crystallization of the fluorides K_2HfF_6 and K_2ZrF_6 (mentioned above) is used now only for the concentration of hafnium. The solubilities of K_2HfF_6 in water and $KHfF_5$ in 0.7 M HF are about 1.5 and 2.2 times as much as those of K_2ZrF_6 and $KZrF_5$ in the respective solvent thereby allowing the accumulation of Hf in solution. The different solubilities of the zirconium and hafnium phosphates in strong acid media, of the cupferronates (*see Cupferron*) in HF solutions, and of their hydroxides allow their separation by fractional precipitation.

Separation of the tetrahalides can be achieved from their solutions in molten salts (K_2ZrF_6, NaCl, $SnCl_2$) or under pressure (10–70 atm). However, distillation of the adducts of the tetrachlorides with $POCl_3$ is a more convenient route. Borohydrides and alkoxides of Zr and Hf are more volatile, but their complicated syntheses and high air-sensitivity limit their usefulness.

There are a few differences in the chemical behavior of zirconium and hafnium that can be exploited for their separation. The equilibrium constant of the reaction shown in equation (1) for Zr is greater than 10 orders of magnitude larger than for Hf. Therefore, reaction of a mixture of MCl_4 vapors with O_2 and Cl_2 at 500–900 °C selectively oxidizes Zr to ZrO_2 and leaves $HfCl_4$. On heating a mixture of MCl_4 with Zr or Al metal in vacuo at 400–450 °C, most of the $ZrCl_4$ is reduced to nonvolatile $ZrCl_3$ while $HfCl_4$ is left unchanged and can be distilled from the reaction mixture. Electrolysis of K_2MF_6 in molten NaCl–KCl mixture at 650–700 °C first gives MCl_2 but ultimately yields mainly metallic Zr.

$$MCl_4 + O_2 \rightleftharpoons MO_2 + Cl_2 \qquad (1)$$

Ion exchange and chromatography are used most often in analytical chemistry, due to the low concentration of the final solutions. Zr and Hf can be separated in anionic forms in sulfuric acid or concentrated HCl or HF with anion exchange resins like Dowex 2, or in cationic forms in diluted acids with cation exchange resins like Dowex 50.

Liquid extraction methods are based on the differential distribution coefficients of Zr and Hf between aqueous and organic phases. For example, hexone and other ketones (such as cyclohexanone) are used to extract hafnium into the organic phase from acid rhodanide solutions while tributyl phosphate (tbp) extracts zirconium into the organic phase from nitric acid or its mixture with HCl as complexes with one or two tbp ligands. The composition of the extracted species depends on the composition and pH of the aqueous phase. In 5 M HCl/HNO_3 (1:1), the composition of the extracted complex is $ZrOCl(NO_3)\cdot n(tbp)$, while in concentrated nitric acid it is $Zr(NO_3)_4\cdot n(tbp)$. It is assumed that hafnium is extracted as $Hf(NO_3)_4\cdot 2(tbp)\cdot nHNO_3$. From chloric acid solutions the metals are effectively extracted with fluorinated diketones (*see Diketones*), such as thenoyltrifluoroacetone (tta).

3.4 Uses

Zirconium metal has a very high corrosion resistance except toward fluoride ions, *aqua regia*, concentrated sulfuric acid, wet chlorine, and iron(III) and copper(II) chlorides. It has found use alongside stainless steel, titanium, and tantalum in the production of chemical apparatus. Zirconia has a very high melting point (above 2500 °C) and is used to make heat-resistant crucibles, ceramics, and abrasives. The generally low toxicity (except to individual allergic reactivity) has given zirconia use in cosmetics, antiperspirants (as zirconium hydroxychloride in roll-on deodorants), and food packaging.

In the 1940s, zirconium and hafnium metals were brought to prominence by their use in the nuclear industry in nuclear reactors and submarines. Zirconium and hafnium differ completely in their ability to transmit thermal neutrons. Zirconium is practically transparent to these particles (with a cross section for thermal neutron capture of 0.18 barns) whereas hafnium is a powerful absorber (105 barns). Both metals, therefore, are used in the nuclear industry: zirconium is used as a cladding for the uranium dioxide fuel rods of water-cooled nuclear reactors, while hafnium is used as a material for reactor control rods (for example, in nuclear submarines) and for protective screens in reactors. The nuclear industry consumes about 90% of the total world zirconium and hafnium output. The corrosion resistance of pure zirconium is insufficient for nuclear technology, so a series of alloys containing Sn, Fe, Cr, and Ni ('Zircaloys', the cross section of which is only 0.22 barns) have been developed.[6] Zirconium is also used as a getter, as an electrode material, and as a component of a variety of alloys including superconducting niobium-based alloys that retain their superconductivity (*see* ***Superconductivity***) in strong magnetic fields. Zirconium–zinc alloys become magnetic at temperatures below 35 K. The addition of 0.1% Zr to steel increases its hardness and toughness and the element is therefore used in the production of steel armor plate. Zirconium alloys exhibit catalytic activity for ammonia synthesis and conversion of SO_2 to SO_3 (*see Catalysis*).

The uses of zirconium and hafnium compounds based on their thermal and corrosion stability are described in related sections (see below). The most dramatic use of zirconium (in the form of zirconia) is in ultrastrong ceramics. This was developed from the need for tank engines that would tolerate very high temperatures without the need of lubrication or a cooling system. Consequently, these tough, heat-resistant ceramics that are sharper than toughened steel make excellent industrial high-speed cutting tools. They have also found use in consumer goods such as knives, scissors, and golf irons, in addition to medical use as bioceramics in prosthetic joint replacement.

4 OXIDATION STATES, COORDINATION NUMBERS, AND STEREOCHEMISTRY

The chemistry of hafnium has not been studied to nearly the same extent as zirconium, but its behavior very closely resembles that of the lighter metal. The most important oxidation state of these metals is almost exclusively the group oxidation state of IV. Lower oxidation states are only sparsely represented in contrast to titanium for which oxidation state III is also characteristic (*see* ***Titanium: Inorganic & Coordination Chemistry***). The M^{III} state has no aqueous chemistry, since it readily reduces water. Nevertheless, lower oxidation states of zirconium and hafnium have been reported in a few inorganic solids (III, II, I) and recently in organometallic and coordination compounds in nonaqueous solutions (III, II, 0, −II). Ligands such as cyclopentadienyl (*see Cyclopentadienyl*) or dienes (*see Diene Complexes*) effectively stabilize lower oxidation states of Zr and Hf, and a large number of bis- and monocyclopentadienyl M^{III} and M^{II} complexes have been reported (*see* ***Zirconium & Hafnium: Organometallic Chemistry***).

The standard electrode potentials of Zr/Zr^{4+} and Hf/Hf^{4+} couples in aqueous solution are −1.529 and −1.70 V versus SHE, where SHE is the standard hydrogen electrode (*see Redox Properties & Processes*). Hafnium has the most negative reduction potential among the transition metals (*see Transition Metals*). In alkaline solution, the standard electrode potentials (equation 2) shift to the anodic region (−2.36 and −2.50 V, respectively), becoming (for Hf) more negative than those of the actinides. The standard electrode potentials, including intermediate oxidation states, measured in a molten NaCl–KCl mixture at 1000 K are −1.338 V (Zr^{2+}/Zr^0), −0.954 V (Zr^{3+}/Zr^{2+}), and −0.377 V (Zr^{4+}/Zr^{3+}) vs. Ag/AgCl, while the potentials of the Zr^{4+}/Zr^0 and Hf^{4+}/Hf^0 couples are −1.002 and −1.185 V respectively.

$$MO(OH)_2 + H_2O + 4e^- \rightleftharpoons M + 4OH^- \qquad (2)$$

Coordination numbers (CN) of zirconium and hafnium range from 4 to 12, but because of the large values of their ionic and covalent radii (*see Covalent Radii*) (Table 1), their complexes typically have CNs of 6–8 (*see* ***Coordination Numbers & Geometries***). They have a varied stereochemistry (*see Stereochemistry*), as a result of the spherical symmetry of their d^0 configuration and the consequent absence of ligand field effects. Typical coordination polyhedra are listed in Table 2. Thus, for CN 8, the coordination polyhedra most often observed are the dodecahedron (*see Dodecahedral*) and the square antiprism (*see Square Antiprism*). Chelating ligands (*see Chelate Effect*) forming five-membered metallacycles (such as $C_2O_4{}^{2-}$) tend to give a dodecahedral structure, while the preferred geometry for ligands that form six-membered metallacycles (such as acac) is the square antiprism.[7] Analogously, replacing the rather small bidentate ligand $NO_3{}^-$ by the larger $IO_3{}^-$ causes a change from a dodecahedral arrangement of the metal atom to a square antiprismatic one. Maximum CN values of 10 and 12 are noted for the very small hydride ligand, typically in the form of borohydride, $BH_4{}^-$, complexes (*see* ***Hydride Complexes of the Transition Metals***). Coordination numbers of 8 and 7 are typical for small ligands like F^-, O^{2-}, or OH^-, while in most chloride and alkoxide complexes the metal atom has an octahedral arrangement (*see* ***Structure & Property Maps for Inorganic Solids***). An increase of substituent bulk in a second coordination sphere reduces the CN to 5 or even 4 (*see Coordinative Saturation & Unsaturation*).

It should be noted that zirconium and hafnium usually form electron deficient complexes (*see Electron Deficient Compound*), which do not obey the Effective Atomic Number Rule (EAN rule) (*see Effective Atomic Number Rule*) and have a maximum of only 16 electrons. Monomers MX_4 with monodentate ligands are rather strong Lewis acids and readily yield adducts with two, three, or four donor ligands. In MX_4 monomers with π-donor ligands X (*see π-Base*), there is a noticeable shortening of the M−X distances in comparison with the sum of the covalent radii (0.26 Å for X = F; 0.15 Å for X = Cl, NMe_2), thus pointing to some multiple bond character in these compounds.

Structures of di- and monovalent zirconium and hafnium compounds contain octahedra, chains, or layers of metal atoms with metal−metal bonds. It is this that differentiates these compounds from those of M^{III} (MX_3 or molecular $M_2X_6L_4$ complexes) with isolated M–M bonds. A recent reinvestigation of the ZrI_3 structure showed two distinct Zr–Zr distances (3.507 and 3.172 Å); the latter is typical for a Zr–Zr bond (*see Bond Length*).

5 BINARY AND MIXED COMPOUNDS

5.1 Hydrides

Zirconium and hafnium react with hydrogen at temperatures above 700 °C, yielding an α-phase and hydrides with a limiting M:H ratio of 1:2 (*see* ***Hydrides: Solid State Transition Metal Complexes***). Under hydrogen pressure, absorption

Table 2 Coordination numbers and polyhedra of zirconium and hafnium

Oxidation state	Coordination number	Coordination polyhedron	Examples of compounds
IV	4	Tetrahedron	$ZrCl_4$ (gas), $Zr(NMe_2)_4$ (gas and solution, dimeric in solid state), $ZrCl(OAr')_3$
	5	Square pyramid	K_2ZrO_3, $PhNZr(OAr')_2py'_2$
	6	Octahedron	$ZrCl_4{\cdot}2L$, $Tl_2Zr(O^fR)_6$ $[Ph_3C]_2[Hf_2Cl_{10}]$
		Trigonal prism	$[NMe_4][Zr(S_2C_6H_4)_3]$
	7	Pentagonal bipyramid	$Hf(OH)_2SO_4{\cdot}H_2O$, Na_3MF_7, $Zr(SO_4)_2$
		Capped trigonal prism	$(NH_4)_3MF_7$
		Capped octahedron	$Zr_4O(O\text{-}i\text{-}Pr)_{10}(acac)_4$
		Piano stool	ZrO_2 (baddeleyite)
	8	Dodecahedron	$[Zr_4(OH)_8(H_2O)_{16}]^+$, $Zr(NO_3)_4$, $M(C_2O_4)_4$
		Square antiprism	$Zr(TPP)_2$, $Zr(SO_4)_2{\cdot}H_2O$ $Zr(IO_3)_4$, $Zr(acac)_4$
		Cube	$Zr_{13}O_8(OMe)_{36}$, ZrO_2 (cubic)
		Bicapped trigonal prism	K_4ZrTe_{17}, $HfTe_5$,
	9	Irregular	$M_2(PMe_3)_2H_3(BH_4)_5$
	10	Irregular	$Hf_2[N(SiMe_2CH_2PMe_2)_2]_2H_3(BH_4)_3$
	12		$M(BH_4)_4$, $Zr(BH_3Me)_4$
III	6	Octahedron	MCl_3
	7	Pentagonal bipyramid	$Hf_2Cl_6(dippe)_2$, $M_2X_6(PR_3)_4(C_2H_4)$
	8	Irregular	$Zr_2Cl_3(ppp)_3$
II	6	Cage structure	ZrI_2
	7	Piano stool	$(C_6H_6)[HfI_2(PMe_2Ph)_2]$
I	6	Layered structure	ZrCl, HfBr
0	7	Piano stool	$(trmpe)M(CO)_4$
−II	6	Octahedron	$[K(cryptand\text{-}2,2,2)]_2[M(CO)_6]^{2-}$

takes place with the formation of MH_x hydrides by a transformation of the hcp lattice first to distorted cubic ($x < 1.53$), then to face-centered cubic ($1.53 < x < 1.70$), face-centered tetragonal ($1.70 < x < 1.980$), and finally to a body-centered tetragonal lattice for MH_2. During hydrogenation the density of the metal decreases to 5.5 (Zr) and 11.4 (Hf) g cm^{-3} for the dihydride. This is accompanied by cracking of the solid, and this reaction can therefore be used as a method for converting the bulk metals to fine powders. Both hydrides are stable to air and can replace the metals as convenient starting materials for obtaining other binary compounds, and in the manufacture of ceramics and of foam aluminum using zirconium hydride.**[8]**

5.2 Borides

Both elements form borides of composition MB and MB_2, but only zirconium yields a dodecaboride, ZrB_{12}. The structure of the MB phase contains zigzag chains of boron atoms, and planar hexagonal nets of boron atoms exist in the structure of the MB_2 phase. In contrast, the ZrB_{12} phase has an fcc NaCl-type structure (*see* ***Borides: Solid-state Chemistry***).

5.3 Carbides and Silicides

Both metals and their dioxides react with carbon at high temperatures, yielding carbides, ZrC and HfC, with a NaCl structure type. Their enthalpies of formation are 200.6 and 217.4 kJ mol^{-1}, respectively. Very high melting points (3735 and 3890 °C) are characteristic of these compounds and the alloy of composition HfC·4TaC is the highest melting substance known (mp 3990 °C) (*see* ***Carbides: Transition Metal Solid-state Chemistry***). The conductivities of these are as high as those of metals. They resist mineral acids up to 230 °C (100 °C in HNO_3), but they react with halogens, oxygen, and nitrogen when heated.

There are several examples of M–Si systems. Silicides of composition M_2Si, MSi, and MSi_2 are known for both metals. Zirconium also forms the Zr_3Si_2 phase and hafnium the Hf_5Si_3 phase (*see* ***Silicon: Inorganic Chemistry***). All the silicides are insoluble in all mineral acids (except HF), and, unlike $TiSi_2$, in 10% aqueous KOH.

5.4 Pnictides

Yellow nitrides MN are produced by direct interaction of the elements. It is interesting that the rate of reaction of zirconium with nitrogen is higher than that with oxygen, so the burning of the metal in air yields a mixture of nitride, oxide, and oxonitride, Zr_2ON_2. The reaction of MN with carbon is reversible. The nitrides also have a bcc structure, forming an uninterrupted series of solid solutions with the MC carbides. Their melting points are 2950 °C (Zr) and 2980 °C (Hf), and hafnium nitride is the most fire-resistant of all the metal nitrides (*see* ***Nitrides: Transition Metal Solid-state Chemistry***). A brown intermediate zirconium nitride of composition Zr_3N_4 is produced by heating $ZrCl_4$ at 700 °C in a flow of ammonia (equation 3). Decomposition of the adduct $ZrCl_4(NH_3)_2$ also yields Zr_3N_4 via a nitridochloride (ZrClN) stage.[9] Further heating of Zr_3N_4 gives blue ZrN_x ($x = 0.86$–0.94) above 750 °C and ZrN above 1000 °C. Treatment of ZrI_4 with ammonia at 500 °C gives a yellow ZrIN phase, whose structure is made up of Zr–N and Zr–I chains. These phases exhibit a 'metallic' conductivity that is higher than that of the pure metals, and ZrN is a superconductor below 8.9 K.

$$ZrCl_4 + 4NH_3 \longrightarrow ZrCl_4{\cdot}4NH_3 \longrightarrow Zr(NH_2)_4 \longrightarrow Zr_3N_4 \tag{3}$$

Zirconium and hafnium nitrides dissolve in cold 6 M HF but are stable in other acids except when heated (equation 4).

$$2HfN + 3H_2SO_4 + 2H_2O \longrightarrow 2HfOSO_4 + (NH_4)_2SO_4 + H_2 \tag{4}$$

With phosphorus, zirconium and hafnium form phosphides of composition M_3P, MP, and MP_2, which dissolve only in HF/HNO_3 mixtures (*see* ***Phosphides: Solid-state Chemistry***). ZrP_2 can be also obtained by reaction of $ZrCl_4$ with phosphine.

Arsenides of composition MAs and MAs_2 are also known (*see* ***Arsenic: Inorganic Chemistry***).[10]

5.5 Chalcogenides

Zirconium and hafnium react with *Chalcogens* on heating to give compounds of composition ME_2, ME_3, and ME_5. Their thermal stability decreases in the order $E = S > Se > Te$. Oxochalcogenides, MOE, are formed on treatment of the metal dioxides with H_2S. The MS_2 sulfides dissolve in hot hydrochloric acid, but the MS_3 compounds do not react. $ZrTe_2$ has a metallic conductivity, but ZrS_2, $ZrSe_2$, and $HfTe_2$ are semiconductors (*see* ***Semiconductors***), and HfS_2 is an insulator (*see* ***Sulfur: Inorganic Chemistry***). The chalcogenides $(Cu,Cr)ME_4$ with spinel structures are semiconductors. Phases of the compositions $Ba_5Hf_4S_{13}$ and $Ba_6Hf_5S_{16}$ with perovskite blocks are considered as probable prospective materials for superconductors.[11] In the phase $K_4M_3Te_{17}$, the metal atom has a bicapped trigonal prismatic arrangement, as in $HfTe_5$.[12]

5.6 Oxides and Hydroxides

5.6.1 Oxides

Besides the dioxide MO_2, suboxides of zirconium and hafnium of composition M_6O, M_3O, and metastable MO are known (*see* ***Oxides: Solid-state Chemistry***). The dioxides are high melting (mp $ZrO_2 = 2850$ °C, $HfO_2 = 2900$ °C), nonvolatile solids and find uses in the manufacture of fireproof or chemical resistant products. Besides the monoclinic crystal modification stable at room temperature, there are also two high-temperature modifications, tetragonal and cubic. In the presence of a little CaO a stable fluorite structure is formed, which avoids the injurious mechanistic consequences of the phase changes on repeated heating and cooling. Zirconia and hafnia possess an ionic conductivity via O^{2-} ions, in particular as solid solutions with other oxides, such as Y_2O_3 (*see* ***Ionic Conductors***). Zirconium and hafnium dioxides can be obtained both in the direct interaction of metals with oxygen and in the reaction of the tetrachlorides with water at 250 °C, followed by heating in air at 500 °C, or in oxygen at 350 °C on a fluidized bed. Amorphous dioxides suitable for the manufacture of ceramics are produced by the hydrolysis of Zr and Hf alkoxides (see below). At elevated temperatures zirconia and hafnia can be reduced by Ca to the metals and by carbon to the carbides. Anhydrous zirconia is used as a support for metal and oxide catalysts (*see* ***Oxide Catalysts in Solid-state Chemistry***).

5.6.2 Hydroxides

Zirconium hydroxide is precipitated by bases at lower pH than the hafnium compound. Zr and Hf are obviously unable to form true hydroxides, and these compounds are more correctly formulated as $MO_2{\cdot}xH_2O$. Amorphous hydrous zirconia and hafnia (α-phase) transform to microcrystalline forms (β-phase) with noticeable heat evolution. They lose water up to the composition $MO_2{\cdot}H_2O$ at 140 °C (Zr) or 155 °C (Hf). Hydrous zirconia has excellent absorptive capacity, particularly for oxygen-containing anions. For example, the concentration of ${SO_4}^{2-}$ anions over hydrous zirconia is so low that no precipitate forms on the addition of barium salts to the filtrate. While the hydroxides of composition $M(OH)_4$ are not stable, in alkaline solutions, ${M(OH)_5}^-$ are present and even ${M(OH)_6}^{2-}$ anions have been reported in very concentrated alkalis. Salts of these anions, such as $Na_2Hf(OH)_6$, can be isolated.

5.6.3 Zirconates and Hafnates

Zr and Hf hydroxides are rather amphoteric (*see Amphoterism*). The metazirconates and -hafnates, Q_2MO_3, (where Q is a cationic counterion) and the corresponding poly compounds, $Q_2M_2O_7$, $Q_2M_3O_9$, and $Ln_2M_7O_{17}$ (Ln = La, Nd), are known. A common route for their preparation is the firing of zirconia and hafnia with the appropriate metal carbonate or nitrate. In K_2ZrO_3, zirconium has a tetragonal pyramidal arrangement. Zirconates and hafnates of M^{II} cations of composition $M^{II}ZrO_3$ usually possess a perovskite structure, whereas $M^{II}_2ZrO_4$ compounds often have a spinel structure. Lead zirconate, $PbZrO_3$, is a segnetoelectric material, like $PbTiO_3$.

5.6.4 Heteropolyacids

Zirconium forms heteropolyacids with molybdenum, such as $H_8[Zr(Mo_2O_7)_6]$, whose alkali metal derivatives have been isolated. In the first member of the series, of composition $ZrMo_2O_7(OH)_2(H_2O)_2$, the zirconium atom has a pentagonal bipyramidal arrangement (*see* ***Polyoxometalates***).

5.6.5 Peroxo Compounds

Zirconium and hafnium tetrahalides react with hydrogen peroxide in alkali solution to yield $M(OH)_3OOH$. The maximum content of peroxo units per metal atom has been observed in $K_4Zr(O_2)_4{\cdot}6H_2O$, which is a derivative of the unknown orthoperzirconic acid $Zr(OOH)_4$.

5.7 Halides and Oxohalides

Zirconium and hafnium form halides of composition MX_4 and also MX_3, MX_2, and MCl (see below) (*see* ***Fluorides: Solid-state Chemistry*** and ***Halides: Solid-state Chemistry***). All the tetrahalides are colorless (except for the red-brown HfI_4) and volatile solids, melting only under pressure. The tetrachlorides are produced by chlorination of the dioxides in the presence of coke. The tetraiodides are formed in a direct reaction of iodine with the metal, but the use of the hydrides is more convenient. The halides of hafnium are more stable to heat than those of zirconium. Decomposition of tetraiodides to yield pure metals is used in the van Arkel–de Boer process. The tetrahalides (except for the fluorides) readily dissolve in water, with formation of the oxohalides MOX_2. The reaction of MF_4 with water yields $MF_4{\cdot}3H_2O$, which is stable to hydrolysis. $ZrF_4{\cdot}3H_2O$ contains dimers, $(H_2O)_3F_3Zr(\mu\text{-}F)_2ZrF_3(H_2O)$, while the hafnium complex is a polymer with double Hf–F–Hf bridges (*see Bridging Ligand*).**13** The tetrahalides have a monomeric, tetrahedral structure in the gas phase (except for HfF_4, which forms a dimer). In the solid state, the tetrafluorides have a structure with an antiprism of eight fluorides around each metal atom, while tetrachlorides are composed of chains of edge-sharing distorted octahedra of six chlorides.

Depending on the temperature, heating $HfF_4{\cdot}3H_2O$ in air gives oxofluorides that are mostly isomorphous with the corresponding zirconium compounds: Hf_4OF_{14}, $HfOF_2$ or Hf_2OF_6 (no zirconium analog), $Hf_3O_2F_8$, and HfO_2. The differences between Zr and Hf are also evident in the diverse composition of the products of hydrolysis and thermal decomposition of $MF_4{\cdot}3H_2O$:$Zr_4F_{10}(OH)_6{\cdot}3H_2O$ and $Hf_4F_{12}(OH)_4{\cdot}4H_2O$, $Zr_4F_{10}O_3$ and $Hf_4F_{12}O_2$. Anhydrous hygroscopic oxochlorides of zirconium and hafnium $MOCl_2$ were obtained according to equation (5). On heating they disproportionate (equation 6). The hydrated oxochlorides $MOCl_2{\cdot}8H_2O$ decompose above 65 °C, yielding the dioxides.

$$3MCl_4 + Sb_2O_3 \longrightarrow 3MOCl_2 + 2SbCl_3 \qquad (5)$$

$$2MOCl_2 \xrightarrow{65\,^\circ C} MCl_4 + MO_2 \qquad (6)$$

6 SALTS OF OXOACIDS

6.1 Silicates

Silicates of zirconium, $ZrSiO_4$ (zircon), and hafnium, $HfSiO_4$, are the only crystalline phases in the MO_2–SiO_2 system. Their fusion with molten Na_2SiO_3 yields double silicates, Na_2MSiO_5 and $Na_4MSi_2O_8$.

6.2 Nitrates

Anhydrous volatile nitrates $M(NO_3)_4$ are obtained by the interaction of the chlorides with N_2O_5 (equation 7):

$$MCl_4 + N_2O_5 \longrightarrow M(NO_3)_4 + NO_2Cl \qquad (7)$$

They have monomeric structures with bidentate NO_3 groups. $M(NO_3)_4$ and $MO(NO_3)_2$ react with water more slowly than do the titanium analogs, yielding hydrates of composition $M(NO_3)_4{\cdot}5H_2O$ and $MO(NO_3)_2{\cdot}nH_2O$ ($n = 2$, 6); both can be isolated from cold concentrated nitric acid. As in the case of other $MOX_2{\cdot}nH_2O$ salts, there are no ‘zirconyl’ or ‘hafnyl’ units (MO^{2+}) in the structures of these compounds. The absorbance bands around 850–900 cm^{-1} in the IR spectra of these compounds, which were earlier considered evidence for the presence of zirconyl or hafnyl M=O bonds, are now assigned to bridging M–O–M linkages. The eight-coordinate metal atom in $MO(NO_3)_2{\cdot}2H_2O$ is surrounded by two hydroxyl groups, four water molecules, and two monodentate NO_3 groups; in anhydrous $ZrO(NO_3)_2$, on the other hand, oxygen bridged chains are present. ‘Dizirconyl’, $Zr_2O_3(NO_3)_2{\cdot}5H_2O$, and ‘dihafnyl’, $Hf_2O_3Cl_2{\cdot}5H_2O$, salts have no terminal M=O bonds either. Hafnium nitrate forms a volatile adduct $Hf(NO_3)_4{\cdot}N_2O_5$; zirconium nitrate, however, does not. Mixed nitrates, $Q[M(NO_3)_6]$, are known, where $Q = NR_4{}^+$.

6.3 Phosphates

The orthophosphates $M(HPO_4)_2$ are practically insoluble in mineral acids (except HF) and can be precipitated from strong acid solutions as hydrates with one or two water molecules. This is a method for separating Zr and Hf from other metals (except Pa). The Hf salts are less soluble than those of Zr and accumulate in the precipitate from sulfuric acid solution. Both $Zr(HPO_4)_2{\cdot}nH_2O$ phases have a layered structure and can be intercalated by quite large molecules, such as phen or aminoferrocene.**14** The pillared materials so obtained have pore dimensions approaching those found in zeolite Y and can be used as sorbents or catalysts. Heating the orthophosphates transforms them to pyrophosphates, $M(P_2O_7)$. Mixed phosphatosilicates of zirconium and sodium, such as $Na_3Zr_2Si_2PO_{12}$, are Na superionic conductors (*see* ***Phosphates: Solid-state Chemistry***).

6.4 Sulfates

The anhydrous sulfates $M(SO_4)_2$ are produced as white solids by the reaction of the dioxides with $NaHSO_4$. They are relatively stable to heat, but above 500 °C they decompose to yield MO_2. $Zr(SO_4)_2$ has a polymeric structure with two bidentate and three monodentate sulfate groups bound to the seven-coordinate Zr atom. Evaporation of their aqueous solutions or crystallization from 6 M sulfuric acid gives the compounds $M(SO_4)_2{\cdot}4H_2O$. Hydrates of composition $M(SO_4)_2{\cdot}nH_2O$ ($n = 1, 5, 7$) are also known. X-ray analyses of zirconium salts show a polymeric structure with bridging sulfate groups and seven- ($n = 1$) and eight-coordinate zirconium ($n = 4$) and a dimeric structure with eight-coordinate zirconium ($n = 5, 7$). Basic sulfates of composition $MOSO_4{\cdot}2H_2O$, $M_2(OH)_2(SO_4)_3{\cdot}4H_2O$, $M(OH)_2SO_4{\cdot}H_2O$, $M(OH)_2SO_4{\cdot}2H_2O$, and $M_2O(SO_4)_3{\cdot}5H_2O$ have been detected in the MO_2–SO_3–H_2O system. Zirconium sulfates of the composition $4ZrO_2{\cdot}3SO_3{\cdot}15H_2O$ (Hauser's salt) and $5ZrO_2{\cdot}3SO_3{\cdot}15.5H_2O$ are of industrial importance. In most such complexes the metal atom is eight-coordinate, but in $Zr(OH)_2SO_4{\cdot}H_2O$ the zirconium has a pentagonal bipyramidal arrangement with four bridging OH groups and a water molecule in the equatorial plane. It is interesting that the peroxosulfate $Zr_2O_6SO_4{\cdot}8H_2O$ has no Hf analog. Mixed sulfates $Q_2[M(SO_4)_3]{\cdot}nH_2O$ are known for Zr, Hf, and Ti whereas $Q_4[M(SO_4)_4]{\cdot}nH_2O$ are isolated only for Zr and Hf. The structure of $Q_2[Zr(SO_4)_3]{\cdot}nH_2O$, like that of $Zr(SO_4)_2{\cdot}nH_2O$ ($n = 5, 7$), consists of dimeric $[Zr_2(SO_4)_6(H_2O)_4]^{4-}$ units with eight-coordinate Zr. In $[NH_4][Hf(SO_4)_4(H_2O)_2]{\cdot}2H_2O$, the Hf atom is dodecahedrally coordinated by eight oxygen atoms from two water molecules and two bidentate and two monodentate sulfate groups.

6.5 Salts of Other Acids

The anhydrous perchlorates of zirconium and hafnium, $M(ClO_4)_4$, are colorless volatile crystalline solids. The action of water yields the hydrates $MO(ClO_4)_2{\cdot}8H_2O$, which decompose to MO_2 on heating. Mixed perchlorates, $Q_n[M(ClO_4)_{n+4}]$, are documented. Iodates of zirconium and hafnium, $M(IO_3)_4$, with a square antiprismatic anion are, like the phosphates, insoluble in nitric acid.

Ammonium carbonatozirconate, $[NH_4]_3[Zr(OH)(CO_3)_3]{\cdot}2H_2O$, is used in crosslinking of polymers such as polyacrylates. The dialkylcarbamates $M(O_2CNR_2)_4$, prepared by treating MCl_4 with a CO_2–NHR_2 mixture in toluene, have a slightly distorted dodecahedral arrangement around the metal atom (the X-ray structures are known for M = Hf; R = *i*-Pr).[15] Their reaction with anhydrous HCl yields complexes with a $MCl_6{}^{2-}$ anion (equation 8).

$$M(O_2CNEt_2)_4 + 8HCl \longrightarrow [NH_2Et_2]_2[MCl_6] + 2[NH_2Et_2]Cl + 4CO_2 \qquad (8)$$

A dodecahedral anion is also present in trioxalatozirconic acid, $H_4[ZrO(C_2O_4)_3]{\cdot}7H_2O$, and the mixed oxalates $K_4[Zr(C_2O_4)_4]{\cdot}5H_2O$ and $Na_4[Zr(C_2O_4)_4]{\cdot}3H_2O$. It should be noted that very stable oxalate complexes of Zr and Hf are stable to alkalis. α-Hydroxycarboxylic acids react with zirconium ions to form tri- and tetracarboxylatozirconylic acids. In acid solutions, complexones yield very stable eight-coordinate complexes ($K_{ML} = 10^{20}$–10^{35}) with ratio M:L = 1:1 (such as $[M(EDTA)]{\cdot}3H_2O$) and, rarely, 1:2 (such as $[M(NTA)_2]^{2-}$). A recent X-ray analysis showed that EDTA is a true octadentate ligand in these complexes.[16] In neutral solutions, complexes of formula $[M(EDTA)(OH)]_n{}^{n-}$ ($n = 1, 2$) exist, because of hydrolysis. Alkalis precipitate the metal hydroxides from these complexes at pH >9.

The zirconium salts of organic acids are widely applied in industry. Carboxylatozirconylic acids are used in treating dermatitis and in making textiles water repellent, while zirconium acetate, $Zr(OAc)_4$, and the trilactozirconate $Na_2H[Zr(OH)(MeC(OH)CO_2)_3]$ are components of body deodorants, and the 2-ethylhexanoate and naphthenate are used as siccatives.

7 AQUEOUS CHEMISTRY

All salts of zirconium and hafnium tend to hydrolyze in aqueous solutions, though less so than those of titanium. In highly dilute solutions ($<10^{-4}$ M), Zr and Hf exist as the aqueous ions $[M(OH)_n]^{(4-n)+}$, where n is pH-dependent. The hydration energies are 7001 and 7169 kJ mol^{-1} for Zr and Hf respectively. In chloride, perchlorate, and nitrate solutions, hafnium is less hydrolyzed than zirconium, while the reverse is true in sulfate solutions. This is connected with the lower solubility of hafnium compounds in sulfate solutions, even in only slightly acid media. It should be noted that the sulfate anion has a strong affinity for Zr and Hf.

In perchlorate or chloride solutions of moderate ($>10^{-3}$ M) concentration, Zr and Hf are present as $4MO_2{\cdot}16H_2O{\cdot}nH^+$, which is a cyclic tetramer, usually $[M_4(OH)_8(H_2O)_{16}]^{8+}$, in which the metal atoms are bound by two hydroxyl bridges. This moiety has been found in solid $MOCl_2{\cdot}8H_2O$. There is some evidence for the existence of Zr_3 species, probably $[Zr_3(OH)_6(H_2O)_{12}]^{6+}$, in 2.8 M HCl solution. In these solutions, the metal migrates toward the cathode under the influence of an electric field. Their cationic nature prevents them from reacting with cation exchange resins; they form colored precipitates with acid organic dyes. As well as chloride and perchlorate, tetrameric cations also exist in solutions of Zr and Hf salts in the presence of other weakly coordinating anions (bromide, iodide, thiocyanate). An increase in the acidity or the chloride ion concentration converts Zr and Hf into an anionic form. Solutions with an HCl concentration >6 M do not react with cation exchange resins, and complexes of composition $QMCl_5$ and Q_2MCl_6 can be isolated. The stability of the anionic complexes $[MX_{4+n}]^{n-}$ changes in the sequence $X = F \gg Cl > Br > I$, in line with the trend in M–X bond energies. In aqueous solution, the stable complexes MF_5^-, MF_6^{2-}, and MF_7^{3-} have been detected, and their salts with NH_4^+ and alkali metal cations have been obtained.

In the electrolysis of solutions of $M(SO_4)_2{\cdot}4H_2O$, protons move toward the cathode and the metal to the anode, so these compounds can be formulated as $H_2[MO(SO_4)_2]{\cdot}3H_2O$ (disulfatozirconic and -hafnic acids). The reaction of sodium acetate with $ZrOCl_2{\cdot}8H_2O$ yields diacetatozirconic acid (equation 9). They do not precipitate with acid dyes, and they react with anion exchange resins rather than with their cation exchange counterparts.

$$ZrOCl_2{\cdot}8H_2O + 2NaOAc \longrightarrow HZrO(OH)(OAc)_2 + 2NaCl \quad (9)$$

8 COORDINATION COMPOUNDS

8.1 Hydride Complexes

The Zr and Hf tetrahydroborates $M(BH_4)_4$ are the most volatile compounds of these elements, with boiling points of 123 and 118 °C; they are also very sensitive to oxidation and hydrolysis. They can be obtained by the reaction of the chlorides with alkali metal borohydrides or of the complex fluorides $NaMF_5$ with aluminum borohydride (the fluorides MF_4 do not react), followed by distillation from the reaction mixture. According to low-temperature X-ray data, all the borohydride groups are tridentate in both $M(BH_4)_4$ complexes, which have T_d symmetry. The same is true for their substituted $M(BH_3Me)_4$ derivatives, that is, the metal atom is 12-coordinate. Proton NMR indicates fast exchange of bridging and terminal protons on the NMR timescale in these fluxional molecules (*see Fluxional Molecule*).

Treatment of $M(BH_4)_4$ with PMe_3 gives $M_2H_3(BH_4)_5(PMe_3)_2$, in which two metal atoms are bridged by three hydrides. One of them also has three trihapto (*see Hapticity*) BH_4 groups (CN 12) while the second, besides three bridging hydrides, has two phosphines and two dihapto borohydride groups (CN 9).[17] A similar structure with nonequivalent hafnium atoms (CN 9 and 10) has been found for $Hf_2[N(SiMe_2CH_2PMe_2)_2]_2H_3(BH_4)_3$. Reaction of $M(BH_4)_4$ with bidentate phosphines (P–P) gives the mononuclear $MH_2(BH_4)_2(P–P)_2$ complexes.

Surface bound hydrides of zirconium, obtained by the reaction sequence in equation (10) ($n = 2, 3$) (*see* ***Supported Organotransition Metal Compounds***), are of interest because of their high catalytic activity in the polymerization of alkenes, cyclization of dienes and alkynes, and even methane C–H bond (*see* ***Alkane Carbon–Hydrogen Bond Activation***) activation (equation 11).[18]

$$\begin{aligned}[Si](OH)_n + ZrNp_4 &\xrightarrow{-nCMe_4} [Si]O_nZrNp_{4-n}\\ &\xrightarrow{+H_2,\ -CMe_4} [Si]O_nZrH_{4-n} \qquad (10)\end{aligned}$$

$$[Si]O_3ZrH + CH_4 \longrightarrow [Si]O_3ZrMe + H_2 \qquad (11)$$

Hydride-containing clusters can be prepared under very mild conditions by reacting $ZrCl_4$ and various amounts of $HSnBu_3$ followed by the addition of phosphines or halide salts (phosphonium or ammonium) (equation 12).[19]

$$\begin{aligned}ZrCl_4 + HSnBu_3 &\xrightarrow{[R_4E]Cl} [R_4E]_3[Zr_6Cl_{18}H_5] \qquad (E = N, P)\\ ZrCl_4 + HSnBu_3 &\xrightarrow[PR_3]{} Zr_5Cl_{12}H_4(PR_3)_5 + Zr_6Cl_{12}H_4(PR_3)_4 + [HPR_3]_3[Zr_6Cl_{18}H_5] \qquad (12)\end{aligned}$$

A monomeric hydride of a Zr(III) center supported by a cyclopentadienyl ligand and $N(SiMe_2CH_2P(i\text{-}Pr)_2)_2$ can be obtained. Metathesis reactions of the Zr(III) chloride complex with Me_3SiCH_2Li or MeMgBr give the corresponding alkyl derivatives. Reaction of these alkyl species with H_2 (1 atm) proceeds smoothly at room temperature to give $ZrH(\eta^5\text{-}C_5H_5)N(SiMe_2CH_2P(i\text{-}Pr)_2)_2$. The tetrahydroborate complex can also be obtained by reaction with $LiBH_4$ (Scheme 1).[20]

Reaction of the zirconium tetraamide complex $Zr(NMe_2)_4$ with silanes yields aminosilanes, H_2, and amide hydrides such as the unusual trinuclear complex $[(Me_2N)_3Zr(\mu\text{-}H)(\mu\text{-}NMe_2)]_2Zr$ (equation 13).[21]

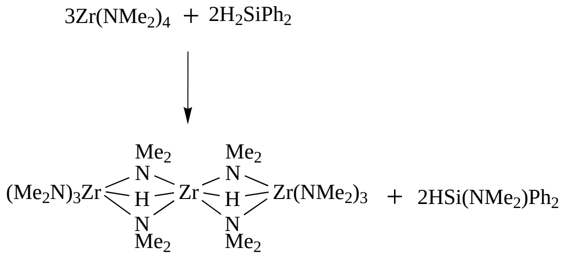

(13)

A zirconium complex of the *meso*-octaethylporphyrinogen ligand reacts with KH to yield a polynuclear hydride. When the reaction is performed in a 1:1 KH:Zr ratio, a dinuclear complex is observed. Using a 2:1 KH:Zr ratio under rigorously controlled reaction conditions leads to the formation of a polynuclear species. In the dinuclear complex, each Zr atom is

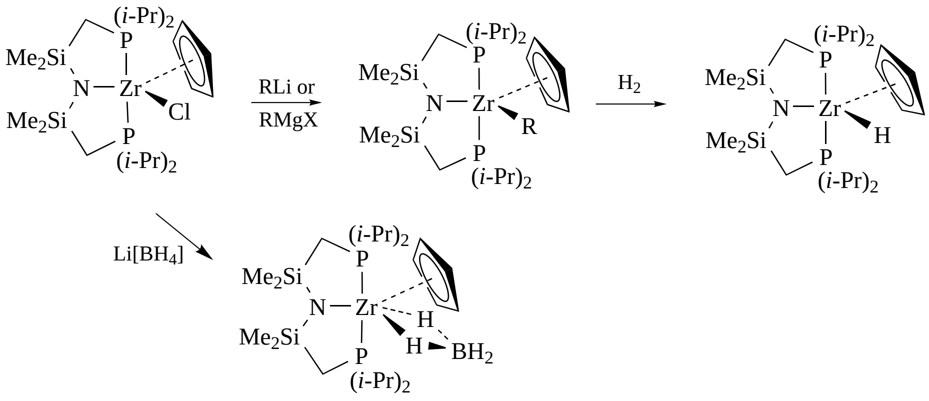

Scheme 1

η^5:η^1:η^5:η^1-bonded to the porphyrinogen ligand, while each potassium cation is η^5-bonded to two pyrrolyl rings to form a bent bis(cyclopentadienyl)-type fragment. The polynuclear complex contains the centrosymmetric unit $K_4Zr_4H_8$. Only four K^+ ions participate in the metal-hydride skeleton, while the other four are bonded to the porphyrinogen periphery (Scheme 2).[22]

A dimeric zirconium(IV) trihydride complex has been synthesized by reaction of $LiBHEt_3$ with the tridentate triaryloxide zirconium chloride complex $ZrCl(THF)_2$(*t*-Bu–L) (H_3(*t*-Bu–L) = 2,6-bis(4-*t*-butyl-6-methylsalicyl)-4-*t*-butylphenol) (equation 14). The solid-state structure shows each zirconium center adopts a trigonal prismatic structure with a Zr–Zr separation of 3.163(1) Å. In solution, the three resulting hydrides appear equivalent on the NMR timescale. Analogous reactivity was observed for the titanium conger. However, in the resulting titanium trihydride, the metals are assigned formal Ti(III) oxidation states.[23]

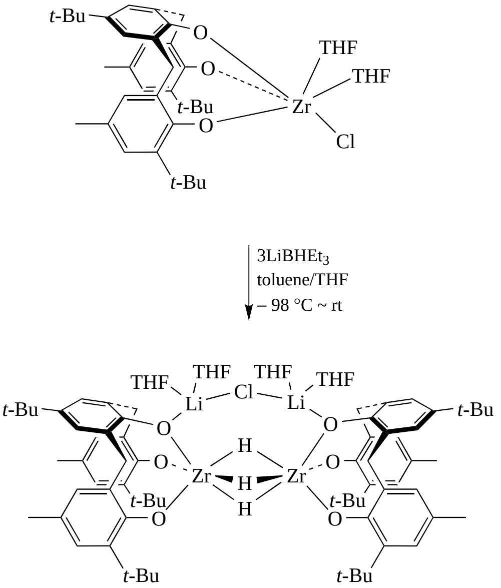

(14)

Sublimation of tetraneopentyl zirconium onto the surface of silica dehydroxylated at 500 °C results in the electrolytic cleavage of one Zr–C bond by a surface proton, with the formation of the tris neopentyl zirconium [Si]-O-$Zr(CH_2CMe_3)_3$ grafted species. Reaction of this supported Zr alkyl with hydrogen at 150 °C leads to the formation of a zirconium hydride. Interestingly, this reaction does not yield neopentane, but rather the formation of methane and ethane are observed. These products are in fact the result of the hydrogenolysis of evolved neopentane catalyzed by the silica-supported zirconium hydride.[24]

8.2 Halide Complexes

8.2.1 Ionic Complexes

Zirconium and hafnium tetrahalides form a variety of double halides with metal halides. The most widespread composition is Q_2MX_6 (Q = monovalent cation) but the QMX_5 complexes and fluoride complexes Q_3MF_7 and Q_4MF_8 are also documented. Q_2MX_6 chlorides and bromides consist of $[MX_6]$ octahedra. The complex chloride anions $[MCl_5]^-$ and $[MCl_6]^-$ have been detected in molten MCl_4 (equation 15):

$$2MCl_4 \rightleftharpoons [MCl_3]^+[MCl_5]^- \rightleftharpoons [MCl_2]^+[MCl_6]^- \quad (15)$$

The structures of complex Zr and Hf fluorides depend on the nature of the cation. For Q_2MF_6 complexes, the following coordination polyhedra are known: an octahedron (Q = Rb), a square antiprism (Q = N_2H_6), and a dodecahedron with four bridging fluorine atoms (Q = K). Two structural types are described for Q_3MF_7 complexes: a pentagonal bipyramid (Q = Na) and a capped trigonal prism (Q = NH_4), like the NbF_7^{2-} anion (*see* ***Niobium & Tantalum: Inorganic & Coordination Chemistry***). The coordination polyhedron

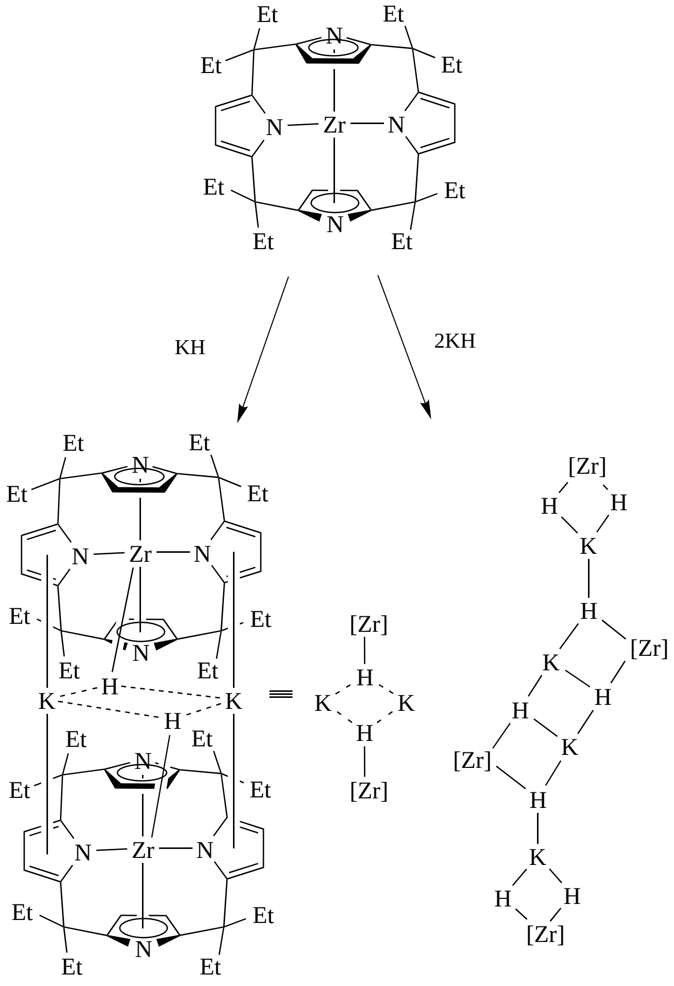

Scheme 2

in Q_4MF_8 is a square antiprism, while, in the structure of $Cu_3[Zr_2F_{14}]\cdot 16H_2O$, two ZrF_8 square antiprisms share a common polyhedral edge. The dimeric anion in the complex $[Ph_3C]_2[Hf_2Cl_{10}]$ consists of edge-sharing octahedra.[25] Reaction of $ZrCl_4$ with $LiNPh_2$ affords two different THF adducts of $LiZrCl_5$, in the forms $[Li(THF)_4][ZrCl_5(THF)]$ and $[(THF)_3Li(\mu\text{-}Cl)ZrCl_4(THF)]$.[26]

8.2.2 Neutral Complexes

The tetrahalides of zirconium and hafnium are strong Lewis acids and form a variety of molecular complexes of composition MCl_4L_2, where L = ether, ester, amine, nitrile, phosphine (see below), and so on. All are monomeric and have a *cis* configuration (*see Isomer, Types of*). With diarsines (*see Arsine & As-donor Ligands*), eight-coordinate dodecahedral complexes $MCl_4(diars)_2$ are produced but the Hf complex, unlike that of Zr, precipitates only after a delay. Reaction of $MCl_4(THF)_2$ with tetradentate Schiff bases (*see Schiff Base*) yields pentagonal bipyramidal complexes $M(salen)Cl_2(THF)$, with trans chlorine atoms. When recrystallized from toluene they lose THF and transform into *cis* octahedral (*see Octahedral*) complexes.[27] $HfCl_4(THF)_2$ is an active catalyst for the esterification of carboxylic acids with alcohols and is more hydrolytically stable than $HfCl_4$. $ZrCl_4$ is also active, but inferior.[28]

8.3 Complexes with Oxygen Donor Ligands

Zirconium and hafnium show a greater preference for O-donors than does titanium.[29] Besides salts of oxygen acids, alkoxides of Zr and Hf and complexes with β-diketones and complexones (*see* ***Water & O-donor Ligands***) have been the most intensively studied. In nitrobenzene solution, MCl_4 forms adducts with two molecules of alcohol (such as $MCl_4(MeOH)_2$), ether or ester, but in a pure alcohol the equilibrium shown in equation (16) ($n = 1$ or 2) exists. Monomeric products of incomplete substitution having the composition $[HNMe_3]_2[ZrCl_4(OMe)(MeOH)]Cl$, with a linear Zr–O–Me bond, and also $(Et_2O)_2Li(\mu\text{-}Cl)_2Zr(tritox)_2$

have been isolated. The addition of a base, such as ammonia, shifts the equilibrium to the right and the alkoxides $M(OR)_4$ are produced quantitatively. Compounds with $R = Me$ or t-Bu can be obtained by alcohol exchange with $M[O(i\text{-Pr})]_4$, isopropanol being separated from the reaction mixture by distillation as an azeotrope with benzene. The best route for the preparation of these compounds is the exchange of $M[O(i\text{-Pr})]_4$ with the appropriate ester (equation 17). The structure of $Zr[O(i\text{-Pr})]_4$ in the solid state is a tetramer, with a Zr_4O_{16} core involving trigonal metaprismatic coordination of Zr, which persists in solution in hydrocarbon solvents.[30] $M(OR)_4$ compounds are colorless volatile solids or liquids, depending on the R group; their degree of association varies from 4 to 1.[31] For very bulky alkoxy groups like 2,6-substituted aryloxides, the substitution of the last chlorine atom in MCl_4 is difficult, and monomers such as $HfCl(OAr')_3$ are obtained. Zirconium methoxide, $Zr(OMe)_4$, is insoluble in MeOH or C_6H_6, while $Zr(OEt)_4$ has rather high solubility and sublimes at 120 °C at 10^{-4} mmHg. Stable *Tetrahedral* monomers, such as $M[OC(t\text{-Bu})_3]_4$, have a vapor pressure of 650 Pa at 90 °C.

$$MCl_4 + n\text{ROH} \rightleftharpoons M(OR)_nCl_{4-n} + n\text{HCl} \qquad (16)$$

$$M(O\text{-}i\text{-Pr})_4 + \text{AcOR} \rightleftharpoons M(OR)_4 + \text{AcO-}i\text{-Pr} \qquad (17)$$

Metal alkoxide complexes with related alcohols are apparently edge-sharing bioctahedral dimers, on the evidence of the X-ray structure of the isopropyl complex. Some stable mixed alkoxides of the type $Q[M_3(OR)_9]$ (Q = Li, Na, K, NH_4, Ca/2) have been reported; they distill in vacuo without decomposition. The X-ray structures of several bimetallic alkoxides obtained by Caulton, $QZr_2[O(i\text{-Pr})]_9$, Q = Li[HO(i-Pr)], K(DME), Ba[O(i-Pr)], show a similar triangular structure with two μ_3 and three μ-OR bridges.[32] The thallium salt of composition $Tl_2Zr(O^fR)_6$ obtained by the reaction shown in equation (18) has a distorted octahedral structure stabilized by six Tl:F contacts.[33]

$$ZrNp_4 + {}^f\text{ROH} \xrightarrow{-4CMe_4} Zr(O^fR)_4 \xrightarrow{TlO^fR} Tl_2Zr(O^fR)_6 \qquad (18)$$

Oxo bridges are found in products of the partial hydrolysis of metal alkoxides. They noticeably stabilize polynuclear structures. In the complex $Zr_{13}O_8(OMe)_{36}$, the central ZrO_8 core is surrounded by 12 zirconium atoms, and the complex has a cubic symmetry. Tetrameric complexes, $Zr_3MO[O(i\text{-Pr})]_{10}(acac)_n$ (M = Zr, Fe, Co), have a tetrahedral metal framework with a μ_4 oxygen atom.[34] Reaction of $KZr_2[O(i\text{-Pr})]_9(DME)$ with two equivalents of KH generates an unusual complex $K_4Zr_2O[O(i\text{-Pr})]_{10}$ containing a K_4Zr_2 octahedron with a μ_6-O^{2-} unit. This complex reacts with $CuCl_2$ in the presence of traces of water, yielding the polynuclear complex $Cu_4Zr_4O_3[O(i\text{-Pr})]_{18}$ with a planar central Cu_4 moiety capped by two $Zr_2[O(i\text{-Pr})]_8$ units and with a planar μ_4-O^{2-} ion.[35] These heterometallic alkoxides are considered the most suitable precursors for Sol–Gel synthesis of solids (*see* ***Sol–Gel Synthesis of Solids***) and chemical vapor deposition (*see Chemical Vapor Deposition*) technology. A rare example of five-coordinate Zr has been found in $(Ar'O)_2Zr[OCH(CH_2Ph)NC_5H_2PhCH(CH_2Ph)O]$, which is produced by carbonylation of $(Ar'O)_2ZrMe_2$ in the presence of pyridine in a 1:1 ratio; with a 1:2 ratio a more usual six-coordinate complex is obtained.[36]

Dihydric and polyhydric alcohols give very stable, apparently monomeric, complexes with zirconium and hafnium. Thus, the monomer $Li_2Zr(OSiPh_2OSiPh_2O)_3\cdot 3py$ has been obtained by treatment of $ZrCl_4$ with the lithium salt of the disilanol.[37] The ability of hydrous zirconia to absorb pyrocatechols is used in medicine in the treatment of dermatitis. By analogy with their titanium counterparts, complexes of calixarenes (*see Calixarenes*), such as Q{4-t-butylcalix[8]arene[MO(i-Pr)]$_2$}, are believed to consist of a central dimeric $M(OR)_2M$ core with six-coordinate metal atoms.[38] The calixarene supported zirconium alkyl species [p-t-Bu-calix[4]-$(OMe)_2(O)_2ZrR_2$] react stepwise with carbon monoxide and isocyanides to give C–C formation products.[39]

β-Diketones form stable MA_4 complexes with six-membered chelate rings (equation 19). These complexes are used in separation of the elements by extraction from acid solutions. The stability constants of these complexes (*see* ***Stability Constants & their Determination***) are linearly dependent on the dissociation constant of the β-diketone. The best extracting agents are β-diketones with a trifluoro group, such as tta. The structures of the $M(acac)_4$ acetylacetonates (mp 194 °C for Zr and 188 °C for Hf) are square antiprismatic, and those of complexes of formula $M(acac)_3Cl$ are distorted pentagonal bipyramidal.

$$MOCl_2 + 4\text{acacH} + Na_2CO_3 \longrightarrow M(acac)_4 + 2NaCl + 2H_2O + CO_2 \qquad (19)$$

Zirconium and hafnium complexes of an amine bis(phenolate) ligand with a THF side-arm donor have been shown to perform living polymerization of 1-hexene when activated with $B(C_6F_5)_3$.[40] The Zr catalysts (**1**) possess very high activities of 21 000 g $mmol^{-1}{}_{cat}\,h^{-1}$. In neat olefin, the reaction is very exothermic and accompanied by various termination processes resulting in a higher polydispersity index than observed when the monomer is diluted in chlorobenzene.

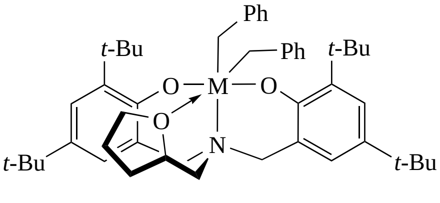

M = Zr, Hf

(**1**)

8.4 Complexes with Nitrogen Donor Ligands

Addition of thiocyanate ions to chloride or perchlorate solutions of zirconium and hafnium yields complexes containing from one to eight isothiocyanate groups per metal atom. These systems are of interest because of the importance of thiocyanate complexes in the extraction and separation of the elements. IR spectroscopy indicates that M–N bonds are present in the violet (Zr) and pink (Hf) complexes $[NEt_4]_2[M(NCS)_6]$; analogous complexes have been obtained with alkali metal cations. In the presence of pyridine, the dodecahedral $Zr(bipy)_2(NCS)_4$ complex is produced (*see **Ammonia & N-donor Ligands***).

The amides of zirconium and hafnium, $M(NR_2)_4$, like the alkoxides, are associated. The degree of association depends on the nature of R.[41] $Zr(NMe_2)_4$ (mp 70 °C, bp 80 °C at 0.05 mmHg) in the solid state adopts the amide-bridged dimeric structure $Zr_2(\mu\text{-}NMe_2)_2(NMe_2)_6$.[42] A monomer–dimer equilibrium is established in solution but only the monomer exists in the gas phase. Gas-phase electron diffraction data indicate that the N atoms are coplanar, as a result of N to Zr p_π to d_π donation (*see p_π–d_π Bonding*).[43]

The ammonolysis of $(tritox)Zr(CH_2Ph)_3$ yields various polynuclear complexes, depending on the ratio of the reagents: $[(tritox)Zr]_6(\mu_6\text{-}N)(\mu_3\text{-}NH)(\mu\text{-}NH_2)_3$ (1:1), $[(tritox)Zr]_5(\mu_5\text{-}N)(\mu_3\text{-}NH)_4(\mu\text{-}NH_2)_4$ (1:1.75), and $[(tritox)Zr]_5(\mu_5\text{-}N)(\mu\text{-}NH_2)_{12}$ (1:2.6). The structures have been confirmed by NMR and X-ray analysis.[44] These polyamidonitriles can be considered as analogs of the known polyoxoanions, such as $(i\text{-}PrOY)_5(\mu_5\text{-}O)(\mu_3\text{-}O\text{-}i\text{-}Pr)_4(\mu\text{-}O\text{-}i\text{-}Pr)_4$.

Several $ZrLCl_2(OR)$ complexes (R = alkyl or aryl) that contain the *Tripodal Ligand* tris(3,5-dimethylpyrazolyl)hydroborate, $HBpz'_3$, which is considered a formal isolobal analog of cyclopentadienide, have been obtained. In all of them the metal atom is six-coordinate, as in $CpZrCl_2(OR)$ complexes.[45]

The bis(porphyrinato) complexes of zirconium, $Zr(OEP)_2$ and $Zr(TPP)_2$, have a sandwich structure and have been obtained by treating $Zr(NEt_2)_4$ with the free porphyrins H_2OEP or H_2TPP (*see Porphyrin*). An X-ray analysis of $Zr(TPP)_2$ and its mono- and di-cations (as salts with the $SbCl_6^-$ anion) indicates a distorted square antiprismatic arrangement around Zr that contracts with increasing charge.[46]

There has recently been an explosion in the use of new multidentate anionic N-donor ligands for group 4 metals. The diamido-donor class of ligands where anionic amido groups flank a central neutral donor atom such as O, N, S, or P have been particularly well studied. Cationic organometallic catalysts based of Zr and Hf complexes of the dianionic $(RNCH_2CH_2)_2NMe$ ligand have shown very high activity for the living polymerization (*see **Oligomerization & Polymerization by Homogeneous Catalysis***) of 1-hexene where R = 2,6-$Cl_2C_6H_3$. For R = Mes, activity

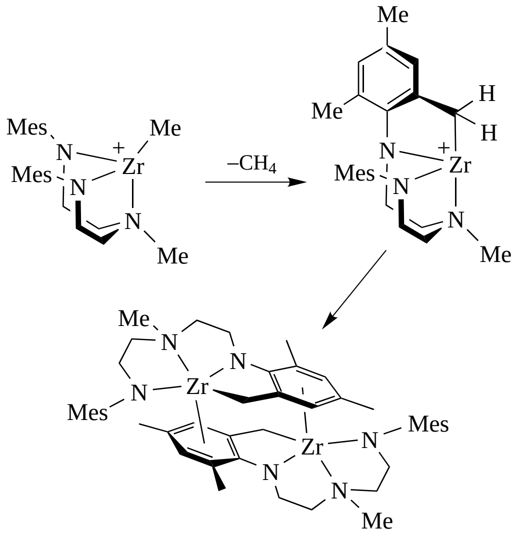

Scheme 3

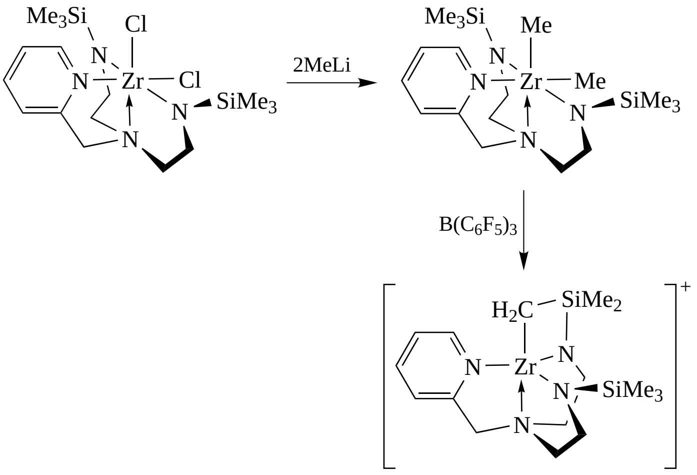

Scheme 4

is hindered by decomposition *via* mesityl methyl hydrogen abstraction. Dimerization of the cyclometallated cation occurs by coordination to an arene ring of another cation (Scheme 3).**47**

One or both chloride ligands in $ZrCl_2(N_2NN')$ can be substituted using organo-magnesium or -lithium reagents forming the mono- and dialkyl derivatives $Zr(CH_2Ph)Cl(N_2NN')$ and $ZrMe_2(N_2NN')$. Treatment of $ZrMe_2(N_2NN')$ with $B(C_6F_5)_3$ or $[CPh_3][B(C_6F_5)_4]$ leads to trimethylsilyl group C−H bond activation yielding a cyclometallated cation (Scheme 4).**48**

Hafnium alkyl complexes stabilized by the diamidopyridine ligand $(RNCH_2)_2C(CH_3)(2\text{-}C_5H_4N)^{2-}$ (R = Mes) (abbreviated $MesN_2py$) have also shown living polymerization activity of 1-hexene at temperatures below 10 °C. Activation of $Hf(i\text{-Bu})_2(MesN_2py)$ with $[Ph_3C][B(C_6F_5)_4]$ gives the *i*-butyl substituted hafnium cation that is considerably more stable than that of the zirconium analog. Addition of 1-hexene causes quantitative polymerization without indication of β-hydride elimination over a period of 2−3 hours at 0 °C.**49**

The tribenzyl complex (i-Pr_2triazacyclononane)$Zr(CH_2Ph)_3$ eliminates toluene upon heating with concomitant ring opening of the ancillary macrocycle to yield $[CH_2{=}CHNCH_2CH_2N(i\text{-Pr})CH_2CH_2N(i\text{-Pr})]Zr(CH_2Ph)$ (equation 20).**50**

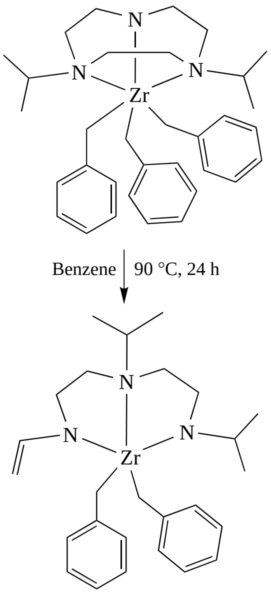

(20)

Group 4 metals in combination with alkali hydrides provide a remarkable method of chemical modification of porphyrinogens to give novel macrocycles (*see Macrocycle*) that cannot be prepared by classical organic methods. The reactivity of the zirconium hydride shown in Scheme 5 is demonstrated by the insertion reactions into the metal-hydride bond, for example, with terminal olefins, isocyanides, and alkynes. Particularly intriguing is the reaction of the oepg-zirconium-hydride species with CO. This formally converts a pyrrole ring of the oepg ligand into a pyridine fragment. The resulting modified ligand can be cleaved by hydrolysis. A subsequent transformation of the resulting pyridine tris(pyrrole) macrocycle using Hf in lieu of Zr leads to the doubly pyridine-modified, protonated ligand.**51**

Reactions of monochloro complexes of zirconium and hafnium stabilized by tripodal trianionic ligands (such as $MeC(CH_2NR)_3{}^{3-}$, $HC(SiMe_2NR)_3{}^{3-}$ and $MeSi(SiMe_2NR)_3{}^{3-}$) with the late transition metal organometallic complexes $K[CpM(CO)_2]$ (M = Fe, Ru) gives heterodinuclear complexes with unbridged metal−metal bonds. These heterobimetallic complexes react with, for example, methylisocyanide to yield insertion products (Scheme 6).**52**

Trinuclear complexes can be made if bis(amido) chelate ligands are used in place of the tripod ligands. The addition of two $CpM'(CO)_2$ units (M′ = Fe, Ru) can be carried out sequentially. However, mixed trinuclear complexes possessing Zr–Ru–Fe metal centers cannot be prepared this way (Scheme 7).**53**

The activation of C–H bonds by d^0 metal centers can be investigated very effectively with complexes of the type $(t\text{-}Bu_3SiNH)_3ZrR$, where R is an alkyl or aryl group, as these compounds undergo reversible elimination of hydrocarbon. In these examples, concerted mechanisms involving R′–H bond interaction at d^0 metal imido complexes, either isolable or transient, give metathesis products via R–H elimination.**54,55**

The reactivity of zirconium imido complexes supported by a dibenzotetraaza[14]annulene (taa) macrocycle ligand toward a range of unsaturated substrates has been examined. Reaction with *t*-butyl isocyanate cleanly generated the cycloaddition product $Zr\{N(2,6\text{-}(i\text{-Pr})_2C_6H_3)C(O)N(t\text{-Bu})\}(Me_4taa)$ (equation 21).**56**

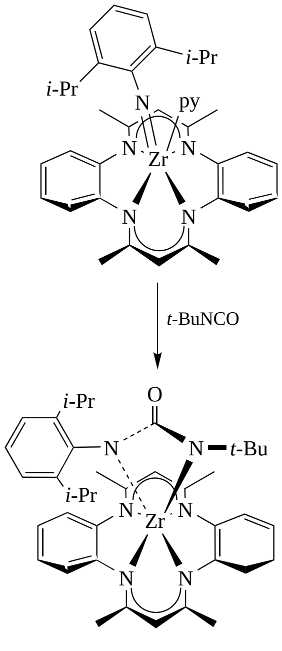

(21)

Group 4 imido chemistry (*see Imide Complexes*) is less well studied than that of the group 5−7 metals. An important reason for this is the change in reactivity of the imido ligand upon coordination to the more electropositive metals. The increased polarity of the M=NR unit in compounds

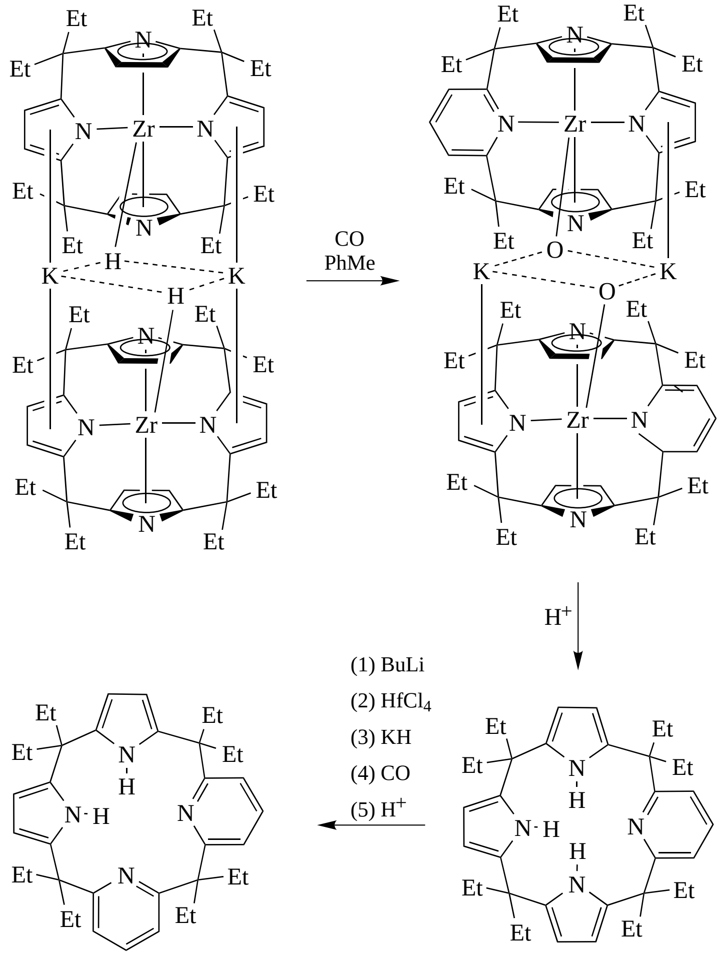

Scheme 5

of group 4 renders the imido ligand the preferential point of attack. One approach for stabilizing the imido unit is the protection of the greater part of the coordination sphere of the metal by a polydentate ligand that not only meets the electronic demand of the highly Lewis acidic early transition metal center but ideally allows the generation of low-coordinate imido species under controlled conditions.

The number of titanium imido complexes characterized greatly outnumbers those of the heavier congeners, particularly for hafnium. Zirconium imides of a variety of diamido-based ligands have been prepared. A zirconium dialkyl complex supported by two alkyl guanidinate ligands reacts with aryl isocyanides to give the corresponding zirconium aryl imide species.[57] The relative instability of imides of zirconium as compared to titanium is apparent in complexes supported by 1,3,5-trialkyltriazacyclohexane (R′tach) and 1,4,7-triazacyclononane (R′tacn) ligands. Whereas crystalline aryl and alkyl imides of the form $TiCl_2(NR)(R'tach)$ and $TiCl_2(NR)(R'tacn)$ (R = *t*-Bu, 2,6-(*i*-Pr)$_2$C$_6$H$_3$, R′ = Me, *t*-Bu) can be readily obtained in excellent yield, the zirconium imide $ZrCl_2(N\text{-}2,6\text{-}(i\text{-}Pr)_2C_6H_3)(Me_3tach)$ can only be prepared on an NMR tube scale.[58]

Treatment of *cis*-(ttp)ZrCl$_2$ (ttp = *meso*-tetra-*p*-tolylporphorynato dianion) with two equivalents of bulky lithium amide reagents, LiNHR (R = 2,4,6-Me$_3$C$_6$H$_2$, 2,4,6-*t*-Bu$_3$C$_6$H$_2$, 2,4,6-Ph$_3$C$_6$H$_2$, 2,6-*i*-Pr$_2$C$_6$H$_3$), in toluene resulted in the formation of terminal imido complexes. The 2,6-diisopropylphenyl derivative was most amenable to isolation and purification. The analogous Hf complex, (ttp)Hf(N-2,6-*i*-Pr$_2$C$_6$H$_3$), could be isolated by the same reaction. The solid-state crystal structures of the two compounds are isomorphous. The geometry about the metals is best described as distorted square pyramidal. Treatment of the Hf imide with excess aniline results in the formation of the bis(amido) complexes, (ttp)Hf(NHPh)$_2$ and (ttp)Hf(NHPh)(NH(2,6-*i*-Pr$_2$C$_6$H$_3$)).[59]

Chiral (*see Chiral*) nitrogen donor ligands have also been developed for enantioselective (*see Enantioselectivity*) catalysis in an effort to diversify this area of chemistry hitherto dominated by ansa-metallocene (*see Metallocene Complexes*) based ancillary groups. Using a diamino-biphenyl backbone, chiral multidentate ligands have been prepared and

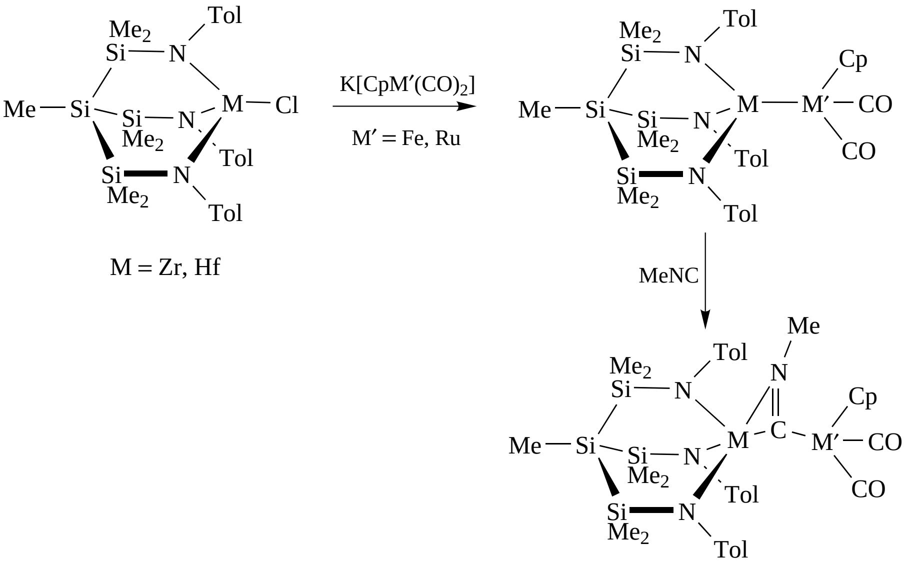

Scheme 6

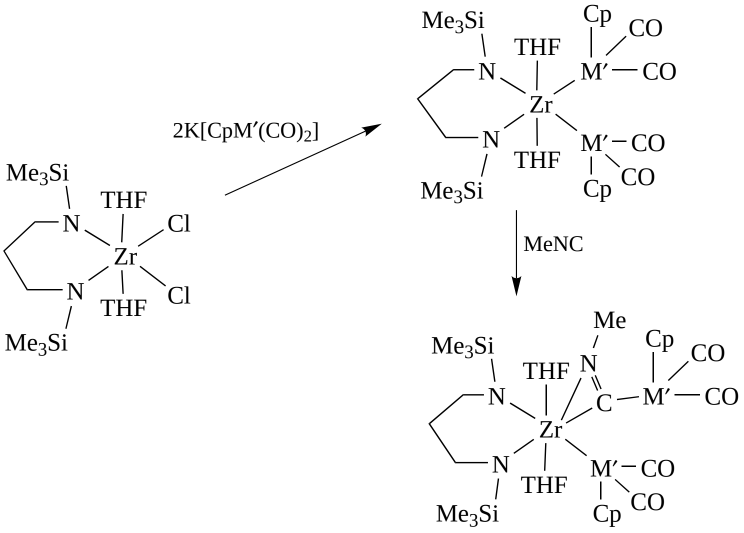

Scheme 7

coordinated to zirconium to give C_2 or other chiral species. Reaction of these amino ligands with $Zr(NMe_2)_4$ yields the metal complexes via protonolysis of two dimethylamido groups. Asymmetric variations of these ligands have also been prepared with different substituents at each amine (Figure 1).[60]

8.5 Dinitrogen Complexes

Coordination and organometallic complexes of zirconium and hafnium have in recent years shown a rich ability to form dinitrogen compounds (*see Dinitrogen & Dinitrogen Complexes*), as well as promoting reactivity at the dinitrogen center. Dinitrogen complexes of Zr and Hf are nearly always bimetallic with the coordinated N_2 fragment bridging the metals in either an end-on or side-on bonding mode. The bonding mode is strongly dependent on the ancillary ligands present. Reduction of $ZrCl_3(N(SiMe_2CH_2PR_2)_2)$ (abbreviated $ZrCl_3(PNP)$, $R = i$-Pr) with sodium amalgam yields the side-on bridging dinitrogen complex $(ZrCl(PNP))_2(\mu\text{-}\eta^2:\eta^2\text{-}N_2)$. The resulting N_2 fragment possesses a highly elongated N−N bond

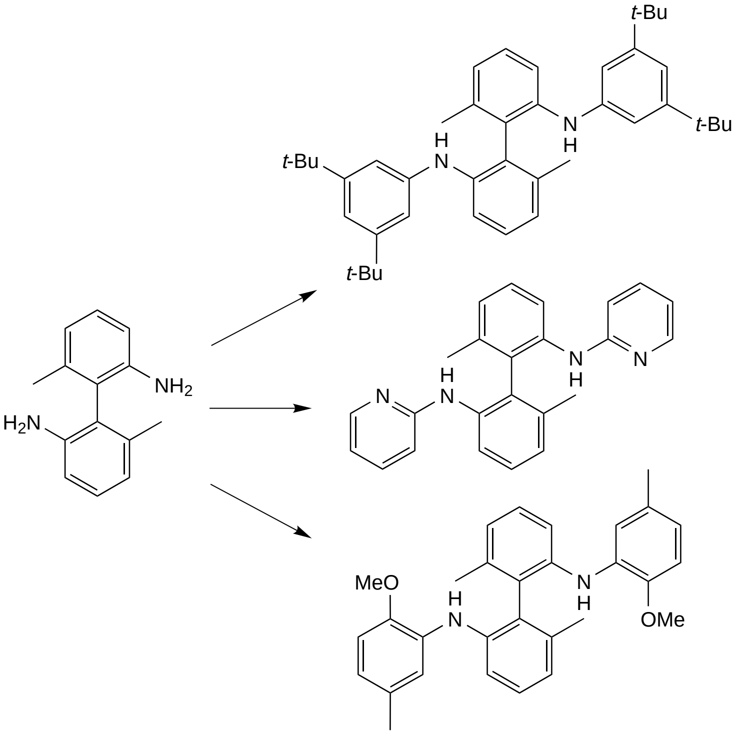

Figure 1 Chiral N-donor ligands used in asymmetric catalysis by Zr

of 1.548(7) Å. Changing the chloride ligand to cyclopentadienyl alters the bonding mode of the dinitrogen unit generating an end-on bridging species $(ZrCp(PNP))_2(\mu\text{-}N_2)$ with a N−N distance of 1.301(3) Å. Replacement of chloride with another hard anionic ligand such as an alkoxide allows the side-on bonding mode of dinitrogen to be maintained. Interestingly, direct metathesis of the chloride-substituted dinitrogen complex with alkoxide or aryloxide transfer reagents results in product decomposition. However, the reduction of $ZrCl_2(OR')(PNP)$ ($R' = 2,6\text{-}Me_2C_6H_3$ or t-Bu) with sodium amalgam under N_2 gives the dinitrogen complex $(Zr(OR')(PNP))_2(\mu\text{-}\eta^2:\eta^2\text{-}N_2)$ with a N−N bond length of 1.528(7) Å (Scheme 8).**[61]**

A zirconium(IV) chloride complex of a macrocyclic ligand derived from the (PNP) system described above has been prepared. Reduction of $ZrCl_2(P_2N_2)$ (where $P_2N_2 = PhP(CH_2SiMe_2NSiMe_2CH_2)_2PPh$) with potassium graphite (KC_8) results in the formation of a dinuclear dinitrogen complex possessing a side-on N_2 unit with a N−N distance of 1.43(4) Å. Reaction of this dinitrogen complex with dihydrogen results in an unprecedented transformation to give a N−H unit and a bridging hydride, probably *via* heterolysis (*see Heterolytic Cleavage*) of the H–H bond. A similar process can be effected with primary silanes to generate silylhydrazido species with a bridging hydride. This transformation probably occurs in a similar manner to the addition of H_2, that is, through heterolytic activation of the H−Si bond (Scheme 9).**[62]**

Zirconium hydride complexes have also exhibited dinitrogen activation. The chiral zirconocene dihydride eliminates dihydrogen spontaneously and in the presence of N_2 forms a dinuclear side-on bridged complex with a resulting N−N bond distance of 1.241(3) Å. The N_2 moiety in $Me_2Si(C_5H_2\text{-}2\text{-}SiMe_3\text{-}4\text{-}CMe_3)_2Zr_2(\mu\text{-}\eta^2:\eta^2\text{-}N_2)$, however, does become displaced upon exposure to PMe_3 to form the Zr(II) species $[rac\text{-}BpZr](PMe_3)_2$ (equation 22).**[63]**

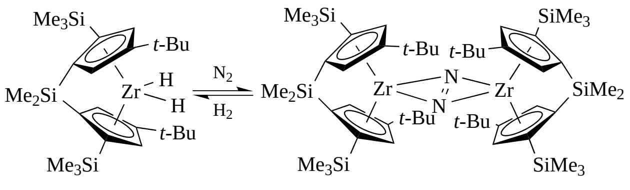

(22)

A related reaction, which yields a zirconocene dinitrogen complex possessing a side-on bound N_2 fragment, proceeds *via* alkane elimination from a zirconium alkyl hydride. Intramolecular C−H activation gives a cyclometallated hydride species, which upon exposure to an atmosphere of dinitrogen at − 35 °C results in a dinitrogen complex with a N−N bond length of 1.47(3) Å, shown in Scheme 10.**[64]**

Heterobimetallic dinitrogen complexes containing a group 4 transition metal have been prepared. Reaction of the anionic dinitrogen complex trans-$[NBu_4][W(NCS)(N_2)(dppe)_2]$ with Cp_2MCl_2 (M = Zr, Hf) or $Cp_2ZrClMe$ gives $W(NCS)(dppe)_2$

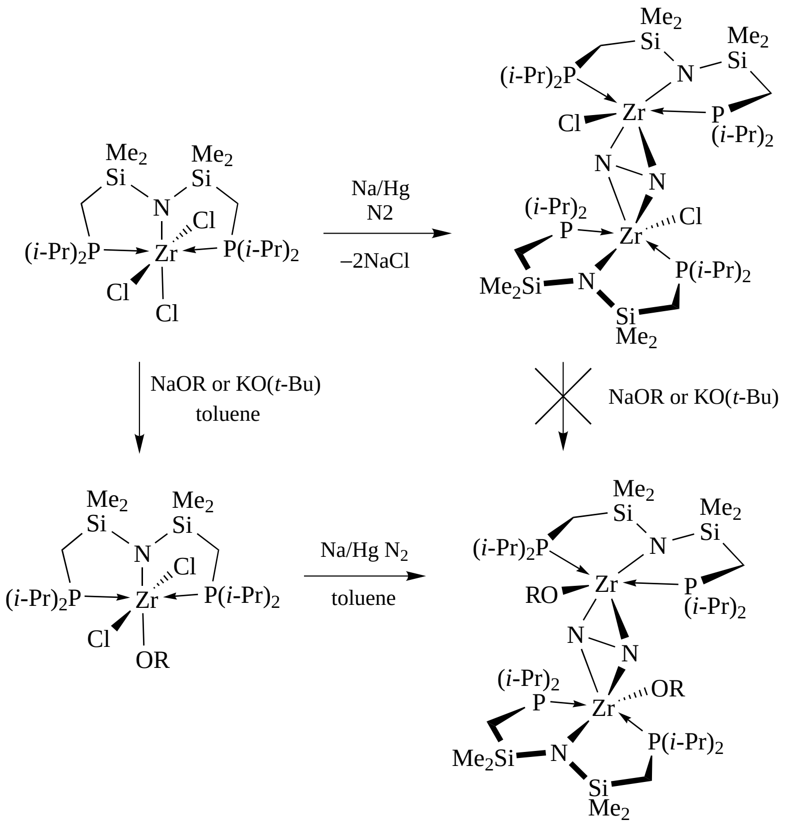

Scheme 8

(μ-N$_2$)MCp$_2$Cl or W(NCS)(dppe)$_2$(μ-N$_2$)ZrCp$_2$Me, respectively (equation 23).[65]

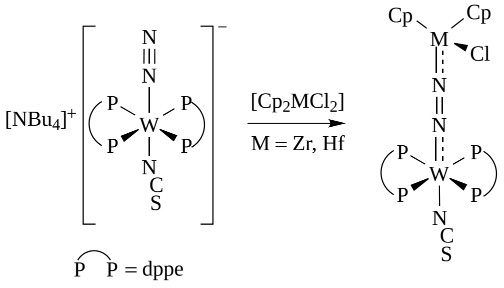

(23)

The products of reactions of laser-ablated zirconium and hafnium atoms with dinitrogen have also been examined and characterized by infrared spectroscopy. Density Functional (DFT) calculations were used to model the vibration bands arising from various metal-dinitrogen and -nitride fragments generated. Spectroscopic evidence suggests that dinuclear rhombic molecules with bridging nitrogen atoms are among the species observed, which provides evidence for the complete activation and bond cleavage of a dinitrogen molecule by two naked metal atoms. Also postulated was the presence of NMN-type dinitrides as well as side-on bound MN$_2$ and bis-η^2-bound M(N$_2$)$_2$ dinitrogen fragments.[66]

8.6 Complexes with Phosphorus and Sulfur Donor Ligands

Zr and Hf tetrachlorides form complexes of composition MCl$_4$(POCl$_3$) and MCl$_4$(POCl$_3$)$_2$ with phosphoryl trichloride. These are used in the separation of the elements by distillation. The distillate has the composition 3MCl$_4$(POCl$_3$)$_2$ and boils (1 atm) at 360 °C (Zr) and 355 °C (Hf). Phosphines react with zirconium halides in an appropriate solvent yielding monomeric adducts whose composition depends on the cone angle (*see Cone Angle*) of the ligand (*see* ***P-donor Ligands***). With PEt$_3$, PBu$_3$ (L) and bulky diphosphines dppe or dbpe (L–L) the six-coordinate ZrX$_4$L$_2$ and ZrX$_4$(L–L) complexes (X = Cl, Br) have been prepared, whereas with smaller chelating phosphines, such as dmpe, eight-coordinate complexes ZrX$_4$(L–L)$_2$ were obtained.[67] Although the structure of the latter is unknown, an analogy is implied with the dodecahedral ligand arrangement in the related complex ZrMe$_4$(dmpe)$_2$.

Zr–S bonds are rather weak. For example, zirconium, unlike other metals, does not form complexes with thioglycolic acid, whereas with glycolic acid the triglycolatozirconic acid derivatives H$_3$[Zr(OH)(OCH$_2$CO$_2$)$_3$] are formed. Nevertheless, insertion (*see Insertion*) of CS$_2$ into a metal–nitrogen

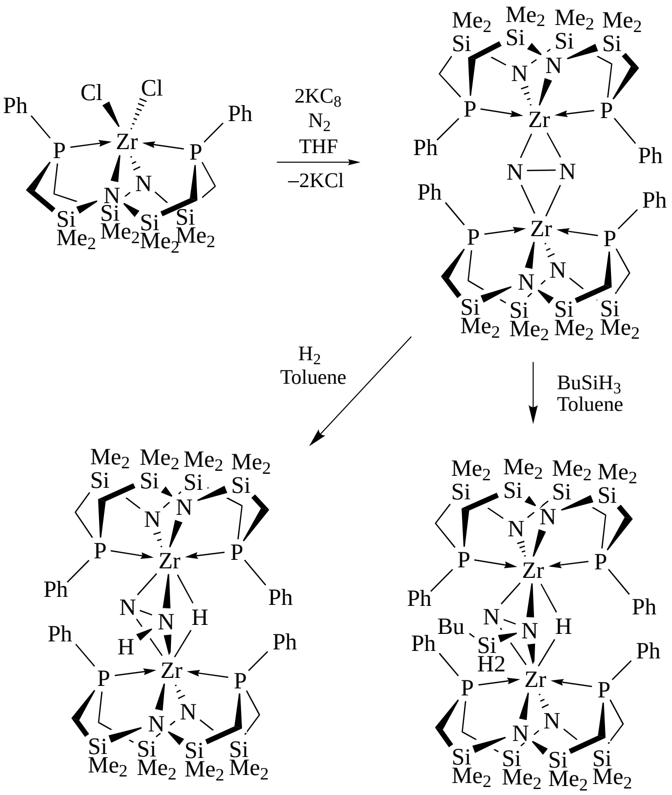

Scheme 9

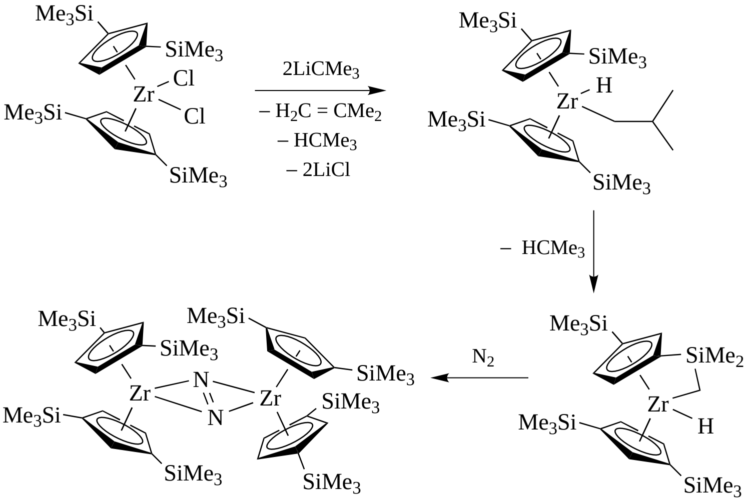

Scheme 10

bond gives a dithiocarbamate (*see Dithiocarbamate*) (equation 24).[68] In the dithiolate $[NMe_4]_2[Zr(S_2C_6H_4)_3]$, the coordination polyhedron is intermediate between a distorted trigonal prism and an octahedron.

$$Zr[N(i\text{-}Pr)_2]_4 + CS_2 \longrightarrow Zr[S_2CN(i - Pr)_2]_4 \qquad (24)$$

Homoleptic anionic zirconium and hafnium phosphine complexes have recently been prepared using bisphosphinine ligands, which are phosphine analogs of the ubiquitous bipyridyl ligand. Structure determinations of the $Li_3(solv)Cl$ salts were performed (solv = DME for M = Zr and THF for M = Hf) show the overall geometry around the metal center to be trigonal prismatic. Disruption of the aromaticity is

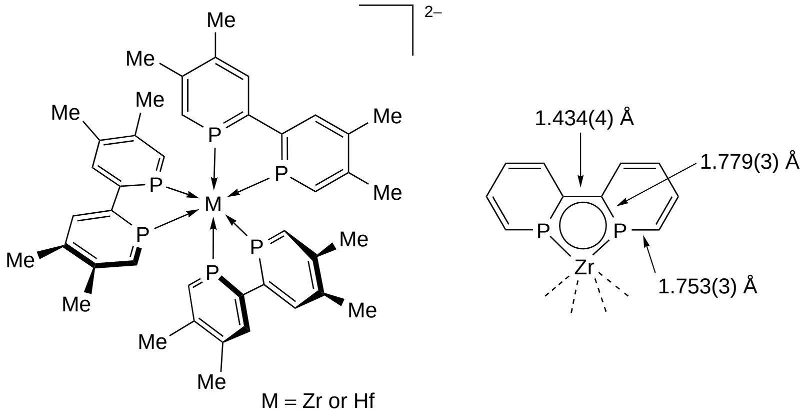

Figure 2 Homoleptic Zr and Hf bisphosphine complexes

observed in each phosphinine subunit. It is suggested that the −2 oxidation state of the complex is only formal; the complex possesses a delocalized character that makes assignment of oxidation state difficult (Figure 2).[69]

8.7 Complexes with Mixed-Donor Ligands

A mononuclear imido complex of Zr has been prepared by reaction of LiNH(*t*-Bu) with $ZrCl_2(PhP(CH_2SiMe_2NSiMe_2CH_2)_2PPh)$ ($ZrCl_2(P_2N_2)$) followed by addition of MeLi. In the formation of Zr(N-*t*-Bu)(P_2N_2), there was no evidence that the putative Zr(NH(*t*-Bu))Me(P_2N_2) was stable with respect to alkane elimination.[70]

During the preparation of dark blue $(Zr(P_2N_2))_2(\mu\text{-}\eta^2:\eta^2\text{-}N_2)$, a small amount (<5%) of a yellow crystalline by-product was sometimes observed. A Pasteur separation of a few crystals of this material allowed analysis by X-ray crystallography and showed that this by-product does not contain dinitrogen; instead, a phosphorus-phenyl group on one $Zr(P_2N_2)$ unit is bound to the zirconium center of another $Zr(P_2N_2)$ fragment. When this reduction is performed in the absence of N_2 (either under argon or in vacuum), good yields of the dimer were obtained (equation 25).[71]

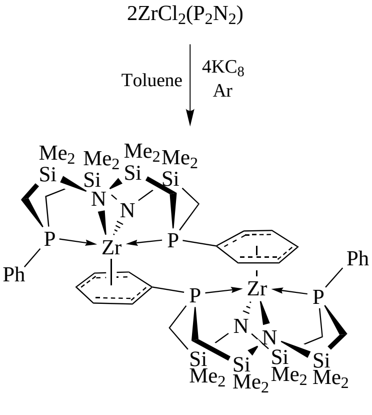

(25)

The reaction of one equivalent of $LiN(SiMe_2CH_2PR_2)_2$ (R = Me, Ph) with MCl_4 yields the six-coordinate $MCl_3(N(SiMe_2CH_2PR_2)_2)$ complexes with meridional (Zr) or facial (Hf) geometries. The same reaction with two equivalents of the lithium salt generates chiral distorted octahedral $MCl_2(N(SiMe_2CH_2PR_2)_2)_2$ complexes with two bidentate hybrid ligands that are inert to nucleophilic attack.[72]

Mixed-donor variations of the diamido-amine ligands, which are discussed above, have been prepared where the central neutral donor atom is a P, O, or S atom. The group 4 chemistry of these coordination complexes has been primarily directed at polymerization catalysis and small molecule activation. The various NON, NPN, and NSN ligands studied include (RN-*ortho*-$C_6H_4)_2D^{2-}$ (D = O, S) and $(RNCH_2CH_2)_2D^{2-}$ (D = O, P) type systems that have shown a tremendous range of reactivity toward, for example, olefin polymerization (*see* ***Oligomerization & Polymerization by Homogeneous Catalysis***) and dinitrogen complex formation. The ligands may bind either meridionally (*mer*) or facially (*fac*) (Figure 3).[73–76]

Addition of two equivalents of MeMgCl or MeLi to $ZrCl_2(N(CH_2SiMe_2N\text{-}t\text{-}Bu)_2)$ yields a dimeric product with two zirconium centers bridged by two imido groups. Although addition of one equivalent of MeLi to the dichloride precursor gives $ZrCl(Me)(N(CH_2SiMe_2N\text{-}t\text{-}Bu)_2)$ in good yield, attempts to replace the second chloride result in ligand degradation by a proposed electron transfer to zirconium followed by elimination of a *t*-Bu radical (Scheme 11).[77]

The desire for new nonmetallocene-based single-site polyolefin catalysts has lead to the use of high-throughput screening techniques to achieve faster identification of catalytically active systems and allow a much broader range of catalyst candidates and conditions to be evaluated. Particularly in the case of highly modifiable ligand systems, that is, those where the donor substituents and donor atoms themselves may be modified, this approach allows for even small variations in electronic and steric properties to be probed. These high-throughput approaches require an efficient method of attaching

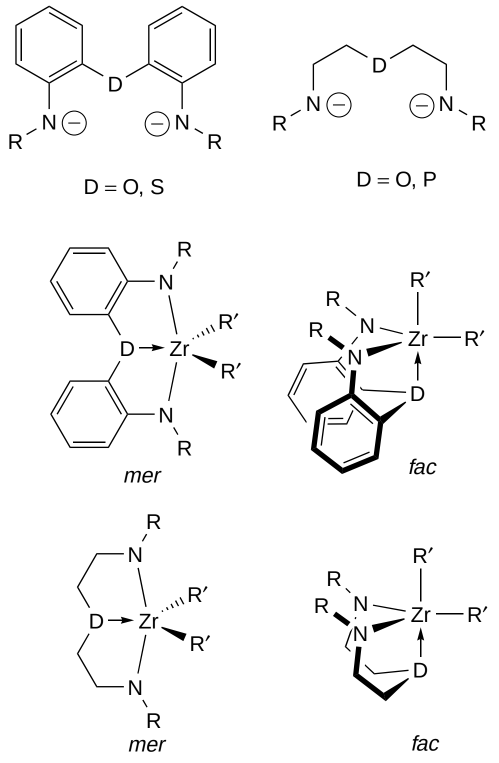

Figure 3 Hybrid diamido-donor ligands

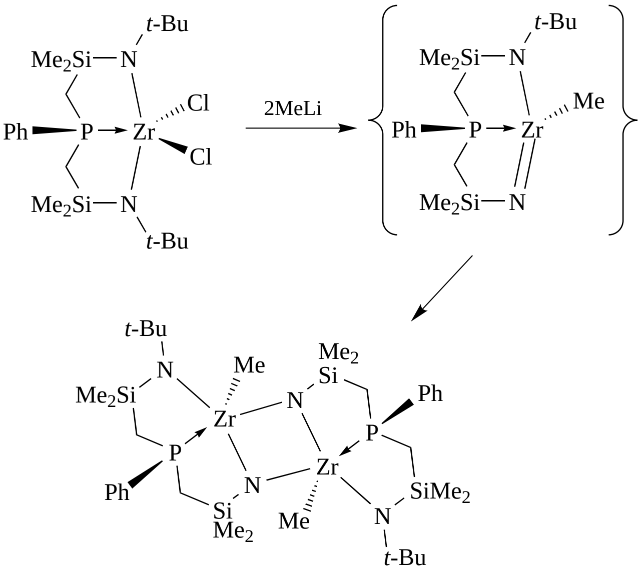

Scheme 11

a ligand to the metal. The most useful approach has been to capitalize on the labile nature of M–C bonds and their susceptibility to elimination by protio ligand derivatives. $M(CH_2Ph)_4$ (M = Zr and Hf) complexes can be used in the preparation of catalyst candidates by reaction with ligands that possess acidic protons, as in the protonated forms of the ligands discussed above.**[78]**

9 LOWER OXIDATION STATES

9.1 Inorganic Compounds

Low oxidation states are not characteristic of zirconium and hafnium. There is no aqueous chemistry of the metals in oxidation state ≤ III, except for the unstable orange aqua ion $[Zr(H_2O)_6]^{3+}$, which is analogous to the stable violet $[Ti(H_2O)_6]^{3+}$ ion. Inorganic compounds of M^{III}, M^{II}, and M^{I} have been studied mainly as halides and chalcogenides, M_2X_3 and MX (X = S, Se, Te). Chalcogenides of the trivalent metals were obtained by the direct reaction of the elements at 800 °C. Some distinction between Zr and Hf is displayed in the structure of M_2S_3: cubic for Zr and hexagonal for Hf. The compounds are stable toward both hot water and air.

The halides MX_3 and MX_2 are intensely colored (from blue-black to olive-green) solids. Trihalides with nonstoichiometric phases MX_x ($x = 2.94–3.03$ for Cl and 2.83–3.43 for I) are known for all halides (except HfF_3); they are obtained by the reduction of the related tetrahalide with the metal (equation 26), or with aluminum in a molten $MCl_4–AlCl_3$ mixture. The reaction shown in equation 26 is carried out under elevated pressure to prevent disproportionation (*see Disproportionation*). Zirconium is reduced more readily than hafnium, so that in the mixture $ZrCl_4/HfCl_4/Zr$, only $ZrCl_3$ is detected. The trihalides MX_3 are rather strong reducing agents. Their vigorous reaction with water is accompanied by oxidation of the metal and evolution of hydrogen; they remove potassium from KNH_2 in liquid ammonia (equation 27).

$$Zr + 3ZrCl_4 \longrightarrow 4ZrCl_3 \qquad (26)$$

$$ZrBr_3 + KNH_2 \xrightarrow{NH_3(l)} K + ZrBr_3NH_2 \qquad (27)$$

On heating, the trihalides MX_3 disproportionate, yielding related dihalides. Further heating produces the subchlorides MCl for X = Cl and the metal for X = Br. HfCl may be also obtained by the electrolysis of molten hafnium chlorides with a zirconium anode. ZrX and HfX (X = Cl, Br) have layered (MMCl=ClMMCl=Cl) structures**[79]** and are better lubricants than graphite in the temperature range 400–1000 °C. ZrCl and ZrBr phases can be intercalated (*see **Intercalation Chemistry***) with oxygen, carbon, nitrogen, and hydrogen, forming $ZrXO_x$, ZrXH, and $ZrXY_{0.5}$ (Y = H, C, N) phases. In the first two of these, oxygen and hydrogen atoms occupy tetrahedral interstices between double zirconium layers, whereas in the last named, interstitial atoms are localized in octahedral holes.**[80]**

In the phases of composition Zr_5Sb_3Z, obtained either by arc melting, vapor-phase transport, or metal flux methods, the interstitial atom Z (C, O, Al, Si, P, etc.) occupies all the zirconium trigonal antiprism sites in the Zr_5Sb_3 host structure.**[81]**

9.2 Coordination Compounds

Reduction of $ZrCl_4$ by sodium amalgam in the presence of phosphines yields dinuclear Zr^{III} complexes of composition $[(PR_3)_2ZrCl_2(\mu\text{-}Cl)]_2$, containing Zr–Zr bonds (CN 7).**[82]** Complexes with the PMe_3 ligand have also been obtained via photolysis of $ZrNp_2Cl_2(PMe_3)_2$. The first analogous hafnium complex with an Hf–Hf bond (3.099 Å), $Hf_2Cl_6(dippe)_2$, has been obtained by the reduction of $HfCl_4$ with Na/K alloy in the presence of the phosphine.**[83]** Recently, iodide analogs $[(PR_3)_2ZrI_2(\mu\text{-}I)]_2$ and complexes with the substituted pyridine bppy have also been prepared. The zirconium complex of a multidentate phosphido ligand, $Zr_2Cl_3[P(CH_2CH_2PMe_2)_2]_3$, has been isolated; it has two bridging phosphorus atoms and one chlorine atom, and an eight-coordinate metal atom.**[84]** The metal–metal distance in such complexes is rather long and lies within the range 3.1–3.4 Å (*see* ***Dinuclear Organometallic Cluster Complexes***).

Triangular zirconium mixed-valence complexes stabilized by arenes, $[Zr_3(\mu\text{-}Cl)_6(\eta^6\text{-}C_6Me_6)_3]^{n+}$ ($n = 1, 2$) (*see Arene Complexes*), have been isolated as salts with the $[Al_2Cl_7]^-$ anion (equation 28).**[85]** Arenes also stabilize divalent hafnium in the complexes $(\mu\text{-}\eta^{12}\text{-}C_6H_5R)[HfI_2(PMe_2Ph)_2]_2$ (R = H, Me), which have a piano stool structure (*see Piano Stool Structure*).**[86]**

$$9ZrCl_4 + 9C_6Me_6 + 4Al + 8AlCl_3 \longrightarrow 3[Zr_3Cl_6(C_6Me_6)_3][Al_2Cl_7]_2 \tag{28}$$

The most exciting feature of low-valent zirconium and hafnium complexes is their ability to coordinate small unsaturated molecules. Thus reduction of the monomeric complex $ZrCl_3(N(SiMe_2CH_2P(i\text{-}Pr)_2)_2)$ by Na/Hg under N_2 yields deep blue crystals of dimeric $\{ZrCl(N(SiMe_2CH_2P(i\text{-}Pr)_2)_2)\}_2(\mu\text{-}N_2)$**[87]** (*see Dinitrogen & Dinitrogen Complexes*); also dimers $M_2X_6(PEt_3)_4$ (M = Zr, Hf; X = Cl, Br) directly react with ethylene under mild conditions to produce metal–alkene complexes (*see Alkene Complexes*) $M_2X_6(PEt_3)_4(\eta^2\text{-}C_2H_4)$.**[88]** In both complexes, the bridging molecules (dinitrogen or ethylene) lie perpendicular to the M–M axis, forming a planar MX_2M moiety. The N–N distance (1.548 Å) is longer than that in hydrazine (1.47 Å), and the C–C distances (>1.5 Å) are close to those of ordinary C–C bonds. This is evidence of the highly reduced state of dinitrogen and ethylene in these complexes. The oxidative addition of pivalonitrile to the Zr–Zr bond yields the complex $[ZrCl_2(bppy)_2]_2(\mu\text{-}Cl)[\mu\text{-}\eta^2\text{-}NC(t\text{-}Bu)]$ with a Zr–Zr distance of 3.55 Å (compared with 3.14 Å for a Zr–Zr single bond).**[89]**

A few examples of zerovalent zirconium and hafnium complexes are known. The reduction of MCl_4 with lithium in the presence of a diamine (bipy, phen) gives air-sensitive, monomeric, diamagnetic $M(L\text{–}L)_4$ complexes.**[90]** Carbonyl complexes of Zr^0 and Hf^0 have been reported (equation 29) that are stabilized by the tripodal phosphine ligand, $(trmpe)M(CO)_4$, and by a triamine, $(ttacn)M(CO)_4$. These are obtained by the reduction of MCl_4 with potassium naphthalenide in the presence of a ligand.**[91]** Further reduction in the presence of macrocyclic ethers (only for Zr) or of cryptands (*see Crown Ethers*; *Cryptands & Cryptates*) yields complexes of zirconium and hafnium in oxidation state −II having the formula $[KL]_2[M(CO)_6]$ (L = 15-crown-5 for zirconium, cryptand [2.2.2] for both metals). The existence of the octahedral $M(CO)_6{}^{2-}$ anion has been confirmed for zirconium by ^{91}Zr NMR studies and by X-ray analysis (Zr–C = 2.210 Å, Hf–C = 2.178 Å).**[92]**

$$MCl_4(THF)_2 + trmpe + 4KC_{10}H_8 + 4CO \tag{29}$$
$$\xrightarrow{\text{DME, }-70\,^\circ\text{C}} (trmpe)M(CO)_4 + 4KCl + 4C_{10}H_8 + 2THF$$

9.3 Clusters

Heating $[(PMe_2Ph)_2ZrCl_2(\mu\text{-}Cl)]_2$ leads to the formation of a $Zr_6Cl_{12}(PMe_2Ph)_6$ cluster consisting of an octahedral zirconium skeleton stabilized by edge-bridging chlorides and terminal phosphines.**[93]** For inorganic Zr_6Cl_{12} cluster phases of the formula $Q_m[Zr_6(Z)Cl_{12}]Cl_n$, an interstitial atom is required in all cases for the stabilization of the Zr_6 cluster (*see* ***Electronic Structure of Clusters***). A large family of these phases with Z = H, Be, B, C, N, and even Mn and Fe has been obtained via both solid state and nonaqueous reactions.**[94]** High-temperature reactions have been used to produce Zr_5Sb_3Z phases containing an interstitial atom (Z = C, O, Al, Si, P, S, etc.) in the centers of all zirconium trigonal antiprism sites in the Zr_5Sb_3 host (see Section 9.1).**[81]**

10 RELATED ARTICLES

Analytical Chemistry of the Transition Elements; Coordination Numbers & Geometries; Coordination & Organometallic Chemistry: Principles; Hydride Complexes of the Transition Metals; Oxide Catalysts in Solid-state Chemistry; Periodic Table: Trends in the Properties of the Elements; Sol–Gel Synthesis of Solids; Structure & Property Maps for Inorganic Solids; Titanium: Inorganic & Coordination Chemistry; Zirconium & Hafnium: Organometallic Chemistry.

11 REFERENCES

1. J. Emsley, ‘Nature’s Building Blocks: An A-Z Guide to the Elements’, Oxford University Press, Oxford, 2001.

2. R. J. H. Clark, D. C. Bradley, and P. Thornton, ‘The Chemistry of Titanium, Zirconium, and Hafnium’, Oxford University Press, Oxford, 1975.
3. F. A. Cotton, G. Wilkinson, C. A. Murillo, and M. Bochmann, ‘Advanced Inorganic Chemistry’, 6th edn., John Wiley & Sons, New York, 1999.
4. N. N. Greenwood and A. Earnshaw, ‘Chemistry of the Elements’, 2nd edn., Pergamon, Oxford, 1997.
5. O. A. Sinegribova and G. A. Jagodin, *Atom. Energy Rev.*, 1966, **4**, 93.
6. J. H. Schemel, ‘ASTM Manual on Zirconium and Hafnium’, American Society for Testing and Materials, Philadelphia, PA, 1977.
7. D. L. Kepert, ‘Inorganic Stereochemistry’, Springer, Berlin, 1982.
8. H. J. Goldschmidt, ‘Interstitial Alloys’, Butterworth, London, 1967.
9. A. Yajima, Y. Segawa, R. Matsuzoki, and Y. Saeki, *Bull. Chem. Soc. Jpn*, 1983, **56**, 2638.
10. T. F. Connolly ed., ‘Groups IV, V, and VI Metals and Compounds’, Plenum, New York, 1972.
11. B. H. Chen, B. W. Eichhorn, and P. E. Fanwick, *Inorg. Chem.*, 1992, **31**, 1788.
12. P. M. Keane and J. A. Ibers, *Inorg. Chem.*, 1991, **30**, 1327.
13. D. Hall, C. E. F. Pickard, and T. N. Waters, *J. Inorg. Nucl. Chem*, 1971, 2395.
14. C. F. Lee, L. K. Myers, K. G. Valentine, and M. E. Thompson, *J. Chem. Soc., Chem. Commun.*, 1992, 201.
15. F. Calderazzo, S. Ianelli, G. Pampaloni, G. Pelizzi, and M. Sperrle, *J. Chem. Soc., Dalton Trans.*, 1991, 693.
16. D. F. Evans, G. W. Griffiths, C. O’Mahoney, D. J. Williams, C. Y. Wong, and J. D. Woolins, *J. Chem. Soc., Dalton Trans.*, 1992, 2475.
17. J. E. Gozum and G. S. Girolami, *J. Am. Chem. Soc.*, 1991, **113**, 3829.
18. F. Quignard, A. Choplin, and J. M. Basset, *J. Chem. Soc., Chem. Commun.*, 1991, 1589.
19. L. F. Chen, F. A. Cotton, and W. A. Wojtczak, *Angew. Chem., Int. Ed. Engl.*, 1995, **34**, 1877.
20. M. D. Fryzuk, M. Mylvaganam, M. J. Zaworotko, and L. R. MacGillivray, *J. Am. Chem. Soc.*, 1993, **115**, 10360.
21. X. Z. Liu, Z. Z. Wu, Z. H. Peng, Y. D. Wu, and Z. L. Xue, *J. Am. Chem. Soc.*, 1999, **121**, 5350.
22. D. Jacoby, S. Isoz, C. Floriani, K. Schenk, A. Chiesi-Villa, and C. Rizzoli, *Organometallics*, 1995, **14**, 4816.
23. T. Matsuo and H. Kawaguchi, *Organometallics*, 2003, **22**, 5379.
24. F. Lefebvre and J. M. Basset, *J. Mol. Catal. A*, 1999, **146**, 3.
25. F. Calderazzo, P. Pallavicini, G. Pampaloni, and P. F. Zanazzi, *J. Chem. Soc., Dalton Trans.*, 1990, 2743.
26. M. Polamo and M. Leskela, *Acta Chem. Scand.*, 1997, **51**, 44.
27. F. Corazza, E. Solari, C. Floriani, A. Chiesi-Villa, and C. Guastini, *J. Chem. Soc., Dalton Trans.*, 1990, 1335.
28. K. Ishihara, S. Ohara, and H. Yamamoto, *Science*, 2000, **290**, 1140.
29. S. A. Cotton and F. A. Hart, ‘The Heavy Transition Metals’, Macmillan, London, 1975.
30. V. W. Day, W. G. Klemperer, and M. M. Pafford, *Inorg. Chem.*, 2001, **40**, 5738.
31. D. C. Bradley, R. C. Mehrotra, and D. P. Gaur, ‘Metal Alkoxides’, Academic Press, New York, 1978.
32. K. G. Caulton and L. G. Hubert-Pfalzgraf, *Chem. Rev.*, 1990, **90**, 969.
33. J. A. Samuels, J. W. Zwanziger, E. B. Lobkovsky, and K. G. Caulton, *Inorg. Chem.*, 1992, **31**, 4046.
34. R. Schmidt, H. Ahamdane, and A. Mosset, *Inorg. Chim. Acta*, 1991, **190**, 237.
35. J. A. Samuels, B. A. Vaarstra, J. C. Huffman, K. L. Trojan, W. E. Hatfield, and K. G. Caulton, *J. Am. Chem. Soc.*, 1990, 9623.
36. C. H. Zambrano, A. K. McMullen, L. M. Kobriger, P. E. Fanvick, and I. P. Rothwell, *J. Am. Chem. Soc.*, 1990, **112**, 6565.
37. M. A. Hossain, M. B. Hursthouse, A. Ibrahim, M. Mazid, and A. C. Sullivan, *J. Chem. Soc., Dalton Trans.*, 1989, 2347.
38. G. E. Hofmeister, E. Alvarado, J. A. Leary, D. I. Yoon, and S. F. Pedersen, *J. Am. Chem. Soc.*, 1990, **112**, 8843.
39. L. Giannini, A. Caselli, E. Solari, C. Floriani, A. Chiesi-Villa, C. Rizzoli, N. Re, and A. Sgamellotti, *J. Am. Chem. Soc.*, 1997, **119**, 9709.
40. S. Groysman, I. Goldberg, M. Kol, E. Genizi, and Z. Goldschmidt, *Inorg. Chim. Acta*, 2003, **345**, 137.
41. M. G. Lappert, P. P. Power, A. R. Sanger, and R. C. Srivastava, ‘Metal and Metalloid Amides’, Wiley, New York, 1980.
42. M. H. Chisholm, C. E. Hammond, and J. C. Huffman, *Polyhedron*, 1988, **7**, 399.
43. K. Hagen, C. J. Howill, D. A. Rice, and J. D. Runnacles, *Inorg. Chem.*, 1988, **27**, 2032.
44. M. M. Banaszak Holl and P. T. Wolczanski, *J. Am. Chem. Soc.*, 1992, **114**, 3854.
45. R. A. Kresinski, L. Isam, T. A. Hamor, C. J. Jones, and J. A. McCleverty, *J. Chem. Soc., Dalton Trans.*, 1991, 1835.
46. H. J. Kim, D. Whang, J. Kim, and K. Kim, *Inorg. Chem.*, 1992, **31**, 3882.
47. R. R. Schrock, P. J. Bonitatebus, and Y. Schrodi, *Organometallics*, 2001, **20**, 1056.
48. M. E. G. Skinner, D. A. Cowhig, and P. Mountford, *Chem. Commun.*, 2000, 1167.
49. P. Mehrkhodavandi, R. R. Schrock, and L. L. Pryor, *Organometallics*, 2003, **22**, 4569.
50. G. R. Giesbrecht, A. Shafir, and J. Arnold, *Chem. Commun.*, 2000, 2135.

51. D. Jacoby, S. Isoz, C. Floriani, A. Chiesi-Villa, and C. Rizzoli, *J. Am. Chem. Soc.*, 1995, **117**, 2793.
52. B. Findeis, M. Schubart, C. Platzek, L. H. Gade, I. Scowen, and M. McPartlin, *Chem. Commun.*, 1996, 219.
53. S. Friedrich, L. H. Gade, I. J. Scowen, and M. McPartlin, *Angew. Chem., Int. Ed. Engl.*, 1996, **35**, 1338.
54. C. P. Schaller and P. T. Wolczanski, *Inorg. Chem.*, 1993, **32**, 131.
55. C. P. Schaller, C. C. Cummins, and P. T. Wolczanski, *J. Am. Chem. Soc.*, 1996, **118**, 591.
56. A. J. Blake, J. M. McInnes, P. Mountford, G. I. Nikonov, D. Swallow, and D. J. Watkin, *J. Chem. Soc. Dalton Trans.*, 1999, 379.
57. T. G. Ong, D. Wood, G. P. A. Yap, and D. S. Richeson, *Organometallics*, 2002, **21**, 1.
58. A. J. Blake, P. E. Collier, L. H. Gade, P. Mountford, J. Lloyd, S. M. Pugh, M. Schubart, M. E. G. Skinner, and D. J. M. Trosch, *Inorg. Chem.*, 2001, **40**, 870.
59. J. L. Thorman, I. A. Guzei, V. G. Young, and L. K. Woo, *Inorg. Chem.*, 1999, **38**, 3814.
60. P. N. O'Shaughnessy, K. M. Gillespie, C. Morton, I. Westmoreland, and P. Scott, *Organometallics*, 2002, **21**, 4496.
61. J. D. Cohen, M. D. Fryzuk, T. M. Loehr, M. Mylvaganam, and S. J. Rettig, *Inorg. Chem.*, 1998, **37**, 112.
62. M. D. Fryzuk, J. B. Love, S. J. Rettig, and V. G. Young, *Science*, 1997, **275**, 1445.
63. P. J. Chirik, L. M. Henling, and J. E. Bercaw, *Organometallics*, 2001, **20**, 534.
64. J. A. Pool, E. Lobkovsky, and P. J. Chirik, *J. Am. Chem. Soc.*, 2003, **125**, 2241.
65. H. Ishino, T. Nagano, S. Kuwata, Y. Yokobayashi, Y. Ishii, and M. Hidai, *Organometallics*, 2001, **20**, 188.
66. G. P. Kushto, P. F. Souter, G. V. Chertihin, and L. Andrews, *J. Chem. Phys.*, 1999, **110**, 9020.
67. M. D. Fryzuk, T. S. Haddad, and D. J. Berg, *Coord. Chem. Rev*, 1990, **99**, 137.
68. A. F. Lindmark and R. C. Fay, *Inorg. Chem.*, 1983, **22**, 2000.
69. P. Rosa, N. Mezailles, L. Ricard, F. Mathey, and P. Le Floch, *Angew. Chem., Int. Ed.*, 2000, **39**, 1823.
70. M. D. Fryzuk, J. B. Love, and S. J. Rettig, *Organometallics*, 1998, **17**, 846.
71. M. D. Fryzuk, C. M. Kozak, P. Mehrkhodavandi, L. Morello, B. O. Patrick, and S. J. Rettig, *J. Am. Chem. Soc.*, 2002, **124**, 516.
72. M. D. Fryzuk, A. Carter, and A. Westerhaus, *Inorg. Chem.*, 1985, **24**, 642.
73. R. Baumann, R. Stumpf, W. M. Davis, L. C. Liang, and R. R. Schrock, *J. Am. Chem. Soc.*, 1999, **121**, 7822.
74. M. Aizenberg, L. Turculet, W. M. Davis, F. Schattenmann, and R. R. Schrock, *Organometallics*, 1998, **17**, 4795.
75. D. D. Graf, R. R. Schrock, W. M. Davis, and R. Stumpf, *Organometallics*, 1999, **18**, 843.
76. L. C. Liang, R. R. Schrock, and W. M. Davis, *Organometallics*, 2000, **19**, 2526.
77. R. R. Schrock, S. W. Seidel, Y. Schrodi, and W. M. Davis, *Organometallics*, 1999, **18**, 428.
78. T. R. Boussie, G. M. Diamond, C. Goh, K. A. Hall, A. M. LaPointe, M. Leclerc, C. Lund, V. Murphy, J. A. W. Shoemaker, U. Tracht, H. Turner, J. Zhang, T. Uno, R. K. Rosen, and J. C. Stevens, *J. Am. Chem. Soc.*, 2003, **125**, 4306.
79. R. L. Daake and J. D. Corbett, *Inorg. Chem.*, 1977, **16**, 2029.
80. S.-J. Hwu, R. P. Ziebarth, S. V. Winbush, J. E. Ford, and J. D. Corbett, *Inorg. Chem.*, 1986, **25**, 283.
81. E. Garcia and J. D. Corbett, *Inorg. Chem.*, 1990, **29**, 3274.
82. J. H. Wengrovius, R. R. Schrock, and C. D. Day, *Inorg. Chem.*, 1981, **20**, 1844.
83. P. M. Morse, S. R. Wilson, and G. S. Girolami, *Inorg. Chem.*, 1990, **29**, 3200.
84. P. G. Edwards, J. A. K. Howard, J. S. Parry, and A.-R. Al-Soudani, *J. Chem. Soc., Chem. Commun.*, 1991, 1385.
85. C. G. Young, *Coord. Chem. Rev.*, 1989, **96**, 89.
86. F. A. Cotton, P. A. Kibala, and W. A. Wojtczak, *J. Am. Chem. Soc.*, 1991, **113**, 1462.
87. M. D. Fryzuk, T. S. Haddad, and S. J. Rettig, *J. Am. Chem. Soc.*, 1990, **112**, 8185.
88. F. A. Cotton and P. A. Kibala, *Inorg. Chem.*, 1990, **29**, 3192.
89. D. M. Hoffman and S. Lee, *Inorg. Chem.*, 1992, **31**, 2675.
90. J. Quirk and G. Wilkinson, *Polyhedron*, 1982, **1**, 209.
91. J. E. Ellis, A. J. DiMaio, A. L. Rheingold, and B. S. Haggerty, *J. Am. Chem. Soc.*, 1992, **114**, 10676.
92. J. E. Ellis and K.-M. Chi, *J. Am. Chem. Soc.*, 1990, **112**, 6022.
93. F. A. Cotton, P. A. Kibala, and W. J. Roth, *J. Am. Chem. Soc.*, 1988, **110**, 298.
94. R. P. Ziebarth and J. D. Corbett, *Acc. Chem. Res.*, 1989, **22**, 256.

Zirconium & Hafnium: Organometallic Chemistry

Philippe Meunier & Nadine Pirio
Université de Bourgogne, Dijon, France

Based in part on the article Zirconium & Hafnium: Organometallic Chemistry by Bernard Gautheron, Roland Broussier, & Philippe Meunier which appeared in the Encyclopedia of Inorganic Chemistry, First Edition.

1 Introduction 1
2 Cyclopentadienyl Complexes of Zr and Hf 3
3 Unusual Coordination Geometries at Carbon Stabilized by Group 4 Metallocenes 13
4 Other Anionic π-Ligands Complexes 15
5 Dinuclear Complexes 17
6 Complexes of Zr^{IV} and Hf^{IV} Lacking π-ligands 19
7 Neutral Organozirconium Complexes in Organic and Organometallic Synthesis 20
8 Cationic Zirconocenes in Organic Synthesis and Catalysis 30
9 Organozirconium Complexes in Asymmetric Catalysis 33
10 Related Articles 35
11 References 35

Abbreviations

Ac = Acetyl; acac = Acetylacetone; Ar = Aryl; binap = 2,2-bis(diphenylphosphanyl)-1,1′-binaphtyl; binol = 2,2′-dihydroxy-1,1′-binaphthyl; Bn = Benzyl; *i*-Bu = *Iso*-butyl; *n*-Bu = Butyl; *t*-Bu = *Tert*-butyl; cod = Cycloocta-1,5-diene; cot = Cyclooctatetraene; Cp = Cyclopentadienyl; Cp′ = Methylcyclopentadienyl; Cp* = Pentamethylcyclopentadienyl; Cy = Cyclohexyl; ds = Diastereoisomeric selectivity; DME = Ethylene glycol dimethyl ether; dmpe = 1,2-bis(dimethylphosphanyl)ethane; dppe = 1,2-bis(diphenylphosphanyl)ethane; ebi = Ethylene-1,2-bis(indenyl); ebthi = Ethylene-1,2-bis(tetrahydroindenyl); ee = Enantiomeric excess; LDA = Lithium diisopropylamide; Et = Ethyl; Hf = Hafnium; HOMO = Highest Occupied Molecular Orbital; Ind = Indenyl; ERP = Electron Paramagnetic Resenance; LUMO = Lowest Unoccupied Molecular Orbital; M = Zr or Hf; MAO = Methylaluminoxane; Me = Methyl; Mes = Mesityl; MOP = Mono *n* octyl phosphate; NMR = Nuclear Magnetic Resonance; Ph = Phenyl; *i*-Pr = *iso*-propyl; *n*-Pr = Propyl; py = Pyridine; tbps = *tert*-butyldiphenylsilyl; Tf = Triflyl (trifluoromethanesulfonyl); thf or THF = Tetrahydrofuran; Ts = Tosyl (4-toluenesulfonyl); vapol = 3,3′-bis(2-phenyl-4-phenanthrol); Zr = Zirconium.

1 INTRODUCTION

Since the discovery of the first organometallic complexes (*see Organometallic Complexes*) Cp_2TiBr_2 and Cp_2ZrBr_2 by Wilkinson in 1953, the literature on this subject has reflected the astonishing extension of the organometallic chemistry of the group 4 transition metals (*see Transition Metals*). This article focuses on modern organometallic chemistry of zirconium and hafnium, while the organotitanium complexes (*see* ***Titanium: Organometallic Chemistry***) appear elsewhere in this encyclopedia.

During the last decade, more than a thousand papers have been published (as during the preceding 40 years) dealing with several thousands of Zr and Hf compounds, largely dominated by organozirconium complexes. In fact, Zr occurs in the lithosphere to the extent of 0.022%. Although it is much less abundant than titanium (0.63%), it is roughly as abundant as carbon. Despite some technical difficulties in the production of pure Zr compounds (due to the presence of about 2% of Hf in the minerals), it is one of the less expensive transition metals. Hf is more difficult to obtain, and commercially available reagents usually also contain some traces of Zr. Very pure derivatives can be obtained by distillation and ion-exchange techniques (*see Ion Exchange*).

Because the ionic radii of the metals are similar ($Zr = 0.79$ Å, $Hf = 0.78$ Å), as are the covalent radii ($Zr = 1.55$ Å, $Hf = 1.54$ Å) (*see Covalent Radii*), their complexes often exhibit a close similarity in their behavior and molecular structure. However, several well-characterized Zr complexes have no counterparts in the Hf series, which always appear the less reactive in accordance with bond dissociation enthalpy measurements (*see Enthalpy*).

Most of the stable complexes have d^0 structure (*see d^n Configuration*) and formally count as having 16 valence electrons surrounding the metal, with an empty d orbital (*see d-Orbitals*) being responsible for the observed reactivity. This number is less than required by the 18-electron rule (*see Eighteen Electron Compounds*) as related to the stability of transition metal complexes. So, for some Zr or Hf organometallics, stabilization is achieved by completing the electronic configuration to 18 electrons, by coordinating an additional neutral ligand (such as a solvent or phosphane molecule) or by reacting with some unsaturated molecules to form zirconocene-ate complexes. The coordination number of the metal for Zr complexes ranges from 4 to 8. For Hf complexes with the same ligands, it is often smaller. A typical example of this effect is the structure of Cp_4Zr, which is consistent with the presence of three pentahapto and one monohapto Cp ligands (*see Hapticity*), while the structure of the Hf analog contains two pentahapto and two monohapto Cp rings. The most common oxidation state (*see Oxidation Number*) for Zr and Hf complexes is +4, as suggested by their electronic configuration (Zr: [Kr] $4d^2 5s^2$; Hf: [Xe] $5d^2 6s^2$). But a significant number of examples with the lower value +2 are known, such as $Cp_2Zr(CO)_2$ or

$Cp_2Zr(PMe_3)_2$. Some complexes, as alkene- and alkyne-$ZrCp_2$ structures can be considered as Zr^{II} complexes, but also as zirconacyclopropanes and zirconacyclopropenes respectively, in which Zr is the +4 oxidation state. They can be represented as resonance hybrids (**1**) and (**2**). On the contrary, Zr^{III} and Zr^{I} compounds are rarer and displayed few synthetically useful transformations.

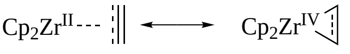

(**1**) (**2**)

Cationic zirconocene complexes are well-known very reactive species with interesting applications owing to their Lewis acidic character (*see Lewis Acids & Bases*). In particular, they are often involved into various catalytic processes including Ziegler-Natta type polymerizations (*see Ziegler–Natta Catalysts*).

The crystal structure of the 16-electron d^0 species (*see Bent Metallocenes*) such as $(RCp)_2MX_2$ (**3**), is a distorted tetrahedron, each Cp ligand (*see Cyclopentadienyl*) occupying a single coordination position. Owing to the steric demand of the Cp ligand, the angle α is larger (and consequently β is smaller) than for a regular tetrahedron. Typically, α and β lie in the range 128–133° and 94–97° respectively, depending on the nature of R and X. In case of *ansa* metallocenes containing a bridge with at least two atoms, the distortion of the tetrahedron is similar. On the contrary, it is more pronounced in *ansa* metallocenes (*see Bridging Ligand*) with a monoatomic bridge (**4**) and largely depends on the nature of Z ($\alpha = 116–129°$; $\beta = 97–101°$). In every case, the Cp ligands can be staggered, eclipsed, or intermediate. Apparently, there is no relation between the relative conformation of the rings and the nature of the α-ligands. Substituents in the two Cp rings are generally opposed to each other in the favored conformation, thus minimizing steric and electronic interactions, but some exceptions have been noted. The distance d_1 lies in the range 2.10–2.32 Å (with an Hf–Cp bond slightly shorter (0.01–0.03 Å) than Zr–Cp bond), whereas d_2 is more largely dependant on the identity of the metal and the X groups.

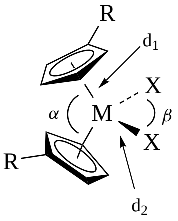

(**3**)

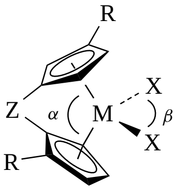

Z = B, C, Si, Ge, P

(**4**)

Spectroscopic techniques are very useful techniques to characterize the group 4 metallocenes (*see Metallocene Complexes*). ^1H NMR is a very convenient method for studying the diamagnetic d^0 complexes (*see Diamagnetism*), for which the proton resonances of the organic ligands generally appear in the range 0–10 ppm downfield from the Me_4Si reference. Exceptions are found, especially for hydrido ligands, where resonances appear at higher field. ^{13}C and ^{31}P NMR are also valuable tools for establishing structures, but ^{91}Zr NMR seems limited to simple and very symmetrical complexes. EPR spectroscopy (*see Electron Paramagnetic Resonance*) affords suitable information about paramagnetic M^{III} complexes (*see Paramagnetism*). Infrared spectra (*see Infrared Spectroscopy*) are typical: for example, dicarbonyl complexes exhibit two strong metal-carbonyl stretching bands with frequencies in the range 1980–1840 cm^{-1}. A normal isotopic pattern is generally detected in mass spectrometry (*see Mass Spectrometry*). Photoelectron spectroscopy (UV) has been used to determine the electronic and conformational structures of these molecules.

Although there are many different types of M^{IV} and M^{II} compounds, roughly 75–80% of the currently known well-characterized organozirconiums or organohafniums are cyclopentadienyl derivatives. In these 16-electron d^0 M^{IV} complexes (**5**), one valence-shell empty orbital is available for coordination. They are therefore fundamentally Lewis acidic and certainly, most of their reactions are governed by interaction of the empty metal orbital with electron donors. Probably for the same reason, apart from the dihalides and a few other compounds, Zr and Hf complexes are air- and moisture-sensitive. They require handling in an inert atmosphere, using, for example, the Schlenk tube technique (*see Schlenk Tube*) or a glove box.

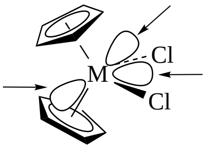

The available coordination sites are indicated by the arrows

(**5**)

Although organozirconium and hafnium compounds are not as well known as Grignard reagents (*see Grignard Reagents*), it seems that the time is apt for synthetic chemists to fully enter the world of that chemistry. Very reactive cationic zirconocenes, often *in situ*-generated from neutral complexes, are very useful catalysts in different fields of chemistry, particularly in stereospecific polymerization process, even in industry. According to the structure of the M^{IV} complexes, the empty Zr or Hf orbital may interact with any proximal electrons, including n electron lone-pair, π electrons, or σ electrons. Such interactions may be intermolecular or intramolecular. These processes, which explain the astonishing development of the synthetical applications of organozirconiums, include σ and π complexations, hydrozirconation (*see Hydrozirconation*) and carbozirconation (*see*

Carbometalation), oxidative addition (*see Oxidative Addition*) and reductive elimination (*see Reductive Elimination*), σ-bond metathesis (*see σ-Bond Metathesis*), and migratory insertion (*see Migratory Insertion*).

An overall review of these most important topics is developed below. This article is not an exhaustive review; it deals only with the main actual aspects of Zr and Hf chemistry, complementary to those developed in the first edition of the Encyclopedia of Inorganic Chemistry.**[1]** For more specific details, readers should consult the references mentioned within the articles cited.

2 CYCLOPENTADIENYL COMPLEXES OF Zr AND Hf

Unquestionably, group 4 complexes containing one or two Cp ligands are the most important and the most versatile reagents that find use in catalytic and stoichiometric reactions.

The most widely used approach for coordination of Cp, as well as the many variations of this ligand, requires use of lithium, sodium, and magnesium (or sometimes thallium or potassium) salts of the ligand anion. They can be obtained by direct reaction of the metal or some organometallic reagents on a suitable cyclopentadiene monomer. Another way for synthesizing substituted Cp ligands is the reduction or alkylation of a parent fulvene at the exocyclic carbon atom. But disadvantages of these procedures include the need to prepare moisture- and air-sensitive ligand anions. So, some alternative methods circumvent these difficulties. In this area, reaction of trimethylsilyl- or stannyl-substituted cyclopentadienyls with transition metal halides is a useful procedure.**[1]** Some more recent reports**[2]** are related to the use of neutral reagents for the preparation of racemic bis indenyl and bis cyclopentadienyl group 4 complexes. In parallel, the reaction of group 4 homoleptic compounds (*see Homoleptic Compound*) with fulvene derivatives gives rise to mono or bis cyclopentadienyl compounds (Scheme 1). Coordination of the *cis*-diene to the metal should encourage transfer of the metal ligands to the exocyclic carbon giving functionalized Cp complexes.**[3]**

Amine elimination process can be used starting from cyclopentadiene derivatives to produce in good yield *ansa* metallocenes.

2.1 Bis Cyclopentadienyls of Zr^{IV} and Hf^{IV} $[(\eta^5\text{-L})(\eta^5\text{-L}')MXY]$

2.1.1 *Dihalides and Related Complexes*

These complexes, which are readily synthesized by transmetalation (*see Transmetalation*) from the appropriate Cp metal and MX_4 ($L = L'$) or (η^5-L)MX_3 ($L \neq L'$), represent a large family of quite always air-stable compounds. The bromides and iodides are also obtained from chlorine exchange reactions with the appropriate boron trihalide. The fluorides can be obtained by metathesis (*see Metathesis*) of chlorides derivatives with Me_3SnF. With only one equivalent of tin reagent per mole of dichloride, partial fluorination occurs affording mixed halide metallocenes. The fluorides are also prepared by chloride/fluoride, by chloride/NMe_2 followed by NMe_2/fluoride exchange, and by oxidative addition (*see Oxidative Addition*).**[4]**

Of course, complexes containing unsubstituted Cp ligands were the first to be prepared, but to date a great variety of certainly many thousands of complexes have been prepared by different very efficient ways. Substituents are consistent with various carbon or main group functionalities. For example, the structures are very different to Zr complexes of the sterically demanding pentaphenylcyclopentadienyl,**[5]** bis fluorenyl derivatives**[6]** or very exciting Zr complex containing a corrannulene-based ligand (equation 1).**[7]** This bowl-shaped ligand has two sides because of the curvature of the molecule: an *endo* (concave) and an *exo* (convex) side (*see Exo & Endo Substituents*). The Zr atom was determined to be found at the

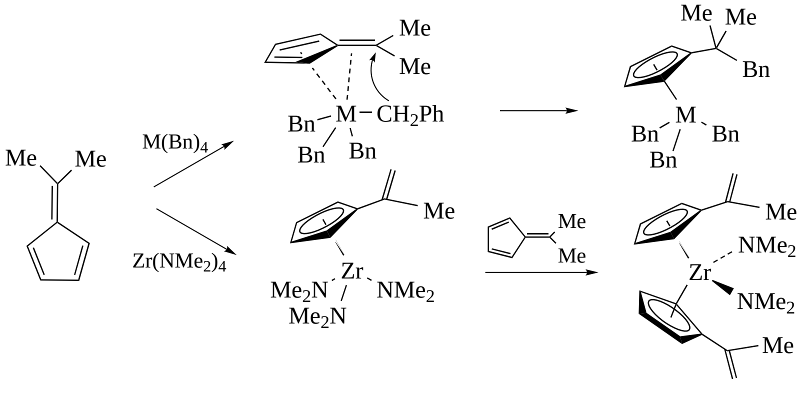

Scheme 1

exo side of the bowl.

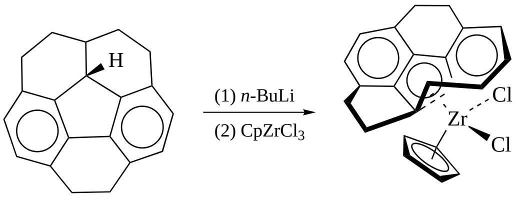

(1)

The stereoselective complexation (*see Stereochemistry*) of the heterotopic faces of Cp ligands can be realized. For example, starting from the isodicyclopentadienyl anion and MCl_4 or (η^5-L)MCl_3, the results clearly indicate the temperature dependence in the stereo differentiation of the two heteropic sides of the anion.[1]

Special attention must be given to the *ansa* organometallics. The bridge linking the two Cp ligands can be very short (B, CR_2, SiR_2, GeR_2, NR, PR, etc.), or longer ($(CH_2)_n$, cyclic derivatives, siloxy chains, etc.). Even, the doubly bridged complexes (**6**) and (**7**) can be prepared.[8,9] An interannular bridge restricts the free rotation of the Cp ligands about the Cp–metal axes with respect to each other changing the dihedral angle between the two Cp ligands.

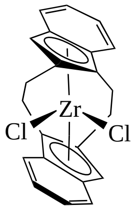

(**6**)

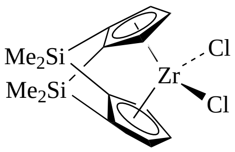

(**7**)

Of course, the nature of the bridge allows varying degrees of stereorigidity and accessibility to the coordination site of the molecule. Some additional ways can be used to prepare *ansa* metallocenes. For example, it is possible to use silastannatetrahydro-s-indacenes as Cp transfer agents for producing silanediyl-bridged zirconocene complexes (equation 2).[10]

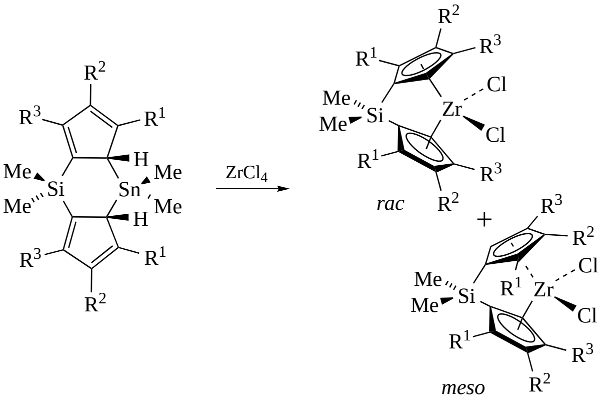

(2)

It is also possible to generate the bridge in a second step by ring-closing metathesis reaction (*see Metathesis*) using the Grubb's catalyst $RuCl_2(=CHPh)(PCy)_3$. *Ansa* metallocenes can be isolated in good conditions by this way (equation 3).[11] The method was extended to diastereoselective kinetic resolution of *meso*- and *dl*-isomeric mixtures and showed excellent selectivity.

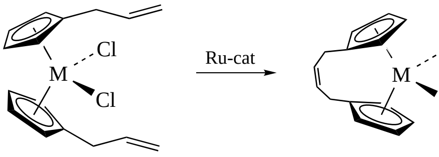

(3)

Another reaction can be used to generate a two-carbon bridge between the Cp ligands.[12] In tetrahydrofuran (THF), the reaction of $ZrCl_4$ with two equivalents of *n*-BuLi, begun at −78 °C and completed at 25 °C, results in a black suspension of $ZrCl_2$ and LiCl, which reacts with fulvenes to provide a high yield of *ansa* zirconocene dichloride (equation 4).

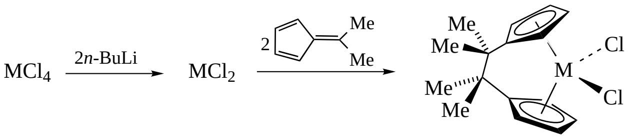

(4)

This reaction can operate starting from a lot of fulvenes. Some allyl-bridged metallocenes can be synthesized by an unusual intramolecular $HNMe_2$ elimination and a fulvene coupling (equation 5).[13]

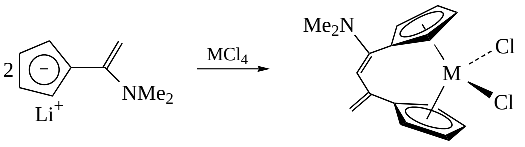

(5)

Different procedures can be used to obtain racemic or even optically active *ansa* metallocenes of great interest for applications in asymmetric reactions (*see Asymmetric Unit*) or polymerization processes (*see Polymer*). For example, reaction of $C_2H_4(Ind)_2Mg(thf)_2$ with zirconium biphenolate complexes gave directly the pure diastereomers.[14] In the more classical metalation of bis indenyl ligands, a good choice of the starting material and the metallic salt can change dramatically the *dl*/*meso* proportion.[15] Starting from the bis anion and $ZrCl_4$, a 1/1 mixture was obtained. On the contrary, pure *dl* racemate can be obtained with amine elimination process.

For the preparation of enantiomerically pure ebthi zirconium derivatives, an efficient procedure using optically pure binol can be used starting from racemic mixture.[16]

2.1.2 Dialkyls, Diarys, and Related Complexes

These important compounds with regards to their reactivity are obtained by transmetalation (*see Transmetalation*) between the appropriate metallocene dichloride (*see Metallocene Complexes*) and an alkyl- or aryl-lithium reagent. Dialkyl and diaryl zirconium complexes are very moisture-sensitive, degrading to form μ-oxo species (see Section 5).

Dimethylzirconocene is thermally stable and can be sublimated *in vacuum*. Its photolysis yields methane together with transient zirconocene species, which can be trapped with several types of electron-donating ligands including dienes, phosphanes, and CO (see Section 2.3). Same behavior is observed for diarylzirconocenes with formation of biaryl products.

Thermolysis of diarylzirconocenes readily affords arynezirconocene complexes (equation 6). These species are best described as metallacyclopropenes, and are versatile reagents in organic synthesis. When $(Cp^*)_2ZrPh_2$ or $(t\text{-}BuCp)_2ZrPh_2$ are heated at 80 °C, cyclometallated complexes (*see Cyclometalation*) are formed by hydrogen transfer from a methyl group to the coordinated benzyne ring.[1]

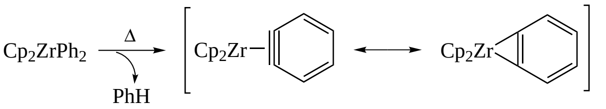

(6)

Other complexes of great interest are the η^4-conjugated diene metallocenes.[1] They are conveniently prepared by the one-pot reaction of the photochemically induced metallocene with the diene at low temperature. Alternative routes include the treatment of the metallocene dichloride with a conjugated diene dianion equivalent or the coupling of alkenyl ligands in the coordination sphere of the metal. The resulting systems show unusual behavior. For example, buta-1,3-diene directly leads to the *s-trans* complex (**8**), which can be thermally equilibrated into the *s-cis* isomer (**9**). This form exhibits a substantial metallacyclopentene character and is best described as a d^2 metal^{IV} (σ^2,π)-type complex (**10**), as shown by X-ray crystal analysis. On the other hand, the *s-trans* isomer should be formally regarded as a real d^2 metal^{II}-alkene π-complex.

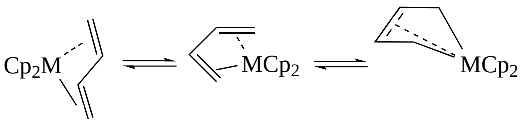

(**8**) (**9**) (**10**)

2.1.3 Hydrides and Related Complexes

Hydrides (*see Hydrides*) or aluminio- and borio-hydrides of Zr and Hf are important intermediates in catalytic processes and organic synthesis. The metal–hydrogen bond can be formed by the reduction of a dihalide metallocene with $LiAlH_4$ or $LiHAl(Ot\text{-}Bu)_3$. An efficient reaction which can be used, in particular, for several substituted Cp systems is the hydrogenolysis of the corresponding dimethyl complexes.[17] In some cases, these reactions can proceed under mild conditions (1 atm H_2, 25 °C). The molecularity of these hydride species was dependent on the substituents on the Cp rings. Monomeric compounds were found for hindered systems while dimeric systems containing hydrogen bridges were obtained for less steric crowded systems.

As a proof of the *ansa* effect, an interesting difference between the *ansa* complex (**11**) and traditional metallocenes can be observed (Scheme 2). Attempts to prepare the *ansa* zirconocene analog of $Cp_2^*ZrH_2$ lead instead to C–H bond activation of benzene to hydride complex (**12**). Performing the reaction in cyclohexane gave the dihydride bridged dimer (**13**) which reacts with benzene to give (**12**) or can be converted to the monomeric derivative (**14**) upon addition of a donor ligand. Compound (**13**) readily reacts with $(CH_2{=}CH_2)_2Mg$ and gives the first structurally characterized zirconocene ethylene-hydride $[\{Me_2Si(C_5Me_4)_2\}Zr(\eta^2\text{-}C_2H_4)H]_2Mg$. This complex might be considered as a model for intermediates in catalytic olefin hydrogenation processes (*see Hydrogenation*) and polymerization. The unique reactivity observed with these *ansa* systems is ascribed to the increased electrophilicity (*see Electrophile*) of their metal center.

Treatment of Cp_2ZrCl_2 with $LiAlH_4$ and then H_3GaNMe_3 or reaction of the preformed hydride Cp_2ZrH_2 with H_3AlNMe_3 affords the heterobimetallic complex (**15**).[18] Boron-containing heterobimetallic complexes (**16**) can be prepared by reaction of metallocene dichlorides with the cyclic hydroborate anion $[H_2BC_5H_{10}]^-$,[19] then reduction of M–Cl bond with LiH.

Dihydrides metallocenes can react with (η^2-diarylketone) zirconocene dimers to yield dimetallic compounds (**17**).[20] These systems contain a dimetallabicyclic framework in which

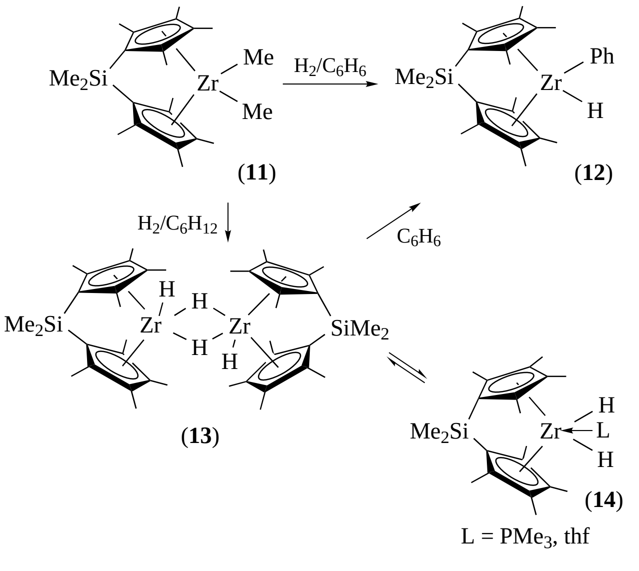

Scheme 2

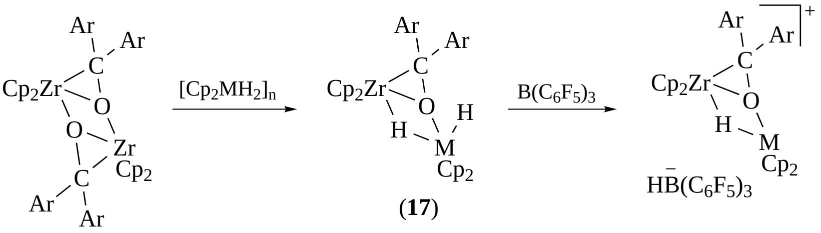

Scheme 3

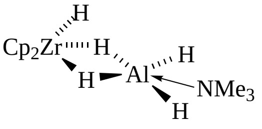

(**15**)

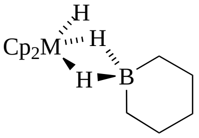

(**16**)

the two metal centers are bridged by the oxygen atom of the η^2-diarylketone ligand and a μ-hydride ligand. The remaining hydride ligand is oriented *trans* to the μ-H moiety of the MCp_2 unit. Treatment of these complexes with $B(C_6F_5)_3$ results in the selective abstraction of the terminal hydride ligand to form dimetallic cation complexes (Scheme 3).

2.1.4 Mono Alkyls and Related Complexes

Halogeno(alkyl)metallocenes are generally obtained from the halides by transmetalations (*see Transmetalation*) with careful control of the stoichiometry and experimental conditions.**[1]** The cleavage using $PbCl_2$ of a Zr–C bond from a dialkyl complex, hydrozirconation (*see Hydrozirconation*) of unsaturated molecules and scrambling reactions (*see Disproportionation*) between dichlorides and dialkyls have also been employed to prepare compounds of this class. They exhibit a rich reactivity by substitution of the chloride moiety. Thus, the reaction of $Cp_2Zr(Me)Cl$ with $PhC{\equiv}CCH_2MgBr$ affords an η^3-propargyl/allenyl zirconocene.**[21]** The complex can be described as two resonance forms in which the allenyl representation (**19**) is more important than the propargyl form (**18**).

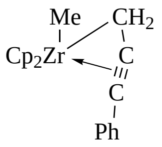

(**18**)

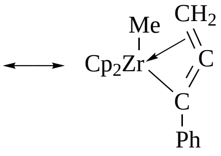

(**19**)

2.1.5 Phosphido Ligands-containing Complexes

Owing to their potentialities in coordination chemistry and catalysis, the chemistry of complexes incorporating Zr–P bonds presents an increasing development.**[22]** Compounds can be synthesized by halide metathesis (*see Metathesis*) from lithium phosphanides and the corresponding dihalogeno or halogeno(methyl)metallocene. In addition, electron-rich lithium phosphanides can reduce Zr^{IV}, affording Zr^{III} dimer (**20**). Others strategies are based on oxidative addition (*see Oxidative Addition*) of P–H bonds to zirconocenes. An efficient synthesis of the phosphanidozirconium complex (**21**) is the treatment of $Cp_2Zr(PHR)_2$ ($R = Me_2(i\text{-}PrMe_2C)Si$) with $Zr(NEt_2)_4$.**[23]**

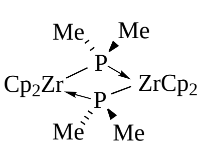

(**20**)

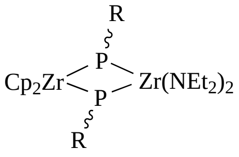

(**21**)

Beside classical Zr–P bond cleavage with the release of the corresponding phosphane, ketones, aldehydes, nitriles, isonitriles, and epoxides have been inserted into the Zr–P bonds of four- or five-membered phosphazirconacycles leading to ring expansion. For example, the equation (7) shows the insertion of acetonitrile in a triphosphanato complex affording an unsymmetrical six-membered ring complex.**[22]**

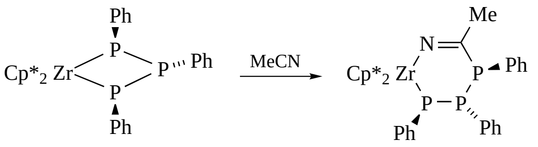

(7)

Finally, the main application of zirconium phosphanido complexes is to use them as metalloligands for coordination with the late transition metals to form phosphorus-bridged early–late heterobimetallic complexes.

2.1.6 Complexes Containing an M=E Bond (E = N, P, O, S, Se, Te)

Early transition metal complexes that contain doubly bonded ligands have been developed in view to synthetical applications. Imido, phosphinidene, and chalcogenido complexes are the most commonly used.[24] They exhibit high reactivity with small unsaturated molecules owing to the nucleophilicity of the main group element combined with high electrophilicity of the metal center. Additionnaly, they have been proposed as the catalytic agents in many organic transformations.

Imido zirconocenes (*see Imide Complexes*) are synthesized from thermolysis of $Cp_2Zr(Me)NHR$. They react with a wide variety of organic substrates (alkynes, imines, azides, carbodiimides, ketones) to yield [2 + 2] cycloaddition products (Scheme 4) (*see Metallacycle*).[25]

Enantioselective chemistry (*see Enantioselectivity*) has been also developed with imido complexes.[26] The stereospecific reaction of *rac*-(ebthi)(thf)Zr=NAr with racemic symmetrically or unsymmetrically 1,3-disubstituted allenes (1,3-diphenylallene, 3,4-heptadiene, 4,5-nonadiene or 1,2-cyclononadiene) provides at room temperature a single diastereoisomeric azazirconacycle (equation 8). In certain cases, this system allows conversion of an allene racemate into a mixture enriched in one enantiomer.

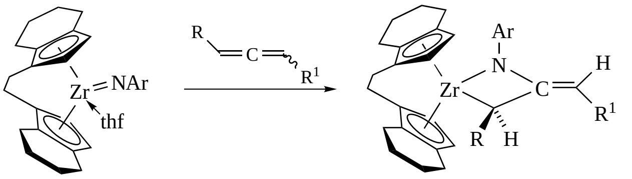

Zr=NAr
thf
R
C
R1
Ar
N
Zr
C
H
R1
R
H

(8)

Different procedures were developed for the obtention of Zr phosphinidene complexes. The first stable complex was obtained *via* the loss of phosphane from an intermediate bis phosphanido complex. Other routes were sought to more readily gain access to these unsaturated complexes. Thus, the addition of a base to a primary phosphanido complex is another opportunity to obtain such complexes.[22] Benzonitrile and dicyclohexylcarbodiimide react with the phosphinidene complex (**22**) by insertion into the Zr=P bond, or by cycloaddition and subsequent rearrangement (Scheme 5).

Starting from the phosphinidene complex (**22**) and ketones, the double-bond metathesis reaction provides access to a phosphaalkene and the zirconocene oxide $(Cp_2ZrO)_n$. A similar situation is also observed in the reaction with epoxides to give the corresponding phosphiranes (Scheme 6).[22]

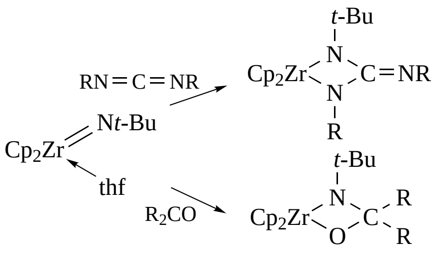

t-Bu
N
Cp2Zr
C=NR
N
R
RN=C=NR
Nt-Bu
Cp2Zr
thf
R2CO
t-Bu
N
Cp2Zr
C
O
R
R

Scheme 4

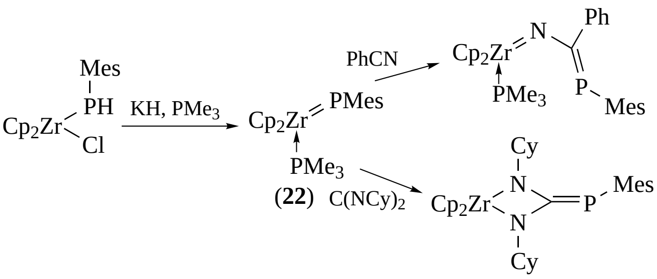

Mes
PH
Cp2Zr
Cl
KH, PMe3
Cp2Zr
PMes
PMe3
(22)
PhCN
Cp2Zr
N
Ph
PMe3
P
Mes
C(NCy)2
Cy
N
Cp2Zr
N
Cy
P
Mes

Scheme 5

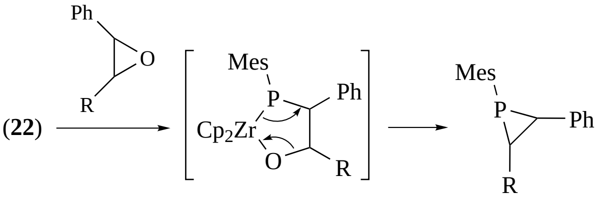

Ph
O
R
(22)
Mes
P
Ph
Cp2Zr
O
R
Mes
P
Ph
R

Scheme 6

Phosphinidene-group transfer reaction to main group elements can also be achieved starting, for example, from Me_2SiCl_2 or t-Bu_2SnCl_2 (Scheme 7).[22]

Terminal chalcogenido zirconium complexes (**23**) are conveniently synthesized by the reactions of dicarbonylzirconocene with either N_2O or the elemental chalcogens (S, Se, Te) (*see Chalcogens*) in the presence of pyridine. The Zr=E bond in these complexes is highly reactive and leads to a variety of 1,2-addition and cycloaddition reactions (Scheme 8).[27,28]

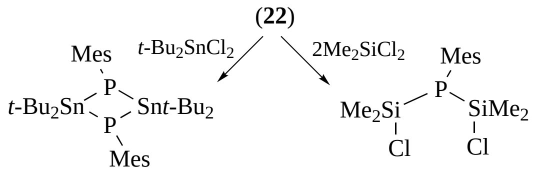

(22)
t-Bu2SnCl2
2Me2SiCl2
Mes
P
t-Bu2Sn
Snt-Bu2
P
Mes
Mes
P
Me2Si
SiMe2
Cl
Cl

Scheme 7

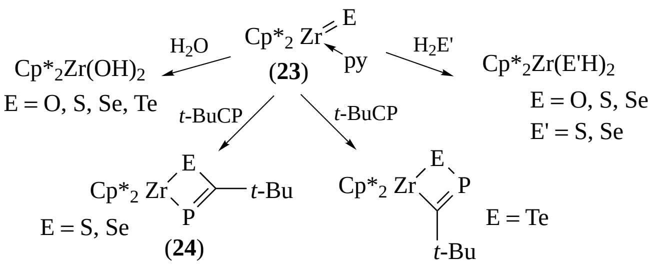

Cp*2 Zr
E
py
(23)
H2O
Cp*2Zr(OH)2
E = O, S, Se, Te
H2E'
Cp*2Zr(E'H)2
E = O, S, Se
E' = S, Se
t-BuCP
t-BuCP
Cp*2 Zr
E
P
t-Bu
E = S, Se
(24)
Cp*2 Zr
E
P
t-Bu
E = Te

Scheme 8

The four-membered ring Zr systems (**24**) can undergo further ring expansion reactions with other chalcogenides, nitriles, and isonitriles (Scheme 9).[28]

2.2 Bis Cyclopentadienyl Complexes of Zr^{III} and Hf^{III}

In contrast to Zr^{IV} complexes, monomeric Zr^{III} complexes are scarcely reported, most of the evidence being drawn by EPR spectra of Zr^{IV} derivatives reduced electrochemically or by chemical agents.[29] Some of them have been structurally characterized, however, such as the zirconocene^{III} diacetylide complex of the tweezer type in equation (9).[30]

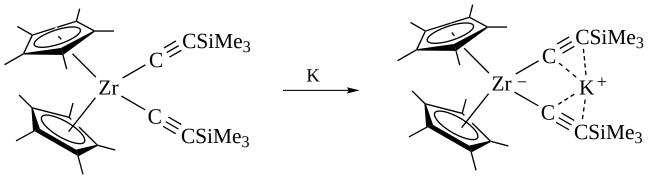

(9)

2.3 Bis Cyclopentadienyl Complexes of Zr^{II} and Hf^{II}

Despite the efforts expended in the synthesis and characterization of 14-electron zirconocenes and hafnocenes, no true monomeric M^{II} complexes have been isolated. Cp_2Zr and Cp_2Hf are transient species with a d^2 configuration. Similarly to titanocene (*see Titanocene*), they possess one electron lone-pair and two vacant orbitals, affording a reactivity comparable to that of carbenes. Consequently, these complexes can be trapped by electron-donating neutral ligands giving, for example, dicarbonyl compounds with CO.[1] Those fragments are able to react with a great number of unsaturated molecules to form a variety of metallacycles. Some of them give with other substrates organic, heterocyclic, or organometallic useful chemical reactions.

Cp_2M^{II} fragments were initially generated by reducing Cp_2MCl_2 and related Cp_2M^{IV} derivatives with $Mg/HgCl_2$, Na/naphtalene and Na/Hg.[31] For use Cp_2M^{II} species in organic synthesis applications, the crucial point is to find ligands that sufficiently stabilize the metallocene fragment, but that can be quantitatively released under mild conditions to generate the unstable and very active core complex. Two main ways have been developed which fill these requirements, as described in the following.

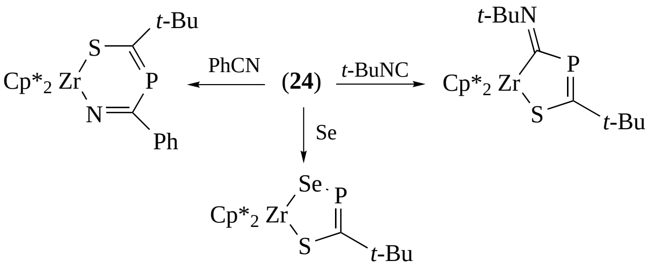

Scheme 9

2.3.1 *1-Butene Zirconocene*

Zirconocene dichloride with two equivalents of *n*-BuLi has been shown to generate Cp_2Zr(1-butene) (zirconocene equivalent also called Negishi's reagent) by a β-H abstraction (*see β-Hydride Elimination*) of dibutylzirconocene (Scheme 10).[1,31] Treatment of Cp_2ZrCl_2 with two equivalents of *t*-BuLi provides also a Cp_2Zr equivalent. Conversion of dialkylzirconocenes into the corresponding zirconacyclopropanes has been shown to be a nondissociative concerted process. Consequently, free Cp_2Zr is not generated at any time.

In the presence of π compounds, alkyne- or alkene-Cp_2Zr derivatives (eventually stabilized by complexation with trimethylphosphane) have been obtained. The potentialities of these reagents in synthetic chemistry will be developed in the Section 7.

2.3.2 *Bis(Trimethylsilyl)Acetylene Complexes*

Among the other potentially useful Cp_2Zr equivalents, the most important are stable and well-defined bis(trimethylsilyl)acetylene complexes (**25–28**).[32,33]

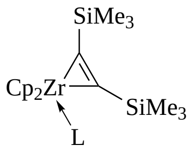

(**25**) L = thf
(**26**) L = py

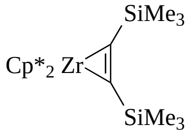

(**27**)

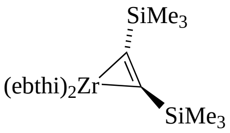

(**28**)

From their resonance forms, these complexes have been considered as acetylenic π-complexes (M^{II}) or as metallacyclopropenes (M^{IV}) which led to coupling reactions

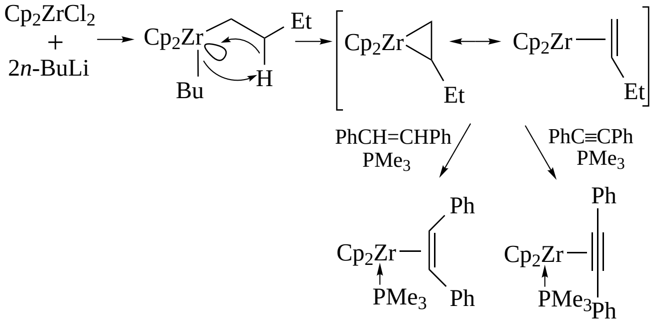

Scheme 10

of the alkyne (insertion into the metallacyclopropene) or to a substitution of the alkyne by a given substrate. Their behavior is, in all cases, best explained by the easy release of the silyl-substituted alkyne. In Zr chemistry, it seems that this result was obtained by an associative mechanism, while for titanium complexes, the substitution can also proceeds *via* a free titanocene (dissociative mechanism). The complexes (**25–28**) are able to react with many unsaturated molecules affording very original structures.

2.3.3 Reaction of Zirconocene Equivalents with Mono or Polyalkynes

The reaction of (**26**) with acetylene at low temperature gives rise to a five-membered zirconacycle that upon warming generates a dimeric complex with a bridging diacetylide group and an agostic (*see Agostic Bonding*) 1-alkenyl ligand (equation 10).**[31]**

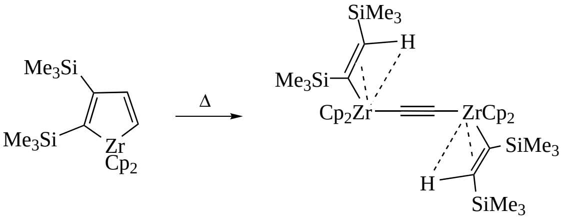

(10)

With not conjugated diynes of general formula RC≡CXC≡CR, a structural diversity is observed depending on the nature of the spacer X. Coordination or *exo–exo* coupling reactions affording metallacyclopentadienes are observed.**[31]** In addition, polymers, cyclodimers, cyclotrimers, cyclotetramers, and macrocycles**[34]** (*see Macrocycle*) that contain the metallacyclopentadiene unit have been obtained starting, for example, from $Me_3SiC{\equiv}C(C_6H_4)_nC{\equiv}CSiMe_3$ ($n = 1–4$), $Me_3SiC{\equiv}CC_6H_4(C_5H_3N)_2C_6H_4C{\equiv}CSiMe_3$, and $Me_3SiC{\equiv}C(C_5H_3N)_2C{\equiv}CSiMe_3$. Bis(alkynyl)silanes give access to an annelated zirconacyclobutene-silacyclobutene complex (Scheme 11).**[35]** The mechanism of the reaction might be rationalized by an initial coupling of the diyne to the zirconocene and a subsequent rearrangement of the intermediate complex *via* a zwitterionic zirconocene-ate (*see Ate Complexes*).

Depending on the nature of the Cp ligands, the metal, the stoichiometry, and the reaction conditions, very different complexes have been obtained by treatment of (**25–28**) with 1,3-butadiynes.**[31]** For instance, the formation of (**29**) and (**30**) results of cleavage of the C–C bond of the alkynes. The coupling of two alkyne units in the coordination sphere of the metal gives (**31**).**[32]**

Original metallacyclocumulenes were obtained from a 1:1 stoichiometric reaction between dialkyne and zirconocene (equation 11).**[36]** The unusual molecular structure of the five-membered zirconacycle (**32**) shows an almost planar arrangement containing three carbon–carbon double bonds.

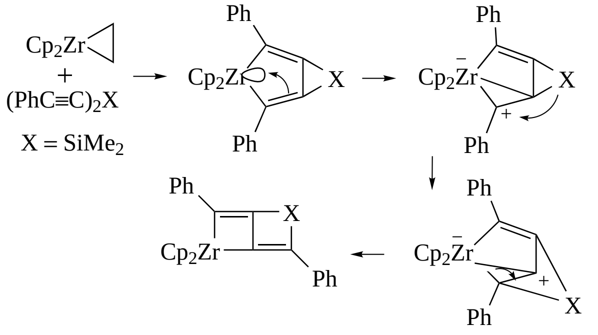

Scheme 11

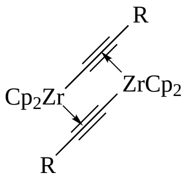

(**29**)

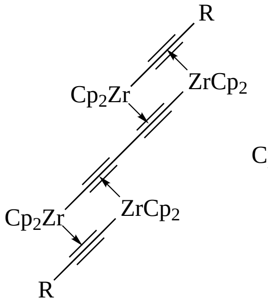

(**30**)

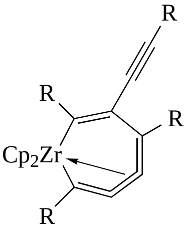

(**31**)

The central one is longer than the two others; this elongation has been ascribed to the intramolecular interaction of this bond with the metal center.

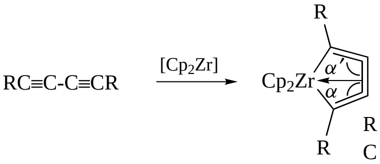

(**32**)

R = *t*-Bu:
C = C : 1.28, 1.31 and 1.29 Å
$\alpha = 150.0°$, $\alpha' = 147.2°$

(11)

In the Cp* series, the same structure has been obtained using the same procedure but as well, by irradiation of $Cp*_2Zr(\sigma\text{-}C{\equiv}CR)_2$. In the case of 2,2,7,7-tetramethyl-3,5-octadiyne, the activation of the methyl groups of a Cp* ligand and C–C coupling with the diyne have been observed (equation 12).**[37]**

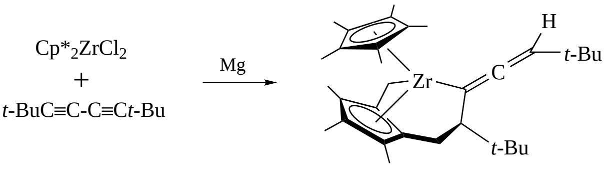

(12)

2.3.4 Reaction of Zirconocene Equivalents with Hetero Unsaturated Compounds

The reactions of complex (**25**) with carbonyl compounds show a strong dependence on the substituents leading to the substitution or elimination of the silyl-substituted acetylene or the insertion into the Zr–C bond.[31] Moreover, the reaction of methacrolein with (**25**) depends strongly of the solvent used: in hexane elimination of bis(trimethylsilyl)acetylene leads to the formation of dimer (**33**) while in THF insertion with the formation of zirconacycle (**34**) is observed.

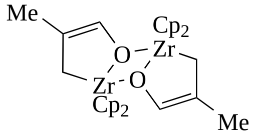

(**33**)

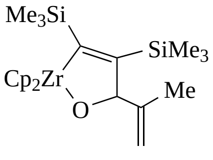

(**34**)

Various phenyl-substituted imines react with (**26**) in a manner that depends on the substituents present but in all cases, elimination of the alkyne is observed.[31] The imine PhN=CMePh affords the η^2-complex (**35**). On the contrary, with the ketimine HN=CPh$_2$, complex (**36**) is generated by hydrogen transfer. Two molecules of the aldimine PhN=CHPh are coupled to give a five-membered diamido complex (**37**). An unusual reaction with 2-vinylpyridine takes place starting from (**26**) or (**28**). Monoazadienes (**38**) are formed, in which the aromaticity of the pyridine ring has been lost.

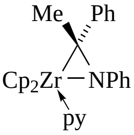

(**35**)

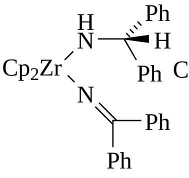

(**36**)

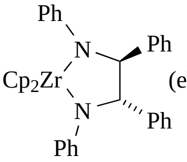

(**37**)

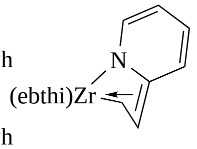

(**38**)

2.4 Mono Cyclopentadienyl Complexes of Zr^{IV} and Hf^{IV}

Mono Cp metallocenes are interesting as starting materials for the synthesis of mixed ring systems. The most efficient access to CpMCl$_3$ compounds is the radical cleavage of a Cp–M bond from Cp$_2$MCl$_2$ under irradiation. Thus the reaction of Cp$_2$ZrCl$_2$ with one equivalent of bromine yields the useful precursor CpZrCl$_2$Br.[38] Transmetalation from main group or alkali metal complexes is another widely used method.[1] Additionally, DME complexes of CpMCl$_3$ can be generated by ligand exchange reactions in good yields (*see Ligand Substitution*).[1]

Unusual nitrogen-stabilized Zr trichloride complex bearing pendant ligand (*see Pendant Groups*) can be obtained by reaction of zirconium tetrachloride on a 1:1 *rac*/*meso* distannyl Cp derivative (equation 13).[39]

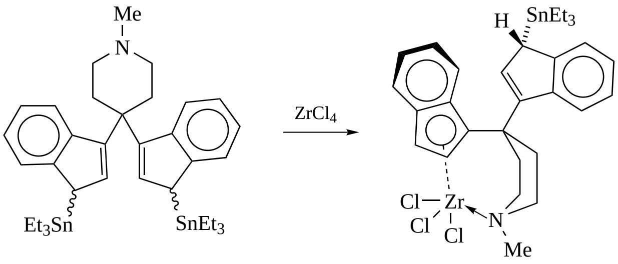

(13)

In general, the solubility of solvent-free complexes is very low. However, coordination of Zr with donor solvents gives more soluble compounds. Depending on the extent of the steric effect of the pentahapto ligand, solvent mono or bis adducts are obtained. However stronger electron-donating molecules such as phosphanes do not form adducts, according to the Lewis acidity of the metal.

2.5 Constrained-geometry (CG) Complexes

In homogeneous polymerization catalysis (*see Kaminsky Catalysts*), constrained-geometry (CG) catalysts differ from bis Cp metallocenes in their ability to readily incorporate α-olefins in copolymerization with ethylene. This ability is due to the open nature of the catalyst active site.

A method of preparation of CG complexes involves the metathetical reaction of the dilithio salt of $[(C_5R_4)X(NR^1)]^{2-}$ with an appropriate metal halide (equation 14). Nitrogen can be replaced by phosphorus atom.

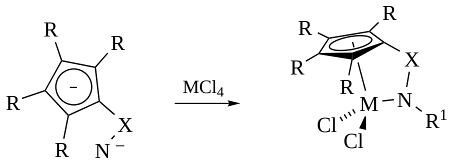

(14)

X = carbon chain
or heteroatom fragment (Si, Ge…)

Amine elimination reaction developed for metallocenes is another method (see Section 2). Immobilized CG complexes can be prepared by this way to form heterogeneous phase systems (*see Heterogenized Catalyst*) (equation 15).[40]

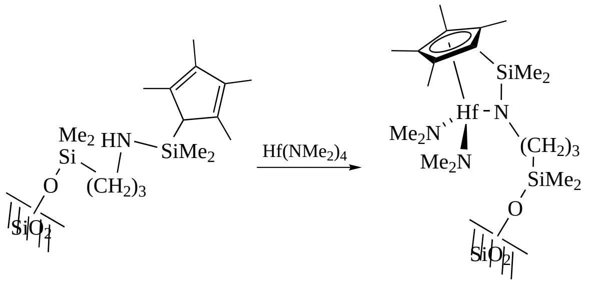

(15)

Independently of the interest of the CG complexes in polymerization catalysis, similar reactivity to that of metallocenes can be observed. For instance, the metathetical reaction of $[(C_5H_4)SiMe_2(N\textit{t}\text{-Bu})]ZrCl_2$ with $[Mg(C_4H_6)(thf)_2]_n$ affords the Zr-butadiene complex (**39**).[41]

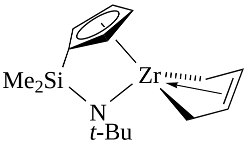

(**39**)

2.6 Mono Cyclopentadienyl Complexes with Low-valent Zr and Hf (M^{III}, M^{II}, and M^0)

Very few complexes of general formula (η^5-L)ZrXY have been characterized by EPR spectroscopy and even less have been isolated. They are generated by Na naphtalenide reduction, by UV irradiation of the appropriate metallocene, or by electroreduction of dialkyls. They can be stabilized by phosphane donors hold by the Cp rings (**40**).[42]

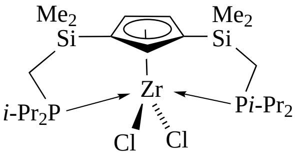

(**40**)

Addition of carbon monoxide to the Zr^{III} complex (**41**) stabilized by a tridentate ligand (*see Tridentate Ligand*) gives rise to an equal mixture of two diamagnetic products among which the rare mono Cp dicarbonyl Zr^{II} complex (**42**) (equation 16).[43]

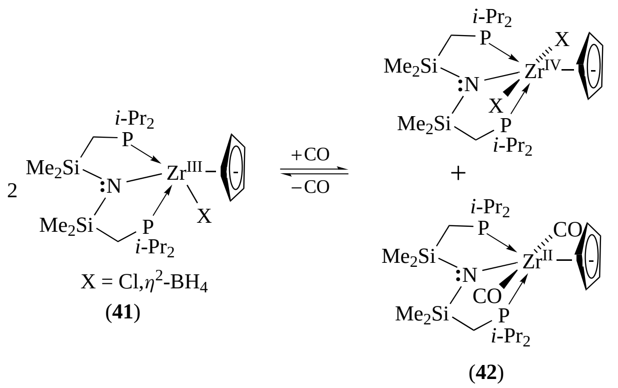

(16)

The metal^0 anionic salt, $CpM(CO)_4^-$ is reported as the result of the alkali metal naphtalenide reduction of the trichloride precursor in the presence of carbon monoxide.[44] Zr^0 and Hf^0 complexes containing α-bonded ligands, without Cp, are also known.[1]

2.7 Cationic Complexes

The chemistry of cationic d^0 16-electron $Cp_2MR(L)^+$ complexes, and d^0 14-electron $Cp_2M(R)^+$ has been largely developed, in particular, because these species can perform Ziegler-type alkene polymerizations (*see Ziegler–Natta Catalysts*) and can also be used as reagents in other organometallic syntheses. Usually, the zirconocene precursors are neutral complexes that first need *in situ*-activation before displaying cationic reactivity. Different general reactions for preparing cationic complexes have been developed.

The Lewis acid $B(C_6F_5)_3$ (*see Lewis Acids & Bases*), as well as the trityl salt $[Ph_3C][B(C_6F_5)_4]$, can abstract a methyl group from Cp_2ZrMe_2 and related zirconocenes to form $[Cp_2ZrMe]^+$.[31] A single-electron oxidation of dialkylzirconocenes with a ferricinium or a silver salt induces the formation of a cationic zirconocene (equation 17).[31]

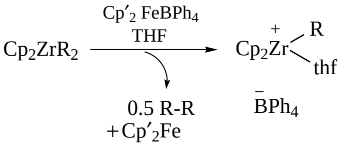

$$Cp_2ZrR_2 \xrightarrow[\text{THF}]{Cp'_2FeBPh_4} \overset{+}{Cp_2Zr}(R)(thf)\ \ \overset{-}{B}Ph_4 \qquad \downarrow 0.5\ R\text{-}R + Cp'_2Fe \tag{17}$$

Finally, the methylaluminoxane (MAO) $[Al(Me)O]_n$ can be involved in several ways in the generation of a cationic zirconocene species. It can serve as a methylation agent (conversion of Zr–Cl to Zr–Me), and as a Lewis acid in abstracting methyl groups. In the generation of polymerization catalysts from Cp_2ZrCl_2 and MAO, the active species has the supposed composition $[Cp_2ZrMe]^+$ $[Me\text{–}MAO]^-$.[45]

The structure of some cationic zirconocenes has been determined by spectroscopic methods and by X-ray crystallography (*see X-ray Crystallography*). None of these cations is ever completely free; they are either coordinated by an additional ligand (typically a solvent molecule), or they interact with their counterions.

The solvent-stabilized cations $[Cp'_2ZrR(solvent)]^+$ shows typical reactivity patterns (Scheme 12). Hydrogenolysis of the

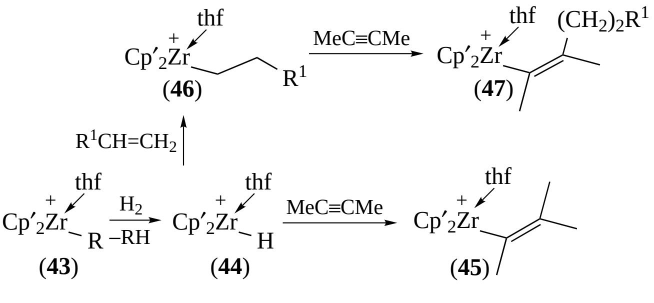

Scheme 12

starting cationic species (**43**) results in the formation of the hydride (**44**) which undergoes insertion of an alkyne or an alkene unit to yield (**45**) or (**46**) respectively. Moreover, the alkylzirconocene (**46**) can insert an alkyne to give an alkenyl zirconocene cation (**47**) (see Section 7.2). All these species can be isolated as complex salts with the counterion BPh_4^-. Hydride (**44**) is also a catalyst for ethene polymerization.[31]

Complexes of the general formula Cp_2ZrY_2 (Y = nonnucleophilic counterion) can be prepared by halide abstraction from Cp_2ZrCl_2 with AgY. The case of $Cp_2Zr(OTf)_2(thf)$ serves as a typical example.[46] Whereas it has been shown by X-ray structure determination that this is a neutral complex with covalently bound triflates, even a weak donor (e.g. solvent, substrate) will cause ionization in solution.

2.8 18-Electron Complexes

2.8.1 Anionic Complexes

Group 4 metallocenes being 16-electron derivatives, have an empty orbital that can undergo organometallate species formation. Thus, the electronegativity of Zr being greater than that of Li, intermediate formation of zirconate species can explain the reactivity of zirconacyclopentadienes with *n*-BuLi (Scheme 13).[31]

The anionic Zr^{II} intermediate (**48**) can also be involved in the photoassisted coupling reaction of alkynyl moieties.[47]

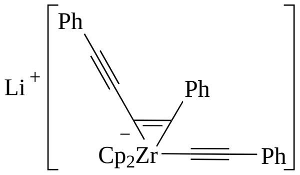

(**48**)

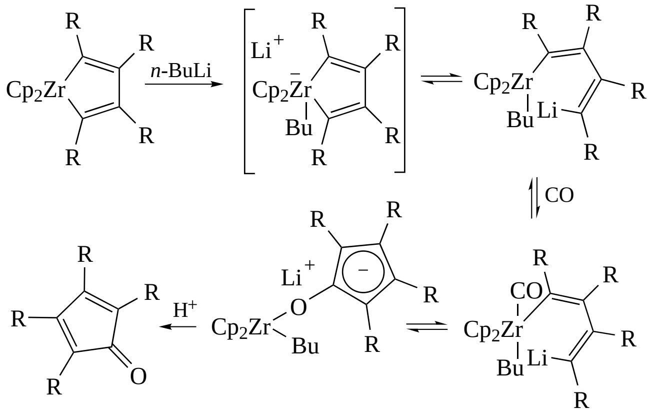

Scheme 13

2.8.2 Zwitterionic Metallocenes

Organozirconates. Zwitterionic zirconocene-ate (*see Ate Complexes*) intermediates have been evoked to explain some reaction mechanisms (see Section 2.3.3). In fact, electron transfer from an organic ligand to 16-electron metal center permits the generation of a carbocationic center which can, then, undergoes isomerization and rearrangement characteristic of carbocations.[48] It is now possible to isolate and characterize stable zwitterionic phosphonium zirconate complexes (equation 18).[49]

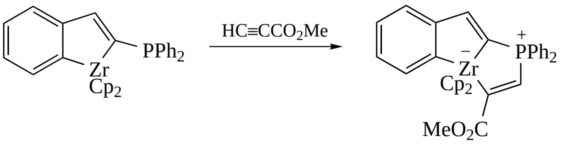

(18)

Similar reactions can be performed starting from various heteroallenes (CO_2, CS_2, RN=C=NR, RN=C=S, RN=C=O) giving stable monomeric five-coordinated anionic complexes. Addition of diazoalkane to phosphanozirconocenes leads to stable N-metal phosphazines (equation 19).

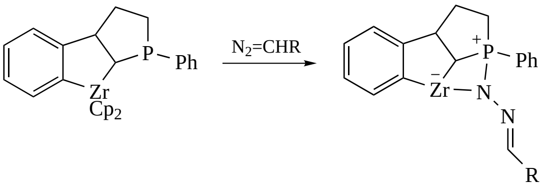

(19)

The formation of zirconate species can be performed even on the surface of dendritic systems, inducing the formation of multizwitterionic species.[50]

Some azazirconacyclopentene-substituted phosphanes activate the X–H bonds (X = C, O, N, P, S) of different reagents (Scheme 14).[51]

This is due to the combination of two factors:

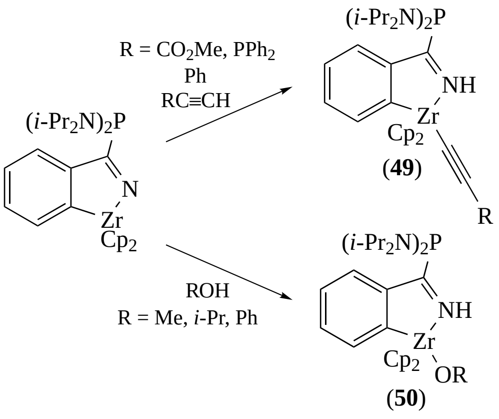

Scheme 14

- the presence of the phosphorus lone-pair in (**49**) or (**50**) increases the basicity of the cyclic imino nitrogen atom through delocalization along the P–C=N unit.
- the existence of a dative zirconium–nitrogen bond in (**49**) or (**50**) stabilizes the metal at 18 valence electrons. Thus, these structures can be described as betaines (**51**).

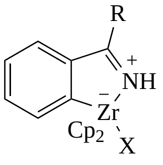

(**51**)

The resulting Zr–X bonds can be readily cleaved as shown by the reaction with diphenylchlorophosphane (equation 20).[51]

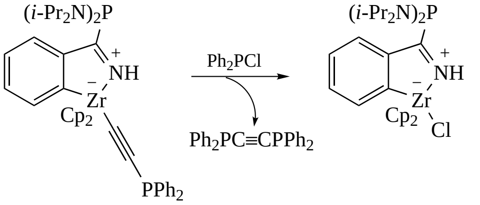

(20)

Zirconocene Boron-betaine. An interesting concept that can be applied to the synthesis of single-component metallocene Ziegler catalyst consists to covalently bind an anionic counterpart to the cationic framework.[52] The counterion can be attached either to an alkyl group linked to the metal or to one of the Cp ring.

Compounds of the first type can be obtained starting from butadiene zirconocene (with or without an *ansa* bridge). In the formation of (**52**), a pronounced property of cationic center is its ability to bind fluoride. The chemistry of these compounds reveals two important features (Scheme 15). First, through reaction of (**52**) with one equivalent of ethylene, a mono insertion product has been characterized. This requires that the next insertion is much slower and implies therefore that at early stages of the polymerization the charges remain in close proximity. Secondly, this type of zwitterions (*see Zwitterion*) is short-lived under catalytic conditions; after several insertions, terminaison occurs to produce a conventional nonzwitterionic active site.

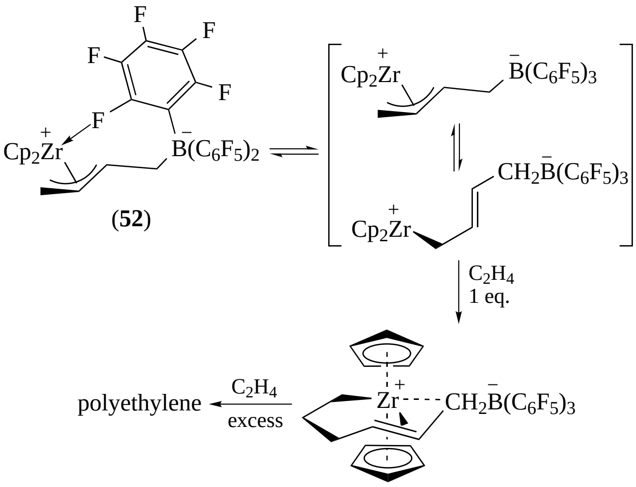

Scheme 15

Starting from half-sandwich zirconium 1,3-diene complexes and boron(trispentafluorophenyl) affords a way for synthesizing a triple-decker sandwich (*see Triple-decker Sandwich*) featuring an *ansa* borole-allyl ligand.[53] Other typical examples of zwitterionic complexes can be obtained starting from bis propynyl zirconocene and tris(pentafluorophenyl)borane.[54] When $B(C_6F_5)_3$ abstracts an alkynyl group from the bis acetylide (**53**), the borate alkyne inserts into the remaining Zr bond yielding zirconocene boron-betaine (**54**), which further reacts with two equivalents of isonitrile (Scheme 16).

Zwitterionic structures with a borate anion covalently attached to a cyclopentadienyl donor can be obtained by a number of synthetic approaches. In the known compounds, the means by which the borate is tethered to the ring has a significant impact on the properties of the zwitterions. In particular, the length of the tether connecting the ring with the borate is crucial for the stability and intramolecular ion–ion contacts. For example tris cyclopentadienyl zirconium betaine complex in which boron atom is directly bonded to Cp can be generated from boron substituted cyclopentadienyl anion (equation 21).[55]

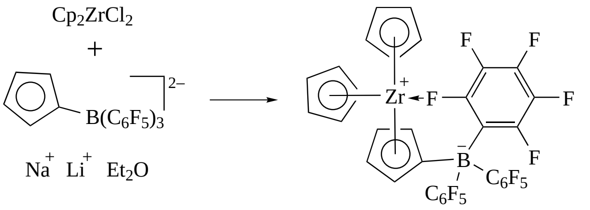

(21)

Most of zirconocene boron-betaines are single-component mediators of olefin polymerization and at least rival conventional catalysts with respect to productivity.

3 UNUSUAL COORDINATION GEOMETRIES AT CARBON STABILIZED BY GROUP 4 METALLOCENES

Independently of the classical four-coordinate tetrahedral, three-coordinate trigonal planar, or two-coordinate linear geometries at carbon (*see Coordination Geometries*), group

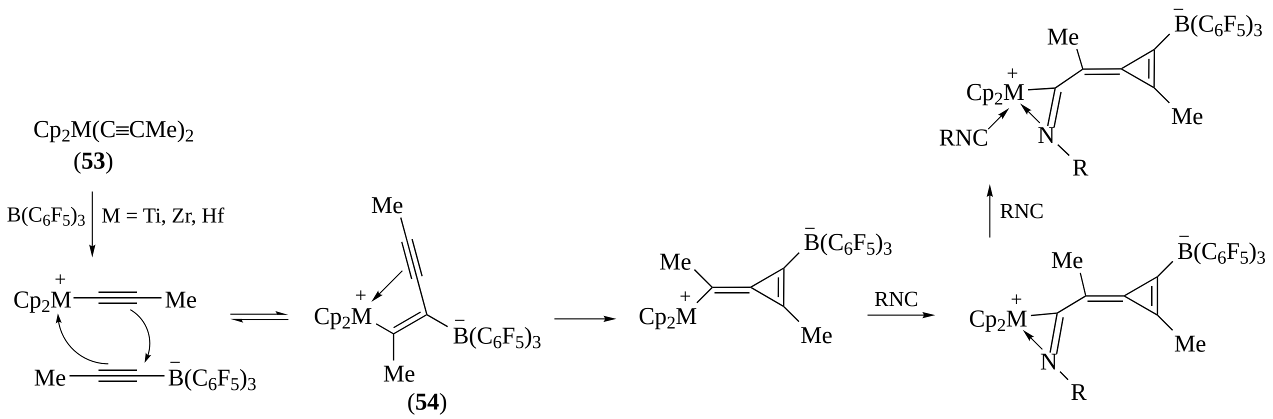

Scheme 16

4 metallocenes offer the opportunity to stabilize other unusual carbon geometries of extraordinary stability.[56] In these complexes, the Cp_2M units may serve as strong σ-donors (*see σ-Donor*) and σ-or π-acceptors. The assistance of the metal system can be obtained by two different ways: internal ion pairing (*see Ion Pairing*) and three-center-two-electron bonds.

3.1 Metal–carbon Ion Pair

When a 2-zirconaindane system is treated with one equivalent of the strong organometallic Lewis acid $B(C_6F_5)_3$ selective addition to one of the two methylene groups takes place (equation 22). The X-ray crystal structure of the obtained product (**55**) reveals the formation of a new ring system, which displays a strong internal ion pair interaction. The C4–B bond is strong (1.682(3) Å). The carbon atom C4 exhibits an ion pair interaction with the Zr center (bond lengths: C4–Zr 2.593(3) Å, C1−Zr 2.264(3) Å; angles C3–C4–B 119.1(3)°, Zr···C4–B 155.3(2)°, Zr···C4–C3 85.4 (2)°, Zr–C1–C2 93.5(2)°).[56]

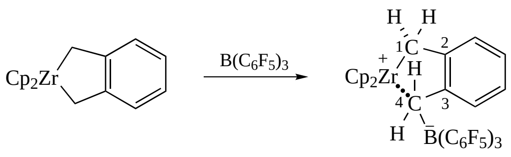

(**55**)

(22)

A similar complex was obtained by treatment of (*s-cis-*η^4-butadiene)(cot)zirconium with tris(pentafluorophenyl)borane (equation 23). As for (**55**), the complex (**56**) shows an internal Zr–C ion pair and gives rise to a five-membered metallacycle.[56]

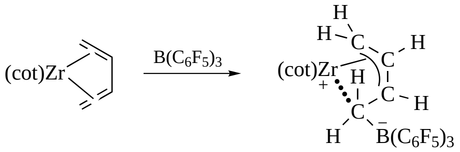

(**56**)

(23)

3.2 Planar-tetracoordinate Carbon

The formation of planar-tetracoordinate carbon is an unusual situation that can be obtained, for instance, by treatment of the *in situ*-generated $[Cp_2Zr–C{\equiv}C–CH_3]^+$ with one equivalent of starting bis(propynyl)zirconocene.[56] In homodimetallic system (**57**), C36 is a planar-tetracoordinate carbon atom. In fact, it is a part of a C=C double bond (C37−C36 1.317(8) Å). C36 is also connected to the acetylene carbon atom C35 by a Csp−Csp$^2\sigma$-bond (C36−C35 1.401(8) Å) and exhibits an unsymmetrical three-center-two-electron interaction with the adjacent Zr atom (C36−Zr1 2.435(6) Å; C36−Zr2 2.530(5) Å). The central core of three atoms around C36 is coplanar. An activation barrier of $\Delta G^{\neq}_{\text{rearr}}(190\,\text{K}) = 9.5 \pm 0.5\,\text{kcal mol}^{-1}$ was determined by studying the dynamic feature of (**57**).

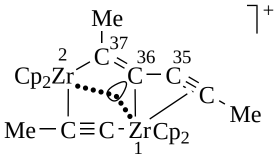

(**57**)

Most of the known examples of complexes incorporating a planar-tetracoordinate carbon contain alkyl, aryl, or even bulky substituents on the carbon center.[57] However, recently a way was found to prepare such compounds bearing hydrogen at this carbon atom.[58] A typical example was obtained by treatment of a dimeric zirconocene complex with the Brönsted acid *N*,*N*-dimethylanilinium tetraphenylborate (equation 24). Moreover, in homodinuclear complex (**58**), the low $^{13}C-^{1}H$ coupling constant (99 Hz) indicates an agnostic (*see Agostic Bonding*) CH···Zr2 interaction.

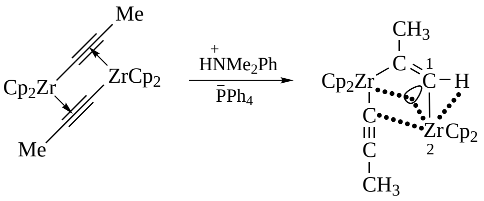

(**58**)

(24)

The formation of complexes containing planar-tetracoordinate carbon atoms is even more favorable by combination of group 4 metallocene and main group compound. A typical preparation involves reaction of dimethylzirconocene with the dimethylaluminium(phenylacetylide) dimer (equation 25).[57]

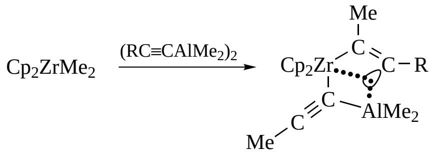

(25)

The group 4 benzynemetallocenes combined with boron, aluminum, and gallium building blocks were successfully employed in the stabilization of planar-tetracoordinate carbon compounds (equation 26).[56]

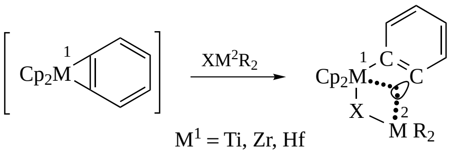

M^1 = Ti, Zr, Hf
M^2 = B, Al, Ga
X = H, alkyl

(26)

3.3 Stable C_{2v}–methane Derivative

A stable organometallic C_{2v}–methane derivative (**59**) was obtained starting from the (μ-vinyl)bis(zirconocene) complex with tris(pentafluorophenyl) borane.[59]

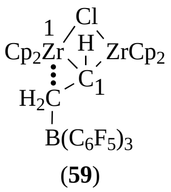

(**59**)

The $Cp_2Zr1\cdots C2H_2$–B interaction is probably electrostatic. It corresponds to an internal ion pair situation (Zr1–C2 2.600(3) Å, C1–C2–B 119.2(2)° and Zr1–C2–B 155.0(2)°) analogous of the complexes described previously (see Section 3.1). It seems that this distorted C_{2v}–methane-like coordination geometry is ca. 5 kcal mol^{-1} less stable than ideal tetrahedral geometry. Certainly the gain of energy afforded by the ion pair formation is responsible for the stability of homodinuclear complex (**59**).

3.4 Distorted Square-pyramidal Hypercoordinated Carbon Compounds

Protonation of (μ-alkenyl)bis(zirconocene) complexes under nonnucleophilic conditions takes a different regiochemical course than the $B(C_6F_5)_3$ addition (equation 27).[60] The X-ray crystal structure of (**60**) is consistent with distorted square-pyramidal pentacoordinated geometry at the central atom C1.

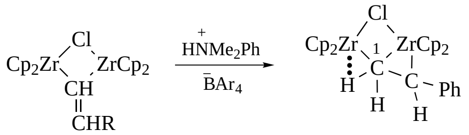

(**60**)

(27)

4 OTHER ANIONIC π-LIGANDS COMPLEXES

A variety of Zr and Hf complexes containing ligands that are isoelectronic to Cp have been developed for the purpose of creating analogs of classical metallocenes. The new ligands which might confer different properties on the derived metal complexes are essentially based on heterocyclic anions with elements of groups 13 to 16.

Substitution of a uninegative 6π electron Cp ligand with a dianionic 6π electron ligand provides a way to prepare metallocene analogs bearing an additional negative charge relative to the corresponding metallocenes. This is the case with aminoborole zirconate and hafnate that are isoelectronic to neutral metallocenes Cp_2MCl_2 (equation 28). These 16-electron derivatives represent an unusual class of molecules having both Lewis acidic and Lewis basic sites (*see Lewis Acids & Bases*) held in relatively close proximity. Aminoborollides were also used in the synthesis of neutral alkyl complexes of the type $Cp^*[C_4H_4BN(CHMe_2)_2]MR$ that are isoelectronic to metallocenium cations $[Cp_2MR]^+$.[61] These 14-electron compounds exhibit a rich reactivity and potentially useful applications in catalysis.

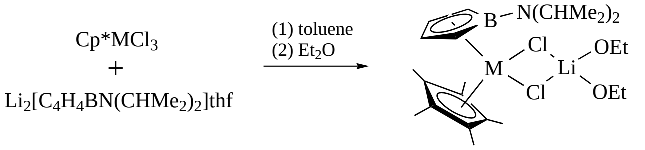

(28)

Other boron-containing ligands like 1,2- and 1,3-thiaborollides or 1,2-benzothiaborollide can also give rise to various metallocenes (**61, 62**) analogous to cyclopentadienyl or indenyl ones.

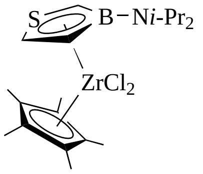

(**61**)

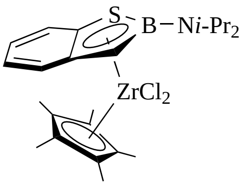

(**62**)

Monoanionic boratabenzene ligands are isoelectronic to cyclopentadienide anion and can be used to synthesize Zr^{IV} equivalent metallocenes (equation 29). A more congested complex of 9-phenyl-9-borata-anthracene (*C*1-symmetry) was obtained by a similar way.[62] Mono and bis boratabenzene complexes can also be prepared by reaction of a neutral boratabenzene-PMe_3 adduct with tetrabenzyl zirconium or hafnium.[63] Boratabenzene *ansa* metallocenes with CH_2–CH_2 or $Si(CH_3)_2$ bridges[64] as well as Cp-boratabenzene mixed complexes[65] or CG complexes were synthesized.

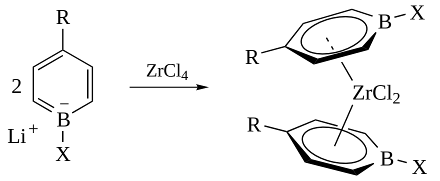

(29)

The coordination mode of those boron-containing ligands is quite different of the one of Cp rings. In 1,2-thiaborole systems, the zirconium atom is slip-distorted away from boron atom and the ligand is very close to η^4-coordination. The boratabenzene ring approached a η^5-coordination with the metal being much closer to the five ring carbon atoms than to the boron atom. In bridged structures by boron atoms, the boratabenzene ligand can be η^6-bonded to the metal center. The coordination mode also differs in oxidation state of the metal. The aminoboratabenzene is η^5-coordinated to the central metal in $(C_4H_4BN\textit{i}\text{-}Pr_2)_2ZrCl_2$ and η^6-bonded in $(C_4H_4BN\textit{i}\text{-}Pr_2)_2Zr(PMe_3)_2$. The reaction of the boratabenzene Zr^{II} complex with ethyne involves an unprecedented ring annelation to afford the complex (**63**), which contains a novel boron-containing ligand (equation 30).[66]

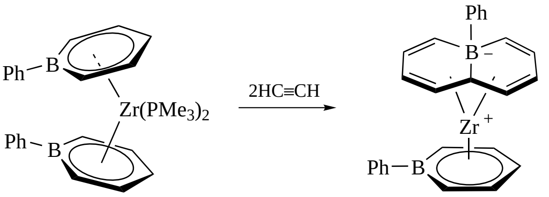

(**63**)

(30)

Another class of compounds whose ligation chemistry has been found to parallel that of Cp are the 7,8-C_2B_9- and 2,3-C_2B_4-carborane dianions. Like Cp, they are donor ligands in which six electrons are delocalized in π-type orbitals around a five-membered ring. The reaction of these carborane ligands with the appropriate metal reagent results in several mixed-ligand sandwich and full- and half-sandwich complexes of zirconium and hafnium.[67]

Neutral silolyl and germolyl metallocenes (**64–65**) have been prepared. The η^4-germole complex of Hf (**66**), resulting from a migration of a methyl group from Hf to Ge can be characterized during the course of these studies.[68]

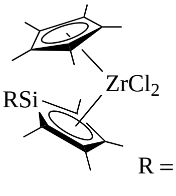

(**64**)

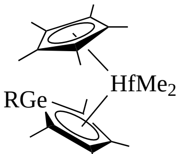

R = $SiMe_3$

(**65**)

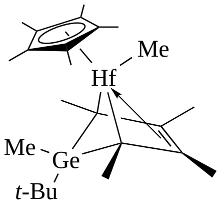

(**66**)

Phospholyl anions are also isoelectronic to Cp ligands, and these species readily complex Zr^{IV}.[1] A reduction reaction of $(C_4Me_4P)_2ZrCl_2$ by magnesium in THF gives transient diphosphazirconocene species which can be trapped by CO, bis trimethylsilyl acetylene, or 2-butyne to yield the corresponding dicarbonyl (**67**), zirconacyclopropene (**68**), and zirconacyclopentadiene (**69**).[69]

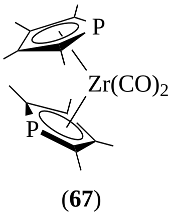

(**67**)

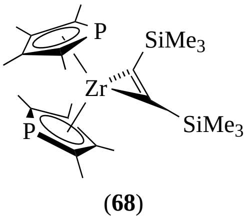

(**68**)

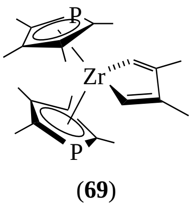

(**69**)

The cyclic π ligand derived from tropine in which an allyl group is completed with nitrogen as a two-electron donor atom leads to the synthesis of bis tropidinyl zirconium dichloride

(equation 31).[70]

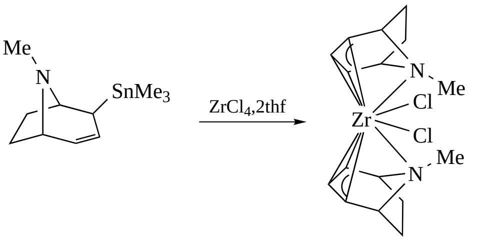

(31)

Complexes containing an open chain are also metallocenes analogs. For instance, pentadienyl anions (*see Pentadienyl Ligand*) form open metallocenes with transition metals as efficiently as do cyclopentadienyls.[1] Half-open metallocenes can be obtained in a similar way starting from $CpZrCl_2Br$ (Scheme 17).[38]

5 DINUCLEAR COMPLEXES

Dinuclear transition metal complexes (*see Dinuclear*) in which two reactive metal centers are maintained in close proximity have been largely studied owing to the opportunity provided to observe a synergism effect. In many cases, interest has focused on complexes containing early (electron deficient) and late (electron rich) transition metals in different oxidation states in which such interactions are more probable. They can combine the Lewis acidity of the early metals and the known ability of the late metals to activate small molecules.[71]

Except for some specific arrangements, homo and hetero dinuclear complexes can be classified within the seven main groups (**70–76**) in which for some of them one of the organometallic moieties can be viewed as a metalloligand for the other part.

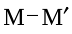

(**70**)

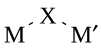

(**71**)

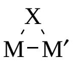

(**72**)

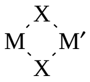

(**73**)

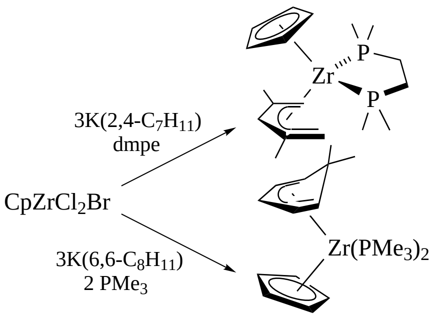

Scheme 17

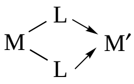

(**74**)

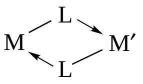

(**75**)

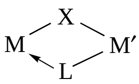

(**76**)

A few stable metal–metal bonded complexes (**70**) have been described. They are synthesized by reaction of a zirconium dichloride complex with an organometallate of iron or ruthenium[72,73] (see following section). CO_2 and CS_2 insertion into the polar metal–metal bond affords hetero dinuclear complexes of the second family (**71**) (Scheme 18).[73]

The μ-oxo complexes are representative complexes of the (**71**) group. They are readily prepared by the smooth hydrolysis of most metallocenes.[1] Arrangement (**71**) is also present in the methyl-bridged homo dinuclear species (**77**) formed by reaction of methylzirconocene cation with Cp_2ZrMe_2.

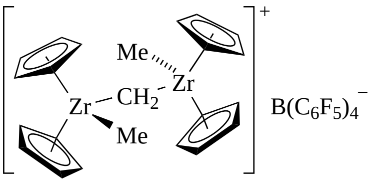

(**77**)

Dimeric association (**71**) can be obtained by an acid-base reaction between alkyl zirconocene and a terminal alkynyl ruthenium complex (equation 32). Surprisingly, the same reaction was observed with an iron acetylide opposed to Schwartz's reagent (*see Schwartz's Reagent*) (equation 33).[74]

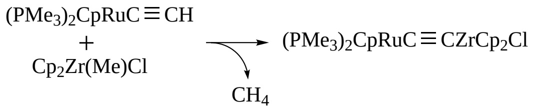

$$\mathrm{(PMe_3)_2CpRuC{\equiv}CH} + \mathrm{Cp_2Zr(Me)Cl} \xrightarrow[\mathrm{CH_4}]{} \mathrm{(PMe_3)_2CpRuC{\equiv}CZrCp_2Cl} \qquad (32)$$

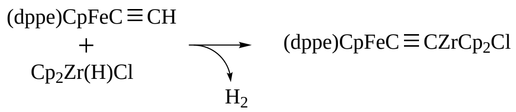

$$\mathrm{(dppe)CpFeC{\equiv}CH} + \mathrm{Cp_2Zr(H)Cl} \xrightarrow[\mathrm{H_2}]{} \mathrm{(dppe)CpFeC{\equiv}CZrCp_2Cl} \qquad (33)$$

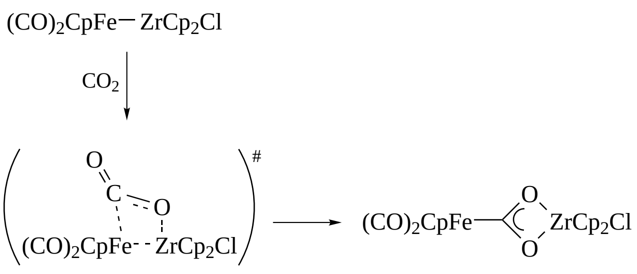

Scheme 18

Another early–late bimetallic complex related to the (**71**) group can be prepared by connecting the two Cp rings by a carbon bridge. Its reaction with an excess of $AlMe_3$ affords a doubly bridged hetero bimetallic complex (equation 34).[75]

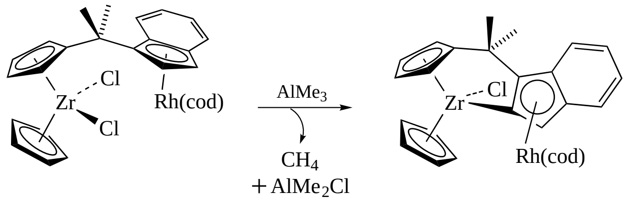

(34)

The complex (**78**) containing a zirconium–iridium bond and an imido bridge is the rare example of type (**72**) (Scheme 19). This early–late bimetallic compound contains two electronically unsaturated transition metals ($Zr = 16e^-$, $Ir = 16e^-$) which can make the structure interesting for testing the cooperative effect. Indeed, its reactivity with a variety of carbon-heteraoatom bonds results in cleavage of the metal–metal bond involving both metal centers. For instance incorporation of carbon dioxide produces a metallacyclopentane with a bridging metallacycle ester moiety.[76]

With various nitriles, two different hetero dinuclear complexes with arrangement (**73**) are obtained (equation 35). The formation of the cyclometalated species (**79**) involves a hydrogen transfer from a Cp* methyl group to the electrophilic carbon center of the nitrile in an intermediate fulvene complex. Kinetic results indicate that a second molecule of nitrile catalyzes the conversion of this fulvene intermediate into (**80**).[76]

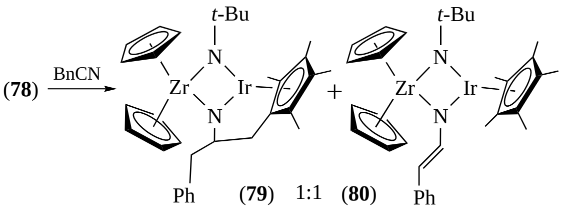

(35)

Many other examples of complexes of group (**73**) have been described. In particular, four-membered homo or hetero bimetallacyclic compounds can be obtained by simple way (equation 36).[76,77] In $Cp_2Zr(\mu\text{-}SMe)_2RuCp^*Cl$, the four atoms of the ZrS_2Ru core lie in a plane, the two methyl groups on the sulfur atoms being in *syn* conformation in solid state. On the contrary, in complex $Cp_2Zr(\mu\text{-}Nt\text{-}Bu)_2IrCp^*$, the four-membered Ir–Zr–N_2 ring is puckered (fold angle 17.6°), and the nitrogen atoms are planar, indicating π-donation to the formally electronically unsaturated Ir and Zr centers. The Zr–Ir distance is 0.3 Å longer than Zr–Ir single bonds, indicating that there is little direct Zr–Ir interaction. A homobimetallic eight-membered ring complex $[Cp_2Zr(\mu\text{-}O_2BPh)]_2$ can be generated by reaction of dimethylzirconocene with phenylboronic anhydride.[78] In this dimer, the metal centers are positioned above and below the approximate plane defined by the boron and oxygen atoms, generating a chair like conformation within the heterometallacycle.

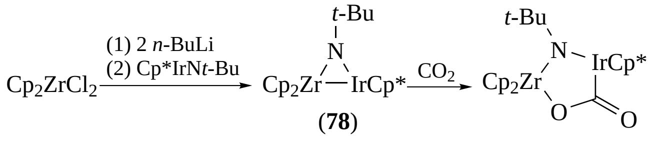

Scheme 19

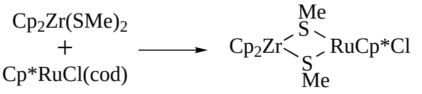

$$Cp_2Zr(SMe)_2 + Cp^*RuCl(cod) \longrightarrow Cp_2Zr(\mu\text{-}SMe)_2RuCp^*Cl \qquad (36)$$

When the arrangement (**74**) is present in early–late transition metal complexes, the bridging ligand can be a substituent of the Cp ligands. For example, hetero bimetallic complex (**81**) is obtained starting from $(Ph_2PCp)_2MCl_2$ and $Re(CO)_5Cl$. The second metal fragment is anchored through the phosphane substituents on the Cp ring.[79] Substitution reactions are very difficult on complex (**81**). Only, careful addition of a stoichiometric amount of $LiAlH_4$ produced a small quantity of a particular dihydride (equation 37).

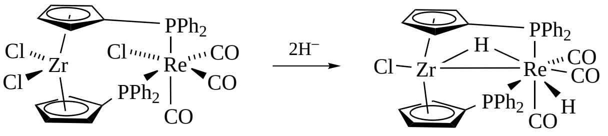

(**81**)

(37)

Even, $C_5H_4PPh_2$-bridged Zr^{II}–Mo^0 complexes (**82**) can be obtained upon treatment of $[Cl(Me)Zr(\mu\text{-}C_5H_4PPh_2)_2Mo(CO)_3L]$ ($L = CO$, PMe_3) with cyclohexenyllithium and trimethylphosphane.

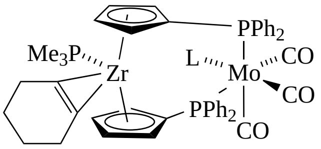

(**82**)

Chiral C_2-symmetric early–late complexes can be obtained *via* similar complexation starting from bis phosphinoenolato zirconocene.[80] Assembly of phenyl-substituted phosphametallocene and $[(binap)Rh(cod)]^+$ leads also to a chiral hetero dinuclear complex. The unprecedented thermal room temperature isomerization of Zr derivative was exploited to achieve its dynamic resolution producing enantiopure bimetallic *ansa* metallocene.[81]

The twofold deprotonation of a hydrosulfide zirconocene with the appropriate rhodium compound results in the clean formation of d^0–d^8 trinuclear complex (equation 38).**[82]**

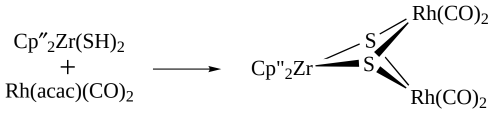

Cp″ = 1,3-disubstituted Cp

(38)

Dimeric associations (**75**) are typical of some low oxidation state and coordinatively unsaturated complexes that spontaneously exhibit a tendency to completely fill the valence electronic shell around the metal. Dinuclear dihydride $[(C_5H_4Me)_2ZrH(\mu\text{-}H)]_2$, for which the two metallocene-H units are joined by two Zr–H–Zr (two-electron-three-center bonds) are examples of this family.**[1]**

Alkynylchalcogenato ruthenium^{II} complexes react with zirconocene to give rise to heterobimetallic early–late dissymmetrically bridged complexes of family (**76**) (equation 39).**[83]** In those specific complexes, the two metal centers are linked by μ-chalcogenido and μ-σ, π-alkynyl moieties. The acetylenic bridge is unsymmetrical because the terminal carbon of alkynyl is σ-bonded to ruthenium, while zirconium interacts with both alkynyl carbons in a side-on fashion.

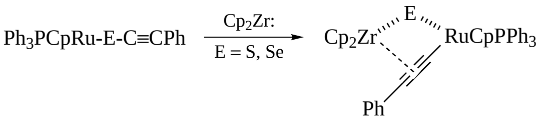

(39)

6 COMPLEXES OF Zr^{IV} AND Hf^{IV} LACKING π-LIGANDS

Beside the historical dominance of metallocenes and other cyclopentadienyl-based complexes, nonmetallocene complexes of group 4 have recently been the subject of renewed interest owing to the fact that new ligand environments might result in novel patterns of reactivity. Several bi, tri, or tetradentate ligands (*see Bidentate Ligand*; *Tridentate Ligand*; *Tetradentate Ligand*) have been employed to build early transition metal complexes. Except for some specific arrangements, such systems can be classified within the following families (**83**) to (**90**).

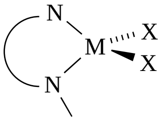

(83)

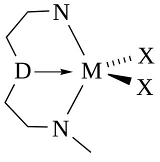

(84)

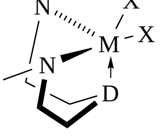

(85)

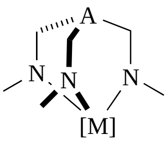

(86)

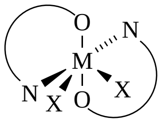

(87)

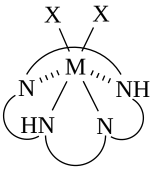

(88)

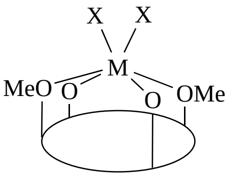

(89)

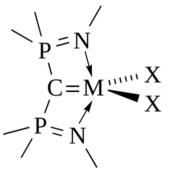

(90)

X = Cl, CH_2Ph
D = donor atom
(N, P)
A = carbon or
boron atom
or carbocycle

The 1,1′-ferrocenediyl-bridged ligand system $Fe[(C_5H_4)NPh]_2$ give access to redox-active chelate complexes of the type (**83**).**[84]**

One of the issues surrounding group 4 complexes of the type (**84**) or (**85**), which have a central donor atom and arms between the donor and the two nitrogen atoms, is that the geometries *mer* (like (**84**)) or *fac* (like (**85**)) mainly influence the reactivity of the metal center. By using phosphorus atom as the donor, it is possible to force the geometry to be *fac*, in order to finely adjust the steric hindrance for catalytic applications (equation 40).**[85]**

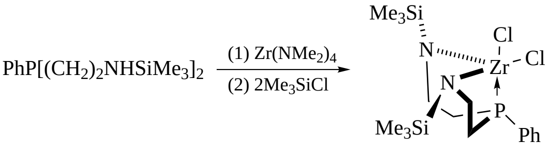

(40)

C_3-symmetrical tripodal ligands have been used to obtain amido complexes of family (**86**). If chiral substituents are present in the ligand periphery, some stereo discrimination is observed in the reaction with several chiral ketones and aldehydes.**[86]** On the other hand, such systems can generate early–late heterobimetallics with metal–metal bonds (equation 41). Reaction of (**91**) with MeNC as well as the heteroallenes CO_2, CS_2, RNCO and RNCS led to insertion into the polar metal–metal bond.**[72]** Tris (pyrazolyl)borate (*see Tris(pyrazolyl)borates*) Zr and Hf complexes are other interesting examples of the type (**86**). In combination with MAO, they give promising results in ethylene and ethylene/hexene polymerizations. Substitution of these sterically crowded ligands allows adjustements of the environment of the active site to the monomer.[87]

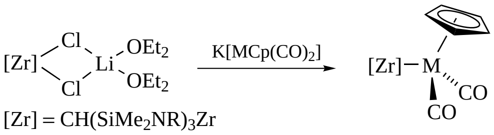

(41)

$[Zr] = CH(SiMe_2NR)_3Zr$
M = Fe, Ru

(**91**)

Bis 8-quinolinato metal complexes are representative examples of distorted octahedral structures of the type (**87**). It was noted that these systems bear a topological resemblance to the chiral, octahedral, active metal sites that have been proposed for supported Ziegler-Natta catalysts, and are interesting for modeling catalytic properties. Similar comportment has been observed with diamine bis (phenolate) ligands.[88]

Tetraazamacrocycles ancillary ligands including porphyrins have been used to prepare numerous group 4 organometallic complexes (**88**). These ligands are formally 12-electron donors to metal centers. Cationic tropocoronand group 4 organometallic complexes were found to generate differences in the Lewis acidity of the metal in comparison with their metallocene analogues. Thus, the use of tropocoronand ligands influences both the insertion chemistry and the structural properties of the resulting complexes.[89]

Similar behavior is observed for calix[4]arene (*see Calixarenes*) complexes of the type (**89**).[90] Moreover, the oxygen donor atoms are particularly appropriate for the oxophilic early transition metals. A rich chemistry has been developed with complexes containing zirconium–carbon bonds. In this area, aryne zirconocene compounds can be thermally generated and isolated without trimethylphosphane additional coordination. Zirconium-butadiene chemistry has been explored as well and constitutes a source of zirconium^{II} complexes.

Complexes of type (**90**) represent a new class of zirconium hydrocarbyl derivatives in which a strong metal carbene interaction in a pincer ligand structure is formed.[91] The crystal structure of such complexes shows a short metal carbon link common to two fused four-membered rings which are almost coplanar.

7 NEUTRAL ORGANOZIRCONIUM COMPLEXES IN ORGANIC AND ORGANOMETALLIC SYNTHESIS

For some years, organozirconium complexes are among the most useful reagents in organic, heterocyclic, and organometallic synthesis.[31] The success of organozirconium reagents in synthesis can be explained in terms of chemo, regio (*see Regioselectivity*), diastereo, and enantioselectivity (*see Enantioselectivity*). These compounds are generally able to discriminate between similar functionalities that differ only slightly in their steric and/or electronic environment.

7.1 Hydrozirconation

The availability of the Schwartz's reagent $Cp_2Zr(H)Cl$ (*see Schwartz's Reagent*) and its versatile behavior explain its extensive use in organic chemistry.[1] The scope of hydrozirconation (*see Hydrozirconation*) with respect to both substrate structure and chemoselectivity lies somewhere between those of hydroboration (*see Hydroboration*) and hydroalumination.

7.1.1 Hydrozirconation and Subsequent Quenching

The clean *cis* addition of the Schwartz's reagent across an alkyne affords a good way to functionalize alkenes. Starting from an alkyne bearing a methyl group, which has been known to favor placement of the zirconium species at the least hindered site, provides extremely valuable access to natural products after hydrozirconation (*see Hydrozirconation*), I_2 quenching and subsequent Stille coupling with vinylstannane (e.g. *reveromycin B*).[92]

Hydrozirconation is a useful way to produce *gem* metallozirconocenes of general formula (**92**) and (**93**), which are interesting reagents in organic synthesis.

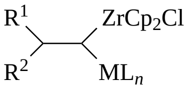

(**92**)

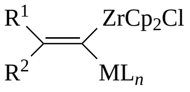

(**93**)

M = Al, B, Li, Ga, Sn, Zn, Zr

In fact, cleavage of the carbon–zirconium bond occurs classically with various electrophiles (*see Electrophile*), generally under mild conditions. In addition, the other carbon–metal bond in *gem* metallozirconocenes undergoes a broad range of transformations. The different reactivities of the carbon–metal and carbon–zirconium bonds are the results of the difference of electronegativity of the two metal centers and the two different bond polarities.

Aluminiozirconocene complexes can be obtained by the addition of an organoaluminium hydride to an alkenylzirconium complex or by the addition of the Schwartz's reagent to an alkenylaluminium derivative.[31] Hydrozirconation of phenyl(trimethylsilyl) acetylene gives the corresponding alkenylzirconocene chloride, that generates by treatment with $AlMe_3$ a stable complex with a planar-tetracoordinate carbon atom (see Section 3).[31] Similar Zr/Al and Zr/Ga structures can also be obtained by trapping a transient μ-alkyne complex with a Lewis acidic main group organometallic. Benzynezirconocene can also give rise to such complexes by treatment with trimethylgallium.[31]

Gem boriozirconocene alkanes can be prepared by either hydrozirconation of alkenylboranes or hydroboration of

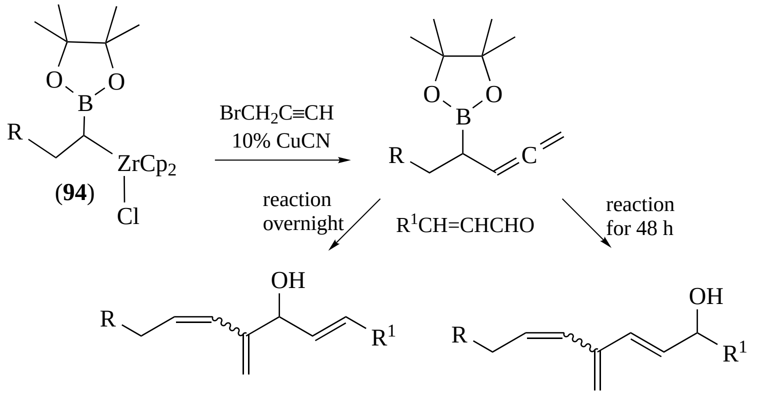

Scheme 20

alkenylzirconium compounds (equation 42).**31** However, these compounds proved to be unstable.

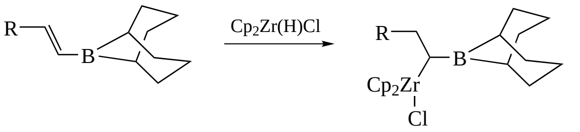

(42)

Boronates are more stable since they are stabilized owing to the donor effect of oxygen lone-pairs to the empty orbital of the boron. The two different carbon–metal bonds afford particular reactivity. For example, addition of propargylbromide on (**94**) in presence of a catalytic amount of copper$^{\text{I}}$ cyanide undergoes a carbon–carbon bond formation with exclusive cleavage of the C–Zr bond. The subsequent borylallene, by treatment with α,β-unsaturated aldehydes, affords two trienes, depending on the reaction conditions (Scheme 20).

Other classical reactions such as halogenation or amination with zirconium and boron compounds respectively are possible starting from 1,1-boriozirconocene complexes.

In boriozirconocene alkenes, the chemistry of Csp^2–Zr and Csp^2–B bonds differ considerably and this feature allows a sequential route to substituted alkenes.**93** Furthermore, cleavage of the two types of bonds generally occurs with retention of geometry. On the other hand, heating of alkynezirconocene complexes with 9-BBN, to 80–90 °C, affords a bimetallic complex (**95**) showing a planar-tetracoordinate carbon and an *iso*-BBN structure.

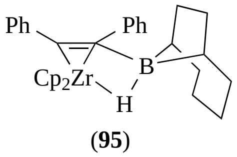

(**95**)

The addition of Cp$_2$Zr(H)Cl to trialkylstannylacetylenes leads to 1,1-stanniozirconocenes that formally represent stereodefined 1,1-dianion equivalents.**31** Starting from this compound and according to the difference of exchange rate Sn/Br and Zr/Br, it is possible to generate with complete stereocontrol (*see Stereochemistry*) bromoiodoalkenes. Combination of Zr-promoted bicyclization and properties of 1,1-stanniozirconocenes offers opportunities to synthesize some natural products.**31**

Addition of Cp$_2$Zr(H)Cl to an alkenylzinc halide affords relatively unstable 1,1-bimetallics of Zn and Zr. Addition of an aldehyde or a ketone is a general way to synthesize (*E*)-alkenes. Remarkably, the hydrozirconation can be applied to functionalized alkenylzinc reagents bearing an ester, chloride or cyano functionality (equation 43).**31**

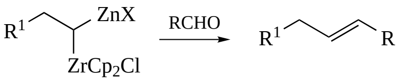

(43)

1,1-siliciozirconocene can be converted as well by quenching with arylselenylbromide to an array of vinylselenides which may be further transformed into chain-elongated materials (equation 44).**31** In these products the selenide and the silane groups can be substituted: the aryl selenide by copper-catalyzed couplings with Grignard reagents, and the silicon by displacement with electrophiles. Analogous procedures using disulfide or sulfonyl chloride as quenching agent give rise to vinyl sulfides and sulfones.**31**

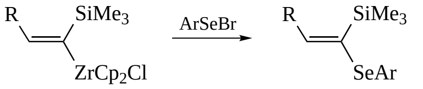

(44)

An overview of the hydrozirconation of alkynyl sulfones reveals many variations in the regiochemistry. Starting from arylacetylenic sulfoxides, the hydrozirconation classically takes place in a *cis* fashion, with zirconium in the α-position

(equation 45).[31]

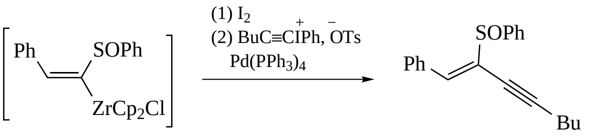
Ph
SOPh
ZrCp$_2$Cl
(1) I$_2$
(2) BuC≡C$\overset{+}{\text{I}}$Ph, $\overset{-}{\text{O}}$Ts
Pd(PPh$_3$)$_4$
SOPh
Ph
Bu

(45)

Hydrozirconation can be applied to heteroatomic systems affording original compounds. In this way, cyanophosphanes react cleanly with the Schwartz's reagent, the metal being linked to the more electronegative atom of the double bond. Quenching with many main group electrophiles affords a large variety of *C*-phosphanyl-*N*-phosphanyl or *N*-boranylimines (**96**) (Scheme 21).

Treatment of dicyanophosphanes with one equivalent of the Schwartz's reagent leads to a substitution that gives the stable hydrocyanophosphanes.[94] Further addition of one equivalent of $Cp_2Zr(H)Cl$ to the latter ones affords the primary phosphane R–PH_2 (R=Me) or the aldimino secondary phosphane (**97**). At room temperature, a [1,3]-H sigmatropic rearrangement is observed for (**97**), giving a *N*-zirconated phosphaalkene (equation 46).

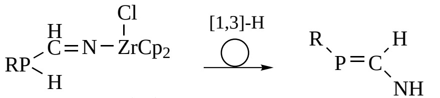

(**97**) R = *t*-Bu, Mes

(46)

Dicyanophosphane (R = N*i*-Pr_2) undergoes a true hydrozirconation reaction with the formation of the aldiminocyanophosphane (**98**) and of a dihydrozirconated compound after further addition of one equivalent of $Cp_2Zr(H)Cl$ (equation 47).[94]

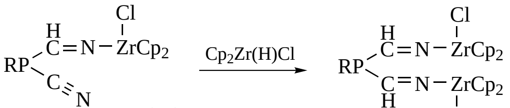

(**98**) R = N*i*-Pr_2

(47)

7.1.2 Ring-forming and Ring-opening Reactions

The Schwartz's reagent (*see Schwartz's Reagent*) allows ring formation from substrates possessing both oxirane and alkene functionalities (equation 48).[31] Based on *in situ* NMR analyses, it has been shown that the mechanism proceeds by clean inversion at the reacting oxirane center. No reaction takes place in the absence of the Lewis acid.

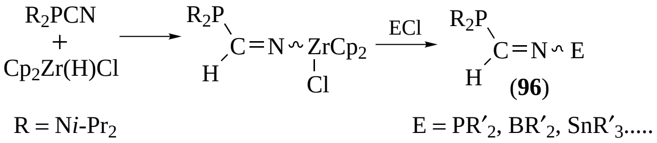

Scheme 21

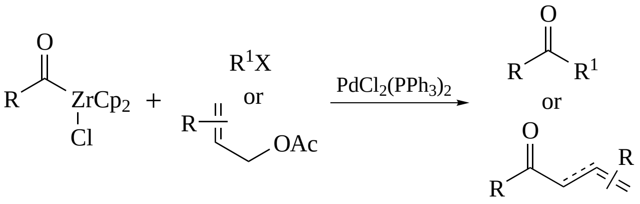

Scheme 22

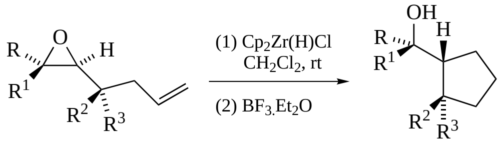

(48)

Hydrozirconation (*see Hydrozirconation*) of phosphaimines, phosphaalkenes, or bis(imino)phosphorane takes place with the formation of various three- or four-membered phosphazirconacycles.[31]

Ring-opening reactions of oxygen heterocycles such as dihydrofuran or dihydropyran are initiated by Schwartz's reagent. The nature of the resulting complex depends on the stoichiometry of the reaction. With one equivalent of $Cp_2Zr(H)Cl$, the linear derivative (**99**) is obtained by migration of the Cp_2ZrCl fragment initiated by the oxophilicity of Zr (equation 49). The action of two equivalents of $Cp_2Zr(H)Cl$ leads directly to a dihydrozirconated complex, precursor of phosphinito-phosphane by a Zr/P exchange.[95]

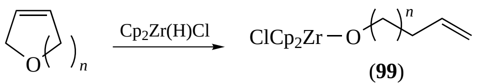

n = 1, 2

(**99**)

(49)

7.1.3 Acyl Zirconocenes

Acylzirconocene chlorides are easily accessible in a one-pot procedure through the hydrozirconation (*see Hydrozirconation*) of alkene or alkyne derivatives with the Schwartz's reagent and subsequent migratory insertion (*see Migratory Insertion*) of carbon monoxide into the alkyl- or alkenyl−zirconium bond. The stability of the acylzirconocene chlorides is remarkable at room temperature, and consequently allows many applications in organic synthesis.

Classically, the acylzirconocene chlorides can be converted into aldehydes, carboxylic acids, esters, and acyl halides. Recently, the usefulness of acylzirconocenes has been extended. In fact, these unmasked acyl anions directly add to aldehydes and imines affording α-hydroxy or α-amino ketones, respectively.[31] The reaction of acylzirconocene chlorides with imines also proceeds under Brønsted acid-catalyzed conditions, even with aqueous acids.[31]

Several palladium-catalyzed processes have also been developed for carbon–carbon bond formation based on acyl zirconocenes. Both alkylations and acylations occurred, the best results being obtained with allylic acetates as coupling partners. Selective additions to α,β-enones can be achieved starting from acylzirconocene chlorides with cyclohexanone in the presence of a palladium catalyst. Even more, the regioselectivity (*see Regioselectivity*) can be very easily controlled by the choice of the catalytic system ($Pd(OAc)_2$,$BF_3{\cdot}Et_2O$ for 1,4-addition and $PdCl_2(PPh_3)_2$ for 1,2-one). An enantioselective (*see Enantioselectivity*) version of the 1,2-addition has been recently developed using (*R*)–MOP ligand in place of triphenylphosphane (66% ee).[31] α,β-ynones can also react with acylzirconocene chlorides affording easily cyclopentenone derivatives.[96]

Metal catalyzed cross-coupling reactions with acylzirconocene chlorides and various organic halides or acetates can give rise to unsymmetrical ketones or a mixture of β,γ- and α,β-unsaturated ketones (Scheme 22). The advantage of the use of a Cu^I catalyst instead of a Pd catalyst is to avoid the undesirable formation of α,β-unsaturated ketone.[31]

7.1.4 Allylic Zirconocenes

Allylic zirconocenes, generated by hydrozirconation (*see Hydrozirconation*) of allenic systems, react with terminal alkynes when activated with MAO to regioselectively afford 1,4-dienes.[31] The same MAO catalyzed process, applied to haloalkynes, leads to excellent yields of the 1,4-enyne (**100**) (Scheme 23).[97]

7.1.5 Cross-coupling Reactions

Combination of hydrozirconation (*see Hydrozirconation*) process with other catalyzed reactions represents a great interest in the synthesis of polyenic natural products. The synthesis of the backbone of the antibiotic *Lissoclinolide* can be realized by hydrozirconation with i-$BuZrCp_2Cl$ and subsequent Pd-catalyzed coupling (*see Coupling*) of the fragments.[98] Similar cross-coupling reactions of vinylzirconocenes can give rise very smoothly to a variety of vinyl selenide containing materials, which can be further transformed into stereodefined butadienes (equation 50).[99]

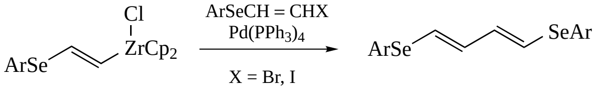

(50)

Treatment of alkyl or alkenylzirconium with Cu^I or Zn^{II} salts *via* stoichiometric or catalytic processes provides new possibilities for improving coupling reactions of these species. For example, cross-coupling reactions of alkylzirconocenes to unsaturated oxazolidinones take place in the presence of $CuBr{\cdot}SMe_2$. Hydrozirconation-transmetalation of terminal alkynes can be effective using Me_2Zn at low temperatures in toluene, the resulting zinc species being able to react with aldehydes to produce racemic allylic alcohols. Even more, a nonracemic version of this reaction has been developed with excellent levels of enantioselectivity (*see Enantioselectivity*).[100] Another combination of hydrozirconation and zinc mediated reactions can produce reductive coupling of allenes and alkynes affording finally an α-adduct *via* a zinca-Claisen rearrangement (equation 51).[31]

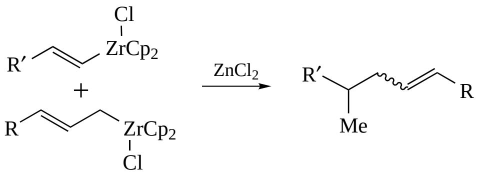

(51)

On the other hand, hydrozirconation-transmetalation to zinc, when carried out in THF, can be used to prepare allylic amines. When carried out in CH_2Cl_2, however, a different reaction pathway is followed (Scheme 24).[101] Even more, with a different order of introduction of the reagents, it is possible to obtain diastereoselectively homoallylic amines instead of the expected aminocyclopropanes.[31]

7.2 Carbozirconation

Migratory insertion (*see Migratory Insertion*) and carbozirconation (*see Carbometalation*) represent two C–C bond formation processes in which Zr–C bonds directly participate. The synthetic scope of migratory insertion in organozirconium

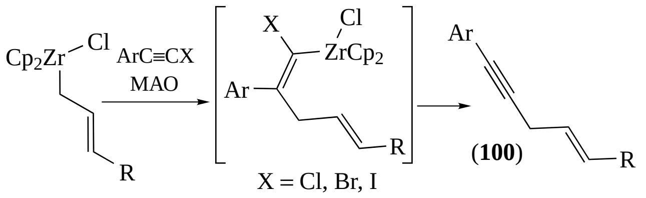

Scheme 23

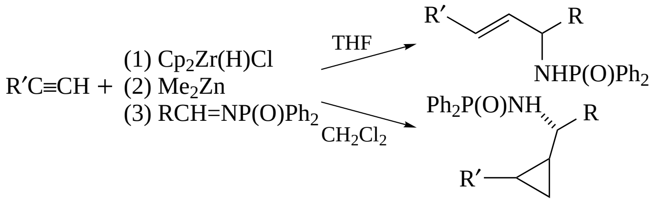

Scheme 24

chemistry is quite limited to the use of carbon monoxide (*see CO Insertion*. Carbozirconation requires dipolar (and mostly bimetallic) activation and/or very reactive small-ring zirconacycles, especially three-membered ones that can undergo cyclic carbozirconation. These reactions can be either stoichiometric or catalytic in Zr.

7.2.1 Stoichiometric Acyclic Carbozirconation

Activation or ate complexation are necessary to obtain acyclic carbozirconation. In fact, no reaction was observed between chloromethylzirconocene and *n*-propylacetylene. On the contrary, carbozirconation occurred starting from aluminated alkyne (Scheme 25).

The reaction of allylzirconocene with alkynes in presence of MAO, which begin with an ate complexation (*see Ate Complexes*) of the alkyne, appears to be mechanistically closely related to the above example (equation 52).**31**

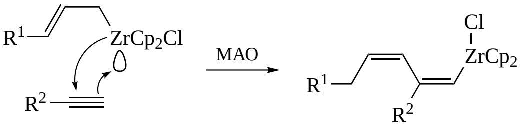

(52)

7.2.2 Stoichiometric Cyclic Carbozirconation

Three-membered zirconacycles (zirconacyclopropanes and zirconacyclopropenes) undergo ring expansion through cyclic carbozirconation (*see Carbometalation*) (Scheme 26).

The enyne bicyclization-carbonylation tandem reaction is of great interest to synthesize various organic compounds. Possible mechanisms have been proposed as follows (Scheme 27).

The subsequent development of $Cp_2Zr(n\text{-}Bu)_2$, which reacts as a Cp_2Zr equivalent, has been the beginning of an interesting organic chemistry, including natural products.**102** A 14-electron species like Cp_2Zr (see Section 2.3) has almost no chance to exist freely, and the equivalents of zirconocene are 16- or even 18-electron species. This has been rationalized by formation of three-membered zirconacycles before subsequent reaction. Three different protocols have been developed: i) by reaction with π-compounds of *in situ*-generated dialkylzirconocenes, ii) by β-H abstraction without the use of π-compounds, and iii) by using bis(trimethylsilyl)acetylene as a labile π-ligand.

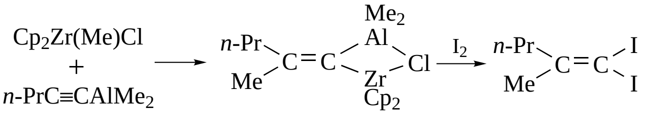

Scheme 25

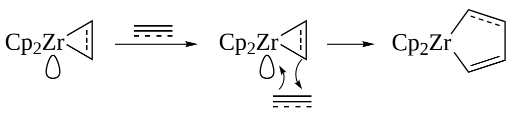

Scheme 26

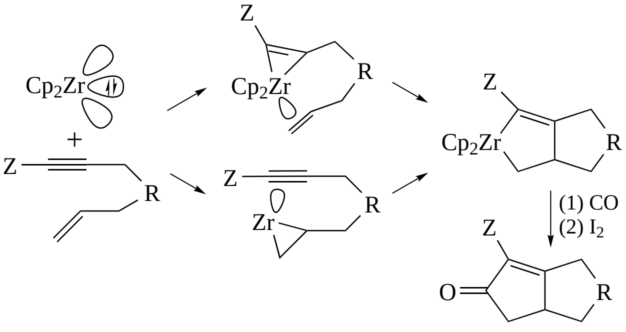

Scheme 27

Interestingly, high regioselectivity (*see Regioselectivity*) and stereoselectivity (*see Stereoselectivity*) have been observed in the reaction of zirconocene equivalents and unsaturated molecules. Thus, alkyl substituents prefer to be β to Zr, whereas aryl and alkenyl ones prefer to be α to Zr. In cases where there are two carbon-bound substituents, they usually prefer to be trans to one another, presumably to minimize steric interactions like in the 1-zirconacyclopent-3-yne (**101**), the first metallocyclopentyne complex.**103**

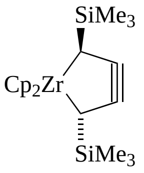

(**101**)

One important aspect of the Cp_2Zr-promoted cyclization that is now well-established is the ready reversibility through decarbozirconation, presumably involving an interaction between the empty Zr-orbital and the Cβ –Cβ′ bond of the five-membered zirconacycle and subsequent displacement of ethylene (equation 53).**31** Reaction of 2-azadienes on zirconocene affords *via* a retro-Brook rearrangement interesting azaoxazirconacycles.**104**

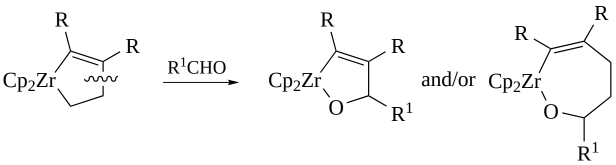

(53)

Interesting consequence of the reversibility of the carbozirconation (*see Carbometalation*) process includes stereo and regioselectivity backbone rearrangement (equation 54).**[31]**

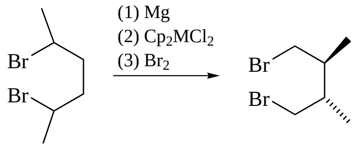

(54)

Another pathway to generate reactive three-membered zirconacycles and zirconaheterocycles is the thermolysis of diphenylzirconocene or related complexes. Many different structures with or without heteroatoms are readily obtained. These strongly constrained compounds are very reactive towards a large variety of polar or nonpolar species.

Similar to the benzynezirconocene, cyclohexyne, cyclopentyne, alkyne, alkene, cycloalkene zirconocenes, and related species insert various substrates such as alkynes, alkenes, aldehydes, ketones, nitriles or phosphaalkynes. They lead in general five-membered zirconacycles, which can be converted by transmetalation or exchange reactions into fused-ring aromatic or heterocyclic compounds.**[1]** The extension of this chemistry to heterobenzyne complexes can be realized, for instance, in phosphinine compounds.**[105]** Consequently, under mild conditions, η^2-phosphabenzyne-zirconocene complexes are formed and can be isolated either as PMe_3 adducts or as dimers when the elimination reaction is carried out without added phosphane (Scheme 28).

With dissymmetrical alkynes or alkenes, very clean reactions are often obtained by regiospecific processes (*see Regioselectivity*).**[1]** For example, the use of phosphorus unsaturated reagents afford the opportunity to generate various mono or diphosphanes and related species (Scheme 29).**[106,107]**

By reaction with buta-1,3-diyne, an unusual complex of a distorted cyclocumulene can be generated (equation 55).**[108]** This structure is stabilized by coordination of the central double bond of the seven-membered ring to the electronically unsaturated zirconium atom.

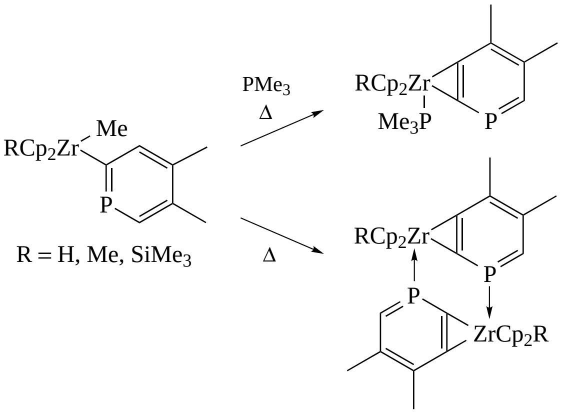

Scheme 28

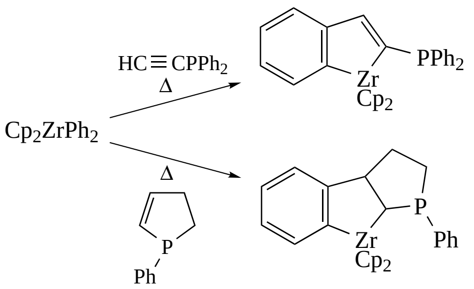

Scheme 29

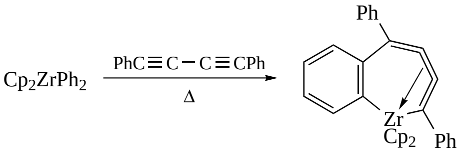

(55)

When the two alkynyl functions are separated by a silyl or a phosphano group, an interesting rearrangement takes place giving rise to tricyclic species (Scheme 30).**[109]** This skeletal rearrangement proceeds *via* intermediate zwitterionic zirconate (**102**). The empty orbital and electrophilicity of Zr are probably the reasons that lead to zwitterionic species containing zirconates and carbocationic centers.

Many zirconaheterocyclic complexes containing oxygen, nitrogen, phosphorus, chalcogens or silicon atoms can be generated by similar ways and offer also interesting reactivity (equations 56–58).**[1,110,111]**

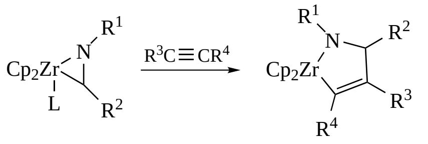

(56)

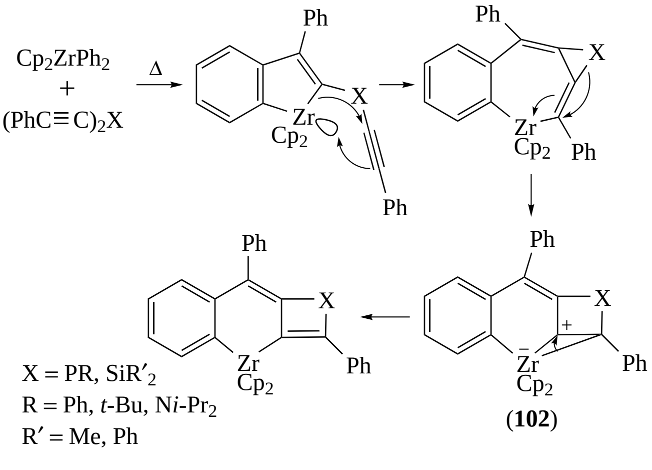

X = PR, SiR′2
R = Ph, *t*-Bu, N*i*-Pr2
R′ = Me, Ph

Scheme 30

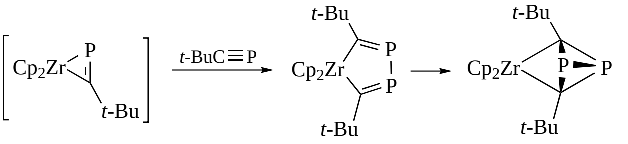

(57)

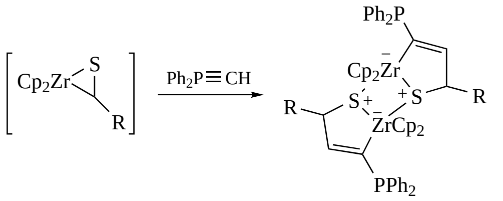

(58)

Even cationic azazirconacycles such as $[Cp_2Zr(\eta^2\text{-picolyl}).thf]^+$ that are isoelectronic (*see Isoelectronic*) to the neutral Zr-benzyne complex exhibit similar insertion reactions (*see Insertion*).[1]

7.2.3 Synthetical Applications of Zircona-cycles and -Heterocycles

As previously demonstrated, zirconacycles can be prepared by coupling (*see Coupling*) a low-valent metal complex and one or two molecules of unsaturated compound. Most of them are very useful starting materials for synthetical applications. Several processes can be employed to transform the metallacycles (*see Metallacycle*) into a variety of organic compounds.

Hydrolysis. Hydrolysis of zirconacyclopentadienes (**103**) with inorganic acid (*see Acids & Acidity*) provides, in a stereocontrolled manner, 1,2,3,4-tetrasubstituted dienes.[31] Protonolysis with weak organic acids such as ethanol gives monoprotonated dienylzirconocene, which can be reacted with electrophiles to yield pentasubstituted diene derivative (Scheme 31).[31] In the same way, β,γ unsaturated amines are obtained by cleavage of Zr–C and Zr–N bonds of azazirconacycles.

Halogenolysis. Halogenolysis of zirconacyclopentadienes (**103**) affords 1,4-dihalodienes. Whereas the iodination of zirconacyclopentadienes in THF with 2 equivalents of I_2 affords mainly the monoiodinated diene, the diiodo diene is the major product in CH_2Cl_2. Iodination carried out in THF in the presence of two equivalents of CuCl undergoes diiodination in 95% yield (equation 59).[31]

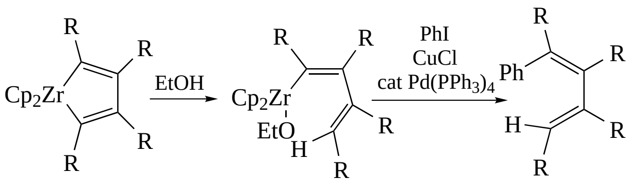

(**103**) R = Et

Scheme 31

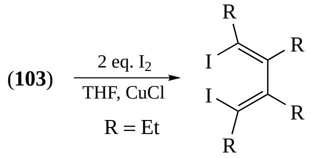

(59)

σ-Bond Metathesis Including Transmetalation. All the complexes that can be obtained through benzynezirconocene and related species can react with different electrophiles affording carbo or heterocycles *via* replacement of zirconium moiety by other carbo or heteroatomic species or by transmetalation reactions (*see Transmetalation*). Reactions of zirconacyclopentadienes with dihalides electrophiles derived from elements of groups 13 to 16 afford heterocyclic systems in good yield.[1] A four-center mechanism involving the availability of an empty orbital on each metal atom is usually proposed as being required for this transformation. In the reported examples, the Cp_2Zr moiety is converted into the very stable Cp_2ZrX_2. The driving force of the heteroatom transfer is presumably the high halophilicity of Zr. This reaction was extended to a lot of zirconacycles and leads original heterocycles (**104–107**).[1,107,109,110] In the particular case of silicon exchange, it is hardly possible to exchange Zr with Si by using R_2SiCl_2. It is difficult with $SiBr_4$, but easy with H_2SiCl_2.[31] Steric constraints reasons have been given to explain these difficulties.

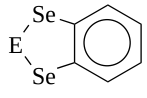

E = $SnMe_2$

(**104**)

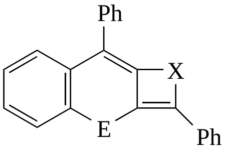

X = PPh, $SiMe_2$
E = AsPh, SbPh

(**105**)

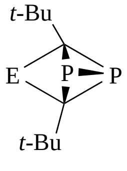

E = BPh, PCl

(**106**)

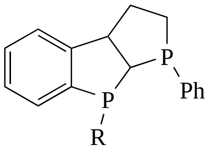

R = Ph, Me, t-Bu, N*i*Pr_2

(**107**)

Transmetalation to Cu, Ni, or Zn is sometimes necessary to release the organic compounds. For instance, treatment of zirconacyclopentadiene with CuCl generates an unstable dicopper complex, which can couple in situ with allyl, benzyl, aryl, thienyl, alkynyl, and alkenyl halides (Scheme 32).[31]

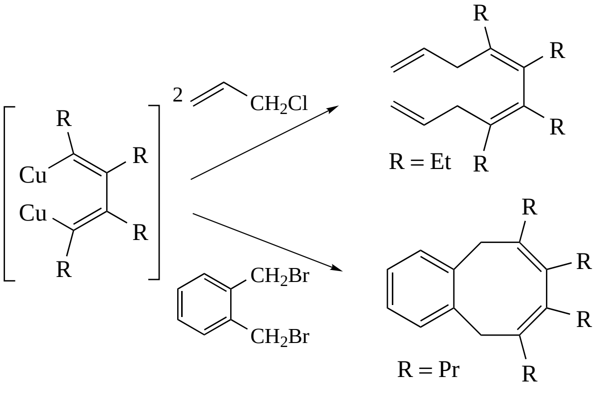

Scheme 32

Reactions of zirconacyclopentadienes with aldehydes in the presence of $AlCl_3$ afford cyclopentadiene derivatives (equation 60). Aluminacyclopentadiene might be an intermediate in this reaction.[112]

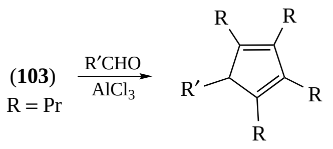

(60)

Addition reactions to Carbon–carbon multiple bonds. 1,1-additions of metallacyclopentadienes to carbon–carbon triple bonds are rare but some interesting examples are described. Particularly, addition of propynoate to zirconacyclopentadienes gives cyclopentadiene derivatives without any transmetalation to other metal.[31] Benzene derivatives can be obtained in high yields *via* reaction of dimethylacetylenedicarboxylate with zirconacyclopentadienes according to a 1,2-addition (Scheme 33).[31]

Starting from azazirconacyclopentadienes, pyridine derivatives can be obtained in the presence of $NiCl_2(PPh_3)_2$ (equation 61).[113]

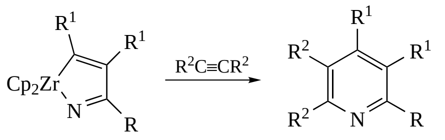

(61)

In a similar way to the above examples, the addition of zirconacyclopentadienes to methylmaleate gives cyclohexadiene derivatives. It is noteworthy that the two ester groups are *cis* in the starting material and *trans* to one another in the product.[31]

Insertion reactions of carbon monoxide and isonitriles. The carbenic character of carbon monoxide and isonitriles, which favors initial donation of an electron pair to the 16-electron Zr atom, is certainly responsible for the success of these processes.

Zirconacyclopentanes and zirconacyclopentenes readily react with CO at −78 °C to give cyclopentanones and cyclopentenones, respectively (Scheme 34). In the same conditions, zirconacyclopentadienes do not react. But reaction can be performed in the presence of $NiCl_2(PPh_3)_2$ to afford cyclopentadienones.[114]

Insertion of isonitriles into zirconacycles affords η^2-iminoacyl complexes that smoothly rearrange to stable η^2-imine zirconocenes.[31] In the case of 2-phosphanozirconaindenes, rearrangement proceeds leading to η^1-imine zirconocenes (Scheme 35). Subsequent formation of a β-phosphano indenoimine is obtained by elimination of Cp_2Zr fragment for the 2,6-dimethylphenyl isocyanide.[115]

7.3 Insertion Reaction of Carbenoids

The carbenoids represent 1-halo-1-lithium species (R^3R^4CLiX) that can cleanly react with organozirconocenes.[31] A

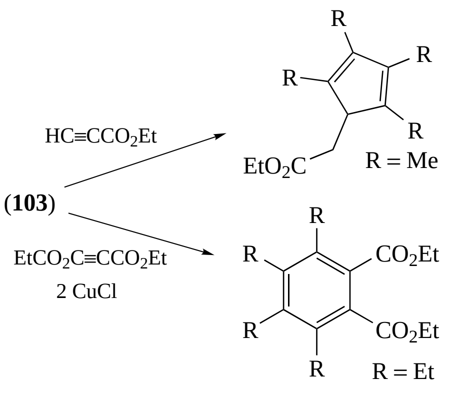

Scheme 33

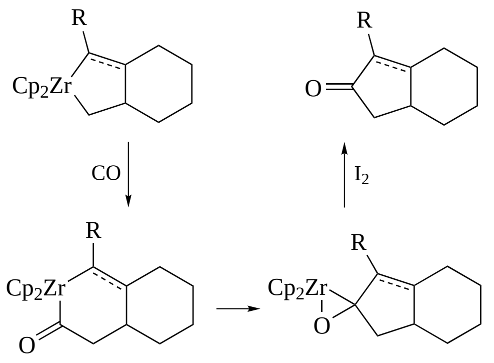

for zirconacyclopentane : R = H
for zirconacyclopentene : R = $SiMe_3$

Scheme 34

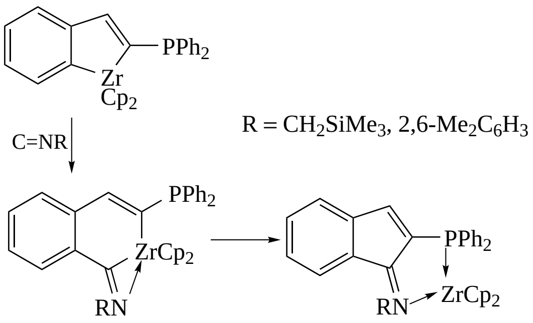

Scheme 35

key feature of this reaction is that the product retains the carbon–zirconium bond functionality of the substrate. Similar to carbon monoxide or isonitriles, compounds containing a lithium atom and a nucleofugal group on the same carbon can react with organozirconium complexes. Initial attack on the 16-electron Zr atom (*see Electron Configuration*) leads to a 18-electron metallate complex (*see Ate Complexes*) that rearranges with loss of halogen to give a novel 16-electron complex (Scheme 36). These complexes can generate several organic molecules by protonolysis or treatment with electrophilic reagents. During the reaction, an inversion of configuration is observed at the carbenoid atom.

Alkenyl carbenoids have been generated by halogen/lithium exchange or by deprotonation of alkenyl halides. 1-halo-1-lithioalkenes insert into Zr–C bonds affording stereodefined alkenes after treatment with an electrophile. In particular, the insertion of 2-monosubstituted alkenyl carbenoids is stereospecific (*see Stereoselectivity*).**31** By elimination of hydrogen chloride followed by α-deprotonation of the alkenyl halide using two equivalents of Li(2,2,6,6-tetramethylpiperidide), (*Z*) or (*E*)-1-chloro-1-lithio-1,3-butadiene can be *in situ*-generated from (*E*) or (*Z*)-1,4-dichloro-2-butene respectively. Similarly, insertion of various carbenoids into mono or bis alkynyl zirconocenes affords dienyne or (*Z*)-enediynes. Insertion of the readily formed (*E*)-1,2-dichloro-1-lithioethene into organozirconocene chlorides generates very useful terminal (*E*)-enynes by elimination of zirconocene dichloride from the intermediate species (Scheme 37).**116**

The insertion of allenyl carbenoids into Zr–C bonds is an interesting process for the generation of cumulenyl zirconium complexes, precursors of enyne products (equation 62).**116**

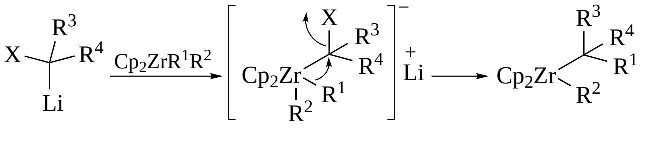

Scheme 36

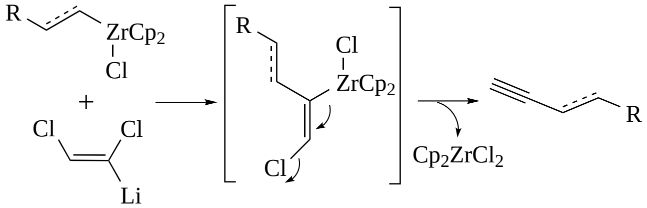

Scheme 37

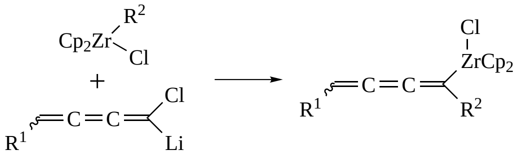

(62)

1-lithio-3-chloro-1-propyne efficiently inserts into zirconacycles to afford η^3-propargyl/allenyl complexes, precursors of various unsaturated organic compounds (equation 63).**31**

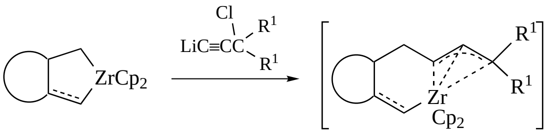

(63)

A ring-expanded process (five- to six-membered zirconacycle) can be observed by a clean insertion (*see Insertion*) of 2,2-disubstituted-1-lithio-1-chloro-alkenes into five-membered zirconacycles (Scheme 38).**31**

Tandem insertion of allyl carbenoids and aldehydes affords some organic compounds resulting from a three-component coupling reaction.**31** The most extensively studied application of this methodology is the insertion of allyl carbenoids into zirconacycles and subsequent elaboration of the formed allylzirconocenes with electrophiles (Scheme 39).**31**

Insertion of benzyl carbenoids into saturated bicyclic zirconacycles gives initially a 1:1 mixture of the diastereoisomeric zirconacyclohexanes (**108**) and (**109**). (**109**) undergoes a complete isomerization in a few minutes at 60 °C to the more stable diastereomer (**108**) (Scheme 40).

Insertion of benzyl carbenoids into zirconacyclopentenes follows a different but mechanistically related process.

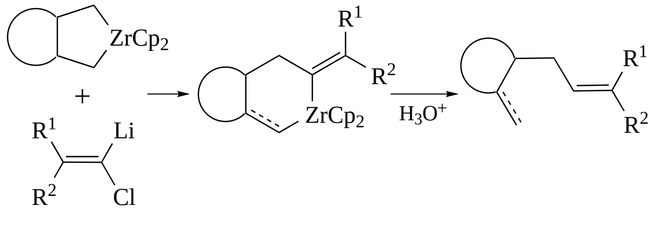

Scheme 38

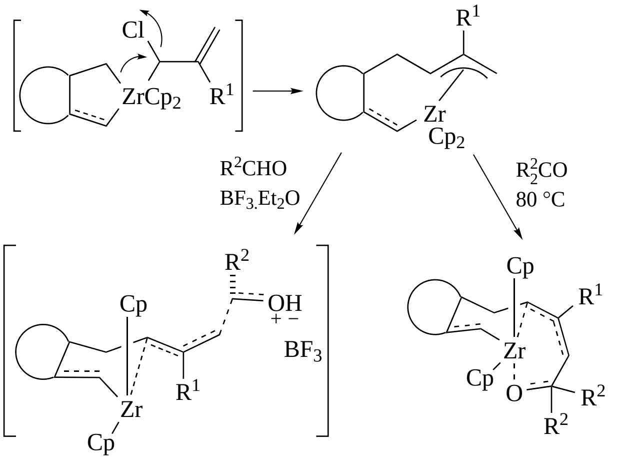

Scheme 39

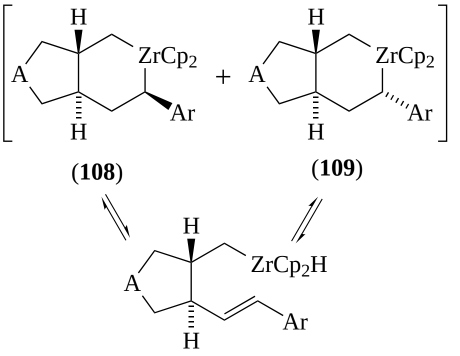

Scheme 40

However, the course of the reaction can be different in relation with the structure of the starting complexes. For five-membered fused zirconacyclopentenes, zirconacyclohexenes (**110**) are formed as a 1:1 mixture of diastereomers (Scheme 41). No equilibrium was observed between (**110**) and zirconocene hydride (**111**). In comparison, monocyclic zirconacyclopentenes and six-membered fused zirconacyclopentenes directly form the product (**112**), resulting of a β-hydride transfer/α-elimination (*see α-Elimination*) in high yield, presumably *via* (**111**). The CG of the fused five-membered ring could be responsible for the absence of β-hydride transfer (*see Hydrides*).

1,1-dihalolithium species are readily accessible by *in situ*-deprotonation of 1,1-dihalides with LDA and efficiently insert into zirconacycles, giving a complex (**113**), which rearranges to form fused cyclopentanes (**114**) (Scheme 42).[117]

Insertion of metalated epoxides into organozirconocenes proceeds *via* 1,2-rearrangement of the ate complex (*see Ate Complexes*) initially generated affording the β-alkoxyzirconocene, which can then undergo stereospecific *syn*-elimination to yield a tetrasubstituted alkene (Scheme 43).

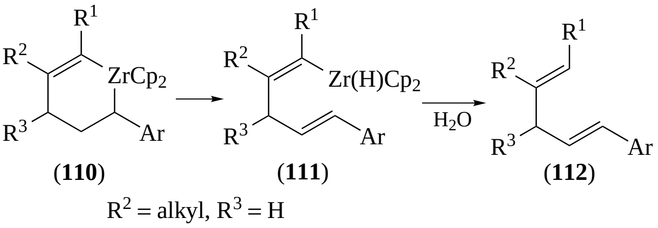

Scheme 41

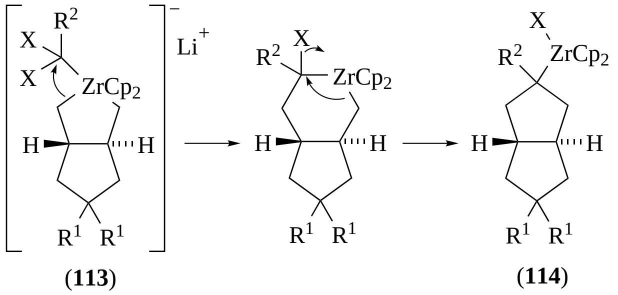

Scheme 42

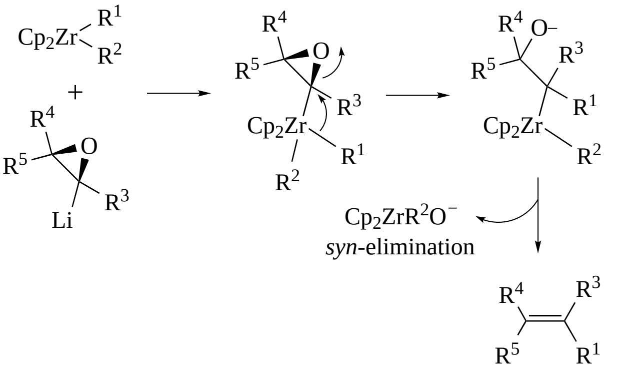

Scheme 43

Insertion of lithiated epoxynitriles into alkenylzirconocenes can afford various cyano derivatives, but not often in a stereospecific way (Scheme 44).[31]

The insertion of metal carbenoids into zirconacyclopentenes that are not α-substituted on the alkyl and the alkenyl sides of the Zr shows only a 2.2:1 selectivity in favor of the alkyl side. In the case of insertion into zirconacyclopentenes in which there is an α-substituent on the alkenyl, a wide variety of metal carbenoids selectively insert into the zirconium–alkyl bond.[31] On the contrary, steric hindrance of the alkyl side leads to complete selectivity in favor of insertion into the alkenyl side. The selectivity cannot be systematically attributed to steric factors (*see Steric Effect*) especially when insertion into the more hindered side is observed. In this case, the observed selectivity can be correlated with the highest

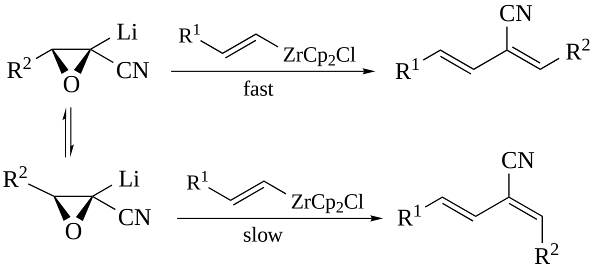

Scheme 44

coefficient of HOMO (*see HOMO*) of the zirconacycle, rather than of the lowest LUMO (*see LUMO*), suggesting that the carbenoid may be attacking as an electrophile.

8 CATIONIC ZIRCONOCENES IN ORGANIC SYNTHESIS AND CATALYSIS

The reactivity of the cationic Zr complexes is a direct consequence of their Lewis acidity (*see Lewis Acids & Bases*): (i) various substitution reactions can occur into the Zr−solvent weak bond, (ii) unsaturated substrates (CO, alkenes, alkynes, or ketones) insert into the Zr–C bond, potentially leading to polymerization reactions (see Section 8.2), (iii) new organic ligands obtained after reaction in the coordination sphere of the metal can be spontaneously released by β-H elimination (*see β-Hydride Elimination*), or (iv) C–H bond activation of suitable ligands can occur.

8.1 Applications in Organic Synthesis

8.1.1 *For Glycosides and Nucleosides Synthesis*

$Cp_2ZrCl_2/AgClO_4$ (1:1) combination and related hafnocene reagents can be used as activator of glycosyl fluorides. For example, the zirconocene-promoted glycosylation was applied in the total synthesis of antitumor monoterpene glycosides.**[31]** It is interesting to note that sometimes $Cp_2HfCl_2/AgClO_4$ (1:2) combination displayed a different chemoselectivity, inducing a Friedel−Crafts cyclization to a chromane skeleton.**[31]** For some years, these procedures have been largely used in various glycosylation processes, including glycopeptide synthesis.

8.1.2 *Cationic Acylzirconocene Complexes*

A cationic η^2-acylzirconocene can be quantitatively generated by treating a cationic zirconocene complex $[Cp_2Zr(R)(L)]^+$ (R = alkyl or alkenyl) with carbon monoxide (T < 23 °C, 1 atm). The use of these complexes has been

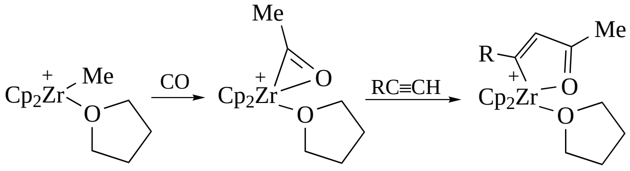

Scheme 45

exemplified by the formation of α,β-unsaturated ketones, 1,4-divinyl ketones, α-lactones, and furans (Scheme 45).**[31]**

The cationic zirconocene acyl complex (O-inside and O-outside isomers) unusually reacts with vinylchloride or methylvinylketone, affording in good yield a dinuclear dicationic complex, which has been characterized by X-ray diffraction (Scheme 46).**[118]**

In spite of the growing number of examples, the thermal instability of d^0 carbonyl complexes (*see Carbonyl Compound*) has often precluded their isolation. The use of an allyl ligand can stabilize the corresponding complex through a strong $\sigma \rightarrow \pi^*$ donation completely inhibiting fluxionality of the complex (equation 64).**[31]**

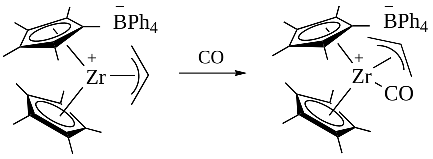

(64)

8.1.3 *Applications in Heterocyclic Chemistry*

Cationic zirconocene alkyl complexes of general type $[Cp_2Zr(R)(L)_n]^+$ (n = 0, 1, L = labile ligand) (*see Labile*) react readily with pyridines and other N-heterocycles by coordination and metalation (*ortho* C–H activation) to yield

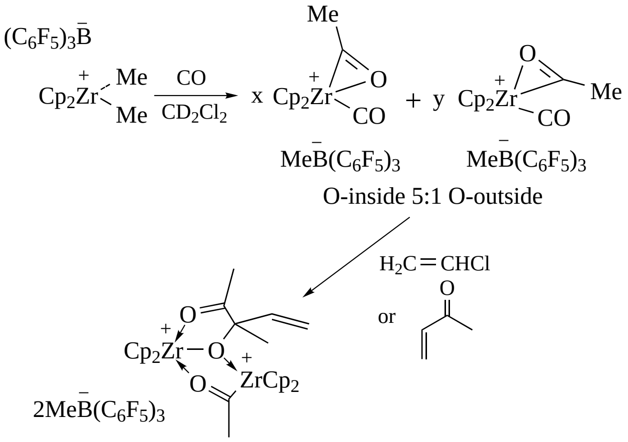

Scheme 46

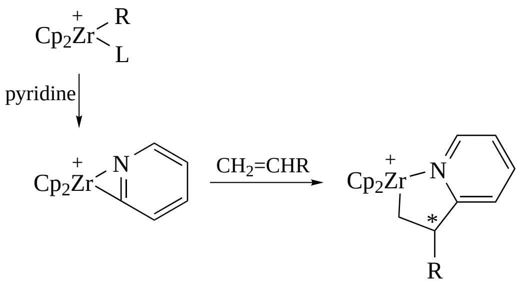

Scheme 47

η^2-pyridyl complexes that are quite reactive and insert α-olefins and other unsaturated substrates to yield ring expansion products (Scheme 47).[119]

The α-olefin insertions proceed regiospecifically in the Zr–C bond, affording 1,2-insertion product, in which a stereogenic center is present at the β-position (relatively to Zr) of the metallacycle. Starting from chiral zirconocene complexes (as *rac*-[(ebi)Zr(η^2-pyridyl)]$^+$), propene insertion occurs with a high level of diastereoselectivity in cases where the η^2-pyridyl ligand contains a six-substituent.[119]

8.1.4 Miscellaneous Reactions

Cationic zirconocene complexes can be employed as Lewis acid catalysts (*see Lewis Acids & Bases*) in several reactions.

The rearrangement of isopent-3-enyl epoxy esters with $Cp_2ZrCl_2/AgClO_4$ yields asymmetric bicyclo octane esters which are base-stable protecting groups for carboxylic acids (Scheme 48). However, the orthoesters are only the kinetic products and can rearrange under reaction conditions to more stable THF derivatives.[120]

Zirconocene dichloride and catalytic amounts of silver perchlorate can easily induce the rearrangement of an epoxide to an aldehyde (equation 65).[31]

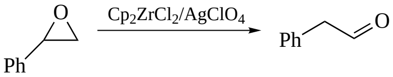

(65)

Cationic zirconocene complexes can induce cycloaddition reactions possibly in an asymmetric manner (see Section 9).

In the Mukaiyama aldol reaction, Zr cationic catalysts can be used. They act very quickly and require only low catalyst loadings (0.5% $[Cp_2Zr(OTf)_2\ thf]$). But, the reactions show only modest diastereoselectivity.[121]

A sequential cyclization–silylation of dienes can be induced by a cation-like permethylzirconocene complex (equation 66).[122]

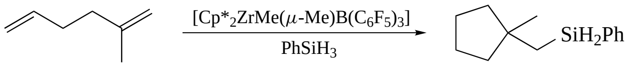

(66)

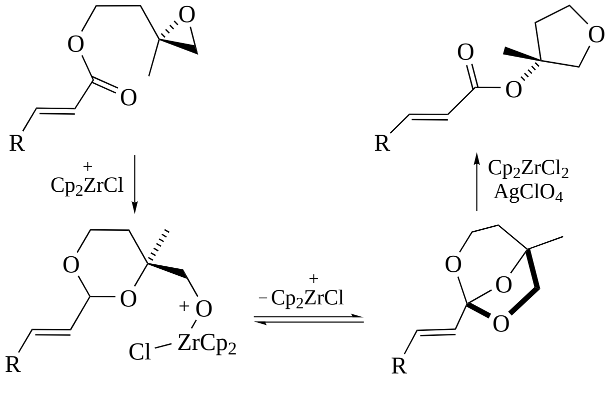

Scheme 48

8.2 Homogeneous Polymerization Catalysis

Cationic 16-electron $[RCp_2Zr(R)(L)]^+$ and 14-electron $[Cp_2Zr(R)]^+$ complexes contain at least one low-lying metal centered empty orbital which can be used for substrate coordination. This feature prompted chemists to use these species as alkene polymerization catalysts. As heterogeneous Ziegler-Natta catalysts (*see Ziegler–Natta Catalysts*) are systems with different active sites, the polymer structure (*see Polymer*) cannot be totally controlled. In comparison, metallocene catalysts are soluble in hydrocarbons. They show only one type of active site and their chemical structures can be easily changed.[123] These properties allow to accurately predicting the properties of the resulting polyolefins. In addition, their catalytic activity is 10–100 times higher than that of the classical Ziegler-Natta systems. In combination with MAO, zirconium and hafnium complexes reveal a very high activity towards olefin polymerization. When metallocenes, especially zirconocenes, are treated with MAO, catalysts allow the polymerization of up to 10^8 g of ethene per gram of Zr. The catalyst can be remained in the polymer at such high activities. The insertion time (for the insertion of one molecule of ethylene into the growing chain) amounts to some 10^{-5} s only. In some respect, such activities compare well with biocatalysts.

It is generally assumed that MAO firstly undergoes a fast ligand exchange reaction with the metallocene dichloride ($Cl \rightarrow Me$). Either Cl^- or $CH_3{}^-$ is further abstracted from the complex by an Al-center from MAO, thus forming a cationic species (step 1). In the step 2, the monomer (alkene) coordinates to the empty orbital of the complex. Step 3 is related to the insertion (*see Insertion*) of the alkene into the zirconium–alkyl bond which generates a new free

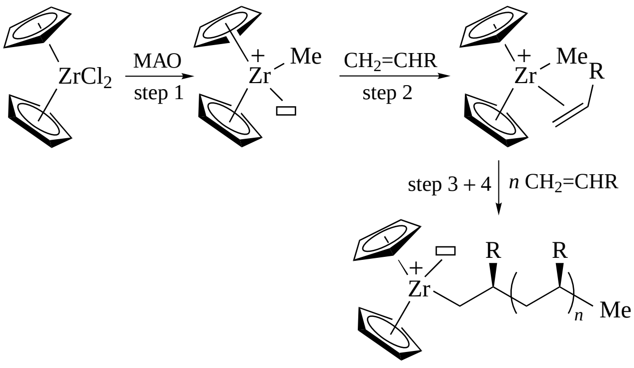

Scheme 49

coordination position. Step 4 is the repetition of step 3, in a very short period of time (about 2000 propene molecules per catalyst molecule per second), providing finally a polymer chain (*see Polymer*). Changing parameters like the nature of the ligand, the cocatalyst and the solvent influences each step (Scheme 49).

For the last twenty years, several hundred complexes have been synthesized with a view to extend properties of the polymer or to improve the activity of the catalysts. Selected typical examples of Zr or Hf precursors (**115–120**) are displayed below.

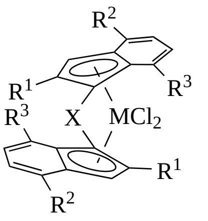

(**115**)

X = C_2H_4, $SiMe_2$
$R^1 = R^2 = R^3 =$ H, Me
or R^1 = Me, R^2 = Ph, R^3 = H

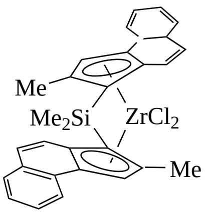

(**116**)

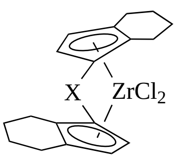

(**117**)

X = C_2H_4, $SiMe_2$

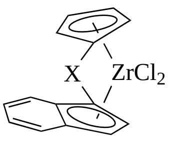

(**118**)

X = CMe_2, CPh_2

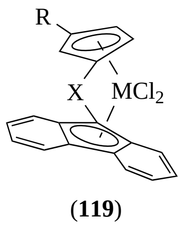

(**119**)

X = CMe_2, CPh_2
R = H, t-Bu, C_6H_{11}

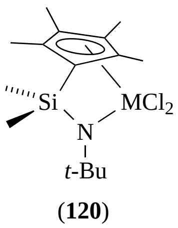

(**120**)

According to the symmetry of the complex and its structural features, very different polymers or copolymers have been obtained. The stereo regulation of α-alkene polymerization is one of the most important aspects of zirconocene or hafnocene-based catalysts. C_2-symmetric complexes (**115**), (**116**), or (**117**) lead to highly isotactic polypropylene, whereas C_s catalysts (**119**) (R = H) induce the syndiotactic arrangement.[1] In recent years, research has increased in the area of C_1-symmetric systems as (**118**) or (**119**) (R = t-Bu, C_6H_{11}), for example, which have been shown to transform propene to polypropylene with varying microstructures from aspecific to stereoblock,[124] to syndiotactic,[125] to hemiisotactic,[126] or to isotactic, depending on the nature of the hapto ligands (*see Hapticity*). This behavior is due to the fact that C_1-symmetric complexes have two coordination sites that are diastereotopically related to each other. As a result, monomer coordination can occur with different stereospecificity at each site, and the polymer chain prefers to occupy the less sterically crowded site. On the other hand, atactic polypropylene is produced when an achiral zirconocene catalyst is employed.

Group 4 metallocene catalysts are, in addition to polyethylene and polypropylene, able to generate syndiotactic polystyrene, to polymerize cycloolefins (cyclopentene, norbornene, and their substituted compounds), and to give access to various copolymers. During the polymerization of cycloolefins, only the double bond is opened and not the ring.

Half-sandwich metallocenes (**120**) (*see Half-sandwich Complexes*) play important role in the copolymerization of ethene and various α-olefins. They are distinguished by a sterically accessible active site. These catalysts are remarkably stable up to polymerization temperatures of 160 °C.

Though metallocene complexes possess excellent activities and stereospecificities for the polymerization of prochiral olefins as well as narrow molecular weight distributions of the generated polymers, they are not directly suitable for industrial applications. So, many efforts have been made to support metallocene catalysts. One approach is the use of organic support materials like cross-linked polystyrene. Another method consists to attach a ligand precursor on a polymeric support and then built up the catalyst.[127] The anchorage of the catalyst can be performed on inorganic support materials by an adsorption process at the surface of the solid particles or by a chemical bond, for instance, with silica. An interesting feature of this type of supported catalyst is that the fixation can change the stereospecificity from syndiotactic to isotactic according to the bulkiness of the support. An efficient way is to synthesize metallocene catalysts with an olefin or alkyne function that can be used as a comonomer in the polymerization process. In this case, the homogeneous catalyst is transferred to a heterogeneous system without using any support. The length of the alkenyl substituent must have some steric influence (*see Steric Effect*) on the rate of the β-hydrogen elimination reaction that terminates the growth of the polymer chain. Thus, the self-immobilization of metallocene complexes provides an elegant way to heterogeneize homogeneous metallocene catalysts

(equation 67).

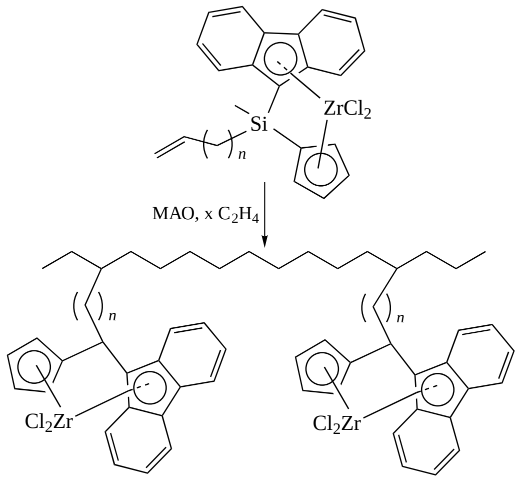

(67)

8.3 Miscellaneous Catalytic Reactions

In addition to the extensive development of applications of group 4 metallocenes in polymerization, other uses have been described concerning different catalytic processes.

The dinuclear Hf dicarbolide methyl complex (η^5-$C_2B_9H_{11}$)Cp*Hf(μ-η^2:η^3-$C_2B_9H_{11}$)HfCp*Me_2 catalyses the regioselective dimerization of terminal alkynes to 2,4-disubstituted but-1-en-3-ynes ($CH_2{=}C(R)C{\equiv}CR$). A great selectivity for dimer formation rather than trimer or higher oligomers has been obtained, owing to a self-correcting mechanism. The intermediate, which could potentially produce trimers or higher rank oligomers, undergoes an intramolecular cyclization reaction. The complex finally obtained is too crowded to produce trimers in subsequent cycles.

The anionic zirconocene trihydride $[Cp_2{}^*ZrH_3]^-$ is able to promote the oligomerization (*see Oligomer*) of PRH_2 to the cyclic polyphosphanes $(PR)_5$. This is evidence of the fact that complexes of early transition metals have a propensity to mediate P–P bond formation.[22]

Group 4 benzamidinate complexes were found to be active catalytic precursors, in the presence of MAO, for the isomerization of aliphatic olefins and the disproportionation (*see Disproportionation*) of 1,4- and 1,3-cyclohexadienes (Scheme 50).[128] The active species is the cationic hydride complex obtained for aliphatic olefins by the insertion of the methyl ligand with concomitant β-hydrogen elimination, and for the alicyclic dienes by an activation of the allylic hydrogen and subsequent elimination of methane.

The silyl chloride complexes (η^5-$C_5H_4SiMe_3)_2Zr[Si(SiMe_3)_3]Cl$ is a catalyst for the dehydropolymerization of both $PhSiH_3$ and n-Bu_2SnH_2 to relatively low-molecular weight polymers. Thus, polysilanes and polystannanes can be obtained.

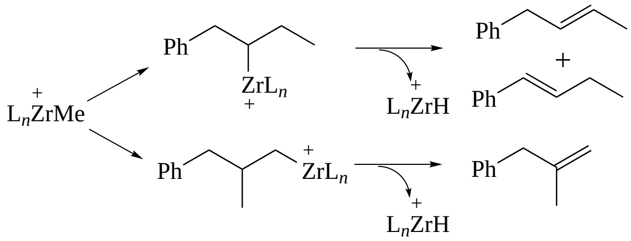

Scheme 50

9 ORGANOZIRCONIUM COMPLEXES IN ASYMMETRIC CATALYSIS

9.1 Zr-catalyzed Enantioselective C–C Bond-forming Reactions

In the area of enantioselective synthesis (*see Enantioselectivity*), the development of catalytic carbon–carbon bond-forming reactions that proceed under mild conditions in an enantioselective fashion (ee $>$ 95%) remains a challenging objective.[129] Among a great variety of metallic complexes, Zr-containing chiral catalysts can promote efficient and highly enantioselective additions of nucleophilic fragments such as alkylmetals and cyanides to C=O and C=N bonds. Moreover, Zr-based metallocenes promote additions of alkylmetals to carbon–carbon double bonds, reactions that do not easily occur with other catalysts. One another important feature is that the product of the asymmetric addition of an alkylmetal to an alkene produces a chiral alkylmetal that can be further functionalized.

Chiral C_2-symmetric ansa metallocenes are often used to promote asymmetric C–C bond-forming transformations.[31] (ebthi)$ZrCl_2$ or its derived binaphtolate and related complexes are intensively utilized in Zr-catalyzed enantioselective alkylation of alkenes with Grignard reagents (*see Grignard Reagents*). Thus in the presence of 2.5 to 10 mol% of these nonracemic complexes and EtMgCl as alkylating agent, five-, six- and seven-membered unsaturated heterocycles undergo facile asymmetric ethylmagnesation. The unsaturated alcohol in equation (68) can be used as a key intermediate in the first enantioselective total synthesis of the antifungal agent *fluvirucin*.[31]

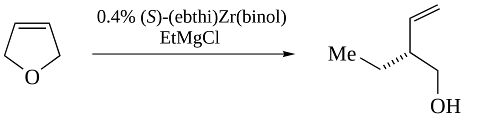

(68)

The catalytic cycle proposed for the enantioselective ethylmagnesation involves the chiral zirconocene–ethylene complex (**121**), formed upon reaction of the dichloride with two equivalents of EtMgCl. Coupling of the alkene substrate leads to the formation of the metallacyclopentane intermediate, which gives the zirconate (**122**) with a third equivalent of EtMgCl. A Zr–Mg ligand exchange yields (**123**). Subsequent β-hydride abstraction, accompanied by intramolecular magnesium alkoxide elimination leads to the final product and regeneration of (**121**). These alkylation processes are useful when used in conjunction with well-known catalytic ring-closing metathesis.[130,131] Intramolecular variants of the above Zr-catalyzed enantioselective alkylations can be performed.[31]

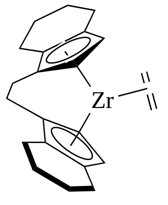

(**121**)

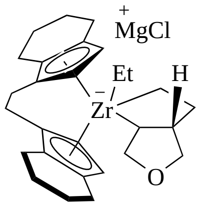

(**122**)

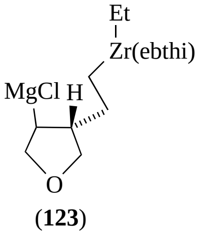

(**123**)

According to the high level of enantioselectivity (*see Enantioselectivity*) obtained in the asymmetric catalytic carbomagnesation and the interaction between the zirconocene–ethylene complex (**121**) and chiral unsaturated pyrans or furans, it is possible to induce differential rates of reaction leading to kinetic resolution. For instance, with a 2-substituted pyran, after 50% conversion, one enantiomer of the chiral alkene can be recovered in high enantiomeric purity. In fact, the favored model for the intermediate is the complex (**124**) that minimizes the steric interactions by preferential association of one pyran enantiomer with (ebthi)Zr complex (**121**). Consequently, in the presence of catalytic amounts of optically active (ebthi)$ZrCl_2$, a variety of chiral pyrans can be resolved in excellent enantiomeric purity (ee > 99%).[31] Moreover, this Zr-catalyzed resolution technology may be applied to medium-ring heterocycles, even if the presence of an aromatic substituent can have an adverse influence on the outcome of the catalytic resolution.[31]

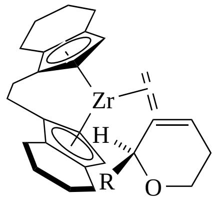

(**124**)

Kinetic resolution of cyclic allylic ethers can be performed by asymmetric Zr-catalyzed carbomagnesation. Six-, seven- or eight-membered ethers can readily be resolved by the Zr-catalyzed protocol (with ee between 81 to 99%). As an example, the tandem Zr-catalyzed kinetic resolution followed by a Ru-catalyzed ring-opening/ring-closing metathesis affords chiral chromenes with high optical purity (ee > 99%).[31]

Enantioselective carboaluminations of inactivated alkenes are promoted by the nonbridged chiral zirconocene (**125**), neutral or in association with $B(C_6F_5)_3$ (equation 69).[31] An unexpected observation is that addition of water leads to substantial acceleration of the C–C bond-forming process.[132]

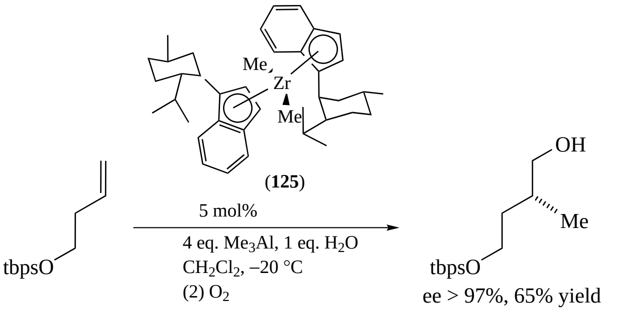

ee > 97%, 65% yield

(69)

Application of Zr-catalyzed enantioselective additions of alkylzinc reagents to imines delivers optically enriched or optically pure amines, a class of compounds having a great significance to medicine and biology.[31] Facile reduction of substrates with Et_2Zn may be due to β-H elimination of the metal–Et complexes which generate active metal hydrides that can promote amine reduction. The catalytic asymmetric protocol can be applied to the synthesis of nonaryl imines to generate homochiral amines. A recent procedure for amine synthesis involves a three-component process with *in situ*-formation of the imine substrate followed by its asymmetric alkylation.[133]

Catalytic asymmetric cyanide addition to imines (Strecker-type reaction) is an interesting carbon–carbon bond-forming reaction. The aminonitriles obtained may be converted to nonproteogenic α-amino acids.[134] In this reaction, the binuclear complex proposed as the active catalytic species was formed starting from two equivalents of Zr(O*t*-Bu)$_4$, 6-Br-binol, and *N*-methylimidazole and one equivalent of 3-Br-binol (equation 70). The protocol can be modified by using a three-component synthesis (aldehyde/aminophenol/HCN) to avoid the use of undesirable stannane reagent. This in situ-procedure is particularly interesting for less stable aliphatic imines. In this case, the aminonitrile synthesized is the precursor of the corresponding aminoesters.[31]

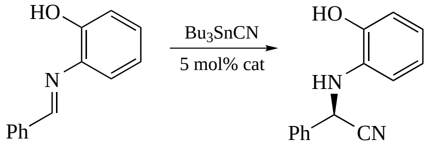

91% ee, 92% yield

(70)

Enantioselective aldol and Mannich reactions and related transformations can be efficiently performed with several zirconium catalysts. Addition of 1-naphtol to ethyl pyruvate mediated with the chiral (diborna-Cp)$ZrCl_3$ complex is reported with an appreciable level of enantioselectivity.[1]

At lower temperatures higher optical purities are obtained, and curiously, addition of water improves the selectivity and the reactivity. In a similar way, additions of ketene and thioketene acetals to a range of aromatic and aliphatic aldehydes have been accomplished and demonstrated the role of protic additives on the yield and the enantiomeric excess.[31] Through the use of the chiral catalyst prepared from Br_2-binol ligand, a range of α,α-disubstituted β-amino esters can be generated by addition of ketene acetals and derivatives to imines.[31] In this catalytic process, when more electron-withdrawing chiral ligands are used (CF_3 substituted binol), enantioselectivity and reactivity levels are often enhanced. Very high ee and yields are observed in similar reactions using chiral vapol-derived catalyts.[135]

Cationic *ansa* metallocenes can be utilized as chiral catalysts in Diels–Alder reactions. For example, in the presence of the cationic zirconocene complex $[(\text{ebthi})\text{Zr}(\text{O}t\text{-Bu})\cdot\text{thf}]^+$, the $[4+2]$ cycloaddition of acrolein and cyclopentadiene proceeds efficiently to afford *endo* and *exo* cycloadducts (equation 71). In reactions in which methyl acrylate is used as the dienophile, cycloadditions occur with lower levels of enantioselection (23% ee), but with significantly higher degrees of diastereoselectivity (17:1 *endo, exo*). In these processes, recent studies demonstrated the great influence of chiral metallocene structure and the dramatic solvent effect.[31]

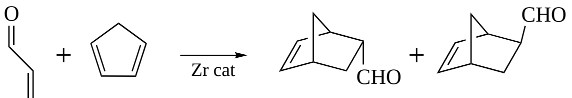

53% ee, 5:1 ds, 93% yield

(71)

In relation with the ability of cationic *ansa* zirconocene complexes to affect stereocontrolled alkene polymerization reactions, it is possible to insert simple alkenes into the $[(\text{ebi})\text{Zr}(\eta^2\text{-pyrid-2-yl})]^+$ and $[(\text{ebthi})\text{Zr}(\eta^2\text{-pyrid-2-yl})]^+$ systems.[31] The derived three-membered azazirconacycles are formed with high levels of diastereoselectivity, depending on the nature of alkene substituents. Thus, the enantiopure ebthi complex catalyzes asymmetric C–C bond-forming reactions (equation 72).

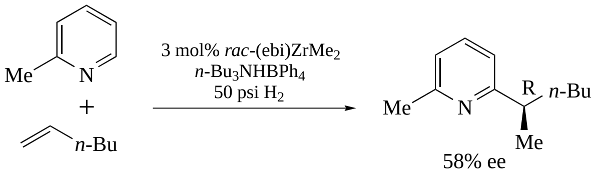

58% ee

(72)

9.2 Zr-catalyzed Enantioselective C–N and C–H Bond-forming Reactions

C–N bond-forming reaction is promoted by $\text{Zr}(\text{O}t\text{-Bu})_4$ in the presence of trimethylsilyl trifluoroacetate and a chiral amine triol (equation 73). This tightly bound multidentate ligand is very effective for transferring chirality.[136]

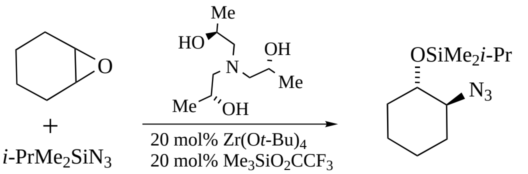

93% ee, 86% yield

(73)

Ansa metallocene-catalyzed hydrogenation of various alkenes can also be performed with low to moderate enantiomeric excess. The most successful hydrogenations involve trisubstituted alkenes, for which enantioselectivity can be in the range 83–99%. However, the use of cationic (ebthi)Zr-catalysts generated with MAO require that the alkene should not be able to polymerize in a facile manner. Thus, whereas with 1-decene as the substrate, only 28% of the hydrogenation product is obtained, 2-methyl-1-pentene affords 97% of the hydrogenation adduct. Tetrasubstituted alkenes can be hydrogenated with an efficient and highly enantioselective Zr-catalyzed process.[137]

10 RELATED ARTICLES

Bonding Energetics of Organometallic Compounds; Carbonyl Complexes of the Transition Metals; Mechanisms of Reaction of Organometallic Complexes; Niobium & Tantalum: Organometallic Chemistry; Oligomerization & Polymerization by Homogeneous Catalysis; Organic Synthesis Using Metal-mediated Metathesis Reactions; Scandium, Yttrium & the Lanthanides: Organometallic Chemistry; Titanium: Organometallic Chemistry.

11 REFERENCES

1. B. Gautheron, R. Broussier, and P. Meunier, ‘Encyclopedia of Inorganic Chemistry’, John Wiley & Sons, 1994, p. 4488.
2. G. M. Diamond, R. F. Jordan, and J. L. Petersen, *Organometallics*, 1996, **15**, 4045.
3. J. S. Rogers, R. J. Lachicotte, and G. C. Bazan, *Organometallics*, 1999, **18**, 3976.
4. E. F. Murphy, R. Murugavel, and H. W. Roesky, *Chem. Rev.*, 1997, **97**, 3425.
5. D. L. Greene, O. A. Villalta, D. M. Macias, A. Gonzalez, W. Tikkanen, B. Schick, and K. Kantardjieff, *Inorg. Chem. Commun.*, 1999, **2**, 311.
6. H. G. Alt and E. Samuel, *Chem. Soc. Rev.*, 1998, **27**, 323.

7. R. M. Chin, M. S. Jarosh, J. D. Russell, and R. J. Lachicotte, *Organometallics*, 2002, **21**, 2027.
8. R. L. Halterman, A. Tretyakov, D. Combs, J. Chang, and M. A. Khan, *Organometallics*, 1997, **16**, 3333.
9. F. J. Fernández, P. Gómez-Sal, A. Manzanero, P. Royo, H. Jacobsen, and H. Berke, *Organometallics*, 1997, **16**, 1553.
10. M. Hüttenhofer, M.-H. Prosenc, U. Rief, F. Schaper, and H.-H. Brintzinger, *Organometallics*, 1996, **15**, 4816.
11. M. Ogasawara, T. Nagano, and T. Hayashi, *J. Am. Chem. Soc.*, 2002, **124**, 9068.
12. J. J. Eisch, F. A. Owuor, and X. Shi, *Organometallics*, 1999, **18**, 1583.
13. S.-D. Bai, X.-H. Wei, J.-P. Guo, D.-S. Liu, and Z.-Y. Zhou, *Angew. Chem. Int. Ed. Engl.*, 1999, **38**, 1926.
14. H.-R. H. Damrau, E. Royo, S. Obert, F. Schaper, A. Weeber, and H.-H. Brintzinger, *Organometallics*, 2001, **20**, 5258.
15. R. L. Halterman, D. Combs, and M. A. Khan, *Organometallics*, 1998, **17**, 3900.
16. B. Chin and S. L. Buchwald, *J. Org. Chem.*, 1997, **62**, 2267.
17. A. J. Hoskin and D. W. Stephan, *Coord. Chem. Rev.*, 2002, **233–234**, 107.
18. K. Khan, C. L. Raston, J. E. McGrady, B. W. Skelton, and A. H. White, *Organometallics*, 1997, **16**, 3252.
19. F.-C. Liu, J. Liu, E. A. Meyers, and S. G. Shore, *Inorg. Chem.*, 1998, **37**, 3293.
20. U. Blaschke, G. Erker, M. Nissinen, E. Wegeluis, and R. Fröhlich, *Organometallics*, 1999, **18**, 1224.
21. P. W. Blosser, J. C. Gallucci, and A. Wojcicki, *J. Organomet. Chem.*, 2000, **597**, 125.
22. D. W. Stephan, *Angew. Chem. Int. Ed. Engl.*, 2000, **39**, 315.
23. M. Driess, J. Aust, and K. Merz, *Eur. J. Inorg. Chem.*, 2002, 2961.
24. E. Hey-Hawkins, *Chem. Rev.*, 1994, **94**, 1661.
25. R. L. Zuckerman and R. G. Bergman, *Organometallics*, 2001, **20**, 1792.
26. Z. K. Sweeney, J. L. Salsman, R. A. Andersen, and R. G. Bergman, *Angew. Chem. Int. Ed. Engl.*, 2000, **39**, 2339.
27. W. A. Howard, T. M. Trnka, M. Waters, and G. Parkin, *J. Organomet. Chem.*, 1997, **528**, 95.
28. S. E. d'Arbeloff-Wilson, P. B. Hitchcock, J. F. Nixon, H. Kawaguchi, and K. Tatsumi, *J. Organomet. Chem.*, 2003, **672**, 1.
29. F. Soleil and R. Choukroun, *J. Am. Chem. Soc.*, 1997, **119**, 2938.
30. V. Varga, J. Hiller, U. Thewalt, M. Polášek, and K. Mach, *J. Organomet. Chem.*, 1998, **553**, 15.
31. I. Marek, 'Titanium and Zirconium in Organic Synthesis', Wiley-VCH Verlag GmbH, Weinheim, 2002.
32. U. Rosenthal, P. Arndt, W. Baumann, V. V. Burlakov, and A. Spannenberg, *J. Organomet. Chem.*, 2003, **670**, 84.
33. D. Thomas, N. Peulecke, V. V. Burlakov, B. Heller, W. Baumann, A. Spannenberg, R. Kempe, U. Rosenthal, and R. Beckhaus, *Z. Anorg. Allg. Chem.*, 1998, **624**, 919.
34. L. L. Schafer, J. R. Nitschke, S. S. H. Mao, F.-Q. Liu, G. Harder, M. Haufe, and T. D. Tilley, *Chem. Eur. J.*, 2002, **8**, 74.
35. Z. Xi, R. Fischer, R. Hara, W.-H. Sun, Y. Obora, N. Suzuki, K. Nakajima, and T. Takahashi, *J. Am. Chem. Soc.*, 1997, **119**, 12842.
36. P.-M. Pellny, F. G. Kirchbauer, V. V. Burlakov, W. Baumann, A. Spannenberg, and U. Rosenthal, *J. Am. Chem. Soc.*, 1999, **121**, 8313.
37. P.-M. Pellny, F. G. Kirchbauer, V. V. Burlakov, W. Baumann, A. Spannenberg, and U. Rosenthal, *Chem. Eur. J.*, 2000, **6**, 81.
38. V. Kulsomphob, A. M. Arif, and R. D. Ernst, *Organometallics*, 2002, **21**, 3182.
39. I. E. Nifant'ev, P. V. Ivchenko, V. V. Bagrov, and L. G. Kuz'mina, *Organometallics*, 1998, **17**, 4734.
40. H. Juvaste, T. T. Pakkanen, and E. I. Iiskola, *Organometallics*, 2000, **19**, 4834.
41. J. W. Strauch and J. L. Petersen, *Organometallics*, 2001, **20**, 2623.
42. M. D. Fryzuk, L. Jafarpour, and S. J. Rettig, *Organometallics*, 1999, **18**, 4050.
43. M. D. Fryzuk, M. Mylvaganam, M. J. Zaworotko, and L. R. MacGillivray, *Organometallics*, 1996, **15**, 1134.
44. J. E. Ellis, S. R. Frerichs, and B. K. Stein, *Organometallics*, 1993, **12**, 1048.
45. H. H. Brintzinger, D. Fischer, R. Mülhaupt, B. Rieger, and R. M. Waymouth, *Angew. Chem. Int. Ed. Engl.*, 1995, **34**, 1143.
46. J. B. Jaquith, C. J. Levy, G. V. Bondar, S. Wang, and S. Collins, *Organometallics*, 1998, **17**, 914.
47. R. Choukroun, J. Zhao, C. Lorber, P. Cassoux, and B. Donnadieu, *Chem. Commun.*, 2000, 1511.
48. R. Chauvin, *Eur. J. Inorg. Chem.*, 2000, 577.
49. Y. Miquel, A. Igau, B. Donnadieu, J.-P. Majoral, N. Pirio, and P. Meunier, *J. Am. Chem. Soc.*, 1998, **120**, 3504.
50. J.-P. Majoral, C. Larré, R. Laurent, and A.-M. Caminade, *Coord. Chem. Rev.*, 1999, **190–192**, 3.
51. V. Cadierno, M. Zablocka, B. Donnadieu, A. Igau, J.-P. Majoral, and A. Skowronska, *Chem. Eur. J.*, 2001, **7**, 221.
52. W. E. Piers, *Chem. Eur. J.*, 1998, **4**, 13.
53. T. J. Woodman, M. Thornton-Pett, D. L. Hughes, and M. Bochmann, *Organometallics*, 2001, **20**, 4080.
54. W. Ahlers, B. Temme, G. Erker, R. Fröhlich, and T. Fox, *J. Organomet. Chem.*, 1997, **527**, 191.
55. N. Kleigrewe, T. Brackemeyer, G. Kehr, R. Fröhlich, and G. Erker, *Organometallics*, 2001, **20**, 1952.
56. G. Erker, *Chem. Soc. Rev.*, 1999, **28**, 307.

57. D. Röttger and G. Erker, *Angew. Chem. Int. Ed. Engl.*, 1997, **36**, 812.
58. J. Schottek, G. Erker, and R. Fröhlich, *Eur. J. Inorg. Chem.*, 1998, 551.
59. J. Schottek, G. Erker, and R. Fröhlich, *Angew. Chem. Int. Ed. Engl.*, 1997, **36**, 2475.
60. J. Schottek, D. Röttger, G. Erker, and R. Fröhlich, *J. Am. Chem. Soc.*, 1998, **120**, 5264.
61. A. Pastor, A. F. Kiely, L. M. Henling, M. W. Day, and J. E. Bercaw, *J. Organomet. Chem.*, 1997, **528**, 65.
62. R. A. Lee, R. J. Lachicotte, and G. C. Bazan, *J. Am. Chem. Soc.*, 1998, **120**, 6037.
63. M. A. Putzer, J. S. Rogers, and G. C. Bazan, *J. Am. Chem. Soc.*, 1999, **121**, 8112.
64. A. J. Ashe III, J. W. Kampf, and M. W. Schiesher, *Organometallics*, 2003, **22**, 203.
65. G. E. Herberich, U. Englert, and A. Schmitz, *Organometallics*, 1997, **16**, 3751.
66. A. J. Ashe III, S. Al-Ahmad, J. W. Kampf, and V. G. Young Jr, *Angew. Chem. Int. Ed. Engl.*, 1997, **36**, 2014.
67. N. S. Hosmane, H. Zhang, L. Jia, T. J. Colacot, J. A. Maguire, X. Wang, S. N. Hosmane, and K. A. Brooks, *Organometallics*, 1999, **18**, 516.
68. J. M. Dysard and T. D. Tilley, *J. Am. Chem. Soc.*, 2000, **122**, 3097.
69. F.-X. Buzin, F. Nief, L. Ricard, and F. Mathey, *Organometallics*, 2002, **21**, 259.
70. G. G. Lavoie and R. G. Bergman, *Angew. Chem. Int. Ed. Engl.*, 1997, **36**, 2450.
71. N. Wheatley and P. Kalck, *Chem. Rev.*, 1999, **99**, 3379.
72. L. H. Gade, H. Memmler, U. Kauper, A. Schneider, S. Fabre, I. Bezougli, M. Lutz, C. Galka, I. J. Scowen, and M. McPartlin, *Chem. Eur. J.*, 2000, **6**, 692.
73. J. R. Pinkes, S. M. Tetrick, B. E. Landrum, and A. R. Cutler, *J. Organomet. Chem.*, 1998, **566**, 1.
74. X. Gu and M. B. Sponsler, *Organometallics*, 1998, **17**, 5920.
75. D. Takeuchi, J. Kuwabara, and K. Osakada, *Organometallics*, 2003, **22**, 2305.
76. J. R. Fulton, T. A. Hanna, and R. G. Bergman, *Organometallics*, 2000, **19**, 602.
77. K.-I. Fujita, M. Ikeda, Y. Nakano, T. Kondo, and T.-A. Mitsudo, *J. Chem. Soc., Dalton Trans.*, 1998, 2907.
78. J. E. Balkwill, S. C. Cole, M. P. Coles, and P. B. Hitchcock, *Inorg. Chem.*, 2002, **41**, 3548.
79. T. Gutmann, E. Dombrowski, N. Burzlaff, and W. A. Schenk, *J. Organomet. Chem.*, 1998, **552**, 91.
80. C. Mattheis, P. Braunstein, and A. Fischer, *J. Chem. Soc., Dalton Trans.*, 2001, 800.
81. T. K. Hollis, L.-S. Wang, and F. Tham, *J. Am. Chem. Soc.*, 2000, **122**, 11737.
82. M. A. F. Hernandez-Gruel, J. J. Pérez-Torrente, M. A. Ciriano, A. B. Rivas, F. J. Lahoz, I. T. Dobrinovitch, and L. A. Oro, *Organometallics*, 2003, **22**, 1237.
83. Y. Sunada, Y. Hayashi, H. Kawaguchi, and K. Tatsumi, *Inorg. Chem.*, 2001, **40**, 7072.
84. U. Siemeling, O. Kuhnert, B. Neumann, A. Stammler, H.-G. Stammler, B. Bildstein, M. Malaun, and P. Zanello, *Eur. J. Inorg. Chem.*, 2001, 913.
85. R. R. Schrock, S. W. Seidel, Y. Schrodi, and W. M. Davis, *Organometallics*, 1999, **18**, 428.
86. L. H. Gade, P. Renner, H. Memmler, F. Fecher, C. H. Galka, M. Laubender, S. Radojevic, M. McPartlin, and J. W. Lauher, *Chem. Eur. J.*, 2001, **7**, 2563.
87. K. Michiue and R. F. Jordan, *Organometallics*, 2004, **23**, 460.
88. T. Toupance, S. R. Dubberley, N. H. Rees, B. R. Tyrrell, and P. Mountford, *Organometallics*, 2002, **21**, 1367.
89. M. J. Scott and S. J. Lippard, *Organometallics*, 1998, **17**, 1769.
90. L. Giannini, A. Caselli, E. Solari, C. Floriani, A. Chiesi-Villa, C. Rizzoli, N. Re, and A. Sgamellotti, *J. Am. Chem. Soc.*, 1997, **119**, 9198.
91. R. P. Kamalesh Babu, R. McDonald, S. A. Decker, M. Klobukowski, and R. G. Cavell, *Organometallics*, 1998, **18**, 4226.
92. K. E. Drouet and E. A. Theodorakis, *Chem. Eur. J.*, 2000, **6**, 1987.
93. L. Deloux, E. Skrzypczak-Jankun, B. V. Cheesman, M. Srebnik, and M. Sabat, *J. Am. Chem. Soc.*, 1994, **116**, 10302.
94. A. Maraval, A. Igau, C. Lepetit, A. Chrostowska, J. M. Sotiropoulos, G. Pfister-Guillouzo, B. Donnadieu, and J.-P. Majoral, *Organometallics*, 2001, **20**, 25.
95. N. Cénac, M. Zablocka, A. Igau, G. Commenges, J.-P. Majoral, and A. Skowronska, *Organometallics*, 1996, **15**, 1208.
96. Y. Hanzawa, A. Kakuuchi, M. Yabe, K. Narita, N. Tabuchi, and T. Taguchi, *Tetrahedron Lett.*, 2001, **42**, 1737.
97. S. Yamanoi, T. Matsumoto, and K. Suzuki, *Tetrahedron Lett.*, 1999, **40**, 2793.
98. C. Xu and E. Negishi, *Tetrahedron Lett.*, 1999, **40**, 431.
99. A.-M. Sun and X. Huang, *Synth. Commun.*, 1999, **29**, 1421.
100. P. Wipf and S. Ribe, *J. Org. Chem.*, 1998, **63**, 6454.
101. P. Wipf, C. Kendall, and C. R. J. Stephenson, *J. Am. Chem. Soc.*, 2001, **123**, 5122.
102. E. Negishi and T. Takahashi, *Bull. Chem. Soc. Jpn.*, 1998, **71**, 755.
103. N. Suzuki, M. Nishiura, and Y. Wakatsuki, *Science*, 2002, **295**, 660.
104. V. Gandon, P. Bertus, and J. Szymoniak, *Tetrahedron*, 2000, **56**, 4467.
105. N. Avarvari, P. Rosa, F. Mathey, and P. Le Floch, *J. Organomet. Chem.*, 1998, **567**, 151.

106. Y. Miquel, A. Igau, B. Donnadieu, J.-P. Majoral, L. Dupuis, N. Pirio, and P. Meunier, *Chem. Commun.*, 1997, 279.

107. M. Zablocka, N. Cénac, A. Igau, B. Donnadieu, J.-P. Majoral, A. Skowronska, and P. Meunier, *Organometallics*, 1996, **15**, 5436.

108. S. Bredeau, G. Delmas, N. Pirio, P. Richard, B. Donnadieu, and P. Meunier, *Organometallics*, 2000, **19**, 4463.

109. N. Pirio, S. Bredeau, L. Dupuis, P. Schütz, B. Donnadieu, A. Igau, J.-P. Majoral, J.-C. Guillemin, and P. Meunier, *Tetrahedron*, 2004, **60**, 1317.

110. P. Binger, B. Biedenbach, C. Krüger, and M. Regitz, *Angew. Chem. Int. Ed. Engl.*, 1987, **26**, 764.

111. E. Ortega, N. Pirio, P. Meunier, and B. Donnadieu, *Chem. Commun.*, 2004, 678.

112. Z. Xi and P. Li, *Angew. Chem. Int. Ed. Engl.*, 2000, **39**, 2950.

113. T. Takahashi, F. Tsai, and M. Kotora, *J. Am. Chem. Soc.*, 2000, **122**, 4994.

114. T. Takahashi, F.-Y. Tsai, Y. Li, and K. Nakajima, *Organometallics*, 2001, **20**, 4122.

115. V. Cadierno, M. Zablocka, B. Donnadieu, A. Igau, J.-P. Majoral, and A. Skowronska, *J. Am. Chem. Soc.*, 1999, **121**, 11086.

116. A. Kasatkin and R. J. Whitby, *J. Am. Chem. Soc.*, 1999, **121**, 7039.

117. N. Vicart and R. J. Whitby, *Chem. Commun.*, 1999, 1241.

118. H. Shen and R. F. Jordan, *Organometallics*, 2003, **22**, 2080.

119. S. Dagorne, S. Rodewald, and R. F. Jordan, *Organometallics*, 1997, **16**, 5541.

120. P. Wipf and D. C. Aslan, *J. Org. Chem.*, 2001, **66**, 337.

121. S. Lin, G. V. Bondar, C. J. Levy, and S. Collins, *J. Org. Chem.*, 1998, **63**, 1885.

122. G. A. Molander and C. P. Corrette, *Tetrahedron Lett.*, 1998, **39**, 5011.

123. W. Kaminsky, *Catal. Today*, 2000, **62**, 23.

124. A. M. Bravakis, L. E. Bailey, M. Pigeon, and S. Collins, *Macromolecules*, 1998, **31**, 1000.

125. M. H. Lee, J.-W. Park, C. S. Hong, S. I. Woo, and Y. Do, *J. Organomet. Chem.*, 1998, **561**, 37.

126. G. Guerra, L. Cavallo, G. Moscardi, M. Vacatello, and P. Corradini, *Macromolecules*, 1996, **29**, 4834.

127. H. G. Alt, *J. Chem. Soc. Dalton Trans.*, 1999, 1703.

128. C. Averbuj and M. S. Eisen, *J. Am. Chem. Soc.*, 1999, **121**, 8755.

129. I. Marek, *J. Chem. Soc. Perkin Trans.*, 1999, **1**, 535.

130. A. Fürstner, *Angew. Chem. Int. Ed. Engl.*, 2000, **39**, 3012.

131. A. H. Hoveyda and R. R. Schrock, *Chem. Eur. J.*, 2001, **7**, 945.

132. S. Ribe and P. Wipf, *Chem. Commun.*, 2001, 299.

133. J. R. Porter, J. F. Traverse, A. H. Hoveyda, and M. C. Snapper, *J. Am. Chem. Soc.*, 2001, **123**, 10409.

134. H. Ishitani, S. Komiyama, Y. Hasegawa, and S. Kobayashi, *J. Am. Chem. Soc.*, 2000, **122**, 762.

135. S. Xue, S. Yu, Y. Deng, and W. D. Wulff, *Angew. Chem. Int. Ed. Engl.*, 2001, **40**, 2271.

136. B. W. McCleland, W. A. Nugent, and M. G. Finn, *J. Org. Chem.*, 1998, **63**, 6656.

137. M. V. Troutman, D. H. Appella, and S. L. Buchwald, *J. Am. Chem. Soc.*, 1999, **121**, 4916.

Acknowledgments

Dr. J.-C. Hierso is gratefully acknowledged for many useful suggestions and discussions during the preparation of this contribution. The authors also want to thank S. Royer for her help in compiling the bibliography.

Alkaline Earth Metals: Organometallic Chemistry

Jacob S. Alexander, Marites Guino-o, Maria Felisa Zuniga, Roger C. Hahn & Karin Ruhlandt-Senge
Syracuse University, Syracuse, NY, USA

1	Introduction	1
2	Synthesis	1
3	Structural Features and Bonding	5
4	Applications	20
5	Conclusions	27
6	References	28

1 INTRODUCTION

The organometallic chemistry of the alkaline earth metals has been predominantly centered on magnesium. (*See* ***Beryllium & Magnesium: Organometallic Chemistry***) Originated by the groundbreaking studies by V. Grignard in 1900, it was shown that organomagnesium halides might easily be prepared by the treatment of an organic halide with magnesium metal in diethylether. The resulting compounds have important roles in synthetic chemistry, prompting extensive studies. Novel developments in this area of chemistry, such as transition metal–catalyzed cross-coupling or magnesium-halogen exchange reactions among others (discussed below) further improved the utility of these important reagents.

In contrast to the magnesium analogs, the heavy group IIA congeners are more reactive and thus more difficult to prepare. In addition, their higher tendency towards aggregation, as caused by the larger ionic radii, often leads to solubility problems. As a result, the organometallic compounds of calcium, strontium and barium were viewed as laboratory curiosities without applications, and it is not a surprise when the recent edition of Greenwood and Earnshaw mentions that from about 50 000 papers on the organometallic compounds of group IIA, less than 1% deal with the heavier triad of alkaline earth metals.[1] Magnesium's lighter congener beryllium has received only little attention owing in part to its reduced nucleophilicity as compared to magnesium. Moreover, beryllium was considered the 'most toxic nonradioactive element'. (*See* ***Beryllium: Inorganic Chemistry***) Even when in the 1990s it became clear that with appropriate precautions beryllium chemistry can be carried out in a safe manner, research intensity did not increase markedly.

The organometallic chemistry of the heavy alkaline earth metals experienced a renaissance in the 1980s when synthetic procedures for the preparation of discrete, soluble cyclopentadienide derivatives were derived, as delineated in several excellent review articles.[2,3] Today, advances in synthetic methodology and characterization techniques have allowed for detailed synthetic and structural investigations of an extended group of organometallic derivatives of the heavy metals. These research efforts are prompted by the numerous applications in a variety of disciplines including synthetic chemistry, materials, and solid-state applications, and polymer chemistry amongst others.[4–12]

This article summarizes some of the recent developments in alkaline earth organometallic chemistry. Several excellent review articles are available for more detailed discussions on the subject areas. It is important to note that radium, the heaviest alkaline earth metal, is radioactive and no organometallic compounds have been reported.

2 SYNTHESIS

2.1 General Considerations

The organometallic chemistry of the Group IIA metals is dominated by the M^{2+} oxidation state. (*See* ***Alkaline Earth Metals: Inorganic Chemistry***) The elements in the group are generally defined with the members loosely partitioned into two general classes. The first class contains the smaller beryllium and magnesium, whose chemistry is often markedly different than that of the larger congeners. The high charge/size ratio observed by these ions, particularly in the case of Be^{2+}, with an ionic radius of 0.41 Å (CN 4), and Mg^{2+} (CN 4) with 0.71 Å leads to an extremely high polarizing power and a chemistry influenced by covalent interactions.[13] Still, the significant difference in electronegativity (EN) between beryllium (1.47), magnesium (1.23) and carbon (2.50) indicates a significant polar bond contribution.[14] In many respects, the chemistry of the lighter analogs mirrors that of zinc rather than that of the heavier members of the group with the coordination sphere of the lighter group IIA metals more easily saturated by relatively small organic ligands. Organomagnesium compounds are well studied as the result of the enormous synthetic utility of the Grignard and diorganomagnesium reagents. Many of the compounds have been isolated and characterized in detail, showing a preference for low-coordination numbers. The composition of the products, especially in solution is not straightforward, as discussed below.

The second class of alkaline earth metals involves the heavier congeners, although radium, as a radioactive element, is not studied in detail. The significant increase in ionic size and reduction in electronegativity experienced by these metals (Ca (CN 6) 1.14 Å, EN = 1.04; Sr (CN 6) 1.27 Å, EN = 0.97;

Ba (CN 6) 1.49 Å, EN = 0.97) leads to chemistry dominated by electrostatic interactions. There are significant similarities between the chemistry of calcium and divalent ytterbium as well as strontium and divalent europium and samarium owing to quite similar size/charge ratios.[15] (*See* ***Scandium, Yttrium & the Lanthanides: Organometallic Chemistry*** and ***Scandium, Yttrium & the Lanthanides: Inorganic & Coordination Chemistry***)

Several distinct trends are exhibited in the chemistry of the heavy alkaline earth metals as one descends the group. In accord with the increased metal coordination sphere, increased metal–ligand and metal-donor lability is observed. Moreover, the increased metal diameter typically requires the presence of sterically demanding ligands often in combination with appropriate donors to sterically saturate the metal coordination sphere and prevent the formation of polymeric species. Still, oligomerization is commonly observed for the heavier metals. Partially as a result of this, and also owing to the predominantly ionic nature of the compounds, solubility generally decreases upon descending the group; most such complexes are sparingly soluble in hydrocarbons unless sterically demanding ligands with considerable methyl substitution are employed to enhance this property.

Work on heavy alkaline earth organometallics was hampered for years owing to lack of suitable synthetic access routes. The extreme air and moisture sensitivity of the compounds (even in comparison to the magnesium analogs) and difficulties in isolating pure products frustrated early work and remains a serious challenge. In addition, early efforts were predicated on straightforward conceptual routes owing to the difficulties involving the preparation of suitable starting materials for more advanced, multistep synthesis. Fortunately, growth in other fields (particularly alkali metal 'superbases' and alkaline earth metal amides) facilitated a concomitant increase in the synthetic arsenal for alkaline earth metal chemists, and now a wide range of applications is available for the preparation of these compounds.

2.2 Synthetic Methodologies

As discussed above the variation of chemical properties observed in group IIA elements requires a range of synthetic methodologies. As such, some preparative methods are not applicable for all metals. Synthetic methodologies for the lighter metals are well established and documented and will be discussed only briefly. In contrast, the development of synthetic routes towards the heavier analogs is far less established and will be discussed in greater detail. Amongst those, the term direct metallation summarizes a selection of synthetic strategies involving the reaction of a metal and neutral ligand, is now gaining prominence for the preparation of the heavier group IIA analogs. Metathesis reactions including salt-elimination, transamination, transmetallation, hydrocarbon elimination, and desilylation represent alternative avenues towards the heavy alkaline earth organometallics and will be discussed in detail below.

2.2.1 Direct Reaction of Organohalogens with the Metal

This is the classical method to prepare the Grignard analogs, and remains the most frequently used synthetic method towards the heteroleptic organomagnesium halides and the diorganomagnesium derivatives if the initial formation of the 'RMgX' is followed by the addition of 1,4 dioxane. The exothermic reaction is typically conducted in ethers and may proceed quite rapidly, especially if small alkyl or aryl substituents are employed.

Essential for the success of this reaction are the quality of the magnesium metal in the reaction since the magnesium oxide layer are all will effectively passivate the metal surface preventing access to the underlying magnesium metal. Several methods of surface activation are available: addition of a few drops of CCl_4 or $BrCH_2CH_2Br$ or a small amount of iodine that will penetrate the protective oxide layer are all commonly employed. Especially effective is the addition of iodine followed by slight heating and extended stirring under inert gas. A more reactive form of magnesium ('Rieke' magnesium) may be prepared by the reduction of a magnesium halide with an alkali metal, lithium naphthalide, on potassium graphite.[16] A recent, powerful activation method focuses on the use of di(isobutyl)aluminum hydride (DIBAH) allowing the preparation of Grignard reagents well below the boiling point of THF.[17]

Grignard-type reactions require the presence of a donor. Typically, diethyl ether is used, whose high volatility provides a vapor barrier above the solution to protect from oxidation and hydrolysis. Nevertheless, an inert gas is needed to ensure optimal yields. The introduction of sterically demanding ligands often coincides with difficulties to initiate the reaction. The presence of bulky ligands also results in reduced reaction rates, and consequent low yields and long reaction times. These problems may be circumvented by external heating, or the use of higher boiling ethers such as THF. It is important to note that the vapor barrier created by the higher boiling solvent is less effective; as such strict inert gas conditions are necessary. In addition to ligand size and the nature of the solvent, the halide substituent has an important role in the overall reaction with organoiodides being the most and organofluorides being the least reactive. Typically, fluorides may be prepared in good yields if highly active magnesium is utilized (equation 1).

$$\mathrm{Mg_{(act.)}} + \mathrm{RX} \xrightarrow{\text{Ether}} \mathrm{RMgX}$$
$$\text{Act.} = \text{activated; X} = \text{F, Cl, Br, I; R} = \text{Alkyl, Aryl} \qquad (1)$$

Use of this route for the heavier metal analogs has been met with limited success with the purity of the alkaline earth metal playing a pivotal role.[18–25] This work indicated that it is especially important to avoid any alkali metal impurities in the alkaline earth metal source.[26] Moreover, the need for an ethereal solvent is frustrated by the commonly observed ether cleavage reactions, making this a less attractive route to prepare the heavy metal analogs.

2.2.2 Direct Metallation

One of the earliest and most straightforward methods employed in the preparation of heavy alkaline earth organometallics involved the reaction of a metal with an acidic ligand substrate (equation 2) in an oxidative addition.

$$\mathrm{Ae_{Act.}} + 2\mathrm{HR} \longrightarrow \mathrm{AeR_2} + \mathrm{H_2}$$
$$\mathrm{Ae} = \mathrm{Ca, Sr, Ba} \quad \mathrm{Act.} = \mathrm{Activated} \qquad (2)$$

This method generally requires activation of the metal and the availability of an oxide-free metal surface. This can be accomplished in several ways, including the reduction of the alkaline earth metal iodides with potassium metal or lithium napthalide,[11,12,27] the utilization of freshly distilled metals,[28] the preparation of surface enhancing amalgams by addition of a few drops of mercury,[19] addition of a small amount of iodine, or (most commonly) the dissolution of the metals in anhydrous, liquid ammonia.[29–31] While the heavy alkaline earth metals dissolve easily in ammonia, this tendency decreases for the lighter metals. Beryllium does not dissolve, and magnesium does so only if highly active magnesium powder is employed. This trend coincides with an increase in reactivity as descending the group, allowing a smooth reaction for barium, while reflux conditions for strontium and calcium (dry ice condenser, −35 °C) are required. Still, calcium reactions are typically quite sluggish. The presence of a secondary donor is often required, even for the heaviest, most reactive alkaline earth metals, and products are only available if such a donor is present. As an example, the reaction of barium with the bulky amine $\mathrm{HN(SiMe_3)_2}$ proceeds smoothly in the presence of THF whereas, no reaction is observed in the absence of THF.[32] Direct metallation has been used successfully to prepare families of amides and aryloxides, but organometallic examples remain rare.[33]

A variant of direct metallation, cocondensation, has been utilized to prepare the first σ-bonded organocalcium complex, $\{\mathrm{(SiMe_3)_2CH}\}_2\mathrm{Ca(1,4dioxane)_2}$,[34] in addition to a transient heteroleptic calcium hydride, $\mathrm{C_6H_5CaH}$ by C–H activation (equation 3).[35] The heteroleptic hydride is highly reactive and decomposes upon warming the reaction vessel above −78 °C. The product has been identified by its reaction with alcohols, affording quantitatively a series of calcium aryloxides.

$$\mathrm{Ca_s} + \mathrm{ArH_{excess}} \xrightarrow[\mathrm{THF}]{\text{cocondensation}} \mathrm{ArCaH(THF)_2}$$
$$\mathrm{Ar} = \text{benzene, toluene, } t\text{Bu-benzene, xylene} \qquad (3)$$

The direct metallation of magnesium with anthracene in THF quantitatively affords a THF solvated magnesium anthracenide in the form of orange yellow crystals.[36–39] While the solubility of the unsubstituted magnesium anthracene derivatives is low, the substitution of the aromatic system with $\mathrm{SiMe_3}$ groups sufficiently increases the solubility to afford crystalline samples. The magnesium anthracenides are the starting material for the formation of magnesium hydride catalysts.[40] The heavier alkaline earth metal anthracenides have been prepared by dissolving the alkaline earth metals and anthracene in a mixture of liquid, anhydrous ammonia, and THF, but solubility problems have prevented their complete characterization and widespread use.[41]

2.2.3 Salt Elimination

Salt elimination is currently an attractive synthetic route to prepare cyclopentadienide derivatives of group IIA. The metal halides require the presence of ethers to enable homogeneous reaction conditions. Amongst the halides, the fluorides are the least soluble, whilst the iodides display the highest solubility. For the heavier metals, homogeneous reaction condition can only be achieved if the iodides are employed. The iodides are preferentially reacted with organopotassium reagents, owing to the high lattice energy of KI, and its subsequent precipitation, even in THF solutions. Moreover, cyclopentadienide potassium salts are easy to prepare and handle, justifying the preference for this route (equation 4). The required presence of etheral solvents does not allow the direct preparation of donor-free products. If desired, an alternative synthetic strategy, such as transmetallation and the use of organomercury reagents is advisable.

While salt elimination has been employed for the preparation of the metallocenes for some time, it remains a challenging route towards an extended group of organometallics owing to the high reactivity of the potassium organometallics. Rare exceptions are the preparations of $\mathrm{Ca(C(SiMe_3)_3)_2}$ and more recently $\mathrm{Ca(THF)_4(CH_2Ph)_2}$.[42,43]

$$\mathrm{AeI_2} + 2\mathrm{KR} \longrightarrow \mathrm{AeR_2} + 2\mathrm{KI}$$
$$\mathrm{Ae} = \mathrm{Be, Ca, Sr, Ba} \quad \mathrm{R} = \text{alkyl, aryl} \qquad (4)$$

The combination of alkaline earth iodides and organopotassium reagents has proven to be advantageous for avoiding problematic solubility and separation issues that can be formidable using this route, especially if the solubility of the product is low. Proven methods to improve product solubility include the addition of various donor systems (such as crown ethers). The success of the reaction route critically depends on the purity of both starting materials; the presence of lithium, as often introduced using potassium organometallics prepared by Schlosser conditions, or any other impurity will complicate the isolation of pure products. The introduction of a novel method for preparing organopotassium reagents in the absence of lithium (desilylation) should help overcome this synthetic obstacle.[44]

2.2.4 *Transamination*

With the development and detailed characterization of the bis(bistrimethylsilyl)amides of the heavy alkaline earth metals, the transamination regime has become an attractive route to prepare a variety of alkaline earth metal derivatives, including organometallics. The attractiveness of the route is due to the good stability and excellent solubility of the metal amides in a variety of solvents (equation 5).

$$\mathrm{Ae(N(SiMe_3)_2)_2(THF)_2 + 2HR \longrightarrow AeR_2 + 2HN(SiMe_3)_2}$$
$$\mathrm{Ae = Ca, Sr, Ba \quad R = alkyl, aryl} \tag{5}$$

The reaction route is quite flexible, but the reactant needs to be more acidic than the liberated amine. Although the alkaline earth metal amides are generally not as basic ($\mathrm{p}K\mathrm{a} = 30-33$) as the potassium organometallics used in the salt-elimination regime, they are nonetheless known to attack both crown ethers and ethereal solvents, necessitating careful control of reaction conditions to circumvent this undesirable side reaction.[45] Other side reactions involve the protonation of the liberated amine by the acid, under formation of a primary amine (equation 6). If excess acid is present, a second protonation may lead to the formation of NH_3. The cleaved $SiMe_3$ group silylates the acid, thus dramatically reducing product yields.[46] The protonation of the amine may partially be suppressed by slow and dilute addition of acid avoiding an excess of acid at all times.

$$\mathrm{HN(SiMe_3)_2 + HR \longrightarrow Me_3SiR + 2H_2NSiMe_3}$$
$$\mathrm{R = Alkyl, Aryl} \tag{6}$$

2.2.5 *Transmetallation*

Transmetallation was used extensively for the preparation of heavy alkali organometallics by reaction of a heavy alkali metal alkoxide or aryloxide with an organolithium reagent under precipitation of lithium alkoxide/aryloxide. The reaction typically proceeds smoothly, the only drawback being the separation of two solid reaction products. As such, careful choice of ligands to enable the facile separation on the basis of different solubility properties is crucial. Use of this route in the preparation of alkaline earth metal organometallics has been reported for the preparation of strontium and barium dibenzyl derivatives.[10,45] Two variants of this reaction have been reported: reaction of an alkoxide (specifically the *tert*-butoxides) with benzyllithium (equation 7), or treatment of the bis(bistrimethylsilyl)amides with the lithium reagent (equation 8). Again, the principal drawbacks of these reactions focus on the separation of the two solid reaction products. Since heavy alkaline earth metal *tert*-butoxides are difficult to prepare in a pure form, it is advantageous to focus on the amide as a starting material.

$$\mathrm{Ae(O}t\mathrm{Bu)_2 + 2Li(C_7H_7) \longrightarrow Ae(C_7H_7)_2 + 2LiO}t\mathrm{Bu}$$
$$\mathrm{Ae = Sr, Ba} \tag{7}$$

$$\mathrm{Ae(N(SiMe_3)_2)_2(THF)_2 + 2LiR \longrightarrow AeR_2 + 2LiN(SiMe_3)_2}$$
$$\mathrm{Ae = Ca, Sr, Ba; R = Alkyl, Aryl} \tag{8}$$

2.2.6 *Metal Exchange*

The use of organomercurials to prepare organometallic reagents has been well documented and is especially powerful where the formation of 'ate' complexes is prevalent.[47] The method has been used extensively to prepare pure organoberyllium or magnesium compounds, especially in cases when a donor-free product is warranted. Even though this route might be quite powerful for the preparation of the heavier alkaline earth metal analogs, past work was limited to the preparation of dibenzyl derivatives. The dearth of further studies is likely due to the reluctance to work with highly toxic organomercurials (equation 9). (*See* ***Mercury: Organometallic Chemistry***).

$$\mathrm{Ae + HgR_2 \longrightarrow AeR_2 + Hg}$$
$$\mathrm{R = Alkyl, Aryl} \tag{9}$$

2.2.7 *Hydrocarbon Elimination*

Until recently, there was no analog in heavy alkaline earth chemistry to the well-established alkane elimination route used to prepare a variety of magnesium amides and chalcogenides.[48] The attractiveness of the route for magnesium is due to the commercial availability of dibutyl magnesium. The gaseous nature of butane allows a simple work-up procedure (equation 10). However, until recently, similar chemistry for the heavier alkaline earth metals was not possible owing to the lack of suitable dialkyl or aryl reactants. Recent reports by Harder *et al.* describe the facile preparation of dibenzyl calcium and barium compounds, giving rise to the intriguing possibility of employing these reagents in a similar reaction scheme (equation 11).[10,42] Work in our group has extended the group of reagents to strontium,[45] making available all heavy alkaline earth metals in this reaction scheme.

$$\mathrm{Mg(C_4H_9)_2 + HR \longrightarrow MgR_2 + 2C_4H_{10}}$$
$$\mathrm{R = amine, thiol, selenol} \tag{10}$$

$$\mathrm{Ae(C_7H_7)_2 + 2HR \longrightarrow AeR_2 + 2C_7H_8}$$
$$\mathrm{Ae = Ca, Sr, Ba \quad R = Alkyl, aryl} \tag{11}$$

So far, dibenzyl derivatives remain the only hydrocarbon source for hydrocarbon elimination reactions, especially since the well-explored bis-cyclopentadienides are not suitable as starting materials for this type of reaction. The high basicity of the benzyl reagents allows for the metallation of many otherwise inactive ligand systems, and the formation of toluene as the side product facilitates the isolation of the target molecules. Owing to the highly reactive nature of the starting materials and their low solubility in apolar solvents, this entry requires the presence of the polar solvent THF at temperatures below −40 °C to prevent ether cleavage chemistry. Efforts to modify solubility properties through substitution of the benzyl moiety are underway.

2.2.8 *Alkaline Earth 'Superbase' Analogs*

An intriguing new possible entry currently under development involves the application of a recently discovered route to heavy alkali organometallics through a simple desilylation reaction in which an alkali metal *tert-butoxide* is reacted directly with a trimethylsilyl substituted ligand yielding the desired product and trimethylsilyl*tert*butylether. In the case of the alkaline earth metals, this reaction requires the presence of an organolithium reagent to afford the desired product (equation 12).

$$\mathrm{Ba(O}t\mathrm{Bu)_2 + 2(SiMe_3)CHR_2 \xrightarrow{n\mathrm{BuLi}} Ba(CHR_2)_2 + 2Me_3SiO}t\mathrm{Bu}$$
$$\mathrm{R = Aryl} \qquad (12)$$

The exact role of the organolithium reagent remains unclear, but it seems plausible that the components function as alkaline earth metal-containing 'superbase' analogs, with a alkali-alkaline earth metal alkoxide/organometallic aggregate as the metallating species.[44]

2.2.9 *Hydride Elimination*

The reaction of metal hydrides MH_2 with acidic hydrocarbons seems an attractive way to prepare the target compound since a commercially available metal source can be utilized. Moreover, the formation of only gaseous by-products ensures a facile work-up (equation 13). However, only few compounds have been prepared using this route owing to the low reactivity of the hydrides caused by their polymeric, insoluble nature. Moreover, the unreliable purity of the commercial hydrides poses significant problems. As such, rather acidic ligands and enforced reaction conditions are required for the reaction to proceed.

$$\mathrm{MH_2 + 2RH \longrightarrow MR_2 + 2H_2}$$
$$\mathrm{M = Be\text{-}Ba,\ R = acidic\ hydrocarbon} \qquad (13)$$

3 STRUCTURAL FEATURES AND BONDING

The structural features in the target compounds are quite diverse and bonding within the target compounds may involve σ- and π-type interactions. The following chapters are divided by ligand type to allow a more direct comparison of trends within the group of metals.

Owing to the significant lability within the target compounds, ligand exchange reactions are frequently observed. This is especially relevant for heteroleptic compounds, where complex solution equilibria complicate the isolation of pure species. As such, solution chemistry of the organometalhalides is discussed below.

3.1 Disproportionation/Redistribution (Schlenk) Equilibria

Despite their role as the most widely used organometallic reagents, the constitution of Grignard reagents in solution has been a source of uncertainty for some time. It is now well established that solutions of Grignard reagents can contain many different species interlinked by complex equilibria. The position of the equilibria depends on many factors including but not limited to (1) the nature of the halogen, (2) the nature of the solvent, (3) the concentration of the solution, (4) the size and electronic properties of the ligand, and (5) the temperature of the solution.[49] Schlenk and Schlenk proposed the now-familiar representation of the organomagnesium halides by an equilibrium between the dihalides and the diorgano compounds (equation 14).

$$\mathrm{MX_2 + R_2Mg \rightleftharpoons 2RMgX}$$
$$\mathrm{X = F, Cl, Br, I;\ R = Alkyl, Aryl} \qquad (14)$$

This suggestion was further justified by extensive VT-NMR studies offering additional useful information on the rate of exchange.[50] In the presence of small groups such as methyl, lowering the temperature allows the observation of distinct signals, rather than averaged resonances allowing the identification of individual components. Lower rates of exchange are also observed if the ligand size increases, as shown for ligands as small as *tert*-butyl. Important information in regards to the equilibria was also obtained on studies involving the heavier alkaline earth metal analogs. Only in the presence of very sterically demanding ligands, such as substituted cyclopentadienides, heteroleptic species may be isolated.[51]

For the magnesium reagents, the influence of 1,4 dioxane or other complexing agents typically results in the formation of the diorganomagnesium species,[49] owing to the precipitation of the dihalide dioxane adduct, which can be removed by filtration (equation 15).

$$\mathrm{2RMgX + C_4H_8O_2 \longrightarrow MgR_2 + MgX_2(C_4H_8O_2)\downarrow}$$
$$\mathrm{X = F, Cl, Br, I;\ R = Alkyl, Aryl} \qquad (15)$$

If the ligand system is sterically demanding, the rates of exchange are very slow allowing the isolation of heteroleptic RMgX. In this case, addition of 1,4 dioxane does not afford the diorganomagnesium reagents, even if reflux conditions are employed. As an example, 2,4,6-$Ph_3C_6H_2MgBr(THF)_2$ (Figure 1) does not afford the diorganomagnesium species even if an excess of 1,4 dioxane and reflux conditions are employed. A likely explanation is based on an unfavorable transition state owing to the large steric demand of the ligand. The smaller size of beryllium and the increased covalency of its bonds allows the more ready isolation of heteroleptic species, especially if sterically demanding ligands such as terphenyl are employed.[52]

3.2 Alkaline Earth Metallocenes

Cyclopentadienide (Cp) derivatives are known for all alkaline earth metals, and trends observed within the group nicely represent the changes in properties within the group of metals.[53] As for the heavy metal triad, cyclopentadienide derivatives remain the largest well-explored group of organometallics known, with the earliest examples dating back as early as 1956.[54] Several excellent review articles summarize trends observed within this group of compounds.[2,3,53,55]

The large variability of the Cp ligand through various substitution patterns on the ring such as pentamethyl, triisopropyl, and tetraisopropyl led to a large selection of compounds, whose structural features are largely driven by steric considerations. Frequently, smaller substituents will result in oligomeric species in the solid state, as shown with the polymeric $(Me_5Cp)_2Ca$ (Figure 2),[56] while bulkier groups on the ring, despite increasing metal radii, will support the formation of monomeric species, as shown in Figure 3.[57]

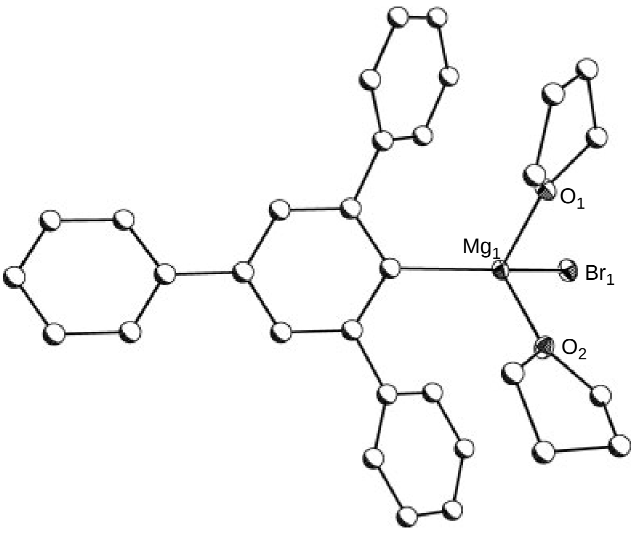

Figure 1 The structure of 2,4,6$Ph_3C_6H_2MgBr(THF)_2$. Hydrogen atoms have been omitted for clarity

Altering the substituents on the Cp rings also has radical effects on a variety of physical properties, including solid-state geometries, solubility, stability to hydrolysis, oxidation, and ligand extrusion, and others.

Cyclopentadienide derivatives appear both as simple complexes, reminiscent of ferrocene, or as heteroleptic systems. Because of the primarily electrostatic bonding models attributed to alkaline earth organometallics, the range of geometries available even for simple homoleptic alkaline earth metallocenes Cp_2M (M = Be–Ba) is surprising.

Beryllocene, Cp_2Be, prepared in 1956 by E. O. Fischer, was intensively examined to determine its structural features. This work quickly abandoned a structural model based on ferrocene, and different bonding modes for the two Cp rings were demonstrated by Cp_2Be's high dipole moment in solution. The slipped sandwich (η^5/η^1) structure, with beryllium disordered between the two nonequivalent Cp rings was confirmed by electron diffraction and crystallographic studies.[58–60] Coinciding with the disordered solid-state

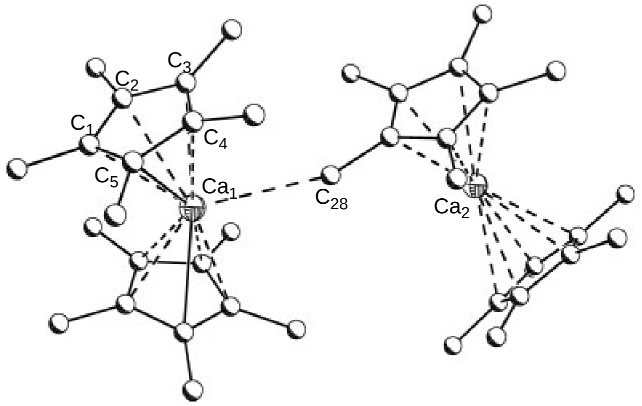

Figure 2 The structure of $[(Me_5Cp)_2Ca)]_n$. Hydrogen atoms have been omitted for clarity

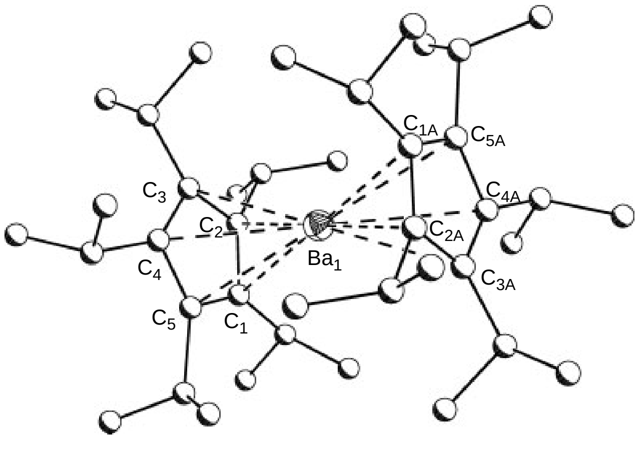

Figure 3 The structure of $[(iPr_5)Cp]_2Ba$. Hydrogen atoms have been omitted for clarity

structure, beryllocene is highly fluctional in solution, with only one set of resonances in both ^{1}H and ^{13}C NMR studies down to −135 °C.[61,62] The fluctional nature of beryllocene may be explained by the small radius of beryllium. The optimal Cp–Be distance is shorter than half the Van der Waals distance between two Cp rings. More details on beryllocene can be found in a comprehensive review on organoberyllium chemistry.[63]

The larger size of magnesium allows a more symmetrical structure of magnesocene, Cp_2Mg. X-ray diffraction studies show the two Cp rings to be antiprismatic with Mg–C distances of 2.304(8) Å.[64] Electron diffraction data indicate an ecliptic orientation of the rings in the gas phase (D_{5h} symmetry) with slightly elongated Mg–C distances of 2.339(4) Å. However, a model with staggered rings (D_{5d}) cannot be ruled out. The permethylated analog displays quite similar structural features.[65,66]

The chemistry of the cyclopentadienide derivatives of the heavier alkaline earth metal derivatives has been summarized in several excellent review articles.[2,3,55,67] The structural features of the heavier cyclopentadienide derivatives are characterized by an increasing trend towards bent geometry upon descending the group–observed both in the gas phase (electron diffraction studies) and the solid state (X-ray diffraction).[68–72] While permethylated magnesocene exhibits a linear structure, the Me_5Cp-Ae-Me_5Cp (centroid) angle deceases to 131° (solid state) and 148° (gas phase) for the analogous barium compound.[73] This trend follows structural pattern also reported for the halides, with the strongest deviation from linear geometry for the corresponding fluorides.[74] With an increasing degree of ionicity in the metal–ligand bond upon descending the group, the exact degree of covalent contribution towards the metal-carbon bond is still the topic of some debate. Several theories have been developed to rationalize the deviation from linear (VSEPR) geometry, with extensive MO calculations showing that the energy needed to obtain a bent structure are small (4–12 kJ mol^{-1}). The bent geometry within the heavier metallocenes is so typical of this group of compounds that examples in which the system does *not* display such behavior in the solid state are particularly noteworthy, such as in $[(iPr_5)Cp]_2Ba$, shown in Figure 3.

The library of substituted cyclopentadienide systems expanded rapidly, most notably by Hanusa *et al.*, and Sitzmann *et al.*[2,3,55,57,67] This work also demonstrated that various base adducts of these complexes could be obtained, resulting in the preparation of compounds with various donors to examine structural changes and concomitant variation in physical properties. In this context, the homoleptic metallocenes were treated with a host of Lewis bases including phosphines,[56] isonitriles, pyrazines,[75] carbonyl[76] and even unsaturated carbon systems such as in $(Me_5Cp)_2(Me_3SiCC{\equiv}CCSiMe_3)Ca$, through weak π-interactions with the alkynyl moieties[77] (Figure 4).

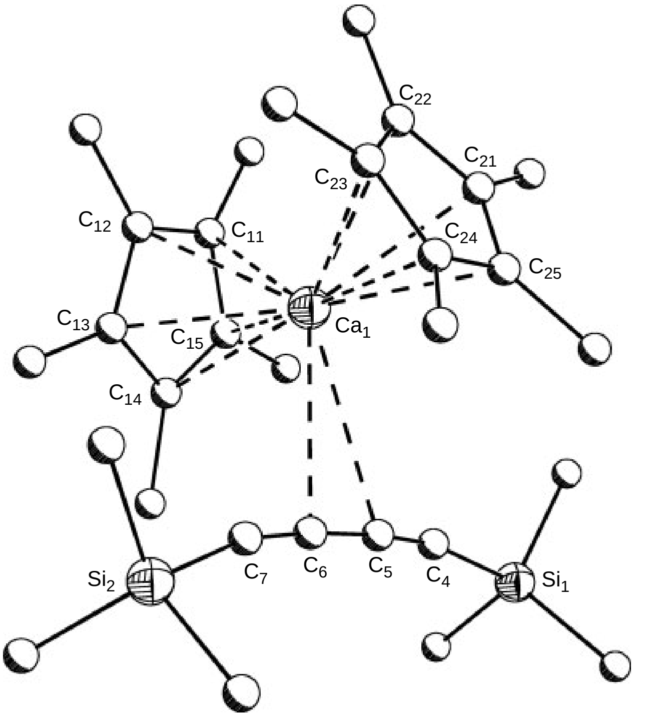

Figure 4 The solid-state structure of $(Me_5Cp)_2(Me_3SiCC\text{-}CCSiMe_3)Ca$. Hydrogen atoms have been omitted for clarity

An interesting class of compounds of this type are the alkaline earth metal carbenes in which the metal center is ligated by two Me_5Cp rings in addition to carbene (1,3,4,5-$Me_4C_3N_2$).[78] Several of these compounds have been isolated and characterized, with both mono- and di-adducts known in the solid state. These compounds all display similar bent geometries as defined by the centroids of the rings through the metal, and the smaller magnesium congener displays a 'slipped' $\eta^5-\eta^3$ coordination with the rings as a result of steric strain by the bulky carbene. The strontium analog is as shown in Figure 5. The strongly donating carbene can displace a wide variety of other donor adducts, even THF, which is often difficult to remove for the smaller metals even under harsh conditions. Interestingly, the variation of Lewis donors in the metallocenes has little influence on the overall bent geometries of these compounds.

An interesting variant of metallocenes is the tripledecker $\{(iPr)_4Cp\}cotBa_2$ (cot = cyclooctatetraene), shown in Figure 6.[79] This centrosymmetrical compound displays a π-coordinated central cyclooctatetraene to two barium atoms, which complete their coordination sphere by two tetraisopropyl-substituted cyclopentadienides.

Related metallocenes utilizing indenyl and fluorenyl ligands have been described. The bis-indenyl and bis-(di-isopropyl)indenyl systems can be easily prepared by metathesis from the potassium indenide and the heavier alkaline earth metal iodides.[80] The resulting compounds adopt the familiar bent geometries despite the large steric bulk of the ligands,

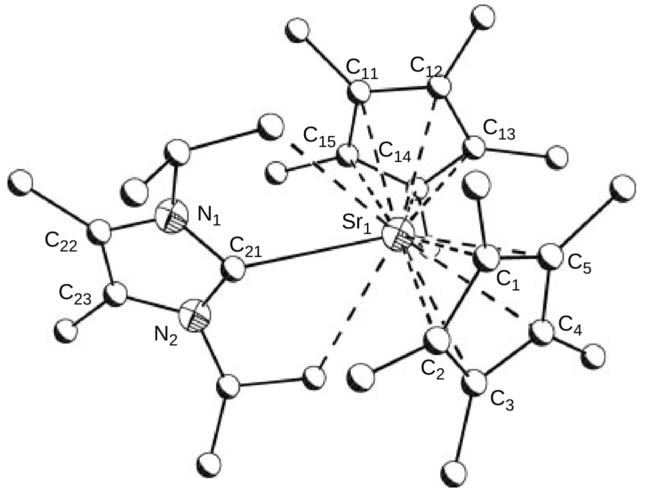

Figure 5 The solid-state structure of $(C_5Me_5)_2Sr(N,N{}^iPr_2 3,4\text{-}Me_2\text{-}C_3N_2)_2$. Hydrogen atoms have been omitted for clarity

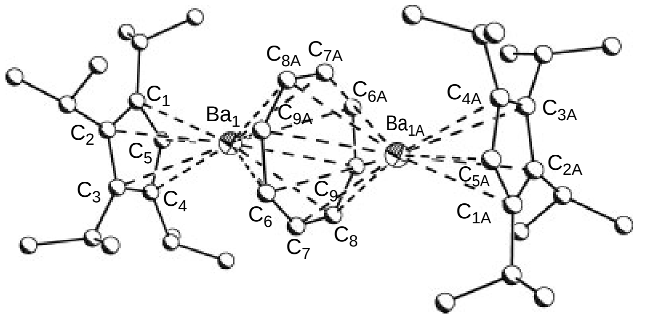

Figure 6 The solid-state structure of $\{(i\text{Pr})_4\text{Cp}\}\text{cotBa}_2$. Hydrogen atoms have been omitted for clarity

although there is variation in the solid state with the calcium and barium structures being monomeric while the strontium congener is a coordination polymer, as shown in Figure 7.

The bent structural motif observed in the cyclopentadienides and the indenides is continued even if the sterically more demanding fluorenyl ligand is coordinated to the metal center, as seen in bis(fluorenyl)barium$(NH_3)_4$, shown in Figure 8.[81] Even though the ligands are large enough to prevent oligomerization, the metal coordination sphere is saturated by the small ammonia donors. The steric bulk of the ligand does not appear to affect the molecular geometry with the compound displaying a centroid–Ba–centroid angle of ca. 115°, considerably deviating from a VSEPR prediction of linearity.

A selection of *ansa*-metallocene derivatives in which two dimethylsilyl or ethyl-bridged Cp, indenyl or fluorenyl moieties encapsulate the alkaline earth metal center have been prepared (see Figure 9).[82,83] The structurally enforced narrow bite angle of these fused ligands correlates well with the bent metallocene geometries observed previously. *Ansa* derivatives may be prepared as chiral compounds, and as such open up possibilities for their application as catalysts or reagents for stereocontrolled organic synthesis.[82] The *ansa* derivatives of the heavier metals exhibit a slightly slipped coordination between the metal center and the ligand, with both of these favoring η^3 or η^5 coordination and the inclusion of higher numbers of donor solvent molecules (three for calcium, four for barium) as opposed to the more centrally mounted magnesium compounds.

3.3 Alkaline Earth Metal Organometallics Exhibiting Metal–Ligand π-Bonding

Several groups of heavy alkaline earth metal derivatives, exhibiting metal–ligand π-bonding, in addition to the metallocenes have been studied resulting in allyl and alkenyl derivatives in addition to 'open metallocenes'.[53,84] The *bis*-allyl calcium complex $(C_3(SiMe_3)_2H_3)_2Ca(THF)_2$, shown in Figure 10, displays a symmetrical orientation of the metal over the π-system.[85] In contrast, magnesium allyl derivatives

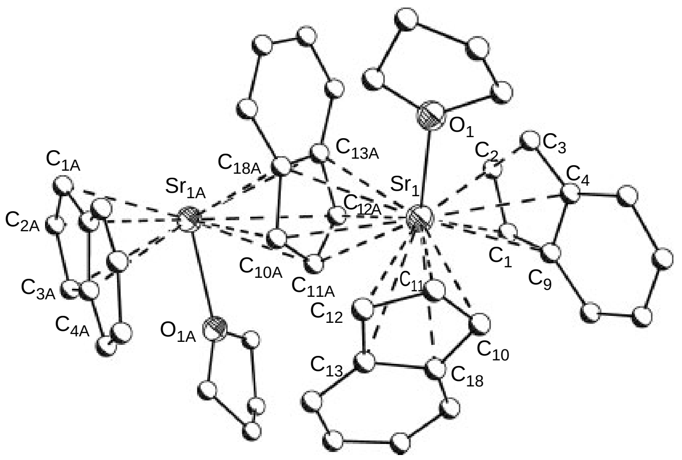

Figure 7 The solid-state structure of bis(indenyl)strontium(THF). Hydrogen atoms have been omitted for clarity

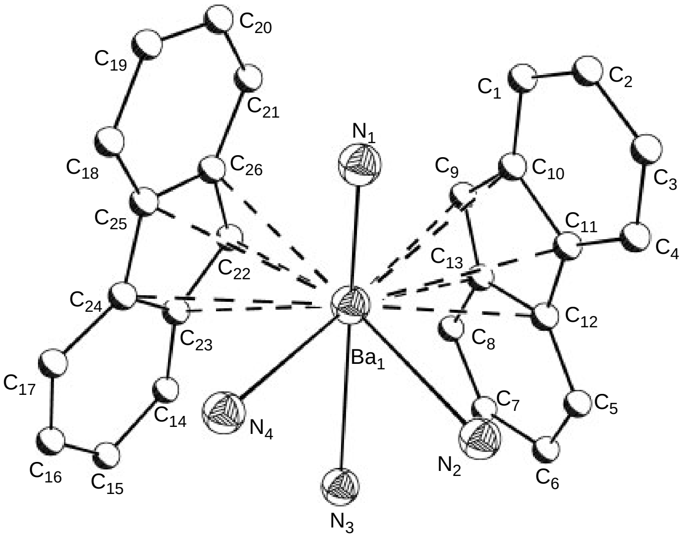
C_{20}
C_{19}
C_{21}
C_{1}
C_{2}
N_{1}
C_{18}
C_{26}
C_{9}
C_{10}
C_{3}
C_{25}
C_{11}
C_{4}
C_{22}
C_{13}
C_{24}
C_{12}
C_{23}
C_{8}
Ba_{1}
C_{17}
C_{7}
C_{5}
C_{14}
N_{4}
N_{2}
C_{16}
C_{15}
C_{6}
N_{3}

Figure 8 The solid-state structure of bis(fluorenyl)barium-tetrakis(ammonia). Hydrogen atoms have been omitted for clarity

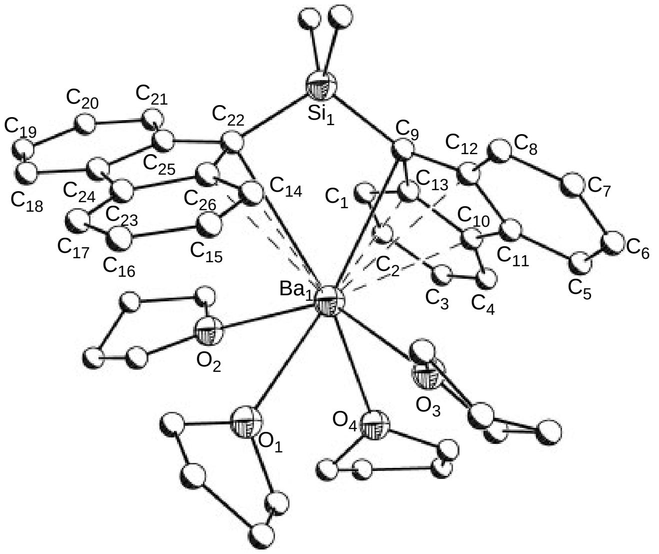
C_{20}
C_{21}
C_{19}
C_{22}
Si_{1}
C_{9}
C_{12}
C_{8}
C_{25}
C_{18}
C_{24}
C_{26}
C_{14}
C_{1}
C_{13}
C_{7}
C_{23}
C_{10}
C_{6}
C_{17}
C_{16}
C_{15}
C_{11}
C_{2}
Ba_{1}
C_{3}
C_{4}
C_{5}
O_{2}
O_{3}
O_{4}
O_{1}

Figure 9 The solid-state structure of $Me_2Si(fluorenyl)_2Ba(THF)_4$. Hydrogen atoms have been omitted for clarity

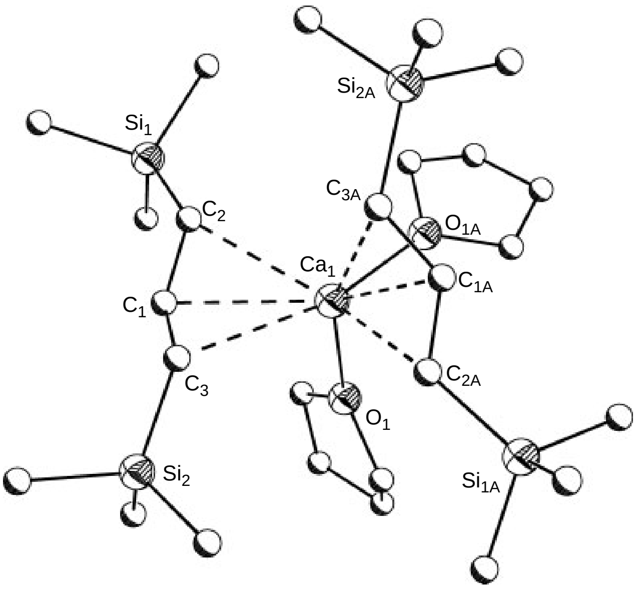
Si_{2A}
Si_{1}
C_{3A}
C_{2}
O_{1A}
Ca_{1}
C_{1A}
C_{1}
C_{2A}
C_{3}
O_{1}
Si_{2}
Si_{1A}

Figure 10 The solid-state structure of $(C_3(SiMe_3)_2H_3)_2Ca(THF)_2$. Hydrogen atoms have been omitted for clarity

feature a σ-bond to the allyl group. The different metal–ligand bonding modes have been put to use by Yamamoto *et al.* with allylbarium reagents to overcome the synthetic obstacles inhibiting comparable organomagnesium compounds.[4–9]

Variation of extension of the π-system and substitution thereof allowed for characterization of several magnesium, calcium, strontium, and barium species. Trimethylsilyl substitution on the alkenyl chain led to the formation of a magnesium TMEDA adduct,[86] while the terminal phenylation of the alkenyl system leads to the formation of monomeric compounds of calcium and strontium with solvation by THF filling the coordination sphere.[87] Similar compounds have been prepared with phosphorus ylids, leading to the characterization of several barium organometallic species bearing phosphorus supported ligands.[88,89] Further substitution can lead to metal-carbon interactions, such as in the coordination of barium to a highly conjugated system bearing a phosphacyclopentadienyl moiety, and a coupled diphenylbutadiyne system to give an intriguing complex, shown in Figure 11.[90]

Further documenting the breadth of metal–ligand π-interactions is an ‘open’ calcocene derived from an acylic pentadienyl ligand.[84] With the addition of trimethylsilyl

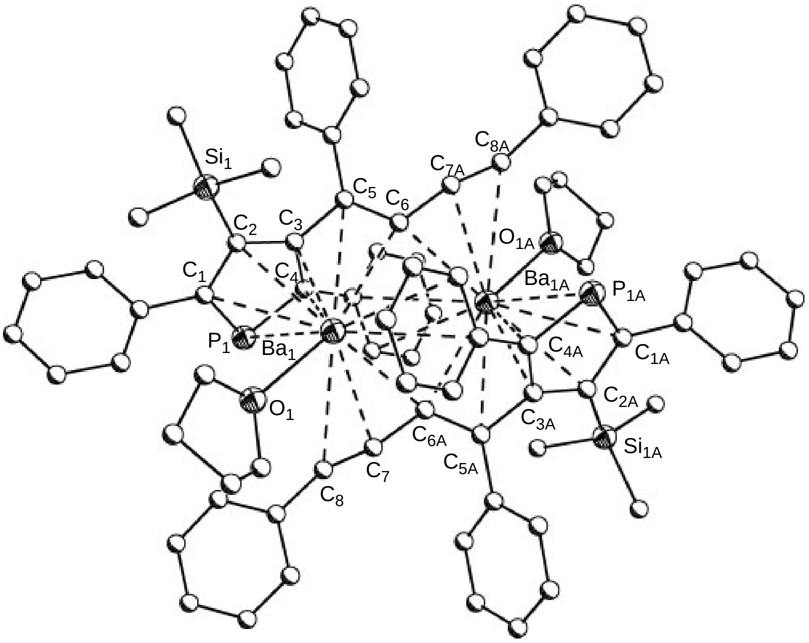

Figure 11 The solid-state structure of [(2,5-diphenyl-3-(1,4-diphenylbutene-3-yne-2-ide-1-yl)-4-TMS-1-phosphacylopentadienide)Ba (THF)]$_2$. Hydrogen atoms have been omitted for clarity

moieties to stabilize the system and assist with solubility, this ligand is of particular interest because of the variety of possible binding modes available. In the solid-state complex, as a single THF solvate, the system displays the ligands in an *anti* orientation with the TMS substituents pointing away from each other. Both π systems display η^5 coordination, and the complex shows the familiar bent geometry so commonly observed in alkaline metal organometallics.

Derived from the reaction of anthracene with the alkaline earth metals in a donor solvent, and of particular interest owing to its utility as a source for highly pure metal, the anthracenide derivatives have received some attention. (Anthracenide)Mg(THF)$_3$, shown in Figure 12, was initially reported in 1967,[91] its structural characterization followed in 1988.[36] The compound is known for its easy reaction with hydrogen in the presence of transition metal catalysts.[40] The resulting MgH_2 can be added to 1-alkenes. Owing to the low solubility of the anthracenides, substitution of the aromatic ring increases solubility to afford a selection of structurally characterized species.[36] In all cases, the metal is bridging the two central carbon atoms. The coordination environment at the metal is completed by three THF donors. Thus far, no structural information is available on the heavier congeners, likely owing to the low solubility of the complexes and associated problems with the growth of suitable single crystals.

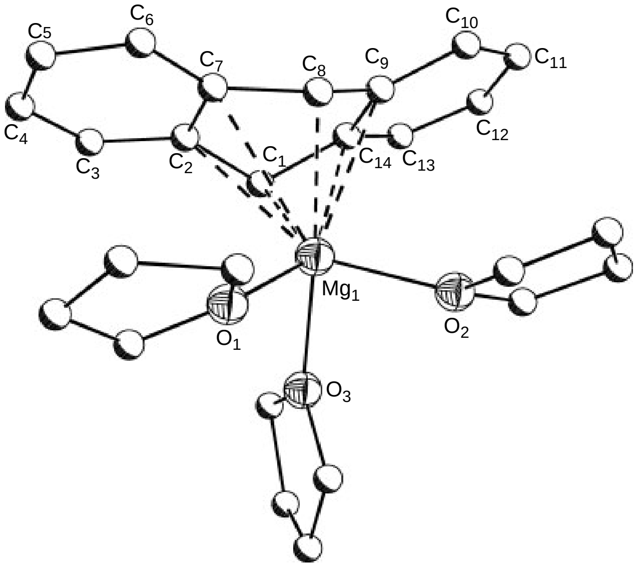

Figure 12 The solid-state structure of (anthracenide)Mg(THF)$_3$. Hydrogen atoms have been omitted for clarity

A variant of these compounds, magnesium anthracenylmagnesiumbromide etherate, shown in Figure 13, displays a dimeric structure with a somewhat surprising metal–ligand σ-interaction.[92] The two magnesium centers do not bind to the central anthracenide ring, rather, a η^1 metal–ligand bond with bridging bromides is completing the magnesium coordination sphere. It is anticipated that the greater need for steric saturation for the heavier metals, together with increased ionic bond character would necessitate an extended coordination sphere, achieved either by additional solvation or aggregation.

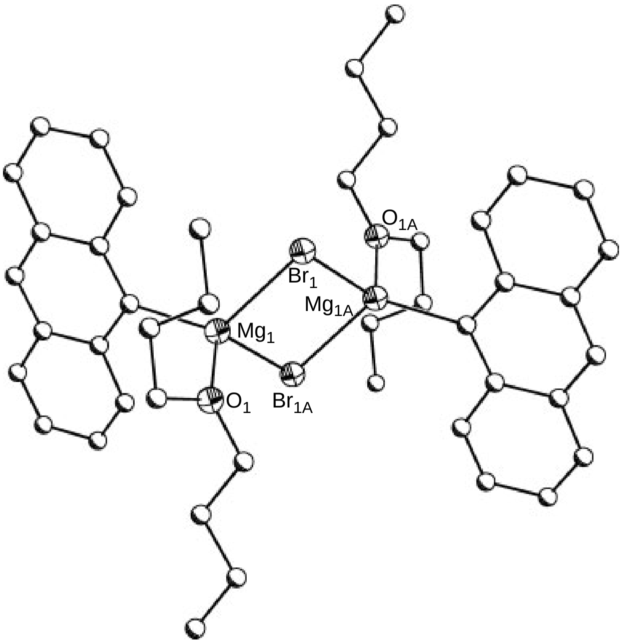

Figure 13 The solid-state structure of (magnesium anthracenyl-magnesiumbromide etherate. Hydrogen atoms have been omitted for clarity

3.4 σ-Bonded Organometallic Systems

A range of σ-bonded organometallic complexes of beryllium and magnesium has been reported, and we will briefly discuss some central structural trends observed within this group of compounds. Owing to the wealth of information, especially in regards to organomagnesium chemistry, we refer to several excellent review articles.[67,93,94] In contrast to the steady progress on metallocenes and π-stabilized compounds for the heavier metals, σ-bonded calcium, strontium, and barium organometallics were languishing in obscurity while simple alkyl derivatives for the larger metals eluded characterization. Partially as a result of the extremely high reactivity, low solubility, and difficulties in characterization posed by these compounds, and partially because of the perceived lack of application as compared to organomagnesium chemistry, it was not until 1991 that the first structurally characterized compounds of this type became available.

By far the largest group of compounds of this type has been reported for magnesium, while the high toxicity of beryllium and its compounds dampened interest. Dimethylberyllium, shown in Figure 14, is a polymeric species, exhibiting four-coordinate beryllium centers through 2e3c-CH_3 bridges.[95] In the gas phase, the compound exhibits monomeric Me_2Be molecules with linear geometry, as analyzed by electron diffraction.[47] An increase in ligand size reduces aggregation tendencies, as demonstrated with $(t\text{Bu})_2Be$, which exhibits a monomeric structure in the solid state.

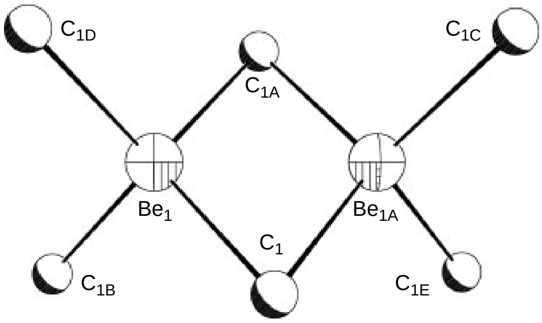

Figure 14 The solid-state structure of $(Me_2Be)_n$. Hydrogen atoms have been omitted for clarity

Even in the presence of bulky ligands, the addition of Lewis bases affords base adducts, as observed for the three coordinate $(2,4,6\text{-}Me_3C_6H_2)_2BeOEt_2$.[96] Heteroleptic beryllium species display the same trend, with a coordination number of two if Lewis bases are absent and the ligands are large, as seen in the terphenyl derivative 2,6-$(2,4,6\text{-}Me_3C_6H_2)_2C_6H_3BeN(SiMe_3)_2$, shown in Figure 15.[97] However, not even extremely bulky ligands such as terphenyl can prevent the addition of donor molecules.

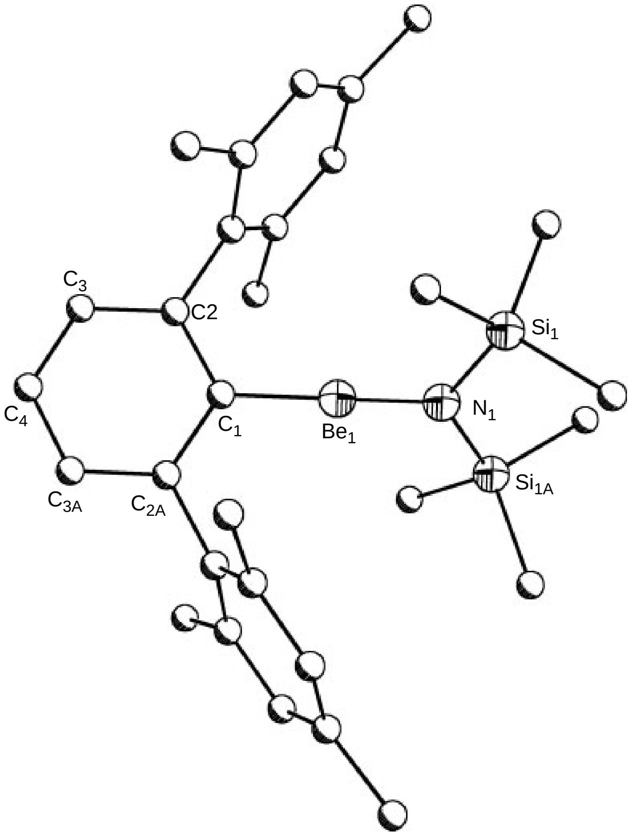

Figure 15 The solid-state structure of 2,6-$(2,4,6\text{-}Me_3C_6H_2)_2C_6H_3$ $BeN(SiMe_3)_2$. Hydrogen atoms have been omitted for clarity

Similar trends are seen for the magnesium species, and the use of bulky ligands in the absence of Lewis bases allows the preparation of rare two-coordinate alkyl magnesium species. Examples include the linear $(Me_3Si)_3C)_2$ Mg.[98] Interestingly, utilization of the bulky Mes* (Mes* $= 2,4,6\text{-}t\mathrm{Bu}_3C_6H_2$) ligand also affords a two-coordinate compound $(2,4,6\text{-}t\mathrm{Bu}_3C_6H_2)_2$ Mg, but with a bent structure, shown in Figure 16.[99] The bent metal geometry might be explained on the basis of agostic interactions originating from the *ortho tert*-butyl groups at the ligand. These interactions are also likely responsible for the lack of donor coordination, even in the presence of THF. The reduction of ligand size affords complexes with a coordination number of four or higher.

The clean isolation and structural characterization of heteroleptic Grignard species remains problematic, owing to complex solution equilibria. Still, a number of compounds have been analyzed in an effort to further understand aspects contributing towards the formation and composition of these important reagents. In all cases, donor-containing compounds were obtained, with the coordination environment of the metal strongly dependent on ligand and donor size and the nature of the halide. Generally, the presence of sterically demanding ligands facilitates the isolation of the heteroleptic species. The bulky ligands also support the isolation of species with a low metal coordination number as demonstrated with the dimeric, four-coordinate $[(2,6\text{-}(2,4,6\text{-}Me_3C_6H_2)_2C_6H_3)MgBr(THF)]_2$,[100] (Figure 17) or the four coordinate, monomeric $(2,4,6\text{-}Ph_3C_6H_2)MgBr(thf)_2$, (Figure 1), $(2,6\text{-}(2,4,6\text{-}i\mathrm{Pr}_3C_6H_2)_2C_6H_3)MgBr(THF)_2$[101] and $PhMgBr(OEt_2)_2$.[102] In the presence of smaller ligands and donors the metal coordination number increases, as demonstrated with the five-coordinate $MeMgBr(THF)_3$.[103] While intense efforts have led to a much-improved understanding of the Schlenk equilibrium and the reagents involved, numerous questions regarding mechanistic rationales and structure-function relationships keep the field active.

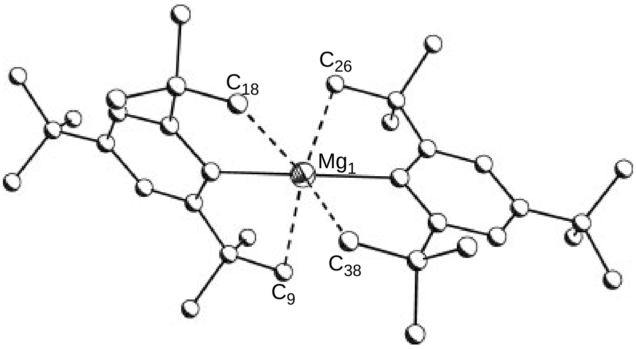

Figure 16 The solid-state structure of $(2,4,6t\text{-}Bu_3C_6H_2)_2Mg$. Hydrogen atoms have been omitted for clarity

Simple alkyl complexes for the heavier congeners, calcium, strontium, and barium remain scarce. Even as information on Grignard reagents became more widely available owing to improved synthetic and spectroscopic techniques (particularly in the field of X-ray crystallography) progress with the larger metals lagged behind. Although several reports of preparation of such compounds were disseminated, little detailed information was provided. As of now, only a few simple alkyl complexes of the heavier alkaline earth metals have been isolated and well characterized, perhaps as the result of the higher demand for electronic and coordinative stabilization required for such compounds as compared to

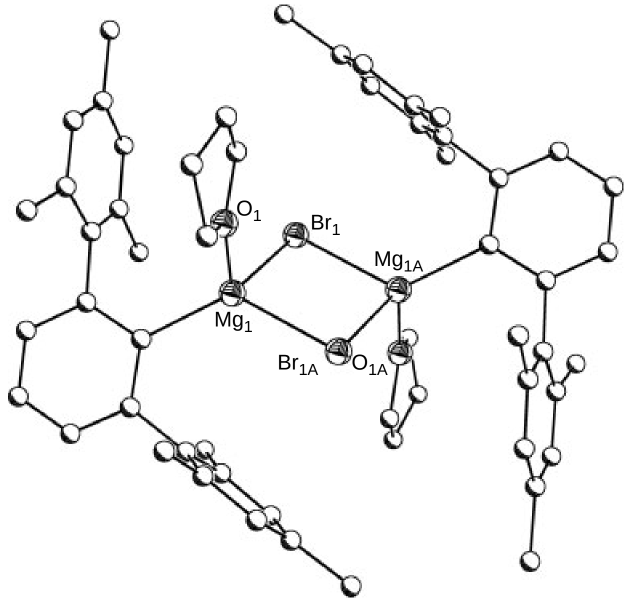

Figure 17 The solid-state structure of $[(2,6\text{-}(2,4,6Me_3C_6H_2)_2C_6H_3)MgBr(THF)]_2$. Hydrogen atoms have been omitted for clarity

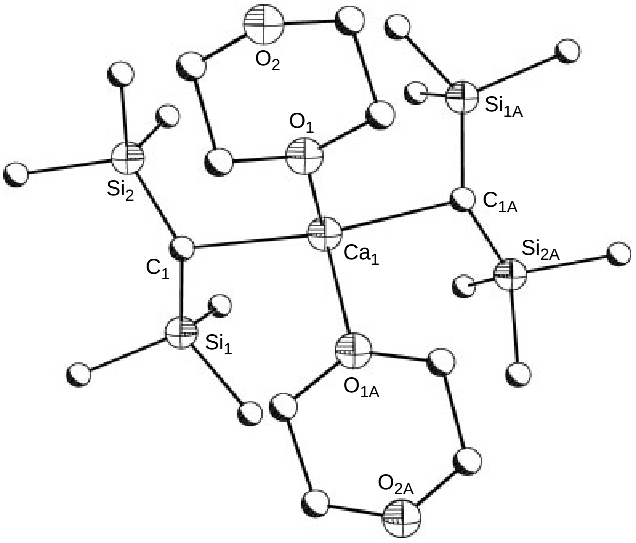

Figure 18 The solid-state structure of $(CH(SiMe_3)_2)_2Ca(dioxane)_2$. Hydrogen atoms have been omitted for clarity

magnesium and beryllium. In addition, the (relatively) more ionic metal-carbon bonds render the metal–ligand bonds more labile without high degrees of stabilization by other donors or solvent molecules contributing to the structure.

Beginning in 1991, the first structurally characterized σ-bound heavy alkaline earth organometallic appeared with the four-coordinate $(CH(SiMe_3)_2)_2Ca(dioxane)_2$ (Figure 18).**[104]** Although the synthetic pathway was highly technical (cocondensation of calcium vapor and the bromoalkyl at 77 K) the final product could be isolated and structurally characterized. Further progress did not come until 1997 with the two-coordinate $((SiMe_3)_3C)_2Ca$, a σ-bonded 'unstabilized' (i.e. lacking other metal-donor interactions beyond the organometallic bond) organometallic (Figure 19), which remains the only example of such a compound. Interestingly, bent metal geometry is observed in this compound, whose origin may be explained on the basis of agostic interactions rather than trends observed for the halides or cyclopentadienide derivatives.**[43]**

With σ-bonded organometallic compounds of the heavy alkaline earth metals still limited to calcium, the expansion of the library of such compounds to the heavier metals was achieved with a family of crown ether stabilized alkaline earth metal acetylides $M(CCSiPh_3)_2$(18-crown-6) (M = Ca, Sr, Ba) (Figure 20).**[105]** The compounds presented important information for the comparison of reactivity and structural trends for the heavy alkaline earth metals. Interestingly, the acetylides display increased bending at the metal center as descending the group, and also increased bending at the ipso-carbon atom within the acetylide ligand. Carbon-metal-carbon angles within the barium compound display values as low as 163° for the L-M-L moiety, with angles at the ipso-carbon atom as narrow as 127 and 141° for the sp hybridized ligand atoms. In contrast, acetylides of magnesium and beryllium display linear geometry at the ipso ligand atom. The deviation from ideal geometry can largely be explained by the low directionality of the sp-hybrid orbital and associated facile distortion from ideal geometry. Interestingly, though, a closely related group of acetylides, M(18-crown-6)$(CC4\text{-}t\mathrm{Bu}C_6H_4)_2$ displays an almost identical deviation from linear geometry with angles at the ipso atom as low as 126°.**[106]**

While the acetylides took advantage of the coordinative and electrostatic stabilization afforded by the crown ethers, other means of stabilizing σ-bonded organometallics involve the use of intramolecularly coordinated ligands, as elegantly applied in the preparation of the simple alkyl complexes $((Me_3Si)_2(MeOMe_2Si)C)_2M(donor)$ (M = Sr (donor = THF); Ba (donor = DME $(MeOCH_2CH_2OMe)$; Figure 21).**[107]**

3.5 Substituted Phenylmethanides and π-stabilized Alkaline Earth Organometallics

Early work on the dibenzyl derivatives of the heavier alkaline earth metal triad suggested that they could be

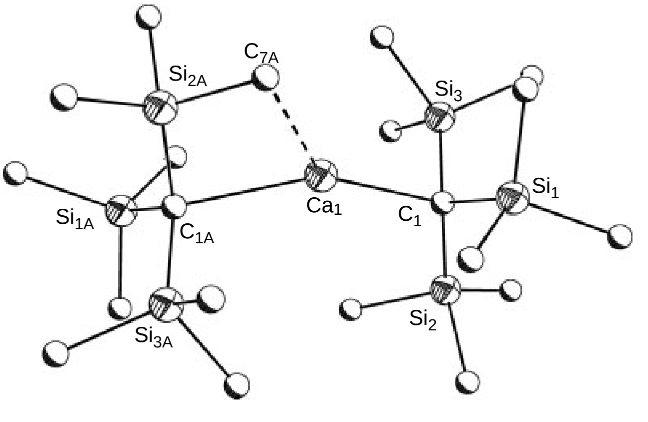

Figure 19 The solid-state structure of $(SiMe_3)_3C)_2Ca$. Hydrogen atoms have been omitted for clarity

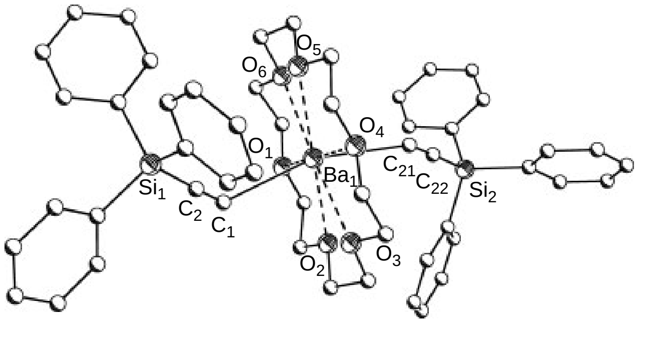

Figure 20 The solid-state structure of $(Ph_3SiCC)_2Ba$(18-crown-6). Hydrogen atoms have been omitted for clarity

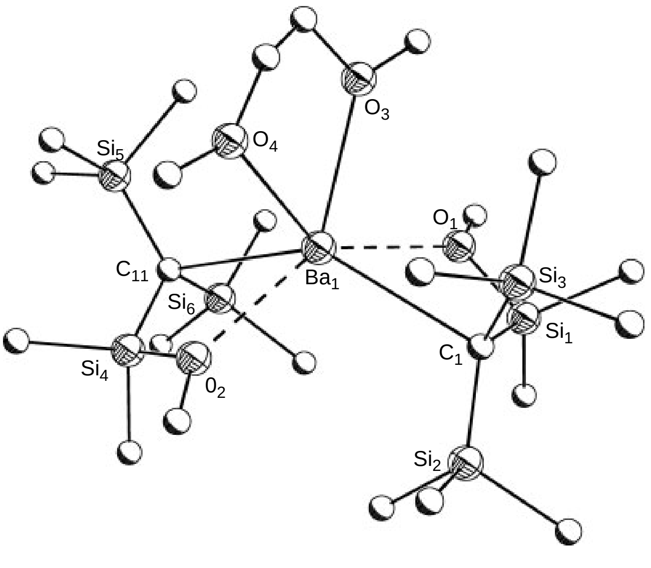

Figure 21 The solid-state structure of $((Me_3Si)_2(MeOMe_2Si)C)_2Ba$ (DME). Hydrogen atoms have been omitted for clarity

valuable reagents to be employed in various polymerization applications.[108,109] However, this work was limited to in situ examinations and NMR studies, and the inability to determine the exact nature of the reagents hampered further progress in this field. It was not until Harder *et al.* developed a facile method for the preparation of pure calcium and barium dibenzyl derivatives including in-depth structural characterization and structure/function studies, that the role of dibenzyl derivatives in polymerization chemistry could began in earnest.[10]

Relying on a transmetallation scheme for the preparation of dibenzylbarium, the common problem of separating the two solid reaction products (see above) was addressed by careful choice of reaction condition.[10] Nevertheless, it remained difficult to isolate the strontium derivative, and further manipulation of the solvent system was needed to allow the isolation of the pure compound.[45] The separation problem was exacerbated for calcium, requiring the use of salt elimination for its preparation.[42]

Shortly after Harder's report of isolable dibenzylbarium, various other related compounds appeared in the literature. Continuing with the approach of tuning solubility, both through substituent effects as well as solvent choice, it was discovered that substitution of toluene with trimethylsilyl substituents allowed for the isolation and characterization of crystalline complexes of *bis*-(α,α-*bis*(trimethylsilyl)benzyl) potassium and calcium.[110] Similar to the proposed structure of dibenzylbarium, the calcium compound was a THF solvate, although the potassium congener (used as a precursor *via* metathesis) was a linear polymer without additional Lewis donor coordination. This compound also displayed interesting deformations in the phenyl rings as a result of metal coordination, which occurred in an η^3 fashion (Figure 22).

While $SiMe_3$ coordination significantly improved the solubility of the complexes, the increased steric demand of the ligand significantly reduced the compound's activity towards styrene polymerization. Continuous work focused on the introduction of alternative substituents, and their introduction in other but the α-positions. As a result of this work, benzyl complexes of calcium have been prepared using the combination of a single $SiMe_3$ substituent on the α-carbon in addition to an *ortho*-dimethylamino moiety (Figure 23).[111] Prepared through metathesis with the corresponding potassium salt, this compound afforded highly pure compounds with a high tendency for crystal formation. Unlike the *bis*-$SiMe_3$ substituted complex, where significant metal-arene interactions are observed, the dimethylamino derivative displays no such interaction, likely owing to the intramolecular stabilization of the ligand.

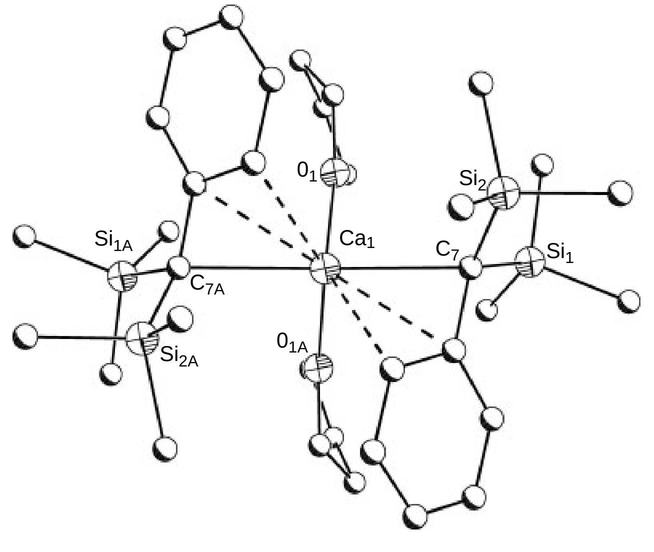

Figure 22 The solid-state structure of $Ca[(SiMe_3)_2CC_6H_5)]_2[THF]_2$. Hydrogen atoms have been omitted for clarity

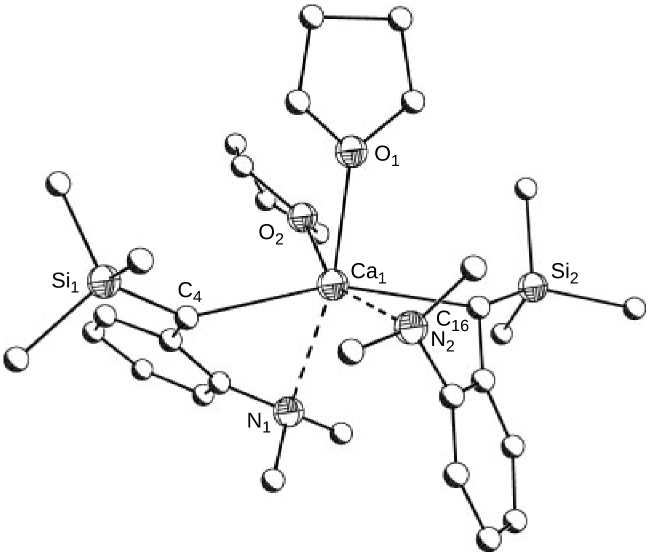

Figure 23 The solid-state structure of $Ca[(SiMe_3)CH(o\text{-}NMe_2)C_6H_4]_2[THF]_2$. Hydrogen atoms have been omitted for clarity

This compound demonstrates two diastereomers in slow exchange as viewed through NMR studies in benzene, although only one set of THF signals is observed. A dissociative mechanism of exchange between disastereomers has been proposed. Unlike the *bis*-Me_3Si-substituted compound, this complex does act as a polymerization initiator, giving predominantly atactic product. The only other example of a heavier alkaline earth metal dibenzyl system is the strontium analog of the calcium dimethylamino stabilized system. This compound is a more effective initiator than the analogous calcium system, likely owing to the more exposed metal center.[112]

The steric bulk of the substituted benzyl ligands allows the preparation of heteroleptic species, examples include the combination of the dimethylamino stabilized dibenzyl reagent and 9-Me_3Si substituted fluorene, as shown in Figure 24.[113] Despite the presence of sterically demanding ligands and intramolecular coordination, this complex still displays additional Lewis base donation, although the steric demand of the fluorene ligand only permits a single THF to

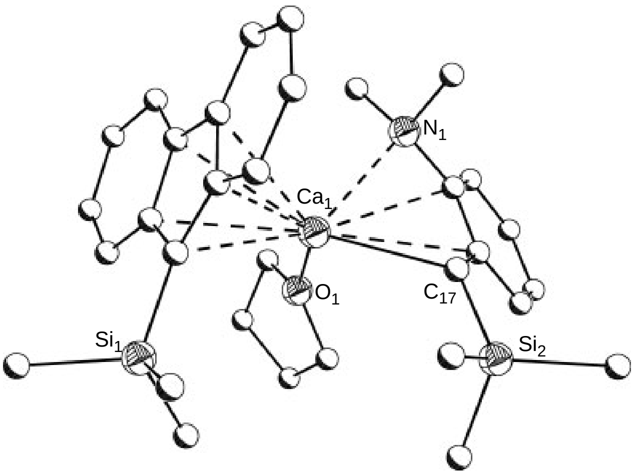

Figure 24 The solid-state structure of [9-$SiMe_3$-fluorene][o-NMe_2-(TMS)CHC_6H_4]Ca. Hydrogen atoms have been omitted for clarity

approach the metal center. The metal sits squarely over the center of the larger π-center while maintaining a single metal-carbon bond to the benzyl carbon as well as an interaction with the dimethylamino moiety. This compound is also an active polymerization initiator, although product control is difficult owing to the inability of the calcium compound to maintain stereochemical integrity during the reaction. However, under certain conditions, the inversion of the compound can be circumvented to produce polymers with high syndiotacticity.

Introduction of secondary stabilization in the form of –NMe_2 functionalities, and removal of the $SiMe_3$ moiety allows the formation of heteroleptic complexes. Unlike the larger Me_3Si substituted ligand, the steric requirements of the metal are fulfilled by dimerization. Examples include products involving the dibenzyl ligand in addition to ligation to 9-Me_3Si fluorene or Me_4EtCp, as shown in Figure 25.[114]

As these studies seemed to indicate that substitution on the benzylic carbon tends to slow activity as a polymerization initiator, attempts were made to isolate simpler compounds with as little crowding near the metal center as possible. This was realized with the preparation of *para*-substituted homoleptic dibenzyl complexes of calcium, as well as the isolation of the elusive unsubstituted dibenzylcalcium derivative by salt elimination.[42] Preparation of the *para*-*t*Bu compound was possible through metathesis of the potassium salt, and led to a six-coordinate tetra-THF solvate. Interestingly, this complex displays η^1 coordination product in the solid state, with the benzyl ligands taking axial positions over four equatorially located THF molecules, shown in Figure 26. This geometry is altered in the unsubstituted dibenzylcalcium compound Figure 26 with the ligands adopting a cis orientation with four THF donors completing the coordination sphere. The somewhat surprising differentiation in coordination geometry is ascribed to the charge localizing effect of the *para* substituent that removes some of the electronic imperative to adopt a trans geometry in the solid state. The dibenzyl compounds appear to be promising metallation reagents for a variety of less acidic compounds, and in fact have been applied in such a manner.

Replacement of one α-carbon atom in the benzyl ligand by a phenyl group affords diphenylmethane, with a second replacement giving triphenylmethane, several compounds of which have been isolated in conjunction with the heavy alkaline earth metals by utilizing the dibenzyl reagents as alkaline earth metal source materials. The di- and triphenylmethanides are easily available owing to the increased acidity of the parent hydrocarbons, as compared to toluene. In the presence of a stabilizing crown ether, a rare example of a compound exhibiting barium-ligand σ-bonding, $(HCPh_2)_2Ba$(18-crown-6), shown in Figure 27, is obtained.[44]

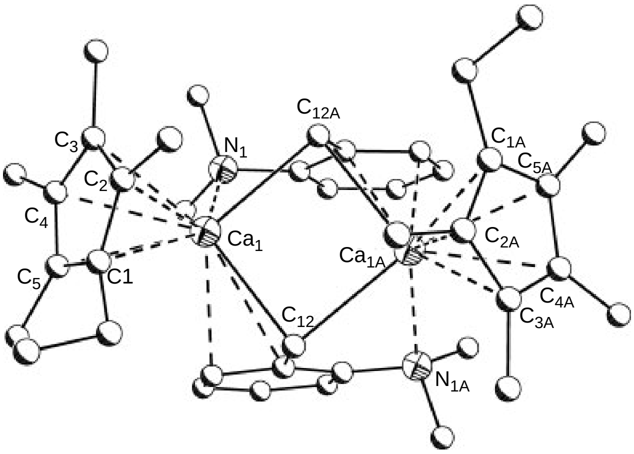

Figure 25 The solid-state structure of [(o-$NMe_2C_7H_6$)(Me_4EtCp) Ca]$_2$. Hydrogen atoms have been omitted for clarity

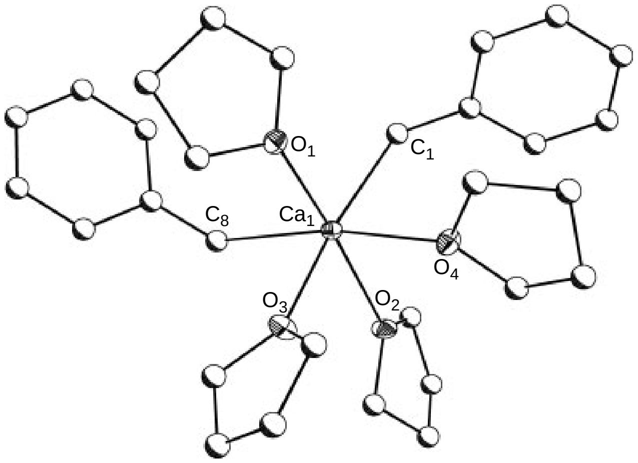

Figure 26 The solid-state structure of $(PhCH_2)_2Ca(THF)_4$. Hydrogen atoms have been omitted for clarity

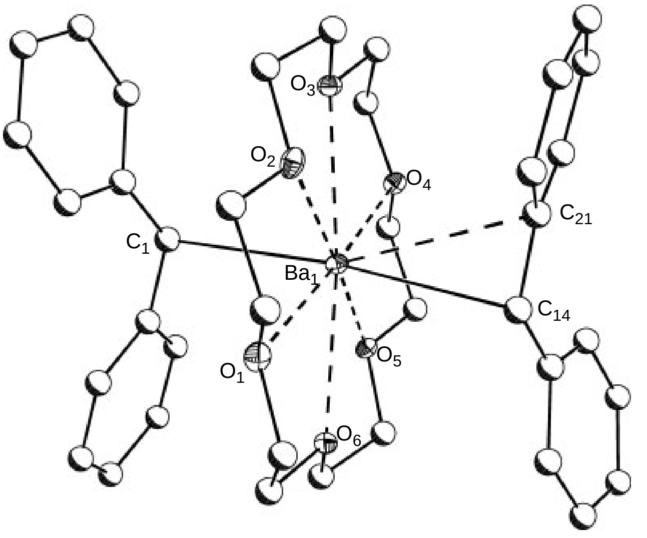

Figure 27 The solid-state structure of $(HCPh_2)_2Ba$(18-crown-6). Hydrogen atoms have been omitted for clarity

This compound displays a slightly pyramidal geometry at the α-carbons, and the phenyl rings are not coplanar, which is typical for sterically congested multiphenyl-substituted ligands of this type. The increased steric demand of the ligand together with the electronic and coordinative stabilization provided by the crown ether enable increased stability as compared to the dibenzyl derivative. Remarkably, crown ether-stabilized barium diphenylmethanide is sufficiently stable to allow for recrystallization from hot THF, whereas dibenzylbarium reacts readily with THF at temperature above −40 °C.

Although these compounds have considerable synthetic difficulties surrounding their preparation and characterization, the interesting questions of metal-carbon bonding and potential application in polymer synthesis ensure further research efforts.

3.6 '-Ate' Complexes of the Alkaline Earth Metals

'Ate' complexes of the alkaline earth metals are most prominent for magnesium, and to a significantly lesser extent for the heavier metals. The compounds are often observed in the presence of encapsulating donors such as crown ethers or cryptates; a representative example is shown in Figure 28.**[115]**

The number of 'ate' complexes for the heavier congeners is smaller, owing to the significantly reduced metal charge density. As such, the polymeric barate $[Bu_4P]$ $[Cp_3Ba]$, shown in Figure 29, represents a significant example of this class of compounds. The barate was prepared through the combination of Cp_2Ba, $Bu_3P{=}CH(CH_2)_2CH_3$ and CpH employing the Wittig reagent to generate the cyclopentadienide anion while avoiding undesirable side products.**[116]** The anions form infinite chains further stabilized by agostic interactions to the phosphonium units.

Not unexpectedly, the Cp–Ba bond lengths within the barate are considerably lengthened as compared to the simple Cp_2Ba systems, and the Cp rings exhibit rotational disorder. The η^4-metal coordination of the Cp rings is particularly interesting. With four such interactions, the metal coordination sphere seems to be sufficiently stabilized rendering further

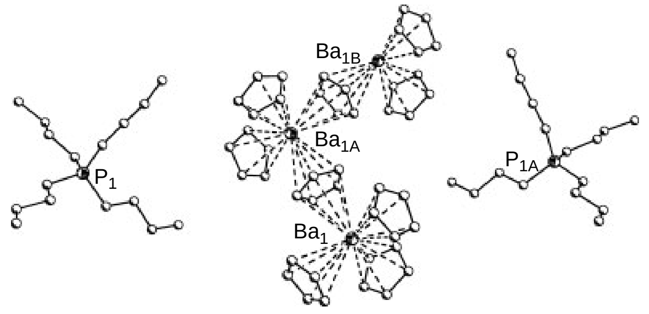

Figure 29 The solid-state structure of $[Bu_4P][Cp_3Ba]$. Hydrogen atoms have been omitted for clarity

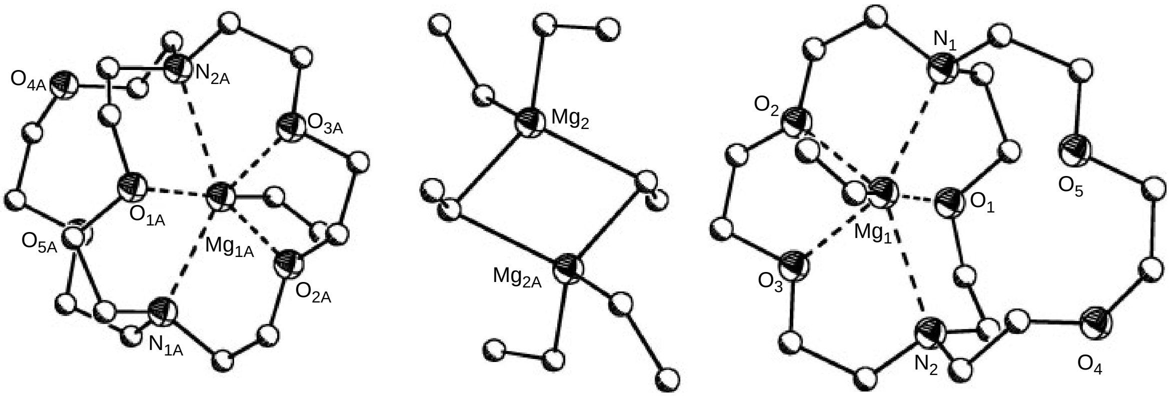

Figure 28 The solid-state structure of $[EtMgL]_2^{+}$ $[Et_6Mg_2]^{2-}$ Hydrogen atoms have been omitted for clarity

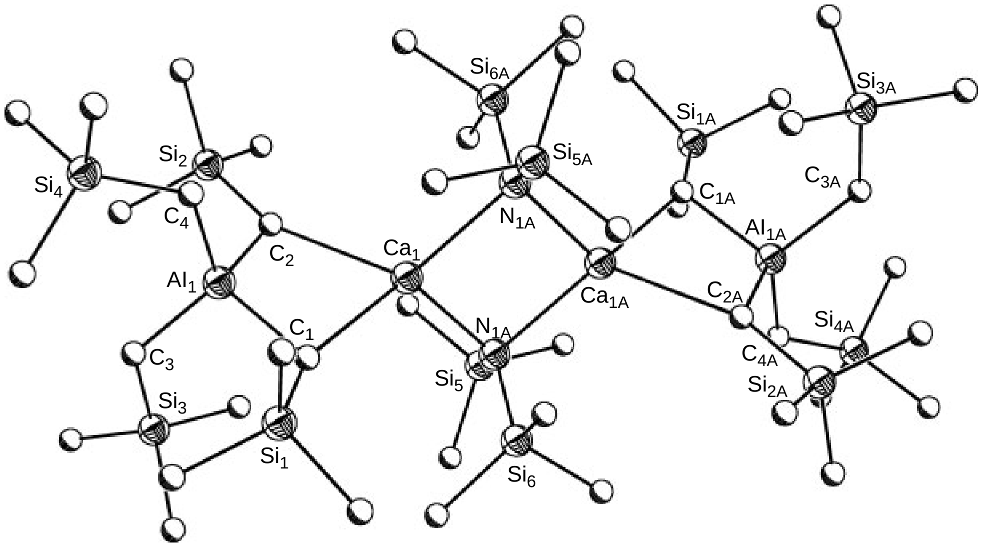

Figure 30 The solid-state structure of $Ca_2[Al(CH_2SiMe_3)_4]_2[N(SiMe_3)_2]_2$. Hydrogen atoms have been omitted for clarity

donor solvent-metal interaction unnecessary. Representing an approximate tetrahedral geometry, the Cp–Ba–Cp angles range from 106.3–114.6°. Other results from this study seem to indicate that it may be possible to prepare the dianionic barate anion, $[Cp_4Ba]^{2-}$.

Led by the efforts of Westerhausen and coworkers, a variety of heavy alkaline earth metal zincates or aluminates under formation of alkaline earth metal-carbon contacts have been prepared. Examples include the reaction of trialkylalanes with donor-free calcium *bis*-amides to afford dimeric aluminates, shown in Figure 30.**[117]** Noteworthy is the planar Ca_2N_2 center of this complex, in addition to close calcium–aluminum contacts, which may indicate the presence of three-center, two-electron bonding.

Other examples of this series include a selection of 'ate' complexes prepared by the treatment of alkylzinc reagents with freshly distilled alkaline earth metals under extrusion of elemental zinc.**[28]** This route was employed to prepare a strontium zincate in which the alkaline earth metal center adopts a distorted octahedral geometry completed by two THF solvent donors.**[28]** Similar reactions with barium metal lead to structurally closely related compounds. Flexibility in solvent choice is noted by the preparation of related complexes in toluene, displaying metal-toluene π-interactions.

The compounds prepared by these reactions are highly susceptible to rearrangements in situ; reaction of barium bis[tris(trimethylsilylmethyl)zincate] with excess barium gives a unique barium cubane, shown in Figure 31.**[118]** Acting through a proposed alkylbarium intermediate, this compound is stabilized by agostic interactions surrounding the metal core. This complex displays carbon atoms in the relatively rare coordination number of six, with extended contacts to the zinc centers.

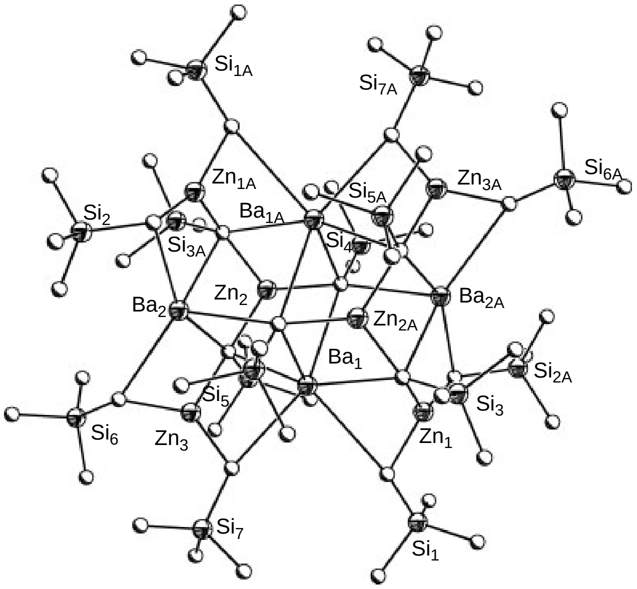

Figure 31 The solid-state structure of $Ba_4[Zn_6(CH_2SiMe_3)_4(CHSiMe_3)_3]_2$. Hydrogen atoms have been omitted for clarity

3.7 Charge-separated Alkaline Earth Organometallics

A category of organometallic alkaline earth complexes does not involve metal–ligand bonding. Such compounds, while common in aqueous solution for many cations, are much less prevalent for the alkaline earth organometallics. Nonetheless, under carefully controlled reaction conditions these highly reactive compounds may be synthesized, isolated, and characterized. In order to accomplish this feat, both the anion and the cation must be appropriately stabilized. A combination of two factors should be considered when attempting to induce

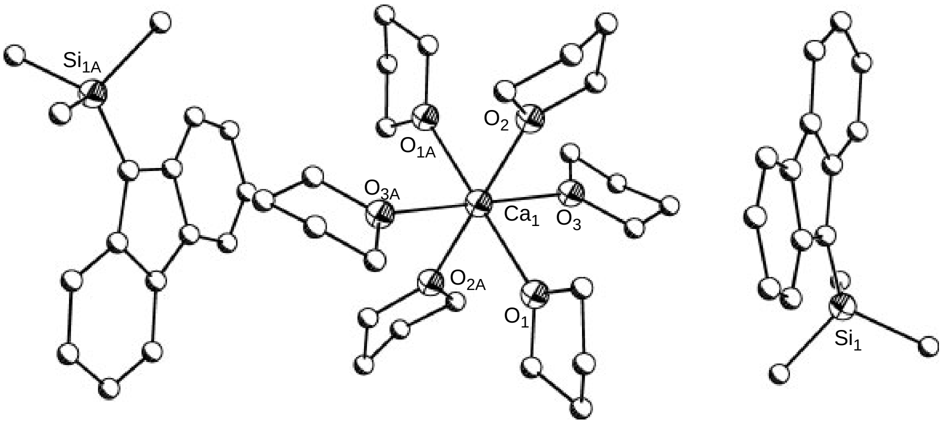

Figure 32 The solid-state structure of $[Ca(THF)_6][Me_3Si(fluorenyl)]_2$. Hydrogen atoms have been omitted for clarity

charge separation in these organometallics. The simplest route involves the application of donor solvents to saturate the cation as a solvent-separated ion pair (SSIP). The formation of separated ions is facilitated if the anion is capable to delocalize the negative charge, as seen in $[Ca(THF)_6]^{2+}$ $[Me_3Si(fluorenyl)]_2{}^{2-}$, shown in Figure 32.**[119]** The extensive resonance stabilization in the anion allows ion separation despite cation coordination to only six monodentate THF donors. Clearly, the highly oxophilic nature of the calcium cation leads to energetically favorable cation interactions that trump the stability offered by direct metal-carbon contacts. Indeed, this balance between metal-donor and metal-carbon favorability is the deciding factor in determining the final solid-state geometry of the complex. This can be predicted with considerable accuracy when taking into account the size and nature of the donors versus the anion as well as the degree of electronic stabilization offered by each of these. Especially for resonance-stabilized anions, it is generally possible to induce separation, although isolation of these highly reactive compounds can be a challenge.

It has been suggested that considerable stability for solvated alkaline earth cations in such systems is granted by the 'metal-in-a-box' model, in which the arrangement of anionic ligands surrounding the solvated cation provides considerable electronic stabilization *via* long-range π-interactions in the presence of benzene as a 'lid' for the box.**[119]** In such systems, considerable stabilization between the THF protons and the anionic π-systems can be envisioned (Figure 33).

An alternative example of the metal-in-a-box model is provided by the monocationic $[(Ph_4B)Ba(thf)_4][BPh_4]$, shown in Figure 34. Here, the metal coordination sphere is completed by π-arene interactions to a BPh_4 anion, which binds in a sandwich-type interaction to the metal. Secondary, nonclassical interactions between the monocation and the noncoordinated anion provide additional stabilization. Interestingly, analogous reaction conditions for the smaller metals calcium and strontium afford the dicationic species $[M(thf)_n][BPh_4]_2$ ($M = Ca$, $n = 6$; $M = Sr$, $n = 7$), that are also stabilized by the nonclassical interactions. Clearly, the large barium center cannot be sufficiently stabilized by THF solvation alone.**[120]**

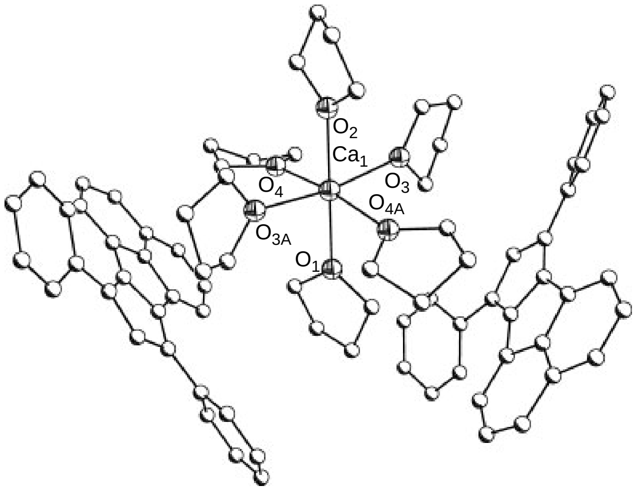

Figure 33 The solid-state structure of $[Ca(THF)_6]$[7,9-diphenyl-cyclopenta [*a*]acenapthadienide$]_2$. Hydrogen atoms have been omitted for clarity

An alternate, though related, approach to the formation of charge-separated ion pairs is to induce separation not through the solvent alone, but rather through application of appropriate donor systems and cosolvents (donor-assisted ion pairs – DAIP) to more effectively encapsulate the cation. This method has been employed most successfully for the larger congeners strontium and barium, whose coordination sphere is less easily filled by small donors such as THF. Most commonly employed for this technique are the versatile crown ethers, and the variety of cavity sizes allows for considerable flexibility in metal-donor bonding design. Also used successfully is the cosolvent hexamethylphosphoramide (HMPA), which is a powerful donor in its own right.

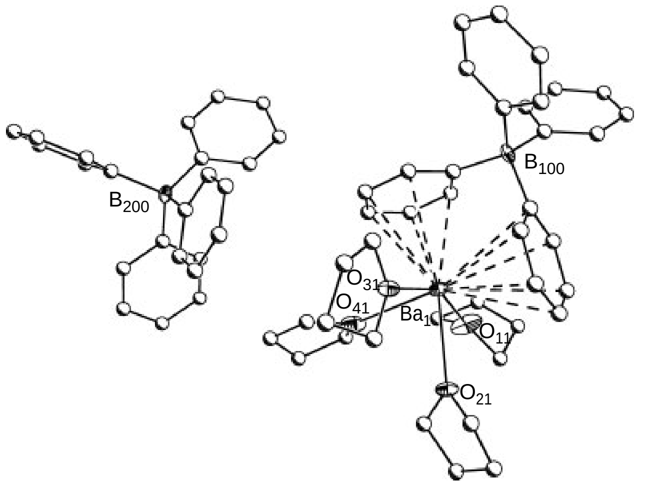

Figure 34 The solid-state structure of $[(Ph_4B)Ba(thf)_4][BPh_4]$. Hydrogen atoms have been omitted for clarity

As noted above, the ability of ligands with multiple phenyl rings positioned to allow resonance stabilization in an anion makes them ideal candidates for DAIP. Recent reports have demonstrated this with the presentation of a family of heavy alkaline earth triphenylmethanides, all of which occur as charge-separated complexes in the solid state.[45] Reaction of dibenzylbarium or strontium with triphenylmethane in the presence of 18-crown-6 and HMPA leads to the isolation of the DAIP triphenylmethanide, the barium compound of which is shown in Figure 35.

In the triphenylmethanides, the metal is coordinatively and electronically saturated by the encompassing crown ether that occupies an equatorial plane around the metal, as well as by the axially located HMPA donors. This favorable cation coordination environment is well established in alkaline earth metal chemistry. The ligands are free to adopt the most conformationally stable orientation, and steric demands force the rings away from planarity and in both the strontium and barium systems the rings display the familiar ‘propeller’ geometry, comparable to that seen for related alkali systems.

The calcium congener, while prepared through similar routes, eluded satisfactory structural determination until the application of pure, substituted benzylcalcium starting materials in the absence of additional donors.[42] While this compound crystallizes as a SSIP, the structural motifs are very similar to those of the DAIP systems, with the octahedrally coordinated calcium center surrounded by the anionic ligands.

The formation of separated ions for both cations, $[Ca(thf)_6]^{2+}$ and $[Ca(18\text{-crown-}6)(HMPA)_2]^{2+}$ points to the effective resonance stabilization in the triphenylmethanide anion. In addition, the high steric demands of the three phenyl rings discourages direct contact between the metal and either the central carbon of the ligand or the π-system of the phenyl rings. π-metal–ligand bonding is also disfavored owing to the effective cation-donor stabilization.

Similar chemistry for the diphenylmethanides demonstrates some interesting facets of the structural chemistry of separated ion pairs. Treatment of dibenzylbarium with diphenylmethane in the presence of 18-crown-6 does not lead to separated ion pairs, but somewhat surprisingly to the contact species $Ba(18\text{-crown-}6)(CHPh_2)_2$, shown in Figure 27.[44] In this compound, the combination of the strength of the metal-carbon bond as well as the decreased steric demands of the smaller diphenylmethanide ligand allow for a contact structure. Coordination with the metal also lends to a pyramidalization of the *ipso* carbons. In addition, the phenyl rings are tipped noticeably away from coplanarity, which is in contrast to similar alkali metal structures.[121] Attempts to induce DAIP through application of additional donors was initially unsuccessful in the presence of the crown ether, but a reaction system involving excess HMPA led to the isolation and partial characterization of a system in which the metal is coordinated by six HMPA molecules in an octahedral orientation with the anions completely separated from the metal center.[44]

Attempts to further pursue this chemistry were plagued with difficulties although significant progress was seen. Concentrations of reaction mixtures containing dibenzylstrontium, crown ether, and diphenylmethane led to dimeric ether

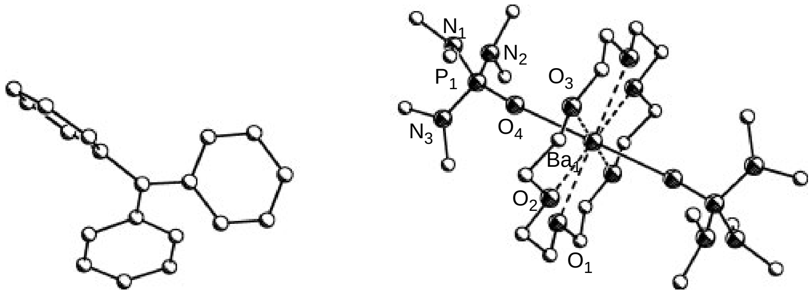

Figure 35 The solid-state structure of $[Ba(18\text{-crown-}6)(HMPA)_2][CPh_3]_2$. Only one of the symmetry equivalent $[CPh_3]^-$ anions is shown. Hydrogen atoms have been omitted for clarity

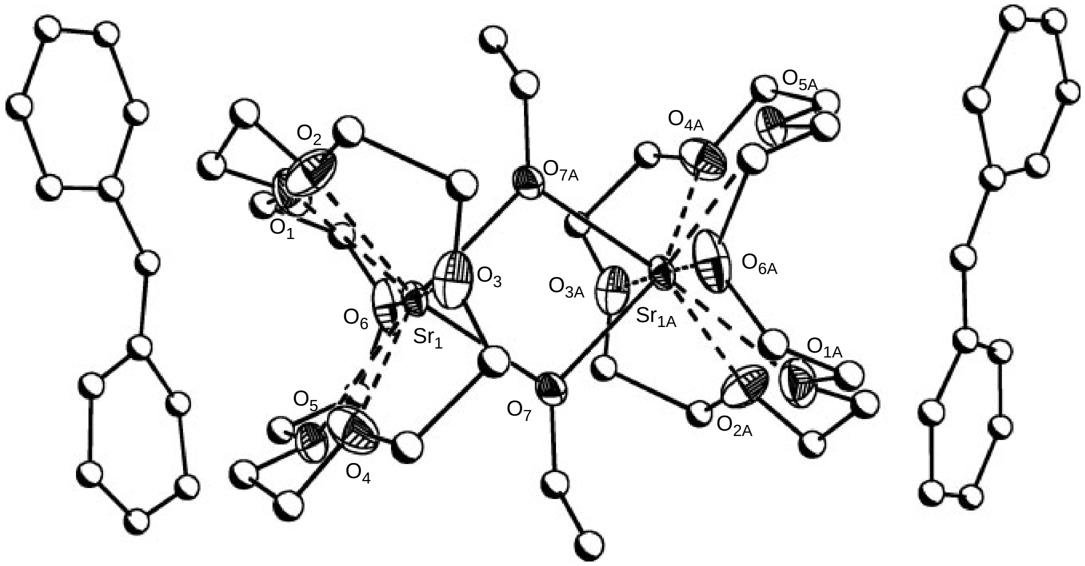

Figure 36 The solid-state structure of Sr(18-crown-6)(HCPh$_2$)(OC$_2$H$_4$)]$_2$. Hydrogen atoms have been omitted for clarity

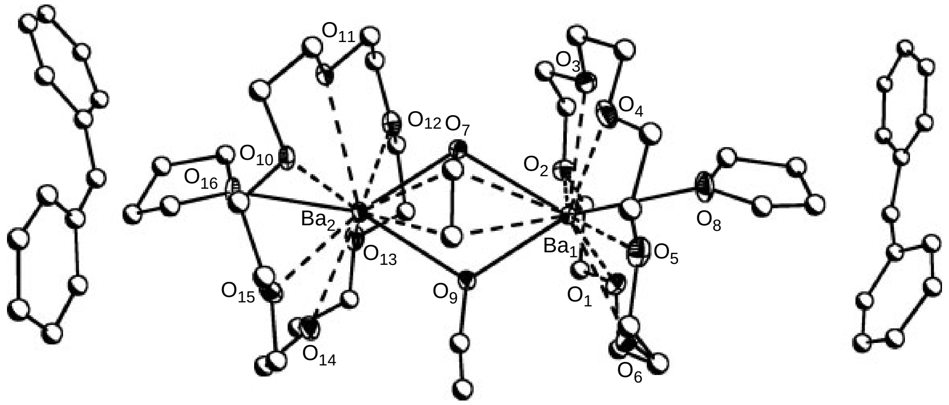

Figure 37 The solid-state structure of [Ba(18-crown-6)(HCPh$_2$)(THF)(OC$_2$H$_4$)]$_2$. Hydrogen atoms have been omitted for clarity

cleavage products in which each strontium center is coordinated by a crown ether and an enolate. Charge neutrality is ensured by a separated diphenylmethanide anion, as shown in Figure 36.

Here, the ligand adopts a planar geometry, while the crown ether is highly folded as the result of the approach of the two bridging enolates taking up a considerable portion of the metal coordination sphere.

Effects of metal size on the coordination environment are nicely demonstrated in the analogous barium compound, obtained in an effort to circumvent the ether cleavage problem using gentler synthetic methods developed for heavy alkali metals. In this method, barium alkoxides were combined with SiMe$_3$ substituted diphenylmethane. While the method did lead to desilylation in the desired location, upon concentration of the mother liquors of these compounds, ether cleavage products were observed as well, as shown in Figure 37.[44]

In this compound, the larger size of the barium cation allows for less steric congestion around the enolate bridges, leading to a dramatically less folded crown ether, permitting the coordination of an additional THF donor. Again, the CHPh$_2$ ligand is separated, adopting an almost identical geometry as in the strontium complex.

4 APPLICATIONS

With applications for the heavy alkaline earth organometallics discussed throughout this article, we will here specifically focus on some recent developments of Grignard reagents in synthetic chemistry.

The huge scope of the chemistry of Grignard reagents reflects the utility of these organometallic species in synthetic chemistry. Most prominently, Grignard reagents participate a) in nucleophilic substitution and addition reactions (uncatalyzed and catalyzed) with various organic functional groups, b) as strong bases by abstracting protons from even weakly acidic substrates, and c) in magnesium-halogen exchange reactions. In-depth accounts of the preparation and uses of organomagnesium reagents and mechanisms of their formation and reactions are found in the *Handbook of Grignard Reagents* (editors Silverman and Rakita, 1996),[122] *Grignard Reagents New Developments* (editor Richey, 2000),[123] and *Magnesium in Organic Synthesis* (Inoue and Oshima, a chapter in *Main Group Metals in Organic Synthesis*, editors Yamamoto and Oshima, 2004);[124] older literature on the reactions of Grignard reagents with nonmetallic substrates is summarized in the classic monograph by Kharasch and Reinmuth.[125] This account focuses on selected areas of Grignard chemistry in which significant progress has been reported since ca. 1997; references are included through part of 2004.

4.1 Halogen–Magnesium Exchange Reactions

Since Grignard's initial work in 1900 until very recently, organomagnesium compounds were prepared almost exclusively by reaction of carbon-halogen bonds with metallic magnesium, under conditions (e.g. in solvents such as Et_2O or THF) that forbade the presence of polar carbon-element multiple bonds (C=O, C=N, C=N, N=O, etc), strained polar carbon-element single bonds (epoxides, aziridines, etc) or even weakly acidic hydrogens (terminal alkynes) in the substrate.[49] By the 1970s, a few examples of formation of Grignard reagents (from Grignard reagents) via bromine- and iodine-magnesium exchange had appeared, enough to show that exchange was facilitated by electronegative structural elements in the organic halide.[126] However, none of the Grignards thus prepared contained any of the above-cited 'incompatible' functional groups. Then, seminal work by Cahiez and Knochel[127] showed that exchange with ^{i}Pr$_2$Mg or ^{i}PrMgBr in THF at −40° could transform aryl iodides containing bromide, ester, amide, or cyano groups to the corresponding functionalized arylmagnesium bromides. These react with allyl bromide or benzaldehyde at low temperature to give very good product yields (equation 16). In 1999, Knochel extended this exchange reaction to functionalized aryl and heteroaryl bromides, particularly those containing electron-withdrawing and/or ortho metallation-directing groups.[128]

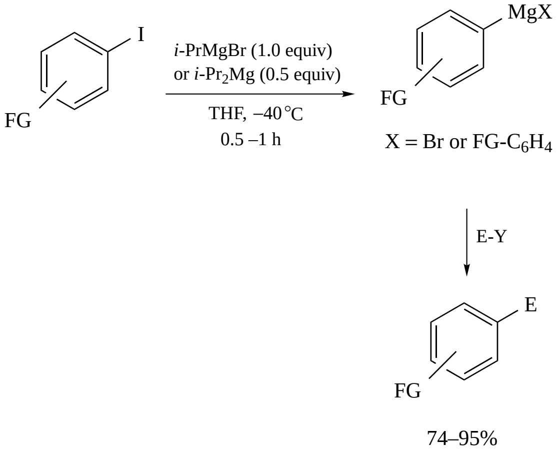

(16)

Functional group (FG) = Br, CONR$_2$, CN, CO$_2$Et, CO$_2t$Bu;
E-Y = aldehyde, allyl bromide

Also in 1999, Cahiez and Knochel prepared functionalized alkenylmagnesium reagents by exchange of functionalized alkenyl iodides with iPr$_2$Mg or iPrMgBr.[129] Soon after, Oshima reported that trialkylmagnesiates (R_3MgLi) can induce facile halogen-magnesium exchange of aryl halides even in the absence of electron-withdrawing groups, and facile halogen-magnesium exchange of unfunctionalized alkenyl iodides and cyclopropyl bromide; the reactivity of the magnesiate can be tuned by the choice of alkyl groups (Me, ^{n}Bu, ^{i}Pr) (equation 17).[130,131] Reactions with electrophiles sometimes are facilitated by the presence of a transition metal catalyst (CuCN·2LiCl).[126,131] In 2003, Knochel's group reviewed the expanding developments and applications of this methodology;[126] selected examples are described briefly here.

$$\mathrm{RX} \xrightarrow[\text{THF, } <0\,^\circ\text{C}]{\mathrm{R'_3MgLi}} \mathrm{RR'_2MgLi} \xrightarrow{\text{Electrophile, E}} \mathrm{RE}$$

$R =$ (un)functionalized aryl, heteroaryl, alkenyl, or cyclopropyl

$R' =$ Me, nBu, i-Pr; X = I, Br (17)

Unfunctionalized aryl Grignard reagents (alkyl Grignards are too reactive) undergo iodine–magnesium exchange with electronegatively functionalized *ortho*-iodonitroarenes. The nitroarylmagnesium products react smoothly with benzaldehyde. In addition stoichiometric transmetallation with CuCN·2LiCl affords arylcopper reagents that couple efficiently with allylic bromides or benzoyl bromide.[126]

2-Chloromethyl-1-iodobenzene and its 3-methoxycarbonyl analog undergo selective iodine–magnesium exchange with ^{i}PrMgBr. The new Grignard can be used to construct various substituted heterocycles; for example, reaction with aldehydes and subsequent intramolecular displacement of chloride affords a range of substituted isobenzofurans (equation 18).[132]

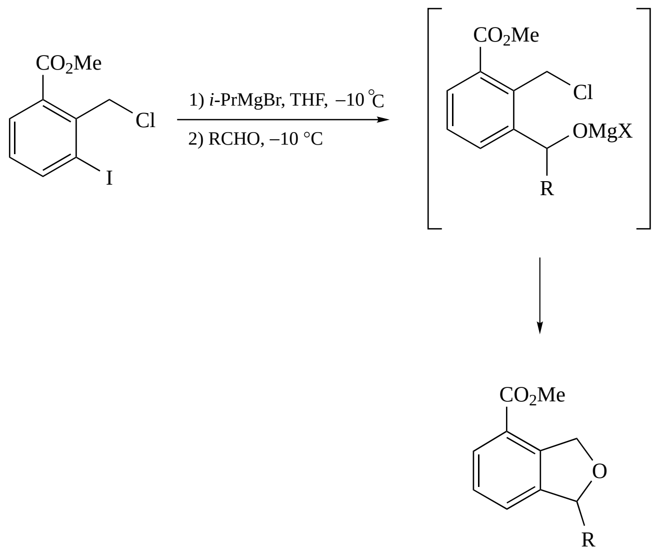
CO2Me
Cl
I
1) i-PrMgBr, THF, −10 °C
2) RCHO, −10 °C
CO2Me
Cl
OMgX
R
CO2Me
O
R

(18)

In a variation of this methodology, Oshima demonstrated the rapidity of the low-temperature iodine–magnesium exchange of ethyl *o*-iodobenzoate with $^{n}\mathrm{Bu_3MgLi}$ by adding the reagent to a mixture of the ester and heptanal. Only 3-hexylphthalide (69%) was obtained, showing that the exchange was much faster than attack of the magnesiate on the aldehyde (equation 19).[131]

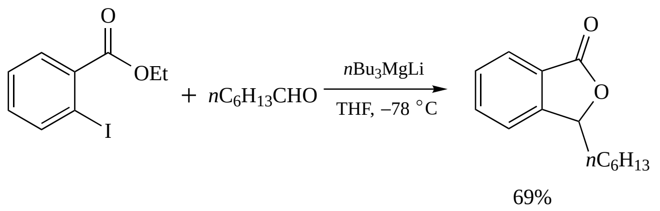
O
OEt
I
+ nC6H13CHO
nBu3MgLi
THF, −78 °C
O
O
nC6H13
69%

(19)

A Merck group, in developing a synthesis of a promising antidepressant/antiemetic, found that the rapid exchange (0 °C) between 3,5-bis(trifluoromethyl)bromo-benzene and *i*PrMgBr is the safest preparation of the potentially explosive aryl Grignard, and suitable for multikilo scale-up.[133]

In 2002, Knochel added aryl- and heteroaryl ketones to the list of functions that can tolerate iodine–magnesium exchange of iodoarenes.[134] Use of *neo*-pentylmagnesium bromide (NpMgBr) instead of $^{i}\mathrm{PrMgBr}$ removed the possibility of competing ketone reduction via hydride transfer, and addition of a polar aprotic cosolvent [N-methylpyrrolidinone (NMP) or *N*,*N*-dimethylacetamide (DMAC)] with THF enabled rapid exchange at −45 °C to −25 °C. Even aryl ketones bearing an α (acidic) proton reacted with minimal enolate formation; transmetallation of the functionalized Grignard to the corresponding organozinc reagent and Cu(I)-catalyzed reaction with an allyl bromide gave the desired ketone in good yield (equation 20).

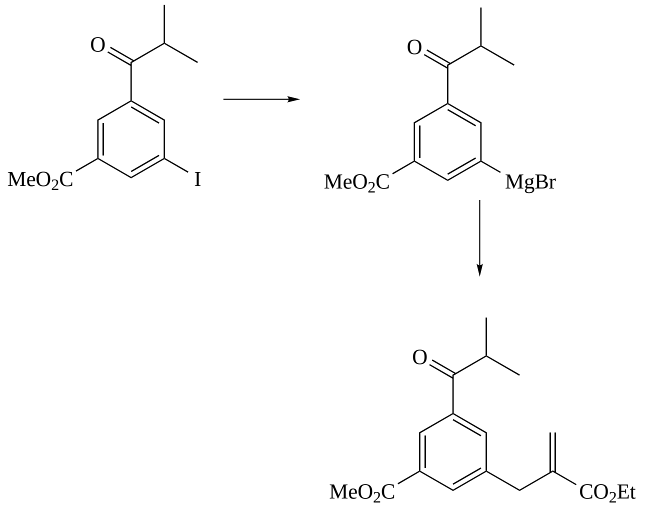
O
MeO2C
I
O
MeO2C
MgBr
O
MeO2C
CO2Et

(20)

Oshima used the halogen-magnesium exchange power of *n*-$\mathrm{Bu_3MgLi}$ in a mild, one-pot preparation of a wide range of functionalized biaryls from functionalized bromo- or iodoarenes (G = esters, amides, and nitriles).[135] Treatment of the assumed butyl diarylmagnesium ate-complexes with $\mathrm{TiCl_4}$ induced oxidative self-coupling to form the biaryls in moderate to good yields (equation 21).

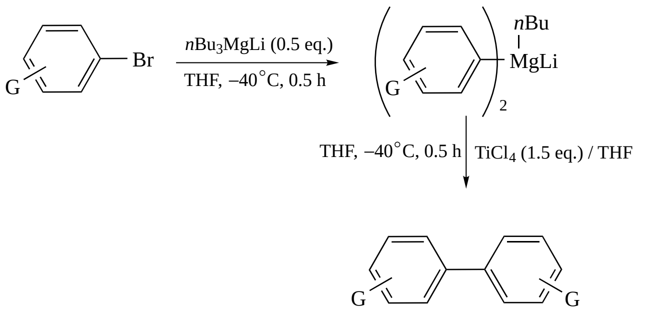
G
Br
nBu3MgLi (0.5 eq.)
THF, −40°C, 0.5 h
G
nBu
MgLi
2
THF, −40°C, 0.5 h
TiCl4 (1.5 eq.) / THF
G
G

(21)

Recent use of *n*-$\mathrm{Bu_3MgLi}$ enabled the first reported iodine–magnesium exchange with sensitive iodoazulenes, and subsequent reaction with a range of electrophiles (equation 22).[136]

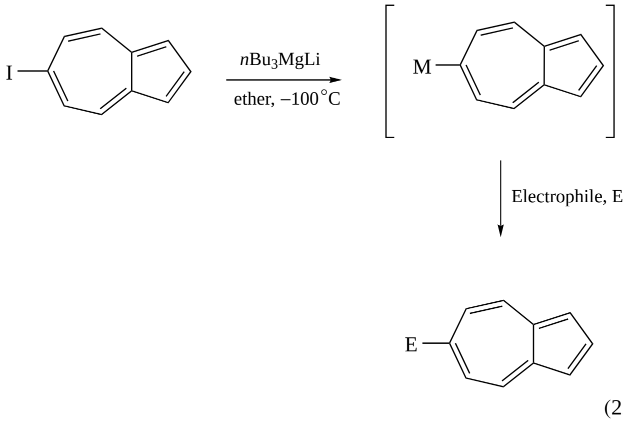
I
nBu3MgLi
ether, −100°C
M
Electrophile, E
E

(22)

The use of halogen-magnesium exchange has been extended to a variety of functionalized heteroaryl bromides and iodides. As with the aryl halides, the nature of the heterocycle greatly influences the rate of the exchange; electron-poor heteroaryls react faster.**[126]** Again, use of trialkylmagneriates results in higher reactivity and selectivity, but $^{n}Bu_3MgLi$ needs to be replaced by $^{n}BuMe_2MgLi$ to avoid side reactions.**[131]** Examples include functionalized iodo-**[126,137]** and bromopyridines,**[126,138]** halogenated diazines,**[126]** iodouracils,**[126]** halogenated imidazoles and antipyrines,**[126,139]** as well as pyrazoles**[140]** and thiophenes.**[126,141]**

After the initial report on preparation of functionalized alkenylmagnesium reagents, Knochel's group studied these systems further.**[126,142]** Alkenyl halides exchange more slowly than do aryl halides, but again, iodides exchange more easily than do bromides, and the presence of proximal/conjugated electron-withdrawing or chelating groups facilitates the process. Vinyl bromides containing certain electron-withdrawing groups (CN, SO_2Ph, CO_2tBu, and $CONEt_2$) geminal to the bromide exchange readily with *i*PrMgBr. A variety of systems and synthetic applications has been explored.**[126,142]** Oshima's reactive magnesiates rapidly undergo exchange with nonactivated alkenyl iodides, with complete retention of configuration of the double bond.**[131]**

Halide-magnesium exchange of alkyl halides rarely has been used to prepare new organomagnesium compounds. Early studies with simple bromides and Grignards in Et_2O or Et_2O-hydrocarbon solvents largely failed to give any observable exchange.**[125]** One of the more positive results of a thorough 1964 study by Zakharkin was a 17% exchange between *n*-pentylmagnesium bromide and CH_3I after 1 h in THF at 0 °C.**[143]** Results with other paired systems showed that Wurtz coupling was a major reaction (also seen in the earlier studies), that the exchange rate for a given R group was RI > RBr > RCl, and that any success could be expected only if the organic moiety in the organomagnesium compound to be produced was more electronegative than the organic moiety in the initial Grignard. Alkyl Grignards were recognized to be more reactive (in several ways) than aryl or alkenyl Grignards, so little effort was expended for many years to prepare functionalized alkyl Grignard reagents. In 2001, knowing that exocyclic cyclopropyl bonds have abnormal s character for a 'saturated' hydrocarbon, Oshima showed that bromocyclopropane and $^{n}Bu_3MgLi$ readily undergo bromine–magnesium exchange; subsequent reaction with benzaldehyde gave a 91% yield of α-cyclopropylbenzyl alcohol (equation 23).**[131]**

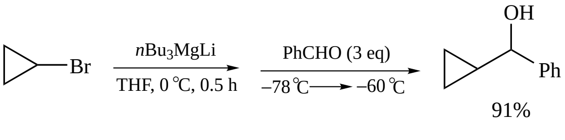

(23)

Soon thereafter, Knochel reported synthesis of the first cyclopropyl Grignards bearing an ester group.**[144]** The cis reagent, stabilized by the chelating ester function, gave good yields of products with a variety of electrophiles, all with retention of configuration (equation 24). The trans isomer, lacking chelation stabilization, nonetheless formed readily, and after transmetallation to the copper derivative, reacted with benzoyl chloride to give the pure trans keto ester in 65% yield.

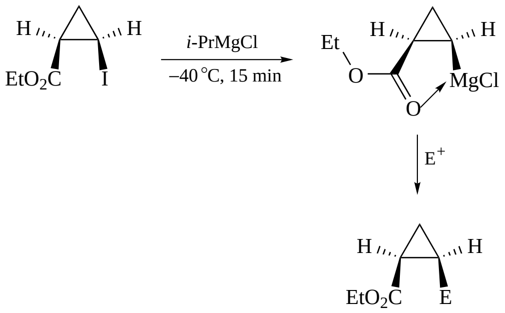

(24)

In 2004, using carefully designed 3-iodomethyl-1-oxacyclopentanes, Oshima was able to achieve iodine–magnesium exchange between the primary iodide and secondary or tertiary Grignard reagents, or $^{n}Bu_3MgLi$ (equation 25).**[145]** Factors in the success of the reaction included an excess of the initial organomagnesium reagent, Et_2O (not THF) as solvent, and a facile intramolecular reaction pathway (cyclopropane ring closure) to drain off the primary Grignard reagent formed in the possibly reversible exchange process.

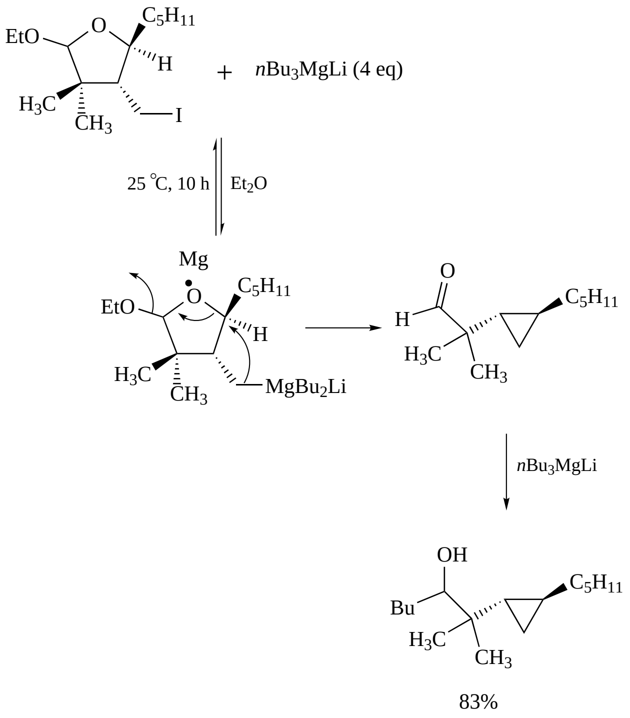

(25)

Fleming has exploited the greater exchangeability of vinylic halides versus alkyl halides to generate γ- and δ-chlorovinyl

Grignards, usable in reactions with cyclic γ-hydroxy-α,β-alkenenitriles to generate bicyclic ring systems in a single operation (equation 26).[146]

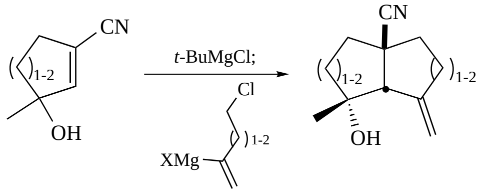

(26)

Magnesium carbenoids (compounds containing a carbon atom bonded to magnesium and to a geminal electron-withdrawing heteroatom), form extremely rapidly at low temperatures (−78 °C) via halogen-magnesium exchange.[126,147] The initial observation of this type of reaction[148] was extended in the 1990s to general preparation of magnesium carbenoids.[126] Knochel further extended this chemistry, performing the exchange between substituted *gem*-dibromocyclopropanes and *i*PrMgCl in Et_2O to stereoselectively prepare cyclopropylmagnesium carbenoids; subsequent reaction with electrophiles proceeds with retention of configuration.[126] Knochel also found that selected iodomethyl carboxylates undergo iodine−magnesium exchange with *i*PrMgCl in THF/*n*-butylpyrrolidinone at −78 °C; the generated carbenoids give very good yields in reaction with a variety of electrophiles.[147] Oshima has worked extensively on the exchange reactions of other substituted *gem*-dibromocyclopropanes and dibromodisilylmethanes with R_3MgLi, and the reactions of the resulting products with various electrophiles.[149]

Satoh has developed a related sulfoxide-magnesium exchange reaction between aryl α-chloroalkyl- and α-chlorovinylsulfoxides, and has extensively studied the chemistry of the resulting magnesium carbenoids and magnesium alkylidene carbenoids.[150]

References in Knochel's review and other recent scattered publications report some applications of halogen-Grignard or halogen-magnesate exchange reactions to synthesis of natural products and pharmaceuticals; these are certain to appear with increasing frequency.

4.2 Nucleophilic Substitution

4.2.1 Displacement at Carbon: Uncatalyzed Cross-coupling Reactions

The formation of a new carbon−carbon bond is a general reaction of organometallic reagents with organic electrophiles. Typically, the 'carbanion' component of the Grignard reagent (RMgX) serves as the nucleophile that displaces various leaving groups of the organic substrate (equation 27).

$$\begin{gathered}\mathrm{RY} + \mathrm{R'MgX} \longrightarrow \mathrm{R\text{-}R'} + \mathrm{MgYX}\\ \mathrm{R} = \text{alkyl, aryl; } \mathrm{Y} = \text{leaving group; } \mathrm{R'} = \text{alkyl, aryl;}\\ \mathrm{X} = \text{halide}\end{gathered} \tag{27}$$

This methodology continues to be important in the preparation of a wide variety of research compounds, pharmaceutical intermediates, and fine chemicals. However, the efficiency of Grignard reagents for cross-coupling reactions often has been restricted by competing reactions that include β-elimination, reduction, magnesium-halogen exchange, and electron-transfer reactions. The exact mechanism of the formation of a new carbon−carbon bond by displacement of a leaving group often is uncertain. Three commonly considered mechanisms are a) an S_N2 (direct nucleophilic substitution) process, b) an S_N1 process wherein a stable carbocation is formed upon Lewis acid-assisted departure of the leaving group, and c) a SET (single electron-transfer) process arising from electron transfer and involving radical intermediates.[151]

Halides in the organic substrates are considered the most useful leaving groups owing to availability and effective polarization of the carbon-halogen bond.[122] Among the halides, iodides usually react most rapidly, but most easily undergo Mg-halogen exchange. Generally, the reactivity of halides follows the trend $\mathrm{I} > \mathrm{Br} \gg \mathrm{Cl} \gg \mathrm{F}$. Before the advent of effective catalysts, simple (unfunctionalized) alkyl halides, except methyl iodide, were not commonly used for coupling, owing to their slow reactions with Grignard reagents.[125] In contrast to simple alkyl halides, allylic and benzylic halides often give useful yields owing to greater ease of displacement (milder reaction conditions).[49] Transition metal-catalyzed reactions will be discussed in detail below.

Another class of leaving groups is the oxyanions, including sulfates and sulfonates (e.g. mesylates, tosylates, and triflates), that often are easily displaced to afford coupling products in good yields. Alkoxy groups incorporated into acetals, ketals, and orthoesters usually do not react with Grignard reagents, but their displacement can be facilitated by coordination of the alkoxy group with the Lewis acidic magnesium ion. The order of reactivity of such leaving groups is aryloxy > alkoxy > thioalkoxy > amino.[152] Other displaceable C–O bonds are found in phosphate esters, carboxylate esters, certain ethers, and epoxides.[151] Nucleophilic ring opening reactions were also demonstrated in the reaction of 3-aza-2-oxabicyclo[2.2.1]hept-5-enes[153] and β-lactones[154] with Grignard reagents.

Uncatalyzed nucleophilic substitution reactions of Grignard reagents with aromatic compounds is much more difficult than with alkyl species, unless the leaving group (sometimes halide; usually alkoxide is preferred) is activated by one or more potent electron-withdrawing substituents, such as an oxazoline, nitro, or ester moiety, most often at the ortho position.[49] Such displacement is hypothesized to follow an addition-elimination pathway.

In 1998, methoxy and halogen substituents *meta* to a highly hindered benzoate ester were found to increase the rate of displacement of the sandwiched *ortho* methoxy leaving group.[155] (equation 28) In 2001, *meta*-alkoxy rate enhancement was found applicable also to displacement of a methoxy group *para* to a benzoate ester.[156]

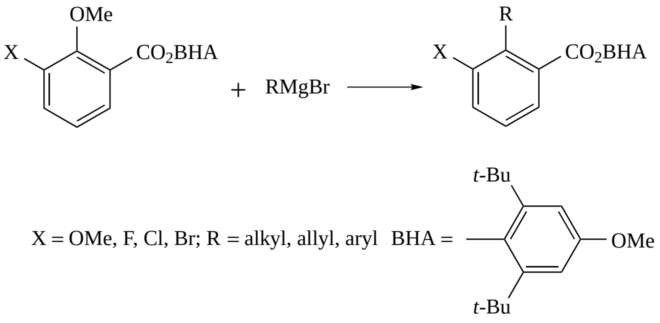

(28)

In 2003, the 2-methoxy substituent in a 2-methoxy-3- or 4-methyl furoate was found to be displaceable by EtMgBr in Et_2O.[157] Hattori and Miyano have applied the alkoxy displacement method to the reaction of 2-methoxy-1-naphthyl Grignard with 1-menthoxy-2-nitro naphthalene; the departing chiral menthoxy group imparted a high level of optical purity (78% ee) to the axially chiral binaphthyl so formed.[158] An Otsuka Pharmaceutical research group has successfully coupled a highly substituted aryl Grignard with a highly substituted *ortho*-methoxybenzoate (with displacement of the methoxy group) to produce (on a multikilo scale) a biphenyl intermediate in the synthesis of a promising pharmaceutical agent.[159]

In 2001, Makosza reported an improvement in the known oxidative nucleophilic substitution of *ortho* hydrogen in *p*-methoxy- and *p*-chloronitroarenes via *ortho* addition of an alkyl group from a Grignard reagent.[160] The intermediate σ^H additive was oxidized to the final alkylated nitroarene by addition of liquid ammonia and powdered $KMnO_4$ to the reaction mixture in THF at −70 °C, producing better yields than previous oxidizing agents.

4.2.2 *Transition Metal–Catalyzed Cross-coupling Reactions*

In tandem with the above-described recent advances in the preparation of Grignard reagents containing functional groups, great strides have been made recently in the development of transition metal-catalyzed cross-coupling reactions of Grignard reagents. The rise of nickel- and palladium-catalyzed coupling of Grignard reagents with alkenyl and aryl halides in the 1970s, and the renaissance of iron-catalyzed coupling that started in the late 1990s have been described in a summary by Fürstner of some of his group's recent extensive work on iron catalysis.[161] Contributions to the field of iron-catalyzed Grignard cross-coupling by the groups of Kochi, Cahiez, and Knochel are cited therein, as well as in the 2003 review by Knochel's group,[126] and in Shinokubo and Oshima's 2004 review.[162] The recent success of iron catalysis in carbon–carbon bond formation has attracted intense interest because of the cheap availability, stability, and environmental compatibility of many iron salts. Fürstner's 2002 paper summarized existing evidence suggesting that an iron species with the formal composition $[Fe(MgX)_2]$ propagates the coupling process.[161] This paper reported high yields of coupling between alkyl Grignards and electron-poor aryl chlorides and tosylates, and electron-rich aryl triflates. Aryl chlorides, triflates, and tosylates are better coupling partners than the corresponding iodides and bromides; the latter tend to undergo competitive reduction. Competing Grignard attack on substituents such as carboxylate and sulfonate esters, sulfonamides, and nitriles was not observed. Heteroarene substrates include a dibenzofuran, a thiophene, and numerous nitrogen-containing arenes. Coupling of aryl Grignards with arene substrates succeeds only with π-electron-deficient heteroaryl chlorides; Figadère had reported a similar finding months earlier.[163]

In 2003, Fürstner's group reported applications of this methodology to total syntheses of some natural products,[164,165] and to the stereospecific S_N2' reaction of alkyl and aryl Grignards with optically enriched propargyl epoxides to yield alkyl- and aryl-substituted 2,3-allenols with high stereochemical fidelity (equation 29).[166]

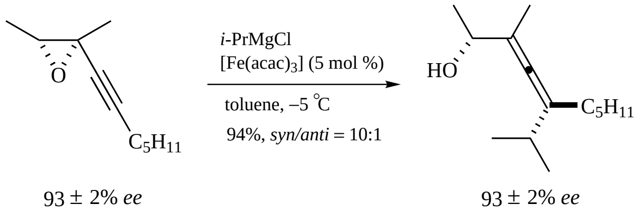

(29)

In 2004, his group described in some detail the iron-catalyzed cross-couplings of alkyl and aryl Grignards with enol triflates, acid chlorides, and dichloroarenes.[167] Enol triflates give good to excellent yields; many substrate functional groups (e.g. esters, enones, carbamates) are tolerated, and several functionalized Grignards work well.

A much broader variety of functionalized acid chlorides was studied than was reported in previous literature; all combinations of aromatic and aliphatic acid chlorides and aryl and alkyl Grignards work very well, proceeding in less than 15 min at −78 °C; attack on the product ketone is negligible. Substrate stereogenic centers are not racemized, and radical intermediates appear to be unlikely. Results of dichloroarene couplings are variable; while good yields of the desired monoalkylated product usually are obtained, *ortho*-substituted substrates can be problematic, and function-bearing Grignards are much less reactive.

Also in 2004, papers by the groups of Hayashi[168] and Nakamura[169] were followed shortly by a Fürstner paper,[170] all reporting efficient iron complex-catalyzed couplings of aryl Grignards with alkyl halides. Each group employed a differently ligated Fe species and different solvents ($\mathrm{Et_2O}$ or THF) and temperatures; each reported results superior to previously reported palladium- and nickel-catalyzed processes, and to stoichiometric arylation with organocopper reagents. Salient features of these couplings include excellent tolerance of polar groups (e.g. ketones, esters, enolates, chlorides, nitriles, isocyanates), greater reactivity of secondary over primary bromides ($\mathrm{RI} > \mathrm{RBr} > \mathrm{RCl}$), and complete racemization during arylation of secondary bromides, indicating formation of radical intermediates.

In the presence of manganese chloride, functionalized aromatic halides and aromatic Grignard reagents cross-couple under mild conditions.[171] Likewise, synthetically important heterocycles cross-couple in the presence of cobalt catalysts.[172]

Although there has been much recent progress in the development of transition metal-catalyzed coupling between alkyl Grignards and, for example, aryl or vinyl halides and triflates, between aryl Grignards and alkyl halides, and the corresponding aryl–aryl and aryl-vinyl combinations (including heteroarenes), satisfactory alkyl–alkyl coupling has remained elusive. Stoichiometric organocuprates can couple with alkyl halides with high yields and chemoselectivity[173] but large excesses of the organocuprate often are needed, and large-scale industrial applications are discouraged by the prospect of disposing of large-scale copper residues; higher order or mixed cuprates have provided some improvement.[174] Fürstner[170] (and others) has discussed some of the problems attending palladium- and nickel-catalyzed cross-coupling involving alkyl halides and/or alkylmetal reagents, and cited some of the groups continuing to work on the alkyl–alkyl coupling problem. In 2000, Cahiez showed that copper-catalyzed coupling of primary, secondary, and tertiary alkyl Grignards with primary alkyl bromides proceed in very good yields, if *N*-methylpyrrolidinone (NMP) was used as a cosolvent with THF.[175] NMP as a cosolvent has also facilitated iron- and manganese-catalyzed Grignard cross-couplings.[161,171,175] The reactions proceed smoothly under mild conditions, even in the presence of esters, nitriles, ketones, and alkyl chlorides. However, secondary bromides do not react. In earlier work (1998),[176] van Koten's group (with Cahiez as coauthor) reported very good coupling of primary, secondary, and tertiary Grignards with primary and secondary alkyl bromides, cocatalyzed by THF-soluble tridentate diamino organo-manganese(II) complexes and CuCl. Ketone and ester functions do not interfere. No follow-up of this promising, little-cited method has been found.

In 2004, Oshima's group reported full details of cobalt-catalyzed cross-coupling of primary, secondary, and tertiary alky halides with allylic and benzylic Grignard reagents.[177] Bis-diphenylphosphinoalkane catalyst ligands sometimes are needed, and iodides and bromides give better yields than chlorides; amides, esters, and carbonates are attacked, even at −78 °C. For facile synthesis of quaternary carbon centers, this method is better than use of palladium, nickel, or copper catalysts; the reaction mechanism probably includes generation of an alkyl radical.

In addition to iron, recent uses of manganese, chromium, and cobalt catalysts for Grignard cross-coupling are described in the Shinokubo–Oshima review.[162]

4.2.3 Displacement at Electrophilic Main Group Elements and Transition Metals

Similar to substitution reactions with organic substrates, the nucleophilic attack of the alkyl or aryl groups of Grignard reagents on main group elements and transition metals requires suitable leaving groups and effective solvent systems. Because these reactions proceed favorably only when the electrophilic centers are more electronegative than magnesium, reactions involving alkali and heavy alkaline earth metals are not viable.

Elements within group 13 (B, Al, Ga, In and Tl), group 14 (Si, Ge, Sn and Pb), group 15 (N, P, As, Sb and Bi), and group 16 (O, S, Se and Te), and a variety of transition metals from groups 3 to 12 are known to undergo alkylation and arylation with Grignard reagents.[152] The products of these reactions have found vast applications in various fields that include catalysis and materials science. Recently, the interaction of Grignard reagents with phosphaalkynes was described to successfully produce phosphavinyl Grignard regents, $[\mathrm{RP{=}C(Bu^{t})MgCl}]$ $\mathrm{R} =$ alkyl or aryl.[178,179] These reagents were subsequently employed for the preparation of phosphovinyl-main group complexes by reaction with several groups 13, 14, and 16 monohalides.[180] Use of these reagents has been extended as well to reactions with transition metal complexes.[181,182]

4.3 Grignard Reagents as Bases

Grignard reagents are very strong bases; parameters that affect their base strength have been reviewed.[122] They are convenient bases (particularly ethylmagnesium bromide) for irreversible deprotonation of terminal alkynes (equation 30). Many uses of the resulting acetylenic Grignards have been described, including addition to a variety of carbonyl compounds, in which they are less prone to side reactions than are the corresponding lithium reagents.[122]

$$\mathrm{RC{\equiv}CH + R'MgX \longrightarrow RC{\equiv}CMgX + R'H}$$

$$\text{where: R, R}' = \text{alkyl, X} = \text{halogen} \tag{30}$$

Grignard reagents readily deprotonate alcohols, secondary amines, and secondary amides; in certain substrates, the resulting magnesiated species can undergo inter- or intramolecular addition, or intramolecular rearrangement.[122]

In 1989, Eaton extended the utility of amido-Grignards, showing that highly hindered magnesium amide bases (e.g. bis(2,2′,6,6′-tetramethylpiperidino)magnesium, $(TMP)_2Mg$)) are much more stable in THF than are the corresponding lithium amides, yet effectively ortho magnesiate, for example, methyl benzoate without attacking the ester function (equation 31).[183] Amide-activated strained systems such as, the carboxamidocyclopropane in equation (32) undergo analogously directed magnesiation in good yield.

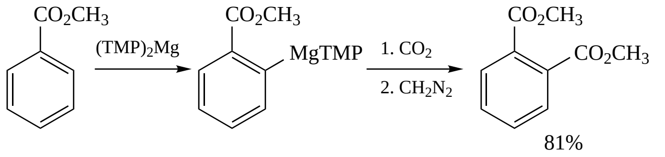

CO2CH3
(TMP)2Mg
CO2CH3
MgTMP
1. CO2
2. CH2N2
CO2CH3
CO2CH3
81%

(31)

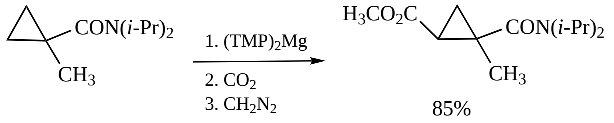

CON(i-Pr)2
CH3
1. (TMP)2Mg
2. CO2
3. CH2N2
H3CO2C
CON(i-Pr)2
CH3
85%

(32)

In 2002, Eaton introduced an even stronger deprotonating/metallating reagent, $BuMgN\textit{i}Pr_2$, which also is usefully stable in THF, and can completely deprotonate amide-activated cyclopropanes by irreversible formation of butane.[184] This process was applied in a new synthetic route to the antidepressant, Milnacipran (equation 33).

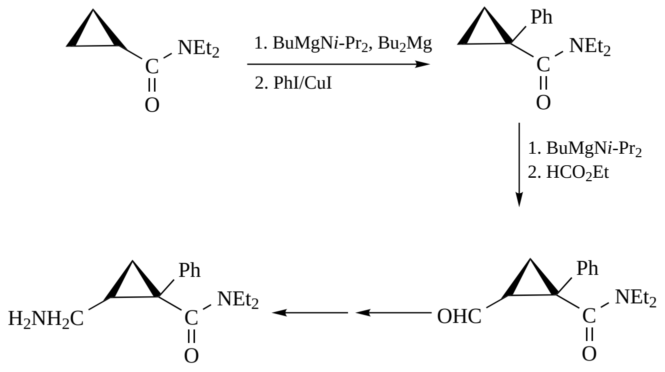

NEt2
C
O
1. BuMgNi-Pr2, Bu2Mg
2. PhI/CuI
Ph
NEt2
C
O
1. BuMgNi-Pr2
2. HCO2Et
Ph
NEt2
C
O
OHC
H2NH2C
Ph
NEt2
C
O

Milnacipran

(33)

More recently, Shuto used $BuMgN\textit{i}Pr_2$ to effect the cis-trans isomerization of the cyclopropanecarboxamide shown below (equation 34),[185] and a Chiron group found $BuMgN\textit{i}Pr_2$ best for deprotonation of a similar substrate in a formal synthesis of the potential anti-HIV agent MIV-150 (equation 35).[186]

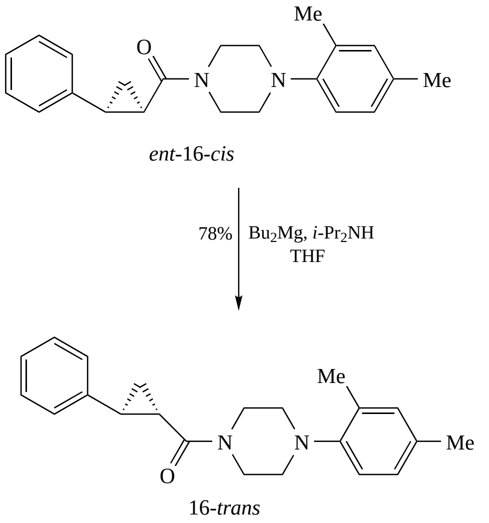

Me
O
N
N
Me
ent-16-cis
78%
Bu2Mg, i-Pr2NH
THF
Me
N
N
Me
O
16-trans

(34)

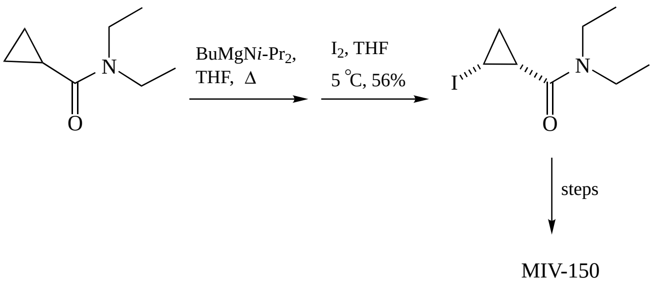

N
O
BuMgNi-Pr2,
THF, Δ
I2, THF
5 °C, 56%
I
N
O
steps
MIV-150

(35)

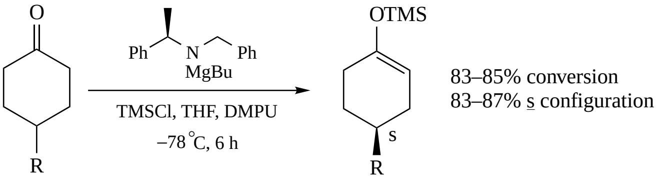

O
R
Ph
N
Ph
MgBu
TMSCl, THF, DMPU
−78 °C, 6 h
OTMS
s
R
83–85% conversion
83–87% s configuration

(36)

Eaton's base also has stimulated use of an enantiopure alkylmagnesium amide for enantioselective deprotonation of a set of 4-substituted cyclohexanones (equation 36);[187] further work in this area can be expected. Finally, efficient ortho-magnesiation of *N*-phenylsulfonylpyrrole has been achieved with an excess of $\textit{i}PrMgCl$ and a catalytic amount (5 mol%) of $\textit{i}Pr_2NH$ to serve as a proton transfer agent; subsequent reaction with a range of electrophiles afforded decent yields of products (equation 37).[188]

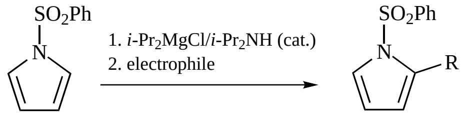

SO2Ph
N
1. i-Pr2MgCl/i-Pr2NH (cat.)
2. electrophile
SO2Ph
N
R

(37)

R = (e.g.) I, alkyl, $SiMe_3$, aryl, heteroaryl

5 CONCLUSIONS

The structural chemistry of the alkaline earth metals is continuing to grow at a rapid rate. New synthetic methods, new applications in a variety of fields and fascinating questions pertaining to the very nature of the chemical bond guarantee that further investigations will continue to be well deserved. Through the work of the several groups pioneering the renaissance in heavy alkaline earth organometallics, a new appreciation for this previously dismissed class of reagents is emerging that will undoubtedly lead to further developments sure to contribute considerably to the library of knowledge of these metals.

6 REFERENCES

1. N. N. Greenwood and A. Earnshaw, 'Chemistry of the Elements', 2nd edn., Butterworth-Heinemann, London, 2002.
2. T. P. Hanusa, *Polyhedron*, 1990, **9**, 1345.
3. T. P. Hanusa, *Organometallics*, 2002, **21**, 2559.
4. A. Yanagisawa, S. Habaue, and H. Yamamoto, *J. Am. Chem. Soc.*, 1991, **113**, 8955.
5. A. Yanagisawa, S. Habue, and H. Yamamoto, *J. Am. Chem. Soc.*, 1991, **113**, 5893.
6. A. Yanagisawa, S. Habue, K. Ysaue, and H. Yamamoto, *J. Am. Chem. Soc.*, 1994, **116**, 6130.
7. A. Yanagisawa, H. Hibino, S. Habaue, Y. Hisada, and H. Yamamoto, *J. Org. Chem.*, 1992, **57**, 6386.
8. A. Yanagisawa, H. Hibino, N. Nomura, and H. Yamamoto, *J. Am. Chem. Soc.*, 1993, **115**, 5879.
9. A. Yanagisawa, K. Ogasawara, K. Ysaue, and H. Yamamoto, *Chem. Commun.*, 1996, 367.
10. S. Harder, H. H. Brintzinger, and A. Weeber, *Organometallics*, 2000, **19**, 1325.
11. T. C. Wu, H. Xiong, and R. D. Rieke, *J. Org. Chem.*, 1990, **55**, 5045.
12. R. A. O'Brien, T. Chen, and R. D. Rieke, *J. Org. Chem.*, 1992, **57**, 2667.
13. R. D. Shannon, *Acta Crystallogr.*, 1976, **A32**, 751.
14. A. L. Allred and E. G. Rochow, *J. Inorg. Nucl. Chem.*, 1958, **5**, 264.
15. W. J. Evans, *Polyhedron*, 1987, **6**, 803.
16. R. D. Rieke, *Acc. Chem. Res.*, 1977, **10**, 301.
17. U. Tilstam and H. Weinmann, *Org. Process Res. Dev.*, 2002, **6**, 906.
18. C. Glacet, *Memoires Presentes Soc Chim*, 1938, **5**, 895.
19. R. Masthoff, H. Schueler, and G. Krieg, *J. Organomet. Chem.*, 1968, **13**, 37.
20. R. Masthoff and C. Vieroth, *J. Prakt. Chem.*, 1968, **38**(3–4), 182.
21. R. Masthoff and G. Krieg, *Z. Chem.*, 1966, **6**, 433.
22. N. Kawabata, A. Matsumura, and S. Yamashita, *Tetrahedron*, 1973, **28**, 1069.
23. N. Kawabata, A. Matsumura, and S. Yamashita, *J. Org. Chem.*, 1973, **38**, 4268.
24. K. Mochida and T. Yamanishi, *J. Organomet. Chem.*, 1987, **332**, 247.
25. B. G. Gowenlock, W. E. Lindsell, and B. Singh, *J. Chem. Soc., Dalton Trans.*, 1978, 657.
26. D. Bryce-Smith and A. Skinner, *J. Chem. Soc. A*, 1963, 577.
27. M. J. McCormick, K. B. Moon, S. P. Jones, and T. P. Hanusa, *J. Chem. Soc., Chem. Commun.*, 1990, 778.
28. M. Westerhausen, C. Gueckel, T. Habereder, M. Vogt, M. Warchhold, and H. Noeth, *Organometallics*, 2001, **20**, 893.
29. J. D. Woolins, 'Inorganic Experiments', VCH, New York, 1994.
30. M. Coles and F. Hart, *J. Organomet. Chem.*, 1971, **32**, 279.
31. S. R. Drake and D. J. Otway, *Polyhedron*, 1992, **11**, 745.
32. W. Vargas and K. Ruhlandt-Senge, *Eur. J. Inorg. Chem.*, 2003, 3472.
33. J. Hitzbleck, A. Y. O'Brien, C. M. Forsyth, G. B. Deacon, and K. Ruhlandt-Senge, *Chem. – Eur. J.*, 2004, **10**, 3315.
34. M. F. Lappert, G. A. Lawless, B. Royo, P. B. Hitchcock, and F. G. N. Cloke, *J. Chem. Soc., Chem. Commun.*, 1991, 724.
35. J. P. Dunne, S. Fox, and M. Tacke, *J. Mol. Struct. (Theochem)*, 2001, **543**, 157.
36. L. M. Engelhardt, S. Harvey, C. Raston, and A. H. White, *J. Organomet. Chem.*, 1988, **341**, 39.
37. B. Bogdanovic, N. Janke, C. Kruger, R. Mynott, K. Schlichte, and U. Westeppe, *Angew. Chem., Int. Ed. Engl.*, 1985, **24**, 960.
38. H. Lehmkuhl, A. Shakoor, K. Mehler, C. Kruger, Y. Angermund, and H. Tsay, *Chem. Ber.*, 1985, **118**, 4239.
39. H. E. Ramsden and J. E. Engelhart, 1967, US 3351646, 4.
40. B. Bogdanovic, S.-T. Liao, M. Schwickardi, P. Sikorsky, and B. Spliethoff, *Angew. Chem.*, 1980, **92**, 845.
41. H. Boennemann, B. Bogdanovic, R. Brinkman, N. Egeler, R. Benn, I. Topalovic, and K. Seevogel, *Main Group Met. Chem.*, 1990, **13**, 341.
42. S. Harder, S. Muller, and E. Hubner, *Organometallics*, 2004, **23**, 178.
43. C. Eaborn, S. Hawkes, P. B. Hitchcock, and J. D. Smith, *Chem. Commun.*, 1997, 1961.
44. J. S. Alexander and K. Ruhlandt-Senge, *Chem. – Eur. J.*, 2004, **10**, 1274.
45. J. S. Alexander and K. Ruhlandt-Senge, *Organometallics*, 2003, **22**, 4933.
46. S. Chadwick, U. Englich, and K. Ruhlandt-Senge, *Angew. Chem., Int. Ed. Engl.*, 1998, **37**, 3007.
47. C. Elschenbroich, 'Organometallchemie', B. G. Teubner Verlag, Wiesbaden, 2003.
48. U. Englich and K. Ruhlandt-Senge, *Coord. Chem. Rev.*, 2000, **210**, 135.

49. M. B. Smith and J. March, ‘Advanced Organic Chemistry’, 5th edn., John Wiley & Sons, New York, 2001.
50. H. Lehmkuhl, K. Mehler, R. Benn, A. Rufinska, and C. Krueger, *Chem. Ber.*, 1986, **119**, 1054.
51. H. Sitzmann, F. Weber, M. D. Walter, and G. Wolmershauser, *Organometallics*, 2003, **22**, 1931.
52. M. Niemeyer and P. P. Power, *Inorg. Chem.*, 1997, **36**, 4688.
53. D. Stalke, *Angew. Chem., Int. Ed. Engl.*, 1994, **33**, 2168.
54. K. Ziegler, H. Froitzheim-Kuehlhorn, and K. Hafner, *Chem. Ber.*, 1956, **89**, 434.
55. T. P. Hanusa, *Chem. Rev.*, 1993, **93**, 1023.
56. C. J. Burns and R. A. Andersen, *J. Organomet. Chem.*, 1987, **325**, 31.
57. H. Sitzmann, T. Dezember, and M. Ruck, *Angew. Chem., Int. Ed. Engl.*, 1998, **37**, 3114.
58. A. Almenningen, A. Haaland, and J. Lusztyk, *J. Organomet. Chem.*, 1979, **170**, 271.
59. K. W. Nugent, J. K. Beattie, T. W. Hambley, and M. R. Snow, *Aust. J. Chem.*, 1984, **37**, 1601.
60. C. H. Wong, T. Y. Lee, J. Chao, and S. Lee, *Acta Crystallogr., Sect. B*, 1972, **28**, 1662.
61. C.-H. Wong and S.-M. Wang, *Inorg. Nucl. Chem.*, 1975, **11**, 677.
62. K. W. Nugent, J. K. Beattie, and L. D. Field, *J. Phys. Chem.*, 1989, **93**, 5371.
63. H. Schmidbaur, ‘Gmelin Handbook of Inorganic Chemistry’, 8th edn., Springer, Berlin, 1987.
64. W. Buender and E. Weiss, *J. Organomet. Chem.*, 1975, **92**, 1.
65. A. Haaland, J. Lusztyk, J. Brunvoll, and K. B. Starowieyski, *J. Organomet. Chem.*, 1975, **85**, 279.
66. R. A. Andersen, J. M. Boncella, C. J. Burns, R. Blom, A. Haaland, and H. V. Volden, *J. Organomet. Chem.*, 1986, **312**, C49.
67. T. P. Hanusa, *Coord. Chem. Rev.*, 2000, **210**, 329.
68. R. A. Andersen, J. M. Boncella, C. J. Burns, R. Blom, A. Haaland, and H. V. Volden, *J. Organomet. Chem.*, 1986, **312**, C49.
69. R. A. Williams, T. P. Hanusa, and J. C. Huffman, *Organometallics*, 1990, **9**, 1128.
70. R. A. Williams, T. P. Hanusa, and J. C. Huffman, *J. Chem. Soc., Chem. Commun.*, 1988, 1045.
71. R. A. Andersen, R. Blom, J. M. Boncella, C. J. Burns, and H. V. Volden, *Acta Chem. Scand.*, 1987, **A41**, 24.
72. R. A. Andersen, R. Blom, C. J. Burns, and H. V. Volden, *J. Chem. Soc., Chem. Commun.*, 1987, 768.
73. R. A. Williams, T. P. Hanusa, and J. C. Huffman, *Organometallics*, 1990, **9**, 1128.
74. M. Guido and G. Gigli, *J. Chem. Phys.*, 1976, **65**, 1397.
75. R. A. Williams and T. P. Hanusa, *J. Organomet. Chem.*, 1992, **429**, 143.
76. P. Selg, H. H. Brintzinger, R. A. Andersen, and I. T. Horvath, *Angew. Chem., Int. Ed. Engl.*, 1995, **34**, 791.
77. R. A. Williams and T. P. Hanusa, *J. Am. Chem. Soc.*, 1990, **112**, 2454.
78. A. J. Arduengo, F. Davidson, R. Krafczyk, W. J. Marshall, and M. Tamm, *Organometallics*, 1998, **17**, 3375.
79. H. Sitzmann, M. D. Walter, and G. Wolmershauser, *Angew. Chem., Int. Ed. Engl.*, 2002, **41**, 2315.
80. J. Overby and T. P. Hanusa, *Organometallics*, 1996, **15**, 2205.
81. G. Mösges, F. Hampel, and P. von Ragué Schleyer, *Organometallics*, 1992, **11**, 1769.
82. H. H. Damrau, A. Geyer, M. Prosenc, A. Weeber, F. Schaper, and H. H. Brintzinger, *J. Organomet. Chem.*, 1998, **553**, 331.
83. S. Harder, M. Lutz, and A. W. G. Straub, *Organometallics*, 1997, **16**, 107.
84. J. Overby and T. P. Hanusa, *Angew. Chem.*, 1994, **106**, 2300.
85. M. H. Harvey, T. P. Hanusa, and V. G. J. Young, *Angew. Chem., Int. Ed. Engl.*, 1999, **38**, 217.
86. M. G. Gardiner, C. Raston, F. G. N. Cloke, and P. B. Hitchcock, *Organometallics*, 1995, **14**, 1339.
87. K. Mashima, H. Sugiyama, N. Kanehisa, Y. Kai, H. Yasuda, and A. Nakamura, *J. Am. Chem. Soc.*, 1994, **116**, 6977.
88. S. Harder and M. Lutz, *Organometallics*, 1997, **16**, 225.
89. H. Schmidbaur, U. Deschler, and B. Milewski-Mahrla, *Chem. Ber.*, 1982, **115**, 3290.
90. M. Westerhausen, W. Digeser, H. Noeth, T. Seifert, and A. Pfitzner, *J. Am. Chem. Soc.*, 1998, **120**, 6722.
91. H. E. Ramsden, 1967, Application: US 3354190, 3.
92. H. Bock, K. Ziemer, and C. Naether, *J. Organomet. Chem.*, 1996, **511**, 29.
93. J. S. Alexander and K. Ruhlandt-Senge, *Eur. J. Inorg. Chem.*, 2002, **11**, 2749.
94. M. Westerhausen, *Angew. Chem. Int. Ed. Engl.*, 2001, **40**, 2975.
95. A. I. Snow and R. E. Rundle, *Acta Crystallogr.*, 1951, **4**, 348.
96. K. Ruhlandt-Senge, R. A. Bartlett, M. Olmstead, and P. P. Power, *Inorg. Chem.*, 1993, **32**, 1724.
97. M. Neimeyer and P. P. Power, *Inorg. Chem.*, 1997, **36**, 4688.
98. S. S. Al-Juaid, C. Eaborn, P. B. Hitchcock, C. A. McGeary, and J. D. Smith, *Chem. Commun.*, 1989, 273.
99. R. J. Wehmschulte and P. P. Power, *Organometallics*, 1995, **14**, 3264.
100. J. J. Ellison and P. P. Power, *J. Organomet. Chem.*, 1996, **526**, 263.
101. C. S. Hwang and P. P. Power, *Bull. Korean Chem. Soc.*, 2003, **24**, 605.
102. G. D. Stucky and R. E. Rundle, *J. Am. Chem. Soc.*, 1964, **86**, 4825.
103. M. Vallino, *J. Organomet. Chem.*, 1969, **20**, 1.

104. F. G. N. Cloke, P. B. Hitchcock, M. F. Lappert, G. A. Lawless, and B. Royo, *J. Chem. Soc., Chem. Commun.*, 1991, 724.
105. D. C. Green, U. Englich, and K. Ruhlandt-Senge, *Angew. Chem., Int. Ed. Engl.*, 1999, **38**, 354.
106. J. S. Alexander and K. Ruhlandt-Senge, *Eur. J. Inorg. Chem.*, 2002, **11**, 2761.
107. K. Izod, S. T. Liddle, and W. Clegg, *J. Am. Chem. Soc.*, 2003, **125**, 7534.
108. B. De Groof, W. Mortier, M. Van Beulen, and M. Szwarc, *Macromolecules*, 1977, **10**, 598.
109. B. De Groof, M. Van Beulen, and M. Szwarc, *Macromolecules*, 1975, **8**, 396.
110. S. Harder and F. Feil, *Organometallics*, 2000, **19**, 5010.
111. S. Harder, F. Feil, and A. Weeber, *Organometallics*, 2001, **20**, 1044.
112. S. Harder and F. Feil, *Organometallics*, 2001, **20**, 4616.
113. S. Harder, F. Feil, and K. Knoll, *Angew. Chem., Int. Ed. Engl.*, 2001, **40**, 4261.
114. S. Harder and F. Feil, *Organometallics*, 2002, **21**.
115. H. G. Richey, *J. Am. Chem. Soc.*, 1985, **107**, 432.
116. S. Harder, *Angew. Chem., Int. Ed. Engl.*, 1998, **37**, 1239.
117. M. Westerhausen, C. Birg, H. Noeth, J. Knizek, and T. Seifert, *Eur. J. Inorg. Chem.*, 1999, 2209.
118. M. Westerhausen, C. Gueckel, and P. Mayer, *Angew. Chem., Int. Ed. Engl.*, 2001, **40**, 2666.
119. S. Harder, F. Feil, and T. Repo, *Eur. J. Chem.*, 2002, **9**, 1991.
120. J. Hitzbleck and K. Ruhlandt-Senge, *in pre paration*.
121. J. S. Alexander, D. G. Allis and K. Ruhlandt-Senge, *in preparation*.
122. G. S. Silverman and P. E. Rakita, ‘Handbook of Grignard Reagents’, Marcel Dekker, New York, 1996.
123. H. G. Richey, ‘Grignard Reagents New Developments’, John Wiley and Sons, Chichester, 2000.
124. A. Inoue and K. Oshima, in ‘Main Group Metals in Organic Synthesis’, eds. H. Yamamoto and K. Oshima, Wiley-VCH, Weinheim, 2004, Vol. 1, p. 51.
125. M. S. Kharasch and O. Reinmuth, ‘Grignard Reactions of Nonmetallic Substances’, Prentice-Hall, New York, 1954.
126. P. Knochel, W. Dohle, N. Gommermann, F. F. Kneisel, F. Kopp, T. Korn, I. Sapountzis, and V. A. Vu, *Angew. Chem., Int. Ed. Engl.*, 2003, **42**, 4302.
127. L. Boymond, M. Rottlander, G. Cahiez, and P. Knochel, *Angew. Chem., Int. Ed. Engl.*, 1998, **37**, 1701.
128. M. Abarbri, F. Dehmel, and P. Knochel, *Tetrahedron Lett.*, 1999, **40**, 7449.
129. M. Rottlaender, L. Boymond, G. Cahiez, and P. Knochel, *J. Org. Chem.*, 1999, **64**, 1080.
130. K. Kitagawa, A. Inoue, H. Shinokubo, and K. Oshima, *Angew. Chem., Int. Ed. Engl.*, 2000, **39**, 2481.
131. A. Inoue, K. Kitagawa, H. Shinokubo, and K. Oshima, *J. Org. Chem.*, 2001, **66**, 4333.
132. T. Delacroix, L. Berillon, G. Cahiez, and P. Knochel, *J. Org. Chem.*, 2000, **65**, 8108.
133. J. L. Leazer Jr, R. Cvetovich, F.-R. Tsay, U. Dolling, T. Vickery, and D. Bachert, *J. Org. Chem.*, 2003, **68**, 3695.
134. F. F. Kneisel and P. Knochel, *Synlett*, 2002, 1799.
135. A. Inoue, K. Kitagawa, H. Shinokubo, and K. Oshima, *Tetrahedron*, 2000, **56**, 9601.
136. S. Ito, T. Kubo, N. Morita, Y. Matsui, T. Watanabe, A. Ohta, K. Fujimori, T. Murafuji, Y. Sugihara, and A. Tajiri, *Tetrahedron Lett.*, 2004, **45**, 2891.
137. L. Berillon, A. Lepretre, A. Turck, N. Ple, G. Queguiner, G. Cahiez, and P. Knochel, *Synlett*, 1998, 1359.
138. W. Cai and D. H. B. Ripin, *Synlett*, 2002, 273.
139. F. Dehmel, M. Abarbri, and P. Knochel, *Synlett*, 2000, 345.
140. J. Eskildsen, N. Ostergaard, P. Vedso, and M. Begtrup, *Tetrahedron*, 2002, **58**, 7635.
141. C. Christophersen, M. Begtrup, S. Ebdrup, H. Petersen, and P. Vedso, *J. Org. Chem.*, 2003, **68**, 9513.
142. J. Thibonnet, V. Anh Vu, L. Berillon, and P. Knochel, *Tetrahedron*, 2002, **58**, 4787.
143. L. I. Zakharkin, O. Y. Okhlobystin, and K. A. Bilevich, *J. Organomet. Chem.*, 1964, **2**, 309.
144. V. A. Vu, I. Marek, K. Polborn, and P. Knochel, *Angew. Chem., Int. Ed. Engl.*, 2002, **41**, 351.
145. T. Tsuji, T. Nakamura, H. Yorimitsu, H. Shinokubo, and K. Oshima, *Tetrahedron*, 2004, **60**, 973.
146. F. F. Fleming, Z. Zhang, Q. Wang, and O. W. Steward, *J. Org. Chem.*, 2003, **68**, 7646.
147. S. Avolio, C. Malan, I. Marek, and P. Knochel, *Synlett*, 1999, 1820.
148. J. Villieras, B. Kirschleger, R. Tarhouni, and M. Rambaud, *Bull. Soc. Chim. Fr.*, 1986, **3**, 470.
149. A. Inoue, J. Kondo, H. Shinokubo, and K. Oshima, *Chem. – Eur. J.*, 2002, **8**, 1730.
150. T. Satoh, A. Kondo, and J. Musashi, *Tetrahedron*, 2004, **60**, 5453, and references therein.
151. A. E. Hill, in ‘Grignard Reagents New Developments’, ed. H. G. Richey, John Wiley and Sons, Chichester, 2000, p. 27.
152. G. S. Silverman, in ‘Handbook of Grignard Reagents’, eds. G. S. Silverman and P. E. Rakita, Marcel Dekker, New York, 1996, p. 307.
153. M. D. Surman, M. J. Mulvihill, and M. J. Miller, *J. Org. Chem.*, 2002, **67**, 4115.
154. S. G. Nelson, Z. Wan, and A. Stan Magdalena, *J. Org. Chem.*, 2002, **67**, 4680.
155. T. Hattori, A. Takeda, K. Suzuki, N. Koike, E. Koshiishi, and S. Miyano, *J. Chem. Soc., Perkin Trans. 1*, 1998, 3661.
156. T. Kojima, T. Ohishi, I. Yamamoto, T. Matsuoka, and H. Kotsuki, *Tetrahedron Lett.*, 2001, **42**, 1709.

157. M. R. Iesce, M. L. Graziano, F. Cermola, S. Montella, and L. Di Gioia, *Tetrahedron Lett.*, 2003, **44**, 5781.
158. T. Hattori, A. Takeda, O. Yamabe, and S. Miyano, *Tetrahedron*, 2002, **58**, 233.
159. S. Aki, Y. Haraguchi, H. Sakikawa, M. Ishigami, T. Fujioka, T. Furuta, and J.-I. Minamikawa, *Org. Process Res. Dev.*, 2001, **5**, 535.
160. M. Makosza and M. Surowiec, *J. Organomet. Chem.*, 2001, **624**, 167.
161. A. Furstner, A. Leitner, M. Mendez, and H. Krause, *J. Am. Chem. Soc.*, 2002, **124**, 13856.
162. H. Shinokubo and K. Oshima, *Eur. J. Org. Chem.*, 2004, 2081.
163. J. Quintin, X. Franck, R. Hocquemiller, and B. Figadere, *Tetrahedron Lett.*, 2002, **43**, 3547.
164. A. Furstner and A. Leitner, *Angew. Chem., Int. Ed. Engl.*, 2003, **42**, 308.
165. A. Furstner, D. De Souza, L. Parra-Rapado, and J. T. Jensen, *Angew. Chem., Int. Ed. Engl.*, 2003, **42**, 5358.
166. A. Fuerstner and M. Mendez, *Angew. Chem., Int. Ed. Engl.*, 2003, **42**, 5355.
167. B. Scheiper, M. Bonnekessel, H. Krause, and A. Furstner, *J. Org. Chem.*, 2004, **69**, 3943.
168. T. Nagano and T. Hayashi, *Org. Lett.*, 2004, **6**, 1297.
169. M. Nakamura, K. Matsuo, S. Ito, and E. Nakamura, *J. Am. Chem. Soc.*, 2004, **126**, 3686.
170. R. Martin and A. Fuerstner, *Angew. Chem., Int. Ed. Engl.*, 2004, **43**, 3955.
171. G. Cahiez, F. Lepifre, and P. Ramiandrasoa, *Synthesis*, 1999, 2138.
172. T. J. Korn, G. Cahiez, and P. Knochel, *Synlett*, 2003, 1892.
173. G. H. Posner, in ‘Organic Reactions’, ed. W. G. Dauben, Wiley, New York, 1975, Vol. 22, p. 253.
174. B. H. Lipshutz, in ‘Organic Reactions’, ed. L. A. Paquette, Wiley, New York, 1992, Vol. 41, p. 135.
175. G. Cahiez, C. Chaboche, and M. Jezequel, *Tetrahedron*, 2000, **56**, 2733.
176. J. G. Donkervoort, J. L. Vicario, J. T. B. H. Jastrzebski, R. A. Gossage, G. Cahiez, and G. van Koten, *J. Organomet. Chem.*, 1998, **558**, 61.
177. H. Ohmiya, T. Tsuji, H. Yorimitsu, and K. Oshima, *Chem. – Eur. J.*, 2004, **10**, 5640.
178. D. E. Hibbs, C. Jones, and A. F. Richards, *J. Chem. Soc., Dalton Trans.*, 1999, 3531.
179. J. Renner, U. Bergstrasser, P. Binger, and M. Regitz, *Eur. J. Inorg. Chem.*, 2000, 2337.
180. S. Aldridge, C. Jones, P. C. Junk, A. F. Richards, and M. Waugh, *J. Organomet. Chem.*, 2003, **665**, 127.
181. M. Brym, C. Jones, and A. F. Richards, *J. Chem. Soc., Dalton Trans.*, 2002, 2800.
182. C. Jones, A. F. Richards, S. Fritzsche, and E. Hey-Hawkins, *Organometallics*, 2002, **21**, 438.
183. P. E. Eaton, C. H. Lee, and Y. Xiong, *J. Am. Chem. Soc.*, 1989, **111**, 8016.
184. M.-X. Zhang and P. E. Eaton, *Angew. Chem., Int. Ed. Engl.*, 2002, **41**, 2169.
185. K. Yamaguchi, Y. Kazuta, H. Abe, A. Matsuda, and S. Shuto, *J. Org. Chem.*, 2003, **68**, 9255.
186. S. Cai, M. Dimitroff, T. McKennon, M. Reider, L. Robarge, D. Ryckman, X. Shang, and J. Therrien, *Org. Process Res. Dev.*, 2004, **8**, 353.
187. E. L. Carswell, D. Hayes, K. W. Henderson, W. J. Kerr, and C. J. Russell, *Synlett*, 2003, 1017.
188. A. Dinsmore, D. G. Billing, K. Mandy, J. P. Michael, D. Mogano, and S. Patil, *Org. Lett.*, 2004, **6**, 293.

Acknowledgment

We gratefully acknowledge support from the National Science Foundation enabling our work in the area of organometallic alkaline earth metals (CHE-0108098). We also thank Dr. Weijie Teng for providing us with the graphical material used in this article.

Biomimetic Synthesis of Nanoparticles

Joseph M. Slocik, Marc R. Knecht & David W. Wright
Vanderbilt University, Nashville, TN, USA

1 Introduction 1
2 Amino Acids as Stabilizing Ligands 1
3 Peptides 5
4 Protein Templates 11
5 Viruses for Nanoparticle Synthesis 15
6 Plant Mediated Nanoparticle Synthesis 18
7 Conclusions 19
8 Related Articles 19
9 References 19

1 INTRODUCTION

Biological systems display exquisite control in the mineralization of nanoparticles (*see Nanocrystals*; ***Semiconductor Nanocrystal Quantum Dots***; ***Metal Nanoparticles, Synthesis of*** and ***Metal Nanoparticles, Organization & Applications of***) as a result of highly developed detoxification mechanisms, regulatory processes, and requisite structural components, by the use of diverse biomolecular templates (*see* ***Biomineralization***). These templates include amino acids, peptides, proteins, and viruses which offer precisely defined metal binding sites, spatial organization, structurally confined cages/cavities/pores, and an environment that protects against oxidizing conditions/nanoparticle aggregation. Consequently, the corresponding biogenic nanoparticles exhibit superior quality (i.e. 24 carat gold), dispersity, crystallinity, morphology, and optical/electronic properties. Presently, synthetic approaches that mimic biomineralization processes have gained interest along with the wealth of viable nanoparticle templates. Herein, we describe the methodology, biologically derived templates and motifs, and the resultant nanoparticle characteristics/properties. The scope of this review will begin by examining synthetic nanoclusters stabilized by individual amino acids and proceed to nanoparticles stabilized by increasing complex peptides (Table 1) and finally proteins and virus templates.

2 AMINO ACIDS AS STABILIZING LIGANDS

2.1 Cysteine

2.1.1 Zero-valent Metals

The most studied single amino acid capping ligand is cysteine. Cysteine is the only free thiolate amino acid occurring within the standard twenty amino acids and represents an ideal ligand for use as a size directing capping ligand with soft metal substrates such as gold, silver, platinum, copper, and type II–VI semiconductors.

Cysteine has been shown to be an excellent monodentate ligand in the formation of zero-valent gold nanoclusters using standard reduction conditions.**[1]** Under anaerobic conditions, free cysteine was added to a solution of Au (III). Subsequently, the gold sol was further reduced using sodium borohydride to form zero-valent Au^0.**[1,2]** With the reduction of gold, the thiolate ligand of the cysteine moiety capped the surface of the newly formed nanoparticle, preventing Oswald ripening and maintaining a monodisperse set of nanoparticles.

The Au^0 nanoclusters formed were relatively monodisperse with a typical size distribution of 3.8 ± 1.0 nm in diameter. Additionally, the cysteine passivated gold nanoclusters were highly crystalline, confirmed by the major diffractions of the (100), (200), (220) and (020) of the face-centered cubic lattice for the gold.**[1]** The overall size dimensions were slightly larger than previously reported values for gold-alkenethiol nanoclusters, but the diffraction patterns from both nanostructures were similar.**[3]**

Gold nanoclusters were also obtained through a place exchange reaction. Taylan *et al*. were able to substitute surface stabilized citrate Au^0 nanoclusters with cysteine by incubation of the particles with the free amino acid,**[4]** providing a handle to conjugate other biologically relevant molecules to the surface of the cluster. This reaction was driven through the surface affinity for the thiolate moiety. As the cysteine thiolate ligands have a stronger binding affinity for gold surfaces than oxygen from the perspective of enthalpic considerations, the thiolate could favorably displace the oxygen moieties and bind to the gold surface.

Many different applications for gold cysteine nanoclusters have been proposed. One application is the use of citrate capped nanoparticles as sensors for the detection of thiol containing structures. This application relies on the fact that thiols can easily displace oxygen coordinated moieties. Zhong *et al*. have studied this process between cysteine and homocysteine to develop an assay for the homocysteine biomarker, a correlate to cardiovascular disease. When citrate stabilized particles of 13 nm were incubated with either thiolate structure, the solution color changed from a dark red to a deep blue. The displacement of citrate by these moieties resulted

Table 1 Summary of amino acid and peptide stabilized nanoparticles

Ligand	Nanoparticle	Diameter (nm)	UV absorbance (nm)	Synthesis method	Reference
Cysteine	Au^0	3.8 ± 1.0	511	Reduction	1
Cysteine	Au^0	123	620	Place Exchange	4,5
Cysteine	Ag^0	4.4 ± 0.3	400	Reduction	1,7
Cysteine	Cu^0	3.5 ± 0.8	398	Reduction	1
Cysteine	Pt^0	16.9 ± 8.4	–	Reduction	1
Cysteine	CdS	2–4	360–400	Metal Sulfide	10
Cysteine	ZnS	–	260–275	Metal Sulfide	11
Cysteine	Ag_2S	9 ± 2.25	300	Metal Sulfide	13
Histidine	Au^0	3.8 ± 1.0	518	Reduction	1
Histidine	Ag^0	10 ± 3.0	393	Reduction	1
Histidine	Cu^0	6.9 ± 2.4	571	Reduction	1
Histidine	Pt^0	3.4 ± 1.0	270	Reduction	1
Histidine	ZnS	4.24 ± 0.66	260–305	Metal Sulfide	15
Histidine	ZnS:Mn	8.3	387 and 412	Metal Sulfide	16
Lysine	Au^0	6.5 ± 0.7	510	Reduction	17
Aspartic Acid	Au^0	24 ± 3	530	Reflux Reduction	18
Glutathione	Au^0	0.9 nm core	675	Reduction	22
Glutathione	Au^0	4.5 ± 1.2	512	Reduction	1
Glutathione	Ag^0	8.6 ± 3.5	486	Reduction	1
Glutathione	Cu^0	9.7 ± 4.3	363	Reduction	1
Glutathione	Pt^0	17.0 ± 6.2	–	Reduction	1
Glutathione	CdS	2.28–2.46	319–364	Metal Sulfide	25
Glutathione	ZnS	1.95–3.45	252–270	Metal Sulfide	28
Glutathione	Ag_2S	9.0 ± 2.25	300	Metal Sulfide	13
HRE	Au^0	9.5	524	Reduction	1,2
HRE	Ag^0	11.2	402	Reduction	1,2
HRE	Cu^0	–	574	Reduction	1,2
HRE	Pt^0	7.9	317	Reduction	1,2
HRE	TiO_2	–	282	Condensation	2
HRE	Ag_2S	11.3	–	Metal Sulfide	2
HRE	ZnS	3.1	288	Metal Sulfide	1
AG3	Ag^0	60–150	440	Peptide Reduced	47
AG4	Ag^0	60–150	440	Peptide Reduced	47

in a noticeable shift of the UV absorbance of the particles from 550 nm to 620 nm.[5] This shift in the plasmon resonance occurs through the formation of self-assembled structures of the nanoparticles though hydrogen bonding interactions of the amine and carboxylate groups of the cysteine and homocysteine substrates once substitution was complete.

Another application for cysteine capped gold nanoparticles is the use as a solid support for oligomerization of amino acids in solution. This application has environmental applications in which free amino acids can be extracted from aqueous solutions. In this method, the amino groups on the surface of the nanoparticle mediates the formation of linkages for oligomerization when a standard peptide coupling agent is added. Following the reaction progress by UV spectroscopy, a plasmon resonance peak shift (510 nm to 598 nm over 1 h) is observed as the result of the formation of larger aggregates. Once a critical oligomer size domain is obtained, the particles precipitate from solution and can be collected by filtration. The oligomers can be recovered by oxidative cleavage from the particle.[6]

A second well studied cysteine stabilized nanocluster is the zero-valent silver nanocluster. Nanoclusters of this type, prepared via $NaBH_4$ reduction, have been reported to have discrete monomodal size distributions on the order of 4.4 ± 0.3 nm. From UV–vis spectroscopy and transmission electron microscopy (TEM), Mandal *et al.* have shown that the silver nanoclusters can self assemble into a larger structure through hydrogen bonding of the capping cysteine ligand. The surface exposed amine and carboxylate formed a network of hydrogen-bonded nanoparticles. The plasmon resonance at 400 nm showed a broadening trend over a 7 hour reaction period, at which point the self-assembly process of Ag^0 nanocluster networks was completed. Further analysis of Ag^0 cysteine stabilized nanoparticles by powder X-ray diffraction (XRD) has shown a high degree of crystallinity and a face-centered cubic lattice constant of 4.34 Å.[1] Thermal studies indicated a stable network to ~55 °C.[7]

Similar to Ag^0, zero-valent platinum nanoclusters were synthesized with cysteine capping ligands under reducing conditions. The platinum clusters showed a larger size distribution of 16.9 ± 8.4 nm and no noticeable plasmon resonance peak in the visible spectrum. The electronic and dielectric properties of platinum gave rise to the featureless spectra, reminiscent of the spectra of polyacrylate stabilized Pt^0 clusters.[8]

Cysteine ligands have also been reported in the synthesis of intricate copper nanoparticles following a literature modified reduction procedure.[2] The Cu^0 nanoclusters revealed a plasmon resonance band at 398 nm and an average size distribution of 3.5 ± 0.8 nm by TEM. Infrared analysis of the stabilized nanoparticles showed a weakened S–H stretch at 2598 cm^{-1} suggesting uncoordinated cysteine thiols, supporting the possible involvement of the amine functional group from the cysteine alpha carbon in particle stabilization.[1] These particles displayed extreme O_2 sensitivity, degrading under aerobic conditions to Cu (I) and then Cu (II) cysteine complexes. Additionally, this sensitivity precluded the convenient determination of nanoparticle crystallinity.[9]

2.1.2 Metal Sulfides Nanoclusters

Cysteine has also been shown to passivate the surface of highly fluorescent CdS bionanocrystallites. These nanocrystals have been of interest owing to their possible use as fluorescent labels and photocatalysts. Generally, the nanoparticles were formed by the addition of inorganic sulfide (Na_2S) to solutions of a cadmium cysteine precursor complex. This synthetic process yielded nanocrystals of a size dimension between 2 and 4 nm in diameter.[10]

The synthetic conditions for CdS formation were explored with different ratios of cadmium:cysteine and cadmium:sulfide in order to further manipulate and refine the resultant nanocrystal properties. While a great deal of reaction space was examined to optimize the ratios of the cluster components, the different ratios of cysteine to cadmium produced little to no tangible difference between reactions. This suggests that prior to the addition of the sulfide nucleating component, the cysteine forms a cadmium/amino acid precursor complex.[10] In contrast, the ratio of sulfide to cadmium was critical in tuning the size of the nanoparticle. As the ratio of sulfide to Cd approached and surpassed 1, the UV absorbance began to shift toward the red indicating the formation of larger capped CdS nanocrystals with higher sulfide ratios. The fluorescence spectra of these particles also showed a dependence on the equivalents of sulfide added, reflecting the characteristic quantum confinement of these nanoparticles. By keeping the amino acid in excess, there was always sufficient capping ligand to stabilize the particle and prevent aggregation to the bulk.

In addition to fluorescent CdS nanocrystals, cysteine represents an excellent ligand for ZnS nanocrystals. Again, inorganic sulfide is incorporated into a zinc cysteine complex to initiate cluster formation. An examination of reaction temperatures suggests optimal formation occurred at 45 °C. Once formed, the clusters were highly fluorescent and gave rise to an absorbance around 274 nm blue shifted from the bulk band gap for ZnS. From the UV data and size fractionation studies monitored by UV–vis, it appeared that the cysteine moiety was able to form clusters of rather uniform size and distribution.[11]

As was previously determined with CdS, titration experiments of sulfide produced varying sizes of ZnS nanoparticles. By maintaining a constant ratio between cysteine and Zn (II) of 1:1, varying equivalents of sulfide (0–1.5 eq.) were added. From UV–vis, the collection of ZnS-(Cys) nanocrystals displayed absorption shoulders between 260–275 nm. As the equivalents of sulfide increased, the shoulder red shifted indicating the formation of larger nanoparticles in solution. Additional characterization by Mehra *et al.* of the ZnS nanocrystal products revealed only a small variation of particle sizes obtained after separation of the reaction mixture by gel permeation chromatographic methods.[11]

Given the unique photophysical properties of semiconductor quantum dots, one potential application of these materials is as photocatalysts. When the ZnS-(Cys) nanoparticles were introduced to paraquat and irradiated with light at 254 nm, efficient reduction of the dye occurred. Ultimately, the photoreducibility offered by ZnS nanoclusters is advantageous to many applications, including wastewater treatment.[11] By using this unique synthetic method, batches of gram scale quantities have been produced that are quite stable for up to 30 months,[12] making ZnS a commercially viable catalyst and environmental agent.

Ag_2S was also effectively stabilized by cysteinyl ligands. These clusters are synthesized using a molar ratio of 2:1 cysteine:silver ions upon which stoichiometric amounts of inorganic sulfide were added to nucleate the nanoparticle, with subsequent size-selective precipitation.[13] The resultant nanoparticles had an absorbance shoulder at 300 nm. Further analysis using high-resolution transmission electron microscopy (HRTEM) revealed a particle size of approximately 9.00 ± 2.25 nm in diameter. Selected area electron diffraction (SAED) analysis also demonstrates the highly crystalline nature of the product.[13]

2.2 Histidine

2.2.1 Zero-valent Metal Nanoclusters

Among metal chelating ligands, histidine exhibits numerous physical properties amenable to nanocluster stabilization including good nucleophilicity, side-chain pK_a, known metal binding, and good hydrogen bonding. Histidine has been shown to stabilize various nanoclusters through the imidazole side chain, which acts as a capping agent to passivate the nanocluster surface. Given the pK_a of the histidine side chain is 6.00,[14] its use as a ligand occurs upon deprotonation at neutral to slightly basic pH. This unique amino acid has been shown to cap several metal nanoclusters, including gold, silver, copper, platinum, and ZnS quantum dots with good results.[1,15]

Based on synthetic methods developed for cysteine stabilized clusters, histidine encapsulated Au^0 nanoclusters were prepared by the formation of a histidine/Au (III) precursor complex with subsequent reduction by $NaBH_4$. UV analysis confirmed the synthesis by the presence of a plasmon resonance peak for Au^0 at 518 nm. Further confirmation by TEM showed particles with an average diameter of 3.8 ± 1.0 nm with a good deal of crystallinity as determined by XRD.[1]

Silver histidine nanoclusters were produced by similar methods, whereby silver ions were complexed to histidine and reduced using $NaBH_4$ for four hours under anaerobic conditions. UV absorbance showed a broad peak at 393 nm indicating formation of the clusters. TEM and XRD analysis revealed nanoclusters on the size dimensions of 10.0 ± 3.0 nm with a high degree of crystallinity.[1]

Interestingly, Pt^0-(His) nanoclusters prepared by standard $NaBH_4$ reduction from precursor complexes of Pt (II) and histidine in aqueous solutions produced nanoclusters with a plasmon resonance at 270 nm as compared to a theoretical maximum plasmon band predicted at 345 nm for particles $\leq$20 nm.[8] A high degree of crystallinity was confirmed by the (100), (200), (220), and (020) diffractions in the powder XRD diffraction peaks. TEM analysis demonstrated a tight distribution of particles with an average diameter of 3.4 ± 1.0 nm.[1]

Novel copper nanoclusters were also synthesized using histidine as the surface ligand. As described for Cu^0-(Cys), these clusters were highly air sensitive, therefore an anaerobic environment was necessary to prevent nanocluster degradation to copper oxides during characterization. UV studies revealed a plasmon resonance at 571 nm with TEM analysis confirming a size distribution of 6.9 ± 2.4 nm.[1]

Further insight into histidine encapsulation of nanoclusters (Au, Ag, Cu, Pt) was provided by infrared spectroscopy. IR spectra of free histidine showed a set of stretching bands for the N–H bond of the amine and strong peaks (1630 cm^{-1}, 1413 cm^{-1}) attributed to an asymmetrical and symmetrical CO_2^- stretch. As a result of nanocluster stabilization and the subsequent formation of a metal-N(His) interface, the N–H stretching frequencies broadened and the number of bands decreased relative to free histidine due to the interactions with the dielectric field at the nanocluster surface.[1]

2.2.2 Metal Sulfide

Histidine has been shown by Mehra *et al.* to stabilize fluorescent nanoparticles of ZnS. Nanoparticle synthesis is similar to ZnS-(Cys) methods (see Section 2.1.2). It was noted that the best ratio for nanoparticle formation is 2:1 for histidine to zinc (II). Titrations of sulfide into solutions of the complexed metal and amino acids showed formation of larger particles as the sulfide equivalents increased. This formation gave rise to many absorbances in the UV between 260 to 305 nm. When only one equivalent of sulfide was added, formation of two peaks appeared in the UV at 265 and 285 nm, indicating the formation of two different populations of nanoclusters synthesized. Fluorescence studies revealed strong fluorescence with peak maxima around 425 nm.[15] By using size exclusion chromatography (SEC), researchers were able to separate the two different populations of ZnS particles, providing a route for improved monodispersity.[15]

Further analysis of the particles using HRTEM confirmed formation of the nanocrystalline material. For nanoparticles of an average diameter of 4.24 ± 0.66 nm, distinct lattice planes could be observed with spacings of 3.0 ± 0.3 Å. Furthermore, SAED patterns displayed a wurtzite crystal structure with diffraction rings at 3.12 Å, 1.92 Å and 1.63 Å.[15]

Based on the above synthetic routes, ZnS-(His) nanoclusters were doped with manganese to improve the photophysical properties of the quantum dots. To synthesize these unique doped clusters, the zinc (II) ions were allowed to complex with the histidine in solution, followed by addition of manganese. During nucleation induced by the addition of sulfide, manganese was doped into the reaction mixture. Each nanocluster was doped with approximately 1% manganese. The resulting ZnS:Mn clusters had a typical absorbance (387 and 412), but exhibited a strong distinctive orange fluorescence originating from the d−d transition of the Mn^{2+} ion.[16]

2.3 Lysine

Similar to histidine, lysine has also been shown to bind gold nanoparticle surfaces through the ε-primary amine of the side chain. The lysine capped Au^0 nanoparticles synthesized from reduction by $NaBH_4$ were approximately 65 ± 7 Å in diameter and showed an initial strong plasmon resonance at 510 nm that broadened and red shifted slightly over time. This broadening was attributed to the formation of a self-assembled structure from hydrogen bonding of surface capping lysines between individual nanoclusters.[17]

Evidence for the formation of the self-assembled structure was based upon the pH behavior of the nanoparticle solution. At acidic pHs, the plasmon resonance showed little to no broadening of the peak. At neutral conditions, the peak broadened due to the formation of larger structures in solution. More basic solutions of nanoclusters produced spectra with even broader plasmon resonances, supporting the hypothesis that the more basic a solution was, the larger the network of hydrogen-bonded nanoparticles. Upon heating the solution, hydrogen bonds were disrupted and the surface plasmon resonance peaks shifted and became much more pronounced. These results were further confirmed with TEM analysis which showed either individualized nanoparticles or tightly associated random networks of particles depending upon the pH of the solution studied.[17]

2.4 Aspartic Acid

Inspired by the citric acid reductive route to gold nanoparticles,[18] aspartic acid was used as both reductant and surface capping ligand. In this method, refluxing chloroauric acid in solution with aspartic acid caused the reduction of gold by the amino acid eventually forming the nanoparticles. UV analysis has shown a typical plasmon resonance peak at 530 nm for these particles. TEM analysis of the particles showed a size distribution of 24 ± 3 nm, which is considerably larger than that reported for the citric acid method.[18] This is likely due to the difference in the inherent reducing ability of the aspartic acid relative to citrate.

2.5 Metathesis/Transmetallation of Amino Acid Stabilized Nanoparticles

In contrast to standard borohydride reductive nanoparticle synthesis, we have developed an alternative strategy to amino acid encapsulated nanoparticles by utilizing a metal nanoparticle (M^0-(Ligand))/metal ion (M^{n+}) precursor redox pair with matched oxidation/reduction potentials. Simply, a metal nanoparticle such as Pt^0-(Cys) acts as the principal reductant to a complimentary selected metal ion of Au^{3+} resulting in a new stabilized metal nanoparticle of Au^0-(Cys) and the oxidation product of the original nanoparticle Pt^{n+}. Malow *et al.* have reported a metathesis/transmetallation type reaction between a platinum colloid and a Au^I cyanide compound.[19] Similarly, we employed a Pt^0-(Cys)/$AuCl_4^-$ pair and 0.5–2.0 equivalents of Au^{III} to Pt^0-(Cys). XRD analysis of the nanoparticle products revealed differences in crystallinity as the equivalents of Au^{3+} were increased, whereby 0.5 and 1.5 equivalents of Au^{3+} yielded low crystalline products likely due to incomplete reactions/substitutions with the platinum lattice (Figure 1). At 1.0 eq. of Au^{3+}, both crystalline Pt^0 and Au^0 are present as observed by two sets of diffractions. Upon addition of 2.0 eq., only one set of diffractions attributed to fcc Au^0 are present. After ethanol purification of oxidized products, the atomic % of gold increased to 95.6% as the atomic % of platinum decreased to 4.4% at 2.0 eq as explained by energy-dispersive system (EDS). Analogously, a Cu^0-(Cys)/Pt^{2+} pair produced stabilized platinum nanoparticles by copper mediated reduction of Pt^{2+}. This approach provides a means to synthesizing a variety of metal nanoparticles which are difficult to synthesize under borohydride reduction via the judicious selection of a redox pair. The choice of metal nanoparticle, oxidation state, and stabilizing ligand are all critical considerations.

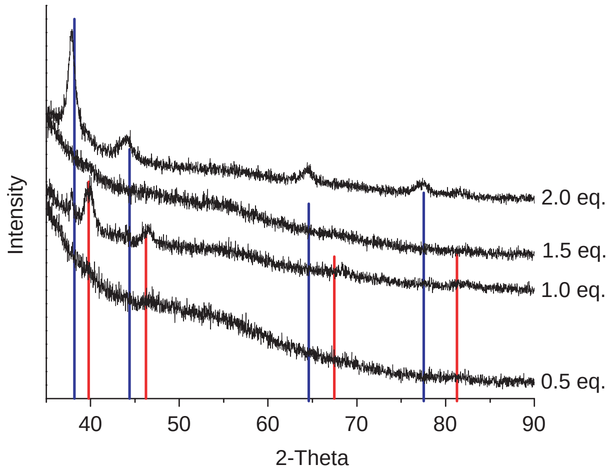

Figure 1 XRD analysis of Pt^0-(Cys)/nAu^{3+} reaction. 0.5–2.0 eq. of Au^{3+} added to 1.0 eq. of Pt^0-(Cys), precipitated, and scanned on a Scintag X_1 θ/θ automated powder diffractometer with a Cu target, a peltier-cooled solid-state detector, and zero background Si (510) sample support. Both line sets of standard diffractions are included for fcc Pt^0 (red lines) and Au^0 (blue lines). Reaction scheme for metathesis/transmetallation reaction between Pt^0-(Cys)/Au^{3+}

3 PEPTIDES

The main inspiration for the formation of nanoparticles from single amino acids arose from the fact that in nature, many particles are formed from short chain peptides that contain a cysteine or histidine amino acid.[1,2,20] These short chain peptides are principally used as a form of detoxification from the effects of high heavy metal ion concentrations *in vivo*. From these biological examples, the chemistry of these peptides has been expanded to form novel zero-valent and semiconductor nanoparticles under *in vitro* conditions (Figure 2).

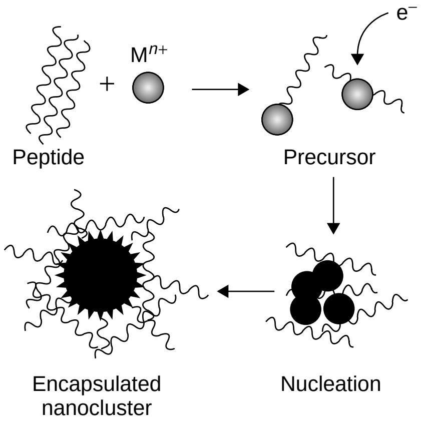

Figure 2 Biomimetic synthesis strategy for peptide encapsulated nanoclusters. Synthesis begins with complexation of peptide ligand to metal ion, followed by borohydride reduction of metal complex, nucleation, and formation of peptide stabilized nanocluster. (Reprinted with permission from Ref. 1. © 2003 American Chemical Society)

3.1 Glutathione (GSH)

The simplest of all peptides used in the formation of biologically relevant nanoclusters is the reducing peptide GSH.[21] Glutathione is a peptide comprised of three amino acid residues with the sequence γECG (**1**).

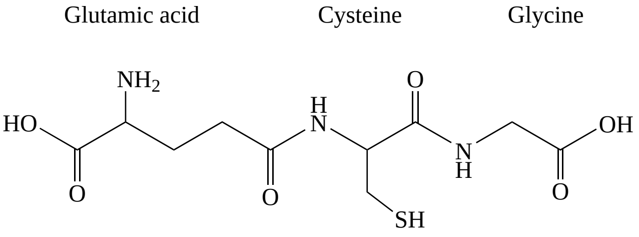

(**1**)

With the free thiolate moiety, this peptide demonstrates similar surface chemistry to cysteine ligands, and as a result is available to bind to the surface of nanoclusters, Au^0, Ag^0, Cu^0, Pt^0, CdS, and ZnS.

3.1.1 *Zero-valent Noble Metals*

Glutathione has been shown to stabilize zero-valent gold nanoclusters through a gold thiol interaction. Whetten *et al.* have used various spectroscopic methods, from mass spectrometry to powder X-ray diffraction, to characterize these nanoparticles. A typical synthesis of Au^0-(GSH) particles starts with the formation of a Au(III)GSH complex which is reduced using a strong reductant to form the nanoparticles in a solution of 2:3 water:methanol. Mass spectrometry analysis of the Au^0 nanoparticle products revealed the zero-charged spectrum had a cluster mass of approximately 10 417 amu corresponding to a formula mass of $Au_{28}(GSH)_{16}$.[22] Powder X-ray diffraction revealed broad peaks which correlated to a face-centered cubic gold structure. Scherrer's analysis of the diffraction peaks estimated a core diameter of approximately 0.9 nm based on peak widths.[22] These glutathione encapsulated particles also showed a plasmon peak at 675 nm.[22] These results, armed with the proof that a GSH monolayer immobilized on a surface remained biochemically active to stabilize glutathione S-transferase on the monolayer,[23] gave rise to speculation that GSH encapsulated zero-valent nanoclusters can be used as a bioremediation agent *in vivo*.

In another study of Au^0-(GSH), Wright *et al.* have synthesized nanoparticles in a completely aqueous media under anaerobic conditions. Following the standard reduction preparations with sodium borohydride, gold nanoparticles were produced with a plasmon resonance band at 512 nm. Powder XRD analysis match a face-centered cubic lattice, while TEM showed that the particles had an average diameter of 4.5 ± 1.2 nm.[1]

Zero-valent silver nanoparticles have also been synthesized using GSH as a surface passivant. Under standard reducing conditions, a preformed Ag(I)GSH complex was reduced to form nanoparticles of Ag^0-(GSH). After isolation and purification of the nanoclusters, characterization showed a plasmon resonance band at 486 nm, a face-centered cubic lattice structure revealed by powder XRD, and a particle diameter of 8.6 ± 3.5 nm by TEM.[1]

Additionally, Pt^0 nanoclusters were synthesized with glutathione as a ligand. Upon reduction of a preformed Pt(II)GSH complex, nanoparticulate material of Pt^0-(GSH) was formed. These nanoparticles had an average diameter of 17.0 ± 6.2 nm and demonstrated no plasmon absorbance due to the electronic and dielectric properties of the metal.[8] Powder XRD analysis confirmed a face-centered cubic lattice structure for the material.[1]

Formation of zero-valent copper clusters with glutathione has been studied anaerobically. The ligand has been reported to provide a substantial degree of surface passivation. Reduction of a Cu(II)-GSH complex produced nanoparticles with a plasmon resonance band at 363 nm. These nanoparticles possessed a diameter of 9.7 ± 4.3 nm as demonstrated by TEM analysis.[1] Under aerobic conditions, the nanoparticles oxidatively degrade as evinced by the loss of the plasmon absorption band over time.

3.1.2 *Metal Sulfide Nanocrystals*

Glutathione has been shown to mediate the formation of CdS semiconductor nanocrystals. GSH encapsulated nanocrystals were first observed *in vivo* in the yeast *Candida glabrata* as a consequence of detoxification processes, when grown under conditions of high Cd^{2+}.[23,24] Mechanistic investigations revealed that the primary step-in CdS formation involved the chelation of glutathione to Cd^{2+} to generate a Cd(II)-$(GSH)_2$ precursor complex. Following complexation, inorganic sulfide was titrated in varying ratios (0.25 to 2.0) to determine the optimal ratio for nanocrystal formation. Ethanol precipitation mediated size separation of CdS nanoclusters in good yield.[25]

Mehra *et al.* noted a red shift in nanocluster absorption when different ratios of sulfide samples were compared. As the ratios increased, the UV–vis peak shifted toward the red corresponding to an increase in nanocluster size.[25] This was undoubtedly from the incorporation of more sulfide into the cluster core to form larger overall nanoparticles. For instance, a ratio of 0.75 (sulfide to cadmium) produced a product that absorbed between 319 and 346 nm, while samples formed from a ratio of 1.0 showed absorbances between 343 and 364 nm.[25] Using the Brus approximation, these nanoclusters had diameters of 22.8 Å and 24.6 Å, respectively.

Research has also been conducted on the ratios of GSH to cadmium for nanocluster formation. Clusters were formed at ratios as high as 1:1, but these reactions did not produce a uniform distribution of particles. In fact, the most reproducible results arose from reactions with Cd:GSH ratios of 0.25 to 0.5. With these ratios, nanoparticles on the order of 10.7 to 20.3 Å were formed, respectively.[26] This small size regime displayed a unique photoreactivity.

Photolytically, CdS-(GSH) nanoclusters reduced *p*-nitrophenol[25] and methylviologen[26] by surface-mediated phenomena. This is most likely due to the potential of photo-generated electrons at the nanocluster surface. Samples with cadmium to sulfide ratios of <1.25 showed a better ability to reduce the organic molecule.[26] The rate of reduction was dependant upon the sample and the pH of the reaction. The reaction proceeded with similar kinetics at pH 8 and 9, while it was significantly slower at pH 10, degrading only 80% of the substrate.[25] Mehra has suggested that such photocatalytic systems may have environmental applications for organic remediation.

As expected, the formation of ZnS-(GSH) nanoclusters is analogous to CdS. Beginning with the $Zn(II)(GSH)_2$ precursor complex, nanocluster formation is initiated by the addition of the sulfide. Mehra *et al*. has shown that the precursor Zn(II)GSH complex does indeed closely follow the synthetic route of CdS-(GSH) nanoparticles.[27] Considering the similarities between the thiol chemistry of zinc and cadmium, studies to optimize ZnS nanocluster formation primarily focused on the ratio of zinc to sulfide ions in solution. Varying equivalents of sulfide (0.1–2.0) were studied for the formation of nanoclusters. An optimal ratio of Zn^{2+}:S^{2-} was obtained at 1:1. The average size of nanoparticles prepared at this ratio was shown to be about 3.45 ± 0.5 nm.[28] Elution profiles from SEC highlighted the dispersity of nanoparticle populations synthesized in aqueous solutions.[27] By size dependent absorption, the reaction mixtures revealed two cluster populations with an approximate diameter of 22.6 Å and 19.54 Å, respectively. Any excess of sulfide added greater than 1 equivalent was volatilized and not incorporated into the nanoclusters.[27]

Another common similarity between the CdS-(GSH) and ZnS-(GSH) nanoparticles was the ability to photoreduce methylviologen[27] and *p*-nitrophenol (PNP)[28] in solution. Under an inert atmosphere, reduction was evident from the clear formation of the characteristic spectrum of reduced methylviologen.[27] *P*-nitrophenol was similar in that an optimal reduction occurred when the ratio of PNP to nanocrystal was approximately five to ten. In fact, when the ratio was higher, a decreased reduction rate was evident. Over time, complete reduction of the PNP occurred.[28]

A third type of metal sulfide nanoparticle stabilized by GSH is Ag_2S. Ag_2S nanoparticle synthesis is challenging particularly in aqueous media due to the tendency to form bulk material rather than discrete nanoparticles. Mehra *et al*. have developed a standard synthesis for efficient production of this material. In this synthesis, silver ions are reacted with GSH to form a $Ag(I)\text{-}(GSH)_n$ complex (where n is undetermined) and after sufficient reaction time, the inorganic sulfide is added to the solution in stoichiometric amounts to induce nucleation of the silver sulfide core. Subsequently, the nanoparticles were precipitated using a size-selective precipitation method.[13] Under this preparation method, Mehra and coworkers have isolated nanoparticles of Ag_2S on the order of 9 ± 2.25 nm. Using HRTEM and SAED, the particles appeared as a highly ordered crystalline material. Furthermore, the electronic absorption spectra obtained from these nanoparticles showed a strong absorbance shoulder at approximately 300 nm.[13]

3.2 Phytochelatin Peptides

An analogue of glutathione is a group of peptides known as phytochelatins (PC). These multi-dentate chelating agents (*see Chelating Ligands*) have the chemical structure of $(\gamma\text{-EC})_n\text{G}$ and are naturally found at rather high concentrations in yeast and plants in response to heavy metals (n ranging from 2 to 11).[23,24,29] The primary structural motif of the phytochelatins is the repeating cysteine subunit making it an excellent heavy metal chelator known to bind many heavy metal ions, including cadmium,[30] copper,[31] lead,[32] silver,[33] and mercury.[34]

Research, pioneered by Dameron and Winge, investigated the formation of CdS nanoclusters with phytochelatins. As with glutathione, synthesis begins with the formation of a stoichiometric metal/peptide complex dependent on the length of the phytochelatin peptide ($[\gamma\text{EC}]_n\text{G}$ where $n = 2\text{–}4$) and the number of reduced cysteine binding sites. Molar equivalences of 0.5, 1 and 1 of peptide produced maximal complexation with peptides of n equal to 2, 3 and 4 respectively.[35] With the ratios of cadmium to peptide known, titrations of sulfide were analyzed for the formation of the nanocluster. The optimal equivalent was different depending upon the peptide used to passivate the nanocluster surface.[35] As an example, the phytochelatin with $n = 3$ was extensively studied for sulfide formation of nanoparticles. As sulfide was increasingly titrated, the absorbance band shifted until a maximal equivalence of 0.57 was added to solution. At this equivalence, the absorbance band became maximally shifted to 318 nm, with fluorescence activity at 430 nm.[35]

3.2.1 *Combinatorial Peptide Library Based upon Phytochelatins*

To understand the mechanistic formation of CdS nanocrystals using phytochelatins, a spatially addressable combinatorial set of peptides (Figure 3) was designed based on the $n = 3$ phytochelatin peptide by Spreitzer *et al*.[36,37] The library was comprised of 125 peptides with the sequence of **X**Cys**Y**Cys**Z**CysGly; whereby X, Y, and Z were varied with the spacer residues of α-Glu, γ-Glu, α-aminobutyric acid (GABA), SerGly, and ε-aminohexanoic acid (ε-Ahx). These linkages were chosen to attenuate the distance between cysteine binding sites by varying the spacing from 3.75 to 8.7 Å.

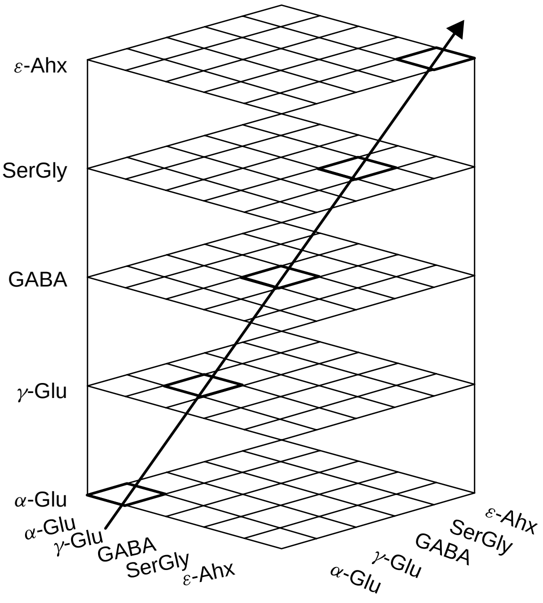

Figure 3 Spatially addressable combinatorial peptide library comprised of 125 peptides with the sequence of **X**Cys**Y**Cys**Z**CysGly, whereby X, Y, and Z are spacer residues of α-Glu, γ-Glu, GABA, SerGly, and ε-aminohexanoic acid (ε-Ahx). (Reproduced by permission of Wiley VCH)

Each peptide was screened for CdS nanoparticle stabilization and characterized by UV–vis, fluorescence, SEC, and photophysical properties to develop selection criteria. Size exclusion results showed nanoclusters with molecular weights of approximately 28 kDa consistent with a composition of 80 Cd atoms, 62 sulfur atoms, and 22 (γ-EC)$_3$G peptides.[36,38] Analysis of the characterization results showed that when an α-linked glutamic acid was substituted in all three positions (X, Y, and Z) and the cysteine spacing was kept small, smaller sized CdS nanoparticles were formed.[30] The analysis of the library elements suggest that the mechanism for nanocluster size selectivity is likely due to the various library peptides trapping growing CdS nanoclusters and the stability of these particles when the surface of the aggregate presents sites which match the spacing of the peptide and/or complex.

To further explore what properties of the stabilizing ligand controlled the distribution of cluster sizes, an informatic analysis based on quantitative structure activity relationships was performed. The results of such an analysis showed there was a correlation between nanocluster molecular weight and the dipole of the peptidyl ligand. Ligands with greater dipoles produced larger sized nanoclusters.[37] This analysis explains the differences in cluster size when different peptides were compared.[36]

3.3 Histidine-rich Peptide

Another important class of metal binding peptides conducive to the formation of metal nanoclusters are histidine-rich peptides. These proteins and peptides have been discovered in the digestive vacuole of the malarial parasite *Plasmodium*,[39] the vitellaria of the liver fluke *Fasciola hepatica*,[40] human saliva,[41] and blood serum;[42] and implicated in the biomineralization of copper, zinc, and heme.[43] In particular, a histidine-rich protein (HRP II) from *Plasmodium falciparum* is responsible for mediating the biomineralization of hemozoin crystallites by functioning as a nucleation template for heme. Examination of HRP II reveals a common repetitive binding domain with the sequence of Ala-His-His-Ala-His-His-Ala-Ala-Asp (HRE) within the protein scaffold.[39] Consequently, this 9-mer linear peptide epitope represents a versatile ligand for the synthesis and stabilization of various nanoclusters by offering several binding sites for metal ions and then multiple surface stabilizing groups.[43,44]

The HRE peptide was shown to mineralize a total of seven nanoclusters, ZnS, Au^0, Ag^0, Pt^0, Cu^0, TiO_2, and Ag_2S. All nanoparticles were formed by mixing appropriate ratios of metal to peptide to form a metal peptide precursor complex. To this solution, sulfide or reductant was added to form the appropriate encapsulated metal nanocluster. Condensation of titanium isopropoxide in the presence of HRE was used for synthesis of TiO_2-(HRE) nanoparticles. Once formed, all of the nanoclusters were characterized using UV–vis, IR, powder XRD, transmission electron microscopy, and an antigen capture assay.[1,2]

Each nanocluster possessed a UV–vis spectrum that was specific to each particle (Figure 4). The absorption maxima for the ZnS nanoclusters was observed at 288 nm with a blue shifted shoulder reminiscent of the spectra from the work of Mehra *et al.* using glutathione.[2,12] The noble metals of gold and silver displayed typical plasmon resonances at 524

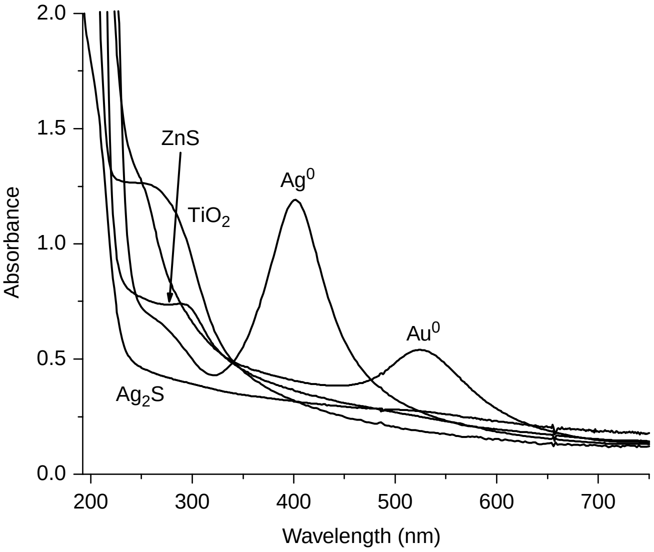

Figure 4 UV–vis absorption spectra of HRE peptide encapsulated nanoclusters. (Reprinted with permission from Ref. 2. © 2002 American Chemical Society)

and 402 nm respectively confirming nanoparticle formation.[2] For nanoparticles of copper and platinum, plasmon resonance bands were observed at 574 nm and 317 nm respectively.[1] Furthermore, the novel TiO_2 nanoclusters absorbed at 282 nm, and are of great interest since they represent the only water-soluble example yet reported. Finally, the Ag_2S nanoclusters displayed no absorbance within the scanned regime.[2]

IR analysis confirmed the existence of peptides bound to the nanocluster surface. Vibrations attributed to the histidine side chains as well as from the amide stretches were present in the purified nanocluster spectra. Also, a loss of the N–H stretching band of histidine was noted, indicating a coordination mode for the peptide-metal nanostructures.[1,2] This analysis confirmed the attachment of the HRE peptide to the surface.

Powder X-ray diffraction showed that most of the clusters formed, ZnS, Au^0, Ag^0, Pt^0, Cu^0, and Ag_2S, were crystalline with the exception of the TiO_2 nanoclusters which showed no discernable crystalline pattern. The lack of crystallinity for the titania was most likely a consequence of the synthetic route adopted. Transmission electron microscopy revealed average nanocluster sizes of 3.1 nm for ZnS, 9.5 nm for Au^0, 11.2 nm for Ag^0, 7.9 nm for Pt^0, and 11.3 nm for Ag_2S.[1,2]

The most fascinating aspect of these biomimetically derived clusters was the biological activity of the HRE peptide recognition elements incorporated onto the nanocluster surface. A commercially available ***Para***sight F test for HRP II of *P. falciparum* malaria was used to screen for antibody recognition of the peptide encapsulated nanoclusters. Consequently, the HRE encapsulated nanoclusters of ZnS, Au^0, Ag^0, Pt^0, and Cu^0 elicited a monoclonal antibody response. This suggests that the HRE peptides adopt a suitable conformation along the surface by repeating itself as multiple epitopes.[1,2] Negative results were observed for TiO_2-(HRE) and Ag_2S-(HRE) due to surface anomalies associated with the crystal lattice structures making it unrecognizable to the antibody.

To study the nonspecific interactions between the metal-HRE peptide interface and a nickel chelating surface, an affinity assay for histidine was conducted. In this study, a nickel nitrolotriacetic acid complex coated on a commercially available well plate (Xenopore) was incubated with Au^0-(HRE), Ag^0-(HRE), and ZnS-(HRE) nanoparticles. Assuming the HRE peptide has histidine residues not involved in surface stabilization and are presented toward the bulk solution, then nanocluster binding to the plate would occur through Ni-(His) coordination. Binding of HRE stabilized nanoparticles was highlighted by binding efficiencies of 79% and 42.4% for silver and gold, respectively. Ni surface binding of ZnS-(HRE) was observed by fluorescence microscopy (Figure 5). These results indicate the presence of uncoordinated histidine residues on the surface of the particles which are available to interact with the nickel surfaces. This also suggests that the peptide interface presented two types of histidines; one type stabilizing particle formation while the opposing type interacted with the nickel coated well plate.[1]

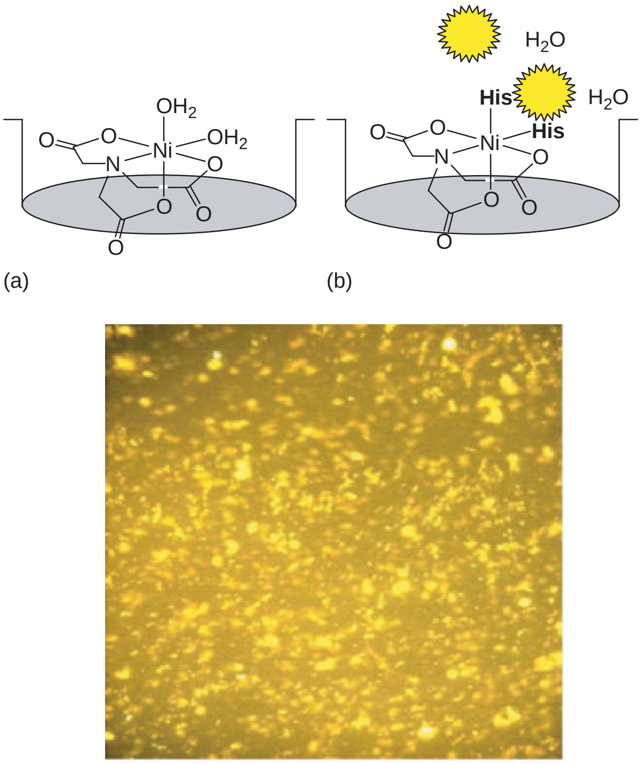

Figure 5 (a) Nickel chelate surface. (b) Binding of ZnS-(HRE) to nickel surface. (yellow spiked circles = ZnS-(HRE)). Fluorescence of ZnS-(HRE) binding to nickel chelate glass cover slip (Xenopore) and imaged on a Leica MZ FL III fluorescence stereo microscope with a Green Fluorescent Protein (GFP) 1 filter, excitation filter (425/60 nm), a Barrier filter 480 nm set, and an integrated digital camera

3.4 Phage Displayed Peptide Libraries

A novel method for the elucidation and isolation of random polypeptides with the ability to form nanoparticles is through phage display (Figure 6). In this process, randomized peptides of the same length are expressed along the coat protein of a nonpathogenic virus. The virus then infects a bacterial sample upon which it rapidly multiplies to yield a vast quantity of phage particles which are then 'biopanned' on receptor surface to determine which peptides on the coat binds to the surface. Nonbinding phages are washed away while binding phage are amplified and the process repeated with increasingly stringent elution conditions.[45] Ultimately, only those peptides most strongly associated with the substrate remain. Using this technique, peptides have been discovered that bind to a metal or metal oxide surface that can further be used to form nanocluster surfaces.[46–48]

3.4.1 Silver Selected Peptides

Phage display was used to screen peptides for the directed self-assembly of zero-valent nanoclusters in which silver

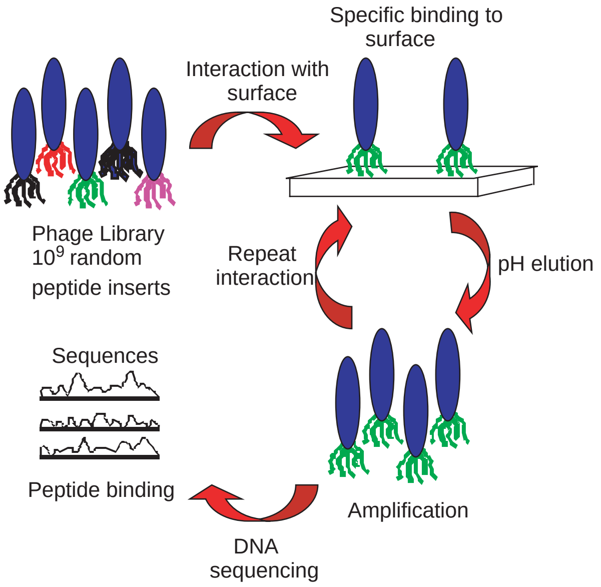

Figure 6 Phage display peptide selection for electronic materials. Random peptides are expressed on the minor phage coat representing 10^9 peptide sequences, peptides are screened for binding affinity to metal surfaces, phages that bind with a specific sequence are eluted from metal surface by lowering pH and amplified by infecting *E. coli* hosts. The amplified phages are reexposed to metal substrate to maximize substrate specificity and binding. This selection process is further repeated to select for the peptide with the highest binding affinity. Finally, the phage DNA is sequenced to reveal the peptide binding sequence

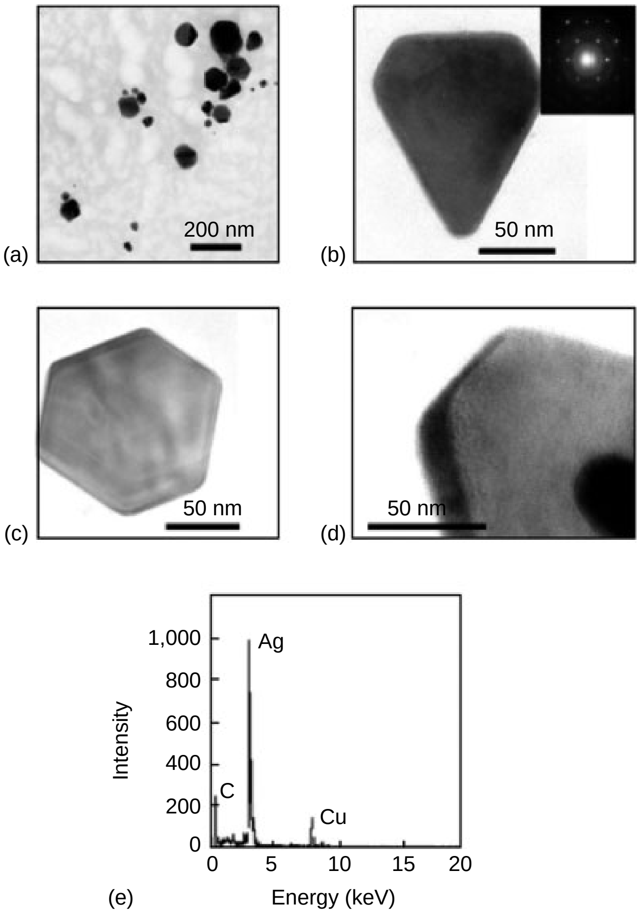

Figure 7 Characterization of silver nanoparticles produced by AG4 clone. (a) TEM micrograph of silver nanocrystal morphologies obtained from AG4 clone. (b&c) TEM micrographs of silver nanoparticles with AG4 peptides. Inset in (b) is electron diffraction pattern from [111] beam direction for fcc crystal. (d) Edge of truncated silver crystal. (e) EDX spectrum indicative for the presence of silver, Cu, and carbon are due to grid. (Reproduced by permission of Nature Publishing Group (www.nature.com))

particles were used as the metal substrate surface. From this analysis, three peptides were isolated with the ability to bind to silver surfaces. These peptides (AG3 - AYSSGAPPMPPF, AG4 - NPSSLFRYLPSD, and AG5 - SLATQPPRTPPV) were isolated and further studied for their ability to generate and reduce silver ions to novel zero-valent silver nanoclusters without the addition of any external reductant.[47]

The properties of the isolated peptides were quite similar in nature, whereby each peptide consisted of 12 amino acids in length and possessed a number of residues with functional side groups that could stabilize nanoclusters. In many instances, these side chains were the hydroxyl-terminated side chains of serine, threonine, and tyrosine. In two of the peptides (AG3 and AG4), the location of the hydroxylated amino acids was conserved within two of the peptides. Similarly, one proline amino acid was conserved throughout all three of the sequences.[47]

Upon incubating each peptide in a solution of silver nitrate with *no* exogenous reductant, a clearly observable plasmon resonance peak arose at 440 nm for AG3 and AG4, but not with AG5. The peak was quite broad, indicative of a disperse size and shape distribution.[49] The main difference between the active peptides and inactive AG5 was an overall basic isoelectric point for AG5.[47] The assays were performed at neutral conditions which would modulate the side-chain dynamics under acidic or basic conditions.

TEM analysis of the nanoparticles produced a wide distribution of sizes between 60 and 150 nm in diameter (Figure 7). Also, different morphological structures of Ag^0 particles were observed which included spherical, triangular, and hexagonal shapes.[47] This broad size distribution and variety of shapes concurred with the broad and tailing plasmon peak of the UV.

3.4.2 *Silica Precipitating Peptides*

In addition to selecting peptides for metal substrates, phage display methods successfully identified peptides capable of forming silica nanospheres. Recently, many groups have isolated proteins and peptides responsible for the *in vivo* production of silica.[50,51] Stone and coworkers have isolated additional novel peptides using phage display that are capable of yielding similar structures under ambient conditions.[46] The isolated peptides were incubated in monosilicic acid for five minutes at neutral pH conditions using phosphate buffer, and as a result formed large silica nanoparticles on the order of approximately 500 nm.[46] From this assay, Stone *et al*. were able to elucidate the characteristics of the peptides that could produce silica nanospheres (Figure 8). All of the peptides possessed hydroxyl amino acids (mostly serine), basic amino acids (lysine or histidine), and had an overall basic isoelectric point.[46]

3.4.3 Metal Sulfides

Belcher *et al*. were able to isolate specific peptides able to direct the synthesis of crystal specific metal sulfide (CdS and ZnS) nanoparticles through phage display.[48] In this study, phages were panned against crystal surfaces, and those which bound were isolated and amplified for further characterization. Two different peptide lengths were studied, a linear 7-mer peptide and a constrained 12-mer. Interestingly, this technique elucidated two different peptide sequences capable of directing the synthesis of CdS and ZnS, one set for each metal sulfide. The peptides specific for CdS did not bind ZnS and vice versa.[48]

The set of 7-mer peptides showed a binding motif in which the arrangements of proline, methionine, and positively charged amino acids (R, H, K) were required for binding to ZnS surfaces. The set of 12 cyclic amino acid peptides (Figure 9) showed similar patterns, positively charged amino acids/proline, followed by methionine or hydroxyl amino acid residue.[48] This similarity is of interest to note because of the fact that two different phage displayed constructs showed similar binding motifs indicative of the overall understanding of peptide binding to ZnS surfaces.

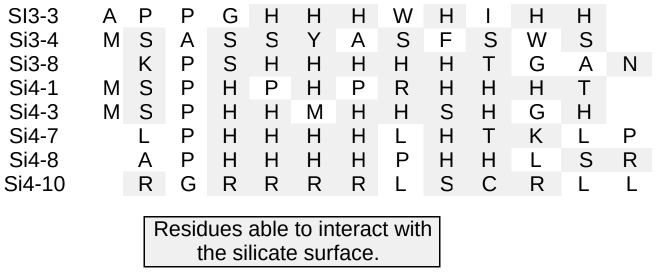

SI3-3	A	P	P	G	H	H	H	W	H	I	H	H	
Si3-4	M	S	A	S	S	Y	A	S	F	S	W	S	
Si3-8		K	P	S	H	H	H	H	H	T	G	A	N
Si4-1	M	S	P	H	P	H	P	R	H	H	H	T	
Si4-3	M	S	P	H	H	M	H	H	S	H	G	H	
Si4-7		L	P	H	H	H	H	L	H	T	K	L	P
Si4-8		A	P	H	H	H	H	P	H	H	L	S	R
Si4-10		R	G	R	R	R	R	L	S	C	R	L	L

Residues able to interact with the silicate surface.

Figure 8 Sequences of peptides discovered from phage display with silica precipitating activity

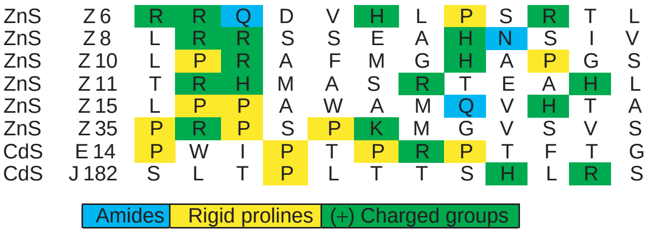

ZnS	Z 6	R	R	Q	D	V	H	L	P	S	R	T	L
ZnS	Z 8	L	R	R	S	S	E	A	H	N	S	I	V
ZnS	Z 10	L	P	R	A	F	M	G	H	A	P	G	S
ZnS	Z 11	T	R	H	M	A	S	R	T	E	A	H	L
ZnS	Z 15	L	P	P	A	W	A	M	Q	V	H	T	A
ZnS	Z 35	P	R	P	S	P	K	M	G	V	S	V	S
CdS	E 14	P	W	I	P	T	P	R	P	T	F	T	G
CdS	J 182	S	L	T	P	L	T	T	S	H	L	R	S

🟦 Amides 🟨 Rigid prolines 🟩 (+) Charged groups

Figure 9 Peptide sequences that exhibit binding affinities for CdS or ZnS from phage display

When specific phages were incubated with nanoparticle reactants, lattice specific ZnS crystals were synthesized. The Z8 phage clone (H_2N-LRRSSEAHNSIV-CO_2H) generated nanoparticles of 4 nm in diameter, while phage A7 peptides (H_2N-CNNPMHQNC-CO_2H) grew crystals of 4 nm by 2 nm in size. Through subsequent characterization, it was elucidated that the A7 clone grew crystals of ZnS with a wurtzite lattice structure, while the phage Z8 produced ZnS nanocrystals with a zinc blend lattice.[48] This characterization gives credence to the biological formation of different crystal structures through different interactions of peptides with metal and metal sulfide surfaces. This specificity is most likely the mechanism through which nature uses to produces intricate structures that are biologically relevant.

4 PROTEIN TEMPLATES

There are a number of physiological functions in organisms that necessitates the biosynthesis of nanoparticles ranging from metal regulation/storage to detoxification to structural assemblies. Consequently, the production of nanoparticles is mediated by various types of protein templates suited to guide nanoparticle formation and function. For instance, they provide a spatially delineated cage which confines nanoparticle synthesis to the physical dimensions of the protein cavity, while encapsulating the newly formed nanoparticle. Additionally, proteins serve as scaffolds for the directed assembly of metal nanostructures. With the current advancements in molecular biology; proteins can be readily expressed, cloned, mutated, and purified, offering an accessible means toward the biomimetic synthesis of inorganic nano-materials. The first protein system shown to mineralize metal nanoparticles was the well known iron storage protein ferritin. By using ferritin as a model template, proteins not typically associated with metals were crafted to mimic ferritin's activity.

4.1 Ferritin Protein

Ferritins are a ubiquitous class of robust proteins involved in the biomineralization of iron oxide particles. Structurally, the protein shell is assembled from 24 peptide subunits (4 helical bundles) of repeating H and L chains which form the fundamental spheroidal shape; provide a large spatially arranged compartment (9.0-nm diameter) for mineralization; and generate hydrophilic and hydrophobic channels with openings of 0.5 nm that lead directly to the cavity

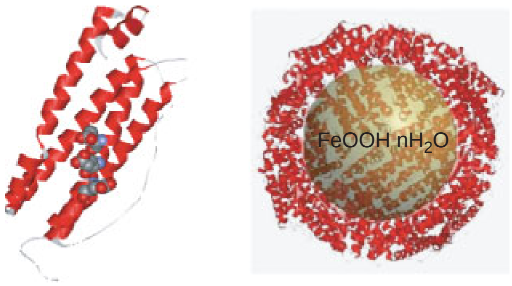

Figure 10 Four helix bundle of the L chain of ferritin showing iron oxide nucleating site (Glu61, Glu64, and Glu67). Quaternary structure of ferritin displaying mineralized ferrihydrite particle

(Figure 10).[52] Besides serving as structural components, each chain performs a complementary function in terms of processing cellular Fe^{II}. Primarily, the H chain catalyzes the oxidation of Fe^{II} to Fe^{III} at a dinuclear ferroxidase site; whereas the L chain contains a putative iron oxide nucleation domain integrated within the 4-helix bundle subunit.[52] This site consists of three glutamic acid residues (Glu 61, 64, and 67) along a helix face directed toward the interior of the protein (Figure 10).[53] As a result, an abundance of iron binding sites with negative charge density is organized within the protein cavity facilitating nucleation of discrete ferric oxyhydroxide mineral cores. Upon forming cores along the protein interior, further mineralization proceeds through an autocatalytic reaction.[52]

Indeed, the protein cage is archetypal in biomineralization by offering a controlled reaction environment that minimizes oxidative hydrolysis anywhere other than within the confines of the protein cavity.[52] Additionally, the soluble protein coat encapsulating the iron mineral prevents the ripening of these particles into larger insoluble aggregates. These inherent properties as well as structural features have prompted an interest in ferritin as a template in the biomimetic synthesis of a collection of various nanoparticles. This collection consists of Fe_3S_4/Fe_2S_3,[54] Fe_3O_4,[55] α-MnOOH,[56] Co(O)OH,[57] UO_2,[58] and CdS[59] nanoparticles.

Ferritin induced nanoparticle synthesis was adapted from a number of different synthetic strategies reliant upon the physical nature of ferritin. For instance, ferritin can readily exist in two stable forms (native ferritin with an intact iron oxide core or apo-ferritin lacking a mineral core) owing to the enhanced structural integrity of the protein shell. As a result, two general reaction schemes were adopted. The first route utilized the iron oxide core of native or reconstituted ferritin as a precursor to different mineral phases and types of iron nanoparticles, while the second invokes mineralization within the empty cavity of apo-ferritin. In the latter approach, the native protein must be demetallated by reductive dissolution with thioglycolic acid to yield apo-ferritin.[58] Ultimately, apo-ferritin provides a widely applicable means to the synthesis of various nanoparticle compositions under many conditions.

Recently, Mann *et al.* have successfully shown the *in situ* biomineralization of iron sulfide nanoparticles from both native and reconstituted iron oxide cores of ferritin by utilizing the permeability of the protein for a sulfur containing source.[54] Basically, a source of aqueous Na_2S was introduced to a de-aerated solution of native (3000 Fe atoms) or reconstituted (500 Fe atoms) horse spleen ferritin under acidic conditions. After 40 min, the iron oxide core had been transformed into an amorphous iron sulfide particle.[54] The particles were characterized by TEM and revealed average sizes of 6.5 nm and <2 nm in diameter for the native and reconstituted ferritin derived reactions. Further analysis by ^{57}Fe Mössbauer spectroscopy indicated some structural and magnetic ordering of the iron sulfide product (effective oxidation state $+2.5$) from the reconstituted based reaction.[54] In contrast, the native ferritin product was determined to possess a $+3$ oxidation state, tentatively identified as 'Fe_2S_3'. From these results, it was hypothesized that the reaction of iron oxide with sulfide proceeds according to the following steps: rapid surface adsorption of sulfide, formation of surface bound ferric sulfide, electron transfer, and dissolution of Fe^{II}.

In a parallel reaction, the synthesis of an ancillary magnetic phase of iron oxide, magnetite, was explored as a means to determining structural specificity occurring during mineralization processes.[55] Also, this would provide an alternative synthetic approach to the development of potential contrast agents for magnetic resonance imaging of tissue, cell labeling, and separation techniques. However within the cavity of ferritin under physiological conditions, the antiferromagnetic mineral form of ferrihydrite ($FeOOH{\cdot}nH_2O$) is kinetically favored leading to its preferential mineralization, as it provides a functional source of labile iron for metabolic use.[55] Synthetically, the controlled formation of magnetite was achieved by the slow oxidation of Fe^{II} over ten sequential additions to apo-ferritin at relatively high temperatures (60 °C) and pH (8.5).[55] The resultant encapsulated particles were spherical with diameters of 6.0 ± 1.2 nm. Exposure to air resulted in a phase transition of the core to maghemite (γ-Fe_2O_3). This synthesis was also further optimized to mineralize only magnetic iron oxide phases, magnetite, and maghemite.[60] Mann *et al.* performed the mineralization under purely anaerobic conditions and stoichiometric amounts of an oxidant, trimethylamine-N-oxide.

In an attempt to elucidate the efficacy of non-iron substrates, the biomimetic synthesis of MnOOH was demonstrated with apo-ferritin templates. The reconstitution of ferritin with manganese oxide was performed by addition of $MnCl_2{\cdot}4H_2O$ at an optimal pH of 8.9–9.2 with theoretical loading of between 1000 to 3000 Mn atoms.[56] Consequently, the synthesis showed signs of non-mineralized proteins and a significant degree of nonspecific oxide precipitation of crystalline Mn_3O_4 in the bulk. This was attributed to isolated and sporadic nucleation events, little or no oxidase activity for Mn ions, and an equivalent mineralization rate for Mn ions without ferritin present in the bulk solution.[56]

Additional metal precursors were examined because of the limited mineralization and deposition of MnOOH particles by ferritin. In particular, Co(O)OH particles were synthesized within ferritin from Co^{II} and H_2O_2 as an external oxidizing agent.[57] The reaction was performed via a stepwise synthesis of the mineral core and monitored by a pH-stat autotitration. Results from the autotitration provided mechanistic detail, whereby it was determined that 2.1 protons are released per Co^{II} in the 2 electron reduction of H_2O_2 to Co^{III} which subsequently underwent hydrolysis.[57] The oxidative hydrolysis proceeded rapidly and was confined entirely within the protein cavity as confirmed by the absence of bulk precipitation with the subsequent addition of excess oxidant.

Undoubtedly the most unlikely substrate for ferritin is $UO_2{}^{2+}$, however, the implications of biomimetically synthesizing uranium oxide loaded ferritin could have use in neutron capture therapy. The synthetic approach utilized ion binding of $UO_2(O_2CCH_3)_2$ according to a known stoichiometry of 12 ions per ferritin molecule, followed by hydrolytic polymerization of metal ions within apoferritin.[58] Characterization by TEM analysis confirmed dense cores of polymerized uranyl oxyhydroxide particles of 6 nm in diameter.

4.2 Ferritin-like Proteins

Interestingly, in the bacterium of *Listeria innocua*, protein systems similar to ferritin have been discovered to possess a cage-like structure.[61] Comparatively, this unusual protein is comprised of only 12 peptide subunits and is substantially smaller in magnitude than native ferritin. As a result, these structural characteristics generate an interior cavity with dimensions of 5 nm capable of holding a maximum of 500 iron atoms (4500 Fe atoms for ferritin). Douglas *et al.* have exploited the smaller cage of this protein in the synthesis of ferromagnetic iron oxide particles following the controlled oxidative hydrolysis method described above.[61] As expected, the mineralized product was 4.4 ± 1.1 nm in diameter according to TEM and identified as the cubic iron oxide phase (γ-Fe_2O_3) by selected area diffraction, consistent with results obtained from the native ferritin system.[61]

Additionally, the *L. innocua* ferritin-like protein served as a template for the controlled mineralization of two cobalt oxide phases Co(O)OH and Co_3O_4 under two reaction temperatures of 23° and 65 °C, respectively.[62] Substantial differences in crystallinity of the cobalt mineral core was observed between the two synthetic routes. The mineralization reaction carried out at higher temperatures yielded more crystalline nanomaterials, while the low-temperature synthesis tended toward amorphous material. The high crystallinity obtained at higher temperatures is most likely due to removal of structural waters present in the protein cavity and the surpassed energy barrier of nucleation at 65 °C.[62]

Synthetic modifications to native ferritin also provided a ferritin-like protein with different intrinisic properties, functions, and mineralization abilities. The exterior protein shell of ferritin was modified by an alkylation reaction using long chain primary amines (C_n, $n = 6$, 9, 12, 14, 18) covalently coupled by nucleophilic substitution at carbodiimide-activated carboxylic acid groups on the protein surface.[63] This resulted in a hydrophobically modified protein that exhibited significant solubility in organic solvents such as dichloromethane. However, reconstitution of the alkylated protein with Fe^{II} was ineffective at *in situ* cavity mineralization of discrete iron oxide cores due to the modified surface chemistry.[63]

4.3 Heat Shock Proteins

Heat shock proteins (Hsp) represent an essential class of proteins which act as molecular chaperones to partially denatured proteins.[64] These proteins are rapidly expressed in all organisms at increased levels in response to cellular stresses such as elevated temperatures, chemical or heavy metal exposure, pH extremes, osmotic variations, and infection or disease state.[65] As a consequence of these external stimuli, normal proteins are then susceptible to unfolding of their native conformational structure. Fortunately, small heat shock proteins favorably interact and stabilize the damaged target protein preventing mutual association, irreversible aggregation, and precipitation of proteinaceous plaques.[65] The Hsp-protein complex forms through the interactions of exposed hydrophobic residues of the damaged protein with the hydrophobic pocket of the heat shock protein. This maintains the solubility of the damaged protein by encompassing it within a structurally defined pore comprised of two supramolecular rings with each ring composed of 7–9 complementary protein subunits with molecular weights of 60 kDa.[65] Conceptually, this pore presents a template conducive toward biomaterials synthesis.

Only recently have heat shock proteins been used in the stabilization of nanoparticles. Aida *et al.* have demonstrated the inclusion of already preformed CdS nanoparticles within the chaperonin proteins of GroEL from *Escherichia coli* and *T.th* cpn from *Thermus thermophilus* HB8.[66] These proteins were chosen as a result of sharing similar structural characteristics: (1) tubular structure measuring 14.6 nm in length, (2) cylindrical cavity with a 4.5-nm diameter, and (3) stability to adverse conditions (pH and temperature). *T.th* cpn, however, contains an additional bowl-shaped capping protein.

The protein-nanoparticle complex was prepared by adding a dimethylformamide (DMF) solution of preformed CdS nanoparticles ranging from 2 to 4 nm to a solution of heat shock protein. As a result, the CdS nanoparticles diffused into the heat shock pore analogous to a damaged protein over a period of 100 h. TEM analysis revealed that as much as 75% of the proteins contained a single discrete nanoparticle core of CdS. Upon subsequent inclusion, the CdS complex displayed intense photoluminescence from 430 to

720 nm for as long as 400 days with GroEL. Additionally, when subjected to heating-cooling cycles over the range of 4–80 °C, the photoluminescence of the *T.th* cpn-CdS complex was quenched at 80 °C but quickly recovered to its original intensity after cooling to 4 °C.[66] In contrast, CdS particles not stabilized by proteins showed an irreversible photoluminescence profile at only 30 °C. The enhanced thermal stability of the *T.th* cpn-CdS complex is entirely dependent on the chaperonin protein.

In an innovative experiment, these protein encapsulated nanoparticles were shown to be responsive to the action of adenosine 5′-triphosphate (ATP) (Figure 11).[66] Inherently, chaperonin proteins react to the binding of ATP in the presence of Mg^{2+} and K^+ by inducing a comformational change in the protein structure. This mediates the opening of the pore and subsequently releases the guest proteins. By analogy, CdS nanoparticles were released upon ATP binding as monitored by size exclusion chromatography. The SEC elution profile showed a peak corresponding to the *T.th* cpn protein and an additional broad peak attributed to ATP and its hydrolyzed products.[66] More importantly, the fluorescence of CdS was absent, consistent with its release from the protein cavity.

The concept of using heat shock proteins as templates for nanoparticle assembly was further explored by Trent *et al.* through genetic manipulation of the 9 β subunits of a heat shock protein isolated from the thermophillic organism of *Sulfolobus shibatae*.[67] This protein offered numerous benefits which made it an optimal system for study; such as stability to adverse conditions, self-assembly into regular double-ring (each ring contains 9 β subunits) structures driven by ATP and Mg^{2+}, and a propensity to crystallize into higher-order periodic structures of 2-D crystals up to 20 µm in diameter.[67]

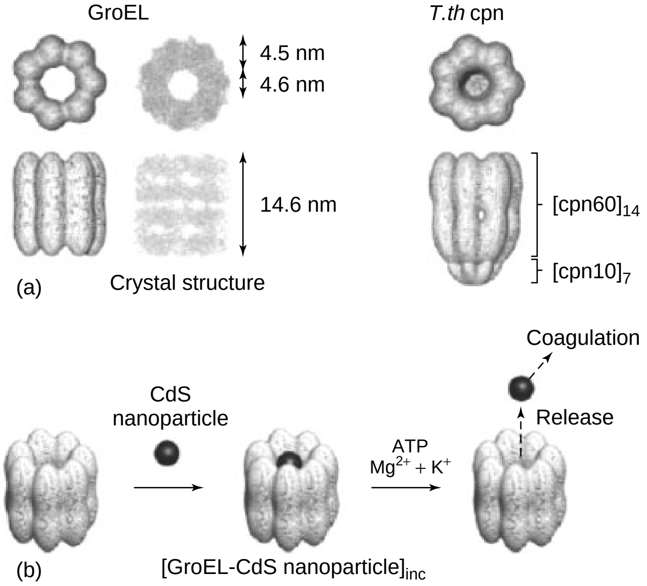

Figure 11 Strategy for nanoparticle inclusion/release by chaperonin protein templates. (a) Structural representation of chaperonin proteins, GroEL, and *T.th* cpn. (b) Scheme depicting inclusion of CdS nanoparticles within chaperonin cavity and their triggered release from the cavity by ATP. (Reproduced by permission of Nature Publishing Group (www.nature.com))

Prior to use as a nanoparticle template, the β subunits were genetically modified by adding cysteine residues at different solvent exposed sites to yield two mutant variations of the β subunits. The two variations consisted of β subunits with exposed 28 amino acid loops and β subunits with these amino acid loops deleted. These β subunits were then assembled into chaperonin proteins upon Mg^{2+}/ATP binding and crystallized into a reactive protein template with a ring of thiol groups that protruded into the protein pore to different extents (3 nm and 9 nm pore diameters).[67]

The two variations of chaperonin proteins containing different pore diameters were used in the size-selective discrimination of Au^0 nanoparticles (5, 10, 15 nm diameters) and CdSe–ZnS quantum dots (4.5 nm). Experimentally, protein samples in hexagonally packed 2-D crystals were applied to formvar coated TEM grids producing a hydrated protein template attached to the TEM substrate. This was followed by additions of aqueous gold nanoparticles passivated with bis(*p*-sulfonatophenyl)phenylphosphine ligands of a particular size. Dependent on the pore diameter, appropriately sized particles either subsequently bound the interior thiol groups of the protein template or were physically restricted. This was definitively demonstrated by the inclusion of only 5 nm Au^0 particles within the mutant protein possessing a 3-nm pore diameter, and the occlusion of 10 and 15 nm particles.[67] In contrast, the proteins with pores of 9 nm in diameter bound predominantly 10 nm Au^0 particles with partial signs of random binding with the 5-nm and 15-nm gold. Core shell CdSe–ZnS particles of 4.5 nm stabilized by trioctyl phosphine oxide (TOPO) were unevenly distributed on the chaperonin templates with 3 nm pores.

This heat shock protein system was also used as a biomimetic template for the synthesis of metal nanoparticles based on the reduction of protein stabilized metal precursor complexes. Accordingly, a heat shock protein template was designed by Jonathan Trent (NASA Ames Research Center) with small peptide binding sites, histidine-rich peptide epitopes (HRE) of AHHAHHAAD previously reported to stabilize a variety of metal nanoparticles, integrated into the central pore of the ((HRE)-Hsp) protein. This served to potentially revert the natural function and hydrophobicity of the protein pore as well as provide nine selective HRE metal binding domains that project into the cavity (1 HRE peptide per β subunit/9 HRE peptides total per protein). Recently in our lab, we prepared nanoparticle/(HRE)-Hsp complexes by saturating the HRE peptides with metal ions of Au^{3+}, Ag^+, or Zn^{2+} that would load the heat shock pore. This was followed by standard borohydride reduction or inorganic sulfide addition resulting in Au^0, Ag^0, or ZnS nanoparticles confined within the heat shock protein cavity (unpublished).

Consequently, the synthesis of protein encapsulated nanoparticles within the heat shock cavity resulted in $<10\%$ of the proteins associated with a nanoparticle (Figure 12). This suggests that the diffusion of hydrated metal precursor ions into the pore was limited by the hydrophobic environment of the protein pore. Ultimately, the integrated HRE peptides within the protein cavity failed to lessen the hydrophobic barrier, and as a result provided ineffectual binding domains for the hydrated metal ions of Au^{3+}, Ag^{+}, and Zn^{2+}. To compensate for the hydrophobic nature of the protein pore, an insoluble Au^{I} precursor complex of $AuClP(CH_3)_3$ was used. The (HRE)-Hsp template was saturated with $AuClP(CH_3)_3$ through (nonspecific/HRE) binding and adsorption of gold. Association with the protein induced solubilization of the chlorotrimethylphosphinegold (I) compound, and upon reduction with $NaBH_4$ resulted in a gold nanoparticle decorated protein. The TEM micrograph of the Au^0/(HRE)-Hsp structure (Figure 9) reveals a discrete Au^0 particle confined within the heat shock pore and surrounded by gold particles bound to the protein surface at each of the nine HRE modified β subunits through nonspecific interactions.

Analogously, Douglas *et al.* have used a small 24 subunit heat shock protein isolated from the hyperthermophillic archaeon, *Methanococcus jannaschii*, as a biomimetic template for the oxidative mineralization of iron.**[68]** Both the wild type and a mutant (glycine at position 41 replaced for cysteine) exhibited ferrihydrite mineralization as determined by an increase in the ligand to metal charge transfer absorbance at 400 nm and the presence of discrete iron oxide particles of 9.0 ± 1.2 nm in diameter from TEM.

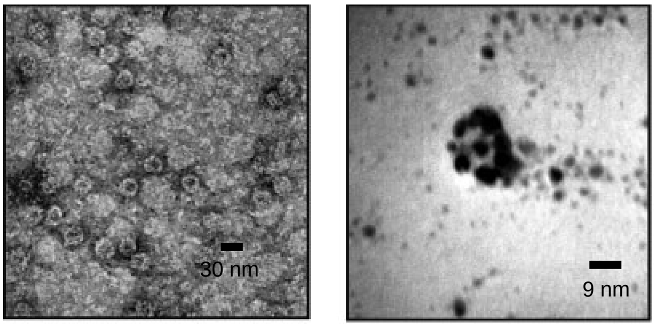

(a) (b)

Figure 12 TEM micrographs of Au^0 nanoparticle synthesis mediated by an HRE peptide integrated heat shock protein (Hsp 60) from *Sulfolobus shibatae*. (a) TEM of Au^0/(HRE)-Hsp complex prepared from addition of $AuCl_4^-$, reduced by citrate, and negatively stained by uranyl acetate. (b) TEM of Au^0/(HRE)-Hsp prepared from insoluble Au^I precursor of $AuClP(CH_3)_3$ and reduced by borohydride (unstained)

5 VIRUSES FOR NANOPARTICLE SYNTHESIS

Viruses represent another example of viable nanoparticle templates resulting from their structural polymorphism and defined composition. In general, viruses exist in a variety of sizes and morphologies ranging from 30 nm spherical viruses to 300 nm rod-like structures. Additionally, all viruses are comprised of a compact self-sustaining packet of genetic material enveloped within a functional protein capsid ideally suited for their survival and propagation. The protein capsid functions by protecting the genome, releasing nucleic acids upon host infection, recognition, and reassembly/externalization of progeny virions. Each related function occurs by highly coordinated large scale structural changes to the capsid such as covalent cross-linking between neighboring subunits and modifications in the secondary and tertiary protein structures. Ultimately, these characteristics have inspired the directed synthesis of nanoparticles using numerous viral templates that results in highly ordered nanoparticle arrays or spatially confined particles.

5.1 Mosaic Virus Templates

5.1.1 *Tobacco Mosaic Viruses (TMV)*

TMV primarily affects tobacco plants by infecting the leaves and roots system of predisposed cultivars. The virulence is manifested in a mottled appearance or mosaic pattern on leaves and inevitably the inhibition of normal growth. TMV is derived from a Japanese strain and attributed to worldwide losses of tobacco crops.**[69]** In particular, TMV particles contain 95% proteins and 5% nucleic acids. The proteins that compose the viral envelope and genome compartment consist of 2130 identical coat protein molecules in total which follow the right-handed helix of an associated RNA strand. The orientation of identical proteins generates a 300-nm long hollow cylinder defined by an 18-nm outer diameter and 4 nm inner diameter.**[69]** The dimensions and repeating proteins presented along the viral surface provided a template for the biomineralization of nanoparticle arrays as documented by Mann *et al.***[70]**

Exposure of wild-type TMV to $[AuCl_4]^-$, $[PtCl_6]^{2-}$, and Ag^+ precursors, followed by hydrazine reduction and photoreduction yielded viruses decorated with zero-valent nanoparticles. Reduction of $[AuCl_4]^-$ and $[PtCl_6]^{2-}$ by hydrazine at an acidic pH induced nucleation at the positively charged lysine and arginine residues along the outer surface of the viral template. As a result, Au^0 and Pt^0 spheroidal nanoparticles of 8.6 ± 3.0 nm and 2.5–5.0 nm, respectively, were locally externalized at the virus surface with Au^0 TMV surface illustrated in (Figure 13).**[70]** Under basic conditions, the positive charges on the surface were reduced while the negative charges of glutamate residues lining the 4-nm channel wall increased, thus promoting the binding of positively charged Ag^+ along the channel interior. Upon photoreduction

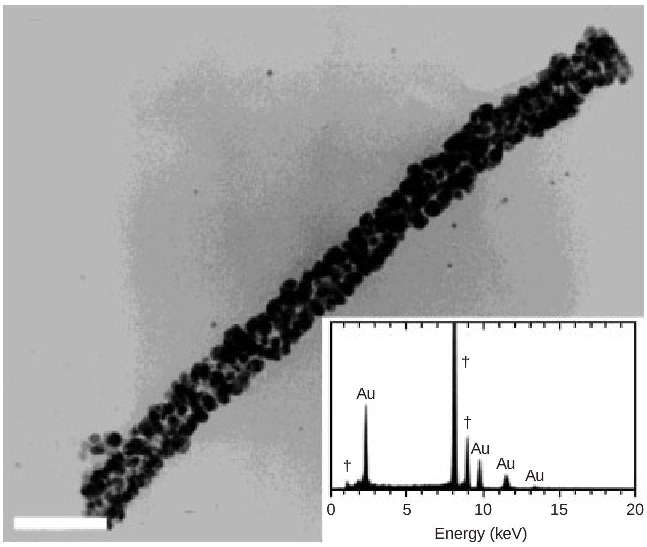

Figure 13 TEM micrograph of wild-type tobacco mosaic virus coated with gold nanoparticles. Scale bar corresponds to 50 nm. Inset shows EDX spectrum and presence of gold (Cu peaks are from grid). (Reprinted with permission from Ref. 70. © 2003 American Chemical Society)

of Ag^+, linear arrays of Ag^0 nanoparticles less than 5 nm in diameter were spatially organized within the virion channel.

Virion templates of TMV were also used in combination with different synthetic routes for CdS, PbS, and Fe oxide nanoparticles.[71] Nanoparticle-virion tubules were prepared by reacting a buffered solution of TMV in $CdCl_2$ (pH 7) or TMV in $Pb(NO_3)_2$ (pH 5) with H_2S gas. The formation of metal sulfide nanoparticles occurred over 6 hours as observed by a uniform coating of CdS and PbS nanocrystals on the TMV surface from TEM analysis. Selected area electron diffraction of the mineralized products indicated a zinc blende crystal structure for CdS particles and a rock salt structure for single domain PbS nanocrystals. The iron oxide nanoparticles were mineralized by the TMV templates by the oxidative hydrolysis of an Fe^{II}/Fe^{III} acidic solution with NaOH.[71] Consequently, a mineral coating of irregular ferrihydrite particles grew on the surface to a thickness of 2 nm.

5.1.2 Brome Mosaic Viruses (BMV)

Brome mosaic viruses (BMV) readily infect different varieties of grasses and to a minor extent maize. Collectively, BMV is among the smallest viruses with an icosahedral protein capsid of 27 nm in diameter, and in contrast to most other viruses, is cationic at pH below 6.5.[72] The architecture of the capsid portion of the virus is constructed from 180 protein capsomeres that are independently stabilized by weak electrostatic interactions with the negatively charged RNA core (3234, 2865, 2114, and 876 nucleotides).[72] Kao *et al.* have developed an approach to replacing this RNA core with negatively charged citrate stabilized Au^0 particles with the intentions of incorporating a potential spectroscopic probe into the virion cavity for the study of single virus particles.[73]

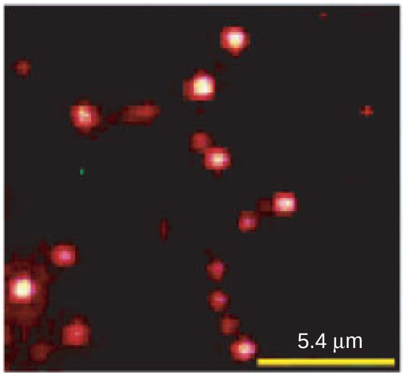

Figure 14 Dark-field optical micrograph of Au^0 nanoparticles encapsulted by brome mosaic virus. (Reprinted with permission from Ref. 73. © 2003 American Chemical Society)

Kao *et al.* performed the replacement of the RNA core of BMV particles with 2.5–4.5 nm Au^0-(citrate) nanoparticles by sequentially disassembling the BMV virions into individual capsomeres, reassembling the BMV virions in the presence of Au^0 nanoparticles, and purifying the resultant BMV encapsulated Au^0 particles.[73] As determined from TEM micrographs, only 2% of the viral capsids appeared to be functionalized with gold nanoparticles. However, some of the functionalized virions contained a pair of Au^0 particles enclosed within the same capsid. Pairing of Au^0 particles was illustrated by a dark-field optical micrograph (Figure 14), whereby the scattered intensity of the brighter spots indicated a Au^0 nanoparticle pair and the lesser intensity was representative of a single gold particle.[73]

5.2 Cowpea Chlorotic Mottle Viruses (CCMV)

As a close relative to the brome mosaic virus; the cowpea chlorotic mottle virus (CCMV) possesses an outer diameter of 28 nm, is assembled from 180 subunits that create an icosahedral type structure, and contains an RNA core.[72,74] Another similarity is the cationic interior surface of the viral capsid which is formed from subunits with highly basic N-termini (6 positively charged arginine and 3 lysine residues) that project into the cavity and stabilize the RNA core.[75] However as a potential biomineralization template, the electrostatic environment of the virion cavity precludes any cationic metal precursors and thus limits its applicability for nanoparticle synthesis.

Recently, Young *et al.* have designed a CCMV virion cage with an anionic interface that favorably binds Fe^{II} and Fe^{III} ions and then subsequently controls the oxidative hydrolysis to size-constrained iron oxide minerals.[75] The anionic cage was prepared by genetically replacing the 9 basic residues at the N-terminus with glutamic acid groups yielding a total of 1620 corresponding anionic binding sites. Based on the synthesis of the iron oxides in ferritin, the modified virus was initially loaded with approximately 2000 iron atoms and air oxidized to yield an iron oxide particle size of 8.2 ± 1.6 nm according to TEM. The virion encapsulated particles were further subjected to iron oxide mineralization by additions of 6000 iron atoms per cage which resulted in nanoparticles with an average size of 24.0 ± 3.5 nm that completely occupied the volume of the cavity (CCMV inner diameter 18–24 nm). To establish the significance of the mutations, the wild-type CCMV empty protein cage (cationic interior) was substituted for the mutant virus in iron oxide mineralization experiments. As expected, the wild-type protein exhibited a lack of control in iron oxide mineralization as observed by bulk precipitation, demonstrating the utility of cationic interface.

As described above, protein capsids are inclined toward reversible changes in their overall structure that induce transfer of the nucleic acid contents through virion pores. Synonymously, CCMV was identified to undergo dynamic structural changes correlated to the opening or closing of these viral gated pores. The molecular gating mechanism occurs by pH- dependent swelling/shrinking of the virion by as much as 10% of the virus dimensions. For example, a pH greater than 6.5 causes a volume expansion of the virion cage and the concerted opening of 60 separate pores with a diameter of 2 nm which allows free molecular exchange. Under acidic conditions ($\mathrm{pH} < 6.5$), the virion contracts to its original non-swollen form by forcing the pores closed and in turn preventing access to the cavity. This pH-dependent structural control was exploited in the oligomerization reactions of tungstate and vanadate ions into confined paratungstate and decavanadate polyanions. The reaction was performed by first removing the viral RNA, swelling the virion capsid by adjusting the pH to greater than 6.5, incubating the empty swollen virions with metal anions, and then lowering the pH below 6.5 to close the gated pores. As a result, the structural transition from open to closed pores resulted in the spatially selective crystallization and entrapment of the paratungstate and decavanadate ions within the virion.

5.3 Engineered Bacteriophages for Nanoparticle Assembly

Bacteriophages are classified as simple viruses which target and infect bacteria. Their appeal as a biological template results from three compositional elements fundamental to the phage construct; a major protein coat (900 nm in length), minor protein coat, and a genetic factory of single stranded DNA (Figure 15). Particularly, the DNA plasmid serves as a source for phage replication after injection into the host bacteria, whereupon more phages are created. Additionally, the plasmid contains a random DNA insert, with no purposeful function to the phage, that expresses a sequence of amino acids in accordance with the minor protein coat. As a result, the insert provides an exceptional means to genetically displaying large peptide combinatorial libraries 10^9 on the minor protein coat surface of filamentous bacteriophages for the screening of evolutionary selected peptides against desired inorganic substrates as described above. Aside from genetically engineering the minor coat, the major protein coat also can be modified to incorporate binding sites along the viral surface as shown by Belcher *et al.* in the templated assembly of quantum dot nanowires.[76]

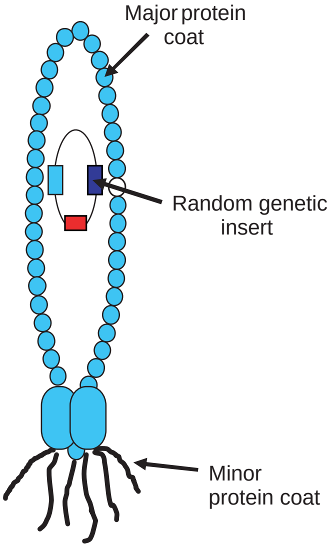

Figure 15 Representation of bacteriophage components

Belcher *et al.* have successfully expressed a group of peptides, that selectively nucleates ZnS and CdS identified from a pIII phage display library, as pVIII fusion proteins into the crystalline helical major coat protein of single M13 phage particles.[76] Subsequently, the integration of nucleating peptides along the viral capsid template was shown to direct the highly oriented, phase specific growth of ZnS or CdS nanocrystals into elaborate nanowires. The viruses were engineered to encode for peptide sequences previously selective for either ZnS or CdS; such as the ZnS peptides of CNNPMHQNC (A7) and VISNHAESSRRL (Z8) or SLTPLTTSHLRS (J140) which recognizes and nucleates CdS.[76] The peptide derivatized templates were added to a solution of $ZnCl_2$ or $CdCl_2$, respectively, for 12 hours to ensure saturation of metal precursor ions at the distinct peptide binding sites. After loading the phage template, Na_2S was introduced into the solution initiating the selective nucleation of metal sulfide nanoparticles at temperatures of 0 °C or −25 °C for 24 h, and then allowed to age at room temperature conditions.

Analysis of the Z8 peptide engineered virus demonstrated preferential growth of ZnS particles oriented in the [001] direction perpendicular to the viral surface.[76] Alternatively, the shorter A7 peptide sequence resulted in high density layers of ZnS (8–16 quantum dots per 10 nm of virus) particles due to an increased register of peptide copies programmed along the surface (Figure 15).[76] Analogous results were observed with CdS (3–6 quantum dots per 10 nm of virus). Additionally, a CdS and ZnS viral heterostructure was obtained with a dual peptide system that presented two nucleation sites specific for CdS or ZnS.

Liquid crystalline systems based on nanoparticle-bacteriophage conjugates were recently developed by Belcher *et al*. that display novel material properties.[77] They used the innate anisotropic shape of bacteriophages to form well ordered liquid crystals (head to tail vertical alignment) and the potential binding sites of the minor coat protein for templating nanoparticle growth. Specifically, the A7 peptide selective for ZnS was expressed in the minor coat, exposed to $ZnCl_2$ solution, and mineralized with Na_2S, to yield a smectic-like lamellar ZnS viral film.[77] As a result, multiple ZnS nanocrystals bound at the A7 peptide and were aligned in the direction of the bacteriophage (Figure 16). Optical characterization elucidated the different liquid crystalline phases of the ZnS-phage hybrid and their transitions under a magnetic field. Examination by scanning electron microscopy (SEM) indicated a periodic length of 895 nm between the 20 nm aggregates of ZnS nanocrystals and A7 phage layers approximately equivalent to the length of a bacteriophage of 880 nm.[77]

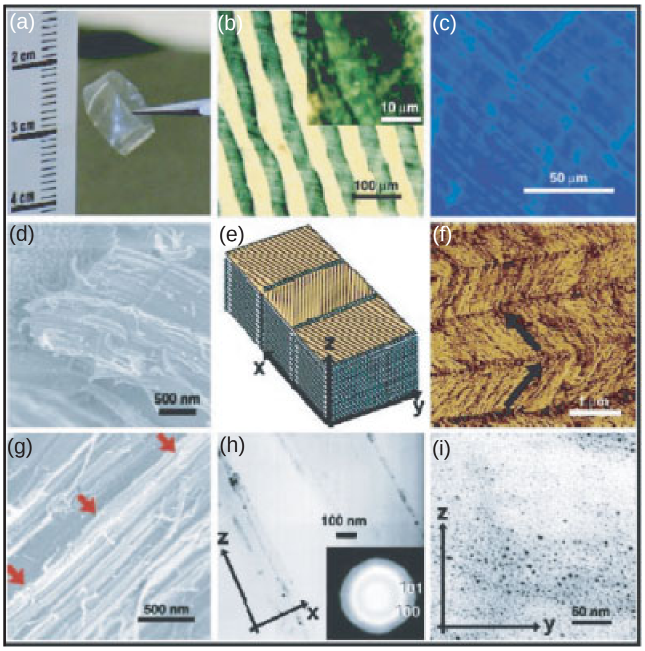

Figure 16 Characterization of A7-ZnS film. (a) Photograph of A7-ZnS film. (b) Polarized optical microscopy (20x) displaying birefringent dark and bright band patterns. (c) Photoluminescent image (ex. 350 nm with filtering below 400 nm). (d) SEM image of highly packed three-dimensional bulk film structure. (e) Schematic structural diagram of A7-ZnS film. (f) Atomic force microscopy (AFM) image of free surface (Arrows indicate the right angles between the adjacent director that result from the parallel aligned herringbone patterns that the phage forms). (g) SEM image of close-packed lamellar structure of phage and nanocrystal layers (red arrows). (h) Low resolution TEM of cross section of A7-ZnS film (inset shows electron diffraction pattern for ZnS wurtzite structure). (i) Low resolution TEM of film in the y-z direction illustrating ZnS nanocrystals. (Reprinted with permission from Lee *et al*., Science 296: 892–5. © 2002 American Association for the Advancement of Science. Permissions from AAAS is required for all other uses (www.sciencemag.org))

6 PLANT MEDIATED NANOPARTICLE SYNTHESIS

Plants display a well known ability to bio-remediate heavy metals, and as a consequence have been used for nanoparticle synthesis. Presently, Gardea-Torresdey *et al*. demonstrated the first living plant system (*Medicago sativa* alfalfa plant) to bio-reduce Au^{3+} into corresponding Au^0 nanoparticles. In addition to the bio-reduction of gold, live alfalfa plants have exhibited reduction activity with silver, whereby exposure to silver containing media results in reduction to Ag^0, followed by absorption and uptake by the roots system, and finally translocation to the shoots as silver nanoparticles.[78] TEM analysis shows mainly spherical nanoparticle morphologies with diameters of 2–20 nm.

Certain plant species have also been reported to biosynthesize silver nanoparticles analogous to alfalfa. After extensive screening of different plant types for silver reduction, Sastry *et al*. have identified geranium leaf (*Pelargonium graveolens*) extracts as successful candidates in the synthesis of silver nanoparticles.[79] Upon exposure of geranium leaf broth to silver nitrate, silver nanoparticles were quickly formed within nine hours. This was substantially faster in comparison to the 24–120 h required for silver reduction by bacteria or fungi. XRD confirmed the presence of metallic silver, although it most likely occurs as a composite with a bioorganic phase as observed by an additional unassigned diffraction peak. Interestingly, the unexposed leaf broth when cast into a film exhibited intense diffractions attributed to the crystalline phase of the magnesium containing metalloprotein, chlorophyll. This is also supported by EDS measurements, whereby magnesium was detected in the sample indicative of chlorophyll. Further analysis by Fourier transform infrared (FTIR) revealed stretching vibrations at $1640\,cm^{-1}$ for an amide I band in the silver leaf broth sample, suggestive of chlorophyll or terpenoids possibly acting in silver reduction.

Jones *et al*. have described an unusual plant extract in the synthesis and stabilization of metal hydroxide particles consisting of an extracted biopolymer of κ-Carrageenan derived from seaweed.[80] κ-Carrageenan features repeating units of hydroxy and sulfate groups which favorably interact with mineral surfaces and represents an exceptional stabilizing ligand for nanoparticles. Addition of Fe^{3+}, Ni^{2+}, or Co^{2+} to κ-Carrageenan and increases of pH yielded solutions of stabilized metal hydroxides as observed by XRD. According to

TEM, morphologies of iron oxyhydroxide particles stabilized by κ-Carrageenan appeared as a gel ‘cage’ and colloidally stable.[80] For nickel hydroxide, the biopolymer prevented aggregation by covering the crystal surface as observed by disperse particles. However, cobalt hydroxide revealed superstructures in the TEM composed of 100–200 nm platelets ‘glued’ together into a 10 µm spherical aggregate. It was determined that κ-Carrageenan interacts with all 3 metal cations through physical cross-linking of the biopolymer by electrostatic interactions of the cations with the ionized sulfate groups initially. At a basic pH of 13, the metal ions are precipitated as the hydroxide resulting in the formation of the colloidal nanoparticles stabilized through reversible electrostatic interactions with the κ-Carrageenan backbone.

7 CONCLUSIONS

Nature has provided a wealth of examples of stabilizing ligands used in the synthesis of various types of nanoparticles ranging in structural diversity from single amino acids to small peptides to large proteins. This structural scale of complexity is best exemplified by small phytochelatin peptides used to detoxify Cd^{2+} and Zn^{2+} into metal sulfide nanoparticles and the iron storage protein ferritin which controls the selective mineralization of iron oxide particles. Conceptually, these biological systems represent exquisite models for biomimetic nanoparticle synthesis by offering functional binding templates, surface passivating agents, and biomolecular recognition elements.

Systematically, a collection of individual amino acids (cysteine, histidine, aspartic acid, and lysine) was shown to stabilize a number of different zero-valent metal and metal sulfide nanoclusters displaying a broad scope of physical properties. These provided a fundamental basis set for nanoparticle synthesis and the further development of higher-order molecules exhibiting protein secondary structure and spatial/structural control over materials synthesis in three-dimensions. Accordingly, the structural and sequence variability of small peptides has had significant implications in nanoparticles synthesis owing to the assembly of nanoparticle-peptide interfaces originating from biomineralization proteins, evolutionary selected by phage displayed peptide libraries, and/or screened from combinatorial peptide libraries. Ultimately, spatial control is highly desired and has recently been achieved with the use of protein and viral templates possessing a defined cavity for the mineralization of atypical nanoparticle substrates. In total, templates derived from biological motifs exhibit control over nanoparticle size, morphology, and crystallinity that mimics the natural function and mineralization activity in nature.

8 RELATED ARTICLES

Biomineralization; Metal Nanoparticles, Organization & Applications of; Metal Nanoparticles, Synthesis of; Semiconductor Nanocrystal Quantum Dots.

9 REFERENCES

1. J. M. Slocik and D. W. Wright, *Biomacromol.*, 2003, **4**, 1135.
2. J. M. Slocik, J. T. Moore, and D. W. Wright, *Nano Lett.*, 2002, **2**, 169.
3. M. M. Maye, W. Zheng, F. L. Leibowitz, N. K. Ly, and C.-J. Zhong, *Langmuir*, 2000, **16**, 490.
4. M. Ozsoz, A. Erdem, K. Kerman, D. Ozkan, B. Tugrul, N. Topcuoglu, H. Ekren, and M. Taylan, *Anal. Chem.*, 2003, **75**, 2181.
5. F. X. Zhang, L. Han, L. B. Israel, J. G. Daras, M. M. Maye, N. K. Ly, and C.-J. Zhong, *Analyst*, 2002, **127**, 462.
6. K. Naka, H. Itoh, Y. Tampo, and Y. Chujo, *Langmuir*, 2003, **19**, 5546.
7. S. Mandal, A. Gole, N. Lala, R. Gonnade, V. Ganvir, and M. Sastry, *Langmuir*, 2001, **17**, 6262.
8. B. G. Ershov and N. L. Sukhov, *Russ. J. Phys. Chem.*, 2001, **75**, 1303.
9. S. Chen, H. Yao, and K. Kimura, *Langmuir*, 2001, **17**, 733.
10. W. Bae, R. Abdullah, and R. K. Mehra, *Chemosphere*, 1998, **37**, 363.
11. W. Bae and R. K. Mehra, *J. Inorg. Biochem.*, 1998, **70**, 125.
12. R. Kho, C. L. Torres-Martínez, and R. K. Mehra, *J. Colloid Interface Sci.*, 2000, **227**, 561.
13. M. C. Brelle, J. Z. Zhang, L. Nguyen, and R. K. Mehra, *J. Phys. Chem. A.*, 1999, **103**, 10194.
14. S. J. Lippard and J. M. Berg, ‘Principals of Bioinorganic Chemistry’, 1st ed., University Science Books, Mill Valley, CA, 1994.
15. R. Kho, L. Nguyen, C. L. Torres-Martínez, and R. K. Mehra, *Biochem. Biophys. Res. Commun.*, 2000, **272**, 29.
16. G. Yi, B. Sun, F. Yang, and D. Chen, *J. Mater. Chem.*, 2001, **11**, 2928.
17. P. R. Selvakannan, S. Mandal, S. Phadtare, R. Pasricha, and M. Sastry, *Langmuir*, 2003, **19**, 3545.
18. S. Mandal, P. R. Selvakannan, S. Phadtare, R. Parischa, and M. Sastry, *Proc. Indian Acad. Sci. (Chem. Sci.)*, 2002, **114**, 513.
19. A. Henglein, B. G. Ershov, and M. Malow, *J. Phys. Chem.*, 1995, **99**, 14129.
20. C. T. Dameron, R. N. Reese, R. K. Mehra, A. R. Kortan, P. J. Carroll, M. L. Steigerwald, L. E. Brus, and D. R. Winge, *Nature*, 1989, **338**, 596.

21. P. C. Jocelyn, ‘Biochemistry of the SH Group: The Occurrence, Chemical Properties, Metabolism and Biological Function of Thiols and Disulfides’, Academic Press, London, 1972.
22. T. G. Schaaff, G. Knight, M. N. Shafigullin, R. F. Borkman, and R. L. Whetten, *J. Phys. Chem. B.*, 1998, **102**, 10643.
23. R. K. Mehra and D. R. Winge, *J. Cell. Biochem.*, 1991, **45**, 30.
24. W. E. Rauser, *Plant Physiol.*, 1995, **109**, 1141.
25. L. Nguyen, R. Kho, W. Bae, and R. K. Mehra, *Chemosphere*, 1999, **38**, 155.
26. W. Bae and R. K. Mehra, *J. Inorg. Biochem.*, 1998, **69**, 33.
27. W. Bae, R. Abdullah, D. Henderson, and R. K. Mehra, *Biochem. Biophys. Res. Commun.*, 1997, **237**, 16.
28. C. L. Torres-Martínez, L. Nguyen, R. Kho, W. Bae, K. Bozhilov, V. Klimov, and R. K. Mehra, *Nanotechnology*, 1999, **10**, 340.
29. M. H. Zenk, *Gene*, 1996, **179**, 21.
30. W. Bae and R. K. Mehra, *J. Inorg. Biochem.*, 1997, **68**, 201.
31. R. K. Mehra and P. Mulchandani, *Biochem. J.*, 1995, **307**, 697.
32. R. K. Mehra, V. R. Kodati, and R. Abdullah, *Biochem. Biophys. Res. Commun.*, 1995, **215**, 730.
33. R. K. Mehra, K. Tran, G. W. Scott, P. Mulchandani, and S. S. Saini, *J. Inorg. Biochem.*, 1996, **61**, 125.
34. R. K. Mehra, J. Miclat, V. R. Kodati, R. Abdullah, T. C. Hunter, and P. Mulchandani, *Biochem. J.*, 1996, **314**, 73.
35. C. T. Dameron and D. R. Winge, *Inorg. Chem.*, 1990, **29**, 1343.
36. G. Spreitzer, J. M. Whitling, J. D. Madura, and D. W. Wright, *Chem. Commun.*, 2000, 209.
37. J. M. Whitling, G. Spreitzer, and D. W. Wright, *Adv. Mat.*, 2000, **12**, 1377.
38. C. T. Dameron and I. T. Dance, ‘Biomimetic Materials Chemistry’, VCH Publishers, New York, 1996.
39. T. E. Wellems and R. J. Howard, *Proc. Natl. Acad. Sci. U.S.A.*, 1986, **83**, 6065.
40. J. H. Waite and A. C. Rice-Ficht, *Biochemistry*, 1989, **28**, 6104.
41. D. Brewer and G. Lajoie, *Rapid Commun. Mass Spectrom.*, 2000, **14**, 1736.
42. W. T. Morgan, *Biochemistry*, 1985, **24**, 1496.
43. D. J. Sullivan Jr, I. Y. Gluuzman, and D. E. Goldberg, *Science*, 1996, **271**, 219.
44. S. Pagola, P. W. Stephens, D. S. Bohle, A. D. Kosar, and S. K. Madsen, *Nature*, 2000, **404**, 307.
45. G. P. Smith, *Science*, 1985, **228**, 1315.
46. R. R. Naik, L. L. Brot, S. J. Clarson, and M. O. Stone, *J. Nanosci. Nanotechnol.*, 2002, **2**, 95.
47. R. Naik, S. J. Stringer, G. Agarwal, S. E. Jones, and M. O. Stone, *Nat. Mat.*, 2002, **1**, 169.
48. C. E. Flynn, C. Mao, A. Hayhurst, J. L. Williams, G. Georgiou, B. Iverson, and A. M. Belcher, *J. Mater. Chem.*, 2003, **13**, 2414.
49. G. C. Schatz and R. P. Van Duyne, ‘Handbook of Vibrational Spectroscopy’, Wiley, New York, 2002.
50. K. Shimizu, J. Cha, G. D. Stucky, and D. E. Morse, *Proc. Natl. Acad. Sci. U.S.A.*, 1998, **95**, 6234.
51. N. Kröger, R. Deutzmann, and M. Sumper, *Science*, 1999, **286**, 1129.
52. N. D. Chasteen and P. M. Harrision, *J. Struct. Biol.*, 1999, **126**, 182.
53. V. J. Wade, S. Levi, P. Arosio, A. Treffry, P. M. Harrision, and S. Mann, *J. Mol. Biol.*, 1991, **221**, 1443.
54. T. Douglas, D. P. E. Dickson, S. Betteridge, J. Charnock, C. D. Garner, and S. Mann, *Science*, 1995, **269**, 54.
55. F. C. Meldrum, B. R. Heywood, and S. Mann, *Science*, 1992, **257**, 522.
56. F. C. Meldrum, T. Douglas, S. Levi, P. Arosio, and S. Mann, *J. Inorg. Biochem.*, 1995, **58**, 59.
57. T. Douglas and V. T. Stark, *Inorg. Chem.*, 2000, **39**, 1828.
58. F. C. Meldrum, V. J. Wade, D. L. Nimmo, B. R. Heywood, and S. Mann, *Nature*, 1991, **349**, 684.
59. K. K. W. Wong and S. Mann, *Adv. Mater.*, 1996, **8**, 928.
60. K. K. W. Wong, T. Douglas, S. Gider, D. D. Awschalom, and S. Mann, *Chem. Mater.*, 1998, **10**, 279.
61. M. Allen, D. Willits, J. Mosolf, M. Young, and T. Douglas, *Adv. Mater.*, 2002, **14**, 1562.
62. M. Allen, D. Willits, M. Young, and T. Douglas, *Inorg. Chem.*, 2003, **42**, 6300 **ASAP**.
63. K. K. W. Wong, H. Cölfen, N. T. Whilton, T. Douglas, and S. Mann, *J. Inorg. Biochem.*, 1999, **76**, 187.
64. M. Ehrnsperger, H. Lilies, M. Gaestel, and J. Buchner, *J. Biol. Chem.*, 1999, **274**, 14867.
65. T. M. Treweek, A. M. Morris, and J. A. Carver, *Aust. J. Chem.*, 2003, **56**, 357.
66. D. Ishii, K. Kinbara, Y. Ishida, N. Ishii, M. Okochi, M. Yohda, and T. Aida, *Nature*, 2003, **423**, 628.
67. R. A. McMillan, C. D. Paavola, J. Howard, S. L. Chan, N. J. Zaluzec, and J. D. Trent, *Nat. Mater.*, 2002, **1**, 247.
68. M. L. Flenniken, D. A. Willits, S. Brumfield, M. J. Young, and T. Douglas, *Nano Lett.*, 2003, **3**, 1573 **ASAP.**
69. M. H. V. V. Regenmortel and H. Fraenkel-Conrat, ‘The Plant Viruses’, Plenum Press, New York, 1986.
70. E. Dujardin, C. Peet, G. Stubbs, J. N. Culver, and S. Mann, *Nano Lett.*, 2003, **3**, 413.
71. W. Shenton, T. Douglas, M. Young, G. Stubbs, and S. Mann, *Adv. Mater.*, 1999, **11**, 253.
72. R. I. B. Francki, ‘The Plant Viruses’, Plenum Press, New York, 1985.
73. B. Dragnea, C. Chen, E. Kwak, B. Stein, and C. C. Kao, *J. Am. Chem. Soc.*, 2003, **125**, 6374.
74. J. A. Speir, S. Munshi, G. Wang, T. S. Baker, and J. E. Johnson, *Structure*, 1995, **3**, 63.

75. T. Douglas, E. Strable, D. Willits, A. Aitouchen, M. Libera, and M. Young, *Adv. Mater.*, 2002, **14**, 415.
76. C. Mao, C. E. Flynn, A. Hayhurst, R. Sweeney, J. Qi, G. Georgiou, B. Iverson, and A. M. Belcher, *Proc. Natl. Acad. Sci. U.S.A.*, 2003, **100**, 6946.
77. S. Lee, C. Mao, C. E. Flynn, and A. M. Belcher, *Science*, 2002, **296**, 892.
78. J. L. Gardea-Torresdey, E. Gomez, J. R. Peralta-Videa, J. G. Parsons, H. Troiani, and M. Jose-Yacaman, *Langmuir*, 2003, **19**, 1357.
79. S. S. Shankar, A. Ahmad, and M. Sastry, *Biotechnol. Prog.*, 2003, **19**, 1627.
80. F. Jones, H. Colfen, and M. Antonietti, *Biomacromol.*, 2000, **1**, 556.

Acknowledgment

This work was supported by an NSF CAREER (CHE-0196540) and NSF 0304124.

Bond Lengths in Inorganic Solids & Liquids

I. David Brown
McMaster University, Hamilton, ON, Canada

1	Introduction	1
2	Early Attempts to Understand Bond Lengths	1
3	An Electrostatic Description of the Chemical Bond	1
4	Bond Lengths, Bond Fluxes and Bond Valences	2
5	Some Theorems about Bond Valences	5
6	Applications	6
7	References	6

1 INTRODUCTION

The chemical bond has resisted all attempts to provide it with a rigorous definition, yet it is one of the most widely used concepts in chemistry. It relies on the assumption that chemistry can be understood by considering only the nearest neighbors of a given atom and ignoring all interactions between more distant neighbors, an assumption that has never been justified theoretically. In spite of this lack of theoretical underpinning, the chemical bond model (*see Localized Bonding*), which predates the discovery of the electron by half a century, has been remarkably successful.

Many properties have been attributed to the chemical bond, but most of these. such as the bond energy (*see Bond Energies*), are difficult to define in a precise way and even more difficult to measure. The only bond property that can be measured with confidence is its length (*see Bond Length*), and many thousands of accurate bond lengths have been reported in the scientific literature (*see* ***Diffraction Methods in Inorganic Chemistry***).[1]

There are currently three different approaches to understanding chemical bonding. Quantum mechanical calculations (*see Ab Initio Calculations*; ***Molecular Orbital Theory***), even though they give the most complete picture, offer few insights into the nature of chemical bonds themselves because the concept of a bond does not arise naturally from a formalism based on the interactions between nuclei and electrons rather than the interaction between atoms. Even though quantum mechanics gives accurate values for measurable properties, its calculations are computer intensive and it becomes more difficult to use the more complex the chemical system.

A simpler approach that avoids the use of quantum mechanics is the two-body potential model (ionic model) that treats a crystal or molecule as a collection of atoms that interact through an empirical classical potential (*see* ***Solids: Computer Modeling***). This model involves a smaller, though still significant, computational load and is frequently used to predict the physical properties of crystals, but the potentials used are long-range and are inconsistent with a picture of localized chemical bonds.[2]

A third approach, the bond valence model (*see Bond Valence Method*), is related to the two-body potential model but is expressed in terms of the electrostatic field rather than the energy. It assumes that the valence electrons of the atoms can be assigned to individual bonds and that these determine the bond length. In spite of its conceptual and computational simplicity, this model gives good predictions of the bond length and provides useful chemical insights.[3]

Each of the above three models has advantages and limitations, but all can predict interatomic distances to an accuracy of a few picometres. Only the last is expressed in terms of the chemical bond and this model will be reviewed here.[3]

2 EARLY ATTEMPTS TO UNDERSTAND BOND LENGTHS

The earliest attempt to explain the observed lengths of chemical bonds in inorganic solids was the ionic model (*see Ionic Bonds*), in which the valence electrons were all assumed to reside on the more electronegative atoms (anions) leaving the more electropositive atoms (cations) with a positive charge (*see Anion* and *Cation*). The ions themselves were assumed to be hard or soft spheres with a fixed radius. Since the ions are held together by the long-range Coulomb potential, this model belongs to the two-body potential class of models and a quantitative treatment requires the summation over all pairs of atoms in the crystal.

When the interacting atoms have a similar electronegativity (*see Electron Spin Echo Envelope Modulation Spectroscopy*), as in organic compounds, a covalent bond model is usually used. Atoms are assumed to be held together by pairs of valence electrons localized between the two bonded atoms. The localized covalent bonds (*see Covalent Bonds*) and the long-range ionic interactions (*see Lithophiles*) represent two extremes of bond character with real bonds lying on the continuum in between. Unfortunately there is no unique way to locate the position of a given bond on this continuum, which makes it difficult to combine these two viewpoints quantitatively.

3 AN ELECTROSTATIC DESCRIPTION OF THE CHEMICAL BOND

It is, however, possible to derive an electrostatic picture of a localized chemical bond that leads naturally to the bond valence model. Atoms consist of an inert *core* (nucleus plus the filled inner electron shells), which carries a positive charge equal and opposite to that of the valence electrons that occupy the partially filled outer shell and are used to form chemical bonds.

When two atoms are brought together, the partially filled valence shells overlap first, with the valence electrons of one atom occupying states in the unfilled valence shell of the other. The overlapping electrons lie between the two positively charged cores attracting both, and pulling them together. The closer the atoms get, the larger the number of valence electrons lying in the overlap region and the greater the attractive force between the nuclei. Eventually the two cores start to overlap and, being unable to accommodate electrons from the other atom, they generate a repulsive force. Equilibrium is reached when the attractive and repulsive forces are equal. If the number of overlapping valence electrons is increased, they pull the atoms closer together, increasing the core repulsion until a new equilibrium is reached. The distance between the two atoms is therefore a measure of both the repulsive and the attractive force, hence of the number of valence electron pairs in the overlap region.

The electrostatic field linking the atom cores to the overlapping valence electrons can be used to define a chemical bond. As shown schematically in Figure 1, this field can be represented by lines of field. The total number of lines of field linking the charges is called the electrostatic flux, and it is equal to the charges on which it starts and terminates. Figure 1(a), which gives an electrostatic picture of a covalent bond, shows that the flux in the bond (proportional to the number of lines of field) is equal to the number of valence electron pairs in the overlap region. This picture of a covalent bond can conceptually be converted from a covalent to an ionic bond by moving the overlapping valence electrons onto the more electronegative atom (the anion) as shown in Figure 1(b). As Figure 1 shows, the electrostatic flux linking the A and X atoms depends only on the number of overlapping valence electrons and not on their location. The model therefore gives a quantitative picture of both ionic and covalent bonds.

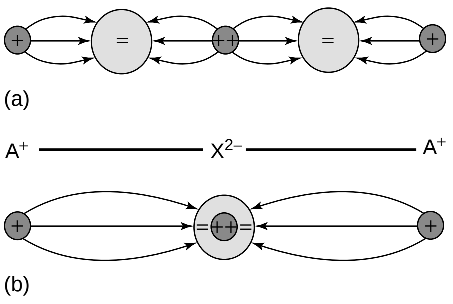

Figure 1 A schematic representation of the electrostatic model of the chemical bonds in a hypothetical $A^+ - X^{2-} - A^+$ molecule: (a) a covalent bond and (b) an ionic bond. The small circles represent the atomic cores, the large circles represent the overlapping valence electrons

4 BOND LENGTHS, BOND FLUXES AND BOND VALENCES

The bond flux is equal to the number of electron pairs associated with the bond, and as expected, this number can be estimated from the bond length, R_{ij}, using equation (1)

$$S_{ij} = \exp\left(\frac{R_0 - R_{ij}}{B}\right) \tag{1}$$

where R_0 and B are empirically determined constants[4–6] (a selection is given in Table 1) that are transferable to all bonds between the same pair of ions. S_{ij} is an estimate of the flux, but as it is subject to the experimental uncertainties associated with R_{ij}, it is not identical to the flux and is conveniently called the *bond valence.* Provided the bond is not sterically strained (see Section 5), the bond valence calculated using equation (1) is a good approximation to the electrostatic flux.[7] The form of equation (1) is shown by the line in Figure 2 for Ca–O bonds. For comparison, the points show the bond fluxes calculated directly from Coulomb's law for a selection of Ca–O bonds in well-determined structures.

According to Gauss' electrostatic theorem, the total bond flux, s_{ij}, leaving the core of atom i is equal to its charge, which is the same as the number of valence electrons, V_i (the formal ionic charge (*see Formal Charge*) or *atomic valence*), that the atom uses in bonding, equation (2).

$$V_i = \sum_j \{s_{ij}\} \tag{2}$$

The constants in equation (1) are fitted for each pair of ion-types to ensure that equation (2) is obeyed when the bond valence, S_{ij}, in equation (1) is substituted for the bond flux, s_{ij}, in equation (2) for a large number of accurately determined coordination environments.[9] While the value of R_0 depends on the sizes of the ions, a value of $B = 0.37$ A is found to work well for many ion pairs.[4] The programs VALENCE and VALIST can be used to determine the bond valence from the bond length.[10,11]

The bond flux can also be calculated by recognizing that in the ionic limit each bond is an electric capacitor (represented by flux linking two opposite charges). The network of atoms and bonds is thus a capacitive electrical circuit, and since in most equilibrium structures all the bond capacitances are empirically found to be equal, the fluxes can be calculated using the Kirchhoff equations (2) and (3) in which the bond capacitances cancel.[12]

$$0 = \sum_{\text{loop}} \{s_{ij}\} \tag{3}$$

where the summation is over any loop in the bond network. The program BONDVAL can be used to solve the Kirchhoff equations.[13]

Table 1 Selected bond valence parameters R_0 ($B = 0.37$ A)^5 (mostly taken from references 4 and 6) and crystal radii from reference 8

	R_0 (for $B = 37$ pm) for different anions (pm)				Shannon crystal radii (pm) for different coordination numbers							
Ion	O^{2-}	F^-	Cl^-	S^{2-}	2	3	4	5	6	7	8	9
Ag^+	184.2	180	209	211.9	81		114	123	129	136	142	
Al^{3+}	162.0	154.5	203.2	213			53	62	67.5			
As^{3+}	178.9	170	216	227.2					72			
As^{5+}	176.7	162.0	214				47.5		60			
Au^{3+}	183.3	181	217				82		99			
B^{3+}	137.1	128.1	174	182		15	25		41			
Ba^{2+}	228.5	218.8	269	276.9					149	152	156	161
Be^{2+}	138.1	128.1	176	183		30	41		59			
Bi^{3+}	209.4	199	248	257.0				110	117		131	
Bi^{5+}	206	197	244						90			
Br^{7+}	181	172	219				39		53			
C^{4+}	139	132	176	180		6	29		30			
Ca^{2+}	196.7	184.2	237	245					114	120	126	132
Cd^{2+}	190.4	181.1	221.2	230.4			92	101	109	117	124	
Ce^{3+}	215.1	203.6	252						115	121	128.3	133.6
Ce^{4+}	202.8	199.5	241						101		111	
Cl^{7+}	163.2	155	200				22		41			
Cl^-									167			
Co^{2+}	169.2	164	203.3				72	81	79(LS), 88.5(HS)		104	
Co^{3+}	163.7	162	205						68.5(LS), 75(HS)			
Cr^{2+}	173	167	209						87(LS), 94(HS)			
Cr^{3+}	172.4	165.7	208						75.5			
Cr^{6+}	179.4	174	212				40		58			
Cs^+	241.7	233	279.1	289					181		188	192
Cu^+	150.4	160	185.8	189.8	60		74		91			
Cu^{2+}	167.9	159.4	200	205.4			71	79	87			
Cu^{3+}	173.5		207.8						68(LS)			
Dy^{3+}	200.1	192.2	241	247					105.2	111	116.7	122.3
Er^{3+}	198.8	190.4	239	246					103.0	108.5	114.4	120.2
Eu^{2+}		204	253	258.4					131	134	139	144
Eu^{3+}	207.4	196.1							108.7	115	120.6	126.0
F^-					114.5	116	117		119			
Fe^{2+}	173.4	165	206	212.5			77		75(LS), 92(HS)		106	
Fe^{3+}	175.9	167.9	209	214.9			63(HS)	72	69(LS), 78.5(HS)		92	
Ga^{3+}	173.0	162	207	216.3			61	69	76.0			
Gd^{3+}	206.5	195	244.5	253					107.8	114	119.3	124.7
Ge^{4+}	174.8	166	214	221.7			53.0		67.0			
H^+	[a]				−4							
Hf^{4+}	192.3	185	230				72		85	90	97	
Hg^+	190	181	228			111			133			
Hg^{2+}	197.2	190	225	230.8	83		110		116		128	
Ho^{3+}	202.5	190.8	240.1						104.1		115.5	121.2
I^-									206			
I^{5+}	200.3	190	238			58			109			
I^{7+}	193	183	231				56		67			
In^{3+}	190.2	179.2	228	237.0			76		94.0		106	
Ir^{5+}	191.6	182	230	238					71			
K^+	213.2	199.2	251.9	259			151		152	160	165	169
La^{3+}	217.2		254.5	264.3					117.2	124	130.0	135.6
Li^+	146.6	136.0	191	194			73.0		90		106	
Lu^{3+}	197.1	187.6	236.1	243					100.1		111.7	117.2
Mg^{2+}	169.3	157.8	208	218			71	80	86.0		103	
Mn^{2+}	179.0	169.8	213.3				80	89	81(LS), 97(HS)		110	
Mn^{3+}	176.0	166	214					72	72(LS), 78.5(HS)			
Mn^{4+}	175.3	171	213				53		67.0			

(cont’d overleaf)

Table 1 cont'd

	R_0 (for $B = 37$ pm) for different anions (pm)				Shannon crystal radii (pm) for different coordination numbers							
Ion	O^{2-}	F^-	Cl^-	S^{2-}	2	3	4	5	6	7	8	9
Mn^{6+}	179						39.5					
Mn^{7+}	179	172	217				39		60			
Mo^{3+}	183.4	176	222						83			
Mo^{4+}	185.6			223.5					79.0			
Mo^{5+}	190.7			228.8			60		75			
Mo^{6+}	190.7	181	228	233.1			55	64	73	87		
N^{3-}							132					
N^{3+}	136.1	137	175						30			
N^{5+}	143.2	136	180			4.4			27			
Na^+	180.3	167.7	215	230.0			113	114	116	126	132	138
Nb^{5+}	191.1	187	227	237			62		78	83	88	
Nd^{3+}	210.5	200.8	249.2	259					112.3	124.9	130.3	
Ni^{2+}	165.4	159.6	202	193.7			69(T), 62(SQ)	77	83.0			
Ni^{3+}				204.0					70(LS), 74(HS)			
Np^{3+}		200	248						115			
Np^{4+}									101		112	
O^{2-}					121	122	124		126		128	
Os^{4+}	181.1	172	219						77.0			
Os^{6+}	203							63	68.5			
P^{5+}	161.7		202	214.5			31	43	52			
Pb^{2+}	211.2	203	253	254.1			112		133	137	143	149
Pb^{4+}	204.2	194	243				79	87	91.5		108	
Pd^{2+}	179.2	174	205				78		100			
Pm^{3+}									111		123.3	128.4
Pr^{3+}	213.8	202.2	250	260					113		126.6	131.9
Pt^{2+}	176.8	168	205				74		94			
Pt^{4+}	187.9	175.9	217						76.5			
Pu^{3+}	211	200	248						114			
Rb^+	226.3	216	265.2	270					166	170	175	177
Re^{5+}	186								72			
Re^{7+}		186	223				52		67			
Rh^{3+}	179.3	171	217						80.5			
Ru^{3+}	177								82			
Ru^{4+}	183.4	174	221						76.0			
Ru^{5+}	190								70.5			
S^{2-}									170			
S^{4+}	164.4	160	202						51			
S^{6+}	162.4	156	203				26		43			
Sb^{3+}	197.3	188.3	235	247.4			90	94	90			
Sb^{5+}	194.2	179.7	230						74			
Sc^{3+}	184.9	176	223	232.1					88.5		101.0	
Se^{2-}									184			
Se^{4+}	181.1	173	222						64			
Se^{6+}	178.8	169	216				42		56			
Si^{4+}	162.4	158	203	212.6			40		54.0			
Sm^{3+}	208.8		197.7	255					109.8	116	121.9	127.2
Sn^{2+}	194	192.5	236									
Sn^{4+}	190.5	184.3	227.6	239.9			69	76	83.0	89	95	
Sr^{2+}	211.8	201.9	251	259					132	135	140	145
Ta^{5+}	192.0	188	230						78	83	88	
Tb^{3+}	203.2	193.6	242.7	251					106.3	112	118.0	123.5
Tc^{4+}									78.5			
Te^{2-}									207			
Te^{4+}	197.7	187	237			66	80		111			

Table 1 cont'd

	R_0 (for $B = 37$ pm) for different anions (pm)				Shannon crystal radii (pm) for different coordination numbers							
Ion	O^{2-}	F^-	Cl^-	S^{2-}	2	3	4	5	6	7	8	9
Te^{6+}	191.7	182	230				57		70			
Th^{4+}	216.7	206.8	255	264					108		119	123
Ti^{3+}	179.1	172.3	217						81.0			
Ti^{4+}	181.5	176	219	224			56	65	74.5		88	
Tl^+	212.4	215	256	254.5					164		173	
Tl^{3+}	200.3	188	232				89		102.5		112	
Tm^{3+}	200.0	184.2	238	245					102.0		113.4	119.2
U^{4+}	211.2	203.8							103	109	114	119
U^{5+}	207.5	196.6	246						90	98		
U^{6+}	207.5				59		66		87	95	100	
V^{3+}	174.3	170.2	219	218.5					78.0			
V^{4+}	178.4	170	216	222.6				67	72		86	
V^{5+}	180.3		216				49.5	60	68			
W^{6+}	191.7	183	227				56	65	74			
Y^{3+}	201.9	190.4	240	248					104.0	110	115.9	121.5
Yb^{3+}	196.5	187.5	237.1	243					100.8	106.5	112.5	118.2
Zn^{2+}	170.4	162	201	209			74	82	88.0		104	
Zr^{4+}	192.8	184.6	233	241			73	80	86	92	98	103

[a] O–H bonds are conveniently modeled with $R_0 = 0.529$, $B = 0.94$ over the range of distances most commonly encountered, but these values do not give good valences for very short and very long bonds.

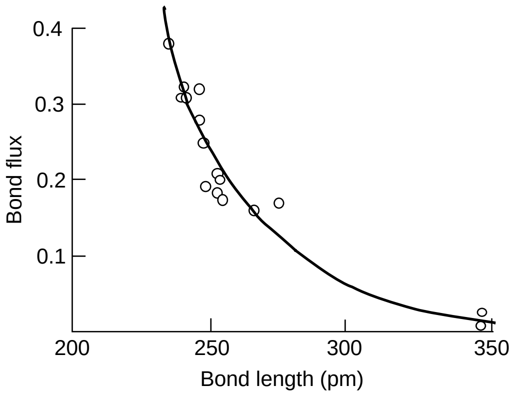

Figure 2 The relation between bond valence and bond length for Ca–O bonds. The line shows equation (1). The points are electrostatic fluxes calculated using Coulomb's law for several different Ca-bearing crystals. (Figure 3.1 from 'The Chemical Bond in Inorganic Chemistry' by Brown, David (2001)). (Ref. 3. Reproduced by permission of Oxford University Press)

5 SOME THEOREMS ABOUT BOND VALENCES

A number of theorems associated with the bond valence model are useful in the analysis of inorganic structures.[14] Equation (2), known as the *valence sum rule,* is central to the model. Since Gauss' theorem is necessarily obeyed by the bond fluxes that terminate at each atom, equation (2) is always obeyed and ensures that if the flux in one bond is changed, the fluxes in all the other bonds in the network will relax, giving rise to the long-range Coulomb effects. However, if bond valences determined from experimental bond lengths are used instead of the fluxes, equation (2) may not be exactly obeyed, particularly if the structure is strained as a result of crowding or incomensurations between its different parts as found, for example, in many perovskites. Important as such deviations are, they are the exception, and equation (2) is widely used to check the chemical validity of a newly determined crystal structure, or to see whether the bonds are strained (*see* ***Diffraction Methods in Inorganic Chemistry***).[15]

The equal valence rule or loop rule equation (3) is less rigorously obeyed, and does not apply to the environments of atoms with electronically driven anisotropies arising from, for example, lone electron pairs (*see Lone Pair*; ***Electronic Structure of Main-group Compounds***) or Jahn–Teller distortions (*see Jahn–Teller Effect*; ***Copper: Inorganic & Coordination Chemistry***).

The concave form of equation (1) shown in Figure 2 leads to the distortion theorem that states that any deviations of the bond lengths in the coordination environment of an atom from their mean causes an increase in the bond valence sum, provided that the average bond length is held constant. A corollary is that any atom located in a cavity that is too large will tend to distort its environment, often by moving away from the center of the cavity, as this will increase the bond valence sum which otherwise would be too small. The best-known example of such a distortion is the O–H···O hydrogen bond (*see* ***Hydrogen Bonding & Dihydrogen Bonding***). The two

O atoms come into contact when the O–O distance is larger that twice the O–H distance expected for a symmetrically two-coordinated H atom. To compensate, the H atom moves off-center until its bond valence sum reaches 1.0 e (electrons), giving rise to the characteristically asymmetric hydrogen bond (*see Hydrogen Bonding*).[16]

6 APPLICATIONS

Before the development of the bond valence model, ionic radii were widely used to predict bond lengths (*see Crystallographic Radius*).[8] Popular listings are provided by Pauling[17] and more recently and comprehensively by Shannon and Prewitt.[18,19] A selection of the latter are given in Table 1. However, since the ionic radii predict that all bonds between a given pair of ions will have the same length, they do not take into account the effects of neighboring atoms and can only reliably predict individual bond lengths in regular cation environments. Nevertheless, they provide a convenient measure of the relative sizes of atoms that can be used for comparative purposes as, for example, in Figure 3. They can also be used to decide whether two cations can substitute for each other, since substitution should be easiest between ions of similar valence and similar size.

For the accurate prediction or analysis of bond lengths a more sophisticated model is needed.[14] If the way in which the atoms are linked by bonds is known, equations (2) and (3) can be used to predict bond fluxes, and equation (1) can then be used to calculate the expected bond distances. Differences between the predicted and observed bond lengths indicate the presence of either electronic or steric strain (or possibly an incorrectly determined structure).[15] Alternatively, using equation (1) experimentally determined bond lengths can be converted to bond valences, which can be checked to see how well equation (2) is obeyed. The root mean square discrepancy between the bond valence sums and the formal valence, V_i, for all the atoms in a crystal, is known as the *global instability index*, (GII). Experimental uncertainties in the bond lengths usually account for GII values of around 0.05 e. Larger values indicate either bond strain or errors in the structure determination. Structures with GII $>$ 0.25 e are unstable and should be checked for possible errors. Figure 3 shows how the GII varies as a function of rare-earth cation radius in Ln_2BaCuO_5. In this series of isostructural crystals, Tm has the least strained structure but the isostructural Nd compound would be so highly strained that Nd_2BaCuO_5 adopts a different structure.[20]

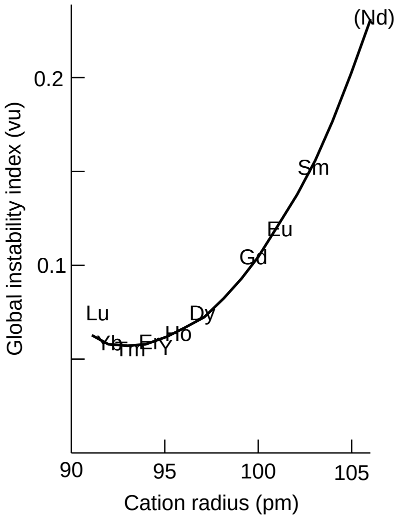

Figure 3 The variation in the Global Instability Index of Ln_2BaCuO_5 as a function of the ionic radius of Ln. The line is a fitted second order equation. Nd adopts a different structure. (Figure 12.3 from 'The Chemical Bond in Inorganic Chemistry' by Brown, David (2001)). (Ref. 3. Reproduced by permission of Oxford University Press)

Other uses for the bond valence sums include the determination of the oxidation states of atoms (*see Oxidation Number*), the examination of the distribution of atoms over different crystallographic sites (*see Crystal Structures*),[21] the location of Ca and Na binding sites in proteins (*see* ***Calcium-binding Proteins***),[22] and the analysis of enzyme mechanisms (*see Protein Determination*; ***Cation-activated Enzymes***).[23] The bond valence model also gives good predictions for chemical properties such as solubility and stability.[24] Compared to other methods of exploring the structure and properties of chemical compounds, the bond valence model, by focussing on localized bonds, is conceptually simple. The insights it provides make it an ideal tool for use in both planning and analyzing the structures of inorganic materials.

7 REFERENCES

1. A. Belsky, M. Hellenbrandt, V. L. Karen, and P. Luksch, *Acta. Cryst.*, 2002, **B58**, 364.
2. C. R. A. Catlow ed. 'Computer Modelling in Inorganic Crystallography', Academic Press, San Diego and London, 1997.
3. I. D. Brown, 'The Chemical Bond in Inorganic Chemistry. The Bond Valence Model', Oxford University Press, Oxford, 2001.
4. I. D. Brown and D. Altermatt, *Acta. Cryst.*, 1985, **B47**, 192.
5. I. D. Brown, Accumulated Table of Bond Valence Parameters: 2001, http://www.ccp14.ac.uk/ccp/web_mirrors/i_d_brown/bond_valence_param.
6. N. W. Brese and M. O'Keeffe, *Acta. Cryst*, 1991, **B47**, 192.
7. I. D. Brown, 'The Chemical Bond in Inorganic Chemistry. The Bond Valence Model', Oxford University Press, Oxford, 2001, p. 26ff.

8. R. D. Shannon, 'Crystal Radii in the Oxides & Fluorides, in the Encyclopedia of Inorganic Chemistry', 1st edn., ed. R. B. King,John Wiley & Sons p. 929.
9. I. D. Brown, 'The Chemical Bond in Inorganic Chemistry. The Bond Valence Model', Oxford University Press, Oxford, 2001, p. 224ff.
10. I. D. Brown, The program VALENCE for calculating bond valences interactively: 2001, http://www.ccp14.ac.uk/ccp/web_mirrors/i_d_brown.
11. A. S. Wills and I. D. Brown, The program VALIST FOR WINDOWS for calculating bond valences from a table of bond lengths: 2001, ftp://ftp.ill.fr/pub/dif/valist/.
12. I. D. Brown, 'The Chemical Bond in Inorganic Chemistry. The Bond Valence Model', Oxford University Press, Oxford, 2001, p. 28.
13. K. A. Popov and I. P. Orlov, Program BONDVAL for predicting bond valences from the connectivity table: 2001, http://www.ccp14.ac.uk/ccp/web_mirrors/bondvalencewizard.
14. M. O'Keeffe, *Struct. Bonding*, 1989, **71**, 161.
15. I. D. Brown, 'The Chemical Bond in Inorganic Chemistry. The Bond Valence Model', Oxford University Press, Oxford, 2001, p. 181ff.
16. I. D. Brown, 'The Chemical Bond in Inorganic Chemistry. The Bond Valence Model', Oxford University Press, Oxford, 2001, p. 75.
17. L. Pauling, 'The Nature of the Chemical Bond', 3rd edn., Cornell, 1960, p. 514.
18. R. D. Shannon and C. T. Prewitt, *Acta Crystallogr.*, 1969, **B25**, 925.
19. R. D. Shannon, *Acta Crystallogr.*, 1976, **A32**, 751.
20. I. D. Brown, 'The Chemical Bond in Inorganic Chemistry. The Bond Valence Model', Oxford University Press, Oxford, 2001, p. 166.
21. I. D. Brown, 'The Chemical Bond in Inorganic Chemistry. The Bond Valence Model', Oxford University Press, Oxford, 2001, p. 181.
22. I. D. Brown, 'The Chemical Bond in Inorganic Chemistry. The Bond Valence Model', Oxford University Press, Oxford, 2001, p. 204.
23. I. D. Brown, 'The Chemical Bond in Inorganic Chemistry. The Bond Valence Model', Oxford University Press, Oxford, 2001, p. 181.
24. I. D. Brown, 'The Chemical Bond in Inorganic Chemistry. The Bond Valence Model', Oxford University Press, Oxford, 2001, p. 53ff.

Metal-related Diseases of Genetic Origin

Bibudhendra Sarkar
University of Toronto, Toronto, ON, Canada

1 Introduction 1
2 Copper-related Diseases 1
3 Iron-related Diseases 7
4 Zinc-related Disease 10
5 Other Rare Genetic Disorders of Metal Metabolism 11
6 Related Articles 11
7 References 11

1 INTRODUCTION

Mutations in the genes encoding proteins that are involved in normal metal metabolism usually result in severe genetic disorders. Wilson and Menkes diseases are two genetic disorders of copper metabolism. They are caused by mutations in the genes *ATP7B* and *ATP7A*, which encode copper-transporting P-type ATPases. The major genetic disorders affecting iron metabolism are hematochromatosis, thalassemia, and aceruloplasminemia. Genetic disorders of zinc metabolism include acrodermatitis enteropathica. There are several other rare genetic disorders of little known genetic factors. They will be discussed very briefly in this article.

2 COPPER-RELATED DISEASES

2.1 Wilson Disease

2.1.1 Clinical and Biochemical Features

Wilson disease is an autosomal recessive disorder of copper transport (Figure 1).[1] It results in the toxic accumulation of copper in various tissues, but mainly in the liver, kidney, and brain. Wilson disease occurs worldwide with an average prevalence of about 1 in 30 000 in most populations.[2] The age of onset for Wilson disease is variable and can extend from 3–4 years into the mid-50s. There are three phases in the progression of the disease. In the first phase, copper accumulates in the cytoplasm of hepatocytes. As more copper is absorbed, in the second phase the increased concentration of cytoplasmic copper results in the induction of large amounts of metallothionein (*see* ***Metallothioneins***). It causes the chelation and storage of copper in the hepatocytes leading to necrosis and release of copper into the blood stream.[3] In the third phase, copper begins to accumulate in other organs such as the brain, kidney, and cornea. Sudden release of high level of copper in the blood circulation due to oxidative damage to erythrocyte membranes leads to hemolytic anemia.[4] Wilson disease patients fall into three categories: those displaying hepatic symptoms, those displaying neurologic symptoms, and those displaying both (Table 1).

One of the important diagnostic features of Wilson disease is the dull brown Kayser-Fleisher (K-F) rings caused by deposition of copper in the cornea.[5] The majority of Wilson disease patients and all patients displaying neurologic disorder demonstrate K-F rings.[6] Patients with an early age of onset usually display predominantly hepatic symptoms, whereas those with a later age of onset display predominantly neurologic symptoms.[7] Liver dysfunction symptoms include jaundice and fatigue; associated conditions include asymptomatic cirrhosis, subacute hepatitis, and hepatitis resembling autoimmune hepatitis.[8] Symptoms of neurologic disorders in Wilson disease include deteriorating coordination, tremors, dysarthria, drooling, personality changes, dementia, slurring of speech, rigidity, and behavioral problems.[9] It is generally believed that the neurologic symptoms of Wilson disease are due to cerebellar or extrapyramidal involvement or combination of both conditions.

The disturbance of copper excretion, primarily due to a defect in the billiary excretion, is consistent with the biochemical findings in patients with Wilson disease. Urinary copper excretion is increased owing to total body overload of copper. Renal dysfunction includes albuminuria and renal rickets.[9] Incorporation of copper in ceruloplasmin is impaired. Thus, there is a greater proportion of copper bound to albumin and amino acid complexes in the serum. But the overall copper concentration in serum is low. Ceruloplasmin is a multicopper oxidase (*see* ***Copper Proteins: Oxidases***) that

Table 1 Clinical and biochemical features of Wilson and Menkes diseases

Laboratory findings	Menkes disease	Wilson disease
	↓Serum copper levels ↓Liver copper levels ↑Intestinal/kidney copper levels	↓Serum copper levels ↑Liver copper levels ↑Urinary copper levels
Defect	Intestinal copper absorption Deficiency of copper enzyme	Decreased billiary excretion of copper Incorporation of copper into ceruloplasmin
Treatment	Daily Cu-histidine injections	Chelation therapy
Genes	X chromosome/recessive	Chromosome 13/recessive

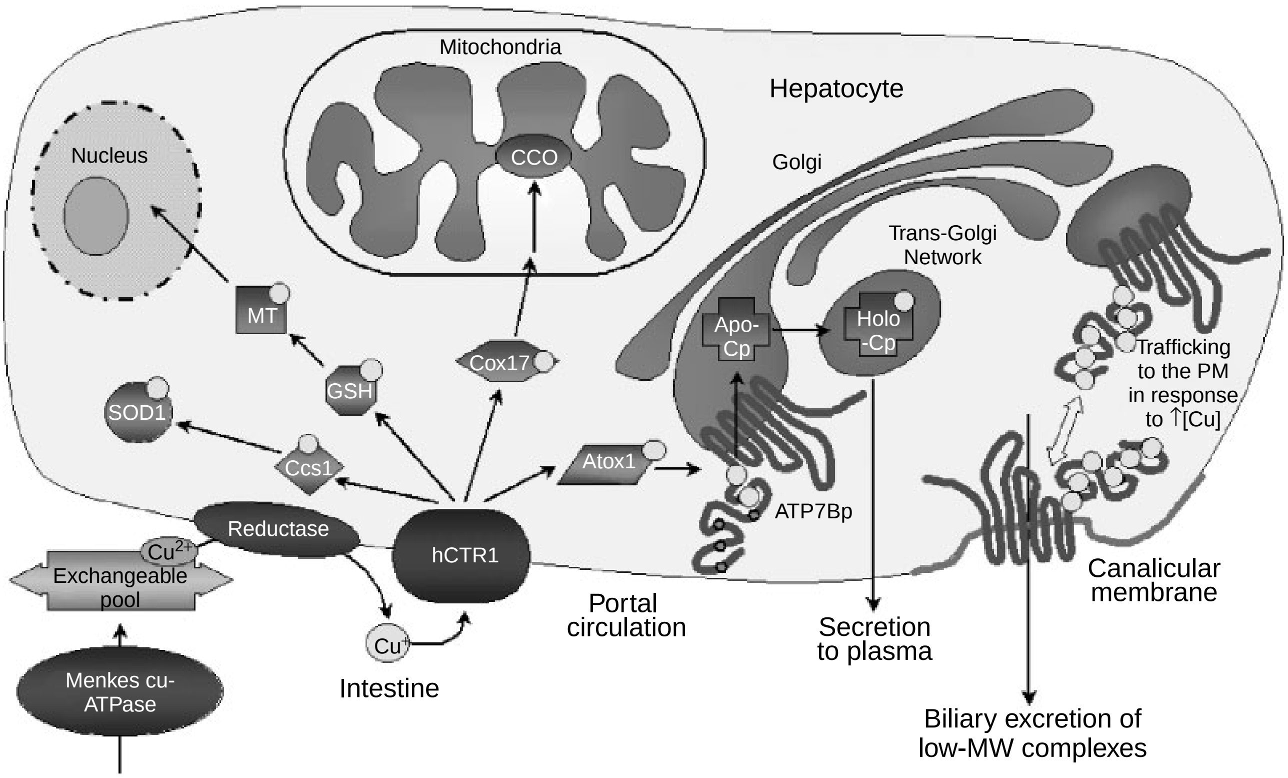

Figure 1 Copper transport pathway. Copper is absorbed in the intestine and becomes bound to amino acids, mainly histidine and albumin. Prior to uptake, Cu(II) is reduced to Cu(I) by a membrane-bound reductase and enters the cell via a passive transporter. Once in the cell, copper becomes bound to copper chaperones responsible for delivering copper to specific proteins. The Wilson/Menkes ATPase accepts copper from these chaperones and pumps it into the Golgi for incorporation into various proteins such as ceruloplasmin (Cp). Ceruloplasmin may also play a role in delivering copper to peripheral tissues via cell-surface receptors that internalize the protein. The Wilson disease ATPase may also play a role in the elimination of copper into the bile

has been implicated in iron metabolism (see section on aceruloplasminemia). The low ceruloplasmin levels in Wilson disease are the result of a disturbance in the transfer of copper to the apoprotein during its synthesis.

2.1.2 *Wilson Disease Gene*

The Wilson disease gene was first assigned to a single locus by linking to the esterase D gene.[10] Later studies placed the gene close to a cluster of polymorphic markers in the q14.3 hand of chromosome 13.[11–13] The localization studies led to the cloning of the gene independently by two groups designated as *ATP7B*.[14,15] The gene consists of 22 exons out of which 21 are expressed in the liver. Exon 22 is expressed in the kidney.[16–18] The size of the exons ranges from 77 bp to 2355 bp.[16] There is a high level of expression of the gene transcript in the liver and kidney with a lower level in the lung and placenta.[14] One finds a good correlation of the pattern of expression and the observed clinical and biochemical features of the disease.

There are missense mutations in the Wilson disease gene in all the exons and rarely in exons 1–5, which encode the six N-terminal metal-binding motifs, and exon 21, which encodes the C-terminal tail of the protein.[18,19] Several other mutations in the Wilson disease gene, with small insertion/deletions, nonsense, frameshift, and splice-site mutations, have been found and they are discussed elsewhere.[18,20–24] Most common missense mutations in many populations are a change from histidine in position 1069 to glutamine. This mutation is found in about 38% of homozygous Wilson disease patients of North European descent. It occurs in a conserved loop motif (SEHPL) that is adjacent to the conserved phosphorylation motif DKTG. It is not clear what specific function is performed by this motif, but it seems to be necessary for the function of the heavy-metal ATPases, as this motif is conserved between the Wilson disease (ATP7B), Menkes disease (ATP7A), and Cop A (bacterial copper ATPase) proteins.[15,25]

Advantage was taken of the high frequency of the His 1069 Glu for a genotype/phenotype analysis of this mutation. In one case study, patients homozygous for the His 1069 Glu mutation had later age of onset as compared to the heterozygous patients, 20 years versus 15.4 years.[19] This His 1069 Glu was found at high frequency in Mediterranean populations. The data from several studies suggest that the His 1069 Glu mutation is the most common molecular defect in the Wilson disease protein and it probably arose from an ancient mutational event.[26]

2.1.3 Wilson Disease Copper-transporting ATPase: ATP7B

The Wilson disease gene is predicted to encode a copper-transporting P-type ATPase, having many features in common with other cation-transporting P-type ATPases including bacterial heavy-metal transporters shown in Figure 2.[27] The predicted structure of the Wilson disease copper-transporting ATPase contains general features conserved among members of the P-type ATPase family. There are the TGEA motif (actuator domain), DKTG motif (phosphorylation domain), and the sequence MXGDGXNDXP found in the hinge region that connects the phosphorylation domain to the transmembrane segment. ATP7B is further classified as a heavy-metal transporting P-type ATPase since it contains six metal-binding motifs, GMTCXXC at the N-terminus of the molecule, the CPC motif in the sixth transmembrane region (TM6), the SEHPL motif in the nucleotide-binding domain and eight transmembrane segments.

Structural Studies of ATP7B. A complete structural description of ATP7B remains unsolved. However, major advances have been made to characterize the N-terminal copper-binding domain of ATP7B. The ATP7B copper-binding N-terminal domain binds copper with the stoichiometry of one copper per metal-binding repeat and this binding occurs through a cooperative mechanism.[28–30] The bound copper is in the +1 oxidation state and is coordinated by two cysteines in a distorted linear geometry. CD experiments have shown that the N-terminal domain undergoes secondary and tertiary conformational changes in response to copper binding. It has been suggested that the conformational changes observed in the ATP7B N-terminal domain induced by copper-binding may signal the protein to traffic between the trans-Golgi network (TGN) and the plasma membrane in a copper-dependent manner.[31] Interestingly, the N-terminal copper-binding domain has the ability to bind different transition metals with varying affinities

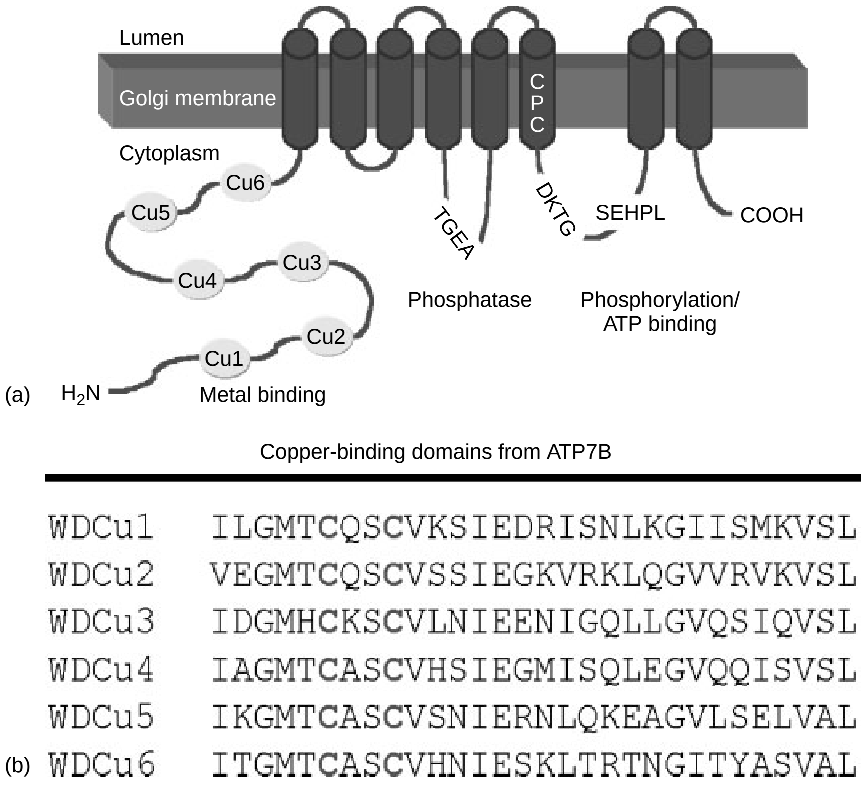

WDCu1	ILGMTCQSCVKSIEDRISNLKGIISMKVSL
WDCu2	VEGMTCQSCVSSIEGKVRKLQGVVRVKVSL
WDCu3	IDGMHCKSCVLNIEENIGQLLGVQSIQVSL
WDCu4	IAGMTCASCVHSIEGMISQLEGVQQISVSL
WDCu5	IKGMTCASCVSNIERNLQKEAGVLSELVAL
WDCu6	ITGMTCASCVHNIESKLTRTNGITYASVAL

Figure 2 Proposed structure of the Wilson/Menkes copper ATPases. (a) The predicted structure contains domains that are similar to other cation-transporting ATPases as well as other heavy-metal transporters. Cu1-6, N-terminal copper-binding motifs; TGEA, transduction motif; CPC, transmembrane motif present in heavy-metal transporters; DKTG, phosphorylation motif; SEHPL, conserved motif found in all heavy-metal transporting ATPases of unknown function. (b) Sequence alignment of metal-binding motifs from the Wilson disease protein (WDCu1-6) and other heavy-metal binding/transporting proteins. ATX1, copper chaperone from *S. cerevisiae*; ATOX1, human copper chaperone; CopA, copper-transporting ATPase from *E. hirae*; MerP, mercury-binding protein from E. coli; CadA, cadmium-transporting ATPase from *S. aureus*

as follows: Cu(II) ≫ Zn(II) > Ni(II) > Co(II). Zinc binds mostly to nitrogen atoms in the N-terminus and not to the copper-binding motif having cysteine residues. The conformational changes induced by zinc binding are completely different from those of copper-binding.[32]

The experimental determination of the 3D structure of the entire ATP7B poses many technical challenges. However, studies have been carried out by homology modeling using gapped-BLAST analysis. The sequence of ATP7B was aligned representing the copper-transporting ATPases with the SERCA1a sequence.[33,34] This sequence alignment generated a structural alignment of homologous regions of ATP7B (Figure 3).

Functional Aspects of ATP7B. Since the discovery of the Menkes and Wilson disease genes, the studies of many research groups revealed various aspects of how these copper-ATPases work. The unique metal-binding cytosolic N-terminal domain of copper ATPases has been the focus of much research. In copper ATPases with multiple copper-binding domains, the closest to the transmembrane region appears to be functionally more important than the ones closest to the amino terminus.[35] Therefore, the role of the N-terminal copper-binding domains may be to increase the overall catalytic rate of the transporter. Conformational studies have shown that the N-terminal domains undergo secondary and tertiary conformational changes in response to copper-binding.[31] It is not known just how the conformational changes in the N-terminal copper-binding domain affect the function of the ATPase. It has been suggested that the conformational changes observed in the ATP7B N-terminal domain induced by copper binding may signal the protein to traffic between the trans Golgi network and the plasma membrane. In addition to its role in trafficking, a regulatory role has also been suggested for the N-terminal domain. Results have shown that the nucleotide/phosphorylation domains interact with the N-terminus and the copper-bound N-terminal domain induces a conformational change in the nucleotide/phosphorylation domain, altering the protein–protein interaction.[36] The copper chaperone ATOX1 was shown to interact with some, but not all, the N-terminal copper-binding repeats.[37,38] Structural homology modeling of the six repeats of ATP7B reveals that they have different electrostatic surfaces from one another and thus not all are equally capable of interacting with the chaperone.[39] Copper binding to the N-terminus weakens its interaction with the nucleotide-binding domain thereby causing them to dissociate.[40] The dissociation of the N-terminus from the nucleotide-binding domain restores the nucleotide-binding affinity of this domain thereby allowing the binding of ATP to the nucleotide-binding site. The successive conformational changes are transmitted to the translocation domain. The transmembrane domains are associated with the transduction channel and contain residues critical to cation binding. The conserved proline residue in the ATPase transmembrane domain 6 is flanked by a pair of cysteine residues to form the highly conserved CPC motif, which is predicted to be one of the copper-binding sites within the channel.[41–43] The hydrolysis of the phosphoenzyme requires the release of copper from the channel to the lumen. The release of cation may cause the movement of the activator domain and allow water to access and hydrolyze the phosphoenzyme.

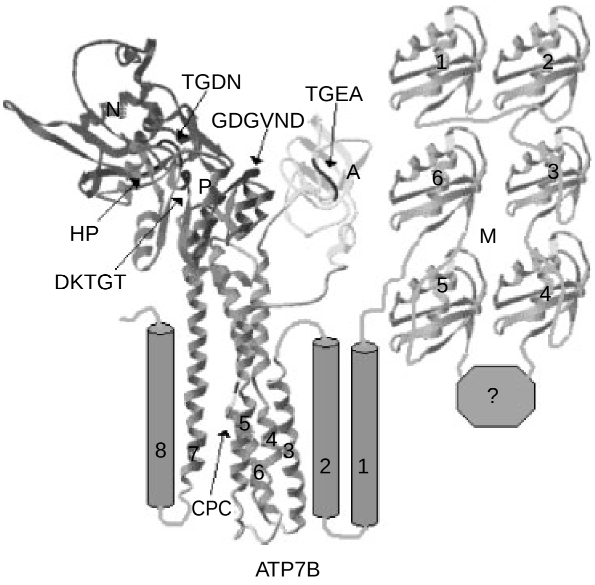

Figure 3 Homology modeling of ATP7B based on the known structure of calcium ATPase. The core of ATP7B encompassing the regions between TM3 and TM7 can be successfully modeled. Actuator domain (A); N-terminal metal-binding domain (M); nucleotide-binding domain (N); phosphorylation domain (P). The important and conserved residues are marked on ATP7B. TM1, TM2, and TM8 do not correspond to any of the transmembrane helices in calcium ATPase and were not modeled. The six copper-binding domains in the N-terminal region of ATP7B each adopt a ferredoxin-like fold found in other metal-binding domains. The region between the 4th and 5th copper-binding domains may contain a domain whose function is yet to be discovered[33]

2.1.4 Treatment of Wilson Disease

For almost 50 years following the description of Wilson disease, there was no effective treatment for this progressive fatal disorder. The damage to vital organs (liver, brain, kidney) in Wilson disease is caused by the toxic action exerted by excessive amounts of copper deposited primarily in these organs. There are several pharmacologic regimens and therapeutic modalities available for the treatment of Wilson disease (Table 2).

It should be pointed out that failure to comply with lifelong therapy led to recurrent symptoms and liver failure, the latter requiring liver transplantation for survival.[44] Treatments used for Wilson disease are described below.

Table 2 Agents for the treatment of Wilson disease

Agent	Mechanism of Action	Daily Adult Dosage
D-Penicillamine[a]	Reduction and chelation of copper. Urinary excretion of copper by mobilizing copper from organs	1–2 g orally in divided doses
Triethylenetetramine (Trientine)	Copper chelator and urinary excretion	0.75–1.5 g orally in divided doses
Zinc salts	Inhibits intestinal absorption of copper by induction of intestinal cell metallothionein; may also induce hepatic metallothionein	150–200 mg of elemental zinc orally in divided doses
British anti-Lewisite (BAL)[b]	Copper chelator	3 mL of 10% BAL in peanut oil IM
Tetrathiomolybdate[c]	Blocking the intestinal absorption of copper and a copper chelator	Up to 2 mg/kg orally in divided doses

[a] Administered with supplementation of 25 mg pyridoxine orally daily; [b] Rarely used. [c] Experimental.

a. BAL (2,3-Dimercaptopropanol)

It was the first agent used to treat Wilson disease as a decoppering agent.[45,46] It must be administered by intramuscular injection; its use was all but abandoned in favor of orally available chelating agents.

b. D-Penicillamine

D-Penicillamine was first introduced in the treatment of Wilson disease in 1956.[47,48] The usual recommended adult dose is 1 g/day. D-Penicillamine acts by reductive chelation.[49,50] It reduces copper bound to protein, which in turn causes the reduction of affinity of the protein for copper and allows D-penicillamine to bind the copper. The immediate and dramatic result of the administration of D-penicillamine is a marked increase in urinary copper excretion. Removal of copper from the liver remains incomplete and hepatic copper levels may remain elevated even after years of therapy.[49] The major problem with D-penicillamine is its high level of toxicity. Approximately 30% of patients are hypersensitive to the drug, which may cause its discontinuation. It has been shown that a significant number of patients with neurologic aspects of the disease may become worse after they are started with this drug.[51] Most of the long-term side effects involve either the immune system or connective tissues.[52] The deleterious effects on connective tissues are a direct result of reaction with D-penicillamine itself. This could also result from an interaction with the enzyme lysyl oxidase, which is a copper enzyme and is responsible for the cross-linking of collagen.

c. Trientine

Trientine (triethylenetetramine) was used in 1982 to treat Wilson disease as an alternative to D-penicillamine.[52] It is also a chelator of copper and increases urinary excretion of copper. There is less experience with the use of trientine compared to D-penicillamine. Its toxicity is relatively unexplored. The initial effect of this treatment is large cupriuresis but its rate diminishes more rapidly than with D-penicillamine. However, it should be pointed out that this treatment is effective especially in situations for which D-penicillamine must be stopped because of adverse side effects. Trientine appears to compete effectively for the copper bound to serum proteins but is not able to do so in the liver.[53]

d. Zinc

Zinc was known to produce copper deficiency in experimental animals. The first report of zinc treatment for Wilson disease was published in 1979.[54] Zinc causes induction of metallothionein in the intestinal cells, which binds copper with high affinity and holds it with high affinity until the intestinal cells are sloughed off. Thus, zinc inhibits absorption of copper from the intestine and increases the fecal excretion of copper. Zinc also blocks the reabsorption of endogenously secreted copper from saliva and gastric juice. A major advantage of zinc treatment is its low toxicity.

e. Tetrathiomolybdate

Molybdate is known to induce copper deficiency. It was found that the administration of molybdenum compounds, particularly with added sulfate, impaired copper metabolism in ruminants.[55] Tetrathiomolybdate has been used to treat patients who were intolerant to D-penicillamine, trientine, and zinc. Tetrathiomolybdate seems to act both by blocking the intestinal absorption of copper and keeping it in a metabolically inert chelated form, which is not taken up by the liver. However, it induces only a modest cupriuresis.[56] There are also known toxic effects of tetrathiomolybdate on the skeletal system of growing animals.[57] Thus one should be extremely careful in administering this compound. It should be considered as an experimental drug.

2.2 Menkes Disease

2.2.1 Clinical and Biochemical Features

Menkes disease is another genetic disorder of copper metabolism characterized by an impairment in the absorption of dietary copper and severe disturbance in the intracellular transport of copper.[58] The disease was first characterized by John Menkes and coworkers in 1962 during the course of study of five patients from the same family who died before the age of three.[59] In their original study, they noticed that the disease seemed to be confined to males and was inherited in a sex-linked recessive manner.

Menkes disease patients are unable to absorb copper and hence suffer from the effect of copper deficiency. The disease has a very early age of onset and affected children suffer from neurodegeneration and die before the age of three years. All patients gain very little weight following birth. Several gross abnormalities are noted with hair. They are coarse and brittle and either twisted or fractured at various intervals. This abnormality of hair in Menkes disease led to the disorder to be referred to as kinky hair syndrome.

The clinical features of the disease include hypothermia, arterial rupture, and bone changes. Patients are found to have extremely low levels of copper in the liver, brain, and serum as well as having very low ceruloplasmin levels. These all are due to the basic biochemical defect of severely reduced ability to absorb copper from the intestine and a disturbance in the intracellular transport of copper.[58,60]

The clinical symptoms of classical Menkes disease can be traced back to developmentally important copper enzymes such as lysyl oxidase, tyrosinase (*see* ***Copper: Hemocyanin/Tyrosinase Models***), cytochrome *c* oxidase (*see* ***Cytochrome Oxidase***), dopamine β-hydroxylase, superoxide dismutase, and amine oxidase (*see Superoxide Dismutase*).[6,61] Lysyl oxidase is needed for the cross-linking of connective tissue; a deficiency in this enzyme causes weakened connective tissue and connective tissue disorder such as arterial ruptures as observed in these patients.[6] Low levels of cytochrome c oxidase cause temperature instability and the absence of tyrosinase explains the hair depigmentation observed in affected individuals.[62]

2.2.2 Menkes Disease Gene

Early genetic work on Menkes disease had mapped the disease locus to band xq13.3.[63–65] Following this road map, the Menkes disease gene (*ATP7A*) was isolated and independently identified by three groups using positional cloning.[66–68] The gene contains 23 exons and spans a genomic region of approximately 150 kb.[69,70] The exons are in the 77 to 726 bp range with introns ranging from 196 bp to 60 kb. After the exon coding for the fifth metal-binding domain (exon five in *ATP7A* and exon 3 in *ATP7B*), the coding region for both the Wilson disease gene (*ATP7B*) and Menkes disease gene (*ATP7A*) are virtually identical.

In the Menkes disease gene, approximately 20% of the mutations are insertion/deletion mutation of varying sizes. In a study of 41 unrelated patients presenting the severe form of Menkes disease, 19 mutations were due to insertion or deletion.[71] The two largest of the deletions are 14 bp deletion in exon 10 and 10 bp deletion in exon 22. These deletions, as well as the others would be predicted to alter the reading frame of the gene, leading to the introduction of a stop codon and premature truncation of the protein. Alternatively, these mutations may lead to the skipping of subsequent mutation-bearing exons, which may result in an internally deleted protein that may still retain some function of the *ATP7A*.[72] Exon 8 codes for the region between metal-binding 6 and the first transmembrane segment of the protein. The exact role this region plays in the function of the ATPase remains unknown but it could play a role in the precise localization of the metal-binding domain relative to the ATPase core. The importance of this region of the protein is exemplified by the finding that individuals carrying mutations in exon 8 present the most severe form of Menkes disease.[71] In the Wilson disease protein, only two mutations have been found in the corresponding region.[26] These findings may indicate that these domains play somewhat different roles in the Wilson and Menkes ATPases, despite their high degree of sequence homology.

2.2.3 Menkes Disease Copper-transporting ATPase: ATP7A

The Menkes disease gene encodes a 1500 amino acid protein, which is predicted to be a copper-transporting P-type ATPase with a high degree of homology with the Wilson disease protein (Figure 4).[68] The overall identity between these two proteins is 57% and this rises to 79% and higher in the phosphatase, transduction-phosphorylation and ATP-binding domains.[14] Although these two proteins have a significant similarity, there are some significant differences, most notably a 78-amino acid insertion between metal-binding domains 1 and 2 in the Menkes protein, which is not the case in Wilson protein. The importance of this insertion is not yet known.

2.2.4 Structure and Function of Menkes Disease Protein

Copper-binding properties of the N-terminal metal-binding domain are similar to that in Wilson disease ATPase. This protein also binds copper in a 1:6 protein to copper ratio.[29]

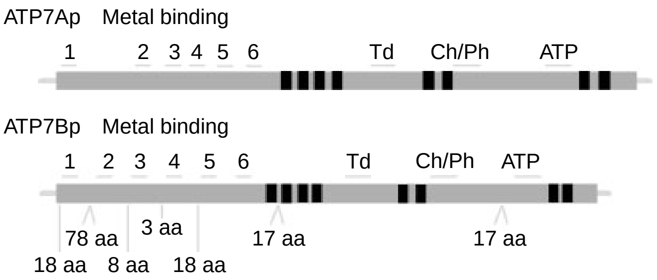

Figure 4 Comparison of Menkes (ATP7A) and Wilson (ATP7B) ATPases. ■ – Transmembrane segments, Td – Transduction, Ch – Channel, Ph – Phosphorylation, ATP – ATP binding, | – Insertion relative to ATP7A, Λ – Deletions relative to ATP7A

The geometry of the copper-binding site is digonal as seen in the case of Wilson protein.[73] Binding of Ag to the fourth domain of the metal-binding segment has been characterized by NMR studies.[74]

The mechanisms of catalysis and copper-dependent trafficking of the Menkes protein have been summarized in a recent review.[75] Biochemical studies indicated that mutation of six metal-binding sites did not abolish the catalytic activity of Menkes ATPase and hence it was considered that these motifs were not essential for copper translocation. However, the binding of copper to these sites increased the affinity of the protein for copper translocation, which would involve the interaction between the binding sites and the cytosolic ATP-binding domain of ATP7A. Much further work is necessary to delineate the mechanism of this process.

2.2.5 *Treatment of Menkes Disease*

Treatment of Menkes patients have concentrated on restoring normal copper levels in the body by administering copper. Since the intestinal absorption of copper is very low in Menkes patients, copper must be administered parenterally. Copper has been administered in various forms including copper chloride, copper sulfate, copper EDTA, and copper-albumin. But none of these copper compounds is able to produce significant clinical improvement, especially in regard to neurodegeneration.[76] The only currently available treatment for Menkes patients is subcutaneous injections of copper-histidine. This complex was originally discovered in human blood and was shown to transport copper across the cell membrane.[1] The structure of copper-histidine has recently been solved by X-ray crystallography.[77] Patients treated with copper-histidine soon after birth have shown significant clinical and biochemical improvements and can achieve normal levels of ceruloplasmin, dopamine β-hydroxylase, norepinephrine, and serum copper.[78–81] A long-term clinical follow-up of copper-histidine treated patients over 10–20 years has been reported (Table 3).[82] Despite the favorable effects on the neurologic symptoms, the residual abnormalities such as connective tissue abnormality can become more severe later in life. Therefore, this treatment should still be regarded as experimental.

3 IRON-RELATED DISEASES

3.1 Hereditary Hemochromatosis

3.1.1 *Clinical and Biochemical Features*

Hereditary hemochromatosis is a disorder of iron metabolism in which the uptake of iron from the digestive

Table 3 Summary of clinical and biochemical features in the menkes disease patients treated with copper-histidine[82]

	1 (MF)	2 (TL)	3 (RH)	4 (GV)
Affected relative	Brother	Maternal uncle	None	maternal half-brother
Gestation at delivery	37 weeks	40 weeks	35 weeks	35 weeks (induced)
Pretreatment features	Facies, hypothermia	None	Hypothermia, failure to thrive, facies bone changes, vascular abnormalities, abnormal hair	
		Treatment		
Cu-his started	3 months	18 months	4 weeks	2 days
Plasma copper levels on Treatment (μmol L^{-1})	4–10.5	10–20	10–20	10–25
Liver copper	NE	Decreased	NE	Normal
		Outcome		
Age (years)	20	17	Died 10.25	10
School performance	Age-appropriate	4 years behind	Age-appropriate	1 year behind
Neurologic deficits	Nil	Ataxia, apraxia (cerebellar vermis hypoplasia)	Nil	Nil
Occipital horns	+	−	−	+
Other skeletal Abnormalities	++	Nil	+	++
Bladder diverticulae	−	−	++	+
Abnormal hair	+	Initially present, now normal	No	++
Postural hypotension	+++	+	++	++
Chronic diarrhea	++	−	++	++

Abbreviations: NE, not estimated; Cu-his, copper-histidine.

system is not downregulated, resulting in excessive iron uptake. The body continues to absorb high levels of dietary iron regardless of the levels of stored iron in the body (*see* ***Iron Proteins for Storage & Transport & their Synthetic Analogs***). Excess iron is slowly deposited in the liver as hemosiderin with a simultaneous increase in plasma iron and saturation of plasma transferrin.[83] Tissue damage becomes evident when the iron store reaches 20 to 50 times normal values. Hence, the age of onset of the disease is late between 40 and 60 years. However, neonatal hemochromatosis and juvenile hemochromatosis have also been described;[84] these are not the same as hereditary hemochromatosis pathophysiologically. Hereditary hemochromatosis seems to be more prevalent in males than in females owing to differences in the rate of iron absorption and loss.[83]

The classic clinical and pathological findings include weakness and lethargy, abdominal pain, diabetes mellitus, amenorrhea, dyspnea, and various neurologic symptoms. The onset of the clinical symptoms of the disease is greatly affected by both genetic and environmental factors. Patients demonstrate asymptomatic elevation of serum alanine aminotransferase and aspartate aminotransferase. Iron is stored in the liver, thyroid, and heart in the form of hemosiderin. An early diagnostic test is to monitor the level of iron and transferrin (*see* ***Iron Proteins for Storage & Transport & their Synthetic Analogs***) saturation in plasma. Measurement of transferrin saturation in the 70% range is usually diagnostic with typical hereditary hemochromatosis patients having values in the 90% range.

Iron being a redox-active metal, it most likely exerts its toxic effects through the generation of hydroxyl radical or by generation of ferryl ion.[85–87] In iron loaded condition, there is generation of radical species leading to lipid peroxidation. Lipid peroxidation of cellular membrane would have deleterious effects on their function and hence on the function of the cell. There is also irreversible oxidation of ascorbic acid. Deficiency of ascorbic acid can lead to a reduction in the amount of iron available for erythropoiesis.

3.1.2 Genetic Aspects of Hemochromatosis

Hereditary hemochromatosis is an autosomal recessive disorder of iron metabolism. The frequency of the homozygous genotype is 1 out of 250 persons, with 1 in 9 being a carrier.[88,89] The disease is most common in European descent and it is the most common genetic disorder in Caucasians known in the United States. Early studies indicated that the gene responsible for hereditary hemochromatosis was linked to the human leukocyte antigen. In 1996, the gene was identified near the major histocompatibility complex (MHC) on chromosome 6, which contained a mutation present in 83% of individual homozygous for hereditary hemochromatosis.[90] The gene, termed HFE, encodes a 343-amino acid protein, which is very similar to MHC class 1 molecules.

3.1.3 HFE protein

Although concrete evidence as to the exact function of the HFE protein is as yet unavailable, many interesting theories have been proposed. A proposed model for the HFE protein is shown in Figure 5.[90] β_2-microglobulin is a protein that is usually found complexed to MHC class 1 proteins on the surface of most cells. If β_2-microglobulin is absent, the complex is destabilized and cell-surface quantities of HLAs are reduced. The Cys 282 Tyr mutation common in hemochromatosis patients is very close to the expected site of β_2-microglobulin binding and would be expected to diminish this interaction. Immunohistochemical studies have localized the HFE protein to various portions of the gastrointestinal tract. These findings correlate well with observation that primary site of iron absorption is affected.[91,92] Based on these observations, it has been proposed that HFE protein is involved in the downregulation of the iron absorption process. There are three proposals regarding the possible role of HFE protein. First, the HFE protein may act as a 'sensor' of body iron concentration by some form of iron chelate. This would in turn tell the enterocyte that iron stores are high and that iron uptake should be downregulated. Secondly, the HFE protein would act as part of a signal transduction pathways, as has been demonstrated in the epidermal growth factor (EGF) receptor systems.[90] Third, it has been suggested that HFE may interact with members of the immune system and indirectly affect iron metabolism. Much further work is necessary to know the exact function of this protein.

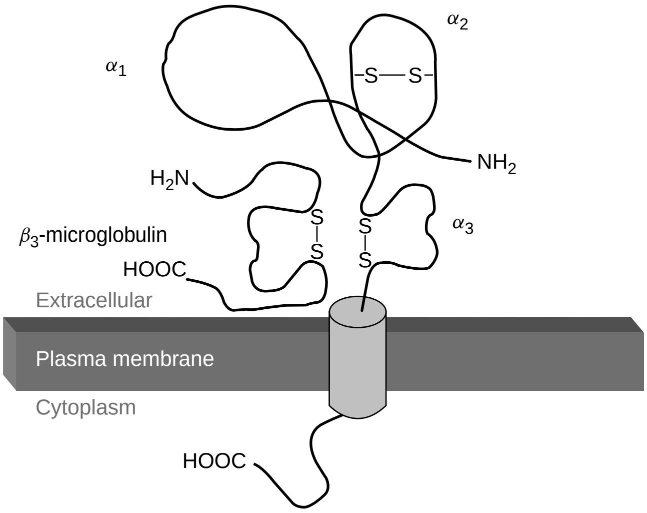

Figure 5 Proposed model for the HFE protein. The model was constructed by homology to other MHC class 1 proteins. The protein has three extracellular domains, which are homologous to the α_1, α_2, and α_3 domains of other MHC class 1 proteins. The protein also has a site for noncovalent interaction with β_2 microglobulin, which is a separate protein. In addition, the protein has a single transmembrane segment and a short cytoplasmic tail

3.1.4 *Treatment for Hereditary Hemochromatosis*

Once diagnosed hereditary hemochromatosis can be treated by weekly venesection of approximately 0.5 L of blood. The amount of iron removed in this way is usually around 250 mg per 0.5 L of blood.[93] The intensive therapy lasts for 2–3 years depending on the iron present. A recent study reported patient compliance with this form of treatment.[93] Another treatment option is chelation therapy by deferoxamine but this is an expensive treatment and the iron removal is slower; its main use is with non-HFE hemochromatosis.

3.2 Thalassemia

3.2.1 *Clinical and Biochemical Features*

Thalassemias are technically not disorders of iron metabolism or iron transport but the severe iron overload is usually the major complication of the disease. The most clinically important forms of thalassemia are α and β-thalassemia caused by the decreased or absent production of one or more globin proteins (*see* ***Iron: Heme Proteins & Dioxygen Transport & Storage***) and those where some chains are synthesized but at greatly reduced rate. Patients with the severe form of the disease suffer from iron overload as a side effect of regular blood transfusion to treat the disorder. The β-globin production in homozygous forms of β-thalassemia is either nonexistent or very low, leading to an excess of α-globin chains in red-cell precursors. Since the α-globins are not able to form a viable tetramer, they precipitate and form inclusion bodies, which leads to the destruction of red-cell precursor and subsequent ineffective erythropoiesis. The end result is hemolysis and general state of anemia and tissue hypoxia. The hypoxic condition stimulates the release of erythropoietin, which, in turn, leads to the increased absorption of intestinal iron and expansion of the bone marrow. Iron loading is further compounded by the fact that blood transfusion is needed to relieve anemia. It causes decrease of intestinal iron but the additional input of iron through transfusion continues to accumulate.

The continued absorption of iron causes its deposition in various tissues starting with liver and spleen and followed by myocardium. Deposition of iron in the myocardium usually results in death by intractable cardiac failure.[94] Patients suffer from hypoparathyroidism and hypogonadism. Patients with the severe form of thalassemia are more susceptible to bacterial infection, possibly due to the increase in serum iron, which may favor bacterial growth. Iron overload is less common in the adult forms of α-thalassemia. This is most likely the result of a fundamental difference between α and β-thalassemia. As mentioned, the excess of α-globin chains cannot form viable tetramers and causes red-cell destruction. The excess β-chains present in α-thalassemia are able to form soluble homodimers and do not precipitate in the bone marrow. This is paralleled in the fetal state when excess γ-chains form soluble homodimers. Hence, α-thalassemia is characterized by a severe degree of inefficient erythropoiesis and a milder degree of anemia.

3.2.2 *Genetic Aspects of Thalassemia*

The underlying cause of the disease is a disturbance in the synthesis of one or more of the globin chains of hemoglobin. There are several different types of hemoglobins, all of which are tetrameric, containing two pairs of different polypeptide chains, and are developmentally regulated. The structure of human hemoglobin shows that each α-chain makes contact with two β-chains creating an α, β and $\alpha_2\beta_2$ interface.[95,96] The six globin genes are divided into two clusters found on two different chromosomes. The α-like gene cluster is located on chromosome 16 while the β-like gene cluster resides on chromosome 11. However, no protein product has yet been isolated and its function remains unknown. Rearrangements within the α and β gene clusters are fairly common and in most cases have no associated clinical condition.

3.2.3 *Treatment of Thalassemia*

The treatment of thalassemia, as in other metal overload disorder, is chelation therapy. The chelating agent most widely used is deferoxamine administered subcutaneously. The search for an orally administered iron chelator has intensified in recent years, leading to clinical trials of many potential new iron chelators such as deferiprone(L1). However, many issues regarding the use of these drugs, such as dose-related toxicity and recommended age of initiation, remain unresolved.[97–101]

3.3 Aceruloplasminemia

3.3.1 *Clinical and Biochemical Features*

In aceruloplasminemia, iron accumulates in various tissues including liver, brain, and in the islets of Langerhans, which causes loss of pancreatic β-cells. There is an increase in iron level in the basal ganglia. Iron also deposits in the microglia and neurons.[102] These findings are consistent with biochemical studies, which suggested direct involvement of ceruloplasmin in the iron metabolism pathway. The ferroxidase activity of ceruloplasmin has been proposed since the 1960s.[103–105] The clinical features of aceruloplasminemia includes neurologic disease, diabetes mellitus, and retinal degeneration.[106] The age of onset of neurologic disorders varies from 38 to 65 years. Patients show involuntary movements such as ataxic gait or slurred speech initially. Patients also develop mental disturbances and intellectual impairment. Once the disease is full-blown, various degrees of neurologic symptoms are observed. All these observations suggest that ceruloplasmin is playing a critical role in the metabolism of iron in brain implying that ceruloplasmin is unable to cross the blood-brain barrier. Thus, the ceruloplasmin gene must occur in the brain. Under normal conditions, iron in the brain is oxidized by astrocyte-secreted ceruloplasmin, followed by incorporating into transferrin, which is synthesized in oligodendrocytes.[102]

Without ceruloplasmin activity the ferrous iron is taken up by brain cells leading to iron overload and cell death. A similar situation occurs in peripheral tissues. This is supported by studies indicating a significant increase in plasma lipid peroxidation in patients with aceruloplasminemia.[107]

3.3.2 Ceruloplasmin Gene

The ceruloplasmin gene is located on chromosome 3, spanning approximately 36 kb and consisting of 19 exons.[108] Mutations in this gene lead to aceruloplasminemia demonstrating progressive neurodegeneration of the retinal and basal ganglia.[102] The disorder is inherited in an autosomal recessive manner. Most of the mutations in this gene result in a shift in the reading frame, such that the amino acid residues at the carboxy terminus essential for the trinuclear copper cluster responsible for oxidase activity are eliminated. This is consistent with the observation of little or no oxidase activity in the plasma of affected individuals. Gene mutations found are heterogeneous in patients with the same ethnic background, though mutation has been shown to be shared by two unrelated Japanese families.[108] All mutations are predicted to produce truncated ceruloplasmin by premature termination in translation.[109]

3.3.3 Ceruloplasmin

Ceruloplasmin is a secreted blue copper protein, which carries 95% of the circulating copper in the body.[110] Copper in ceruloplasmin is not exchangeable. The crystal structure shows that the holoprotein contains six copper atoms, three of which are in a trinuclear copper cluster.[111] The protein is synthesized in the hepatocytes and copper incorporation takes place in the secretory pathway most likely in the Golgi or rough endoplasmic reticulum with N-glycosylation not being required for copper incorporation.[112] The synthesis and secretion of the protein is not dependent on copper incorporation, but apoceruloplasmin lacking oxidase activity is unstable and is rapidly degraded once secreted.[113] Analysis of copper incorporation into apoceruloplasmin in vitro reveals that this process is cooperative and that the failure of copper incorporation into copper-binding site is intrinsic to the mutant proteins.[114] The trinuclear copper cluster is responsible for activating oxygen during the catalytic cycle of the protein. The ligands for the trinuclear cluster originate from both the amino and carboxy termini of the protein. Ceruloplasmin plays a key role in the mobilization and oxidation of iron stores and their incorporation into transferrin.

Human ceruloplasmin is composed of a single polypeptide chain of 1046 amino acid residues.[115] The protein shows a threefold internal homology of amino acid sequence and each homology unit contains 340–350 amino acids. From these data, it is suggested that ceruloplasmin is an evolutionary product of a tandem triplication of ancestral gene.

3.3.4 Treatment

Currently there is no effective treatment for aceruloplasminemia. It is interesting that Wilson disease patients rarely show the symptoms of aceruloplasminemia despite very low levels of ceruloplasmin. It appears that extrahepatic production of ceruloplasmin is enough to carry out iron metabolism. Treatment of aceruloplasminemia involves chelating agent to mobilize and remove iron from various tissues. D-penicillamine therapy was initiated but no clinical effect was demonstrated.[116] Deferoxamine has been used to treat this condition.[117] This chelator has been shown earlier to cross the blood-brain barrier. Initial trials using deferoxamine to treat aceruloplasminemia patients have shown a decrease in neurologic symptoms. But further studies are necessary to provide the basis for treating individuals suffering from aceruloplasminemia.

4 ZINC-RELATED DISEASE

4.1 Acrodermatitis Enteropathica

4.1.1 Clinical and Biochemical Features

Acrodermatitis enteropathica is a rare autosomal recessive disease.[118] It was demonstrated that the disorder was caused by the inability to absorb sufficient zinc.[119] This disease is not present at birth but usually develops in the early months of life soon after weaning from breastfeeding. It causes classic symptoms of zinc deficiency, such as dermatological lesions, changes in the gastric mucosa, associated digestive system problems, lack of weight gain, and immune, and reproductive problems. Neuropsychiatric signs include irritability, emotional disorders, tremors, and occasional cerebellar ataxia.

4.1.2 Genetic Aspects

The linkage analysis revealed that the acrodermatitis enteropathica gene is located on chromosome 8q24.3 and the SLC39A4 gene has been found to be the cause for this disorder.[120–123] The SLC39A4 gene encodes one member of a human zinc–iron regulated transporter-like protein (hZIP) family, hZIP4. The gene consists of a total of 12 exons. Mutations in hZIP4 were found in patients, which strongly suggested that the disorder is caused by a defect in this gene.

4.1.3 Protein Encoded by the Gene

The gene encodes a polypeptide of 647 amino acids, having eight transmembrane domains organized in two blocks of three and five. A histidine-rich region, which is considered to be the zinc-binding site, resides between the two blocks of transmembrane domains.[121,122,124] This gene is expressed abundantly in the small intestine, stomach, colon, and kidney. The presumed zinc-uptake protein is localized in the apical membrane of the enterocyte.

Little is known, however, about the function of hZIP4, although three other members of the ZIP family (hZIP1, hZIP2, and hZIP3) have been shown to transport zinc into the cytoplasm.[125,126]

4.1.4 Treatment

The symptoms of the disease can be ameliorated by dietary zinc supplementation. The differential diagnosis of the disease includes acquired zinc deficiency condition owing to low-zinc level in mother's milk because both conditions are very similar in terms of onset and clinical features. As soon as the low-zinc breastfed infants are weaned, they no longer require supplemental zinc, but acrodermatitis enteropathica patients experience recurrence of symptoms if they discontinue oral zinc therapy.

5 OTHER RARE GENETIC DISORDERS OF METAL METABOLISM

There are several less common genetic disorders of metal metabolism.[127] Occipital Horn Syndrome is a mild allelic form of Menkes disease causing skeletal dysplasia but with little neurologic impairment except developmental delay. The genetic basis is mutation in *ATP7A*. Serum copper, ceruloplasmin, and lysyl oxidase activity in this disease are low. TFR2-deficiency is a rare form of hemochromatosis caused by mutations in transferrin receptor-2 gene, which maps to chromosome 7q22. Clinical features are related to mutations in HFE.[128] Ferroportin deficiency is related to hereditary hemochromatosis not related to the HFE locus. Ferroportin is the main iron export pump in macrophages and hepatocytes. Mutations are found in the gene *SLC11A3* in chromosome 2q32.[129] Tricho-hepatic-enteric syndrome is a combination of hair abnormality, hepatic dysfunction with iron overload, and diarrhea. This disorder may be related to perinatal hemochromatosis but the basis of the disease is unknown. GRACILE Syndrome (Fellman Syndrome) is caused by mutations in *BCS1L* gene, which encodes a protein in the mitochondrial inner membrane required for assembly of complex III in the mitochondrial respiratory chain.[130] Accumulation of iron in this disorder may be a secondary feature. Iron accumulation becomes less severe as the affected child gets older. There is no effective treatment for this condition. Congenital cholestasis with hepatic zinc accumulation is an extremely rare disease. The pathogenesis of this zinc overload liver disease is not yet determined.

6 RELATED ARTICLES

Metal-based Drugs; Metal-based Imaging Agents.

7 REFERENCES

1. B. Sarkar, *Chem. Rev.*, 1999, **99**, 2535.
2. M. Frydman, *J. Gastroenterol. Hepatol.*, 1990, **5**, 483.
3. P. E. Hunziker and I. Sternlieb, *Eur. J. Clin. Invest.*, 1991, **21**, 466.
4. W. B. Dobyns, N. P. Goldstein, and H. Gordon, *Mayo Clin. Proc.*, 1979, **54**, 35.
5. I. H. Scheinberg and I. Sternlieb, 'Wilson's Disease', Saunders, Philadelphia, 1984.
6. D. M. Danks, in 'Metabolic Basis of Inherited Disease', McGraw Hill, New York, 1995, p. 2211.
7. C. D. Vulpe and S. Packman, *Annu. Rev. Nutr.*, 1995, **15**, 293.
8. A. P. Mowat, 'Liver Disorders in Childhood', 3rd edn., Butterworth-Heinemann, Cambridge, MA, 1994.
9. J. M. Walshe, *Lancet*, 1989, **2**, 228.
10. M. Frydman, B. Bonne-Tamir, L. A. Farrer, P. M. Conneally, A. Magazanik, S. Ashbel, and Z. Goldwitch, *Proc. Natl. Acad. Sci. U.S.A.*, 1985, **82**, 1819.
11. A. M. Bowcock, L. A. Farrer, L. L. Cavalli-Sforza, J. M. Hebert, K. K. Kidd, M. Frydman, and B. Bonne-Tamir, *Am. J. Hum. Genet.*, 1987, **41**, 27.
12. A. M. Bowcock, L. A. Farrer, J. M. Hebert, M. Agger, I. Sternlieb, I. H. Scheinberg, C. H. Buys, H. Scheffer, M. Frydman, T. Chajek-Saul, B. Bonne-Tamir, and L. L. Cavalli-Sforza, *Am. J. Hum. Genet.*, 1988, **43**, 664.
13. V. Yuzbasiyan-Gurkan, G. J. Brewer, E. Boerwinkle, and P. J. Venta, *Am. J. Hum. Genet.*, 1988, **42**, 825.
14. P. C. Bull, G. R. Thomas, J. M. Rommens, J. R. Forbes, and D. W. Cox, *Nat. Genet.*, 1993, **5**, 327.
15. R. E. Tanzi, K. Petrukhin, I. Chernov, J. L. Pellequer, W. Wasco, B. Ross, D. M. Romano, E. Parano, L. Pavone, L. M. Brzustowicz, M. Devoto, J. Peppercorn, A. I. Bush, I. Sternlieb, M. Piratsu, J. F. Gusella, O. Evgrafov, G. K. Penchaszadeh, B. Honig, I. S. Edelman, M. B. Soares, I. H. Scheinberg, and T. C. Gilliam, *Nat. Genet.*, 1993, **5**, 344.
16. K. Petrukhin and T. C. Gilliam, *Curr. Opin. Pediatr.*, 1994, **6**, 698.
17. D. W. Cox, *Am. J. Hum. Genet.*, 1995, **56**, 828.
18. G. R. Thomas, J. R. Forbes, E. A. Roberts, J. M. Walshe, and D. W. Cox, *Nat. Genet.*, 1995, **9**, 210.
19. A. B. Shah, I. Chernov, H. T. Zhang, B. M. Ross, K. Das, S. Lutsenko, E. Parano, L. Pavone, O. Evgrafov, I. A. surIvanova-Smolenskaya, G. Anneren, K. Westermark,

F. H. Urrutia, G. K. Penchaszadeh, I. Sternlieb, I. H. Scheinberg, T. C. Gilliam, and K. Petrukhin, *Am. J. Hum. Genet.*, 1997, **61**, 317.

20. N. Shimizu, C. Kawase, H. Nakazono, H. Hemmi, H. Shimatake, and T. Aoki, *Biochem. Biophys. Res. Commun.*, 1995, **217**, 16.
21. L. M. Chuang, H. P. Wu, M. H. Jang, T. R. Wang, W. C. Sue, B. J. Lin, D. W. Cox, and T. Y. Tai, *J. Med. Genet.*, 1996, **33**, 521.
22. G. Loudianos, V. Dessi, A. Angius, M. Lovicu, A. Loi, M. Deiana, N. Akar, P. Vajro, A. Figus, A. Cao, and M. Pirastu, *Hum. Genet.*, 1996, **98**, 640.
23. M. S. Nanji, V. T. Nguyen, J. H. Kawasoe, K. Inui, F. Endo, T. Nakajima, T. Anezaki, and D. W. Cox, *Am. J. Hum. Genet.*, 1997, **60**, 1423.
24. A. Odermatt, H. Suter, R. Krapf, and M. Solioz, *J. Biol. Chem.*, 1993, **268**, 12775.
25. K. Petrukhin, S. G. Fischer, M. Pirastu, R. E. Tanzi, I. Chernov, M. Devoto, L. M. Brzustowicz, E. Cayanis, E. Vitale, J. J. Russo, D. Matseoane, B. Boukhgalter, W. Wasco, A. L. Figus, J. Loutianos, A. Cao, I. Sternlieb, O. Evgrafov, E. Parano, L. Pavone, D. Warburton, J. Ott, G. K. Penchaszadeh, I. H. Scheinberg, and T. C. Gilliam, *Nat. Genet.*, 1993, **5**, 338.
26. A. Figus, A. Angius, G. Loudianos, C. Bertini, V. Dessi, A. Loi, M. Deiana, M. Lovicu, N. Olla, G Sole, S. D. Virgiliss, F. Lilliu, A. M. G. Farci, A. Nurchi, R. Giacchino, A. Barabino, M. Marazzi, L. Zancan, N. A. Greggio, M. Marcellini, A. Solinas, A. Deplano, C. Barbera, M. Devoto, S. Ozsoylu, N. Kocak, N. Akar, S. Karayalcin, V. Mokini, P. Cullufi, A. Balestrieri, A. Cao, and M. Pirastu, *Am. J. Hum. Genet.*, 1995, **57**, 1318.
27. B. Sarkar, *J. Inorg. Biochem.*, 2000, **79**, 187.
28. M. DiDonato, S. Narindrasorasak, J. R. Forbes, D. W. Cox, and B. Sarkar, *J. Biol. Chem.*, 1997, **272**, 33279.
29. S. Lutsenko, K. Petrukhin, M. J. Cooper, C. T. Gilliam, and J. H. Kaplan, *J. Biol. Chem.*, 1997, **272**, 18939.
30. P. Y. Jensen, N. Bonander, L. B. Moller, and O. Farver, *Biochim. Biophys. Acta*, 1999, **1434**, 103.
31. M. DiDonato, H. F. Hsu, S. Narindrasorasak, L. Que Jr, and B. Sarkar, *Biochemistry*, 2000, **39**, 1890.
32. M. DiDonato, J. Zhang, L. Que Jr, and B. Sarkar, *J. Biol. Chem.*, 2002, **277**, 13409.
33. N. Fatemi and B. Sarkar, *Inorg. Chim. Acta*, 2002, **339**, 179.
34. N. Fatemi and B. Sarkar, *Environ. Health Perspect.*, 2002, **110**,(Suppl. 5), 695.
35. J. R. Forbes, G. Hsi, and D. W. Cox, *J. Biol. Chem.*, 1999, **274**, 12408.
36. R. Tsivkovskii, J. F. Eisses, J. H. Kaplan, and S. Lutsenko, *J. Biol. Chem.*, 2001, **24**, 24.
37. D. Larin, C. Mekios, K. Das, B. Ross, A. S. Yang, and T. C. Gilliam, *J. Biol. Chem.*, 1999, **274**, 28497.
38. I. Hamza, M. Schaefer, L. W. Klomp, and J. D. Gitlin, *Proc. Natl. Acad. Sci. U.S.A.*, 1999, **96**, 13363.
39. D. L. Huffman and T. V. O'Halloran, *Annu. Rev. Biochem.*, 2001, **70**, 677.
40. R. Tsivkovskii, B. C. MacArthur, and S. Lutsenko, *J. Biol. Chem.*, 2001, **276**, 2234.
41. K. D. Bissig, H. Wunderli-Ye, P. W. Duda, and M. Solioz, *Biochem. J.*, 2001, **357**, 217.
42. J. R. Forbes and D. W. Cox, *Am. J. Hum. Genet.*, 1998, **63**, 1663.
43. I. Voskoboinik, J. Mar, D. Strausak, and J. Camakaris, *J. Biol. Chem.*, 2001, **276**, 28620.
44. E. A. Roberts and M. L. Schilsky, *Hepatology*, 2003, **37**, 1475.
45. J. N. Cummings, *Brain*, 1951, **74**, 10.
46. D. Denny-Brown and H. Porter, *N. C. Med. J.*, 1951, **245**, 917.
47. J. M. Walshe, *Am. J. Med.*, 1956, **21**, 487.
48. J. Peisach and W. E. Blumberg, *Mol. Pharmacol.*, 1969, **5**, 200.
49. I. H. Scheinberg, M. E. Jaffe, and I. Sternlieb, *N. Engl. J. Med.*, 1987, **317**, 209.
50. I. H. Scheinberg, I. Sternlieb, M. Schilsky, and R. J. Stockert, *Lancet*, 1987, **2**, 95.
51. G. J. Brewer, V. Yuzbasiyan-Gurkan, and A. B. Young, *Semin. Neurol.*, 1987, **7**, 209.
52. J. M. Walshe, *Lancet*, 1982, **1**, 643.
53. B. Sarkar, A. Sass-Kortsak, R. Clarke, S. H. Laurie, and P. Wei, *Proc. R. Soc. Med.*, 1977, **70**,(Suppl. 3), 13.
54. T. U. Hoogenraad, R. Koevoet, and E. G. de Ruyter Korver, *Eur. Neurol.*, 1979, **18**, 205.
55. J. Mason, *Ir. Vet. J.*, 1982, **36**, 164.
56. J. M. Walshe, *Q. J. Med.*, 1986, **58**, 81.
57. J. A. Spence, N. F. Suttle, G. Wenham, T. El-Gallad, and I. Bremner, *J. Comp. Pathol.*, 1980, **90**, 139.
58. D. M. Danks, E. Cartwright, B. J. Stevens, and R. R. Townley, *Science*, 1973, **179**, 1140.
59. J. H. Menkes, M. Alter, G. K. Steigleder, D. R. Weakley, and J. H. Sung, *Pediatrics*, 1962, **29**, 764.
60. S. M. Herd, J. Camakaris, R. Christofferson, P. Wookey, and D. M. Danks, *Biochem. J.*, 1987, **247**, 341.
61. M. DiDonato, S. Narindrasorasak, and B. Sarkar, 'Copper Transport and its Disorders: Molecular and Cellular Aspects', Plenum Publishing, New York, 1999.
62. A. Bankier, *J. Med. Genet.*, 1995, **32**, 213.
63. V. Verga, B. K. Hall, S. R. Wang, S. Johnson, J. V. Higgins, and T. W. Glover, *Am. J. Hum. Genet.*, 1991, **48**, 1133.
64. Z. Tümer, J. Chelly, N. Tommerup, Y. Ishikawa-Brush, T. Tonnesen, A. P. Monaco, and N. Horn, *Hum. Mol. Genet.*, 1992, **1**, 483.
65. Z. Tümer, N. Tommerup, T. Tonnesen, J. Kreuder, I. W. Craig, and N. Horn, *Hum. Genet.*, 1992, **88**, 668.

66. J. Chelly, Z. Tumer, T. Tonnesen, A. Petterson, Y. Ishikawa-Brush, N. Tommerup, N. Horn, and A. P. Monaco, *Nat. Genet.*, 1993, **3**, 14.

67. J. F. Mercer, J. Livingston, B. Hall, J. A. Paynter, C. Begy, S. Chandrasekharappa, P. Lockhart, A. Grimes, M. Bhave, D. Siemieniak, and T. W. Glover, *Nat. Genet.*, 1993, **3**, 20.

68. C. Vulpe, B. Levinson, S. Whitney, S. Packman, and J. Gitschier, *Nat. Genet.*, 1993, **3**, 7.

69. H. A. Dierick, L. Ambrosini, J. Spencer, T. W. Glover, and J. F. Mercer, *Genomics*, 1995, **28**, 462.

70. Z. Tümer, B. Vural, T. Tonnesen, J. Chelly, A. P. Monaco, and N. Horn, *Genomics*, 1995, **26**, 437.

71. Z. Tümer and N. Horn, *J. Med. Genet.*, 1997, **34**, 265.

72. S. Das, B. Levinson, S. Whitney, C. Vulpe, S. Packman, and J. Gitschier, *Am. J. Hum. Genet.*, 1994, **55**, 883.

73. M. Ralle, M. J. Cooper, S. Lutsenko, and N. J. Blackburn, *J. Am. Chem. Soc.*, 1998, **120**, 13525.

74. J. Gitschier, B. Moffat, D. Reilly, W. I. Wood, and W. J. Fairbrother, *Nat. Struct. Biol.*, 1998, **5**, 47.

75. I. Voskoboinik, J. Camakaris, and J. F. Mercer, *Adv. Protein Chem.*, 2002, **60**, 123.

76. A. D. Garnica, *Eur. J. Pediatr.*, 1984, **142**, 98.

77. P. Deschamps, P. P. Kulkarni and B. Sarkar, *Inorg Chem.*, 2004, **43**, 3338.

78. G. Sherwood, B. Sarkar, and A. S. Sass-Kortsak, *J. Inherit. Metab. Dis.*, 1989, **12**, 393.

79. J. Kreuder, A. Otten, H. Fuder, Z. Tumer, T. Tonnesen, N. Horn, and D. Dralle, *Eur. J. Pediatr.*, 1993, **152**, 828.

80. B. Sarkar, K. Lingertat-Walsh, and J. T. Clarke, *J. Pediatr.*, 1993, **123**, 828.

81. Z. Tümer, N. Horn, T. Tonnesen, J. Christodoulou, J. T. Clarke, and B. Sarkar, *Nat. Genet.*, 1996, **12**, 11.

82. J. Christodoulou, D. M. Danks, B. Sarkar, K. E. Baerlocher, R. Casey, N. Horn, Z. Tumer, and J. T. Clarke, *Am. J. Med. Genet.*, 1998, **76**, 154.

83. T. H. Bothwell, R. W. Charlton, and A. G. Motulsky, ‘Metabolic Basis of Inherited Disease’, McGraw-Hill, New York, 1995, p. 2237.

84. G. J. Escobar, M. B. Heyman, W. B. Smith, and M. M. Thaler, *Pediatrics*, 1987, **80**, 549.

85. B. R. Bacon and R. S. Britton, *Hepatology*, 1990, **11**, 127.

86. R. J. Ward, A. L. Florence, D. Baldwin, C. Abiaka, F. Roland, M. H. Ramsey, D. P. Dickson, T. J. Peters, and R. R. Crichton, *Eur. J. Biochem.*, 1991, **202**, 405.

87. J. M. Gutteridge, *Acta Paediatr. Scand. Suppl.*, 1989, **361**, 78.

88. C. E. McLaren, V. R. Gordeuk, A. C. Looker, V. Hasselblad, C. Q. Edwards, L. M. Griffen, J. P. Kushner, and G. M. Brittenham, *Blood*, 1995, **86**, 2021.

89. D. L. Witte, W. H. Crosby, C. Q. Edwards, V. F. Fairbanks, and F. A. Mitros, *Clin. Chim. Acta*, 1996, **245**, 139.

90. J. N. Feder, A. Gnirke, W. Thomas, Z. Tsuchihashi, D. A. Ruddy, A. Basava, F. Dormishian, R. Domingo Jr, M. C. Ellis, A. Fullan, L. M. Hinton, N. L. Jones, B. E. Kimmel, G. S. Kronmal, P. Lauer, V. K. Lee, D. B. Loeb, F. A. Mapa, E. McClelland, N. C. Meyer, G. A. Mintier, N. Moeller, T. Moore, E. Morikang, C. E. Prass, L. Quintana, S. M. Starnes, R. C. Schatzman, K. J. Brunke, D. T. Drayna, N. J. Risch, B. R. Bacon, and R. K. Wolff, *Nat. Genet.*, 1996, **13**, 399.

91. B. R. Bacon, *Gastroenterology*, 1997, **113**, 995.

92. S. Parkkila, A. Waheed, R. S. Britton, J. N. Feder, Z. Tsuchihashi, R. C. Schatzman, B. R. Bacon, and W. S. Sly, *Proc. Natl. Acad. Sci. U.S.A.*, 1997, **94**, 2534.

93. B. L. Hicken, D. C. Tucker, and J. C. Barton, *Am. J. Gastroenterol.*, 2003, **98**, 2072.

94. D. Weatherall, J. B. Clegg, D. R. Higgs, and W. G. Wood, ‘Metabolic Basis of Inherited Disease’, McGraw Hill, New York, 1995, p. 3417.

95. J. M. Baldwin, *J. Mol. Biol.*, 1980, **136**, 103.

96. G. Fermi, M. F. Perutz, B. Shaanan, and R. Fourme, *J. Mol. Biol.*, 1984, **175**, 159.

97. N. F. Olivieri, G. M. Brittenham, C. E. McLaren, D. M. Templeton, R. G. Cameron, R. A. McClelland, A. D. Burt, and K. A. Fleming, *N. Engl. J. Med.*, 1998, **339**, 417.

98. I. R. Wanless, G. Sweeney, A. P. Dhillon, M. Guido, A. Piga, R. Galanello, M. R. Gamberini, E. Schwartz, and A. R. Cohen, *Blood*, 2002, **100**, 1566.

99. A. Piga, C. Gaglioti, E. Fogliacco, and F. Tricta, *Haematologica*, 2003, **88**, 489.

100. T. F. Tam, R. Leung-Toung, W. Li, Y. Wang, K. Karimian, and M. Spino, *Curr. Med. Chem.*, 2003, **10**, 983.

101. C. Wong and D. R. Richardson, *Int. J. Biochem. Cell Biol.*, 2003, **35**, 1144.

102. E. D. Harris, Y. Qian, and M. C. Reddy, *Mol. Cell. Biochem.*, 1998, **188**, 57.

103. S. Osaki, D. A. Johnson, and E. Frieden, *J. Biol. Chem.*, 1966, **241**, 2746.

104. G. R. Lee, S. Nacht, J. N. Lukens, and G. E. Cartwright, *J. Clin. Invest.*, 1968, **47**, 2058.

105. S. Osaki, D. A. Johnson, and E. Frieden, *J. Biol. Chem.*, 1971, **246**, 3018.

106. J. I. Logan, K. B. Harveyson, G. B. Wisdom, A. E. Hughes, and G. P. Archbold, *Q. J. Med.*, 1994, **87**, 663.

107. H. Miyajima, Y. Takahashi, T. Kamata, H. Shimizu, N. Sakai, and J. D. Gitlin, *Ann. Neurol.*, 1997, **41**, 404.

108. W. Takahashi, F. Yoshii, and Y. Shinohara, *J. Neuroimaging*, 1996, **6**, 246.

109. K. Yoshida, ‘Metals and Genetics’, Klewar Academic/Plenum, New York, 1999, p. 301.

110. E. Frieden, *Clin. Physiol. Biochem.*, 1986, **4**, 11.

111. V. N. Zaitsev, I. Zaitseva, M. Papiz, and P. F. Lindley, *J. Biol. Inorg. Chem.*, 1999, **4**, 579.

112. M. Sato and J. D. Gitlin, *J. Biol. Chem.*, 1991, **266**, 5128.

113. J. D. Gitlin, J. J. Schroeder, L. M. Lee-Ambrose, and R. J. Cousins, *Biochem. J.*, 1992, **282**(Pt 3), 835.

114. N. E. Hellman, S. Kono, H. Miyajima, and J. D. Gitlin, *J. Biol. Chem.*, 2002, **277**, 1375.

115. N. Takahashi, T. L. Ortel, and F. W. Putnam, *Proc. Natl. Acad. Sci. U.S.A.*, 1984, **81**, 390.

116. H. Morita, S. Ikeda, K. Yamamoto, S. Morita, K. Yoshida, S. Nomoto, M. Kato, and N. Yanagisawa, *Ann. Neurol.*, 1995, **37**, 646.

117. H. Miyajima, Y. Takahashi, M. Serizawa, E. Kaneko, and J. D. Gitlin, *Free Radical Biol. Med.*, 1996, **20**, 757.

118. N. Danbolt and K. Closs, *Acta Derm. Venereol. Suppl. (Stockh)*, 1943, **23**, 127.

119. P. M. Barnes and E. J. Moynahan, *Proc. R. Soc. Med.*, 1973, **66**, 327.

120. K. Wang, E. W. Pugh, S. Griffen, K. F. Doheny, W. Z. Mostafa, M. M. al-Aboosi, H. el-Shanti, and J. Gitschier, *Am. J. Hum. Genet.*, 2001, **68**, 1055.

121. S. Kury, B. Dreno, S. Bezieau, S. Giraudet, M. Kharfi, R. Kamoun, and J. P. Moisan, *Nat. Genet.*, 2002, **31**, 239.

122. K. Wang, B. Zhou, Y. M. Kuo, J. Zemansky, and J. Gitschier, *Am. J. Hum. Genet.*, 2002, **71**, 66.

123. A. Nakano, H. Nakano, K. Nomura, Y. Toyomaki, and K. Hanada, *J. Invest. Dermatol.*, 2003, **120**, 963.

124. M. L. Guerinot, *Biochim. Biophys. Acta*, 2000, **1465**, 190.

125. L. A. Gaither and D. J. Eide, *J. Biol. Chem.*, 2000, **275**, 5560.

126. L. A. Gaither and D. J. Eide, *J. Biol. Chem.*, 2001, **276**, 22258.

127. E. A. Roberts, ‘Physician’s Guide to the Treatment and Follow-up of Metabolic Diseases’, Springer, Heidelberg, In press, 2005.

128. A. Roetto, F. Daraio, F. Alberti, P. Porporato, A. Cali, M. De Gobbi, and C. Camaschella, *Blood Cells Mol. Dis.*, 2002, **29**, 465.

129. O. T. Njajou, N. Vaessen, M. Joosse, B. Berghuis, J. W. van Dongen, M. H. Breuning, P. J. Snijders, W. P. Rutten, L. A. Sandkuijl, B. A. Oostra, C. M. van Duijn, and P. Heutink, *Nat. Genet.*, 2001, **28**, 213.

130. I. Visapaa, V. Fellman, J. Vesa, A. Dasvarma, J. L. Hutton, V. Kumar, G. S. Payne, M. Makarow, R. Van Coster, R. W. Taylor, D. M. Turnbull, A. Suomalainen, and L. Peltonen, *Am. J. Hum. Genet.*, 2002, **71**, 863.

Acknowledgments

I would like to thank Drs. Eve A. Roberts and Prasad P. Kulkarni for fruitful discussions. Research in the author’s laboratory is supported by grant MOP-1800 from the Canadian Institutes of Health Research.

Hard & Soft Acids and Bases

R. Bruce Martin
University of Virginia, Charlottesville, VA, USA

1 Hard and Soft Definitions 1
2 Substitution Reactions 1
3 Metal Ion Scales 2
4 Ligand Scale 3
5 Comparisons of Metal Ion Scales 4
6 Conclusions 4
7 References 5

1 HARD AND SOFT DEFINITIONS

Almost 50 years ago, metal ions were divided into two groups: a majority labeled class (a), for which the anion binding strength in aqueous solutions is greatest for F^- and generally follows the order $F > Cl > Br > I$, and a minority class (b), in which F^- binding is weaker than at least one of the heavier anions and that generally follows the order $F < Cl < Br < I$ (in the gas phase all metal ions follow the first order).[1] The same trends occur in other columns in the periodic table; for example, class (a) metal ions tend to favor binding to oxygen and class (b) metal ions to sulfur ligands. Subsequently Pearson extended the application and changed the terminology so that class (b) metal ions became soft and class (a) metal ions were subdivided into hard and borderline groups.[2] The greater popularity of the altered nomenclature is partly because it is easier to say harder or softer than more (a) character or more (b) character. Thus fluoride and chloride are described as hard, bromide as borderline, and iodide as soft.

The proposal by Pearson that hard acids prefer to coordinate with hard bases, and soft acids to soft bases, has become well known. All alkali, alkaline earth, and lanthanide metal ions are classified as hard as are the five small metal ions Be^{2+}, Al^{3+}, Cr^{3+}, Ga^{3+}, and Fe^{3+}, and also Mn^{2+}, Sc^{3+}, and In^{3+}. Borderline metal ions include the last five dipositive ions of the first transition row and Sn^{2+}, Pb^{2+}, and Bi^{3+}. Soft metal ions include Pd^{2+}, Ag^+, Cd^{2+}, Hg^{2+}, CH_3Hg^+, Tl^+, and Tl^{3+}. In addition to the assignments of the halides already mentioned, hard ligands include most oxygen donor ligands and aliphatic amines, while aromatic amines are borderline. Soft ligands include sulfhydryl groups and CN^-, SCN^-, and $S_2O_3{}^{2-}$. Despite the popularity of the hard–soft designation, a quarter of a century elapsed before Pearson proposed a quantitative scale. Pearson defined softness as the reciprocal of hardness and presented quantitative absolute hardness values for metal ions and ligands (in which the hardness of an atom and an anion such as F and F^- are surprisingly identical).[3] Subsequently Pearson disavowed his quantitative hardness scales for at least some cations and anions.[4] In any case, the hardness values for metal ions do not correlate at all with the stability constants of complexes, which are correlated best by the electron affinity of the metal ion.[5] Though often spoken of by chemists as if it is the determining factor in complex stability, the contribution of hardness or softness may pale compared to the intrinsic stability, which often dominates the binding strength.[4,5]

2 SUBSTITUTION REACTIONS

Just what does the typical chemist imply when she/he uses the terms hard and soft? To few if any does it correspond to Pearson's quantitative scale derived from gas-phase parameters and where hardness is the reciprocal of softness. More likely it expresses features of stabilities where, for example, though Cu^{2+} binds NH_3 more avidly than Mg^{2+}, the latter metal ion interacts more strongly with F^- than does Cu^{2+}. Comparisons of this kind and the stability orders of halide complexes of various metal ions mentioned at the beginning are equivalent to describing the extent of substitution reactions. If M and N are two different metal ions and X and Y two different ligands, we may compare the hardness of a metal ion by considering the substitution on the metal ion of one ligand by another

$$MX + Y \rightleftharpoons X + MY \tag{1}$$

for which the free energy change is proportional to $\log K_{MY} - \log K_{MX}$, where K_{MY} and K_{MX} are the stability constants for complexes MY and MX, respectively. An advantage of such a comparison is that it greatly reduces the overlooked effect of a reduction in coordination number from the aqueous ion for several soft metal ions in augmenting stability constants by powers of 10.[6] Similarly, we may compare the hardness of a ligand by considering the substitution on the ligand of one metal ion for another

$$MX + N \rightleftharpoons M + NX \tag{2}$$

for which the free energy change is proportional to the stability constant difference: $\log K_{NX} - \log K_{MX}$. By considering such substitution reactions one gains consistency in application of the principle of hard and soft acids and bases. The scales presented below are practical scales dependent only upon experimental stability constants determined in aqueous solutions, and they do not involve any other quantities such as electron affinities and other parameters from gas-phase reactions, heats of hydration, or heats of reaction.

Nor do the scales assume a model or rely on derived parameters with arbitrary scaling. These other factors have been discussed many times.[7,8] The scales probably represent what most investigators imply when they use the terms hardness and softness.

3 METAL ION SCALES

To avoid influence of chelate ring bite size on complex stabilities unidentate ligands are emphasized. Extensive stability constant values are available for four unidentate hard ligands: F$^-$, OH$^-$, acetate, NH$_3$, and borderline Br$^-$. Though somewhat limited in scope, the ligands encompass donor atoms of interest to many chemists. From a careful tabulation of stability constants for 28 metal ions with the five unidentate ligands, stability constant differences for a single metal ion with two different ligands yield the ordering in the following metal ion scales.[9] The number in parentheses following a metal ion is the log stability constant difference.

3.1 Fluoride Minus Bromide: Halide Scale

Among the common halides, iodide is the softest member but a limited number of stability constants have been published. For this reason we employ the more extensive values for bromide. Ordering of metal ion stabilities with soft I$^-$ is virtually identical to that of borderline Br$^-$. Differences in the stability constant logarithms for a metal ion with F$^-$ minus that for the same metal ion with Br$^-$ give the halide scale. These differences are ordered in the following halide scale where after each of the 22 metal ions the difference appears in parentheses, and a greater than sign (>) indicates a factor of about 10. Not considering the proton at the beginning of the scale, the span of differences is 14.3 log units, and there are 14 greater than signs among the metal ions.

H$^+$(11.9)>>>>>>Sc(6.3) > Be(5.5),
Fe(III)(5.5) > Ga(4.5), Y(4.1), **Sn**(3.8),
Lu(3.7) > Ce(3.3), La(3.0) > Mg(2.7), **Bi**(2.4) > In(1.7),
Zn(1.4), Mn(1.0), **Cu**(0.9), **Ni**(0.9),
Co(0.8) > **Pb**(0.3) > *Cd*(−0.8)>>>>*Ag*(−4.6),
CH$_3$*Hg*(−5.0)>>>*Hg*(−8.0).

Halide scale

The only change required by considering iodide instead of bromide is to reverse the order of Bi^{3+}, In^{3+}, and Zn^{2+}. The change from positive to negative signs occurs after Pb^{2+} for either bromide or iodide ligands. This sign change corresponds to the class (a) and class (b) division mentioned in the first sentence of the Introduction. Metal ions assigned by Pearson as hard appear in normal type, borderline in bold, and soft in italics.

Metal ions favoring fluoride appear at the beginning of the scale and those favoring bromide (and iodide) at the end. The ordering in the halide scale corresponds closely to the three categories described by Pearson: nine hard metal ions and borderline Sn^{2+}, are followed by six borderline metal ions and also hard In^{3+} and Mn^{2+}, and completed by four soft metal ions. As the multiple greater than signs indicate, the last three cases involving Ag$^+$ and Hg(II) are much softer than all others in the list. The above halide scale serves as a quantitative guide to the relative hardness and softness of 22 metal ions toward halide ions in aqueous solutions.

3.2 Hydroxide Minus Ammonia: OH–N scale

More relevant to many investigators than differences among halide stability constants are comparisons involving oxygen and nitrogen donor atoms. These differences are ordered in the following hydroxide−ammonia (OH–N) scale, where after each of the 25 metal ions the difference between stability constant logs appears in parentheses, and a greater than sign indicates a factor of about 10. The span is 10.3 log units and there are 10 greater than signs.

Sc(9.0) > Ga(8.4), Fe(III)(8.0) > Al(6.7),
H$^+$(6.5) > In(6.0), Y(5.9), Lu(5.7), Ce(5.3),
La(5.3) > **Pb**(4.7), *Tl*(*III*)(4.3) > *Pd*(3.4) > **Zn**(2.7),
Cu(2.4), Mg(2.3), **Co**(2.3), *CH*$_3$*Hg*(2.3),
Mn(2.2) > *Hg*(1.8), *Tl*(*I*)(1.7), Ca(1.4),
Ni(1.4), *Cd*(1.3) > Li(0.7)>>*Ag*(−1.3).

OH–N scale

Again, metal ions assigned by Pearson as hard appear in normal type, borderline in bold, and soft in italics.

Metal ions favoring hydroxide appear at the beginning of the OH–N scale and those favoring ammonia at the end. The OH–N scale begins with nine hard metal ions, followed by nine metal ions with an intermingling of all three types, and finally concluding with four soft metal ions, but also with hard Ca^{2+} and Li$^+$ and borderline Ni^{2+} embedded therein.

3.3 Acetate Minus Ammonia: O–N Scale

As an oxygen donor ligand, hydroxide may not be typical, and for some applications acetate may offer a more representative oxygen donor ligand than hydroxide. For acetate−ammonia, 22 log stability constant differences yield the following acetate−ammonia (O−N) scale. The scale spans 8.0 log units and each of the eight greater than signs indicates a factor of near 10.

Sc(2.8) > La(1.6), Ce(1.5), Y(1.3), Lu(1.2) > *Tl*(*I*)(0.8),
Ca(0.7), Li(0.6), **Pb**(0.6), Mg(0.3) > Fe(III)(−0.4),
Mn(−0.4), In(−0.5) > **Co**(−1.0), *Cd*(−1.1),
Zn(−1.2) > **Ni**(−2.0), **Cu**(−2.3) > *Ag*(−2.9),
Tl(*III*)(−2.9) > *CH*$_3$*Hg*$^+$(−4.1), H$^+$(−4.5) > *Hg*(−5.2).

O–N scale

Once again Pearson's hard metal ions appear in normal type, borderline in bold, and soft in italics.

Metal ions favoring acetate appear at the beginning of the O−N scale and those favoring ammonia at the end. Of the first 13 metal ions, 11 are hard, but in this group there is one soft (Tl^+) and one borderline (Pb^{2+}) metal ion. Next a group of four borderline metal ions also contains one soft metal ion (Cd^{2+}). The scale ends with four soft metal ions, but also with the hard proton.

3.4 Carboxylate Minus Sulfhydryl: O–S Scale

Unfortunately, it is impossible to develop a comparable hardness scale with unidentate sulfur donor ligands as so few reliable experimentally determined stability constants are available. Polymerization has gone unrecognized in many of the determinations. Many of the constants involve chelate rings that introduce the additional variable of chelate ring bite size. Ag^+ and Hg^{2+} prefer linear coordination, making formation of five- and even six-membered chelate rings highly strained.[6]

Nonetheless, by relaxing the requirement for unidentate ligands, we may compare the tendency of some metal ions to bind to oxygen or sulfhydryl donor atoms. Stability constants have been tabulated for binding to substituted iminodiacetates, $R–N(CH_2COO^-)_2$.[10] For $R = –CH_2COO^-$ (nitrilotriacetate) and $R = –CH_2CH_2S^-$, the difference in stability constant logs for the former minus the latter tridentate ligand is given in parentheses, in sequence, after each dipositive metal ion.

Ca(1.5), Sr(1.4), Ba(1.3), Mg(1.1) ⋙
Mn(−1.9), **Ni**(−2.2), **Fe**(−2.9) ≫
Zn(−5.3), **Pb**(−5.6), *Cd*(−6.9), *Hg*(< −8).

O–S scale

Similar differences and sequence are obtained with $R = –CH_2CH_2OH$ as the oxygen donor, with the addition of poorly chelating Hg^{2+}, still with the greatest negative value.[10] Metal ions in the O−S scale falls distinctly into three groups: alkaline earths with differences from +1.5 to +1.1, transition metal ions from −1.9 to −2.9, and filled d orbital ions from −5.3 to <−8. The spans within the first two groups are narrower than the gaps between the three groups. For oxygen−sulfhydryl binding, the alkaline earths may be designated as hard, the three transition metal ions as borderline, and the four filled d shell metal ions as soft. The recognized avidity of Zn^{2+} for sulfhydryl donors is confirmed. Though assigned as hard by Pearson, by this grouping, Mn^{2+} is emphatically borderline. This borderline designation for Mn^{2+} is also more consistent with other scales presented above.

4 LIGAND SCALE

To create a ligand scale, corresponding to the second substitution reaction of Section 2, we consider the differences between stability constant logarithms for soft and hard metal ions for several ligands. Hg^{2+} stands as the preeminent soft metal ion. Sc^{3+} is the hardest metal ion in all three of the above scales, but results are limited. More ligands may be included if results for the smaller and heavier lanthanides are considered for the hard metal ion. For 16 ligands, the difference between the stability constant logarithms for Hg^{2+} minus a lanthanide in parentheses is as follows.

F^-(−3), H_2O(0), acetate(2), HCO_3^-(4), CO_3^{2-}(5),
OH^-(5) > **pyridine**(6), **benzimidazole**(6), **imidazole**(7),
Cl^-(7), NH_3(8), SCN^-(9), $\mathbf{Br}^-$(9) > I^-(13),
CN^-(13), $\mathit{S_2O_3}^{2-}$(14).

Ligand scale

Ligands assigned by Pearson as hard appear in normal type, borderline in bold, and soft in italics. For Pearson, aliphatic amines are hard and aromatic amines borderline. Since imidazole binds metal ions through a borderline pyridine-type nitrogen,[11] imidazole is also classed as borderline in the ligand scale. Use of CH_3Hg^+ in place of Hg^{2+} yields a virtually identical ordering with a lesser span of 13 log units.

The hardest ligands appear at the beginning of the ligand scale, which spans 17 log units. Cyanide and thiocyanate are ambivalent ligands; virtually all metal ions bind to CN^- through the carbon atom. Even upon binding the first CN^-, Cu^+, Ag^+, and Hg^{2+} undergo a reduction to two-coordination. A reduction to four-coordination occurs upon binding of the second CN^- to Ni^{2+} and Zn^{2+}.[6] A reduction in coordination number strengthens binding.

Log stability constant plots of the four amines against one another correlate tightly ($R^2 > 0.98$) for seven metal ions. With the values for ammonia on the x-axis, straight lines produced by plotting on the y-axis give slopes of 0.71 for pyridine, 0.77 for benzimidazole, and 0.88 for imidazole. These slopes provide factors that yield quantitative hardness values on the ligand scale from ammonia(8): $0.71 \times 8 = 6$ for pyridine, $0.77 \times 8 = 6$ for benzimidazole, and $0.88 \times 8 = 7$ for imidazole. Thus the order of increasing softness is pyridine(6) < benzimidazole(6) < imidazole(7) < ammonia(8); the aliphatic amine is softer than all three aromatic amines, opposite to the Pearson assignment. The new order is confirmed by quantitatively considering exchange reactions between ammonia and pyridine (or imidazole) with soft CH_3Hg^+ (or Ag^+) and any borderline or hard metal ion: ammonia always pairs preferentially with the soft metal ion.

The above order of increasing softness of the amines is also the order of increasing basicity. The influence of greater basicity in yielding increasing softness is also illustrated by two other comparisons in the ligand scale: H_2O(0) < OH^-(5) and HCO_3^-(4) < CO_3^{2-} (5). These sequences point up a general feature of metal ion stabilities: greater basicity yields greater metal ion stability, which in turn provides greater discrimination among metal ions, which in turn gives rise to softness. Often, however, other factors overwhelm the influence of basicity: among the halides fluoride is both the strongest base and the hardest.

The ligand scale serves as a quantitative indication of the relative hardness and softness of ligands. Wide applicability of the ligand scale is supported by ordering identical to the above for the seven common ligands in a scale derived from heats of formation of solid compounds of identically charged and similarly sized Ca^{2+} and Cd^{2+}.[7] In the ligand scale, the first six ligands are assigned as hard by Pearson; of the next closely spaced seven ligands, two are hard, four borderline, and one soft. The ligand scale ends with three soft ligands. In the ligand scale, the relative softness of the presumably hard ammonia(8), comparable to borderline bromide(9) and soft thiocyanate(9), emerged unexpectedly. Based on the quantitative results of the ligand scale, previously hard ammonia and chloride and soft thiocyanate are more appropriately switched into the borderline group. These switches more consistently place all amines, aliphatic, and aromatic, in the same borderline group. The recommended designations lead to a consistent sequence of six hard, seven borderline, and three soft ligands, as indicated by the two inequality signs between the three groups. Thus all oxygen donor ligands are designated hard and now all nitrogen donors borderline. Within the borderline group, aliphatic amines are softer than aromatic amines.

5 COMPARISONS OF METAL ION SCALES

5.1 Correlations

Though there is a wide measure of sequence agreement among the three metal ion scales, there are also differences. For example, of the three scales, in only the OH–N scale is Ag^+ the softest metal ion, in the other two scales it is Hg^{2+}. Departures from an identical ordering demonstrate that the degree of metal ion hardness and softness depends on the ligands considered, and that finding absolute values applicable to all cases in aqueous solutions is not possible. Thus one uses the scales applicable to ligands being considered: for example, the O–N scale for many biological systems.

5.2 Pb^{2+}

Lead (Pb^{2+}) presents a case that demonstrates limitations in the hard-soft concept. The first stability constant logarithms for lead and the halide ions, all at 25° C and 1.0 M ionic strength, appear in parentheses: $F(1.44) > Cl(0.90) < Br(1.10) < I(1.26)$.[12] The increasing trend for the last three halides describes class (b) behavior, while the greatest value for F^- characterizes a class (a) metal ion. Pb^{2+} interacts relatively strongly with both oxygen (hard) and sulfur (soft) donor ligands, and relatively weakly with nitrogen donor ligands, as illustrated in the stability ruler (see Section 5 in ***Metal Ion Toxicity***). Despite the presence of a free sulfhydryl group on the proteins, Pb^{2+} binding occurs exclusively at the Ca^{2+} sites, composed solely of O donors, of oncomodulin and chick vitamin D induced intestinal calcium-binding protein.[13] Pb^{2+} also combines with the components of nucleic acids.[14] In many examples, Pb^{2+} eschews borderline (is antiborderline) and opts for either hard or soft behavior, making the simple hard–soft concept ineffective for use with this metal ion. In contrast, compared to other metal ions, Ni^{2+} exhibits a tendency to prefer nitrogen over oxygen or sulfur donors (except when two or more sulfur donors promote a diamagnetic complex).

6 CONCLUSIONS

Note again that the quantitative values associated with hardness and softness in this article are based wholly on experimentally determined log stability constant differences determined in aqueous solutions at room temperature. The values are not absolute; addition of more metal ions might extend the scales in either direction. Small differences between metal ions should not be overinterpreted. The relative difference scales are linear in log stability constant, stretching from very hard at one end to very soft at the other. As hardness decreases, softness correspondingly increases, and vice versa. These practical scales are difficult to relate to that of Pearson, where absolute hardness values are derived from gas-phase parameters, and softness is the reciprocal of hardness.[3]

In practice, the principle of hard and soft acids and bases is often contorted so as to provide nonfalsifiable explanations for almost any observation.[5] The limitations of the principle need greater exposure. The very hard Sc^{3+} and the very soft CH_3Hg^+ both bind strongly and nearly equally to the hard ligands hydroxide on one hand and acetate on the other.[9] Though both metal ions are considered as very soft, Hg^{2+} is among the strongest binders to hydroxide and acetate, and Ag^+ among the weakest. With the exception only of Ag^+, hydroxide forms stronger complexes with all metal ions than do ammonia or bromide. It is only when differences of stability constant logs are compared that one finds some quantitative justification for the principle of hard and soft acids and bases. Such differences are sequenced in the scales of this article. The principle of hard and soft acids and bases finds its most consistent application, not in direct stability constant comparisons, but rather in the free energy or log stability constant differences of the substitution reactions of Section 2.

7 REFERENCES

1. S. Ahrland, J. Chatt, and N. R. Davies, *Q. Rev. Chem. Soc.*, 1958, **12**, 265.
2. R. G. Pearson, *J. Am. Chem. Soc.*, 1963, **85**, 3533.
3. R. G. Pearson, *Inorg. Chem.*, 1988, **27**, 734.
4. R. G. Pearson, *Inorg. Chim. Acta*, 1995, **240**, 93.
5. R. B. Martin, *Inorg. Chim. Acta*, 1998, **283**, 30.
6. R. B. Martin, *Comments Inorg. Chem.*, 1996, **18**, 249.
7. R. J. P. Williams and J. D. Hale, *Struct. Bonding*, 1966, **1**, 249.
8. R. G. Pearson, ‘Hard and Soft Acids and Bases’, Dowden, Hutchinson and Ross, Stroudsberg, PA., 1973.
9. R. B. Martin, *Inorg. Chim. Acta*, 2002, **339**, 27.
10. R. B. Martin and H. Sigel, *Comments Inorg. Chem.*, 1988, **6**, 285.
11. R. J. Sundberg and R. B. Martin, *Chem. Rev.*, 1974, **74**, 471.
12. A. E. Martell and R. M. Smith, ‘Critical Stability Constants’, Plenum, New York, 1974–1989, Vols. 1–6.
13. C. S. Fullmer, S. Edelstein, and R. H. Wasserman, *J. Biol. Chem.*, 1985, **260**, 6816.
14. H. Sigel, C. P. DaCosta, and R. B. Martin, *Coord. Chem. Rev.*, 2001, **219–221**, 435.

Long-range Electron Transfer in Biology

Jay R. Winkler
California Institute of Technology, Pasadena, CA, USA

1 Introduction 1
2 Electron-transfer Theory 1
3 Chemically Modified Proteins 3
4 Protein−Protein Reactions 6
5 Photosynthesis and Respiration 8
6 Concluding Remarks 10
7 Related Articles 10
8 References 10

1 INTRODUCTION

Electron-transfer (ET) reactions, the simplest chemical transformations, play vital roles in a diverse ensemble of biological processes. Biological electron transfer is an extraordinarily vibrant field of inquiry, responsible for thousands of original research articles during the past decade. This chapter will focus on studies of ET in chemically modified proteins, protein−protein complexes, and two key biological energy transduction pathways, photosynthesis (*see* ***Photosynthesis***) and respiration (*see* ***Cytochrome Oxidase***).

Aerobic organisms derive most of the energy needed for life processes by the burning of foodstuffs with molecular oxygen in air.[1] In the first part of the respiratory process, hydrogen atoms are extracted from organic molecules. The hydrogen carriers provide reducing equivalents to the respiratory chain located in cell organelles (mitochondria) or, in bacteria, in the cell membrane. These chains consist of a series of membrane-bound protein complexes in which the hydrogen atoms are split into protons and electrons. The electrons are passed down the chain and reduce molecular oxygen to water, whereas protons are left behind on one specific side of the membrane. In addition, the electron current through the chain is coupled to the pumping of additional protons from water to the same side of the membrane.[2] The two proton currents lead to an increased positive charge and decreased pH on this side. The resulting electrochemical potential across the membrane drives the synthesis of ATP, the universal energy currency of living cells.

Photosynthesis is the natural complement to respiration. Photons from the sun induce charge separation in a membrane-bound redox chain, ultimately producing a transmembrane potential for ATP synthesis. In green plants, algae, and cyanobacteria, the photogenerated holes oxidize water to oxygen. The photochemically generated reducing equivalents produce NADPH that, along with ATP, is used in carbon dioxide fixation.

Highly optimized ET reactions are essential for the operation of these biochemical machines. Much of the research on biological electron transfer aims to define the electronic and structural factors that regulate the rates and efficiencies of these essential transformations. This chapter will focus on studies of ET through proteins, particularly metalloproteins. ET processes involving DNA molecules have been the subject of extensive research as well,[3–6] but this work is beyond the scope of this chapter.

2 ELECTRON-TRANSFER THEORY

The unique simplicity of ET reactions has fostered the development of a powerful theoretical formalism that describes the rates of these processes in terms of a small number of parameters.[7] The conceptual breakthrough that led to the development of ET theory involved the recognition of the pivotal role played by the Franck−Condon principle.[8,9] Owing to the much higher electron velocities, nuclei remain fixed during the actual electron transfer from donor to acceptor. The transition state for this reaction must lie at a point in nuclear-configuration space where the reactant and product states are degenerate (Figure 1). Hence, through fluctuations of the reacting molecules and their surroundings, the transition-state configuration will be reached and an electron can transfer.

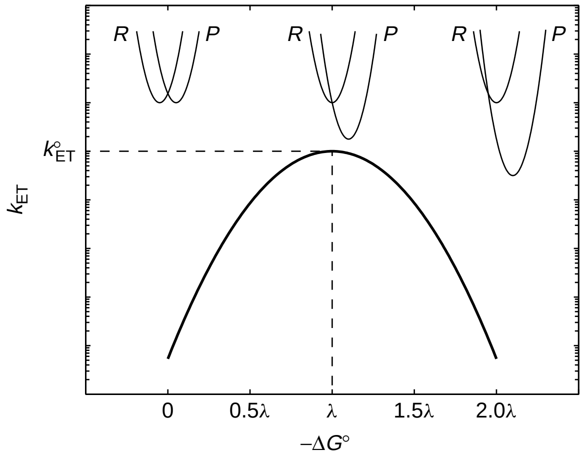

Figure 1 Driving-force dependence of ET rates predicted by semiclassical theory (equation 1). Rates increase with driving force until they reach a maximum value (k°_{ET}) at $-\Delta G^\circ = \lambda$. Rates then decrease at higher driving forces (inverted effect)

2.1 Activation Barriers

According to classical (Marcus) theory, the activation barrier for an adiabatic ET reaction depends on two parameters, the driving force ($-\Delta G^\circ$) and the reorganization energy (λ).[7] The reorganization parameter reflects the extent of outer-sphere (λ_{OUT}) and inner-sphere (λ_{IN}) nuclear rearrangement that accompanies charge transfer. The λ values for a cross reaction between two different reagents can be estimated from the average of the electron self-exchange reorganization energies for each redox partner (i.e. $\lambda_{12} \approx \lambda_{11}/2 + \lambda_{22}/2$). The unique prediction from Marcus theory is that rates reach a maximum when the driving force equals the reorganization energy. At higher driving forces, rates are predicted to decline (inverted effect) owing to less favorable Franck–Condon factors for the electron transfer. The central lesson of classical theory is that nuclear rearrangements accompanying ET must be compensated by reaction driving force (Figure 1). The balance between ΔG° and λ is a direct consequence of protein structure.

Electron transfer in proteins generally involves redox centers separated by long distances. The electronic interaction between redox sites is relatively weak and the transition state for the ET reaction must be formed many times before there is a successful conversion from reactants to products; the process is electronically nonadiabatic. A Landau–Zener treatment of the reactant-product transition probability produces the familiar semiclassical expression for the rate of nonadiabatic electron transfer between a donor (**D**) and acceptor (**A**) held at fixed distance (equation 1).[7] Biological electron flow over long distances with a relatively small release of free energy is possible because the protein fold creates a suitable balance between ΔG° and λ as well as adequate electronic coupling between distant redox centers.

$$k_{\mathrm{ET}} = \sqrt{\frac{4\pi^3}{h^2 \lambda RT}}\, H_{\mathrm{AB}}^2 \exp\left\{-\frac{(\Delta G^\circ + \lambda)^2}{4\lambda RT}\right\} \qquad (1)$$

2.1.1 Redox Potentials

The reduction potentials of redox-active proteins are exquisitely sensitive to the structure of the polypeptide.[10–13] It is well known that homologous proteins from different organisms can have quite disparate amino acid sequences yet nearly identical three-dimensional structures.[14,15] Nevertheless, single-point mutations can destroy redox function without disrupting structure. Indeed, substitution of a single amino acid in myoglobin can shift the Fe(III/II) reduction potential by as much as 200 mV, effecting greater than a thousand-fold change in the equilibrium constant for reaction with a redox partner.[16]

The secondary and tertiary structures of a protein can modulate the reduction potential of a single cofactor by more than 500 mV. The Fe(III/II) reduction potential of a free heme in aqueous solution is approximately −200 mV versus the normal hydrogen electrode (NHE), the potential of cytochrome *c* is 260 mV, and that of cytochrome *f* reaches 450 mV.[17] The shift in reduction potential is reflected in a differential folding free energy of the oxidized and reduced proteins.[18] In the case of cytochrome *f*, the Fe(II) protein is more stable toward unfolding than the oxidized protein;[19] the redox potential indicates a stability differential of some 650 meV (63 kJ mol^{-1}). In order for cytochrome *f* to be a viable redox protein, the folding free energy of the oxidized form must be at least $2\,k_{\mathrm{B}}$T ($\sim$5 kJ mol^{-1} at 298 K), requiring that the folding free energy of the reduced protein be greater than 68 kJ mol^{-1} (700 meV).

2.1.2 Reorganization Energy

The protein fold plays a central role in lowering the reorganization energy of a biological ET reaction.[10] A large part of the λ-reduction results from sequestering a redox center from the aqueous solvent environment. Continuum models suggest that embedding a redox center inside a low dielectric cavity can lower the outer-sphere reorganization energy by as much as 50%.[20] Moreover, by constraining the coordination environment around metal centers, inner-sphere reorganization energy can be reduced as well.[10] Indeed, metals that are typically poor redox reagents because of large reorganization barriers can be extremely efficient when embedded in protein interiors. The reorganization energy for electron self-exchange in $\mathrm{Cu(phen)_2}^{2+/+}$, for example, is $\sim$2.4 eV; the value for Cu(II/I) in *Pseudomonas aeruginosa* azurin is 0.7 eV. The 1.7-eV reduction in λ reflects the transition-state stabilization imposed by the azurin fold.[10,21]

It is important to remember that the reorganization energy is a composite parameter rather than a fundamental physical quantity. Refinements to the semiclassical theory usually arise from quantum mechanical treatments of vibrational motions.[22] The increased rigor associated with these models, however, is rarely accompanied by the extra data required to cope with the influx of new parameters. The approximations involved in its definition, and the errors associated with its measurement dictate that λ should never be expressed with great precision.

2.2 Electronic Coupling

The ability to control redox potentials and reorganization energies in proteins comes at a price: ET partners buried within insulating polypeptides cannot come into close contact to exchange electrons. The essential electronic interaction between redox cofactors must be mediated by the polypeptide matrix. Extensive experimental and theoretical efforts have been aimed at elucidating the factors that regulate distant electronic couplings between redox sites in proteins.[21,23,24]

The electronic coupling matrix element (H_{AB}) reflects the strength of the interaction between reactants and products at the nuclear configuration of the transition state. Square-barrier ET tunneling models predict that the coupling will depend exponentially on the distance (r) between redox centers (equation 2).[25] A square tunneling barrier implies that a homogeneous medium separates the donor and acceptor. This model is appropriate for electron tunneling across a vacuum ($\beta = 3\text{–}5\,\text{Å}^{-1}$) and is a reasonable approximation for tunneling through glassy solvents (H_2O, $\beta = 1.65\,\text{Å}^{-1}$;[26] 2-methyltetrahydrofuran, $\beta = 1.2\,\text{Å}^{-1}$[27]). Superexchange models are better suited to the description of tunneling through inhomogeneous media. In 1961, McConnell described a superexchange model for electron tunneling from a donor to an acceptor across a bridge composed of n identical repeat units.[28] The electronic coupling matrix element is a function of the couplings between redox sites and the bridge (h_{Ab}, h_{bB}), the coupling between bridge elements (h_{bb}), and the gap ($\Delta\varepsilon$) between the energy of tunneling electron (or hole) and reduced (or oxidized) bridge states (equation 3).

$$H_{\text{AB}}(r) = H_{\text{AB}}(r_o)\exp\left\{-\tfrac{1}{2}\beta(r - r_o)\right\} \tag{2}$$

$$H_{\text{AB}} = \frac{h_{\text{Ab}}}{\Delta\varepsilon}\left(\frac{h_{\text{bb}}}{\Delta\varepsilon}\right)^{n-1} h_{\text{bB}} \tag{3}$$

The medium separating redox sites in proteins is comprised of a complex array of bonded and nonbonded contacts and an *ab initio* calculation of coupling strengths is a formidable challenge.[29] The homologous-bridge superexchange model (equation 3) is not suitable because of the diverse interactions in proteins. Beratan and Onuchic developed a generalization of the McConnell superexchange coupling model that accommodates the structural complexity of a protein matrix.[30] In this tunneling-pathway model, the medium between **D** and **A** is decomposed into smaller subunits linked by covalent bonds, hydrogen bonds, or through-space jumps. Each link is assigned a coupling decay (ε_{C}, ε_{H}, ε_{S}), and a structure-dependent searching algorithm is used to identify the optimum coupling pathway between the two redox sites. The total coupling of a single pathway is given as a repeated product of the couplings for the individual links (equation 4). The variation of ET rates with r depends upon the coupling-decay factors for hydrogen bonds (ε_{H}), van der Waals contacts (ε_{S}), and single covalent bonds (ε_{C}). Equation (3) suggests that the magnitude of ε_{C} should depend critically upon the energy of the tunneling electron relative to the energies of the bridge hole and electron states. Clear demonstrations of this energy dependence in the tunneling regime have been elusive. Studies, however, have shown that electron transport over exceptionally long distances is possible when hole or electron states of the bridge can be populated as real intermediates.[31,32] In comparing ET data from different protein systems, then, it is important to consider the tunneling-energy gap and the possibility of forming oxidized or reduced intermediates in the bridging medium.

$$H_{\text{AB}} = \Pi\varepsilon_{\text{C}}\Pi\varepsilon_{\text{H}}\Pi\varepsilon_{\text{S}} \tag{4}$$

The tunneling-pathway model has proven to be one of the most useful methods for estimating distant electronic couplings.[21,23,30,33] The original tunneling-pathway model successfully described the distance dependence of protein ET reactions when a single pathway dominated the coupling.[30] The model was less successful when multiple pathways contributed to the overall coupling. More elaborate computational protocols have since been developed to describe in greater detail the factors that determine distant couplings in proteins.[29,33–38]

3 CHEMICALLY MODIFIED PROTEINS

3.1 Ru-modified Proteins

Semiclassical theory provides a framework for understanding biological electron flow; what is necessary on the experimental front are systematic investigations of the response of rates to variations in ET parameters (ΔG°, λ, r). Early efforts involving studies of bimolecular ET reactions were frustrated by the effects of diffusion. A simple bimolecular ET reaction can be broken into a sequence of three steps: diffusive formation of an encounter or precursor complex (**DA**); ET from donor to acceptor within the precursor complex ($\mathbf{DA} \rightarrow \mathbf{D}^{+}\mathbf{A}^{-}$); and dissociation of the successor complex to give products. The precursor and successor complexes are rarely observed in ET reactions; it is reasonable to employ a steady-state approximation to describe the time dependence of the [**DA**] concentration (i.e. $\partial[\mathbf{DA}]/\partial t = 0$). Within the limits of this approximation, the observed second-order rate constant for a bimolecular ET reaction (equation 5) depends on the rates of formation and dissociation of the precursor complex ($k_{+\text{D}}$ and $k_{-\text{D}}$, respectively) and the ET rate within the complex (k_{ET}, equation 1). Below the diffusion limit (i.e. $k_{\text{ET}} \ll k_{-\text{D}}$), k_{obs} is equal to $K_{[\text{DA}]}k_{\text{ET}}$ (where $K_{[\text{DA}]} = k_{+\text{D}}/k_{-\text{D}}$ is the equilibrium constant for precursor-complex formation). Since the value of $K_{[\text{DA}]}$ is usually not known, it is quite difficult to extract accurate values of λ and H_{AB} from low-driving-force bimolecular ET rates. At high driving forces, reaction rates become masked by diffusion (i.e. $k_{\text{ET}} \gg k_{-\text{D}}, k_{\text{obs}} = k_{+\text{D}}$), frustrating efforts to observe inverted driving-force behavior.

$$k_{\text{obs}} = \frac{k_{+\text{D}}k_{\text{ET}}}{k_{-\text{D}} + k_{\text{ET}}} \tag{5}$$

In order to circumvent these difficulties, experimentalists developed methods to study the rates of intraprotein ET reactions.[21,23,24,39] One early approach involved metalloproteins that had been surface-labeled with redox-active metal complexes.[40,41]

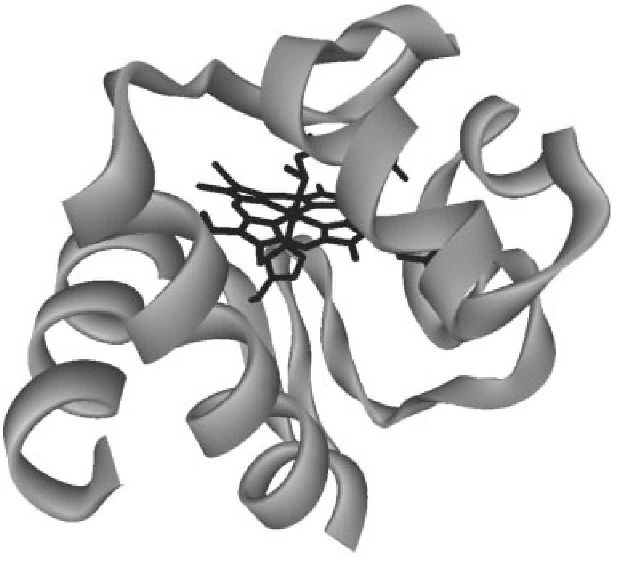

Figure 2 Ribbon representation of the peptide backbone in horse heart cytochrome c. The heme and its axial ligands are shown in black

3.2 Reorganization Energy

3.2.1 Cytochrome c

Investigations of intramolecular ET in heme proteins have focused on cytochrome c (104 amino acids in the horse protein; 12.5 kDa; $E^\circ = 0.26$ V *vs.* NHE) (*see* ***Iron: Heme Proteins & Electron Transport***) (Figure 2).[14,15] Early work with the Ru–ammine modified protein involved the replacement of the native Fe center with Zn. Long-range ET reactions were initiated by visible-light excitation of the resulting Zn-porphyrin (ZnPor) to its long-lived (>10 ms), strongly reducing ($E^\circ \sim -0.8$ V *vs.* NHE) triplet-excited state. A driving-force study of ET rates in $Ru(NH_3)_4L$(His33)-modified Zn-substituted cytochrome c ($L = NH_3$, pyridine, isonicotinamide) was consistent with $\lambda_{12} = 1.2$ eV.[23,42] The self-exchange reorganization energies for Ru-ammine complexes (λ_{11}) are in the vicinity of 1.6 eV. Intramolecular ET kinetics, then, suggest that $\lambda_{22} = 0.8$ eV for Zn-cytochrome c.[42]

Studies of high-driving-force ET in heme and nonheme proteins were made possible by Ru-diimine labeling protocols and the 'flash-quench' triggering method.[43] The driving-force dependence of ET in Ru(diimine)$_2$(im)(His33)-modified Fe-cytochrome c (im = imidazole) is best described by $\lambda_{12} = 0.8$ eV.[21,23] This value is lower than that found for Ru-ammine-modified Zn-cytochrome c because the diimine ligands coordinated to the Ru center are larger and more hydrophobic than ammines. Consequently, the self-exchange reorganization energy for Ru(diimine)$_2$(im)(His)$^{3+/2+}$ is substantially smaller ($\lambda_{11} = 0.8$ eV) than that of the ammine.[23,42] The combined results from ET measurements in the Ru–ammine and Ru–diimine proteins suggest that the reorganization energy for electron exchange between Fe(II)- and Fe(III)-cytochrome c is 0.8(1) eV.

3.2.2 Azurin

The flash-quench method made it possible to examine high-driving-force ET in labeled copper proteins. *P. aeruginosa* azurin (Figure 3) has a Cu(II/I) reduction potential of 0.31 V *vs.* NHE.[24] Analysis of the driving-force dependence of Cu(I) → M(III) (M = Ru, Os) ET in M(diimine)$_2$(im)(His83)-azurin gives a reorganization energy of 0.8 eV.[44] In accord with this finding, the temperature independence (240–300 K) of Cu(I) → Ru(III) ET in Ru(bpy)$_2$(im)(His83)-azurin can be described by $\lambda_{12} = 0.7 \pm 0.1$ eV, although the observed twofold increase in rate constant as the temperature is lowered to 160 K cannot be explained by changes in the exponential term of the semiclassical rate expression.[45] It is more likely

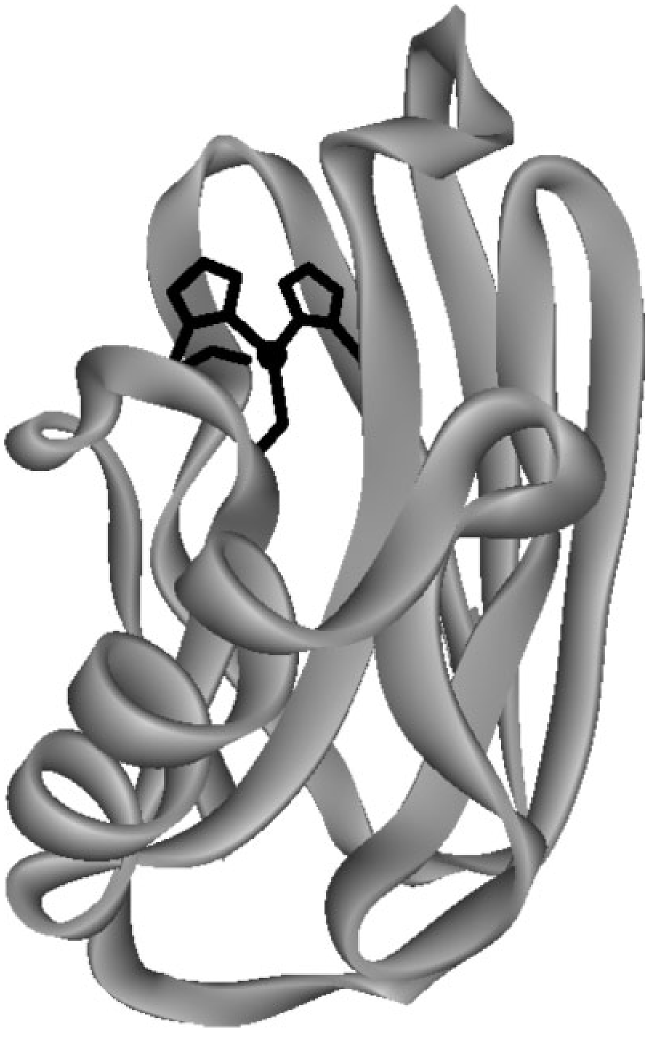

Figure 3 Ribbon representation of the peptide backbone in *P. aeruginosa* azurin. The Cu cofactor and its ligands are shown in black

that the Ru–Cu electronic coupling increases as the protein is cooled to 170 K.

Rates of Ru(III) and Os(III) reduction by Cu(I) have been measured in single crystals of *P. aeruginosa* M(diimine)$_2$(im)(His83)-azurin. In these cases, protein conformation and surface solvation are precisely defined by high-resolution X-ray structure determinations.[46] The time constants for electron tunneling in crystals are roughly the same as those measured in solution, indicating very similar protein structures in the two states. High-resolution structures of the oxidized (1.5 Å) and reduced (1.4 Å) forms of Ru(tpy)(bpy)(im)(His83)-azurin (tpy = 2,2′:6,2″-terpyridine; bpy = 2,2′-bipyridine) establish that very small changes in copper coordination accompany reduction.[46] Although Ru(bpy)$_2$(im)(His83)-azurin is less solvated in the crystal lattice, the reorganization energy for Cu(I) → Ru(III) electron transfer falls in the same range (0.6–0.8 eV) determined experimentally for the reaction in solution. It is striking that driving forces, reorganization energies, and rates of Cu(I) → M(III) (M = Ru, Os) ET are virtually unchanged when labeled azurins lose one-third of their solvent-accessible surface upon transfer from dilute solutions to crystal lattices with just 40% water. These observations suggest that bulk water plays a minor role in azurin ET reactions; what little solvent reorganization occurs is likely to involve only the ordered waters of hydration.

3.3 Tunneling Timetables

Theoretical analyses of coupling pathways in proteins suggest that the efficiency of long-range electron tunneling depends on the secondary structure of the polypeptide between the redox centers.[47] The distance dependence of ET in azurin provides insight into the efficiency of coupling across β-sheet structures.[23] The copper center in azurin is situated at one end of an eight-stranded β-barrel, ligated in a trigonal plane by two imidazoles (His46, His117) and a thiolate (Cys112); in addition, there are weak axial interactions (Met121 thioether sulfur, Gly45 carbonyl oxygen) (Figure 3).[48] The azurin from *P. aeruginosa* has two additional His residues, one of which (His83) reacts readily with Ru-labeling reagents. An H83Q base mutant was prepared and individual mutant His residues were introduced at five locations on β-strands extending from the Cys112 and Met121 ligands (K122H, T124H, T126H, Q107H, M109H). Measurements of Cu(I) → Ru(bpy)$_2$(im)(HisX)$^{3+}$ ET ($-\Delta G^\circ = 0.7$ eV) provide a calibration for the distance dependence of ET along β-strands (Figure 4). The driving-force-optimized electron tunneling timetable for azurin reveals an exponential distance dependence, with a decay constant (β) of 1.1 Å^{-1}, and an intercept at close contact ($r_o = 3$ Å) of 10^{13} s^{-1}. This decay constant is quite similar to that found for superexchange-mediated tunneling across saturated alkane bridges ($\beta \approx 1.0$ Å^{-1}),[49] strongly indicating that a similar coupling mechanism is operative in the polypeptide.

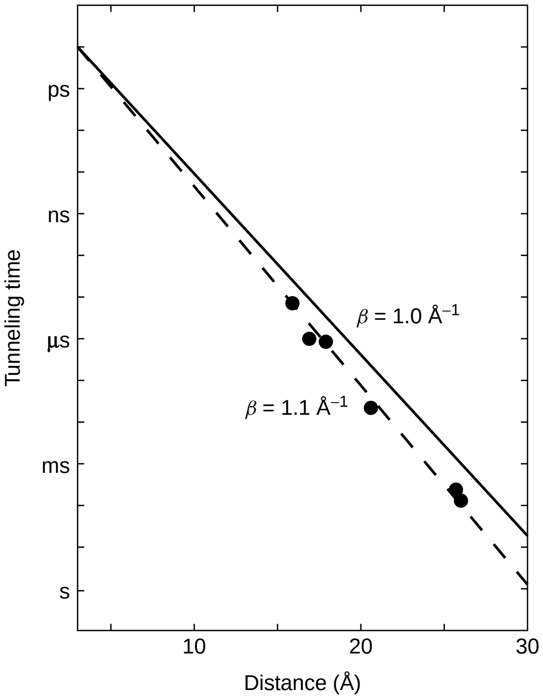

Figure 4 Distance dependence of driving-force-optimized electron tunneling times in Ru-labeled *P. aeruginosa* azurin. The solid line is the distance decay predicted by the tunneling-pathway model for ET along an ideal β-strand ($\beta = 1.0$ Å^{-1}). The dashed line is the best fit to the data ($\beta = 1.1$ Å^{-1})[23]

The validity of the azurin tunneling timetable rests on the assumption that Ru-azurin structures are not very different in crystals and aqueous solutions. Measurements of ET kinetics on crystalline samples of labeled azurins directly test this assumption;[46] the rate constants for oxidation of Cu(I) by Ru(III) and Os(III) in solutions and crystals are nearly identical for each donor–acceptor pair. It follows that the crystal structures of reduced and oxidized azurin are the relevant reactant and product states for solution ET.

It is important to distinguish between superexchange-mediated electron tunneling and multistep mechanisms that also can move charge over large molecular distances.[31,32] In tunneling processes, quantum mechanical mixing of localized donor and acceptor states with oxidized (and/or reduced) bridge states couples the reactant and product states, producing an avoided crossing between the free-energy surfaces at the transition state. Neither oxidized nor reduced bridge states are populated in tunneling reactions; ET occurs in a single elementary reaction step. There is a practical upper limit to the separation distance between redox sites; if charges must be transferred farther than this range, then multiple tunneling steps are required. Long-range ET can proceed by either single or multistep tunneling, but each mechanism has distinct energetic and coupling requirements, and can respond quite differently to changes in reaction parameters (e.g. T, ΔG°).

The energy gap between the donor/acceptor redox levels and those of oxidized or reduced intermediate states is the primary criterion in determining when multistep tunneling becomes important. In proteins with a single redox cofactor, the opportunities for multistep tunneling are limited. Extreme redox potentials are necessary to oxidize and reduce polypeptide backbones; thus multistep tunneling via backbone states will not contribute to observed ET kinetics under most solution conditions. The side chains of certain amino acids (e.g. Tyr, Trp) have redox potentials that are more accessible than those of the peptide backbone.[50,51] Oxidized Trp and Tyr residues have been characterized spectroscopically in a large number of proteins, although direct evidence for their involvement in multistep tunneling reactions is hard to come by.[52]

The $Ru(bpy)_2(im)(His)^{3+/2+}$ reduction potential ($E^\circ = 1.0\,V$ *vs.* NHE) is not high enough to oxidize Trp or Tyr residues in Ru-azurin; photogenerated holes in $Ru(bpy)_2(im)(HisX)^{3+}$ complexes remain localized on the Ru center. The energy gap between the Ru(III) hole state and oxidized bridge states must therefore be greater than 75 meV ($3k_B T$ at 295 K). The fact that oxidized bridge states lie at higher energy than the Ru(III) hole does not rule out multistep tunneling; endergonic steps can be compensated by favorable reactions later in a sequence.[32] Endergonic reactions, however, become less effective as the temperature decreases, so that multistep tunneling with highly endergonic steps will exhibit a strong dependence on temperature. The finding that the rate of Cu(I) → Ru(III) ET in $Ru(bpy)_2(im)(HisX)$-azurin is nearly independent of temperature between 240 and 300 K, coupled with the observation that decreasing the temperature to 160 K produces a twofold increase in the ET rate, demonstrate that multistep tunneling cannot explain long-range ET in Ru-azurin.[45] Instead, the data shown in Figure 4 provide a calibration standard for superexchange-mediated electron tunneling in proteins.

The rates of high-driving-force ET reactions have been measured for more than 30 Ru(diimine)-labeled metalloproteins.[21,23,24] Only modest corrections are required to scale these rates to driving-force-optimized values, permitting comparisons of ET in different proteins. The results are summarized in the electron tunneling timetable of Figure 5. The reported distances are all metal-to-metal measures; in the case of metal clusters, the closest metal was chosen. Tunneling times range from a few nanoseconds (12.2-Å ET in the high-potential iron–sulfur protein from *C. vinosum*) to 10 milliseconds (26-Å ET in *P. aeruginosa* azurin).

The Ru–protein data points are scattered around the Ru–azurin $\beta = 1.1\,\text{Å}^{-1}$ exponential distance decay. More than three-fourths of the Ru–protein ET rates fall in a 1.0 to $1.3\,\text{Å}^{-1}$ β-value zone. The data in Figure 5 suggest that a canonical distance decay constant will not describe long-range electron tunneling in proteins. Rates at a single distance can differ by as much as a factor of 10^3 and **D/A** distances that differ by as much as 5 Å can produce identical rates. The absence of a simple exponential distance dependence in the Ru–protein rate data is likely a reflection of the heterogeneity of the coupling medium. The efficiency of the coupling between redox centers is determined by the three-dimensional structure of the intervening polypeptide. While the azurin β-barrel structure supports a relatively uniform distance decay, highly helical proteins (myoglobin, cytochrome b_{562})[21,24] exhibit far more heterogeneous behavior. The protein fold is the key determinant of biological ET rates: it establishes the driving force, the reorganization energy, and the electronic coupling.

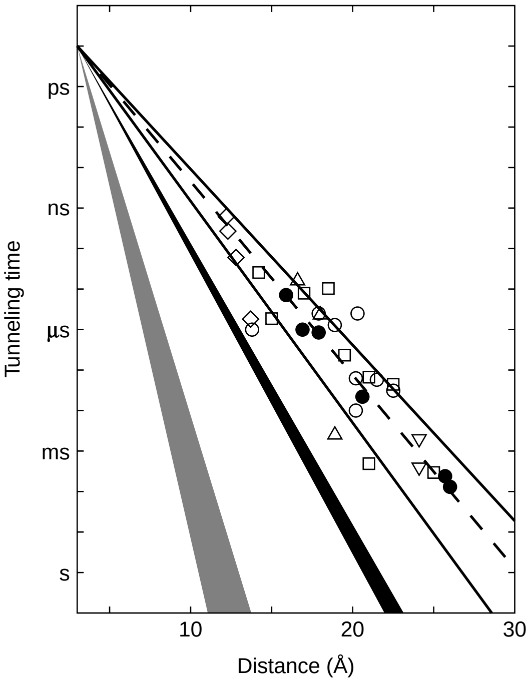

Figure 5 Tunneling timetable for ET in Ru-modified proteins: azurin (●); cytochrome *c* (○); myoglobin (△); cytochrome b_{562} (□); HiPIP (◇); and Fe:Zn-cytochrome *c* crystals (▽). The solid lines illustrate the tunneling-pathway predictions for coupling along β-strands ($\beta = 1.0\,\text{Å}^{-1}$) and α-helices ($\beta = 1.3\,\text{Å}^{-1}$); the dashed line illustrates a 1.1-Å^{-1} distance decay. Distance decay for electron tunneling through water is shown as a black wedge. Estimated distance dependence for tunneling through vacuum is shown as the grey wedge[21,23]

4 PROTEIN–PROTEIN REACTIONS

In low ionic-strength buffers, many proteins of opposite charge will form relatively tightly bound complexes.[53,54] With the aid of rapid triggering methods, it is possible to measure rates of long-range ET between redox sites in protein–protein complexes.[55,56] In many complexes, there are multiple binding sites and it is not uncommon to find that the ET kinetics often are regulated by the dynamics of conformational changes in the complex.[54] The usual interpretation is that surface diffusion of the two proteins produces a transient complex with significantly better electronic coupling and faster electron transfer. Consequently, rates depend strongly on solvent viscosity rather than intrinsic ET parameters (ΔG°, λ, r). A further complication associated with studies of protein–protein ET in solution is that binding sites and, hence, locations of redox cofactors, often are unknown. Issues of conformational change and structural ambiguity have been addressed recently with measurements of protein–protein ET kinetics in protein crystals.

4.1 Hemoglobin Hybrids

Kinetics measurements on crystallographically characterized metal-substituted hemoglobin (Hb) hybrids provided some of the earliest insights into interprotein ET rates.[57] Because Hb is a very strongly bound complex of four polypeptide subunits, ET measurements are not complicated by the dynamical problems that plague interpretation of rates in more weakly bound complexes. Replacement of the native Fe center in the β-subunits of Hb with Zn or Mg creates the opportunity for photoinitiated ET reactions. The reacting metal centers in the Hb hybrids are separated by 25 Å so that rates are relatively slow even at high driving forces. The time constant for ET from a triplet-excited ZnPor in the β-subunit to an Fe(III) center in the α-subunit is about 16 ms. Extensive studies of temperature dependences of hybrid Hb ET rates led to the conclusion that the reorganization energy for these reactions ($\lambda \sim 1$ eV) is dominated by outer-sphere contributions.[58] Measurements of ET rates in cryogenic glasses suggest that the polypeptide is the primary outer-sphere medium for the reaction and that bulk solvent reorganization does not play an important role in the reaction. Moreover, it was suggested that even at room temperature, the protein medium in Hb acts like a frozen glass. Results from measurements on Ru-azurin crystals also indicate that bulk solvent makes only a minor contribution to protein ET reorganization energies.[46]

4.2 Cytochrome *c*/cytochrome b_5 Complexes

The ET reaction between cytochrome *c* and cytochrome b_5 has been the subject of experimental and theoretical investigations for more than forty years.[59,60] Modeling both bimolecular and intracomplex ET between these proteins has been an active field of study. The detailed structural model proposed by Salemme in 1976 for the precursor complex of this protein pair stimulated a great deal of experimental work.[61] Careful spectroscopic studies revealed that these oppositely charged proteins form a stable 1:1 complex at low ionic strength.[59]

McLendon and Miller employed a combination of photochemical and pulse-radiolytic methods to probe the driving-force dependence of heme–heme ET in this complex.[53] The ET rates exhibit a near-Gaussian free-energy dependence, in excellent agreement with a 0.8-eV reorganization energy. The significance of this result is that, although this is a relatively low value of λ for ET between transition metal complexes in aqueous solution, it is by no means optimized. Most biological ET processes release less than 0.3 eV of free energy; with a 0.8-eV reorganization energy, rates will be 1–2 orders of magnitude below their maximum values.

Evidence for more complex ET processes came from studies in which photochemically generated reductants injected electrons into preformed Fe-cytochrome b_5/Fe-cytochrome *c* complexes. In one study, the rate of $b_5 \rightarrow c$ ET ($1.7 \times 10^3\ \mathrm{s}^{-1}$) was reported to depend on viscosity and surface mutations.[62] A later laser-flash photolysis study found a rate-limiting second-order reduction of Fe-cytochrome b_5/Fe-cytochrome *c* complexes and no sign of saturation, suggesting that the intracomplex ET rate was greater than $10^4\ \mathrm{s}^{-1}$.[59]

Ru-modified cytochrome b_5 and photochemical triggering methods were used to examine the kinetics of ET in cytochrome b_5/c complexes.[60] Rapid intraprotein reduction ($<$100 ns) of Fe(III)-cytochrome b_5 by excited $\mathrm{Ru(bpy)_3}^{2+}$ made it possible to probe $b_5 \rightarrow c$ ET kinetics. Two concentration-independent ET rates ($4 \times 10^5\ \mathrm{s}^{-1}$, $3.4 \times 10^4\ \mathrm{s}^{-1}$) were observed, suggesting that two cytochrome b_5/c species are present in solution. Studies of ionic-strength dependences and the effects of mutations suggest that the slower Fe(III)-cytochrome *c* reduction phase may be limited by conformational changes within one of the complexes.[60]

4.3 Cytochrome *c*/cytochrome *c* Peroxidase Complexes

Cytochrome *c* peroxidase (C*c*P) catalyzes the two-electron reduction of H_2O_2 by ferrocytochrome *c*. Hydrogen peroxide reacts rapidly with the resting ferric form of C*c*P to produce a species referred to as compound I, which contains a ferryl ($\mathrm{Fe(IV)O}^{2+}$) heme and a protein radical located on Trp191. The ET reactions involving these physiological redox partners have been studied in great detail.[54] At low ionic strength, acidic C*c*P and basic cytochrome *c* form a stable complex. A model of a 1:1 complex, based on the crystal structures of the two independent proteins, was proposed by Poulos and Kraut in 1980.[63] Twelve years later, Pelletier and Kraut reported the crystal structure of a 1:1 complex of the two yeast proteins.[64] Interestingly, the complex between yeast C*c*P and horse cytochrome *c* exhibited a slightly different structure. Analysis of the yeast/yeast complex suggested an electronic coupling pathway from the cytochrome *c* heme to the C*c*P heme via Trp191. On the basis of these crystallographic results, Pelletier and Kraut argued that C*c*P and cytochrome *c* form a highly specific 1:1 ET complex.

Hoffman and coworkers have employed metal-substituted C*c*P and cytochrome *c* to explore the ET kinetics between these two proteins.[54] Results from four-dimensional quenching studies, temperature and ionic-strength dependences, species variations, and electrostatic modeling provide compelling evidence for two distinct cytochrome *c* binding sites on C*c*P. The higher affinity binding site is the locus for Trp191 radical reduction by cytochrome *c*. Heme (C*c*P) reduction by cytochrome *c* can occur from either the high or low affinity binding site but, when exchange between the two is rapid, reduction from the low affinity site dominates.[54] These studies of C*c*P/cytochrome *c* ET, as well as those of cytochrome b_5/c, reveal the considerable mechanistic complexity of protein–protein ET processes.

4.4 Zn-cytochrome *c*/Fe-cytochrome *c* Crystals

Studies of C*c*P/cytochrome *c* and cytochrome b_5/c reactions highlight the difficulty of extracting ET parameters when donors and acceptors are not held at fixed distances and orientations. Crystals containing photoactivatable donors and acceptors at specific lattice sites are ideal media for investigating tunneling between proteins. In crystal lattices of tuna cytochrome *c*, chains of cytochrome *c* molecules form helices with a 24.1-Å separation between neighboring metal centers.[65] All other metal–metal distances in the lattice are greater than 30 Å. Thus, the heme groups can be treated as ordered in a one-dimensional chain, separated by identical protein and solvent media. By doping Zn-cytochrome *c* into this lattice, interprotein ET was probed using laser-flash transient spectroscopy. ET from the triplet-excited Zn-porphyrin to a neighboring Fe(III)-cytochrome *c* proceeded with a rate constant of $4(1) \times 10^2\,\mathrm{s}^{-1}$; the rate of charge recombination was about four times faster ($2.0(5) \times 10^3\,\mathrm{s}^{-1}$).[65]

Rapid relay of electrons involving at least one soluble redox enzyme requires the formation of short-lived, weakly bound protein–protein complexes. The recognition sites between proteins in such complexes tend to be smaller ($<1200\,\text{Å}^2$) and include more water molecules than the interfaces between subunits in oligomeric proteins. The interprotein interactions in crystals of tuna cytochrome *c* involve relatively few contacts: $760\,\text{Å}^2$ of surface area is buried in an interface with 31 van der Waals contacts ($3.2 \leq d \leq 3.9$ Å) and 16 water molecules (3 of which form bridging hydrogen bonds across the interface) but only one direct hydrogen bond bridging the two proteins. Indeed, the cytochrome *c* – cytochrome *c* interface is reminiscent of that between the natural redox partners, cytochrome *c* and cytochrome *c* peroxidase ($770\,\text{Å}^2$),[64] and may be typical of the interaction zones for soluble redox proteins. The Zn–Fe separation in doped tuna cytochrome *c* crystals is similar to that in Zn–Fe–hemoglobin hybrids (24.7 Å, T-state), although the tetrameric heme protein has many more contacts between subunits and a greater atom density at the interface. Nevertheless, $^*\mathrm{ZnPor} \rightarrow \mathrm{Fe(III)}$ and $\mathrm{Fe(II)} \rightarrow \mathrm{ZnPor}^{+\bullet}$ ET rates in Hb hybrids[57] and Zn-doped tuna cytochrome *c* crystal are quite similar and fall well within the range that has been established in studies of Ru-modified proteins.[21,23,24] The protein crystal ET data demonstrate that small interaction zones of low density are quite effective in mediating interprotein redox reactions.

5 PHOTOSYNTHESIS AND RESPIRATION

5.1 Photosynthetic Reaction Centers

Bacterial photosynthetic reaction centers (PRC) have been among the most actively studied ET proteins since DeVault and Chance first measured *C. vinosum* tunneling rates in the early 1960s.[66,67] In many cases, measurements of ET kinetics preceded determination of the three-dimensional structure of the membrane-bound protein assembly. It was not until the X-ray crystal-structure determinations of the *Rhodopseudomonas (Rps.) viridus*[68] and *Rhodobacter (Rb.) sphaeroides*[69] PRCs that distances could be assigned to specific rate constants. The recent crystal structures of photosystems I[70,71] and II[72,73] from cyanobacteria promise to clarify critical aspects of the ET mechanisms in oxygenic PRC.[74,75]

Photosynthetic reaction centers are ideal substrates for investigations of long-range electron transfer.[76–78] Charge separation in anoxygenic bacterial PRCs arises from a series of highly optimized ET processes (Figure 6). The primary photochemical event involves 2-ps ET over 17.8 Å from an electronically excited chlorophyll special pair ($^*(\mathrm{Bchl})_2$) to a pheophytin (Bphe) acceptor.[79] The rate of this reaction increases by about a factor of two as the temperature is lowered from 295 to 4 K. The absence of thermal activation indicates that the reorganization energy for $^*(\mathrm{Bchl})_2 \rightarrow \mathrm{Bphe}$ ET must be close to the driving force (0.2 eV). The reduced pheophytin delivers an electron to a quinone ($\mathrm{Q_A}$) 14.5 Å away in 100 ps. This productive reaction is 500 times faster than charge recombination with the hole in the bacteriochlorophyll special pair ($(\mathrm{Bchl})_2{}^{\bullet+}$). In 100 ps, approximately half of the 1.3 eV excitation

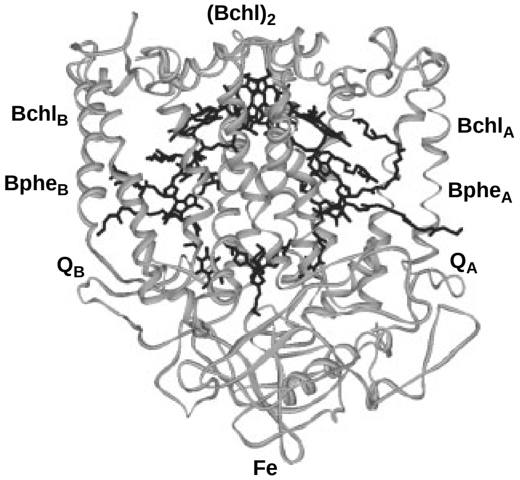

Figure 6 Model of the X-ray crystal structure of the photosynthetic reaction center from *Rb. sphaeroides*.[69] The bacteriochlorophyll special pair ($(\mathrm{Bchl})_2$), accessory bacteriochlorophylls (Bchl), bacteropheophytins (Bphe), quinones (Q), and iron complex (Fe) are shown in black. Electron transfer proceeds primarily along the A branch

energy of *(Bchl)$_2$ has been used to produce a 28.7 Å charge separation.[80] The charge on Q_A is subsequently transferred to a second quinone (Q_B) in a proton-coupled ET step.[81,82]

The hole in the bacteriochlorophyll special pair is filled by electron transfer from a cytochrome. In *Rps. viridis*, the cytochrome donor is tightly bound to the PRC at the membrane surface. This subunit contains four hemes in a nearly linear array oriented perpendicular to the membrane.[68] The reduction potentials of the hemes alternate from high ($\geq$250 mV *vs.* NHE) to low ($\leq$50 mV) as the distance from (Bchl)$_2$ increases.[83] The heme closest to the special pair, cytochrome c_{559}, has the highest potential and fills the (Bchl)$_2$$^{\bullet+}$ hole in about ~200 ns.[84] The next well-characterized process is ET from cytochrome c_{556} to cytochrome c_{559} in ~2 μs over a distance of 27.9 Å.[84]

In *Rb. sphaeroides*, (Bchl)$_2$$^{\bullet+}$ is reduced by a soluble single heme protein, cytochrome c_2. Several *Rb. sphaeroides* PRC mutants with altered (Bchl)$_2$$^{\bullet+/0}$ potentials have been prepared. In all, $E°$((Bchl)$_2$$^{\bullet+/0}$) values range from a low of 0.410 V to a high of 0.765 V *vs.* NHE (the wild-type value is 0.505 V).[85] A driving-force study of Fe(II) → (Bchl)$_2$$^{\bullet+}$ ET in cytochrome c_2/PRC complexes gave $\lambda = 0.5$ eV.[86] Global analysis of temperature and driving-force dependences of these ET rates indicated that $\lambda = 0.96 \pm 0.07$ eV, and H_{AB} values were not constant for all of the mutants.[87] The kinetics of ET from cytochrome c_2 to (Bchl)$_2$$^{\bullet+}$ in the PRC from *Rb. sphaeroides* have been measured in structurally characterized crystals.[88] The rate ($1.1 \times 10^6\ \mathrm{s}^{-1}$), driving force (0.16 eV), and donor–acceptor distance (21.2 Å) are quite similar to those for ET from cytochrome c_{559} to (Bchl)$_2$$^{\bullet+}$ in *Rps. viridis*.

Photosynthesis works because charge separation is more efficient than energy-wasting charge recombination. By blocking appropriate steps in the charge-separation sequence, it has been possible to determine the rates of PRC charge-recombination reactions. The near-linear arrangement of redox cofactors forms a redox potential gradient that favors short-range charge-separation reactions. In all cases, charge recombinations are many orders of magnitude slower than competing charge-separation reactions.[80]

Many of the PRC ET reactions exhibit only modest variations with temperature. The rate of the primary photochemical event increases at cryogenic temperature.[79] Several other reaction rates decrease by only small factors when temperatures are lowered.[87] For charge separation, this behavior can be attributed to driving-force-optimized reactions.

5.2 Cytochrome *c* Oxidase

In the terminal reaction of the respiratory chain, membrane-bound cytochrome *c* oxidase (C*c*O) receives electrons from soluble cytochrome *c* and passes them on to O_2.[1] C*c*O is a multisubunit membrane-bound enzyme with four redox cofactors (Cu$_A$, cytochrome *a*, cytochrome a_3, Cu$_B$). The locations of these metal complexes in C*c*O were revealed in the 1990s by the X-ray crystal structures of bacterial[89] and bovine enzymes (Figure 7).[90,91] The ET reactions of C*c*O have been the subjects of extensive investigation.[92,93] Cu$_A$, a binuclear Cu site with bridging S(Cys) atoms, is the primary electron acceptor from soluble cytochrome *c*.[94] Studies with Ru-modified cytochrome *c* reveal rapid ($6 \times 10^4\ \mathrm{s}^{-1}$)[95] electron injection from Fe(II) into Cu$_A$ at low driving force ($\Delta G° = -0.03$ eV).[96] Modeling suggests that cytochrome *c* binds to the bovine enzyme at an acidic patch on subunit II with an Fe–Cu distance of 17.8 Å.[97] The cytochrome *c* heme in the model is within 3.3 Å of the Trp104 (subunit II) indole ring, a residue that appears from mutagenesis experiments to be critical for rapid cytochrome *c*/Cu$_A$ ET. A possible electron tunneling path from this cytochrome *c* binding site through Trp104 to the bridging S(Cys200) ligand on Cu$_A$ has been identified.[98]

The 19.6-Å electron transfer from Cu$_A$ to cytochrome *a* proceeds rapidly at low driving force ($1.8 \times 10^4\ \mathrm{s}^{-1}$; $\Delta G° = -0.05$ eV).[95] Multiple electronic coupling pathways

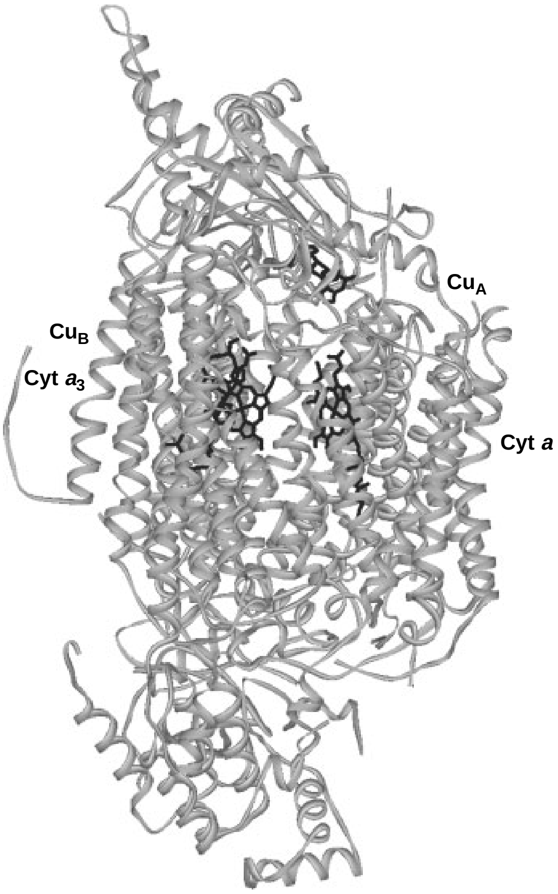

Figure 7 Model of the X-ray crystal structure of the bovine cytochrome *c* oxidase.[90,91] The dimeric Cu$_A$ site, cytochromes *a* and a_3, and the Cu$_B$ center are shown in black. Electrons enter the enzyme through Cu$_A$ and oxygen is activated at the cytochrome a_3/Cu$_B$ active site

have been proposed for this reaction. One postulated coupling route proceeds from Cu_A ligand His204 (subunit II) across one hydrogen bond to Arg438 (subunit I) (H204(Nε)-R438(O), 3.36 Å), and another H– bond (2.95 Å) from the Arg438 N–amide to the cytochrome *a* heme-propionate.[1,99–101] A tunneling-currents analysis suggested a slightly different Cu_A-cytochrome *a* coupling route through His204.[102] More recent work suggests that, owing to strong Cu–S(Cys) electronic interactions, pathways involving the bridging Cys residues are important for mediating coupling even though they involve more bonds than do routes through His204. Two independent analyses indicated that the sequence Cys200/Ile199/Arg439/heme-propionate (cytochrome *a*) is the dominant coupling route between Cu_A and cytochrome *a*.[101,102]

The coupling between cytochrome *a* and cytochrome a_3 has also been examined.[99,102] Nearly equivalent coupling routes between the two hemes involving the axial His residues (His378(cytochrome *a*), His376(cytochrome a_3)) were identified. One pathway proceeds through the intervening Phe377 residue; the other two involve a hydrogen bond between His378 and Val374. From Ala375, one pathway goes directly to His376 and the other involves a hydrogen bond to Tyr372 (which is hydrogen bonded to His376). A second study identified three major cytochrome *a*/cytochrome a_3 pathways: one is the direct jump from heme *a* to heme a_3; one has the aromatic ring of Phe377 as the only intermediate group; and the third involves His378 and the Phe377 aromatic ring. In spite of the similarity in Cu_A-cytochrome *a* (19.6 Å) and Cu_A-cytochrome a_3 (22.4 Å) distances, pathway analyses do not find important coupling pathways between the Cu_A center and cytochrome a_3.[99,102]

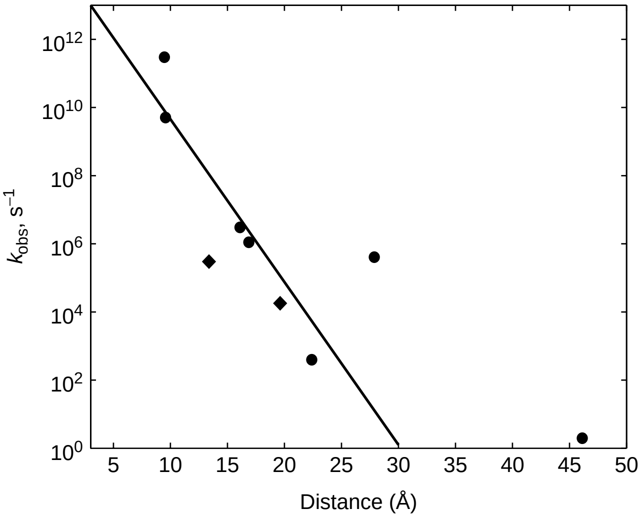

Figure 8 Distance dependence of observed ET rates in C*c*O (♦) and the PRC (●).[92,104] The solid line shows the average distance dependence found for driving-force-optimized ET in Ru-modified proteins ($\beta = 1.1$ Å^{-1})

6 CONCLUDING REMARKS

It is interesting to compare rates of electron tunneling in C*c*O and PRC with results from Ru-modified proteins (Figure 8).[80,92] The solid line in the figure corresponds to the average distance dependence of driving-force-optimized ET rates in Ru-proteins ($\beta = 1.1$ Å^{-1}; 10^{13} s^{-1} intercept). Most of the observed tunneling rates in C*c*O and the PRC lie near or *above* this line, indicating that the natural ET reactions are highly optimized, both in terms of reorganization energy and electronic coupling. Three of the *Rps. viridis* PRC reactions are at least two orders of magnitude faster than would be expected for activationless ET: the initial charge-separation event; ET from cytochrome c_{556} to cytochrome c_{559}; and charge recombination from reduced Q_A to cytochrome c_{559}. These unusually high ET rates may signal the presence of multistep tunneling processes.[79,88,103] It is interesting that neither the $Q_A^- \rightarrow (Bchl)_2^{\bullet +}$ nor the $Q_A^- \rightarrow$ cytochrome c_{559} charge-recombination reaction is unusually slow. This contrasts with the $Bphe^- \rightarrow (Bchl)_2^{\bullet +}$ reaction, which is 10^3 times slower than expected for a driving-force-optimized process at the same distance.[80] Inverted driving-force behavior may be responsible for retarding $Bphe^- \rightarrow (Bchl)_2^{\bullet +}$ ET, but multistep tunneling may nullify its effects in the longer-range reactions. The rate of ET from Cu_A to cytochrome *a* in C*c*O is close to that expected for an optimized reaction, yet the reaction driving force is just 50 meV. Clearly, both reorganization energies and electronic coupling pathways in C*c*O have been finely tuned to achieve a high level of electron transport efficiency.

7 RELATED ARTICLES

Copper Proteins with Type 1 Sites; Cytochrome Oxidase; Electron Transfer in Coordination Compounds; Electron Transfer Reactions: Theory; Iron: Heme Proteins & Electron Transport; Iron: Heme Proteins, Peroxidases, Catalases & Catalase-peroxidases; Photosynthesis.

8 REFERENCES

1. B. E. Ramirez, B. G. Malmström, J. R. Winkler, and H. B. Gray, *Proc. Natl. Acad. Sci. U.S.A.*, 1995, **92**, 11949.
2. P. Brzezinski and G. Larsson, *Biochim. Biophys. Acta Bioenerg.*, 2003, **1605**, 1.
3. B. Giese, *Curr. Opin. Chem. Biol.*, 2002, **6**, 612.
4. M. E. Núñez and J. K. Barton, *Curr. Opin. Chem. Biol.*, 2002, **4**, 199.
5. F. D. Lewis, in ‘Electron and Charge Transport Processes in DNA’, eds. H. B. Gray and J. R. Winkler, Weinheim, Germany, 2001.

6. N. M. Jackson and M. G. Hill, *Curr. Opin. Chem. Biol.*, 2001, **5**, 209.
7. R. A. Marcus and N. Sutin, *Biochim. Biophys. Acta*, 1985, **811**, 265.
8. R. A. Marcus, *Angew. Chem., Int. Ed. Eng.*, 1993, **32**, 1111.
9. R. A. Marcus, *Adv. Chem. Phys.*, 1999, **106**, 1.
10. H. B. Gray, B. G. Malmström, and R. J. P. Williams, *J. Biol. Inorg. Chem.*, 2000, **5**, 551.
11. C. N. Schutz and A. Warshel, *Proteins: Struct., Funct., Genet.*, 2001, **44**, 400.
12. P. J. Stephens, D. R. Jollie, and A. Warshel, *Chem. Rev.*, 1996, **96**, 2491.
13. F. A. Armstrong and G. S. Wilson, *Electrochim. Acta*, 2000, **45**, 2623.
14. G. R. Moore and G. W. Pettigrew, 'Cytochromes *c*: Evolutionary, Structural, and Physicochemical Aspects', Springer-Verlag, 1990.
15. R. A. Scott and A. G. Mauk, in 'Cytochrome *c* – A Multidisciplinary Approach', University Science Books, Sausalito, CA, 1996.
16. E. L. Raven and A. G. Mauk, *Adv. Inorg. Chem.*, 2001, **51**, 1.
17. F. A. Tezcan, J. R. Winkler, and H. B. Gray, *J. Am. Chem. Soc.*, 1998, **120**, 13383.
18. J. R. Telford, P. Wittung-Stafshede, H. B. Gray, and J. R. Winkler, *Acc. Chem. Res.*, 1998, **31**, 755.
19. P. Wittung-Stafshede, *Acc. Chem. Res.*, 2002, **35**, 201.
20. T. Simonson, *Rep. Prog. Phys.*, 2003, **66**, 737.
21. H. B. Gray and J. R. Winkler, *Q. Rev. Biophys.*, 2003, **36**, 341.
22. M. Bixon and J. Jortner, *Adv. Chem. Phys.*, 1999, **106**, 35.
23. H. B. Gray and J. R. Winkler, *Annu. Rev. Biochem.*, 1996, **65**, 537.
24. J. R. Winkler, A. Di Bilio, N. A. Farrow, J. H. Richards, and H. B. Gray, *Pure Appl. Chem.*, 1999, **71**, 1753.
25. J. J. Hopfield, *Proc. Natl. Acad. Sci. U.S.A.*, 1974, **71**, 3640.
26. A. Ponce, H. B. Gray, and J. R. Winkler, *J. Am. Chem. Soc.*, 2000, **122**, 8187.
27. K. V. Mikkelsen and M. A. Ratner, *Chem. Rev.*, 1978, **87**, 113.
28. H. M. McConnell, *J. Chem. Phys.*, 1961, **35**, 508.
29. A. A. Stuchebrukhov, *Adv. Chem. Phys.*, 2001, **118**, 1.
30. J. N. Onuchic, D. N. Beratan, J. R. Winkler, and H. B. Gray, *Annu. Rev. Biophys. Biomol. Struct.*, 1992, **21**, 349.
31. M. Bixon and J. Jortner, *J. Chem. Phys.*, 1997, **107**, 5154.
32. C. C. Page, C. C. Moser, and P. L. Dutton, *Curr. Opin. Chem. Biol.*, 2003, **7**, 551.
33. W. B. Curry, M. D. Grabe, I. V. Kurnikov, S. S. Skourtis, D. N. Beratan, J. J. Regan, A. J. A. Aquino, P. Beroza, and J. N. Onuchic, *J. Bioenerg. Biomembr.*, 1995, **27**, 285.
34. J. J. Regan and J. N. Onuchic, *Adv. Chem. Phys.*, 1999, **107**, 497.
35. I. A. Balabin and J. N. Onuchic, *J. Phys. Chem. B*, 1998, **102**, 7497.
36. S. S. Skourtis and D. N. Beratan, *J. Biol. Inorg. Chem.*, 1997, **2**, 378.
37. K. Kumar, I. V. Kurnikov, D. N. Beratan, D. H. Waldeck, and M. B. Zimmt, *J. Phys. Chem. A*, 1998, **102**, 5529.
38. A. A. Stuchebrukhov, *J. Chem. Phys.*, 1996, **105**, 10819.
39. F. Millett and B. Durham, *Biochemistry*, 2002, **41**, 11315.
40. K. M. Yocom, J. B. Shelton, J. R. Shelton, W. E. Schroeder, G. Worosila, S. S. Isied, E. Bordignon, and H. B. Gray, *Proc. Natl. Acad. Sci. U.S.A.*, 1982, **79**, 7052.
41. J. R. Winkler, D. G. Nocera, K. M. Yocom, E. Bordignon, and H. B. Gray, *J. Am. Chem. Soc.*, 1982, **104**, 5798.
42. J. R. Winkler and H. B. Gray, *Chem. Rev.*, 1992, **92**, 369.
43. I.-J. Chang, H. B. Gray, and J. R. Winkler, *J. Am. Chem. Soc.*, 1991, **113**, 7056.
44. A. J. Di Bilio, M. G. Hill, N. Bonander, B. G. Karlsson, R. M. Villahermosa, B. G. Malmström, J. R. Winkler, and H. B. Gray, *J. Am. Chem. Soc.*, 1997, **119**, 9921.
45. L. K. Skov, T. Pascher, J. R. Winkler, and H. B. Gray, *J. Am. Chem. Soc.*, 1998, **120**, 1102.
46. B. R. Crane, A. J. Di Bilio, J. R. Winkler, and H. B. Gray, *J. Am. Chem. Soc.*, 2001, **123**, 11623.
47. D. N. Beratan, J. N. Betts, and J. N. Onuchic, *Science*, 1991, **252**, 1285.
48. E. T. Adman, *Adv. Protein Chem.*, 1991, **42**, 145.
49. J. F. Smalley, H. O. Finklea, C. E. D. Chidsey, M. R. Linford, S. E. Creager, J. P. Ferraris, K. Chalfant, T. Zawodzinsk, S. W. Feldberg, and M. D. Newton, *J. Am. Chem. Soc.*, 2003, **125**, 2004.
50. J. Stubbe and W. A. van der Donk, *Chem. Rev.*, 1998, **98**, 705.
51. J. Stubbe, D. G. Nocera, C. S. Yee, and M. C. Y. Chang, *Chem. Rev.*, 2003, **103**, 2167.
52. M. C. Y. Chang, C. S. Yee, J. Stubbe, and D. G. Nocera, *Proc. Natl. Acad. Sci. U.S.A.*, 2004, **101**, 6882.
53. G. McLendon and R. Hake, *Chem. Rev.*, 1992, **92**, 481.
54. J. M. Nocek, J. S. Zhou, S. DeForest, S. Priyadarshy, D. N. Beratan, J. N. Onuchic, and B. M. Hoffman, *Chem. Rev.*, 1996, **96**, 2459.
55. V. L. Davidson, *Acc. Chem. Res.*, 2000, **33**, 87.
56. G. Tollin, *J. Bioenerg. Biomembr.*, 1995, **27**, 303.
57. B. M. Hoffman, M. J. Natan, J. M. Nocek, and S. A. Wallin, *Struct. Bonding*, 1991, **75**, 85.
58. L. A. Dick, I. Malfant, D. Kuila, S. Nebolsky, J. M. Nocek, B. M. Hoffman, and M. A. Ratner, *J. Am. Chem. Soc.*, 1998, **120**, 11401.
59. A. G. Mauk, M. R. Mauk, G. R. Moore, and S. H. Northrup, *J. Bioenerg. Biomembr.*, 1995, **27**, 311.
60. B. Durham, J. L. Fairris, M. McLean, F. Millett, J. R. Scott, S. G. Sligar, and A. Willie, *J. Bioenerg. Biomembr.*, 1995, **27**, 331.

61. F. R. Salemme, *J. Mol. Biol.*, 1976, **102**, 563.
62. L. Qin, K. K. Rodgers, and S. G. Sligar, *Mol. Cryst. Liq. Cryst.*, 1991, **194**, 311.
63. T. L. Poulos and J. Kraut, *J. Biol. Chem.*, 1980, **255**, 10322.
64. H. Pelletier and J. Kraut, *Science*, 1992, **258**, 1748.
65. F. A. Tezcan, B. R. Crane, J. R. Winkler, and H. B. Gray, *Proc. Natl. Acad. Sci. U.S.A.*, 2001, **98**, 5002.
66. D. De Vault and B. Chance, *Biophys. J.*, 1966, **6**, 825.
67. D. De. Vault, J. H. Parkes, and B. Chance, *Nature*, 1967, **215**, 642.
68. J. Deisenhofer, O. Epp, I. Sinning, and H. Michel, *J. Mol. Biol.*, 1995, **246**, 429.
69. H. Komiya, T. O. Yeates, D. C. Rees, J. P. Allen, and G. Feher, *Proc. Natl. Acad. Sci. U.S.A.*, 1988, **85**, 9012.
70. P. Jordan, P. Fromme, H. T. Witt, O. Klukas, W. Saenger, and N. Krauß, *Nature*, 2001, **411**.
71. P. Fromme, P. Jordan, and N. Krauß, *Biochim. Biophys. Acta*, 2001, **1507**, 5.
72. A. Zouni, H. T. Witt, J. Kern, N. Krauß, W. Saenger, and P. Orth, *Nature*, 2001, **409**, 739.
73. N. Kamiya and J. R. Shen, *Proc. Natl. Acad. Sci. U.S.A.*, 2003, **100**, 98.
74. N. Krauß, *Curr. Opin. Chem. Biol.*, 2003, **7**, 540.
75. J. H. A. Nugent, *Eur. J. Biochem.*, 1996, **237**, 519.
76. Govindjee, J. T. Beatty, and H. Gest, *Photosynth. Res.*, 2003, **76**, 1.
77. Govindjee and H. Gest, *Photosynth. Res.*, 2002, **73**, 1.
78. K. Mobius, *Chem. Soc. Rev.*, 2000, **29**, 129.
79. C. Kirmaier and D. Holten, *Photosynth. Res.*, 1987, **13**, 225.
80. S. Franzen, R. F. Goldstein, and S. G. Boxer, *J. Phys. Chem.*, 1993, **97**, 3040.
81. M. Y. Okamura, M. L. Paddock, M. S. Graige, and G. Feher, *Biochim. Biophys. Acta Bioenerg.*, 2000, **1458**, 148.
82. R. I. Cukier and D. G. Nocera, *Annu. Rev. Phys. Chem.*, 1998, **49**, 337.
83. F. Baymann and F. Rappaport, *Biochemistry*, 1998, **37**, 15320.
84. J. M. Ortega and P. Mathis, *Biochemistry*, 1993, **32**, 1141.
85. X. Lin, H. A. Murchison, V. Nagarajan, W. W. Parson, J. P. Allen, and J. C. Williams, *Proc. Natl. Acad. Sci. U.S.A.*, 1994, **91**, 10265.
86. X. Lin, J. C. Williams, J. P. Allen, and P. Mathis, *Biochemistry*, 1994, **33**, 13517.
87. G. Venturoli, F. Drepper, J. C. Williams, J. P. Allen, X. Lin, and P. Mathis, *Biophys. J.*, 1998, **74**, 3226.
88. H. L. Axelrod, E. C. Abresch, M. Y. Okamura, A. P. Yeh, D. C. Rees, and G. Feher, *J. Mol. Biol.*, 2002, **319**, 501.
89. S. Iwata, C. Ostermeier, B. Ludwig, and H. Michel, *Nature*, 1995, **376**, 660.
90. T. Tsukihara, H. Aoyama, E. Yamashita, T. Tomizaki, H. Yamaguchi, K. Shinzawa-Itoh, R. Nakashima, R. Yaono, and S. Yoshikawa, *Science*, 1995, **269**, 1071.
91. S. Yoshikawa, K. Shinzawa-Itoh, R. Nakashima, R. Yaono, E. Yamashita, N. Inoue, M. Yao, J. M. Fei, C. P. Libeu, T. Mizushima, H. Yamaguchi, T. Tomizaki, and T. Tsukihara, *Science*, 1998, **280**, 1723.
92. J. R. Winkler, B. G. Malmström, and H. B. Gray, *Biophys. Chem.*, 1995, **54**, 199.
93. Ó. Einarsdóttir and I. Szundi, *Biochim. Biophys. Acta Bioenerg.*, 2004, **1655**, 263.
94. H. Beinert, *Eur. J. Biochem.*, 1997, **245**, 521.
95. L. M. Geren, J. R. Beasley, B. R. Fine, A. J. Saunders, S. Hibdon, G. J. Pielak, B. Durham, and F. Millett, *J. Biol. Chem.*, 1995, **270**, 2466.
96. L. P. Pan, S. Hibdon, R.-Q. Liu, B. Durham, and F. Millett, *Biochemistry*, 1993, **32**, 8492.
97. V. A. Roberts and M. E. Pique, *J. Biol. Chem.*, 1999, **274**, 38051.
98. R. K. Szilagyi and E. I. Solomon, *Curr. Opin. Chem. Biol.*, 2002, **6**, 250.
99. J. J. Regan, B. E. Ramirez, J. R. Winkler, H. B. Gray, and B. G. Malmström, *J. Bioenerg. Biomembr.*, 1998, **30**, 35.
100. D. R. Gamelin, D. W. Randall, M. T. Hay, R. T. Houser, T. C. Mulder, G. W. Canters, S. de Vries, W. B. Tolman, Y. Lu, and E. I. Solomon, *J. Am. Chem. Soc.*, 1998, **120**, 5246.
101. S. D. George, M. Metz, R. K. Szilagyi, H. Wang, S. P. Cramer, Y. Lu, W. B. Tolman, B. Hedman, K. O. Hodgson, and E. I. Solomon, *J. Am. Chem. Soc.*, 2001, **123**, 5757.
102. D. M. Medvedev, I. Daizadeh, and A. A. Stuchebrukhov, *J. Am. Chem. Soc.*, 2000, **122**, 6571.
103. C. C. Page, C. C. Moser, X. Chen, and P. L. Dutton, *Nature*, 1999, **402**, 47.
104. H. B. Gray and W. R. Ellis Jr, in ‘Electron Transfer’, eds. I. Bertini, H. B. Gray, S. J. Lippard, and J. S. Valentine, University Science Books, Mill Valley, CA, 1994.

Acknowledgments

I thank Brian S. Leigh for assistance with the graphics. This research is supported by the National Science Foundation and the National Institutes of Health.

Luminescence Behavior & Photochemistry of Organotransition Metal Compounds

Vivian Wing-Wah Yam[1] & Kenneth Kam-Wing Lo[2]
[1]*The University of Hong Kong, Hong Kong, China*
[2]*City University of Hong Kong, Hong Kong, China*

1	Introduction	1
2	Carbonyl, Isocyanide, and Cyanide Systems	2
3	Alkynyl Systems	10
4	Alkenyl, Arene, and Aryl Systems	17
5	Alkylidenes and Alkylidyne Systems	18
6	Cyclometalated Systems	23
7	Alkyl Systems	27
8	Related Articles	28
9	References	28

Abbreviations

10-MePTZ = 10-methylphenothiazine; 2,3-dpp = 2,3-bis (2-pyridyl)pyrazine; 2,9-Me$_2$-4,7-Ph$_2$-phen = 2,9-dimethyl-4,7-diphenyl-1,10-phenanthroline; 2,9-Me$_2$-phen = 2,9-dimethyl-1,10-phenanthroline; 3,4,7,8-Me$_4$-phen = 3,4,7,8-tetramethyl-1,10-phenanthroline; 4,4′-{NH$_2$}$_2$-bpy = 4,4′-diamino-2,2′-bipyridine; 4,4′-Me$_2$-bpy = 4,4′-dimethyl-2,2′-bipyridine; 4, 4′-Ph$_2$-bpy = 4,4′-diphenyl-2,2′-bipyridine; 4, 4′-^{t}Bu$_2$-bpy = 4,4′-di-*tert*-butyl-2,2′-bipyridine; 4,7-Me$_2$-phen = 4,7-dimethyl-1,10-phenanthroline; 4-MeOPh-HPhbpy = 4′-(4-methoxyphenyl)-6′-phenyl-2,2′-bipyridine; 4-Me-phen = 4-methyl-1,10-phenanthroline; 5,6-Me$_2$-phen = 5,6-dimethyl-1,10-phenanthroline; 5-Ph-phen = 5-phenyl-1,10-phenanthroline; bimy = benzimidazol-2-ylidene; biq = 2,2′-biquinoline; bpy = 2,2′-bipyridine; bpy-dvb-bpy = 1,4-bis[2-(4′-methyl-2,2′-bipyrid-4-yl)ethenyl]benzene; bpy-pyr1 = 4-(2-pyrrol-1-ylethyl)-4′-methyl-2,2′-bipyridine; bpy-pyr2 = 4,4′-bis((3-pyrrol-1-ylpropyloxy)carbonyl)-2,2′-bipyridine; BSA = bovine serum albumin; BTA = bis(trimethylsilyl)acetylene; chrysi = 5,6-chrysenequinone diimine; COD = 1,5-cyclooctadiene; DAB = 1,4-diaza-1,3-butadiene; DFT = density functional theory; dmb = 1,8-diisocyano-*p*-menthane; dmb-tol = 4-methyl-4′-(*N*-methyl-*p*-tolylaminomethyl)-2,2′-bipyridine; dmpe = 1,2-bis(dimethylphosphino)ethane; dmpm = bis(dimethylphosphino) methane; dpmp = bis(diphenylphosphinomethyl)phenylphosphine; dppb = 1,2-bis(diphenylphosphino)benzene; dppe = 1,2-bis(diphenylphosphino)ethane; dpp-HCNN = 2,9-diphenyl-1,10-phenanthroline; dppm = bis(diphenylphosphino)methane; dppn = benzo[*i*]dipyrido[3,2−*a*:2′,3′−*c*] phenazine; dppz = dipyrido[3,2−*a*:2′,3′−*c*]phenazine EHMO = Extended Hückel Molecular Orbital; EPA = ether/isopentane/ethanol (5:5:2 by volume); EPR = Electron Paramagnetic Resonance; H(pyCH$_2$)$_2$im = 1,3-bis(2-pyridinylmethyl)-1*H*-imidazolium; H$_2$bph = biphenyl; Hacac = acetylacetone; HAT = 1,4,5,8,9,12-hexaazatriphenylene; Hbsn = 2-(1-naphthyl)benzothiazole; Hbt = 2-phenylbenzothiazole; Hbtp = 2-(2-benzothienyl)pyridine; Hbzq = 7,8-benzoquinoline; HCpy$_3$ = tris(2-pyridyl)methane; Hhfac = 1,1,1,5,5,5-hexafluoroacetylacetone; Hmppy = 3-methyl-1-phenylpyrazole; HOMO = highest-occupied molecular orbital; Hpba = 4-(2-pyridyl)benzaldehyde; Hpic = picolinic acid; Hppy = 2-phenylpyridine; Hppz = 1-phenylpyrazole; Hpq = 2-phenylquinoline; HSA = human serum albumin; Hsal = *N*-methylsalicylimine; Hthpy = 2-(2-thienyl)pyridine; IL = intraligand; im = imidazole; ^{i}Pr-DAB = *N*,*N*′-diisopropyl-1,4-diaza-1,3-butadiene; LLCT = ligand-to-ligand charge-transfer; LMCT = ligand-to-metal charge-transfer; LUMO = lowest-unoccupied molecular orbital; MC = metal-centered; Me$_3$TACN = 1,4,7-trimethyl-1,4,7-triazacyclononane; MeP$_3$ = 1,1,1-tris(diphenylphosphinomethylethane); Mes = mesityl; MLCT = metal-to-ligand charge-transfer; MMLCT = metal-metal-to-ligand charge-transfer; MO = molecular orbital; MV^{2+} = methyl viologen; pby-HCNN = 6-phenyl-2,2′-bipyridine; PEG = poly(ethylene glycol); phen = 1,10-phenanthroline; phi = 9,10-phenanthrene quinone diimine; phpy4,5p(*R*,*R*) py = (8*R*,10*R*)-2-(2′-phenyl)-4,5-pinenopyridine; PMMA = poly(methyl methacrylate); Ppy$_3$ = tris(2-pyridyl)phosphine; py-4-COOH = isonicotinic acid; py-4-Et = 4-ethylpyridine; py-4-Me = 4-methylpyridine; py-CH$_2$NHbiotin = *N*-[(4-pyridyl)methyl]biotinamide; py-PTZ = 10-(4-picolyl)phenothiazine; pz = pyrazolyl; SBLCT = sigma-bond-to-ligand charge-transfer; SCE = standard calomel electrode; SDS = sodium dodecylsulfate; SSCE = sodium saturated calomel electrode; TACN = 1,4,7-triazacyclononane; TAP = 1,4,5,8-tetraazaphenanthrene; ^{t}Bu$_3$-terpy = 4,4′,4″-tri-*tert*-butyl-2,2′:6′,2″-terpyridine; TCNQ = tetracyanoquino-*p*-dimethane; terpy = 2,2′:6′,2″-terpyridine; thpy4,5p(*R*,*R*) py = (8*R*,10*R*)-2-(2′-thienyl)-4,5-pinenopyridine; tmb = 2, 5-diisocyano-2′,5′-dimethylhexane; TMEDA = tetramethylethylenediamine; TMPTA = trimethylolpropane triacrylate; TPA = 1,3,5-triaza-7-phosphaadamantane; XLCT = halide-to-ligand charge-transfer.

1 INTRODUCTION

The fluorescence (*see Fluorescence*) properties of organic compounds are well known and extensively studied. Many compounds, especially the polyaromatics, exhibit intense fluorescence with tunable energy upon variation in electronic and structural factors. The emission origin is usually limited to $^1(\pi \rightarrow \pi^*)$, $^1(\text{n} \rightarrow \pi^*)$, or intramolecular charge-transfer (*see Charge Transfer*) although in many cases excimer and exciplex formation has been observed. The synthesis, structures, and chemical reactivity of a number of organotransition metal compounds have received much attention over the past decades. Factors such as a wide choice of carbon-containing ligands, the flexible bonding modes of these ligands, and the diversity of molecular structures, can result in the formation of novel organometallic compounds with characteristic physical and chemical properties. In particular, the luminescence and photochemical studies of organotransition metal compounds contribute to an important aspect of modern photochemistry.

Incorporation of transition metal centers to organic ligands enables efficient spin-orbit coupling, leading to the population of excited states (*see Excited State*) of triplet (*see Triplet State*) character and enhancement of the phosphorescence of organic compounds or phosphorescence (*see Phosphorescence*) characteristic of the organometallic compounds. Basically, coordination of transition metal centers to organic compounds can enrich the emission properties by providing new excited-state character that is unable to achieve otherwise. For example, metal-to-ligand charge-transfer transitions are commonly observed in transition metal complexes containing d electrons and organic ligands with low-lying empty π^* orbitals. Ligand-to-metal charge-transfer transitions are also common for electron-rich organic ligands and electron-deficient (*see Electron Deficient Compound*), high-valent transition metal centers. In addition, short metal–metal separations, which could be an implication of weak metal–metal interactions, have been observed in many polynuclear organotransition metal systems (*see* ***Polynuclear Organometallic Cluster Complexes*** and ***Dinuclear Organometallic Cluster Complexes***), especially those with a d^8 and d^{10} electronic configuration. The metal–metal interaction can destabilize the filled d_{z^2} orbitals (due to the formation of $d\sigma^*$) and stabilize the empty p_z orbitals (due to the formation of $p\sigma$ orbitals). Thus, the HOMO-LUMO gap (*see HOMO–LUMO Gap*) can be reduced, leading to low-energy $(d\sigma^* \rightarrow p\sigma)$ transitions.

In this article, a number of selected d-block organotransition metal compounds are introduced and their remarkable luminescence and photochemical properties are described and discussed. Emphasis is placed on the interrelationship between the nature of the transition metal centers, identity and bonding mode of the organic ligands, the photophysical and photochemical properties, and the character of the emissive states. Novel luminescent organotransition metal complexes with potential application values in different areas are also included here. Meanwhile, readers are referred to a selection of book chapters and review articles on the photophysics and photochemistry of transition metal complexes.**[1–7]**

2 CARBONYL, ISOCYANIDE, AND CYANIDE SYSTEMS

2.1 Carbonyl Systems (*See Carbonyl Complexes of the Transition Metals*)

2.1.1 Luminescence Properties

Hexacarbonyl complexes $[\text{M(CO)}_6]$ (M = Cr, Mo, W) can react with a diimine ligand (N–N) to form highly colored complexes $[\text{M(CO)}_4\text{(N–N)}]$.**[8]** The photophysical properties of these complexes have received much interest. The electronic absorption spectra of $[\text{M(CO)}_4\text{(N–N)}]$ (M = Cr, Mo, W) displayed two bands in the visible region. The absorption band at higher energy (ca. 400 nm) was proposed to be an admixture of ^{1}MLCT and d-d transitions, while the lower energy one at ca. 460–600 nm was assigned to an ^{1}MLCT $(d\pi(\text{M}) \rightarrow \pi^*(\text{N–N}))$ transition. Excitation of the complexes $[\text{M(CO)}_4\text{(N–N)}]$ (M = Mo, W) in degassed benzene at room temperature resulted in dual luminescence with emission bands at ca. 606 and 739 nm. The origin of both bands has been assigned to an ^{3}MLCT excited state, with the higher-energy band perturbed by a nearby ^{3}LF state.**[3]**

There have been many photophysical and photochemical studies of the rhenium(I) carbonyl diimine complexes $[\text{Re(CO)}_3\text{(N–N)X}]$ (N–N = diimine ligands, X = monodentate ligands such as carbonyl, halides, pyridines, and phosphines).**[1–4,8]** In the presence of the diimine ligand, relatively intense ^{1}MLCT $(d\pi(\text{Re}) \rightarrow \pi^*(\text{N–N}))$ absorption bands appear in the visible region. In most cases, excitation of the complexes gives rise to intense and long-lived emission in the visible region. The lifetime falls into the submicrosecond to microsecond timescales, and the emission is phosphorescence in nature. An excited state of ^{3}MLCT $(d\pi(\text{Re}) \rightarrow \pi^*(\text{N–N}))$ character has been assigned to many complexes of this type.**[1–4,8]**

The ^{3}MLCT emission properties of many rhenium(I) carbonyl diimine complexes have been used to demonstrate the energy-gap law. For example, the complexes $[\text{Re(N–N)(CO)}_3\text{(L)}]$ (N–N = bpy, phen, 5-Ph-phen; L = substituted pyridines or quinoline) displayed ^{3}MLCT $(d\pi(\text{Re}) \rightarrow \pi^*(\text{N–N}))$ phosphorescence at room temperature.**[9]** The radiationless decay-rate constants depended on the emission energy as described in the energy-gap law $(\ln k_{\text{nr}} \approx \text{A} - \text{B}\ E_{\text{em}})$. From the Hammett constant of the substituent, both the emission energy and lifetime of related complexes can be predicted.**[9]**

A special property of these luminescent carbonyl diimine complexes is their solvatochromic behavior.**[1–4,8]** The MLCT absorption bands exhibit a noticeable red shift when the polarity of the solvents decreases (negative solvatochromism). For example, the ^{1}MLCT transition of $[\text{Re(CO)}_3\text{(bpy)Cl}]$ occurred at 370 and 400 nm in CH_3CN and benzene respectively.**[3]** Similar solvatochromism was also observed for the charge-transfer bands of other carbonyl complexes

$[M(CO)_4(N–N)]$ (M = Cr, Mo, W).[1–4,8] The hypsochromic shift of the MLCT absorption band with increasing solvent polarity has been accounted for by assuming that the charge transfer in the MLCT excited state occurs antiparallel to the ground-state dipole moment. The higher transition energy in more polar solvents may be due to dominating ground-state stabilization. The ^{3}MLCT emission of these complexes displays a small blue shift with an increase in emission lifetimes in more non-polar solvents. For example, the complex $[Re(CO)_3(bpy)Cl]$ showed ^{3}MLCT emission in CH_3CN at 622 nm ($\tau_o = 25$ ns) while the emission occurred at 615 nm ($\tau_o = 70$ ns) in benzene.[3] These solvent effects have also been interpreted mainly on the basis of the energy-gap law.[10]

These luminescent carbonyl diimine MLCT emitters also display interesting luminescence rigidochromism.[1–4,8,10,11] The emission maxima of these complexes exhibit a distinct shift to higher energy upon cooling the sample solutions from room temperature to glass at low temperature. This phenomenon is associated with the rigidity change in the medium rather than simply a temperature effect because it was found that even at room temperature, significant hypsochromic shifts were noticed when these MLCT emitters were incorporated in a rigid polyester resin.[11] The blue shift was a consequence of the destabilization of the excited state of the complex since the solvent molecules cannot freely reorient themselves around the excited complex in a rigid environment. As an example, the complex $[W(CO)_4(4\text{-Me-phen})]$ displayed a weaker emission band at 553 nm and a stronger one at 765 nm in EPA at 293 K.[11] Upon lowering the temperature from 293 to 80 K, the overall emission intensity increased by 100 fold, and the higher-energy band became more dominant. Both bands displayed significant hypsochromic shifts to ca. 533 and 647 nm, respectively, at 80 K. On the basis of the sensitivity of the luminescence properties of these organometallic complexes on the rigidity of their local environment, these complexes have been exploited as spectroscopic probes in the cross-linking polymerization of photosensitive thin films.[11] To illustrate this, the luminescent rhenium(I) complex $[Re(CO)_3(4,7\text{-}Ph_2\text{-phen})Cl]$ has been used to monitor the acrylate cross-linking reaction. The ^{3}MLCT emission of the complex added to a TMPTA/PMMA system containing the photoinitiator 2,2-dimethoxy-2-phenylacetophenone experienced a blue shift (from 576 to 562 nm) with an increase in emission intensity and lifetime when polymerization proceeded. The change in the emission intensity and lifetimes essentially resulted from the increased rigidity of the polymer environment and the corresponding decrease of the matrix free volume. This rhenium(I) complex and its analogues such as $[Re(CO)_3(phen)Cl]$ and $[Re(CO)_3(4,7\text{-}Ph_2\text{-phen})I]$ were also used as probes in the curing of photosensitive epoxy-based materials.[11]

The emission properties of rhenium(I) polypyridine complexes have been utilized in biological studies. Activation of the coordinated isonicotinic acid of the complex $[Re(CO)_3(2,9\text{-}Me_2\text{-}4,7\text{-}Ph_2\text{-phen})(py\text{-}4\text{-}COOH)]^+$ by *N*-hydroxysuccinimide allowed the conjugation of the complex to biomolecules such as human serum albumin.[12] The HSA conjugate displayed intense emission at 550 nm ($\tau_{average} = 2.7\,\mu s$) in oxygenated aqueous solution. The emission polarization of the rhenium-HSA conjugate was sensitive to the binding of anti-HSA due to the increase in molecular weight and a substantial enhancement in anisotropy. This luminescent conjugate was employed in a competition immunoassay for HSA.

Schanze and coworkers connected an anthracene unit to a rhenium(I)-bpy chromophore via a flexible tether to give complexes such as $[Re(CO)_3(bpy)(py\text{-}4\text{-}CH_2NHCO(CH_2)_3NHCH_2\text{-}9\text{-anthracene})]^+$.[13] In an aqueous solution, the rhenium(I)-bpy unit interacted with the hydrophobic anthracene and the ^{3}MLCT luminescence was significantly quenched by exchange triplet–triplet energy transfer. However, in the presence of double-stranded DNA molecules, anthracene intercalated strongly into the double-helix, leading to an increased separation between the rhenium(I)-bpy and anthracene units. The efficiency of the intramolecular energy transfer quenching was lowered and the ^{3}MLCT emission was thus resumed (Figure 1).

The ^{3}MLCT emission properties of a series of rhenium(I) polypyridine complexes attached with a biotin moiety $[Re(CO)_3(N–N)(py\text{-}CH_2NH\text{-biotin})](PF_6)$ have been studied.[14] While common organic fluorescent biotin conjugates suffer from significant self-quenching due to resonance-energy transfer upon binding to the protein avidin, these rhenium(I) biotin complexes displayed luminescence enhancement and lifetime elongation upon binding to avidin. These

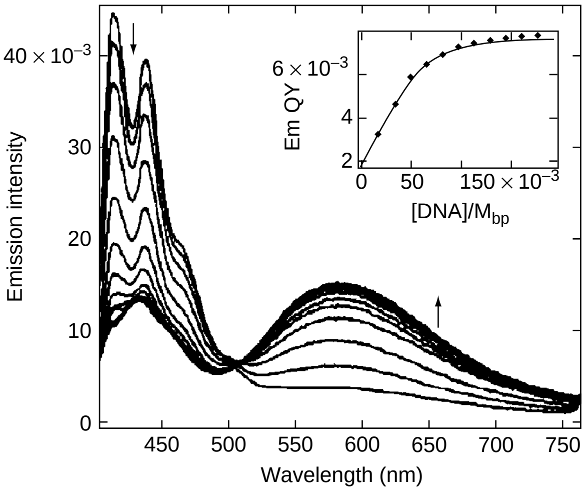

Figure 1 Corrected emission spectra of $[Re(CO)_3(bpy)(py\text{-}4\text{-}CH_2NHCO(CH_2)_3NHCH_2\text{-}9\text{-anthracene})]^+$ as a function of [DNA]/[Re]. [DNA]/[Re] ratios: 0, 0.5, 1.0, 1.5, 2.0, 2.5, 3.0, 3.5, 4.0, 4.5, 5.0, and 5.5. Inset shows a plot of Φ_{em}^{MLCT} versus [DNA] for the same emission titration experiment. Conditions: Tris buffer; pH = 7.0; [Re] = 33 μM. (Reprinted with permission from Ref. 13. © 1993 American Chemical Society)

observations suggested that the complexes could be exploited as a new class of a luminescent probe for avidin, biotin, and biotinylated species.

2.1.2 Nature of Excited States

It is noteworthy that the excited-state lifetimes of $[Re(CO)_3(N–N)X]$ increased significantly upon changing the axial ligand X from Cl to Br and then to I, while the emission energy did not change.[15] The transient absorption difference spectra of $[Re(CO)_3(bpy)X]$ revealed the absorption of the bpy$\cdot^-$ anion radical at ca. 375 and 470 nm together with an absorption band associated with the halide ligand. For $X = Cl$, it occurred as a very weak red tail of the bpy$\cdot^-$ anion radical band, and for $X = Br$, it became a distinct low-energy shoulder. However, for $X = I$, a separate and intense band occurred at 780 nm. Time-resolved IR spectra showed that the carbonyl stretching frequencies shifted to higher values upon irradiation, an observation due to the reduced π-back bonding (*see Back Bonding*) of the rhenium center to the carbonyl in the charge-transfer excited state. The force constants of the CO bonds decreased in the order: $X = Cl$ ($82\,N\,m^{-1}$) $>$ $X = Br$ ($76\,N\,m^{-1}$) $\gg$ $X = I$ ($55\,N\,m^{-1}$), suggesting that the HOMO of the complexes contained substantial Re–X ($d\pi$-$p\pi$) antibonding character (Figure 2). The halide participation in the HOMO increased in the order $Cl < Br \ll I$ because of its better electronegativity from Cl to I, and the excited state of the iodo complex $[Re(CO)_3(bpy)I]$ should be best described as XLCT in character.

The dinuclear rhenium(I) thiolate complexes $[\{Re(N–N)(CO)_3\}_2(\mu\text{-S-}C_6H_4\text{-X-p})](CF_3SO_3)$ showed low-energy ^{1}MLCT ($d\pi$(Re) $\rightarrow$ π^*(N–N)) absorption bands at ca. 430 nm in CH_2Cl_2.[16] Excitation of the complexes resulted in intense yellow–green luminescence at ca. 606–615 nm ($\tau_o = 100–140$ ns). On the basis of the relatively small dependence of the emission energy on the nature of the thiolate ligands, the emission was assigned to an ^{3}MLCT ($d\pi$(Re) $\rightarrow$ π^*(N–N)) excited state, mixed with some ^{3}LLCT (p(S) $\rightarrow$ π^*(N–N)) character. Related mixed-metal rhenium(I) thiolate and selenolate complexes $[\{Re(N–N)(CO)_3(\mu\text{-E-}C_6H_4\text{-X-}p)\}_2M(bpy)_2]^{2+}$ (M = Zn(II), Cd(II)) were also studied.[17]

When more conjugated diimine or pyridine ligands are used, the excited states of rhenium(I) carbonyl complexes can have substantial ^{3}IL character.[18] While the ^{3}MLCT emission is often broad, with a lifetime in the submicrosecond to microsecond timescale, the ^{3}IL emission usually has noticeable structural features, even in fluid solutions at ambient temperature. The emission lifetime is usually very long. A simple and widely applicable approach is to evaluate the ratio of the emission quantum yield and the emission lifetime (the product of the intersystem crossing efficiency and radiative decay-rate constant).[18] Experimental values of

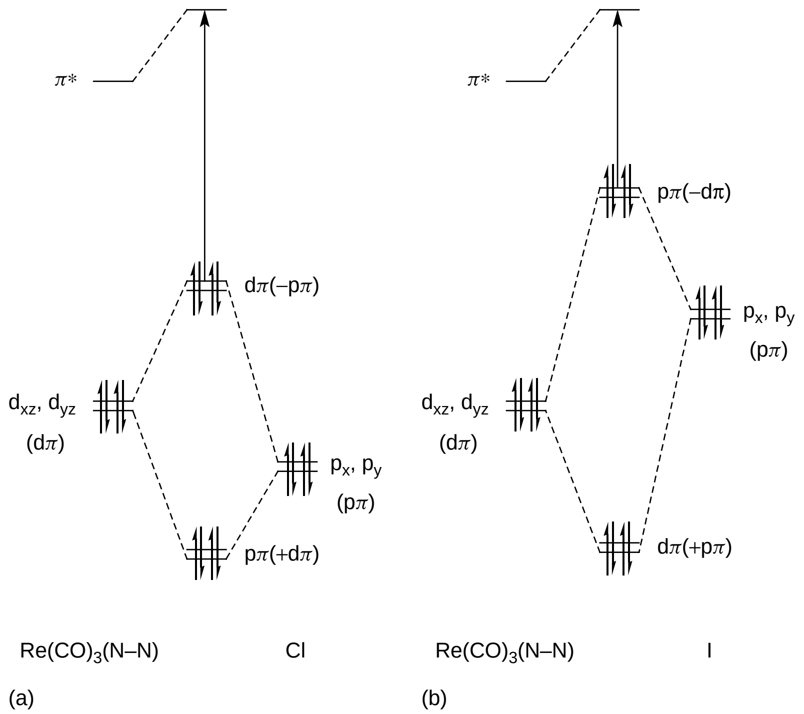

Figure 2 Simplified MO schemes showing the effect of π-interaction between the rhenium atom and the halide axial ligand on the character of the lowest electronic transition of $[Re(CO)_3(N–N)X]$. The two highest-occupied molecular orbitals of the chloro (a) and iodo (b) complexes were predominantly of metal $d\pi$(Re) and iodo $p\pi$ character, respectively, giving rise to essentially ($d\pi$(Re) $\rightarrow$ π^*(N–N)) MLCT and (p(I) $\rightarrow$ π^*(N–N)) LLCT lowest transitions, respectively. (Reprinted from Ref. 15, © 1998, with permission from Elsevier)

this ratio being $<10^4\,s^{-1}$ suggest that the intersystem crossing (*see Intersystem Crossing*) efficiency to populate the ^{3}MLCT state is less than unity, implying the population of ^{3}IL or other triplet states such as an LF state directly from the ^{1}MLCT state: for example, the products ($\eta_{ISC} \cdot k_{nr}$) for the dppz (**1**) and bpy-dvb-bpy (**2**) complexes of rhenium(I), $[Re(CO)_3(dppz)(py\text{-}4\text{-}Me)]^+$, and $[Re(CO)_3(bpy\text{-}dvb\text{-}bpy)(CH_3CN)]^+$, were 11 and $<20\,s^{-1}$, respectively, reflecting significant ^{3}IL character in their emissive states. In addition, the transient absorption difference spectra of these complexes showed remarkable difference to those of common rhenium(I) diimine ^{3}MLCT emitters, but resembled those of the free ligands dppz and bpy-dvb-bpy, respectively.

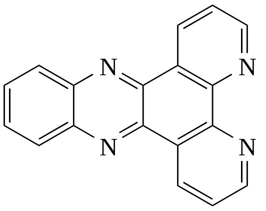

dppz

(**1**)

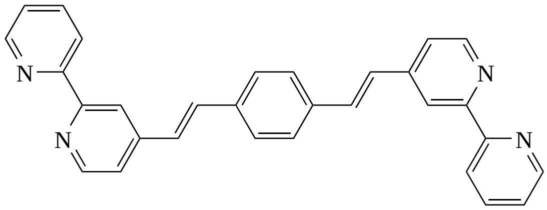

bpy-dvb-bpy

(**2**)

Time-resolved, step-scan FT-IR spectroscopy has been used to monitor the ν(CO) frequencies of rhenium(I) carbonyl polypyridine complexes and hence to study the excited-state electronic structures of these systems.**[19]** The MLCT and IL character in the emissive states of $[Re(CO)_3(phen)(py\text{-}4\text{-}Me)]^+$ and $[Re(CO)_3(dppz)(PPh_3)]^+$, respectively, has been studied by this technique. The presence of two close-lying states of MLCT and IL character for the complex $[Re(CO)_3(4,4'\text{-}\{NH_2\}_2\text{-}bpy)(py\text{-}4\text{-}Et)]^+$ was also confirmed.

The complexes $[Re(CO)_3(N\text{–}N)(L)]^+$ (N–N = dppz or dppn (**3**), L = pyridine or 4-methylpyridine) have been prepared and their luminescence properties studied.**[20,21]** Luminescence and transient absorption spectroscopy indicated that this class of complexes exhibited a triplet IL excited state. The intercalative binding of the complexes to double-stranded calf thymus DNA and synthetic oligonucleotides was investigated, and cleavage of the plasmid pBR322 upon visible light irradiation was observed. It appeared that the excited complex $[Re(CO)_3(dppz)(py)]^{+*}$ directly oxidized the DNA molecule. However, in the case of the dppn analogue, the reactive species responsible for the cleavage was identified to be superoxide radicals and hydroxyl radicals, both of which were produced from the reduction of dioxygen by the excited complex. In a related study, the ^{3}IL (dppz) nature of the excited state of the complex $[Re(CO)_3(dppz)(py)]^+$ has been investigated using visible and infrared transient absorption and resonance Raman spectroscopy (*see Resonance Raman Spectroscopy*) on the picosecond and nanosecond timescales.**[22]**

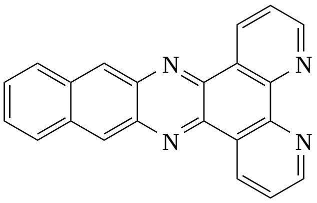

dppn

(**3**)

The emission properties of another class of complexes $[Re(CO)_3(N\text{–}N)(py)]^+$ containing alkyl and aryl-substituted phenanthroline ligands (N–N) (3,4,7,8-Me_4-phen, 2,9-Me_2-4,7-Ph_2-phen, 4,7-Me_2-phen, 5,6-Me_2-phen, 5-Ph-phen, 2,9-Me_2-phen and phen), have been investigated.**[23]** In particular, the temperature dependence of the solution emission was studied. Most of the complexes showed a steady increase in the observed decay-rate constant with temperature from 150 to 320 K, which can be rationalized by the thermal population of a short-lived ^{1}MLCT or d-d state, which was higher in energy than the usual ^{3}MLCT state. Interestingly, the rate constant of the 3,4,7,8-Me_4-phen complex first decreased from 150 to 230 K before rising from 230 to 320 K. Fitting of the data suggested the presence of a longer-lived state lying about $130\,cm^{-1}$ above the ^{3}MLCT state. For this particular complex, the long-lived state was assigned to an ^{3}IL state associated with the 3,4,7,8-Me_4-phen ligand. The presence of IL character in the solution emission of this complex can be revealed by its extraordinarily long emission lifetime (13 µs in CH_2Cl_2 at 298 K) and structured emission spectra.

The intriguing luminescence properties of the platinum(II) carbonyl biphenyl complex $[Pt(bph)(CO)_2]$ have been studied.**[24]** The low-energy absorption bands at ca. 301 and 330 nm were assigned to ^{1}MLCT (d(Pt) $\rightarrow \pi^*$(bph)) transitions. In the solid state, the crystals were green and absorbed at ca. 650 nm. The absorption band was assigned to a $^1(d\sigma^* \rightarrow \pi^*$(bph)) transition. The complex showed excitation wavelength-dependence and structured emission bands in low-temperature glass. Such multiple emission behavior is characteristic of the presence of more than one emitting species. The emission bands that occurred at ca. 525 and 660 nm were related to the presence of dimeric species and higher-nuclearity aggregates formed as the solution cooled. The solid sample showed an intense emission band at 726 nm, which was proposed to be related to the columnar structure of the solid in which the complex molecules were stacked alternatively with a Pt–Pt distance of ca. 3.24 Å.

2.1.3 Photochemical Properties

The photoredox properties of rhenium(I) polypyridine complexes have been well studied. Reductive quenching of luminescent rhenium(I) systems by amines, and oxidative quenching by pyridinium ions have been described.[1–4,8] When these quenchers are linked covalently to a rhenium(I) center, photoinduced intramolecular electron transfer reactions are anticipated. The intramolecular electron transfer chemistry of rhenium(I) polypyridine complexes has been investigated in detail by Meyer and coworkers.[25] The complex $[\mathrm{Re(CO)_3(bpy)(py\text{-}PTZ)}]^+$ contained a reductive quencher ligand py-PTZ (**4**). In 77-K alcohol glass, the photophysical properties of the complex were essentially the same as that of its pyridine counterpart. However, in $\mathrm{CH_3CN}$ at room temperature, excitation of the ^{1}MLCT chromophore was followed by rapid appearance of transient absorption features at 350 and 500 nm, consistent with the formation of charge-separated states $[\mathrm{Re(CO)_3(bpy^{\bullet-})\ (py\text{-}PTZ^{\bullet+})}]^+$. Kinetic measurements revealed that this charge-separated transient species decayed to the ground state with a rate constant that was three orders of magnitude smaller than that of the back-electron-transfer within the model association complex $\{[\mathrm{Re(CO)_3(bpy^{\bullet-})\ (py\text{-}4\text{-}Et)}]^0$, $\mathrm{10\text{-}MePTZ^{\bullet+}}\}$. The relatively small decay-rate constant for the intramolecular electron transfer was accounted for by the restricted relative orientation of the electron donor and acceptor. The photophysical properties of a related complex $[\mathrm{Re(CO)_3(dmb\text{-}tol)Cl}]$ containing the quencher dmb-tol (**5**) were also investigated.[26]

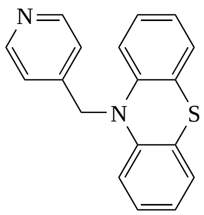

py-PTZ

(**4**)

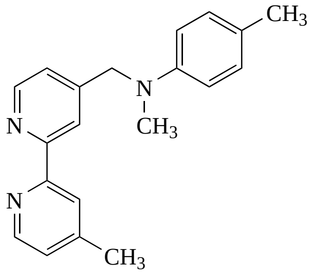

dmb-tol

(**5**)

In view of the strong photooxidizing properties of $[\mathrm{Re(CO)_3(phen)(im)}]^+$,[27] azurin from *Pseudomonas aeruginosa* has been modified with a rhenium(I) diimine unit via a histidine residue to give the derivative $[\mathrm{Re(CO)_3(phen)(His83)}]^+$-$\mathrm{AzCu^+}$. Direct photoinduced oxidation of Cu(I) to Cu(II) was observed.[27] In a related study, the photogeneration of tryptophan and tyrosyl radicals by rhenium(I) complexes conjugated to azurin involving the flash-quench technique has been demonstrated.[28] The EPR spectra of frozen solutions of irradiated $[\mathrm{Re(CO)_3(phen)(H83)}]^+$-$\mathrm{AzZn^{2+}/[Co(NH_3)_5Cl]^{2+}}$ and $[\mathrm{Re(CO)_3(phen)(H107)}]^+$-$\mathrm{AzZn^{2+}/[Co(NH_3)_5Cl]^{2+}}$ (Y72F mutant, leaving only one tyrosin, Y108, in the protein) revealed the presence of W48• and Y108• radicals, respectively, formed by the oxidizing rhenium(II) species.

Transient FTIR and UV-vis spectroscopy have been used to study the excited-state properties of mononuclear $[\mathrm{Re(CO)_3(4,4'\text{-}Me_2\text{-}bpy)(CH_3CN)}](\mathrm{PF_6})$ and dinuclear $[\mathrm{Re(CO)_3(4,4'\text{-}Me_2\text{-}bpy)}]_2$ in $\mathrm{CH_3CN}$ or THF.[29] The one-electron reduced monomer $[\mathrm{Re(CO)_3(4,4'\text{-}Me_2\text{-}bpy)(Sol)}]$ (Sol = $\mathrm{CH_3CN}$ or THF), formed from (1) the reductive quenching of the excited states of $[\mathrm{Re(CO)_3(4,4'\text{-}Me_2\text{-}bpy)(CH_3CN)}](\mathrm{PF_6})$ by triethylamine or (2) the homolysis of $[\mathrm{Re(CO)_3(4,4'\text{-}Me_2\text{-}bpy)}]_2$, underwent dimerization slowly in THF. The reaction of $[\mathrm{Re(CO)_3(4,4'\text{-}Me_2\text{-}bpy)(Sol)}]$ with $\mathrm{CO_2}$ was slow and competed with the dimerization. Photolysis of $[\mathrm{Re(CO)_3(4,4'\text{-}Me_2\text{-}bpy)}]_2$ in the presence of $\mathrm{CO_2}$ produced CO with a 25–50% yield based on [Re]. A $\mathrm{CO_2}$-bridged dimer, $[\mathrm{(4,4'\text{-}Me_2\text{-}bpy)(CO)_3Re{-}C(O)O{-}Re(CO)_3(4,4'\text{-}Me_2\text{-}bpy)}]$ was identified as an intermediate and both $[\mathrm{Re(CO)_3(4,4'\text{-}Me_2\text{-}bpy)}]_2(\mathrm{OCO_2})$ and $[\mathrm{Re(CO)_3(4,4'\text{-}Me_2\text{-}bpy)(OC(O)OH)}]$ were detected as oxidation products.

The photochemical properties of $[\mathrm{Ru(CO)_3(dmpe)}]$ (dmpe = 1,2-bis(dimethylphosphino)ethane) have been studied by matrix isolation at 12 K and laser flash photolysis with UV-vis and IR detection at ambient temperatures.[30] UV photolysis ($\lambda_{\mathrm{ex}} = 234$–$376$ nm) in a matrix resulted in the formation of $[\mathrm{Ru(CO)_2(dmpe)\cdot S}]$ (S = matrix host). Laser flash photolysis in heptane solution ($\lambda_{\mathrm{ex}} = 266$ or 308 nm) revealed that $[\mathrm{Ru(CO)_2(dmpe)\cdot(heptane)}]$ was a short-lived intermediate fragment that reacted rapidly with $[\mathrm{Ru(CO)_3(dmpe)}]$.

2.1.4 Polynuclear Systems

A number of tetranuclear rhenium(I) cyclophane complexes have been isolated by the reaction of $[\mathrm{Re(CO)_5Cl}]$ with excess bridging pyridine ligands such as pyrazine, 4,4′-bipyridine, 1,2-bis(4-pyridyl)ethylene, and bridging porphyrin units including 2,8,12,18-tetrabutyl-3,7,13,17-tetramethyl-5,15-bis(4-pyridyl)$\mathrm{(H)_2}$porphyrin and its zinc(II)-coordinated counterpart.[31] The cavity lengths of these molecular squares varied from ca. 3 to 20 Å. Heterometallic molecular squares have been constructed by the reaction of the monomer $[\mathrm{Re(CO)_3(4,4'\text{-}bpy)Cl}]$ and $\mathrm{M(dppp)(OTf)_2}$ (M = Pd(II) or Pt(II)). Most of these rhenium(I) squares displayed ^{3}MLCT emission upon photoexcitation and the emission maxima occurred at ca. 584–661 nm in $\mathrm{CH_2Cl_2}$ at room temperature. It is noteworthy that the emission intensity of the $\mathrm{Re_2Pd_2}$ square increased in the presence of anions such as $\mathrm{BF_4^-}$, $\mathrm{OTf^-}$, and $\mathrm{ClO_4^-}$. The potential applications of these cyclophanes in differentiating molecules of various sizes were investigated.

The luminescence of a thin film coated with $[Re(CO)_3(\mu\text{-}4,4'\text{-bipyridine})Cl]_4$ was quenched by nitrobenzene vapor because of electron transfer. Recently, mesoporous thin films of $[Re(CO)_3(\mu\text{-}L)Cl]_4$ (L = 4,4′-pyrazine or 4,4′-bipyridine) have been utilized as sensors for volatile organic compounds (VOCs). The host-guest interaction between the rhenium cyclophanes and VOCs was confirmed by quartz crystal microbalance studies.

Luminescent π-conjugated polymers obtained from Pd-mediated cross-coupling of $[Re(CO)_3(bpy\{C{\equiv}CH\}_2)Cl]$, 4,4′-diethynylbiphenyl, and $1,4\text{-}(I)_2\text{-}2,5\text{-}(C_{18}H_{37}O)_2\text{-}C_6H_2$ have been isolated and characterized.[32] The synthesis of these polymers is illustrated in Scheme 1. Four polymers with various mole fractions (from 0 to 0.5) of the rhenium(I) carbonyl unit showed intense $^1IL(\pi \rightarrow \pi^*)$ (polymer backbone) emission at 435 nm in THF solutions. The emission quantum yield and lifetime decreased with increasing mole fraction of rhenium(I), suggesting that the diffusing $^1IL(\pi \rightarrow \pi^*)$ exciton was dynamically quenched by the rhenium(I) traps. In low-temperature glass, the polymers showed $^1IL(\pi \rightarrow \pi^*)$ fluorescence. For those polymers that contained the rhenium(I) units, additional emission bands at 643 and 700 nm were also observed. The former was the $^3IL(\pi \rightarrow \pi^*)$ phosphorescence of the polymer, while the latter was the $^3MLCT(d\pi(Re) \rightarrow \pi^*(\text{polymer}))$ phosphorescence. Both the $^3IL(\pi \rightarrow \pi^*(\text{polymer}))$ states and the $^3MLCT(d\pi(Re) \rightarrow \pi^*(\text{polymer}))$ states were observed in the transient absorption difference spectra of those polymers containing the rhenium(I) carbonyl unit. The photophysics of related rhenium(I)-phenylene-ethynylene oligomers have also been studied by UV-vis transient absorption spectroscopy and time-resolved, step-scan Fourier transform infrared spectroscopy, establishing the $^3IL(\pi \rightarrow \pi^*)$ nature of the lowest-lying excited state.[33]

The optoelectronic properties of conjugated polymers containing the rhenium diimine unit $[Re(CO)_3(phen)Cl]$ have been studied.[34] Charge-carrier mobility measurements showed that the presence of metal complexes could facilitate the charge-transport process, and the enhancement in carrier mobility was dependent on the metal content in the polymer. The use of transition metal complexes for both photovoltaic and electroluminescence applications was demonstrated.

Ishitani and coworkers reported the photophysical properties of polynuclear luminescent rhenium(I) diimine complexes with bridging pyridine and phosphine ligands.[35] The tetranuclear complex $[\{Re(bpy)(CO)_3(dppe)Re(bpy)(CO)_2\}_2(4,4'\text{-bpy})]^{4+}$ emitted at 695 nm with a very weak emission shoulder at ca. 540 nm. The low-energy emission was assigned to an $^3MLCT\ (d\pi(Re) \rightarrow \pi^*(bpy))$ state involving the central $[\{(dppe)Re(bpy)(CO)_2\}_2(4,4'\text{-bpy})]$ unit, while the high energy one to another ^3MLCT state involving the terminal $[Re(bpy)(CO)_3(dppe)]$ unit. Intramolecular energy transfer from the terminal Re-bpy units to the central Re-bpy units was suggested. For the trinuclear complex $[Re(bpy)(CO)_3(dppe)Re(bpy)(CO)_2(4,4'\text{-bpy})\text{-}Re(bpy)(CO)_3]^{3+}$, dual luminescence at ca. 540 and 670 nm was observed. The 540-nm emission was assigned to an ^3MLCT state of the $Re(bpy)(CO)_3(4,4'\text{-bpy})$ unit, while the 670 nm emission was assigned to another ^3MLCT state of the central $[\text{-dppe-}Re(bpy)(CO)_2(4,4'\text{-bpy})\text{-}]$ unit. Similar energy transfer was proposed to occur from the terminal rhenium(I) units to the central one.

Thin films of $poly[Ru(L)(CO)_2Cl_2]$ complexes (L = bpy-pyr1 (**6**) or bpy-pyr2 (**7**)) have been prepared by

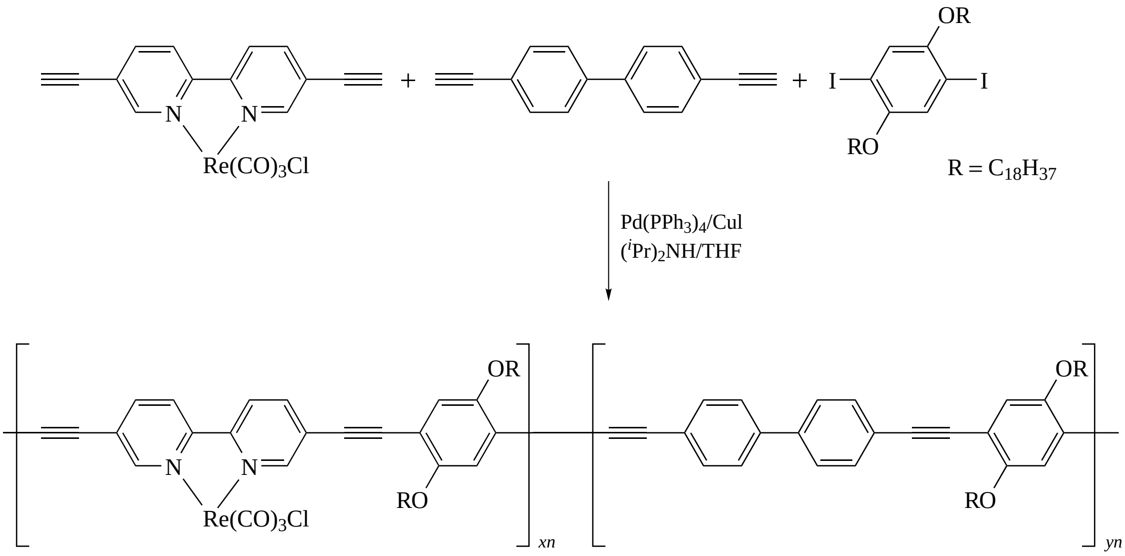

Scheme 1 Synthesis of π-conjugated polymer incorporated with rhenium(I) 2,2′-bipyridine units. The values of x and y varied from 0 to 0.5 and 1 to 0.5, respectively

anodic electropolymerization of the corresponding monomeric complexes on platinum and indium–tin oxide electrodes.[36] Photolysis ($\lambda_{ex} = 366$ nm) of the films immersed in CH_3CN led to successive photosubstitutions of the two CO ligands and one Cl^- ligand by CH_3CN for the bpy-pyr1 polymer while only photosubstitutions of the CO ligands occurred for the bpy-pyr2 analogue. On the basis of the photochemistry, images can be created in the films by using masking techniques.

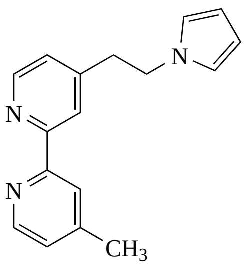

bpy-pyr1

(**6**)

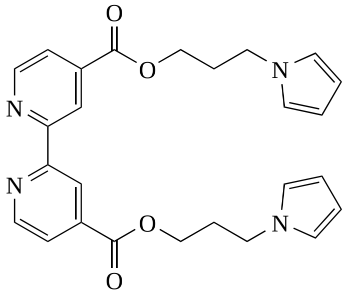

bpy-pyr2

(**7**)

2.2 Isocyanide Systems

Isocyanides are versatile ligands (*see Isocyanide Ligands*) that have been coordinated to many transition metal centers to give novel organometallic compounds. In particular, the ligands tmb (**8**) and dmb (**9**) have been extensively used to coordinate to metal centers to give dimeric and polymeric materials, and many of which showed attractive spectroscopic and luminescence properties. The dinuclear rhodium(I) isocyanide complex $[Rh_2(dmb)_4]^{2+}$ showed very long Rh–Rh bond distances in the solid states (3.861–4.48 Å).[37] The solution absorption spectrum of the complex displayed an intense $^1(d_{xz}, d_{yz} \rightarrow p\sigma)$ band at 314 nm, where the $p\sigma$ orbital is the bonding MO formed between the $5p_z$ orbitals of the rhodium(I) centers. The $^1(d\sigma^* \rightarrow p\sigma)$ (where the $d\sigma^*$ is the antibonding MO formed between the $4d_{z^2}$ orbitals of the rhodium(I) centers) transition appeared as an asymmetric absorption band at ca. 420–440 nm with a long tailing shoulder at ca. 480 nm. The corresponding $^3(d\sigma^* \rightarrow p\sigma)$ transition occurred at ca. 3000 cm^{-1} lower in energy in the polarized single-crystal spectra. Symmetric fluorescence and phosphorescence bands at ca. 546–600 nm and 660–714 nm, respectively, were observed in various media under different conditions. The MM2 calculation results revealed a very shallow ground-state ($^1A_{1g}$) surface with a minimum at 4.75 Å, and an extremely anharmonic excited-state ($^3A_{2u}$) surface with a well-defined minimum at 3.35 Å.

The luminescence properties of the gold(I) isocyanide complex $[Au_2(dmb)(CN)_2]$ have been studied.[38] The crystal structure of the complex showed an intramolecular gold–gold separation of 3.536 Å. The solid sample displayed an emission band at 456 nm ($\tau_o = 0.59\ \mu s$) and a weaker broad emission band at around 600–700 nm. The complex only displayed a high-energy band at 458 nm ($\tau_o = 0.13\ \mu s$) in dichloromethane solution. Other related $[Au_2(diiso)(C{\equiv}CPh)_2]$ and $[Au_2(diiso)(CN)_2]$ (diiso = tmb or dmb) have been shown to display luminescence behavior.[39] Excited states of ^{3}MLCT ($d(Au) \rightarrow \pi^*(diiso)$) and $^3(d\sigma^* \rightarrow p\sigma)$ character were responsible for the emission of the alkynyl and cyano complexes, respectively.

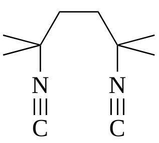

tmb

(**8**)

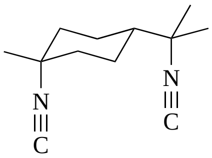

dmb

(**9**)

The crystal structure of $[Ir(CN\text{-}CH_3)_2Au(\mu\text{-}dppm)_2](PF_6)_2$ consisted of a nearly planar $Ir(CN\text{-}CH_3)_2P_2$ unit that was connected to a very linear AuP_2 unit through two bridging dppm ligands.[40] The fluorescence and phosphorescence of the complex in CH_2Cl_2 occurred at 540 and 668 nm, respectively, which were assigned to singlet and triplet excited states of $(d\sigma^* \rightarrow p\sigma)$ character, respectively.

The M–M bonds of dinuclear d^9–d^9 complexes $[Pd_2(L)_nX_2]$ (X = Cl, Br, py; $n = 1$, L = dmb, tmb; $n = 4$, L = CNR) have been investigated using resonance Raman spectroscopy and UV-vis measurements of the $d\sigma$–$d\sigma^*$ absorption band at various temperatures.[39] There was a clear relationship between the $\lambda_{abs}(d\sigma - d\sigma^*)$ and the internuclear distances between the two palladium(I) centers. The longest $d(Pd_2)$ data gave the smallest $d\sigma - d\sigma^*$ gap and hence, the lowest transition energy. Polymeric d^{10} materials $[\{M(dmb)_2Y\}_n]$ (M = Cu, Ag; Y = PF_6^-, BF_4^-, NO_3^-, ClO_4^-, $CH_3CO_2^-$) exhibited a linear structure where the $M(dmb)_2^+$ units were linked together in a double bridging fashion. These polymers displayed emission in the solid state and glass at 77 K upon irradiation. Density functional theory calculations indicated that the HOMO was mainly metal-based in character, while the LUMO was π^*(isocyanide) in nature, and the emission was assigned to an excited state of ^{3}MLCT character. The copper polymer $[\{Cu(dmb)_2TCNQ\}_n]$/TCNQ was photoconducting, and photovoltaic cells were designed using this material.[41]

Mann and coworkers reported the remarkable solvatochromic behavior of luminescent platinum(II) isocyanide/palladium(II) cyanide (*see Cyanides* and ***Cyanide Complexes of the Transition Metals***) complexes $[Pt(p\text{-}CN\text{-}C_6H_4\text{-}C_nH_{2n+1})_4][Pd(CN)_4]$ (n = 6, 10, 12, 14).[42] A film of $[Pt(p\text{-}CN\text{-}C_6H_4\text{-}C_{10}H_{21})_4][Pd(CN)_4]$ on a microscopy slide changed its color from pink when it was exposed to air saturated with chloroform vapor. The emission band of the solid also displayed a red shift from at 640 to 658 nm. Other volatile organic vapors gave shifts to different extents. As an example, the emission spectra of a related complex $[Pt(p\text{-}CN\text{-}cyclododecyl)_4][Pt(CN)_4]$ under increasing concentrations of methanol vapor showed a blue shift (Figure 3). The solid

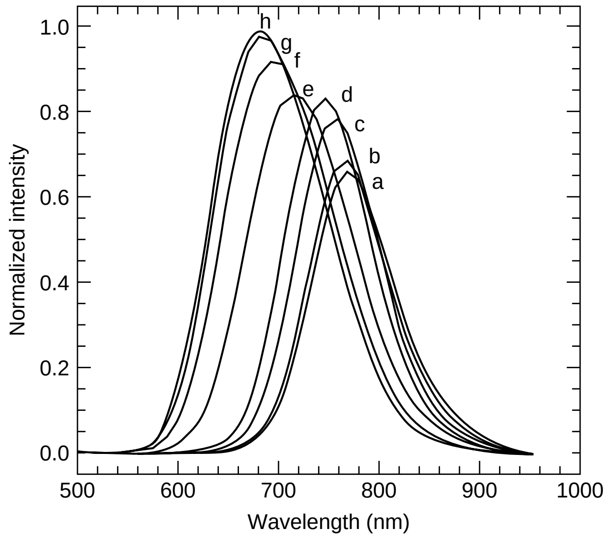

Figure 3 Emission spectra of [Pt(p-CN-cyclododecyl)$_4$][Pt(CN)$_4$] under varying concentrations of methanol vapor at 25 ± 1 °C. Concentrations (percent saturation): a, 0; b, 1; c, 6; d, 11; e, 22; f, 54; g, 78; h, 100. (Reprinted with permission from Ref. 43. © 2002 American Chemical Society)

of these complexes consisted of infinite stacks of alternating cations and anions with considerable metal–metal interactions along the chains propagated through interionic d_{z^2} and p_z interactions. The large size mismatch between the cation and anion produced a structure with a relatively large free volume, facilitating the rapid and reversible sorption of the volatile organic compounds. The shifts of the absorption and emission bands were attributed to the interactions between the guest molecules and the linear chain chromophore in the ground and/or excited state. As an important step in the development of an ‘electronic nose’, a three-channel cross-reactive sensor array bead based on related vapoluminescent platinum(II) double-salt materials such as [Pt(CN-cyclododecyl)$_4$][Pt(CN)$_4$], [(phen)Pt(CN-cyclohexyl)$_2$][Pt(CN)$_4$], [Pt(CN-n-tetradecyl)$_4$][Pt(CN)$_4$], and [(phen)Pt(CN-cyclohexyl)Cl]$_2$[(phen)Pt(CN-cyclohexyl)$_2$]$_2$[Pt(CN)$_4$]$_3$ was fabricated.[43]

A series of luminescent mononuclear [(C^N^N)Pt(CNR)]$^+$ (HC^N^N = 6-phenyl-2,2′-bipyridine; R = ^{t}Bu, ^{n}Bu, ^{i}Pr, cyclohexyl, 2,6-Me$_2$C$_6$H$_3$) and dinuclear [{(C^N^N)Pt}$_2$(μ-CN(CH$_2$)$_3$NC)]$^{2+}$ isocyanide complexes has been synthesized, and their spectroscopic and photophysical properties investigated.[44] Close π–π intermolecular contacts (3.4–3.6 Å) and a metal–metal distance 3.3831(9) Å were observed in the mononuclear complexes. At high concentrations, the complex [(C^N^N)Pt(CN^{n}Bu)]$^+$ displayed a weak MMLCT (dσ^*(Pt–Pt) $\rightarrow$ π^*(C^N^N)) absorption shoulder at 511 nm ($\varepsilon = 120\ \mathrm{dm^3\,mol^{-1}\,cm^{-1}}$). The room-temperature emission spectrum of [(C^N^N)Pt(CN-cyclohexyl)]$^+$ for complex concentrations $\geq 7 \times 10^{-3}\ \mathrm{mol\,dm^{-3}}$ showed a low-energy ^{3}MMLCT band at 710 nm. The mononuclear complexes at high concentration in 77 K glass displayed π–π excimeric emission at 600–625 nm.

2.3 Cyanide Systems (*See Cyanide Complexes of the Transition Metals*)

The pressure-dependent emission properties of M[Au(CN)$_2$] (M = K, Cs) and Cs$_2$Na[Au(CN)$_2$]$_3$ have been investigated.[45] For example, the emission of the single crystals of K[Au(CN)$_2$] showed a large bathochromic shift from 397 to 521 nm when the applied hydrostatic pressure was increased from 1 to 30 kbar. The emission spectra of the single crystals of these complexes at various pressures are shown in Figure 4. The shift was suggested to result from the quasi-one-dimensional metal–metal interactions and the quasi-two dimensional formation of electronic energy bands.

The complexes K[Au(CN)$_2$] and K[Ag(CN)$_2$] in water and methanol displayed intense luminescence that was dependent on the concentration, solvent, temperature, and excitation wavelength.[46] The emission spectra of the gold complex in aqueous solution at ambient conditions showed dual luminescence at ca. 400–410 nm (HE band) and 430–470 nm (LE

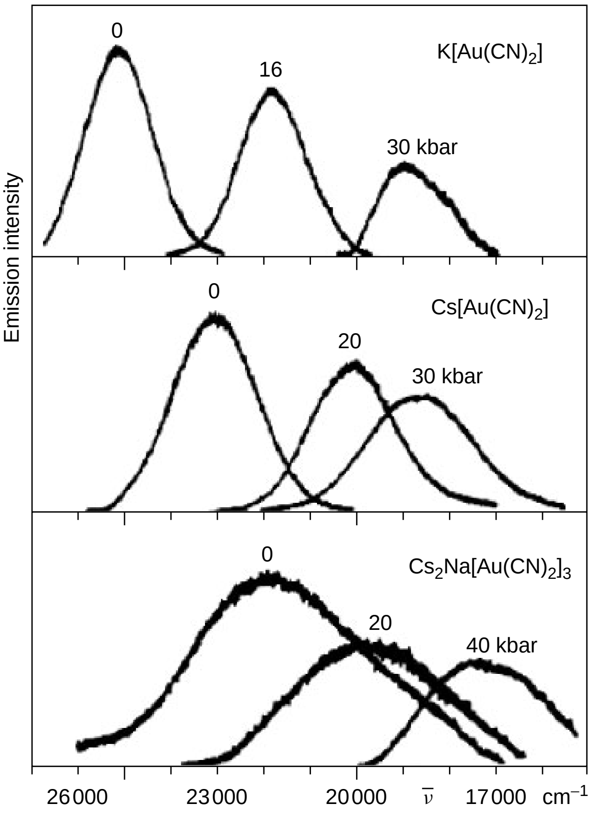

Figure 4 Emission spectra of different M[Au(CN)$_2$] single crystals for various pressures at 295 K (λ_{ex} = 325 nm). (Reprinted with permission from Ref. 45. © 1995 American Chemical Society)

band). As the concentration of the complex was increased, enhancement in the relative intensity of the LE/HE bands and a red shift of the LE band were observed. The luminescence was assigned to $^*[Au(CN)_2{}^-]_n$ and $^*[Ag(CN)_2{}^-]_n$ excimers and exciplexes of different n and geometries. MP2 calculations on the lowest-energy triplet excited state of staggered $[Au(CN)_2{}^-]_2$ showed the formation of a gold–gold σ-bond with an internuclear distance of 2.66 Å. The assignment of exciplex emission was based on the large Stokes' shifts and the structureless feature of the emission bands, which suggested very distorted excited states. EHMO calculations using the models $[M(CN)_2{}^-]_n$ and $^*[M(CN)_2{}^-]_n$ ($M = Au$, Ag; $n = 2$, 3) also suggested the formation of M–M bonds in the first excited electronic states.

A linear chain with weak gold···gold interactions was observed in the crystal structure of $[(TPA)_2Au][Au(CN)_2]$, while a helical chain was observed in (TPA)AuCl.[47] Intrachain Au···Au separations of 3.457(1) and 3.396(2) Å were observed in these compounds, respectively. Although single crystals of $[(TPA)_2Au][Au(CN)_2]$ were nonemissive even at cryogenic temperature, the finely ground sample displayed excitation wavelength-dependent and intense blue to green emission. The chloro complex (TPA)AuCl emitted at 580 nm at 78 K. Owing to the absence of significant metal–metal interactions in the crystal structures of these complexes, it was suggested that localized surface defects comprising dimeric or oligomeric units were responsible for the emission of the powder.

3 ALKYNYL SYSTEMS

3.1 Rhenium(I) (*See Rhenium: Organometallic Chemistry*) Alkynyls

A series of rhenium(I) complexes $[Re(CO)_3(N–N)(\{C{\equiv}C\}_n–R)]$ containing conjugated alkynyl ligands displayed remarkable luminescence properties.[48,49] The origin of the emission was assigned to an ^{3}MLCT ($d\pi(Re) \rightarrow \pi^*(N–N)$) excited state. It is interesting to note that the emission energy of these complexes increased with an increasing degree of conjugation in the alkynyls (E_{em} ($n = 3$) > E_{em} ($n = 2$) > E_{em} ($n = 1$)). EHMO calculations revealed a LUMO (*see LUMO*) of significant π^*(N–N) character, while the HOMO (*see HOMO*) was mainly the antibonding overlap between $d\pi$(Re) and $\pi(C{\equiv}C)$ orbitals. Lengthening the alkynyl unit would raise the $\pi(C{\equiv}C)$ level and result in a closer energy match between the $d\pi$(Re) and $\pi(C{\equiv}C)$ orbitals. This was expected to increase the energy of the HOMO and led to a decrease in the HOMO–LUMO gap. However, such a decrease in emission energy was not observed upon the lengthening of the alkynyl unit, and a possible reason was that the overlap integral between the $d\pi$(Re) and $\pi(C{\equiv}C)$ orbitals was reduced because of the more delocalized electron density in the alkynyl. Dinuclear rhenium(I) alkynyl complexes $[Re(CO)_3(N–N)\{C{\equiv}C\}_nRe(CO)_3(N–N)]$ ($n = 2$, 4, 6) and mixed-metal alkynyl complexes $[\{\eta^2\text{-}Re(CO)_3(N–N)(C{\equiv}CPh)\}_2M]^+$, $[M_3(P\text{-}P)_3\{\mu_3-\eta^1\text{-}C{\equiv}C–[C_6H_2R_2\text{-}2,5]_n–C{\equiv}C\text{-}4\text{-}Re(CO)_3(N–N)\}_2]^+$ ($M =$ Cu, Ag; $n = 0$, 1), such as (**10**) and $[Ag_6(\mu\text{-dppm})_4\{\mu_3\text{-}C{\equiv}CC{\equiv}C–Re(N–N)(CO)_3\}_4]^{2+}$ (**11**) were isolated and shown to display rich emission properties.[50,51] An ^{3}MLCT ($d\pi(Re) \rightarrow \pi^*(N–N)$) excited state, possibly mixed with some ^{3}LLCT ($\pi(C{\equiv}C) \rightarrow \pi^*(N–N)$) character, was identified for these systems.

A redox-driven luminescence switch constructed from the linking of the rhenium(I) alkynyl to an iron(II) alkynyl has been synthesized.[52] The complex $[Re(bpy)(CO)_3(C{\equiv}C–C_6H_4–C{\equiv}C\text{-}p)Fe(C_5Me_5)(dppe)]$ was nonluminescent because the emissive ^{3}MLCT ($d\pi(Re) \rightarrow \pi^*(bpy)$) state was quenched effectively by the low-lying MLCT and LF excited state of the iron(II) moiety. However, the one-electron oxidized form of the complex, $[Re(bpy)(CO)_3(C{\equiv}C–C_6H_4–C{\equiv}C\text{-}p)Fe(C_5Me_5)(dppe)]^+$, displayed typical ^{3}MLCT ($d\pi(Re) \rightarrow \pi^*(bpy)$) emission at 590 nm in CH_2Cl_2 at 298 K due to the absence of the intramolecular quenching pathway.

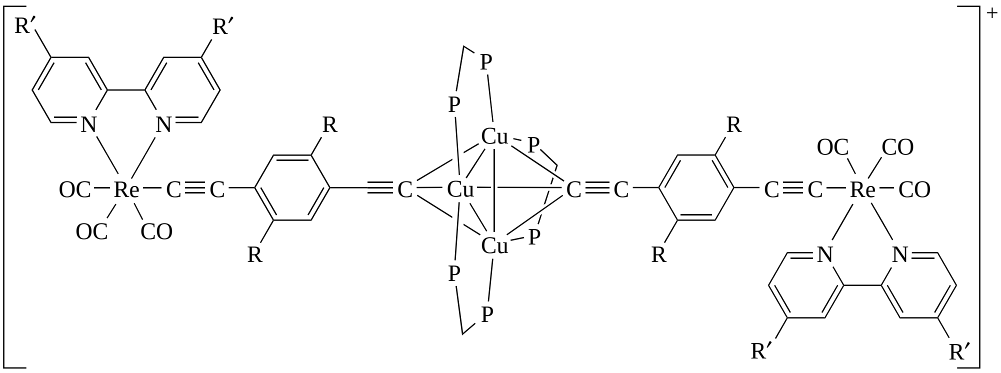

$[Cu_3(P\text{-}P)_3\{\mu_3\text{-}\eta^1\text{-}C{\equiv}C\text{-}(C_6H_2R_2\text{-}2,5)\text{-}C{\equiv}C\text{-}4\text{-}Re(CO)_3(N\text{-}N)\}_2]^+$

(**10**)

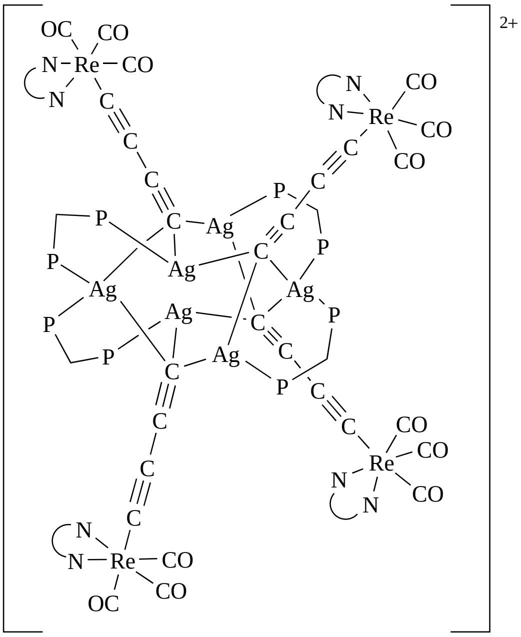

$[Ag_6(\mu\text{-dppm})_4\{\mu_3\text{-C}{\equiv}CC{\equiv}C\text{-Re(CO)}_3(N\text{–}N)\}_4]^{2+}$

(11)

3.2 Platinum(II) (*See Platinum: Organometallic Chemistry*) and Palladium(II) (*See Palladium: Organometallic Chemistry*) Alkynyls

The luminescence properties of *trans*-$Pt(C{\equiv}CH)_2(PEt_3)_2$ and *trans*-$Pt(C{\equiv}CPh)_2(PEt_3)_2$ have been investigated.[53,54] The complex *trans*-$Pt(C{\equiv}CPh)_2(PEt_3)_2$ displayed an intense structured emission in the solid state and in glass at 77 K. The presence of vibrational progressions in $\nu(C{\equiv}C)$ mode (and additional phenyl-localized modes in the phenylalkynyl complex) in the emission spectra of these complexes, together with the nonemissive nature of *trans*-$[PtCl_2(PEt_3)_2]$ suggested that the emission originated from an ^{3}MLCT ($d\pi(Pt) \rightarrow \pi^*(C{\equiv}C)$) excited state.[54] A similar ^{3}MLCT excited state, probably with some mixing of ^{3}IL ($\pi \rightarrow \pi^*(PhC{\equiv}C)$) character, was also proposed to the emission of the related complex *trans*-$[Pt(C{\equiv}CPh)_2(\text{dppm-}P)_2]$. The assignment was supported by resonance Raman (*see Resonance Raman Spectroscopy*) spectroscopic results[55] and EHMO studies on the model complex *trans*-$[Pt(C{\equiv}CPh)_2(\text{dmpm-}P)_2]$.[56]

Yam and coworkers extended the photophysical studies from the mononuclear to the dinuclear platinum(II) A-frame $[Pt_2(\mu\text{-dppm})_2(\mu\text{-C}{\equiv}CR)(C{\equiv}CR)_2]^+$ (**12**) and face-to-face $[Pt_2(\mu\text{-dppm})_2(C{\equiv}CPh)_4]$ (**13**) alkynyl complexes.[54] The low-temperature emission spectra revealed rich vibronic-structured bands with progressional spacings typical of the $\nu(C{\equiv}C)$ mode. The absorption and emission bands of these complexes occurred at lower energy than those of the mononuclear complexes. The solid-state emission energy increased with the increasing $\pi^*(C{\equiv}CR)$ orbital energy. These observations suggest that the origins of the absorption and phosphorescence were MMLCT ($d\sigma^* \rightarrow p\sigma/\pi^*(C{\equiv}CPh)$) in nature. The alkynyl moieties can be used to coordinate to other transition metal centers: for example, the mixed-metal alkynyl complex $[Pt_2(\mu\text{-dppm})_2(C{\equiv}CPh)_4\{Cu(CH_3CN)\}_2]^{2+}$ (**14**) has been isolated.[57] The MMLCT absorption and emission of this complex occurred at lower energy than those of the parent diplatinum complex $[Pt_2(\mu\text{-dppm})_2(C{\equiv}CPh)_4]$ because of a shortening of the Pt···Pt distance as well as an enhanced π-accepting ability of the C≡CPh groups upon the π-coordination to copper(I). The narrowing of the HOMO-LUMO energy gap due to these factors is illustrated in Figure 5.

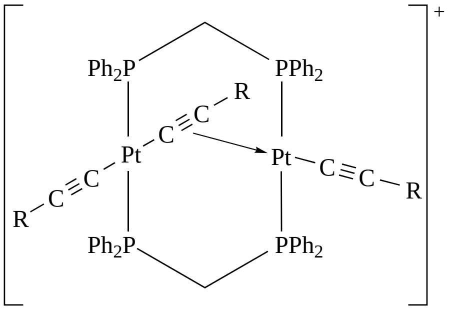

$[Pt_2(\mu\text{-dppm})_2(\mu\text{-C}{\equiv}CR)(C{\equiv}CR)_2]^+$

(12)

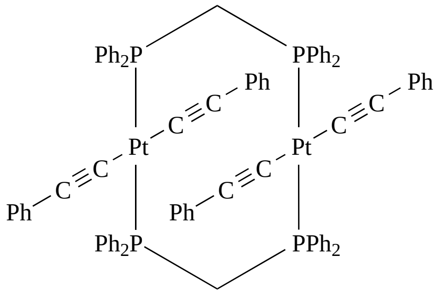

$[Pt_2(\mu\text{-dppm})_2(C{\equiv}CPh)_4]$

(13)

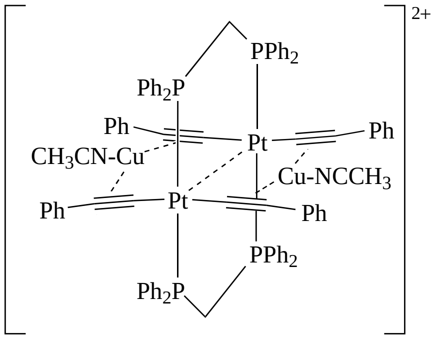

$[Pt_2(\mu\text{-dppm})_2(C{\equiv}CPh)_4\{Cu(CH_3CN)\}_2]^{2+}$

(14)

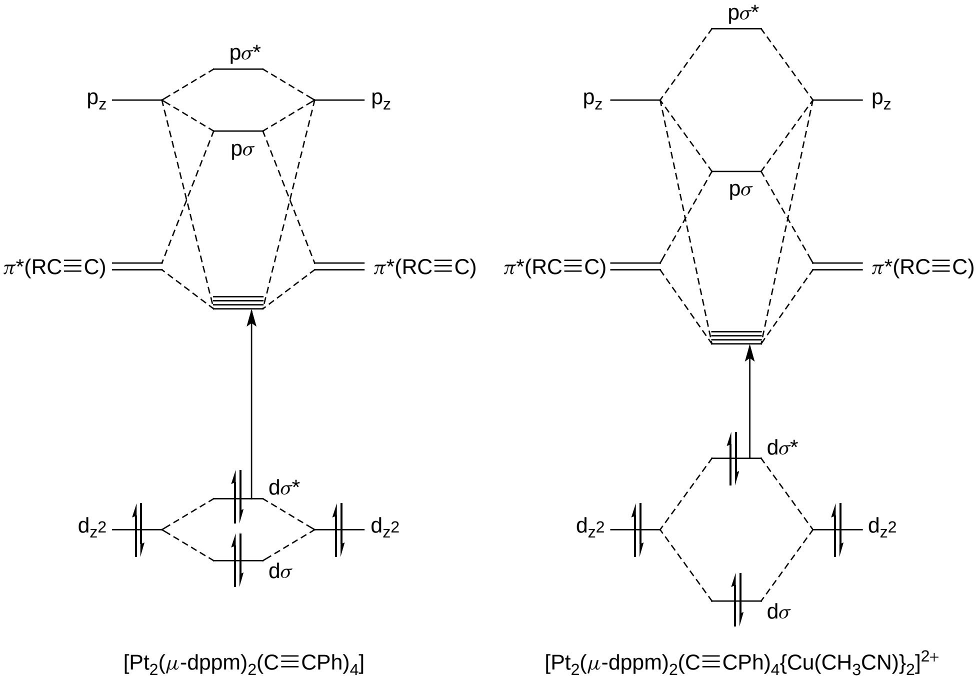

$[Pt_2(\mu\text{-dppm})_2(C{\equiv}CPh)_4]$ $[Pt_2(\mu\text{-dppm})_2(C{\equiv}CPh)_4\{Cu(CH_3CN)\}_2]^{2+}$

Figure 5 Diagrams showing the narrowing of HOMO-LUMO energy gap of the face-to-face dinuclear platinum(II) complex $[Pt_2(\mu\text{-dppm})_2(C{\equiv}CPh)_4]$ upon copper(I) coordination. (Reprinted with permission from Ref. 54. © 2002 American Chemical Society)

Other mixed-metal platinum(II) alkynyl complexes such as $[Pt_2M_4(C{\equiv}CR)_8]$ (M = Cu, Ag) (**15**) and their dimers, trimers, and higher aggregates such as $[\{Pt_2Ag_4(C{\equiv}C^tBu)_8\cdot(bpy)\}]_n$, have been shown to display photoluminescence in the solid state and in frozen solutions.[58,59] The emission of $[Pt_2M_4(C{\equiv}CR)_8]$ was assigned to an ^{3}LMCT (RC≡C → Pt_2M_4) or ^{3}LMMCT (RC≡C → $M_4Pt{-}PtM_4$) state. The polymer $[\{Pt_2Ag_4(C{\equiv}C^tBu)_8\cdot(bpy)\}]_n$ showed intense and long-lived bluish-green emission. The higher intensity and longer lifetime of this emission with respect to the parent complex $[Pt_2Ag_4(C{\equiv}C^tBu)_8]$ suggested a substantial reduction in the overall deactivation via nonradiative mechanism. The higher aggregates were shown to emit at lower energy than the respective monomers.[59]

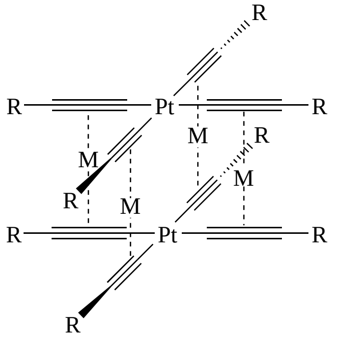

$[Pt_2M_4(C{\equiv}CR)_8]$

(**15**)

A series of branched palladium(II) and platinum(II) complexes containing the rigid conjugated arylalkynyl ligand 1,3,5–$(HC{\equiv}CC_6H_4{-}C{\equiv}C{-}p)_3C_6H_3$ has been synthesized and characterized.[60,61] A red shift in the absorption energy upon going from the palladium(II) complex to its platinum(II) counterpart was observed, suggestive of the presence of ^{1}MLCT (dπ(M) → π*(C≡CR)) (M = Pd, Pt) character in the transitions. The emission of these complexes at low temperature was assigned to an excited state of mixed ^{3}IL (π(C≡CR) → π*(C≡CR))/^{3}MLCT (dπ(M) → π*(C≡CR)) character.

Polymeric species $\{Pt(X^nBu_3)_2{-}C{\equiv}C{-}(C{\equiv}C)_m{-}C{\equiv}C\}_n$ and $\{Pt(X^nBu_3)_2{-}(C{\equiv}C)_m{-}C_6H_4{-}(C{\equiv}C)_m{-}p\}_n$ $(m = 0,\ 1)$ have been synthesized.[62] The absorption and emission spectra of these complexes showed extended π-electron conjugation through the metal sites on the chain, with a lower π–π* energy gap for the triacetylenic than for the diacetylenic polymers. Well-resolved vibronic structure associated with the ν(C≡C) frequency was observed in both the absorption and emission spectra, indicating strong electron-phonon coupling for these polymers.

Apart from phosphine ligands, polypyridine ligands have been incorporated into platinum(II) alkynyl moieties to give luminescent complexes. The use of polypyridine ligands is interesting because their planar structure and the square-planar coordination geometry of the d^8 platinum(II) center could modify the excited state of these luminescent complexes by π–π and/or Pt···Pt interactions. The complex

$[\mathrm{Pt(4,4'\text{-}Ph_2\text{-}bpy)(C{\equiv}C{-}Ph)_2}]$ showed intermolecular π-stacking of the alkynyl and phenyl moieties with the bipyridine group.[63] Excitation of these complexes gave ^{3}MLCT (5d(Pt) $\rightarrow$ π^*(N–N)) emission. The complex $[\mathrm{Pt(4,4'\text{-}{}^{t}Bu_2\text{-}bpy)(C{\equiv}C{-}C{\equiv}C{-}Ph)_2}]$ showed structured emission spectra in the solid state and rigid glass. The low-energy shoulder at 603 nm in the 77 K solid-state emission was suggested to be excimeric emission. The electroluminescence properties of these platinum(II) diimine alkynyls were investigated. A related series of cyclometalated platinum(II) alkynyl complexes $[\mathrm{Pt(bzq)(C{\equiv}CR)_2}]^-$ (R = ^{t}Bu, SiMe$_3$, Ph, Tol, $\mathrm{C_6H_4CF_3}$-4, $\mathrm{C_5H_4N}$-2) has also been synthesized, characterized and shown to be strongly emissive in the solid state and in frozen solutions.[64]

The solvent-induced aggregation of a platinum(II) terpyridine alkynyl complex has been studied.[65] X-ray crystallography revealed that the complex $[\mathrm{Pt(terpy)(C{\equiv}C{-}C{\equiv}CH)}]^+$ crystallized in two forms: (1) a dark green form in which platinum atoms formed a linear chain and were equally spaced, with partial stacking of the terpy units; and (2) a red form that showed a dimeric structure with alternating short and long Pt···Pt distances arranged in a zig-zag fashion. Both forms dissolved in acetonitrile and acetone to form yellow solutions with high-energy ^{1}IL ($\pi \rightarrow \pi^*$(C≡C–C≡CH)) absorption bands at 313, 329, and 340 nm, and a less intense ^{1}MLCT (d(Pt) $\rightarrow$ π^*(C≡C–C≡CH)) band at ca. 416 nm. Addition of diethyl ether into such solutions changed the color from yellow to green, and then to blue, with the appearance of a new absorption band at ca. 615 nm in the spectra (Figure 6a). These observations were absent for the structural analogue $[\mathrm{Pt({}^{t}Bu_3\text{-}terpy)(C{\equiv}C{-}C{\equiv}CH)}]^+$, which did not exhibit any π–π or Pt···Pt interactions in its crystal structure. The changes displayed by the platinum(II) terpy complex were likely to result from the aggregation of the complex induced by the addition of diethyl ether, and the low-energy absorption band was assigned to an ^{1}MMLCT ($\mathrm{d}\sigma^*(\mathrm{Pt})_n \rightarrow \pi^*$(C≡C–C≡CH)) transition. The appearance of the absorption band was accompanied by a new emission band at 785 nm (Figure 6b), which was likewise assigned to an ^{3}MMLCT ($\mathrm{d}\sigma^*(\mathrm{Pt})_n \rightarrow \pi^*$(C≡C–C≡CH)) excited state. These remarkable changes in the absorption and emission properties of the complex induced by the solvent composition could be utilized as versatile reporters and probes of environmental changes.

Three novel luminescent dinuclear platinum(II) complexes with bridging alkynyls have been studied.[66] The complexes $[\mathrm{Pt({}^{t}Bu_3\text{-}terpy){-}\{C{\equiv}C\}_n{-}Pt({}^{t}Bu_3\text{-}terpy)}]$ (n = 1, 2, 4) showed intense high-energy ^{1}IL (alkynyl and ^{t}Bu$_3$-terpy) absorption bands at ca. 308–342 nm. Low-energy absorption bands at ca. 428–522 nm were assigned to ^{1}MLCT (dπ(Pt) $\rightarrow$ π^*(^{t}Bu$_3$-terpy)) transitions mixed with ^{1}LLCT (π(alkynyl) $\rightarrow$ π^*(^{t}Bu$_3$-terpy)) character. Remarkably, the low-energy absorption bands shifted to higher energy upon elongation of the alkynyl units. A similar observation has been made and explained for a series of rhenium(I) alkynyl complexes. A blue shift in the 77-K glass-emission energy was also observed for the platinum(II) complexes on going from $n = 1$ to 2. A highly structured emission spectrum was, however, observed for the complex $[\mathrm{Pt({}^{t}Bu_3\text{-}terpy)\{C{\equiv}C\}_8Pt({}^{t}Bu_3\text{-}terpy)}]$, which was likely to be a consequence of the involvement of a high degree of ^{3}IL (alkynyl) character in the emissive state.

Weder and coworkers reported the use of the dinuclear platinum(II) alkene complex $[\mathrm{Pt_2(\mu\text{-}Cl)_2(PhCH{=}CH_2)_2Cl_2}]$

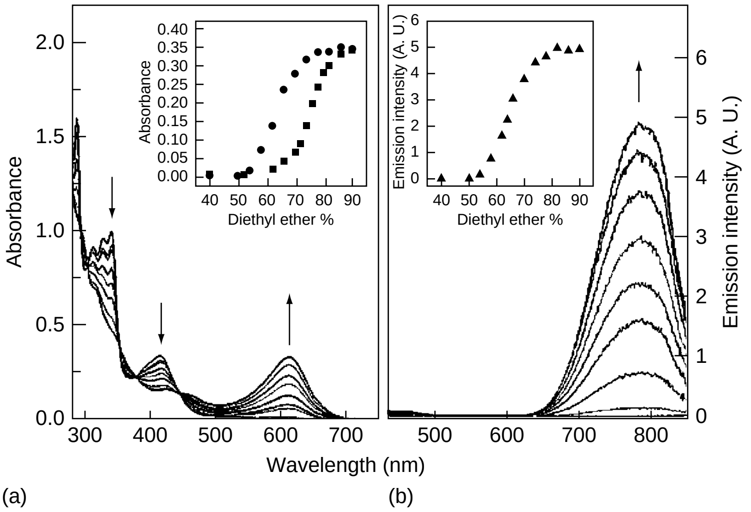

Figure 6 (a) UV-vis absorption changes of $[\mathrm{Pt(terpy)(C{\equiv}C{-}C{\equiv}CH)}]^+$ (concentration = 1.47×10^{-4} M) in acetonitrile with increasing diethyl ether content. Inset: Plot of absorbance vs. diethyl ether composition in acetonitrile at 615 nm (■) and in acetone at 610 nm (●). (b) Emission enhancement of $[\mathrm{Pt(terpy)(C{\equiv}C{-}C{\equiv}CH)}]^+$ (concentration = 1.47×10^{-4} M) in acetone upon increasing diethyl ether content. Inset: Plot of corrected emission intensity as a function of diethyl ether composition (▲). (Reprinted with permission from Ref. 65. © 2002 American Chemical Society)

in the formation of a three-dimensionally cross-linked, conjugated poly(p-phenylene ethynylene)-platinum(II) network, in which the ethynylene moieties of the polymer are coordinated to the platinum(II) centers.[67] The formation of these polymeric materials is shown in Scheme 2. The photoluminescence of the PPE polymer was significantly quenched after the platinum(II) coordination. The observations were suggested to be a result of exciton migration along the polymer main chains to

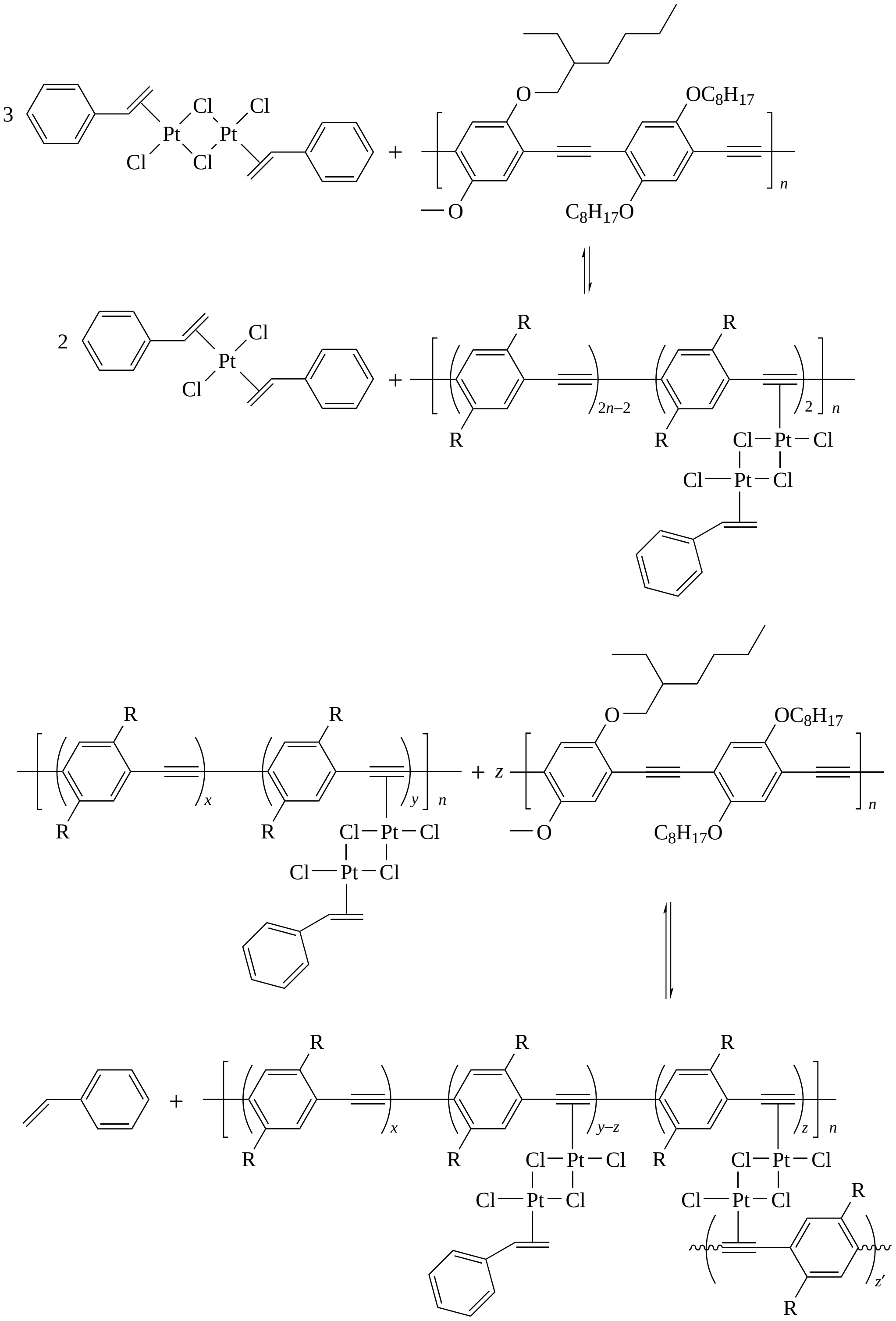

3
Cl
Cl
Pt
Pt
Cl
Cl
+
O
OC8H17
n
O
C8H17O
2
Cl
Pt
Cl
+
R
R
2n–2
2
n
R
R
Cl—Pt—Cl
Cl—Pt—Cl
x
y
n
+ z
Cl—Pt—Cl
Cl—Pt—Cl
y–z
z
z′

Scheme 2 Suggested equilibria for the reaction of $[Pt_2(\mu\text{-}Cl)_2(PhCH{=}CH_2)_2Cl_2]$ and poly(p-phenylene ethynylene) the complexation sites, which seemed to represent low-energy states and provided pathways for nonemissive radiation processes. In a related study, a PPE derivative was reacted with a platinum(0) styrene complex [Pt(styrene)$_3$] to form a polymer network in which the platinum(0) centers were π-bonded to the ethynylene moieties of the polymer chains.[68] A similar decrease in the photoluminescence intensity of the polymer was also observed.

A hexanuclear luminescent platinum(II) complex [Pt$_2$(μ-dppm)$_2$(C≡C-py-4)$_4${Pt(terpy)}$_4$](CF$_3$SO$_3$)$_8$ has been isolated and characterized.[69] The slight red shift of the ^{3}MMLCT emission band relative to that of the parent complex [Pt$_2$(μ-dppm)$_2$(C≡C-py-4)$_4$] was attributed to the increased Pt···Pt interaction due to a shrinkage of the Pt···Pt bond distance in the Pt$_2$(dppm)$_2$ core in the hexanuclear structure and an increase in the π-accepting ability of the ethynylpyridine units upon coordination of the Pt(terpy) moieties.

Luminescent platinum(II) alkynyl polymers *trans*-[–Pt(PBu$_3$)$_2$C≡CRC≡C–]$_n$ (R = 9,9-dihexylfluorene-2,7-diyl; 9-butylcarbazole-3,6-diyl) have been prepared.[70] The absorption and luminescence spectra were compared to those of the monomeric model complexes *trans*-[Pt(Ph)(PEt$_3$)$_2$C≡CRC≡CPt(Ph)(PEt$_3$)$_2$] and other fluorene derivatives. The optical gap and intersystem crossing from the singlet excited state to the triplet excited state were found to increase with a decreasing degree of conjugation. The photoconducting properties of these polynuclear platinum alkynyl complexes were also investigated.

3.3 Copper(I) (*See Copper: Organometallic Chemistry*), Silver(I) (*See Silver: Organometallic Chemistry*) and Gold(I) (*See Gold: Organometallic Chemistry*) Alkynyls

The photophysical properties of a wide range of copper(I) alkynyl complexes have been studied.[49,71] These examples can be classified into the following groups: a dinuclear complex with bridging alkynyls, [Cu$_2$(PPh$_2$CH$_3$)$_2$(μ-η^1-C≡CPh)$_2$], trinuclear complexes with one or two μ_3-bridging alkynyls, [Cu$_3$(P-P)$_3$(μ_3-η^1-C≡CR)]$^{2+}$ (**16**), [Cu$_3$(P-P)$_3$(μ_3-η^1-C≡CR)$_2$]$^+$ (**17**), and [Cu$_3$(P-P)$_3$(μ_3-η^1-C≡CR)(μ_3-η^1-C≡CR′)]$^+$, mixed chloro- and alkynyl-bridged trinuclear complexes, [Cu$_3$(P-P)$_3$(μ_3-η^1-C≡CR)(μ_3-Cl)]$^+$, tetranuclear metallocubane-type complexes with four or three μ_3-bridging alkynyls, [Cu$_4$(PR$''_3$)$_4$(μ_3-η^1-C≡CR)$_4$] (**18**) and [Cu$_4$(PPh$_3$)$_4$(μ_3-η^1,η^1,η^2-C≡C–C$_6$H$_4$O-CH$_3$-4)$_3$]$^+$ (**19**), tetranuclear complexes with a C$_2$ bridging alkynyl, [Cu$_4$(P-P)$_4$(μ_4-η^1,η^2-C≡C)]$^{2+}$ (**20**), and hexanuclear complexes with a bis(μ_3-bridging alkynyl), [Cu$_3$(P-P)$_3$(μ_3-η^1-C≡C–C$_6$H$_4$–C≡C-4)Cu$_3$(P-P)$_3$]$^{4+}$ (**21**). All these copper(I) alkynyls showed intense and long-lived green to orange emission upon irradiation. Systematic variations on the identity of the phosphine ligands, and substituents on the alkynyls revealed that the nature of the emissive state was ^{3}LMCT (alkynyl → Cu$_n$)/^{3}MC(3d → 4s/4p) with predominantly ^{3}LMCT (alkynyl → Cu$_n$) character. The mixing

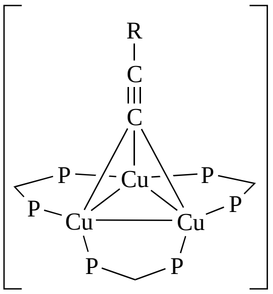

[Cu$_3$(P-P)$_3$(μ_3-η^1-C≡CR)]$^{2+}$

(**16**)

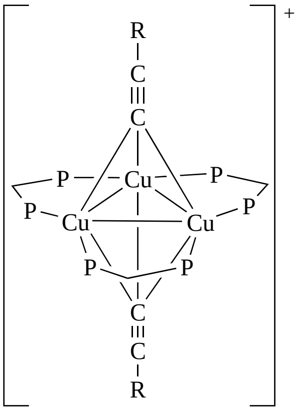

[Cu$_3$(P-P)$_3$(μ_3-η^1-C≡CR)$_2$]$^+$

(**17**)

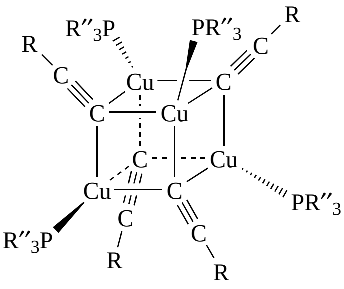

[Cu$_4$(PR$''_3$)$_4$(μ_3-η^1-C≡CR)$_4$]

(**18**)

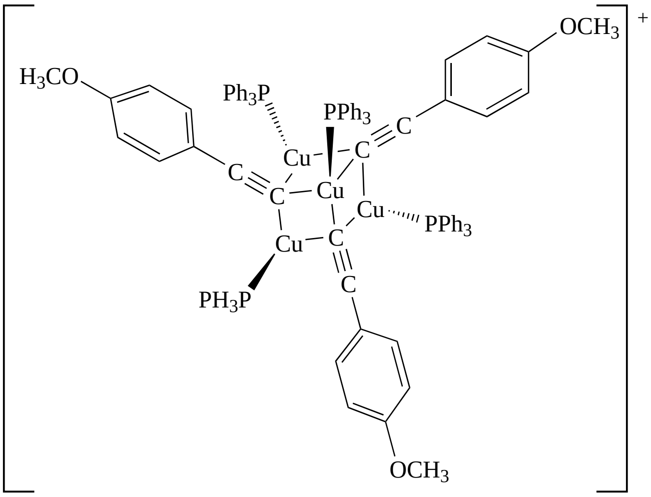

[Cu$_4$(PPh$_3$)$_4${μ_3-η^1,η^1,η^2-C≡C-C$_6$H$_4$OCH$_3$-4)$_3$]$^+$

(**19**)

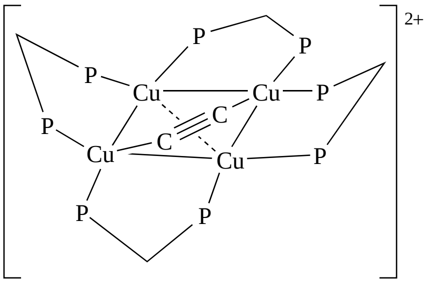

$[Cu_4(P\text{-}P)_4(\mu_4\text{-}\eta^1,\eta^2\text{-}C{\equiv}C)]^{2+}$

(**20**)

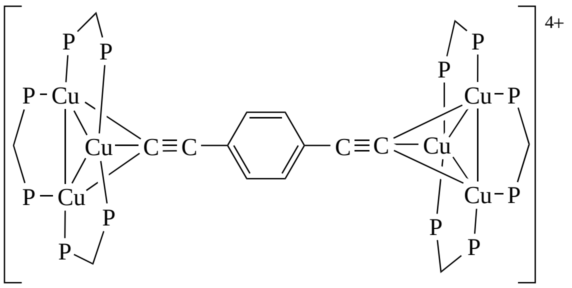

$[Cu_3(P\text{-}P)_3(\mu_3\text{-}\eta^1\text{-}C{\equiv}C\text{-}C_6H_4\text{-}C{\equiv}C\text{-}4)Cu_3(P\text{-}P)_3]^{4+}$

(**21**)

of ^{3}MC (3d → 4s/4p) character, resulted from Cu···Cu interaction, into the excited state was proposed on the basis of the short Cu···Cu distances revealed by crystallographic studies. However, ^{3}IL (alkynyl) character existed in the excited states of some of these examples, especially those with highly conjugated alkynyl ligands such as $–C{\equiv}C–C_6H_4–C{\equiv}C\text{-}4$ and $–C{\equiv}C–C{\equiv}C–R$ and alkynyl ligands with a strong electron-withdrawing substituent such as $–C{\equiv}C–C_6H_4–NO_2\text{-}4$. A small blue shift in the emission energy was observed for the silver(I) analogues of some of these complexes such as $[Ag_3(P\text{-}P)_3(\mu_3\text{-}\eta^1\text{-}C{\equiv}CR)]^{2+}$ and $[Ag_3(P\text{-}P)_3(\mu_3\text{-}\eta^1\text{-}C{\equiv}C–C_6H_4–C{\equiv}C\text{-}4)Ag_3(P\text{-}P)_3]^{4+}$, which was in agreement with the assignment of an ^{3}LMCT (alkynyl → M_n)/^{3}MC (d → s/p) mixed state.

The copper(I) alkynyls displayed rich photochemistry and particularly strong photoreducing properties. The transient absorption difference spectrum of $[Cu_3(dppm)_3(\mu_3\text{-}\eta^1\text{-}C{\equiv}CPh)_2]^+$ and the electron acceptor 4-(methoxycarbonyl)-*N*-methylpyridinium ion showed an intense characteristic pyridinyl radical absorption band at ca. 400 nm. An additional broad near-infrared absorption band was also observed and it was assigned as an intervalence-transfer transition of the mixed-valence transient species $[Cu^ICu^ICu^{II}(dppm)_3(\mu_3\text{-}\eta^1\text{-}C{\equiv}CPh)_2]^{2+}$. The interesting photophysical and photochemical properties of other copper(I) alkynyl complexes such as [Cu(BTA)(hfac)],[72] $[Cu_{16}(hfac)_8(C{\equiv}C^tBu)_8]$,[73] and $[Cu_{20}(hfac)_8(C{\equiv}CCH_2Ph)_{12}]$[73] have also been studied.

Luminescent dinuclear gold(I) alkynyl complexes $[PCy_3–Au–\{C{\equiv}C\}_n–Au–PCy_3]$ ($n = 1, 2, 3, 4$) have been isolated and their spectroscopic properties investigated.[74] Bonding of the C_n moieties to gold(I) centers enabled the lowest-energy ^{3}IL ($\pi \rightarrow \pi^*$(C≡C)) excited states to acquire sufficient allowedness via gold spin-orbit coupling to appear prominently in both the absorption and emission spectra. The spectra showed very rich vibronic structures with the appearance of the characteristic ν(C≡C) mode. The origin lines were observed at 331, 413, 502, and 574 nm for $n = 1$, 2, 3 and 4 respectively. A plot of ν_{0-0} versus $1/n$ gave an estimation of the ν_{0-0} for $[PCy_3–Au–\{C{\equiv}C\}_\infty–Au–PCy_3]$ to be ca. 11 000 cm^{-1} ($\lambda_{0-0} = 909$ nm). The excited state of $[PCy_3–Au–\{C{\equiv}C\}_2–Au–PCy_3]$ was a powerful reducing agent as revealed by an excited-state reduction potential $E°(Au_2{}^+/Au_2^*)$ of ≤ -1.85 V versus SSCE.

The isolation and photophysical studies of conjugated polymeric gold(I) complexes $[–Au–C{\equiv}C–Ar–C{\equiv}C–Au–LL–]_n$ (Ar = aryl; LL = diphosphine or bis(isocyanide))[75] and dinuclear gold(I) ring complexes such as $[C_6H_4(OCH_2C{\equiv}CAu)_2\{\mu\text{-}Ph_2P(CH_2)_nPPh_2\}]$ containing bridging diphosphine and dialkynyl ligands[76] have been reported. The alkynyl ligands and Au···Au interactions were found to play an important role in the emission properties of these systems.

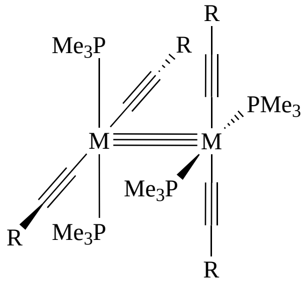

$[M_2(C{\equiv}CR)_4(PMe_3)_4]$

(**22**)

3.4 Molybdenum(II) (*See Molybdenum: Organometallic Chemistry*) and Tungsten(II) (*See Tungsten: Organometallic Chemistry*) Alkynyls

The electronic and resonance Raman spectra of dinuclear metal–metal bonded alkynyl complexes $[M_2(C{\equiv}CR)_4(PMe_3)_4]$ (M = Mo, W; R = CMe_3, $SiMe_3$, $CHMe_2$, Ph, (*see also* ***Dinuclear Organometallic Cluster Complexes***)) (**22**) displayed an unprecedented degree of ligand orbital mixing with the formally metal-metal-localized δ and δ^* frontier orbitals.[77,78] In particular, the $^1(\delta \rightarrow \delta^*)$ transitions of these complexes occurred at substantially lower energy with higher intensity than those of their structural counterparts $[M_2(X)_4(PMe_3)_4]$ (X = halides, Me, NCO, NCS). The 77 K absorption spectrum of $[Mo_2(C{\equiv}CSiMe_3)_4(PMe_3)_4]$ showed progressional spacings that were greater than the ground-state metal–metal stretch. An assignment to the ν(MoC) was therefore proposed instead of the common $\nu(Mo_2)$ mode. It was suggested that the $^1(\delta \rightarrow \delta^*)$ transitions displayed significant frontier orbital mixing between the $[\delta,\delta^*]$ orbitals of the M_2 core and the $[\pi,\pi^*]$ orbitals of the alkynyl ligands.

4 ALKENYL, ARENE, AND ARYL SYSTEMS

4.1 Alkenyl Systems

Similar to other d^8–d^8 systems, the dinuclear iridium(I) complex $[Ir(\mu\text{-pz})(COD)]_2$ (**23**) showed spin-allowed and spin-forbidden $(d\sigma^* \rightarrow p\sigma)$ absorption bands at 498 and 585 nm, respectively.[79,80] Under ambient conditions, the complex displayed fluorescence at 564 nm and phosphorescence at 687 nm, which were assigned to singlet and triplet excited states of $(d\sigma^* \rightarrow p\sigma)$ character. The triplet excited state of the complex was a powerful reductant with an excited-state reduction potential $E°$ $(Ir_2^{+/0*})$ of -1.81 V vs. SSCE. Facile electron transfer reactions occurred between the excited complex and methyl viologen and other pyridinium acceptors. The absence of an inverted effect for the forward electron transfer reactions, and the presence of such inverted behavior for the back-electron-transfer reactions were observed and explained.[80]

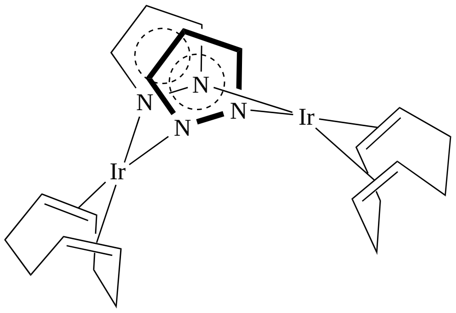

$[Ir(\mu\text{-pz})(COD)]_2$

(**23**)

Irradiation of the complexes *trans*-$[W(CO)_4(\eta^2\text{-alkene})_2]$ (alkene = propene, 1-butene, cyclopentene) in an alkane solution led to the loss of alkene and CO.[81] The liberation of alkene was accompanied by the formation of 16-electron coordinatively unsaturated species: *trans*- and *cis*-$[W(CO)_4(\eta^2\text{-alkene})(\text{solvent})]$. In the case of propene and 1-butene, these species transformed into *cis*-$[WH(\eta^3\text{-allyl})(CO)_4]$. In the presence of excess alkenes, the 16-electron species bound alkene to give *cis*-$[W(CO)_4(\eta^2\text{-alkene})_2]$. The CO loss upon irradiation of *trans*-$[W(CO)_4(\eta^2\text{-alkene})_2]$ led to the formation of *mer*- and *fac*-$[W(CO)_3(\eta^2\text{-alkene})_2(\text{solvent})]$, which transformed to *mer*- and *fac*-$[W(CO)_3(\eta^2\text{-alkene})_3]$ in the presence of excess alkenes.

Perutz and coworkers demonstrated that photoreaction of $[Rh(\eta^5\text{-}C_5H_5)(PPh_3)(C_2H_4)]$ with SiR_3H (R = ^{i}Pr, Et) and hexafluorobenzene produced $[Rh(\eta^5\text{-}C_5H_5)(PPh_3)(SiR_3)(H)]$ and $[Rh(\eta^5\text{-}C_5H_5)(PPh_3)(\eta^2\text{-}C_6F_6)]$, respectively.[82] Oxidative addition of the C–H bonds of partially fluorinated arenes C_6F_5H and 1,3-$C_6F_2H_4$ led to the formation of $[Rh(\eta^5\text{-}C_5H_5)(PPh_3)(Ar_F)(H)]$ ($Ar_F = C_6F_5$, 2,6-$C_6H_3F_2$). Oxidative addition of benzene may be detected following photolysis in benzene-THF mixtures at 233 K ($\lambda_{ex} < 400$ nm), but the product decomposed upon warming. Recent work showed that photolysis of the bis-alkene complex $[Rh(\eta^5\text{-}C_5H_5)(C_2H_4)_2]$ with pyridine compounds such as 4-methylpyridine, 4,4′-Me_2-bpy and 2,2′-dipyridylketone gave a variety of products.[83]

4.2 Arene and Aryl Systems

Tyler and coworker reported photochemically active polymers $[CONH(CH_2)_2(\eta^5\text{-}C_5H_4)(CO)_3Mo\text{-}Mo(CO)_3(\eta^5\text{-}C_5H_4(CH_2)_2NHCO)(CH_2)_m]_n$ ($m = 4, 8$) (**24**).[84] Owing to the presence of metal–metal bonds along the backbone, the polyamides were photochemically reactive. Metal–metal bond photolysis reactions similar to the $Cp_2Mo_2(CO)_6$ dimer were observed, as evidenced by the disappearance of the $^1(d\pi \rightarrow \sigma^*)$ (508 nm) and $^1(\sigma \rightarrow \sigma^*)$ (388 nm) bands in the absorption spectrum. It was proposed that the reaction occurred by photolysis of the Mo–Mo bond followed by trapping of the metal radicals with atmospheric oxygen. This proposal has been confirmed by a related polymer system in which built-in metal-radical traps (chlorine atoms) were incorporated into the polymers.[85] The effect of radical size, chain length, and mass on the cage recombination efficiency of photochemically generated radical cage pairs of related polymers were studied in detail.[86]

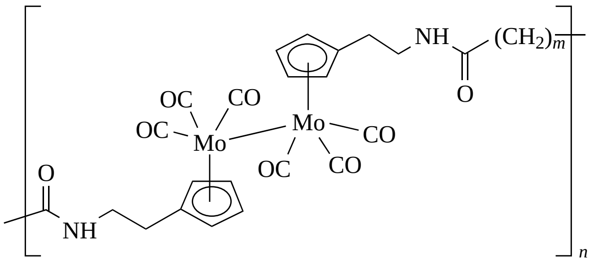

$[CONH(CH_2)_2(\eta^5\text{-}C_5H_4)(CO)_3Mo\text{-}Mo(CO)_3(\eta^5\text{-}C_5H_4(CH_2)_2NHCO)(CH_2)_m]_n$

(**24**)

The MLCT states of d^6 complexes with polypyridine ligands are well known. Analogous systems of organometallic d^6 complexes with arenes as 6π-electron ligands are expected to exhibit interesting luminescence properties. Unfortunately, the MLCT states of such complexes are apparently located above the LF states and therefore these complexes do not exhibit luminescence. However, for d^{10} systems, such LF states are absent and thus, emission properties of d^{10} arene complexes are anticipated. The copper(I) benzene complex $Cu_2(CF_3SO_3)_2(C_6H_6)$ showed an absorption band at 315 nm ($\varepsilon = 1200\,dm^3\,mol^{-1}\,cm^{-1}$) in benzene solution, which was assigned to an ^{1}MLCT (d(Cu) → $\pi^*(C_6H_6)$) transition.**87** While the complex was not emissive in solution, excitation of a solid sample of the complex resulted in intense ^{3}MLCT (d(Cu) → $\pi^*(C_6H_6)$) emission at 518 nm ($\tau_o = 0.5\,\mu s$).

The basic reaction of the tricarbonyl(cyclohexadienyl)iron cation $[(C_6H_7)Fe(CO)_3]^+$ consists of an addition of a nucleophile to the cyclohexadienyl ligand yielding a substituted cyclohexadiene ligand.**88** Assuming the cation contains an iron(0) center and a coordinated cyclohexadienyl cation, the complex was expected to have low-lying MLCT (Fe(0) → $C_6H_7^+$) transitions. Photolysis of the complex in solution resulted in the formation of 1,3-cyclohexadiene and 1,3,5,-hexatriene. The photolysis was also accompanied by the evolution of CO, a rise in pH and the formation of Fe^{2+}. In the MLCT excited state, the Fe(II) and $C_6H_7^-$ were expected to be formed. In contrast to the ground state, this excited state was expected to facilitate an electrophilic attack at the cyclohexadienyl ligand. In aqueous solution, the attack of protons led to the formation of $[(C_6H_8)Fe(CO)_3]^{2+}$ which was unstable and susceptible to the attack by water molecules to give $[Fe(H_2O)_6]^{2+}$. This mechanism also explained the release of CO and a rise in pH of the reaction mixture during irradiation.

Different techniques have been used to study the products of photoreactions of organometallic compounds: for example, irradiation of the arene complexes $[CpFe(\eta^6\text{-arene})]^+$ resulted in the substitution of the arene by solvent or other potential ligands present in solution.**89** In solutions containing an epoxide monomer, this photochemical reaction generated a species that initiated polymerization. Ion cyclotron resonance Fourier transform mass spectrometry and electrospray ionization mass spectrometry were used to elucidate the mechanism of these photoinitiated polymerizations.

The alkane C−H bond activation reaction by arene complexes such as $[(\eta^5\text{-}C_5H_5)Rh(CO)_2]$ has attracted much interest. Subpicosecond infrared spectroscopic measurements revealed that the reactive intermediate in the cyclohexane activation by $[(\eta^5\text{-}C_5H_5)Rh(CO)_2]$ was associated with an absorption band at 1963 cm^{-1}.**90** This transient intermediate was identified to be the cyclohexane solvate $[(\eta^5\text{-}C_5H_5)Rh(CO)(C_6H_{12})]$. The mechanism of the photolysis of $[(\eta^5\text{-}C_5H_5)Ir(CO)_2]$ in cyclohexane has also been studied.**91** About 20% of the excited molecules underwent dissociation to lose a CO ligand, leading to $[(\eta^5\text{-}C_5H_5)Ir(CO)]$ or a solvate of this species, which were responsible for the activation of the alkane.

The crystal structures of the aryl complex $[Au(C_6Cl_5)_2]_2[Tl(OPPh_3)][Tl(OPPh_3)(L)]$ (L = THF, acetone) showed extended unsupported chains with short intermolecular interactions between alternating gold(I) and thallium(I) centers (3.0529(3)−3.3205(3) Å).**92** At room temperature, the THF and acetone complexes emitted at 497 and 501 nm, respectively. At low temperature, the luminescence was dependent on the excitation wavelengths. DFT and time-dependent DFT calculations on simplified model systems revealed that the site-selective excitation behavior was due to the different thallium(I) environments. The vaporchromic behavior of a related polymeric complex $\{Tl[Au(C_6Cl_5)_2]\}_n$ has also been reported recently.**93** This polymer showed a wide range of emission wavelengths in the presence of different volatile organic compounds. These observations were suggested to be due to weak interaction of the Tl(I) centers with the organic compounds.

5 ALKYLIDENES (*See Carbene Complexes*) AND ALKYLIDYNE SYSTEMS

5.1 Gold (*See Gold: Organometallic Chemistry*) and Silver (*See Silver: Organometallic Chemistry*) Alkylidenes

Balch and coworkers described the solvent-induced luminescence properties of the organometallic complex $[Au_3(\mu\text{-}CH_3N{=}COCH_3)_3]$ (**25**).**94,95** Intense and long-lived yellow luminescence was observed when a solvent such as $CHCl_3$ was in contact with the solid sample of the complex that had been irradiated with ultra-violet light. Upon photoexcitation, the complex emitted at 446 nm ($\tau_o = 1$ ms) and 552 nm ($\tau_o = 1.4$, 4.4 and 31 s) in the solid state and at 422 nm in $CHCl_3$. Gold···gold contacts of 3.308(2) Å were observed in the trimeric structure of the complex. The triangular units also showed some stacking interactions, leading to intermolecular gold···gold distances of ca. 3.346(1) Å. The solvent-induced luminescence was suggested to result from the supramolecular aggregation of the complex.

Several trinuclear complexes of gold(I) interact with silver and thallium salts to intercalate Ag^+ and Tl^+ cations, thereby forming chains in the crystal structures.**96** The complexes $[\{(\mu\text{-C,N-L})_3Au_3\}_2M]X$ (μ-C,N-L = 1-benzylimidazolate, 1-methylimidzaolate, $C(OEt){=}NC_6H_4\text{-}CH_3\text{-}p$; M = Ag^+, Tl^+; X = BF_4^-, PF_6^-, ClO_4^-) have been isolated. The sandwich (*see Sandwich Compound*) clusters center the cations between the planar trinuclear moieties producing structures of $(B_3AB_3B_3AB_3)_n$ units. Short Au···Au contacts (ca. 3.0 Å) were observed between BAB molecular centers. Crystalline sample of the complexes showed intense luminescence:

for example, $[\{(\mu\text{-1-benzylimidazolate})_3Au_3\}_2Ag](BF_4)$ displayed green emission at 535 nm ($\tau_o = 550$ and 115 ns) at 298 K. Upon cooling to 77 K, the solid showed orange emission at 570 nm ($\tau_o = 1100$ and 220 ns). The emission was assigned to excited states of Au···Au character delocalized along the crystallographic axis of the chain. Thermal contraction led to a reduction in the intermolecular metal–metal distances along the chain and thus a decrease in the band gap and emission energy.

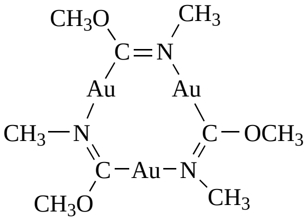

$[Au_3(\mu\text{-}CH_3N{=}COCH_3)_3]$

(**25**)

The crystal structures and luminescence properties of three gold(I) alkylidene complexes $[Au\{C(NHMe)_2\}_2](PF_6)$ (**26**), $[Au\{C(NHMe)_2\}_2](BF_4)$, and $[Au\{C(NMe_2)(NHMe)\}_2](PF_6)$ (**27**) have been reported.[97] Solid samples of $[Au\{C(NHMe)_2\}_2](PF_6)$ and $[Au\{C(NHMe)_2\}_2](BF_4)$ emitted at 484 and 482 nm at room temperature. Their close structural analogue $[Au\{C(NMe_2)(NHMe)\}_2](PF_6)$ did not show emission in the solid state at room temperature or 77 K. The solid-state emission of $[Au\{C(NHMe)_2\}_2](PF_6)$ and $[Au\{C(NHMe)_2\}_2](BF_4)$ was attributed to the formation of extended chains of gold(I) centers that were connected through aurophilic attractions and an excited state of metal-centered $^3(d\sigma^* \rightarrow p\sigma)$ character was assigned. This assignment was supported by the short Au···Au distances for $[Au\{C(NHMe)_2\}_2](PF_6)$ (3.1882(1) Å) and $[Au\{C(NHMe)_2\}_2](BF_4)$ (3.4615(2) Å).

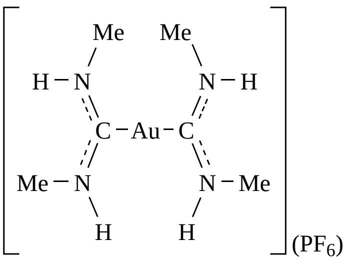

$[Au\{C(NHMe)_2\}_2](PF_6)$

(**26**)

Although shorter Au···Au distances were observed for the halide salts $[Au\{C(NHMe)_2\}_2](X)$ (3.1231(3) and 3.1297(4) Å for X = Cl and Br, respectively), solid samples of these complexes emitted at apparently higher energy, at 391 and 412 nm for X = Cl and Br, respectively, than their PF_6^- and BF_4^- counterparts.[98] This observation was attributed to the fact that $[Au\{C(NHMe)_2\}_2](X)$ existed as dimeric units in the crystals. In contrast, infinite gold chains were observed for both the PF_6^- and BF_4^- complexes.

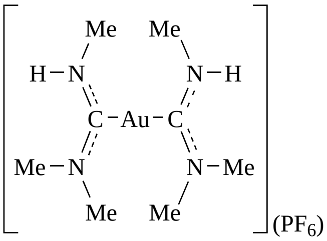

$[Au\{C(NMe_2)(NHMe)\}_2](PF_6)$

(**27**)

The trinuclear complex $[(\mu\text{-1-benzylimidazolate})_3Au_3]$ has a strong tendency to form stacked compounds. Reaction with TCNQ and C_6F_6 gave dark green $[\{(\mu\text{-1-benzylimidazolate})_3Au_3\}_2(TCNQ)]_n$ and colorless $[\{(\mu\text{-}C(OEt){=}NC_6H_4\text{-}CH_3\text{-}p)_3Au_3\}_2(C_6F_6)]_n$ polymers, respectively.[99] While the gold(I) trimer displayed blue photoluminescence, the adduct $[\{(\mu\text{-}C(OEt){=}NC_6H_4\text{-}CH_3\text{-}p)_3Au_3\}_2(C_6F_6)]_n$ was nonemissive. X-ray crystallographic studies revealed that the presence of C_6F_6 disrupted the intermolecular aurophilic bonding in the $[\mu\text{-}C(OEt){=}NC_6H_4\text{-}CH_3\text{-}p_3Au_3]$ units. When the adduct was immersed in a solvent that does not dissolve the gold(I) trimer, such as diethyl ether, the adduct lost its crystallinity and the resulting power exhibited the blue emission of the gold(I) trimer, indicating that C_6F_6 was liberated. Other stacked assemblies formed by gold(I) trimers such as $[(\mu,\text{-1-benzylimidazolate})_3Au_3]$ and $[(\mu\text{-}C(OEt){=}NC_6H_4\text{-}CH_3\text{-}p)_3Au_3]$ with the trinuclear mercury(II) complex $[Hg_3(\mu\text{-}C,C\text{-}C_6F_4)_3]$ (**28**) have been isolated and shown to exhibit remarkable luminescence properties.[100]

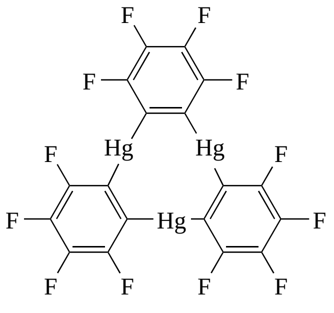

$[Hg_3(\mu\text{-}C,\ C\text{-}C_6F_4)_3]$

(**28**)

Recently, the adducts formed between $[Hg_3(\mu\text{-}C,C\text{-}C_6F_4)_3]$ and polyaromatics including pyrene, naphthalene, and biphenyl, respectively, have been isolated.[101] The crystalline samples of the adducts showed red, green, and blue phosphorescence, respectively, at 77 K and room temperature (Figure 7). Owing to the heavy atom effects, these adducts

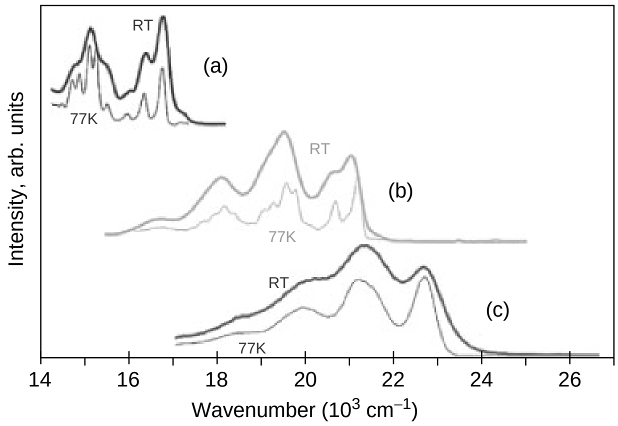

Figure 7 Emission spectra of crystalline solids formed between $[Hg_3(\mu\text{-}C,C\text{-}C_6F_4)_3]$ and polyaromatics including (a) pyrene, (b) naphthalene, and (c) biphenyl. Intensities of different spectra were adjusted arbitrarily for clarity. (Reprinted with permission from Ref. 101. © 2003 American Chemical Society)

exhibited very long $^3(\pi \rightarrow \pi^*)$ phosphorescence lifetimes (454–712 μs) at room temperature.

Luminescent silver(I) alkylidene complexes $[((pyCH_2)_2im)_2Ag](X)$ ($X = BF_4^-$, Cl^-), $[((pyCH_2)_2im)_3Ag_3](BF_4)_3$ (**29**)[102] and related silver(I) *N*-heterocyclic alkylidene complexes,[103] and gold(I) alkylidene complexes $[Au(R_2\text{-}bimy)L]$ ($R = Et, Me$; $L = Cl, Br, I, bimy, SC_6H_5, C{\equiv}CPh$)[104] have been synthesized and found to display intense luminescence.

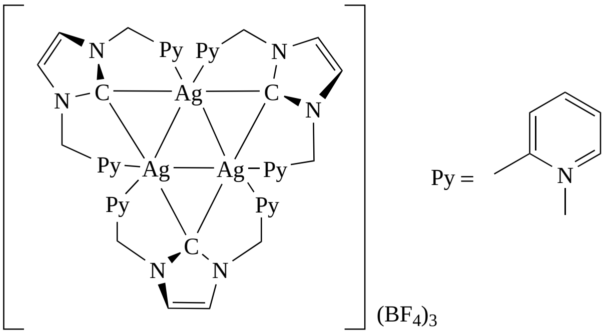

$[((pyCH_2)_2im)_3Ag_3](BF_4)_3$

(**29**)

5.2 Ruthenium (*See Ruthenium: Organometallic Chemistry*) and Rhenium (*See Rhenium: Organometallic Chemistry*) Alkylidenes

A series of luminescent ruthenium(II) cyclometalated aminoalkylidene complexes (*see Alkylidene*) $[Ru(N\text{–}N)_2\{{=}C(CH_2R)NR'C_6H_3R''\}](OTf)$ (N–N = bpy, phen; $R = C_6H_5$, C_6H_3S, $C_6H_4\text{-}Cl\text{-}p$; $R' = H, CH_3$; $R'' = H$, $OCH_3\text{-}p$, $Br\text{-}p$, $CF_3\text{-}p$) such as (**30**) has been shown to exhibit ^{3}MLCT ($d\pi(Ru) \rightarrow \pi^*(N\text{–}N)$) luminescence at ca. 782–813 nm.[105] The assignment was supported by EHMO calculations, which showed that the HOMO was mainly ruthenium-based, while the LUMO had substantial diimine character. A related luminescent ruthenium(II) alkylidene complex containing a benzo-15-crown-5 ring (*see Crown Ethers*) has also been isolated recently.[106] The uptake of sodium and lithium ions by this crown-ether complex was investigated by spectroscopic titrations and mass spectrometry.

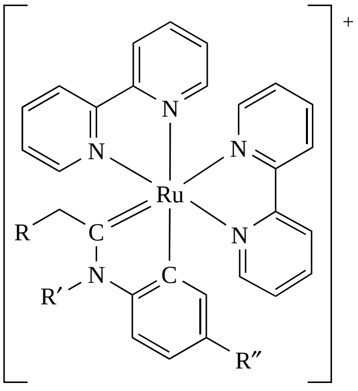

$[Ru(bpy)_2\{=C(CH_2R)NR'C_6H_3R''\}]^+$

(**30**)

A series of rhenium alkylidene complexes $[HNCH_2CH_2NHCRe(CO)_3(N\text{–}N)]^+$ has been successfully isolated.[107] HF-SCH and MP2 MO calculations on $[HNCH_2CH_2NHCRe(CO)_3(NHCHCHNH)]^+$ and its fragments $[Re(CO)_3(NHCHCHNH)]^+$ and $[HNCH_2CH_2NHC]$ showed that the HOMO was essentially the nonbonding $d_{xz}(Re)$ orbital (z-axis taken as the Re–C(alkylidene) axis), which was close in energy to the nonbonding $d_{yz}(Re)$ and $d_{x^2-y^2}(Re)$ orbitals. The LUMO comprised p_z(N–N) and p_z(alkylidene). Thus, the lowest-energy transition could be formulated as $d(Re) \rightarrow \pi^*(N\text{–}N)$ mixed with a small amount of $d(Re) \rightarrow \sigma^*$(alkylidene) character. A single configuration interaction (CIS) calculation suggested that the absorption band of $[HNCH_2CH_2NHCRe(CO)_3(phen)]^+$ at ca. 363 nm and the less intense shoulder at ca. 450 nm were ^{1}MLCT and ^{3}MLCT ($d(Re) \rightarrow \pi^*(phen)$) transitions, respectively. The complexes displayed photoluminescence and the emission was assigned to an $^3(d_{xz}(Re) \rightarrow \pi^*(N\text{–}N))$ excited state with partial $^3(d_{xz}(Re) \rightarrow p_z(\text{alkylidene C}))$ character.

5.3 Platinum (*See Platinum: Organometallic Chemistry*) Alkylidenes

The luminescence properties of a series of dinuclear platinum alkenylidene complexes $[Pt_2(\mu\text{-}C{=}CHPh)(C{\equiv}CPh)$

$(PEt_3)_3(X)]^{n+}$ (X = PEt_3 ($n = 1$), halide, SPh ($n = 0$)) (**31**) and their structural analogues have been studied.**108** The complexes displayed $^1(Pt_2 \rightarrow C{=}C)$ absorption bands at ca. 370–494 nm. Most of the complexes were emissive at low-temperature alcohol glass. The emission occurred at 546–710 nm ($\tau_o = 10{-}330\ \mu s$) and was assigned to an excited state of $^3(Pt_2 \rightarrow C{=}C)$ CT character.

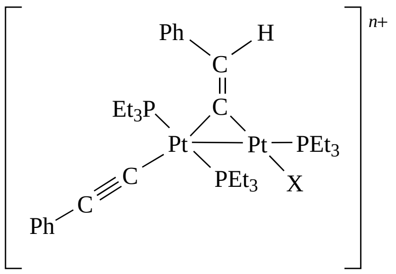

$[Pt_2(\mu\text{-}C = CHPh)(C{\equiv}CPh)(PEt_3)_3(X)]^{n+}$

(**31**)

The hexanuclear Pt(II) alkylidene complex $[\{Pt(CN)(C_{10}H_{21}N_4)\}_6]$ (**32**) was synthesized.**109** The absorption spectrum of this complex displayed an intense band at 356 nm ($\varepsilon = 18\,000\ dm^3\ mol^{-1}\ cm^{-1}$), attributed to an ^{1}MLCT (Pt → π^*(alkylidene)) transition. The emission of the complex at 507–519 nm was assigned to an excited state of ^{3}MLCT (Pt → π^*(alkylidene)) parentage.

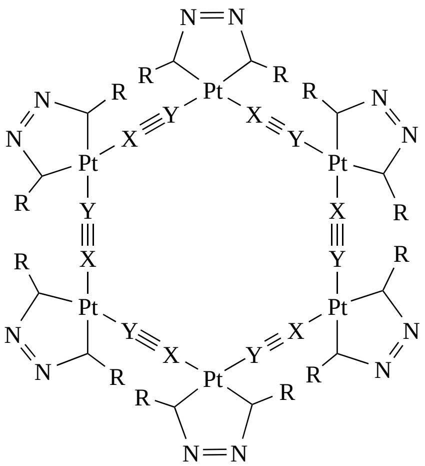

$X{\equiv}Y = C{\equiv}N$ or $N{\equiv}C$; R = $NHCH_3$

$[\{Pt(CN)(C_{10}H_{21}N_4)\}_6]$

(**32**)

Mononuclear platinum(II) alkylidene complexes $[(CNN)Pt\{C(NHR^1)(NHR^2)\}]^+$ and its dinuclear counterpart, $[\{(CNN)Pt\}_2\mu\text{-}\{C(NH^tBu)(NH(CH_2)_3)\}_2NMe]^{2+}$ (**33**) have been synthesized and characterized.**110** The ^{3}MLCT (d(Pt) → π^*(CNN)) emission of the mononuclear complexes occurred at 542–558 nm in CH_3CN at 298 K. The emission maximum of the dinuclear complex occurred at 545 nm, and fell within the range observed for its mononuclear counterparts. This suggested the absence of interactions between the platinum(II) centers because Pt–Pt and/or ligand–ligand interactions would yield MMLCT emission at $\lambda_{em} >$ 600 nm. The photochemistry of these platinum(II) alkylidene complexes was investigated. Two related platinum(II) alkylidene complexes $[(C_{10}H_{21}N_4)Pt(CN)(CN^tBu)]$ and $[(C_{10}H_{21}N_4)Pt(CN^tBu)_2]^+$ have also been synthesized and characterized.**111** The solvent- and pH-dependent photophysical properties of these complexes have also been studied.

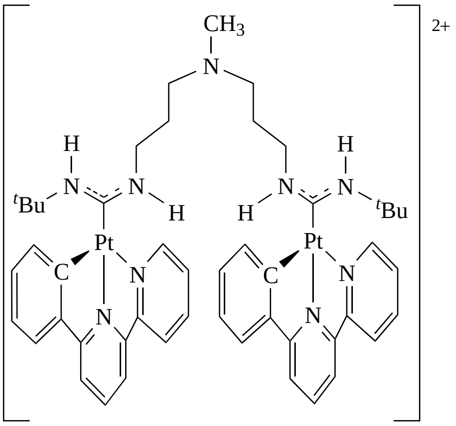

$[\{(CNN)Pt\}_2\mu\text{-}\{C(NH^tBu)(NH(CH_2)_3)\}_2NMe]^{2+}$

(**33**)

5.4 Tungsten (*See Tungsten: Organometallic Chemistry*) and Molybdenum (*See Molybdenum: Organometallic Chemistry*) Alkylidynes

Bocarsly and Mayr first reported the luminescence properties of transition metal alkylidyne (*see Alkylidyne*) complexes $[XW(CO)_2(L_2)(CPh)]$ (X = halides, L_2 = TMEDA, $(py)_2$ or dppe).**112** The complexes exhibited broad and structureless emission bands at ca. 625–640 nm, which was attributable to an excited state of ^{3}MLCT (d_{xy}(W) → π^*(W≡C)) character. With an extension of the alkylidyne unit, the complexes $[XW(CO)_2(L_2)(C\text{-}C_6H_4\text{-}p\text{-}(C{\equiv}C\text{-}C_6H_4\text{-}p\text{-})_n\text{-}N{\equiv}C)]$ (L_2 = TMEDA, dppe; $n = 0$, 1) containing an isocyanide moiety have been shown to possess rich luminescence properties.**113** Perturbation of the absorption and emission properties of the complexes by coordination of the isocyanide moiety to metal-containing fragments such as *fac*-$ReCl(CO)_3$, *cis*-$PdCl_2$, *trans*-PdI_2, and *trans*-PtI_2 was also studied.

Irradiation of the alkylidyne-carbonyl tungsten complexes *cis*-$[ClW(CO)_2(PMe_2R)_2(CPh)]$ (R = Me or Ph) with visible light in the presence of electrophiles ECl (E = H, $C(O)CMe_3$, $C(O)C_6H_4\text{-}OCH_3\text{-}p$, $Si(CMe_3)_2Ph$) afforded the complexes *trans*-$[(Cl)_2W(CO)(PMe_2R)_2(EOC{\equiv}CPh)]$ that contained a four-electron-donor alkyne ligand.**114** The reactions were accompanied by the photoinduced cis–trans isomerization of the starting complex. Therefore, the same products were produced when the trans-isomers were used. This photoinduced alkylidyne-carbonyl coupling reaction was an efficient method for the synthesis of metal-coordinated ynols and alkyne derivatives.

The lowest-energy absorption bands of the metallobutadiyne complexes $[HC{\equiv}W(dmpe)_2(C{\equiv}CR)]$ (R = H, $SiMe_3$, Ph, C_6H_4-($C{\equiv}CPr^n$-*p*)) occurred at ca. 449–494 nm and were assigned to a $^1(d_{xy} \rightarrow \pi^*(W{\equiv}C))$ transition.[115] The energy decreased with increasing π-conjugation of the alkynyl ligand. Concerning the HOMO of $[HC{\equiv}W(dmpe)_2(C{\equiv}CR)]$, the energy and orbital interactions of the tungsten d_{xy} orbital were independent of the nature of the axial ligands, since this orbital was nonbonding with respect to the HC≡W–C≡CR axis. However, for the LUMO, mixing of the $\pi^*(W{\equiv}C)$ and $\pi^*(C{\equiv}CR)$ orbitals was symmetry-allowed and the former was stabilized while the later was destabilized. This mixing resulted in a red shift of the $^1(d_{xy} \rightarrow \pi^*(W{\equiv}C))$ transition energy of these complexes relative to $[HC{\equiv}W(dmpe)_2(X)]$ (X = Cl, I, ^{n}Bu).

Two tungsten alkylidyne polymers $[W({\equiv}C\text{–}(4\text{-}NC_5H_2\text{-}3,5\text{-}Me_2))(O^tBu)_3]_n$ (**34**) and $[W({\equiv}C\text{–}(3\text{-}NC_5H_4))(O^tBu)_3]_n$ (**35**) displayed emission at 635 and 640 nm, respectively, in the solid state at 77 K.[116] Under similar conditions, the monomeric $[W({\equiv}CR)(O^tBu)_3]$ (R = aryl, alkyl) complexes were nonemissive. It was proposed that the [W≡C–pyridine] π-system contributed significantly to the frontier orbitals of these luminescent polymeric materials.

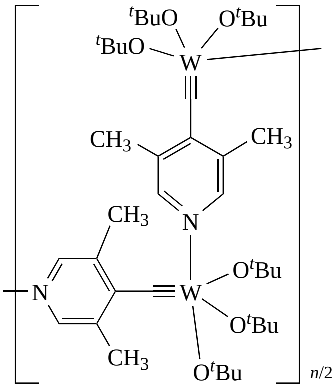

$[W({\equiv}C\text{-}(4\text{-}NC_5H_2\text{-}3,5\text{-}Me_2))(O^tBu)_3]_n$

(**34**)

Che and coworkers reported a series of luminescent molybdenum and tungsten alkylidyne complexes $[(\eta^3\text{-}L)Cl(CO)_2M{\equiv}CPh]^+$ (M = Mo, W; L = $HCpy_3$, Ppy_3, MeP_3, TACN, Me_3TACN) containing a tridentate ligand L.[117] The complexes displayed orange–red emission at ca. 614–669 nm (τ_o = 9–250 ns), which was assigned to an excited state of $^3(d_{xy} \rightarrow d_{\pi^*}(d_{xz}, d_{yz}))$ character.

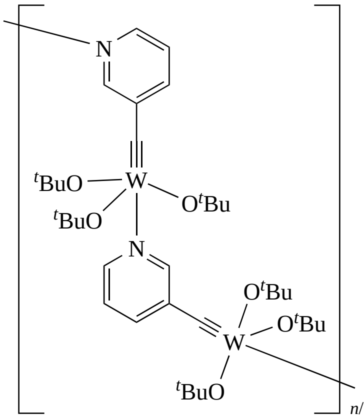

$[W({\equiv}C\text{-}(3\text{-}NC_5H_4))(O^tBu)_3]_n$

(**35**)

McElwee–White and coworkers investigated the luminescence and photochemical properties of the molybdenum and tungsten alkylidyne complexes $[(\eta^5\text{-}C_5H_5)(L)_2M{\equiv}CR]$ (M = Mo, W; L = $P(OMe)_3$, CO; R = Ph, Me, cyclo-C_3H_5).[118] Upon excitation, $[(\eta^5\text{-}C_5H_5)(CO)\{P(OMe)_3\}M{\equiv}CPh]$ in THF solutions at room temperature emitted at ca. 696 and 705 nm, for M = Mo and W, respectively. The origin of the emission was assigned to an ^{3}MLCT ($d(M) \rightarrow \pi^*(M{\equiv}C)$) excited state. The emission of $[(\eta^5\text{-}C_5H_5)(CO)\{P(OMe)_3\}W{\equiv}CPh]$ was quenched in the presence of anthracene and the mechanism was triplet-state energy transfer in nature. In the presence of halocarbons such as $CHCl_3$, the complexes $[(\eta^5\text{-}C_5H_5)(L)_2M{\equiv}CR]$ (M = Mo, W; L = $P(OMe)_3$, CO; R = aryl, alkyl) underwent photo-oxidation to give a 17-electron cation radical, which exhibited both metal-centered and ligand-centered reactivity.[119] Transient absorption spectroscopic studies revealed that the triplet excited states of $[(\eta^5\text{-}C_5H_5)(CO)\{P(OMe)_3\}M{\equiv}CPh]$ showed absorption bands at ca. 440–445 nm, with distinct shoulders at ca. 395 and 420 nm.[120] However, the transient absorption difference spectrum of $[(\eta^5\text{-}C_5H_5)(CO)\{P(OMe)_3\}W{\equiv}C\text{-}Np\text{-}2]$ showed a featureless band at lower energy (ca. 460 nm), suggesting that the excited state of this complex involved some π or π^* levels of the aryl unit. The ^{3}MLCT ($d(W) \rightarrow \pi^*(W{\equiv}CPh)$) emission of the complex $[(\eta^5\text{-}C_5H_5)(CO)\{P(OPh)_3\}W{\equiv}CPh]$ at ca. 710 nm (τ_o = 192 ns) was quenched by pyridinium ions and nitroaromatics via an electron transfer mechanism.[121] The total reorganization energy and the excited-state reduction potential $E°([W]^{+/0*})$ were determined to be 0.40 eV and −1.85 V versus SCE. The highly negative potential indicated the strongly reducing nature of the excited alkylidyne complex.

5.5 Osmium (*See Osmium: Organometallic Chemistry*) and Rhenium (*See Rhenium: Organometallic Chemistry*) Alkylidynes

Sullivan reported the photophysical properties of the luminescent osmium alkylidyne complex

$[(NH_3)_5Os{\equiv}CPh](CF_3SO_3)_3$.[122] The high-energy band of this complex at ca. 292 nm ($\varepsilon = 14\,300\,dm^3\,mol^{-1}\,cm^{-1}$) was assigned to an $^1IL(\pi \rightarrow \pi^*)$ transition associated with the alkylidyne moiety in conjugation with the phenyl ring, and the low-energy absorption band at 462 nm ($\varepsilon = 200\,dm^3\,mol^{-1}\,cm^{-1}$) was assigned to a $^1(d_{xy} \rightarrow d\pi^*(d_{xz}, d_{yz}))$ transition. For the C_{2v} symmetry of $[(NH_3)_5Os{\equiv}CPh]^{3+}$, the d_{xz} and d_{yz} orbitals were split into orbitals of different energy by interaction with the phenyl π-system. The emission of the complex at 632 nm ($\tau_o = 55$ ns) was quenched by pyridine and its derivatives. It was suggested that the proton-transfer mechanism from the excited complex to the pyridines was most probable on the basis of (1) isotope studies using $[(ND_3)_5Os{\equiv}CPh]^{3+}$, and (2) the very high quenching rate for pyridine ($k_q = 5 \times 10^9\,mol\,dm^{-3}\,s^{-1}$). The proposal was in agreement with the more electropositive character of the metal center in the excited state due to the promotion of metal-based electron to an orbital of significant carbon character.

Che and coworkers reported a series of luminescent rhenium(V) benzylidyne complexes $[Re(CC_6H_2Me_3\text{-}2,4,6)(dppb)_2Cl]^+$, $[Re(CC_6H_2Me_3\text{-}2,4,6)(L)_2(CO)(H_2O)Cl]^+$ (L = monodentate phosphines), $[Re(CC_6H_2Me_3\text{-}2,4,6)(dppe)(CO)_2Cl]^+$, and $[Re(CC_6H_2Me_3\text{-}2,4,6)(N\text{–}N)(CO)_2Cl]^+$.[123] Different substituents (R) including H, OMe, Me, Cl, Br, and CN were introduced to the benzylidyne moiety to give $[Re(CC_6H_4\text{-R-}p)(dppe)(CO)_2(OTf)]^+$. Excitation of the complexes in CH_2Cl_2 at room temperature resulted in emission at ca. 520–610 ($\tau_o = 0.02$–$4.84\,\mu s$). The emission of the phosphine complexes was assigned to a $^3(\pi(Re{\equiv}C\text{–}Ph) \rightarrow \pi^*(Re{\equiv}C\text{–}Ph))$ state. This assignment was supported by the observations that electron-donating substituents R increased the emission energy of the complexes $[Re(CC_6H_4\text{-R-}p)(dppe)(CO)_2(OTf)]^+$ while electron-withdrawing ones decreased the energy. The excited state of the diimine complexes $[Re(CC_6H_2Me_3\text{-}2,4,6)(N\text{–}N)(CO)_2Cl]^+$ was suggested to be $^3MLCT\ (d\pi(Re) \rightarrow \pi^*(N\text{–}N))$ because a red shift in the emission energy was observed for the diimine ligands that contain electron-withdrawing substituents.

6 CYCLOMETALATED SYSTEMS

6.1 Rhodium(III) (*See Rhodium: Organometallic Chemistry*) and Iridium(III) (*See Iridium: Organometallic Chemistry*) Cyclometalates

Watts and coworkers reported the luminescence properties of cyclometalated iridium(III) and rhodium(III) complexes (*see Cyclometalation*).[124] The dichloro-bridged dimers $[M_2(N^{\wedge}C)_4Cl_2]$ (M = Ir, Rh; $HN^{\wedge}C$ = Hppy, Hbzq) displayed intense emission with structural features in $EtOH/MeOH/CH_2Cl_2$ (4:1:1: v:v) glass at 77 K. The emission of the rhodium(III) dimers was assigned to an ^3IL excited state in view of the extraordinarily long lifetimes ($\tau_o = 93\,\mu s$ and 2.7 ms for $N^{\wedge}C$ = ppy and bzq, respectively). However, the excited state of the iridium(III) complexes involved significant $^3MLCT\ (d\pi(Ir) \rightarrow \pi^*(N^{\wedge}C))$ character. Relatively intense and structureless emission at ca. 520–550 nm was observed for the iridium(III) dimers in fluid solutions at room temperature, and the emission was assigned to an ^3MLCT excited state. However, the rhodium(III) dimers did not display any emission in fluid solutions at room temperature.

Reactions of the dichloro-bridged rhodium(III) and iridium(III) dimers with diimine ligands resulted in the formation of the luminescent mononuclear complexes $[M(N^{\wedge}C)_2(N\text{–}N)]^+$ (M = Ir, Rh; $N^{\wedge}C$ = ppy, bzq; N–N = bpy, phen).[125] The electronic absorption and emission spectra of these complexes are shown in Figure 8. The rhodium(III) complexes displayed very long-lived emission in

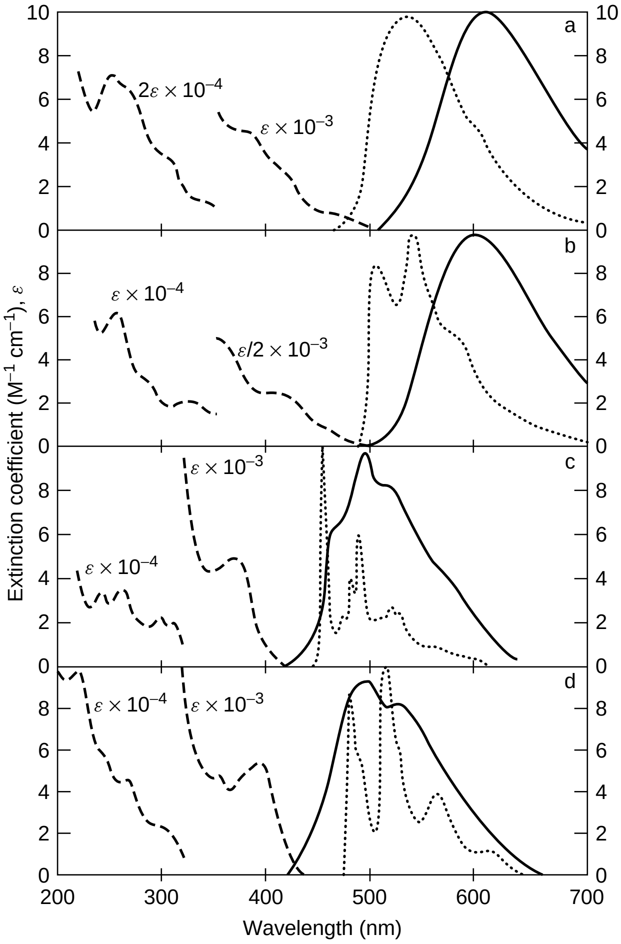

Figure 8 Absorption and emission spectra of mixed-ligand complexes: (- - - -) absorption in methanol at room temperature; (· · · ·) emission in ethanol-methanol (4:1) at 77 K; (———) emission at room temperature in ethanol-methanol (4:1) for iridium(III) complexes and in acetonitrile for rhodium(III) complexes. (a) $[Ir(ppy)_2(bpy)]^+$; (b) $[Ir(bzq)_2(phen)]^+$; (c) $[Rh(ppy)_2(bpy)]^+$; (d) $[Rh(bzq)_2(phen)]^+$. (Reprinted with permission from Ref. 125. © 1987 American Chemical Society)

77 K glass ($\lambda_{em} = 457-538$ nm, $\tau_o = 177-4250\,\mu$s), which was assigned to an excited state of ^{3}IL ($\pi \rightarrow \pi^*$(N^C)) character. Dual emission was observed for the cyclometalated iridium(III) diimine complexes under similar conditions, and charge-transfer excited states involving the cyclometalating and diimine ligands were identified.

The photophysics and excited-state properties of cyclometalated rhodium(III) and iridium(III) complexes $[M(N^\wedge C)_2(N–N)]^+$ (M = Rh(III), Ir(III); N^C = ppy, thpy; N–N = bpy, en) have been investigated.**126** The lowest excited states for the rhodium(III) complexes were ^{3}IL ($\pi \rightarrow \pi^*$) (N^C), while those for the iridium(III) counterparts can be ^{3}IL or ^{3}MLCT in character, depending on the environment.

The absorption and emission properties of the cyclometalated rhodium(III) complexes $[Rh(N^\wedge C)_2(N–N)]^+$ (N^C = ppy, thpy, N–N = bpy, phen, biq) have been studied.**127,128** The complexes showed intense ^{1}MLCT (dπ(Rh) $\rightarrow \pi^*$(N^C)) bands at ca. 360–380 nm. At 77 K, these complexes emitted strongly at 454–546 nm ($\tau_o = 0.04-5$ ms). The luminescence was assigned to predominantly ^{3}IL involving (1) the cyclometalating ligand for the bpy and phen complexes, and (2) the diimine ligands for the biq complexes.

Vogler and coworker reported the interesting photoluminescence properties of the cyclometalated rhodium(III) complexes with cyanide ligands $[Rh(ppy)_2(CN)_2]^-$.**129** The yellow complex showed intense absorption bands at 264, 302, and 363 nm. It is noteworthy that the complex displayed bluish-green luminescence in CH_3CN at room temperature, which was uncommon for rhodium(III) ppy complexes because the low-lying LF states of rhodium(III) prevented these complexes from emitting at room temperature. In contrast, the strong LF strength of the CN^- ligand shifted the d-d states to higher energy and thus allowed the complex to emit at room temperature. The emission spectrum displayed vibronic features at 460, 490, 520 (sh), 565 (sh), and 610 (sh) nm and the emission was assigned to an ^{3}IL excited state involving the ppy ligands.

A series of *facial* homoleptic cyclometalated iridium(III) complexes has been synthesized and their photophysical properties investigated.**130** The ^{3}MLCT emission of the complexes in toluene 298 K occurred at 558–652 nm ($\tau_o = 0.74-4.7\,\mu$s). An OLED device that used $[Ir(1\text{-phenylisoquinolinato})_3]$ as a phosphorescent dopant produced pure-red emission with very high efficiency.

The intense and long-lived luminescence of these complexes has been utilized in the development of the oxygen sensor.**131** Four mononuclear and dinuclear cyclometalated iridium(III) diimine complexes were immobilized in polymerized poly(ethylene glycol) ethyl ether methacrylate matrices, and the oxygen quenching on the luminescence of the films was studied. Linear Stern–Volmer plots were obtained. Despite the difference in the luminescence energy and lifetimes of the complexes, similar Stern–Volmer slopes were observed. The size and charge of the complexes played an important role in the sensitivity of the systems.

In another example, the cyclometalated iridium complex $[Ir(ppy)_2(4\text{-vinylpyridine})Cl]$ has been attached via hydrosilation (*see Hydrosilation*) to hydride-terminated poly(dimethylsiloxane) to produce a luminescent material.**132** Evaluation of this material as a luminescent oxygen sensor revealed significantly improved sensitivity over dispersions of the original vinyl pyridine complex in poly(dimethylsiloxane). The luminescent material was blended with polystyrene to give a new sensor that exhibited increased sensitivity and maintained short response times to rapid changes in air pressure.

In contrast to common luminescent rhodium(III) systems, the complexes $[Rh(ppy)_2(TAP)]^+$ (**36**) and $[Rh(ppy)_2(HAT)]^+$ (**37**) showed structureless emission spectra in fluid solutions at room temperature and in rigid glass at 77 K.**133** In addition to the observation of the irreversible oxidation wave, the emission was assigned to an ^{3}SBLCT (σ(Rh–C) $\rightarrow \pi^*$(TAP or HAT)) excited state. The iridium(III) complex $[Ir(ppy)_2(HAT)]^+$ displayed dual emissions in 77 K glass, which was assigned to excited states of ^{3}MLCT (dπ(Ir) $\rightarrow \pi^*$(HAT)) and ^{3}SBLCT (σ(Ir–C) $\rightarrow \pi^*$(HAT)) character. Recently, optically active cyclometalated rhodium(III) complexes Δ-[Rh(thpy4,5p(*R*,*R*)py)$_2$(TAP)]Cl (**38**), Λ-[Rh (thpy4,5p(*S*,*S*)py)$_2$(TAP)]Cl (**39**), and Δ-[Rh(phpy4, 5p(*R*,*R*)py)$_2$(TAP)]Cl (**40**) have been prepared, characterized, and their photophysical properties studied.**134** The nature of the excited states was investigated by time-dependent DFT calculations.

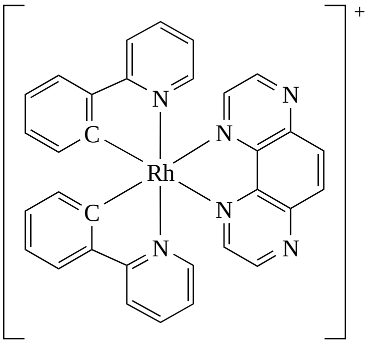

$[Rh(ppy)_2(TAP)]^+$

(**36**)

Campagna and coworkers reported the synthesis and photophysical studies of a number of luminescent cyclometalated mononuclear and dinuclear rhodium(III) and iridium(III) complexes such as $[M^1\{(2,3\text{-dpp})M^2(ppy)_2\}_3]^{5+}$ (M^1 = Ru, Os, M^2 = Rh, Ir).**135** For the rhodium(III) complexes, the emission was assigned to ^{3}MLCT states involving the ruthenium(II) or osmium(II) center and the bridging 2,3-dpp ligand. However, for the heterometallic iridium(III) complexes $[Ru\{(2,3\text{-dpp})Ir(ppy)_2\}_3]^{5+}$ and $[Os\{(2,3\text{-dpp})Ir(ppy)_2\}_3]^{5+}$, the emission originated from ^{3}MLCT excited states of (dπ(Ir) $\rightarrow \pi^*$(2,3-dpp)) and (dπ(Os) $\rightarrow$

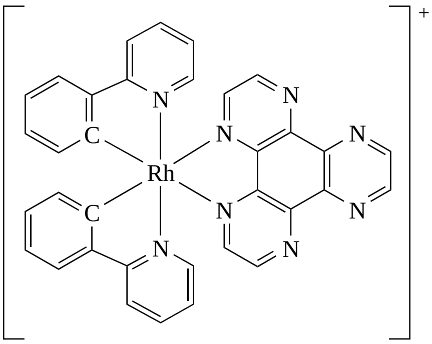

[Rh(ppy)$_2$(HAT)]$^+$

(**37**)

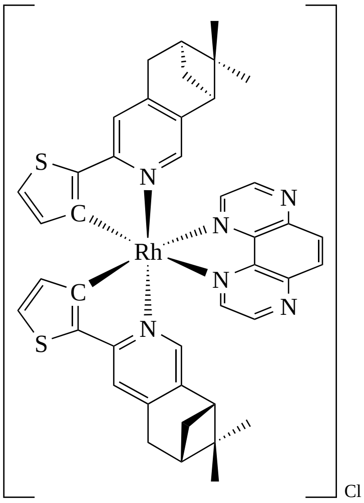

Λ-[Rh(thpy4,5p(*S*,*S*)py)$_2$(TAP)]Cl

(**39**)

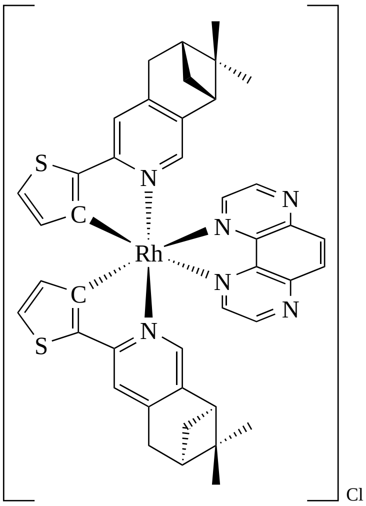

Δ-[Rh(thpy4,5p(*R*,*R*)py)$_2$(TAP)]Cl

(**38**)

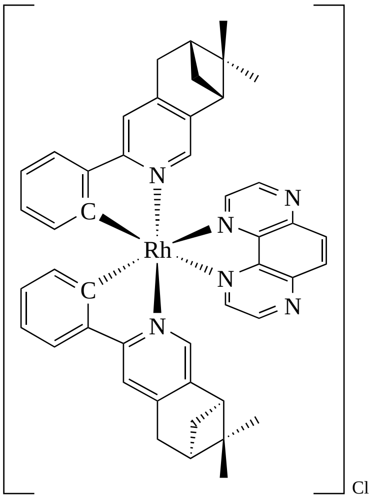

Δ-[Rh(phpy4,5p(*R*,*R*)py)$_2$(TAP)]Cl

(**40**)

π^*(2,3-dpp)) character, respectively. Other luminescent dinuclear cyclometalated iridium(III) complexes have been synthesized using bridging diimine ligands with an ester-linked chelating site.[136]

Barton and coworker reported the preparation of two cyclometalated rhodium(III) complexes [Rh(ppy)$_2$(chrysi)]$^+$ and [Rh(ppy)$_2$(phi)]$^+$ and their spectral properties.[137] Both complexes bound to DNA and caused cleavage upon photoactivation. While [Rh(ppy)$_2$(chrysi)]$^+$ caused photocleavage of DNA selectively at the single CC mismatch, the phi analogue cleaved B-DNA nonspecifically. However, compared to the bpy analogue [Rh(bpy)$_2$(chrysi)]$^{3+}$, the binding of [Rh(ppy)$_2$(chrysi)]$^+$ to DNA was decreased by a factor of 14 because of the lower charge of the complex. The overall DNA-photocleavage efficiencies of the ppy complexes were significantly lower than those of their bpy counterparts because of the reduced photoefficiencies.

Thompson and coworkers reported a class of neutral cyclometalated iridium(III) complexes [Ir$_2$(N^C)$_4$Cl$_2$] and [Ir(N^C)$_2$(LX)] (HN^C = Hppy (**41**), Hmppy (**42**), Hbzq (**43**), Hbt (**44**), Hbsn (**45**), Hpq (**46**), Hbtp (**47**); HLX = Hacac (**48**), Hpic (**49**), Hsal (**50**)).[138,139] Upon photoexcitation, the mononuclear complexes displayed long-lived and intense emission in CH$_2$Cl$_2$ at 77 K and under ambient conditions. The emission wavelengths varied from 512 to 612 nm and the lifetimes from 1.4 to 5.8 µs at room temperature. The emission energy was sensitive to the identity of the cyclometalating ligand N^C and, to a less extent, the anionic ancillary ligand LX. The emission was assigned to an excited state of predominantly ^{3}IL ($\pi \rightarrow \pi^*$(N^C)) character. Since heavy metal complexes, particularly those containing platinum and iridium, can serve as efficient phosphors in organic light-emitting devices,[140] three of the acac complexes were used as dopants for OLEDs.**139** The OLEDs fabricated using the complexes [Ir(ppy)$_2$(acac)], [Ir(bt)$_2$(acac)], and [Ir(btp)$_2$(acac)] displayed green, yellow, and red electroluminescence respectively, with very similar current-voltage characteristics and high external quantum efficiencies (from 6 to 12.3%). The high efficiencies resulted from efficient trapping and radiative relaxation of the singlet and triplet excitons formed in the electroluminescent process.

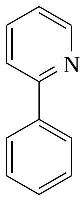
Hppy
(**41**)

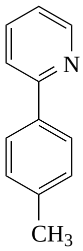
Hmppy
(**42**)

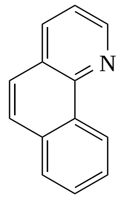
Hbzq
(**43**)

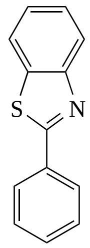
Hbt
(**44**)

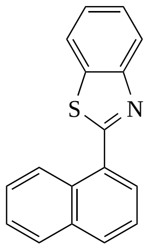
Hbsn
(**45**)

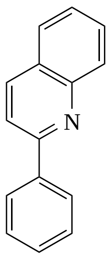
Hpq
(**46**)

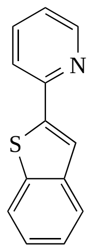
Hbtp
(**47**)

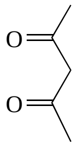
Hacac
(**48**)

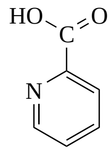
Hpic
(**49**)

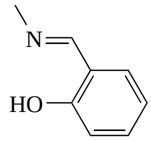
Hsal
(**50**)

The luminescent iridium(III) complexes [Ir(pba)$_2$(N–N)](PF$_6$) displayed indistinguishable and structured emission spectra with very long emission lifetimes (4.3–5.7 µs) in fluid solutions at 298 K.**141** These observations suggested that the emissive state of these complexes was ^{3}IL ($\pi \rightarrow \pi^*$(pba)) in nature. Since the aldehyde moieties of these complexes can react with the primary amine groups of biomolecules to form stable secondary amines after reductive amination, the protein avidin was labeled with these complexes to give luminescent conjugates. The intense and long-lived ^{3}MLCT ($d\pi$(Ir) $\rightarrow \pi^*$(N–N)) emission of the bioconjugates was exploited in the design of a competitive bioassay for biotin.

6.2 Platinum(II) (*See Platinum: Organometallic Chemistry*) and Gold(III) (*See Gold: Organometallic Chemistry*) Cyclometalates

A series of mono and multinuclear dicyclometalated platinum(II) complexes [Pt(C^N^C)L^1], [Pt$_2$(C^N^C)$_2$(μ-L^2)], and [Pt$_3$(C^N^C)$_3$(μ_3-dpmp)] (HC^N^CH = 2,6-diphenylpyridine; L^1 = monodentate pyridine, isocyanide, and phosphine derivatives, L^2 = bidentate pyridine and phosphine derivative) has been synthesized and characterized.**142** X-ray crystallographic studies revealed π–π interactions between the planar Pt(C^N^C) units and, in some cases, between the phenyl rings of ligands. Some of the complexes displayed vibronically structured emission bands at 508–526 nm in 77 K alcohol glass, which was assigned to ^{3}IL excited states. Both π–π^* excimeric and ^{3}MLCT emissions were observed in these examples.

A sol-gel oxygen sensor based on such luminescent complexes has been reported.**143** The complex [Pt(MeOPh-C^N^N)X] (MeOPh-HC^N^N = 3-phenyl-5-*p*-methoxylphenyl-2,2′-bipyridine, X = NH$_2$(CH$_2$)$_3$Si(OCH$_2$CH$_3$)$_3$) was homogeneously incorporated into sol-gel glass by condensation with Si(OCH$_2$CH$_3$)$_4$. The emission spectrum of the film displayed a peak at ca. 520 nm and a shoulder at 650 nm, and was assigned to an excited state of ^{3}MLCT (d(Pt) $\rightarrow \pi^*$(MeOPh-C^N^N)) character. Owing to its triplet nature, the emission was quenched by oxygen. This oxygen sensor had the advantage of a large quenching response because of the very long excited-state lifetime ($\tau_o = 7.3$ µs) of the immobilized luminescent complex in the absence of oxygen.

A dinuclear cyclometalated platinum(II) complex [Pt$_2$L$_2$(dppm)]$^{2+}$ (L = 4-(*p*-diethylphosphonophenyl)-6-phenyl-2,2′-bipyridine) has been employed as a luminescent probe for SDS micelles.**144** Addition of SDS micelles to an aqueous solution of the complex led to an emission band at 530 nm, which was similar to the ^{3}MLCT emission of mononuclear species. The observations were attributed to the absence of intramolecular and/or intermolecular Pt(II)–Pt(II) interactions when the complex was incorporated in the SDS micelles. Addition of NaCl solution into a micellar solution of the complex resulted in an additional ^{3}MMLCT (($d\sigma^*$) $\rightarrow$ (π^*)) emission band at 650 nm. It was suggested that addition of sodium cations would force two cyclometalated platinum(II) units sufficiently close for intramolecular metal–metal and/or ligand–ligand interactions to occur, and thus the observation of ^{3}MMLCT luminescence.

The cyclometalated platinum(II) complex attached with a PEG substituent [Pt(NNC-PEG)Cl] displayed a weak and broad emission band at ca. 543 nm in water at low concentrations of the complex.**145** At [Pt] $\geq 10^{-4}$ M, a new emission band at 710 nm due to Pt–Pt and/or ligand-ligand interaction was observed. In the presence of BSA, the emission intensity of the complex was significantly enhanced, which was attributed to the binding of the complex to the hydrophobic regions of the protein. A binding constant of 2.7×10^4 mol^{-1} dm^3 was estimated. Upon addition of urea, the emission intensity was first enhanced and eventually reduced. These observations were interpreted in terms of (1) tighter binding of the complex by the BSA molecule at low urea concentrations, and (2) denaturing of the protein that occurred at high urea concentrations.

Luminescent cyclometalated platinum(II) and gold(III) complexes $[Pt(dpp\text{-}CNN)(MeCN)]^+$,[146] $[Pt_2(pby\text{-}CNN)_2(dppm)]^{2+}$,[146] and [Au(4-MeOPh-Phbpy)Cl][147] have been prepared and their interactions with calf thymus DNA and synthetic oligonucleotide duplexes poly(dG-dC)$_2$ and poly(dA-dT)$_2$ have been investigated. An intercalative binding mode was proposed for these complexes.

A series of luminescent cyclometalated platinum(II) complexes containing crown-ether (*see Crown Ethers*) pendants [Pt(C^N^C)(L)] (HC^N^CH = 2,6-diphenylpyridine, L = monodentate phosphine-crown ether and pyridine-crown ether ligands) and their crown ether-free and terpyridine derivatives have been isolated and characterized.[148] The complexes showed high-energy structured ^{3}IL emission bands in alcohol glass at 77 K. In CH_2Cl_2 at room temperature, an additional broad emission band at 620–625 nm was also observed when the concentration of the complexes was increased. The emission was suggested to be derived from a ground-state oligomerization or aggregation process due to Pt–Pt and/or ligand-ligand interactions. The binding of sodium, barium, and potassium ions by the crown-ether complexes was investigated. The neutral cyclometalated crown-ether complexes bound the cations with a higher binding constant than their positively charged terpyridine analogues.

The intense absorption band of the cyclometalated platinum(II) complex $[Pt(thpy)_2]$ at 420 nm was assigned to an ^{1}MLCT (d(Pt) $\rightarrow \pi^*$(thpy)) transition.[149] In degassed CH_3CN, the complex displayed ^{3}MLCT luminescence at ca. 580 nm ($\tau_o = 2.4\,\mu s$). In contrast, in CH_2Cl_2, $CHCl_3$, or a mixture of CH_3CN and CH_2Cl_2, the complex underwent photooxidative addition reactions with the formation of [Pt(thpy)(Cl)(R)] (R = CH_2Cl, $CHCl_2$). The results were interpreted on the basis of a mechanism involving generation of $Pt(thpy)_2Cl\cdot$ and $CH_2Cl\cdot$ radicals via (1) a charge-transfer-to-solvent CTTS excited sate, populated from the IL and LMCT states obtained by light absorption and (2) the thermally relaxed ^{3}MLCT emissive state through the conversion to CTTS or bimolecular reaction with CH_2Cl_2.

The pressure- and temperature-dependent emission properties of $[Pt(thpy)_2]$ doped into an n-decane Shpol'skii matrix have been studied.[150] The emitting state was of ^{3}IL ($\pi \rightarrow \pi^*$(thpy)) character with a significant MLCT admixture. The luminescence properties of a related mixed-ligand cyclometalated platinum(II) complex [Pt(thpy)(ppz)] have also been studied and a mechanism involving excimer formation has been suggested for the observed quenching and annihilation reactions.[151] High-resolution optical spectroscopy and optically detected magnetic resonance spectroscopy have been used to study the emitting state of cyclometalated complex [Pt(thpy)(CO)Cl] at 1.2 K and compared to that of other related cyclometalated complexes.[152]

A series of cyclometalated platinum(II) phosphine complexes $[Pt(bzq)(P\text{-}P)](PF_6)$ (P-P = dppm, dppe, dppp) has been synthesized and structurally characterized.[153] The absorption bands at ca. 300 nm ($\varepsilon \approx 2 \times 10^4\,dm^3\,mol^{-1}\,cm^{-1}$) were assigned to ^{1}IL ($\pi \rightarrow \pi^*$) transitions, while the weaker absorption features at lower energy (ca. 340–402 nm) were assigned to ^{1}MLCT (dπ(Pt) $\rightarrow \pi^*$(bzq)) transitions. In 77-K alcohol glass, the complex $[Pt(bzq)(dppm)](PF_6)$ displayed structural ^{3}IL (bzq) emission bands at ca. 466, 500, and 538 nm ($\tau_o = 204\,\mu s$).

The structures and emission properties of a series of related complexes $[Pt(N^\wedge C)(dppm)]^+$ (HN^C = Hppy, Hmppy, Hpq) and [Pt(bph)(dppm)] have been investigated.[154] The electronic absorption spectra of the complexes showed high-energy ^{1}IL ($\pi \rightarrow \pi^*$(N^C)) and low-energy ^{1}MLCT (dπ(Pt) $\rightarrow \pi^*$(N^C)) bands. All the complexes displayed long-lived structured intraligand/charge-transfer emission in low-temperature glass.

Thompson and coworkers reported the synthesis, electrochemistry, and photophysics of a series of cyclometalated platinum(II) complexes [Pt(N^C)(L)] containing a monoanionic cyclometalating ligand N^C and a β-diketonato ligand L. DFT calculations were carried out on both the ground (singlet) and excited (triplet) states of these complexes.[155] The HOMO levels were a mixture of Pt and ligand orbitals, while the LUMO was predominantly N^C-based. The structured emission of the complexes ranged from 438 to 612 nm in 2-Me-THF. High emission quantum efficiencies (0.02–0.25) and lifetimes in the microsecond timescale were observed.

7 ALKYL SYSTEMS

Kaim and coworkers attached the ligand 1,4-diaza-1,3-butadiene and its derivatives (R-DAB, where R = alkyl, aryl) to a series of organoplatinum fragments such as $PtMe_2$, $PtMe_4$, and $PtMes_2$.[156] All the complexes displayed low-energy ^{1}MLCT (d(Pt^{II}) $\rightarrow \pi^*$(R-DAB)) and ^{1}SBLCT (σ(Pt^{IV}-C) $\rightarrow \pi^*$(R-DAB)) absorption bands at ca. 304–634 nm. The assignments were supported by DFT calculations on model complexes involving the ligand HN=CHCH=NH. The platinum(II) complexes showed weak ^{3}MLCT emission at ca. 460–630 nm. In contrast, the organoplatinum(IV) complexes show chemical reactivity upon irradiation. For example, in chlorinated solvents such as CH_2Cl_2 and $CHCl_3$, the complexes $[PtMe_4(R\text{-}DAB)]$ (R = ^{t}Bu, p-Tol) reacted with the solvents to form $[PtMe_3Cl(R\text{-}DAB)]$.

Alkyl ligands are strong σ-donors, and coordination of such ligands to metal centers such as rhenium(I) and ruthenium(II) would perturb the electronic structures of the metal centers and give complexes with remarkable photochemical properties.[15] Irradiation of the complexes $[Re(CO)_3(R)(4,4'\text{-}Me_2\text{-}bpy)]$ (R = Et, ^{i}Pr, Bz) into their visible ^{1}MLCT absorption bands (ca. 400–500 nm) resulted in extremely efficient homolytic cleavage of the Re–R bonds with the formation of the radicals $[Re(CO)_3(4,4'\text{-}Me_2\text{-}bpy)]\cdot$ and R$\cdot$.[157,158] The methyl analogue underwent a similar photochemical reaction, but with a quantum yield of only 0.4. It was proposed that the ^{1}MLCT (dπ(Re) $\rightarrow$ π^*(4,4′-Me$_2$-bpy)) excited state of this complex may either pass a barrier of 1560 cm^{-1} to the dissociative ^{1}SBLCT (σ(Re−C) $\rightarrow$ π^*(4,4′-Me$_2$-bpy)) state and decompose into radicals or simply undergo radiative decay to the ground state, giving typical ^{3}MLCT emission.

The photophysical properties of related ruthenium(II) alkyl complexes [Ru(CO)$_2$(L$_1$)(L$_2$)(N–N)] have been studied.**159** The complex [Ru(CO)$_2$(Cl)(Me)(^{i}Pr-DAB)] showed an ^{1}MLCT (dπ(Ru) $\rightarrow$ π^*(^{i}Pr-DAB)) absorption band at 450 nm and an ^{3}MLCT (dπ(Ru) $\rightarrow$ π^*(^{i}Pr-DAB)) emission band at 650 nm ($\tau_o = 0.3\,\mu$s) in 2-Me-THF glass at 90 K. Interestingly, the lowest-energy excited state of the iodo complex [Ru(CO)$_2$(I)(Me)(^{i}Pr-DAB)] was ^{3}XLCT (p(I) $\rightarrow$ π^*(N–N)) in nature. Meanwhile, the lowest-lying excited states for the complexes [Ru(CO)$_2$(L$_1$)(L$_2$)(N–N)] (L$_1$ = X; L$_2$ = ^{i}Pr, Bz) were ^{3}SBLCT (σ(Ru−C) $\rightarrow$ π^*(N–N)) in character. In these cases, the σ-orbital was delocalized with contributions from 5p(Ru) and the antisymmetric combination of the σ-orbitals of L$_1$ and L$_2$. Upon irradiation under ambient conditions, the weaker σ-bond (Ru−L$_1$ or Ru−L$_2$) was broken to form radicals.

The synthesis and photochemistry of related rhodium(III) bis(alkyl) complexes *cis,cis*-[Rh(R)$_2$(I)(CO)(dmb)] (R = Me, ^{i}Pr) have been studied.**160** The complexes showed an ^{1}IL (π $\rightarrow$ π^*(dmb)) absorption band at ca. 295 nm. There was another band at ca. 370 nm for both complexes, which was assigned to an ^{1}XLCT (p(I) $\rightarrow$ π^*(dmb)) transition. Irradiation of both complexes in solution resulted in Rh−R bond homolysis, as evidenced by IR, UV-vis, and spin-trap EPR investigations. The photoreaction was proposed to occur after crossing from the XLCT state to the reactive SBLCT state.

8 RELATED ARTICLES

Carbene Complexes; Carbonyl Complexes of the Transition Metals; Cyanide Complexes of the Transition Metals; Dinuclear Organometallic Cluster Complexes; Electron Transfer in Coordination Compounds; Electron Transfer Reactions: Theory; Electronic Structure of Organometallic Compounds; Luminescence; Nucleic Acid−Metal Ion Interactions; Photochemistry of Transition Metal Complexes; Photochemistry of Transition Metal Complexes: Theory; Polynuclear Organometallic Cluster Complexes.

9 REFERENCES

1. A. J. Lees, *Chem. Rev.*, 1987, **4**, 711.
2. V. Balzani and F. Scandola, ‘Supramolecular Photochemistry’, Ellis Horwood, Chichester, 1990.
3. K. Kalyanasundaram, ‘Photochemistry of Polypyridine and Porphyrin Complexes’, Academic Press, London, 1992.
4. D. M. Roundhill, ‘Photochemistry and Photophysics of Metal Complexes: Modern Inorganic Chemistry’, Plenum Press, New York, 1994.
5. V. W. W. Yam and K. K. W. Lo, Luminescence Behavior of Polynuclear Metal Complexes of Copper(I), Silver(I), and Gold(I), in ‘Molecular and Supramolecular Photochemistry’, Vol. 4, Multimetallic and Macromolecular Inorganic Photochemistry, eds. V. Ramamurthy and K. S. Schanze, Marcel Dekker, New York, 1999, p. 31.
6. V. W. W. Yam and K. K. W. Lo, *Chem. Soc. Rev.*, 1999, **28**, 323.
7. H. Yersin and D. Donges, *Top. Curr. Chem.*, 2001, **214**, 81.
8. A. Vlček Jr, *Coord. Chem. Rev.*, 2002, **230**, 225.
9. J. V. Caspar, E. M. Kober, B. P. Sullivan, and T. J. Meyer, *J. Am. Chem. Soc.*, 1982, **104**, 630.
10. E. M. Kober, B. P. Sullivan, and T. J. Meyer, *Inorg. Chem.*, 1984, **23**, 2098.
11. A. J. Lees, *Coord. Chem. Rev.*, 1998, **177**, 3.
12. X.-Q. Guo, F. N. Castellano, L. Li, and J. R. Lakowicz, *Anal. Chem.*, 1998, **70**, 632.
13. N. B. Thornton and K. S. Schanze, *Inorg. Chem.*, 1993, **32**, 4994.
14. K. K. W. Lo, W. K. Hui, and D. C. M. Ng, *J. Am. Chem. Soc.*, 2002, **124**, 9344.
15. D. J. Stufkens and A. Vlček Jr, *Coord. Chem. Rev.*, 1998, **177**, 127.
16. V. W. W. Yam, K. M. C. Wong, and K. K. Cheung, *Organometallics*, 1997, **16**, 1729.
17. V. W. W. Yam, Y. L. Pui, K. M. C. Wong, and K. K. Cheung, *Chem. Commun.*, 2000, 1751.
18. A. I. Baba, J. R. Shaw, J. A. Simon, R. P. Thummel, and R. H. Schmehl, *Coord. Chem. Rev.*, 1998, **171**, 43.
19. J. R. Schoonover, G. F. Strouse, R. B. Dyer, W. D. Bates, P. Chen, and T. J. Meyer, *Inorg. Chem.*, 1996, **35**, 273.
20. H. D. Stoeffler, N. B. Thornton, S. L. Temkin, and K. S. Schanze, *J. Am. Chem. Soc.*, 1995, **117**, 7119.
21. V. W. W. Yam, K. K. W. Lo, K. K. Cheung, and R. Y. C. Kong, *J. Chem. Soc., Dalton Trans.*, 1997, 2067.
22. J. Dyer, W. J. Blau, C. G. Coates, C. M. Creely, J. D. Gavey, M. W. George, D. C. Grills, S. Hudson, J. M. Kelly, P. Matousek, J. J. McGarvey, J. McMaster, A. W. Parker, M. Towrie, and J. A. Weinstein, *Photochem. Photobiol. Sci.*, 2003, **2**, 542.
23. L. Wallace, D. C. Jackman, D. P. Rillema, and J. W. Merkert, *Inorg. Chem.*, 1995, **34**, 5210.
24. G. Y. Zheng and D. P. Rillema, *Inorg. Chem.*, 1998, **37**, 1392.
25. P. Chen, T. D. Westmoreland, E. Danielson, K. S. Schanze, D. Anthon, P. E. Neveux Jr, and T. J. Meyer, *Inorg. Chem.*, 1987, **26**, 1116.

26. C. M. Partigianoni, S. Chodorowski-Kimmes, J. A. Treadway, D. Striplin, S. A. Trammell, and T. J. Meyer, *Inorg. Chem.*, 1999, **38**, 1193.
27. W. B. Connick, A. J. Di Bilio, M. G. Hill, J. R. Winkler, and H. B. Gray, *Inorg. Chim. Acta*, 1995, **240**, 169.
28. A. J. Di Bilio, B. R. Crane, W. A. Wehbi, C. N. Kiser, M. M. Abu-Omar, R. M. Carlos, J. H. Richards, J. R. Winkler, and H. B. Gray, *J. Am. Chem. Soc.*, 2001, **123**, 3181.
29. Y. Hayashi, S. Kita, B. S. Brunschwig, and E. Fujita, *J. Am. Chem. Soc.*, 2003, **125**, 11976.
30. M. K. Whittlesey, R. N. Perutz, I. G. Virrels, and M. W. George, *Organometallics*, 1997, **16**, 268.
31. R. V. Slone, K. D. Benkstein, S. Bélanger, J. T. Hupp, I. A. Guzei, and A. L. Rheingold, *Coord. Chem. Rev.*, 1998, **171**, 221.
32. K. D. Ley, C. E. Whittle, M. D. Bartberger, and K. S. Schanze, *J. Am. Chem. Soc.*, 1997, **119**, 3423.
33. K. A. Walters, D. M. Dattelbaum, K. D. Ley, J. R. Schoonover, T. J. Meyer, and K. S. Schanze, *Chem. Commun.*, 2001, 1834.
34. P. K. Ng, X. Gong, S. H. Chan, L. S. M. Lam, and W. K. Chan, *Chem. Eur. J.*, 2001, **7**, 4358.
35. O. Ishitani, K. Kanai, Y. Yamada, and K. Sakamoto, *Chem. Commun.*, 2001, 1514.
36. M.-N. Colomb-Dunand-Sauthier, A. Deronzier, and R. Ziessel, *J. Phys. Chem.*, 1993, **97**, 5973.
37. V. M. Miskowski, S. F. Rice, H. B. Gray, R. F. Dallinger, S. J. Milder, M. G. Hill, C. L. Exstrom, and K. R. Mann, *Inorg. Chem.*, 1994, **33**, 2799.
38. C. M. Che, W. T. Wong, T. F. Lai, and H. L. Kwong, *J. Chem. Soc., Chem. Commun.*, 1989, 243.
39. P. D. Harvey, *Coord. Chem. Rev.*, 2001, **219**, 17.
40. A. L. Balch and V. J. Catalano, *Inorg. Chem.*, 1991, **30**, 1302.
41. P. D. Harvey and D. Fortin, *Coord. Chem. Rev.*, 1998, **171**, 351.
42. C. L. Exstrom, J. R. Sowa Jr, C. A. Daws, D. Janzen, and K. R. Mann, *Chem. Mater.*, 1995, **7**, 15.
43. S. M. Drew, D. E. Janzen, and K. R. Mann, *Anal. Chem.*, 2002, **74**, 2547.
44. S. W. Lai, H. W. Lam, W. Lu, K. K. Cheung, and C. M. Che, *Organometallics*, 2002, **21**, 226.
45. H. Yersin and U. Riedl, *Inorg. Chem.*, 1995, **34**, 1642.
46. M. A. Rawashdeh-Omary, M. A. Omary, H. H. Patterson, and J. P. Fackler Jr, *J. Am. Chem. Soc.*, 2001, **123**, 11237.
47. A. Assefa, M. A. Omary, B. G. McBurnett, A. A. Mohamed, H. H. Patterson, R. J. Staples, and J. P. Fackler Jr, *Inorg. Chem.*, 2002, **41**, 6274.
48. V. W. W. Yam, *Chem. Commun.*, 2001, 789.
49. V. W. W. Yam, K. K. W. Lo, and K. M. C. Wong, *J. Organomet. Chem.*, 1999, **578**, 3.
50. V. W. W. Yam, W. Y. Lo, C. H. Lam, W. K. M. Fung, K. M. C. Wong, V. C. Y. Lau, and N. Zhu, *Coord. Chem. Rev.*, 2003, **245**, 39.
51. V. W. W. Yam, W. Y. Lo, and N. Y. Zhu, *Chem. Commun.*, 2003, 2446.
52. K. M. C. Wong, S. C. F. Lam, C. C. Ko, N. Zhu, V. W. W. Yam, S. Roué, C. Lapinte, S. Fathallah, K. Costuas, S. Kahlal, and J.-F. Halet, *Inorg. Chem.*, 2003, **42**, 7086.
53. L. Sacksteder, E. Baralt, B. A. DeGraff, C. M. Lukehart, and J. N. Demas, *Inorg. Chem.*, 1991, **30**, 2468.
54. V. W. W. Yam., *Acc. Chem. Res.*, 2002, **35**, 555.
55. C. L. Choi, Y. F. Cheng, C. Yip, D. L. Phillips, and V. W. W. Yam, *Organometallics*, 2000, **19**, 3192.
56. H. K. Yip, H. M. Lin, Y. Wang, and C. M. Che, *J. Chem. Soc., Dalton Trans.*, 1993, 2939.
57. K. M. C. Wong, C. K. Hui, K. L. Yu, and V. W. W. Yam, *Coord. Chem. Rev.*, 2002, **229**, 123.
58. V. W. W. Yam, K. L. Yu, and K. K. Cheung, *J. Chem. Soc., Dalton Trans.*, 1999, 2913.
59. I. Ara, J. Forniés, J. Gómez, E. Lalinde, and M. T. Moreno, *Organometallics*, 2000, **19**, 3137.
60. V. W. W. Yam, L. J. Zhang, C. H. Tao, K. M. C. Wong, and K. K. Cheung, *J. Chem. Soc., Dalton Trans.*, 2001, 1111.
61. V. W. W. Yam, C. H. Tao, L. J. Zhang, K. M. C. Wong, and K. K. Cheung, *Organometallics*, 2001, **20**, 453.
62. J. Lewis, M. S. Khan, A. K. Kakkar, B. F. G. Johnson, T. B. Marder, H. B. Fyfe, F. Wittman, R. H. Friend, and A. E. Dray, *J. Organomet. Chem.*, 1992, **425**, 165.
63. S. C. Chan, M. C. W. Chan, Y. Wang, C. M. Che, K. K. Cheung, and N. Zhu, *Chem. Eur. J.*, 2001, **7**, 4180.
64. S. Fernández, J. Forniés, B. Gil, J. Gómex, and E. Lalinde, *Dalton Trans.*, 2003, 822.
65. V. W. W. Yam, K. M. C. Wong, and N. Zhu, *J. Am. Chem. Soc.*, 2002, **124**, 6506.
66. V. W. W. Yam, K. M. C. Wong, and N. Zhu, *Angew. Chem., Int. Ed. Engl.*, 2003, **42**, 1400.
67. C. Huber, F. Bangerter, W. R. Caseri, and C. Weder, *J. Am. Chem. Soc.*, 2001, **123**, 3857.
68. A. Kokil, I. Shiyanovskaya, K. D. Singer, and C. Weder, *J. Am. Chem. Soc.*, 2002, **124**, 9978.
69. C. K. Hui, B. W. K. Chu, N. Zhu, and V. W. W. Yam, *Inorg. Chem.*, 2002, **41**, 6178.
70. W. Y. Wong, G. L. Lu, K. H. Choi, and J. X. Shi, *Macromolecules*, 2002, **35**, 3506.
71. V. W. W. Yam, K. K. W. Lo, W. K. M. Fung, and C. R. Wang, *Coord. Chem. Rev.*, 1998, **17**, 17.
72. H. Kunkely and A. Vogler, *Inorg. Chem. Commun.*, 2003, 543.
73. C. W. Baxter, T. C. Higgs, A. C. Jones, S. Parsons, P. J. Bailey, and P. A. Tasker, *J. Chem. Soc., Dalton Trans.*, 2002, 4395.

74. C. M. Che, H. Y. Chao, V. M. Miskowski, Y. Li, and K. K. Cheung, *J. Am. Chem. Soc.*, 2001, **123**, 4985.
75. M. J. Irwin, J. J. Vittal, and R. J. Puddephatt, *Organometallics*, 1997, **16**, 3541.
76. W. J. Hunks, M.-A. MacDonald, M. C. Jennings, and R. J. Puddephatt., *Organometallics*, 2000, **19**, 5063.
77. T. C. Stoner, R. F. Dallinger, and M. D. Hopkins, *J. Am. Chem. Soc.*, 1990, **112**, 5651.
78. K. D. John, T. C. Stoner, and M. D. Hopkins, *Organometallics*, 1997, **16**, 4948.
79. J. L. Marshall, S. R. Stobart, and H. B. Gray, *J. Am. Chem. Soc.*, 1984, **106**, 3027.
80. H. B. Gray, J. R. Winkler, and D. Wiedenfeld, *Coord. Chem. Rev.*, 2000, **200**, 875.
81. T. Szymańska-Buzar, K. Kern, and D. J. Stufkens, *New J. Chem.*, 1998, 1539.
82. S. N. Heaton, M. G. Partridge, R. N. Perutz, S. J. Parsons, and F. Zimmermann, *J. Chem. Soc., Dalton Trans.*, 1998, 2515.
83. C. Godard, S. B. Duckett, S. Parsons, and R. N. Perutz, *Chem. Commun.*, 2003, 2332.
84. G. F. Nieckarz and D. R. Tyler, *Inorg. Chim. Acta*, 1996, **242**, 303.
85. G. F. Nieckarz, J. J. Litty, and D. R. Tyler, *J. Organomet. Chem.*, 1998, **554**, 19.
86. E. Schutte, T. J. R. Weakley, and D. R. Tyler, *J. Am. Chem. Soc.*, 2003, **125**, 10319.
87. H. Kunkely and A. Vogler, *Chem. Phys. Lett.*, 2003, **368**, 49.
88. H. Kunkely and A. Vogler, *Inorg. Chem. Commun.*, 2003, **6**, 830.
89. C. A. Turner, W. Ding, I. J. Amster, and C. Kutal, *Coord. Chem. Rev.*, 2002, **229**, 9.
90. J. B. Asbury, H. N. Ghosh, J. S. Yeston, R. G. Bergman, and T. Lian, *Organometallics*, 1998, **17**, 3417.
91. J. B. Asbury, K. Hang, J. S. Yeston, J. G. Cordaro, R. G. Bergman, and T. Lian, *J. Am. Chem. Soc.*, 2000, **122**, 12870.
92. E. J. Fernández, A. Laguna, J. M. López-de-Luzuriaga, F. Mendizabal, M. Monge, M. E. Olmos, and J. Pérez, *Chem. Eur. J.*, 2003, **9**, 456.
93. E. J. Fernández, J. M. López-de-Luzuriaga, M. Monge, M. E. Olmos, J. Pérez, A. Laguna, A. A. Mohamed, and J. P. Fackler Jr, *J. Am. Chem. Soc.*, 2003, **125**, 2022.
94. J. C. Vickery, M. M. Olmstead, E. Y. Fung, and A. L. Balch, *Angew. Chem., Int. Ed. Engl.*, 1997, **36**, 1179.
95. E. Y. Fung, M. M. Olmstead, J. C. Vickery, and A. L. Balch, *Coord. Chem. Rev.*, 1998, **171**, 151.
96. A. Burini, R. Bravi, J. P. Fackler Jr, R. Galassi, T. A. Grant, M. A. Omary, B. R. Pietroni, and R. J. Staples, *Inorg. Chem.*, 2000, **39**, 3158.
97. R. L. White-Morris, M. M. Olmstead, F. Jiang, D. S. Tinti, and A. L. Balch, *J. Am. Chem. Soc.*, 2002, **124**, 2327.
98. R. L. White-Morris, M. M. Olmstead, F. Jiang, and A. L. Balch, *Inorg. Chem.*, 2002, **41**, 2313.
99. M. A. Rawashdeh-Omary, M. A. Omary, and J. P. Fackler Jr, *J. Am. Chem. Soc.*, 2001, **123**, 9689.
100. A. Burini, J. P. Fackler Jr, R. Galassi, T. A. Grant, M. A. Omary, M. A. Rawashdeh-Omary, B. R. Pictroni, and R. J. Staples, *J. Am. Chem. Soc.*, 2000, **122**, 11264.
101. M. A. Omary, R. M. Kassab, M. R. Haneline, O. Elbjeirami, and F. P. Gabbaï, *Inorg. Chem.*, 2003, **42**, 2176.
102. V. J. Catalano and M. A. Malwitz, *Inorg. Chem.*, 2003, **42**, 5483.
103. K. M. Lee, H. M. J. Wang, and I. J. B. Lin, *J. Chem. Soc., Dalton Trans.*, 2002, 2852.
104. H. M. J. Wang, C. Y. L. Chen, and I. J. B. Lin, *Organometallics*, 1999, **18**, 1216.
105. V. W. W. Yam, B. W. K. Chu, C. C. Ko, and K. K. Cheung, *J. Chem. Soc., Dalton Trans.*, 2001, 1911.
106. V. W. W. Yam, C. C. Ko, B. W. K. Chu, and N. Zhu, *Dalton Trans.*, 2003, 3914.
107. W. M. Xue, M. C. W. Chan, Z. M. Su, K. K. Cheung, S. T. Liu, and C. M. Che, *Organometallics*, 1998, **17**, 1622.
108. L. Sacksteder, E. Baralt, B. A. DeGraff, C. M. Lukehart, and J. N. Demas, *Inorg. Chem.*, 1991, **30**, 3955.
109. S. W. Lai, K. K. Cheung, M. C. W. Chan, and C. M. Che, *Angew. Chem. Int. Ed.*, 1998, **37**, 182.
110. S. W. Lai, M. C. W. Chan, K. K. Cheung, and C. M. Che, *Organometallics*, 1999, **18**, 3327.
111. S. W. Lai, M. C. W. Chan, Y. Wang, H. W. Lam, S. M. Peng, and C. M. Che, *J. Organomet. Chem.*, 2001, **617**, 133.
112. A. B. Bocarsly, R. E. Cameron, H. D. Rubin, G. A. McDermott, C. R. Wolff, and A. Mayr, *Inorg. Chem.*, 1985, **24**, 3976.
113. A. Mayr, M. P. Y. Yu, and V. W. W. Yam, *J. Am. Chem. Soc.*, 1999, **121**, 1760.
114. A. Mayr, C. M. Bastos, R. T. Chang, J. X. Haberman, K. S. Robinson, and D. A. Belle-Oudry, *Angew. Chem., Int. Ed. Engl.*, 1992, **31**, 747.
115. J. Manna, S. J. Geib, and M. D. Hopkins, *J. Am. Chem. Soc.*, 1992, **114**, 9199.
116. T. P. Pollagi, S. J. Geib, and M. D. Hopkins, *J. Am. Chem. Soc.*, 1994, **116**, 6051.
117. F. W. Lee, M. C. W. Chan, K. K. Cheung, and C. M. Che, *J. Organomet. Chem.*, 1998, **552**, 255.
118. J. D. Carter, K. B. Kingsbury, A. Wilde, T. K. Schoch, C. J. Leep, E. K. Pham, and L. McElwee-White, *J. Am. Chem. Soc.*, 1991, **113**, 2947.
119. K. E. Torraca and L. McElwee-White, *Coord. Chem. Rev.*, 2000, **206**, 469.
120. T. K. Schoch, A. D. Main, R. D. Burton, L. A. Lucia, E. A. Robinson, K. S. Schanze, and L. McElwee-White, *Inorg. Chem.*, 1996, **35**, 7769.
121. C. C. S. Cavalheiro, K. E. Torraca, K. S. Schanze, and L. McElwee-White, *Inorg. Chem.*, 1999, **38**, 3254.

122. S. Trammell, B. P. Sullivan, L. M. Hodges, W. D. Harman, S. R. Smith, and H. H. Thorp, *Inorg. Chem.*, 1995, **34**, 2791.
123. W. M. Xue, Y. Wang, M. C. W. Chan, Z. M. Su, K. K. Cheung, and C. M. Che, *Organometallics*, 1998, **17**, 1946.
124. S. Sprouse, K. A. King, P. J. Spellane, and R. J. Watts, *J. Am. Chem. Soc.*, 1984, **106**, 6647.
125. Y. Ohsawa, S. Sprouse, K. A. King, M. K. DeArmond, K. W. Hanck, and R. J. Watts, *J. Phys. Chem.*, 1987, **91**, 1047.
126. M. G. Colombo, A. Hauser, and H. U. Güdel, *Top. Curr. Chem.*, 1994, **171**, 143.
127. M. Maestri, D. Sandrini, V. Balzani, U. Maeder, and A. von Zelewsky, *Inorg. Chem.*, 1987, **26**, 1323.
128. D. Sandrini, M. Maestri, V. Balzani, U. Maeder, and A. von Zelewsky, *Inorg. Chem.*, 1988, **27**, 2640.
129. H. Kunkely and A. Vogler, *Chem. Phys. Lett.*, 2000, **319**, 486.
130. A. Tsuboyama, H. Iwawaki, M. Furugori, T. Mukaide, J. Kamatani, S. Igawa, T. Moriyama, S. Miura, T. Takiguchi, S. Okada, M. Hoshino, and K. Ueno, *J. Am. Chem. Soc.*, 2003, **125**, 12971.
131. G. Di Marco, M. Lanza, A. Mamo, I. Stefio, C. Di Pietro, G. Romeo, and S. Campagna, *Anal. Chem.*, 1998, **70**, 5019.
132. M. C. DeRosa, P. J. Mosher, G. P. A. Yap, K. S. Focsaneanu, R. J. Crutchley, and C. E. B. Evans, *Inorg. Chem.*, 2003, **42**, 4864.
133. P. Didier, I. Ortmans, A. Kirsch-De Mesmaeker, and R. J. Watts., *Inorg. Chem.*, 1993, **32**, 5239.
134. L. Ghizdavu, O. Lentzen, S. Schumm, A. Brodkorb, C. Moucheron, and A. Kirsch-De Mesmaeker, *Inorg. Chem.*, 2003, **42**, 1935.
135. S. Serroni, A. Juris, S. Campagna, M. Venturi, G. Denti, and V. Balzani, *J. Am. Chem. Soc.*, 1994, **116**, 9086.
136. F. Neve, A. Crispini, S. Serroni, F. Loiseau, and S. Campagna, *Inorg. Chem.*, 2001, **40**, 1093.
137. J. L. Kisko and J. K. Barton, *Inorg. Chem.*, 2000, **39**, 4942.
138. S. Lamansky, P. Djurovich, D. Murphy, F. Abdel-Razzaq, R. Kwong, I. Tsyba, M. Bortz, B. Mui, R. Bau, and M. E. Thompson, *Inorg. Chem.*, 2001, **40**, 1704.
139. S. Lamansky, P. Djurovich, D. Murphy, F. Abdel-Razzaq, H.-E. Lee, C. Adachi, P. E. Burrows, S. R. Forrest, and M. E. Thompson, *J. Am. Chem. Soc.*, 2001, **123**, 4304.
140. M. A. Baldo, D. F. O’Brien, Y. You, A. Shoustikov, S. Sibley, M. E. Thompson, and S. R. Forrest, *Nature*, 1998, **395**, 151.
141. K. K. W. Lo, C. K. Cheung, and N. Zhu, *Chem. Eur. J.*, 2003, **9**, 475.
142. W. Lu, M. C. W. Chan, K. K. Cheung, and C. M. Che, *Organometallics*, 2001, **20**, 2477.
143. Y. G. Ma, T. C. Cheung, C. M. Che, and J. Shen, *Thin Solid Films*, 1998, **333**, 224.
144. L. Z. Wu, T. C. Cheung, C. M. Che, K. K. Cheung, and M. H. W. Lam, *Chem. Commun.*, 1998, 1127.
145. C. M. Che, J. L. Zhang, and L. R. Lin, *Chem. Commun.*, 2002, 2556.
146. H. Q. Liu, T. C. Cheung, and C. M. Che, *Chem. Commun.*, 1996, 1039.
147. H. Q. Liu, T. C. Cheung, S. M. Peng, and C. M. Che, *Chem. Commun.*, 1995, 1787.
148. V. W. W. Yam, R. P. L. Tang, K. M. C. Wong, X. X. Lu, K. K. Cheung, and N. Zhu, *Chem. Eur. J.*, 2002, **8**, 4066.
149. D. Sandrini, M. Maestri, V. Balzani, L. Chassot, and A. von Zelewsky, *J. Am. Chem. Soc.*, 1987, **109**, 7720.
150. H. Yersin, D. Trümbach, and H. Wiedenhofer, *Inorg. Chem.*, 1999, **38**, 1411.
151. M. Maestri, D. Sandrini, A. von Zelewsky, and C. Deuschel-Cornioley, *Inorg. Chem.*, 1991, **30**, 2476.
152. H. Yersin, D. Donges, W. Humbs, J. Strasser, R. Sitters, and M. Glasbeek, *Inorg. Chem.*, 2002, **41**, 4915.
153. J. DePriest, G. Y. Zhen, C. Woods, D. P. Rillema, N. A. Mikirova, and M. E. Zandler, *Inorg. Chim. Acta*, 1997, **264**, 287.
154. J. DePriest, G. Y. Zheng, N. Goswami, D. M. Eichhorn, C. Woods, and D. P. Rillema, *Inorg. Chem.*, 2000, **39**, 1955.
155. J. Brooks, Y. Babayan, S. Lamansky, P. I. Djurovich, I. Tsyba, R. Bau, and M. E. Thompson, *Inorg. Chem.*, 2002, **41**, 3055.
156. W. Kaim, A. Klein, and S. Hasenzahl, *Organometallics*, 1998, **17**, 237.
157. C. J. Kleverlaan, D. J. Stufkens, I. P. Clark. M. W. George, J. J. Turner, D. M. Martino, H. van Willigen, and A. Vlček Jr, *J. Am. Chem. Soc.*, 1998, **120**, 10871.
158. C. J. Kleverlaan and D. J. Stufkens, *Inorg. Chim. Acta*, 1999, **284**, 61.
159. J. van Slageren, F. Hartl, D. J. Stufkens, D. M. Martino, and H. van Willigen, *Coord. Chem. Rev.*, 2000, **208**, 309.
160. J. van Slageren, A. L. Vermeer, D. J. Stufkens, M. Lutz, and A. L. Spek, *J. Organomet. Chem.*, 2001, **626**, 118.

Acknowledgments

VWWY thanks the Hong Kong Research Grants Council and The University of Hong Kong for financial support. KKWL thanks the Hong Kong Research Grants Council and City University of Hong Kong for financial support.

Metal-based Drugs

C. Frank Shaw III
Illinois State University, Normal, IL, USA

1	Introduction	1
2	Gold-based Antiarthritics	1
3	Silver Antibacterial Agents	8
4	Pt-based Antitumor Agents	10
5	Vanadium Insulin Mimics and Enhancers	15
6	Lithium	19
7	Other Metallodrugs – in Use or in Development	21
8	Concluding Remarks	25
9	Further Reading	26
10	References	26

1 INTRODUCTION

The study of metals in medicine forms an important subdiscipline of inorganic biochemistry.[1–4] The use of metal-based drugs predates the emergence of inorganic biochemistry in the 1970s and 1980s and even the development of modern medicinal chemistry in the period between World War I and World War II. In prehistoric times and through the age of the alchemists, metal-based therapies were at best empirical and more often pseudoscientific preparations used to treat of a wide variety of diseases. For example, gold salts were used in the late nineteenth century to treat alcoholism, opium addiction, and neurasthemia (Figure 1(b)), although modern medicine finds no value for such treatments. The third edition of the *National Formulary*, published in 1906, lists 454 preparations, of which 149, or roughly one-third, are metal-based.[5] They were formulated as elixirs, ointments, powders, pills, and tinctures that contain either a single metal species or mixtures of several metal species. In some cases, metal ions were combined with other substances, including herbal extracts such as gentian or cinchona, organic medicinals such as quinine, strychnine, and opium, cod liver oil, and even sherry wine.[5] The inorganic elements found in the 1906 *National Formulary* are shown in the periodic table of Figure 2. It is quite different from the periodic table featured on the cover of a recent student textbook on metals in medicine[3] that prominently featured Li, V, Mn, Fe, Pt, and Au.

The German physicians Paul Ehrlichmann and Robert Koch made pioneering contributions to modern medicine, including scientific approaches to the development of arsenicals and gold compounds, respectively, for treatment of various diseases. The contribution of Paul Ehrlichmann, who is considered the father of modern immunology, included investigation of the medicinal properties of arsenicals, and the final version of the German 200 DM note, Figure 1(a), celebrating his career, depicts the modern crystal structure of the phenylarsine hexamer, $[PhAs]_6$. Robert Koch's research on the antibacterial activity of $K[Au(CN)_2]$ in the search for a treatment for tuberculosis led eventually to the successful use of gold thiolates for treating rheumatoid arthritis. Despite these and other successes, the increasing ability of medicinal chemists to synthesize and screen large numbers of organic compounds for optimal medicinal activity and the concurrent recognition that the chronic and, sometimes, acute toxicity of traditionally used inorganic agents based on arsenic, mercury, and lead inter alia became evident, leading to curtailed use of inorganic medicinals after World War II.

Until the 1960s, research on metal ions in biochemistry and medicine was typically pursued in the realms of clinical medicine, nutritional science and toxicology. Starting in that decade, increasingly powerful physicochemical methods became available to study the roles of metal ions in biological systems. Atomic absorption and emission spectroscopy, later coupled to inductively coupled plasma methods of sample introduction, and the availability of useful isotopes for tracer experiments allowed precise measurement of metal accumulation and fluxes. Powerful techniques including extended X-ray absorption fine structure (EXAFS) and Raman and Mössbauer spectroscopies became available to directly probe the chemical environment of metal ions in biological macromolecules and even tissue preparations ex vivo, providing information about structure, electronic states, ligation and reactivity. Electron spin resonance (ESR) and nuclear magnetic resonance (NMR) methods complemented one another: ESR probes paramagnetic metal ions such as high-spin Fe^{2+} and Fe^{3+}, and low-spin Fe^{3+}, while NMR has been applied to a host of inorganic nuclei including Li, V, Ag, Pt, and Hg among medicinally used species. A renaissance of research on metals in medicine, which benefited from and helped to drive these improvements in physicochemical methods, was stimulated by Professor Barnett Rosenberg's discovery that diamminedichloroplatinum(II), $(H_3N)_2PtCl_2$, has potent antitumor activity (*see* ***Platinum-based Anticancer Drugs***).[6] This chapter concentrates on the roles of gold, silver, platinum, vanadium, and lithium in modern medicine, and briefly reviews current and potential uses of other inorganic medicinal agents.

2 GOLD-BASED ANTIARTHRITICS

2.1 Introduction and History

Gold is arguably the first pure element known to early man, since it could be found in stream beds and other geological formations and was visually attractive and easily workable. Medical treatises from ancient civilizations in Egypt, China,

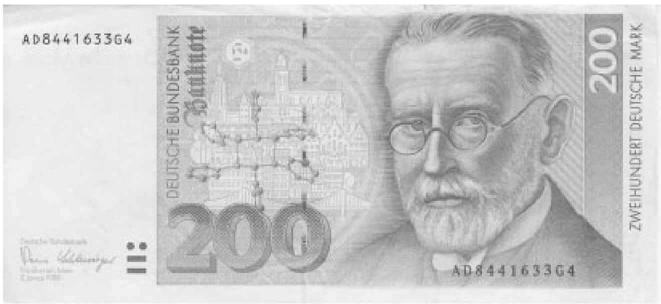

(a)

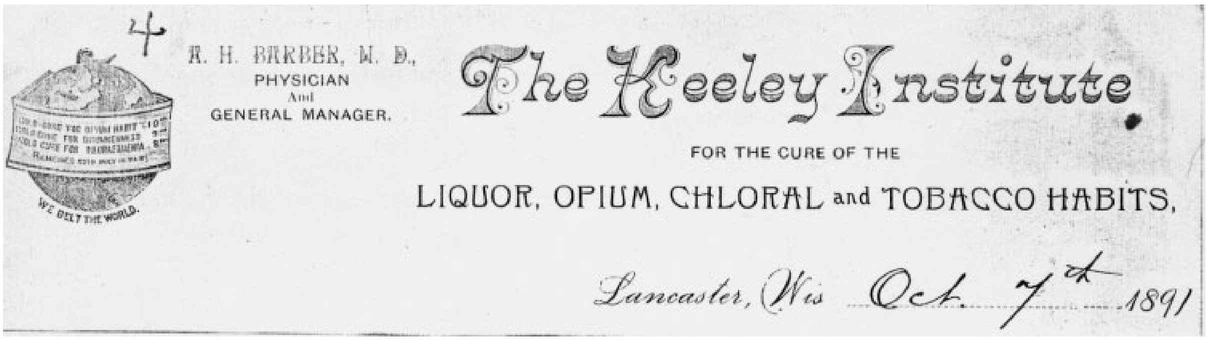

4

R. H. BARBER, M. D.,
PHYSICIAN
And
GENERAL MANAGER.

The Keeley Institute

FOR THE CURE OF THE
LIQUOR, OPIUM, CHLORAL and TOBACCO HABITS,

Lancaster, Wis Oct. 7th 1891

WE BELT THE WORLD.

(b)

Figure 1 (a) The 200 Deutschmark note commemorating Paul Ehrlichmann's contributions to biomedical science included the structure of $(PhAs)_6$, which he developed as a medicinal agent. (b) Letterhead for the Keeley Institute in Lancaster, WI, highlighting the use of gold preparations to treat opium addiction, drunkenness, and neurasthemia in the 1890s

Elements Used in the 1906 *National Formulary*

1	2	3	4	5	6	7	8	9	10	11	12	13	14	15	16	17	18
H																	
Li												B	C	N	O	F	
Na	Mg											Al	Si	P	S	Cl	
K	Ca					Mn	Fe			Cu	Zn			As		Br	
																I	
										Au	Hg		Pb	Bi			

Figure 2 A periodic table highlighting elements found in preparations given in the *National Formulary* of 1906

Greece, and elsewhere included numerous uses of gold for treating a wide variety of ailments.[4] These ancient civilizations attributed magical and healing powers to items fashioned from gold and preparations containing powdered gold.[7,8] As Chinese, Arabic, and European alchemists learned to prepare compounds of gold, these agents were also used to treat a wide variety of ailments.[7,8] Gold found many medical uses derived from these traditions late into the 19th century, as exemplified by the gold treatments shown in Figure 1(b). The modern use of gold treatments, now known as chrysotherapy, after Chryses, a golden-haired maiden of Greek mythology, trace their scientific origins to the pioneering work of Dr. Robert Koch, a German physician, who studied the antibacterial properties of potassium aurocyanide, $K[Au(CN)_2]$, while screening potential chemotherapeutic agents against *tubercle bacilli*. This led to the experimental, but ultimately unsuccessful, use of other gold compounds to treat tuberculosis for a period of time in the late nineteenth and early twentieth centuries.[9,10] The Parisian physician Jacque Forestier, who noted beneficial effects of gold treatments on the rheumatoid arthritis of some patients, initiated its use for that disease. A double-blind trial by British Rheumatism Council after World War II demonstrated that it was efficacious for many patients and generated long lasting remissions of the disease state for some patients. Starting in the early 1970s, Dr. Blaine Sutton at Smith, Kline & French Laboratories developed an oral gold preparation, auranofin, which was finally licensed in the late 1980s.[11] In modern medicine, gold compounds have found use in treating rheumatoid arthritis and related disease states, and are being actively synthesized and screened for antitumor, antiparasitic, and antiviral activity.

2.2 The Element and Oxidation States

Gold (Z = 79), which is found in the sixth row of the periodic table, between platinum and mercury, belongs to group Ib (or group 11) and lies below copper and silver, with which it shares common properties (*see* ***Periodic Table: Trends in the Properties of the Elements***). This triad is referred to as the coinage metals. Elemental gold is a shiny, yellow substance, which is malleable and ductile and a good conductor of heat and electricity. The reduction potential for gold(I) is strongly positive, resulting in a natural inertness, which befits its description as a noble metal:

$$Au^+ + e^- = Au^\circ \qquad E^0{}_{1/2} = +1.68 \text{ volts} \qquad (1)$$

It is inert to common acids and can be dissolved by using aqua regia (~3:1 HCl:HNO_3) or liquid bromine for laboratory purposes. The inertness of gold, its yellow color, and the unusual preference of gold(I) for two-coordination can all be traced to the uniquely strong influence of relativistic effects on the 6s orbital. This effect is maximal at gold, compared to platinum, mercury and more distant neighbors along the sixth period of elements.[12]

Compounds in oxidation states −I through V are known.[13,14] The common and stable oxidation states that dominate the aqueous chemistry of gold are Au(I) and Au(III). The aquated ions are unstable to reduction, but many complexes are stabilized by a variety of soft ligands. The remaining oxidation states (−I, II, IV, V) exhibit interesting chemical and physicochemical properties, but have not yet found medicinal applications.

Gold in the +1 oxidation state, which has a d^{10} electron configuration, can form complexes with two, three, or four bound ligands. Relativistic effects operating on the 6s orbital generate a large s-p energy gap that favors linear, two-coordination over three- and four-coordination.[12] As a result gold(I) reacts with the heavier halides and cyanide to form $AuX_2{}^-$ ions, but not the corresponding $AuX_3{}^{2-}$ or $AuX_4{}^{3-}$ complexes, in contrast to silver(I) and copper(I), which have smaller s-p gaps and form numerous three- and four-coordinate species in addition to two-coordinate linear complexes with these anions. Gold in the +3 oxidation state forms principally square-planar, four-coordinate complexes typical of d^8 transition metal ions (Figure 3). A limited number of complexes with five-coordination have been characterized, and typically contain a chelating ligand such as *o*-phenanthroline or biphenyl with one donor atom coordinated in the square plane and the second at an elongated distance along the perpendicular axis.

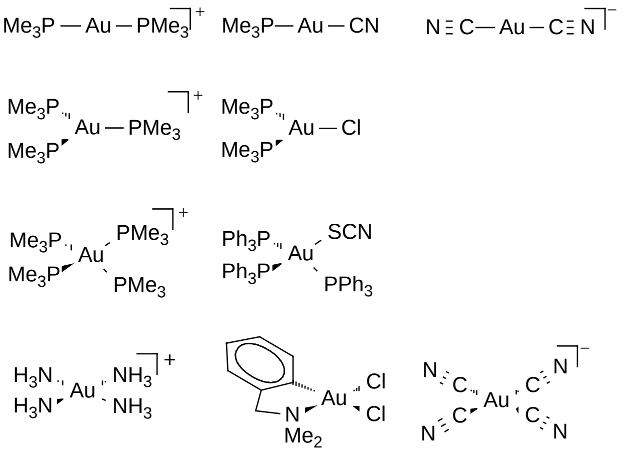

Figure 3 Coordination geometries for gold(I) and gold(III) complexes: examples of (a) negative, neutral and positively charged linear gold(I) complexes; (b) trigonal and tetrahedral gold(I) complexes and (c) square-planar gold(III) complexes (Et = ethyl; Me = methyl; Ph = phenyl; SG = glutathionate-(S))

2.3 Antiarthritic (Chrysotherapy) Agents

The compounds currently in clinical use for treating rheumatoid arthritis, shown in Figure 4, are all gold(I) thiolates.[15] The first-generation drugs include, sodium bis(thiosulfato)gold(I) (sanochrysin), which has a well-defined stoichiometry and structure, and three oligomeric gold(I) thiolates with thiomalate (myochrysine), thioglucose (solgonal) or thiopropanolsulfonate (allochrysin) ligands in approximately 1:1 ratio to the gold. None of the oligomeric preparations have been amenable to crystallization, although a close analog of myochrysine, $CsHNa_2(AuSTm)_2$, was crystallized by a vapor deposition method.[16] This elegant structure consists of double-helical strands of polymer with 1:1 ratio of gold and thiomalate stabilized by gold–gold interactions between the intertwined strands (Figure 5). Viewed along the helical axes, alternating helices spiral clockwise and counterclockwise and contain exclusively R- or exclusively S-thiomalate to facilitate helical packing. Other model compounds form discrete structures: $[Au(S\text{-}C_6H_2\text{-}i\text{Pr}_3)]_6$ crystallizes in hexameric rings formed by alternate linear gold(I) ions and bridging thiolate ligands. Recently reported catenated ring structures found for the *p*-*t*-butylphenylthiolato and *o*-*t*-butylphenylthiolato complexes of gold(I) have the stoichiometries, $[RSAu]_{10}$ and $[RSAu]_{12}$, respectively (Figure 6).[17] The first consists of two linked pentamers and the second of two linked hexamers. The ability to form both catenane structures, stabilized by gold–gold interactions, and simpler oligomers suggest why

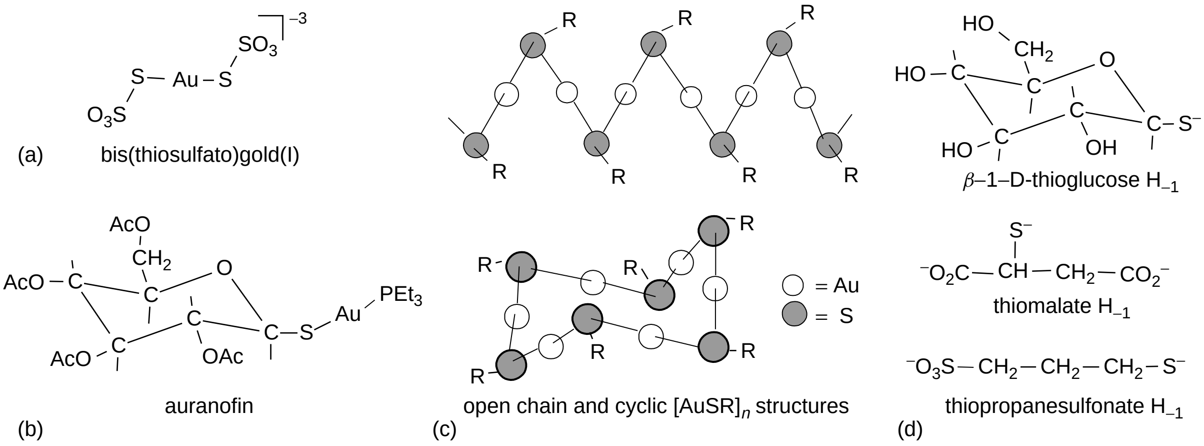
–3
SO3
S— Au – S
O3S
(a)
bis(thiosulfato)gold(I)
R
R
R
R
R
R
R
HO
CH2
HO – C
O
C
C
C– S⁻
HO
OH
β–1–D-thioglucose H–1
AcO
CH2
AcO – C
O
C
C
C–S
Au
PEt3
AcO
OAc
auranofin
(b)
R
R
R
R
R
R
= Au
= S
open chain and cyclic [AuSR]n structures
(c)
S⁻
⁻O2C— CH — CH2 — CO2⁻
thiomalate H–1
⁻O3S— CH2— CH2— CH2– S⁻
thiopropanesulfonate H–1
(d)

Figure 4 Structures of clinically used antiarthritic gold complexes

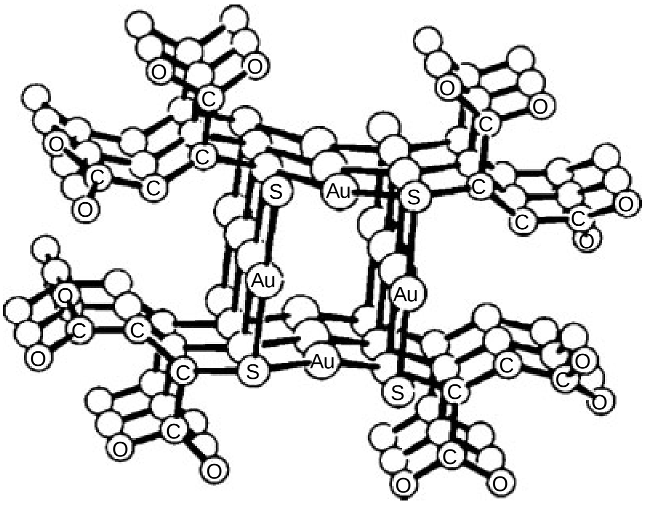
O
O
C
O
O
C
O
C
C
C
C
S
Au
S
C
O
C
C
O
O
Au
Au
O
C
C
O
C
S
Au
S
C
C
O
O
O
C
O
O
C
O
O

Figure 5 The structure of a single helix in $[CsHNa_2(AuSTm)_2]$, viewed along the helical axis. Alternating helices contain exclusively R- or S-thiomalate and coil clockwise and counterclockwise in the structure. Aurophilic interactions, arising from relativistic effects on the gold 6s orbital, stabilize the helices and are evident in the figure

the oligomeric gold(I) thiolates have been so difficult to crystallize.

Only one second-generation drug, auranofin (2,3,4,6-tetraacetyl-*β*-1-D-thioglucopyranosato-*S*-(triethylphosphine) gold(I)), has been clinically tested and approved for use against arthritis. It is a discrete, well-characterized monometallic species (Figure 4(b)) having essentially linear coordination (∠S-Au-P = 174°) to the tetraacetylthioglucose and phosphine ligands. The simpler analogues Et_3PAuCl and $Et_3PAuSTg$, Tg = *β*-1-D-thioglucopyranosato-*S*, exhibit similar antiarthritic activity, but the chloride compound induced severe intestinal distress when administered to patients, and the thioglucose analogue is hygroscopic, which severely limited shelf life of the medicinal preparation. Both untoward side effects are absent with the acetylated sugar moiety of auranofin. In vivo, the tetraacetylthioglucose ligand is rapidly displaced in ligand exchange reactions and the phosphine is more slowly displaced over about 24 hours. The phosphine ligand renders the compound lipophilic, thereby allowing oral administration, and allows it to enter cells more rapidly.

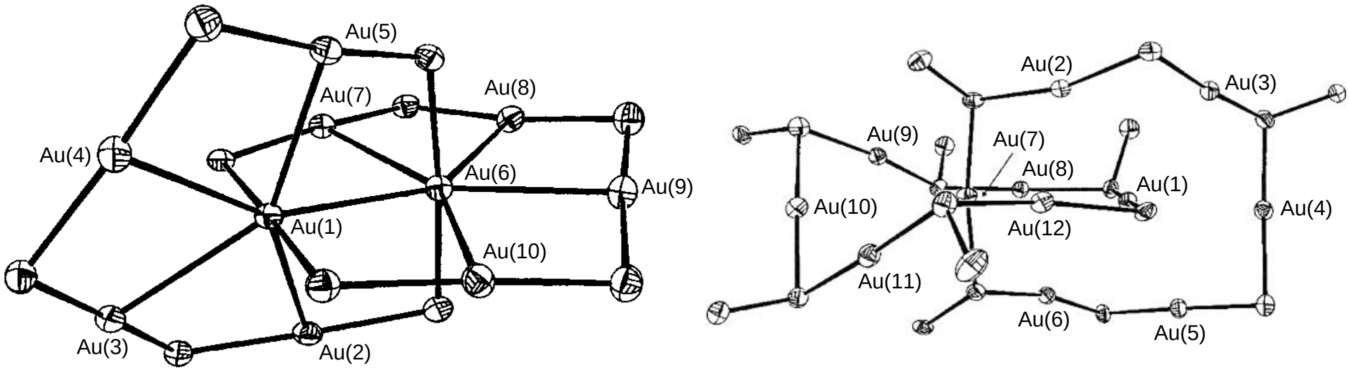
Au(5)
Au(7)
Au(8)
Au(4)
Au(6)
Au(9)
Au(1)
Au(10)
Au(3)
Au(2)
Au(2)
Au(3)
Au(9)
Au(7)
Au(8)
Au(1)
Au(10)
Au(4)
Au(12)
Au(11)
Au(6)
Au(5)

Figure 6 Structures of the gold(I) monothiolate catanes, $[AuSR]_{10}$ and $[AuSR^1]_{12}$, R = *p*-*t*Bu-$C_6H_4S^-$ and R^1 = *o*-*t*Bu-$C_6H_4S^-$. The ability to form stable catenated ring systems may explain the difficulties encountered in preparing crystalline forms of the gold(I) thiolates used clinically.[17]

2.4 Chrysotherapy for Rheumatiod Arthritis

Rheumatoid Arthritis (RA) is an autoimmune disease, in which the synovial tissues that line and lubricate the joints are under attack by the immune system. To date, neither a triggering agent (viral, microbial, etc.) nor a self-antigen has been identified. Gold drugs are considered to be disease modifying anti-rheumatic drugs (DMARDS) that retard and sometimes cause remission of the disease state.[18] The response of patients to gold therapy is typically manifest only after 3 to 6 months. Since RA is a cyclic disease with flare-ups and quiescent periods, it is frequently difficult to evaluate the effectiveness of various treatments. One accepted effect of chrysotherapy is its anti-inflammatory activity.[18,19] Additional mechanisms of action that may contribute to chrysotherapy are inhibition of various enzymes, antimicrobial activity, reduction of humoral immunity, inhibition of the complement pathway, effects on lymphocytes, monocytes, or neutrophils – especially inhibition of T-cell proliferation and of polymorphonuclear monocyte activation. Multiple mechanisms of action may be acting in concert, and there is not wide acceptance of any one or combination as the primary biological action underlying chrysotherapy.[18,19] Auranofin, which is orally administered, exhibits fewer toxic side effects than the conventional parenteral agents, but a metaanalysis of 66 clinical trials establishes that it is somewhat less effective than the latter.[20] Both oral and parenteral drugs are still used clinically although improved, competing therapies have decreased the use of chrysotherapy worldwide.

2.5 Pharmacology – Prodrugs

The parenterally administered gold drugs are absorbed into the blood stream and the resulting gold concentration reaches a maximum within several hours and then decreases to a basal level. Auranofin is administered orally and several weeks are required to achieve substantial blood concentrations of gold. Although there is no direct correlation of blood gold levels with therapeutic benefit, concentrations in excess of 300 mg dL^{-1} are typically considered to carry increased probability of side effects. Because auranofin carries a phosphine ligand and is lipophilic, unlike the parenteral drugs, its metabolism differs in the blood and especially at the cellular level. Absorption of gold from auranofin in the intestines is accompanied by hydrolysis of the acetyl groups from the tetraacetylthioglucose by enzymes in the intestinal wall lining,[21] but gold from the parenteral drugs is not absorbed by the gut or intestines. Gold accumulated from the parenteral drugs is excreted primarily via the kidneys and urine, but when auranofin is administered a large fraction is excreted via the bile, which establishes a reabsorption cycle with the intestines.[22]

Table 1 Protein complexes of gold drugs & metabolites[15]

Complex	Au ligation	d(Au-X)/pm
Alb–S–$(\mathrm{AuSTm})_{0.4}$	S–Au–S	228 (S)
Alb–S–(AuSAtg)	S–Au–S	228 (S)
Alb–S–$\mathrm{AuPEt_3}$	S–Au–P	227 (S), 230 (P)
Alb–$\mathrm{N_{his}}$–$\mathrm{AuPEt_3}$	N–Au–S	–
Alb–SH·$[\mathrm{Au(CN)_2}]$	C–Au–C	
Alb–SH·$[\mathrm{Au(CN)_2}]_3$	C–Au–C	
Hb–S$(\mathrm{AuPEt_3})$	S–Au–P	
Au,Cd,Zn-MT	S–Au–S	229 (S)
$(\mathrm{TmSAu})_{20}$MT	S–Au–S	230 (S)
Cyclophilin – $\mathrm{N_{his}}$–Au[26]	N–Au–P	206 (N), 227 (P)

In vivo studies indicate that gold-based chrysotherapy agents are prodrugs, species that undergo transformation after administration to form the active species.[15] The metabolism occurs rapidly by ligand exchange reactions. Radiotracer studies of $[\mathrm{Au^{35}STm}]_n$, $[\mathrm{Au^{35}Stg}]_n$, and $\mathrm{Et_3{}^{32}PAu^{35}SATg}$ administered to laboratory animals demonstrate that within hours, substantial displacement of the thiolate ligands from gold has taken place. In the case of auranofin, the tetraacetylthioglucose ligand is essentially displaced within less than an hour and the triethylphosphine within a day. Gold present in the serum is bound primarily to serum albumin; only relatively small concentrations of low-molecular weight (so-called 'free') gold species are present. Extensive studies of albumin-gold adducts have identified cysteine-34 as the primary binding site at which reactions of the gold drugs take place. Table 1 lists complexes that have been characterized by a variety of physical methods including crystallography, EXAFS, Mössbauer, NMR, and other spectroscopic techniques.[15]

The crystal structure of human albumin located Cysteine-34 at the turn between helices h2 and h3 with the side chain sulfhydryl group oriented toward the protein interior,[23] consistent with EPR studies suggesting that it is 950 pm below the surface.[24] Sadler has demonstrated by ^{1}H NMR studies that the cys-34 residue must move outward from the crevice created by the helices before it can react to form disulfide bonds or bind to $\mathrm{Et_3PAu^+}$ derived from auranofin.[25] These structural observations are consistent with the kinetic mechanism for the reactions of albumin with auranofin and its triisopropylphosphine analogue, which revealed a slow crevice opening reaction in equilibrium between open and closed forms of albumin. The kinetic model accounts for a process that is first order in protein when the auranofin is present in excess,

$$\mathrm{rate} = \mathrm{k_1[AlbSH]}, \tag{2}$$

which is controlled by the rate of the crevice opening, and the second order kinetics observed when equilibrium mixtures of reactants and products are examined by ^{31}P NMR methods:

$$\begin{aligned} \mathrm{rate_f} &= \mathrm{k_2[AlbSH][R_3PAuSAtg]} \\ \mathrm{rate_r} &= \mathrm{k_{-2}[AlbSAuPR_3][AtgSH]}. \end{aligned} \tag{3}$$

Extrapolation to the physiological situation, in which albumin (ca. 440 μM) is in excess of auranofin (10–25 μM), predicts a rapid reaction of auranofin with the open-crevice form,

$$\text{rate} = k_4[\text{AlbSH}][\text{R}_3\text{PAuSAtg}],\ k_4 = (8 \pm 2) \times 10^2\,\text{M}^{-1}\text{s}^{-1}, \quad (4)$$

that is consistent with the rapid loss of ATgSH from auranofin in animal model studies.

Metallothionein (MT), a metal-binding protein rich in cysteine residues, which binds Cu^+ and Zn^{2+} under normal physiological conditions and Cd^{2+} after accumulation of the metallotoxin (*see* ***Metallothioneins***), also binds gold(I) after exposure of organisms to gold drugs and complexes. AuSTm and Et_3PAuCl react with Cd,Zn-MT to displace Zn^{2+} preferentially and on exposure to excess gold Cd^{2+}. The gold may bind with loss or retention of the carrier ligands depending on conditions. Et_3PAu^+ from Et_3PAuCl is transferred to Cys-β92 of hemoglobin (*see* ***Iron: Heme Proteins & Dioxygen Transport & Storage***), but auranofin does not react. This establishes a relative affinity of thiols for gold as Albumin Cys-35 > AtgSH > Hemoglobin Cys-β92 > Chloride.

In contrast to albumin, hemoglobin and metallothionein, in which gold(I) coordination to cysteine thiol residues has been clearly established by physicochemical methods, the binding of gold to cyclophilin is unusual in that the Et_3PAu^+ moiety binds to a histidine residue in preference to the two free thiols present in the protein structure.[26] When cysteine-34 of albumin is blocked by chemical modification, Et_3PAuCl, but not auranofin, will bind to the numerous histidine residues present.

Because the triethylphosphine ligand used in auranofin is pyrophoric (i.e. it spontaneously catches fire on exposure to air), its separation from auranofin and subsequent fate in vivo is a consequential matter. In vivo, it is readily, although less spectacularly, oxidized to triethylphosphine oxide ($Et_3P{=}O$), which is quite water soluble and harmlessly excreted in the urine.[15,22,27] Triethylphosphine, when directly added to a solution of albumin, is oxidized at the expense of the protein disulfide bonds.[28] Either by allowing $AlbS\text{-}AuPEt_3$ formed in vitro to remain in the presence of the displaced AtgSH or by adding a thiol such as glutathione after purifying it, the formation of $Et_3P{=}O$ is stimulated, which suggests a likely mechanism for the displacement and subsequent oxidation of Et_3P in biological systems. Red blood cells (RBCs) also contribute to phosphine oxidation. After taking up Et_3PAu^+ from auranofin, they release the gold concomitantly with glutathione to form an extracellular albumin adduct, AlbS-Au-SG, where GS^- is the anion of glutathione, and release the phosphine as $Et_3P{=}O$.

Although they are significant intermediates in the in vivo ligand exchange reactions that metabolize the gold drugs and transport gold in vivo, the albumin complexes formed by direct reaction with the clinically used chrysotherapy agents, Table Au-1, are unlikely to be the active therapeutic agents. Additional metabolic reactions, recognized in the late 1980s, further alter the nature of gold in vivo. Graham and colleagues investigated the role of immunogenerated cyanide,[29,30] and Gleichmann and his colleagues in Germany observed evidence for the oxidation of gold drugs to gold(III) species,[31,32] a possibility long noted, especially by Smith and coworkers.[33] Interestingly, both processes involve a common enzyme, myleoperoxidase (MPO; *see* ***Iron: Heme Proteins, Peroxidases, Catalases & Catalase-peroxidases***), a participant in the oxidative burst of immune cells.

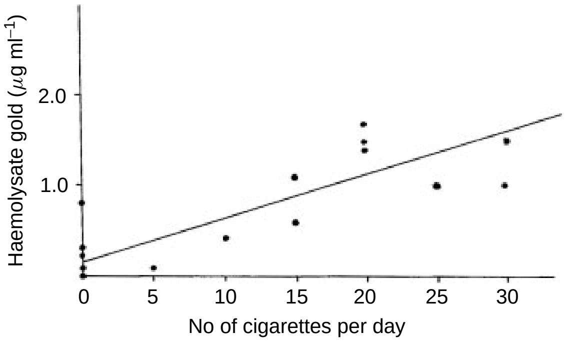

Figure 7 A plot of the gold concentrations in red blood cell lysates as a function of the patient's smoking habits. (Reprinted from Ref. 33. © 1991, with permission from Elsevier)

Tobacco-smoking patients exhibit higher levels of gold in their red blood cells (Figure 7), even when taking the parenteral drugs that don't lead to RBC uptake of gold in vitro.[34,35] Graham *et al.* showed that cyanide, present in tobacco smoke at ca. 1700 ppm,[36] alters the blood distribution of gold by forming $[Au(CN)_2]^-$, which is accumulated by RBCs.[33,34,37] Macrophage cells can generate cyanide from thiocyanate, and in the presence of thiocyanate and polymorphonuclear monocytes stimulated to undergo the oxidative burst, aurothiomalate is converted to aurocyanide.[29,30] The aurocyanide, in turn, inhibits the macrophages from further release of reactive oxygen species, which may be involved in joint damage.[29] Aurocyanide, $[Au(CN)_2]^-$, has been observed in the urine and blood of patients treated with any of the three gold drugs used clinically in the US.[38] The low levels of free aurocyanide found in their serum may be in equilibrium with albumin to which aurocyanide binds at multiple sites and remains intact, based on the characteristic Mössbauer spectrum for the linear ion.

The oxidation of gold(I) to gold(III) metabolites was detected in mice by use of the popliteal lymph node assay,[31,32] which is a classical test to distinguish the immunoreactivity of metabolites from their progenitor substances. The significance for chrysotherapy was confirmed by showing an amanestic response of T-cells from chrysotherapy patients to gold(III) but not to the gold(I) thiolates that were administered to them.[39] In vitro studies with hypochlorite generated by the action of myleoperoxidase demonstrated that AuStm, AuStg, auranofin and $[Au(CN)]_2{}^-$ are all oxidized to gold(III) under biomimetic conditions[40,41] Further, MPO and its substrates H_2O_2 and

Cl^-, from which hypochlorite is generated, are sufficient to oxidize AuSTm to gold(III).[40] The gold(III) species are not immunogenic but likely react with proteins to generate antigenic species and may carry oxidizing equivalents from the site of the oxidative burst to other cells or macromolecules.

The uptake and release of gold by a variety of cell types, especially the red blood cell and various immune cells, has been investigated. The rate, extent, and mechanism of uptake vary according to the cell type and the gold complex. Based on studies of the transfer of Et_3PAu^+ into macrophage cells, Mirabelli *et al.* developed the sulfhydryl shuttle model (Figure 8).[27] The Et_3PAu^+ moiety is transferred from auranofin and other ligands in the extracellular environment to membrane proteins containing sulfhydryl groups, which then transport it through the membrane to the intracellular environment, where it may react with a variety of thiol or selenocysteine containing ligands (e.g. glutathione, hemoglobin, Se-dependent glutathione peroxidase, and thiol-proteases) in RBCs and other cells. Gold may efflux from RBCs either as the original Et_3PAu^+ moiety[27] or as a thiolate complex, such as glutathionatogold(I). The latter forms an AlbS-Au-SG complex in the extracellular environment, which in effect results in a phosphine for glutathione ligand exchange reaction.[42] The parenteral drugs do not typically deliver gold into cells, except in the case of phagocytic cells, which can incorporate the oligomeric complexes,[43] or in the presence of cyanide.[30,33–35] Consequently, metallothionein (*see* ***Metallothioneins***), the inducible heavy-metal-binding protein, is synthesized in CHO cells that are exposed to auranofin[43,44] but not when the cells are exposed to AuSTm.[45] Even CHO cells that are stimulated to overproduce MT are not resistant to the growth inhibitory effects of AuSTm. Smith, Reglinski, *et al.* have observed that the effects of AuSTm on cells can be effected via interactions with cell membranes without its incorporation into the cytosol or organelles.[33,46]

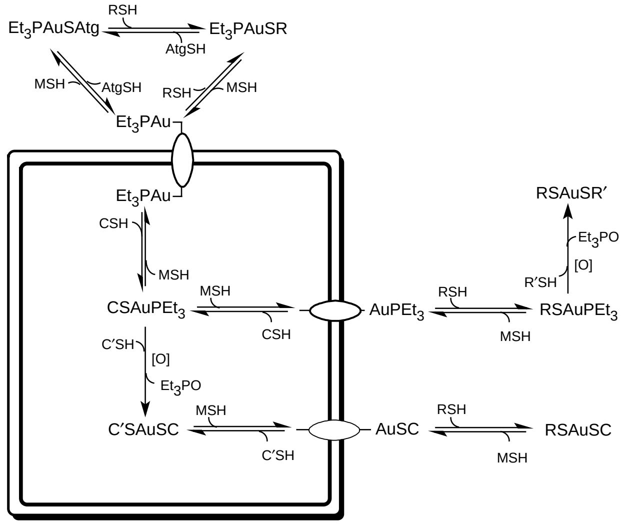

Figure 8 The sulfhydryl shuttle model for Et_3PAu^+ accumulation and efflux through cellular membranes. CSH and RSH = cellular and extracellular thiols, protein, or small molecule; MSH = membrane sulfhydryl-dependent transport systems

Enzyme inhibition has been extensively explored as a source of the antiarthritic activity of gold compounds and may play a role in the anti-inflammatory effects by inhibiting enzymes in the prostaglandin biosynthesis pathway. An early tabulation of data[47] has not been updated although many additional enzymes and gold complexes have been studied. Many thiol-dependent enzymes are inhibited by gold complexes, which are presumed to undergo reactions with active site thiols in a manner analogous to their reactions with Cys-34 of albumin. The measured inhibition constants, as tabulated previously, range from millimolar to the micromolar level. Since only 10–25 μM gold concentrations are achieved in vivo during therapy, only those enzymes with smaller K_i values are likely to be inhibited.[47] Selenols (RSeH) have a much higher affinity for gold(I) than do the corresponding thiols (RSH), and as a result, selenium-dependent enzymes are readily inhibited at gold concentrations comparable to and sometimes significantly lower than the therapeutically relevant gold concentrations. Examples include Se-dependent glutathione peroxidase and Se-dependent thioredoxins.[48–50]

2.6 Cancer Chemotherapy

Gold compounds have been tested extensively for antitumor activity and many active compounds have been examined in cell culture and sometimes in animal models in vivo.[15,51,52] Three rationales are frequently cited: (1) analogies of gold(III) square-planar complexes to their platinum(II) analogues; (2) immunomodulatory properties related to use against RA, and (3) complexation of gold(I) and gold(III) compounds with active organic chemotherapy agents to modulate the properties of metal and ligand. The screening of numerous auranofin analogues with variations in the phosphine and thiolate ligands, led to the development of a promising antitumor agent, $[Au(DPPE)_2]Cl$ (DPPE = bis(diphenylphosphino)ethylene), which was identified as a stable metabolite of a dinuclear gold compound by Berners-Price *et al.*:[53]

$$(\mu\text{-DPPE})(\text{AuCl})_2 \longrightarrow [\text{Au}(\text{DPPE})_2]^+ \qquad (5)$$

Unfortunately, development of this compound was thwarted by the discovery of significant cardiovascular toxicity caused by the inhibition of mitochondrial function. This represents a demonstrable targeting of gold to a particular organelle and suggests that better delivery of gold to inflamed joints in chrysotherapy may be achievable with ligands that are less labile than the currently used monodentate thiolates. Early screening of gold(III) complexes for antitumor activity was not fruitful. In contrast, (dimethylaminomethylphenyl)dichlorogold(III) and its acetate analogue, are stabilized by the chelating C,N donor ligand that generates a neutral complex and stabilizes the gold(III) against reduction in vivo. They show promising activity, with a different mechanism of action than cisplatin, but clinical trials have not been undertaken.[54]

2.7 Anti-HIV and Antiparasitic Activities

Gold complexes have been tested and shown to have anti-HIV activity, as reviewed elsewhere.[15] Gold thioglucose (AuStG) showed promising activity against the KL4-3 strain of HIV. It reacts with Cys-532 on the viral coat protein gp 160, but the activity is specific to this strain and it is not effective against more virulent strains. AuStG is also effective against reverse transcriptase (RTase) in cell-free extracts, but is not an effective inhibitor of HIV in cell cultures since it does not enter the cell. Aurocyanide, $[Au(CN)_2{}^-]$, inhibits the proliferation of the T-9 strain of CD4+ T-cells in vitro, and is effective at doses as low as 20 nm. These promising leads have not led to more extensive investigations of gold-based anti-HIV drugs, even though a clinical report suggests that auranofin treatment stimulated CD4+ T-cell counts in an AIDS patient undergoing gold treatment for psoriatic arthritis but not anti-HIV therapy.

Gold compounds are being actively explored for the treatment of a variety of parasites. Antimalarial activity of gold has been investigated, based in part on the observation that antimalarial drugs, for example, chloroquine, are also effective against rheumatoid arthritis. The chloroquine complex of triphenylphosphinegold(I) is more active against *Plasmodium falciparum* (see $IC_{50} = 5.1 \times 10^{-9}$ M) and *Plasmodium berghei* (2.3×10^{-8} M) than chloroquinediphosphate or other metal complexes.[48] *Schistosoma mansoni*, another tropical parasite, is dependent on a novel thioredoxin glutathione reductase enzyme (*Sm*-TGR) to protect it from oxidative stress in the host organism. *Sm*-TGR combines thioredoxin reductase and glutathione reductase activities in a single selenium-dependent enzyme. The IC_{50} values for inhibition of the glutathione reductase and thioredoxin reductase by auranofin are 10 and 7 nM, respectively, suggesting that gold complexes have potential use against this disease.[49]

3 SILVER ANTIBACTERIAL AGENTS

3.1 Introduction and History

Silver has long been known to exhibit antibacterial properties, which may have been an unwitting advantage to those who could afford silver vessels and tableware. Silver sulfadiazine is a widely used and very effective burn ointment, and silver-treated catheters greatly reduces the rate of infection associated with their use. The element is not known to be essential, although trace amounts (<1 mg total body burden) are accumulated, with blood levels typically below $10\,\mu g\,L^{-1}$.[55]

An early record that the ancients recognized and exploited silver's microcidal properties is the report by Herodotus that the King of Persia stored boiled water in silver urns for his military campaigns.[56] Raulin showed as early as 1869 that silver vessels prevented the growth of *Aspergillus niger* in their contents.[57] Uses of silver in modern medicine are based on its effective antibacterial and antifungal actions, including topical application of silver sulfadiazine for burns, and antimicrobial coatings for catheters that reduce the frequency of infections.[58,59] The once prevalent use of silver nitrate to treat opthalmia neonatorum has been discontinued owing to rare but serious complications and the availability of safer alternatives. C. L. Fox, Jr, introduced silver sulfadiazine in the late 1960s as a treatment of surgical wounds and burns.[60–62] Various forms of silver are also used in some water purification devices to eliminate microbial contamination.[58]

3.2 The Element and Ion

Silver (Z = 47) falls in group IB (group 11), between copper and gold, and has intermediate chemical and physical properties (*see* ***Periodic Table: Trends in the Properties of the Elements***). The elemental form is a shiny white color and tarnishes by forming a black residue, particularly in polluted urban environments. It is more reactive than gold and less reactive than copper. There are two stable isotopes, ^{107}Ag (51.82% abundance) and ^{109}Ag (48.18% abundant). Both are NMR active with nuclear spins, $I = 1/2$, and have reasonable receptivity.[63] The $5s^1\ 4d^{10}$ electron configuration of atomic silver favors formation of a stable Ag^+ ion, having a d^{10} electron configuration, which forms salts with halides, nitrate, sulfate and a wide variety of other common anions. Ag(I) readily forms linear two-coordinate, trigonal-planar three-coordinate and tetrahedral four-coordinate complexes. Silver–silver interactions have been noted in many cases. It also forms Ag(II) and Ag(III) complexes under a variety of conditions, but these oxidation states are less common and more reactive than the simple monovalent ion. The standard electrode potential for formation of silver metal from silver ion is positive,

$$Ag^+ + e^- = Ag^\circ \qquad E^0{}_{1/2} = +0.7996 \text{ volts} \tag{6}$$

as generations of introductory students learned after splashes of silver nitrate on their skin generated black splotches of colloidal silver stain. Ligands such as cyanide, thiolates and phosphines stabilize silver against reduction and reverse the sign of the reduction potential.

3.3 Medical Applications

Silver sulfadiazine (AgSD; Figure 9) is a preferred antimicrobial agent for severe burn cases, and is applied after debridement of the wounds as an ointment containing

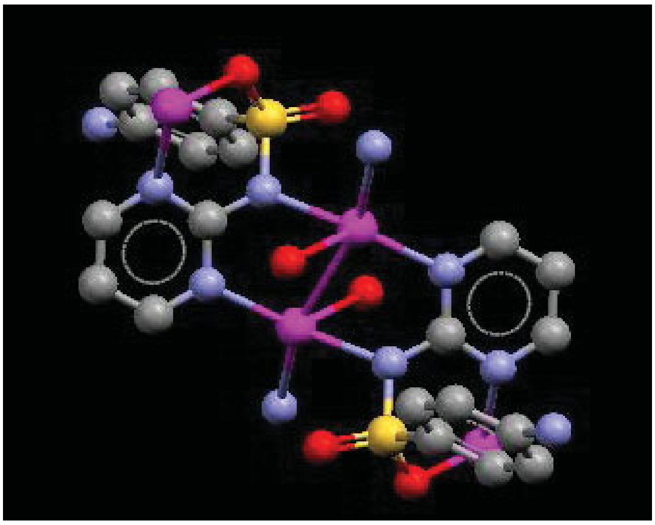

Figure 9 The coordination of silver in silver sulfadiazine, the topical agent for burns and wound treatment: the Ag–Ag dimeric unit stabilized by two head-to-tail bridging sulfadiazine ligands bound via pyrimidinyl and sulfamido nitrogen donor atoms; only the nitrogen and sulfur donor atoms of the third sulfadiazine ligands are shown. SULPMS from the Cambridge Crystallography Database

1% micronized AgSD. Only a very few orally active antibiotics are also suitable as topical applications, whereas AgSD, which is stable to light and over time and relatively insoluble, is very effective in topical applications. It is active against a wide variety of bacterial species and yeasts (fungi). The sulfadiazine ligand is a classical sulfa drug, generated by a sulfonamide linkage between *para*-amino sulfonic acid and 2-aminopyrimidine. The crystal structure of the silver complex consists of bridging silver cations coordinated to four donor atoms provided by three different sulfadiazine molecules to generate a complex, double-stranded polymer.[64,65] Interestingly, silver ions are paired in an arrangement with short silver–silver distances, 2.916 Å, linked by two bridging sulfadiazine molecules arranged in a head-to-tail fashion so that each silver binds to the sulfonamide nitrogen of one ligand and a pyrimidine ring nitrogen of the opposing ligand. Each silver is also coordinated by a pyrimidine ring nitrogen and a sulfonamide oxygen from a chelating sulfadiazine as shown in Figure 9.[64,65] The associated silver atom and four donor atoms are arranged in a distorted trigonal-bipyramidal array (Figure 9). Although the AgSD structure is often simplified and presented either as (i) a cationic silver associated with a deprotonated sulfadiazine or (ii) silver coordinated to a monodentate sulfadiazine via the deprotonated sulfonamide nitrogen or (iii) silver chelated by the pyrimidine nitrogen and sulfonamide oxygen, it is, in fact, the complex ligation into a double-stranded polymer that explains the low solubility and great stability of AgSD.

An important advantage of AgSD for chemoprophylaxis of burn wounds is that most bacterial species are unable to develop resistance against it.[60] After the infectious bacterium *Pseudomonas aeruginosa* was successively recultured 10 times through subinhibitory doses of various antibiotics, the MIC (mimimum inhibitory concentration) was determined and compared to the values measured before the passages (Table 2). The susceptibility of AgSD decreased only marginally, 1.6-fold, while the organic antibiotics showed 40- to 130-fold decreases.

Table 2 Susceptibility of *P. aeruginosa* to antimicrobial drugs after ten passages through subinhibitory concentrations[60]

Antimicrobial agent(s)	MIC (nmol mL^{-1}) Before passage	MIC (nmol mL^{-1}) After passage	Decrease in susceptibility
AgSD	50	80	1.6-fold
Norfloxacin	5	200	40-fold
Ofloxacin	5	200	40-fold
Pefloxacin	5	500	100-fold
Fortaz	1.5	200	130-fold
AgSD + Norflaxacin	7.7	75	10-fold
AgSD + Ofloxacin	3	50	17-fold
AgSD + Fortaz	12	100	8-Fold

Silver sulfadiazine is quite insoluble and releases the silver slowly, thereby maintaining a constant concentration of the free silver ion, which is the therapeutic agent. Although sulfadiazine itself has antimicrobial activity, the evidence that silver ion itself is the principle agent of AgSD arises from the following key observations: (1) *para*-aminobenzoic acid, a sulfadiazine antagonist, does not inhibit the action of AgSD, (2) using both ^{35}S- and ^{110}Ag-labelled AgSD preparations, it was shown that the silver was associated with the bacteria, but ^{35}S was not incorporated into it.[66] Norflaxacin, pefloxacin and oflaxacin are quinolone drugs that are also effective antibiotics, but subject to the development of bacterial resistance. They exhibit synergistic activity when used in combination with Ag–SD,[60,65–68] and the development of resistance to the organic agents is significantly reduced (Table 2).

3.4 Bacterial Silver Resistance

Long-term concerns about the potential for development of silver-resistant bacteria and fungi, especially in hospital and clinical settings, have led to extensive investigations of bacterial silver resistance.[69] Early studies were directed at studying the phenomenon as a function of the microorganism and exposure conditions. More recently, cellular and molecular biology approaches have allowed the mechanisms of silver resistance to be unraveled and compared to bacterial resistance to other metal ions. A gene family, silA, silB, silC, silE, silP, silR, silS, was identified as a silver resistance determinant on the plasmid of a hospital burn-ward *Salmonella* isolate.[70,71] The corresponding proteins coded by these genes have homologues in bacterial resistance genes to other metals. SilS and SilR, which resemble the CzcS and CzcR proteins of the cadmium, zinc, cobalt resistance mechanism, are a membrane-bound silver ion sensor and an aspartyl phosphate

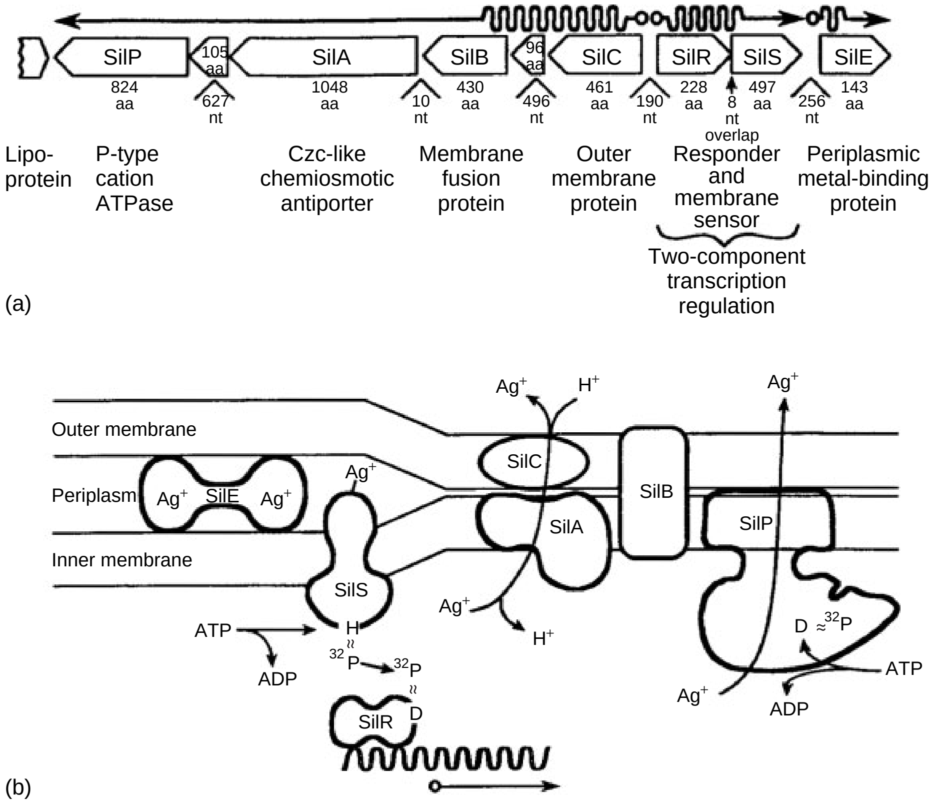
SilP
105 aa
SilA
SilB
96 aa
SilC
SilR
SilS
SilE
824 aa
627 nt
1048 aa
10 nt
430 aa
496 nt
461 aa
190 nt
228 aa
8 nt overlap
497 aa
256 nt
143 aa
Lipo-protein
P-type cation ATPase
Czc-like chemiosmotic antiporter
Membrane fusion protein
Outer membrane protein
Responder and membrane sensor
Periplasmic metal-binding protein
Two-component transcription regulation
(a)
Outer membrane
Periplasm
Inner membrane
Ag$^+$
SilE
Ag$^+$
Ag$^+$
SilS
ATP
ADP
H
^{32}P
^{32}P
D
SilR
Ag$^+$
H$^+$
SilC
SilA
Ag$^+$
H$^+$
SilB
Ag$^+$
SilP
D ≈ ^{32}P
ATP
ADP
Ag$^+$
(b)

Figure 10 The silver resistance genes, transcripts and the organization of the protein products in the membrane of *Salmonella*.[70,71] (a). Top line shows the mRNAs. The open boxes indicate different genes or open reading frames (ORFs) and their orientations. The nucleotides between the genes (nt) and the amino acids of the proteins (AA) are indicated. (b). The proposed functions and organization of the protein products relative to the bacterial structure are indicated. (Ref. 71. Reproduced by permission of Nature Publishing Group (www.nature.com))

transcriptional responder (Figure 10). The silA, silB, silC, and silP genes are cotranscribed to generate a SilABC complex that functions as a cation–proton antitransporter and SilP, an ATP-dependent active transporter that also generates a silver efflux.[71,72] A detailed understanding of the structure-function relationships of this protein family may suggest treatment protocols, such as combination therapy with two active antibacterial agents, that will retard the development and widespread transference of resistance.

3.5 Screening of New Complexes for Antimicrobial Activity

Exploration of new complexes with useful antimicrobial activities has stimulated extensive development of synthetic chemistry of silver(I) complexes. The incorporation of novel ligands can moderate the physical and chemical properties of complexes. For example, the bis(diphosphine)silver(I) complexes (which are analogues of the bis(diphosphine)gold(I) complexes with promising antitumor activity compromised by their antimitochondrial activity) were examined for antitumor and antimicrobial activity by Berners-Price *et al.*[73] 2-Substituted benzimidazole derivatives of silver(I) are more effective than the copper analogues against *Staphylococcus aureus* (MIC $= 9.8$ vs 78 and 9.8 vs $156\,\mu\mathrm{g\,mL^{-1}}$) when the substituents are 2-pyridyl and 5-methyl-2-pyridyl.[74] These and two related complexes showed similar MIC values (9.8 to $39\,\mu\mathrm{g\,mL^{-1}}$) against a panel of 7 additional infectious agents including *P. aeruginosa* and *Candida albicans*. Five sulfacetamide silver derivatives, which introduce two sulfonamide linkages, were tested against two *Aspergillus* species (*niger* and *flavus*) and *C. albicans*.[75] The silver complexes were more effective (MIC range $3–12\,\mu\mathrm{g\,mL^{-1}}$) than the zinc analogues ($13–22\,\mu\mathrm{g\,mL^{-1}}$) or the ligands ($>88\,\mu\mathrm{g\,mL^{-1}}$).

4 Pt-BASED ANTITUMOR AGENTS (*See also Platinum-based Anticancer Drugs*)

4.1 Introduction and History

The serendipitous discovery of antitumor activity for platinum compounds by Professor Barnett Rosenberg occurred during research based on the novel premise that the organization of the chromosomes of dividing cells resemble the patterns of magnetic field lines and, therefore, bacterial growth might be altered in electric fields. Cells grown in electric fields generated with gold or silver electrodes reproduced indistinguishably from the controls, whereas cell growth in cultures where the field was generated by platinum electrodes was inhibited.[6,76] Further investigation revealed that *cis*-diamminedichloroplatinum(II) and *cis*-diamminetetrachloroplatinum(IV) formed in the latter culture were responsible for the growth inhibition. In vitro and in vivo testing demonstrated the effectiveness of the Pt(II) complex against leukemia and other tumor cells. Subsequent clinical trials established the utility of cisplatin for treating ovarian and testicular cancer, in particular, and for other tumors in combination therapy with organic antitumor agents. Since then thousands of platinum(II) and platinum(IV) agents have been tested as potential antitumor agents, and nearly 30 have proceeded through at least phase I clinical testing.

4.2 The Metal and Its Oxidation States

Platinum (Z = 78) is a whitish, noble metal found in group 10 (or VIIIB) of the periodic table, in the triad with and lying below nickel and palladium (*see* ***Periodic Table: Trends in the Properties of the Elements***). It can be found in elemental form in the mountains of Columbia, where the pre-Columbian natives used it. European chemists discovered and reported it in the mid-1700s. Like gold and silver, it has a positive reduction potential:

$$\mathrm{Pt}^{2+} + 2\mathrm{e}^{-} = \mathrm{Pt}^{0} \qquad \mathrm{E}^{0}{}_{1/2} = \sim +1.2 \text{ volts} \tag{7}$$

The metal does not react with oxygen, even when heated, and is resistant to the actions of either nitric or hydrochloric acid.

The principal oxidation states are Pt(II) and Pt(IV). Pt(II) is the prototypical d^8 ion and forms square-planar, four-coordinate complexes, which are somewhat sluggish in their ligand exchange reactions. Pt(IV) is a d^6 metal ion and forms octahedral 6-coordinate complexes, which exhibit the typical kinetic inertness associated with the d^6 configuration. Pt(IV) is an oxidizing agent and is reduced to Pt(II) under biological conditions by agents such as thiols. The oxidation states Pt(I) and Pt(III) are also known, primarily in complexes with Pt–Pt bonds. The Pt(0) oxidation state has a d^{10} configuration and forms linear 2-coordinate, trigonal 3-coordinate and tetrahedral 4-coordinate complexes. It is principally Pt(II) and Pt(IV) that are relevant to the medicinal chemistry of antitumor agents.

4.3 Clinically Used Platinum Antitumor Agents

The five platinum-based antitumor agents that are presently licensed[77,78] are shown in Figure 11 and listed in Table 3. Cisplatin (Figure 11(a)), as described above, was the first to be licensed, and remains an important and widely used clinical treatment. Used in combination therapy with a variety of organic drugs, it has found exceptional application against ovarian and testicular cancers and is also used to treat a wide variety of tumors including melanoma, bladder carcinoma, neuroblastomas, cervical carcinoma, oropharyngeal carcinoma, osteosarcoma, and lymphoma. It is one of the three leading antitumor drugs in worldwide clinical use, but nonetheless suffers from undesirable side effects including nephrotoxicity and frequent instances of drug resistance that limit its usefulness.

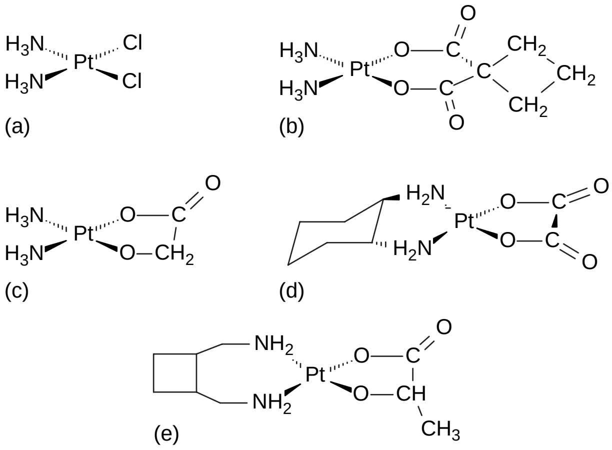

Figure 11 Clinically used platinum antitumor agents: (a) cisplatin; (b) carboplatin; (c) nedaplatin; (d) oxaliplatin; (e) lobaplatin

Table 3 Platinum antitumor agents approved for clinical use[80–83]

Structure[a]	Name	Effective against	Mode	Limiting toxicity	Approval
a	cisplatin	testicular, ovarian[b]	IV	nephrotoxicity	worldwide
b	carboplatin	testicular, ovarian[b]	IV	thrombocytopenia	worldwide
c	nedaplatin	head and neck, lung	IV	myleosuppression	Japan
d	oxaliplatin	colorectal cancer	IV	sensory neuropathy	France
e	lobaplatin	myelogenous leukemia		thrombocytopenia	China

[a] Figure 11. [b] Also used in combination therapy for a range of additional tumors.

The success of cisplatin in the clinic has stimulated the synthesis and preclinical testing of over 3000 related and unrelated platinum compounds since Rosenberg's initial report in 1965. It also spawned extensive searches for antitumor activity by complexes of other metals including gold, rhenium, ruthenium, tin, titanium and rhodium.[79] Four additional platinum-based drugs are presently licensed. Carboplatin (Figure 11(b)) retains the *cis*-diammine structure of cisplatin, but substitutes a chelating dicarboxylato ligand for the chloride ligands. It exhibits similar therapeutic profiles and is a safer drug with fewer side effects.[77,80] Like cisplatin it is licensed for use worldwide.

Three complexes, nedaplatin, oxaliplatin and lobaplatin (Table 3), have been licensed in particular countries for specific uses and are undergoing active clinical trials elsewhere. All three retain the *cis*-nitrogen donor atom arrangement found in cisplatin and have a bidentate oxygen-donor ligand. Nedaplatin (Figure 11(c)) contains the *cis*-diammineplatinum core with a chelating glyoxylate ligand, coordinated through the alkoxide oxygen and a carboxylate group oxygen atom. It has been approved in Japan for use against head and neck, testicular, nonsmall cell lung, oesophageal, ovarian, and cervical cancers.[81] In oxaliplatin (Figure 11(d)), the nitrogen donor atoms are provided by the chelating ligand *trans*-L-DACH (*trans*-L-1,2-diaminocyclohexane) and the labile ligand is a chelated oxalate ion.[80] It is licensed in France for colorectal cancer and is being tested in phase I trials in combination therapy with irinotecan (CPT-11), an agent able to block a resistance-developing repair mechanism, and in phase II trials with raltitrexed (taxol). Clinical trials against other tumor types are also under way: phase II trials in combination with 5-fluoruracil against metastatic prostate cancer and phase I trials in combination with irinotecan and 5-fluorouracil against advanced gastrointestinal malignancies. The presence of the bulky DACH ligand may contribute to its lack of cross-resistance to cisplatin.[77] Lobaplatin contains a chelating butylenediamine ligand, in which the internal carbons form one side of a cyclobutane ring (Figure 11(e)). The remaining coordination positions are occupied by a chelating lactate ligand bound through a carboxylate oxygen and the hydroxyl oxygen.[77,80,82] It has been licensed in China for treatment of myelogenous leukemia. A variety of tumor types respond to lobaplatin and some tumors that readily develop cisplatin resistance are not cross-resistant to it, which is an important therapeutic advantage.[82]

In addition to the compounds approved for use worldwide or in specific countries, at least eight other experimental Pt-based drugs are in phase I or II clinical testing (Table 4). Given the effectiveness of cisplatin and carboplatin against a variety of targets, there is strong interest in developing additional compounds, in which unique ligands may enhance activity against various types of tumors that are refractory to cisplatin or that develop resistance to it.

Three slow-release formulations of platinum compounds are in clinical trials. L-NDDP is a complex of *trans*-R,R-1,2-DACH with two bound neodecanoate ligands (Figure 12(a)) that is formulated in a multilamellar liposome preparation and administered intraperitoneally.[84] The Pt concentrations observed in the peritoneal cavity are approximately 20- to 50-fold greater than that in the plasma and are maintained for prolonged periods.[84] SPI-77 is a liposomal formulation of cisplatin and has been shown to reduce toxicity. It releases the platinum slowly, leading to half-lives for the platinum in vivo in the range of 60–80 hours, compared to ca. 1 hour for traditional IV administration of cisplatin. Lipoplatin, presently in Phase I and II trials, uses an alternative liposomal formulation to deliver cisplatin, which also leads to reduced side effects. Their effectiveness is comparable to cisplatin, and the reduced side effects are a significant clinical benefit.

Five additional complexes that have entered phase I or II trials (Table 4 and Figure 12(b–f)) reflect novel approaches to designing new Pt-based agents. Cycloplatam is a mixed amine-ammine complex, ammine(cyclopentylamine)-S(-)malatoplatinum(II) (Figure 12(b)), which is being developed in Russia and has entered phase II trials there.[85] Reported to be more effective and less toxic than cisplatin, it can be given by oral or intracavitary administration and is being tested against lung, ovarian and prostate cancers. ZD 0473 is also a mixed amine-ammine species, with a 2-methylpyridine ligand replacing one ammine of cisplatin. The methyl group is positioned over the coordination plane of the platinum, which results in steric hindrance to ligand exchange of the chlorides and slower transformation

Table 4 Platinum antitumor agents in Phase I or II clinical trials

Structure[a]	Name	Code	Mode	Limiting toxicity	Phase
a		L-NDDP	ip	neutropenia, thrombocytopenia	I
	Stealth cisplatin	SPI-77		Tbd	II
	Lipoplatin™			Tbd	II
b	cycloplatam		oral, ic	Myleosuppresion	II
c	satraplatin	JM-216	oral	Myleosuppresion	II
d	heptaplatin	SKI-2053R	iv	hepatotoxicity, myleosuppresion, renal	I
e		ZD-0473	oral	thrombocytopenia, neutropenia	II
f		BBR-3464		neutropenia, vomiting	I

[a] Refer to Figure 12.

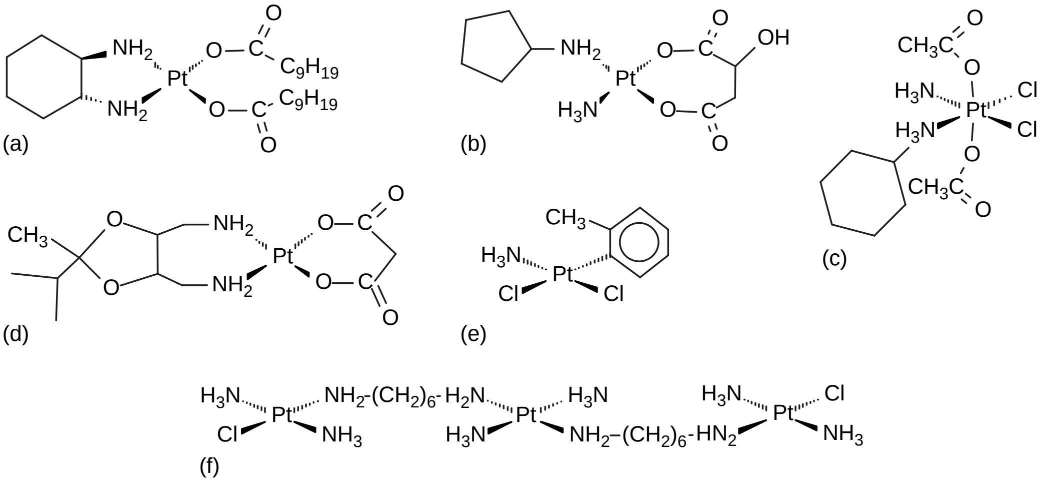

Figure 12 Compounds in clinical phase I, II or III testing as antitumor agents: (a) L-NDDP; (b) cycloplatam; (c) JM-216; (d) SKI-2053R; (e) ZD-0473; (f) BRR-3463

into metabolites.[77,80,84] It is active against cisplatin- and carboplatin-resistant tumor lines and is being tested against a variety of tumor types including breast cancer. Heptaplatin (SKI 2053R), which contains a bidentate malonato ligand opposite a substituted butylenediamine ligand (Figure 12(d)), is in phase I clinical trials. It is a less toxic substance than cisplatin, and is also administered intravenously. It is being applied to advanced malignancies. Satraplatin (JM 216, [*cis,cis,trans*-$(CyH_2N)(H_3N)Cl_2(OAc)_2Pt(II)$], Figure 12(c)) the only Pt(IV) complex presently undergoing extensive clinical trials, is an octahedral complex with mutually trans acetate ligands, mutually cis chlorides and mutually cis ammine and cyclohexylamine ligand pairs arranged so that the chlorides are each trans to a nitrogen donor as in cisplatin. The complex can be taken orally and is not cross-resistant to cisplatin in certain tumor lines. Satraplatin's antitumor action is apparently preceded by reduction to a Pt(II) species. BBR 3463 is a trinuclear complex belonging to a large family of potential di- and polynuclear Pt antitumor agents developed by Farrell and coworkers.[86] It is the first multinuclear complex to enter clinical trials and appears to generate a new array of DNA adducts, which may explain the widespread lack of cross-resistance to cisplatin when tested against tumor cell lines.

Approximately 18 additional compounds that had entered clinical trials have been withdrawn from further development, because they lack broader activity than cisplatin or exhibit greater toxicity, or for economic and marketing reasons. Iproplatin (*cis,trans,cis*-bis(isopropylamine)dihydroxodichloroplatinum(IV); [*cis,trans,cis*-$(i\mathrm{PrH_2N})_2(OH)_2Cl_2Pt(II)$]), for example, showed promise in preclinical testing against tumors and in animal studies, but during clinical testing proved to be more toxic than cisplatin and less effective because the toxicity limited the dosage that could be used.

4.4 Metabolism and Mechanism of Action of Pt-based Antitumor Drugs

Cisplatin and the mononuclear analogues that either have been approved or are presently in clinical trials share a number of traits. Most important are the presence of two mutually cis amine ligands, which are critical to the in vivo activity, and two leaving groups such as chloride or carboxylate ligands. Early structure-function studies established that optimal activity resulted when the ligands trans to the nitrogen donor ligands have intermediate affinities for the Pt(II) center. Weakly bound ligands such as acetate ions decrease the activity compared to cisplatin, as do very strongly bound ligands, for example, the additional ammines in $[Pt(NH_3)_4{}^{2+}]$.[77]

The ligation of platinum in cell culture and in vivo is modified by a series of crucial equilibrium reactions. Using cisplatin as the example, the chloride ions are displaced by water to form sequentially the mono aquo and then diaquo complexes. The resulting aquated ions are involved in acid-base equilibria, which generate the corresponding hydroxo complexes. Under physiological conditions, the hydrolysis is repressed in the serum where the chloride concentration is relatively high (~150 mM), thereby maintaining the parent drug, whereas after entering the low chloride environment of the cell cytosol ($[Cl^-] \sim 4\,\mathrm{mM}$), the diaquo metabolite is formed. The diaquo cation is more reactive to ligand exchange reactions, which facilitate a further reaction of the platinum with DNA, leading to the adducts responsible for the antitumor activity.

These reactions can be used to understand many of the structure-function relationships among the approved drugs and those that have undergone clinical testing. For example, carboplatin retains the *cis*-diammineplatinum(II) center, but the chlorides have been replaced by the cyclobutanedicarboxylate ligand. The similar array of

Table 5 Hydroylsis and plasma clearance half-lives for cisplatin and carboplatin[87,88]

Drug	Hydrolysis[a] $t_{1/2,\text{hydrolysis}}$ (hrs)	Total platinum clearance[b] $t_{1/2,\text{fast}}$ (min)	Total platinum clearance[b] $t_{1/2,\text{slow}}$ (hrs)	Free platinum clearance[b] $t_{1/2,\text{fast}}$ (min)	Free platinum clearance[b] $t_{1/2,\text{slow}}$ (hrs)
cisplatin	2.4	18–37	44–190	22–78	unobserved
carboplatin	268	98	7– > 24	87	354

[a]pH 7 in chloride-free phosphate buffer. [b]Plasma platinum levels measured by flameless atomic absorption spectrometry; 'free Pt' is that passing through a 50 000 Dalton ultrafiltration membrane.

antitumor activities of cisplatin and carboplatin are in part a consequence of the common hydrolysis products that form when the chloride ions and dicarboxylate ligand, respectively, are displaced to form the *cis*-diamminediaquoplatinum(II) as a common metabolite. Yet, the kinetics of the hydrolysis to the diaquo species are dramatically slowed by the chelating dicarboxylate ligand of carboplatin (Table 5). The slow hydrolysis, in turn, exerts a profound effect on the pharmacokinetics of drug clearance from the body. In particular, the long lasting availability of low-molecular weight (''free'') platinum may contribute to the therapeutic profile of carboplatin. The presence of a chelating amine ligand will also affect the metabolism of platinum-based drugs. Since the ammine ligands of cisplatin are retained in complexes formed with DNA, the DACH-containing drug, oxaliplatin (Figure 11(d)), will retain the chelating 1,2-diaminocychohexane ligand when it binds to DNA. The greater bulk and affinity for platinum are likely to confer additional resistance to DNA repair mechanisms, consistent with the in vitro activity of oxaliplatin against certain Pt-resistant cell lines.

The movement of Pt drugs into the cell is modeled in Figure 13, again using cisplatin as the example. When the drug crosses the cell plasma membrane, it encounters a low chloride concentration and is hydrolyzed to the diaquo complex. The target of the drug is DNA, which is encapsulated behind the double membrane of the nucleus. Platinum reacts via ligand exchange principally at the N-7 position of guanine residues to form intra- and interstrand crosslinks with duplex (*see* ***Nucleic Acid–Metal Ion Interactions***).[89] Guanine-Pt-guanine linkages account for 60–65% of the bound Pt. To lesser extent it also reacts to form adenine-Pt-guanine instrastrand crosslinks that account for about 20–25% of the DNA-bound Pt.[86–88] The effect of the crosslinks is to introduce lesions that disrupt the normal base pairing and cause kinks in the double-helical structure of the DNA (Figure 14). In some cell types these lesions are not readily removed or repaired, and the resulting inhibition of replication and transcription adversely affects the cells, leading to apoptosis. Other cells, unfortunately, are able to repair the lesions or develop other means of resistance such as enhanced biosynthesis of metallothionein, a metal-binding protein (*see* ***Metallothioneins***),[89,91] or glutathione, a cellular

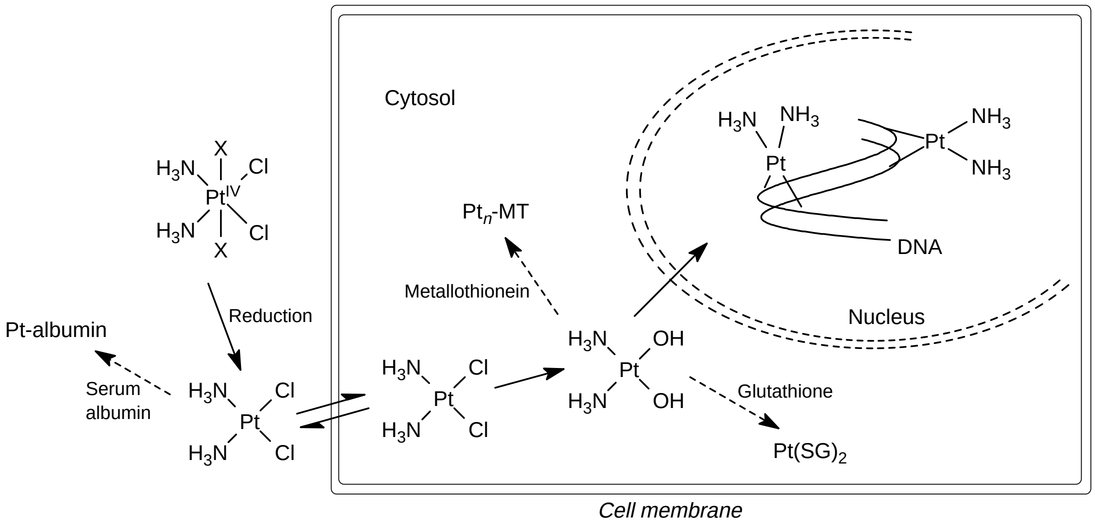

Figure 13 Mechanism of action and competing cellular targets of cisplatin. Solid arrows delineate the normal progression to formation of DNA lesions and dashed arrows represent nonproductive, dead-end reactions with other substances

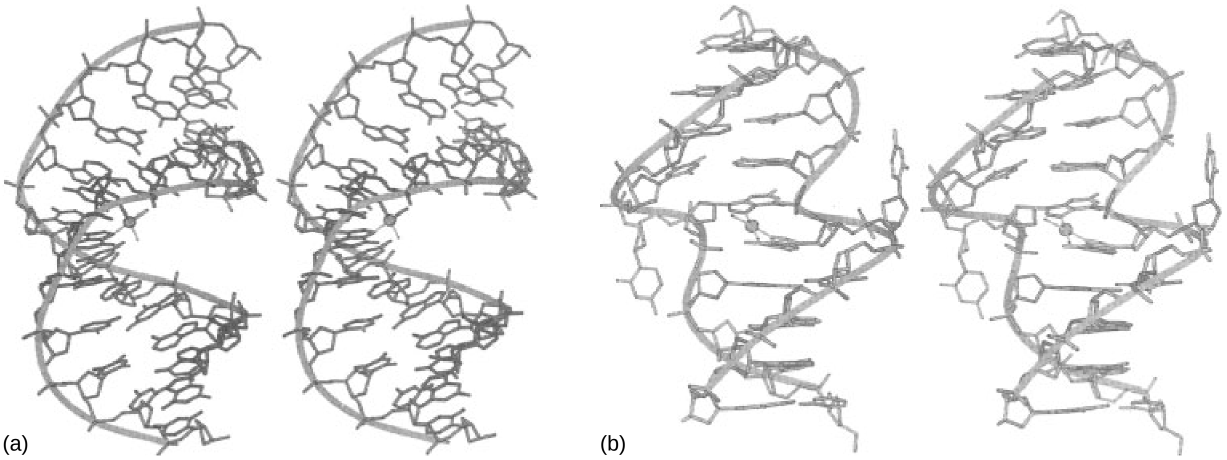

Figure 14 Stereoviews of the NMR solution structures of platinated DNA sequences illustrating the deformation of the normal double-helical structure. (a) intrastrand *cis*-GG crosslink in d(CCTCTG*G*TCTCC)-d(GGAGACCAGAGG); (b) interstrand *cis*-GG crosslink in the palindromic sequence d(CATAG*CTATG)-d(CATAG*CTATG); * represents the donor nucleotides. (Reprinted with permission from Ref. 90. © 1999 American Chemical Society)

reductant with an affinity for heavy metal ions, which both bind Pt(II) very tightly.

While binding of cisplatin and its analogues favors the N-7 position of guanine among many possible donor sites in the DNA structure, the reaction is not highly favored over the many alternative non-DNA sites that compete for the platinum.[92] Thioethers can react with cisplatin and in some cases can even displace the amine ligands, but they can in turn be displaced slowly by nucleotides such as guanidine. Sadler carried out interesting competition experiments between methionine, an amino acid with a thioether side chain, and the nucleotide 5′-GMP for $[Pt(dien)Cl^+]$. The sulfur of methionine initially displaces the chloride ion, but is then slowly displaced by the guanine, which reacts at N-7. The biological reductant, glutathione, found at millimolar concentrations in many cells also reacts effectively with cisplatin and analogues.[92,93] In contrast to the reversibility of thioether binding, glutathione is not readily displaced from Pt(II) by nucleotides. MT is another target with a high affinity for Pt(II); it has the ability to react directly with cisplatin without preliminary hydrolysis to the aqueous species.[89,91] MT is a small cysteine-rich metal-binding protein that occurs naturally in cells with Zn^{2+}, and sometimes Cu^+, ions bound to it; exogenous toxic and medicinal metal ions, including Cd(II), Hg(II), Au(I), Ag(I), Pt(II), and Bi(III), react with it after entering cells. Pt(II) complexes react with MT in vivo and in vitro to displace bound Zn^{2+} and the more tightly bound Cd^{2+}.[89,91] The ^{14}C-radiolabelled ethylenediamine ligand in the cisplatin analogue, $[(en)PtCl_2]$, is effectively displaced in reaction with MT, suggesting that both the chloride and ammonia ligands of cisplatin are displaced and that the Pt is fully ligated by cysteine thiolato groups.[89,92]

5 VANADIUM INSULIN MIMICS AND ENHANCERS

5.1 Introduction

Vanadium complexes are under intensive investigation as insulin-enhancing drugs for the treatment of diabetes.[94–97] Because they are orally absorbed, they are potentially very useful for the treatment of diabetes, an increasingly prominent disease in the United States and other nations. Vanadium is found in most plant and animal tissues at low levels and at significantly higher concentrations in tunicates (*see* ***Vanadium in Biology***). It is suggested to be a nutritional trace element, but a specific biological function, which is the sine qua non for essentiality, has not been identified in higher organisms, whereas in many marine organisms and microbes, biological roles for vanadium are now well defined.[98,99] A vanadium-containing nitrogenase enzyme can be biosynthesized by certain bacteria in the absence of molybdenum. Like the molybdenum-containing analogues, the vanadium enzymes have multiple protein subunits and the vanadium is associated with an FeV Cofactor (FeVCo) that has a V:Fe:S ratio of 1:19:19 for the $\alpha\beta_2$ form and 2:30:34 ratio in the $\alpha_2\beta_2$ form in *A. vinelandii*.[98] Lichen and algae also utilize vanadium-dependent enzymes. The brown algae *Ascophyllum nodosum* generates a haloperoxidase that contains two V(V) ions at the active site.[100,101] A vanadium-dependent nitrate reductase, which also has a porphyrin (heme c) cofactor and an N-terminal sequence that is not homologous to the molybdenum-dependent nitrate reductases, has recently been identified in an anaerobic chemolithoautotrophic bacterium. Some species of marine tunicates (in the chordate phylum) accumulate vanadium into their blood cells, imparting a greenish color and, hence, the name vanadocytes, but no function has been assigned to the accumulated vanadium.[102,103]

5.2 The Element and Ions

Vanadium (Z = 23), was named for the Scandinavian goddess, Vanadis, because of the many brightly colored compounds that it forms (*see* ***Periodic Table: Trends in the Properties of the Elements***). It falls in group 5 (or Vb) of the periodic table and is the lightest element of its triad. The elemental form is bright white in appearance, ductile and soft. Naturally occurring vanadium is almost entirely ^{51}V (99.76% abundance) with a trace of ^{50}V (0.24%). ^{51}V is a useful NMR-active isotope, even though it is a quadrupolar nucleus (I = 7/2). The ^{48}V isotope is a beta emitter having a half-life of 16.0 days, which makes it useful as a tracer in metabolic studies. Complexes in oxidation states from $-$I to $+$V have been characterized. The aqueous ions of the lower oxidation states, $[V^{II}(OH_2)_6]^{2+}$ and $[V^{III}(OH_2)_6]^{3+}$, are readily oxidized by air. The principle aqueous ions of the higher oxidation states are the oxo ions, $V^{IV}O^{2+}{}_{(aq)}$ (vanadyl ion) and $V^{v}O_4{}^{3-}$ (vanadate), which at neutral pH exists as an equilibrium mixture of $H_2V^VO_4{}^-$ and $HV^VO_4{}^{2-}$ with a pK_a value of 7.8. The anions are analogous to phosphate ions, but $H_3V^VO_4$, a phosphoric acid analogue, is not stable, and at low pH ($\leq$1) the $V^VO_2{}^+{}_{(aq)}$ is the dominant species. The oxidation states III, IV, and V are most relevant to the aqueous chemistry under biomimetic conditions, and most compounds under consideration for diabetes therapy contain either V(IV) or V(V), although an active V(III) complex of maltol has been identified.

5.3 Insulin-enhancing Vanadium Compounds for Diabetes Mellitus

Diabetes mellitus (DM) is an increasingly common disease of sugar metabolism. Juvenile-onset diabetes, also known as Type I or insulin-dependent diabetes (IDDM), is an autoimmune disease that results in decreased release of insulin by the pancreas. Late-onset diabetes, also known as Type II or non-insulin-dependent diabetes (NIDDM), results from reduced sensitivity of cells to the insulin signal. A convenient animal model for studying diabetes and testing alternative therapies is the streptozotocin-treated diabetic rat. Streptozotocin (STZ) attacks the pancreas and decreases insulin production and release, thus, mimicking many aspects of the human disease.[104] Since insulin is not orally absorbed, the oral administration of vanadium compounds that are insulin-mimetic or insulin-enhancing would be a very attractive therapy[94–97]

The inorganic, bioinorganic and medicinal chemistry of vanadium compounds in the oxidation states III, IV, and V has been studied extensively in this regard. Active compounds of all three oxidation states have been reported to act favorably to improve glucose metabolism. The inorganic salts, particularly sodium vanadate ($NaVO_3$) and vanadyl sulfate ($VOSO_4$) have been carried through phase II clinical testing. They lower gluconeogenesis in the liver, enhance the uptake and oxidation of glucose by adipocytes and stimulate its conversion into glycogen.[94] Although vanadium compounds are sometimes described as insulin mimics, current mechanistic studies suggest that the in vivo actions can better be described as enhancing insulin activity.[105]

The most promising compounds to date are those of V(IV). Figure 15 shows the structures of a variety of vanadyl complexes with chelating ligands that have been prepared and tested in various model systems. The ligands typically function as monoanionic chelating agents, which render the complexes neutral and, therefore, lipophilic, thereby allowing them to pass more easily through cellular membranes by passive diffusion.[94] Table 6 provides further information about their properties. BMOV (bis(maltolato)oxovanadium(IV), Figure 15(a)) has become a benchmark compound for comparison to newer complexes. It is a square pyramidal structure with an axial oxo group, in which vanadium is chelated in a bidentate fashion by two maltol ligands that coordinate via their alkoxy and ketone oxygen atoms. Daily, oral administration of BMOV (0.4 mmol kg^{-1} day^{-1}, which was then lowered to 0.2 mmol kg^{-1} day^{-1}) either in drinking water or by oral gavage (direct introduction to the stomach) produced normalization of blood glucose levels in the STZ-treated diabetic rat. VPA, VO-MPA, VCME, and Naglivan (Figure 15(d–g)) also contain bidentate organic chelates and are also effective when orally administered within the range of 0.1 to 0.7 mmol kg^{-1} day^{-1}.[94] VO-Salen contains a tetradentate Schiff's base ligand (Figure 15(b)). VO-metf (Figure 15(c)), which uses biguanidine ligands, is an example of a metallodrug that incorporates a medicinal ligand effective for the same disorder (metformin or Glucophage™) in the expectation that the metal and ligand will work synergistically.

Bisperoxovanadates with the formulas $[(VO(O_2)_2(L\text{–}L')]^{n-}$ and $[VO(O_2)_2L)]^{n-}$ and monoperoxovanadates with the formulas $[VO(O_2)(OH_2)_2(L\text{–}L')]^{n-}$ and $[VO(O_2)(L\text{–}L')_2]^{n-}$, in which the peroxo ligands bind in an η^2 configuration to form a three-membered ring with the central V(V) center, have also shown good activity in laboratory animals. Their structures are distorted pentagonal bipyramids when a bidentate ligand (L–L′) is used, and a distorted pentagonal pyramid when the ligand are monodentate. The bisperoxo complexes with L–L′ = phenanthroline ($n = 1-$), dimethylphenanthroline ($n = 1-$) and picolinate ($n = 2-$), are effective at much lower doses ($\sim$1–6 µmol kg^{-1}) than the vanadyl complexes when administered IV, i.p., or subcutaneously, but only the phenanthroline complex was active (20–200 µmol kg^{-1}) when administered by oral gavage. The neutral oxoperoxodiaquopicolinatovanadium(V) complex with L–L′ = picolinate ($n = 0$) was effective at 0.4 µmol kg^{-1}, whereas the trianionic oxoperoxobis(oxalato)vanadium(V) complex ($n = 3-$) exhibited only marginal activity.

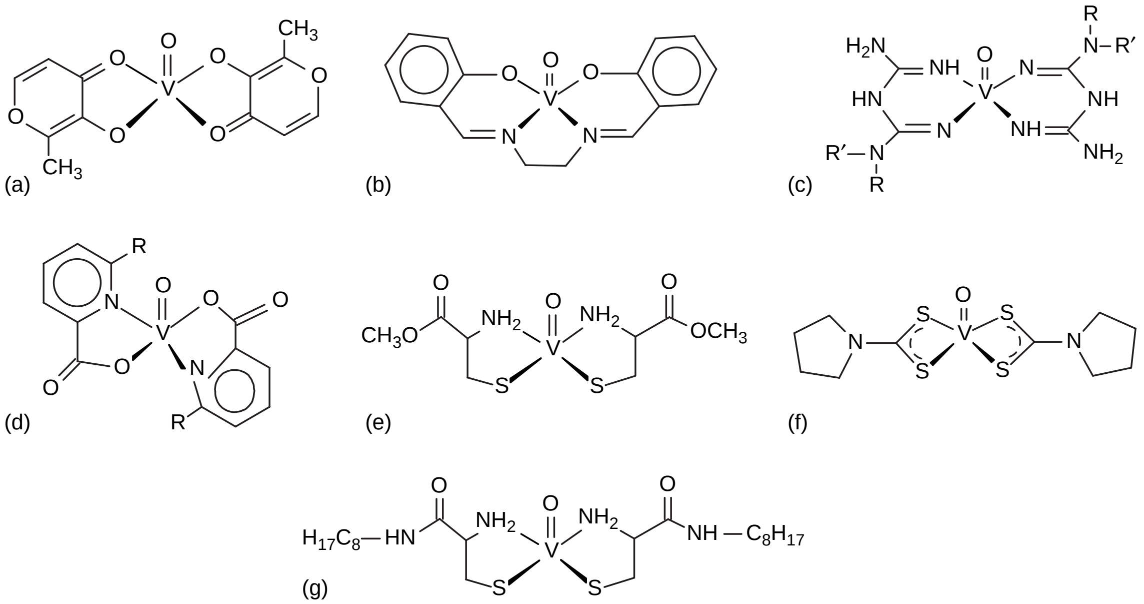

Figure 15 Structures of vanadium complexes with insulin-enhancing activity: (a) BMOV; (b) VO-Salen; (c) VO-metf; (d) VPA; (e) VCME; (f) VP; (g) Naglivan

Table 6 Vanadyl complexes ([VO(L–L′)$_2$]) exhibiting insulin-enhancing properties[a]

Structure[b]	Abbreviation	Ligand	$\nu_{V=O}$/cm^{-1}
a	BMOV	maltol	995
b	VO-Salen	*N*,*N*′-disalicylidineethylenediamine	981
c	VO-metf	biguanidine	929
d	VPA	picolinate	980
d	VO-MPA	3-methylpicolinate	948
e	VCME	cysteine methyl ester	956,945
f	VP	pyrrolidine-*N*-carbodithiolate	
g	Naglivan	*N*-octylcysteineamide	

[a]Doses typically ca. 10 mg V kg^{-1} day^{-1}.[94] [b]Refers to Figure 15.

The synthesis, properties, and biological activities of tris(maltolato)vanadium(III) and three analogues have been reported (Table 7). The structures of the [V(ma)$_3$] complex and the ligands are shown in Figure 16. Blood glucose levels in STZ-diabetic rats were determined after 24 hours in comparison to BMOV. The only compound showing significant activity is the tris(maltato)complex, which has activity comparable to that of BMOV, that is, reducing the 24-hr blood glucose level to <9 mM in diabetic rats.

Table 7 Response of STZ-treated diabetic rats to vanadium(III) compounds[106]

	Intraperitoneal administration		Oral gavage
Non-platinum	[glucose]$_{24h}$/mM	Positive responses[a]	[glucose]$_{24h}$/mM
BMOV control	8.2 ± 3.0	4 of 5	15.7 ± 2.2
[V(ema)$_3$]	10.5 ± 1.8	0 of 5	19.0 ± 3.2
[V(ma)$_3$]	12.3 ± 3.7	3 of 5	14.5 ± 3.2
[V(koj)$_3$]	19.7 ± 0.4	0 of 5	n/d[b]
[V(dpp)$_3$]	19.9 ± 0.9	0 of 5	n/d[b]
untreated control	> 20 mM	–	19.0 ± 0.3

[a]Number of animals with [glucose]$_{24h}$ < 9 mM out of 5 animals. [b]Not determined.

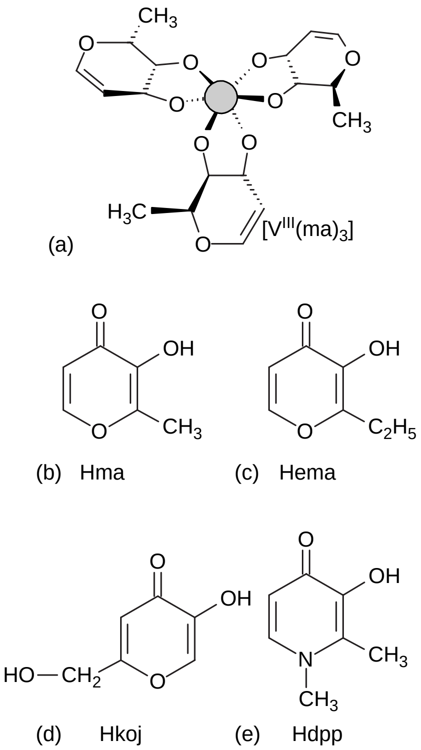

(a)

(b) Hma (c) Hema

(d) Hkoj (e) Hdpp

Figure 16 Structure of (a) tris(maltolato)vanadium(III) and the ligands (b) maltol, (c) ethylmaltol, (d) kojic acid, and (e) 1,2-dimethyl-3-hydroxy-4-pyridinone

5.4 Metabolism of Vanadium Compounds

Vanadium accumulates in the liver, kidney, and bones of mammals including humans. ^{48}V tracer studies of radiolabeled BMOV, VPA and vanadyl sulfate showed that the liver:kidney:bone ratios of tissue vanadium accumulation were 8:3:2 for ^{48}V-BMOVand 6:4:1 for ^{48}V-$VOSO_4$, with an almost threefold greater overall accumulation of BMOV, clearly demonstrating that the distribution among tissues and the total accumulation are both dependent on the ligation of the complex administered.[91] No toxic or harmful effects of bone accumulation have been reported. The major side effects observed in animal testing and human clinical trials of the vanadium insulin-enhancing agents are episodes of gastrointestinal intolerance and limited weight gain.[96] Green tongue, a phenomenon reminiscent of the greenish vanadocytes in tunicates, has been reported after occupational exposure to airborne compounds in vanadium refineries or to vanadium residues encountered in fuel-fired boiler maintenance operations. The effect is reversible after cessation of exposure and without long-term consequences.

Vanadate enters cells by an active transport process that depends on the structural and electronic similarity to phosphate ion transport, since the isoelectronic species, HZO_4^{2-} and $H_2ZO_4^{-}$, are dominant species for $Z = P$ or V at physiological pH. Neutral vanadyl complexes such as BMOV and $[VO(acac)_2]$, in contrast, enter cells by passive diffusion, which is advantageous for medicinal applications. Accumulating evidence suggests that oxidation-reduction reactions and ligand exchange by hydrolysis and by reaction with endogenous ligands alters the ligation of vanadium and its oxidation states. The binding of vanadium compounds to proteins in the blood alters their bioavailability and transport. A number of studies summarized in recent reviews establish that the order of binding preference tends to be[94,99] transferrin $>$ albumin $>$ immunoglobins.

While the affinity of transferrin (*see* ***Iron Proteins for Storage & Transport & their Synthetic Analogs***) for vanadyl is ~10-fold greater than that of albumin, the latter can bind up to 20 vanadyl ions including a specific interaction with cys-34, the only reduced cysteine residue in the protein.

5.5 Possible Mechanisms of Action

As for other several other inorganic medicinal agents, there is not a well-established and generally accepted mechanism of action for vanadium insulin enhancers. After its secretion from the pancreas, insulin concentrations are greatest and its activity is most essential in the liver, muscle and adipose tissue of the body. Crans *et al.* have documented three possible mechanisms that may explain their actions.[99] The most widely studied mechanism is the inhibition of phosphatase enzymes that catalyze the phosphorylation of regulatory proteins. The first enzyme of the insulin regulatory cascade, protein phosphatase 1B (pp1B) is sensitive to vanadium inhibition. Elimination or inhibition of this enzyme leads to increased insulin activity and reduced obesity in mice by preventing phosphorylation of the insulin receptor. Peroxovanadates act as irreversible inhibitors of cysteine-dependent phosphatases by oxidizing the active site cysteines. Vanadyl complexes are competitive inhibitors of phosphatase activity. The overall activity of the drugs in vivo does not, however, correlate with their in vitro inhibitory activity, which may reflect their metabolism in vivo and likely the existence of additional biological actions of the vanadium compounds and metabolites. Reactions of vanadium compounds with transferrin are another mechanism by which metabolic changes can be induced. Binding of vanadyl cation or fragments of vanadium complexes formed by partial ligand displacement may alter metal transport and also the transport of vanadium metabolites in an organism. A third mechanism is the interaction of vanadium complexes with the cellular mechanisms for redox homeostasis. Glutathione, a cellular reductant, is known to reduce vanadium compounds. Since oxidative stress apparently plays a role in the development of the diabetic condition and in the proliferation of complications that can lead to the loss of limbs and other side effects, the interaction of vanadium with the redox state of cells may be an important aspect of its mechanism of action.

Given that the V(III), V(IV), and V(V) oxidation states are all active and that reasonable routes exist for in vivo oxidation-reduction reactions to interconvert the three states, a redox equilibrium seems quite likely. Since cellular and subcellular environments vary in pH, redox potential, availability of ligands and enzyme activities, a very variable array of metabolites may be present in different tissues and organelles. Indeed, different insulin-enhancing activities may be affected by different oxidation states generated in vivo. For example, peroxovanadates function as irreversible inhibitors of phosphatase enzymes, while vanadyl complexes are reversible inhibitors and much less effective. There is emerging awareness that the vanadium drugs under study may, in fact, be prodrugs that are activated in vivo by redox and ligand exchange processes.

It is interesting that maltol complexes of both V(III) and V(IV) are more active than other analogues with vanadium in the same oxidation state – an observation that suggests some maltol metabolite may have unique or superior activity at one or more sites of action. The finding that $[MoO_2]^{2+}$ and Co(II) complexes of maltol show insulin-mimetic activity – albeit weaker than that of BMOV – is not inconsistent with this suggestion. As a better understanding of vanadium metabolism and the role of the medicinal ligands are delineated, the design of more effective drug molecules can be anticipated.

6 LITHIUM

6.1 Introduction and History

Lithium carbonate (Li_2CO_3) treatment is used worldwide for the prophylactic treatment of bipolar affective disorder. Although the molecular mechanism(s) of action remains uncertain, the efficacy is well-demonstrated and can be maintained by continued use of the drug. Lithium succinate is used to treat seborrheic dermatitis, a skin disorder. Other uses currently being explored include treating immunological disorders and cancers.[107,108] Schrauzer has proposed that lithium may be an essential trace element and has suggested a daily intake of 1.00 mg day^{-1}.[109]

Dr. J. F. J. Cade, an Australian psychiatrist, first reported on the beneficial use of a lithium compound for a psychiatric disorder, namely, manic behavior in 1949.[110] The early human trials were undertaken after initial experiments on rats, which became quite lethargic after treatment with lithium urate.[110,111] Fairly large doses were required for treating manic behavior and its use for this disorder has been displaced by organic drugs that carry less risk. His report, however, led to its current use as a treatment for bipolar affective disorder (also known as manic-depressive disorder).[112,113] Its use in the United States was curtailed for a decade and a half by the US. Food and Drug Administration (FDA), which based its decision on incidental poisonings due to overuse of a lithium-based table salt substitute, despite a safe record of controlled psychiatric applications in Europe.[114] It has been estimated that by 1985 lithium treatments had saved the world at least 17.5 billion in medical expenses and by reduction of lost productivity.[115]

6.2 The Element and Ion

Lithium (Z = 3) is the smallest of the alkali metals in group I (*see* ***Periodic Table: Trends in the Properties of the Elements***). It occurs naturally in brines and pegmatites and is found in river water at concentrations of $\sim 2\,\mu M$.[116] Plants accumulate it and transfer it to humans and animals at low concentrations.[109] Elemental lithium is a soft, pale silvery substance that can be cut with a butter knife and is easily deformed. Naturally occurring lithium consists of two isotopes, ^6Li and ^7Li, which are 7.42 and 92.58% abundant. The three additional isotopes that have been prepared synthetically, ^5Li, ^8Li, and ^9Li have half-lives of $\sim 10^{-21}$ sec, 0.86 sec, and 0.18 sec, respectively, which are too short to allow effective use as radiotracers in biological experiments. The ^6Li and ^7Li nuclei are both quadrupolar, $\mu_{^6Li} = 1$ and $\mu_{^7Li} = 3/2$, respectively. The ^7Li isotope has proved extremely useful for NMR experiments both in vitro and in vivo. Lithium forms a single stable ion, Li^+, by loss of a single electron from the outer 2s subshell. The very negative standard reduction potential indicates that oxidation to Li^+ is favorable:

$$Li^+ + e^- = Li^0 \qquad E_o{}^2 = -3.045 \text{ volts.} \tag{8}$$

As a consequence, it is reactive toward air and forms lithium hydroxide by reaction with oxygen and moisture in the air, necessitating storage under oil or an inert environment. Its chemistry is that of the 1+ ion, since the inner core electrons are not easily removed. The very small ionic radius, 0.60 Å, causes Li^+ to be strongly hydrated in aqueous solution. Thus, the effective ionic radius increases to 3.40 Å in solution; the 5.6-fold increase from free ion to aqueous ion is far greater than for any other alkali metal ion. The large charge-to-radius ratio makes it atypical of the heavier alkali metal ions and more like magnesium in some of its chemical properties. For example, both tend to form polar-covalent organometallic species, RLi and RMgX, whereas the heavier group I and II elements form less stable and more reactive ionic species.

6.3 Psychiatric Uses

Manic depression currently affects up to 2 percent of the world's population. Clinical studies demonstrate proven effectiveness of lithium treatment for bipolar affective disorder.[113,117,118] Lithium is taken orally and has been used successfully by some patients for periods exceeding a decade. The action is prophylactic, meaning that it is able to prevent the occurrence of the manic and depressive mood swing phases of the disease once the patient has been taking it for a period of time. It functions very well in typical cases of bipolar disorder and is more efficacious than the anticonvulsant carbamazepine (5H-dibenz[b,f]azepine)-carboxamide.[113,117,118] It is effective in cases with mood-incongruent psychotic features or with rapid cycling,[117] but may not be as effective as carbamazepine for cases with atypical manifestations.[118] A recent metaanalysis of previous studies confirms the efficacy of lithium therapy for relapse prevention and suggests that it prevents manic episodes more effectively than depressive episodes. On the other hand, there is a clearly documented reduction of suicides among patients receiving lithium treatments,[117,118] and Schou, who had an important role in the development and acceptance of lithium therapy, recommends it, on the basis of an extensive literature review, for patients at high risk of committing suicide.[117]

A double-blind, placebo-controlled trial of the use of lithium to augment antidepressant medication for treating unipolar major depression has shown it to be beneficial for patients receiving continuation therapy following acute therapy for a major depressive episode.[119,120] The 14 patients in the lithium-treated group suffered no relapses over 4 months, while seven of the 15 patients in the placebo-treated group experienced relapses including one suicide.[119]

A number of competing hypotheses have been proposed to explain the action of lithium against affective bipolar disorder. As with other metallodrugs that are widely distributed in the body, it is difficult to identify the causative biological activities when many systems and pathways are incidentally inhibited or stimulated. It is not clear that a single mechanism explains both the antimanic and the antidepressant activities that are observed clinically.[107,108,117] Three principal hypotheses for the mechanism of action are presently being investigated. Lithium inhibits the normal phosphoinositide signaling system, leading to depletion of inositol in the hypothalmus, and also inhibits adenylate cyclase, which in turn lowers cyclic-AMP levels. Both effects have been suggested to contribute to the clinical benefits.[107,108] It has been pointed out, however, that the brain levels of inositol in humans are higher than those in laboratory animal models, and that, therefore, the role of phosphoinositide signaling system may not be central to the action of lithium in affective bipolar disorder. Inhibition of Mg^{2+}-dependent G-protein activation has also been proposed as a mechanism of action, which would also affect cell signal transduction pathways in the brain.[121] The third proposed mechanism is based on a specific membrane disorder in bipolar disorders.[122] Interestingly, there is evidence for a genetic predisposition for responses to lithium therapy.[123]

6.4 Pharmacology

Following oral administration, lithium is widely distributed in the body with the largest accumulations in bones (>1 mmol kg^{-1} wet weight) and teeth (Figure 17) based on a metaanalysis of nine independent studies.[107] The kidney, thyroid, and adrenal glands accumulate between 0.3 and 0.4 mmol kg^{-1} wet weight, while the brain concentrations are somewhat below 0.2 mmol kg^{-1} wt weight.[107] Oral dosing of patients with lithium carbonate (250 mg in previously untreated subjects) leads to plasma levels of ca. 0.2 mmol L^{-1} after 1 to 4 hours, followed by a decay over the next 72 hours (Figure 18). Excretion is through the kidneys, and the decay is multiphasic, but has an approximate half-life of $t_{1/2} = 24$ hours. Dosage varies up to 2.0 g (~30 mmol) of lithium carbonate per day, and is typically in the range of 800 mg (~11 mmol) of Li_2CO_3, which is formulated with a binder such as guar gum or

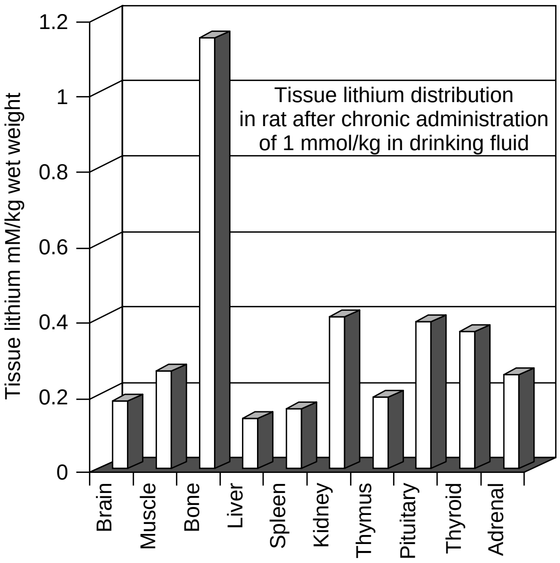

Figure 17 Distribution of lithium among organs of the rat after chronic ingestion 1 mmol kg^{-1} of lithium carbonate in the drinking water, normalized databased on a metaanalysis of 9 studies, as reported in Ref. 107. (Reprinted with permission from © 1999 American Chemical Society)

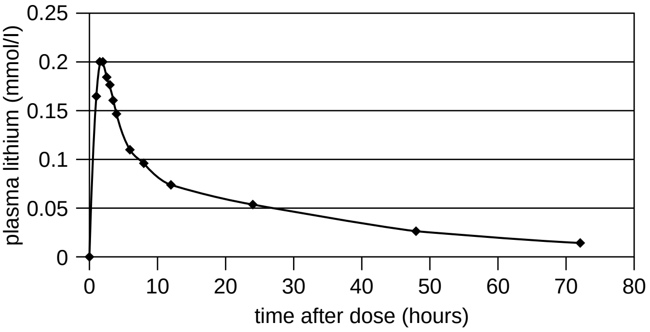

Figure 18 Plasma levels of lithium following a single dose of oral lithium carbonate (250 mg Li) in previously untreated subjects. (Reprinted with permission from Ref. 107 © 1999 American Chemical Society)

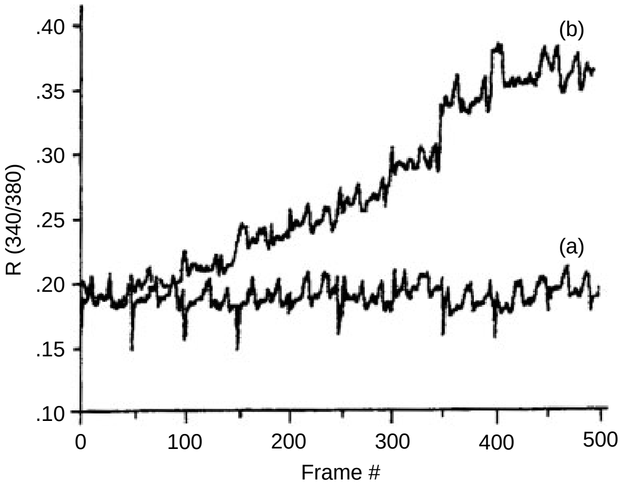

Figure 19 Time-dependent fluorescent monitoring of free Mg^{2+} in neuroblastomas cells demonstrates the Li^{+}/Mg^{2+} competition that releases bound Mg^{2+} (curve B) Li-perfused cells, compared to untreated cells (curve A). Each frame represents 0.33 seconds. (Ref. 124. Reproduced by permission of Biophysical Society)

methyl cellulose.[107] The target serum levels are in the range 0.4–0.8 $\text{mmol}\,l^{-1}$, which is achieved cumulatively after multiple, daily doses.

The ability of Li^{+} to compete with Na^{+} in cell membranes and with Mg^{2+} in a variety of sites has been well documented in biochemical and cellular systems. Fluorescence spectroscopy, using, for example, the dye furaptra, ^{7}Li NMR, and to a lesser extent ^{31}P NMR methods have all been applied to examining the competition.[124] Figure 19 shows fluorescent monitoring of the displacement of Mg^{2+} from cellular binding sites in the neuroblastomas cell line SH-Sy5Y after exposure to Li^{+}, leading to an increase in free Mg^{2+}. Similar results were obtained by ^{31}P NMR spectroscopic monitoring of the ATP α and β phosphate chemical shifts, which increase upon Li^{+}/Mg^{2+} exchange.[124] Table 8 compares the affinity of Li^{+} and Na^{+} for cell membrane sites in (unsealed) RBC ghost cells and cytoskeleton-depleted cells (csd-RBCs), studied by ^{23}Na and ^{7}Li NMR methods.

The cytoskeleton causes a reversal of the expected affinity of the monovalent cations for membrane binding sites, leading to the order $Na^{+} > Li^{+}$, whereas its depletion causes the binding preference to revert to the electrostatically expected order, $Li^{+} > Na^{+}$.[124]

Table 8 Li^{+} and Na^{+} binding constants for red blood cell membranes[124]

Constant	Unsealed RBC Membranes	csd-RBC Membranes
K_{Li}	$209\,M^{-1}$	$321\,M^{-1}$
K_{Na}	$292\,M^{-1}$	$262\,M^{-1}$

6.5 Topical Applications

Lithium succinate (Efalith)[125–127] and lithium gluconate[128] are effective topical treatments for seborrheic dermatitis, which affects the face and other oil-secreting areas of the body. The causative agent has been identified as the yeast, *Pityrosporum ovale*.[126,129] Two British multicenter double-blind, randomized studies and another in Belgium, which compared lithium succinate (8%) ointment to the vehicle, have demonstrated that the succinate successfully treats the majority of the patients.[129,130] The benefits are observed within days after onset of treatment and last significantly beyond the cessation of treatment. It has been found specifically useful for AIDS patients,[130] among whom a high incidence of infection is observed.[129,130] The action of the lithium succinate is apparently directed against the lipid metabolism of the yeast,[126] but not its growth,[127] and may exert an anti-inflammatory response in the patients.[130]

6.6 Potential New Uses

Lithium compounds are under investigation for a number of additional medical uses. Salzman has reviewed 21 additional potential uses of lithium in psychiatry that have been reported in the literature.[120] Lithium has been shown to inhibit herpes, pox and adenoviruses in vitro and lithium succinate ointment is useful in treating herpes simplex infections.[131] Interestingly, patients with dipolar disorder who are treated with oral lithium carbonate exhibit a reduction in the frequency of labial herpes recurrence.[132] Lithium reduces brain damage in animal models of certain neurodegenerative diseases and has been shown to inhibit expression of apoptotic proteins, p53 and Bax, which leads to the possibility that it may be useful in treating neurodegenerative diseases.[133]

7 OTHER METALLODRUGS – IN USE OR IN DEVELOPMENT

7.1 Introduction

This section briefly reviews a number of additional classes of metallodrugs that are of interest at the intersection of biological inorganic chemistry and modern medicine. Antimony and arsenic have important, life-saving antiparasitic activities, while bismuth is a key antiulcer treatment and useful for other gastrointestinal disorders. The success of cisplatin and its analogues has stimulated intensive searches for complexes of other metal ions with antitumor activity.[134–136] Although many promising candidates with suitable cytotoxicity and bioavailability have been identified, toxicity concerns, patent issues and other factors have kept most from reaching even Phase I clinical testing. The examples listed in Table 9 are discussed briefly in this section,

Table 9 Non-platinum metals under investigation as antitumor agents

Metal	Z	Examples	Refs.
Ruthenium	44	*trans*-$[Cl_4(Ind)_2Ru^{III}]^-$, *trans*-$[Cl_4Im_2Ru^{III}]^-$, *trans*-$[Cl_4(Me_2SO)ImRu^{III}]^-$	134,135
Gallium	31	$Ga(NO_3)_3$, [(8-quinolinolato)$_3$ Ga^{III}]	134,138,139
Gold	79	$[Au^I(Ph_2PCH_2CH_2PPh_2)_2]^+$, [(damp)$Au^{III}Cl_2$]	53,54
Titanium	22	*cis*-$[(CH_3CH_2O)_2(bzac)_2Ti^{IV}]$, $[(\eta^5\text{-}C_5H_5)_2Ti^{IV}Cl_2]$	134,140,141
Tin	50	$(n\text{-}Bu)_3Sn\text{-}S\text{-}CH_2\text{-}CH_2\text{-}NH_3^+$	134,142
Vanadium	23	$V^{IV}OSO_4$, NaV^VO_4, $[V^{IV}O(maltolato)_2]$	134
Arsenic	33	As_2O_3	143–146

except for gold antitumor agents, discussed in Section 2.6. Recent overviews of the metallodrugs under development as antitumor agents can be consulted for further detail.[134–137]

7.2 Ruthenium Antitumor and Nitrogen Oxide Scavenging Agents

Ruthenium complexes have shown considerable promise as antitumor agents, and some may act via mechanisms other than DNA binding.[134,135] Octahedral Ru^{III}polyam(m)ine (Am) complexes, $[Ru^{III}(Am)_nX_{6-n}]^{+/0/-}$ (Figure 20) exhibit favorable cytotoxicity in cell culture and are correspondingly active in animal models against a variety of tumor lines. Correlations between their DNA binding ability and biological activity have been observed. Trichloro and tetrachloro complexes exhibit the best activity. *mer*-$[Ru^{III}L^3Cl_3]$ complexes, where L^3 represents planar tridentate ligands such as terpyridine have activities comparable to cisplatin. Tetrachloro complexes such as *trans*-$[Ru^{III}Cl_4(Im)_2]^-$ (Im = imidazole) are typically more active against a wide variety of tumors, especially with ImH^+ as the counterion. The compound *trans*-$[Cl_4(Ind)_2Ru^{III}]^-$ (Ind = indazole; KP1019, Figure 20(c)) has entered clinical trials.[147]

The trinuclear ruthenium red complex, $[(H_3N)_5Ru^{III}ORu^{IV}(NH_3)_4ORu^{III}(NH_3)_5]^{6+}$ accumulates in the mucopolysaccharide coat of tumor cells and inhibits their growth.[134] Active, octahedral Ru^{III} and Ru^{II} complexes of EDTA-like ligands (polyaminopolycarboxylates) damage and alter the conformation of DNA molecules, which inhibits DNA recognition. Pyrimidines bind via η^2 coordination of the C_5-C_6 double bond or by forming η^1 links to N_1 and N_3 positions. *cis*-$[Ru^{III}Cl_2(pdta)]$ stimulates the respiratory burst of neutrophil cells and the NADPH oxidase-dependent release of superoxide, which is potentially a second mechanism of cytotoxicity.

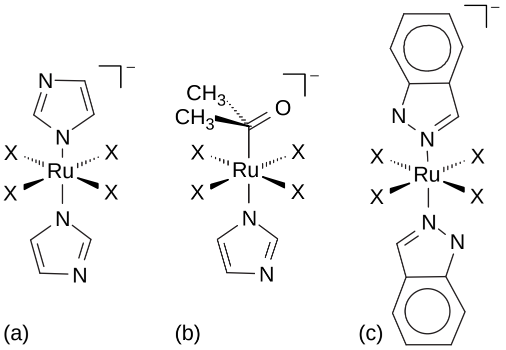

Figure 20 Structures of (a) *trans*-$[Ru(Im)_2X_4]^-$; (b) *trans*-[Ru(DMSO)(Im)$X_4]^-$ (Im = imidazole), the anionic constituent of NAMI and NAMI-A; (c) *trans*-$[Ru(Ind)_2X_4]^-$ (Ind = indazole) the anionic constituent of KP1019

NAMI and NAMI-A, the respective imidizolium and sodium salts of *trans*-$[Cl_4(Me_2SO)(Im)Ru^{III}]^-$ (Figure 20(b)) show promise against metastatic tumors, which are generally refractory to treatment. They appear to act extracellulary rather than by DNA binding. The activity of metalloproteinases is lowered at the transcriptional level by down-regulating the levels of mRNA for the matrix metalloproteinase MMP-2 relative to that for TMP-2, an inhibitor for MMP-2. This, in turn, slows metastasis of tumors and may find use in postsurgical or postradiation therapies.[134,135]

Ruthenium complexes have also been explored as potential NO scavengers.[148,149] NO is generated in vivo by the constitutive nitric oxide synthetase enzyme (c-NOS) as a messenger in the course of normal physiological signaling processes (especially in vasodilation), but is also generated by an inducible nitric oxide synthase (i-NOS) in macrophage cells, which overproduces it in certain disease states (diabetes, arthritis, inflammation, epilepsy, which are chronic diseases, and septic shock, which is acute and sometimes fatal) (*see* ***Nitrogen Monoxide (Nitric Oxide): Bioinorganic Chemistry***). K[Ru^{III}(Hedta)Cl], JM1226, acts as a scavenger and has potential use in treating such disease states. It undergoes hydrolysis to the corresponding aquo species, $[Ru^{III}(Hedta)(OH_2)]$, which reacts by ligand exchange to form the nitrosyl complex, $[Ru^{II}(edta)(OH_2)NO]^+$, formally a ruthenium(II) species bound to the NO^+ ion.[148,149]

7.3 Gallium Antitumor and Hypercalcemia Treatments

Gallium (Z = 31) in group 3(A) of the periodic table (*see* ***Periodic Table: Trends in the Properties of the Elements***) is an effective antitumor agent for lymphomas and bladder carcinoma.[134,138,139,147] It is most often administered as a slow infusion of gallium nitrate, $Ga(NO_3)_3$. Although the fully aquated ion $[Ga(OH_2)_6]^{3+}$ is quite acidic and precipitates as amorphous hydroxides, it reacts with transferrin in vivo in the blood serum almost completely, partially displacing iron, at the therapeutic concentrations of 10–15 μM.[134,138] The ability to mimic iron is important in the delivery of gallium to tumor cells by transferrin and also in the likely mechanism of action, as Ga^{3+} binds to and inhibits the iron-enzyme ribonucleotide reductase (*see* ***Iron Proteins with Dinuclear Active Sites***), which converts ribonucleotides to deoxyribonucleotides, thus depriving tumor cells of DNA precursor molecules needed for replication. Complexes of gallium have been explored as alternate means of administration and delivery to tumor cells. Complexation by the iron-siderophore, deferoxamine, inhibits cell growth and induces apoptosis. Chelating ligands such as citrate, 8-hydroxyquinoline and 3-hydroxy-4-pyrones increase bioavailability, in part by reducing the extent of hydrolysis. tris-(8-Quinolinolato)gallium(III) (KP46) has entered clinical trials.

Gallium nitrate is used clinically, at lower doses than for treating tumors, to treat hypercalcemia associated with bone cancers.[134,139] It incorporates into bone at very low levels and prevents calcium resorption, leading also to higher phosphate and collagen levels, and hence sturdier bone structure.[134,139]

7.4 Titanium Antitumor Agents

Titanium ($Z = 22$) is the lightest element of the group 4 (4B) triad of the periodic table (*see* ***Periodic Table: Trends in the Properties of the Elements***). Ti(IV) is the most stable oxidation state, but Ti(III) and Ti(II) complexes are also commonly encountered. The antitumor activity of titanium(IV) compounds has been investigated extensively,[134,140,141] Titanocene dichloride $[(\eta^5\text{-}C_5H_5)_2Ti^{IV}Cl_2]$ and budotitane (Figure 21) are among the few non-platinum metal compounds to enter clinical trials. They show activity against a variety of tumor types and are most effective against gastrointestinal tumors.[134,140,141] The titanocenes are the most active of a series of $[(\eta^5\text{-}C_5H_5)_2MX_2]$ complexes ($M = $ Ti, V, Nb, Mo; $X = $ halide) to exhibit significant activity. They are prodrugs that undergo rapid hydrolysis and subsequent acid dissociation,[134] not unlike cisplatin. The most acidic diaquo complex is diaquotitanocene, $pK_{a1} = 3.51$ and $pK_{a2} = 4.35$, which generates the neutral dihyroxo species, $[(\eta^5\text{-}C_5H_5)_2Ti(OH)_2]$, at physiological pH. Transferrin may play a role in delivering Ti^{IV} to tumor cells.[138] Titanocene dichloride blocks collagenase IV activity (a Zn-dependent matrix metalloproteinase enzyme) and may act by preventing angiogenesis.

Budotitane, $[(EtO)_2(bzac)_2Ti^{IV}]$, exists in solution as three equilibrating structural isomers resulting from differing orientations of the benzylacetonate ligands relative to the mutually cis ethoxy groups. The isomers are in thermal equilibrium: *cis-cis-cis*, Figure 21(b), 60%; *cis-trans-cis*, 21%; and *cis-cis-trans*, 19%. Only recently has one of the isomers, *cis-cis-trans*-budotitane with the acetate oxygens mutually trans, been isolated and crystallized.[150] The availability of a single pure isomer may facilitate further clinical studies.

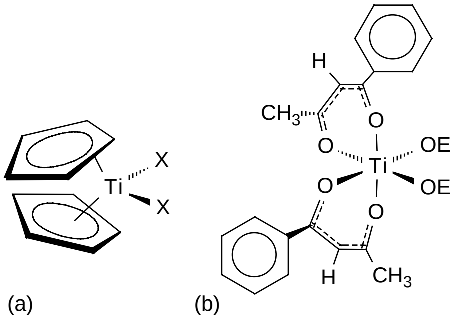

Figure 21 Structures of (a) titanocene dihydroxide, the dominant hydrolysis product of titanocene dichloride; (b) *cis-cis-cis*-budotitane (*cis-cis-cis*-$[(EtO)_2(bzac)_2Ti^{IV}]$), the dominant solution isomer in an equilibrium with the *cis-trans-cis*- and *cis-cis-trans*-isomers

7.5 Tin Antitumor Agents

Many classes of organotin(IV) compounds (*see* ***Tin: Organometallic Chemistry***) have been tested for antitumor activity.[134,151] Organotin compounds have a wide range of biological activities and have had widespread use as biocides in paints, although their use as marine-antifouling agents has been curtailed.[142] The general order of toxicities is $R_3SnX > R_2SnX_2 > RSnX_3$. The nature of the R group affects their solubility and biological activity. The *n*-butyl group and to a lesser extent the phenyl and benzyl groups show the greatest promise in balancing solubility and lipophilicity. Serious neurotoxic effects, especially for shorter-chain trialkyltin complexes, and immunosuppressive effects are the most serious side effects. A wide variety of mono-, di-, and polydentate inorganic ligands have been tested. A series of tri- and di-*n*-butyltin cysteaminates and *N,N*-dimethylcysteaminates have been examined and found to have much lower ID_{50} values than cisplatin, etoposide, or 5-fluorouracil when tested against a panel of seven human tumor lines.[152]

7.6 Arsenicals Past and Present

Arsenic is in group 15 (VA) of the periodic table, lying between phosphorus and antimony (*see* ***Periodic Table: Trends in the Properties of the Elements***). Arsenic has two principle oxidation states, As(III) and As(V). It is a highly toxic element that is carcinogenic and also a classical poison (*see* ***Metal Ion Toxicity***). In some regions of the world, most notably Bangladesh, arsenic in the drinking water is a serious public health concern.[153] Solid forms of arsenic present in geological formations can be mobilized by prokaryotes that utilize oxyanions of arsenic for energy generation under

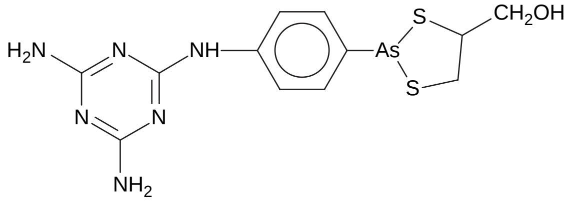

Figure 22 Melarsoprol contains a phenylarsine moiety coordinated by dimercaptopropanol (BAL) linked to a para-melamine functional group

anaerobic conditions and release the arsenic to the aqueous phase.**[154]**

Paul Ehrlich developed arsenicals in parallel efforts to cure syphilis and trypanosomiasis (African sleeping sickness), which is transmitted by mosquitoes. A considerable number of organoarsenicals, especially substituted phenyl derivatives were prepared and tested against these infectious diseases. Loevenhart and Stratman-Thomas's 1928 review of Ehrlich's work provides a fascinating view of medicinal chemistry in its early stages.**[155]** While syphilis is no longer treated with arsenicals, melarsoprol (Figure 22) finds continuing use in the treatment of the second stage of trypanosomiasis, when the trypanosomes reside in the cerebrospinal fluid, where they are no longer accessible to other treatments (pentamidine and suramin) that are effective in the earlier stage of infection.**[156]** The structure of melarsoprol is based on a phenylarsine moiety, in which the arsenic is coordinated by dimercaptopropanol (BAL) and a melamine functional group is para-substituted on the phenyl ring.

Arsenic trioxide (As_2O_3, ATO) had historical applications against leukemia, but was then set aside for a period of time. In the 1990s, it was shown to be effective against acute promyelocytic leukemia (APL),**[143]** and has been approved by the FDA (Trisenox™)**[144]** Its success in this therapy has led to testing against related tumors, notably myelodysplastic syndrome (MDS)**[143]** and multiple myeloma (MM),**[145]** which remains uncurable. Phase II clinical trials have demonstrated the effectiveness of As_2O_3.**[145]** Its actions include up-regulation of lymphokine-activated-killer (LAK) cells and degradation of the PML-RARalpha chimeric gene that blocks differentiation of the host-organism granulocytes, a class of immune cells.**[146]** At the molecular level, As_2O_3 reacts with thiols to inhibit a variety of enzymes related to the cancer growth. High concentrations act on mitochondria in a thiol-dependent manner to induce cell apoptosis.

7.7 Antimony Antiparasitic Agents

Antimony (Z = 51) lies between arsenic and bismuth in group 15 (*see* ***Periodic Table: Trends in the Properties of the Elements***). It has been used medicinally since the age of the alchemists. Like other members of its group it readily forms compounds of the +3 and +5 states. Although relatively little attention has been paid to this element by the inorganic biochemistry community, several compounds have important medicinal properties. Tartar emetic ($K_2[Sb_2(d\text{-}C_4O_6H_2)_2]\cdot 3H_2O$) has been used for over 300 years in the treatment of schistomiasis and leishmaniasis. The compound consists of two Sb(III) ions linked by two tartaric acid molecules. Sodium stibogluconate, which contains two Sb(V) ions linked to two gluconic acid molecules, remains an important treatment for leishmaniasis. As with other antibiotics, the evolution of resistant parasite strains is reducing the effectiveness of antimonicals in the tropical nations where its use is most important. Research on the mechanisms of induction of resistance and the structures of the proteins involved in resistance gives hope that cotreatment with an antimony compound and an inhibitor of either the induction mechanism or the resistance conferring proteins will allow effective treatments to continue.

7.8 Bismuth Antiulcer Complexes

Bismuth has a well-accepted role in the treatment of ulcers and other forms of gastric distress including diarrhea, dyspepsia, and general gastric distress. Indeed, bismuth might be rated the foremost of all metallodrugs based on (i) sheer mass of bismuth compounds consumed for medicinal purposes, over 700 tons per annum in just the United Kingdom and United States and (ii) the unusual validation by present-day scientific knowledge and medical practices of a treatment first reported in the 15th century. In complementary reviews, Sun and Sadler describe the inorganic basis of bismuth medicinal agents and their mechanisms of action as presently understood,**[157]** while Briand and Burford have impressively catalogued the literature on bismuth compounds and their formulations and uses, organized in a series of extensive tables that facilitate retrieval of over 1000 references.**[158]**

Bismuth (Z = 83) is the heaviest stable element in group 15 (VA) of the periodic table (*see* ***Periodic Table: Trends in the Properties of the Elements***). The ^{201}Bi isotope, which is 100% abundant, has a 9/2 nuclear spin. ^{212}Bi, an alpha emitter is used in nuclear medicine as a radiotherapeutic agent.**[159,160]** Bismuth has two stable oxidation states: Bi(V), corresponding to complete loss of the valence electrons, and Bi(III), a lower oxidation state that retains two valence electrons. Both oxidation states are diamagnetic. The latter is more stable and more common since Bi(V) has a large reduction potential:

$$\mathrm{Bi(V)} + 2e^- = \mathrm{Bi(III)} \qquad E^0{}_{1/2} = 2.03\ \mathrm{V} \tag{9}$$

Bismuth occurs in nature as Bi_2O_3 and as bismuth sulfide ores. This reflects the fact that Bi(III) is an intermediate acid in the Pearson's classification of hard and soft acids-bases (*see* ***Hard & Soft Acids and Bases***). Interestingly, over-the-counter drug formulations involve primarily oxygen-donor ligands such as salicylate, citrate, and nitrate, while in vivo reactions include formation of bismuth metallothionein complexes, for which Bi–S ligation is extremely important. Bi(III) has a rich coordination chemistry with complexes ranging from three to ten-coordinate. Three-coordinate structures such as Me_3B and $Bi(SAr)_3$ are trigonal pyramidal owing to the presence of a stereochemically active lone pair, as found for the lighter group V elements such as nitrogen and phosphorus. The nonaaquo complex, $[Bi(OH_2)_9]^{3+}$ found in the trifluoromethylsulfonate salt is a tricapped trigonal prism,[161] but in aqueous solution a variety of oxo- and hydroxy-bridged species such as $[Bi_6O_6]^{6+}$, $[Bi_6O_4(OH)_4]^{6+}$, $[Bi_6O_6(OH)_3]^{3+}$ and $[Bi_6(OH)_{12}]^{6+}$ are present at various pH conditions. The triethylenetetraminehexaacetate complex contains a 10-coordinate Bi(III) ion.[162]

In the medicinal agents used to treat ulcers, Bi(III) is complexed to oxygen-donor ligands (Table 10). Bismuth-subsalicylate (BSS) is marketed as Pepto-Bismol™, CBS as De-Nol™ and RBC as Tritec™ and Pylorid™. Ranitidine is an organic H_2 antagonist that works synergistically with bismuth in RBC. Although the bacterium *Helicobacter pylori* had been known for over a century, it was discovered to be the causative agent for ulcers only in 1983. It uses two metalloenzymes, urease, which has two nickel ions at the active site (*see* ***Nickel Enzymes & Cofactors***), and a manganese-dependent catalase (*see* ***Manganese Proteins with Mono- & Dinuclear Sites***). The urease catalyzes cleavage of urea into ammonia and CO_2 thereby neutralizing its immediate environment in the normally acidic stomach mucosa, while the Mn-catalase catalyzes the disproportionation of H_2O_2 to oxygen and water to protect the bacterium against neutrophil cells activated by the immune system. The composition and structures of the bismuth antiulcer formulations are sensitive to pH and concentration effects and many variants can be identified by NMR and electrochemical studies of the solutions and by crystallization and X-ray structure determination.[157,158]

Newer agents under investigation include tris(tropolonato) Bi(III) and nitratobis(tropolonato)Bi(III); a host of bis (mercaptoethanol)Bi(III) complexes, which are formed with O,S-bidentate chelation, with and without deprotonation of the hydroxyl oxygen and usually having an axial fifth ligand; and sialic acid derivatives of Bi(III).[157] The interactions of Bi(III) and its compounds with metallothionein, serum albumin and transferrin have been studied by a variety of groups, as have a number of enzymes that may be related to the mechanism(s) of action of bismuth in treating ulcers.

In the 1930s and 1940s, bismuth formulations were used extensively to treat syphilis,[158] but they have since been supplanted by more effective antibiotics. More recently, bismuth complexes have been examined for antitumor activity,[163,164] Tiekink compared the literature results for antimony(III), antimony(V), and bismuth(III) with the conclusion that Bi(III) was most promising among these possibilities.[164]

8 CONCLUDING REMARKS

As a scientific discipline, metals in medicine (or inorganic medicinal chemistry) is healthy and active. Potential new metal-based drugs directed at a wide variety of pathological conditions are reported every year. Specialists in the field have developed an increasingly sophisticated understanding of how metal ion activity and toxicity can be targeted and modulated (or tuned) by altering the oxidation states and ligation of the metal ion. A variety of proteins (e.g. serum albumin, metallothionein, transferrin) that can alter the chemical state and bioavailability of metal ions and their complexes have been identified and characterized. Similarly, small molecule redox-active species and ligands are known and their reactions well characterized. The roles of oxidation-reduction reactions, ligand exchange reactions and aggregation in metallodrug metabolism have been identified. Useful screening models have been developed for many target diseases, but remain lacking for other, sometimes equally important diseases. Despite these advances, only a disappointingly small number of compounds have proceeded through clinical trials to approval by national drug agencies. This reflects in part concerns of large drug firms about toxicity and liability issues and conservatism on the part of regulatory agencies. Patent issues are also a concern since the greatest activity in the field remains in academic laboratories. One hopeful sign is the formation and evolution of small entrepreneurial companies that are targeting metallodrug discovery and development. With almost a hundred elements beyond carbon, nitrogen, oxygen, and phosphorus, the periodic table, in combination with many thousands of unique ligands, remains a relatively unexplored source of new compounds that may exceed the potential of the world's rainforests.

Table 10 Bismuth-based antihelicobacter pylori formulations[157]

Compound	Formula	Aqueous solubility	MIC_{50}/nM
Bismuth subnitrate	$Bi(O)NO_3$	Insoluble	0.45
Bismuth subgallate	$Bi(OH)C_7H_4O$	Insoluble	0.04
Bismuth subsalicylate	$Bi(O)C_7H_5O_3$	very low	0.09
CBS[a]	$K_3(NH_4)_2[Bi_6O_3(OH)_5(C_6H_5O_7)_4]$	soluble	0.04
RBC[a]	$[ranitidine]^+$ Bi(citrate)	soluble	0.011

[a] CBS = colloidal bismuth subcitrate; RBC = ranitidine bismuth citrate; approximate formulas.

9 FURTHER READING

P. E. Glennas, J. S. Hunziker, J. H. R. Garvey, H. E. R. Kägi, *Biochem. Pharmacol.*, 1986, **35**, 2033.

C. Srinivasan, M. Minadeo, J. Toon, D. Graham, D. Mota de Freitas, and C. F. G. C. Geraldes, *J. Mag. Res.*, 1999, **140**, 206.

10 REFERENCES

1. C. Orvig and M. J. Abrams, *Chem. Rev.*, 1999, **99**(9), 2201.
2. M. J. Clarke and P. J. Sadler eds, 'Metallopharmaceuticals I & II', Springer Verlag, Berlin, 1999.
3. N. P. Farrell ed., 'Uses of Inorganic Chemistry in Medicine', Royal Society of Chemistry, Cambridge, 1999.
4. K. H. Thompson and C. Orvig, *Science*, 2003, **300**, 936.
5. American Pharmaceutical Association, 'The National Formulary of Unofficial Preparations', 3rd edn., American Pharmaceutical Association, Baltimore, 1906.
6. B. Rosenberg, L. VanCamp, and T. Krigas, *Nature*, 1965, **205**, 698.
7. G. J. Higby, *Gold Bull.*, 1982, **15**, 130.
8. H. Zhao and Y. Ning, *Gold Bull.*, 2001, **33**, 24.
9. C. Voegtlin, in 'Chemistry in Medicine', ed. J. Stieglitz, The Chemical Foundation, New York, 1929, p. 712.
10. W. D. Block and K. Van Goor, 'Metabolism, Pharmacology and Therapeutic Uses of Gold Compounds', Charles C. Thomas Publishers, Springfield, IL, 1956.
11. B. M. Sutton, in 'Bioinorganic Chemistry of Gold Coordination Compounds', eds. B. M. Sutton and R. G. Franz, Smith Kline & French Laboratories, Philadelphia, PA, 1983, p. 6.
12. P. Pyykko, *Chem. Rev.*, 1988, **88**, 563.
13. H. Schmidbaur ed., 'Gold: Chemistry, Biochemistry and Technology', Wiley & Sons, New York, 1999.
14. R. J. Pudephatt, 'The Chemistry of Gold', Elsevier Publishing Company, Amsterdam, 1978.
15. C. F. Shaw III, *Chem. Rev.*, 1999, **99**, 2589.
16. R. Bau, *J. Am. Chem. Soc.*, 1998, **120**, 9380.
17. M. R. Wiseman, P. A. Marsh, P. T. Bishop, B. H. Brisdon, and M. F. Malon, *J. Am. Chem. Soc.*, 2000, **122**, 12598.
18. P. Lipsky, in 'Arthritis: Etiology, Diagnosis and Management', eds. P. D. Utsinger, N. J. Zvaifler, and G. E. Ehrlich, Lippincott, Philadelphia, PA, 1989, Chap. 35, p. 601.
19. D. A. Gordon, in 'Textbook of Rheumatology', eds. W. W. Kelly, E. D. Harris, D. Ruddy, and C. B. Sledge, W.B. Saunders, New York, 1989, Chap. 48, p. 804.
20. D. T. Felson, J. J. Anderson, and R. F. Meenan, *Arthritis Rheum.*, 1990, **33**, 1449.
21. R. C. Elder and K Tepperman, *Science*, 1984, **225**, 430.
22. A. P. Intoccia, T. L. Flanagan, D. T. Walz, L. Gutzait, J. E. Swagzdis, J. Flagiello Jr, B. Y. H. Hwang, R. Dewey, H. Noguchi, 'Bioinorganic Chemistry of Gold Coordination Compounds', eds. B. M. Sutton and R. G. Franz, Smith Kline & French Laboratories, Philadelphia, PA, 1983, p. 21.
23. D. C. Carter and J. X. Ho, *Adv. Protein Chem.*, 1994, **45**, 153.
24. H. H. Hull, R. Chang, and L. Kaplan, *Biochim. Biophys. Acta*, 1975, **400**, 132.
25. J. Christodoulou, P. J. Sadler, and A. J. Tucker, *Eur. J. Biochem.*, 1994, **225**, 363.
26. J. Zou, P. Taylor, J. Dornan, S. P. Robinson, M. D. Walkinshaw, and P. J. Sadler, *Angew. Chem., Int. Ed. Engl.*, 2000, **39**, 2931.
27. R. M. Snyder, C. Mirabelli, and S. J. Crooke, *Biochem. Pharmacol.*, 1986, **35**, 923.
28. A. T. Razi, G. Otiko, and P. J. Sadler, *Am. Chem. Soc., Symp. Ser.*, 1983, **209**, 371.
29. G. G. Graham and A. J. Kettle, *Biochem. Pharmacol.*, 1998, **56**, 307.
30. G. G. Graham and M. W. Whitehouse, *Inflamm. Res.*, 1996, **45**, 579.
31. D. Schumann, M. Kubicka-Muranyi, J. Mircheva, J. Günther, P. Kind, and E. Gleichmann, *J. Immunol.*, 1990, **145**, 2132.
32. K. Takahashi, P. Griem, C. Goebel, J. Gonzalez, and E. Gleichmann, *Met.-Based Drugs*, 1994, **1**, 483.
33. W. E. Smith and J. Reglinski, *Perspect. Bioinorg. Chem.*, 1991, **1**, 183.
34. G. G. Graham, T. M. Haavisto, P. J. McNaught, C. D. Browne, and G. D. Champion, *J. Rheumatol.*, 1982, **9**, 527.
35. D. W. James, N. W. Ludvigsen, L. G. Cleland, and S. C. Milazzo, *J. Rheumatol.*, 1982, **9**, 532.
36. US Department of Health, Education, and Welfare, Smoking and Health: Report of the Advisory Committee to the Surgeon General of the Public Health Service, U.S. Public Health Service Publication 1103, Washington DC, p. 1103.
37. G. G. Graham, T. M. Haavisto, H. M. Jones, and G. D. Champion, *Biochem. Pharmacol.*, 1984, **33**, 1257.
38. R. C. Elder, Z. Zhao, Y. Zhang, J. G. Dorsey, E. V. Hess, and K. Tepperman, *J. Rheumatol.*, 1993, **20**, 268.
39. J. Verwilghen, G. H. Kingsley, L. Gambling, and G. S. Panayi, *Arthr. Rheum.*, 1992, **35**, 1413.
40. C. F. Shaw III, S. Schraa, E. Gleichmann, Y. P. Grover, L. Dunemann, and A. Jagarlamudi, *Met.-Based Drugs*, 1994, **1**, 351.
41. A. Canumalla, N. Al-Zamil, M. Phillips, A. A. Isab, and C. F. Shaw III, *J. Inorg. Biochem.*, 2001, **85**, 67.
42. C. F. Shaw III, A. A. Isab, M. T. Coffer, and C. K. Mirabelli, *Biochem. Pharmacol.*, 1990, **40**, 1227.
43. K. Ugai, M. Ziff, and P. E. Lipsky, *Arthritis Rheum.*, 1979, **22**, 1352.

44. B. P. Mania, T. R. Butt, C. K. Mirabelli, D. J. Eckerd, E. Steinberg, and S. T. Crooke, *Mol. Pharmacol.*, 1987, **13**, 21.
45. M. A. Nedelman, R. C. Elder, and K. Tepperman, *Proc. Soc. Exp. Biol. Med.*, 1989, **191**, 179.
46. W. E. Smith, J. Reglinski, S. Homey, D. H. Brown, and R. Struck, *Inorg. Chem.*, 1990, **29**, 5190.
47. C. F. Shaw III, *Inorg. Perspect. Biol. Med.*, 1979, **2**, 287.
48. M. Navarro, H. Pérez, and R. A. Sánchez-Delgado, *J. Med. Chem.*, 1997, **40**, 1937.
49. H. M. Alger and D. L. Williams, *Mol. Biochem. Parasitol.*, 2002, **121**, 129.
50. K. Becker, S. Gromer, R. H. Schirmer, and S. Muller, *Eur. J. Biochem.*, 2000, **267**, 6118.
51. C. F. Shaw III, ‘Metal Compounds in Cancer Therapy’, ed. S. P. Fricker, Chapman & Hall, 1994, p. 46.
52. E. R. Tiekink, *Crit. Rev. Oncol. Hematol.*, 2002, **42**, 225.
53. S. J. Berners-Price, P. S. Jarrett, and P. J. Sadler, *Inorg. Chem.*, 1987, **26**, 3074.
54. S. P. Fricker, *Met.-Based Drugs*, 1999, **6**, 291.
55. G. Perrelli and G. Piolatto, *Sci. Total Environ.*, 1992, **120**, 93.
56. E. H. Blakeney ed., ‘The History of Herodotus’, Translated by G. Rawlinson, Dent, London, 1945.
57. J. Raulin, *Sci. Nat.*, 1869, **11**, 93.
58. J. L. Clement and P. S. Jarrett, *Mater. Med.*, 1994, **1**, 467.
59. R. B. Beard, M. DeLaurent, K. Pourrezaei, and S. Adrian, *Mater. Med.*, 1994, **1**, 445.
60. S. M. Modak, L. Sampath, and C. L. Fox Jr, ‘Proceedings of the First International Conference on Gold and Silver in Medicine’, eds. C. R. Merril, C. F. Shaw, J. A. Spadaro, S. F. Etris, The Gold and Silver Institutes, Washington, DC, 1987, p. 205.
61. C. L. Fox Jr, *Arch. Surg.*, 1968, **96**, 1840.
62. C. L. Fox Jr, B. W. Rappole, and W. Stanford, *Surg. Gynecol. Obstet.*, 1969, **128**, 1021.
63. C. F. Shaw III NMR and ESR Spectroscopy Applied to Gold and Silver Compounds in ‘The Chemistry of Organic Derivatives of Gold and Silver’, John Wiley & Sons, 1999, p. 67.
64. D. S. Cook and M. F. Turner, *J. Chem. Soc.*, 1975, 1021.
65. N. C. Baenziger and A. W. Struss, *Inorg. Chem.*, 1976, **15**, 1807.
66. S. M. Modak and C. L. Fox, *Biochem. Pharmacol.*, 1973, **22**, 2391.
67. S. M. Modak, L. Sampath, and C. L. Fox Jr, *J. Burn Care Rehabil.*, 1988, **9**, 359.
68. S. Modak, J. Stanford, J. Friedlaender, P. Fox, and C. L. Fox Jr, *Burns Incl. Therm. Inj.*, 1984, **10**, 170.
69. A. D. Russell and W. B. Hugo, *Prog. Med. Chem.*, 1994, **31**, 351.
70. S. Silver, *FEMS Microbiol. Rev.*, 2003, **27**, 341.
71. A. Gupta, K. Matsui, J. F. Lo, and S. Silver, *Nat. Med.*, 1999, **5**, 183.
72. S. Silver, A. Gupta, K. Matsui, and F. J. Lo, *Mater. Med.*, 1999, **6**, 315.
73. R. K. Johnson, A. J. Giovenella, L. F. Faucette, C. K. Mirabelli, and P. J. Sadler, *J. Inorg. Biochem.*, 1988, **33**, 2285.
74. B. Ulküseven, A. Tavman, and G. Otük, *Met.-Based Drugs*, 1999, **6**, 163.
75. A. Mastrolorenzo and C. T. Supuran, *Met.-Based Drugs*, 2000, **7**, 49.
76. B. Rosenberg, L. VanCamp, E. B. Grimley, and A. J. Thompson, *J. Biol. Chem.*, 1965, **242**, 1347.
77. E. Wong and C. M. Giandomenico, *Chem. Rev.*, 1999, **99**, 2451.
78. Z. Guo and P. J. Sadler, *Adv. Inorg. Chem.*, 2000, **49**, 183.
79. S. P. Fricker ed., ‘Metal Compounds in Cancer Therapy’, Chapman & Hall, London, 1994.
80. J. T. Hartmann and H. P. Lipp, *Expert Opin. Pharmacother.*, 2001, **4**, 889.
81. B. Desoize and C. Madoulet, *Crit. Rev. Oncol. Hematol.*, 2002, **42**, 317.
82. M. J. McKeague, *Expert Opin. Investig. Drugs*, 2001, **10**, 119.
83. J. H. Schiller, *Oncology*, 2002, **63**, 105.
84. E. Q. Cosaert, *Brit. J. Cancer*, 2002, **87**, 825.
85. A. Nersesyan, E. Perrone, P. Roggieri, and C. Bolognesi, *Chemotherapy*, 2003, **49**, 132.
86. N. P. Farrell and S. Spinelli, Dinuclear and Trinuclear Anticancer Agents, in ‘Uses of Inorganic Chemistry in Medicine’, ed. N. P. Farrell, Royal Society of Chemistry, Cambridge, 1999, p. 124.
87. L. R. Kellend, Platinum Anticancer Drugs, in ‘Metal Compounds in Cancer Therapy’, ed. S. P. Fricker, Chapman & Hall, London, 1994 p. 32.
88. L. R. Kellend, Cisplatin-based Anticancer Agents, in ‘Uses of Inorganic Chemistry in Medicine’, ed. N. P. Farrell, Royal Society of Chemistry, Cambridge, 1999, p. 109.
89. A. Pattanaik, G. Bachowski, J. Laib, D. Lemkuil, C. F. Shaw III, D. H. Petering, A. Hitchcock, and L. Saryan, *J. Biol. Chem.*, 1992, **267**, 16121.
90. E. R. Jamieson and S. J. Lippard, *Chem. Rev.*, 1999, **99**, 2467.
91. D. C. Lemkuil, D. Nettesheim, C. F. Shaw III, and D. H. Petering, *J. Biol. Chem.*, 1994, **269**, 24792.
92. J. Reedijk, *Chem. Rev.*, 1999, **99**, 1499.
93. K. J. Barnham, M. I. Djuran, Pd. S. Murdoch, J. D. Ranford, and P. J. Sadler, *J. Chem. Soc., Dalton Trans.*, 1995, 3721.
94. K. H. Thompson, J. H. McNeill, and C. Orvig, *Chem. Rev.*, 1999, **99**, 2561.
95. H. Sakurai, *Chem. Rev.*, 2002, **2**, 237.
96. K. H. Thompson, J. H. McNeill, and C. Orvig, in ‘Metallopharmaceuticals II’, ed. P. J. Sadler, Springer Verlag, 1999, p. 141.

97. C. Orvig, K. H. Thompson, M. C. Cam, and J. H. McNeill, in 'Uses of Inorganic Chemistry in Medicine', ed. N. Farrell, Royal Society of Chemistry, Cambridge, 1999, p. 91.
98. R. Eady, *Chem. Rev.*, 1996, **96**, 3013.
99. D. C. Crans, J. J. Smee, E. Gaidamausksa, and L. Yang, *Chem. Rev.*, 2004, **104**, 849.
100. J. M. Arber, E. deBoer, C. D. Garner, S. S. Hasnain, and R. Wever, *Biochemistry*, 1989, **28**, 7968.
101. R. A. Tschirret-Guth and A. Butler, *J. Am. Chem. Soc.*, 1994, **116**, 411.
102. M. Henze, *Hoppe-Seyler's Z. Physiol. Chem.*, 1911, **72**, 494.
103. F. H. Nielsen, in 'Metal Ions in Biological Systems', eds. H. Siegel and A. Sigel, Marcel Decker, New York, 1995, Vol. 31, p. 543.
104. R. H. J. Bell and R. J. Hye, *Surg. Res.*, 1983, **35**, 433.
105. K. H. Thompson and C. Orvig, *J. Chem. Soc., Dalton Trans.*, 2000, 2885.
106. M. Melcher, S. J. Retting, B. D. Liberian, K. H. Thompson, V. G. Yuen, J. H. McNeill, and C. Orvig, *Inorg. Chem.*, 2001, **40**, 4686.
107. N. J. Birch, *Chem. Rev.*, 1999, **99**, 2659.
108. N. J. Birch, in 'Uses of Inorganic Chemistry in Medicine', ed. N. P. Farrell, The Royal Society of Chemistry, Cambridge, 1999, p. 11.
109. G. N. Schrauzer, *J. Am. Coll. Nutr.*, 2002, **21**, 14.
110. J. F. J. Cade, *Med. J. Aust.*, 1949, **36**, 349.
111. G. Walter, *Psychiatr. Serv.*, 1999, **50**, 969.
112. M. Schou, *Pharmacol. Rev.*, 1957, **9**, 17.
113. A. Coppen, *Bipolar Disord.*, 1999, **1**, 3.
114. F. N. Johnson, 'The History of Lithium Therapy', Macmillan, London, 1984.
115. W. D. Rubinstein and H. L. Rubinstein, 'Menders of the Mind: A History of the Royal Australian and New Zealand College of Psychiatrists, 1946–1996', Oxford University Press, 1996.
116. L. S. Kszos and A. J. Stewart, *Ecotoxicology*, 2003, **12**, 439.
117. M. Maj, *Bipolar Disord.*, 2003, **5**, 180.
118. M. Schou, *Bipolar Disord.*, 1999, **1**, 5.
119. M. Bauer, T. Bschor, D. Kunz, A. Berghöfer, A. Ströhle, and B. Müller-Oerlinghausen, *Am. J. Psychiatry*, 2000, **157**, 1429.
120. C. Salzman, *Harv. Rev. Psychiatry*, 2003, **11**, 230.
121. S. Avissar, G. Schreiber, A. Danon, and R. H. Belmaker, *Nature*, 1998, **331**, 440.
122. H. L. Metzler, *Biol. Psychiatry*, 1991, **30**, 1071.
123. M. Alda, *J. Psychiatry Neurosci.*, 1999, **24**, 154.
124. L. Amari, B. Layden, J. Nickolakopoulos, Q. Rong, D. Mota de Freitas, G. Baltazar, M. M. C. A. Castro, and C. F. G. C. Geraldes, *Biophys. J.*, 1999, **76**, 2934.
125. D. F. Horrobin, in 'Lithium and the Cell: Pharmacology and Biochemistry', ed. N. J. Birch, Academic Press, London, 1991, p. 273.
126. D. J. Gould, P. S. Mortimer, C. Proby, M. G. Davis, P. J. W. Kersey, R. Lindskov, A. Oxholm, A. M. M. Strong, E. Hamill, K. Kenicer, C. Greene, J. J. Cream, R. J. Clayton, J. D. Wilkinson, A. Davis, B. R. Allen, R. Marks, L. Lever, M. Y. Moss, P. F. Morse, S .I. Wright, D. F. Horrobin, and J. C. M. Stewart, *Am. Acad. Dermatol*, 1992, **26**, 452.
127. C. Cuelenaere, J. De Bersaques, and A. Kint, *Dermatology*, 1992, **183**, 194.
128. B. Dreno and D. Moyse, *Eur. J. Dermatol*, 2002, **12**, 549.
129. A. K. Gupta and R. Bluhm, *J. Eur Acad. Dermatol Venereol*, 2004, **18**, 13.
130. J. A. Langtry, C. M. Rowland-Payne, R. C. Staughton, J. C. Stewart, and D. F. Horrobin, *Clin. Exp. Dermatol*, 1997, **22**, 216.
131. G. R. B. Skinner, C. Hartley, A. Buchan, L. Harper, and P. Gallimore, *Med. Microbiol. Immunol.*, 1980, **168**.
132. J. K. Rybakowski, *Pharmacopsychiatry*, 2003, **33**, 159.
133. D. M. Chuang, R. W. Chem, E. Chalecka-Frauaszek, M. Reu, R. Hashimoto, V. Senatorov, H. Kauai, C. Hough, T. Hiroi, and P. Leeds, *Bipolar Disorders.*, 2002, **4**, 129.
134. M. P. Clarke, F. Zhu, and D. R. Frasca, *Chem. Rev.*, 1999, **99**, 2511.
135. S. P. Fricker ed., 'Metal Compounds in Cancer Therapy', Chapman & Hall, 1994.
136. C. X. Zhang and S. J. Lippard, *Curr. Opin. Chem. Biol.*, 2003, **7**, 481.
137. M. P. Clarke, F. Zhu, and D. R. Fasca, *Chem. Rev.*, 1999, **99**, 2511.
138. H. Sun, H. Li, and P. J. Sadler, *Chem. Rev.*, 1999, **99**, 2817; 1994, 65.
139. C. R. Chitamber, *Semin. Oncol.*, 2003, **30**(2 Suppl. 5), 1.
140. F. Caruso and M. Rossi, *Met. Ions Biol. Syst.*, 2004, **42**, 353.
141. F. Caruso and M. Rossi, *Mini. Rev. Med. Chem.*, 2004, **4**, 49.
142. I. Omae, *Chem. Rev.*, 2003, **103**, 3431.
143. A. List, M. Beran, J. DiPersio, J. Slack, N. Vey, C. S. Rosenfeld, and P. Greenberg, *Leukemia*, 2003, **17**, 1499.
144. J. Mayorga, C. Richardson-Hardin, and K. A. Dicke, *Clin. J. Oncol. Nurs.*, 2002, **6**, 341.
145. M. A. Hussein, *Cancer Control*, 2003, **10**, 370.
146. J. Fang, S. J. Chen, J. H. Tong, Z. G. Wang, G. Q. Chem, and Z. Chen, *Cancer Biol. Ther.*, 2002, **1**, 614.
147. M. A. Jakupec and B. K. Keppler, *Met. Ions Biol. Syst.*, 2004, **42**, 425.
148. S. P. Fricker, *Platinum Met. Rev.*, 1995, **39**, 150.
149. S. P. Fricker, *Met. Ions Biol. Syst.*, 2004, **41**, 421.
150. E. Dubler, R. Buschman, and H. W. Schmalle, *J. Inorg. Biochem.*, 2003, **95**, 97.
151. M. Gielen, M. Biesemans, D. de Vos, and R. Willem, *J. Inorg. Biochem.*, 2000, **79**, 1.
152. M. Gielen, K. Handir, M. Hollein, and D. de Vos, *Met.-Based Drugs*, 2000, **7**, 233.

153. J. C. Ng, J. Wang, and A. Shraim, *Chemosphere*, 2003, **52**, 1353.
154. R. S. Oremland and J. F. Stolz, *Science*, 2003, **300**, 939.
155. A. S. Loevenhart and W. K. Stratman-Thomas, in ‘Chemistry in Medicine’, ed. J. Steiglitz, The Chemical Foundation, 1928, p. 665.
156. A. J. Nok, *Parisitol. Res.*, 2003, **90**, 71.
157. H. Sun and P. J. Sadler, in ‘Metallopharmaceuticals II: Diagnosis and Therapy’, eds. P. J. Sadler and M. J. Clarke, Springer Verlag, 2001, p. 159.
158. G. G. Briand and N. Burford, *Chem. Revs.*, 1999, **99**, 2601.
159. S. Hassfjell and M. W. Brechbiel, *Chem. Rev.*, 2001, **101**, 2019.
160. M. W. Brechbiel, *Exp. Biol. Med.*, 2001, **226**, 627.
161. W. Frank, G. J. Reis, and J. Schneider, *Angew. Chem.*, 1995, **34**, 2416.
162. H. Wullens, M. Devillers, B. Tinant, and J. P. Declercq, *J. Chem. Soc., Dalton Trans.*, 1996, 2023.
163. P. Köpf-Meir, *Eur. J. Clin. Pharmacol.*, 1994, **47**, 1.
164. E. R. Tiekink, *Crit. Rev. Oncol. Hematol.*, 2002, **42**, 217.

Metal-based Imaging Agents

Lynn C. Francesconi, Melchor V. Cantorias & Robertha C. Howell

Hunter College and the Graduate School of the City University of New York, New York, NY, USA

Based in part on the article Metal-based Drugs & Imaging Agents by R. C. Elder & Katherine Tepperman which appeared in the Encyclopedia of Inorganic Chemistry, First Edition.

1	Introduction	1
2	Technetium	1
3	Other Metal Diagnostic Agents	13
4	Concluding Remarks	17
5	Related Articles	17
6	References	17

1 INTRODUCTION

Radiopharmaceuticals are drugs that contain a radionuclide and are routinely used for diagnosis and treatment of disease. This entry discusses imaging agents that are useful for diagnosis (*see* ***Metal-based Drugs***), focusing on the growing class of metal-based imaging agents, wherein the radionuclide is a transition metal or posttransition metal. The most widely used radionuclide for radiopharmaceuticals is technetium-99m, ^{99m}Tc.[1–3] The radionuclides ^{67}Ga, ^{111}In, ^{210}Tl, ^{57}Co, and ^{51}Cr are used in the clinic as well.[4] There are a number of radioisotopes, including ^{64}Cu, ^{67}Cu, ^{68}Ga, that show promise for diagnostic purposes.[5]

1.1 Requirements for a Diagnostic Imaging Agent

The physical properties of the radionuclide are paramount for its use in diagnostic imaging (Table 1). First, the radionuclide should emit penetrating radiation, either gamma or positron emission, that is detected outside the body. γ-ray emission is the basis of Single Photon Emission Computed Tomography (SPECT), used for imaging radiopharmaceuticals based on ^{99m}Tc, ^{111}In, ^{67}Ga, or $^{123/131}$I. The energies of the emitted gamma photon should be in the range of 100–250 keV, the window of current gamma cameras. Radiopharmaceuticals for Positron Emission Tomography (PET) emit a positron (β^+) that results in the production of two 511 keV annihilation photons that are emitted at an angle of 180° (with respect to each other). PET scanners contain a circular array of detectors with coincidence circuits designed to specifically detect the 511 keV photons emitted in opposite directions. The most widely used PET radiopharmaceutical is ^{18}F fluorodeoxyglucose (FDG) for imaging glucose metabolism. Radiometal positron emitters for diagnostic imaging under investigation include ^{62}Cu, ^{64}Cu, and ^{68}Ga.

Other requirements for an effective radiopharmaceutical include a half-life that is long enough to synthesize, purify the radiopharmaceutical, inject the drug into the patient, allow it to localize and image the desired area with PET or SPECT instrumentation. The half-life should be commensurate with the procedure. For example, small molecule heart and brain perfusion-based agents require shorter half-lives because they reach the target quickly. Radionuclides with longer half-lives are generally required for imaging with monoclonal antibodies because they take longer to reach the target. Also, the radionuclide should decay to a relatively stable daughter without any accompanying α- or β-particle emission. Finally, the cost and availability of the radionuclide are important parameters as well. The development of parent–daughter generator systems, in which a longer-lived parent decays to a shorter-lived daughter that is eluted from a chromatographic column, has increased the availability of some radionuclides. The development of the ^{99}Mo/^{99m}Tc generator was instrumental in the widespread availability of the radionuclide ^{99m}Tc that is a mainstay in nuclear medicine procedures. Another generator system approved by the US Food and Drug Administration (FDA) for clinical use is the ^{82}Sr/^{82}Rb system, which is a direct-infusion generator allowing the use of ^{82}Rb that has a 76 sec half-life for myocardial imaging. Other generator systems with potential utility, discussed herein, are the ^{68}Ge/^{68}Ga and the ^{62}Zn/^{62}Cu systems.[1,5,6]

1.2 Diagnostic Radioisotope Production Methods

The two methods for production of radioisotopes that are used in imaging involve either an accelerator or cyclotron or application of a generator system. Production of radionuclides has been reviewed comprehensively.[5,6] Accelerator or cyclotron-produced radiometals are more expensive, since the cyclotron or accelerator can produce one isotope at a time. Targetry and separations (usually ion extraction or ion exchange) methods have to be worked out as well. The development of parent–daughter generator systems has increased the availability of some radionuclides. Parent–daughter generators are systems in which a longer-lived parent decays to a shorter-lived daughter that is eluted from a chromatographic column. A classic example of such as system is the ^{99}Mo/^{99m}Tc generator.

2 TECHNETIUM

2.1 Physical Properties

Technetium, as ^{99m}Tc, is the most widely used radionuclide in the nuclear medicine clinic and is used in over 85%

Table 1 Common γ- and positron-emitting radionuclides

Radionuclide	Half-life	Production methods	Maximum particle emission^a	γ-emission (keV)
^{99m}Tc	6.2 h	^{99}Mo/^{99m}Tc generator	IT	141
^{67}Ga	3.26 days	Cyclotron	EC (100%)	91,93,185,296,388
^{68}Ga	67.63 min	^{68}Ge/^{68}Ga generator	1.899 MeV β^+ (90%)	1077 (3.3%)
			EC decay (10%)	511 (176%)
^{66}Ga	9.5 h	Cyclotron	4.153 MeV β^+ (57%)	2752 (23.5%)
			EC decay (43%)	1039 (38.4%)
				834 (6.1%)
				511 (117.3%)
^{62}Cu	9.74 min	^{62}Zn/^{62}Cu generator	2.96 MeV β^+ (97.8%)	511
			EC decay (2.2%)	
^{64}Cu	12.7 h	Cyclotron	0.63 MeV β^+ (19%)	511
			EC decay (41%)	
^{67}Cu	2.58 days	Accelerator	0.577 MeV β^-	184.6 (46.7%)
				93.3 (16.6%)
				91.3 (7.3%)
^{111}In	2.83 days	Cyclotron	EC decay	245 (94%)
				171 (91%)

^{a}IT = Isomeric transition; EC = Electron capture.

of nuclear medicine scans. The physical characteristics (γ ray = 142 keV, half-life = 6.02 h) of ^{99m}Tc are ideal for nuclear medicine scans to study organs lying deep in the body using current SPECT technology. The short half-life allows more activity to be injected with minimal radiation burden to the patient. ^{99m}Tc decays to ^{99}Tc, a very weak β^- emitter, that provides no interference or degradation of image quality. ^{99m}Tc is conveniently obtained from the $^{99}\text{Mo} \rightarrow {}^{99m}\text{Tc}$ generator using saline as an eluent (Scheme 1). The parent, ^{99}Mo (66 h half-life), as $^{99}\text{MoO}_4{}^{2-}$ adsorbed on an alumina column, continuously decays to the daughter, ^{99m}Tc (6 h half-life). The separation of ^{99m}Tc from ^{99}Mo is accomplished by selective elution of $^{99m}\text{TcO}_4{}^-$ with saline owing to the charge difference. The generator can be prepared at a production site and shipped to remote locations and will dispense eluate of suitably high activity for nuclear medicine scans for one week.

Sodium pertechnetate, $\text{Na}^{99m}\text{TcO}_4{}^-$ from the generator is the starting material for all radiopharmaceuticals based on ^{99m}Tc. The generator eluate, $^{99m}\text{TcO}_4{}^-$, is introduced into a ‘radiopharmaceutical instant kit’ containing the ligand, a reductant, usually stannous ion, and buffers. Incubation at room temperature or elevated temperature for a prescribed period of time, leads to the formation of the technetium imaging agents. The reaction to form the reduced ^{99m}Tc radiopharmaceutical must be quick and of high radiochemical purity.

2.2 Chemistry of Technetium

Technetium is a transition metal that lies in the middle of the transition series and possesses a diverse chemistry. Complexes are known where the range of Tc oxidation states is −1 to +7, having various coordination geometries (4–9) with a variety of ligands filling the coordination requirements. For production of radiopharmaceuticals, $\text{Na}^{99m}\text{TcO}_4$ must be reduced from the +7 oxidation state to a lower oxidation state for complexation with chelating ligands. Reduction of $\text{TcO}_4{}^-$ is most commonly accomplished by stannous chloride. The

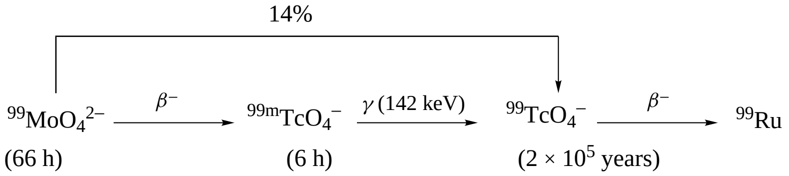

Decay Scheme of $^{99}\text{MoO}_4{}^{2-}$ to $^{99m}\text{TcO}_4{}^-$: the chemistry of the ^{99m}Tc generator

Scheme 1

coordinating ligand has a profound effect on the oxidation state and the Tc core that is formed vide infra.

The concentration of Tc (both ^{99m}Tc and ^{99}Tc) eluted as pertechnetate from the generator is generally in the range of 10^{-7} to 10^{-10} M. These 'no-carrier-added' concentrations preclude characterization of its complexes using routine analytical techniques available to inorganic chemists. The long-lived ^{99}Tc isotope (β^-: 243 keV; $t_{1/2}$: 2×10^6 years) is available in macroscopic quantities and has enabled the use of standard methods of chemical characterization to determine the structure and chemistry and physiochemical properties of these Tc radiopharmaceuticals. Rhenium, the third row transition metal congener of Tc, has also been used for characterization. However, the kinetic inertness of Re compared to Tc, as well as the higher reduction potential, can result in significant differences in the chemistry and, using Re as a nonradioactive surrogate for Tc, should be practiced with caution. Most of the ^{99m}Tc based radiopharmaceuticals on the market since the 1980s have been characterized by performing the ^{99}Tc chemistry, characterization using routine analytical tools and relating back to the tracer radiopharmaceutical by high performance liquid chromatography (HPLC) concordance experiments.

2.3 Technetium Cores

The chelating ligands that are present upon reduction of TcO_4^- with stannous ion determine the coordination complex that forms. Complexes of a variety of oxidation states, structures, and ligand composition can form. Certain stable motifs, often called 'technetium cores' (Figure 1), form the basis of small coordination compounds and molecules that can be linked to biomolecules.

2.3.1 *Tc=O^{3+} Core*

The Tc=O^{3+} core is ubiquitous in radiopharmaceutical chemistry. This core forms upon reduction of pertechnetate in the presence of a diaminodithiol or N_3S tetradentate ligand and other ligands, including amine-oxime ligand systems. Generally, one or more amine or amide nitrogens deprotonate upon complexation forming strong bonds to the Tc^V. These complexes are square pyramidal with the Tc=O in the apical position. The strong bonds (thiolate S, amide N) to the Tc(V) render these complexes very stable and tetradentate N_2S_2 or N_3S ligands form a significant cohort of the ligands studied as bifunctional chelates (BFC). Diastereomers, wherein a substituent is syn or anti to the Tc=O group, commonly form when a chiral carbon is incorporated in the ligand.

2.3.2 *O=Tc=O$^+$ Core*

The O=Tc=O$^+$ core forms when pertechnetate is reduced in the presence of amines such as linear or macrocyclic tetraamines, such as cyclam and also phosphines. In this case, the donor atoms do not bond as strongly to the Tc^V.

2.3.3 *Tc(Co)$_3^+$ Core*

In the mid- to late 1990s, Alberto prepared water-soluble, air-stable $Tc(CO)_3(H_2O)_3^+$ species, both on the tracer, ^{99m}Tc, and on the macroscopic, ^{99}Tc, levels.**[7–10]** These species undergo ligand exchange in water to form stable octahedral complexes that possess the $Tc(CO)_3^+$ core. $^{99m}Tc(OH_2)(CO)_3^+$ is available in a kit formulation from Mallinckrodt, St. Louis, MO, where potassium boranocarbonate $K(H_3BCO_3H)$ is employed as the in situ

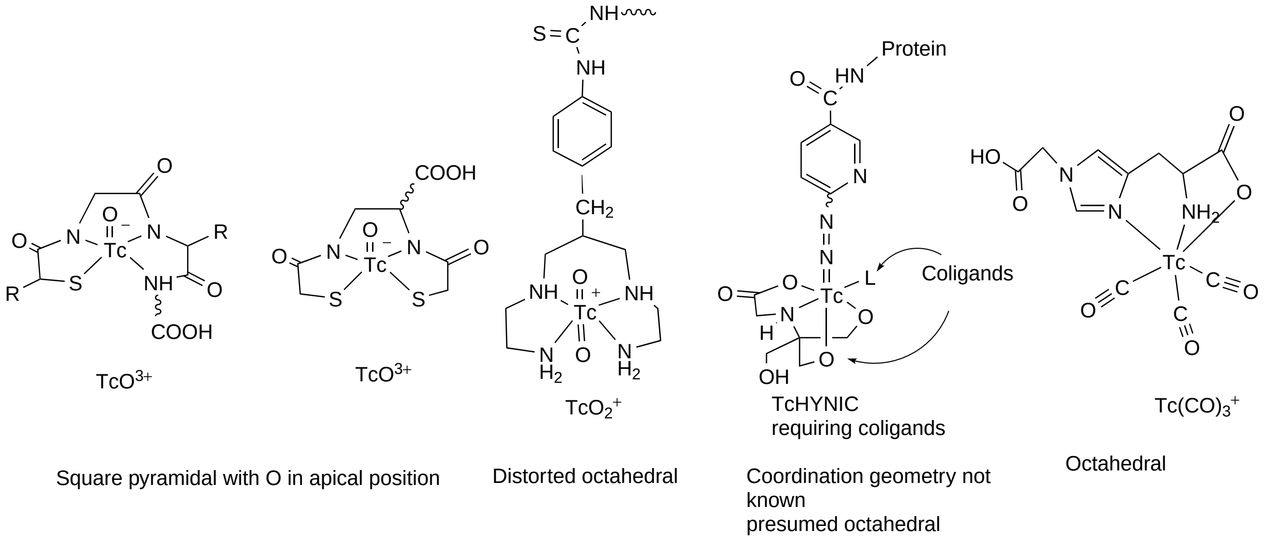

Figure 1 Technetium cores

CO source and $NH_3{\cdot}BH_3$ serves as a reductant.[9] On the macroscopic scale, $MX_3(CO)_3{}^{2-}$ (M=^{99}Tc, Re), which forms the *fac*-$M(CO)_3{}^+$ unit in water, can be prepared via a low pressure synthesis.

The water molecules are substitutionally labile and the 'soft' $M(I)(CO)_3{}^+$ species reacts with ligands containing both hard and soft ligands, for example, thioethers, histidine, and carboxylates, to form kinetically stable octahedral complexes. In fact, histidine in a peptide is such a strong binding ligand that it often competes with the intended bifunctional ligand.

Ligands containing three donor atoms, including heterocyclic amines and carboxylate groups, provide the most stable ^{99m}Tc tricarbonyl complexes, and such tridentate ligands have been incorporated into peptides and receptor-specific molecules for successful radiolabeling with the $^{99m}Tc(CO)_3{}^+$ moiety.[11,12] Single amino acids that can be incorporated directly into peptide syntheses have been derivatized with N-heterocyclic tridentate ligands for complexation of $^{99m}Tc(CO)_3$.[13,14] A potential problem with the $^{99m}Tc(CO)_3{}^+$ core is the high affinity for histidine, often requiring 'prelabeling' procedures that are not amenable to radiopharmaceutical kit formulation.

2.3.4 Tc HYNIC Core

The N-hydroxysuccinimidyl hydrazinonicotinate (S-HYNIC) moiety forms a very stable ^{99m}Tc complex and provides excellent images.[15,16] HYNIC has been successfully coupled to peptides and antibodies for imaging thrombosis and sites of infection.[17,18] HYNIC also has been used for attachment to Annexin for in vivo imaging of apoptosis at the molecular level.[19,20]

The hydrazinopyridine moiety can bind to Tc using one or two coordination sites requiring the use of coligands, such as tricene, ethylenediaminediacetic acid (EDDA) and glucoheptonate. The advantage of using HYNIC as a bifunctional chelating agents(BFCA) is its high labeling efficiency and the choice of coligands allows easy modification of the hydrophilicity and pharmacokinetics of ^{99m}Tc-labeled small peptides. However, the difficulty that arises from multiple products and the lack of clarity as to the oxidation state of the Tc may impede the development of HYNIC-peptides into radiopharmaceutical kits.[17,21]

2.4 Technetium Radiopharmaceuticals

The development of the 'instant radiopharmaceutical kit' in the 1970s was followed by the development of technetium imaging agents for renal, skeletal, and hepatobiliary imaging. At that time, the coordination chemistry of technetium was not well understood and as a result, the early radiopharmaceuticals are not fully characterized. Studies of the coordination chemistry of technetium intensified in the late 1970s leading to the discovery of Tc brain, heart, and renal agents. These agents are considered 'Tc essential,' because the size, charge, and lipophilicity of the Tc complex (properties that result from the combination of Tc and the coordinating ligand) dictate the biological localization of the radiometal complex. Most of the early radiopharmaceuticals, and, indeed, the radiopharmaceuticals in clinical usage, are considered Tc essential.

Another category of Tc agents that have been under investigation from the mid-1980s to present are 'technetium tagged' radiopharmaceuticals. In this broad class, the Tc, bound to a ligand, is connected to a biologically active molecule via a linker (Scheme 2). Targeted technetium molecules distribute in the body according to a targeting vector, generally, an antibody targeted towards an antigen on a tumor site, or a peptide or hormone or small molecule targeted towards a receptor. The targeting vector is connected via a 'linker' to an organic ligand that forms a coordination complex with the metal ion, often called a metal chelate. The organic ligand and the linker are often called a bifunctional chelate.

2.4.1 Tc-essential Radiopharmaceuticals

The early technetium imaging agents have been reviewed in earlier versions of this Encyclopedia and in other references.[2,3] This section is intended to be an overview highlighting developments in technetium chemistry.

Brain Agents. ^{99m}Tc radiopharmaceuticals that penetrate the blood–brain barrier (BBB) are generally small, neutral, and lipophilic. Moreover, to be useful for imaging, the molecules must possess some mechanism of retention. Clinical brain imaging studies with ^{99m}Tc, aimed at detection of regional cerebral blood flow changes, are performed with D, L-^{99m}Tc-HMPAO, Ceretec™, or L, L-^{99m}Tc-ECD, Neurolite™ (Figure 2). Both are small, neutral molecules that cross the BBB and are retained in the brain.

^{99m}Tc ethyl-cysteine-dimer (ECD) is based on a tetradentate N_2S_2 chelate. ECD has two chiral centers and can be synthesized as the L, L-ECD or D, D-ECD isomers. Both form similar chiral, symmetric square-pyramidal Tc(V) oxo complexes that are neutral and lipophilic. However, the in

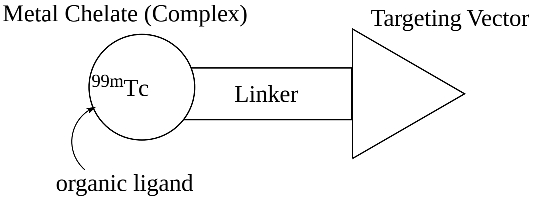

Generalized Scheme for targeted ^{99m}Tc and other radiometal diagnostic agents.

Scheme 2

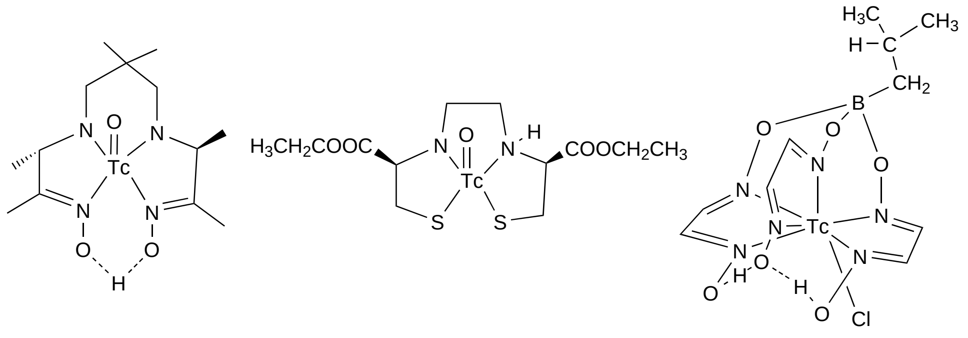

^{99m}TcO(d,l- HMPAO) Ceretec^{TM}

^{99m}TcO (L,L,-ECD) Neurolite^{TM}

^{99m}Tc DMG-2MP

Figure 2 Brain imaging agents

vivo behavior is quite different; while both penetrate the intact blood–brain barrier, the L,L-isomer is stereoselectively hydrolyzed to the acid, forming a charged species that is trapped in the brain.**[22]** Other brain perfusion agents that have been studied in humans include the Tc-boronic acid adducts of dioximes (Tc-BATO), particularly the 2-methylpropyl derivative.

Heart Agents. Routine myocardial perfusion imaging in nuclear medicine started with ^{201}Tl thallous chloride. While ^{201}Tl^{+} is efficiently perfused into the myocardium, the long half-life and imaging characteristics are not optimal for nuclear medicine imaging and cationic ^{99m}Tc-based perfusion agents were desired.

The hexakis *tert*-butylisonitrile Tc(I) complex, Tc(TBI)$_6{}^{+}$, was the first complex to image human myocardial tissue; however, its high lipophilicity resulted in high lung and liver uptake. Optimization of the organometallic Tc(I) hexakis isonitrile family of compounds led to the development of hexakis(2-methoxyisobutylisonitrile)Tc(I), Tc(I)(MIBI)$_6{}^{+}$ (Cardiolite™ or sestamibi), an FDA-approved agent for clinical myocardial perfusion imaging (Figure 3).

Other lipophilic cations that have been approved as myocardial perfusion agents include a Tc(III) ^{99m}Tc-teboroxime cryptate, (Cardiotec™), the trans-dioxo technetium(V) bisphosphine complex, ^{99m}Tc-tetrofosmin (Myoview™) and the mixed ligand Tc(III) Schiff-base bisphosphine Tc-Q12 complex, ^{99m}Tc-furifosmin (TechneScan) (Figure 3).

Renal Agents. ^{99m}Tc MAG3 (TechneScan™; Figure 4) is used to assess renal function.**[23,24]** After intravenous injection, this tracer passes through the kidneys and is rapidly excreted primarily by active tubular secretion. ^{99m}TcMAG3 has no chiral centers and thus does not form diastereomers. On coordination of the MAG3 ligand to the Tc(V) center, the thiolate sulfur and three amide nitrogens each lose their protons to yield an anionic complex, exhibiting square-pyramidal geometry with the oxo group in the apical position. The carboxylate group is not coordinated to the metal. A free carboxylate group is necessary for efficient renal excretion of an anion. The MAG3 ligand and derivatives are used as bifunctional chelates to link Tc to biomolecules.

Agents for Hypoxia. Determining the oxygen status of solid human tumors and identifying viable versus hypoxic (low oxygen content) tissue following myocardial infarction, ischemia, and strokes is important to determine treatment regime. Hypoxic tissue can be differentiated from oxic tissue (normal oxygen concentrations) and necrotic tissue (dead or nonviable tissue) on the basis of differences in reduction potential within the cells. A hypoxic tissue radiopharmaceutical must be able to enter the cell and it must be selectively reduced in hypoxic tissue, but not normal tissue. Once inside the cell, the compound should be reduced and trapped in the hypoxic area.

Recent ^{99m}Tc-based imaging agents, shown in Figure 5, for hypoxic tissue are in development. These include nitroimidazole derivatives, BSM-181321 and BRU-59-2, based on the ^{99m}Tc-propyleneamine oxime (PNAO) complexes. Both contain the 2-nitroimidazole functionality, that is the active component of the oxygen mimetic molecule, ^{19}F-2-nitroimidazole,**[25]** and have been shown in vivo to localize in ischemic tissue. The BnAO chelate also displays uptake in hypoxic tissue. The mechanism is unknown, however, electrochemical studies show an irreversible reduction at biologically accessible potentials.

2.4.2 Receptor Specific Agents-technetium Tagged Radiopharmaceuticals

The mid- to late 1980s saw an increasing emphasis on designing technetium radiopharmaceuticals that have specific interaction with cellular proteins and/or receptors.

Monoclonal Antibodies and Large Proteins. Monoclonal antibodies (mAb) that target cellular antigens can be labeled

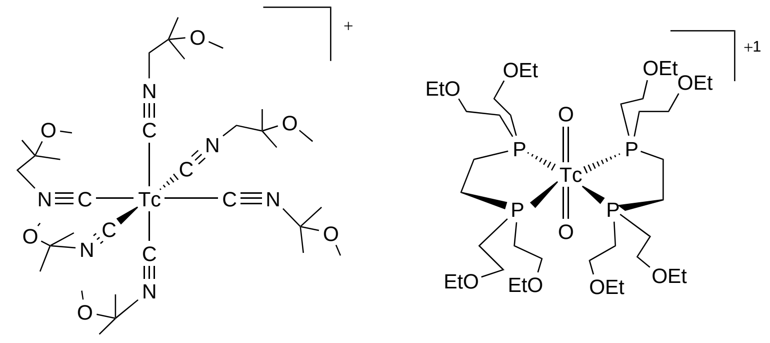

Tc^{I} (MIBI)$_6^+$
sestamibi
cardiolite^{TM}
[Tc^{I}]$^+$

Tc-tetrofosmin
myoview^{TM}
[Tc^{V}O$_2$]$^+$

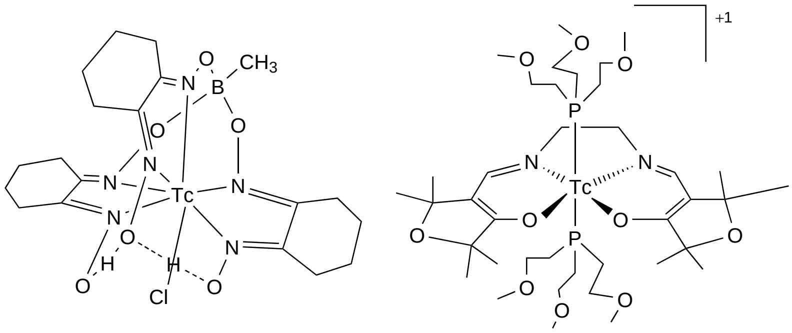

Tc-teboroxime
cardiotec^{TM}
[Tc^{III}]^0

Tc- furifosmin
techneScan Q12
[Tc^{III}]$^+$

Figure 3 Heart imaging agents showing variation in the Tc cores

with ^{99m}Tc by direct labeling or with BFC conjugates. The long time required for mAbs to localize at their target antigen in vivo has hindered their widespread use for ^{99m}Tc agents. However, various ^{99m}Tc-labeled antibody fragments have been used clinically to image cancers and melanoma.[26] Also, ‘pretargeting’ strategies have been developed wherein the antibody, covalently linked to a molecule, such as streptavidin, is administered first and allowed to circulate and bind to antigen. Administration of a clearing agent, such as galactosylated protein, that has a high-affinity, noncovalent interaction with streptavidin will remove the mAbs from circulation, but allow them to remain in the tumor. A small effector molecule, for example, biotin linked to the chelated radiometal, is then administered. Pretargeting strategies allow the radiolabeled small molecule to bind to the tumor with rapid excretion of residual radioactivity.[27,28]

Labeling of ^{99m}Tc to annexin, a small 36 kDa endogenous protein that binds to phosphoserine headgroups in phosphatidyl serine with affinity of ca 10^{-9} M, has been used to detect apoptosis in vivo in animal models of transplant rejection, to visualize apoptotic cells and to assess chemotherapy of xenographs. The potential for using ^{99m}Tc labeled Annexin to visualize apoptosis in a wide array of pathologies is under investigation.[19,20,29,30]

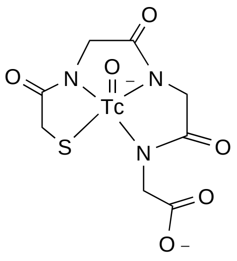

Figure 4 ^{99m}Tc MAG3

Receptor-specific Small Molecules. Receptor imaging in nuclear medicine has been performed with small receptor-specific molecules radiolabeled with ^{123}I (reactor produced),

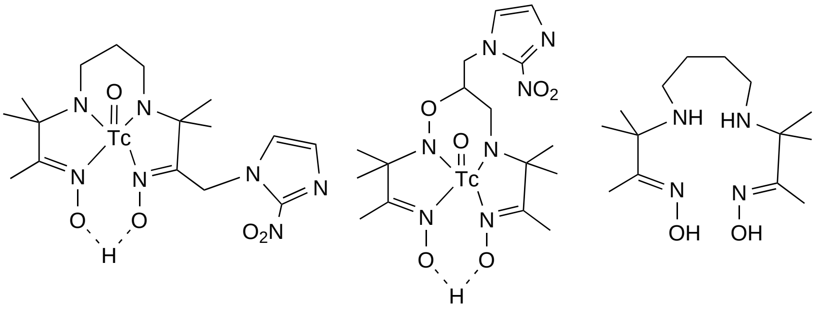

^{99m}Tc-BMS-181321 ^{99m}Tc-BRU-59-2 BNAO

Figure 5 ^{99}Tc complexes for imaging hypoxic tissue

^{18}F, and ^{11}C (cyclotron produced). These isotopes can be incorporated into biomolecules with relative ease and with no or minor alteration of the structure of the biomolecule and, generally, the bioactivity remains the same or similar. The high costs and relative unavailability for routinely producing receptor-specific agents with these isotopes provided the impetus for developing similar agents labeled with ^{99m}Tc. Unlike ^{123}I, ^{18}F, and ^{11}C, labeling with ^{99m}Tc requires incorporation of a ligand or coordinating atoms within or appended to the molecular framework of the receptor ligand to stabilize ^{99m}Tc. Generally, the approach that is taken is to 'tag' the biologically active molecule with a ligand for complexation of ^{99m}Tc, although there are a few examples where the biologically active molecule is templated by ^{99m}Tc. These have been called the 'conjugate design' and 'integrated design,' respectively.[31,32]

The general design criteria applied in the development of these complexes, discussed in detail in previous reviews,[31,32] are dictated by (1) the location of the receptor in the organ or body and (2) the structure of the receptor and nature of its interaction with ligands. Some receptors, such as the integrin gpIIB/IIIA and somatostatin receptors, are located in the vascular or peripheral system and do not need to cross the BBB or cellular membranes to reach the target receptor. In these cases, there is more tolerance for the size and charge of the receptor-specific radiopharmaceutical. Receptor-specific ^{99m}Tc molecules for neurotransmitter receptors, located in the brain, must traverse the BBB. Receptor-specific molecules for intracellular steroid hormones need to cross plasma membranes.

The structure of the receptor and the nature of its interaction with the receptor-specific molecule will determine the degree to which large ^{99m}Tc molecules or ^{99m}Tc molecules with large substituents will be tolerated. Other important concerns include receptor density, affinity of the complex, and nonspecific binding of the complex.

Receptor-specific ^{99m}Tc labeled molecules can be divided into two broad categories: small molecules and peptides. The following discussion presents an overview of this large area with specific examples that are in clinical trials or on the market.

Small ^{99m}Tc Labeled Receptor-specific Organic Molecules

Neuroreceptors/Transporters[2,3,33]. Noninvasive neuroreceptor imaging could greatly aid in understanding, diagnosis, and monitoring various neurologic diseases. An important consideration in the design of these radiopharmaceuticals is that they must cross the blood–brain barrier. Thus, the complexes must be small, neutral, lipophilic, and stable in vivo as well as possess high affinity for the targeted receptor with minimal nonspecific binding to other proteins and receptors.

Two promising agents target the dopamine transporter (DAT) and have shown receptor-specific localization in primate and human brains. The DAT, located in high density on the presynaptic dopamine neurons concentrated in the striatum of the brain, plays a vital role in regulating endogenous dopamine concentration in the synaptic cleft. The DAT has been implicated in Parkinson's disease and schizophrenia. Several groups have targeted the DAT using tropane analogs, shown in Figure 6, that are derivatives of well-known DAT antagonists, β-CIT or β-CFT.

^{99m}Tc-TRODAT is a tropane derivative in which the diaminodithiol ligand is linked via a methylene group to the 2β-position of tropane. Two diastereomers form on coordination of the ligand to the TcO^{3+} core, both syn relative to the TcO group. Both diastereomers show nanomolar binding affinities for DAT in rat striatal homogenate. The tracer localizes in the basal ganglia consistent with DAT binding.[34] ^{99m}Tc-Technepine is also a tropane derivative which is conjugated to the amine nitrogen of a dithiol-amide-amine ligand coordinated to the TcO^{3+} core.[35,36] Two diastereomers, both syn relative to the TcO group, show nanomolar IC_{50} values for the DAT in cynomologous monkey brain homogenates. Modifications of the structures increase selectivity for the DAT versus the serotonin receptor.[3] A '3 + 1' ^{99m}Tc-tropanol is a motif wherein the Tc=O core is bound to a tridentate dithiol ligand and a monodentate thiol that is itself linked to the tropane moiety.[37] TROTEC is a tropane derivatized with the $Tc(CO)_3{}^{+}$ core.[38]

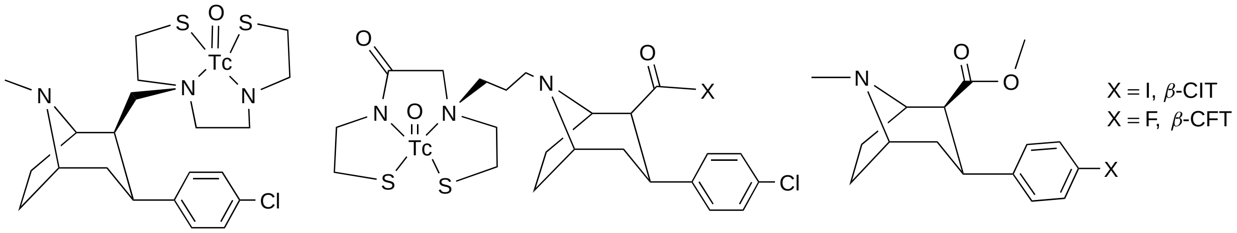

^{99m}Tc-TRODAT ^{99m}Tc-Technepine, X = OMe, OEt

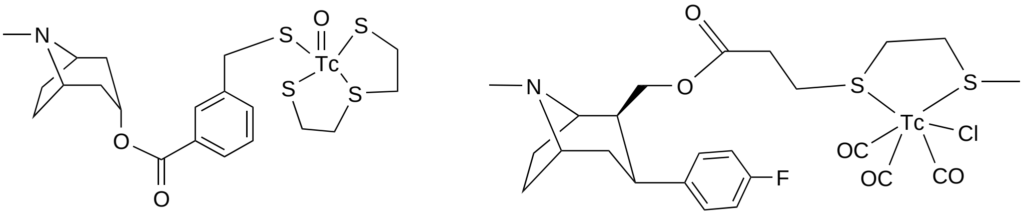

^{99m}Tc-3+1-a-tropanol ^{99m}Tc-TROTEC-1

Figure 6 ^{99m}Tc complexes for imaging the dopamine transporter

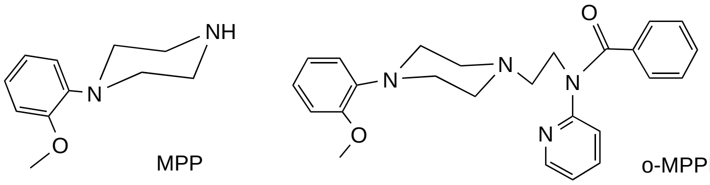

MPP o-MPPI

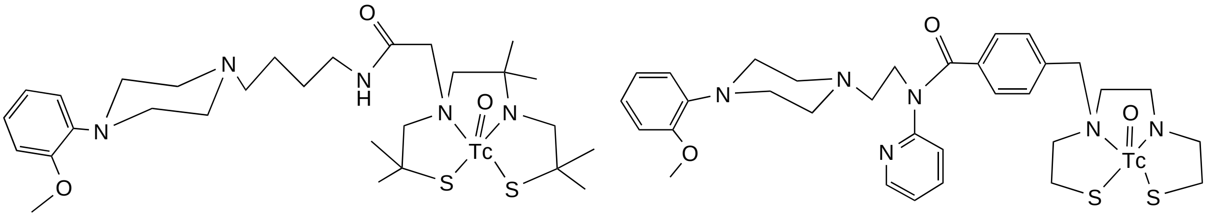

^{99m}Tc-MPP analog ^{99m}Tc- o-MPPI analog

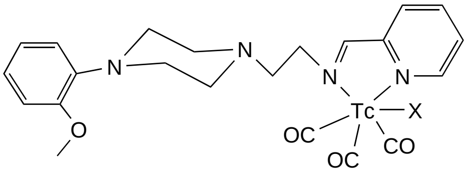

^{99m}Tc(CO)$_3$-MPPI analog

Figure 7 ^{99m}Tc complexes for imaging the serotonin receptor

Alteration of serotonin receptors is implicated in a variety of anxiety disorders, depression, schizophrenia, and Alzheimer's disease. The 5-HT$_{1A}$ and 5-HT$_{2A}$ subtypes have received the most attention with respect to developing ^{99m}Tc-labeled receptor-specific complexes. These tracer complexes must also penetrate the BBB. Most of the ^{99m}Tc complexes investigated for serotonin 5-HT$_{1A}$ receptors are analogs of high-affinity antagonists at the 5-HT$_{1A}$ receptor that possess 1-(2-methoxyphenylpiperazine) (MPP) as the receptor-binding moiety (Figure 7). The diaminodithiol chelate linked to 2-methoxyphenyl piperazine via alkyl chains or via linkages that contain both a 2-pyridyl substituent and an aromatic

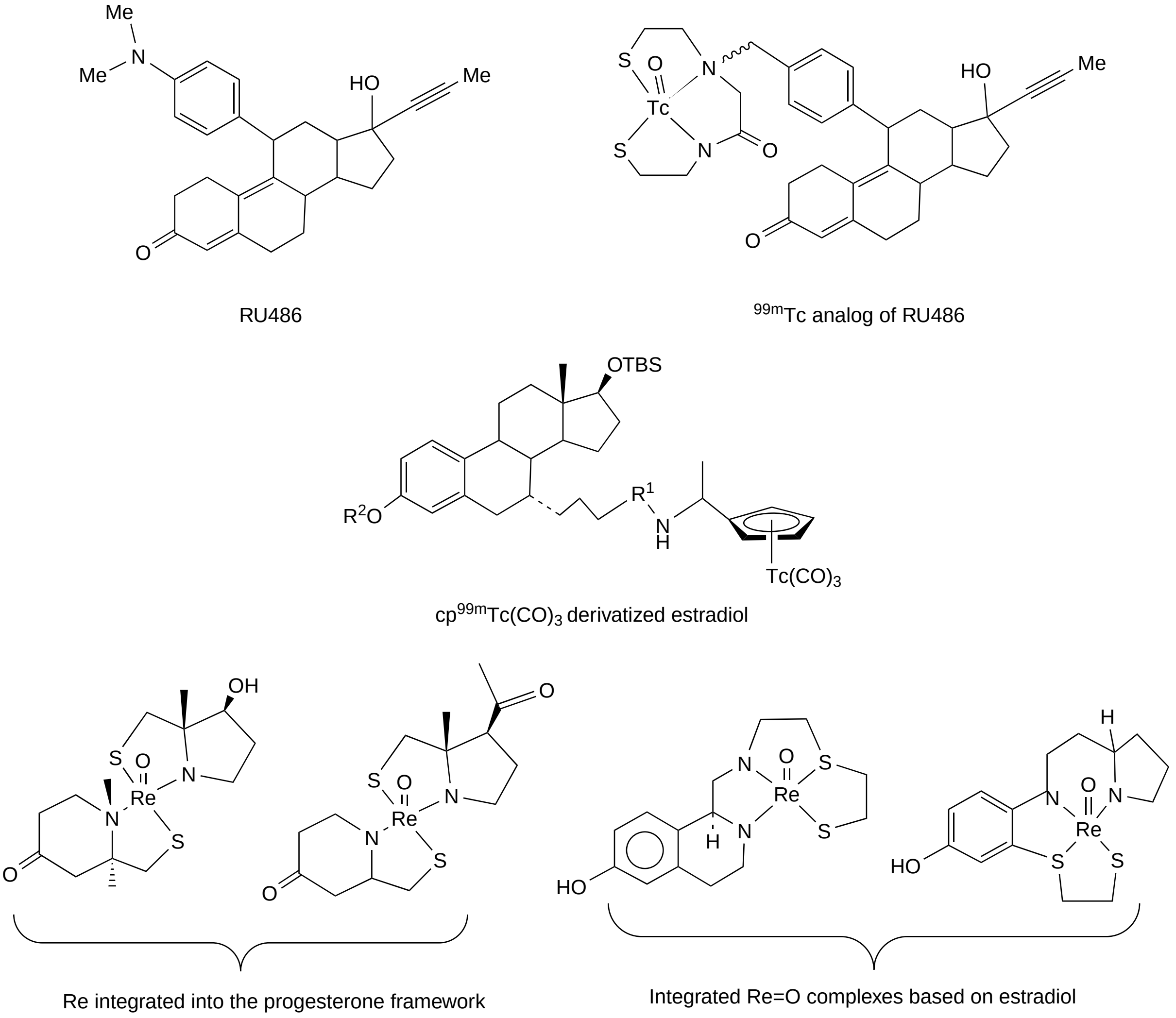

RU486

^{99m}Tc analog of RU486

cp^{99m}Tc(CO)$_3$ derivatized estradiol

Re integrated into the progesterone framework

Integrated Re=O complexes based on estradiol

Figure 8 Tc and Re derivatives of progesterone and estradiol

benzamide show high affinity for the 5-HT$_{1A}$ receptor; however, brain uptake is low. Other MPP analogs have been reported, including one based on the Tc(CO)$_3$$^+$ core.[33]

Steroid Receptors. Steroid receptors such as estrogen, progesterone, and androgen receptors are overexpressed in breast, ovarian, and prostate cancers. Estrogen and progesterone receptors are present in about 65% of human breast cancers. The presence or absence of these receptors in cases of breast carcinoma assists the determination of the therapeutic strategy (hormonal or chemical) that is likely to be effective. The successful Tc complex must cross the membrane lipid bilayer of the cell, and thus, the size and lipophilicity of the complex must be balanced with receptor-binding affinity.

Katzenellenbogen and coworkers have done extensive research in the area of steroid receptor ligands.[31,32] Appending N$_2$S$_2$ chelates onto progestin at the 11β position, based on the drug RU486 (Figure 8), resulted in ^{99m}Tc complexes that showed moderate to high affinity for the progestin receptor. However, nonspecific binding and uptake in nontarget organs were observed.[39,40] Attempts to reduce the molecular mass and lipophilicity lead to design of integrated complexes wherein the Tc=O group is integrated within the ring system of 5-α-hydroxytestosterone or estradiol. The binding affinities were found to be low but this integrated approach where the ^{99m}Tc templates the structure of the overall complex appears to be a promising strategy.[41] Other designs where the tricarbonyl moiety have been tethered to estradiol have been examined.

Other Receptors. The above examples show the design criteria of stabilizing ^{99m}Tc either appended to or integrated within the framework of small receptor-specific molecules. There have been other receptors such as sigma receptors, muscareinic acetylcholine receptors, and dopamine D2

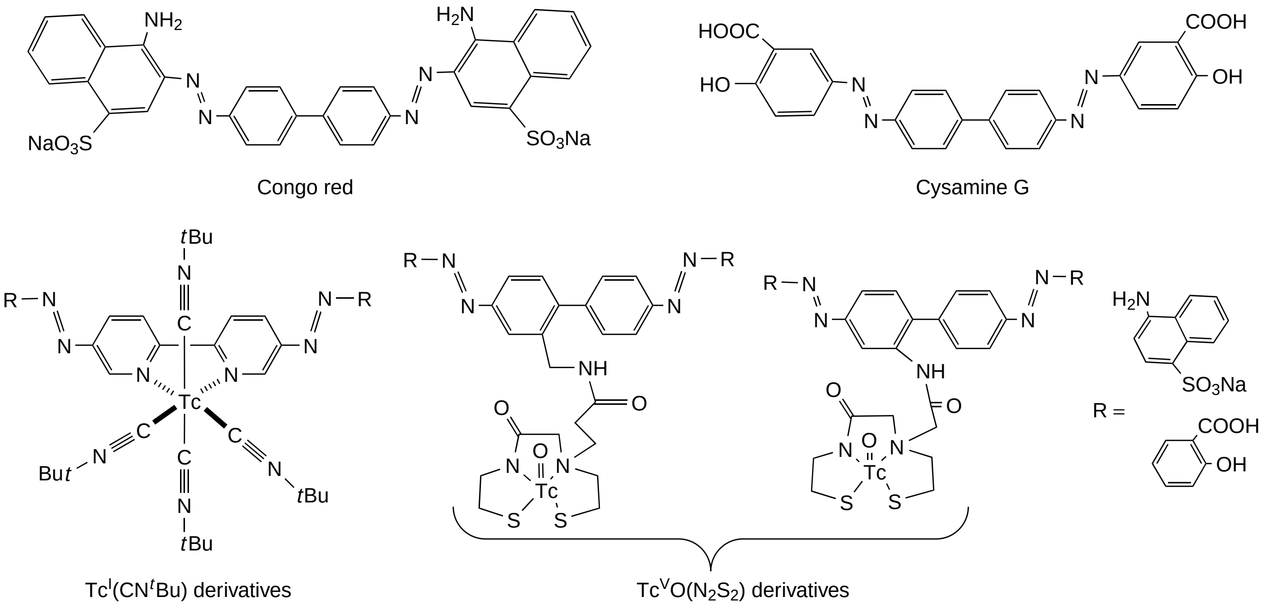

Congo red

Cysamine G

Tc^{I}(CN^{t}Bu) derivatives

Tc^{V}O(N$_2$S$_2$) derivatives

Figure 9 Tc complexes for binding to β-amyloid fibrils

receptors that have been targeted with ^{99m}Tc labeled small molecules. These can be found in recent reviews.[2,3,33]

Other Targets

Amyloid Plaque. Staining by aromatic azo dyes such as congo red and chrysamine G displays extensive amyloid deposits in postmortem brain tissues from Alzheimer's patients. Incorporating the basic dye structures within Tc complexes by an integrated approach in which a central bipyridyl group capable of bidentate coordination to Tc is introduced in place of the biphenyl group in the azo dyes results in Tc(I) complexes, shown in Figure 9, that display submicromolar binding affinity to β-amyloid fibrils.[42,43] The charges of the molecules preclude brain uptake. Alternative approaches using pendant amineamide chelates have been reported for these azo dyes as well as their uncharged ester derivatives. In vivo studies show low brain uptake even for neutral derivatives, perhaps due to their large size.[44,45]

Multidrug Resistance Targeting Molecules. Multidrug resistance (MDR) is a phenomenon in which cancer cells become resistant to chemotherapeutic drugs with differing modes of action. This is believed to be one of the primary reasons for treatment failure in cancer patients. The most well-characterized source of MDR arising from cancer cells is the P-glycoprotein (Pgp) expressed by the human MDR1 gene. Pgp is a transmembrane protein and is believed to confer drug resistance by pumping cytotoxic material out of the cell. Functional measurement of the MDR status in vivo by SPECT or PET would be useful in determining the resistance status of a tumor. ^{99m}TcMIBI, a myocardial perfusion agent, is a substrate for Pgp and thus does not accumulate in MDR-active cells and experiences increased washout rate from tumors expressing Pgp.[46,47] Other lipophilic cationic ^{99m}Tc complexes such as ^{99m}Tc-tetrofosmin and the ^{99m}Tc-Q complexes have also been shown to be substrates for Pgp in both in vitro and in vivo animal tumor models.[48] Efforts to optimize the differential uptake between drug-sensitive and drug-resistant tumors and to minimize nonspecific binding have identified variants of the ^{99m}Tc-Q series.

^{99m}Tc Labeled Receptor-specific Peptides.[17] The success of ^{111}In diethylenetriaminepentaacetic acid (DTPA)-octreotide (OctreoScan™), the first radiolabeled peptide in the nuclear medicine clinic (vide infra) stimulated the search for receptor-specific imaging agents based on ^{99m}Tc peptides. These ^{99m}Tc-labeled peptides target cell surface receptors. For example, tagging a ^{99m}Tc chelate to cyclic peptides targeted towards gpIIb/IIIa receptors have proven successful for imaging Deep Vein Thrombosis (DVT). A thrombus is an aggregate of fibrin, platelets, and red blood cells within blood vessels. In a rapidly growing thrombus, activated platelets express gpIIb/IIIa receptors that recognize peptides and proteins such as fibrinogen containing a tripeptide Arg-Gly-Asp (RGD) motif. The RGD unit has been incorporated into high-affinity antagonists of the gpIIb/IIIa receptor. Ligands that bind ^{99m}Tc have been appended to these high-affinity receptor-specific cyclic species. For example, DMP 757, an RGD containing conformationally constrained cyclic high-affinity gpIIb/IIIa antagonist, has been derivatized with the N_2S_2 ligand and the HYNIC moiety to give, upon labeling with ^{99m}Tc, the radiolabeled analogs, RP419 and DMP444, respectively (Figure 10). Both ^{99m}Tc-labeled agents show rapid uptake in thrombi and clear visualization 15–30 minutes after injection.

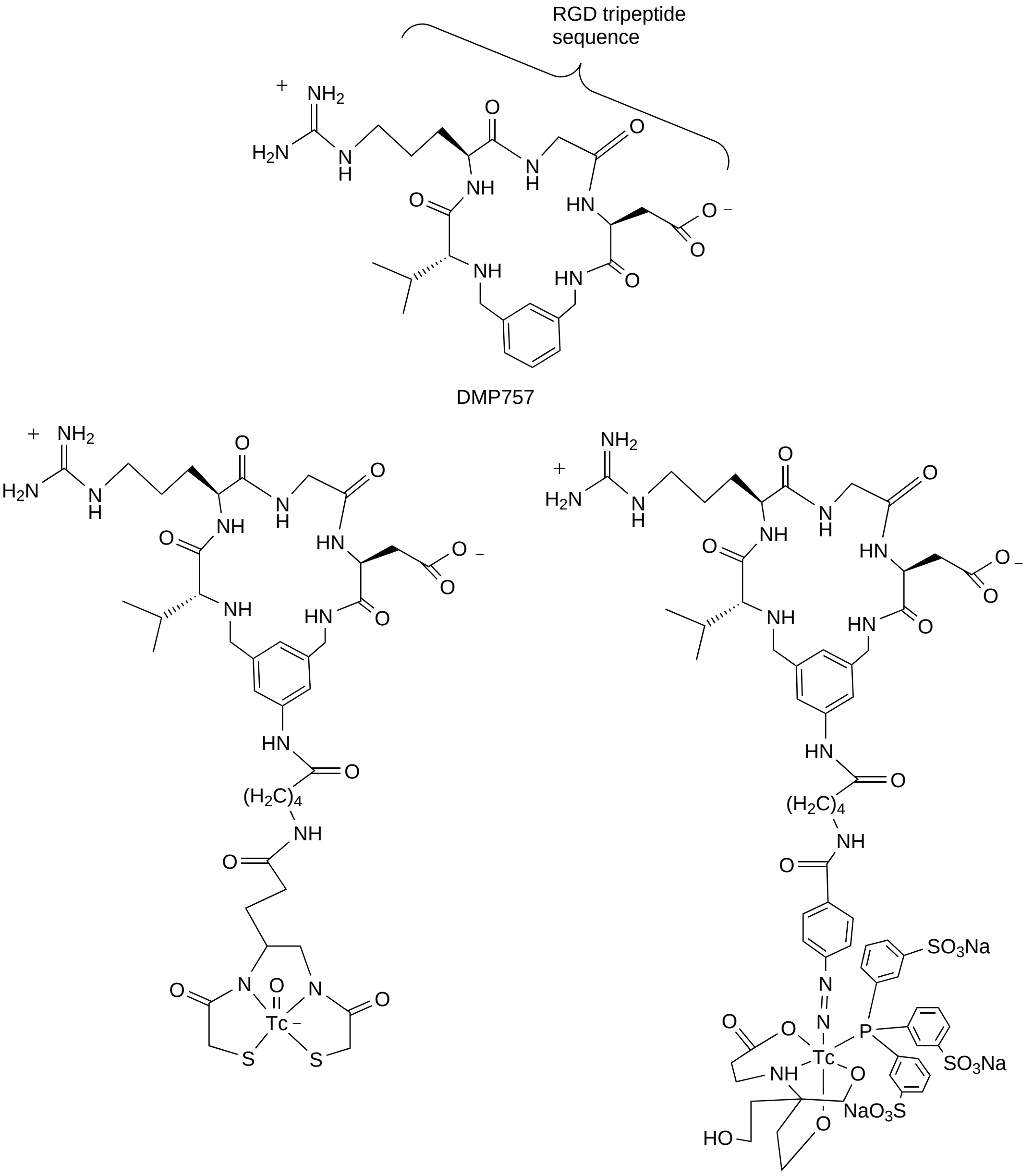

DMP757

RP419
$^{99m}Tc^{V}O\ N_2S_2$ derivatized DMP757

DMP444
^{99m}Tc HYNIC derivatized DMP757

Figure 10 ^{99m}Tc derivatives of DMP757 for imaging thrombosis

The first ^{99m}Tc-radiolabeled peptide in the nuclear medicine clinic was ^{99m}TcO apcitide (^{99m}TcO(P246); Figure 11), the technetium complex of the 13-amino acid apcitide, *cyclo*-(D-Tyr-Apc-Gly-Asp-Cys)-Gly-Gly-Cys(Acm)-Gly-Cys(Acm)-Gly-Gly-Cys-NH_2, where Apc is L-S-(3-aminopropyl)cysteine (an arginine mimetic) and Acm is the acetamidomethyl protecting group. ^{99m}TcO apcitide has high affinity and selectivity for the gpIIb/IIIa receptor.[49,50] Bibapcitide, a 26-amino acid, bis-succinimidomethyl ether-linked dimer of the peptide apcitide, has been formulated as a single-vial, lyophilized kit having the trade name AcuTect™. When sodium pertechnetate ($^{99m}TcO_4^-$) is added to the AcuTect™ radiopharmaceutical kit and the resulting kit is heated, ^{99m}TcO apcitide forms (Figure 11). The ^{99m}Tc is complexed to the terminal Gly-Gly-Cys of apcitide (N_3S donor set).[51]

The second ^{99m}Tc-labeled peptide to enter clinical use is ^{99m}Tc depreotide (^{99m}Tc P829, NeoTect™) for lung tumor imaging (Figure 12). The pharmacophore, cyclic-Tyr-D-Trp-Lys-Val receptor-binding sequence is restrained in

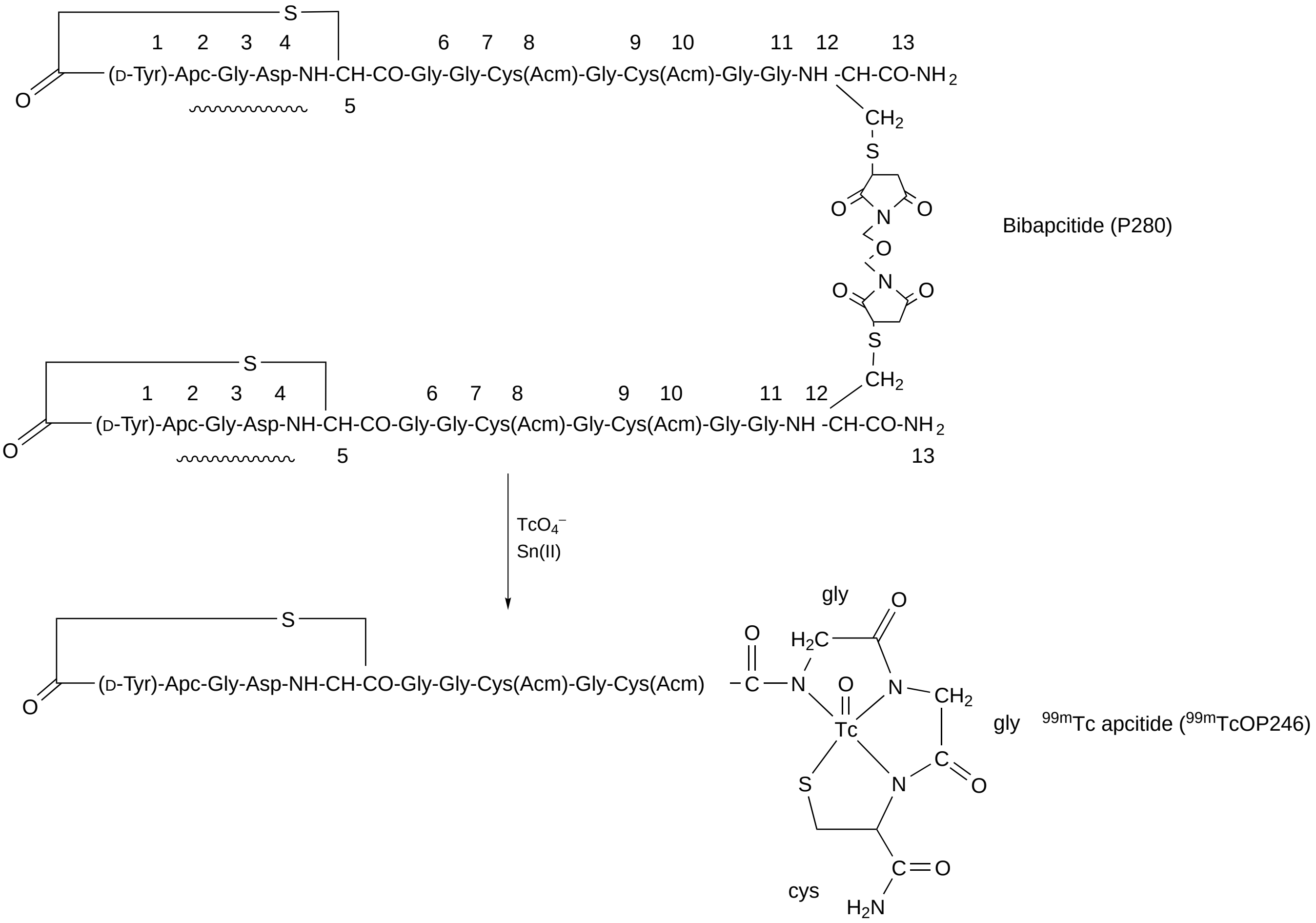
(D-Tyr)-Apc-Gly-Asp-NH-CH-CO-Gly-Gly-Cys(Acm)-Gly-Cys(Acm)-Gly-Gly-NH -CH-CO-NH2
Bibapcitide (P280)
TcO4−
Sn(II)
(D-Tyr)-Apc-Gly-Asp-NH-CH-CO-Gly-Gly-Cys(Acm)-Gly-Cys(Acm)
gly
cys
99mTc apcitide (99mTcOP246)

Figure 11 Bibapcitide and ^{99m}Tc apcitide (AcuTect™) for imaging Deep Vein Thrombosis

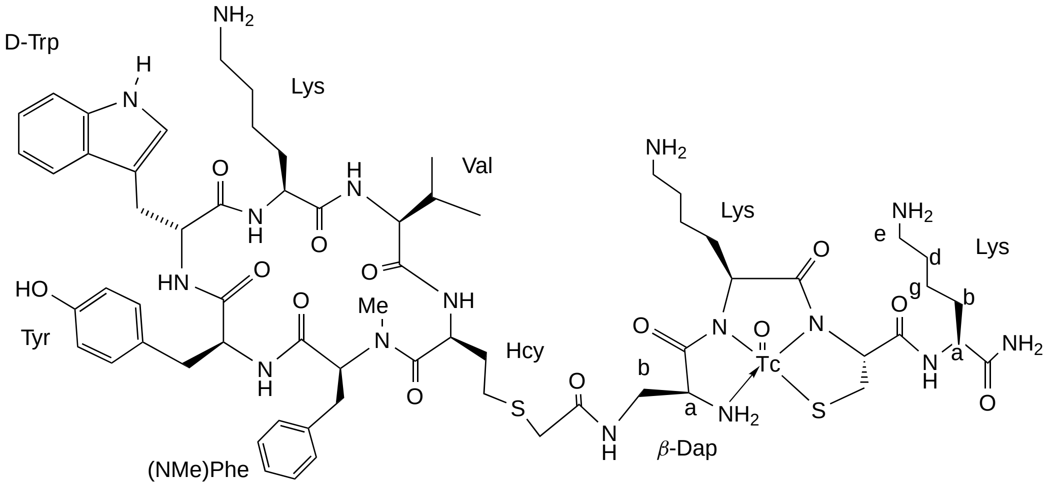
D-Trp
Lys
Val
HO
Tyr
Me
Hcy
Lys
Lys
β-Dap
(NMe)Phe

Figure 12 ^{99m}Tc depreotide (P829) NeoTect™

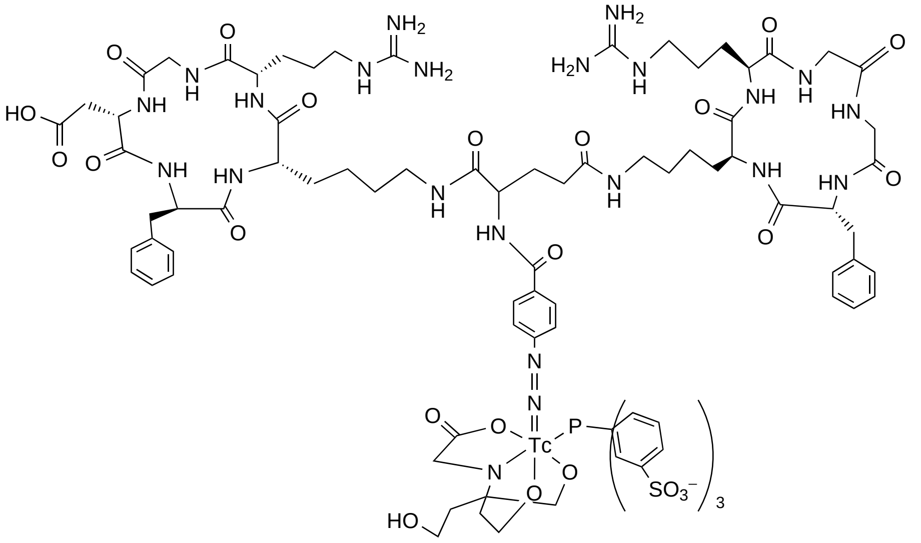

Figure 13 A ^{99m}Tc labeled vitronectin receptor antagonist for tumor imaging

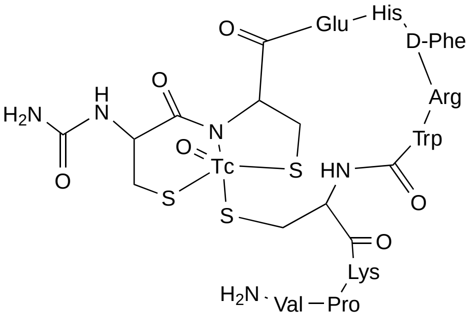

Figure 14 Cyclic ^{99m}Tc α-MSH analog

a cycle and tethered to a β-diaminopropionate-Lys-Cys-Lys that comprises the ^{99m}Tc binding region, shown in Figure 12. Two ^{99m}Tc-labeled depreotide diastereomers form upon treatment with $^{99m}TcO_4^-$ and stannous ion, where the pendant group (containing the cyclic pharmacophore) is disposed syn or anti to the Tc=O group. The diastereomers have nanomolar affinities for the somatostatin receptor.**[52]**

Many antagonists to the vitronectin receptor, an integrin receptor, inhibit tumor-induced angiogenesis and tumor growth. A dimeric vitronectin receptor antagonist, RP593, labeled with ^{99m}Tc (Figure 13) shows high affinity in vitro receptor assays and studies in animal tumor models indicate rapid blood clearance with tumor uptake.**[53]**

There are few examples of the integrated design in radiolabeled peptides. One example is found in the α-melanocyte stimulating hormone (α-MSH) receptor-binding peptides that are expressed on murine and human melanoma tumors. In this case, the ^{99m}Tc templates the cyclization of a tridecapeptide by binding to cysteine residues at the N- and C-terminals to produce enzymatically stable ^{99m}Tc (Figure 14) and ^{188}Re analogs that display significant tumor localization in vivo. This metal-cyclized peptide binds to the α-melanocyte stimulating hormone (α-MSH) receptor.**[54–56]**

3 OTHER METAL DIAGNOSTIC AGENTS

3.1 Gallium, Indium

^{67}Ga and ^{111}In are presently clinically used in diagnostic imaging. The positron-emitting ^{68}Ga ($t_{1/2} = 68$ min) is generator produced (^{68}Ge/^{68}Ga) and is potentially useful for PET imaging.

3.1.1 General Information

Ga(III) and In(III) (Group IIIB) have properties similar to Fe(III) except that their reduction potential to the +2 species is much lower and not attained under physiological conditions. Thus, the +3 oxidation state is exclusively observed in radiopharmaceutical chemistry. The formation of hydrolysis products and formation of transferrin complexes (Ga(III)-transferrin: log $K_1 = 20.3$;**[57]** In(III)-transferrin: log $K_1 = 18.74$**[58]**) must be considered in the design of radiopharmaceuticals based on Ga(III) and In(III) (*see* ***Iron Proteins for Storage & Transport & their Synthetic Analogs***). Therefore, the majority of Ga(III) and In(III) coordination complexes used as radiopharmaceuticals or as BFCA, to link Ga(III) and In(III) to antibodies or

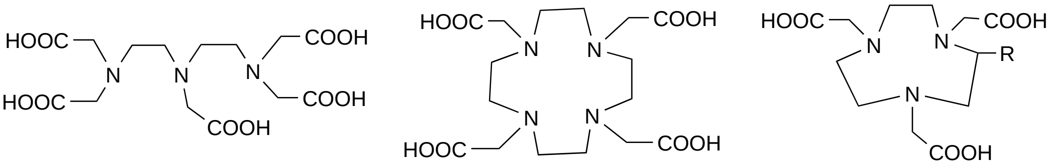

DTPA DOTA NOTA

Figure 15 Ligands for Gallium(III) and Indium(III)

peptides, have very high thermodynamic stability and/or are kinetically inert to exchange with transferrin in vivo. Macrocyclic or linear aminocarboxylates (Figure 15) are typically employed although others have been and are studied. Ligand development for radiopharmaceutical use has been thoroughly reviewed.[6] The coordination chemistry, analytical chemistry, and radiopharmaceutical applications have been reviewed.[5,6,59]

3.1.2 Radiopharmaceuticals Containing ^{67}Ga and ^{111}In Currently in Use

Approved Radiopharmaceuticals for Imaging Based on Monoclonal Antibodies

The DTPA ligand is linked to antibodies via a carbohydrate-glycyl-tyrosyl-lysine linkage in the commercial products ProstaScint and OncoScint. ProstaScint is a whole IgG1, murine monoclonal antibody that was generated from a human prostatic cell line. This product is used to determine extent of prostate cancer. OncoScint is based on the monoclonal antibody B72.3 or CYT-103 directed against an antigen TAB-72 that is expressed on colorectal adenocarcinomas and ovarian cancers. Another commercially available product, MyoScint, is an anti-myosin Fab fragment antibody with an attached DTPA chelate that localizes in necrotic myocardial tissue and is used to detect myocardial infarcts.

Radiopharmaceuticals for Tumor and Infection Imaging

^{67}Ga-citrate has been used to image tumors since 1969 and infection since 1972. ^{67}Ga citrate scintigraphy is the best available functional imaging modality for evaluating patients with non-Hodgkin's lymphoma and Hodgkin's disease and is also in clinical use for diagnosis of lung cancer, malignant melanoma, and leukemia. The role of ^{67}Ga scintigraphy is primarily to assess the viability of tumors, that is, to differentiate between the presence of viable lymphoma, which requires further treatment, or benign tissues.

^{67}Ga citrate is not stable in blood and the actual radiopharmaceutical in vivo is ^{67}Ga transferring (*see* ***Iron Proteins for Storage & Transport & their Synthetic Analogs***).[60,61] The mechanism of ^{67}Ga-citrate/transferrin uptake into tumors has been debated. The most recent theory is that after intravenous injection of ^{67}Ga citrate, ^{67}Ga is transported in the blood bound to transferrin (an iron-transport protein). ^{67}Ga transferrin binds to transferrin receptors (CD71) that are increased and upregulated on tumor cells and is incorporated by receptor-mediated endocytosis into intracellular lysosomes.[62] The result is enhanced ^{67}Ga uptake in malignant cells.

^{67}Ga-citrate is also commonly used for imaging infection and inflammation.[63,64] At sites of inflammation, the gallium-transferrin complex leaks into the extracellular space and ^{67}Ga is transchelated from transferrin in blood to lactoferrin and siderophores (*see* ***Iron Transport: Siderophores***), which are released by leukocytes and bacteria. Imaging with ^{67}Ga takes place usually 24–72 h following injection.

^{111}In-labeled white blood cells (WBC) have also been clinically used for infection and inflammation imaging. The neutral, lipid-soluble ^{111}In(oxine)$_3$ (oxine = 8-hydroxyquinoline) complex penetrates cellular membranes and is used to label WBC.[65] After diffusing intracellularly, the ^{111}In(oxine)$_3$ complex dissociates and the ^{111}In is bound to nuclear and cytoplasmic proteins. Labeling of WBCs is done in plasma to avoid transchelation with transferrin in blood. The procedure consists of withdrawal of blood from patient, separation of red blood cells from white blood cells, purification of leucocytes, radiolabeling, followed by reinjection of the radiolabeled cells into the patient. The WBCs migrate to inflamed area and can lead to positive imaging.

Disadvantages of using ^{111}In-labeled WBCs include the laborious procedure, specialized equipment and the exposure to potentially contaminated blood that can lead to transmission of blood-born pathogens. An alternative to white blood cell labeling is labeling IgG, a nonspecific immunoglobulin, with ^{111}In using the chelator DTPA. ^{111}In-DTPA-IgG accumulates by binding to receptors present on inflammatory cells.[66] DTPA-IgG, formulated as an instant kit (MacroScint™, RW Johnson Pharmaceutical Research Institute) is used for detection of infectious bone and joint disease.

A disadvantage of ^{111}In-labeled IgG is the lengthy time between injection of radiopharmaceutical and imaging (generally 1–3 days). This problem has been addressed by a 3-step pretargeting procedure[67] as well as the use of faster clearing molecules such as chemotactic peptides,[68] that also bind to receptors expressed on white blood cells with high affinity. Chemotactic peptides show promise for imaging infection and inflammation although issues such as undesired biological activity may impede clinical development.[69]

Radiolabeled Receptor Ligands for Tumor Imaging
The first peptide-based receptor-binding radiopharmaceutical is ^{111}In-DTPA-octreotide, known as ^{111}In-OctreoScan™.**[70,71]** Octreotide (Figure 16) is a shortened peptide analog of somatostatin, a cyclic disulfide-containing peptide hormone of 14 amino acids that is present throughout the central nervous system. Somatostatin receptors (sstr) are overexpressed on many neuroendocrine tumors. Octreotide and metal-derivatized octreotide analogs exhibit high affinity for sstr2 receptors, one of the five different human somatostatin receptor types that has been cloned. Imaging and therapy of neuroendocrine tumors with octreotide and other small peptide somatostatin derivatives has been reviewed.**[71–83]**

^{111}In-DTPA-D-Phe-octreotide binds to sst receptors and is internalized via invagination of the plasma membrane and coated vesicles. Once in the cell, the receptor dissociates from ^{111}In-DTPA-octreotide and is externalized. The polarity of the DTPA-conjugated radiometabolites such as ^{111}In-DTPA-D-Phe prevents passage of the radioactivity out of the cell.**[84]**

Studies to improve receptor uptake and selectivity**[85]** and to tailor the peptide for other radiometals for SPECT and PET imaging followed the introduction of ^{111}In-DTPA-D-Phe-octreotide in the clinic. The differences in coordination chemistry of the radiometal may influence biological behavior. For example, the ^{67}Ga complex of DOTA derivatized Tyr^3-octreotide showed higher stability in human serum, high affinity to the somatostatin receptor and high tumor and low kidney uptake compared to the ^{111}In and ^{90}Y congeners. Gallium(III) is hexacoordinate, bound to four nitrogen atoms of the DOTA and two carboxylate oxygen atoms, while the In(III) and Y(III) analogs are seven-coordinate. It is likely that the free carboxylate group of the ^{67}Ga derivative contributes to the favorable handling of the radiopeptide by the kidneys.**[86]** ^{67}Ga labeled DOTA-Tyr^3-octreotate showed improved affinity for the sstr2 receptor.**[87]** The positron-emitting ^{68}Ga-DOTA-Tyr^3-octreotide showed high sensitivity in identifying carcinoid tumors in patients by PET compared to ^{111}In-octreotide. The combination of the high tumor to nontumor contrast, excellent clearance properties, and sensitivity of PET bode well for the use of ^{68}Ga in somatostatin receptor PET imaging.**[88]**

3.2 Copper

Copper offers many radionuclides of interest for diagnostic imaging and for radiotherapy. The positron-emitting ^{64}Cu has been investigated for labeling proteins, peptides, and molecules with long blood clearance. ^{60}Cu and ^{62}Cu are of interest for agents that reach their targets and clear the blood quickly.**[89,90]**

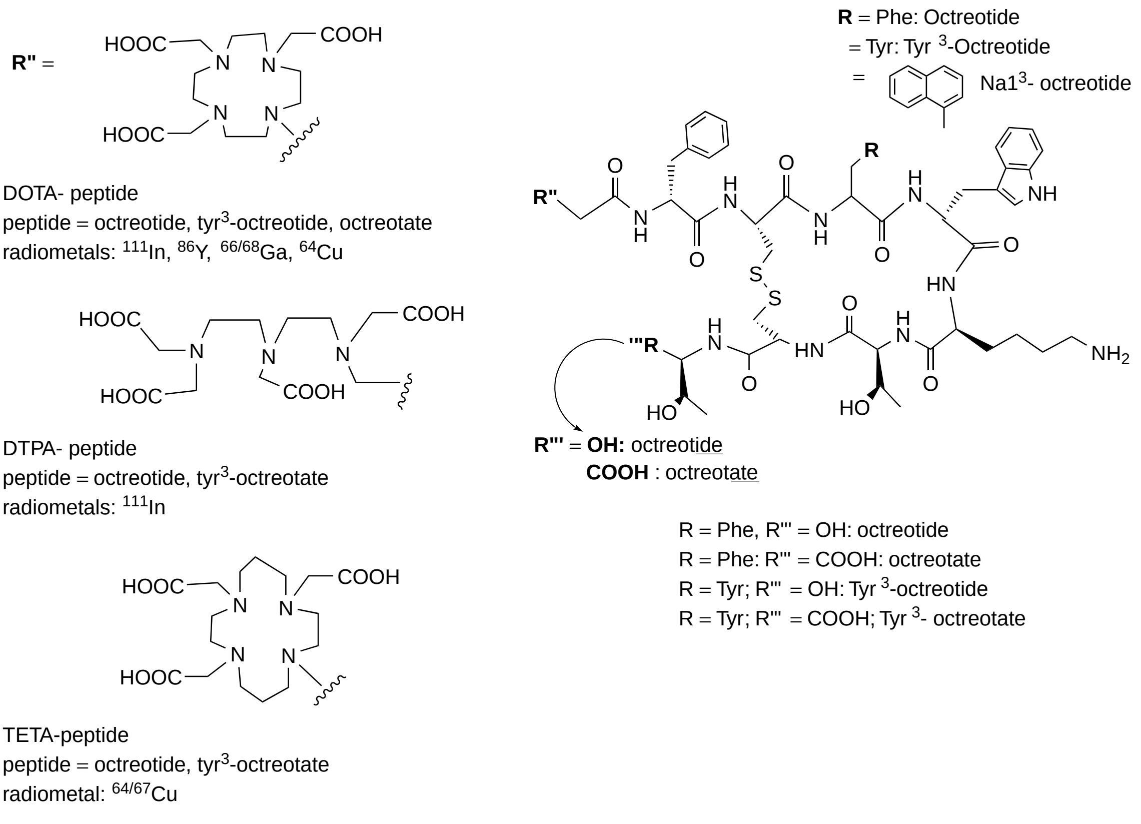

DOTA- peptide
peptide = octreotide, tyr^3-octreotide, octreotate
radiometals: ^{111}In, ^{86}Y, $^{66/68}$Ga, ^{64}Cu

DTPA- peptide
peptide = octreotide, tyr^3-octreotate
radiometals: ^{111}In

TETA-peptide
peptide = octreotide, tyr^3-octreotate
radiometal: $^{64/67}$Cu

R = Phe, R''' = OH: octreotide
R = Phe: R''' = COOH: octreotate
R = Tyr; R''' = OH: Tyr ^{3}-octreotide
R = Tyr; R''' = COOH; Tyr ^{3}- octreotate

Figure 16 Octreotide and derivatives

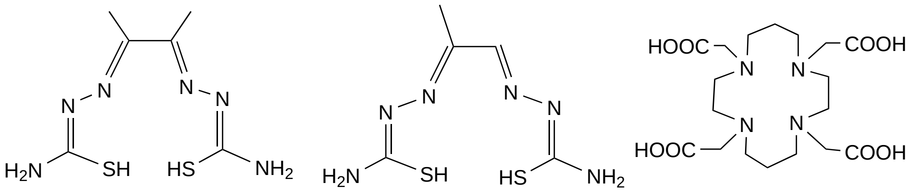

ATSM PTSM TETA

Figure 17 Ligands for Cu^{II}

Two classes of ligands, shown in Figure 17, have been extensively investigated for complexation of copper: bis(thiosemicarbazones), represented by diacetyl-bis(N4-methylthiosemicarbazone) (ATSM) and pyruvaldehyde bis-(N4-methylthiosemicarbazone) (PTSM) and macrocyclic ligands exemplified by 1,4,8,11-tetraaza-cyclotetradecane-N,N',N'',N'''-tetraacetic acid (TETA).

3.2.1 *Bis(thiosemicarbazones)*

ATSM and PTSM form small neutral, lipophilic square-planar complexes with radiocopper that can easily traverse the blood–brain barrier.**[91–93]** ^{67}Cu-PTSM is rapidly extracted into cells and the Cu(II) is reduced to Cu(I) by intracellular thiols, followed by dissociation of the resulting labile Cu(I)-PTSM and binding of the Cu(I) to intracellular proteins, thus constituting the trapping mechanism. Details of this process are discussed in a review by Blower.**[89]** The high lipophilicity of Cu-PTSM may preclude its use as a blood flow tracer.**[94–96]**

^{64}Cu-ATSM is selectively trapped in highly reducing hypoxic tissue but not in less reducing normal tissue. On the other hand, Cu-PTSM is reduced in both normoxic and hypoxic tissue. Hypoxia selectivity has been correlated to the reduction potential of the molecule that is in turn related to the alkyl group substitution.**[97]** The reduction potential of Cu-ATSM is about 100 mV lower than that of Cu-PTSM. Density Functional Theory and chemical reactivity studies attempt to correlate the structure and redox properties of bis(thiosemicarbazones) with the characteristics of the LUMOs (metal or ligand based) and chemical reactivity.**[98]** The fast and selective uptake of $^{64/62}$Cu-ATSM in hypoxic tissue will allow rapid quantitative and qualitative detection of hypoxic regions in tumors with PET before a radiotherapy or chemotherapy regime.**[91,93,99,100]**

3.2.2 *Macrocyclic Ligands*

While acyclic polyaminocarboxylate (DTPA, ethylenediaminetetraacetic acid (EDTA)) complexes of copper(II) have high thermodynamic stability, these complexes are kinetically labile to ligand exchange. Cu(II) has been found to have much greater kinetic stability (and consequently greater serum stability) with macrocyclic chelates, such as TETA and DOTA, than with aliphatic ligands.**[101]** Consequently, TETA or DOTA have been used to conjugate radiocopper to biomolecules.**[102]** Many studies suggest that negatively charged complexes may have more favorable clearance properties when used as BFCs.

Studies over the last decade show that ^{64}Cu-TETA linked to antibodies shows tumor uptake and provides impetus for the use of PET in combination with ^{64}Cu for imaging of tumors.**[103–105]** Also, the β^- emissions of ^{64}Cu and ^{67}Cu have been used to advantage in radiotherapy applications when these isotopes are conjugated to antibodies.**[106–108]** Recent advances in genetically engineered fragments**[109]** and pretargeting strategies**[110]** show rapid access and high retention in tumor tissue combined with rapid blood clearance.

^{64}Cu has also been conjugated to octreotide and modified octreotide analogs using TETA and cyclam derivatives (Figure 16).**[105,106]** Biological studies show that tyrosine substitution in position 3 and replacement of the C-terminal alcohol with a C-terminal COOH enhance receptor-binding and tumor cell uptake with the addition of the C-terminal COOH contributing more.**[106]**

In analysis of the liver metabolism in rats treated with anti-colorectal carcinoma mAb 1A3 radiolabeled with ^{67}Cu through three different macrocyclic bifunctional chelates, it was apparent that the radiocopper was transchelated and bound to proteins such as superoxide dismutase (SOD; *see* ***Copper Proteins with Type 2 Sites***). Transchelation of the copper radiolabel appears to be a major factor for liver accumulation of the $^{64/67}$Cu-labeled BFC-1A3 conjugates.**[111]** After extensive evaluation, experimental results are consistent with in vivo transchelation of ^{64}Cu from TETA-octreotide to superoxide dismutase (SOD) in rat liver.**[112]**

New ligands that show improved biological kinetic stability are needed to form stable Cu(II) bifunctional complexes. For this purpose, a series of ligands that sequester radiocopper have been developed. 1-N-(4-aminobenzyl)-3,6,10,13,16,19-hexaazabicyclo(6.6.6)eicosane-1,8-diamine (SarAr, Figure 18) was designed for conjugation to proteins and complexes metals within 30 min at pH 6–8.**[113]** The ^{64}Cu(SarAr) is found to be kinetically inert to dissociation of the radiocopper and is rapidly excreted through the renal system; these qualities make it an attractive prospect for use in nuclear medicine.**[113]** Cross-bridged cyclam ligands (Figure 18) have been developed, have high stability with copper, and appear

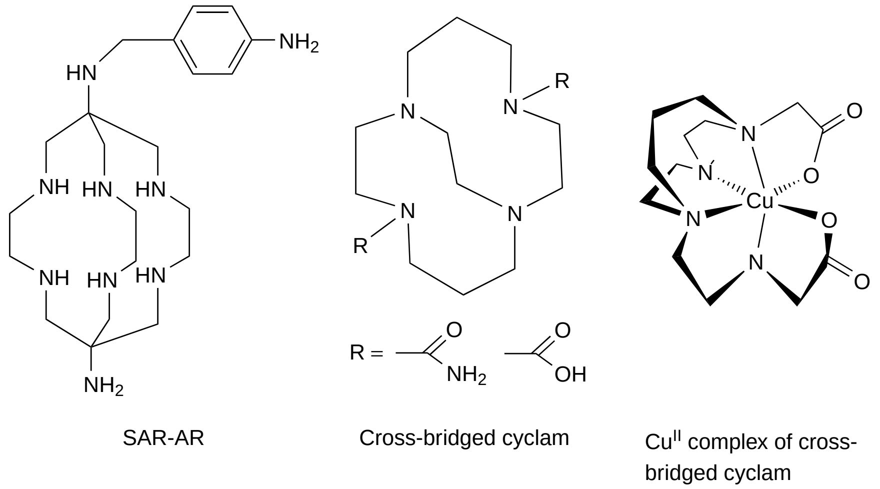

SAR-AR

Cross-bridged cyclam

Cu^{II} complex of cross-bridged cyclam

Figure 18 Macrocyclic ligands for stabilization of ^{67}Cu, ^{64}Cu

to have improved kinetic stability.[114,115] Thus, these cross-bridged cyclam ligands may sequester Cu(II) appropriately for nuclear medicine applications.[116]

4 CONCLUDING REMARKS

Diagnostic imaging has grown significantly with the introduction of new metal-based imaging agents, including ^{99m}Tc agents for brain, heart, and renal imaging as well as the introduction of targeted peptide receptor-specific agents (both ^{111}In and ^{99m}Tc) in the clinic. An increased understanding of the requirements of small molecule receptor-specific interactions, coupled with the development of the coordination chemistry of ^{99m}Tc and other radiometals, result in new potential imaging radiopharmaceuticals, many of which are in clinical trials.

5 RELATED ARTICLES

Iron Proteins for Storage & Transport & their Synthetic Analogs; Metal-based Drugs; Metal-related Diseases of Genetic Origin.

6 REFERENCES

1. S. S. Jurisson, D. Berning, W. Jia, and D. Ma, *Chem. Rev.*, 1993, **93**, 1137.
2. S. S. Jurisson and J. D. Lydon, *Chem. Rev.*, 1999, **99**, 2205.
3. A. Mahmood and A. G. Jones, in ‘Handbook of Radiopharmaceuticals’, eds. M. J. Welch and C. S. Redvanly, John Wiley and Sons, West Sussex, 2003.
4. S. Jurisson, D. Berning, W. Jia, and D. Ma, *Chem. Rev.*, 1993, **93**, 1137.
5. C. J. Anderson and M. J. Welch, *Chem. Rev.*, 1999, **99**, 2219.
6. S. Z. Lever, J. D. Lydon, C. S. Cutler, and S. S. Jurisson, Radioactive metals in imaging and therapy, in ‘Comprehensive Coordination Chemistry II’, eds. T. Meyer, J. McLeverty, Elsevier Ltd., London, 2004, Vol. 9, p. 883.
7. R. Alberto, R. Schibli, P. A. Schubiger, U. Abram, R. Huebener, H. Berke, and T. A. Kaden, *Chem. Commun.*, 1996, **11**, 1291.
8. R. Alberto, R. Schibli, A. Egli, and A. Schubiger, *J. Am. Chem. Soc.*, 1998, **120**, 7987.
9. R. Alberto, K. Ortner, N. Wheatley, R. Schibli, and P. A. Schubiger, *J. Am. Chem. Soc.*, 2001, **123**, 3135.
10. R. Schibli, R. Schwarzbach, R. Alberto, K. Ortner, H. Schmalle, C. Dumas, A. Egli, and P. A. Schubiger, *Bioconjug. Chem.*, 2002, **13**, 750.
11. R. Schibli, R. LaBella, and R. Alberto, *Bioconjug. Chem.*, 2000, **11**, 245.
12. E. Garcia-Garayoa, P. Blauenstein, M. Bruehlmeier, A. Blanc, K. Iterbeke, P. Conrath, D. Tourwe, and P. A. Schubiger, *J. Nucl. Med.*, 2002, **43**, 374.
13. K. A. Stephenson, J. Zubieta, S. R. Banerjee, M. K. Levadala, L. Taggart, L. Ryan, N. McFarlance, D. R. Boreham, K. P. Maresca, J. W. Babich, and J. F. Valliant, *Bioconjug. Chem.*, 2004, **15**, 128.
14. S. R. Banerjee, M. K. Levadala, N. Lazarova, L. Wei, J. F. Valliant, K. A. Stephenson, J. W. Babich, K. P. Maresca, and J. Zubieta, *Inorg. Chem.*, 2002, **41**, 6417.
15. M. J. Abrams, M. Juweid, C. I. tenKate, D. A. Schwartz, M. M. Hauser, F. E. Gaul, A. J. Fuccello, R. H. Rubin,

H. W. Strauss, and A. J. Fischman, *J. Nucl. Med.*, 1990, **31**, 2022.

16. S. K. Larsen, H. F. Solomon, G. Caldwell, and M. J. Abrams, *Bioconjug. Chem.*, 1995, **6**, 635.
17. S. Liu and D. S. Edwards, *Chem. Rev.*, 1999, **99**, 2235.
18. D. S. Edwards, S. Liu, M. C. Ziegler, A. R. Harris, A. C. Crocker, S. J. Heminway, J. A. Barrett, G. J. Bridger, M. J. Abrams, and J. D. Higgins III, *Bioconjug. Chem.*, 1999, **10**, 884.
19. F. G. Blankenberg, P. D. Katsikis, J. F. Tait, E. R. Davis, L. Naumovski, K. Ohtsuki, S. Kopiwoda, M. J. Abrams, S. Darkes, R. C. Robbins, H. T. Maecker, and H. W. Strauss, *Proc. Natl. Acad. Sci. U.S.A.*, 1998, **95**, 6349.
20. F. G. Blankenberg, J. F. Tait, K. Ohtsuki, and H. W. Strauss, *Nucl. Med. Commun.*, 2000, **21**, 241.
21. D. S. Edwards, S. Liu, J. A. Barrett, A. R. Harris, R. J. Looby, M. C. Ziegler, S. J. Heminway, and T. R. Carroll, *Bioconjug. Chem.*, 1997, **8**, 146.
22. R. C. Walovitch, T. C. Hill, St. Garrity, E. H. Cheesman, B. A. Burgess, D. H. O'Leary, A. D. Watson, M. V. Ganey, R. A. Morgan, and S. J. Williams, *J. Nucl. Med.*, 1989, **30**, 1892.
23. D. L. Nosco and J. A. Beaty-Nosco, *Coord. Chem. Rev.*, 1999, **184**, 91.
24. G. Grummon, R. Rajagopalan, G. Palenik, A. Koziol, and D. Nosco, *Inorg. Chem.*, 1995, **34**, 1764.
25. A. Nunn, K. Linder, and H. W. Strauss, *Eur. J. Nucl. Med.*, 1995, **22**, 265.
26. A. N. Serafini, *J. Nucl. Med.*, 1993, **34**, 533.
27. H. Karacay, R. M. Sharkey, W. J. McBride, G. L. Griffiths, Z. Qu, K. Chang, H. J. Hansen, and D. M. Goldenberg, *Bioconjug. Chem.*, 2002, **13**, 1054.
28. D. M. Goldenberg, *J. Nucl. Med.*, 2002, **43**, 693.
29. K. Verbeke, D. Kieffler, J. L. Vanderheyden, C. Reutelingsperger, N. Steinmetz, A. Green, and A. Verbruggen, *Nucl. Med. Biol.*, 2003, **30**, 771.
30. G. J. Kemerink, X. Liu, D. Kieffler, S. Ceyssens, L. Mortelmans, A. M. Verbruggen, N. D. Steinmetz, J. L. Vanderheyden, A. M. Green, and K. Verbeke, *J. Nucl. Med.*, 2003, **44**, 947.
31. R. K. Hom and J. A. Katzenellenbogen, *Nucl. Med. Biol.*, 1997, **24**, 485.
32. J. A. Katzenellenbogen, in 'Handbook of Radiopharmaceuticals: Radiochemistry and Applications', eds. M. J. Welch and C. S. Redvanly, John Wiley and Sons, West Sussex, 2003.
33. B. Johannsen and H.-J. Pietzsch, *Eur. J. Nucl. Med.*, 2002, **29**, 263.
34. H. F. Kung, H.-J. Kim, M. P. Kung, S. K. Meegalla, K. Plossl, and H.-K. Lee, *Eur. J. Nucl. Med.*, 1996, **23**, 1527.
35. B. K. Madras, A. G. Jones, A. Mahmood, R. E. Zimmerman, B. Garada, B. L. Holman, A. Davison, P. Blundell, and P. C. Meltzer, *Synapse*, 1996, **22**, 239.
36. P. C. Meltzer, P. Blundell, A. G. Jones, A. Mahmood, B. Garada, R. E. Zimmerman, A. Davison, B. L. Holman, and B. K. Madras, *J. Med. Chem.*, 1997, **40**, 1835.
37. B. Johannsen, R. Berger, P. Brust, H.-J. Pietzsch, M. Scheunemann, S. Seifert, H. Spies, and R. Syhre, *Eur. J. Nucl. Med.*, 1997, **24**, 316.
38. A. Hoepping, M. Reisgys, P. Brust, S. Serifert, H. Spies, R. Alberto, and B. Johannsen, *J. Med. Chem.*, 1998, **41**, 4429.
39. J. P. Dizio, R. Fiaschi, A. Davison, A. G. Jones, and J. A. Katzenellenbogen, *Bioconjug. Chem.*, 1991, **2**, 353.
40. J. P. Dizio, C. J. Anderson, A. Davison, G. J. Ehrhardt, K. E. Carlson, M. J. Welch, and J. A. Katzenellenbogen, *J. Nucl. Med.*, 1992, **33**, 558.
41. R. K. Hom and J. A. Katzenellenbogen, *J. Org. Chem.*, 1997, **62**, 6290.
42. H. Han, C.-G. Cho, and P. T. Lansbury Jr, *J. Am. Chem. Soc.*, 1996, **118**, 4506.
43. P. T. Lansbury Jr and K. S. Kosik, *Chem. Biol.*, 2000, **7**, R9.
44. W. Zhen, H. Han, M. Anguiano, C. A. Lemere, C.-G. Cho, and P. T. Lansbury Jr, *J. Med. Chem.*, 1999, **42**, 2805.
45. N. Dezutter, T. de Groot, D. Crombez, H. Vanbilloen, D. Moechars, G. Bormans, F. Van Leuven, and A. Verbruggen, in 'Technetium, Rhenium and other Metals in Chemistry and Nuclear Medicine', eds. M. Nicolini and U. Mazzi, Servizi Grafici, Padova, 1999, Vol. 5.
46. D. Piwnica-Worms, M. L. Chiu, M. Budding, J. F. Kronauge, R. A. Kramer, and J. M. Croop, *Cancer Res.*, 1993, **53**, 977.
47. V. Sharma and D. Piwnica-Worms, *Chem. Rev.*, 1999, **99**, 2545.
48. J. R. Ballinger, J. Bannerman, I. Boxen, P. Firby, N. G. Hartman, and M. J. Moore, *J. Nucl. Med.*, 1996, **37**, 1578.
49. J. Lister-James, L. C. Knight, A. H. Maurer, L. R. Bush, B. R. Moyer, and R. T. Dean, *J. Nucl. Med.*, 1996, **37**, 775.
50. J. Lister-James and R. T. Dean, in 'Technetium, Rhenium and other Metals in Chemistry and Nuclear Medicine', eds. M. Nicolini, and U. Mazzi, Servizi Grafici Editoriali, Padova, 1999.
51. L. C. Francesconi, Y. Zheng, J. Bartis, M. Blumenstein, C. Costello, and M. DeRosch, *Inorg. Chem.*, 2004, **43**, 2867.
52. J. Lister-James, D. A. Pearson, M. A. De Rosch, J. E. Cyr, R. Manchanda, J. V. Rutkovski, C. A. Nelson, B. R. Moyer, L. C. Francesconi, R. T. Dean eds, 'Tc-99m P829: Characterization of a Technetium-99-Labeled Somatostatin Receptor-Binding Peptide', SGE Editoriali, Padovi, 1999, Vol. 5.
53. S. Liu, D. S. Edwards, M. C. Ziegler, A. R. Harris, S. J. Heminway, and J. A. Barrett, *Bioconjug. Chem.*, 2001, **12**, 624.
54. M. Giblin, S. Jurisson, and T. Quinn, *Bioconjug. Chem.*, 1997, **8**, 347.
55. M. Giblin, N. Wang, T. Hoffman, S. Jurisson, and T. Quinn, *Proc. Natl. Acad. Sci. U.S.A.*, 1998, **95**, 12814.

56. J. Chen, M. Giblin, N. Wang, S. S. Jurisson, and T. P. Quinn, *Nucl. Med. Biol.*, 1999, **26**, 687.
57. W. R. Harris and V. L. Pecoraro, *Biochemistry*, 1983, **22**, 292.
58. W. R. Harris, Y. C. Chen, and K. Wein, *Inorg. Chem.*, 1994, **33**, 4991.
59. R. E. Weiner and M. L. Thakur, in 'Handbook of Radiopharmaceuticals: Radiochemistry and Applications', eds. M. J. Welch and C. S. Redvanly, John Wiley and Sons, West Sussex, 2003.
60. E. I. O. Even-Sapir, *Eur. J. Nucl. Med. Mol. Imaging*, 2003, **30**, S65.
61. D. M. Schuster and N. A. Alazraki, *Semin. Nucl. Med.*, 2002, **32**, 193.
62. F. Nejmeddine, M. Raphael, and A. Martin, *J. Nucl. Med.*, 1999, **40**, 40.
63. D. K. Hughes, *J. Nucl. Med. Technol.*, 2003, **31**, 196.
64. H. J. J. M. Rennen, O. C. Boerman, W. J. G. Oyen, and F. H. M. Corstens, *Eur. J. Nucl. Med.*, 2001, **28**(2), 241.
65. J. G. McAfee and M. L. Thakur, *J. Nucl. Med.*, 1976, **17**, 480.
66. A. J. Fischman, R. H. Rubin, J. A. White, E. Locke, R. A. Wilkinson, M. Nedleman, R. J. Callahan, B. A. Khaw, and H. W. Strauss, *J. Nucl. Med.*, 1990, **31**, 1199.
67. O. C. Boerman, J. van Eerd, W. J. Oyen, and F. H. Corstens, *J. Nucl. Med.*, 2001, **42**, 1405.
68. A. J. Fischman, M. C. Pike, D. Kroon, A. J. Fucello, D. Rexinger, C. ten Kate, R. Wilkinson, R. H. Rubin, and H. W. Strauss, *J. Nucl. Med.*, 1991, **32**, 483.
69. J. W. Babich, Q. Dong, W. Graham, M. Barzana, K. Ferrill, M. C. Pike, and A. J. Fischman, *J. Nucl. Med.*, 1997, **38**, 268P.
70. E. P. Krenning, D. J. Kwekkeboom, W. H. Bakker, P. P. M. Kooij, H. Y. Oei, M. van Hagen, P. T. E. Postema, M. de Jong, J. C. Reubi, T. J. Visser, A. E. M. Reijs, L. J. Hofland, J. W. Koper, and S. W. J. Lamberts, *Eur. J. Nucl. Med.*, 1993, **20**, 716.
71. A. J. van der Lely, W. W. deHerder, E. P. Krenning, and D. J. Kwekkeboom, *Endocrine*, 2003, **20**, 307.
72. E. Bombardieri, M. Maccauro, E. deDeckere, G. Savelli, and A. Chiti, *Ann. Oncol.*, 2001, **12**, S51.
73. K. Oberg, *Chemotherapy*, 2001, **47**, 40.
74. C. Scarpignato and I. Pelosini, *Chemotherapy*, 2001, **47**, 1.
75. S. Froidevaux and A. N. Eberle, *Biopolymers (Pept. Sci.)*, 2002, **66**, 161.
76. W. W. de Herder and S. W. J. Lamberts, *Curr. Opin. Oncol.*, 2002, **14**, 53.
77. S. Mather, *Nucl. Med. Commun.*, 2000, **21**, 507.
78. R. E. Weiner and M. L. Thakur, *Appl. Radiat. Isot.*, 2002, **57**, 749.
79. T. M. Behr, M. Gotthardt, A. Barth, and M. Behe, *Q. J. Nucl. Med.*, 2001, **45**, 189.
80. W. A. Breeman, M. deJong, D. J. Kwekkeboom, R. Valkema, W. H. Bakker, P. P. M. Kooij, T. J. Visser, and E. P. Krenning, *Eur. J. Nucl. Med.*, 2001, **28**, 1421.
81. I. Virgolini, T. Traub, C. Novotny, M. Leimer, B. Fuger, S. R. Li, P. Patri, T. Pangerl, P. Angelberger, M. Raderer, F. Andreae, A. Kurtaran, and R. Dudczak, *Q. J. Nucl. Med.*, 2001, **45**, 153.
82. I. Virgolini, T. Traub, C. Novotny, M. Leimer, B. Futer, S. R. Li, P. Patri, T. Pangeri, P. Angelberger, M. Raderer, G. Burggasser, F. Andreae, A. Kurtaran, and R. Dudczak, *Curr. Pharm. Des.*, 2002, **8**, 1781.
83. I. Virgolini, K. Britton, J. Buscombe, R. Moncayo, G. Paganelli, and P. Riva, *Semin. Nucl. Med.*, 2002, **32**, 148.
84. J. R. Duncan, M. T. Stephenson, H. P. Wu, and C. J. Anderson, *Cancer Res.*, 1997, **57**, 649.
85. D. Wild, J. S. Schmitt, M. Ginj, H. R. Macke, B. F. Bernard, E. Krenning, M. DeJong, S. Wenger, and J. C. Reubi, *Eur. J. Nucl. Med. Mol. Imaging*, 2003, **10**, 1338.
86. A. Heppeler, S. Froidevaux, H. R. Macke, E. Jermann, M. Behe, P. Powell, and M. Hennig, *Chem. – Eur. J.*, 1999, **5**, 1974.
87. J. C. Reubi, J. C. Schar, B. Waser, S. Wenger, A. Heppeler, J. S. Schmitt, and H. R. Macke, *Eur. J. Nucl. Med.*, 2000, **27**, 273.
88. M. Hoffmann, H. Maecke, A. R. Borner, E. Weckesser, P. Schoffski, M. L. Oel, J. Schumacher, M. Henze, A. Heppeler, G. J. Meyer, and W. H. Knapp, *Eur. J. Nucl. Med.*, 2001, **28**, 1751.
89. P. J. Blower, J. S. Lewis, and J. Zweit, *Nucl. Med. Biol.*, 1996, **23**, 957.
90. C. J. Anderson, M. A. Green, and Y. Fujibayashi, in 'Handbook of Radiopharmaceuticals', eds. M. J. Welch and C. S. Redvanly, John Wiley and Sons, West Sussex, 2003.
91. H. Taniuchi, Y. Fujibayashi, Y. Yonekura, J. Knoishi, and A. Yokoyama, *J. Nucl. Med.*, 1997, **38**, 1130.
92. M. A. Green, *Nucl. Med. Biol.*, 1987, **14**, 59.
93. J. S. Lewis and M. J. Welch, *Q. J. Nucl. Med.*, 2001, **45**, 183.
94. M. A. Green, C. J. Mathias, M. J. Welch, A. H. McGuire, D. Perry, F. Fernandez-Rubio, J. S. Perlmutter, M. E. Raichle, and S. R. Bergmann, *J. Nucl. Med.*, 1990, **31**, 1989.
95. M. E. Shelton, M. A. Green, C. J. Mathia, M. J. Welch, and S. R. Bergmann, *Circulation*, 1990, **82**, 990.
96. H. Young, P. Carnochan, J. Zweit, J. Babich, S. Cherry, and R. Ott, *Eur. J. Nucl. Med.*, 1994, **21**, 336.
97. J. L. J. Dearling, J. S. Lewis, G. E. D. Mullen, M. J. Welch, and P. J. Blower, *J. Biol. Inorg. Chem.*, 2002, **7**, 249.
98. R. I. Maurer, P. J. Blower, J. R. Dilworth, C. A. Reynolds, Y. Zheng, and G. E. D. Mullen, *J. Med. Chem.*, 2002, **45**, 1420.
99. J. S. Lewis, D. W. McCarthy, T. J. McCarthy, Y. Fujibayashi, and M. J. Welch, *J. Nucl. Med.*, 1999, **40**, 177.

100. Y. Fujibayashi, H. Taniuchi, Y. Yonekura, H. Ohtani, H. Konishi, J. Konishi, and A. Yokoyama, *J. Nucl. Med.*, 1997, **38**, 1155.
101. W. C. Cole, S. J. DeNardo, C. F. Meares, M. J. McCall, G. L. DeNardo, and A. L. Epstein, *Int. J. Appl. Radiat. Isot. Part B. Nucl. Med. Biol.*, 1986, **13**, 363.
102. D. L. Kukis, H. Diril, D. P. Greiner, S. J. Denardo, G. L. DeNardo, and Q. A. Salako, *Cancer*, 1994, **73**, 779.
103. C. J. Anderson, J. M. Connett, S. W. Schwarz, P. A. Rocque, L. W. Guo, G. W. Philpott, K. R. Zinn, C. F. Meares, and M. J. Welch, *J. Nucl. Med.*, 1992, **33**, 1685.
104. C. J. Anderson, S. W. Schwarz, J. M. Connett, P. D. Cutler, L. W. Guo, C. J. Germain, G. W. Philpott, K. R. Zinn, D. P. Greiner, and C. F. Meares, *J. Nucl. Med.*, 1995, **36**, 850.
105. C. J. Anderson, F. Dehdashti, P. D. Cutler, S. W. Swartz, R. Laforest, L. A. Bass, J. S. Lewis, and D. W. McCarthy, *J. Nucl. Med.*, 2001, **42**, 212.
106. J. S. Lewis, M. R. Lewis, A. Srinivasan, M. A. Schmidt, J. Wang, and C. J. Anderson, *J. Med. Chem.*, 1999, **42**, 1341.
107. R. T. O’ Donnell, G. L. DeNardo, D. L. Kukis, K. R. Lamborn, S. Shen, A. Yuan, D. S. Goldstein, G. R. Mirick, and S. J. DeNardo, *J. Nucl. Med.*, 1999, **140**, 2014.
108. J. M. Connett, C. J. Anderson, L. W. Guo, S. W. Schwartz, K. R. Zinn, B. E. Rogers, B. A. Siegel, G. W. Philpott, and M. J. Welch, *Proc. Natl. Acad. Sci. U.S.A.*, 1996, **93**, 6814.
109. A. M. Wu, P. J. Yazaki, S. Tsai, K. Nguyen, A. L. Anderson, D. W. McCarthy, T. Toyokuni, M. E. Phelps, and S. S. Gambhir, *PNAS*, 2000, **97**, 8495.
110. M. R. Lewis, M. Wang, D. B. Axworthy, L. J. Theodore, R. W. Mallet, A. R. Fritzberg, M. J. Welch, and C. J. Anderson, *J. Nucl. Med.*, 2003, **44**, 1284.
111. B. E. Rogers, C. J. Anderson, J. M. Connett, L. W. Guo, W. B. Edwards, E. L. C. Sherman, K. R. Zinn, and M. J. Welch, *Bioconjug. Chem.*, 1996, **7**, 511.
112. L. A. Bass, M. Wang, M. J. Welch, and C. J. Anderson, *Bioconjug. Chem.*, 2000, **11**, 527.
113. N. M. DiBartolo, A. M. Sargeson, T. M. Donlevy, and S. V. Smith, *J. Chem. Soc., Dalton Trans.*, 2001, 2303.
114. G. R. Weisman, E. H. Wong, D. C. Hill, M. E. Rogers, D. P. Reed, and J. C. Calabrese, *J. Chem. Soc., Chem. Commun.*, 1996, 947.
115. E. H. Wong, G. R. Weisman, D. C. Hill, D. P. Reed, M. E. Rogers, J. S. Condon, M. A. Fagan, J. C. Calabrese, K.-C. Lam, I. A. Guzei, and A. L. Rheingold, *J. Am. Chem. Soc.*, 2000, **122**, 10561.
116. S. Sun, M. Wuest, G. R. Weisman, E. H. Wong, D. P. Reed, A. Boswell, R. Motekaitis, A. E. Martell, M. J. Welch, and C. J. Anderson, *J. Med. Chem.*, 2002, **45**, 469.

Acknowledgment

We are grateful to the NIH-SCORE program and NSF for support.

Metal-mediated Protein Modification

James W. Whittaker
Oregon Health and Science University, Beaverton, OR, USA

1 Introduction 1
2 Metalloenzyme-mediated Protein Modification 1
3 Metalloprotein Self-processing 6
4 Modifications Mediated by Small Complexes 11
5 Related Articles 12
6 References 12

Abbreviations

TPQ = 2,4,5-trihydroxyphenylalanine quinone; LTQ = lysine tyrosylquinone; ROS = reactive oxygen species; Asc = ascorbate.

1 INTRODUCTION

Proteins perform many of the most essential functions in biology, from structure and recognition to catalysis and regulation, representing an extraordinarily diverse range of functions for a single family of molecules. This diversity is possible because of the unique organization of the folded polypeptide chain and the variety of functional groups provided by the 20 naturally occurring L-amino acids. The primary structure of the linear polypeptide chain is uniquely determined by its genetic template and the ‘universal genetic code’. Expansion of the genetic code in certain special cases allows incorporation of at least two additional rare amino acids, selenocysteine (*see* ***Selenium Proteins Containing Selenocysteine***) and pyrrolysine, into proteins that utilize the unique reactivity of these groups in enzyme catalysis.

The functionality of protein structures may be further extended through posttranslational modifications to the polypeptide chain, generating novel amino acid residues. Some of these modified residues (like *m*-hydroxyphenylalanine (**1**), *o,o*′-dityrosine (**2**), dihydroxyphenylalanine (**3**)) bear a strong resemblance to familiar amino acids, while others form hyper-modified structures (like histidinomerdesmosine (**4**) and desmosine (**5**)). Generally these modifications can only be detected through direct analysis of the protein structure using high-resolution methods like X-ray crystallography or mass spectrometry, although in some cases (e.g. formation of a chromophore or a cross-link) the unusual behavior of the modified protein has allowed detection by more conventional biochemical techniques. There is a growing recognition that covalent modification of protein structure is important for biological function, and investigating these modifications is a rapidly emerging area in proteomics research.[1] Metal ions are known to participate in some way in many of the processing events giving rise to protein modifications. This overview focuses on these metal-dependent processing reactions, within which we will broadly distinguish among metalloenzyme-mediated protein modifications, metalloprotein self-processing reactions, and reactions of inorganic complexes leading to covalent modification of protein structure (Table 1).

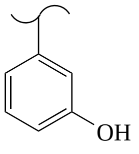

(**1**)

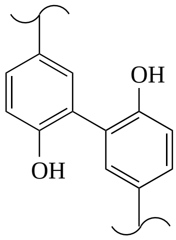

(**2**)

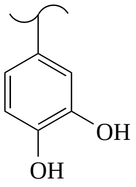

(**3**)

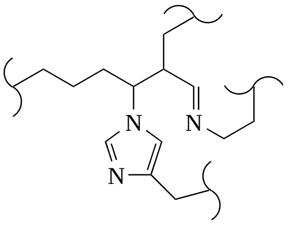

(**4**)

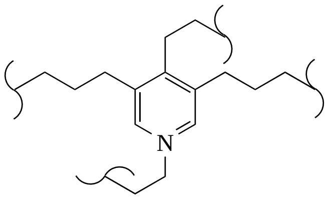

(**5**)

2 METALLOENZYME-MEDIATED PROTEIN MODIFICATION

Enzymatic processing of proteins allows new functionality to be introduced in a highly selective fashion with one protein serving as a macromolecular substrate in the reaction. The inherent structural specificity of enzyme catalysis allows the recognition of individual amino acid side chains in a specific structural context for modification, and this type of processing is an important step in the maturation of many proteins, particularly those that are secreted into the extracellular space. Typical modification reactions include the oxygenation of amino acid side chains (by a class of enzymes known as oxygenases), oxidation of side chains (by oxidases), glycosylation of residues (by glycosyl transferases), and site-specific cleavage of polypeptide chains (by metalloproteases).

Table 1 Metal-mediated posttranslational modification of proteins

Mediating Complex	Metal	Modification product
A. Metalloenzyme-mediated modification		
Proline hydroxylase	Fe	γ-hydroxyproline
Lysine hydroxylase	Fe	δ-hydroxylysine
Peptidylglycine α-amidating hydroxylase	Cu	α-hydroxyglycine
Lysyl oxidase	Cu	α-aminoadipic δ-semialdehyde
Tyrosinase	Cu	dihydroxyphenylalanine
Peroxidase	Fe	dityrosine
Galactosyl transferase	Mn	galactosyl peptide
Peptidylamidoglycolate lyase	Zn	amidated peptide
Matrix metalloproteases	Zn	peptides
B. Metalloprotein self-processing		
Amine oxidase	Cu	trihydroxyphenylalanine (TPQ)
Lysyl oxidase	Cu	lysine tyrosyl quinone (LTQ)
Galactose Oxidase	Cu	cysteinyl-tyrosine
Hemocyanin	Cu	cysteinyl-histidine
Diphenol oxidase	Cu	cysteinyl-histidine
Cytochrome *c* oxidase	Cu	histidinyl-tyrosine
Nitrile hydratase	Fe,Co	cysteine sufenate/sulfinate
C. Modification by small complexes		
Artificial peptidases	Cu, Fe	peptides
Fenton reaction	Fe,Cu,Cr	nonspecific oxidation
Substitution-inert complexation	Cr,Co,Ru	complex conjugation

2.1 Oxygenases

Enzymes that insert oxygen atoms from molecular oxygen into unactivated C–C and C–H bonds are known generically as oxygenases (*see* ***Iron: Heme Proteins, Mono- & Dioxygenases***). Monooxygenases insert a single atom from dioxygen into substrate, reducing the other atom of oxygen to water. Dioxygenases, on the other hand, insert both atoms of dioxygen into products. All of the oxygenases that are known to be involved in protein modification contain essential metal cofactors.

2.1.1 Proline Hydroxylase [E.C. 1.14.11.2]

Hydroxylation of peptidyl proline residues is an essential step in the maturation of collagen, a proline- and glycine-rich structural protein that is the most abundant single polypeptide in the human body.[2–5] Collagen serves as the matrix material in bone and is the major polymer in tendon, skin, and blood vessels. The strength and flexibility of collagen is a consequence of its unique structure, a protein triple-helix formed by assembly of three polypeptides whose backbones are extensively interconnected by hydrogen bonding. This structure is further stabilized by hydrogen bonding between backbone amide groups and hydroxyl groups of hydroxyproline residues formed posttranslationally by oxygenation of proline residues in a (Gly-Pro-Pro)-sequence motif that is repeated many times within the protein. The enzyme that catalyzes the oxygenation reaction, proline hydroxylase, is a nonheme iron enzyme that requires 2-oxoglutarate as a reducing cosubstrate.[6]

Proline hydroxylase has been isolated and characterized and is known to contain a mononuclear nonheme ferrous iron center that is the catalytic active site of the enzyme, coordinated by two histidine and one aspartate side chains. The requirement for Fe(II) is reflected in the in vivo sensitivity of collagen formation to chelators specific for ferrous ion (e.g. 2,2′-dipyridyl). In addition to the catalytic metal cofactor, the reaction requires a reducing cosubstrate, 2-oxoglutarate, dioxygen, and the procollagen peptide (equation 1).

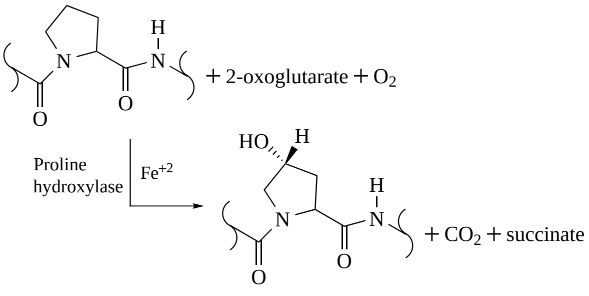

(**6**)

(1)

Hydroxylation primarily occurs at the γ-position of the proline ring to form γ-hydroxyproline (**6**), although β-hydroxyproline is also formed in smaller amounts. These two products apparently result from two closely related enzymes exhibiting distinct substrate regioselectivity.

The active site metal center reductively activates dioxygen during the catalytic turnover cycle. Oxygenation of the ferrous [Fe(II)] metal center in the resting enzyme is thought to generate a metal-bound peroxide adduct of 2-oxoglutarate whose decay results in transient formation of a highly reactive oxidized oxo-ferryl [Fe(IV)=O] species.[7] This aggressive oxo intermediate is capable of inserting an oxygen atom into unactivated C–H bonds. The specificity of the enzyme for C–H bonds in proline side chains in collagen is a consequence of substrate selectivity determined by the extended active site environment rather than the metal complex.

Although the reaction cycle returns the active site to the resting ferrous state during turnover, uncoupling between metal oxidation and substrate hydroxylation sometimes occurs, converting the enzyme to a catalytically inactive ferric complex. Ascorbate is required to maintain the protein-bound iron in the resting enzyme in the ferrous oxidation state. This ascorbate requirement of proline hydroxylase is expressed in the clinical connection between dietary ascorbate deficiency and scurvy, a disease resulting from incomplete collagen processing.[8] This example clearly illustrates the importance of metal ions in protein modification and biological function.

2.1.2 Lysine Hydroxylase [E.C. 1.14.11.4]

A second posttranslation modification that occurs in the maturation of collagen is the oxygenation of lysine residues to form δ-*erythro*-hydroxylysine, which serves as an anchor for attachment of carbohydrates in a glycosylation process (equation 2).

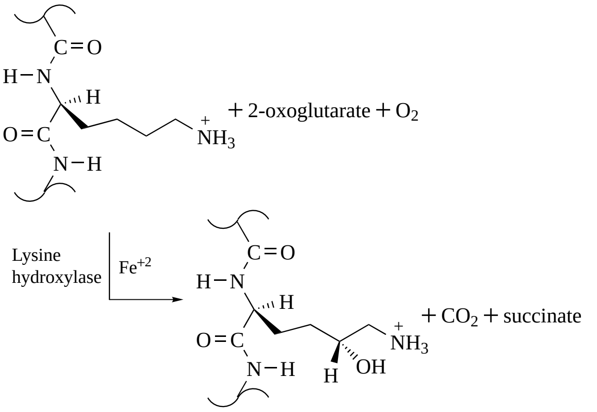

(**7**)

(2)

The enzyme that catalyzes this reaction, lysine hydroxylase, is, like prolyl hydroxylase, a Fe(II)/2-oxoglutarate dependent dioxygenase[6] but exhibits a distinct substrate specificity.

2.1.3 Peptidylglycine α-hydroxylating Monooxygenase [E.C. 1.14.17.3]

Many neuropeptides and peptide hormones are posttranslationally modified by C-terminal amidation, in which a C-terminal glycine residue is first hydroxylated, then cleaved to generate a carboxamido terminal group.[9] The amidated peptide does not serve as a substrate for carboxypeptidases (which recognize a C-terminal carboxyl group) and modification thus extends the lifetime of the peptide in circulation. The peptide hormones oxytocin and vasopressin exhibit this type of C-terminal amidation. The amidating reaction is performed by a bifunctional copper- and zinc-dependent protein-processing enzyme peptidylglycine α-amidating monooxygenase, which is comprised of an N-terminal monooxygenase domain (peptidylglycine α-hydroxylating monooxygenase) and a C-terminal lyase domain (peptidylamidoglycolate lyase)(*vide infra*).

Peptidylglycine α-hydroxylating monooxygenase is a copper metalloenzyme containing two Type 2 mononuclear copper sites (*see* ***Copper Proteins with Type 2 Sites***), each having a distinct coordination environment. X-ray crystallography shows that one copper ion has a $[(His)_2Met(H_2O)]$ ligand set, while the other has $[(His)_3(H_2O)]$ coordination. The oxidized [Cu(II)] centers in the resting enzyme are reduced to Cu(I) during turnover by two molecules of ascorbate (Asc), which are oxidized by one electron to semiascorbyl free radicals (Asc•). The Cu(I)-containing enzyme binds the peptide substrate and dioxygen to form a ternary complex within which the monooxygenation reaction occurs, inserting an oxygen atom into the unactivated C–H bond at the alpha carbon of the carboxy terminal glycine residue to form α-hydroxyglycine (**8**) (equation 3).

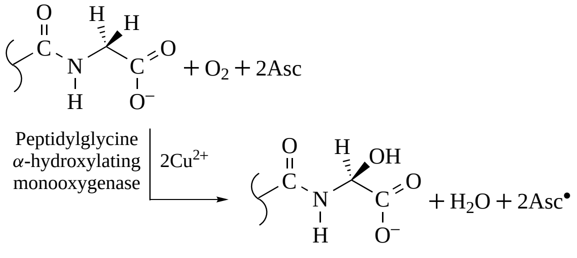

(**8**)

(3)

Amidating enzymes related to peptidylglycine α-hydroxylating monooxygenase are involved in regulation of a wide range of biological processes, including the vascularization of tissue (angiogenesis), which is recognized as an important target for cancer therapy. The copper-dependence of the glycine monooxygenase suggests the possibility of controlling tumor growth using metal-specific chelation. In fact, depletion of copper in tissues by treatment with a sulfide donor, tetrathiomolybdate, has been shown to have antitumor activity, possibly as a result of inactivation of amidating enzymes responsible for angiogenesis hormone processing.

2.2 Oxidases

Oxidases are enzymes that catalyze oxidation–reduction processes that do not involve insertion of oxygen atoms. Modification of proteins by oxidases allows the introduction of covalent cross-links between polypeptide chains.

2.2.1 *Lysyl Oxidase [E.C. 1.4.3.13]*

Lysyl oxidases catalyze the oxidation of the ε-amino group in the side chain of lysine residues in proteins, producing a reactive aldehyde functional group, which can form Schiff-base adducts with unmodified lysine residues or undergo aldol addition, creating covalent cross-links between polypeptide chains.[10–12] Lysyl oxidases are widespread in nature, and have been isolated from organisms ranging from yeast to man.

Lysyl oxidase contains a single Type 2 copper center (*see* ***Copper Proteins with Type 2 Sites***) at the active site, bound by three histidine residues. The metal ion appears not to be redox active during turnover, and the oxidation chemistry is instead performed by a covalently attached cofactor, lysine tyrosyl quinone, derived from a tyrosine residue in the protein (*vide infra,* Section 3.1). The overall reaction involves oxidation of the primary amine group of a peptide-bound lysine residue, reduction of dioxygen to hydrogen peroxide, and release of ammonium ion (equation 4).

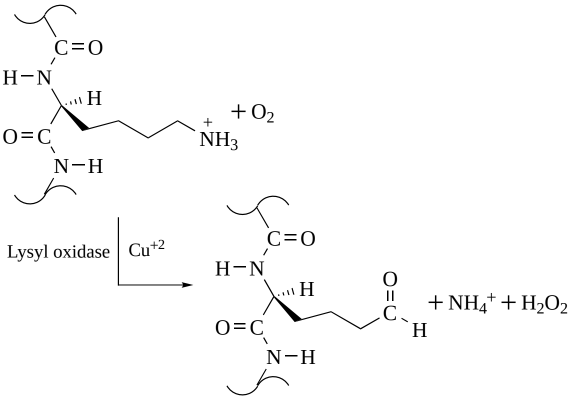

(**9**)

(4)

The peptidyl lysine substrate is converted to an α-aminoadipic δ-semialdehyde (allysine) residue in this process. This reaction is important in the maturation of the extracellular matrix proteins collagen and elastin, in which multiple allysine residues condense to form complex cross-links between polypeptide chains creating the unusual amino acids histidinomerdesmosine (**4**) and desmosine (**5**). The formation of these cross-links in collagen and elastin is important in determining their physical properties. Increasing the extent of cross-linking with age leads to loss of flexibility. Conversely, defects in cross-linking between chains may result in hyperextensible (rubbery) skin. Lysyl oxidases appear to have other, less well-characterized roles in tumor suppression, developmental control, and chemotaxis.

2.2.2 *Tyrosinase [E.C. 1.4.18.1]*

Tyrosinase (*see* ***Copper Proteins with Dinuclear Active Sites***), a copper metalloenzyme with a very broad phylogenetic distribution, is responsible for the browning of fruits and mushrooms.[13–15] Tyrosinase is a bifunctional phenol oxidase that is able to both hydroxylate monophenols like tyrosine (monooxygenase reaction, (equation 5)) and subsequently oxidize the diphenol product to the corresponding quinone (oxidase reaction, (equation 6)) at a single Type 3 binuclear copper active site.

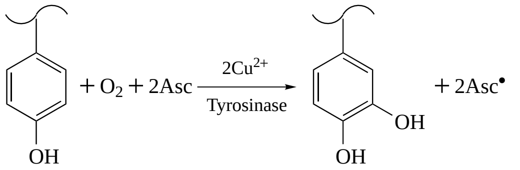

(5)

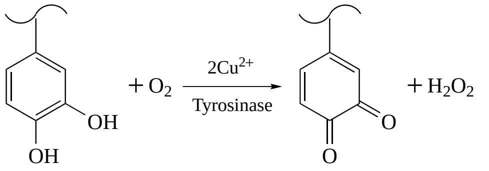

(6)

(**10**)

While tyrosinase substrates are generally small molecule phenolic compounds, the enzyme also appears to be responsible for the formation of dihydroxyphenylalanine (dopa) in molluscan proteins, including adhesive proteins (‘mussel glue’) that allow barnacles, limpets, and mussels to anchor themselves to wetted surfaces.[16] The presence of dopa residues in these polyphenolic proteins leads to cross-linking (probably *via* a peptidyl tyrosyl *o*-quinone (**10**) intermediate) forming an extremely strong polymeric resin. This unique bioadhesive is currently being investigated for potential biomedical applications.

2.3 Transferases and Lyases

2.3.1 *Galactosyl Transferase [E.C. 2.4.1.44]*

Many extracellular proteins are glycoconjugates, containing covalently bound polysaccharides that contribute to stability of the protein and may have a signaling function in cellular targeting. Carbohydrate residues are attached to proteins during secretion from the cell by specialized glycosyl transferases localized in the secretory pathway

(equation 7).

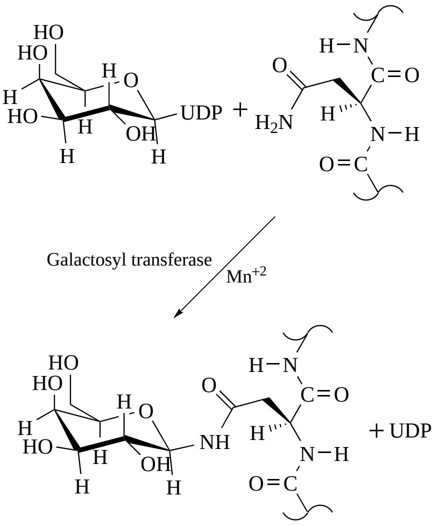

(7)

Many of these enzymes are known to be manganese dependent (*see* ***Manganese Proteins with Mono- & Dinuclear Sites***), containing a mononuclear divalent manganese ion in their active site.[17] The structures of a number of glycosyl transferases have recently been solved by X-ray crystallography, revealing a metal ion bound in mixed amine/carboxylate $[(Asp)_2(His)_1]$ coordination. The divalent metal ion is strictly required for activity, possibly functioning to activate the phosphorylated substrate. Further evidence for the importance of manganese-mediated glycosylation is provided by observation that mutational inactivation of the golgi manganese ion transporter (Pmr1p) in yeast results in aberrant processing of secretory proteins and 'supersecretion' behavior.

2.3.2 *Peptidylamidoglycolate lyase [E.C. 4.3.2.5]*

Peptidylamidoglycolate lyase completes the peptide amidation process initiated by peptidylglycine α-hydroxylating monooxygenase (*vide supra*, Section 2.1.3).[9] This zinc-dependent function converts the hydroxyglycine containing peptide to the amidated form and releases glyoxalate (equation 8):

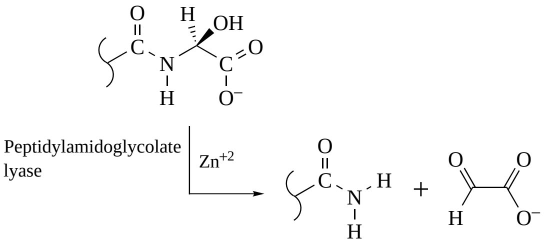

(**11**)

(8)

The role of the zinc ion in this reaction is not clearly understood, but might involve activation of coordinated water serving as a specific base in the reaction.

2.4 Metalloproteases

Proteolytic cleavage (peptide bond hydrolysis) is another way that metal-mediated posttranslational modification of proteins may occur.[18–21] Site-specific cleavage of polypeptides is essential for maturation of the protein and conversion of prohormones and cytokine precursor proteins to their biologically active forms, and proteolysis is also an important mechanism for regulating the protein activity through irreversible degradation.

2.4.1 *Methionine Aminopeptidase [E.C. 3.4.11.18]*

Virtually all proteins expressed in cells undergo processing to remove the N-terminal methionine residue encoded by the 'start codon', ATG. Cleavage of this initiation methionine from newly formed polypeptide chains is catalyzed by the enzyme methionine aminopeptidase (equation 9).

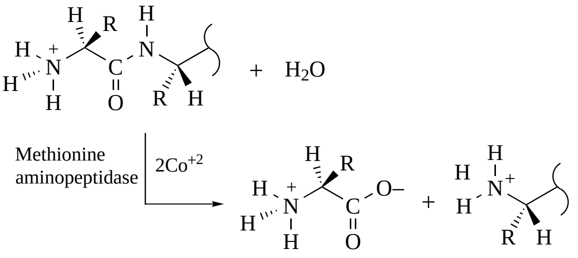

(9)

The active site of methionine aminopeptidase contains a binuclear cobalt complex that is required for activity, although a number of divalent metal ions support turnover to varying degrees. X-ray crystallographic studies on the enzyme in complexes with transition state analogs suggests that the binuclear metal cluster serves to stabilize the tetrahedral intermediate in peptide hydrolysis.[21]

2.4.2 *Zinc Metalloproteases*

Zinc metalloproteases (*see* ***Zinc Enzymes***) form an important class, distinguished by a strict requirement for a tightly bound mononuclear zinc ion cofactor. The role of the zinc ion in the hydrolytic mechanism is to polarize and activate both the coordinated peptide carbonyl and a coordinated solvent nucleophile, stabilizing the tetrahedral intermediate

(equation 10).

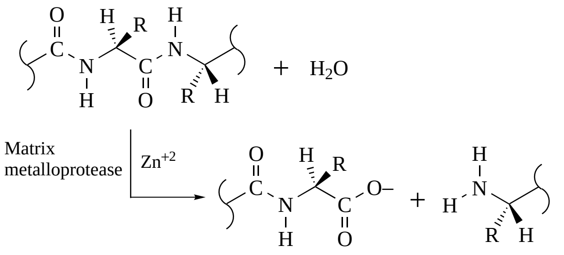

(10)

The central role of proteolytic processing by metalloproteases is illustrated by the essential functions in which they are involved. Carboxypeptidase A is a degradative enzyme that is important for recycling proteins, cleaving the C-terminal peptide bond to release free amino acids. The angiotensin converting enzyme (ACE) membrane secretase, which is responsible for the release of a peptide (angiotensin) that is involved in regulation of blood pressure, is a zinc metalloprotease that is an important target for pharmaceuticals aimed at controlling hypertension. Matrix metalloproteases are a family of zinc enzymes that have important roles in cellular regulation. Collagenase and elastase are involved in remodeling tissues during development. The ADAMs ('a disintegrin and metalloproteinase') family of zinc enzymes includes secretases and enzymes that process prohormones for release from cells. These enzymes are responsible for activating cytokines (bioactive cellular messenger molecules) including pro-TNF-α (tumor necrosis factor α), a peptide that is involved in programmed cell death. One of the matrix metalloproteases (disintegrin) has been implicated in the cleavage of β-amyloid precursor protein leading to Alzheimer's plaque formation. The specific zinc requirement of this family of proteases makes them sensitive to metal chelators (EDTA, 1,10-phenanthroline) and hydroxamate substrate analogs, features that are taken advantage of in the design of new pharmaceuticals targeting these enzymes.**[18–20]**

2.5 Peroxidase Coupling

Peroxidases are heme metalloenzymes (*see* ***Iron: Heme Proteins, Peroxidases, Catalases & Catalase-peroxidases***) that catalyze oxidation of a variety of substrates coupled to reduction of hydrogen peroxide to water. During the catalytic cycle, hydrogen peroxide oxidizes the heme to an oxy-ferryl porphyrin π cation radical species [$(P^{+\bullet})Fe(IV){=}O$] known as Compound I, which undergoes two 1-electron reduction steps. As a result, peroxidases are able to efficiently oxidize organic substrates to free radical products. Typically, the substrates for these enzymes are small organic molecules, but peroxidases have also been shown to catalyze the formation of cross-links in proteins in vitro, producing o,o'-dityrosine (**2**) dimers through a free radical coupling mechanism.**[22]** Dityrosine has been used as a biomarker for pathological protein oxidation. Covalent cross-links between tyrosine residues have been found in the egg coat proteins of certain invertebrates, suggesting the possibility of a structural role for dityrosine in biology.

3 METALLOPROTEIN SELF-PROCESSING

The simple coordination chemistry characteristic of the majority of protein–metal interactions is replaced in certain cases by irreversible covalent modifications of the protein mediated by the metal ion. These modifications are essential for the function and are templated by the structure of the protein, as no other proteins are required for the reaction to occur. These self-processing reactions result in the biogenesis of redox cofactors in some enzymes (amine oxidases, galactose oxidase, cytochrome *c* oxidase) and activation of hydrolytic sites in others (nitrile hydratase). The active sites of all of these enzymes are bifunctional, directing not only the catalytic turnover reaction of the mature enzyme but the modification steps required for maturation.

3.1 Quinocofactors

Enzymes that perform oxidation–reduction catalysis generally require some type of cofactor to store electrons (and protons) during the catalytic cycle. The cofactors are usually low-molecular weight species that reversibly bind to the enzyme, but in some cases are intrinsic elements of the protein structure. For example, *quinoenzymes* contain covalently bound quinones derived from tyrosine or tryptophan residues in the protein. These *quinocofactors* represent a striking extension of protein side-chain reactivity.**[23–27]**

There is a great deal of interest in understanding how the quinocofactors are formed. The mechanisms for the biogenesis of the tyrosine-derived quinocofactors, 2,4,5-trihydroxyphenylalanine quinone (TPQ, (**12**)) and lysine tyrosylquinone (LTQ, (**13**)) have been most extensively studied.

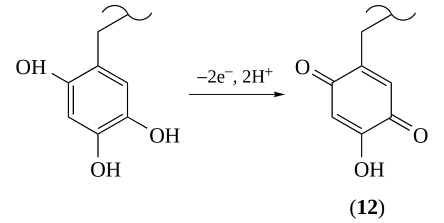

(**12**)

(11)

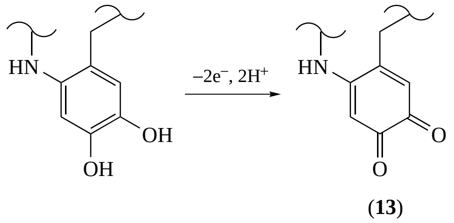

(**13**)

(12)

3.1.1 Topaquinone

Amine oxidases [E.C. 1.4.3.6] are a family of enzymes that are distributed over both prokaryotic and eukaryotic life, with the enzymes from bacteria (*Escherichia coli*, *Arthrobacter globiformis*) and plants (pea seedling) being most extensively studied (*see* ***Copper Proteins with Type 2 Sites***). All of these enzymes contain a mononuclear copper ion and a TPQ quinocofactor (**12**) that serves as both a redox center and an electrophile in the oxidation of primary amines (equation 11). Peptide mapping and gene sequencing have proven that the cofactor is derived from a tyrosyl residue in the protein, which undergoes posttranslational oxygenation to form the quinone.**28–30**

The protein is expressed in a precursor form, lacking both copper and quinocofactor. In vitro experiments have demonstrated that only copper and O_2 are required for the biogenesis reaction to occur. X-ray crystallographic studies on the self-processing reaction of *A. globiformis* amine oxidase have taken advantage of the availability of diffraction-quality crystals of the precursor apoprotein and the possibility of performing the cofactor biogenesis reaction within the crystal. The crystals are exposed to Cu^{+2} and dioxygen under controlled conditions, and the progress of the reaction followed using microspectrophotometry. The crystals are freeze-trapped for structure determination, yielding X-ray snapshots of species formed during the biogenesis of the quinocofactor.**31** This approach has provided important structural characterization of processing intermediates, as a basis for the biogenesis mechanism, illustrated in Scheme 1.**24–36**

The reaction is thought to be initiated by binding Cu^{+2} ion to the apoprotein, forming a complex in which the metal ion is coordinated by three histidine side chains and the phenolate form of the tyrosine residue that forms the cofactor (**14**). In a twist from the usual metalloprotein chemistry, dioxygen is thought to bind at a nonmetal site within the protein (**15, 16**). The presence of O_2 is thought to somehow induce a shift in the electron delocalization within the tyrosinate-Cu^{+2} charge transfer complex, stabilizing the phenoxyl radical species (**16**). The phenoxyl radical is expected to react readily with triplet dioxygen, yielding a peroxide adduct (**17**) that can lose the elements of water to form a peptidyl-dopaquinone that initially binds to the metal ion (**18**) and then dissociates (**19**). This first oxygenation product has been detected as an early intermediate in the X-ray snapshots.

The second hydroxyl group is introduced into the tyrosine side chain through attack by a metal-activated solvent molecule rather than dioxygen. Hydroxide attack at the open para-position yields trihydroxy phenylalanine (**20**), which undergoes oxidation by dioxygen to form the mature quinocofactor-containing protein (**21**) (equation 11).

3.1.2 Lysine Tyrosylquinone

The active site of lysyl oxidase contains a chromophoric quinocofactor that is distinct from, but related to TPQ.**23–26** Structural characterization (by mass spectrometry) has shown that in lysyl oxidase, a lysine side chain adds to the quinocofactor forming a covalent cross-link within the protein. This novel cofactor, which has been given the trivial name lysine tyrosyl quinone (LTQ) (**13**), is immobilized by this linkage, and exhibits an altered pattern of reactivity, forming an *o*-quinone (equation 11) rather than the *p*-quinonoid structure stabilized by TPQ (equation 12).

3.2 Cross-linked Amino Acids

Covalent linkage between two amino acid side chains within a single polypeptide chain appears to be a surprisingly common modification that may serve a function in the structure or reactivity of the protein. In addition to the cross-linked *o,o*′-dityrosine dimers (*vide supra*, Section 2.5) and the quinocofactor, LTQ (*vide supra*, Section 3.1.2), a number of other covalent structures have been identified, mainly by X-ray crystallography. These cross-linked amino acid derivatives include cysteinyl-tyrosine (**22**), histidyl-tyrosine (**23**), and cysteinyl-histidine (**24**).

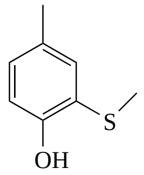

(**22**)

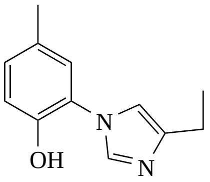

(**23**)

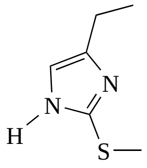

(**24**)

3.2.1 Cysteinyl-tyrosine Cofactor

The radical copper oxidases (*see* ***Copper Proteins with Type 2 Sites***), including galactose oxidase [E.C. 1.1.3.9] and glyoxal oxidase, have active sites that contain a nonquinone redox cofactor formed by covalently cross-linking cysteine and tyrosine residues to create a thioether-bridged structure, cysteinyl-tyrosine (**22**).**37,38** Unlike the TPQ cofactor in quinoproteins, the cysteinyl-tyrosine cofactor is restricted to one-electron oxidation–reduction chemistry, stabilizing a protein-free radical in the catalytically active form of the enzyme. The radical serves as a ligand to the Type 2 Cu^{+2} metal center, forming a two-electron redox unit that transfers electrons from reducing substrates (generally alcohols or simple aldehydes) to dioxygen, generating hydrogen peroxide. The presence of a modified tyrosine residue in galactose oxidase that functions as a free radical site in catalysis was recognized initially from spectroscopic studies, and the novel thioether linkage of one of the tyrosines in the active site was subsequently revealed by X-ray crystallography (Figure 1).**37,38**

The origin of the cysteinyl-tyrosine cofactor is intriguing, and early studies showed that a precursor form of the enzyme,

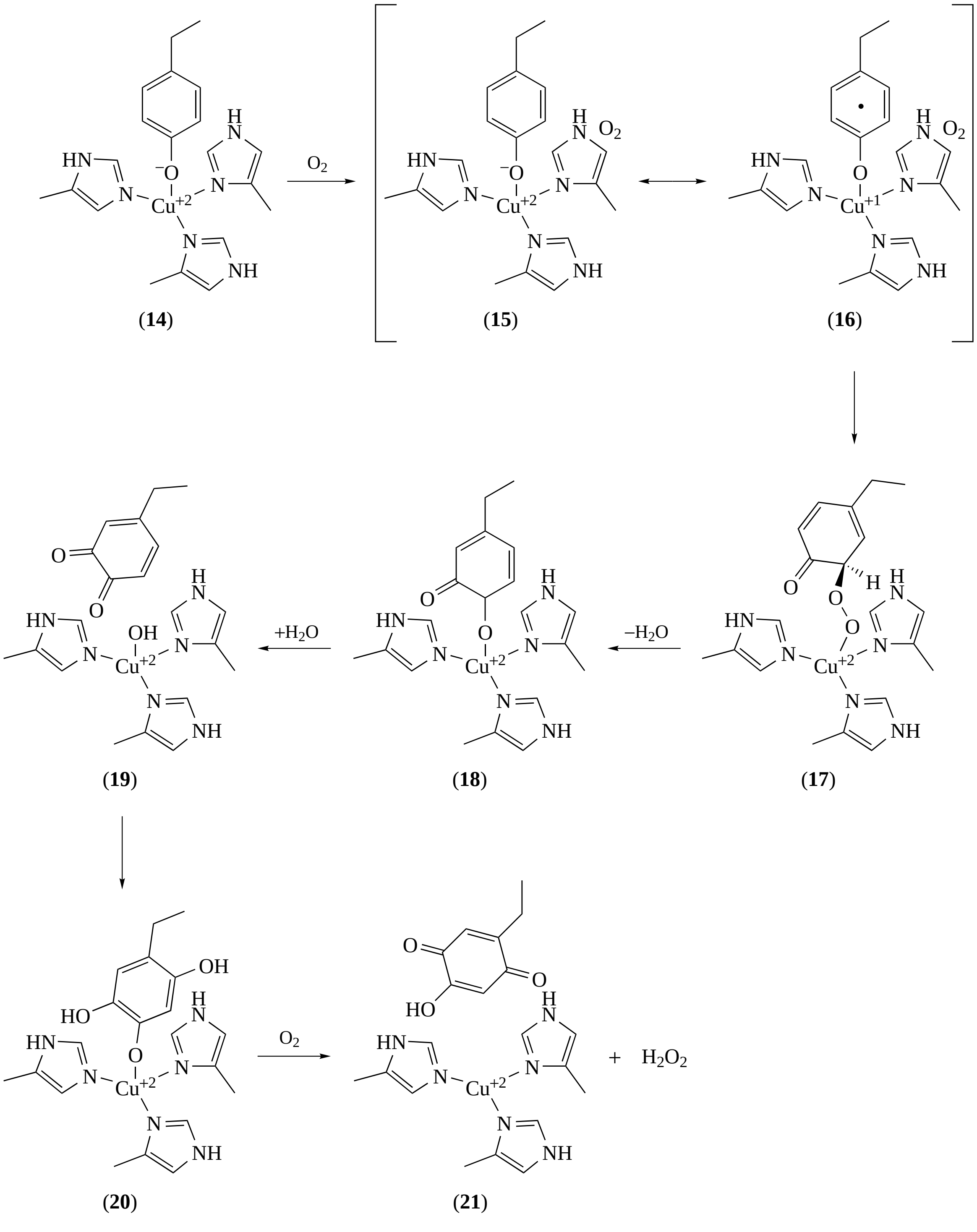

Scheme 1

lacking the cross-link, could spontaneously form the cofactor in the presence of copper and dioxygen, without assistance from any other proteins.[39] This indicates that, as seen for the amine oxidases, the active site is able to direct all of the chemistry required for cofactor biogenesis. Recent in vitro studies on the mechanism of cofactor biogenesis in galactose oxidase, using recombinant precursor protein, have demonstrated that it is a Cu^{+1}-dependent reaction.[40] Although Cu^{+2} also supports cofactor biogenesis in galactose oxidase, the reaction is >4000-fold slower when oxidized metal ion is used, and may still require slow reduction of Cu^{+2} by adventitious reductants for the reaction to proceed.

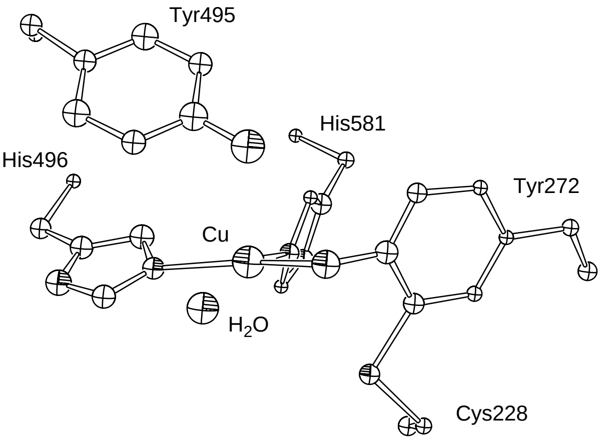

Figure 1 The active site of galactose oxidase, showing the covalent cross-link between Cys228 and Tyr272. Heteroatoms (N,O,S) are indicated by a shaded quadrant. [ortep-III view based on PDB ID 1GOG]

The mechanism for cysteinyl-tyrosine cofactor biogenesis in galactose oxidase is outlined in Scheme 2.**[40]** The metal-free precursor protein (**25**) binds Cu^{+1} in the active site (**26**) and reacts with dioxygen to form an oxygenated species related to Cu^{+2}-superoxide adduct (**27**). This reactive complex may abstract a hydrogen atom from cysteine thiol to form a thiyl radical (**28**) or oxidize the tyrosine residue to form a phenoxyl radical (**29**). Reaction of either of these radical species would generate a covalent adduct (**30**). Loss of a proton restores the conjugation of the aromatic ring system and at the same time reduces the metal ion. This mature, cross-linked Cu^{+1} complex (**31**) represents the reduced form of the active enzyme, and subsequent reaction with O$_2$ completes the biogenesis process, forming catalytically active, free radical containing active enzyme as the product (**32**).

3.2.2 Histidyl-tyrosine

The dioxygen reduction site of the key respiratory enzyme, cytochrome *c* oxidase [E.C. 1.9.3.1], is a bimetallic catalytic center comprised of a heme iron adjacent to a Type 2 mononuclear copper center (*see* ***Cytochrome Oxidase***). The recent solution of the X-ray crystal structure of this enzyme revealed an entirely unanticipated covalent modification of the protein structure, a cross-link between a histidine and tyrosine side chain (**23**) within the active site (Figure 2).**[41]** This extraordinary posttranslational modification has been confirmed by peptide mapping and mass spectrometry, and has been detected as a conserved element in cytochrome *c* oxidases isolated from organisms ranging from bacteria to cows.**[42,43]** The role of the cross-linked structure in the function of cytochrome *c* oxidase is still controversial.**[44–46]** A number of possibilities have been suggested, including a role in modulating the acidity of the active site tyrosine hydroxyl group, stabilizing a possible phenoxyl free radical intermediate during turnover, stabilizing an unusual oxidation of copper, or a structural role as rigid scaffolding supporting the metal coordination spheres. The mechanism for formation of this feature is at present entirely unknown, but is likely a self-processing reaction of the protein mediated by the metal ions.

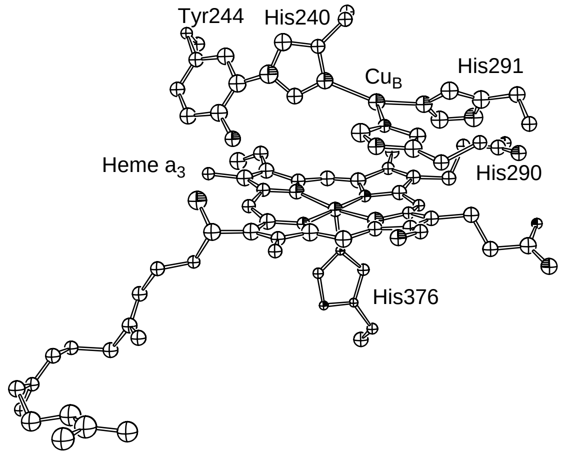

Figure 2 Oxygen-reducing Heme a$_3$-Cu$_B$ active site of fully reduced bovine cytochrome *c* oxidase, showing the covalent cross-link between His240 and Tyr244. Heteroatoms (N,O) are indicated by a shaded quadrant. [ortep-III view based on PDB ID 1OCR]

3.2.3 Cysteinyl-histidine

Cysteinyl-histidine (**24**) was first identified as a posttranslational modification of tyrosinase, detected during protein sequence analysis.**[47]** Like cysteinyl-tyrosine (**22**), it contains a thioether linkage, the sulfur being attached to the imidazole δ-carbon within the histidine side chain. Subsequent studies have identified cysteinyl-histidine in hemocyanin, the oxygen carrier protein of arthropods and molluscs that, like tyrosinase, contains a dinuclear copper site**[48]** (*see* ***Copper Proteins with Dinuclear Active Sites***). The X-ray crystal structures of the octopus oxygen transport protein hemocyanin and sweet potato catechol oxidase (Figure 3) have revealed that this protein modification is associated with the redox-active binuclear copper metal cluster, suggesting a metal-mediated origin for cysteinyl-histidine.**[49,50]**

3.3 Hydrolytic Sites

3.3.1 Nitrile Hydratase [E.C. 4.2.1.84]

Nitrile hydratase is a key enzyme involved in the microbial degradation of nitriles in the environment, catalyzing the hydration of a nitrile to an amide (*see* ***Iron Proteins with***

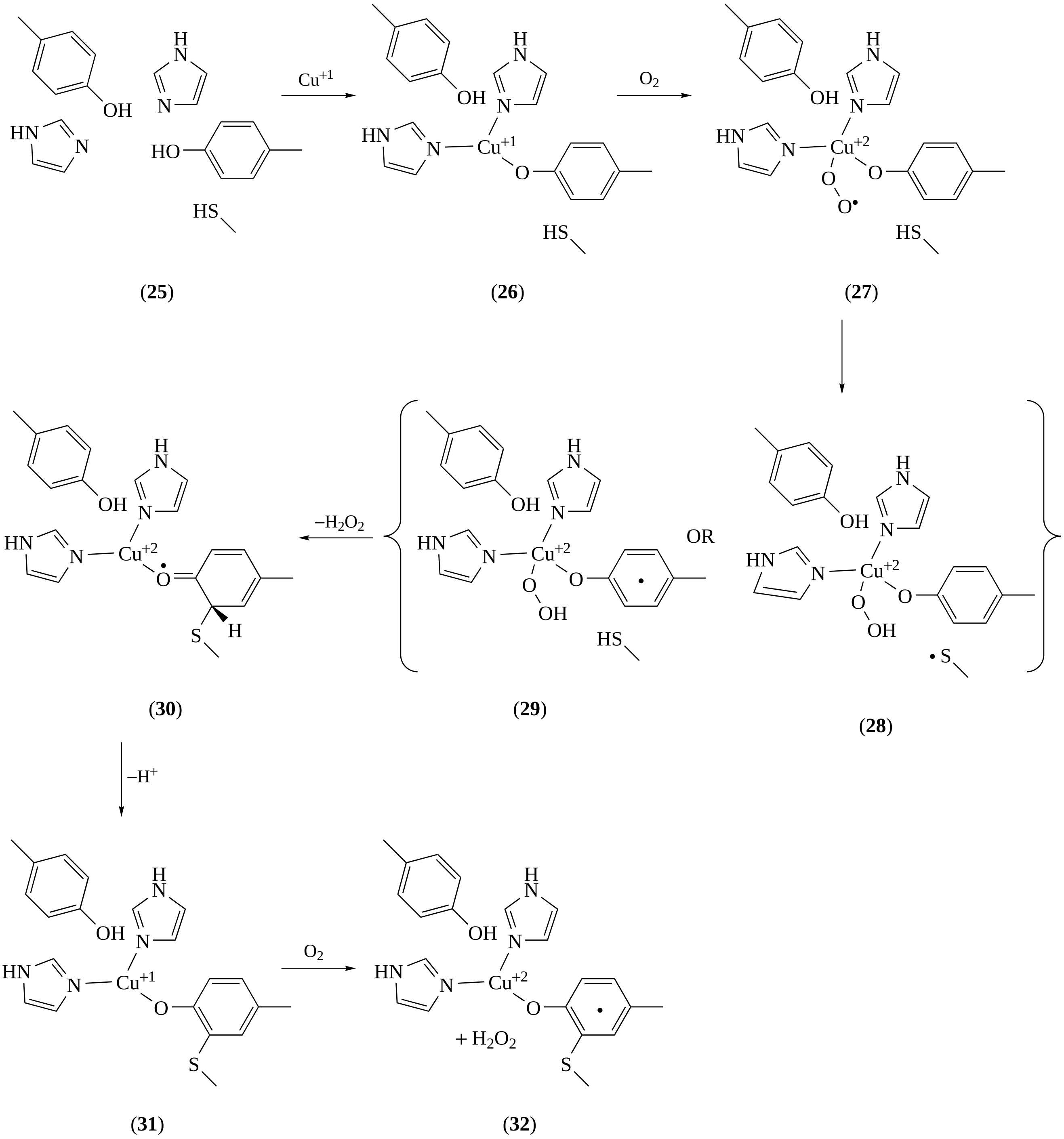

Scheme 2

Mononuclear Active Sites). This reaction has important commercial applications, and nitrile hydratase has been used industrially for enzymatic production of acrylamide from acrylonitrile. The enzyme contains a mononuclear Fe(II) (or Co(II)) active site, the metal ion being bound in a highly unusual coordination involving two deprotonated peptide amides together with three cysteine side chains (Figure 4). The two cysteines that are bound trans to the peptide ligands have been found (by X-ray crystallography) to be modified by oxygenation to cysteine-sulfenic acid (Cys-SOH (**34**)) and cysteine-sulfinic acid (Cys-SO_2H (**35**)) derivatives.[51]

Enzyme lacking these modifications is catalytically inactive, and the oxygenation occurs spontaneously when the anaerobically prepared precursor protein is exposed to O_2. The

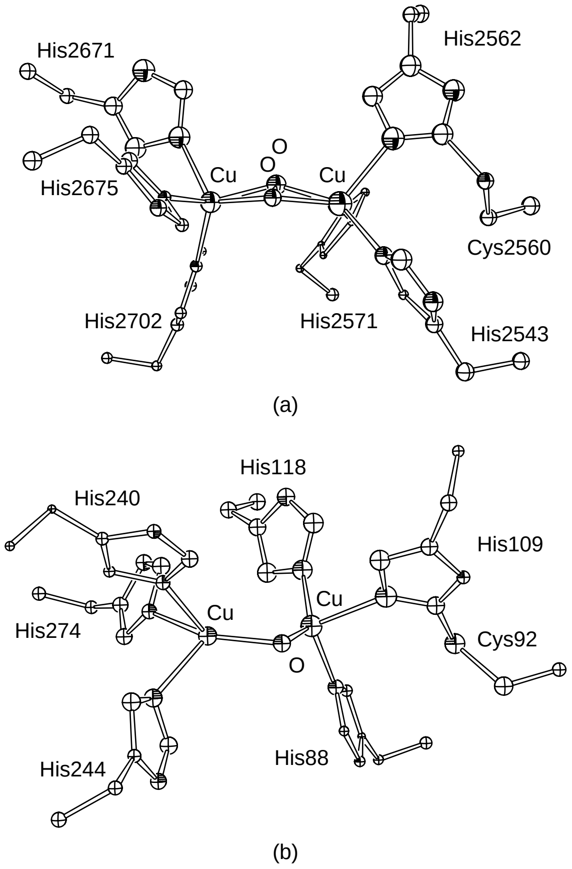

Figure 3 Binuclear copper complexes in octopus hemocyanin (a) and sweet potato catechol oxidase (b) showing the thioether linkage between a cysteine residue and a directly coordinating histidine imidazole. Heteroatoms (N,O,S) are indicated by a shaded quadrant. [ortep-III views based on PDB ID 1JS8 and 1BT1]

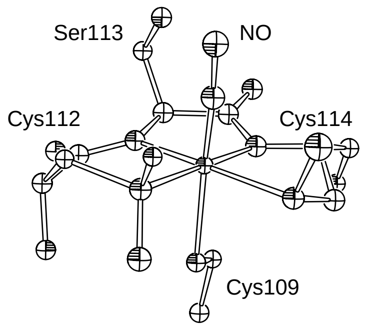

Figure 4 Active site structure of iron nitrile hydratase from *Rhodococcus erythropolis* showing modified cysteine metal ligands, Cys112-SO_2H and Cys114-SOH. [ortep-III view based on PDB ID 2AJH]

three oxygen atoms that are introduced in this self-processing reaction form a claw of hydrogen-bonding groups that may be involved in activating the nitrile substrate or coordinated water.

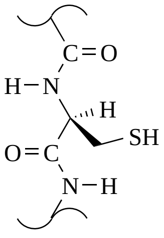

(**33**)

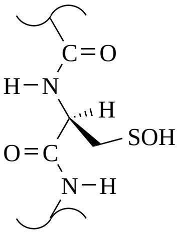

(**34**)

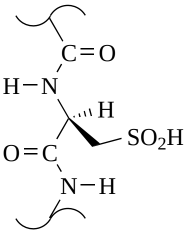

(**35**)

4 MODIFICATIONS MEDIATED BY SMALL COMPLEXES

4.1 Artificial Proteases

The understanding of the mechanistic principles underlying the catalytic chemistry of metalloproteases has been applied in the design and synthesis of a number of biomimetic metal complexes that function as artificial proteases. These complexes include mononuclear water-activating complexes, and multinuclear complexes that combine carboxyl terminal recognition, peptide carbonyl polarization, and water nucleophile activation functions.[52]

Surprisingly, the most successful artificial proteases operate by a completely nonbiomimetic mechanism, using peroxide activated by metal complexes for peptide bond cleavage. Iron chelate-mediated protein cleavage may operate through a number of different mechanisms, involving bound oxygen species or diffusible hydroxyl radicals. This approach has been refined as a tool for mapping protein–protein interactions, using tethered cutting reagents to footprint the contact surfaces between two proteins.[53]

4.2 Fenton Chemistry

Proteins are susceptible to attack by a wide variety of metal-associated oxidants resulting in covalent modifications that impair, rather than enhance, their biological function. This observation has given rise to a view that many aspects of human health (disease, aging, and cancer) are linked to oxidative stress induced by reactive oxygen species (ROS) including superoxide radical ($O_2^{-\bullet}$), hydrogen peroxide (H_2O_2), and hydroxyl radical ($HO^\bullet$), products of partial reduction of dioxygen by metal complexes.[54,55] The one-electron reactivity characteristic of transition metal complexes makes them especially potent mediators of these oxidative modifications.

The reaction of dioxygen with reduced metal complexes generates the entire series of reductively activated dioxygen species, ultimately forming the very aggressive hydroxyl radical. The aggressive oxidation chemistry associated with reductive cleavage of hydrogen peroxide by metal complexes was first reported by Fenton more than 100 years ago and these reactions are often loosely described as 'Fenton chemistry' (equation 13).[56]

$$\mathrm{Fe}^{+2} + \mathrm{H_2O_2} \xrightarrow{\mathrm{H}^+} \mathrm{Fe}^{+3} + \mathrm{HO}^{\bullet} + \mathrm{H_2O} \qquad (13)$$

In the presence of reductants (such as ascorbate), the oxidized metal complex is rereduced and is able to support redox cycling, catalytically forming ROS. The hydroxyl radical formed in this reaction is highly reactive, and can insert unselectively into virtually any C–H bond in a protein. The lack of specificity in this modification tends to make the products of protein attacked by ROS extremely heterogeneous. Biomarkers used to monitor protein oxidation include *o,o′*-dityrosine (**2**), dopa (**3**), *o*-tyrosine, methionine sulfoxide, cysteine sulfenic (**34**) and sulfinic (**35**) acids, cysteic acid (Cys-SO_3H), and kynurenine (from tryptophan).[57] Iron and copper complexes are particularly well-suited for this type of chemistry, accounting for the biological safeguards imposed on the intracellular trafficking of those metal ions.

4.3 Oxidation by Metal Complexes

In some cases, proteins react directly with metal complexes. This type of metal-mediated modification is particularly common for metals in higher oxidation states, and is thought to contribute to the toxicity of high-valent chromium [Cr(VI)] in the environment (*see* ***Chromium: Biological Relevance***). Protein side chains that are relatively easily oxidized (including tyrosine, tryptophan, and cysteine) may form free radicals. Subsequent reaction of these radicals with O_2 forms reactive oxygen species, driving Fenton chemistry (*vide supra*, Section 4.2). Copper has been implicated in biomedically important protein oxidative modifications, including oxidation of low density lipoprotein leading to atherosclerosis, and damage to neurofilaments leading to nerve cell death.[58] It is not generally possible to resolve the contributions of the metal in direct oxidation and redox cycling in vivo.

4.4 Conjugation with Substitution-inert Metal Complexes

While the majority of metal-mediated protein modifications covered in this survey involve activation of small molecules (e.g. O_2, H_2O) by metal complexes, there are some instances in which complexation of the metal ion itself serves as the mechanism of modification. Complexes with low-valent cobalt and chromium undergo relatively rapid ligand exchange, permitting solution complexes to coordinate with exposed amino acid side chains (e.g. histidine) on the surface of proteins. Oxidation of this adduct converts the complex to a substitution-inert species. The extreme inertness of Cr(III) and Co(III) complexes toward ligand-substitution reactions may be understood as a consequence of the strong ligand field stabilization of the fully coordinated ground state relative to the lower coordinate complex that corresponds to the transition state for ligand exchange. The extreme stability of these adducts (exchange lifetime >10 days) results in an essentially permanent alteration of the protein. The biological consequences of this type of modification are less severe than similar modifications of DNA, which are mutagenic, but extensive protein modification will always have a deleterious effect on cells, contributing to concerns about the widespread use of Cr(III) dietary supplements[59,60] (*see* ***Chromium: Biological Relevance***). In vitro, the stability of substitution-inert metal complexes can be used to engineer protein–metal conjugates and to introduce photochemically reactive groups for special applications.[61]

5 RELATED ARTICLES

Cobalt: Inorganic & Coordination Chemistry; Copper: Inorganic & Coordination Chemistry; Copper Proteins: Oxidases; Copper Proteins with Dinuclear Active Sites; Copper Proteins with Type 2 Sites; Cytochrome Oxidase; Iron: Heme Proteins, Peroxidases, Catalases & Catalase-peroxidases; Iron Proteins with Mononuclear Active Sites; Metal Ion Toxicity; Metal-related Diseases of Genetic Origin; Metallocenter Biosynthesis & Assembly; Metalloregulation; Peptide–Metal Interactions; Zinc Enzymes.

6 REFERENCES

1. M. Mann and O. N. Jensen, *Nat. Biotechnol.*, 2003, **21**, 255.
2. H. M. Kagan, *Acta Trop.*, 2000, **77**, 147.
3. R. J. McCormick, *Poult. Sci.*, 1999, **78**, 785.
4. K. I. Kivirikko and T. Pihlajaniemi, *Adv. Enzymol. Relat. Areas Mol. Biol.*, 1998, **72**, 325.
5. T. Pihlajaniemi, R. Myllylla, and K. I. Kivirikko, *J. Hepatol.*, 1991, **13**(Suppl. 3), S2.
6. M. J. Ryle and R. P. Hausinger, *Curr. Opin. Chem. Biol.*, 2002, **6**, 193.
7. J. C. Price, E. W. Barr, B. Tirupati, J. M. Bollinger Jr, and C. Krebs, *Biochemistry*, 2003, **42**, 7497.
8. S. Englard and S. Seifter, *Ann. Rev. Nutr.*, 1986, **6**, 365.
9. S. T. Prigge, R. E. Mains, B. A. Eipper, and L. M. Amzel, *Cell Mol. Life Sci.*, 2000, **57**, 1236.
10. L. I. Smith-Mungo and H. M. Kagan, *Matrix Biol.*, 1998, **16**, 387.
11. H. M. Kagan, *Path. Res. Pract.*, 1994, **190**, 910.

12. R. B. Rucker, T. Kosonen, M. S. Clegg, A. E. Mitchell, B. R. Rucker, J. Y. Uriu-Hare, and C. L. Keen, *Am. J. Clin. Nutr.*, 1998, **67**(Suppl. 5), 996S.
13. S. Y. Seo, V. K. Sharma, and N. Sharma, *J. Agric. Food Chem.*, 2003, **51**, 2837.
14. J. C. Garcia-Borron and F. Solano, *Pigment Cell Res.*, 2002, **15**, 162.
15. C. Gerdemann, C. Eicken, and B. Krebs, *Acc. Chem. Res.*, 2002, **35**, 183.
16. L. O. Burzio, V. A. Burzio, T. Silva, L. A. Burzio, and J. Pardo, *J. Curr. Opin. Biotechnol.* 1997, **8**, 309.
17. J. D. Crowley, D. A. Traynor, and D. C. Weatherburn, *Met. Ions Biol. Syst.*, 2000, **37**, 209.
18. M. D. Sternlicht and Z. Werb, *Ann. Rev. Cell. Dev. Biol.*, 2001, **17**, 463.
19. N. M. Hooper, E. H. Karran, and A. J. Turner, *Biochem. J.*, 1997, **321**, 265.
20. N. M. Hooper and A. J. Turner, *Bioch. Soc. Trans.*, 2000, **28**, 441.
21. W. T. Lowther, Y. Zhang, P. B. Sampson, J. F. Honek, and B. W. Matthews, *Biochemistry*, 1999, **38**, 14810.
22. O. M. Lardinois and P. R. de Montellano, *J. Biol. Chem.*, 2001, **276**, 23186.
23. T. E. Stites, A. E. Mitchell, and R. B. Rucker, *J. Nutr.*, 2000, **130**, 719.
24. D. M. Dooley, *J. Inorg. Biol. Chem.*, 1999, **4**, 1.
25. K. Tanizawa, *J. Biochem. (Tokyo)*, 1995, **118**, 671.
26. B. Schwartz and J. P. Klinman, *Vitam. Horm. (San Francisco)*, 2001, **61**, 219.
27. J. P. Klinman, *Proc. Natl. Acad. Sci. U.S.A.*, 2001, **98**, 14766.
28. S. M. Janes, D. Mu, D. Wemmer, A. J. Smith, S. Kaur, D. Maltby, A. L. Burlingame, and J. P. Klinman, *Science*, 1990, **248**, 981.
29. R. Matsuzaki, S. Suzuki, K. Yamaguchi, T. Fukui, and K. Tanizawa, *Biochemistry*, 1995, **34**, 4524.
30. C. E. Ruggiero, J. A. Smith, K. Tanizawa, and D. M. Dooley, *Biochemistry*, 1997, **36**, 1953.
31. M. Kim, T. Okajima, S. Kishishita, M. Yoshimura, A. Kawamori, K. Tanizawa, and H. Yamaguchi, *Nat. Struct. Biol.*, 2002, **9**, 591.
32. J. E. Dove, B. Schwartz, N. K. Williams, and J. P. Klinman, *Biochemistry*, 2000, **39**, 3690.
33. D. Cai and J. P. Klinman, *J. Biol. Chem.*, 1994, **269**, 32039.
34. Y. H. Choi, R. Matsuzaki, T. Fukui, E. Shimizu, T. Yorifuji, H. Sato, Y. Ozaki, and K. Tanizawa, *J. Biol. Chem.*, 1995, **270**, 4712.
35. C. E. Ruggiero and D. M. Dooley, *Biochemistry*, 1999, **38**, 2892.
36. B. Schwartz, J. E. Dove, and J. P. Klinman, *Biochemistry*, 2000, **39**, 3699.
37. J. W. Whittaker, *Adv. Prot. Chem.*, 2002, **60**, 1.
38. N. Ito, S. E. V. Phillips, C. Stevens, Z. B. Ogel, M. J. McPherson, J. N. Keen, K. D. S. Yadav, and P. F. Knowles, *Nature*, 1991, **350**, 87.
39. M. S. Rogers, A. J. Baron, M. J. McPherson, P. F. Knowles, and D. M. Dooley, *J. Am. Chem. Soc.*, 2000, **122**, 990.
40. M. M. Whittaker and J. W. Whittaker, *J. Biol. Chem.*, 2003, **278**, 22090.
41. S. Yoshikawa, K. Shinzawa-Itoh, R. Nakashima, R. Yaono, E. Yamashita, N. Inoue, M. Yao, M. J. Fei, C. P. Libeu, T. Mizushima, H. Yamaguchi, T. Tomizaki, and T. Tsukihara, *Science*, 1998, **280**, 1723.
42. C. Ostermeier, A. Harrenga, U. Ermler, and H. Michel, *Proc. Natl. Acad. Sci. U.S.A.*, 1997, **94**, 10547.
43. G. Buse, T. Soulimane, M. Dewor, H. E. Meyer, and M. Bluggel, *Prot. Sci.*, 1999, **8**, 985.
44. F. MacMillan, A. Kannt, J. Behr, T. Prisner, and H. Michel, *Biochemistry*, 1999, **38**, 9179.
45. T. K. Das, C. Pecoraro, F. L. Tomson, R. B. Gennis, and D. L. Rousseau, *Biochemistry*, 1998, **37**, 14471.
46. E. Pinakoulaki, U. Pfitzner, B. Ludwig, and C. Varotsis, *J. Biol. Chem.*, 2002, **277**, 13563.
47. K. Lerch, *J. Biol. Chem.*, 1982, **257**, 6414.
48. C. Gielens, N. De Geest, X. Q. Xin, B. Devreese, J. Van Beeumen, and G. Preaux, *Eur. J. Biochem.*, 1997, **248**, 879.
49. M. E. Cuff, K. I. Miller, K. E. van Holde, and W. A. Hendrickson, *J. Mol. Biol.*, 1998, **278**, 855.
50. T. Klabunde, C. Eicken, J. C. Sacchettini, and B. Krebs, *Nat. Struct. Biol.*, 1998, **5**, 1084.
51. A. Miyanaga, S. Fushinobu, K. Ito, and T. Wakagi, *Biochem. Biophys. Res. Commun.*, 2001, **288**, 1169.
52. J. Suh, *Acc. Chem. Res.*, 2003, **36**, 562.
53. S. A. Datwyler and C. F. Meares, *TIBS*, 2000, **25**, 408.
54. G. J. Brewer, *J. Cell. Mol. Med.*, 2003, **7**, 11.
55. E. R. Stadtman, *Ann. N.Y. Acad. Sci.*, 2001, **938**, 22.
56. H. J. H. Fenton, *Proc. Roy. Soc.*, 1893, **9**, 113.
57. H. R. Griffiths, *Free Rad. Res.*, 2000, **33**, S47.
58. M. J. Burkitt, *Arch. Biochem. Biophys.*, 2001, **394**, 117.
59. D. S. Lamson and S. M. Plaza, *Altern. Med. Rev.*, 2002, **7**, 218.
60. Z. N. Kenkare and D. G. Federman, *Compr. Ther.*, 2002, **28**, 148.
61. H. B. Gray and J. R. Winkler, *Annu. Rev. Biochem.*, 1996, **65**, 537.

Acknowledgment

Partial support for this work by the National Institutes of Health (GM 46749) is gratefully acknowledged.

Metallocenter Biosynthesis & Assembly

Scott B. Mulrooney & Robert P. Hausinger
Michigan State University, East Lansing, MI, USA

1 Introduction 1
2 Reversible Metal Ion Binding 1
3 Metallochaperone Delivery of Metal Ion or Cofactor 2
4 Enzymatically Catalyzed Posttranslational Modification at the Metal-binding Site 3
5 Synergistic Binding of Metal with Another Component 4
6 Synthesis of Metal-containing Cofactors and Use of Scaffold Proteins 5
7 Metal Incorporation Coupled to Electron Transfer 5
8 Requirement for an Apoprotein-specific Molecular Chaperone 6
9 Related Articles 7
10 References 7

Abbreviations

CCS = copper chaperone for superoxide dismutase; Moco = molybdenum cofactor; MPT = molybdopterin; FeMoco = iron-molybdenum cofactor of nitrogenase, SOD1 = Cu/Zn superoxide dismutase.

1 INTRODUCTION

Although metalloproteins have been characterized intensively for decades, investigators have only recently focused on the mechanisms of biological metallocenter assembly.[1,2] Here, we briefly describe several recurring themes (summarized in Table 1) that are used, often in a combined manner, for cellular synthesis of metal sites. This summary draws from a recent, more comprehensive treatment of this subject.[3] In the simplest situation, metal binding to a biological ligand occurs by reversible thermodynamic control. The prevalence of buried metallocenters, the exceedingly low concentrations of free metal ions within cells, and the sophisticated structures of many metal-containing active sites provide evidence that alternative approaches also must exist. In some cases, metallochaperones are used to deliver the metal of interest to an apoprotein. In other cases, the target protein undergoes posttranslational modification at the metal-binding site, either prior to or after the metal is bound. Many metallocenters contain additional components that are added along with the metal ion or used to form an independent metal-containing cofactor, perhaps with the assistance of a scaffolding protein. Electron transfer reactions involving the metal, an added compound, or the protein ligand can participate in activation. Finally, molecular chaperones that bind to and alter the conformation of the target apoprotein may be utilized. In many cases, the function of the molecular chaperone is coupled to nucleotide triphosphate hydrolysis. Additional complications of metallocenter biosynthesis exist within cells, but are not highlighted here: uptake of metal ions,[4] sensing and controlling of cellular metal levels (*see* ***Metalloregulation*** and ***Metallochaperones & Metal Ion Homeostasis***),[5] and intercompartmental trafficking of metals and metal-containing proteins.[6]

2 REVERSIBLE METAL ION BINDING

The interactions between some biological macromolecules (L) and their requisite metal ions (M^{n+}) are governed simply by thermodynamic control, such as that illustrated in equation (1).

$$\mathrm{L} + \mathrm{M}^{n+} \rightleftharpoons \mathrm{L{\cdot}M}^{n+} \qquad (1)$$

In these situations, the ligand's specificity and affinity for the metal ion as well as the metal ion's coordination geometry depend both on the metal ion properties and on factors associated with the macromolecular ligand.[7,8] Metal ions vary in their charge, radius, ligand exchange lability, ligand preference (e.g. hardness/softness; *see* ***Hard & Soft Acids and Bases***), and position in the Irving-Williams series. Similarly, the fold of a protein or other biological macromolecule, its rigidity, and the properties of its side chains (e.g. pK_a, polarizability, and location in a particular secondary structure) dictate its interactions with the metal ions.

Intracellular Ca-regulated proteins (*see* ***Calcium-binding Proteins***) provide a nice illustration of reversible metal ion binding.[9] For example, calmodulin, a small acidic protein involved in the regulation of selected phosphatases, kinases, and other enzymes, reversibly binds four Ca^{2+} ions.[10] Each of the hard Ca^{2+} ions is coordinated by 7 hard oxygen ligands contributed by amino acid side chains that comprise the so-called 'EF hand' helix-loop-helix motif. Analogous sites are found in troponin C, parvalbumin, calbindins, and additional Ca-binding proteins. For calmodulin, the reversible interaction shown in equation (1) is oversimplified because binding of the first two Ca^{2+} ions occurs in a cooperative manner with an average binding constant of approximately $2 \times 10^5\,\mathrm{M}^{-1}$ whereas the third and fourth ions are associated with binding constants of about $3 \times 10^4\,\mathrm{M}^{-1}$. The binding of calcium ions leads to the exposure of hydrophobic sites

Table 1 General mechanisms of metallocenter biosynthesis[a]

Mechanism	Equation(s) representing the indicated mechanism[b]
1. Reversible metal ion binding	$\mathrm{L} + \mathrm{M}^{n+} \rightleftharpoons \mathrm{L{\cdot}M}^{n+}$
2. Metallochaperone delivery of metal ion or cofactor	$\mathrm{L_1{\cdot}M}^{n+} + \mathrm{L_2} \rightleftharpoons \mathrm{L_1} + \mathrm{L_2{\cdot}M}^{n+}$
3. Enzymatically catalyzed posttranslational modification to create a metal-binding site	$\mathrm{L} \longrightarrow \mathrm{L}^*$ *and* $\mathrm{L}^* + \mathrm{M}^{n+} \rightleftharpoons \mathrm{L^*{\cdot}M}^{n+}$
4. Synergistic binding of metal with another component	$\mathrm{L} + \mathrm{M}^{n+} + \mathrm{X} \rightleftharpoons \mathrm{L{\cdot}M}^{n+}{\cdot}\mathrm{X}$
5. Synthesis of metal-containing cofactors and use of scaffold proteins	$\mathrm{Y} + \mathrm{M}^{n+} \longrightarrow \mathrm{Y{\cdot}M}^{n+}$ *and* $\mathrm{Y{\cdot}M}^{n+} + \mathrm{L} \rightleftharpoons \mathrm{L{\cdot}Y{\cdot}M}^{n+}$
6. Metal incorporation coupled with electron transfer	$\mathrm{L} + \mathrm{M}^{n+} \longrightarrow \mathrm{L{\cdot}M}^{(n+)+1} + \mathrm{e}^-$ *or* $\mathrm{L} + \mathrm{M}^{n+} + \mathrm{X}^{y+} + \mathrm{z\ e}^- \longrightarrow \mathrm{L{\cdot}M}^{n+}{\cdot}\mathrm{X}^{y+(-z)}$
7. Requirement for an apoprotein-specific molecular chaperone	$\mathrm{C{\cdot}L} + \mathrm{M}^{n+}(+\mathrm{NTP}) \longrightarrow \mathrm{L{\cdot}M}^{n+} + \mathrm{C}(+\mathrm{NDP} + \mathrm{P_i})$

[a]These mechanisms are not mutually exclusive. Many examples of metallocenter synthesis utilize multiple mechanisms. In addition, it is important to note that metallocenter assembly can be driven by nucleotide hydrolysis reactions, typically involving mechanism 7. [b]L, protein ligand; L*, covalently modified ligand; X, non-metal component of a metallocenter; Y, component required for the synthesis of a metal-containing cofactor; C, molecular chaperone.

on calmodulin, likely responsible for its interaction with the calmodulin-associated proteins listed above.

Investigators studying metallocenter properties can exploit such thermodynamic control to substitute alternate metal ions into selected proteins.**11** In this process, the original metal ions are removed by chelation, often using extreme conditions such as low pH/denaturants, and the resulting apoproteins are incubated with high concentrations of the desired metal ions to obtain the metal-substituted species. For example, the metal sites of many Zn-containing enzymes (*see **Zinc Enzymes***) have been replaced by Co to facilitate spectroscopic analyses. Five-coordinate Co^{2+} often exhibits intense ligand-to-metal charge-transfer transitions, and Co^{2+} is paramagnetic so that EPR spectroscopy can be used to monitor the metal site. While such an approach can help define the properties of selected metallocenters, this method of metal incorporation may have little relevance to the in vivo mechanism of metallocenter assembly.

Significantly, thermodynamic control cannot explain many metal ion–protein interactions.**12** This point is highlighted by the Cu-containing proteins (*see **Copper Proteins with Type 1 Sites***) that form despite the reported absence of free copper ions in the cell.**13,14** This claim is based on the measured zeptomolar (10^{-21} M) sensitivity of the *Escherichia coli* copper regulatory protein CueR and on the estimation of less than 10^{-18} M Cu in yeast, determined on the basis of superoxide dismutase activity measurements; for comparison, one atom of free Cu per yeast cell (10^{-14} liters) would correspond to a concentration of 10^{-10} M. An analogous situation may well exist for Zn,**15** where the intracellular concentration is estimated at 10^{-11} M.**16** It is still unclear whether Fe, Mo, Ni, Co, and other biologically important metal ions exist at significant concentrations as the ‘‘free’’ species (i.e. the hydrated metal ions) in the cell.**12** Not unexpectedly, expression of genes encoding metal transporters and permeases that accumulate these ions are tightly regulated (*see **Metalloregulation***).**5** In this way, cells strike a balance in which metal concentrations are maintained at levels sufficient for growth while preventing deleterious effects. The low concentrations of free metal ions observed within cells imply that reversible metal ion binding to ligands is unlikely to account for the synthesis of most metallocenters. Furthermore, the metallocenters of many proteins are buried within a rigid framework. This finding demands that the metal ions must bind to the ligand during the folding process, an unlikely scenario, or that an alternative mechanism exists for incorporating the metal (Sections 3 through 8).

3 METALLOCHAPERONE DELIVERY OF METAL ION OR COFACTOR

Metallochaperones (*see **Metallochaperones & Metal Ion Homeostasis***) are metal-binding proteins ($\mathrm{L_1}$) designed to deliver the appropriate metal ion or metal cofactor to a target ligand ($\mathrm{L_2}$), as illustrated in equation (2).

$$\mathrm{L_1{\cdot}M}^{n+} + \mathrm{L_2} \rightleftharpoons \mathrm{L_1} + \mathrm{L_2{\cdot}M}^{n+} \qquad (2)$$

It is important to note the distinction between metallochaperones and molecular chaperones that assist in protein folding. The best-studied protein chaperones, such as GroEL, Hsp70, and Hsp40,**17** prevent the misfolding or stimulate the refolding of a wide range of proteins by processes that generally require nucleotide triphosphate hydrolysis. These generalized or ‘housekeeping’ protein chaperones are certain to play a role in the synthesis of many metalloproteins. In addition, Section 8 describes a subset of metalloprotein-specific molecular chaperones that bind to a target apoprotein and confer an appropriate conformation needed to bind a metal ion or cofactor. Nucleotide triphosphate hydrolysis is carried out by a subset of these chaperones, presumably to provide a driving force for their reactions. In contrast to such molecular chaperones that bind proteins, metallochaperones bind metal ions or metal cofactors and deliver them to their highly specific targets.

Perhaps the clearest examples of metallochaperones are small, cytoplasmic proteins (e.g. Atx1 in yeast, Atox1 (or Hah1) in humans, or CopZ in bacteria) that function to deliver Cu^{1+} to secretory pathway ATPases.[6,18–22] Three-dimensional structures are known for these three proteins and for domain 4 of a target protein (the Menkes disease protein, Mnk4) in various metal-bound states. Both the metallochaperones and the target proteins bind Cu^{+1} using two Cys residues found in a MT/HCXXC motif, and a model of the Hah1:Mnk4 complex identifies other critical residues likely to be needed for protein:protein interactions. The mechanism of Cu^{1+} transfer between the metallochaperone and the target domain is proposed to involve ligand exchange reactions with two- and three-coordinate intermediates. Significantly, reversible Cu^{1+} transfer between the two proteins occurs with an equilibrium constant near unity. This equilibrium does not provide enough thermodynamic driving force for efficient metallocenter assembly; thus, these metallochaperones are hypothesized to function like enzymes that provide kinetic control. The mechanism by which Cu^{+1} initially becomes bound to the metallochaperones has not been elucidated.

Other copper metallochaperones exhibit a range of more complex behaviors. For example, a protein often considered to be a mitochondrial copper metallochaperone, Cox17, contains a polynuclear copper site coordinated by thiolate ligands,[18,19] as opposed to a single metal ion binding site. The copper chaperone for superoxide dismutase (CCS) has three domains: domain I is related to Atx1, domain II structurally resembles the target enzyme, and domain III contains a critical Cys-X-Cys motif. Cu/Zn superoxide dismutase (SOD1) activation likely initiates by the swapping of domain II in dimeric CCS with one subunit of dimeric Zn-containing SOD1, yielding two molecules of the heterodimer. Domain I of CCS obtains Cu^{1+} from an unknown source and transfers the metal ion to domain III. Domain III then rotates its position to deliver Cu to the SOD1 active site. Of note, this transfer involves a change in Cu coordination from Cys ligation to binding by His ligands and appears to require an oxygen-dependent step.[19] A reasonable scenario is that this step involves both oxidation of the metal and oxidation of Cys229 in CCS and Cys55 of SOD1 to form a disulfide bond, thus propping open the active site, followed by disulfide exchange to yield a Cys55-Cys144 disulfide in SOD1. The CCS:SOD1 complex has been structurally characterized.[19]

Three Ni-containing enzymes (*see* ***Nickel Enzymes & Cofactors***) appear to utilize Ni metallochaperones for enzyme activation.[23,24] UreE appears to function in Ni^{2+} delivery to urease. The *Klebsiella aerogenes* protein binds ∼6 Ni per dimer, whereas that from *Bacillus pasteurii* binds a single Ni per dimer. The metal content differences arise from a His-Asp-His sequence near the middle and a histidine-rich region at the carboxyl terminus of the former protein. Truncated *K. aerogenes* UreE protein, missing the His-rich region, and UreE variants lacking the His-Asp-His motif also function in urease activation. Structures of the truncated *K. aerogenes* protein and full-length *B. pasteurii* UreE reveal nearly identical protein folds, with a conserved Ni binding site located at the dimer interface. Surprisingly, the Ni-binding domain of UreE closely resembles the fold of the Cu-binding Atx1 metallochaperone. The UreE proteins contain a second module that structurally resembles a domain of an Hsp40-type molecular chaperone protein.[23] It may be that the chaperone-like module participates in UreE docking to its partner protein while the metal-binding domain transfers Ni to urease apoprotein. The metallochaperone functions even in the presence of chelators, indicating that UreE is not simply a reversible carrier of Ni in this process. HypA and HypB can be considered to serve as Ni metallochaperones for hydrogenase activation. HypA binds stoichiometric levels of Ni and forms a complex with HypB.[25] In some microorganisms, HypB also binds multiple Ni atoms using an *N*-terminal histidine-rich motif, reminiscent of the situation for some UreE proteins involved in urease activation. Finally, carbon monoxide dehydrogenase appears to use a Ni metallochaperone (CooJ) for enzyme activation.[23,24]

Metallochaperones alternatively can bind metal cofactors rather than metal ions, as illustrated by the heme chaperone involved in synthesis of *c*-type cytochromes.[26] Biosynthesis of cytochrome *c* in *Escherichia coli* requires the products of eight cytochrome *c* maturation (*ccm*) genes as well as several multipurpose proteins.[27] The apoprotein is secreted across the cytoplasmic membrane into the periplasmic space by the Sec system, and the apoprotein thiols are reduced in order to react with the heme vinyl groups. Meanwhile, the heme is transported across the membrane by a still poorly understood process that might involve CcmA and CcmB. Within the periplasm, heme is covalently bound to a His residue of CcmE, acting as a heme chaperone.[28] CcmC is essential for heme attachment, but CcmD, CcmA, and CcmB facilitate this process. In the last step of biosynthesis, heme is transferred from CcmE to the reduced cytochrome *c* apoprotein. This process appears to use CcmF as a bacterial heme lyase, perhaps in association with CcmG and/or CcmH. The thioether linkages of heme to the protein ensure that cytochrome *c* remains a stable redox cofactor.

4 ENZYMATICALLY CATALYZED POSTTRANSLATIONAL MODIFICATION AT THE METAL-BINDING SITE

Some proteins tightly bind their cognate metal ion only after the nascent apoprotein (L) undergoes a covalent modification reaction (producing L*), as shown in equations (3) and (4).

$$L \longrightarrow L^* \quad (3)$$

$$L^* + M^{n+} \rightleftharpoons L^*{\cdot}M^{n+} \quad (4)$$

Several blood clotting factors, other plasma proteins, and bone proteins are modified at selected glutamyl groups by the action of a vitamin K-dependent carboxylase.[29,30] The resulting γ-carboxyglutamic acid residues chelate Ca^{2+} and aid in maintaining protein:protein and protein:membrane interactions. Similarly, a specific interaction with Ca^{2+} occurs in proteins containing enzymatically derivatized epidermal growth factor domains, such as those present in coagulation factors, complement proteins, and transforming growth factors.[30] Specific aspartyl and asparaginyl groups in these proteins are hydroxylated by an α-ketoglutarate-dependent dioxygenase to produce β-hydroxyaspartyl and β-hydroxyasparaginyl residues that bind the metal ions. Calcium ions also interact tightly with dentin or bone phosphoproteins that are very rich in phosphoserine residues.[31] These promote deposition of calcium phosphate or calcium hydroxylapatite during tooth and bone development. As a final example, the egg yolk protein phosvitin contains adjacent phosphoserine residues that form a tight complex (binding constant near $10^{18}\,M^{-1}$) with Fe^{3+}, important for trace metal ion storage during embryonic development.[32]

A related type of posttranslational modification accompanying metal binding involves proteolysis. An excellent example of such a situation is associated with hydrogenase activation.[23,33,34] In this case, a protease recognizes the Ni-containing large subunit precursor and proteolysis leads to a conformational change that buries the metallocenter. A similar proteolysis-based process may function in the stable incorporation of manganese into the oxygen-evolving complex.[35]

Posttranslational modifications alternatively can occur after a metal ion binds to a protein (*see* ***Metal-mediated Protein Modification***), in some cases involving a change in metal redox state or chemical transformations of another component. The resulting modifications may impart a specific enzymatic activity to the protein, tune the reactivity of the protein metallocenter, stabilize metal ion binding, or inactivate the enzyme. Often, the modifications derive from autocatalytic reactions directly involving the bound metal; however, accessory enzymes may be needed to recognize the metal-bound form of the protein and catalyze the chemical changes. Galactose oxidase contains a tyrosyl side chain linked by a thioether bond to a cysteine residue. The tyrosine that becomes modified first binds Cu^{1+} and is oxidized to a tyrosyl radical (as the metal is oxidized to Cu^{2+}) then reacts with the cysteine side chain.[36,37] Cytochrome *c* oxidases (*see* ***Cytochrome Oxidase***) contain a crosslink between tyrosine and histidine side chains, where the histidine is a ligand to Cu. The precise role of this modification is controversial, but its presence in enzymes from both bacteria and higher eukaryotes highlights its importance. Various other types of oxidations can occur on tyrosine[38,39] or cysteinyl[40] side chains after metal ion binding. In addition, self-hydroxylations of aromatic amino acids near the active sites of many nonheme iron oxygenases are known to occur,[41] often accompanied by enzyme inactivation.

5 SYNERGISTIC BINDING OF METAL WITH ANOTHER COMPONENT

The interaction of metal ions with some proteins is accompanied by the binding of another nonmetal component (X), as illustrated in equation (5).

$$L + M^{n+} + X \rightleftharpoons L\cdot M^{n+}\cdot X \qquad (5)$$

The identity of the accessory compound can range widely, as shown by the following examples. The metallocenter of ribulosebisphosphate carboxylase/oxygenase is comprised of both Mg^{2+} and an activating CO_2 molecule.[42,43] Assembly of this site proceeds in a stepwise fashion with CO_2 reacting with the ε-amino group of a specific lysyl residue to form a carbamate that serves as one of the metal ligands. Analogous CO_2-dependent metal-binding reactions occur during activation of a number of dinuclear hydrolases including phosphotriesterase[44] and urease.[45] In these enzymes, the carbamate bridges the two metal ions bound to the active site. The metallocenter of transferrin consists of both ferric ion and the carbonate dianion, with the carbonate acting as a bridge between the protein and the metal.[46] Kinases and phosphotransferases often bind their required metal ions concurrently with their substrate (e.g. the MgATP complex). Proteins containing Fe–S clusters[47–49] require a source of inorganic sulfur and this is provided by accessory proteins. In pioneering studies, the *Azotobacter vinelandii* NifS was shown to be a pyridoxal phosphate-dependent L-cysteine desulfurase that creates an enzyme-bound persulfide for use in the production of Fe–S clusters in nitrogenase proteins (*see* ***Nitrogenase Catalysis & Assembly***).[50,51] Essentially all organisms subsequently have been shown to possess homologous activities for use in the Fe–S cluster synthesis.[52,53] As a final example, Fe-only hydrogenases[34,54] and NiFe-hydrogenases[23,33] possess Fe sites with bound cyanide and carbon monoxide molecules. Cyanide synthesis involves HypF and HypE proteins for *E. coli* hydrogenase.[55,56] Critical insight into this process was obtained by experiments with an *E. coli carAB* mutant, deficient in carbamoylphosphate synthesis, that requires carbamoylphosphate for hydrogenase activation. Purified HypF transfers the carbamoyl group from carbamoyladenylate to the carboxyl terminus of HypE.[56,57] HypE dehydrates the protein-bound thiocarbamate to yield an enzyme thiocyanate which, after reduction, provides the cyanide ligand.[56] CO ligands may derive from similar chemistry with an added hydrolysis step. The activation of these enzymes requires that both the metal ions and the diatomic molecules be incorporated.

6 SYNTHESIS OF METAL-CONTAINING COFACTORS AND USE OF SCAFFOLD PROTEINS

Activation of selected metalloproteins requires the prior synthesis of a cofactor that contains both metal and an additional organic or inorganic component (Y), as shown in equations (6) and (7).

$$\mathrm{Y} + \mathrm{M}^{n+} \longrightarrow \mathrm{Y{\cdot}M}^{n+} \tag{6}$$

$$\mathrm{Y{\cdot}M}^{n+} + \mathrm{L} \rightleftharpoons \mathrm{L{\cdot}Y{\cdot}M}^{n+} \tag{7}$$

Perhaps the best-characterized example of this mechanism involves the synthesis of heme cofactors and their subsequent incorporation into various hemoproteins (*see* ***Iron: Heme Proteins & Electron Transport***). Succinctly, enzyme-catalyzed reactions convert either succinyl-CoA or glutamate into δ-aminolevulinic acid. This molecule is further converted through a series of intermediates to form protoporphyrin IX, the metal-free cofactor, into which Fe is inserted by ferrochelatase.[58] Analogous reactions are required for the synthesis of other tetrapyrrole macrocycles such as the cobalamins (*see* ***Cobalt: B_{12} Enzymes & Coenzymes***), various types of chlorophylls, and the methanogen coenzyme F_{430} (containing Co, Mg, or Ni, respectively). Co- and Mg-chelatases have been described for insertion of these metals into the appropriate tetrapyrrolic ring structures.[59,60]

Molybdenum-containing enzymes (*see* ***Molybdenum: Organometallic Chemistry***), with the exception of nitrogenase described below, possess a complex with Mo coordinated to one or two molecules of a tricyclic pyranopterin (also known as molybdopterin, MPT) forming the molybdenum cofactor (Moco).[61–63] Moco biosynthesis has been extensively detailed in *Escherichia coli* by using a combination of biochemical, genetic, and structural approaches, and additional insights are provided by studies in other microorganisms and eukaryotes. The first step involves the conversion of GTP or a closely related compound into precursor Z by MoaA and MoaC. In this remarkable reaction, the C-8 carbon of the guanine base is inserted between the $2'$ and $3'$ carbons of the ribose ring. The detailed mechanism of this reaction is unknown, but the sequence of MoaA indicates similarity to members of the ‘radical SAM’ family of proteins that catalyze radical-based reactions using *S*-adenosylmethionine and Fe–S clusters.[64] The role of MoaC in the reaction is unclear, but its structure has been elucidated. The second phase of Moco synthesis involves conversion of precursor Z to MPT in reactions catalyzed by MoaD, MoaE, and MoeB. Biochemical and structural studies involving complexes formed by MoeB plus MoaD and MoaD plus MoaE reveal that MoeB activates the *C*-terminus of MoaD by adenylation, and activated MoaD is modified by a sulfur transferase using cysteine-derived sulfur, resulting in a protein ending in a thiocarboxylate. The sulfur atoms from two MoaD thiocarboxylates are transferred by MoaE onto precursor Z to form the dithiolene group of MPT. MogA, a potential MPT carrier,[65] has been structurally characterized. MoeA appears to facilitate incorporation of Mo into MPT.[65,66] Its structure reveals four domains including one that resembles MogA, consistent with a role in MPT or Moco binding. In most prokaryotic Mo-containing enzymes, Moco is further modified by conversion to the guanine, cytosine, or hypoxanthine dinucleotide forms. For example, MobA transforms Moco into molybdopterin guanine dinucleotide. The structure of MobA has been determined and the biochemical properties of this reaction unraveled. These enzymes appear to be structurally and functionally similar to previously characterized nucleotide diphospho sugar transferases.

Some metallocenters are first synthesized on a scaffold protein and subsequently incorporated into the target enzyme. For example, the iron-molybdenum cofactor (FeMoco) of nitrogenase (*see* ***Nitrogenase Catalysis & Assembly***) is first assembled on NifEN (i.e. the products of the *nifE* and *nifN* genes) and then transferred into the NifDK enzyme apoprotein.[50,67] Notably, the two scaffold proteins are structurally related to the nitrogenase subunits. Scaffold proteins need not always be related in sequence to the final protein targets as demonstrated by accessory protein components involved in the synthesis of Fe–S cluster proteins (*see* ***Iron–Sulfur Proteins***).[52,53] A series of proteins (e.g. NifU, IscU, IscA, SufA) accept sulfur from L-cysteine desulfurases and appear to function as scaffolds for Fe–S cluster synthesis. Various biophysical approaches have been used to demonstrate that the sulfur donor and cognate sulfur acceptor proteins form complexes.[51,68] Questions remain about the precise types of interactions occurring between the donor/acceptor proteins, the source of Fe, and the possible types of clusters that can be generated in the scaffold proteins. Nevertheless, the overall pattern is conserved, with these proteins being acceptors of the Fe and S for cluster synthesis.

7 METAL INCORPORATION COUPLED TO ELECTRON TRANSFER

The synthesis of some metallocenters is coupled to one or more electron transfer reactions. Depending on the example, the redox step may involve the metal, another component, or a side chain of the protein. Direct metal oxidation during metallocenter assembly (equation 8) is nicely illustrated by synthesis of the ferrihydrite core of ferritin (*see* ***Iron Proteins for Storage & Transport & their Synthetic Analogs***) or formation of the tetramanganese cluster in the oxygen-evolving photoreaction center (*see* ***Manganese: The Oxygen-evolving Complex & Models***).

$$\mathrm{L} + \mathrm{M}^{n+} \longrightarrow \mathrm{L{\cdot}M}^{(n+)+1} + \mathrm{e}^- \tag{8}$$

Ferritin is an iron storage protein comprised of 24 subunits (a mixture of H subunits with M_r 22–24 kDa and L subunits with M_r 20–22 kDa) that associate to form a hollow sphere capable of binding up to 4500 iron atoms.[69,70] Nucleation of the iron core is initiated at a ferroxidase site that binds two Fe^{2+} ions, reacts with oxygen to form a transient peroxodiferric species,[71] and releases H_2O_2 while yielding a μ-hydroxo (or oxo) diferric precursor. After its nucleation, the core grows primarily by oxidative processes on the surface of the mineral particle. In contrast, the water-oxidizing complex of photosystem II is formed by stepwise binding and oxidation of four Mn^{2+},[72] with the electrons transferred to other components of the photosynthetic system. More generally, synthesis of Cu^{2+} and Fe^{3+} sites in proteins often involves initial binding of Cu^{1+} and Fe^{2+} followed by oxidation to stabilize the metal ions.

Other examples illustrate how reduction of an accessory component may be required for metallocenter synthesis (equation 9).

$$\mathrm{L} + \mathrm{M}^{n+} + \mathrm{X}^{y+} + z\,\mathrm{e}^- \longrightarrow \mathrm{L}\cdot\mathrm{M}^{n+}\cdot\mathrm{X}^{y+(-z)} \qquad (9)$$

For example, incorporation of nickel into carbon monoxide dehydrogenase of *Rhodospirillum rubrum* requires the prior reduction of an Fe–S cluster.[73] Structural studies of this protein reveal that the added Ni completes a unique [1Ni-4Fe-4S] center that is required for activity.[74] Another example of a reductive activation step occurs during NiFe-hydrogenase biosynthesis, perhaps involving participation of the Fe–S cluster in HypD.[55] Yet a third example from the Ni-enzyme literature involves the synthesis of methyl-*S*-coenzyme M reductase, a methanogen enzyme that contains the Ni-tetrapyrrole cofactor F_{430}.[23] Formation of active enzyme requires both the reduction of Ni^{2+} to Ni^{1+} and reduction of a C=N bond in the organic macrocycle.[75]

The third redox-dependent process involved in metallocenter assembly requires changes to the protein, typically involving cysteine residues. For example, disulfide bonds that are spontaneously generated or enzymatically formed in periplasmic proteins must be reduced to create metal-binding thiolates or for cytochrome *c* biosynthesis. The opposite reaction, oxidation of cysteines during metallocenter assembly appears to be required for SOD1 activation.

8 REQUIREMENT FOR AN APOPROTEIN-SPECIFIC MOLECULAR CHAPERONE

Several metalloproteins incorporate their metal centers by processes that appear to involve apoprotein-specific molecular chaperones (C). These proteins stabilize a required conformation of the target apoprotein, often catalyze nucleotide triphosphate hydrolysis, and dissociate after activation (equation 10); thus, they bind the apoprotein but are not part of the final holoprotein.

$$\mathrm{C}\cdot\mathrm{L} + \mathrm{M}^{n+}(+\mathrm{NTP}) \longrightarrow \mathrm{L}\cdot\mathrm{M}^{n+} + \mathrm{C}(+\mathrm{NDP} + \mathrm{P_i}) \qquad (10)$$

These apoprotein-specific molecular chaperones target only their particular apoprotein partners, but otherwise resemble in function the well-studied molecular chaperones such as GroEL, Hsp70, and Hsp40 that bind to and prevent misfolding or stimulate refolding of a wide range of proteins.[17,76]

UreG and HypB are putative GTP-dependent apoprotein-specific molecular chaperones for urease and hydrogenase.[23] GTP-dependent urease activation requires a nucleotide-binding site located within UreG. Hydrogenase biosynthesis involves the HypB- and GTP-dependent insertion of Ni into a $Fe(CO)(CN)_2$-containing HypC:pre-HycE complex. Of interest, HypB is related in sequence to UreG and exhibits low levels of GTPase activity.[33]

Apoprotein-specific chaperones also are implicated in the biosynthesis of Fe–S cluster proteins and Moco-containing enzymes. Hsc20 and Hsc66, encoded by genes within the *isc* (iron–sulfur cluster biosynthesis) operon, are related to the known molecular chaperones DnaK and DnaJ. Surface plasmon resonance and titration calorimetry approaches reveal that a scaffold protein containing an Fe–S cluster forms a complex with Hsc20, which directs it to Hsc66.[77] This interaction stimulates Hsc66 ATPase activity by 480-fold via interaction with the Hsc66 substrate binding site.[78] The incorporation of Moco and its modified forms into molybdoenzymes often requires an additional protein component, as first noted for maturation of nitrate reductase where NarJ participates after Moco synthesis was complete.[61,62] NarJ and related proteins (e.g. TorD involved in activation of trimethylamine *N*-oxide)[79] are suggested to play molecular chaperone-type roles in the activation process.

At least two molecular chaperone-like activities are associated with nitrogenase biosynthesis. In one case, the γ or NifY proteins form complexes with nitrogenase lacking its FeMoco.[50,67] These proteins prop open and allow access to the enzyme active site, bind and insert FeMoco, and then dissociate from the nitrogenase holoprotein. Formation of the complex between γ or NifY proteins and FeMoco-free nitrogenase is achieved by action of the second nitrogenase-related chaperone, dinitrogenase reductase, in an ATP-dependent manner.[50] Of interest, the [4Fe-4S] center of dinitrogenase reductase is required for its function in electron delivery to nitrogenase, but not for its action as a chaperone.

A final example of an apoprotein-specific molecular chaperone involved in metallocenter activation is associated with *Streptomyces* tyrosinase. Insertion of Cu into the tyrosinase apoprotein (encoded by *melC2*) requires complex formation with the product of *melC1* that stabilizes an appropriate apoprotein conformation, inserts the metal, and assists in secretion of the active enzyme.[80]

9 RELATED ARTICLES

Calcium-binding Proteins; Copper Enzymes in Denitrification; Copper Proteins with Type 1 Sites; Copper Proteins with Type 2 Sites; Iron: Heme Proteins & Electron Transport; Iron–Sulfur Proteins; Metal-mediated Protein Modification; Metallochaperones & Metal Ion Homeostasis; Molybdenum: MPT-containing Enzymes; Nickel Enzymes & Cofactors, Nitrogenase Catalysis & Assembly; Zinc Enzymes.

10 REFERENCES

1. R. P. Hausinger, *BioFactors*, 1990, **2**, 179.
2. R. P. Hausinger, G. L. Eichhorn, and L. G. Marzilli, ‘Mechanisms of Metallocenter Assembly’, VCH Publishers, New York, 1996.
3. J. Kuchar and R. P. Hausinger, *Chem. Rev.*, 2004, **104**, 509.
4. D. J. Eide, *Adv. Microb. Physiol.*, 2000, **43**, 1.
5. S. Silver and W. Walden, ‘Metal Ions in Gene Regulation’, Chapman & Hall, New York, 1998.
6. T. V. O’Halloran and V. C. Culotta, *J. Biol. Chem.*, 2000, **275**, 25057.
7. S. J. Lippard, and J. M. Berg, ‘Principles of Bioinorganic Chemistry’, University Science Books, Mill Valley, CA, 1994.
8. J. J. R. Fraùsto da Silva and R. J. P. Williams, ‘The Biological Chemistry of the Elements’, Clarendon Press, Oxford, 1991.
9. S. Forsén and J. Kördel, Calcium in Biological Systems, in ‘Bioinorganic Chemistry’, eds. I. Bertini, H. B. Gray, S. J. Lippard, and J. S. Valentine, University Science Books, Mill Valley, CA, 1994, p. 107.
10. D. Chin and A. R. Means, *Trends Cell Biol.*, 2000, **10**, 322.
11. D. S. Auld, *Meth. Enzymol.*, 1995, **248**, 228.
12. L. A. Finney and T. V. O’Halloran, *Science*, 2003, **300**, 931.
13. T. D. Rae, P. J. Schmidt, R. A. Pufahl, V. C. Culotta, and T. V. O’Halloran, *Science*, 1999, **284**, 805.
14. A. Changela, K. Chen, Y. Xue, J. Holschen, C. E. Outten, T. V. O’Halloran, and A. Mondragón, *Science*, 2003, **301**, 1383.
15. C. E. Outten and T. V. O’Halloran, *Science*, 2001, **292**, 2488.
16. R. J. P. Williams, *Coord. Chem. Rev.*, 2001, **216–217**, 583.
17. F. U. Hartl and M. Hayer-Hartl, *Science*, 2002, **295**, 1852.
18. S. Puig and D. J. Thiele, *Curr. Opin. Chem. Biol.*, 2002, **6**, 171.
19. A. C. Rosenzweig, *Chem. Biol.*, 2002, **9**, 673.
20. A. C. Rosenzweig, *Acc. Chem. Res.*, 2001, **34**, 119.
21. D. L. Huffman and T. V. O’Halloran, *Annu. Rev. Biochem.*, 2001, **70**, 677.
22. M. D. Harrison, C. E. Jones, M. Solioz, and C. T. Dameron, *Trends Biochem. Sci.*, 2000, **25**, 29.
23. S. B. Mulrooney and R. P. Hausinger, *FEMS Microbiol. Rev.*, 2003, **27**, 239.
24. R. K. Watt and P. W. Ludden, *Cell. Mol. Life Sci.*, 1999, **56**, 604.
25. N. S. Mehta, J. W. Olson, and R. J. Maier, *J. Bacteriol.*, 2003, **185**, 726.
26. L. Thöny-Meyer, *Biochemistry*, 2003, **42**, 13099.
27. L. Thöny-Meyer, *Biochem. Soc. Trans.*, 2002, **30**, 633.
28. H. Schultz, H. Hennecke, and L. Thöny-Meyer, *Science*, 1998, **281**, 1197.
29. B. Furie, B. A. Bouchard, and B. C. Furie, *Blood*, 1999, **93**, 1798.
30. T. Drakenberg, M. Sunnerhagen, and J. Stenflo, Generation of Calcium-binding Sites in Proteins by Formation of δ-carboxyglutamic Acid and β-hydroxyaspartic Acid/β-hydroxyasparagine, in ‘Mechanisms of Metallocenter Assembly’, eds. R. P. Hausinger, G. L. Eichhorn, and L. G. Marzilli, VCH Publishers, New York, 1996, p. 41.
31. W. T. Butler, *Eur. J. Oral Sci.*, 1998, **106**, 204.
32. J. Hegenauer, P. Saltman, and G. Nace, *Biochemistry*, 1979, **18**, 3865.
33. L. Casalot and M. Rousset, *Trends Microbiol.*, 2001, **9**, 228.
34. P. M. Vignais, B. Billoud, and J. Meyer, *FEMS Microbiol. Rev.*, 2001, **25**, 455.
35. B. A. Diner, D. Ries, B. N. Cohen, and J. G. Metz, *J. Biol. Chem.*, 1988, **263**, 8972.
36. M. M. Whittaker, D. P. Ballou, and J. W. Whittaker, *Biochemistry*, 1998, **37**, 8426.
37. M. S. Rogers and D. M. Dooley, *Curr. Opin. Chem. Biol.*, 2003, **7**, 189.
38. N. K. Williams and J. P. Klinman, *J. Mol. Catal. B*, 2000, **8**, 95.
39. R. P. Pesavento and W. A. van der Donk, *Adv. Prot. Chem.*, 2001, **58**, 317.
40. I. Endo, M. Nojiri, M. Tsujimura, M. Nakasako, S. Nagashima, M. Yohda, and M. Odaka, *J. Inorg. Biochem.*, 2001, **83**, 247.
41. M. J. Ryle and R. P. Hausinger, *Curr. Opin. Chem. Biol.*, 2002, **6**, 193.
42. W. W. Cleland, T. J. Andrews, S. Gutteridge, F. C. Hart8man, and G. H. Lorimer, *Chem. Rev.*, 1998, **98**, 549.
43. D. Walther, M. Ruben, and S. Rau, *Coord. Chem. Rev.*, 1999, **182**, 67.
44. F. M. Rauschel and H. M. Holden, *Adv. Enzymol. Rel. Areas Mol. Biol.*, 2000, **74**, 51.
45. R. P. Hausinger and P. A. Karplus, Urease, in ‘Handbook of Metalloproteins’, eds. K. Wieghardt, R. Huber, T. L. Poulos, and A. Messerschmidt, John Wiley & Sons, West Sussex, 2001, p. 867.
46. O. Zak, K. Ikuta, and P. Aisen, *Biochemistry*, 2002, **41**, 7416.
47. H. Beinert, R. H. Holm, and E. Münck, *Science*, 1997, **277**, 653.

48. H. Beinert, *J. Biol. Inorg. Chem.*, 2000, **5**, 2.
49. D. C. Rees and J. B. Howard, *Science*, 2003, **300**, 929.
50. J. Frazzon and D. R. Dean, *Metal Ions Biol. Syst.*, 2002, **39**, 163.
51. H. Mihara and N. Esaki, *Appl. Microbiol. Biotechnol.*, 2002, **60**, 12.
52. J. Frazzon and D. R. Dean, *Curr. Opin. Chem. Biol.*, 2003, **7**, 166.
53. R. Lill and G. Kispal, *Trends Biochem. Sci.*, 2000, **25**, 352.
54. Y. Nicolet, C. Cavazza, and J. C. Fontecilla-Camps, *J. Inorg. Biochem.*, 2002, **91**, 1.
55. M. Blokesch, A. Paschos, E. Theodoratou, A. Bauer, M. Hube, S. Huth, and A. Böck, *Biochem. Soc. Trans.*, 2002, **30**, 674.
56. S. Reissmann, E. Hochleitner, H. Wang, A. Paschos, F. Lottspeich, R. S. Glass, and A. Böck, *Science*, 2003, **299**, 1067.
57. A. Paschos, A. Bauer, A. Zimmermann, E. Zehelein, and A. Böck, *J. Biol. Chem.*, 2002, **277**, 49945.
58. H. A. Dailey, T. A. Dailey, C. K. Wu, A. E. Medlock, K. F. Wang, J. P. Rose, and B. C. Wang, *Cell. Mol. Life Sci.*, 2000, **57**, 1909.
59. E. Raux, H. L. Schubert, and M. J. Warren, *Cell. Mol. Life Sci.*, 2000, **57**, 1880.
60. C. J. Walker and R. D. Willows, *Biochem. J.*, 1997, **327**, 321.
61. H. Schindelin, C. Kisker, and K. V. Rajagopalan, *Adv. Prot. Chem.*, 2001, **58**, 47.
62. R. R. Mendel and G. Schwarz, *Metal Ions Biol. Syst.*, 2002, **39**, 317.
63. R. R. Mendel and R. Hänsch, *J. Exp. Bot.*, 2002, **53**, 1689.
64. J. Cheek and J. B. Broderick, *J. Biol. Inorg. Chem.*, 2001, **6**, 209.
65. J. Nichols and K. V. Rajagopalan, *J. Biol. Chem.*, 2002, **277**, 24995.
66. C. Sandu and R. Brandsch, *Arch. Microbiol.*, 2002, **178**, 465.
67. J. Frazzon and D. R. Dean, *Met. Ions Biol. Syst.*, 2002, **39**, 163.
68. T. Kurihara, H. Mihara, S. Kato, T. Yoshimura, and N. Esaki, *Biochim. Biophys. Acta*, 2003, **1647**, 303.
69. M. A. Carrondo, *EMBO J.*, 2003, **22**, 1959.
70. N. D. Chasteen and P. M. Harrison, *J. Struct. Biol.*, 1999, **126**, 182.
71. J. Hwang, C. Krebs, B. H. Huynh, D. E. Edmondson, E. C. Thiel, and J. E. Penner-Hahn, *Science*, 2000, **287**, 122.
72. A.-F. Miller and G. W. Brudvig, *Biochemistry*, 1990, **29**, 1385.
73. S. A. Ensign, M. J. Campbell, and P. W. Ludden, *Biochemistry*, 1990, **29**, 2162.
74. C. L. Drennan, J. Heo, M. D. Sintchak, E. Schreiter, and P. W. Ludden, *Proc. Natl. Acad. Sci. U.S.A.*, 2001, **98**, 11973.
75. Q. Tang, P. E. Carrington, Y.-C. Horng, M. J. Maroney, S. W. Ragsdale, and D. F. Bocian, *J. Am. Chem. Soc.*, 2002, **124**, 13242.
76. P. Wittung-Stafshede, *Acc. Chem. Res.*, 2002, **35**, 201.
77. K. G. Hoff, J. J. Silberg, and L. E. Vickery, *Proc. Natl. Acad. Sci. U.S.A.*, 2000, **97**, 7790.
78. J. J. Silberg, K. G. Hoff, T. L. Tapley, and L. E. Vickery, *J. Biol. Chem.*, 2001, **276**, 1696.
79. M. Ilbert, V. Méjean, M.-T. Giudici-Orticoni, J.-P. Samama, and C. Iobbi-Nivol, *J. Biol. Chem.*, 2003, **278**, 28787.
80. Y. H. W. Lee, Role of MelC1 as a Chaperone for Streptomyces Tyrosinase Copper Assembly, in ‘Mechanisms of Metallocenter Assembly’, eds. R. P. Hausinger, G. L. Eichhorn, and L. G. Marzilli, VCH Publishers, New York, 1996, p. 223.

Acknowledgments

Research on metallocenter biosynthesis in the authors’ laboratory is supported by NIH grant DK45686 (to R.P.H.).

Metallochaperones & Metal Ion Homeostasis

Valeria C. Culotta
Johns Hopkins University Bloomberg School of Public Health, Baltimore, MD, USA

1 Introduction 1
2 Metal Trafficking Pathways Involving Copper 2
3 Metal Trafficking Pathways Involving Manganese 5
4 Perspectives 6
5 Related Articles 6
6 References 6

Glossary

ATX1: copper chaperone for the Cu transporting P-type ATPase in the Golgi
CCS: copper chaperone for the largely cytosolic Cu/Zn superoxide dismutase
Copper transporting P-type ATPase: a membrane transporter for copper that uses energy derived from ATP hydrolysis to drive copper transport
COX17: copper carrying molecule for the mitochondria
IMS: intermembrane space of mitochondria, lying between the inner and outer membranes of this organelle
Metal chaperone: molecule that binds a specific metal and helps insert this ion into the metal binding site of a metalloprotein
Metalloprotein: protein that binds a specific metal ion and requires that metal ion for proper function
Metal transporter: transmembrane protein responsible for the translocation of metal ions across a lipid bilayer
MTM1: mitochondrial inner membrane transporter needed for activating SOD2 with manganese
SCO: Copper carrying molecule, possibly the copper chaperone or copper insertion factor for cytochrome oxidase
SMF2: intracellular metal transporter essential for manganese trafficking
SOD1: copper and zinc containing form of superoxide dismutase, a superoxide anion scavenging enzyme
SOD2: manganese containing form of superoxide dismutase localized in the mitochondrial matrix

1 INTRODUCTION

1.1 The Notion of 'Metal Trafficking'

The proteins that require metal ions as cofactors are numerous and are assorted in diverse cellular locations. How is it that these vastly different proteins all acquire their partner metal ion in an accurate and efficient manner? The process is quite complex and involves the cooperation of membrane transporters and metal carrying metallochaperones.

In order for a metal ion to reach its intracellular protein target, a number of complex barriers must be crossed. First, the metal existing in the extracellular environment must traverse the plasma membrane of the cell. The lipid bilayers of cellular membranes are generally impermeable to metals and cellular uptake of the ion requires the action of metal transport proteins. A host of membrane transporters reside at the cell surface, some of which are specific for certain ions (e.g. only copper or only zinc), while others are more promiscuous in their choice of metal ion substrate (e.g. can transport both copper and zinc). But all are designed to ensure that cells acquire proper levels of the essential heavy metal ions such as copper, zinc, iron, and manganese.

Once inside the cell, the metal is subjected to one of several fates. For example, the ion may be directly shuttled to metal requiring enzymes in the soluble cytosol. But many metalloproteins reside within membrane bound organelles (e.g. the Golgi or mitochondria) and the metal needs to traverse an additional membrane. As with cell surface transport, the translocation of metals across intracellular membranes is facilitated by heavy metal transporters.

In addition to the membrane bound transporters, the delivery of certain metals to their cognate metalloprotein involves the action of highly specific 'metal chaperone' or 'metallochaperone' proteins. These metal carriers are often soluble, as opposed to membrane associated, and act to directly insert the metal into the proper site of the metalloprotein.

Overall, a metal ion is not permitted to freely move about within a cell, but instead is personally escorted to its destination through the combined action of metal transporters and metal chaperones working in concert. This process of moving metals inside cells is commonly referred to as 'metal trafficking'. And many such highways exist in eukaryotic cells (reviewed in[1]).

1.2 Why do Metals Need Trafficking?

The requirement for metal ion trafficking is not intuitively obvious, as it might seem less energy intensive to move the ion by random diffusion. In a test tube setting, a metal ion will generally insert itself into the correct site of a metalloprotein with ease; most metalloproteins in fact exhibit a high affinity for their partner metal ion. However, the situation inside a living cell is not so simple. Although metals may accumulate in cells to concentrations that far exceed the binding affinity of their cognate metalloprotein, the fraction of the total metal which is actually bioavailable is extraordinarily low. Through elegant studies in the laboratory of Tom O'Halloran, it has been estimated that in spite of the micromolar quantities of copper or zinc accumulated by a cell, not a single atom is freely available to react in the cytoplasm.[2,3]

Metals such as zinc, copper, iron, and manganese are not only essential for life, but are potentially toxic and if left unchecked, these ions can cause much havoc to the cell. In fact, all organisms are equipped with a host of metal detoxification pathways that act to sequester or remove metals, thereby preventing these ions from reacting with biomolecules. An example of one such metal detoxification system is the metal binding metallothionein protein (MT). Genes that encode the MTs are induced under metal toxicity conditions and the encoded MT proteins serve to 'mop up' excess metals, preventing toxicity from these ions. With such efficient metal scavenging systems, it seems quite a challenge for metalloproteins to find their cognate cofactor. This challenge is overcome in part through the action of metal trafficking proteins, specifically the aforementioned metal chaperones that act to spare a few ions from detoxification and ensure the safe delivery of metals to metalloproteins. It would then appear that the metal detoxification and metal trafficking pathways are at odds with one another. While the detoxification systems protect the *cell from the metal*, the metallochaperones protect the *metal from the cell*.

2 METAL TRAFFICKING PATHWAYS INVOLVING COPPER

Much of the current state of knowledge regarding metal trafficking pathways has emerged from studies on copper. Copper is a redox-active metal that can readily donate or accept electrons, and as such, serves as an ideal catalytic cofactor for reactions involving oxygen chemistry.

In eukaryotes, extracellular copper can enter the cell via a cell surface high affinity transporter for the metal. The first of this type of copper transporter, known as CTR1, was originally discovered in baker's yeast by Andrew Dancis.[4] Homologues exist in humans and other eukaryotes as well. A mouse containing a homozygous deletion in CTR has been created in the laboratory of Dennis Theile and this mouse exhibited profound developmental defects and embryonic lethality.[5] Hence this single pathway of high affinity copper uptake is essential for mammalian development and viability.

Once copper has entered the cell, it is subject to one of several fates. When the metal is readily abundant or present in excess, a large fraction of copper is subject to detoxification, largely by sequestration within MTs (Figure 1). This is thought to represent a dead-end fate of the metal. However, a separate pool of the metal is spared from detoxification and enters one of three major copper trafficking pathways. These pathways independently supply copper to proteins in the secretory pathway, in the cytoplasm, and in the mitochondria (Figure 1). These three pathways will now be discussed independently.

2.1 Delivering Copper to Enzymes in the Secretory Pathway

A number of copper requiring enzymes are located at the cell surface or are exported into the extracellular milieu. Examples of such 'secretory Cu-enzymes' include copper requiring ferroxidases that function in iron transport (e.g. ceruloplasmin, CP), enzymes for neurotransmission (peptidyl amidating enzyme and dopamine β hydroxylase), an extracellular superoxide dismutase (SOD) that functions in antioxidant defense and enzymes for formation of connective tissue (lysyl oxidase), and pigments (tyrosinase) (reviewed in[6]). En route to their designated location, each of these enzymes passes through a specialized compartment of the late Golgi where copper insertion takes place.

Copper enters the late Golgi compartment through the action of a specialized membrane copper transporter. This transporter is a member of a family of so-called 'P-type' ATPase transporters that derive energy from ATP hydrolysis to translocate copper from the cytoplasm across the Golgi membrane into the lumen of the Golgi. Two such copper transporters have been identified in humans and these are known as the Wilson disease and Menkes disease proteins (*see* ***Metalloregulation***).[6] Mutations in the corresponding genes have been linked to inherited disorders of copper transport and metabolism in humans. Homologues to these transporters have been identified in virtually every eukaryotic cell and in each case, the transporter protein contains at its amino terminus, a repeat of 2–6 short protein domains that have the capacity to bind copper.

The copper that serves as the substrate for the copper transporting ATPase finds it way to the transporter via the action of a cytosolic copper chaperone known as ATX1 (yeast)[7] or ATOX1/HAH1 (mammals).[8] We originally identified ATX1 in 1995 as a potential antioxidant protein in yeast, hence the name ATX1. Yet in follow-up studies, it became clear that this small copper binding protein actually serves to shuttle cytosolic copper to the copper transporting ATPase in the Golgi.[9] In fact, ATX1 exhibits significant homology to the aforementioned copper binding repeats found at the N-terminus of the copper transporter. In all these ATX1-like protein domains, there exists a single copper binding motif CXXC (C = cysteine copper binding ligand and X = any amino acid). Since both the donor (ATX1) and recipient (Cu ATPase) for copper transfer harbor this novel copper binding site, copper is able to move from one site to the other by rapid

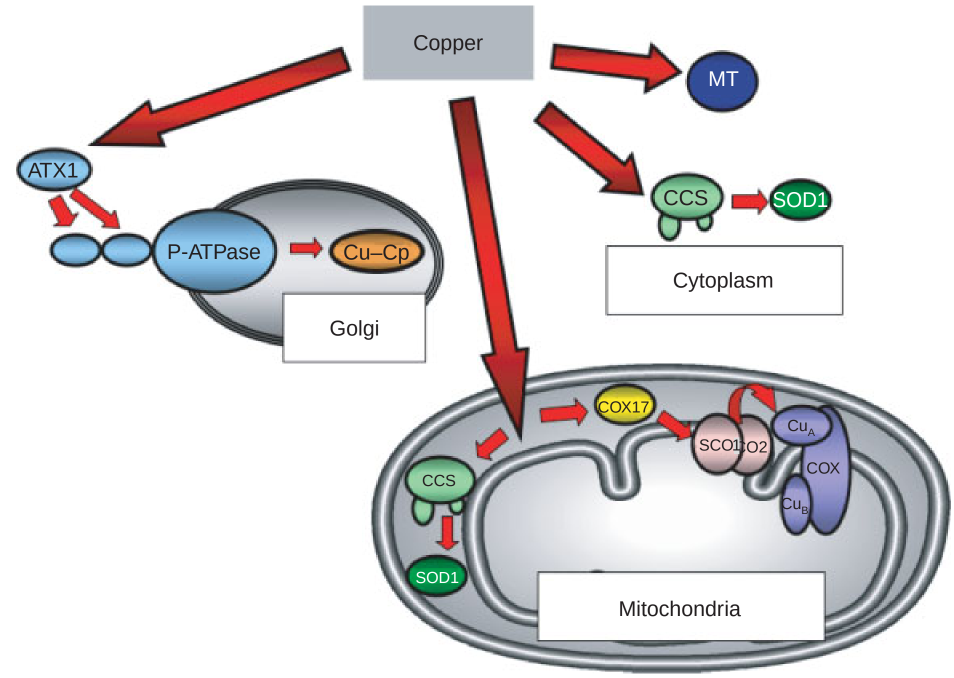

Figure 1 Metal trafficking pathways involving copper. Shown is a cartoon of a typical eukaryotic cell with various pathways of copper trafficking, indicated in red arrows. Much of the metal is sequestered by detoxification factors such as metallothioneins (‘MT’). Alternatively, the metal can be delivered to two copper chaperones in the cytosol: (1) ATX1 (in light blue) which carries the copper to the P-type copper transporting ATPase (‘P-ATPase’) in the Golgi. This transporter pumps copper into Golgi lumen for activation of copper enzymes in the secretory pathway, such as ceruloplasmin (CP); (2) Cytosolic CCS (light green) also captures copper, which is then delivered to the copper/zinc superoxide dismutase (SOD1). Copper may also be delivered by some unknown mechanism to the mitochondrial IMS, where it can be taken up by a mitochondrial localized CCS that in turn activates mitochondrial SOD1. IMS copper that is destined for cytochrome oxidase is first captured by soluble COX17, then delivered to SCO1 (or SCO2) in the inner membrane, and finally inserted into the Cu_A site of cytochrome oxidase (COX)

exchange of its cysteine ligands. This was the first mechanism of copper transfer reported for any copper chaperone and was originally proposed by Thomas O’Halloran and colleagues in 1997.[9]

2.2 Delivery of Copper to the Cytosol: The Copper Requiring Superoxide Dismutase Enzyme

Another pathway of copper trafficking functions specifically to deliver copper to a single enzyme in the cytoplasm, the copper and zinc containing SOD1 (*see* ***Copper Proteins with Type 2 Sites***). SOD1 acts to catalytically disproportionate two molecules of superoxide to oxygen and hydrogen peroxide, and it is the redox cycling of copper at the active site that drives the chemistry. By removing toxic superoxide anion radicals, SOD enzymes represent the first line of defense against oxidative damage. SOD1 is ubiquitously expressed among eukaryotes and in certain cells, this enzyme can represent as much as 1% of the total cellular protein.

The vast majority of SOD1 ($\geq$95%) localizes to the cytosol and therefore, there is no intracellular membrane barrier for delivering copper to this enzyme. However, owing to the virtual absence of available copper in the cytosol, SOD1 relies on a copper chaperone for acquiring the metal. This molecule has been denoted as CCS, for copper chaperone for SOD1.

We first identified CCS in 1997 by genetic studies in the baker’s yeast *S. cerevisiae*;[10] CCS was subsequently found to be well conserved throughout eukaryotes. CCS is a rather large copper chaperone, consisting of three domains (I, II, III) that serve distinct functions in inserting copper into SOD1.[11] The N-terminal domain I of CCS exhibits extensive homology to the ATX1 copper chaperone and contains the signature CXXC copper site. However, unlike ATX1, the CXXC of CCS is not essential for inserting copper into SOD1, rather this sequence appears important for capturing copper under conditions of copper limitation. In the central region of CCS, a larger domain II exhibits strong homology to SOD1, but lacks the SOD1 copper site. This homology facilitates the formation of a transient heterodimer between CCS and SOD1 that is the prelude to copper transfer. The structure of this heterodimer has been solved by X-ray crystallography and most notably, the interactions between CCS domain II and a monomer of SOD1 very closely mirror the interactions stabilizing the homodimer of SOD1 itself.[12] Lastly, the extreme carboxyl terminus (domain III) of CCS harbors a short copper binding site (CXC) that facilitates copper insertion into

SOD1. In fact, in the crystallographic analysis of CCS-SOD1 heterodimer, domain III is closely juxtaposed to the active site of SOD1. Interestingly, one of the CCS CXC cysteines forms an intermolecular disulfide bridge with an essential cysteine in SOD1, perhaps representing an intermediate in the copper transfer process.[12]

Unlike ATX1, where the chemistry of copper transfer is well understood, the mechanism of copper transfer from CCS to SOD1 remains unclear. For example, a dramatic change in metal ion coordination chemistry must accompany the copper transfer process in this case. Copper is bound to CCS in the reduced Cu(I) form via sulfhydral ligands, while in SOD1, copper is oxidized to the cupric Cu(II) state and is coordinated in an all-nitrogen environment to four histidines. The driving force for this large change in coordination chemistry is still poorly understood, but may involve an external oxidant, such as the superoxide substrate itself.

2.3 Delivery of Copper to the Mitochondria

The inner membrane of mitochondria is the site of respiratory electron transport and within the inner membrane and the intermembrane space (IMS) of mitochondria are two important copper containing enzymes. First, cytochrome c oxidase (COX) represents the terminal electron acceptor in the respiratory chain and two subunits of this large complex enzyme contain copper sites. A second enzyme in the mitochondria that requires copper is SOD1, as described above. Although the vast majority of SOD1 is cytosolic, a small fraction of this enzyme enters the IMS of the mitochondria where it is believed to directly scavenge superoxide anions produced as a by-product of the electron transport chain.

The copper that is trafficked to the mitochondrial IMS for SOD1 and COX must first cross the outer membrane of the mitochondria. The mitochondrial outer membrane has large pores that could accommodate the transport of solutes and small molecules. However the molecular state of the copper as it transits the outer membrane and enters the IMS is not understood. Once copper does enter the IMS, it is known to be captured by two copper binding proteins that facilitate delivery of the metal to the copper requiring SOD1 and COX enzymes. These copper capturing molecules include the mitochondrial form of CCS (described above) and the copper carrier for COX, known as COX17.

2.3.1 The Mitochondrial Form of CCS

Approximately 5% of the total cellular CCS can enter the mitochondria and this serves to metallate the fraction of SOD1 that resides in the IMS.[13] The exact mechanism by which CCS and SOD1 enters the IMS is unknown, but our studies indicate that apo SOD1 can move freely in either direction across the outer membrane, presumably through the outer membrane pores. But once this enzyme is metallated by CCS in either the cytosol or the IMS, the copper containing enzyme is trapped in the respective compartment (Figure 2). Indeed, increasing the metallation of SOD1 by mitochondrial CCS serves to shift the equilibrium of SOD1 towards the mitochondria. As such, CCS not only plays an important role in inserting copper into SOD1, but also in influencing the cellular location of this enzyme (Figure 2).[14]

2.3.2 Copper Delivery to Cytochrome Oxidase

As described above, COX of the respiratory chain has two subunits that require metallation with copper: the Cu_A site in subunit 2 contains 2 copper ions, while subunit 1 of the enzyme harbors a single copper atom in the Cu_B site. The Cu_A site acquires copper through two sets of accessory proteins in the mitochondria: COX17 and SCOI/SCOII. Assembly of the Cu_B site involves separate accessory factors including mitochondrial COX11. In this review, we shall specifically focus on assembly of the Cu_A site.

As is the case with the ATX1 and CCS copper chaperones, all the assembly factors for the Cu_A site of COX were originally discovered by genetic studies in baker's yeast, through work largely pioneered by Glerum and Tzagoloff in 1996.[15]

COX17 is a small cysteine rich protein that can bind copper in the form of a binuclear cuprous-thiolate cluster.[16] The COX17 protein has been localized to both the cytoplasm and mitochondria, and because of this dual location, COX17 was proposed to shuttle copper ions between these two compartments. However, work by D. Winge has shown that only the mitochondrial form of COX17 is needed for copper activation of cytochrome oxidase.[17] The role of the cytoplasmic form is not understood. In any case, mitochondrial COX17 is believed to capture IMS copper and then transfer the metal to a second set of accessory proteins for the Cu_A site of cytochrome oxidase: SCO1 and SCO2.

SCO1 and SCO2 are two homologous molecules that lie in the inner membrane of the mitochondria.[18] The copper binding site of these molecules bears striking resemblance to the target of copper delivery in cytochrome oxidase. The SCO1 and SCO2 proteins are believed to accept copper from COX17 and then transfer the metal to the Cu_A site of cytochrome oxidase (see cartoon of Figure 1) (reviewed in[19,20]). It is noteworthy that in humans, mutations in *SCO2* have been associated with a fatal disease in infants, hypertrophic cardioencephalomyopathy.[21]

3 METAL TRAFFICKING PATHWAYS INVOLVING MANGANESE

By far the greatest amount of information involving metal trafficking has surfaced from studies on copper. But more

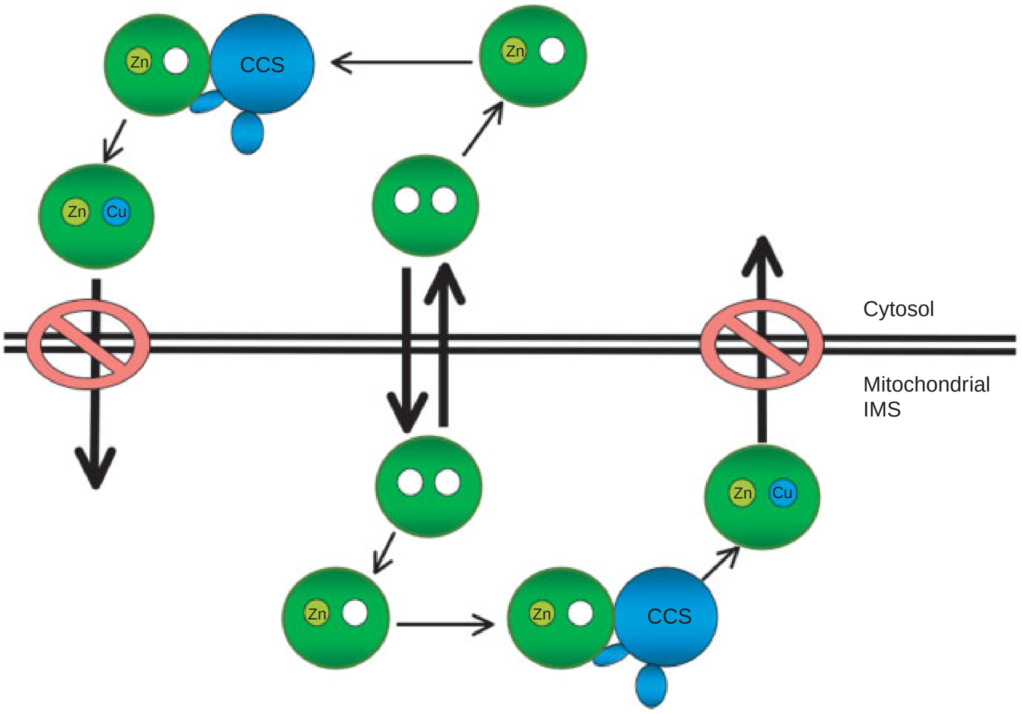

Figure 2 Partitioning SOD1 between the mitochondria and cytosol via the action of CCS. The double line represents the outer membrane of the mitochondria. Light arrows indicate maturation steps in the metallation of SOD1, whereas heavy arrows indicate movement of SOD1 across the outer mitochondrial membrane. The apo or unmetallated form of SOD1 can readily traverse the membrane in either direction. Once copper is inserted via CCS, SOD1 can no longer cross the membrane and becomes trapped within the corresponding compartment, either the cytosol or intermembrane space (IMS) of the mitochondria as indicated. This model shows zinc loading of SOD1 prior to copper metallation, but the exact order by which this occurs in vivo is not clear

recently, findings have emerged regarding the movement of manganese ions within the cell (reviewed in[1]). For the purposes of this discussion, we shall focus on studies completed in the baker's yeast *S. cerevisiae* that address the delivery of manganese ions to a manganese containing SOD2 (*see* ***Manganese Proteins with Mono- & Dinuclear Sites***) in the mitochondria.

Like the copper containing SOD1, SOD2 in the mitochondria serves to remove toxic superoxide anion radicals. SOD2 is strictly localized to the matrix of the mitochondria and acts to scavenge superoxide released on the matrix side of the respiratory chain. Our recent studies have shown that SOD2 can only obtain manganese when the protein is in the mitochondria. Therefore, there must exist a specific pathway for routing manganese ions to the heart of the mitochondria where the metal can activate SOD2.

3.1 Transmembrane Transporters for Manganese

Virtually all that is known regarding the transport and trafficking of manganese has come from studies in yeast and it is anticipated that similar mechanisms exist in higher eukaryotes including humans. Manganese that originates in the extracellular environment is first taken up by the cell via high affinity transport systems on the cell surface. One such system is represented by the yeast SMF1 transporter. SMF1 is a member of the Nramp family of divalent metal/proton symporters that have been well conserved from bacteria to humans. Yeast SMF1 primarily functions in the uptake of extracellular manganese under conditions of manganese limitation (reviewed in[1]). Once inside the cell, the metal is delivered to an intracellular vesicle where it then serves as the substrate for a second Nramp transporter, known as SMF2. SMF2 bears striking homology to SMF1, but never resides at the cell surface, only in intracellular vesicles. In one model of manganese transport, the metal is sequentially passed down from SMF1 at the cell surface to the SMF2 containing vesicles.[22] SMF2 then acts to transport the metal out of the vesicle for eventual delivery to other sites in the cell, including the mitochondria (see cartoon of Figure 3).

The metal ion transported by SMF2 is indeed utilized by the mitochondria for activation of SOD2. Yeast cells lacking SMF2 express a SOD2 polypeptide that is virtually devoid of manganese ions.[22] However, the role of SMF2 in delivering manganese to SOD2 is not direct. Rather SMF2 acts far upstream in the trafficking pathway. Other transporters or metal chaperones that operate downstream of SMF2 serve to pass the metal on to the mitochondria for utilization by SOD2. Once such downstream molecule is MTM1.

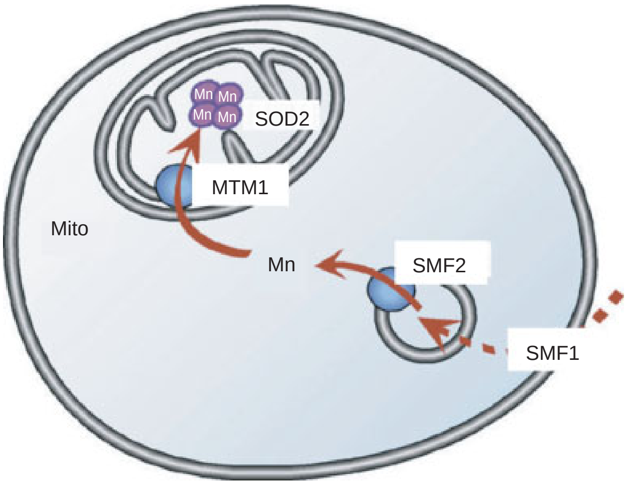

Figure 3 Pathway of trafficking manganese to mitochondrial SOD2. The model shown is based on factors identified in the baker's yeast *S. cerevisiae.* Extracellular manganese can enter the cell by a high affinity manganese transporter, SMF1. The metal is then trafficked to intracellular vesicles and then exported via a second manganese transporter known as SMF2. The metal that exits the SMF2-containing vesicles can then be escorted to the mitochondria where it is ultimately inserted into SOD2. The MTM1 transporter of the mitochondrial inner membrane is essential for activating SOD2 with manganese and may itself transport manganese or facilitate activation of SOD2 by transporting another mitochondria solute

3.2 The MTM1 Mitochondrial Factor for Activation of SOD2 with Manganese

We identified yeast MTM1 as a protein of the mitochondrial inner membrane that is needed to activate SOD2 with manganese.[23] MTM1 is a member of a large family of mitochondrial solute transporters known as MCF, for mitochondrial carrier family. All eukaryotic organisms express 30–40 distinct MCF molecules that serve to transport solutes in and out of the mitochondria. Substrates include ATP/ADP, precursors and products of the TCA cycle, and so on. Although the precise substrate for transport by MTM1 is not known, manganese is a likely candidate. Yeast cells lacking MTM1 show a deficiency in manganese incorporation into SOD2, although the mitochondria organelle itself is not deficient in manganese.[23] Therefore, if MTM1 indeed transports manganese, it must be specific for delivering manganese directly to SOD2. In one model, MTM1 or an accessory protein interact with SOD2 molecules and directly insert the metal ion cofactor (see Figure 3).

4 PERSPECTIVES

The findings presented here on metal trafficking have been limited to copper and manganese ions. However, it is conceivable that analogous pathways will emerge for other metals as well. Metals such as iron and even zinc are known to be toxic, but essential nutrients. As such, it is critical that cells maintain strict guidance and regulation of these ions to ensure accurate incorporation into metalloproteins without metal ion toxicity.

5 RELATED ARTICLE

Metalloregulation.

6 REFERENCES

1. E. Luk, L. T. Jensen, and V. C. Culotta, *J. Biol. Inorg. Chem.*, 2003, **8**, 803.
2. C. E. Outten and T. V. O'Halloran, *Science*, 2001, **292**, 2488.
3. T. D. Rae, P. J. Schmidt, R. A. Pufahl, V. C. Culotta, and T. V. O'Halloran, *Science*, 1999, **284**, 805.
4. A. Dancis, S. Yuan, D. Haile, C. Askwith, D. Eide, C. Moehle, J. Kaplan, and R. Klausner, *Cell*, 1994, **76**, 393.
5. J. Lee, J. R. Prohaska, and D. J. Thiele, *Proc. Natl. Acad. Sci. U.S.A.*, 2001, **98**, 6842.
6. V. C. Culotta and J. D. Gitlin, in 'Disorders of Copper Transport', eds. C. R. Scriver, A. L. Beaudet, W. S. Sly, and D. Valle, McGraw Hill, New York, 2001.
7. S. Lin and V. C. Culotta, *Proc. Natl. Acad. Sci. U.S.A.*, 1995, **92**, 3784.
8. L. W. J. Klomp, S. J. Lin, D. Yuan, R. D. Klausner, V. C. Culotta, and J. D. Gitlin, *J. Biol. Chem.*, 1997, **272**, 9221.
9. R. Pufahl, C. Singer, K. L. Peariso, S. J. Lin, P. Schmidt, C. Fahrni, V. C. Culotta, J. E. Penner-Hahn, and T. V. O'Halloran, *Science*, 1997, **278**, 853.
10. V. C. Culotta, L. Klomp, J. Strain, R. Casareno, B. Krems, and J. D. Gitlin, *J. Biol. Chem.*, 1997, **272**, 23469.
11. P. Schmidt, T. D. Rae, R. A. Pufahl, T. Hamma, J. Strain, T. V. O'Halloran, and V. C. Culotta, *J. Biol. Chem.*, 1999, **274**, 23719.
12. A. L. Lamb, A. S. Torres, T. V. O'Halloran, and A. C. Rosenzweig, *Nat. Struct. Biol.*, 2001, **8**, 751.
13. L. A. Sturtz, K. Diekert, L. T. Jensen, R. Lill, and V. C. Culotta, *J. Biol. Chem.*, 2001, **276**, 38084.
14. L. S. Field, Y. Furukawa, T. V. O'Halloran, and V. C. Culotta, *J. Biol. Chem.*, 2003, **278**, 28052.
15. D. M. Glerum, A. Shtanko, and A. Tzagoloff, *J. Biol. Chem.*, 1996, **271**, 14504.
16. D. N. Heaton, G. N. George, G. Garrison, and D. R. Winge, *Biochemistry*, 2001, **40**, 743.

17. A. B. Maxfield, D. N. Heaton, and D. R. Winge, *J. Biol. Chem.*, 2004, **279**, 35334.
18. D. M. Glerum, A. Shtanko, and A. Tzagoloff, *J. Biol. Chem.*, 1996, **271**, 20531.
19. D. R. Winge, *Structure*, 2003, **11**, 1313.
20. H. S. Carr and D. R. Winge, *Acc. Chem. Res.*, 2003, **36**, 309.
21. M. Jaksch, I. Ogilvie, J. Yao, G. Kortenhaus, H. G. Bresser, K. D. Gerbitz, and E. A. Shoubridge, *Hum. Mol. Genet.*, 2000, **9**, 795.
22. E. Luk and V. C. Culotta, *J. Biol. Chem.*, 2001, **276**, 47556.
23. E. Luk, M. Carroll, M. Baker, and V. C. Culotta, *Proc. Natl. Acad. Sci. U.S.A*, 2003, **100**, 10353.

Acknowledgments

Much of the work described in this chapter was supported by funding from the JHU NIEHS center and by NIH grants GM 50016 and ES 08996 awarded to VC.

Metalloprotein Design & Engineering

Yi Lu
University of Illinois at Urbana-Champaign, Urbana, IL, USA

1	Introduction	1
2	Rational Design: Consensus Sequence/Structure Approach	1
3	Rational Design: Modular Approach	20
4	Combinatorial Design	22
5	Design of Metalloproteins with Structures and Functions Unprecedented in Nature	24
6	Summary and Outlook	25
7	Related Articles	28
8	References	28

1 INTRODUCTION

Metalloproteins play important roles in biology. They account for about 1/3 of structurally characterized proteins and about 1/2 of all proteins.[1] The availability of different metal ions with various redox states, ligands, and geometries about the metal ion allows for fine-tuning of the reactivity of proteins at the highest level. As shown in other sections of this encyclopedia, studies of native metalloproteins and their variants have provided numerous insights. Design and engineering of metalloproteins can serve as a touchstone whereby the principles obtained from the studies are tested, and help determine whether the *necessary* features identified from the studies are *sufficient* to confer the structure and function of the proteins. Since it is a bottom-up approach of building the proteins that is complementary to the top-down approach of native protein studies, it can offer new insights. Furthermore, it is possible to design metalloproteins with unprecedented structural and functional properties. Finally, most designed proteins are smaller than the native proteins, making them easier for practical applications.

A number of excellent reviews on metalloprotein design and engineering have appeared in the literature.[2–28] This review will focus mainly on advances in creating new metal-binding sites in proteins.

2 RATIONAL DESIGN: CONSENSUS SEQUENCE/STRUCTURE APPROACH

Metalloproteins always contain highly conserved amino acid residues around the metal-binding sites, including the ligands to the metal ions. The consensus sequence/structure approach often involves a sequence homology search of a large number of proteins in the same family, identification of conserved sequences responsible for common metal-binding motifs, and then application of this knowledge to the design.

2.1 Design of Metallopeptide Models

Metallopeptide models refer to systems that are mostly unstructured in solution in the absence of metal ions.[21] It is applicable to design of metal-binding sites whose conserved residues appear mostly in a single peptide that is often much shorter than the whole protein. Designing metalloproteins using only the peptide with the consensus sequence, often called a motif, represents the minimalist approach in its purest sense. These motifs typically contain His, Cys, or both residues. In addition, metalloporphyrin-containing peptides have also been made to mimic basic features in heme proteins.

2.1.1 Metallopeptide Models with His-Containing Motifs

An interesting example of designed metal-peptide models is based on the amino terminal Cu^{II} and Ni^{II}-binding motif found first in serum albumin, and then later in other proteins such as neuromedins C and K, human sperm protamine P2a, and histatins.[29,30] The motif contains a simple tripeptide Xaa-Xaa-**His** (where Xaa is an α-amino acid, and amino acid side chains that are ligated to metal ions are shown in bold) with a free NH_2-terminus. This peptide binds Cu^{II} and Ni^{II} specifically through the histidine imidazole nitrogen, two intervening deprotonated amide nitrogens, and the terminal α-amine (Figure 1a). While the histidine at the third position is required, the identity of the first two amino acids seems to exert little effect on metal complexation at or above physiological pH. Based on this motif, a number of Cu^{II} and Ni^{II}-binding peptides have been designed. The designed motifs, either alone or incorporated into a protein, are effective cleavage agents for nucleic acids and proteins. Another interesting finding is that the $Ni^{II}\cdot$Xaa-Xaa-**His** metallopeptide can target either the minor groove of B–form DNA or loop regions of structured RNA molecules.

While the Xaa-Xaa-**His** motif can bind metal ions and form a stable structure alone, almost all other metal-binding motifs have to be associated with either a peptide, a de novo designed protein, or a native protein scaffold. For example, the **His**-X_3-**His** motif (Figure 1b), common to zinc finger proteins (*see* ***Zinc: DNA-binding Proteins***), hemocyanin (*see* ***Copper: Hemocyanin/Tyrosinase Models*** and ***Copper Proteins with Dinuclear Active Sites***), and the EF-hand calcium-binding motif, found in calcium proteins (*see* ***Calcium-binding Proteins***), are often designed as part of another protein domain instead of as an individual unit alone. They will be covered in the Section 3.1 (Rational Design: Modular Approach) below.

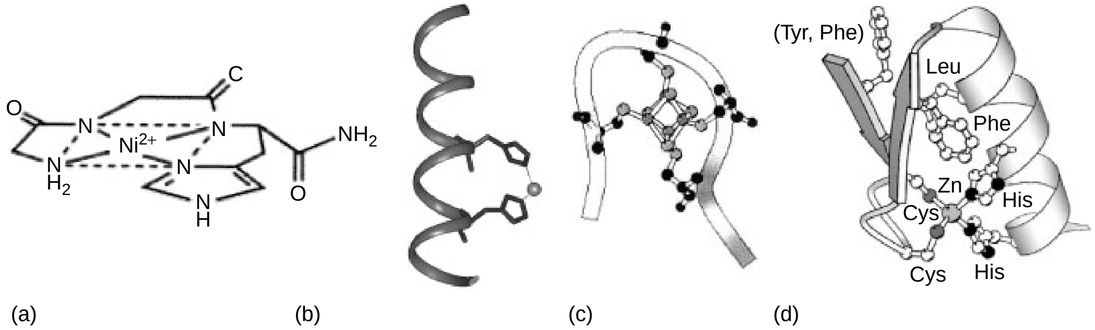

Figure 1 Metal-binding motifs and domains. (a) Ni^{II}·Xaa-Xaa-**His** motif. (Reprinted with permission from Ref. 30. © 1999 the American Chemical Society); (b) **His**-X_3-**His** motif. (Reprinted with permission from Ref. 23. © 2001 the American Chemical Society); (c) **Cys**-Xaa-Xaa-**Cys** motif. (Reprinted with permission from B.R. Gibney, S.E. Mulholland, F. Rabanal, and P.L. Dutton, *Proc. Natl. Acad. Sci. U.S.A.*, 1996, **93**, 15041. © 1996 National Academy of Sciences, USA); (d) Zinc finger domain. (Reprinted with permission from Ref. 28. © 2004 the American Chemical Society)

2.1.2 Metallopeptide Models with Cys-containing Motifs

The **Cys**-Xaa-Xaa-**Cys** motif, occurs in rubredoxins, ferredoxins (*see* ***Iron–Sulfur Proteins***), and metallothionins (*see* ***Metallothioneins***). Based on the consensus sequence of ferredoxins, -**Cys**-$(Xaa)_2$-**Cys**-$(Xaa)_2$-**Cys**-$(Xaa)_{10-50}$-Cys, a 16-amino acid peptide (LysLeu**Cys**GluGlyGly**Cys**IleAla**Cys**Gly Ala**Cys**GlyGlyTrp) has been designed and shown to incorporate a ferredoxin-like [4Fe-4S] cluster under physiological conditions (Figure 1c).[31] This sequence was later truncated to seven amino acids (**Cys**IleAla**Cys**GlyAla**Cys**) that still maintain most of the spectral features of ferredoxins. This motif has been incorporated into de novo designed four α-helical bundles to formal mixed ferredoxin-heme-containing center, or bridged $[Ni^{II}\text{-}(\mu_2\text{-}S_{Cys})\text{-}Fe_4S_4]$-containing assembly (see Section 3.2). A rubredoxin-like $Fe^{II/III}$(**Cys**)$_4$ has also been designed using two β-hairpin peptides with each containing the **Cys**-Xaa-Xaa-**Cys** motif.[32] Instead of relying strictly on conserved primary sequence alignment, the authors designed the rubredoxin-like metallopeptide based on the three dimensional structure of native rubredoxin, through which they identified the minimal structure unit around the metal-binding site and incorporated it into the 11-mer peptide. Design of peptide models for blue copper proteins has also been reported.[33,34] Finally, an NMR study of the GlyMetThr**Cys**AlaAla**Cys** motif, commonly found in heavy metal-binding and transporter proteins such as MerP (*see* ***Metallochaperones & Metal Ion Homeostasis***), showed that the structure of the motif in an 18-mer peptide is similar to that in the 72-residue MerP protein (Figure 2).[35] This result suggests that carefully designed metal-binding sites in metallopeptides can maintain the same structure as in native proteins.

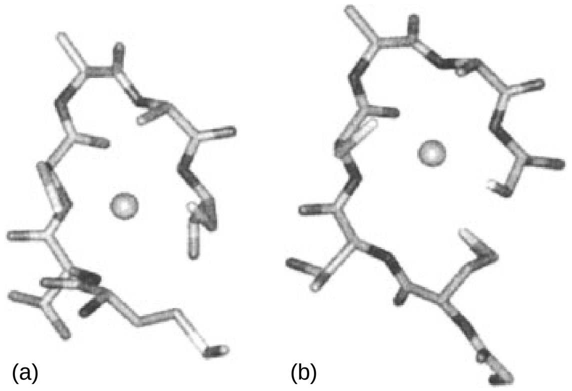

Figure 2 Structural comparison of GlyMetThr**Cys**AlaAla**Cys** motif in a designed 18 residue metallopeptide model (a) and its corresponding loop in MerP protein (b). (Reprinted with permission from Ref. 35. © 2000 the American Chemical Society)

2.1.3 Metallopeptide Models with His and Cys-containing Zinc Finger Domains

The metallopeptides discussed above, although stable in solution, are mostly part of an overall structural unit in proteins. A few other metallopeptides, on the other hand, can fold into separate structure units (called domains), which are different from other parts of the proteins. Zinc finger domains (*see* ***Zinc: DNA-binding Proteins***) are a primary example of metal-binding domains, with the Cys_2His_2 finger as the most common in the family.[28] Based on a database of 131 sequences from 18 different proteins, a 26-mer peptide was designed with the consensus sequence (see Figure 1d).[36] Remarkably, the Zn^{II}-binding affinity of this designed peptide ($K_d \sim 2$ pM) is higher than those of any natural zinc fingers known, demonstrating that protein design can result in new proteins with unprecedented properties. This peptide was further modified to include a minimal number of amino acids.[37] This 'minimalist' zinc finger, containing mostly Ala in noncritical positions, has comparable Zn^{II}-binding affinity to those of native zinc fingers. This result showed that protein design can reveal, in the most unequivocal way, the key structural features of metalloproteins.

2.1.4 *Metalloporphyrin-peptides as Models for Heme Proteins*

Heme proteins are one of the largest classes of metalloproteins studied to date (*see* ***Iron: Heme Proteins & Dioxygen Transport & Storage***; ***Iron: Heme Proteins, Peroxidases, Catalases & Catalase-peroxidases***).[38] More than 5% of protein structures in the Protein Data Bank contain at least one heme moiety.[27] It is no wonder that designing heme proteins has been one of the most active areas of research. Since the dominant secondary structure in heme proteins is α-helices (accounting for $\sim$77% of all secondary structures in known heme proteins),[27] a number of α-helix-containing metalloporphyrin-peptides have been synthesized using either covalent or noncovalent approaches.[17,18,22,27]

A classic metalloporphyrin-peptide was made by proteolytic digestion of the natural protein cytochrome *c*. The resulting metallopeptides, called microperoxidases, contain the **Cys**-Xaa-Xaa-**Cys-His** motif that binds to the heme covalently through the two Cys residues.[39] They are one of the few metalloporphyrin-peptides that are five-coordinate with an open binding site. Therefore they exhibit oxidation and oxygenation activities, such as peroxidase and cytochrome P450 activities. They have also been used as biosensors for H_2O_2.

To expand the sequence and structure diversity of the microperoxidases, other peptides have been covalently linked to different metalloporphyrins (Figure 3). For example, an undecapepetide whose sequence was derived from a natural protein was covalently attached to the deuteroporphyrin through its propionate group (Figure 4a).[40,41] Ligands to the heme center were provided either through addition of free ligands such as imidazole, or through covalent attachment of the histidine to the second heme propionate. In addition, by covalently attaching a chelating ligand for copper to the

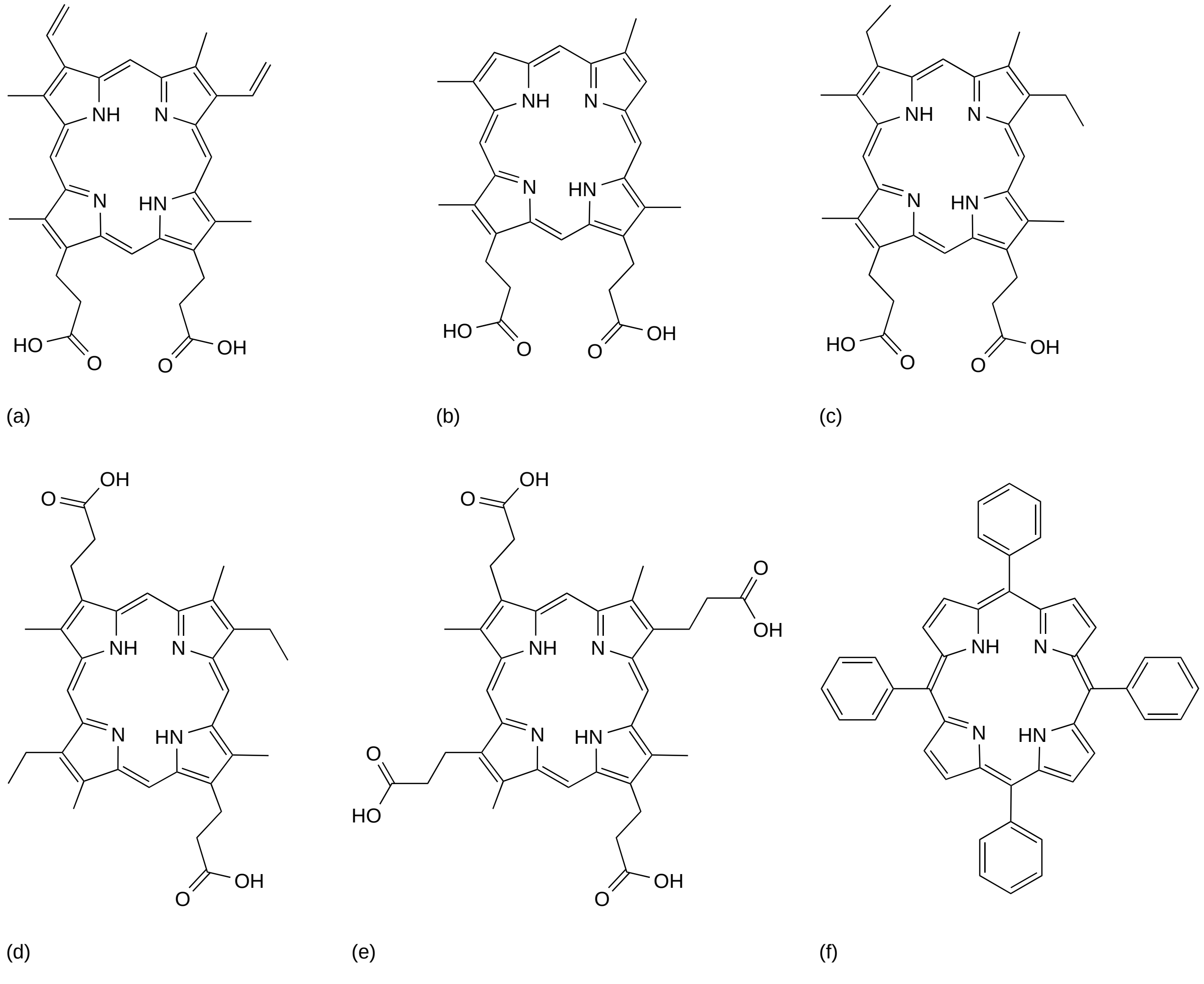

Figure 3 Chemical structures of porphyrins used in metallopeptide design. (a) protoporphyrin IX; (b) deuteroporphyrin IX; (c) mesoporphyrin IX; (d) mesoporphyrin II; (e) coproporphyrin; (f) *meso*-tetraphenylporphyrin[22]

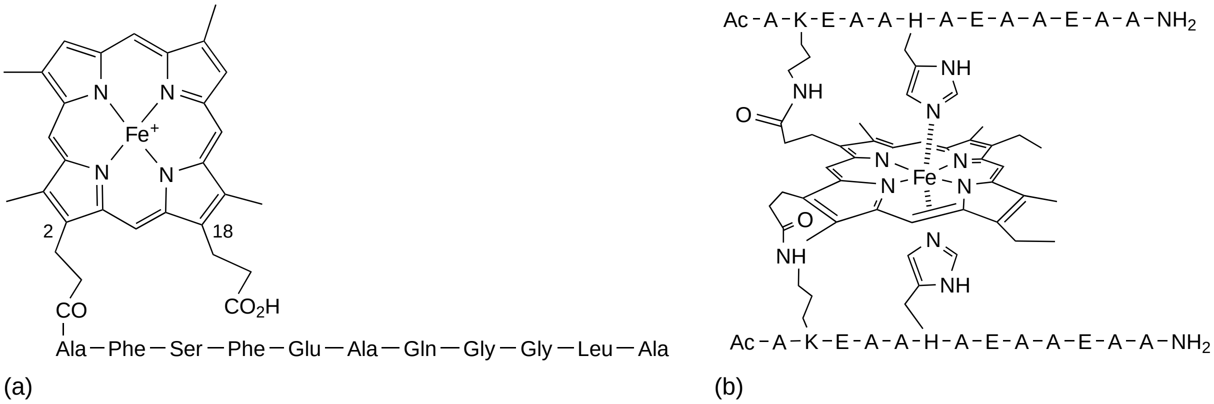
Fe+
2
18
CO
CO2H
Ala—Phe—Ser—Phe—Glu—Ala—Gln—Gly—Gly—Leu—Ala
(a)
Ac-A-K-E-A-A-H-A-E-A-A-E-A-A-NH2
NH
NH
O
N
Fe
O
NH
N
NH
Ac-A-K-E-A-A-H-A-E-A-A-E-A-A-NH2
(b)

Figure 4 Metalloporphyrin-peptides models with covalent linkage through porphyrin propionate. (a) peptide deuteroporphyrin system (b) peptide sandwiched mesoporphyrin system

second heme propionate, this system also provided interesting models for cytochrome *c* oxidase (*see* ***Cytochrome Oxidase***).

One or two peptides have been attached to mesoheme through an amide linkage between the heme propionate and the Lys N-ε nitrogen (Figure 4b).[42] Investigation of this peptide sandwiched mesoporphyrin system showed that His to heme ligation is mainly responsible for the peptide transformation from random coil to helix. Independently, the same propionate-Lys linkage strategy has been exploited to attach deuteroporphyrin to peptides whose sequence is derived from the F helix of hemoglobin β-chain.[22,43,44] Detailed structural analysis of the resulting metallopeptides, called mimochromes, showed that diastereomerism may occur when polypeptides coordinate to metal ions (Figure 5). Finally, five-coordinate hemes have been obtained in both peptide sandwiched mesoporphyrin and mimochrome systems, paving the way for studies of their enzymatic activities.

In addition to the propionate group, other positions on metalloporphyrins have also been used as sites for attaching peptides, including modified tetraphenylporphyrins coupled to peptides through a thioether linkage (Figure 6a)[45] or through copper coordination (Figure 6b).[46] In both cases, proper positioning of key amino acids on the peptide for the covalent linkage to the porphyrins is critical for the porphyrin-peptide assembly and induction of α-helical content. To create the thioether linkage, two Cys residues at position 2 and 13 of the 14-mer peptide are necessary to react with iodoacetamide-modified free base tetraphenylporphrin. To form the copper coordination, two pairs of His residues at positions at 4, 8, 15, and 19 (forming the His-X_3-His motif) of the 22-mer peptide are required, together with modified tridentate *meso*-phenyl groups.

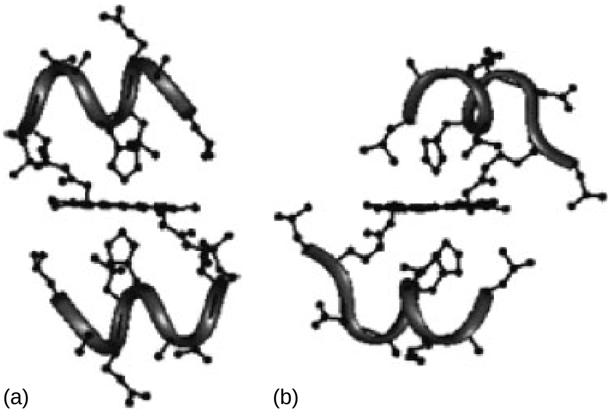

Figure 5 NMR structures of two diastereomers of Co^{III}-mimochrome I. (a) Δ isomer; (b) Λ isomer. (Reprinted with permission from Ref. 22. © 2001 the American Chemical Society)

The above described covalent approach to the design of metalloporphyrin-peptide models has the advantages of ensuring proper peptide/porphyrin stoichiometry and positioning, and reducing axial ligand dissociation. However, it requires multistep syntheses, making it difficult to introduce a number of variants of the peptide sequences. In addition, it may not be able to offer insight into folding and noncovalent interactions of a large number of heme proteins, such as globins, peroxidases, and oxidases, without covalent linkage between heme and peptide. Therefore metalloporphyrin-peptide models through spontaneous assembly of peptides around metalloporphyrins have been made. Without the covalent linkage, the challenges are to construct peptides that can fold into a unique conformation and can maximize both the interactions between the peptide and metalloporphyrin and the binding of ligand to the heme center. Toward these goals, several systems have been designed. With few exceptions, most systems utilize two α-helical peptides dimerized by a disulfide linkage through the N-terminal Cys residues, with His residues placed in the center of the two peptides for ligation to the metalloporphyrin center. These peptides spontaneously assemble around metalloporphyrins (such as Co^{III}coproporphyrin/Co^{III}octaethylporphyrin,[47] Fe^{III}mesoporphyrin,[48] or Fe^{III}coproporphyrin (Figure 7)[49–51]).

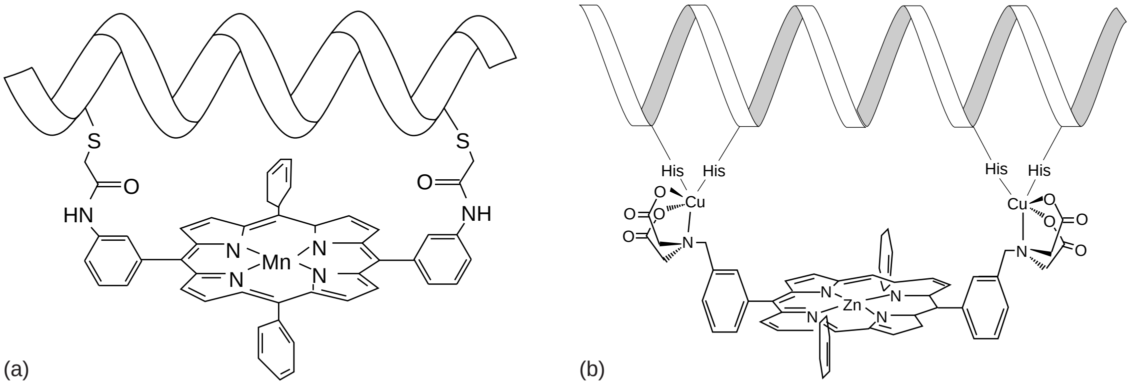

Figure 6 Metalloporphyrin-peptides models with covalent linkage through a thioether linkage (a);[45] or copper coordination (b)[46]

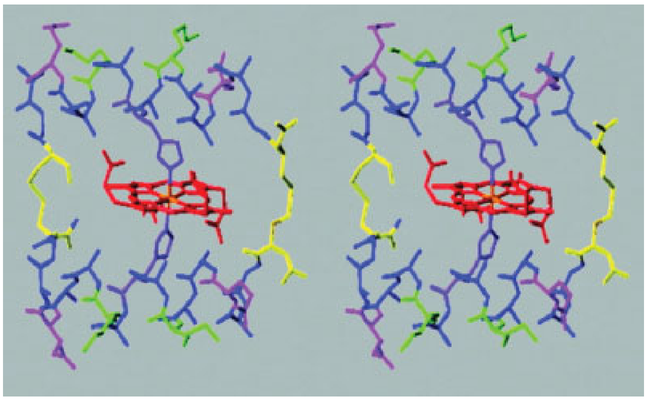

Figure 7 Two stereo side view of NMR structure of a self assembled metalloporphyrin-peptides model. (Reprinted with permission from M.M. Rosenblatt, J. Wang, and K.S. Suslick, *Proc. Natl. Acad. Sci. U.S.A.*, 2003, **100**, 13140. © 2003 National Academy of Sciences, USA)

Strong evidence has been obtained about the roles of metal-ligand ligation and the disulfide linkage in promoting α-helix formation. Other effects have also been noted. For example, neutral and positively charged peptides bind to the negatively charged metalloporphyrins more strongly than anionic peptides.[51] Different degrees of hydrophobic interactions between the peptides and the metalloporphyrin can result in binding constants that span a range of ~6000 fold.[49]

2.2 Design of Metal-binding Sites into De Novo Designed Proteins

The metallopeptide systems described in the last section represent metalloprotein design at the most 'minimalistic' level. Successful designs of metallopeptides that mimic natural metalloproteins can not only reveal dominant factors determining the structural and functional properties, but also provide much simpler alternatives for practical applications. However, many of the peptides lack built-in secondary structure and, as demonstrated experimentally, require binding of metal cofactors to form stable structures.

This approach works fine for design of metalloproteins such as heme proteins and zinc finger proteins where metal cofactor binding plays an important role in protein folding and structure formation. However, a number of other metalloproteins fold independently of metal cofactor binding. In a few cases, such as type 1 blue copper proteins (*see* ***Copper Proteins with Type 1 Sites***), the protein scaffolds are believed to enforce metal-site geometry. Mimicking of those proteins is more likely to be successful using more rigid proteins as scaffolds. Toward this goal, de novo designed proteins with rigid scaffolds, such as four α-helical bundle proteins, have been used for metal-binding site design.

2.2.1 *Introducing Heme into De Novo Designed Proteins*

In an extension to the covalent approach in the metalloporphyrin models described above, metalloporphyrins have been used as a template to induce α-helical folding and formation of four α-helical bundles, a common heme protein scaffold. In these systems, metalloporphyrins play both a catalytic role in terms of performing electron transfer or oxidative function, and a structural role in terms of helping to position the four peptides to form a bundle without collapsing. The first example, called helichrome, was made by linking the N-termini of four identical 15-mer peptides to the four propionate groups of coproporphyrin I (Figure 8a).[52] The peptides are amphiphilic, resulting in a hydrophobic substrate-binding pocket in the folded four α-helical bundle. Therefore it displays interesting cytochrome P450-like activity (*see* ***Iron: Heme Proteins, Mono- & Dioxygenases***) by oxidation of aniline to *p*-aminophenol. The second example employed a structurally more rigid and chemically more stable tetraphenylporphyrin, and attached the N-termini of four hydrophobic 21-residue peptides to *meso*-tetrakis(*m*-carboxyphenyl)porphyrin through *m*-carboxyamido linkages (Figure 8b).[53] The resulting metalloporphyrin-peptides, called tetraphilins, mimic the ion-channel proteins. The presence

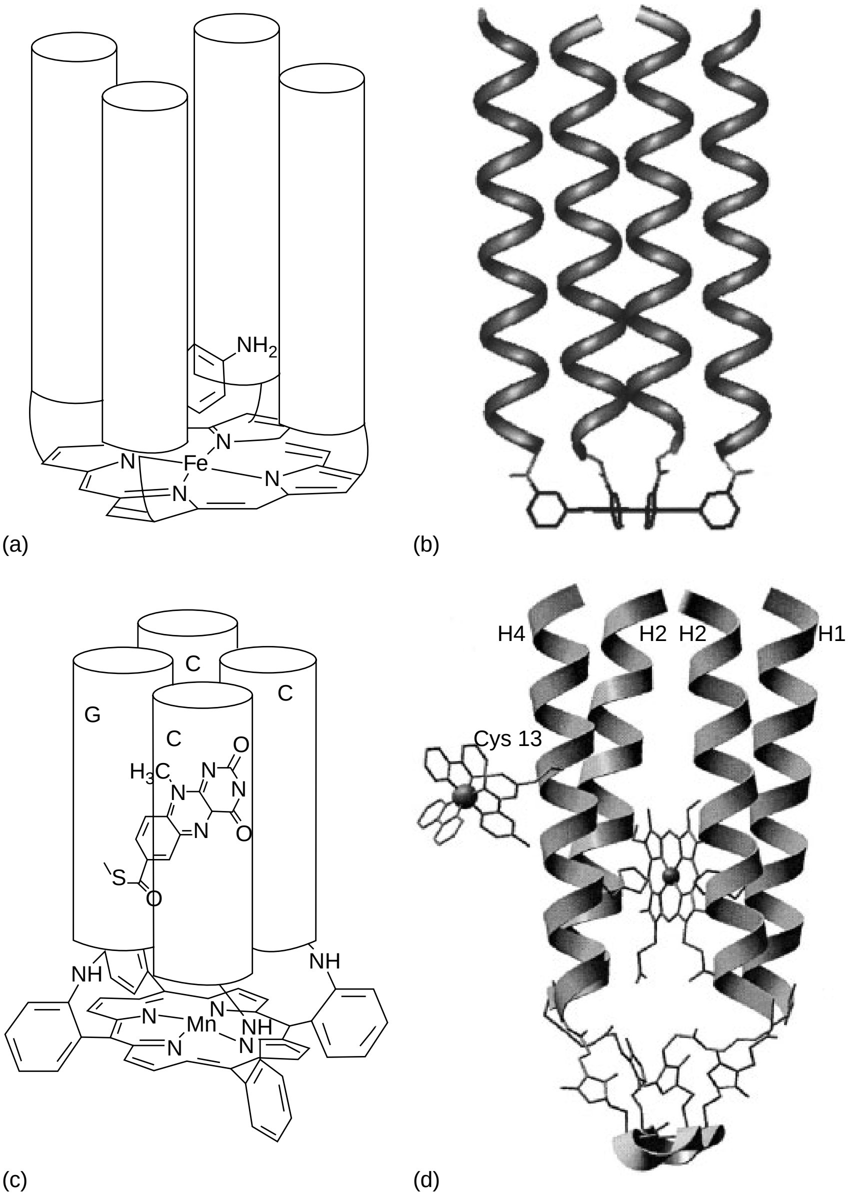

Figure 8 Template approach to de novo heme protein design using metalloporphyrins as templates. (a) helichrome; (b) tetraphilins; (c) artificial membrane proteins. (Reprinted with permission from Ref. 22. © 2001 the American Chemical Society); (d) helical proteins based on Cys-containing cyclic peptide. (Reprinted with permission from H.K. Rau, N. DeJonge, and W. Haehnel, *Proc. Natl. Acad. Sci. U.S.A.*, 1998, **95**, 11526. © 1998 National Academy of Sciences, USA)

of the porphyrin increased the conductance lifetime and eliminated the voltage dependence of the peptide ion channel. Finally, a similar strategy has also been used to design *meso*-tetrakis(m-carboxyphenyl)porphyrin-linked four α-helical bundles that can penetrate into membranes (Figure 8c).[54] This was made possible by using peptides whose sequences were derived from the C- and G-helices of the transmembrane regions of bacteriorhodopsin. An artificial electron transfer system was designed into the system by insertion of $\mathrm{Mn^{III}}$ into the porphyrin and covalent attachment of a flavin in the middle of the four α-helical bundles.

In addition to metalloporphyrins, other molecules have been used as templates for building artificial metalloproteins. Among those, cyclic peptides containing four cysteines with different protection groups offer considerable opportunities, as this system allows coupling of unprotected peptides either at the N-terminus or the ε-amino group of a C-terminal Lys.[55] In this way, both parallel or antiparallel four α-helical bundles can be made. For example, an antiparallel four α-helical bundle protein that mimics the heme-binding core of the b-subunit of the cytochrome bc_1 complex has been made this way through incorporation of two His residues in the middle of the peptides.[55,56] To demonstrate the versatility and modularity of this approach, a ruthenium-tris(bipyridine) complex was also covalently attached to the surface of the model protein (Figure 8d), allowing a detailed investigation of distance-dependent electron transfer in this system.[56]

While the above template based approach has several advantages over the nontemplate approach in overcoming topology and folding issues in protein design, there are not many such examples of metalloproteins in nature. A more challenging design is through spontaneous assembly of linear peptides. A remarkable achievement in protein design was the design of four α-helical bundle proteins based on first principles.[16,57] Since then several heme-containing four α-helical bundle proteins have been made based on the design.[16–18,22,27,57] For example, a series of helix-loop-helix peptides containing one His residue was designed to dimerize via N-terminal Cys residues and form four α-helical bundles with bis-His ligated heme parallel to the helices in the bundle core (Figure 9a).[58] They also showed that the mere presence of two His residues is insufficient to achieve specific binding of heme; introducing a hydrophobic cavity is also required. In addition, multi-heme proteins have been designed using helix-disulfide-helix peptides (Figure 9b).[59] In this way, a di-α-helical peptide containing two bis-His heme groups has been synthesized and assembled into a four α-helical bundle with four parallel heme groups in the middle. The sequence design was based on the heme-binding site of cytochrome bc_1 complex, including the spacing of the two His ligands and the presence of other amino acid residues, such as Phe and Arg in the heme-binding site. The resulting proteins resemble native heme proteins in their spectral and electrochemical properties, including heme–heme redox interaction.

In the above multi-heme proteins, all heme planes are parallel to each other. In other multi-heme proteins in nature, such as heme a and heme a_3 center in cytochrome c oxidases (*see* ***Cytochrome Oxidase***), the heme planes are perpendicular to each other. Four heme groups with heme perpendicular to one another have been designed into four α-helical bundles through the use of a side-chain packing algorithm, called CORE (Figure 9c).[60] The same program also helps to design artificial electron transfer centers where a bis-His ligated heme is situated in the middle of the four α-helical bundle and a Ru(bpy)$_2$ attached to the end of the bundle.[61]

2.2.2 *Introducing Nonheme Di-iron Centers into De Novo Designed Proteins*

Dinuclear iron centers are found in a large number of metalloproteins with diverse functions (*see* ***Iron Proteins with Dinuclear Active Sites***). Despite very different overall folds, most of the proteins position the di-iron centers within a four-helix bundle, with conserved Glu-X-X-His motifs on two of the four helices.[62] Each of the remaining two helices also contributes a Glu residue. Introducing six polar ionizable groups in the hydrophobic core of the helix bundle represent a grand challenge. This task was accomplished by using a retrostructural analysis and computational design approach.[62,63] In addition to placing the above six residues (Glu$_4$His$_2$) in positions analogous to the native di-iron proteins, residues around the metal-binding site that play structural and functional roles have also been introduced. They include residues in the secondary coordination sphere that form hydrogen bonds to ligands of the metal ions,

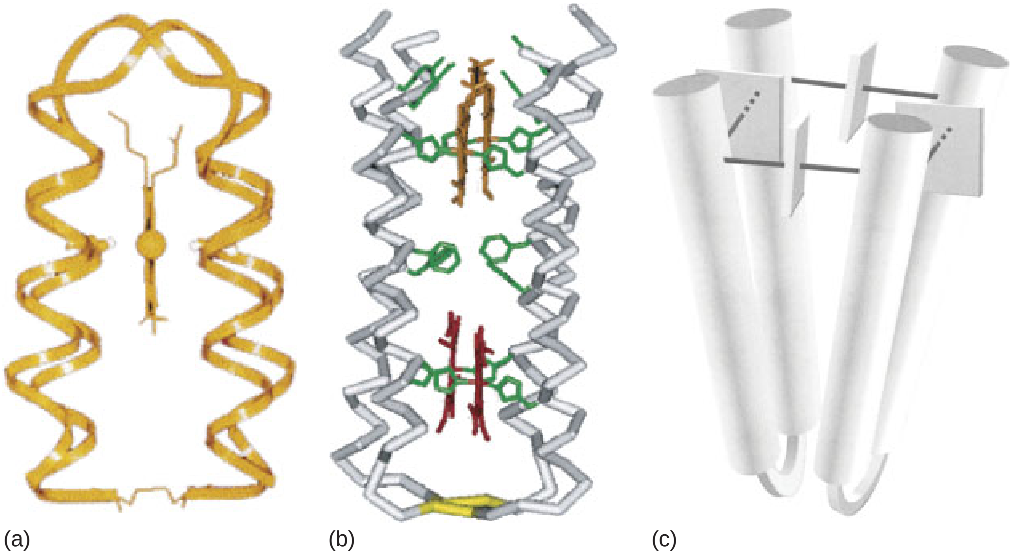
(a) (b) (c)

Figure 9 Self assembly approach to de novo heme protein design. (a) bis-His ligated single heme parallel to the helices in the four α-helical bundle; (b) bis-His ligated multi-hemes parallel to the helices in the four α-helical bundle. (Reprinted with permission from Ref. 27. © 2004 the American Chemical Society); (c) bis-His ligated multi-hemes perpendicular to each other in the four α-helical bundle. (Reprinted with permission from Ref. 60. © 2001 the Protein Society)

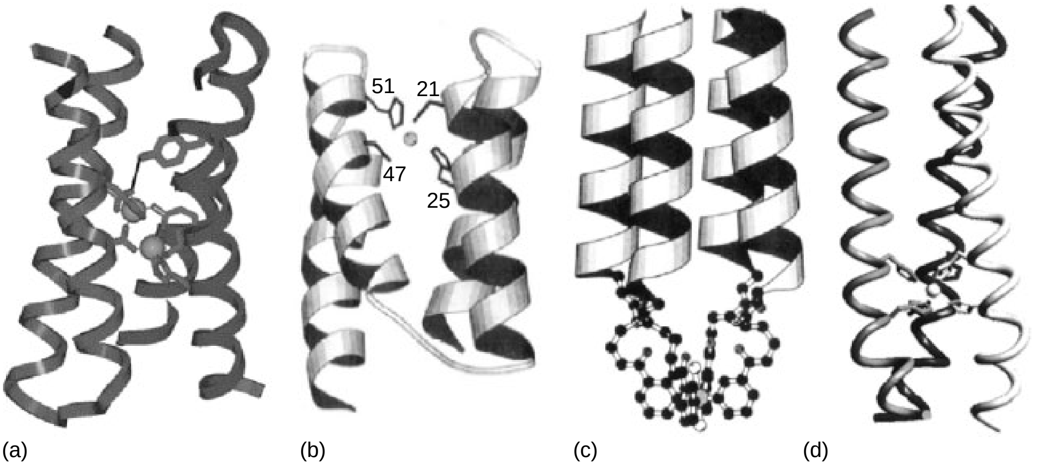

Figure 10 Incorporation of nonheme metal-binding sites into de novo designed proteins. (a) X-ray structure of a di-Zn^{II} derivative of Due Ferro 1. (Reprinted with permission from Ref. 57. © 2000 the American Chemical Society); (b) Computer model of $Zn^{II}(His)_2(Cys)_2$ site in a four-helical bundle. (Reprinted with permission from Ref. 65. © 1995 the American Chemical Society); (c) computer model of Ru^{II}-directed assembly of a four-helical bundle. (Reprinted with permission from Ref. 66. © 1992 the American Chemical Society); (d) Metal-ion induced assembly of a three-helcial bundle. (Reprinted with permission from Ref. 67. © 1998 the American Chemical Society)

such as a Tyr residue hydrogen-bonded to one of the Glu ligands, which is found in the di-iron center of R2 subunit of ribonucleotide reductase from Escherichia coli (*E. coli*). A crystal structure of the di-Zn^{II} derivative of the designed protein showed that the experimentally determined structure and the designed models are very similar (Figure 10a).**63** Since then significant progress has also been made in designing substrate accessible dinuclear metal centers by reducing the bulk of two hydrophobic Leu residues that blocked access to the metal sites.**64** This work paved the way for designing catalytically active metalloenzymes.

2.2.3 Introducing Other Metal-binding Sites into De Novo Designed Proteins

In addition to heme and nonheme di-iron, Zn^{II} has been introduced into the de novo designed four-helical bundle proteins. In one case, a $Zn^{II}(His)_3$ site has been introduced into two antiparallel helical pairs, with two His separated on a single turn of helix and the third one from the neighboring helix.**68,69** In another case, a $Zn^{II}(His)_2(Cys)_2$ site was created by two adjacent helices, each of which contributes a Cys and a His residue (Figure 10b).**5,70** The Cys and His residues are separated by about one turn of the helix. Unlike metal ion-induced metallopeptide folding, Zn^{II}-binding in these designed proteins resulted in no significant change of secondary structure. However, the metal binding did result in substantial stabilization of the protein toward denaturation.

As discussed in Section 2.2.1, metalloporphyrins or cyclic peptides have been used as a template for synthesis of topologically predetermined metallopeptides and proteins. The same strategy has been used to introduce other metal-binding sites into de novo designed proteins. A good example is the use of exchange-inert Ru^{II} or Co^{III} complexes to direct synthesis of three- and four-helix bundle proteins (Figure 10c).**66,71** Amphiphilic peptides functionalized with $2,2'$-bipyridine at the N-terminus were designed and shown to undergo spontaneous self assembly in the presence of metal ions. The oligomeric state and orientation of the helix bundle can be controlled through the intrinsic binding energy and stringent geometric requirements of the metal coordination. This approach has been extended to design a heterodinuclear three helix bundle protein where the Ru^{II} is located at one end and a $Cu^{II}(His)_3$ site at the opposite end.**72** Since Ru^{II} and Co^{III} complexes at the end of the designed helix proteins are redox active, placing another redox partner at defined location of the peptide allowed a systematic study of electron transfer influenced by such factors as distance, formation, and presence of hydrogen bonds.

Metal ion-induced assembly of designed helical bundle proteins has also been shown by introducing His or Cys residues in the middle of the peptides instead of the end of the peptide.**67** In addition, rather than using metal complexes to direct the assembly of designed proteins, one can use designed helical proteins to enforce unusual geometry and coordination numbers of metal ions.**73** A nice example is the use of three-stranded helical peptides to impose a three-coordinate trigonal Hg^{II}-binding site, even though Hg^{II} normally prefers two-coordinate linear geometry.**74** This was accomplished by introducing one Cys in the middle of each of the three helical peptides that has been designed to form three helical bundles. This driving force to form three helical bundles makes Hg^{II} adopt its unusual geometry.

While de novo designed helical proteins are the predominant scaffolds for incorporation of metal-binding sites, use of other de novo designed scaffolds for metalloprotein design is emerging. A good example is introducing a transition metal-binding site (with binding selectivity of $\mathrm{Cu^{II}} > \mathrm{Zn^{II}} \gg \mathrm{Cd^{II}} > \mathrm{Co^{II}}$) in a de novo designed all β-proteins.[75] The protein was designed based on a portion of heavy chain variable domain of an immunoglobin. Three His residues were then incorporated into two loops between the β-strands, with two on one loop and the third one on another loop.

2.3 Design of Metal-binding Sites into Native Protein Scaffolds

The design of metal-binding sites in de novo designed scaffolds described in the above section represents the ultimate goal of protein design and is considered de novo design in its most fundamental and challenging form. However, the number of de novo designed scaffolds is limited to a few well-characterized ones, such as helix bundles. In contrast, close to 600 different natural scaffolds are available in the Protein Data Bank.[76] It has been shown that the same protein scaffold is used many times in different proteins, with different metal-binding sites crafted into its scaffold. Therefore, the design of metal-binding sites into native scaffolds offers more scaffold choices at the present time and thus presents more opportunity to test our knowledge and to build proteins with novel properties.[23] In addition, most native scaffolds have high thermodynamic stability and extraordinary tolerance for residue substitution, deletion, and insertion, making drastic changes of the scaffold's metal-binding site more likely to succeed. Finally, years of research in native proteins make the construction, purification, and characterization (including X-ray crystallography) of the protein scaffolds a common laboratory practice. As the understanding of protein structure improves, de novo designed proteins will become more attractive as scaffolds. But until then, working with existing native scaffolds affords equal advantages.

2.3.1 Redesign of an Existing Metal-binding Site to a New Site with Dramatically Different Structure and Function

Redesign bypasses not only the design of the overall scaffold, but also the initial creation of the metal-binding site. In addition to being more technically feasible with a better chance of success than other methods, this approach best reveals the role of specific residues responsible for a particular structural or functional feature of the metal-binding site of interest.

A. Redesign of Heme Proteins. Heme proteins are one of the most diverse groups of metalloenzymes with functions ranging from electron transfer, small molecule transport and sensing, to oxygen activation (*see* ***Iron: Heme Proteins & Dioxygen Transport & Storage***; ***Iron: Heme Proteins, Peroxidases, Catalases & Catalase-peroxidases***). Key factors that determine functional specificity include the types of hemes, nature of the proximal ligands, and the architecture of the distal site. Therefore redesign has focused on these three areas.

Redesign of One Type of Heme Protein into Another Type. Different types of hemes, such as heme a, b, c, d, d_1, o, chloroheme, heme P460, and siroheme (*see* ***Iron Porphyrin Chemistry***), share a common skeleton and differ in structural details owing to substitutions at the various positions.[38,77] Most of those hemes bind to the protein noncovalently. Redesigning those types of heme proteins into another often involves making the apo-protein, through either heme extraction or protein expression under controlled conditions, and then incorporating different types of hemes. However, c-type heme proteins contain covalent linkage to the protein through the Cys residues and the thioether bond formation is believed to be assisted by proteins such as heme lyase. Therefore redesign involving c-type hemes entails additional challenges. Interestingly, both cytochrome b_5 and cytochrome b_{562} have been redesigned into c-type heme proteins without the requirement of heme lyase. The redesign of cytochrome b_5 was accomplished through mutation of a surface Asn residue to Cys that placed the thiol group 3–3.5 Å from the heme 4-vinyl group,[78] while the redesign of cytochrome b_{562} was aided by a structural homology between the cytochrome b_{562} and a major class of c-type cytochromes.[79] Cysteine residues were then introduced in positions of cytochrome b_{562} homologous to those in the c-type cytochromes. In addition, a c-type cytochrome, cytochrome c_{552}, was converted into a b-type cytochrome after both heme-binding cysteines were replaced with alanine, either individually[80] or together.[81] These studies suggest that assembly of certain c-type cytochromes may be a consequence of spontaneous thioether bond formation after binding of heme to a prefolded polypeptide.[81,82] The redesigned proteins with a c-type thioether attachment have a significantly increased stability, while conversion of the c-type to the b-type heme proteins resulted in decreased stability.

Redesign of Heme Protein Through Change of Axial Ligands. The axial ligands often play dominant roles in modulation of structure and function of heme proteins. Among the ligands, histidine is by far the most common and found in many types of heme proteins such as cytochromes, globins, and peroxidases. Cysteine and tyrosine are found in a few classes of heme enzymes such as cytochrome P450, chloroperoxidase (CPO), and catalase. Therefore changing the axial ligands is an effective way to redesign heme proteins. For example, the bis-His cytochrome b_5 (Figure 11a)[83] and cytochrome c_3[84,85] have been converted to His-Met cytochromes, commonly found in cytochrome c, by mutation of one of the His

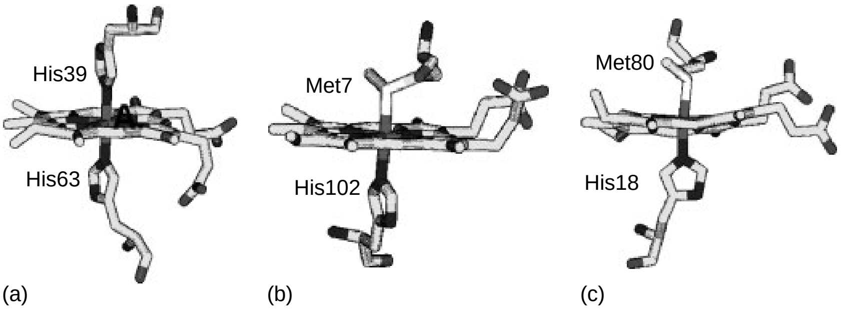

Figure 11 Cytochromes with different axial ligand coordination. (a) cytochrome b_5; (b) cytochrome b_{562} and (c) cytochrome *c*. (Reprinted with permission from Ref. 23. © 2001 the American Chemical Society)

ligands to Met. In the latter case, the mutation resulted in a 160–180 mV increase in reduction potential.[84,85] A still further increase in reduction potential was observed when the His-Met coordinated cytochrome b_{562} (Figure 11b) was changed to bis-Met.[86,87]

Both the axial Met and His ligands of cytochrome *c* (Figure 11c) have been replaced by other amino acids.[88–90] These studies indicated that replacement of the axial Met80 could lead to a dramatic change in the heme reduction potential. The His-to-Cys change resulted in ∼650 mV decrease in reduction potential, by far the largest change of reduction potentials from axial ligand mutations. In addition, by changing the Met ligand to a noncoordinating amino acid such as Ala using either protein semi-synthesis[91,92] or site-directed mutagenesis,[93] cytochrome *c* has been converted into an oxygen-binding protein such as myoglobin (Mb); the variant possessing a similar binding site for dioxygen and other exogenous ligands as in Mb. Similarly, cytochrome b_{562} was redesigned to a heme protein that binds exogenous ligands like CO, by changing Met to Gly or Ala.[94] In a redesign in the reverse direction, myoglobin (Figure 12a) has also been converted into a cytochrome like the bis-His cytochrome b_5 when the distal valine was replaced with a histidine.[95–97] Interestingly, the mutation resulted in ∼170 mV decrease in the reduction potential of myoglobin.

Oxidative degradation of heme is an important catabolic step in biology. The reaction is catalyzed by heme oxygenase (HO) (Figure 12b), which degrades heme to hydroxyheme, then to verdoheme, and finally to biliverdin.[98] Both cytochrome b_5 (with bis-His ligation) and b_{562} (with His-Met ligation) have been redesigned to mimic HO, through mutation of one of the His axial ligands to Met.[99–101] Further mutation of the remaining His in cytochrome b_5 to Val resulted in degradation of heme beyond verdoheme and to biliverdin, the final product of HO activity.[102]

Axial thiolate ligation from Cys is important for the reactivity and spectral characteristics of many heme enzymes such as P450, NOS, CPO, and CooA. In order to gain insight into the role of this ligation, the axial ligand His has been changed to Cys in both the human[103–105] and horse heart[106] myoglobins. This mutation resulted in not only a ∼280 mV decrease in reduction potential (which is consistent with thiol ligation to the heme iron), but also ∼5-fold increase in P450-type monooxygenase activity. Similarly, mutation of the proximal His to Cys was also made in heme oxygenase (Figure 12b).[107]

Unlike human Mb, the His-to-Cys mutation alone in horse heart Mb did not result in heme-thiolate ligation. However, an additional mutation of the distal histidine to either a valine or isoleucine resulted in a P450-like protein in its

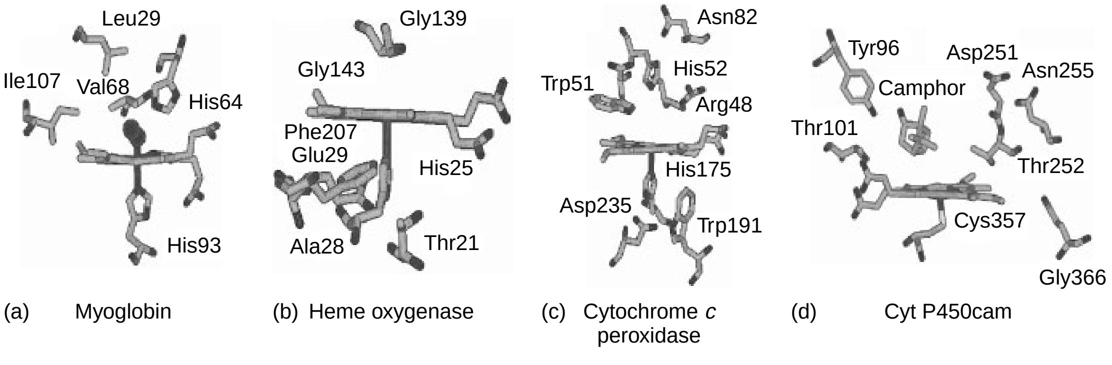

Figure 12 Heme proteins with one open coordination site. (a) myoglobin; (b) heme oxygenase; (c) cytochrome *c* peroxidase; (d) cytochrome P450. (Reprinted with permission from Ref. 23. © 2001 the American Chemical Society)

resting ferric state (*see* ***Iron: Heme Proteins, Mono- & Dioxygenases***).[106] This effect, termed the trans effect by the authors, makes a significant contribution to the axial ligand binding and stability. Similarly, mutation of the axial His ligand to Cys in cytochrome *c* peroxidase (C*c*P) (Figure 12c) resulted in a very unstable ligand that was rapidly oxidized to cysteic acid.[108] It was then recognized that a nonpolar residue next to the Cys is conserved in P450 proteins, while the analogous amino acid in C*c*P is an aspartic acid (see Figure 3b). Therefore, a further mutation of this Asp to Leu resulted in a stable, penta-coordinate, high-spin heme with thiolate ligation.[109] The study also marked the first time a stable cyanoferric complex and ferrous state of a model P450 was made.[109,110] Stable cysteine thiolate coordination in the ferrous-CO derivative of an engineered protein was obtained by mutations of the His and Met axial ligands in cytochrome b_{562} to Cys and Gly, respectively.[111] The key to the success was to replace two glutamate residues, which make energetically unfavorable interactions with the heme propionate groups through electrostatic repulsion, to Ser. These works demonstrated the importance of the secondary coordination sphere around the primary coordination ligands in stabilizing metal-ligand ligation.

In a heme redesign in the opposite direction to the above work, the axial Cys ligand in CPO[112] and cytochrome P450 (Figure 12d)[113,114] was changed to a His. Replacing the axial Cys with His in cytochrome P450$_{\text{cam}}$ resulted in a greatly decreased camphor oxidation rate, elevated uncoupling rate, slower electron transfer rate from redox partner putidaredoxin, and much greater peroxidase activity. These results suggest that the proximal cysteine is essential for protein folding, substrate binding, and electron transfer and P450 monooxygenase activity.

Finally, the proximal histidines of myoglobin[103,104,115,116] and heme oxygenase[107] have also been mutated to tyrosine in order to convert these proteins to a catalase. As expected, replacement of His with Tyr in Mb resulted in a ~250 mV decrease in reduction potential because of the negative charge of Tyr. Surprisingly, this mutation had little effect on myoglobin's ability to carry out heterolytic or homolytic O–O cleavage.

Redesign of Heme Protein Through Change of Distal Site. With the exception of cytochromes, the residues around the distal side of the heme do not coordinate to the iron directly, and they exert their influence by fine-tuning the properties of heme proteins. For example, a distal His is present in globins and many peroxidases (in addition to the common proximal His ligand). Despite this similarity, globins are oxygen carriers and only react with H_2O_2 at a much slower rate ($\sim 10^2\,M^{-1}\,s^{-1}$) than peroxidases (with a rate of $\sim 10^7\,M^{-1}\,s^{-1}$). Furthermore, unlike peroxidases, globins cleave the O–O bond of peroxide both heterolytically and homolytically. Watanabe and coworkers were the first to recognize the importance of the location of the two distal His residues in Mb and in CcP; the distances between the N_ε of the distal His and the ferric heme iron are normally 4.1–4.6 Å for globins and 5.5–6.0 Å for peroxidases (Figure 13).[24,117,118] Therefore, a series of variants were made that include His64Leu (to eliminate the distal His in Mb), His64Leu/Phe43His (to introduce a distal His at a similar position/distance as in peroxidases) and His64Leu/Leu29His (to introduce a distal His at a farther position/distance than in peroxidases). While His64Leu and His64Leu/Leu29His variants reacted with $H_2O_2 \sim 100$ and $\sim 3-6$ times slower than the native Mb, the His64Leu/Phe43His variant exhibited ~11 fold higher activity. These changes in reactivity were rationalized in terms of the roles of the distal histidines as general acid-base catalysts.[24,118] The His64 in native Mb functioned only as a general base by enhancing the binding of H_2O_2 through hydrogen-bonding to both oxygen atoms of the peroxide, and it was too close to the heme center to support heterolysis of the peroxide bond. In contrast, the His43 in His64Leu/Phe43His variant was at a similar position and distance as in most peroxidases and thus can work both as a general base to enhance the binding of H_2O_2 through deprotonation of the peroxide, and as a general acid to facilitate the heterolytic cleavage of the peroxide O–O bond. The His29 in His64Leu/Leu29His was too far away to serve any of these purposes. This work was a beautiful demonstration that proper positioning of the distal histidine is essential for the activation of H_2O_2 by heme enzymes.

Another structure-based redesign has been demonstrated in the conversion of human heme oxygenase-1 (HO-1) into a peroxidase.[119] The crystal structure of HO-1 suggests that Gly139 interacts directly with iron bound ligands (Figure 12b). When this glycine was mutated to Ala, Leu, Phe, Trp, His, or Asp, the resulting protein gained peroxidase activity by reacting with H_2O_2 to form a ferryl species that catalyzed the peroxidation of guaiacol. Displacement of the distal helix, which shifted owing to steric interactions between the larger amino acid side chains introduced by the mutations and the heme group, appears to be responsible for the new reactivity. Therefore, the authors concluded that the ferryl species formation responsible for the peroxidase activity was a default reaction, and the principal role of the HO active site may be to suppress this unwanted reaction with respect to HO activity. The gain in peroxidase activity in HO-1 was also observed with mutations of Asp140, another distal side residue that may participate in a hydrogen-bonding network involving ligands coordinated to the heme iron.[120,121]

B. Redesign of Nonheme Iron Proteins. In heme protein redesign described above, the heme prosthetic group largely dictates the active site structure. Redesign focuses mainly on the proximal and distal sides of the heme, causing minimal effects on the overall protein scaffolds. This is not necessarily the case for nonheme metalloproteins in which metal sites are not as dominant and small changes may have more dramatic effects on the protein folds and stability.

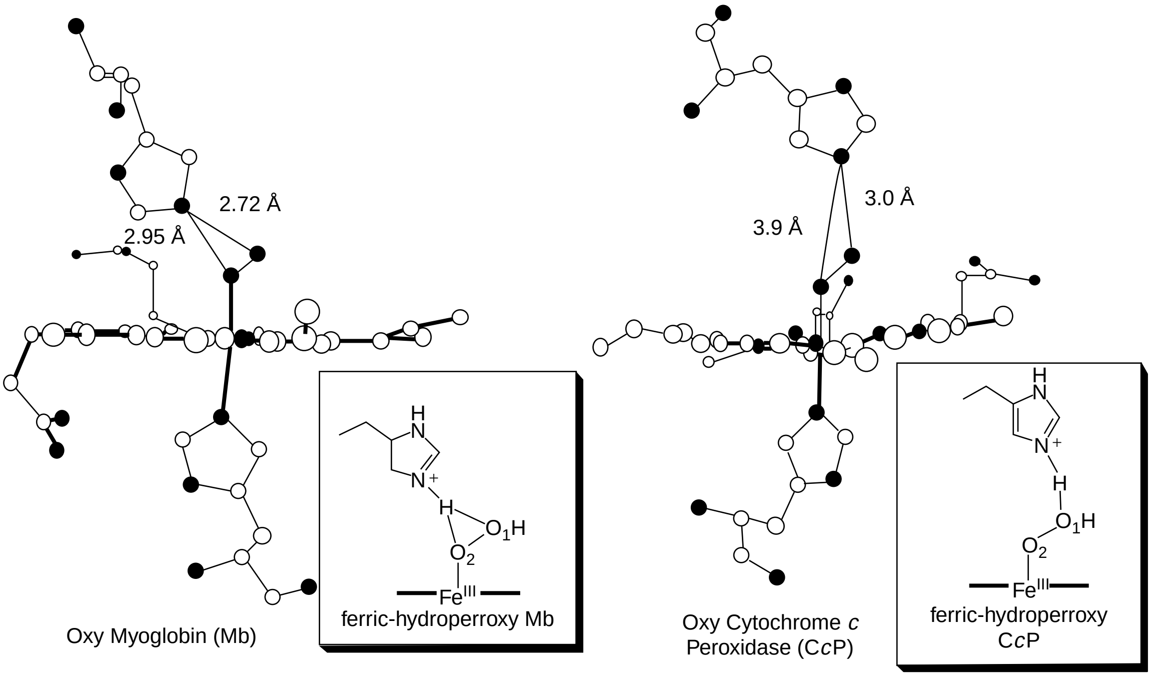

Figure 13 X-ray crystal structures of oxy forms of cytochrome *c* peroxidase mutant (W191F C*c*P) and myoglobin (Mb), used to postulate structures of ferric-hydroperoxy species, a precursor of compound I, as depicted in insets. (Reprinted with permission from Ref. 118. © 2001 the American Chemical Society)

From Rubrerythrin to Ribonucleotide Reductase. Dinuclear iron proteins (*see* ***Iron Proteins with Dinuclear Active Sites***) are an important class of nonheme iron proteins that share a similar di-iron oxo core and yet perform a variety of different functions ranging from dioxygen binding (hemerythrin, Hr), to ribonucleotide reduction (ribonucleotide reductase, RnR), and methane activation (methane monooxygenase, (MMO)). The majority of dinuclear iron proteins, including RnR and MMO, contain six ligands from 2 pairs of **Glu**X$_{30-32}$**Glu**XX**His** motifs. Only five of the six ligands are found at the corresponding positions in rubrerythrin (Rr) from *Desulfovibrio vulgaris*, a protein whose physiological role remains to be determined, (Figure 14). The putative sixth ligand, His56, is too far away to serve as a ligand to the nearest iron in Rr. Instead, Glu97 provides the sixth ligand at the other end, and it is believed to be a unique ligand for Rr proteins.[122] The di-iron oxo site of Rr was redesigned by mutation of Glu97 to Ala.[123] The X-ray crystal structure of the redesigned protein indicated that His56 was an iron ligand and this coordination was not a result of His56 moving closer to the iron. Instead the iron moved $\sim$1.6 Å relative to the same iron in the native Rr. The di-iron oxo site of the new variant is very similar to that of RnR.

Since Tyr122 plays a critical role in RnR function, an effort was also made to introduce a Tyr at a similar position in Rr.[123] Even though a Tyr102 was present in Rr that seemed to correspond to Tyr122 in RnR, a sequence homology search indicated that a nonconserved residue (Leu60) in Rr corresponded to Tyr122 in RnR. Therefore, a Leu60Tyr mutation was made and the crystal structure of the variant was obtained. According to the structure, the side chain of the introduced Tyr60 was now in a similar position as the Tyr122 in RnR. While the introduction of the Tyr into Rr was successful, no Tyr radical was detected in the redesigned protein. This result was explained based on the difference that Tyr122 in RnR made direct hydrogen bonds to an iron-coordinating terminal carboxylate while the Tyr60 in the redesigned protein did not. Both the Glu97Ala and Leu60Tyr mutation studies suggested that significant local structural changes might occur. These changes may not be readily predicted without homology information.

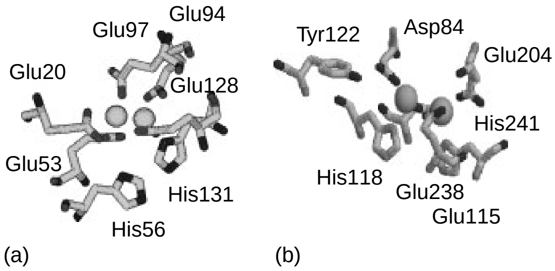

Figure 14 The di-iron oxo sites in rubrerythrin (a) and ribonucleotide reductase (b). (Reprinted with permission from Ref. 23. © 2001 the American Chemical Society)

From Ribonucleotide Reductase to Methane Monooxygenase. Redesign of the di-iron site of ribonucleotide reductase (RnR) introduced a methane monooxygenase (MMO) type function.**[124]** The metal site of RnR is surrounded by hydrophobic residues. A tyrosine (Tyr122) close to the dinuclear iron center is proposed to form a radical, initiating the catalytic cycle of RnR (Figure 14b). To examine the importance of the hydrophobic environment around the iron oxo site of RnR, Phe208 was mutated to a Tyr, placing another phenolic group near the site. UV-vis and RR spectral studies of the variant showed that it contains a ferric catecholate instead of a Tyr radical. The mechanism for generation of this protein derived dihydroxyphenylalanine was proposed to be similar to that of MMO.

From One Type to Another Type of Fe–S Cluster. Iron–sulfur clusters, such as [2Fe–2S], [3Fe–4S], and [4Fe–4S], are found in proteins (*see* ***Iron–Sulfur Proteins***). One of the most interesting aspects of the iron–sulfur proteins is their ready conversion from one type to another through chemical oxidation and reduction, pH changes, or site-directed mutagenesis.**[125–128]** More importantly, several studies have indicated that some of the cluster conversions are physiologically relevant in that they play important roles in regulation of enzyme activity.

C. Redesign of Copper Proteins. Copper proteins are classified into three types according to their spectroscopic properties (*see* ***Copper Proteins with Dinuclear Active Sites***; ***Copper Proteins with Type 1 Sites***; ***Copper Proteins with Type 2 Sites***). Type 1 copper proteins, commonly called 'blue copper' proteins, usually have an intense blue color owing to a strong absorption around 600 nm. They also have a very small $A_{\|}$, which is the hyperfine splitting with the molecular z axis (d_z2 in the case of Cu(II) proteins) oriented parallel to the external magnetic field, in electronic paramagnetic resonance spectroscopy (EPR). Type 2 copper proteins have spectroscopic properties just like simple copper complexes. Type 3 copper proteins are a group of binuclear copper proteins that have no EPR signal in the oxidized state owing to antiferromagnetic coupling of the two neighboring Cu(II) ions. Recently, new classes of copper centers, such as the purple Cu_A (*see* ***Cytochrome Oxidase***) and the Cu_z (*see* ***Copper Enzymes in Denitrification***) sites, have been identified.

From One Type 2 Copper Protein to Another Type 2 Copper Protein. It has been shown that a type 2 copper protein called copper–zinc superoxide dismutase (CuZnSOD) (Figure 15b) shares the same overall scaffold as its copper chaperone protein called copper chaperone for SOD (CCS).**[129–131]** All of the zinc site ligands and three of four copper site histidine ligands in CuZnSOD are conserved in human CCS (hCCS). The zinc site in hCCS displayed the same structure as in CuZnSOD.**[132]** The fourth ligand in the copper site of CuZnSOD is replaced by an aspartate residue in hCCS. Although aspartate could be a ligand to copper, no copper binding is evident from the X-ray structure of hCCS,**[132]** and hCCS exhibits no SOD activity.**[133]** Based on this analysis, the Asp residue in hCCS was converted to His as in CuZnSOD.**[133]** The resulting protein gained significant SOD activity, indicating that this mutation allows the formation of a new catalytically active copper site as in CuZnSOD and is critical in conferring the SOD activity. Furthermore, they demonstrated that this mutation did not inhibit the protein from functioning as a copper chaperone. This work strongly suggests that the aspartate residue is present in hCCS to preclude the deleterious SOD reaction as a result of copper binding, so that hCCS can function as a pure copper chaperone. Furthermore, it indicates that both the location and the exact nature of the amino acid residues are important for the formation of the metal-binding sites in proteins.

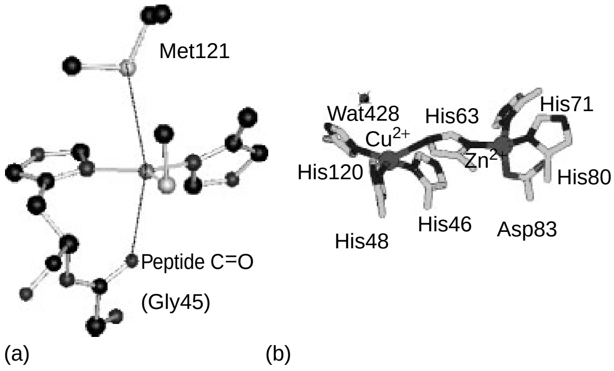

Figure 15 Structures of type 1 copper protein, Azurin (a) and Type 2 copper protein, Copper, zinc superoxidase dismutase (b). (Reprinted with permission from Ref. 23. © 2001 the American Chemical Society)

From A Type 2 Copper Protein to A Type 1 Blue Copper Protein. The essential features of type 1 copper proteins appear to be two histidine imidazoles and a cysteine thiolate coordinated to Cu(II) in a trigonal planar (or distorted tetrahedral) geometry with one or two additional weak axial ligands such as methionine (Figure 15a) (*see* ***Copper Proteins with Type 1 Sites***).**[134]** To elucidate the relationship between the type 1 and type 2 copper proteins and to take advantage of predefined scaffolds and metal-binding sites in the design of the unusual type 1 copper center, Lu *et al.* introduced cysteines into the metal-binding sites of yeast CuZnSOD (Figure 15b), a type 2 copper protein.**[135–139]** When a cysteine was substituted for a histidine in the copper site, a site having a distorted square-planar geometry (Figure 15b), a strong new absorption around 400 nm and a typical type 2 or 'normal' EPR were observed, suggesting that the presence of cysteine was not sufficient in itself to produce the unusual type 1 or 'blue' copper spectra.**[135,139]** On the other hand, substitution of a cysteine for a histidine in the zinc site, a site possessing a distorted tetrahedral geometry, resulted in a type 1 copper protein.**[135–138]** All three His-to-Cys mutant proteins reacted with ascorbate much faster than the wild type protein, indicating that the presence of a thiolate greatly increased the redox reactivity of the metal-binding site, consistent with the thiolate providing an efficient superexchange pathway for electron transfer.[138] The bridging histidine in CuZnSOD was also replaced with a cysteine by Banci *et al.*, but the resulting protein did not display any S-to-Cu(II) charge transfer absorption, indicating the lack of a Cu-cysteine bond.[140] These studies demonstrated that both the cysteine ligand and the geometry define the structural and functional properties of type 1 blue copper proteins.

From A Type 1 Blue Copper Protein to A Type 2 Copper Protein. The type 1 blue copper protein azurin from *Pseudomonas aeruginosa* has been converted into a type 2 copper protein through mutation of the Cys ligand (Figure 15a) to Asp.[141] The mutation resulted in not only a type 2, five-coordinate copper site, with both oxygens of the aspartate residue serving as potential ligands to copper,[142,143] but also in a dramatically reduced electron self exchange rate and intramolecular electron transfer rate compared to the native azurin.[144] The type 1 to type 2 copper conversion has also been accomplished by replacing one of the histidines in the type 1 blue copper azurin with glycine.[145–147] Interestingly the blue copper site can be restored by addition of external ligands such as N-methyl imidazole. Despite this restoration, the protein was not able to rapidly interconvert between the Cu(II) and Cu(I) forms, indicating that the covalent attachment of the ligand at the histidine position to the protein backbone is essential for the electron transfer function of the protein.

D. Redesign of Other Metalloproteins.

Redesign of Ca^{II}/Mg^{II} Specificity. Proteins in the calmodulin superfamily (including troponin C, parvalbumin (PV) and oncomodulin (OM)) share similar overall structure and yet have different selectivity for Ca^{II} and Mg^{II} (*see* ***Calcium-binding Proteins***; ***Cation-activated Enzymes***). For example, PV and OM have four helix-turn-helix domains, two of which contain mixed Ca^{II}/Mg^{II} sites and two Ca^{II}-specific sites. The mixed Ca^{II}/Mg^{II} sites have been converted to Ca^{II}-specific sites by replacing amino acids with the corresponding residues in the Ca^{II}-specific site.[148–150]

Redesign of Mg^{II}/Mn^{II} Specificity. Many endonucleases require divalent metal cofactors for DNA cleavage.[151] Like most endonucleases, EcoRV prefers Mg^{II} over Mn^{II}. However, mutation of Ile91 to Leu reversed the preference to Mn^{II} over Mg^{II}.[152] Surprisingly, Ile91 does not interact with the metal or recognition site, but points away from it into a hydrophobic core. The Ile91Leu mutation thus indirectly alters the coordination sphere providing better coordination of Mn^{II}. This result shows again that selectivity can be altered without directly replacing any of the metal ligands.

Redesign of Mg^{II}/Zn^{II} specificity. Mammalian alkaline phosphatase (AP) contains a tetrahedral Zn^{II} site (*see* ***Zinc Enzymes***), whereas *E. coli* AP has an octahedral Mg^{II} at the corresponding location. Mutation of a single amino acid (D153H) in *E. coli* AP, converted the specificity and geometry of the site to that of mammalian AP.[153]

Redesign of Fe^{II}/Mn^{II} Specificity. Among the many interesting cases of metal-ion specificity in proteins, the difference in specificity of Fe- and Mn-containing superoxide dismutase (SOD) is perhaps the most intriguing.[154,155] Both FeSOD and MnSOD share the same sequence and structural homologies. The overall structures and metal-binding sites of both proteins are virtually identical. However, even though FeSOD binds nonnative Mn ions, it is active only with Fe ions. The reverse is true for MnSOD. Since the primary coordination spheres of FeSOD and MnSOD are quite similar, efforts in redesigning their metal-ion specificity have been focused on the secondary coordination sphere, including a conserved glutamate residue (Glu170) in the dimer interface of MnSOD, and conserved glutamine residues believed to be central to the hydrogen-bonding network of FeSOD and MnSOD. For example, mutation of Glu170 to Ala in MnSOD resulted in purified protein that binds exclusively Fe, with similar spectroscopy to that of FeSOD, but no SOD activity.[156] When the histidine in FeSOD from *Mycobacterium tuberculosis* is mutated to Gln to mimic that in MnSOD, the variant protein was still found to bind Fe preferentially.[157] On the other hand, similar mutations in *Porphyromonas gingivalis* Cambialistic SOD made to mimic MnSOD resulted in a variant whose electronic absorption spectrum resembled more closely that of MnSOD.[158] More importantly, the variant displayed increased SOD activity over the wild type enzyme when Mn was in the metal-binding site. Finally, a mutation in MnSOD, to incorporate a Gln corresponding to that in FeSOD, did not result in a new, FeSOD-like active site. However, the MnSOD variant gained new SOD activity (~7% that of FeSOD) when Fe was in the metal-binding site.[159] These studies suggest that the presence and the position of the glutamine residue is important but not the sole determinant of the metal-ion specificity of FeSOD and MnSOD. Major differences in other conserved residues need to be elucidated before a successful redesign of metal-ion specificity can be accomplished.

2.3.2 Design and Engineering of New Metal-binding Sites

While redesign of existing metal-binding sites provides insight into the critical differences between the template and target proteins, it cannot address the roles of important residues that are common to both proteins. Designing new metal-binding sites provides such opportunities.

A. Design Through Homology. New metal-binding sites can be created based on either sequence or structural homology between a starting protein lacking the metal-binding site and the target protein with the metal-binding site. This approach relies on guidance from homology and offers a better chance of success than design by inspection. It is an important exercise for protein designers, especially in the early stages of protein design when our knowledge of creating metal-binding sites is limited.

Creation of a New Zn^{II}-binding site. New Zn$^{\mathrm{II}}$-binding sites have been created in several proteins based on structural homology. For example, the X-ray structure of the 37 amino acid protein, charybdotoxin, was examined for a Zn(II) binding site analogous to that in carbonic anhydrase.**[160–162]** A region containing two antiparallel strands of β-sheet was identified in charybdotoxin and the appropriate residues were mutated to His, as in carbonic anhydrase. A few other sterically conflicting residues were also mutated. The same metal-ion specificity as carbonic anhydrase, with Cu(II) preferred over Zn(II), was obtained with the new metal-binding site. This study demonstrated the success obtained from careful modeling and structural homology searches.

The stabilization of an adenylate kinase was achieved by placing the metal-binding site common to one protein family member into another member of the protein family. For the adenylate kinase family, those from gram-positive bacteria contain a Zn$^{\mathrm{II}}$ site while those from gram-negative bacteria do not. The Cys-X$_2$-CysX$_{16}$-Cys-X$_2$-Cys zinc binding motif of adenylate kinases from gram-positive organisms was engineered into a gram-negative protein.**[163,164]** The resulting protein displayed increased thermal stability. Similarly, a mammalian serum retinal binding protein (RBP) variant was also stabilized with the introduction of a Zn$^{\mathrm{II}}$ site.**[165]** The Zn$^{\mathrm{II}}$ site was modeled after the carbonic anhydrase (CA) site. As in CA, three residues on adjacent antiparallel β-strands of the RBP were mutated to His.

Creation of a New Mn(II)-binding Site in Peroxidases: Toward A New Manganese Peroxidase. Cytochrome *c* peroxidase (C*c*P) and manganese peroxidase (MnP) are members of the plant peroxidase superfamily (*see* ***Iron: Heme Proteins, Peroxidases, Catalases & Catalase-peroxidases***). C*c*P catalyzes the oxidation of ferrocytochrome *c* while MnP plays a key role in the oxidative biodegradation of lignin and many aromatic pollutants. Despite the limited sequence homology (less than 20%) between the two peroxidases, the overall structural folds of the two enzymes are quite similar (Figure 16a).**[166]** One major difference is that C*c*P lacks the Mn$^{\mathrm{II}}$-binding site found in MnP (Figure 16b). On the basis of a comparison of X-ray structures of the two peroxidases, the Lu group**[167–169]** and Goodin group**[170]** succeeded in engineering a Mn$^{\mathrm{II}}$-binding site in C*c*P by introducing amino acids found in MnP into the corresponding positions in C*c*P.**[171]** More importantly, they showed that the introduction of the new Mn$^{\mathrm{II}}$-binding site resulted in a significant increase in Mn$^{\mathrm{II}}$ oxidation activity. Similarly Tien group created a Mn$^{\mathrm{II}}$-binding site in lignin peroxidase, another peroxidase that shares similar overall structural and heme-binding site, but lacks the Mn$^{\mathrm{II}}$-binding site.**[172]** The resulting enzyme was able to oxidize Mn$^{\mathrm{II}}$ and still retain lignin peroxidase activity.

Creation of A New Cation-binding Site in Cytochrome c Peroxidase: Toward a Cation-controlled Molecular Switch. Heme peroxidases catalyze oxidation of a variety of substrates using H$_2$O$_2$ (*see* ***Iron: Heme Proteins, Peroxidases, Catalases & Catalase-peroxidases***). Structural comparison showed that a cation-binding site is present in ascorbate peroxidase (APX) and many plant peroxidases (a K$^+$ site for APX and a Ca$^{\mathrm{II}}$ for most other peroxidases), while only a water molecule was present at the same location in cytochrome *c* peroxidase (C*c*P). To engineer a protein whose activity can be controlled by a designed cation site, Poulos' group introduced the APX K$^+$-binding site into C*c*P based on a strong structural homology between the two proteins, and showed that long-range electrostatic effects can control the reactivity of a redox active amino acid chain.**[173,174]** Furthermore, based on a structural homology between C*c*P and Ca$^{\mathrm{II}}$-containing peroxidases such as lignin peroxidase and manganese peroxidase, the same group replaced amino acid

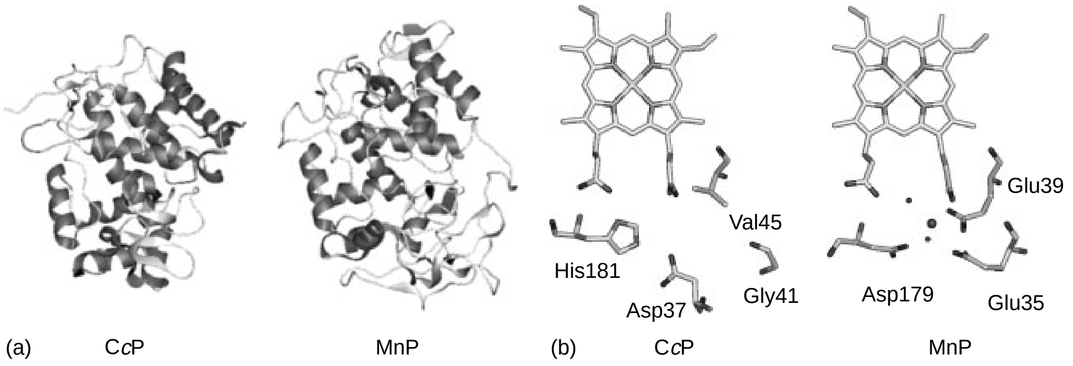

Figure 16 (a) Overall structure of C*c*P and MnP; (b) active site structure of C*c*P and MnP. (Reprinted with permission from Ref. 23. © 2001 the American Chemical Society)

residues in the C*c*P variant with those responsible for binding Ca^{II}.[175] The success of conversion was confirmed by X-ray crystallography. In contrast to what was observed with the C*c*P variant containing K^+-binding site, the EPR signal and enzyme activity of the new variant are much more selective for Ca^{II} than for K^+.

B. Design by Inspection. While design through homology is effective in the design of new metal-binding sites, like protein redesign, it cannot address the roles of important residues that are common to both proteins. Metalloprotein design in proteins with little homology represents a new level of challenge. To meet the challenges, several methods have been applied, including design by inspection, through using automated computer search algorithms, and structural based design.

Design by inspection is the method of choice in early metalloprotein design without homology. It relies on the knowledge of both starting proteins and target metal-binding sites. In the simplest case, metal-binding sites were created by introducing a single amino acid, such as His and Cys, or a series of His residues. Then those conserved metal-binding motifs described in the metallopeptide section (Section 2.1) were inserted into a protein. Finally, an even higher level of metal-site design is apparent from work where two or more metal-chelation residues were introduced at specific locations. The work in introducing conserved metal-binding motifs into native protein scaffolds has been covered in Section 2.1 and Section 3.1. Here we focus mainly on incorporating two or more chelating residues in a special defined way. To create these metal-binding sites, more intricate design strategies were necessary. These sites were generally created either through a knowledge of secondary structure or by analyzing the three-dimensional structure of the target protein. Residues thought to be in close proximity and capable of binding were changed to histidine or cysteine and the success of the site was tested by experiments. In many cases it remained to be shown if all of the designed ligands actually coordinated to the metal ion. Despite this concern, the designed metal-binding sites have been used in a variety of applications such as elucidation of protein topology, increase in protein stability, aid in protein purification, regulation of enzyme activity and selectivity, and creation of new enzymatic activities.

To Elucidate Protein Topology. Numerous examples have been presented in the literature in which two His residues have been created at two different locations and then metal-binding used to identify helix position, orientation, or other types of protein topology.[23] For example, a transmembrane segment in the human dopamine transporter (hDAT) was probed with new metal-binding sites.[176] A bis-histidine site was created with a residue at position 375 plus neighboring residues. Inhibition of the transporter with Zn(II) coordination was observed only with histidine residues located at position 375 and those located at residue 371, 377, 378, or 379. The results from Zn(II) binding to the mutants suggested that the transmembrane segment was helical, ending at position 375 and then changing to another loop structure beyond there.

To Stabilize Proteins. Metal-binding sites were created between helices or domains in the same subunit, or between subunits of multimeric proteins to help stabilize their interactions. For example, a Leu58His mutation in one of the helices together with the naturally occurring His39 on a neighboring helix in iso-1-cytochrome *c* was used to chelate metal complexes, $[Ru(2,2'bipyridine)_2]^{2+}$,[177] or $[Cu(iminodiacetate)]^{2+}$,[178] which resulted in 16.5 and 5 °C increases in melting temperature, respectively, over the wild type protein.[177,178] Increase of thermal stability was also observed when a metal-binding site was incorporated between two domains of the serine protease trypsin.[179] Finally. cross-linking of the helices with Zn(II) sites were designed into the interface of two GFP variants, yellow (YFP) and cyan (CFP) fluorescent proteins to stabilize the heterodimer.[180]

To Aid in Protein Purification. In addition to the increase of protein stability, the His58/His39 chelating site of iso-1-cytochrome *c* later became an important part of a dual gene/protein system for the homologous expression and purification of nonfunctional cytochrome *c*.[181] Homologous expression of nonfunctional mutant proteins of iso-1-cytochrome *c* in yeast *Saccharomyces cerevisiae* lacking the wild type cytochrome *c* gene was not possible because the yeast cells lacking this essential electron transfer protein could not grow. A strategy was designed to overcome this problem by coexpressing both the nonfunctional cytochrome *c* variant and a functional cytochrome *c*.[181] To separate the two proteins of similar properties, a Leu58His mutation was made on the functional cytochrome *c* so that a bis-His site was formed with the His39 originally in the protein. The functional cytochrome *c* was then easily separated from the nonfunctional cytochrome *c* by a metal affinity column.

To Regulate Enzyme Activity and Substrate Selectivity. Engineered metal-binding sites have been used to control the activity and substrate specificity of enzymes.[23] For example, addition of Zn^{II} to the Arg96His variant of rat trypsin switched off enzyme catalysis, while subsequent addition of EDTA restored full activity.[182] The inhibition is due to Zn^{II}-binding to both the engineered His96 and the naturally existing His57, an important residue for catalysis. The metal-dependent stabilization of protein–protein interface is also used as a way to induce enzyme activation. For example, substitution of opposing residues at the dimer interface of glycogen phosphorylase to His allowed the use of a Ni^{II} ion to lock the enzyme in the dimeric form and activate the enzyme.[183] Furthermore, bis-His variants of trypsin were made around the substrate-binding pocket of trypsin to modulate substrate specificity by metal binding.[184–186]

To Create New Activities. Section 2.3.2 describes a few studies of using design by homology to create a Mn^{II}-binding site in cytochrome *c* peroxidase and lignin peroxidase that mimic a structurally homologous manganese peroxidase. A similar Mn^{II}-binding site has been created in myoglobin by inspection even though there is no homology between myoglobin and manganese peroxidase.**187** The Mn^{II}-site was created at the exposed heme edge of myoglobin through mutations of two Lys to Glu. The resulting protein exhibits increased manganese peroxidase activity.

C. Design using Automated Computer Search Algorithms. To help design new metal-binding sites in proteins with little structural homology between the starting and target proteins, a number of computer algorithms have been written. Among several of these reported algorithms, two programs called Metal-Search**188** and Dezymer**189** have been the most successful in guiding metalloprotein design. Both Metal-Search and Dezymer algorithms make predictions based on strict geometric principles.**190** They assume a fixed protein backbone and search for optimal locations of ligands using different amino acid side chain rotamers. In the Metal-Search program, the idealized metal positions at every residue, including its side chain and rotamer are precalculated and those substitutions that result in idealized metal positions near each other are then grouped and evaluated. The Dezymer program, on the other hand, starts with an anchor point of an amino acid substitution with a selected rotamer, and systematically searches for additional coordinating residues that can satisfy the desired geometry of the designed site. Once a site and its substitution are identified, other changes in the surrounding area may be needed to avoid steric conflicts and to optimize packing of the site. In its current form, the Metal-Search program is used mainly for design of tetrahedral metal-binding sites while the Dezymer program is more versatile in this regard. Discussed below are several successful examples.

Design of A Tetrahedral Zn^{II}-Binding Site Containing Cys and His. Using the Metal-Search program, a tetrahedral His_3Cys metal-binding site has been designed into the B1 domain of IgG-binding protein G.**191** Solvent-exposed residues were chosen as places to put ligands in order to avoid major perturbations to the overall structure of this small, 56-residue scaffold. In addition to the four metal ligands, additional mutation of a residue that was in a predicted steric conflict with one of the introduced histidines was also carried out. In a complementary approach, several tetrahedral Zn^{II}-binding sites have also been designed into the deeper hydrophobic core of thioredoxin using the Dezymer program.**192** Spectroscopic studies showed that the designed proteins by both programs bind metal ions in the predicted tetrahedral environment and prefer binding Zn^{II} over Co^{II} by 100- to 1000-fold. With estimated constants on the order of a few nanomolar, the strong binding affinity in both studies is remarkable for a designed protein.

The importance of the secondary coordination sphere in improving metal-binding affinity has been demonstrated in one of the designed proteins.**193** Inspired by the work of Christianson and Firke's groups on the study of zinc protein carbonic anhydrase,**8** Marino and Regan placed Glu, Gln, Asp, or Asn close to each of the three histidine ligands in the designed $Zn(II)His_3Cys$ tetrahedral site of the B1 domain so that they could form hydrogen-bonding interactions with the imidazole nitrogens of the histidine ligands. These mutations resulted in 1.5- to 6.4-fold enhancement of affinity. Double mutations in the secondary coordination sphere resulted in even further enhancement and the effects appeared additive. An intriguing find from the study is that the above mutant proteins with enhanced metal-binding affinity unexpectedly shared little secondary structure with the parent protein, probably because many of the mutations caused major perturbations of the protein scaffold.

Design of iron–sulfur clusters. The mononuclear $[Fe(Cys)_4]$ rubredoxin center has been designed into native protein scaffolds using both the Metal-Search**194** and Dezymer**195** programs. The Dezymer program was used to convert a disulfide bond in thioredoxin to a mononuclear $[Fe(Cys)_4]$ rubredoxin center (Figure 17a).**195** The protein was capable of undergoing several successive cycles of air oxidation and reduction by β-mercaptoethanol.**195** In another study, the Metal-Search program was used to design the same mononuclear $[Fe(Cys)_4]$ center into the B1 domain of the IgG-binding protein G.**194** From these studies, Farinas and Regan recognized a limitation of the Dezymer and Metal-Search programs. Both programs used the fixed backbone of protein coordinates from either X-ray or average NMR structures. Small backbone movements can occur in solution and are sometimes necessary to accommodate slight changes associated with introducing new amino acid ligands. Therefore, the authors decided to select at random six out of 60 calculated NMR structures to apply the Metal-Search program.**194** Indeed, they found that, while certain sites can be identified in both the average and the individual structures, some sites could only be found in the individual structures. Since this strategy does not change the program algorithms, it can be applied to protein design using other programs or computer modeling packages. More study using this strategy is needed to find out how useful it is in metalloprotein design.

Most of the design of metal-binding sites has been limited to mononuclear centers. The design of tetranuclear $[Fe_4S_4]$ clusters into proteins represents a new challenge. In this case the Dezymer program was used to search for backbone positions of thioredoxin to place Cys side chains to match the $[Fe_4S_4]$ structures of a HiPIP protein.**197** In addition, two cysteines in the native thioredoxin were removed to avoid their competing chelation. A final isosteric Asp-to-Leu mutation was also included to improve the stability of the designed protein. The successful design of the center in thioredoxin was supported by the optical and EPR studies that showed similar

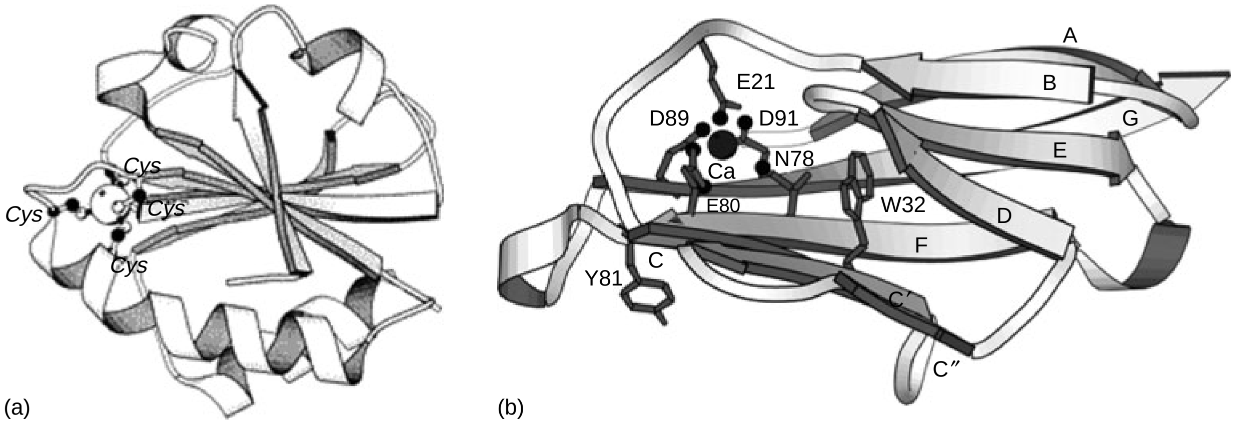

Figure 17 Computer models of designed metal-binding site using automated computer search algorithms. (a) A mononuclear [Fe(Cys)$_4$] center in thioredoxin. (Reprinted with permission from Ref. 195. © 1998 the American Chemical Society); (b) A Ca^{II}-binding site in N-terminal domain of rat CD2. (Reprinted with permission from Ref. 196. © 2003 the American Chemical Society)

spectral signatures as that in HiPIP proteins. Furthermore, the [Fe$_4$S$_4$] cluster was much more stable in the designed protein than when it was free in solution.

Design of A Calcium-binding Protein. A Ca^{II}-binding site has been introduced into a noncalcium-binding protein, domain 1 of the rat cell surface adhesion receptor CD2 using the Dezymer program (Figure 17b).**[196]** A survey of a number of calcium-binding proteins indicate that, despite the great diversity in the composition of ligand residues and bond angles and lengths of calcium-binding sites, common local structural parameters can be used to identify and design calcium-binding proteins, the most common geometry being pentagonal bipyramidal.**[198]** The defined parameter was used to search for locations in CD2. The resulting candidates (~7000) from the program were further filtered by several known criteria for calcium-binding sites, such as solvent accessibility, side-chain steric conflict, hydrogen bonding, hydrophobic, and electrostatic environment around the designed site. The final designed protein selectively binds Ca^{II} over Mg^{II} with Ca^{II}-binding affinity comparable to that of natural extracellular calcium-binding proteins (K_d of 50 μM).**[196]**

Design of A Blue Copper Center. Design of a blue copper center in proteins represents a still further challenge in metalloprotein design. For most successful examples of metalloprotein designs described so far, construction of a geometrically correct, sterically compatible primary coordination sphere was sufficient to reproduce the dominant features of the structure and function of the desired centers. However, certain metal-binding sites in proteins are unique in that metal ions are not necessarily in their preferred state and, to design such sites correctly, special caution has to be taken to prevent many alternative reactivities and coordination geometries.**[199]** Type 1 blue copper centers are a primary example. These centers contain a mononuclear copper with CysHis$_2$ in a trigonal plane and another weak axial ligand, usually Met (Figure 15a). Since this geometry is not preferred by either Cu(I) or Cu(II), blue copper proteins display many unusual spectroscopic properties, such as an intense blue color and very small $A_{\|}$ in electron spin resonance spectroscopy. In addition to the challenge of designing a site that allows incorporation of copper ions into a geometry that is not preferred, the assembly of the designed protein has to overcome the alternative reactivity of disulfide bond formation between proteins. This competing reaction is especially efficient in the presence of redox active metal ions such as Cu(II). Despite these complications, the Dezymer program was used to carry out a series of four primary designs and 32 variants.**[189,199,200]** The most successful variant of the designed thioredoxin was able to mimic the type 1.5 copper center after a strong, exogenous ligand, azide, was introduced axially into the designed center. By using an iterative strategy of design, characterization, and evaluation, the author provided many valuable insights into the metalloprotein design process. These included the need to surround the designed primary coordination sphere with a hydrophobic shell to ensure the absence of potential alternative coordinating residues or even solvent (water) and the requirement of forming a strong Cu(II)-thiolate bond in order to destabilize disulfide bond formation. It demonstrated that negative design (i.e. destabilization of competing reactions and coordination) is a crucial aspect of the protein design process.

Design of Mononuclear Nonheme Iron Centers with Catalytic Activities. Perhaps the biggest challenge in protein design is the introduction of catalytic activity into proteins, which requires a careful design of open coordination sites for binding small molecules like O$_2$, as well as substrates. Using the X-ray structure of the trigonal bipyramidal iron site in iron superoxide dismutase (SOD) as a guide, Pinto *et al.***[201]** used the Dezymer program to search thioredoxin and identify positions to place one Asp and two His in a plane. Another His at the axial position was also chosen so that an open coordination site was created on the opposite end. Additional mutations were introduced to prevent competing chelation by two internal cysteines and one histidine and to improve packing for the designed site. The electronic absorption spectrum of the designed protein as well as its N_3^- and F^- adducts are similar to those of native iron SOD and the iron has a dissociation constant of less than 1 μM. More importantly, comparative studies with the unrelated *E. coli* iron SOD indicated that the designed protein can catalyze superoxide dismutation with a rate on the order of 10^5 $M^{-1}s^{-1}$. Even though the catalytic rate is still about 10^4 fold slower than the native SOD, the rate is quite impressive considering that many of the long-range structural features in the native SOD have not been introduced into the designed protein.

The above work was extended by Benson *et al.*,**[202]** who designed six mononuclear iron-binding sites with three histidines and at least one open site at three different locations of thioredoxin. Unfavorable steric clashes were eliminated through further mutations. In almost all cases, the designed proteins were found to bind one Fe(III) with a K_d less than 5–10 μM. Two of the designs exhibit SOD activities appreciably above the background, with one of them approaching 1% of native *E. coli* SOD activity. An apparent correlation between the SOD activity and the number of positive charges in the vicinity of the designed site was also noted. This observation confirms the importance of electrostatic interactions between the superoxide anion and protein side chains in SOD activity.

D. Design using a Combination of Strategies. So far we have discussed two approaches to designing new metal-binding sites in proteins with little structural homology. Design by inspection relies heavily on the knowledge of the designer while design using automated computer algorithms requires correct input of parameters to define unique metal-binding sites. Owing to lack of knowledge, a number of metal-binding sites, such as blue copper proteins and heteronuclear metal assemblies (e.g. heme-copper centers) remain difficult to define and application of the automated computer algorithms have not been successful. The third approach uses a combination of the two strategies, by combining visual inspection of proteins to find proper locations for creating new metal-binding sites, and computer program evaluation for the energetics of positioning appropriate amino acid residues. It is most suitable for creating new metal-binding sites where location of the site is fairly certain from previous knowledge or study. As in the design by inspection approach, this approach uses previous knowledge to locate the site and thus bypasses the exhaustive search process of theoretical approaches. At the same time, this approach uses similar rigorous methods for evaluation of energetics of positioning appropriate amino acid residues for the site formation.

Design and Creation of A New Metal-binding Site in Antibodies and Green Fluorescent Proteins. Both antibodies and green fluorescent proteins have found wide applications in biology. Engineering metal binding into either protein would be an interesting way of increasing their functional diversity. By examining the morphology of Zn^{II} sites in PDB structures of carbonic anhydrase and carboxypeptidase, and then the structure of the anti-fluorescein antibody 4-4-20, multiple potential Zn^{II} sites were identified.**[203]** Many of the designed proteins successfully bound Zn^{II} in addition to other divalent metal ions. It remains to be seen if the sites can successfully catalyze a reaction. One particular protein was also used as a metal-ion sensor.**[204]** Similarly, work towards using the green fluorescent protein (GFP) as a metal-ion sensor was accomplished by creating a metal-binding site on its surface.**[205]** The coordination of metal ions in these designed proteins resulted in quenching of the protein's fluorescence. The first round of design was a bis-histidine site that loosely bound Ni^{II}. The second round of design involved the addition of a third metal-coordinating residue, aspartate. This variant yielded an effective metal site for Cu^{II}, Ni^{II}, or Co^{II} with binding constants in the low micromolar range.

Design and Creation of a Cu_B Center in Myoglobin and Cytochrome c Peroxidase: Toward A Novel Heme-copper Oxidase. Heme-copper oxidases (HCO's) are a superfamily of terminal oxidases in the respiratory chains of both eukaryotic mitochondria and bacteria (*see* ***Cytochrome Oxidase***). At the heart of these enzymes is a dinuclear center consisting of a heme with a proximal histidine and a Cu(II) with three histidines (Figure 18). One major difference between heme-copper oxidases and other heme proteins is the presence of the Cu(II), called the Cu_B center. It would be quite interesting to find out how to design and engineer a Cu_B center into other heme proteins at a similar location with respect to the heme center, and whether the presence of the new Cu_B center can transform heme proteins such as globins and peroxidases into an oxidase. Toward this goal, the Cu_B-site

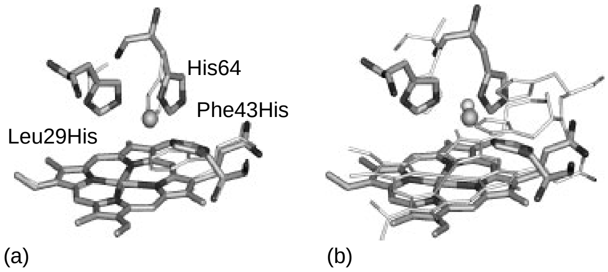

Figure 18 (a) Overlay of the crystal structure of WTMb (thin) and the a structural model of Cu_BMb based on computer modeling and energy minimization (thick); (b) Overlay of the crystal structure of heme-cooper center in C*c*O (thin) and the same structural model of Cu_BMb (thick) as in (a). (Reprinted with permission from Ref. 207. © 2000 the American Chemical Society)

has been designed into both cytochrome *c* peroxidase[206] and myoglobin.[207] It was accomplished through a careful overlay of the heme-copper center in cytochrome *c* oxidase (C*c*O) with the heme site in either C*c*P or Mb (Figure 18). Different orientations of the C*c*P/Mb active-sites were sampled until an appropriate match of residues in C*c*P/Mb to the histidine ligands of the Cu_B-site in C*c*O were found. The matched residues in C*c*P/Mb were then mutated to histidines and the energetic parameters after energy minimization of the resulting proteins were evaluated and compared with the parameters of wild type proteins. Spectroscopic studies confirm the creation of a single Cu(II)-binding site in both Mb and C*c*P. In addition, the study also revealed that the presence of Cu(II) and Ag(I) (as a Cu(I) mimic) increased the affinity of heme for diatomic ligands such as CN^- and O_2. More importantly, further studies showed that the Cu_B center plays a critical role in O_2 binding and reduction, and proton delivery during the O_2 reduction is important to avoid heme degradation and to promote the HCO reaction.[208]

3 RATIONAL DESIGN: MODULAR APPROACH

In addition to the consensus sequence/structure approach described above, the modular approach is also very effective in designing new metalloproteins. This approach involves transplanting a conserved structural unit from one protein into another. It is commonly used by Nature to create new structures and functions since gene shuffling and recombination is often observed in biological systems. Therefore learning this ‘trick’ is an important step in metalloprotein design and engineering.

3.1 Application to Metallopeptide Models

Zinc finger proteins (*see* ***Zinc: DNA-binding Proteins***) are a good example where the modular approach can be applied, since the proteins almost always contain two or more zinc finger domains, which have to work together to achieve high activity (i.e. DNA binding). It has been shown that one zinc finger domain interacts primarily with three base pairs of DNA; the identity of amino acids at the −1, 2, 3 and 6 positions (numbered relative to the start of helix) defines the specificity of the DNA base pairs they recognize. Three zinc finger domains can recognize nine base pairs. By swapping one zinc finger domain with another, the specific DNA sequences that the zinc finger proteins can recognize have been altered. A number of these designed zinc finger proteins have already been applied as artificial transcription factors for different DNA sequences.

Incorporating common structural motifs such as the His- and Cys-containing motifs and the zinc finger domain discussed above onto other proteins has resulted in new hybrid proteins with dual functionality. Two strategies have been used to achieve this goal. In the first strategy, the metal-binding motifs or domains are fused by a linker to either the N- or C-terminus of another protein. For example, the Ni^{II}·Xaa-Xaa-**His** peptide (see Section 2.1.1) has been fused onto the N-terminus of the DNA-binding domain of Hin recombinase and the resulting hybrid metalloenzyme can carry out sequence specific (due to Hin recombinase) oxidative cleavage (due to Ni^{II}·Xaa-Xaa-**His** peptide). The incorporation of a series of histidines (∼4–6 residues) at the N- or C- termini of proteins formed functional metal-binding sites. It is an efficient way of creating nonspecific metal sites of relatively high binding affinity. The histidine repeats, including histidine tags, are widely used in protein purification with the technique called immobilized metal affinity chromatography (IMAC),[209] to sense or remove metal ions, or to immobilize proteins to a surface for structure determination. Finally, site-specific DNA methylases or restriction enzymes have also been obtained when the zinc finger domains were combined in this way with *S*-adenosyl methionine-dependent methylase or the type IIS restriction enzyme *Fok*I, respectively.

In the second strategy, metal-binding structural motifs are crafted in the middle of another protein domain that shares similar structural homology. For example, an arginine-rich α-helix from HIV-1 Rev was engineered into the zinc finger framework by replacing the α-helix of the zinc finger protein while keeping the metal-binding histidine ligand (Figure 19a).[210] The new hybrid protein can now bind RNA (HIV-1 Rev response element) instead of DNA in a Zn^{II}-dependent manner. The His-X_3-His motif (Figure 1b) can be incorporated into proteins with only a few residue substitutions.[209,211] For example, the His-X_3-His motif was engineered into T4 lysozyme to aid the determination of distances between residues by measuring the EPR relaxation of a nitroxide spin label attached to a cysteine by a Cu^{II} ion

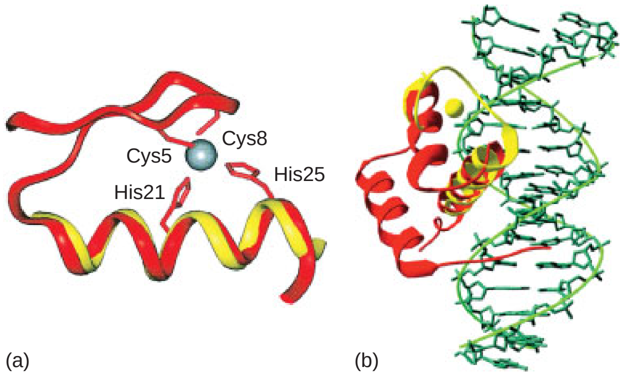

Figure 19 (a) Computer model of a designed zinc finger-Rev peptides. Overlap between the α-helical segment of Zif finger 2 (magenta) (3) and residues 34–47 of the Rev peptide (yellow). (Reprinted with permission from Ref. 210. © 1999 National Academy of Sciences, USA); (b) Computer model of a designed Ca^{II}-binding site by merging the calcium-binding EF-hand of calmodulin (yellow) and the helix-turn-helix DNA-binding domain of engrailed homeodomain (red) (cocrystallized with DNA). (Reprinted from Ref. 215. © 2001, with permission of Elsevier)

bound to the engineered His-X_3-His motif.[212] The His-X_3-His arrangement was also engineered into iso-1-cytochrome *c* through Lys4His/Thr8His mutations to create a more stable variant resistant to thermal and chemical denaturation,[178,213] and to aid in protein separation in the presence of metal ions.[214]

The EF-hand calcium-binding motif was engineered onto a loop in human lysozyme for increased stability,[216] or between two green fluorescent protein (GFP) variants to form an effective calcium sensor.[217,218] Interestingly it has been recognized that the EF-hand Ca^{II}-binding motif and a helix-turn-helix DNA-binding motif are almost superimposable (Figure 19b).[215] By crafting ligands to the Ca^{II} site into the helix-turn-helix motif and replacing Ca^{II} with lanthanide, a sequence-selective peptide nuclease has also been obtained.[210,215,219,220]

3.2 Application to Designing Metal-binding Site in De Novo Designed Proteins

A demonstration of the modular approach in de novo designed proteins appeared in 1996, in which a metallopeptide model of a ferredoxin-like [4Fe-4S] cluster (described in Section 2.1.2) has been incorporated into the loop region of a de novo designed di-heme protein (described in Section 2.2.1).[31] Normally the loop regions of the four-helix bundle proteins play a structural role. By replacing the loop of the de novo designed di-heme proteins with conserved loop derived from ferredoxins, a multicofactor metalloprotein containing [4Fe-4S] cluster at one end and a di-heme center in the middle was obtained. This approach has been extended to design bridged $[Ni^{II}\text{-}(\mu_2\text{-}S_{Cys})\text{-}Fe_4S_4]$-containing assembly into the four-helix bundle.[221] In the design, the Fe_4S_4 ferredoxin motif [Cys-Ile-Ala-Cys-Gly-Ala-Cys] was used, with the fourth cysteine positioned to serve as the bridging ligand between the cluster and Ni^{II}. Three other binding residues (either N_3S (His_3Cys) or N_2S_2 (His_2Cys_2)) were incorporated in appropriate positions to constitute a binding site for Ni^{II}. Finally, the template-assisted assembly of metalloproteins described in Section 2.2.1 may also make the modular design possible. For example, the cyclic peptides containing four cysteines with different protection groups allow coupling of different peptides with different functional groups. In this way different metal-binding centers can be attached to different peptides.

3.3 Application to Designing Metal-binding Site in Native Protein Scaffolds

3.3.1 *Gene Shuffling and Recombination*

Gene shuffling and recombination has been used as a tool to engineer heme proteins. This research endeavor is aided by identification of exons and their corresponding protein structural units called modules.[222,223] For example, human hemoglobin contains two α- and two β-subunits. Amino acids associated with the $\alpha_1\beta_1$ interface are located in a single module. Replacing this module from the β-subunit with the module in the α-subunit resulted in a chimeric hemoglobin that binds preferentially to the β-subunit.[224] Furthermore, a heme-binding module was also identified. Substitution of the heme-binding module in myoglobin with that in α-subunit of hemoglobin makes the heme environment of the chimeric myoglobin resemble more of α-subunit of hemoglobin, including the orientation of proximal His.[225] These successes suggest small structural modules can be defined and used for design and engineering of metalloproteins.

3.3.2 *Loop-directed Mutagenesis*

On average, loops account for ∼30% of globular protein structural elements. They are highly tolerant of amino acid replacement, insertion, and deletion; this feature makes it an ideal place to design different metal-binding sites without changing or disrupting the overall scaffolds of the proteins. Therefore a number of metal-binding sites are in between loops, and transplanting the active site in the loop from one protein into another can be a general approach of designing novel proteins. Analogous to site-directed mutagenesis, the replacement of one loop with another loop is termed loop-directed mutagenesis (LDM).

Grafting of Calcium-binding Loop to Increase Stability. In a complementary approach to using automated computer algorism to designing Ca^{II}-binding sites in domain 1 of the rat cell surface adhesion receptor CD2 (see section 'Creation of A New Mn(II)-binding Site in Peroxidases: Toward A New Manganese Peroxidase'), the EF-hand calcium-binding loop III from calmodulin was inserted with glycine linkers into the same protein and shown to bind Ca^{II}.[226] To increase protein stability, the Ca^{II}-binding ω loop containing 10 amino acids in thermophilic thermolysin was introduced into homologous mesophilic neutral protease to replace a seven-residue loop in the corresponding position.[227] While maintaining similar activity as the native enzyme, the designed neutral protease binds a new calcium ion with a K_d ∼0.1 mM, and was 2-fold more stable than the native protein in the presence of Ca^{II}. Similarly, replacing a loop in mesophilic subtilisin BPN′ with the corresponding Ca^{II}-binding loop of a homologous thermophilic thermitase resulted in a new Ca^{II}-binding site with a K_d ∼0.1 mM, and 10-fold more stability to irreversible inactivation at 60 °C.[228]

Introduction of Metal-binding Loop to Regulate Activity. In an extension of their work on metal-ion regulation of enzyme activity (see section 'Creation of A New Zn^{II}-binding Sites'), Halfon and Craik succeeded in regulating trypsin activity by introducing a metal-binding loop from its homologous protein called tonin.[229] Based on computer modeling, two histidines in the loop, together with the catalytic histidine of trypsin, could complex metal ions. Addition of $\mathrm{Cu^{II}}$, $\mathrm{Ni^{II}}$, or $\mathrm{Co^{II}}$ ions to the engineered protein substantially inhibited the proteolytic activity of trypsin and the inhibition can be fully reversed by removal of the metal ions using EDTA. Significantly, LDM made it possible to create a tridentate histidine ligand set, resulting in much higher metal-binding affinity (∼100 nM for Cu(II)) and tighter regulation of enzyme activity than the previously reported bidentate histidine ligand sets based on site-directed mutagenesis.

Incorporation of Metal-binding Loop to Create New Functionality. LDM can also be used to introduce new metal-binding sites and functionality into proteins. This principle has been demonstrated in several cases of protein design study based on the Greek key β-barrel scaffold. For example, it was recognized that subunit II of cytochrome *c* oxidase (C*c*OII) was structurally and functionally homologous to the CyoA subunit of cytochrome *o* quinol oxidase, and shared the same Greek key β-barrel fold. However, the CyoA did not contain the $\mathrm{Cu_A}$ center as in C*c*OII. A careful sequence alignment revealed that the amino acids capable of forming the $\mathrm{Cu_A}$ center were replaced by those that could not coordinate copper and those amino acids were clustered in a loop between two β strands F and G (called the FG loop) (Figure 20).[230] Replacing the whole loop sequence of CyoA with the corresponding loop sequence of C*c*OII restored the $\mathrm{Cu_A}$ center.[230]

Similar sequence alignments also revealed that C*c*OII shared similar structural homology with the mononuclear type 1 blue copper proteins and the main difference between the two families of proteins resided in the FG loop sequence (Figure 20).[230–233] The conversion of the blue copper center into a $\mathrm{Cu_A}$ center using LDM is more challenging because the blue copper protein had to accommodate not only the extra copper ion, but also the longer C*c*OII FG loop. The LDM was successfully carried out in azurin[233,234] and amicyanin[232,235] (Figure 20). The X-ray structures of the engineered $\mathrm{Cu_A}$ center in CyoA[236] and in azurin[237] indicated that, with the exception of the FG loop region, the protein backbones of the engineered proteins were superimposable on that of the wild type proteins. Azurin was able to accommodate the insertion of extra amino acids and the additional copper ion by a simple ‘breathing’ motion of ∼3 Å.[237] These findings are encouraging because they suggest that protein scaffolds can be rigid enough to withstand large changes in the loop region, and at the same time are fluid enough to accommodate incorporation of new and very different metal-binding sites. Therefore, in addition to its value in protein design, LDM may be a general way to introduce metal-binding sites with known sequences but unknown structures into a well-characterized protein for facile spectroscopic and X-ray crystallographic study. Indeed, LDM was used to convert one blue copper protein into another blue copper protein with different spectroscopic and redox properties,[238] and from a $\mathrm{Cu_A}$ center in C*c*O to a blue copper protein.[239]

4 COMBINATORIAL DESIGN

While the rational design approach described above is an effective tool for optimizing and altering protein function, one drawback is that the structure and mechanism of the proteins to be designed must be understood. Unfortunately, the number of structures in the protein databases is increasing dramatically and our knowledge about protein structure and function is quite limited. Furthermore, it is extremely difficult to predict long-range effects of residues far from the active site on structure and function. More studies show that those long-range effects are important in protein design. Design

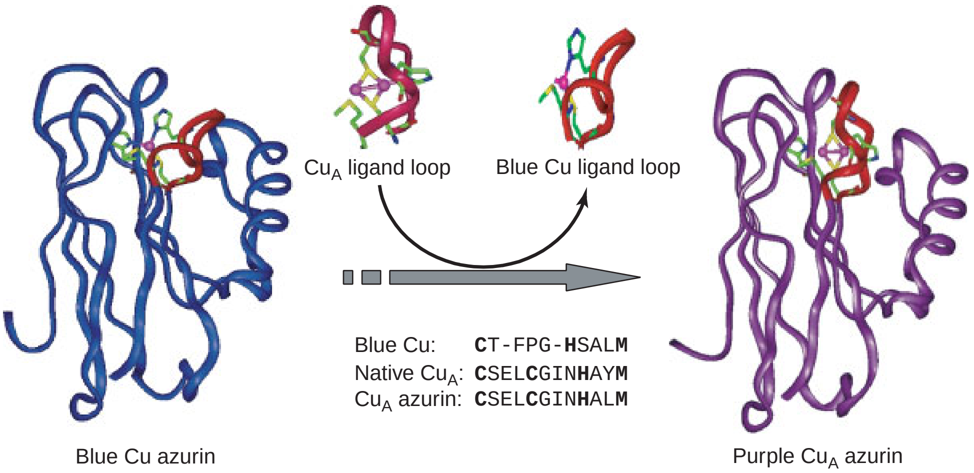

Figure 20 Schematic illustration of engineering the $\mathrm{Cu_A}$ center into azurin through loop-directed mutagenesis.

through combinatorial and evolution methods requires little prior knowledge of the protein structure.

4.1 Application to Metallopeptide Models

While rational designs have enjoyed much success on well-characterized proteins, it has been difficult to apply the same principles to proteins with unknown structure or function. For example, zinc finger peptides have been designed based on consensus sequence to recognize certain DNA sequences specifically. The modular approach has expanded the DNA sequences zinc finger proteins can bind by domain swapping (see Section 3.1). However, the range of DNA sequences that the designed protein can recognize is still limited as only a limited number of zinc finger proteins are known and key structural features responsible for binding a specific DNA sequence have been elucidated in only selected cases. In addition, even if new zinc finger proteins have been designed, the binding affinity and selectivity may not be optimal. Therefore, new zinc finger proteins have been obtained through a phage display method, where proteins of interest are presented on the surface of phage. By randomizing residues in contact with DNA and selecting those proteins with the highest affinity for a given DNA sequence, zinc finger proteins have been selected to recognize new DNA sequence with high affinity and selectivity.[28,240,241] The selected protein bound the target DNA with high affinity (nanomolar dissociation constants) and specificity (greater than 20 000-fold discrimination against nonspecific DNA). Interestingly, some of the selected zinc finger proteins have been tested in cell cultures and were shown to block DNA transcription.[242]

4.2 Application to Designing Metal-binding Site in De Novo Designed Proteins

The template-assembled synthetic protein based on cysteine-containing cyclic peptides was described in Section 2.2.1 as an effective approach for modular design of helical bundle proteins that bind heme and other cofactors. This system has also been used to generate combinatorial libraries of helical bundles to select for the most stable variants that bind heme[243] or copper.[244] Instead of varying every amino acid in every positions of the four helices, the authors restricted variation to only those hydrophobic amino acids of different sizes and a few polar ones (Gly, Ala, Val, Leu, Ile, Phe, Tyr, and Gln) and only at positions that form the hydrophobic core of the helix bundle. For the copper protein library, potential ligands of His residues and a single Cys residue were positioned next to each other in the hydrophobic core. In addition, residues adjacent to these ligands were also varied to optimize packing and prevent Cys oxidation. This combination of rational design principle with combinatorial protein assembly makes the libraries manageable (462 combinations of two of the four helices for the heme protein library and 96 combinations of three of the four helices for the copper protein library). Screening by UV-vis absorption spectra resulted in heme proteins with a more positive midpoint potential than that of the de novo designed heme proteins. The selection also resulted in stable copper-thiolate proteins with UV-vis and EPR spectra similar to the redesigned CuZnSOD when a Cys is introduced into the tetragonal copper center (see Section 2.3.1).[135,139]

While the above work was designed to bind metal cofactors specifically, work from the Hecht group has shown that it is possible to obtain heme proteins from libraries that were not explicitly designed to bind heme.[245] The group has demonstrated the design of libraries of helical proteins based on 'binary patterning' of polar and nonpolar amino acids, which create amphipathic segments of secondary structures with one face containing only polar residues and the other face containing only nonpolar residues. Surprisingly half of the 30 members of binary libraries could bind heme with a broad range of affinities and with spectroscopic features resembling those of natural cytochromes, even though no selection for binding was performed.[246] The library did include potential heme-binding ligands such as His and Met residues. More interestingly, the heme proteins from the library were shown to bind CO with kinetic association and dissociation rates similar to those of natural heme proteins.[247] Several of them exhibit peroxidase activities, the best of which had a catalytic turnover rate approaching that of horseradish peroxidase (only 3.5 times slower).[248]

4.3 Application to Designing Metal-binding Sites in Native Protein Scaffolds

Selection of Metalloproteins Through Phage display. Similar to selection of zinc finger peptides (see Section 4.1), variants of carbonic anhydrase containing random mutations in the hydrophobic residues surrounding the metal-binding site have been displayed on phage.[249] Those with high metal-binding affinity have been selected and enriched, and consensus residues at each position were identified. A correlation between the dissociation constant and catalytic activity of the variants and the volume of the amino acids at selected positions were noted.

Search for New Metallo-antibodies. In an approach that is complementary to the rational design of metal-binding sites in antibodies (see Section 2.3.2), preparing antibodies against metal complexes such as metalloporphyrins or the transition state analogs of the reactions they catalyze has resulted in new metalloproteins with catalytic functions. For example, monoclonal antibodies have been prepared using metalloporphyrin,[250,251] or transition state analogs of porphyrin metallation[252] as antigens. The antibodies isolated were found to bind the antigen metal complexes more tightly than other similar complexes.[250] More importantly, by choosing the porphyrin antigens carefully, several groups have been able to obtain metalloporphyrin-containing antibodies that can catalyze a variety of reactions such as porphyrin metallation,[252] electron transfer,[253,254] peroxidation,[255–261] mono-[251,262,263] and dioxygenation.[264]

Directed Evolution of Heme Enzymes. Directed evolution of horse heart Mb has been carried out to select variants with enhanced peroxidase activity.[265] After subjecting the Mb gene to several cycles of PCR random mutagenesis, the expressed variants were selected against a low concentration of a common peroxidase substrate (2,2-azino-bis-(3-ethyl)-benzothiazoline-6-sulfonic acid (ABTS)). Among the selected variants, one variant contains four substitutions in the heme pocket and exhibits ~25-fold higher peroxidase activity than WTMb. In another study, directed evolution of cytochrome P450 was carried out to improve its hydroxylation reactivity by more than 20-fold over that of the native enzyme.[266] The investigators were able to efficiently screen for the improved variant P450s by coexpressing them with horseradish peroxidase, which converts the products of the P450 reaction into fluorescent compounds amenable to digital image screening.[267] In both studies, the mutations found in the selected variants with enhanced activities were not obvious and would have been difficult to uncover using a rational design approach.

5 DESIGN OF METALLOPROTEINS WITH STRUCTURES AND FUNCTIONS UNPRECEDENTED IN NATURE

As shown in the above sections, important progresses have been made in designing metalloproteins that closely mimic those in nature. However, natural metalloproteins use only 20 amino acids, only less than 10 of which are potential metal ligands. Furthermore, they employ only a small sub-set of metal ions listed in the periodic table and of metal-containing prosthetic groups synthesized by inorganic chemists. Therefore introducing unnatural amino acid and nonnative metal ions or metal-containing prosthetic groups into a designed protein can dramatically expand the repertoire of its functionalities and thus its range of applications.[268]

5.1 Introducing Unnatural Amino Acids into Metal-binding Sites of Designed Proteins

Since solid-state peptide synthesis is commonly used in both peptide models and de novo designed proteins, introducing unnatural amino acids is relatively straightforward, as one can replace the natural amino acids with unnatural ones in the synthesis. One nice example is replacing bis-His ligation with bis-pyridine ligation to heme in a de novo designed four-α-helix bundle, through incorporation of 4-β-(pyridyl)-L-alanines in place of His residues.[269] The ligation change resulted in 287 mV change in heme reduction potential.

Introducing unnatural amino acids into native proteins is more challenging when the proteins are used as scaffolds for metalloprotein design because of its size. A classic way is global replacement of one type of natural amino acids in the protein with an unnatural amino acid when growing cells lacking the particular amino acid (called auxotroph) and supplementing with an analog of the natural amino acids. For example, all of the Met residues in azurin[270] and cytochrome P450[271] have been replaced by selenoMet and Norleucine, respectively, using a Met auxotroph supplemented with the replacement amino acid. The approach is restricted by which amino acids can be replaced and by the analogs available. The location of replacement is also not specific as all of the natural amino acids of a given type will be replaced. A more specific way of introducing unnatural amino acids is by cavity complementation.[272] This approach involves replacing one of the metal-ion ligands with either Gly or Ala to create a cavity. Addition of exogenous ligands of the appropriate size and character complement the cavity created by the replacement. For example, different ligands have been introduced into a cavity created by replacing the promixal His ligand in both myoglobin[273] and cytochrome *c* peroxidase.[274] However, the cavity complementation approach is useful only when a cavity can be generated with enough rigidity and the added unnatural ligand has strong enough affinity to the cavity because the ligand is not covalently linked. If one wants to introduce unnatural amino acids covalently linked to other residues, one effective approach is to synthesize the proteins in smaller pieces, and then use the recently developed technique called native chemical ligation to join the peptides together forming a native peptide bond at the junction. This technique has been used by Low and coworkers to probe the roles of aromatic residues in rubredoxin,[275] the backbone amide-ligand interactions in High-Potential Iron Proteins,[276] and heme axial ligand in cytochrome b_{562}.[277] For large proteins, chemical synthesis of peptides can be quite expensive and low yielding. Another high cost and low yield system is the use of tRNA molecules charged with unnatural amino acids during in vitro translation.[278] Extension of the system in vivo has resulted in significant saving in cost and increase in yield.[279] However, only certain analogs of natural amino acids can be incorporated using the method. Therefore few applications of such methods in metalloproteins have been reported.

Semi-synthesis where a bacterially expressed peptide is coupled with a synthetic peptide containing the unnatural amino acids is a nice balance between the costs and efficiency because large quantities of large peptides are expressed in bacteria at low cost.[91,92] Recent progress with the expressed protein ligation (EPL) method, enables the coupling without the requirement of protecting groups thus increasing overall yields.[280] The only limitation is the requirement of a cysteine residue at the union of the

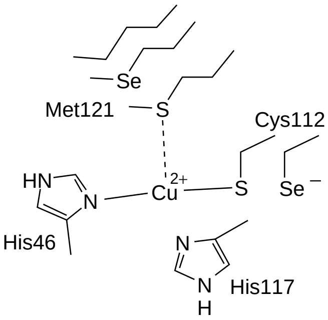

Figure 21 Introducing unnatural amino acids into type 1 blue copper azurin to fine-tune the properties with minimal structural perturbation

expressed protein and the synthetic peptide containing the unnatural amino acid. This limitation may be removed with innovative methods developed recently.[277,281] Using this method, both Cys and Met ligands in type 1 blue copper Azurin have been replaced specifically with selenoCys[282] and selenoMet/norleucine,[283] respectively (Figure 21). This allowed fine-tuning of the structural and functional properties (such as reduction potentials) of the proteins. Similarly, introducing citrulline into the recognition helix of a zinc finger protein by EPL demonstrated the use of unnatural amino acids to tailor the protein to recognize a broad range of DNA sites.[284]

5.2 Introducing Nonnative Metal Ions or Metal-Containing Prosthetic Groups into Designed Proteins

Like unnatural amino acid introduction described above, it is relatively straightforward to incorporate nonnative metal ions or metal-containing prosthetic groups into de novo designed metallopeptides and proteins. For example, a ruthenium complex has been used as a template to assemble helical bundle proteins (see Section 2.2.1). To introduce nonnative metal-containing prosthetic groups into native proteins, one way is to replace natural prosthetic groups with artificially synthesized ones. A nice example is replacing heme in myoglobin with metalloporphyrins such as protoporphyrin IX modified at the two propionate groups that created effective binding domains for protein−protein and protein-small molecule recognition and electron transfer (Figure 22a).[25] Furthermore, when the heme is replaced with iron porphycene[285] or modified by flavin at one of the propionate groups,[286] dramatically enhanced O_2-binding affinity or O_2 activation activities have been observed, respectively.

Covalent attachment of ligand or the whole metal complex to a specific site through bioconjugation to either Cys or Lys is another effective strategy. For example, 1,10-*o*-phenanthroline-copper, an effective DNA cleavage agent, has been attached to several DNA-binding proteins.[289] The combination of high cleavage activity of the metal complex with specific DNA recognition selectivity makes the artificial metalloproteins very effective nucleases. Fe-EDTA has been incorporated into proteins for the same reason.[290] Another remarkable achievement is the incorporation of copper-phenanthroline and rhodium-diphosphine complexes into proteins that turns the proteins into highly efficient asymmetric catalysts.[291,292]

To design artificial enzymes with asymmetric catalytic activities, one has to control chemo- and enantioselectivity. Since the native protein scaffolds have not evolved to tightly bind artificial metal complexes in a single conformation, three approaches have been used to design proteins with high enantioselective selectivity. In the noncovalent approach (Figure 22b), structure-based design of the protein and modification of the metal complexes has been shown to be important.[287,293–295] In the single point covalent attachment approach (Figure 22c), carefully selecting a protein host so that the metal complex can bury deep into a substrate accessible pocket is shown to be effective.[291,292] In the two-point covalent attachment approach (Figure 22d), careful positioning of the two attachment points limited the number of conformational states available to the metallocomplex inside the protein and by so doing significantly improved both rate of reaction and enantioselectivity.[288]

6 SUMMARY AND OUTLOOK

6.1 Summary

This review covers recent advances in metalloprotein design, with focus on different approaches to the design. Impressive progress has been made in designing metal-binding sites in peptides, de novo designed proteins, and native protein scaffolds. The approach can be rational or combinatorial. Under rational design, redesigning an existing metal-binding site to a new site with dramatically different structure and function complements well the design of new metal-binding sites by revealing the role of specific residues responsible for a particular structural or functional feature of the metal-binding site of interest. To create a new metal-binding site, several approaches have been used, including design based on structural homology, by inspection, using automated computer search algorithms, or combination of above approaches. In addition, the modular approach in which a conserved structural unit is transplanted from one protein into another has also been shown to be effective. Design through combinatorial and evolution methods has also been successful as it requires little prior knowledge of the protein structure. Finally introducing unnatural amino acids or nonnative metal ions/prosthetic groups to expand the repertoires of metalloproteins have been demonstrated. So which systems should one choose to work on and which approaches should one use? The answer depends on the goals of the design and experience and knowledge of the designers.

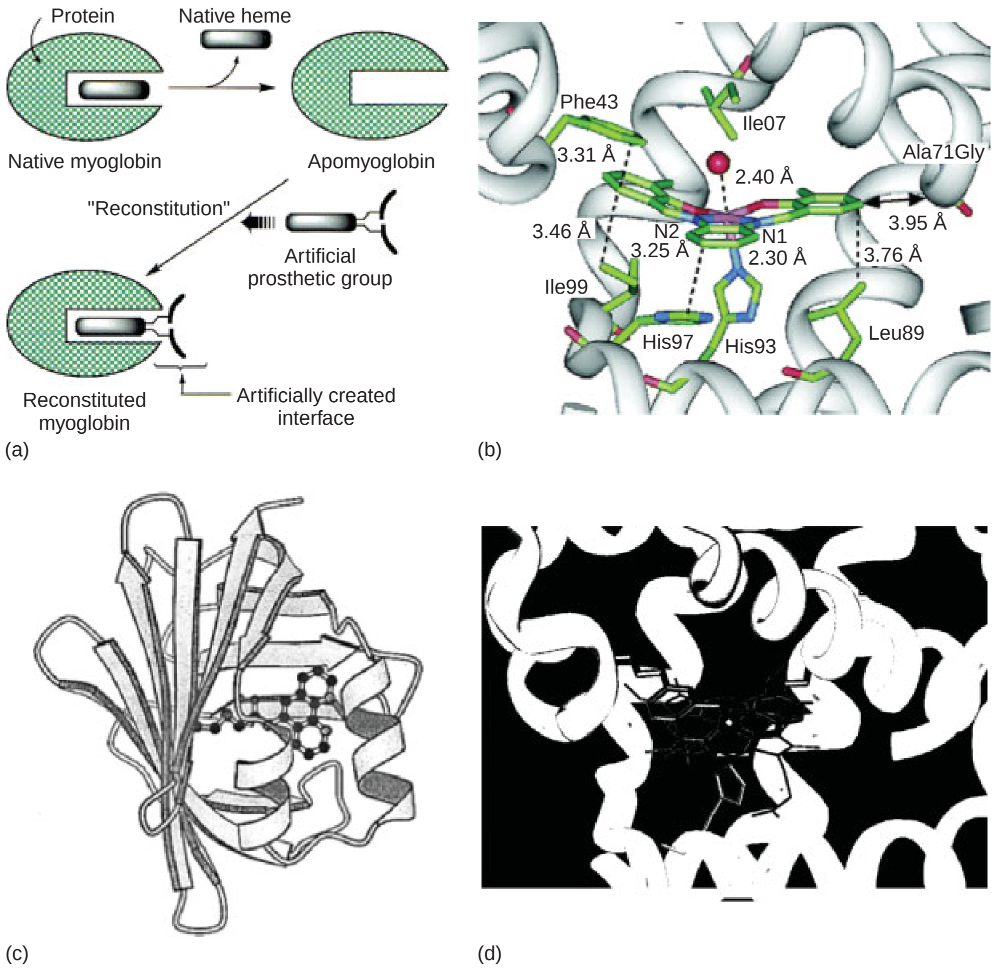

Figure 22 Introducing nonnative prosthetic group into metalloproteins. (a) by chemical modification of heme propionate. (Reprinted with permission from Ref. 25. © 2002 the American Chemical Society); (b) by noncovalent addition strategy. The crystal structure of the $Fe^{III}(3,3'-Me_2$-salophen) incorporated into Ala17GlaMb. (Reprinted with permission from Ref. 287. © 2004 the American Chemical Society); (c) by a single attachment strategy. The computer model of adipocyte lipid binding protein-phenanthroline complex. (Reprinted with permission from Ref. 291. © 1997 the American Chemical Society); (d) by a dual covalent attachment strategy. The computer model of Mb(L72C/Y103C) with a Mn^{III}-Salen complex covalently attached at two-points and overlayed with heme. (Reprinted with permission from Ref. 288. © 2004 the American Chemical Society)

6.1.1 System Choice

Metallopeptide design represents the minimalist design in its purest sense. If a small metallopeptide can replicate large metalloproteins, it is the best approach to reveal essential features of the metal-binding sites and to be used for practical applications because of its small size. It is more likely to be successful if all the ligands in the native proteins are in a short segment of peptide and if metal binding directs the folding of the peptides and formation of the sites. However, a number of ligands span a large distance in the peptide chain and the rigid protein scaffolds play an important role in formation of many metal-binding sites, for example, enforcing distorted geometry that the metal ion may not prefer. Therefore designing metal-binding sites in protein scaffolds may be a preferred choice for designing those metalloproteins.

To design metal-binding sites into protein scaffolds, one can choose de novo designed proteins or native proteins. Designing metal-binding sites in de novo designed proteins represents the most fundamental and challenging endeavor. It is the ultimate goal of metalloprotein design and its success is the measure of progress in the field. However, the number of de novo designed scaffolds is quite limited when compared with large number of available native protein scaffolds. More importantly, nature has been shown to use the same native scaffold for many different metalloproteins. Therefore designing metal-binding sites in native scaffolds is part of metalloprotein design endeavor.

When designing metal-binding sites in native protein scaffolds, one can design new metal-binding sites or redesign the existing metal-binding sites. Designing new metal-binding sites should be a preferred choice. However, owing to lack of knowledge, some metal-binding sites, such as type 1 blue copper center, are simply difficult to design. In those cases, redesign offers a better chance of success and offers equally important insights, although redesign often misses common factors existing between the starting and target proteins.

6.1.2 Approach Choice

The rational approach is the best at testing our knowledge. Both success and failure from the rational design may offer deep insight. Rational design using automated computer search algorithms has clear advantages for efficient crafting of metal centers and judicious choice of the best amino acid side chains for the formation of the metal-binding sites. It is best used for creation of new metal-binding sites in proteins where neither site location nor side chain choice can be determined based on the investigator's knowledge or protein homology. It is especially useful for designing metal-binding sites where construction of a geometrically correct, sterically compatible primary coordination sphere is sufficient to reproduce the dominant features of the structure and function of the desired center. Tetrahedral Zn(II) centers, iron–sulfur clusters, and mononuclear nonheme iron centers are primary examples of the successful designs.

For many other metal centers, such as blue copper and purple Cu_A centers, construction of a geometrically correct, sterically compatible primary coordination may not be sufficient to result in the desired metal-binding sites because their formation may be opposed by several alternative reactivities and geometries. Most metal-binding sites in proteins are not in idealized geometries as in their small metal complex counterparts. For example, the geometry of the blue copper center is preferred by neither Cu(II) nor Cu(I). Without a careful design that includes secondary coordination sphere or even longer range interactions, the amino acid side chains may be flexible enough to accommodate the geometry of the free metal ions and ruin the computer program design. Until now few effective programs are known to overcome these problems and much iteration, mostly based on knowledge and inspection, are needed for a successful design. Moreover, structural features responsible for protein selectivity of one metal ion over the other still remains to be fully understood. Thus, it is difficult to write programs capable of designing metal-binding sites selectively. In this regard, protein redesign, rational design by homology or modular approach may offer a better chance of success by gaining insight into the structure and function of the centers one (or a few) residue(s) at a time. This advantage is demonstrated by the successful redesign of a type 2 copper protein CuZnSOD into a type 1 blue copper protein (see Section 2.3.1)[135–138] or transformation of type 1 blue copper proteins into purple Cu_A proteins by loop-directed mutagenesis (see Section 3.3.2).[230,232–235]

Another equally attractive empirical approach is the design of new metal-binding sites based on protein homology. This approach depends strongly on the degree of sequence or structural homology. Generally speaking, higher homology often leads to a better chance of success. At the same time, factors that are common to both template protein and the target protein cannot be revealed from the design exercise. This problem also applies to the protein redesign approach. Despite these limitations, both approaches are extremely useful at elucidating the role of specific structural features in protein design and function, and at revealing principles of protein design.

Design of metal-binding sites by inspection is one of the early forms of protein design. Although it appears less elegant than other methods, design by inspection has produced proteins with many practical applications, such as proteins with a His-X_3-His chelating site on the surface and with poly-His tags for protein purification. The designed metal-binding sites also resulted in proteins with increased stability, altered activities, altered selectivity, new functions, and elucidated protein topologies. It can be an effective approach for creating metal-binding sites with more complexity if the investigators are armed with a thorough understanding of the structure and function of both the target and the template proteins, and have a reasonably good idea where the metal site can be created. This approach can be enhanced further if it can utilize computer programs to help evaluate and modify the initial design through energy minimization. This is the basis of the combined approach. On one hand, the combined approach is similar to design by inspection in that it relies on the investigator's knowledge to pinpoint the location of the metal-binding site. On the other hand, the approach resembles the automated computer algorithm approach in that it uses rigorous computer programs to evaluate the initial design and to suggest better designs with better energetic terms.

All the rational methods described above rely heavily on our knowledge of principles governing the structure and function of metal-binding sites. However, despite much progress made so far, our knowledge is still quite limited. For example, the high affinity and selectivity of many metal-binding sites remains to be elucidated. Fascinating new metal centers are being discovered. To fill the gap of our knowledge and to keep pace with the rapid development of the field, combinatorial design of metal-binding sites is of great value. However, this approach requires a clear and convenient selection scheme.

Modular approaches may bridge the gap between rational design and combinatorial engineering. It allows easier rational generation of a site by swapping structural elements, such as a loop, that are important for the formation of the metal-binding site. At the same time, it is easier to search combinatorially for optimal sequences since the search is narrowly focused on the region of difference and its surrounding areas.

6.2 Outlook

Given this vast and rapidly developing field, it is very difficult to predict the future. All one can do is to offer the best possible path to the future based on what we have learned. One focus for future research should be on design of geometrically strained metal-binding sites, such as the blue copper center, and multinuclear (particularly heteronuclear) metal centers. It is a test of our knowledge and ability. One way to improve success is to combine the advantages of two or more approaches. For example, rational approaches can be used to create a new metal-binding site and combinatorial searches can then be used to fine-tune the metal-binding affinity, selectivity, or in the case of catalytic sites, the substrate-binding pocket. Furthermore, automated computer programs can be used to design or redesign geometrically strained metal-binding sites, such as the blue copper center, in proteins with high homology to these proteins. This strategy offers a higher chance of success. Study of the designed protein may help improve the programs.

Another focus of future research should be the role of the secondary coordination sphere in metalloprotein design. With few exceptions, most designed metal-binding sites have a binding affinity that is orders of magnitude weaker than that in the native proteins. The role of secondary coordination sphere in tuning the properties of metal-binding sites has been well recognized.[8] Recent work has strongly suggested the importance of negative design, for example, to avoid steric conflict, to prevent solvent exposure and to inhibit ligand oxidation. Positive interactions such as hydrogen bonding and electrostatic interactions are also very important.[106,109,111,193] Introducing those positive design elements has been shown to be essential for successful metalloprotein design.[106,109,111]

The importance of three-dimensional structural characterization of the designed proteins should also be recognized. Spectroscopy has been the main tool to demonstrate the success of the design. However, the spectroscopic signatures can indicate only part of the designed metal-binding sites. Three-dimensional structures of the designed protein, whether confirming the design or revealing surprises, will be quite valuable for further design.

Finally, in addition to structurally defined metal-binding sites, designing catalytically active metal centers will be another exciting area of research. It is the best way to realize the potentials of metalloprotein design.

7 RELATED ARTICLES

Copper Proteins: Oxidases; Copper Proteins with Dinuclear Active Sites; Copper Proteins with Type 1 Sites; Copper Proteins with Type 2 Sites; Cytochrome Oxidase; Iron: Heme Proteins & Dioxygen Transport & Storage; Iron: Heme Proteins & Electron Transport; Iron: Heme Proteins, Mono- & Dioxygenases; Iron: Heme Proteins, Peroxidases, Catalases & Catalase-peroxidases; Iron Proteins with Dinuclear Active Sites; Iron Proteins with Mononuclear Active Sites; Iron–Sulfur Proteins; Peptide–Metal Interactions; Zinc: DNA-binding Proteins; Zinc Enzymes.

8 REFERENCES

1. A. J. Thomson and H. B. Gray, *Curr. Opin. Chem. Biol.*, 1998, **2**, 155.
2. J. A. Tainer, V. A. Roberts, and E. D. Getzoff, *Curr. Opin. Biotechnol.*, 1991, **2**, 582.
3. J. A. Tainer, V. A. Roberts, and E. D. Getzoff, *Curr. Opin. Biotechnol.*, 1992, **3**, 378.
4. J. M. Berg, *Curr. Opin. Struct. Biol.*, 1993, **3**, 585.
5. L. Regan, *Annu. Rev. Biophys. Biomol. Struct.*, 1993, **22**, 257.
6. L. Regan, *Trends Biochem. Sci.*, 1995, **20**, 280.
7. D. J. Matthews, *Curr. Opin. Biotechnol.*, 1995, **6**, 419.
8. D. W. Christianson and C. A. Fierke, *Acc. Chem. Res.*, 1996, **29**, 331.
9. H. W. Hellinga, in ‘Protein Eng.’, eds. J. L. Cleland and C. S. Craik, Wiley-Liss, New York, 1996, p. 369.
10. H. W. Hellinga, *Curr. Opin. Biotechnol.*, 1996, **7**, 437.
11. L. Regan, *Adv. Mol. Cell Biol.*, 1997, **22A**, 51.
12. Y. Lu and J. S. Valentine, *Curr. Opin. Struct. Biol.*, 1997, **7**, 495.
13. B. R. Gibney, F. Rabanal, and P. L. Dutton, *Curr. Opin. Chem. Biol.*, 1997, **1**, 537.
14. H. W. Hellinga, *Folding Des.*, 1998, **3**, R1.
15. D. E. Benson, M. S. Wisz, and H. W. Hellinga, *Curr. Opin. Biotechnol.*, 1998, **9**, 370.
16. W. F. DeGrado, C. M. Summa, V. Pavone, F. Nastri, and A. Lombardi, *Annu. Rev. Biochem.*, 1999, **68**, 779.
17. B. R. Gibney and P. L. Dutton, *Adv. Inorg. Chem.*, 2001, **51**, 409.
18. M. L. Kennedy and B. R. Gibney, *Curr. Opin. Struct. Biol.*, 2001, **11**, 485.
19. G. Gilardi, A. Fantuzzi, and S. J. Sadeghi, *Curr. Opin. Struct. Biol.*, 2001, **11**, 491.
20. L. Baltzer and J. Nilsson, *Curr. Opin. Biotechnol.*, 2001, **12**, 355.
21. G. Xing and V. J. DeRose, *Curr. Opin. Chem. Biol.*, 2001, **5**, 196.
22. A. Lombardi, F. Nastri, and V. Pavone, *Chem. Rev.*, 2001, **101**, 3165.
23. Y. Lu, S. M. Berry, and T. D. Pfister, *Chem. Rev.*, 2001, **101**, 3047.
24. Y. Watanabe, *Curr. Opin. Chem. Biol.*, 2002, **6**, 208.
25. T. Hayashi and Y. Hisaeda, *Acc. Chem. Res.*, 2002, **35**, 35.
26. P. D. Barker, *Curr. Opin. Struct. Biol.*, 2003, **13**, 490.
27. C. J. Reedy and B. R. Gibney, *Chem. Rev.*, 2004, **104**, 617.
28. D. Jantz, B. T. Amann, G. J. Gatto Jr, and J. M. Berg, *Chem. Rev.*, 2004, **104**, 789.
29. C. Harford and B. Sarkar, *Acc. Chem. Res.*, 1997, **30**, 123.
30. E. C. Long, *Acc. Chem. Res.*, 1999, **32**, 827.

31. B. R. Gibney, S. E. Mulholland, F. Rabanal, and P. L. Dutton, *Proc. Natl. Acad. Sci. U.S.A.*, 1996, **93**, 15041.
32. A. Lombardi, D. Marasco, O. Maglio, L. Di Costanzo, F. Nastri, and V. Pavone, *Proc. Natl. Acad. Sci. U.S.A.*, 2000, **97**, 11922.
33. R. Fattorusso, G. Morelli, A. Lombardi, F. Nastri, O. Maglio, G. D'Auria, C. Pedone, and V. Pavone, *Biopolymers*, 1995, **37**, 401.
34. R. G. Daugherty, T. Wasowicz, B. R. Gibney, and V. J. DeRose, *Inorg. Chem.*, 2002, **41**, 2623.
35. G. Veglia, F. Porcelli, T. DeSilva, A. Prantner, and S. J. Opella, *J. Am. Chem. Soc.*, 2000, **122**, 2389.
36. B. A. Krizek, B. T. Amann, V. J. Kilfoil, D. L. Merkle, and J. M. Berg, *J. Am. Chem. Soc.*, 1991, **113**, 4518.
37. S. F. Michael, V. J. Kilfoil, M. H. Schmidt, B. T. Amann, and J. M. Berg, *Proc. Natl. Acad. Sci. U.S.A.*, 1992, **89**, 4796.
38. P. Turano and Y. Lu, in 'Handbook on Metalloproteins', eds. I. Bertini, H. Sigel, and A. Sigel, Marcel Dekker, New York, 2001, p. 269.
39. P. A. Adams, D. A. Baldwin, and H. M. Marques, in 'Cytochrome C', eds. R. A. Scott and A. G. Mauk, University Science Books, Sausalito, CA, 1996, p. 635.
40. L. Casella, M. Gullotti, L. De Gioia, E. Monzani, and F. Chillemi, *J. Chem. Soc., Dalton Trans.*, 1991, 2945.
41. F. Montanari and L. Casella eds, 'Metalloporphyrins Catalyzed Oxidations', [In: Catal. Met. Complexes, 1993; 17], Kluwer, Dordrecht, Netherlands, 1994.
42. D. R. Benson, B. R. Hart, X. Zhu, and M. B. Doughty, *J. Am. Chem. Soc.*, 1995, **117**, 8502.
43. F. Nastri, A. Lombardi, G. Morelli, O. Maglio, G. D'Auria, C. Pedone, and V. Pavone, *Chem. – Eur. J.*, 1997, **3**, 340.
44. G. D'Auria, O. Maglio, F. Nastri, A. Lombardi, M. Mazzeo, G. Morelli, L. Paolillo, C. Pedone, and V. Pavone, *Chem. – Eur. J.*, 1997, **3**, 350.
45. G. R. Geier III and T. Sasaki,*Tetrahedron*, 1999, **55**, 1859.
46. T. B. Karpishin, T. A. Vannelli, and K. J. Glover, *J. Am. Chem. Soc.*, 1997, **119**, 9063.
47. P. A. Arnold, W. R. Shelton, and D. R. Benson, *J. Am. Chem. Soc.*, 1997, **119**, 3181.
48. S. Sakamoto, S. Sakurai, A. Ueno, and H. Mihara, *Chem. Commun.*, 1997, 1221.
49. D. L. Huffman, M. M. Rosenblatt, and K. S. Suslick, *J. Am. Chem. Soc.*, 1998, **120**, 6183.
50. M. M. Rosenblatt, D. L. Huffman, X. Wang, H. A. Remmer, and K. S. Suslick, *J. Am. Chem. Soc.*, 2002, **124**, 12394.
51. M. M. Rosenblatt, J. Wang, and K. S. Suslick, *Proc. Natl. Acad. Sci. U.S.A.*, 2003, **100**, 13140.
52. T. Sasaki and E. T. Kaiser, *J. Am. Chem. Soc.*, 1989, **111**, 380.
53. K. S. Akerfeldt, R. M. Kim, D. Camac, J. T. Groves, J. D. Lear, and W. F. DeGrado, *J. Am. Chem. Soc.*, 1992, **114**, 9656.
54. H. Mihara, K.-Y. Tomizaki, T. Fujimoto, S. Sakamoto, H. Aoyagi, and N. Nishino, *Chem. Lett.*, 1996, 187.
55. H. K. Rau and W. Haehnel, *J. Am. Chem. Soc.*, 1998, **120**, 468.
56. H. K. Rau, N. DeJonge, and W. Haehnel, *Proc. Natl. Acad. Sci. U.S.A.*, 1998, **95**, 11526.
57. R. B. Hill, D. P. Raleigh, A. Lombardi, and W. F. DeGrado, *Acc. Chem. Res.*, 2000, **33**, 745.
58. C. T. Choma, J. D. Lear, M. J. Nelson, P. L. Dutton, D. E. Robertson, and W. F. DeGrado, *J. Am. Chem. Soc.*, 1994, **116**, 856.
59. D. E. Robertson, R. S. Farid, C. C. Moser, J. L. Urbauer, S. E. Mulholland, R. Pidikiti, J. D. Lear, A. J. Wand, W. F. DeGrado, and P. L. Dutton, *Nature*, 1994, **368**, 425.
60. Z. Xu and R. S. Farid, *Protein Sci.*, 2001, **10**, 236.
61. L. Cristian, P. Piotrowiak, and R. S. Farid, *J. Am. Chem. Soc.*, 2003, **125**, 11814.
62. C. M. Summa, A. Lombardi, M. Lewis, and W. F. DeGrado, *Curr. Opin. Struct. Biol.*, 1999, **9**, 500.
63. A. Lombardi, C. M. Summa, S. Geremia, L. Randaccio, V. Pavone, and W. F. DeGrado, *Proc. Natl. Acad. Sci. U.S.A.*, 2000, **97**, 6298.
64. L. Di Costanzo, H. Wade, S. Geremia, L. Randaccio, V. Pavone, W. F. DeGrado, and A. Lombardi, *J. Am. Chem. Soc.*, 2001, **123**, 12749.
65. M. Klemba and L. Regan, *Biochemistry*, 1995, **34**, 10094.
66. M. R. Ghadiri, C. Soares, and C. Choi, *J. Am. Chem. Soc.*, 1992, **114**, 4000.
67. K. Suzuki, H. Hiroaki, D. Kohda, H. Nakamura, and T. Tanaka, *J. Am. Chem. Soc.*, 1998, **120**, 13008.
68. T. Handel and W. F. DeGrado, *J. Am. Chem. Soc.*, 1990, **112**, 6710.
69. T. M. Handel, S. A. Williams, and W. F. DeGrado, *Science*, 1993, **261**, 879.
70. L. Regan and N. D. Clarke, *Biochemistry*, 1990, **29**, 10878.
71. M. R. Ghadiri, C. Soares, and C. Choi, *J. Am. Chem. Soc.*, 1992, **114**, 825.
72. M. R. Ghadiri and M. A. Case, *Angew. Chem.*, 1993, **105**, 1663; *Angew. Chem., Int. Ed. Engl.*, 1993, **1632**(1611), 1594.
73. B. T. Farrer and V. L. Pecoraro, *Curr. Opin. Drug Disc. Develop.*, 2002, **5**, 937.
74. G. R. Dieckmann, D. K. McRorie, D. L. Tierney, L. M. Utschig, C. P. Singer, T. V. O'Halloran, J. E. Penner-Hahn, W. F. DeGrado, and V. L. Pecoraro, *J. Am. Chem. Soc.*, 1997, **119**, 6195.
75. A. Pessi, E. Bianchi, A. Crameri, S. Venturini, A. Tramontano, and M. Sollazzo, *Nature*, 1993, **362**, 367.
76. 2001, http: //scop.mrc-lmb.cam.ac.uk/scop/count.html.

77. A. B. P. Lever and H. B. Gray, ‘Physical Bioinorganic Chemistry Series’, Addison-Wesley, Reading, MA, 1983, p. 286.

78. P. D. Barker, J. C. Ferrer, M. Mylrajan, T. M. Loehr, R. Feng, Y. Konishi, W. D. Funk, R. T. A. MacGillivray, and G. Mauk, *Proc. Natl. Acad. Sci. U.S.A.*, 1993, **90**, 6542.

79. P. D. Barker, E. P. Nerou, S. M. V. Freund, and I. M. Fearnley, *Biochemistry*, 1995, **34**, 15191.

80. E. J. Tomlinson and S. J. Ferguson, *J. Biol. Chem.*, 2000, **275**, 32530.

81. E. J. Tomlinson and S. J. Ferguson, *Proc. Natl. Acad. Sci. U.S.A.*, 2000, **97**, 5156.

82. P. D. Barker and S. J. Ferguson, *Structure*, 1999, **7**, R281.

83. S. G. Sligar, K. D. Egeberg, J. T. Sage, D. Morikis, and P. M. Champion, *J. Am. Chem. Soc.*, 1987, **109**, 7896.

84. I. Mus-Veteau, A. Dolla, F. Guerlesquin, F. Payan, M. Czjzek, R. Haser, P. Bianco, J. Haladjian, B. J. Rapp-Giles, J. D. Wall, G. Voordouw, and M. Bruschi, *J. Biol. Chem.*, 1992, **267**, 16851.

85. A. Dolla, L. Florens, P. Bianco, J. Haladjian, G. Voordouw, E. Forest, J. Wall, F. Guerlesquin, and M. Bruschi, *J. Biol. Chem.*, 1994, **269**, 6340.

86. P. D. Barker, E. P. Nerou, M. R. Cheesman, A. J. Thomson, P. de Oliveira, and H. A. O. Hill, *Biochemistry*, 1996, **35**, 13618.

87. P. D. Barker and S. M. V. Freund, *Biochemistry*, 1996, **35**, 13627.

88. T. N. Sorrell, P. K. Martin, and E. F. Bowden, *J. Am. Chem. Soc.*, 1989, **111**, 766.

89. A. L. Raphael and H. B. Gray, *Proteins: Struct., Funct., Genet.*, 1989, **6**, 338.

90. C. J. A. Wallace, *FASEB J.*, 1993, **7**, 505.

91. C. J. A. Wallace and I. Clark-Lewis, *J. Biol. Chem.*, 1992, **267**, 3852.

92. K. L. Bren and H. B. Gray, *J. Am. Chem. Soc.*, 1993, **115**, 10382.

93. Y. Lu, D. R. Casimiro, K. L. Bren, J. H. Richards, and H. B. Gray, *Proc. Natl. Acad. Sci. U.S.A.*, 1993, **90**, 11456.

94. T. Uno, A. Yukinari, Y. Moriyama, Y. Ishikawa, Y. Tomisugi, J. A. Brannigan, and A. J. Wilkinson, *J. Am. Chem. Soc.*, 2001, **123**, 512.

95. J. Qin, G. N. La Mar, Y. Dou, S. J. Admiraal, and M. Ikeda-Saito, *J. Biol. Chem.*, 1994, **269**, 1083.

96. E. Lloyd, D. P. Hildebrand, K. M. Tu, and A. G. Mauk, *J. Am. Chem. Soc.*, 1995, **117**, 6434.

97. Y. Dou, S. J. Admiraal, M. Ikeda-Saito, S. Krzywda, A. J. Wilkinson, T. Li, J. S. Olson, R. C. Prince, I. J. Pickering, and G. N. George, *J. Biol. Chem.*, 1995, **270**, 15993.

98. P. R. Ortiz de Montellano and A. Wilks, *Adv. Inorg. Chem.*, 2001, **51**, 359.

99. J. C. Rodriguez and M. Rivera, *Biochemistry*, 1998, **37**, 13082.

100. J. C. Rodriguez, T. Desilva, and M. Rivera, *Chem. Lett.*, 1998, 353.

101. J. K. Rice, I. M. Fearnley, and P. D. Barker, *Biochemistry*, 1999, **38**, 16847.

102. L. Avila, H.-W. Huang, J. C. Rodriguez, P. Moënne-Loccoz, and M. Rivera, *J. Am. Chem. Soc.*, 2000, **122**, 7618.

103. S. Adachi, S. Nagano, Y. Watanabe, K. Ishimori, and I. Morishima, *Biochem. Biophys. Res. Commun.*, 1991, **180**, 138.

104. S. Adachi, S. Nagano, K. Ishimori, Y. Watanabe, I. Morishima, T. Egawa, T. Kitagawa, and R. Makino, *Biochemistry*, 1993, **32**, 241.

105. T. Matsui, S. Nagano, K. Ishimori, Y. Watanabe, and I. Morishima, *Biochemistry*, 1996, **35**, 13118.

106. D. P. Hildebrand, J. C. Ferrer, H.-L. Tang, M. Smith, and A. G. Mauk, *Biochemistry*, 1995, **34**, 11598.

107. Y. Liu, P. Moeenne-Loccoz, D. P. Hildebrand, A. Wilks, T. M. Loehr, A. G. Mauk, and P. R. Ortiz de Montellano, *Biochemistry*, 1999, **38**, 3733.

108. K. Choudhury, M. Sundaramoorthy, A. Hickman, T. Yonetani, E. Woehl, M. F. Dunn, and T. L. Poulos, *J. Biol. Chem.*, 1994, **269**, 20239.

109. J. A. Sigman, A. E. Pond, J. H. Dawson, and Y. Lu, *Biochemistry*, 1999, **38**, 11122.

110. R. Perera, M. Sono, J. A. Sigman, T. D. Pfister, Y. Lu, and J. H. Dawson, *Proc. Natl. Acad. Sci. U.S.A.*, 2003, **100**, 3641.

111. T. Uno, A. Yukinari, Y. Tomisugi, Y. Ishikawa, R. Makino, J. A. Brannigan, and A. J. Wilkinson, *J. Am. Chem. Soc.*, 2001, **123**, 2458.

112. X. Yi, M. Mroczko, K. M. Manoj, X. Wang, and L. P. Hager, *Proc. Natl. Acad. Sci. U.S.A.*, 1999, **96**, 12412.

113. S. Yoshioka, S. Takahashi, H. Hori, K. Ishimori, and I. Morishima, *Eur. J. Biochem.*, 2001, **268**, 252.

114. K. Auclair, P. Moeenne-Loccoz, and P. R. Ortiz de Montellano, *J. Am. Chem. Soc.*, 2001, **123**, 4877.

115. K. D. Egeberg, B. A. Springer, S. A. Martinis, S. G. Sligar, D. Morikis, and P. M. Champion, *Biochemistry*, 1990, **29**, 9783.

116. D. P. Hildebrand, D. L. Burk, R. Maurus, J. C. Ferrer, G. D. Brayer, and A. G. Mauk, *Biochemistry*, 1995, **34**, 1997.

117. S.-I. Ozaki, T. Matsui, and Y. Watanabe, *J. Am. Chem. Soc.*, 1996, **118**, 9784.

118. S.-I. Ozaki, M. P. Roach, T. Matsui, and Y. Watanabe, *Acc. Chem. Res.*, 2001, **34**, 818.

119. Y. Liu, L. K. Lightning, H.-W. Huang, P. Moenne-Loccoz, D. J. Schuller, T. L. Poulos, T. M. Loehr, and P. R. O. De Montellano, *J. Biol. Chem.*, 2000, **275**, 34501.

120. L. K. Lightning, H.-W. Huang, P. Moenne-Loccoz, T. M. Loehr, D. J. Schuller, T. L. Poulos, and P. R. O. De Montellano, *J. Biol. Chem.*, 2001, **276**, 10612.

121. H. Fujii, X. Zhang, T. Tomita, M. Ikeda-Saito, and T. Yoshida, *J. Am. Chem. Soc.*, 2001, **123**, 6475.

122. F. deMare, D. M. Kurtz Jr, and P. Nordlund, *Nat. Struct. Biol.*, 1996, **3**, 539.

123. F. deMare, P. Nordlund, N. Gupta, N. V. Shenvi, X. Cui, and D. M. Kurtz Jr, *Inorg. Chim. Acta*, 1997, **263**, 255.

124. M. Ormo, F. deMare, K. Regnstrom, A. Aberg, M. Sahlin, J. Ling, T. M. Loehr, J. Sanders-Loehr, and B. M. Sjoberg, *J. Biol. Chem.*, 1992, **267**, 8711.

125. M. K. Johnson, in 'Encyclopedia of Inorganic Chemistry', ed. R. B. King, John Wiley & Sons, Chichester, 1994, p. 1896.

126. H. Beinert, R. H. Holm, and E. Munck, *Science*, 1997, **277**, 653.

127. M. K. Johnson, *Curr. Opin. Chem. Biol.*, 1998, **2**, 173.

128. S. Bian and J. A. Cowan, *Coord. Chem. Rev.*, 1999, **190–192**, 1049.

129. J. S. Valentine and E. B. Gralla, *Science*, 1997, **278**, 817.

130. T. V. O'Halloran and V. C. Culotta, *J. Biol. Chem.*, 2000, **275**, 25057.

131. A. C. Rosenzweig, *Acc. Chem. Res.*, 2001, **34**, 119.

132. A. L. Lamb, A. K. Wernimont, R. A. Pufahl, T. V. O'Halloran, and A. C. Rosenzweig, *Biochemistry*, 2000, **39**, 1589.

133. P. J. Schmidt, M. Ramos-Gomez, and V. C. Culotta, *J. Biol. Chem.*, 1999, **274**, 36952.

134. Y. Lu, in 'Biocoordination Chemistry', eds. L. Que Jr and W. B. Tolman, Elsevier, Oxford, 2004, Vol. 8, p. 91.

135. Y. Lu, E. B. Gralla, J. A. Roe, and J. S. Valentine, *J. Am. Chem. Soc.*, 1992, **114**, 3560.

136. Y. Lu, L. B. LaCroix, M. D. Lowery, E. I. Solomon, C. J. Bender, J. Peisach, J. A. Roe, E. B. Gralla, and J. S. Valentine, *J. Am. Chem. Soc.*, 1993, **115**, 5907.

137. J. Han, T. M. Loehr, Y. Lu, J. S. Valentine, B. A. Averill, and J. Sanders-Loehr, *J. Am. Chem. Soc.*, 1993, **115**, 4256.

138. Y. Lu, J. A. Roe, E. B. Gralla, and J. S. Valentine, in 'Bioinorg. Chem. of Copper', eds. K. D. Karlin and Z. Tyeklar, Chapman & Hall, New York, 1993, p. 64.

139. Y. Lu, J. A. Roe, C. J. Bender, J. Peisach, L. Banci, I. Bertini, E. B. Gralla, and J. S. Valentine, *Inorg. Chem.*, 1996, **35**, 1692.

140. L. Banci, I. Bertini, M. Borsari, M. S. Viezzoli, and R. A. Hallewell, *Eur. J. Biochem.*, 1995, **232**, 220.

141. T. J. Mizoguchi, A. J. Di Bilio, H. B. Gray, and J. H. Richards, *J. Am. Chem. Soc.*, 1992, **114**, 10076.

142. S. Faham, T. J. Mizoguchi, E. T. Adman, H. B. Gray, J. H. Richards, and D. C. Rees, *J. Biol. Inorg. Chem.*, 1997, **2**, 464.

143. M. Piccioli, C. Luchinat, T. J. Mizoguchi, B. E. Ramirez, H. B. Gray, and J. H. Richards, *Inorg. Chem.*, 1995, **34**, 737.

144. S. DeBeer, C. N. Kiser, G. A. Mines, J. H. Richards, H. B. Gray, E. I. Solomon, B. Hedman, and K. O. Hodgson, *Inorg. Chem.*, 1999, **38**, 433.

145. T. den Blaauwen, M. Van de Kamp, and G. W. Canters, *J. Am. Chem. Soc.*, 1991, **113**, 5050.

146. T. den Blaauwen and G. W. Canters, *J. Am. Chem. Soc.*, 1993, **115**, 1121.

147. G. van Pouderoyen, C. R. Andrew, T. M. Loehr, J. Sanders-Loehr, S. Mazumdar, H. A. O. Hill, and G. W. Canters, *Biochemistry*, 1996, **35**, 1397.

148. I. Durussel, T. L. Pauls, J. A. Cox, and M. W. Berchtold, *Eur. J. Biochem.*, 1996, **242**, 256.

149. T. L. Pauls, I. Durussel, I. D. Clark, A. G. Szabo, M. W. Berchtold, and J. A. Cox, *Eur. J. Biochem.*, 1996, **242**, 249.

150. R. E. Reid and R. M. Procyshyn, *Arch. Biochem. Biophys.*, 1995, **323**, 115.

151. A. Jeltsch, C. Wenz, W. Wende, U. Selent, and A. Pingoud, *Trends Biotechnol.*, 1996, **14**, 235.

152. I. B. Vipond, B.-J. Moon, and S. E. Halford, *Biochemistry*, 1996, **35**, 1712.

153. J. E. Murphy, X. Xu, and E. R. Kantrowitz, *J. Biol. Chem.*, 1993, **268**, 21497.

154. A.-F. Miller and D. L. Sorkin, *Comments Mol. Cell Biophys.*, 1997, **9**, 1.

155. J. W. Whittaker, in 'Metal Ions in Biological Systems', eds. A. Sigel and H. Sigel, Marcel Dekker, New York, 2000, Vol. 37, p. 587.

156. M. M. Whittaker and J. W. Whittaker, *J. Biol. Chem.*, 1998, **273**, 22188.

157. K. Bunting, J. B. Cooper, M. O. Badasso, I. J. Tickle, M. Newton, S. P. Wood, Y. Zhang, and D. Young, *Eur. J. Biochem.*, 1998, **251**, 795.

158. B. Y. Hiraoka, F. Yamakura, S. Sugio, and K. Nakayama, *Biochem. J.*, 2000, **345**, 345.

159. A. L. Schwartz, E. Yikilmaz, C. K. Vance, S. Vathyam, R. L. Koder, and A.-F. Miller, *J. Inorg. Biochem.*, 2000, **80**, 247.

160. C. Vita, C. Roumestand, F. Tom, and A. Menez, *Proc. Natl. Acad. Sci. U.S.A.*, 1995, **92**, 6404.

161. B. Pierret, H. Virelizier, and C. Vita, *Int. J. Pept. Protein Res.*, 1995, **46**, 471.

162. E. Drakopoulou, S. Zinn-Justin, M. Guenneugues, C. Leon, I. Segalas, B. Gilquin, A. Menez, and C. Vita, in 'Perspectives on Protein Engineering '96, Montpellier, France', BIODIGM, Bingham, UK, 1996, p. 18.

163. V. Perrier, S. Burlacu-Miron, S. Bourgeois, W. K. Surewicz, and A.-M. Gilles, *J. Biol. Chem.*, 1998, **273**, 19097.

164. S. Burlacu-Miron, V. Perrier, A.-M. Gilles, E. Pistotnik, and C. T. Craescu, *J. Biol. Chem.*, 1998, **273**, 19102.

165. H. N. Müller and A. Skerra, *Biochemistry*, 1994, **33**, 14126.

166. M. Sundaramoorthy, K. Kishi, M. H. Gold, and T. L. Poulos, *J. Biol. Chem.*, 1994, **269**, 32759.

167. B. K. Yeung, X. Wang, J. A. Sigman, P. A. Petillo, and Y. Lu, *Chem. Biol.*, 1997, **4**, 215.

168. X. Wang and Y. Lu, *Biochemistry*, 1999, **38**, 9146.

169. A. Gengenbach, S. Syn, X. Wang, and Y. Lu, *Biochemistry*, 1999, **38**, 11425.

170. S. K. Wilcox, C. D. Putnam, M. Sastry, J. Blankenship, W. J. Chazin, D. E. McRee, and D. B. Goodin, *Biochemistry*, 1998, **37**, 16853.

171. A. Gengenbach, X. Wang, and Y. Lu, in 'Fundamentals and Catalysis of Oxidative Delignification Processes', ed. D. S. Argyropoulos, American Chemical Society, Washington, D.C., 2001, Vol. 785, p. 487.

172. T. Mester and M. Tien, *Biochem. Biophys. Res. Commun.*, 2001, **284**, 723.

173. C. A. Bonagura, M. Sundaramoorthy, H. Pappa, W. R. Patterson, and T. L. Poulos, *Biochemistry*, 1996, **35**, 6107.

174. C. A. Bonagura, M. Sundaramoorthy, B. Bhaskar, and T. L. Poulos, *Biochemistry*, 1999, **38**, 5538.

175. C. A. Bonagura, B. Bhaskar, M. Sundaramoorthy, and T. L. Poulos, *J. Biol. Chem.*, 1999, **274**, 37827.

176. L. Norregaard, I. Visiers, C. J. Loland, J. Ballesteros, H. Weinstein, and U. Gether, *Biochemistry*, 2000, **39**, 15836.

177. A. Muheim, R. J. Todd, D. R. Casimiro, H. B. Gray, and F. H. Arnold, *J. Am. Chem. Soc.*, 1993, **115**, 5312.

178. P. Umana, J. T. Kellis Jr, and F. H. Arnold, *ACS Symp. Ser.*, 1993, **516**, 102.

179. J. W. Wray, W. A. Baase, G. J. Ostheimer, X. J. Zhang, and B. W. Matthews, *Protein Eng.*, 2000, **13**, 313.

180. K. K. Jensen, L. Martini, and T. W. Schwartz, *Biochemistry*, 2001, **40**, 938.

181. Y. Lu, D. R. Casimiro, K. L. Bren, J. H. Richards, and H. B. Gray, *Proc. Natl. Acad. Sci. U.S.A.*, 1993, **90**, 11456.

182. J. N. Higaki, R. J. Fletterick, and C. S. Craik, *Trends Biochem. Sci.*, 1992, **17**, 100.

183. M. F. Browner, D. Hockos, and R. Fletterick, *Nat. Struct. Biol.*, 1994, **1**, 327.

184. W. S. Willett, S. A. Gillmor, J. J. Perona, R. J. Fletterick, and C. S. Craik, *Biochemistry*, 1995, **34**, 2172.

185. W. S. Willett, L. S. Brinen, R. J. Fletterick, and C. S. Craik, *Biochemistry*, 1996, **35**, 5992.

186. L. S. Brinen, W. S. Willett, C. S. Craik, and R. J. Fletterick, *Biochemistry*, 1996, **35**, 5999.

187. C. L. Hunter, R. Maurus, M. R. Mauk, H. Lee, E. L. Raven, H. Tong, N. Nguyen, M. Smith, G. D. Brayer, and A. G. Mauk, *Proc. Natl. Acad. Sci. U.S.A.*, 2003, **100**, 3647.

188. N. D. Clarke and S.-M. Yuan, *Proteins: Struct., Funct., Genet.*, 1995, **23**, 256.

189. H. W. Hellinga and F. M. Richards, *J. Mol. Biol.*, 1991, **222**, 763.

190. J. R. Desjarlais and N. D. Clarke, *Curr. Opin. Struct. Biol.*, 1998, **8**, 471.

191. M. Klemba, K. H. Gardner, S. Marino, N. D. Clarke, and L. Regan, *Nat. Struct. Biol.*, 1995, **2**, 368.

192. M. S. Wisz, C. Z. Garrett, and H. W. Hellinga, *Biochemistry*, 1998, **37**, 8269.

193. S. F. Marino and L. Regan, *Chem. Biol.*, 1999, **6**, 649.

194. E. Farinas and L. Regan, *Protein Sci.*, 1998, **7**, 1939.

195. D. E. Benson, M. S. Wisz, W. Liu, and H. W. Hellinga, *Biochemistry*, 1998, **37**, 7070.

196. W. Yang, L. M. Jones, L. Isley, Y. Ye, H.-W. Lee, A. Wilkins, Z.-R. Liu, H. W. Hellinga, R. Malchow, M. Ghazi, and J. J. Yang, *J. Am. Chem. Soc.*, 2003, **125**, 6165.

197. C. D. Coldren, H. W. Hellinga, and J. P. Caradonna, *Proc. Natl. Acad. Sci. U.S.A.*, 1997, **94**, 6635.

198. W. Yang, H.-W. Lee, H. Hellinga, and J. J. Yang, *Proteins: Struct., Funct., Genet.*, 2002, **47**, 344.

199. H. W. Hellinga, *J. Am. Chem. Soc.*, 1998, **120**, 10055.

200. H. W. Hellinga, J. P. Caradonna, and F. M. Richards, *J. Mol. Biol.*, 1991, **222**, 787.

201. A. L. Pinto, H. W. Hellinga, and J. P. Caradonna, *Proc. Natl. Acad. Sci. U.S.A.*, 1997, **94**, 5562.

202. D. E. Benson, M. S. Wisz, and H. W. Hellinga, *Proc. Natl. Acad. Sci. U.S.A.*, 2000, **97**, 6292.

203. V. A. Roberts and E. D. Getzoff, *FASEB J.*, 1995, **9**, 94.

204. J. D. Stewart, V. A. Roberts, M. W. Crowder, E. D. Getzoff, and S. J. Benkovic, *J. Am. Chem. Soc.*, 1994, **116**, 415.

205. T. A. Richmond, T. T. Takahashi, R. Shimkhada, and J. Bernsdorf, *Biochem. Biophys. Res. Commun.*, 2000, **268**, 462.

206. J. A. Sigman, B. C. Kwok, A. Gengenbach, and Y. Lu, *J. Am. Chem. Soc.*, 1999, **121**, 8949.

207. J. A. Sigman, B. C. Kwok, and Y. Lu, *J. Am. Chem. Soc.*, 2000, **122**, 8192.

208. J. A. Sigman, H. K. Kim, X. Zhao, J. R. Carey, and Y. Lu, *Proc. Natl. Acad. Sci. U.S.A.*, 2003, **100**, 3629.

209. F. H. Arnold and B. L. Haymore, *Science*, 1991, **252**, 1796.

210. D. J. McColl, C. D. Honchell, and A. D. Frankel, *Proc. Natl. Acad. Sci. U.S.A.*, 1999, **96**, 9521.

211. F. H. Arnold, *Bio-Technology*, 1991, **9**, 151.

212. J. Voss, L. Salwinski, H. R. Kaback, and W. L. Hubbell, *Proc. Natl. Acad. Sci. U.S.A.*, 1995, **92**, 12295.

213. J. T. Kellis Jr, R. J. Todd, and F. H. Arnold, *Bio/Technology*, 1991, **9**, 994.

214. R. J. Todd, M. E. Van Dam, D. Casimiro, B. L. Haymore, and F. H. Arnold, *Proteins: Struct., Funct., Genet.*, 1991, **10**, 156.

215. S. J. Franklin, *Curr. Opin. Chem. Biol.*, 2001, **5**, 201.

216. R. Kuroki, Y. Taniyama, C. Seko, H. Nakamura, M. Kikuchi, and M. Ikehara, *Proc. Natl. Acad. Sci. U.S.A.*, 1989, **86**, 6903.

217. V. A. Romoser, P. M. Hinkle, and A. Persechini, *J. Biol. Chem.*, 1997, **272**, 13270.

218. A. Miyawaki, J. Llopis, R. Helm, J. M. McCaffery, J. A. Adams, M. Ikura, and R. Y. Tsien, *Nature*, 1997, **388**, 882.

219. J. T. Welch, M. Sirish, K. M. Lindstrom, and S. J. Franklin, *Inorg. Chem.*, 2001, **40**, 1982.
220. R. T. Kovacic, J. T. Welch, and S. J. Franklin, *J. Am. Chem. Soc.*, 2003, **125**, 6656.
221. C. E. Laplaza and R. H. Holm, *J. Am. Chem. Soc.*, 2001, **123**, 10255.
222. M. Go, *Nature*, 1981, **291**, 90.
223. W. A. Eaton, *Nature (London, United Kingdom)*, 1980, **284**, 183.
224. K. Wakasugi, K. Ishimori, K. Imai, Y. Wada, and I. Morishima, *J. Biol. Chem.*, 1994, **269**, 18750.
225. K. Inaba, K. Ishimori, and I. Morishima, *J. Mol. Biol.*, 1998, **283**, 311.
226. Y. Ye, S. Shealy, H.-W. Lee, I. Torshin, R. Harrison, and J. J. Yang, *Protein Eng.*, 2003, **16**, 429.
227. S. Toma, S. Campagnoli, I. Margarit, R. Gianna, G. Grandi, M. Bolognesi, V. De Filippis, and A. Fontana, *Biochemistry*, 1991, **30**, 97.
228. S. Braxton and J. A. Wells, *Biochemistry*, 1992, **31**, 7796.
229. S. Halfon and C. S. Craik, *J. Am. Chem. Soc.*, 1996, **118**, 1227.
230. J. van der Oost, P. Lappalainen, A. Musacchio, A. Warne, L. Lemieux, J. Rumbley, R. B. Gennis, R. Aasa, T. Pascher, B. G. Malmström, and M. Saraste, *EMBO J.*, 1992, **11**, 3209.
231. G. J. Steffens and G. Buse, *Hoppe-Seyler's Z. Physiol. Chem.*, 1979, **360**, 613.
232. C. Dennison, E. Vijgenboom, S. de Vries, J. van der Oost, and G. W. Canters, *FEBS Lett.*, 1995, **365**, 92.
233. M. Hay, J. H. Richards, and Y. Lu, *Proc. Natl. Acad. Sci. U.S.A.*, 1996, **93**, 461.
234. M. T. Hay, M. C. Ang, D. R. Gamelin, E. I. Solomon, W. E. Antholine, M. Ralle, N. J. Blackburn, P. D. Massey, X. Wang, A. H. Kwon, and Y. Lu, *Inorg. Chem.*, 1998, **37**, 191.
235. L. H. Jones, A. Liu, and V. L. Davidson, *J. Biol. Chem.*, 2003, **278**, 47269.
236. M. Wilmanns, P. Lappalainen, M. Kelly, E. Sauer-Eriksson, and M. Saraste, *Proc. Natl. Acad. Sci. U.S.A.*, 1995, **92**, 11955.
237. H. Robinson, M. C. Ang, Y.-G. Gao, M. T. Hay, Y. Lu, and A. H. J. Wang, *Biochemistry*, 1999, **38**, 5677.
238. C. Dennison, E. Vijgenboom, W. R. Hagen, and G. W. Canters, *J. Am. Chem. Soc.*, 1996, **118**, 7406.
239. V. Zickermann, A. Wittershagen, B. O. Kolbesen, and B. Ludwig, *Biochemistry*, 1997, **36**, 3232.
240. D. J. Segal and C. F. Barbas III, *Curr. Opin. Chem. Biol.*, 2000, **4**, 34.
241. S. A. Wolfe, L. Nekludova, and C. O. Pabo, *Annu. Rev. Biophys. Biomol. Struct.*, 2000, **29**, 183.
242. Y. Choo, I. Sanchez-Garcia, and A. Klug, *Nature*, 1994, **372**, 642.
243. H. K. Rau, N. DeJonge, and W. Haehnel, *Angew. Chem., Int. Ed. Engl.*, 2000, **39**, 250.
244. R. Schnepf, P. Hoerth, E. Bill, K. Wieghardt, P. Hildebrandt, and W. Haehnel, *J. Am. Chem. Soc.*, 2001, **123**, 2186.
245. D. A. Moffet and M. H. Hecht, *Chem. Rev.*, 2001, **101**, 3191.
246. N. R. L. Rojas, S. Kamtekar, C. T. Simons, J. E. McLean, K. M. Vogel, T. G. Spiro, R. S. Farid, and M. H. Hecht, *Protein Sci.*, 1997, **6**, 2512.
247. D. A. Moffet, M. A. Case, J. C. House, K. Vogel, R. D. Williams, T. G. Spiro, G. L. McLendon, and M. H. Hecht, *J. Am. Chem. Soc.*, 2001, **123**, 2109.
248. D. A. Moffet, L. K. Certain, A. J. Smith, A. J. Kessel, K. A. Beckwith, and M. H. Hecht, *J. Am. Chem. Soc.*, 2000, **122**, 7612.
249. J. A. Hunt and C. A. Fierke, *J. Biol. Chem.*, 1997, **272**, 20364.
250. A. W. Schwabacher, M. I. Weinhouse, M. T. M. Auditor, and R. A. Lerner, *J. Am. Chem. Soc.*, 1989, **111**, 2344.
251. E. Keinan, S. C. Sinha, A. Sinha-Bagchi, E. Benory, M. C. Ghozi, Z. Eshhar, and B. S. Green, *Pure Appl. Chem.*, 1990, **62**, 2013.
252. A. G. Cochran and P. G. Schultz, *Science*, 1990, **249**, 781.
253. A. Harada, H. Yamaguchi, K. Okamoto, H. Fukushima, K. Shiotsuki, and M. Kamachi, *Photochem. Photobiol.*, 1999, **70**, 298.
254. H. Yamaguchi, M. Kamachi, and A. Harada, *Angew. Chem., Int. Ed. Engl.*, 2000, **39**, 3829.
255. A. G. Cochran and P. G. Schultz, *J. Am. Chem. Soc.*, 1990, **112**, 9414.
256. T. Imanaka and M. Takagi, *ACS Symp. Ser.*, 1995, **604**, 138.
257. M. Takagi, K. Kohda, T. Hamuro, A. Harada, H. Yamaguchi, M. Kamachi, and T. Imanaka, *FEBS Lett.*, 1995, **375**, 273.
258. K. Kohda, M. Kakehi, Y. Ohtsuji, M. Tagaki, and T. Imanaka, *FEBS Lett.*, 1997, **407**, 280.
259. A. Harada, H. Fukushima, K. Shiotsuki, H. Yamaguchi, F. Oka, and M. Kamachi, *Inorg. Chem.*, 1997, **36**, 6099.
260. Y. Kawamura-Konishi, A. Asano, M. Yamazaki, H. Tashiro, and H. Suzuki, *J. Mol. Catal. B: Enzym.*, 1998, **4**, 181.
261. S. de Lauzon, B. Desfosses, D. Mansuy, and J.-P. Mahy, *FEBS Lett.*, 1999, **443**, 229.
262. X. Liu, S. Chen, Y. Feng, G. Gao, and T. Yang, *Ann. N. Y. Acad. Sci.*, 1998, **864**, 273.
263. S. Nimri and E. Keinan, *J. Am. Chem. Soc.*, 1999, **121**, 8978.
264. K. Ohkubo, H. Ishida, T. Sagawa, K. Urabe, K. Seri, and M. Suga, *Chem. Lett.*, 1993, 61.
265. L. Wan, M. B. Twitchett, L. D. Eltis, A. G. Mauk, and M. Smith, *Proc. Natl. Acad. Sci. U.S.A.*, 1998, **95**, 12825.
266. H. Joo, Z. Lin, and F. H. Arnold, *Nature*, 1999, **399**, 670.
267. H. Joo, A. Arisawa, Z. Lin, and F. H. Arnold, *Chem. Biol.*, 1999, **6**, 699.
268. Y. Lu, *Curr. Opin. Chem. Biol.*, 2005, **9**, 118.
269. H. K. Privett, C. J. Reedy, M. L. Kennedy, and B. R. Gibney, *J. Am. Chem. Soc.*, 2002, **124**, 6828.

270. P. Frank, A. Licht, T. D. Tullius, K. O. Hodgson, and I. Pecht, *J. Biol. Chem.*, 1985, **260**, 5518.

271. P. C. Cirino, Y. Tang, K. Takahashi, D. A. Tirrell, and F. H. Arnold, *Biotechnol. Bioeng.*, 2003, **83**, 729.

272. D. Barrick, *Curr. Opin. Biotechnol.*, 1995, **6**, 411.

273. G. D. DePillis, S. M. Decatur, D. Barrick, and S. G. Boxer, *J. Am. Chem. Soc.*, 1994, **116**, 6981.

274. D. E. McRee, G. M. Jensen, M. M. Fitzgerald, H. A. Siegel, and D. B. Goodin, *Proc. Natl. Acad. Sci. U.S.A.*, 1994, **91**, 12847.

275. D. W. Low and M. G. Hill, *J. Am. Chem. Soc.*, 1998, **120**, 11536.

276. D. W. Low and M. G. Hill, *J. Am. Chem. Soc.*, 2000, **122**, 11039.

277. D. W. Low, M. G. Hill, M. R. Carrasco, S. B. H. Kent, and P. Botti, *Proc. Natl. Acad. Sci. U.S.A.*, 2001, **98**, 6554.

278. L. Wang and P. G. Schultz, *Chem. Commun.*, 2002, 1.

279. A. J. Link, M. L. Mock, and D. A. Tirrell, *Curr. Opin. Biotechnol.*, 2003, **14**, 603.

280. T. W. Muir, D. Sondhi, and P. A. Cole, *Proc. Natl. Acad. Sci. U.S.A.*, 1998, **95**, 6705.

281. L. Z. Yan and P. E. Dawson, *J. Am. Chem. Soc.*, 2001, **123**, 526.

282. S. M. Berry, M. D. Gieselman, M. J. Nilges, W. A. Van der Donk, and Y. Lu, *J. Am. Chem. Soc.*, 2002, **124**, 2084.

283. S. M. Berry, M. Ralle, D. W. Low, N. J. Blackburn, and Y. Lu, *J. Am. Chem. Soc.*, 2003, **125**, 8760.

284. D. Jantz and J. M. Berg, *J. Am. Chem. Soc.*, 2003, **125**, 4960.

285. T. Hayashi, H. Dejima, T. Matsuo, H. Sato, D. Murata, and Y. Hisaeda, *J. Am. Chem. Soc.*, 2002, **124**, 11226.

286. T. Matsuo, T. Hayashi, and Y. Hisaeda, *J. Am. Chem. Soc.*, 2002, **124**, 11234.

287. T. Ueno, M. Ohashi, M. Kono, K. Kondo, A. Suzuki, T. Yamane, and Y. Watanabe, *Inorg. Chem.*, 2004, **43**, 2852.

288. J. R. Carey, S. K. Ma, T. D. Pfister, D. K. Garner, H. K. Kim, J. A. Abramite, Z. Wang, Z. Guo, and Y. Lu, *J. Am. Chem. Soc.*, 2004, **126**, 10812.

289. C.-H. B. Chen, L. Milne, R. Landgraf, D. M. Perrin, and D. S. Sigman, *ChemBioChem*, 2001, **2**, 735.

290. S. A. Datwyler and C. F. Meares, *Met. Ions Biol. Syst.*, 2001, **38**, 213.

291. R. R. Davies and M. D. Distefano, *J. Am. Chem. Soc.*, 1997, **119**, 11643.

292. D. Qi, C.-M. Tann, D. Haring, and M. D. Distefano, *Chem. Rev.*, 2001, **101**, 3081.

293. M. E. Wilson and G. M. Whitesides, *J. Am. Chem. Soc.*, 1978, **100**, 306.

294. M. Ohashi, T. Koshiyama, T. Ueno, M. Yanase, H. Fujii, and Y. Watanabe, *Angew. Chem., Int. Ed. Engl.*, 2003, **42**, 1005.

295. J. Collot, J. Gradinaru, N. Humbert, M. Skander, A. Zocchi, and T. R. Ward, *J. Am. Chem. Soc.*, 2003, **125**, 9030.

Acknowledgments

Yi Lu wishes to acknowledge the contributions from Lu group members and collaborators whose names are cited in the references. The research in the Lu group has been generously supported by the US National Science Foundation and the National Institutes of Health.

Multi-Heme Cytochromes & Enzymes

Inês A. C. Pereira & António V. Xavier
Instituto de Tecnologia Química e Biologica, Oeiras, Portugal

1 Introduction 1
2 The Cytochrome c_3 Family 2
3 The Hydroxylamine Oxidoreductase Family 9
4 Other Multiheme c Cytochromes 14
5 Related Articles 14
6 References 15

Abbreviations

9HCc_3 = Nine-heme cytochrome c_3; 16HCc_3 = Sixteen-heme high molecular mass cytochrome c_3; 3HCc_3 = Three-heme cytochrome c_7; HAO = Hydroxylamine oxidoreductase; Ffr = Flavocytochrome c fumarate reductase; Stc = Small tetraheme cytochrome c; 4HCc_3TpI = Type I cytochrome c_3; H$_2$ase = Hydrogenase; TETC = Transmembrane electron transfer complex; Di4HCc_3 = Dimeric cytochrome c_3; 4HCc_3TpII = Type II cytochrome c_3; cNiR = Cytochrome c nitrite reductase; Ssc = Split-Soret cytochrome; NapAB = Periplasmic nitrate reductase.

1 INTRODUCTION

Most known multiheme cytochromes and enzymes belong to the family of cytochromes c (*see* ***Iron: Heme Proteins & Electron Transport***), which contain Fe-protoporphyrin IX covalently attached to the polypeptide chain by two thioether bonds, formed by addition of two cysteinyl residues to the vinyl side-chains of the porphyrin ring. The two cysteines form a characteristic amino acid sequence motif CXXCH, usually indicative of heme c ligation, and where the histidine is the axial fifth ligand to the iron. For some cytochromes (see Section 2), the number of residues between the two cysteines can be three or four. The heme redox potentials in cytochromes c cover a wide range and are tuned by several factors, usually dominated by the type of axial ligation and the extent of solvent exposure of the heme.[1,2]

Bacterial cytochromes c are either periplasmic or attached to the periplasmic side of the membrane, and this led to the suggestion by Wood that the covalent attachment of heme evolved as a way of preventing its loss from periplasmic proteins to the external medium.[3] However, there are some observations that go against this idea, namely, the fact that there are both extracellular and periplasmic proteins that contain noncovalently bound hemes. It has been argued that there are a number of reasons that justify the advantage of having heme covalently attached to the polypeptide.[4,5] Studies, in which a c-type cytochrome was converted to a b-type, or a b-type to a c-type, show that covalent attachment of the heme confers increased stability to a cytochrome. Furthermore, covalent attachment enables a tight binding of heme with much less polypeptide required, and permits the clustering of spatially very close hemes in well defined arrangements. Such dense packing of hemes, as observed in multiheme proteins, probably allows for extremely fast electron transfer between them.[6]

The biogenesis of cytochromes c involves quite complex assembly systems that differ between organisms. The simplest one is found in mitochondria of fungal, vertebrate, and invertebrate cells, but is unrelated to both the bacterial system I (the *ccm* system), found in some gram-negative bacteria, and to system II (the *ccs* system) found in other classes of gram-negative bacteria, gram-positive bacteria, cyanobacteria, and in plant and algal chloroplasts.[7–9] These systems are involved in the transport of apocytochrome and heme across the membrane, maintaining the cysteine residues of the heme-binding motif in a reduced state, and in covalent attachment of heme catalyzed by a heme lyase.

The most widely known protein containing a heme c is the mitochondrial cytochrome c (*see* ***Iron: Heme Proteins & Electron Transport***) that, together with similar bacterial cytochromes, form the family of monoheme cytochromes c. These are characterized by histidine-methionine coordination, and a low solvent exposure of the heme, resulting in positive redox potentials. Their fold can be found as a domain of more complex proteins like the cytochrome cd_1 nitrite reductase, caa_3 and cbb_3-type oxidases (*see* ***Cytochrome Oxidase***), and several diheme cytochromes such as cytochrome c peroxidases, cytochrome c_4 from *Pseudomonas stutzeri*, and the cytochrome subunit of the flavocytochrome c sulfide dehydrogenase from *Allochromatium vinosum*. An interesting protein related to this family is SoxAX, a heterodimeric c-type cytochrome involved in the oxidation of thiosulfate.[10] The two hemes of the SoxA subunit constitute the first example of hemes c with histidine/cysteine ligation, and the catalytic heme 2 (the heme numbering used throughout this text follows the order of the heme-binding site in the polypeptide sequence from the N-terminus) is further unusual in that its cysteinyl ligand suffers a posttranslational modification to form cysteinyl persulfide.

Multiheme c cytochromes and enzymes form distinct families from the monoheme c cytochromes. They are characterized by a low amino acid residues to heme ratio (resulting in significant exposure of heme to the solvent) and bis-histidinyl coordination, with few known exceptions. These two characteristics are responsible for the low heme redox potentials of this family. In some cases, the multiheme *c* domain is part of more complex proteins. The hemes may be six coordinated and low spin or pentacoordinated and high spin, and it is generally assumed that the low-spin hemes have an electron transfer function, whereas the high-spin hemes have a catalytic function, owing to the possibility of binding a substrate. However, there are two examples of proteins containing one high-spin heme, the high molecular mass cytochrome c_3 (see Section 2.3) and cytochrome c_{554} (see Section 3.2), for which a purely electron transfer function is proposed and no enzymatic activity has, so far, been detected.

A striking feature apparent from the structures of multiheme proteins described to date, is that the hemes are found clustered in structural arrangements that are quite conserved among, otherwise, totally unrelated proteins in amino acid sequence or polypeptide fold. Indeed, most hemes in these proteins are part of diheme packing motifs where the two heme planes are found either parallel but offset ('heme stacking motif') or perpendicular to each other ('diheme elbow motif') (Figure 1).[11] In the parallel motif the interheme iron distances are around 10 Å and the heme planes are separated by a distance of less than 4 Å. In the perpendicular motif, the heme iron distances are around 12 Å. Furthermore, these diheme motifs may form larger structural heme motifs (superheme motifs) that are almost superimposable, and the similarity may also extend to the folding of the polypeptide chain surrounding the hemes.[4,12] The functional significance of these heme structural arrangements is not yet understood, and they possibly reflect favorable arrangements to tune heme–heme redox potential interactions and/or warrant very fast electron transfer.

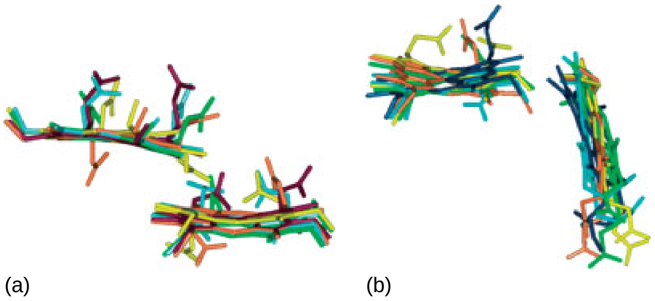

Figure 1 (a) Superposition of heme pairs displaying the parallel heme stacking motif. The hemes shown are from the *D. desulfuricans* ATCC 27774 Split-Soret cytochrome (PDB code 1DCC, hemes 1 and 2, magenta), *N*. europaea HAO (PDB code 1FGJ, hemes 3 and 5, yellow), *W. succinogenes* NrfA (PDB code 1FS7, hemes 3 and 4, green), *N*. europaea cytochrome c_{554} (PDB code 1FT5, hemes 1 and 3, orange) and *S. oneidensis* MR-1 Stc (PDB code 1M1Q, hemes 2 and 3, light blue). (b) Superposition of heme pairs displaying the perpendicular diheme elbow motif. The hemes shown are from the *D. vulgaris* Hildenborough 4HCc_3TpI (PDB code 2CHT, hemes 1 and 3, dark blue), *N. europaea* HAO (PDB code 1FGJ, hemes 7 and 8, yellow), *W. succinogenes* NrfA (PDB code 1FS7, hemes 2 and 3, green), *N. europaea* cytochrome c_{554} (PDB code 1FT5, hemes 3 and 5, orange) and *S. oneidensis* MR-1 Stc (PDB code 1M1Q, hemes 3 and 4, light blue)

Most multiheme *c* proteins for which the structure has been determined can be divided into two families of similar superheme motifs. The first one is the cytochrome c_3 family, which includes proteins containing one or more tetraheme arrangements (see Section 2). In this tight and closely spaced arrangement, the perpendicular motif is predominant, since both of the most distant hemes, 1 and 4 (almost parallel to each other) are perpendicular to both hemes 2 and 3 (Figure 2). This heme core architecture is found in other members of the family like the nine-heme cytochrome c_3 (9HCc_3), the sixteen-heme high molecular mass cytochrome c_3 (16HCc_3), and even the three-heme cytochrome c_7 (3HCc_3). Since the larger proteins of this family are assemblies of cytochrome c_3-like heme motifs, they are here also named as cytochromes c_3.

The second family is more diverse and includes proteins like the eight-heme hydroxylamine oxidoreductase (HAO), its redox partner the tetraheme cytochrome c_{554}, the five-heme NrfA nitrite reductase, the tetraheme domain of the flavocytochrome *c* fumarate reductase (Ffr), and the small tetraheme cytochrome *c* (Stc) of *Shewanella* sp. Several of the hemes of each protein have almost identical orientation to groups of hemes in the other proteins. Taking HAO as a reference, the four hemes of cytochrome c_{554} are superimposable on hemes 3–6 of HAO, the five hemes of the NrfA are superimposable on hemes 4–8 of HAO, the four hemes of the Stc are superimposable on hemes 5–8 of HAO and hemes 1–3 of the Ffr are superimposable on hemes 5–7 of HAO (Figure 3). This family includes both stacked and perpendicular diheme motifs with the interesting feature that the two motifs alternate.

In the two following sections, several proteins belonging to each family are discussed. In the third section, a brief overview of other multiheme *c* proteins is presented.

2 THE CYTOCHROME c_3 FAMILY

A very high cellular content of multiheme cytochromes *c* is a characteristic of a specialized group of gram-negative δ-proteobacteria that use sulfate as terminal electron acceptor. *Desulfovibrio* (*D*.), from which the first known multiheme cytochrome was isolated, is the best studied genus. Most of these cytochromes are related in terms of sequence and structure forming a family that is characterized by a low polypeptide to heme ratio, low redox potentials, and a tetraheme globular arrangement where the perpendicular motif is predominant.[13] The prototype of this family is the Type I cytochrome c_3 (4HCc_3TpI), which was the third cytochrome *c* to be identified and is the most studied member of the family.

2.1 Type I Cytochrome c_3

The 4HCc_3TpI is a periplasmic cytochrome that is highly abundant in all *Desulfovibrio* species described so far,[13] and is

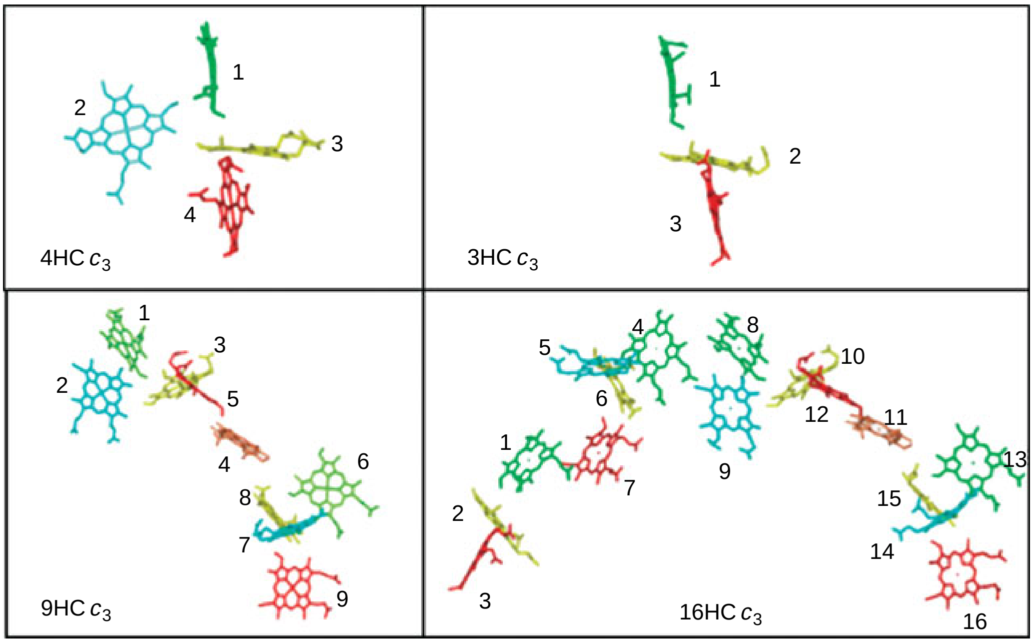
4HC c_3
1
2
3
4
3HC c_3
1
2
3
9HC c_3
1
2
3
4
5
6
7
8
9
16HC c_3
1
2
3
4
5
6
7
8
9
10
11
12
13
14
15
16

Figure 2 Heme structures of multiheme *c* proteins belonging to the cytochrome c_3 family: *D. vulgaris* Hildenborough 4HCc_3TpI (PDB code 2CHT), *Dsm. acetoxidans* 3HCc_3 (PDB code 1HH5), *D. desulfuricans* ATCC 27774 9HCc_3 (PDB code 19HC) and *D. vulgaris* Hildenborough 16HCc_3 (PDB code 1H29). The hemes are colored according to the corresponding heme in the 4HCc_3TpI (heme 1 green, heme 2 blue, heme 3 yellow, heme 4 red). Hemes 4 in 9HCc_3 and 11 in 16HCc_3 are not part of tetraheme arrangements and are colored orange

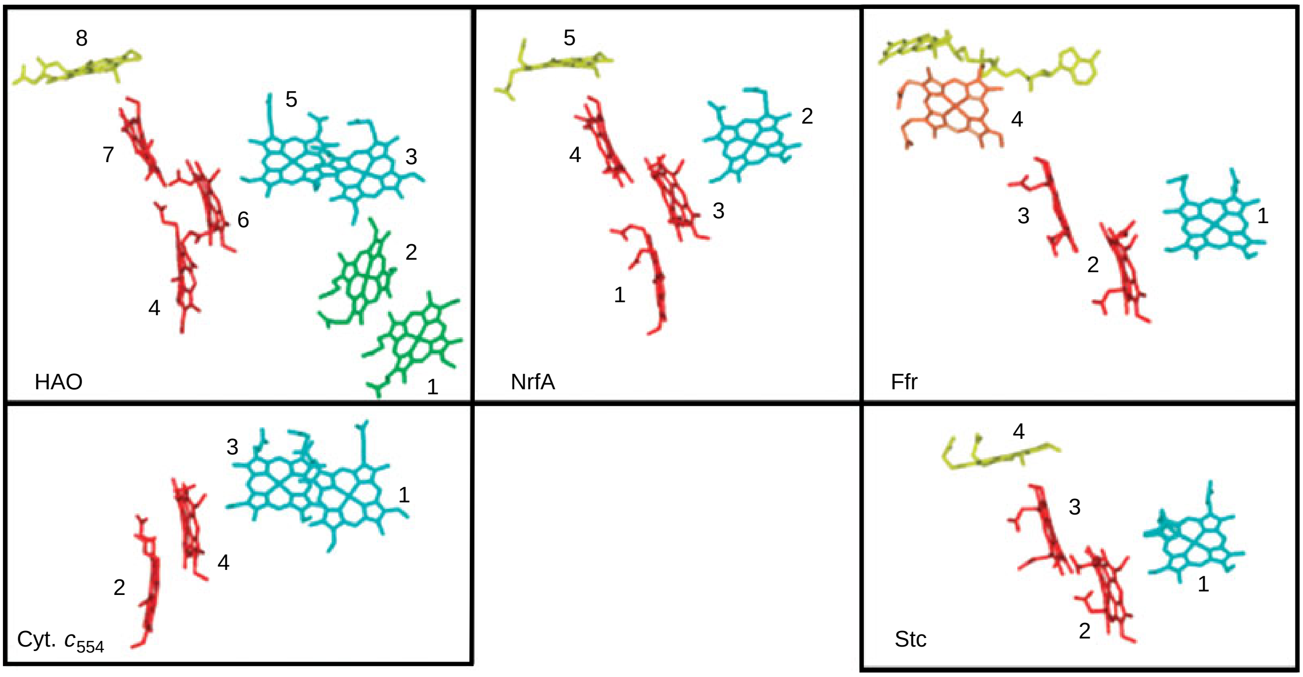
HAO
1
2
3
4
5
6
7
8
NrfA
1
2
3
4
5
Ffr
1
2
3
4
Cyt. c_{554}
1
2
3
4
Stc
1
2
3
4

Figure 3 Heme structures of multiheme *c* proteins belonging to the HAO family: *N. europaea* HAO (PDB code 1FGJ), *W. succinogenes* NrfA (PDB code 1FS7), *S. frigidimarina* NCIMB400 Ffr (PDB code 1QJD), *N. europaea* cytochrome c_{554} (PDB code 1FT5) and *S. oneidensis* MR-1 Stc (PDB code 1M1Q). The hemes are colored according to the four-heme clusters of HAO. Hemes in the same color are superimposable. Heme 4 of Ffr is colored orange, since it shows a considerable deviation from heme 8 in HAO. The flavin group of Ffr is shown in yellow

also present in other sulfate-reducing bacteria such as *Desulfomicrobium*, *Desulfobulbus*, and *Thermodesulfobacterium*. The designation of Type I stems from the fact that recently a second type of tetraheme cytochrome c_3 was identified (see Section 2.3). The 4HCc_3TpI has a central role in the bioenergetic metabolism of *Desulfovibrio* sp., working as a coupling protein between hydrogenase (H_2ase) and one of several possible transmembrane electron transfer complexes (TETC), which transport electrons from the periplasm to the reduction of sulfate in the cytoplasm (see Section 2.3). It is a small (∼14 kDa), monomeric protein containing four hemes *c* with bis-histidinyl coordination. The four hemes are quite exposed to the solvent and have low redox potentials in the range of −200 to −400 mV. The 4HCc_3TpI is a very stable protein that has been studied by a wide range of techniques, making it one of the most well-characterized electron transfer proteins in terms of structure-function relationship. The detailed characterization of some 4HCc_3TpIs includes: (1) thorough microscopic thermodynamic characterization of their relevant redox and protolytic centers, including their pairwise homotropic (heme–heme redox potential) and heterotropic (heme redox potential and p*K*a of specific groups, known as redox-Bohr effect, rB) cooperativities; (2) X-ray crystal and/or solution nuclear magnetic resonance (NMR) structures in different redox and/or protonation states; and (3) elucidation of the molecular bases that govern the functional cooperativities.[14] These studies indicate that the 4HCc_3TpI has two characteristics that are fundamental for its function: it performs a two-electron step and is capable of electron-to-proton energy transduction.

The 3D-structure of the 4HCc_3TpIs shows no similarity to other known tetraheme cytochromes *c* like cytochrome c_{554} (see Section 3.2), the *Shewanella* small tetraheme cytochrome (which was initially also referred to as a cytochrome c_3) (see Section 3.4), or the tetraheme cytochrome of the photosynthetic reaction center.[15] The structure of 4HCc_3TpI is very compact, displays little secondary structure and is dominated by the characteristic heme arrangement where all the closest hemes are perpendicular to each other (Figure 4). Remarkably, 4HCc_3TpIs have a small number of conserved residues, with approximately 20% sequence identity. Nevertheless, they form a very conserved structural family, having an almost identical polypeptide fold and heme core architecture. This is due to the fact that the conserved residues include the 16 that constitute the four hemes binding motifs (2 His and 2 Cys per heme), and the order of these residues in the polypeptide chain is crucial in determining the globular structure of the protein. One of the most important characteristics of cytochromes c_3 is its folding: although it has only few and small secondary structure elements it comprises two domains of approximately the same length (Figure 5). Interestingly, the N-terminal domain has all the ligands of heme 1 and the C-terminal all those of heme 4. Hemes 2 and 3 have ligands from both domains and are nestled in the interdomain region. The resulting tight globular folding is largely controlled by the interwound positioning of the histidinyl ligands in the polypeptide sequence. Another interesting characteristic feature of 4HCc_3TpIs is the presence of the conserved motif CX_2CHH where the two consecutive histidines are axial ligands to hemes 1 and 2, respectively. In addition, two heme-binding sites in 4HCc_3TpIs are unusual in that they have four residues between the two cysteines that bind hemes 2 and 4. However, this is not important for the tetraheme structural motif, since it is not observed in some members of the cytochrome c_3 family (see Section 2.3). A further conserved feature of 4HCc_3TpIs is the presence of a positive surface region surrounding heme 4 that is proposed to be the site of interaction with a negative region of hydrogenase.[16,17]

The 4HCc_3TpI from *D. vulgaris* Hildenborough captures both electrons and protons resulting from the oxidation of

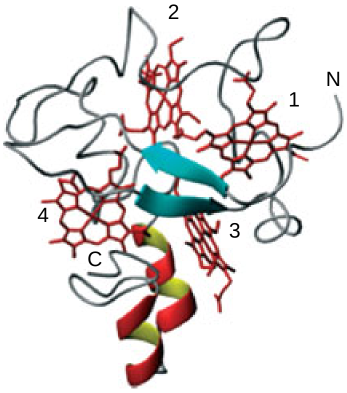

Figure 4 Structure of *D. vulgaris* Hildenborough 4HCc_3TpI (PDB code 2CHT)[18]

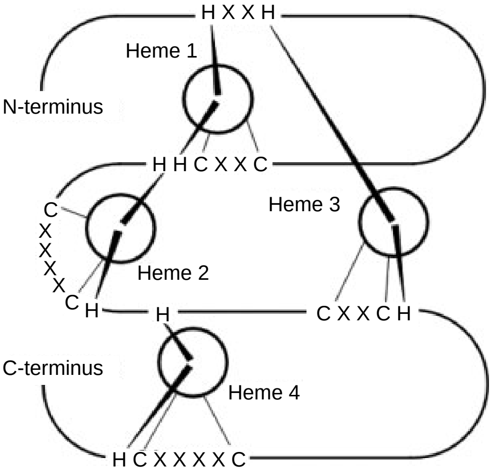

Figure 5 Schematic representation of 4HCc_3TpI, depicting the N- and C-terminal domains, each embedding one of hemes 1 and 4, respectively. The other two hemes are in the groove between the two domains

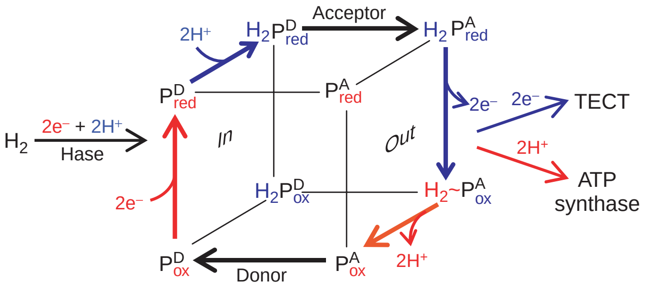

Figure 6 Mechanism proposed for the energy transducing role of 4HCc_3TpI that leads to energy conservation.[14] The cube paradigm, generally accepted to describe this type of activity, is adapted so that the In and Out faces represent the stepwise recognition of the energy transducer protein (P) by the donor (D) and acceptor (A) proteins. These specific recognitions must be redox/protonation state specific in order to avoid short circuits, and warrant vectoriality to the process. Blue (deenergized) and red (energized) are used for comparative purposes

H_2 by hydrogenase,[19] and the heterotropic cooperativities between redox and protic centers, are essential for the electron-to-proton energy transduction role of 4HCc_3TpI (Figure 6).[14] This crucial function involves the electrons and protons produced by oxidation of hydrogen and subsequently given to the cytochrome:: $H_2 \rightarrow 2e^{-*} + 2H^{+} \rightarrow 2e^{-} + 2H^{+*}$, where the asterisks represent energized electrons (i.e. in centers with low redox potential) and energized protons (i.e. bound to protic groups with low pK_a). Thus, acidified protic groups are obtained, as high reducing energy originating from oxidation of hydrogen is transferred via the cytochrome to deenergized redox centers of the acceptor (TETC) (see Section 2.3). Concomitantly, a protic rB center is energized (i.e. acidified). Thus, working as an electro-protonic energy transducer, 4HCc_3TpI performs a ‘proton thrusting’ mechanism that can activate ATP synthase and lead to energy conservation.[19]

Both *D. vulgaris* and *D. gigas* 4HCc_3TpIs receive the two electrons produced by the oxidation of H_2 in a concerted two-electron step, which results from a positive homotropic redox cooperativity between two hemes. Thus, there is a stabilization of the protein states with these two hemes in the same oxidation state and a concerted binding (release) of two electrons. This process cannot be explained by direct electrostatic considerations (Coulomb’s law) that imply a repulsive effect between charges of the same sign. Consequently, this cooperative effect must involve a redox-linked structural modification, such that reduction of one center induces a structural modification, resulting in an overall anti-Coulomb effect.[14] It should be stressed that the structural rearrangement that stabilizes the new conformation need not involve large structural modifications.[20]

Like other low redox potential cytochromes, the 4HCc_3TpIs can catalyze the reduction of several molecules such as sulfur, polysulfides, Fe^{III}, Cr^{VI}, U^{VI}, and other metal oxides. This has been suggested to be a nonspecific property driven by the difference in reduction potential and high exposure of the heme groups in these cytochromes. Moreover, other proteins with redox centers of low potential, like hydrogenase, display the same property,[21] and even hemin has been shown to reduce chromate.[22] However, an NMR study revealed that the binding of the negatively charged $CrO_4{}^{2-}$ to cytochrome c_7 (see Section 2.4) is not unspecific, but occurs close to heme 4, probably due to the positive surface area surrounding this heme.[23] Interestingly, this is the same heme that is proposed to be involved in electron transfer from hydrogenase.

2.2 Dimeric Cytochrome c_3

A dimeric cytochrome c_3 (Di4HCc_3), containing two tetraheme subunits, is also present in some sulfate-reducers, having been isolated from *D. gigas*, *D. africanus*, and *Desulfomicrobium norvegicum*. It is also named as cytochrome c_3 (M_r 26 000) and was previously known as cytochrome cc_3.[24] This cytochrome is a periplasmic homodimer of two 13 500 Da tetraheme subunits, both in *Dsm. norvegicum* and in *D. gigas*. In this last case the two subunits are linked by two disulphide bridges. The reduction potentials of the *Dsm. baculatum* Di4HCc_3 hemes are as low as those of 4HCc_3TpI, in agreement with the bis-histidinyl coordination for the four hemes.

The crystal structures of the Di4HCc_3 from *Dsm. baculatum* and *D. gigas* have been obtained.[25,26] The two structures are very similar and show that each monomer has a polypeptide fold and heme arrangement identical to that observed for 4HCc_3TpIs. The dimer interface is formed by the surface region around heme 1 of each monomer. As in the case of 4HCc_3TpIs the exposed heme 4 is surrounded by a positive surface region.

The physiological role of Di4HCc_3 has not been extensively investigated. However, it has been shown that it can be reduced by the main hydrogenase isolated from the organism (a [NiFe] hydrogenase for *D. gigas* and a [NiFeSe] hydrogenase for *D. africanus* and *Dsm. norvegicum*) in a similar way to 4HCc_3TpI. The *D. gigas* Di4HCc_3 was shown to stimulate the reduction of thiosulfate by a partially purified extract, using H_2/hydrogenase as electron donor, but strangely this was not observed with purified thiosulfate reductase. In the case of *Dsm. norvegicum*, reduction of the Di4HCc_3 by the [NiFeSe] was slower than reduction of the 4HCc_3TpI, indicating that 4HCc_3TpI is the preferred electron acceptor for this hydrogenase. Furthermore, the rate of reduction of the Di4HCc_3 is increased in the presence of small amounts of the 4HCc_3TpI.[27] However, in *D. africanus* the [NiFeSe] hydrogenase displays a lower K_m for reduction of Di4HCc_3 than for reduction of 4HCc_3TpI.[28] Interestingly, analysis of the preliminary genome data available for *D. vulgaris* Hildenborough and *Desulfovibrio desulfuricans* G20 shows that the gene for a Di4HCc_3 homolog is encoded in the same transcription unit as a second [NiFe] hydrogenase isoenzyme. This suggests that in these organisms the Di4HCc_3 is the physiological partner for this hydrogenase. In *D. vulgaris* Hildenborough, the [NiFe] hydrogenase isoenzyme 1 has been well characterized and its physiological partner is the 4HCc_3TpI. The [NiFe] hydrogenase isoenzyme 2 and the Di4HCc_3 have so far not been detected in this organism, suggesting they will be expressed under different conditions to the [NiFe] hydrogenase isoenzyme 1 and the 4HCc_3TpI.

2.3 Membrane-associated Cytochromes

Several multiheme cytochromes of the cytochrome c_3 family are associated with membrane−bound redox complexes. These cytochromes are targeted to the periplasmic side of the membrane as indicated by the presence of signal peptide sequences in the corresponding genes. The strength of their association with the membrane is variable since some can be isolated from the soluble periplasmic fraction. The members of this subgroup are a tetraheme cytochrome known as Type II cytochrome c_3 (4HCc_3TpII), a nine-heme cytochrome c_3 (9HCc_3) and a 16-heme cytochrome c_3 (16HCc_3). The last two cytochromes are composed of tetraheme-like domains with the typical heme arrangement of the cytochrome c_3 family. This suggests they originated from gene duplication events and/or that the tetraheme arrangement found in this family is a structural module with a specialized function shared by the whole family. However, the results so far do not support the latter idea, but rather indicate that the membrane-associated cytochromes do not have the same functional properties as the 4HCc_3TpI and form a separate group that evolved to perform a different function (see below).

The Type II Tetraheme Cytochrome. Type II cytochromes c_3 (4HCc_3TpII) are a second group of tetraheme cytochromes c_3 that have structural, genetic, and reactivity features that distinguish them from the previously characterized 4HCc_3TpIs.[29] *D. africanus* was the first *Desulfovibrio* sp. reported to contain a 4HCc_3TpII, and was referred to as 'acidic cytochrome c_3'.[28,30] A homolog of this cytochrome was later characterized from *D. vulgaris* Hildenborough, and a 4HCc_3TpII is also encoded in the genome of *D. desulfuricans* G20. The nomenclature of 'acidic' and 'basic' cytochromes c_3 is not appropriate, since 4HCc_3TpIs can have low pIs (e.g. 4HCc_3TpI from *D. gigas*) and 4HCc_3TpIIs may be not very acidic.

The macroscopic reduction potentials of the *D. vulgaris* Hildenborough 4HCc_3TpII hemes (−170, −235, −260, and −325 mV) are similar to those commonly observed for the 4HCc_3TpIs. In the case of the *D. africanus* 4HCc_3TpII, the four reduction potentials obtained by cyclic voltammetry were quite close (−210, −240, −260, and −270 mV).

Comparison of the crystal structure of the *D. africanus* 4HCc_3TpII[31] with a theoretical model for the structure of the *D. vulgaris* Hildenborough cytochrome shows that, although its four-heme arrangement is identical, and the overall protein fold is similar to 4HCc_3TpI, it displays some localized differences that can affect the heme's reactivity, reflecting a different physiological role. The 4HCc_3TpII cytochromes lack the characteristic positive surface region around heme 4, proposed to be the site of interaction and electron exchange with a negatively charged region of the redox partner hydrogenase. In addition, 4HCc_3TpIIs have a more exposed heme 1 that is surrounded by a negative surface region, indicating that this may be the heme involved in electron transfer with the physiological partner. In fact, the rate of reduction of the 4HCc_3TpIIs by hydrogenase is stimulated by catalytic amounts of 4HCc_3TpI. Thus, although the four-heme structural motif is conserved in both the 4HCc_3TpI and 4HCc_3TpII, they have different properties that are the result of only small structural differences, and have evolved to perform different physiological functions. All of the heme-binding sites present in the 4HCc_3TpII display the typical motif CXXCH, whereas a characteristic of 4HCc_3TpIs is the presence of one or more heme-binding sites with four residues between the two cysteines (CX$_4$CH).

The gene coding for the *D. vulgaris* Hildenborough 4HCc_3TpII is part of an operon with genes coding for two other proteins that are related to predicted proteins of the 9HCc_3 and 16HCc_3 operons. One of them is an integral membrane protein that belongs to the family of heme *b*-containing subunits of respiratory complexes, which are involved in electron transfer with the membrane quinone pool. The other is a hydrophilic protein, probably located in the cytoplasmic face of the membrane that is related to the catalytic subunits of heterodisulfide reductases present in methanogenic archaea. It contains two [4Fe4S] centers and a conserved five-cysteine motif that has been proposed to bind another iron−sulfur center, responsible for reduction of the heterodisulfide of CoM and CoB to the corresponding thiols.[32] Thus, this operon encodes a transmembrane protein complex with redox centers in the periplasm, membrane, and cytoplasm, which is likely to have a role in the respiratory electron transfer (Figure 7). Such a complex is also encoded in the genome of *D. desulfuricans* G20, and in the case of *D. africanus* the partial sequence available reveals an incomplete open reading frame upstream of the TpII-c_3 gene encoding a FeS protein homologous to the one found in the *D. vulgaris* Hildenborough genome. The *D. vulgaris* Hildenborough 4HCc_3TpII cannot be detected in the soluble fraction indicating it has a strong association with the membrane complex, in contrast to the corresponding cytochrome from *D. africanus*, which was isolated as a soluble protein. Nevertheless, *D. vulgaris* Hildenborough 4HCc_3TpII is also a hydrophilic protein with no membrane-associated domains, that remains soluble after the detergent is removed.

The Nine-heme Cytochrome c_3. The nine-heme cytochrome c_3 (9HCc_3), originally reported to contain 12 hemes, was referred to as the dodecaheme cytochrome c.[34] Only when its structure became available was the correct number of hemes established as nine.[35] This cytochrome of 37.8 kDa has been isolated from *D. desulfuricans* strains ATCC 27774

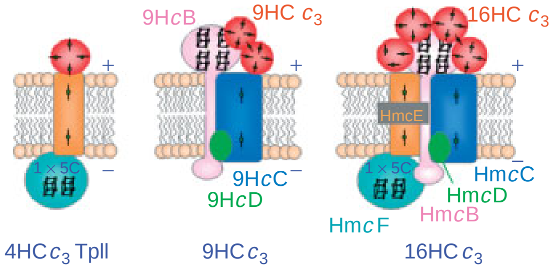

Figure 7 Schematic representation of the membrane-bound complexes associated with 4HCc_3TpII, 9HCc_3, and 16HCc_3 as deduced from sequence data.[33] Related subunits are in similar colors

and Essex, which are sulfate-reducing bacteria that can also use nitrate as electron acceptor.[36] The structure shows that this cytochrome has two tetraheme motifs similar to those of cytochrome c_3, with an extra heme located between the two (Figures 2 and 8). The N-terminal motif contains hemes 1, 2, 3, and 5 and heme 4 is the isolated heme. The two tetraheme regions display some of the characteristics of the 4HCc_3TpII cytochrome, including all of the heme-binding sites of the form CXXCH, an exposed first heme surrounded by a negative surface charge, and a heme that corresponds to 4HCc_3TpI heme 4 in the C-terminal domain (heme 9), that lacks the positive surface charge. The structure of the reduced form shows significant changes surrounding hemes 1 and 4, and thermodynamic simulations indicate that the hemes belonging to the N-terminal domain have, in general, a lower redox potential than those found in the C-terminal domain, suggesting electrons will flow from the former to the latter.[37]

Like the 4HCc_3TpII, 9HCc_3 from *D. desulfuricans* 27774 can be reduced by hydrogenase but this reduction is faster in the presence of catalytic amounts of 4HCc_3TpI. Modeling studies indicate a specific interaction between the negative 9HCc_3 N-terminal region surrounding hemes 1 and 2 and the positive heme 4 region of 4HCc_3TpI.[38]

The 9HCc_3 sequence is similar to the C-terminal region of the high molecular mass cytochrome c_3 16HCc_3 (see below), and the 9HCc_3 gene is the first of an operon (*9hc*) encoding three other proteins that have a strong similarity to predicted proteins of the 16HCc_3 operon.[39] They are an integral transmembrane subunit possibly containing hemes *b* (similar to HmcC), a small membrane subunit (similar to HmcD) and a periplasmic subunit with binding sites for four [4Fe4S] clusters (similar to HmcB) (Figure 7). Thus, the *9hc* operon encodes a membrane-bound redox complex and given the similarity between 9HCc_3 and the two C-terminal domains of 16HCc_3 it is likely that the 9Hc complex replaces the Hmc complex in *D. desulfuricans* 27774, as also suggested by the fact that the 16HCc_3 is not detected in this organism. Expression of the *9hc* operon in *D. desulfuricans* 27774 is higher on sulfate than on nitrate, in agreement with a possible role of this complex as a substitute for the Hmc complex in electron transport to the reduction of sulfate. The 9HCc_3 cytochrome can be found both in the soluble and in the membrane fraction indicating that it may dissociate from the 9Hc complex.

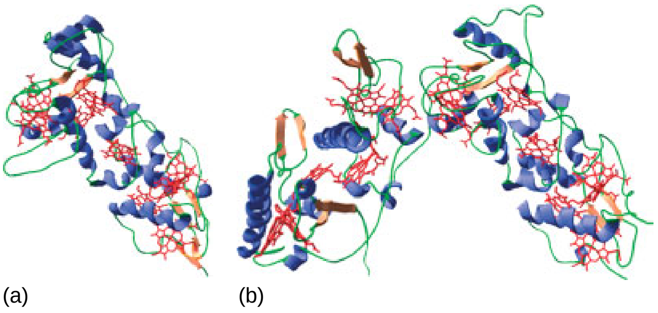

Figure 8 (a) Structure of 9HCc_3 from *D. desulfuricans* ATCC 27774 (PDB code 19HC).[35] (b) Structure of 16HCc_3 from *D. vulgaris* Hildenborough (PDB code 1H29)[33]

The Sixteen-heme Cytochrome c_3. The high molecular mass cytochrome c_3 (16HCc_3) is the largest in the cytochrome c_3 family, containing 16 hemes *c* and a mass of around 65 kDa. It is the cytochrome with the highest number of hemes in a single polypeptide known so far. 16HCc_3 may be isolated as a soluble protein from *D. vulgaris* Hildenborough, *D. vulgaris* Miyazaki, and *D. gigas*, but it is found in higher amounts in the membrane fraction. The presence of high-spin heme(s) in both oxidized and reduced form of 16HCc_3 was detected by visible, EPR, and Mössbauer spectroscopies.[40] In *D. vulgaris* 16HCc_3, the reduction potentials of the 16 hemes span a large range and can be roughly divided into three groups: 4 to 5 hemes have redox potentials of −30 to −100 mV, 3 to 4 hemes around −170 mV and 7 to 8 hemes −250 to −280 mV. Several of these reduction potentials are strongly pH dependent. The 16HCc_3 cytochrome is only very slowly reduced by the hydrogenases but, like the other membrane-associated cytochromes 4HCc_3TpII and 9HCc_3, its rate of reduction is stimulated by addition of catalytic amounts of 4HCc_3TpI.

The structure of the *D. vulgaris* Hildenborough 16HCc_3 is organized in four tetraheme cytochrome c_3-like heme motifs (Figures 2 and 8).[33,41] The first motif is incomplete and contains only three hemes, and the final two, including an isolated heme connecting them, show great similarity to the 9HCc_3 from *D. desulfuricans*. The four motifs are spatially arranged in two different regions: an N-terminal region that comprises the first two cytochrome c_3-like motifs, and a C-terminal region that is similar to 9HCc_3. These two elongated regions are at an angle thus giving the 16HCc_3 molecule the shape of a stretched ‘V’. An interesting aspect of 16HCc_3 is that the heme groups of the N-terminal region are not positioned according to their order in the sequence. Thus, the N-terminus and heme 1 are not present at one extremity of the molecule, but in the region between the first two motifs, and heme 4 (the first heme of the second motif) is placed between the second and third tetraheme motifs, whereas it is heme 7 that is closest to the first motif (Figure 2). This situation is not found in the C-terminal 9HCc_3-like region in which the hemes are found according to their order in the sequence (with the exception of the isolated heme 11) with heme 16 located at the C-terminus extremity. This peculiar heme arrangement of the 16HCc_3 N-terminal region results in a symmetry between the two regions, with hemes equivalent to cytochrome c_3 heme 4 (16HCc_3 hemes 3 and 16) at each extremity of the molecule and with hemes equivalent to cytochrome c_3 heme 1 (16HCc_3 hemes 4 and 8) at the V-angle. The four-heme cytochrome c_3-like regions of 16HCc_3 have more similarities with 4HCc_3TpII than with 4HCc_3TpI, and all of the heme-binding sites are of the CXXCH form. The first heme motif is missing heme 2 of tetraheme cytochromes c_3, and for this reason has been considered to be similar to cytochrome c_7 (3HCc_3) (see Section 2.4). However, this first motif is considerably larger than 3HCc_3 and indeed resembles more the tetraheme cytochrome c_3 fold, particularly that of 4HCc_3TpII than that of the triheme cytochrome (which is not surprising considering that 3HCc_3 is present in phylogenetically more distant bacteria). The C-terminal region is strikingly similar to the 9HCc_3 structure, including the isolated heme between the two tetraheme domains, heme 11 in 16HCc_3. The main difference is that heme 15 (heme 8 of 9HCc_3) is only coordinated by one axial ligand and is the high-spin heme of 16HCc_3. The histidine that binds heme 8 in 9HCc_3 is replaced by an isoleucine, which is positioned in van der Waals contact distance to the heme iron. The presence of a high-spin heme is suggestive of a substrate-binding site and an enzymatic activity. However, no enzymatic activity has yet been found for 16HCc_3. Furthermore, binding of a substrate would require a considerable conformational change to expose the free iron coordination site. The fact that 9HCc_3 has no high-spin heme also argues against an enzymatic activity of 16HCc_3 and it is possible that heme 15 may have lost its His ligand without affecting the physiological function. The presence of such a high-spin heme in a cytochrome is also observed in cytochrome c_{554} (see Section 3.2).

The gene for 16HCc_3, named *hmcA*, was cloned in *D. vulgaris* Hildenborough and found to be part of a large operon (the *hmc* operon) encoding a transmembrane complex of six proteins, having redox centers in the periplasm, membrane, and cytoplasm (Figure 7).[42] The 16HCc_3 is a periplasmic hydrophilic cytochrome with no transmembrane helices and its association with the membrane probably occurs *via* interaction with the other proteins in the complex. The gene *hmcB* encodes a transmembrane protein with a periplasmic hydrophilic N-terminal domain containing four [4Fe4S] cluster binding motifs and a cytoplasmic C-terminal tail; *hmcC*, *hmcD*, and *hmcE* encode integral membrane proteins, of which HmcC and HmcE may bind hemes *b*, and *hmcF* encodes a cytoplasmic protein having two [4Fe4S] cluster binding motifs, that is related to the catalytic subunits of heterodisulfide reductases. This complex has been proposed to be an important component in the sulfate respiratory chain by performing the electron transfer between periplasmic hydrogen oxidation and cytoplasmic sulfate reduction. Evidence for such a role of the Hmc complex could be found in the case where hydrogen is used as sole energy source. Indeed, expression of the *hmc* operon increases when hydrogen is used as electron donor when compared to either lactate or pyruvate.[43,44] In *D. vulgaris* Hildenborough, the *hmc* operon is adjacent to two genes (*rrf1* and *rrf2*) encoding expression regulating proteins. A mutant containing a deletion of the *rrf1* and *rrf2* genes overexpresses the *hmc* operon three times, and grows faster than the wild type on hydrogen but slower on lactate.[43] A second mutant, in which the *hmc* operon is deleted, grows normally with either lactate or pyruvate as electron donor, and can still grow with hydrogen as sole energy source, but with a slower rate than the wild type.[45] These results implicate the Hmc complex in the metabolism of hydrogen but not of lactate, and support the proposal that it is involved in the transfer of electrons from periplasmic hydrogen oxidation to the cytoplasmic reduction of sulfate. The fact that deletion of the *hmc* operon in *D. vulgaris* Hildenborough does not prevent growth on hydrogen indicates that there are other proteins that can fulfill the same role, and a likely candidate is the complex associated with the 4HCc_3TpII.

2.4 Cytochrome c_7

Cytochrome c_7 (3HCc_3) is the only member of the cytochrome c_3 family that is not present in sulfate-reducing bacteria. It is found in members of the *Geobacteraceae* like the marine *Desulfuromonas acetoxidans*, *Geobacter metallireducens*, and *Geobacter sulfurreducens*, all of which perform dissimilatory Fe^{III} reduction.[46,47] It is a periplasmic cytochrome of about 9 kDa containing three hemes *c*, with bis-histidinyl coordination and redox potentials of −140, −210, and −240 mV. The structure of the *D. acetoxidans* 3HCc_3 has been obtained both by NMR[48] and X-ray crystallography.[49] The overall protein fold and heme arrangement of this cytochrome is similar to cytochromes c_3, but it lacks the heme corresponding to heme 2 in these cytochromes (Figure 2). As in 4HCc_3TpIs, there is a region of positive surface charge surrounding heme 4, suggesting a similar mode of reactivity involving this heme. 3HCc_3 can be reduced by a recently identified hydrogenase from *D. acetoxidans*,[50] and also by *Desulfovibrio* hydrogenases. However, this cytochrome has different kinetic and thermodynamic properties from 4HCc_3TpIs, and does not present a redox-Bohr effect or perform a concerted two-electron step.[51]

The physiological function of 3HCc_3 is not completely established. The cytochrome from *D. acetoxidans*, has a high polysulfide reductase activity and was therefore proposed to act as the terminal reductase when this bacterium is growing with elemental sulfur as electron acceptor.[52] It also displays high activity in the reduction of several metal oxides (see Section 2.1), suggesting a possible direct role in the dissimilatory reduction of metals, although the periplasmic location of 3HCc_3 precludes such a role in the case of insoluble metal oxides. In *G. sulfurreducens* a knockout mutant of the 3HCc_3 homolog (designated by PpcA) is affected in the reduction of Fe^{III}, U^{VI}, and anthraquinone 2,6-disulfonate (a humic acid analog) with acetate, but not with hydrogen, as the electron donor.[53] The acetate-dependent reduction of fumarate is also not affected. The results indicate that the triheme cytochrome is involved in electron transfer across the periplasm to the reduction of Fe^{III} by proteins in the outer membrane, but may be directly involved in periplasmic reduction of U^{VI} and antraquinone 2,6-disulfonate. The periplasmic location of hydrogenase overcomes the need for electron transfer across the periplasm, explaining why the PpcA mutant is not affected in growth with hydrogen.

3 THE HYDROXYLAMINE OXIDOREDUCTASE FAMILY

HAO is the largest member of the family of multiheme *c* proteins that share a similar superheme structural motif characterized by stacked diheme pairs generally interconnected by perpendicular heme arrangements. The members of this family show no apparent sequence identity or overall structural similarity, but there is local similarity in the polypeptide fold surrounding the hemes. This group includes both enzymes and electron transfer proteins, and the cases that have been more thoroughly investigated and for which there is structural information available will be discussed in particular. For two of the cases presented, the catalytic subunit is actually a multiheme *c* protein: HAO and cytochrome *c* nitrite reductase, which, interestingly, both act on nitrogen oxide compounds. In the two cases the electron donor/acceptor is also a multiheme *c* protein. There are also several examples of enzymes in which the catalytic subunit does not contain hemes *c*, but these are found in an electron transferring subunit, as in NapB subunit of the periplasmic nitrate reductase. In other cases, the multiheme *c* domain is actually fused to the catalytic domain, as in the case of the flavocytochrome *c* fumarate reductase.

3.1 Hydroxylamine Oxidoreductase

HAO catalyzes the four-electron oxidation of hydroxylamine to nitrite.[54] It is present in autotrophic nitrifying bacteria, like *Nitrosomonas*, which are obligate chemolithotrophs that use the oxidation of ammonia as their sole energy source.[55] For each cycle of hydroxylamine oxidation, two electrons are returned for the initial step of ammonia oxidation and the other two are either transferred to the terminal oxidase *via* the components of the respiratory chain, or used to generate NADH by reverse electron transport.

HAO from *Nitrosomonas europaea* is a homotrimer of 64 kDa subunits that is located in the periplasm. Each subunit contains eight hemes *c*, bound by typical CXXCH motifs. The catalytic heme has a third covalent bond to the protein between the 5-meso carbon of the porphyrin and the Cε1 ring carbon of tyrosine467 from a different subunit, thus providing the cross-link covalent attachment of the three subunits.[56,57] This heme has a Soret band at 463 nm in the reduced form, and is designated by heme P460.

The gene coding for HAO is expressed as a monocistronic transcript. There are three widely separated copies of this gene in the *N. europaea* genome, which are identical except for one nucleotide difference in one gene copy.[55] Mutants with any one copy of *hao* disrupted, or double mutants, show no growth differences to the wild type.[58] The nucleotide sequences of the two hao_1 and hao_2 gene copies are nearly identical for 160 bp upstream of the start codon, which includes the transcription start sites. The nucleotide sequence of the hao_3 gene copy diverges from the other two 15 bp upstream of the start codon.

The crystal structure of HAO has been determined.[57] The three subunits form a conical structure at the bottom of which a cavity is formed. There is also a cleft between the subunits that is negatively charged, and is proposed to be the docking site for the electron acceptor, cytochrome c_{554}, which is positively charged. Each subunit has three domains: the N-terminal domain contains hemes 1–3 and 5; the central domain is dominated by long α-helices and includes heme 8, while hemes P460 (heme 4), 6 and 7 are located in a pocket between these first two domains; the C-terminal domain is flexible and is not resolved in the electron density map. All *c*-type hemes have bis-histidinyl coordination, and heme P460 is five coordinate. The 24 hemes of the HAO trimer are in close contact to each other (Fe–Fe distances less than 12.8 Å) forming a circular structure. The three P460 hemes are located above a ring formed by 18 *c* hemes (all except the three hemes 1, which are not part of the ring). The hemes in each subunit are organized in three clusters showing parallel arrangements and an isolated heme (heme 8). In the triheme cluster formed by hemes P460, 6 and 7, hemes 6 and 7 form a typical parallel stacking motif, whereas hemes P460 and 6 are antiparallel (Figure 3). The two other clusters, formed by the diheme pairs 1/2 and 3/5, present also a parallel stacking motif. An interesting feature of HAO, observed in other multiheme proteins like the NrfA nitrite reductase or the small tetraheme cytochrome of *Shewanella* sp. is that the parallel motifs are connected by perpendicular motifs (see Section 1), formed by the heme pairs 2/3, 5/6, and 7/8 (Figure 3).

The peculiar heme arrangement of HAO is proposed to be linked to the two two-electron oxidation steps of hydroxylamine (NH_2OH) with HNO as an enzyme-bound intermediate.[54] The cross-linkage of heme P460 with Tyr467 may allow these two components to remove two electrons from NH_2OH, which will be transferred to the 6/7 heme pair and successively to the pairs 5/3 and 2/1. Heme 1 is exposed to the solvent at the negatively charged cleft where cytochrome

c_{554} is proposed to bind, and may thus be the electron exit heme. Cytochrome c_{554} also has two coplanar diheme pairs, which may indicate that it can also accept two electrons simultaneously. This cytochrome then transfers electrons to the membrane-bound tetraheme cytochrome c_{m552} (see Section 4), which is a good candidate to reduce the membrane ubiquinone pool, from where electrons are partitioned between the ammonia monooxygenase reaction, the aerobic respiratory chain, and reverse electron transport.[59]

The redox and spectroscopic properties of HAO have been closely investigated.[54] The EPR spectrum of HAO displays three types of signals, and show that four of the hemes are magnetically isolated and noninteracting, two hemes are weakly spin-coupled, and the remaining pair of hemes (which includes the high-spin heme P460) are exchange-coupled and give an integer-spin resonance. The EPR signals have been attributed to the hemes in the structure, with the pair P460/6 originating the strongly exchange-coupled signal, the pair 3/5 the weakly spin-coupled signal, and the hemes 1, 2, 7, and 8 the magnetically isolated heme signal.[60] Thus, magnetic heme interactions are only observed for the parallel heme pairs and not the perpendicular ones. Apparently the pair 1/2 does not present an exchange interaction, although it has a parallel arrangement similar to the pair 3/5. However, it may have an isotropic exchange coupling, in which case the signal is indistinguishable from the mononuclear species. The observed exchange interactions are probably derived from direct electronic overlap of the porphyrin orbitals in the stacked hemes. Interestingly, heme coupling in HAO is weaker than that observed for both cytochrome c_{554} and the NrfA nitrite reductase, although all the hemes in these two proteins can be spatially overlaid to equivalent ones of HAO (Figure 3).

3.2 Cytochrome c_{554}

The periplasmic cytochrome c_{554} is the electron acceptor for HAO. It is a monomeric protein of 25 kDa that binds four c-type hemes.[61] Its crystal structure is mainly α-helical, and has been determined for both oxidation states.[11,12] Three of the hemes have bis-histidinyl coordination (hemes 1, 3, and 4) and heme 2 is five coordinate and high spin. Heme 1 is unusual since it is the first example of a heme iron coordinated by the N_δ atom of a histidine. The macroscopic redox potentials of hemes 1 to 4 are $+47$, $+47$, -147, and -276 mV, respectively.[62] The four hemes of cytochrome c_{554} have a structural arrangement identical to hemes 3–6 of HAO, and hemes 2–4 of cytochrome c_{554} are equivalent to hemes 1–3 of NrfA (Figure 3). This similarity is also extended to the polypeptide chain surrounding the hemes, despite no obvious sequence similarity between these proteins. The four hemes are organized in two diheme pairs with a stacked parallel arrangement (hemes 1/3 and 2/4) perpendicular to each other. As observed for HAO, the hemes in each parallel pair are spin-coupled but there is no detectable magnetic interaction between the perpendicular hemes.[62] Treatment of cytochrome c_{554} with HAO and hydroxylamine results in reduction of two hemes,[63] supporting the idea that these two proteins perform two-electron transfer steps.

The presence of a high-spin heme in cytochrome c_{554} suggests the possibility of a catalytic function for this protein. However, this heme does not bind small ligands such as CN^-, F^-, CO, or NO in a pH range of 4–10,[62] and there is no evidence for a catalytic activity for this cytochrome. The crystal structure shows that the vacant coordination position of heme 2 is shielded from binding an exogenous ligand by the presence of three residues, Thr154, Pro155, and Phe156. The unusual presence of a high-spin heme in an electron transfer protein is also observed in the case of the sixteen-heme high molecular mass cytochrome from *Desulfovibrio* spp. (see Section 2.3).

There are three copies of the *hcy* (or *cyc*) gene coding for cytochrome c_{554}, each located 1,162-bp downstream of each copy of *hao*.[55] Two of the copies have been sequenced and are identical. The membrane-bound cytochrome c_{m552} (see Section 4) is encoded by genes contiguous with two of the three copies of *hcy*, but this does not happen for the third copy. It is likely that cytochrome c_{m552} is cotranscribed with cytochrome c_{554} and acts as its electron acceptor.

3.3 Cytochrome *c* Nitrite Reductase

There are four different types of nitrite reductases: the copper-containing protein ***Copper Enzymes in Denitrification*** and cytochrome cd_1 perform a one-electron reduction of nitrite to nitric oxide, and are involved in denitrification;[64–67] the siroheme-containing protein and the cytochrome c nitrite reductase (cNiR)[68,69] both perform the complete, six-electron reduction, of nitrite to ammonia. The cNiR is present in the γ, δ or ε-subclasses of proteobacteria, and is encoded by the *nrf* operon (*n*itrite *r*eduction with *f*ormate), which has different gene composition in the different classes of bacteria,[68] having in common only the gene for the catalytic subunit, *nrfA*.

In the γ-proteobacteria (like *E. coli* or *Haemophilus influenzae*), the *nrf* operon has the structure *nrfABCDEFG*, where NrfB is a periplasmic pentaheme cytochrome that probably acts as electron donor to NrfA, and NrfC a periplasmic iron–sulfur protein that together with the membrane-bound NrfD acts as a quinol oxidase to transfer electrons to NrfB.[70] The products of the *nrfEFG* genes form a NrfA-specific heme lyase required for attachment of a heme group to the active site.[71] In the ε-proteobacteria (e.g. *Wolinella succinogenes* or *Sulfurospirillum deleyianum*), the *nrf* operon includes *nrfHAIJ*, in which NrfH is a membrane-anchored tetraheme cytochrome that transfers electrons directly from the quinol pool to NrfA,[72] and NrfHI are involved in the heme attachment to the active site.[73] In the δ-proteobacteria (e.g. *D. vulgaris* or *G. sulfurreducens*), no accessory genes are present in the operon that is formed only by *nrfAH*.

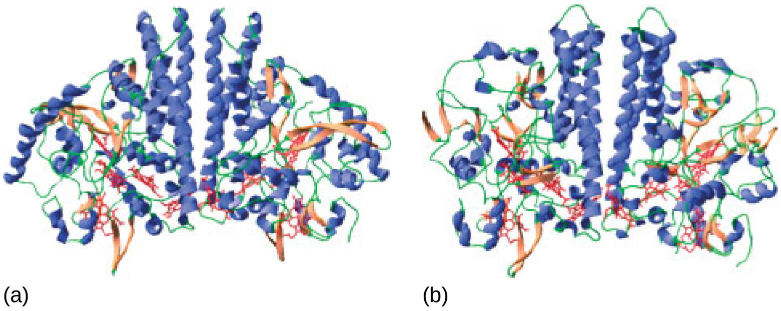

Figure 9 Structure of NrfA dimer from (a) *Wolinella* succinogenes (PDB code 1FS7)[76] and (b) *D. desulfuricans* ATCC27774 (PDB code 1OAH)[78]

NrfA is a 55–65 kDa protein that for a long time was considered to bind six hemes *c*: There are a great deal of spectroscopic data on this protein interpreted on the basis of this assumption! When the sequence of the *E. coli* enzyme became available, it revealed the presence of four typical heme *c* binding sites (CXXCH),[74] and an unconventional motif with a lysine replacing the histidine (CXXCK), later shown to bind a fifth heme.[71] NrfA is thus a pentaheme cytochrome and the unusual lysine-bound heme is the high-spin catalytic site. There are now several crystal structures available for NrfA from several organisms,[75–78] all of which show a very conserved arrangement of the five hemes. In all cases, the protein crystallizes as a homodimer, and the hemes in each monomer are in close contact allowing electron transfer between the monomers. The dimer is stabilized by the presence of long α-helices that interact across the dimer interface (Figure 9a). Despite a relatively low sequence identity, the polypeptide fold of the *S. deleyianum*, *W. succinogenes*, and *E. coli* NrfA are very similar, whereas that for *D. desulfuricans* ATCC 27774 shows more differences (Figure 9b). In all structures, hemes 2–5 are bis-histidinyl coordinated, and heme 1 is coordinated by a lysine with the other site being available to bind an external ligand. There are two conserved calcium ions, one near the active site and a second one coordinated by the propionates of hemes 3 and 4, and it has been shown that calcium is required for maximal activity of NrfA.[79] Another common feature of all the structures is the presence of two channels that lead from the surface to the active-site heme: a positively charged channel that is a putative inlet pathway for nitrite, and a negatively charged one that is a putative exit pathway for ammonia.

The five-heme groups in the NrfA monomer are tightly packed together on one side of the molecule with Fe–Fe distances of less than 12.8 Å. All the hemes are involved in the heme pair arrangements found in other multiheme proteins. The hemes 1, 3, and 4 are in parallel planes, forming two pairs of stacked hemes (1/3 and 3/4). The pairs 2/3 and 4/5 form diheme elbow motifs where the heme planes are almost perpendicular to each other. All of the hemes in NrfA can be superimposed on hemes 4 to 8 of HAO, including the two high-spin catalytic hemes (1 in NrfA and 4 in HAO) (Figure 3).

The solvent-exposed heme 2 is surrounded by a surface area of positive electrostatic potential, proposed as the site of interaction of the *S. deleyianum*, *W. succinogenes*, and *D. desulfuricans* NrfA with the physiological partner NrfH. In *E. coli*, NrfA has a different physiological partner, NrfB, and this correlates with some differences observed in the area around heme 2, that is, a more acidic surface region and a seven-residue insertion, only observed in the sequence of NrfA from organisms that have a *nrfB* rather than a *nrfH* gene in the *nrf* operon.

The NrfA protein is isolated in distinct forms from different groups of proteobacteria. In the γ-proteobacteria (like *E. coli*), NrfA is purified as a single protein either from the periplasm or from the membrane fraction and there is no evidence for the formation of a stable complex with its electron donor NrfB. In the ε-proteobacteria, such as *W. succinogenes* and *S. deleyianum*, NrfA can be isolated either as a soluble protein from the periplasm, or in the form of a complex with NrfH from the membrane fraction. In the δ-proteobacteria, such as *D. desulfuricans* and *D. vulgaris*, it can only be isolated from the membranes in the form of a tight complex with NrfH, which can only be dissociated in the two subunits in the presence of denaturing agents.[80,81]

The *c*NiR has been extensively investigated by spectroscopic techniques, including EPR, MCD, and Mössbauer. This enzyme has quite interesting spectroscopic features owing to the presence of magnetic interactions between the hemes. However, many of these studies are hampered by the fact that their interpretation was performed before it was known that NrfA contains five hemes and/or that NrfA is present in a complex with the tetraheme cytochrome NrfH. Recent analysis of the NrfA spectroscopic properties have overcome these problems.[77,81]

NrfA catalyzes the final step of the respiratory chain in dissimilatory nitrite ammonification. Proteoliposomes containing the formate dehydrogenase, menaquinone, and NrfAH complex from *W. succinogenes* catalyze electron transport from formate to nitrite, which is associated with the development of an electrochemical proton potential across the membrane.[72] However, oxidation of a menaquinol analog by nitrite does not generate a membrane potential, indicating that the site of energy conservation is the formate dehydrogenase. Further than the six-electron reduction of nitrite to ammonia, NrfA also catalyzes the five-electron reduction of nitric oxide and the two-electron reduction of hydroxylamine, both of which are possible intermediates in the reduction of nitrite, as well as the six-electron reduction of sulfite to sulfide.[82] A detailed mechanism has been proposed for the reduction of nitrite,[83] and the reduction of both nitrite and hydroxylamine have been probed by protein film voltammetry.[84] Interestingly, the ability of NrfA to reduce nitric oxide may have an important role in the survival of several enteric pathogenic bacteria to this toxic agent.[85] There is also evidence that in these bacteria the *c*NiR works in coordination with the periplasmic nitrate reductase, Nap, which is responsible for the reduction of nitrate when low levels of nitrate are available, for example, in body fluids.[66] The two systems (*c*Nir and Nap) have similar transcriptional regulation and may form a multimeric complex in the periplasm.

The *c*NiR has also been proposed to have a role in the detoxification of nitrite, since it is present in organisms that cannot use this compound for growth, but where it has a role in preventing growth inhibition by nitrite.[80,86]

3.4 Flavocytochrome *c* Fumarate Reductase and *Shewanella* Small Tetraheme Cytochrome

Flavocytochrome Fumarate Reductase. The flavocytochrome fumarate reductase (Ffr) is a soluble periplasmic protein from *Shewanella* spp. that reduces fumarate but does not oxidize succinate, in contrast to the membrane-bound fumarate reductases that are related to succinate dehydrogenases, and transfer electrons from quinol to fumarate. It is a monomeric protein of 63.8 kDa that is composed of three domains. The N-terminal domain contains four *c*-type hemes, and the flavin domain contains noncovalently bound FAD and is related to flavoprotein subunits of membrane-bound fumarate reductases and succinate dehydrogenases. There is also a third domain in the flavocytochromes that has considerable flexibility and may be involved in controlling access of substrate to the active site. The macroscopic redox potentials of the four hemes of Ffr are −102, −146, −196, and −238 mV, while that of FAD is −152 mV.[87] The low redox potential of FAD in Ffr compared to that in membrane-bound fumarate reductase (−55 mV)[88] may explain why it is unable to oxidize succinate.

The physiological electron donor of Ffr is likely to be the membrane-anchored tetraheme cytochrome CymA (see Section 4), since a soluble form of this cytochrome can transfer electrons efficiently to Ffr.[89] In *S. frigidimarina* (formerly *S. putrefaciens* NCIMB400), the Ffr gene is expressed under microaerobic and all anaerobic growth conditions. A null mutant lacking this enzyme is unable to grow anaerobically with fumarate, indicating that this protein is the physiological fumarate reductase.[90] However, a second tetraheme cytochrome similar to Ffr is induced during growth of this bacterium in the presence of Fe^{III}, and was named Ifc for iron-induced flavocytochrome.[91] Although Ifc does have a high fumarate reductase activity it is not expressed during growth with fumarate, during microaerobic growth or anaerobic growth with electron acceptors other than Fe^{III}. The physiological role of Ifc is proposed to be the electron transport to soluble Fe^{III} compounds. A mutant strain deficient in this cytochrome can still grow with Fe^{III} but this leads to overexpression of soluble and membrane-bound *c*-type cytochromes.

The crystal structures of Ffr from two *Shewanella* spp. and Ifc have been determined and are very similar to each other.[92–94] The FAD domain of these flavocytochromes has significant structural similarity to other FAD-binding proteins. The heme-binding domain shows very little secondary structure. All of the hemes are coordinated by two histidines and are in close distance to each other. Hemes 1 and 2 are positioned in a perpendicular motif, whereas hemes 2 and 3 are in a parallel stacked motif. These three hemes can be superimposed to hemes 5–7 of HAO and 2–4 of NrfA (Figure 3). Heme 4 of Ffr is deviated from the corresponding heme 8 position in HAO, because it is oriented toward the FAD group.

The structural similarity of the flavin domain and the conservation of a few residues of the active site in soluble and membrane-bound fumarate reductases suggest a common catalytic mechanism for these enzymes.[93] A series of studies involving site-directed mutagenesis have helped to elucidate this mechanism (for a recent reference see Ref. 95). A key arginine residue acts as the active-site catalyst by acting both as a Lewis acid (stabilizing a negative charge in the transition state) and a Brønsted acid (delivering a proton to the substrate).[96,97]

Shewanella Small Tetraheme Cytochrome. The small tetraheme cytochrome (Stc) isolated from *Shewanella* spp. has this designation owing to the fact that it is the smallest tetraheme cytochrome *c* known to date, having only 86 residues and a molecular mass of 11.8 kDa. This cytochrome was initially designated as a cytochrome c_3, but determination of the elongated heme core architecture by NMR revealed that it is completely different from the globular one found in the cytochrome c_3 family, as expected from a primary sequence alignment that depicts quite different motifs for the residues that bind hemes 2 and 3, which are essential for the globular folding of cytochrome c_3 (Figure 5).[98] The Stc is encoded by the monocistronic gene *cctA*, and is involved in periplasmic electron transfer of the respiratory chain when Fe^{III} is the terminal electron acceptor. A mutant strain lacking this cytochrome shows no difference relative to the wild type in aerobic growth, or anaerobic growth in the presence of other electron acceptors, but respiration with Fe^{III} as electron acceptor is severely, although not completely, impaired.[99]

The crystal structure of *Shewanella oneidensis* MR-1 Stc has been determined, both in oxidized and reduced forms.[100] The heme structural arrangement is similar, but not identical, to that observed in *Shewanella* Ffr, with the main difference being heme 4, which is oriented toward the FAD group in Ffr (Figure 3). The hemes in Stc show the typical diheme arrangement of this family, with the pairs 1/2 and 3/4 in a perpendicular orientation and the pair 2/3 in a parallel stacked motif. Hemes 1 to 4 of the Stc can be superimposed on hemes 5–8 of HAO and 2–5 of NrfA. Reduction induces small changes in the position of several residues, resulting in decreased solvent exposure of the hemes and removal of the single positive charge from the molecular surface. The surface charge of *S. oneidensis* MR-1 Stc is mainly negative but homogeneous, with no obvious binding sites for redox partners. In the *S. frigidimarina* Stc, the pH dependence of the microscopic heme redox potentials is small.[101]

3.5 Split-Soret Cytochrome and NapB

Split-Soret Cytochrome. The split-Soret cytochrome (Ssc) and NapB proteins have no relationship except the fact that both contain a single stacked parallel diheme motif. Ssc is a dimer of two identical 26.3 kDa subunits, which has so far been isolated only from the *D. desulfuricans* ATCC 27774, a species that can use sulfate or nitrate as terminal electron acceptors. Each monomer contains two *c*-type hemes with bis-histidinyl coordination and redox potentials of −168 and −330 mV. The name of this cytochrome derives from the fact that the reduced form displays a split-Soret band with maxima at 420 nm and a shoulder at 415 nm.

A model of the three-dimensional structure of Ssc shows that this protein has unique features, and does not belong to the cytochrome c_3 family.[102] The heme groups are attached at a C-terminal domain of the molecule and exposed to the solvent, in a parallel stacked motif. In the Ssc dimer, the four hemes are very close together, and the sixth histidinyl ligand of heme 1 is provided by the chain of the other monomer, indicating that the dimer is the functional unit of Ssc. This cytochrome also contains an α-helical N-terminal domain where four cysteines are positioned at an open surface pocket of the protein suggesting the binding of a FeS center. Indeed, the presence of a [2Fe2S] cluster in Ssc had been proposed on the basis of Mössbauer data,[103] and it could be confirmed by EPR spectroscopy of anaerobically purified Ssc.[104] This cluster is very oxygen-labile as indicated by nonheme iron quantification of aerobically and anaerobically prepared Ssc, and the fact that it is not observed in the structure of the aerobically purified Ssc. Modeling of the [2Fe2S] center suggests a possible unusual coordination by only three of the available cysteines, leaving one free coordination position in one of the irons that is accessible from the outside of the molecule and thus pointing to a not yet found enzymatic activity.

The physiological function of Ssc has not been elucidated. Cloning and sequencing of the *D. desulfuricans* ATCC 27774 Ssc gene revealed that the cytochrome is encoded by a monocistronic operon, and contains a signal peptide sequence indicating that the protein is periplasmic. Transcriptional analysis revealed that sulfate-grown cells contained only 9% of the Ssc mRNA levels of nitrate-grown cells.[104] A homolog of the Ssc cytochrome gene is found in the genomes of *D. desulfuricans* G20, *S. oneidensis*, *Desulfitobacterium hafniense* but not *D. vulgaris* Hildenborough. In the genome of the sulfate-reducing archaeon, *Archaeoglobus fulgidus*, a putative homolog of Ssc is encoded, which contains only the N-terminal domain that binds the FeS cluster, but not the C-terminal heme *c* domain.

NapB. NapB is a subunit of the heterodimeric periplasmic nitrate reductase (NapAB) and transfers electrons to the catalytic NapA molybdoprotein. Nap systems are found in a number of bacteria, including enterobacteria, aerobic denitrifiers, and nonsulfur purple photosynthetic bacteria.[66,105] Their physiological function is different in these groups of bacteria and includes redox balancing using nitrate as an electron sink to dispose of excess reductant, aerobic denitrification, and nitrate scavenging in nitrate-limited environments.

NapB is a 13–19 kDa diheme cytochrome *c*, usually isolated in a strong complex with NapA, although in some cases it is possible to separate the two subunits. The redox potentials of the hemes vary in different bacterial species, probably reflecting the diverse physiological roles. NapB is essential for Nap activity since deletion mutants in *E. coli* and *Rhodobacter sphaeroides* have very low nitrate reductase activity. It receives electrons from the quinol pool *via* the membrane-anchored tetraheme cytochrome NapC. The crystal structure of a proteolyzed form of recombinant NapB from *H. influenzae* was determined[106] and, more recently, that of the NapAB complex from *Rb. sphaeroides* was also obtained.[107] The two hemes in NapB are bis-His coordinated, and display the typical diheme stacked arrangement. The structure of *H. influenzae* NapAB shows that NapB has extensive interactions with NapA, explaining the high affinity of this complex. The two proteins are bound such that heme II of NapB is in close contact to the iron–sulfur cluster of NapA, whereas heme I is exposed to the solvent, and is thus the heme likely to receive electrons from NapC. A comparison of the cofactors redox potentials in the bound and isolated subunits shows that there is a strong effect of complex formation on the redox potential of the [4Fe4S] cluster (a change of +180 mV), and a smaller, but significant, change for heme 2 (+40 mV). The increase in the redox potentials are due to the decrease in solvent exposure of the cofactors, and lead to favorable electron transfer steps between the cofactors.

4 OTHER MULTIHEME *c* CYTOCHROMES

An important family of multiheme proteins are the tetra or pentaheme *c*-type cytochromes that are bound to the membrane by an N-terminal hydrophobic anchor, usually referred to as the NapC family of cytochromes, since this was the first one to be recognized.**[108,109]** These cytochromes act as quinol dehydrogenases, transferring electrons from the quinone pool to periplasmic proteins involved in the reduction of various electron acceptors like nitrate, nitrite, fumarate, Fe^{III}, trimethylamine N-oxide, and dimethylsulfoxide. Phylogenetic analyses show these novel quinol dehydrogenases are more widely distributed among the *Proteobacteria* than the bc_1 complex. Examples include: NapC, which is involved in reduction of the periplasmic nitrate reductase NapAB; NirT, which is thought to donate electrons to the periplasmic cd_1 nitrite reductase; NrfH, the electron donor of the NrfA nitrite reductase; TorC, which is involved in the reduction of trimethylamine N-oxide reductase; DmsC and DorC, which are likely electron donors to dimethylsulfoxide reductases; and FccC, which is suggested to transfer electrons to a periplasmic methacrylate reductase. Two further interesting members of this family are the CymA from *Shewanella* spp. and cytochrome c_{m552} of *N. europea*. CymA is not specific for any one reductase, since it is involved in reduction of nitrate, nitrite, fumarate, DMSO, Fe^{III}, and Mn^{IV}, thus having to interact with a range of redox partners.**[89,110]** Cytochrome c_{m552} (or CycB) of *N. europea* probably operates in reverse of the rest of the family by reducing the quinone pool with electrons derived from the periplasmic oxidation of hydroxylamine.**[59]** Despite the importance of this family of cytochromes in electron transfer chains, no structure has yet been determined.

The common feature of these proteins is the presence of a tetraheme periplasmic domain that is attached to the membrane through a single α-helical anchor. In TorC and DorC, there is an additional C-terminal monoheme domain.**[111]** The four hemes have bis-histidinyl coordination and low redox potentials, whereas the monoheme has a high redox potential. There is evidence to indicate that the tetraheme globular domain is formed by two diheme domains, which show sequence similarity to each other, and may be related to the diheme binding segments of cytochromes of the HAO family (see Section 3).**[108]** In the case of CymA and NapC, the membrane anchor is apparently not necessary for interaction of the heme domain with quinols.

Multiheme cytochromes *c* play an important role in bacterial iron respiration.**[47,112]** In this process, soluble Fe^{III} chelates or insoluble Fe^{III} oxides serve as terminal electron acceptors of the anaerobic respiratory chain. In *Shewanella* and *Geobacter* spp., the two most studied Fe^{III}-reducing organisms, a great increase in cellular multiheme *c*-type cytochromes is observed upon growth by iron respiration. In the case of the genus *Shewanella,* electron transport to Fe^{III} involves CymA in the cytoplasmic membrane, and several periplasmic and outer membrane cytochromes. These include the products of the *mtrDEF-omcA-mtrCAB* gene cluster, which encodes two periplasmic decaheme cytochromes *c* (MtrA and MtrD), two putative outer membrane β-barrel proteins (MtrB and MtrE) and three outer membrane decaheme cytochromes *c* (OmcA, MtrC, which is also designated by OmcB, and MtrF).**[113,114]** In addition, the periplasmic Stc and Ifc proteins (see Section 3.4) may also play a role in Fe^{III} reduction. The periplasmic cytochromes may be involved in direct reduction of soluble Fe^{III} chelates that may enter the periplasm, or in electron transport between CymA and the outer membrane cytochromes that are most likely responsible for reduction of the insoluble Fe^{III} oxides. The outer membrane cytochrome OmcA was purified from *S. frigidimarina* cells and shown to bind 10 bis-His ligated hemes, with redox potentials centered at -243 and -324 mV.**[115]** A mutant deleted in OmcA is affected in its ability to reduce MnO_2, but not Fe^{III}.**[113]** Its paralog, MtrC (OmcB), seems to play a more significant role in Fe^{III} reduction, as is the case for the periplasmic cytochrome MtrA and the outer membrane MtrB.**[114]** MtrB is required for incorporation of cytochromes in the outer membrane.**[116]** A recombinant form of the periplasmic MtrA cytochrome has been characterized.**[117]** It is a 32 kDa cytochrome containing 10 bis-His coordinated hemes *c* that reduce over the potential range of -100 to -400 mV. Sequence analysis of MtrA suggests that six of the hemes may be organized in parallel diheme pair motifs similar to hemes 2/3 of Stc. MtrA can reduce several Fe^{III} chelates and transfer electrons to the *E. coli* host NrfA and NapAB. This indicates that, as in Stc, the surface-exposed hemes may be involved in nonspecific electron transfer, which is probably a general property for cytochromes with a low amino acid to heme ratio.

In *G. sulfurreducens*, two outer membrane cytochromes, designated as OmcB and OmcC, are also implicated in Fe^{III} reduction.**[118]** They are 79% identical and both contain 12 hemes *c*. OmcB is about twofold more abundant than OmcC, and an OmcB-deficient mutant is greatly impaired in its ability to reduce Fe^{III}, which is not observed for the OmcC-deficient mutant. The periplasmic triheme cytochrome *c* PpcA is also involved in electron transfer across the periplasm to the reduction of Fe^{III} (see Section 2.4). A great number of genes coding for multiheme cytochromes are present in the *G. sulfurreducens* genome. Several of these are high molecular mass cytochromes with an astonishing number of hemes per polypeptide (e.g. 18, 24, 27, and 33 hemes!). This reveals there are still a number of multiheme *c* proteins to be investigated, the study of which may bring new insights to this group of proteins.

5 RELATED ARTICLES

Electron Transfer Reactions: Theory; Iron: Heme Proteins & Dioxygen Transport & Storage; Iron: Heme Proteins

& Electron Transport; Iron: Heme Proteins, Mono- & Dioxygenases; Iron: Heme Proteins, Peroxidases, Catalases & Catalase-peroxidases.

6 REFERENCES

1. G. R. Moore and G. W. Pettigrew, 'Cytochrome *c*. Evolutionary, Structural and Physicochemical Aspects', Springer-Verlag, 1990.
2. F. A. Tezcan, J. R. Winkler, and H. B. Gray, *J. Am. Chem. Soc.*, 1998, **120**, 13383.
3. P. M. Wood, *Biochim. Biophys. Acta*, 1991, **1058**, 5.
4. P. D. Barker and S. J. Ferguson, *Structure Fold. Des.*, 1999, **7**, R281.
5. J. W. A. Allen, O. Daltrop, J. M. Stevens, and S. J. Ferguson, *Philos. Trans. R. Soc. London, B*, 2003, **358**, 255.
6. C. C. Page, C. C. Moser, and P. L. Dutton, *Curr. Opin. Chem. Biol.*, 2003, **7**, 551.
7. M. D. Page, Y. Sambongi, and S. J. Ferguson, *Trends Biochem. Sci.*, 1998, **23**, 103.
8. R. Kranz, R. Lill, B. Goldman, G. Bonnard, and S. Merchant, *Mol. Microbiol.*, 1998, **29**, 383.
9. L. Thony-Meyer, *Biochem. Soc. Trans.*, 2002, **30**, 633.
10. V. A. Bamford, S. Bruno, T. Rasmussen, C. Appia-Ayme, M. R. Cheesman, B. C. Berks, and A. M. Hemmings, *EMBO J.*, 2002, **21**, 5599.
11. T. M. Iverson, D. M. Arciero, B. T. Hsu, M. S. P. Logan, A. B. Hooper, and D. C. Rees, *Nat. Struct. Biol.*, 1998, **5**, 1005.
12. T. M. Iverson, D. M. Arciero, A. B. Hooper, and D. C. Rees, *J. Biol. Inorg. Chem.*, 2001, **6**, 390.
13. I. A. C. Pereira, M. Teixeira, and A. V. Xavier, *Struct. Bonding*, 1998, **91**, 65.
14. A. V. Xavier, *FEBS Lett.*, 2002, **532**, 261.
15. C. R. D. Lancaster and H. Michel, in Photosynthetic Reaction Centers of Purple Bacteria, in 'Handbook of Metalloproteins', eds. A. Messerschmidt, R. Huber, T. Poulos, and K. Wieghardt, John Wiley & Sons, New York, 2001, p. 119.
16. P. M. Matias, C. M. Soares, L. M. Saraiva, R. Coelho, J. Morais, J. Le Gall, and M. A. Carrondo, *J. Biol. Inorg. Chem.*, 2001, **6**, 63.
17. L. ElAntak, X. Morelli, O. Bornet, C. Hatchikian, M. Czjzek, A. Dolla, and F. Guerlesquin, *FEBS Lett.*, 2003, **548**, 1.
18. P. M. Matias, C. Frazao, J. Morais, M. Coll, and M. A. Carrondo, *J. Mol. Biol.*, 1993, **234**, 680.
19. R. O. Louro, T. Catarino, J. LeGall, and A. V. Xavier, *J. Biol. Inorg. Chem.*, 1997, **2**, 488.
20. L. Brennan, D. L. Turner, A. C. Messias, M. L. Teodoro, J. LeGall, H. Santos, and A. V. Xavier, *J. Mol. Biol.*, 2000, **298**, 61.
21. B. Chardin, M. T. Giudici-Orticoni, G. De Luca, B. Guigliarelli, and M. Bruschi, *Appl. Microbiol. Biotechnol.*, 2003, **63**, 315.
22. E. Lojou, P. Bianco, and M. Bruschi, *J. Electroanal. Chem.*, 1998, **452**, 167.
23. M. Assfalg, I. Bertini, M. Bruschi, C. Michel, and P. Turano, *Proc. Natl. Acad. Sci. U.S.A.*, 2002, **99**, 9750.
24. M. Bruschi, *Methods Enzymol.*, 1994, **243**, 140.
25. M. Czjzek, F. Guerlesquin, M. Bruschi, and R. Haser, *Structure*, 1996, **4**, 395.
26. C. Frazao, L. Sieker, G. Sheldrick, V. Lamzin, J. LeGall, and M. A. Carrondo, *J. Biol. Inorg. Chem.*, 1999, **4**, 162.
27. C. Aubert, M. Brugna, A. Dolla, M. Bruschi, and M. T. Giudici-Orticoni, *Biochim. Biophys. Acta*, 2000, **1476**, 85.
28. L. Pieulle, J. Haladjian, J. Bonicel, and E. C. Hatchikian, *Biochem. Biophys. Acta*, 1996, **1273**, 51.
29. F. M. Valente, L. M. Saraiva, J. LeGall, A. V. Xavier, M. Teixeira, and I. A. Pereira, *Chembiochem*, 2001, **2**, 895.
30. V. Magro, L. Pieulle, N. Forget, B. Guigliarelli, Y. Petillot, and E. C. Hatchikian, *Biochim. Biophys. Acta*, 1997, **1342**, 149.
31. S. Norager, P. Legrand, L. Pieulle, C. Hatchikian, and M. Roth, *J. Mol. Biol.*, 1999, **290**, 881.
32. E. C. Duin, C. Bauer, B. Jaun, and R. Hedderich, *FEBS Lett.*, 2003, **538**, 81.
33. P. M. Matias, A. V. Coelho, F. M. A. Valente, D. Plácido, J. LeGall, A. V. Xavier, I. A. C. Pereira, and M. A. Carrondo, *J. Biol. Chem.*, 2002, **277**, 47907.
34. A. V. Coelho, P. M. Matias, L. Sieker, J. Morais, M. A. Carrondo, J. Lampreia, C. Costa, J. J. G. Moura, I. Moura, and J. LeGall, *Acta Crystallogr.*, 1996, **D52**, 1202.
35. P. M. Matias, R. Coelho, I. A. Pereira, A. V. Coelho, A. W. Thompson, L. C. Sieker, J. L. Gall, and M. A. Carrondo, *Structure*, 1999, **7**, 119.
36. M. A. Carrondo, C. M. Soares, and P. M. Matias, Nine-heme Cytochrome *c*, in 'Handbook of Metalloproteins' eds. A. Messerschmidt, R. Huber, T. Poulos, and K. Wieghardt, John Wiley & Sons, New York, 2001, p. 147.
37. I. Bento, V. H. Teixeira, A. M. Baptista, C. M. Soares, P. M. Matias, and M. A. Carrondo, *J. Biol. Chem.*, 2003, **278**, 36455.
38. P. M. Matias, L. M. Saraiva, C. M. Soares, A. V. Coelho, J. LeGall, and M. A. Carrondo, *J. Biol. Inorg. Chem.*, 1999, **4**, 478.
39. L. M. Saraiva, P. N. da Costa, C. Conte, A. V. Xavier, and J. LeGall, *Biochim. Biophys. Acta*, 2001, **1520**, 63.
40. I. A. C. Pereira, J. LeGall, A. V. Xavier, and M. Teixeira, *J. Biol. Inorg. Chem.*, 1997, **2**, 23.
41. M. Czjzek, L. ElAntak, V. Zamboni, X. Morelli, A. Dolla, F. Guerlesquin, and M. Bruschi, *Structure*, 2002, **10**, 1677.

42. M. Rossi, W. B. Pollock, M. W. Reij, R. G. Keon, R. Fu, and G. Voordouw, *J. Bacteriol.*, 1993, **175**, 4699.
43. R. G. Keon, R. Fu, and G. Voordouw, *Arch. Microbiol.*, 1997, **167**, 376.
44. J. L. Steger, C. Vincent, J. D. Ballard, and L. R. Krumholz, *Appl. Environ. Microbiol.*, 2002, **68**, 1932.
45. A. Dolla, B. K. Pohorelic, J. K. Voordouw, and G. Voordouw, *Arch. Microbiol.*, 2000, **174**, 143.
46. D. R. Lovley and J. D. Coates, *Curr. Opin. Microbiol.*, 2000, **3**, 252.
47. I. Schroder, E. Johnson, and S. de Vries, *FEMS Microbiol. Rev.*, 2003, **27**, 427.
48. M. Assfalg, L. Banci, I. Bertini, M. Bruschi, M. T. Giudici-Orticoni, and P. Turano, *Eur. J. Biochem.*, 1999, **266**, 634.
49. M. Czjzek, P. Arnoux, R. Haser, and W. Shepard, *Acta Crystallogr. D Biol. Crystallogr.*, 2001, **57**, 670.
50. M. Brugna, W. Nitschke, R. Toci, M. Bruschi, and M. T. Giudici-Orticoni, *J. Bacteriol.*, 1999, **181**, 5505.
51. I. J. Correia, C. M. Paquete, R. O. Louro, T. Catarino, D. L. Turner, and A. V. Xavier, *Eur. J. Biochem.*, 2002, **269**, 5722.
52. I. A. Pereira, I. Pacheco, M. Y. Liu, J. LeGall, A. V. Xavier, and M. Teixeira, *Eur. J. Biochem.*, 1997, **248**, 323.
53. J. R. Lloyd, C. Leang, A. L. Hodges Myerson, M. V. Coppi, S. Cuifo, B. Methe, S. J. Sandler, and D. R. Lovley, *Biochem. J.*, 2003, **369**, 153.
54. N. Igarashi and N. Tanaka, Hydroxylamine Oxidoreductase, in 'Handbook of Metalloproteins', eds. A. Messerschmidt, R. Huber, T. Poulos, and K. Wieghardt, John Wiley & Sons New York, 2001, p. 454.
55. D. J. Arp, L. A. Sayavedra-Soto, and N. G. Hommes, *Arch. Microbiol.*, 2002, **178**, 250.
56. D. M. Arciero, A. B. Hooper, M. Cai, and R. Timkovich, *Biochemistry*, 1993, **32**, 9370.
57. N. Igarashi, H. Moriyama, T. Fujiwara, Y. Fukumori, and N. Tanaka, *Nat. Struct. Biol.*, 1997, **4**, 276.
58. N. G. Hommes, L. A. Sayavedra-Soto, and D. J. Arp, *Arch. Microbiol.*, 2002, **178**, 471.
59. M. Whittaker, D. Bergmann, D. Arciero, and A. B. Hooper, *Biochim. Biophys. Acta*, 2000, **1459**, 346.
60. M. P. Hendrich, D. Petasis, D. M. Arciero, and A. B. Hooper, *J. Am. Chem. Soc.*, 2001, **123**, 2997.
61. T. M. Iverson, M. P. Hendrich, D. M. Arciero, A. B. Hooper, and D. C. Rees, Cytochrome c_{554}, in 'Handbook of Metalloproteins' eds. A. Messerschmidt, R. Huber, T. Poulos, and K. Wieghardt, John Wiley & Sons New York, 2001, p. 136.
62. A. K. Upadhyay, D. T. Petasis, D. M. Arciero, A. B. Hooper, and M. P. Hendrich, *J. Am. Chem. Soc.*, 2003, **125**, 1738.
63. D. M. Arciero, C. Balny, and A. B. Hooper, *Biochemistry*, 1991, **30**, 11466.
64. S. J. Ferguson, *Curr. Opin. Chem. Biol.*, 1998, **2**, 182.
65. D. J. Richardson and N. J. Watmough, *Curr. Opin. Chem. Biol.*, 1999, **3**, 207.
66. L. Potter, H. Angove, D. Richardson, and J. Cole, *Adv. Microb. Physiol.*, 2001, **45**, 51.
67. I. Moura and J. J. Moura, *Curr. Opin. Chem. Biol.*, 2001, **5**, 168.
68. J. Simon, *FEMS Microbiol. Rev.*, 2002, **26**, 285.
69. O. Einsle, in Cytochrome *c* Nitrite Reductase, in 'Handbook of Metalloproteins', eds. A. Messerschmidt, R. Huber, T. Poulos, and K. Wieghardt, John Wiley & Sons, New York, 2001, p. 440.
70. H. Hussain, J. Grove, L. Griffiths, S. Busby, and J. Cole, *Mol. Microbiol.*, 1994, **12**, 153.
71. D. J. Eaves, J. Grove, W. Staudenmann, P. James, R. K. Poole, S. A. White, I. Griffiths, and J. A. Cole, *Mol. Microbiol.*, 1998, **28**, 205.
72. J. Simon, R. Gross, O. Einsle, P. M. Kroneck, A. Kroger, and O. Klimmek, *Mol. Microbiol.*, 2000, **35**, 686.
73. R. Pisa, T. Stein, R. Eichler, R. Gross, and J. Simon, *Mol. Microbiol.*, 2002, **43**, 763.
74. A. Darwin, H. Hussain, L. Griffiths, J. Grove, Y. Sambongi, S. Busby, and J. Cole, *Mol. Microbiol.*, 1993, **9**, 1255.
75. O. Einsle, A. Messerschmidt, P. Stach, G. P. Bourenkov, H. D. Bartunik, R. Huber, and P. M. Kroneck, *Nature*, 1999, **400**, 476.
76. O. Einsle, P. Stach, A. Messerschmidt, J. Simon, A. Kroger, R. Huber, and P. M. Kroneck, *J. Biol. Chem.*, 2000, **275**, 39608.
77. V. A. Bamford, H. C. Angove, H. E. Seward, A. J. Thomson, J. A. Cole, J. N. Butt, A. M. Hemmings, and D. J. Richardson, *Biochemistry*, 2002, **41**, 2921.
78. C. A. Cunha, S. Macieira, J. M. Dias, G. Almeida, L. L. Goncalves, C. Costa, J. Lampreia, R. Huber, J. J. Moura, I. Moura, and M. J. Romao, *J. Biol. Chem.*, 2003, **278**, 17455.
79. P. Stach, O. Einsle, W. Schumacher, E. Kurun, and P. M. Kroneck, *J. Inorg. Biochem.*, 2000, **79**, 381.
80. I. A. Pereira, J. LeGall, A. V. Xavier, and M. Teixeira, *Biochim. Biophys. Acta*, 2000, **1481**, 119.
81. M. G. Almeida, S. Macieira, L. L. Goncalves, R. Huber, C. A. Cunha, M. J. Romao, C. Costa, J. Lampreia, J. J. Moura, and I. Moura, *Eur. J. Biochem.*, 2003, **270**, 3904.
82. I. C. Pereira, I. A. Abreu, A. V. Xavier, J. LeGall, and M. Teixeira, *Biochem. Biophys. Res. Commun.*, 1996, **224**, 611.
83. O. Einsle, A. Messerschmidt, R. Huber, P. M. Kroneck, and F. Neese, *J. Am. Chem. Soc.*, 2002, **124**, 11737.
84. H. C. Angove, J. A. Cole, D. J. Richardson, and J. N. Butt, *J. Biol. Chem.*, 2002, **277**, 23374.
85. S. R. Poock, E. R. Leach, J. W. Moir, J. A. Cole, and D. J. Richardson, *J. Biol. Chem.*, 2002, **277**, 23664.
86. E. A. Greene, C. Hubert, M. Nemati, G. E. Jenneman, and G. Voordouw, *Environ. Microbiol.*, 2003, **5**, 607.

87. K. L. Turner, M. K. Doherty, H. A. Heering, F. A. Armstrong, G. A. Reid, and S. K. Chapman, *Biochemistry*, 1999, **38**, 3302.
88. J. J. Van Hellemond and A. G. Tielens, *Biochem. J.*, 1994, **304**(Pt 2), 321.
89. C. Schwalb, S. K. Chapman, and G. A. Reid, *Biochemistry*, 2003, **42**, 9491.
90. E. H. Gordon, S. L. Pealing, S. K. Chapman, F. B. Ward, and G. A. Reid, *Microbiology*, 1998, **144**(Pt 4), 937.
91. P. S. Dobbin, J. N. Butt, A. K. Powell, G. A. Reid, and D. J. Richardson, *Biochem. J.*, 1999, **342**(Pt 2), 439.
92. V. Bamford, P. S. Dobbin, D. J. Richardson, and A. M. Hemmings, *Nat. Struct. Biol.*, 1999, **6**, 1104.
93. P. Taylor, S. L. Pealing, G. A. Reid, S. K. Chapman, and M. D. Walkinshaw, *Nat. Struct. Biol.*, 1999, **6**, 1108.
94. D. Leys, A. S. Tsapin, K. H. Nealson, T. E. Meyer, M. A. Cusanovich, and J. J. Van Beeumen, *Nat. Struct. Biol.*, 1999, **6**, 1113.
95. E. L. Rothery, C. G. Mowat, C. S. Miles, M. D. Walkinshaw, G. A. Reid, and S. K. Chapman, *Biochemistry*, 2003, **42**, 13160.
96. M. K. Doherty, S. L. Pealing, C. S. Miles, R. Moysey, P. Taylor, M. D. Walkinshaw, G. A. Reid, and S. K. Chapman, *Biochemistry*, 2000, **39**, 10695.
97. C. G. Mowat, R. Moysey, C. S. Miles, D. Leys, M. K. Doherty, P. Taylor, M. D. Walkinshaw, G. A. Reid, and S. K. Chapman, *Biochemistry*, 2001, **40**, 12292.
98. M. Pessanha, L. Brennan, A. V. Xavier, P. M. Cuthbertson, G. A. Reid, S. K. Chapman, D. L. Turner, and C. A. Salgueiro, *FEBS Lett.*, 2001, **489**, 8.
99. E. H. Gordon, A. D. Pike, A. E. Hill, P. M. Cuthbertson, S. K. Chapman, and G. A. Reid, *Biochem. J.*, 2000, **349**, 153.
100. D. Leys, T. E. Meyer, A. S. Tsapin, K. H. Nealson, M. A. Cusanovich, and J. J. Van Beeumen, *J. Biol. Chem.*, 2002, **277**, 35703.
101. M. Pessanha, R. O. Louro, I. J. Correia, E. L. Rothery, K. L. Pankhurst, G. A. Reid, S. K. Chapman, D. L. Turner, and C. A. Salgueiro, *Biochem. J.*, 2003, **370**, 489.
102. P. M. Matias, J. Morais, A. V. Coelho, R. Meijers, A. Gonzalez, A. W. Thompson, L. Sieker, J. LeGall, and M. A. Carrondo, *J. Biol. Inorg. Chem.*, 1997, **2**, 507.
103. B. Devreese, C. Costa, H. Demol, V. Papaefthymiou, I. Moura, J. J. Moura, and J. Van Beeumen, *Eur. J. Biochem.*, 1997, **248**, 445.
104. I. A. Abreu, A. I. Lourenco, A. V. Xavier, J. LeGall, A. V. Coelho, P. M. Matias, D. M. Pinto, M. Armenia Carrondo, M. Teixeira, and L. M. Saraiva, *J. Biol. Inorg. Chem.*, 2003, **8**, 360.
105. D. Richardson, B. C. Berks, D. A. Russel, S. Spiro, and C. J. Taylor, *Cell. Mol. Life Sci.*, 2001, **58**, 165.
106. A. Brige, D. Leys, T. E. Meyer, M. A. Cusanovich, and J. J. Van Beeumen, *Biochemistry*, 2002, **41**, 4827.
107. P. Arnoux, M. Sabaty, J. Alric, B. Frangioni, B. Guigliarelli, J. M. Adriano, and D. Pignol, *Nat. Struct. Biol.*, 2003, **10**, 928.
108. M. L. Cartron, M. D. Roldan, S. J. Ferguson, B. C. Berks, and D. J. Richardson, *Biochem. J.*, 2002, **368**, 425.
109. J. Simon, R. Eichler, R. Pisa, S. Biel, and R. Gross, *FEBS Lett.*, 2002, **522**, 83.
110. C. R. Myers and J. M. Myers, *J. Bacteriol.*, 1997, **179**, 1143.
111. S. Gon, M. T. Giudici-Orticoni, V. Mejean, and C. Iobbi-Nivol, *J. Biol. Chem.*, 2001, **276**, 11545.
112. D. R. Lovley, *ASM News*, 2002, **68**, 231.
113. J. M. Myers and C. R. Myers, *Appl. Environ. Microbiol.*, 2001, **67**, 260.
114. A. S. Beliaev, D. A. Saffarini, J. L. McLaughlin, and D. Hunnicutt, *Mol. Microbiol.*, 2001, **39**, 722.
115. S. J. Field, P. S. Dobbin, M. R. Cheesman, N. J. Watmough, A. J. Thomson, and D. J. Richardson, *J. Biol. Chem.*, 2000, **275**, 8515.
116. C. R. Myers and J. M. Myers, *Appl. Environ. Microbiol.*, 2002, **68**, 5585.
117. K. E. Pitts, P. S. Dobbin, F. Reyes-Ramirez, A. J. Thomson, D. J. Richardson, and H. E. Seward, *J. Biol. Chem.*, 2003, **278**, 27758.
118. C. Leang, M. V. Coppi, and D. R. Lovley, *J. Bacteriol.*, 2003, **185**, 2096.

Semiconductor Nanocrystal Quantum Dots

Jennifer A. Hollingsworth
Los Alamos National Laboratory, Los Alamos, NM, USA

1 Introduction 1
2 Colloidal Nanosynthesis 1
3 Inorganic Surface Modification 8
4 Shape Control 12
5 Phase Transitions and Phase Control 18
6 Related Articles 20
7 References 20

1 INTRODUCTION

An important parameter of a semiconductor material is the width of the energy gap that separates the conduction from the valence energy bands (Figure 1(a), left). In semiconductors of macroscopic sizes, the width of this gap is a fixed parameter, which is determined by the material's identity. However, the situation changes in the case of nanoscale semiconductor particles with sizes smaller than ~10 nm (Figure 1(a), right). This size range corresponds to the regime of quantum confinement for which electronic excitations 'feel' the presence of the particle boundaries and respond to changes in the particle size by adjusting their energy spectra. This phenomenon is known as the *quantum size effect*, while nanoscale particles that exhibit it are often referred to as quantum dots (QDs).

As the QD size decreases, the energy gap increases, leading, in particular, to a blue shift of the emission wavelength. In the first approximation, this effect can be described using a simple 'quantum box' model. For a spherical QD with radius R, this model predicts that the size-dependent contribution to the energy gap is simply proportional to 1/R[1] (Figure 1(b)). In addition to increasing energy gap, quantum confinement leads to a collapse of the continuous energy bands of the bulk material into discrete, 'atomic' energy levels. These well-separated QD states can be labeled using atomic-like notations (1S, 1P, 1D, etc.), as illustrated in Figure 1(a). The discrete structure of energy states leads to the discrete absorption spectrum of QDs (schematically shown by vertical bars in Figure 1(c)), which is in contrast to the continuous absorption spectrum of a bulk semiconductor (Figure 1(c)).

Semiconductor QDs bridge the gap between cluster molecules and bulk materials. The boundaries between molecular, QD, and bulk regimes are not well defined and are strongly material dependent. However, a range from ~100 to ~10 000 atoms per particle can be considered as a crude estimate of sizes for which the nanocrystal regime occurs. The lower limit of this range is determined by the stability of the bulk crystalline structure with respect to isomerization into molecular structures. The upper limit corresponds to sizes for which the energy level spacing is approaching the thermal energy kT, meaning that carriers become mobile inside the QD.

Semiconductor QDs have been prepared by a variety of 'physical' and 'chemical' methods. Some examples of physical processes, characterized by high-energy input, include molecular beam epitaxy (MBE) and metalorganic-chemical-vapor-deposition (MOCVD) approaches to quantum dots[1–3] and vapor-liquid solid (VLS) approaches to quantum wires.[4,5] High-temperature methods have also been applied to chemical routes, including particle growth in glasses.[6,7] Here, however, we emphasize 'soft' (low-energy-input) colloidal chemical synthesis of crystalline semiconductor nanoparticles that we will refer to as nanocrystal quantum dots (NQDs). NQDs comprise an inorganic core overcoated with a layer of organic ligand molecules. The organic capping provides electronic and chemical passivation of surface dangling bonds, prevents uncontrolled growth and agglomeration of the nanoparticles, and allows NQDs to be chemically manipulated like large molecules with solubility and reactivity determined by the identity of the surface ligand. In contrast to substrate-bound epitaxial QDs, NQDs are 'freestanding.' In this discussion, we concentrate on the most successful synthesis methods, where success is determined by high crystallinity, adequate surface passivation, solubility in nonpolar or polar solvents, and good size monodispersity. Size monodispersity permits the study and, ultimately, the use of materials-size-effects to define novel materials properties. Monodispersity in terms of colloidal nanoparticles (1–15 nm size range) requires a sample standard deviation of $\sigma \leq 5\%$, which corresponds to ± one lattice constant.[8] Because colloidal monodispersity in this strict sense remains relatively uncommon, preparations are included in this chapter that achieve approximately $\sigma \leq 20\%$, in particular where other attributes, such as novel compositions or shape control, are relevant. In addition, we discuss 'soft' approaches to NQD chemical and structural modification.

2 COLLOIDAL NANOSYNTHESIS

The most successful NQD preparations with respect to nanocrystal quality and monodispersity entail pyrolysis of metal-organic precursors in hot coordinating solvents (120–360 °C). Understood in terms of La Mer and Dinegar's studies of colloidal particle nucleation and growth,[8,9] these preparative routes involve a temporally discrete nucleation event followed by relatively rapid growth from solution-phase monomers and finally slower growth by Ostwald

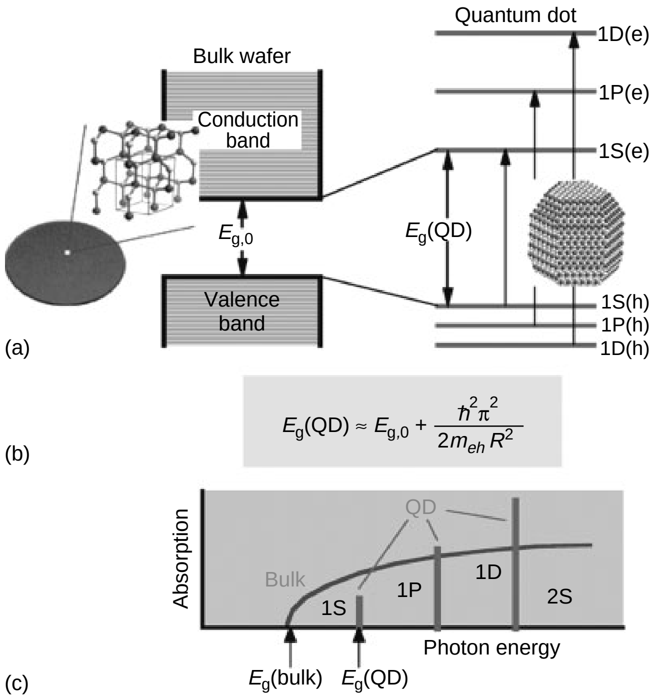
Quantum dot
Bulk wafer
Conduction band
1D(e)
1P(e)
1S(e)
$E_{g,0}$
E_g(QD)
Valence band
1S(h)
1P(h)
1D(h)
(a)
$E_g(QD) \approx E_{g,0} + \frac{\hbar^2\pi^2}{2m_{eh}R^2}$
(b)
Absorption
QD
Bulk
1S
1P
1D
2S
Photon energy
E_g(bulk)
E_g(QD)
(c)

Figure 1 (a) A bulk semiconductor has continuous conduction and valence energy bands separated by a 'fixed' energy gap, E_{g0} (left), while a QD is characterized by discrete atomic-like states with energies that are determined by the QD radius R (right). (b) The expression for the size-dependent separation between the lowest electron [1S(e)] and hole [1S(h)] QD states (QD energy gap) obtained using the 'quantum box' model [$m_{eh} = m_e m_h/(m_e + m_h)$, where m_e and m_h are effective masses of electrons and holes, respectively]. (c) Schematic of the continuous absorption spectrum of a bulk semiconductor (curved line), compared to the discrete absorption spectrum of a QD (vertical bars)

ripening (referred to as recrystallization or aging) (Figure 2). Nucleation is achieved by quick injection of precursor into the hot coordinating solvents, resulting in thermal decomposition of the precursor reagents and supersaturation of the formed 'monomers' that is partially relieved by particle generation. Growth then proceeds by addition of monomer from solution to the NQD nuclei. Monomer concentrations are below the critical concentration for nucleation, and, thus, these species only add to existing particles, rather than form new nuclei.[10] Once monomer concentrations are sufficiently depleted, growth can proceed by Ostwald ripening. Here, sacrificial dissolution of smaller (higher-surface-energy) particles results in growth of larger particles and, thereby, fewer particles in the system.[8]

Alternatively, supersaturation and nucleation can be triggered by a *slow* ramping of the reaction temperature. Precursors are mixed at low temperature and slowly brought to the temperature at which precursor reaction and decomposition occur sufficiently quickly to result in supersaturation.[11] Supersaturation is again relieved by a 'nucleation burst', after which temperature is controlled to avoid additional nucleation events, allowing monomer addition to existing nuclei to occur more rapidly than new nuclei formation. Thus, nucleation does not need to be instantaneous, but it should be a single, temporally discreet event to provide for the desired nucleation-controlled narrow size dispersions.[10]

2.1 Tuning Particle Size and Maintaining Size Monodispersity

Size and size dispersion can be controlled during the reaction, as well as post-preparatively. In general, time is a key

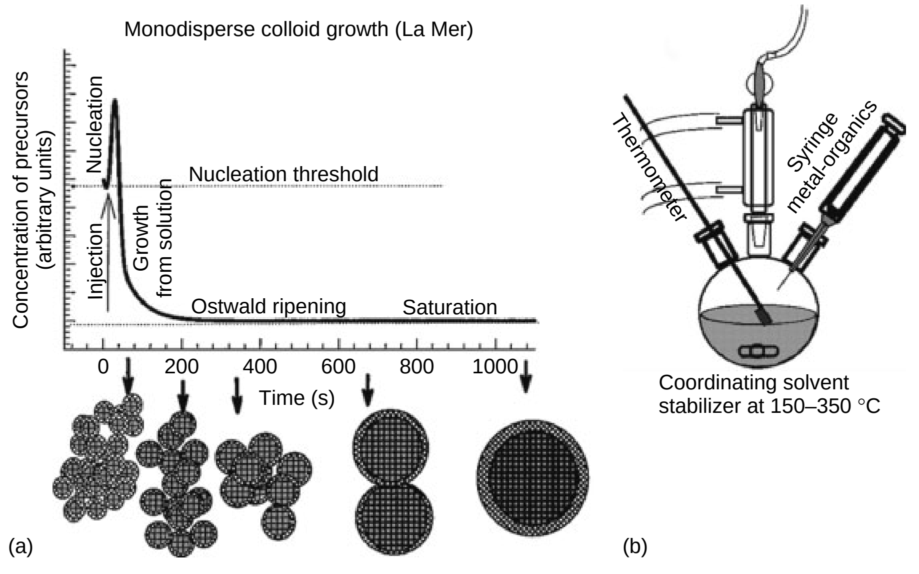
Monodisperse colloid growth (La Mer)
Concentration of precursors (arbitrary units)
Nucleation
Nucleation threshold
Injection
Growth from solution
Ostwald ripening
Saturation
0
200
400
600
800
1000
Time (s)
(a)
Thermometer
Syringe metal-organics
Coordinating solvent stabilizer at 150–350 °C
(b)

Figure 2 (a) Schematic illustrating La Mer's model for the stages of nucleation and growth for monodisperse colloidal particles. (b) Representation of the synthetic apparatus employed in the preparation of monodisperse NQDs. (Reprinted, with permission, from the Annual Reviews of Materials Science, Volume 30 © 2000 by Annual Reviews www.annualreviews.org) variable; longer reaction times yield larger average particle size. Nucleation and growth temperatures play contrasting roles. *Lower* nucleation temperatures support lower monomer concentrations and can yield larger-size nuclei. Whereas, *higher* growth temperatures can generate larger particles as the rate of monomer addition to existing particles is enhanced. Also, Ostwald ripening occurs more readily at higher temperatures. Precursor concentration can influence both the nucleation and the growth processes, and its effect is dependent upon the surfactant/precursor-concentration ratio and the identity of the surfactants (i.e. the strength of interaction between the surfactant and the NQD or between the surfactant and the monomer species). All else being equal, higher precursor concentrations promote the formation of fewer, larger nuclei and, thus, larger NQD particle size. Similarly, low stabilizer:precursor ratios yield larger particles. Also, weak stabilizer-NQD binding supports growth of large particles and, if too weakly coordinating, agglomeration of particles into insoluble aggregates.[10] Stabilizer-monomer interactions may influence growth processes, as well. Ligands that bind strongly to monomer species may permit unusually high monomer concentrations that are required for very fast growth (see Section 4),[12] or they may promote reductive elimination of the metal species (see below).[13]

The steric bulk of the coordinating ligands can impact the rate of growth subsequent to nucleation. Coordinating solvents typically comprise alkylphosphines, alkylphosphine oxides, alkylamines, alkylphosphates, alkylphosphites, alkylphosphonic acids, alkylphosphoramide, alkylthiols, fatty acids, and so on of various alkyl chain lengths and degrees of branching. The polar head group coordinates to the surface of the NQD, and the hydrophobic tail is exposed to the external solvent/matrix. This interaction permits solubility in common nonpolar solvents and hinders aggregation of individual nanocrystals by shielding the van der Waals attractive forces between NQD cores that would otherwise lead to aggregation and flocculation. The NQD-surfactant connection is dynamic, and monomers can add or subtract relatively unhindered to the crystallite surface. The ability of component atoms to reversibly come on and off of the NQD surface provides a necessary condition for high crystallinity – particles can anneal while particle aggregation is avoided. Relative growth rates can be influenced by the steric bulk of the coordinating ligand. For example, during growth, bulky surfactants can impose a comparatively high steric hindrance to approaching monomers, effectively reducing growth rates by decreasing diffusion rates to the particle surface.[10]

The two stages of growth (the relatively rapid first stage and Ostwald ripening) differ in their impact on size dispersity. During the first stage of growth, size distributions remain relatively narrow (dependent upon the nucleation event) or can become more focused. In contrast, sizes tend to defocus during Ostwald ripening as smaller particles begin to shrink and eventually dissolve in favor of growth of larger particles.[14] The benchmark preparation for CdS, CdSe, and CdTe NQDs,[15] which dramatically improved the overall quality of the nanoparticles prepared until that point, relied on Ostwald ripening to generate size series of II–VI NQDs. For example, CdSe NQDs from 1.2–11.5 nm in diameter were prepared.[15] Size dispersions of 10–15% were achieved for the larger-size particles and had to be subsequently narrowed by size-selective precipitation. The size-selective process simply involves first titrating the NQDs with a polar ‘nonsolvent,’ typically methanol, to the first sign of precipitation plus a small excess, resulting in precipitation of a small fraction of the NQDs. Such controlled precipitation preferentially removes the largest dots from the starting solution, as these become unstable to solvation before the smaller particles do. The precipitate is then collected by centrifugation, separated from the liquids, redissolved, and precipitated again. This iterative process separates larger from smaller NQDs and can generate the desired size dispersion of $\leq 5\%$.

More recently, preparations for II–VI semiconductors have been developed that specifically avoid the Ostwald-ripening growth regime. In one such method, the regime of relatively fast growth (the ‘size-focusing’ regime) is maintained by the addition of precursor monomer to the reaction solution after nucleation has occurred but before Ostwald growth has begun. The additional monomer is not sufficient to nucleate more particles, that is, not sufficient to again surpass the nucleation threshold. Instead, monomers add to existing particles and promote relatively rapid particle growth. Sizes focus as the monomer preferentially adds to smaller particles rather than to larger ones.[14] High monodispersity is evident in transmission electron micrograph (TEM) images (Figure 3). A slowly reacting precursor can provide a similar effect. For example, in the preparation of PbSe from lead oleate and trioctylphosphine selenide (see Section 2.3), the initial nucleation event consumes only a small fraction of the lead precursor. The lead oleate is relatively stable in phenyl ether, a reaction solvent. The unspent precursor present in solution

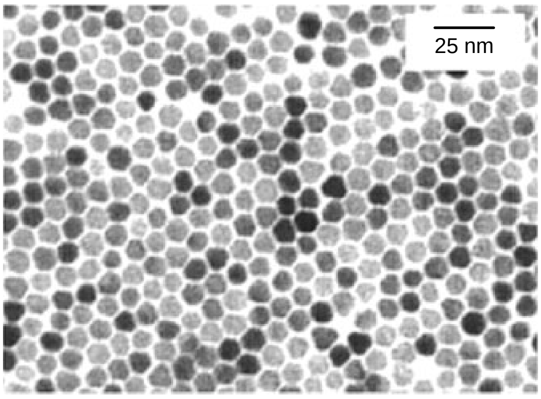

Figure 3 TEM of 8.5-nm diameter CdSe nanocrystals demonstrating the high degree of size monodispersity achieved by the ‘size-focusing’ synthesis method. (Reprinted with permission from Ref. 14. © 1998 American Chemical Society)

is sufficient to maintain growth in the size-focusing regime until particle sizes are reached that are several times those obtained in the initial stage of nucleation and growth ($\sim$3 nm to $\sim$12 nm). Alternatively, growth can simply be stopped during the fast-growth stage (by removing the heat source), and sizes are limited to those relatively close to the initial nucleation size. Because nucleation size can be manipulated by changing precursor concentration or reaction injection temperature, narrow size dispersions of controlled average particle size can be obtained by this method, as well.

2.2 CdSe NQDs – the 'Model' System

Owing to the ease with which high-quality samples can be prepared, the II–VI compound, CdSe, has comprised the 'model' NQD system and been the subject of much basic research into the electronic and optical properties of NQDs. CdSe NQDs can be reliably prepared from pyrolysis of a variety of cadmium precursors, including alkyl cadmium compounds (e.g. dimethylcadmium)[15] and various cadmium salts (cadmium oxide, cadmium acetate, and cadmium carbonate),[16] combined with a selenium precursor prepared simply from Se powder dissolved in trioctylphosphine (TOP) or tributylphosphine (TBP). Initially, the surfactant-solvent combination, technical-grade trioctylphosphine oxide (tech-TOPO) and TOP, was used, where tech-TOPO performance was batch specific owing to the relatively random presence of adventitious impurities.[15] More recently, tech-TOPO has been replaced with 'pure' TOPO to which phosphonic acids have been added to controllably mimic the presence of the technical-grade impurities.[17] In addition, TOPO has been replaced with various fatty acids, such as stearic and lauric acid. The fatty-acid systems are compatible with the full range of cadmium precursors, but are most suited for growth of larger NQDs ($>$6 nm in diameter), compared to the TOPO/TOP system, since growth proceeds relatively more quickly.[16] Further, the choice of fatty acid can influence particle growth, as shorter alkyl chain lengths yield relatively faster growth (likely improving monomer access to particle surfaces). The cadmium precursor is typically dissolved in the fatty acid at moderate temperatures, converting the Cd compound to cadmium stearate, for example. Alkyl amines were also successfully employed as CdSe growth media.[16] Incompatible systems are those that contain the anion of a strong acid (present as the surfactant ligand or as the cadmium precursor) and thiol-based systems.[16] Perhaps the most successful system, in terms of producing high quantum yields (QYs) in emission and monodisperse samples, uses a complex mixture of surfactants: stearic acid, TOPO, hexadecylamine, TBP, and dioctylamine.[18]

2.3 Optimizing Photoluminescence

High QYs are indicative of a well-passivated surface. NQD emission can suffer from the presence of unsaturated, 'dangling' bonds at the particle surface that act as surface traps for charge carriers. Recombination of trapped carriers leads to a characteristic emission band ('deep-trap' emission) on the low-energy side of the 'band-edge' photoluminescence (PL) band. Band-edge emission is associated with recombination of carriers in NQD 'interior' quantized states. Coordinating ligands help to passivate surface trap sites, enhancing the relative intensity of band-edge emission compared to the deep-trap emission. The complex mixed-solvent system, described above, has been used to generate NQDs having QYs as high as 70 – 80%. These remarkably high PL efficiencies are comparable to the best achieved by inorganic epitaxial-shell surface-passivation techniques (see Section 3). They are attributed to the presence of a primary amine ligand, as well as to the use of excess selenium in the precursor mixture (ratio Cd:Se of 1:10). The former alone (i.e. coupled with a 'traditional' Cd:Se ratio of 2:1 or 1:1) yields PL QYs that are higher than those typically achieved by organic passivation (40–50% compared to 5–15%). The significance of the latter likely results from the unequal reactivities of the cadmium and selenium precursors. Accounting for the relative precursor reactivities by using such concentration-biased mixed precursors may permit improved crystalline growth and, hence, improved PL QYs.[18] Further, in order to achieve the very high QYs, reactions must be conducted over limited time spans from 5–30 min. PL efficiencies reach a maximum in the first half of the reaction and decline thereafter (Figure 4). Optimized preparations yield rather large NQDs, emitting in the orange–red. However, high-QY NQDs representing a variety of particle sizes are possible. By controlling precursor identity, total precursor concentrations, the identity of the solvent system, the nucleation and growth temperatures, and the growth time, NQDs emitting with $>$30% efficiency from $\sim$510 nm to 650 nm can be prepared.[18] Finally, the important influence of the primary amine ligands may result from their ability to pack more efficiently on the NQD surfaces. Compared to TOPO and TOP, primary amines are less sterically hindered and may simply allow for a higher capping density.[19] However, the amine-CdSe NQD linkage is not as stable as for other more strongly bound CdSe ligands.[20] Thus, growth solutions prepared from this procedure are highly luminescent but washing or processing into a new liquid or solid matrix can dramatically impact the QY. Multidentate amines may provide both the desired high PL efficiencies and the necessary chemical stabilities.[18]

High-quality NQDs are no longer limited to cadmium-based II–VI compounds. Preparations for III-V semiconductor NQDs are also well developed (see Section 3). Exclusively band-edge UV to blue emitting ZnSe NQDs ($\sigma = 10\%$) exhibiting QYs from 20 – 50% have been prepared by pyrolysis of diethylzinc and TOPSe at high temperatures (nucleation: 310 °C; growth: 270 °C). Successful reactions employed hexadecylamine (HDA)/TOP as the solvent system (elemental analysis indicating that bound surface ligands comprised two-thirds HDA and one-third TOP), while the

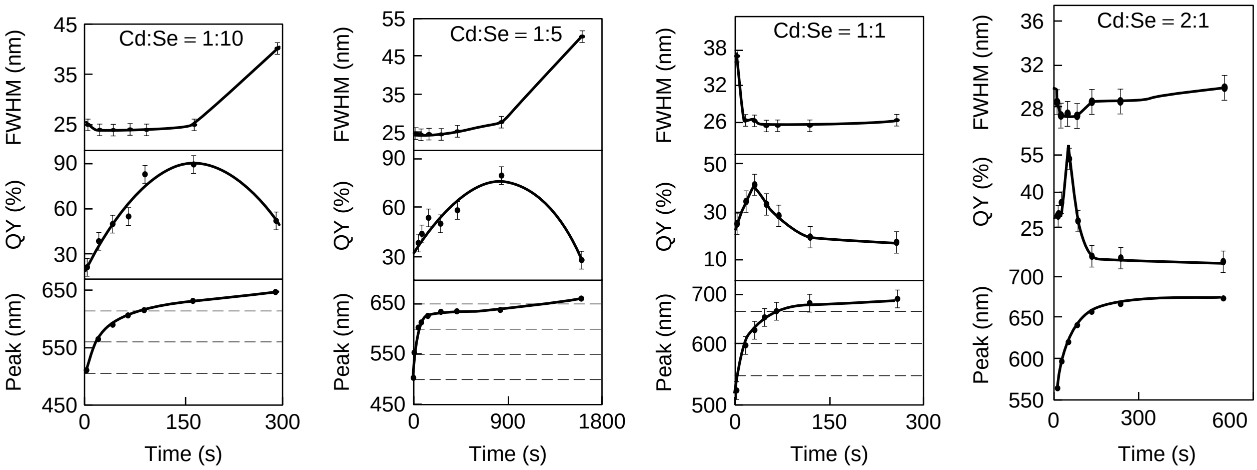

Figure 4 Temporal evolution of the full-width-at-half-maximum (FWHM) of the PL band, the PL QY, and the PL peak position for identical reactions differing only with respect to their initial Cd:Se precursor ratios (see top boxes). (Reprinted with permission from Ref. 18. © 2002 American Chemical Society)

TOPO/TOP combination did not work for this material. Indeed, the nature of the reaction product was very sensitive to the TOPO/TOP ratio. Too much TOPO, which binds strongly to Zn, generated particles so small that they could not be precipitated from solution by addition of a nonsolvent. Too much TOP, which binds very weakly to Zn, yielded particles that formed insoluble aggregates. As somewhat weaker bases compared to phosphine oxides, primary amines constitute ligands of intermediate strength, and, in addition, may provide enhanced capping density (as discussed earlier).[19] HDA, in contrast with shorter-chain primary amines (octylamine and dodecylamine), provided good solubility properties and permitted sufficiently high growth temperatures for reasonably rapid growth of highly crystalline ZnSe NQDs.[19]

High-quality NQDs absorbing and emitting in the infrared have also been prepared by way of a surfactant-stabilized pyrolysis reaction. PbSe colloidal quantum dots can be synthesized from the precursors: lead oleate (prepared *in situ* from lead(II)acetate trihydrate and oleic acid)[21] and TOPSe.[10,21] TOP and oleic acid are present as the coordinating solvents, while phenyl ether, a noncoordinating solvent, provides the balance of the reaction solution. Injection and growth temperatures are varied (injection: 180–210 °C; growth: 110–130 °C) to control particle size from ~3.5 nm–~9 nm in diameter.[21] The particles respond to 'traditional' size-selection precipitation methods, allowing the narrow as-prepared size dispersions ($\sigma \leq 10\%$) to be further refined ($\sigma = 5\%$) if desired.[10] Oleic acid provides excellent capping properties as photoluminescence (PL) quantum efficiencies, relative to IR dye no. 26, are ~85%.[21] PbSe NQDs afford an important alternative to their organic-dye counterparts, which suffer from low QYs in PL (<0.5%) and poor photostability. NQD emission is not limited to the near IR. By preparing large-size PbSe NQDs (>10 nm) (Figure 5), we recently achieved efficient emission in the mid-infrared (to 4 µm) (Figure 6), obtaining several-percent quantum efficiencies at this very red wavelength.[22]

2.4 Aqueous-based Synthetic Routes and the Inverse-micelle Approach

In addition to the moderate (~150 °C) and high-temperature (>200 °C) preparations discussed above, many room-temperature reactions have been developed. The two most prevalent schemes entail thiol-stabilized aqueous-phase growth and inverse-micelle methods. We will briefly consider these approaches here, and the former is discussed in some detail in Section 3 as it pertains to core/shell nanoparticle growth. In general, the low-temperature methods suffer from relatively poor size dispersions ($\sigma > 20\%$) and often exhibit significant, if not exclusively, trap-state PL. The latter is inherently weak and broad compared to band-edge PL, and it is less sensitive to quantum-size effects and particle-size control. Further, low-T aqueous preparations are limited in their applicability to relatively ionic materials. Higher temperatures are required to prepare *crystalline* covalent compounds (barring reaction conditions that may reduce the energetic barriers to crystalline growth, for example, catalysts and templating structures). Thus, II–VI compounds, which are more ionic compared to III–V compounds, have been successfully prepared at low temperatures (room T or less), while III-V compound semiconductors have not.[23]

The processes of nucleation and growth in aqueous systems are conceptually similar to those observed in their higher-temperature counterparts. Typically, the metal perchlorate salt is dissolved in water, and the thiol stabilizer is added (commonly, 1-thioglycerol). After the pH is adjusted to >11 (or from 5–6 if ligand is a mercaptoamine[24]) and the solution is deaerated, the chalcogenide is added as the hydrogen

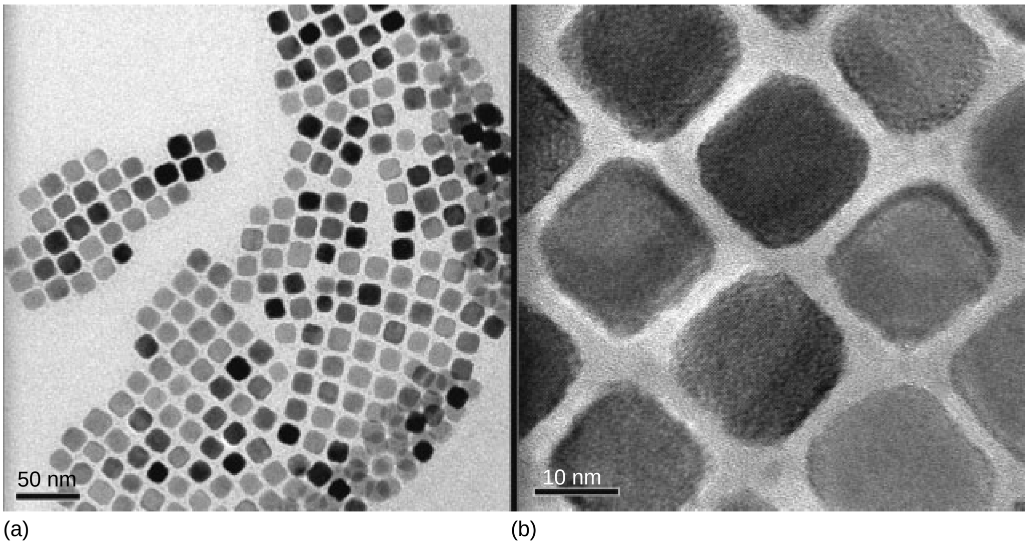

Figure 5 (a) Lower-magnification TEM imaging reveals the nearly uniform size and shape of the large-size PbSe NQDs (here, 17 nm). (b) High-resolution (HR) TEM of the PbSe NQDs, where the internal crystal lattice is evident for several of the particles

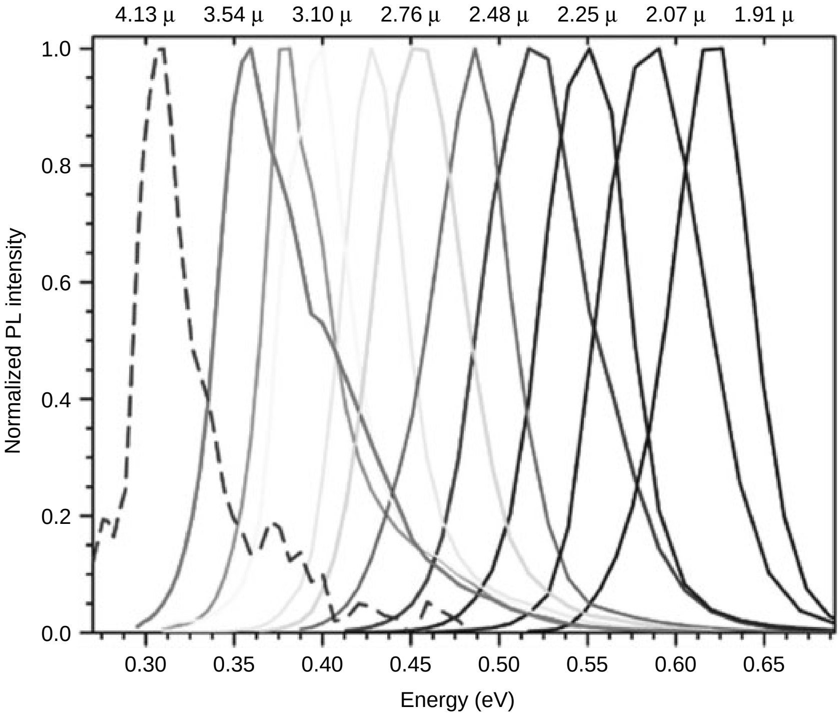

Figure 6 With large-size PbSe QDs (>8 nm in diameter) we demonstrated efficient PL in the mid-IR: Normalized spectra of a size series of PbSe QDs at RT, showing excellent tunability and narrow size distributions ($\sigma \sim 10\%$). The dashed spectrum was collected at 77 K from a sample with a peak at 0.34 eV at RT, exhibiting a red shift and narrowing

chalcogenide gas.[23,25,26] Addition of the chalcogenide induces particle nucleation. The nucleation process appears not to be an ideal, temporally discrete event, as the initial particle-size dispersion is large, as evidenced, for example, in broad PL spectra. Growth, or ‘ripening’, is allowed to proceed over several days, after which a redshift in the PL spectrum is observed, and the spectrum is still broad.[23] For example, fractional precipitation of an aged CdTe growth solution yields a size series exhibiting emission spectra centered from 540 nm to 695 nm, where the full width at half maximum (FWHM) of the size-selected samples are at best 50 nm,[23] compared to ∼25 nm for the best high-temperature reactions. In Cd-based systems, the ripening process can be accelerated by warming the solution; however, in Hg-based systems heating the solution results in particle instability and degradation.[23] Initial particle size can be roughly 'tuned' by changing the identity of the thiol ligand. The thiol binds to metal ions in solution prior to particle nucleation, and extended X-ray absorption fine structure (EXAFS) studies have demonstrated that the thiol stabilizer binds exclusively to metal surface sites in the formed particles.[27] By changing the strength of this metal–thiol interaction, larger or smaller particle sizes can be obtained. For example, decreasing the bond strength by introducing an electron withdrawing group adjacent to the sulfur atom leads to larger particles.[24,27]

The advantage of room-temperature, aqueous-based reactions lies in their ability to produce nanocrystal compositions that are, as yet, unattainable by higher-temperature pyrolysis methods. Of the II–VI compounds, Hg-based materials are thus far restricted to the temperature/ligand combination afforded by the aqueous thiol-stabilized preparations. The nucleation and growth of mercury chalcogenides have proven difficult to control in higher-temperature, nonaqueous reactions. Relatively weak ligands, fatty acids and amines (stability constant $K < 10^{17}$), yield fast growth and precipitation of the mercury chalcogenide, while stronger ligands, polyamines, phosphines, phosphine oxides, and thiols (stability constant $K > 10^{17}$), promote reductive elimination of metallic mercury at elevated temperatures.[13] Very high PL efficiencies (up to 50%) are reported for HgTe NQDs prepared in water.[26] However, the as-prepared samples yield approximately featureless absorption spectra and broad PL spectra. Further, the PL QYs for NQDs that emit at >1 µm have been determined in comparison with Rhodamine 6G, which has a PL maximum at ∼550 nm. Typically, spectral overlap between the NQD emission signal and the reference organic dye is required to ensure reasonable QY values by taking into account the spectral response of the detector.

An alternative low-temperature approach that has been applied to a variety of systems, including mercury chalcogenides, is the inverse-micelle method. In general, the reversed-micelle approach entails preparation of a surfactant/polar-solvent/nonpolar-solvent microemulsion, where the content of the spontaneously generated spherical micelles is the polar-solvent fraction and that of the external matrix is the nonpolar solvent. The surfactant is commonly dioctyl sulfosuccinate, sodium salt (AOT). Precursor cations and anions are added and enter the polar phase. Precipitation follows, and particle size is controlled by the size of the inverse-micelle 'nanoreactors', as determined by the water content, W, where $W = [H_2O]/[AOT]$. For example, in an early preparation, AOT was mixed with water and heptane, forming the microemulsion. Cd^{2+}, as $Cd(ClO_4)_2{\cdot}6H_2O$, was stirred into the microemulsion allowing it to become incorporated into the interior of the reverse micelles. The selenium precursor was subsequently added and, upon mixing with cadmium, nucleated colloidal CdSe. Untreated solutions were observed to flocculate within hours, yielding insoluble aggregated nanoparticles. Addition of excess water quickened this process. However, promptly evaporating the solutions to dryness, removing micellar water, yielded surfactant-encased colloids that could be redissolved in hydrocarbon solvents. Alternatively, surface passivation could be provided by first growing a cadmium shell via further addition of Cd^{2+} precursor to the microemulsion followed by addition of phenyl(trimethylsilyl)selenium (PhSeTMS). PhSe-surface passivation prompted precipitation of the colloids from the microemulsion. The colloids could then be collected by centrifugation or filtering and redissolved in pyridine.[28]

More recently, the inverse-micelle technique has been applied to mercury-chalcogenides as a means to control the fast growth rates characteristic of this system (see above).[13] The process employed is similar to traditional micelle approaches; however, the metal and chalcogenide precursors are phase segregated. The mercury precursor (e.g. mercury(II)acetate) is transferred to the aqueous phase, while the sulfur precursor [bis (trimethylsilyl) sulfide $(TMS)_2S$] is introduced to the nonpolar phase. Additional control over growth rates is provided by the strong mercury ligand, thioglycerol, similar to thiol-stabilized aqueous-based preparations. Growth is arrested by replacing the sulfur solution with aqueous or organometallic cadmium or zinc solutions. The Cd or Zn add to the surface of the growing particles and sufficiently alter surface reactivity to effectively halt growth. Interestingly, addition of the *organometallic* metal sources results in a significant increase in PL QY to 5–6%, whereas, no observable increase accompanies passivation with the aqueous sources. Wide size dispersions are reported ($\sigma = 20$–30%). Nevertheless, absorption spectra are sufficiently well developed to clearly demonstrate that associated PL spectra, red-shifted with respect to the absorption band edge, derive from band-edge luminescence and not deep-trap-state emission. Finally, ligand exchange with thiophenol permits isolation as aprotic-polar-soluble NQDs, while exchange with long-chain thiols or amines permits isolation as nonpolar-soluble NQDs.[13]

The inverse-micelle approach may also offer a generalized scheme for the preparation of monodisperse metal-oxide nanoparticles.[29] The reported materials are ferroelectric oxides and, thus, stray from our emphasis on optically active semiconductor NQDs. Nevertheless, the method demonstrates an intriguing and useful approach: the combination of sol-gel techniques with inverse-micelle nanoparticle synthesis (with *moderate*-temperature nucleation and growth). Monodisperse barium titanate, $BaTiO_3$, nanocrystals, with diameters controlled in the range from 6–12 nm, were prepared. In addition, proof-of-principle preparations were successfully conducted for TiO_2 and $PbTiO_3$. *Single-source* alkoxide precursors are used to ensure proper stoichiometry in the preparation of complex oxides (e.g. bimetallic oxides) and are commercially available for a variety of systems. The precursor is injected into a stabilizer-containing solvent (oleic acid in diphenyl ether; 'moderate' injection temperature: 140 °C). The hydrolysis-sensitive precursor is, up to this point, protected from water. The solution temperature is then reduced to 100 °C (growth temperature), and 30 wt% hydrogen peroxide solution (H_2O/H_2O_2) is added. Addition of the H_2O/H_2O_2 solution generates the microemulsion state and prompts a vigorous exothermic reaction. Control over particle size is exercised either by changing the precursor/stabilizer ratio or the amount of H_2O/H_2O_2 solution that is added. Increasing either results in an increased particle size, while decreasing the precursor/stabilizer ratio leads to a decrease in particle size. Following growth over 48 h, the particles are extracted into nonpolar solvents such as hexane. The extreme monodispersity of these relatively unique nano-oxides was evident following preparation of highly ordered superlattices, exhibiting periodicity over several microns, by slow precipitation from hexane (polydisperse samples yield disordered 2-D and 3-D arrays).[29]

3 INORGANIC SURFACE MODIFICATION

Surfaces play an increasing role in determining nanocrystal structural and optical properties as particle size is reduced. For example, owing to an increasing surface-to-volume ratio with diminishing particle size, surface trap states exert an enhanced influence over photoluminescence properties, including emission efficiency, and spectral shape, position and dynamics. Further, it is often through their surfaces that semiconductor nanocrystals interact with 'their world', as soluble species in an organic solution, reactants in common organic reactions, polymerization centers, biological tags, electron/hole donors/acceptors, and so on. Controlling organic and inorganic surface chemistry is key to controlling the physical and chemical properties that make NQDs unique compared to their epitaxial quantum-dot counterparts. In the previous section, we discussed the impact of organic ligands on particle growth and particle properties. In this section, we review surface modification techniques that utilize *inorganic* surface treatments. NQDs overcoated with a semiconductor layer are generally referred to as (core)shell NQDs. Thus far, the core-shell motif has permitted enhanced photoluminescence,[20,30–34] improved stability against photochemical oxidation,[20,31,35] enhanced processibility,[36] and band-structure engineering ('Type-II structures' – optical transition energies are not limited to band-gap energies).[37]

3.1 (Core)Shell NQDs

Overcoating highly monodisperse CdSe with epitaxial layers of either ZnS[30,31] or CdS (Figure 7)[20] has become routine and typically provides almost an order of magnitude enhancement in PL efficiency compared to the exclusively organic-capped starting nanocrystals [5–10% efficiencies can yield 30–70% efficiencies (Figure 8)]. The enhanced quantum efficiencies result from enhanced coordination of surface unsaturated, or dangling, bonds, as well as from improved confinement of electrons and holes to the particle core. The latter effect occurs when the band gap of the shell material is larger than that of the core material, as is the case for (CdSe)ZnS and (CdSe)CdS (core)shell particles. Successful overcoating of III-V semiconductors has also been reported.[32–34]

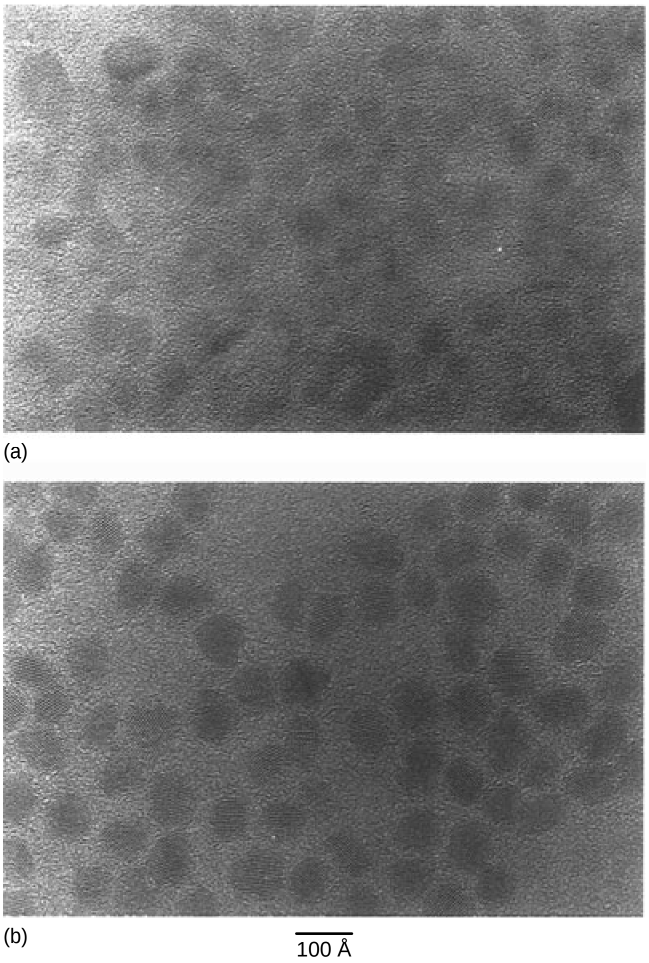

Figure 7 Wide-field HR-TEMs of (a) 3.4-nm diameter CdSe core particles and (b) (CdSe)CdS (core)shell particles prepared from the core NQDs in (a) by overcoating with a 0.9-nm thick CdS shell. Where lattice fringes are evident, they span the entire nanocrystal, indicating epitaxial (core) shell growth. (Reprinted with permission from Ref. 20. © 1997 American Chemical Society)

The various preparations share several synthetic features. First, the best results are achieved if initial particle size distributions are narrow, as some size-distribution broadening occurs during the shell-growth process. Because absorption spectra are relatively unchanged by surface properties, they

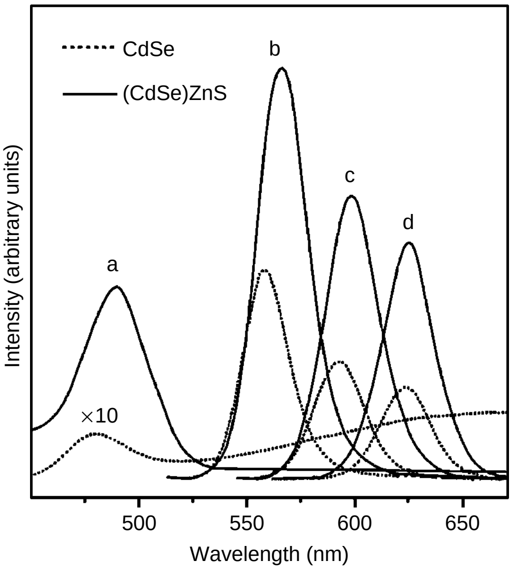

Figure 8 PL spectra for CdSe NQDs and (CdSe)ZnS (core)shell NQDs. Core diameters are (a) 2.3, (b) 4.2, (c) 4.8, and (d) 5.5 nm. (Core)shell PL QYs are (a) 40, (b) 50, (c) 35, and (d) 30%. Trap-state emission is evident in the (a) core-particle PL spectrum as a broadband to the red of the band-edge emission and absent in the respective (core)shell spectrum. (Reprinted with permission from Ref. 30. © 1997 American Chemical Society)

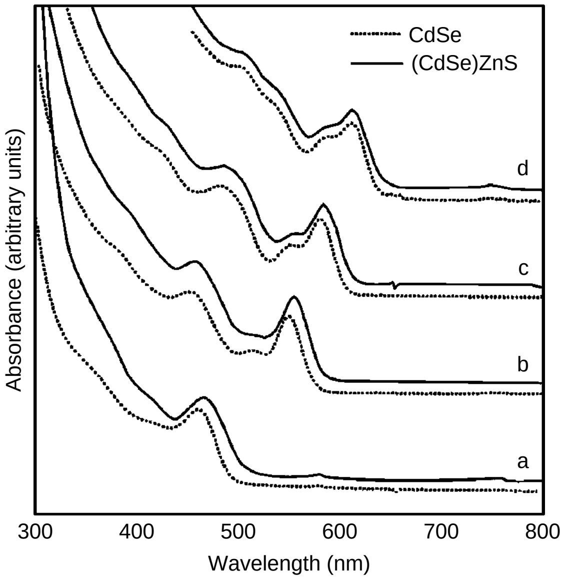

Figure 9 Absorption spectra for bare (dashed lines) and 1–2 monolayer ZnS-overcoated (solid lines) CdSe NQDs. (Core)shell spectra are broader and slightly red-shifted compared to the core counterparts. Core diameters are (a) 2.3, (b) 4.2, (c) 4.8, and (d) 5.5 nm. (Reprinted with permission from Ref. 31. © 1997 American Chemical Society)

can be used to monitor the stability of the nanocrystal core during and following growth of the inorganic shell. Further, if the conduction band offset between the core and the shell materials is sufficiently large (i.e. large compared to the electron confinement energy), then significant redshifting of the absorption band edge should not occur, as the electron wave function remains confined to the core (Figure 9). A large red shift in (core)shell systems, having sufficiently large offsets (determined by the identity of the core/shell materials and the electron and hole effective masses), indicates growth of the core particles during shell preparation. A small broadening of absorption features is common and results from some broadening of the particle size dispersion (Figure 9). Alloying, or mixing of the shell components into the interior of the core, would also be evident in absorption spectra if it were to occur. The band edge would shift to some intermediate energy between the band energies of the respective materials comprising the alloyed nanoparticle.

PL spectra can be used to indicate whether effective passivation of surface traps has been achieved. In poorly passivated nanocrystals, deep-trap emission is evident as a broad tail or hump to the red of the sharper band-edge emission spectral signal. The broad, trap signal will disappear and the sharp, band-edge luminescence will increase following successful shell growth (Figure 8(a)). Note: The trap-state emission signal contribution is typically larger in smaller (higher relative-surface-area) nanocrystals than in larger nanoparticles (Figure 8(a)).

Homogeneous nucleation and growth of shell-material as discrete nanoparticles may compete with *heterogeneous* nucleation and growth at core-particle surfaces. Typically, a combination of relatively low precursor concentrations and reaction temperatures is used to avoid particle formation. Low precursor concentrations support undersaturated-solution conditions and, thereby, shell growth by heterogeneous nucleation. The precursors, diethylzinc and bis(trimethylsilyl) sulfide in the case of ZnS shell growth, for example, are added dropwise at relatively low temperatures to prevent buildup and supersaturation of unreacted precursor monomers in the growth solution. Further, employing relatively low reaction temperatures avoids growth of the starting core particles.[20,31] ZnS, for example, can nucleate and grow as a crystalline shell at temperatures as low as 140 °C[31] and CdS shells have been successfully prepared from dimethylcadmium and bis(trimethylsilyl) sulfide at 100 °C,[20] thereby avoiding complications owing to homogeneous nucleation and core-particle growth. Additional strategies for preventing particle growth of the shell material include using organic capping ligands that have a particularly high affinity for the shell metal. The presence of a strong binding agent seems to lead to more controlled shell growth, for example, TOPO is replaced with TOP in CdSe shell growth on InAs cores, where TOP (softer Lewis base) coordinates more tightly than TOPO (harder Lewis base) with cadmium (softer Lewis acid).[34] Finally, the ratio of the cationic to anionic precursors can be used to prevent shell-material homogeneous nucleation. For example, increasing the concentration of the chalcogenide in a cadmium–sulfur precursor mixture hinders formation of unwanted CdS particles.[20]

Successful overcoating is possible for systems where relatively large lattice mismatches between core and shell crystal structures exist. The most commonly studied (core)shell system (CdSe)ZnS, is successful despite a 12% lattice mismatch. Such a large lattice mismatch could not be tolerated in flat heterostructures, where strain-induced defects would dominate the interface. It is likely that the highly curved surface and reduced facet lengths of nanocrystals relax the structural requirements for epitaxy. Indeed, two types of epitaxial growth are evident in the (CdSe)ZnS system: coherent (with large distortion or strain) and incoherent (with dislocations), the difference arising for thin (approximately one to two monolayers, where a monolayer is defined as 3.1 Å) versus thick (> two monolayers) shells, respectively.[31] High-resolution TEM images of thin-shell-ZnS-overcoated CdSe QDs reveal lattice fringes that are continuous across the entire particle, with only a small ‘bending’ of the lattice fringes in some particles indicating strain. TEM imaging has also revealed that thicker shells (>2 monolayers) lead to the formation of deformed particles, resulting from uneven growth across the particle surface. Here, too, however, the shell appeared epitaxial, oriented with the lattice of the core (Figure 10). Nevertheless, wide-angle X-ray scattering (WAXS) data showed reflections for both CdSe and ZnS, indicating that each was exhibiting its own lattice parameter in the thicker-shell systems. This type of structural relationship between the core and the shell was described as *incoherent* epitaxy. It was speculated that at low coverage, the epitaxy is coherent (strain is tolerated), but that at higher coverages, the high lattice mismatch can no longer be sustained without the formation of dislocations and low-angle grain boundaries. Such defects in the core-shell boundary provide non-radiative recombination sites and lead to diminished PL efficiency compared to coherently epitaxial thinner shells. Further, in all cases studied where more than a single monolayer of ZnS was deposited, the shell appeared to be continuous. X-ray photoelectron spectroscopy (XPS) was used to detect the formation of SeO_2 following exposure to air. The SeO_2 peak was observed only in bare TOPO/TOP-capped dots and dots having less than one monolayer of ZnS overcoating. Together, the high-resolution TEM images and XPS data suggest complete, epitaxial-shell formation in the highly lattice-mismatched system of (CdSe)ZnS.

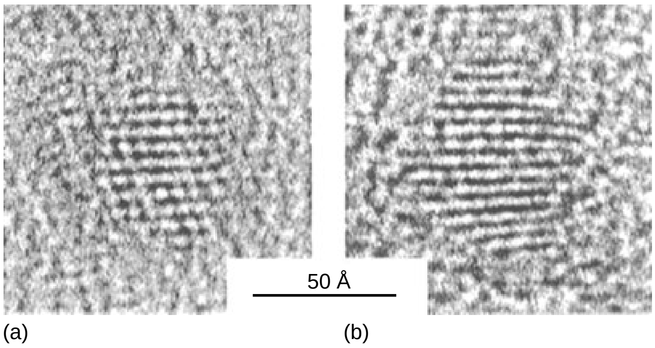

Figure 10 HR-TEM of (a) CdSe core particle and (b) a (CdSe)ZnS (core)shell particle (2.6 monolayer ZnS shell). Lattice fringes in (b) are continuous throughout the particle, suggesting epitaxial (core)shell growth. (Reprinted with permission from Ref. 31. © 1997 American Chemical Society)

The effect of lattice mismatch has also been studied in III-V semiconductor core systems. Specifically, InAs has been successfully overcoated with InP, CdSe, ZnS, and ZnSe.[34] The degree of lattice mismatch between InAs and the various shell materials differed considerably, as did the PL efficiencies achieved for these systems. However, no direct correlation between lattice mismatch and QY in PL was observed. For example, (InAs)InP produced quenched luminescence while (InAs)ZnSe provided up to 20% PL QYs, where the respective lattice mismatches are 3.13% and 6.44%. CdSe shells, providing a lattice *match* for the InAs cores, also produced up to 20% PL QYs. In all cases, shell growth beyond two monolayers (where a monolayer equals the d_{111} lattice spacing of the shell material) caused a decrease in PL efficiencies, likely due to the formation of defects that could provide trap sites for charge carriers [as observed in (CdSe)ZnS[31] and (CdSe)CdS[20] systems]. The perfectly lattice-matched CdSe shell material should provide the means for avoiding defect formation; however, the stable crystal structures for CdSe and InAs are different under the growth conditions employed. CdSe prefers the wurtzite structure while InAs prefers cubic. For this reason, this ‘matched’ system may succumb to interfacial defect formation with thick shell growth.[34]

The larger contributor to PL efficiency in the (InAs)shell systems was found to be the size of the energy offset between the respective conduction and valence bands of the core and shell materials. Larger offsets provide larger potential energy barriers for the electron and hole wave functions at the (core)shell interface. For InP and CdSe, the conduction band offset with respect to InAs is small. This allows the electron wave function to experience the surface of the nanoparticle. In the case of CdSe, fairly high PL efficiencies can still be achieved because native trap sites are less prevalent than they are on InP surfaces. Both ZnS and ZnSe provide large energy offsets. The fact that the electron wave function remains confined to the core of the (core)shell particle is evident in the absorption and PL spectra. In these confined cases, no red shifting was observed in the optical spectra following shell growth.[34] The observation that PL enhancement to only 8% quantum yield was possible using ZnS as the shell material may have been due to the large lattice mismatch between InAs and ZnS of ∼11%. Otherwise, ZnS and ZnSe should behave similarly as shells for InAs cores.

Shell chemistry can be precisely controlled to achieve unstrained (core)shell epitaxy. For example, the zinc–cadmium alloy, $ZnCdSe_2$ was used for the preparation of (InP) $ZnCdSe_2$ nanoparticles having essentially zero lattice mismatch between the core and the shell.[32] High-resolution TEM images demonstrated the epitaxial relationship between the layers, and very thick epilayer shells were grown – up to 10 monolayers, where a monolayer was defined as 5 Å. The shell layer successfully protected the InP surface from oxidation, a degradation process to which InP is particularly susceptible.

3.2 Quantum-dot/Quantum-well Structures

Optoelectronic devices comprising two-dimensional quantum-well structures are generally limited to material pairs that are well lattice-matched owing to the limited strain tolerance of such planar systems; otherwise, very thin well layers are required. In order to access additional quantum-well-type structures, more strain-tolerant systems must be employed. As already alluded to, the highly curved quantum-dot nanostructure is ideal for lattice-mismatched systems. Several quantum-dot/quantum-well (QD/QW) structures have been successfully synthesized, ranging from the well lattice-matched CdS(HgS)CdS[38–40] (quantum dot, quantum well, cladding) to the more highly strained ZnS(CdS)ZnS.[41] The former provides emission color tunability in the infrared spectral region, while the latter yields access to the blue–green spectral region. In contrast to the very successful (core)shell preparations discussed earlier in this section, the QD/QW structures have been prepared using ion displacement reactions, rather than heterogeneous nucleation on the core surface (Figure 11). These preparations have been either aqueous or polar-solvent based and conducted at low temperatures (room temperature to – 77 °C). They entail a series of steps that first involves the preparation of the nanocrystal cores (CdS and ZnS, respectively). Core preparation is followed by ion-exchange reactions in which a salt precursor of the 'well' metal ion is added to the solution of 'core' particles. The solubility product constant (K_{sp}) of the metal sulfide corresponding to the added metal species is such that it is significantly less than that of the metal sulfide of the core metal species. This solubility relationship leads to precipitation of the added metal ions and dissolution of the surface layer of core metal ions via ion exchange. Analysis of absorption spectra during addition of 'well' ions to the nanoparticle solution revealed an apparent concentration threshold, after which addition of the 'well' ions produced no more change in the optical spectra. Specifically, in the case of the CdS(HgS)CdS system, ion exchange of Hg^{2+} for Cd^{2+} produced a redshift in absorption until a certain amount of 'well' ions had been added. According to inductively coupled plasma-mass spectrometry (ICP-MS), which was used to measure the concentration of free ions in solution for both species, up until this threshold concentration was reached the concentration of free Hg^{2+} ions was essentially zero, while the Cd^{2+} concentration increased linearly. After the threshold concentration was reached, the Hg^{2+} concentration increased linearly (with each externally provided addition to the system), while the Cd^{2+} concentration remained approximately steady. These results agree well with the ion-exchange reaction scenario, and, perhaps more importantly, suggest a certain natural limit to the exchange process. It was determined that in the example of 5.3 nm CdS starting core nanoparticles, approximately 40% of the Cd^{2+} was replaced with Hg^{2+}. This value agrees well with the conclusion that one complete monolayer has been replaced, as the surface-to-volume ratio in such nanoparticles is 0.42. Further dissolution of Cd^{2+} core ions is prevented by formation of the complete monolayer-thick shell, which also precludes the possibility of island-type shell growth.[39]

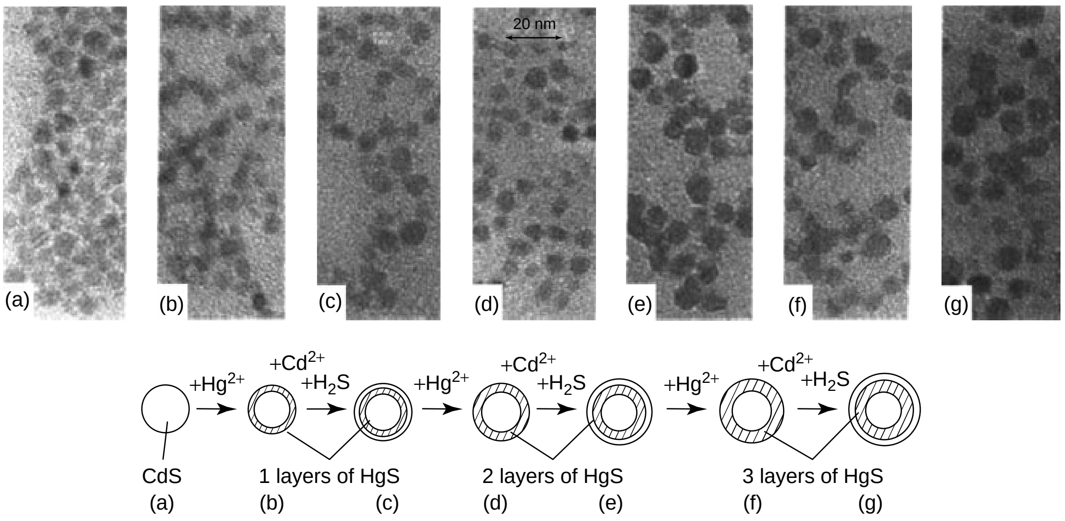

Figure 11 TEMs of CdS(HgS)CdS at various stages of the ion displacement process, where the latter is schematically represented in the figure. (Reprinted with permission from Ref. 39. © 1994 American Chemical Society)

Subsequent addition of H_2S or Na_2S causes the precipitation of the off-cast core ions back onto the particles. The ion replacement process, requiring the sacrifice of the newly re-deposited core metal ions, can then be repeated in order to increase the thickness of the 'well' layer. This process has been successfully repeated for up to three layers of well material. The 'well' is then capped with a re-deposited layer of core metal ions to generate the full QD/QW structure. The thickness of the cladding layer could be increased by addition in several steps (up to 5) of the metal and sulfur precursors.[39]

The nature of the QD/QW structure and its crystalline quality have been analyzed by high-resolution TEM. In the CdS(HgS)CdS system, evidence has been presented for both approximately spherical particles, as well as faceted particle shapes such as tetrahedrons and twinned tetrahedrons. In all cases, well and cladding growth is epitaxial as evidenced by the absence of amorphous regions in the nanocrystals and in the smooth continuation of lattice fringes across particles. Analysis of HR-TEM micrographs also reveals that the tetrahedral shapes are terminated by (111) surfaces that can be *either* cadmium or sulfur faces.[40] The choice of stabilizing agent – an anionic polyphosphate ligand – favors cadmium faces and likely supports the faceted tetrahedral structure that exposes exclusively cadmium-dominated surfaces (Figure 12). In addition, both the spherical particles and the twinned tetrahedral particles provide evidence for an embedded HgS layer in the presumed QD/QW structure. Owing to differences in their relative abilities to interact with electrons (HgS more strongly than CdS), contrast differences are evident in HR-TEM images as bands of HgS surrounded by layers of CdS (Figure 12).

Size dispersions in these low-temperature, ionic-ligand stabilized reactions are reasonably good (∼20%), as indicated by absorption spectra, but poor compared to those achieved using higher-temperature pyrolysis and amphiphilic coordinating ligands (4–7%). Nevertheless, the polar-solvent-based reactions give us access to colloidal materials, such as mercury chalcogenides, thus far difficult to prepare using pyrolysis-driven reactions (Section 2). Further, the ion-exchange method provides the ability to grow well and shell structures that appear to be precisely 1, 2, or 3 monolayers deep. Heterogeneous nucleation provides less control over shell thicknesses, resulting in incomplete and variable multilayers (e.g. 1.3 or 2.7 monolayers *on average*, etc.). Stability of core/shell materials against solid-state alloying is an issue, at least for the CdS(HgS)CdS system. Specifically, cadmium in a CdS/HgS structure will, within minutes, diffuse to the surface of the nanoparticle where it is subsequently replaced by a Hg^{2+} solvated ion.[39] This process is likely supported by the substantially greater aqueous solubility of Cd^{2+} compared to Hg^{2+}, as well as the structural compatibility between the two lattice-matched CdS and HgS crystal structures.

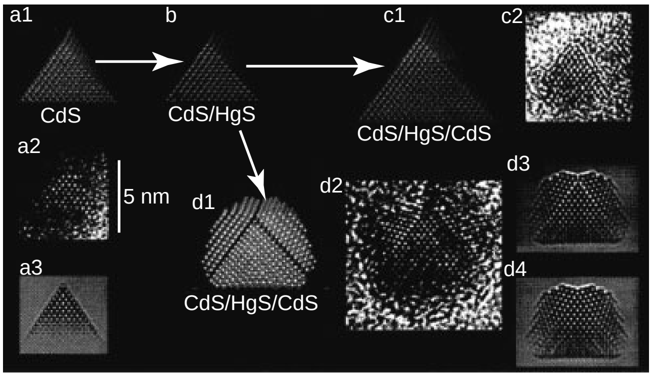

Figure 12 HR-TEM study of the structural evolution of a CdS core particle to a (CdS) (core)shell particle to the final CdS(HgS)CdS nanostructure. (a1) molecular model showing that all surfaces are cadmium terminated (111). (a2) TEM of a CdS core that exhibits tetrahedral morphology. (a3) TEM simulation agreeing with (a2) micrograph. (b) Model of the CdS particle after surface modification with Hg. (c1) Model of a tetrahedral CdS(HgS)CdS nanocrystal. (c2) A typical TEM of a tetrahedral CdS(HgS)CdS nanocrystal. (d1) Model of a CdS(HgS)CdS nanocrystal after twinned epitaxial growth, where the arrow indicates the interfacial layer exhibiting increased contrast owing to the presence of HgS. (d2) TEM of a CdS(HgS)CdS nanocrystal after twinned epitaxial growth. (d3) Simulation agreeing with model (d1) and TEM (d2) showing increased contrast owing to presence of HgS. (d4) Simulation assuming all Hg is replaced by Cd – no contrast is evident. (Reprinted Figure 1 with permission from A. Mews, A.V. Kadavanich, U. Banin, and A.P. Alivisatos, *Phys. Rev. B.*, **53**, R13242-R13245 (1996). © 1996 by the American Physical Society)

4 SHAPE CONTROL

The nanoparticle growth process described in Section 2, where fast nucleation is followed by slower growth, typically leads to the formation of spherical or approximately spherical particles. Such essentially isotropic particles represent the thermodynamic, lowest energy, shape for materials having relatively isotropic underlying crystal structures. For example, under this growth regime, the wurtzite crystal structure of CdSe, having a c/a ratio of $\sim$1.6, fosters the growth of slightly prolate particles, typically exhibiting aspect ratios of approximately 1.2. Furthermore, even for materials whose underlying crystal structure is more highly anisotropic, nearly spherical nanoparticles often result owing to the strong influence of the surface in the nanosize regime. Surface energy is minimized in spherical particles, compared to more anisotropic morphologies.

4.1 Kinetically Driven Growth of Anisotropic NQD Shapes – CdSe As the Model System

Under a different growth regime, one that promotes fast, kinetic growth, more highly anisotropic shapes, such as rods and wires, can be obtained. In semiconductor nanoparticle synthesis, such growth conditions have been achieved using high precursor, or monomer, concentrations in the growth solution. As discussed previously (Section 2), particle-size distributions can be ‘focused’ by maintaining relatively high monomer concentrations that prevent the transition from the fast-growth to the slow-growth (Ostwald ripening) regime.[14] Even higher monomer concentrations can be used to effect a transition from thermodynamic to kinetic growth. Access to the regime of very fast, kinetic growth allows control over particle shape. The system is essentially put into ‘kinetic overdrive,’ where dissolution of particles is minimized as the monomer concentration is maintained at levels higher than the solubility of all of the particles in solution. Growth of all particles is, thereby, promoted.[14] Further, in this regime, the rate of particle growth is not limited by diffusion of monomer to the growing crystal surface, but, rather, by how fast atoms can add to that surface. In this way, the relative growth rates of different crystal faces strongly influence the final particle shape.[42] Specifically, in systems where the underlying crystal lattice structure is anisotropic, for example, the wurtzite structure of CdSe, simply the presence of high monomer concentrations (kinetic growth regime) at and immediately following nucleation can accentuate the differences in relative growth rates between the unique *c*-axis and the remaining lattice directions, promoting rod growth. In other words, the monomer-concentration-dependent transition from slower-growth to fast-growth regimes coincides with a transition from diffusion controlled to reaction-rate-controlled growth and from dot to rod growth. In general, longer rods are achieved with higher initial monomer concentrations, and rod growth is sustained over time by maintaining high monomer concentrations using multiple-injection techniques. Finally, the relative rates of different crystallographic faces can be further controlled by judicious choice of organic ligands.[12,17]

In order to more precisely tune the growth rates controlling CdSe rod formation, high monomer concentrations are used in conjunction with appropriate organic ligand mixtures. In this way, a wide range of rod aspect ratios has been produced (Figure 13).[12,17,42] Specifically, the ‘traditional’ trioctylphosphine oxide (TOPO) ligand is supplemented with alkyl phosphonic acids. The phosphonic acids are strong metal (Cd) binders and may influence rod growth by changing the relative growth rates of the different crystal faces.[42] CdSe rods form by enhanced growth along the crystallographically unique *c*-axis (taking advantage of the anisotropic wurtzite crystal structure). Interestingly, the fast growth has been shown to be unidirectional – exclusively on the (001) face.[42] The (001) facets comprise alternating Se and Cd layers, where the Cd atoms are relatively unsaturated (three dangling bonds per atom). In contrast, the related (001) facet exposes relatively saturated Cd faces having one dangling bond per atom (Figure 14). Thus, compared to (001), the (001) face (opposite *c*-axis growth) and {110} faces (*ab* growth), for example, are slow growing, and *unidirectional* rod growth is promoted. The exact mechanism by which the phosphonic acids alter the relative growth rates is not certain. Their influence may be in inhibiting the growth of (001) and {110} faces or it may be in directly promoting growth of the (001) face by way of interactions with surface metal sites.[42]

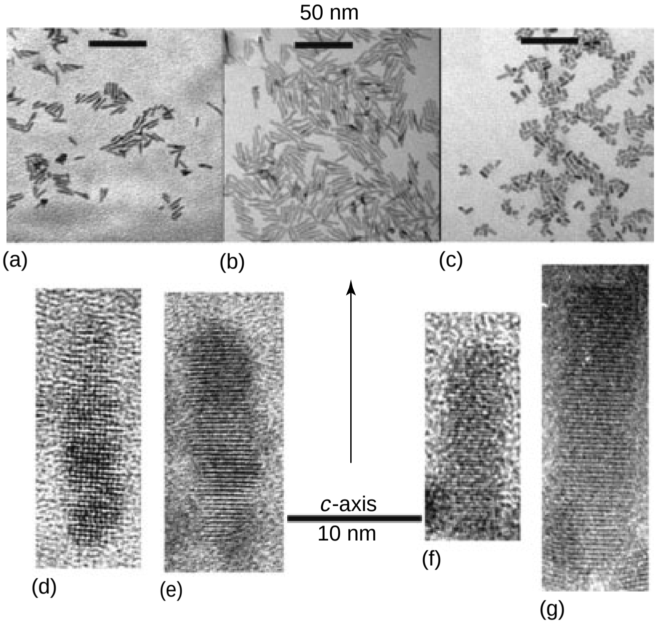

Figure 13 (a-c) TEMs of CdSe quantum rods demonstrating a variety of sizes and aspect ratios. (d-g) HR-TEMs of CdSe quantum rods revealing lattice fringes and rod growth direction with respect to the crystallographic *c*-axis. (Ref. 17. Reproduced by permission of Nature Publishing Group (www.nature.com))

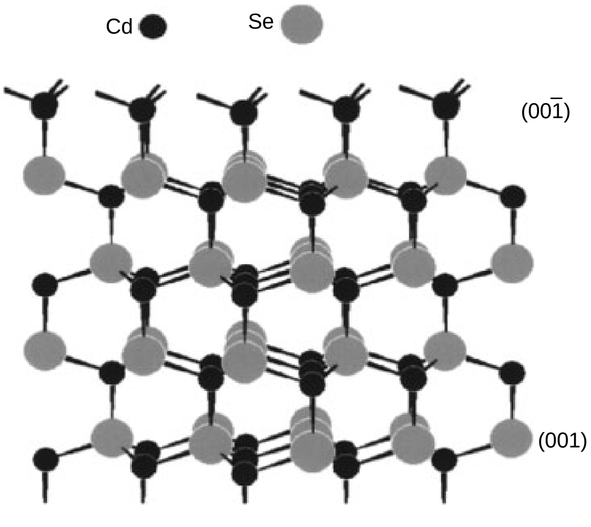

Figure 14 Atomic model of the CdSe wurtzite crystal structure. The (001) and the (001) crystal faces are emphasized to highlight the different number of dangling bonds associated with each Cd atom (three and one, respectively). (Reprinted with permission from Ref. 42. © 2000 American Chemical Society)

Alternatively, it has been proposed that a more important contribution to the formation of rod-shaped particles by the strong metal ligands is their influence on 'monomer' concentrations, where monomer again refers to various molecular precursor species. Specifically, the phosphonic acids may simply *permit* the high monomer concentrations that are required for kinetic, anisotropic growth. As strong metal binders, they may coordinate Cd monomers, stabilizing them against decomposition to metallic Cd.[12]

More complex shapes, such as 'arrows', 'pine trees', and 'teardrops' have also been prepared in the CdSe system, and the methods used are an extension of those applied to the preparation of CdSe rods. Once again, CdSe appears to be the 'proving ground' for semiconductor nanoparticle synthesis. Several factors influencing growth of complex shapes have been investigated, including the time evolution of shape and the ratio of TOPO to phosphonic acid ligands,[42] as well as the steric bulk of the phosphonic acid.[12] Predictably, reaction temperature also influences the character of the growth regime.[12,42] In the regime of rod growth, that is, fast kinetic growth, complex shapes can evolve over time. Rods and 'pencils' transform into 'arrows' and 'pine-tree-shaped' particles (Figure 15). The sides of the arrow or tree points comprise wurtzite (101) faces. As predicted by traditional crystal-growth theory, these slower growing faces have replaced the faster growing (001) face, permitting the evolution to more complex structures.[42] Shape and shape evolution dynamics were also observed to be highly dependent upon phosphonic acid concentrations. Low concentrations (< 10 mol%) of hexylphosphonic acid (HPA), for example, relative to TOPO produced approximately spherical particles, while moderate amounts (20 mol%) yielded rods, and high concentrations (60 mol%) resulted in arrow-shaped particles. As discussed previously, HPA appears to enhance the growth of the (001) face *relative* to other crystallographic faces, and higher concentrations simply permit even higher relative growth rates. Therefore, shape evolution to the arrow and tree morphologies proceeds more quickly in the presence of high HPA concentrations. The growth of single-headed arrows, as opposed to double-headed, results from the characteristic unidirectional growth, that is, growth from the (001) face only, and not from the (001) face.

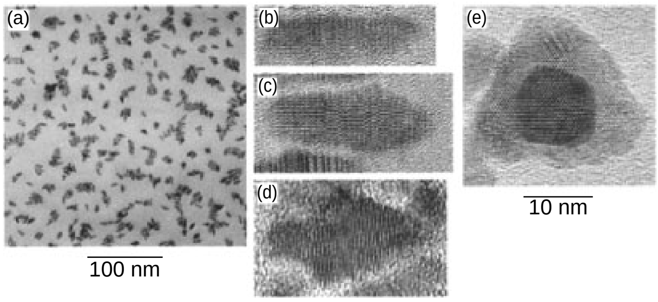

Figure 15 (a) TEMs of a CdSe NQD sample dominated by arrow-shaped particles (60% HPA reaction). (b-d) HR-TEMs demonstrating the shape evolution from (b) pencil- to (c) arrow- to (d) pine-tree-shaped CdSe NQDs. (e) Pine-tree-shaped particle looking down the [001] direction, that is, the long axis. Analysis of lattice spacings obtained by HR-TEM imaging revealed that wurtzite is the dominate phase for each shape and that the angled facets of the arrows comprise the (101) faces. (Reprinted with permission from Ref. 42. © 2000 American Chemical Society)

'Teardrop-shaped' particles also arise from the tendency toward unidirectional growth. In this case, rod-shaped crystals are exposed to growth conditions favoring spherical particle shapes, that is, equilibrium slow growth and low-monomer concentrations, causing the rods to become rounded. Monomer concentration is then quickly increased to force elongation of the 'droplet' from one end into particles resembling tadpoles.[42] The growth regime governing the evolution of rods to spherical particles has been termed '1-D to 2-D intraparticle ripening.[12]' Nanoparticle volumes and total numbers remain approximately constant (as do monomer concentrations), while nanoparticle shape changes dramatically. Intraparticle diffusion of *c*-axis atoms to other crystal faces may explain this transformation. The process is distinguished from 'interparticle ripening,' or Ostwald ripening, that is observed at even lower monomer concentrations. Intraparticle ripening is thought to occur when a 'diffusion equilibrium' exists between the nanoparticles and the monomers in the bulk solution.[12] Alternatively, it has also been shown that nanodots can be used to 'seed' the growth of nanorods. Here, the spherical particles are exposed to high monomer concentrations that promote one-dimensional growth from the template particles. Improved short-axis and aspect-ratio distributions have been reported for these rods (Figure 16).[12]

Rod growth dynamics also depend upon the identity of the phosphonic acid. The effectiveness of the phosphonic acid in promoting rod growth depends critically on its steric bulk, or the length of its alkyl chain. Shorter-chain phosphonic acids, such as HPA, more effectively promote rod growth compared to longer-chain phosphonic acids, such as tetradecylphosphonic acid (TDPA). Combinations of longer- and shorter-chain phosphonic acids can be used to readily tune rod aspect ratios[12] and control shape evolution dynamics.

The above morphologies reflect the underlying wurtzite crystal structure of CdSe. Occasionally, however, CdSe nucleates in the zinc-blende phase. When this occurs, a different type of morphology, the tetrapod, is observed. Here, the zinc-blende nuclei expose four equivalent (111) faces that comprise the crystallographic equivalent of the wurtzite (001) faces (alternating planes of Cd or Se). From these (111) surfaces, four wurtzite 'arms' grow unidirectionally. Further addition of monomer either lengthens the wurtzite arms, in the case of 'purely' wurtzite arms, or generates dendritic-like wurtzite branches, when zinc-blende stacking faults are present in the arm ends (Figure 17).[42]

CdSe rod QYs in PL are typically relatively low, ca. 1 to 4%. Like their spherical counterparts, however, rods can be overcoated with a higher band gap inorganic

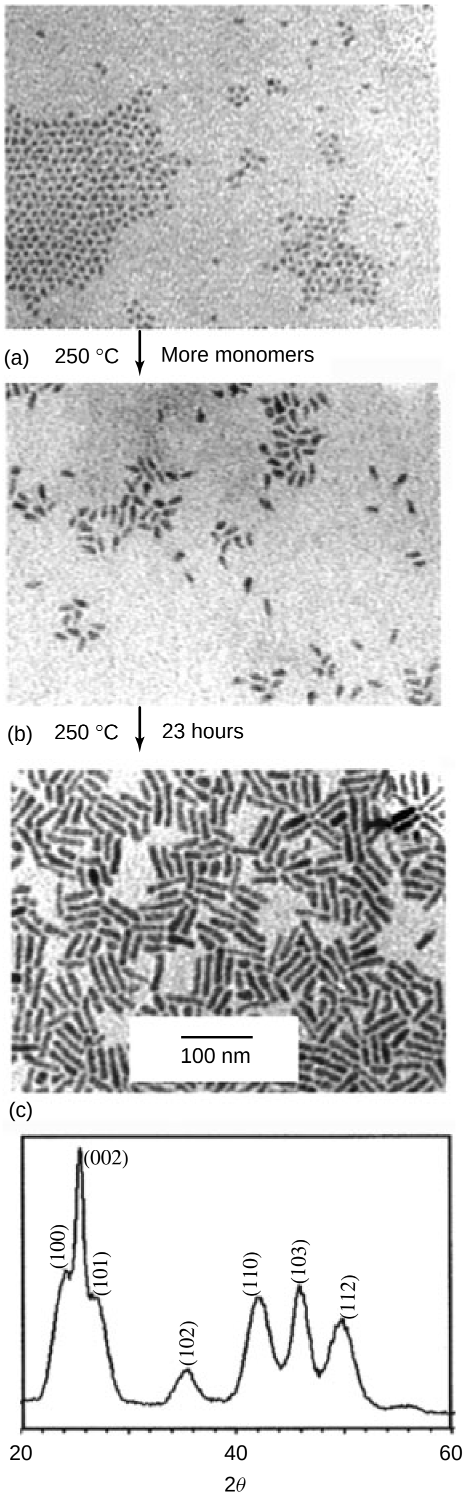

Figure 16 ‘Seeding’ CdSe NQD rod growth for improved size monodispersity. (a) TEM of CdSe dots prepared in 13% TDPA using an injection temperature of 360 °C and a growth temperature of 250 °C. (b) TEM of NQD rods grown from the dot seeds following injection of additional monomer (c) TEM of NQD rods after 23 h of growth. (d) XRD pattern for CdSe rods from (c). (Reprinted with permission from Ref. 12. © 2001 American Chemical Society)

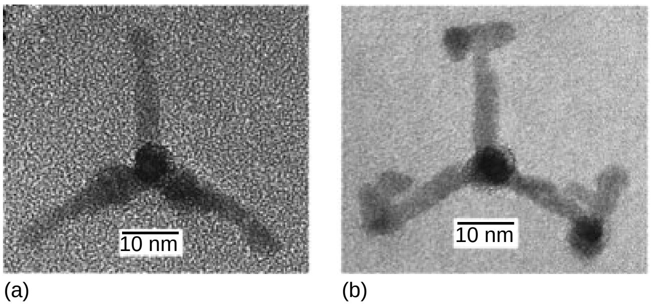

Figure 17 HR-TEMs of CdSe tetrapods. (a) Image down the [001] direction of one of the four arms. All arms are wurtzite phase, as confirmed by analysis of lattice spacings. (b) ‘Dendritic’ tetrapod, where branches have grown from each arm. Some stacking faults are present in the branches, and zinc-blende layers are present at the ends of the original four arms. (Reprinted with permission from Ref. 42. © 2000 American Chemical Society)

semiconductor, increasing QYs to 14–20%.**[43,44]** Lattice mismatch requirements for rods are somewhat more severe than for spherical particles, and synthetic steps unique to rod overcoating have been employed in the most successful preparations.**[44]** As discussed previously (Section 3), spherical nanoparticle systems benefit from having highly curved surfaces, compared to less-strain-tolerant planar systems. Nanorods provide an intermediate case. The average curvature of rods lies between that of dots and films, and, owing to their larger-size/surface area compared to dots, more interfacial strain can accumulate leading to the formation of dislocations. The 12% lattice mismatch between ZnS and CdSe is, therefore, less well tolerated in rods. CdS can be used as a lattice-mismatch ‘buffer layer’ between CdSe and ZnS (only ∼4% lattice mismatch with CdSe and ∼8% with ZnS). Addition of a small amount of Cd precursor to the shell precursor solution (Cd:Zn of 0.12:1.0) appears to lead to the preferential formation of CdS at the surface of the rods. ZnS growth then proceeds on the CdS. High-resolution TEM images demonstrate uniform and epitaxial growth. Interestingly, QYs remain low, and the benefits of inorganic overcoating in the graded epitaxial approach are only fully realized following photochemical annealing (via laser irradiation) of the rod particles (Figure 18).**[44]**

4.2 Shape Control Beyond CdSe

Solution-phase preparations of unusually shaped and highly anisotropic particles that are soluble, relatively monodisperse, and sufficiently small to exhibit quantum-confinement effects are thus far limited, but not exclusive to CdSe. CdS and CdTe rods can be prepared using phosphonic-acid-controlled reactions. In addition, CdS rods and multipods can be prepared in a monosurfactant system in which hexadecylamine (HDA) serves both as the stabilizing ligand and as the shape-determining ligand.**[45]** Here, rod and multipod formation

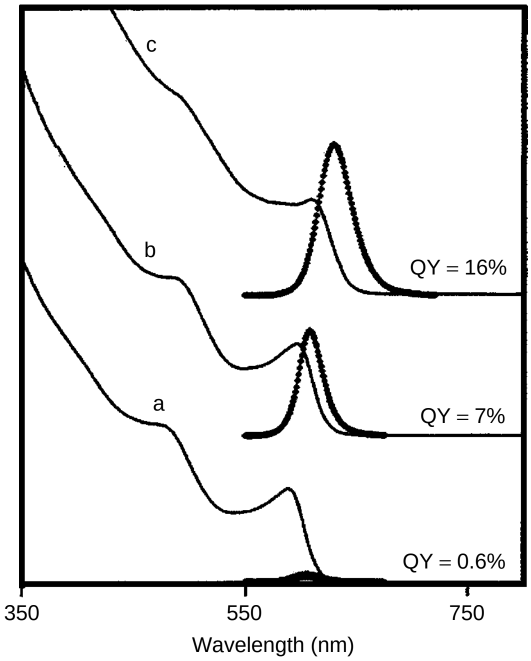

Figure 18 Absorption (solid line) and PL (dashed line) spectra for medium-length (3.3 × 21 nm) CdSe nanorods. (a) Core nanorods without ZnS shell. (b) (Core)shell nanorods with thin CdS-ZnS shells (~2 monolayers of shell material, where the CdS 'buffer' shell comprises ~35% of the total shell). (c) (Core)shell nanorods with medium CdS-ZnS shells (~4.5 monolayers of shell material, where the CdS 'buffer' shell comprises ~22% of the total shell). PL spectra were recorded following photoannealing of the samples[44]

is temperature dependent. Rods form at high temperatures (~300 °C), while bipods, tripods, and tetrapods dominate at lower temperatures (120–180 °C). The dependence of shape on temperature likely results from preferential formation of wurtzite CdS nuclei (thermodynamic phase) at high temperatures and zinc-blende nuclei (kinetic phase) at lower temperatures. As in the CdSe system, the zinc blende {111} faces can support fast growth of (001) wurtzite 'arms.' Significantly, this method allows isolation of tetrapods in ~82% yield (compared to 15–40% by the HPA method) at 120 °C. Size control is less well developed, and particles are relatively large compared to their HPA-derived counterparts. Nevertheless, it is the first significant report of solution-based growth of bipod and tripod morphologies in the II–VI system and provides a more predictable method of producing tetrapods.[45]

The same monosurfactant system can be applied to shape-controlled preparation of the magnetic semiconductor, MnS.[46] At low solution-growth temperatures (120–200 °C), MnS prepared from the single-source precursor, $Mn(S_2CNEt_2)_2$, can nucleate in either the zinc-blende or the wurtzite phase, while at high temperatures (>200 °C) MnS nucleates in the rock-salt phase. Low-temperature growth yields a variety of morphologies: highly anisotropic nanowires, bipods, tripods and tetrapods (120 °C), nanorods (150 °C), and spherical particles (180 °C). The 'single pods' comprise wurtzite cores with wurtzite-phase arms. In contrast, the multipods comprise zinc-blende cores with wurtzite arms, where the arms grow in the [001] direction from the zinc-blende {111} faces, as discussed previously with respect to the Cd-chalcogenide system. Dominance of the isotropic spherical particle shape in reactions conducted at moderate temperatures (180 °C) implies a shift from predominantly kinetic control to predominantly thermodynamic control over the temperature range from 120 to 180 °C.[46] Formation of 1-D particles at low temperatures results from kinetic control of relative growth rates. At higher temperatures, differences in activation barriers to growth of different crystal faces are more easily surmounted, equalizing relative growth rates. Finally, high-temperature growth supports only the thermodynamic rock-salt structure, large cubic crystals. Also, by combining increased growth times with low growth temperatures, shape evolution to 'higher-temperature' shapes is achieved.[46]

Extension of the ligand-controlled shape methodology to highly symmetric cubic crystalline systems is also possible. Specifically, PbS, having the rock-salt structure, has been prepared as rods, tadpole-shaped monopods, multipods (bipods, tripods, tetrapods, and pentapods), stars, truncated octahedra, and cubes.[47] The rod-based particles, including the mono and multipods, retain short-axis dimensions that are less than the PbS Bohr exciton radius (16 nm) and, thus, can potentially exhibit quantum-size effects. These highly anisotropic particle shapes represent truly metastable morphologies for the inherently isotropic PbS system. The underlying PbS crystal lattice is the symmetric rock-salt structure, the thermodynamically stable manifestations of which are the truncated octahedra and the cubic nanocrystals. The PbS particles are prepared by pyrolysis of a single-source precursor, $Pb(S_2CNEt_2)_2$, in hot phenyl ether in the presence of a large excess of either a long-chain alkyl thiol or amine. The identity of the coordinating ligand and the solvent temperature determine the initial particle shape following injection (Figure 19). Given adequate time, particle shapes evolve from the metastable rods to the stable truncated octahedron and cubes, with star-shaped particles comprising energetically intermediate shapes.[47]

As in the CdSe system, the particle shape in the cubic PbS system depends intimately on the ligand concentration and its identity. The highest ligand concentrations yield a reduced rate of growth from the {111} faces compared to the {100} faces, which experience enhanced *relative* growth rates. Further, alkylthiols are more effective at controlling relative growth rates compared to alkylamines. The latter, a weaker Pb binder, consistently leads to large, thermodynamically stable cubic shapes. Finally, reaction temperature plays a key role in determining particle morphology. The lowest temperatures (140 °C) yield the metastable rod-based morphologies, with intermediate star shapes generated at moderate temperatures (180–230 °C) and truncated octahedra isolated at the highest temperatures (250 °C). Interestingly, the rod structures appear

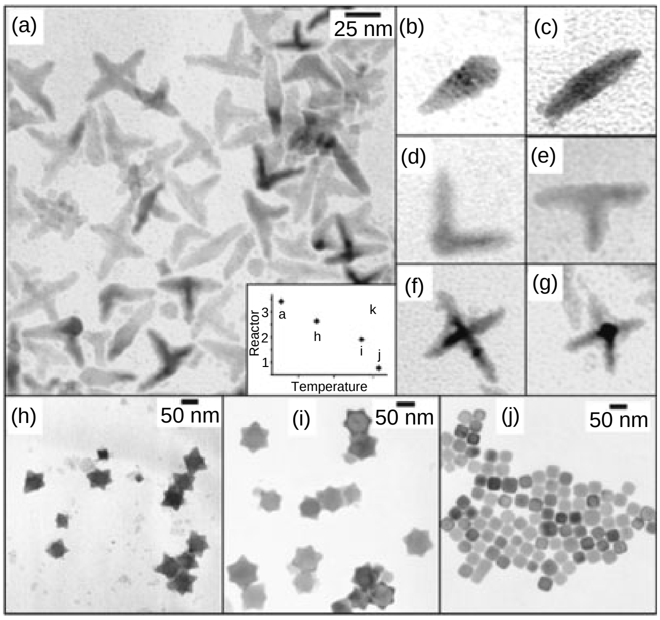

Figure 19 TEMs showing the variety of shapes obtained from the PbS system grown from the single-source precursor, $Pb(S_2CNEt_2)_2$, at several temperatures. (a) Multipods prepared at 140 °C. (b) Tadpole-shaped monopod (140 °C). (c) I-shaped bipod (140 °C). (d) L-shaped bipod (140 °C). (e) T-shaped tripod (140 °C). (f) Cross-shaped tetrapod (140 °C). (g) Pentapod (140 °C). (h) Star-shaped nanocrystals prepared at 180 °C. (i) Rounded star-shaped nanocrystals prepared at 230 °C. (j) Truncated octahedra prepared at 250 °C. (Reprinted with permission from Ref. 47. © 2002 American Chemical Society)

to form by preferential growth of {100} faces from truncated octahedra seed particles. For example, the 'tadpole' shaped monopods are shown by HR-TEM studies to comprise truncated octahedra 'heads' and [100]-axis 'tails,' resulting from growth from a (100) face. The star-shaped particles that form at 180 °C are characterized by six triangular corners, comprising each of the six {100} faces. The {100} faces have 'shrunk' into these six corners as a result of their rapid growth, similar to the replacement of the (001) face by slower growing faces during the formation of arrow-shaped CdSe particles (see above). The isolation of star-shaped particles at intermediate temperatures suggests that the relative growth rates of the {100} faces remain enhanced compared to the {111} faces at these temperatures. Further, the overall growth rate is enhanced as a result of the higher temperatures. The star-shaped particles that form at 230 °C are rounded and represent a decrease in the differences in relative growth rates between the {100} faces and the {111} faces, the latter, higher-activation-barrier surface benefiting from the increase in temperature. A definitive shift from kinetic growth to thermodynamic growth is observed at 250 °C (or at long growth times). Here, the differences in reactivity between the {100} and the {111} faces are negligible given the high thermal energy input that surmounts either face's activation barrier. The thermodynamic cube shape is, therefore, approximated by the shapes obtained under these growth conditions. In all temperature studies, the alkylthiol:precursor ratio was ~80:1, and monomer concentrations were kept high, conditions supporting controlled and kinetic growth, respectively.

III-V semiconductors have proven amenable to solution-phase control of particle shape using an unusual synthetic route. Specifically, the method involves the solution-based catalyzed growth of III-V nanowhiskers.[48] In this method, referred to as the 'solution-liquid-solid mechanism,' a dispersion of nanometer-sized indium droplets in an organometallic reaction mixture serves as the catalytic sites for precursor decomposition and nanowhisker growth. As initially described, the method afforded no control over nanowhisker diameters, producing very broad diameter distributions and mean diameters far in excess of the strong-confinement regime for III-V semiconductors. Additionally, the nanowhiskers were insoluble, aggregating, and precipitating upon growth. However, recent studies have demonstrated that the nanowhisker mean diameters and diameter distributions are controlled through the use of near-monodisperse metallic-catalyst nanoparticles.[49,50] The metallic nanoparticles are prepared over a range of sizes by heterogeneous seeded growth.[51] The solution-liquid-solid mechanism in conjunction with the use of these near-monodisperse catalyst nanoparticles and polymer stabilizers affords soluble InP and GaAs nanowires having diameters in the range of 3.5–20 nm and diameter distributions of ±15–20% (Figure 20). The absorption spectra of the InP quantum wires contain discernible excitonic features from which the size dependence of the band gap has been determined, and quantitatively compared to that in InP quantum dots.[50] Preliminary results indicate that II-VI quantum wires can be grown similarly.[52] A similar approach was applied to growth of insoluble, but size-monodispersed in diameter (4–5 nm), silicon nanowires. Here, reactions were conducted at elevated temperature and pressure (500 °C and 200–270 bar) using alkanethiol-coated

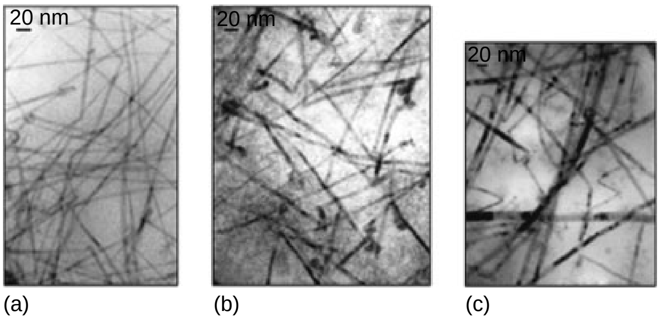

Figure 20 TEM images of InP quantum wires. Mean diameters: (a) 4.49 ± 0.75 nm [±17%; grown from 9.88 ± 0.795 (±8.0%) In-catalyst nanoparticles]; (b) 6.61 ± 1.03 nm; (c) 11.01 ± 2.29 nm. (Ref. 49. Reproduced by permission of Nature Publishing Group (www.nature.com))

gold nanoclusters (2.5 ± 0.5-nm diameter) as the nucleation and growth 'seeds'.[53]

5 PHASE TRANSITIONS AND PHASE CONTROL

5.1 NQDs Under Pressure

NQDs have been used as model systems to study solid–solid phase transitions.[54–57] The transitions, studied in CdSe, CdS, InP, and Si nanocrystals,[56] were induced by pressure applied to the nanoparticles in a diamond anvil cell by way of a pressure-transmitting solvent medium, ethylcyclohexane. Such transitions in bulk solids are typically complex and dominated by multiple nucleation events, the kinetics of which are controlled by crystalline defects that lower the barrier height to nucleation.[54,57] In nearly defect-free nanoparticles, the transitions can exhibit single-structural-domain behavior and are characterized by large kinetic barriers (Figure 21). In contrast to original interpretations, which described the phase transition in nanocrystals as 'coherent' over the entire nanocrystal,[54] the nucleation of the phase transition process was recently shown to be localized to specific crystallographic planes.[57] The simple unimolecular kinetics of the transition still support a single nucleation process; however, the transition is now thought to result from plane sliding as opposed to a coherent deformation process. Specifically, the sliding-plane mechanism involves shearing motion along the (001) crystallographic planes, as supported by detailed analyses of transformation times as a function of pressure and temperature.

Because of the large kinetic barriers in nanocrystal systems, their phase transformations are characterized by hysteresis loops (Figure 21).[54,55,57] The presence of a strong hysteresis signifies that the phase transition does not occur at the thermodynamic transition pressure and that time is required for the system to reach an equilibrium state. This delay is fortunate in that it permits detailed analysis of the transition kinetics even though the system is characterized by single-domain (finite-size) behavior. As alluded to, these analyses were used to determine the structural mechanism for transformation. Specifically, kinetics studies of transformation times as a function of temperature and pressure were used to determine relaxation times, or average times to overcome the kinetic barrier, and, thereby, rate constants. The temperature dependence of the rate constants led to the determination of activation energies for the forward and reverse transitions, and the pressure dependence of the rate constants led to the determination of activation volumes for the process.[57] The latter represents the volume change between the starting structure and an intermediate transitional structure. Activation volumes for the two directions, wurtzite to rock salt and rock salt to wurtzite, respectively, were unequal and smaller for the latter, implying that the intermediate structure more closely resembles the 4-coordinate structure. The activation volumes were also shown to be of opposite sign, indicating that the mechanism by which the phase transformation takes place involves a structure whose volume is in between that of the two end phases. Most significantly, the magnitude of the activation volume is small compared to the total volume change that is characteristic of the system ($\sim$0.2% vs. 18%). The activation volume is equal to the critical nucleus size responsible for initiating the phase transformation – *defining the volume change associated with the nucleation event.*

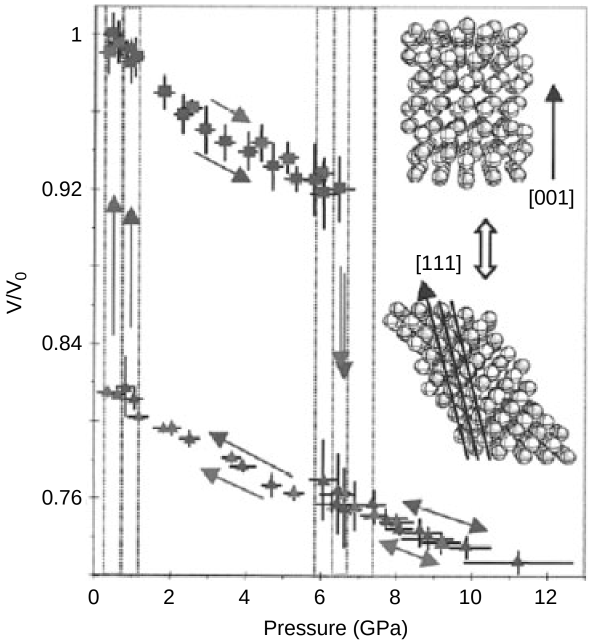

Figure 21 Two complete hysteresis cycles for 4.5 nm CdSe NQDs presented as unit cell volumes for the wurtzite sixfold-coordinated phase (triangles) and the rock-salt fourfold-coordinated phase (squares) versus pressure. Solid arrows indicate the direction of pressure change, and dotted boxes indicate the mixed-phase regions. Unlike bulk phase transitions, the wurtzite to rock-salt transformation in nanocrystals is reversible and occurs without the formation of new high-energy defects, as indicated by overlapping hysteresis loops. The shape change that a sliding-plane transformation mechanism (see text) would induce is shown schematically on the right. (Reprinted figure with permission from J.N. Wickham, A.B. Herhold, and A.P. Alivisatos, *Phys. Rev. Lett.*, 2000, **84**, 923. © 2000 by the American Physical Society)

The small-size of the activation volume suggests that the structural mechanism for transformation cannot be a coherent one involving the entire nanocrystal.[57] Spread out over the entire volume of the nanocrystal, the activation volume would amount to a volume change smaller than that induced by thermal vibrations in the lattice. Therefore, a mechanism involving some fraction of a nanocrystal was considered. The nucleus was determined not to be three-dimensional, as a sphere the size of the activation volume would be less than a single unit cell. Also, activation volumes were observed to increase with increasing particle size (in the direction of increasing pressure). There is no obvious mechanistic reason for a spherically shaped nucleus to increase in size with an increase in particle size. Further, additional observations have been made: (1) particle shape changes from cylindrical or elliptical to slab-like upon transformation from the 4-coordinate to the 6-coordinate phase,[55] (2) the stacking-fault density increases following a full pressure cycle from the 4-coordinate through the 6-coordinate and back to the 4-coordinate structure,[55] and (3) the entropic contribution to the free-energy barrier to transformation increases with increasing size (indicating the nucleation event can initiate from multiple sites).[57] Together, the various experimental observations suggest that the mechanism involves a directionally dependent nucleation process that is not coherent over the whole nanocrystal. The specific proposed mechanism entails shearing of the (001) planes, with precedent found in martensitic phase transitions (Figure 22).[55,57] Further, the early observation that activation energy increases with size[54] likely results from the increased number of chemical bonds that must be broken for plane sliding to occur in large nanocrystals, compared to that in small nanocrystals. Such a mechanistic-level understanding of the phase transformation processes in nanocrystals is important as nanocrystal-based studies, owing to their simple kinetics, may ultimately inform a better understanding of the hard-to-study, complex transformations that occur in bulk materials and geologic solids.[57]

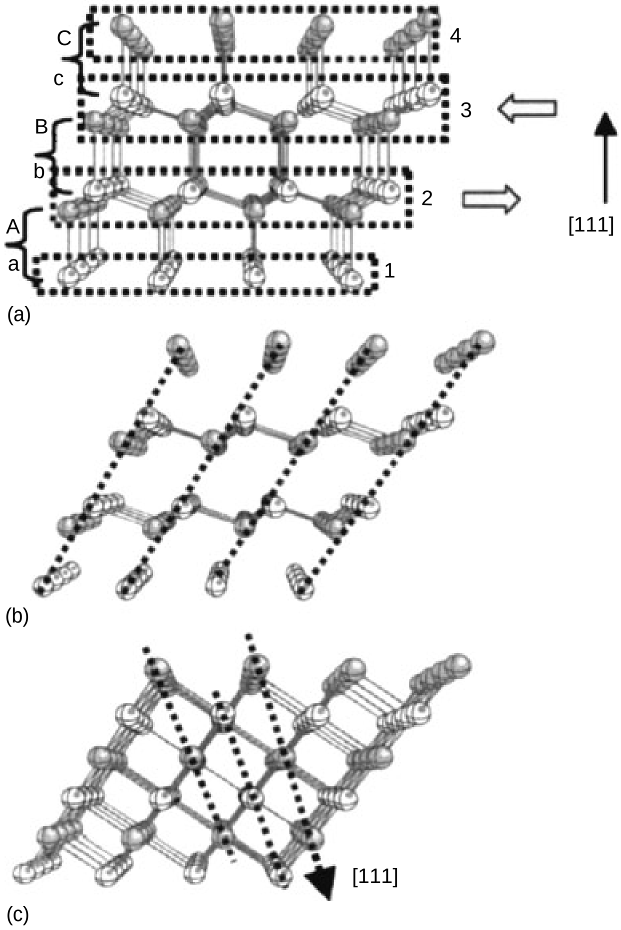

Figure 22 Schematic illustrating the sliding-plane transformation mechanism. (a) Zinc-blende structure, where brackets denote (111) planes, dashed boxes show planes that slide together, and arrows indicate the directions of movement. (b) Structure of (a) after successive sliding has occurred. (c) Rock-salt structure, where dashed lines denote (111) planes. Structures are oriented the same in (a-c). (Reprinted with permission from J.N. Wickham, A.B. Herhold, and A.P. Alivisatos, *Phys. Rev. Lett.*, 2000, **84**, 923. © 2000 by the American Physical Society)

5.2 NQD Growth Conditions Yield Access to Non-thermodynamic Phases

Phase control, much like shape control (Section 4), can be achieved in nanocrystal systems by operating in kinetic growth regimes. Materials synthesis strategies have typically relied upon the use of reaction conditions far from standard temperature and pressure (STP) to obtain nonmolecular materials such as ceramics and semiconductors. The crystal-growth barriers to covalent nonmolecular solids are high and have historically been surmounted by employing relatively extreme conditions, comprising a direct assault on the thermodynamic barriers to solid-state growth. The interfacial processes of adsorption-desorption and surface migration permit atoms initially located at non-lattice sites on the surface of a growing crystal to relocate to a regular crystal lattice position. When these processes are inefficient or not functioning, amorphous material can result. Commonly, synthesis temperatures of $\geq 400\,^{\circ}C$ are required to promote these processes leading to crystalline growth.[58,59] Such conditions can preclude the formation of kinetic, or higher-energy, materials and can limit the selection of accessible materials to those formed under thermodynamic control – the lowest-energy structures.[60,61] In contrast, biological and organic-chemical synthetic strategies, often relying on catalyzed growth to surmount or lower energy barriers, permit access to both lowest-energy and higher-energy products,[60] as well as access to a greater variety of structural isomers compared to traditional, solid-state synthetic methods. The relatively low-temperature, surfactant-supported, solution-based reactions employed in the synthesis of NQDs provide for the possibility of forming kinetic phases, that is, those phases that form the fastest under conditions that prevent equilibrium to the lowest-energy structures. Formation of the CdSe zinc-blende phase, as opposed to the wurzite structure, is likely a kinetic product of low-temperature growth. In general, however, examples are relatively limited. More examples are to be found in the preparation of nonmolecular *solid* thin films: electrodeposition onto single-crystal templating substrates,[62] chemical vapor deposition using single-source precursors having both the target elements and the target structure built-in,[63] and reaction of nano-thin-film, multilayer reactants to grow metastable, superlattice compounds.[64–66] One clear

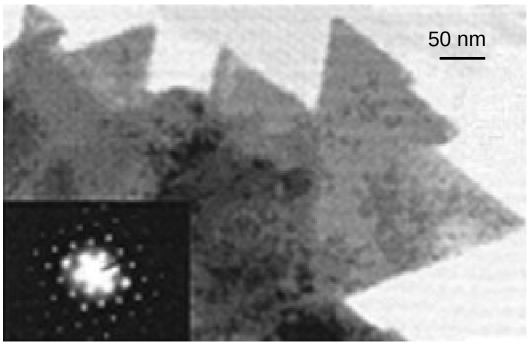

Figure 23 TEM of InS platelets with triangular features; inset, electron-diffraction pattern collected along the [0001] zone axis of a platelet

example from the solution phase is that of the formation of the metastable, previously unknown, rhombohedral InS (R-InS) phase.[67] The organometallic precursor, t-Bu_3In, was reacted with $H_2S(g)$ at ∼200 °C in the presence of a protic reagent, benzenethiol. This reagent provided the apparent dual function of catalyzing efficient alkyl elimination and supplying some degree of surfactant stabilization. While the starting materials were soluble, the final product was not. Nevertheless, characterization by TEM (Figure 23) and powder X-ray diffraction (XRD) revealed that the solid-phase product was a new layered InS phase, structurally distinct from the thermodynamic network structure, orthorhombic β-InS. The new phase was 10.6% less dense compared to β-InS, consistent with a low-T, kinetic structure. Further, TEM imaging revealed that the new phase was prepared as nanocrystal platelets (5–20 nm) that self- assembled to form large, micron-scale sheets (Figure 23). The van der Waals surfaces of the nanocrystal *ab* plane (the large-area plane in the platelets) are low-energy, coordinatively saturated ‘faces’, while the edges of the nanocrystallites are characterized by higher-energy unsaturated sites. Therefore, it is at the edges that the nano-platelets likely attached, generating the larger sheets. Electron-diffraction patterns collected perpendicular to the large-area sheet surfaces and over large areas (collection radii ≈150 nm) demonstrated not only that the crystallographic *c* axes were indeed perpendicular to the sheet surfaces but that the sheets diffracted coherently, as single crystals would (Figure 23). Assembly and attachment of platelets into sheets, therefore, proceeded in a crystallographically coherent fashion resembling a self-assembly process known in natural mineral systems as ‘oriented attachment’.[68,69]

6 RELATED ARTICLES

Biomimetic Synthesis of Nanoparticles; Metal Nanoparticles, Organization & Applications of; Metal Nanoparticles, Synthesis of; Sol–Gel Encapsulation of Metal and Semiconductor Nanocrystals.

7 REFERENCES

1. D. Bimberg, M. Grundmann, and N. N. Ledentsov, *MRS Bull.*, 1998, **23**, 31.
2. P. M. Petroff and G. Medeiros-Riberio, *MRS Bull.*, 1996, **21**, 54.
3. A. D. Yoffe, *Adv. Phys.*, 2001, **50**, 1.
4. J. Hu, T. W. Odom, and C. M. Lieber, *Acc. Chem. Res.*, 1999, **32**, 435.
5. L. J. Lauhon, M. S. Gudiksen, D. Wang, and C. M. Lieber, *Nature*, 2002, **420**, 57.
6. N. F. Borelli and D. W. Smith, *J. Non-Cryst. Solids*, 1994, **180**, 25.
7. A. Lipovskii, E. Kolobkova, V. Petrikov, I. Kang, A. Olkhovets, T. Krauss, M. Thomas, J. Silcox, F. Wise, Q. Shen, and S. Kycia, *Appl. Phys. Lett.*, 1997, **71**, 3406.
8. C. B. Murray, C. R. Kagan, and M. G. Bawendi, *Annu. Rev. Mater. Sci.*, 2000, **30**, 545.
9. V. K. La Mer and R. H. Dinegar, *J. Am. Chem. Soc.*, 1950, **72**, 4847.
10. C. B. Murray, S. Sun, W. Gaschler, H. Doyle, T. A. Betley, and C. R. Kagan, *IBM J. Res. Dev.*, 2001, **45**, 47.
11. A. J. Nozik and O. I. Micic, *MRS Bull.*, 1998, **23**, 24.
12. Z. A. Peng and X. Peng, *J. Am. Chem. Soc.*, 2001, **123**, 1389.
13. K. A. Higginson, M. Kuno, J. Bonevich, S. B. Qadri, M. Yousuf, and H. Mattoussi, *J. Phys. Chem.*, 2002, **106**, 9982.
14. X. Peng, J. Wickham, and A. P. Alivisatos, *J. Am. Chem. Soc.*, 1998, **120**, 5343.
15. C. B. Murray, D. J. Norris, and M. G. Bawendi, *J. Am. Chem. Soc.*, 1993, **115**, 8706.
16. L. Qu, Z. A. Peng, and X. Peng, *Nano Lett.*, 2001, **1**, 333.
17. X. Peng, L. Manna, W. Yang, J. Wickham, E. Scher, A. Kadavanich, and A. P. Alivisatos, *Nature*, 2000, **404**, 59.
18. L. Qu and X. G. Peng, *J. Am. Chem. Soc.*, 2002, **124**, 2049.
19. M. Hines and P. Guyot-Sionnest, *J. Phys. Chem. B*, 1998, **102**, 3655.
20. X. Peng, M. C. Schlamp, A. V. Kadavanich, and A. P. Alivisatos, *J. Am. Chem. Soc.*, 1997, **119**, 7019.
21. B. L. Wehrenberg, C. J. Wang, and P. Guyot-Sionnest, *J. Phys. Chem. B*, 2002, **106**, 10634.
22. J. M. Pietryga, R. D. Schaller, D. Werder, M. H. Stewart, V. I. Klimov, J. A. Hollingsworth *J. Am. Chem. Soc.*, 2004, **126**, 11752.
23. S. V. Kershaw, M. Harrison, A. L. Rogach, and A. Kornowski, *J. Select. Top. Quantum Elect.*, 2000, **6**, 534.

24. N. Gaponik, D. V. Talapin, A. L. Rogach, K. Hoppe, E. V. Shevchenko, A. Kornowski, A. Eychmüller, and H. Weller, *J. Phys. Chem. B*, 2002, **106**, 7177.
25. T. Vossmeyer, L. Katsikis, M. Giersig, I. G. Popovic, K. Diesner, A. Chemseddine, A. Eychmüller, and H. Weller, *J. Phys. Chem.*, 1994, **98**, 7665.
26. A. Rogach, S. Kershaw, M. Burt, M. Harrison, A. Kornowski, A. Eychmüller, and H. Weller, *Adv. Mater.*, 1999, **11**, 552.
27. J. Rockenberger, L. Troger, A. L. Rogach, M. Tischer, M. Grundmann, A. Eychmüller, and H. Weller, *Ber. Bunsen-Ges. Phys. Chem.*, 1998, **102**, 1.
28. M. L. Steigerwald, A. P. Alivisatos, J. M. Gibson, T. D. Harris, R. Kortan, A. J. Muller, A. M. Thayer, T. M. Duncan, D. C. Douglas, and L. E. Brus, *J. Am. Chem. Soc.*, 1988, **110**, 3046.
29. S. O'Brien, L. Brus, and C. B. Murray, *J. Am. Chem. Soc.*, 2001, **123**, 12085.
30. M. A. Hines and P. Guyot-Sionnest, *J. Phys. Chem.*, 1996, **100**, 468.
31. B. O. Dabbousi, J. Rodriguez-Viejo, F. V. Mikulec, J. R. Heine, H. Mattoussi, R. Ober, K. F. Jensen, and M. G. Bawendi, *J. Phys. Chem. B*, 1997, **101**, 9463.
32. O. I. Micic, B. B. Smith, and A. J. Nozik, *J. Phys. Chem. B*, 2000, **104**, 12149.
33. Y. W. Cao and U. Banin, *Angew. Chem. Int. Ed.*, 1999, **38**, 3692.
34. Y. W. Cao and U. Banin, *J. Am. Chem. Soc.*, 2000, **122**, 9692.
35. M. A. Correa-Duarte, M. Giersig, and L. M. Liz-Marzán, *Chem. Phys. Lett.*, 1998, **286**, 497.
36. M. Danek, K. F. Jensen, C. B. Murray, and M. G. Bawendi, *Chem. Mater.*, 1996, **8**, 173.
37. S. Kim, B. Fisher, H.-J. Eisler, and M. G. Bawendi, *J. Am. Chem. Soc.*, 2003, **125**, 11466.
38. A. Eychmuller, A. Mews, and H. Weller, *Chem. Phys. Lett.*, 1993, **208**, 59.
39. A. Mews, A. Eychmüller, M. Giersig, D. Schoos, and H. Weller, *J. Phys. Chem.*, 1994, **98**, 934.
40. A. Mews, A. V. Kadavanich, U. Banin, and A. P. Alivisatos, *Phys. Rev. B*, 1996, **53**, R13242.
41. R. B. Little, M. A. El-Sayed, G. W. Bryant, and S. Burke, *J. Chem. Phys.*, 2001, **114**, 1813.
42. L. Manna, E. C. Scher, and A. P. Alivisatos, *J. Am. Chem. Soc.*, 2000, **122**, 12700.
43. M. Kazes, D. Y. Lewis, Y. Ebenstein, T. Mokari, and U. Banin, *Adv. Mater.*, 2002, **14**, 317.
44. L. Manna, E. C. Scher, L. S. Li, and A. P. Alivisatos, *J. Am. Chem. Soc.*, 2002, **124**, 7136.
45. Y. Jun, S. M. Lee, N. M. Kang, and J. Cheon, *J. Am. Chem. Soc.*, 2001, **123**, 5150.
46. Y. Jun, Y. Jung, and J. Cheon, *J. Am. Chem. Soc.*, 2002, **124**, 615.
47. S. M. Lee, Y. Jun, S. N. Cho, and J. Cheon, *J. Am. Chem. Soc.*, 2002, **124**, 11244.
48. T. J. Trentler, K. M. Hickman, S. C. Goel, A. M. Viano, P. C. Gibbons, and W. E. Buhro, *Science*, 1995, **270**, 1791.
49. H. Yu and W. E. Buhro, *Adv. Mater.*, 2003, **15**, 416.
50. H. Yu, J. Li, R. A. Loomis, L-W. Wang, and W. E. Buhro, *Nature Mater.*, 2003, **2**, 517.
51. H. Yu, P. C. Gibbons, K. F. Kelton, and W. E. Buhro, *J. Am. Chem. Soc.*, 2001, **123**, 9198.
52. H. Yu, J. Li, R. A. Loomis, P. C. Gibbons, L-W. Wang, and W. E. Buhro, *J. Am. Chem. Soc.*, 2003, **125**, 16168.
53. J. D. Holmes, K. P. Johnston, R. C. Doty, and B. A. Korgel, *Science*, 2000, **287**, 1471.
54. C. C. Chen, A. B. Herhold, C. S. Johnson, and A. P. Alivisatos, *Science*, 1997, **276**, 398.
55. J. N. Wickham, A. B. Herhold, and A. P. Alivisatos, *Phys. Rev. Lett.*, 2000, **84**, 923.
56. A. B. Herhold, C. C. Chen, C. S. Johnson, S. H. Tolbert, and A. P. Alivisatos, *Phase Transitions*, 1999, **68**, 1.
57. K. Jacobs, D. Zaziski, E. C. Scher, A. B. Herhold, and A. P. Alivisatos, *Science*, 2001, **293**, 1803.
58. A. Stein, S. W. Keller, and T. E. Mallouk, *Science*, 1993, **259**, 1558.
59. W. E. Buhro, K. M. Hickman, and T. J. Trentler, *Adv. Mater.*, 1996, **8**, 685.
60. L. Brus, *Science*, 1997, **276**, 373.
61. B. Parkinson, *Science*, 1995, **270**, 1157.
62. J. A. Switzer, M. G. Shumsky, and E. W. Bohannan, *Science*, 1999, **284**, 293.
63. E. G. Gillan and A. R. Barron, *Chem. Mater.*, 1997, **9**, 3037.
64. H. Sellinschegg, S. L. Stuckmeyer, M. D. Hornbostel, and D. C. Johnson, *Chem. Mater.*, 1998, **10**, 1096.
65. M. Noh and D. C. Johnson, *J. Am. Chem. Soc.*, 1996, **118**, 9117.
66. M. Noh, J. Thiel, and D. C. Johnson, *Science*, 1995, **270**, 1181.
67. J. A. Hollingsworth, D. M. Poorjay, A. Clearfield, and W. E. Buhro, *J. Am. Chem. Soc.*, 2000, **122**, 3562.
68. J. F. Banfield, S. A. Welch, H. Zang, T. T. Ebert, and R. L. Penn, *Science*, 2000, **289**, 751.
69. J. A. Hollingsworth and V. I. Klimov, 'Soft' Chemical Synthesis and Manipulation of Semiconductor Nanocrystals, in 'Semiconductor and Metal Nanocrystals: Synthesis and Electronic and Optical Properties', ed. V. I. Klimov, Marcel Dekker, New York, 2004, p. 1.

Acknowledgment

The author would like to acknowledge her husband, Howard Coe, for editing the text, transcribing and organizing references, and making graphical improvements to the figures. Jennifer would also like to thank Howard for his patience, support and sense of humor throughout this project. She would like to thank members of the LANL C-PCS Softmatter Nanotechnology and Advanced Spectroscopy Team, as well:

Dr. Victor Klimov (Team Leader), Dr. Jeffrey Pietryga (NQD synthesis), Dr. Richard Schaller (NQD spectroscopy), and Don Werder (TEM).

Organic Synthesis Using Metal-mediated Metathesis Reactions

Rebecca M. Kissling[1] **& Steven P. Nolan**[2]
[1]*State University of New York, Binghamton, NY, USA*
[2]*University of New Orleans, New Orleans, LA, USA*

1 Introduction 1
2 New Catalysts and Approaches 1
3 Mechanism and Theory 4
4 Recent Methodology Developed Utilizing Olefin Metathesis 6
5 Application of Olefin Metathesis Toward Total Synthesis Problems 23
6 Olefin Metathesis for the Formation of Polymers and Materials 33
7 Green Chemistry Utilizing Olefin Metathesis Catalysts 35
8 Summary 41
9 Related Articles 41
10 References 41

1 INTRODUCTION

The discovery of transition metal catalyzed olefin metathesis reactions is one of the most important developments in organic chemistry of the last 40 years.[1] These reactions include ring-closing metathesis (RCM), ring-opening metathesis (ROM), ring-opening metathesis polymerization (ROMP), acyclic diene metathesis polymerization (ADMET) and cross metathesis (CM) (Scheme 1). Chauvin described the mechanism that is currently accepted today. It and a fundamental mechanism for RCM are outlined in Scheme 2.[2] The potency of the olefin metathesis reactions lies in the interrelationship of the various reactions, the reversibility of the metathesis steps, and the fact that the reaction conditions can be readily tailored to give desired product outcomes.

Early olefin metathesis catalysts were transition metal salts combined with main group alkylating agents and reactivity was limited to unfunctionalized olefins because of the harsh operating conditions.[3] The olefin metathesis chemistry of the late 1970s through the early 1990s was dominated by well-defined early and mid transition metal complexes of which (**1a**) (Scheme 3), developed by Schrock, is an excellent example.[4] Complex (**1a**) exhibited remarkable activity for ADMET and ring closure to tri- and even tetra-substituted cyclic products.[5–7] Along with the extraordinary activity, some drawbacks accompanied the group VI-type catalysts, including catalyst synthesis, high sensitivity to oxygen and moisture, and a somewhat narrow substrate scope due to functional group sensitivity.

In 1992, the discovery of late metal alkylidene complexes of the type ($L_2X_2Ru{=}CHR$) that could catalyze RCM and ROMP was reported by Grubbs.[8,9] The ruthenium complex (**2a**) (Scheme 3) was more stable, tolerant of a wide range of functional groups and capable of operating under less stringent reaction conditions than the group VI catalysts, although less active. This type of complex was particularly useful for RCM and ROM of highly functionalized molecules as well as ROMP of strained cyclic olefins. The ‘user friendliness’ of complex (**2a**) made olefin metathesis an attractive new reaction for organic chemists and throughout the last 10 years the chemical literature was rich with new applications for olefin metathesis reactions catalyzed by Mo or Ru complexes. These complementary catalysts gave rise to an olefin metathesis revolution for approaching synthetic problems, particularly those in total synthesis.[10]

In 2000 and 2001, reviews on olefin metatheis by Fürstner[11] and Grubbs respectively that outlined the development and progress of olefin metathesis up through the turn of the century[12] focused on the functional group tolerance, scope of reactivity, and mechanism of action of Grubbs ruthenium-based olefin metathesis catalyst (**2a**), and the discoveries of more active catalysts (**2b**),[13] (**3a**),[14–16] and (**4a**).[17,18] Since that time there has been rapid progress in the creation of new catalysts, both ruthenium and molybdenum based, including successful chiral OM catalysts, further elucidation of the mechanism, new methodologies, and an even stronger presence of olefin metathesis as a key reaction in the construction of complex carbon skeletons. The following is an account of the most recent developments in olefin metathesis chemistry.

2 NEW CATALYSTS AND APPROACHES

A number of new ruthenium and molybdenum olefin metathesis catalysts have been developed since the turn of the century. These new, very active catalysts build upon prior successful catalysts and insight gained from systematic mechanistic studies.

A family of phosphine-free ruthenium-based olefin metathesis catalysts has been developed over the last few years. First, work done independently by Hoveyda and Blechert resulted in the H_2Mes isopropoxybenzylidene (**4b**), a highly active air-stable ruthenium (pre)catalyst for olefin metathesis (Scheme 4).[19,20] Hoveyda described (**4b**) as a recyclable monomeric catalyst also with high activity for ring-opening, ring-closure, and cross metathesis that tolerates

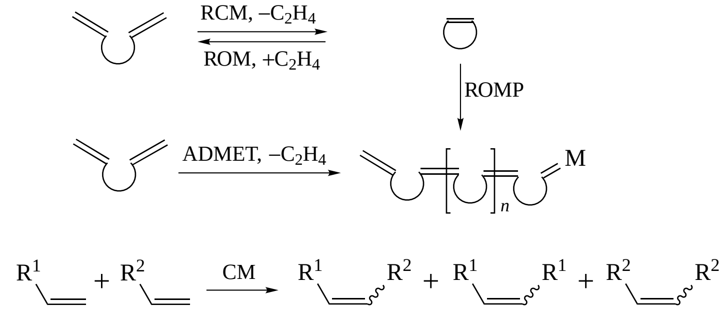
RCM, $-C_2H_4$
ROM, $+C_2H_4$
ROMP
ADMET, $-C_2H_4$
M
n
R^1
R^2
CM
R^1
R^2
R^1
R^1
R^2
R^2

Scheme 1 Types of olefin metathesis reactions

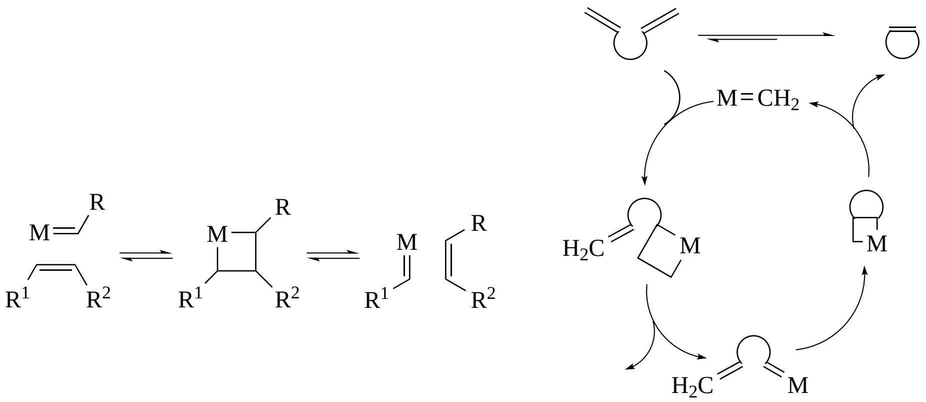
M
R
R^1
R^2
M
R
R^1
R^2
M
R
R^1
R^2
$M=CH_2$
H_2C
M
M
H_2C
M

Scheme 2 Mechanism of olefin metathesis and proposed cycle for RCM

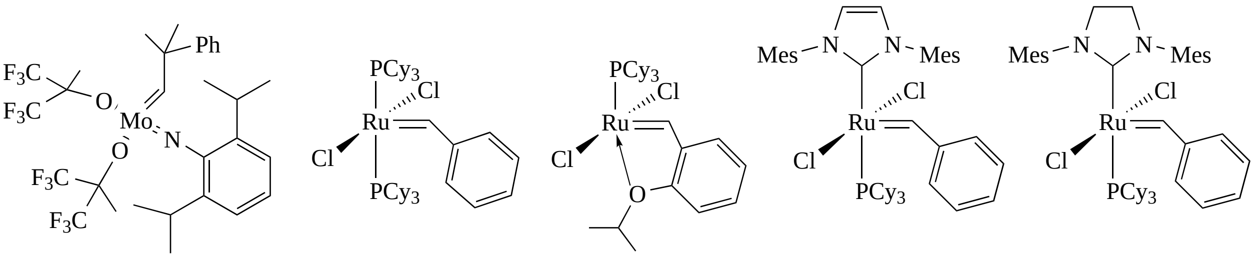
F_3C
F_3C
O
Mo
Ph
N
O
F_3C
F_3C
PCy_3
Cl
Ru
Cl
PCy_3
PCy_3
Cl
Ru
Cl
O
Mes
N
N
Mes
Cl
Ru
Cl
PCy_3
Mes
N
N
Mes
Cl
Ru
Cl
PCy_3

(**1a**) (**2a**) (**2b**) (**3a**) (**4a**)

Scheme 3 Some successful olefin metathesis catalysts

the steric bulk of up to trisubstituted substrates or products. Blechert's report on (**4b**) concludes that the catalytic behaviors of (**4a**) and (**4b**) are distinct and that (**4b**) favors cross metathesis activity. This catalyst prototype led to a number of new catalysts based on aryl alkyl ethers bound to the alkylidene. The first of these was the binol-derived catalyst (**4c**), initially developed for enantioselective catalysis.[21] While reactions with this catalyst were not stereoselective, (**4c**) was air stable yet significantly more active than (**4a**) for RCM with initial rates 10-fold that of the previous benchmark by (**4a**). Catalyst (**4c**) completely converted classical RCM substrates like diallyl diethyl malonate and substrates like *N*-(but-3-enyl)-*N*-tosylbut-3-en-1-amine that have very low reactivity for RCM, while (**4a**) gave only moderate to low conversions under the same conditions. Cross metathesis reaction of linear olefins and electron-poor alkenes with very high trans:cis ratios were also effected by (**4c**).

Blechert then discovered the related catalyst (**4d**) while trying to elucidate the factors that made (**4c**) more active than (**4b**).[22] The ligand structure of (**4d**) is similar to that of (**4c**) in that the benzylidene ether ligand has a bulky group ortho to the ruthenium-coordinating ether moiety. Catalyst(**4d**) is so

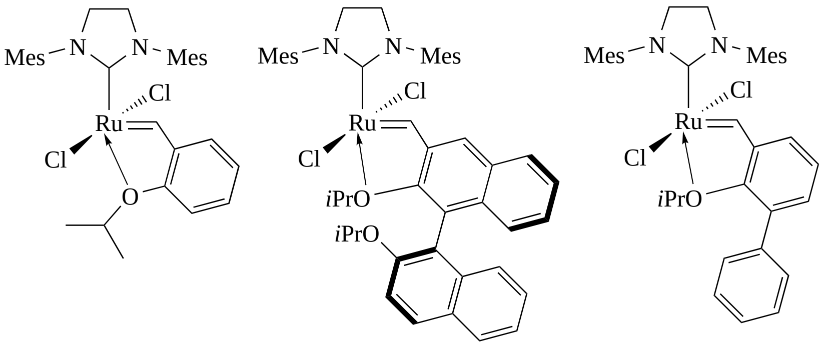

(**4b**) (**4c**) (**4d**)

Scheme 4 Phosphine-free ruthenium complexes for olefin metathesis

active that 1 mol% ring-closes *N*-tosyldiallylamine in 90 min at 0 °C. For all reactions tested, including RCM, CM, RCM-CM, and ROMP, (**4d**) was significantly more active than (**4a**). The high activity of this catalyst is thought to be because of the rapid dissociation of the bulky ligand leading to the active 14-electron species. Catalyst (**4d**) is the most functional group tolerant Ru containing olefin metathesis catalyst reported to date. It successfully mediates ROM-CM reactions of unprotected amines and sulfur containing compounds with metathesis partners of varying degrees of bulk giving products in high yield.[23]

Fürstner developed ruthenium indenylidene (readily accessible from commercially available diphenyl propargyl alcohol) (**2c**) and (**3b**) (Scheme 5) versions of the alkylidene (**2a**) and (**3a**) with (**2c**) being superior to (**3b**) in yield, reaction rate, and tolerance to polar functional groups.[24] Catalyst (**2c**) was more active than (**2a**) for RCM and it was applied to RCM to form functionalized rings from 5 to 21 members. For all reported ring closures, compared cases (**2c**) was equal to or superior to (**2a**). The functional group tolerance and activity made (**2c**) the best catalyst for the RCM approach to the synthesis of the ADE ring system of Nakadomarin A.

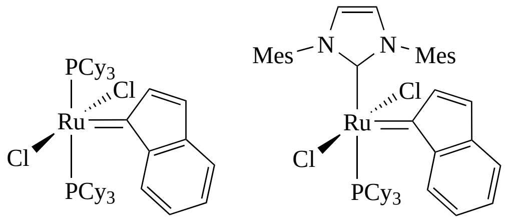

(**2c**) (**3b**)

Scheme 5 Indenylidene versions of olefin metathesis active complexes

Grubbs synthesized and characterized a series of (**2a**), (**3a**), and (**4a**) analogs with electron-rich alkylidenes having the general structure $LPCy_3Cl_2Ru{=}C(H)ER$, ($L = PCy_3$, IMes, H_2IMes) (ER = OEt, SEt, SPh, N(carbazole), N(pyrrolidinone)) and determined their efficacy as olefin metathesis catalysts of electron-rich olefins with the goal of developing a general metathesis method for creating difunctional olefins (Scheme 6).[25] These Fischer-carbene complexes (*see Fischer-type Carbene Complexes*) have similar X-ray structures to their parent complexes, but were

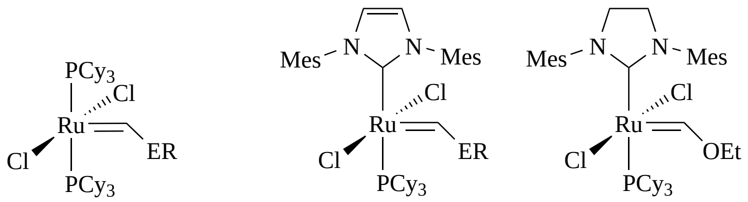

ER = OEt **(2d)**
SEt **(2e)**
SPh **(2f)**
N(carbazole) **(2g)**
N(pyrrolidinone) **(2h)**

ER = OEt **(3c)**
SEt **(3d)**
N(carbazole) **(3e)**
N(pyrrolidinone) **(3f)**

(**4e**)

Scheme 6 Electron-rich analogues of olefin metathesis active complexes more stable than their parent complexes and significantly lower in activity with the overall reactivity trend $E = C > N > S > O$ with even the O analogs exhibiting some activity. In this report, synthesis of difunctional olefins was not achieved because methylidene intermediates are not formed and the reaction cannot proceed by the metathesis mechanism.

Very recently, Grubbs and coworkers completed an analysis based on insight from mechanistic work on the relative rates of phosphine dissociation and olefin coordination (vide infra) in ruthenium alkylidene catalyzed olefin metathesis reactions. The study was based on numerous analogues of (**4a**), having different phosphine groups, for example, (**4e**), (**4f**), and (**4g**). Rates for ROMP of cyclooctadiene with the most potent of these new complexes were 340-fold greater than with (**4a**) (Scheme 7).[26]

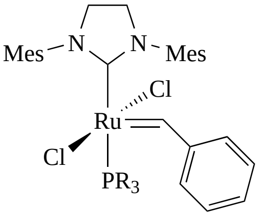

$PR_3 =$	$P(p\text{-}CF_3C_6H_4)_3$	(**4f**)
	$P(p\text{-}ClC_6H_4)_3$	(**4g**)
	$P(p\text{-}FC_6H_4)_3$	(**4h**)
	$P(C_6H_5)_3$	(**4i**)
	$P(p\text{-}CH_3C_6H_4)_3$	(**4j**)
	$P(p\text{-}CH_3OC_6H_4)_3$	(**4k**)

Scheme 7 Electron deficient analogues of (**4a**)

3 MECHANISM AND THEORY

The mechanism of (**2a**) was extensively explored during the late 1990s.[27] These studies supported two different pathways for the potential mechanism of the Ru type olefin metathesis catalysts, described in Scheme 8. The first pathway (a) begins with olefin coordination followed by phosphine dissociation and alkylidene rotation where alkylidene and olefin are cis to each other and undergo metallacyclobutane (*see Metallacycle*) formation and formation of product. The other pathway (b) considered begins with phosphine dissociation and olefin coordination trans to the remaining phosphine, and metallacyclobutane formation trans to the phosphine. Experiments favor the latter hypothesis; although the mechanism in Scheme 9 best fits the overall experimental data. Bulkier electron-donating phosphine ligands in the (**2**) family increase activity, which is suggested to be caused by the electron richness provided by phosphine to metal center donation that allows one phosphine to dissociate and also can stabilize the 14-electron metallacyclobutane intermediate. Recently developed catalysts of the (**2**), (**3**), and (**4**) families have activities that could only partially be explained by ligand donation, prompting many groups to reexamine the mechanism of ruthenium-catalyzed olefin metathesis.[13–17] Since the catalysts discussed above can be varied by a modular approach, all that was needed was for the appropriate mechanistic questions to be asked.

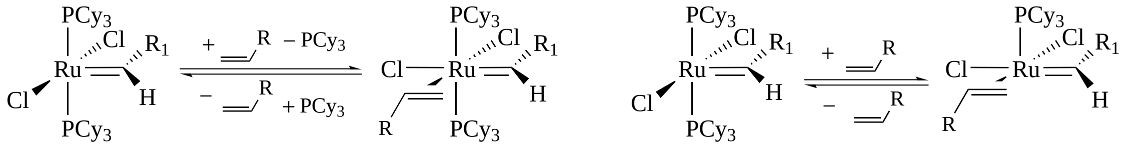

(a) (b)

Scheme 8 Proposed associative (a) and dissociative (b) olefin coordination

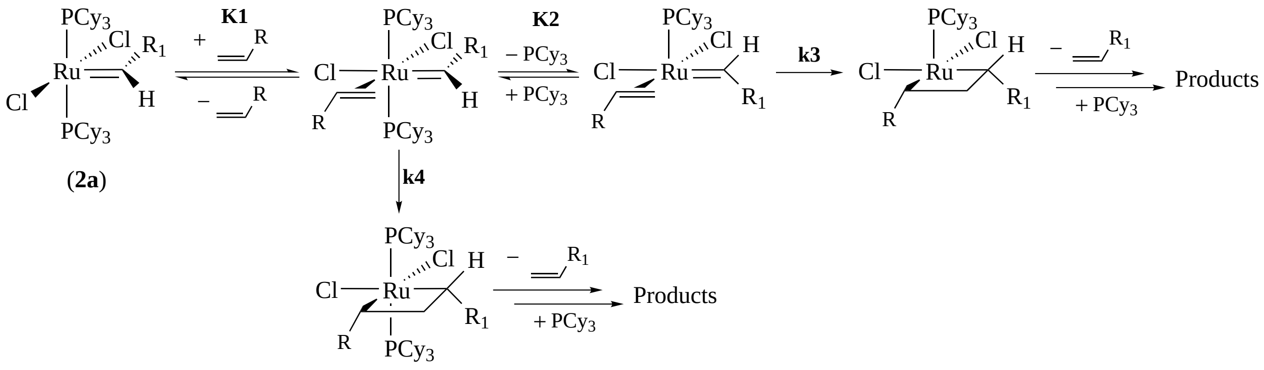

Scheme 9 Mechanism supported by evidence in 1997 study

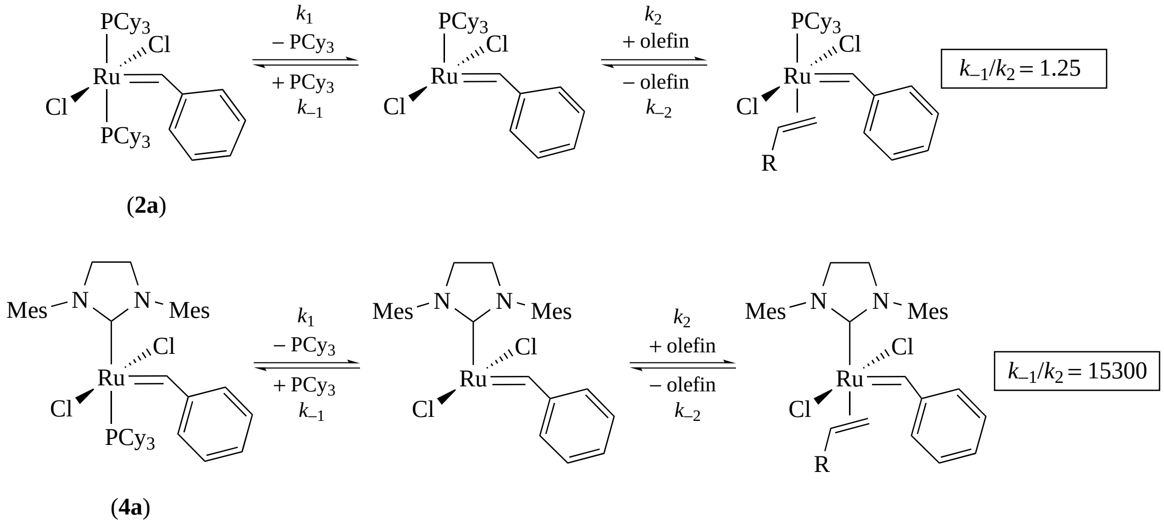

Scheme 10 Ratio of phosphine reassociation to olefin coordination

3.1 Experimental Results

Grubbs took a closer look at mechanism with regard to the greater activity of (**4a**) versus (**2a**).**[28]** To this point, it had been argued that the greater catalytic activity of (**4a**) was caused by the dihydroimidazolinium ligand's better ability to promote dissociation of phosphine through its higher steric bulk (*see Steric Effect*) and greater electron donation; leading more quickly to the active 14-electron species.**[14,17]** Careful kinetic analysis of phosphine exchange reactions and reactions with ethyl vinyl ether supported a dissociative pathway and showed that during the progress of the reaction neither did phosphine dissociate faster in (**4a**) nor were the initiation rates faster. What appeared to matter was the ratio of the rate of phosphine rebinding to olefin binding, that is, k_{-1}/k_2. This ratio is lower in (**4a**) by four orders of magnitude than in (**2a**) (Scheme 10). Thus, even though (**4a**) is slower to dissociate phosphine than (**2a**), once phosphine is dissociated, the 14-electron species prefers to bind olefin rather than rebind phosphine. A related result was determined by work on ADMET kinetics of 1,9-decadiene by Wagener. This study revealed a stronger temperature dependence on reaction rate for (**4a**) when compared to (**2a**). The rate of polymerization at 30 °C, for reactions catalyzed by (**2a**), was twice that for (**4a**). At higher temperatures, (**4a**) was the more active catalyst. The reason for the greater temperature sensitivity of (**4a**) was postulated to be the difference in phosphine dissociation rates for the two precatalysts.**[29]**

3.2 Theoretical Work

A number of theoretical studies support the results of the experimental work by Grubbs and Wagener. Chen performed a quantum mechanical/molecular mechanics (QM/MM) study on the olefin metathesis reaction comparing (**2a**) and (**4a**). The enthalpy of activation predictions from this study is consistent with the experimental values found by Grubbs in that the shape of the ligand, threefold symmetry of phosphine and twofold symmetry of carbene, influenced the dissociation energetics. The QM/MM results indicate that phosphine dissociation is always rate limiting for (**4a**), while the rate-limiting step of (**2a**) has a metallocylobutane structure.**[30]**

Cavallo performed density functional theory (DFT) (ADF) calculations on (**2a**), (**3a**), (**4a**), and their various proposed catalytic cycle intermediates.**[31]** The data from this work agrees with experimental results in the activation energies for phosphine exchange and binding energies for ethene; heteroleptic (*see Heteroleptic Compound*) phosphine/NHC-based complexes have a higher propensity to bind olefin (longer C=C and shorter Ru-olefin distances) than bisphosphine complexes. Each of the energy barriers measured was found to be less than 8 kcal mol^{-1}, with (**3a**) and (**4a**) having a lower olefin insertion barrier than (**2a**). Metallacycles were slightly more stable than olefin bound intermediates for (**3a**) and (**4a**) while the (**2a**)-derived metallacycle was higher in energy, consistent with Chen's QM/MM work.**[30]** The bulky NHC ligand's major role appears to be to crowd the alkylidene moiety and thus destabilize the phosphine-free, olefin-free intermediate, *not* to promote phosphine dissociation electronically.

Thiel performed DFT calculations on a more simplified data set, utilizing PH_3 in place of PCy_3 and imidazol-2-ylidene for IMes, looking at the electronics of both associative and dissociative pathways for the mechanism (*see* ***Mechanisms of Reaction of Organometallic Complexes***).**[32]** This study showed that the dissociative mechanism with trans olefin coordination is favored and that the relative rates of phosphine dissociation and olefin coordination can be affected by phosphine choice. The results of the calculations are rationalized by a steric analysis, arguing that the C_2-symmetric NHC is less able to exert steric pressure on the C_3-symmetric

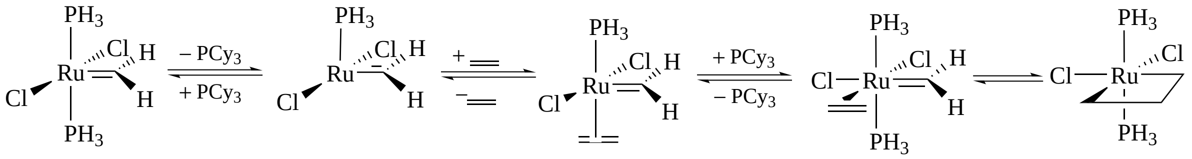

(**5**) +18.86 kcal mol^{-1} +10.13 kcal mol^{-1} +5.11 kcal mol^{-1} +3.96 kcal

Scheme 11 Intermediates in pathway A

phosphines. Thiel concludes that the most effective catalysts will have one weak and one strong σ-donor ligand.

The low-energy barrier to the rate-determining step in olefin metathesis using (**2a**) was supported by DFT (B3LYP) studies on the orbital interactions of (**2a**) with particular interest in the ruthenacyclobutane.[33] A C–C α-agostic (*see Agostic Bonding*) interaction in the metallacyclobutane gives a flat potential energy surface going from ruthenium alkylidene coordinated olefin to ruthenium alkylidene' and olefin'. In addition, strong ruthenium alkylidene/olefin π orbital interactions agree with the low-energy barrier to the rate-determining step of olefin metathesis.

A DFT (B3LYP) study on the mechanism of (**2a**) in olefin metathesis was also recently published using bisphosphine methylidene models.[34] The authors concluded from this work that the active catalyst in olefin metathesis is $(PR_3)_2Cl_2Ru{=}CH_2$, not the higher energy carbenoid complex $((PR_3)_2ClRu–CH_2Cl)$, and that there exist three reaction pathways, A, B, and C. Pathway A is most consistent with a dissociative pathway (Scheme 11). Pathway B and C both have higher activation energies than does A and begin with ethylene coordination to the bisphosphine complex, forming a low-energy (-2.01 kcal mol^{-1}) intermediate; pathway B loses a phosphine, which leads to a high energy barrier to formation of the metallacyclobutane. The energetics of pathway C are dictated by formation of carbenoid species en route to the metallacyclobutane.

Nolan and Cavallo showed only small metrical differences in bond length among the various ligands like IMes and H_2IMes even though there was a large difference in the efficacy of the corresponding catalysts (**3a**) and (**4a**). This was taken to indicate that catalytic ability is quite sensitive to the donor properties of the ligands.[35]

Grubbs and coworkers performed a systematic study on a large number of olefin metathesis initiators that differed only in the phosphine ligand; wherein the phosphine dissociation rate constants, relative rates of phosphine reassociation, RCM, and ROMP rates were determined.[26] A linear free energy (LFE) relationship was found between the strength of the phosphine σ-donation and catalyst initiation rate but no LFE relationship was found with reassociation rates. Overall, among the initiators examined, the p-CF_3triphenylphosphine substituted species had the highest relative reactivity to (**4a**): 340 higher rate in polymerization of COD (cyclooctadiene) and an eightfold increase in rate for RCM of diethyl 2-allyl-2-cinnamylmalonate (Table 1).

These recent findings indicate overall that the ligand that remains on the metal affects the energetics of the catalytic cycle, specifically olefin coordination, and the accessibility of the metallocyclobutane structure, the properties of the phosphane ligand control initiation rates, and thus how much of the catalyst can enter the catalytic cycle. The results of these careful analyses (Table 2) are sure to germinate the next generation of efficacious olefin metathesis catalysts.

4 RECENT METHODOLOGY DEVELOPED UTILIZING OLEFIN METATHESIS

4.1 Advances in the Construction of Small Heterocycles and Carbocycles

The predictable construction of heterocycles and highly functionalized carbocycles with or without intracycle asymmetry is paramount to synthesis of biologically important compounds and other areas of organic synthesis.[36–38] A number of methodological advances have been reported utilizing RCM for the construction of previously inaccessible rings.[39]

Table 1 Relationship of rates and activities (polymerization of cod) of various catalysts of type (**4**)

Complex	Precatalyst phosphine	k_1 (s^{-1})	k_{-1}/k_2	Activity relative to (**4a**)
(**4a**)	PCy_3	0.13 ± 0.01	1.25	1
(**4f**)	$P(p\text{-}CF_3C_6H_4)_3$	48 ± 2	7.3	340
(**4g**)	$P(p\text{-}ClC_6H_4)_3$	17.9 ± 0.4	45	95
(**4i**)	$P(C_6H_5)_3$	7.5 ± 0.6	2.3	50
(**4k**)	$P(p\text{-}CH_3OC_6H_4)_3$	1.8 ± 0.1	7.5	10

Table 2 Summary of recent experimental and theoretical mechanistic work

Author	Method	Mechanism support
Grubbs	Phosphine exchange reaction kinetics on (**3a**) and (**4a**)	The ratio of rates of olefin coordination to phosphine reassociation dictate rate of reaction, and permit the slower to initiate heteroleptic (**3a**) and (**4a**) to be more active catalysts.
Wagener	ADMET kinetics (**2a**) and (**4a**)	Reaction rates using (**4a**) were much more temperature dependant than those using (**2a**). Indicating that phosphine dissociation is an energy barrier for (**4a**) processes.
Chen	QM/MM (**2a**) and (**4a**)	Ligand shape (phosphine vs. NHC) is linked to rate of dissociation of trans phosphine. Phosphine dissociation is always slow step for (**4a**) while metallocyclobutane formation is the energetic barrier for (**2a**)
Cavallo	DFT (ADF) (**2a**), (**3a**) and (**4a**)	Lower lower insertion barriers for NHC-precatalysts than for (**2a**). (**2a**) had higher energy metallacyclobutane
Thiel	DFT (BP86) Analogues of (**2a**) and (**3a**)	Dissociative, trans olefin coordination, phosphine geometry superior to NHC geometry for dissociating phosphine
Suresh and Koga	DFT (B3LYP) Analogue of (**2a**)	Nearly flat potential energy surface going from Ru-alkylidene with coordinated olefin to ruthenacyclobutane to ruthenium alkylidene' with coordinated olefin' caused by C–C agostic interactions
Bottoni	DFT (B3LYP) Analogue of (**2a**)	3 Competing pathways support associative and dissociative mechanisms and finds carbenoids significant contributors as intermediates
Grubbs	Kinetics on heteroleptic compounds	Sigma donation of phosphine directly related to initiation rates in heteroleptic compounds rates of phosphine reassociation not directly linked
Cavallo and Nolan	Calorimetry and crystal-structure measurements (**3a**) and (**4a**)	Electron donation is main difference between (**3a**) and (**4a**) activity

Much of the increase in scope is linked to the higher functional group tolerance and activity of (**4a**).

A need for a synthetic entry toward simple and structurally complex alkaloids prompted development of methodology to prepare a variety of azabicyclo[*n*.3.1] alkenes in good yields utilizing protected 2,6-*cis*-dialkenyl piperidines, prepared from glutarimide or 4-methoxy pyridine and catalyzed by (**2a**) and (**4a**) (equation 1).[40,41]

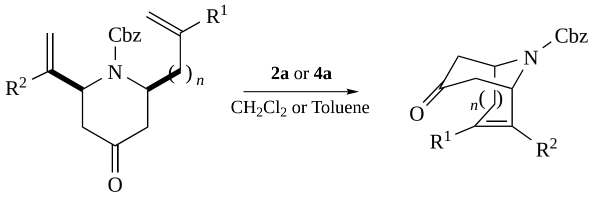

(6a–d) **(7a–d)**

a: $n = 0$; R^1, $R^2 = H$
b: $n = 1$; $R^1 = H$, $R^2 = CH_3$
c: $n = 1$; R^1, $R^2 = CH_3$
d: $n = 0$; $R^1 = H$, $R^2 = CH_3$

(1)

Madsen was able to synthesize conduritols (cyclic polyalcohols) via RCM metathesis of tartaric acid or sugar derivatives using (**2a**) or (**4a**), making available a number of the possible conduritol diastereomers in just a few steps from the chiral pool (Table 3).[42]

The 1,2-dihydroquinoline and quinoline structural units, ubiquitous in natural products, were synthesized utilizing ene–ene or ene–enol RCM.[43] The authors explored catalysis with (**2a**) and found it brought many substrates to >90% isolated products (50 °C, 1 h) while (**4a**) took all substrates reported to nearly quantitative conversion (Table 4).

Complex (**3a**) proved to be efficient for the formation of a variety of adjacent cyclic ethers via triple RCM from readily synthesized acyclic hexaenes.[44] The reaction, which proceeds under mild to somewhat forcing conditions, gives moderate to good yields of the desired tricyclic ethers over the alternative RCM products (equation 2).

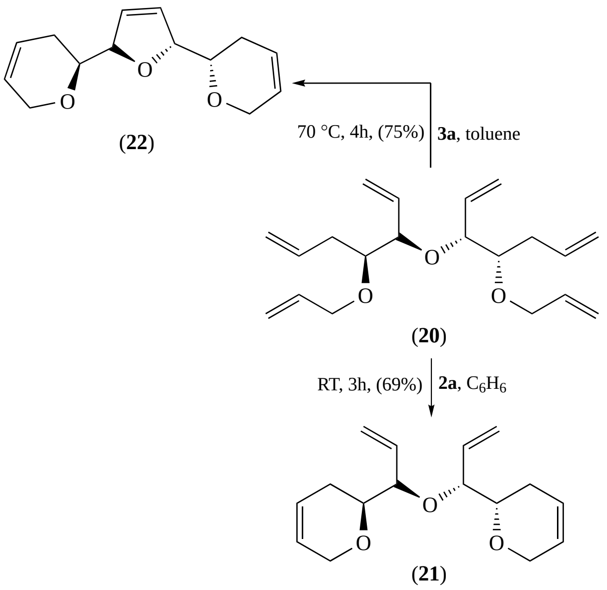

(**22**) (**20**) (**21**)

(2)

Table 3 Formation of conduritols by RCM

Entry	Substrate	Products	Catalyst	mol%	Yield
1	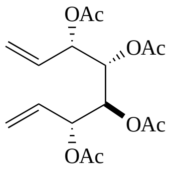 (**8**)	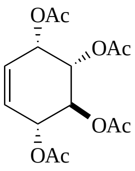 (**9**)	(**2a**) (**4a**)	10 7.5	81 95
2	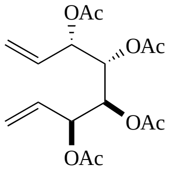 (**10**)	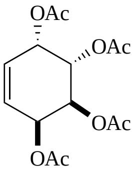 (**11**)	(**4a**)	7.5	96
3	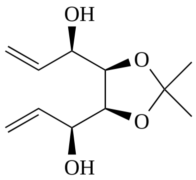 (**12**)	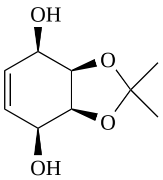 (**13**)	(**4a**)	5	72

Table 4 Synthesis 1,2-dihydroquinolines

Entry	Substrate	Precatalyst	Product	Yield
1	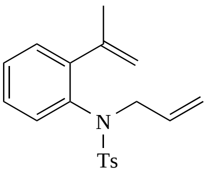 (**14**)	(**2a**)	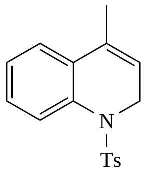 (**15**)	92
2	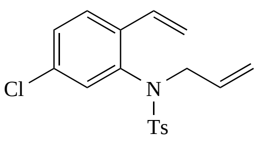 (**16**)	(**2a**)	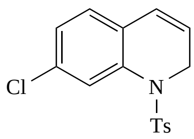 (**17**)	74
3		(**4a**)		100
4	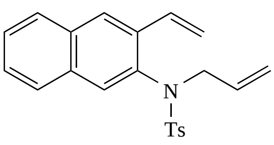 (**18**)	(**2a**)	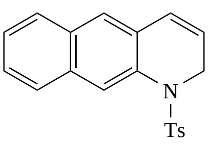 (**19**)	98

Liu and coworkers prepared a number of bicyclic ethers by applying en-yne-ene metathesis with (**2a**) or (**4a**) to chiral bisallyloxybut-1-ynes to give various bicyclic ethers with interesting biological properties from a common starting material.[45] Using 3 mol% (**2a**), the 3,4-bisallyloxybutynes gave a [4.4.0] bicycle as the major product with small amounts of [5.3.0] bicycle. The 3-allyloxy4-but-2-enyloxy analogue gave only [5.3.0] bicyclic ethers when 2 mol% (**4a**) was used (Table 5).

α-Phosphono lactone analogues of cytidine and cytosine arabinose diphosphates were constructed via a Lewis acid (*see Lewis Acids & Bases*) catalyzed asymmetric allyl addition to arabinose aldehyde followed by RCM.[46] The RCM step was examined using (**2a**) and (**4a**), with (**4a**) giving better conversion to lactone product in good yields (equation 3).

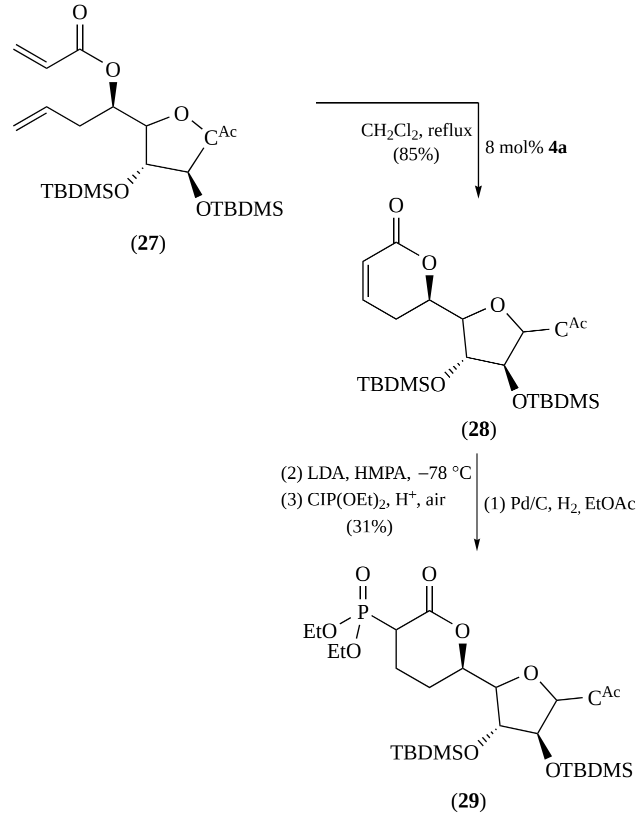

(27)
TBDMSO
OTBDMS
C^{Ac}
CH_2Cl_2, reflux
(85%)
8 mol% **4a**
(28)
(2) LDA, HMPA, −78 °C
(3) CIP(OEt)$_2$, H$^+$, air
(31%)
(1) Pd/C, H_2, EtOAc
EtO
EtO
P
(29)

(3)

Table 5 Tandem en-yn-ene metathesis

3,4-bisallyloxybut-1-yne $\xrightarrow[2\,\text{mol\% }\mathbf{4a},\ 48\,\text{h}]{\text{ethylene (1 atm)}}$ fused bicyde product

Entry	Substrate	Product	Yield[a]
1	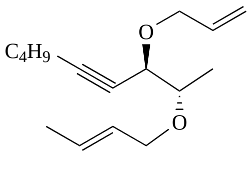 (**23**)	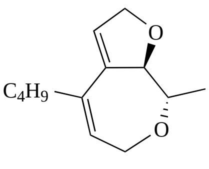 (**24**)	82%
2	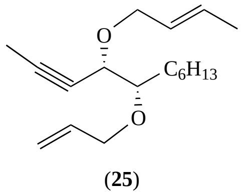 (**25**)	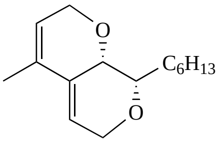 (**26**)	84%

[a] Isolated yield.

Efficient routes to α-trifluoromethylated nitrogen heterocycles of various sizes for applications in synthesis of CF_3 tagged bioactive molecules were achieved in two steps from α-(trifluoromethyl)homoallylamines via ene–ene or ene–yne metathesis catalyzed by (**2a**) and with better conversions by (**4a**) (equation 4).[47]

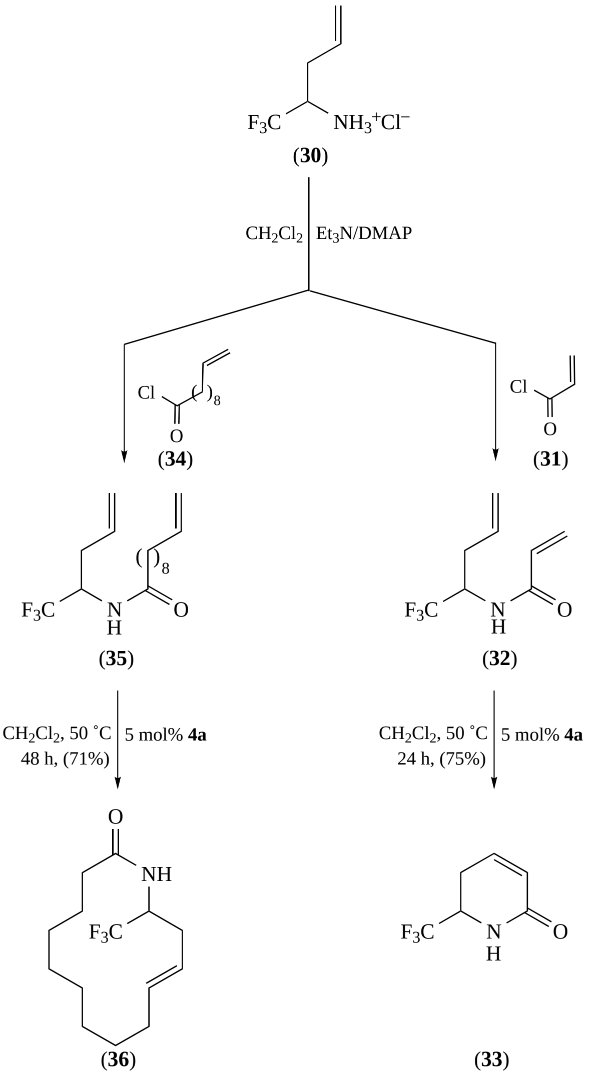

F_3C
$NH_3^+Cl^-$
(30)
CH_2Cl_2
Et_3N/DMAP
Cl
(34)
(31)
(35)
(32)
CH_2Cl_2, 50 ˚C
48 h, (71%)
5 mol% **4a**
CH_2Cl_2, 50 ˚C
24 h, (75%)
5 mol% **4a**
NH
(36)
(33)

(4)

An efficient new methodological pathway for the preparation of the polyhydroxylated alkaloids, indolizidines, and quinolizidines was developed through (**4a**) catalyzed RCM/allylic amination or, alternatively, RCM/haloamination strategies (equation 5), starting from a methyl furanoside precursor.[48]

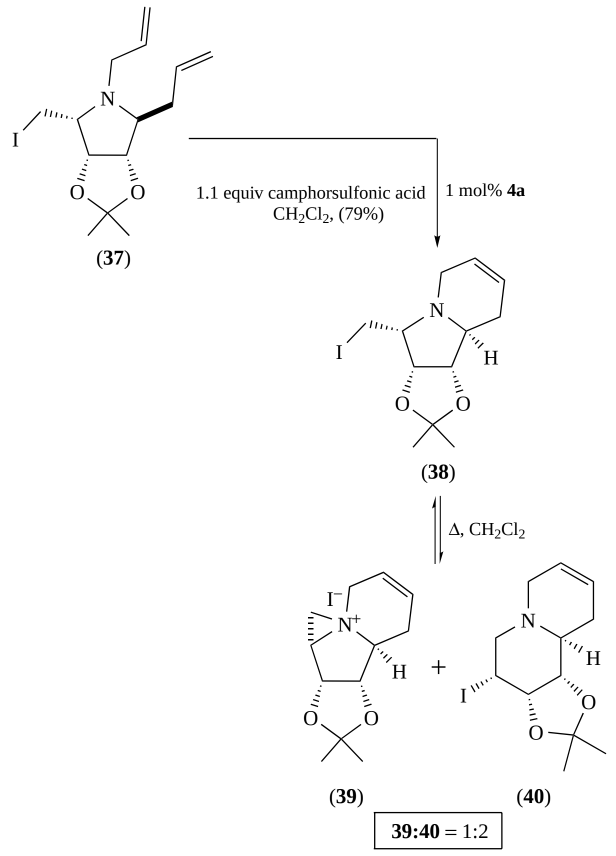
I
N
O
O
1.1 equiv camphorsulfonic acid
CH2Cl2, (79%)
1 mol% 4a
N
H
I
O
O
Δ, CH2Cl2
I−
N+
H
+
O
O
N
H
I
O
O
39:40 = 1:2

(37) (38) (39) (40)

(5)

Meyers used (**2a**) under a variety of conditions to ring close a number of enantiopure lactams to form spirocycles ranging in size from 5 to 8 members in 18–24 h reaction times that could then be converted to different targets in just a few steps (Table 6).[49]

Snieckus developed a RCM approach to analogues of ergot alkaloids employing (**2a**). This route is the first to access *seco-C*/D ring ergot alkaloid cores and it does so with good efficiency (equation 6).[50]

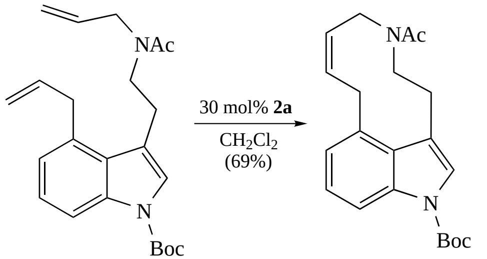
NAc
N
Boc
30 mol% 2a
CH2Cl2
(69%)
NAc
N
Boc

(**47**) (**48**)

(6)

The synthesis of unsymmetrical nonadjacently linked tetrahydrofurans was accomplished by Mootoo through (**4a**) catalyzed cross metathesis of the protected substituted-tetrahydrofuran components.[51] These compounds are potential intermediates for acetogenins having potent antitumor activity

Table 6 Ring closure metathesis to give a variety of spirocycles

Entry	Lactam	Product	%de	%yield
1	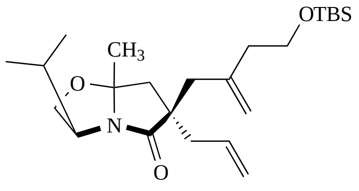 OTBS CH3 O N O (**41**)	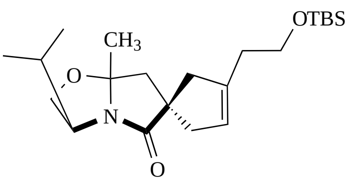 OTBS CH3 O N O (**42**)	95	95
2	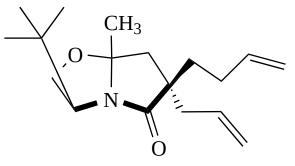 (**43**)	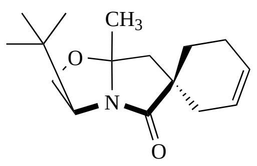 (**44**)	95	97
3	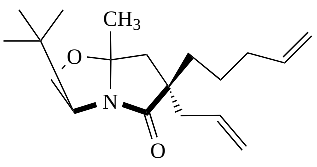 (**45**)	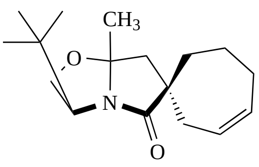 (**46**)	95	90

(equation 7).

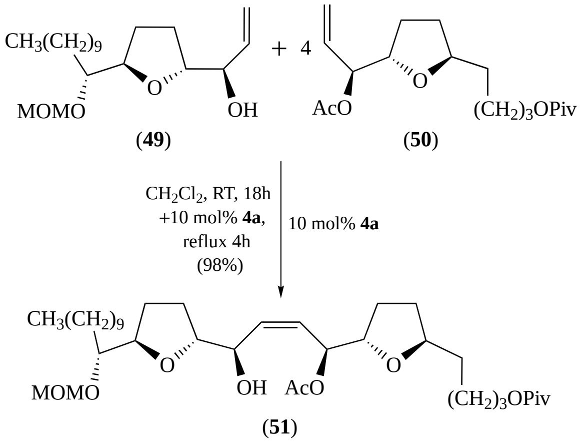
CH3(CH2)9
MOMO
OH
+ 4
AcO
(CH2)3OPiv
(49)
(50)
CH2Cl2, RT, 18h
+10 mol% 4a,
reflux 4h
(98%)
10 mol% 4a
CH3(CH2)9
MOMO
OH AcO
(CH2)3OPiv
(51)

(7)

Rutjes utilized (**2a**) and (**3a**) for ring-closing olefin metathesis of enamides.[52] The five and six-membered ring products were available in good yields for the most part, although forcing conditions were sometimes required (equation 8). Hanson pursued the synthesis of cyclic enol phosphates via RCM utilizing (**4a**).[53] Five- and six-membered heterocycles (X = O, NTs, S, SO_2) were achieved in good to excellent yields with 5 mol% catalyst (equation 9).

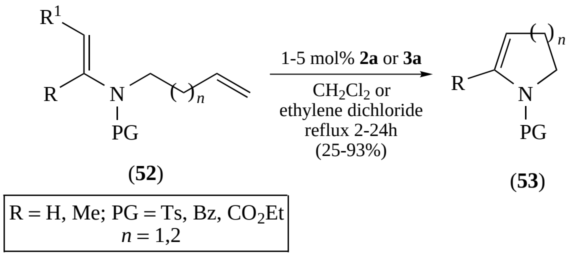
R1
R
N
PG
n
1-5 mol% 2a or 3a
CH2Cl2 or
ethylene dichloride
reflux 2-24h
(25-93%)
R
N
PG
n
(52)
(53)
R = H, Me; PG = Ts, Bz, CO2Et
n = 1,2

(8)

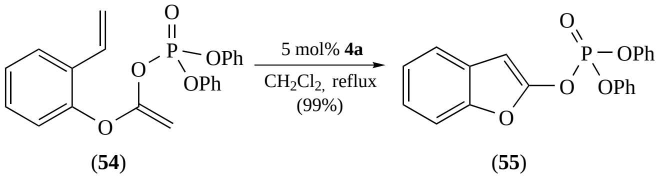
O
P
OPh
OPh
O
O
5 mol% 4a
CH2Cl2, reflux
(99%)
O
P
OPh
O
OPh
O
(54)
(55)

(9)

The high selectivity of olefin metathesis with (**2a**) was key in the formation of diverse nonracemic vinyl cyclopropanes from chiral homoallylic alcohols and allyl chlorodimethylsilane in three steps, or allyl trimethylsilane in two steps, giving diastereomerically pure cis or trans isomers.[54]

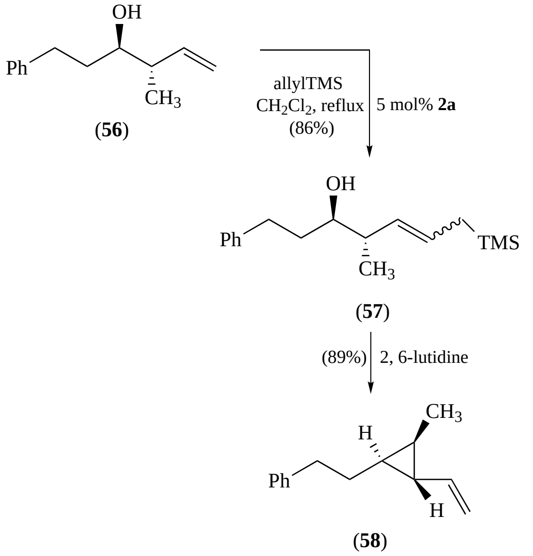
OH
Ph
CH3
(56)
allylTMS
CH2Cl2, reflux
(86%)
5 mol% 2a
OH
Ph
CH3
TMS
(57)
(89%)
2, 6-lutidine
CH3
H
Ph
H
(58)

(10)

4.2 Macrocycles and Supramolecular Structures

Naturally occurring macrocycles are often highly functionalized, often having heterocycles in the ring. In many cases, successful synthesis of macrocycles hinged on ring-closing lactonizations and lactamizations.[55–59] With the advent of efficient RCM, macrocycle synthesis gained a new avenue of approach that allowed the formation of rings without the reliance on functional group transformations.[60–62] Numerous reports utilizing (**2a**) for the formation of macrocycles have been published, while (**4a**) has allowed the scope of this type of transformation to broaden significantly. Similarly, olefin metathesis has been an important synthetic route in the formation of supramolecular structures; this section covers some recent advances in these areas utilizing (**2a**).

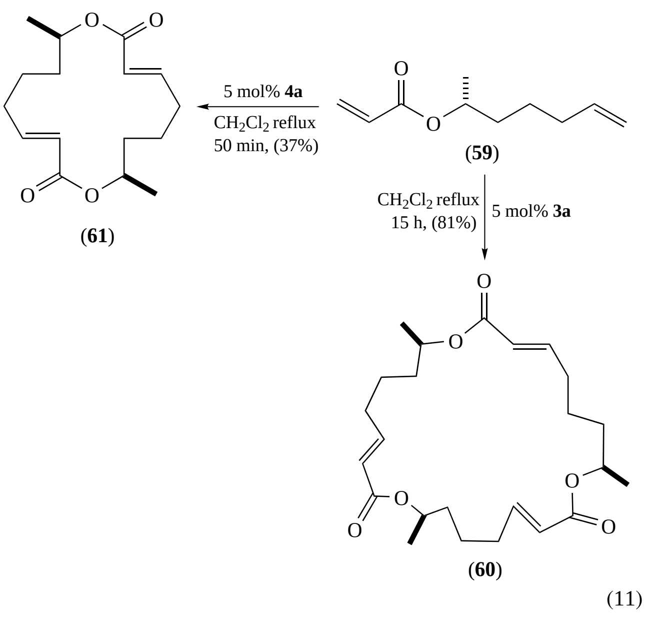
O
O
O
O
(61)
5 mol% 4a
CH2Cl2 reflux
50 min, (37%)
O
O
(59)
CH2Cl2 reflux
15 h, (81%)
5 mol% 3a
O
O
O
O
O
O
(60)

(11)

Table 7 Formation of macrolactones from α,β-unsaturated esters catalyzed by (**4a**)

Entry	Diene	[], mM	Product(yield)
1	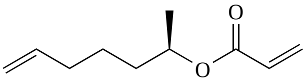 (**62**)	6	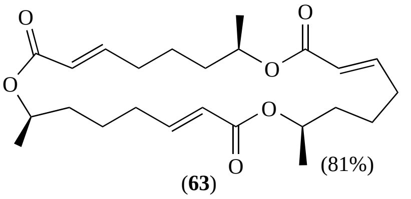 (**63**) (81%)
2	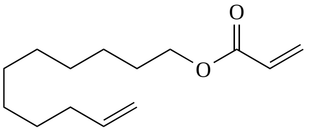 (**64**)	3	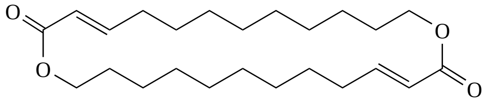 (**65**) (82%)
3	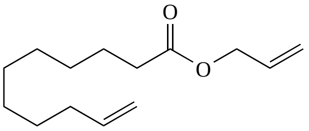 (**66**)	1	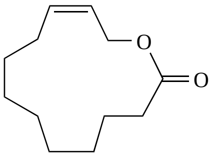 (**67**) (78%)

Olefin metathesis has become a leading method for assembling macrocycles. Of particular efficacy in these reactions are the second-generation catalysts like (**4a**). Fürstner reported that dienes with ester functionality could be cyclized to form 14-membered lactones as the thermodynamic products. Chiral macrocycles were also achieved by ring-closing dimerizations and trimerizations of chiral dienes (equation 11).[63] Grubbs also reported successful use of (**4a**) to ring close, dimerize, and trimerize ester-containing dienes to form a variety of macrolactones. The driving force for formation of RCM products over CM products was seen to be the low concentrations (Table 7).[64] In related work, Grubbs was able to access a variety of macrocycles that were derived from differing parent compounds. Ring sizes from 18 to 36 members were obtained in low to moderate yield via ring expansion utilizing functionalized straight chain dienes and cyclopentenes and cyclooctenes at low concentrations (equation 12). The strength of this strategy lies in the ease of access to a variety of ring sizes through adjustment of stoichiometry and concentrations.[65]

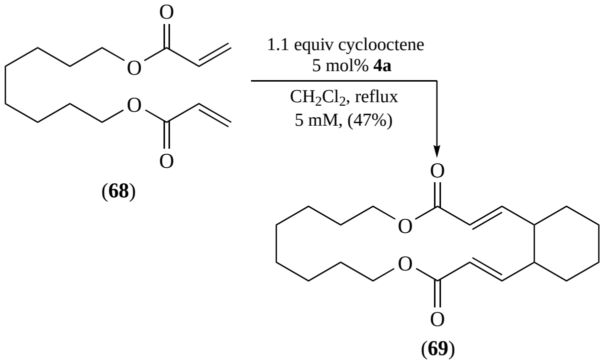

(**68**)

(**69**)

(12)

Olefin metathesis was successfully applied in the creation of end functionalized polybutadiene oligomers employing self-metathesized (using **2a**) viologen-based pseudo[2]rotaxane dimers as chain transfer agents in the polymerization of 1,5 cyclooctadiene catalyzed by (**4a**) to create porphyrin containing [3]rotaxanes.[66] This report expands upon methodology for end functionalizing polybutadienes reported by Grubbs.[67,68]

Paddlanes having a bicyclo[1.1.1]pentane core have been synthesized from dicarboxylate esters and 1,3 difunctionalized bicyclo[1.1.1]pentanes using (**2a**) catalyzed olefin metathesis (equations 13 and 14).[69]

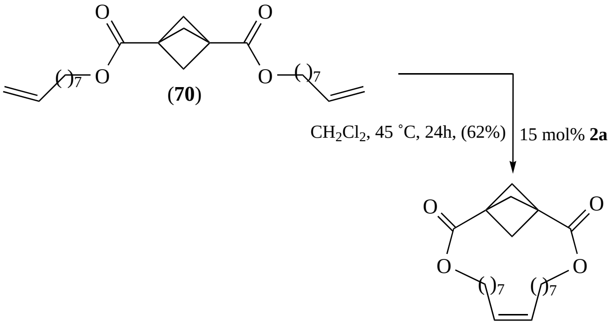

(**70**)

(**71**)

(13)

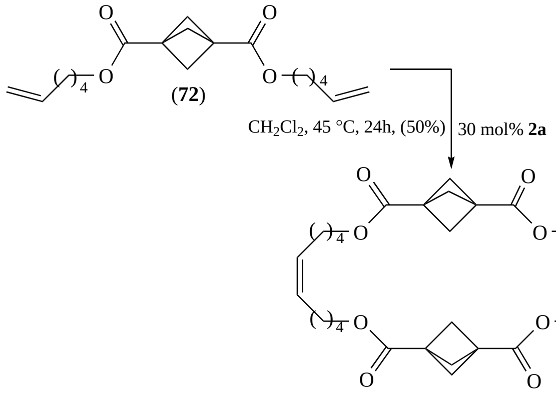

(**72**)

(**73**)

(14)

[3]Catenane synthesis was achieved by utilizing alkene terminated pseudorotaxanes of various lengths and (**2a**) expanding on work reported earlier by Smith,**[70]** resulting in modest concentration and ring size dependent yields (2–35%) of desired products, equation (15).**[71]**

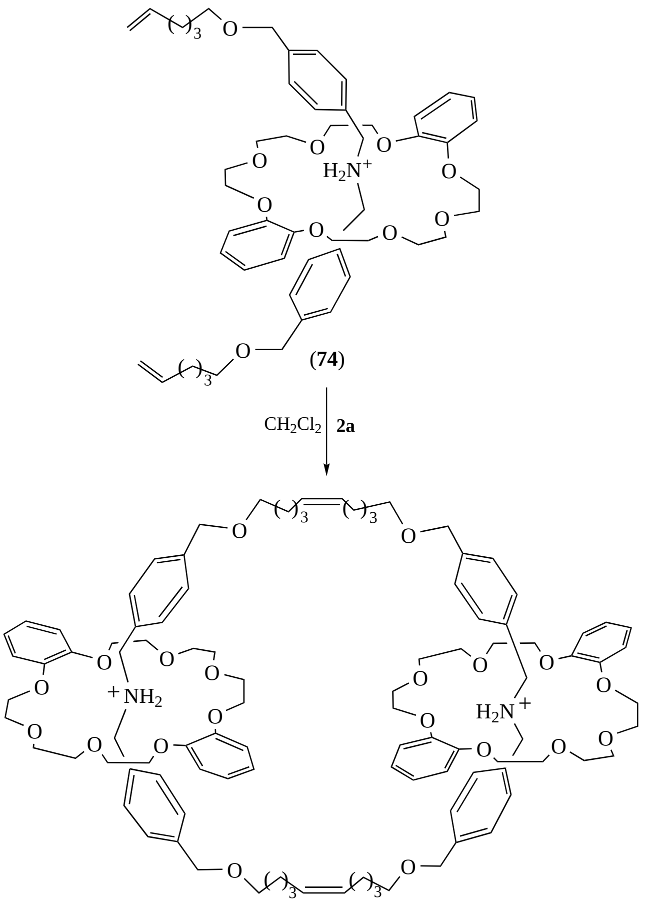

(**74**)

(**75**)

(15)

Van Koten and coworkers took advantage of the combination of a shape persistent reusable cationic template and olefin metathesis to form trigonal functionalized macrocycles from 2,6-diolefin substituted pyridines catalyzed by (**2a**) in moderate to good yields (equation 16).**[72]** The controllable binding modes allow easy liberation of the macrocycle from the template. Upon reduction of the alkenes, these flexible macrocycles were efficient hosts for the parent template. This strategy can be utilized for the formation of nitrogen and oxygen functionalized macrocycles.

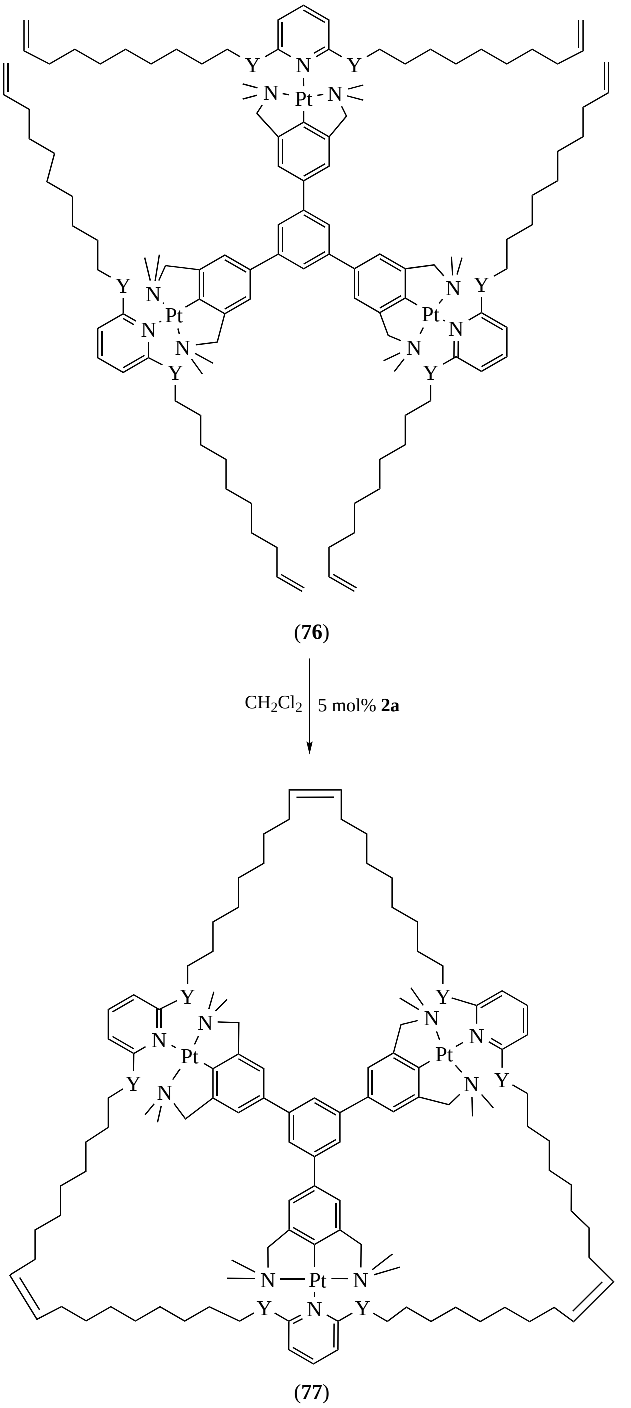

(**76**)

(**77**)

(16)

4.3 Cross Metathesis

It was recognized early that efficient olefin cross metathesis could provide new methods for the synthesis of complex molecules. However, neither (**1a**) nor (**2a**) were very effective at *intermolecular* cross metathesis owing to poor reaction selectivity (cross vs. intramolecular metathesis) and low E:Z ratios (*see (E) & (Z) Isomers*).[73–75] The advent of more active and functional group tolerant olefin metathesis catalysts recently made cross metathesis a viable route for constructing a large variety of functionalized acyclic alkenes.

Grubbs used (**4a**) to efficiently install functional groups that might otherwise be added via C–H activation or allylic oxidation pathways (Scheme 12). Among the breadth of compound types accessible through these cross metathesis strategies were substituted vinyl-phosphonic, boronic, and carbonyl esters, which were synthesized in good to excellent yields.[76]

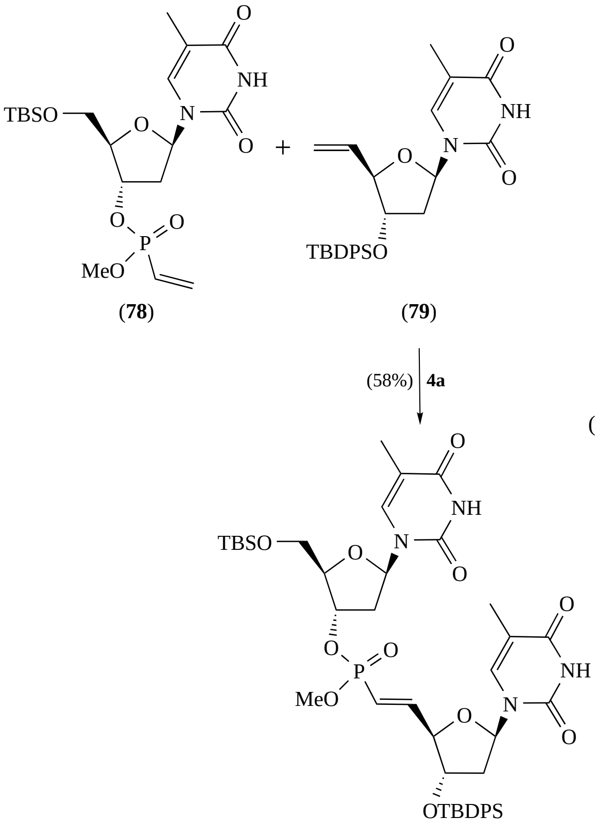

(**78**) (**79**) (**80**)

(17)

Several examples of the use of (**4a**) catalyzed cross metathesis of protected allylic sugars, or vinyl substituted heterocycles or vinylated functional groups have been reported. Vinylphosphonate-linked nucleotide dimers were synthesized by cross metathesis using complex (**4a**), achieving products with E:Z ratios of >20:1 in moderate to good yields (equation 17).[77] A metal-mediated route to acyclic nucleosides developed by Agrofoglio and coworkers produced nucleosides in two steps from parent pyrimidines and purines.[78] The first step is Pd catalyzed allylation, and the second step is (**3a**) catalyzed cross metathesis of a protected allylic diol with yields over the two-step process in the 40–60% range (equation 18).

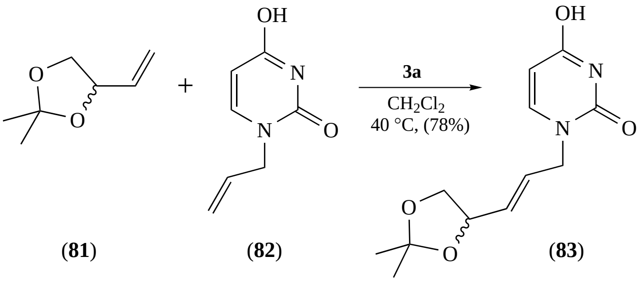

(**81**) (**82**) (**83**)

(18)

Complex (**4a**) gave cross metathesis products of protected allyl-galactosides and allyl halides as a convenient route to substituted-allylhalides in good yields and high E:Z selectivities, illustrating the power of cross metathesis to bring functionalities together in few steps.[79] Protected olefinic carbohydrate was linked during peptide assembly, or to a peptide fragment, in the development of strategies for forming C-neoglycopeptides designed for modeling cellular recognition and its relationship to disease.[80] Many different C-glycoside/amino acid combinations were successfully linked although the E:Z ratios were not described. Efficient access to iminosugar C-glycoside building blocks was provided by (**4a**) catalyzed cross metathesis. The methodology is general and gives access to these structurally diverse bioanalogous compounds for potential application in biomimetic chemistry.[81] Examples of cross metathesis with protected sugars and glycosides are illustrated in Scheme 13.

Grubbs found that (**4a**) ring-opened cyclic olefins, and then react with an acrylate to produce end functionalized linear olefins, giving a ring-opened cross metathesis product (ROCM) with two olefins with differing reactivity (equation 19).[82] Key to the distribution of products was the relative rates of ring-opening and cross metathesis with the functionalized olefin.

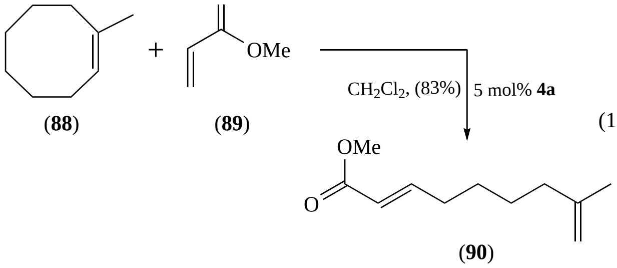

(**88**) (**89**) (**90**)

(19)

Taylor reported kinetically controlled cross metathesis of homoallylic alcohols and allyl trimethyl silane with (**4a**) gave products with high E-olefin selectivity and good yields via a five-membered chelate intermediate (equation 20).[83]

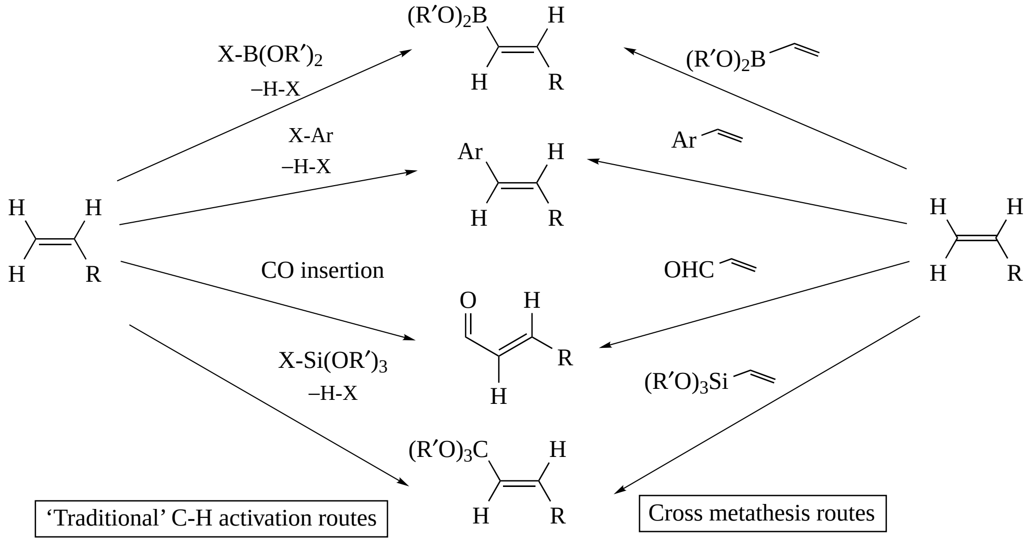
X-B(OR′)₂
–H-X
X-Ar
–H-X
CO insertion
X-Si(OR′)₃
–H-X
(R′O)₂B
Ar
OHC
(R′O)₃Si
'Traditional' C-H activation routes
Cross metathesis routes

Scheme 12 Cross metathesis as a reaction equivalent to vinyl C–H activation processes of substitution and insertion

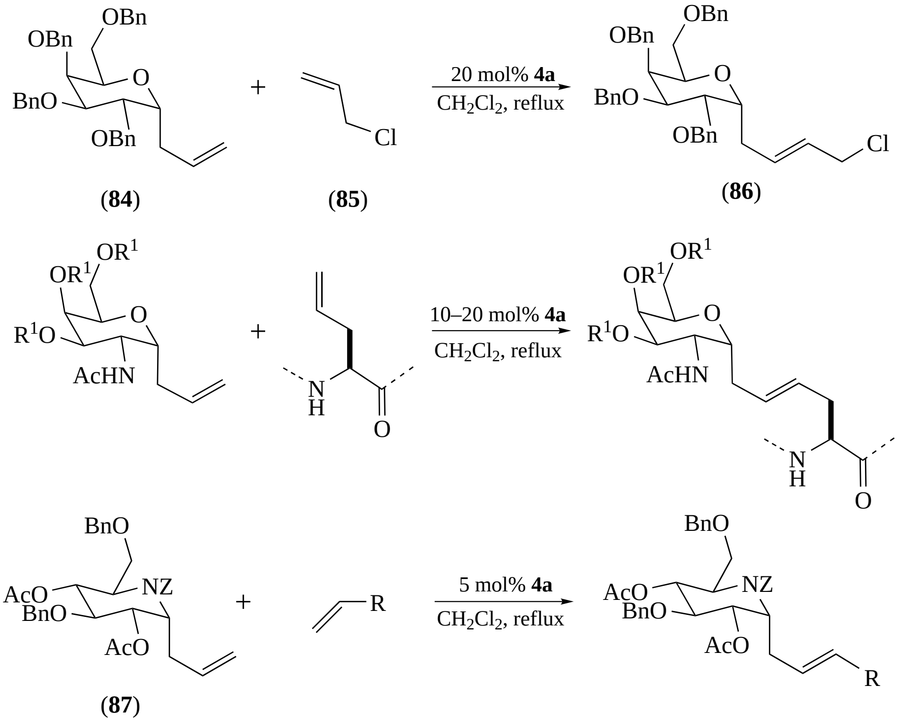
(84)
(85)
(86)
(87)
20 mol% 4a
CH₂Cl₂, reflux
10–20 mol% 4a
CH₂Cl₂, reflux
5 mol% 4a
CH₂Cl₂, reflux

Scheme 13 Cross metathesis of protected sugars catalyzed by (**4a**)

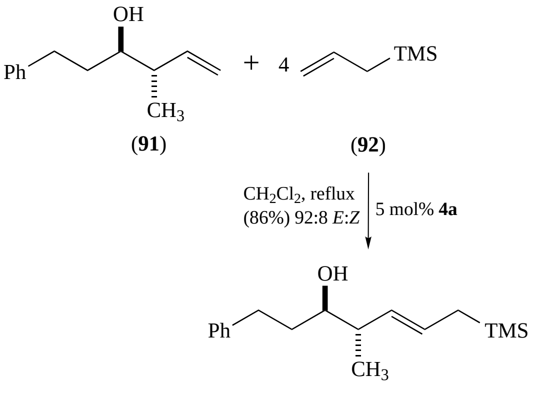

(93)

(20)

Grubbs reported the use of (**4a**) in the synthesis of symmetrical trisubstituted olefins, wherein isomer selectivity is not an issue.[84] Isolated yields using neat isobutylene or 2-methyl-2-butene as both reactant and solvent and a variety of functionalized metathesis partners were good to excellent under low catalyst loadings, providing a viable alternative to the Wittig reaction (equation 21).

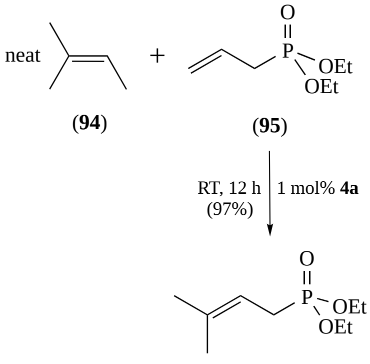

(96)

(21)

Cross metathesis of chiral allylic alcohol or amine moieties and styrene to create phenyl analogues of the parent compounds was achieved using (**4a**). The phenyl group, in conjugation with the parent molecule, lends a stronger extinction coefficient to the molecules, making the species more amenable for analysis by circular dichroism.[85]

4.4 Asymmetric Olefin Metathesis

Along with better efficacy in cross metathesis, one of the areas of olefin metathesis that was awaited eagerly is the area of asymmetric olefin metathesis. As of 2000, only a few reports for evidence of asymmetric induction, all of which were catalyzed by molybdenum complexes, had been published.[86–89]

Schrock and Hoveyda have reported the synthesis and activity of a number of chiral molybdenum-based catalysts for enantioselective olefin metathesis (for example, **97a, b**) (Scheme 14); to date, the majority of successful enantioselective (*see Enantioselectivity*) olefin metathesis has been reported from their labs utilizing this family of compounds.[90] Key to the success of these catalysts is the enantiopure diolate ligands, the substituted biphenolate or binaphtholate, that limit the trajectory of olefin approach. These catalysts have been applied to both asymmetric ring-opening and ring-closing metathesis (AROM and ARCM) respectively as well as tandem AROM-cross-metathesis reactions. Initial successful entries in this category are the biphenolate (**97a**) and the binaphtholate (**97b**). The octahydrobinaphtholate, (**97c**), was successful in kinetic resolution of racemic polyenes, achieving $k_{\text{rel}} = >25$ for a variety of substrates. Complexes (**97a**), (**97b**), and (**97c**) all promoted desymmetrization but (**97c**) gave consistently high k_{rel} in kinetic resolutions (Table 8) as well as good desymmetrization results.

A later report describes AROM/CM of norbornyl alkenes and styrene coupling partners to create asymmetrically functionalized cyclopentanes with alkenyl groups that can be further elaborated.[91] High yields (>98%) of trans (>98) cross metathesis products (predominantly the desired ring-opened, A–B metathesis product) can be achieved using (**97a**) (equation 22).

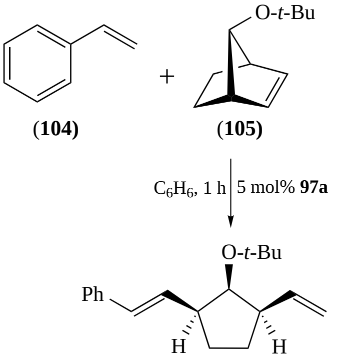

(22)

(106)

>98% conversion
>98% conversion to product
>98% *trans*
92% yield >98% ee

A variety of new catalysts has been developed through the Schrock/Hoveyda collaboration. Analogs of (**97a**) having silyl groups para to the hydroxy positions were created with the aim of attaching the catalyst to a support to increase ease of catalyst/product separation and to retard bimolecular decomposition of alkylidene intermediates.[92] These silyl substituted analogues, (**97d**) and (**97e**), have comparable capabilities to the parent compound (Table 9), and thus are attractive candidates for synthesis of heterogenized analogs.

Schrock reported catalysts related to (**97c**) with a variety of substituents at the 3,3′ position of the octahydrobinaphtholate ligand including benzhydryl, (**97f**), and mesityl, (**97g**) (Scheme 15).[93] This ligand type is easier to access than either biphenol or binaphthol derived species, since the axially chiral biaryl construct is already in place and substitutions are nearly

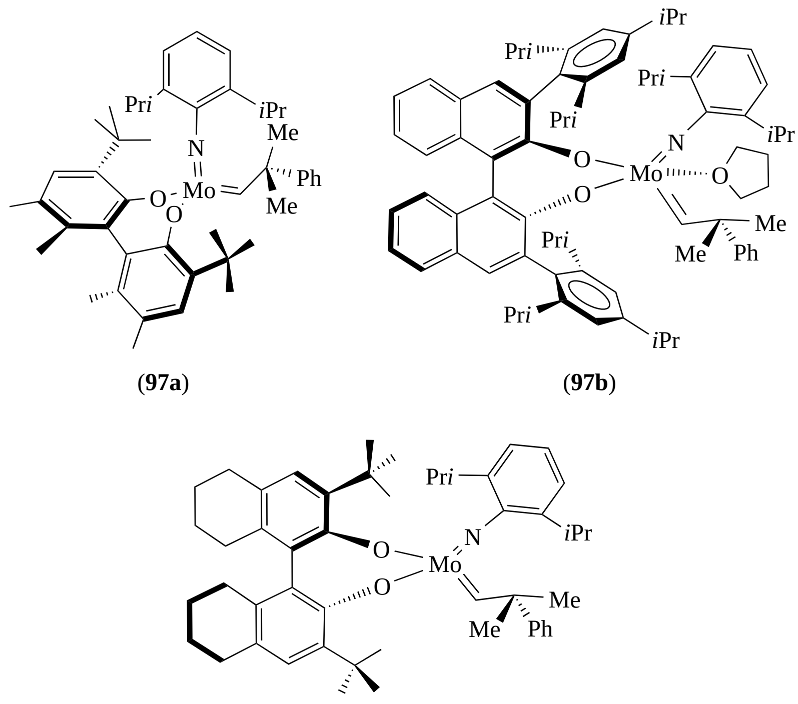
Pr*i*
*i*Pr
N
Mo
O
O
Me
Ph
Me
(**97a**)
*i*Pr
Pr*i*
Pr*i*
Pr*i*
*i*Pr
N
O
Mo
O
O
Me
Me
Ph
Pr*i*
Pr*i*
*i*Pr
(**97b**)
Pr*i*
*i*Pr
N
O
Mo
O
Me
Me
Ph

(**97c**)

Scheme 14 Chiral molybdenum-based catalysts for asymmetric olefin metathesis

Table 8 Molybdenum catalyzed ARCM kinetic resolutions

Entry	Substrate	Product	Catalyst	k_{rel}
1	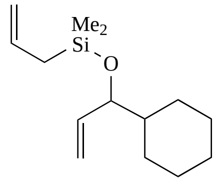 (±)-**98**	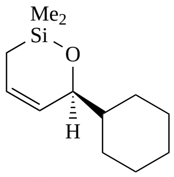 (*S*)-**99**	(**97a**)	>25
2			(**97b**)	3.0
3			(**97c**)	>25
4	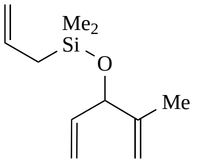 (±)-**100**	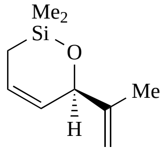 (*R*)-**101**	(**97a**)	<2
5			(**97b**)	5
6			(**97c**)	20
7	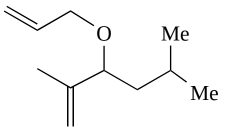 (±)-**102**	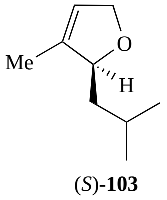 (*S*)-**103**	(**97a**)	11
8			(**97b**)	<2
9			(**97c**)	25

Table 9 Desymmetrization by ring-closing metathesis utilizing (**97a, d–g**)

Entry	Substrate	Product	Catalyst	Time (h)	% Conv.	% ee
1	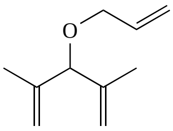 (**107**)	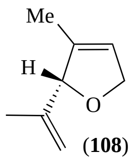 (**108**)	(**97d**)	1	89	97
2			(**97e**)	1.5	88	97
3			(**97a**)	6	94	93
4			(**97f**)	2	>95	93
5			(**97g**)	3	84	93

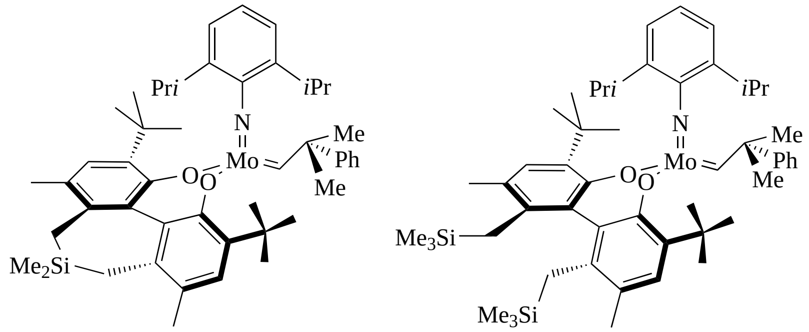
Pri
iPr
N
Mo
Me
Ph
Me
O
O
Me2Si
Me3Si
Me3Si

(**97d**) (**97e**)

Scheme 15 Chiral molybdenum olefin metathesis catalysts with benzhydryl and mesityl substituted bitet ligands

exclusive at the 3,3′ positions. These complexes and others in the family were effective for desymmetrization of allylic ethers (Table 9, entries 4 and 5) and asymmetric ring closure of tertiary *and* unprotected secondary amines.[94] Results from the secondary amine metathesis illustrated that the aryloxy bond to the Mo is robust enough to withstand potential N–H-based protonation (equation 23).

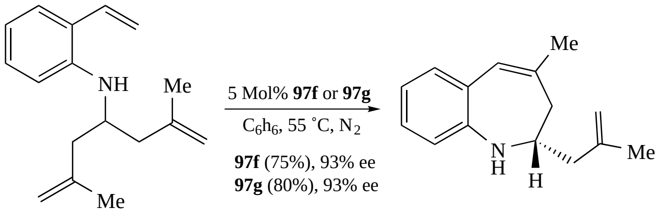
NH
Me
Me
5 Mol% 97f or 97g
C6h6, 55 ˚C, N2
97f (75%), 93% ee
97g (80%), 93% ee
Me
N
H
H
Me

(**109**) (**110**)

(23)

Analogs of (**97a**), (**97b**), (**97f**), and (**97g**), with 2,6-dichlorophenylimido instead of 2,6-diisopropylphenylimido (**97h**), (**97i**), (**97j**), and (**97k**), respectively (Scheme 16) were also synthesized.[93] These complexes were found to have similar activity and scope to the parent complexes, giving enantioselective RCM of unprotected tertiary amines with good yields and enantioselectivities exceeding 90%.[95]

A related catalyst (**97i**), bears an alkylimido ligand instead of an arylimido (Figure 1).[96] This catalyst exists as the syn isomer and has activities not available in the arylimido species, effecting AROM/CM of norbornyl ethers and allyl boronate in 90% ee and good yield with a 13:1 trans:cis ratio (equation 24).

Promising results were obtained for the AROM/RCM of norbornyl trienes with (**97i**) (ees up to 96% and 80% yield of the desired product were reported) (equation 25).

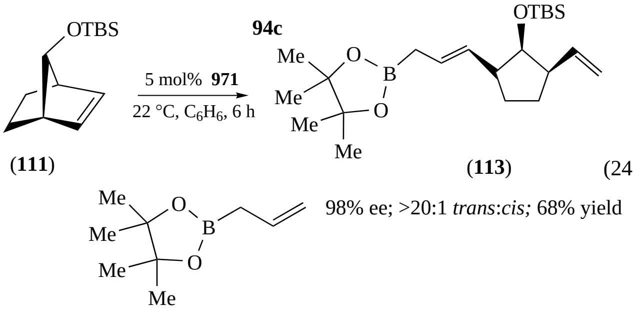
OTBS
94c
5 mol% 971
22 °C, C6H6, 6 h
Me
Me
Me
Me
O
B
O
OTBS
Me
Me
Me
Me
O
B
O
98% ee; >20:1 trans:cis; 68% yield

(**111**) (**113**) (24)

(**112**)

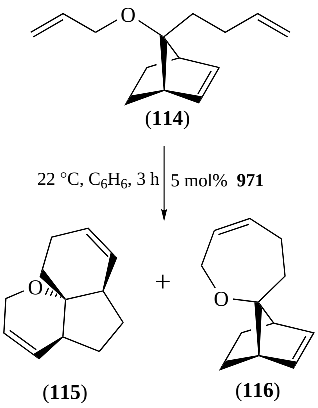
O
22 °C, C6H6, 3 h
5 mol% 971
O
+
O

(**114**)

(25)

(**115**)
80% yield
96% ee

(**116**)
20% yield

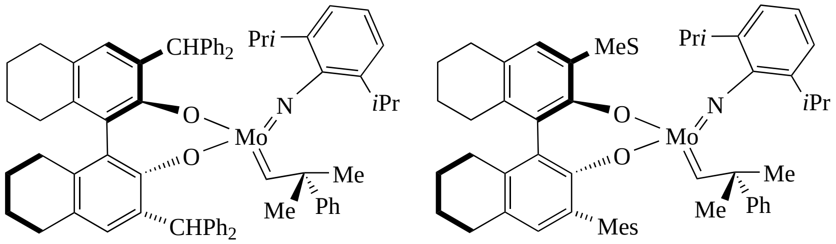

(**97f**) (**97g**)

Scheme 16 Chiral molybdenum olefin metathesis catalysts with 2,6-dichlorophenylimido ligands. Mo-coordinated THF omitted for clarity

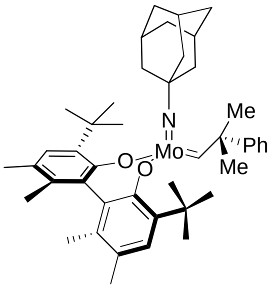

(**97l**)

Figure 1 Adamantylimido substituted chiral molybdenum olefin metathesis catalyst

As with many catalytic systems, additives can play an important role. During optimization of the asymmetric rearrangement of cyclopentenyl tertiary ethers to chiral cyclohexenyl tertiary ethers, Hoveyda found a strong solvent effect on the enantioselectivity of the reaction using (**97b**).[97] Lewis basic (*see Lewis Acids & Bases*) additives were used to modify the catalyst since (**97i**) is Lewis acidic and coordination could change the equilibration of the Mo-alkylidene isomers and, thus, could alter the enantioselectivity. Coordination of Lewis base to the metal center might also change the 'fit' of the chiral pocket. Addition of 10 equiv (vs. substrate) of THF substantially increased the enantiomeric excess of the product in the model transformation (Table 10). It was surmised that the effect was coordinative rather than an effect of the change in solvent polarity. The discovery of this additive effect led to the successful synthesis of enantioenriched spyrocylcic ethers in up to 96% ee without yield erosion.

Hoveyda explored the development of a robust chiral catalyst that would operate in air and was recoverable or recyclable.[98] To accomplish this, he turned to ruthenium-based catalysts and applied some of what had been learned about effective olefin metathesis catalysis to date. First, there is improved performance when the dissociating ligand is an ether tethered to the alkylidene at the 2 position, rather than a phosphine. Second, an electron-rich ligand such as H_2IMes gives improved catalyst stability. Utilizing these concepts in conjunction with a large chiral element on the imidazolinium ligand led to (**119a**) in good yield (Scheme 17). The racemic version of this new catalyst performed RCM only sluggishly under forcing conditions, but 90% of the catalyst was recovered after 98% conversion to products. Asymmetric AROM/CM of tricyclic norbornenes and styrene by (**119a**) under moderate conditions led to nearly quantitative conversions, moderate yields, high trans:cis ratios, high ees, and approximately 90% recovered catalyst. Complex (**119a**) operated in air using undistilled tetrahydrofuran to give AROM/CM of 7-oxonorbornenes and styrene to give similar results in yield, isomer ratios, and ees as seen under rigorously dry and air-free conditions. Hoveyda and coworkers then systematically explored the effect of substituents on the binaphtholate moiety and the aryl alkyl ether alkylidene

Table 10 The effect of adding THF to enantioselective rearrangement reactions catalyzed by (**97i**)

Entry	Substrate	Product	Equiv THF	% Conv./% yield	% ee
1	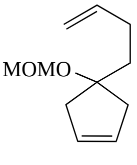 (**113**)	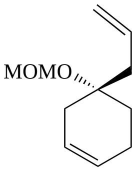 (**114**)	0	>98;nr[a]	78
2			2	>98;nr	85
3			10	>98;93	92

[a]nr = not reported.

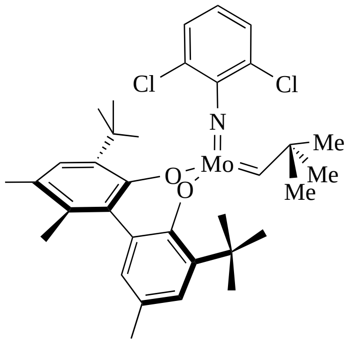

(**97h**)

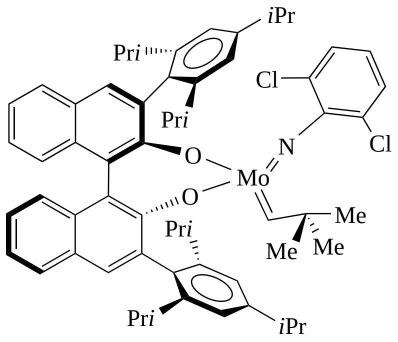

(**97i**)

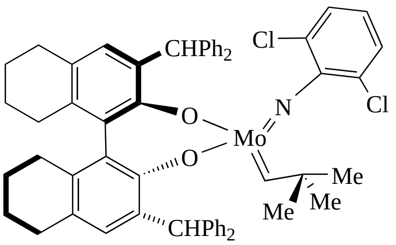

(**97j**)

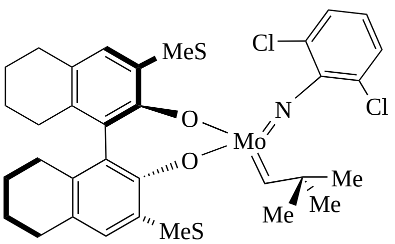

(**97k**)

Scheme 17 Chiral ruthenium olefin metathesis catalysts

Table 11 Results for AROM/CM catalyzed by (**119a–c**)

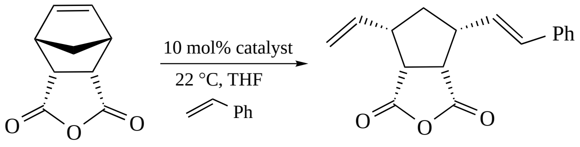

(**120**) (**104**) (**121**)

Entry	Catalyst	Relative activity	Time	% Conversion	% Yield	% ee
1	(**119a**)	1	1	>98	63	70
2	(**119b**)	130	0.4	>98	60	70
3	(**119c**)	160	0.4	>98	85	nr[a]

[a] Reported to be between 75% and 82% ee.

to optimize this type of catalyst for activity.[99] The most successful catalysts, (**119b**) and (**119c**), had steric crowding near the ether group to enhance activation to the 14-electron species. In addition, (**119c**) had a CF_3 group at the 6-position of the naphthol portion of the chiral element (Scheme 17, Table 11).

Grubbs examined the effect that a C_2 symmetric imidazolinium ligand would have on dichloro-, dibromo-, and diiodo-ruthenium alkylidene catalysts (**112a–f**) (Scheme 18).[100] The new complexes had activities and stabilities similar to the parent complex (**4a**) and were thus tested for asymmetric induction in enantioselective desymmetrization reactions. The k_{rel} using these new complexes were low, leading to very low ees; however, selectivity was strongly boosted, with NaI as an additive (k_{rel} = up to 19). The selectivity results were rationalized to be a result of side-on olefin coordination followed by halide ligand reorganization.

Schreiber applied (**4a**)-catalyzed RCM in the development of some of the facets of diversity-oriented synthesis toward the stereochemical control of macrocycle skeletal diversity. In this work, he showed that a chiral element such as an amino alcohol, even many bonds from the ring closure, can influence the stereochemical outcome of RCM of otherwise identical complex substrates like a chiral auxiliary via diastereomeric transition states. Depending on which isomer is used, a completely different reaction pathway is observed.[101]

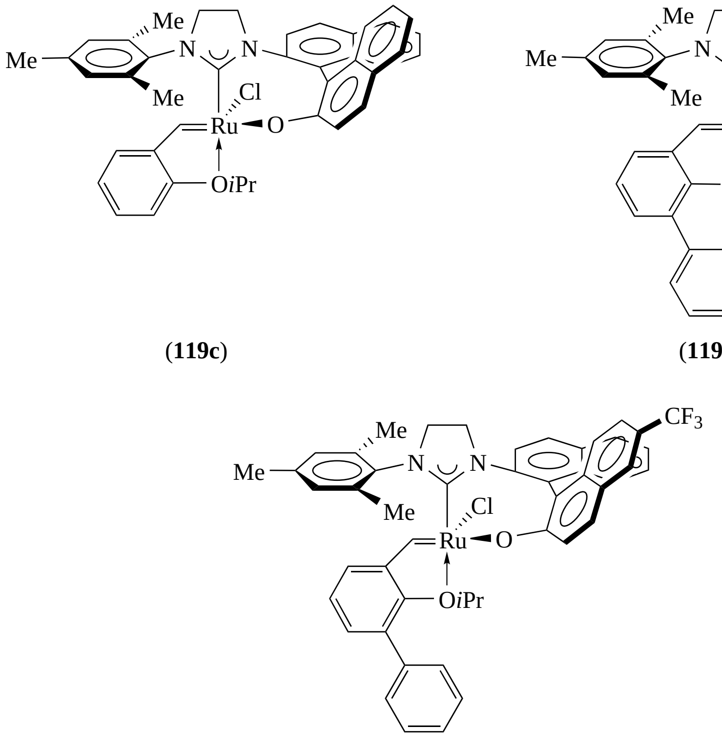

(**119c**) (**119b**)

(**119C**)

Scheme 18 Ruthenium olefin metathesis catalysts with C_2-symmetric imidazolinium ligands

4.5 Tandem and Sequential Reactions

Organometallic catalysts and reagents normally mediate a single transformation; however, their expense requires high turn over efficiency. Another way to increase their efficiency is to participate in sequential reactions where multiple transformations are performed sequentially in the same pot by a single catalyst or with complementary catalysts.

Grubbs reported tandem olefin metathesis/hydrogenation as a means to make saturated cyclic products and a one-pot RCM/transfer dehydrogenation/hydrogenation route to (*R*)-(−)-Muscone utilizing (**4a**) (Scheme 19).[102] Snapper and coworkers took advantage of the isomerization side reaction that occurs in unpurified OM catalysts to generate cyclic enol ethers using catalyst (**4a**) in moderate to good overall yields from acyclic dienes (equation 26).[103]

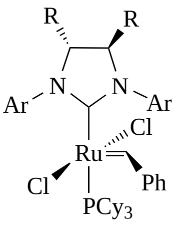

	R	Ar
(**122a**)	$-(CH_2)_4-$	mesityl
(**122b**)	$-(CH_2)_4-$	*o*-methylphenyl
(**122c**)	$-(CH_2)_4-$	*o*-isopropylphenyl
(**122d**)	Ph	mesityl
(**122e**)	Ph	*o*-methylphenyl
(**122f**)	Ph	*o*-isopropylphenyl

Scheme 19 Silyl substituted chiral olefin metathesis catalysts

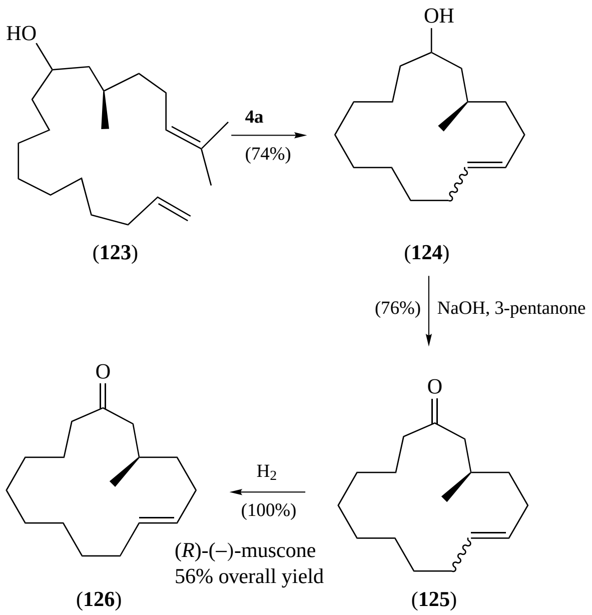

(**123**) (**124**) (**126**) (**125**)

(26)

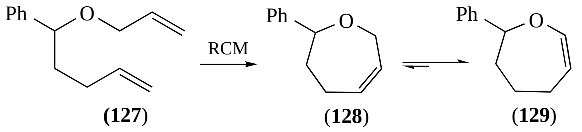
Ph
O
RCM
Ph
O
Ph
O
(127)
(128)
(129)

(27)

A combination of palladium catalyzed allylic acetate isomerization and ruthenium-catalyzed RCM effected 3-acetylcyclopentenes and tertiary cyclopentenols in one-pot in moderate to good yields.[104,105] Grigg explored sequential reactions utilizing palladium catalyzed allene insertion/nucleophile incorporation and (**4a**) for RCM to give in two steps a variety of five- and six-membered heterocycles in overall good yields (equation 28).[106] A similar process was reported by Ruitijes.[52] In related work, Grigg also explored allenylation/RCM/1,3-dipolar cycloaddition from aryl iodides, allene, CO, and allylic sulfonamides to construct complex heterocycles as products of sequential Pd and Ru (**4a**) catalyses.[107]

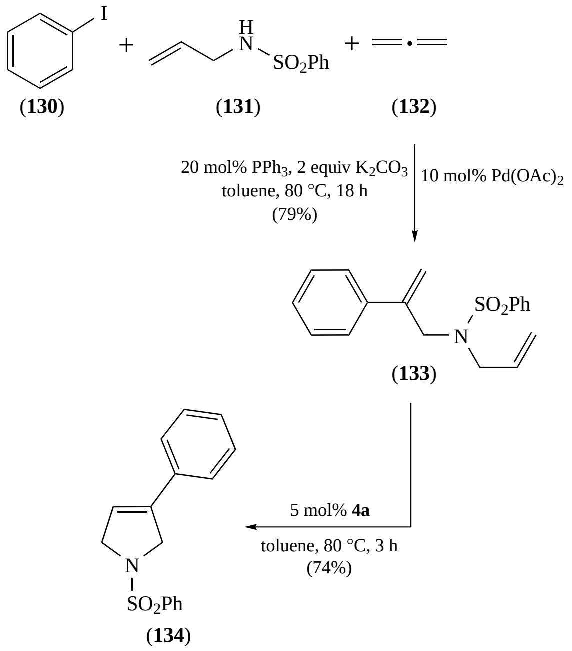
I
H
N
SO2Ph
(130)
(131)
(132)
20 mol% PPh3, 2 equiv K2CO3
toluene, 80 °C, 18 h
(79%)
10 mol% Pd(OAc)2
SO2Ph
N
(133)
5 mol% 4a
toluene, 80 °C, 3 h
(74%)
N
SO2Ph
(134)

(28)

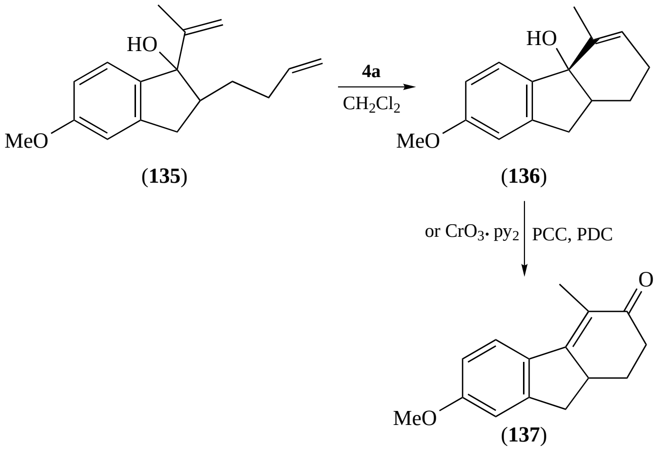
HO
MeO
(135)
4a
CH2Cl2
HO
MeO
(136)
or CrO3· py2
PCC, PDC
O
MeO
(137)

(29)

A synthetic route to α,β-disubstituted cycloalkenones via a four step one-pot synthesis employed (**4a**) for RCM and then oxidative rearrangement giving products in low to moderate overall yields as a way to access estrogen receptor ligand tetrahydrofluorenones (equation 29).[108] Crimmins reported an asymmetric aldol-olefin metathesis approach to the synthesis of functionalized cyclopentenes exploiting the acyclic stereocontrol of the aldol reaction with efficient (**2a**) catalyzed RCM (equation 30).[109]

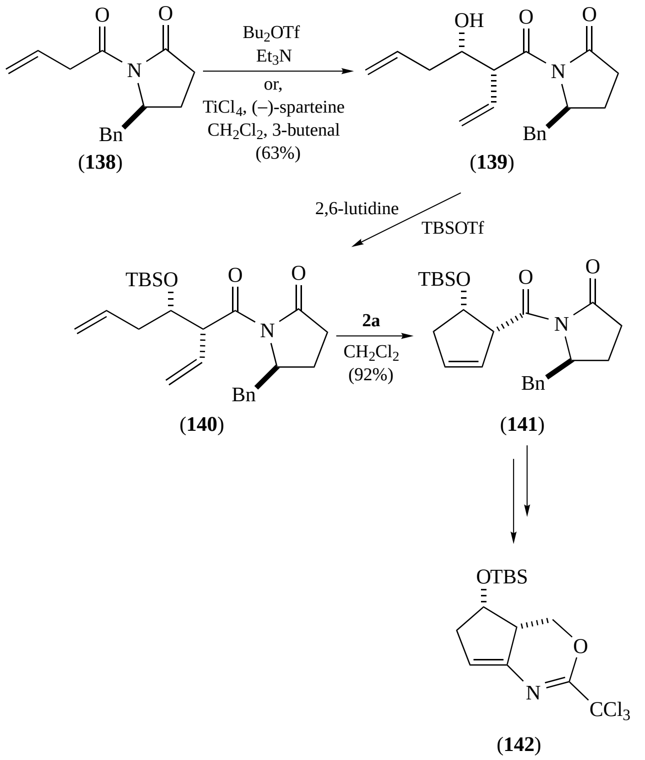
O
O
N
Bn
(138)
Bu2OTf
Et3N
or,
TiCl4, (−)-sparteine
CH2Cl2, 3-butenal
(63%)
OH
O
O
N
Bn
(139)
2,6-lutidine
TBSOTf
TBSO
O
O
N
Bn
(140)
2a
CH2Cl2
(92%)
TBSO
O
O
N
Bn
(141)
OTBS
O
N
CCl3
(142)

(30)

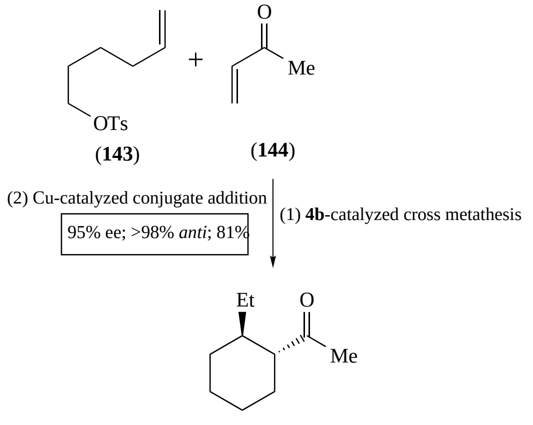
OTs
(143)
O
Me
(144)
(2) Cu-catalyzed conjugate addition
95% ee; >98% anti; 81%
(1) 4b-catalyzed cross metathesis
Et
O
Me
(145)

(31)

Hoveyda and coworkers recently developed sequential catalytic cross metathesis/asymmetric conjugate addition utilizing (**4b**) to make acyclic aliphatic enones (equation 31).[110] Blechert developed a synthetic route toward bicyclic N-heterocycles that hinged on cross metathesis and double reductive amination to access compounds like

R below using (**4b**) (equation 32).[111] Snapper utilized (**4a**) and (**4b**) for ring-opening cross metathesis/oxy-Cope rearrangement, giving medium ring-containing bicycles as well as stereochemical insight for these transformations (equation 33).[112] Lee and coworkers utilized (**4a**) to achieve one-pot, stereoselective three-component tandem Enyne/cross metathesis/Diels–Alder reactions in good to excellent yields (equation 34).[113]

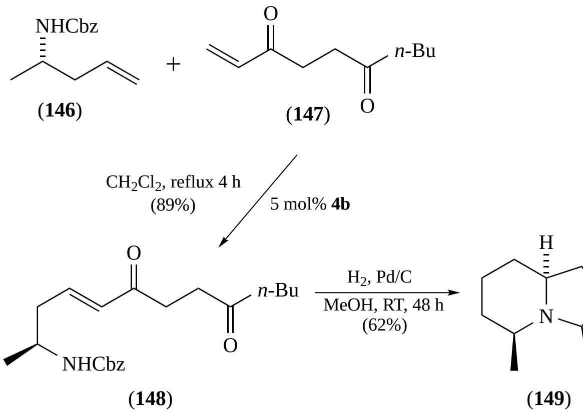
NHCbz
+
O
n-Bu
O
(146)
(147)
CH2Cl2, reflux 4 h
(89%)
5 mol% 4b
O
n-Bu
O
NHCbz
(148)
H2, Pd/C
MeOH, RT, 48 h
(62%)
H
N
n-Bu
(149)

(32)

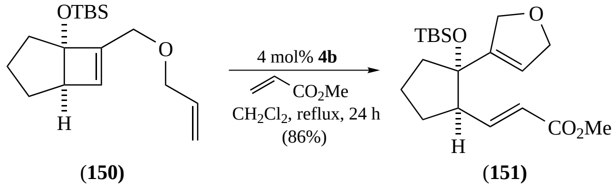
OTBS
O
H
(150)
4 mol% 4b
CO2Me
CH2Cl2, reflux, 24 h
(86%)
TBSO
O
H
CO2Me
(151)

(33)

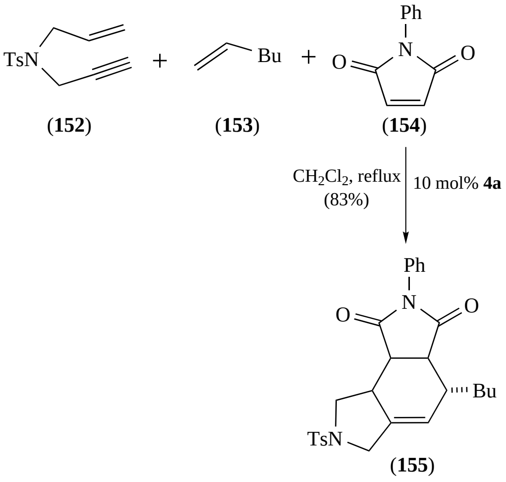
TsN
+
Bu
+
Ph
N
O
O
(152)
(153)
(154)
CH2Cl2, reflux
(83%)
10 mol% 4a
Ph
N
O
O
Bu
TsN
(155)

(34)

4.6 Other Methodological Developments

Some of the progress in catalyst development has been made by simple application modifications like the suspension of (**4a**) in paraffin, allowing for ease of benchtop use.[114] The solid had acceptable activity even after benchtop storage without precaution for nearly two years and the paraffin was readily removed via flash chromatography.

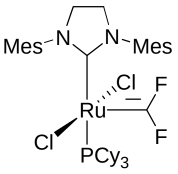
Mes
N
N
Mes
Cl
F
Ru
Cl
F
PCy3

(**4m**)

Figure 2 Electron-poor alkylidene complex (**4m**)

RCM using (**4a**) was reported to be strongly accelerated by microwave radiation, giving quantitative conversions of substrates like diethyl diallylmalonate in 15 min while thermal conversions for the same time was only 3%.[115] Chang and coworkers expanded the scope of substrates for cross and RCM conjugated eneynes utilizing the bis-bromopyridine substituted catalyst (**41**) (equation 35). The reaction requires elevated temperatures and long reaction times but gives products in up to 70% yield with as much as a 25:1 *Z*:*E* isomer ratio.[116]

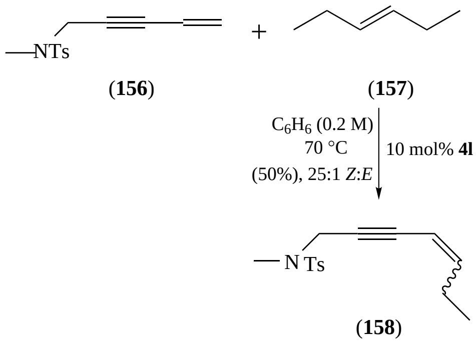
NTs
+
(156)
(157)
C6H6 (0.2 M)
70 °C
(50%), 25:1 Z:E
10 mol% 4l
N Ts
(158)

(35)

Grubbs and coworkers used (**4a**) to perform olefin metathesis with 1,1-difluoroethelyene; a metathesis partner that had theretofore been unavailable for reaction consideration.[117] While metathesis did occur, the difluoro carbene Ruthenium complex (**4m**) (Figure 2) was not an effective catalyst itself; thus, little if any turnover was observed, although this did provide a potential convenient pathway for constructing dihalocarbene-metal complexes.

5 APPLICATION OF OLEFIN METATHESIS TOWARD TOTAL SYNTHESIS PROBLEMS

Much of the bias of the foregoing section was on methodology that could be geared to the synthesis of classes of natural products and biologically relevant molecules (vide supra). What follows are some specific recent highlights in syntheses of small, medium, and large ring compounds formed by RCM, and larger molecules constructed or elaborated by cross metathesis. The diverse synthetic strategies are unified by the integral role olefin metathesis played in the successful completion of the target compounds.

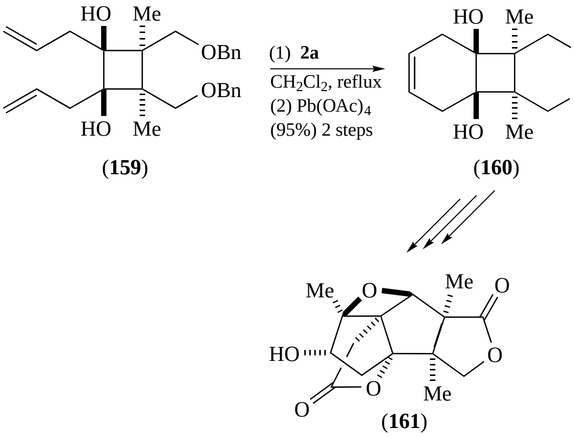
HO
Me
OBn
OBn
HO
Me
(1) 2a
CH_2Cl_2, reflux
(2) $Pb(OAc)_4$
(95%) 2 steps
HO
Me
OBn
OBn
HO
Me
Me
O
Me
O
HO
O
O
O
Me

(159) (160) (161)

(36)

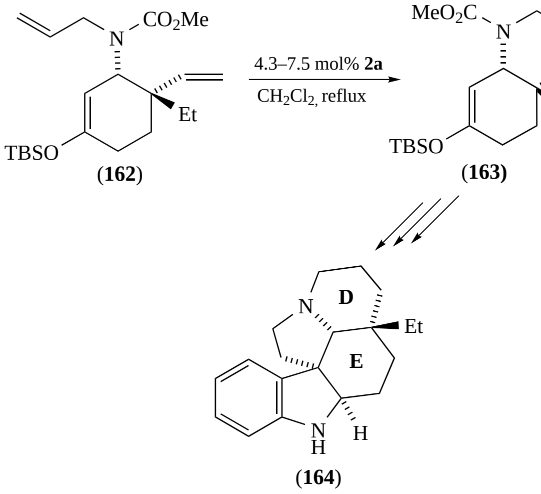
CO_2Me
N
Et
TBSO
4.3–7.5 mol% 2a
CH_2Cl_2, reflux
MeO_2C
N
Et
TBSO
N
D
Et
E
N
H
H

(162) (163) (164)

(37)

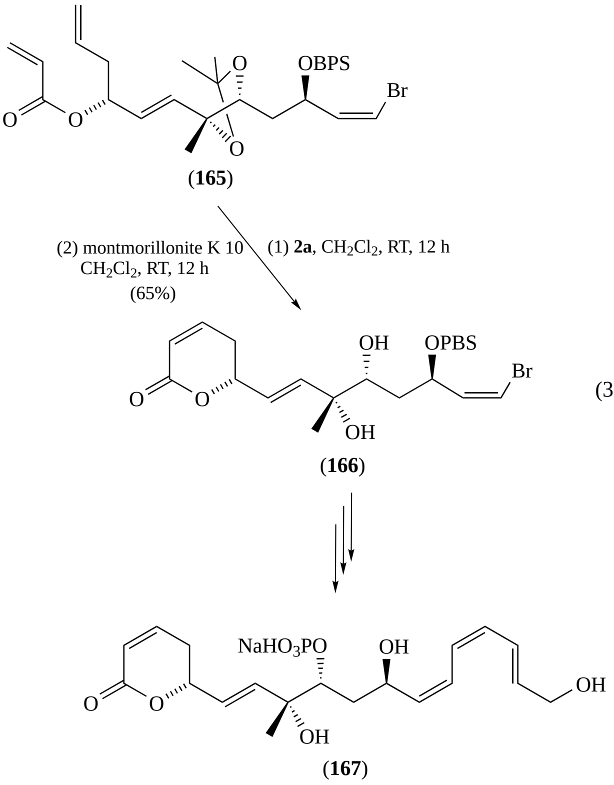
O
O
O
O
OBPS
Br
O
(2) montmorillonite K 10
CH_2Cl_2, RT, 12 h
(65%)
(1) 2a, CH_2Cl_2, RT, 12 h
O
O
OH
OPBS
Br
OH
O
O
$NaHO_3PO$
OH
OH
OH

(165) (166) (167)

(38)

5.1 Synthesis of Natural Products Containing Small Rings

Functionalized five- and six-membered rings are ubiquitous in natural products. Often RCM is a critical step for the successful synthesis of these carbocycles and heterocycles. Inoue and Hirama utilized (**2a**) for RCM of the *meso* diene precursor which could then be modified through a desymmetrization protocol to the desired merrilactone A (equation 36).**118** Rawal's syntheses of the pentacyclic aspidosperma alkaloids utilized olefin metathesis in the construct of the DE ring using (**1a**) to obtain the desired product in 88% isolated yield for this system. There was a significant difference between the performance of (**1a**) and (**2a**), the molybdenum catalyst providing complete conversion in 1 h at 60 °C as compared to only partial conversion in 10 h at the same temperature for (**2a**). However, the catalyst of choice for gram scale reactions was (**2a**) (equation 37).**119** Falck used (**2a**) catalyzed for the ring closure of the chiral six-membered lactone in the total synthesis of (+)-Fostriecin with good yield under mild conditions (equation 38).**120** Kibayashi and coworkers reported the asymmetric total synthesis of (−)-Adaline where and acyl protected amine diene underwent quantitative ring closure to form the Δ^3homotropane using 25 mol% (**2a**) or 15 mol% (**4a**) (equation 39).**121** One mol% (**2a**) accomplished ring closure in the bicyclic core of the marine natural product Dysinosin A in nearly quantitative yield by Hanessian and coworkers (equation 40).**122**

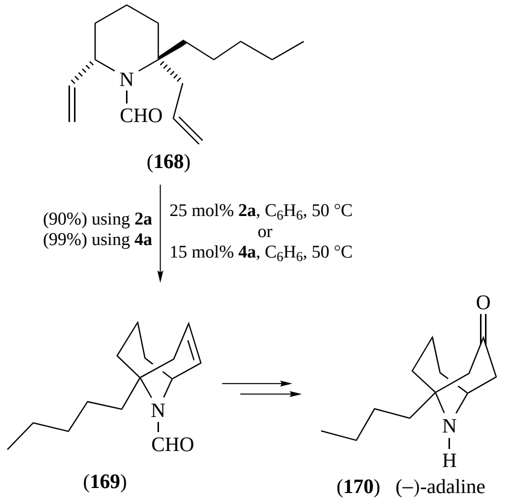
N
CHO
(90%) using 2a
(99%) using 4a
25 mol% 2a, C_6H_6, 50 °C
or
15 mol% 4a, C_6H_6, 50 °C
N
CHO
O
N
H

(168) (169) (170) (−)-adaline

(39)

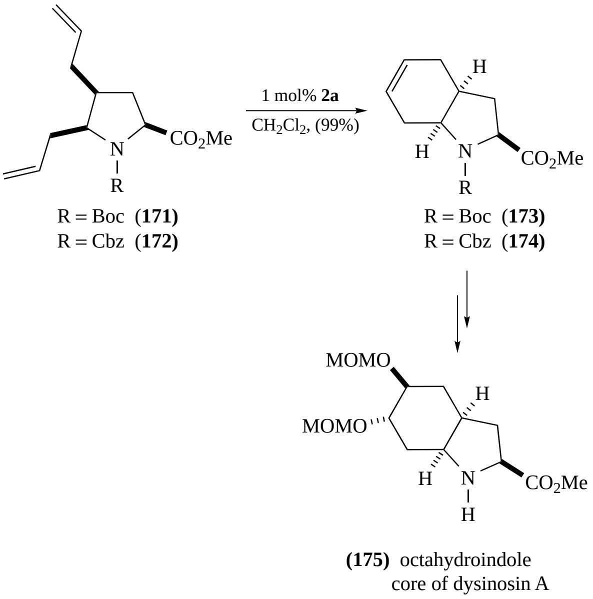
CO2Me
N
R
1 mol% 2a
CH2Cl2, (99%)
H
H
N
CO2Me
R
R = Boc (171)
R = Cbz (172)
R = Boc (173)
R = Cbz (174)
MOMO
MOMO
H
H
N
CO2Me
H
(175) octahydroindole
core of dysinosin A

(40)

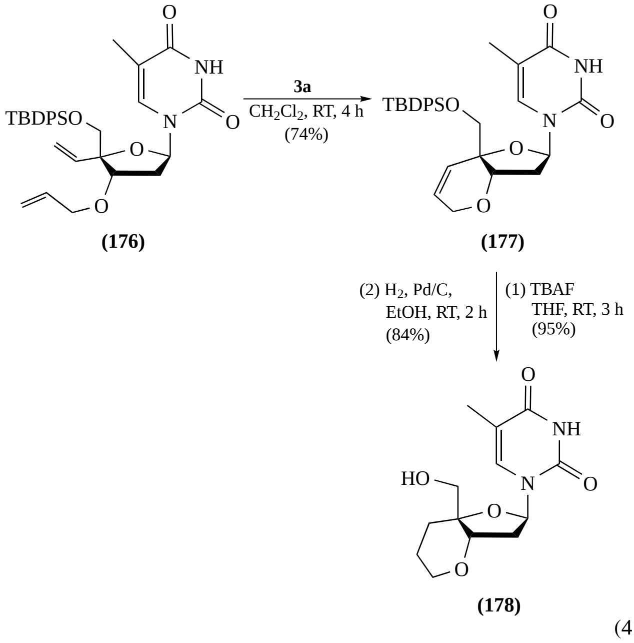
O
NH
N
O
TBDPSO
O
O
3a
CH2Cl2, RT, 4 h
(74%)
O
NH
N
O
TBDPSO
O
O
(176)
(177)
(2) H2, Pd/C,
EtOH, RT, 2 h
(84%)
(1) TBAF
THF, RT, 3 h
(95%)
O
NH
N
O
HO
O
O
(178)

(41)

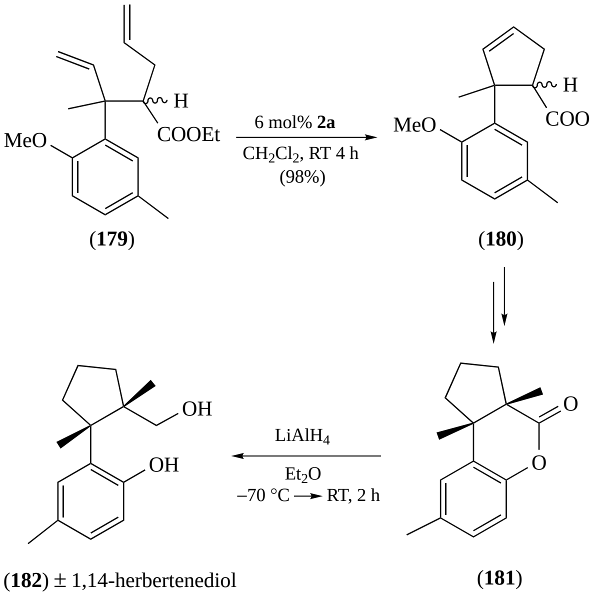
H
MeO
COOEt
6 mol% 2a
CH2Cl2, RT 4 h
(98%)
MeO
H
COOEt
(179)
(180)
OH
OH
LiAlH4
Et2O
−70 °C → RT, 2 h
O
O
(182) ± 1,14-herbertenediol
(181)

(42)

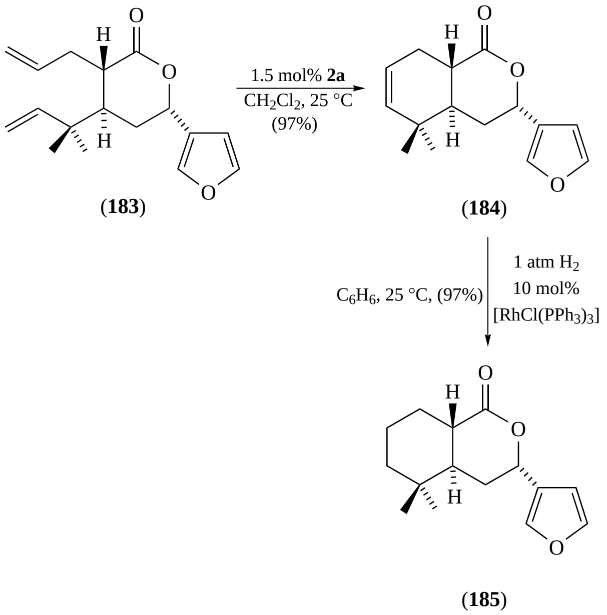
O
H
O
H
O
1.5 mol% 2a
CH2Cl2, 25 °C
(97%)
O
H
O
H
O
(183)
(184)
C6H6, 25 °C, (97%)
1 atm H2
10 mol%
[RhCl(PPh3)3]
O
H
O
H
O
(185)

(43)

RCM with (**3a**) and reduction are the final steps in Lebreton's syntheses of bicyclic thymidine nucleoside analogues as part of a program of development of less toxic anti-AIDS drugs (equation 41).[123] Srikrishna used a RCM inspired strategy and (**2a**) for the construction of the five-membered carbocycle in (±)-1,14-herbertenediol (equation 42), and (±)-11-*epi*-herbertenolide.[124] Metz used RCM catalyzed by (**2a**) or less effectively (**4a**) in the formation of both six-membered rings as part of the enantioselective syntheses of Ricciocarpins A and B (equation 43).[125] RCM with (**2a**) to form a five-membered chiral lactone was the key step in Singh's synthesis of (−)-acaterin from a Baylis-Hillman adduct in good overall yield (equation 44).[126]

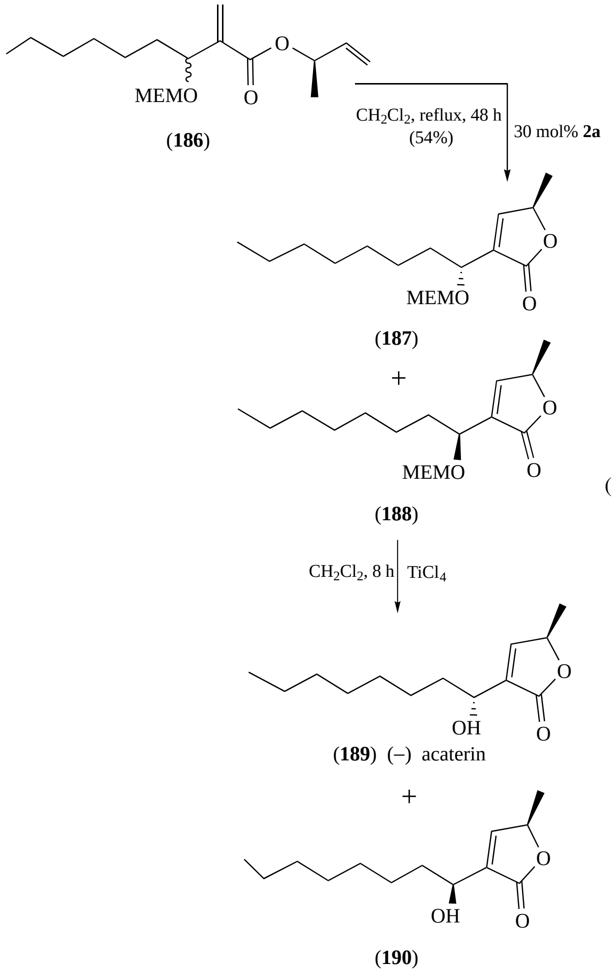
MEMO
O
(186)
CH2Cl2, reflux, 48 h
(54%)
30 mol% 2a
MEMO
O
(187)
+
MEMO
O
(188)
CH2Cl2, 8 h
TiCl4
OH
O
(189) (−) acaterin
+
OH
O
(190)

(44)

5.2 Synthesis of Natural Products Containing Medium Rings

The formation of medium size rings (8–10-membered) presents challenges based on strain and entropy (Scheme 20).[39,127] Reitz utilized RCM by (**2a**) of diallyl glycine to give the eight-membered cyclic olefin in equation (45).[128] Two steps convert it to a scaffold for peptidomimetic synthesis.

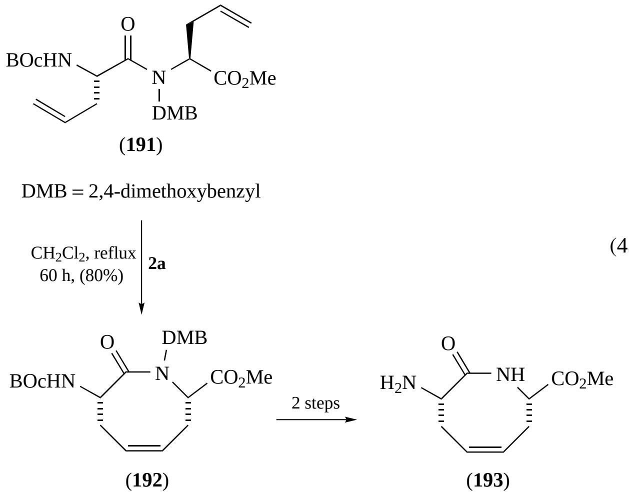
BOcHN
O
N
CO2Me
DMB
(191)
DMB = 2,4-dimethoxybenzyl
CH2Cl2, reflux
60 h, (80%)
2a
O
DMB
BOcHN
N
CO2Me
(192)
2 steps
O
H2N
NH
CO2Me
(193)

(45)

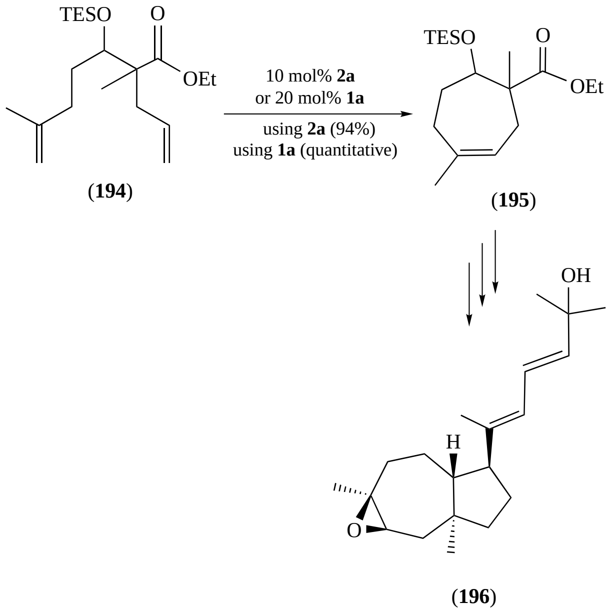
TESO
O
OEt
(194)
10 mol% 2a
or 20 mol% 1a
using 2a (94%)
using 1a (quantitative)
TESO
O
OEt
(195)
OH
H
O
(196)

(46)

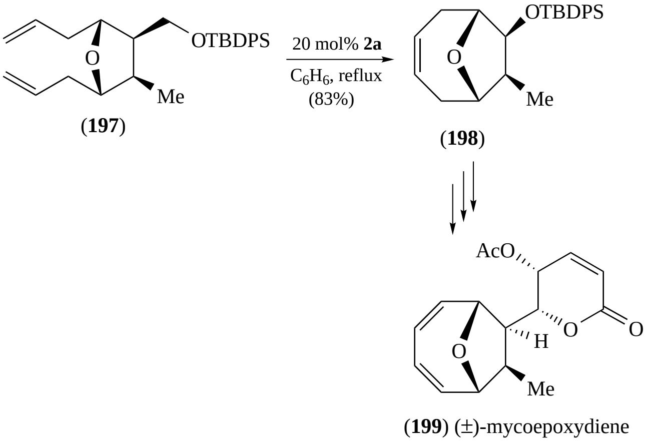
OTBDPS
O
Me
(197)
20 mol% 2a
C6H6, reflux
(83%)
OTBDPS
O
Me
(198)
AcO
O
O
H
O
Me
(199) (±)-mycoepoxydiene

(47)

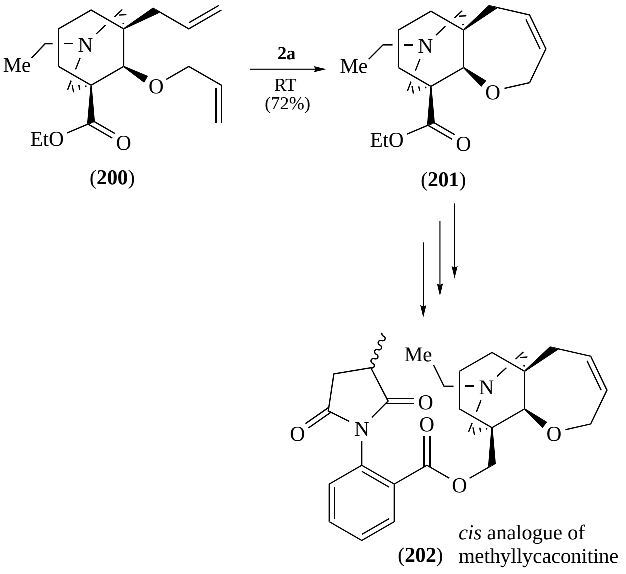
Me
N
O
EtO
O
(200)
2a
RT
(72%)
Me
N
O
EtO
O
(201)
Me
N
O
O
O
N
O
O
O
(202)
cis analogue of
methyllycaconitine

(48)

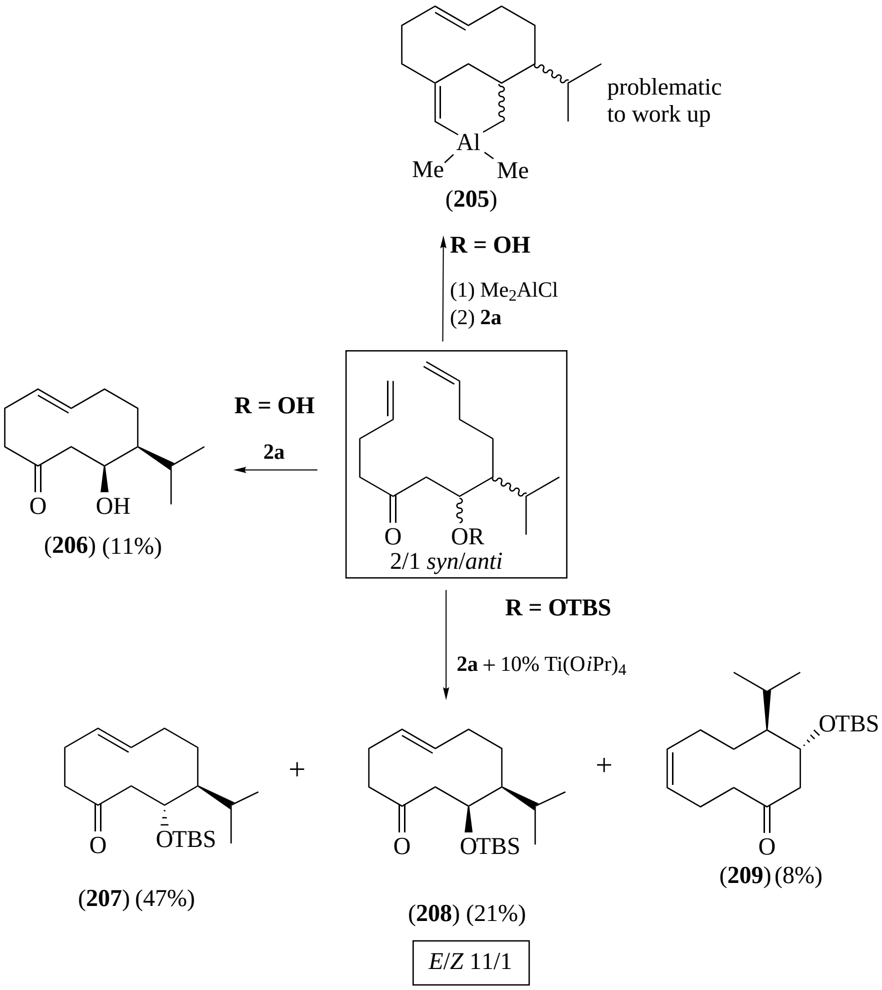
problematic
to work up
Al
Me
Me
(205)
R = OH
(1) Me$_2$AlCl
(2) 2a
R = OH
2a
O
OH
(206) (11%)
O
OR
2/1 syn/anti
R = OTBS
2a + 10% Ti(O*i*Pr)$_4$
OTBS
+
+
O
OTBS
(207) (47%)
O
OTBS
(208) (21%)
E/Z 11/1
O
(209) (8%)

Scheme 20 Various ring closure routes to form 10-membered rings en route to sesquiterpene natural products

Similar in difficulty to formation of the 8–10-membered rings is the synthesis of trisubstituted seven-membered rings.[129] Tori prepared these seven-membered carbocycles in good to high yield utilizing (**2a**) (equation 46).[130] Elaboration of these intermediates led to the successful total synthesis of liverwort diterpenes. Ring-closing olefin metathesis is often used late in a synthetic strategy to obtain functionalized cyclic compounds. Tadano, on the other hand, used (**2a**) catalyzed RCM relatively early in the synthetic scheme with many steps of further elaboration to arrive at (±)-mycoepoxydiene.[131] Brimble utilized (**2a**) to achieve late stage RCM to form the seven-membered B ring in high yield as a part of the stereodivergent synthesis of ABE ring analogs of methyllycaconitine, a potent antagonist of the α7 nAChR in mammalian neuronal membranes (equation 48).[132] Martin disclosed an efficient formal synthesis of (−)-Peduncularine where the key step is near quantitative ring closure using (**4a**) catalyst (equation 49). Closure with (**2a**) required protection of the alcohol and led to the product with much lower yield.[133] Koskinen reported the first 10-membered carbocycle formed by olefin metathesis in moderate yield and high E/Z selectivity using (**2a**) combined with Ti(O*i*-Pr)$_4$. This reaction protocol led to the successful synthesis of a pine foliage sesquiterpene.[134]

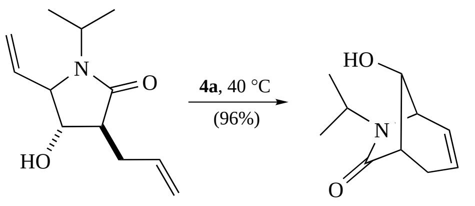
N
O
HO
4a, 40 °C
(96%)
HO
N
O

(49)

(**203**) (**204**) (−)-peduncularine

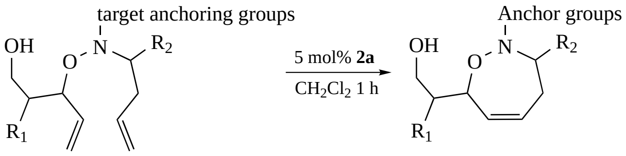
target anchoring groups
OH
O
N
R$_2$
R$_1$
5 mol% 2a
CH$_2$Cl$_2$ 1 h
Anchor groups
OH
O
N
R$_2$
R$_1$

(50)

Verdine utilized RCM as a key step in the synthesis of a library of bifunctional small molecules to screen for heterodimerizer (potential synthetic antitumor agents) (equation 50).[135] Again, the key step to the success of the scheme is ring-closing olefin metathesis to make the tetrahydro-oxazepine skeleton in all possible isomers, which was accomplished utilizing (**2a**).

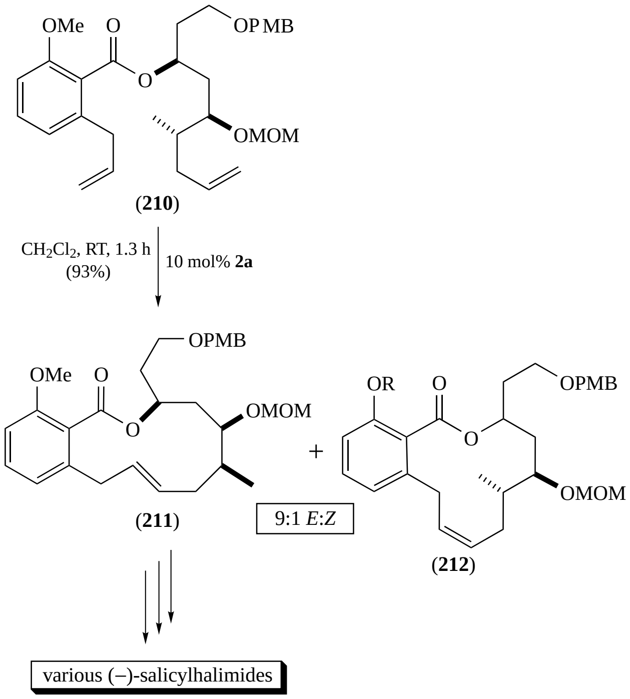
OMe
O
OPMB
O
OMOM
(210)
CH2Cl2, RT, 1.3 h
(93%)
10 mol% 2a
OPMB
OMe
O
O
OMOM
(211)
9:1 E:Z
+
OR
O
OPMB
O
OMOM
(212)
various (−)-salicylhalimides

(51)

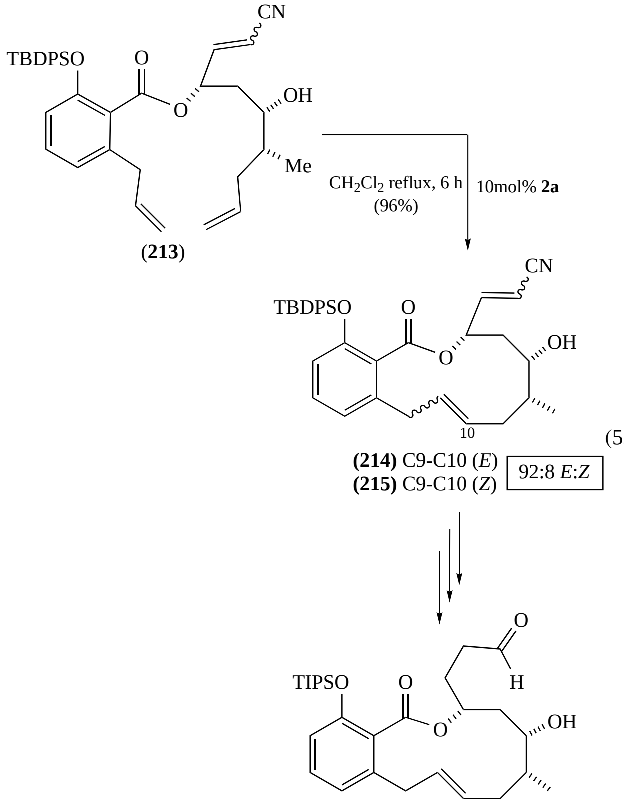
CN
TBDPSO
O
O
OH
Me
(213)
CH2Cl2 reflux, 6 h
(96%)
10mol% 2a
CN
TBDPSO
O
O
OH
10
(214) C9-C10 (E)
(215) C9-C10 (Z)
92:8 E:Z
O
TIPSO
O
H
O
OH

(52)

(216) precursor to the (+)-salicylhalimides (26%) over 13 steps

5.3 Macrocyclic Natural Product Synthesis

The synthesis of functionalized macrocycles becomes increasingly important with the discovery of more and more key, biologically active natural products, and the desire to increase the efficacy of these agents while reducing their human toxicity through medicinal chemistry discovery. De Brabander reported the total synthesis of Salicylhalamide A and related compounds. The 12-membered benzolactone ring contains an *E*-alkene that was selectively formed during RCM using (**2a**) (equation 51). Catalyst (**4a**) was efficient at ring closure but for these substrates had a much lower *E*:*Z* selectivity.[136] Georg and coworkers targeted the salicylihalamides as well, utilizing a chiral pool approach with ring closure by olefin metathesis. While the route differed, the *E*-selectivity for the ring bound olefin remained a challenge. This group also found that (**2a**) had superior selectivity leading to chromatographically separable products in a 2:1 ratio (equation 52).[137]

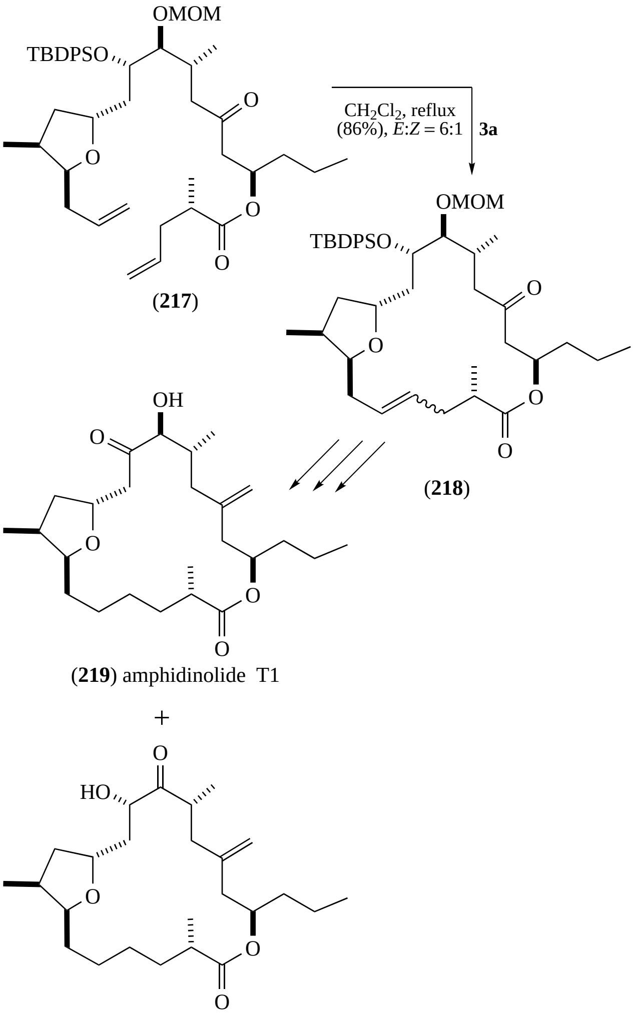
OMOM
TBDPSO
O
O
O
O
(217)
CH2Cl2, reflux
(86%), E:Z = 6:1
3a
OMOM
TBDPSO
O
O
O
O
(218)
OH
O
O
O
O
(219) amphidinolide T1
+
O
HO
O
O
O
(220) amphidinolide T4

(53)

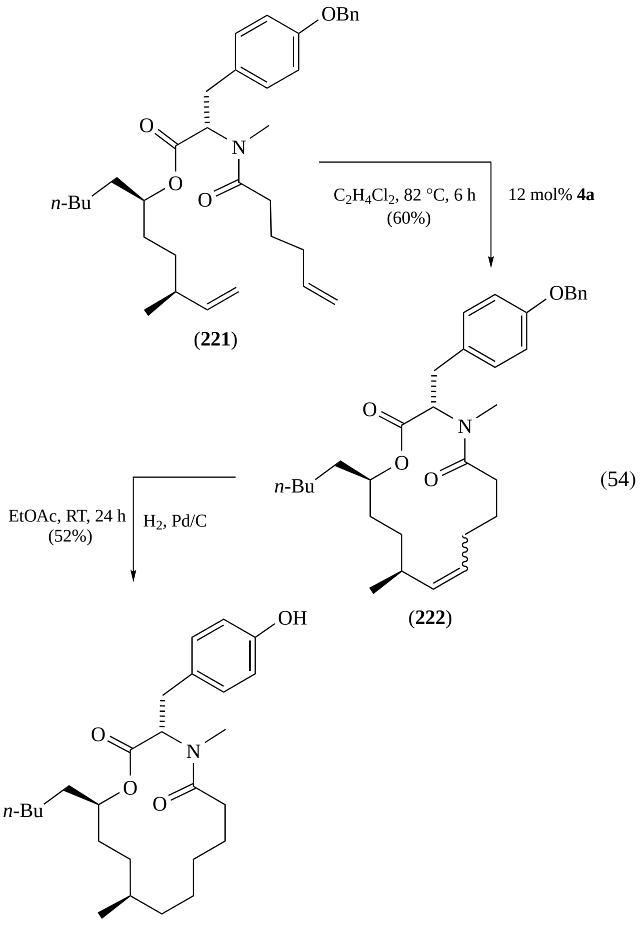
OBn
n-Bu
O
N
$C_2H_4Cl_2$, 82 °C, 6 h
(60%)
12 mol% **4a**
OBn
EtOAc, RT, 24 h
(52%)
H_2, Pd/C
OH

(**221**)

(**222**)

(54)

(**223**) PF1163B

Fürstner utilized (**3a**)-catalyzed RCM to close the 19-membered ring of various amphidinolides (equation 53). The E:Z ratio was approximately 6:1 although selectivity was not crucial since the alkene moiety was reduced by palladium catalyzed hydrogenation. Complex (**4a**) was used for ring closure to access another diastereomer.[138] The key step in Gesson's total synthesis of antifungal agent (−)-PF1163B was (**4a**) catalyzed ring closure to the 13-membered ring, which was achieved in good yield (equation 54).[139]

Burke utilized (**2a**) to catalyze RCM in his design of a globally constrained Grb2 SH2 inhibitor (equation 55). Here the parent compound is an open-chain molecule and olefin metathesis provides an avenue for rigidifying that functionalized skeleton.[140] Kingston synthesized paclitaxel analogues designed to favor the T-paclitaxel conformation using (**2a**) catalyzed olefin metathesis as the ring-closing step.[141] The total synthesis of Woodrosin I, a glycoside macrocycle, relied on the efficacy of RCM. In this case, Fürstner successfully utilized both (**2a**) and (**2c**) to give nearly quantitative closure of the diolefinic precursor.[142] Nicolaou was able to apply RCM to as part of his synthesis of coleophomones B and C, which differ only at the alkene moiety, B being E and C being Z. The success of this synthetic pathway was a combination of the efficacy of (**4a**) with the discovery of a single step that gave the isomeric RCM precursors in high yield and easily separable from one another (Scheme 21).[143]

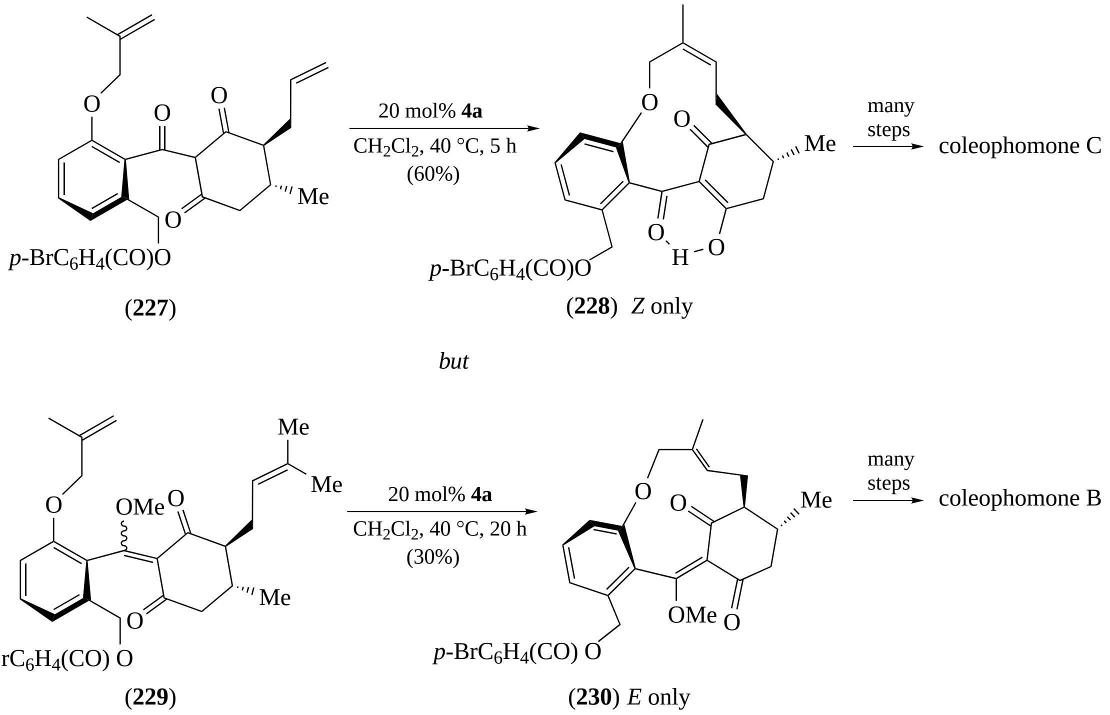
O
Me
p-BrC$_6$H$_4$(CO)O
20 mol% **4a**
CH_2Cl_2, 40 °C, 5 h
(60%)
many steps
coleophomone C
O
H
but
OMe
20 mol% **4a**
CH_2Cl_2, 40 °C, 20 h
(30%)
many steps
coleophomone B
p-BrC$_6$H$_4$(CO) O

(**227**)

(**228**) Z only

(**229**)

(**230**) E only

Scheme 21 Small differences in dienes lead to exclusively Z or E ring-closed products in synthetic strategy for coleophomones B and C

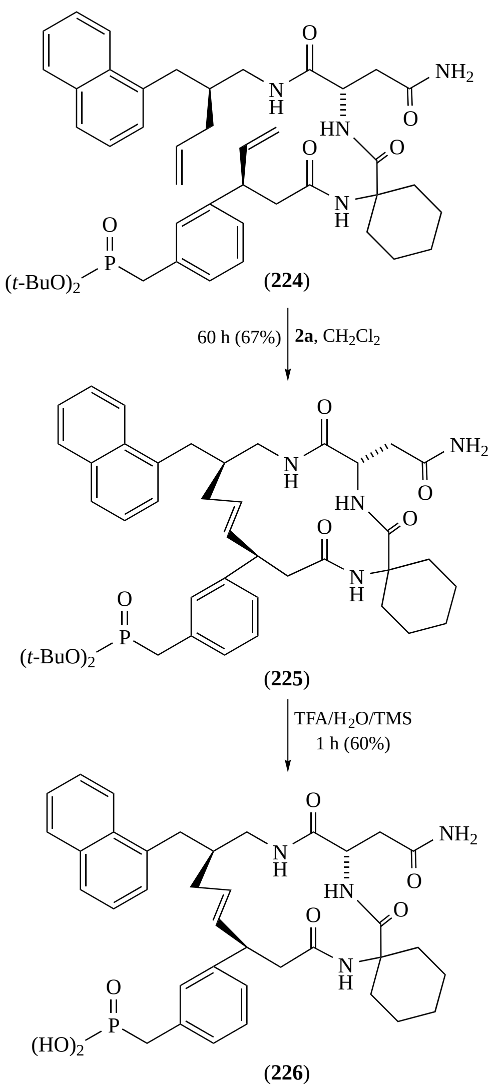
(224)
(t-BuO)₂
60 h (67%)
2a, CH₂Cl₂
(225)
TFA/H₂O/TMS
1 h (60%)
(226)
(HO)₂

(55)

Nantermet constructed 20-membered thrombin inhibitors from highly functionalized diolefin scaffolds using (**2a**)-catalyzed RCM. The stereochemistry of the ring closure was 3.5:1 *E*:*Z*, although the alkene was ultimately reduced (equation 56).**144** Fürstner utilized RCM to complete the synthesis of the phytotoxic lactones herbarumin I and II (equation 57). These 10-membered macrocycles contain an *E*-alkene, which was obtained in high yield and stereoselectivity 7:1 *E*:*Z* using (**2c**) under kinetic control while (**3a**) provided only the *Z*-isomer.**145** Stereospecific total synthesis of trans- and cis-resorcylide from a common precursor was achieved by allowing or blocking hydrogen bonding to access the two isomers and ring closing with (**4a**) to give the 12-membered ring (equation 58).**146**

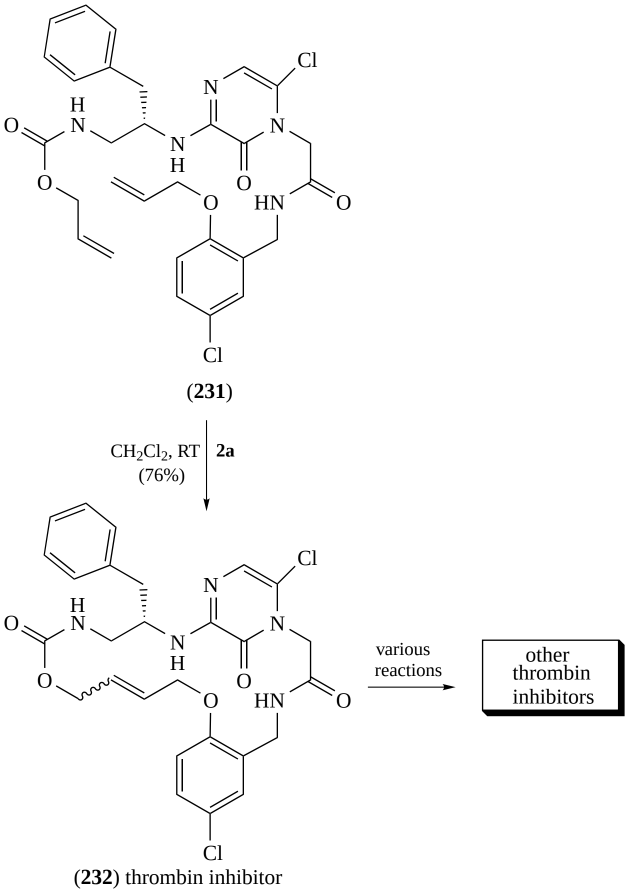
(231)
CH₂Cl₂, RT
(76%)
2a
various reactions
other thrombin inhibitors
(232) thrombin inhibitor

(56)

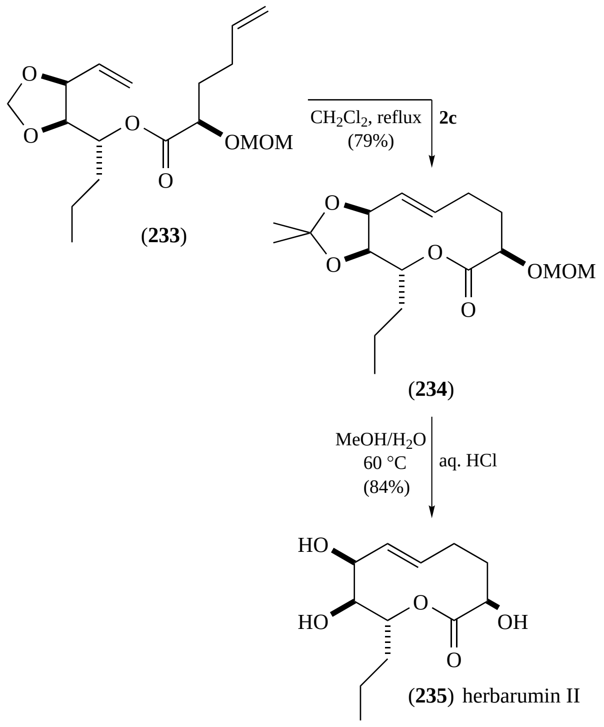
(233)
CH₂Cl₂, reflux
(79%)
2c
(234)
MeOH/H₂O
60 °C
(84%)
aq. HCl
(235) herbarumin II

(57)

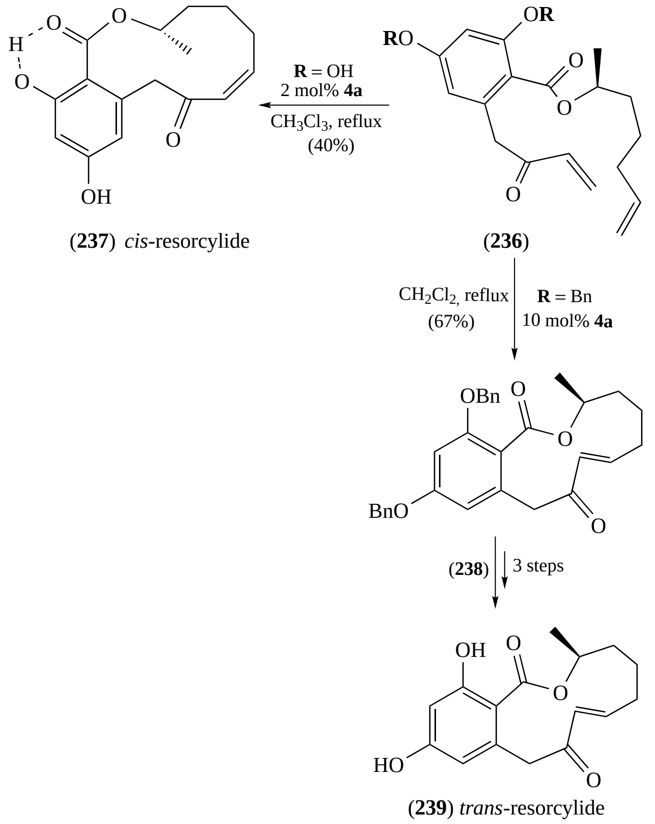

(**237**) *cis*-resorcylide

(**236**)

(**238**)

(**239**) *trans*-resorcylide

(58)

Epothilone macrolides are an emerging class of potent antitumor agents that might have high potential in cancer chemotherapy via microtubule stabilization. Olefin metathesis has played an important role in the Danishefsky laboratories in the syntheses of epothilones, illustrated in Scheme 22. Key to the Danishefsky strategy was to utilize (**4a**) catalyzed RCM for ring closing only on terminal monosubstituted olefin and then to reduce the disubstituted olefin to the alkane. This route is highly efficient for ring closure and reduces the optimization and separation necessary for the relative stereochemistry of the 12,13-trisubstituted olefin that was completed in a separate step prior to ring closure.[147] Numerous epothilone analogs became easily in reach using this convergent RCM strategy (Scheme 22a, b), allowing biological structure-reactivity studies to be completed on a series of related epothilones, lending insight to the import of ring size to the antitumor efficacy of this class of compounds.[148] This strategy allowed the Danishefsky group to explore the effect of trifluoromethyl analogues of epothilones leading to an effective antitumor agent that is more stable than the parent compound (Scheme 22c).[149] This work ultimately led to a group of epothilone analogues whose accessibility is clearly due to the efficient convergent synthetic route (Scheme 22d).[150] This family of compounds in early studies proves to be better potential drug candidates than the naturally derived parent compounds provided by the designed in features that give more stable and bioavailable agents.

5.4 Cross Metathesis in Synthesis

With the advent of efficient cross metathesis catalysis, this reaction is being seen in a variety of total syntheses and analogue synthesis strategies. Two areas where cross metathesis has been particularly useful are the addition of side chains or heterodimerization and the formation of homodimers.

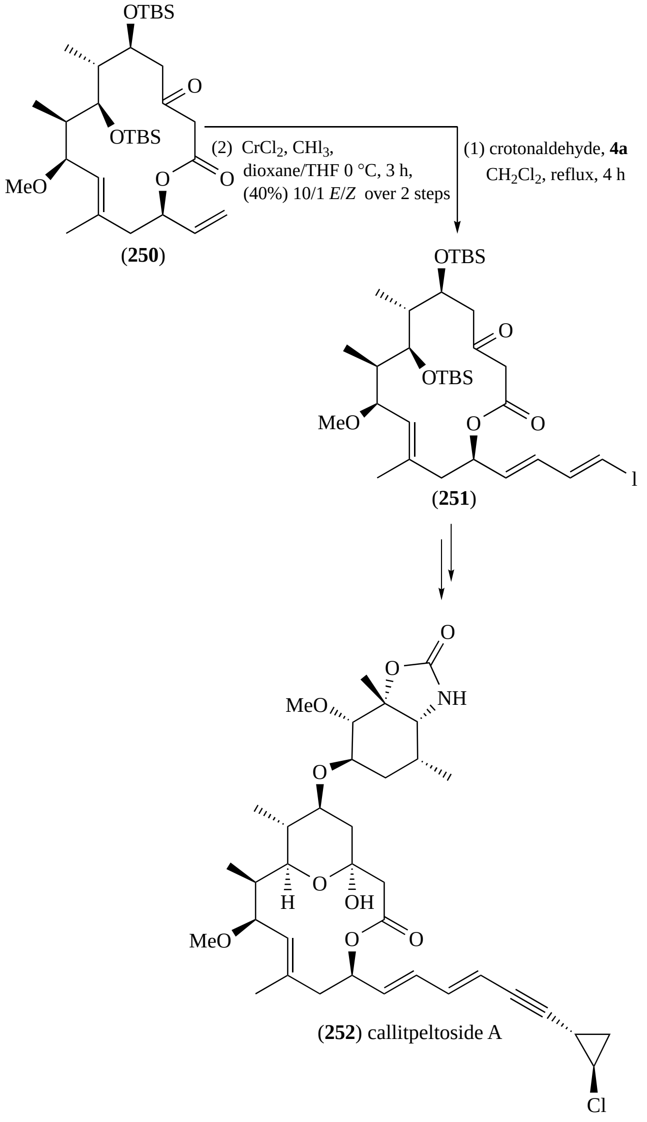

(**250**)

(**251**)

(**252**) callitpeltoside A

(59)

Trost used (**4a**) catalyzed cross metathesis as a part in the construction of callipeltoside side chains with both high yield and high *E*:*Z* ratio (equation 59).[151] Diver also used (**4a**) catalyzed cross metathesis to modify the MeBmt side chain of cyclosporin A to give resin bound protein affinity agents.[152] Stoltz used (**4a**) catalyzed prenylation to elaborate one of the side chains in his work toward the synthesis of Garsubellin A and related phloroglucins (equation 60).[153] Miller reported high-yielding hetero cross metathesis of a Proline–Glycine

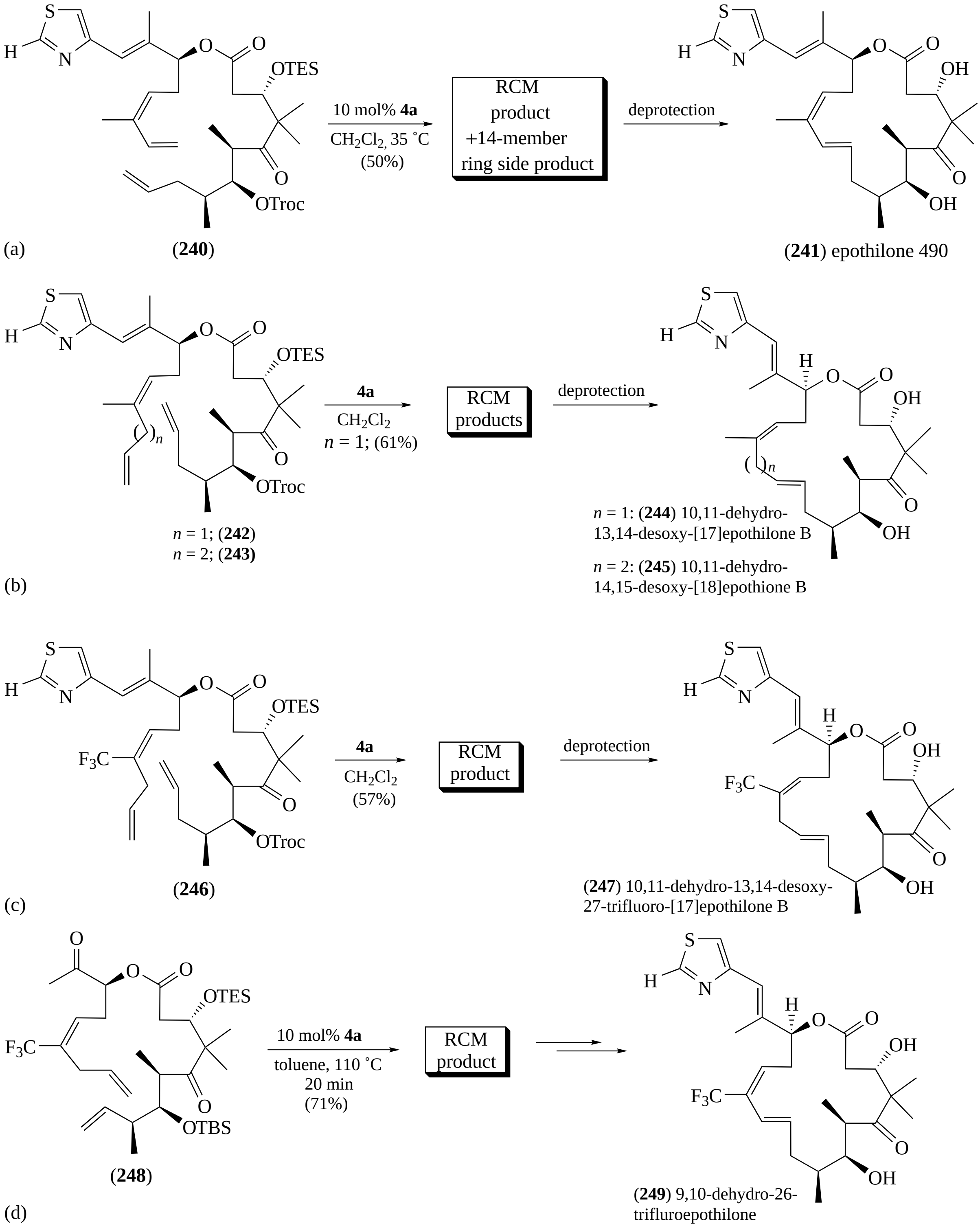
(a)
(240)
10 mol% 4a
CH2Cl2, 35 ˚C
(50%)
RCM product +14-member ring side product
deprotection
(241) epothilone 490
(b)
n = 1; (242)
n = 2; (243)
4a
CH2Cl2
n = 1; (61%)
RCM products
deprotection
n = 1: (244) 10,11-dehydro-13,14-desoxy-[17]epothilone B
n = 2: (245) 10,11-dehydro-14,15-desoxy-[18]epothione B
(c)
(246)
4a
CH2Cl2
(57%)
RCM product
deprotection
(247) 10,11-dehydro-13,14-desoxy-27-trifluoro-[17]epothilone B
(d)
(248)
10 mol% 4a
toluene, 110 ˚C
20 min
(71%)
RCM product
(249) 9,10-dehydro-26-trifluroepothilone
S
N
H
O
OTES
OTroc
OTBS
OH
F3C

Scheme 22 Use olefin metathesis to access different epothilones isostere to give 83% yield of the desired product in high E:Z ratio under optimized conditions with (**4a**) (equation 61).[154]

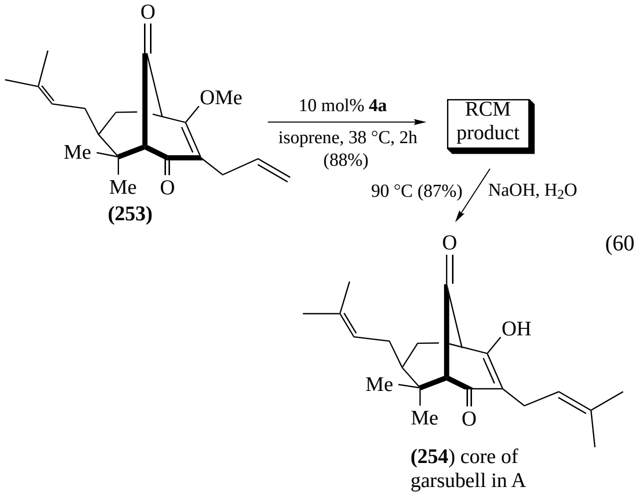
O
OMe
Me
Me O
(253)
10 mol% 4a
isoprene, 38 °C, 2h
(88%)
RCM product
90 °C (87%)
NaOH, H2O
O
OH
Me
Me O
(254) core of garsubell in A

(60)

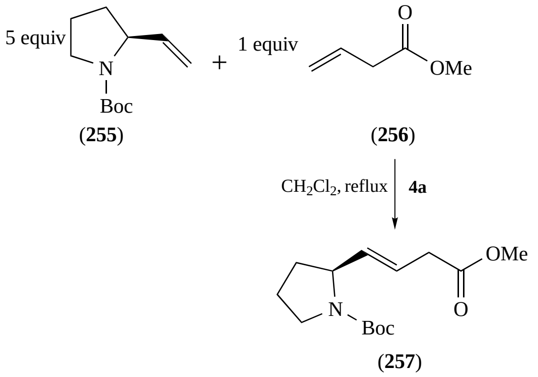
5 equiv
N
Boc
(255)
+
1 equiv
O
OMe
(256)
CH2Cl2, reflux
4a
OMe
N
Boc
O
(257)

(61)

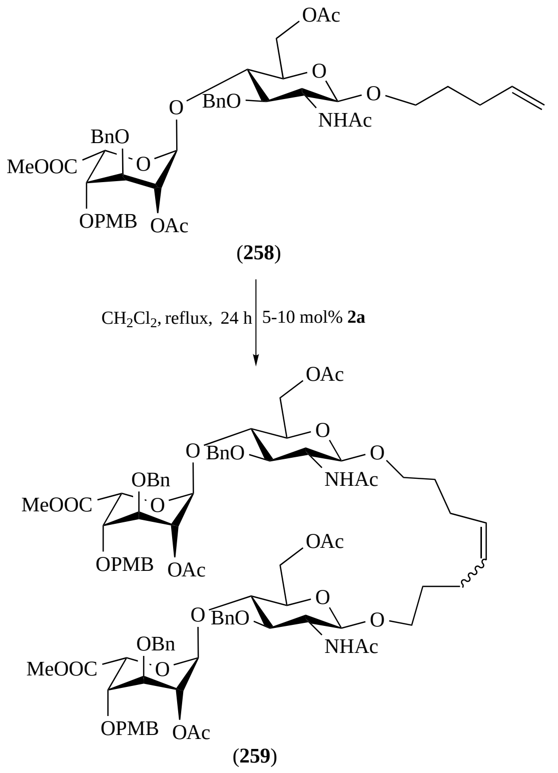
OAc
O
O
BnO
O
NHAc
BnO
MeOOC
O
OPMB
OAc
(258)
CH2Cl2, reflux, 24 h
5-10 mol% 2a
OAc
O
O BnO
O
NHAc
OBn
MeOOC
O
OPMB
OAc
OAc
O
O BnO
O
NHAc
OBn
MeOOC
O
OPMB
OAc
(259)

(62)

Chaikof and coworkers used (**2a**) to effect the homo cross metathesis on derivatives of heparan sulfate and hyaluronan to explore how neutral tether dimers compare to the parent compounds as agonists of antagonists of GAG dependent events (equation 62).[155] Wood also prepared dimers of K252a in 87% yield via cross metathesis with (**2a**) and subsequent Rh hydrogenation to explore the chemical biological effect of dimerization with a 14-carbon linker at the C7 position.[156] Smith utilized (**1a**), (**2a**), and (**4a**) catalyzed cross metathesis to access (−)-cylindrophanes A and F via dimerization of a precursor diolefin (equation 64). It was surmised that the reversible nature of olefin metathesis results in the desired head to tail homodimers, the thermodynamically preferred product, with (**1a**) giving the most efficient results. An extension of this strategy was to start with a head to tail acyclic dimer and subject that to ring closure. This also led to the only desired product in 15 to 20% higher yield than when using the monomers.[157]

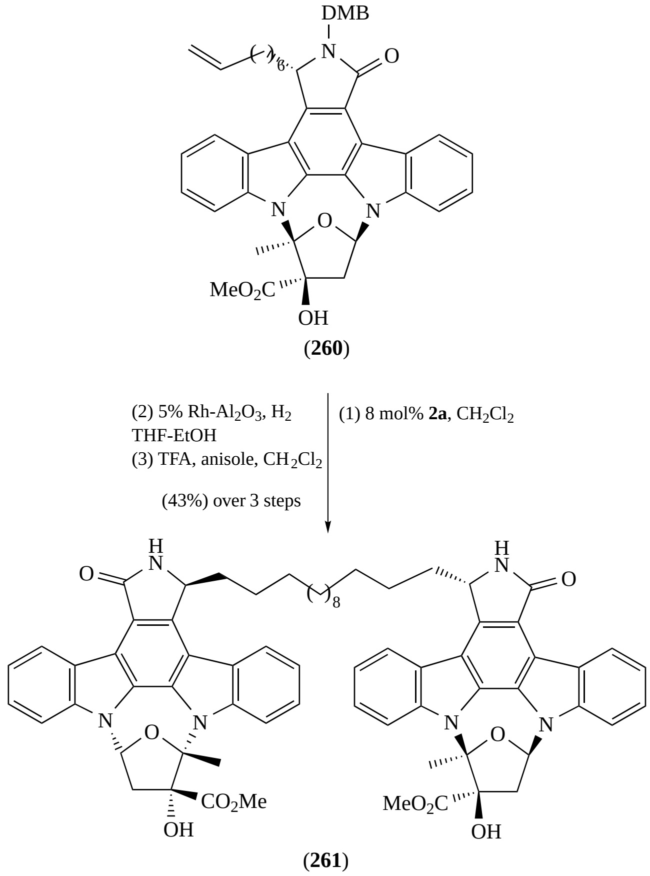
DMB
N
O
8
N
O
N
MeO2C
OH
(260)
(2) 5% Rh-Al2O3, H2
THF-EtOH
(3) TFA, anisole, CH2Cl2
(43%) over 3 steps
(1) 8 mol% 2a, CH2Cl2
H
N
O
8
H
N
O
N
O
N
CO2Me
OH
N
O
N
MeO2C
OH
(261)

(63)

6 OLEFIN METATHESIS FOR THE FORMATION OF POLYMERS AND MATERIALS

Coughlin and Emrick utilized a benzyl phosphine oxide substituted styrene in olefin metathesis by (**2a**) to make

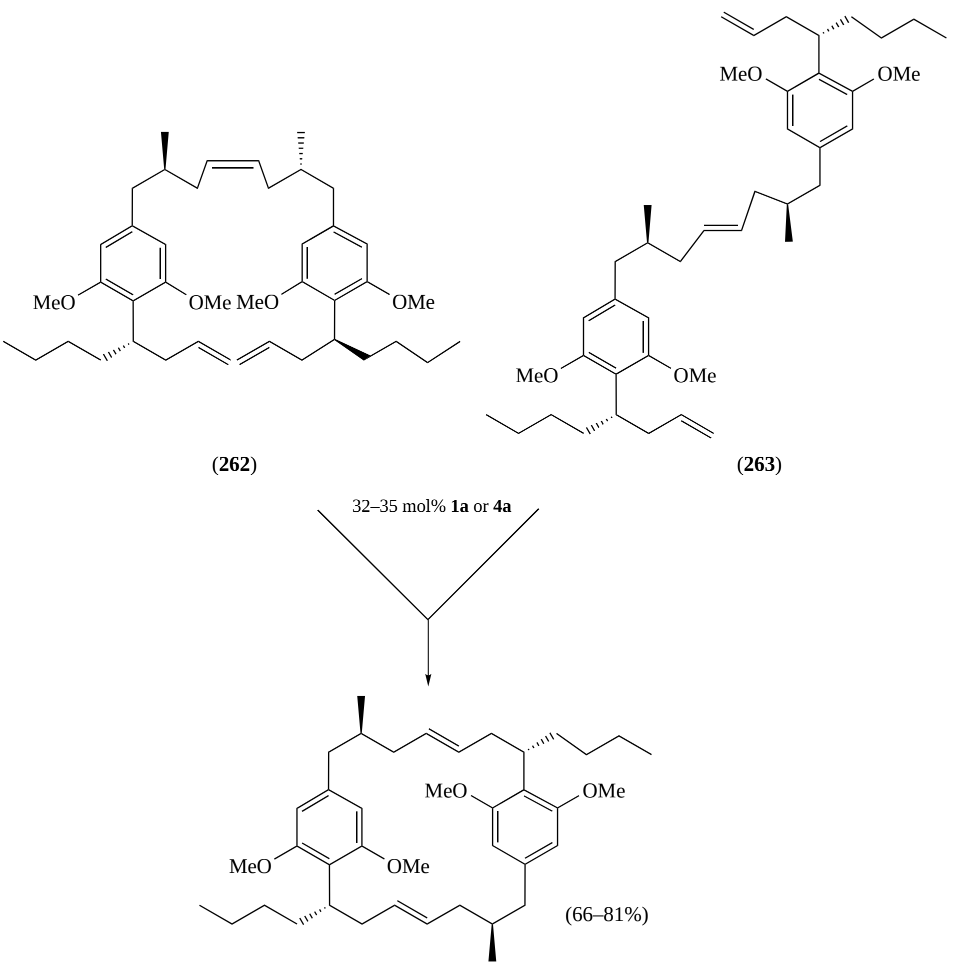
MeO
OMe
MeO
OMe
MeO
OMe
MeO
OMe
32–35 mol% **1a** or **4a**
MeO
OMe
MeO
OMe
(66–81%)

(**262**)

(**263**)

(64)

(**264**) cylindrophane

polyolefin–cadmium selenide composites where the radiating olefin chains help keep the CdSe particles (*see* ***Semiconductor Nanocrystal Quantum Dots***) dispersed.[158]

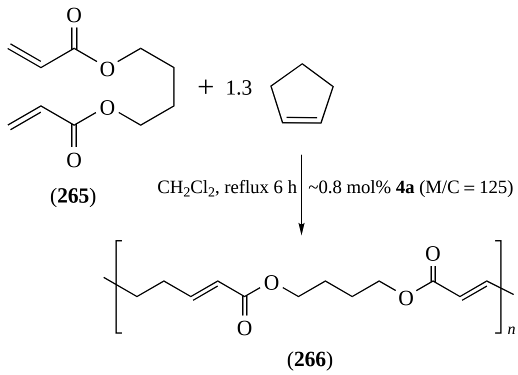
O
O
O
O
+ 1.3
CH_2Cl_2, reflux 6 h
~0.8 mol% **4a** (M/C = 125)
O
O
O
O
n

(**265**)

(65)

(**266**)

(75%); 96% A/B alternating; PDI = 1.58

Ruthenium complex (**4a**) provided a new general route to alternating copolymerization utilizing cyclooctene and diacrylates via olefin metathesis (equation 65).[159] Nuclear magnetic resonance (NMR) studies demonstrated that under the reaction conditions cyclic monomers like cyclooctene undergo ROMP at a high rate while acyclic diacrylate monomers insert into the chain slowly. The overall process, coined as ROIMP (ring-opening insertion metathesis polymerization), results in polymers with A,B alternation ranging from 94 to 99% in yields ranging from 75 to 99% and having moderate PDI (1.43–2.06), with a careful balance of catalyst loading and reaction concentration key to successful, highly alternating polymerizations.

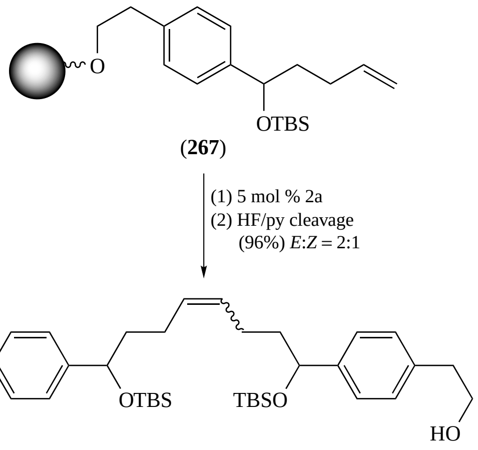
O
OTBS
(1) 5 mol % 2a
(2) HF/py cleavage
(96%) *E*:*Z* = 2:1
OTBS
TBSO
OH
HO

(**267**)

(66)

(**268**)

Schreiber utilized intra-site olefin metathesis as a key step in synthesizing C_2-symmetric functionalized dimeric molecules for the close association of proteins.[160] Both (**2a**) and (**4a**) were effective at 5 mol% giving very high conversions to the dimerized product (equation 66). The E:Z ratios of the linked bead dimerized molecules were similar to what was found in analogous solution reactions.

Olefin metathesis under mild conditions was instrumental in the preparation of pthalocyanine polymers of high molecular weight without use of a radical initiator by Kimura and Shirai using (**2a**).[161]

(**2a**) was also utilized in the attachment of polymer to a silica face (*see* ***Supported Organotransition Metal Compounds***).[162] In this strategy, an allyl group is attached to the substrate bound silicon that then reacts in a cross metathesis fashion with (**2a**). Then this surface bound Ru-alkylidene catalyzes ROMP of norbornene to give alkyl silicon terminated polymer film that is thus attached to the surface in controllable density and polymer thickness.

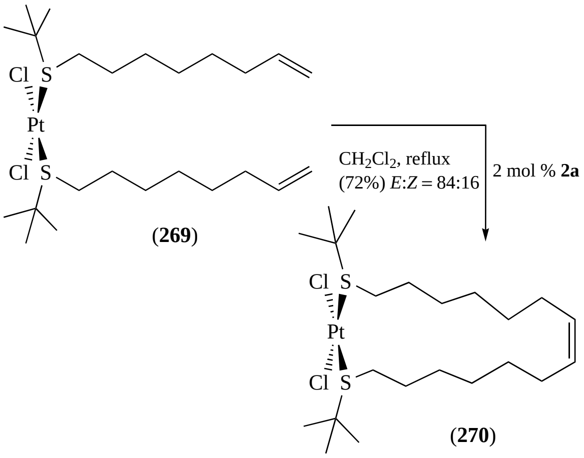

(**269**)

(**270**)

(67)

Gladysz has relied on the functional group tolerance and efficiency of olefin metathesis reactions catalyzed by (**2a**) to develop a variety of transition metal containing ligands and other functionalities with a central theme of creating metalamacrocycles, equation (67).[163,164] The types of transformations accomplished on a variety of olefin bearing organometallic fragments include intermolecular linking of olefin-substituted cyclopentadiene, intramolecular cyclizations of platinum thioethers, and allyl substituted phosphines. Terminal olefins on of metal-bound phosphanes also underwent intramolecular cross metathesis of cis-, trans-, and fac- ligands.

Overkleeft and van Boom utilized the (**4a**) catalyst to develop mannitol-derived fused oxacycle scaffold for the construction of combinatorial libraries.[165] The RCM of the highly functionalized conformationally fused cyclic products also cleaves it from the library bead, (equation 68).

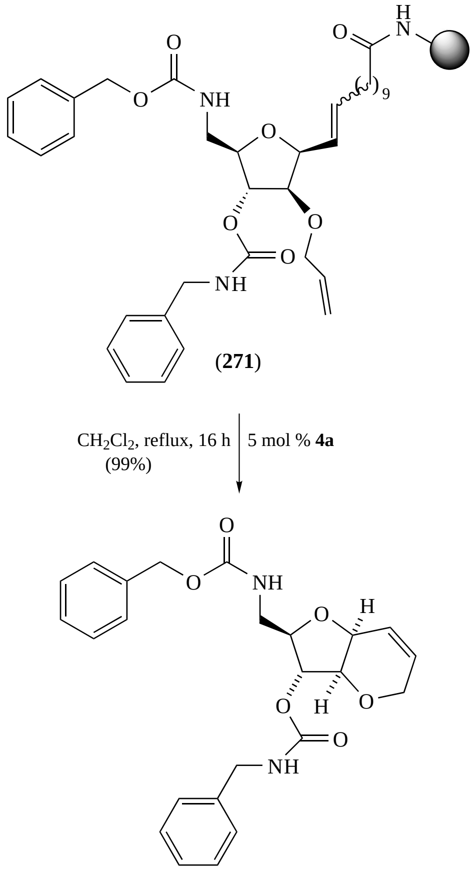

(**271**)

(**272**)

(68)

7 GREEN CHEMISTRY UTILIZING OLEFIN METATHESIS CATALYSTS

One of the areas garnering attention in catalysis research has been the development of ‘green’ or environmentally benign catalytic systems. For olefin metathesis, the trend has been to develop catalytic systems that can be efficiently recycled. Success in this area has multiple implications for OM processes. First, a recyclable catalyst will give overall more turnovers per catalyst molecule, and thereby be more economical. Second, a catalyst that can be efficiently recycled (low loss of activity over repeated uses) leaches less Ruthenium into the product and thus less expensive processing costs. To this end immobilization of the olefin metathesis catalysts on a variety of solid supports and utilization of nonorganic solvent systems have been explored.

A few examples of polymer supported olefin metathesis have been reported recently. Hoveyda formed styrenyl ether complexes of several ruthenium-based olefin metathesis catalysts that were then incorporated into a dendrimer structure (**273**) (Scheme 23), reporting good conversions over 6 cycles albeit with diminishing ruthenium content.[19,20] Yao used a similar chelating ligand to incorporate olefin

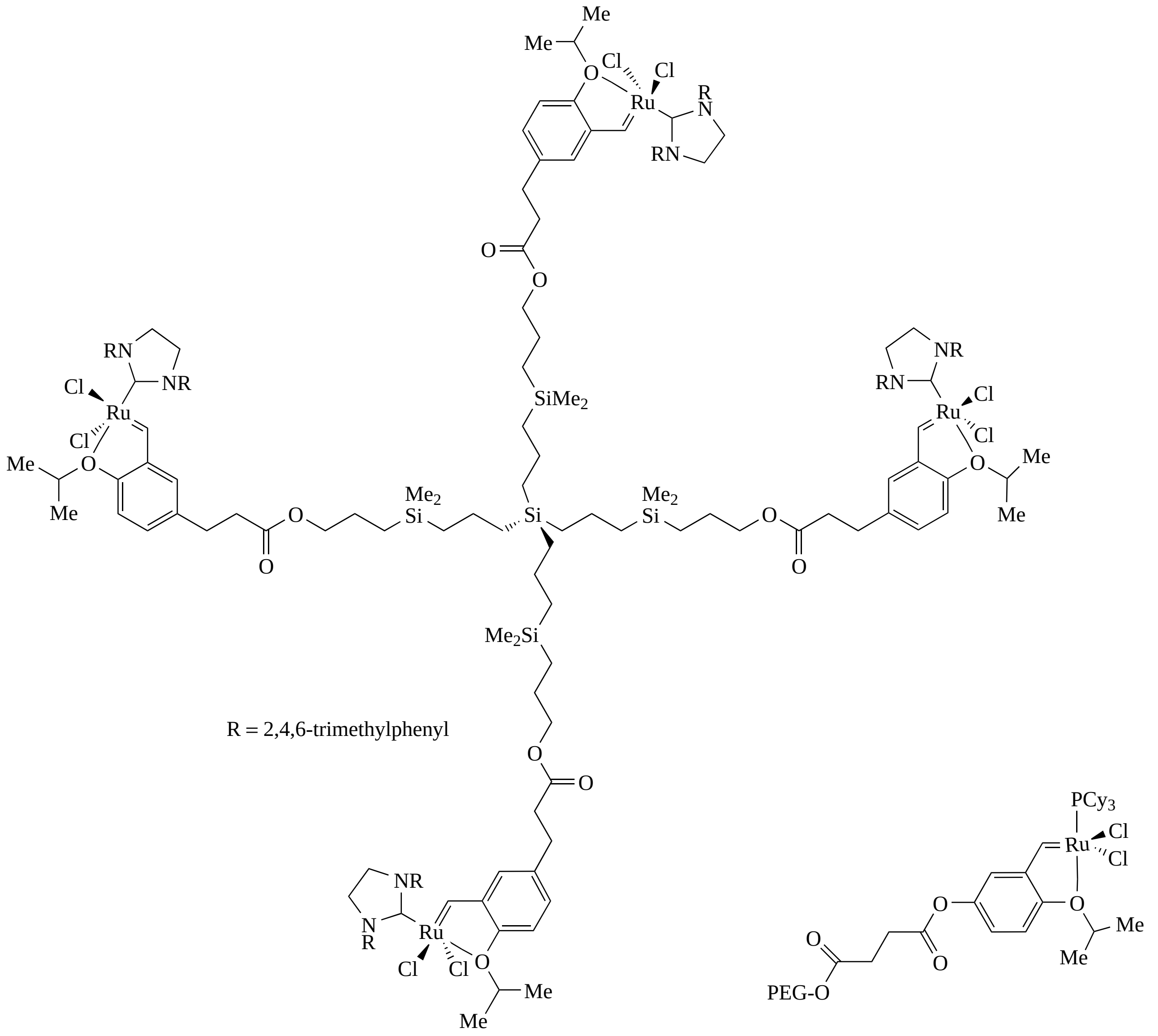

(**273**) (**274**)

Scheme 23 Recoverable catalysts

metathesis catalysts into polyethylene glycol (PEG) showing only minor loss of activity for RCM over 8 cycles (**274**) (Scheme 23).[166]

Blechert took advantage of the fact that the alkylidene group of any of the family of the ruthenium-based RCM catalysts can be substituted by a reaction with a pendant vinyl group of a divinyl benzene-containing polymer. Applying this idea, he created a PEG based system in which the styrenyl ether is pendant from the polymer backbone.[167] The strategy for building the catalyst relies on the ROMP of isoproxystyrene-oxanorbornene ether utilizing (**4a**) as catalyst and CuCl as phosphine scavenger (equation 69). The resulting red polymeric product has a high level of ruthenium incorporation and shows good activity with a variety of RCM ROM-CM and tandem metathesis reactions giving quantitative conversions. Recovery of the catalyst is achieved by adding hexane or diethyl ether to the reaction mixture. The RCM of *N*-tosyldiallylamine was tested for catalyst recyclability. The catalyst performed without visible loss of reactivity giving quantitative conversions in 1 h for the first 5 runs, with reactivity tailing off for runs 6 and 7; although quantitative conversion was still achieved, cycle 8 proved to be the limit of the performance of this catalyst. Ruthenium content of the products of the first four cycles was less than 0.004%. The parent homogeneous complexes react with the polymer to give a known catalyst loading

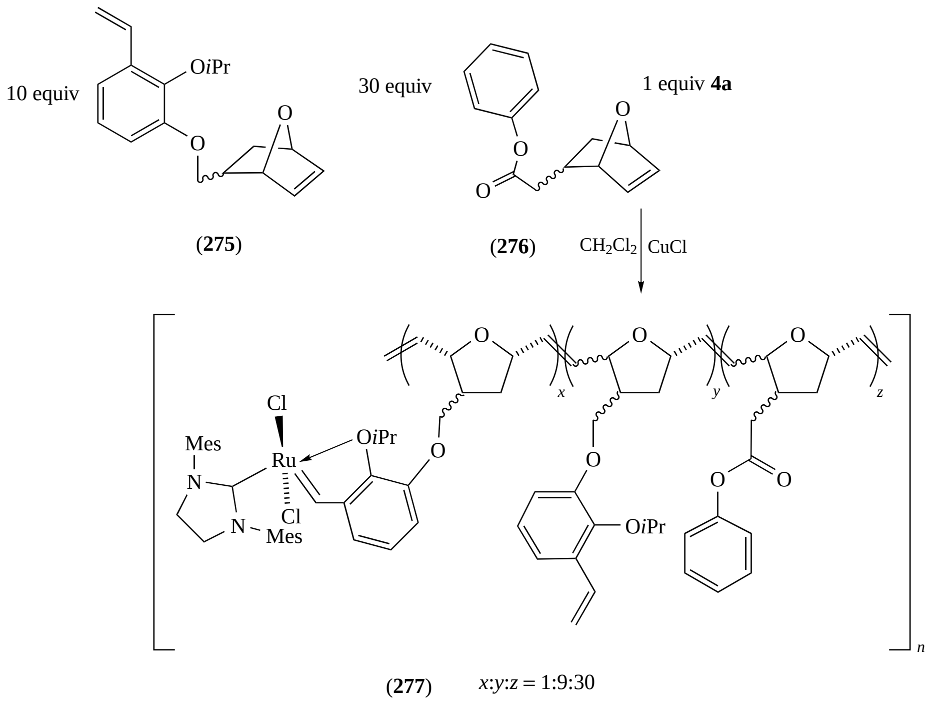

(69)

per gram of polymer. Because of the nature of RCM, the catalyst is free during the course of the RCM reaction and is recaptured by the support when the catalyst is not turning over, thus providing benefits of both homogeneous (solvated catalyst substrate complex) and heterogeneous (recoverable, recyclable) catalyst behavior.

A number of researchers have heterogenized olefin metathesis active complexes in polymers containing pendant vinyl groups via different methodologies. Barrett and coworkers formed (**278**) via reaction of (**3a**) with a lightly cross-linked solvent swellable vinylated polystyrene**[168]** or Merrifield resin to form a bead-supported catalyst that could be directly compared to their previously reported similarly supported (**2a**) (**279**) (Scheme 24).**[169]** Results from this study are described in Table 12.

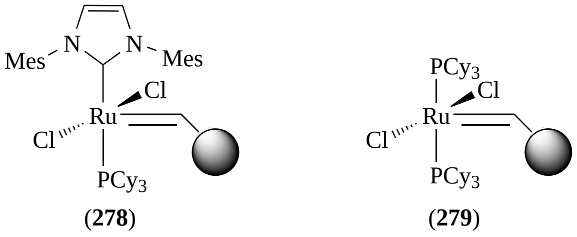

Scheme 24 Olefin metathesis catalysts bound to Merrifield resin

The formation of (**281**) from (**280**) is nearly quantitative for the first 4 cycles under the described reaction conditions (Table 6, entry 1); these results compare favorably to those for (**279**) under different reaction conditions (entry 2). Although these results are not strictly comparable, (**278**) appears to have greater longevity overall. The heterogenized catalyst is also active for the formation of heterocycles with only slight attenuation of efficacy (entries 3 and 4). For the described system, additives are quite important to the successful recycling of the catalyst. Addition of 5 mol%

Table 12 Comparison of efficacy of (**274**) and (**275**) over many reaction cycles. For the ring closure of diethyl diallylmalonate

				Conversion each cycle					
Entry	Substrate	Product	Catalyst	1	2	3	4	5	6
1	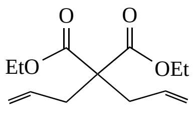 (**280**)	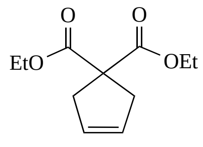 (**281**)	(**278**)	100	100	97	86	60	32
2			(**279**)[a]	100	100	50	10	–	–

Entry 1. Toluene 50 °C for 2 h, 2.5 mol% (**274**), 10 mol% 1-octene. Entry 2. CH_2Cl_2 at 25 °C for 40 min, 5 mol% (**275**), 10 mol% 1-hexene.

triphenylphosphine promoted quantitative conversion of (**280**) to (**281**) with just 0.25 mol% (**278**). Blechert also used a Merrifield resin to heterogenized olefin metathesis catalyst through an ether linkage on the backbone of (**4a**).[170]

Jafarpour and Nolan developed (**282**), (**283**), and (**284**) (Scheme 25) through the reactions of (**2a**), (**3a**), and (**4a**) with a highly cross-linked polydivinyl benzene macroporus polymer or monolith.[171,172] These polymers, developed for molecular imprinting,[173] have a permanent pore structure and do not need to be swollen by solvent for substrate access to the pendant catalyst. Results from the ring closure of (**280**) are described in Table 13. The polymer bound analogs have similar or better activity when compared to the free parent catalysts. The activity of these catalysts (particularly **284**) is maintained at over at least 4 cycles without the use of additives. There is, on average, a loss of 5% of total ruthenium from the polymer after 4 cycles using this methodology.

Kobayashi took advantage of π arene-ruthenium complexes (*see Arene Complexes*) to develop a polystyrene-OM catalyst system in which the catalyst was not connected to the polymer via an alkylidene; instead, the cationic ruthenium reacts through an appended allenylidine, (**285**) (Figure 3).[174] Upon appropriate activation conditions, the catalyst gives moderate to good conversions using high catalyst loadings (20 mol%) and long reaction times.

Lamaty reported olefin metathesis catalysts supported by various connectivities to PEG (Scheme 26).[175] These catalysts are soluble yet can be recovered upon addition of nonpolar solvent. The best of these catalysts, an analog of (**4b**), where the isopropyl group is replaced by PEG (**287**), could be recycled five times with only moderate loss in reactivity.

Table 13 Comparison of monolith bound catalysts to their free catalyst counterparts

Entry	Catalyst precursor	Cycle	Yield
1	(**2a**)	–	85[a]
2	(**282**)	1	97
3	(**282**)	4	81
4	(**3a**)	–	92[a]
5	(**283**)	1	97
6	(**283**)	4	81
7	(**4a**)	–	100
8	(**284**)	1	100
9	(**284**)	4	100

All reactions performed in CH_2Cl_2 at 25 °C for 0.5 h, 5 mol% catalyst precursor. GC yields. [a]NMR yields.

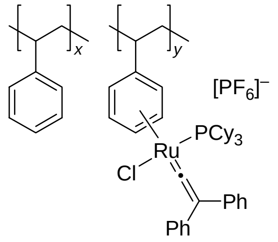

(**285**)

Figure 3 Recyclable ruthenium π-arene catalyst

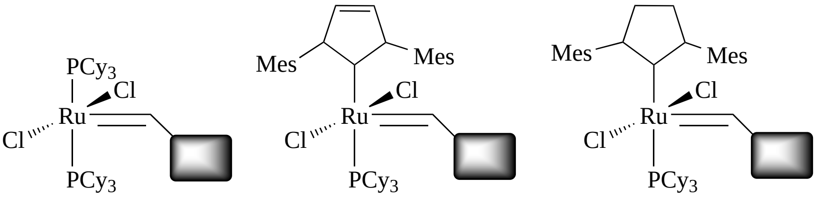

(**282**) (**283**) (**284**)

Scheme 25 Olefin metathesis complexes bound to (poly)divinylbenzene monoliths

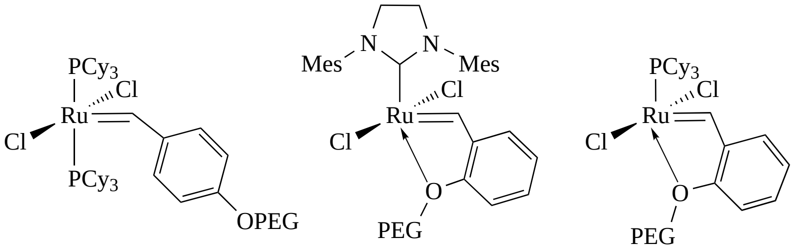

(**286**) (**287**) (**288**)

Scheme 26 PEG-bound olefin metathesis catalysts

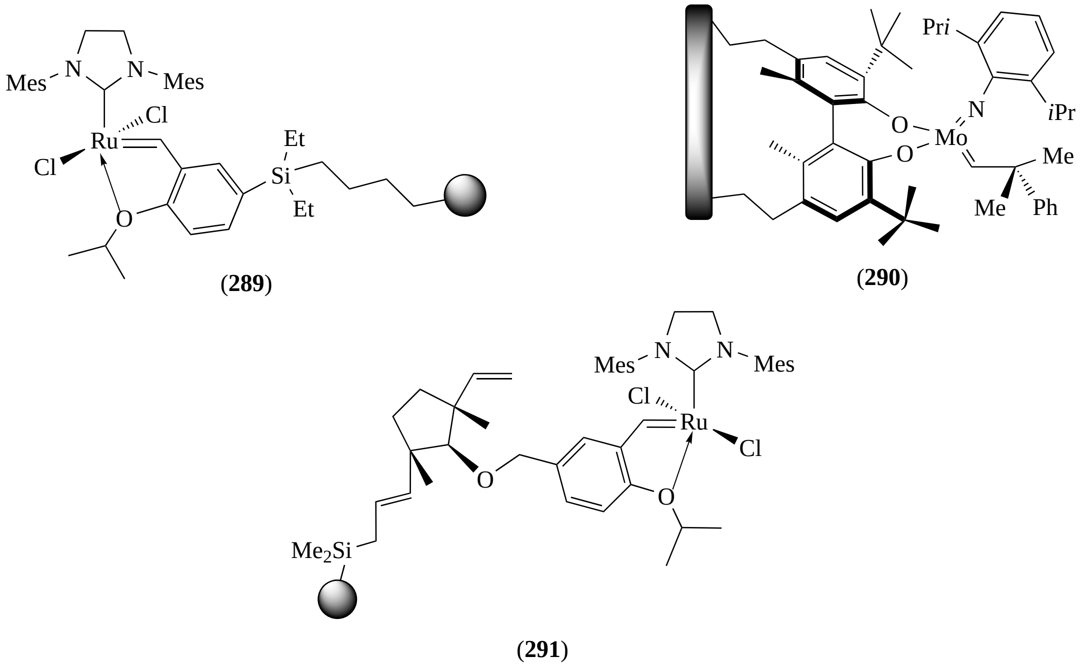

Scheme 27 Other types of recoverable olefin metathesis catalysts

Grela and coworkers attached (**4b**) to butyl diethyl silyl polystyrene to yield catalyst (**289**) in three steps.[176] The catalyst had good activity toward formation of trisubstituted alkene products in RCM and CM processes. The catalysts retained efficacy for up to 6 cycles and could be used sequentially on different substrates without cross contamination.

Hoveyda and Schrock attached (**97a**) to polymer via attached styrene groups yielding the first reported supported chiral molybdenum olefin metathesis catalyst, (**290**) (Scheme 27).[177] Supported complex (**290**) is less active than (**97a**), but it gives similar ranges of *ee*s for enantioselective transformations like desymmetrization. The catalyst is recyclable and, even though the conversions have eroded, the enantioselectivity is still relatively high, Table 14.

Fourkas and Hoveyda immobilized (**4b**) on sol–gel via a norbornyl ester linkage combining the release return mechanism with the ease of a monolith-type heterogeneous system; one such supported catalyst is (**291**).[178] This strategy provides a number of potential advantages in that the support substrate is macroscopic and can be manipulated using tweezers. Commercial grade sol gels give consistent loading and invariant porosity under different reaction conditions. Utilizing this system in CH_2Cl_2, the authors found conversion to analytically pure products with low ruthenium leaching under the same conditions for 4 cycles; with additional reaction time allowances, the sol–gel catalysts were active to 15 cycles without using additives to increase the efficiency of ruthenium rebinding to the support. Table 15 illustrates the capabilities of (**291**) as a recyclable catalyst for the same reaction or from one reaction type to another.

Another strategy for recovering and reusing catalysts is to depart from traditional solvents. Fürstner utilized complex (**2d**) in catalysis in supercritical CO_2 ($scCO_2$), an ecologically benign reaction medium that can be used in place of organic solvents in an increasing number of organic transformations.[179] Even though (**2d**) is not soluble in $scCO_2$, isolated yields of products are similar to those under homogeneous reaction conditions, although the reaction times are much greater in general. Table 16 outlines the results for $scCO_2$ reactions catalyzed by (**2d**) from an initial study in this area.

Buijsman and coworkers found the ionic liquid 1-butyl-3-methylimidazolium hexafluorophosphate ([bmim]PF_6) to be an efficient solvent for RCM using (**2a**) and (**4a**)[180] and an alternative that allowed recycling of the catalyst, albeit at higher temperatures than typical RCM in dichloromethane. The good reactivity and the green solvent characteristics of ionic liquids makes this initial study notable. A further development in this area was made by Mauduit and Guillemin synthesizing a variant of the (**4b**) catalysts with a more cationic Ru center but tethered to a [bmim]PF_6-like center, (**314**).[181] This catalyst was successfully recycled 10 times yielding >95% for *N*,*N*-diallyltosylamine, while the nontethered analog gave high yields only under the first cycle. The catalyst was also successfully recycled 3–8 times on other substrates. Yao reported a similar tethered ionic liquid catalyst, (**315**), that also gave good levels of recyclability.[182]

Table 14 Comparison of recoverable catalyst (**290**) with well-defined complex (**97a**)

				Isolated catalyst, (**97a**)			Supported catalyst, (**290**)		
Entry	Substrate	Product	*t*(h)	Conv. (%)	Yield (%)	ee (%)	Conv. (%)	Yield (%)	ee (%)
1	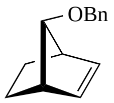 + **104** (**292**)	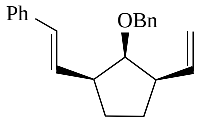 (**293**)	0.5	>98	89	>98	>98	92	98
2	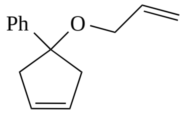 (**294**)	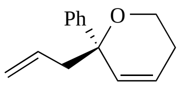 (**295**)	24	93	88	19	57	45	33
3	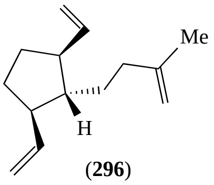 (**296**)	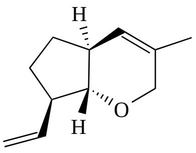 (**297**)	2	93	84	>98	57	41	93

Table 15 Olefin metathesis using sol–gel bound olefin metathesis catalysts

Cycle		Conv. (%)	Yield (%)
1	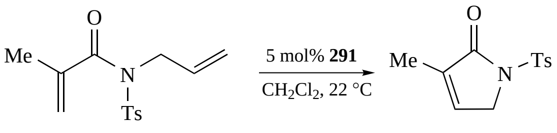 (**298**) $\xrightarrow[\mathrm{CH_2Cl_2},\ 22\ ^{\circ}\mathrm{C}]{5\ \mathrm{mol\%}\ \mathbf{291}}$ (**299**)	>98	>98
2		>98	>98
3		>98	>98
4		>98	>98
	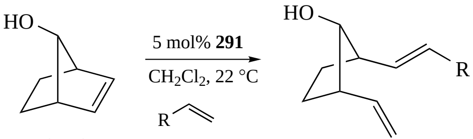 (**300**) $\xrightarrow[\mathrm{CH_2Cl_2},\ 22\ ^{\circ}\mathrm{C}]{5\ \mathrm{mol\%}\ \mathbf{291}}$		
5	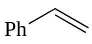 (**104**) (**301**)	>98	>98
6	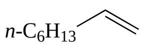 (**302**) (**303**)	>98	>98
7	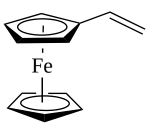 (**304**) (**305**)	>98	>98
8	═ (**306**) (**307**)	>98	>98

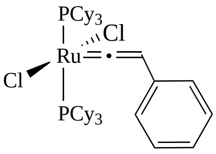

(**2d**)

Table 16 Olefin metathesis in supercritical carbon dioxide

Entry	Substrate	Product	Yield
1	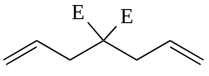 (**280**)	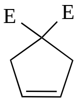 (**281**)	85
2	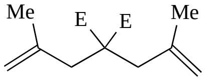 (**308**)	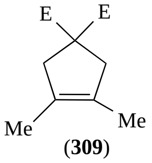 (**309**)	51[a]
3	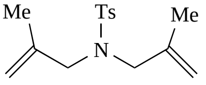 (**310**)	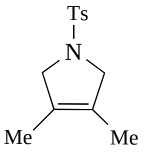 (**311**)	83
4	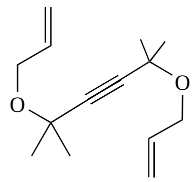 (**312**)	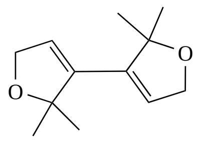 (**313**)	62

E = CO_2Et. Conditions: 2.5 mol% (**2d**), T = 40 °C, $d(CO_2)$ = 0.75 g mol^{-1} t = 24 h. [a]GC yield: t = 120 h.

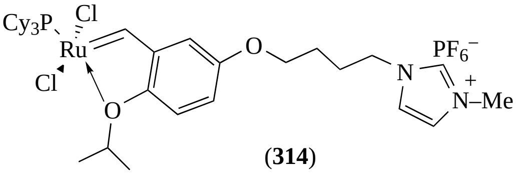

(**314**)

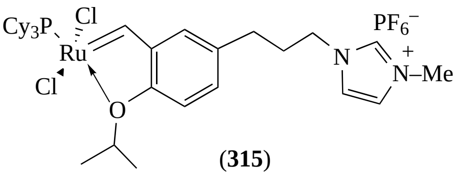

(**315**)

Even with immobilized catalysts being developed, removal of ruthenium by-products remains an important challenge. Georg and coworkers found that addition of 50 equiv (relative to ruthenium) of dimethyl sulfoxide or triphenylphosphine oxide brought ruthenium levels in reaction mixtures down from 50 to 1–2 μg mg^{-1}.[183] The ruthenium levels in purified products are similar to those reported by Grubbs, where the metal was removed as trishydroxymethylphosphine complexes,[184] and those from the $Pb(OAc)_4$ oxidation of ruthenium reported by Paquette.[185]

8 SUMMARY

Olefin metathesis is a class of reaction that is evolving both in the quality of the catalysts and in the myriad of synthetic goals in which the reaction can play a part. With each year, our mechanistic understanding grows, and with this comes insightful research exploiting new findings, pushing the boundaries of performance and scope. The modular nature of these catalysts, and reversibility of many of the steps in the catalytic cycle, has allowed rapid progress in: (1) catalytic activity; (2) functional group tolerance; (3) new reaction pathway development; (4) exploration of an ever broadening range of substrate types; (5) cascading reactions and tandem reaction; (6) enantioselective olefin metathesis with both molybdenum and ruthenium; (7) development of different routes to make these catalysts more environmentally friendly. In light of the rapid advances seen since 2001, it is likely that we will be treated to even more exciting reports in this area in the years to come.

9 RELATED ARTICLES

Mechanisms of Reaction of Organometallic Complexes; Multi-Heme Cytochromes & Enzymes; Palladium: Organometallic Chemistry; Ruthenium: Organometallic Chemistry; Semiconductor Nanocrystal Quantum Dots; Supported Organotransition Metal Compounds.

10 REFERENCES

1. N. Calderon, *Acc. Chem. Res.*, 1972, **5**, 127.
2. J.-L. Herrison and Y. Chauvin, *Macromol. Chem.*, 1971, **141**, 161.
3. K. J. Ivin and J. C. Mol, ‘Olefin Metathesis and Metathesis Polymerization’, Academic Press, London, 1997.
4. R. R. Schrock, J. S. Murdzek, G. C. Bazan, J. Robbins, M. DiMare, and M. O’Regan, *J. Am. Chem. Soc.*, 1990, **112**, 3875.
5. R. R. Schrock, *Tetrahedron*, 1999, **55**, 8141.
6. R. R. Schrock, *Acc. Chem. Res.*, 1990, **23**, 158.
7. R. R. Schrock, *Chem. Rev.*, 2002, **102**, 145.
8. S. T. Nguyen, L. K. Johnson, R. H. Grubbs, and J. W. Ziller, *J. Am. Chem. Soc.*, 1992, **114**, 3974.
9. S. T. Nguyen, R. H. Grubbs, and J. W. Ziller, *J. Am. Chem. Soc.*, 1993, **115**, 9856.
10. R. H. Grubbs and S. Chang, *Tetrahedron*, 1998, **54**, 4413.
11. A. Fürstner, *Angew. Chem., Int. Ed. Engl.*, 2000, **39**, 3012.
12. T. M. Trnka and R. H. Grubbs, *Acc. Chem. Res.*, 2001, **34**, 18.

13. J. S. Kingsbury, J. P. A. Harrity, P. J. Bonitatebus, and A. H. Hoveyda, *J. Am. Chem. Soc.*, 1999, **121**, 791.
14. M. Scholl, T. M. Trnka, J. P. Morgan, and R. H. Grubbs, *Tetrahedron Lett.*, 1999, **40**, 2247.
15. J. Huang, E. D. Stevens, and S. P. Nolan, *J. Am. Chem. Soc.*, 1999, **121**, 2674.
16. T. Weskamp, F. J. Kohl, W. Hieringer, D. Gliech, and W. A. Hermann, *Angew. Chem., Int. Ed. Engl.*, 1999, **38**, 2416.
17. J. P. Morgan and R. H. Grubbs, *Org. Lett.*, 2000, **2**, 3153.
18. M. Scholl, S. Ding, C. W. Lee, and R. H. Grubbs, *Org. Lett.*, 1999, **1**, 953.
19. S. B. Garber, J. S. Kingsbury, B. L. Gray, and A. H. Hoveyda, *J. Am. Chem. Soc.*, 2000, **122**, 8168.
20. S. Gessler, S. Randl and S. Blechert, *Tetrahedron Lett.*, 2000, **41**, 9973.
21. H. Wakamatsu and S. Blechert, *Angew. Chem., Int. Ed. Engl.*, 2002, **41**, 794.
22. H. Wakamatsu and S. Blechert, *Angew. Chem., Int. Ed. Engl.*, 2002, **41**, 2403.
23. A. M. Dunne, S. Mix, and S. Blechert, *Tetrahedron Lett.*, 2003, **44**, 2733.
24. A. Fürstner, O. Guth, A. Düffels, G. Seidel, M. Liebl, B. Gabor, and R. Mynott, *Chem. – Eur. J.*, 2001, **7**, 4811.
25. J. Louie and R. H. Grubbs, *Organometallics*, 2002, **21**, 2153.
26. J. A. Love, M. S. Sanford, M. W. Day, and R. H. Grubbs, *J. Am. Chem. Soc.*, 2003, **125**, 10103.
27. E. L. Dias, S. T. Nguyen, and R. H. Grubbs, *J. Am. Chem. Soc.*, 1997, **119**, 3887.
28. M. S. Sanford, M. Ulman, and R. H. Grubbs, *J. Am. Chem. Soc.*, 2001, **123**, 749.
29. S. E. Lehman Jr and K. B. Wagener, *Macromolecules*, 2002, **35**, 48.
30. C. Adlhart and P. Chen, *Angew. Chem., Int. Ed. Engl.*, 2002, **41**, 4484.
31. L. Cavallo, *J. Am. Chem. Soc.*, 2002, **124**, 8965.
32. S. F. Vybioshchikov, M. Bühl, and W. Thiel, *Chem. – Eur. J.*, 2002, **8**, 3962.
33. C. H. Suresh and N. Koga, *Organometallics*, 2004, **23**, 76.
34. F. Bernardi, A. Bottoni, and G. P. Miscione, *Organometallics*, 2003, **22**, 940.
35. A. C. Hillier, W. J. Sommer, B. S. Yong, J. L. Peterson, L. Cavallo, and S. P. Nolan, *Organometallics*, 2003, **22**, 4322.
36. L. Yet, *Chem. Rev.*, 2000, **100**, 2963.
37. G. Mehta and S. Singh, *Chem. Rev.*, 1999, **99**, 881.
38. I. Ojima, M. Tzamarioudaki, Z. Li, and R. J. Donovan, *Chem. Rev.*, 1996, **96**, 635.
39. G. Illuminati and L. Mandolini, *Acc. Chem. Res.*, 1981, **14**, 95.
40. C. E. Niepp and S. F. Martin, *Tetrahedron Lett.*, 2002, **43**, 1779.
41. C. E. Niepp and S. F. Martin, *J. Org. Chem.*, 2003, **68**, 8867.
42. M. Jørgensen, E. H. Iversen, A. L. Paulsen, and R. Madsen, *J. Org. Chem.*, 2001, **66**, 4630.
43. M. Arisawa, C. Theeraladanon, A. Nishida, and M. Nakagawa, *Tetrahedron Lett.*, 2001, **42**, 8029.
44. M.-P. Heck, C. Baylon, S. P. Nolan, and C. Mioskowski, *Org. Lett.*, 2001, **3**, 1989.
45. C.-J. Wu, L. Reniguntala, R. J. Madhushaw, and R.-S. Liu, *J. Org. Chem.*, 2003, **68**, 7889.
46. X. Chen and D. F. Wiemer, *J. Org. Chem.*, 2003, **68**, 6597.
47. S. Gille, A. Ferry, T. Billard, and B. R. Langlois, *J. Org. Chem.*, 2003, **68**, 8932.
48. S. H. L. Verhelst, B. P. Martinez, M. S. M. Timmer, G. Lodder, G. A. van der Marel, H. S. Overkleeft, and J. H. van Boom, *J. Org. Chem.*, 2003, **68**, 9598.
49. R. C. Hughes, C. A. Dvorak, and A. I. Meyers, *J. Org. Chem.*, 2001, **66**, 5545.
50. A. V. Kalinin, B. A. Chauder, S. Rakhit, and V. Snieckus, *Org. Lett.*, 2003, **5**, 3519.
51. L. Zhu and D. R. Mootoo, *Org. Lett.*, 2003, **5**, 3475.
52. S. S. Kinderman, J. H. van Maarseveen, H. E. Schoemaker, H. Hiemstra, and F. P. J. T. Rutjes, *Org. Lett.*, 2001, **3**, 2045.
53. A. Whitehead, J. D. Moore, and P. R. Hanson, *Tetrahedron Lett.*, 2003, **44**, 4275.
54. R. E. Taylor, F. C. Engelhardt, M. J. Schmitt, and H. Yuan, *J. Am. Chem. Soc.*, 2001, **123**, 2964.
55. A. K. Ghosh and S. Liu, *J. Am. Chem. Soc.*, 2003, **125**, 2374.
56. T. R. Hoye and M. Hu, *J. Am. Chem. Soc.*, 2003, **125**, 9576.
57. B. Zhu and J. P. Panek, *Org. Lett.*, 2000, **2**, 2575.
58. D. L. Boger, S. H. Kim, Y. Mori, J.-H. Weng, O. Rogel, S. L. Castle, and J. J. McAtee, *J. Am. Chem. Soc.*, 2001, **123**, 1862.
59. A. B. Smith III and Z. Wan, *Org. Lett.*, 1999, **1**, 1491.
60. A. Fürstner and K. Langemann, *J. Org. Chem.*, 1996, **61**, 3942.
61. S. J. Miller, H. E. Blackwell, and R. H. Grubbs, *J. Am. Chem. Soc.*, 1996, **118**, 9606.
62. K. C. Nicolaou, Y. He, H. Vourloumis, F. Vallberg, F. Roschangar, F. Sarabia, S. Ninkovic, Z. Yang, and J. I. Trujillo, *J. Am. Chem. Soc.*, 1997, **119**, 7960.
63. A. Fürstner, O. R. Thiel, and L. Ackermann, *Org. Lett.*, 2001, **3**, 449.
64. C. W. Lee and R. H. Grubbs, *J. Org. Chem.*, 2001, **66**, 7155.
65. C. W. Lee, T.-L. Choi, and R. H. Grubbs, *J. Am. Chem. Soc.*, 2002, **124**, 3224.
66. R. G. E. Coumans, J. A. A. W. Elemans, R. J. M. Nolte, and A. E. Rowan, *Angew. Chem., Int. Ed. Engl.*, 2003, **42**, 650.
67. M. A. Hillmyer, S. T. Nguyen, and R. H. Grubbs, *Macromolecules*, 1997, **30**, 178.
68. C. W. Bielwaski, O. A. Sherman, and R. H. Grubbs, *Polymer*, 2001, **41**, 4939.

69. L. A. W. Paquette and J. Méndez-Andino, *Tetrahedron Lett.*, 2001, **42**, 967.
70. A. B. Smith III, C. M. Adams, and D. V. Paone, *J. Am. Chem. Soc.*, 2000, **122**, 4984.
71. H. Iwamoto, K. Itoh, H. Nagamiya, and Y. Fukazawa, *Tetrahedron Lett.*, 2003, **44**, 5773.
72. A. V. Chuchuryukin, H. P. Dijkstra, B. M. Suijkerbuijk, G. P. M. van Klink, A. M. Mills, A. L. Spek, and G. van Koten, *Angew. Chem., Int. Ed. Engl.*, 2003, **42**, 228.
73. W. E. Crowe and D. R. Goldberg, *J. Am. Chem. Soc.*, 1995, **117**, 5162.
74. O. Brummer, A. Ruckert, and S. Blechert, *Chem. – Eur. J.*, 1997, **3**, 441.
75. H. E. Blackwell, D. J. O'Leary, A. K. Chatterjee, D. A. Washenfelder, R. A. Bussmann, and R. H. Grubbs, *J. Am. Chem. Soc.*, 2000, **123**, 6543.
76. A. K. Chatterjee and R. H. Grubbs, *Angew. Chem., Int. Ed. Engl.*, 2002, **41**, 3171.
77. M. Lera and C. J. Hayes, *Org. Lett.*, 2001, **3**, 2765.
78. F. Amblard, S. P. Nolan, I. Gillaizeau, and L. A. Agrofoglio, *Tetrahedron Lett.*, 2003, **44**, 9177.
79. B. Liu, S. K. Das, and R. Roy, *Org. Lett.*, 2002, **4**, 2723.
80. G. J. McGarvey, T. E. Benedum, and F. W. Schmidtmann, *Org. Lett.*, 2002, **4**, 3591.
81. G. Godin, P. Compain, and O. R. Martin, *Org. Lett.*, 2003, **5**, 3269.
82. J. P. Morgan, C. Morrill, and R. H. Grubbs, *Org. Lett.*, 2002, **4**, 67.
83. F. C. Engelhardt, M. J. Schmitt, and R. E. Taylor, *Org. Lett.*, 2001, **3**, 2209.
84. A. K. Chatterjee, D. P. Sanders, and R. H. Grubbs, *Org. Lett.*, 2002, **4**, 1939.
85. K. Tanaka, K. Nakanishi, and N. Berova, *J. Am. Chem. Soc.*, 2003, **125**, 10802.
86. O. Fujimura and R. H. Grubbs, *J. Am. Chem. Soc.*, 1996, **118**, 2499.
87. O. Fujimura and R. H. Grubbs, *J. Org. Chem.*, 1998, **63**, 824.
88. J. B. Alexander, D. S. La, D. R. Cefalo, and A. H. Hoveyda, *J. Am. Chem. Soc.*, 1998, **120**, 4041.
89. S. S. Zhu, D. R. Cefalo, D. S. La, J. Y. Jamieson, W. M. Davis, and A. H. Hoveyda, *J. Am. Chem. Soc.*, 1999, **121**, 8251.
90. S. L. Aeilts, D. R. Cefalo, P. J. Bonitatebus Jr, J. H. Houser, A. H. Hoveyda, and R. R. Schrock, *Angew. Chem., Int. Ed. Engl.*, 2001, **40**, 1452.
91. D. S. La, E. S. Sattely, J. G. Ford, R. R. Schrock, and A. H. Hoveyda, *J. Am. Chem. Soc.*, 2001, **123**, 7767.
92. K. C. Hultzsch, P. J. Bonitatebus, J. Jernelius, R. R. Schrock, and A. H. Hoveyda, *Organometallics*, 2001, **20**, 4705.
93. R. R. Schrock, J. Y. Jamieson, S. J. Dolman, S. A. Miller, P. J. Bonitatebus, and A. H. Hoveyda, *Organometallics*, 2002, **21**, 409.
94. S. J. Dolman, R. R. Schrock, and A. H. Hoveyda, *Org. Lett.*, 2003, **5**, 4899.
95. S. J. Dolman, E. S. Sattely, A. H. Hoveyda, and R. R. Schrock, *J. Am. Chem. Soc.*, 2002, **124**, 6991.
96. W. C. P. Tsang, J. A. Jernelius, G. A. Cortes, G. S. Weatherhead, R. R. Schrock, and A. H. Hoveyda, *J. Am. Chem. Soc.*, 2003, **125**, 2591.
97. X. Teng, D. R. Cefalo, R. R. Schrock, and A. H. Hoveyda, *J. Am. Chem. Soc.*, 2002, **124**, 10779.
98. J. J. Van Veldhuizen, S. B. Garber, J. S. Kingsbury, and A. H. Hoveyda, *J. Am. Chem. Soc.*, 2002, **124**, 4954.
99. J. J. Van Veldhuizen, D. G. Gillingham, S. B. Garber, O. Kataoka, and A. H. Hoveyda, *J. Am. Chem. Soc.*, 2003, **125**, 12502.
100. T. J. Seiders, D. W. Ward, and R. H. Grubbs, *Lett.*, 2001, **3**, 3225.
101. J. K. Sello, P. R. Andreana, and S. L. Schreiber, *Org. Lett.*, 2003, **5**, 4125.
102. J. Louie, C. W. Bielawski, and R. H. Grubbs, *J. Am. Chem. Soc.*, 2001, **123**, 11312.
103. A. E. Sutton, B. A. Seigal, D. F. Finnegan, and M. L. Snapper, *J. Am. Chem. Soc.*, 2002, **124**, 13390.
104. D. C. Braddock and A. J. Wildsmith, *Tetrahedron Lett.*, 2001, **42**, 3239.
105. D. C. Braddock and A. Matsuno, *Tetrahedron Lett.*, 2002, **43**, 3305.
106. H. A. Dondas, G. Balme, B. Clique, R. Grigg, A. Hodgson, J. Morris, and V. Sridharan, *Tetrahedron Lett.*, 2001, **42**, 8673.
107. R. Grigg, A. Hodgson, J. Morris, and V. Sridharan, *Tetrahedron Lett.*, 2002, **43**, 1023.
108. D. Meng and D. L. Parker Jr, *Tetrahedron Lett.*, 2002, **43**, 9035.
109. M. T. Crimmins and E. A. Tabet, *J. Org. Chem.*, 2001, **66**, 4012.
110. H. Mizutani, S. J. Degrado, and A. H. Hoveyda, *J. Am. Chem. Soc.*, 2002, **124**, 779.
111. S. Randl and S. Blechert, *J. Org. Chem.*, 2003, **68**, 8879.
112. B. H. White and M. L. Snapper, *J. Am. Chem. Soc.*, 2003, **125**, 14901.
113. H.-Y. Lee, H. Y. Kim, H. Tae, B. G. Kim, and J. Lee, *Org. Lett.*, 2003, **5**, 3439.
114. D. F. Taber and K. J. Frankowski, *J. Org. Chem.*, 2003, **68**, 6047.
115. K. G. Mayo, E. H. Nearhoof, and J. J. Kiddle, *Org. Lett.*, 2002, **4**, 1567.
116. B. Kang, D. Kim, Y. Do, and S. Chang, *Org. Lett.*, 2003, **5**, 3041.
117. T. M. Trnka, M. W. Day, and R. H. Grubbs, *Angew. Chem., Int. Ed. Engl.*, 2001, **40**, 3441.
118. M. Inoue, T. Sato, and M. Hirama, *J. Am. Chem. Soc.*, 2003, **125**, 10772.

119. S. A. Kozmin, T. Iwama, Y. Huang, and V. H. Rawal, *J. Am. Chem. Soc.*, 2002, **124**, 4628.

120. Y. K. Reddy and J. R. Falck, *Org. Lett.*, 2002, **4**, 969.

121. T. Itoh, N. Yamazaki, and C. Kibayashi, *Org. Lett.*, 2002, **4**, 2469.

122. S. Hanessian, R. Margarita, A. Hall, S. Johnstone, M. Tremblay, and L. Parlanti, *J. Am. Chem. Soc.*, 2002, **124**, 13342.

123. M. Montembault, N. Bourgougnon, and J. Lebreton, *Tetrahedron Lett.*, 2002, **43**, 8091.

124. A. Srikrishna and M. S. Rao, *Tetrahedron Lett.*, 2002, **43**, 151.

125. C. Held, R. Fröhlich, P. Metz, *Angew. Chem., Int. Ed. Engl.*, 2001, **40**, 1058.

126. R. V. Anand, S. Baktharaman, and V. K. Singh, *Tetrahedron Lett.*, 2002, **43**, 5393.

127. A. Fürstner and K. Radkowski, *Chem. Commun.*, 2001, 671.

128. C. J. Creighton and A. B. Reitz, *Org. Lett.*, 2001, **3**, 893.

129. M. E. Maier, *Angew. Chem., Int. Ed. Engl.*, 2000, **39**, 2073.

130. K. Nakashima, K. Inoue, M. Sono, and M. Tori, *J. Org. Chem.*, 2002, **67**, 6034.

131. K. Takao, G. Watanabe, H. Yasui, and K. Tadano, *Org. Lett.*, 2002, **4**, 2941.

132. D. Barker, M. D. McLeod, M. A. Brimble, and G. P. Savage, *Tetrahedron Lett.*, 2002, **43**, 6019.

133. D. G. Washburn, R. W. Heidebrecht Jr, and S. F. Martin, *Org. Lett.*, 2003, **5**, 3523.

134. M. Nevalainen and A. M. P. Koskinen, *Angew. Chem., Int. Ed. Engl.*, 2001, **40**, 4060.

135. K. Koide, J. M. Finkelstein, Z. Ball, and G. L. Verdine, *J. Am. Chem. Soc.*, 2001, **123**, 398.

136. Y. Wu, X. Liao, R. Wang, X.-S. Xie, and J. K. De Brabander, *J. Am. Chem. Soc.*, 2002, **124**, 3245.

137. K. L. Yang, B. Blackman, W. Diederich, P. T. Flaherty, C. J. Mossman, S. Roy, Y. M. Ahn, and G. I. Georg, *J. Org. Chem.*, 2003, **68**, 10030.

138. C. Aïssa, R. Riveiros, J. Ragot, and A. Fürstner, *J. Am. Chem. Soc.*, 2003, **125**, 15512.

139. F. Bouazza, B. Renoux, C. Bachmann, and J.-P. Gesson, *Org. Lett.*, 2003, **5**, 4049.

140. Y. Gao, C. Q. Wei, and T. R. Burke Jr, *Org. Lett.*, 2001, **3**, 1617.

141. B. B. Metaferia, J. Hoch, T. E. Glass, S. L. Bane, S. K. Chatterjee, J. P. Snyder, A. Lakdawala, B. Cornett, and D. G. I. Kingston, *Org. Lett.*, 2001, **3**, 2461.

142. A. Fürstner, F. Jeanjean, P. Razon, C. Wirtz, and R. Mynott, *Chem. – Eur. J.*, 2003, **9**, 320.

143. K. C. Nicolaou, G. Vassilikogiannakis, and T. Montagnon, *Angew. Chem., Int. Ed. Engl.*, 2002, **41**, 3276.

144. P. G. Nantermet and H. G. Selnick, *Tetrahedron Lett.*, 2003, **44**, 2401.

145. A. Fürstner, K. Radkowski, C. Wirtz, R. Goddard, C. W. Lehmann, and R. Mynott, *J. Am. Chem. Soc.*, 2002, **124**, 7061.

146. E. A. Couladouros, A. P. Mihou, and E. A. Bouzas, *Org. Lett.*, 2004, **6**, 977.

147. K. Biswas, H. Lin, J. T. Njardarson, M. D. Chappell, T.-C. Chou, Y. Guan, W. P. Tong, L. He, S. B. Horwitz, and S. J. Danishefsky, *J. Am. Chem. Soc.*, 2002, **124**, 9825.

148. A. Rivkin, J. T. Njardarson, K. Biswas, T.-C. Chou, and S. J. Danishefsky, *J. Org. Chem.*, 2002, **67**, 7737.

149. A. Rivkin, K. Biswas, T.-C. Chou, and S. J. Danishefsky, *Org. Lett.*, 2002, **4**, 4081.

150. T.-C. Chou, H. Dong, A. Rivkin, F. Yoshimura, A. E. Gabarda, Y. S. Cho, W. P. Tong, and S. J. Danishefsky, *Angew. Chem., Int. Ed. Engl.*, 2003, **42**, 4762.

151. B. M. Trost, J. L. Gunzner, O. Dirat, and Y. H. Rhee, *J. Am. Chem. Soc.*, 2002, **124**, 10396.

152. J. A. Smulik, S. T. Diver, F. Pan, and J. O. Liu, *Org. Lett.*, 2002, **4**, 2051.

153. S. J. Spessard and B. M. Stoltz, *Org. Lett.*, 2002, **4**, 1943.

154. M. M. Vasbinder and S. J. Miller, *J. Org. Chem.*, 2002, **67**, 6240.

155. S. M. Rele, S. S. Iyer, and E. L. Chaikof, *Tetrahedron Lett.*, 2003, **44**, 89.

156. K. Tamaki, E. W. D. Huntsman, D. T. Petsch, and J. L. Wood, *Tetrahedron Lett.*, 2002, **43**, 379.

157. A. B. Smith III, C. M. Adams, S. A. Kozmin, and D. V. Paone, *J. Am. Chem. Soc.*, 2001, **123**, 5925.

158. H. Skaff, M. F. Ilker, E. B. Coughlin, and T. Emrick, *J. Am. Chem. Soc.*, 2002, **124**, 5729.

159. T.-L. Choi, I. M. Rutenburg, and R. H. Grubbs, *Angew. Chem., Int. Ed. Engl.*, 2002, **41**, 3839.

160. H. E. Blackwell, P. A. Clemons, and S. L. Schreiber, *Org. Lett.*, 2001, **3**, 1185.

161. M. Kimura, K. Wada, K. Ohta, K. Hanabusa, H. Shirai, and N. Kobayashi, *Macromolecules*, 2001, **34**, 4706.

162. A. Juang, O. A. Scherman, R. H. Grubbs, and N. S. Lewis, *Langmuir*, 2001, **17**, 1321.

163. J. Ruwwe, J. M. Martín-Alvarez, C. R. Horn, E. B. Bauer, S. Szafert, T. Lis, F. Hampel, P. C. Cagle, and J. A. Gladysz, *Chem. – Eur. J.*, 2001, **7**, 3931.

164. E. B. Bauer, F. Hampel, and J. A. Gladysz, *Organometallics*, 2003, **22**, 5567.

165. M. S. M. Timmer, M. Verdoes, L. A. J. M. Sliedregt, G. A. van der Marel, J. H. van Boom, and H. S. Overkleeft, *J. Org. Chem.*, 2003, **68**, 9406.

166. Q. Yao, *Angew. Chem., Int. Ed. Engl.*, 2000, **39**, 3896.

167. S. J. Connon, A. M. Dunne, and S. Blechert, *Angew. Chem., Int. Ed. Engl.*, 2002, **41**, 3835.

168. M. Ahmed, T. Arnauld, A. G. M. Barrett, D. C. Braddock, and P. A. Procopiou, *Synlett*, 2000, **7**, 1007.

169. M. Ahmed, A. G. M. Barrett, D. C. Braddock, S. M. Cramp, and P. A. Procopiou, *Tetrahedron Lett.*, 1999, **40**, 8657.

170. S. C. Schürer, S. Gessler, N. Buschmann, and S. Blechert, *Angew. Chem., Int. Ed. Engl.*, 2000, **39**, 3898.

171. L. Jafarpour and S. P. Nolan, *Org. Lett.*, 2000, **2**, 4075.

172. L. Jafarpour, M.-P. Heck, B. Baylon, H. M. Lee, C. Mioskowski, and S. P. Nolan, *Organometallics*, 2002, **21**, 671.

173. L. Canali and D. C. Sherrington, *Chem. Soc. Rev.*, 1999, **28**, 85.

174. R. Akiyama and S. Kobayashi, *Angew. Chem., Int. Ed. Engl.*, 2002, **41**, 2602.

175. S. Varray, R. Lazaro, J. Martinez, and F. Lamaty, *Organometallics*, 2003, **22**, 2426.

176. K. Grela, M. Tryznowski, and M. Bieniek, *Tetrahedron Lett.*, 2002, **43**, 9055.

177. K. C. Hultzsch, J. A. Jernelius, A. H. Hoveyda, and R. R. Schrock, *Angew. Chem., Int. Ed. Engl.*, 2002, **41**, 589.

178. J. S. Kingsbury, S. B. Garber, J. M. Giftos, B. L. Gray, M. M. Okamoto, R. A. Farrer, J. T. Fourkas, and A. H. Hoveyda, *Angew. Chem., Int. Ed. Engl.*, 2001, **40**, 4251.

179. A. Fürstner, L. Ackermann, K. Beck, H. Hori, D. Koch, K. Langemann, M. Liebl, C. Six, and W. Leitner, *J. Am. Chem. Soc.*, 2001, **123**, 9000.

180. R. C. Buijsman, E. van Vuuren, and J. G. Sterrenburg, *Org. Lett.*, 2001, **3**, 3785.

181. N. Audic, H. Clavier, M. Mauduit, and J. C. Guillemin, *J. Am. Chem. Soc.*, 2003, **125**, 9248.

182. Q. Yao and Y. Zhang, *Angew. Chem., Int. Ed. Engl.*, 2003, **42**, 3395.

183. Y. M. Ahn, K. Yang, and G. I. Georg, *Org. Lett.*, 2001, **3**, 1411.

184. H. D. Maynard and R. H. Grubbs, *Tetrahedron Lett.*, 1999, **40**, 4137.

185. L. A. Paquette, J. D. Schloss, I. Efremov, F. Fabris, F. Gallou, J. Mendez-Andino, and J. Yang, *Org. Lett.*, 2000, **2**, 1259.

Organic Synthesis Using Metal-mediated Coupling Reactions

Felix E. Goodson & Melissa B. Cichowicz
West Chester University of Pennsylvania, West Chester, PA, USA

1 Introduction 1
2 Coupling of Organic Substrates with Grignard Reagents 2
3 Coupling of Organic Substrates with Terminal Acetylenes 4
4 Coupling of Organic Substrates with Organozinc Reagents 6
5 Coupling of Organic Substrates with Organotin Reagents 7
6 Coupling of Organic Substrates with Organoboron Reagents 9
7 Coupling of Organic Substrates with Organosilicon Reagents 12
8 Catalytic Amination of Organic Electrophiles 14
9 Applications 17
10 Conclusions and Future Outlook 17
11 Related Articles 17
12 References 17

1 INTRODUCTION

Reactions that form carbon–carbon bonds are of fundamental importance in organic synthesis. Given this, it is somewhat surprising that the cross-coupling reaction, arguably the most powerful tool for this purpose available to the modern-day synthetic organic chemist, rarely makes it into the curriculum of the typical introductory course in organic chemistry. However, as this reaction continues to gain importance in academic and industrial laboratory settings, this oversight will probably be remedied in the near future.

Indeed, one does not need to look far in the literature to see how the cross-coupling reaction has gained prominence in recent years. At the time of writing this contribution (May, 2004), a keyword search on the Chemical Abstracts Database for ‘cross, coupling, palladium’ retrieves over 2700 articles, 1200 since the year 2000. Recent compilations of reviews have also been plentiful. Diederich’s and Stang’s *Metal-Catalyzed Cross-Coupling Reactions*,[1] and Negishi’s all-encompassing *Handbook of Organopalladium Chemistry for Organic Synthesis*[2] are two must-haves for any chemist performing research in this area. Furthermore, recent issues of the *Journal of Organometallic Chemistry* and *Topics in Current Chemistry* have been completely devoted to the subject.

A cross-coupling reaction can be partially defined by equation (1), where Nu is a carbon (or heteroatom) nucleophile (*see Nucleophile*), R–X is an electrophilic substrate, X is a halogen or other appropriate leaving group, and M is a metal or metalloid. At first glance, it would appear that simple nucleophilic substitution reactions should fall under this definition. However, what makes the cross-coupling chemistry special is its ability to perform transformations that cannot be accomplished with simple substitution chemistry.

$$\mathrm{R{-}X + M{-}Nu} \xrightarrow[\text{Catalyst}]{\text{Transition metal}} \mathrm{R{-}Nu + MX} \qquad (1)$$

Consequently, to narrow the definition a bit further, we will adhere to Negishi’s suggestion[3] and define cross-coupling reactions as those that follow some variation of the mechanism depicted in Scheme 1 (where Mt is a transition metal, L is an ancillary ligand (*see Ancillary Ligand*), and n is the oxidation state of the reduced metal in the catalytic cycle). This mechanism is supported by stoichiometric studies on isolated metal complexes (mostly where Mt = Pd, $n = 0$, L = triphenylphosphine) thought to be the intermediates in this cycle.

This is not to say that all cross-coupling reactions follow the same reaction pathway. Indeed, recent studies performed under conditions that more closely match those of the cross-coupling catalysis indicate that the actual mechanism depends upon the catalyst precursor, as well as the identities and concentrations of anions (which change as the reaction progresses) and cations (including the identity of M) present in the reaction.[4] The situation is muddied further by the fact that sterically hindered phosphines, chelating ligands, and metals other than palladium are increasingly being used in cross-coupling protocols. Conclusions drawn from studies on classical palladium complexes do not necessarily hold for these new systems.

Nevertheless, most would agree that whatever the details, the fundamental steps of oxidative addition (*see Oxidative Addition*), transmetallation (*see Transmetalation*), and reductive elimination (*see Reductive Elimination*) are intimately involved in the catalytic cycle, and Scheme 1 provides us with a starting point for rationalizing why certain protocols work better than others. Furthermore, for the synthetic organic chemist, what matters is that the reactions work, not so much the hows and whys of the process. So, for most of us, the understanding provided by this mechanism is sufficient. This does not mean, however, that the details are unimportant. For the organometallic chemist, on whose shoulders lie the development of next generations of catalysts, a thorough understanding of the microscopic steps is essential for the rational design of more advanced systems.

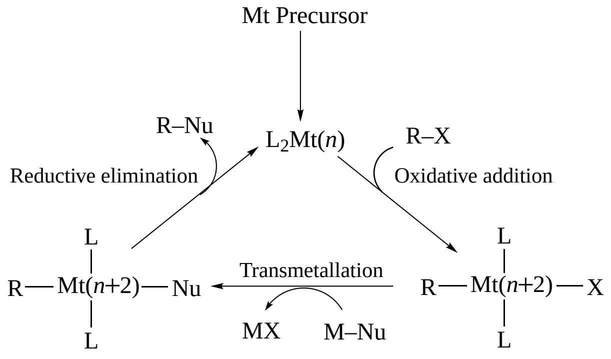

Scheme 1 General mechanism for cross-coupling reactions catalyzed by transition metals

Over the past 30+ years, cross-coupling protocols utilizing a wide variety of metals and metalloids have been studied. However, we will cover only those that have been applied the most often in organic synthesis. Furthermore, the related Heck (*see Heck Reaction*) and Tsuji–Trost reactions, which follow different mechanisms (and hence, do not fall under our more narrow definition), are beyond the scope of this entry.

2 COUPLING OF ORGANIC SUBSTRATES WITH GRIGNARD REAGENTS (*See Grignard Reagents*)

2.1 History and Overview

In 1972, Kumada[5] and Corriu[6] independently disclosed what has come to be known as the Kumada–Corriu protocol for the nickel-catalyzed cross-coupling reaction of Grignard reagents (*see Grignard Reagents*) with organic substrates (equation 2). In a classic example of rational catalyst design, the authors of the first paper showed that the primary side reaction, β-hydride elimination (*see β-Hydride Elimination*) from the intermediate dialkylnickel(II) species, could be minimized if a chelating phosphine were present in the reaction. Thus, using the catalyst $NiCl_2$(dppp) (dppp = diphenylphosphinopropane, (**1**)), viable yields could be obtained even when the Grignard reagent contained β-hydrogens. Furthermore, later studies showed that aryl chlorides provided better results than those obtained with the other halogens, in marked contrast to the trend observed with the corresponding palladium catalysis (vide infra). In fact, despite the vast amount of research performed in this field since 1972, the Kumada–Corriu protocol remains one of the best methods for synthesizing alkylarenes from aryl chlorides.

$$\text{R–X} + \text{R}'\text{–MgX}' \xrightarrow[(-\text{MgXX}')]{\text{Ni catalyst}} \text{R–R}' \qquad (2)$$

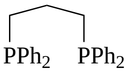

(**1**)

In the following years, a number of researchers reported on the analogous palladium-catalyzed cross coupling of alkenyl and aryl halides with Grignard reagents. The best results were obtained with bromide and iodide substrates, and palladium complexes with triphenylphosphine ligands were typically used as catalysts. In addition to broadening the scope of the reaction to include the other halides, the palladium catalysts also provided for higher E/Z stereoselectivity than what was obtainable with the nickel systems.

One serious drawback for the early nickel and palladium systems was that when secondary alkyl Grignard reagents were employed, a significant amount of 2° to 1° isomerization took place resulting in the competing formation of n-alkyl-substituted by-products (equation 3). Hayashi found that this side reaction could be limited when $PdCl_2$(dppf) (dppf = 1,1′-bis(diphenylphosphino)ferrocene, (**2**)) was used as the catalyst.[7] The authors argued that the superior activity and selectivity for this complex was due to its unusually large P–Pd–P angle of 99°, which served to decrease the C–Pd–C bond angle in the dialkylpalladium intermediate causing an increase in its rate of reductive elimination.

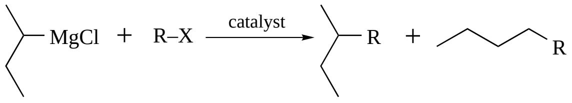

(3)

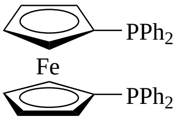

(**2**)

While organic chlorides, bromides, and iodides are still the most common substrates, recently the scope has been expanded to include organic fluorides, nitriles, ethers, triflates, phosphates, iodonium salts, and substrates with various chalconide-leaving groups. Of the different cross-coupling reactions covered in this article, the Kumada–Corriu protocol has been the least reviewed. However, the topic has been covered in recent historical treatments.[3,8,9]

2.2 Recent Improvements in Catalyst Development

Most of the research in terms of methodology improvement has proceeded along three fronts: the development of asymmetric coupling reactions,[10] the use of new nickel and palladium catalysts with specifically designed ancillary ligands, and the investigation of how different transition metals could be used to catalyze the reaction. While importance of the first area of research is obvious, the second is driven by the tendency of homogeneous nickel and palladium catalysts to decompose during the reactions they mediate, resulting in decreased activity and product contamination.[11] Finally, the expense of palladium and the toxicity of nickel have spurred others to investigate different transition metal alternatives.

There are two primary applications of asymmetric Grignard cross-coupling reactions that researchers have attempted to optimize over the years. The first of these is the reaction of an alkenyl or aromatic substrate with a secondary alkyl Grignard reagent. The challenge in this type of reaction lies in the fact that these Grignard species undergo a rapid racemization; however, with the appropriate asymmetric catalyst, optically enriched cross-coupling products can be obtained (equation 4).

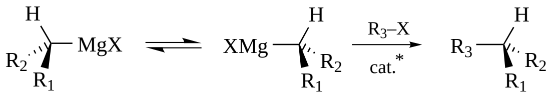

(4)

A large fraction of the catalysts investigated for this purpose is on the basis of palladium or nickel complexes with chiral ferrocenylphosphine derivatives. This interest was spurred by the early work of Hayashi and Kumada who achieved the asymmetric coupling depicted in equation (5) ($R' = H$) in 68% ee using phosphine (**3**) to provide chirality at the catalytic center.[10] More recently, Knochel synthesized bisphosphine derivative (**4**) ($R = Ph$) which gave results similar to (**3**) when vinyl bromide was the substrate (equation 5, $R' = H$, 63% ee).[12] However, when the reaction was performed with β-bromostyrene ($R' = Ph$), the enantioselectivity (*see Enantioselectivity*) increased to 93%.

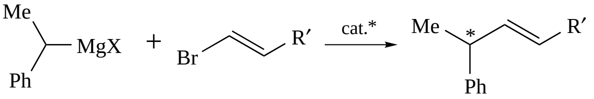

(5)

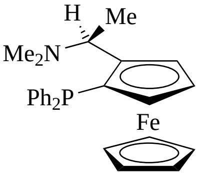

(**3**)

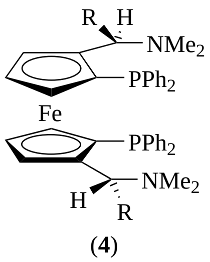

(**4**)

Researchers have also speculated on whether the optical induction provided by (**3**) was because of the ferrocene backbone or to the P–N chelate. Hayashi and Kumada attempted the reaction in equation (5) ($R' = H$) with several β-(dialkylamino)alkylphosphines and found that enantioselectivies as high as 83% could be achieved when the ligands contained bulky groups on the stereogenic carbons (i.e. (**5**)).[10] Another more recent improvement was the development of ligand (**6**), in which the chelating nitrogen atom is itself a stereogenic center. When equation (5) ($R' = H$) was performed with this phosphine and a nickel catalyst, an 86% ee was obtained.[13]

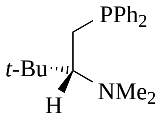

(**5**)

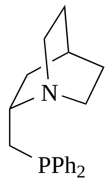

(**6**)

The other primary application of asymmetric Grignard coupling reactions has been in the synthesis of axially chiral binaphthyl and biphenyl derivatives. Hayashi performed a binaphthyl synthesis (equation 6) in 95% ee using a nickel catalyst and ligand (**7**),[10] a P–O chelating analog to (**3**). For a similar synthesis of chiral biaryls (equation 7) ligand, (**8**) was found to yield the most successful results (93% ee).[10]

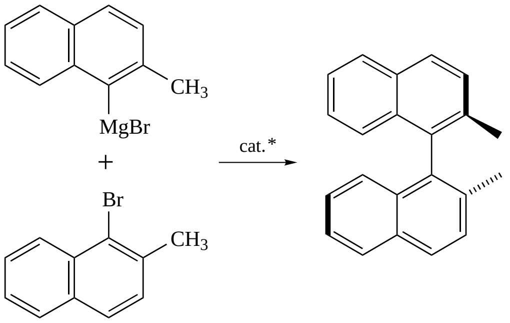

(6)

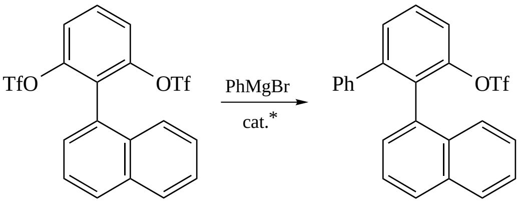

(7)

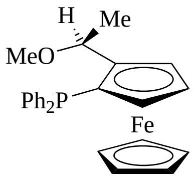

(**7**)

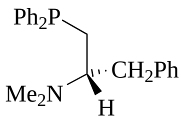

(**8**)

In order to address the issue of phosphine-derived by-products in nickel-catalyzed systems, a number of researchers have investigated the use of alternative ligands to promote cross-coupling reactions. In particular, Herrmann and coworkers have successfully applied N-heterocyclic carbene ligands (e.g. (**9**)), as well as the commercially available monodentate tri(*tert*-butyl)phosphine, in the nickel-catalyzed Kumada–Corriu protocol.[14] Similarly, Kambe recently reported an alkyl–alkyl Grignard cross-coupling reaction catalyzed by nickel salts in the presence of a butadiene additive.[15]

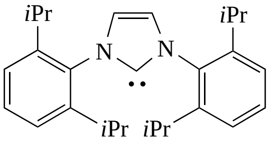

(**9**)

Much of the effort in recent palladium catalyst development has been geared toward improving the activity and selectivity of the original Pd-dppf system. The critical parameter in this regard is believed to be the P–Pd–P bond angle, or phosphine bite angle. In their recent compilation of bite angle effects in homogeneous catalysis,[16] van Leeuwen and coworkers indicated that the optimal values for this parameter were between 96° and 102°. Hayashi recently showed that diphenylphosphinobiphenyl (dpbp, (**10**)) produced results comparable to those generated by dppf, even though the bite angle for this ligand (92°) was less than the optimal range.[17] The authors noted, however, that in the $PdCl_2$ complex with this phosphine, the Cl–Pd–Cl angle (88.2°) was only slightly larger than that for the dppf complex (87.8°), suggesting that this may be the more important parameter for catalyst optimization.

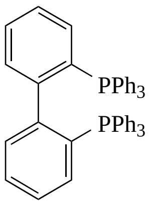

(**10**)

A significant amount of research has also been devoted to the development of phosphine alternatives in palladium catalysis. Investigators have used heterocyclic carbene ligands in a variety of cross-coupling reactions.[18,19] In particular, (**9**) was found to promote the palladium-catalyzed coupling of aryl halides (including chlorides) with aryl Grignard reagents to form substituted biphenyls in nearly quantitative yields. Li has used a combinatorial approach to design phosphinous acid derivatives (e.g. (**11**)) which can be deprotonated in situ to yield electron-rich ligands that are similarly able to activate aryl chlorides during Pd-catalyzed Grignard cross-coupling reactions.[20]

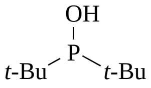

(**11**)

Although the disclosures of Kumada and Corriu are generally regarded as the progenitors of the cross-coupling reaction, these papers were actually preceded by two catalytic systems reported by Kochi. The first of these was a copper catalyzed coupling between alkyl halides and alkyl Grignard reagents.[21] Slight modifications have expanded the scope to include the use of alkyl tosylates, and more recently dienyl triflates, to form 2-substituted 1,3-dienes (equation 8).[22]

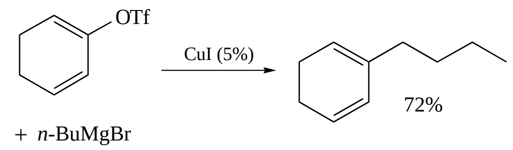

(8)

Kochi's other harbinger system was a vinylation of Grignard reagents catalyzed by iron species generated in situ from $FeCl_3$.[23] Despite this early success, iron catalysts for this reaction have received little attention until recently. One problem preventing their use in organic synthesis was that a large excess of halide substrate was required to generate the favorable yields. However, Cahiez spurred the more recent interest by showing that this excess could be eliminated if the reaction were performed in the presence of a dialkyl amide cosolvent (such as DMF or NMP) (equation 9).[24] Fürstner later extended the scope of this reaction to include aryl and heteroaryl chlorides, triflates, and tosylates – without the amide cosolvent.[25] While Kochi proposed a mechanism analogous to Scheme 1, in which the iron shuttles between the +1 and +3 oxidation states,[26] Fürstner suggested that the active species is an 'inorganic Grignard reagent' $[Fe(MgX)_2]$, and that the cycle proceeds through iron in the 0 and −2 oxidation states,[25] isoelectronic with the proposed intermediates in the traditional nickel and palladium systems.

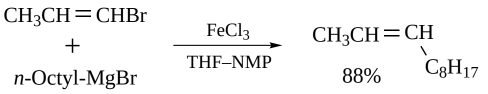

$$\mathrm{CH_3CH{=}CHBr} + n\text{-Octyl-MgBr} \xrightarrow[\text{THF–NMP}]{\mathrm{FeCl_3}} \underset{88\%}{\mathrm{CH_3CH{=}CH{-}C_8H_{17}}} \qquad (9)$$

3 COUPLING OF ORGANIC SUBSTRATES WITH TERMINAL ACETYLENES

3.1 History and Overview

The palladium-catalyzed coupling of organic substrates with terminal acetylenes (equation 10),[27,28] owes its nascence

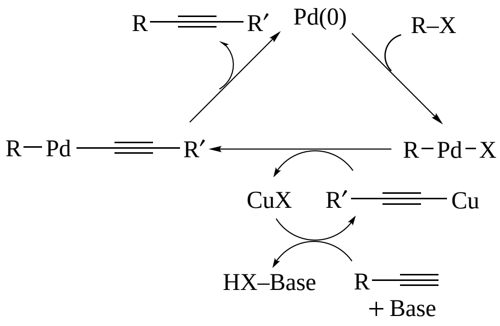

Scheme 2 Dual cycle mechanism for the Sonogashira protocol

originally to the Stephens–Castro reaction.[29] This procedure, developed in 1963, involves the stoichiometric nucleophilic attack of copper acetylides onto aryl iodide substrates. Twelve years later, two independent reports showed that the related palladium-catalyzed olefination reaction (Heck coupling (*see Heck Reaction*)) could be extended to terminal alkynes, albeit at high temperatures.[30,31] Concurrently, Sonogashira disclosed the standard protocol in which the transformation takes place under much lower temperatures in the presence of a copper(I) cocatalyst.[32] While the mechanism of the copper-free protocols probably involves an alkyne insertion/β-hydride elimination pathway (analogous to the Heck coupling reaction), Sonogashira proposed a dual-cycle mechanism for the copper-assisted reaction involving the traditional cross-coupling steps of oxidative addition, transmetallation, and reductive elimination (Scheme 2).[27]

$$\mathrm{R{-}X} + \mathrm{R'{-}{\equiv}} \xrightarrow[\text{Base}]{\text{Pd/Cu}} \mathrm{R'{-}{\equiv}{-}R} \qquad (10)$$

Unlike other cross-coupling reactions, for which the scope has rapidly expanded in recent years, the range of electrophilic substrates that can be used successfully in the Sonogashira protocol is still rather limited. Vinylic substrates (iodides, bromides, chlorides, triflates, and more recently tosylates) typically yield the best results. For aromatic substrates, iodides and triflates are preferred over bromides, which in turn give far better yields than aryl chlorides. This latter aspect of the reaction is particularly frustrating when one considers the recent advances in the activation of aryl chloride substrates for reactivity in other cross-coupling protocols.[33]

3.2 Methodology Development

Another serious drawback to the Sonogashira protocol is the occasional occurrence of side reactions. These include oxidative homocoupling of the terminal alkyne coupling partner, exchange of the aryl groups in the $\mathrm{ArPd(PPh_3)_2X}$ intermediates, and reductive dehalogenation of aryl halide substrates. Furthermore, the greater reactivity of terminal alkynes relative to acetylene renders the synthesis of monosubstituted alkynes problematic utilizing the original conditions. Fortunately, recent efforts have led to significant improvements in methodology and catalyst development that have addressed many of these issues.

The difficulty in synthesizing monosubstituted alkynes was resolved first through the use of protecting groups. For example, trimethylsilylacetylene can be coupled to aryl halides under the standard conditions, after which removal of the trimethylsilyl group results in the monosubstituted alkyne.[34] This route has since become the standard procedure for the synthesis of the terminal acetylene coupling partners in Sonogashira reactions, as these compounds can be subsequently coupled to form asymmetric alkyne derivatives. Alternatively, this process can be streamlined further through the use of a one-pot procedure (e.g. equation 11).[35] Here, the terminal acetylene is generated in situ and subsequently coupled in the same reaction mixture.

$$\begin{array}{c}\mathrm{Ph{-}{\equiv}{-}SiMe_3}\\ +\\ \mathrm{R{-}X}\end{array} \xrightarrow[\substack{\text{Piperidine}\\ \text{THF/MeOH}\\ \mathrm{K_2CO_3}}]{\mathrm{Pd(PPh_3)_4,\ CuI}} \mathrm{Ph{-}{\equiv}{-}R} \qquad (11)$$

As has been the case with the other cross-coupling reactions, a great deal of effort has gone into the development and screening of different ligands in order to improve the scope, reactivity, and selectivity of the catalysts used in the Sonogashira protocol. Tri(*o*-tolyl)phosphine has long been a favorite in the related Heck coupling reaction, and palladium complexes of this ligand have also been successfully applied here. Furthermore, the metallacycle (*see Metallacycle*) (**12**) formed from palladium acetate and this phosphine has also achieved high turnovers (as high as 8000) for Sonogashira coupling reactions with aryl bromides.[36] In another recent development, Buchwald and Fu showed that room temperature Sonogashira reactions can be achieved when tri(*t*-butyl)phosphine-ligated catalysts are used.[37]

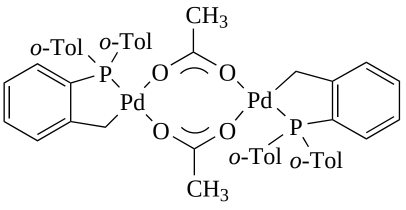

(**12**)

The problem of product contamination with phosphine-derived by-products has led others to investigate the use of phosphine alternatives in Sonogashira coupling reactions. N-heterocyclic carbenes (e.g. (**9**)) have found use in a wide variety of cross-coupling reactions,[18,19] including the Sonogashira protocol. Similarly, Nájera showed that oxime

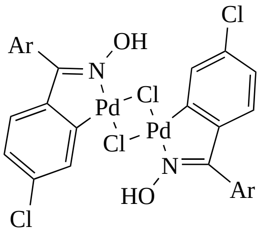

(**13**)

palladacycles (**13**)[38] could successfully catalyze Sonogashira and other coupling reactions.

A number of researchers have tried to tackle catalyst removal/recovery/recycling issues by using systems in which the palladium has been embedded on a solid support. Perhaps the most encouraging example in terms of activation of aryl chlorides is Choudary's heterogeneous layered double hydroxide supported nanopalladium catalyst.[39] This material promotes the coupling of aryl chlorides to phenylacetylene in yields ranging from 60 to 95%.

4 COUPLING OF ORGANIC SUBSTRATES WITH ORGANOZINC REAGENTS

4.1 History and Overview

Building upon the success of the Kumada–Corriu protocol, Negishi and coworkers investigated tandem hydrometallation/cross-coupling methodologies for the stereoselective synthesis of substituted alkenes. The metal that first yielded the sought-after result was aluminum. Hence, the original Negishi coupling entailed a hydroalumination of an alkyne, followed by subsequent coupling of the resulting alkenylalane with an alkenyl halide (equation 12, $M = Al$).[40] The following year, the authors disclosed an analogous hydrozirconation (*see Hydrozirconation*)/cross-coupling protocol (equation 12, $M = Zr$),[41] as well as coupling between aryl halides and organozinc reagents (equation 13).[42] Of the three metals, zinc was found to be the most reactive, the most functional group tolerant, and since then the most widely used.[3,43]

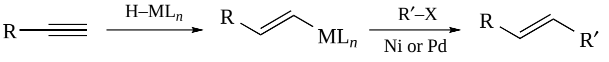

(12)

$$R\text{–}ZnX + R'\text{–}X \xrightarrow{\text{Pd or Ni}} R\text{–}R' + ZnX_2 \qquad (13)$$

The traditional scope for this reaction involved coupling alkenyl or aryl iodides or bromides with aryl, alkenyl, or alkynylzinc halides. However, recent modifications have allowed the scope to be extended to include additional electrophiles (*see Electrophile*) such as aryl and vinyl chlorides, sulfonate esters, aryl ethers, and substrates with various chalconide-leaving groups. Other improvements on couplings with alkynylzinc nucleophiles have made this reaction a viable alternative to the Sonogashira reaction, particularly for vinyl and aryl chloride substrates. Finally, recent modifications in reaction protocols have led to coupling reactions that can stitch together two sp^3-hybridized carbon centers. While these procedures are air and moisture sensitive, they can be performed in the presence of a wide variety of functional groups on either or both of the coupling partners.

4.2 Methodology Development

The Negishi protocol is relatively free of side reactions, the most prevalent being the competing homocoupling of two substrate-derived groups, and β-hydrogen elimination (*see β-Hydride Elimination*) of alkene from intermediate alkylmetal complexes. Head-to-head comparisons have shown coupling with zinc reagents to be the most active of the commonly used cross-coupling protocols,[43] typically occurring in minutes at room temperature or even below. As a result, many of the catalyst-derived side reactions that can be problematic with other protocols do not compete with the desired coupling process here.

The palladium catalyst used in the original example was $Pd(PPh_3)_2$, formed in situ by treating $PdCl_2(PPh_3)_2$ with diisobutylaluminum hydride prior to adding the reagents. However, simple $Pd(PPh_3)_4$ was later found to yield equivalent results. For typical sp^2–sp^2 coupling procedures, this system is perfectly sufficient. However, for coupling of sp^2 substrates with alkylzinc reagents, palladium complexes with dppf (**2**) were found to be more active and more selective for the desired product.[7] Other phosphines that have seen more recent use include tri(*tert*-butyl)phosphine and tri(cyclopentyl)phosphine, for the coupling of aryl chloride[33] and alkyl halide[44] substrates, respectively. Nonphosphine-based palladium catalyst systems, such as Li's phosphinous acid ligands (e.g. (**11**)),[45] have also been utilized, as have palladacycle (**12**)[36] and ligandless systems without added phosphine.

As was the case with the Kumada–Corriu protocol, a significant amount of research has been devoted to the development of asymmetric Negishi coupling reactions.[10] In fact, for the standard asymmetric coupling reaction (equation 14), the enantioselectivity for the reaction performed with the organozinc reagent (86% ee) was significantly higher than that attained with the Grignard reagent (equation 5, 65% ee). This increased enantioselectivity for zinc relative to magnesium has been seen in other asymmetric coupling reactions,[12] although it is not universal. The best enantioselectivity for this reaction (93%) was realized utilizing the zinc reagent with phosphine (**4**) ($R = Me$).[10] A significant improvement in the asymmetric Negishi reaction was the discovery that unlike their magnesium counterparts, configurationally stable chiral alkylzinc reagents can undergo cross coupling with retention of configuration (equation 15).[46]

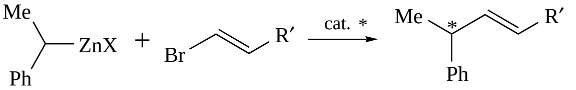

(14)

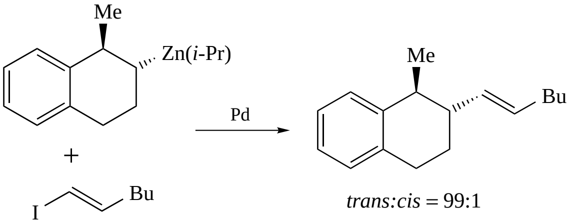

trans:cis = 99:1

(15)

Another recent improvement to the Negishi protocol has been the extension of the scope to include alkyl substrates. Knochel showed that coupling reactions between alkyl substrates and alkylzinc reagents could be performed if they were run in the presence of an electron-poor alkene such as p-trifluoromethylstyrene.[47] The authors suggested that the alkene serves as a π-acid, removing electron density from the catalyst center, and thereby increasing the rate of reductive elimination relative to possible side reactions. Finally, Fu and coworkers approached the problem by screening different catalysts. They noted that a palladium system with the electron-rich tri(cyclopentyl)phosphine ligand was optimal for the coupling of primary alkyl substrates (halides, tosylates),[44] while a nickel system with the ligand Pybox (**14**) worked best for the coupling of secondary alkyl bromides and iodides (equation 16).[48]

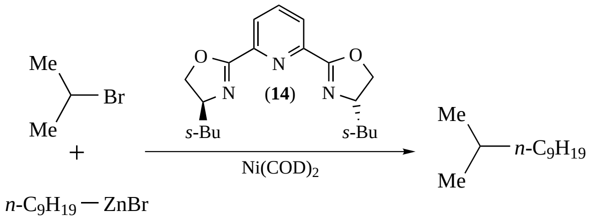

(16)

5 COUPLING OF ORGANIC SUBSTRATES WITH ORGANOTIN REAGENTS

5.1 History and Overview

The development of the reaction between an organic electrophile (*see Electrophile*) and an organotin reagent (equation 17)[49–51] was arguably the most significant single step forward in cross-coupling methodology. While organozinc and Grignard reagents are incompatible with acidic and some electrophilic functional groups, organotin reagents show a remarkable functional group tolerance, due largely to the relative nonpolarity of the C–Sn bond. Eaborn set the groundwork for this reaction by showing in 1976 that a group could be transferred from a tin reagent to an organic halide in the presence of a palladium catalyst (equation 18).[52] The first carbon–carbon bond forming reaction involving tin nucleophiles was performed by Kosugi in 1977,[53] a year prior to Stille's first paper on the coupling of acyl chlorides with organotin reagents.[54] Nevertheless, it was Stille who developed the reaction and performed the seminal mechanistic experiments through the 1980s.

$$\text{R–X} + \text{R}'\text{–SnR}''_3 \xrightarrow{\text{catalyst}} \text{R–R}' + \text{X–SnR}''_3 \qquad (17)$$

$$\text{Ar–X} + \text{R}''_3\text{Sn–SnR}''_3 \xrightarrow{\text{Pd}} \text{Ar–SnR}''_3 + \text{X–SnR}''_3 \qquad (18)$$

The traditional scope[55] of the reaction included acyl, aryl, vinyl, benzyl, and allyl substrates with bromide, iodide, and triflate leaving groups. More recently, the scope has been extended to include alkyl halides and substrates with chloride, fluoride, fluorosulfonate, nonaflate (nonafluoro-1-butanesulfonate), and sulfonium salt leaving groups. Even metal halides can be activated during this protocol, opening the door for the formation of carbon–metal bonds mediated by palladium catalysis.[56] Thus, the Kosugi–Stille protocol has come a long way since its early development in the late 1970s. However, it is still not without its problems, and efforts to improve this methodology are continually being pursued.

5.2 Methodology Development

Two of the most significant drawbacks of the Kosugi–Stille protocol are direct consequences of the reaction's sought-after mildness. Often the reactions are quite sluggish, which necessitates that they be carried out at elevated temperatures. Also, the nonpolarity of the C–Sn bond renders the transmetallation step rate determining. Thus, side reactions promoted by RPdL_2X species,[11] the resting state of the triphenylphosphine-based catalysts most commonly used, can have a particularly detrimental effect on the yield and purity of the desired product. Most notable among these are the alkyl–aryl (equation 19, R = alkyl)[57] and aryl–aryl (equation 19, R = aryl)[58,59] exchange reactions. When this occurs during the catalytic cycle, phosphine-derived rather than substrate-derived groups are incorporated into the cross-coupled product mixture. Furthermore, oxidative homocoupling of the tin reagents, participation of the tin-derived dummy ligands (R″ in equation 17), and cine substitution of α-substituted vinyl stannanes are other prevalent side reactions endemic to this protocol.

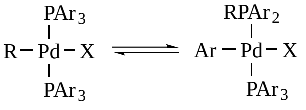

$$\text{R}-\underset{\text{PAr}_3}{\overset{\text{PAr}_3}{\text{Pd}}}-\text{X} \rightleftharpoons \text{Ar}-\underset{\text{PAr}_3}{\overset{\text{RPAr}_2}{\text{Pd}}}-\text{X} \qquad (19)$$

In order to improve the activity and selectivity of this reaction, a veritable witches brew of additives has been incorporated into the standard procedure. Chief among these is lithium chloride. Originally, this was employed by Stille in coupling reactions of vinyl triflates in order to prevent the formation of a catalytically inactive Pd species that was observed via ^{31}P NMR. However, the more recent use of LiCl to promote couplings that do not involve triflates**[60]** suggests that the role of this additive may be a bit more complicated. One possibility is that the chloride coordinates to the Sn, renders it hypervalent (*see Hypercoordination*), and thus, more reactive toward transmetallation.**[60]** Others have used tetrabutylammonium fluoride in this same capacity, given the known tendency of fluoride to coordinate to tin.

Another common additive is cuprous iodide, the role of which appears to be twofold.**[61]** Firstly, it provides an alternate pathway involving transmetallation first from tin to copper and then from copper to palladium, both of which appear to be faster than the original tin to palladium process. Secondly, it can act as a scavenger for excess triphenylphosphine, which is known to retard the transmetallation step of this cross-coupling reaction.

One other significant drawback to the Kosugi–Stille protocol is that it generates a stoichiometric amount of a toxic trialkyltin halide by-product that has to be removed from the product mixture. One development geared toward mitigating this problem is Maleczka's tandem hydrostannylation/Kosugi–Stille coupling procedure in which tin is used in catalytic amounts (Scheme 3).**[62]** Here, the stoichiometric reagents are a vinyl halide and an alkyne, the latter of which is hydrostannylated with trimethyltin hydride to form the vinylstannane. At this point, the cross coupling yields the product and trimethyltin halide, which is subsequently reduced by carbonate and poly(methylhydrosiloxane) (PMHS) back to the tin hydride. By employing this procedure, tin usage can be reduced by 96%.

Some of the most significant improvements in catalyst development were the discoveries of alternative palladium ligands made by Farina in the early 1990s. In particular, tri(2-furyl)phosphine (**15**) and triphenylarsine proved to be far superior to triphenylphosphine when used as ligands in palladium-catalyzed Kosugi–Stille reactions.**[63]** Perhaps just as importantly, this discovery showed that significant improvements in methodology could be achieved by tailoring the structure of the ancillary ligands bound to the catalytic center. This in turn opened the gates for a flood of research on the synthesis and screening of ligands designed to improve the protocol further. A few notable examples include Elsevier's rigid bidentate imine ligands (**16**),**[64]** Mathey's tetraphosphole macrocycle (**17**),**[65]** and Shirakawa's iminophosphine ligands (**18**).**[66]** Palladacycles such as (**12**),**[36]** (**13**),**[38]** and (**19**) have also been successfully applied, the last of which produced turnover numbers as high as 830 000 in the coupling of 4-bromoacetophenone with phenyltributyltin.**[67]** In terms of activating aryl chloride substrates,**[33]** trialkylphosphines such as tri(t-butyl)phosphine have seen the most success. Recent catalyst systems based upon N-heterocyclic carbene ligands**[18,19]** have also been applied in the Kosugi–Stille protocol, with (**9**) being successful at promoting the reaction with aryl bromides and chlorides.

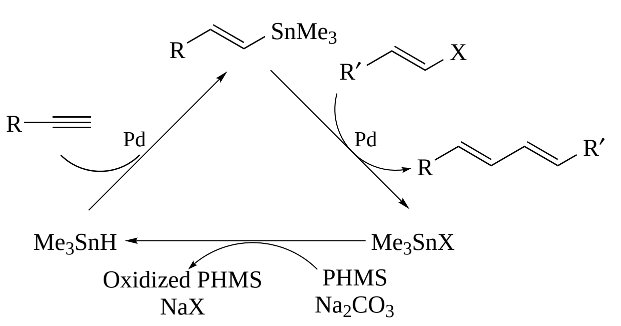

Scheme 3 One-pot tandem hydrostannylation/Kosugi–Stille coupling procedure that is catalytic in tin

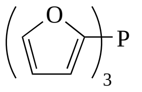

(**15**)

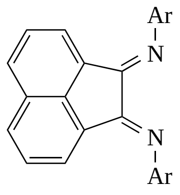

(**16**)

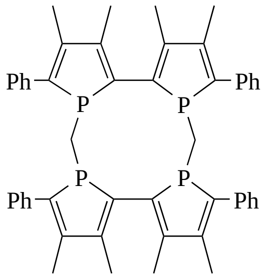

(**17**)

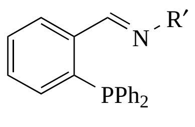

(**18**)

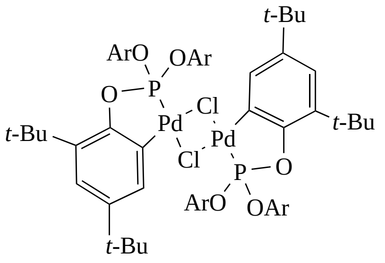

(**19**)

5.3 Recent Mechanistic Insights

Of the different cross-coupling protocols, the Kosugi–Stille reaction is the one for which the mechanism has been studied in the greatest detail. Indeed, our basic picture (Scheme 1) for the mechanism of cross-coupling reactions in general is due in no small part to the extensive mechanistic work performed on this reaction by Stille and coworkers through the early 1980s.**[55]** As of 1993, the least-understood step of the catalytic cycle was the transmetallation reaction. Consequently, most of the recent mechanistic work has been done on this final rate-determining step in the catalysis.

This recent interest was piqued by the observation of Louie and Hartwig[68] that the rate of transmetallation was inversely dependent upon the concentration of added phosphine, suggesting a mechanism involving predissociation of this ligand. This prompted Casado and Espinet to study the kinetics of the coupling reaction between an aryl iodide and vinyltributyltin.[69] A large, negative entropy of activation led them to propose a mechanism involving an associative substitution in which the nucleophile directly replaces the ancillary ligand (Scheme 4). Such a mechanism is analogous to an S_E2(cyclic) substitution in which the electrophilic Pd accepts electrons from the front lobe of the Sn–C bonding orbital (Scheme 5). This implies that a stereogenic carbon bound to tin would undergo transmetallation with retention of configuration, in line with certain examples in the literature. However, other instances have been shown to proceed with inversion of configuration in line with an S_E2(open) mechanism (Scheme 5) in which the electrophilic palladium accepts electrons from the back lobe of the Sn–C bonding orbital. In a later study,[70] Espinet and coworkers showed that the key to this discrepancy was the presence of halide in the coordination sphere of the palladium. When aryl triflates were coupled to tin nucleophiles in the absence of halide, the authors found evidence for an S_E2(open) pathway. However, when LiCl was added to the reaction mixture, the cross coupling reverted to the S_E2(closed) mechanism.

Other efforts in the mechanistic study of the Kosugi–Stille protocol have been geared toward directly observing and/or isolating the transmetallation products. This is a nontrivial undertaking since the subsequent reductive elimination is generally rapid. However, Echavarren and coworkers were able to synthesize complex (**20**) which cleanly transmetallated to complex (**21**), isolation of which was made possible by its reluctance to form the three-membered ring upon reductive elimination (equation 20).[71] Lo Sterzo showed that the transmetallation product formed between the reaction of tributyltinacetylides with metal iodide complex (**22**) could also be isolated and characterized (equation 21).[56] Furthermore, kinetics experiments revealed that this process similarly followed two different pathways analogous to the S_E2(open) and S_E2(closed) mechanisms mentioned above.

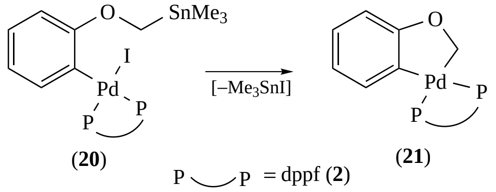

(20)

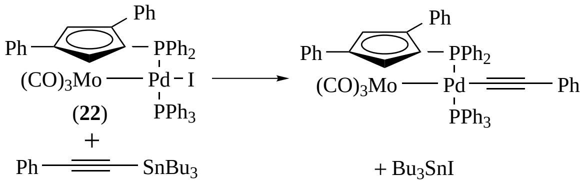

(21)

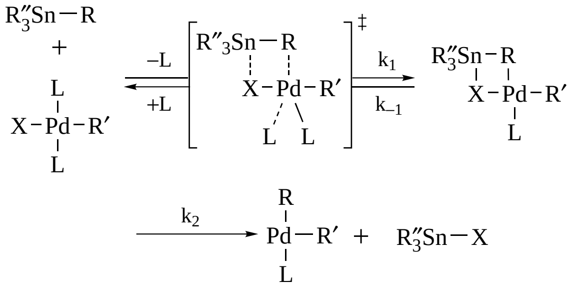

Scheme 4 Associative substitution mechanism for transmetallation

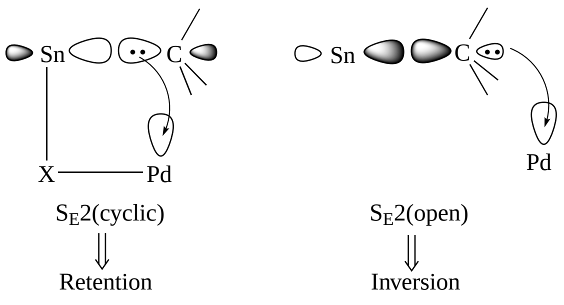

Scheme 5 S_E2(cyclic) vs. S_E2(open) transmetallation pathways

6 COUPLING OF ORGANIC SUBSTRATES WITH ORGANOBORON REAGENTS

6.1 History and Overview

The first example of the use of boron reagents in palladium-catalyzed coupling reactions was supplied in 1975 by Heck, who showed that alkenyl boronic acids could serve as substrates (in lieu of alkenyl halides) in the analogous Heck coupling reaction (*see Heck Reaction*) with alkenes.[72] However, early attempts by Negishi to involve boranes in catalytic cross-coupling reactions were not realized, despite his success at utilizing the analogous aluminum reagents.[40] In 1979, Miyaura and Suzuki noted that the catalytic cross coupling between aryl halide substrates and alkenyl boranes could be achieved if the reaction were run in the presence of a stoichiometric amount of base, such as hydroxide or alkoxide (e.g. equation 22).[73] This procedure, now known as the Suzuki–Miyaura reaction,[74–79] provided the advantages of the Kosugi–Stille protocol, namely, functional group tolerance and mildness of reaction conditions, without its chief downside, the resulting formation of toxic tin by-products.

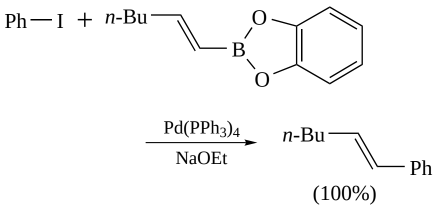

(22)

The traditional scope of this reaction entailed the use of alkenyl, alkynyl, or aryl bromides or iodides coupled with aryl or alkenyl boronic acids or esters. More recently, the range of substrates has been expanded to include aryl chlorides, activated aryl fluorides, and sulfonate esters, as well as iodonium, trimethylammonium, diazonium, and sulfonium salts. Furthermore, the development of bicyclic alkyl boron reagents enabled the transfer of alkyl groups in this reaction.[74] Finally, with new modifications that allow for the coupling of alkyl substrates with β-hydrogens,[80] it is now possible to couple virtually any imaginable combination of organic electrophile and organoboron reagent.

6.2 Methodology Development

The conditions for the traditional methodology involved performing the reactions in an arene solvent (benzene or toluene) along with aqueous base and tetrakis(triphenylphosphine)palladium(0) as the catalyst precursor. However, several side reactions resulting in reduced yield of products can also occur under these conditions. Chief among these is the hydrolytic deboronation of the boron reagent (equation 23), which has long been known to be catalyzed by base and metal cations, such as cadmium, magnesium, and nickel.[81] Aryl–aryl exchange[58,59] between Pd- and P-bound aryl groups can result in phosphine-derived coupling products contaminating product mixtures, particularly when the reaction is performed with electron-rich aryl substrates. Reductive dehalogenation of the substrate and oxidative homocoupling of the boron reagents have also been noted during this protocol.

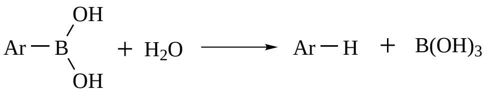

$$\text{Ar}-\text{B}(\text{OH})_2 + \text{H}_2\text{O} \longrightarrow \text{Ar}-\text{H} + \text{B(OH)}_3 \qquad (23)$$

The last two side reactions are fairly easy to control. The reductive dehalogenation appears to be caused by the concomitant oxidation of a primary alcohol (either from the boronic ester or from an alcohol cosolvent).[82] Consequently, it can be minimized simply by utilizing boronic esters from tertiary alcohols (such as pinacol) and by avoiding the use of alcohol cosolvents. Since oxidative homocoupling is facilitated by ambient oxygen, the impact of this side reaction can be reduced by rigorously excluding oxygen from the cross-coupling mixtures. The other two side reactions, however, can be more problematic. Consequently, a great deal of effort has gone into optimizing the various parameters of this protocol (solvent, base, catalyst, etc.) so as to minimize their effect on product yields.

As there is no clear consensus on the best solvent to use, this unfortunately remains a parameter that should be screened for a given reaction. Water-free protocols have been developed, and they can be useful for moisture-sensitive substrates and for minimizing the competing protodeboronation.[82] However, there is evidence that some water is required in order to facilitate the cross coupling,[83] though the water of hydration typically present in the inorganic base appears to be sufficient.[82] Other research has been devoted toward the other extreme, the development of all-aqueous Suzuki–Miyaura reactions.[84] Water-soluble substrates such as carboxylic acids and phenols react cleanly at room temperature, while water-insoluble substrates can be coupled successfully by either increasing the temperature to 100 °C or adding a water-miscible organic cosolvent such as acetone or DMF. Further work has shown that a surfactant can replace the organic cosolvent,[85] and that the higher temperatures can be achieved more efficiently (allowing successful reactions in minutes) through the use of microwave irradiation.[86]

The fact that stronger bases speed up both the coupling and the hydrolytic deboronation means that the choice of base is not always obvious. Although aqueous carbonate is the one most commonly used, stronger alkoxide bases appear to yield the best results for sterically hindered boronic acids.[87] For base-sensitive substrates, bicarbonate can be used successfully when THF is the organic cosolvent.[88] However, this base is less successful when employed with mostly nonaqueous reaction conditions.[83] On the other hand, fluoride, an even weaker base, appears to work well with both aqueous and nonaqueous protocols.[89]

By far the greatest amount of research, in terms of methodology development, has gone into the search for more active and more general catalyst systems that promote fewer side reactions. Early on, researchers noted that the yields of typical Suzuki–Miyaura reactions could be improved by replacing the triphenylphosphine-based catalysts with those using sterically hindered triaryl phosphines such as tris(2-methoxyphenyl)phosphine and tri(*o*-tolyl)phosphine. The success of these systems can be explained by the fact that aryl–aryl exchange is inhibited by steric hindrance close to the metal.[59] More recently, Buchwald and coworkers discovered that electron-rich dialkylphosphinobiphenyl ligands (e.g. (**23**)) could perform nonaqueous Suzuki–Miyaura reactions at room temperature on not only aryl bromide substrates, but with nonactivated aryl chlorides as well.[90] Concurrently, Fu and coworkers showed that simple sterically hindered trialkylphosphines such as tri(*t*-butyl)phosphine and tri(cyclohexyl)phosphine could form highly active catalysts that also coupled aryl chloride, bromide, and triflate substrates under mild conditions.[91] Of particular import with this system is the phosphine to palladium ratio. Interestingly, the authors noted that $Pd[P(t\text{-Bu})_3]_2$ was not as effective as a catalyst formed in situ from $Pd_2(dba)_3$ and $P(t\text{-Bu})_3$ with one phosphine per palladium atom. Other bulky trialkylphosphines based upon an adamantane framework (e.g. (**24**)) have been similarly developed and used in Suzuki–Miyaura reactions.[92]

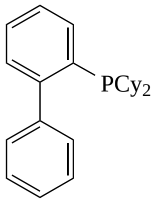

(**23**)

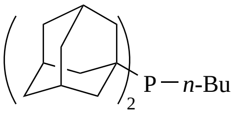

(**24**)

Efforts have also gone toward new strategies to enforce the optimal 1:1 P to Pd ratio. Bei, Guram, and coworkers showed that P–O chelating ligand (**25**) forms a 1:1 P to Pd complex upon reaction with $Pd(dba)_2$ (equation 24).[93] However, the dibenzylidineacetone ligand still present has been shown to hinder the reactivity of palladium toward oxidative addition.[4] In support of this, Beller pointed out that catalyst (**26**) is more active than those formed in situ from the phosphine and $Pd_2(dba)_3$.[94] Similarly, Hartwig's Pd(I) dimer (**27**), with one phosphine per palladium and no supporting alkene ligands of any kind, is one of the most active catalysts screened to date.[95]

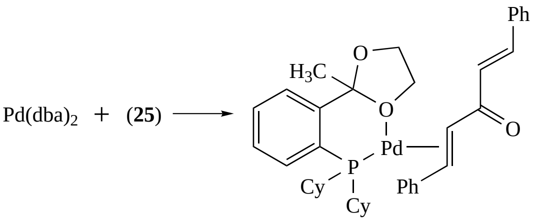

(24)

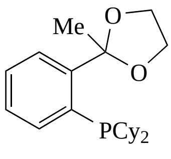

(**25**)

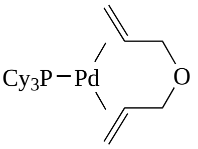

(**26**)

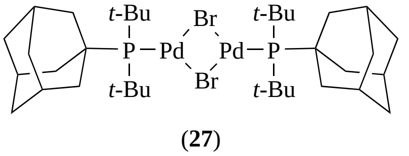

(**27**)

Significant research has also been devoted to extending this electron-rich sterically hindered ligand strategy to nonphosphine-based catalysts. In particular, N-heterocyclic carbene ligands such as (**9**) have seen increasing use in Suzuki coupling reactions of various substrates.[18,19] Li's phosphinous acid catalysts also fall into this category,[45] as do other systems based upon phosphite[67] and diazabutadiene[19] ligands.

Another strategy for catalyst development was based upon the discovery of Beller and coworkers, that the palladacycle (**12**) could catalyze the nonaqueous Suzuki coupling of aryl bromide and chloride substrates with efficiencies greater than what had been observed up until that time.[96] Since then, palladacycles based upon a variety of functional groups have been developed and screened in Suzuki–Miyaura coupling reactions.[97] Particularly noteworthy is the observation of Bedford and coworkers that the most active catalysts are obtained from single phosphine adducts of these palladacycles.[98] They surmise that the true catalyst is a monoligated Pd–L species formed in situ from the adducts under the reaction conditions. Thus, once again the importance of the proper L:Pd ratio becomes apparent in the optimal catalyst design for this protocol.

Considering all the work that has gone into catalyst development, it is interesting that excellent activities can be obtained when simple palladium salts are used as catalysts. This 'ligandless' methodology for aqueous Suzuki–Miyaura coupling reactions was first disclosed by Bumagin, Bykov, and Beletskaya in the late 1980s, and summarized in a more recent full paper by Bumagin and Bykov.[84] Wallow and Novak demonstrated that simple palladium acetate is significantly more efficient than triphenylphosphine-based catalysts, and that the ligandless methodology works best in water, with a water-miscible cosolvent such as acetone.[99] In terms of how these systems are able to function, Reetz has provided evidence that palladium nanoparticles are responsible for the actual catalytic activity.[100]

In order to address catalyst separation, recovery, and recycling issues, a great deal of work has been devoted toward the development of heterogeneous catalyst systems. One obvious strategy is to exploit the heterogeneity already present in the traditional protocol, that is, to force the palladium to partition into the aqueous phase of the reaction. Genêt recently demonstrated that the water-soluble triarylphosphine (**28**) can promote efficient Suzuki–Miyaura reactions from which it was possible to recycle the catalyst up to three times.[101] Water-soluble versions of the newly developed nonaqueous catalysts have also been investigated. Miyaura demonstrated the effectiveness of a carbohydrate-substituted Buchwald phosphine (**29**),[102] while Shaughnessy has shown the utility of water-soluble versions of hindered, electron-rich trialkylphosphines.[103] Finally, heterogeneous catalysts in the form of, for example, palladium nanoparticles,[104] have also been extensively investigated.

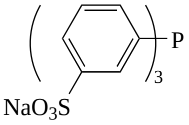

(**28**)

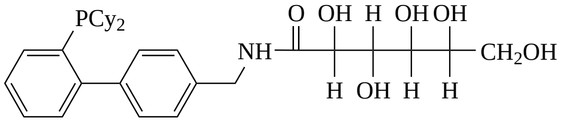

(**29**)

6.3 Recent Mechanistic Insights

Most of the mechanistic work on this reaction has been devoted to determining the role of the base. Its most obvious function would be to complex the Lewis-acidic boron reagent, rendering it nucleophilic and thus activating it toward transmetallation. However, Miyaura, Suzuki, and coworkers noted that an electron-rich tetracoordinate boronate complex was less reactive than a trivalent boronic ester.[105] From this, they surmised that the role of the base was not to activate the boron toward transmetallation, but rather to transform the palladium halide intermediate to the hydroxide or alkoxide species, which would then be more reactive toward boron. However, in a mass spectrometry study of a reaction between a pyridyl halide substrate and an aryl boronic acid, Aliprantis and Canary saw no evidence of palladium hydroxide or alkoxide intermediates, despite observing signals in the mass spectra assignable to every other palladium intermediate of the proposed catalytic cycle.[106]

In a more recent study, Matos and Soderquist noted that trialkylboranes such as (**30**) reacted much more quickly than alkylborinates (e.g. (**31**)),[107] and they explained this with the fact that the former can complex hydroxide, while the latter cannot. This led the authors to speculate that the two boron reagents reacted via two different mechanisms (Scheme 6). For species such as (**30**), which are capable of forming nucleophilic hydroxide complexes, the top cycle is active; while, for species such as (**31**), the bottom cycle – analogous to that proposed by Miyaura and Suzuki – predominates.

To complicate matters further, Smith and coworkers noted that for reactions with arylboronic acid coupling partners, the rate-determining step for aryl bromide substrates was oxidative addition, while for aryl iodide substrates it was transmetallation.[83] Thus, the exact mechanism for a particular coupling reaction depends upon the substrate, the activity of the coupling partner, and doubtless the conditions under which the reaction is performed. Finally, one further observation[107] showed that coupling with chiral alkyl boron reagents proceeds with retention of configuration, suggesting that transmetallation occurs via an S_E2(cyclic) pathway as described above in the Stille–Kosugi protocol.

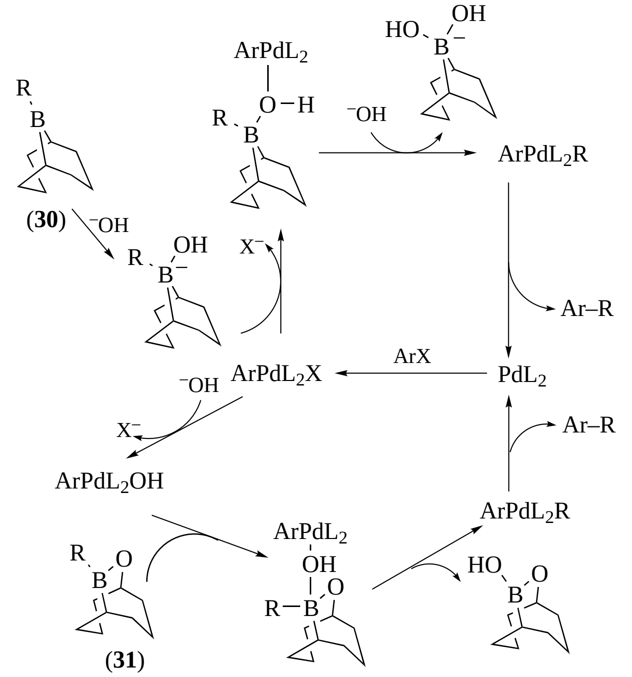

Scheme 6 Possible mechanistic cycles for Suzuki–Miyaura reactions

7 COUPLING OF ORGANIC SUBSTRATES WITH ORGANOSILICON REAGENTS

7.1 History and Overview

The first cross coupling of organosilicon reagents, which in this case were in the form of organopentafluorosilicate salts,[108] was reported by Kumada in 1982. Soon afterwards, Kikukawa[109] and Hallberg[110] independently disclosed the coupling of alkenyltrimethylsilanes with aryl diazonium salts and aryl iodides, respectively. However, these reactions were not stereoselective, leading the authors to postulate a mechanism involving carbometallation (*see Carbometalation*) rather than the transmetallation more typical of cross-coupling reactions. In 1988, Hiyama showed that this transformation could occur under much milder conditions (50 °C) with retention of stereochemistry, when performed in the presence of a source of fluoride (e.g. equation 25).[111] This idea of activating silicon for cross coupling by rendering it pentavalent upon treatment with a base is a central theme to what has become known as the

Hiyama protocol.[112–115]

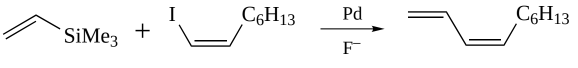

(25)

Traditionally, this reaction could be performed on alkenyl, alkynyl, or aryl substrates with iodide, bromide, or triflate leaving groups. However, recent methodology improvements have expanded the scope to include aryl chlorides and nonaflates. Furthermore, with the observation that functionalized alkyl groups can be transferred from silicon,[116] a wide array of cross-coupling procedures can now be performed. Other advantages of this protocol include excellent functional group compatibility, the low cost of the silicon reagents, and the lack of toxic byproducts.

7.2 Methodology Development

The majority of the methodological improvements to this reaction have been in the development of new organosilane coupling partners. This research was spurred by the discovery that organofluorosilanes (**32**) react more quickly than the nonfluorinated analogs.[112] Interestingly, while monofluorosilane reagents ($n = 2$) work best for the transmetallation of alkenyl groups, aryl silanes require two fluorine atoms ($n = 1$) for effective coupling to occur. The analogous chlorosilanes can also be effective coupling partners, provided that they are treated with fluoride beforehand or used in the presence of hydroxide. A more recent development allows for the coupling of alkyl groups from the silicon.[116] Here three fluorine atoms ($n = 0$) are required to promote the reaction. Similarly, Ito and coworkers disclosed that alkenylalkoxysilanes (**33**) were also effective coupling partners, proving that the electronegative atoms other than halogens could serve to activate the silicon.[117] Shibata[118] and DeShong[119] have since shown that arylalkoxysilanes could be used to synthesize biphenyl derivatives upon coupling with aryl halide substrates.

$R_T{-}SiMe_nF_{(3-n)}$ $\quad$ $R_T{-}SiMe_n(OR)_{(3-n)}$

(**32**) (**33**)

In 1999, Denmark disclosed that silacyclobutane derivatives (**34**) were very effective coupling partners for the transfer of alkenyl and aryl groups.[115] The original theory was that the release of strain energy upon treatment with fluoride to make the silicon pentacoordinate is what made these species so active. However, later studies showed that under the conditions of the cross-coupling reactions, silacyclobutanes formed silanols (**35**) and disoloxanes (**36**), which themselves proved to be efficient transmetallating species. Finally, Yoshida and coworkers have developed the cross-coupling chemistry of 2-pyridylsilane derivatives (**37**).[120] Of interest here is, the fact that conditions can be tailored so as to toggle between either the Heck or Hiyama coupling of these compounds (equation 26).

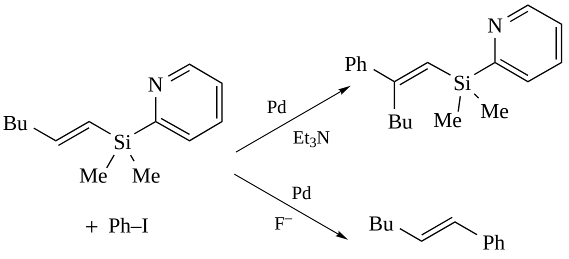

(26)

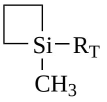

(**34**)

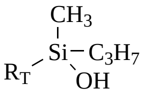

(**35**)

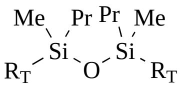

(**36**)

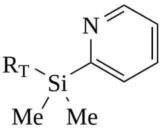

(**37**)

R_T = Group that is transferred to palladium

As was the case with the other coupling protocols, side reactions can limit the yields of the desired products. In particular, reductive dehalogenation of aryl substrates, protodesilylation of the organosilicon reagent, homocoupling of one or both components, cine substitution, and participation of the dummy silicon ligands have all been observed in Hiyama coupling reactions. Again, as with the other protocols, different catalyst systems have been utilized in order to minimize the impact of these competing processes.

In Hiyama's original publication, the major catalyst system consisted of the allylpalladium(II)chloride without added ligands.[111] Consequently, the majority of the silicon cross-coupling reactions have been performed with this or similar ligandless protocols. However, researchers have occasionally had success in improving the reaction by performing it with added triphenylphosphine, triphenylarsine, triethylphosphite, or tri(*o*-tolyl)phosphine ligands. A more recent development is that aryl chloride substrates can participate if catalyst systems based upon trialkylphosphines, Buchwald's ligand (**23**), or N-heterocyclic carbenes (e.g. (**9**)) are employed.[33]

7.3 Recent Mechanistic Insights

Information on the transmetallation step was obtained by monitoring the coupling of optically active silane derivatives (equation 27).[112] At lower temperatures, the reaction proceeds with the retention of configuration, suggesting an S_E2(cyclic) transition state, while higher temperatures result primarily in inversion, in line with an S_E2(open) pathway. Also, Echavarren and coworkers were able to monitor the transmetallation step directly using their 'frustrated coupling cycle' strategy (equation 28).[121] Intriguingly, the platinum analog transmetallated without the addition of a fluoride activator.

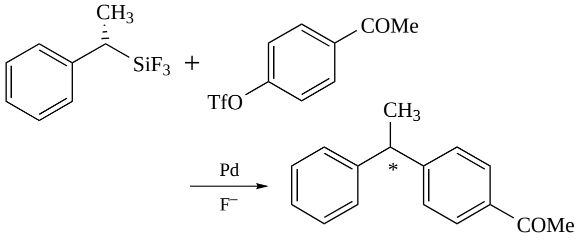

(27)

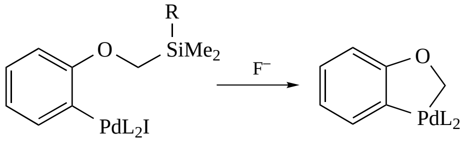

(28)

8 CATALYTIC AMINATION OF ORGANIC ELECTROPHILES (*See Electrophile*)

8.1 History and Overview

Arguably the most significant advance of the past 10 years in the field of cross-coupling reactions has been the development of the catalytic amination of organic electrophiles.[122,123] Despite the relative youth of this procedure, its history can be traced back to the turn of the previous century with the venerable Ullmann reaction, which entails heating an amine with aryl halide in the presence of copper powder and base. However, the spark that truly ignited the development of this protocol came in 1983, with Kosugi's coupling of aryl bromides with tin amides (equation 29).[124]

$$\mathrm{Ph{-}Br} + \mathrm{Bu_3Sn{-}NEt_2} \xrightarrow[{[-\mathrm{Bu_3SnBr}]}]{\mathrm{Pd}} \mathrm{Ph{-}NEt_2} \qquad (29)$$

A tantalizing observation made by Kosugi was that triphenylphosphine-based catalysts were far inferior to $PdCl_2(o\text{-tolyl}_3P)_2$ for the coupling of aryl halides with tin amides.[124] In 1994, the groups of Buchwald and Hartwig began publishing work in which this catalyst was used as a starting point to improve vastly the scope and utility of this reaction. The true breakthrough came the following year when both groups concurrently disclosed a procedure entailing the direct reaction of an amine with an aryl bromide in the presence of base (sodium *tert*-butoxide[125] or lithium hexamethyldisilazide[126]) and a palladium tri(*o*-tolyl)phosphine catalyst (equation 30). This was a significant improvement in that it provided relatively mild reaction conditions and eliminated the concomitant formation of toxic tin by-products.

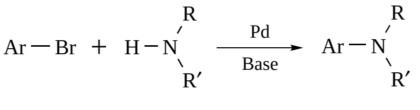

$$\mathrm{Ar{-}Br} + \mathrm{H{-}NRR'} \xrightarrow[\text{Base}]{\text{Pd}} \mathrm{Ar{-}NRR'} \qquad (30)$$

The original procedure involved the coupling of aryl bromides with secondary amines. However, since then the scope has been expanded to include substrates such as aryl iodides, chlorides, fluorides, triflates, tosylates, nonaflates, iodonium salts, and even boronic acids. While the reaction has not been extensively utilized with vinyl or alkynyl substrates, it can be performed with various heteroaryl halides. Similarly, numerous types of nitrogen-containing coupling partners, including primary amines, imines, various azoles, lactams, and simple amides, can now be used in this reaction.

8.2 Methodology Development

Despite the success of the original Hartwig–Buchwald protocol, this procedure was not without its drawbacks. The scope was limited to aryl bromide substrates and secondary amine coupling partners, and the requirement of a strong *tert*-butoxide or amide base meant that substrates with base-sensitive functional groups would not be compatible. While this latter constraint has since been obviated by the discovery that weaker bases such as Cs_2CO_3 can promote the reaction, the extension of the scope has required some sophisticated catalyst development (vide infra).

A second issue is that catalytic aminations are plagued by several notable side reactions. Most prevalent among these is β-hydride elimination (*see β-Hydride Elimination*) of imine from the intermediate Pd-amido complex (equation 31). This reaction also produces a Pd–H species, which can then reduce the substrate to form arene, the generation of which can be considered a second side reaction. Furthermore, aryl–aryl exchange has also been noted in amination reactions, and, for the monoarylation of primary amines, by-products caused by overarylation (equation 32) to form tertiary amines pose an additional difficulty.

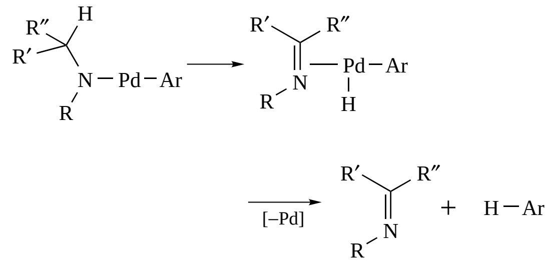

(31)

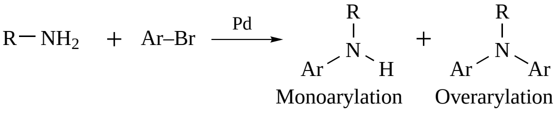

(32)

In order to tackle the β-hydrogen elimination problem, researchers took a page from the methodology developed for the Kumada–Corriu protocol. Buchwald and Hartwig concurrently divulged that this side reaction could be minimized when aminations were performed with the chelating ligands BINAP (**38**)[127] and dppf (**2**).[128] These encouraging results then led researchers to experiment with other chelating phosphines, such as Xantphos (**39**),[129] and DPEphos (**40**)[130] which proved to be particularly active. Others have investigated ligands that chelated through atoms besides phosphorus, again with impressive results. In particular, (**7**) was shown to be extremely active and selective for the arylation of acyclic secondary amines,[131] a transformation that had previously proved troublesome.

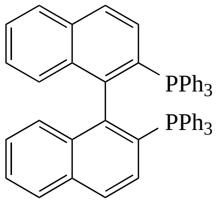

(**38**)

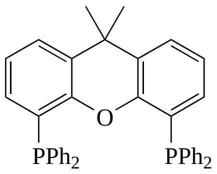

(**39**)

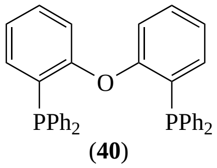

(**40**)

While these investigations were occurring, researchers in Japan showed that sterically hindered electron-rich trialkylphosphines such as tri(*tert*-butyl)phosphine[132] were extremely effective at promoting the amination of aryl halides, including aryl chlorides. Afterwards, Hartwig disclosed that the best activity was obtained when the tri(*tert*-butyl)phosphine to palladium ratio was strictly held to 1:1 (rather than the 2:1 or greater typically seen with other types of phosphines), and that the scope of this catalyst system could be expanded to include the coupling of a variety of aryl halide substrates with various nitrogen coupling partners.[133] This strict ratio can be enforced through the use of Pd(I) dimers such as (**27**), which promote the rapid amination of aryl chlorides and bromides at room temperature.[95]

The next generation of catalysts combined the structural elements discussed in the previous paragraphs. In particular, Hartwig noted that dppf analog (**41**) promoted room temperature amination of aryl bromides and iodides, and elevated-temperature aminations of aryl chlorides and tosylates.[134] Soon afterwards, Buchwald reported similar activity with (**42**), which incorporated chelation through a nitrogen atom.[135] Guram and coworkers also reported effective amination of chloride substrates with (**25**), which similarly promotes chelation through a nearby oxygen atom.[136] A significant step forward was Buchwald's development of phosphinobiphenyl ligands (e.g. (**23**)) which provide for catalytic activity and generality in scope similar to tri(*tert*-butyl)phosphine with the additional advantage of being air stable.[137]

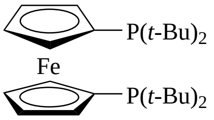

(**41**)

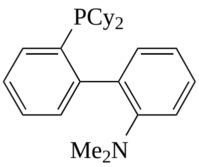

(**42**)

As was the case in the other coupling reactions, nonphosphine-based catalysts have also been applied in amination chemistry. In particular, N-heterocyclic carbenes such as (**9**) have provided successful results for a wide variety of amination transformations.[18,19] Similarly, catalysts based upon phosphinous acid ligands (e.g. (**11**)) have also found success in the amination of aryl chloride substrates.[138]

The amination of aryl chlorides was first accomplished utilizing the palladacycle catalyst (**12**).[139] This initial success spurred a significant amount of research that has gone into the synthesis and study of various palladacycles in order to see if the activity of this type of catalyst could be improved further.[36,97] Recently, systems that consist of a palladacycle plus an added ligand have proven to be some of the most active yet. The theory here is that these species act as precursors to the actual Pd–L catalysts in which, once again, the P:Pd ratio is restricted to its optimal 1:1 value.[98]

8.3 Recent Mechanistic Insights

A general mechanism for the palladium-catalyzed amination of aryl halides is presented in Scheme 7.[122] This picture has been developed from studies performed largely upon isolated complexes, with the oxidative addition and reductive elimination steps being investigated in the greatest detail. On

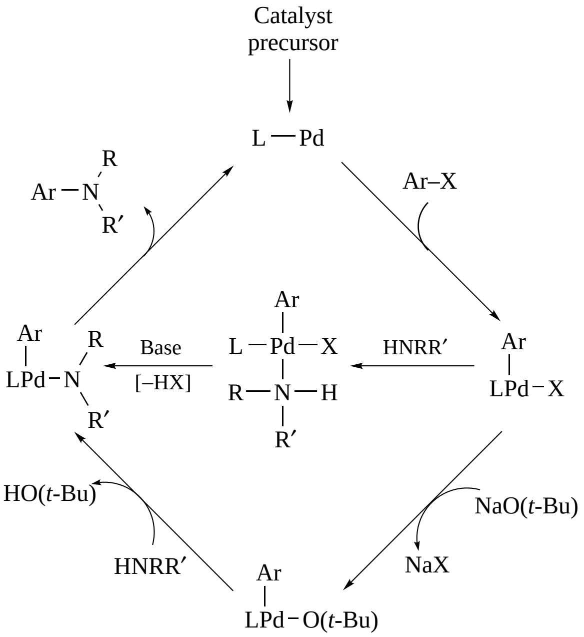

Scheme 7 General mechanism for catalytic amination of organic electrophiles

the face, this process does not seem to be markedly different from the general mechanism cited for carbon–carbon bond forming cross-coupling reactions. However, the fact that many nontraditional catalysts are used for amination reactions suggests that many subtle mechanistic differences, leading to less subtle differences in reactivity, should operate for the different catalyst systems.

For the case of tri(*o*-tolyl)phosphine-ligated catalysts, the upper pathway appears to predominate. Oxidative addition occurs first via loss of a ligand from the bisphosphine precursor to form the oxidative adduct, which exists as a dimer bridged through the halogen atoms (equation 33).[122] This dimer is broken up by amine, the coordination of which to palladium renders its proton acidic. Subsequent deprotonation by base leads to the amido complex, which can then reductively eliminate to form the product. When *tert*-butoxide is used as the base, the rate is limited by formation of and reductive elimination from the amido complex, while for the stronger hexamethyldisilazide, the rate-determining step appears to be oxidative addition.[126]

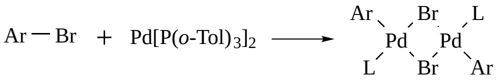

(33)

For the case of chelating phosphines, Hartwig noted that palladium alkoxide complexes can be formed by treatment of the corresponding halides with base, and that amido complexes can, in turn, be formed from the alkoxide.[122] This observation opened the possibility that alkoxide intermediates lie on the catalytic cycle (lower pathway in Scheme 7). Van Leeuwen and coworkers studied the kinetics for the amination of aryl triflates and bromides using different Xantphos catalyst systems.[140] For triflate amination, they found the rate to be first order in amine and *tert*-butoxide, but zero order in aryl triflate. From this, they concluded that a mechanism similar to the upper pathway in Scheme 7 was operating, with the deprotonation of coordinated amine being the rate-determining step. For aryl bromides, however, the rate was dependent on the concentration of *tert*-butoxide, but not amine or aryl bromide. Thus, under these conditions, the lower pathway – with the replacement of halide by *tert*-butoxide as the rate-limiting step – was postulated to be the operating mechanism.

Hartwig and coworkers have studied the amination reaction of aryl halides catalyzed by $Pd(BINAP)_2$ and $Pd(dppf)_2$.[141] They similarly observed kinetics that were zero order in aryl halide; however, their rates were independent of the concentrations of base and amine. From this, they suggested a mechanism in which loss of a chelating ligand (prior to oxidative addition) was the rate-determining step. Furthermore, NMR evidence led them to suggest that $Pd(BINAP)_2$ was the resting state of the catalytic cycle, as predicted from the results of their kinetics experiments. However, in a subsequent paper, they found that the rate did depend upon aryl halide at higher substrate concentrations, suggesting that another mechanism may be operating under these conditions.[142]

More recently, Blackmond, Buchwald, and coworkers investigated the kinetics of catalytic aminations via in situ reaction calorimetry.[143] They maintained that the apparent zero-order kinetics observed by others was in fact caused by an induction period during which the active catalytic species was gradually introduced into the mechanistic cycle. For the case of $Pd(BINAP)_2$, they argued that this complex was external to the catalytic cycle, with the active catalyst being the monoligated species (which enters the cycle via a slow dissociation of BINAP from $Pd(BINAP)_2$). Furthermore, they observed rates that were dependent upon the concentrations of both aryl halide and amine (though not on base), suggesting a mechanism in which amine coordinates to palladium prior to oxidation addition of the aryl halide (Scheme 8).

Others have investigated the kinetics of amination reactions mediated by catalyst systems employing the new electron-rich monodentate ligands. In particular, Hartwig has shown that for catalysis by a 1:1 palladium to tri(*tert*-butyl)phosphine system, a mechanism in which oxidative addition of aryl chlorides follows coordination of base to the palladium competes with the standard nonanionic pathway.[144] Finally, Caddick, Cloke, and coworkers have studied amination reactions of aryl chlorides performed by palladium complexes of N-heterocyclic carbene ligands.[145] They found the rate to be limited by the oxidative addition step, which occurs first through the dissociation of an NHC ligand.

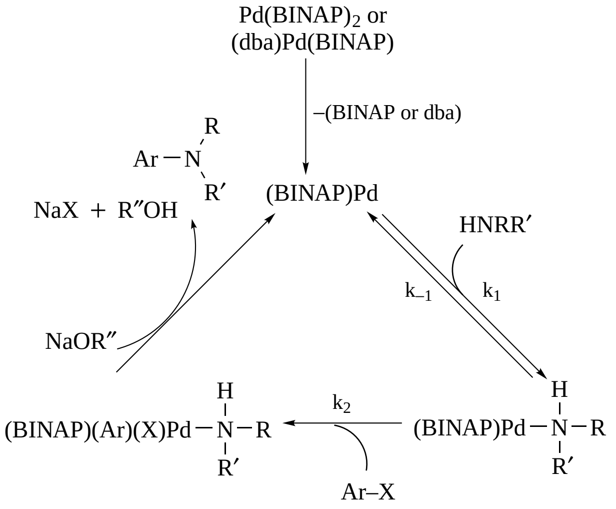

Scheme 8 Modified amination mechanism involving amine coordination prior to oxidative addition

9 APPLICATIONS

Discoveries made in the late 1970s of electrical conductivity in conjugated polymers spawned a monumental interest in the study of these materials, which are ideally suited for synthesis via cross-coupling reactions. Yamamoto was the first to realize this possibility with a regiochemically defined synthesis of poly(*p*-phenylene) formed via the Kumada–Corriu protocol.[146] Since then, various cross-coupling reactions have been applied in condensation polymerization reactions,[147,148] with the Suzuki[149] and Sonogashira[150] protocols gaining the most widespread use.

Cross-coupling reactions have also seen increasing utilization in the synthesis of natural products,[151] as well as in the generation of combinatorial libraries[152] for both pharmaceutical[153] and materials[154] applications. Finally, other reviews note the importance of cross-coupling reactions in the formation of porphyrins[155] as well as in the industrial synthesis of commercial pharmaceuticals[156] and industrial fine chemicals.[157]

10 CONCLUSIONS AND FUTURE OUTLOOK

Given the prolific use of cross-coupling chemistry in such a wide array of applications, it is easy to see that these reactions have matured remarkably from the academic curiosity they were a mere 20–30 years ago. As industry comes to rely more heavily on this chemistry, future developments will doubtlessly be driven by economics. Strategies for catalyst recovery and recycling have been developed, but there is clearly room for improvement. Furthermore, the fact that palladium is one of the most expensive elements in the periodic table will drive the search for systems based upon more abundant metals, an area of research that we are now just beginning to explore. Thus, while our understanding of this chemistry has indeed come a long way, there is still a great deal more to be learned.

11 RELATED ARTICLES

Beryllium & Magnesium: Organometallic Chemistry; Boron: Organoboranes; Mechanisms of Reaction of Organometallic Complexes; Palladium: Organometallic Chemistry; Silver: Inorganic & Coordination Chemistry; Tin: Organometallic Chemistry; Zinc: Organometallic Chemistry.

12 REFERENCES

1. F. Diederich and P. J. Stang, eds. ‘Metal-Catalyzed Cross-Coupling Reactions’, Wiley-VCH Verlag GmbH, Weinheim, Germany, 1998.
2. E. Negishi, ed. ‘Handbook of Organopalladium Chemistry for Organic Synthesis’. John Wiley & Sons, Hoboken, NJ, 2002.
3. E. Negishi, *J. Organomet. Chem.*, 2002, **653**, 34.
4. C. Amatore and A. Jutand, Structural and Mechanistic Aspects of Palladium-Catalyzed Cross-Couplings, in ‘Handbook of Organopalladium Chemistry for Organic Synthesis’, ed. E. Negishi, John Wiley & Sons, Hoboken, NJ, 2002, p. 943.
5. K. Tamao, K. Sumitami, and M. Kumada, *J. Am. Chem. Soc.*, 1972, **94**, 4374.
6. R. J. P. Corriu and J. P. Masse, *J. Chem. Soc., Chem. Commun.*, 1972, 144.
7. T. Hayashi, M. Konishi, Y. Kobori, M. Kumada, T. Higuchi, and K. Hirotsu, *J. Am. Chem. Soc.*, 1984, **106**, 158.
8. K. Tamao, *J. Organomet. Chem.*, 2002, **653**, 23.
9. S.-I. Murahashi, *J. Organomet. Chem.*, 2002, **653**, 27.
10. T. Hayashi, Palladium-Catalyzed Asymmetric Cross-Coupling, in ‘Handbook of Organopalladium Chemistry for Organic Synthesis’, ed. E. Negishi, John Wiley & Sons, Hoboken, NJ, 2002, p. 791.
11. P. W. N. M. van Leeuwen, *Appl. Cat. A.*, 2001, **212**, 61.
12. L. Schwink and P. Knochel, *Chem. Eur. J.*, 1998, **4**, 950.
13. C. Saluzzo, J. Breuzard, S. Pellet-Rostaing, M. Vallet, F. Le Guyader, and M. Lemaire, *J. Organomet. Chem.*, 2002, **643–644**, 98.
14. V. P. W. Böhm, T. Weskamp, C. W. K. Gstöttmayr, and W. A. Herrmann, *Angew. Chem. Int. Ed.*, 2000, **39**, 1602.

15. J. Terao, H. Watanabe, A. Ikumi, H. Kuniyasu, and N. Kambe, *J. Am. Chem. Soc.*, 2002, **124**, 4222.
16. P. W. N. M. van Leeuwen, P. C. J. Kamer, J. N. H. Reek, and P. Dierkes, *Chem. Rev.*, 2000, **100**, 2741.
17. M. Ogasawara, K. Yoshida, and T. Hayashi, *Organometallics*, 2000, **19**, 1567.
18. W. A. Herrmann, *Angew. Chem. Int. Ed.*, 2002, **41**, 1290.
19. A. C. Hillier, G. A. Grasa, M. S. Viciu, H. M. Lee, C. Yang, and S. P. Nolan, *J. Organomet. Chem.*, 2002, **653**, 69.
20. G. Y. Li, *J. Organomet. Chem.*, 2002, **653**, 63.
21. M. Tamura and J. K. Kochi, *Synthesis*, 1971, 303.
22. A. S. E. Karlström, M. Rönn, A. Thorarensen, and J.-E. Bäckvall, *J. Org. Chem.*, 1998, **63**, 2517.
23. M. Tamura and J. Kochi, *J. Am. Chem. Soc.*, 1971, **93**, 1487.
24. G. Cahiez and H. Avedissian, *Synthesis*, 1998, 1199.
25. A. Fürstner, A. Leitner, M. Méndez, and H. Krause, *J. Am. Chem. Soc.*, 2002, **124**, 13856.
26. J. K. Kochi, *J. Organomet. Chem.*, 2002, **653**, 11.
27. K. Sonogashira, *J. Organomet. Chem.*, 2002, **653**, 46.
28. K. Sonogashira, Sonogashira Alkyne Synthesis, in 'Handbook of Organopalladium Chemistry for Organic Synthesis', ed. E. Negishi, John Wiley & Sons, Hoboken, NJ, 2002, p. 493.
29. C. E. Castro and R. D. Stephens, *J. Org. Chem.*, 1963, **28**, 2163.
30. L. Cassar, *J. Organomet. Chem.*, 1975, **93**, 253.
31. H. A. Dieck and F. R. Heck, *J. Organomet. Chem.*, 1975, **93**, 259.
32. S. Sonogashira, Y. Tohda, and N. Hagihara, *Tetrahedron Lett.*, 1975, 4467.
33. A. F. Littke and G. C. Fu, *Angew. Chem. Int. Ed.*, 2002, **41**, 4176.
34. S. Takahashi, Y. Kuroyama, K. Sonogashira, and N. Hagihara, *Synthesis*, 1980, 627.
35. D. A. Shultz, K. P. Gwaltney, and H. Lee, *J. Org. Chem.*, 1998, **63**, 4034.
36. W. A. Herrmann, V. P. W. Böhm, and C.-P. Reisinger, *J. Organomet. Chem.*, 1999, **576**, 23.
37. T. Hundertmark, A. F. Littke, S. L. Buchwald, and G. C. Fu, *Org. Lett.*, 2000, **2**, 1729.
38. D. A. Alonso, C. Nájera, and M. C. Pacheco, *Org. Lett.*, 2000, **2**, 1823.
39. B. M. Choudary, S. Madhi, N. S. Chowdari, M. L. Kantam, and B. Sreedhar, *J. Am. Chem. Soc.*, 2002, **124**, 14127.
40. S. Baba and E. Negishi, *J. Am. Chem. Soc.*, 1976, **98**, 6729.
41. E. Negishi and D. E. Van Horn, *J. Am. Chem. Soc.*, 1977, **99**, 3168.
42. E. Negishi, A. O. King, and N. Okukado, *J. Org. Chem.*, 1977, **42**, 1821.
43. E. Negishi, Overview of the Negishi Protocol with Zn, Al, Zr, and Related Metals, in 'Handbook of Organopalladium Chemistry for Organic Synthesis', ed. E. Negishi, John Wiley and Sons, Hoboken, NJ, 2002, p. 229. Editor.
44. J. Zhou and G. C. Fu, *J. Am. Chem. Soc.*, 2003, **125**, 12527.
45. G. Y. Li, *J. Org. Chem.*, 2002, **67**, 3643.
46. A. Boudier, C. Darcel, F. Flachsmann, L. Micouin, M. Oestreich, and P. Knochel, *Chem. Eur. J.*, 2000, **6**, 2748.
47. A. E. Jensen and P. Knochel, *J. Org. Chem.*, 2002, **67**, 79.
48. J. Zhou and G. C. Fu, *J. Am. Chem. Soc.*, 2003, **125**, 14726.
49. M. Kosugi and K. Fugami, Overview of the Stille Protocol with Sn, in 'Handbook of Organopalladium Chemistry for Organic Synthesis', ed. E. Negishi, John Wiley & Sons, Hoboken, NJ, 2002, p. 263.
50. M. Kosugi and K. Fugami, *J. Organomet. Chem.*, 2002, **653**, 50.
51. K. Fugami and M. Kosugi, *Top. Curr. Chem.*, 2002, **219**, 87.
52. D. Azarian, S. S. Dua, C. Eaborn, and D. R. M. Walton, *J. Organomet. Chem.*, 1976, **117**, C55.
53. M. Kosugi, K. Sasazawa, Y. Shimizu, and T. Migita, *Chem. Lett.*, 1977, 301.
54. D. Milstein and J. K. Stille, *J. Am. Chem. Soc.*, 1978, **100**, 3636.
55. J. K. Stille, *Angew. Chem. Int. Ed.*, 1986, **25**, 508.
56. A. Ricci and C. Lo Sterzo, *J. Organomet. Chem.*, 2002, **653**, 177.
57. D. K. Morita, J. K. Stille, and J. R. Norton, *J. Am. Chem. Soc.*, 1995, **117**, 8576.
58. K.-C. Kong and C.-H. Cheng, *J. Am. Chem. Soc.*, 1991, **113**, 6313.
59. F. E. Goodson, T. I. Wallow, and B. M. Novak, *J. Am. Chem. Soc.*, 1997, **119**, 12441.
60. M. Fujita, H. Oka, and K. Ogura, *Tetrahedron Lett.*, 1995, **36**, 5247.
61. V. Farina, S. Kapadia, B. Krishnan, C. Wang, and L. S. Liebeskind, *J. Org. Chem.*, 1994, **59**, 5905.
62. W. P. Gallagher, I. Terstiege, and R. E. Maleczka Jr, *J. Am. Chem. Soc.*, 2001, **123**, 3194.
63. V. Farina and B. Krishnan, *J. Am. Chem. Soc.*, 1991, **113**, 9585.
64. R. van Asselt and C. J. Elsevier, *Tetrahedron*, 1994, **50**, 323.
65. F. Mercier, F. Laporte, L. Ricard, F. Mathey, M. Schröder, and M. Regitz, *Angew. Chem. Int. Ed.*, 1997, **36**, 2364.
66. E. Shirakawa and T. Hiyama, *J. Organomet. Chem.*, 1999, **576**, 169.
67. D. A. Albisson, R. B. Bedford, S. E. Lawrence, and P. N. Scully, *Chem. Commun.*, 1998, 2095.

68. J. Louie and J. F. Hartwig, *J. Am. Chem. Soc.*, 1995, **117**, 11598.
69. A. Casado and P. Espinet, *J. Am. Chem. Soc.*, 1998, **120**, 8978.
70. A. Casado, P. Espinet, and A. M. Gallego, *J. Am. Chem. Soc.*, 2000, **122**, 11771.
71. C. Mateo, D. J. Cárdenas, C. Fernández-Rivas, and A. M. Echavarren, *Chem. Eur. J.*, 1996, **2**, 1596.
72. H. A. Dieck and R. F. Heck, *J. Org. Chem.*, 1975, **40**, 1083.
73. N. Miyaura and A. Suzuki, *J. Chem. Soc., Chem. Commun.*, 1979, 866.
74. S. R. Chemler, D. Trauner, and S. J. Danishefsky, *Angew. Chem. Int. Ed.*, 2001, **40**, 4545.
75. A. Suzuki, Overview of the Suzuki Protocol with B, in 'Handbook of Organopalladium Chemistry for Organic Synthesis', ed. E. Negishi, John Wiley & Sons, Hoboken, NJ, 2002, p. 249.
76. A. Suzuki, *J. Organomet. Chem.*, 2002, **653**, 83.
77. S. Kotha, K. Lahiri, and D. Kashinath, *Tetrahedron*, 2002, **58**, 9633.
78. N. Miyaura, *Top. Curr. Chem.*, 2002, **219**, 12.
79. N. Miyaura, *J. Organomet. Chem.*, 2002, **653**, 54.
80. M. R. Netherton, C. Dai, K. Neuschütz, and G. C. Fu, *J. Am. Chem. Soc.*, 2001, **123**, 10099.
81. H. G. Kuivila, J. F. Reuwer, and J. A. Mangravite, *J. Am. Chem. Soc.*, 1964, **86**, 2666.
82. Y. Urawa, H. Naka, M. Mayazawa, S. Souda, and K. Ogura, *J. Organomet. Chem.*, 2002, **653**, 269.
83. G. B. Smith, G. C. Dezeny, D. L. Hughes, A. O. King, and T. R. Verhoeven, *J. Org. Chem.*, 1994, **59**, 8151.
84. N. A. Bumagin and V. V. Bykov, *Tetrahedron*, 1997, **53**, 14437.
85. D. Badone, M. Baroni, R. Cardamone, A. Ielmini, and U. Guzzi, *J. Org. Chem.*, 1997, **62**, 7170.
86. C. G. Blettner, W. A. König, W. Stenzel, and T. Schotten, *J. Org. Chem.*, 1999, **64**, 3885.
87. H. Zhang, F. Y. Kwong, Y. Tian, and K. S. Chan, *J. Org. Chem.*, 1998, **63**, 6886.
88. C. Kowitz and G. Wegner, *Tetrahedron*, 1997, **53**, 15553.
89. S. W. Wright, D. L. Hageman, and L. D. McClure, *J. Org. Chem.*, 1994, **59**, 6095.
90. J. P. Wolfe, R. A. Singer, B. H. Yang, and S. L. Buchwald, *J. Am. Chem. Soc.*, 1999, **121**, 9550.
91. A. F. Littke, C. Dai, and G. C. Fu, *J. Am. Chem. Soc.*, 2000, **122**, 4020.
92. A. Zapf, A. Ehrentraut, and M. Beller, *Angew. Chem. Int. Ed.*, 2000, **39**, 4153.
93. X. Bei, H. W. Turner, H. Weinberg, and A. S. Guram, *J. Org. Chem.*, 1999, **64**, 6797.
94. M. G. Andreu, A. Zapf, and M. Beller, *Chem. Commun.*, 2000, 2475.
95. J. P. Stambuli, R. Kuwano, and J. F. Hartwig, *Angew. Chem. Int. Ed. Engl.*, 2002, **41**, 4746.
96. M. Beller, H. Fischer, W. A. Herrmann, K. Öfele, and C. Brossmer, *Angew. Chem. Int. Ed.*, 1995, **34**, 1848.
97. J. Dupont, M. Pfeffer, and J. Spencer, *Eur. J. Inorg. Chem.*, 2001, 1917.
98. R. B. Bedford, C. S. J. Cazin, S. J. Coles, T. Gelbrich, P. N. Horton, M. B. Hursthouse, and M. E. Light, *Organometallics*, 2003, **22**, 987.
99. T. I. Wallow and B. M. Novak, *J. Org. Chem.*, 1994, **59**, 5034.
100. M. T. Reetz and E. Westermann, *Angew. Chem. Int. Ed.*, 2000, **39**, 165.
101. C. Dupuis, K. Adiey, L. Charrault, V. Michelet, M. Savinac, and J.-P. Genêt, *Tetrahedron Lett.*, 2001, **42**, 6523.
102. M. Nishimura, M. Ueda, and N. Miyaura, *Tetrahedron*, 2002, **58**, 5779.
103. K. H. Shaughnessy and R. S. Booth, *Org. Lett.*, 2001, **3**, 2757.
104. M. B. Thathagar, J. Beckers, and G. Rothenberg, *J. Am. Chem. Soc.*, 2002, **124**, 11858.
105. N. Miyaura, K. Yamada, H. Suginome, and A. Suzuki, *J. Am. Chem. Soc.*, 1985, **107**, 972.
106. A. O. Aliprantis and J. W. Canary, *J. Am. Chem. Soc.*, 1994, **116**, 6985.
107. K. Matos and J. A. Soderquist, *J. Org. Chem.*, 1998, **63**, 461.
108. J. Yoshida, K. Tamao, H. Yamamoto, T. Kakui, T. Uchida, and M. Kumada, *Organometallics*, 1982, **1**, 542.
109. K. Ikenaga, K. Kikukawa, and T. Matsuda, *J. Chem. Soc., Perkin Trans. 1*, 1986, 1959.
110. K. Karabelas and A. Hallberg, *J. Org. Chem.*, 1986, **51**, 5286.
111. Y. Hatanaka and T. Hiyama, *J. Org. Chem.*, 1988, **53**, 918.
112. T. Hiyama and E. Shirakawa, *Top. Curr. Chem.*, 2002, **219**, 62.
113. T. Hiyama, *J. Organomet. Chem.*, 2002, **653**, 58.
114. S. E. Denmark and R. F. Sweis, *Chem. Pharm. Bull.*, 2002, **50**, 1531.
115. S. E. Denmark and R. F. Sweis, *Acc. Chem. Res.*, 2002, **35**, 835.
116. H. Matsuhashi, S. Asai, K. Hirabayashi, Y. Hatanaka, A. Mori, and T. Hiyama, *Bull. Chem. Soc. Jpn.*, 1997, **70**, 437.
117. K. Tamao, K. Kobayashi, and Y. Ito, *Tetrahedron Lett.*, 1989, **30**, 6051.
118. K. Shibata, K. Miyazawa, and Y. Goto, *Chem. Commun.*, 1997, 1309.
119. M. E. Mowery and P. DeShong, *J. Org. Chem.*, 1999, **64**, 1684.
120. K. Itami, K. Mitsudo, T. Nokami, T. Kamei, T. Koike, and J. Yoshida, *J. Organomet. Chem.*, 2002, **653**, 105.
121. C. Mateo, C. Fernández-Rivas, D. J. Cárdenas, and A. M. Echavarren, *Organometallics*, 1998, **17**, 3661.

122. J. F. Hartwig, Palladium-Catalyzed Amination of Aryl Halides and Related Reactions, in ‘Handbook of Organopalladium Chemistry for Organic Synthesis’, ed. E. Negishi, John Wiley & Sons, Hoboken, NJ, 2002, p. 1051.
123. A. R. Muci and S. L. Buchwald, *Top. Curr. Chem.*, 2002, **219**, 131.
124. M. Kosugi, M. Kameyama, and T. Migita, *Chem. Lett.*, 1983, 927.
125. A. S. Guram, R. A. Rennels, and S. L. Buchwald, *Angew. Chem. Int. Ed. Engl.*, 1995, **34**, 1348.
126. J. Louie and J. F. Hartwig, *Tetrahedron Lett.*, 1995, **36**, 3609.
127. J. P. Wolfe, S. Wagaw, and S. L. Buchwald, *J. Am. Chem. Soc.*, 1996, **118**, 7215.
128. M. S. Driver and J. F. Hartwig, *J. Am. Chem. Soc.*, 1996, **118**, 7217.
129. Y. Guari, D. S. van Es, J. N. H. Reek, P. C. J. Kamer, and P. W. N. M. van Leeuwen, *Tetrahedron Lett.*, 1999, **40**, 3789.
130. J. P. Sadighi, M. C. Harris, and S. L. Buchwald, *Tetrahedron Lett.*, 1998, **39**, 5327.
131. J.-F. Marcoux, S. Wagaw, and S. L. Buchwald, *J. Org. Chem.*, 1997, **62**, 1568.
132. M. Nishiyama, T. Yamamoto, and Y. Koie, *Tetrahedron Lett.*, 1998, **39**, 617.
133. J. F. Hartwig, M. Kawatsura, S. I. Hauck, K. H. Shaughnessy, and L. M. Alcazar-Roman, *J. Org. Chem.*, 1999, **64**, 5575.
134. B. C. Hamann and J. F. Hartwig, *J. Am. Chem. Soc.*, 1998, **120**, 7369.
135. D. W. Old, J. P. Wolfe, and S. L. Buchwald, *J. Am. Chem. Soc.*, 1998, **120**, 9722.
136. X. Bei, A. S. Guram, H. W. Turner, and W. H. Weinberg, *Tetrahedron Lett.*, 1999, **40**, 1237.
137. J. P. Wolfe, H. Tomori, J. P. Sadighi, J. Yin, and S. L. Buchwald, *J. Org. Chem.*, 2000, **65**, 1158.
138. G. Y. Li, *Angew. Chem. Int. Ed.*, 2001, **40**, 1513.
139. M. Beller, T. H. Riermeier, C.-P. Reisinger, and W. A. Herrmann, *Tetrahedron Lett.*, 1997, **38**, 2073.
140. Y. Guari, G. P. F. van Strijdonck, M. D. K. Boele, J. N. H. Reek, P. C. J. Kamer, and P. W. N. M. van Leeuwen, *Chem. Eur. J.*, 2001, **7**, 475.
141. L. M. Alcazar-Roman, J. F. Hartwig, A. L. Rheingold, L. M. Liable-Sands, and I. A. Guzei, *J. Am. Chem. Soc.*, 2000, **122**, 4618.
142. L. M. Alcazar-Roman and J. F. Hartwig, *Organometallics*, 2002, **21**, 491.
143. U. K. Singh, E. R. Strieter, D. G. Blackmond, and S. L. Buchwald, *J. Am. Chem. Soc.*, 2002, **124**, 14104.
144. L. M. Alcazar-Roman and J. F. Hartwig, *J. Am. Chem. Soc.*, 2001, **123**, 12905.
145. A. Kd. K. Lewis, S. Caddick, F. G. N. Cloke, N. C. Billingham, P. B. Hitchcock, and J. Leonard, *J. Am. Chem. Soc.*, 2003, **125**, 10066.
146. T. Yamamoto and A. Yamamoto, *Chem. Lett.*, 1977, 353.
147. T. Yamamoto, *J. Organomet. Chem.*, 2002, **653**, 195.
148. A.-D. Schlüter and Z. Bo, Synthesis of Conjugated Polymers for Materials Science, in ‘Handbook of Organopalladium Chemistry for Organic Synthesis’, ed. E. Negishi, John Wiley & Sons, Hoboken, NJ, 2002, p. 825.
149. A. D. Schlüter, *J. Polym. Sci., Polym. Chem. Ed.*, 2001, **39**, 1533.
150. U. H. F. Bunz, *Chem. Rev.*, 2000, **100**, 1605.
151. Z. Tan and E. Negishi, Synthesis of Natural Products via Palladium-Catalyzed Cross-Coupling, in ‘Handbook of Organopalladium Chemistry for Organic Synthesis’, ed. E. Negishi, John Wiley & Sons, Hoboken, NJ, 2002, p. 863.
152. S. Bräse, J. Köbberling, and N. Griebenow, Organopalladium Reactions in Combinatorial Chemistry, in ‘Handbook of Organopalladium Chemistry for Organic Synthesis’, ed. E. Negishi, John Wiley & Sons, Hoboken, NJ, 2002, p. 3031.
153. S. Wendeborn, A. de Mesmaeker, W. K.-D. Brill, and S. Berteina, *Acc. Chem. Res.*, 2000, **33**, 215.
154. M.-S. Schiedel, C. A. Briehn, and P. Bäuerle, *J. Organomet. Chem.*, 2002, **653**, 200.
155. W. M. Sharman and J. E. van Lier, *J. Porphyrins Phthalocyanines*, 2000, **4**, 441.
156. N. Yasuda, *J. Organomet. Chem.*, 2002, **653**, 279.
157. A. Zapf and M. Beller, *Top. Catal.*, 2002, **19**, 101.

Acknowledgments

The authors are indebted to Ms. Tia Carter, Mr. Dinakar Gnanamgari, Mr. Charan Singh, and the WCU library staff for their assistance in obtaining the articles necessary to complete this manuscript.

Porous Inorganic Materials

Xiqing Wang,[2] Xianhui Bu[1] & Pingyun Feng[2]
[1]*California State University, Long Beach, CA, USA*
[2]*University of California Riverside, Riverside, CA, USA*

---

1 Introduction 1
2 Microporous Materials 2
3 Mesoporous Materials 3
4 Macroporous Materials 14
5 Hierarchical Porous Structures 16
6 Related Articles 17
7 References 17

Glossary

M41S: A family of mesoporous materials including MCM-41, MCM-48, and MCM-50
MSU-1,2,3,4: Michigan State University no. 1, 2, 3, 4, a series of wormhole mesoporous materials prepared in the presence of nonionic surfactants
Pluronic: polyethylene oxide–polypropylene oxide triblock surfactant, $(EO)_m(PO)_n(EO)_m$, for example, P123 = $(EO)_{20}(PO)_{70}(EO)_{20}$
SBA-x: Santa Barbara no. x, a series of mesoporous materials
Tergitol: alkyl–polyethylene oxide surfactant, $C_nH_{2n+1}(EO)_m$
Triton-X: alkylaryl–polyethyleneoxide surfactant, $C_nH_{2n+1}Ph(EO)_m$

Abbreviations

2D or 3D = 2 or 3 dimensional; 3DOM = 3-dimensional ordered macroporous materials; CMK-1,2, 3 = Carbon mesostructured by KAIST (Korea Advanced Institute of Science and Technology) no. 1, 2, 3; CTAB = Cetyltrimethylammonium bromide, $[C_{16}H_{33}N(CH_3)_3]^+Br^-$; HMS = Hexagonal molecular sieves. ICF-*m* = Inorganic chalcogenide framework, no. *m*; MCF = Mesostructured cellular foams; MCM-41, 48, 50 = Mobil composition of matter no. 41, 48, and 50; MMS = Mesoporous molecular sieves; PCH = porous clay heterostructures; SEM = Scanning electron microscopy; TEM = Transmission electron microscopy; TEOS = Tetraethoxysilane.

---

1 INTRODUCTION

Porous materials are of great interest because of their wide commercial applications as ion exchangers, adsorbents, and catalysts. There are a variety of porous materials differing in chemical composition, pore geometry and size, and degree of crystallinity. According to the IUPAC definition,[1] porous materials are classified into three groups on the basis of pore size: microporous materials are porous solids with pore size below 2 nm, mesoporous materials are porous solids with pore size between 2 and 50 nm, and macroporous materials are those with pore size larger than 50 nm (Figure 1).

Pores with different sizes show characteristic physical adsorption effects as manifested in the isotherm.[2] The isotherm shows the relationship between the amount of a given gas taken up or released by a solid as a function of the gas pressure under a constant temperature. The type-I isotherm shows a steep increase at very low pressures and a long saturation plateau and is characteristic of microporous materials. The type-IV isotherm exhibits a steep increase at high relative pressure and, in many cases, a hysteresis loop, which is associated with capillary condensation in mesopores.

The development of microporous materials started in late 1940s with the synthesis of synthetic zeolites by Barrer, Milton, Breck, and their coworkers. Some commercially important microporous materials such as zeolites A, X, and Y were made in the first several years of Milton and Breck's work. In the following 30 years, zeolites with various topologies and chemical compositions were prepared, culminating in the synthesis of ZSM-5 and its aluminum-free pure silica form in 1970s. A breakthrough leading to an extension of crystalline microporous materials to nonsilicates occurred in 1982 when Flanigen *et al.* reported the synthesis of aluminophosphate molecular sieves. Since the late 1980s and the early 1990s, crystalline microporous materials have been made in many other compositions including chalcogenides and metal–organic frameworks.

Prior to the 1990s, materials with pore size in the meso range such as silica gels and activated carbons show disordered pore structure with a broad distribution of pore size. In 1992, by using cationic surfactants as template, Mobil scientists

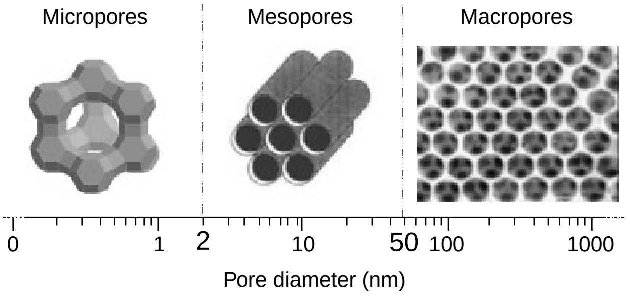

Figure 1 The IUPAC classification of porous materials on the basis of pore diameter

prepared a family of mesoporous silicas (denoted M41S) with hexagonal and cubic symmetry and highly uniform pore sizes ranging from 2 to 10 nm. There has been a widespread interest in ordered mesoporous materials since the discovery of M41S.

Following the discovery of ordered mesoporous materials, the templated approach was also employed for the synthesis of ordered macroporous materials. Macroporous materials with uniform pore sizes are predicted to have useful optical properties and may have applications as photonic crystals with optical band gaps.[3]

This article focuses on ordered mesoporous materials that have undergone a rapid growth in the past decade. For completeness, the concurrent progresses in the areas of crystalline microporous and ordered macroporous materials are briefly described.

2 MICROPOROUS MATERIALS[4]

Microporous materials are formed with hydrated inorganic cations or organic species located within cavities of the extended inorganic or inorganic–organic hybrid host framework. Extra-framework organic species are usually protonated amines, quaternary ammonium cations, or neutral solvent molecules. Dehydration (or desolvation) and calcination are two methods frequently used to remove extra-framework species and generate microporosity.

Even though crystalline microporous materials include those with pore size between 10 and 20 Å (called extra-large pore materials), few of them have a pore size within this range. This limits the applications of microporous materials to small molecules. There has always been a desire to increase the pore size of a crystalline material to more than 10 Å while maintaining adequate thermal or hydrothermal stability required for various applications.[5] Recent advances in chalcogenide and metal–organic framework materials have shown much promise for the preparation of extra-large pore materials.

In addition to the desire for an increase in the pore size, there has been a strong interest in generating multifunctional materials in which crystalline microporosity is integrated with other useful properties such as framework chirality, ferromagnetism, semiconductivity, or ion conductivity.[6]

2.1 Microporous Silicates and Germanates

Microporous materials are typified by natural and synthetic zeolites that are crystalline 3D aluminosilicates with open channels or cages. Synthetic and structural concepts of zeolites have to a large extent shaped the development of microporous materials during the past 50 years. For example, the use of organic structure-directing agents in the synthesis of high-silica zeolites and their all-silica polymorphs contributed to the later discovery of aluminophosphate molecular sieves. A comprehensive review on the synthesis and structure of zeolites and related materials has been given by Dyer and will not be repeated here.[7]

The commercial importance of zeolites has prompted numerous efforts aimed at the synthesis of new microporous materials. One commonly used approach is through the substitution of framework cations (i.e. Al^{3+} or Si^{4+}) in zeolites by other cations such as Ga^{3+}, Ge^{4+}, and P^{5+}. Because of the close resemblance to zeolites, gallosilicates and alumino- (or gallo-) germanates were among the earliest nonzeolite microporous materials being prepared. In general, gallosilicates and alumino- (or gallo-) germanates do not possess framework topologies not previously found among zeolites. However, the recent use of organic structure-directing agents in the synthesis of germanates has resulted in a number of materials with unprecedented framework topologies.[8]

In general, each compositional system has a unique range of the T–O bond length and the T–O–T angle (where T refers to tetrahedral atoms) and has its own preference for certain types of framework topology. For example, structures with strained double four-ring units are more likely to occur as germanates. Another example is the synthesis of UCSB-7. It could be prepared under a variety of experimental conditions as either a gallogermanate or aluminogermanate.[9] However, it has not been prepared as a silicate. It is thus not surprising to find that by incorporating the germanium source into the synthesis mixture of silicates, new microporous materials could be synthesized.[10]

2.2 Microporous Phosphates and Arsenates[11]

The synthesis of aluminophosphate molecular sieves in 1980s represents a breakthrough in the development of microporous materials. Since then, much of the worldwide synthetic efforts have been directed toward nonsilicate microporous materials. Many novel framework topologies could be found with phosphates, and many other elements could be incorporated into phosphates to produce additional new framework topologies or new compositions.

Aluminophosphate molecular sieves, as originally prepared, have a neutral framework and generally require organic amines or alkylammonium cations as extra-framework species. However, it was soon discovered that both Si^{4+} and many metal cations (in particular divalent metal cations) could be incorporated into the aluminophosphate framework to generate a negative framework similar to high-silica zeolites. A complete substitution of Al^{3+} sites by divalent cations such as Zn^{2+} or Be^{2+} gives a series of zinco- or beryllo-phosphates that are similar to low-silica zeolites. The negative framework charge and the associated extra-framework charge-balancing cations are useful for many applications of microporous materials; however, the stability of microporous materials generally decreases with increasing negative charge on the framework.

Of great significance is the synthesis of an extra-large pore microporous material in the aluminophosphate composition. VPI-5, a hydrated aluminophosphate, has a unidimensional channel with a window size formed by 18 tetrahedral cations. At the time of its discovery, the largest window size for zeolites was only 12. Thus, the discovery of VPI-5 inspired new efforts aimed toward the synthesis of extra-large pore microporous materials. Since then, a number of extra-large pore phosphates and silicates have been synthesized. Chalcogenide and metal–organic framework materials offer new promises for the development of extra-large pore materials.

Compared with microporous phosphates, there are few microporous arsenates. The syntheses and structures of arsenates are similar to those of phosphates when divalent metal cations such as Zn^{2+} and Be^{2+} are employed as framework tetrahedral atoms.[12] However, there is very little similarity between alumino- (or gallo-) arsenates and the corresponding phosphates. In the intermediate range where both divalent and trivalent metal cations are present, some similarities between arsenates and phosphates have been observed.[13]

2.3 Microporous Sulfides and Selenides[14,15]

The replacement of framework anions (i.e. O^{2-}) with chalcogens (e.g. S^{2-}) represents a more recent approach for generating microporous materials. The efforts to make microporous chalcogenides began with germanium or tin sulfides. However, germanium or tin sulfides do not form microporous materials similar to all-silica polymorphs of zeolites. It was later found that the incorporation of low-valent cations such as Mn^{2+} into the Ge–S composition helped to generate 3D frameworks.

Three-dimensional sulfide and selenide frameworks have also been made in the indium and gallium chalcogenide compositions. In addition, the incorporation of mono or divalent cations into indium or gallium chalcogenide compositions has produced some new framework chalcogenides often based on the assembly of chalcogenide clusters.

The combination of trivalent (M^{3+}) and tetravalent (M^{4+}) cations in chalcogenides has led to a series of framework chalcogenides, among which the microporous behavior has been demonstrated. The M^{4+} to M^{3+} ratio in these chalcogenides, however, can be much smaller than that in zeolites and so far falls within the range from about 0.21 to 0. Despite the low M^{4+} to M^{3+} ratio, some sulfides in this series possess adequate stability toward ion exchange and thermal treatment. The Cs^{+} exchanged UCR-20GaGeS-TAEA (TAEA = tris(2-aminoethyl)amine) exhibits the type-I isotherm and its pore size is as large as 9.5 Å.[16]

Similar to zeolites, chalcogenides could be prepared with either inorganic or organic cations as extra-framework species. A family of hydrated sulfides and selenides were made recently. These materials, denoted as ICF-*m*, were prepared in aqueous solutions from simple inorganic salts. One of the most interesting properties of these inorganic chalcogenides is fast-ion conductivity at room temperature and moderate to high humidity. In particular, lithium compounds such as ICF-22 and ICF-26 exhibit ionic conductivity significantly greater than previously known crystalline lithium compounds.[6]

2.4 Inorganic–Organic Hybrid Microporous Materials[17]

A rapidly developing field in the microporous materials involves metal–organic framework materials. These materials are prepared by using multidentate organic ligands (e.g. nitriles, carboxylates, amines) to link together metal cations with a low valence (usually divalent cations such as Zn^{2+}). The resulting materials are now called metal–organic frameworks or MOFs.

One promising application of metal–organic frameworks is in the area of gas storage. Several metal–organic framework materials have been found to have a high capacity for methane or hydrogen storage. Through proper design of organic ligands and their assembly with metal centers, noncentrosymmetric or chiral frameworks can be prepared. Moreover, because MOFs generally involve transition metal cations, they open up new opportunities in the design of magnetic microporous materials.

3 MESOPOROUS MATERIALS[18,19]

3.1 Synthesis Pathways and Formation Mechanisms[20,21]

3.1.1 *Base Synthesis*

The synthesis of ordered mesoporous materials in the past decade greatly expanded the range of ordered porous materials and opened up many new opportunities in the design and applications of materials. Of particular importance is the synthetic methodology that is used for the preparation of these materials. Prior to this, the synthesis of porous materials generally involved the use of individual molecules or hydrated clusters of simple ions. In the synthesis of ordered mesoporous materials, however, it is the assembly of surfactant molecules that directs the condensation of inorganic precursors.

Inspired by the similarity between M41S and surfactant/water liquid crystal phases, Mobil scientists proposed two general pathways (Figure 2).[20,21] The first model suggests that the water-surfactant liquid crystal phase serves as the structure-directing element. This model could not explain observations that surfactant-silicate mesophases could form at surfactant concentration as low as 1%, which is too low to form a liquid crystal phase. The second model suggests that the presence of the silicate somehow mediates the ordering of surfactant micelles into the hexagonal (or cubic Ia3d) arrangement. This model was later further developed by Monnier *et al.* into a more general cooperative assembly mechanism.

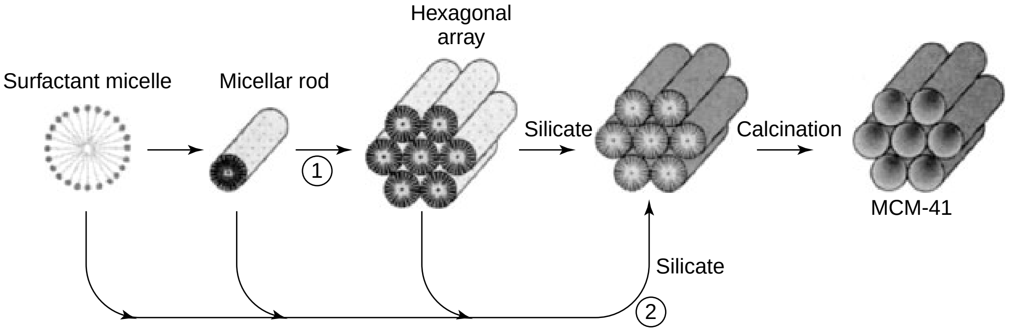

Figure 2 The proposed two possible pathways, (1) and (2), to the formation of MCM-41. (Reprinted with permission from Ref. 21. © 1992 American Chemical Society)

The model by Monnier *et al.* presented a more detailed mechanism by which silicate species can prompt the formation of inorganic–organic composite mesophases.[22] This mechanism suggests that the direct cooperative multidentate binding between cationic surfactants and negatively charged silicate oligomers, preferential polymerization of silicates at the interface, and charge-density matching across the silicate-surfactant interface are crucial factors for the formation of mesophases.

3.1.2 Acid Synthesis

The direct interaction between surfactants and inorganic precursors was later found to be not the only pathway for the formation of mesophases. A major discovery following Mobil's work is the synthesis of mesophases through the assembly of cationic inorganic species with cationic surfactants in acidic solutions. Here, the interaction between cationic silica species and cationic surfactant headgroups is suggested to be mediated by halide anions.

The synthetic results under both basic and acidic conditions allowed Huo *et al.* to propose a generalized mechanism[23,24] for the formation of mesostructured inorganic/organic composites. This mechanism involves electrostatic interactions between the inorganic precursor I and the surfactant headgroup S (Figure 3). Both direct and mediated modes are possible between charged inorganic precursors (cationic I^+, anionic I^-) and charged surfactant headgroups (cationic S^+, anionic S^-), resulting in four synthetic routes: (S^+I^-), (S^-I^+), $(S^+X^-I^+)$, and $(S^-M^+I^-)$. The (S^+I^-) and $(S^-M^+I^-)$ routes occur when the base conditions are used, whereas the (S^-I^+) and $(S^+X^-I^+)$ routes are associated with the acid synthesis. The discovery of the acid synthesis approach and the four proposed pathways has had a profound impact on the later development of mesoporous materials.

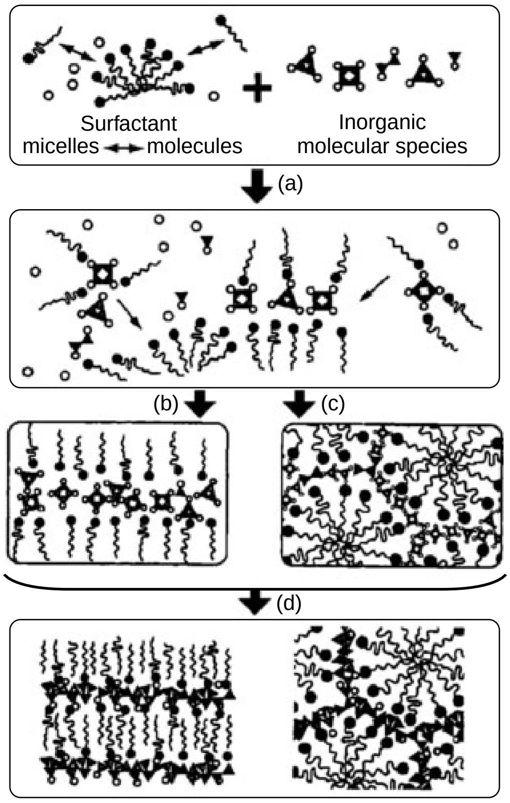

Figure 3 Schematic illustration of interaction between surfactants and inorganic species. (Reprinted with permission from Ref. 24. © 1994 American Chemical Society)

Zhao *et al.*[25,26] greatly extended the utility of the acid synthesis approach when they used amphiphilic triblock copolymers to prepare a series of periodically ordered mesoporous silicas, SBA-*n* ($n = 11$, 12, 14, 15, and 16), with uniform pore sizes well beyond 100 Å. Prior to this work, mesoporous materials with pore size in this range either did not exist or had much lower ordering compared to SBA-*n*. The formation of SBA-*n* from block copolymers was proposed to go through the (S^0H^+) (X^-I^+) pathway in the acidic media involving a combination of electrostatic and hydrogen-bonding interactions.[26] The use of the acidic media is a major difference between this work and the earlier work by Pinnavaia *et al.*

In the above work by Zhao *et al.*, when the amount of the swelling agent (i.e. 1,3,5-trimethylbenzene) was gradually increased, a structural transition from the hexagonally ordered mesophases into mesostructured cellular foams (MCFs) occurred.[27] The MCFs were made from a system composed of aqueous HCl, triblock copolymer P123, 1,3,5-trimethylbenzene (TMB), and ethanol. Tetraethoxysilane (TEOS) was hydrolyzed at the organic–inorganic interface at the surface of P123-coated TMB droplets in aqueous HCl to form hydrophilic cationic silica species that subsequently condensed around the organic assemblies. The MCFs possess uniform spherical cells with controllable diameter ranging from 24 to 42 nm, depending on the amount of TMB and aging temperature.[28]

3.1.3 Neutral Synthesis

Pinnavaia *et al.*[29] used neutral alkylamines as templates to form disordered mesoporous silica, named hexagonal molecular sieves (HMS). The S^0I^0 formation mechanism was proposed between neutral amine micelles (S^0) and neutral inorganic precursors (I^0). The interactions between S^0 and I^0 were assumed to be hydrogen bonding. The resulting HMS has a 'worm-like' pore structure, with thicker framework walls and smaller X-ray scattering domain sizes compared to M41S.

Mesoporous silica could also be prepared using nonionic amphiphilic surfactants (N^0)[30] with a polyethylene oxide (PEO, EO_n) hydrophilic headgroup. Through the proposed neutral N^0I^0 assembly pathway, worm-like disordered mesoporous silica or amorphous silica are formed using nonionic PEO surfactants or triblock copolymers. The low structural order may be related to the absence of sufficiently strong electrostatic or hydrogen-bonding interactions.

The above N^0I^0 pathway was later modified by Pinnavaia *et al.* by introducing small metal cations ($M^{n+} = Li^+$, Co^{2+}, Ni^{2+}, Mn^{2+}, and Zn^{2+}) into the assembly process, affording mesoporous silica with improved structural order.[31] This approach was denoted $(N^0M^{n+})I^0$, wherein hydrogen bonds were formed between cationic metal complexes containing nonionic $R(EO)_nH$ surfactants (N^0) and the neutral inorganic precursors (I^0). Electrostatic forces were enhanced through the complexation of small M^{n+} cations by the EO groups of N^0. As summarized in Table 1, various types of interactions between the organic surfactants and the inorganic precursors, including electrostatic charge matching (S^+I^-, S^-I^+, $S^+X^-I^+$, and $S^-M^+I^-$), H-bonding (S^0I^0 and N^0I^0), covalent interactions or their combination ($(S^0H^+)(X^-I^+)$ and $(N^0M^{n+})I^0$), may play significant roles in the formation of mesostructured materials.

3.1.4 Ligand-assisted Templating Mechanism

Antonelli and Ying prepared hexagonally packed mesoporous niobium oxide (2D-hexagonal, *p*6m), named Nb-TMS1, using alkyl amines as the structure-direct agent.[32] A new mechanism called 'ligand-assisted templating' (LAT) was suggested. The proposed mechanism involves direct covalent interactions between the Nb alkoxide precursor and the amine ligand through the N–Nb bond prior to the hydrolysis and condensation of the preformed alkoxide-surfactant precursor. After removal of the surfactant by extraction, mesostructures are retained. This approach provides control of mesostructured phases by simple adjustment of the metal/surfactant ratio, resulting in a family of mesoporous transition metal oxides ('$P6_3/mmc$' hexagonal Nb-TMS2, cubic *Pm*3*n* Nb-TMS3, and lamellar Nb-TMS4).[33]

3.1.5 Direct Liquid Crystal Templating Mechanism[34]

Mesoporous materials described so far are prepared under surfactant concentrations that are generally too low to form long-range ordered lyotropic liquid crystal phases in a surfactant/water system. The coorganization between inorganic and organic species is prompted by various forms of interfacial interactions, and in general, the stronger the interaction, the more ordered the resulting mesophases.

Mesoporous materials can also be prepared at high surfactant concentrations at which long-range liquid crystals can form even in the absence of inorganic precursors. Attard *et al.* demonstrated this approach by using the liquid crystal phases of the nonionic surfactants such as octaethylene glycol monododecyl ether ($C_{12}EO_8$) or octaethylene glycol monohexadecyl ether ($C_{16}EO_8$) as templates. This synthesis approach is reminiscent of pathway 1 of the original liquid crystal templating mechanism for MCM-41 proposed by Mobil scientists.

In Attard's approach, tetramethylorthosilicate (TMOS) was hydrolyzed and condensed in the aqueous domain of the liquid crystal phase at pH of about 2, leading to mesostructured hexagonal, cubic, or lamellar silica. Methanol from the hydrolysis of TMOS destroys the long-range order of the liquid crystal; however, upon the removal of methanol, the lyotropic liquid crystal is restored and serves as the template phase for the further condensation of silicates. The resulting pore system replicates the shape of the lyotropic mesophase, so this process is also termed 'nanocasting'.

Feng *et al.* prepared a series of periodically ordered mesoporous silica by using high concentrations of triblock copolymers in multicomponent ternary (surfactant/cosurfactant/water) and quaternary (surfactant/cosurfactant/oil/water) systems.[35] One key feature to Feng's approach is that methanol is removed under vacuum prior to the mixing between silicate precursors and surfactants. Thus the lyotropic liquid crystal phase, once formed, maintains its long-range ordering throughout the whole silicate condensation process. The removal of methanol prior to mixing with surfactant/cosurfactant/oil is also advantageous because the presence of surfactant, cosurfactant, or oil could make the

Table 1 The general scheme of the various types of interaction between surfactants and inorganic precursors

Pathway[a]	Interaction	Schematic representation	pH	Typical examples of phases formed	Reference
S^+I^-	electrostatic	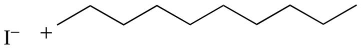	11–13	MCM-41, hexagonal MCM-48, cubic MCM-50, lamellar	Mobil, 1992[20,21]
S^-I^+	electrostatic	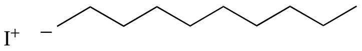	<5	Metal Oxides, lamellar	Stucky, 1994[23,24]
$S^+X^-I^+$	electrostatic	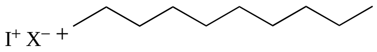	<2	Silica, hexagonal, cubic, lamellar	Stucky, 1994[23,24]
$S^-M^+I^-$	electrostatic	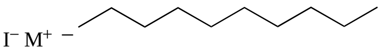	>8	ZnO, Al_2O_3, lamellar	Stucky, 1994[23,24]
S^0I^0	H-bonding	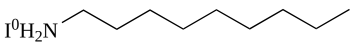	~9	HMS, worm-like	Pinnavaia, 1995[29]
N^0I^0	H-bonding	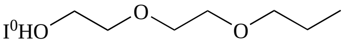	≤7	MSU family, worm-like	Pinnavaia, 1995[30]
LAT (S-I)	Covalent	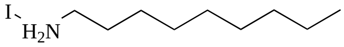		Nb-TMS, M41S analogs	Ying, 1996[32]
$(S^0H^+)(X^-I^+)$	Electrostatic + H-bonding	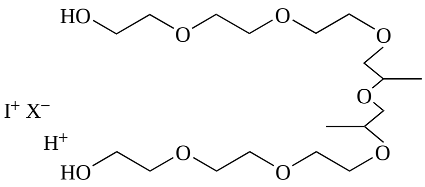	<1	SBA-15, hexagonal	Stucky, 1998[25,26]
$(N^0M^{n+})I^0$	Electrostatic + H-bonding	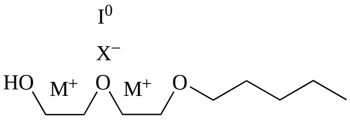	~7	Hexagonal or 3D faulted hexagonal and cubic	Pinnavaia, 1999[31]

[a] S = surfactants; I = inorganic species; M^{n+} = metal cations; X^- = halide anions; N = nonionic surfactants.

efficient removal of methanol difficult. The use of cosurfactants and oils provides additional variables for the control of a number of structural features of resulting mesophases including pore size and wall thickness.

During the direct liquid crystal templating, the condensation of inorganic precursors occurs in the aqueous domain of preformed lyotropic liquid crystals. With this approach, the interaction between inorganic precursors and surfactant headgroups could disrupt the long-range order of liquid crystals and should therefore be minimized. For silicates, performing reactions at pH of about 2, which is the isoelectric point of silicates, helps to reduce such interaction.

3.1.6 Evaporation-induced Self-assembly (EISA)

Brinker *et al.* developed a simple evaporation-induced self-assembly (EISA) process that allows the rapid production of patterned porous or nanocomposite materials in the form of films, fibers, or spheres.[36] Starting from a homogeneous solution of soluble silica and surfactant below the critical micellar concentration, evaporation of ethanol increased surfactant concentration, driving self-assembly of silica-surfactant micelles and their further organization. By adjusting the initial alcohol/water/surfactant molar ratio, 2D hexagonal, cubic, 3D hexagonal, and lamellar silica-surfactant mesophases could be made.

3.2 Structure[37]

The pore structure, such as pore geometry and pore size, of mesoporous materials is one of the key parameters for practical applications, especially those dependent on size and shape selectivity and ready access to porosity. Considerable efforts have been devoted to control the pore structure of mesoporous materials.

3.2.1 Pore Geometry Control

The pore geometry is associated with the symmetry of mesophases and can be ill defined when the ordering of the mesophases is very low. However, highly ordered mesophases can be prepared under a variety of experimental conditions. By tuning synthetic parameters, it is possible to control the topological features of resulting mesophases. The original Mobil work led to the synthesis of a 2D ordered hexagonal phase with unidimensional channels (p6m) and a 3D ordered cubic phase with 3D bicontinuous channels (Ia3d). The use of the acidic medium and the surfactant $C_{16}H_{33}N(C_2H_5)_3^+$ or $C_{16}H_{33}N(C_2H_5)(C_5H_{10})^+$ (cetylethylpiperidinium) allowed Huo *et al.* to discover a new cubic phase (Pm3n), SBA-1.[24] In addition, SBA-2[38] (acid synthesis) and SBA-7[39] (base synthesis) with previously unknown pore structure were also prepared by using divalent quaternary ammonium surfactants with the general formula $C_nH_{2n+1}N(CH_3)_2(CH_2)_sN(CH_3)_3^{2+}$ (denoted C_{n-s-1}, $n = 12$, 13, 16, 18, 20, $s = 2$, 3, 6). Two new cubic mesoporous silica SBA-11 (*Pm*-3*m*) and SBA-16 (*Im*-3*m*) have been synthesized by Zhao *et al.* from $C_{16}EO_{10}$ and $EO_{106}PO_{70}EO_{106}$,[26] respectively, in addition to SBA-12 that is similar in structure to SBA-2.

The use of surfactant molecules with different charges and geometrical features is an effective way to control the structure of mesophases. According to the cooperative self-assembly formation mechanism, inorganic species interact with surfactant micelles at the interface through electrostatic interaction or hydrogen bonding. So phase transitions are expected to be associated with changes in the curvature of interface. In classical micelle chemistry, micellar organization is related to the local effective surfactant packing parameter, $g = V/a_0l$, where V is the total volume of the hydrophobic chains, a_0 is the effective headgroup area at the micelle surface, and l is the kinetic surfactant tail length. The expected mesophase depends on the value of g (Table 2). Huo *et al.* first applied this concept to explain and predict product structure and phase transition.[38,40]

Other factors that affect the structure of mesophases include the concentration ratio between surfactants and inorganic precursors. For example, MCM-41 was prepared at a $C_{16}H_{33}(CH_3)_3N^+$/Si ratio of less than 1. As the $C_{16}H_{33}(CH_3)_3N^+$ /Si ratio increases beyond 1, the cubic phase (Ia3d) can be produced. Similarly, Nb-TMS1 (p6m), Nb-TMS2 ($P6_3/mmc$), Nb-TMS3 (*Pm*-3*n*), and Nb-TMS4 (p2) were prepared at various surfactant to Nb ratios.[33]

3.2.2 Pore Size Engineering

Surfactant Chain Length. Under comparable reaction conditions, the pore size generally increases with the chain length of surfactants. For example, when quaternary ammonium surfactants (C_nTMABr) with different alkyl tails ($n = 8$, 9, 10, 12, 14, and 16) were used, the pore size of resulting materials increased from 18 to 37 Å with the increase in the chain length.[21]

Table 2 Different g values and related mesophases

g	Mesophase	Space group	Examples
<1/3	3D hexagonal	$P6_3/mmc$	SBA-2
1/3	Cubic	*Pm*3*n*	SBA-1
1/3–1/2	2D hexagonal	*p*6*m*	SBA-3, MCM-41
1/2–2/3	Cubic	*Ia*3*d*	MCM-48
>1	Lamellar	*p*2	MCM-50

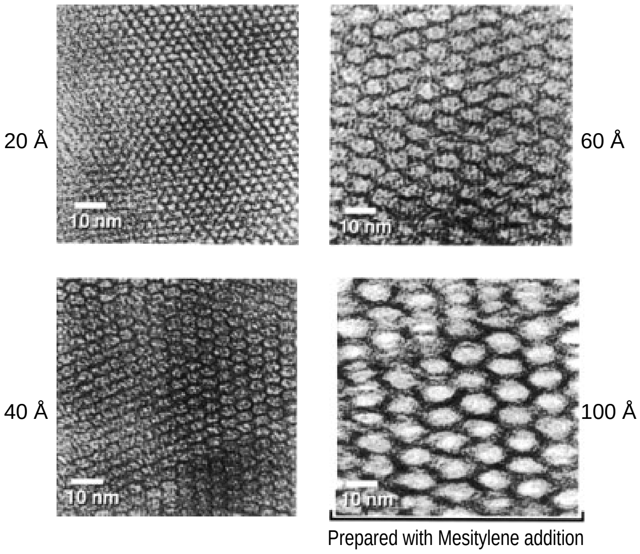

Figure 4 TEM images of MCM-41 with different pore sizes up to 100 Å. (Reprinted with permission from Ref. 21. © 1992 American Chemical Society)

Addition of Swelling Agents. In Mobil's original work on M41S, 1,3,5-TMB was used as the swelling agent to increase the pore size of mesoporous materials. By adjusting the TMB/C_{16}TMABr ratios, the pore size of MCM-41 was enhanced up to 100 Å (Figure 4). Other aromatic hydrocarbons, alkanes, and amines have also been used as pore expanders. Owing to their hydrophobicity, organic auxiliaries can be incorporated into the core of micelles to increase the size of micelles. The increase in the pore size of resulting mesophases is related to this phenomenon.

Temperature[41]. The N^0I^0 synthetic pathway can be used to control the pore size by choice of the assembly temperature. In the case of MSU-1 silica assembled with Tergitol 15-S-12, pore size increases from 21 to 45 Å when the synthesis temperature is increased from 25 to 65 °C. With increasing temperature, PEO segments of the surfactant become more hydrophobic, thus decreasing the size of hydrophilic headgroups and, consequently, enlarging the diameter of hydrophobic core, which determines the pore size. The hydrogen bonding between the shortened hydrophilic PEO segments of surfactants and inorganic species, which is related to the wall thickness, can become weaker at elevated temperatures. This mechanism is supported by the evidence of a decrease in the wall thickness accompanied by an increase in the pore size.

Postsynthesis Treatment[42]. As-synthesized mesoporous silica can contain a significant concentration of the OH^- group, particularly if made at low synthesis temperatures and in short times, and their pore size can be modified by the postsynthesis treatment. Tailoring the pore size through this method is commonly achieved by hydrothermal restructuring of as-synthesized materials at a higher temperature. A gradual pore size expansion to about 70 Å was observed by treatment of as-made MCM-41 in the mother liquid at 150 °C for a period of 1 to 10 days.[43] Huo and coworkers found that the pore size of MCM-41 could be enlarged by hydrothermal treatment of the predried, as-made samples at 100 °C, affording high-quality materials with the pore size up to 60 Å.[24]

Water is thought to enter the pore space to solvate the silicate framework, surfactants, and their counterions, leading to silica dissolution, transport, and redeposition. It is shown that the hydrothermal restructuring process is very sensitive to both the temperature and the duration. While an excessive hydrothermal treatment can cause dramatic decreases of pore volumes and surface areas, neutral amines and alkenes generated in situ by the decomposition of some quaternary ammonium surfactants can act as swelling agents. The water-amine postsynthesis treatment provides further support for the swelling effect of neutral amines. Sayari *et al.* reported pore size expansion by up to threefold when as-synthesized MCM-41 was treated in aqueous emulsions of an appropriate long-chain amine, such as N,N-dimethylhexadecylamine (DMHA).[44] An unprecedented enlargement of pore size (from 31.5 to 250 Å) and pore volume (from 0.85 to 3.31 $cm^3\ g^{-1}$) was achieved by hydrothermal treatment in the presence of dimethyldecylamine (DMDA).[45]

3.3 Composition

3.3.1 Silica and Doped Silica

A large variety of mesoporous silica has been prepared. These mesoporous silicas differ in a number of features including space group symmetry, degree of ordering, pore size and wall thickness, and degree of polymerization. As shown in Table 3, these differences are generated by a number of synthetic factors such as pH, types of surfactants, and auxiliary reagents such as oils and inorganic ions. Many different names exist for mesoporous silica, and these different names designate materials prepared under specific conditions used by different individual research groups.[46–52]

Numerous efforts have been spent on doping silica with other elements, most of which are transition metal elements. In many cases, the goal of these syntheses is to introduce or enhance acidic or redox catalytic activity into mesoporous silica. Depending on the individual element and synthetic procedures, the doping level spans a wide range of values from about 5 to over 3000 for the Si/dopant molar ratio.[54]

3.3.2 Phosphates

Because of the similarity between aluminophosphate and silica molecular sieves, the synthesis of mesoporous silica was soon followed by the efforts aimed toward the synthesis of mesoporous aluminophosphates. Both lamella and hexagonally ordered aluminophosphate mesostructures have been prepared.[55,56]

Recently, Zhao *et al.* proposed that the interaction between two or more inorganic precursors, guided by 'acid–base pair' principles, plays an important role in the formation of ordered multicomponent mesoporous structures, in particular phosphates.[57] They suggested that to form multicomponent mesoporous materials, stable pairs of different species during nucleation are necessary. The larger the acidity or alkalinity difference between the metallic and nonmetallic precursors, the more likely that the pairs will form. No extra acid or base is required to adjust the pH of the synthesis system. This method is particularly effective for metal phosphates. A series of mesoporous materials including TiPO, ZrPO, AlPO, NbPO, and CePO were prepared by using this approach.

3.3.3 Metal Oxides

Mesoporous metal oxides encompass a variety of chemical compositions. In general, these compositions are not as stable as mesoporous silica, or they are not as ordered as silica. However, the combination of mesoporosity with other unique properties afforded by these compositions (e.g. semiconductivity, redox activity) has inspired considerable efforts in the synthesis of these mesostructured materials. In the study of synthetic pathways for the formation of mesoporous materials, Huo *et al.* reported a series of mesostructured oxides based on Sb, W, and Al and so on. by using cationic or anionic surfactants.[24] Another significant progress in the templated synthesis of mesoporous oxides was reported by Yang *et al.* when they used block copolymers to synthesize a range of mesoporous oxides including TiO_2, ZrO_2, HfO_2, Nb_2O_5, Ta_2O_5, WO_3, Al_2O_3, SiO_2, and SnO_2.[58] Yang's approach is also applicable to the synthesis of mixed oxides such as Al_2TiO_y and $ZrTiO_y$. The following gives a discussion of some selected mesoporous oxides.

Titania. Mesoporous TiO_2 is very attractive because of the excellent photocatalytic activity associated with TiO_2. Among the three crystalline polymorphs of titania (anatase, rutile, and brookite), anatase is the most suitable phase for photocatalysis because of its large band gap and suitable redox potential. The early attempts to prepare mesoporous titania used surfactants with phosphate headgroups, and the resulting mesophases contain phosphate groups even after calcinations.[59,60] Phosphorus-free mesoporous titania was reported by Antonelli by using dodecylamine.[61] Using block copolymers, Yang *et al.* reported the synthesis of

Table 3 A summary of various silicate mesophases

Name	Mesophase	Space group	Surfactant	Pathway
MCM-41[20,21]	Hexagonal	$p6m$	alkylammonium, e.g. CTAB	S^+I^-
MCM-48[20,21]	Cubic	$Ia3d$	alkylammonium, e.g. CTAB	S^+I^-
MCM-50[20,21]	Lamellar	$p2$	alkylammonium, e.g. CTAB	S^+I^-
MSU-1[30]	Wormhole/disordered		Tergitol, e.g. $C_{11-15}EO_9$	S^0I^0
MSU-2[30]	Wormhole/disordered		Triton-X, e.g. C_8PhEO_8	S^0I^0
MSU-3[30]	Wormhole/disordered		Pluronic, e.g. $EO_{13}PO_{30}EO_{13}$	S^0I^0
MSU-4[30]	Wormhole/disordered		Tween	S^0I^0
MSU-G[46]	3D vesicular	L_3	gemini diamines, e.g. $C_{10}H_{21}NH(CH_2)_2NH_2$	N^0I^0
HMS[29]	Wormhole/disordered		amines, e.g. C_8NH_2	N^0I^0
SBA-1[24]	Cubic	Pm-$3n$[51]	alkylammonium	$S^+X^-I^+$
SBA-2[38]	3D hexagonal	$P6_3/mmc$	divalent quaternary ammonium	S^+I^-
SBA-3[20]	hexagonal	$p6m$	quaternary ammonium (acid synthesis)	$S^+X^-I^+$
SBA-4[39]	lamellar	$P2$		base
SBA-5[39]	cubic	$R3c$		base
SBA-6[39]	cubic	Pm-$3n$[51]	$18B_{4\text{-}3\text{-}1}$ gemini[a]	base
SBA-7[39]	3D hexagonal	$P6_3/mmc$		$S^+X^-I^+$
SBA-8[53]	2D rectangular	cmm	cationic bolaform[b]	S^+I^-
SBA-11[26]	cubic	$Pm3m$	alkyl-polyethylene oxide, e.g. $C_{16}EO_{10}$	$(S^0H^+)(X^-I^+)$
SBA-12[26]	3D hexagonal	$P6_3/mmc$	alkyl-polyethylene oxide, e.g. $C_{18}EO_{10}$	$(S^0H^+)(X^-I^+)$
SBA-14[26]	cubic	$Pm3n$	alkyl-polyethylene oxide, e.g. $C_{12}EO_4$	$(S^0H^+)(X^-I^+)$
SBA-15[25,26]	2D hexagonal	$p6m$	block copolymer, e.g. $EO_{20}PO_{70}EO_{20}$	$(S^0H^+)(X^-I^+)$
SBA-16[26]	cubic	Im-$3m$[51]	block copolymer, e.g. $EO_{106}PO_{70}EO_{106}$	$(S^0H^+)(X^-I^+)$
FDU-1[47]	cubic, caged	$Fm3m$[52]	$EO_{39}BO_{47}EO_{39}$	$(S^0H^+)\ (X^-I^+)$
KIT-1[48]	disordered		$[C_{16}H_{33}N(CH_3)_3]^+Cl^-$	S^+I^-
FSM-16[49]	layered		$[C_{16}H_{33}N(CH_3)_3]^+Cl^-$	sheets folding
PCH[50]	layered		intercalated quaternary ammonium and neutral amine	gallery-templated

[a] Gemini surfactant 18B4-3-1 = $C_{18}H_{37}OC_6H_4OC_4H_8N(CH_3)_2C_3H_6N(CH_3)_3Br_2$. [b] Bolaform surfactant $(CH_3)N\text{–}(CH_2)_n\text{–}O\text{–}(C_6H_4)_2\text{–}O\text{–}(CH_2)_n\text{–}N(CH_3)_3Br_2$, $n = 4, 6, 8, 10, 12$.

2D hexagonal titania from $EO_{20}PO_{70}EO_{20}$ and cubic titania ($Im3m$) from $EO_{75}BO_{45}$.[58]

Very recently, mesoporous TiO_2 with anatase, rutile, bicrystalline mixture (anatase and rutile) with controlled phase composition, and tricrystalline mixture (anatase, rutile, and brookite) were reported by using triblock copolymer as template and $TiCl_4$ as precursor.[62] The resulting crystalline titanias are thermally stable and have high surface area and large pore size up to 16 nm.

Zirconia. Mesoporous zirconia was first reported by Knowles and Hudson[63] with cationic alkyltrimethylammonium surfactants.[64] Starting from zirconium sulfate or propoxide, Schüth[65] and Ciesla *et al.*[66] synthesized hexagonal mesoporous zirconia using alkyltrimethylammonium surfactants as templates. Reddy and Sayari[67] obtained hexagonal or lamellar phases of mesostructured zirconia using quaternary ammonium surfactants and acidified primary alkylamine, respectively. Mesoporous zirconia has also been synthesized with amphoteric[68] and anionic[69,70] templates.

In a detailed study,[71] mesostructured zirconia has been prepared by using various amphiphilic surfactants with different headgroups (anionic and nonionic) and different tail lengths (1–18 carbons) as templates. Removal of surfactants leads to the loss of structural order and a decrease of the surface area. However, the presence of phosphates and sulfates in the walls may improve the stability.

Alumina. Mesoporous aluminas with high surface area are of great interest because of their potential use as catalysts and catalyst supports. The first successful synthesis of mesoporous aluminas was reported by Bagshaw and Pinnavaia through N^0I^0 assembly process.[72] Aluminas accessible through this route (designated as MSU-X aluminas) have wormhole pore structures with surface area around 400 to

$500\ m^2\ g^{-1}$. Similar wormhole mesoporous aluminas were also prepared using cationic[73] or anionic[74] surfactants as templates.

Mesostructured alumina with hexagonal structure can be synthesized in the presence of sodium dodecyl sulfate (SDS), but it was not stable upon surfactant removal.[75] Thermally stable mesoporous alumina has been obtained by using triblock copolymer as templates in ethanol solution. Most alumina mesophases consist of amorphous or semicrystalline framework. Recently, Pinnavaia and coworkers developed a novel three-step assembly method to prepare mesostructured alumina with framework walls composed of crystalline, lathlike γ-Al_2O_3 nanoparticles.[76,77]

3.3.4 Carbons[78]

Porous carbonaceous materials are important in many application areas because of their remarkable properties, such as high surface areas, chemical inertness, and good mechanical stability. Carbon molecular sieves that are amorphous and microporous are commercially important for the separation of nitrogen from air, and activated carbons with a wide pore size distribution are also useful adsorbents for various applications.

Recently, there has been an increasing interest in the synthesis of ordered mesoporous carbons,[79] since such materials are very promising as adsorbents, catalyst supports, and electrochemical double-layer capacitors.[80,81] Ordered mesoporous silicas have been shown as suitable templates to prepare periodic mesoporous carbons with various pore shapes and connectivity. The synthesis procedure involves impregnation of the mesoporous silica with an appropriate carbon precursor, carbonization of carbon source, and subsequent removal of silica using an aqueous solution of HF or NaOH.[78]

Ryoo *et al.* reported the first ordered mesoporous carbon, CMK-1, using cubic MCM-48 as template and sucrose as carbon source.[79] CMK-1 exhibited a highly ordered cubic structure, as confirmed by transmission electron microscopy (TEM). However, x-ray powder diffraction patterns indicated that CMK-1 underwent a structural transformation upon the silica removal due to the two disconnected porous systems separated by the silica wall.[82,83]

Similarly, cubic SBA-1 and disordered HMS have also been used as templates to prepare periodic mesoporous carbons (designated as CMK-2[79] and SNU-2[84] respectively). On the other hand, MCM-41 that has a hexagonal structure with unidimensional channels was found unsuitable as the template for the preparation of mesoporous carbons. Using SBA-15 as a template resulted in the first-ordered mesoporous carbon, designated as CMK-3,[85] which is exactly an inverse replica of the silica template. Although SBA-15 possesses the hexagonal mesostructure ($p6$m) similar to MCM-41, the microporosity[86] or the mesotunnels[87] within the silica walls could be responsible for the successful replication of ordered CMK-3.[88] Recent work on periodic mesoporous carbons includes improving structural integrity and thermal stability,[89] developing a low-cost synthesis route,[90] controlling the pore diameters,[91] and preparing carbons with graphitic pore walls.[92]

3.3.5 Periodic Mesoporous Organosilicas (PMOs)

Periodic mesoporous organosilicas (PMOs) are a new kind of organic–inorganic hybrid materials. However, unlike hybrid mesoporous materials made by grafting organic groups on the pore surface, PMOs contain organic groups as an integral component of silica-based framework.[93–95] The synthesis of PMOs involves the hydrolysis and condensation of tailor-made bridged organosilica precursor $((R'O)_3Si)_nR$ ($n = 2$ or 3, $R' =$ methyl or ethyl) in the presence of surfactant assemblies. The surfactant templates can be removed by solvent extraction or ion exchange. Essential to the synthesis of PMOs is the design and selection of the organosilica precursors. Various synthetic routes, such as Grignard, alcoholysis, hydrosilation, Pd-catalyzed Heck coupling, hydroboration, lithiation, and silylation of halides have been applied to prepare the molecular poly(trialkoxysilyl)organic precursors.[96] So far, various organic groups (Figure 5) including methane, ethane, ethylene, and benzene have been integrated into the framework of PMOs.[96,97] Since the first three contributions to PMOs were reported in 1999, some new synthetic strategies have been developed for the preparation of PMOs, resulting in many mesophases including wormhole structures,[95] cubic structures,[98] 2D hexagonal structures similar to MCM-41[93] or SBA-15,[99] and a 3D hexagonal structure with unknown space group.[94] One of the most intriguing successes is the report of a 2D hexagonal mesoporous benzene-silica with a crystal-like wall structure, exhibiting structural periodicity with a spacing of 7.6 Å along the channel direction.[100]

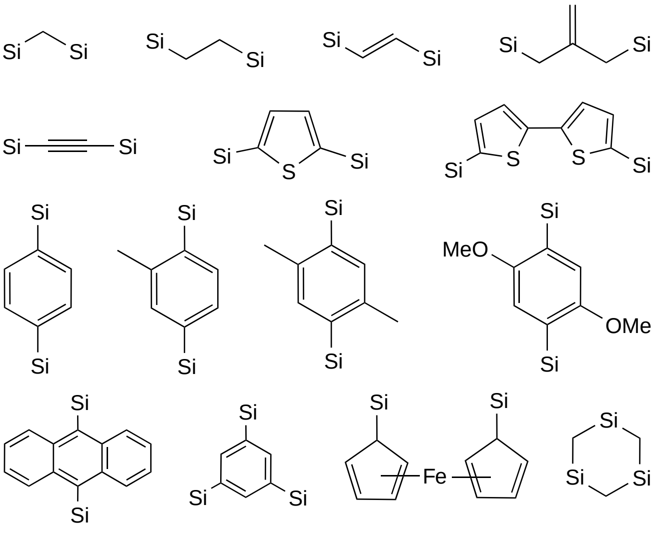

Figure 5 Examples of organic and organometallic bridging groups that have been incorporated into PMOs

Advantages[101] of PMOs include homogeneous distribution of bridged organic groups with high and tunable concentrations, large free void space, and consequently easily accessible functional groups. PMOs are expected to provide interesting electronic, optical, magnetic, catalytic, and mechanical properties.[96,101,102]

3.3.6 Chalcogenides

Germanium Sulfides. Metal chalcogenides are among the earliest nonoxide mesostructured materials being studied.[15] Because of the similarity to silicates, germanium or tin chalcogenides have received considerable attention. Through the room temperature reaction of aqueous solutions of $Na_4Ge_4S_{10}$ with solutions of various surfactant alkyltrimethylammonium bromide salts, Kanatzidis *et al.* prepared several surfactant-inorganic phases with the general formula of $[C_nH_{2n+1}N(CH_3)_3]_4Ge_4S_{10}$ ($n = 12$, 14, 16, and 18).[103] All four phases contain unconnected $[Ge_4S_{10}]^{4-}$ clusters and are fully crystalline with the space group P−1, unlike a typical amorphous mesoporous solid.

Ozin *et al.* subsequently prepared hexagonal mesostructured germanium sulfides by using low-valent metal cations such as Co^{2+}, Ni^{2+}, Cu^+, and Zn^{2+} to connect $[Ge_4S_{10}]^{4-}$ clusters around cetyltrimethylammonium bromide (CTAB).[104] This approach is similar to the synthesis of microstructured $[(CH_3)_4N]_4Mn[Ge_4S_{10}]$. However, Ozin's approach used formamide as the solvent instead of water.

Mesostructured germanium sulfides containing wormhole-like pores were prepared by Kanatzidis *et al.* by using divalent metal cations such as Zn^{2+}, Cd^{2+}, Hg^{2+}, Ni^{2+}, and Co^{2+} in aqueous medium with cationic surfactants $[C_nH_{2n+1}N(CH_3)_3]Br$ ($n = 12, 14, 16,$ and 18). A hexagonally ordered mesostructured manganese germanium sulfide was prepared under hydrothermal conditions with Mn^{2+} as the linking agent and mesityltrimethylammonium surfactant.[105] New hexagonally ordered mesophases could also be made by using Pt^{2+} as the linker in the presence of alkylpyridinium surfactants $[C_nH_{2n+1}NC_5H_5]Br$ ($n = 12$, 14, 16, 18, 20, and 22).[106]

In addition to divalent metal cations, trivalent and tetravalent cations (i.e. In^{3+}, Ga^{3+}, Sb^{3+}, and Sn^{4+}) were also effective as linking agents to organize $[Ge_4S_{10}]^{4-}$ clusters to form hexagonally ordered mesostructures.[107,108] In this case, cetylpyridinium bromide was used as the surfactant, and formamide served as the solvent. The mesophases made with Ga^{3+} and Sb^{3+} showed intense visible photoluminescence at 77 K.

In all the above cases, metal cations are used as linking agents to connect together $[Ge_4S_{10}]^{4-}$ clusters. It can be envisioned that it might also be possible to employ metal clusters to link $[Ge_4S_{10}]^{4-}$. One such cluster is the biologically relevant cubane Fe_4S_4. Starting from $K_4Ge_4S_{10}$ and substitutionally labile $[Fe_4S_4Cl_4]^{2-}$ clusters, a novel hexagonally ordered mesostructured sulfide built from both $[Ge_4S_{10}]^{4-}$ and $[Fe_4S_4Cl_4]^{2-}$ clusters was synthesized from a formamide solution containing the surfactant cetylpyridinium bromide.[109]

Tin Sulfides. Kessler *et al.* reported a crystalline phase synthesized from $SnCl_4$, Na_2S, and dodecylamine in the ethanol-water system at room temperature. This new tin sulfide has the formula of $(C_{12}H_{25}NH_3)_4[Sn_2S_6]\cdot 2H_2O$, and the $[Sn_2S_6]^{4-}$ dimers are formed by two edge-sharing $[SnS_4]$ tetrahedra.[110] Hexagonally ordered mesostructured tin sulfides were synthesized by Kanatzidis *et al.* by linking $[Sn_2S_6]^{4-}$ clusters with metal cations (i.e. Zn^{2+}, Cd^{2+}, Ga^{3+}). These photoluminescent mesophases were made in the presence of cetylpyridinium surfactant in the formamide solution under basic conditions and are semiconductors in the energy range from 2.5 to 3.1 eV.[111]

Germanium Selenides. Mesostructured germanium selenides are chemically and structurally similar to the corresponding sulfides. By following strategies similar to those developed for sulfides, Kanatzidis *et al.* have prepared a series of mesostructured germanium selenides. By using Zn^{2+}, Cd^{2+}, Hg^{2+}, Ni^{2+}, and Co^{2+} to link $[Ge_4Se_{10}]^{4-}$ clusters, mesostructured germanium selenides with wormholes were prepared in the presence of cationic surfactants $[C_nH_{2n+1}N(CH_3)_3]Br$ ($n = 12$, 14, 16, and 18).[112] Hexagonally mesostructured selenides were prepared by linking $[Ge_4Se_{10}]^{4-}$ clusters with Pt^{2+}, Sb^{3+}, Sn^{4+} or Fe_4S_4 clusters as linker agents and cetylpyridinium as the surfactant.

Tin Selenides. A series of mesostructured tin selenides were prepared by Kanatzidis *et al.* by linking $[SnSe_4]^{4-}$ anions with divalent metal cations.[113] These materials have the general formula of $(CP)_{4-2x}M_xSnSe_4$, where CP is cetylpyridinium; $1.0 < x < 1.3$; M = Mn, Fe, Co, Zn, Cd, and Hg. The d-spacing for the lowest peak ranges from 35 to 40 Å, and the pore arrangement based on wormhole, hexagonal, and cubic types has been observed. These phases are medium band gap semiconductors with band gap varying from 1.4 to 2.5 eV.

In addition to $[SnSe_4]^{4-}$ anions, $[Sn_2Se_6]^{4-}$ dimers could also form mesophases in combination with Pt^{2+} in the presence of long-chain pyridinium surfactants (C_nPyBr, $n = 18, 20$).[114] In this case, the cubic symmetry with the space group Ia-3d was preferred. The surfactant molecules could be ion-exchanged reversibly and without loss of the cubic structure and particle morphology. This Pt−Sn−Se phase has a low-energy band gap of 1.7 eV.

Similar to germanium sulfides or selenides, $[Sn_4Se_{10}]^{4-}$ adamantine clusters also exist and have been found to form mesostructured semiconductors with Pt^{2+} when templated by the lyotropic liquid-crystalline phase of alkylpyridinium surfactant $[C_{16}H_{33}NC_5H_5]Br$. This mesophase designated as $C_{16}PyPtSnSe$ has a band gap of 1.5 eV.

Other Chalcogenides. In addition to germanium (or tin) sulfides and selenides, mesostructured chalcogenides have also been made in other compositions. For example, Stupp *et al*. prepared hexagonally ordered mesostructured CdS by reacting H_2S with cadmium salts within the ordered environment of the preformed liquid crystal mesophase.[115] The mesophase was formed using oligoethylene oxide oleyl ether ($C_{18}H_{35}(OCH_2CH_2)_{10}OH$) mixed with an equal volume of aqueous 0.1 M Cd^{2+} salt. The symmetry and long-range order of the liquid crystal are preserved during the precipitation of the inorganic–organic mesophase.

3.3.7 *Metals*

By using preformed lyotropic liquid crystals of nonionic surfactants, Attard and coworkers have prepared mesostructured Pt and Sn.[116–118] This methodology can be applied to other elements such as Se and Te or metal alloys such as Pt–Ru or Pt–Pd.[119–121] The ordered mesostructured metals can be obtained by either chemical or electrochemical reduction of metal salts that are dissolved in the aqueous domain of lyotropic liquid crystals formed from oligoethylene oxide nonionic surfactants. The pore diameter can be tuned by the length of the alkyl chain of the surfactants, and the topology of metallic mesophases can be controlled by the symmetry of lyotropic liquid crystals.

The chemical reduction method generally produces mesostructured metals with granular morphology. The mesostructures of the metals formed by this method are casts of the structures of the liquid crystals used in the syntheses. During this process, the product is formed in the aqueous domain of the preorganized liquid crystals without disrupting the long-range ordering of the liquid crystals.

The electrochemical reduction method can produce mesostructured metals in the form of thin films. By electrodeposition of plating mixtures made from appropriate salts, mesostructured metal films can be produced on the electrode surface with high surface areas and good mechanical and electrochemical stability. The ability to produce ordered mesostructured metal films may lead to new types of electrode materials for applications such as batteries, fuel cells, and sensors.

3.4 Morphology Control

Mesoporous materials were originally synthesized in irregular bulk or powder forms, which could limit their applications in separation, optics, electronics, and so on. Thus, it is highly desirable to produce mesoporous materials with controllable macroscopic forms. So far, mesoporous materials have been synthesized in a variety of forms including thin films, spheres, fibers, monoliths, rods, single crystals, and nanoparticles. The acidic synthetic route ($S^+X^-I^+$) developed by Huo *et al*. appears to be the most appropriate for the morphological control of mesostructures.

3.4.1 *Thin Films*

The interests in thin films of silica-surfactant mesostructured materials arise from their potential applications in membrane-based separations, sensors, heterogeneous catalysis, and microelectronics.[122] Thin films of mesoporous silicas were first prepared by spin-coating an aqueous mixture of surfactants and prehydrolyzed silica precursors on a substrate followed by drying.[123,124] In addition to the spin-coating method, supported films can also be made by directly growing on substrates[125,126] or by dip-coating.[127,128] The film growth is generally faster by spin- or dip-coating. Free-standing films can be grown at liquid–vapor (e.g. water–air)[129,130] and liquid–liquid (e.g. oil–water) interfaces.[131] In addition to mesostructured silica, thin films of mesostructured titania,[132] zirconia,[133] tin oxide,[134] and organosilica[135] have also been successfully achieved.

3.4.2 *Spheres*

The use of emulsion biphase chemistry allows the preparation of both hollow[136] and hard[137] mesoporous silica spheres. Through a modified Stöber method,[138] spherical mesoporous silicas with particle sizes ranging from submicrometers to micrometers (∼2 µm) have been achieved.[139,140] Recent efforts have focused on control of the size and monodispersity. Ward and coworkers have achieved highly monodisperse mesoporous silica spheres with controllable particle size by EISA of precursor microdroplets produced by a vibrating orifice aerosol generator (VOAG).[141] Pseudomorphic transformation of preformed amorphous silica spheres to MCM-41 has demonstrated another promising way for the control of the size and morphology.[142]

3.4.3 *Monoliths*

There is an increasing interest in transparent monoliths with periodic mesoporous structures due to their potential applications in optics. Using the direct liquid crystal templating approach, Feng *et al*. prepared monolithic mesostructured silica templated by microemulsion liquid crystals.[143] By adjusting the synthetic composition, many different highly ordered mesophases, such as cubic spherical micellar $Im3m$, 3D hexagonal $P6_3/mmc$, bicontinuous cubic $Ia3d$, and primitive-centered cubic $Pn3m$, were obtained.[144] Careful control of evaporation of the solvent by a thin layer of mineral oil also helped the preparation of crack-free monoliths.[145]

3.4.4 *Fibers*

Early attempts to prepare mesoporous silica fibers employed mechanical drawing[146] or emulsion biphase chemistry.[147] The latter method resulted in fibers with a single-crystal-like mesostructure where the pore channels run circularly around the fiber axis.[148] Recently, Stucky and coworkers reported a simple one-phase route to mesostructured fibers.[149] The most intriguing aspect of this route is that the internal architecture of such nanofibers can be readily controlled via the synthesis.

3.5 Structural Stability

For applications of mesoporous materials, their structural stability is among the most important considerations and has therefore been studied extensively. Cassiers and coworkers[150] systematically investigated the thermal, hydrothermal, and mechanical stabilities of the most well-known mesoporous silicas. They found that the thermal stability is strongly dependent on the silica source and the wall thickness. M41S materials prepared with fumed silica show higher thermal stability than those made from TEOS. Transformation of layered silicates to mesoporous silica allows the resulting porous clay heterostructures (PCH) and FSM-16 to possess more condensed and ordered walls than M41S materials. It is well known that SBA-15 consists of thicker walls, and is thus expected to exhibit good thermal stability. The following stability trend has been observed by Cassiers *et al.*: MCM-41 (fumed silica), MCM-48 (fumed silica), KIT-1 (colloidal silica) > SBA-15(TEOS) > FSM-16 (layered silicate), PCH (layered silicate) > MCM-41 (TEOS), MCM-48 (TEOS), HMS (TEOS).

The hydrothermal stability is mainly dependent on the wall thickness and the degree of polymerization. KIT-1 and SBA-15 are highly resistant to hydrothermal treatment due to their highly polymerized and thicker walls. Under mild steaming conditions, the pore structure might lead to different hydrothermal stability for materials with comparable wall thickness. Cubic MCM-48 exhibits less structural degradation than the hexagonal mesoporous materials. A complete hydrothermal stability order reported by Cassiers *et al.* is as follows: KIT-1 > SBA-15 > MCM-48 (fumed silica and TEOS), PCH > FSM-16, MCM-41 (fumed silica and TEOS), HMS.

Unlike the thermal and hydrothermal stabilities, the mechanical stability seems less dependent on the nature of mesoporous materials. All materials gradually collapse with the increase of pressure, accompanied with the decrease of surface area and pore volume.[151] Recent studies show that cubic SBA-1 and MCM-48 are more mechanically stable than hexagonal mesoporous materials such as MCM-41 and SBA-15.[152] Hydrolysis of Si–O–Si bonds by water adsorbed onto the silanol groups under compression was found as the main reason for mechanical instability.[153] Organically functionalized materials are more hydrophobic than unmodified counterparts, and thus show enhanced mechanical stability due to the water repelling ability.[154]

3.6 Application

Since the discovery of ordered mesoporous materials, researchers have explored many possible applications that can take advantage of the unique compositional or structural features of mesoporous materials. In addition to applications in traditional areas such as catalysis, separation, and ion exchange, new applications that might involve mesoporous materials include stationary phases in HPLC, bio and macromolecular separations, low dielectric constant materials, enzyme immobilization, optical host materials, templates for fabrication of porous carbons, and reactions in confined environments.

3.6.1 Catalysis[155,156]

The potential application in catalysis is one of the most important uses of ordered mesoporous materials. Mesoporous materials can be used as catalysts in either acid or redox catalysis. To help increase acidity, trivalent cations such as Al and B are often incorporated into siliceous mesoporous framework to generate more acid sites. The acidity can also be generated by dispersing heteropoly acids or by grafting organic functional groups onto the surface of mesoporous solids. Many modified MCM-41 type materials have been found to be catalytically active in selected acid-catalyzed processes, However, owing to their disordered framework, mesoporous materials have only moderate acidity. And this limits their applications in petroleum refining and fine chemical synthesis.

For redox catalysis, efforts have been spent on preparing transition metal modified mesoporous materials. These materials are capable of extending the catalytic oxidation chemistry to large molecules. The selective catalytic activity has also been demonstrated, for example, in the oxidation of aromatic compounds by using titanium-containing mesoporous silica (Ti-MCM-41 and Ti-HMS).[157]

In addition to their direct use as catalysts, mesoporous materials are also useful as catalyst supports because of their high surface area, high thermal stability, and low cost. Extensive studies have been done on the preparation and catalytic activity of metals (e.g. Pt, Pd, Ru, Cu) and metal oxides (e.g. TiO_2, VO_x, ZrO_2, Fe_2O_3) supported on ordered mesoporous materials. The impact of mesoporous materials has also been felt in organometallic chemistry, as shown by a new series of composites being made by functionalizing mesoporous materials with organometallic compounds.[158]

3.6.2 Environmental Remediation and Separation

Removal of heavy-metal ions has been a major focus in environmental remediation and cleanup. Various materials, such as activated charcoal, clays, silica gels, and ion-exchange resins have been used as adsorbents. Functionalized mesoporous silicas have recently proved to be a promising or even better alternative.[159,160] Mercier *et al.* prepared a highly effective Hg^{2+} adsorbent by grafting thiol moieties to the framework walls of mesoporous silica, denoted MP-HMS.[159] Because of the uniform and large pore structure, MP-HMS showed an improved access of guest species to the binding sites along with a high loading capacity of 310 mg g^{-1} (1.5 mmol g^{-1}), compared to those made from disordered porous materials, such as silica gel. Concurrently, Feng and coworkers reported a similar heavy-metal ion adsorbent by modifying large-pore MCM-41 with a cross-linked monolayer of mercaptopropylsilane with thiol terminal groups.[160] The resulting adsorbent, functionalized monolayers on mesoporous supports (FMMS), was extremely effective for the removal of Hg^{2+} and other heavy-metal ions. The high relative surface coverage of monolayers (up to 76%) led to a remarkable adsorption capacity of 505 mg g^{-1} for Hg^{2+}. To simplify the synthesis procedure, Mercier *et al.* developed a one-step method by cocondensation of TEOS with 3-mercaptopropyltrimethoxysilane in the presence of surfactants.[161]

Unlike the previously studied mercaptopropyl ligand, the thiourea ligands are expected to have weaker bonding to mercury ions in comparison to thiol group, which should facilitate the adsorbent regeneration.[162] A good example is large-pore MCM-41 grafted with 1-allyl-3-propylthiourea,[163] which could be conveniently regenerated under mild conditions. Recent work in this area has focused on the improvement of mercury adsorption capacity. A logical strategy to increase capacity is the use of multifunctional ligands.[162] Grafting of (1,4)-bis(triethoxysilyl)propane tetrasulfide onto the surface of SBA-15 has led to an adsorbent with an unprecedented loading capacity of 13.5 mmol Hg^{2+} g^{-1}.[164] Functionalized mesoporous silicas for the removal of other metal ions, such as Pb^{2+}, Cu^{2+}, and Zn^{2+}, have also been reported.[165]

3.6.3 Chromatography

Commercial chromatography silica stationary phases were prepared by the polymerization induced colloidal assembly (PICA) method,[166] subsequently exhibiting an interparticle (textural) pore structure with moderate surface area (100–550 $m^2\,g^{-1}$) and broad pore-size distribution. Ordered mesoporous silicas show a high surface area up to 1600 $m^2\,g^{-1}$ coupled with tunable and uniform pore size arising from intraparticle (structural) porosity, and are thus expected to provide superior chromatographic performance as stationary phases. MCM-41 was first tested as chromatographic matrix for normal-phase high-performance liquid chromatography (HPLC)[167] and size-exclusion chromatography.[168] The most intriguing advantage of MCM-41 is the ability to separate different types of analytes (basic, acidic, and neutral) with good column efficiency within reasonable analysis times.[167] Gallis *et al.*[169] used acid-prepared mesoporous spheres (APMS) to separate ferrocene from acetylferrocene by normal-phase flash liquid chromatography, exhibiting better separating ability (e.g. longer retention time, higher selectivity) than commercial silicas. Similar results have also been obtained in normal-phase, reversed-phase, and chiral HPLC based on APMS and spherical MCM-48.[170,171] Boissiere and coworkers[172] used MSU-1 spheres to separate polycyclic aromatic hydrocarbons (PAHs) by normal-phase HPLC. Separation of biomolecules was accomplished on spherical SBA-15 by reversed-phase HPLC.[173] In comparison to their applications in HPLC, there are only few efforts to use mesoporous silicas in gas chromatography (GC).[174]

4 MACROPOROUS MATERIALS

4.1 Synthesis

Ordered macroporous materials can be templated by colloidal crystals or emulsions. In comparison to microporous and mesoporous materials, the synthesis strategy of macroporous materials is relatively simple.

4.1.1 Colloidal Crystal Templating

A general three-step procedure[175,176] for the formation of macroporous materials by colloidal crystal templating is illustrated in Figure 6. In the first step, monodispersed colloidal spheres assemble into ordered 3D or sometimes 2D arrays to serve as templates. Secondly, the voids of colloidal crystals are filled by precursors that subsequently solidify to form composites. Finally, the original spheres are removed, creating a solid framework with interconnected voids, which faithfully replicate the template arrays.

Latex and silica spheres are the most commonly used templates for the colloidal crystal assembly, because they are highly monodisperse and commercially available. Many crystallization methods have been used to form close-packed structures, including sedimentation, centrifugation, filtration, convective deposition, slit filling, and pressing. All these methods result in polycrystalline domains, usually with face-centered cubic (fcc) packing or randomly stacked hexagonal close-packed planes (rhcp), affording 26-vol% void space. Sometimes colloidal crystals are sintered or annealed to increase their stability and ensure interconnection.

The design of the interstices filling in colloidal crystals with appropriate media and subsequently fluid–solid transformation is central to the whole synthesis. Fluid precursors in the voids of crystal arrays can solidify by polymerization[177] and sol-gel hydrolysis.[178] More recently, many methods[179] have been developed including salt precipitation and chemical conversion, chemical vapor deposition (CVD), spraying techniques (spray pyrolysis, ion spraying, and laser spraying), nanocrystal deposition and sintering, oxide and salt reduction, electrodeposition, and electroless deposition.

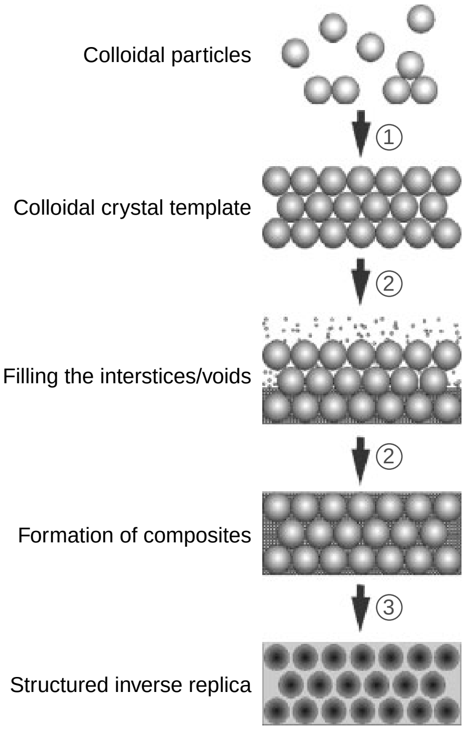
Colloidal particles
①
Colloidal crystal template
②
Filling the interstices/voids
②
Formation of composites
③
Structured inverse replica

Figure 6 A schematic of the general procedure for preparing ordered macroporous materials by colloidal crystal templating. (1) Assembly of colloidal particles to form colloidal crystal template; (2) Filling the interstices/voids with precursors to form composites; and (3) Removal of templates. (Reprinted from Ref. 175, © 2000, with permission from Elsevier)

Templates should be removed from the composites to yield porous structures. Polymer templates can be removed by calcination, by dissolution with appropriate solvents, or by photo degradation, while silicas are eliminated by dissolution in aqueous HF or NaOH solution.

4.1.2 *Emulsion Templating*[180,181]

Imhof and Pine have demonstrated that a highly uniform dispersion of emulsion droplets can serve as templates to prepare macroporous materials of titania, silica, and zirconia. In their work, treatment of polydisperse emulsions by shearing and/or fraction resulted in uniform emulsion droplets around which alkoxide precursors are deposited through a sol-gel process. Subsequent drying and heat treatment yielded solid materials with spherical pores left behind by the emulsion droplets (see Figure 7). Macroporous materials templated by emulsion droplets possess highly uniform pores in a wide range from 50 nm to 10 µm, unlike those prepared by colloidal crystal templating whose pore sizes are within 100 to 1000 nm. The materials can be adjusted with any desired porosity up to 90%.

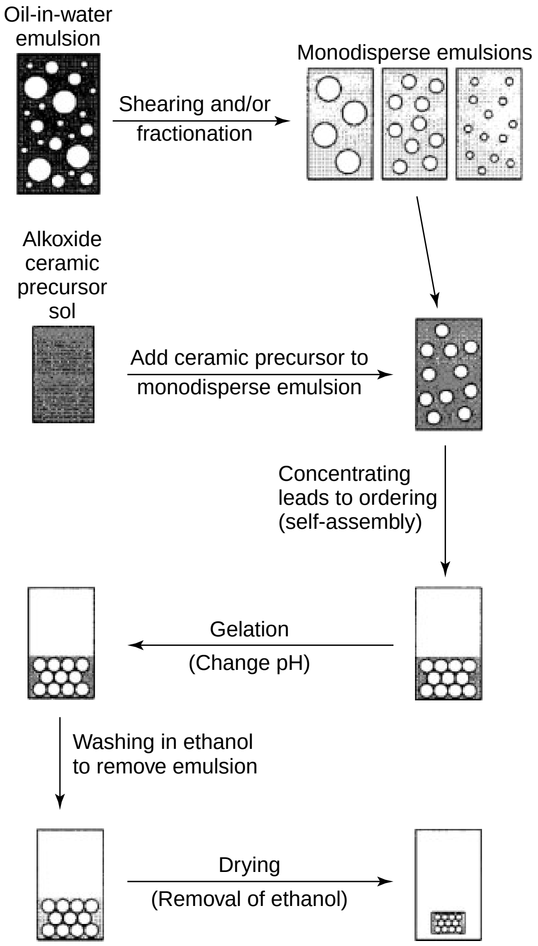
Oil-in-water emulsion
Shearing and/or fractionation
Monodisperse emulsions
Alkoxide ceramic precursor sol
Add ceramic precursor to monodisperse emulsion
Concentrating leads to ordering (self-assembly)
Gelation
(Change pH)
Washing in ethanol to remove emulsion
Drying
(Removal of ethanol)

Figure 7 A schematic of procedure to macroporous materials using emulsion droplets as templates. (Reproduced by permission of Wiley VCH)

4.2 Composition and Wall Structures

A summary of ordered macroporous materials with different compositions is given elsewhere.[182,183] Many compositions have been made, ranging from oxides,[177] polymers,[184] and carbons,[185] to semiconductors[186] and metals.[187] The wall structures of macroporous materials can be amorphous, crystalline, with mesopores or micropores, organically modified, or with surface catalysts.[188]

4.3 Applications

Because macroporous materials have 3D periodicity on a length scale comparable to the wavelength of visible light, 3DOM materials have potential use as photonic crystals.[183] Other potential applications include catalysts, bioglasses, sensors, and substrates for surface-enhanced Raman scattering spectroscopy (SERS).[176,179]

5 HIERARCHICAL POROUS STRUCTURES

Hierarchical porous materials are solids that are ordered at different length scales. Materials with multiple porosities are of high interest for applications in catalysis and separation, because these applications can take advantages of different pore structures. For example, microporous–mesoporous composites have shown superior catalytic activities by the combination of strong acidity from zeolites with high reactant or product mobility due to large uniform mesopores.[189] Several approaches have been reported on the design and synthesis of hierarchical porous materials, as discussed below.

5.1 Multiple Templating

As discussed previously, organic molecules, supramolecular micelles (or liquid crystals), and colloidal crystals (or emulsions) are employed as templates to prepare microporous, mesoporous, and macroporous materials, respectively. Combining different templates into one synthesis is expected to generate hierarchical porous materials. Yang *et al.* have demonstrated a simple procedure to fabricate hierarchical ordered oxides (silica, niobia, and titania) by concurrently or sequentially combining latex sphere templating, cooperative assembly, and micromolding using polydimethylsiloxane (PDMS) stamps (Figure 8a).[190] In their work, the PDMS mold with micrometer-scale patterns was placed on a substrate, creating accessible channels between the mold and the substrate in which the latex spheres organized into a close-packed array. The voids of the array were filled with a sol-gel block copolymer precursor solution. After sufficient time for cross-linking and polymerization, the mold was removed and the organic templates were eliminated by calcination. The resulting materials exhibited surface patterns of macroporous structures with mesoporous walls (Figure 8, b–e).

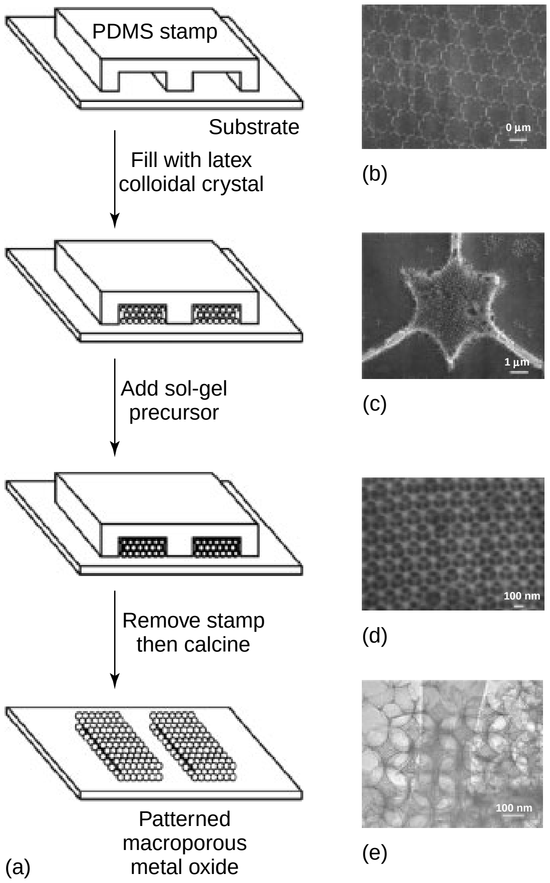
PDMS stamp
Substrate
Fill with latex colloidal crystal
Add sol-gel precursor
Remove stamp then calcine
Patterned macroporous metal oxide
(a)
0 µm
(b)
1 µm
(c)
100 nm
(d)
100 nm
(e)

Figure 8 Schematic of the fabrication of hierarchical ordered oxides (a) (Reprinted from Ref. 179, © 2001, with permission from Elsevier) scanning electron microscopy (SEM) images (b, c, d), at different magnifications, of hierarchical ordered mesoporous silica display a high-quality surface pattern (∼1000 nm), which is made up of a macroporous (∼100 nm) framework of cubic mesoporous silica (∼11 nm), as shown in TEM image (e). (Reprinted with permission from P. Yang *et al.*, *Science*, 1998, **282**, 2244)

Stein and coworkers have synthesized a macroporous silicate with zeolitic microporous frameworks by a ‘dual templating’ method using latex spheres and tetrapropylammonium hydroxide.[191] Similarly, in situ or simultaneous synthesis of macroporous silica with mesoporous wall[192] and micro/mesoporous composites[193] has been reported in the presence of appropriate dual templates. Microporous/mesoporous materials can also be prepared by a two-step synthetic process, where mesoporous materials are synthesized first, followed by transformation of amorphous mesopore walls into a microporous crystalline (or semicrystalline) phase. Huang *et al.* prepared a MCM-41/ZSM-5 composite containing interconnected mesopore and micropore.[194] Trong On *et al.* demonstrated a general method for the preparation of large-pore mesoporous materials with semicrystalline zeolitic frameworks, involving a templated solid-state secondary crystallization of zeolites from amorphous mesopore walls.[195] Unlike the previous work, Goto and coworkers described a ‘reversed’ two-step approach to prepare microporous/mesoporous composites using zeolites as the silica-alumina source for mesoporous materials.[196]

5.2 Assembly from Building Blocks

Colloidal zeolites have been used as building blocks to fabricate hierarchical porous materials. Infiltrating ethanol sol of zeolite nanoparticles into an ordered array of polystyrene spheres resulted in macroporous zeolites, which involves a self-assembly process.[197] After ethanol evaporation, zeolite nanoparticles were aggregated by capillary forces. High concentration of external silanol groups favored the formation of hydrogen bonds between particles and eventually Si–O–Si bonds after calcination. The method has been further developed to produce transparent and self-standing zeolite membranes with controlled mesoporosity.[198] Concurrently, the preformed zeolite-coated polystyrene spheres have been used as building blocks to assemble hierarchical materials with ordered nano, meso, and macroporosity.[199] The core-shell building blocks were fabricated through a 'layer-by-layer' method[200] by alternate adsorption of zeolite nanoparticles and positively charged macromolecules onto latex spheres. This allows the wall thickness of the resulting macroporous monoliths to be fine-tuned by the layer numbers.

5.3 Bulk Dissolution and Structural Rearrangement

The strategy of this method is to utilize the inherent porosity of bulky substrates in the construction of hierarchical structures by incorporating additional pore systems. Diatoms are unicellular algae whose walls are composed of silica with an internal pore diameter at submicron to micron scales. Zeolitization of diatoms, in which zeolite nanoparticles are dispersed on the surface of diatoms followed by a hydrothermal conversation of a portion of the diatom silicas into zeolites, resulted in the formation of a micro/mesoporous composite material.[201] Similarly, wood has also been used as a substrate to prepare meso/macroporous composites and meso/macroporous zeolites. After the synthesis, wood is removed by calcination.[202]

6 RELATED ARTICLES

Self-assembled Inorganic Architectures; Sol–Gel Synthesis of Solids; Zeolites.

7 REFERENCES

1. K. S. W. Sing, D. H. Everett, R. A. W. Haul, L. Moscou, R. A. Pierotti, J. Rouquerol, and R. Siemieniewska, *Pure Appl. Chem.*, 1985, **57**, 603.
2. S. J. Gregg and K. S. W. Sing, 'Adsorption, Surface Area and Porosity', Academic Press, San Diego, CA, 1982.
3. J. D. Joannopoulos, P. R. Villeneuve, and S. Fan, *Nature*, 1997, **386**, 143.
4. Ch. Baerlocher, W. M. Meier, and D. H. Olson, 'Atlas of Zeolite Framework Types', Elsevier, New York, 2001.
5. M. E. Davis, *Nature*, 2002, **417**, 813.
6. N. Zheng, X. Bu, and P. Feng, *Nature*, 2003, **426**, 428.
7. A. Dyer, in 'Encyclopedia of Inorganic Chemistry', ed. B. R. King, John Wiley & Sons, New York, 1994, p. 4364.
8. M. O'Keeffe and O. M. Yaghi, *Chem. Eur. J.*, 1999, **5**, 2796.
9. X. Bu, P. Feng, T. E. Gier, D. Zhao, and G. D. Stucky, *J. Am. Chem. Soc.*, 1998, **120**, 13389.
10. A. Corma, M. J. Diaz-Cabanas, J. Martinez-Triguero, F. Rey, and J. Rius, *Nature*, 2002, **418**, 514.
11. A. K. Cheetham, G. Ferey, and T. Loiseau, *Angew. Chem., Int. Ed. Engl.*, 1999, **38**, 3269.
12. T. E. Gier and G. D. Stucky, *Nature*, 1991, **349**, 508.
13. P. Feng, T. Zhang, and X. Bu, *J. Am. Chem. Soc.*, 2001, **123**, 8608.
14. X. Bu and P. Feng, in 'The Chemistry of Nanostructured Materials', ed. P. Yang, World Scientific, Singapore, 2003, p. 1, and references therein.
15. R. W. J. Scott, M. J. Mac Lachlan, and G. A. Ozin, *Curr. Opin. Solid State Mater. Sci.*, 1999, **4**, 113.
16. N. Zheng, X. Bu, and P. Feng, *Science*, 2002, **298**, 2366.
17. O. M. Yaghi, M. O'Keeffe, N. W. Ockwig, H. K. Chae, M. Eddaoudi, and J. Kim, *Nature*, 2003, **423**, 705.
18. U. Ciesla and F. Schüth, *Micropor. Mesopor. Mater.*, 1999, **27**, 131.
19. F. Di Renzo, A. Galarneau, P. Trens, and F. Fajula, in 'Handbook of Porous Solids', eds. F. Schüth, K. S. W. Sing, and J. Weitkamp, John Wiley & Sons, Weinheim, 2002, p. 1311.
20. C. T. Kresge, M. E. Lonowicz, W. J. Roth, J. C. Vartuli, and J. S. Beck, *Nature*, 1992, **359**, 710.
21. J. S. Beck, J. C. Vartuli, W. J. Roth, M. E. Lonowicz, C. T. Kresge, K. T. Schmitt, C. T.-W. Chu, D. H. Olson, E. W. Sheppard, S. B. McCullen, J. B. Higgins, and J. L. Schlenker, *J. Am. Chem. Soc.*, 1992, **114**, 10834.
22. A. Monnier, F. Schüth, Q. Huo, D. Kumar, D. Margolese, R. S. Maxwell, G. D. Stucky, M. Krishnamurty, P. Petroff, A. Firouzi, M. Janicke, and B. F. Chmelka, *Science*, 1993, **261**, 1299.
23. Q. Huo, D. I. Margolese, U. Ciesla, P. Feng, T. E. Gier, P. Sieger, R. Leon, P. M. Petroff, F. Schuth, and G. D. Stucky, *Nature*, 1994, **368**, 317.
24. Q. Huo, D. I. Margolese, U. Ciesla, D. G. Demuth, P. Feng, T. E. Gier, P. Sieger, A. Firouzi, B. F. Chmelka, F. Schuth, and G. D. Stucky, *Chem. Mater.*, 1994, **6**, 1176.
25. D. Zhao, J. Feng, Q. Huo, N. Melosh, G. H. Fredrickson, B. F. Chmelka, and G. D. Stucky, *Science*, 1998, **279**, 548.
26. D. Zhao, Q. Huo, J. Feng, B. F. Chmelka, and G. D. Stucky, *J. Am. Chem. Soc.*, 1998, **120**, 6024.
27. P. Schmidt-Winkel, W. W. Lukens Jr, D. Zhao, P. Yang, B. F. Chmelka, and G. D. Stucky, *J. Am. Chem. Soc.*, 1999, **121**, 254.
28. P. Schmidt-Winkel, W. W. Lukens Jr, P. Yang, D. I. Margolese, J. S. Lettow, J. Y. Ying, and G. D. Stucky, *Chem. Mater.*, 2000, **12**, 686.
29. P. T. Tanev and T. J. Pinnavaia, *Science*, 1995, **267**, 865.
30. S. A. Bagshaw, E. Prouzet, and T. J. Pinnavaia, *Science*, 1995, **269**, 1242.
31. W. Zhang, B. Glomski, T. R. Pauly, and T. J. Pinnavaia, *Chem. Commun.*, 1999, 1803.
32. D. M. Antonelli and J. Y. Ying, *Angew. Chem., Int. Ed. Engl.*, 1996, **35**, 426.

33. D. M. Antonelli, A. Nakahira, and J. Y. Ying, *Inorg. Chem.*, 1996, **35**, 3126.
34. G. S. Attard, J. C. Glyde, and C. G. Goltner, *Nature*, 1995, **378**, 366.
35. P. Feng, X. Bu, and D. Pine, *Langmuir*, 2000, **16**, 5304.
36. C. J. Brinker, Y. Lu, A. Sellinger, and H. Fan, *Adv. Mater.*, 1999, **11**, 579.
37. N. K. Raman, M. T. Anderson, and C. J. Brinker, *Chem. Mater.*, 1996, **8**, 1682.
38. Q. Huo, R. Leon, P. M. Petroff, and G. D. Stucky, *Science*, 1995, **268**, 1324.
39. G. D. Stucky, Q. Huo, A. Firouzi, B. F. Chmelka, S. Schacht, I. G. Voigt-Martin, and F. Schüth, in 'Progress in Zeolite and Microporous Materials, Studies in Surface Science and Catalysis', eds. H. Chon, S.-K. Ihm, and Y. S. Uh, Elsevier, Amsterdam, 1997, Vol. 105, p. 3.
40. Q. Huo, D. I. Margolese, and G. D. Stucky, *Chem. Mater.*, 1996, **8**, 1147.
41. E. Prouzet and T. J. Pinnavaia, *Angew. Chem., Int. Ed. Engl.*, 1997, **36**, 516.
42. A. Sayari, M. Kruk, M. Jaroniec, and I. L. Moudrakovshi, *Adv. Mater.*, 1998, **10**, 1376.
43. D. Khushalani, A. Kuperman, G. A. Ozin, K. Tanaka, J. Garces, M. M. Olken, and N. Coombs, *Adv. Mater.*, 1995, **7**, 842.
44. A. Sayari, Y. Yang, M. Kruk, and M. Jaroniec, *J. Phys. Chem. B*, 1999, **103**, 3651.
45. A. Sayari, *Angew. Chem., Int. Ed. Engl.*, 2000, **39**, 2920.
46. S. S. Kim, W. Zhang, and T. J. Pinnavaia, *Science*, 1998, **282**, 1302.
47. C. Yu, Y. Yu, and D. Zhao, *Chem. Commun.*, 2000, 575.
48. R. Ryoo, J. M. Kim, C. H. Ko, and C. H. Shin, *J. Phys. Chem.*, 1996, **100**, 17718.
49. S. Inagaki, Y. Fukushima, and K. Kuroda, *J. Chem. Soc., Chem. Commun.*, 1993, 680.
50. A. Galarneau, A. Barodawalla, and T. J. Pinnavaia, *Nature*, 1995, **374**, 529.
51. Y. Sakamoto, M. Kaneda, O. Terasaki, D. Zhao, J. M. Kim, G. D. Stucky, H. J. Shin, and R. Ryoo, *Nature*, 2000, **408**, 449.
52. J. R. Matos, M. Kruk, L. P. Mercuri, M. Jaroniec, L. Zhao, T. Kamiyama, O. Terasaki, T. J. Pinnavaia, and Y. Liu, *J. Am. Chem. Soc.*, 2003, **125**, 821.
53. D. Zhao, Q. Huo, J. Feng, J. Kim, Y. Han, and G. D. Stucky, *Chem. Mater.*, 1999, **11**, 2668.
54. J. Y. Ying, C. P. Mehnert, and M. S. Wong, *Angew. Chem., Int. Ed. Engl.*, 1999, **38**, 56.
55. P. Feng, Y. Xia, F. Jiang, X. Bu, and G. D. Stucky, *Chem. Commun.*, 1997, 949.
56. D. Zhao, Z. Luan, and L. Kevan, *Chem. Commun.*, 1997, 1009.
57. B. Tian, X. Liu, B. Tu, C. Yu, J. Fan, L. Wang, S. Xie, G. D. Stucky, and D. Zhao, *Nat. Mater.*, 2003, **2**, 159.
58. P. Yang, D. Zhao, D. I. Margolese, B. F. Chmelka, and G. D. Stucky, *Nature*, 1998, **396**, 152.
59. D. Antonelli and J. Y. Ying, *Angew. Chem., Int. Ed. Engl.*, 1995, **34**, 2014.
60. V. F. Stone Jr and R. J. Davis, *Chem. Mater.*, 1998, **10**, 1468.
61. D. M. Antonelli, *Micropor. Mesopor. Mater.*, 1999, **30**, 315.
62. H. Luo, C. Wang, and Y. Yan, *Chem. Mater.*, 2003, **15**, 3841.
63. J. A. Knowles and M. J. Hudson, *J. Chem. Soc., Chem. Commun.*, 1995, 2083.
64. M. J. Hudson and J. A. Knowles, *J. Mater. Chem.*, 1996, **6**, 89.
65. F. Schueth, *Ber. Bunsen-Ges. Phys. Chem.*, 1995, **99**, 1306.
66. V. Ciesla, S. Schacht, G. D. Stucky, K. K. Unger, and F. Schüth, *Angew. Chem., Int. Ed. Engl.*, 1996, **35**, 541.
67. J. S. Reddy and A. Sayari, *Catal. Lett.*, 1996, **38**, 219.
68. A. Kim, P. Bruinsma, Y. Chen, L.-Q. Wang, and J. Liu, *Chem. Commun.*, 1997, 161.
69. G. Pacheco, E. Zhao, A. Garcia, A. Sklyarov, and J. J. Fripiat, *Chem. Commun.*, 1997, 491.
70. G. Pacheco, E. Zhao, A. Garcia, A. Sklyarov, and J. J. Fripiat, *J. Mater. Chem.*, 1998, **8**, 219.
71. M. S. Wong and J. Y. Ying, *Chem. Mater.*, 1998, **10**, 2067.
72. S. A. Bagshaw and T. J. Pinnavaia, *Angew. Chem., Int. Ed. Engl.*, 1996, **35**, 1102.
73. S. Cabrera, J. El Haskouri, J. Alamo, A. Beltran, D. Beltran, S. Mendioroz, M. D. Marcos, and P. Amoros, *Adv. Mater.*, 1999, **11**, 379.
74. F. J. P. Vaudry, S. Khodabandeh, and M. E. Davis, *Chem. Mater.*, 1996, **8**, 1451.
75. M. Yada, M. Machida, and T. Kijima, *Chem. Commun.*, 1996, 769.
76. Z. Zhang, R. W. Hicks, T. R. Pauly, and T. J. Pinnavaia, *J. Am. Chem. Soc.*, 2002, **124**, 1592.
77. Z. Zhang and T. J. Pinnavaia, *J. Am. Chem. Soc.*, 2002, **124**, 12294.
78. R. Ryoo, S. H. Joo, M. Kruk, and M. Jaroniec, *Adv. Mater.*, 2001, **13**, 677.
79. R. Ryoo, S. H. Joo, and S. Jun, *J. Phys. Chem. B*, 1999, **103**, 7743.
80. J. Lee, S. Yoon, T. Hyeon, S. M. Oh, and K. B. Kim, *Chem. Commun.*, 1999, 2177.
81. S. H. Joo, S. J. Choi, I. Oh, J. Kwak, Z. Liu, O. Terasaki, and R. Ryoo, *Nature*, 2001, **412**, 169.
82. M. Kruk, M. Jaroniec, R. Ryoo, and S. H. Joo, *J. Phys. Chem. B*, 2000, **104**, 7960.
83. S. H. Joo, S. Jun, and R. Ryoo, *Micropor. Mesopor. Mater.*, 2001, **44/45**, 153.
84. J. Lee, S. Yoon, S. M. Oh, C.-H. Shin, and T. Hyeon, *Adv. Mater.*, 2000, **12**, 359.

85. S. Jun, S. H. Joo, R. Ryoo, M. Kruk, M. Jaroniec, Z. Liu, T. Hosanna, and O. Terasaki, *J. Am. Chem. Soc.*, 2000, **122**, 10712.

86. M. Kruk, M. Jaroniec, C. H. Ko, and R. Ryoo, *Chem. Mater.*, 2000, **12**, 1961.

87. J. Fan, C. Yu, L. Wang, B. Tu, D. Zhao, Y. Sakamoto, and O. Terasaki, *J. Am. Chem. Soc.*, 2001, **123**, 12113.

88. C. Yu, J. Fan, B. Tian, D. Zhao, and G. D. Stucky, *Adv. Mater.*, 2002, **14**, 1742.

89. S. B. Yoon, J. Y. Kim, and J.-S. Yu, *Chem. Commun.*, 2001, 559.

90. S.-S. Kim and T. J. Pinnavaia, *Chem. Commun.*, 2001, 2418.

91. J.-S. Lee, S. H. Joo, and R. Ryoo, *J. Am. Chem. Soc.*, 2002, **124**, 1156.

92. T.-W. Kim, I.-S. Park, and R. Ryoo, *Angew. Chem., Int. Ed. Engl.*, 2003, **42**, 4375.

93. T. Asia, M. J. Mac Lachlan, N. Coombs, and G. A. Ozin, *Nature*, 1999, **402**, 867.

94. S. Inagaki, S. Guan, Y. Fukushima, T. Hosanna, and O. Terasaki, *J. Am. Chem. Soc.*, 1999, **121**, 9611.

95. B. J. Melded, B. T. Holland, C. F. Branford, and A. Stein, *Chem. Mater.*, 1999, **11**, 3302.

96. T. Asia, G. A. Ozin, H. Grundy, M. Kruk, and M. Jaroniec, in ‘Nonporous Materials III, Studies in Surface Science and Catalysis’, eds. A. Sayari and M. Jaroniec, Elsevier, Amsterdam, 2002, Vol. 141, p. 1.

97. C. Yeshiva-Ishii, T. Asia, N. Coombs, M. J. Mac Lachlan, and G. A. Ozin, *Chem. Commun.*, 1999, 2539.

98. S. Guan, S. Inagaki, T. Hosanna, and O. Terasaki, *Micropor. Mesopor. Mater.*, 2001, **44–45**, 165.

99. H. Zhu, D. J. Jones, J. Zodiac, J. Rosier, and R. Duarte, *Chem. Commun.*, 2001, 2568.

100. S. Inagaki, S. Guan, T. Hosanna, and O. Terasaki, *Nature*, 2002, **416**, 304.

101. M. J. Mac Lachlan, T. Asia, and G. A. Ozin, *Chem. Eur. J.*, 2000, **6**, 2507.

102. T. Asia, C. Yeshiva-Ishii, M. J. Mac Lachlan, and G. A. Ozin, *J. Mater. Chem.*, 2000, **10**, 1751.

103. F. Bonhomie and M. G. Kanatzidis, *Chem. Mater.*, 1998, **10**, 1153.

104. M. J. Maculation, N. Coombs, and G. A. Ozin, *Nature*, 1999, **397**, 681.

105. K. K. Rang an, S. J. L. Billing, V. Pekoe, J. Heisting, and M. G. Kanatzidis, *Chem. Mater.*, 1999, **11**, 2629.

106. P. N. Realities, K. K. Rang an, and M. G. Kanatzidis, *J. Am. Chem. Soc.*, 2002, **124**, 2604.

107. K. K. Rang an, P. N. Realities, and M. G. Kanatzidis, *J. Am. Chem. Soc.*, 2000, **122**, 10230.

108. K. K. Rang an, P. N. Realities, T. Bakes, and M. G. Kanatzidis, *Chem. Commun.*, 2001, 809.

109. P. N. Realities, T. Bakes, V. Papaefthymiou, and M. G. Kanatzidis, *Angew. Chem., Int. Ed. Engl.*, 2002, **39**, 4558.

110. J. Li, B. Marler, H. Kessler, M. Soulard, and S. Kallus, *Inorg. Chem.*, 1997, **36**, 4697.

111. K. K. Rangan, P. N. Trikalitis, C. Canlas, T. Bakas, D. P. Weliky, and M. G. Kanatzidis, *Nanostruct. Lett.*, 2002, **2**, 513.

112. M. Wachhold, K. K. Rangan, M. Lei, M. F. Thorpe, S. J. L. Billinge, V. Petkov, J. Heising, and M. G. Kanatzidis, *J. Solid State Chem.*, 2000, **152**, 21.

113. P. N. Trikalitis, K. K. Rangan, T. Bakas, and M. G. Kanatzidis, *Nature*, 2001, **410**, 671.

114. P. N. Trikalitis, K. K. Rangan, T. Bakas, and M. G. Kanatzidis, *J. Am. Chem. Soc.*, 2002, **124**, 12255.

115. P. Braun, P. Osenar, and S. I. Stupp, *Nature*, 1996, **380**, 325.

116. G. S. Attard, C. G. Goltner, J. M. Corker, S. Henke, and R. H. Templer, *Angew. Chem., Int. Ed. Engl.*, 1997, **36**, 1315.

117. G. S. Attard, P. N. Bartlett, N. R. B. Coleman, J. E. Elliott, J. R. Owen, and J. H. Wang, *Science*, 1997, **278**, 838.

118. A. H. Whitehead, J. M. Elliott, J. R. Owen, and G. S. Attard, *Chem. Commun.*, 1999, 331.

119. G. S. Attard, S. A. A. Leclerc, S. Maniguet, A. E. Russell, I. Nandhakumar, B. R. Gollas, and P. N. Bartlett, *Micropor. Mesopor. Mater.*, 2001, **44–45**, 159.

120. G. S. Attard, S. A. A. Leclerc, S. Maniguet, A. E. Russell, I. Nandhakumar, B. R. Gollas, and P. N. Bartlett, *Chem Mater.*, 2001, **13**, 1444.

121. S. Guerin and G. S. Attard, *Electrochem. Commun.*, 2001, **3**, 544.

122. S. Pevzner, O. Regev, and R. Yerushalmi-Rozen, *Curr. Opin. Colloid Interface Sci.*, 2000, **4**, 420.

123. M. Ogawa, *J. Am. Chem. Soc.*, 1994, **116**, 7941.

124. M. Ogawa, *Chem. Commun.*, 1996, 1149.

125. I. A. Aksay, M. Trau, S. Manne, I. Honma, N. Yao, L. Zhou, P. Fenter, P. M. Eisenberger, and S. M. Gruner, *Science*, 1996, **273**, 892.

126. H. Yang, A. Kuperman, N. Coombs, S. Mamiche-Afara, and G. A. Ozin, *Nature*, 1996, **379**, 703.

127. Y. Lu, R. Ganuli, C. Drewien, M. Anderson, C. J. Brinker, W. Gong, Y. Guo, H. Soyez, B. Dunn, M. Huang, and J. Zink, *Nature*, 1997, **389**, 364.

128. D. Zhao, P. Yang, D. I. Margolese, B. F. Chmelka, and G. D. Stucky, *Chem. Commun.*, 1998, 2499.

129. H. Yang, N. Coombs, I. Sokolov, and G. A. Ozin, *Nature*, 1996, **381**, 589.

130. A. S. Brown, S. A. Holt, T. Dam, M. Trau, and J. W. White, *Langmuir*, 1997, **13**, 6363.

131. S. Schacht, Q. Huo, I. G. Voigt-Martin, G. D. Stucky, and F. Schuth, *Science*, 1996, **273**, 768.

132. P. C. A. Alberius, K. L. Frindell, R. C. Hayward, E. J. Kramer, G. D. Stucky, and B. F. Chmelka, *Chem. Mater.*, 2002, **14**, 3284.

133. E. L. Crepaldi, G. Jde. A. A. Soler-Illia, D. Grosso, P.-A. Albouy, and C. Sanchez, *Chem. Commun.*, 2001, 1582.

134. H. Miyata, M. Itoh, M. Watanabe, and T. Noma, *Chem. Mater.*, 2003, **15**, 1334.

135. K. Landskron, B. D. Hatton, D. D. Perovic, and G. A. Ozin, *Science*, 2003, **302**, 266.

136. S. Schacht, Q. Huo, I. G. Voigt-Martin, G. D. Stucky, and F. Schuth, *Science*, 1996, **273**, 768.

137. Q. Huo, J. Feng, F. Schüth, and G. D. Stucky, *Chem. Mater.*, 1997, **9**, 14.

138. M. Grün, I. Lauer, and K. K. Unger, *Adv. Mater.*, 1997, **9**, 254.

139. G. Büchel, M. Grün, K. K. Unger, A. Matsumoto, and K. Tsutsumi, *Supramol. Sci.*, 1998, **5**, 253.

140. K. Schumacher, M. Grün, and K. K. Unger, *Micropor. Mesopor. Mater.*, 1999, **27**, 201.

141. G. V. Rama Rao, G. P. Lopez, J. Bravo, H. Pham, A. K. Datye, H. Xu, and T. L. Ward, *Adv. Mater.*, 2002, **14**, 1301.

142. T. Martin, A. Galarneau, F. Di Renzo, F. Fajula, and D. Plee, *Angew. Chem., Int. Ed. Engl.*, 2002, **41**, 2590.

143. P. Feng, X. Bu, G. D. Stucky, and D. J. Pine, *J. Am. Chem. Soc.*, 2000, **122**, 994.

144. S. A. El-Safty and T. Hanaoka, *Adv. Mater.*, 2003, **15**, 1893.

145. H. Yang, Q. Shi, B. Tian, S. Xie, F. Zhang, Y. Yan, B. Tu, and D. Zhao, *Chem. Mater.*, 2003, **15**, 536.

146. P. Yang, D. Zhao, B. F. Chmelka, and G. D. Stucky, *Chem. Mater.*, 1998, **10**, 2033.

147. Q. Huo, D. Zhao, J. Feng, K. Weston, S. K. Buratto, G. D. Stucky, S. Schacht, and F. Schüth, *Adv. Mater.*, 1997, **9**, 974.

148. F. Marlow, B. Spliethofff, B. Tesche, and D. Zhao, *Adv. Mater.*, 2000, **12**, 961.

149. J. Wang, J. Zhang, B. Y. Asoo, and G. D. Stucky, *J. Am. Chem. Soc.*, 2003, **125**, 13966.

150. K. Cassiers, T. Linssen, M. Mathieu, M. Benjelloun, K. Schrijnemakers, P. Van Der Voort, P. Cool, and E. F. Vansant, *Chem. Mater.*, 2002, **14**, 2317.

151. N. Bai, Y. Chi, Y. Zou, and W. Pang, *Mater. Lett.*, 2002, **54**, 37.

152. A. Vinu, V. Murugesan, and M. Hartmann, *Chem. Mater.*, 2003, **15**, 1385.

153. T. Tatsumi, K. A. Koyano, Y. Tanaka, and S. Nakata, *J. Porous Mater.*, 1999, **6**, 13.

154. N. Igarashi, K. Hashimoto, and T. Tatsumi, *J. Mater. Chem.*, 2002, **12**, 3631.

155. A. Sayari, *Chem. Mater.*, 1996, **8**, 1840.

156. D. Trong On, D. Desplantier-Giscard, C. Danumah, and S. Kaliaguine, *Appl. Catal., A: Gen.*, 2003, **253**, 545.

157. P. T. Tanev, M. Chibwe, and T. J. Pinnavaia, *Nature*, 1994, **368**, 321.

158. R. Anwander, *Chem. Mater.*, 2001, **13**, 4419.

159. L. Mercier and T. J. Pinnavaia, *Adv. Mater.*, 1997, **9**, 500.

160. X. Feng, G. E. Fryxell, L.-Q. Wang, A. Y. Kim, J. Liu, and K. M. Kemner, *Science*, 1997, **276**, 923.

161. J. Brown, R. Richer, and L. Mercier, *Micropor. Mesopor. Mater.*, 2000, **37**, 41.

162. V. Antochshuk, O. Olkhovyk, M. Jaroniec, I.-S. Park, and R. Ryoo, *Langmuir*, 2003, **19**, 3031.

163. V. Antochshuk and M. Jaroniec, *Chem. Commun.*, 2002, 258.

164. L. Zhang, W. Zhang, J. Shi, Z. Han, Y. Li, and J. Yan, *Chem. Commun.*, 2003, 210.

165. A. M. Liu, K. Hidajat, S. Kawi, and D. Zhao, *Chem. Commun.*, 2000, 1145.

166. R. K. Iler and H. J. McQueston, *U.S. Patent*, 4,010,242, 1977.

167. M. Grün, A. A. Kurganov, S. Schacht, F. Schuth, and K. K. Unger, *J. Chromatogr., A*, 1996, **740**, 1.

168. A. Kurganov, K. Unger, and T. Issaeva, *J. Chromatogr., A*, 1996, **753**, 177.

169. K. W. Gallis, J. T. Araujo, K. J. Duff, J. G. Moore, and C. C. Landry, *Adv. Mater.*, 1999, **11**, 1452.

170. K. W. Gallis, A. G. Eklund, S. T. Jull, J. T. Araujo, J. G. Moore, and C. C. Landry, *Stud. Surf. Sci. Catal.*, 2000, **129**, 747.

171. C. Thoelen, K. Van de Walle, I. F. J. Vankelecom, and P. A. Jacobs, *Chem. Commun.*, 1999, 1841.

172. C. Boissiere, M. Kummel, M. Persin, A. Larbot, and E. Prouzet, *Adv. Funct. Mater.*, 2001, **11**, 129.

173. J. Zhao, F. Gao, Y. Fu, W. Jin, P. Yang, and D. Zhao, *Chem. Commun.*, 2002, 752.

174. M. Raimondo, G. Perez, M. Sinibaldi, A. De Stefanis, and A. A. G. Tomlinson, *Chem. Commun.*, 1997, 1343.

175. O. D. Velev and A. M. Lenhoff, *Curr. Opin. Colloid Interface Sci.*, 2000, **5**, 56.

176. A. Stein, *Micropor. Mesopor. Mater.*, 2001, **44/45**, 227.

177. O. D. Velev, T. A. Jede, R. F. Lobo, and A. M. Lenhoff, *Nature*, 1997, **389**, 447.

178. B. T. Holland, C. F. Blanford, and A. Stein, *Science*, 1998, **281**, 538.

179. A. Stein and R. C. Schroden, *Curr. Opin. Solid State Mater. Sci.*, 2001, **5**, 553.

180. A. Imhof and D. J. Pine, *Nature*, 1997, **389**, 948.

181. A. Imhof and D. J. Pine, *Adv. Mater.*, 1998, **10**, 697.

182. O. D. Velev and E. W. Kaler, *Adv. Mater.*, 2000, **12**, 531.

183. Y. Xia, B. Gates, Y. Yin, and Y. Lu, *Adv. Mater.*, 2000, **12**, 693.

184. S. H. Park and Y. Xia, *Chem. Mater.*, 1998, **10**, 1045.

185. A. A. Zakhidov, R. H. Baughman, Z. Iqbal, C. Cui, I. Khayrullin, S. O. Dantas, J. Marti, and V. G. Ralchenko, *Science*, 1998, **282**, 897.

186. Y. A. Vlasov, N. Yao, and D. J. Norris, *Adv. Mater.*, 1999, **11**, 165.

187. K. M. Kulinowski, P. Jiang, H. Vaswani, and V. L. Colvin, *Adv. Mater.*, 2000, **12**, 833.

188. C. F. Blanford, H. Yan, R. C. Schroden, M. Al-Daous, and A. Stein, *Adv. Mater.*, 2001, **13**, 401.

189. A. Corma, V. Fornes, J. Martinez-Triguero, and S. B. Pergher, *J. Catal.*, 1999, **186**, 57.

190. P. Yang, T. Deng, D. Zhao, P. Feng, D. Pine, B. F. Chmelka, G. M. Whitesides, and G. D. Stucky, *Science*, 1998, **282**, 2244.

191. B. T. Holland, L. Abrams, and A. Stein, *J. Am. Chem. Soc.*, 1999, **121**, 4308.

192. Q. Luo, L. Li, B. Yang, and D. Zhao, *Chem. Lett.*, 2000, 378.

193. A. Karlsson, M. Stocker, and R. Schmidt, *Micropor. Mesopor. Mater.*, 1999, **27**, 181.

194. L. Huang, W. Guo, P. Deng, Z. Xue, and Q. Li, *J. Phys. Chem. B*, 2000, **104**, 2817.

195. D. Trong On and S. Kaliaguine, *Angew. Chem., Int. Ed. Engl.*, 2001, **40**, 3248.

196. Y. Goto, Y. Fukushima, P. Rath, Y. Imada, Y. Kubota, Y. Sugi, M. Ogura, and M. Matsukata, *J. Porous Mater.*, 2002, **9**, 43.

197. L. Huang, Z. Wang, J. Sun, L. Miao, Q. Li, Y. Yan, and D. Zhao, *J. Am. Chem. Soc.*, 2000, **122**, 3530.

198. L. Huang, Z. Wang, H. Wang, J. Sun, Q. Li, D. Zhao, and Y. Yan, *Micropor. Mesopor. Mater.*, 2001, **48**, 73.

199. K. H. Rhodes, S. A. Davis, F. Caruso, B. Zhang, and S. Mann, *Chem. Mater.*, 2000, **12**, 2832.

200. F. Caruso, R. A. Caruso, and H. Mohwald, *Science*, 1998, **282**, 1111.

201. M. W. Anderson, S. M. Holmes, N. Hanif, and C. S. Cundy, *Angew. Chem., Int. Ed. Engl.*, 2000, **39**, 2707.

202. A. Dong, Y. Wang, Y. Tang, N. Ren, Y. Zhang, Y. Yue, and Z. Gao, *Adv. Mater.*, 2002, **14**, 926.

Self-assembled Inorganic Architectures

Jitendra K. Bera,[1] John Bacsa & Kim R. Dunbar[2]
[1]*Indian Institute of Technology, Kanpur, India*
[2]*Texas A&M University, College Station, TX, USA*

1 Introduction 1
2 Classification of Structure 2
3 N-heterocycles and Related Ligands 2
4 Cyanide 13
5 Carboxylate Ligands 24
6 Hydrogen Bonding 31
7 Supramolecular Assembly Dynamics 40
8 Inorganic Assemblies with Functionality 42
9 Related Articles 43
10 References 43

Glossary

Assembly descriptor: a formula-like notation that expresses the number of binding sites and the topicity of molecular building units
Default structures: high-symmetry structures that are ubiquitous for all building blocks with a particular symmetry and coordination number
Double molecular box: molecular architecture that resembles two cubes (or boxes) fused at one corner
Functional materials: molecular materials that are designed to perform specific function(s)
Isoreticular structures: a series of molecular architectures with identical network topologies but with different functionalities and dimensions
Linkers: a molecular component that acts as a bridge between molecular entities
Metal-organic-framework (MOF): three-dimensional architectures composed of metal ions and organic ligands
Molecular loop: dinuclear molecules with two bridging ligands with an approximate geometry resembling that of a loop
Octahedral SBU: a octahedral molecular building block whose geometry plays a decisive role in determining the three-dimensional structure of the solid
Paddlewheel: dinuclear metal complexes with four bridging ligands arranged in a paddle-wheel fashion
Secondary building unit (SBU): molecular fragment that is not necessarily an isolable entity but is rather a principle building block of an architecture and that determines the topology of the three-dimensional structure
Single-molecule-magnets: molecules that have the ability to be magnetized when a field is applied and exhibit slow paramagnetic relaxation; the effect is due to an individual molecule rather than to a long-range ordering as in bulk magnets
Square SBU: a molecular fragment with the shape of a square whose geometry plays an important role in determining the three-dimensional structure of the solid
Supramolecular: assembly of molecules of higher complexity than the molecules themselves, held together and organized by means of intermolecular noncovalent interactions

Abbreviations

4,4′-H_2bpy = 4,4′-bipyridinium di-cation; BINAP = Binaphthalene; bpm = bis-(1-pyrazolyl)methane; bptz = 3,6-bis-(2-pyridyl)tetrazine; bpy = Bipyridine; bpym = Bipyrimidine; BU = Building units; Cp = Cyclopentadienyl; *p*-cymene = 4-Isopropyltoluene; DABCO = 1,4-diazabicyclo [2.2.2]octane; DaniF = N,N'-di(p-anisyl)formamidinate; dmpby = 5,5′-dimethyl-2,2′-bipyridine; dbbpy = di-t-butylbipyridine; DMF = N,N'-dimethylformamide; DMSO = Dimethyl sulfoxide; dppm = Bis-diphenylphosphinomethane; dppp = Diphenylphosphinopropane; ESI-MS = Electrospray ionization mass spectroscopy; en = Ethylenediamine; Et = Ethyl; H_2BDC = 1,4-benzenedicarboxylic acid; BDC = 1,4-benzenedicarboxylate; *fac* = Facial; Hbim = 2,2′-biimidazolate; impy = 2-(2-pyridyl)-4,4,5,5-tetramethyl-4,5-dihydro-1H-imidazolyl-1-oxy; MOF = Metal-organic framework; MOP = Metal-organic polyhedron; OTf = Triflate ion; PB = Prussian blue; phen = Phenanthroline; Ph = Phenyl; Py = Pyridine-based ligand; SBU = Secondary building unit; tacn = 1,4,7-triazacyclononane; tbp = Trigonal-bipyramidal; tmphen = Tetramethylphenanthroline; triphos = 1,1,1-tris(diphenylphosphinomethyl)ethane.

1 INTRODUCTION

The self-assembly (*see Self-assembly*) of metal cations (*see Cation*) with multidentate ligands (*see Ligand*) results in the formation of a variety of inorganic architectures. Given that a range of products is possible for the same combination of starting materials, it is remarkable that the molecular self-assembly generally favors one particular architecture over the others. This situation is even more favored when the chemistry involves labile (*see Labile*) metal–ligand interactions that allow for healing of defects throughout the reaction profile. Although the outcome of these self-assembly processes is often unpredictable, the formation of one product in high yield typically can be rationalized on the basis of the interplay between kinetic and thermodynamic factors.

The field of inorganic supramolecular chemistry is motivated, to a large extent, by a desire to prepare new types of functional materials, but the research area also has contributed a great deal to fundamental coordination chemistry as well. This short review is dedicated to highlighting key advances in this area with an emphasis on novel structures. The article is organized according to broad categories of bridging ligands (*see Bridging Ligand*) that have been used to prepare self-assembled inorganic architectures. The terms 'self-assembly' and 'self-assembled structures' include molecular metallomacrocycles, cages/clusters, hydrogen-bonded networks as well as oligomers and polymers.

2 CLASSIFICATION OF STRUCTURE

Self-assembly of ligands with metal ions has led to the isolation of a wide variety of molecular architectures of which discrete two- and three-dimensional structures (metallocyclic polygons and polyhedra) constitute a significant proportion. As their approximate molecular symmetries resemble regular polygons, they are referred to as molecular triangles, squares, pentagons, hexagons, cubes, and so on. An early attempt to develop a notation for describing the building blocks that lead to particular geometries was introduced by Peter J. Stang[1] and later modified by G. F. Swiegers.[2] The assembly descriptor nomenclature employs a formula-like notation to describe the number of binding sites and the topicity of the building blocks involved in the formation of a particular structure. Advantages of this notation are the efficient identification of acceptor(metal)–donor(ligand) combination that is required for the formation of a particular product and the rapid comparison of compounds of different structures. A consideration of the basic manner in which building blocks combine aids in the conceptual development of new architectures. The usefulness of the assembly descriptor notation system is illustrated by the following example. The symbol A^{3a} indicates an 'angular' building block with 'three' identical 'acceptor' sites, with the 'linear' unit having two different 'donor' sites symbolized as L^{1d1d}. An assembly consisting of two A^{3a} and three L^{1d1d} units, as shown in Scheme 1, is given the description $A_2^{3a}L_3^{1d1d}$. Examples of self-assembled A_4^{1a1d} and mixed-assembled $A_2^{2a}A_2^{2d}$ structures are complex (**1**) and (**2**) respectively. Clearly these descriptors provide valuable information, at a glance, about the building units and their modes of binding in the self-assembled architectures.

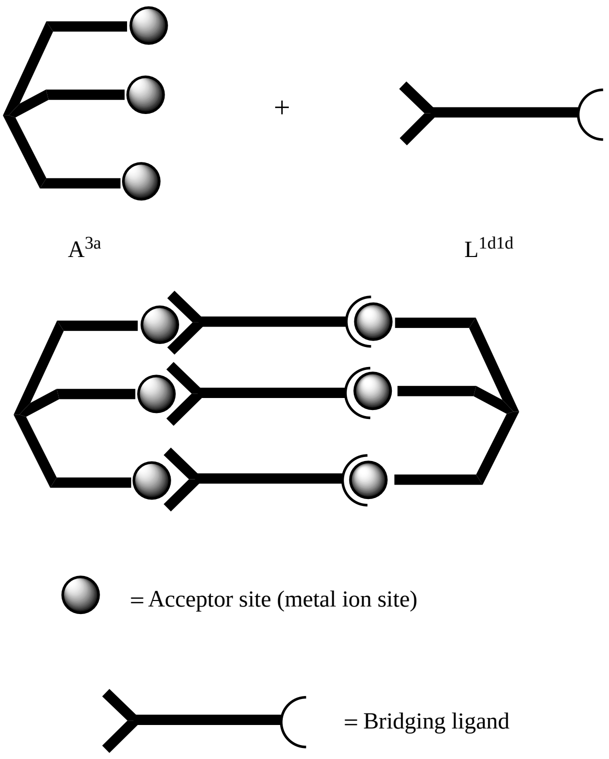

Scheme 1

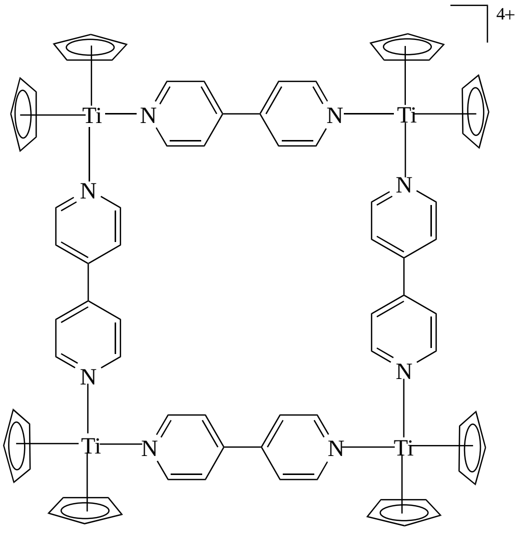

A_4^{1a1d}

(**1**)

3 N-HETEROCYCLES AND RELATED LIGANDS

Multidentate ligands derived from pyridine have been widely used for the assembly of transition metals (*see*

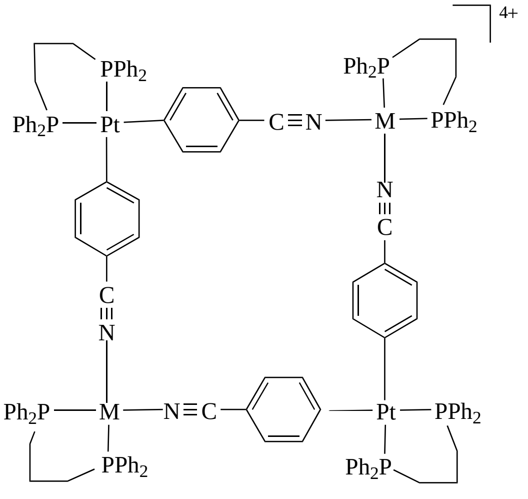

M = Pt, Pd

$A_2^{2a}A_2^{2d}$

(**2**)

Transition Metals) into oligomers as well as polymers (*see Polymer*). The use of bridging ligands to connect metal precursors that possess capping ligands has produced a large number of discrete molecular structures of varying shapes and sizes. Pioneering work in this area by Fujita[3] and Stang[4] involved the synthesis of specialized ligands and tailored metal precursors, and their subsequent self-assembly into cyclic molecules. Companion spectroscopic and structural studies of the resulting inorganic architectures and investigations of the reaction dynamics led to a comprehensive body of work that has inspired many others to explore the field of inorganic supramolecular chemistry.[5] The following sections describe various structures that have appeared in the literature over the years and that serve to illustrate the rich variety of molecular species that can be accessed by this chemistry. An examination of this body of work provides valuable insight into the topologies of the molecular components that are required for the construction of molecular architectures of particular sizes, shapes and dimensions.

3.1 Dinuclear (*see Dinuclear*) Macrocycles

Reactions of (en)Pd(ONO_2)$_2$ (en = ethylenediamine) with bidentate ligands (*see Bidentate Ligand*) of the type Py-X-Py (Py = a pyridine-based ligand) produce the dinuclear metallomacrocycles (**3–7**) (Scheme 2).[6] As indicated, the organic linker can be varied to generate a host of structures upon coordination to the Pd(II) complex. The ability of these metallocyclophanes to encapsulate organic guests was investigated; for example, the fluorinated macrocycle (**6**) is capable of recognizing electron-rich (*see Electron Rich Compound*) aromatic species such as napthalene in aqueous solutions.[7] The introduction of diazacycloalkanes or chiral (*see Chiral*) groups into the organic backbones yields the analogous metallomacrocycles (**8**)[8] and (**9**)[9] respectively.

In a similar manner, reactions of bis-(triethylphosphine)-M(II)-bis-triflates with bis-pyridine ligands provide access to dinuclear metallomacrocycles. The reaction of equimolar amounts of $(Et_3P)_2M(II)(OTf)_2$ (OTf = triflate ion) (M = Pt, Pd) with bis-heteroaryl-iodonium triflate (**10**) yields the molecular squares (**11**) and (**12**) respectively (Scheme 3).[10]

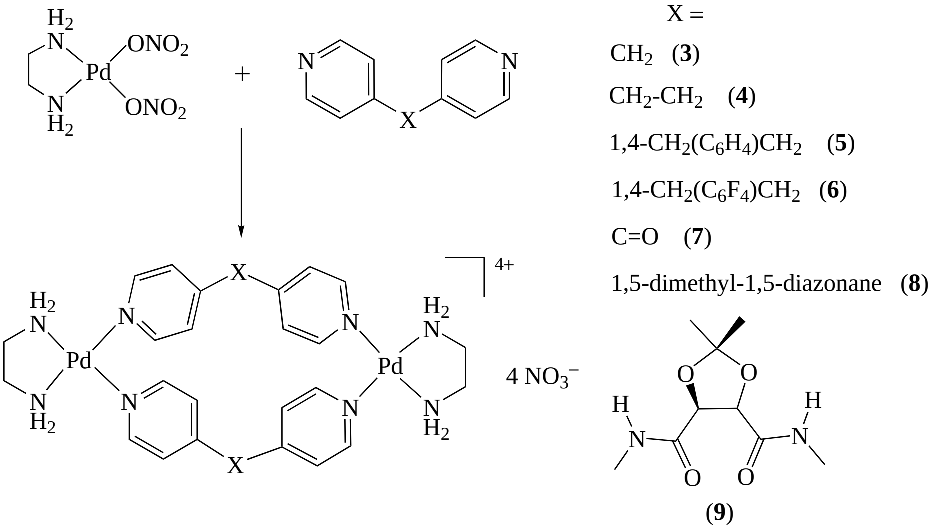

Scheme 2

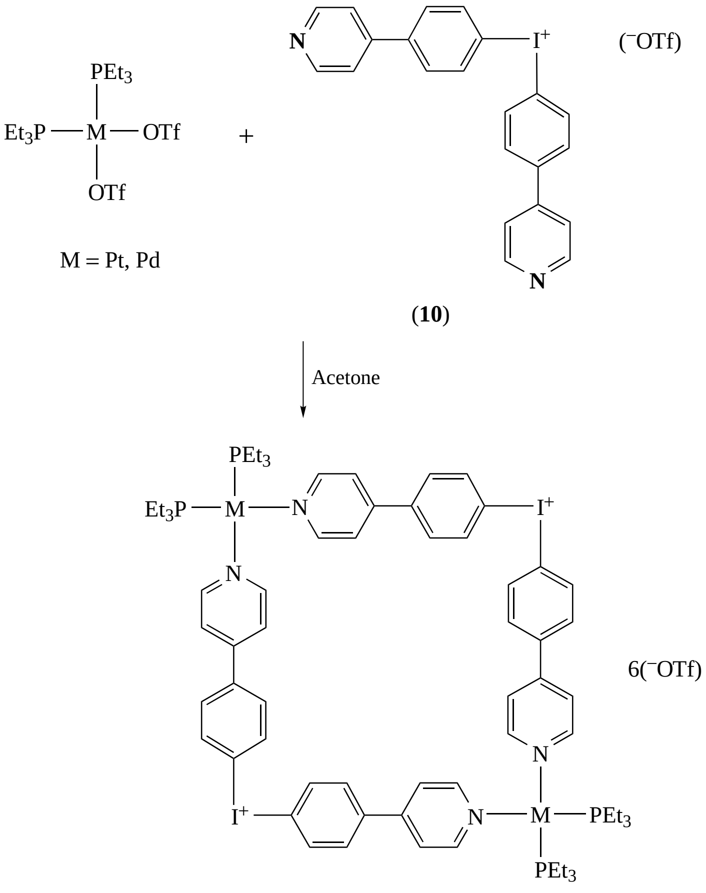
PEt3
Et3P — M — OTf
OTf
M = Pt, Pd
+
N
I+
(−OTf)
N
Acetone
PEt3
Et3P
M
N
I+
6(−OTf)
I+
N
M
PEt3
PEt3

(10)

(11) (Pt)
(12) (Pd)

Scheme 3

The solid-state structure of (**12**) reveals that it consists of a planar, rhomboidal molecule with N–Pd–N angle of 84° and a C–I–C corner angle of 99°. Bis-pyridine ligands can be varied in numerous ways to yield a variety of diverse structures; these include macrocycles containing bis-pyridine functionalized C_{60} molecules (**13**)[11] and the bis-pyridine incorporated porphyrin compound (**14**).[12]

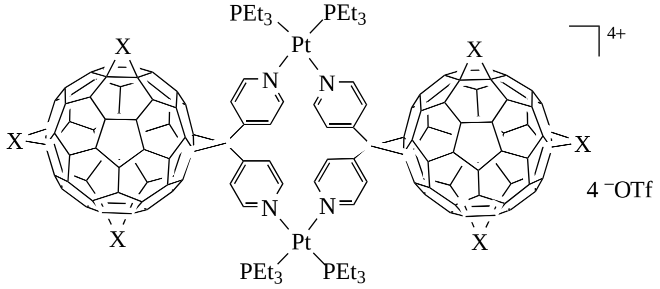
PEt3
PEt3
Pt
X
X
N
N
4+
X
X
4 −OTf
N
N
X
Pt
X
PEt3
PEt3

(**13**)

$X = C(CO_2Et)_2$

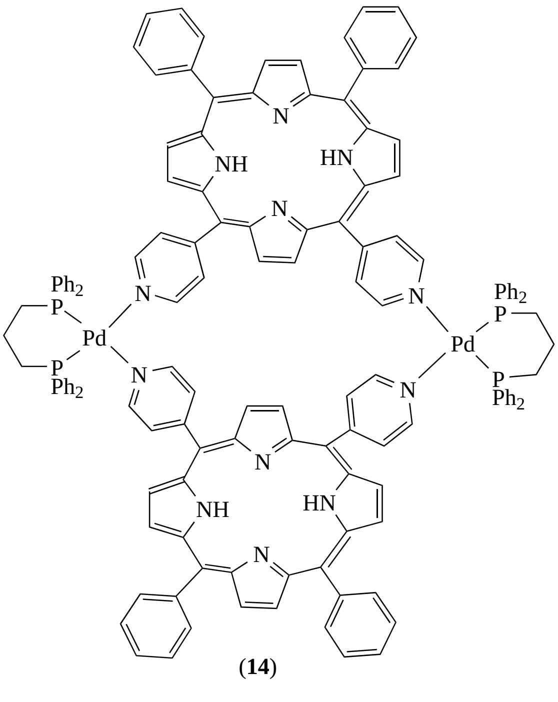
N
NH
HN
N
Ph2
P
Pd
P
Ph2
N
N
N
Ph2
P
Pd
P
Ph2
N
N
N
NH
HN
N

(**14**)

Diphosphine ligands have also been employed as site-protecting groups. Chirality (*see Chiral*) was introduced to the chemistry by using phosphine-modified binapthalene (BINAP) ligands. In this manner, the chiral molecular square (**16**) was prepared by the reaction of (**15**) with (**10**) (Scheme 4).[13] The induced chirality is entirely due

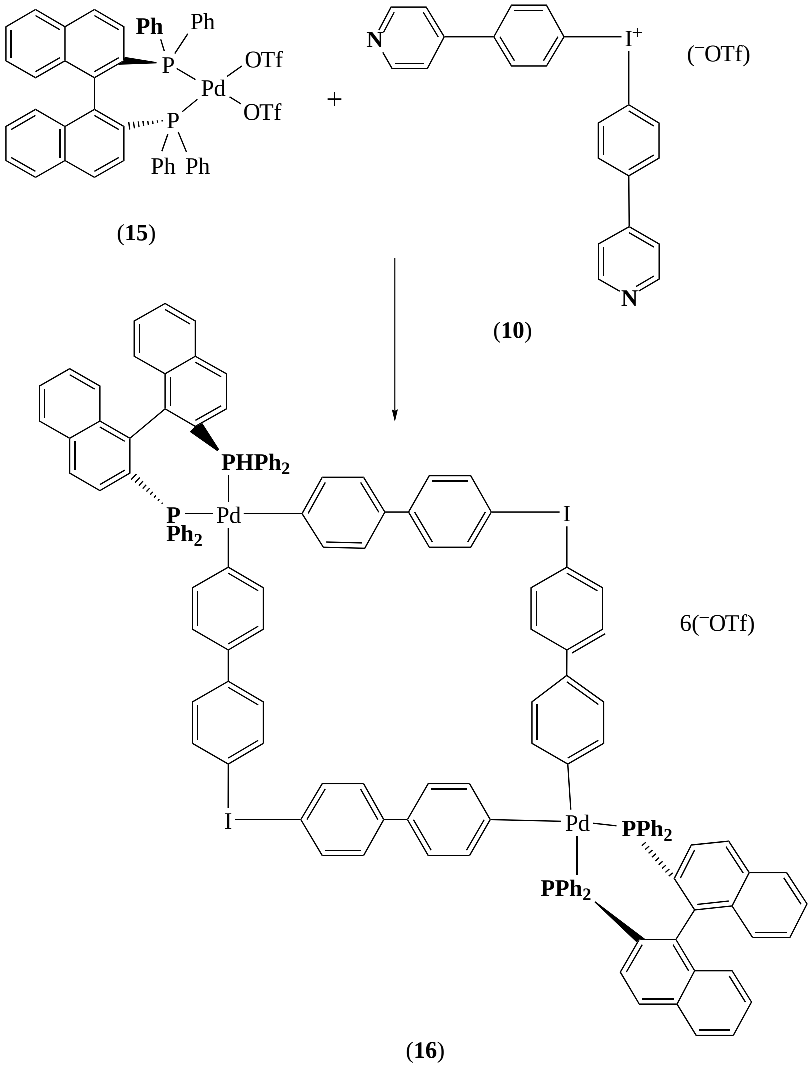
Ph
Ph
P
Pd
OTf
OTf
P
Ph Ph
(15)
+
N
I+
(⁻OTf)
N
(10)
PHPh2
P Ph2
Pd
I
6(⁻OTf)
I
Pd
PPh2
PPh2
(16)

Scheme 4

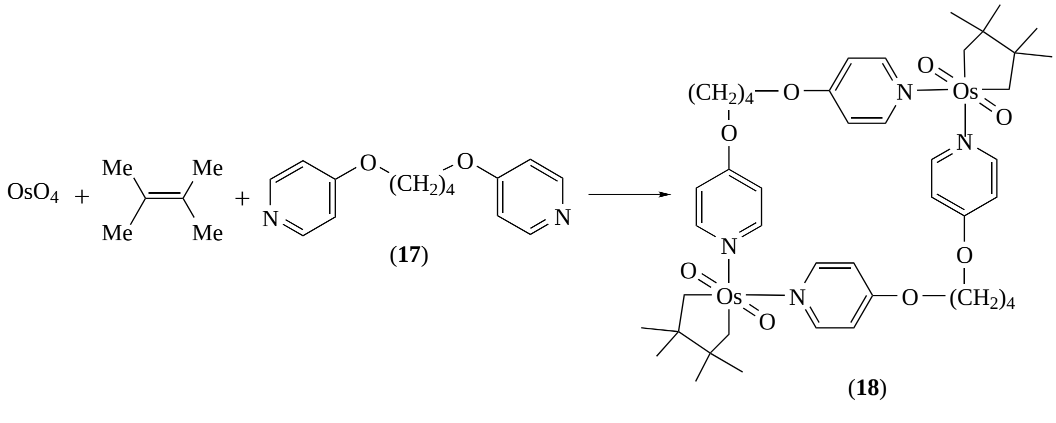
OsO4
+
Me
Me
Me
Me
+
N
O
(CH2)4
O
N
(17)
(CH2)4
O
N
Os
O
O
N
O
(CH2)4
O
N
O
Os
O
N
(18)

Scheme 5

to the BINAP ligand rather than to the symmetry of the overall molecule.

Relatively few dinuclear metallomacrocycles with metal ions other than Pd(II) or Pt(II) are known. Among the reported examples is the neutral macrocyclic structure (**18**)[**14**] isolated from the reaction of OsO_4, 2,3-dimethyl-2-butene and the bis-pyridyl ligand (**17**) (Scheme 5). The self-assembly of a tetrahedral (*see Tetrahedral*) Cu(I) salt with 4-thiomethyl-6-(3′-pyridyl)-2,2′-bipyridine leads to the dinuclear metallomacrocycle (**19**).[**15**] Mass spectroscopic and single-crystal X-ray studies confirmed the composition of the complex. Use of the acetate salt of Cd(II) yields a similar macrocycle but with each metal atom having an irregular octahedral (*see Octahedral*) geometry consisting of bidentate acetate ligands with methanol molecules occupying the additional coordination sites.

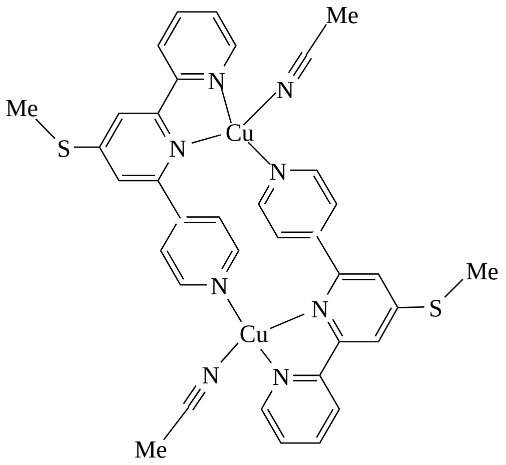

(**19**)

3.2 Molecular Triangles and Trinuclear Macrocycles

Molecular triangles are less well-known as compared to dinuclear and tetranuclear structures. Fujita and coworkers isolated a series of triangles (**20–23**) by reacting linearly disposed bis-heteroaryls with (en)$Pd(ONO_2)_2$ (Scheme 6).[**16**] These molecular triangles are in equilibrium with the corresponding molecular squares, and the composition varies depending on the flexibility of bridging ligands, the protecting groups on the metal ions, the solvent, and concentrations and identities of potential templates. Electrospray ionization mass spectroscopic (ESI-MS) studies on solutions of (**21**) indicated an equilibrium mixture with the corresponding square (**24**). The results of ^1H NMR studies performed on this system revealed that, at moderate concentrations, the square is the major product whereas at low concentrations the formation of the triangle is favored. Oligomers were noted to form at very high concentrations. Addition of di-sodium salts of 1,3-adamantanedicarboxylic acid in water to the equilibrium mixture shifts the equilibrium to the square structure with the anionic guest being located inside the cavity of the square (**25**) (Scheme 7).[**17**]

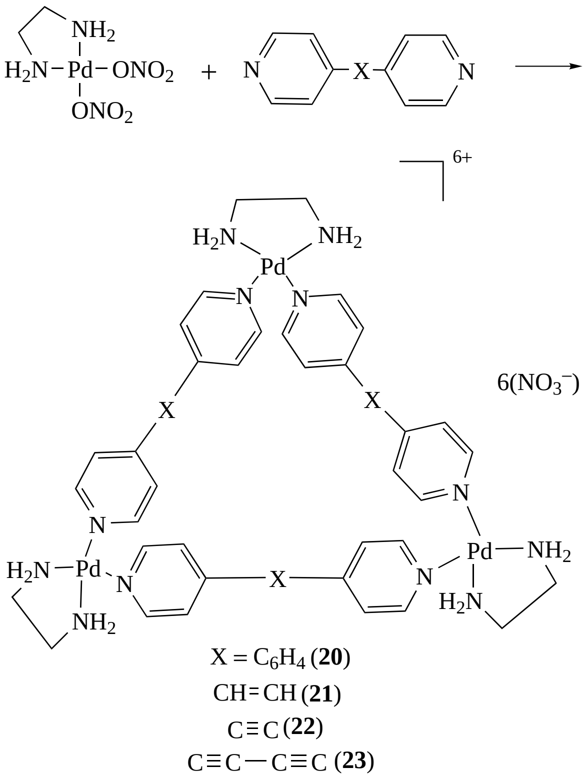

Scheme 6

It is reasonable to expect that the use of rigid 60° angular building blocks with 180° linear linking units would provide triangular structures. Indeed, this has been demonstrated by the self-assembly of 4,7-phenanthroline and the linear phenyl-bridged bis-palladium complex, which yields the triangle (**26**).[**18**]

A trinuclear metallomacrocycle (**27**) has been synthesized using 2,2′-bipyrazine and (en)$Pt(ONO_2)_2$.[**19**] The solid-state structure of (**27**) reveals that the two pyrazine rings of the bipyrazine ligand are twisted with respect to each other, which is an essential ingredient for the formation of the triangle. Subsequent addition of (en)$Pd(ONO_2)_2$ to the molecular triangle leads to a hexanuclear complex in which Pd(II) ions are coordinated to the free 2 and 2′ nitrogen atoms of bipyrazine. Rotation about the C–C single bond allows for chelation to other metal ions and thereby provides access to Pt_6, Pd_6 and Pt_3Pd_3 triangles.[**20**] Interestingly, the corresponding Pd complex forms a mononuclear chelating bipyrazine complex, which illustrates the unpredictable nature of these reactions.

The high-yield synthesis of a luminescent trinuclear structure (**28**) in which deprotonated benzimidazole acts as the

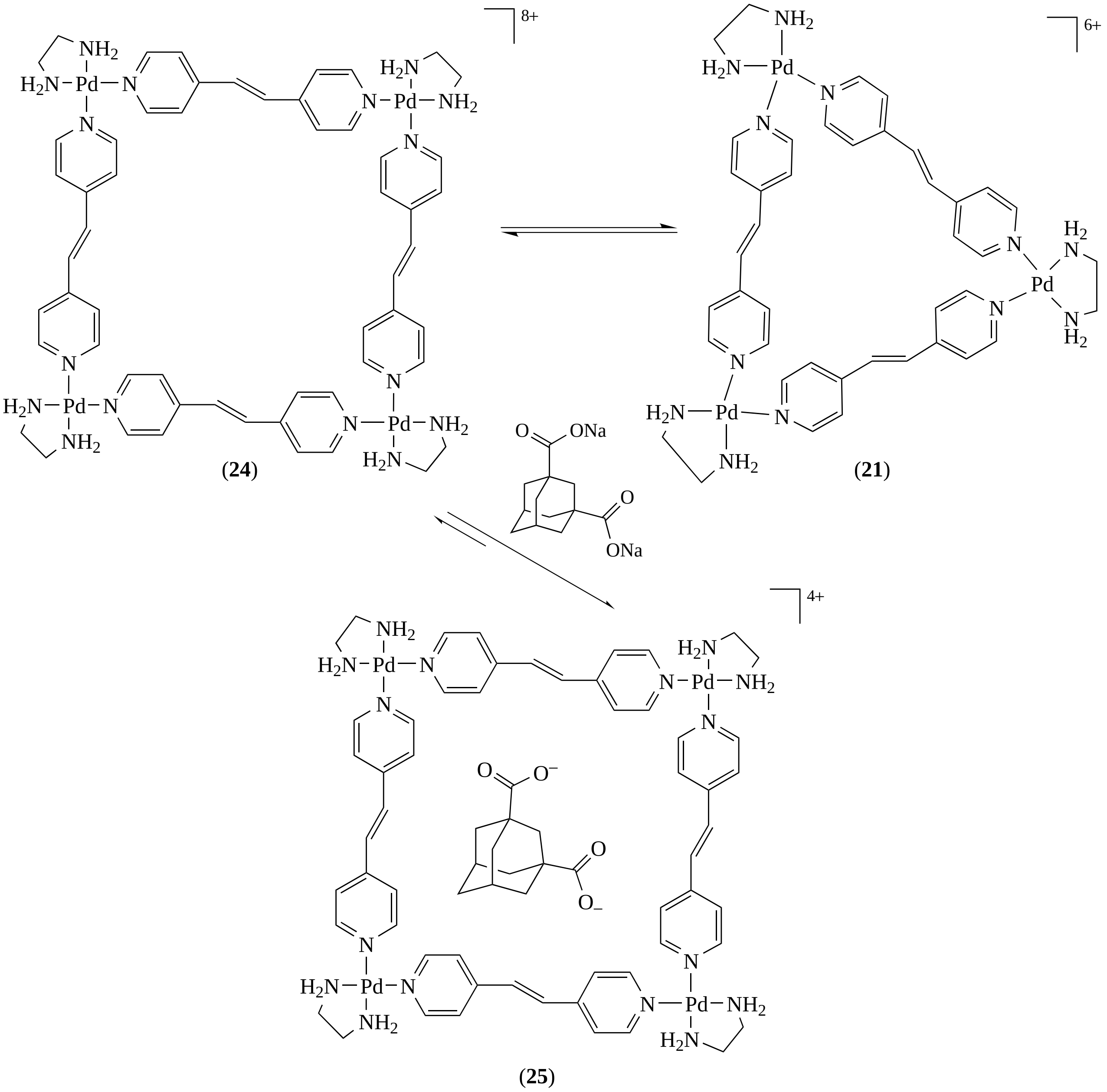

Scheme 7

bridge between cyclometallated Pt(II)-2-(2-thienyl)pyridine units has been reported.[21] The three Pt atoms in this structure occupy the corners of a triangle and the three imidazole ligands span the edges. The N–Pt–N angles at the vertices are close to 90°, which is larger than the expected angles for trinuclear cyclic systems with rigid linkers. Flexible linkers such as 1,2-bis-(3,5-dimethylpyrazol-1-yl)ethane (**29**) also form trinuclear metallomacrocycles with $PdCl_2$. For example, in complex (**30**), the ligand coordinates to *trans*-$PdCl_2$ and is highly strained (Scheme 8).[22] Interactions between methylene protons (of the ligand) and the palladium and chloride ions presumably increase the overall stability of the trimeric structures.

3.3 Molecular Squares and Tetrameric Structures

Among the various polygonal assemblies that inorganic architectures can adopt, molecular squares are the most common. This fact can be attributed to the tendency of transition metals to form cis complexes with L–M–L bond angles of 90° and to the widespread availability of linear-bridging ligands. In this vein, Stang and coworkers

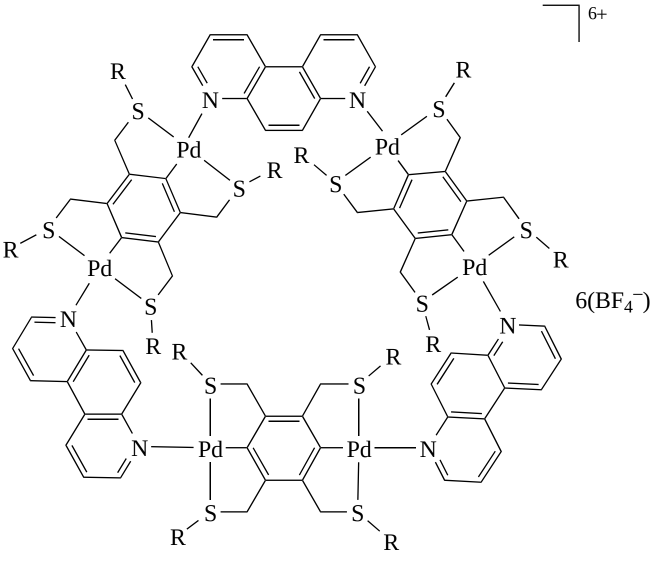

R = *n*-Bu, Ph

(**26**)

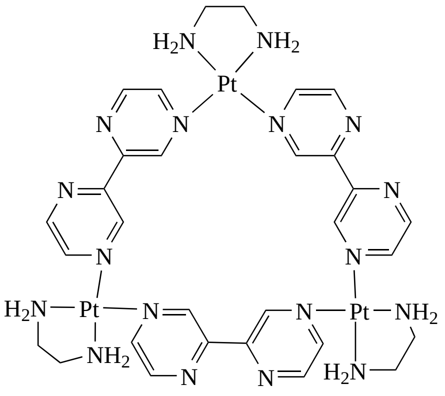

(**27**)

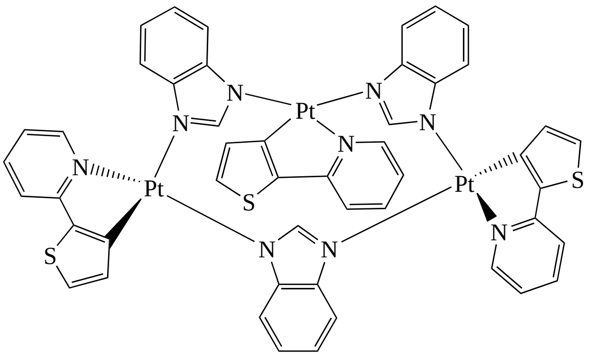

(**28**)

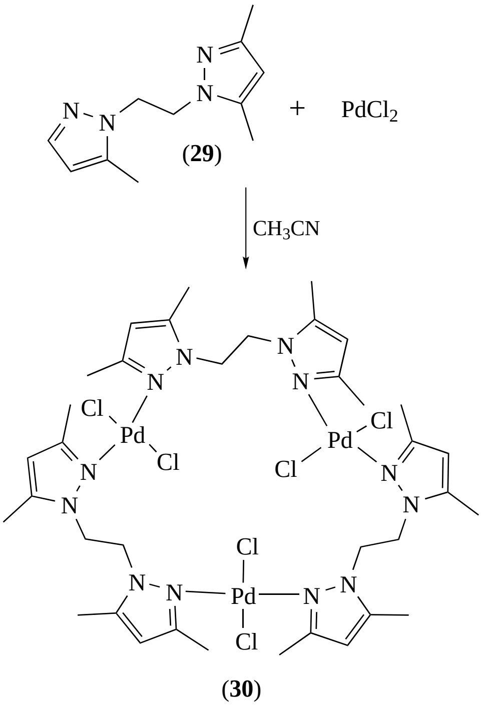

Scheme 8

have used Pt and Pd phosphine-containing precursors as the vertices and 4,4′-bipyridine ligands as the edges for the assembly of squares. Reactions of $(Et_3P)_2M(OTf)_2$ (M = Pd, Pt) with equimolar amounts of linearly disposed *N*-aryl ligands yield molecular squares (**31–36**) with varied cavity sizes (Scheme 9).[23] Bis-phosphine ligands also have been used to block the cis positions of square-planar Pt(II) and Pd(II) complexes. Reactions of (dppp)Pt(II)$(OTf)_2$ (dppp = diphenylphosphinopropane) with 4,4′-bipyridine in chlorinated solvents provide the molecular square (**37**)[24] in which the metal ions occupy the corners and the organic ligands span the edges. The diagonal and edge-to-edge metal–metal distances are approximately 15 Å and 11 Å respectively.

Fujita *et al.* pioneered the use of bis-amine ligands in molecular square chemistry. A typical metal precursor that has been used is (en)$Pd(ONO_2)_2$. A quantitative yield of the molecular square (**38**) was obtained from the reaction of (en)Pd(II)$(ONO_2)_2$ with 4,4′-bipyridine (Scheme 10).[16,25] Molecular structure of the resulting 8×8 Å^2 square was established by NMR spectroscopy, mass spectrometry (*see Mass Spectrometry*), and single-crystal X-ray diffraction (*see X-ray Diffraction*) studies. Although the Pd(II) complex produces molecular squares almost exclusively, the Pt(II) analog yields a mixture of oligomers. With heating, the thermodynamically favored square molecules were found to be the predominant products.

The aforementioned examples primarily involve the use of bis-heteroaryl ligands. Transition metal complexes with appended N-donor ligands, however, can also act as donor ligands for metal acceptors. The organometallic complex (*see Organometallic Complexes*) (**39**) reacts with $(Et_3P)_2Pd(OTf)_2$ to afford the heterometallic square (**40**) (Scheme 11).[26] The

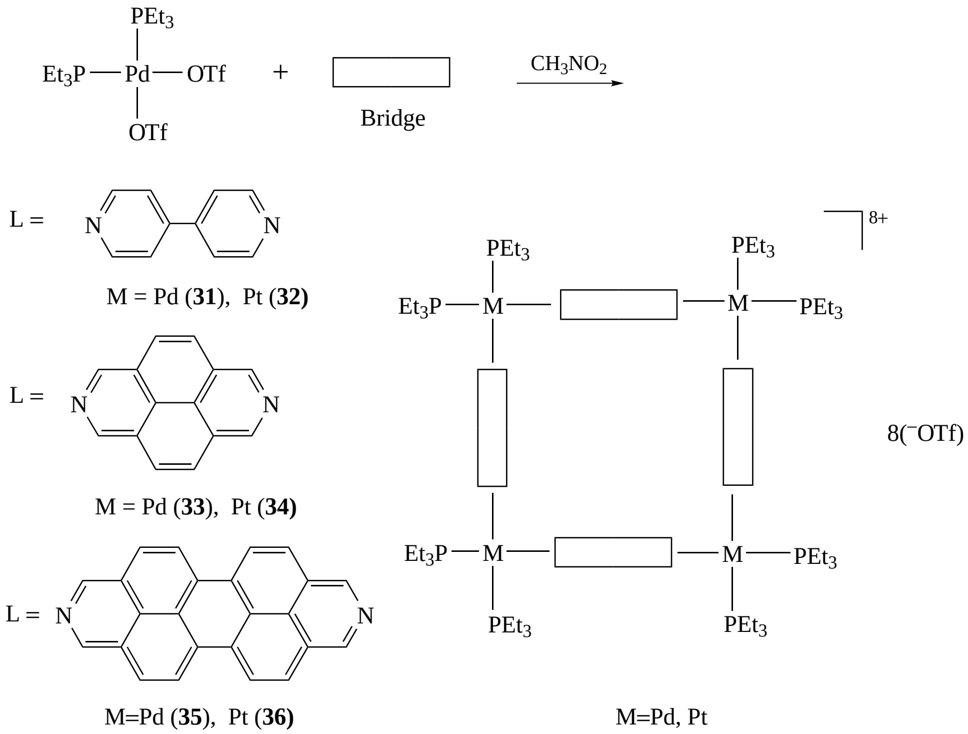
PEt3
Et3P
Pd
OTf
OTf
+
Bridge
CH3NO2
L =
N
N
M = Pd (31), Pt (32)
L =
N
N
M = Pd (33), Pt (34)
L =
N
N
M=Pd (35), Pt (36)
8+
PEt3
Et3P
M
PEt3
8(⁻OTf)
M=Pd, Pt

Scheme 9

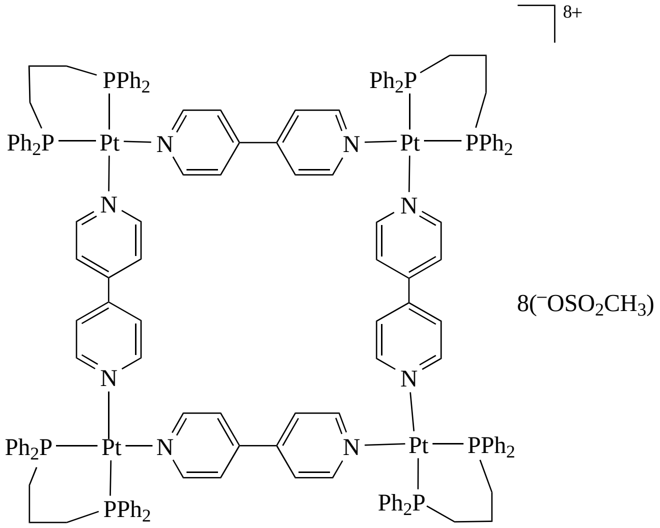
8+
PPh2
Ph2P
Pt
N
8(⁻OSO2CH3)

(**37**)

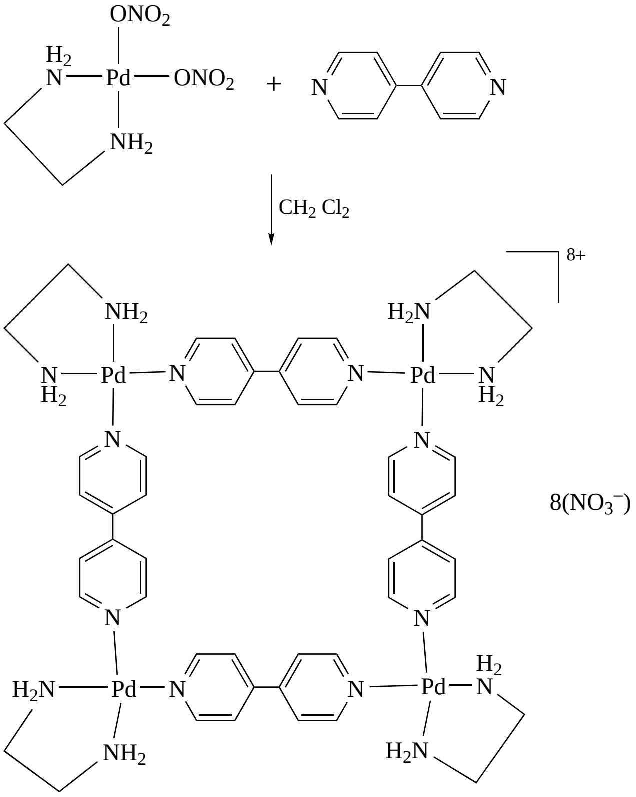
ONO2
H2
N
Pd
ONO2
NH2
+
N
N
CH2 Cl2
8+
NH2
H2N
Pd
N
H2
8(NO3⁻)

(**38**)

Scheme 10

acetylene units along the edges of the square are capable of binding to soft-metal ions as evidenced by the existence of the silver complex (**41**), whose identity has been established by NMR spectroscopy and mass spectrometry.[27] Dissolution of (**41**) in solvents that contain molecules such as pyrazine, phenazine, and so on results in the formation of host–guest complexes (Scheme 12). The solid-state structure of the square with the phenazine guest, (**42**), has been established.[28] The

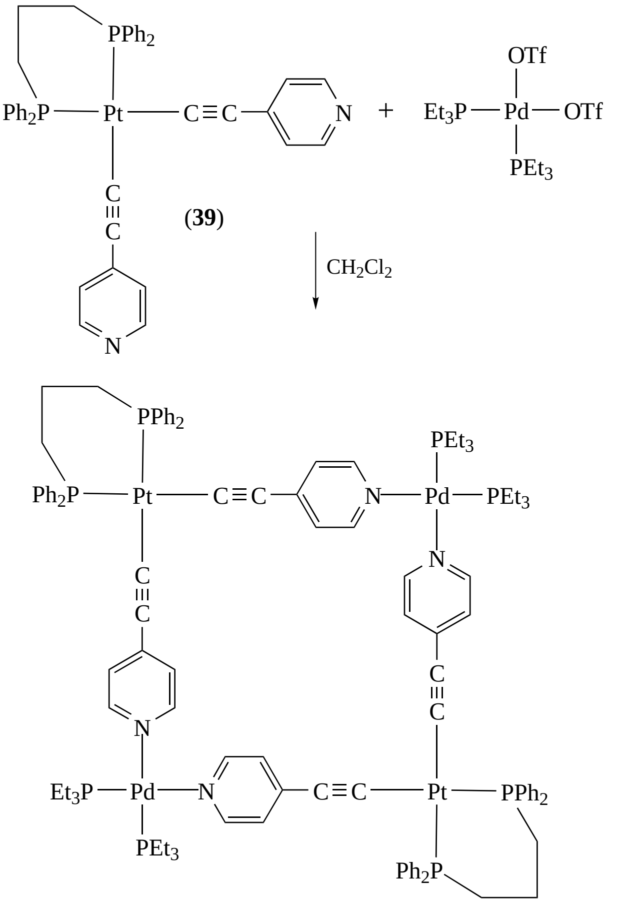
PPh2
Ph2P
Pt
C≡C
N
+
OTf
Et3P
Pd
PEt3
(39)
CH2Cl2
PEt3
(40)

Scheme 11

phenyl rings of the host molecule are nearly in the same plane, with the phenazine guest being orientated orthogonal to the rings. The interatomic distances confirm that each Ag^+ ion is π-coordinated to alkyne groups and further linked to N-atoms of phenazine. Structure (**43**) is another example of a transition metal complex that behaves as a ligand. Reaction of (dppp)Pd(OTf)$_2$ with (**43**) gives the heterometallic, luminescent (*see **Luminescence Behavior & Photochemistry of Organotransition Metal Compounds***) molecular square (**44**) in high yields (Scheme 13).[29] This

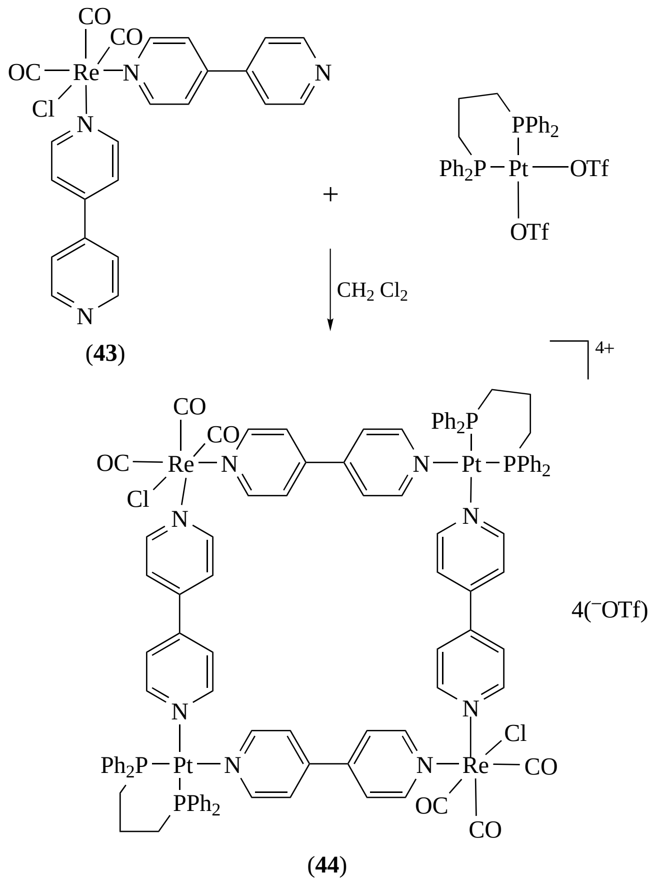
CO
OC
Re
Cl
N
+
PPh2
Ph2P
Pt
OTf
CH2 Cl2
(43)
4+
4(⁻OTf)
(44)

Scheme 13

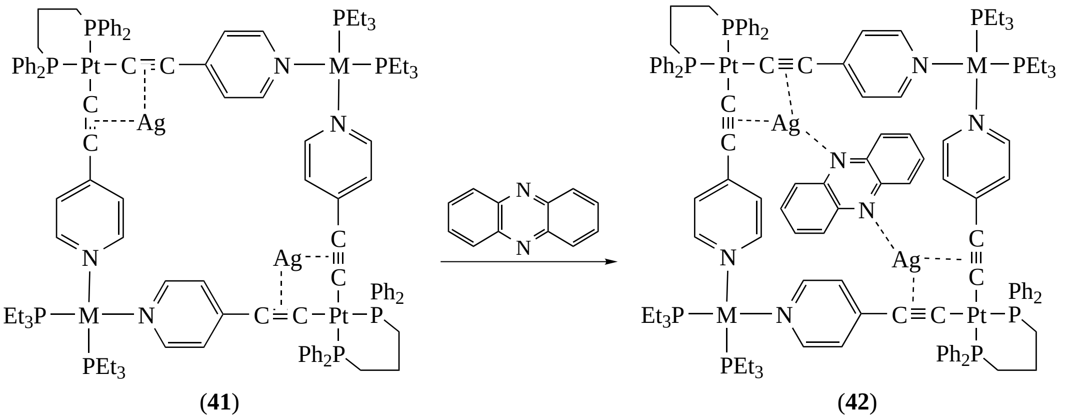
PPh2
Ph2P
Pt
Ag
PEt3
M
N
(41)
(42)

Scheme 12

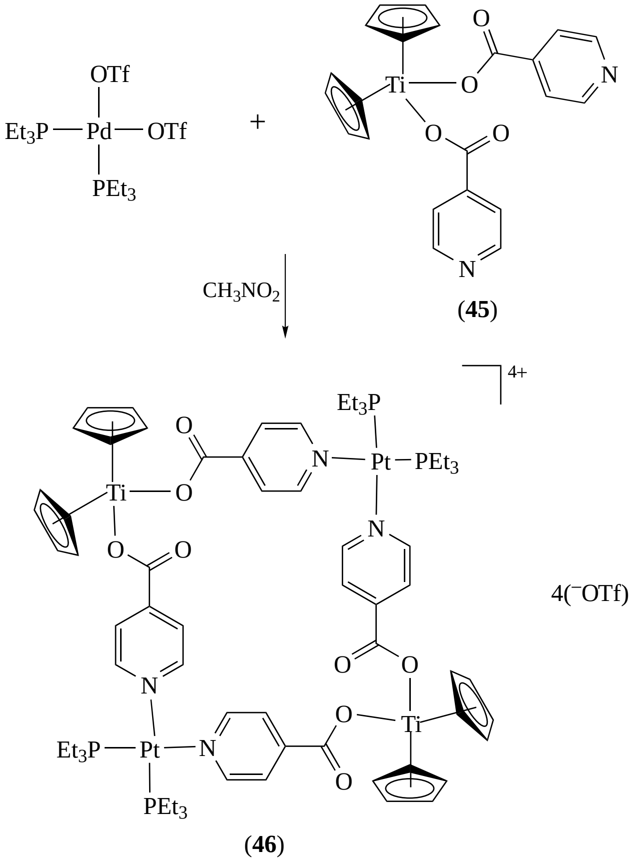

Scheme 14

chemistry allows for the investigation of the self-assembly process by photophysical methods. The early transition metal complex (**45**) has been incorporated into a molecular square by an elegant design (Scheme 14). Interaction of (**45**) with $(Et_3P)_2Pt(OTf)_2$ in nitromethane produces the molecular square (**46**).[30] This orange compound was characterized by mass spectrometry, and exhibits a prominent doubly charged molecular ion peak.

Porphyrin (*see Porphyrin*) molecules containing peripheral pyridine groups act as corners or 180° linkers depending on the positions of the pyridyl donor atoms. Reaction of $(dppp)Pd(OTf)_2$ with (**47**) yields the molecular square (**14**)[12] while a larger square (**49**)[31] was obtained by employing a modified porphyrin (**48**) in which the two pyridine units are trans to each other (Scheme 15). The results of these reactions demonstrate that the ability of the molecular components to act as corners or linkers depends on their topologies. Bis-pyridyl-porphyrin (**47**) reacts with *cis*- and *trans*-$(PhCN)_2PdCl_2$ to yield the molecular squares (**50**) and (**51**), respectively, with varied dimensions.[32] These squares have been characterized by NMR spectroscopy and mass spectrometry combined with UV-visible spectroscopy (*see UV–Visible Spectroscopy*) and vapor-phase osmometry.

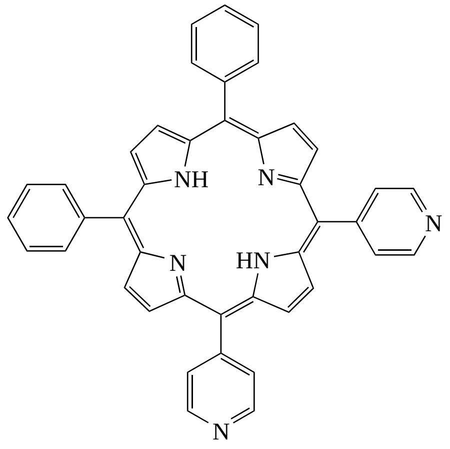

(**47**)

Two remarkable structures (**52**) and (**53**) have been prepared with ‘(dppp)M’ (M = Pt(II), Pd(II)) corners and a ligand based on perylene-bis-imide.[33] This square is exceptionally large with a diagonal M–M distance of 3.4 nm. An interesting aspect of this molecule is that the organic ligands retain their photophysical and electrochemical properties in the complex. Another nanoscale platinum macrocycle (**55**) that has been reported consists of Pt(II) corners (**39**) and Pt(II) linkers (**54**) (Scheme 16).[34] It was noted that the formation of these squares is concentration dependent, and that the monomer is favored at lower concentrations. At higher concentrations, the tetramer is the main product, and, in the limit of high concentrations, polymer formation dominates.

Self-assembly of labile transition metal ions with N-based multidentate ligands produces metallocyclophanes as in the case of the reaction of (**56**) with $Ni(NO_3)_2$ in water to yield the tetranuclear Ni_4L_4 complex.[35] Recrystallization of this compound from DMSO (dimethyl sulfoxide) in the presence of excess $NaClO_4$ produced crystals that contain one nitrate anion (*see Anion*) inside the square cavity of Ni_4L_4 square. The seven perchlorate anions are located in the interstices of the structure. In this context, the role of anions in the self-assembly of metallocyclophanes is being investigated by Dunbar and coworkers with 3,6 bis-(2-pyridyl)tetrazine (bptz). Reaction of the acetonitrile solvated complexes $M(II)(CH_3CN)_6(X)_2$ ($M = Ni$, Zn; $X = BF_4^-$, ClO_4^-) with bptz leads to high yields of the compounds (**57–60**) (Scheme 17). The X-ray and solution NMR studies confirm the location of one anion inside the cavity of the $[M_4(bptz)_4]^{8+}$ unit. The structure of $[\{Ni_4(bptz)_4(CH_3CN)_8\}\subset ClO_4]$ in (**58**) and $[\{Zn_4(bptz)_4(CH_3CN)_8\}\subset BF_4]$ in (**59**) is shown in Figure 1.[36] The coordination geometry (*see* ***Coordination Numbers & Geometries***) around each M(II) ion is distorted octahedral, with four sites being occupied by two different bridging bptz ligands and the two remaining sites being occupied by acetonitrile solvent molecules.

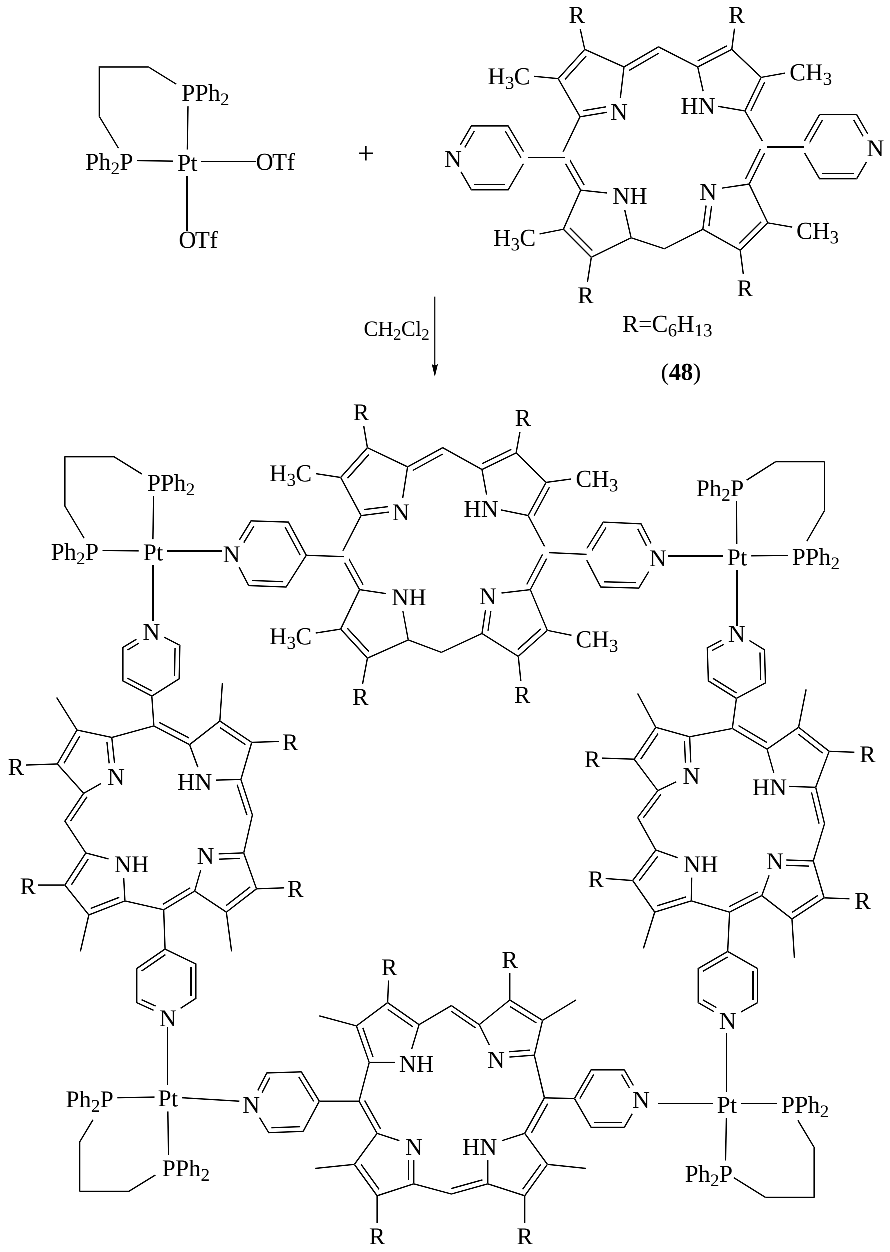

(48)

(49)

Scheme 15

3.4 Molecular Pentagons

Pentagons based on metal-coordination complexes (*see Coordination Complexes*) are quite rare. The first example was reported by Lehn and coworkers who reacted (**61**) with $FeCl_2$ in ethylene glycol at 170°C to produce the pentagon (**62**) in nearly quantitative yield (Scheme 18). An X-ray structural determination confirmed that the molecule is a pentagon with a chloride anion tightly bound within the central cavity. The encapsulated chloride was said to be essential for the formation of the pentagon.[37] Reaction of (**61**) with $FeSO_4$ under identical conditions followed by precipitation with NH_4PF_6 produced the hexameric structure (**63**) in high yield (Scheme 19).[38] Evidence of the nuclearity was confirmed by ESI-MS. Dunbar and coworkers reported a molecular pentagon $Ni_5(bptz)_5(CH_3CN)_{10}(SbF_6)_{10}$ (**64**) from the reaction of $Ni(CH_3CN)_6(SbF_6)_2$ with bptz (Scheme 20). An X-ray structure and a mass spectrometric study confirmed the pentagonal structure of $\{Ni_5(bptz)_5(CH_3CN)_{10}\}\subset SbF_6$ (Figure 2). The templating (*see Templating*) effect of the $[SbF_6]^-$ anion in stabilizing the pentagon has been established.[39] Reactions between Ni(II) ions and bptz in the

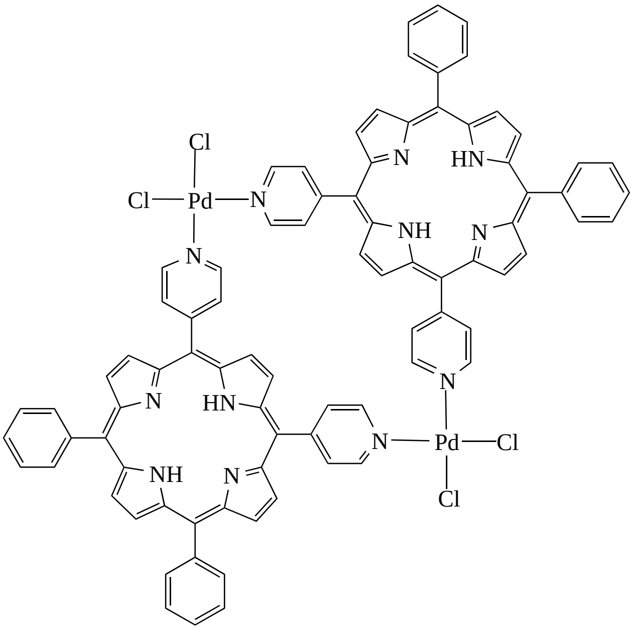

(**50**)

presence of smaller, tetrahedral anions such as $[BF_4]^-$ or $[ClO_4]^-$ lead to the formation of molecular squares under identical conditions.

4 CYANIDE (*See Cyanides*)

The cyanide ligand forms linear bridges and imparts relatively strong electronic and magnetic coupling between metal centers. Metal-cyanide chemistry has been investigated for many years,**[40]** with the most well-known compound in the family being Prussian blue (PB *see Prussian Blue*), $Fe_4[Fe(CN)_6]_3 \cdot nH_2O$, which was discovered by the German artist Diesbach in 1704. PB has been used in many applications over the years including as a pigment in the manufacture of inks and paints. Prussian blue is readily prepared by the addition of $[Fe(II)(CN)_6]^{4-}$ to Fe(III) ions in aqueous solution. The PB family of compounds exhibit defective face-centered cubic frameworks with cavities capable of encapsulating small molecules or charge balancing ions. The different distribution of the vacancies leads to various space group modifications

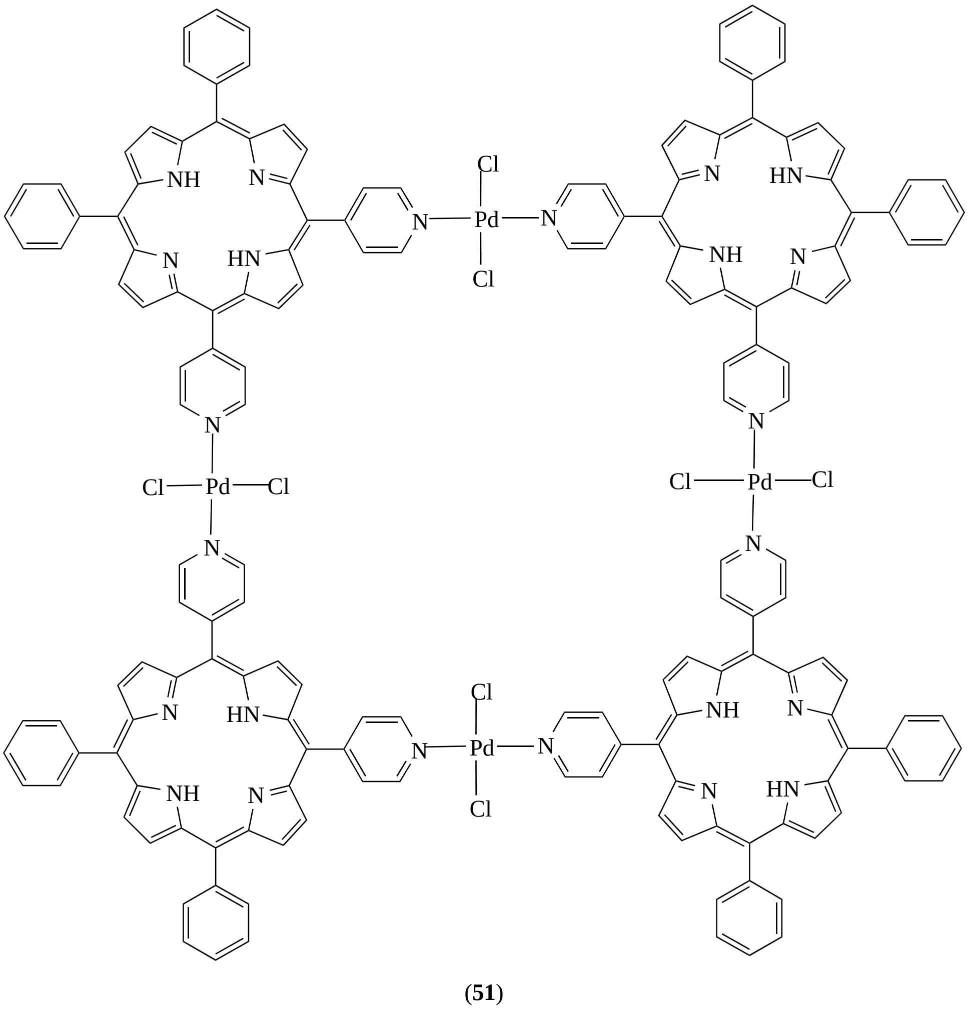

(**51**)

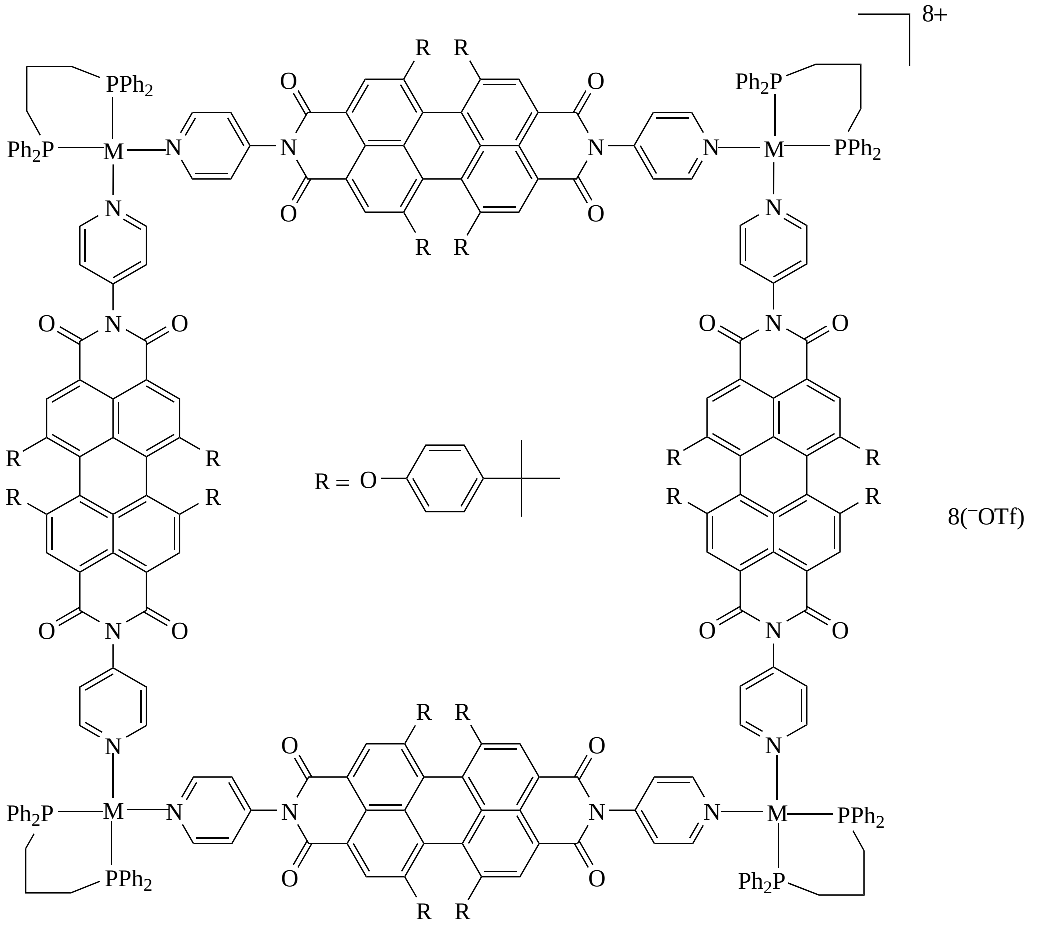

M = Pd (**52**)
Pt (**53**)

depending on the crystal growth conditions. The extent of deviation for Prussian blue ranges from a high-symmetry cubic space group (Fm3m) with a random distribution of vacancies occupied by water molecules to a lower-symmetry Pm3m space group with an ordering of the defects. These compounds are typically extremely insoluble, and the 'soluble forms' of PB are, in fact, colloidal suspensions with various degrees of potassium content.

The Prussian blue analogs $M^cM^a[M^b(CN)_6]\cdot nH_2O$ ($M^c = K^+, Cs^+$ etc.; M^a and M^b = transition metal ions) comprise a family of complexes, many of which exhibit high-magnetic-ordering temperatures. Modification of the PB compounds with the aim of reducing the complexity and dimensionality of the network structure has been achieved by using metal precursors with some of the coordination sites blocked by capping ligands. This chemistry has been fueled by the recognition that large-spin paramagnetic molecules can exhibit slow paramagnetic relaxation or single-molecule magnetic behavior.[41] Researchers are using convergent precursors to favor the deliberate formation of molecular architectures such as squares, cubes, and so on. Unlike the extensive use of square-planar (*see Square Planar*) transition metal ions such as Pd(II) and Pt(II) with the N-heterocyclic based ligands described earlier, molecular components for these magnetic materials consist of six-coordinate transition metals with unpaired electrons. It is necessary to protect four coordination sites at the metal ion to access molecular squares or two-dimensional, infinite networks. In a similar manner, three sites can be capped for accessing three-dimensional structures such as cubes. A number of precursors with two accessible sites available for coordination that have been structurally characterized in recent years include $[M(bpy)_2(OTf)_2]$ (2,2′-bpy = 2,2′-bipyridine) (M = Mn(II) (**65**), Co(II) (**66**)), $[Ni(bpy)_2(H_2O)_2](OTf)_2$ (**67**) and $[Mn(2,2'\text{-}bpym)_2(H_2O)_2](BF_4)_2$ (bpym = bipyrimidine) (**68**). The two cyanide ligands in $[Mn(bpy)_2(CN)_2]$ (**69**) are in cis positions and act as donors to other metal ions.[42]

Slow addition of $Zn(bpy)_2Cl_2$ to an aqueous solution of $K_3[Fe(CN)_6]$ results in the formation of the trinuclear structure $[\{Zn(bpy)_2(H_2O)\}_2\{Fe(CN)_6\}]Cl$ (**70**).[43] An X-ray structure revealed that two $[Zn(bpy)_2(H_2O)]$ units are coordinated to a central $[Fe(CN)_6]^{3-}$ unit in a trans fashion.

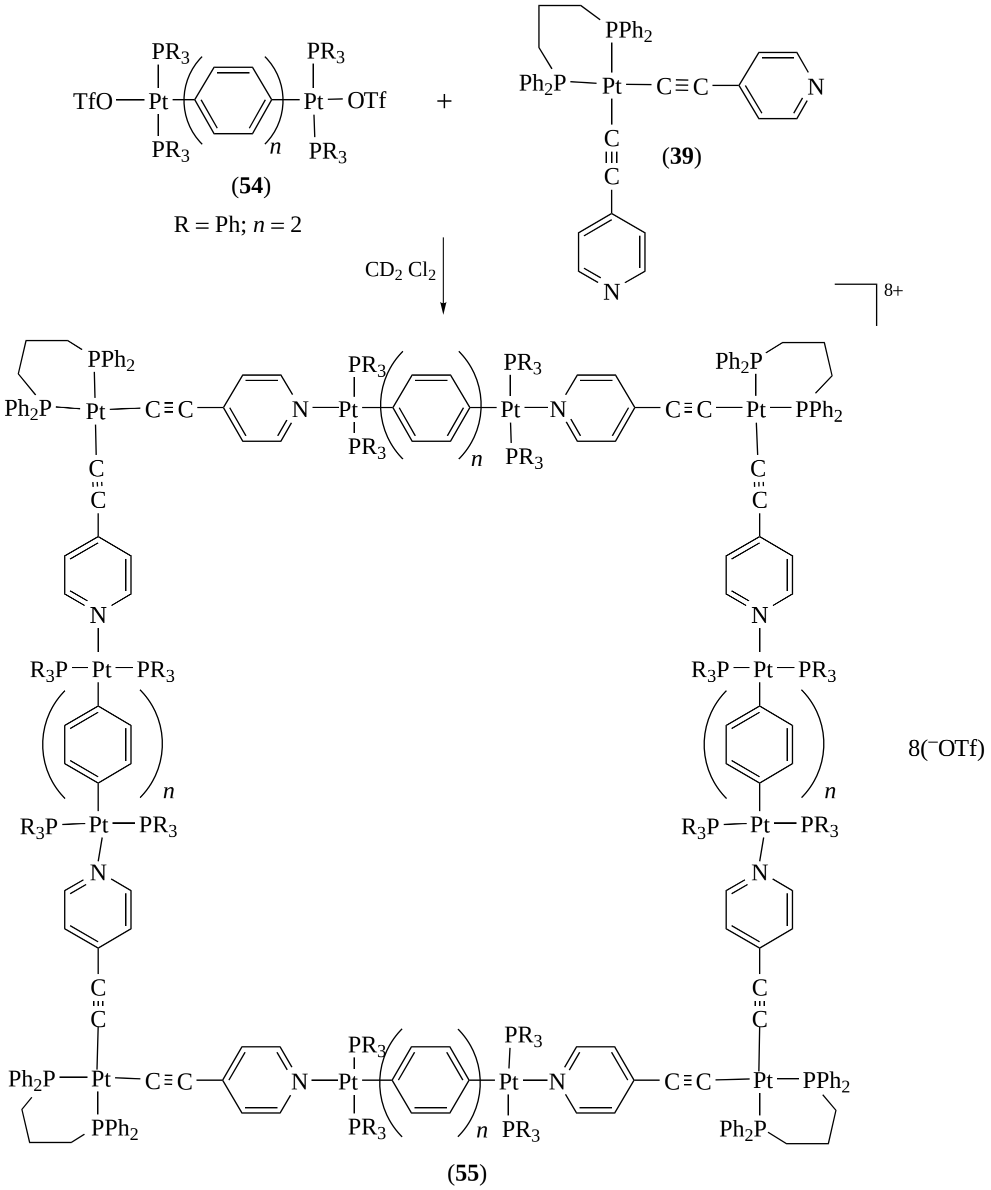
PR3
TfO
Pt
OTf
n
+
PPh2
Ph2P
Pt
C≡C
N
C
C
CD2 Cl2
8+
8(⁻OTf)
R3P
PR3
Ph2P
PPh2

(**54**)

R = Ph; *n* = 2

(**39**)

(**55**)

Scheme 16

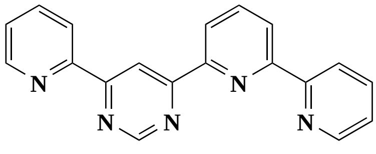

(**56**)

$$[M(CH_3CN)_6(X)_2] + \text{bptz} \xrightarrow{CH_3CN} [M_4(\text{bptz})_4(CH_3CN)_8(X)_8]$$

$M = Ni^{II}$; $X = BF_4^-$ (**57**)

$M = Ni^{II}$; $X = ClO_4^-$ (**58**)

$M = Zn^{II}$; $X = BF_4^-$ (**59**)

$M = Zn^{II}$; $X = ClO_4^-$ (**60**)

Scheme 17

The coordinated water molecule is stabilized by hydrogen bonding to a CN^- ligand of $[Fe(CN)_6]^{3-}$. The complex $[Zn(phen)_3]_2[\{Zn(phen)_2\}_2\{Fe(CN)_6\}_2]$ (**71**) was obtained from the reaction of $[Zn(phen)_2(NO_3)_2]$ with $[Fe(CN)_6]^{3-}$, which contains a central bimetallic $[Zn_2Fe_2]$ square unit.**[43]** The $[Fe(CN)_6]^{3-}$ units reside at opposite vertices of the square with the other two vertices being occupied by Δ and Λ $[Zn(phen)]^{2+}$ units. Similar molecules are accessible with

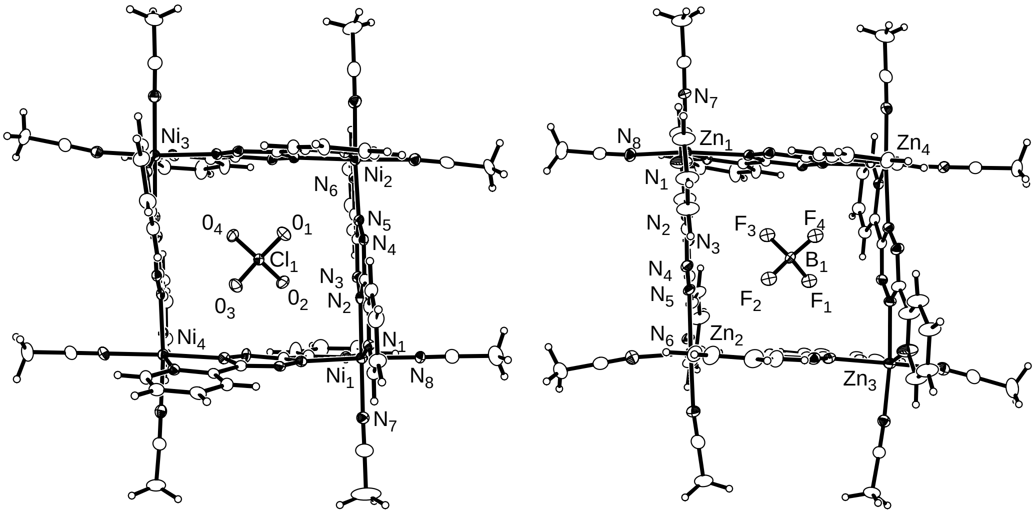
Ni$_3$
Ni$_2$
N$_6$
N$_5$
N$_4$
O$_4$
O$_1$
Cl$_1$
N$_3$
N$_2$
O$_3$
O$_2$
Ni$_4$
N$_1$
Ni$_1$
N$_8$
N$_7$
N$_7$
N$_8$
Zn$_1$
Zn$_4$
N$_1$
N$_2$
N$_3$
F$_3$
F$_4$
B$_1$
N$_4$
N$_5$
F$_2$
F$_1$
N$_6$
Zn$_2$
Zn$_3$

Figure 1 Displacement ellipsoidal plots of the molecular structures of [{$Ni_4(bptz)_4(CH_3CN)_8$}⊂ClO_4] in (**58**) and [{$Zn_4(bptz)_4(CH_3CN)_8$}⊂BF_4] in (**59**)

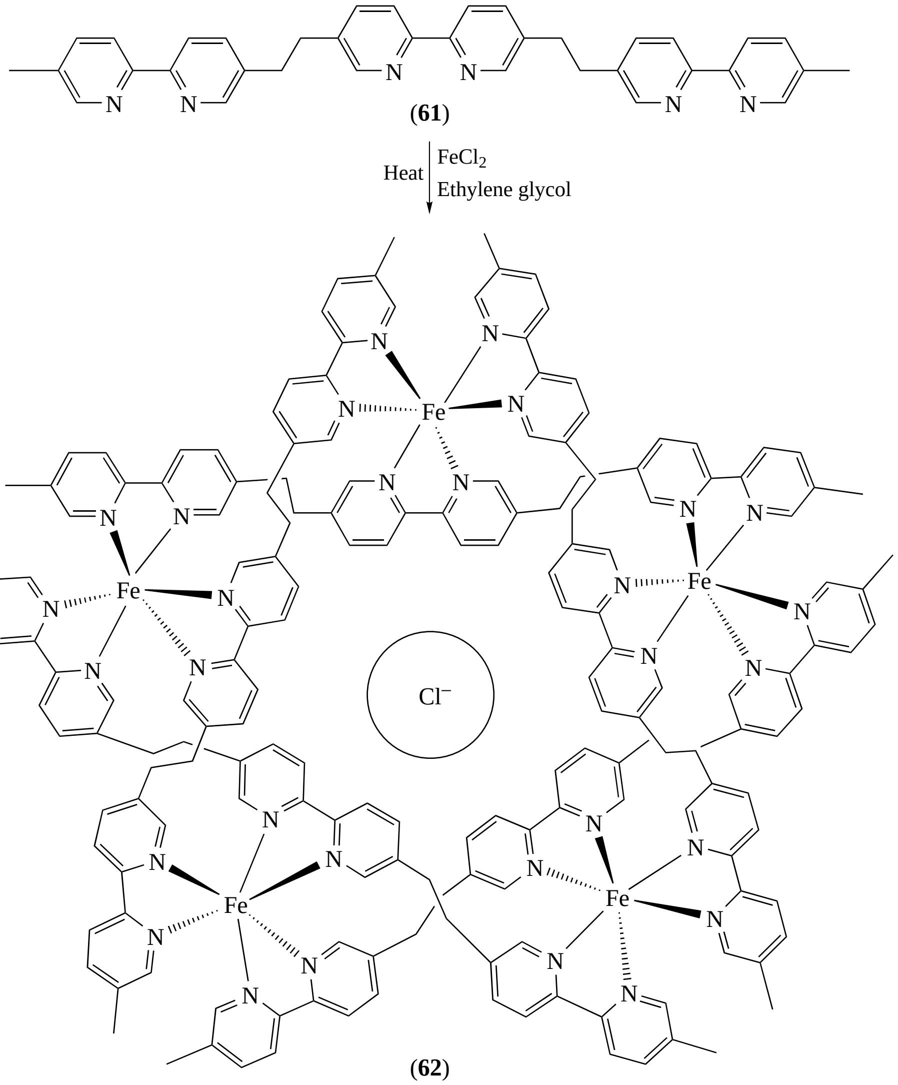
(**61**)
Heat
$FeCl_2$
Ethylene glycol
Cl$^-$
(**62**)

Scheme 18

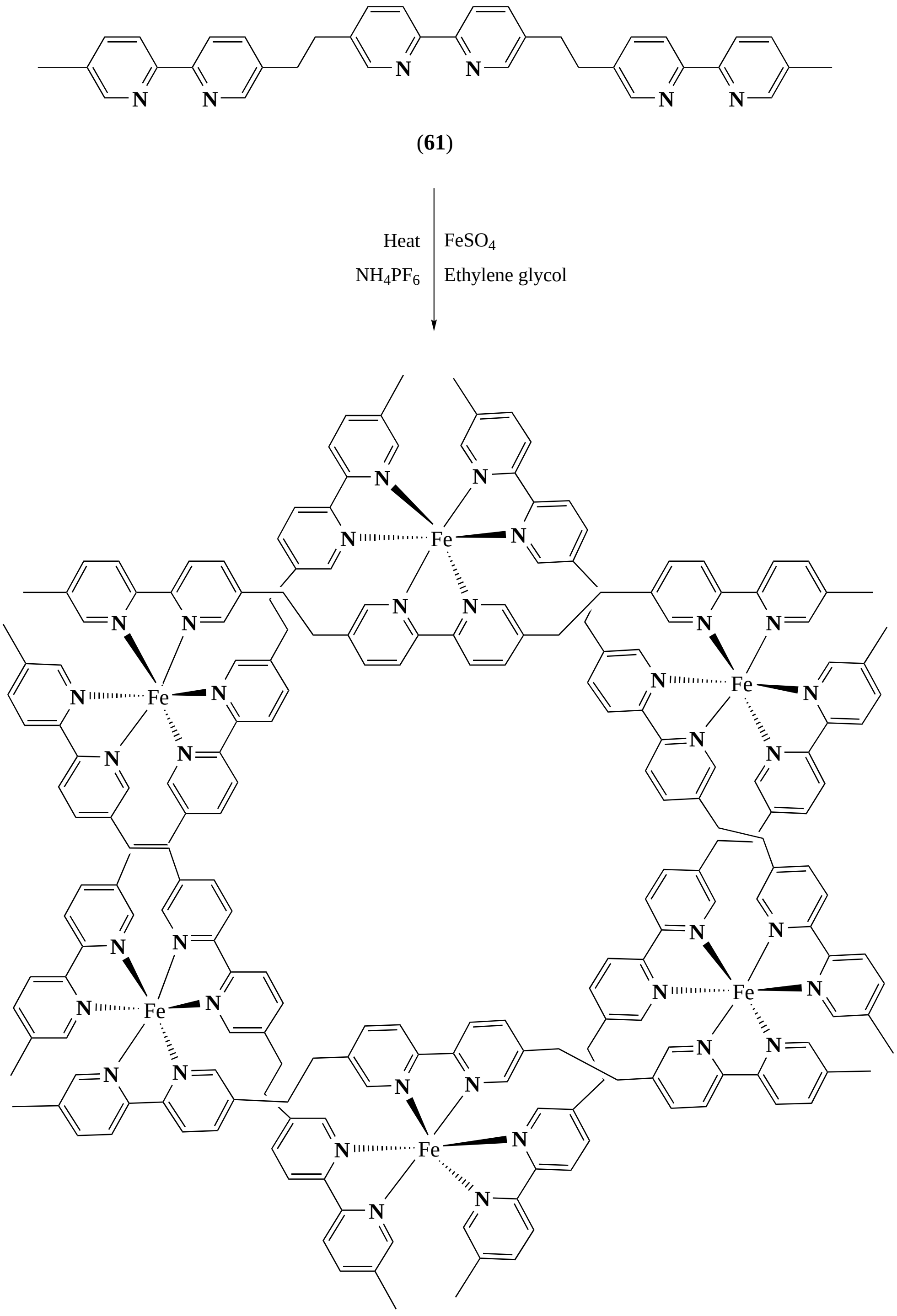
Heat
NH4PF6
FeSO4
Ethylene glycol
N
Fe

(**61**)

(**63**)

Scheme 19

$$\mathrm{Ni(CH_3CN)_6(SbF_6)_2 + bptz \xrightarrow{CH_3CN} Ni_5(bptz)_5(CH_3CN)_{10}(SbF_6)_{10}} \quad (\mathbf{64})$$

Scheme 20

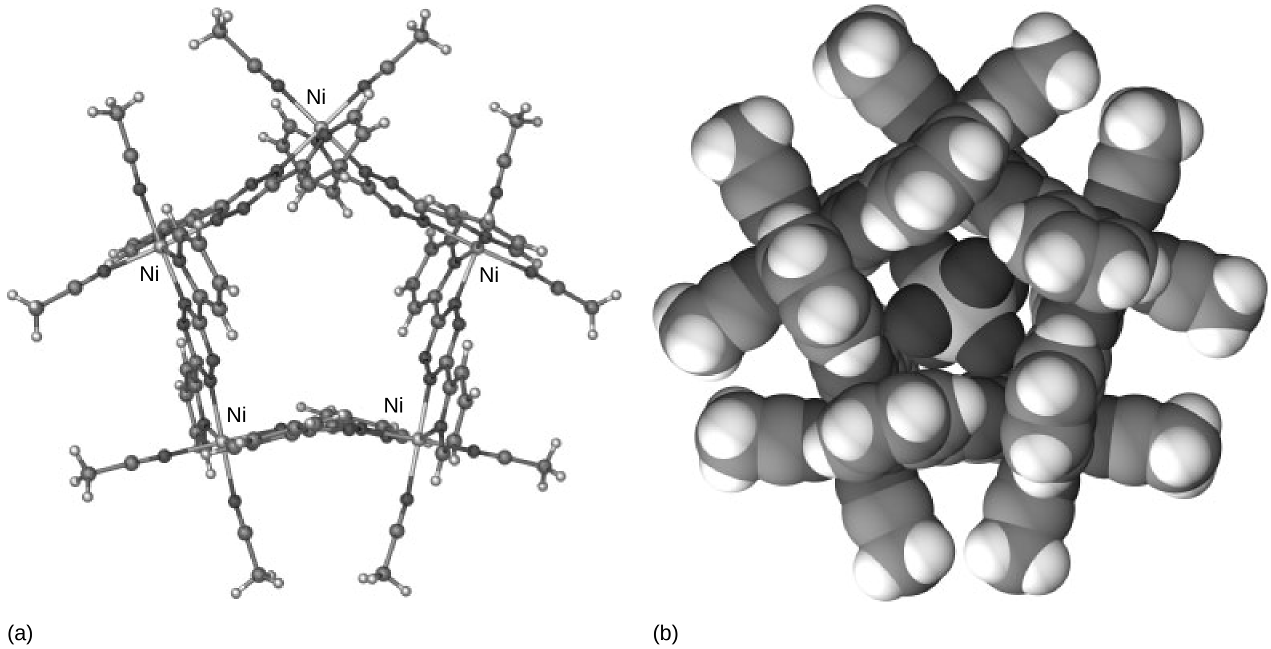

Figure 2 (a) Plot of the molecular structure of the pentagonal $\{Ni_5(bptz)_5(CH_3CN)_{10}\}$ unit in (**64**) and (b) a space filling diagram of $\{Ni_5(bptz)_5(CH_3CN)_{10}\}\subset SbF_6$ with the encapsulated anion

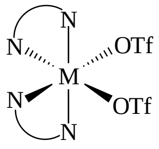

M = Mn^{II} (**65**)
Co^{II} (**66**)

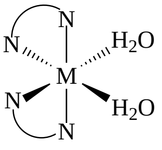

Ni^{II} (**67**)
Mn^{II} (**68**)

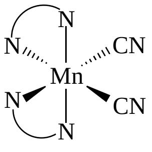

(**69**)

N N = 2,2′-(bipyridine) or 2,2′-(bipyrimidine)

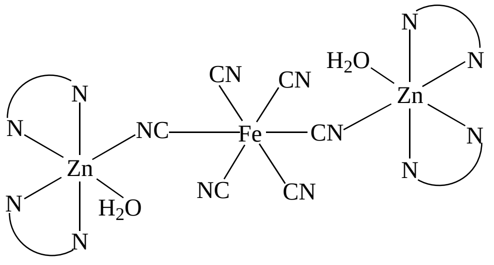

(**70**)

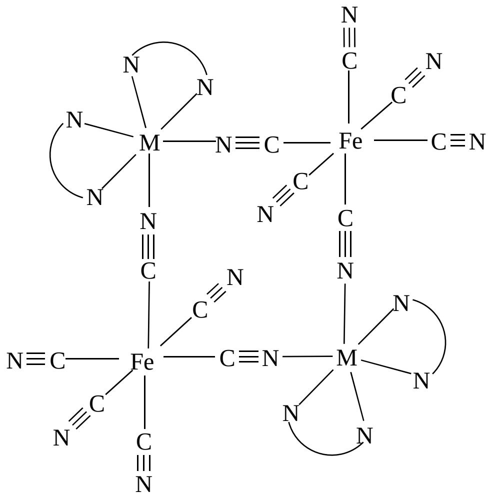

N N = phenanthroline
(**71**)

bipyridyl ligands. Oshio and coworkers reported Fe(II)/Cu(II) and Fe(III)/Cu(II) squares based on metal–cyanide complexes (*see* ***Cyanide Complexes of the Transition Metals***). Reactions of $Fe(dmbpy)_2(CN)_2$ or $[Fe(dmbpy)_2(CN)_2](NO_3)$ (dmbpy = 5,5′-dimethyl-2,2′-bipyridine) with $[Cu(ClO_4)_2]$ and imply (impy = 2-(2-pyridyl)-4,4,5,5-tetramethyl-4,5-dihydro-1H-imidazolyl-1-oxy) yield (**72**) and (**73**), respectively.[44]

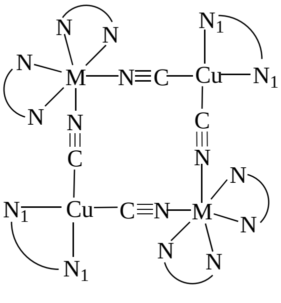

N N = 4,4′-dimethyl-2,2′-bipyridine

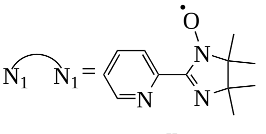

M = Fe^{II} (**72**)
M = Fe^{III} (**73**)

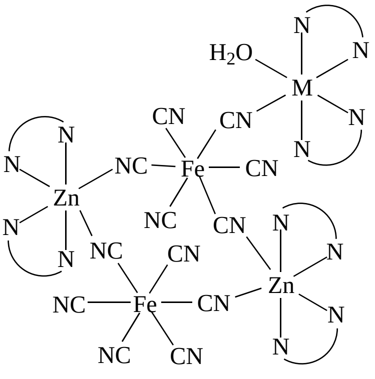

N N = 2,2-bipyridine

M = Ni (**74**), Zn (**75**)

One advantage of the use of hexacyanometallates in the aforementioned reactions is that the free cyanides (*see Cyanides*) can be used for the elaboration of squares into larger assemblies. The molecular pentamer $[\{Ni(bpy)_2(H_2O)\}\{Ni(bpy)_2\}_2\{Fe(CN)_6\}_2\}]$ (**74**) has been isolated from the reaction of $[Ni(bpy)_2(H_2O)_2](OTf)_2$ with $K_3[Fe(CN)_6]$ in water.[42] The formation of the pentanuclear species can be viewed as the addition of an additional $[Ni(bpy)_2(H_2O)]$ unit to the $[\{Ni(bpy)_2\}_2\{Fe(CN)_6\}_2]$ square. The molecule is neutral, which accounts for its preferential crystallization from the reaction solution. An analogous compound was isolated with Zn(II), namely $\{Zn(bpy)_2(H_2O)\}[\{Zn(bpy)_2\}_2\{Fe(CN)_6\}]_2$ (**75**).[43] The concept of adding building blocks to the central square unit can be extended to the formation of even larger molecules, as evidenced by the isolation of the highly unusual decanuclear cluster (*see Cluster*) $[\{Zn(phen)_2\}\{Fe(CN)_6\}]_2[\{Zn(phen)_2\}\{Zn(phen)_2(H_2O)\}\{Fe(CN)_6\}]_2$ (**76**) from $Zn(phen)_2(NO_3)_2$ and $K_3Fe(CN)_6$.[43]

Other molecular geometries besides squares have been isolated from a building-block approach. Slow diffusion of solutions of $[K[18]crown\text{-}6)]_3[Mn(CN)_6]$ and $[Mn(tmphen)_3(NO_3)_2]$ (tmphen = tetramethylphenanthroline) in acetonitrile leads to the formation of the cyanide cluster $\{Mn(tmphen)_2\}_3\{Mn(CN)_6\}_2\}$ (**77**) as shown in Figure 3. The molecular symmetry of (**77**) is nearly that of a trigonal bipyramid (tbp) (*see Trigonal Bipyramidal*) in which low-spin Mn(III) ions occupy the apical positions and high-spin (*see High-spin & Low-spin Compounds*) Mn(II) ions reside in the equatorial plane. Each apical Mn(III) ion is linked to Mn(II) centers via three linear cyanide bridges and is capped by three terminal cyanide ligands. The Mn(II) ions are coordinated to cis tmphen ligands as well as to the N ends of two cyanide bridges. The Mn(II) centers in each molecule are homochiral, but the molecules crystallizes as a racemic mixture in the centrosymmetric space group $P2_1/c$. Magnetic studies of the compound reveal that it behaves as a single-molecule-magnet.[45] Reactions of $[Co(bpy)_3(ClO_4)_2]$ and $K_3Fe(CN)_6$ produce a similar tbp molecule $[\{Co(bpy)_2\}_3\{Fe(CN)_6\}_2](ClO_4)$ (**78**).[42] It was noted that complex (**78**) is the result of a spontaneous redox

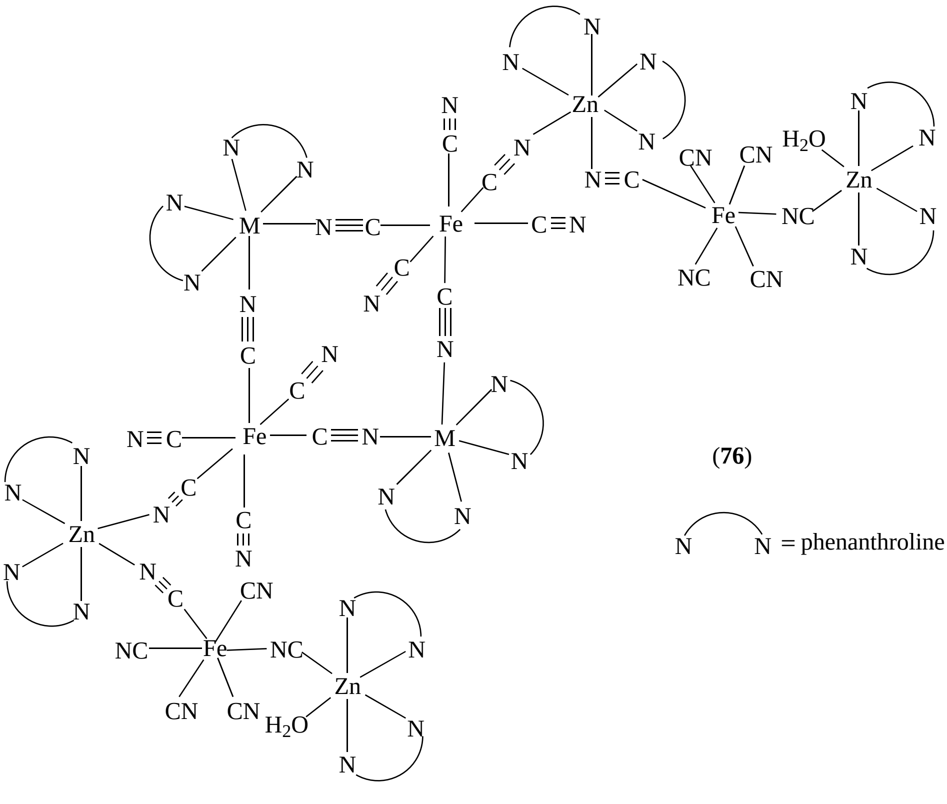

(**76**)

N N = phenanthroline

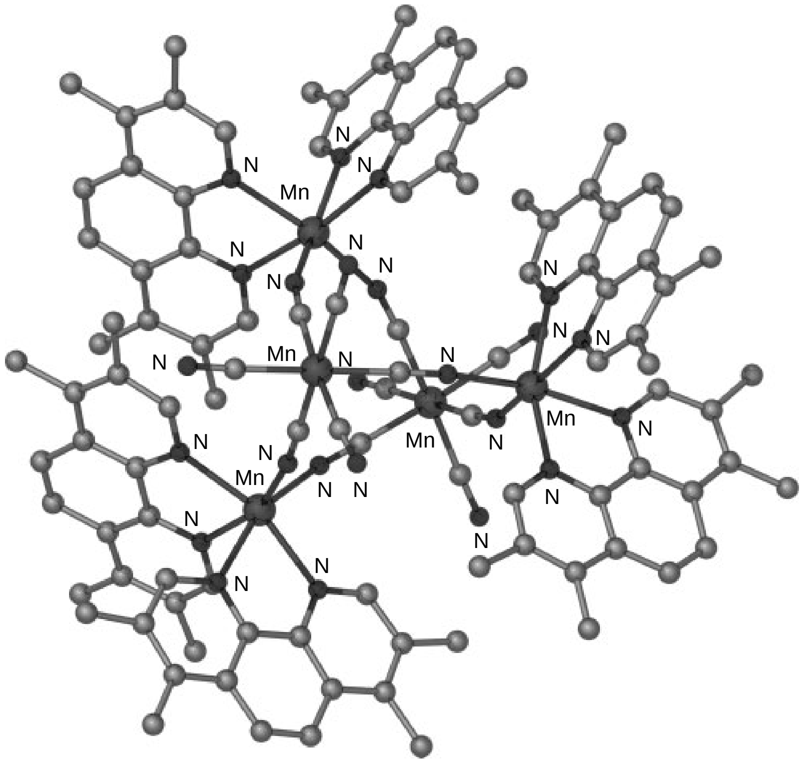

Figure 3 Plot of the molecular structure of $\{Mn(tmphen)_2\}_3\{Mn(CN)_6\}_2$ (**77**)

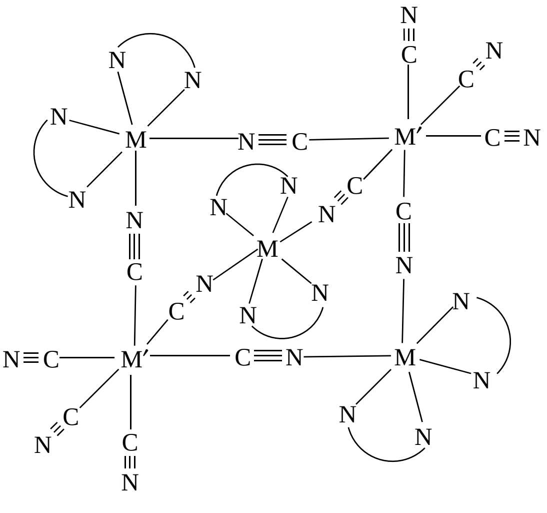

NN	M	M′	Code
bpy	Co	Fe	**78**
bpm	Ni	Fe	**79**
tmphen	Ni	Fe	**80**
impy	Ni	Cr	**81**

Scheme 21

reaction. This conclusion was based on the fact that this compound is diamagnetic and contains two low-spin Fe(II) and Co(III) ions. Similar tbp structures having the general formula $[\{Ni(bpm)_2\}_3\{Fe(CN)_6\}_2]$ (bpm = bis-(1-pyrazolyl)methane) (**79**)[46] and tmphen (**80**)[47] have also been characterized. A similar structure for the $[\{Ni(impy)_2\}_3\{Cr(CN)_6\}_2]$ (**81**) has been proposed (Scheme 21).[48] The use of the bulky radical ligand precludes the formation of an extended network structure and also increases the ground state (*see Ground State*) spin value.

Considerable efforts have been made to synthesize discrete clusters that are analogues of a single cube unit of PB structures. To prevent the formation of a three-dimensional framework, ligands such as 4-isopropyltoluene (*p*-cymene), 1,4,7-triazacyclononane (tacn), triphos (triphos = 1,1,1-tris(diphenylphosphinomethyl)ethane) and cyclopentadienyl (*see Cyclopentadienyl*) (Cp) ligands have been used to cap one face of an octahedron whose other three *fac* (Facial) positions are occupied by CN ligands. Assembly of these tricyanometallate building blocks with three mutually orthogonal, dangling CN ligands has led to a series of molecular cube compounds. For example, the reaction of $[Et_4N][Cp^*Rh(CN)_3]$ and $[\{Cp^*RhCl_2\}_2]$ reported by Rauchfuss and coworkers produces the molecular square (**82**) with Rh atoms at the vertices. The structure of the compound was confirmed by X-ray crystallography (*see X-ray Crystallography*). Analogous mixed-metal $[Rh_2Ru_2]$ (**83**) and $[Co_2Rh_2]$ (**84**) squares have

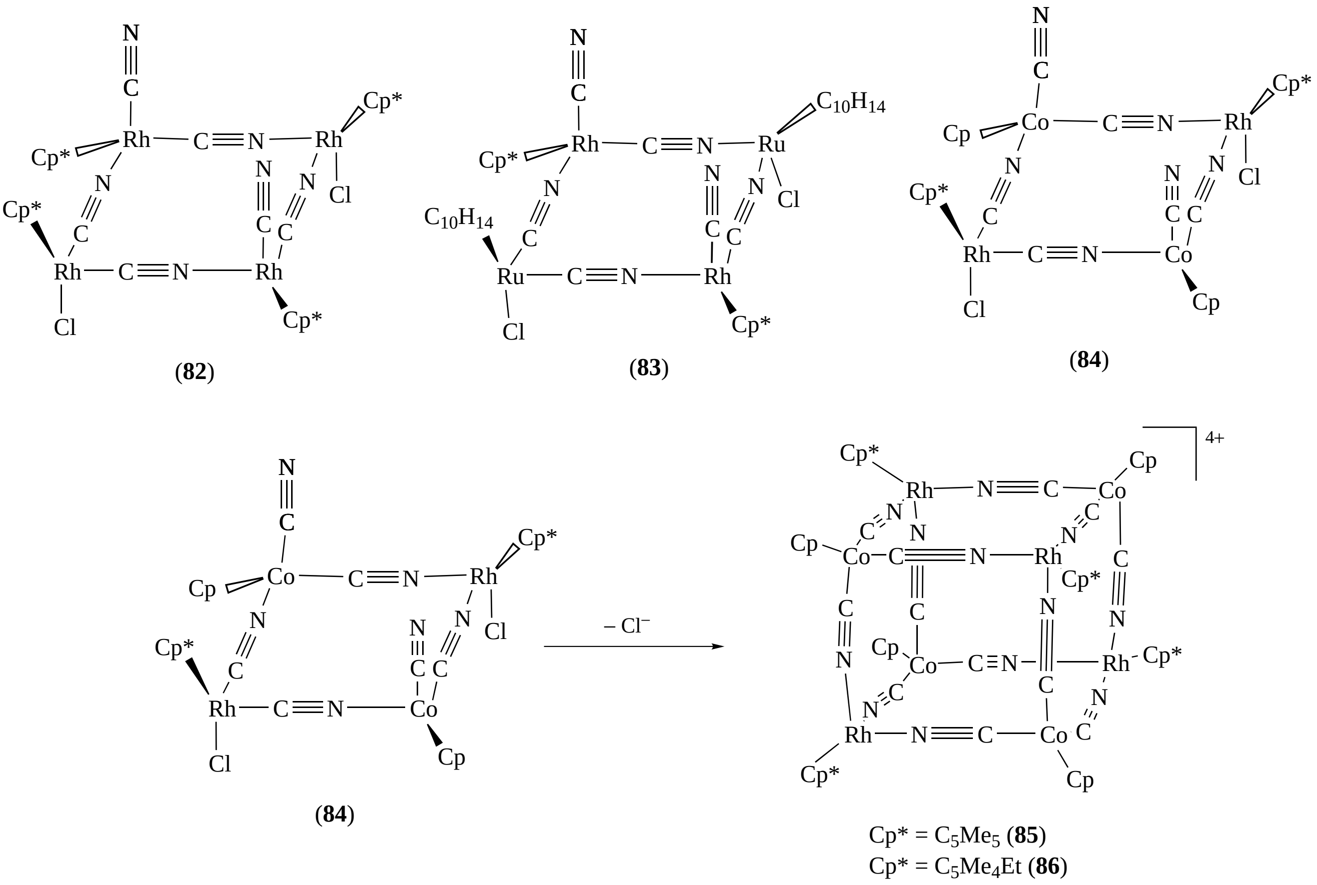

(**82**) (**83**) (**84**)

(**84**)

Cp* = C_5Me_5 (**85**)
Cp* = C_5Me_4Et (**86**)

Scheme 22

also been reported. Upon removal of the Cl^- ligands from (**84**), the $[Rh_4Co_4]$ cube (**85**) is formed (Scheme 22). Compound (**85**) was characterized by ESI-MS studies. The crystal structure (*see Crystal Structures*) of (**86**) was obtained, which confirmed the cubic architecture and the presence of C_5Me_4Et as the capping ligand.**[49]**

In related reactions, Rauchfuss explored condensation reactions of $[Et_4N][CpCo(CN)_3]$ and $[Cp^*Ru(NCMe)_3][PF_6]$ in the presence of cesium ions. This reaction leads to the formation of $[Cs\subset\{CpCo(CN)_3\}_4\{Cp^*Ru\}_4]$ (**87**), a molecular cage with an encapsulated cesium ion.**[50]** Although a myriad of other cations such as Cs^+, K^+, Rb^+, $NH_4{}^+$, $MeNH_3{}^+$ can be encapsulated by this cage, when the reaction is carried out in the presence of $EtNH_3{}^+$ ions, the empty molecular box $[\{CpCo(CN)_3\}_4\{Cp^*Ru\}_4]$ is formed in high purity.**[51]** Reaction of $[Et_4N][CpCo(CN)_3]$, $[Cp^*Ru(NCMe)_3][PF_6]$ and CsOTf in a 4:3:1 ratio in acetonitrile led to the isolation of the incompletely formed cube (**88**) (Scheme 23). The ESI-MS of (**88**) exhibits a molecular ion peak at $m/z = 1649$ and an absence of signals for the cube (**87**). Apart from the structural features of (**88**), this molecule represents an opportunity to incorporate other metal ions into the assembly, by a reaction described as a 'box-completion' process. Treatment of (**88**) with $[Cp^*Rh(NCMe)_3](PF_6)_2$ gives the Cs^+ encapsulated box (**89**). The product was characterized by ESI-MS and NMR spectroscopy. Treatment of (**88**) with $NaPF_6$ produces the 'double molecular box' fused at one corner. The structure of $[Na\{Cs\subset \{CpCo(CN)_3\}_4\{Cp^*Ru\}_3\}_2]\,PF_6$ (**90**) consists of two $Cs\subset \{CpCo(CN)_3\}_4\{Cp^*Ru\}_3$ cages conjoined at a Na^+ ion. The Cs^+ ions are situated at the center of two *pseudo* boxes. The smaller Na^+ ion is coordinated to six terminal cyanides from two incomplete box structures in an octahedral arrangement.

Long and coworkers have contributed a considerable body of work to the area of paramagnetic cube molecules based on bridging cyanide ligands. Formation of the $[Cr_4Co_4]$ cube $[Cr_4Co_4(CN)_{12}(tacn)_8][OTf]_{12}$ (**91**) has been reported to occur from the reaction of equimolar amounts of $[Cr(H_2O)_3(tacn)][OTf]_3$ and $[Co(CN)_3(tacn)]$ in water. The molecular cube $[Co_8(CN)_{12}(tacn)_8][OTs]_{12}$ (**92**), with eight Co atoms at the vertices, has also been reported and characterized by X-ray crystallography. A high R-factor for this structure was attributed to anion disorder but is also likely to be a result of the high symmetry of the cubic clusters. As in the case of fullerenes (*see* ***Carbon: Fullerenes***), these clusters exhibit rotational disorder that greatly affects the quality of

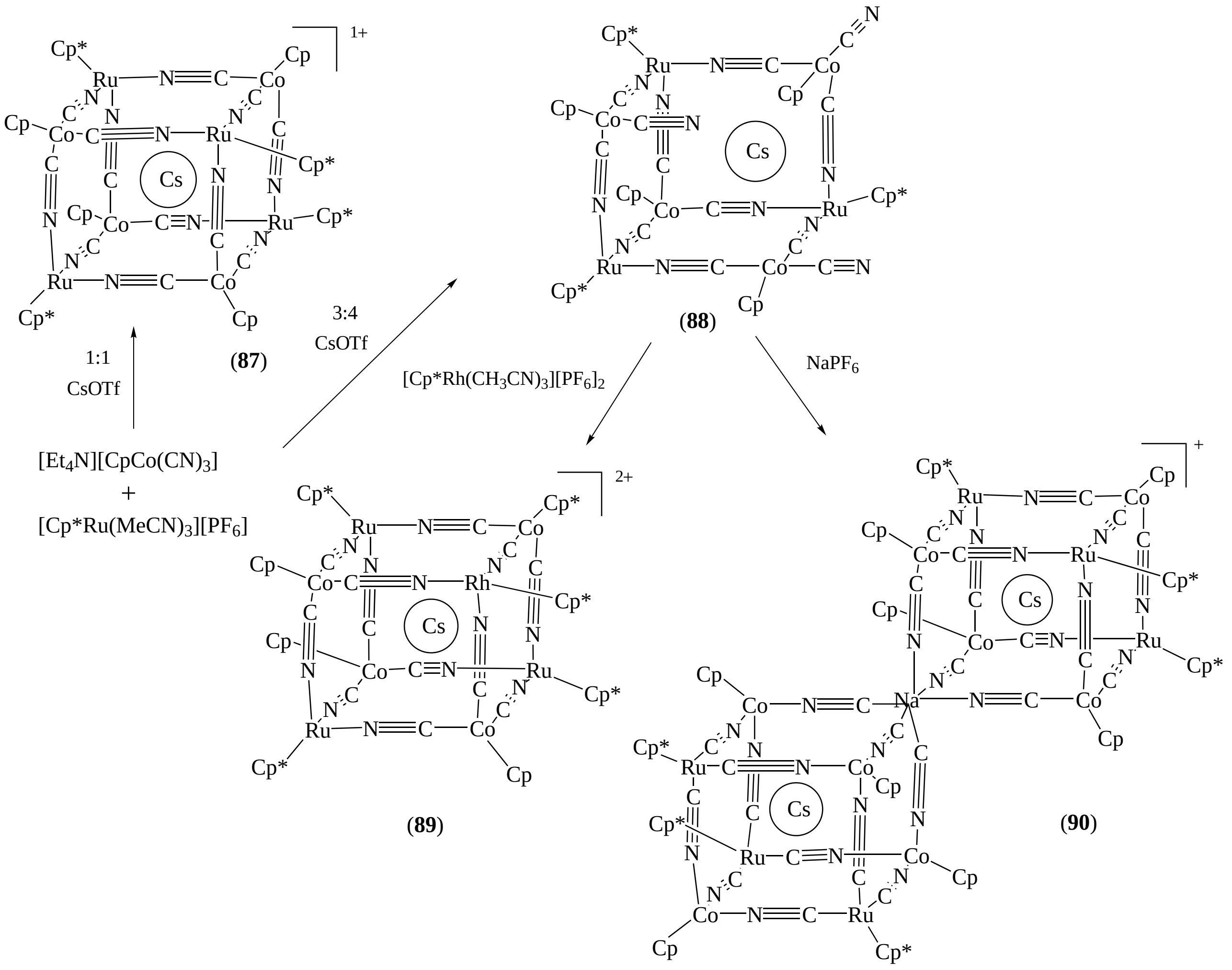
1+
(87)
1:1
CsOTf
[Et4N][CpCo(CN)3]
+
[Cp*Ru(MeCN)3][PF6]
3:4
CsOTf
(88)
[Cp*Rh(CH3CN)3][PF6]2
NaPF6
2+
(89)
+
(90)
Cs
Cp*
Cp
Ru
Co
Rh
Na

Scheme 23

$4[M(H_2O)_3(tacn)]^{y+} + 4[M'(CN)_3(tacn)]^{x-} \longrightarrow [M_4M'_4(CN)_{12}(tacn)_8]^{4(y-x)+}$

$[Cr_4Co_4(CN)_{12}(tacn)_8][OTf]_{12}$ **(91)**

$[Co_8(CN)_{12}(tacn)_8][OTs]_{12}$ **(92)**

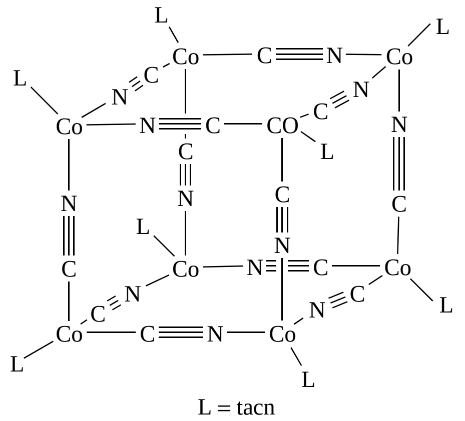

L = tacn

(**92**)

Scheme 24

the diffraction data.[52] Complex (**92**) was synthesized using the same protocol (Scheme 24) described for the preparation of (**91**), which is clearly a general method for synthesizing molecular cubes with metal ions at the vertices. In a similar vein to tacn, the triphos ligand coordinated to paramagnetic Re(II) (d^5) ions ($[Re(triphos)(CH_3CN)_3][BF_4]_2$ (**93**) and $Et_4N[Re(triphos)(CN)_3]$ (**94**)) has been successfully exploited by Dunbar and coworkers for the purpose of making cubes. Self-assembly reactions of (**94**) with MCl_2 in CH_3CN (M = Mn, Fe, Co, Ni, Cu, Zn)[53] provides a family of molecular cubes of general formula $[\{Re(triphos)(CN)_3\}\{MCl\}]_4$. The Oak Ridge Thermal Ellipsoid Plot (ORTEP) diagram (*see ORTEP Diagram*) for one such cube $[\{Re(triphos)(CN)_3\}\{MnCl\}]_4$ (**95**) is shown in Figure 4.[54]

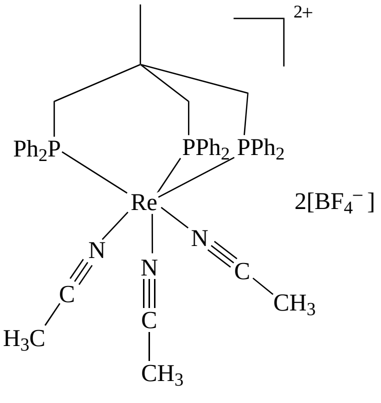

(**93**)

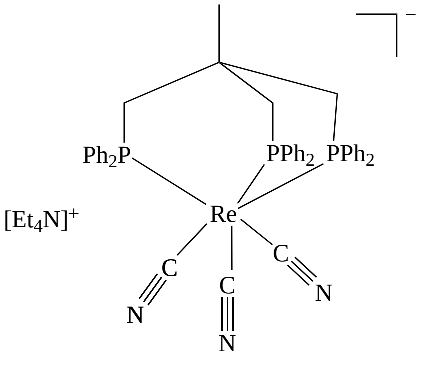

(**94**)

Precursors for cubes based on carbonyl ligands can be prepared from $Mo(CO)_6$, for example, the molecule $(C_6H_3Me_3)Mo(CO)_3$ reacts with $Et_4N[Cp^*Rh(CN)_3]$ in the presence of alkali metal ions to give $(Et_4N)_3[M_a \subset \{Cp^*Rh(CN)_3\}_4\{Mo(CO)_3\}_4]$ (M_a = Cs (**96**), K (**97**)).[55] The cubic architectures of these complexes were established by crystallography. Self-assembly of $Mo(CO)_3(CH_3CN)_3$ molecules in the presence of $[Et_4N]CN$ and KPF_6 ions leads to the formation of the trigonal prismatic (*see Trigonal Prism*) cage compound $(Et_4N)_8[K\subset \{Mo_6(CN)_{19}(CO)_{18}\}]$ (**98**).[56] The crystallographic analysis revealed the existence of a $Mo_6(CN)_{19}$ cage with idealized D_{3h} symmetry. A potassium ion is located near the center of the cage.

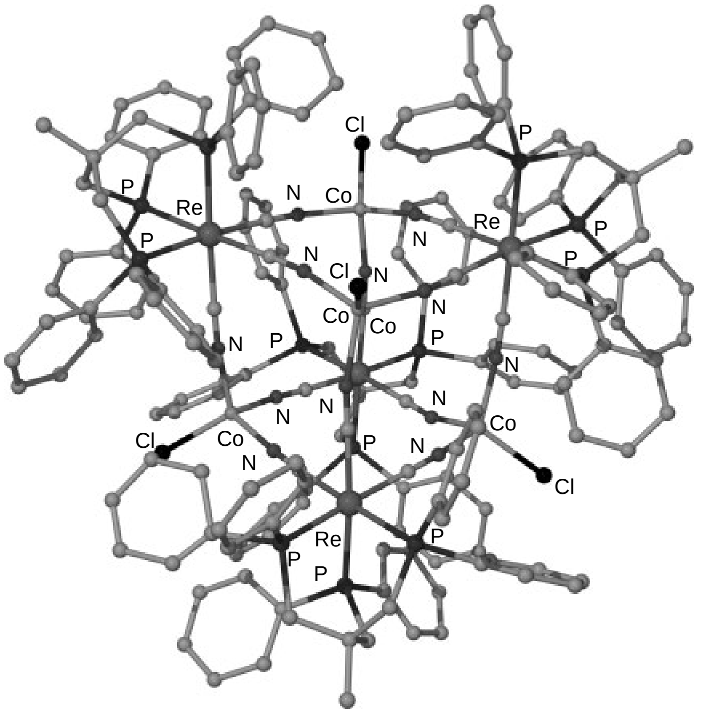

Figure 4 Plot of the X-ray crystal structure of (**95**)

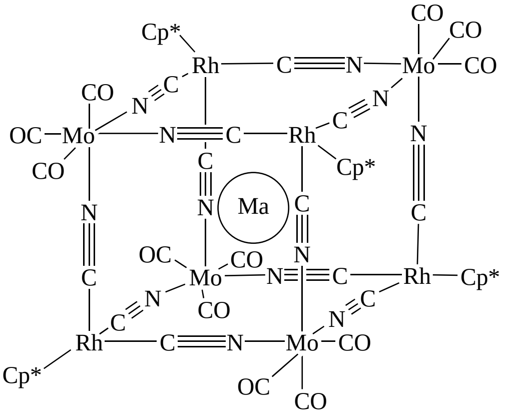

Ma = Cs (**96**); K (**97**)

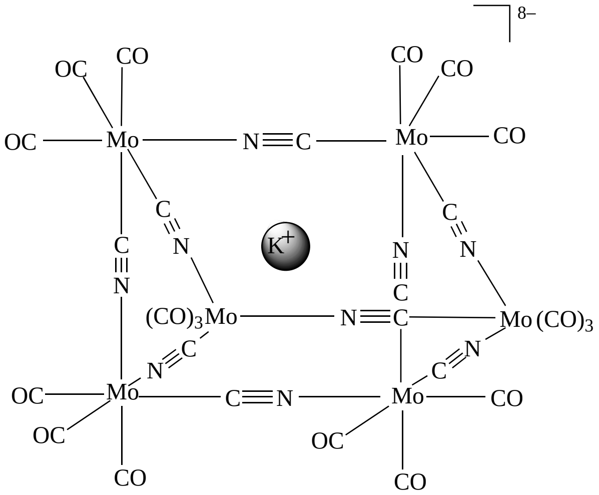

(**98**)

A large body of work has been devoted to the synthesis of discrete clusters as well as one, two, and three-dimensional extended structures by employing site-protected metal complexes with cyanometalates.[57] Strategies for assembling $[M(CN)_6]^{3-}$ with mononuclear metal complexes $[M'L_4(H_2O)_2]^{n+}$ and $[M'L_5(H_2O)]^{n+}$ bearing tetradentate (L_4) (*see Tetradentate Ligand*) and pentadentate (L_5) ligands (*see Pentadentate Ligand*) have been developed. The coordinated water molecules are labile and can be displaced by the N end of the cyanide ligands of a cyanometalate to produce discrete molecules. The multidentate ligands restrict the dimensionality and molecules with high-spin ground states are obtained. The tetra- and penta-amines and their corresponding mononuclear complexes have been synthesized. A series of trinuclear $\{M^{III}(CN)_4\}\{NCM'^{II}L\}_2\}^+$ (M = Cr, Co; M′ = Ni, Co, Cu), tetranuclear $\{M^{III}(CN)_3\}\{NCM'^{II}L\}_3\}^{3+}$ (M = Cr; M′ = Co), and heptanuclear $\{M^{III}\{NCM'^{II}L\}_6\}^{9+}$ (M = Cr, Co; M′ = Ni, Mn, Cu) complexes were isolated and their structures established by X-ray crystallography.[58] The neutral trinuclear bimetallic complex (**99**) is a typical example.[59]

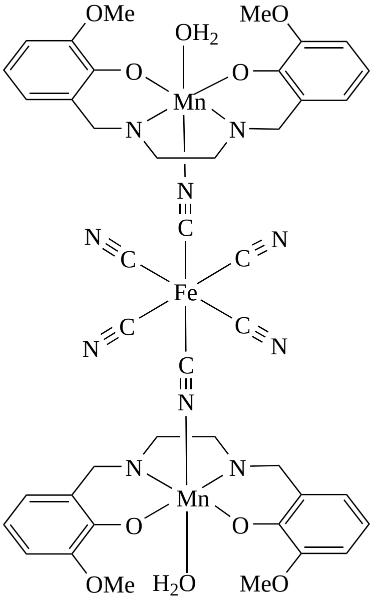

(**99**)

5 CARBOXYLATE LIGANDS

A perusal of the literature indicates that there is a general lack of control on the outcome of reactions of transition metal ions and nitrogen donor ligands. This uncertainty arises from the fact that metal–ligand interactions tend to be weaker than other covalent bonds (*see Covalent Bonds*) and that coordination angles about metal ions are flexible. This situation is in sharp contrast to the formation of organic molecules, for which traditional rules of covalent bonding apply. In organic chemistry, a small set of building blocks, in principle, can be used to build practically any larger organic molecule. The introduction of metal ions results in a much higher degree of complexity owing to a larger variation in bonding patterns and structures. Clearly, developing a set of building blocks for predictable self-assembly of inorganic compounds is a challenge. The use of well-defined and rigid molecular building blocks whose structural integrity is maintained throughout the construction process, however, has been shown to result in predetermined structures.

The term ‘building units’ (BU) has been used to define a group of atoms with a certain geometry, the condensation of which results in a three-dimensional solid. Such units can be molecules, inorganic polyhedra, or metal centers coordinated by organic ligands. The term ‘secondary building units’ (SBU) was introduced by Yaghi and coworkers to describe a conceptual building block[60] that is not necessarily an isolable, chemically distinct entity, but rather a fragment whose geometry plays an important role in determining the three-dimensional structure of the solid. The structural rigidity of certain metal–carboxylate clusters has been exploited for the formation of well-defined structures. For example, the

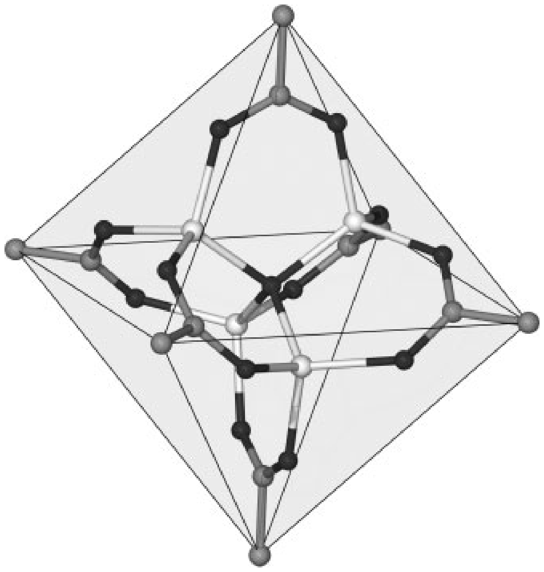

$Zn_4O(CCO_2)_6$
Octahedral SBU

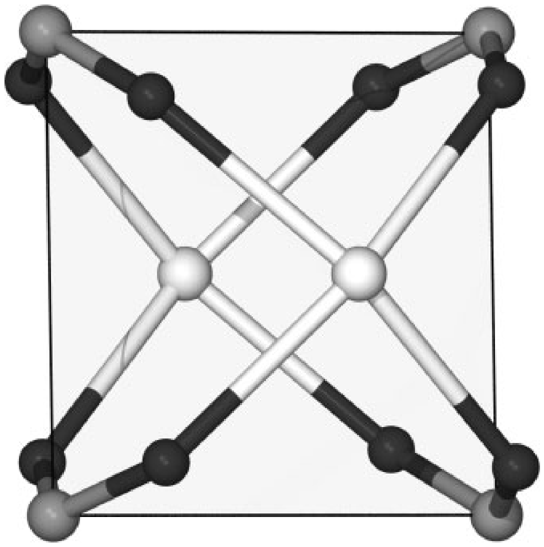

$M_2(CO_2)_4$
Square SBU

Scheme 25

four ZnO_4 tetrahedra (having a common vertex) and the six carboxylate C atoms of $Zn_4O(CO_2)_6$ units (Scheme 25) define an octahedral building block. Similarly, the paddle-wheel unit $M_2(CO_2)_4$ constitutes an example of a square building block. The reaction conditions that yield the paddlewheel (square SBU) and the basic zinc acetate (octahedral SBU) have been identified.

Organic SBUs are pre-assembled, rigid and have well-defined geometries. Condensation of symmetric building blocks results in topologies with high symmetry that are referred to as default structures.[61] For example, addition of the organic ligand adamantine tetracarboxylate (a tetrahedral SBU) to the paddlewheel (square SBU) gives the *default* PtS structure. Similarly, addition of benzenetricarboxylate (a triangular SBU) to the square paddle-wheel SBU results in the *default* Pt_3O_4 structure.[62] The successful synthesis of complexes with low-symmetry topologies requires the use of more complex building blocks coded for the specific product. External influences such as templates have also been noted to be instrumental for achieving the desired product.

Diffusion of triethylamine into a solution of $Zn(NO_3)_2$ and H_2BDC (1,4-benzenedicarboxylic acid) in N,N'-dimethylformamide (DMF)/chlorobenzene results in the formation of a three-dimensional metal-organic-framework (MOF) structure with the composition $Zn_4O(BDC)_3$. A single-crystal X-ray diffraction study revealed a simple cubic topology (Figure 5) in which the vertices are occupied by $Zn_4O(CO_2)_6$ units and the edges are the phenyl moieties of the BDC molecules. The octahedral SBU consists of a single O atom bonded to four Zn atoms forming a regular Zn_4O tetrahedron. Each edge of the Zn tetrahedron is capped by a $-CO_2$ group to form a $Zn_4O(CO_2)_6$ cluster.[63]

In the area of SBU chemistry, there is considerable effort being applied to the design of structures with the same skeleton but with different functionalities and dimensions. In this respect, a total number of sixteen isoreticular structures involving octahedral zinc acetate SBU and dicarboxylate linkers of varying length and ring substituents have been synthesized.[64] Each structure exhibits the same network

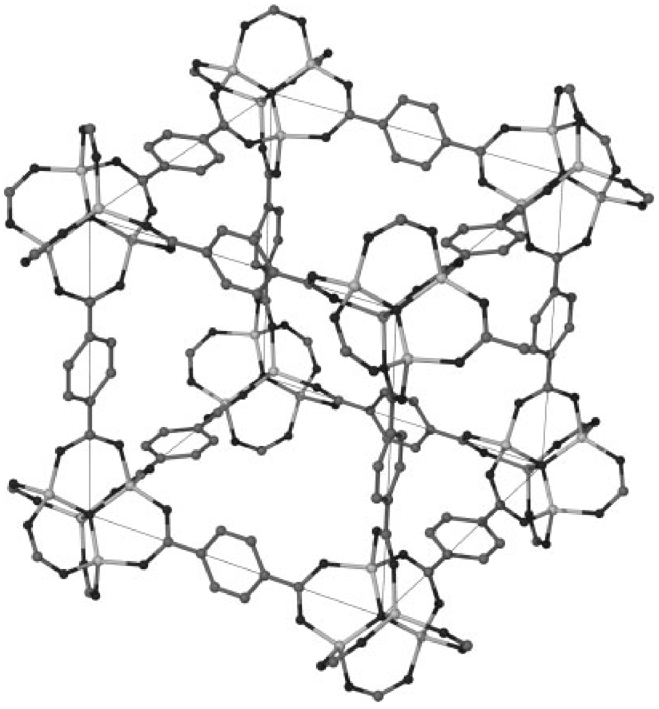

Figure 5 The cube topology of the 3-D extended structure of $Zn_4O(BDC)_3$

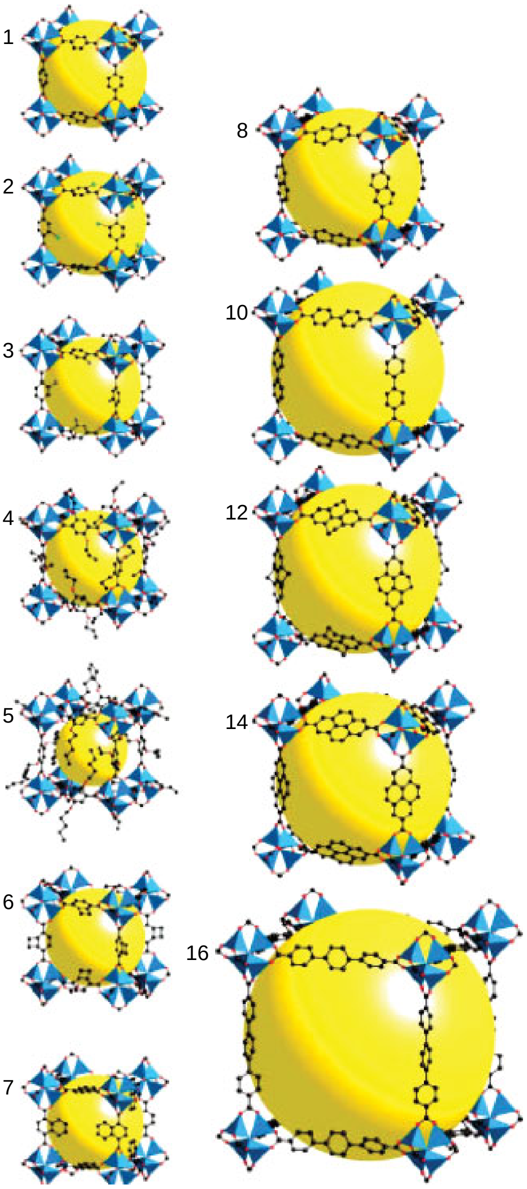

Figure 6 Isoreticular structures having the same network topology but with different linkers. (Reproduced from N.L. Rosi, M. Eddaoudi, J. Kim, M. O'Keeffe, O.M. Yaghi, *CrystEngComm.*, 2002, **4**, 401 by permission of Royal Society for Chemistry)

topology and has been synthesized using exactly the same synthetic parameters except for the desired linkers (Figure 6).

For a given inorganic SBU, the geometry of the organic SBU (linker) has a dramatic influence on the resulting MOF. The use of benzenedicarboxylates with square paddle-wheel SBU's illustrates this point. A truncated cuboctahedron (zero dimensional) structure MOP-1 (metal-organic polyhedron) results with 1,3-benzenedicarboxylate in which the paddle-wheel units are at 120°.[65] The 1,4-benzenedicarboxylate places the paddlewheel at 180° to each other and gives MOF-1 with the square grid structure (two-dimensional).[66] The linker 2-bromo-1,4-benzenedicarboxylate, which places the paddlewheel at 90° angles, yields MOF-2 exhibiting the expected NbO network (Figure 7).[67]

Exquisite control over the outcome of reticular synthesis has also been developed using site-blocked dimetal complexes that dictate certain angular requirements for bonding. The use of site-blocked paddle-wheel dimetal precursors lead to molecular architectures as opposed to the network structures discussed in the preceding section. The use of dicarboxylate bridging ligands to link multiply-bonded dimetal complexes into open-chain oligomers and polymers was first reported by Chisholm and coworkers over ten years ago.[68] Recently, Cotton and coworkers have reported a variety of supramolecular arrays that involve dimetal units.[69] A generic paddle-wheel complex contains eight equatorial and two axial sites (Scheme 26). The precursors are designed such that some of the equatorial positions of the paddlewheel are occupied by nonlabile groups such as formamidinate or diphosphine, while the remaining coordination sites are coordinated by easily substituted ligands such as acetonitrile,

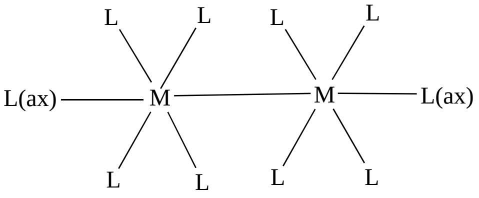

Scheme 26

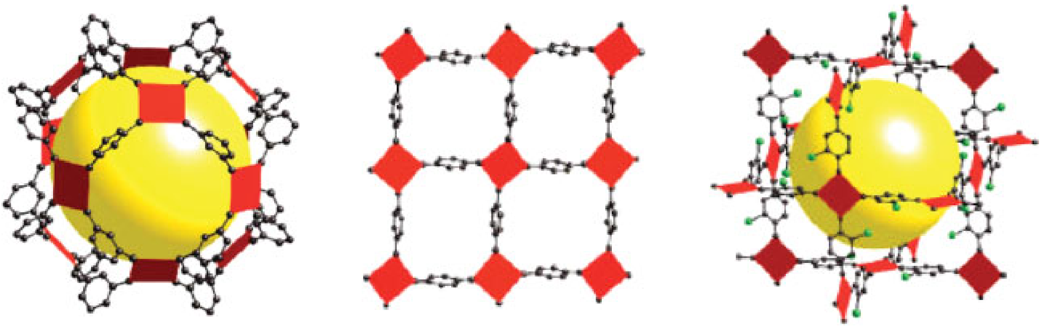

Figure 7 0-D truncated cuboctahedron (MOP-1), 2-D square grid framework (MOF-1) and 3-D network structure (MOF-2). (Reproduced from N.L. Rosi, M. Eddaoudi, J. Kim, M. O'Keeffe, O.M. Yaghi, *CrystEngComm.*, 2002, **4**, 401 by permission of Royal Society for Chemistry)

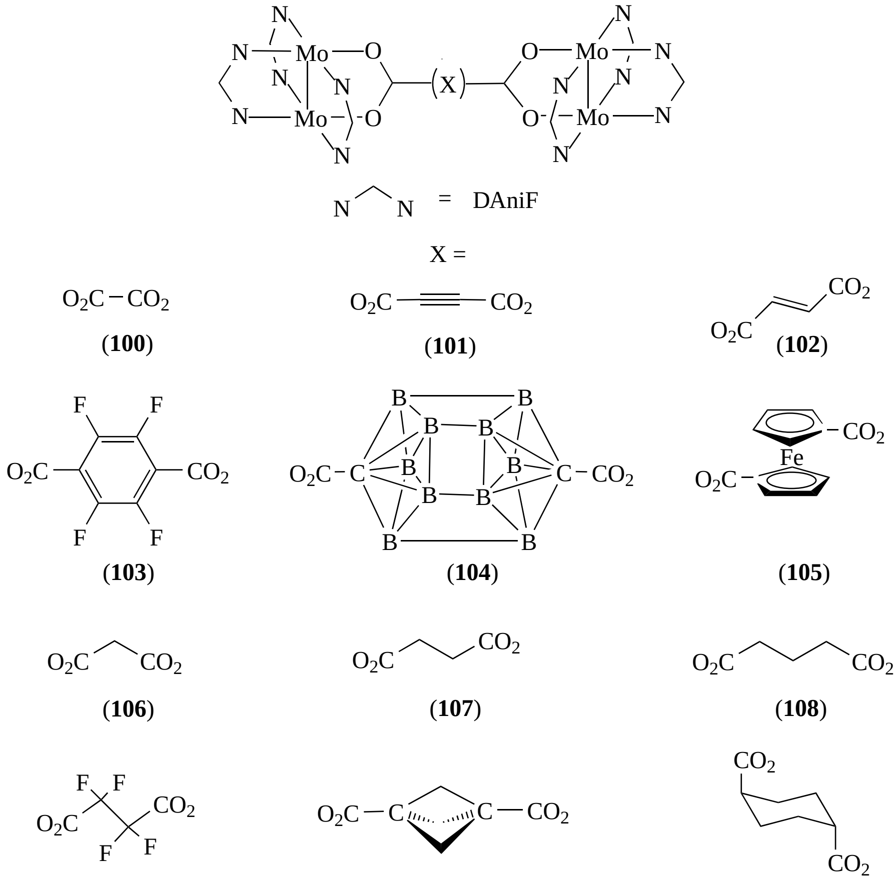

acetate, and so on. Two M_2 units can be assembled by three basic modes, namely by equatorial linkers, by axial linkers, and by both equatorial and axial linkers.

Precursors based on Mo_2^{4+} and Rh_2^{4+} cores have been used in combination with dicarboxylate linkers to construct supramolecular arrays. Dimer-of-dimers, trimer-of-dimers (molecular triangles), and tetramer-of-dimers (molecular squares) have been prepared using this approach. Judicious selection of precursors and linkers are essential for the successful synthesis of the desired molecular architectures. A total of twelve dimer-of-dimers (**100–111**) of general formula $[(DAniF)_3Mo_2]O_2C\text{-}X\text{-}CO_2Mo_2[(DAniF)_3]$ (DAniF = *N*,*N*′-di(*p*-anisyl)formamidinate) have been synthesized in which two Mo_2 units are connected by bridging dicarboxylates.**[70]** These compounds were prepared in one-pot reactions (Scheme 27). It is important to note that the six equatorial positions of the precursors are blocked in order to produce exclusively dimer-of-dimers products. The two M_2 units are nearly coplanar in all of these molecules except for the case of the carboxylates $O_2C–C{=}C{=}C–CO_2$. It has also been demonstrated that the two $[M_2]$ units are coupled perpendicular to each other when the tetrahedral linkers EO_4^{2-} are used (E = S (**112**), Mo (**113**), W (**114**)).**[71]**

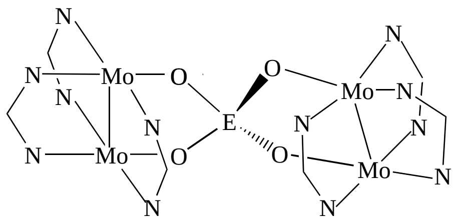

E = S (**112**); Mo (**113**); W (**114**)

$$2\ Mo_2(DAniF)_3(CH_3CN)_2(BF_4) + (Et_4N)_2\ (O_2C\text{-}X\text{-}CO_2) \xrightarrow{CH_3CN} (DAniF)_3Mo_2(O_2C\text{-}X\text{-}CO_2)\ 3Mo_2(DAniF)_3 + 2\ Et_4NBF$$

(DAniF = N,N′-di-p-anisylformamidinate)

Scheme 27

The use of cis-protected $[M_2]$ units provides right angles between the planes defined by the metal atoms and the labile equatorial ligands. Molecular loops, triangles and squares have been designed by a specific choice of the placement of carboxylate functionalities in the linker ligands. Reaction of [*cis*-$Mo_2(DAniF)_2(CH_3CN)_4](BF_4)_2$ with the bent dicarboxylate linkers malonic acid, 1,4-phenylenediacetic and *trans* cyclopentane-1,2-dicarboxylic acid yield the corresponding molecular loops (**115**), (**116**), and (**117**) respectively.[72] A similar reaction of [*cis*-$Mo_2(DAniF)_2(CH_3CN)_4](BF_4)_2$ with *trans* 1,4-cyclohexanedicarboxylate produces the molecular triangle (**118**).[73] The midpoints of the Mo_2 bond vectors define a triangle with the average distance between vertices being 11.16 Å. The neutral triangle (**119**) based on Rh_2 units bridged by oxalate was synthesized by treating [*cis*-$Rh_2(DAniF)_2(CH_3CN)_4](BF_4)_2$ with the oxalate anion in a 1:1 ratio.[74] An excess of the ligand, however, leads to formation of the molecular square [*cis*-$Rh_2(DAniF)_2(O_2CCO_2)_4$] (**120**). This is the only known example of a reaction involving dimetal units wherein both triangle and square structures exist for the same linker. The ^{1}H NMR spectra of these two compounds are identical, but their electrochemical signatures are different, which helps to identify them in a mixture.

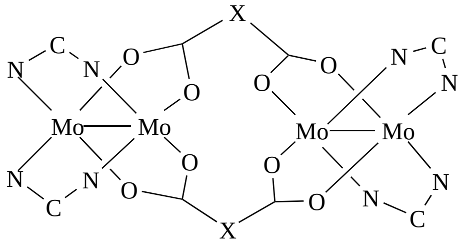

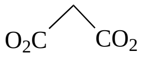
(**115**)

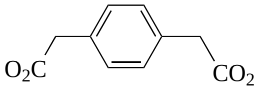
(**116**)

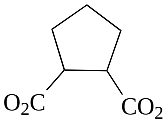
(**117**)

Reactions that involve cis-protected '$Mo_2(DAniF)_2$' units have led to a variety of square structures with dicarboxylate anions. The linkers that have been used are oxalate (**121**), fumarate (**122**), ferrocenedicarboxylate (**123**) and 4,4′-biphenyldicarboxylate (**124**).[75] The midpoints of the Mo_2 units constitute a square, and their structures have been confirmed by ^{1}H NMR spectroscopy and X-ray studies. Similar molecular squares containing Rh_2^{4+} units have been prepared with linkers such as oxalates (**120**), bicyclo[1.1.1]pentane-1,3-dicarboxylate (**125**), tetrafluoroterephthalate (**126**), 1,4-cubanedicarbboxylate (**127**), terephthalate (**128**), fumarate (**129**) and *trans* 1,4-cyclohexanedicarboxylate (**130**). The structures of these molecules have been established by spectroscopic and single-crystal diffraction studies. Detailed electrochemical investigations of these complexes have also been undertaken.[76]

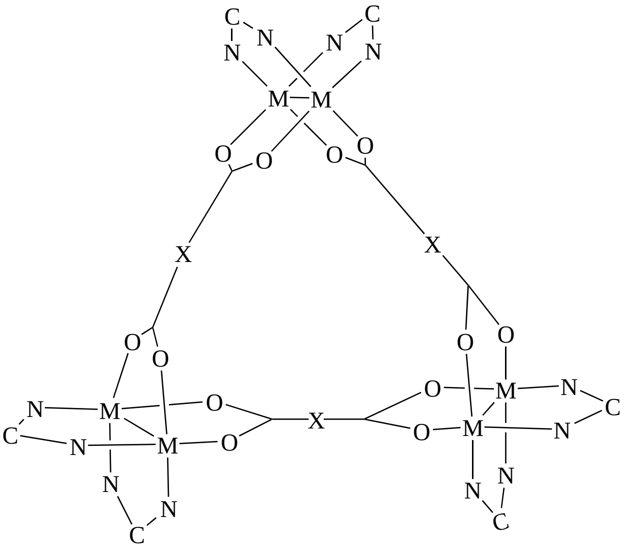

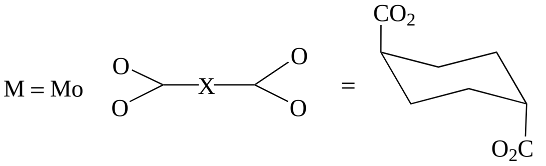

(**118**)

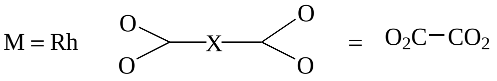

(**119**)

The use of 1,3,5-tricarboxylic-substituted benzene ligands positions the three M_2 units in a triangular disposition. An X-ray structural analysis of $[(DAniF)_3Mo_2]_3(1,3,5\text{-}C_6H_3(CO_2)_3)$ (**131**) revealed a highly symmetrical structure in which each $(DAniF)_3Mo_2$ unit is bound to each of the three carboxylate groups of the trimesic acid anion.[77] The three carboxylate groups are canted out of the plane of the aryl group, which leads to a molecular propeller shape. The three-dimensional cage molecules have been isolated from reactions of [*cis*-$M_2(DAniF)_2(CH_3CN)_4](BF_4)_2$ [M = Mo, Rh] with the trimesate anion.[78] The ^{1}H NMR spectra of the products indicated that the structures are symmetrical. A single-crystal X-ray diffraction study confirmed the structures as being three-dimensional cage molecules involving six $M_2(DAniF)_2$ units and four trimesate anions. The centers of the four benzene rings of the carboxylate linkers define a tetrahedron, and the midpoints of the six M_2 units define an octahedron. The core structure with Mo_2 cage is shown in Figure 8.

In all the discrete structures described above, the axial sites are either open or bound to a weak donor ligand. A number of extended structures have been made by reacting $[\{cis\text{-}Rh_2(DAniF)_2\}(O_2CCH_2CO_2)]_2$ and $[\{cis\text{-}Rh_2(DAniF)_2\}(O_2CCO_2)]_4$ with the polypyridine or polynitrile ligands. The resulting structures include one, two-, and three-dimensional molecular tubes that are described in detail elsewhere.[79]

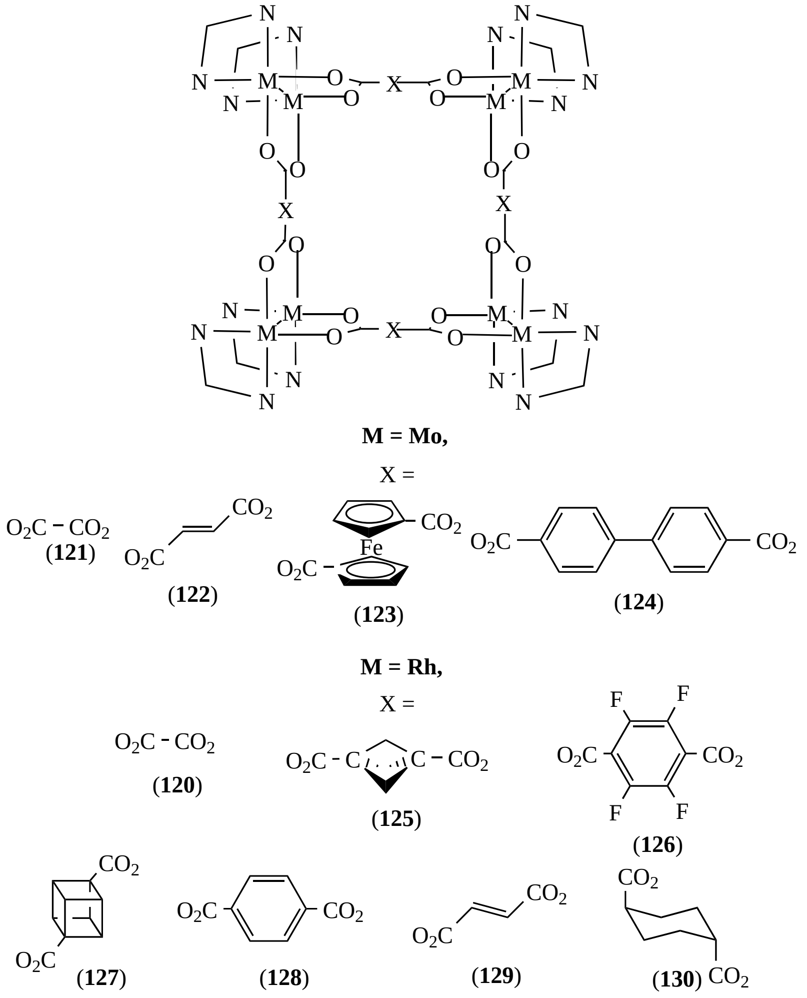
M = Mo,
X =
(121)
(122)
(123)
(124)
M = Rh,
X =
(120)
(125)
(126)
(127)
(128)
(129)
(130)

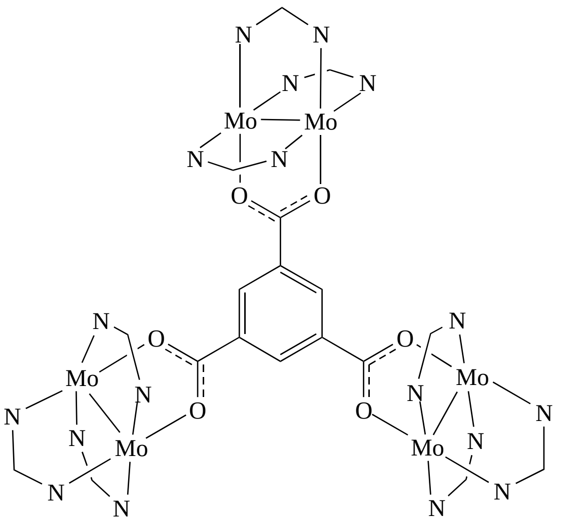

(131)

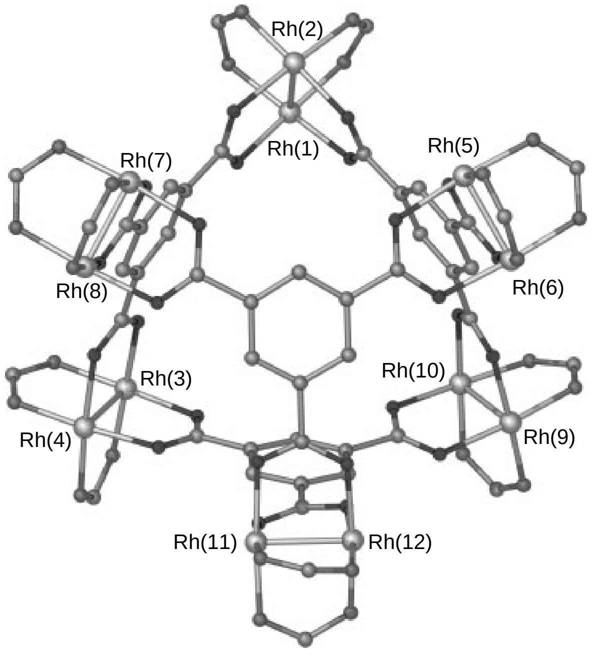
Rh(1)
Rh(2)
Rh(3)
Rh(4)
Rh(5)
Rh(6)
Rh(7)
Rh(8)
Rh(9)
Rh(10)
Rh(11)
Rh(12)

Figure 8 The core of the cage structure (**131**) consisting of six *cis*-$Rh_2(DAniF)_2$ and four trimesate anions

Analogous chemistry has been developed by employing the diphosphine ligands bis-diphenylphosphinomethane (dppm) as protecting ligands for Re_2 cores. The complexes $Re_2Cl_2(dppm)_2(O_2CCH_3)$ and *cis*-$Re_2Cl_2(dppm)_2(O_2CCH_3)_2$

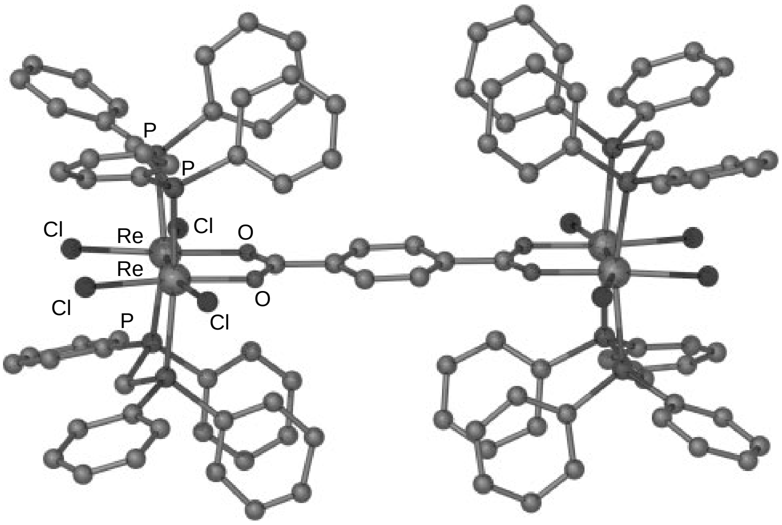

Figure 9 Single-crystal X-ray structure of (**132**)

were reacted with terephthalic acid to form the dimer-of-dimers [*cis*-$Re_2Cl_2(dppm)_2]_2[O_2CC_6H_4CO_2]$ (**132**) and the molecular triangle [*cis*-$Re_2Cl_2(dppm)_2(O_2CC_6H_4CO_2)]_3$ (**133**).[80] The molecular structures of (**132**) and (**133**) are shown in Figure 9 and 10 respectively. Interestingly, the ferrocenedicarboxylate does not produce the expected molecular triangle or square but rather *cis*-$Re_2Cl_2(dppm)_2(O_2C\text{-Fc-}CO_2)$ (**134**) (Figure 11).[81]

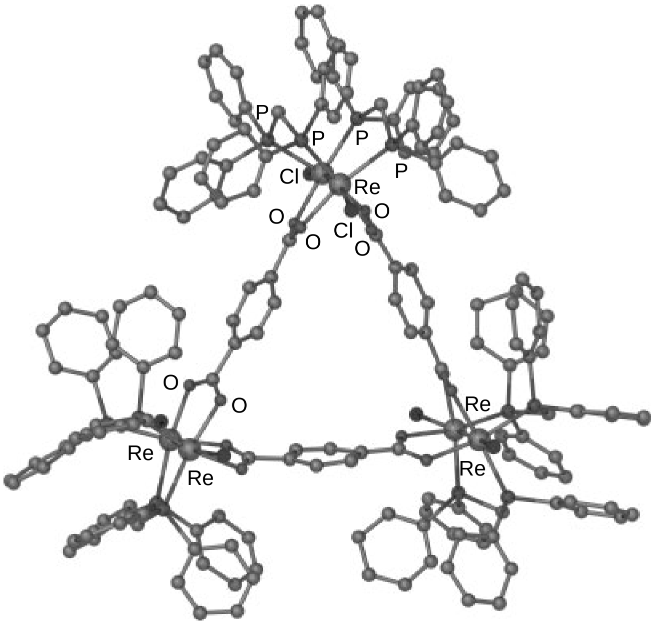

Figure 10 Single-crystal X-ray structure of (**133**)

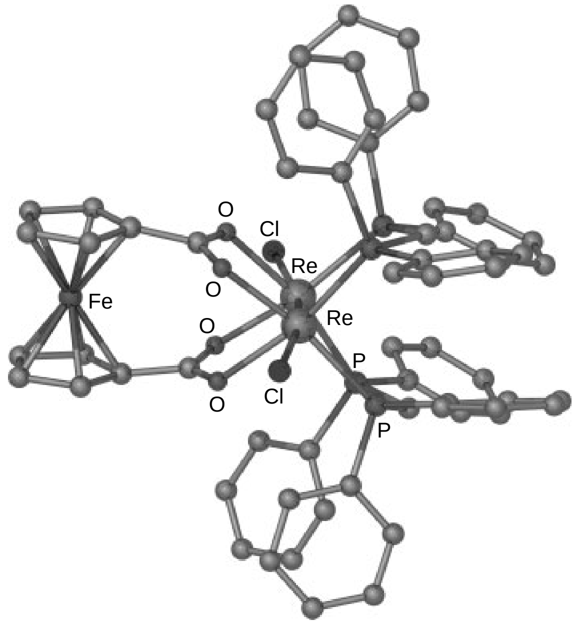

Figure 11 Single-crystal X-ray structure of (**134**)

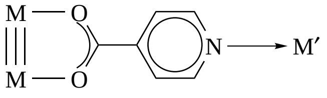

Scheme 28

With the goal of connecting M_2 and M′ units, the isonicotinate ligand, whose possible coordinating motives are depicted in Scheme 28, has been employed. Specifically, the precursor molecule *cis*-$Re_2Cl_2(dppm)_2(O_2CC_5H_4N)_2$ (**135**) was synthesized (Figure 12). A variety of building blocks have been used in reactions of (**135**), including $Pt(dbbpy)(OTf)_2$ (dbbpy = di-tertbutyl bipyridine), $ZnCl_2$,

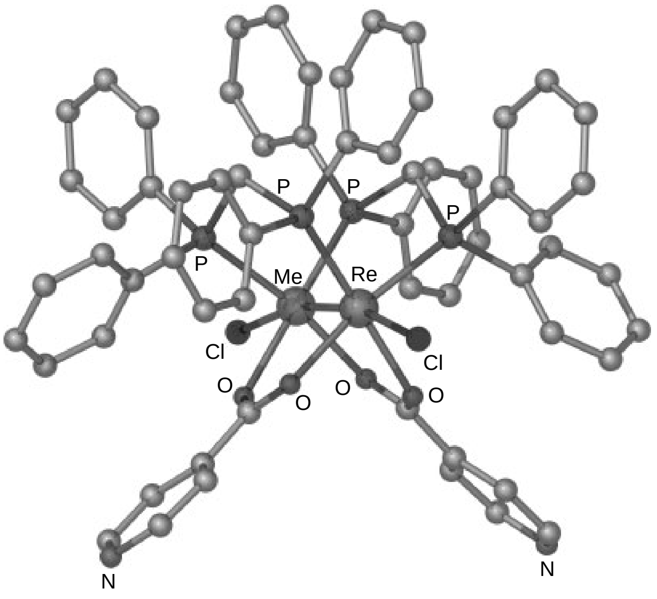

Figure 12 Single-crystal X-ray structure of (**135**)

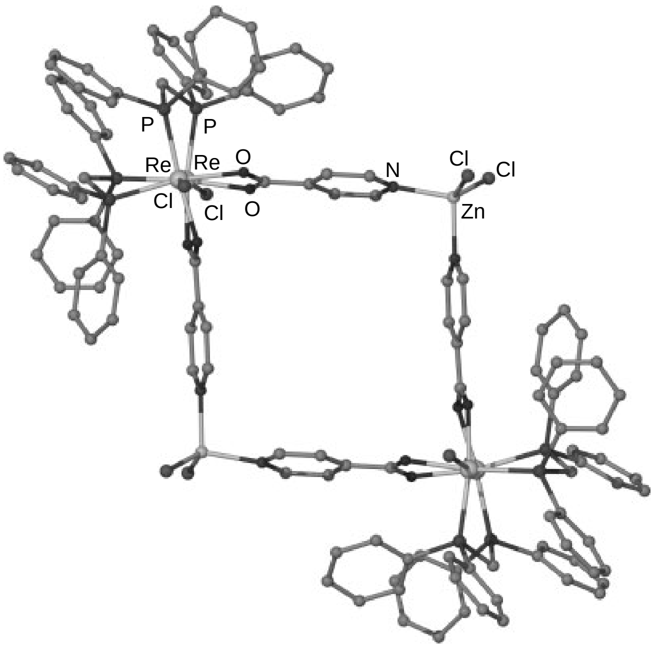

Figure 13 Single-crystal X-ray structure of $[\{Re_2(dppm)_2(O_2CC_5H_4N)_2\}\{Pt(dbbpy)\}]_2$ (**136**)

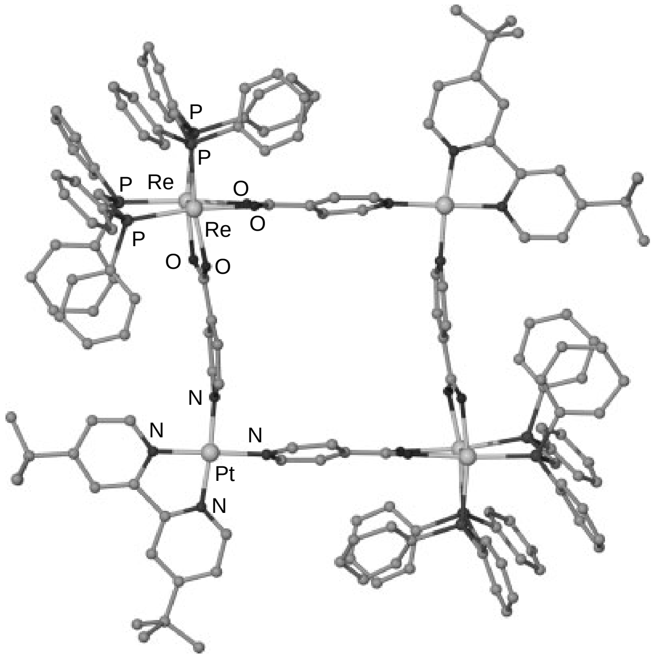

Figure 14 Single-crystal X-ray structure of (**137**)

Ag(OTf), *cis*-$Re_2Cl_4(O_2CCH_3)_2(H_2O)_2$ and $Rh_2(O_2CCH_3)_4$. All of these precursors have at least two positions available for facile substitution, but they differ in the geometry and disposition of available metal binding sites. The *hybrid* molecular squares $[\{cis\text{-}Re_2(OTf)_2(dppm)_2(O_2CC_5H_4N)_2\}\{Pt(dbbpy)\}]_2[OTf]_4$ (**136**) (Figure 13) and $[\{cis\text{-}Re_2Cl_2(dppm)_2(O_2CC_5H_4N)_2\}\{ZnCl_2\}]_2$ (**137**) (Figure 14), composed of alternating Re$_2$(II,II) and M(II) (M = Pt and Zn) corners, were isolated from the reactions of (**135**) with $Pt(dbbpy)(OTf)_2$ and $ZnCl_2$, respectively.[82] In contrast, the reactions of (**135**) with AgOTf, *cis*-$Re_2Cl_4(O_2CCH_3)_2(H_2O)_2$ and $Rh_2(O_2CCH_3)_4$ yield the open-chain polymeric structures $[\{cis\text{-}Re_2(OReO_3)_2(dppm)_2(O_2CC_5H_4N)_2\}\{Ag\bullet ReO_4\}]_\infty$ (**138-a**), $[\{cis\text{-}Re_2Cl_2(dppm)_2(O_2CC_5H_4N)_2\}\{cis\text{-}Re_2Cl_4(O_2CCH_3)_2\}]_\infty$ (**138-b**) and $[\{cis\text{-}Re_2Cl_2(dppm)_2(O_2CC_5H_4N)_2\}\{Rh_2(O_2CCH_3)_4\}]_\infty$ (**138-c**), respectively (Figure 15).[83]

6 HYDROGEN BONDING (*See Hydrogen Bonding & Dihydrogen Bonding*)

Numerous large, complex assemblies have been isolated by taking advantage of the formation of hydrogen bonds.[84] Most of the early studies were restricted to organic molecules, but in the quest for new electronic and magnetic materials, considerable effort has been launched towards the construction of inorganic and organometallic architectures that combine metal–coordination and hydrogen bonds.[85] Pyridine-carboxylic acid and carboxyamides have been used together with a variety of metal ions to form hydrogen-bonded frameworks as shown in Scheme 29. Coupling (*see Coupling*) of two PtBr(4,4′-di-t-butyl-2,2′-bipyridine)$(CH_3)_2(CH_2C_6H_4COOH)$ molecules (**139**) through bridging bis-pyridyl ligands yields (**140**) and (**141**). The carboxylic acid groups appended to the alkyl–platinum

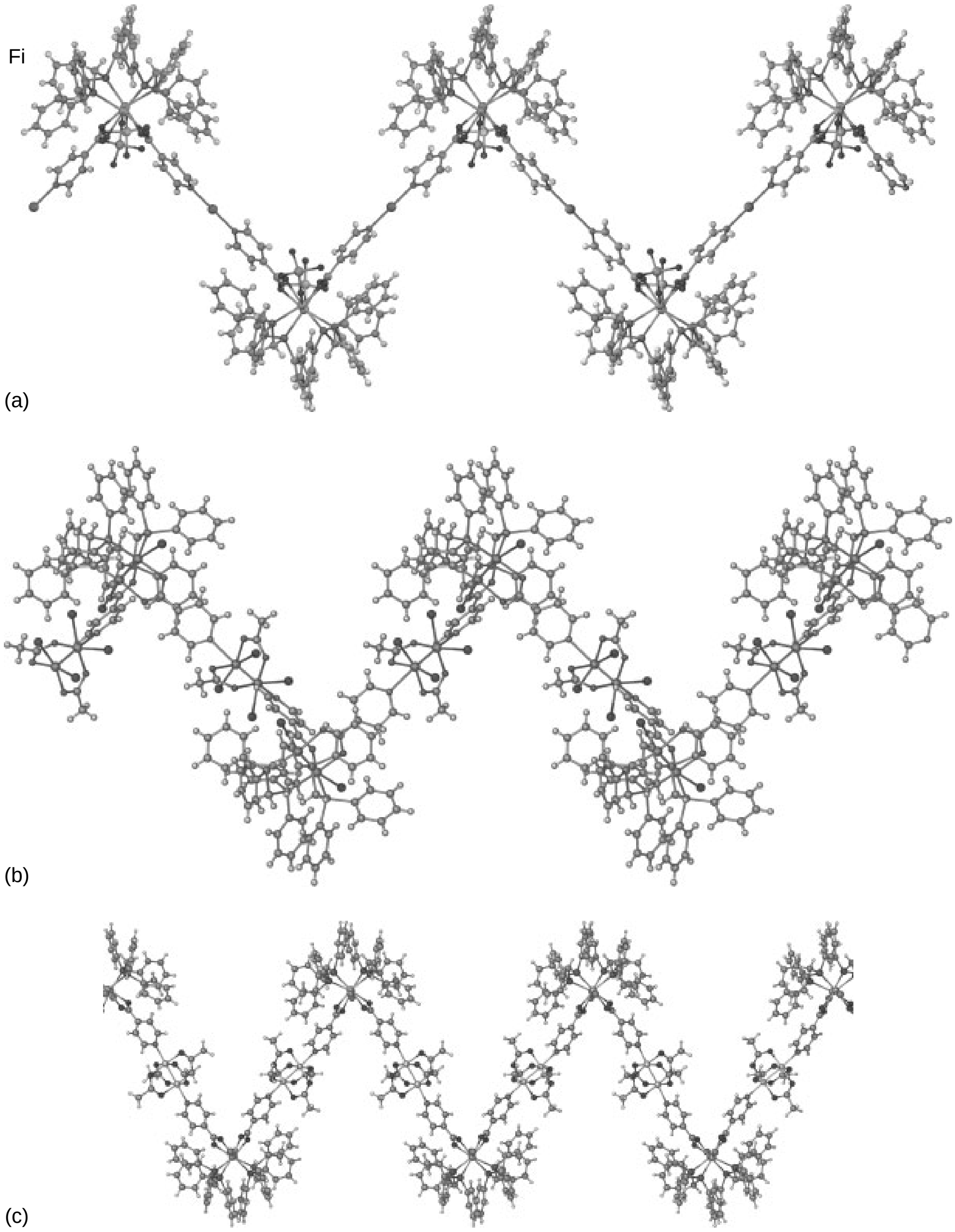

Figure 15 Plots of the open-chain polymeric structures of (a) $[\{Re_2(dppm)_2(O_2CC_5H_4N\text{-}4)_2\}\{Ag\}]_\infty$ in (**138-a**), (b) (**138-b**), and (c) (**138-c**)

unit engage in intermolecular (*see Intermolecular*) hydrogen bonding to form a one-dimensional polymer. In addition, the amide groups of 4-py-$CH_2NHCOCONHCH_2$-py-4 in complex (**141**) induce long-range helicity.**[86]** The twists at the two CCH_2N and CCH_2Pt groups leads to the formation of a helical loop in such a way that the two carboxylic acid groups are positioned in an *anti* conformation that facilitates the formation of hydrogen-bonding interactions. The di-cation has approximate C_2 symmetry, but there is no crystallographically imposed symmetry; the result is an isotactic polymer chain with the pitch of the helix being 26.1 Å.

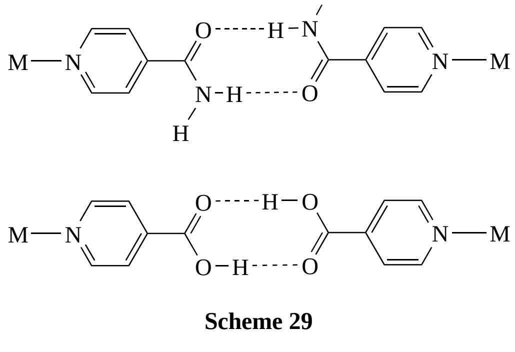

Scheme 29

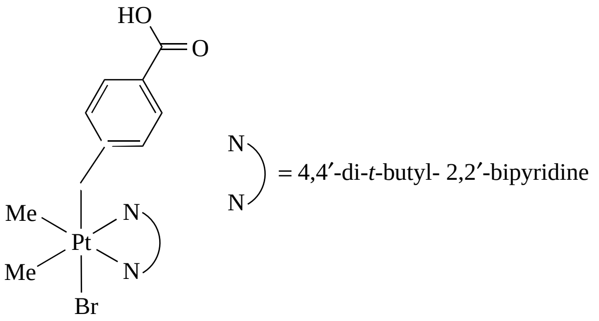

(**139**)

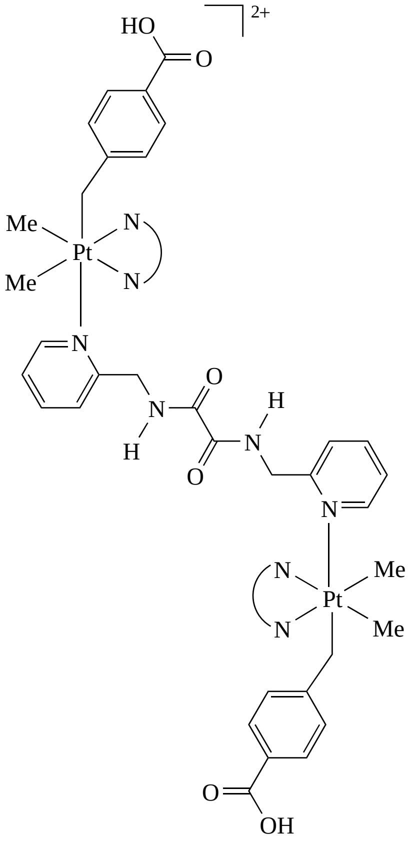

(**140**)

In a similar fashion, the cation $[cis\text{-}(Et_3P)_2Pt(NC_5H_4CONH_2)]^{2+}$ (**142**) crystallizes via interactions involving the amide functionality resulting in infinite, parallel zig-zag chains. In contrast, $[(C_5Me_5)Rh(NC_5H_4CONH_2)_3]^{2+}$ (**143**) crystallizes via the same amide functionality to produce infinite, double-stranded, interwoven chains.[87] Dunbar *et al.* have used nicotinamide and isonicotinamide to form assemblies of multiply-bonded dimetal building units via a combination of coordinate bonds and intermolecular hydrogen bond interactions.[88] The compounds *cis*-$Re_2Cl_4(O_2CCH_3)_2$ (**144**) and $Rh_2(O_2CCH_3)_4$ (**145**)[89] have been used in these reactions owing to the fact that they have a strong tendency to engage in axial interactions with pyridine-based ligands.

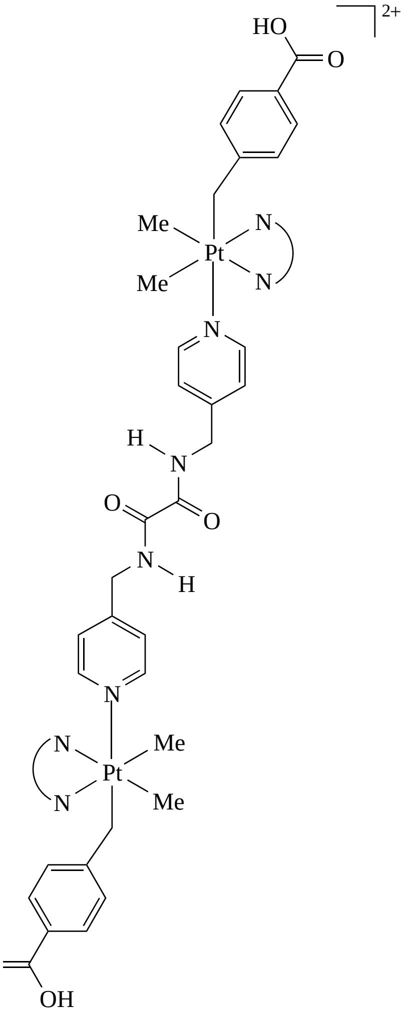

(**141**)

Polymeric networks of the linear, zigzag and sinusoidal varieties were isolated depending on the ligands and metal precursors involved (Figure 16).[88]

Puddephatt and coworkers have reported a series of complexes of general formula *trans*-$PdCl_2L_2$ in which L is a pyridine or quinoline ligand with one or two carboxylic acid functionalities.[90] The complexes $[PdCl_2(NC_5H_4\text{-}4\text{-}COOH)_2]$ (**146**), $[PdCl_2(NC_5H_4\text{-}3\text{-}COOH)_2]$ (**147**), and $[PdCl_2(2\text{-}Ph\text{-}NC_9H_5\text{-}4\text{-}COOH)_2]$ (**148**) form one-dimensional polymers through O–H···O hydrogen−bonding interaction as shown in Scheme 30. It has been demonstrated in this study that the presence of polar solvents such as DMSO or DMF leads to a disruption of the extended H−bonding network.

Two-dimensional structures result when pyridine-dicarboxylic acids are used. The complex *trans*-$PdCl_2L_2$ (L = 2,6-dimethyl pyridine-3,5-dicarboxylic acid) (**149**) self-assembles to yield a two-dimensional sheet structure that involves hydrogen bonding between the carboxylic acid groups mediated by methanol solvent molecules (Scheme 31).

The coordination of four *n*-butylnicotinamide ligands to a Pt(II) center provides access to organized amide H−bond

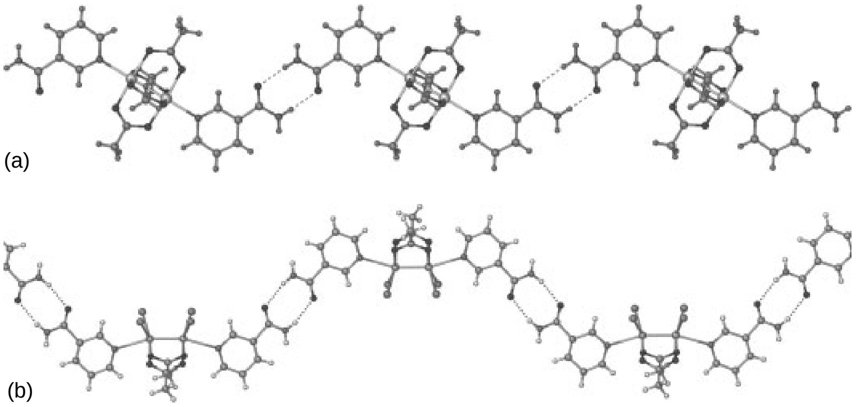

Figure 16 Molecular chain structures of the polymeric compounds formed from axial interactions of (**144**) and (**145**) with pyridine-based ligands

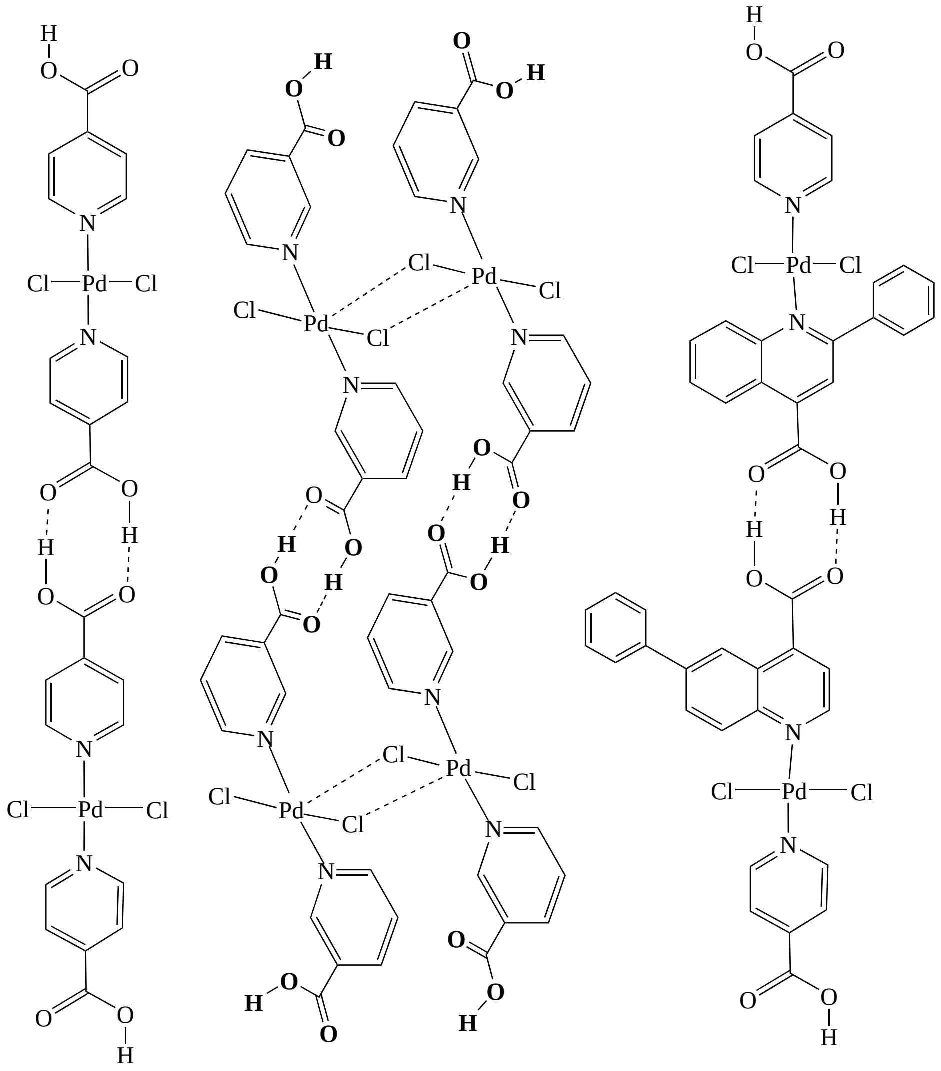

(**146**) (**147**) (**148**)

Scheme 30

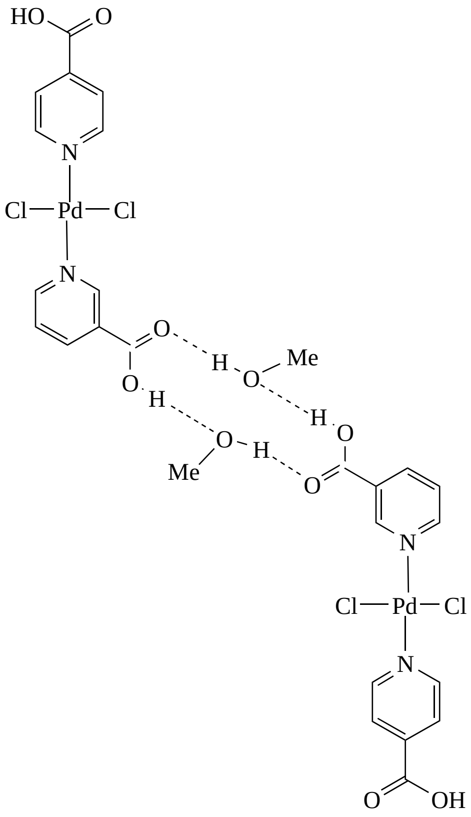

(**149**)

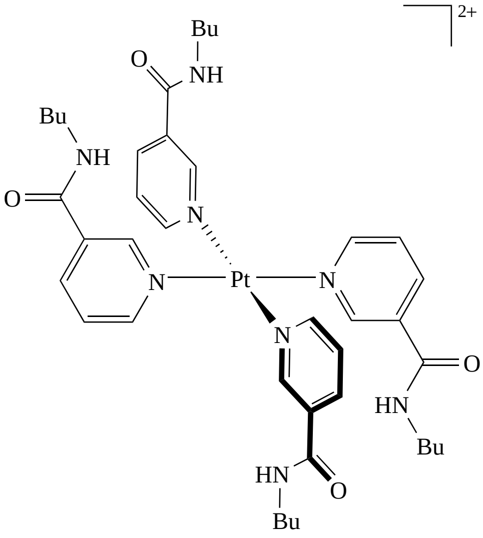

(**150**)

Scheme 31

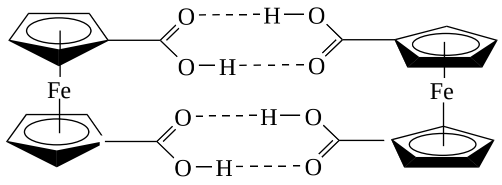

(**151**)

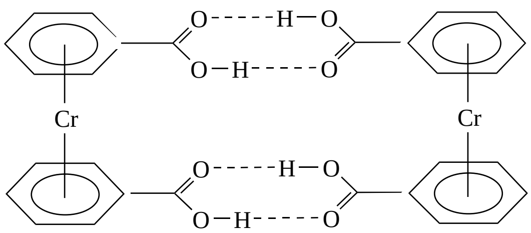

(**152**)

Scheme 32

donors that are suitable for anion binding. ^{1}H NMR studies confirmed the 1:1 binding of (**150**) with ReO_4^-, $CF_3SO_3^-$ and HSO_4^-.[91] An X-ray structure of [(**150**)·ReO_4]ReO_4 revealed hydrogen-bonding interactions between amide hydrogens and CH hydrogens of the ligand and oxygen atoms of the perrhenate anion.

Metallocenedicarboxylic (*see Metallocene Complexes*) acids form dimeric structures in the solid-state. Two typical examples include [Fe(II)(η^5-$C_5H_4COOH)_2$] (**151**) and [Cr((η^6-$C_6H_5COOH)_2$] (**152**) (Scheme 32).[92] Complex (**151**) is known in two polymorphic modifications (the monoclinic and triclinic form) that contain the same dimeric unit but with different arrangement in the solid-state.[93] Self-assembly of (**151**) with DABCO (1,4-diazabicyclo[2.2.2]octane) in a 1:1 ratio occurs with grinding in the solid-state to form [Fe(II)(η^5-C_5H_4COOH)(η^5-C_5H_4COO)($HC_6H_{12}N_2$)] (**153**). The X-ray structure of (**153**) confirms the presence of linear hydrogen-bonded chains mediated through the N-atoms of DABCO.[94] Upon heating, complex (**153**) loses DABCO and reverts to (**151**) in quantitative yields. Grinding (**151**) and DABCO in ratios other than a 1:1 stoichiometry leads to mixtures of (**153**) with excess, unreacted reagent.

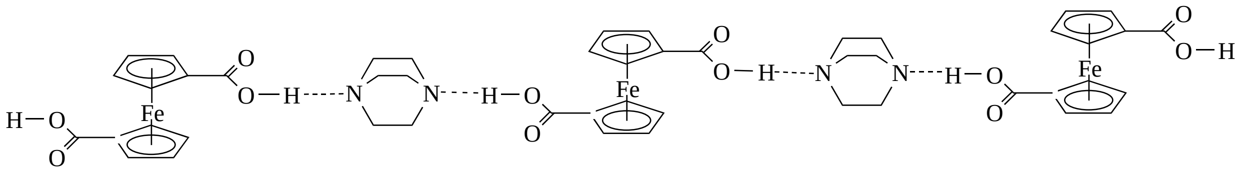

(**153**)

The organometallic receptor (**154**) was designed for complexation to ureas and barbitals through hydrogen-bonding interactions. The formation of 1:1 complexes via the formation of complementary hydrogen bonds was established by NMR spectroscopy and X-ray crystallography.[95] The role of the spacer group in the binding ability of the receptors was emphasized in this study. In the acyclic receptor (**155**), where the spacer is the 1,3-isophthalic acid group, the binding constant with barbital is one-order of magnitude greater than that between (**154**) and barbital. Both geometric and electronic factors have been attributed to this effect.

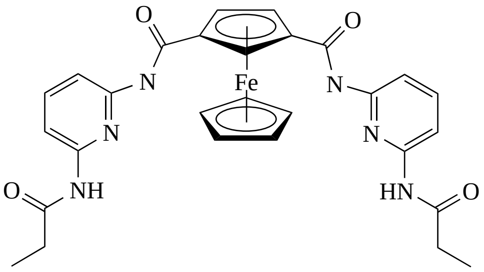

(**154**)

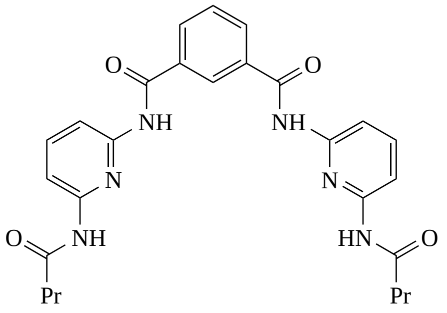

(**155**)

Supramolecular synthons composed of H–bonding interactions between metal–X acceptor and N–H donors (Scheme 33) have been exploited to form hydrogen-bonded network solids.[96,97] Three classes of tetrachlorometallate salts of stoichiometry [4,4′-H_2bpy][MCl_4] have been prepared. For the square-planar anions $[MCl_4]^{2-}$ (M = Pt, Pd), linear hydrogen-bonded ribbons are formed (Scheme 34).[98] In contrast, a cyclic dimer motif (Scheme 35) was reported for [4,4′-H_2bpy][$CoCl_4$].[99] Low-temperature diffraction data of [4,4′-H_2bpy][MCl_4] [M = Zn, Hg, Co] revealed one short NH· · ·Cl hydrogen bond and an additional CH· · ·Cl interaction with a second chloride ligand and an ortho-CH group as shown in Scheme 36. The solid-state structure of the hydrogen-bonded dimeric ring in [4,4′-H_2bpy][$ZnCl_4$] is shown in

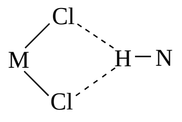

Scheme 33

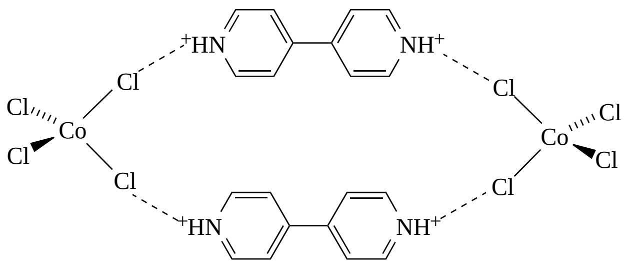

Scheme 35

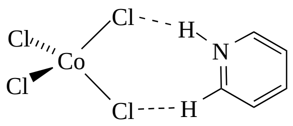

Scheme 36

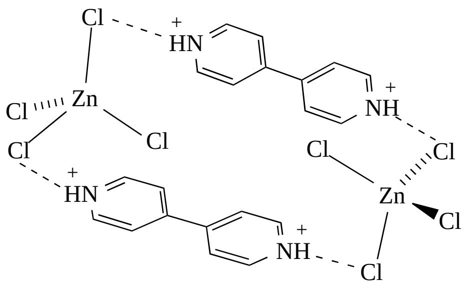

Scheme 37

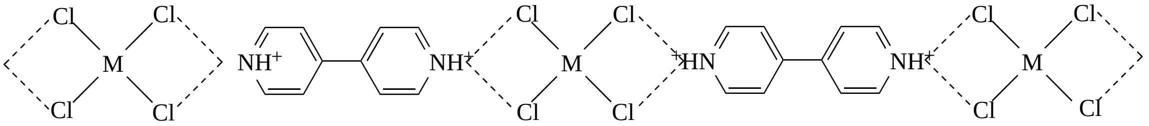

M = Pd(II), Pt(II)

Scheme 34

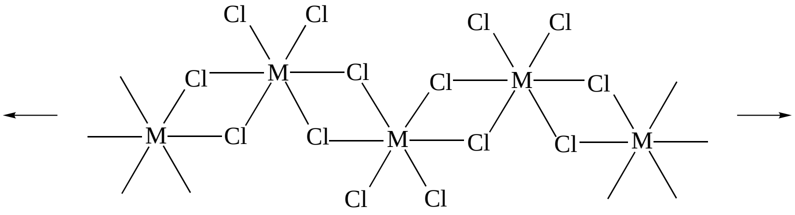

Scheme 38

Scheme 37. When M = Mn, Pb or Cd, the $[MCl_4]^{2-}$ moiety is polymerized and forms the zig-zag edge-sharing octahedral chains shown in Scheme 38. The $[\{MCl_4\}_n]^{2n-}$ chains are cross-linked by hydrogen bonds at both ends of the di-cation as shown in Scheme 39 and at both sides of the $[\{MCl_4\}_n]^{2n-}$ unit as shown in Scheme 40.[100]

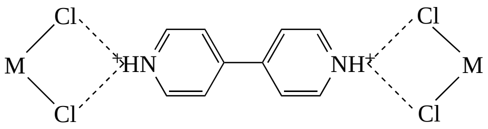

Scheme 39

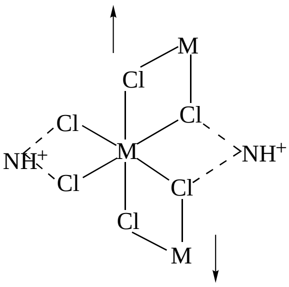

Scheme 40

In the simple salt [4,4′-H_2bpy]Cl_2, ribbons of the type shown in Scheme 41 are observed. Analogously, the structure of [4,4′-H_2bpy][Cu_2Cl_6] consists of a planar anion with the two square-planar metals that are in place of the two chlorides (Scheme 42). The same bonding patterns are noted in [4,4′-H_2bpy][MCl_6]·(M = Os, Pt) and [4,4′-H_2bpy][$FeCl_5$], albeit in a form in which the chloride is also bonded to a metal ion.[101] The ribbons are cross-linked by the metal ions such that the trans-chloride ligands on the metal centers belong to different ribbons (Scheme 43).

The 2,2′-biimidazolate mono-anion ($Hbim^{-1}$) forms metal–chelate complexes and also provides access to intermolecular complementary H–bonding with two sets of NH donors and N acceptors as shown in Scheme 44.[102] By altering the metal-coordination sphere, a variety of neutral metal–$Hbim^{-1}$ complexes with hydrogen-bonded infinite superstructures have been synthesized. The [Cu(II)(Hbim)(SalenNMe$_2$)] complex forms a H–bonded dimer of the type as described in Scheme 45. The cation $[Cu(II)(Hbim)(tacn)]^+$, however, forms a H–bonding interaction with the $[ClO_4]^-$ anion rather than forming self-complementary NH···N interactions between the $Hbim^{-1}$ ligands.[103] The authors concluded that the neutral complexes are better precursors than the charged species for the formation of regular self-assembled superstructures.

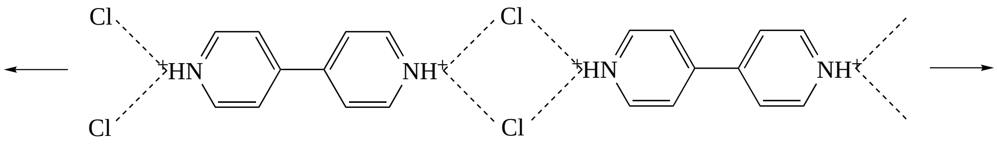

Scheme 41

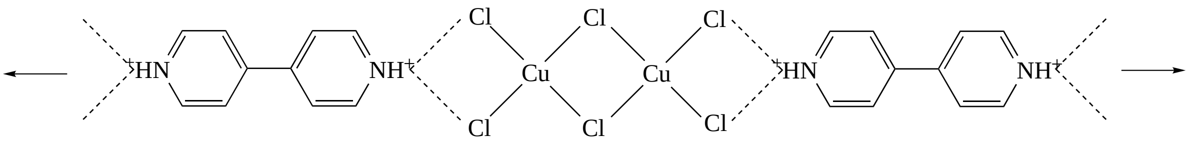

Scheme 42

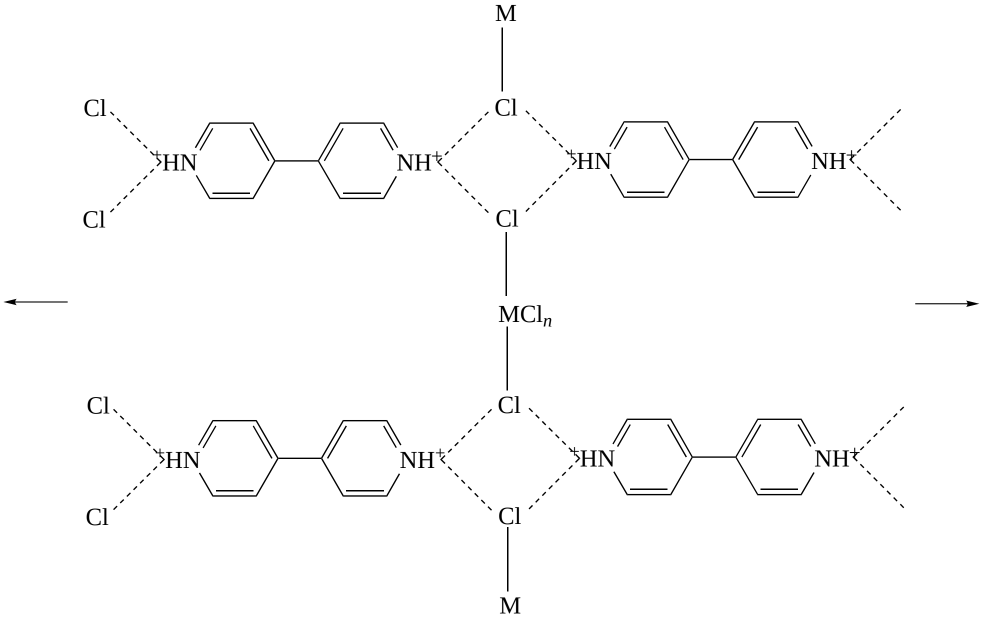

M = Pt(IV), Os(IV), Fe(III)

Scheme 43

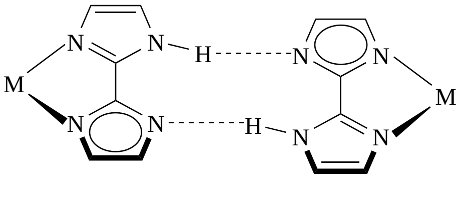

Scheme 44

M = Cu(SalenNMe$_2$)

Scheme 45

The complex *trans*-Ni(II)(Hbim)$_2$(t-Bupy)$_2$ contains two Hbim ligands that engage in intermolecular self-complementary H−bonding interactions, which leads to the formation of linear chains (Scheme 46). The two Hbim ligands engaged in H−bonding interactions occupy the equatorial positions of a distorted octahedron with the two axial positions being occupied by two monodentate t-Bupy ligands (*see Monodentate Ligand*). The linear chain motif can be altered to a one-dimensional zig-zag ribbon structure by changing the disposition of the H−bonding sites in the building blocks. A zig-zag ribbon is formed from Ni(II)(Hbim)$_2$(bpy), which consists of one-dimensional ordered arrays formed by alternating H−bonding between different optical isomers Δ and Λ (Scheme 47). The neutral, racemic complex [Ru(II)(Hbim)$_3$] with D_3 symmetry crystallizes in a two-dimensional honeycomb sheet of the type shown in Scheme 48. All three Hbim ligands are involved in the intermolecular H−bonding interactions and alternative between optical isomers Δ and Λ. In contrast, the two chiral building units of Δ-[Co(III)(Hbim)$_3$] and Λ-[Co(III)(Hbim)$_3$] form one-dimensional helical chains with a left-handed and right-handed chirality respectively.

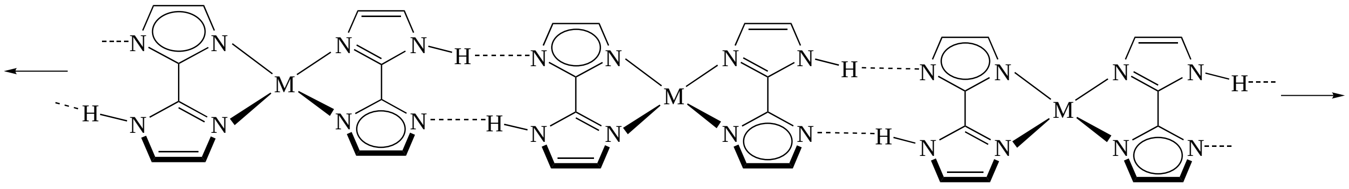

M = *trans*-Ni (t-Bupy)$_2$

Scheme 46

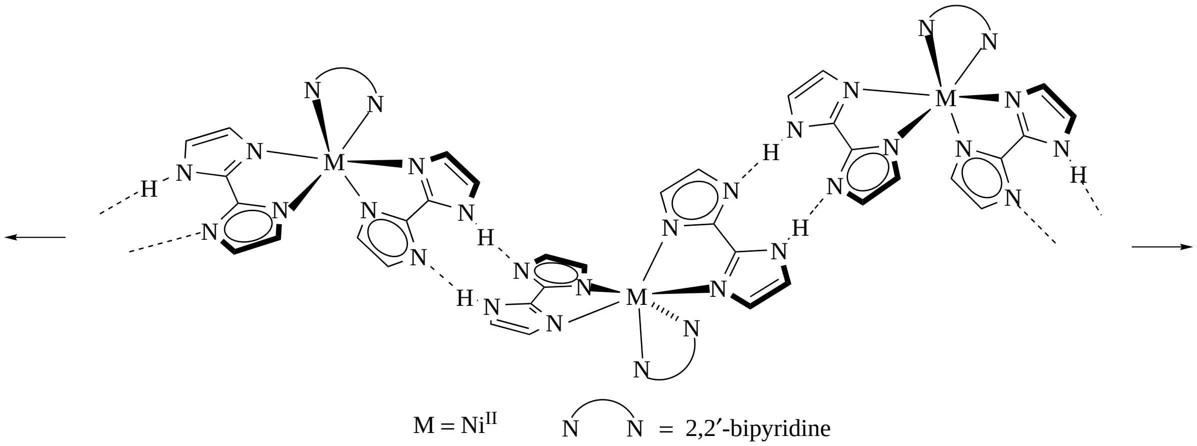

Scheme 47

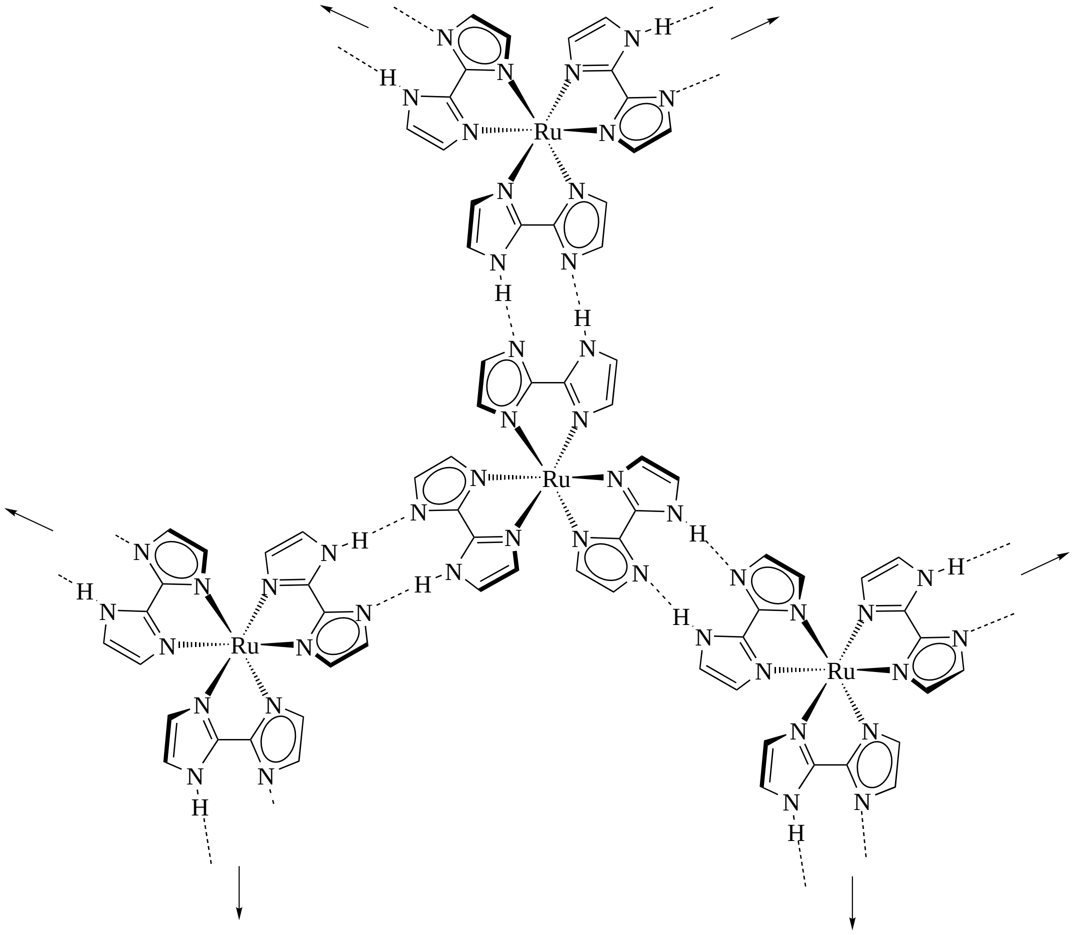

Scheme 48

Each one-dimensional helical chain involves intermolecular H–bonds between the same optical isomers with two of the three Hbim ligands being involved (Scheme 49). A third Hbim moiety is blocked by H–bonds to interstitial 2-propanol molecules and therefore does not participate in the helical-chain architecture.

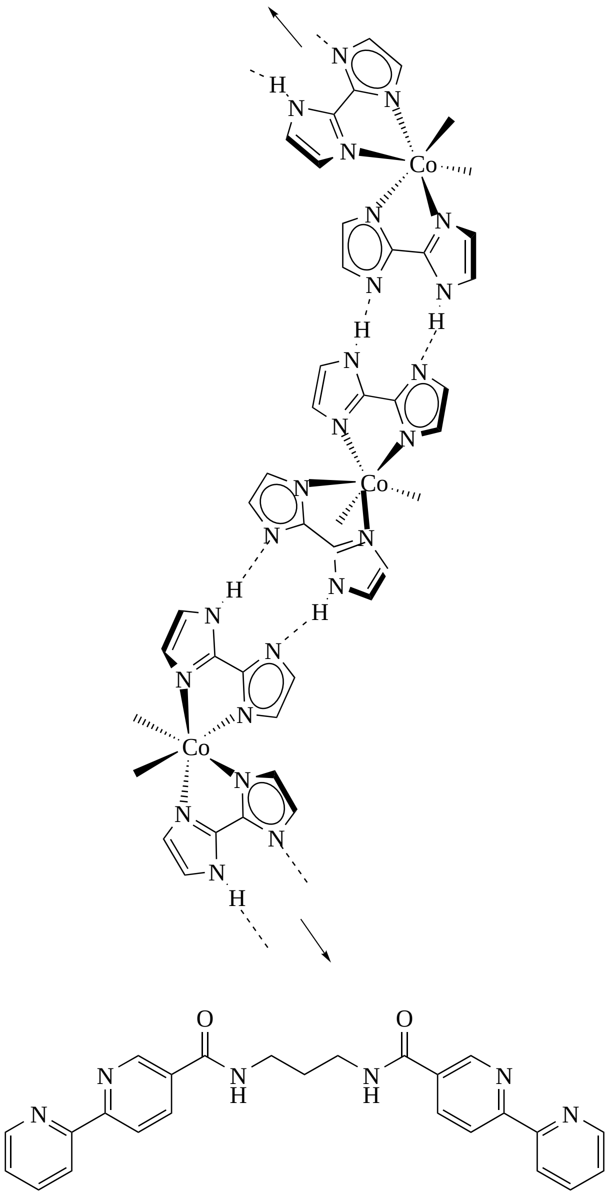

L

Scheme 49

7 SUPRAMOLECULAR ASSEMBLY DYNAMICS

A self-assembly reaction that involves the connection of individual building blocks via noncovalent interactions permits the rational integration of desired functional groups into the resulting molecules. Transition metal coordination bonds have been exploited in the synthesis of numerous metal–based supramolecular architectures in recent years. Complexation of metal ions to multidentate ligands generates equilibrium mixtures of various structures based on numerous possible combinations of metals and ligands.[104] In the situation of thermodynamic control (*see Thermodynamics: Laws*), the product distribution depends on a combination of enthalpic (*see Enthalpy*) and entropic (*see Entropy*) considerations. The factors that influence the geometry of these structures are complex and include the number, relative strength, and directionality of the metal–ligand interactions. The product distribution also depends on the concentration, that is, dilute solutions favor ring closure whereas concentrated solutions yield higher-order oligomers culminating in polymer formation at the limit of high-monomer concentrations. The self-assembly reaction also depends on a variety of parameters such as temperature, pressure, and solvent identity.[105]

Inorganic supramolecular chemistry is dynamic by nature because of the kinetic lability (*see Kinetic Lability*) of the coordinate bonds. The reversibility of the association process of metal and ligands permits a continuous alteration of the products. Intrinsic factors such as the stability of a particular species or extrinsic factors such as the presence or absence of a template allow for the isolation of a particular product. In this vein, the dynamic self-assembly of helicates has been studied by Albrecht–Gary, Lehn, and coworkers in detail. Several kinetic intermediates were identified in the spectroscopic studies of the double-stranded helicates M_3L_2. These misaligned kinetic species engage in structural self-correction that results in the eventual formation of the thermodynamic product.[106] In a mixture of building units, self-selection occurs when the structural instructions are ‘strong’. For example when a mixture of the two tris-bipyridine ligands (**61**) and (**156**) are reacted with Cu(I) and Ni(II), only the double helicates (**157**) and triple helicate (**158**) products are formed. These systems are the result of self-assembly of helicates with self-recognition (Scheme 50).[107]

Armed with an increasing knowledge of supramolecular interactions,[108] chemists are applying the tools of molecular recognition for the optimization of reaction conditions to favor a particular product at the expense of others in the equilibrium mixtures. One useful approach in this regard is to use a chemical species that selectively recognizes and stabilizes one of the products in a mixture via supramolecular interactions. These species are commonly referred to as templates, and their role in a thermodynamic process may be likened to that of catalyst in a kinetically controlled synthesis.[104] For example, Raymond and coworkers have reported the slow conversion of a dinuclear triple-stranded helicate ($M_2L'_3$) to a tetranuclear tetrahedron ($M_4L'_6$) with the addition of the Me_4N^+ guest (Scheme 51). The conversion takes place at 70 °C over 24 h duration and no intermediate species were detected.[109] Selective encapsulation of various cationic guests $Me_2Pr_2N^+$ and Pr_4N^+ has been observed for the tetrahedral $[M_4L''_6]^{12-}$ anionic hosts. A ^{1}H NMR study revealed that the alkali metal ion K^+ does not interact with the interior of the cluster,[110] but that the corresponding alkali ion–crown ether complex is encapsulated into the host molecule.[111] In a similar vein, Lehn and coworkers have reported the conversion of a triferrous linear triple helicate to a pentaferrous circular helicate (**62**) with the addition of chloride as a guest.[37]

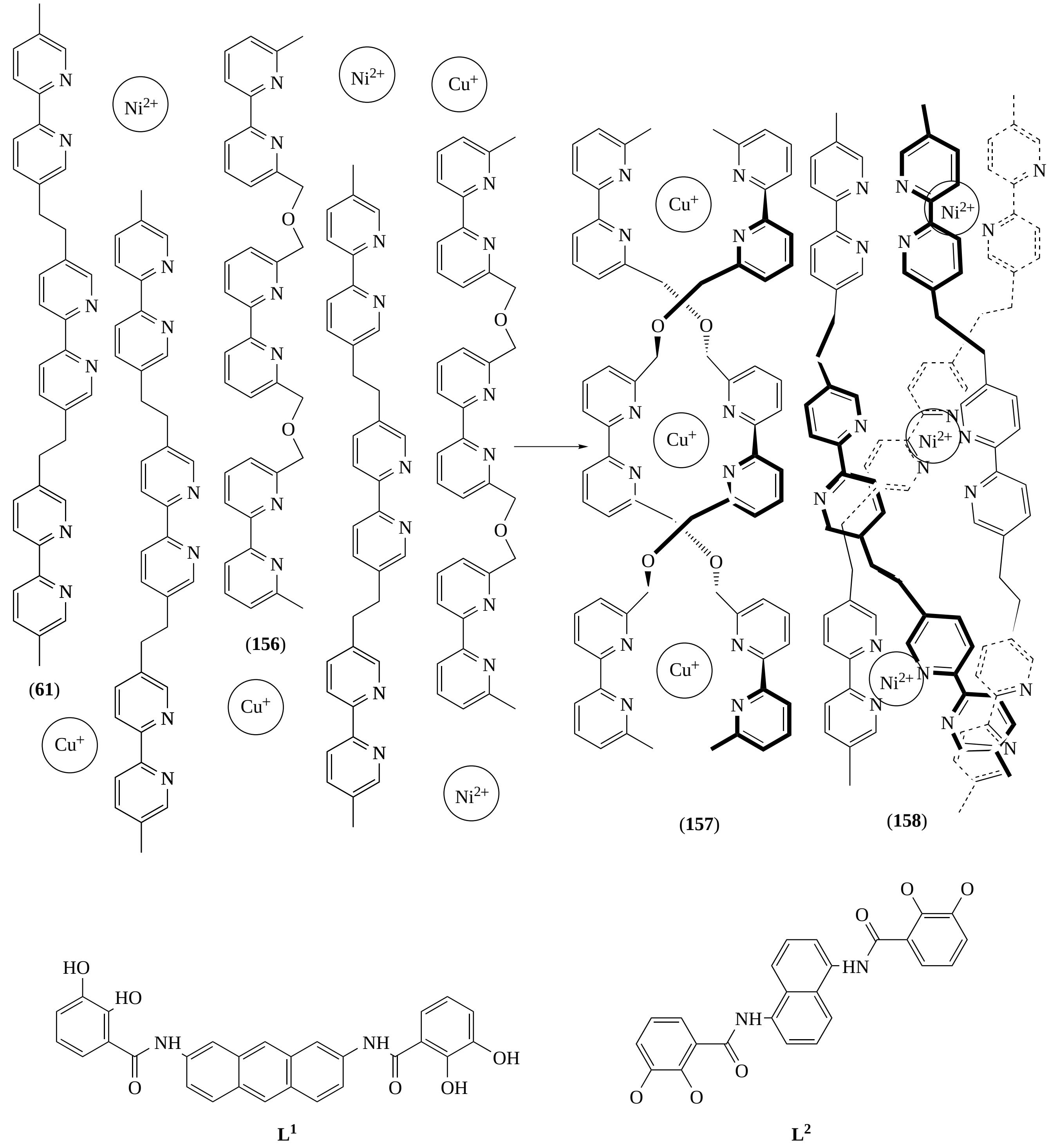

(**61**)

(**156**)

(**157**)

(**158**)

L^1

L^2

Scheme 50

In related work, Dunbar *et al.* recently described the anion templated (*see Templating*) self-assembly reactions of solvated metal ions with bptz. The role of the anions in the preferred stabilization of metallocyclophanes of varying nuclearity has been examined in detail both in solution and in the solid-state. Reactions of the mononuclear precursors [M(II)(CH$_3$CN)$_4$][X]$_2$ (X = BF$_4$ or ClO$_4$; M = Ni and Zn) with bptz in a 1:1 molar ratio afford molecular squares (**57–60**) of the type [M$_4$(bptz)$_4$ $\subset$X]$^{7+}$.**36** Analogous reaction of [Ni(CH$_3$CN)$_6$][SbF$_6$]$_2$ with bptz yields the

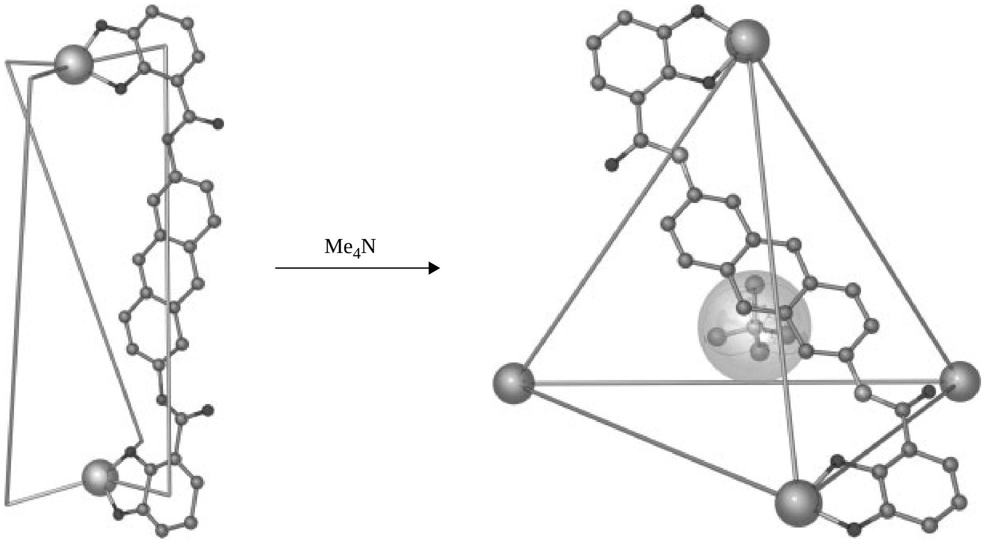

$M_2L^1_3$ $M_4L^1_6$

Scheme 51

molecular pentagon $[\{Ni_5(bptz)_5(CH_3CN)_{10}\}\subset SbF_6](SbF_6)_9$ (**64**) rather than the squares. ESI-MS studies confirmed that the molecular squares are the major products when $[BF_4]^-$, and $[ClO]_4{}^-$ are present and exclusively a molecular pentagon, when $[SbF_6]^-$ is present, respectively.[39] The dimeric $[Ni_2(bptz)(CH_3CN)_8][ClO_4]_4$ complex and the polymer $\{[Mn(bptz)(CH_3CN)_2][BF_4]_2\}_\infty$ were isolated as minor products, indicating their presence in equilibrium mixtures. The templating abilities of anions in the organization of squares and pentagons have been linked to the weak anion-π interaction of the anion and tetrazine unit of the bptz ligands.[112]

8 INORGANIC ASSEMBLIES WITH FUNCTIONALITY

The field of inorganic supramolecular chemistry has witnessed tremendous growth in recent years. An increasing understanding of noncovalent interactions has prompted many inorganic chemists to explore new structures with supramolecular interactions. Recent advances in X-ray technology with the advent of the CCD detector have enabled us to obtain reliable structural information on tiny, weakly diffracting crystals whose structural determination would have been impossible a few years ago. The future of the field, however, lies in our ability to prepare functionally important systems. Indeed, progress is being made towards this goal; for example Fujita and coworkers have demonstrated that the cavities of their structures not only act as reaction vessels, but also serve as molds for product synthesis.[113] The availability of a nanoscale reaction vessel is an attractive approach for the synthesis of new materials. One example of this methodology is the synthesis of a reactive phosphonium–acetone adduct inside the M_4L_6 cavity in aqueous media.[114] The free adducts decompose rapidly in aqueous solution and can be stabilized only with the protection of the hydrophobic cavity of the molecular tetrahedron.

The use of inorganic supramolecular compounds in catalysis has also been successful in recent years. Hupp *et al.* incorporated a Mn(III)-porphyrin (*see Porphyrin*) epoxidation catalyst inside a molecular square,[115] a system that shows enhanced catalyst stability and substrate selectivity as compared to the free catalyst. In another example, chiral metallocyclophanes were constructed from $Pt(PEt_3)_2$ units and enantiopure atropoisomeric 1,1′-binapthyl-6,6′-bis-(acetylenes) and used in enantioselective diethyl zinc addition to aldehydes to afford chiral secondary alcohols.[116] The first organometallic triangle based on Pt(II) and alkyne-di-substituted-binaphthyl system was reported and found to effect asymmetric catalysis reactions of aldehydes to alcohols with excellent conversion rates and enantiomeric excess.[117]

Apart from the use of molecular reaction vessels, there is much promise for the use of solids prepared by Yaghi and others which are highly porous and serve as excellent host structures. The MOFs of composition $Zn_4O(BDC)_3$ with a cubic three-dimensional extended porous structure absorbs hydrogen gas up to 4.5 wt %, that is, 17 hydrogen molecules/formula unit at 78 K and 1.0 wt % at room temperature and pressure of 20 bar, respectively.[118]

Chirality can also be introduced into these framework solids as evidence by the work of Lin and coworkers, who used specifically designed ligands to create hosts that offer chiral discrimination.

Supramolecular chemistry is poised to make a big impact on numerous fields of science including molecular biology as well as chemistry. Complex structures that would be impossible to prepare in a stepwise fashion with covalent bonds are easily formed by the self-assembly process. The advances to date notwithstanding, there is much to learn about the molecular basis of self-organization. Given that one of the 'holy grails' of chemistry is to unravel the processes of evolution and adaptation displayed by biological systems, it is clear that supramolecular chemists have their work cut out for them.

9 RELATED ARTICLES

Cobalt: Organometallic Chemistry; Cyanide Complexes of the Transition Metals; Iron: Inorganic & Coordination Chemistry; Luminescence Behavior & Photochemistry of Organotransition Metal Compounds; Manganese: Inorganic & Coordination Chemistry; Nickel: Inorganic & Coordination Chemistry; Palladium: Inorganic & Coordination Chemistry; Platinum: Inorganic & Coordination Chemistry; Platinum: Organometallic Chemistry; Rhodium: Inorganic & Coordination Chemistry; Ruthenium: Organometallic Chemistry; Technetium & Rhenium: Inorganic & Coordination Chemistry; Zinc: Inorganic & Coordination Chemistry.

10 REFERENCES

1. P. J. Stang and B. Olenyuk, *Acc. Chem. Res.* 1997, **30**, 502; P. J. Stang, *Chem. – Eur. J.* 1998, **4**, 19; B. Olenyuk, A. Fechtenkötter, and P. J. Stang, *J. Chem. Soc., Dalton. Trans.* 1998, 1707.
2. G. F. Swiegers and T. J. Malefetse, *Chem. – Eur. J.* 2001, **7**, 3637; G. F. Swiegers and T. J. Malefetse, *Chem. Rev.* 2000, **100**, 3483.
3. M. Fujita, *Chem. Soc. Rev.*, 1998, **27**, 417.
4. S. Leininger, B. Olenyuk, and P. J. Stang, *Chem. Rev.*, 2000, **100**, 853.
5. B. J. Holliday and C. A. Mirkin, *Angew. Chem., Int. Ed. Engl.*, 2001, **40**, 2022.
6. M. Fujita, F. Ibukuro, H. Hagihara, and K. Ogura, *Nature*, 1994, **367**, 720; M. Fujita, F. Ibukuro, H. Seki, O. Kamo, M. Imanari, and K. Ogura, *J. Am. Chem. Soc.* 1996, **118**, 899; M. Fujita, F. Ibukuro, K. Yamaguchi, and K. Ogura, *J. Am. Chem. Soc.* 1995, **117**, 4175; M. Fujita, M. Aoyagi, K. Ogura, *Inorg. Chim. Acta* 1996, **246**, 53; M. Fujita, M. Aoyagi, F. Ibukuro, K. Ogura, and K. Yamaguchi, *J. Am. Chem. Soc.* 1998, **120**, 611.
7. M. Fujita, S. Nagao, M. Iida, K. Ogata, and K. Ogura, *J. Am. Chem. Soc.*, 1993, **115**, 1574.
8. R. Schneider, M. W. Hosseini, J.-M. Planeix, A. D. De Cian, and J. Fischer, *J. Chem. Soc. Chem. Commun.*, 1998, 1625.
9. G. Ma, Y. S. Jung, D. S. Chung, and J.-I. Hong, *Tetrahedron Lett.*, 1999, **40**, 531.
10. P. J. Stang and K. Chen, *J. Am. Chem. Soc.* 1995, **117**, 1667; P. J. Stang, K. Chen, and A. M. Arif, *J. Am. Chem. Soc.* 1995, **117**, 8793.
11. T. Habicher, J.-F. Nierengarten, V. Gramlich, and F. Diederich, *Angew. Chem., Int. Ed. Engl.*, 1998, **37**, 1916.
12. M. Schmitz, S. Leininger, J. Fan, A. M. Arif, and P. J. Stang, *Organometallics*, 1999, **18**, 4817.
13. B. Olenyuk, J. A. Whiteford, and P. J. Stang, *J. Am. Chem. Soc.*, 1996, **118**, 8221.
14. K.-S. Jeong, Y. L. Cho, J. U. Song, H.-Y. Chang, and M.-G. Choi, *J. Am. Chem. Soc.* 1998, **120**, 10982; K.-S. Jeong, Y. L. Cho, S.-Y. Chang, and H.-Y. Chang, *Angew. Chem., Int. Ed. Engl.* 2000, **39**, 1692.
15. J. M. Hannon, C. L. Painting, and W. Errington, *J. Chem. Soc. Chem. Commun.*, 1997, 307.
16. M. Fujita, O. Sasaki, T. Mitsuhashi, T. Fujita, J. Yazaki, K. Yamaguchi, and K. Ogura, *Chem. Commun.*, 1996, 1535.
17. S. B. Lee, S. G. Hwang, D. S. Chung, H. Yun, and J.-I. Hong, *Tetrahedron Lett.*, 1998, **39**, 873.
18. J. Hall, S. J. Loeb, G. K. H. Shimizu, and G. P. A. Yap, *Angew. Chem., Int. Ed. Engl.*, 1998, **37**, 121.
19. R.-D. Schnebeck, L. Randaccio, E. Zangrando, and B. Lippert, *Angew. Chem., Int. Ed. Engl.*, 1998, **37**, 119.
20. R.-D. Schnebeck, E. Freisinger, and B. Lippert, *Angew. Chem., Int. Ed. Engl.*, 1999, **38**, 168.
21. S.-W. Lai, M. C.-W. Chan, S.-M. Peng, and C.-M. Che, *Angew. Chem., Int. Ed. Engl*, 1999, **38**, 669.
22. A. T. Baker, J. K. Crass, M. Maniska, and D. C. Craig, *Inorg. Chim. Acta.*, 1995, **230**, 225.
23. P. J. Stang, D. H. Cao, S. Saito, and A. M. Arif, *J. Am. Chem. Soc.*, 1995, **117**, 6273.
24. P. J. Stang and D. H. Cao, *J. Am. Chem. Soc.*, 1994, **116**, 4981.
25. M. Fujita, J. Yazaki, and K. Ogura, *J. Am. Chem. Soc.*, 1990, **112**, 5645.
26. J. A. Whiteford, C. V. Lu, and P. J. Stang, *J. Am. Chem. Soc.*, 1997, **119**, 2524.
27. P. J. Stang and J. A. Whiteford, *Organometallics*, 1994, **13**, 3776.
28. J. A. Whiteford, P. J. Stang, and S. D. Huang, *Inorg. Chem.*, 1998, **37**, 5595.
29. R. V. Slone, D. I. Yoon, R. M. Calhoun, and J. T. Hupp, *J. Am. Chem. Soc.*, 1995, **117**, 11813.
30. P. J. Stang and N. E. Persky, *J. Chem. Soc. Chem. Commun.*, 1997, 77.
31. P. J. Stang, J. Fan, and B. Olenyuk, *J. Chem. Soc. Chem. Commun.*, 1997, 1453.

32. M. C. Drain and J. M. Lehn, *J. Chem. Soc. Chem. Commun.*, 1994, 2313.
33. F. Würthner and A. Sautter, *Chem. Commun.*, 2000, 445.
34. J. Manna, C. J. Kuehl, J. A. Whiteford, P. J. Stang, D. C. Muddiman, S. A. Hofstadler, and R. D. Smith, *J. Am. Chem. Soc.*, 1997, **119**, 11611.
35. R. Krämer, L. Kovbasyuk, and H. Pritzkow, *New J. Chem.*, 2002, **26**, 516.
36. C. S. Campos-Fernández, R. Clérac, and K. R. Dunbar, *Angew. Chem., Int. Ed. Engl.* 1998, **38**, 3477; X.-H. Bu, H. Morishita, K. Tanaka, K. Biradha, S. Furusho, M. Shionoya, *Chem. Commun.* 2000, 971.
37. B. Hasenknopf, J. M. Lehn, G. Baum, B. O. Kneisel, and D. Fenske, *Angew. Chem., Int. Ed. Engl.*, 1996, **35**, 1838.
38. B. Hasenknopf, J. M. Lehn, N. Boumediene, A. Dupont-Gervais, A. van Dorsselaer, B. Kneisel, and D. Fenske, *J. Am. Chem. Soc.*, 1997, **119**, 10956.
39. C. S. Campos-Fernández, R. Clérac, J. M. Koomen, D. H. Russell, and K. R. Dunbar, *J. Am. Chem. Soc.*, 2001, **123**, 773.
40. K. R. Dunbar and R. A. Heintz, *Prog. Inorg. Chem.*, 1997, **45**, 283. and references therein.
41. Z. J. Zhong, H. Seino, Y. Mizobe, M. Hidai, A. Fujishima, S. Ohkoshi, and K. J. Hashimoto, *J. Am. Chem. Soc.*, 2000, **122**, 2952; J. Larionova, G. Mathias, M. Pilkington, H. Andres, H. Stoeckli-Evans, H. U. Gudel, and S. Decurtins, *Angew. Chem., Int. Ed. Engl.* 2000, **39**, 1605.
42. J. A. Smith, J.-R. Galán-Mascarós, R. Clérac, J.-S. Sun, X. Ouyang, and K. R. Dunbar, *Polyhedron*, 2001, **20**, 1727.
43. C. P. Berlinguette, J. A. Smith, J.-R. Galán-Mascarós, and K. R. Dunbar, *C. R. Chimie*, 2002, **5**, 665.
44. H. Oshio, M. Yamamoto, and T. Ito, *Inorg. Chem.*, 2002, **41**, 5817.
45. C. P. Berlinguette, D. Vaughn, C. Cañada-Vilalta, J.-R. Galán-Mascarós, and K. R. Dunbar, *Angew. Chem., Int. Ed. Engl.*, 2003, **42**, 1523.
46. K. Van Langenberg, S. R. Batten, K. J. Berry, D. C. R. Hockless, B. Moubaraki, and K. S. Murray, *Inorg. Chem.*, 1997, **36**, 5006.
47. C. P. Berlinguette, J.-R. Galán-Mascarós, and K. R. Dunbar, *Inorg. Chem.*, 2003, **42**, 3416.
48. A. Marvilliers, Y. Pei, J. C. Boquera, K. E. Vostrikova, C. Paulsen, E. Rivière, J.-P. Audière, and T. Mallah, *Chem. Commun.*, 1999, 1951.
49. K. K. Klausmeyer, T. B. Rauchfuss, and S. R. Wilson, *Angew. Chem., Int. Ed. Engl.*, 1998, **37**, 1694.
50. S. M. Contakes, M. L. Kuhlman, M. Ramesh, S. R. Wilson, and T. B. Rauchfuss, *Proc. Natl. Acad. Sci. U.S.A.*, 2002, **99**, 4889.
51. S. C. N. Hsu, M. Ramesh, J. H. Espenson, and T. B. Rauchfuss, *Angew. Chem., Int. Ed. Engl.*, 2003, **42**, 2663.
52. J. L. Heinrich, P. A. Berseth, and J. R. Long, *Chem. Commun.*, 1998, 1231.
53. E. J. Schelter, J. K. Bera, J. Bacsa, J. R. Galán-Mascarós, and K. R. Dunbar, *Inorg. Chem.*, 2003, **42**, 4256.
54. E. J. Schelter, A. V. Prosvirin, W. M. Reiff, K. R. Dunbar, *Angew. Chem., Int. Ed. Engl.*, 2004, **43**, 4912.
55. K. K. Klausmeyer, S. R. Wilson, and T. B. Rauchfuss, *J. Am. Chem. Soc.*, 1999, **121**, 2705.
56. S. M. Contakes and T. B. Rauchfuss, *Angew. Chem., Int. Ed. Engl.*, 2000, **39**, 1984.
57. D. Babel, *Comments Inorg. Chem.* 1986, **5**, 285; W. R. Entley, and G. S. Girolami, *Science*, 1995, **268**, 397; T. Mallah, S. Thiebaut, M. Verdaguer, and P. Veillet, *Science*, 1993, **262**, 1554; S. Ferlay, T. Mallah, R. Ouhaces, P. Veillet, and M. Verdaguer, *Nature*, 1996, **378**, 701; M. Ohba and H. Okawa, *Coord. Chem. Rev.* 2000, **198**, 313.
58. M. Verdaguer, A. Bleuzen, V. Marvaud, J. Vaissermann, M. Seuleiman, C. Desplanches, A. Scuiller, C. Train, R. Garde, G. Gelly, C. Lomenech, I. Rosenman, P. Veillet, C. Cartier, and F. Villain, *Coord. Chem. Rev.*, 1999, **190–192**, 1023; T. Mallah, C. Auberger, M. Verdaguer, and P. Veillet, *J. Chem. Soc., Chem. Commun.*, 1995, 61; A. Scuiller, T. Mallah, A. Nivorozkhin, J.-L. Tholence, M. Verdaguer, and P. Veillet, *New J. Chem.*, 1996, **20**, 1; F. Thétiot, S. Triki, J. S. Pala, C. J. Gómez-García, and S. Golhen, *Chem. Commun.* 2002, 1078.
59. M. Clemente-León, E. Coronado, J. R. Galán-Mascarós, C. J. Gómez-García, T. Woike, and J. M. Clemente-Juan, *Inorg. Chem.*, 2001, **40**, 87.
60. O. M. Yaghi, M. O'Keeffe, N. W. Ockwig, H. K. Chae, M. Eddaoudi, and J. Kim, *Nature*, 2003, **423**, 705.
61. M. O'Keeffe, M. Eddaoudi, H. Li, T. Reineke, and O. M. Yaghi, *J. Solid State Chem.*, 2000, **152**, 3.
62. N. L. Rosi, M. Eddaoudi, J. Kim, M. O'Keeffe, and O. M. Yaghi, *CrystEngComm.*, 2002, **4**, 401.
63. H. Li, M. Eddaoudi, M. O'Keeffe, and O. M. Yaghi, *Nature*, 1999, **402**, 276.
64. M. Eddaoudi, J. Kim, N. Rosi, D. Vodak, J. B. Wachter, M. O'Keeffe, and O. M. Yaghi, *Science*, 2002, **295**, 469.
65. M. Eddaoudi, J. Kim, J. B. Wachter, H. K. Chac, M. O'Keeffe, and O. M. Yaghi, *J. Am. Chem. Soc.*, 2001, **123**, 4368.
66. H. Li, M. Eddaoudi, T. L. Groy, and O. M. Yaghi, *J. Am. Chem. Soc.*, 1998, **120**, 8571.
67. M. Eddaoudi, J. Kim, M. O'Keeffe, and O. M. Yaghi, *J. Am. Chem. Soc.*, 2002, **124**, 376.
68. R. H. Cayton, M. H. Chisholm, J. C. Huffman, and E. B. Lobkovsky, *J. Am. Chem. Soc.*, 1991, **113**, 8709.
69. F. A. Cotton, C. Lin, and C. A. Murillo, *Acc. Chem. Res.*, 2001, **34**, 759 and references therein.
70. F. A. Cotton, C. Lin, and C. A. Murillo, *J. Chem. Soc. Dalton. Trans.* 1998, 3151; F. A. Cotton, J. P. Donahue, C. Lin, and C. A. Murillo, *Inorg. Chem.* 2001, **40**, 1234.
71. F. A. Cotton, J. P. Donahue, and C. A. Murillo, *Inorg. Chem.*, 2001, **40**, 2229.

72. F. A. Cotton, C. Lin, and C. A. Murillo, *Inorg. Chem.*, 2001, **40**, 472.
73. F. A. Cotton, C. Lin, and C. A. Murillo, *Inorg. Chem.*, 2001, **40**, 575.
74. F. A. Cotton, L. M. Daniels, C. Lin, and C. A. Murillo, *J. Am. Chem. Soc.*, 1999, **121**, 4538.
75. F. A. Cotton, C. Lin, and C. A. Murillo, *Inorg. Chem.*, 2001, **40**, 478.
76. F. A. Cotton, C. Lin, C. A. Murillo, and S.-Y. Yu, *J. Chem. Soc., Dalton Trans.*, 2001, 502.
77. F. A. Cotton, C. Lin, and C. A. Murillo, *Inorg. Chem. Commun.*, 2001, **4**, 130.
78. F. A. Cotton, L. M. Daniels, C. Lin, and C. A. Murillo, *Chem. Commun.* 1999, 841; F. A. Cotton, C. Lin, C. A. Murillo, *Inorg. Chem.* 2001, **40**, 6413.
79. F. A. Cotton, C. Lin, and C. A. Murillo, *Proc. Natl. Acad. Sci. U.S.A.*, 2002, **99**, 4810.
80. J. K. Bera, P. Angaridis, F. A. Cotton, M. A. Petrukhina, P. E. Fanwick, and R. A. Walton, *J. Am. Chem. Soc.*, 2001, **123**, 1515.
81. J. K. Bera, R. Clérac, P. E. Fanwick, and R. A. Walton, *J. Chem. Soc., Dalton Trans.*, 2002, 2168.
82. J. K. Bera, B. W. Smucker, R. A. Walton, and K. R. Dunbar, *Chem. Commun.*, 2001, 2562.
83. J. K. Bera, J. Bacsa, B. W. Smucker, and K. R. Dunbar, *Eur. J. Inorg. Chem.*, 2004, 368.
84. L. J. Prins, D. N. Reinhoudt, and P. Timmerman, *Angew. Chem., Int. Ed. Engl.*, 2001, **40**, 2382 and references therein.
85. G. R. Desiraju, *J. Chem. Soc., Dalton Trans.*, 2000, 3745.
86. C. S. A. Fraser, D. J. Eisler, M. C. Jennings, and R. J. Puddephatt, *Chem. Commun.*, 2002, 1224.
87. C. J. Kuehl, F. M. Tabellion, A. M. Arif, and P. J. Stang, *Organometallics*, 2001, **20**, 1956.
88. J. K. Bera, T.-T. Vo, R. A. Walton, and K. R. Dunbar, *Polyhedron*, 2003, **22**, 3009.
89. F. A. Cotton, E. V. Dikarev, M. A. Petrukhina, M. Schmitz, and P. J. Stang, *Inorg. Chem.* 2002, **41**, 2903; Y. Ding, S. S. Lau, P. E. Fanwick, and R. A. Walton, *Inorg. Chim. Acta.* 2000, **300–302**, 505.
90. Z. Qin, M. C. Jennings, and R. J. Puddephatt, *Inorg. Chem.*, 2002, **41**, 5174.
91. C. R. Bondy, P. A. Gale, and S. J. Loeb, *Chem. Commun.*, 2001, 729.
92. D. Braga, L. Maini, F. Grepioni, C. Elschenbroich, F. Paganelli, and O. Schiemann, *Organometallics*, 2001, **20**, 1875.
93. F. Takusagawa and T. F. Koetzle, *Acta Crystallogr., Sect. B*, 1979, **35**, 2888.
94. D. Braga, L. Maini, M. Polito, L. Mirolo, and F. Grepioni, *Chem. Commun.*, 2002, 2960.
95. S. R. Collinson, T. Gelbrich, M. B. Hursthouse, and J. H. R. Tucker, *Chem. Commun.*, 2001, 555.
96. A. L. Gillon, G. R. Lewis, A. G. Orpen, S. Rotter, J. Starbuck, X.-M. Wang, Y. Rodriguez-Martin, and C. Ruiz-Perez, *J. Chem. Soc., Dalton Trans.*, 2000, 3897.
97. L. Brammer, J. K. Swearingen, E. A. Bruton, and P. Sherwood, *Proc. Natl. Acad. Sci. U.S.A.*, 2002, **99**, 4956.
98. G. R. Lewis and A. G. Orpen, *Chem. Commun.*, 1998, 1873.
99. L. J. Barbour, L. R. MacGillivray, and J. L. Atwood, *Supramol. Chem.*, 1996, **7**, 167.
100. A. L. Gillon, A. G. Orpen, J. Starbuck, X.-M. Wang, Y. Rodriguez-Martin, and C. Ruiz-Perez, *Chem. Commun.*, 1999, 2287.
101. B. Dolling, A. L. Gillon, A. G. Orpen, J. Starbuck, and X.-M. Wang, *Chem. Commun.*, 2001, 567.
102. M. Tadokoro, H. Kanno, T. Kitajima, H. Shimada-Umemoto, N. Nakanishi, K. Isobe, and K. Nakasuji, *Proc. Natl. Acad. Sci. U.S.A.*, 2002, **99**, 4950.
103. M. Tadokoro and K. Nakasuji, *Coord. Chem. Rev.*, 2000, **198**, 205.
104. R. L. E. Furlan, S. Otto, and J. K. M. Sanders, *Proc. Natl. Acad. Sci. U.S.A.*, 2002, **99**, 4801.
105. A. V. Davis, R. M. Yeh, and K. N. Raymond, *Proc. Natl. Acad. Sci. U.S.A.*, 2002, **99**, 4793.
106. N. Fatin-Rouge, S. Blanc, E. Leize, A. Van Dorsselaer, P. Baret, J.-L. Pierre, and A.-M. Albrecht-Gary, *Inorg. Chem.* 2000, **39**, 5771; N. Fatin-Rouge, S. Blanc, A. Pfeil, A. Marquis-Rigault, A.-M. Albrecht-Gary, and J.-M. Lehn, *Helv. Chim. Acta* 2001, **84**, 1694.
107. J.-M. Lehn, *Science*, 2002, **295**, 2400; R. Kramer, J.-M. Lehn, A. Marquis-Rigault, *Proc. Natl. Acad. Sci. U.S.A.*, 1993, **90**, 5394.
108. W. B. Jennings, B. M. Farrell, and J. F. Malone, *Acc. Chem. Res.* 2001, **34**, 885; K. Müller-Dethlefs and P. Hobza, *Chem. Rev.* 2000, **100**, 143; W. B. Jennings, B. M. Farrell, and J. F. Malone, *Acc. Chem. Res.* 2001, **34**, 885.
109. M. Scherer, D. L. Caulder, D. W. Johnson, and K. N. Raymond, *Angew. Chem., Int. Ed. Engl.*, 1999, **38**, 1588.
110. T. N. Parac, D. L. Caulder, and K. N. Raymond, *J. Am. Chem. Soc.*, 1998, **120**, 8003.
111. T. N. Parac, M. Scherer, and K. N. Raymond, *Angew. Chem., Int. Ed. Engl.*, 2000, **39**, 1239.
112. J. K. Bera, K. R. Dunbar, unpublished result.
113. M. Yoshizawa, T. Kusukawa, M. Fujita, S. Sakamoto, and K. Yamaguchi, *J. Am. Chem. Soc.*, 2001, **123**, 10454.
114. M. Ziegler, J. L. Brumaghim, and K. N. Raymond, *Angew. Chem., Int. Ed. Engl.*, 2000, **39**, 4119.
115. M. L. Merlau, M. P. Mejia, S. T. Nguyen, and J. T. Hupp, *Angew. Chem., Int. Ed. Engl.*, 2001, **40**, 4239.
116. H. Jiang, A. Hu, and W. Lin, *Chem. Commun.*, 2003, 96.
117. S. J. Lee, A. Hu, and W. Lin, *J. Am. Chem. Soc.*, 2002, **124**, 12948.
118. N. L. Rosi, J. Eckert, M. Eddaoudi, D. T. Vodak, J. Kim, M. O’Keeffe, and O. M. Yaghi, *Science*, 2003, **300**, 1127.

Periodic Table: Historical Aspects

Dennis H. Rouvray
University of Georgia, Athens, GA, USA

1 Introduction 1
2 Early Notions of the Elements 1
3 Discovery of the Chemical Elements 2
4 Relationships among the Elements 4
5 The Advent of the Periodic Table 4
6 Coping with the Anomalies 6
7 The Long End of the Table 7
8 Further Reading 9
9 References 9

1 INTRODUCTION

The periodic table is one of the great classifications of the natural world and ranks on a par with several other major classifications, including the classification of plant species by Linnaeus in the 1750s, the classification of stars by Hertzsprung and Russell in 1913, and the classification of subnuclear particles by Gell-Mann and Ne'eman in the 1950s. The periodic table has for its primary purpose the classification of the chemical elements, the basis for this being the analogies they exhibit in their physical and chemical properties. As the story of the periodic table is closely entwined with that of the elements, we shall explore these two concepts concomitantly here. From this broad perspective, some of the most colorful events that have occurred in chemical history over the past 2600 years are encompassed. In developing our theme, we shall endeavor to stimulate a greater interest in and bring a new awareness of the very rich legacy bequeathed to us by our pioneering predecessors. It is our hope that such an approach may in some way compensate for the often rather cursory treatment afforded our theme in elementary chemistry textbooks and foundational courses.

Because there can be no periodic table without an understanding of the nature of the elements, we shall start by delving into the history of the chemical elements. First, we mention the somewhat ironic fact that around nine genuine elements were known in ancient times, these being carbon, sulfur, copper, iron, lead, tin, mercury, silver, gold, and possibly antimony, though none of them was recognized as an element. Like everything else that was material, these true elements were thought to be composed of metaphysical entities such as essences or principles. The notion that all material objects consisted of essences or principles was a remarkably enduring one that was to persist for well over 2000 years. In fact, this notion remained dominant until the end of the alchemical era was reached toward the end of the eighteenth century. In the Western World, the conception of metaphysical elements is usually traced back to and considered to originate from certain of the natural philosophers of ancient Greece. However, it is important to point out that all of the other major civilizations of the past paid homage to the idea that physical reality manifests itself in terms of metaphysical entities that were regarded as elements. There was even substantial overlap in these entities in different civilizations. Thus, virtually all of the early civilizations conceived of air and fire as elements.

Before probing further into the history of the elements, a brief comment on the etymological derivation of the word *element* seems appropriate. The first usage of the term element was made by the Greek philosopher Plato (427–347 BCE) in the fifth century BCE.[1] The actual word he employed was *στοιχειον* (*stoicheion*), which has the basic meaning shape because it was believed at the time that objects assumed differing shapes or forms when they were fashioned from supposedly amorphous primary matter. The Latin equivalent of this Greek term is *elementum*, and this was first used by the Roman poet Lucretius (ca. 97–55 BCE) in his famous poem *De Rerum Natura* (*On the Nature of Things*) extolling the virtues of an atomic conception of the world.[2] While on the subject of words, we mention in passing the origin of the word quintessence. It was thought by the ancient Greeks that four elements comprised all of the matter on Earth whereas the celestial sphere was constituted from only one transcendent element referred to as the *ether* or the *quinta essentia*, the fifth essence, from which our modern word quintessence is derived. Interestingly, the ether turned out to be by far the longest lived of the Greek elements, for it was not until the dawn of the twentieth century that belief in the ether was finally abandoned.

2 EARLY NOTIONS OF THE ELEMENTS

The earliest philosophers of ancient Greece came to the conclusion that everything in the physical world consisted of one single reality, even though it was manifested in many different forms. This single reality, or single element in modern parlance, was variously interpreted. Thales (650–546 BCE) thought that it was water, Anaximenes (560–500 BCE) that it was air, while Heraclitus (536–470 BCE) maintained that it was fire. As no general agreement could be reached, their several ideas were eventually incorporated into a multielement theory of reality. This theory was put forward by Empedocles (490–430 BCE) who asserted that the world was derived from four basic roots, these being earth, air, fire, and water. He was thus the originator of the much celebrated concept of the four terrestrial elements that was to dominate scholastic thinking for the next two millennia. Plato (427–347 BCE) adopted the four elements and introduced a fifth element, the ether or quinta essentia mentioned earlier, that he believed was the constituent of all matter in the celestial sphere. Plato also associated each of these five elements with one of the five Platonic polyhedra: fire with the tetrahedron, air with the octahedron, water with the icosahedron, earth with the hexahedron (cube), and the ether with the dodecahedron.

Because of the association of the elements with the Platonic polyhedra, it was argued[3] that the elements were constructed from two distinct types of triangle: an isosceles right-angled triangle (two sides equal) and a scalene right-angled triangle (no sides equal). Moreover, it was supposed that the elements air, fire, and water were mutually interconvertible, a supposition that gave rise to the alchemical notion of the transmutation of the elements. Thus, an icosahedron of water (with 20 faces) could be partitioned into two octahedra of air (with a total of $2 \times 8 = 16$ faces) and one tetrahedron of fire (with four faces). The element earth was thought to be too stable to partake in such splitting and the element ether was deemed to be too exalted to do so. The greatly varying characteristics of the materials extant on Earth could be accounted for in terms of (1) the differing sizes of the triangles from which they were constructed, (2) the distinct ratios of the elements of which they were composed, and (3) the varying proportions they contained of the four qualities of dryness, wetness, hotness, and coldness. The behavior of the elements could also be correlated with their specific shapes. Because fire, for instance, consisted of tetrahedral particles with comparatively sharp points, it was thought that fire could cut into and therefore dissolve many material substances. That such notions persisted well into the seventeenth century is seen from Figure 1 which reproduces a depiction of the elements by Kepler[4] dating from 1619.

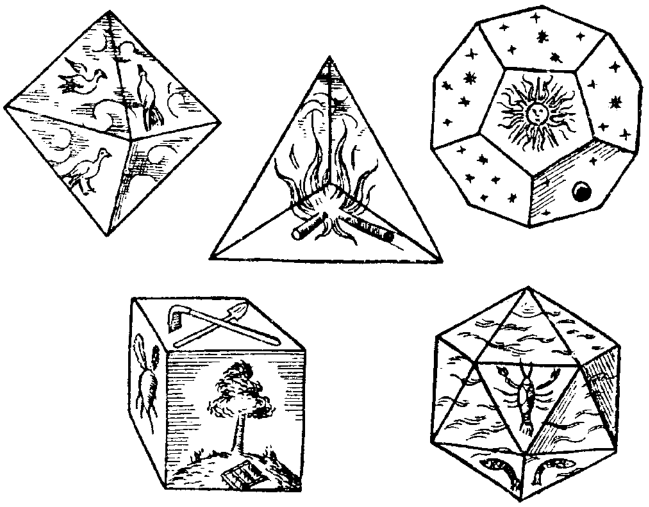

Figure 1 A depiction of the five elements shown here as the five Platonic solids. From Johann Kepler's book *Harmonices Mundi* of 1619

It was during the Middle Ages that the number of the metaphysical elements began to increase. In the eighth century, the somewhat obscure Arab alchemist Jabir ibn Hayyan (ca. 721–815) added two new elements. He argued that all metals are comprised of the elements mercury and sulfur, the element mercury being coagulated by the element sulfur to form individual metals. The specific metal that was formed depended on the relative amounts of the mercury and sulfur it contained. Reference was made here not to the substances mercury and sulfur themselves but to their essences, which were thought to be so rarified that they could not be obtained experimentally. In the sixteenth century, Theophrastus von Hohenheim (1493–1541), also known as Paracelsus, introduced the concept of the *tria prima*, the three principles, which developed the thinking of Jabir ibn Hayyan. Paracelsus asserted that the three fundamental principles were sulfur (the combustible principle), mercury (the liquidity principle), and salt (the incombustibility principle). This trio of elements was allegedly present in all materials whether they be of animal, vegetable, or mineral origin. Mercury was considered to be the spirit of the material, with sulfur its soul, and salt its physical body. By the end of the Middle Ages, the number of metaphysical entities regarded as elements had thus increased to eight.

3 DISCOVERY OF THE CHEMICAL ELEMENTS

The gradual move away from the notion that elements were metaphysical in nature toward a broad acceptance that they are real substances occurred during the seventeenth century. From around the 1630s the conventional wisdom of the day began to be questioned. One of the first to do so was the German alchemist Joachim Jungius (1587–1657), who doubted that the elements were metaphysical entities but saw them rather as corpuscular in structure and comprised of pure and simple substances.[5] In his celebrated book The *Sceptical Chymist*, published in 1661, Robert Boyle (1627–1691) put forward[6] a new definition of an element. It was his intention to discredit the prevailing thinking of the time and to point out that elements always consisted of actual substances. In what is now regarded as the first modern definition of an element, Boyle stated that elements were 'primitive and simple, or perfectly unmingled bodies; which not being made of any other bodies, or of one another, are the ingredients of which all of those called perfectly mixed bodies are immediately compounded, and into which they are ultimately resolved'. This definition found little resonance among Boyle's contemporaries and so was largely ignored during Boyle's lifetime.

In fact, a century elapsed before Boyle's definition began to be taken seriously and put into practice. One of the great luminaries of science, the French chemist Antoine-Laurent Lavoisier (1743–1794), sometimes called the father of modern chemistry, decided to put Boyle's arguments to the test. To determine which substances were elements,

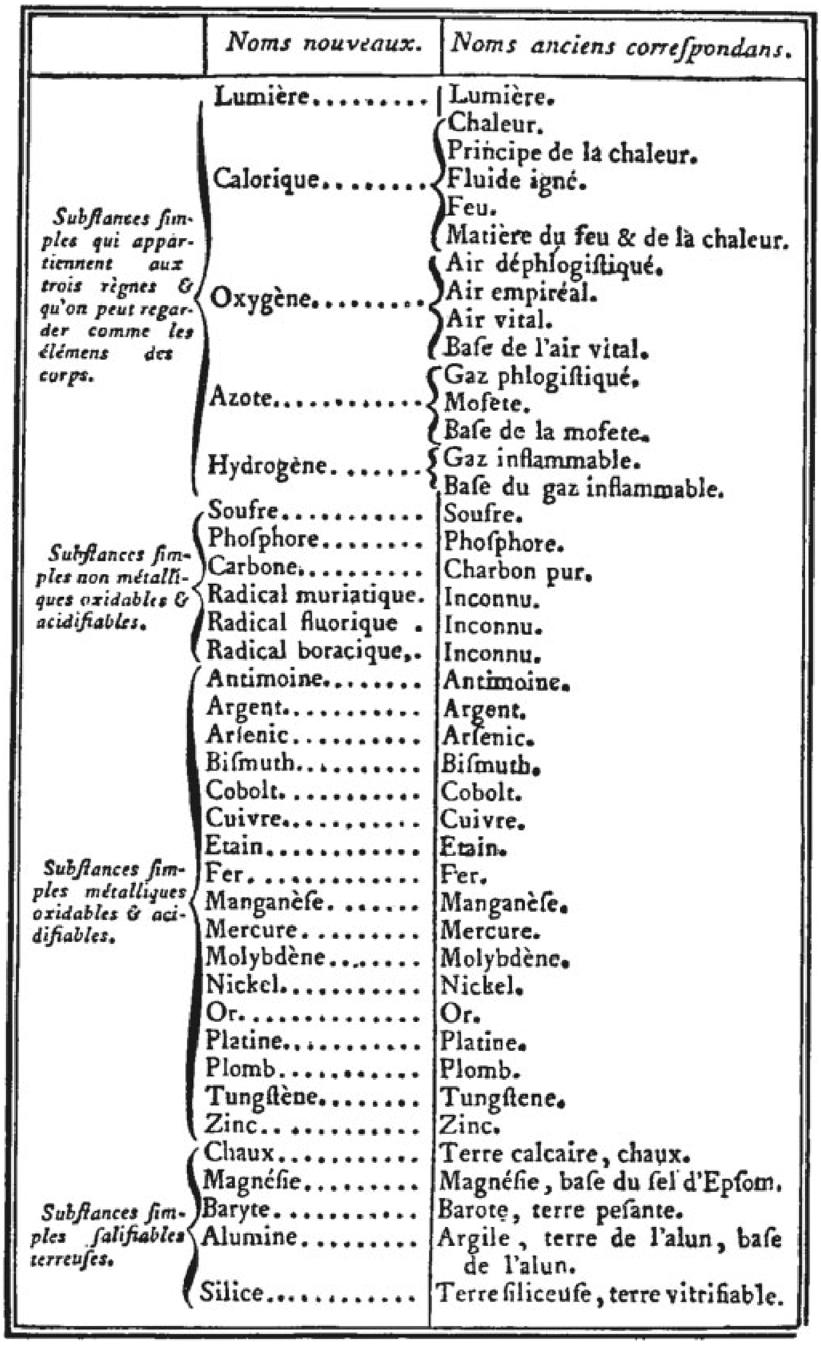

	Noms nouveaux.	Noms anciens correſpondans.
Subſtances ſimples qui appartiennent aux trois règnes & qu'on peut regarder comme les élémens des corps.	Lumière	Lumière.
	Calorique	Chaleur. Principe de la chaleur. Fluide igné. Feu. Matière du feu & de la chaleur.
	Oxygène	Air déphlogiſtiqué. Air empiréal. Air vital. Baſe de l'air vital.
	Azote	Gaz phlogiſtiqué. Mofete. Baſe de la mofete.
	Hydrogène	Gaz inflammable. Baſe du gaz inflammable.
Subſtances ſimples non métalliques oxidables & acidifiables.	Soufre	Soufre.
	Phoſphore	Phoſphore.
	Carbone	Charbon pur.
	Radical muriatique.	Inconnu.
	Radical fluorique	Inconnu.
	Radical boracique	Inconnu.
Subſtances ſimples métalliques oxidables & acidifiables.	Antimoine	Antimoine.
	Argent	Argent.
	Arſenic	Arſenic.
	Biſmuth	Biſmuth.
	Cobolt	Cobolt.
	Cuivre	Cuivre.
	Etain	Etain.
	Fer	Fer.
	Manganèſe	Manganèſe.
	Mercure	Mercure.
	Molybdène	Molybdène.
	Nickel	Nickel.
	Or	Or.
	Platine	Platine.
	Plomb	Plomb.
	Tungſtène	Tungſtene.
	Zinc	Zinc.
Subſtances ſimples ſalifiables terreuſes.	Chaux	Terre calcaire, chaux.
	Magnéſie	Magnéſie, baſe du ſel d'Epſom.
	Baryte	Barote, terre peſante.
	Alumine	Argile, terre de l'alun, baſe de l'alun.
	Silice	Terre ſiliceuſe, terre vitrifiable.

Figure 2 A listing of the chemical elements according to Antoine-Laurent Lavoisier. From his book *Traité Élémentaire de Chimie* of 1789

Lavoisier resolved materials into their ultimate constituents, that is, he decomposed them chemically until ‘the last point that analysis is capable of reaching’. By this means, he was able to draw up a table of simple substances that he claimed were elements. This table was published[7] in his groundbreaking book *Traité Élémentaire de Chimie*, which appeared in 1789. The reproduction of his table here in Figure 2 shows that it contained many substances that are now considered to be elements. The table also includes light and caloric, the latter being regarded by Lavoisier as a material fluid that functioned to separate the particles of elementary substances and thereby maintain them in the gaseous state. However, the rejection by Lavoisier of the alchemical notion of phlogiston, which he considered had made chemistry ‘obscure and unintelligible’, rendered possible a much more realistic understanding of the reactions that the elements entered into and thus afforded new insights into the nature of the elements themselves.

The next major step toward construction of the periodic table was taken in 1803 by the English chemist John Dalton (1766–1844). He demonstrated[8] that, if the hydrogen atom be assumed to have unit weight, then it was possible to assign relative weights to all of the other atoms. This he did by taking the combining weights of various pairs of elements and making the further assumption that the elements combined in a ratio of 1:1. Thus, it was known to Dalton that 12.6 parts of hydrogen combined with 87.4 parts of oxygen by weight. Taking the formula of water to be HO, he deduced that the oxygen atom must be 87.4/12.6 times heavier than the hydrogen atom. In other words, he had determined that the atomic weight of oxygen was seven (rounded to the nearest integer). Although the underlying reasoning was sound, there were two problems with Dalton's approach. First, the combining weights were not accurately known at the time and this led to errors. Second, and more seriously, Dalton's assumption that the elements combined in a 1:1 ratio, and that the formulas for water and ammonia were respectively HO and NH, generated a chaotic situation that was not cleared up for another 60 years. Dalton had, however, pioneered the way in showing that a natural number, that is, the atomic weight, could be associated with each element.

4 RELATIONSHIPS AMONG THE ELEMENTS

The idea that patterns of behavior were to be discerned among the elements was first established by the German chemist Johann Döbereiner (1780–1849). Early in the nineteenth century he began a series of extensive studies on groups of three elements that exhibited analogous behavior. The first group he investigated consisted of the trio *calcium-strontium-barium*. He demonstrated that these elements not only behaved in a chemically similar fashion but also were connected by a mathematical relationship. Döbereiner had shown that the equivalent weight of strontium oxide was almost exactly the mean of the equivalent weights of calcium oxide and barium oxide. In many other respects, the element strontium possessed properties that placed it precisely between the elements calcium and barium.[9] Several additional studies on element trios, including *lithium-sodium-potassium*, *chlorine-bromine-iodine*, and *sulfur-selenium-tellurium*, revealed that similar relationships applied in a number of other cases.[10] Trios of analogous chemical elements began to be referred to as triads and the mathematical relationship they satisfied was called the law of triads.

Important new insights into the various ways in which the elements could be interrelated were gained during the middle decades of the nineteenth century. The German chemist Leopold Gmelin (1788–1853) pointed out[11] in 1843 that whereas in some triads the atomic weights hardly differed at all, for example, in *chromium-manganese-iron*, in other triads the difference was considerable, for example, in *chlorine-bromine-iodine*. It was even shown[12] in 1850 by the German chemist Max von Pettenkofer (1818–1901) that some triads, for example, *fluorine-chlorine-bromine*, did not satisfy the law of triads. Further work also enabled von Pettenkofer to introduce the concept of the tetrad of elements, after he had studied the tetrads *magnesium-calcium-strontium-barium* and *oxygen-sulfur-selenium-tellurium*. Among many other relationships between the elements that were discovered around this time, mention has to be made of the existence of pentads of elements. In 1858, the French chemist Jean Dumas (1800–1884) first discovered[13] the pentad *nitrogen-phosphorus-arsenic-antimony-bismuth*. The earliest attempt to classify all of the elements into natural families was made[14] in 1857 by the English chemist William Odling (1829–1921). The 13 families he devised have a familiar ring to them. In group I, the elements fluorine, chlorine, bromine, and iodine were included; in group II, oxygen, sulfur, selenium, and tellurium; and in group III, nitrogen, phosphorus, arsenic, antimony, and bismuth. By developing such a scheme, Odling came close to discovering the periodic table, a feat he achieved seven years later in 1864.

In 1857, the time was not ripe for the advent of the periodic table because until the early 1860s the great uncertainty surrounding the true values of the atomic weights resulted in considerable confusion. Indeed, it was not unknown for chemists to use their own individual sets of atomic weights! The problem was finally resolved shortly after the first major international gathering of chemists held in Karlsruhe, Germany in September, 1860. At the end of this meeting, the Italian chemist Stanislao Cannizzaro (1826–1910) had a pamphlet distributed that revealed how reliable atomic weights could be calculated. Basically, Cannizzaro had reformulated the earlier work of his compatriot Amadeo Avogadro (1776–1856) who in 1811 had put forward a hypothesis now known as Avogadro's law. The updated version of this law stated[15] that 'the different quantities of the same element contained in different molecules are all whole multiples of one and the same quantity, which, always being entire, has the right to be called an atom'. This new formulation had a dramatic impact on many of the chemists who attended the conference. The German chemist Lothar Meyer (1830–1895) commented after reading it that 'the scales fell from my eyes, doubts vanished, and a feeling of calm certainly came in their place'.

5 THE ADVENT OF THE PERIODIC TABLE

As soon as accurate atomic weights for the elements became available, all of the necessary groundwork had been laid for the appearance of the periodic table. In fact, it was only some 18 months after the Karlsruhe Congress that the first periodic table was published.[16] The French mineralogist Alexandre

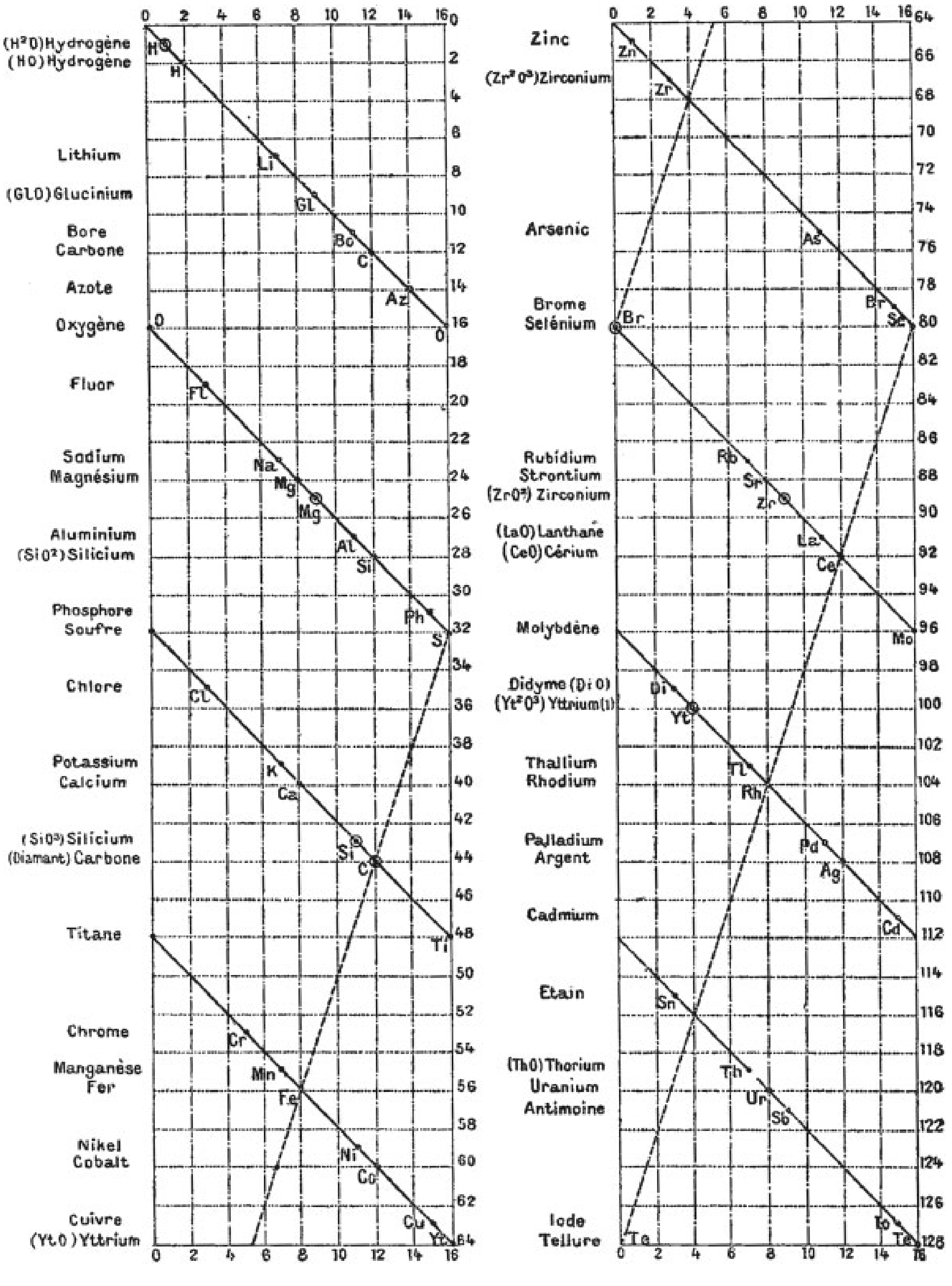
0 2 4 6 8 10 12 14 16
(H²O)Hydrogène
(HO)Hydrogène
Lithium
(GLO)Glucinium
Bore
Carbone
Azote
Oxygène
Fluor
Sodium
Magnésium
Aluminium
(SiO²)Silicium
Phosphore
Soufre
Chlore
Potassium
Calcium
(SiO³)Silicium
(Diamant) Carbone
Titane
Chrome
Manganèse
Fer
Nikel
Cobalt
Cuivre
(YtO)Yttrium
H
H
Li
GL
Bo
C
Az
O
O
FL
Na
Mg
Mg
AL
Si
Ph
S
CL
K
Ca
Si
C
Ti
Cr
Mn
Fe
Ni
Co
Cu
Yt
0 2 4 6 8 10 12 14 16 18 20 22 24 26 28 30 32 34 36 38 40 42 44 46 48 50 52 54 56 58 60 62 64
Zinc
(Zr²O³)Zirconium
Arsenic
Brome
Selénium
Rubidium
Strontium
(ZrO²) Zirconium
(LaO)Lanthane
(CeO)Cérium
Molybdène
Didyme (DiO)
(Yt²O³) Yttrium(?)
Thallium
Rhodium
Palladium
Argent
Cadmium
Etain
(ThO)Thorium
Uranium
Antimoine
Iode
Tellure
Zn
Zr
As
Br
Se
Br
Rb
Sr
Zr
La
Ce
Mo
Di
Yt
TL
Rh
Pd
Ag
Cd
Sn
Th
Ur
Sb
Io
Te
Te
64 66 68 70 72 74 76 78 80 82 84 86 88 90 92 94 96 98 100 102 104 106 108 110 112 114 116 118 120 122 124 126 128

Figure 3 The first prototype of the periodic table put forward by the French mineralogist Alexandre Beguyer de Chancourtois in 1862

Beguyer de Chancourtois (1819–1886), who was seeking for a way to classify geological rock specimens, discovered a prototype version of the periodic table in April, 1862. His prototype assumed the form of a continuous line of the elements ordered according to the recently revised atomic weights. The element line was wound around a right cylinder from the top at an angle of 45°, an arrangement that permitted analogous elements to be aligned along vertical lines drawn on the surface of the cylinder. The first winding of the element line through 360° included all of the elements up to oxygen, the second 360° winding the elements from fluorine to sulfur, and so on until all 59 of the then known elements had been accommodated. This new device was designated as the Telluric Screw, from the Latin word *tellus* that signified both the Earth from which all of the elements derive and the fact that the element tellurium was located at the center of the device. A two-dimensional representation of de Chancourtois' prototype of the periodic table is reproduced in Figure 3.

Following the pioneering work of de Chancourtois, no fewer than five other authors independently put forward periodic tables during the succeeding seven years. Shortly after de Chancourtois' breakthrough, the British chemist John

Newlands (1837–1898) published his first table in 1864 and noted[17] that '. . . the eighth element starting from a given one is a kind of repetition of the first, like the eighth note of an octave of music'. By a remarkable coincidence, the third periodic table author came from the same district of London as Newlands and published his table in the same year, 1864. William Odling (1829–1921) not only managed to include 57 of the 60 elements then known, but also drew a clear distinction between main group and subgroup elements.[18] The fourth discoverer of the periodic table was the Danish American Gustavus Hinrichs (1836–1923) who developed[19] a system for the natural classification of the elements in 1867. In 1868, the fifth author, the German Lothar Meyer (1830–1895) produced a full periodic table that assumed the form of 15 columns of elements, though this was not published immediately. By the time it was eventually published[20] early in 1870, the sixth and final discoverer of the periodic table, the Russian Dmitrii Mendeleev (1834–1907), had already published a 63-element version of the periodic table. The first printed version of the periodic table developed by Mendeleev was intended for distribution to his colleagues. We reproduce it here as Figure 4. A listing of the six independent discoverers of the periodic table is presented in the compilation below.

Discoverer	Date	Designation for the representation
de Chancourtois	1862	Telluric screw
Newlands	1864	Law of octaves
Odling	1864	System of the elements
Hinrichs	1867	Natural classification of elements
Meyer	1868	System of the elements
Mendeleev	1869	System of the elements

A listing of the various designations adopted for the periodic table by its six independent discoverers during the years 1862–1869.

Because Mendeleev is nowadays often regarded as the sole discoverer of the periodic table, it seems fitting to take a closer look at his contributions. A book offering a comprehensive review of his life and times appeared recently.[21] Mendeleev made a point of explicitly formulating the law underlying the periodic table and this he termed the periodic law.[22] Although he presented his law in the form of eight statements, only the first is necessary to grasp the law as the other seven are essentially embellishments of the first. The first statement reads: When the elements are arranged according to their atomic weights, they show an evident periodicity in their properties. This law, however, was not a strict one and even Mendeleev was not averse to making exceptions when these seemed to be called for. Thus, he reversed the order of the elements tellurium and iodine in his table, even though in terms of their atomic weights iodine should precede tellurium.

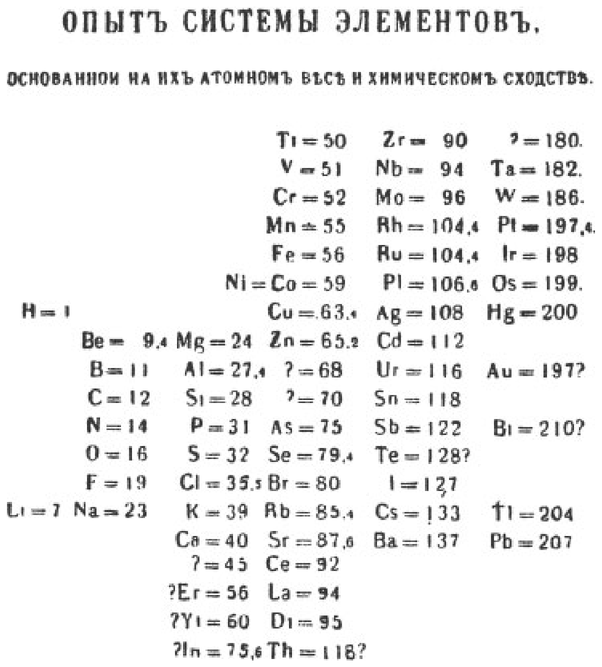

ОПЫТЪ СИСТЕМЫ ЭЛЕМЕНТОВЪ,

ОСНОВАННОЙ НА ИХЪ АТОМНОМЪ ВѢСѢ И ХИМИЧЕСКОМЪ СХОДСТВѢ.

			Ti = 50	Zr = 90	? = 180.
			V = 51	Nb = 94	Ta = 182.
			Cr = 52	Mo = 96	W = 186.
			Mn = 55	Rh = 104,4	Pt = 197,4.
			Fe = 56	Ru = 104,4	Ir = 198
			Ni = Co = 59	Pl = 106,6	Os = 199.
H = 1			Cu = 63,4	Ag = 108	Hg = 200
	Be = 9,4	Mg = 24	Zn = 65,2	Cd = 112	
	B = 11	Al = 27,4	? = 68	Ur = 116	Au = 197?
	C = 12	Si = 28	? = 70	Sn = 118	
	N = 14	P = 31	As = 75	Sb = 122	Bi = 210?
	O = 16	S = 32	Se = 79,4	Te = 128?	
	F = 19	Cl = 35,5	Br = 80	I = 127	
Li = 7	Na = 23	K = 39	Rb = 85,4	Cs = 133	Tl = 204
		Ca = 40	Sr = 87,6	Ba = 137	Pb = 207
		? = 45	Ce = 92		
		?Er = 56	La = 94		
		?Yt = 60	Di = 95		
		?In = 75,6	Th = 118?		

Figure 4 The first printed form of the periodic table put forward by the Russian chemist Dmitrii Mendeleev in 1869

Mendeleev trusted the periodic law enough to leave gaps in his table for elements that were unknown at the time. He predicted the existence of the elements germanium, gallium, and scandium and gave a forecast of their properties that proved to be spectacularly accurate.[23] All three of these elements were discovered within 15 years of the prediction of their existence and this caused excitement in the chemical community and raised Mendeleev's profile. But it should not be forgotten that Mendeleev made around 20 such predictions in all and, apart from the three great successes, his other predictions proved to be either fortuitous guesses or completely wrong. Especially misconceived were his predictions of the elements newtonium (atomic weight 0.17) and coronium (atomic weight 0.4) as well as six new elements that allegedly existed between hydrogen and lithium.

6 COPING WITH THE ANOMALIES

Toward the end of the nineteenth century it became increasingly clear that the periodic law was subject to a number of violations and even Mendeleev himself came to regard it as no more than rough and ready manifestation of some much stricter, mathematical law that remained to be identified. The periodic law was put to the test and found to be wanting when the noble gases began to be discovered in the 1890s by William Ramsey (1852–1916) and his collaborators. The periodic law had not been able to predict the existence of the noble gases, could give no explanation of their unusual properties (they appeared to be completely unreactive chemically), and there seemed to be no space to accommodate them in the periodic table.[24] To cope with the apparently intractable problem posed by the noble gases, Ramsey suggested to Mendeleev in 1900 that an extra group be added to the periodic table. After much soul searching, Mendeleev incorporated a new group 0 into his periodic table to make room for the noble gases. It was quickly realized that this new group, which was initially placed at the extreme left of the table and then immediately to the right of the halogens, fitted naturally into the periodic table. Mendeleev spoke of a 'magnificent survival' of the periodic law in what had proved to be a 'critical test' for it.[25]

The next of the problems to be confronted was one that threatened the very existence of the periodic table and ultimately had the effect of modifying the periodic law as stated by Mendeleev. In 1919, Francis Aston (1877–1945) had demonstrated that in general the elements are comprised of isotopes, that is they consist of atoms with the same number of protons but differing numbers of neutrons.[26] This new insight soon unleashed vigorous debate on whether the periodic table was capable of accommodating all of the elemental isotopes that were beginning to be discovered in large numbers by Aston and several other workers. There was a widespread sentiment that the periodic table would have to be replaced by some much more complex and cumbersome structure that could incorporate all of the isotopes. Just as talk of an abandonment of the conventional periodic table was reaching a peak, the day was saved by experimental work[27] that showed that the presence of isotopes in an element had no effect on its chemical behavior. The only exception to this universal rule was the element hydrogen, the isotopes of which were found to differ quite markedly in their chemical and physical properties. Thus, apart from the case of hydrogen, the substitution of one isotope by another in a given element was of no chemical significance, a finding that meant there was no need to alter either the group or the period structure of the periodic table.

Recognition of the fact that elements always displayed the same chemical behavior – regardless of their isotopic composition – led to a reformulation of the periodic law. The idea that each element was characterized by a unique number had already been demonstrated experimentally by Henry Moseley (1887–1915). By studying the X-ray diffraction patterns produced by a variety of elements, he discovered[28] that the frequencies of the K lines differed from element to element in a predictable and consistent fashion. He went on to show that 'the frequency of any line in the X-ray spectrum is approximately proportional to $A(N-b)^2$, where A and b are constants' and N is an integer that he termed the atomic number of the element. Moseley was able to identify the number N with the number of protons in the atomic nucleus. Plots of the square root of the frequency for the K and L lines in the X-ray spectra of the elements versus their atomic number, reproduced in Figure 5, show almost straight lines. From this work, it became clear why the order in which certain element pairs appeared in the periodic table needed to be reversed. The pairs in question are argon (39.95) and potassium (39.10); cobalt (58.93) and nickel (58.69); and tellurium (127.60) and iodine (126.91), the atomic weights being given in parentheses. The reversal was necessary because the atomic weights of the element pairs, that is, the mean weights averaged overall of the isotopes present, were out of step with the atomic numbers. The periodic law formulated by Mendeleev thus needed to be updated to read: When the elements are arranged according to their atomic numbers, they show an evident periodicity in their properties.

7 THE LONG END OF THE TABLE

The headway made by the physicist Moseley meant that it became possible to determine which substances were elements and also which elements were missing from the periodic table. Moseley himself had pointed out that three elements were missing, that is, the elements numbered 43 (technetium), 61 (promethium), and 72 (hafnium). These anticipated elements were eventually found, though only hafnium occurred naturally, the remaining two being artificially synthesized. The so-called rare earth elements began to be studied in the latter half of the eighteenth century and the last such element (lutetium) was discovered in 1907. The rare earths comprised an eclectic group thought to number up to 32 elements that clearly did not fit neatly into the periodic table and even created doubts about the table itself. Mendeleev remarked[29] that 'a whole large period is wanting between Ce = 140 and Ta = 183 . . . and therefore this portion of the periodic system is, in a way, broken and requires fresh researches'. It has even been observed that, had a majority of the rare earth elements been known in the 1860s, it is unlikely that the periodic table would have been discovered during that decade. The term 'rare earths' is no longer in current use both because it is ill-defined and the materials so characterized are not now regarded as rare.

The difficulties encountered in attempting to classify the rare earth elements were not satisfactorily resolved for several decades. In fact, a major breakthrough in our understanding of atomic physics was required before the issue could be said to be concluded. From the 1880s, versions of the periodic table that broadened out as the table progressed began to be proposed, this being done to allow extra space for the rare earth elements. Early examples of such tables were devised by Hans Thomsen (1826–1909) in 1895[30] and Alfred Werner (1866–1919) in 1905.[31] An important advance in shaping these expanded, two-dimensional periodic tables was made in 1922 when the renowned Danish physicist Niels Bohr (1885–1962) put forward[32] the table reproduced in Figure 6. Although this table had its origins in Bohr's preceding work on the electronic structure of atoms, the structures for many of the heavier atoms were still undetermined at the time. In the case of the rare earth elements, Bohr was thus forced to rely on spectroscopic data. These confirmed that the rare earth elements should indeed occupy a separate location in the periodic table and so he placed the elements

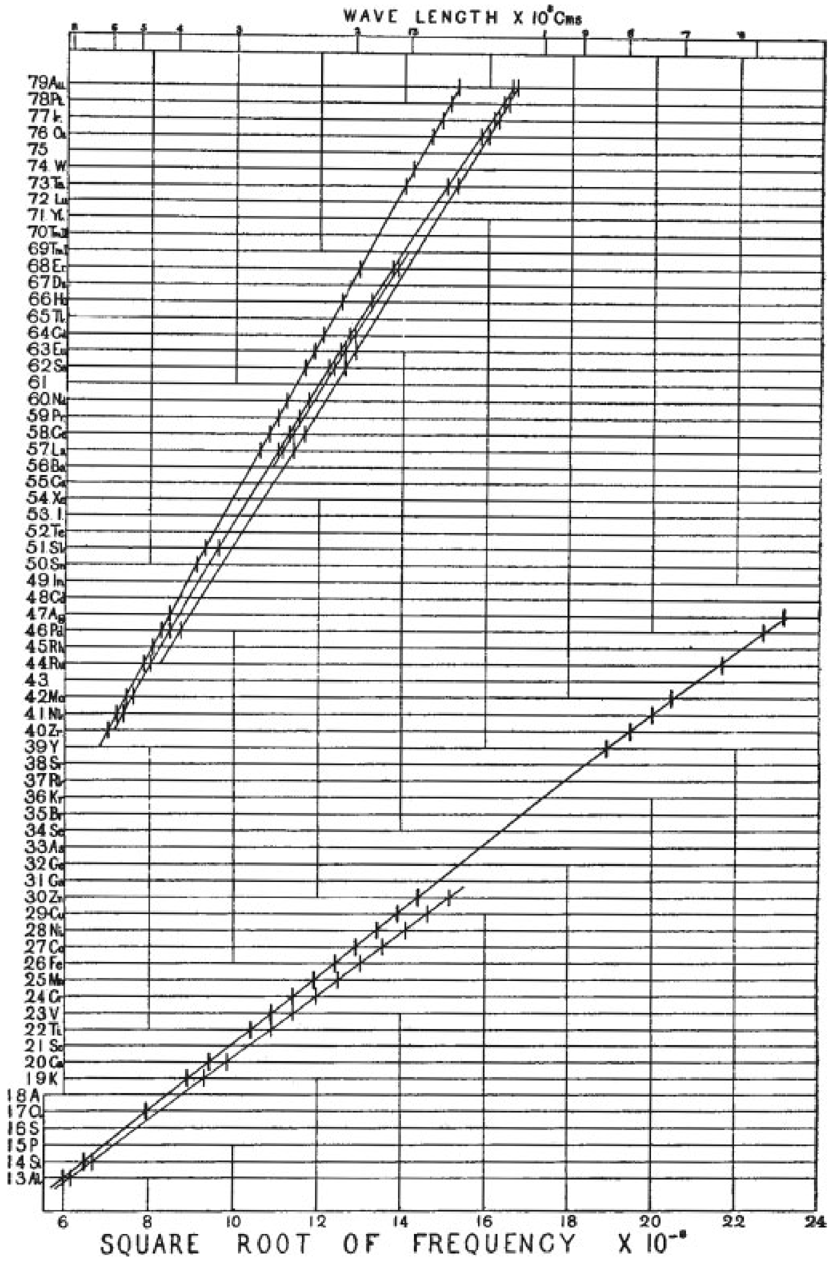

Figure 5 Plots of the square root of the characteristic X-ray frequencies of the elements against their atomic number. Published by Henry Moseley in 1914[28]

cerium through ytterbium in a box within a box. The reason for their singular behavior became clear a few years later when it was realized that in these elements the inner 4f orbitals were being successively filled with electrons. The outer, valence electrons are largely unaffected by this and so all of these elements exhibit remarkably similar chemical behavior.

The elements Bohr had placed in a double box became known as the lanthanides (or lanthanons) because they followed directly after element 57 (lanthanum). Bohr's ideas sparked considerable debate and nowadays element 71 (lutetium) is included among the lanthanides, this being the element at which the 4f orbitals became completely filled. Moreover, there remains some uncertainty whether the element lanthanum itself should be regarded as a lanthanide. From Bohr's periodic table in Figure 6 it can be seen that he left an additional double box for another series of elements that he believed would be analogous to the lanthanides. As he was not sure where this second series might begin, he placed it immediately after element 92 (uranium). However, in 1944, Glenn Seaborg (1912–1999) reconsidered this positioning and decided[33] that the series should start after element 89

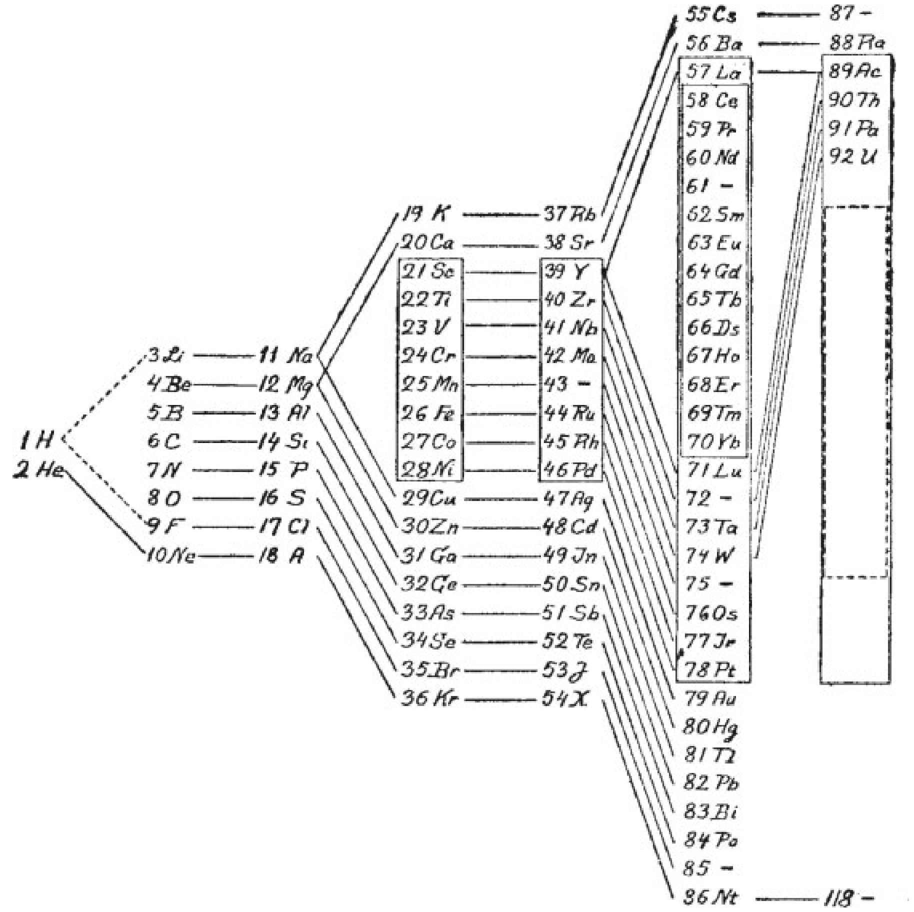
1 H
2 He
3 Li
4 Be
5 B
6 C
7 N
8 O
9 F
10 Ne
11 Na
12 Mg
13 Al
14 Si
15 P
16 S
17 Cl
18 A
19 K
20 Ca
21 Sc
22 Ti
23 V
24 Cr
25 Mn
26 Fe
27 Co
28 Ni
29 Cu
30 Zn
31 Ga
32 Ge
33 As
34 Se
35 Br
36 Kr
37 Rb
38 Sr
39 Y
40 Zr
41 Nb
42 Mo
43 –
44 Ru
45 Rh
46 Pd
47 Ag
48 Cd
49 Jn
50 Sn
51 Sb
52 Te
53 J
54 X
55 Cs
56 Ba
57 La
58 Ce
59 Pr
60 Nd
61 –
62 Sm
63 Eu
64 Gd
65 Tb
66 Ds
67 Ho
68 Er
69 Tm
70 Yb
71 Lu
72 –
73 Ta
74 W
75 –
76 Os
77 Jr
78 Pt
79 Au
80 Hg
81 Tl
82 Pb
83 Bi
84 Po
85 –
86 Nt
87 –
88 Ra
89 Ac
90 Th
91 Pa
92 U
118 –

Figure 6 The periodic table of the elements put forward by Niels Bohr in his book *The Theory of Spectra and Atomic Constitution* in 1922[32]

(actinium). The series thus became known as the actinides and there are again 14 of them because in these elements the 5f orbitals are being filled. This series started with the known elements 90 (thorium), 91 (protactinium) and 92 (uranium) and thereafter the elements had to be synthesized beginning with element 93 (neptunium) in 1940[34] and ending with element 102 (lawrencium) in 1961.[35] Several reviews on the synthesis of transuranic elements are now available.[33,36,37] After element 122, it is now generally thought that yet another special series known as the superactinides begins with the filling of the 6f orbitals, but this is a story that remains to be told.

8 FURTHER READING

J. Emsley, 'Nature's Building Blocks: An A–Z Guide to the Elements', Oxford University Press, Oxford, 2001.

D. C. Hoffman, A. Ghiorso, and G. T. Seaborg, 'The Transuranium People: The Inside Story', Imperial College Press, London, 2000.

D. H. Rouvray and R. B. King, eds., 'The Periodic Table: Into the Twenty-First Century', Research Studies Press, Baldock, Herts, UK, 2004.

J. W. van Spronsen, 'The Periodic System of Chemical Elements: A History of the First Hundred Years', Elsevier, Amsterdam, 1969.

9 REFERENCES

1. J. R. Partington, 'A History of Chemistry', Macmillan, London, 1970, Vol. 1, p. 55.
2. T. Lucretius Carus, in 'De Rerum Natura (On the Nature of Things)', ed. M. F. Smith, Hackett, Indianapolis, IN, 2001, Book 1, p. 22.
3. D. Knight, 'Ideas in Chemistry: A History of the Sciences', Rutgers University Press, New Brunswick, NJ, 1992, Chap. 2.
4. J. Kepler, 'Harmonices Mundi (The Harmonies of the World)', Plank, Linz, 1619.
5. C. Meinel, *Sudhoffs Archiv*, 1982, **66**, 313.

6. R. Boyle, ‘The Sceptical Chymist’, Caldwell, London, 1661, Reprinted in 1911 and 1964 by Dent, London, Part 6, p. 187.
7. A.-L. Lavoisier, ‘Traité Élémentaire de Chimie’, Cuchet, Paris, 1789; R. Kerr, ed., ‘Elements of Chemistry’, Creech, Edinburgh, 1790, p. 175.
8. J. Dalton, *Mem. Manchester Lit. Philos. Soc.*, 1805, **1**(2), 271; J. Dalton, ‘A New System of Chemical Philosophy’, Bickerstaff, London, 1808, Part 1, p. 212.
9. J. W. Döbereiner, *Ann. Phys. (Gilbert)*, 1817, **56**, 331.
10. J. W. Döbereiner, *Ann. Phys. (Poggendorf)*, 1829, **15**, 301.
11. L. Gmelin, ‘Handbuch der Chemie’, 4th edn., Winter, Heidelberg, 1843, Vol. 1, p. 52, p. 456.
12. M. Pettenkofer, *Gelehrte Anzeigen Akad. Wiss. München*, 1850, **30**, 165, 261.
13. J. Dumas, *C. R. Acad. Sci. Paris*, 1858, **47**, 1026.
14. W. Odling, *Philos. Mag.*, 1857, **13**(4), 423, 480.
15. S. Cannizzaro, *Nuovo Cim.*, 1858, **7**, 321.
16. A. E. Beguyer de Chancourtois, *C. R. Acad. Sci. Paris*, 1862, **54**, 757, 840, 967.
17. J. A. R. Newlands, *Chem. News*, 1864, **10**, 94.
18. W. Odling, *Q. J. Sci.*, 1864, **1**, 642.
19. G. D. Hinrichs, ‘Programm der Atomechanik, Oder die Chemie eine Mechanik der Panatome’, Hinrichs, Iowa City, IA, 1867, p. 6; C. A. Zapffe, *Isis*, 1969, **60**, 461.
20. J. L. Mayer, *Ann. Chem. Pharm.*, 1870, **7**, 354.
21. M. D. Gordin, ‘A Well-Ordered Thing: Dmitrii Mendeleev and the Shadow of the Periodic Table’, Basic Books, New York, 2004.
22. D. I. Mendeleev, *Zhur. Russ. Fiz.-Khim. Obshch.*, 1869, **1**, 60; H. M. Leicester and H. S. Klickstein, eds, ‘A Source Book in Chemistry: 1400 – 1900’, Harvard University Press, Cambridge, MA, 1952, p. 438.
23. E. R. Scerri and J. Worrall, *Stud. Hist. Philos. Sci.*, 2001, **32**, 407.
24. C. J. Giunta, *Found. Chem.*, 2001, **3**, 105.
25. D. I. Mendeleev, *Chem. News J. Phys. Sci.*, 1879, **40**, 78.
26. F. W. Aston, *Philos. Mag.*, 1919, **38**, 707.
27. F. A. Paneth and G. von Hevesy, *Sitzung. Kaisl. Akad. Wiss. Wien*, 1914, Abt. 2A, **122**, 1037.
28. H. G. J. Moseley, *Philos. Mag.*, 1913, **26**, 1024; 1914, **27**, 703.
29. D. I. Mendeléeff, ‘The Principles of Chemistry’, 7th edn., Longmans, London, 1905, Vol. 1, p. xvii.
30. J. Thomsen, *Z. Anorg. Chem.*, 1895, **9**, 190.
31. A. Werner, *Chem. Ber.*, 1905, **38**, 914.
32. N. Bohr, ‘The Theory of Spectra and Atomic Constitution’, Cambridge University Press, Cambridge, MA, 1922, p. 70.
33. G. T. Seaborg and W. D. Loveland, ‘The Elements Beyond Uranium’, Wiley-Interscience, New York, 1990, p. 66.
34. E. M. McMillan and P. A. Abelson, *Phys. Rev.*, 1940, **57**, 1185.
35. A. Ghiorso, T. Sikkeland, A. E. Larsh, and R. M. Latimer, *Phys. Rev. Lett.*, 1961, **6**, 473.
36. S. Hofmann and G. Münzenberg, *Rev. Mod. Phys.*, 2000, **72**, 733.
37. S. Hofmann, ‘On Beyond Uranium: Journey to the End of the Periodic Table’, Taylor & Francis, London, 2002.

Hydrogen Bonding & Dihydrogen Bonding

Robert H Crabtree
Yale University, New Haven, CT, USA

1 Introduction 1
2 Nature, Structure, and Spectroscopy 1
3 Applications 2
4 Hydrogen Bonding Involving Metal Complexes 3
5 Dihydrogen Bonding 3
6 Distinction between Hydrogen Bonding and Sigma Complexation 4
7 References 5

Glossary

A–H: a weak acid, A being an electronegative element or group
B: a weak base
DHB: dihydrogen bond (A–H···H–E)
E–H: an element−hydrogen bond

1 INTRODUCTION

The hydrogen bond involves the interaction of a weak acid OH, NH, or similar bond A–H with a weak O or N or similar base, B, to give a linear adduct A–H···B (**1**). Arguably, the most important intermolecular interaction in chemistry, it is responsible for the strength of materials such as wood and spider silk and for many of the physical properties of water such as its surface tension and elevated melting and boiling points relative to its non-hydrogen-bonding analogue, H_2S. Numerous monographs have been devoted to the phenomenon since Pimentel and McClellan's[1] classic 1960 book, *The Hydrogen Bond*, including some very useful recent books.[2,3] From a historical perspective, it was Pauling's[4] celebrated 1939 book *The Nature of the Chemical Bond* that brought the hydrogen bond to the attention of a wide audience, and the early (1950s) recognition of its key role in both the protein alpha helix and the nucleic acid double helix underlined its central importance in biology.

The hydrogen bond has taken center stage with the rise of supramolecular chemistry and molecular recognition.[5,6] It constitutes one of the forces employed in this field, together with aromatic stacking, ion pairing, and coordinate bonding. Hydrogen bonding is particularly important because it is directional and undergoes rapid make and break equilibria that allow a thermodynamically stable structure to be attained rapidly. Important processes like protein folding, enzyme action, and nucleic acid strand recognition rely on these aspects of hydrogen bonding.

In a recent and specifically inorganic development (1990s), dihydrogen bonding has been recognized as a class of hydrogen bonding in which the weak acid A–H component of the hydrogen bond interacts with a hydridic element hydrogen bond H–E, to give an adduct A–H···H–E (**2**) having similar energetics to the classical A–H···B case. Its name, the dihydrogen bond, or DHB, comes from the presence of two hydrogens in close proximity.[7–9] The involvement of an inorganic E–H bond makes it particularly relevant to inorganic chemistry. The ease of calculation in such a simple system has also attracted strong theoretical interest. In spite of its recent discovery, there are already hundreds of papers on the topic. Brammer,[10] who characterized the A–H···M (**3**) hydrogen bond has reviewed the whole area of hydrogen bonding in transition metal chemistry (Scheme 1).

2 NATURE, STRUCTURE, AND SPECTROSCOPY

The hydrogen bond results from the interaction of a weak base, B, (hydrogen bond acceptor) with a weak acid, AH, (hydrogen bond donor) to give the structure A–H···B where the dotted line represents the hydrogen bond.[1–4] This is usually weaker and longer than a normal bond, the bond strength typically amounting to 4−10 kcal mol^{-1} and the bond length to about 0.2−0.7 A less than a van der Waals contact. It is the presence of the hydrogen bridge that gives it the name hydrogen bond. In the terminology of the field, the weak acid component AH is termed a hydrogen bond donor because it donates a proton, and B is likewise termed a hydrogen bond acceptor (i.e. proton acceptor). This can be confusing because in every other area of acid−base chemistry, a base is considered as a donor of a lone pair of electrons and an acid an acceptor. The hydrogen bond can be considered as a structure that results from incomplete proton transfer because AH is too weak an acid and B too weak a base to consummate the transfer. Hydrogen-bonded species are likely transient intermediates in proton transfers in general.

The interaction is predominantly electrostatic (**4**), the A–H dipole interacting with the negatively charged lone pair of electrons on B. For the interaction to be significant, both A and B have to be electronegative groups, as in the water dimer $HO–H\cdots OH_2$. The approximate linearity of the A–H···B system can be explained on the basis of the electrostatic repulsion of the A and B groups (or as the preferential approach of B along the A–H σ^* direction). This type of hydrogen bond typically shows a double minimum potential energy well as in the case of $[PhO–H\cdots OPh]^-$, where by symmetry the proton can be transferred to the phenolate ion base to give $[PhO\cdots H–OPh]^-$.

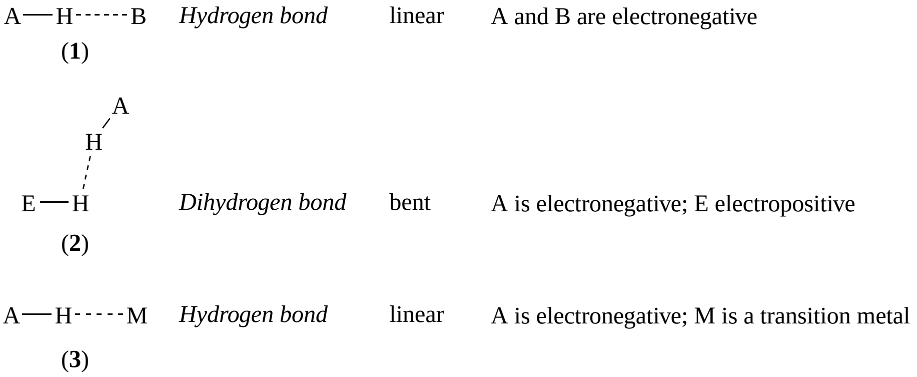
A—H------B
(1)
Hydrogen bond
linear
A and B are electronegative
A
H
E—H
(2)
Dihydrogen bond
bent
A is electronegative; E electropositive
A—H-----M
(3)
Hydrogen bond
linear
A is electronegative; M is a transition metal

Scheme 1 Types of hydrogen bonds

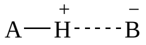

$\overset{+}{A{-}H}\cdots\overset{-}{B}$

(**4**)

$F{-}H{-}F$

(**5**)

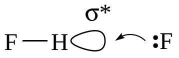

(**6**)

A class of strong hydrogen-bonded species has a single symmetrical potential energy well, leading to a symmetrical structure; these have a high covalent contribution to the bonding. The outstanding example of a strong hydrogen bond is the bifluoride ion, $[F–H–F]^-$ (**5**). The bond lengths are now only slightly longer than in HF itself and the hydrogen bond strength (27 kcal mol^{-1}) becomes very large. In such a case, the covalency of the H–F bonds becomes significant, and the bonding can be considered to involve donation from the F^- lone pair into the HF σ^* orbital (**6**). This is exactly analogous to the bonding situation found in hypervalent main group species such as SF_6, where the F^- lone pair donates into the σ^* orbital of the SF bond trans to itself; another way to view the bifluoride ion is therefore as an example of a hypervalent 2-coordinate 4-electron hydrogen. When hypervalency was believed to require d orbital participation, such an identification would have been unacceptable but modern theories**[11]** of hypervalency have abandoned this old idea of d-participation. Disorder in the crystal containing $[X–H\cdots X]^-$ can lead an unsymmetrical hydrogen bond to appear symmetrical, so care needs to be taken in the interpretation of structural data. Neutron diffraction provides the most reliable data. Interesting metal bifluoride complexes are now known.**[12]**

Because of the soft potential of hydrogen bonds relative to normal bonds, deformations can occur in crystals where the presence of other forces can lead to problems in trying to estimate relative hydrogen bond strengths from the observed bond lengths.**[13]** A good example of hydrogen bond lengths in an inorganic species not following bond strengths is given by Brammer.**[10]** Use of X-ray structural data leads to a systematic error in the H distances, and A–H distances are therefore normalized to their expected neutron diffraction distance before estimating the $H\cdots B$ bond length. Ideally, neutron-diffraction structures are used to characterize important new examples of hydrogen bonding.

Spectroscopic methods are useful for characterization. The A–H stretching frequency in the IR spectrum typically falls on hydrogen bond formation and the AH proton resonance also shifts to high field. Where A or B has a nuclear spin (e.g. ^{19}F), the coupling constant between A or B and H can be used as long as exchange is not too rapid. For example, in the gas phase, HF has an H,F coupling constant near 600 Hz, but in amine$\cdots$H–F adducts, this value falls to about 450 Hz.**[14]**

3 APPLICATIONS

Along with aromatic stacking and hydrophobic forces, hydrogen bonds are applied widely in supramolecular chemistry.**[15]** For example, $N–H\cdots X$ hydrogen bonds are commonly used in anion receptor molecules (X = anion) such as catapinates**[16]** and isophthalamides,**[17]** and in crystal engineering.**[18]** Etter's rules**[19]** have been used to try to rationalize hydrogen bonding patterns in crystals. Anion receptors such as (**7**), based on redox-active metal complexes, have been used for anion sensing.**[20]** Much of this work relates more to organic than inorganic chemistry, however, so in what follows we concentrate on the inorganic applications.

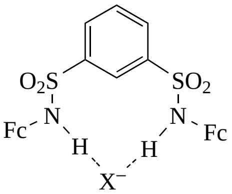

[Fc = ferrocenyl]

(**7**)

4 HYDROGEN BONDING INVOLVING METAL COMPLEXES

In inorganic chemistry, interest has centered recently on unconventional hydrogen bonds of different sorts. For example, it has proved possible to replace both the AH and B components of the A–H···B system by inorganic groups. Substitution of the hydrogen bond acceptor (weak base) has been the most common. Several classes of substitution have proved successful where the weak base is: (1) a metal-based nonbonding pair of electrons or (2) a lone pair of a ligand bound to the metal or (3) an M–H bond (see Section 5). In case 2, the classical hydrogen bond lone pair is still present, in case 1 it is replaced by a metal-based nonbonded electron pair, but in case 3 no lone pair is involved at all and the base is a bonding electron pair.

A–H···M hydrogen bonds (type 1, **3**) were studied by Brammer,[10] who used neutron diffraction to unambiguously characterize the structure. An example is (**8**). Basic metal centers that can protonate with strong acids are particularly likely to show hydrogen bond structures with weak acids. The AHM system is linear and A is an electronegative element, as in the classical hydrogen bond.

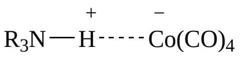

$$R_3N-\overset{+}{H}\text{-----}\overset{-}{Co}(CO)_4$$

(**8**)

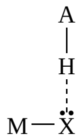

(**9**)

A–H···X–M hydrogen bonds[7,8] (type 2, **9**) have been seen on numerous occasions. Brammer[10] has again done much to characterize these interactions structurally. The M–X···H angle is usually bent because of the presence of sp^3 (F) or p (Cl–I) lone pairs; the preferred angle is smaller for Cl–I than for F. A cis MX_2 unit is a particularly good hydrogen bond acceptor because an approach of the AH between the two X groups allows interaction with both X groups within the favorable range of angles.

Intramolecular proton transfer is also possible via a hydrogen-bonded form in the case shown in equation (1), where the size of the L groups determines which isomer is stabler.[21] This arises from ion pairing with the counterion, as shown by combined theoretical/experimental studies. If L is small (e.g. PMe_2Ph), the anion can bind close to the metal at the preferred binding site and the H_2 complex is formed. If this site is blocked by employing a large L (e.g. PPh_3 or $P(cyclohexyl)_3$), then the anion binds at the remote $-NH_3^+$ site, in which case proton transfer occurs to make this site a better anion acceptor. The same system can stabilize HF binding (**10**), where the F–H···N hydrogen bond is essential to stabilization of the complex; the high J_{HF} of 440 Hz, observed by NMR spectroscopy at low temperature, identifies the species as having an H–F bond.

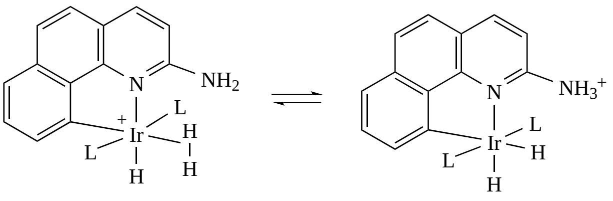

(1)

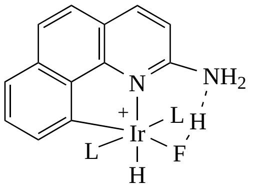

(**10**)

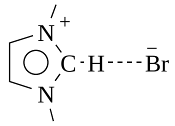

(**11**)

The usual OH or NH acid component of the hydrogen bond can be replaced by an acidic CH, as in the acid 2-position of an imidazolium salt (**11**) where the anion forms an ion pair, aided by the accompanying hydrogen bond. Ion pairing of this sort has been shown to strongly influence the outcome of metallation reactions of imidazolium salts to give normal (C2) versus abnormal (C4,5) metallated carbenes, depending on the strength of hydrogen bonding.[22]

The area of hydrogen bonding in inorganic chemistry has seen a great increase in activity in the last decade and may even find application in homogeneous catalysis in the years to come. In metal-free 'organocatalysts', hydrogen bonding clearly plays a dominant role.[23]

5 DIHYDROGEN BONDING

The possibility that a protonic and a hydridic hydrogen could show an attractive interaction was first raised[24] (1990) in relation to Milstein's complex, *cis*-$[L_4Ir(OH)H]BF_4$, where the OH was pointing towards the adjacent Ir–H. The HH distance, d_{HH}, was a long 2.4 Å, however, equal to the sum of the covalent radii for two H atoms, so the interaction was clearly weak. Later theoretical work[25] showed that this species does not contain a true hydrogen bond, but the general principle suggested in the 1990 work was nonetheless valid even if the particular example was flawed. In the same year, a very close d_{HH} (1.86 Å) was seen by neutron diffraction in a $[L_3Ru(H_2)H_2]$ species (**12**), where the acidic H_2 ligand interacts with the cis Ru–H group.[26] The origin of this effect was correctly identified as the attraction of oppositely charged H atoms. This complex was therefore the first authentic example of the effect.

The concept of the proton−hydride interaction or dihydrogen bonding (DHB) was generalized by Morris[27]

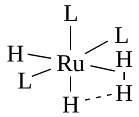

[L = PEt$_2$Ph]

(**12**)

and by Crabtree[28,29] from 1994, who described a series of compounds in which a variety of OH and NH bonds interact with metal hydrides, in both intra- and intermolecular fashion. The d_{HH} values typically associated with such structures proved to range from 1.7–2.1 Å. A particularly convincing case was the neutron-diffraction structure of the adduct [$ReH_5(PPh_3)_2$·indole], where the indole NH was found to be very close (1.753 Å) to one of the ReH hydrides.[30] Being an intermolecular adduct, one could no longer consider that the two H atoms were merely being forced into apparent association by conformational forces. Subsequent work has shown that in many cases, a dihydrogen-bonded adduct can form in solution, but on crystallization, the pure hydride crystallizes without the Lewis acid component. $ReH_5(PPh_3)_2$ and indole were specifically chosen for this work because they crystallize poorly; indeed, indole is a liquid.

One possible ambiguity with the interpretation of the DHB as a proton–hydride attraction was still unresolved, however. Transition metals of the type mentioned above have nonbonding d_π electron pairs, analogous to lone pairs, pointing toward the A–H group. There was still legitimate doubt about whether these compounds were just special examples of A–H· · ·M systems (type 2) since the main interaction might be with a 'lone pair' on the metal, not with the M–H bond. Such interactions, mentioned in Section 4, do indeed genuinely exist. To remove this ambiguity,[31] BH_3NH_3 was studied by a variety of techniques with the conclusion that exactly the same type of bond exists in this species where there are no lone pairs as in [$ReH_5(PPh_3)_2$·indole]. The interaction was therefore termed the dihydrogen bond to emphasize this point.

Just as proton transfer within A–H· · ·B gives A^- and BH^+, proton transfer within A–H· · ·H–M gives A^- and (H_2)–M^+, a dihydrogen complex. Cases are even known (equation 2) where proton transfer occurs to the hydride initially, followed by rearrangement to the more stable dihydride form.[32] The kinetic product being an (H_2)–M species is consistent with protonation requiring a hydrogen bond adduct as an intermediate and with this adduct being of the A–H· · ·H–M type.

$$\text{Cp*FeH(dppe)} + \text{H}^+ \xrightarrow{-80\,^\circ\text{C}} \text{Cp*Fe(H–H)(dppe)}^+ \xrightarrow{\text{warm}} \text{Cp*Fe(H)}_2\text{(dppe)}^+ \quad (2)$$

Applications of dihydrogen bonding have been reported. Jackson[9] has shown how the attack of borohydride on a hydroxyketone shows a high selectivity for hydride addition from the same face of the ketone as the OH group is located. He showed that the BH_4 anion interacts with the OH via a DHB (**13**) by blocking the effect with a F anion and by demonstrating that no borate ester is formed under the conditions used. Dihydrogen-bond-promoted catalysis has recently been seen in the catalytic hydration of nitriles with an indenylruthenium hydride complex, [(η^5-C_9H_7)Ru(dppm)H] (dppm = bis(diphenylphosphino)methane). In this reaction, water is proposed to bind to Ru–H as Ru–H· · ·H–O–H, causing the water oxygen to be correctly placed for a nucleophilic attack at the nitrile carbon.[33]

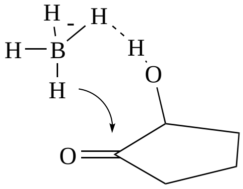

(**13**)

Weak C–H· · ·H–M dihydrogen bonds have been proposed in a number of PPh_3-substituted hydride complexes, to account for the abnormally close (1.6–2.1 A) contacts very commonly found in these species.[34]

6 DISTINCTION BETWEEN HYDROGEN BONDING AND SIGMA COMPLEXATION

In an inorganic context, there are two possible types of E–H–M bridge (E = element). The two cases need to be carefully distinguished.[35] In a hydrogen bond,[9] EH contains an electronegative element, typically NH or OH, but an activated CH bond is possible. The geometry is linear (**14**) and the EH proton shows a low-field proton NMR shift on adduct formation, just as in classical hydrogen bonds.

Sigma complexes,[36–38] including agostic and dihydrogen complexes, also have an E–H–M bridge, but E is a less electronegative element, typically, H, C, B, or M. The bridge is bent, as EH binds side-on to M (**15**), and the H shows a high-field proton NMR shift on adduct formation.

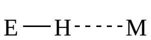

(**14**)

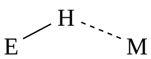

(**15**)

Hydrogen bonds contain linear 4e,3-center E–H–M bridge bonds with hypervalent hydrogen, while sigma complexes contain bent 2e,3-center E–H–M bridge bonds with electron-deficient hydrogen. In the former, the metal acts as a weak base, while in the latter it acts as a weak acid. In principle, intermediate situations are possible where both interactions compete but information is still sparse in this area.

7 REFERENCES

1. G. C. Pimentel and A. L. McClellan, ‘The Hydrogen Bond’, Freeman, San Francisco, 1960.
2. G. A. Jeffrey and W. Saenger, ‘Hydrogen Bonding in Biological Structures’, Springer, Berlin, 1991.
3. G. A. Jeffrey, ‘An Introduction to Hydrogen Bonding’, Oxford University Press, Oxford, 1997.
4. L. Pauling, ‘The Nature of the Chemical Bond’, Cornell University Press, Ithaca, New York, 1939.
5. J.-M. Lehn, ‘Supramolecular Chemistry: Concepts and Perspectives’, VCH, Weinheim, New York, 1995.
6. H. J. Schneider and A. Yatsimirsky, ‘Principles & Methods in Supramolecular Chemistry’, Wiley, New York, 2000.
7. R. H. Crabtree, *Science*, 1998, **282**, 2000, refs cited.
8. R. H. Morris, *Can. J. Chem.*, 1996, **74**, 1907.
9. R. Custelcean and J. E. Jackson, *Chem. Rev.*, 2001, **101**, 1963.
10. L. Brammer, *J. Chem. Soc., Dalton Trans.*, 2003, 3145.
11. A. E. Reed and P. V. Schleyer, *J. Am. Chem. Soc.*, 1990, **112**, 1434.
12. N. A. Jasim and R. N. Perutz, *J. Am. Chem. Soc.*, 2000, **122**, 8685.
13. D. Braga, F. Grepioni, and J. J. Novoa, *Chem. Commun.*, 1998, 1959.
14. B. Patel, D.-H. Lee, A. L. Rheingold, and R. H. Crabtree, *Organometallics*, 1999, **18**, 1615.
15. J. W. Steed and J. L. Atwood, ‘Supramolecular Chemistry’, Wiley, New York, 2001.
16. C. H. Park and H. E. Simmons, *J. Am. Chem. Soc.*, 1968, **90**, 2431.
17. K. Kavallieratos, S. R. de Gala, D. J. Austin, and R. H. Crabtree, *J. Am. Chem. Soc.*, 1997, **119**, 2325.
18. D. Braga, F. Grepioni, and G. R. Desiraju, *Chem. Rev.*, 1998, **98**, 1375.
19. M. C. Etter, *Acc. Chem. Res.*, 1990, **23**, 120.
20. P. D. Beer and P. A. Gale, *Angew. Chem., Int. Ed. Engl.*, 2001, **40**, 487.
21. K. Gruet, E. Clot, O. Eisenstein, D. H. Lee, B. Patel, A. Macchioni, and R. H. Crabtree, *New J. Chem.*, 2003, **27**, 80.
22. A. Kovacevic, S. Gründemann, J. R. Miecznikowski, E. Clot, O. Eisenstein, and R. H. Crabtree, *Chem. Commun.*, 2002, 2580.
23. P. R. Schreiner, *Chem. Soc. Rev.*, 2003, **32**, 289.
24. R. C. Stevens, R. Bau, D. Milstein, O. Blum, and T. F. Koetzle, *Dalton. Trans.*, 1990, 1429.
25. M. J. Calhorda and P. E. M. Lopes, *J. Organomet. Chem.*, 2000, **609**, 53.
26. L. S. Vandersluys, J. Eckert, O. Eisenstein, J. H. Hall, J. C. Huffman, S. A. Jackson, T. F. Koetzle, G. J. Kubas, P. J. Vergamini, and K. G. Caulton, *J. Am. Chem. Soc.*, 1990, **112**, 4831.
27. S. H. Park, R. Ramachandran, A. J. Lough, and R. H. Morris, *Chem. Commun.*, 1994, 2201.
28. J. C. Lee, E. Peris, A. L. Rheingold, and R. H. Crabtree, *J. Am. Chem. Soc.*, 1994, **116**, 11014.
29. R. H. Crabtree, P. E. M. Siegbahn, O. Eisenstein, A. L. Rheingold, and T. F. Koetzle, *Acc. Chem. Res.*, 1996, **29**, 348.
30. B. P. Patel, J. Wessel, W. B. Yao, J. C. Lee, E. Peris, T. F. Koetzle, G. P. A. Yap, J. B. Fortin, J. S. Ricci, G. Sini, A. Albinati, O. Eisenstein, A. L. Rheingold, and R. H. Crabtree, *New J. Chem.*, 1997, **21**, 413.
31. W. T. Klooster, T. F. Koetzle, P. E. M. Siegbahn, T. B. Richardson, and R. H. Crabtree, *J. Am. Chem. Soc.*, 1999, **121**, 6337.
32. P. Hamon, L. Toupet, J. R. Hamon, and C. Lapinte, *Organometallics*, 1992, **11**, 1429.
33. W. K. Fung, X. Huang, M. L. Man, S. M. Ng, M. Y. Hung, Z. Lin, and C. P. Lau, *J. Am. Chem. Soc.*, 2003, **125**, 11539.
34. T. B. Richardson, T. F. Koetzle, and R. H. Crabtree, *Inorg. Chim. Acta*, 1996, **250**, 69.
35. W. B. Yao, O. Eisenstein, and R. H. Crabtree, *Inorg. Chim. Acta*, 1997, **254**, 105.
36. M. Brookhart, M. L. H. Green, and L. L. Wong, *Prog. Inorg. Chem.*, 1988, **36**, 1.
37. R. H. Crabtree, *Angew. Chem., Int. Ed. Engl.*, 1993, **32**, 789.
38. G. J. Kubas, ‘Metal Dihydrogen and Sigma Bond Complexes’, Kluwer, Amsterdam, 2001.

Dihydrogen Complexes & Related Sigma Complexes

Robert H. Crabtree
Yale University, New Haven, CT, USA

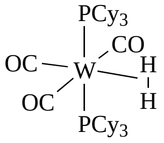

(**1**)

1 Introduction 1
2 Structure and Bonding 2
3 Spectroscopy 3
4 Dynamics and Energetics 3
5 Synthesis 4
6 Reactions 4
7 Other Sigma Complexes 5
8 Related Articles 5
9 References 5

Glossary

Dihydrogen complex: complex of H_2 which retains the H–H bond
Nonclassical hydride: hydride with H···H interactions, for example an H_2 complex
Polyhydride: complex of the type L_nMH_x ($x > 3$)

1 INTRODUCTION

The Kubas[1] dihydrogen complex (1984), $[W(H_2)(CO)_3(P\{C_6H_{11}\}_3)_2]$ (**1**) was the first recognized example of simple dihydrogen binding to a metal without cleavage of the H–H bond or other subsequent process taking place. It was important because the $M(H_2)$ bond provides the simplest and clearest cut case of a σ-complex,[1,2] one in which a sigma bonding electron pair acts as the donor to a metal in a coordination complex. The field of coordination chemistry originated with lone pair donor ligands (e.g. Cl^-, NH_3). The recognition from the 1950s that ligand π-bonding electrons (e.g. $C_5H_5^-$) could also donate to a metal in a complex led to the development of organometallic chemistry. Although σ-complexes were first seen in the 1970s, they were not given special attention until the 1980s, a development that was strongly accelerated by the discovery of complex (**1**). There are now (2004) well over a thousand papers on H_2 complexes.

These complexes are sometimes called 'nonclassical' hydrides because prior classical hydrides always had terminal M–H bonds or M–H–M bridges. Dihydrogen complexes are often indicated using the notation $M(\eta^2\text{-}H_2)$ or $M(H_2)$. The early examples all had H···H distances, d_{HH}, below 1 Å, and most had d_{HH} in the range 0.8–0.9 Å. Only later[3] did it become clear that rare examples of dihydrogen complexes have H···H distances much longer than this, typically in the range $d_{HH} = 1.1–1.5$ Å.[4] These 'stretched' or 'elongated' dihydrogen complexes are clearly on the way to forming dihydrides where the 'nonbonding' H···H distances are typically above 1.6 Å.

A very useful monograph[4] on H_2 complexes, a key resource in the field, also covers alkane and silane sigma complexes $M(\eta^2\text{-}H\text{-}XR_3)$ (X = C, Si), both fully covered in a recent review.[2]

Since H atoms are not accurately located by X-ray diffraction, and neutron diffraction studies cannot be carried out on a routine basis, spectroscopic methods have proved most useful in this area. The best way to characterize dihydrogen complexes relies on NMR spectroscopy: a large $^1J(H,D)$ of the corresponding HD complex reveals the presence of the H–D sigma bond.

Some polyhydrides, for example, $Fe(H_2)H_2L_3$ (L = a series of phosphines), are in fact nonclassical dihydrogen complexes. In such cases, rapid fluxionality can occur. The true structure (**2**, M = Fe) is not readily apparent from the resulting spectrum because all the hydrides appear equivalent. In such a case the $^1J(H,D)$ measurement is not usually useful. To cover this class of complex we[5,6] proposed the T_1 method, arguing that the close approach of two hydrogens would lead to observable changes in the NMR relaxation time. Morris[7] developed the most useful analysis of the data that even allows the d_{HH} extracted, given certain assumptions.[8] In certain cases, the ν(H–H) stretching mode can be detected in the IR spectrum.[4] While the Kubas complex was the first recognized H_2 complex, we were able to provide evidence that several polyhydrides that had been in the literature for many years were in fact also (H_2) complexes. $RuH_4(PPh_3)_3$, first reported in 1976,[9] was identified by Singleton[10] in 1976 as having a 'dihydrogen-like nature' but no physicochemical evidence was obtained until our 1986 report[11] of the T_1 data. As early as 1971, Aresta[12] had called attention to an unusual IR band in $FeH_4(PEtPh_2)_3$ not suspecting it was an H–H stretching frequency. Our T_1 data and proposal of an (H_2) complex followed in 1986. The 1990 neutron diffraction work by Caulton and Koetzle[13] settled the issue – the complex is in fact $[Fe(H_2)(H)_2(PPh_3)_3]$ (**2**, M = Fe).

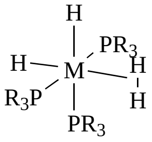

(**2**)

2 STRUCTURE AND BONDING

Following Saillard and Hoffman,[14] the bonding is generally considered to involve a Chatt-Dewar scheme with $H_2(\sigma)$ as the donor and $H_2(\sigma^*)$ as the acceptor. Some back donation is required for an isolable H_2 complex to be formed, because pure Lewis acids like $[Eu(fod)_3]$ do not give isolable adducts.

Good structural evidence comes from neutron diffraction data but this is only obtainable for a very restricted number of complexes.[13] The librational motion of the H_2 can cause problems even in neutron diffraction by making the d_{HH} seem smaller than it is. Modeling the motion more realistically gives better data.

Zilm's[15] solid-state powder NMR method, which measures the H–H dipolar coupling, is less affected by motional problems and may give a better estimate of d_{HH}. Ligand deuteriation is, however, usually needed for optimum results. The kind of accuracy that can be achieved is illustrated by the d_{HH} for Kubas complex, 0.890 ± 0.006 Å. In the absence of neutron data, X-ray diffraction has been used but its reliability is questionable for H_2 complexes. If $^1J(H,D)$ is observable in the corresponding HD complex, Morris' equation[16] can be used. This reliably relates the $^1J(H,D)$ value directly to d_{HH} (and to the bond order).

$$d_{HH}(\AA) = 1.42 - 0.0167\{J_{HD}(Hz)\} \tag{1}$$

Considering first the unstretched H_2 complex, by far the commonest class, the elongation of the H_2 on binding is rather small (from 0.74 Å in free H_2 to 0.8–0.9 Å in the complexes) consistent with the idea that the main interaction $H_2(\sigma)$ to $M(d_\sigma)$ donation, with a relatively minor contribution from $M(d_\pi)$ to $H_2(\sigma^*)$ back donation (Scheme 1). The consequence is that the H_2, depleted of negative charge in the complex, acts as an acid. Some H_2 complexes even have negative pK_a's and so are strong acids.[4]

The stretched class with $d_{HH} = 1.1–1.5$ Å are clearly associated with a much enhanced degree of $M(d_\pi)$ to $H_2(\sigma^*)$ back donation. As a consequence, the H_2 remains more nearly neutral in charge terms in the complex and is less acidic. The first such case[3] was $[ReH_5(H\cdots H)(P\{p\text{-}CH_3C_6H_4\}_3)_2]$ and a few tens of examples are now well-established.

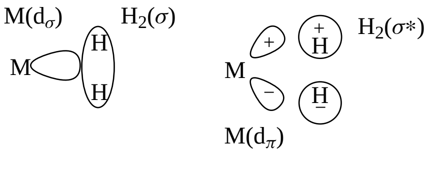

Scheme 1

Interestingly, some systems, such as (**1**) itself, show a tautomeric equilibrium between an H_2 complex and a classical dihydride form; others show a stretched H_2. In the first case we have a double minimum on the potential energy surface (PES) (H_2 and dihydride) and in the other a single minimum. The difference appears to lie[3,17] in the motion of the heavy ligands that produces a barrier to the dihydrogen/dihydride tautomerism and where there are no such heavy atom rearrangements, the barrier disappears and a stretched H_2 becomes possible.

The relative simplicity of density functional theory (DFT) calculations involving H has made this area extremely well served by computational studies. Excellent reviews are available.[18–20] Oxidative addition of H_2 can proceed with low or zero barrier for the most exothermic reactions. In contrast to $Pt + H_2$ that gave a low barrier oxidative addition of this sort, the $Pd + H_2$ system was shown to have a stable $Pd(H_2)$ in matrix in 1986.[21]

The energy difference between (H_2) and $(H)_2$ forms has been related to the singlet triplet (S/T) gap in the metal fragment. A small S/T gap favors the (H_2) form because H_2 complexation requires the S form while oxidative addition involves the T form.

Recent Mossbauer data suggests H_2 can be a better back bonder than originally thought.[22]

The ligand trans to the H_2 plays a key role. High trans effect ligands like CO or H are most effective in promoting the H_2 form. In $[IrHCl_2(H_2)(PR_3)_2]$, the d_{HH} increases from ca. 0.8 to 1.4 Å on moving from the isomer with Cl trans to (H_2) to that with H trans to (H_2).[23]

According to the valence bond order concept as applied to the case of stretched H_2 complexes by Limbach,[24] there is a significant H–H bond order p_{HH} even at $d_{HH} = 1.6$ Å, implying that stretched dihydrogen complexes are not usefully considered as 'compressed dihydrides'.

Stretched H_2 complexes are often poorly modeled in DFT work because the PES is very flat. Lluch and Lledos[25] combined DFT with nuclear motion calculations to suggest that the time-averaged d_{HH} should be temperature dependent, explaining the unusual temperature dependence of the J_{HD} in $[Cp^*Ru(H_2)dppm]^+$, and the isotope dependence of J_{HT} and J_{DT} values.[26]

Eisenstein[27] showed computationally that there is a cis interaction in $[Fe(H_2)(H)_2(PEtPh_2)_3]$ (**2**, M = Fe) by which a protonic H of the H_2 ligand is attracted to a hydridic H of a cis-terminal hydride. This can now be seen as an example of a 'dihydrogen bond'.

Finally, Eisenstein[28] was also able to show that the H_2 splitting reaction in equation (2) was governed by the ability of the counterion to ion pair. For small PR_3, this ion pairing takes place at the coordinated H_2. For large PR_3, the ion pairing occurs at the more remote pendant NH_2, in which case the proton transfer occurs to minimize charge separation in the low dielectric solvent used (CD_2Cl_2).

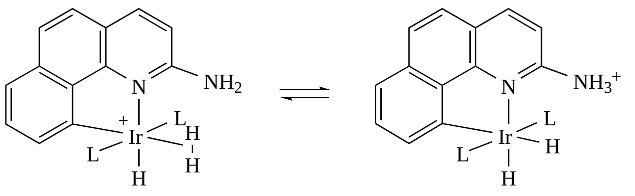

(2)

3 SPECTROSCOPY

As a result of the close approach of the two H atoms, the T_1 relaxation of an H_2 complex can be very much shorter than that of the other resonances. The H_2 resonance can be broad – often even broader than the T_1 value would lead one to expect.[29] In such cases it now seems likely that tight ion pairing with the F-rich counterion may be responsible for the excess broadening via unresolved coupling to ^{19}F.

The short T_1 allows the H_2 signal to be selectively nulled by a suitable inversion recovery sequence. Such a study allowed Kubas *et al.*[1,4] to observe the full hydride NMR spectrum of the minor tautomer, $[W(H)_2(CO)_3(P\{C_6H_{11}\}_3)_2]$ at $-82\,°C$ ($T_1 = 1.7\,s$), which was normally obscured by that of the major species, $[W(H_2)(CO)_3(P\{C_6H_{11}\}_3)_2]$ ($T_1 = 4\,ms$). Where alternative H sites are present, fast exchange usually occurs on the NMR timescale, and it can be hard to correctly identify the situation. If the complex is partially deuterated, the light isotope shows a marked preference for the site with the softer vibrational potential. Deuterium therefore prefers classical sites in complexes of type $[L_nM(H_2)_xH_y]$ because of zero point energy differences and this can lead to isotope perturbation effects[12] even in the high-temperature limit where site exchange is fast; these effects are magnified when tritium partial labeling is employed. Each isotopomer now resonates at a different chemical shift and analysis of the temperature dependence of the signals allows the chemical shifts associated with each site to be deduced.[30]

Normally, an H_2 ligand rotates too fast about the $M-(H_2)$ bond for separate rotamers to be observable. In d^2 complexes, however, where only one d orbital is available, back donation is only possible in one plane but not at right angles to that plane. This means that the H_2 loses all the back donation stabilization when it has rotated 90° from its preferred conformation. This in turn provides a significant rotation barrier leading to the phenomenon of blocked rotation, detected by Chaudret and Sabo-Etienne[31] in compounds of the type $[Cp_2TaH_2L]^+$ (**3**), where barriers of up to $11\,kcal\,mol^{-1}$ were found.

Apart from NMR studies, IR data has been the next most useful technique in the area. The selection rules normally forbid $\nu(HH)$ from having significant intensity, but in some cases, such as (**1**), the vibration can gain intensity from mixing with allowed bands such as $\nu(CO)$. Raman studies have generally been disappointing since the irradiation commonly leads to decomposition, but success has been achieved in some cases.[32]

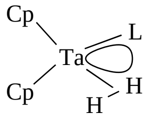

(**3**)

An η^2-HD complex has an IR spectrum that is not simply a superposition of that for the η^2-D_2 as would be the case for the classical $M(H)_2$ analogues. Instead ν(H–D) of the HD complex appears approximately halfway between the corresponding ν(H–H) and ν(D–D). The $\nu(H_2)$ stretching band, typically appearing near 2700 cm, does not correlate with binding strength because of extensive mixing of the many modes.

4 DYNAMICS AND ENERGETICS

The dynamics of $M(H_2)$ systems have been probed in detail by Eckert[33,34] using inelastic neutron scattering (INS), which is sensitive to the small rotational barriers, typically $1-2\,kcal\,mol^{-1}$, involved in unstretched d^6 H_2 complexes. The method also gives an indication of any differential back donation as the H_2 rotates, because the $M–H_2$ sigma bonding does not contribute to the barrier. From theoretical work,[35] some H_2 complexes can have somewhat higher rotation barriers (e.g. $4.8\,kcal\,mol^{-1}$) for $Cr(H_2)_2(CO)_4$ but these are in a range that no current experimental method can probe effectively. Even symmetrical H_2 complexes can have small barriers[4] (e.g. $0.7\,kcal\,mol^{-1}$ for *trans*-$Mo(H_2)CO(dppe)_2$) that are probably related to the small rearrangements of the heavy ligands that accompany H_2 rotation. A more sophisticated model[34] that takes account of additional H_2 motion is required to fully account for the INS data.

In the case of unstretched H_2 complexes, the H_2 binding energy, obtained by time-resolved IR spectroscopy or photoacoustic spectroscopy, lies in the range $\Delta H = 10-20\,kcal\ mol^{-1}$, and is comparable to that of relatively weak ligands like N_2 or H_2O.[4] For stretched complexes like $[Os(H_2)(NH_3)_4L]^{n+}$, calculations[36] predict much larger values in the range $23-50\,kcal\,mol^{-1}$, depending on L, that are comparable – at least at the upper end of the range – with binding energies seen in the case of full oxidative addition to give a classical dihydride. As a result, stretched H_2 ligands are not readily displaced from the metal.

Polyhydrides that contain both (H_2) ligands and terminal hydrides are often highly fluxional on the NMR timescale. This is normally thought to occur via oxidative addition of the (H_2) and rearrangement of the resulting intermediate.

Occasional suggestions of an associative mechanism via an (H_3) transition state have been made.**37** Likewise, $Cp^*Zr(H)_2$ exchanges with D_2 presumably via a transient $Cp^*Zr(H)_2(D_2)$ and an associative pathway. An oxidative addition is not available in this d^0 system.**38** These data suggest that an isolation or at least detection of an (H_3) complex, so far unknown, is feasible.

Quantum mechanical exchange coupling (QMC) is a rare but interesting property of some polyhydrides in which different terminal hydrogen ligands need to be present in different chemical environments but must not exchange fast on the NMR timescale. For example, in $[CpIr(L)(H)_3]^+$ the three H's lie in a plane with two flanking H_a sites and one H_b in the middle position and with a d_{HH} of ca. 1.68 Å.

The variable-temperature NMR spectrum shows a highly temperature-dependent coupling between the two sites.**39** The size of the coupling can attain thousands of Herz and so not a plausible value for a conventional J coupling. This has been identified by Weitekamp**40** and by Zilm**41** as a tunneling phenomenon associated with the close approach of H_a and H_b during their thermal motion. While a fully formed (H_2) intermediate is not proposed, a close approach of the two hydrogens is undoubtedly assisted by the involvement of a stretched (H_2) interaction during the close approach. Calculations support these proposals.**42**

5 SYNTHESIS

All of the synthetic methods that give hydrides can in principle also give H_2 complexes, but the great majority have so far been synthesized either (1) by H_2 addition to a 16e species or intermediate, or (2) protonation of a classical hydride. Examples are given below. In the tungsten case, the starting material has an agostic CH bond which is displaced by H_2. In the Ir case, the product avoids being Ir(VII), an unknown oxidation state for this element by becoming a bis-dihydrogen complex of Ir(III); the conversion of a classical dihydride to a dihydrogen complex can be considered as an internal redox step in which two hydrogen atoms are oxidized by 1e $(H(-1) => H(0))$ and the metal is reduced by two units.

$$[W(CO)_3(PCy_3)_2] + H_2 = [W(H_2)(CO)_3(PCy_3)_2] \qquad (3)$$

$$[IrH_5(PPh_3)_2] + HBF_4 = [IrH_2(H_2)_2(PPh_3)_2]BF_4 \qquad (4)$$

In the case of a protonation, the acid must normally have a noncoordinating counterion, like BF_4 in the above example, to avoid subsequent displacement of the H_2 by the anion. Initial protonation can take place at the hydride to give an H_2 complex, even when the proton subsequently migrates to the metal to give a classical hydride. The reason seems to be that acid (A–H) tends to form a dihydrogen bond (*see* ***Alkane Carbon–Hydrogen Bond Activation***) with the metal bound hydride (M–H) to give a structure of the type M–H···H–A, which leads to transfer of the proton to the hydride, at least initially. Likewise, coordinated H_2 is often the site of highest kinetic acidity.**43,44**

6 REACTIONS

The most striking feature of H_2 binding, at least for unstretched cases, is the astonishingly high degree of acidification that results, specially for cationic systems.**44** Free H_2 has a pK_a of ca. 35, while H_2 complexes can have pK_a's in the range 15 to -5. The acidification of hydrogen, from $pK_a = 35$ for free H_2 to a pK_a as low as -5 for the most acidic H_2 complexes, is very much greater than that for lone pair donor ligands such as OH_2. This is presumably related to the weakness of the $M-(H_2)$ bond compared to the strength of the M–H formed on deprotonation. In this case it is the weak binding of H_2 that gives rise to such a high degree of activation.

$$M\text{–}(H_2) + B = [M\text{–}H]^- + [BH]^+ \qquad (5)$$

$$(B = \text{base})$$

The acidification of H_2 may also be involved in hydrogenase action, where H_2 is believed to bind to an Fe(II) center.**4** Isotope exchange between H_2 and D_2O is catalyzed by the enzyme (*see* ***Nickel Enzymes & Cofactors***; ***Nickel: Models of Protein Active Sites***; ***Iron–Sulfur Proteins***.). Similar isotope exchange can also occur in H_2 complexes.**45**

Oxidative addition to give a classical dihydride is also a common reaction. $[W(H_2)(CO)_3(PCy_3)_2]$ is in equilibrium with about 20% of the dihydride in solution. This can lead to subsequent hydrogenolysis of M–C bonds as in the case of a cyclometallated phenylpyridine complex of Ir(III).**46**

Loss of H_2 generates an unsaturated intermediate that can be trapped by subsequent reaction, so H_2 complexes can be used as starting materials for the synthesis of the other species.

Binding energies of H_2 have been determined for several systems,**4** for example, the enthalpy of binding for Kubas complex itself is $9.4 \pm 0.9\,\text{kcal mol}^{-1}$. In this case, the H_2-OH form has an agostic CH so the enthalpy cited refers to the difference in the values for CH and H_2. Allowing for this factor, the binding energy to the 16-electron $W(CO)_3L_2$ system is estimated as $20 \pm 7\,\text{kcal mol}^{-1}$. Stretched (H_2) complexes seem to have much higher binding energies $(25-50\,\text{kcal mol}^{-1})$.

pK_a's for coordinated H_2 are normally measured by NMR measurements in THF.**47** When an (H_2) and corresponding $(H)_2$ complex are in equilibrium but have the same conjugate base, the relative acidities of the two species are governed by the equilibrium constant between them, the minor isomer being more acidic.

$$\mathrm{p}K_a\{\mathrm{M(H_2)}\} = \mathrm{p}K_a\{\mathrm{M(H)_2}\} - \log K \qquad (6)$$

For a complex with terminal H ligands and an (H_2) ligand, the pK_a's of the sites are the same because they both give the same final product. The (H_2) site is usually a better kinetic acid, however, as was shown for the Ir benzoquinolinate complex of equation (2).

This implies that protonation of the corresponding terminal hydride of the neutral complex is also kinetically preferred. Such protonation probably occurs via an intermediate in which the acid is associated with the terminal hydride in a dihydrogen bond. (*see* ***Hydrogen Bonding & Dihydrogen Bonding***)

7 OTHER SIGMA COMPLEXES[3,4]

CH bonds can bind to metals as sigma complexes. Most commonly these are agostic species, where a ligand is already held to the metal by a strong M–L bond but a CH bond somewhere in the ligand's substituents binds to the metal. These have been reviewed by Brookhart and Green.[48] Much rarer are examples of alkane complexes where only the CH bond holds the ligand to the metal (*see* ***Alkane Carbon–Hydrogen Bond Activation***). Silane sigma complexes[49] are strongly held and do not need chelation. Sigma complexes of X–Y bonds lacking at least one H are very rare.[50]

8 RELATED ARTICLES

Alkane Carbon−Hydrogen Bond Activation.

9 REFERENCES

1. G. J. Kubas, R. R. Ryan, B. I. Swanson, P. J. Vergamini, and H. J. Wasserman, *J. Am. Chem. Soc.*, 1984, **106**, 451.
2. R. H. Crabtree, *Angew. Chem., Int. Ed. Engl.*, 1993, **32**, 789.
3. L. Brammer, J. A. K. Howard, O. Johnson, T. F. Koetzle, J. L. Spencer, and A. M. Stringer, *Chem. Commun.*, 1991, 241.
4. G. J. Kubas, 'Metal Dihydrogen and Sigma Bond Complexes', Kluwer, 2001, a) Chap. 7. b) Chap. 10.
5. X.-L. Luo and R. H. Crabtree, *Inorg. Chem.*, 1990, **29**, 2788.
6. X.-L. Luo, J. A. K. Howard, and R. H. Crabtree, *Magn. Reson. Chem.*, 1991, **29**, S89.
7. K. A. Earl, G. Jia, P. A. Maltby, and R. H. Morris, *J. Am. Chem. Soc.*, 1991, **113**, 3027.
8. J. Y. Corey and J. Braddock-Wilking, *Chem. Rev.*, 1999, **99**, 175.
9. W. H. Knoth, *J. Am. Chem. Soc.*, 1968, **90**, 7172.
10. T. V. Ashworth and E. Singleton, *Chem. Commun.*, 1976, 705.
11. R. H. Crabtree and D. G. Hamilton, *J. Am. Chem. Soc.*, 1986, **108**, 3124.
12. M. Aresta, P. Giannocaro, M. Rossi, and A. Sacco, *Inorg. Chim. Acta*, 1971, **5**, 115.
13. L. S. Vandersluys, J. Eckert, O. Eisenstein, J. H. Hall, J. C. Huffman, S. A. Jackson, T. FKoetzle, G. J. Kubas, P. J. Vergamini, and K. G. Caulton, *J. Am. Chem. Soc.*, 1990, **112**, 4831.
14. J.-Y. Saillard and R. Hoffman, *J. Am. Chem. Soc.*, 1984, **106**, 2006.
15. W. A. King, X. L. Luo, B. L. Scott, G. J. Kubas, and K. W. Zilm, *J. Am. Chem. Soc.*, 1996, **118**, 6782.
16. P. G. Jessop and R. H. Morris, *Coord. Chem. Rev.*, 1992, **121**, 155.
17. R. H. Crabtree, X. Luo, and D. Michos, *Chemtracts-Inorg. Chem.*, 1991, **3**, 245.
18. F. Maseras, A. Lledos, E. Clot, and O. Eisenstein, *Chem. Rev.*, 2000, **100**, 601.
19. S. Niu and M. B. Hall, *Chem. Rev.*, 2000, **100**, 353.
20. A. Dedieu, *Chem. Rev.*, 2000, **100**, 43.
21. G. A. Ozin and J. Garcia-Prieto, *J. Am. Chem. Soc.*, 1986, **108**, 3099.
22. R. H. Morris and M. Schlaf, *Inorg. Chem.*, 1994, **33**, 1725.
23. A. Albinati, V. I. Bakhmutov, K. G. Caulton, E. Clot, J. Eckert, O. Eisenstein, D. G. Gusev, V. V. Grushin, B. E. Hauger, W. T. Klooster, T. F. Koetzle, R. K. Mcmullan, T. J. Ooughlin, M. Pelissier, J. S. Ricci, M. P. Sigalas, and A. B. Vymenits, *J. Am. Chem. Soc.*, 1993, **155**, 7300.
24. S. Grundemann, H. H. Limbach, G. Buntkowsky, S. Sabo-Etienne, and B. Chaudret, *J. Phys. Chem. A*, 1999, **103**, 4752.
25. R. Gelabert, M. Moreno, J. M. Lluch, and A. Lledos, *J. Am. Chem. Soc.*, 1998, **120**, 8168.
26. J. K. Law, H. Mellows, and D. M. Heinekey, *J. Am. Chem. Soc.*, 2002, **124**, 1024.
27. S. A. Jackson and O. Eisenstein, *J. Am. Chem. Soc.*, 1990, **112**, 7203.
28. K. Gruet, E. Clot, E. Eisenstein, D.-H. Lee, B. Patel, A. Macchioni, and R. H. Crabtree, *New J. Chem.*, 2003, **27**, 80.
29. W. Yao, J. W. Faller, and R. H. Crabtree, *Inorg. Chim. Acta*, 1997, **259**, 71.
30. W. J. Oldham, A. S. Hinkle, and D. M. Heinekey, *J. Am. Chem. Soc.*, 1997, **119**, 11028; J. K. Law, H. Mellows, and D. M. Heinekey, *J. Am. Chem. Soc.*, **124**(6), 1024.
31. S. Sabo-Etienne, V. Rodriguez, B. Donnadieu, B. Chaudret, H. A. el Makarim, J. C. Barthelat, S. Ulrich, H. H. Limbach, and C. Moise, *New J. Chem.*, 2001, **25**, 55.

32. M. Chopra, K. M. Wong, G. Jia, and N. T. Yu, *J. Mol. Struct.*, 1996, **379**, 93.
33. J. Eckert, *Spectrochim. Acta*, *Part A*, 1992, **48**, 363.
34. E. Clot and J. Eckert, *J. Am. Chem. Soc.*, 1999, **121**, 8855.
35. G. Pacchioni, *J. Am. Chem. Soc.*, 1990, **112**, 80.
36. G. B. Bacskay, I. Bytheway, and N. S. Hush, *J. Am. Chem. Soc.*, 1996, **118**, 3753.
37. X. L. Luo and R. H. Crabtree, *J. Am. Chem. Soc.*, 1990, **112**, 6912.
38. H. H. Brintzinger, *J. Organomet. Chem.*, 1979, **171**, 337.
39. D. M. Heinekey and J. M. Millar, *J. Am. Chem. Soc.*, 1990, **112**, 909.
40. D. H. Jones, J. A. Labinger, and D. P. Weitekamp, *J. Am. Chem. Soc.*, 1989, **111**, 3087.
41. K. W. Zilm and J. M. Millar, *Adv. Mag. Res.*, 1990, **15**, 163.
42. E. Clot, C. L. LeForestier, O. Eisenstein, and M. Pelissier, *J. Am. Chem. Soc.*, 1995, **117**, 1797.
43. R. H. Crabtree and M. Lavin, *Chem. Commun.*, 1985, 794.
44. M. S. Chinn and D. M. Heinekey, *J. Am. Chem. Soc.*, 1987, **109**, 5865.
45. A. C. Albeniz, D. M. Heinekey, and R. H. Crabtree, *Inorg. Chem.*, 1991, **30**, 3632.
46. A. C. Albeniz, G. Schulte, and R. H. Crabtree, *Organometallics*, 1992, **11**, 242.
47. K. Abdur-Rashid, T. P. Fong, B. Greaves, D. G. Gusev, J. G. Hinman, S. E. Landau, A. J. Lough, and R. H. Morris, *J. Am. Chem. Soc.*, 2000, **122**, 9155.
48. M. Brookhart and M. L. H. Green, *J. Organomet. Chem.*, 1983, **250**, 395.
49. U. Schubert, *Adv. Organomet. Chem.*, 1990, **30**, 151.
50. F. Maseras and R. H. Crabtree, *Inorg. Chim. Acta*, 2004, **357**, 345.

Carbon–Carbon & Carbon–Heteroatom Activation

Robert H. Crabtree
Yale University, New Haven, CT, USA

1 Introduction 1
2 CC Bond Complexes 1
3 CC Bond Activation 1
4 Halocarbon Complexes 3
5 CX Activation 4
6 Conclusion 5
7 References 5

1 INTRODUCTION

As a natural development of the intense activity in CH activation (*see* ***Alkane Carbon–Hydrogen Bond Activation***) since the 1970s, interest has arisen more recently in the closely allied area of CC activation. This process is much more difficult than CH activation and has so far been studied for its mechanistic interest rather than for any practical benefit. CX activation, on the other hand, is a major area of study because it is an initial step in many important and commercially valuable homogeneous catalytic reactions, such as Mizoroki–Heck, Suzuki–Miyaura, and Hartwig–Buchwald reactions. Here, an important practical goal is to avoid having to use the expensive iodides and bromides as ArX reagents in catalytic reactions and to work instead with chlorides and tosylates.

Activation involves binding of the intact C–C or C–X bond to the metal followed by C–C or C–X bond cleavage. The first goal is to understand how CC and CX bonds bind to metals without bond breaking. The next step is the bond breaking process itself, a step that is expected to proceed from the initial adduct. Reviews on metal binding of both halocarbons[1] and of sigma bonds[2] are available, and a book-length studies on sigma complexes[3] and on the activation[4] of a wide variety of bonds by transition metal complexes have very recently appeared.

2 CC BOND COMPLEXES

The first complex in which a CC bond was proposed to bind to a transition metal without CC cleavage was $[(C_5H_4MeEt)Ir(PPh_3)_2]^+$ (**1**). More recently, this species was shown not to have an agostic C–C bond – instead there is just a close metal-ligand contact. Two criteria were proposed to make this distinction: (1) there must be an empty orbital capable of overlap with the C–C bond in question, often leading to a distortion of the geometry at the metal, (2) there must be also some evidence, either from calculation or spectroscopic data, of weakening of the agostic C–C bond.[5] In the case of (**1**), the empty orbital is in the square plane remote from the CC bond and DFT calculations, which reproduced the geometry, showed no elongation of the vicinal CC bond.

True examples of agostic CC bonds are still extremely rare and usually occur only when the system is strongly constrained so that no CH bond is available as an alternative ligand.[6–9] Some examples are shown in diagrams (**2**–**3**).

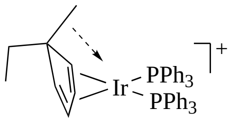

(**1**)

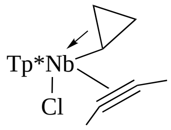

(**2**)

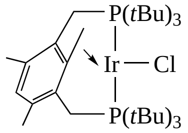

(**3**)

3 CC BOND ACTIVATION

While C–H activations are often relatively fast, C–C activations are commonly slow. This is usually ascribed to the omnidirectional character of the H(1s) orbital allowing it to form strong bonds in the transition state, as well as to the lesser steric hindrance in the C–H case.

For the late metals where M–C bonds are less strong, CC bond activation seems always to need some special driving force, such as relief of strain, chelate assistance, or attainment of an aromatic product. For early metals, M–C bonds can be much stronger and simple CC bonds can be more easily cleaved. A classic early example from Watson[10] (equation 1) requires chelate assistance but C–C cleavage can be competitive with the alternate CH bond cleavage (beta-elimination) that normally dominates:

$$Cp^*{}_2LuCH_2CHMe_2 \longrightarrow Cp^*{}_2LuMe + CH_2{=}CHMe \qquad (1)$$

Many examples of such eliminations have now been seen for the f-block and for d^0 metals.[11] This type of β-alkyl elimination is recognized as an important chain transfer step in Ziegler–Natta and metallocene polymerization catalysis.[12] When it occurs the polymer chain terminates in a C=C bond (equation 2) and in certain cases the alkene chain end can undergo reinsertion and get back into the polymer growth cycle.

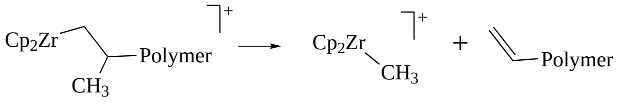

(2)

In the late metals, the classic example comes from Tipper's[13] 1955 reaction of cyclopropane with Pt(II) chloride to give a metallacyclobutane. This relies on ring strain to overcome the normally large barrier. The original formulation of the product as a simple CC bond complex of an intact cyclopropane, although plausible given the unsaturated character of the ring, proved to be incorrect; the true platinacyclobutane structure was determined by Chatt[14] with NMR and IR spectroscopic studies on the *bis*(pyridine) adduct. The platinacyclobutane product reacts with several nitrogen donor ligands (L = pyridine, 2-, 3-, and 4-methylpyridine...) to give a platinata(IV)cyclobutane derivative (equation 3). In addition to the relief of ring strain, the high reactivity of cyclopropane is associated with the fact that the C–C bond HOMO and LUMO have more p orbital character than in unstrained alkanes, which allows better interaction with the metal d orbitals.

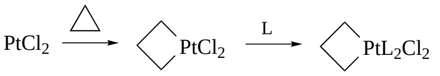

(3)

This was followed by a long series of studies in which the rearrangement of other strained organic ring systems was catalyzed by transition metal salts or complexes. A typical example is the conversion of quadricyclene to norbornadiene, catalyzed by Rh(I) or Pd(II) (equation 4),[15] for which Halpern[16] provided the accepted mechanism. An extensive review[17] of this early work is available.

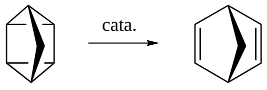

(4)

Surprisingly, mechanistic studies by Bergman *et al.* on the reaction of cyclopropane with the photogenerated Cp*Rh(PMe$_3$) fragment revealed that cyclopropane undergoes C–H activation prior to the rearrangement to a ring-opened product (equation 5).[18]

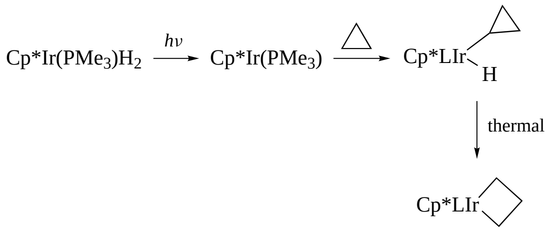

(5)

CC bonds between sp^2 carbons are more easily activated. While the Ph–Ph C–C bond is quite strong, diphenylene (**4**), with a 4-membered ring and lack of steric hindrance, allowing out-of-plane attack by the metal, readily gives CC bond cleavage[19,20] (equation 6). Even in this favorable case, temperatures of over 100 °C are often required. For example, Cr(CO)$_6$ was shown to give fluorenone at 225 °C.[21]

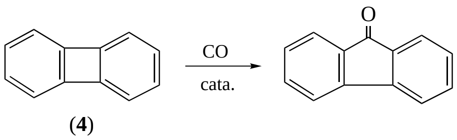

(6)

Opening of the diphenylene ring also led to a number of unusual five-coordinate complexes with a distorted structure intermediate between T- and Y-shape. The high trans effect of the phenylene rings may be part of the reason for the low-coordination number for Ir(III) (equation 7).[22]

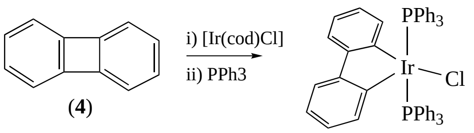

(7)

Initial insertion into an arene CH bond can be followed by CC cleavage[23] as shown in equation (8).

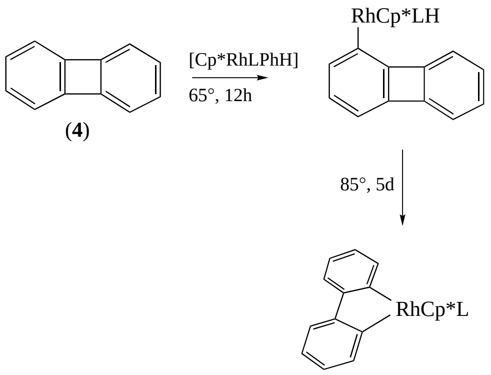

(8)

Suggs and Jun[24,25] used cyclometallation that involved *reversible* CC cleavage to achieve the reaction shown in equation (9) (R = benzyl).

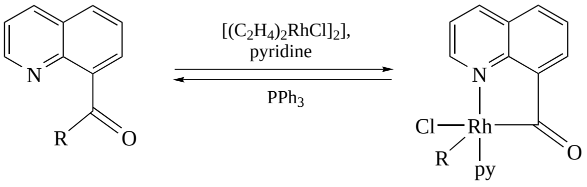

(9)

The ease of activation of CC bonds is inversely related to the bond strength: sp−sp > sp^2−sp^2 > sp^3−sp^3. This suggests that the enhanced accessibility of the sp−sp and sp^2−sp^2

bonds may facilitate reaction. Indeed, the CC bonds in the Suggs examples were often sp^2–sp, easier to activate than sp^3–sp^3.[25] Jun[26,27] has used this general principle to effect some conversions that have promise for application in organic synthesis. Milstein[28–30] found chelate-assisted examples with Rh(I) and Ir(I).

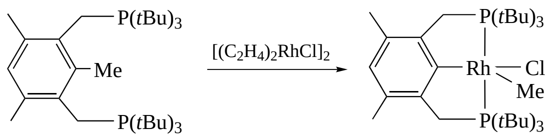

(10)

Aromatization of a cyclopentadiene to a cyclopentadienyl can occur with CC bond breaking.[31] Green reported an interesting reversible migration of an ethyl group from a cyclopentadienyl ring to a Mo metal, resulting in aromatization of the ring. The energy gain from the formation of the aromatic Cp must add 25 kcal mol^{-1} of stability to the product. Eilbracht[32] studied this class of reaction (equation 11) in detail. An alkane[33] CC cleavage reaction proved possible via initial dehydrogenation to a coordinated diene and then alkyl migration (equation 12) as in the reaction studied by Eilbracht and by Green. The migration is reversible as could be shown for the case of equation (13).

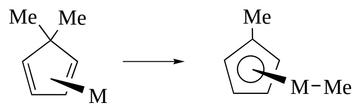

(11)

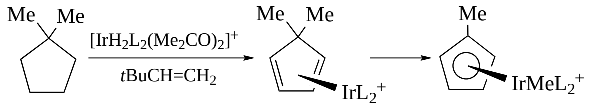

(12)

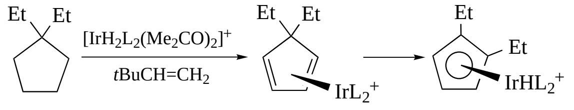

(13)

A number of catalytic reactions involve CC bond cleavage, often driven by strain. For example,[34] biphenylene can be converted to tetraphenylene with $Ni(cod)(PMe_3)_2$ at 100 °C or $Pt(PR_3)_3$ at 120 °C (equation 14). In the Pt case, a series of intermediates could be isolated that suggest a pathway involving double oxidative addition of the biphenylene CC bond, as in the stoichiometric reactions previously discussed, followed by double reductive elimination to give the product.

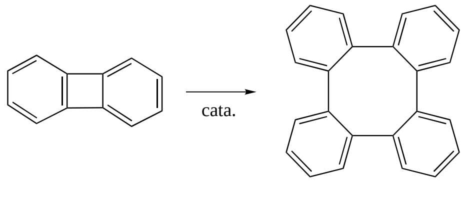

(14)

Equation (15) and (16) shows unusual cases[35] where a catalytic CC cleavage occurs with little or no acceleration via relief of strain, but the reactions are very slow and go in low yield.

Chaudret[36] induced aromatization of the B-ring of a number of 5,7-dienyl steroids by a CC cleavage reaction that removed the angular methyl group. This was possible using the electrophilic ruthenium fragment $[Cp^*Ru]^+$ as stoichiometric reagent.

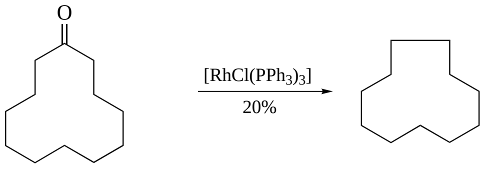

(15)

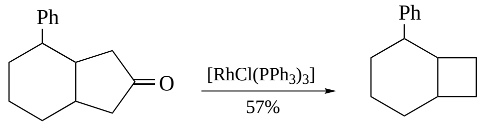

(16)

Suzuki[37] has shown how the triruthenium cluster $Cp^*{}_3Ru_3H_5$ readily gives CH and CC reactions with a wide variety of substrates.

It is also possible to activate a C–C bond by using bare transition metal ions, generated by ionization in the gas phase.[38] Using an ion-beam instrument, Armentrout and Beauchamp[39] were able to show that the reaction of Co^+ with n-butane to give $CoC_2H_4{}^+$ goes exothermally via a C–C insertion to the metal followed by β-hydrogen elimination and reductive elimination of ethane. In this case, the corresponding Co–C bond strengths are much higher than in the case of a metal complex and of course the Co^+ reagent is extremely unhindered.[40]

4 HALOCARBON COMPLEXES

In the earliest authentic halocarbon complex (1982), o-diiodobenzene was found to chelate to cationic Ir(III) as shown in diagram (**5**).[41] An earlier proposed example proved to be misidentified when the crystal structure was carried out. To be stable, any such complex must resist oxidative addition, hence the use of an oxidation state, Ir(III), that is only oxidized with difficulty. The normally rather weakly basic halocarbon lone pairs are often reluctant to bind, but chelation and involvement of the least electronegative halide, iodine, favor binding as does the cationic character of the complex. A series of such complexes was soon found, including complexes of Ir(I)[42] and a series of weakly bound dichloromethane complexes for certain systems.[43] These solvento complexes can be very labile and so find use as precursors for binding of other weakly basic ligands. Even fluorocarbon complexes proved viable.[44] A review of the area is available.[1] It now seems likely that many oxidative addition reactions of halocarbons go via initial formation of halocarbon complexes. In such a complex, the C–X σ^* orbital is presented to the metal ready for electron transfer (**6**), a process that leads to the radical pathway for halocarbon oxidative addition, or for transfer of a pair of electrons, which would lead to the concerted oxidative addition pathway (see Section 5).

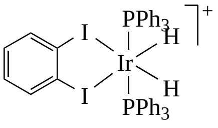

(**5**)

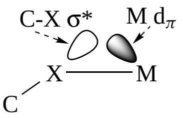

(**6**)

5 CX ACTIVATION

Oxidative addition of a C–X bond to a metal is of central importance to organometallic chemistry and specially to its application in organic synthesis. Apart from the classic Grignard synthesis of RMgX and related species, a multitude of palladium catalyzed reactions (Mizoroki–Heck, Suzuki–Miyaura, Hartwig–Buchwald . . .) go by this initial step.

Among stoichiometric cases, Vaska's complex, IrClCO $(PPh_3)_2$, is the classic transition metal example.[45] It reacts with a number of alkyl halides such as MeI to give a trans adduct (equation 17).

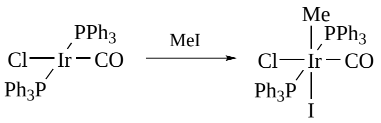

$$\mathrm{Cl{-}Ir(PPh_3)_2{-}CO} \xrightarrow{\mathrm{MeI}} \mathrm{Cl{-}Ir(Me)(I)(PPh_3)_2{-}CO} \qquad (17)$$

One key goal of catalyst development is to move from the more expensive alkyl and aryl iodides and bromides to the cheaper chlorides and the environmentally more desirable tosylates. The latter tend to react less well but the use of basic, bulky ligands like $P(t\mathrm{Bu})_3$ and a number of ferrocenyl-substituted phosphines has improved the situation.

Three mechanisms[46] are usually considered for oxidative addition of alkyl and aryl halides: S_N2, radical and concerted. In the S_N2 pathway, the metal acts as a nucleophile, displacing the halide from RX, followed by coordination of the halide to the metal. The oxidation state of the metal rises by two units.

$$\mathrm{RX} + \mathrm{ML}_\eta \longrightarrow \mathrm{RML}_\eta{}^+ + \mathrm{X}^- \longrightarrow \mathrm{(R)(X)ML}_\eta \qquad (18)$$

The order of reactivity (1° > 2° > 3° alkyl) and the inversion of configuration at α-carbon both follow the precedent of the organic S_N2 case. The $\Delta S^\ddagger$ is typically strongly negative (~ -40 eu). The second step of equation (18) requires a vacant site on the metal. Where this is not present, the process may halt after the first step, as in equation (19).

$$\mathrm{CpIr(CO)_2} + \mathrm{MeI} \longrightarrow \mathrm{[CpIrMe(CO)_2]^+I^-} \qquad (19)$$

In concerted oxidative addition, the C–X bond breaking occurs with concerted formation of M–C and M–X bonds. Such is often the case for aryl halides where the S_N2 process is not applicable. In contrast with the trans product of equation (17), the initial concerted oxidative addition product is often cis. The concerted mechanism is also associated with negative $\Delta S^\ddagger$ (ca. -20 eu) because the transition state is highly organized.

Prior ligand dissociation sometimes occurs, as in the case of $\mathrm{Pd\{P(O\text{-}CH_3C_6H_4)_3\}_2}$ and aryl bromide, where the active intermediate is the highly unsaturated species, $\mathrm{Pd(PAr_3)}$.[47]

Radical processes involve single electron transfer with a change of oxidation state by one unit in the first step. The classic case[48] is that of $\mathrm{Ni(PR_3)_4}$, where the reactive species is $\mathrm{Ni(PR_3)_3}$ (equation 20). Radical chain pathways have also been proposed in certain cases, where the addition of a radical trap drastically slows the rate.

$$\mathrm{NiL_4} \rightleftharpoons \mathrm{NiL_3} \xrightarrow{\mathrm{PhBr}} \mathrm{[NiL_3]^+[PhBr]^-} \longrightarrow \mathrm{[NiBrL_2]} + \mathrm{Ph}\bullet \longrightarrow \mathrm{[NiPhBrL_2]} \qquad (20)$$

Radical clock[49] rearrangements can be used to provide evidence for radical intermediates; these include the ring opening of cyclopropylmethyl radical and the ring closing of the hexenyl radical (equation 21).

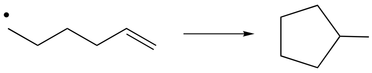

(21)

The pathways differ in outcome with substrates of defined configuration: racemization for the radical path, inversion for the S_N2, and retention for the concerted route.

C–F bond activation is attracting increasing interest in connection with green chemistry. Perfluoroarenes are more reactive than the corresponding perfluoroalkanes, possibly because of the easier access to the C–F bond in C_6F_6 versus C_6F_{12}. Photochemical routes are common as in equation (22).[50]

$$\mathrm{Cp^*RhH_2PMe_3} + \mathrm{C_6F_6} = \mathrm{Cp^*Rh(F)(C_6F_5)} + \mathrm{H_2} \qquad (22)$$

The thermal process requires pyridine solvent and gives quite a different product of equation (23).[51]

$$\mathrm{Cp^*RhH_2PMe_3} + \mathrm{C_6F_6} + \mathrm{C_5H_5N} = \mathrm{Cp^*Rh(H)(C_6F_5)} + \mathrm{[C_5H_5NH]F} \qquad (23)$$

Catalytic reactions involving steps of this type have been developed by Milstein[52] (equation 24–25).

$$C_6F_6 + R_3SiH \xrightarrow{\text{cata.}} C_6F_5H + R_3SiF \qquad (24)$$

$$C_6F_6 + R_3N + H_2 \xrightarrow{\text{cata.}} C_6F_5H + [R_3\,NH]F \qquad (25)$$

Perutz and Eisenstein[53] have used a computational (DFT) approach to estimate the M–C bond energies of a series of partially fluoronated aryl ligands. They show that the main structural predictor of the M–C bond strength is the number of F atoms in the ortho positions, n_F. Higher M–C bond strengths are associated with larger n_F. This study shows the growing importance of computational work, particularly in cases like this where experimental determinations of the data are unreliable or unavailable.

Perfluoroalkanes are much less reactive but the classic 1959 work by Tatlow[54] in *Nature* attracted attention by showing that partial reduction to give definite products could occur (equation 26). In this work, perfluorodecalin (PFD) was reduced to perfluoronaphthalene (PFN) by NaSAr. Since then, several PFD conversions have been reported with transition metal reagents, either via photochemical or thermal routes.[55–57] For example, hot sodium oxalate (465 °C) aromatizes perfluorodecalin to give perfluorotetralin and perfluoronaphthalene (equation 27).[58] Decomposition of solid sodium oxalate at temperatures above 450 °C involves initial formation of elemental carbon that catalyzes the subsequent decomposition of oxalate, leading to the presence of an induction period in the overall decomposition reaction. Prior incipient decomposition of sodium oxalate to carbon and sodium carbonate is necessary for this reagent to effect aromatization.

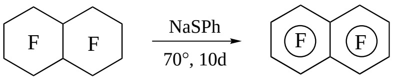

(26)

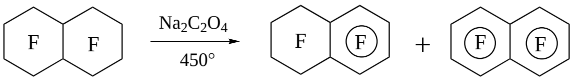

(27)

6 CONCLUSION

CC activation is an emerging problem, where general solutions are still lacking. The reaction is rare and whenever CH activation can occur, it often dominates. Coupling reactions involving aryl halides are among the small group of transition metal catalyzed reactions that are most intensely used in organic synthesis. Carbon-halogen activation is well understood for Cl, Br, and I, and considerable progress has been made in moving from ArI and ArBr to the less reactive but cheaper ArCl as substrates in these reactions. CF activation, however, remains very hard and is still much less understood. The whole area of carbon-halogen activation has also been affected by the rise of the green chemistry[59] in which one goal is the destruction of persistent halogenated materials and another is replacement of halogenated materials by alternate substrates for coupling and related processes.

7 REFERENCES

1. R. J. Kulawiec and R. H. Crabtree, *Coord. Chem. Rev.*, 1990, **99**, 89.
2. R. H. Crabtree, *Angew. Chem., Int. Ed. Engl.*, 1993, **32**, 789.
3. G. J. Kubas, ‘Metal Dihydrogen and Sigma Bond Complexes’, Kluwer Academic, New York, 2001.
4. H. Kurosawa and A. Yamamoto, ‘Fundamentals of Molecular Catalysis’, Elsevier, Amsterdam, 2003.
5. F. Maseras and R. H. Crabtree, *Inorg. Chim. Acta*, 2004, **357**, 345.
6. R. Tomaszewski, I. Hyla-Kryspin, C. L. Mayne, A. M. Arif, R. Gleiter, and R. D. Ernst, *J. Am. Chem. Soc.*, 1998, **120**, 2960.
7. G. Lanza, I. L. Fragala, and T. J. Marks, *J. Am. Chem. Soc.*, 2000, **122**, 12764.
8. A. Vigalok and D. Milstein, *Acc. Chem. Res.*, 2001, **34**, 798.
9. J. Jaffart, M. Etienne, M. Reinhold, J. E. McGrady, and F. Maseras, *Chem. Commun.*, 2003, 876.
10. P. L. Watson and G. W. Parshall, *Acc. Chem. Res.*, 1985, **18**, 51.
11. M. Etienne, R. Mathieu, and B. Donnadieu, *J. Am. Chem. Soc.*, 1997, **119**, 3218, and refs cited.
12. J. J. W. Eshuis, Y. Y. Tan, J. H. Teuben, and J. Renkema, *J. Mol. Catal.*, 1990, **62**, 277.
13. C. H. F. Tipper, *J. Chem. Soc.*, 1955, 2045.
14. D. M. Adams, J. Chatt, R. Guy, and N. Sheppard, *J. Chem. Soc.*, 1961, 738; R. D. Gillard, M. Keeton, and R. Mason, *J. Organomet. Chem.*, 1971, **33**, 247.
15. H. Hogeveen and H. C. Volger, *J. Am. Chem. Soc.*, 1967, **89**, 2486.
16. L. Cassar and J. Halpern, *Chem. Commun.*, 1970, 1082.
17. K. C. Bishop, *Chem. Rev.*, 1976, **76**, 461.
18. R. A. Periana and R. G. Bergman, *J. Am. Chem. Soc.*, 1986, **108**, 7346.
19. H. Schwager, S. Spyroudis, and K. O. C. Vollhardt, *J. Organomet. Chem.*, 1990, **191**, 382.
20. B. L. Edelbach, R. J. Lachicotte, and W. D. Jones, *J. Am. Chem. Soc.*, 1998, **120**, 2843.
21. E. R. Atkinson, P. L. Levins, and T. E. Dickelman, *Chem. Ind.*, 1964, 934.
22. Z. Lu, C. H. Jun, S. R. de Gala, M. Sigalas, O. Eisenstein, and R. H. Crabtree, *Chem. Commun.*, 1993, 1877.

23. C. Perthuisot and W. D. Jones, *J. Am. Chem. Soc.*, 1994, **116**, 3647.
24. J. W. Suggs and C.-H. Jun, *J. Am. Chem. Soc.*, 1984, **106**, 3054.
25. J. W. Suggs and C.-H. Jun, *J. Am. Chem. Soc.*, 1986, **108**, 4679.
26. D. Y. Lee, B. S. Hong, E. G. Cho, H. Lee, and C. H. Jun, *J. Am. Chem. Soc.*, 2003, **125**, 6372.
27. C. H. Jun, C. W. Moon, H. Lee, and D. Y. Lee, *J. Mol. Catal. A*, 2002, **189**, 145.
28. M. Gandleman, A. Vigalok, L. J. W. Shimon, and D. Milstein, *Organometallics*, 1997, **16**, 3981.
29. M. E. van der Boom, H. B. Kraatz, L. Hassner, Y. Ben-David, and D. Milstein, *Organometallics*, 1999, **18**, 3873.
30. D. Milstein, *Pure Appl. Chem.*, 2003, **75**, 445.
31. F. W. S. Benfield and M. L. H. Green, *J. Chem. Soc., Dalton Trans.*, 1974, 1324.
32. P. Eilbracht, *Chem. Ber-Recl.*, 1976, **109**, 1429.
33. R. H. Crabtree, R. P. Dion, D. J. Gibboni, D. V. McGrath, and E. M. Holt, *J. Am. Chem. Soc.*, 1986, **129**, 7222.
34. B. L. Edelbach, R. J. Lachicotte, and W. D. Jones, *J. Am. Chem. Soc.*, 1998, **120**, 2483, and refs cited.
35. M. Murakami, H. Amii, K. Shigeto, and Y. Ito, *J. Am. Chem. Soc.*, 1996, **118**, 8285.
36. M. A. Halcrow, F. Urbanos, and B. Chaudret, *Organometallics*, 1993, **12**, 955.
37. H. Suzuki, Y. Takaya, T. Takemori, and M. Tanaka, *J. Am. Chem. Soc.*, 1994, **116**, 10779.
38. K. Eller and H. Schwarz, *Chem. Rev.*, 1991, **91**, 1121.
39. P. B. Armentrout and J. L. Beauchamp, *J. Am. Chem. Soc.*, 1981, **103**, 784.
40. P. E. M. Siegbahn and M. R. A. Blomberg, *J. Am. Chem. Soc.*, 1992, **114**, 10548.
41. R. H. Crabtree, J. W. Faller, M. F. Mellea, and J. M. Quirk, *Organometallics*, 1982, **1**, 1361.
42. M. J. Burk, R. H. Crabtree, and E. M. Holt, *Organometallics*, 1984, **3**, 638.
43. S. K. Agbossou, C. Roger, A. Igau, and J. A. Gladysz, *Inorg. Chem.*, 1992, **31**, 419.
44. R. H. Crabtree, E. M. Holt, M. Lavin, and R. J. Kulawiec, *Inorg. Chem.*, 1987, **26**, 2559.
45. L. Vaska, *Acc. Chem. Res.*, 1976, **9**, 175 and refs cited.
46. R. H. Crabtree, 'The Organometallic Chemistry of the Transition Metals', Wiley, New York, 2001.
47. J. F. Hartwig and F. Paul, *J. Am. Chem. Soc.*, 1995, **117**, 5373.
48. T. T. Tsou and J. K. Kochi, *J. Am. Chem. Soc.*, 1979, **101**, 6319.
49. R. R. Conry and J. M. Mayer, *Organometallics*, 1991, **10**, 3160.
50. S. T. Belt, M. Helliwell, W. D. Jones, M. G. Partridge, and R. N. Perutz, *J. Am. Chem. Soc.*, 1993, **115**, 1459.
51. B. L. Edelbach and W. D. Jones, *J. Am. Chem. Soc.*, 1997, **199**, 7734.
52. M. Aizenberg and D. Milstein, *Science*, 1994, **265**, 359.
53. E. Clot, B. Oelckers, A. H. Klahn, O. Eisenstein, and R. N. Perutz, *Dalton Trans.*, 2003, **(21)**, 4065.
54. B. Gething, C. R. Patrick, M. Stacey, and J. C. Tatlow, *Nature*, 1959, **183**, 588.
55. J. Burdeniuc, B. Jedlicka, and R. H. Crabtree, *Chem. Ber-Recl.*, 1997, **130**, 145.
56. W. D. Jones, *J. Chem. Soc., Dalton Trans.*, 2003, **(21)**, 3991.
57. T. Braun, and R. N. Perutz, *Chem. Commun.*, 2002, **(23)**, 2749.
58. L. H. McAlexander, C. M. Beck, J. J. Burdeniuc, and R. H. Crabtree, *J. Fluorine Chem.*, 1999, **99**, 67.
59. P. T. Anastas and M. M. Kirchhoff, *Acc. Chem. Res.*, 2002, **35**, 686.

Carbene Complexes

Robert H. Crabtree
Yale University, New Haven, CT, USA

1 Introduction 1
2 Fischer versus Schrock Carbenes 1
3 Carbenes: Synthesis, Spectra, and Reactivity 2
4 Carbynes: Synthesis, Spectra, and Reactivity 5
5 Bridging Carbenes 6
6 Alkene Metathesis 7
7 Further Reading 7
8 References 7

1 INTRODUCTION

This article is adapted with permission from Chapter 11 of the author's book,[1] *The Organometallic Chemistry of the Transition Metals*. Carbenes of type CR_2 form complexes with a variety of transition metal fragments, for example, $Cl_2(Cy_3P)_2Ru{=}CHPh$ (**1**). Carbene complexes were first recognized in the 1960s but they have been a source of a succession of new and remarkable results ever since and interest in them is currently at a high point as a result of the success of the alkene metathesis reaction, for which complex (**1**) is perhaps the best-known catalyst.[2] This proceeds via carbene intermediates and has found a wide variety of uses both in organic synthesis and in polymer synthesis, as well as being of inorganic mechanistic interest.

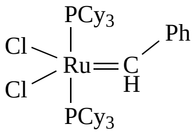

(1)

2 FISCHER VERSUS SCHROCK CARBENES

The two extreme types of coordinated carbene, the Fischer[3] and the Schrock[4] type, can be thought of as complexes of singlet and triplet carbenes, respectively. Carbene complexes, $L_nM{=}CR_2$, have Fischer character where the substituents are π-donors and the empty p orbital of the singlet carbene is needed for back donation from the metal or from π-donor substituents R, such as –OMe or $–NMe_2$. Fischer carbenes are favored for low metal oxidation states, and for late transition metals having π-acceptor ligands. Such a carbene is electrophilic and broadly resembles other lone pair donor ligands such as CO or PPh_3. The M–C bond is essentially single, as illustrated by diagram (**2**).

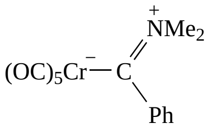

(2)

In contrast, Schrock character is shown by carbenes that form true double bonds to the metal (**3**), as is the case for higher oxidation state, early transition metals, having non π-acceptor ligands. Non π-donor R groups on the carbon such as H or alkyl are preferred since these do not stabilize the singlet form. In this case, the carbene behaves as a nucleophile, having a ∂^- carbon; indeed, a metala-ylid form can be considered as a description of the structure. Cases intermediate between the two extremes are especially common for $M{=}CHal_2$ because the halide has intermediate π-donor strength between H and –OMe.[5]

$$CpCl_2Ta{=}CHPh$$

(3)

The term alkylidene refers to carbenes, CR_2 with alkyl substituents; for example, $MeCH{=}ML_n$ is an ethylidene complex but 'alkylidene' is sometimes used as a synonym for 'Schrock carbene' in the older literature because the first alkylidenes were of the Schrock type. There are electrophilic Fischer alkylidenes as well as Schrock ones, however, so the terms should be kept separate. For example, $[Cp_2W({=}CH_2)Me]^+$ and $Cp_2Ta({=}CH_2)Me$ are isoelectronic, but the former is electrophilic (Fischer) and the latter nucleophilic (Schrock) at the carbene carbon;[6] the net positive charge on the tungsten complex must stabilize the $M(d_\pi)$ levels and is therefore probably the main reason for the difference. Carbyne complexes contain an $M{\equiv}CR$ triple bond and are also known both for low and high oxidation states. We can look at the low-spin carbyne fragment as having an sp lone pair and a single electron in one of the two p orbitals (**4**). In the Fischer bonding scheme, we can consider that in forming its three bonds to the metal, the carbyne: (1) acts as a σ-donor via the C(sp) lone pair, (2) forms a normal π-covalency by the combination of its singly occupied C(p)-orbital with a singly occupied M(d)-orbital, and (3) accepts back-bonding from a filled M(d)-orbital into its empty C(p)-orbital. In the Schrock carbyne deriving from a high-spin ligand, we can consider the resulting $M{\equiv}CR$ bond as a true triple covalent bond. Oxidation states are usually counted by considering CR_2 as a neutral ligand for a Fischer and a dianionic ligand for a Schrock case; in intermediate cases both models can be found, leading to oxidation state ambiguity.[1] N-Heterocyclic carbenes (NHCs), like (**5**), are a class of Fischer carbenes attracting increasing attention as spectator ligands in catalysis, where they can have superior properties versus phosphines, the most common current spectator ligands.[7]

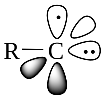

(4)

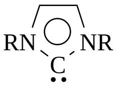

(5)

3 CARBENES: SYNTHESIS, SPECTRA, AND REACTIVITY

Fischer recognized the first carbene complexes in 1964.[3,8] They were formed by the attack of an alkyllithium on a metal carbonyl followed by methylation (equations 1 and 2). Resonance form (**2**), considered as the dominant one in the heteroatom stabilized Fischer carbenes, shows the multiple character of this carbon–heteroatom bond. This effect is responsible for the restricted rotation often observed for this bond in nuclear magnetic resonance (NMR) studies. For example cis and trans isomers (**6**) and (**7**) of methoxymethyl carbenes rapidly interconvert at room temperature, but can be frozen out in the proton NMR at −40 °C.[9] By contrast, the M–C bond is close to single and often rotates freely.

$$\mathrm{(OC)_5Cr{-}CO + MeLi \longrightarrow (OC)_5Cr{=}C(OLi)Me} \qquad (1)$$

$$\mathrm{(OC)_5Cr{=}C(OLi)Me + MeI \longrightarrow (OC)_5Cr{=}C(OMe)Me} \qquad (2)$$

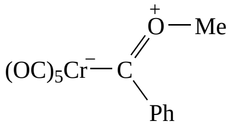

(6)

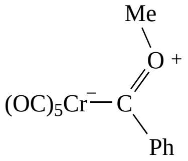

(7)

The key synthetic routes for Fischer carbenes fall into one of three general categories, illustrated by equations (1–3). In equation (2) an acyl or similar species (often but not always formed by a nucleophilic attack on a CO or a similar ligand) is treated with an electrophile to give a Fischer carbene. In equation (3), an H^- (Fischer case) or an H^+ (Schrock case) is abstracted from the α-position of an alkyl and in equation (5) a traditional carbene source is used.

$$\mathrm{L}_n\mathrm{M{-}CHR_2} - \mathrm{H}^+ \longrightarrow [\mathrm{L}_n\mathrm{M{=}CR_2}]^- \qquad (3)$$

$$\mathrm{L}_n\mathrm{M{-}CHR_2} - \mathrm{H}^- \longrightarrow [\mathrm{L}_n\mathrm{M{=}CR_2}]^+ \qquad (4)$$

$$\mathrm{L}_n\mathrm{M} + \mathrm{N_2CR_2} \longrightarrow [\mathrm{L}_n\mathrm{M{=}CR_2}] + \mathrm{N_2} \qquad (5)$$

As an example related to equation (1), isonitriles are very sensitive to nucleophilic attack, and a wide range of bis-heteroatom stabilized carbenes can be obtained (equation 6).[10]

$$\mathrm{[(MeNC)_4Pt]^{2+} + 4Me_2\,NH \longrightarrow [Pt\{{=}C(NHMe)_2\}_4]^{2+}} \qquad (6)$$

Chugaev[11] obtained carbene complexes like these as early as 1915, but the right structure was only assigned much later.[12] Acetylides $\mathrm{L}_n\mathrm{M{-}C{\equiv}CR}$ are unexpectedly good bases[13] via their resonance form $\mathrm{L}_n\mathrm{M^+{=}C{=}C^-{-}R}$. They can react with acid in alcohol solution to give the carbenes shown in equations (7) and (11). An intermediate vinylidene cation probably undergoes nucleophilic attack by the alcohol.[14] In this case, the usual order of attack of equations (1) and (2) – nucleophile, then electrophile – is inverted.

$$\begin{aligned}\mathrm{ClL_2M{-}C{\equiv}CR + HOEt} &= \mathrm{[ClL_2M{=}C{=}CHR]^+ + {}^-OEt}\\ &= \mathrm{ClL_2M{=}C(OEt){-}CH_2R} \qquad (7)\end{aligned}$$

Electrophilic abstraction from an alkyl complex (equation 4) is illustrated in the reactions of equations (8) and (9); equation (9) is driven by the high Si–F bond strength.

$$\begin{tikzcd}\mathrm{Cp(CO)_2FeCH_2OMe + H^+} \arrow[r] & \text{‘}\mathrm{Cp(CO)_2Fe{=}CH_2}^+ \arrow[d] \\ & \text{other products} \end{tikzcd} \qquad (8)$$

$$\begin{aligned}&\mathrm{Cl(CO)(MeCN)L_2RuCF_3 + Me_3SiCl} \longrightarrow\\ &\quad\mathrm{Cl_2(CO)L_2Ru{=}CF_2 + Me_3SiF} \qquad (9)^{15}\end{aligned}$$

Alkylidenes can sometimes be made from organic carbene precursors such as diazomethane[16] or $\mathrm{R_2CCl_2}$.[17]

In ^{13}C NMR spectroscopy, the carbene carbon resonates at ca. 140–400 ppm to low field of $\mathrm{SiMe_4}$. This is probably a result of the existence of low-energy electronic excited states for the complex, which leads to a large ‘paramagnetic’ contribution to the shift. A proton substituent at the carbene carbon resonates from +10 to +20 ppm.

Thermal decomposition of carbene complexes usually leads to one or both of two types of alkenes:[18] one type is formed by rearrangement, and the other by dimerization of the carbene. Equation (10)[19] shows both types of products. The reaction does not go via the free organic carbene, because cyclobutanone, which is known to be formed in the rearrangement of the free carbene, was not detected in the products.

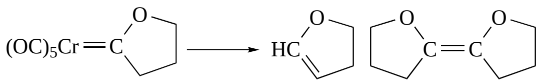

(10)

Fischer carbenes without a heteroatom substituent are very reactive.[20] The protonation of vinyl complexes is one route to such species (equation 11):

$$\mathrm{Cp(CO)_2Fe{-}CH{=}CH_2 + H^+ = Cp(CO)_2Fe{=}CH{-}CH_3}^+ \qquad (11)$$

the addition of base reverses the reaction by a nucleophilic abstraction. The ethylidene complex readily gives a 1,2-shift of the β-proton to give the thermodynamically more stable alkene complex. Even carbenes which lack β-hydrogens are unstable: $[Cp(CO)_2Fe{=}CH{-}CMe_3]^+$ and $[Cp(CO)_2Fe{=}CH{-}CMe_2Ph]^+$ both rearrange by a 1,2-shift of a methyl or a phenyl group, respectively, to the electron-deficient carbene carbon (equations 11 and 12).[21] This reaction, analogous to the Wagner-Meerwein rearrangement in carbonium ions, is fast because of the electron-deficient character of the carbene carbon in this complex.

$$Cp(CO)_2Fe{=}CH{-}CMe_2Ph + H^+ = [Cp(CO)_2Fe(PhCH{=}CMe_2)]^+ \quad (12)$$

$[Cp(Ph_2PCH_2CH_2PPh_2)Fe{=}CH{-}CMe_3]^+$ does not rearrange, however, probably because the increased back donation by the more electron-rich phosphine-substituted iron center decreases the electron deficiency at the carbene carbon.[22]

Oxidative cleavage of a carbene ligand can be achieved with reagents such as Ce(IV) compounds, pyridine N-oxide, dmso, or even with air. The product is normally the ketone corresponding to the starting carbene. This reaction is not only useful for synthetic purposes but also for characterizing the original carbene (equation 13).[23]

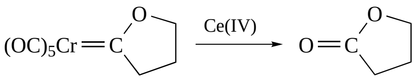

(13)

The synthesis of equation (14) illustrates another useful reaction of Fischer carbenes, the abstraction of a proton β to the metal by a base such as an organolithium reagent. The resulting negative charge can be delocalized on to the metal,[24] and is therefore stabilized. The anion can be alkylated by carbon electrophiles as shown.

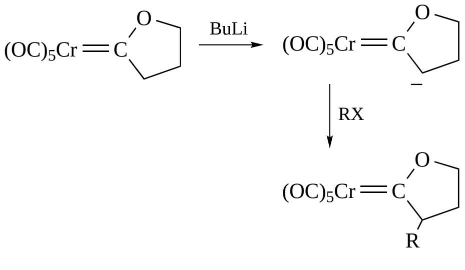

(14)

Fischer carbenes readily undergo nucleophilic attack at the carbene carbon, as shown in equation (15).[25] The attack of amines can give the zwitterionic intermediate shown, or by loss of methanol, the aminocarbene. Mentally replacing the $(CO)_5Cr$ group by an oxygen atom, shows the relation of this reaction to the aminolysis of esters to give amides.

$$(OC)_5Cr{=}C(OMe)Me + H_2NR \longrightarrow (OC)_5Cr{=}C(NHR)Me + HOMe \quad (15)$$

Schrock carbenes are obtained by α-elimination. High-valent metal alkyls, especially of the early metals, can undergo proton abstraction at the α-carbon to give nucleophilic Schrock[26] carbenes. The first high oxidation state carbene was formed in an attempt to make TaR_5 ($R = CH_2CMe_3$, or neopentyl), by the reaction of TaR_3Cl_2 with LiR – interestingly, Wittig was trying to make Ph_3PMe_2 when he discovered $Ph_3P{=}CH_2$. In fact the product is $R_3Ta{=}CH(t\text{-}Bu)$ (equation 16). The reaction probably goes via TaR_5, which then loses neopentane by an α-proton abstraction from one possibly agostic (*see* ***Dihydrogen Complexes & Related Sigma Complexes***) R ligand by another.[4,27]

$$R_3TaCl_2 + 2LiR \longrightarrow R_3TaR_2 \longrightarrow R_3Ta{=}CH\text{-}t\text{Bu} \quad (16)$$

One of the requirements for this α-elimination is that the molecule be crowded. Substitution of a halide in R_2TaCl_3 with a Cp group (equation 17)[28] is enough to do this, for example, as is addition of a PMe_3 (equation 18).[2] The corresponding benzyl complexes require one of the more bulky pentamethylcyclopentadienyls, Cp^* (equation 19),[29] or two plain Cp groups (equation 20).[28]

$$R_2TaCl_3 + TlCp \longrightarrow CpCl_2Ta{=}CH\text{-}t\text{Bu} + t\text{Bu}{-}Me \quad (17)$$

$$R_2TaCl_3 + 2PMe_3 \longrightarrow [(Me_3P)Cl_2Ta{=}CH\text{-}t\text{Bu}(\mu\text{-Cl})]_2 \quad (18)$$

$$(PhCH_2)_3TaCl_2 + 2LiCp^* \longrightarrow Cp^*ClTa{=}CH\text{-}t\text{Bu}(CH_2Ph) \quad (19)$$

$$(PhCH_2)_3TaCl_2 + 2LiCp \longrightarrow Cp_2Ta{=}CH\text{-}t\text{Bu}(CH_2Ph) \quad (20)$$

By adding two PMe_3 ligands, the α-proton of a benzylidene can now undergo abstraction to give a benzylidyne (equations 11 and 25).

$$Cp^*ClTa{=}CH\text{-}t\text{Bu}(CH_2Ph) + 2PMe_3 \longrightarrow Cp^*Ta({\equiv}CPh)(PMe_3)_2Cl + PhCH_3 \quad (21)$$

The methyl group is so sterically undemanding that it does not α-eliminate under the same conditions (equation 22). The synthesis of a methylene complex requires a deprotonation of a methyl complex by a strong base. A net positive charge on the complex activates the methyl for this reaction. Equations (23) and (24) show how this can be done by an electrophilic abstraction of Me^-.

$$Me_3TaCl_2 + 2LiCp \longrightarrow Cp_2TaMe_3 \quad (22)^{26}$$

$$Cp_2TaMe_3 + Ph_3C^+ \longrightarrow [Cp_2TaMe_2]^+ + Ph_3CMe \quad (23)^{30}$$

$$[Cp_2TaMe_2]^+ + CH_2PMe_3 \longrightarrow Cp_2TaMe({=}CH_2) + [PMe_4]^+ \quad (24)^{31}$$

Early metal complexes often avoid the 18e configuration – Me_3TaCl_2 is ostensibly 10e, for example. This can provide coordinative unsaturation at the metal: Schrock carbene complexes with <18e commonly have agostic C–H bonds (*see* ***Alkane Carbon–Hydrogen Bond Activation***; ***Dihydrogen Complexes & Related Sigma Complexes***). When

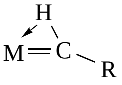

(8)

this happens, the proton on the carbene carbon bends back toward the metal, the M=C bond becomes shorter, and the C–H bond becomes longer (**8**).

Agostic binding leads to a high-field shift for this proton and a lowering of the C, H coupling constant in the ^{1}H NMR spectrum, together with a lowering of ν(C–H) in the infrared (IR). In 18e carbene complexes, such protons are not agostic and usually appear at 12δ with a J(C,H) of 105–130 Hz; in the complexes with <18e, they can come as high as -2δ with a J(C,H) of 75–100 Hz. At the same time, a ν(C–H) band appears in the IR at a position indicating that it has been weakened by the interaction, for example, at 2510 cm^{-1} for CpTa{CH(*t*-Bu)}Cl_2. Crystal structures[32] show that the M=C–R angle can open up to as much as 175°, while the M=C–H angles fall to as little as 78°. The M=C bond length is always short (at least 0.2 Å shorter than an M–C single bond) in all cases studied, but is even shorter in the complexes with <18e. Interestingly, the oxo alkylidene $Cl_2(PEt_3)_2W(=O)(=CHCMe_3)$ has a much less distorted alkylidene group. This is probably because the lone pairs on the oxo group are more basic and so more available for the metal than the C–H bonding pair.[33]

In the structure of $Cp_2TaMe(=CH_2)$ (**9**, by neutron diffraction), the orientation of the methylene group is not the one predicted on steric grounds, with the CH_2 lying in the mirror plane of the molecule, but nearly at right angles (88°) to this plane, with the proton substituents pointing in the direction of the Cp groups. A countersteric conformation like this often indicates that an electronic factor is at work. Here, the filled p_z-orbital of the CH_2 group is interacting with one of the empty orbitals on the metal. Since these orbitals are in the mirror plane of the molecule, this fixes the orientation of the CH_2. The larger CHR alkylidenes deviate only slightly from the orientation shown by CH_2, and so the two Cp groups become inequivalent. The ^{1}H NMR spectrum of the complexes shows this inequivalence but the resonances for the two Cp groups coalesce on warming. In the transition state, the alkylidene probably lies in the mirror plane and has no π-interaction with the metal. The rotation barrier deduced from the data, 25 kcal mol^{-1}, therefore gives an estimate of the strength of the Ta=C π-bond.

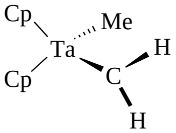

(9)

Reactions of Schrock carbenes illustrate their nucleophilic character. For example, they form adducts with the Lewis acid $AlMe_3$ (equation 25).

$$Cp_2TaMe(=CH_2) + AlMe_3 \longrightarrow Cp_2TaMe(\text{–}CH_2\text{–}AlMe_3) \quad (25)$$

They also react with ketones in the same way as a Wittig reagent (equation 26).[34]

$$R_3Ta(=CH\mathit{t}\text{-Bu}) + Me_2CO \longrightarrow Me_2C{=}CH\mathit{t}\text{-Bu} + \text{‘}R_3TaO_x\text{’} \quad (26)$$

Alkenes react with carbenes to give metalacycles. The alkene may coordinate to the metal first, if only transiently. The carbene carbon then attacks the coordinated alkene to give the product. The metalacycle can decompose in several ways (equations 11 and 30), either by reversal of the formation reaction to give alkene and a carbene, by reductive elimination to give a cyclopropane, or by β-elimination to give an alkene.[26] As might be expected, the more electropositive Ti forms even more nucleophilic carbene complexes. One of the most interesting species of this class is Tebbe's reagent, formed from Cp_2TiCl_2 and $AlMe_3$ (equation 27).[35]

$$Cp_2TiCl_2 + AlMe_3 = Cp_2Ti(Cl)(CH_2)AlMe_2 \quad (27)$$

This is an example of a bridging carbene, but in its reactions it almost always loses Me_2AlCl first to give the mononuclear 16e $Cp_2Ti{=}CH_2$; a base like NEt_3 is sometimes added to help remove the aluminum fragment by complexation. This reagent even gives a Wittig type product with esters, substrates that are not methylenated with $Ph_3P{=}CH_2$. In addition, Tebbe's reagent does not racemize enolizable ketones as do the phosphorus ylids.[36]

$$\text{‘}Cp_2Ti{=}CH_2\text{’} + PhCOOMe \longrightarrow Ph(OMe)C{=}CH_2 \quad (28)$$

Acyl halides, on the other hand, do not methylenate, but give an enolate.[37] Tebbe's complex reacts with alkenes to give stable metalacyclobutanes (equation 29), which are more convenient precursors for the '$Cp_2Ti{=}CH_2$' carbene than is Tebbe's reagent itself. The metalacycles undergo a number of useful reactions.[36] Protonation gives the propanes. Bromination gives the 1,3-dibromides. Oxidation with I_2 leads to net reductive elimination to give the cyclopropane.

$$\text{‘}Cp_2Ti{=}CH_2\text{’} + CH_2{=}CMe_2 \longrightarrow Cp_2Ti(\text{–}CH_2\text{–}CMe_2\text{–}CH_2\text{–}) \quad (29)$$

Intermediate cases between Fischer and Schrock character are known. In the Os complex of equations (30) and (31), Roper[15] has a carbene with intermediate character between the Fischer and Schrock extremes because it reacts both with electrophiles like SO_2 (equation 30), or H^+ and with nucleophiles (e.g. CO, equation 31), or CNR. This is reasonable based on the bonding picture. The osmium has π-donor (Cl), as well as π-acceptor (NO) ligands, the metal is in an intermediate oxidation state (Os(II) if we count the carbene as a Fischer, Os(IV) if a Schrock type), and the carbene carbon has non π-donor substituents (H).

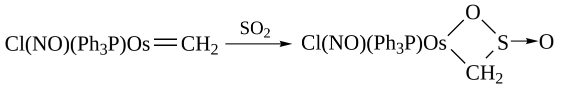

(30)

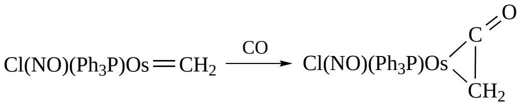

(31)

N-Heterocyclic carbenes (or NHCs, **5**), a class of Fischer carbenes, deserve closer attention. Arduengo[38] (1991) isolated a series of stable carbenes by deprotonation of N,N'-disubstituted imidazolium salts with bulky substituents. These were stable enough for crystal structures to be obtained. This finding reignited interest in carbene complexes derived from the imidazolium ring system that were discovered in the period 1968–1973 by Wanzlick,[39] Öfele,[40] and Lappert.[41] Herrmann[42] showed that these ligands are not only excellent for stabilizing a variety of transition metals but that the resulting complexes are active in a variety of homogeneous catalytic reactions such as Heck and Suzuki coupling. Many more catalytically active complexes have been discovered since, of which perhaps the most striking example is the greatly improved Grubbs metathesis catalyst,[43] $[(NHC)(PR_3)Cl_2Ru{=}CHR]$ (**10**, Ar = mesityl), obtained by replacing one phosphine in the classic catalyst by an NHC.

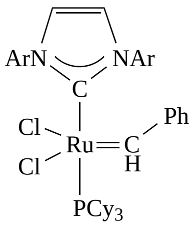

(10)

IR studies of metal carbonyls show that the NHCs are very strongly donating groups, much more so than even the most basic phosphine. NHCs have sometimes been compared with phosphines. It is true that NHCs, like phosphines, stabilize a wide range of complexes and promote catalytic activity in these complexes but there are as many differences as similarities in the behavior of the two classes. One difference, for example, is that carbenes are firmly attached and do not dissociate from the metal significantly, while phosphines can do so with much greater ease.

The synthesis of these NHCs has most often been carried out by first deprotonating the imidazolium salt with nBuLi and then introducing the metal salt. This can be unsatisfactory for systems such as chelating and pincer carbenes which require milder conditions. To cover such cases, direct metallation, transmetallation, and oxidative addition have all proved satisfactory. In direct metallation, the imidazolium salt is treated with a metal precursor having a leaving group, such as an acetate salt. The acetate would then deprotonate the imidazolium salt after initial binding has activated the 2CH bond.[44] For transmetallation, the imidazolium salt is often treated with Ag_2O to give the silver carbene[45] which undergoes subsequent transmetallation to the metal of interest.[46] Oxidative addition can be carried out with Pd(0) to give bis-carbene species, for example.[47] Occasionally, there are surprises, such as in the attempted direct metallation of $IrH_5(PPh_3)_2$, where metallation took place, not at the normal C2 position but at the C4(5) position.[48] These abnormal carbenes are even more strongly electron donating than their normal counterparts. NHCs derives from triazole, oxazole, and other heterocyclic carbenes have also been studied and show distinct differences in behavior from the imidazole versionsm.

4 CARBYNES: SYNTHESIS, SPECTRA, AND REACTIVITY

Fischer[49] first prepared carbyne complexes (1973) by electrophilic abstraction of methoxide ion from a methoxy methyl carbene.

$$\begin{array}{l} L(CO)_4M{=}C(OMe)Me + BX_3 \\ \qquad \longrightarrow [L(CO)_4M{\equiv}CMe]^+BX_4^- + BX_2(OMe) \\ \qquad\qquad \downarrow \\ \qquad\qquad X(CO)_4M{\equiv}CMe \end{array} \tag{32}$$

If L is CO, then the halide ion (Cl, Br, or I) displaces the CO trans to the carbyne in the intermediate cationic complex; this shows the high trans effect of the carbyne. On the other hand, if L is PMe_3, then the cationic species is the final product. Oxidation states for Fischer carbynes are normally assigned by considering CR as an LX ligand, CR^-, that is, $X(CO)_4M{\equiv}CMe$ is M(II). By carefully controlled oxidation, Mayr[50] has been able to remove the carbonyl ligands in a Fischer carbyne to give a Schrock carbyne, thus making a direct link between the two types. This also allows synthesis of Schrock carbenes and carbynes with substituents other than the ones which can be obtained by the standard methods. In equation (33), we can think of the Br_2 oxidizing the metal by two units. This destabilizes the metal d_π orbitals relative to the carbon p orbitals, and so switches the polarity of the metal–carbon multiple bond. Note how the coligands change on going from the soft carbonyls in the W(II) starting material to the hard dme ligand in the W(VI) product. Schrock carbynes are nearly always d^0 (counting the carbyne as an X_3 ligand) as here.

$$\mathrm{Br(CO)_4\,W{\equiv}CMe \xrightarrow{Br_2,\ dme} Br_3(dme)W{\equiv}CMe}$$
$$\mathrm{(dme = MeOCH_2CH_2OMe)} \qquad (33)$$

Otherwise, Schrock carbynes can be made by deprotonation of an α-CH (equation 34), by an α-elimination, in which this CH bond in effect oxidatively adds to the metal (equation 35) or in rare cases by a remarkable metathesis reaction[51] (equation 36). This reaction fails for coligands other than t-butoxide, showing the sensitivity of the different reaction pathways to the electronic and steric environment of the metal. MeCN is cleaved in the same way to a carbyne and a nitride $(t\text{-BuO})_3\mathrm{W{\equiv}N}$.

$$\mathrm{CpCl_2Ta{=}CHR \xrightarrow[ii)\ Ph_3P{=}CH_2]{i)\ PMe_3,} CpCl(PMe_3)Ta{\equiv}CR} \qquad (34)$$

$$\mathrm{Cp^*Br_2Ta{=}CH}t\text{-}\mathrm{Bu \xrightarrow[ii)\ Na/Hg]{i)\ dmpe,} Cp^*(dmpe)HTa{\equiv}C}t\text{-}\mathrm{Bu} \qquad (35)$$

$$(t\text{-BuO})_3\mathrm{W{\equiv}W(O}t\text{-Bu})_3 + t\mathrm{BuC{\equiv}C}t\text{-Bu} \longrightarrow 2(t\text{-BuO})_3\mathrm{W{\equiv}C}t\text{-Bu} \qquad (36)$$

The structural and spectral characteristics follow the pattern of the carbenes. The carbyne ligand is linear, having sp hybridization and the M≡C bond is very short (1st row: 1.65–1.75 Å, 2nd and 3rd row: 1.75–1.90 Å). The ^{13}C NMR shows a characteristic low field resonance for the carbyne carbon at +250 to +400 ppm. Moving to reactivity, a carbyne can couple[52] with another carbyne to give an alkyne or alkyne complex.[53] For instance, $\mathrm{Br(CO)_4Cr{\equiv}CPh}$ reacts with Ce(IV) to give free PhC≡CPh. Carbynes also have extensive photochemistry.[54] In the Fischer series, the carbyne carbon is electrophilic and subject to nucleophilic attack, for example, by $\mathrm{PMe_3}$, pyridine RLi or isonitrile (=Nu) to give a carbene of the type $\mathrm{L}_n\mathrm{M{=}CR(Nu)}$.[49] Alternatively, the nucleophile may attack the metal in $\mathrm{L}_n\mathrm{(CO)M{\equiv}CR}$ and produce a ketenyl complex $\mathrm{L}_n\mathrm{(Nu)M}(\eta^2\text{-OC{=}CR})$ or $\mathrm{L}_n\mathrm{(Nu)_2M}(\eta^1\text{-OC{=}CR})$. On the other hand, Schrock carbynes are nucleophilic and subject to attack by electrophiles, for instance, $(t\text{-BuO})_3\,\mathrm{W{\equiv}C}(t\text{-Bu})$ reacts with HCl to give $(t\text{-BuO})_2\mathrm{Cl_2\ W{=}CH}(t\text{-Bu})$.

5 BRIDGING CARBENES

Like CO, carbenes can act as bridging ligands,[55] usually accompanied by a metal–metal bond (**11**). In bridging, carbenes lose some of their unsaturation, and therefore the very high reactivity of their mononuclear analogs. Fischer methylenes are very reactive and barely isolable, while bridging methylenes are well known and relatively stable. This is reflected in the ^{13}C NMR resonance positions of the carbene carbon for terminal and bridging cases: terminal groups resonate at 250–500δ, while bridging groups appear at 100–210δ if an M–M bond is present and at 0–10δ, if not; for comparison, simple metal alkyls resonate at −40 to 0δ. These values probably reflect the change in hybridization required by the carbon atom to form bonds at the angles required by the geometry of the complex. If no M–M bond is present (**12**), then these will be close to 109°, appropriate for sp^3 C. If an M–M bond is present, the M–C–M angle closes to 75–85° and for a terminal carbene, the angle is 0° and an sp^2 C is needed.

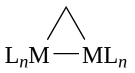

(11)

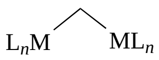

(12)

One of the most valuable synthetic routes to bridging carbenes involves the use of diazomethane (equation 37) and related free carbene precursors;[56] the product of equation (37) has a type (**11**) structure.

$$\mathrm{CpMn(CO)_2(thf) + CH_2N_2 = [\{CpMn(CO)_2\}_2(\mu\text{-}CH_2)] + N_2} \qquad (37)$$

Diazomethane adds not only to monomeric metal complexes but also to compounds containing metal–metal double bonds (equation 38), a reaction that has analogy with the addition of a free carbene to a C=C double bond to give a cyclopropene.[57]

$$\mathrm{[Cp^*{}_2Rh_2(\mu\text{-}CO)_2] + CH_2N_2 = [Cp^*{}_2Rh_2(\mu\text{-}CO)(\mu\text{-}CH_2)] + CO} \qquad (38)$$

The product retains the Rh=Rh double bond in what is really a substitution of CO by $\mathrm{CH_2}$. Insertion of $\mathrm{CH_2}$ into a metal–metal single bond is seen in the synthesis of the platinum ‘A-frame’ complex shown in equation (39),[58] a rare example of a bridging methylene complex without an M–M bond (structure of type (**12**)).

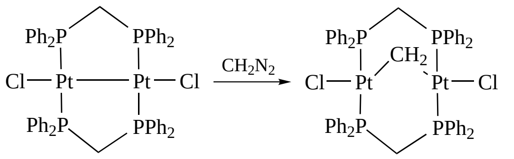

(39)

Comparison of the ^{13}C NMR resonance positions of the carbene carbon for terminal and bridging carbenes reflects the greater unsaturation of the terminal type. Terminal groups resonate at 250 to 500δ, while bridging groups appear at 100 to 210δ if an M–M bond is present, and at 0 to 10δ if not; for comparison, simple metal alkyls resonate at −40 to 0δ. These values probably reflect the change in hybridization required for the carbon atom to form bonds at the angles required by the geometry of the complex. If no metal–metal bond is present (**12**), then these angles will be close to 109° apart and no special rehybridization is required. If an M–M bond is present, the two M–C bonds are usually 75–85° apart. In a terminal carbene, the two bonds are of course formed with the same metal atom.

Carbynes can also bridge three metals, as in the long-known and very stable tricobalt complex (**13**).

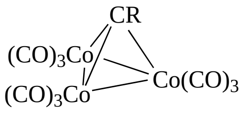

(13)

6 ALKENE METATHESIS

The alkene metathesis reaction[41] (*see Alkene Metathesis*) exchanges alkylidene groups between different alkenes, and is catalyzed by a variety of high oxidation state, early transition metal species (equation 40). The reaction is of interest because it is the strongest bond in the alkene, the C=C bond, that is broken during the reaction. It is also commercially important in the Shell higher olefins process and in the polymerization of cycloalkenes. It is relevant to this article because carbenes are the key intermediates, and the best-known catalyst, (**1**), is a carbene complex.

$$\mathrm{RCH{=}CHR} + \mathrm{R'CH{=}CHR'} \rightleftharpoons \mathrm{RCH{=}CHR'} \qquad (40)$$

The availability of a very recent monograph[2] means that the topic will not be covered in full detail here.

The mechanism of the reaction remained mysterious for many years. Several early papers, the first by Chauvin,[59] suggested the correct solution, but this was not generally accepted until much later. The question was whether the two alkenes bound to the metal and underwent rearrangement (called the pairwise mechanism), or whether the alkenes reacted one at a time (the nonpairwise mechanism). The *Chauvin Mechanism*, equation (41), is now the accepted pathway, and was a particularly imaginative suggestion at a time when both the required metalacyclobutane formation and fragmentation reactions and nonhetroatom substituted carbenes were unknown.

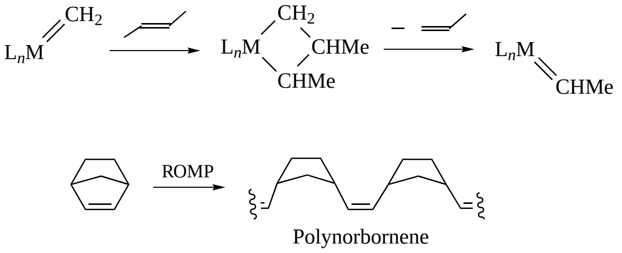

(41)

Metathesis catalysts also have important applications in alkene polymerization via *Ring Opening Metathesis Polymerization*, or ROMP, which leads to the formation of an unsaturated polymer, which means it can be vulcanized, or cross-linked, for greater strength. Commercial norbornene polymerization (mol. wt. $> 2 \times 10^6$) dates from 1976 (CdF Chimie, France). Both Schrock[60] and Grubbs[61,62] have shown that carbene complexes can be active in ROMP. Very good control of chainlength is achieved, and a block copolymer (. . .AAABBB. . .) can be made by adding a second cycloalkene when the first has been consumed. Catalysts that keep their activity even after the substrate has been consumed are *living systems*. Poly(1,4-phenylenevinylene), (p-C_6H_4–CH=CH–)$_n$, obtained in a similar way, has high conductivity when doped, and has useful optical and photochemical properties but is too insoluble to be processable.

7 FURTHER READING

K. H. Doetz, ed. 'Metal Carbenes in Organic Synthesis (Topics in Organometallic Chemistry)', Springer, 2004.

8 REFERENCES

1. R. H. Crabtree, 'The Organometallic Chemistry of the Transition Metals', Wiley, 2001.
2. R. H. Grubbs ed., 'Handbook of Metathesis', Wiley-VCH, Weinheim, 2003.
3. E. O. Fischer and A. Maasbol, *Angew. Chem., Int. Ed. Engl.*, 1964, **3**, 580.
4. R. R. Schrock, *J. Am. Chem. Soc.*, 1974, **96**, 6796.
5. P. J. Brothers and W. R. Roper, *Chem. Rev.*, 1988, **88**, 1293.
6. N. J. Cooper, *Pure Appl. Chem.*, 1984, **56**, 25.
7. G. Bertrand, *Chem. Rev.*, 2000, **100**, 39.
8. K. H. Doetz, 'Transition Metal Carbene Complexes', Verlag Chemie, Weinheim, 1983.
9. E. O. Fischer and A. Maasbol, *Chem. Ber.*, 1967, **100**, 2445.
10. J. S. Miller and A. L. Balch, *Inorg. Chem.*, 1972, **11**, 2069.
11. L. Chugaev, *J. Russ. Chem. Soc.*, 1915, **47**, 776.
12. W. M. Butler, Enemark, J. Parks, A. L. Balch, *Inorg. Chem.*, 1973, **12**, 451.
13. M. Bullock, *J. Am. Chem. Soc.*, 1987, **109**, 8087.
14. R. A. Bell, M. H. Chisholm, D. A. Couch, and L. A. Rankel, *Inorg. Chem.*, 1977, **16**, 677.
15. M. A. Gallop and W. R. Roper, *Adv. Organomet. Chem.*, 1986, **25**, 121.
16. W. Herrmann, B. Reiter, and H. Biersack, *J. Organomet. Chem.*, 1975, **97**, 245.

17. K. Öfele, *Angew. Chem. Int. Ed. Engl.*, 1968, **7**, 950.
18. E. O. Fischer, U. Schubert, and H. Fischer, *Pure Appl. Chem.*, 1978, **50**, 857.
19. C. P. Casey and R. L. Anderson, *Chem. Commun.*, 1975, 895.
20. T. Bodner and A. R. Cutler, *J. Organomet. Chem.*, 1981, **213**, C31.
21. R. S. Bly and R. K. Bly, *Chem. Commun.*, 1986, 1046.
22. A. Davidson and J. P. Selegue, *J. Am. Chem. Soc.*, 1980, **102**, 2455.
23. C. P. Casey and R. L. Anderson, *J. Am. Chem. Soc.*, 1974, **96**, 1230.
24. K. H. Doetz, *J. Organomet. Chem.*, 1979, **182**, 489.
25. H. Werner, E. O. Fischer, B. Heckl, and C. G. Kreiter, *J. Organomet. Chem.*, 1971, **28**, 367.
26. R. R. Schrock, *Science*, 1983, **219**, 13.
27. R. R. Schrock and J. D. Fellmann, *J. Am. Chem. Soc.*, 1978, **100**, 3359.
28. R. R. Schrock, L. W. Messerle, C. D. Wood, and L. J. Guggenberger, *J. Am. Chem. Soc.*, 1978, **100**, 3793.
29. S. J. Mclain, C. D. Wood, L. W. Messerle, R. R. Schrock, F. J. Hollander, W. J. Youngs, and M. R. Churchill, *J. Am. Chem. Soc.*, 1978, **100**, 5962.
30. R. R. Schrock, *J. Am. Chem. Soc.*, 1975, **97**, 6577.
31. R. R. Schrock and P. R. Sharp, *J. Am. Chem. Soc.*, 1978, **100**, 2389.
32. A. J. Schultz, R. K. Brown, J. M. Williams, and R. R. Schrock, *J. Am. Chem. Soc.*, 1981, **103**, 169.
33. J. H. Wengrovius and R. R. Schrock, *Organometallics*, 1982, **1**, 148.
34. R. R. Schrock, *J. Am. Chem. Soc.*, 1976, **98**, 5399.
35. F. N. Tebbe, G. W. Parshall, and G. S. Reddy, *J. Am. Chem. Soc.*, 1978, **100**, 3611.
36. K. A. Brown-Wensley, Sl. Buchwald, L. Cannizzo, L. Clawson, S. Ho, D. Meinhardt, J. R. Stille, D. Straus, and R. H. Grubbs, *Pure Appl. Chem.*, 1983, **55**, 1733.
37. J. R. Stille and R. H. Grubbs, *J. Am. Chem. Soc.*, 1983, **105**, 1664.
38. A. J. Arduengo, R. L. Harlow, and M. Kline, *J Am Chem Soc.*, 1991, **113**, 361.
39. H. W. Wanzlick and H. J. Schonher, *Angew Chem Int Ed. Engl.*, 1968, **7**, 141.
40. K. Ofele and C. G. Kreiter, *Chem Ber-Recl.*, 1972, **105**, 529.
41. D. J. Cardin, B. Cetinkaya, E. Cetinkaya, M. F. Lappert, E. W. Randall, and E. Rosenberg, *J. Chem. Soc. Dalton Trans.*, 1973, 1982.
42. W. A. Herrmann, *Angew Chem Int Ed. Engl.*, 2002, **41**, 1291.
43. T. M. Trnka, J. P. Morgan, M. S. Sanford, T. E. Wilhelm, M. Scholl, T. L. Choi, S. Ding, M. W. Day, and R. H. Grubbs, *J Am Chem Soc.*, 2003, **125**, 2546.
44. E. Peris, J. A. Loch, J. Mata, and R. H. Crabtree, *Chem. Commun.*, 2001, 201.
45. H. M. Wang and I. J. B. Lin, *Organometallics*, 1998, **17**, 972.
46. A. R. Chianese, X. W. Li, M. C. Janzen, J. W. Faller, and R. H. Crabtree, *Organometallics*, 2003, **22**, 1663.
47. S. Gründemann, M. Albrecht, A. Kovacevic, J. W. Faller, and R. H. Crabtree, *J. Chem. Soc. Dalton Trans.*, 2002, 2163.
48. S. Gründemann, A. Kovacevic, M. Albrecht, J. W. Faller, and R. H. Crabtree, *J. Am. Chem. Soc.*, 2002, **124**, 10473.
49. H. Fischer, ‘Carbyne Complexes’, VCH, Weinheim, 1988.
50. A. Mayr and G. A. McDermott, *J. Am. Chem. Soc.*, 1986, **108**, 548.
51. A. Mayr, M. F. Asaro, and T. J. Glines, *J. Am. Chem. Soc.*, 1987, **109**, 580.
52. S. F. Pedersen, R. R. Schrock, M. R. Churchill, and H. J. Wasserman, *J. Am. Chem. Soc.*, 1982, **104**, 6808.
53. E. O. Fischer, G. Huttner, T. L. Lindner, A. Frank, and F. R. Kreissl, *Angew. Chem. Int. Ed. Engl.*, 1976, **15**, 157.
54. J. D. Carter, K. B. Kingsbury, A. Wilde, T. K. Schoch, C. J. Leep, E. K. Pham, and L. McElwee-White, *J. Am. Chem. Soc.*, 1991, **113**, 2947.
55. W. A. Herrman, *Adv. Orgmet. Chem.*, 1982, **20**, 159.
56. K. K. Mayer and W. A. Herrman, *J. Organometal. Chem.*, 1979, **182**, 361.
57. F. Takusagawa, A. Fumagalli, T. F. Koetzle, and W. A. Herrmann, *Inorg Chem.*, 1981, **20**, 3060.
58. M. P. Brown, J. R. Fisher, R. J. Puddephatt, and K. R. Seddon, *Inorg. Chem.*, 1979, **18**, 2808.
59. J. L. Hérisson and Y. Chauvin, *Makromol. Chem.*, 1970, **141**, 161.
60. R. R. Schrock, *Accts. Chem. Res.*, 1990, **24**, 158.
61. R. H. Grubbs and W. Tumas, *Science*, 1989, **243**, 907.
62. V. P. Conticello, D. L. Gin, and R. H. Grubbs, *J. Am. Chem. Soc.*, 1992, **114**, 9708.

Low Coordinated Group 13 Chelates

Samuel Dagorne
Chimie de la Matière Condensée (CNRS), Ecole Nationale Supérieure de Chimie de Paris, Paris, France

1 Introduction 1
2 Tri-coordinate Cationic Group 13 Chelates 1
3 Low-coordinate Monovalent Group 13 Chelates 2
4 Recent Advances in Homogeneous Catalysis by Neutral Tri-coordinate Al Chelates 3
5 Related Articles 3
6 References 3

Abbreviations

$({}^i\mathrm{Pr})_2\mathrm{ATI}^- = N,N'$-diisopropyl-aminotroponiminate; Trip = 2,4,6-triisopropylphenyl; Ar = 2,6-diisopropylphenyl; $\mathrm{Pz}^{\mathrm{R,R'}}$ = 3-R-5-R′-pyrazole.

1 INTRODUCTION

Low-coordinate group 13 complexes have received great attention in the last decade because the often quite electrophilic metal center in these species may be the source of unusual reactivity and thus mediates new chemical transformations. The use of appropriately designed and thus very crowded chelate ligands (*see Chelating Ligands*) has shown a major way to access such low-coordinate compounds because the resulting steric protection of the metal center may strongly limit exchange/redistribution reactions and avoid the formation of aggregates, which are well-known features in group 13 chemistry.[1]

This article mainly focuses on the two major and recent breakthroughs in the area of low-coordinate group 13 chelates: (1) tri-coordinate cationic group 13 chelates and (2) monovalent group 13 chelates. Recent advances in homogeneous catalysis involving more ‘classical’ tri-coordinate Al(III) complexes are also briefly mentioned.

2 TRI-COORDINATE CATIONIC GROUP 13 CHELATES

2.1 Aluminum, Gallium, and Indium Chelates

Although various types of four- to six-coordinate cationic Al chelate species have been developed in the last twenty years and have found applications in catalysis due to their enhanced Lewis acidity (*see Lewis Acids & Bases*),[2] the synthesis and structure of the first tri-coordinate chelate Al cation $\{\mathrm{HC(CMeNAr)_2}\}\mathrm{AlMe}^+$ (**1**) was only recently reported by Jordan.[3] Cation (**1**) can be cleanly obtained as a $\mathrm{B(C_6F_5)_4}^-$ salt by the reaction of the β-diketoiminate neutral precursor $\{\mathrm{HC(CMeNAr)_2}\}\mathrm{AlMe_2}$ with the trityl salt $[\mathrm{Ph_3C}][\mathrm{B(C_6F_5)_4}]$, which proceeds by Me^- abstraction at the metal center (Scheme 1). A weak interaction between the cationic metal center and one meta fluorine of $\mathrm{B(C_6F_5)_4}^-$ (Al−F contact = 2.151(1) Å) is observed in the solid-state structure of the (**1**) $[\mathrm{B(C_6F_5)_4}]$ salt (*see Noncoordinating Anion or Cation*). As a result, the geometry at Al is slightly distorted from planar to pyramidal. The Al–N and Al–C bond distances in (**1**) are slightly shorter than those in the neutral precursor that was ascribed to the increased ionic character of these bonds resulting from the cationic charge (*see Ionic Character*).

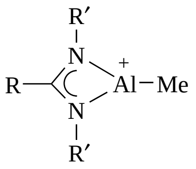

(**2**)

$\mathrm{RC(NR')_2AlMe^+}$

$\mathrm{R = R' = {}^tBu}$

$\mathrm{R = 2,6\text{-}(2,4,6\text{-}Me_3Ph)_2Ph,\ R' = {}^iPr}$

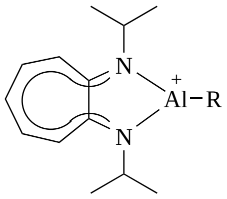

(**3**)

(ATI)AlR$^+$

R = Et, Pr

Thorough studies on various tri-coordinate $\{\mathrm{L\text{-}X}\}\mathrm{AlR}^+$ species (**1–3**) bearing dinitrogen-based bidentate ligands ($\mathrm{L\text{-}X^- = RC(NR')_2}^-$,[4–6] $\mathrm{HC(CMeNAr)_2}^-$,[1,7] and $({}^i\mathrm{Pr})_2\mathrm{ATI}^-$ [8–10]) concluded that such species, which combine a low-coordination number and a charge at Al are highly electrophilic and can be obtained provided two key requirements are fulfilled: (1) the use of a crowded $\mathrm{L\text{-}X^-}$ bidentate ligand that forms a stable Al chelate moiety and (2) the use of an inert counterion (*see Noncoordinating Anion or Cation*).[5,10]

In general, the reactivity of tri-coordinate $\{\mathrm{L\text{-}X}\}\mathrm{AlR}^+$ chelate cations is dominated by their potent Lewis acid character as they form robust four-coordinate cationic $\{\mathrm{L\text{-}X}\}\mathrm{Al(R)(L)}^+$ with Lewis bases such as $\mathrm{NMe_2Ph}$, acetone, and

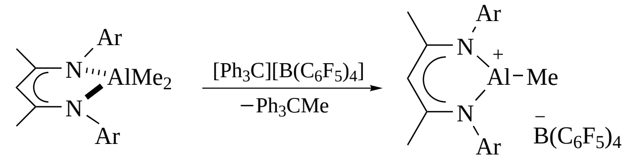

$\mathrm{Ar = 2,6\text{-}{}^iPr_2Ph}$

(**1**)

Scheme 1

acetonitrile. A PhCl adduct $\{(^i\mathrm{Pr})_2\mathrm{ATI}\}\mathrm{Al(Et)(PhCl)}^+$ was also X-ray characterized.**11** This high Lewis acidity is probably responsible for the excellent activity of $\{(^i\mathrm{Pr})_2\mathrm{ATI}\}\mathrm{AlR}^+$ cations in the polymerization of isobutene, propene oxide and, in some cases, of methyl methacrylate. In contrast, studies on the $\{(^i\mathrm{Pr})_2\mathrm{ATI}\}\mathrm{AlR}^+$ species have revealed a poor insertion reactivity in the Al–C bond. In fact, in this regard, these cations appear less reactive than neutral AlR_3 species. Rather, they show a selective and exclusive preference for β-hydride transfer to unsaturated substrates such as ethylene and acetone.**10** The reactivity trends observed for these cations versus those of the AlR_3 neutral species agree with theoretical calculations.**12,13** Apart from this, it is also noteworthy that $\{(^i\mathrm{Pr})_2\mathrm{ATI}\}\mathrm{AlEt}^+$ catalytically dimerize $^t\mathrm{BuC{\equiv}CH}$ via an insertion/σ-bond metathesis cycle (*see σ-Bond Metathesis*).**10**

The synthesis of the Ga and In tri-coordinate chelates $\{(^i\mathrm{Pr})_2\mathrm{ATI}\}\mathrm{MMe}^+$ (M = Ga, In) was also reported.**11,14** These cations, which both crystallize as weakly four-coordinated PhCl adducts, exhibit an enhanced Lewis acidity versus that of the corresponding MMe_3.

2.2 Boron Chelates

A significant contribution in the area of low-coordinate boron chemistry was realized by Corey with the synthesis of chiral tri-coordinate and cationic oxaborolidine complexes such as (**4**), for use in asymmetric catalysis.**15,16** These compounds can be obtained by reaction of the desired chiral aminophenol with BBr_3, and they are highly effective catalysts for enantioselective Diels–Alder reactions. Smith also reported the generation of the tri-coordinate boron cation $\{\mathrm{HC(CMeNAr)}_2\}\mathrm{BMe}^+$, obtained by a Me^- abstraction reaction of $\{\mathrm{HC(CMeNAr)}_2\}\mathrm{BMe}_2$ by $\mathrm{B(C_6F_5)_3}$.**17** This boron cation appears to be much less Lewis acidic than its Al counterpart.

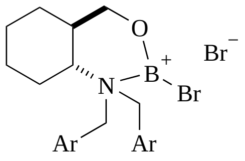

Ar = 3,5-$\mathrm{Me_2Ph}$

(**4**)

3 LOW-COORDINATE MONOVALENT GROUP 13 CHELATES

3.1 Tri-coordinate Monovalent Group 13 Chelates

Nearly unknown 10 years ago, stable monovalent and monomeric group 13 species have been the subject of a few reports since then. In 1994, Piggott reported that the reaction of the bulky tridentate hydroboratotris(pyrazolyl) $\mathrm{HB(Pz^{Ph,H})^-}$ (*see Tris(pyrazolyl)borates*) with InI yields the air-stable, three-coordinate In(I) complex $\{\mathrm{HB(Pz^{Ph,H})_3}\}\mathrm{In}$ (**5**), which is the first monomeric and monovalent group 13 complex (Tl excluded).**18** In this complex, the arrangement of the tridentate ligand-phenyl rings forms a pocket about the In center and its lone pair of electrons, which may be crucial for its stabilization. The closely related tri-coordinate Ga(I) complex $\{\mathrm{HB(Pz^{Ph,H})_3}\}\mathrm{Ga}$ and several other tri-coordinate hydroboratotris(pyrazolyl) In(I) species were subsequently synthesized.**19,20**

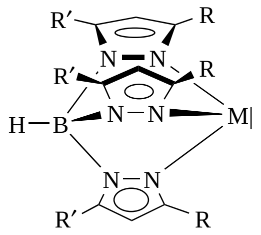

M = In, R = Ph, R′ = H
M = In, R = R′ = ^{t}Bu
M = Ga, R = R′ = ^{t}Bu

(**5**)

3.2 Two-coordinate Monovalent Group 13 Chelates

There has recently been an increasing interest in the design and synthesis of stable monovalent two-coordinate bidentate group 13 complexes, which are isoelectronic to carbene species. The use of bulky bidentate L-X^- or $\mathrm{X_2}^{2-}$-type ligands combined with the appropriate synthetic methodology has opened the way to these unique species whose structural and reactivity studies remain an ongoing effort.

In 1999, Schmidbaur reported that the reduction by potassium metal of the dinuclear Ga(II) compound (**6**), previously synthesized by Cowley,**21** affords the two-coordinate Ga anion (**7**) as a $\mathrm{K(18\text{-}crown\text{-}6)(THF)_2}^+$ (*see Crown Ethers*) salt (Scheme 2).**22** This anion is the first two-coordinate chelate group 13 complex and was X-ray characterized. The $4\mathrm{s}^2$ lone pair of electrons on the Ga atom and the two-electron pairs donated by the nitrogen

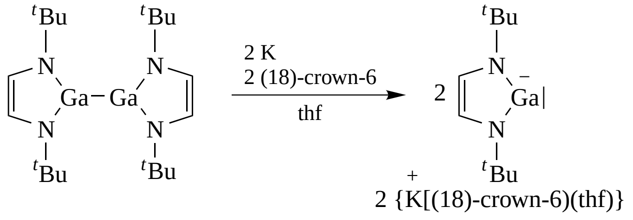

(**6**) (**7**)

Scheme 2

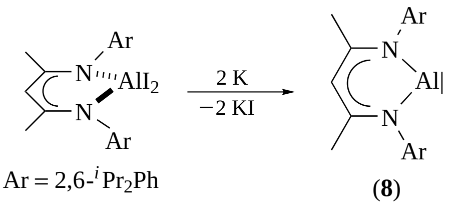

Scheme 3

atoms make up for a sextet configuration. In the present case, the Ga anion may be stabilized by the steric bulk of the bidentate combined with the 6π-electrons system of the heterocycle.

More recently, Roesky and Power showed that the very crowded β-diketoiminate $HC(CMeNAr)_2^-$ was suitable for the preparation of the neutral two-coordinate monovalent Al and Ga species. While the Ga derivative $\{HC(CMeNAr)_2\}Ga$ was directly accessible via a salt metathesis reaction (*see Metathesis*) between $[HC(CMeNAr)_2]Li$ and GaI, the Al derivative $\{HC(CMeNAr)_2\}Al$ (**8**) was obtained by reduction of the Al(III) di-iodo precursor $\{HC(CMeNAr)_2\}AlI_2$ with potassium (Scheme 3).[23,24] The work on Al has been very recently reviewed.[25] X-ray diffraction and theoretical studies on (**8**) suggest that its excellent stability most likely results from the significant steric protection afforded by the Ar groups and the presence of an sp-like hybrid lone pair of electrons at the metal center pointing outside the chelate ring. The Al–N bond distances are longer in $\{HC(CMeNAr)_2\}Al$ than those in the related Al(III) species, which was ascribed to the less Lewis acidic Al(I) versus Al(III).

Reactivity studies of two-coordinate chelate group 13 species have just begun and appear particularly interesting because such species may exhibit both a Lewis acid character (due to the sextet configuration at the metal center) and a Lewis base one (due the lone pair of electrons at the metal center) (*see Lewis Acids & Bases*). For instance, the two-coordinate Ga chelate $\{HC(CMeNAr)_2\}Ga$ reacts with $B(C_6F_5)_3$ to form the gallium–boron donor-acceptor complex $\{HC(CMeNAr)_2\}Ga \rightarrow B(C_6F_5)_3$, showing that such low-coordinate species can behave as effective Lewis bases.[26] Alternatively, the Al(I) and Ga(I) complexes $\{HC(CMeNAr)_2\}M$ (M = Al, Ga) behave like Lewis acids when reacted with the bulky azide compound $TripN_3$ to yield, along with N_2 formation, the first monomeric Al and Ga imide complexes $\{HC(CMeNAr)_2\}M–N(Trip)$ with M = Al and Ga, respectively.[27] In the case of the Ga imide complex (**9**), experimental data and theoretical calculations support a multiple bond character for the exocyclic Ga–N bond.

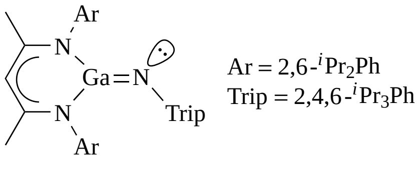

(**9**)

4 RECENT ADVANCES IN HOMOGENEOUS CATALYSIS BY NEUTRAL TRI-COORDINATE Al CHELATES

The use of Al(III) complexes as catalysts in Lewis acid–mediated reactions has been known for years.[28] However, recent years have witnessed interesting developments in this area with the use of ingeniously designed neutral tri-coordinate Al(III) chelates. Representative examples involving such chelates as catalysts include: (1) asymmetric acyl halide-aldehyde cyclocondensations,[29–31] (2) asymmetric Meerwein–Schmidt–Ponndorf–Verley reduction of prochiral ketones,[32] (3) aldol transfer reactions[33] and (4) asymmetric rearrangement of α-amino aldehydes to access optically active α-hydroxy ketones.[34] It is important to point out that, in most cases, the use of a chelating ligand appears critical for effective catalytic activity and enantioselectivity.

5 RELATED ARTICLES

Aluminum: Organometallic Chemistry; Gallium: Organometallic Chemistry; Hard & Soft Acids and Bases; Indium: Organometallic Chemistry.

6 REFERENCES

1. K. B. Starowiejski, in ‘Chemistry of Aluminium, Gallium, Indium and Thallium’, ed. A. J. Downs, Chapman & Hall, London, 1993, p. 322.
2. D. A. Atwood, *Coord. Chem. Rev.*, 1998, **176**, 407.
3. C. E. Radzewich, I. A. Guzei, and R. F. Jordan, *J. Am. Chem. Soc.*, 1999, **121**, 8673.
4. M. P. Coles and R. F. Jordan, *J. Am. Chem. Soc.*, 1997, **119**, 8125.
5. S. Dagorne, I. A. Guzei, M. P. Coles, and R. F. Jordan, *J. Am. Chem. Soc.*, 2000, **122**, 274.

6. J. A. R. Schmidt and J. Arnold, *Organometallics*, 2002, **21**, 2306.
7. C. E. Radzewich, I. A. Guzei, and R. F. Jordan, *J. Am. Chem. Soc.*, 1998, **120**, 9384.
8. E. Ihara, V. G. Young Jr, and R. F. Jordan, *J. Am. Chem. Soc.*, 1998, **120**, 8277.
9. A. V. Korolev, I. A. Guzei, and R. F. Jordan, *J. Am. Chem. Soc.*, 1999, **121**, 11605.
10. A. V. Korolev, E. Ihara, I. A. Guzei, V. G. Young Jr, and R. F. Jordan, *J. Am. Chem. Soc.*, 2001, **123**, 8291.
11. A. V. Korolev, F. Delpech, S. Dagorne, I. A. Guzei, and R. F. Jordan, *Organometallics*, 2001, **20**, 3367.
12. G. Talarico and P. H. M. Budzelaar, *Organometallics*, 2000, **19**, 5691.
13. G. Talarico and V. Busico, *Organometallics*, 2001, **20**, 5691.
14. F. Delpech, I. A. Guzei, and R. F. Jordan, *Organometallics*, 2001, **20**, 1167.
15. Y. Hayashi, J. J. Rohde, and E. J. Corey, *J. Am. Chem. Soc.*, 1996, **118**, 5502.
16. K. T. Sprott and E. J. Corey, *Org. Lett.*, 2003, **5**, 2465.
17. B. Qian, S. W. Baek, and M. R. Smith III, *Polyhedron*, 1999, **18**, 2405.
18. A. Frazer and B. Piggott, *J. Am. Chem. Soc.*, 1994, **116**, 4127.
19. M. C. Kuchta, J. B. Bonanno, and G. Parkin, *J. Am. Chem. Soc.*, 1996, **118**, 10914.
20. M. C. Kuchta, H. V. R. Dias, S. G. Bott, and G. Parkin, *Inorg. Chem.*, 1996, **35**, 943.
21. D. S. Brown, A. Decken, and A. H. Cowley, *J. Am. Chem. Soc.*, 1995, **117**, 5421.
22. E. S. Schmidt, A. Jockisch, and H. Schmidbaur, *J. Am. Chem. Soc.*, 1999, **121**, 9758.
23. C. Cui, H. W. Roesky, H.-G. Schmidt, M. Noltemeyer, H. Hao, and F. Cimpoesu, *Angew. Chem., Int. Ed. Engl.*, 2000, **39**, 4274.
24. N. J. Hardman, B. E. Eichler, and P. P. Power, *Chem. Commun.*, 2000, 1991.
25. M. N. Sudheendra Rao, H. W. Roesky, and G. Anantharaman, *J. Organomet. Chem.*, 2002, **646**, 4.
26. N. J. Hardman, P. P. Power, J. D. Gorden, C. L. B. Macdonald, and A. H. Cowley, *Chem. Commun.*, 2001, **125**, 1866.
27. N. J. Hardman, C. Cui, H. W. Roesky, W. H. Fink, and P. P. Power, *Angew. Chem.*, 2001, **113**, 2230.
28. J. J. Eisch, in ‘Comprehensive Organometallic Chemistry II’, eds. E. W. Abel, F. G. A. Stone, and G. Wilkinson, Elsevier, Oxford, 1995, Vol. 11, Chap. 6.
29. S. G. Nelson, C. Zhu, and X. Shen, *J. Am. Chem. Soc.*, 2004, **126**, 14.
30. Z. Wan and S. G. Nelson, *J. Am. Chem. Soc.*, 2000, **122**, 10470.
31. S. G. Nelson, T. J. Peelen, and Z. Wan, *J. Am. Chem. Soc.*, 1999, **121**, 9742.
32. E. J. Campbell, H. Zhou, and S. T. Nguyen, *Angew. Chem.*, 2002, **114**, 1062.
33. I. Simpura and V. Nevalainen, *Angew. Chem.*, 2000, **112**, 3564.
34. T. Ooi, A. Saito, and K. Maruoka, *J. Am. Chem. Soc.*, 2003, **125**, 14.

Main Group Carbenes

Claire J. Carmalt
University College London, London, UK

1 Introduction 1
2 Groups 1 and 2 1
3 Group 13 4
4 Group 14 10
5 Carbene Adducts of Phosphorus, Arsenic, and Antimony 12
6 Carbene Complexes of the Chalcogens 15
7 Carbene Adducts of Chlorine, Bromine, and Iodine 16
8 Related Articles 17
9 References 17

Abbreviations

TMP = 2,2,6,6-tetramethylpiperidide; Cp* = pentamethylcyclopentadienyl (C_5Me_5); Mes = mesitylene (2,4,6-$Me_3C_6H_2$); THF = tetrahydrofuran; OTf = triflate (OSO_2CF_3) Mes* = 2,4,6-tri-*tert*-butylphenyl (2,4,6-t-$Bu_3C_6H_2$).

1 INTRODUCTION

There has been considerable interest in main group carbene complexes since 1993. Many fascinating advances have been made particularly concerning the solid-state structure of these carbene complexes, which has resulted in an understanding of their electronic structure. Undoubtedly, the isolation of stable crystalline carbenes (**1–4**) has enabled the chemistry of these compounds to be investigated,[1–5] and owing to their high nucleophilicity they can be used as ligands in the formation of both transition and main group complexes.[6,7] These carbenes even form stable complexes with metals that normally show no tendency for π back-donation. Carbenes (**1–4**) represent carbon compounds in oxidation state II and as such are good reducing agents. Generally, the singlet carbene acts as a two-electron donor in a similar manner to tertiary phosphines (*see* ***P-donor Ligands***). Thus, N-heterocyclic carbenes (**1–4**) are reported to complex with around 50 elements, as highlighted in a review by Herrmann and Köcher.[7]

Recently, significant progress has been made in the characterization of main group adducts of these carbenes.[8] This chapter will deal only with carbene compounds of the main group elements reported since 1993 and excludes transition metal carbene compounds (such compounds may be found in the article ***Carbene Complexes***).

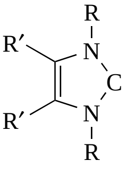
(**1**)

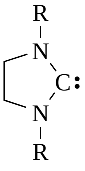
(**2**)

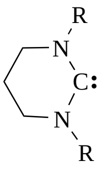
(**3**)

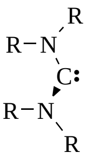
(**4**)

2 GROUPS 1 AND 2

2.1 Complexation of Stable Carbenes with Alkali Metals

There are few examples of carbene complexes of group 1 metals. This is surprising since N-heterocyclic carbenes, such as compounds (**1–4**), are generally synthesized via the C-deprotonation of formamidinium using bases with alkali metal counterions, for example, KO-t-Bu.[1–5] The structural characterization of alkali metal carbene complexes would give information on the interactions between carbenes and alkali metals and thus lead to some understanding of the reactivity properties of these complexes in solution. The first example of an alkali metal–carbene complex (**5**) was isolated from the reaction of (**3**) (R = i-Pr) with $KN(SiMe_3)_2$.[9] The structure of (**5**) showed that dimeric molecules are present with the $N(SiMe_3)_2$ groups acting as bridging ligands. The K–carbene interaction is largely of an electrostatic ion–dipole nature as suggested by the K···C distance of 3.00 Å.

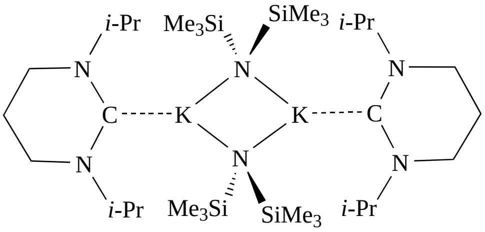
(**5**)

The interaction of $[MN(SiMe_3)_2]$ (M = Li, Na, K) and LiTMP with carbenes (**1**) (R = i-Pr, R′ = Me), (**3**) (R = i-Pr) and (**4**) (R = Me) in solution was also reported.[9] Evidence of complexation of these carbenes with the Li, Na, and K species in solution was given by the ^{13}C NMR shifts for the relevant carbene center. Recently, the reaction of carbene (**1**) with lithium 1,2,4-tris(trimethylsilyl)cyclopentadienide was reported to result in monomeric carbene complexes with 1:1 stoichiometry (R′ = H; R = t-Bu (**6**), adamantyl (**7**), or 2,4,6-trimethylphenyl(**8**)).[10] The crystal structure of (**6**) showed that the cyclopentadienyl ring is coordinated in an η^5-fashion to the lithium center (*see* ***Alkali Metals: Organometallic Chemistry***) and there is a single σ-interaction present between the lithium and the carbene center (Li–C(carbene) 2.155 Å).

Recently, a novel homoleptic carbene–lithium complex (**9**) was isolated from the deprotonation of a monoanionic, tridentate hydrotris(3-methylimidazolin-2-ylidene)borate carbene ligand with n-BuLi (equation 1).[11] An X-ray structure determination of compound (**9**) showed an unusual solvent-free complexation of each lithium atom by four carbene carbon atoms. Thus, terminal binding to the lithium centers of two carbon atoms from each hydrotris(3-methylimidazolin-2-ylidene)borate anion occurs, with the third carbene carbon atom adopting a bridging mode of coordination. The Li–C bonds to the terminal carbene atoms are 2.138(4) and 2.147(4) Å, which are similar to those observed in compound (**6**). In contrast, the Li–C bond distances to the bridging carbon atoms vary and are much longer (2.210(4) and 2.311(4) Å).

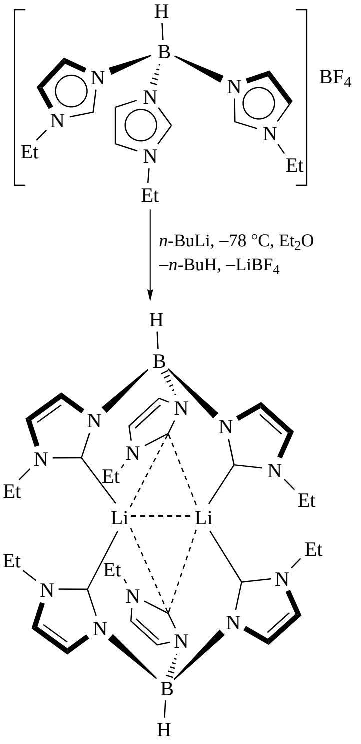

(1)

(**9**)

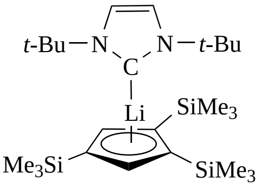

(**6**)

2.2 Carbenes Complexes of Alkaline Earth Metals

The reaction of polymeric beryllium chloride $(BeCl_2)_n$ with nucleophilic carbene (**1**) (R = Me, R′ = H) is reported (equation 2) to yield a cationic carbene complex (**10**).[12] The structure of the cation in (**10**) consists of the beryllium center adopting a distorted tetrahedral coordination. Although the Be–Cl bond distance (2.083 Å) is long when compared with other tetravalent complexes (*see* ***Beryllium: Inorganic Chemistry***), the addition of excess carbene failed to displace the second chloride ion. The Be–C(carbene) bond distances observed are similar to Be–C single bond distances and all the ring distances of the carbene correspond to those found in the free carbene.[1]

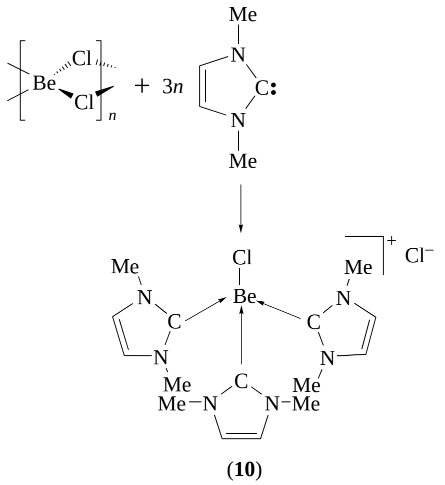

(2)

(**10**)

Reaction of carbene (**1**) (R = Mes or adamantyl, R′ = H) with one equivalent of diethyl magnesium resulted in the formation of the 1:1 adduct, that is, (**1**)·$MgEt_2$, as shown in Scheme 1.[13] The solid-state structure of (**1**)·$MgEt_2$ (**11**, R = Mes) is dimeric via bridging ethyl groups. However, due to greater steric protection provided by adamantyl groups, the structure of (**1**)·$MgEt_2$ (**12**, R = adamantyl) is monomeric with the Mg center adopting a trigonal planar coordination geometry.[13]

Carbene complexes of alkaline earth metal amides[7] and metallocenes have also been reported.[14,15] Reaction of calcium, strontium, and barium bis(trimethylsilyl)amides $[M\{N(SiMe_3)_2\}_2(thf)_2]$ (M = Ca, Sr, Ba) with two equivalents

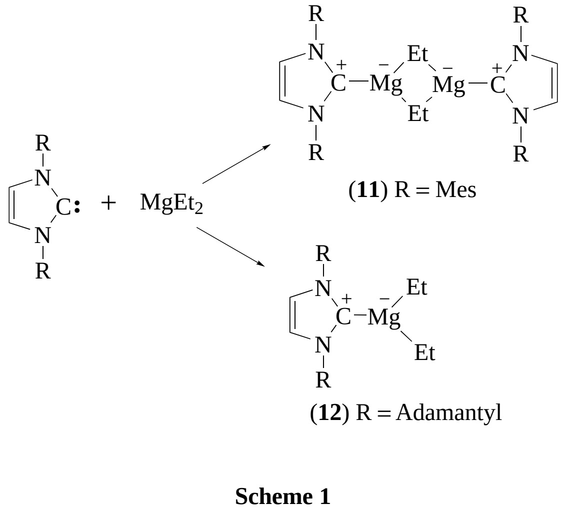

Scheme 1

of (**1**) (R = Me or *t*-Bu, R′ = H) resulted in the displacement of two thf molecules (equation 3) to yield the biscarbene adducts (**13**).[7] The solubility and stability of the adducts was observed to decrease Ca to Ba.

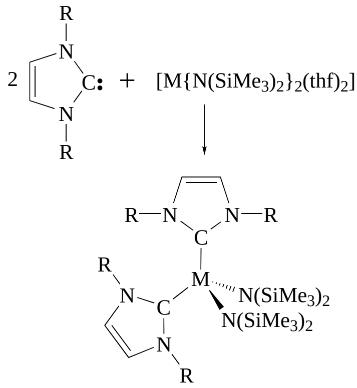

(3)

(**13**) M = Ca, Sr, Ba; R = Me, *t*-Bu

Carbene adducts of alkaline earth metallocenes may be prepared by the 1:1 reaction of carbene (**1**) (R = R′ = Me) with Cp^*_2M (M = Mg, Ca, Sr, Ba).[14] The structure of the magnesium adduct (**1**)·$MgCp^*_2$ (**14**) revealed two different bonding modes for the Cp* ligands (*see* ***Alkaline Earth Metals: Organometallic Chemistry***). Thus, one is coordinated in a η^5-manner (av. Mg–C 2.477(20) Å), whereas the second Cp* ring exhibits a ‘slipped’ geometry (three carbon atoms closest to Mg have an av. Mg–C distance of 2.460(85) Å). Interestingly, the closest Mg–C interaction is with the carbene center (2.192(2) Å). The Mg center in (**14**) adopts a trigonal planar geometry. In contrast to the magnesium adduct, the structures of carbene adducts of the heavier analogues (Ca and Ba) show that both Cp* ligands adopt an η^5-coordination (**15**). Unfortunately, the structure of the Sr analogue is not available. Overall, the carbene ligands show a preference for σ-bonding to the alkaline earth metal center and the metal–carbene distance is always smaller than the M–C(Cp*) distance irrespective of whether the ligand is π- or σ-bonded.

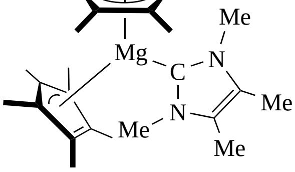

(**14**)

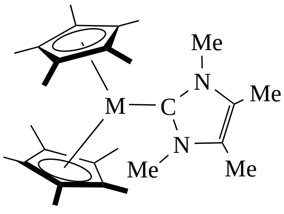

(**15**)

The heavier alkaline earth metals can also form bis(carbene) adducts, of the type $(\mathbf{1})_2\cdot MgCp^*_2$ (M = Sr, Ba; R = R′ = Me).[14] An X-ray structure determination of the strontium adduct (**16**) showed that the strontium center adopts a pseudotetrahedral geometry with two carbenes and two Cp* ligands (Sr–C(carbene) 2.854(5) and 2.868(5) Å; av. Sr–C(Cp*) 2.917(12) Å). The coordinated carbene ligands show a geometry that is similar to unligated carbene.

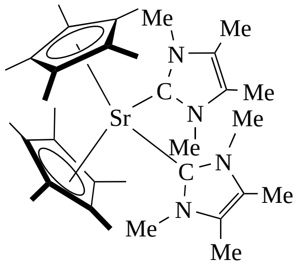

(**16**)

Recently, a series of carbene complexes of new metallocenes of group II elements were reported.[15] Thus, reaction of carbene (**1**) (R = *i*-Pr, R′ = Me) with Cp'_2Mg or $[(C_5Me_4R'')_2M(L_x)(L_y)]$ (M = Ca: R″ = H, $L_x = NH_3$, Ly = THF or R″ = *i*-Pr, L_x = THF; M = Ba, R″ = *t*-Bu, $L_x = L_y$ = THF; M = Sr, R″ = Me, $L_x = L_y$ = THF) afforded the 1:1 adducts (**1**)·$MgCp'_2$ (Cp′ = C_5Me_4H (**17**) or C_5H_3-1-($SiMe_3$)-3-*t*-Bu (**18**)) and (**1**)·$M(C_5Me_4R'')_2$ (**19**). The structures of (**17**) and (**19**) are similar to (**14**) and (**15**) described above, such that the metal center adopts a pseudo-trigonal planar geometry and both Cp′ ligands are coordinated in an η^5-fashion, except with magnesium where one Cp′ ligand is slipped to an η^3 bond. The M–C(carbene) distances are also comparable to (**14**) and (**15**) and confirm that the bond strength of these bonds are dependent on the alkaline earth metal size. As expected, bulky Cp ligands result in longer metal to carbene carbon bonds.

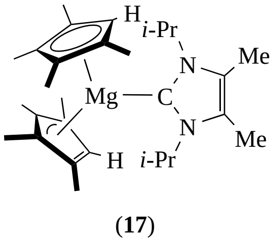

(**17**)

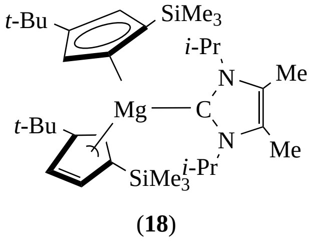

(**18**)

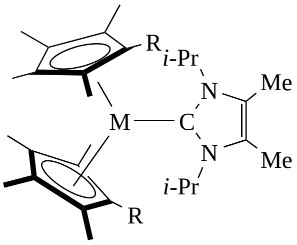

(**19**: M = Ca: R″ = H or *i*-Pr; M = Ba, R″ = *t*-Bu; M = Sr, R″ = Me)

3 GROUP 13

3.1 Carbene Adducts of Group 13 Hydrides

Aluminum and gallium trihydrides and their adducts with N−, P− or O− donor Lewis bases have been extensively studied (*see* ***Aluminum: Inorganic Chemistry*** and ***Ammonia & N-donor Ligands***).[16] Recent interest in these complexes is the result of their potential applications in a wide range of areas such as organic synthesis[17] and chemical vapor deposition (*see Chemical Vapor Deposition*) of 13−15 semiconductors.[18] Complexation of carbenes with the heavier group 13 trihydrides have only been studied recently.[19–25] However, the chemistry of borane adducts of carbenes have been investigated and when (**1**) (R = Me, Et, *i*-Pr, R′ = Me) was allowed to react with $Me_2S{\cdot}BH_3$, the first carbene−BH_3 adduct (**20**) was isolated, as shown in Scheme 2.[26] Both the X-ray structure and ab initio calculations (*see Ab Initio Calculations*) on (**20**) indicate that weak π-interactions between the C=C unit and the N–C–N moiety and within the ring are present with alternating bond lengths. Accordingly, the electronic structure for the imidazole fragment can be described as intermediate between that of a fully delocalized imidazolium ion and a free carbene. The ^{11}B NMR chemical shifts for (**20**) were typical of a ylide-borane adduct ($\delta = -35$) and the $^{1}J(^{1}H,^{11}B)$ coupling constant is similar to that of an anionic complex, that is, $[(C_6H_5)BH_3]^-$. Recently, the reaction of carbene (**1**) and $BH_4{\cdot}THF$ was reported to also yield a carbene−BH_3 adduct (**20**, R = Mes, R′ = H).[27] The structure of (**20**) revealed head-to-tail alignment of (**1**)$\cdot BH_3$ in the solid state with the closest intermolecular contact occurring through a [C–H···H–B] hydrogen bond.

A range of carbene−metal trihydride complexes (**21–27**) were formed from the reaction of (**1**) (R = *i*-Pr, R′ = Me; R = Mes, R′ = H; also when M = Al, R = 2,6-*i*-$Pr_2C_6H_3$, R′ = H) with $[MH_3(NMe_3)]$ (M = Al, Ga, In) or $[LiMH_4]$ (M = Al, Ga), as shown in Scheme 2.[19–24] Although 2:1 adducts of *N*-heterocyclic carbene with indium halides have been isolated (Section 3.2),[28] attempts to form 2:1 adducts via the addition of two equivalents of carbene to $[InH_3(NMe_3)]$ failed. This is presumably due to the fact that InX_3 (X = Cl, Br) is more Lewis acidic than InH_3. The crystal structures of (**21–25**) and (**27**) are all similar and showed that the complexes are monomeric. The group 13 metal center adopts a distorted tetrahedral environment with long M–C(carbene) bond lengths when compared to typical M–C single bonds. As for compound (**20**), the carbene ligand in (**21–25**) and (**27**) exhibits a degree of delocalization somewhere between that of the free carbene and the fully delocalized imidazolium cation. The thermal stability of (**21–27**) was found to decrease in the order (**21**) > (**22**) > (**23**) > (**26**) > (**24**) > (**27**) > (**25**). Moreover, the indane complex, (**25**), is unstable in solution above −20 °C and decomposes in the solid state above −5 °C, depositing indium metal and generating a gas.[20–22] In contrast, compound (**27**) is stable in the solid state (under an inert atmosphere) up

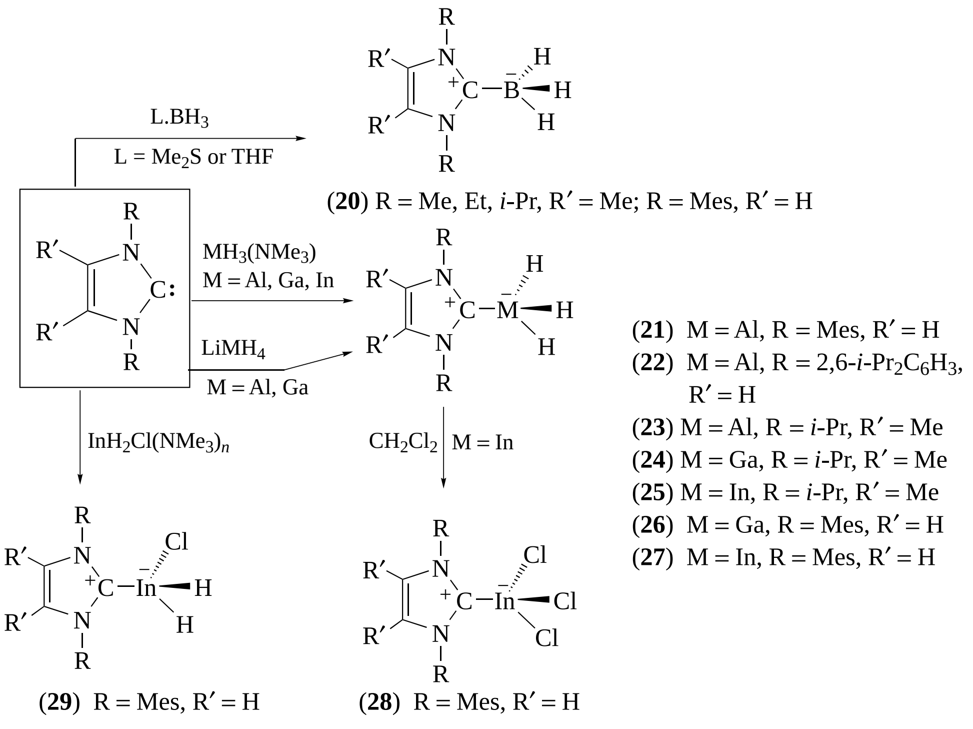

L.BH3
L = Me2S or THF
(20) R = Me, Et, i-Pr, R′ = Me; R = Mes, R′ = H
MH3(NMe3)
M = Al, Ga, In
LiMH4
M = Al, Ga
InH2Cl(NMe3)n
CH2Cl2
M = In
(21) M = Al, R = Mes, R′ = H
(22) M = Al, R = 2,6-i-Pr2C6H3, R′ = H
(23) M = Al, R = i-Pr, R′ = Me
(24) M = Ga, R = i-Pr, R′ = Me
(25) M = In, R = i-Pr, R′ = Me
(26) M = Ga, R = Mes, R′ = H
(27) M = In, R = Mes, R′ = H
(29) R = Mes, R′ = H
(28) R = Mes, R′ = H

Scheme 2

to 115 °C.[23] In solution, the stability of (**27**) is dependent on the solvent. For example, toluene solutions of (**27**) are stable at room temperature for over three months. However, CH_2Cl_2 solutions of (**27**) are unstable and chloride abstraction from the CH_2Cl_2 solvent takes place at 25 °C and the adduct (**1**)·$InCl_3$ (**28**) is formed in moderate yield, as shown in Scheme 2. The high thermal stability of (**27**) is probably a result of a combination of the large steric bulk and high nucleophilicity of carbene (**1**) ($R = Mes$, $R' = H$). Indeed, the high nucleophilicity of the N-heterocyclic carbene is shown by the alane and gallane complexes, (**21–24**) and (**26**), which have much greater stability than normally observed for Lewis base adducts of the group 13 trihydrides (*see* ***Aluminum: Inorganic Chemistry*** and ***Gallium: Inorganic Chemistry***). Such complexes usually decompose cleanly to the metal, hydrogen, and ligand.[19–24] The greater stability of (**27**) versus (**25**) is thought to be due to (**25**) decomposing via a different pathway that involves metallation of the isopropyl carbene substituents by InH_3 with concomitant loss of H_2. However, compound (**27**) decomposes via ligand loss or dihydroimidazole formation.

The carbene adduct (**1**)·InH_3 (**27**, $R = Mes$, $R' = H$), has been used as a selective reducing agent for unsaturated organic functionalities.[29] In addition, the reactivity of (**27**) toward a variety of transition metal complexes has been reported.[30] In general, InH_3 acts as a carbene and/or a hydride transfer reagent to transition metal centers rather than forming heterobimetallic complexes.

A mixed indium hydride halide complex, (**1**)·InH_2Cl (**29**) has been prepared from the 1:1 reaction of $[InH_2Cl(NMe_3)_n]$ with carbene (**1**) ($R = Mes$, $R' = H$), as shown in Scheme 2.[23] The structure of (**29**) is monomeric with the geometry at the In center close to tetrahedral. The In−C distance (2.244(6) Å) is similar to those observed in (**28**) (2.200(7) Å) and (**25**) (2.253(5) Å). A related mixed gallium hydride iodide complex (**1**)·GaH_2I (**30**) has been isolated from the reaction of (**26**) with ‘GaI’, with concomitant deposition of gallium metal.[24] Complex (**30**) is isostructural with the related indium complex (**29**) and has a Ga−C bond distance of 2.022(4) Å.

Bidentate N-heterocyclic carbene complexes of group 13 hydrides have been reported recently.[25] Treatment of carbene (**31**) with two equivalents of $[MH_3(NMe_3)]$ ($M = Al$, Ga, In) or $LiInH_4$ (equation 4) resulted in the formation of the 1:2 adducts (**32–34**). The Al and Ga analogues are moderately thermally stable (*dec.* 122−124 and 168−171 °C) but less stable than compounds (**21–24**) and (**26**). In contrast, the indane adduct (**34**) decomposes at 10−12 °C. The structures of (**32**) and (**34**) were determined and found to be isostructural. Both (**32**) and (**34**) are monomeric and the bidentate carbene ligand (**31**) bridges two MH_3 fragments in a similar manner to bisphosphine complexes.

It is worth noting that recently a novel biscarbene complex of a polyhedral borane was reported.[31] Hydration of the known dicarbonyl $B_{12}H_{10}(CO)_2$ resulted in the formation of the bis(dihydroxy-carbene) complex $B_{12}H_{10}[C(OH)_2]_2·4H_2O$ (**35**). Bond order calculations show negligible π-bonding between the cluster and the carbene diol groups (B−C 1.589(1) Å).

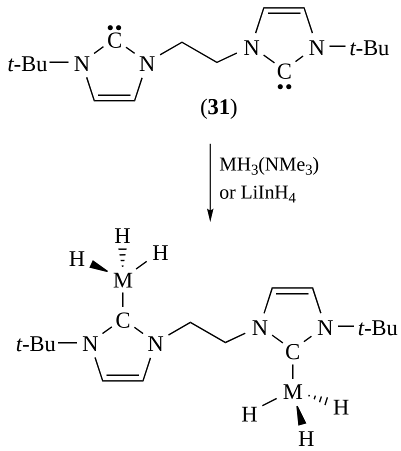

(4)

(**32**) M = Al
(**33**) M = Ga
(**34**) M = In

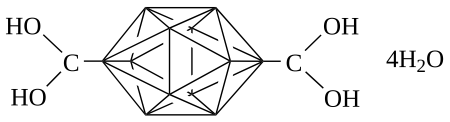

(**35**)

3.2 Carbene Complexes of Group 13 Halides

Reaction of (**1**) ($R = Me$, Et, *i*-Pr, $R' = Me$; $R = Mes$, $R' = H$, Cl) with $BF_3(OEt_2)$ (equation 5) resulted in the isolation of the 1:1 adduct with BF_3 (**36**).[26,32,33] Usually, carbene ligands cannot be stabilized by electron-poor coordination fragments because traditional carbenes show a pronounced tendency toward metal-to-ligand π back-donation. However, N-heterocyclic carbenes do not rely on back-donation for stabilization because of the delocalization of the nitrogen lone pair in these carbenes (e.g. carbene **1**). Thus, compound (**36**) was found to be thermally stable and could be sublimed without decomposition. The structure of (**36**) ($R = R' = Me$; $R = Mes$, $R' = H$, Cl) was determined and the geometry was found to be similar to the borane (BH_3) adduct (**20**), except that the B–C(carbene) bond distance was longer (B–C(carbene): 1.635(5) Å ($R = Mes$, $R' = H$), 1.669(6) Å ($R = Mes$, $R' = Cl$), and 1.603(3) Å for **20**).[26,33] The longer B–C(carbene) bond distance when $R' = Cl$ versus $R' = H$, suggests that the boron−carbon bond is weaker due to the electron-withdrawing chlorine atoms.[33]

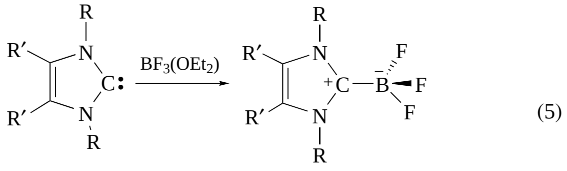

(**36**) R = Me, Et, *i*-Pr, R′ = Me
R = Mes, R′ = H or Cl

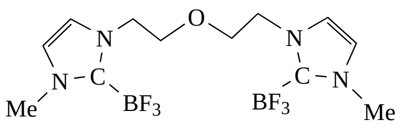

(**37**)

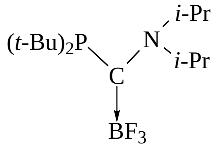

(**38**)

Two further carbene adducts of BF_3 have been reported recently.[34,35] A boron trifluoride adduct (**37**) of a bidentate nucleophilic heterocyclic carbene was obtained as a by-product from the reaction of di-silver-bis-[bis-(2-(3-methylimidazolin-2-yliden-1-yl))ethyl]ether di-tetrafluoroborate with $ZrCl_4$.[34] The geometry at each boron center is similar to that observed in (**36**) and the B–C(carbene) distance is 1.644(2) Å. An acyclic $(i\text{-Pr}_2N)(t\text{-Bu}_2P)C{\cdot}BF_3$ adduct (**38**) has been prepared from the reaction of a (amino)(phosphino)carbene with $BF_3(OEt_2)$.[35] Compound (**38**) was characterized by NMR spectroscopy. Both the ^{11}B ($\delta = -14.6$) and ^{19}F ($\delta = -62.0$) NMR signals appear as quartets ($^1J_{BF} = 43$ Hz) without any coupling with phosphorus, showing that the BF_3 group is only interacting with the carbene center. Interestingly, the softer Lewis acid BH_3 interacts selectively with the phosphorus lone pair rather than the carbene center.[35]

Recently, a series of complexes between indium(III) halides and carbene (**1**) have been reported, as shown in Scheme 3.[22,28,36] The reaction of carbene (**1**) with one equivalent of InX_3 (X = Cl, Br) resulted in the isolation of 1:1 adducts with InX_3 (X = Cl, R = *i*-Pr, R′ = Me (**39**); X = Br: R = *i*-Pr, R′ = Me (**40**); R = Mes, R′ = H (**41**), R = 2,6-$i\text{-Pr}_2C_6H_3$, R′ = H (**42**)). The X-ray structures of (**40–42**) (X = Br) showed that all the compounds are monomeric and the indium center adopts a distorted tetrahedral geometry, with the In–Br bond distances almost equivalent. The In–C(carbene) bond lengths range from 2.195(2)–2.212(8) Å and are relatively long compared to single In–C bond distances. The bond lengths and angles within the carbene heterocycle indicate a degree of delocalization within the ring, for example, the N–C–N angle of ∼106° lies between the normal value for free carbenes (∼102°) and imidazolium cations (∼108°).[1] For the synthesis of the adduct (**1**)·$InCl_3$ (**28**: R = Mes, R′ = H), see Section 3.1 and Scheme 2.[23]

Biscarbene adducts of indium(III) halides (**43–44**) can be prepared from the reaction of InX_3 with two equivalents of carbene (**1**) (R = *i*-Pr, R′ = Me), according to Scheme 3.[28] The crystal structure of (**43**) and (**44**) showed that in both structures the indium center adopts a distorted trigonal bipyramidal geometry. In previously reported neutral 2:1 adducts of InX_3, the halides occupy the equatorial sites (*see* ***Indium: Inorganic Chemistry***), however, in complexes (**43**) and (**44**), one halide and the carbon atoms of (**1**) are present in the equatorial sites, with two halides occupying the apical

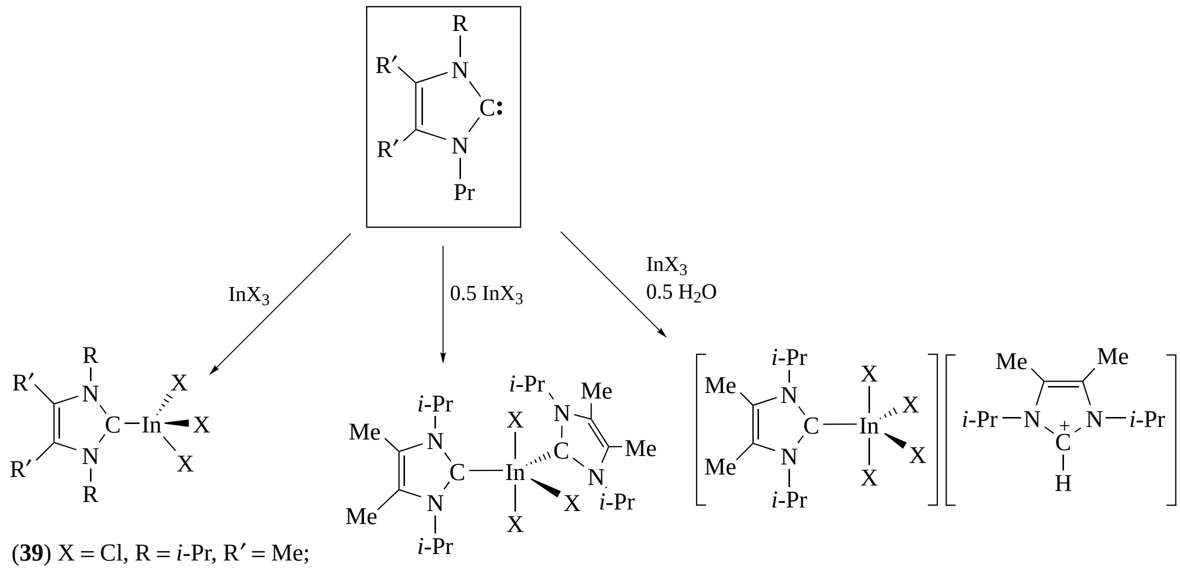

(**39**) X = Cl, R = *i*-Pr, R′ = Me;
(**40**) X = Br, R = *i*-Pr, R′ = Me
(**41**) X = Br, R = Mes, R′ = H
(**42**) X = Br, R = 2,6-$i\text{-Pr}_2C_6H_3$, R′ = H

(**43**) X = Cl
(**44**) X = Br

(**45**) X = Cl
(**46**) X = Br

Scheme 3

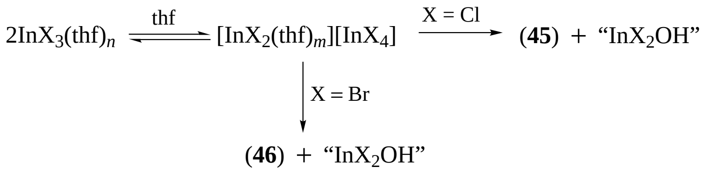
2InX3(thf)n
thf
[InX2(thf)m][InX4]
X = Cl
(45) + "InX2OH"
X = Br
(46) + "InX2OH"

Scheme 4

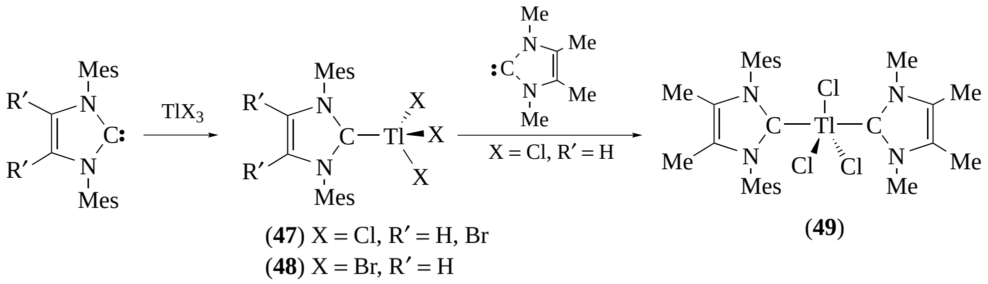
Mes
R′
N
C:
R′
N
Mes
TlX3
C—Tl
X
X
X
Me
N
Me
:C
N
Me
Me
X = Cl, R′ = H
Cl
Tl
Cl
Cl
(47) X = Cl, R′ = H, Br
(48) X = Br, R′ = H
(49)

Scheme 5

positions. It is unclear why (**43**) and (**44**) adopt this sterically unfavorable arrangement of the ligands. The In–C(carbene) distances in (**43**) (*av.* 2.228 Å) and (**44**) (*av.* In–C 2.230 Å) are slightly longer than in (**40–42**), as expected, with the geometries within the planar heterocyclic rings being similar.

An ionic compound is formed when the 1:1 reaction between InX_3 and (**1**) (R = *i*-Pr, R′ = H) is carried out in the presence of water (**45**, X = Cl; **46**, X = Br).[28] The anion comprises a carbene adduct of $[InX_4]^-$, which illustrates the high nucleophilicity of the carbene ligand. The mechanism of the formation of (**45**) and (**46**) is thought to involve the adduct $[InX_3(thf)_n]$ in equilibrium with its ionic isomer in thf solution, as shown in Scheme 4. The other product of the reaction is believed to be an indium hydroxide, $[InX_2OH]$, although this compound was not isolated.

A number of stable carbene–thallium(III) complexes have been prepared via the reaction of carbene (**1**) with TlX_3 (R = Mes: X = Cl, R′ = H or Br (**47**); X = Br, R′ = H (**48**)), as shown in Scheme 5.[37] The structure of (**47**) (R′ = H) is monomeric with a distorted tetrahedral geometry at the thallium center. The geometry of the heterocycle is similar to the indium analogue (**28**) with a Tl–C bond distance of 2.154 Å. The formation of a bis(carbene) adduct of $TlCl_3$ (**49**) was achieved via the reaction of (**47**) with carbene (**1**) (R = R′ = Me). Unfortunately, no structural data for (**49**) is available but it is assumed that the geometry about the thallium center is trigonal bipyramidal with the chloride ligands in the equatorial positions.[37]

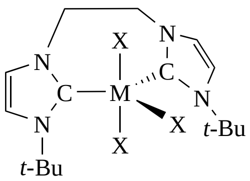
N
X
N
C
N
C—M
N
X
t-Bu
X
t-Bu

(**50**) M = In, X = Br
(**51**) M = Tl, X = Cl

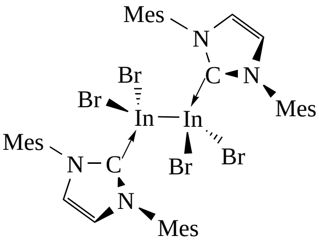
Mes
N
Br
C
N
Br
In—In
Mes
Mes
N—C
Br
Br
N
Mes

(**52**)

Bidentate N-heterocyclic carbene complexes of $InBr_3$ and $TlCl_3$ have been described recently.[25] Reaction of carbene (**31**) with one equivalent of MX_3 resulted in the formation of the 1:1 adducts (**50**, M = In, X = Br; **51**, M = Tl, X = Cl). The isolation of 1:1 adducts rather than a similar 2:1 adduct observed for MH_3 (**32–34**) gives further evidence that $InBr_3$ is a stronger Lewis acid than InH_3. An X-ray structure determination of compound (**50**) shows that the molecule is monomeric with the carbene ligating the indium center in a chelating mode. The geometry at the indium center is distorted trigonal bipyramidal with the carbenes residing in two equatorial positions, similar to the biscarbene–indium halide complexes (**43** and **44**).[36]

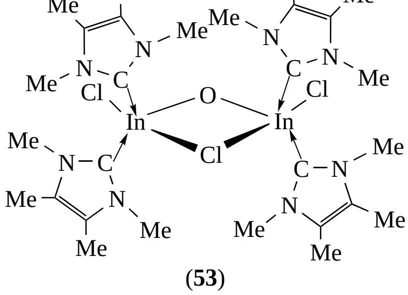
Me
Me
Me
Me
N
Me
Me
N
Me
N—C
C—N
Me
Me
Cl
O
Cl
In
In
Cl
Me
N—C
C—N
Me
Me
N
N
Me
Me
Me
Me
Me

(**53**)

The reactivity of N-heterocyclic carbenes with group 13 metal(I) halide complexes has been studied to a limited extent (*see* ***Low Oxidation State Main Group***).[38–40] The reaction of 0.5 or 1 equivalent of carbene (**1**) (R = Mes, R′ = H) with InBr resulted in the isolation of a thermally robust carbene–indium(II) bromide complex (**52**) with concomitant deposition of indium metal.[38] The mechanism for the formation of (**52**) is thought to involve the intermediate complex (**1**)·InBr, which undergoes a disproportionation reaction to yield (**52**) and indium metal. In the solid state, compound (**52**) is dimeric and both indium centers adopt a distorted tetrahedral geometry with the two [(**1**)·$InBr_2$] fragments staggered with respect to each other. All bond lengths and angles are in the normal range. Reaction of a less sterically hindered N-heterocyclic carbene (**1**) (R = Me, R′ = Me) with InCl afforded the oxo-bridged dimer (**53**) in low yield, due to adventitious oxidation.[39] In contrast, reaction of a very hindered carbene (**1**) (R = 2,6-*i*-$Pr_2C_6H_3$, R′ = H) with 'GaI' resulted in the deposition of gallium metal and the formation of a ionic complex (**54**). The presence of only one coordinated carbene in (**54**), in comparison to the two carbene ligands in (**52**), may be due to the greater steric bulk of the carbene ligand and the smaller covalent radius of the metal atom in the former complex.[38,39] The structure of (**54**) showed that both gallium centers have distorted tetrahedral coordination geometries with a long Ga–Ga bond distance (2.4739(12) Å).

The synthesis and characterization of a thallium(I) triscarbene complex has been described.[40] The reaction of a chelating tripodal carbene ligand 1,3,5-{tris(3-*tert*-butylimidazol-2-ylideno)methyl}-2,4,6-trimethylbenzene with Tl(OTf) resulted in the formation of the triscarbene thallium(I) complex (**55**). An X-ray structural determination showed that the tripodal carbene ligand coordinates with the thallium(I) ion in (**55**) in the expected tridentate conformation. All three imidazole rings are almost perpendicular to the mesitylene moiety, however, the three carbene centers in (**55**) are bound asymmetrically (Tl–C 2.893(4), 2.979(4) and 2.985(5) Å). This is thought to be due to steric or crystal packing effects rather than electronic reasons.

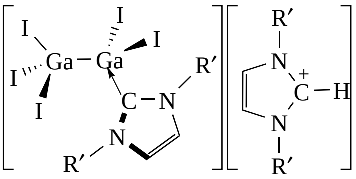

(**54**, R′ = 2,6-*i*-$Pr_2C_6H_3$)

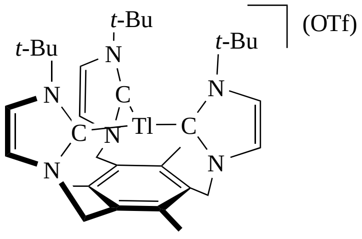

(**55**)

3.3 Carbene Adducts of Organo and Amido Group 13 Complexes

Trialkylboron–carbene adducts have been prepared via a novel synthetic route, as shown in Scheme 6.[41] The initial first step involves reaction of BEt_3 with 1,4,5-trimethylimidazole (**56**) to afford the BEt_3 adduct (**57**), followed by deprotonation and rearrangement to give an ionic species (**58**). The triethylboron–carbene adduct is generated in the final step by way of

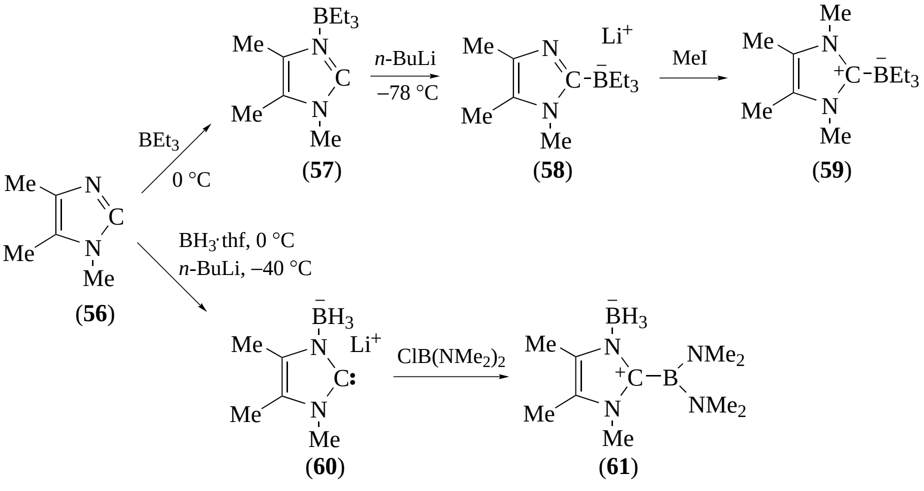

Scheme 6

a methylation with MeI (**59**). Compound (**59**) was characterized by NMR (^{1}H-, ^{13}C- and ^{11}B) and mass spectroscopy; the ^{11}B NMR chemical shift observed for (**59**) was δ −12.6.

Compound (**56**) can also be used to synthesize an amidoboron–carbene adduct.[41] Thus, the intermediate carbene (**60**) was formed by reaction of $BH_3{\cdot}THF$ with (**56**), followed by deprotonation using n-BuLi. Addition of $ClB(NMe_2)_2$ to (**60**) results in the ylidene (**61**), the ^{11}B NMR of which had chemical shifts of δ−21.8 (BH_3) and δ 27.8 ($BNMe_2$). In the solid state, compound (**60**) is dimeric.[42] The synthesis of a range of transition metal complexes with the anion in compound (**60**) have been reported recently, demonstrating that (**60**) is a suitable reagent for introducing the carbene ligand.[43]

N,O–heterocyclic carbenes have also been shown to form adducts with triorganoboron complexes.[44] Triphenylboron–carbene adducts (**62**) were isolated from the reaction of an isocyanide adduct of BPh_3 with methanol (equation 6), in the presence of a catalytic amount of KF. An X-ray structural determination showed that (**62**) consists of a tetrahedrally coordinated boron atom with all four B–C bond distances equal (within experimental error).

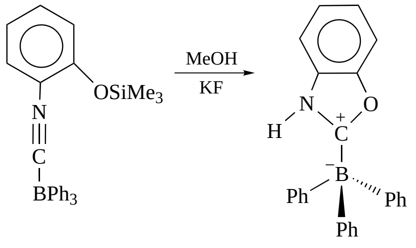

(**62**)

(6)

A related triarylboron–carbene adduct (**64**) was isolated from the attempted recrystallization of the 1-butyl-3-methylimidazolium tetraarylborate salt (**63**) in warm MeOH/H_2O (equation 7).[45] The solid-state structure of (**64**) comprises a distorted tetrahedral boron center with all four B–C bond distances similar, as observed in compound (**62**).[44]

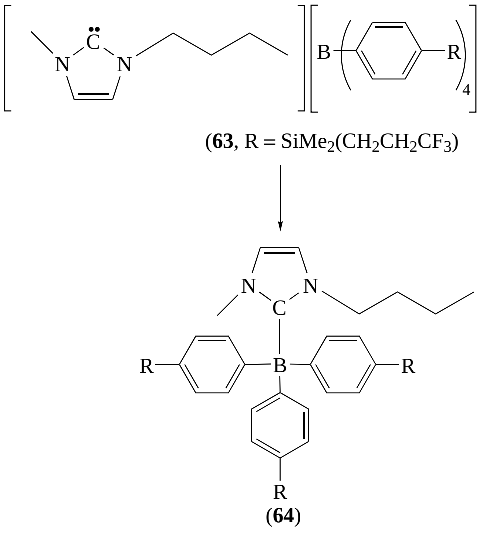

(**63**, R = $SiMe_2(CH_2CH_2CF_3)$)

(7)

(**64**)

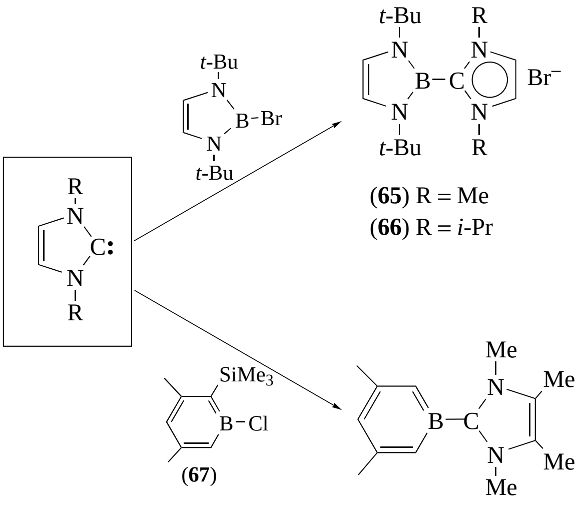

(**65**) R = Me
(**66**) R = i-Pr

(**67**)

(**68**)

Scheme 7

The reactivity of nucleophilic carbenes with 2-bromo-2,3-dihydro-1H-1,3,2-diazaborole has also been described.[46] Reaction of a benzene solution of (**1**) (R = Me, i-Pr; R′ = H) with t-BuNCH=CH(t-Bu)BBr (Scheme 7) resulted in the formation of an ionic compound (**65**, R = Me; **66**, R = i-Pr). The halide displacement observed in the aforementioned reaction is similar to those previously reported in the reactions of carbenes with Me_3SiI.[47] The crystal structure of (**65**) was determined and showed that both heterocyclic rings are planar with an interplanar angle of 92.9°; the B–C(carbene) bond distance of 1.580(11) Å corresponds to that found in (**20**) (1.603(3) Å). A carbene adduct of borabenzene has also been reported, as shown in Scheme 7.[48] Treatment of the highly reactive silylated chloroborabenzene (**67**) with carbene (**1**) (R = R′ = Me) afforded an immediate precipitation of the carbene–borabenzene adduct (**68**). The structure of (**68**) consists of a planar borabenzene and carbene ring with an interplanar angle of 34.75(6)°. The B–C(carbene) bond distance of 1.596(2) Å is comparable to that observed in (**65**).[46]

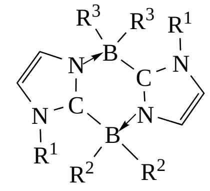

dimeric N-borane adduct (**69a**)

A range of imidazabole derivatives have been described recently.[49] These compounds may be considered as aza- (**69a**) or carbene–borane (**69b**) adducts. However, NMR and X-ray diffraction data of these compounds (**69**) indicate that they are dimers of carbene–borane adducts rather than dimers of

N–borane adducts, as shown by the geometry of the imidazole ring, which is consistent with the former.

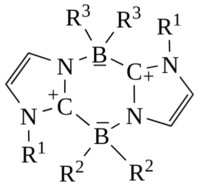

dimeric carbene-borane adduct (**69b**)

$R^1 = CH_3$, $R^2 = R^3 = H$, F, Cl or CH_2CH_3
$R^1 = CH_2C_6H_5$, $R^2 = R^3 = H$
$R^1 = CH_3$, $R^2 = F$, $R^3 = H$

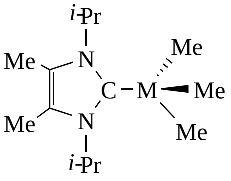

(**70**) M = Al
(**71**) M = Ga

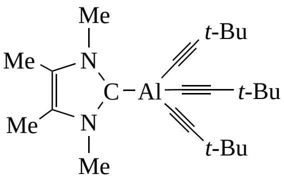

(**72**)

Reports of triorgano group 13 carbene adducts involving the heavier group 13 elements are limited to carbene complexes of $AlMe_3$, $GaMe_3$, and Al(C≡C-*t*-Bu)$_3$.[50,51] Thus, when (**1**) (R = *i*-Pr, R′ = Me) was allowed to react with MMe_3, stable 1:1 adducts of Me_3M (**70**, M = Al; **71**, M = Ga) were formed. X-ray structural determinations showed that the group 13 metal centers in (**70**) and (**71**) are tetrahedrally coordinated with long M–C(carbene) bond lengths (**70**, Al–C(carbene) 2.124(6) Å *cf.* Al–C(methyl) 1.940(5) Å and 2.062(7) Å; (**71**), Ga–C(carbene) 2.13(2) Å *cf.* Ga–C(methyl) 1.95(1) Å and 2.08(2) Å). The Al–C(carbene) distance in (**70**) is much longer than that observed in the related alane complex (**23**) (2.034(3) Å), which is probably a result of greater steric hindrance of $AlMe_3$ versus AlH_3.[21] Similarly, the Ga–C(carbene) bond length in (**71**) is much longer than that found in the gallane complex (**24**) (2.071(15) Å).[21]

The first carbene adduct of a substituted aluminum ethynyl derivative (**72**) was isolated from the reaction of $AlBr_3$ with three equivalents of LiC≡C-*t*-Bu in the presence of carbene (**1**) (R = *i*-Pr, R′ = Me).[51] The structure of (**72**) is similar to compound (**70**), such that the aluminum atom adopts a tetrahedral coordination geometry.

Phosphinosilylcarbene group 13 adducts have also been reported. Reaction of $\{(R_2N)_2P\}(Me_3Si)C$: with BEt_3 (R = cyclohexyl) or MCl_3 (M = Al, Ga or In; R = *i*-Pr) afforded the 1:1 adducts $[\{(R_2N)_2P\}(Me_3Si)C{:}BEt_3]$ and $[\{(R_2N)_2P\}(Me_3Si)C{:}MCl_3]$ (**73**).[52,53] However, reaction of $\{(R_2N)_2P\}(Me_3Si)C$: with MMe_3 resulted in the isolation of phosphorus ylids $[\{(R_2N)_2P(Me)\}(Me_3Si)CMMe_2]$ (**74**), probably via the initial formation of the carbene–MMe_3 adducts.[53] Carbene adducts of constrained geometry aluminum and gallium complexes have been reported recently.[54] The bridged amidocyclopentadienide ligand $[Me_2Si(\eta\text{-}C_5Me_4)(N\text{-}t\text{-}Bu)]^{2-}$ was reacted with $MeMCl_2$ (M = Al, Ga), followed by treatment with carbene (**1**) (R = R′ = Me), to yield the adducts $[Me_2Si(\eta\text{-}C_5Me_4)(N\text{-}t\text{-}Bu)]MMe.(\mathbf{1})$ (**75**).

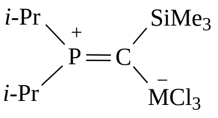

(**73**) M = Al, Ga, In

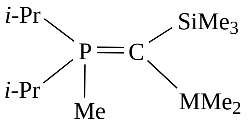

(**74**) M = Al, Ga

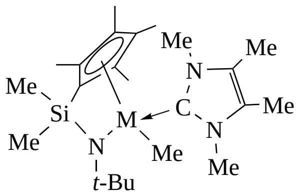

(**75**) M = Al, Ga

4 GROUP 14

Nucleophilic carbenes have been reported to react with Lewis acidic group 14 complexes with the isolation of neutral or ionic compounds via simple adduct formation or displacement of a halide ion.[47,55–60] The range of carbene complexes of silicon, germanium, tin, and lead, as well as some related cyclopropenylidene complexes are described below.

4.1 Carbene Complexes of Silicon

When tetrachlorosilane was allowed to react with (**1**) (R = Me, Et, *i*-Pr; R′ = Me), the somewhat labile 1:1 adduct with $SiCl_4$ (**76**) was formed, according to Scheme 8.[47] The solid-state structure of (**76**), when R = *i*-Pr, showed that the silicon center adopts an essentially trigonal bipyramidal geometry with the carbene ligand in an equatorial position. The bond lengths and angles within the carbene heterocycle indicate a degree of delocalization within the ring (N–C–N angle of 107.1(6)°) and the Si–C(carbene) bond distance is 1.9711(7) Å.

Pentavalent silicon adducts (**78,79**) can be isolated from the reaction of dialkyl- or diaryl-dichlorosilanes with (**1**) (R = Et, *i*-Pr; R′ = Me), whereas when Me_3SiI is reacted with (**1**), ionic imidazolium salts are formed (**77**).[47] Unfortunately, no information regarding the structure of these compounds is available. A crystalline carbene–silylene adduct 1,2-$C_6H_4[N(R)]_2C\text{-}Si[N(R)]_2C_6H_4$-1,2 (**80**, R = CH_2-*t*-Bu) has

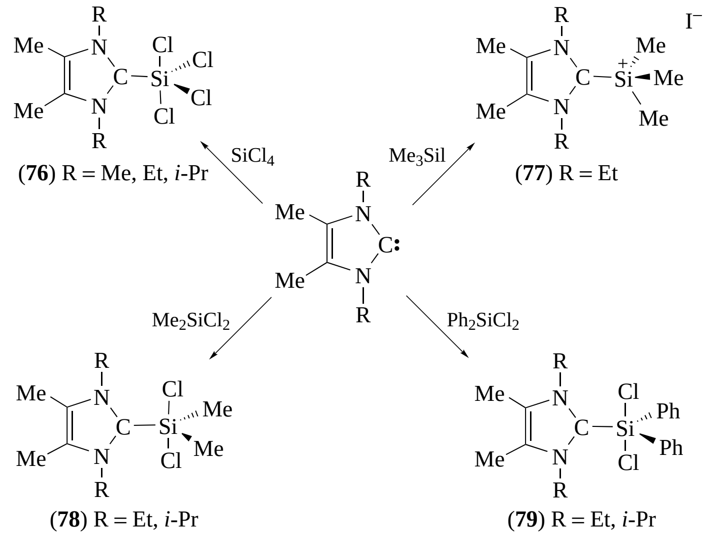

(**76**) R = Me, Et, *i*-Pr

(**77**) R = Et

(**78**) R = Et, *i*-Pr

(**79**) R = Et, *i*-Pr

Scheme 8

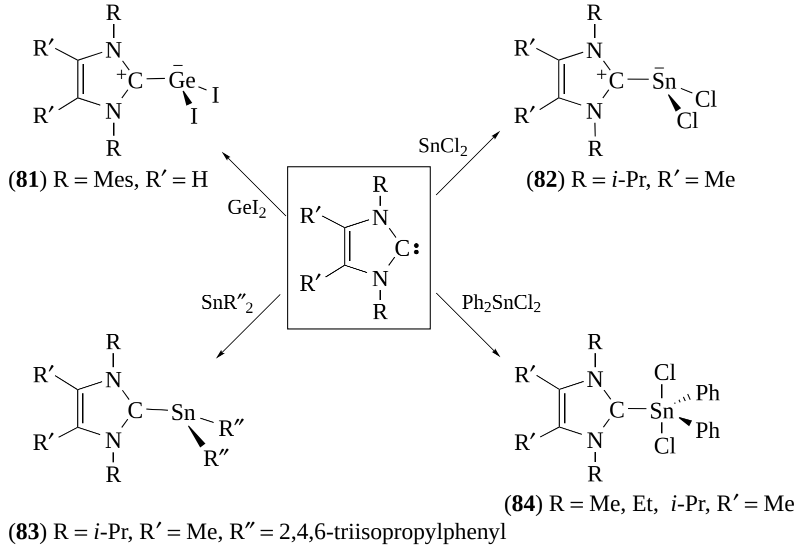

(**81**) R = Mes, R′ = H

(**82**) R = *i*-Pr, R′ = Me

(**84**) R = Me, Et, *i*-Pr, R′ = Me

(**83**) R = *i*-Pr, R′ = Me, R″ = 2,4,6-triisopropylphenyl

Scheme 9

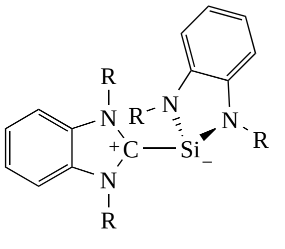

(**80**) R = CH_2-*t*-Bu

been reported recently.[55] Compound (**80**) is a monomer with a long central bond of 2.162(5) Å between the carbene carbon and Si atoms. The carbene carbon is almost planar, however, the silicon is in a pyramidal coordination environment.

4.2 Carbene Adducts of Germanium and Tin

Carbene adducts of germanium and tin have also been reported, as shown in Scheme 9.[56–58] A model for the dimerization of singlet carbenes along a non-least-motion pathway was provided by the reaction of GeI_2 with carbene (**1**) (R = Mes, R′ = H).[56] The formation of a polarized Ge–C bond, rather than a true double bond, was indicated by the ^{13}C NMR chemical shift of the carbene atom ($\delta = 60.88$) in the resulting germene−carbene adduct (**81**). The solid-state structure of (**81**) consists of pyramidal coordination geometry at the Ge center with a long Ge−C bond distance (2.102(12) Å). Interestingly, due to steric interaction between the iodine and mesityl substituents, the two halves of the adduct are twisted with respect to one another.

Stable carbene adducts of tin(II) may be prepared from the reactions of $SnCl_2$ or SnR''_2 ($R'' = 2,4,6$-triisopropylphenyl) with (**1**) ($R = i$-Pr; $R' = Me$).[47,57] The crystal structure of the $SnCl_2$ adduct (**82**) is similar to (**81**), in that a pyramidal geometry is adopted at the Sn center with a Sn−C(carbene) bond distance of 2.290(5) Å. As expected, the Sn−C(carbene) bond distance in the SnR''_2 adduct (**83**, Sn−C(carbene) 2.379(5) Å) is longer than that observed in (**82**) and greater than Sn−C(aryl) bond lengths (2.321(2) Å and 2.308(2) Å). The long Sn−C(carbene) bond distances in (**82**) and (**83**) indicate that these complexes are examples of simple Lewis acid−Lewis base adducts.

Pentavalent tin adducts have also been reported and were isolated from the reaction of (**1**) ($R = i$-Pr, $R' = Me$) with Ph_2SnCl_2.[47] An X-ray structure determination of the Ph_2SnCl_2 adduct (**84**) showed that the Sn(IV) center adopts a distorted trigonal bipyramidal geometry and the three organic substituents occupy the equatorial positions. The Sn−C(carbene) bond distance of 2.179(3) Å in (**84**) is shorter than the Sn−C(carbene) bond distances found in the Sn(II) adducts (**82** and **83**) but longer than the Sn−C(phenyl) bond lengths (2.122(5) Å and 2.139(3) Å).

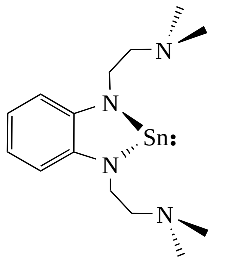

(**85**)

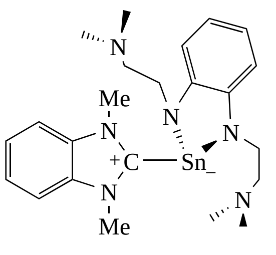

(**86**)

A zwitterionic (*see Zwitterion*) carbene−stannylene adduct has been prepared via the cleavage of a dibenzotetraazafulvalene by a stannylene.[58] Thus, reaction of the tetraamine $1,2\text{-}C_6H_4\text{-}[NHCH_2CH_2NMe_2]_2$ with bis(bis(trimethylsilyl)amido)tin(II) yielded the N-heterocyclic stannylene (**85**). Treatment of stannylene (**85**) with *N,N′N″N‴*-tetramethyl dibenzotetraazafulvalene results in C=C bond cleavage in the dibenzotetraazafulvalene to give the carbene−stannylene adduct (**86**). An X-ray structure determination showed that compound (**86**) is zwitterionic with a partially cationic carbene subunit and a partially anionic stannylene unit. The structure of (**86**) is similar to that of the carbene−silylene (**80**) such that the carbene plane and the stannylene plane are orientated in an almost perpendicular manner.

4.3 Carbene Adducts of Lead

There is only one report of a carbene−plumbylene adduct.[59] Addition of carbene (**1**) ($R = i$-Pr, $R' = Me$) to a toluene solution of PbR''_2: ($R'' = 2,4,6\text{-}i\text{-}Pr_3C_6H_2$) afforded the 1:1 adduct (**87**). An X-ray structure determination revealed that (**87**) is monomeric with an unusually long Pb−C(carbene) distance of 2.540(5) Å. The structure of (**87**) is similar to the silylene− (**80**) and stannylene−carbene (**86**) adduct such that the carbene carbon is almost planar with a pyramidal lead atom. Therefore, of the two possible electronic forms of (**87**) (the plumbene (**87a**) and the zwitterionic (**87b**)), the latter dominates.

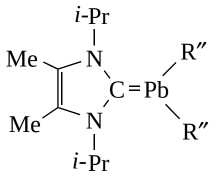

(**87a**, $R'' = 2,4,6\text{-}i\text{-}Pr_3C_6H_2$)

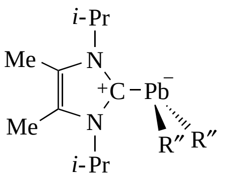

(**87b**, $R'' = 2,4,6\text{-}i\text{-}Pr_3C_6H_2$)

4.4 Cyclopropenylidene Complexes of Germanium, Tin, and Lead

Recently, cyclopropenylidene adducts of divalent germanium, tin, and lead have been reported.[60] Treatment of the cyclopropenylium salt (**88**) with n-BuLi afforded the bis(diisopropylamino)cyclopropenylidene (**89**), as shown in Scheme 10. For germanium and lead, cyclopropenylidene adducts of $E(N(SiMe_3)_2)_2$ (**90**, E = Ge; **91**, E = Pb) can be formed directly via the reaction of (**89**) with $E(N(SiMe_3)_2)_2$. In contrast, the analogous tin compound (**92**) is only accessible from the reaction of $SnCl_2$ with (**89**) followed by amidation of the intermediate carbene adduct. Compounds (**90–92**) are all isolated as thermally stable yellow crystals and have the same structures. Thus in each structure, the group 14 element is pyramidal with E−C(carbene) distances (**90**, Ge−C(carbene) 2.085(3) Å; **91**, Sn−C(carbene) 2.303(9) Å; **92**, Pb−C(carbene) 2.423(8) Å) that suggest a ylidic resonance structure corresponding to the imidazol-2-ylidene adducts described above.[56,57]

5 CARBENE ADDUCTS OF PHOSPHORUS, ARSENIC, AND ANTIMONY

5.1 Carbene Complexes of Phosphorus(III) and Arsenic(III)

The first examples of p-block pnictinidenes were recently reported.[61,62] It was found that the N-heterocyclic carbenes are sufficiently nucleophilic to enable depolymerization of

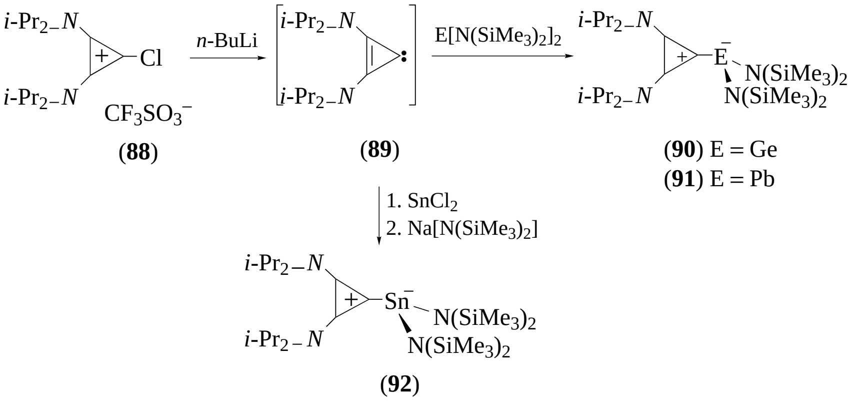

Scheme 10

cyclopolyphosphines and cyclopolyarsines to occur (equation 8) with the isolation of carbene–pnictinidene (**93–97**) adducts.**[61,62]**

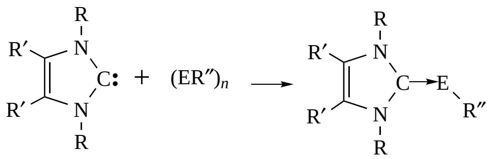

(8)

(**93**) R = R′ = Me; E = P; R″ = Ph; *n* = 5
(**94**) R = Mes; R′ = H; E = P; R″ = Ph; *n* = 5
(**95**) R = Mes; R′ = H; E = P; R″ = C_6F_5; *n* = 4
(**96**) R = Mes; R′ = H; E = P; R″ = CF_3; *n* = 4
(**97**) R = Mes; R′ = H; E = As; R″ = Ph; *n* = 6

The carbene–pnictinidene (**93–97**) adducts can be represented by two extreme canonical forms (**98** and **99**). The canonical form (**99**) represents a conventional phosphaalkene with a C=P double bond, whereas form (**98**) corresponds to a phosphinidene adduct of a carbene and features a C–P dative bond order of one. Structural data for compounds (**93–97**) showed that the E–C(Carbene) bond is ∼4% longer than typical single bonds and that the E–C(R″) moiety is twisted out of the carbene plane by 26–46°.**[61,62]** These data, along with the high-field ^{31}P chemical shifts of (**93**,**94**) and (**96**), indicate the predominance of structure (**98**).

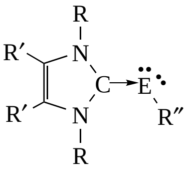

(**98**)

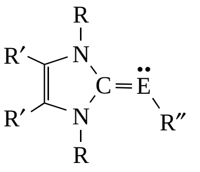

(**99**)

Further support for structure (**98**) was obtained from the reaction of $BH_3{\cdot}THF$ with compound (**94**) (equation 9), which resulted in the isolation of the bis(borane) adduct (**100**). The formation of (**100**) confirms the availability of two lone pairs on the phosphorus center in (**94**).**[63]**

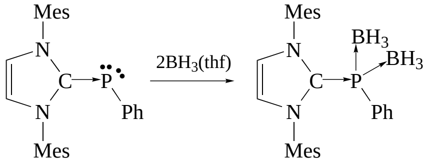

(**94**) (**100**)

(9)

The carbene–phosphinidene adducts described above were prepared from cyclopolyphosphines, which in turn are formed via reduction of higher-oxidation state phosphines, such as $PhPCl_2$. However, in some cases, carbene–phosphinidene adducts (**101**) can be prepared by direct reaction of a nucleophilic carbene with $PhPCl_2$ (equation 10) and a separate reduction step is not required.**[61]** In contrast, reaction of Ph_2PCl with carbene (**1**) (R = *i*-Pr, R′ = Me) resulted in the formation of the corresponding phosphino-imidazolium salt (**102**), which has been structurally characterized as (**103**) on treatment with $AlCl_3$ (equation 11).**[64]** The related phosphino-imidazolium salt (**104**) was isolated from the reaction of $[Ph_3PPh_2][OTf]$ with carbene (**1**) (R = *i*-Pr, R′ = H) with concomitant formation of Ph_3P.**[65]**

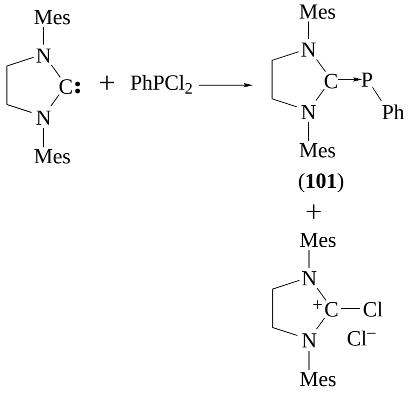

(10)

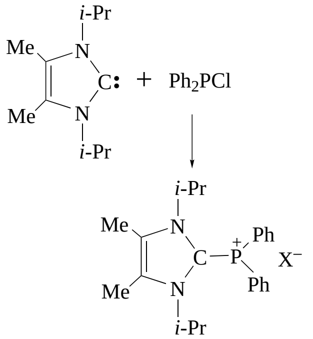

(11)

(**102**) X = Cl
(**103**) X = AlCl$_4$
(**104**) X = OTf

Carbene complexes of iminophosphines have also been reported.[66] Thus, treatment of carbene (**1**) (R = i-Pr, R$'$ = H) with Mes*PNCl or Mes*PNOTf affords the 1:1 adducts (**105**) and (**106**). The structures of (**105**) and (**106**) indicate that π-interaction between the nitrogen centers and the methylene center is favored over that between a planar phosphorus center and a methylene center.

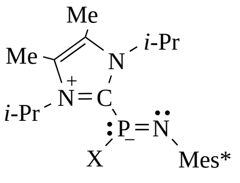

(**105**) X = Cl
(**106**) X = OTf

5.2 Carbene Complexes of Phosphorus(V)

Recently, the formation of the first carbene complex of a phosphorus(V) center was reported.[67] The direct reaction of carbene (**1**) (R = Mes, R$'$ = H) with phenyltetrafluorophosphorane (equation 12) results in the formation of perphosphoranide (**107**) in quantitative yield. An X-ray structural determination showed that the phosphorus center in (**107**) adopts an octahedral geometry with a long P–C(carbene) bond length (P–C(carbene) 1.91 Å *cf.* P–C(phenyl) 1.84 Å). The ^{31}P resonance in (**93**,**94**) and (**96**) are at a substantially higher field than the value in (**107**), which is expected and reflects the change from a two–coordinate to a six–coordinate P center.

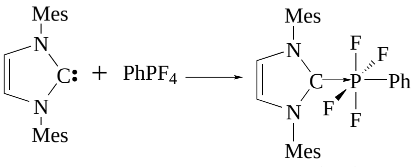

(**107**)

(12)

Carbene adducts of phosphorus pentafluoride have also been reported.[32] Reaction of carbene (**1**) (R = Mes, R$'$ = H) with PF$_5$ affords (**1**)$\cdot$PF$_5$ (**108**) as a minor product with concomitant formation of 1,3-dimesitylimidazolium hexafluorophosphate, (**1**)$\cdot$PF$_6$. However, treatment of carbene (**1**) (R = Mes, R$'$ = Cl) with PF$_5$ resulted in a 60% yield of the 1:1 adduct, (**1**)$\cdot$PF$_5$ (**109**). The improvement in the yield of the adduct is thought to be due to moderation of the carbene's nucleophilic reactivity by the inductive effect of the two chlorine substituents in the formation of (**109**). An X-ray determination showed that the structure of (**109**) is similar to (**107**) with the phosphorus atom adopting an octahedral coordination geometry and a P–C bond distance of 1.893(3) Å.[32,67] Overall, the NMR and structural data support the valence bond structure of (**109**) as zwitterionic. Heterocyclic carbenes have also been used to stabilize metaphosphoric acid fragments.[68] Reaction of carbene (**1**) (R = i-Pr, R$'$ = Me) with POCl$_3$ resulted in the isolation of the corresponding POCl$_3$ carbene adduct (**110**). The metaphosphoric acid–carbene adduct (**111**) was subsequently obtained from the partial hydrolysis of (**110**). The X-ray structure of (**111**) revealed that it is monomeric with a long P–Cl bond (2.070 Å) and a P–C bond distance of 1.843(2) Å.

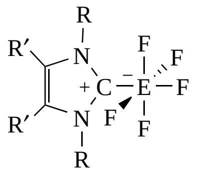

(**108**) E = P, R = Mes, R$'$ = H
(**109**) E = P, R = Mes, R$'$ = Cl
(**112**) E = As, R = Mes, R$'$ = Cl
(**113**) E = Sb, R = Mes, R$'$ = Cl

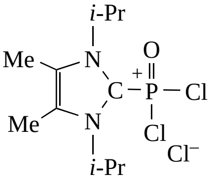

(**110**)

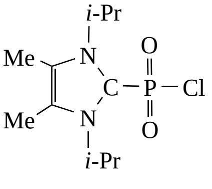

(**111**)

5.3 Carbene Complexes of Arsenic and Antimony

Carbene adducts of the heavier pnictogen pentafluorides have been reported.[32] Reaction of AsF$_5$ or SbF$_5$ with carbene (**1**) (R = Mes, R$'$ = Cl) in 1,3-bis(trifluoromethyl)benzene resulted in the isolation of (**1**)$\cdot$AsF$_5$ (**112**) and (**1**)$\cdot$SbF$_5$ (**113**). The crystallographic analysis for (**112**) and (**113**) reveals the expected octahedral geometry at the pnictogen center with a long As–C (2.009(5) Å) and Sb–C (2.175(5) Å) bond distance respectively. Recently, a novel hypervalent antimonide complex was reported.[69] The nucleophilic addition of carbene (**1**) (R = Mes, R$'$ = H) to Sb(CF$_3$)$_3$ (equation 12) resulted in the formation of the 1:1 adduct with $Sb(CF_3)_3$ (**114**). An X-ray investigation of compound (**114**) showed that the antimony center adopts a pseudo-trigonal bipyramidal coordination geometry with a Sb–C(carbene) bond distance of 2.821 Å and *av.* Sb–$C(CF_3)$ of 2.22 Å. Therefore, the average antimony–carbon distance to the CF_3 groups in (**114**) more closely resemble the Sb–C(carbene) distance in (**113**).

6 CARBENE COMPLEXES OF THE CHALCOGENS

N-heterocyclic carbene adducts of sulfur have been known for many years as a result of their industrial applications in catalysis. These complexes have been described in various reviews[6–8] and this section will be confined to carbene complexes of the chalcogenides reported since 1993.

The reaction of imidazol-2-ylidenes with selenium and tellurium (equation 13) affords the selenones (**115**) and tellurones (**116**).[70–73] In general, tellurocarbonyl compounds, for example, telluroaldehydes, can only be isolated by stabilization with metals, however, compound (**116**) is relatively stable.[69] An X-ray investigation of (**115**) and (**116**) shows that rather than a formal double bond, an ylidic structure is adopted in both cases with long Ch–C(carbene) bond distances (**115** Se–C(carbene): 1.853(4) Å ($R = i$-Pr, $R' =$ Me), 1.884(9) Å ($R =$ Me, $R' =$ H); (**116**) Te–C(carbene) 2.087(4) Å ($R = i$-Pr)). Further support for the ylidic structure for (**115**) and (**116**) was obtained by the ^{74}Se and ^{125}Te NMR spectra, in which the signals resonate upfield when compared to other chalcocarbonyl compounds. This shielding is accounted for by the presence of π-delocalization in the heterocyclic rings (**115** N–C–N 106.4° ($R = i$-Pr, $R' =$ Me), 106.8° ($R =$ Me, $R' =$ H); **116** N–C–N 106.7°). It has also been reported that oxygen, sulfur, and selenium react with 1,2,4-triazol-5-ylidenes (equation 13) in a similar manner to give the 1:1 adducts (**117**).[75]

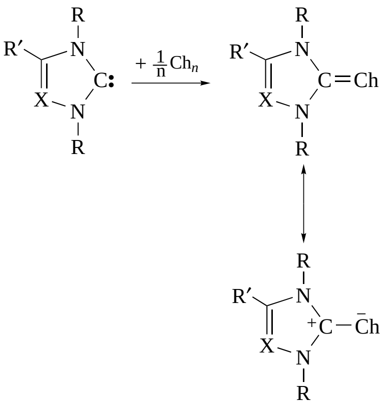

(**115**) Ch = Se, X = CR′, R = Me, Et, *i*-Pr, R′ = Me; R = Me, R′ = H
(**116**) Ch = Te, X = CR′, R = Me, Et, *i*-Pr, R′ = Me; R = Mes. R′ = H, Cl
(**117**) Ch = O, S, Se; X = N, R = R′ = Ph

(13)

Carbene adducts of a range of sulfur compounds have also been isolated.[75–77] Carbene (**1**) ($R = i$-Pr, $R' =$ Me) reacts with sulfur dichloride or thionyl chloride to yield the hypervalent sulfur derivatives (**118**) and (**119**).[76] Similarly, reaction of carbene (**2**) ($R = t$-Bu) with SO_2 led to the formation of the 1:1 adduct (**2**)·SO_2 (**120**).[77] In contrast, reaction of carbene (**1**) ($R = i$-Pr, $R' =$ Me) with SO_2Cl_2 affords the 2-chloro-1,3-diisopropyl-4,5-dimethylimidazolium chlorosulfite salt (**121**).[74] A carbene adduct of SO_3 (**122**) can then be isolated through hydrolysis of (**121**) in the presence of cyanide.

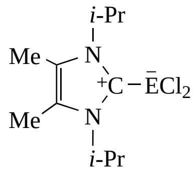

(**118**) E = S
(**119**) E = S=O

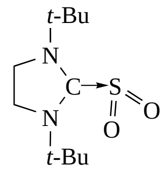

(**120**)

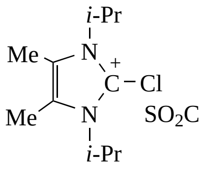

(**121**)

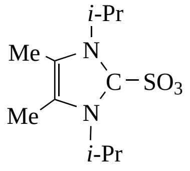

(**122**)

A carbene adduct of $SeBr_2$ (**123**) may be prepared via reaction of (**115**) ($R =$ Me, $R' =$ H) with bromine.[71] However, if only half an equivalent of bromine is reacted with (**115**) ($R =$ Me, $R' =$ H), the diselenide (**124**) is formed.

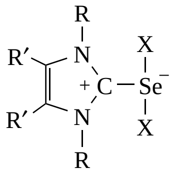

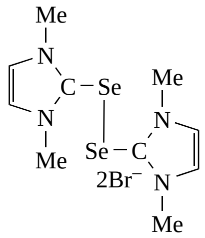

(**123**) X = Br, R = Me, R′ = H
(**125**) X = I, R = *i*-Pr, R′ = Me

(**124**)

The reaction of iodine with seleno- and telluroimidazolines results in the formation of the adducts of SeI_2 (**125**) and TeI_2 (**126**) respectively.[78–80] X-ray diffraction of (**125**) showed that the molecule is monomeric, with the Se center adopting an equatorially vacant trigonal bipyramidal geometry.[78] The axial positions are occupied by the iodine atoms and the Se–I bonds are long (*av.* Se–I 2.811(1) Å; I–Se–I 175.4°). The Se–C(carbene) bond distance of 1.900(4) Å in (**125**) is longer than that observed in (**115**). In the solid-state structure of (**125**), weak iodine–iodine interactions are present (I···I 3.719(1) Å). An Se-methyl ionic compound (**127**) may be prepared by refluxing (**115**) (R = Me, R′ = H) with iodomethane.

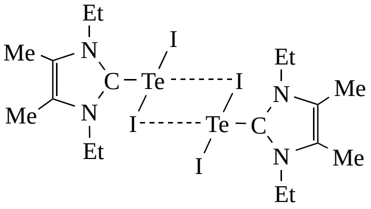

(**126**)

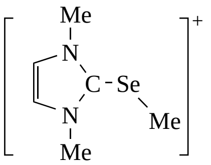

(**127**)

The solid-state structure of the tellurium analogue (**126**) is dimeric and a square-planar geometry is adopted by each tellurium atom.[78] The Te_2I_2 unit is planar and each tellurium has two short Te–I bonds (2.989(1) Å and 2.897(1) Å) and one long Te–I bond (3.564(1) Å). As expected, the Te–C(carbene) distance of 2.120(3) Å is longer than that observed in (**116**) (2.087(4) Å).

7 CARBENE ADDUCTS OF CHLORINE, BROMINE, AND IODINE

Carbene adducts of iodine have been published prior to 1993 and are described in a number of reviews.[7,8] More recently, nucleophilic carbenes, such as (**1**), have been shown to react with I_2 (equation 14) to form 2-iodoimidazolium salts (**128–130**).[80,81] Weak interactions in the solid state, between the iodine in the 2-position of the imidazole ring and the iodide counterion (**128**, I···I 3.348 Å; **129**, I···I 3.249 Å), are present in the imidazolium salts (**128**) and (**129**). The almost linear arrangement of the C–I···I unit indicates a hypervalent central iodine atom and hence the C–I bond distances are long when compared to iodoarenes (**128**, C–I 2.104 Å, C–I···I 176.0°; **129**, C–I 2.113 Å, C–I···I 179.2°). The N–C–N angles of 109.3° and 107.0° in (**128**) and (**129**) respectively are typical of an imidazolium ion. The imidazolium salt (**130**) is similar with a weak interaction in the solid state between the triiodide counterion and the iodine bonded to the carbene (I···I 3.310 Å, C–I 2.131 Å, C–I···I 173.1°, N–C–N 109.5°).

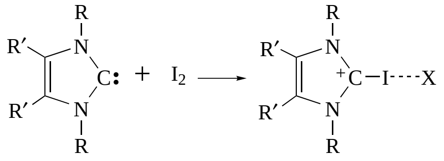

(14)

(**128**) X = I^-, R = Et, R′ = Me
(**129**) X = I^-, R = Mes, R′ = H
(**130**) X = I_3^-, R = adamantyl, R′ = H

The iodide ion in (**129**) can be substituted by tetraphenylborate (**131**), presenting an interesting comparison to (**128–130**), because the anion is unable to interact covalently with the 2-iodoimidazolium cation (equation 15).[80] As expected, the C–I bond distance in (**131**) is shorter than in (**128–130**) at 2.042 Å and the N–C–N internal ring angle is smaller at 107.7°. It is interesting to note that in the crystal structure of (**131**), the C–I bond of the cation resides along a twofold crystallographic axis and the boron atom lies along this same axis at a distance of 4.42 Å from the iodine.

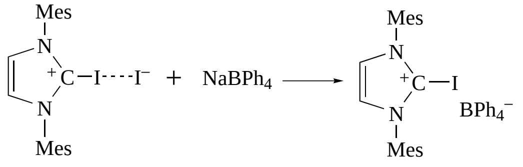

(15)

(**131**)

Cationic bis(carbene) adducts of the hypervalent iodine (**132** and **133**) may be prepared by reaction of the imidazolium salts (**128**) and (**130**) with carbene (equation 16).[81] The ^{1}H and ^{13}C NMR spectra of (**132**) and (**133**) are identical, indicating that the anions do not play an important role in the bonding of the hypervalent iodine cation. X-ray diffraction of (**133**) showed that the central C–I–C unit (177.5°) is almost linear with slightly longer C–I bond distances than those observed in (**128–130**) and (**133**, C–I 2.286 Å and 2.363 Å). The structure of (**133**) suggests that the C–I–C interaction in (**133**) is stronger than the C–I···I interactions in (**128**) and (**129**).

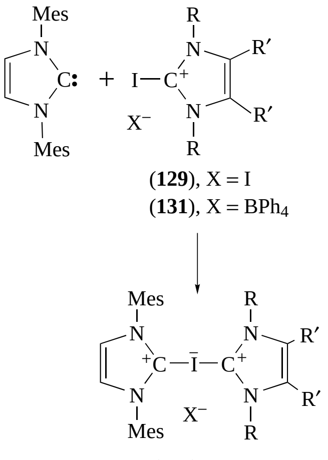

(**129**), X = I
(**131**), X = BPh_4

(16)

(**132**), X = I
(**133**), X = BPh_4

Recently, the reactivity of N-heterocyclic carbenes with bromine and some chloride sources were reported.[82,83] Imidazolium chloride salts are sometimes obtained as side products when carbene (**1**) is reacted with main group species to produce main group carbene adducts.[53,74] However, they can be prepared directly from the reaction of carbene (**1**) ($R = $ Mes, $R' = H$) with chloroalkanes, such as hexachloroethane in acetonitrile (**134**). Reaction of carbene (**1**) ($R = $ Mes, $R' = H$) with Br_2 or 1,2-dibromoethane affords the 2-bromo-1,3-bis(2,4,6-trimethylphenyl) imidazolium bromide (**135**).

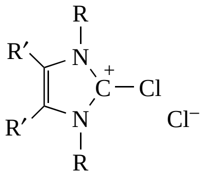

(**134**, R = Mes, R′ = H;
R = *i*-Pr, Et, Me, R′ = Me)

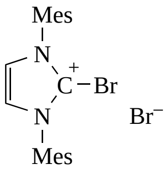

(**135**)

8 RELATED ARTICLES

Alkali Metals: Inorganic Chemistry; Alkali Metals: Organometallic Chemistry; Aluminum: Inorganic Chemistry; Aluminum: Organometallic Chemistry; Antimony: Inorganic Chemistry; Antimony: Organometallic Chemistry; Arsenic: Inorganic Chemistry; Arsenic: Organoarsenic Chemistry; Beryllium & Magnesium: Organometallic Chemistry; Boron Hydrides; Boron: Inorganic Chemistry; Carbene Complexes; Chalcogenides: Solid-state Chemistry; Chlorine, Bromine, Iodine, & Astatine: Inorganic Chemistry; Gallium: Inorganic Chemistry; Germanium: Organometallic Chemistry; Indium: Inorganic Chemistry; Indium: Organometallic Chemistry; Lead: Inorganic Chemistry; Lead: Organometallic Chemistry; Phosphorus: Inorganic Chemistry; Selenium: Inorganic Chemistry; Silicon: Inorganic Chemistry; Silicon: Organosilicon Chemistry; Sulfur: Inorganic Chemistry; Tellurium: Inorganic Chemistry; Tin: Inorganic Chemistry; Tin: Organometallic Chemistry.

9 REFERENCES

1. A. J. Arduengo, H. V. R. Dias, R. L. Harlow, and M. Kline III, *J. Am. Chem. Soc.*, 1992, **114**, 5530.
2. A. J. Arduengo, J. R. Goerlich, and W. J. Marshall III, *J. Am. Chem. Soc.*, 1995, **117**, 11027.
3. R. W. Alder, P. R. Allen, M. Murray, and A. G. Orpen, *Angew. Chem., Int. Ed. Engl.*, 1996, **35**, 1121.
4. A. J. Arduengo III, J. R. Goerlich, and W. J. Marshall, *Liebigs Annl Recl.*, 1997, 365.
5. R. W. Alder, C. P. Butts, and A. G. Orpen, *J. Am. Chem. Soc.*, 1998, **120**, 11526.
6. D. Bourissou, O. Guerret, F. P. Gabbaï, and G. Bertrand, *Chem. Rev.*, 2000, **100**, 39.
7. W. A. Herrmann and C. Köcher, *Angew. Chem., Int. Ed. Engl.*, 1997, **36**, 2162.
8. C. J. Carmalt and A. H. Cowley, *Adv. Inorg. Chem.*, 2000, **50**, 1.
9. R. W. Alder, M. E. Blake, C. Bortolotti, S. Bufali, C. P. Butts, E. Linehan, J. M. Oliva, A. G. Orpen, and M. J. Quayle, *Chem. Commun.*, 1999, 241.
10. A. J. Arduengo III, M. Tamm, J. C. Calabrese, F. Davidson, and W. J. Marshall, *Chem. Lett.*, 1999, 1021.
11. R. Fränkel, C. Birg, U. Kernbach, T. Habereder, H. Nöth, and W. P. Fehlhammer, *Angew. Chem., Int. Ed. Engl.*, 2001, **40**, 1907.
12. W. A. Herrmann, O. Runte, and G. R. J. Artus, *J. Organomet. Chem.*, 1995, **501**, C1.
13. A. J. Arduengo, H. V. R. Dias, F. Davidson, and R. L. Harlow III, *J. Organomet. Chem.*, 1993, **462**, 13.
14. A. J. Arduengo, F. Davidson, R. Krafczyk, W. J. Marshall, and M. Tamm III, *Organometallics*, 1998, **17**, 3375.
15. H. Schumann, J. Gottfriedsen, M. Glanz, S. Dechert, and J. Demtschuk, *J. Organomet. Chem.*, 2001, **617–618**, 588.
16. M. G. Gardiner and C. L. Raston, *Coord. Chem. Rev.*, 1997, **166**, 1.
17. C. L. Raston, A. F. H. Siu, C. J. Tranter, and D. J. Young, *Tetrahedron Lett.*, 1994, **35**, 5915.
18. M. G. Simmonds and W. L. Gladfelter, in ‘The Chemistry of Metal CVD’, eds. T. Kodas and M. Hampden-Smith, VCH, Weinheim, 1994.
19. A. J. Arduengo, H. V. R. Dias, J. C. Calabrese, and F. Davidson III, *J. Am. Chem. Soc.*, 1992, **114**, 9724.
20. D. E. Hibbs, M. B. Hursthouse, C. Jones, and N. A. Smithies, *Chem. Commun.*, 1998, 869.
21. M. D. Francis, D. E. Hibbs, M. B. Hursthouse, C. Jones, and N. A. Smithies, *J. Chem. Soc., Dalton Trans.*, 1998, 3249.
22. R. J. Baker, A. J. Davies, C. Jones, and M. Kloth, *J. Organomet. Chem.*, 2002, **656**, 203.
23. C. D. Abernethy, M. L. Cole, and C. Jones, *Organometallics*, 2000, **19**, 4852.
24. R. J. Baker and C. Jones, *Appl. Organomet. Chem.*, 2003, **17**, 807.
25. R. J. Baker, M. L. Cole, C. Jones, and M. F. Mahon, *J. Chem. Soc., Dalton Trans.*, 2002, 1992.
26. N. Kuhn, G. Henkel, T. Kratz, J. Kreutzberg, R. Boese, and A. H. Maulitz, *Chem. Ber.*, 1993, **126**, 2041.
27. T. Ramnial, H. Jong, I. D. McKenzie, M. Jennings, and J. A. C. Clyburne, *Chem. Commun.*, 2003, 1722.
28. D. E. Hibbs, M. B. Hursthouse, C. Jones, and N. A. Smithies, *Main Group Chem.*, 1998, **2**, 293.

29. C. D. Abernethy, M. L. Cole, A. J. Davies, and C. Jones, *Tetrahedron Lett.*, 2000, **41**, 7567.
30. C. D. Abernethy, R. J. Baker, M. L. Cole, A. J. Davies, and C. Jones, *Transition Met. Chem.*, 2003, **28**, 296.
31. M. A. Fox, J. A. K. Howard, J. M. Moloney, and K. Wade, *Chem. Commun.*, 1998, 2487.
32. A. J. Arduengo, F. Davidson, R. Krafczyk, W. J. Marshall, and R. Schmutzler III, *Monatsh. Chem.*, 2000, **131**, 251.
33. N. Kuhn, R. Fawzi, H. Kotowski, and M. Steimann, *Z. Kristallogr.*, 1997, **212**, 259.
34. D. J. Neilsen, K. J. Cavell, B. W. Skelton, and A. H. White, *Inorg. Chim. Acta*, 2003, **352**, 143.
35. N. Merceron, K. Miqueu, A. Baceiredo, and G. Bertrand, *J. Am. Chem. Soc.*, 2002, **124**, 6806.
36. S. J. Black, D. E. Hibbs, M. B. Hursthouse, C. Jones, K. M. A. Malik, and N. A. Smithies, *J. Chem. Soc., Dalton Trans.*, 1997, 4313.
37. M. L. Cole, A. J. Davies, and C. Jones, *J. Chem. Soc., Dalton Trans.*, 2001, 2451.
38. R. J. Baker, R. D. Farley, C. Jones, M. Kloth, and D. M. Murphy, *Chem. Commun.*, 2002, 1196.
39. R. J. Baker, H. Bettentrup, and C. Jones, *Eur. J. Inorg. Chem.*, 2003, 2446.
40. H. Nakai, Y. Tang, P. Gantzel, and K. Meyer, *Chem. Commun.*, 2003, 24.
41. A. Wacker, H. Pritzkow, and W. Siebert, *Eur. J. Inorg. Chem.*, 1998, 843.
42. A. Wacker, H. Pritzkow, and W. Siebert, *Eur. J. Inorg. Chem.*, 1999, 789.
43. A. Wacker, C. G. Yan, G. Kaltenpoth, A. Ginsberg, A. M. Arif, R. D. Ernst, H. Pritzkow, and W. Siebert, *J. Organomet. Chem.*, 2002, **641**, 195.
44. M. Tamm, F. E. Lugger, and F. E. Hahn, *Organometallics*, 1996, **15**, 1251.
45. J. van der Broeke, M. Stam, M. Lutz, H. Kooijman, A. L. Spek, B. J. Deelman, and G. van Koten, *Eur. J. Inorg. Chem.*, 2003, 2798.
46. L. Weber, E. Dobbert, H.-G. Stammler, B. Neumann, R. Boese, and D. Bläser, *Chem. Ber.*, 1997, **130**, 705.
47. N. Kuhn, T. Kratz, D. Bläser, and R. Boese, *Chem. Ber.*, 1995, **128**, 245.
48. X. Zheng and G. E. Herberich, *Organometallics*, 2000, **19**, 3751.
49. I. I. Padilla-Martínez, F. J. Martínez-Martínez, A. López-Sandoval, K. I. Girón-Castillo, M. A. Brito, and R. Contreras, *Eur. J. Inorg. Chem.*, 1998, 1547.
50. X. W. Li, J. R. Su, and G. H. Robinson, *Chem. Commun.*, 1996, 2683.
51. M. Schiefer, N. D. Reddy, H.-J. Ahn, A. Stasch, H. W. Roesky, A. C. Schlicker, H.-G. Schmidt, M. Noltemeyer, and D. Vidovic, *Inorg. Chem.*, 2003, **42**, 4970.
52. G. Alcaraz, R. Reed, A. Baceiredo, and G. Bertrand, *J. Chem. Soc., Chem. Commun.*, 1993, 1354.
53. A. H. Cowley, F. P. Gabbaï, C. J. Carrano, L. M. Mokry, M. R. Bond, and G. Bertrand, *Angew. Chem., Int. Eg. Engl.*, 1994, **33**, 578.
54. J. M. Pietryga, J. D. Gordon, C. L. B. Macdonald, A. Voigt, R. J. Wiacek, and A. H. Cowley, *J. Am. Chem. Soc.*, 2001, **123**, 7713.
55. W. M. Boesveld, B. Gehrhus, P. B. Hitchcock, M. F. Lappert, and P. von Ragué Schleyer, *Chem. Commun.*, 1999, 755.
56. A. J. Arduengo, H. V. R. Dias, J. C. Calabrese, and F. Davidson III, *Inorg. Chem.*, 1993, **32**, 1541.
57. A. Schäfer, M. Weidenbruch, W. Saak, and S. Pohl, *Chem. Commun.*, 1995, 1157.
58. F. E. Hahn, L. Wittenbecher, M. Kühn, T. Lügger, and R. Fröhlich, *J. Organomet. Chem.*, 2001, **617–618**, 629.
59. F. Stabenow, W. Saak, and M. Weidenbruch, *Chem. Commun.*, 1999, 1131.
60. H. Schumann, M. Glanz, F. Girgsdies, F. Ekkehardt Hahn, M. Tamm, and A. Grzegorzewski, *Angew. Chem., Int. Ed. Engl.*, 1997, **36**, 2232.
61. A. J. Arduengo, J. C. Calabrese, A. H. Cowley, H. V. R. Dias, J. R. Goerlich, W. J. Marshall, and B. Riegel III, *Inorg. Chem.*, 1997, **36**, 2151.
62. A. J. Arduengo III, H. V. R. Dias, and J. C. Calabrese, *Chem. Lett.*, 1997, 143.
63. A. J. Arduengo III, C. J. Carmalt, J. A. C. Clyburne, A. H. Cowley, and R. Pyati, *Chem. Commun.*, 1997, 981.
64. N. Kuhn, J. Fahl, D. Bläser, and R. Boese, *Z. Anorg. Allg. Chem.*, 1999, **625**, 729.
65. N. Burford, T. S. Cameron, P. J. Ragogna, E. Ocando-Mavarez, M. Gee, R. McDonald, and R. E. Wasylishen, *J. Am. Chem. Soc.*, 2001, **123**, 7947.
66. N. Burford, T. S. Cameron, D. J. LeBlanc, A. D. Philips, T. E. Concolino, K.-C. Lam, and A. L. Rheingold, *J. Am. Chem. Soc.*, 2000, **122**, 5413.
67. A. J. Arduengo, R. Krafczyk, W. J. Marshall, and R. Schmutzler III, *J. Am. Chem. Soc.*, 1997, **119**, 3381.
68. N. Kuhn, M. Ströbele, and M. Walker, *Z. Anorg. Allg. Chem.*, 2003, **629**, 180.
69. A. J. Arduengo, R. Krafczyk, R. Schmutzler, W. Mahler, and W. J. Marshall III, *Z. Anorg. Allg. Chem.*, 1999, **625**, 1813.
70. N. Kuhn, G. Henkel, and T. Kratz, *Z. Naturforsch.*, 1993, **48b**, 973.
71. D. J. Williams, M. R. Fawcett-Brown, R. R. Raye, D. Van-Derveer, and R. L. Jones, *Heteroatom Chem.*, 1993, **4**, 409.
72. N. Kuhn, G. Henkel, and T. Kratz, *Chem. Ber.*, 1993, **126**, 2047.
73. F. E. Hahn, L. Wittenbecher, R. Boese, and D. Bläser, *Chem. Eur. J.*, 1999, **5**, 1931.
74. N. Kuhn, K. Eichele, and M. Walker, *Z. Anorg. Allg. Chem.*, 2001, **627**, 2565.

75. D. Enders, K. Breuer, G. Raabe, J. Runsink, J. H. Teles, J. P. Melder, K. Ebel, and S. Brode, *Angew. Chem., Int. Ed. Engl.*, 1995, **34**, 1021.
76. N. Kuhn, H. Bohnen, J. Fahl, D. Bläser, and R. Boese, *Chem. Ber.-Recl.*, 1996, **129**, 1579.
77. M. K. Denk, K. Hatano, and A. J. Lough, *Eur. J. Inorg. Chem.*, 2003, 224.
78. N. Kuhn, T. Kratz, and G. Henkel, *Chem. Ber.*, 1994, **127**, 849.
79. N. Kuhn, T. Kratz, and G. Henkel, *Z. Naturforsch.*, 1996, **51b**, 295.
80. A. J. Arduengo, M. Tamm, and J. C. Calabrese III, *J. Am. Chem. Soc.*, 1994, **116**, 3625.
81. N. Kuhn, T. Kratz, and G. Henkel, *J. Chem. Soc., Chem. Commun.*, 1993, 1778.
82. M. L. Cole, C. Jones, and P. C. Junk, *New. J. Chem.*, 2002, **262**, 1296.
83. N. Kuhn, J. Fahl, R. Fawzi, C. Maichle-Mossmer, and M. Steimann, *Z. Naturforsch.*, 1998, **53b**, 720.

Main Group: Multiple Bonding

Gregory H. Robinson
The University of Georgia, Athens, GA, USA

1 Introduction 1
2 Group 13 Multiple Bonds 1
3 Group 14 Multiple Bonds 2
4 Group 15 Multiple Bonds 5
5 Related Articles 6
6 References 6

1 INTRODUCTION

The proposition of multiple bonding is, arguably, the most compelling concept throughout the whole of chemistry. While the general concept of multiple bonding is well established and easily embraced in organic chemistry, this is not the case for much of organometallic chemistry. In particular, multiple bonding involving homonuclear compounds of the heavier main group elements is a relatively recent phenomenon. The criteria that are routinely employed to assign double and triple bond character in organic compounds, that is, bond distance and bond strength, are of little significance in many cases involving the heavier main group elements. For example, the $E{=}E$ ($E = Sn, Pb$) double bond is both *longer* and *weaker* than the corresponding E–E single bond. Quite obviously, such behavior stands in stark contrast to that of carbon and other lighter main group elements. This is most prominently manifested in the structure of the resulting compounds: 'trans-bent' geometries are preferred over linear structures where triple bonds of the heavier main group elements are concerned. Indeed, a compelling case can be made on the basis of the premise that the behavior of carbon is the exception, rather than the rule, where multiple bonding of many main group elements is concerned. This article will discuss some of the more significant recent discoveries in the chemistry of main group 13, 14, and 15 elements relative to the concept of homonuclear multiple bonding.

2 GROUP 13 MULTIPLE BONDS

2.1 Aluminum Multiple Bonds

The first compound containing an Al–Al bond was reported in 1988 with tetrakis[bis(trimethylsilyl)methyl]dialane, $[(SiMe_3)_2CH]_2Al–Al[CH(SiMe_3)_2]_2$. This compound was prepared by the potassium reduction of bis[bis(trimethylsilyl) methyl]aluminum chloride (equation 1).[1]

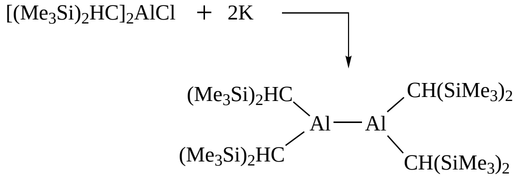

(1)

The Al–Al bond distance is 2.660(1) Å. It is noteworthy that the aluminum atoms were shown to reside in trigonal planar environments about a nearly planar $C_2Al–AlC_2$ core.

In an attempt to approach a measure of π-bonding between two aluminum atoms, Uhl *et al.* examined the alkali metal reduction of $[(SiMe_3)_2CH]_2Al–Al[CH(SiMe_3)_2]_2$. Specifically, sodium or potassium reduction of $[(SiMe_3)_2CH]_2Al–Al[CH(SiMe_3)_2]_2$ in dimethoxyethane (DME) afforded dark blue colored crystals of the $[(SiMe_3)_2CH]_2Al–Al[CH(SiMe_3)_2]_2{}^{\bullet-}$ radical anion (equation 2).[2]

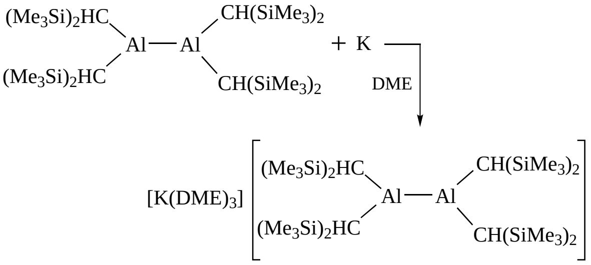

(2)

This species, characterized by ESR, UV-VIS, and IR, demonstrated remarkable stability.

The lithium reduction of $[(SiMe_3)_2CH]_2Al–Al[CH(SiMe_3)_2]_2$, in the presence of TMEDA (tetramethylethylenediamine), gives an 'Al–Al one-electron π-bond' in the $[(SiMe_3)_2CH]_2Al–Al[CH(SiMe_3)_2]_2{}^{\bullet-}$ radical anion as fine black crystals (equation 3).[3]

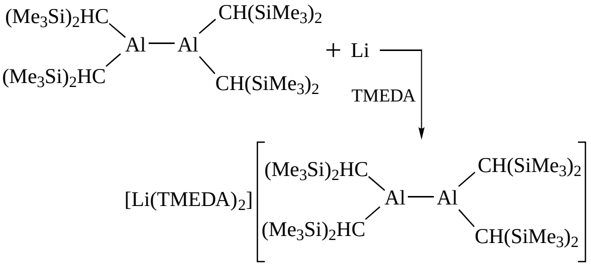

(3)

The solid-state structure of $[(SiMe_3)_2CH]_2Al–Al[CH(SiMe_3)_2]_2{}^{\bullet-}$ is very interesting when compared with that of the neutral dialane. The C–Al–C bond angle of 111.9(2)° is smaller than that reported for the neutral dialane (116.7(1)°), while the Al–C bond distances in the radical anion (2.0420(5) Å) are lengthened compared to those of the neutral dialane (1.982(5) Å). The Al–Al bond in the radical anion of 2.53(1) Å is considerably shorter than that observed in the neutral dialane (2.660(1) Å). Certainly, this decrease in the Al–Al bond distance (in going from the neutral dialane to the radical anion) is consistent with an interaction of some level of multiple bond character.

The radical anion $[\mathrm{Pr}^i_3\mathrm{C}_6\mathrm{H}_2]_2\mathrm{Al}$–$\mathrm{Al}[\mathrm{C}_6\mathrm{H}_2\mathrm{Pr}^i_3]_2{}^{\bullet -}$ was prepared by the lithium reduction of the neutral dialane. The Al–Al bond distance decreased from 2.647(3) Å in the neutral dialane, $[\mathrm{Pr}^i_3\mathrm{C}_6\mathrm{H}_2]_2\mathrm{Al}$–$\mathrm{Al}[\mathrm{C}_6\mathrm{H}_2\mathrm{Pr}^i_3]_2$, to 2.470(2) in the radical anion, $[\mathrm{Pr}^i_3\mathrm{C}_6\mathrm{H}_2]_2\mathrm{Al}$–$\mathrm{Al}[\mathrm{C}_6\mathrm{H}_2\mathrm{Pr}^i_3]_2{}^{\bullet -}$, thus providing evidence of multiple bond character.[4]

The evidence substantially supports a one-electron π-bond between two aluminum atoms. However, a RAl=AlR compound containing a two-electron π-bond has not been reported.

2.2 Gallium Multiple Bonds

The first compound containing a Ga–Ga bond, $[(\mathrm{SiMe}_3)_2\mathrm{CH}]_2$ Ga–Ga$[\mathrm{CH}(\mathrm{SiMe}_3)_2]_2$, was prepared by the reaction of $\mathrm{Ga}_2\mathrm{Br}_4(\mathrm{dioxane})_2$ with $\mathrm{LiCH}(\mathrm{SiMe}_3)_2$.[5] The Ga–Ga bond distance was 2.541(1) Å in this yellow crystalline digallane. Reaction of $\mathrm{Ga}_2\mathrm{Cl}_4(\mathrm{dioxane})_2$ and $(\mathrm{Pr}^i_3\mathrm{C}_6\mathrm{H}_2)\mathrm{MgBr}$ affords $[\mathrm{Pr}^i_3\mathrm{C}_6\mathrm{H}_2]_2$ Ga–Ga$[\mathrm{C}_6\mathrm{H}_2\mathrm{Pr}^i_3]_2$, with a Ga–Ga bond distance of 2.515(3) Å.[6] Upon treatment of $[\mathrm{Pr}^i_3\mathrm{C}_6\mathrm{H}_2]_2$ Ga–Ga$[\mathrm{C}_6\mathrm{H}_2\mathrm{Pr}^i_3]_2$ with an excess of lithium powder, followed by the addition of 12-crown-4, dark brown-red crystals of [Li(12-crown-4)]$[\mathrm{Pr}^i_3\mathrm{C}_6\mathrm{H}_2]_2$ Ga–Ga$[\mathrm{C}_6\mathrm{H}_2\mathrm{Pr}^i_3]_2$ (**1**) were isolated.

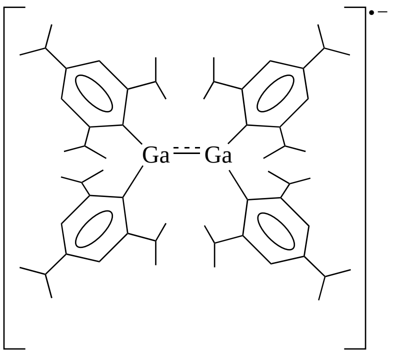

(**1**)

A comparison of the neutral gallane with the radical anion reveals a number of intermolecular structural changes. The Ga–Ga bond was shortened to 2.343(2) Å, thus providing support for a Ga–Ga one-electron π-bond. In addition, the torsion angle between the two $\mathrm{C}_2\mathrm{Ga}$ planes decreased to 15.5° compared to the neutral digallane. The nature of the radical anion was supported by a strong ESR signal.

The utilization of sterically demanding *m*-terphenyl ligands facilitated an interesting, if provocative, period in organogallium chemistry. The *m*-terphenylgallium dichloride compound, $[2{,}6\text{-}(\mathrm{Pr}^i_3\mathrm{C}_6\mathrm{H}_2)_2\mathrm{C}_6\mathrm{H}_3]\mathrm{GaCl}_2$, was prepared from reaction of $[2{,}6\text{-}(\mathrm{Pr}^i_3\mathrm{C}_6\mathrm{H}_2)_2\mathrm{C}_6\mathrm{H}_3]\mathrm{Li}$ with GaCl_3.[7] Sodium metal reduction of $[2{,}6\text{-}(\mathrm{Pr}^i_3\mathrm{C}_6\mathrm{H}_2)_2\mathrm{C}_6\mathrm{H}_3]\mathrm{GaCl}_2$ yields dark red (almost black) crystals of $\mathrm{Na}_2[\mathrm{RGa{\equiv}GaR}]$ (R = 2,6-$(\mathrm{Pr}^i_3\mathrm{C}_6\mathrm{H}_2)_2\mathrm{C}_6\mathrm{H}_3$) (equation 4).[8]

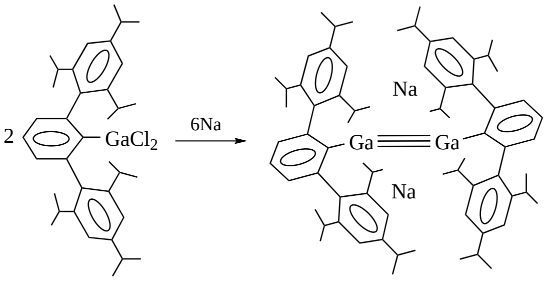

(4)

This provocative compound, with a Ga–Ga bond distance of 2.319(3) Å, was referred to as a ‘digallyne’, thus indicating the first compound containing a Ga–Ga triple bond, albeit a weak triple bond. The C–Ga–Ga–C backbone was decidedly nonlinear with bond angles about the gallium centers of 128.5(4)° and 133.5(4)°. Indeed, this geometry was described as ‘trans-bent’. An alternative interpretation of the bonding as being closer to a Ga–Ga double bond was subsequently proposed by another group.[9] Importantly, bond order values for the –GaGa– interaction have been calculated ranging from 2.794[10] to 3.02,[11] clearly supporting the triple bond formulation. Studies by various research groups on the nature of the Ga–Ga interaction in the digallyne also provide compelling support for the triple bond formulation.[12–14] Indeed, few compounds in the realm of multiple bonding among heavier main group elements have been studied as extensively as the digallyne. This area has recently been reviewed.[15–17] It is important to note that the general mode of preparation employed for the gallyne, the trans-bent structure, and the premise that the heavier main group elements exhibit a different means of hybridization from carbon, have all been repeatedly, and consistently, observed in recent reports of triple bond stabilization for silicon and alkyne analogs for germanium, tin, and lead (vide infra).

3 GROUP 14 MULTIPLE BONDS

Multiple bonds involving the lightest member of group 14 are ubiquitous (i.e. alkenes and alkynes) and traditional chemical bonding theories such as Valence Bond Theory can adequately describe such interactions. The chemistry of compounds containing silicon–silicon multiple bonds, disilenes, and disilynes has not developed in parallel with that of carbon. Nonetheless, significant advances have recently been made, most prominently the report of the first example of a –Si≡Si– triple bond.

3.1 Silicon Multiple Bonds

The concept of multiple bonding becomes slightly more complicated concerning silicon. The first compound containing a Si=Si double bond, tetramesityldisilene, $Mes_2Si{=}SiMes_2$ (Mes = mesityl), was reported in 1981 (equation 5).[18]

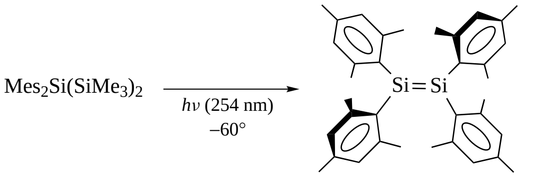

(5)

This seminal compound was isolated as yellow crystals in high yield. The X-ray crystal structure[19] of $Mes_2Si{=}SiMes_2$ revealed a Si=Si double bond distance of 2.15 Å (while typical Si–Si single bond distances approach 2.35 Å). Moreover, the geometry around the silicon atoms was not trigonal planar, as would be expected for carbon, but rather 'trans-bent' (with the silicon atoms residing in pseudopyramidal environments). This clearly suggests that multiple bonding involving heavier main group elements may behave differently than carbon.

The concept of a compound containing a Si–Si triple bond, R–Si≡Si–R, has fascinated chemists for decades. In particular, computational and theoretical chemists have long predicted that large bulky ligands will be necessary to stabilize the Si≡Si interaction and that the linear geometry is not a global minimum but the trans-bent geometry is favored.[20,21] Furthermore, it has been predicted that the bonding between two such silicon atoms would best be described as two dative (donor–acceptor) bonds and one π-bond. This bonding model is at odds with the traditional manner to describe a triple bond between two carbon atoms: one σ-bond and two π-bonds.

Quite recently, this most sought after prize was won: A group of workers succeeded in synthesizing a stable compound containing a –Si≡Si– triple bond. Sekiguchi and coworkers isolated 1,1,4,4-tetrakis[bis(trimethylsilyl)methyl]-1,4-diisopropyl-2-tetrasilyne from reaction of 2,2,3,3-tetrabromo-1,1,4,4-tetrakis[bis(trimethylsilyl)methyl]-1,4-diisopropyl-tetrasilane with four equivalents of potassium graphite in tetrahydrofuran (equation 6).[22]

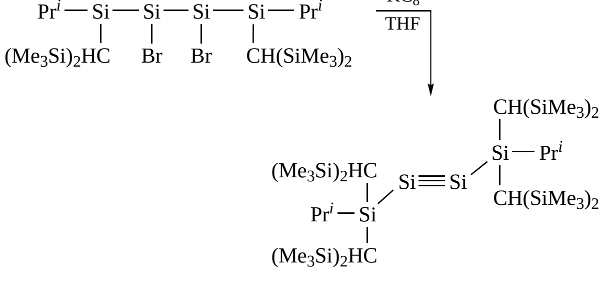

(6)

The air- and moisture sensitive disilyne was isolated as green crystals. The –Si≡Si– triple bond distance was shown to be 2.0622(9) Å via single crystal X-ray diffraction. Perhaps most importantly, the two silicon atoms engaged in the triple bond reside in a 'trans-bent' environment about a bond angle of 137.44(4)°.

3.2 Germanium Multiple Bonds

An early report discussed the synthesis and structure of a cyclotrigermane, hexakis(2,6-dimethylphenyl) cyclotrigermane, and its photoconversion to a digermene (which was not structurally characterized).[23] Reaction of $MgClR(OEt_2)$ ($R = CH(SiMe_3)_2$) with $GeCl_2$(dioxane) produced bright yellow crystals of $[(Me_3Si)_2HC]_2Ge{=}Ge[CH(SiMe_3)_2]_2$: the first solid-state compound containing a Ge=Ge double bond (**2**).[24]

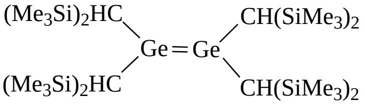

(**2**)

The compound was reported to have C_{2h} symmetry about the Ge_2C_4 core with a fold angle of 32°. Furthermore, the germanium environment was described as being between pyramidal and planar. The Ge=Ge double bond distance was reported as 2.347(2) Å.

Masamune and coworkers subsequently reported the structure of tetrakis(2,6-diethylphenyl)digermene, isolated from the photoconversion of the corresponding cyclotrigermane (**3**).[25] The Ge=Ge bond distance of 2.213 Å in $[2,6\text{-}Et_2C_6H_3]_2Ge{=}Ge[C_6H_3\text{-}2,6\text{-}Et_2]_2$ is considerably shorter than that in (**2**) (2.347(2) Å).

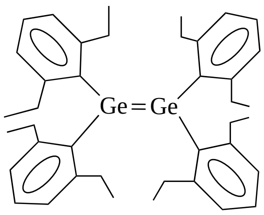

(**3**)

Recently, the $[2,6\text{-}Mes_2C_6H_3]_2Ge{=}Ge[C_6H_3\text{-}2,6\text{-}Mes_2]_2$ digermene has been reported utilizing a sterically demanding *m*-terphenyl ligand.[26] In addition, a germanium analog of an alkyne, albeit with significant electron lone-pair character on the metal atoms and 'bond orders that are less than three', has been reported.[27]

3.3 Tin Multiple Bonds

The first compound containing a Sn=Sn double bond was reported nearly three decades ago. Reaction of tin(II) chloride with bis(trimethylsilyl)methyllithium, $Li[CH(SiMe_3)_2]$, gave the diamagnetic species $\mathbf{:}Sn[CH(SiMe_3)_2]_2$ in solution. However, upon crystallization, the species dimerizes into $[(Me_3Si)_2HC]_2Sn{=}Sn[CH(SiMe_3)_2]_2$ – the first distannene containing ‘a tin–tin (‘bent’ double) bond’ (equation 7).**[28]**

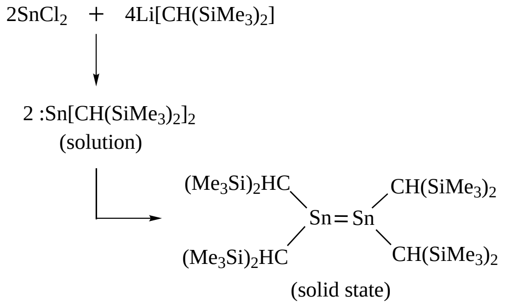

(7)

Again, the molecule resides in a ‘trans-bent’ configuration with the tin atoms in pyramidal geometries. The Sn=Sn double bond distance was shown to be 2.76 Å with the mean Sn–Sn–C bond angle of 115° and the C–Sn–C bond angle of 112°. The authors regarded the dimerization as ‘aggregation of two singlet bent monomers, whereby the approximately sp_xp_y [sp^2] lone-pair hybrid filled orbital on the tin atom of one of the partners overlaps with the vacant p_z orbital of the other’ (**4**). Concluding, the authors stated, ‘‘The molecule is thus considered as having a ‘bent’ and weak SnSn double bond, which also accounts for the relative disposition of the two sets of R groups with respect to each other.’’

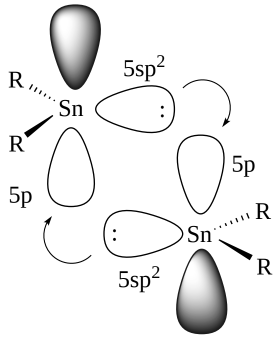

(**4**)

The Sn=Sn double bond distance of 2.76 Å for $[(Me_3Si)_2HC]_2Sn{=}Sn[CH(SiMe_3)_2]_2$ compares to a value of 2.770(4) Å for hexaphenyldistannane,**[29]** $Ph_3Sn–SnPh_3$: within experimental error the Sn=Sn double bond distance and the Sn–Sn single bond distance are equivalent.

Recently, a striking distannene, prepared from the reaction of $Bu^t_2MeSiNa$ and $SnCl_2$(dioxane) in tetrahydrofuran (equation 8), in the form of $[Bu^t_2MeSi]_2Sn{=}Sn[SiMeBu^t_2]_2$ was reported.**[30]**

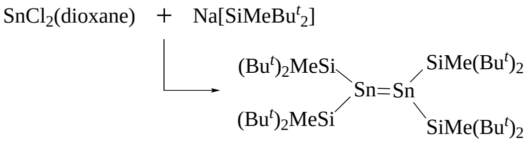

(8)

The most intriguing aspect of this compound is the fact that the Sn=Sn double bond remains intact both in solution and in the solid state. This behavior is in marked contrast to other distannenes that exhibit monomeric behavior in solution. As described by the authors, this compound serves up a number of interesting points structurally. The Sn=Sn bond distance of 2.6683(10) Å is the shortest of all distannenes. Continuing, the sp^2 Sn atoms reside in planar environments – this is in sharp contrast to all other distannenes that unambiguously display trans-bent environments. A last significant point concerns a twist angle of the Sn=Sn double bond of 44.62(7)°. It is most surprising that the Sn=Sn bond remains intact under such a twist angle.

Similar to the case for germanium, a stable tin ‘analog’ of an alkyne, albeit with significant electron lone-pair character on the metal atoms and ‘bond orders that are less than three’, has been reported in RSnSnR ($R = 2,6\text{-}(2,4,6\text{-}Pr^i_3C_6H_2)_2C_6H_3$) by the potassium reduction of RSnCl.**[31]** The Sn–Sn bond distance was reported as 2.6675(4) Å with a Sn–Sn–C bond angle of 125.24(7)°. The overall geometry is trans-bent. It should be noted that the general structure and description of the bonding in this compound is quite similar to the $RGaGaR^{2-}$ digallyne.

3.4 Lead Multiple Bonds

A compound containing an unambiguous example of a double bond between atoms of the heaviest member of group 14, lead, has only recently been reported. This compound, $(Pr^i_3C_6H_2)_2Pb{=}Pb(C_6H_2Pr^i_3)_2$ (**5**), was prepared by reaction of lead(II) chloride with 2,4,6-triisopropylphenylmagnesium bromide at low temperature.**[32]** Reaction gave a violet solution, from which red crystals were isolated. The crystals were reported to be thermally stable, but light- and air-sensitive. The compound resides in a trans-bent geometry with a Pb=Pb double bond distance of 3.0515(3) Å.

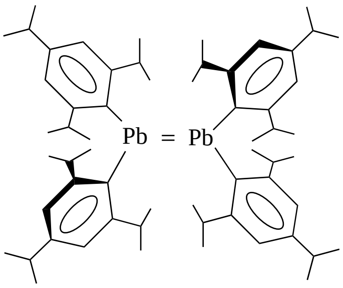

(**5**)

The Pb=Pb double bond distance of 3.0515(3) Å is easily compared to the Pb–Pb single bond distances of 2.83 Å for $Ph_3Pb–PbPh_3$ (Ph = phenyl)[29] or 2.8697(10) Å for $Bp_3Pb–PbBp_3$ (Bp = biphenyl).[33] Here again is an example of a heavier main group element engaging in multiple bond formation. However, the heavier main group atoms display a resistance to hybridize in the same fashion as carbon. Rather, the Pb=Pb double bond is depicted (**6**) showing the orbital overlap in two donor–acceptor interactions.

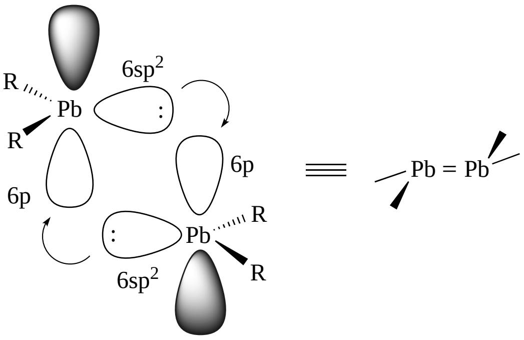

(**6**)

The authors pointed out that bond distances and bond strengths, unlike the case for carbon, are of little significance where multiple bonding of the heavier main group metals is concerned.

Reaction of $LiAlH_4$ with Pb(Br)R (R = 2,6-$(Pr^i_3C_6H_2)_2C_6H_3$) has been reported to yield a lead analog of an alkyne.[34] The Pb–Pb bond distance of 3.188(1) Å for RPbPbR is longer than the Pb=Pb distance of 3.0515(3) Å for $(Pr^i_3C_6H_2)_2Pb{=}Pb(C_6H_2Pr^i_3)_2$. The fact that the C–Pb–Pb bond angle for RPbPbR is 94.26(4)° is perhaps suggestive that the most important contributing resonance structure should be the one with considerable lone-pair electron character on the two lead atoms (**7**).

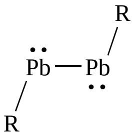

(**7**)

4 GROUP 15 MULTIPLE BONDS

The iconic molecule of multiple bonding of the group 15 elements is obviously dinitrogen, N_2. The $:N{\equiv}N:$ triple bond and the chemistry that springs from it are ubiquitous. The chemistry of multiple bonds of the heavier group 15 elements is not as well developed. However, significant progress and important discoveries have recently been made in this area.

4.1 Phosphorus Multiple Bonds

Bis(2,4,6-tri-*tert*-butylphenyl)diphosphene, (2,4,6-$Bu^t)_3C_6H_2P{=}PC_6H_2$(2,4,6-$Bu^t)_3$, the first compound with a formal P=P double bond, was prepared from the magnesium reduction of (2,4,6-$Bu^t)C_6H_2PCl_2$ (**8**).[35]

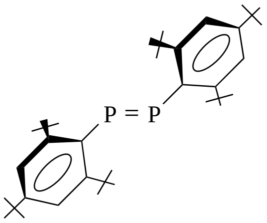

(**8**)

The P=P double bond distance of 2.03 Å for (2,4,6-$Bu^t)_3C_6H_2P{=}PC_6H_2$(2,4,6-$Bu^t)_3$ compares with the P–P single bond distance of 2.23 Å for P_4.

Even though great advances in the chemistry of the P=P double bond have taken place over the past two decades,[36] new and interesting diphosphenes, some utilizing sterically demanding *m*-terphenyl ligands continue to be reported.[37–39]

4.2 Arsenic Multiple Bonds

The chemistry of the As=As double bond is quite similar to that of phosphorus. Stabilization of the As=As double bond has been known for almost two decades. The As=As bond distance in bis[tris(trimethylsilyl)methyl]diarsene, $(SiMe_3)_3CAs{=}AsC(SiMe_3)_3$, prepared by reaction of $(Me_3Si)_3CAsCl_2$ and *tert*-butyllithium, is typical at 2.45 Å.[40]

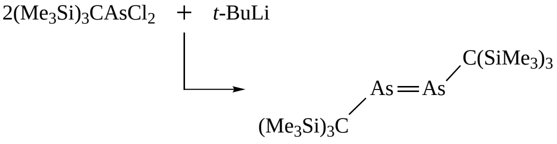

(9)

4.3 Antimony Multiple Bonds

The first stable compound containing an Sb=Sb double bond was only reported in 1998 with (Tbt)Sb=Sb(Tbt) (Tbt = 2,4,6-tris[bis(trimethylsilyl)methyl]phenyl) (**9**).[41] The molecule was prepared in high yield as deep green crystals. The molecule has a trans-bent geometry.

The Sb=Sb double bond was reported as 2.642(1) Å. Interestingly, (Tbt)Sb=Sb(Tbt) undergoes reaction with molecular oxygen to yield a di-μ-oxo dimeric species, (Tbt)Sb(μ-O)$_2$Sb(Tbt), while still maintaining the Sb–Sb bond (although considerably lengthened at Sb–Sb: 3.039(1) Å).[41]

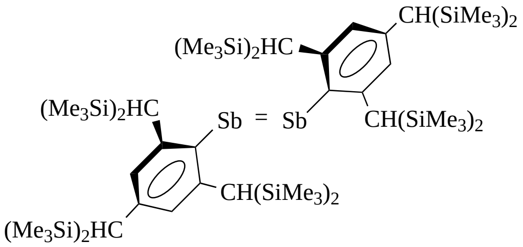

(**9**)

4.4 Bismuth Multiple Bonds

The synthesis of the first stable compound containing a Bi=Bi double bond, (Tbt)Bi=Bi(Tbt) (Tbt = 2,4,6-tris[bis(trimethylsilyl)methyl]phenyl), (**10**),**42** was achieved by a rather involved procedure concerning the deselenation of triselenatribismane with a phosphine reagent.**43** The key intermediate in this synthesis a triselenatribismane. The synthetic procedure continued with the treatment of this intermediate with an excess amount of hexamethylphosphorus triamide and heating for 12 h. Finally, the dibismuthene was isolated as deep purple single crystals. This was a significant discovery: a homonuclear double bond involving the heaviest stable (i.e. nonradioactive) element on the periodic table.

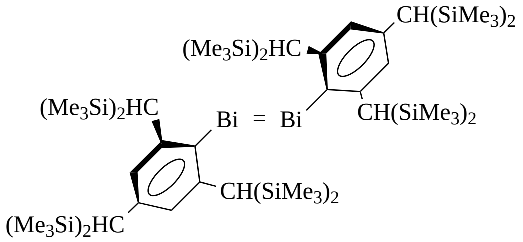

(**10**)

The Bi=Bi double bond distance in (Tbt)Bi=Bi(Tbt) of 2.8206(8) Å compares to the Bi–Bi single bond distance of 2.990(2) Å for $Ph_2Bi–BiPh_2$.**43**

5 RELATED ARTICLES

Gallium: Inorganic Chemistry; Germanium: Organometallic Chemistry; Lead: Organometallic Chemistry; Phosphorus: Inorganic Chemistry.; Silicon: Inorganic Chemistry; Tin: Organometallic Chemistry.

6 REFERENCES

1. W. Uhl, *Z. Naturforsch.*, 1988, **43b**, 1113.
2. W. Uhl, A. Vester, W. Kaim, and J. Poppe, *J. Organomet. Chem.*, 1993, **454**, 9.
3. C. Pluta, K.-R. Pörschke, C. Kruger, and K. Hildenbrand, *Angew. Chem., Int. Ed. Engl.*, 1993, **32**, 388.
4. R. J. Wehmschulte, K. Ruhlandt-Senge, M. M. Olmstead, H. Hope, B. E. Sturgeion, and P. P. Power, *Inorg. Chem.*, 1993, **32**, 2983.
5. W. Uhl, M. Layh, and T. Hildenbrand, *J. Organomet. Chem.*, 1989, **364**, 289.
6. X. He, R. A. Barlett, M. M. Olmstead, K. Ruhlandt-Senge, B. E. Sturgeon, and P. P. Power, *Angew. Chem., Int. Ed. Engl.*, 1993, **32**, 717.
7. J. Su, X.-W. Li, and G. H. Robinson, *Chem. Commun.*, 1998, 2015.
8. J. Su, X.-W. Li, R. C. Crittendon, and G. H. Robinson, *J. Am. Chem. Soc.*, 1997, **119**, 5471.
9. F. A. Cotton, A. H. Cowley, and X. Feng, *J. Am. Chem. Soc.*, 1998, **120**, 1795.
10. Y. Xie, R. S. Grev, J. Gu, H. F. Schaefer, Pv. R. Schleyer, J. Su, X.-W. Li, and G. H. Robinson, *J. Am. Chem. Soc.*, 1998, **120**, 3773.
11. Y. Xie, H. F. Schaefer, and G. H. Robinson, *Chem. Phys. Lett.*, 2000, **317**, 174.
12. K. W. Klinkhammer, *Angew. Chem., Int. Ed. Engl.*, 1997, **36**, 2320.
13. I. Bytheway and Z. Lin, *J. Am. Chem. Soc.*, 1998, **120**, 12133.
14. H. Grützmacher and T. F. Fässler, *Chem. – Eur. J.*, 2000, **6**, 2317.
15. G. H. Robinson, *Acc. Chem. Res.*, 1999, **32**, 773.
16. G. H. Robinson, *Chem. Commun.*, 2000, 2175.
17. G. H. Robinson, *Adv. Organomet. Chem.*, 2001, **47**, 283.
18. R. West, M. J. Fink, and J. Michl, *Science*, 1981, **214**, 1343.
19. M. J. Fink, M. J. Michalczyk, K. J. Haller, R. West, and J. Michl, *Organometallics*, 1984, **3**, 793.
20. K. Kobayashi and S. Nagase, *Organometallics*, 1997, **16**, 2489.
21. K. Kobayashi, N. Takagi, and S. Nagase, *Organometallics*, 2001, **20**, 234.
22. A. Sekiguchi, R. Kinjo, and M. Ichinohe, *Science*, 2004, **305**, 1755.
23. S. Masamune, Y. Hanzawa, and D. J. Williams, *J. Am. Chem. Soc.*, 1982, **104**, 6136.
24. P. B. Hitchcock, M. F. Lappert, S. J. Miles, and A. J. Thorne, *J. Chem. Soc., Dalton Trans.*, 1984, 480.
25. J. T. Snow, S. Murakami, S. Masamune, and D. J. Williams, *Tetrahedron Lett.*, 1984, **25**, 4191.
26. B. Twamley, C. D. Sofield, M. M. Olmstead, and P. P. Power, *J. Am. Chem. Soc.*, 1999, **121**, 3357.
27. L. Pu, A. D. Phillips, A. F. Richards, M. Stender, R. S. Simmons, M. M. Olmstead, and P. P. Power, *J. Am. Chem. Soc.*, 2003, **125**, 11626.

28. D. E. Goldberg, D. H. Harris, M. F. Lappert, and K. M. Thomas, *Chem. Commun.*, 1976, 261.
29. V. H. Preut, H.-J. Haupt, and F. Huber, *Z. Anorg. Allg. Chem.*, 1973, **396**, 81.
30. T. Fukawa, F. Y. Lee, M. Nakamoto, and A. Sekiguchi, *J. Am. Chem. Soc.*, 2004, **126**, 11758.
31. A. D. Phillips, R. J. Wright, M. M. Olmstead, and P. P. Power, *J. Am. Chem. Soc.*, 2002, **124**, 5930.
32. M. Stürmann, W. Saak, H. Marsmann, and M. Weidenbruch, *Angew. Chem., Int. Ed. Engl.*, 1999, **38**, 187.
33. Y. Wang, B. Quillian, P. Wei, X.-J. Yang, and G. H. Robinson, *Chem. Commun.*, 2004, 1234.
34. L. Pu, B. Twamley, and P. P. Power, *J. Am. Chem. Soc.*, 2000, **122**, 3524.
35. M. Yoshifuji, I. Shima, N. Inamoto, K. Hirotsu, and T. Higuchi, *J. Am. Chem. Soc.*, 1981, **103**, 4587.
36. L. Weber, *Chem. Rev.*, 1992, **92**, 1839.
37. R. C. Smith, T. Ren, and J. D. Protasiewicz, *Eur. J. Inorg. Chem.*, 2002, 2779.
38. R. C. Smith, E. Urnezium, K.-C. Lam, A. L. Rheingold, and J. D. Protasiewicz, *Inorg. Chem.*, 2002, **41**, 5296.
39. S. Shah, T. Concolino, A. L. Rheingold, and J. D. Protasiewicz, *Inorg. Chem.*, 2000, **39**, 3860.
40. A. H. Cowley, N. C. Nicholas, and M. Pakulski, *J. Chem. Soc., Dalton Trans.*, 1985, 383.
41. N. Tokitoh, Y. Arai, T. Sasamori, R. Okazaki, S. Nagase, H. Uekusa, and Y. Soashi, *J. Am. Chem. Soc.*, 1998, **120**, 433.
42. F. Calderazzo, R. Poli, and G. Pelizzi, *J. Chem. Soc., Dalton Trans.*, 1984, 2365.
43. N. Tokitoh, Y. Arai, R. Okazaki, and S. Nagase, *Science*, 1997, **277**, 78.

Acknowledgments

The author wishes to thank a number of gifted coworkers and students for their contributions. In addition, gratitude is expressed to the National Science Foundation and to the Petroleum Research Fund, administered by the American Chemical Society, for financial support.

Copper Proteins with Type 2 Sites

Michele A. McGuirl[1] **& David M. Dooley**[2]
[1]*The University of Montana, Missoula, MT, USA*
[2]*Montana State University, Bozeman, MT, USA*

1 Introduction 1
2 Type 2 Copper Proteins: Overview 1
3 Cu, Zn Superoxide Dismutase 2
4 Dopamine-β-Monooxygenase (DβM) and Peptidylglycine α-Amidating Monooxygenase (PAM) 6
5 Quercetinase 11
6 Galactose Oxidase 12
7 Amine Oxidase and Lysyl Oxidase 17
8 Related Articles 23
9 References 23

Abbreviations

2,3QD = Quercetin 2,3-dioxygenase (quercetinase); DβM = Dopamine-β-monooxygenase (dopamine-β-hydroxylase); DDC = Diethyldithiocarbamate; PAM = Peptidylglycine α-amidating monooxygenase; PHM = peptidylglycine α-hydroxylating monooxygenase; PAL = Peptidyl α-hydroxyglycine α-amidating lyase.

1 INTRODUCTION

The copper enzymes covered in this article span a wide range in terms of both their structural and reactivity properties. Yet the copper centers in each share similar coordination geometries and have been designated 'Type 2 (or II)' copper proteins. Type 2 copper proteins lack the unique spectroscopic or magnetic signatures that typify the so-called Type 1 and Type 3 copper proteins, and the unique tetranuclear cluster found in nitrous oxide reductase (*see* ***Copper Proteins with Dinuclear Active Sites***; ***Copper Proteins: Oxidases***; ***Copper Proteins with Type 1 Sites***, and ***Copper Enzymes in Denitrification***). Indeed, the basis for classifying proteins as Type 2 was that the EPR (Electron Paramagnetic Resonance) spectra of the oxidized (resting) forms of these proteins closely resembled the spectra of 'normal' tetragonal Cu^{II} complexes, with $g_{\parallel} > g_{\perp} > 2.00$, and $A_{\parallel} > 120$ G at X-band. It was generally surmised that the coordination environments of the copper sites in such enzymes were unexceptional, with five- or six-coordinate structures composed of N, O ligands. As is often the case in science, many fascinating and totally unexpected structural and chemical phenomena turned out to be concealed behind this deceptively 'normal' facade. Each of the Type 2 enzymes covered here (superoxide dismutase, amine oxidase, lysyl oxidase, galactose oxidase, dopamine-β-monooxygenase, peptidylglycine α-hydroxylating monooxygenase, and quercetinase) displays unique active-site properties.

Elucidating and elaborating structure/function relationships for these enzymes has been greatly aided by the availability of high-resolution crystal structures for one or more enzymes from each group: superoxide dismutase, galactose oxidase, amine oxidase, peptidyglycine α-hydroxylating monooxygenase, and quercetinase. These have generally corroborated the fairly detailed structural models that were developed from extensive spectroscopic studies. At the same time, the 3D structures have revealed many surprising details of the active sites. Indeed, the roles of copper in these 'normal' Type 2 copper centers are more diverse than ever imagined.

2 TYPE 2 COPPER PROTEINS: OVERVIEW

As noted above, a copper-containing protein could be classified on the basis of its EPR spectrum. Type 2 proteins display EPR spectra similar to that of bovine Cu, Zn superoxide dismutase (SOD) shown in Figure 1(a).**[1]** In the absence of additional chromophores, a Type 2 protein would display an absorption spectrum like that of Figure 1(b). These spectral features, particularly the lack of an intense, low-energy ligand-to-metal charge-transfer (LMCT) transition, immediately suggest the absence of cysteine in the first coordination shell of the enzyme Cu^{II}. A classic analysis of the EPR spectra of Cu^{II} proteins and model complexes, based on correlating $g_{\parallel}$ and $A_{\parallel}$ values with the identities of ligand donor atoms, also indicated that Type 2 copper sites were composed primarily of N, O ligands.**[2]** Using peptide and amino acid complexes of Cu^{II} as a guide (*see* ***Peptide–Metal Interactions***), the most plausible ligands for Type 2 centers are histidine imidazole, tyrosine phenolate, amide side chains, peptide carbonyl or nitrogen groups, and water or hydroxide. The basic spectroscopic properties of Type 2 sites**[3]** (Figure 1) further established that these centers contained magnetically isolated $S = 1/2$ Cu^{II} ions in tetragonal five- or six-coordinate geometries. In other words, such a copper site would be mononuclear with a set of four ligands that roughly define a plane, the so-called equatorial plane, with one or two ligands above or below the plane (the axial ligands). Cu^{II} sites with trigonal or tetrahedral coordination geometries, or that are multinuclear, are expected to have spectroscopic properties that differ substantially from those of Type 2 centers.**[4]** Cu^{II} with a tetragonal coordination geometry has a d$_{x^2-y^2}$ ground state, that is, this would be the d orbital that is half-filled, and a ligand-field energy diagram (*see* ***Ligand Field Theory & Spectra***) that simply gives the relative energies of the five 3d valence orbitals, similar to that shown in Figure 2.

Many spectroscopic experiments strongly suggested that water (or hydroxide) was a Cu^{II} ligand in most Type 2 proteins.[5] Facile binding of exogenous ligands by Type 2 Cu^{II} centers is commonly observed and is consistent with the presence of a readily substituted group, for example, a nonprotein ligand, in the first coordination shell of the copper. This aspect of the reactivity of Type 2 copper sites has been previously reviewed.[6] The 3D structural data confirm that water binds to Type 2 coppers. In galactose oxidase, superoxide dismutase, and quercetinase, rapid ligand substitution (substrate binding) at Cu^{II} is involved in the catalytic cycle. Additionally, ligand substitution by tyrosine is part of the copper-catalyzed self-processing mechanisms that create redox-active organic cofactors in galactose oxidase, amine oxidase, and lysyl oxidase. For peptidylglycine α-hydroxylating monooxygenase, substrate has been proposed to be a part of the electron transfer pathway between the two Type II copper centers. More generally, oxygen activation via coordination at Cu^{I} may be an important process in Type 2 copper enzymes.

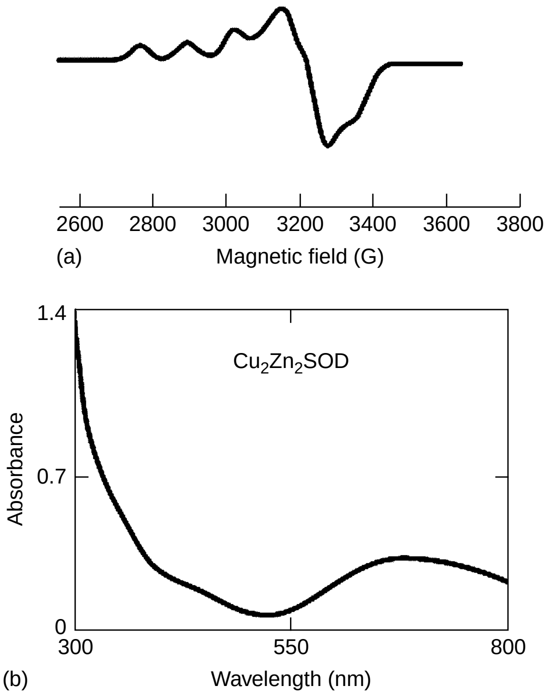

Figure 1 Spectral characteristics of oxidized Cu, Zn SOD (a) X-band EPR spectrum, 77 K (Used with permission from Ref. 1. © 1985 Division of Chemical Education, Inc); (b) room-temperature electronic absorption spectrum [protein] = $35\,mg\,mL^{-1}$

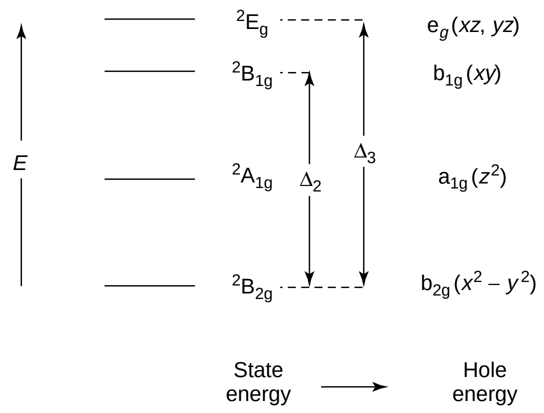

Figure 2 Orbital and state energy-level diagram for Cu^{II} complexes assuming D_{4h} symmetry. This will be approximately correct for a variety of tetragonal or near-tetragonal Cu^{II} complexes. (Reprinted from Ref. 4. © 1986, with permission from Elsevier)

As discussed in the following sections, the catalytic diversity of enzymes containing Type 2 copper is striking. Much progress has been made in understanding how the protein environments modulate a tetragonal Cu^{II} site to achieve these varied activities. Key information has been obtained from NMR and/or X-ray structures of the Type 2 enzymes.

3 Cu, Zn SUPEROXIDE DISMUTASE

This protein is probably the most extensively studied copper-containing enzyme. Cu, Zn superoxide dismutase was the first copper protein to be structurally characterized via X-ray crystallography.[7] Cu, Zn SOD is a very widespread and homologous class [EC 1.15.1.1] of enzymes among eukaryotes. The enzyme has also been identified in several prokaryotes, although here there is considerable diversity in primary sequence and quaternary structure. In addition, Ni-, Mn-, and Fe-containing superoxide dismutases (SODs) are also known. Ni SOD and Fe SOD are found in prokaryotes whereas the Mn SOD is found in prokaryotes and in mitochondria. The Fe and Mn SODs are homologous but structurally unrelated to the Ni SOD, or the Cu, Zn SOD discussed here (*see* ***Iron Proteins with Mononuclear Active Sites***; ***Manganese Proteins with Mono- & Dinuclear Sites***, and ***Nickel Enzymes & Cofactors***). All four types of SOD catalyze the dismutation of superoxide (*see* ***Oxygen: Inorganic Chemistry*** and equation 1).

$$\bullet O_2^- + \bullet O_2^- + 2H^+ \longrightarrow O_2 + H_2O_2 \tag{1}$$

The catalyzed reaction is extremely rapid with a second-order rate constant on the order of $10^9\,M^{-1}s^{-1}$ at ambient temperature and neutral pH.[8] This is well within the range of diffusion-controlled reactions in aqueous solutions under these conditions. Reaction (1) is generally regarded to proceed in two steps involving cyclical reduction/oxidation of the active-site metal ion, as shown in equations (2) and (3).[9]

$$\text{E-Cu}^{\text{II}} + {\bullet}\text{O}_2{}^{-} \longrightarrow \text{E-Cu}^{\text{I}} + \text{O}_2 \tag{2}$$

$$\text{E-Cu}^{\text{I}} + {\bullet}\text{O}_2{}^{-} + 2\text{H}^{+} \longrightarrow \text{E-Cu}^{\text{II}} + \text{H}_2\text{O}_2 \tag{3}$$

Kinetics studies have shown that the rates of the electron-transfer steps are faster than the encounter rate between $\bullet O_2{}^-$ and the enzyme. The encounter rate is independent of the copper oxidation state. K_M for $\bullet O_2{}^-$ is high ($\sim$3.5 mM),[10] which means that, under nearly all conditions, superoxide dismutase turnover is far from saturated.

The overall structure of Cu, Zn SOD is shown in Figure 3;[11] details of the oxidized and reduced forms of the active site are shown in Figure 4.[12] To date, crystal or solution structures are available for Cu, Zn SODs from human, bovine, yeast, spinach, frog, and Gram-negative bacterial sources, in oxidized, reduced, apo-, metal-substituted and/or amino acid mutant forms. (See PDB entries 1Q0E, 1P1V, 1PU0, 1PTZ, 1HL5, 1OAL, 1F1G, 1F1D, 1F1A, 1F18, 1N19, 1N18, 1KMG, 1L3N, 1IBH, 1IBF, 1IBD, 1IBB, 1IB5, 1E9Q, 1E9P, 1E9O, 1EQW, 1DSW, 1EJ8, 1YAZ, 1SXZ, 1SXS, 1QUP, 1P4T, 1B4L, 1FUN, 2JCW, 1MFM, 1BZO, 1CBJ, 1CB4, 2APS, 1BA9, 1ESO, 1AZF, 1SXW, 1YAI, 1YSO, 1JCV, 1SXA, 1SXB, 1SXC, 1XSO, 3SOD, 2SOD, 1SRD, 1SPD, 1SOS, 1SDY, 1SDA, and 1COB, and associated references.) The eukaryotic proteins are dimers composed of two identical 16 kD subunits. In contrast, the prokaryotic enzymes are isolated in either monomeric or dimeric forms, depending on the bacterial species. The principal structural features are highly conserved among the proteins. The overall protein fold is a cylindrical β-barrel composed of eight antiparallel β-strands with three external loops (Figure 3).[11,13] Two of these loops modulate zinc binding or substrate/anion access to the active site. Although the overall fold is conserved across species, the bacterial enzymes use internal β-strands to form the dimer interface whereas the eukaryotic proteins juxtapose the N- and C-terminal β-strands. In all cases, subunit interactions are due mainly to hydrophobic interactions. Additional differences among the two classes of SODs are evident in the loop responsible for electrostatic guidance of the substrate into the active site.

The ligands of the metal centers of Cu, Zn SODs are highly conserved across species and are identical in sequence order, coordination geometry, and intersubunit separation. Cu, Zn SODs are notable for several interesting

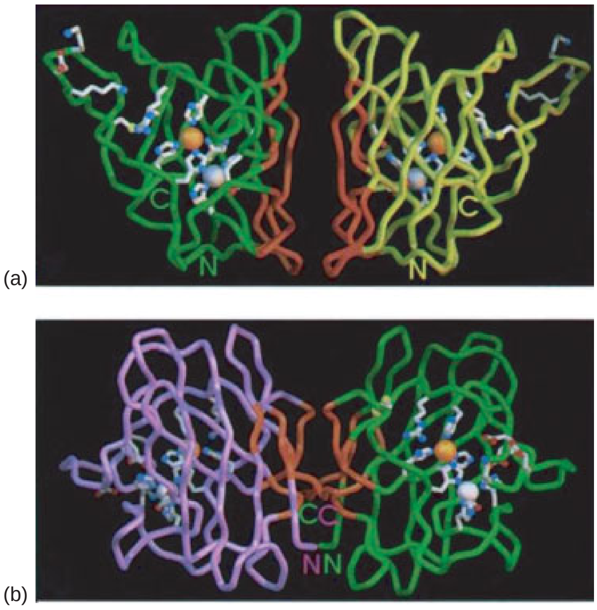

Figure 3 Comparison of the folds and dimer assemblies of (a) prokaryotic CuZnSOD with (b) bovine CuZnSOD. Functionally important side chains for the active site, disulfide cysteines, and electrostatic recognition residues are displayed with white bonds and atom-colored spheres. Dimer interface regions are highlighted in orange; metals are shown as spheres: copper (orange) and zinc (silver). (Reproduced from Y. Bourne, S.M. Redford, H.M. Steinman, J.R. Lepock, J.A. Tainer, and E.D. Getzoff, *Proc. Natl. Acad. Sci. USA*, 1996, **93**, 12774. © 1996 National Academy of Sciences, USA)

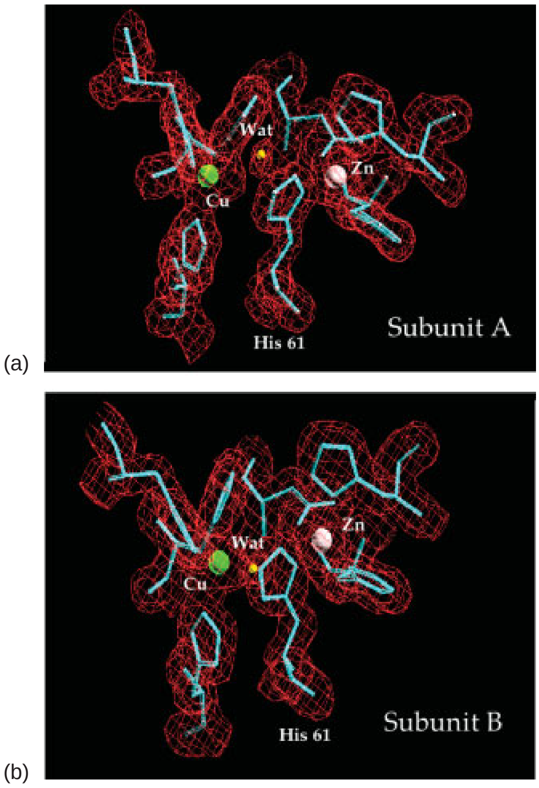

Figure 4 Close-up view of the Cu, Zn SOD active site in (a) reduced and (b) oxidized form. Copper is represented by the yellow spheres, zinc by the blue spheres. Water molecules are represented by the smaller, cyan, spheres. The shifts of water and the bridging His61 are clearly visible in (a), the reduced site. (Reprinted from Ref. 12. © 1999, with permission from Elsevier)

or novel aspects of their active-site structure and metal-ion coordination (Figure 4). The Cu^{II} ion is at the bottom of a deep channel; metal ion ligands form the floor of the channel. There is a potential binding site for superoxide positioned between the copper and a guanidinium side chain from a conserved arginine residue. A deprotonated imidazole group (imidazolate) from a histidine residue bridges the Cu^{II} and Zn^{II} ions in the oxidized form; the distance between the Cu^{II} and Zn^{II} is ~6 Å.[11–13] Not surprisingly, the Zn^{II} coordination geometry is approximately tetrahedral, but the Cu^{II} is in a distorted square pyramidal geometry with four coordinated histidine imidazoles at an average distance of 2.1 Å (including the bridging group) and a coordinated water molecule at about the same or a slightly longer distance. A reasonable way to formulate the structure is to think of the four imidazole nitrogens as roughly defining the equatorial 'plane', but with a pronounced tetrahedral distortion, and to assign the water molecule to an axial position. The coordinated water molecule exchanges very rapidly with solvent water.[5]

Numerous experiments have established that the copper center has the role of a redox catalyst, as shown in equations (2) and (3). A plausible mechanism, based on the premise that Cu^{II}/Cu^{I} cycling is important and emphasizing the role of the essential arginine, is presented in Scheme 1.[13] Recent structural studies[11,12] have confirmed spectroscopic observations that the bridging His ligand is broken upon copper reduction. The coordinating water is also displaced and the Cu(I) center becomes trigonal planar, as indicated in Figure 4(b). Zn^{II} does not appear to be catalytically important since a copper-containing, zinc-depleted form of SOD is nearly fully active.[14] Hence Zn^{II} appears to have primarily a structural role both in organizing the metal-binding region and stabilizing the native conformation. Consistent with a structural role, the Zn^{II} ion is not accessible to solvent and, with a tetrahedral four-coordinate geometry around a d^{10} metal ion, is effectively coordinatively saturated (*see* ***Coordination Numbers & Geometries***).

Since superoxide is a small anion, and since cells contain high concentrations of anions, the problem of substrate

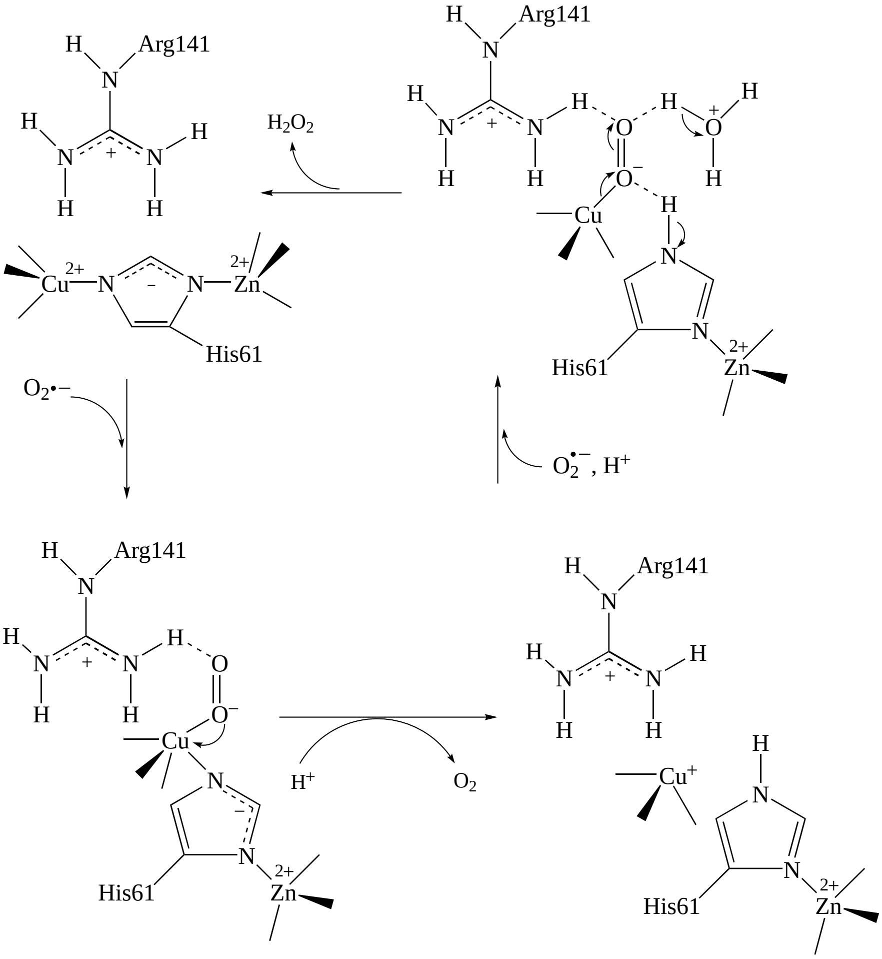

Scheme 1 A possible mechanism for superoxide dismutation catalyzed by Cu, Zn SOD, emphasizing Cu^{II}/Cu^{I} cycling. (Ref. 13. Reproduced by permission of Nature Publishing Group)

recognition by superoxide dismutase appears to be an intriguing one. An experimental indication of this may be the unusual ionic strength dependence of the SOD rate. Most Cu, Zn SODs have a net negative charge, as does superoxide. However, the reaction rate decreases with increasing ionic strength (at constant pH), in contrast to expectations based on simple diffusion models for encounters of ions with the same type of charge.[9,15] Superoxide substrate is electrostatically guided into the active site through interactions with charged amino acid side chains that line the substrate channel. The channel progressively narrows as it approaches the active site; the essential arginine residue and an active site threonine prevent the binding of large nonsubstrate anions.[15–17]

Several anions are known to bind to Cu^{II}, probably occupying the axial binding site between Cu^{II} and the arginine, thereby inhibiting the SOD activity. This chemistry has been thoroughly investigated because small anions may be regarded as substrate analogs; excellent reviews are available.[5,6] Of special interest is the reaction of SOD with bicarbonate, an anion that is present at high concentrations in the blood. Bicarbonate binding is associated with peroxidase activity, leading to the generation of reactive oxygen radicals as shown in Scheme 2.[17] It is postulated that initial formation of peroxycarbonate is followed by the production of a reactive oxygen radical species, O•. In turn, this species may interact with exogenous substrates that are too large to access the active site. Alternatively, oxidization of one of the histidyl copper ligands may occur, leading to loss of the copper ion and subsequent enzyme inactivation.

Over 90 mutations in human Cu, Zn SOD have been associated with familial amyotrophic lateral sclerosis (FALS), a fatal disease in which motor neurons are destroyed (*see* ***Metal-related Diseases of Genetic Origin***).[18] Several roles of SOD in FALS have been proposed; numerous reviews describe these in considerable depth.[19] Rather than the disease being caused by a decrease in SOD activity, it appears that FALS is associated with an as yet undefined gain of function by the SOD protein itself. Possible roles include higher peroxidase/oxidant reactivity and/or the formation of aberrant protein aggregates. Interestingly, the mutations are spread throughout the structure (Figure 5).[18] They may be classified into two groups based on their metal content and activity. More severe forms of FALS are associated with missense mutations in either the metal ligands or in the loops associated with electrostatic steering or zinc binding; these have compromised thermal stabilities as well as lower affinities for both copper and zinc. Hence, it is unlikely that this class of FALS mutants, termed metal-binding region mutants by Valentine *et al.*, causes oxidative damage, since this would require copper-loaded, active SOD. It is known that metal binding strongly influences the stability of the β-barrel. One hypothesis is that the lack of active-site metal ions leads to the unraveling of the edge strands of the β-barrel, which then form toxic aggregates.

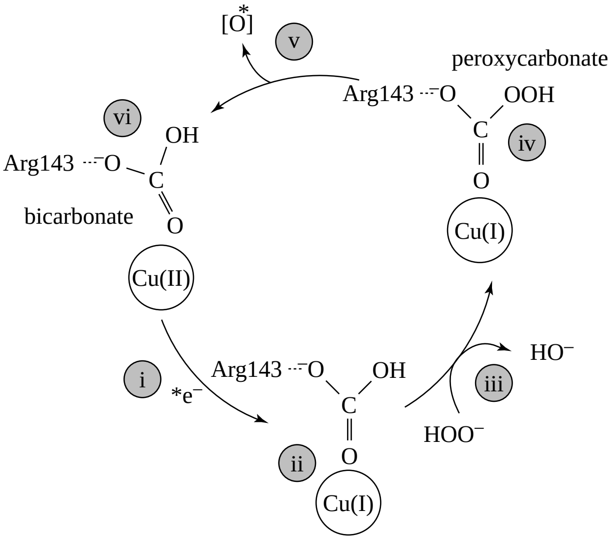

Scheme 2 Proposed mechanism for bicarbonate-mediated peroxidation in SOD. After Cu(II) reduction (i), bicarbonate binds to the anion-binding site (ii). In (iii), HOO^- reacts with bicarbonate to form peroxycarbonate (iv). In (v), the oxygen radical species formed [O*] may oxidize endogenous or exogenous substrates. This leaves bicarbonate bound to the anion-binding site (vi). (Ref. 17. Reproduced by permission of American Society for Biochemistry & Molecular Biology)

In contrast, metal and structural analyses of the second group of FALS mutants show that these proteins are fully capable of binding metals and retain enzymatic activity, if they are properly folded. Thus, they have been termed wild-type-like. It is postulated that these mutants have higher prooxidant activity (possibly via bicarbonate-mediated inactivation, see Scheme 2). Self-inactivation could lead to metal loss and similar aggregation effects described for the metal-binding-region mutants.

In vitro, both metals in the active site of SOD can be reversibly removed. This behavior has been elegantly expanded to produce a variety of metal-substituted derivatives.[20] Co^{II}, Ni^{II}, and Ag^{I} derivatives, where the added metal ion may occupy the copper site or the zinc site (and in some cases both), have proven especially valuable in providing new spectroscopic probes of metal-site structure and reactivity in Cu, Zn SOD. Application of in vitro metal substitution to several of the FALS wild-type-like mutants has shown that these variants readily misfold and often exhibit altered metal ion binding.[21] In addition to the in vitro metal studies, recent work has centered on the mechanism of in vivo copper incorporation. CCS is a copper chaperone protein that forms a heterodimer with Zn-loaded SOD to insert copper and activate the enzyme (*see* ***Metallochaperones & Metal Ion Homeostasis***).

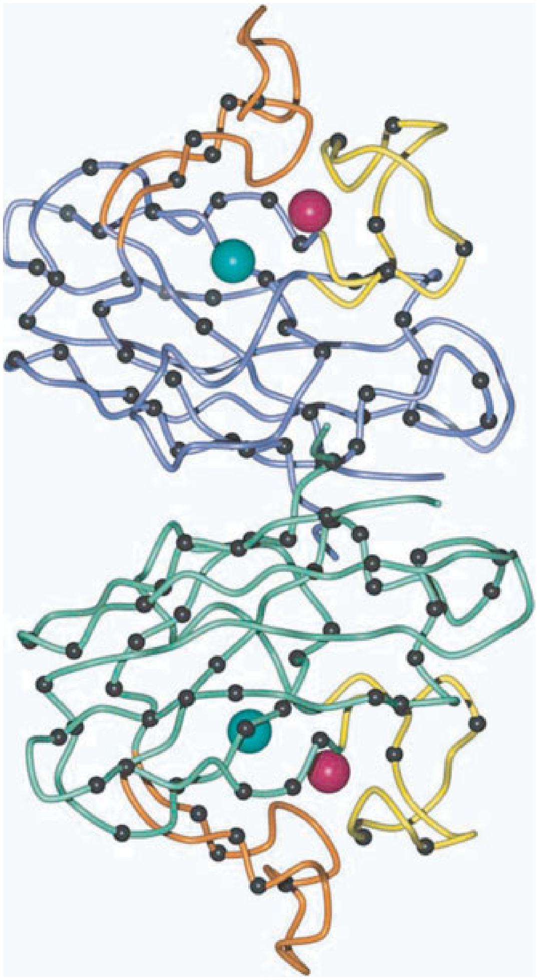

Figure 5 Backbone structure of CuZnSOD dimer showing zinc (red sphere), copper (green sphere), and the positions of FALS missense mutations (small black spheres). The β-barrel of the monomer is colored either green or blue. The electrostatic loop on each monomer is shown in orange while the zinc loop is colored yellow. (R.A. Steiner, K.H. Kalk and B.W. Dijkstra, *Proc. Natl. Acad. Sci. USA*, 2002, **99**, 16625. © 2002 National Academy of Sciences, USA)

4 DOPAMINE-β-MONOOXYGENASE (DβM) AND PEPTIDYLGLYCINE α-AMIDATING MONOOXYGENASE (PAM)

Dopamine β-monooxygenase (DβM, EC 1.14.17.1) and peptidylglycine α-amidating monooxygenase (PAM, EC 1.14.17.3) are related enzymes of the central nervous system.[22,23] DβM (also known as dopamine β-hydroxylase) is the enzyme responsible for the hydroxylation of dopamine to form norepinephrine, as shown in equation (4). Both substrate and product are hormones/neurotransmitters. PAM is a bifunctional enzyme; one domain, called peptidylglycine α-hydroxylating monooxygenase (PHM, EC 1.14.17.3) catalyzes a mechanistically similar reaction to DβM–the hydroxylation of Gly-terminal peptides. The second domain contains peptidyl α-hydroxyglycine α-amidating lyase (PAL, EC 4.3.2.5) activity, which subsequently hydrolyzes the initially formed α-hydroxyglycyl derivative to produce an α-amidated, bioactive peptide and glyoxylate (equation 5). Despite the marked differences in substrate specificities, the two enzymes utilize the same general mechanism.[22–24] Hence, information gleaned about the structure and mechanism of one enzyme has often been applied to the other.

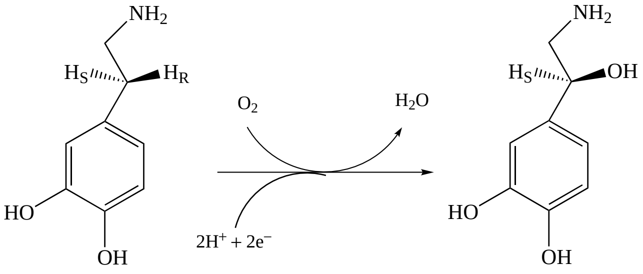

(4)

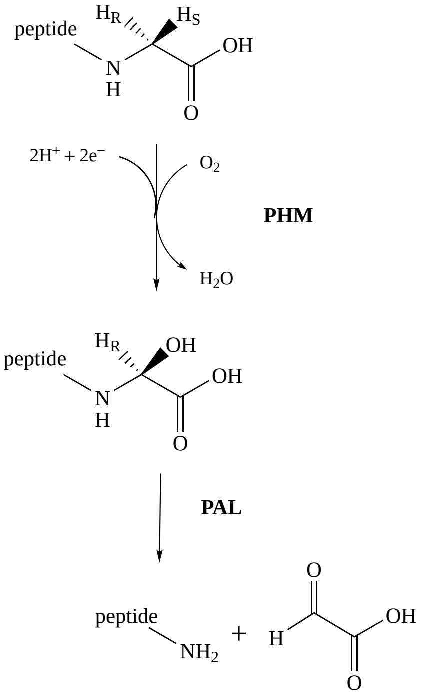

(5)

DβM is located in the chromaffin granules of the adrenal medulla and in synaptic vesicles of the sympathetic nervous system.[22] Owing to its critical role in neurotransmitter metabolism, DβM is of great pharmaceutical interest. DβM exists in both soluble and membrane-bound forms, with the membrane form retaining the amino-terminal signal peptide. The soluble enzyme is a tetramer with a total $M_r \approx 290$ kD; the subunit $M_r \approx 75$ kD. The subunits are arranged in disulfide-linked pairs. DβM is a glycoprotein, with approximately 4% carbohydrate by weight. PAM catalyzes the *C*-terminal amidation of peptides from the nervous and endocrine systems; over half of all bioactive peptides are processed in this way.[23] PAM activity appears to be restricted to neuronal and endocrine tissues. Multiple forms of PAM have been identified in these tissues, resulting from alternative splicing that governs the presence of a transmembrane domain and/or a domain that triggers the cleavage of the PAL domain by endoproteases. When expressed as a 35-kDa monomer, the catalytic core of the PHM domain is fully active.

The active sites of DβM and PHM contain two catalytically essential copper ions. EPR spectra of the oxidized forms of these proteins are typical for Type 2 copper with N, O donor ligands.[24,25] The copper centers are not coupled and are at least 5 Å apart.[22,23] Note the stereochemistry of hydroxylation in equations (4) and (5); both reactions proceed with retention. ^{18}O tracer experiments for the enzymes provided direct evidence for the incorporation of molecular oxygen into the substrate, and both exhibit large deuterium kinetic isotope effects.[22,26,27] In both cases, ascorbate is the physiological reductant. These biochemical similarities are confirmed by sequence comparisons, which pinpoint a conserved catalytic domain.[23] The copper ligands of both the oxidized or reduced states of DβM and PHM are conserved; the H–X–L (L = His or Met) motif is a common copper-binding sequence.

A large body of work in the 1980s and early 1990s strongly suggested that bovine DβM uses a radical mechanism during catalysis.[22] The two copper ions are first reduced by ascorbate. The substrates O_2 and dopamine then bind at one of the copper centers. In the presence of the physiological activator fumarate, dopamine binds first in a preferred order mechanism, similar to the order of substrate binding for PHM.[23] Electron transfer from the second copper center is thought to produce an activated Cu(II)-oxygen species. This moiety abstracts an H atom from the organic substrate, cleaving the C–H bond. It has been shown that O–O bond cleavage occurs prior to the H−atom abstraction step. For many years, it was postulated that a tyrosine residue was involved in oxygen activation.[22]

The field was reenergized by the elucidation of the crystal structure of the catalytic core of PHM in 1997.[28] While that work and subsequent structures confirmed the spectroscopically derived models of copper coordination in the oxidized form (*see* ***Copper: Inorganic & Coordination Chemistry***), new questions and considerable debate arose about the structures of the reduced copper centers, the mechanism of electron transfer, and the nature of the reactive oxygen species.[23,29] These issues have been addressed by several groups and new catalytic mechanisms have emerged. Although there is not yet consensus on each catalytic step, there is general agreement that DβM and PHM are quite similar mechanistically.

The PHM crystal structure shown in Figure 6 corroborates that the copper centers are far apart (∼11 Å), being separated by a solvent-filled channel.[23] Cu_A (often referred to as Cu_H in PHM) is ligated by three His and water in the oxidized form; it has historically been assigned as the electron-transfer site. Oxidized Cu_B (Cu_M in PHM) is coordinated by two His and water, and has a long bond to the sulfur of Met. The latter site has long been identified with substrate binding and hydroxylation chemistry. As depicted in Figure 6(b), changes in copper site geometry or distance are not observed in reduced vs. oxidized PHM crystals.[29] Instead, the only significant difference occurs at the $Cu_{A/H}$ His108 ligand. In reduced PHM, His108 is H-bonded to Gln170, whereas a water molecule bridges the two residues in the oxidized form. The shortest electron transfer pathway connecting the copper centers via covalent and H-bonds is ∼80 Å, which is prohibitively long. No obvious electron transfer pathway across the channel exists in these structures (*see* ***Long-range Electron Transfer in Biology***).

The 3D structure of substrate-bound, oxidized PHM has also been determined.[29] The binding energy associated with the E·S complex is derived primarily from protein interactions with the peptide backbone of the substrate (*N*-α-acetyl-3,5-diiodotyrosylglycine); since few interactions with substrate side chains occur, PHM is able to amidate a diverse pool of peptides. The copper centers remain ∼11 Å apart. The hydrophobic residue of the substrate contacts the Met ligand of $Cu_{B/M}$ and a water molecule bridges the substrate carboxylate and Gln170 via H-bonding. The substrate carbon that undergoes hydroxylation is 4.4 Å from $Cu_{B/M}$; the H_S atom that is abstracted (see equation 5) points toward the solvent atom that is bound to $Cu_{B/M}$. These data support the hypothesis that $Cu_{B/M}$ is the center of substrate binding and hydroxylation. By comparing and combining the substrate/oxidized and reduced structures, Prigge *et al.* have offered a mechanism in which the substrate mediates electron transfer.[23] The proposed pathway is shown in Figure 7 and Scheme 3. The electron passes from $Cu_{A/H}$ through its His108 ligand to Gln170 via the H-bond that is present in the reduced form. From there, the electron moves through the bridging water molecule that is present between Gln170 and the substrate carboxylate in the substrate/oxidized form, through the substrate to $Cu_{B/M}$.

The reduced PHM structure contrasts strongly with the wealth of spectroscopic evidence for both DβM and PHM, which indicates that the coordination numbers of both sites decrease upon reduction to Cu(I).[30–32] The spectroscopically deduced model of the copper centers is presented in Figure 8;[33] both coppers lose their coordinated waters, and the long bond between $Cu_{B/M}$ and Met is considerably shortened. The spectroscopic data are sensible from an inorganic chemistry perspective: three-coordinate Cu^I complexes with N-donor ligands tend to be very reactive towards oxygen (*see* ***Copper: Inorganic & Coordination Chemistry***). In this light, it has been noted that crystallographic conditions can sometimes lead to the generation of photo-reduced species and/or metal centers that are trapped in intermediate geometries between the oxidized and reduced states.[34]

The discrepancy in the proposed reduced copper structures, along with the observation that under certain conditions both coppers of PHM are able to bind the O_2 analog carbon monoxide ($Cu_{A/H}$ only in the presence of substrate),[31,32,35]

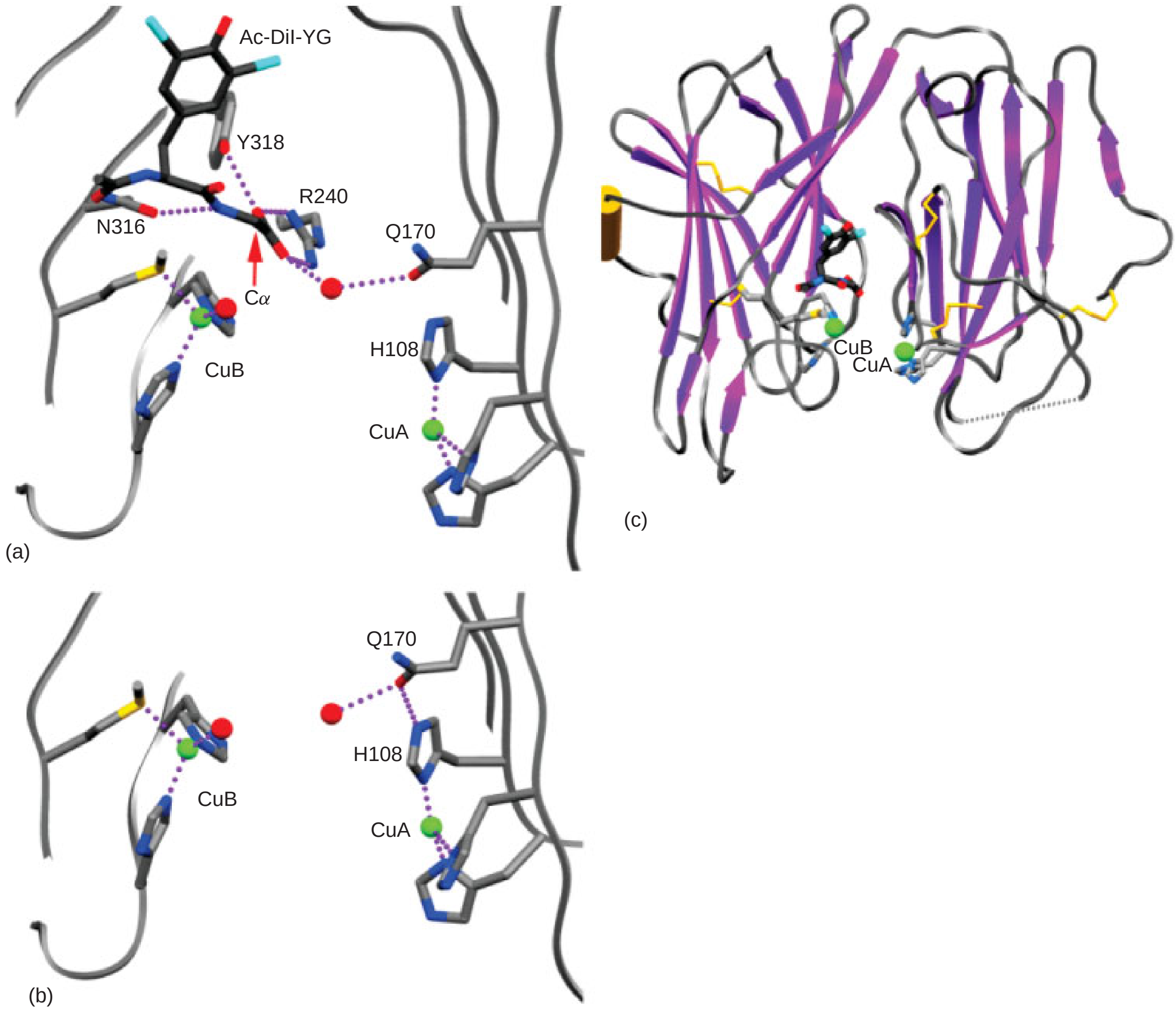

Figure 6 Structure of PHM: (a) active site in oxidized form with complexed peptide substrate, (b) active site in reduced form, (c) overall structure showing the large solvent cleft separating the two copper centers. (Ref. 23. Reproduced by permission of Birkhäuser Verlag AG)

has led to the development of other hypotheses to explain the oxygen activation and electron transfer pathway. These include the idea that O_2 initially binds at $Cu_{A/M}$, is reduced to superoxide and migrates across the channel.[35] Alternatively, it has been proposed that substrate also migrates from $Cu_{B/M}$ to $Cu_{A/H}$, and that the catalytic roles are reversed so that $Cu_{B/M}$ is the electron transfer site and $Cu_{A/H}$ becomes the site of O_2 activation and hydroxylation.[36] The latter hypothesis is based on the observation that mutation of Gln170 has little effect on PHM kinetics and so cannot mediate electron transfer.

Recent publications by Klinman and coworkers reevaluated older work in light of new experiments that (a) rule out Tyr as an activator of O_2 and (b) invoke nonclassical hydrogen tunneling to explain the observed isotope effects.[26,27,37] They have also expanded the mechanistic and kinetics data available for both DβM and PHM. In a key experiment with DβM and its very slow substrate 4-trifluoromethyl-phenethylamine, it was shown that O_2 and substrate activation are tightly coupled, and no paramagnetic species (Cu^{II} or a Cu^{I}-O-O• radical) is detectable by EPR.[27] These data have been used to support the formation of a spin-coupled, diamagnetic Cu^{II}-$O_2{}^{-}$• activated oxygen species that forms prior to electron transfer from the second copper. Klinman's working mechanism is depicted in Scheme 4. Note that the electron transfer pathway is proposed to occur over ~8 Å through H-bonded water molecules, which is predicted to be sufficiently fast even when substantial ligand reorganization of the copper sites is included (*see* ***Long-range Electron Transfer in Biology***), as suggested by the spectroscopically deduced models (Figure 8).[27,37] Moreover, this intriguing mechanism includes a role for Met ligand reorganization in mediating the reversibility of the first reduction step, thus contributing to the driving force for substrate oxidation.[27] Klinman also notes that this mechanism is compatible with substrate-mediated electron transfer for PHM (in lieu of the water molecules) and/or substrate migration. Although the

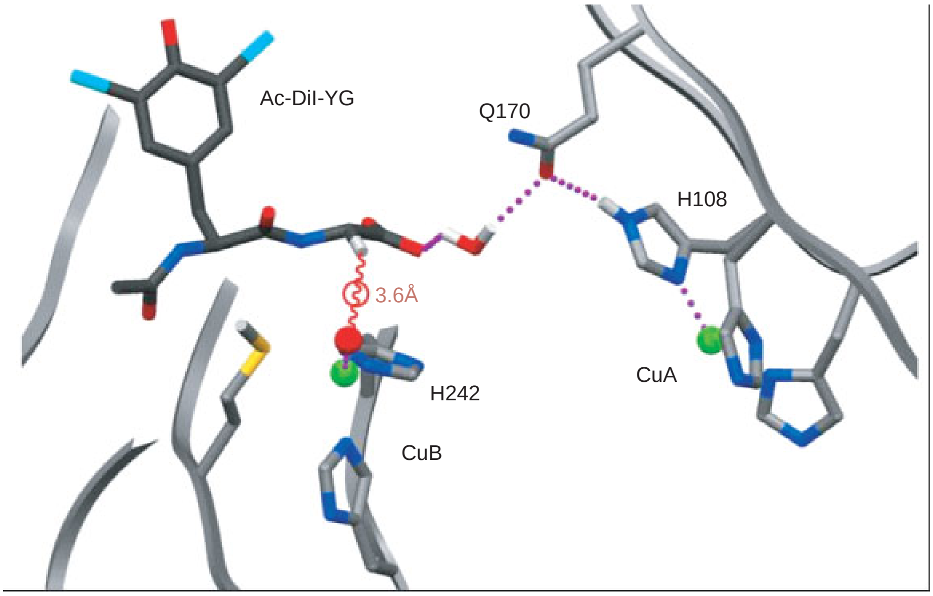
Ac-DiI-YG
Q170
H108
3.6Å
H242
CuB
CuA

Figure 7 Proposed electron transfer pathway between copper ions via substrate. (Ref. 23. Reproduced by permission of Birkhäuser Verlag AG)

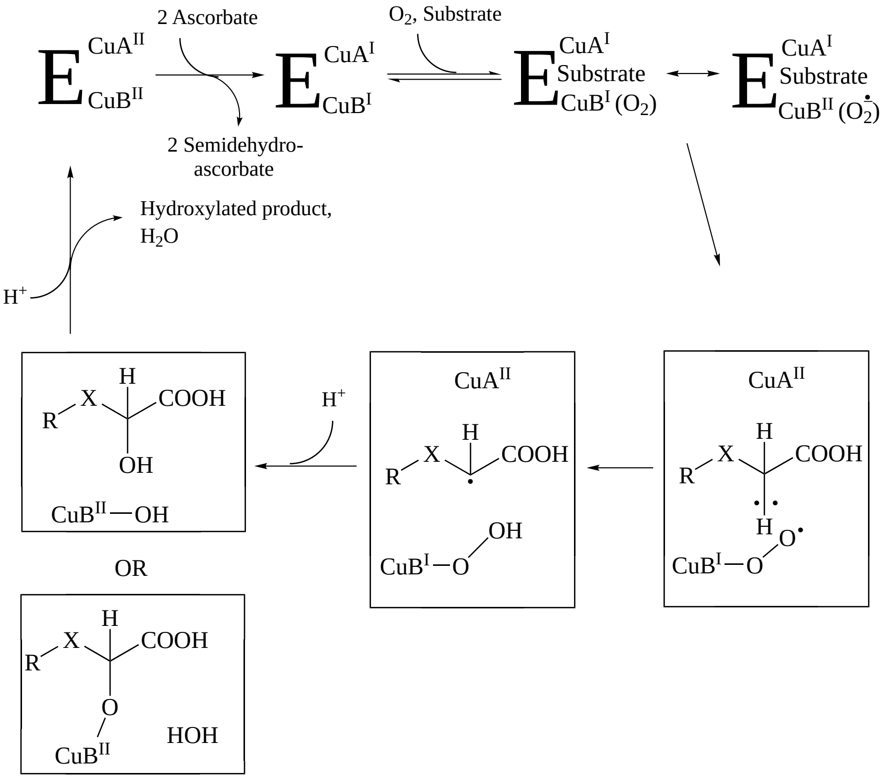
2 Ascorbate
2 Semidehydro-ascorbate
O_2, Substrate
E CuA^{II} CuB^{II}
E CuA^{I} CuB^{I}
E CuA^{I} Substrate CuB^{I} (O_2)
E CuA^{I} Substrate CuB^{II} ($O_2^{\bullet}$)
Hydroxylated product, H_2O
H$^+$
CuB^{II}—OH
OR
HOH
CuB^{II}
CuA^{II}
CuB^{I}—O
CuA^{II}
CuB^{I}—O
R
X
H
COOH
OH

Scheme 3 Proposed catalytic mechanism of PHM involving substrate-mediated electron transfer. (Ref. 23. Reproduced by permission of Birkaüser Verlag AG)

mechanism does not require it, the roles of the two copper centers may also be reversed in Scheme 4.

In summary, the PHM structures have provoked new controversies over the details of substrate hydroxylation by PHM and DβM. It has become evident that the enzymes share a common catalytic mechanism, and that any proposed mechanism must account for the wealth of experimental data available for both proteins.

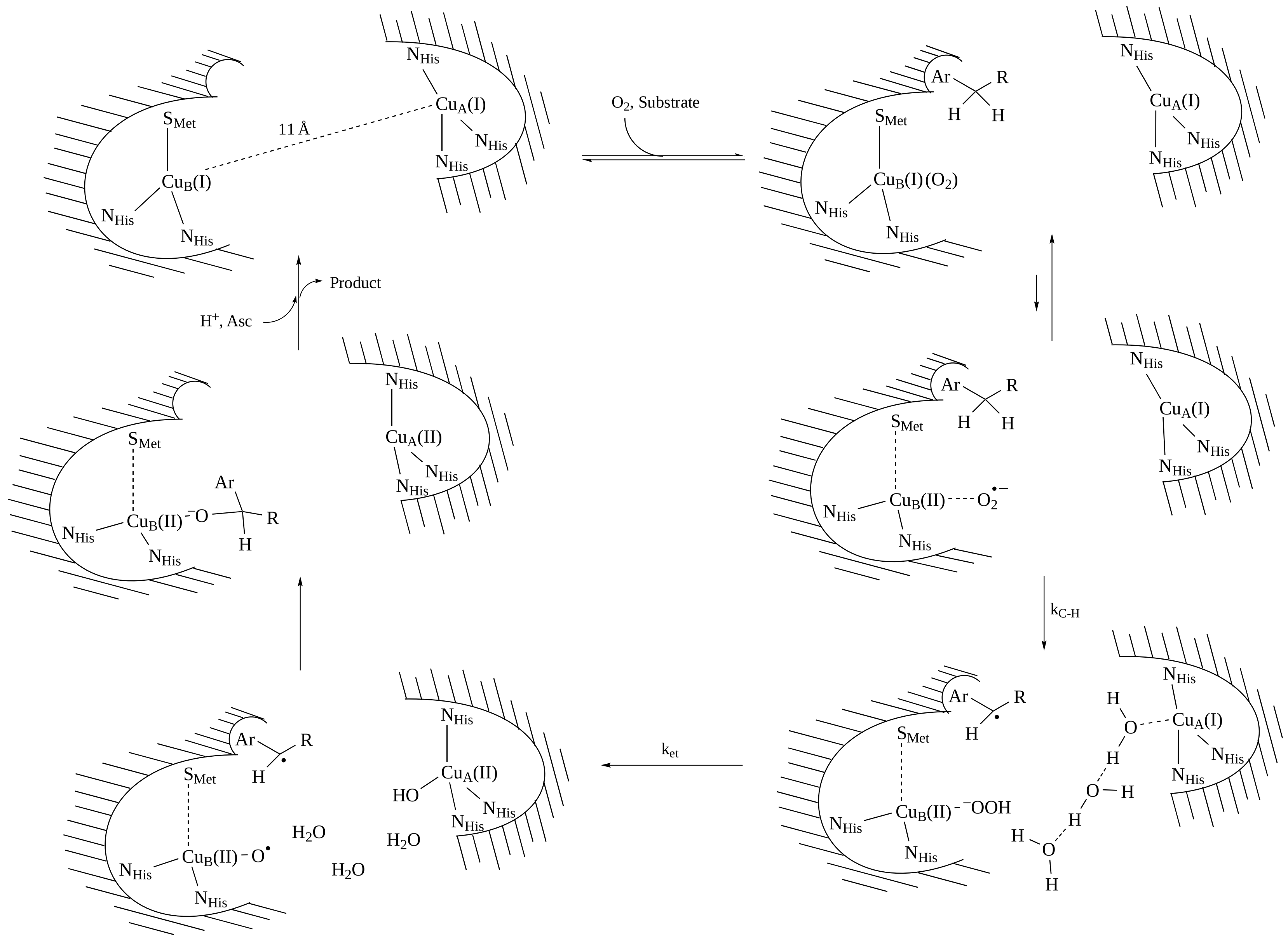
S$_{Met}$
Cu$_B$(I)
N$_{His}$
N$_{His}$
11 Å
Cu$_A$(I)
N$_{His}$
N$_{His}$
N$_{His}$
O$_2$, Substrate
Ar
R
H
H
Cu$_B$(I)(O$_2$)
Cu$_B$(II)
O$_2^{\bullet-}$
k$_{C-H}$
Cu$_B$(II)$^-$OOH
O–H
Cu$_A$(I)
k$_{et}$
Cu$_B$(II)$-$O$^\bullet$
H$_2$O
H$_2$O
H$_2$O
HO
Cu$_A$(II)
Cu$_B$(II)$^-$O
H$^+$, Asc
Product

Scheme 4 Proposed catalytic mechanism of PHM and DβM showing the reactive ternary complex. Proposed structure of the intermediate formed after reaction of Cu$_B$(II)$-$O$_2^\bullet$ with substrate to form a substrate-derived free radical and Cu$_B$(II)$-$OOH. This illustrates a possible pathway for electron transfer from Cu$_A$(I) to Cu$_B$(II)$-$OOH through the solvent-filled cleft and the changes in copper ligation that accompany oxidation. With the exception of reactive intermediates, the water molecules complexed to the copper sites have been omitted. (Ref. 27. Reproduced by permission of American Society for Biochemistry and Molecular Biology)

5 QUERCETINASE

Quercetinase (quercetin 2,3-dioxygenase, 2,3QD, EC1.13.11.24) is the first noniron dioxygenase (*see* ***Iron Proteins with Dinuclear Active Sites*** and ***Iron Proteins with Mononuclear Active Sites***) to be structurally characterized. 2,3QD is a homodimeric enzyme of ~100–148 kDa and is heavily glycosylated.[38,39] 2,3QD catalyzes the cleavage of the O-heterocyclic ring of flavones such as quercetin, with concomitant production of carbon monoxide (equation 6).[38] Both atoms of molecular oxygen are incorporated into the reaction products.

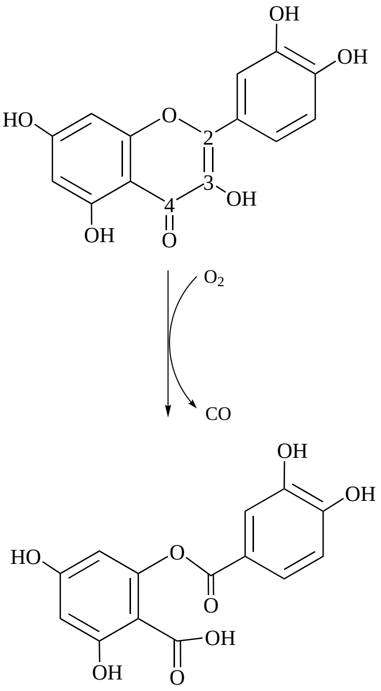

(6)

Although 2,3QD has been isolated from several fungal species,[38–40] the enzyme from *Aspergillus japonicus* has been extensively characterized and will be described herein. A partially deglycosylated form of 2,3QD from *A. japonicus* has been crystallized in its resting form[40] and in anaerobic complexes with substrates or metal chelators.[41,42] The enzyme fold is shown in Figure 9. Each 2,3QD monomer is composed of two structurally related β-sandwich domains (residues 1–145 and 206–350) that are connected by a 60-residue loop.[40] Whereas hydrophobic contacts mediate the interdomain interactions, H-bonds between loop residues and mediating waters largely comprise the dimerization interface. 2,3QD is a member of the cupin superfamily, which includes several nonmetalloenzymes, the manganese-containing enzyme oxalate oxidase (*see* ***Manganese Proteins with Mono- & Dinuclear Sites***), and the iron-containing homogentisate 1,2-dioxygenase (*see* ***Iron: Heme Proteins, Mono- & Dioxygenases***).[43] The metal centers of the metalloenzymes are quite similar in structure, supporting the hypothesis that Type 2 copper centers may have arisen from Mn- or Fe-containing ancestors.[40,44]

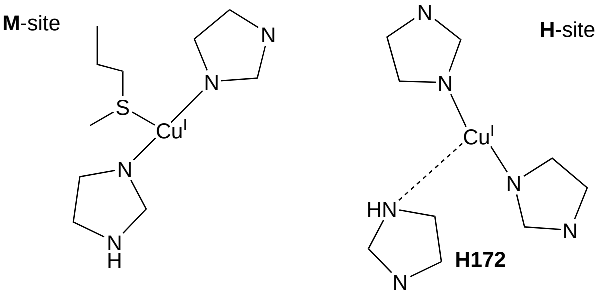

Figure 8 Model of the copper center geometries in reduced PHM, as determined spectroscopically[33]

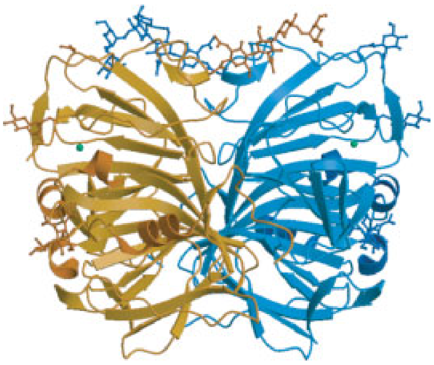

Figure 9 Ribbon diagram of quercetinase. The copper ions are shown as spheres; the carbohydrates are drawn in stick form. (Reprinted from Ref. 40. © 2002, with permission from Elsevier)

Each N-terminal domain of 2,3QD contains a mononuclear Cu(II) ion separated by ~40 Å.[40–42] As isolated, the copper coordination is modeled as two geometries, depicted in Figure 10. Approximately 70% of the copper is present in a distorted tetrahedral geometry with three His and one water molecule (W1) as ligands (Figure 10(b)). A trigonal bipyramidal coordination is also seen, in which a carboxylate oxygen from Glu73 becomes an axial ligand and the water shifts into the His plane (represented by W2) (Figure 10(c)). This is the first enzyme known in which a carboxylate oxygen from the side chain of Glu or Asp serves as a copper ligand.

As seen in Figure 11, EPR spectroscopy confirms that two states of Type 2 copper coordination exist in the resting enzyme at pH 6.[45] The minor species becomes dominant at pH 10. The EPR spectrum also changes upon the anaerobic addition of substrates or the metal chelator diethyldithiocarbamate (DDC), as indicated in the Peisach–Blumberg plot[46] in Figure 12. The spectrum of the DDC adduct indicates that copper has taken up a square pyramidal geometry with three His and two sulfurs from the chelator. This has been confirmed by X-ray crystallography.[41] The EPR,[45] X-ray,[41] and extended X-ray absorption fine structure (EXAFS)[47] data strongly suggest that substrate binds to copper in a monodentate manner during catalysis (Figure 13), replacing the water molecule. Glu73 is also a ligand in the substrate-bound form.[41] Peisach–Blumberg

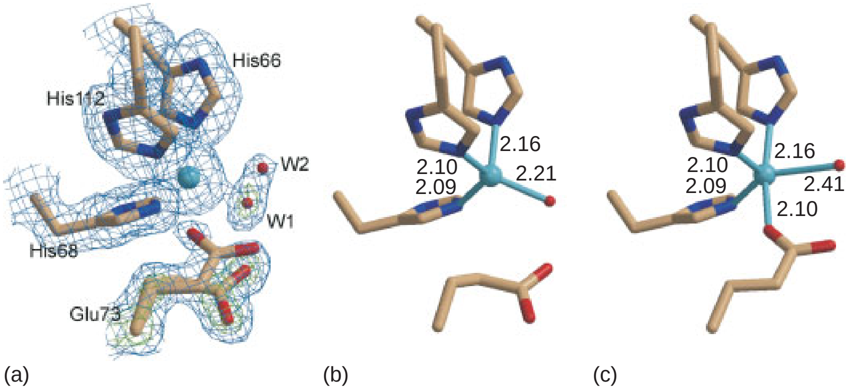

Figure 10 Copper coordination geometries in 2,3QD. (a) Experimental map contoured at the 1.0 r (blue) and 2.5 r (green, only for Glu73 and the solvent molecule) levels. (b) Major distorted tetrahedral coordination. (c) Minor trigonal bipyramidal coordination with a strong square pyramidal component. (Ref. 45. Reproduced by permission of Blackwell)

analysis of the EPR spectra of the anaerobic enzyme-substrate complex indicates that the copper center has undergone changes to a form intermediate between Type 1 and Type 2 centers. In the presence of dioxygen, an adduct ascribed to the copper-depside product is detected. It should be noted that for the *Aspergillus niger* enzyme, no changes in the EPR spectrum were observed upon substrate binding.[38]

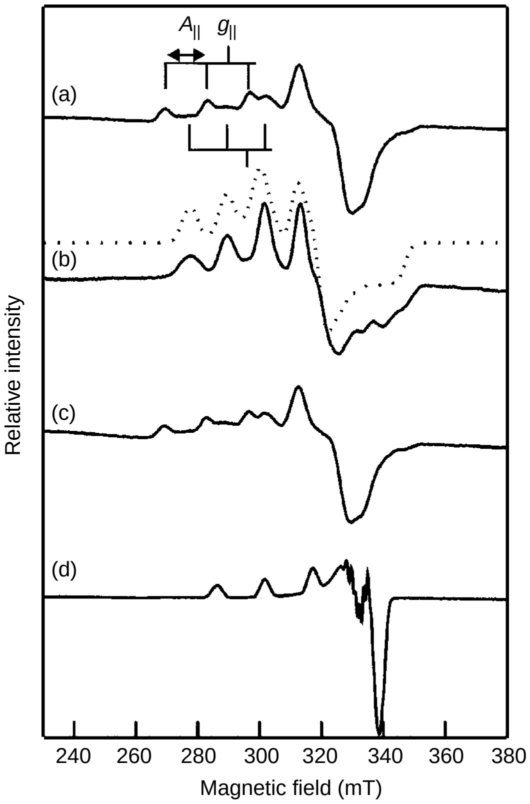

Figure 11 EPR spectra of 2,3QD. (a) 2,3QD at pH 6; (b) 2,3QD at pH 10 (dotted line is simulated data); (c) sample B after the pH has been brought back to pH 6; (d) DDC-inhibited 2,3QD at pH 6. (Ref. 45. Reproduced by permission of Blackwell)

The inherent flexibility in Glu73 ligation and its requirement for activity suggests that its coordination modulates the reactivity of the active site. Glu73 may serve as an active-site base to deprotonate the C3 hydroxyl group.[42] Alternatively, the noted flexibility in Glu73 ligation may modulate the redox potential of Cu(II). A Cu(I)-flavonol radical has been proposed to be a catalytic intermediate,[42] although no organic radical was detected by EPR at 77K, the only temperature examined.[38,45] This flavonol radical intermediate would be remarkably similar to the Cu(I)-TPQ semiquinolamine radical detected in amine oxidases (see Section 7); that radical is in a temperature-sensitive equilibrium with the Cu(II)-TPQ-quinolamine form and is only detectable near room temperature.

The structural and spectroscopic data along with biomimetic studies support the catalytic mechanism outlined in Scheme 5.[42,48,49] The flavonol substrate coordinates to Cu(II) in a monodentate manner, replacing water and shifting the metal center to a square pyramidal geometry (**2**). This is accompanied by the movement of several linker peptidyl residues, which sequesters the active site from solvent. The Glu73 residue may directly deprotonate the flavonol substrate, or it might store the proton for subsequent protononation of the depside product. A Cu(I)-flavonoxy radical tautomer of (**2**) is postulated, since its reaction with triplet O_2 (**2taut** → **3a**) is not spin-forbidden. Alternatively, O_2 may bind directly to the Cu(I) ion (**2taut** → **3b**). CO is released from the endoperoxide intermediate (**4**). Protonation of the depside product signals product release; the mouth of the substrate channel reopens.

6 GALACTOSE OXIDASE

Galactose oxidase [E.C. 1.1.3.9] is an extracellular fungal enzyme named for its ability to oxidize the C-6 position of galactose to an aldehyde (*see* ***Oxidation Catalysis by***

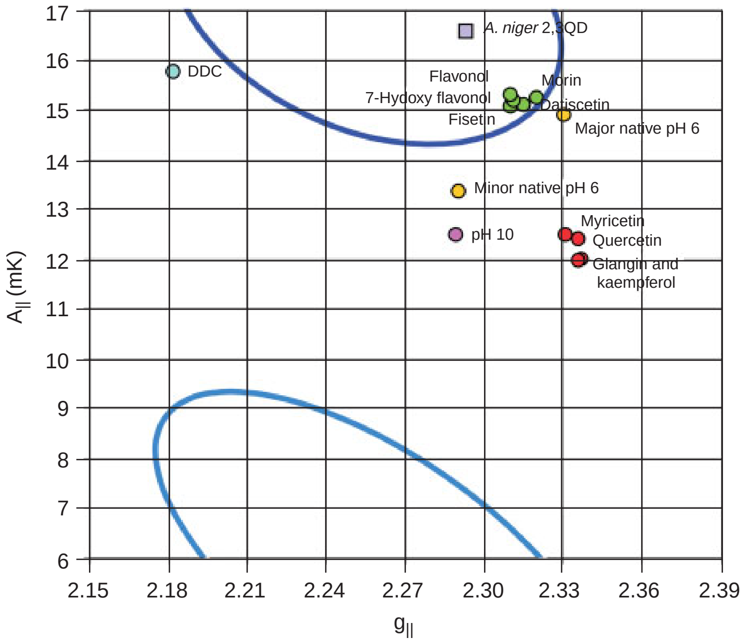

Figure 12 Peisach–Blumberg plot.[46] Plot of $g_{||}$ and $A_{||}$ values from EPR of various flavonol complexes. Area circled in dark blue: the region where Type 2 Cu sites in proteins are found; light blue, where Type 1 sites are found. (Ref. 45. Reproduced by permission of Blackwell)

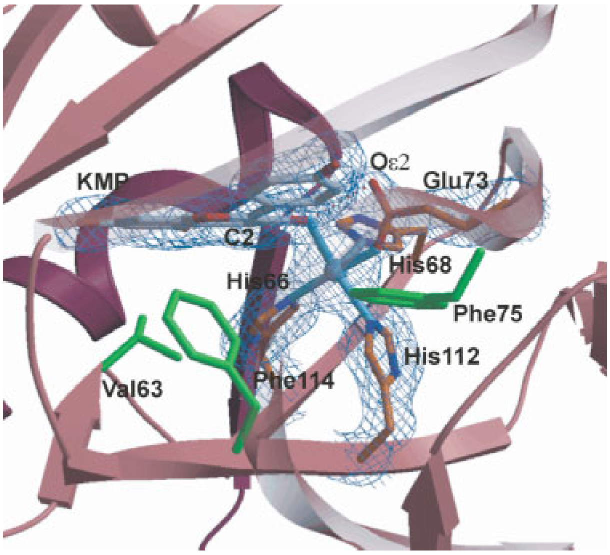

Figure 13 The active site of 2,3QD-substrate complex. Protein copper ligands are represented by orange sticks, substrate is in gray, and the residues in van der Waals contact with the substrate are in green (Reproduced from R.A. Steiner, K.H. Kalk, and B.W. Dijkstra, *Proc. Natl. Acad. Sci. USA*, 2002, **99**, 16625. © 2001 National Academy of Sciences, USA)

Transition Metal Complexes), using oxygen as the oxidant and reducing it to hydrogen peroxide, as illustrated in equation (7). The enzyme acts on a broad range of alcohols and is not specific for galactose, which is actually only an average substrate. Several excellent reviews have recently been published and provide exceptional insight into the structure, catalytic mechanism, and cofactor biogenesis of galactose oxidase.[50–53]

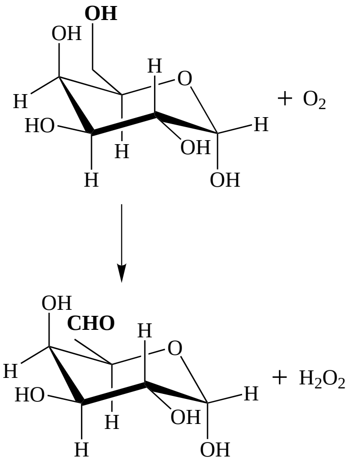

(7)

The most extensively studied galactose oxidase is that secreted from the fungus *Fusarium* spp. (formerly known as *Dactylium dendroides* and *Polyporus circinatus*). Homologs include the fungal glyoxal oxidase and the putative prokaryotic FbfB protein, which is involved in *Stigmatella aurantiaca* fruiting body formation. The peroxide produced during the catalytic cycle of glyoxal oxidase fuels the peroxidases that degrade lignin.[53] However, the biological role of galactose oxidase has not been completely defined. Galactose oxidase

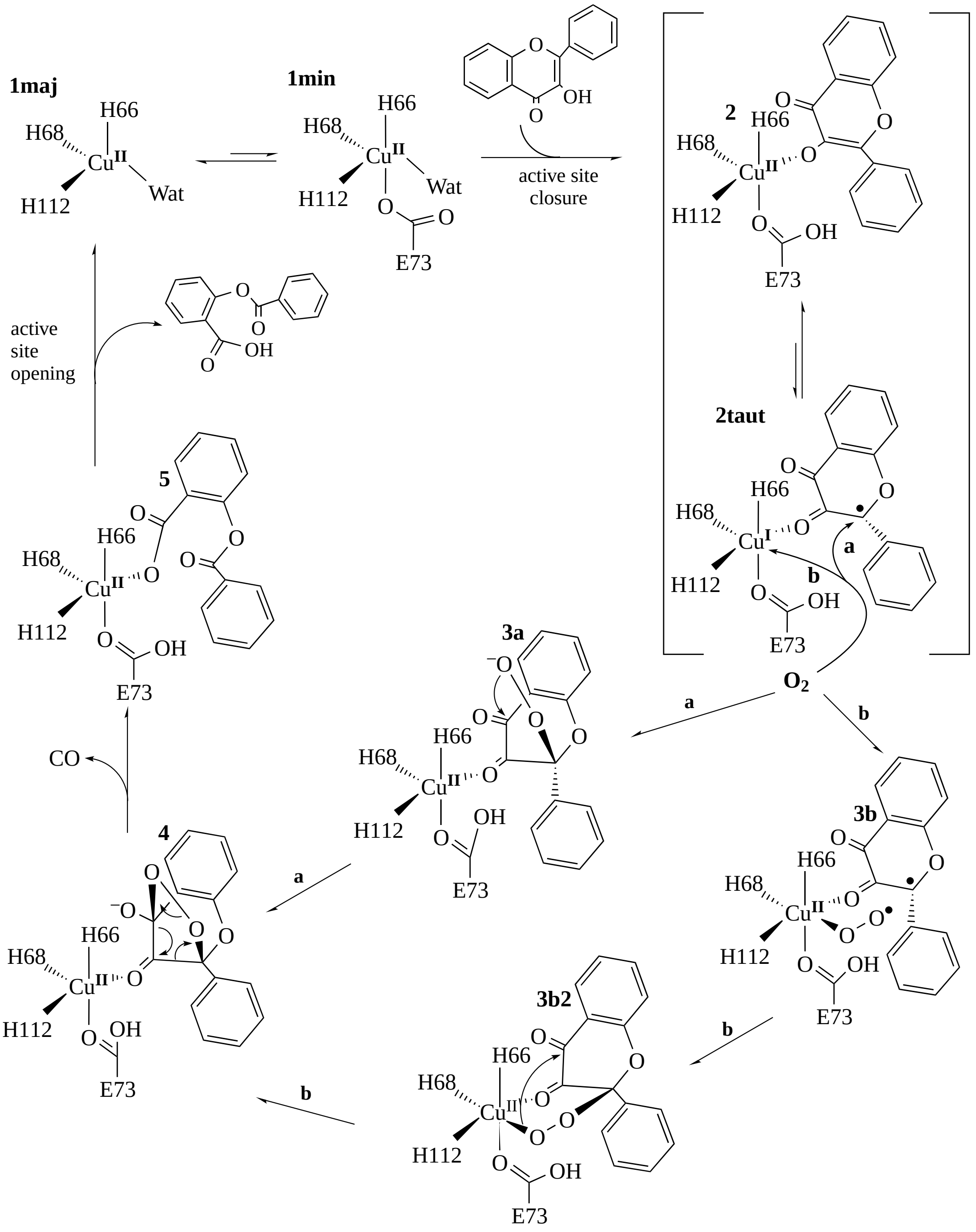
1maj
H66
H68
Cu^II
Wat
H112
1min
H66
H68
Cu^II
Wat
H112
O
O
E73
O
OH
O
active site closure
2
O
H66
O
H68
Cu^II
O
H112
O
OH
E73
2taut
O
H66
O
H68
Cu^I
O
a
b
H112
O
OH
E73
O2
a
b
active site opening
O
O
O
OH
5
O
H66
O
H68
Cu^II
O
O
H112
O
OH
E73
CO
3a
⁻O
O
O
O
H66
H68
Cu^II
O
OH
H112
O
E73
a
4
O
⁻O
H66
O
O
H68
Cu^II
O
H112
O
OH
E73
3b
O
H66
O
H68
Cu^II
O
O•
O
H112
O
OH
E73
b
3b2
O
H66
O
H68
Cu^II
O
O
O
H112
O
OH
E73
b

Scheme 5 Mechanism of 2,3-QD. (Ref. 42. Reproduced by permission of The National Academy of Sciences of the United States of America)

might also be involved in polysaccharide processing or act as a bacteriostat through its production of peroxide.

Galactose oxidase is a monomer composed of a single polypeptide chain ($M_r = 68\,\text{kD}$), with two disulfide bridges, and a single copper ion that is essential for catalytic activity. A second redox center in the active site is provided by a tyrosyl radical (Tyr272).[50–53] The enzyme as isolated is a mixture of active and inactive forms. The inactive form of the enzyme has a typical Type 2 Cu^{II} EPR signal which is abolished by one-electron oxidation to the active form. These observations have led to a model that invokes oxidation of a tyrosine residue to a tyrosine radical on the active enzyme; the unpaired electron on the tyrosine radical is magnetically coupled to the odd electron on Cu^{II}, thereby producing an ‘EPR-silent’ state (see Figure 14).[54] If the active-site copper is removed, an EPR signal that is attributable to a modified tyrosine radical (Figure 15) can be detected.

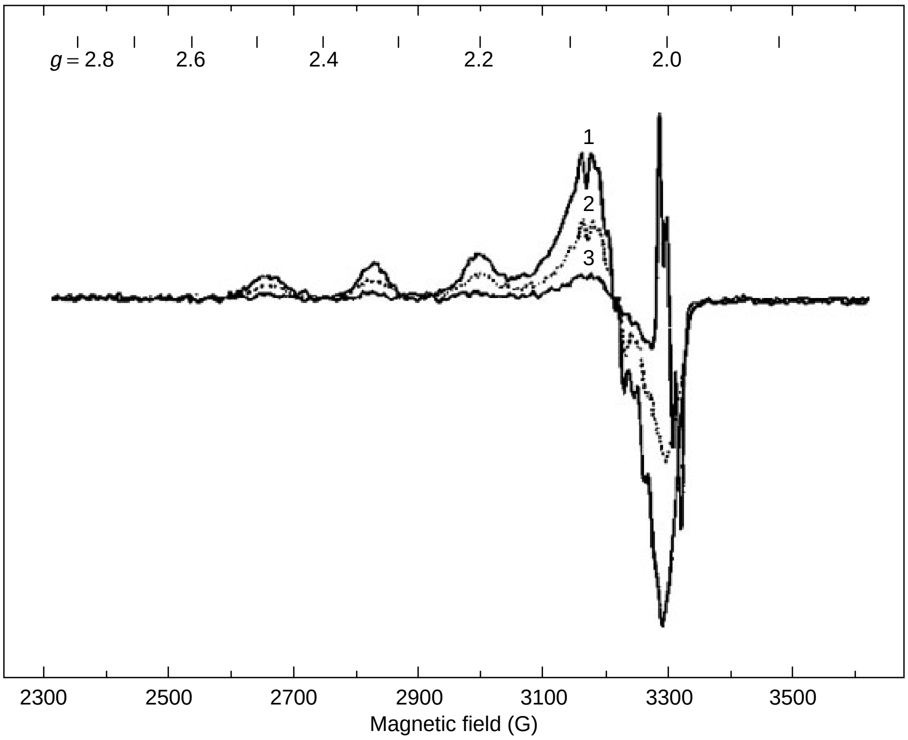

Figure 14 X-band EPR spectra of galactose oxidase at 30 K. 1, reductively inactivated; 2, native (as isolated); 3, oxidized. (Ref. 54. Reproduced by pemission of American Society for Biochemistry & Molecular Biology)

The three-dimensional structure of this enzyme has been solved at atomic resolution (1.7 Å).[55,56] The overall structure of galactose oxidase is shown in Figure 16(a). There are three domains, each composed mostly of β structure; the copper is located on the solvent-accessible surface of the second domain, opposite to the bulk of the third domain. Figure 16(b) provides details of the copper-site structure. Two histidine imidazoles (His496 and His581), a tyrosine (Tyr272), and water (acetate in pH 4.5 buffer conditions) make up the equatorial plane. A second tyrosine (Tyr495) is coordinated axially, with a bond length of 2.69 Å. The equatorial tyrosine (Tyr272) is covalently bonded to Cys228, which results from post-translational processing (vide infra; *see* ***Metal-mediated Protein Modification***). The aromatic ring of Trp290 stacks over the Tyr–Cys unit, shielding the Cys–Tyr cofactor from solvent.

Mutagenesis and spectroscopic studies have revealed much about the active-site structure, the roles of the active-site residues and the catalytic mechanism (see Scheme 6). Oxidized, active galactose oxidase has remarkable electronic absorption spectral features associated with its copper center, as seen in Figure 17. The band at 810 nm has been assigned as being an interligand charge transfer band (Y495 → Y272•) mediated by copper ion wave functions. These have been discerned from multiple detailed studies on the enzyme, mutants, and model compounds.[52]

Kinetic analyses indicate that the losses of catalytic activity in the mutants (see Table 1) is attributable to changes in k_{cat} with only minor perturbations in K_M for galactose.[52] The spectroscopic signatures of the radical present in apogalactose oxidase (resonance Raman, high-field EPR, and ENDOR) are consistent with a thio-substituted tyrosyl radical, establishing Tyr272 as the redox-active residue. Additionally, the Tyr495Phe mutant retains the ability to form a radical, despite being catalytically impaired. The reduction potential of the cofactor is quite low (~400 mV vs NHE) compared with normal tyrosyl radicals (800 – 1000 mV) and is largely controlled by the coordination of copper and the thio-ether linkage to Cys228, as shown in Table 1. Tyr495 and Trp290

Table 1 Properties of galactose oxidase and active-site mutants. (Adapted from Refs. 52, 57 and 58)

Enzyme form	Activity/Cu	Proton uptake	Radical formation/ E'^0 at pH 7.5 (mV)
Wild type	1.0	Yes	Yes/400
Wild type + azide	$K_I = 20\,\mu M$	Yes	Yes/393
Wild type Apo-enzyme	Copper-free	n.d.	Yes/570
Tyr272Phe	none	n.d.	No/ –
Tyr495Phe	0.001	No	Yes/450
Cys228Gly	0.0001	Yes	Yes/630
Trp290His	0.0005	Yes	Yes/730

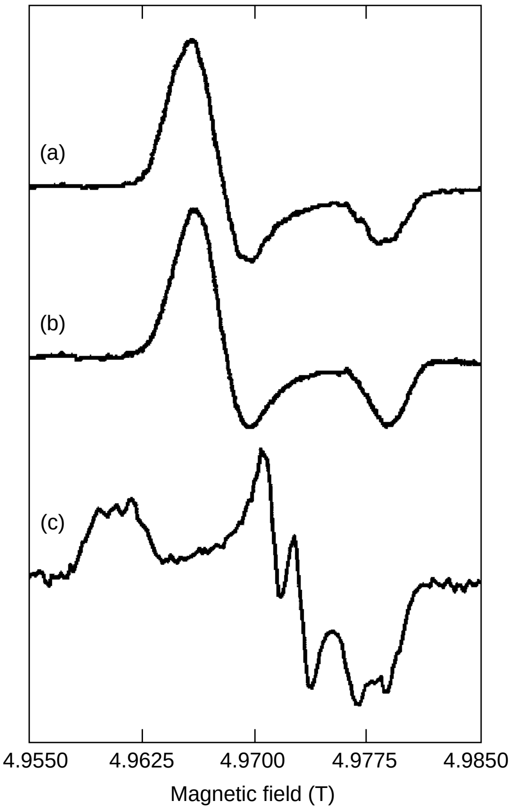

Figure 15 High-frequency (139.5 GHz) EPR spectra for biological free radicals. (a) Apogalactose oxidase free radical. (b) 2-(Methylthio)cresyl phenoxyl free radical. (c) Ribonucleotide reductase free radical. (Reprinted with permission from Ref. 52. © 2003 American Chemical Society)

also influence the potential. The Cu(II)/Cu(I) potential in wild-type enzyme is ∼150 mV, which is similar to aqueous copper.

Spectroscopic studies of the Tyr495Phe mutant have suggested that the axial ligand Tyr495 functions as a general base, abstracting a proton from the substrate and activating it toward oxidation.[51,52] The Tyr495Phe mutant is not competent for proton uptake, as is normally observed for the wild-type protein in the presence of anions. Anions displace the solvent ligand from copper and are analogous to substrate binding. Both spectroscopic studies and computer modeling of enzyme–galactose interactions indicate that galactose can coordinate to $\mathrm{Cu^{II}}$ via O6 at the equatorial position occupied by solvent (see Scheme 6).[54,59]

These data have led to the development of a catalytic mechanism, shown in Scheme 6, that has been further refined by kinetic isotope effect (KIE) experiments.[52,53] Substrate binds to Cu(II), replacing bound solvent. The metal coordination facilitates the deprotonation of the substrate hydroxyl group. The proton is transferred to Tyr495, which dissociates from copper. The temperature and pH dependence of the visible absorption and circular dichroism spectra indicate that galactose oxidase exists as an equilibrium of the Tyr495-Cu(II) form ($\mathrm{Tyr_{ON}}$) and the protonated Tyr495 state, where the phenolate is no longer a copper ligand ($\mathrm{Tyr_{OFF}}$). For some substrates under some conditions, a significant solvent KIE has been observed, indicating that proton transfer may become rate-limiting. Electron transfer from substrate to Cu(II) occurs next, resulting in the formation of a Cu(I)-substrate alkoxyl radical. Ionization of the substrate alcohol lowers its redox potential, facilitating oxidation of the alcohol. Subsequent C–H bond cleavage via H atom transfer to the Tyr272 radical occurs next, producing fully oxidized substrate aldehyde and the fully reduced state of the enzyme, Cu(I)-$\mathrm{Tyr_{red}}$. A large substrate KIE has been measured for C–H bond cleavage, indicating that hydrogen tunneling contributes to H atom transfer.

The second half-reaction of galactose oxidase turnover involves reduction of O_2 to form peroxide, H_2O_2. Although much less is known about this mechanistic step, it is thought that O_2 binds to Cu(I). Both substrate-derived protons are transferred to the peroxide product, as determined from the large substrate (alcohol) KIE on O_2 reduction; evidently hydrogen transfer is fully rate limiting for O_2 reduction. Additional work is necessary to develop a more detailed mechanism of O_2 reduction.

The biogenesis of the unique Tyr272-Cys228 cofactor of galactose oxidase requires only copper and O_2, and does not involve any accessory proteins or enzymes.[60] Another self-processing event, cleavage of the 17 N-terminal residues of the prosequence, is also copper/O_2-dependent. The order of these autocatalytic reactions has not been definitively determined and it is not clear if prosequence cleavage is linked to thio-ether bond formation in vivo.[60,61] The cross-linked cofactor of galactose oxidase is formed when the enzyme is expressed in *Pichia pastoris* without its prosequence.[61]

The crystal structure of progalactose oxidase has been determined.[62] Although it is generally quite similar to that of the mature enzyme, several loops show significant changes (see Figure 16(c) and 16(d)). The prosequence is not near the active site, suggesting that it does not function in copper transport into the active site. Rather, it has been proposed that the prosequence positions the active-site residues so that thio-ether bond formation is favored. The positions of the copper ligands His496, His581, and Tyr495 are nearly identical in both the pro- and mature forms of the enzyme. In contrast, both Tyr272 and Cys228 are rotated significantly. Additionally, Cys228 shows additional electron density at the sulfur atom, which is postulated to be the sulfenic acid (-SOH) oxidized form of Cys. It is likely that this form is a result of X-ray damage. The loop containing Trp290 is also significantly shifted from its final position. This opens up the active site and exposes Cys228 and Tyr272 to solvent.

Based on biochemical and structural studies, several mechanisms of biogenesis have been proposed. As shown in Scheme 7(a), one mechanism involves activation of the phenol group of Tyr272 (or the thiol of Cys228) by coordination to Cu(II) and is similar to the mechanism

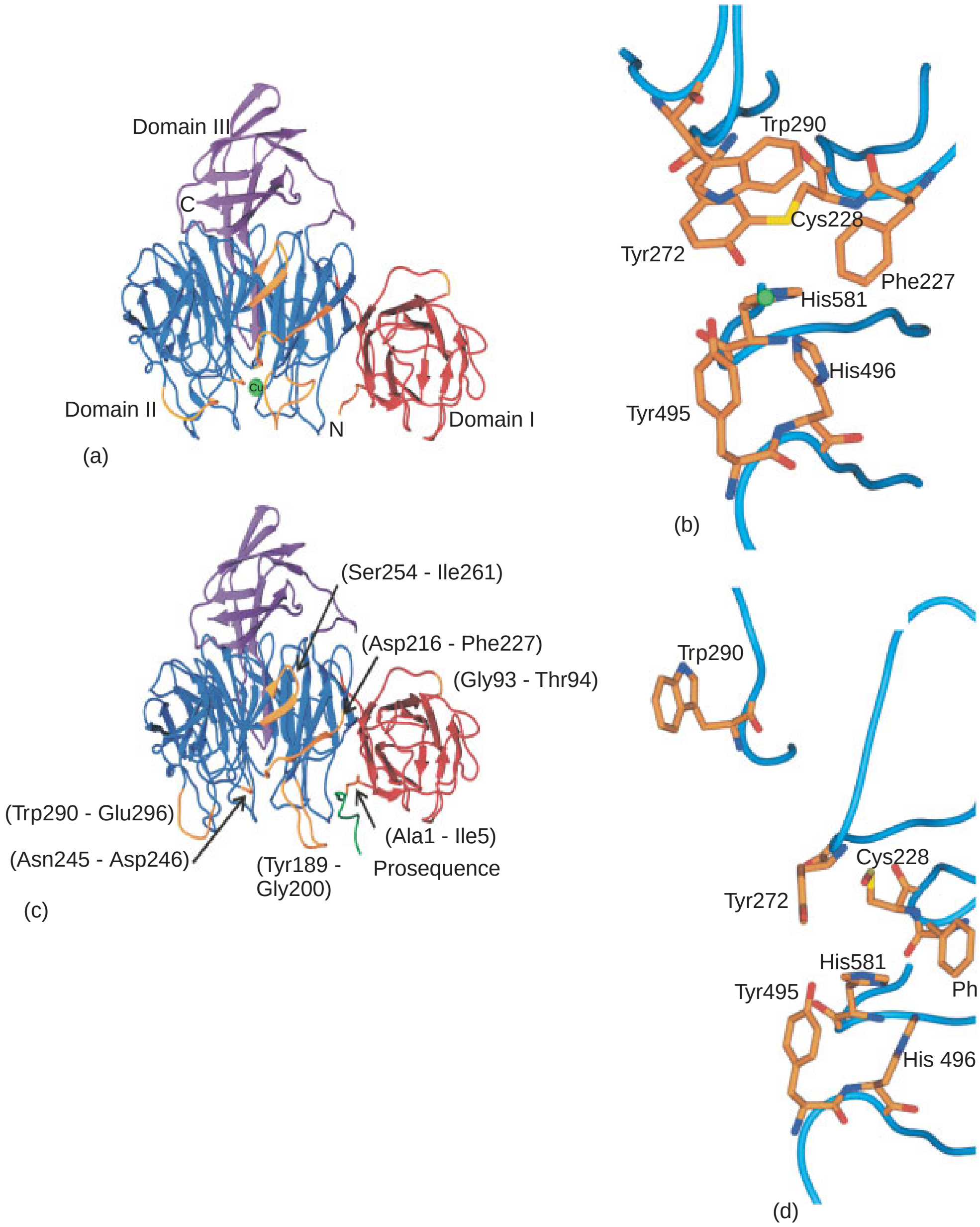
Domain III
C
Domain II
Cu
N
Domain I
(a)
Trp290
Cys228
Tyr272
Phe227
His581
His496
Tyr495
(b)
(Ser254 - Ile261)
(Asp216 - Phe227)
(Gly93 - Thr94)
(Trp290 - Glu296)
(Asn245 - Asp246)
(Tyr189 - Gly200)
(Ala1 - Ile5)
Prosequence
(c)
Trp290
Cys228
Tyr272
His581
Tyr495
Ph
His 496
(d)

Figure 16 Comparison of the overall structures (a,c) and copper-binding/active-site regions (b,d) of processed, active galactose oxidase (a,b) with its precursor proform (c,d). (Reproduced from Ref. 62. © 2001 National Academy of Sciences, USA)

proposed for the biogenesis of the quinone cofactor of amine oxidase.[62] A second proposed mechanism shown in Scheme 7(b) is based on recent kinetic studies of the Cu(I) form of the unprocessed protein. Whittaker *et al*. show that, in vitro, Cu(I)-activated thio-ether bond formation is significantly faster than Cu(II)-mediated cross-linking and is associated with an active-site group ionizing with a $pK_a = 7.3$.[61] In this mechanism, O_2 binding to Cu(I) ultimately produces a Cys228 thiolate radical, which attacks Tyr272 to form the thio-ether bond. Additional studies are needed to elucidate the details of cofactor biogenesis at the molecular level, and to determine if Cu(I)- or Cu(II)-based biogenesis is more likely to occur under physiological conditions.

7 AMINE OXIDASE AND LYSYL OXIDASE

Copper-containing amine oxidases [E.C. 1.4.3.6] are one of the most widely distributed classes of Type 2 copper enzymes.[63] They have been highly purified from bacteria,

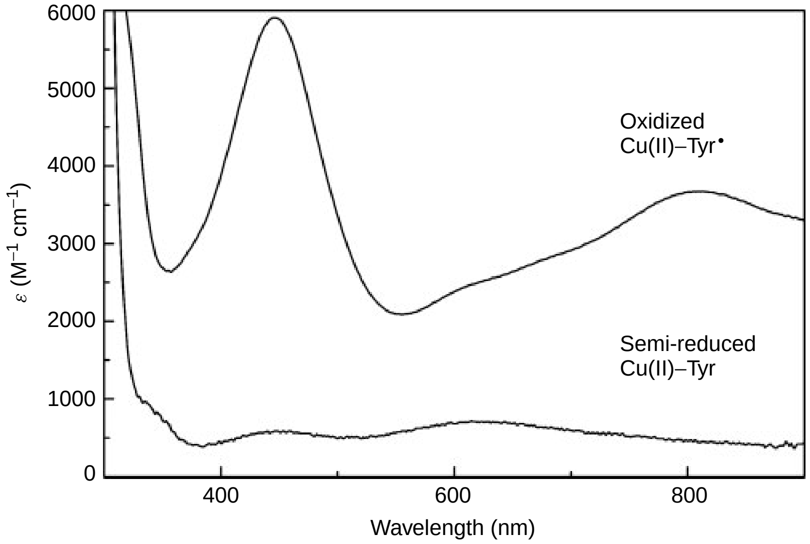

Figure 17 Visible absorption spectra of oxidized, active galactose oxidase and the semireduced, inactive form

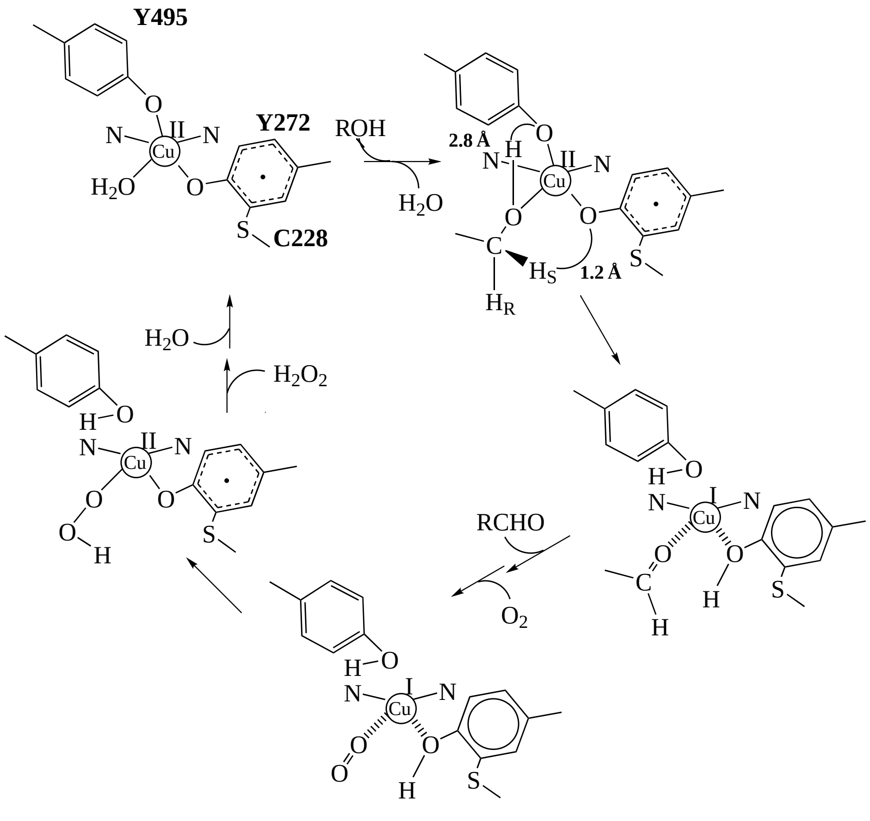

Scheme 6 Catalytic mechanism of galactose oxidase. (Reprinted with permission from Ref. 52. © 2003 American Chemical Society)

yeasts, plants, and mammals. Generally these enzymes are dimers composed of two identical subunits with a total $M_r \sim 130-150$ kD. Amine oxidases catalyze the oxidative deamination of primary amines in a ping pong mechanism (equations 8 and 9).

$$\mathrm{RCH_2NH_2 + E_{ox} \longrightarrow RCHO + E_{red}} \qquad (8)$$

$$\mathrm{E_{red} + O_2 + H_2O \longrightarrow E_{ox} + H_2O_2 + NH_3} \qquad (9)$$

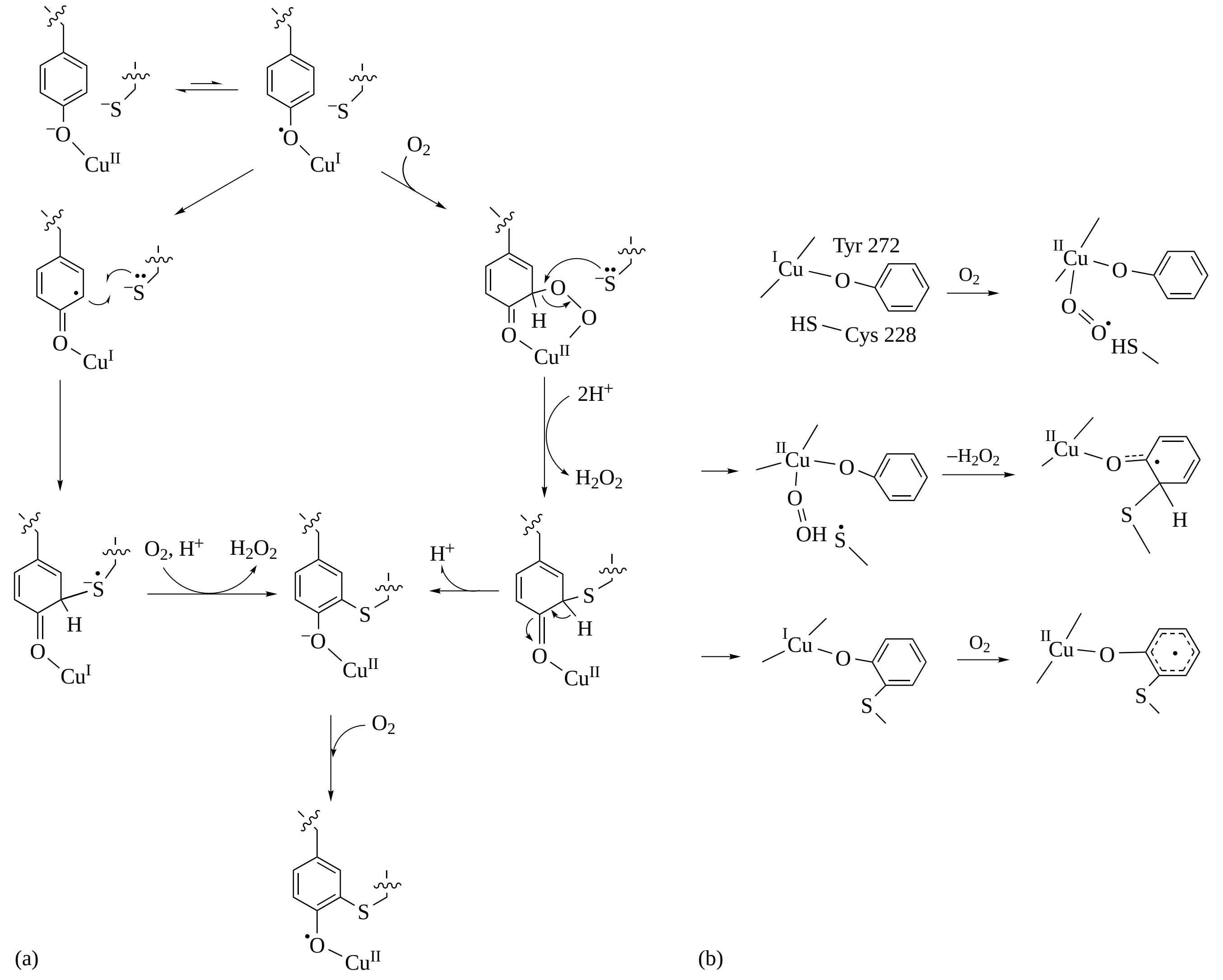

Scheme 7 Two possible mechanisms of thio-ether bond formation based on either (a) Cu(II) and a tyrosyl radical or (b) Cu(I) and a thiyl radical ((a) S.J. Firbank, M.S. Rogers, C.M. Wilmot, D.M. Dooley, M.A. Halcrow, P.F. Knowles, M.J. McPherson, and S.E. Phillips. *Proc. Natl. Acad. Sci. USA*, 2001, **98**, 12932. © 2001 National Academy of Sciences, USA and (b) Ref. 61. Reproduced by permission of The American Society for Biochemistry & Molecular Biology)

Substrate specificities depend on the enzyme source but nearly all biogenic primary amines are included, that is, histamine, tyramine, tryptamine, dopamine, serotonin, norepinephrine, mescaline, 1,5-diaminopentane, 1,4-diaminobutane, spermine, and spermidine. The physiological functions include nutrient metabolism in prokaryotes, regulation of physiological amine concentrations, and mediation of cell-cell interactions through adhesion and apoptosis. Another type of amine oxidase, known as lysyl oxidase, has been discovered in connective tissue.[63] Lysyl oxidases are responsible for the cross-linking of connective tissue in aorta, lung, and cartilage; their primary substrates are peptidyl lysines of elastin and collagen. The severe pathology of dietary copper deficiency and lathyrism is associated with extremely low levels or inhibition of lysyl oxidase. The molecular properties of lysyl oxidase are strikingly different from the soluble amine oxidases. Lysyl oxidase has $M_r = 30-32$ kD and is relatively insoluble in aqueous solution owing to severe aggregation. Lysyl oxidase is initially synthesized as a ~46 kD precursor polypeptide, which is subsequently cleaved to yield the native ~32 kD enzyme.

Both amine and lysyl oxidases possess a single Type 2 copper center and a redox-active cofactor per subunit. As shown in Figure 18, amine oxidases contain 2,4,5-trihydroxyphenylalanine quinone (TPQ) and lysyl oxidase contains lysyl tyrosine quinone (LTQ), in which a lysine side chain has been cross-linked to TPQ. These cofactors are produced from the oxidation of a specific active-site tyrosine residue via novel self-processing events that require only copper and O_2 (*see* ***Metal-mediated Protein Modification***).

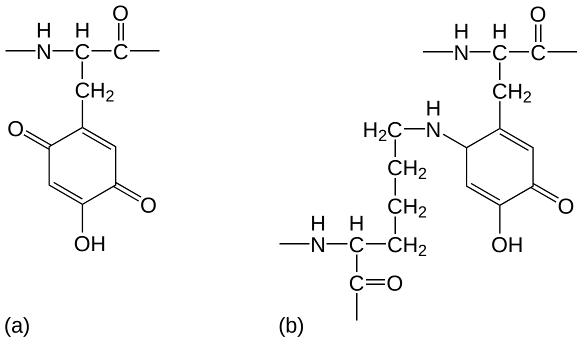

Figure 18 Tyrosine-derived quinone cofactors. (a) TPQ, 2,4,5-trihydroxyphenylalanine quinone; (b) LTQ, lysyl tyrosyl quinone

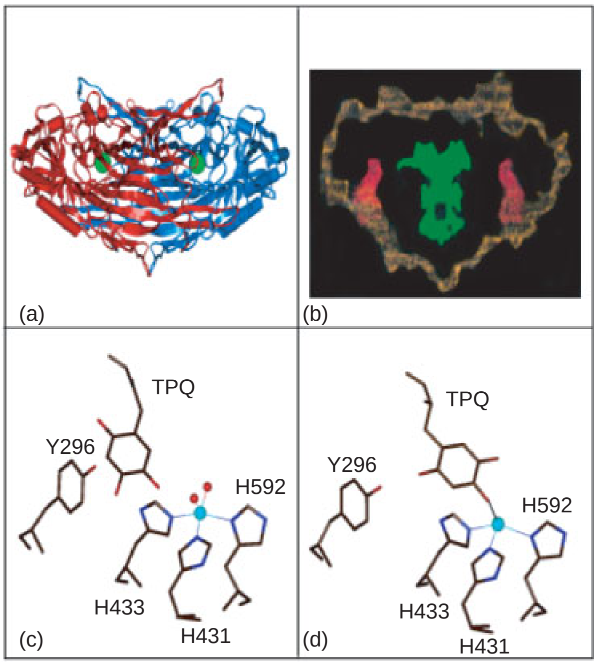

Figure 19 Structure of amine oxidase from *A. globiformis*. (a) ribbon diagram showing subunits in blue and red, copper as green spheres; (b) solvent map showing the substrate channels in red and the inland 'lake' in green; (c) close-up of the copper center showing the active TPQ_{off} conformation; (d) close-up of the copper center showing the inactive TPQ_{on} conformation. (Reprinted with permission from Ref. 69. © 1997 American Chemical Society)

Although the two enzymes in this class are mechanistically similar, much more information is available on the structure and catalytic cycle of amine oxidase than lysyl oxidase. Therefore, only amine oxidases will be discussed in detail here; readers are directed to several excellent reviews for additional information on lysyl oxidase.[64,65]

The structures of five amine oxidases have been solved by X-ray crystallography: two are bacterial (*Escherichia coli*[66–68] and *Arthrobacter globiformis*[69]); two are from yeast (*Hansenula polymorpha*[70] and *P. pastoris*[71]); and one is from pea seedling.[72] Collectively these enzymes exhibit considerable structural homology. The structure of oxidized, resting-state *Arthrobacter globiformis* amine oxidase (AGAO) is shown in Figure 19(a). The actives sites are located within the large β-sandwich core domains, which surround a large, solvent-filled cavity (Figure 19(b)). Two β-hairpin arms extend from the central domain of one subunit across the surface of the other subunit; residues at the end of one arm form part of the entrance to the active-site channel. In most structures, this channel is long and narrow, as shown in Figures 19(b) and 20. An exception to this is the enzyme from *P. pastoris*, in which the substrate channel resembles a broad funnel that is able to accommodate the larger lysyl peptide substrates oxidized by this enzyme.[71] The shape of the substrate channel, along with variations in the numbers and types of residues in the hairpin arms, account for the wide ranges of substrate specificities noted for amine oxidases, which have highly conserved active-site structures (Figures 19(c) and 19(d)). A second metal site believed to bind calcium is present in numerous amine oxidases, although its function remains unknown.[72,73]

The active-site copper ion is coordinated in a distorted square pyramidal geometry by three conserved histidine residues (His431, His433, and His592 in AGAO) and two water molecules, one axial and the other equatorial, confirming the predictions of earlier spectroscopic experiments.[63] TPQ is in close proximity to the copper ion. Several conformations of TPQ have been noted in the available structures. Figure 19(c) shows the active, 'TPQ off' orientation where O-2 is hydrogen bonded to the axial water ligand and O-4 is hydrogen bonded to a conserved tyrosine residue (Tyr296). This orientation of TPQ places the nucleophilic C-5 in close proximity to the conserved active-site base (Asp298) and the substrate access channel. In the 'TPQ on' orientation (Figure 19(d)), TPQ is rotated and ligated to copper via O-4. Although the latter form is not immediately suited for reaction with substrate, the available data suggest that it is in facile equilibrium with the properly oriented form. Moreover, the availability of various TPQ conformations or orientations that have similar energies may be required for its biogenesis from tyrosine (vide infra).

The crystal structures of substrate-reduced amine oxidases have been solved,[67] along with site-directed mutants,[69,74,75] metal-substituted forms,[76,77] enzyme complexes with inhibitors,[67,75] the O_2 mimic nitric oxide (NO) and peroxide.[66] These have been correlated with a wealth of biochemical and spectroscopic data[78] that form the basis for the catalytic mechanism proposed in Scheme 8. A Schiff base complex species (b) is formed between substrate amine and TPQ C-5. Base-catalyzed proton abstraction from substrate α-methylene group, via the conserved active-site aspartate residue, yields the reduced cofactor in a product Schiff-base complex, species (c). Hydrolysis releases product aldehyde, leaving the cofactor in the reduced aminoquinol form, species (d).

The mechanism of O_2 reduction remains a central question; how does the enzyme activate dioxygen for a two-electron

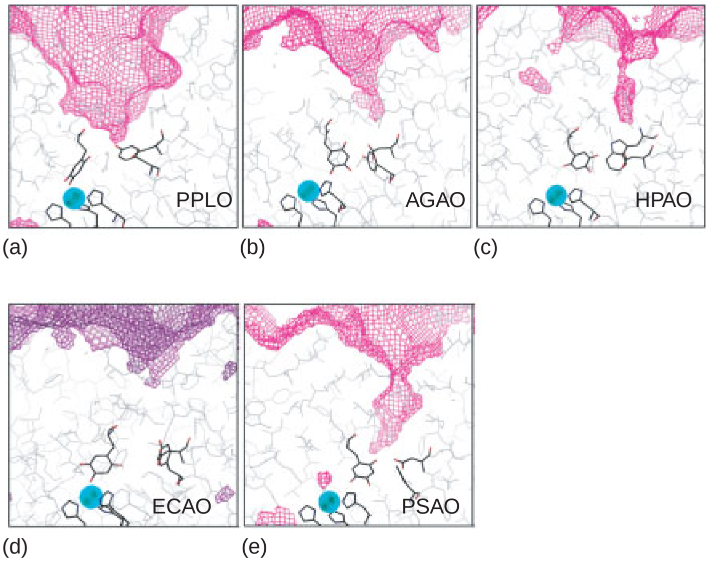
PPLO
AGAO
HPAO
(a)
(b)
(c)
ECAO
PSAO
(d)
(e)

Figure 20 Views of the active-site channels in the known CuAO structures. (a) *P. pastoris*, (b) *A. globiformis*, (c) *H. polymorpha*, (d) *E. coli*, and (e) pea seedling. The surface of each funnel is shown as a blue mesh. The residues in the interior of a protein are drawn in gray, the copper atom is a cyan sphere, and the copper ligands, TPQ, active-site base, and 'gate' residues are drawn with heavy lines. A small portion of the interior lake is seen, colored magenta, at the bottom of some views. (Reprinted with permission from Ref. 71. © 2003 American Chemical Society)

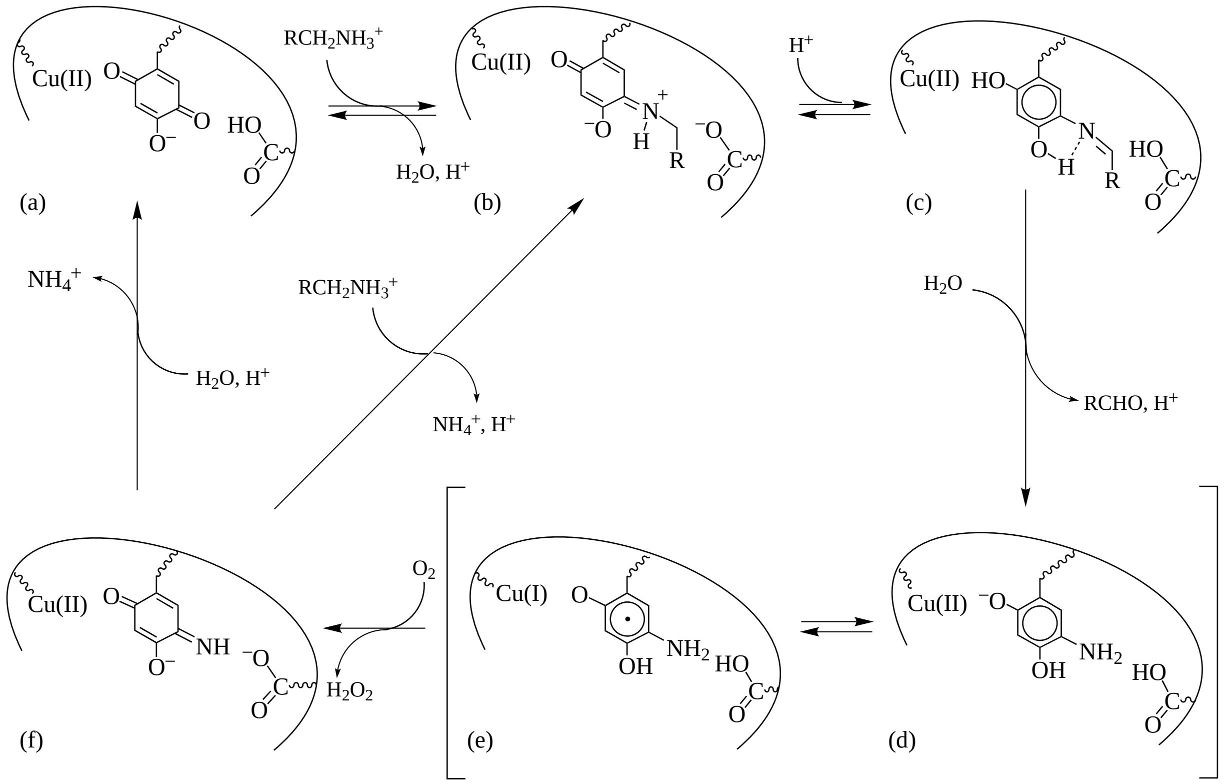
Cu(II)
RCH2NH3+
H2O, H+
H+
(a)
(b)
(c)
NH4+
H2O, H+
RCH2NH3+
NH4+, H+
H2O
RCHO, H+
O2
H2O2
Cu(I)
(f)
(e)
(d)

Scheme 8 Mechanism of amine oxidase. (Ref.73. Reproduced by permission of Springer Verlag) reduction to hydrogen peroxide? The anaerobic substrate-reduced enzyme has been shown by EPR to be an equilibrium mixture of Cu(II)–aminoquinol and Cu(I)–semiquinone radical species (d) and (e), and the Cu(I)–semiquinone species would be expected to react readily with O_2.[63] Formation of the Cu(I)–semiquinone has been shown to be kinetically competent in bacterial and plant enzymes. However, an obligatory role for a Cu(I)–semiquinone intermediate in the oxidative half-reaction of copper amine oxidases is not established, and other viable mechanistic alternatives have been presented. Recent solvent isotope effect, ^{18}O isotope effect, and solvent viscosity effect work using bovine serum amine oxidase indicates that the first electron transfer to O_2, and not oxygen binding, is the rate-determining step for the oxidative half-reaction.[78] Assuming that Cu(I) reduction of O_2 is expected to be relatively fast, Klinman proposes that O_2 is prebound and the rate-limiting, first electron transfer (to produce superoxide) occurs at a site other than the Cu(I) center. A hydrophobic pocket in the *H. polymorpha* active site was identified and suggested to be the site of O_2 binding and initial reduction.[79] The second electron transfer, resulting in the reduction of superoxide to peroxide, could either occur in the hydrophobic pocket or after superoxide binds to Cu(II). More recent work of Mills and Klinman using the cobalt-substituted *H. polymorpha* enzyme lends support to a non-redox role for copper in TPQ reoxidation.[80]

The structure of the anaerobic substrate-reduced enzyme from *E. coli* complexed with the O_2 mimic nitric oxide shows that NO binds between the TPQ-aminoquinol and copper and is not in the hydrophobic pocket thought to bind O_2 in *H. polymorpha*.[66] Additionally, a copper-oxygen species has been directly trapped by equilibrium turnover methods.[66] Here, the Cu–O distance of 2.8 and 3.0 Å and the Cu–O–O bond angle of 88° are consistent with the geometry expected for copper-bound peroxide. The peroxide replaces the axial water ligand to copper and occupies a similar position as NO does in the anaerobically reduced sample. The results also support solution studies that suggest both protons needed to form H_2O_2 are derived from TPQ.[78] These structures show a close interaction of the copper ion, TPQ cofactor, and O_2 or its mimic, NO. These intimate contacts strongly suggest all three entities work as a cohesive catalytic unit in amine oxidases.

One of the most fascinating questions concerning these enzymes is the mechanism of oxidation of the active-site tyrosine residue to form TPQ. This is a posttranslational, self-processing, six-electron oxidation that requires only the apo protein, Cu(II), and $2O_2$ per TPQ.[81] The structures

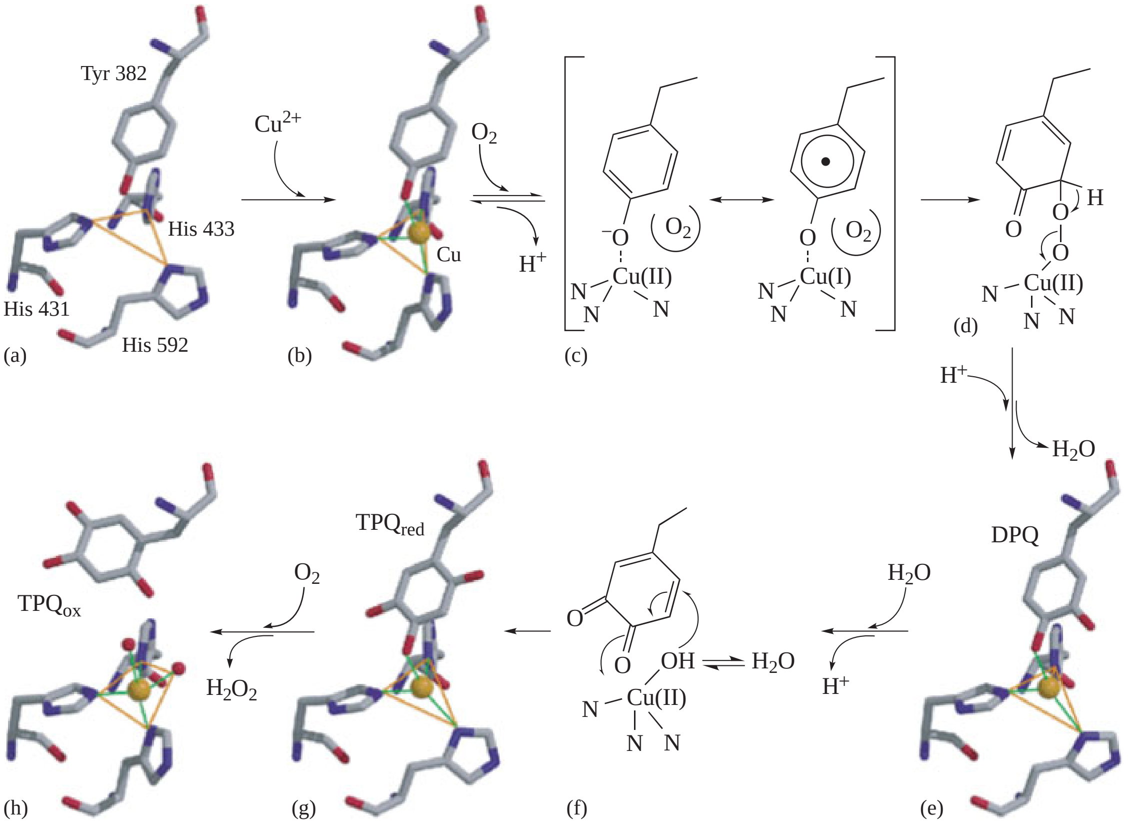

Scheme 9 Proposed mechanism of TPQ formation from tyrosine. Species drawn in stick figures have been structurally characterized. (Reproduced from Ref. 82)

of unprocessed AGAO with and without Cu(II) have been determined.[69,81] The copper is ligated by the three His and by the hydroxyl group of the TPQ-precursor tyrosine (2.5 Å) in a trigonal bipyramidal geometry; the site is preformed to accept the metal. The formation of a transient LMCT band (*see* ***Ligand Field Theory & Spectra***) between tyrosinate and Cu(II) has been observed in the biogenesis of TPQ in *H. polymorpha* amine oxidase.[78] These observations lead to the hypothesis that tyrosine coordination to Cu(II) activates the phenol ring for oxidation by O_2. Few intermediates have been observed in solution because the rate-limiting step occurs early in the mechanism and involves the reaction of the first molecule of O_2. Yet several intermediates have been freeze-trapped in crystals; these are incorporated into a plausible biogenesis mechanism that is illustrated in Scheme 9.[82] Species (c) is drawn to suggest ring activation via coordination; no evidence for radical intermediates in the tyrosine oxidation reaction has been obtained at this time. Note the need for conformational flexibility of the cofactor ring as it rotates nearly 180° ((e) → (f)). The addition of H_2O to the ring, illustrated as (e) → (f) → (g) → (h), has also been demonstrated in solution.[83]

Elucidating all the fascinating details of this reaction will require further mechanistic, structural, and model studies. Finally, the discovery of self-processing redox enzymes[84] (see Section 6; *see* ***Metal-mediated Protein Modification***) may be relevant to understanding aspects of the evolution of enzymes. Metal-ion mediated redox chemistry with oxygen can modify several amino acids, especially tyrosine, tryptophan, cysteine, and histidine. This may have provided a path to generate new redox cofactors prior to the advent of the complex biosynthetic pathways.

8 RELATED ARTICLES

Copper Proteins: Oxidases; Copper Proteins with Dinuclear Active Sites; Copper Proteins with Type 1 Sites; Metallochaperones & Metal Ion Homeostasis.

9 REFERENCES

1. J. S. Valentine and D. Mota de Freitas, *J. Chem. Educ.*, 1985, **62**, 990.
2. J. Peisach and W. E. Blumberg, *Arch. Biochem. Biophys.*, 1974, **165**, 691.
3. E. I. Solomon, M. D. Lowery, L. B. LaCroix, and D. E. Root, *Methods Enzymol.*, 1993, **226**, 1.
4. D. M. Dooley and M. A. McGuirl, *Inorg. Chim. Acta*, 1986, **123**, 231.
5. D. M. Dooley, *Life Chem. Rep.*, 1987, **5**, 91.
6. R. Lontie ed., 'Copper Proteins and Copper Enzymes', CRC Press, Boca Raton, FL, 1984, Vol. II.
7. J. Richardson, K. A. Thomas, B. H. Rubin, and D. C. Richardson, *Proc. Natl. Acad. Sci. U.S.A.*, 1975, **72**, 1349.
8. E. M. Fielden, P. B. Roberts, R. C. Bray, D. J. Lowe, G. N. Mautner, G. Rotilio, and L. Calabrese, *Biochem. J.*, 1974, **139**, 49.
9. E. M. Fielden and G. Rotilio, in 'Copper Proteins and Copper Enzymes', ed. R. Lonti, CRC Press, Boca Raton, FL, 1984, p. 27.
10. J. A. Fee and C. Bull, *J. Biol. Chem.*, 1986, **261**, 13000.
11. Y. Bourne, S. M. Redford, H. M. Steinman, J. R. Lepock, J. A. Tainer, and E. D. Getzoff, *Proc. Natl. Acad. Sci. U.S.A.*, 1996, **93**, 12774.
12. M. A. Hough and S. S. Hasnain, *J. Mol. Biol.*, 1999, **287**, 579.
13. J. A. Tainer, E. D. Getzoff, J. S. Richardson, and D. C. Richardson, *Nature*, 1983, **306**, 284.
14. M. W. Pantoliano, J. S. Valentine, A. R. Burger, and S. J. Lippard, *J. Inorg. Biochem.*, 1982, **17**, 325.
15. E. D. Getzoff, J. A. Tainer, P. K. Weiner, P. A. Kollman, J. S. Richardson, and D. C. Richardson, *Nature*, 1983, **306**, 287.
16. L. J. Hayward, J. A. Rodriguez, J. W. Kim, A. Tiwari, J. J. Goto, D. E. Cabelli, J. S. Valentine, and R. H. Brown Jr, *J. Biol. Chem.*, 2002, **277**, 15923.
17. J. S. Elam, K. Malek, J. A. Rodriguez, P. A. Doucette, A. B. Taylor, L. J. Hayward, D. E. Cabelli, J. S. Valentine, and P. J. Hart, *J. Biol. Chem.*, 2003, **278**, 21032.
18. S. Z. Potter and J. S. Valentine, *J. Biol. Inorg. Chem.*, 2003, **8**, 373.
19. J. S. Valentine and P. J. Hart, *Proc. Natl. Acad. Sci. U.S.A.*, 2003, **100**, 3617.
20. J. Valentine and M. W. Pantoliano, in 'Copper Proteins', ed. T. G. Spiro, Wiley, New York, 1981, p. 291.
21. J. J. Goto, H. Zhu, R. J. Sanchez, A. Nersissian, E. B. Gralla, J. S. Valentine, and D. E. Cabelli, *J. Biol. Chem.*, 2000, **275**, 1007.
22. J. P. Klinman, *Chem. Rev.*, 1996, **96**, 2541.
23. S. T. Prigge, R. E. Mains, B. A. Eipper, and L. M. Amzel, *Cell Mol. Life Sci.*, 2000, **57**, 1236.
24. J. S. Boswell, B. J. Reedy, R. Kulathila, D. Merkler, and N. J. Blackburn, *Biochemistry*, 1996, **35**, 12241.
25. D. J. Merkler, R. Kulathila, Y. S.D., J. Freeman, and J. J. Villafranca, in 'Bioinorganic Chemistry of Copper', eds. K. D. Karlin and Z. Tyeklar, Chapman & Hall, New York, 1993, p. 196.
26. W. A. Francisco, M. J. Knapp, N. J. Blackburn, and J. P. Klinman, *J. Am. Chem. Soc.*, 2002, **124**, 8194.
27. J. P. Evans, K. Ahn, and J. P. Klinman, *J. Biol. Chem.*, 2003, **278**, 49691.
28. S. T. Prigge, A. S. Kolhekar, B. A. Eipper, R. E. Mains, and L. M. Amzel, *Science*, 1997, **278**, 1300.

29. S. T. Prigge, A. S. Kolhekar, B. A. Eipper, R. E. Mains, and L. M. Amzel, *Nat. Struct. Biol.*, 1999, **6**, 976.
30. R. A. Scott, R. J. Sullivan, W. E. DeWolf, Jr, R. E. Dolle, and L. I. Kruse *Biochemistry*, 1988, **27**, 5411.
31. N. J. Blackburn, F. C. Rhames, M. Ralle, and S. Jaron, *J. Biol. Inorg. Chem.*, 2000, **5**, 341.
32. N. J. Blackburn, S. S. Hasnain, T. M. Pettingill, and R. W. Strange, *J. Biol. Chem.*, 1991, **266**, 23120.
33. S. Jaron, R. E. Mains, B. A. Eipper, and N. J. Blackburn, *Biochemistry*, 2002, **41**, 13274.
34. D. C. Rees, *Annu. Rev. Biochem.*, 2002, **71**, 221.
35. S. Jaron and N. J. Blackburn, *Biochemistry*, 1999, **38**, 15086.
36. J. Bell, R. El Meskini, D. D'Amato, R. E. Mains, and B. A. Eipper, *Biochemistry*, 2003, **42**, 7133.
37. W. A. Francisco, N. J. Blackburn, and J. P. Klinman, *Biochemistry*, 2003, **42**, 1813.
38. H. K. Hund, J. Breuer, F. Lingens, J. Huttermann, R. Kappl, and S. Fetzner, *Eur. J. Biochem.*, 1999, **263**, 871.
39. T. Oka, F. J. Simpson, J. J. Child, and C. Mills, *Can. J. Microbiol.*, 1971, **18**, 493.
40. F. Fusetti, K. H. Schroter, R. A. Steiner, P. I. van Noort, T. Pijning, H. J. Rozeboom, K. H. Kalk, M. R. Egmond, and B. W. Dijkstra, *Structure (Camb.)*, 2002, **10**, 259.
41. R. A. Steiner, W. Meyer-Klaucke, and B. W. Dijkstra, *Biochemistry*, 2002, **41**, 7963.
42. R. A. Steiner, K. H. Kalk, and B. W. Dijkstra, *Proc. Natl. Acad. Sci. U.S.A.*, 2002, **99**, 16625.
43. V. Anantharaman, L. Aravind, and E. V. Koonin, *Curr. Opin. Chem. Biol.*, 2003, **7**, 12.
44. B. Abolmaali, H. V. Taylor, and U. Weser, *Struct. Bonding*, 1998, **91**, 91.
45. I. M. Kooter, R. A. Steiner, B. W. Dijkstra, P. I. van Noort, M. R. Egmond, and M. Huber, *Eur. J. Biochem.*, 2002, **269**, 2971.
46. J. Peisach and W. E. Blumberg, *Arch. Biochem. Biophys.*, 1974, **165**, 691.
47. R. A. Steiner, I. M. Kooter, and B. W. Dijkstra, *Biochemistry*, 2002, **41**, 7955.
48. E. Balogh-Hergovich, J. Kaizer, G. Speier, G. Huttner, and A. Jacobi, *Inorg. Chem.*, 2000, **39**, 4224.
49. G. Speier, in 'Dioxygen Activation and Homogeneous Catalytic Oxidation', ed. L. I. Simandi, Elsevier, Amsterdam, 1991, p. 269.
50. M. S. Rogers and D. M. Dooley, *Adv. Protein Chem.*, 2001, **58**, 387.
51. J. W. Whittaker, *Adv. Protein Chem.*, 2002, **60**, 1.
52. J. W. Whittaker, *Chem. Rev.*, 2003, **103**, 2347.
53. M. S. Rogers and D. M. Dooley, *Curr. Opin. Chem. Biol.*, 2003, **7**, 189.
54. M. M. Whittaker and J. W. Whittaker, *J. Biol. Chem.*, 1988, **263**, 6074.
55. N. Ito, S. E. Phillips, K. D. Yadav, and P. F. Knowles, *J. Mol. Biol.*, 1994, **238**, 794.
56. N. Ito, S. E. Phillips, C. Stevens, Z. B. Ogel, M. J. McPherson, J. N. Keen, K. D. Yadav, and P. F. Knowles, *Nature*, 1991, **350**, 87.
57. C. Wright and A. G. Sykes, *J. Inorg. Biochem.*, 2001, **85**, 237.
58. C. G. Saysell, T. Barna, C. D. Borman, A. J. Baron, M. J. McPherson, and A. G. Sykes, *J. Biol. Inorg. Chem.*, 1997, **2**, 702.
59. P. F. Knowles, R. D. Brown III, S. H. Koenig, S. Wang, R. A. Scott, M. A. McGuirl, D. E. Brown, and D. M. Dooley *Inorg. Chem.*, 1995, **34**, 3895.
60. M. S. Rogers, A. J. Baron, M. J. McPherson, P. F. Knowles, and D. M. Dooley, *J. Am. Chem. Soc.*, 2000, **122**, 990.
61. M. M. Whittaker and J. W. Whittaker, *J. Biol. Chem.*, 2003, **278**, 22090.
62. S. J. Firbank, M. S. Rogers, C. M. Wilmot, D. M. Dooley, M. A. Halcrow, P. F. Knowles, M. J. McPherson, and S. E. Phillips, *Proc. Natl. Acad. Sci. U.S.A.*, 2001, **98**, 12932.
63. D. M. Dooley, *J. Biol. Inorg. Chem.*, 1999, **4**, 1.
64. J. Molnar, K. S. Fong, Q. P. He, K. Hayashi, Y. Kim, S. F. Fong, B. Fogelgren, K. M. Szauter, M. Mink, and K. Csiszar, *Biochim. Biophys. Acta*, 2003, **1647**, 220.
65. H. M. Kagan and W. Li, *J. Cell. Biochem.*, 2003, **88**, 660.
66. C. M. Wilmot, J. Hajdu, M. J. McPherson, P. F. Knowles, and S. E. Phillips, *Science*, 1999, **286**, 1724.
67. C. M. Wilmot, J. M. Murray, G. Alton, M. R. Parsons, M. A. Convery, V. Blakeley, A. S. Corner, M. M. Palcic, P. F. Knowles, M. J. McPherson, and S. E. Phillips, *Biochemistry*, 1997, **36**, 1608.
68. M. R. Parsons, M. A. Convery, C. M. Wilmot, K. D. Yadav, V. Blakeley, A. S. Corner, S. E. Phillips, M. J. McPherson, and P. F. Knowles PF, *Structure*, 1995, **3**, 1171.
69. M. C. Wilce, D. M. Dooley, H. C. Freeman, J. M. Guss, H. Matsunami, W. S. McIntire, C. E. Ruggiero, K. Tanizawa, and H. Yamaguchi, *Biochemistry*, 1997, **36**, 16116.
70. R. Li, J. P. Klinman, and F. S. Mathews, *Structure*, 1998, **6**, 293.
71. A. P. Duff, A. E. Cohen, P. J. Ellis, J. A. Kuchar, D. B. Langley, E. M. Shepard, D. M. Dooley, H. C. Freeman, and J. M. Guss, *Biochemistry*, 2003, **42**, 15148.
72. V. Kumar, D. M. Dooley, H. C. Freeman, J. M. Guss, I. Harvey, M. A. McGuirl, M. C. Wilce, and V. M. Zubak, *Structure*, 1996, **4**, 943.
73. B. O. Elmore, J. A. Bollinger, and D. M. Dooley, *J. Biol. Inorg. Chem.*, 2002, **7**, 565.
74. J. M. Murray, C. G. Saysell, C. M. Wilmot, W. S. Tambyrajah, J. Jaeger, P. F. Knowles, S. E. Phillips, and M. J. McPherson, *Biochemistry*, 1999, **38**, 8217.
75. C. G. Saysell, W. S. Tambyrajah, J. M. Murray, C. M. Wilmot, J. S. E. Phillips, M. J. McPherson, and P. F. Knowles, *Biochem. J.*, 2002, **365**, 809.

76. Z. Chen, B. Schwartz, N. K. Williams, R. Li, J. P. Klinman, and F. S. Mathews, *Biochemistry*, 2000, **39**, 9709.
77. S. Kishishita, T. Okajima, M. Kim, H. Yamaguchi, S. Hirota, S. Suzuki, S. Kuroda, K. Tanizawa, and M. Mure, *J. Am. Chem. Soc.*, 2003, **125**, 1041.
78. J. P. Klinman, *Biochim. Biophys. Acta*, 2003, **1647**, 131.
79. Y. Goto and J. P. Klinman, *Biochemistry*, 2002, **41**, 13637.
80. S. A. Mills, Y. Goto, Q. Su, J. Plastino, and J. P. Klinman, *Biochemistry*, 2002, **41**, 10577.
81. C. E. Ruggiero and D. M. Dooley, *Biochemistry*, 1999, **38**, 2892.
82. M. Kim, T. Okajima, S. Kishishita, M. Yoshimura, A. Kawamori, K. Tanizawa, and H. Yamaguchi, *Nat. Struct. Biol.*, 2002, **9**, 591.
83. E. L. Green, N. Nakamura, D. M. Dooley, J. P. Klinman, and J. Sanders-Loehr, *Biochemistry*, 2002, **41**, 687.
84. N. M. Okeley and W. A. van der Donk, *Chem. Biol.*, 2000, **7**, R159.

Copper Enzymes in Denitrification

David M. Dooley & Jeannine M. Chan
Montana State University, Bozeman, MT, USA

1 Introduction 1
2 Nitrite Reductase 3
3 Nitrous Oxide Reductase 6
4 Related Articles 9
5 References 9

1 INTRODUCTION

Denitrification was identified as an important biochemical process over 100 years ago.[1] It is now recognized as a critical component of the global nitrogen cycle,[2] illustrated in Figure 1, and is the critical pathway for balancing the cycle, returning fixed nitrogen to the atmosphere.[3] The elucidation of denitrification at the molecular level is therefore essential to a comprehensive understanding of nitrogen metabolism. As stated concisely by Zumft,[4] 'Denitrification is a bacterial respiratory process that couples electron-transport phosphorylation to the stepwise, sequential reduction of nitrogenous oxides.' Strictly speaking, denitrification is characterized by growth on nitrate (NO_3^-) or nitrite (NO_2^-) with the concomitant evolution of NO, N_2O, or N_2 (*see* ***Nitrogen Monoxide (Nitric Oxide): Bioinorganic Chemistry***; ***Nitrogen: Inorganic Chemistry***). The central roles of nitrate and nitrite in the global nitrogen cycle are apparent in Figure 1. Note that both nitrate and nitrite are common to the denitrification *and* assimilation pathways, suggesting that enzymes controlling the metabolic fates of these compounds will be key points for regulation.[1] The ecology of nitrogen fixation, assimilation, and denitrification substantially impacts agricultural productivity and water quality.[1] Denitrification by soil bacteria leads to major losses of fertilizer nitrogen.[1,5] Yet, a benefit of denitrification may be its use to remove nitrates and nitrites from water supplies and industrial gas emissions.[6–8] Partial denitrification releases N_2O to the atmosphere, contributing to ozone depletion and global warming.[5] Denitrification can be viewed as composed of three somewhat independent components: nitrate respiration, nitrite respiration, and nitrous oxide respiration. Table 1 summarizes the reactions associated with denitrification. Complete denitrification is represented by (e) in Table 1, but the various partial reactions are also observed, as noted above.

Metalloenzymes have prominent roles in all of the redox reactions of denitrification (Figure 2, *see* ***Molybdenum: MPT-containing Enzymes***; ***Multi-Heme Cytochromes & Enzymes***; ***Iron: Inorganic & Coordination Chemistry***; ***Iron Proteins with Dinuclear Active Sites*** for information on the other types of metalloproteins).[9–11] Indeed, as an energy-conserving metabolic pathway, denitrification presents an extremely broad range of interesting issues in metallobiochemistry. This chapter focuses on the structures, mechanisms, and assembly of copper-containing nitrite reductases and nitrous oxide reductases. Nitrite reductases characterized to date are either copper enzymes or belong to the cytochrome cd_1 class.[1,2,4,9–11] Nitrous oxide reductases are generally multicopper enzymes, although the enzyme from *Wolinella succinogenes* is reported to contain a heme *c* center in addition to copper.[12] Nitrite reductases and nitrous oxide reductases have long been recognized as possessing unusual, even unique, spectroscopic properties. Both these enzymes are central to the denitrification pathway of soil and marine bacteria. Nitrite reductases contain a classic blue (Type 1, *see* ***Copper Proteins: Oxidases***) copper center and also contain a Type 2 copper site (*see* ***Copper Proteins with Type 2 Sites***). Nitrous oxide reductases have been shown to contain two unusual types of copper center, one of which is identical to the Cu_A center of cytochrome *c* oxidase (*see* ***Cyanide Complexes of the Transition Metals***). Elucidating and elaborating structure/function relationships for nitrite reductases and nitrous oxide reductases have been greatly aided by the availability of multiple crystal structures for these enzymes. In addition, fairly detailed descriptions of the electronic structures of the copper sites have been developed from extensive spectroscopic and computational studies.

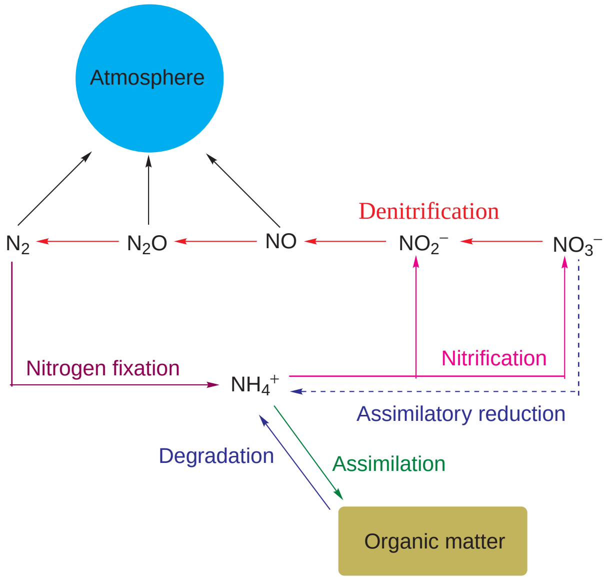

Figure 1 The global nitrogen cycle

Table 1 Redox conversions of nitrogenous oxides during denitrification

Type of reaction	Number of electrons	Formal valence change	E'_0 (mV)[a]	$\Delta G'_0$ (kJ mol^{-1})[b]
(a) Nitrate respiration				
$NO_3^- + [H_2] \longrightarrow NO_2^- + H_2O$	2	+5/+3	+420	−161.1
(b) Nitrite respiration				
$2NO_2^- + 2H^+ + 2[H_2] \longrightarrow N_2O(g) + 3H_2O$	4	+3/+1	+777	−459.2
(c) Nitrous oxide respiration				
$N_2O(g) + [H_2] \longrightarrow N_2(g) + H_2O$	2	+1/0	+1352	−339.5
(d) Nitrate respiration combined with nitrite respiration				
$NO_3^- + 2H^+ + 4[H_2] \longrightarrow N_2O(g) + 5H_2O$	8	+5/+1	+599	−781.9
(e) Nitrate respiration combined with nitrite and nitrous oxide respiration				
$2NO_3^- + 2H^+ + 5[H_2] \longrightarrow N_2(g) + 6H_2O$	10	+5/0	+749	−1121.2
(f) Nitrite respiration combined with nitrous oxide respiration				
$2NO_2^- + 2H^+ + 3[H_2] \longrightarrow N_2(g) + 4H_2O$	6	+3/0	+970	−799.9
(g) Nitric oxide formation and reduction				
$NO_2^- + 0.5[H_2] + H^+ \longrightarrow NO(g) + H_2O$	1	+3/+2	+374	−76.2
$2NO(g) + [H_2] \longrightarrow N_2O(g) + H_2O$	2	+2/+1	+1177	−306.3

[a] These values are for pH 7.0. E'_0 refers to the nitrogenous pair. [b] $\Delta G'_0$ values calculated versus the pair $H_2/2H^+$.

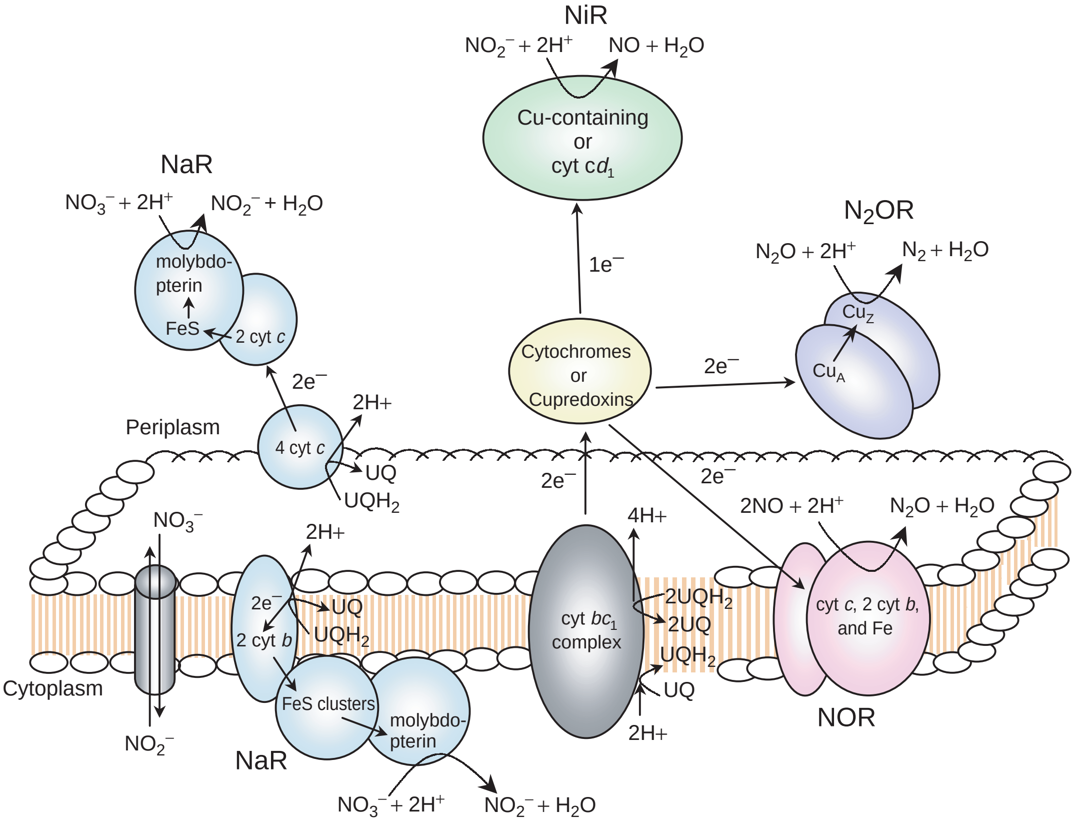
NiR
NO2− + 2H+
NO + H2O
Cu-containing or cyt cd1
NaR
NO3− + 2H+
NO2− + H2O
molybdo-pterin
FeS
2 cyt c
1e−
N2OR
N2O + 2H+
N2 + H2O
CuZ
CuA
Cytochromes or Cupredoxins
2e−
2e−
2H+
Periplasm
4 cyt c
UQ
UQH2
2e−
2e−
NO3−
2H+
4H+
2NO + 2H+
N2O + H2O
2e−
UQ
2 cyt b
UQH2
cyt bc1 complex
2UQH2
2UQ
UQH2
cyt c, 2 cyt b, and Fe
UQ
Cytoplasm
FeS clusters
molybdo-pterin
2H+
NOR
NO2−
NaR
NO3− + 2H+
NO2− + H2O

Figure 2 The dissimilatory denitrification pathway. NO_3^- is reduced to NO_2^- by a membrane-bound or periplasmic nitrate reductase(NaR). NO_2^- is reduced to NO by either a cytochrome cd_1 or copper nitrite reductase (NiR). NO is reduced to N_2O by nitric oxide reductase (NOR). N_2O is reduced to N_2 by nitrous oxide reductase (N_2OR). Electron transport from ubiquinol (UQH_2) at NaR and the cyt bc_1 complex is coupled to generation of a proton gradient

2 NITRITE REDUCTASE

Copper-containing nitrite reductases [E.C. 1.7.2.1] have been highly purified from several organisms, including, *Alcaligenes xylosoxidans*, *Alcaligenes faecalis* S-6, *Pseudomonas aureofaciens*[1,2,4,9–11] and *Haloferax denitrificans*, the first example from an Archeon.[13] Crystal structures have been determined for multiple forms of the first three enzymes.[14–21] Although there are significant variations in some of their reported properties, copper nitrite reductases appear to be trimers of identical subunits and to contain one Type 1 copper per subunit. Interestingly, some nitrite reductases are green in color, in marked contrast to the distinctive blue color of the classic Type 1 copper center. Figure 3 illustrates the electronic spectral differences between the Type 1 center of 'green' nitrite reductases and the canonical features of plastocyanin. The distinctive 480-nm band of the 'green' nitrite reductase results from the pseudo σ Cys(S) $\rightarrow$ Cu^{II} ligand-to-metal charge-transfer band gaining intensity from a distortion in the nitrite reductase site relative to the plastocyanin site.[22] This distortion is a result of the shorter Cu–S(Met) bond, which increases the ligand field strength (*see* ***Ligand Field Theory & Spectra***) and changes the orientation of the $d_{x^2-y^2}$ orbital such that the pseudo σ interaction with the S(Cys) is enhanced. A similar conclusion, based on analysis of resonance Raman spectra, was reached by Sanders-Loehr and coworkers.[23] The structurally characterized enzymes also contain a Type 2 copper site, which serves as the substrate binding site and is required for catalytic activity.[15–17,19,20,24–26] *Achromobacter cycloclastes* nitrite reductase was the first nitrite reductase to be structurally characterized (at 2.3 Å resolution).[14] A schematic view of the structure is shown in Figure 4; the protein crystallizes as a trimer (α_3) with the three subunits arranged in a head-to-tail arrangement around the crystallographic threefold axis. This structural motif is also observed in the other structures.[14–21] Each monomeric unit is composed of two domains each with a Greek key type of β-sheet topology. A Type 1 copper site is located in the amino-terminal domain. A second copper site is located at the interface between subunits in the trimer and is ligated by two histidine imidazoles from one molecule and a histidine imidazole of another molecule (Figure 4). Thus this copper site helps to stabilize the trimeric structure, in addition to the numerous amino acid contacts in the interfacial regions. The coordinated Cys in the Type 1 site and a His residue in the second site are adjacent, such that the two copper ions are separated by about 12.5 Å, a structural arrangement that is very similar to that seen in ascorbate oxidase and other multicopper oxidases (*see* ***Copper Proteins with Dinuclear Active Sites***). An especially interesting result from the crystallographic analysis is the structure of the Type 2 copper site (Figure 5). This Cu^{II} is coordinated by three histidine imidazoles and a solvent-derived ligand,

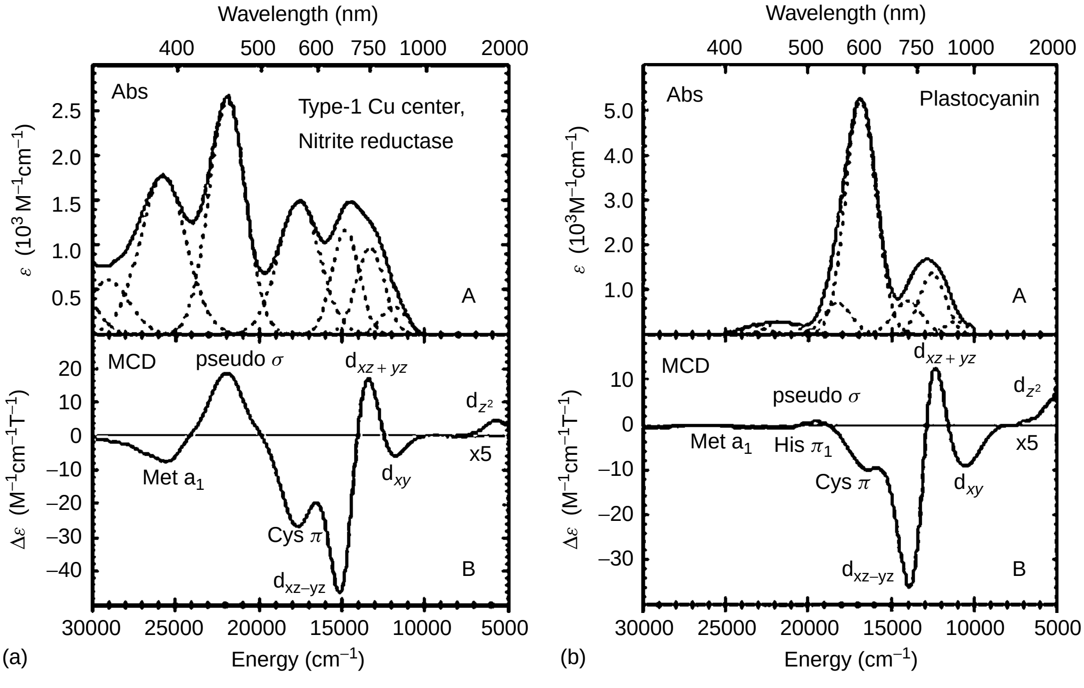

Figure 3 Electronic absorption (A) and magnetic circular dichroism (B) spectra of the Type 1 Cu site of *Achromobacter cycloclastes* nitrite reductase (a) and spinach plastocyanin (b). Absorption data were obtained at 120 K for nitrite reductase and at 25 K for plastocyanin. MCD spectra were obtained at 4.2 K. Gaussian resolution of bands in the absorption spectra is based on a simultaneous linear least-squares fit of Abs, MCD, and CD data for each. MCD data from 5000 to 8000 cm^{-1} have been multiplied by a factor of 5. (Reprinted with permission from Ref. 22. © 1996 American Chemical Society)

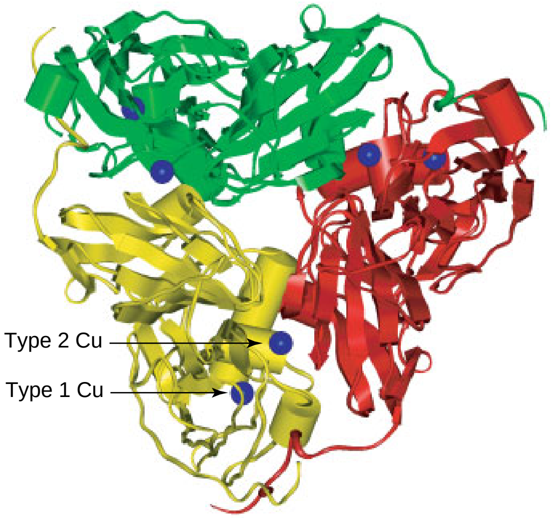

Figure 4 X-ray crystal structure of oxidized copper-containing nitrite reductase from *Alcaligenes faecalis* at 2.0 Å resolution. Coordinates are from PDB entry 1AS7[17]

which is certainly a Type 2 ligand-donor set, but the geometry is distorted towards tetrahedral. Nevertheless, the Type 2 EPR signals associated with *Achromobacter* and other nitrite reductases are consistent with a $d_{x^2-y^2}$ ground state. Note that a fourth histidine is near but not coordinated to the 'Type 2' copper; this residue appears to influence nitrite binding to Cu^{II} via a hydrogen-bonding network in the active site (Figure 5).[24] Both crystallographic and spectroscopic results established that nitrite binds to the Type 2 copper,[15,17,19,27–29] displacing the solvent-derived ligand. Multiple structures of nitrite complexes of nitrite reductases have revealed bidentate O(2) coordination of nitrite, or in a few cases, monodentate O-coordination.[24] In no case has N-ligated nitrite been observed, but it has been pointed out that Cu^{II} complexes of nitrite are generally O-ligated, whereas Cu^{I} may prefer N-coordination with nitrite.[28] (*see* ***Copper: Hemocyanin/Tyrosinase Models*** for a discussion of copper coordination chemistry). Bound nitrite forms a hydrogen bond with an active site aspartic acid residue, which is also connected to the fourth histidine (see above) through H-bonds with a solvent molecule. The H-bond between coordinated nitrite and the aspartic acid residue is believed to be critical for catalysis.[24–27]

Nitrite reductases catalyze both of the reactions below; the physiological electron donors are either *c*-type cytochromes or small blue-copper proteins (equations 1 and 2).[10,11,28] The Type 1 center acts as an electron-accepting site, which then transfers the electron to the Type 2 copper where substrate binding and reduction occur.

$$NO_2^- + e^- + 2H^+ \longrightarrow NO + H_2O \qquad (1)$$

$$2NO_2^- + 4e^- + 6H^+ \longrightarrow N_2O + 3H_2O \qquad (2)$$

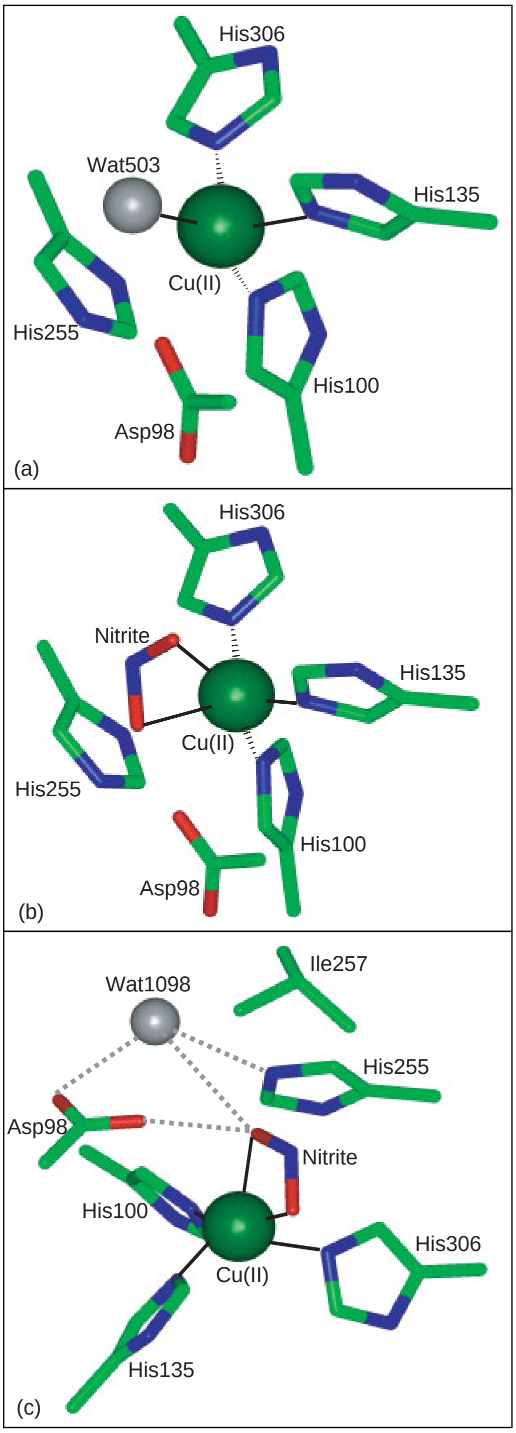

Figure 5 X-ray crystal structures of the Type 2 copper active site of nitrite reductase from *Alcaligenes faecalis* (a) oxidized and (b) nitrite-soaked. Panel (c) is a rotated view of (b) and shows the hydrogen-bonding network. Coordinates are from PDB entries 1AS7 and 1AS6[17]

The capability of nitrite reductases to catalyze both reactions initially raised the obvious question of which reaction occurred in vivo and whether NO was an obligatory intermediate in the denitrification pathway. It is now generally agreed that nitrite reduction in most organisms proceeds stepwise with NO as an intermediate.[28–30] Mechanistic studies are consistent with the blue-copper center serving an electron-transfer function, as expected. An excellent electron-transfer pathway exists between the cysteine ligand of the Type 1 site and the His ligand of the Type 2 site (see above and ***Long-range Electron Transfer in Biology*** and ***Copper Proteins with Dinuclear Active Sites***). Proposed mechanisms for nitrite reduction, based on the structural results as well as kinetics studies of the enzymes, are shown in Figure 6. These mechanistic proposals are based on results from steady-state

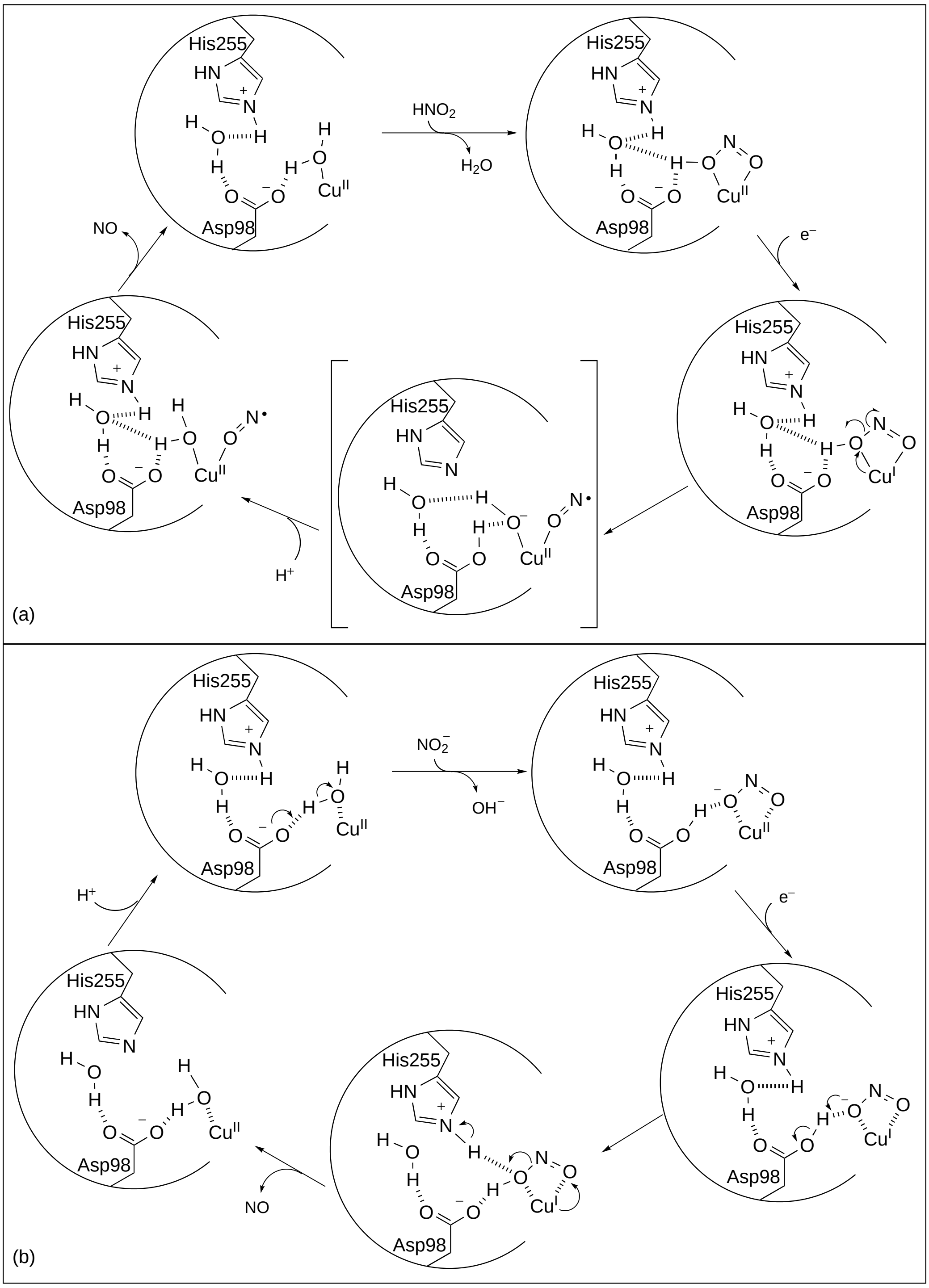

Figure 6 Proposed mechanisms for copper-containing nitrite reductase (a) via an O-bonded nitrosyl[25] or (b) a bound HONO intermediate[30]

and stopped-flow kinetics, pH effects, and the characteristics of enzyme variants produced by site-directed mutagenesis. Note that one mechanism (a) invokes an O-bonded nitrosyl, whereas b postulates a bound HONO intermediate. It should be noted however that the existing data do not completely rule out a Cu^I–NO^+ species as an intermediate, although no direct evidence for such an intermediate is available. A Cu^I nitrosyl intermediate would be analogous to the ferrous–nitrosyl intermediate established for the cytochrome cd_1 nitrite reductases and is well precedented in model copper chemistry.**[28]** Indirect evidence for a Cu^I–NO^+ species as an intermediate in nitrite reduction has been presented.**[31,32]** Further experiments are clearly required to establish the identity of the key intermediates in turnover.

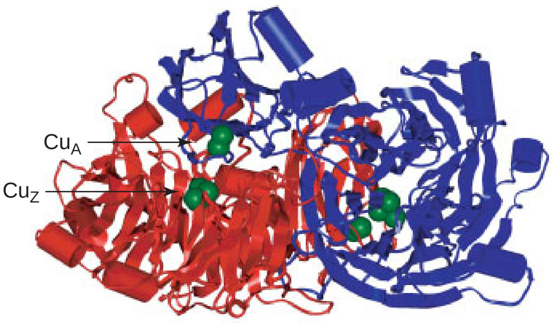

Figure 7 X-ray crystal structure of N_2O reductase from *Paracoccus denitrificans* at 1.6 Å resolution. Coordinates are from PDB entry 1FWX**[50]**

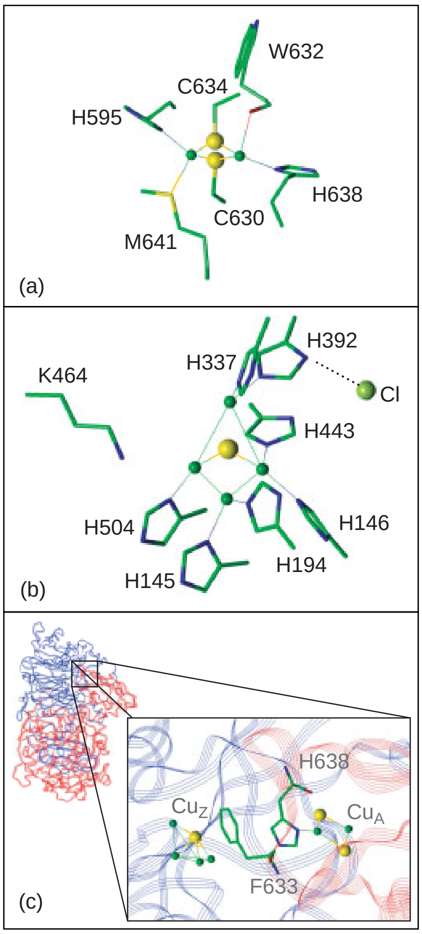

Figure 8 X-ray crystal structure of *Paracoccus denitrificans* N_2O reductase showing (a) the Cu_A site, (b) the Cu_Z site, and (c) the proposed electron-transfer path between the copper sites. Coordinates are from PDB entry 1FWX**[50]**

3 NITROUS OXIDE REDUCTASE

Nitrous oxide reductase [E.C. 1.7.99.6] catalyzes the two-electron reduction of N_2O to N_2 (equation 3).

$$N_2O + 2e^- + 2H^+ \longrightarrow N_2 + H_2O \tag{3}$$

This is a remarkable reaction because the transition metal chemistry of N_2O is sparse, especially with copper. Most N_2O reductases are soluble, periplasmic homodimers; however, there are examples of membrane-associated enzymes.**[33,34]** The best characterized N_2O reductases are from *Paracoccus denitrificans*, *Pseudomonas nautica*, and *Pseudomonas stutzeri*, and most of the information presented here is derived from experiments on these enzymes. Where comparable data are available, N_2O reductases from various organisms appear to be fairly similar, with the exception of the enzyme from *Wolinella succinogenes*,**[12]** as noted above. The crystal structures of N_2O reductase from *P. nautica*,**[35]** and more recently from *P. denitrificans*,**[36]** show two distinct copper clusters per subunit: a bis-thiolate bridged dinuclear electron-transfer site (Cu_A), which is analogous to the Cu_A site in cytochrome *c* oxidase (*see* ***Cyanide Complexes of the Transition Metals***),**[37–43]** and a novel four-copper cluster ligated by seven histidines, the catalytic copper site (Cu_Z), where N_2O is thought to bind and be reduced.**[44–46]** Cu_Z was proposed to be a copper-histidine cluster on the basis of the presence of nine strictly conserved histidine residues,**[47]** and this was supported by a ^1H NMR study that identified two non-Cu_A associated resonances that were assigned as copper-histidine N–H protons.**[48]**

The crystal structure of the *P. denitrificans* N_2O reductase (Figures 7 and 8) established that each monomer consists of an N-terminal, seven-bladed β-propeller fold containing the Cu_Z center and a C-terminal cupredoxin fold containing the Cu_A center.**[36]** The dimer exhibits domain sharing, with the Cu_A site from one monomer interacting with the Cu_Z site from the other monomer. Several intersubunit contacts between Cu_A and Cu_Z ligands have been identified and are thought to provide a pathway for electron transfer. F633 is conserved and located at the dimer interface; it is postulated to be involved in the

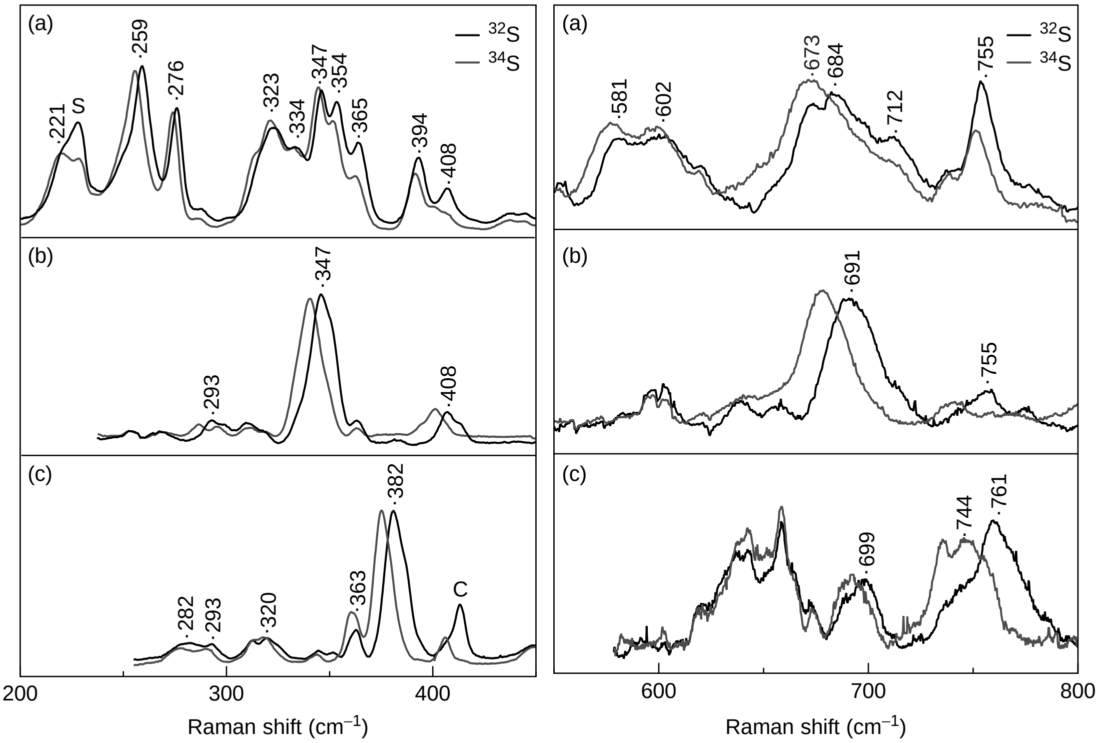

Figure 9 Sulfur isotope dependence of resonance Raman vibrational frequencies for (a) the [Cu(1.5)•Cu(1.5)] mixed-valence Cu_A site, obtained with 488-nm excitation; (b) the [2Cu(I)2Cu(II)] Cu_Z site in semireduced N_2O reductase, obtained with 568-nm excitation; and (c) the dithionite-reduced Cu_Z site, obtained with 647-nm excitation. S denotes 230-cm^{-1} ice mode from frozen solvent. C denotes a band believed to arise from an altered Cu_A site. (Reprinted with permission from M.L. Alvarez, J. Ai, W.G. Zumft, J. Sanders-Loehr, and D.M. Dooley, *J. Am. Chem. Soc.*, 2001, **123**, 476. © 2001 American Chemical Society)

intramolecular electron transfer.[35,36] Additionally, there is a Cl^- ion bound near the Cu_Z center (Figure 8(b)) and two Ca^{2+} ions lie near the dimer interface. Sulfide analysis of native and mutant forms of N_2O reductase, as well as the observation of sulfur isotope shifts in the resonance Raman of N_2O reductase (Figure 9), revealed the presence of inorganic sulfide as the bridging ligand in the Cu_Z center.[49] The recent crystal structure of N_2O reductase from *P. denitrificans*,[36,50] spectroscopic data, and chemical analysis has confirmed the structure of Cu_Z as a μ_4-sulfide bridged tetranuclear Cu center (Figures 8 and 10).[35,49,51] Variable-temperature, variable-field MCD, Q-band EPR, X-ray absorption spectroscopy (XAS), and density functional theory calculations (DFT) showed that the Cu_Z center in the dithionite-reduced enzyme from *P. nautica* is in an $S = 1/2$ state with 3Cu(I)/1Cu(II).[51,52] The DFT calculations predict a delocalized wave function with ~40% of the spin density found on Cu1 (the oxidized Cu). The μ_4-bridging sulfur forms significant σ-bonding interactions with Cu1 and Cu2, allowing the latter to hold 14% of the spin density and contributing to significant delocalization of the unpaired electron.[51] Two variants of the Cu_Z center identified as Cu_Z and $Cu_Z{}^*$ have been characterized from *Paracoccus pantotrophus*. While the variants have distinct spectral properties, they appear to share the same basic Cu_4S structure.[53] Spectroscopic

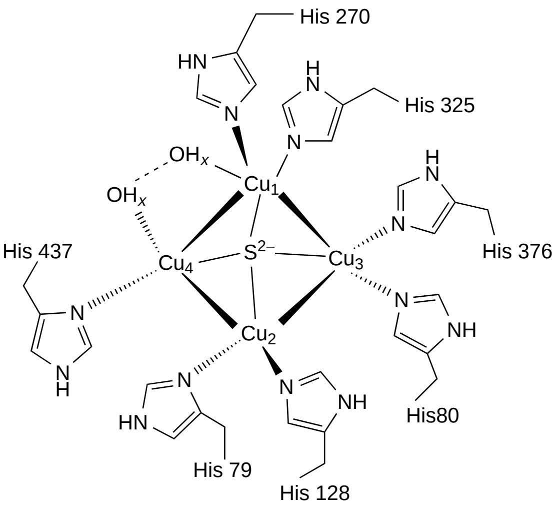

Figure 10 Model of the Cu_Z site in N_2O reductase. (Reprinted with permission from M.L. Alvarez, J. Ai, W.G. Zumft, J. Sanders-Loehr, and D.M. Dooley, *J. Am. Chem. Soc.*, 2001, **123**, 476. © 2001 American Chemical Society)

studies in conjunction with molecular orbital calculations have produced a detailed description of the electronic structure of the [Cu(1.5)•Cu(1.5)] mixed-valence Cu_A site.[54–57] The structure of the Cu_A site is exquisitely designed for its electron-transfer role.[47,54,58–65] Pronounced covalency and electronic delocalization are characteristic of the Cu_2S_2 unit and may influence or dictate both the redox potential and the electron-transfer pathway.[56,57] Detailed analysis of the ground-state wave function of Cu_A by XAS has provided important implications for electron transfer in model systems.[66]

It is reported that approximately 50 genes are required for bacterial denitrification.[67] Their arrangement and location are organism specific, although typically the structural genes for the four key reductases are organized in clusters containing the necessary genes for regulation, cofactor assembly, and protein maturation.[10,68] (*see* ***Metallocenter Biosynthesis & Assembly*** and ***Metallochaperones & Metal Ion Homeostasis*** for general information on these topics.) The organization of the *nos* (N_2O reductase) cluster is illustrated in Figure 11, along with a schematic representation of mature protein localization. The *nos* cluster is composed of four transcriptional units, *nosR, nosZ, nosDFYL*, and *nosX*. Full sequence data for the *nosRZDFYL* clusters of *P. denitrificans*,[69] *Pseudomonas stutzeri*,[70] *Achromobacter cycloclastes*,[71] *Sinorhizobium meliloti*,[72] and *Bradyrhizobium japonicum*[73] are available. *nosR* is located upstream of the N_2O reductase structural gene, *nosZ*, and codes for a regulatory protein with two C-terminal Cys clusters similar to [4Fe-4S] binding motifs of bacterial ferredoxins (*see* ***Iron–Sulfur Proteins***). Another potential metal binding site in NosR, consisting of two CXXXCP motifs, has been identified.[71,74] *nosDFYL* contains genes for proper copper insertion or metal-cluster assembly.[70] *nosX* is located in the *nos* cluster in *S. meliloti*, *P. denitrificans*, *B. japonicum*, and *A. cycloclastes*, but is absent in *P. stutzeri* (but may be located elsewhere). Preliminary data indicate that *nosX* is required for denitrification, but its function is uncertain.[75] NosX may be involved in transcriptional regulation[75] or in the formation of the Cu_A center of N_2O reductase.[76] Transcription of the operon *nosDFYL* (Figure 11) is obligatory for the production of enzymatically active N_2O reductase[70,77] and is likely to contain the genes necessary for Cu_Z biosynthesis.[70] Preliminary characteristics of NosD, F, Y, and L have been deduced from their translated sequences and provide useful clues into their functions. NosD may be a chaperone that keeps apo N_2O reductase in a conformation amenable to copper insertions,[70] or might directly assist in copper cluster assembly. Analysis of NosD sequences has revealed the presence of two CASH (carbohydrate binding protein and sugar hydrolase) domains.[78] Additionally, the C-terminal portion of Nos D (residues 210–440) is 50% similar to NosX. NosF has sequence homology to the family of nucleotide-binding proteins of the ABC transporters and contains an ATP/GTP-binding motif.[79] A maltose binding protein, NosF fusion protein, was shown to have ATPase activity, suggesting that Cu_Z assembly involves an energy-requiring step.[80] NosY appears to be an integral membrane protein of unknown function,[71] perhaps involved in transport. NosL is a Cu(I) protein that may function as a metallochaperone (*see* ***Metallochaperones & Metal Ion Homeostasis***), providing a source of copper under limiting conditions and/or conferring metal specificity to the bioassembly process.[81] NosL has been expressed and characterized and has been shown to specifically bind Cu(I) in a 1:1 stoichiometry (Figure 12).[81] *nosD,F,Y,L* have similarities to ABC transporter families. The nucleotide-binding protein in these systems is found in the cytoplasm like NosF, with a transmembrane protein like NosY, and 1–2 periplasmic components like NosD/L. Results from transposon mutagenesis experiments in *Pseudomonas stutzeri* and reconstitution experiments in the nondenitrifier *Pseudomonas putida* indicated NosD, NosF, and NosY were required to produce functional N_2O reductase,[70,77,82] whereas NosL was not.[80] Copper chaperones are known to be involved in the insertion of copper into several proteins, and this has been suggested to be a general phenomenon

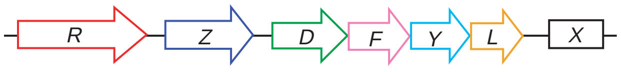

(a) *P. denitrificans*, *A. cycloclastes nos* cluster

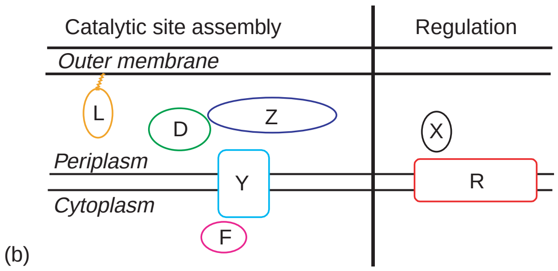

Figure 11 (a) The organization of the *nos* cluster from *Achromobacter cycloclastes* and *Paracoccus denitrificans*. (b) The predicted locations of Nos proteins

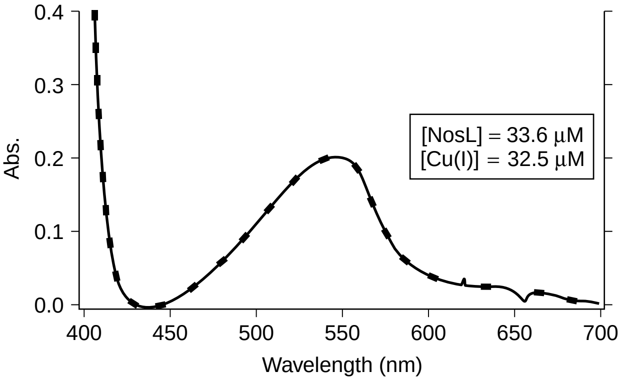

Figure 12 Reaction of NosL, anaerobically stored, with the Cu(I)-selective reagent 2,2′-biquinoline, which forms a purple complex with Cu(I) that absorbs at 546 nm; (dashed line) protein as isolated, (solid line) protein reduced with ascorbate. (Ref. 81. Reproduced by permission of Springer Verlag)

for cytoplasmic or mitochondrial proteins,[83] but may not be absolutely required for periplasmic proteins. In this context it has been suggested that the *nosDFY* ABC transporter system facilitates sulfur transfer from the cytoplasm to the Cu_Z center, with copper provided by NosL.[77] The discovery that several metalloproteins require other proteins for metal-site assembly or proper protein folding, or both, has opened an interesting and important area of research in metallobiochemistry.[81]

4 RELATED ARTICLES

Copper Proteins: Oxidases; Copper Proteins with Dinuclear Active Sites; Cyanide Complexes of the Transition Metals; Iron: Inorganic & Coordination Chemistry; Iron Proteins with Dinuclear Active Sites; Long-range Electron Transfer in Biology; Metallocenter Biosynthesis & Assembly; Metallochaperones & Metal Ion Homeostasis; Molybdenum: MPT-containing Enzymes; Multi-Heme Cytochromes & Enzymes; Nitrogen: Inorganic Chemistry; Nitrogen Monoxide (Nitric Oxide): Bioinorganic Chemistry.

5 REFERENCES

1. W. J. Payne, ‘Denitrification’, John Wiley & Sons, New York, 1981.
2. W. G. Zumft, A. Viebrock, and H. Körner, Biochemical and Physiological Aspects of Denitrification, in ‘The Nitrogen and Sulphur Cycles’, eds. J. A. Cole and S. J. Ferguson, Cambridge University Press, Cambridge, 1988, p. 245.
3. S. J. N. Burgmayer and E. I. Stiefel, *J. Chem. Educ.*, 1985, **62**, 943.
4. W. G. Zumft, The Denitrifying Prokaryotes, in ‘The Prokaryotes’, 2nd edn., eds. A. Balows, H. G. Trüper, M. Dworkin, W. Harder, and K.-H. Schleifer, Springer-Verlag, New York, 1992, p. 554.
5. A. R. Mosier and D. S. Schimel, *Chem. Ind. London*, 1991, **23**, 874.
6. W. T. Potter, U. Le, S. Ronda, J.-G. Cho, R. Shanmugasundram, A. Chirkis, and K. L. Sublette, *Appl. Biochem. Biotechnol.*, 1995, **51–52**, 771.
7. S. Cizinska, V. Mateju, J. Krejci, T. Janoch, and E. Kyslikova, *J. Chem. Technol. Biotechnol.*, 1992, **55**, 33.
8. M. H. Thiemens and W. C. Trogler, *Science*, 1991, **251**, 932.
9. L. I. Hochstein and G. A. Tomlinson, *Annu. Rev. Microbiol.*, 1988, **42**, 231.
10. B. C. Berks, S. J. Ferguson, J. W. B. Moir, and D. J. Richardson, *Biochim. Biophys. Acta*, 1995, **1232**, 97.
11. D. J. Richardson and N. J. Watmough, *Curr. Opin. Chem. Biol.*, 1999, **3**, 207.
12. S. Teraguchi and T. C. Hollocher, *J. Biol. Chem.*, 1989, **264**, 1972.
13. K. Inatomi and L. I. Hochstein, *Curr. Microbiol.*, 1996, **32**, 72.
14. J. W. Godden, S. Turley, D. C. Teller, E. T. Adman, M. Y. Liu, W. J. Payne, and J. LeGall, *Science*, 1991, **253**, 438.
15. M. Kukimoto, M. Nishiyama, M. E. Murphy, S. Turley, E. T. Adman, S. Horinouchi, and T. Beppu, *Biochemistry*, 1994, **33**, 5246.
16. M. E. Murphy, S. Turley, M. Kukimoto, M. Nishiyama, S. Horinouchi, H. Sasaki, M. Tanokura, and E. T. Adman, *Biochemistry*, 1995, **34**, 12107.
17. M. E. Murphy, S. Turley, and E. T. Adman, *J. Biol. Chem.*, 1997, **272**, 28455.
18. R. W. Strange, F. E. Dodd, Z. H. L. Abraham, J. G. Grossman, T. Bruser, R. R. Eady, B. E. Smith, and S. S. Hasnain, *Nature Struct. Biol.*, 1995, **2**, 287.
19. F. E. Dodd, J. Van Beeumen, R. R. Eady, and S. S. Hasnain, *J. Mol. Biol.*, 1998, **282**, 369.
20. R. W. Strange, L. M. Murphy, F. E. Dodd, Z. H. L. Abraham, R. R. Eady, B. E. Smith, and S. S. Hasnain, *J. Mol. Biol.*, 1999, **287**, 1001.
21. T. Inoue, M. Gotowda, M. Kataoka, K. Yamaguchi, S. Suzuki, H. Watanabe, M. Gohow, and Y. Kai, *J. Biochem.*, 1998, **124**, 876.
22. L. B. LaCroix, S. E. Shadle, Y. Wang, B. A. Averill, B. Hedman, K. O. Hodgson, and E. I. Solomon, *J. Am. Chem. Soc.*, 1996, **118**, 7755.
23. C. R. Andrew and J. Sanders-Loehr, *Acc. Chem. Res.*, 1996, **29**, 365.
24. M. J. Boulanger and M. E. P. Murphy, *Protein Sci.*, 2003, **12**, 248.
25. M. J. Boulanger and M. E. P. Murphy, *Biochemistry*, 2001, **40**, 9132.
26. M. J. Boulanger, M. Kukimoto, M. Nishiyama, S. Horinouchi, and M. E. P. Murphy, *J. Biol. Chem.*, 2000, **275**, 23957.
27. K. Kataoka, H. Furusawa, K. Yamaguchi, and S. Suzuki, *J. Biochem.*, 2000, **127**, 345.
28. B. A. Averill, *Chem. Rev.*, 1996, **96**, 2951.
29. S. Suzuki, K. Kataoka, K. Yamaguchi, T. Inoue, and Y. Kai, *Coord. Chem. Rev.*, 1999, **190**, 245.
30. S. Suzuki, K. Kataoka, and K. Yamaguchi, *Acc. Chem. Res.*, 2000, **33**, 728.
31. C. L. Hulse, B. A. Averill, and J. M. Tiedje, *J. Am. Chem. Soc.*, 1989, **111**, 2322.
32. M. A. Jackson, J. M. Tiedje, and B. A. Averill, *FEBS Lett.*, 1991, **291**, 41.
33. A. M. Jones, T. C. Hollocher, and R. Knowles, *FEMS Microbiol. Lett.*, 1992, **92**, 205.

34. U. H. Hole, K. U. Vollack, W. G. Zumft, E. Eisenmann, R. A. Siddiqui, B. Friedrich, and P. M. H. Kroneck, *Arch. Microbiol.*, 1996, **165**, 55.

35. K. Brown, M. Tegoni, M. Prudencio, A. S. Pereira, S. Besson, J. J. Moura, I. Moura, and C. Cambillau, *Nature Struct. Biol.*, 2000, **7**, 191.

36. T. Haltia, K. Brown, M. Tegoni, C. Cambillau, M. Saraste, K. Mattila, and K. Djinovic-Carugo, *Biochem. J.*, 2003, **369**, 77.

37. W. E. Antholine, D. H. W. Kastrau, G. C. M. Steffens, G. Buse, W. G. Zumft, and P. M. H. Kroneck, *Eur. J. Biochem.*, 1992, **209**, 875.

38. P. M. H. Kroneck, W. A. Antholine, J. Riester, and W. G. Zumft, *FEBS Lett.*, 1989, **248**, 212.

39. R. A. Scott, W. G. Zumft, C. L. Coyle, and D. M. Dooley, *Proc. Natl. Acad. Sci. U.S.A.*, 1989, **86**, 4082.

40. M. Kelly, P. Lappalainen, G. Talbo, T. Haltia, J. Van der Oost, and M. Saraste, *J. Biol. Chem.*, 1993, **268**, 16781.

41. N. J. Blackburn, M. E. Barr, W. H. Woodruff, J. Van der Oost, and S. de Vries, *Biochemistry*, 1994, **33**, 10401.

42. T. Tsukihara, H. Aoyama, E. Yamashita, T. Tomizaki, H. Yamaguchi, K. Shinzawa-Itoh, R. Nakashima, R. Yaono, and S. Yoshikawa, *Science*, 1995, **269**, 1069.

43. S. Iwata, C. Ostermeier, B. Ludwig, and H. Michel, *Nature*, 1995, **376**, 660.

44. J. A. Farrar, A. J. Thomson, M. R. Cheesman, D. M. Dooley, and W. G. Zumft, *FEBS Lett.*, 1991, **294**, 11.

45. D. M. Dooley, M. McGuirl, A. C. Rosenzweig, J. A. Landin, R. A. Scott, W. G. Zumft, F. Devlin, and P. J. Stephens, *Inorg. Chem.*, 1991, **30**, 3006.

46. D. M. Dooley, M. L. Alvarez, A. C. Rosenzweig, R. S. Hollis, and W. G. Zumft, *Inorg. Chim. Acta*, 1996, **242**, 239.

47. J. A. Farrar, W. G. Zumft, and A. J. Thomson, *Proc. Natl. Acad. Sci. U.S.A.*, 1998, **95**, 9891.

48. R. C. Holz, M. L. Alvarez, W. G. Zumft, and D. M. Dooley, *Biochemistry*, 1999, **38**, 11164.

49. T. Rasmussen, B. C. Berks, J. Sanders-Loehr, D. M. Dooley, W. G. Zumft, and A. J. Thomson, *Biochemistry*, 2000, **39**, 12753.

50. K. Brown, K. Djinovic-Carugo, T. Haltia, I. Cabrito, M. Saraste, J. J. G. Moura, I. Moura, M. Tegoni, and C. Cambillau, *J. Biol. Chem.*, 2000, **275**, 41133.

51. P. Chen, S. DeBeer George, I. Cabrito, W. Antholine, J. J. Moura, I. Moura, B. Hedman, K. O. Hodgson, and E. I. Soloman, *J. Am. Chem. Soc.*, 2002, **124**, 744.

52. P. Chen, I. Cabrito, J. J. Moura, I. Moura, and E. I. Solomon, *J. Am. Chem Soc.*, 2002, **124**, 10497.

53. T. Rasmussen, B. C. Berks, J. N. Butt, and A. J. Thompson, *Biochem. J.*, 2002, **364**, 807.

54. J. A. Farrar, F. Neese, P. Lappalainen, P. M. H. Kroneck, M. Saraste, W. G. Zumft, and A. J. Thomson, *J. Am. Chem. Soc.*, 1996, **118**, 11501.

55. M. Hay, M. Ang, D. Gamelin, E. Solomon, W. Antholine, M. Ralle, N. Blackburn, and P. Massey, *Inorg. Chem.*, 1998, **37**, 191.

56. D. Gamelin, D. Randall, M. Hay, R. Houser, T. Mulder, G. Canters, S. de Vries, W. Tolman, Y. Lu, and E. Solomon, *J. Am. Chem. Soc.*, 1998, **120**, 5246.

57. F. Neese, R. Kappl, J. Huttermann, W. G. Zumft, and P. M. H. Kroneck, *J. Biol. Inorg. Chem.*, 1998, **3**, 53.

58. M. Wilmanns, P. Lappalainen, M. Kelly, E. Sauer-Eriksson, and M. Saraste, *Proc. Natl. Acad. Sci. U.S.A.*, 1995, **92**, 11955.

59. T. Tsukihara, H. Aoyama, E. Yamashita, T. Tomizaki, H. Yamaguchi, K. Shinzawa-Itoh, R. Nakashima, R. Yaono, and S. Yoshikawa, *Science*, 1996, **272**, 1136.

60. C. R. Andrew, J. Han, S. de Vries, J. van der Oost, B. A. Averill, T. M. Loehr, and J. Sanders-Loehr, *J. Am. Chem. Soc.*, 1994, **116**, 10805.

61. F. Neese, W. G. Zumft, W. E. Antholine, and P. M. H. Kroneck, *J. Am. Chem. Soc.*, 1996, **118**, 8692.

62. C. Dennison, A. Berg, and G. W. Canters, *Biochemistry*, 1997, **36**, 3262.

63. I. Bertini, K. L. Bren, A. Clemente, J. A. Fee, H. B. Gray, C. Luchinat, B. G. Malmström, J. H. Richards, D. Sanders, and C. E. Slutter, *J. Am. Chem. Soc.*, 1996, **118**, 11658.

64. C. Luchinat, A. Soriano, K. Djinovic-Carugo, M. Saraste, B. G. Malmström, and I. Bertini, *J. Am. Chem. Soc.*, 1997, **119**, 11023.

65. J. Salgado, G. Warmerdam, L. Bubacco, and G. W. Canters, *Biochemistry*, 1998, **37**, 7378.

66. S. D. George, M. Metz, R. K. Szilagyi, H. Wang, S. P. Cramer, Y. Lu, W. B. Tolman, B. Hedman, K. O. Hodgson, and E. I. Soloman, *J. Am. Chem. Soc.*, 2001, **123**, 5757.

67. K. U. Vollack, E. Hartig, H. Koerner, and W. G. Zumft, *Mol. Microbiol.*, 1999, **31**, 1681.

68. C. Braun and W. G. Zumft, *J. Bacteriol.*, 1992, **174**, 2394.

69. F. U. Hoeren, B. C. Berks, S. J. Ferguson, and J. E. McCarthy, *Eur. J. Biochem.*, 1993, **218**, 49.

70. W. G. Zumft, A. Viebrock-Sambale, and C. Braun, *Eur. J. Biochem.*, 1990, **192**, 591.

71. M. A. McGuirl, L. K. Nelson, J. A. Bollinger, Y. K. Chan, and D. M. Dooley, *J. Inorg. Biochem.*, 1998, **70**, 155.

72. P. Holloway, W. McCormick, R. J. Watson, and Y. K. Chan, *J. Bacteriol.*, 1996, **178**, 1505.

73. E. J. Bedmar, GenBank Acession# AJ002531, 1998, NCBI Web Page; http://www.ncbi.nlm.nih.gov/entrez/viewer.fcgi?db=nucleotide&val=3850613.

74. H. Cuypers, A. Viebrock-Sambale, and W. G. Zumft, *J. Bacteriol.*, 1992, **174**, 5332.

75. Y. K. Chan, W. A. McCormick, and R. J. Watson, *Microbiology*, 1997, **143**, 2817.

76. N. F. W. Saunders, J. J. Hornberg, W. N. M. Reijnders, H. V. Westerhoff, S. de Vries, and R. J. M. Van Spanning, *J. Bacteriol.*, 2000, **182**, 5211.

77. P. Wunsch, M. Herb, H. Wieland, U. M. Schiek, and W. G. Zumft, *J. Bacteriol.*, 2003, **185**, 887.
78. F. D. Ciccarelli, R. R. Copley, T. Doerks, R. B. Russell, and P. Bork, *Trends Biochem Sci.*, 2002, **27**, 59.
79. M. J. Fath and R. Kolter, *Microbiol. Rev.*, 1993, **57**, 995.
80. U. Honisch and W. G. Zumft, *J. Bacteriol.*, 2003, **185**, 1895.
81. M. A. McGuirl, J. A. Bollinger, N. Cosper, R. A. Scott, and D. M. Dooley, *J. Biol. Inorg. Chem.*, 2001, **6**, 189.
82. A. Dreusch, J. Riester, P. M. H. Kroneck, and W. G. Zumft, *Eur. J. Biochem.*, 1996, **237**, 447.
83. T. D. Rae, P. J. Schmidt, R. A. Pufahl, V. C. Culotta, and T. V. O'Halloran, *Science*, 1999, **284**, 805.

Beryllium: Inorganic Chemistry

Timothy S. Keizer & T. Mark McCleskey
Los Alamos National Laboratory, Los Alamos, NM, USA

1 Introduction 1
2 Beryllium Hydroxo Speciation 1
3 Inorganic Ligands with Beryllium 2
4 Organic Ligands with Beryllium 4
5 Related Articles 5
6 References 5

Glossary

Catechol: 1,2-dihydroxybenzene
CBD: chronic beryllium disease
Chromotropic acid: 4,5-dihydroxynaphthalene-2,7-disulfonic acid
GME: gmelinite
Tiron: 4,5-dihydoxybenzene-1,3-disulfonic acid

1 INTRODUCTION

Beryllium is a lightweight, nonmagnetic, X-ray transparent, robust metal with a high melting point (1285 °C), and a stiffness six times that of steel.[1] Two forms of beryllium dominate in nature: bertrandite, $Be_4(OH)_2Si_2O_7$, and beryl, $Al_2Be_3Si_6O_{18}$ (Figure 1). Beryl is best known for its gemstone forms, emerald, and aquamarine. Beryl is converted to beryllium oxide or beryllium hydroxide by heating with sodium fluorosilicate, then extracting with water (the Copaux process), or by decomposing beryl with sulfuric acid.[2] Beryllium metal is usually prepared by generating the appropriate beryllium halide (*vide infra*), followed by electrolysis of beryllium chloride, or magnesium reduction of beryllium fluoride. Beryllium metal is used in airplanes and satellites for its combined lightness and strength, and as a window in many X-ray applications (*see* ***Diffraction Methods in Inorganic Chemistry***). The largest use of beryllium is in alloys with other metals that can produce unique properties, such as copper–beryllium, which increases in strength 6-fold with just 2% beryllium and is used in a variety of applications including nonsparking tools (*see* ***Alloys***). Beryllium oxide is a good electronic insulator with excellent thermal conductivity and is used for demanding electronic applications including supercomputers and cell phones.

Beryllium is toxic, both as a carcinogen, and as the agent that initiates chronic beryllium disease (CBD) (*see* ***Metal-related Diseases of Genetic Origin***). CBD, a granulomatous lung disease, is an uncontrolled cell-mediated immune response from inhaling beryllium in 6 to 20% of exposed individuals. The onset of CBD can be delayed for 10 to 40 years after exposure, and no strong correlation is known between dose of the beryllium and the development of CBD, although it is clear that very low levels of beryllium exposure can lead to the development of CBD. The nature and effects of CBD have been well studied,[3] but the molecular level mechanism of how beryllium triggers CBD is not well understood.[4,5] The areas of biological and environmental effects of beryllium have been the main focus of study, and far less effort has been devoted to the speciation and interactions of beryllium under physiological conditions. Despite the high toxicity of beryllium, it is still widely used for its unique properties. The use of beryllium in industry and government has increased over time and shows no sign of decline, making it imperative to understand the speciation of beryllium and its interactions with biological systems.

2 BERYLLIUM HYDROXO SPECIATION

Beryllium speciation in water, in the absence of ligands other than H_2O and OH has been well characterized (*see* ***Water & O-donor Ligands***).[6] One interesting result is the tendency of beryllium to form clusters in solution. Above pH 5.5, beryllium begins to precipitate as polymeric beryllium hydroxide $[Be(OH)_2]_n$. It is known that the hydrolysis of the aquo cation $[Be(H_2O)_4]^{2+}$ between pH 3 and pH 6 gives both monomeric and polynuclear species. The compounds $[Be_3(OH)_3]^{3+}$ and $[Be_2(OH)]^{3+}$ have been indicated as dominant species, and their corresponding formation constants have been precisely determined (Figure 2).[6,7] Additional species for beryllium hydroxo complexes are formed at intermediate Be^{2+} to OH^- ratios; in most studies, the best fit to the data was obtained with the addition of the $[Be_5(OH)_6]^{4+}$ and $[Be_6(OH)_8]^{4+}$ species (Figure 2). Using this data, a speciation diagram (Figure 3) displays the concentration of species present in solution at a given pH. The formation of different hydrolysis species is dependent on the concentration of the beryllium solution. As the concentration of the beryllium is decreased, the polynuclear species decrease in concentration, and at 10^{-6} M Be^{2+}, only Be^{2+} and $Be(OH)_2$(s) are present in solution.

Beryllium is amphoteric and the $Be(OH)_2$(s) at pH > 12 begins to dissolve, forming ${Be(OH)_3}^-$ and ${Be(OH)_4}^{2-}$ species. The ^{9}Be NMR gives a narrow peak at 2 ppm, which is most likely due to the ${Be(OH)_4}^{2-}$ species.

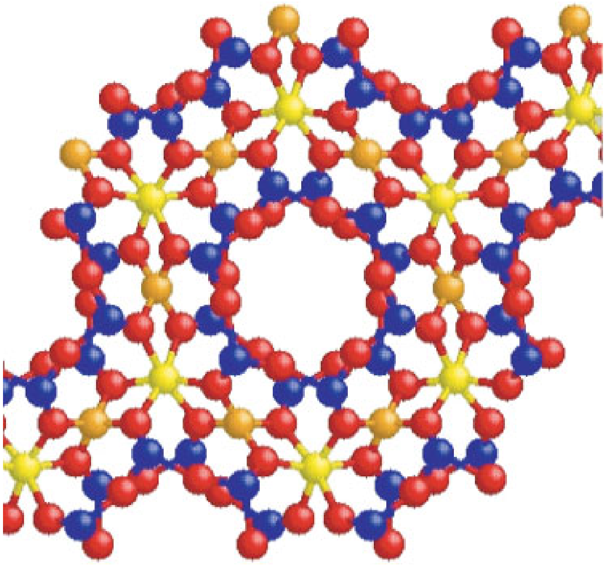

Figure 1 Structure of beryl, $Al_2Be_3Si_6O_{18}$ (Al = yellow, Be = orange, Si = blue, O = red)

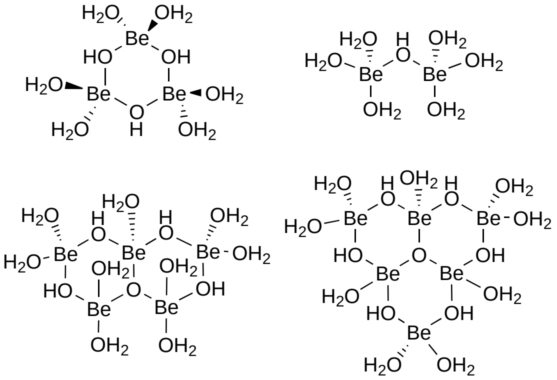

Figure 2 Proposed structures of beryllium hydroxo complexes under acidic conditions

3 INORGANIC LIGANDS WITH BERYLLIUM

Most inorganic ligands do not form stable complexes with beryllium ions under aqueous conditions because of beryllium's high affinity for oxygen donor ligands such as water. The fluoride ion exhibits the highest affinity for the Be^{2+} ion in aqueous conditions, and can contend with water for the Be^{2+} ion.[6] Fluoride can form all four substitution products with water, $[Be(H_2O)_{4-n}F_n]$ ($n = 1-4$). The fluoride ion competes with water $<$ pH 8 at which point $Be(OH)_2(s)$ precipitates. Equilibrium constants from literature were used to form the speciation diagram in Figure 4.[6] The diagram illustrates that the $Be(H_2O)_2F_2$ and $Be(H_2O)F_3$ are the dominate complexes of beryllium at pH ranging from 0.5 to 8, although changing the concentration or varying the Be^{2+}/F^- ratio does result in the formation of the different species.

The speciation of beryllium fluoride has been monitored by NMR.[6,7] The ^9Be NMR of a mixture of the four species gives a spectrum that is complicated due to the overlap of the multiplet resonances. Beryllium NMR has a narrow range in chemical shifts and line broadening caused by the quadrupolar beryllium nuclei ($S = 3/2$). NMR techniques such as selective cross-polarization are used to distinguish the species from each other,[8] but the ^{19}F nuclei allows for a better distinction of the species in solution. The ^{19}F spectrum of the beryllium species exhibits a 1:1:1:1 quartet splitting due to ^9Be having an S-value of 3/2 (Figure 5). The three species $[BeF(H_2O)_3]^+$, $[BeF_2(H_2O)_2]$, and $[BeF_3(H_2O)]^-$ are easily distinguished as separate signals. The quartet in the ^{19}F NMR indicates the fluorides are connected to one beryllium atom, and no bridging fluorides are observed in solution. In

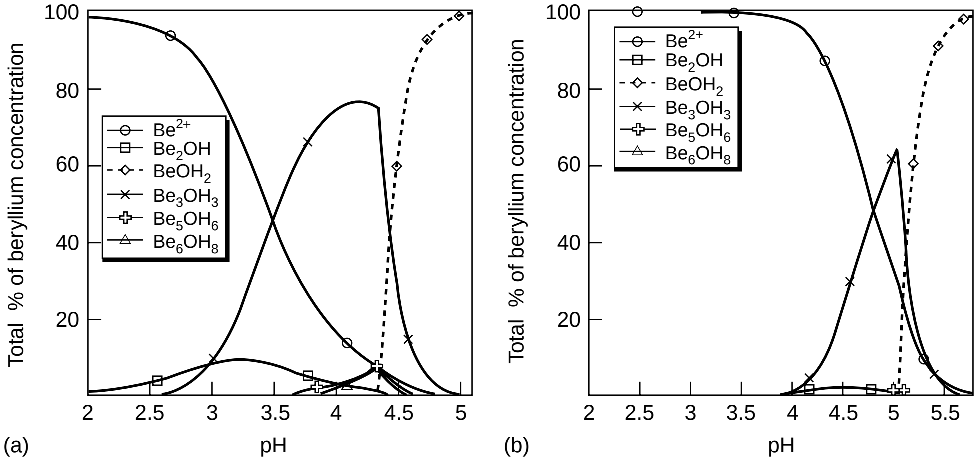

Figure 3 Speciation diagrams of beryllium hydroxo species. (a) $C_{Be} = 0.2\,M$, (b) $C_{Be} = 0.002\,M$

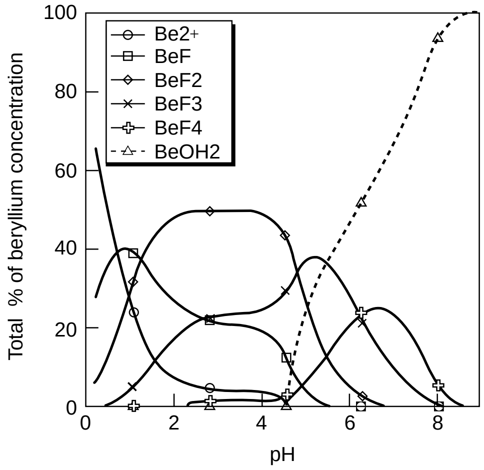

Figure 4 Speciation diagram of beryllium fluoro complexes in solution. $C_{Be} = 0.25\,M$ $C_F = 0.5\,M$

the solid-state structures of beryllium fluoride complexes, the fluorides usually form bridges between beryllium atoms. The ^{9}Be and ^{19}F chemical shifts with coupling constants for the four species are in Table 1.

$$Be(OH)_2 + NH_4F \xrightarrow{230-260°} (NH_4)_2BeF_4 + 2NH_4OH \qquad (1)$$

Table 1 ^{19}F and ^{9}Be NMR data for beryllium fluoride complexes

	^{19}F NMR δ (ppm)	$^1J_{FBe}$ (Hz)	^{9}Be NMR δ (ppm)
$[Be(H_2O)_3F]^+$	−95.55 – −93.98	41.2	0.53 – 0.68
$[Be(H_2O)_2F_2]$	−92.65 – −91.11	39.3	0.17 – 0.33
$[Be(H_2O)F_3]^-$	−90.22 – −88.81	36.3	−0.13 – 0.02
$[BeF_4]^{2-}$	−87.71 – −87.41	33.6	−0.34 – −0.28

$$(NH_4)_2BeF_4 \xrightarrow{>270°} BeF_2 + 2NH_4F \qquad (2)$$

$$BeO + Cl_2 + C \xrightleftharpoons{600-800°} BeCl_2 + CO \qquad (3)$$

$$Be + 2NH_4I \longrightarrow BeI_2 + H_2 \qquad (4)$$

$$Be + 2KNH_2 \longrightarrow Be(NH_2)_2 + 2K \qquad (5)$$

Beryllium halides are not easily prepared in the presence of water.[2] The dehydration of $BeX_2 \bullet 4H_2O$ (X = F, Cl, Br, and I) often leads to hydrolysis products; thus other methods are utilized. Beryllium fluoride is produced by thermally decomposing $(NH_4)_2BeF_4$ (equations 1 and 2). One of the common methods for the synthesis of $BeCl_2$, is heating BeO and Cl_2 gas in the presence of activated carbon at high temperatures (equation 3). Beryllium bromide can be synthesized in a similar manner as $BeCl_2$ (equation 3), using higher temperatures (1100–1200°).[2] The iodide form, BeI_2, can be prepared by heating beryllium oxide with aluminum iodide in a sealed tube. BeI_2 can also be prepared by dissolving beryllium metal in a solution of ammonium iodide in liquid ammonia (equation 4). Other inorganic beryllium compounds can be formed in liquid ammonia such as $Be(NH_2)_2$ (equation 5). Most inorganic beryllium compounds are very hydroscopic.

Little solution work has been performed with beryllium phosphate complexes. Solutions of beryllium phosphate precipitates above pH 2.5. Even chelating ligands, such as citric acid and salicylic acid, cannot solubilize beryllium in the presence of phosphate. The only reported beryllium phosphate structures known are zeolite-type structures (*see* ***Zeolites***), which are formed under elevated temperature and pressure. In recent years, a number of zeolite-type framework structures have been made.[9–11] One, beryllophosphate, forms a gmelinite framework ($BePO_4$-GME) depicted in Figure 6. The beryllophosphates are usually templated with an amine. $BePO_4$-GME used triethylene tetramine as the template. A few beryllium-containing phosphorus type ligands

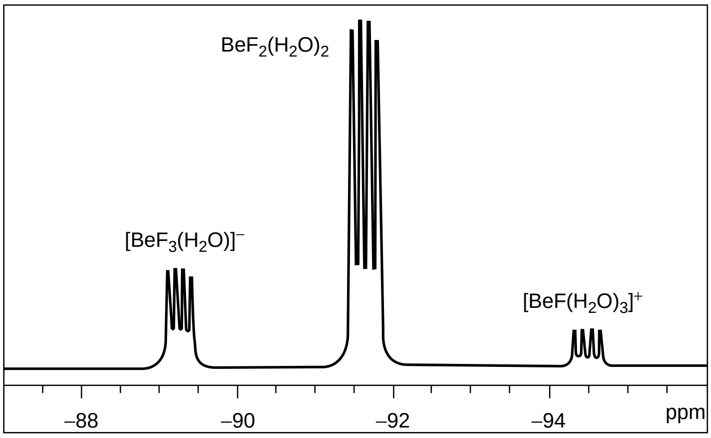

Figure 5 ^{19}F-NMR spectrum of an aqueous solution of beryllium difluoride at room temperature (Reprinted from Ref. 7, © 2001, with permission from Elsevier)

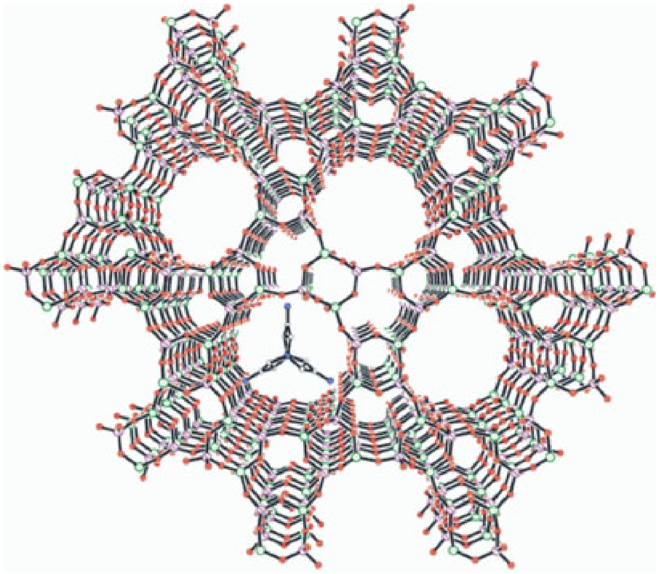

Figure 6 Framework of beryllophosphate $BePO_4$-GME viewed along the *c*-axis, showing the channels enclosed by 12-membered tetrahedral rings. (Reprinted from Ref. 10, © 2001, with permission from American Chemical Society)

such as phosphonate have been made and structurally characterized.[12,13]

4 ORGANIC LIGANDS WITH BERYLLIUM

There has been a significant amount of research on the interactions of organic ligands with beryllium due to the toxicity of beryllium and the role beryllium plays in CBD.[14,15] Most of the research has focused on mononuclear species at low pH, which is mainly due to the precipitation of $Be(OH)_2$ above pH ~5.8, and the formation of polynuclear species. Only a few ligands are able to compete with the formation of $Be(OH)_2$ ($K_{sp} = 1 \times 10^{-20}$).

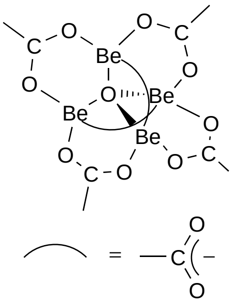

Figure 7 Beryllium acetate structure $[Be_4O(O_2CMe)_6]$ showing the Be_4O core

There are few monodentate ligands that interact with beryllium at higher pH in aqueous conditions; acetates show some affinity for beryllium and have been the most studied. Similar to the hydroxide speciation, there is a tendency for the formation of polynuclear species such as $Be_4(OAc)_6$, where the six acetates act as bridging ligands for the four beryllium atoms to form a tetrahedral Be_4O core (Figure 7).

Aliphatic bidentate carboxylate ligands have increased binding, but are still unable to compete with hydroxide precipitation at pH >6. The stable complexes of beryllium usually form at a 1:1 or 2:1 L:Be species ratio such as $Be(H_2O)_3L$, $BeL_2{}^{2-}$, or $[Be_3(OH)_3(L)_3]^{3-}$. The stability constants for some bidentate ligands are listed in Table 2. Bidentate and multidentate aliphatic hydroxycarboxylic acids are relatively poor ligands for beryllium, with binding constants ranging from 1×10^3 to 1×10^5. Coordination of these ligands is typically weak due to the weak acidity of the hydroxide, and the larger bite size caused by the sp^3 carbon alpha to the hydroxide. Citric acid (CA) on the other hand is an excellent ligand for beryllium. Citric acid solubilizes beryllium at molar concentration across the entire pH range.[16] The speciation of beryllium complexes of citric acid at high beryllium concentrations is determined by using NMR, and it shows that the dominant beryllium complex has a CA:Be ratio of 1:2. The binding features a central Be-O-Be unit with the oxygen coming from the central RO^- of CA, and one carboxylate bound on each side of the two berylliums (Figure 8). Ligands similar to citric acid (Citramalic acid, malic acid, and 3-hydroxy-3-methylglutaric acid), which provide a bridging RO^- and two carboxylates capable of forming 5 and 6 member rings upon binding to Be, also form stable complexes up to pH 9.[16] The addition of a hydroxide group on one of the methylene carbons, as in tartaric acid, dramatically disrupts the Be-O-Be motif, resulting in the precipitation at pH > 5.8.

Table 2 Stability constants for aliphatic bidentate complexes of beryllium

Ligand	K_1	β_2
Oxalate	4.08, 3.26	5.91, 5.32
Malonate	5.73, 5.35	9.28, 8.85
Succinate	4.69, 2.74	6.43, 4.36
Maleate	4.33	6.46
Folate	4.65, 5.15	8.35, 9.05

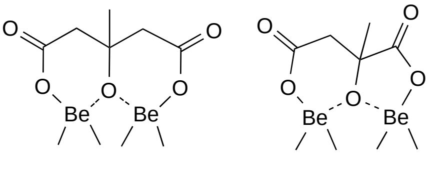

Figure 8 Citric acid binding pockets for beryllium

Aromatic hyrdroxycarboxylic acids and dihydroxy ligands form very stable complexes with beryllium. Salicylic acid type ligands, namely 5-sulfosalicyclate, have been broadly studied over the years for use as a chelation agent for beryllium poisoning.[6] Two main species are formed with these bidentate ligands, BeL and $[BeL_2]^{2-}$ (Figure 9). Catechols and other dihydoxy ligands form complexes similar to the salicylates. Stability constants for some of the higher binding beryllium ligands are listed in Table 3. Chromotropic acid forms the most stable bidentate complex with beryllium reported in literature. 2-hydroxyisophthalic acid and 2,3-dihydroxybenzoic acid form the highest stable complexes utilizing a similar motif of citric acid.[17]

Beryllium prefers to form 5-membered and 6-membered chelated rings with ligands. Seven-membered rings can be formed, but produce weaker complexes. Beryllium tends to favor the 6-membered ring, although 5-membered chelate rings with ligands such as tiron are also very stable. Where the ligand binds two berylliums, the ideal structures contain one six-membered and one five-membered rings, such as in the case of citric acid derivatives.[16,17] Functional groups also play a large part in determining whether a ligand forms a stable complex with beryllium. Hydroxides, carboxylates, or a combination of the two tend to form the majority of the stable complexes in the literature. Chromotropic acid, with a high stability constant, contains two phenolic oxygens, and forms a 6-membered ring with beryllium.[18]

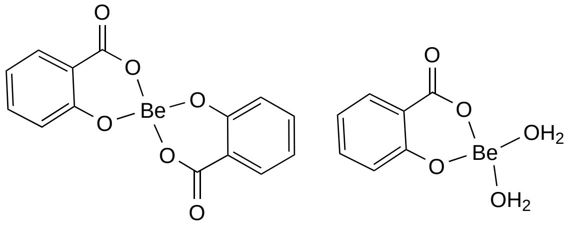

Figure 9 Structures of BeL_2 and $BeL(H_2O)_2$

Table 3 Stability constants for aromatic bidentate complexes of beryllium

Ligand	K_1	β_2
Chromotropic acid	16.2 16.34	28.2 28.19
Tiron	12.2 13.5	21.5 26.0
Catechol	13.7 13.52	25.72 23.35
5-Sulfosalicylic acid	11.2 11.74	19.7 20.66
5-nitrosalicylic acid	10.1 9.64	18.1 17.17

Beryllium is a quadrupolar nucleus ($S = 3/2$), but NMR can be a useful characterization technique. Aqueous beryllium sulfate ($Be(H_2O)_4{}^{2+}$) is used as the standard reference peak at 0 ppm. Although the frequency is affected by the concentration of the solution, at higher concentration, an upfield shift in frequency is observed. Beryllium-9 NMR is used to help determine the number of ligands and waters bound to a beryllium atom, and can also determine the size of the chelating ring formed with beryllium. As water is exchanged by anionic ligands on the beryllium, the beryllium resonance shifts downfield. The ring size also causes a shift in resonance frequency. Beryllium, in a 5-membered ring, is shifted downfield, and as ring size increases, the resonance frequency shifts upfield. The shift in frequency is more notable from a 5-membered ring to a 6-membered ring, than a 6-membered ring to a 7-membered ring chelate.

5 RELATED ARTICLES

Alkaline Earth Metals: Inorganic Chemistry; Beryllium & Magnesium: Organometallic Chemistry.

6 REFERENCES

1. R. G. Bellamy and N. A. Hill, in ‘Internation Series of Monographs on Nuclear Energy’, ed. J. V. Dunworth, The Macmillan Company, New York, 1963, Vol. 1.
2. D. A. Everest, ‘The Chemistry of Beryllium, Topics in Inorganic Chemistry and General Chemistry’, Elsevier, Amsterdam, 1964, Vol. I.
3. C. Saltini and M. Amicosante, *Am. J. Med. Sci.*, 2001, **321**, 89.
4. M. Eisenbud, *Appl. Occup. Environ. Hyg.*, 1998, **13**, 25.
5. C. Saltini, M. Amicosante, A. Franchi, G. Lombardi, and L. Richeldi, *Eur. Respir. J.*, 1998, **12**, 1463.
6. L. Alderighi, P. Gans, S. Midollini, and A. Vacca, in ‘Advances in Inorganic Chemistry: Main Group Chemistry’, eds. A. G. Sykes, and A. H. Cowley, Academic Press, New York, 2000, Vol. 50, p. 109.
7. H. Schmidbaur, *Coord. Chem. Rev.*, 2001, **215**, 223.
8. T. R. Eykyn, D. J. Philp, and P. W. Kuchel, *J. Chem. Phys.*, 2003, **118**, 6997.
9. X. Bu, T. E. Gier, and G. D. Stucky, *Microporous Mesopor. Mater.*, 1998, **26**, 61.
10. H. Zhang, M. Chen, Z. Shi, X. Bu, Y. Zhou, X. Xu, and D. Zhao, *Chem. Mater.*, 2001, **13**, 2042.
11. T. E. Gier and G. D. Stucky, *Nature*, 1991, **349**, 508.
12. L. Alderighi, A. Vacca, F. Cecconi, S. Midollini, E. Chinea, S. Dominguez, A. Valle, D. Dakternieks, A. Duthie, *Inorg. Chim. Acta*, 1999, **285**, 39.

13. N. M. Dyatlova, V. V. Medyntsev, T. Y. Medved, M. I. Kabachnik, *J. Gen. Chem. USSR (engl. Transl.)*, 1968, **38**, 1025.
14. C. Y. Wong, J. D. Woolins, *Coord. Chem. Rev.*, 1994, **130**, 243.
15. M. D. Rossman, *Environ. Health Perspect.*, 1996, **104**, Suppl. 5, 945.
16. T. S. Keizer, N. N. Sauer, T. M. McCleskey, *J. Inorg. Bio. Chem.*, (in press).
17. T. S. Keizer, N. N. Sauer, T. M. McCleskey, *J. Am. Chem. Soc.*, 2004, **126**, 9484.
18. P. G. Plieger, K. D. John, T. S. Keizer, T. M. McCleskey, A. K. Burrell, R. L. Martin, *J. Am. Chem. Soc.*, 2004, **126**, 14651.

Low Oxidation State Main Group

Charles L. B. Macdonald & Bobby D. Ellis
University of Windsor, Windsor, ON, Canada

1 Introduction 1
2 Group 13 Elements 2
3 Group 14 Elements 7
4 Group 15 Elements 8
5 Related Articles 11
6 References 11

Abbreviations

An = Anion; Ch = Group 16 element, 'Chalcogen'; Cp′ = Any cyclopentadienyl ligand; D = General electron donor; Dip = 2,6-diisopropylphenyl; E = Group 14 element, 'Tetrel'; M = Group 13 element, 'Triel'; Mes* = 2,4,6-tri-*t*-butylphenyl; *n* = Principal quantum number; Pn = Group 15 element, 'Pnictogen'; R = Substituent; TM = Transition metal; VSEPR = Valence shell electron pair repulsion; X = Group 17 element, 'Halogen'.

1 INTRODUCTION

1.1 Oxidation States and Their Consequences

The concept of an atom's oxidation state (*see Oxidation Number*) can provide fundamental information about the structure and reactivity of the compound in which the atom is found. In fact, it can be argued that oxidation states provided the basis for Medeleev's initial organization of the periodic table. For the main group elements, the relative stability of lower oxidation states within a given group increases as the atomic number increases. This trend in the periodic table (*see* ***Periodic Table: Trends in the Properties of the Elements***) is generally attributable to the presence of an inert s pair (*see Inert Pair Effect*) caused by relativistic effects (*see Relativistic Effects*).

Whereas discrete low oxidation state compounds of the transition metals are common in organometallic chemistry, the most typical series of examples being the transition metal carbonyl compounds (*see Carbonyl Compound*), there are at present significantly fewer classes of compounds containing main group elements in low oxidation states. An element in a low oxidation state formally has more valence electrons than it would in higher oxidation states. For the transition metals, these valence electrons are generally found in VSEPR-inactive d orbitals. In contrast, for the main group elements, the electrons are in VSEPR-active valence s and p orbitals. Thus a further consequence of having a lower oxidation state is that the main group element will tend to be coordinatively unsaturated (*see Coordinative Saturation & Unsaturation*). Overall, the combination of low-coordination number, incompletely filled orbitals and available electrons makes compounds containing elements in low oxidation states significantly more reactive than their higher oxidation state relatives and the modes of reactivity are often distinct. For example, a low oxidation state can make a group 13 element that typically acts as an acceptor act as a donor instead. In addition to the fundamental chemical insights such compounds provide, the unique structural and chemical properties of low oxidation state main group compounds has resulted in their use as catalysts and as precursors for the formation of new and useful materials.

1.2 Scope

The types of molecules considered in this work are those that have structural or chemical features that are manifestly different than are those of their more common oxidation state counterparts. Because of the breadth of this subject, selected examples are presented to illustrate typical behavior. The properties of the types of compounds containing the elements in more typical oxidation states may be found in the *Inorganic* and *Organometallic* sections describing each element or group and will not be discussed in this article. Similarly, minerals, metal phosphides, metal carbides, and compounds where the oxidation state of the element is low based on formal electron counting techniques (as in some catenated *Catenation* group 14 compounds), but that do not result in unusual chemistry, are not included.

The chemistry of the elements in the second period is generally different from that of their heavier analogues and is only mentioned in certain illustrative cases. The very electropositive elements of the s-block lose their valence electrons readily and do not tend to form stable compounds containing the elements in low oxidation states. For group 1, the lowest typical oxidation state is the elemental form. Similarly, for group 2, while the possibility of the +1 oxidation state exists, the low electronegativity of the elements in conjunction with lattice energy considerations render the lower oxidation state unfavorable. Conversely, the more electronegative elements from groups 16–18 are typically found in the lowest available oxidation state (having an ns^2np^6 electron configuration) and the typical chemistry of such compounds is covered in the appropriate entries on each of the elements of those groups.

Apart from some important reactive intermediates, the compounds considered in this article are 'stable' in that they may be made, characterized, used and perhaps stored under conditions that are conveniently accessible in a modern inorganic laboratory. This caveat requires that the compounds have lifetimes of at least 30 minutes in an inert gas or vacuum atmosphere at temperatures greater than −198 °C (preferably at least −78 °C). In this light, the vast amount of spectroscopic and matrix-isolation (*see Matrix Isolation*) work that has been performed on numerous diatomic and other small molecules is not discussed explicitly – in most cases, information on such species may be found in the appropriate *Inorganic* chemistry section of the particular element or group.

2 GROUP 13 ELEMENTS

In discrete molecules, the elements of group 13 are most typically found in the +3 oxidation state. There are major exceptions to this rule, such as the polyhedral boranes (*see* ***Boron Hydrides***) and carboranes (*see* ***Boron: Polyhedral Carboranes*** and ***Boron: Metallacarbaboranes***), which formally contain B^{I} and are outlined elsewhere in this Encyclopedia, and the compounds of thallium (Tl), which typically contain Tl^{I} for the reasons described above.[1] Thus, in this section, compounds containing group 13 elements in the atypical +1 and +2 oxidation states are presented.

2.1 Oxidation State +1

2.1.1 Synthesis

Compounds containing group 13 elements in the +1 oxidation state are synthesized using a number of different methods, usually through the reduction of a group 13 element in a higher oxidation state.[2,3] As illustrated in Scheme 1, the reduction of M^{III} dihalides with reducing agents such as alkali metals, alkaline earth metals, and other agents produces M^{I} compounds. In the case of In, oxidation of the metal has also been shown to produce In^{I} compounds.[4,5] Likewise, it should be noted that in some cases metallic group 13 elements can be oxidized to form RM^{I} and naked M^{I} ligands in the coordination sphere of transition metals.[6] In theory, the products of most of the preceding preparations are compounds of the form RM^{I}, which have a lone pair and two vacant *n*p orbitals and one substituent in their valence shell, as depicted in Figure 1. Such compounds are typically indicated by the suffixes '−diyl' or '−ylene', for example, RB may be called a 'borylene' or a 'boranediyl'.

Alkyl, aryl, silyl and amido substituents are all amenable to the in situ reduction protocol and similar RM^{I} compounds may also be made from univalent halides.[2,3] The structures of the compounds produced in such reactions are dependent on the nature of the substituent; for most substituents, oligomeric polyhedral clusters are obtained. The use of sterically demanding substituents tends to result in the formation of smaller clusters and oligomers, examples of which are shown in Figure 2 and can even result in monomeric compounds such as (**1**).[7] Similarly, the presence of electron-donating substituents, such as amido groups, can influence the geometry and stability of the oligomer adopted, as exemplified by $(BNMe_2)_6$ (**2**), which adopts a cyclic structure instead of a more typical octahedral arrangement.[8]

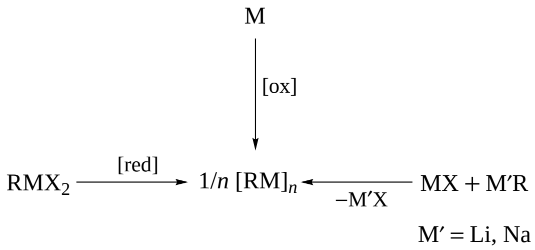

Scheme 1

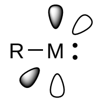

Figure 1 Depiction of the valence electronic structure of a monomeric RM^{I} compound

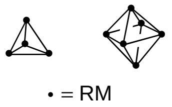

Figure 2 Some typical polyhedral oligomeric structures for $(RM)_n$ compounds

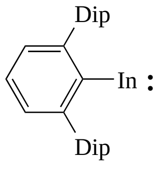

(**1**)

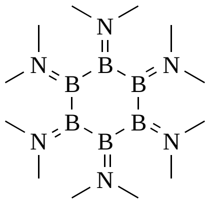

(**2**)

Univalent group 13 compounds also form spontaneously from certain M^{II} precursors. Dissolution of $X_2M{-}MX_2$ (M = Ga, In, Tl) in aromatic solvents results in a disproportionation to produce mixed valence salts of the form $[M\cdot \text{arene}_n][MX_4]$.[9] This process is reversed upon addition of other donors (D), as depicted in Scheme 2.

A more direct method used to prepare M^{I} compounds is through metathesis reactions with reagents that already contain

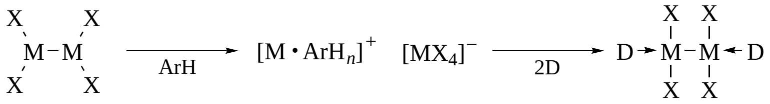

Scheme 2

$$M_{(g)} + HX_{(g)} \xrightarrow[-1/2\ H_2]{} MX \xrightarrow[\text{base}]{} [MX \cdot \text{base}]_n$$

Scheme 3

univalent group 13 elements. Whereas M^IX salts are common for In and Tl, the corresponding salts of the lighter elements have only been prepared since the late 1980s by Schnöckel and coworkers.[2,3,10] All of the univalent halides M^IX ($M = Al, Ga$) are prepared by the high-temperature gas-phase reaction of the appropriate metal atoms with HX, as illustrated in Scheme 3, using a specially designed apparatus (*see* ***Metallic Materials Deposition: Metal-organic Precursors***). The univalent metal halides may be stored at low temperature as metastable solutions in donor solvents; some examples M^IX have been crystallized and these exist as donor-stabilized oligomers in the solid state.

Until recently, the only unusual M^IX reagent that could be prepared using conventional synthetic procedures was the compound know as 'GaI'.[11] As shown in equation (1), this material is prepared by the sonication (*see Sonication*) of Ga metal and 0.5 equivalents of I_2 in toluene at 50 °C; however, the exact composition has not been determined.[12] Similar preparations using different stoichiometries of I_2 have resulted in other subvalent reagents such as 'Ga_2I_3', 'Ga_3I_5', and so on.

$$\text{Ga} + \tfrac{1}{2}\text{I}_2 \longrightarrow \text{``GaI''} \qquad (1)$$

Some of the most extensively explored univalent group 13 compounds are the various cyclopentadienyl 'half-sandwich' complexes of the general formula Cp′M, where Cp′ is any cyclopentadienyl ligand and M is Al, Ga, In, and Tl.[13,14] For Al and Ga, these compounds are typically prepared by the reduction of suitable dihalogenated M^{III} precursors, as outlined in Scheme 4, and they may also be prepared from available univalent halide precursors. For Cp′ ligands bearing relatively small substituents, Cp′M compounds tend to form polyhedral $(Cp'M)_n$ clusters in the solid state and dissociate into monomers in both solution and the gas phase; a depiction of representative oligomeric and monomeric structures is presented in Figure 3. The relative stability of the monomeric form is attributable to the ability of the η^5-Cp′ ligand to donate electron density into both of the formally empty np orbitals on the M^I atom (providing for a valence octet of electrons around M) in addition to the steric demands of the ligand.[15]

$$\text{Cp}'\text{MX}_2 \xrightarrow{[\text{red}]} \text{Cp}'\text{M} \xleftarrow[-\text{M}'\text{X}]{} \text{MX} + \text{M}'\text{Cp}'$$
$$\text{M}' = \text{Li, Na}$$

Scheme 4

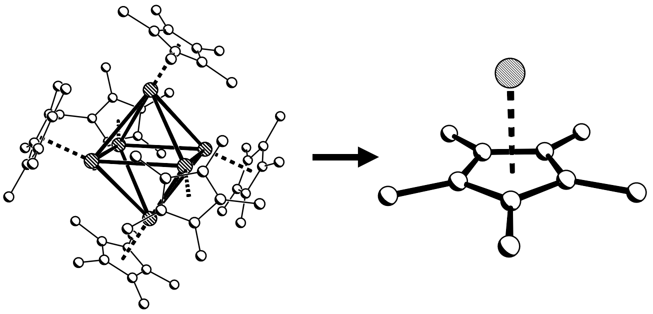

Solid state

Solution and gas phase

Figure 3 Oligomeric and monomeric structures of Cp*M (M = Ga, In)

It has been demonstrated that the presence of even a single Cp′ substituent can, in some cases, alter the thermodynamic preference of certain systems to favor lower oxidation state products.[16] Because of its relative stability, Cp*In provides an alternative route to univalent indium pseudohalides by way of the protonolysis of Cp*H using nonoxidizing protic acids, such as HOTf or HBF_4, as illustrated in equation (2); such reactions may be applicable to the lighter congeners.[17]

$$\text{Cp}^*\text{–In} + \text{HAn} \xrightarrow[-\text{Cp}^*\text{H}]{} \text{In}^+\ \text{An}^- \qquad (2)$$
$$\text{An} = \text{OTf, BF}_4$$

A number of compounds bearing ligands that are isolobal (*see Isolobal Analogy*) with Cp′, such tris(pyrazolyl)borate, $({}^t\text{BuC})_4\text{P}^-$, or $({}^t\text{BuC})_3\text{P}_2{}^-$ and even fullerides, have also been investigated and have chemistry similar to that of the cyclopentadienyl analogues. Similarly, some other chelating ligands have been used to isolate stable, monomeric M^I compounds. Of particular note are the neutral β-diketeniminate (nacnac) complexes (**3**)[18,19] and the anionic diazabutadiene complexes (**4**)[20,21] shown below. These monomeric compounds formally have six electrons in their valence shells and are potentially group 13 analogues of carbenes (*see* ***Main Group Carbenes***).[22]

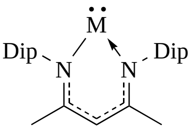

M = Al,Ga

(**3**)

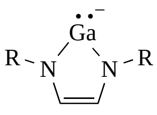

R = Ar, *t*-Bu

(**4**)

2.1.2 *Reactivity*

The reactivity of univalent group 13 compounds has generally been studied for compounds that dissociate, to a significant extent, into monomers in solution.**23** The electronic structure of monomeric RM^I compounds has a group 13 metal with one lone pair of electrons opposite the R ligand and two formally vacant np orbitals, as shown in Figure 1. The presence of the lone pair of electrons allows RM^I compounds to be used as donor ligands and such compounds have been used to synthesize a large number of transition metal complexes. In general, the complexes are prepared by the reaction of the RM^I donor with a transition metal complex bearing at least one readily lost ligand, as illustrated in Scheme 5, and complexes containing more than one RM^I ligand can be made in this way. The RM^I donors can act either as terminal ligands or as bridging ligands in polynuclear complexes. The molecular structure of one such transition metal complex is depicted in Figure 4.

Although no monomeric boranediyl species have yet been prepared, such ligands have been prepared in the coordination sphere of transition metals through the reaction of RBX_2 with alkali metallates such as $K_2Fe(CO)_4$.**24** Such an approach has also been used to prepare transition metal complexes for other RM^I ligands that do not dissociate into monomers in solution. Many of the transition metal complexes of univalent group 13 ligands have proved to be useful precursors for the MOCVD (*see Metal–Organic Chemical Vapor Deposition* and *Organometallic Chemical Vapor Deposition*) preparation of intermetallic (*see Intermetallics*) films and materials.**25**

The bonding between the transition metal and the group 13 element has been studied extensively by computational methods.**26** Because RM^I compounds have a valence electronic structure consisting of a filled orbital of σ symmetry and two unfilled orbitals of π symmetry, they are analogous to carbonyl ligands in that they can act as sigma donors and pi acceptors (*see π-Acid Ligand*). Such an electronic structure allows for numerous possible descriptions of the nature of the bond between the group 13 element and the transition metal; bonding models ranging from mostly ionic to multiple bonded covalent have been proposed.**26,27** The actual amount of transition metal to ligand back-bonding (*see Back Bonding*) is influenced by the nature of the R group on the RM^I ligand and π-acceptor ability of any other ligands on the transition metal.

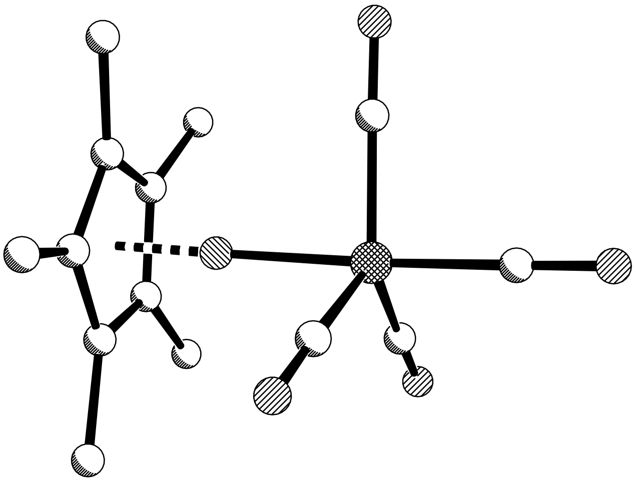

Figure 4 Molecular structure of a terminal $RM-TML_n$ complex: $Cp^*B-Fe(CO)_4$

Donor–acceptor complexes of univalent group 13 ligands have also been prepared with a variety of main group acceptors.**16,28–31** Such complexes are generally synthesized through the reaction of monomeric RM^I compounds with the desired Lewis acid as illustrated in Scheme 6. In particular, the reaction of a series Cp*M compounds (M = Al, Ga, In) with the strong Lewis acids $M'(C_6F_5)_3$ (M' = B, Al, Ga, In) is illustrative. Stable donor–acceptor complexes are obtained

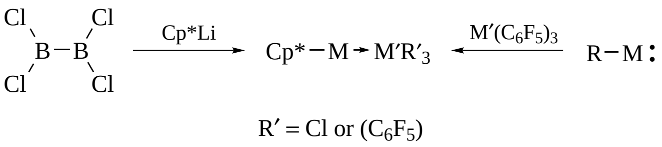

Scheme 6

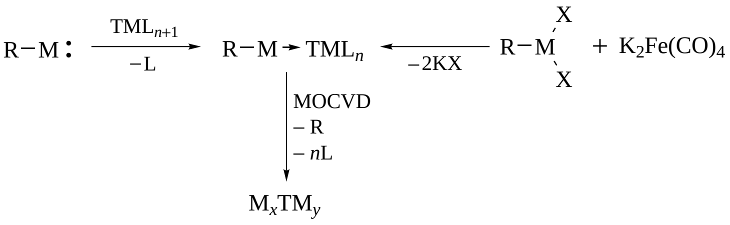

Scheme 5

in many cases and the structural features of complexes suggest that Cp*M donors are comparable in strength to triphenylphosphine. In contrast, the reaction of Cp*Al with $In(C_6F_5)_3$ results in the formation of $Cp^*Al(C_6F_5)_2$ and $[In(C_6F_5)]_n$ because of the relative stabilities of the M^I and M^{III} oxidation states for Al and In.

As summarized in Schemes 7 and 8, oxidation of the group 13 element in RM^I compounds is another common mode of reactivity. The reaction of RM^I with reagents such as $R'_3P{=}O$, $Me_3N–O$, S_8, Se, Te, or $R'N_3$ produces oligomeric M^{III} compounds of the general form $[RMCh]_n$ or $[RMNR']_n$ presumably via transient double-bonded compounds of the type RM=Ch or RM=NR′. The size of the oligomers obtained appears to be dependent on the size of the substituent(s) present. Small substituents tend to produce dimers (**5**), tetramers (heterocubanes), (**6**) and other clusters.[32] Similar clusters containing ligand-free group 15 elements, such as (**7**), can be obtained through the reaction of RM^I compounds with some of the low oxidation state group 15 compounds described in Section 4. Sterically demanding substituents can allow for the isolation of the double-bonded monomers, such as in the cases of (nacnac)M=NR′ (**8**)[33] or for TpM=Ch (**9**).[34] Similarly, various RM^I compounds insert into reactive bonds in transition metal, main group, or organic compounds to produce M^{III} species. This process is analogous to the oxidative addition process observed for some organometallic species and such reactivity has resulted in the use of RIn^I salts as catalysts for various C–C bond-forming reactions.[4]

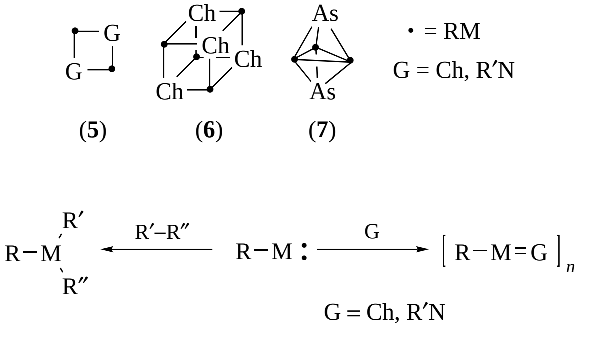

Scheme 7

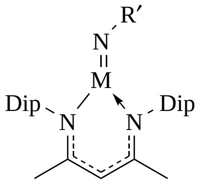

(**8**)

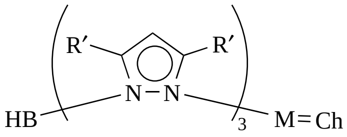

(**9**)

The oxidation of the reactive M^IR compounds through cycloaddition with organic multiple-bonded reagents, such as alkynes, dienes, and heterodynes, produces heterocyclic compounds that contain M^{III} (Scheme 8). In the case of Al^ICl, the initial cycloaddition products often oligomerize to form larger heterocycles and clusters compounds.

Reduction or disproportionation of univalent group 13 compounds generally results in the formation of multiple-bonded species, clusters, and metals (equation 3).[35–37] Such reactivity has been exploited for the production of indium nanoparticles (y = 0) by the solvothermal decomposition of CpIn.[38] Similarly, the thermal decomposition of many RM^I compounds (M = Al, Ga, In) results in the elimination of a portion of the substituents and produces metal-rich group 13 clusters of various sizes; the clusters obtained are thought to be intermediates on the pathway to the formation of bulk metal.[39]

$$\text{R–M}\colon \xrightarrow[-(x-y)\text{R}]{\Delta} \text{M}_x\text{R}_y \text{ clusters} \qquad (3)$$

$$y < x$$

2.2 Oxidation State +2

2.2.1 *Synthesis*

As outlined in Scheme 9, compounds containing group 13 elements in the +2 oxidation state are generally synthesized either by the alkali metal reduction of suitable halogenated precursor R_2MX or by metathesis reactions with available $X_2M–MX_2$ compounds that contain M^{II}.[40] The ligands that have been introduced using this method include aryl, alkoxy, and diketonates, but the most extensively examined series of compounds bear either the bis(trimethylsilyl)methyl ('disyl'),

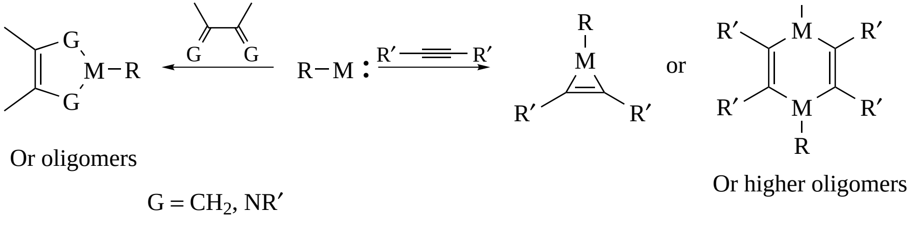

Scheme 8

tris(trimethylsilyl)methyl (‘trisyl’) or other bulky silyl ligands. The general name for compounds of the type $R_2M–MR_2$ is ‘dimetallane’; thus a compound containing an Al–Al bond is termed a ‘dialane’.

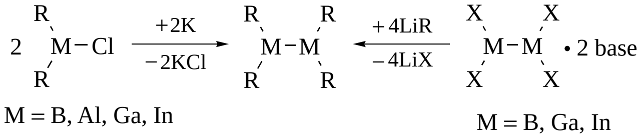

Scheme 9

2.2.2 *Reactivity*

Compounds containing M–M bonds can be further reduced, typically through the action of alkali metals and some alkyllithium reagents, to produce either multiple-bonded radical anions or M^I compounds; examples of such reduction products compounds are depicted in Figure 5.[41]

Some of the most extensively explored classes of reactivity of M^{II} compounds are oxidation of the group 13 elements either by insertion of a molecule into the M–M bond, cleavage of the M–M bond, or addition of a molecule to the M–M bond. Selected examples of such reactions are depicted in Schemes 10 and 11.[41]

The reaction of $R_2M–MR_2$ compounds with carboxylic acids provides different M^{III} products depending on the group 13 element, as summarized in Scheme 12. For Al, the reaction results in the cleavage of the Al–Al bond and the formation of a carboxylate-bridged and hydrogen-bridged dinuclear aluminum compound. For indium, the reaction also results in the cleavage of the In–In bond and yields In^{III} products and indium metal. For gallium, the Ga–Ga bond remains intact and two of the R ligands are cleaved instead.[42]

The transition metal ligand chemistry of M^{II} compounds has largely been restricted to the diboranes $R_2B–BR_2$, which

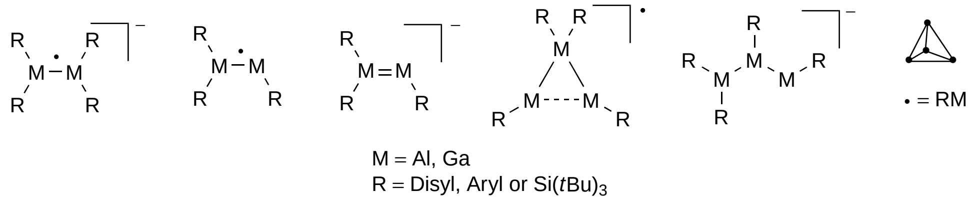

Figure 5 Some products obtained from the reduction of $R_2M–MR_2$ compounds

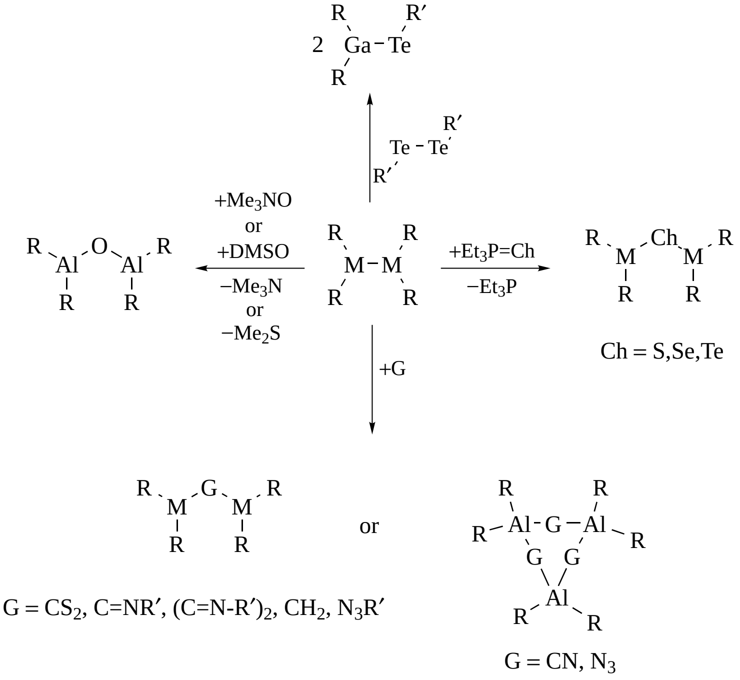

Scheme 10

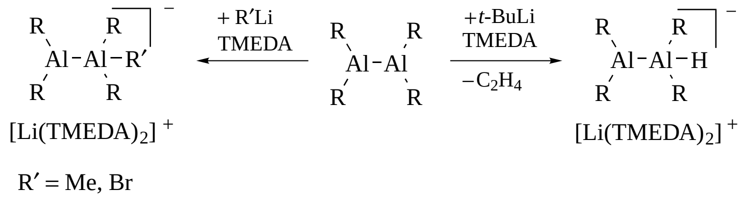

Scheme 11

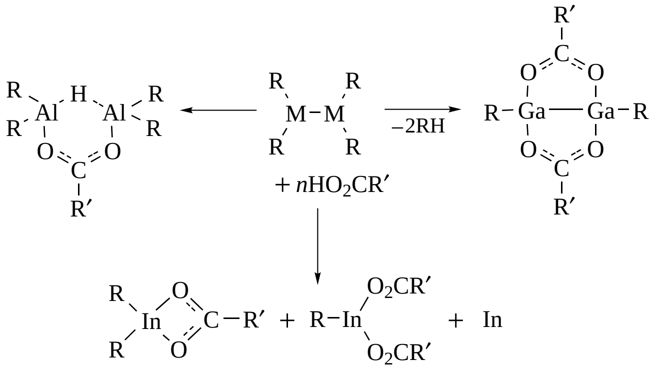

Scheme 12

produce boryl ligands through the cleavage of the B–B bond (equation 4).[43] The boryl groups can act as either terminal or bridging ligands and the transition metal complexes have been investigated extensively as reagents for hydroboration reactions.[44]

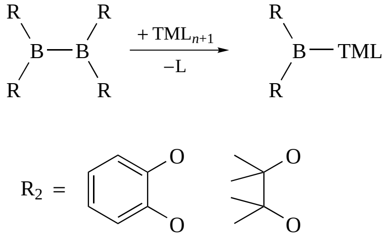

(4)

3 GROUP 14 ELEMENTS

The typical oxidation state for the lighter group 14 elements is +4 and because of periodic trends, the +2 oxidation state is common for the heavier elements such as Sn and Pb. There are numerous cluster compounds, known as Zintl compounds (*see **Zintl Compounds***), that contain group 14 elements in formally low oxidation states and that are described elsewhere in this Encyclopedia. Likewise, the group 14 carbene analogues (*see **Main Group Carbenes***) and multiply bonded compounds (*see **Main Group: Multiple Bonding***) that contain formally univalent or divalent group 14 elements are presented in the appropriate entries. Similarly, compounds containing E–E bonds are not discussed; thus only group 14 elements with oxidation states of less than +2 are considered in this section.

The only E^{I} halide yet reported is $[GeBr]_n$, which was made by the gas-phase reaction of Ge atoms and HBr.[45] While the structure of the bromide compound has yet to be determined, it has been used to make Ge_xR_y clusters ($y < x$) through the metathesis reaction with silyl-lithium or sodium reagents as shown in Scheme 13.[46,47] The formal oxidation state of the Ge atoms in the metal-rich clusters is less than one.

A few compounds containing R–E fragments have been made by the reduction of chlorinated E^{II} precursors bearing very bulky aromatic or silyl substituents. In the absence of other reagents, the univalent group 14 fragments dimerize to form multiple-bonded compounds. If the reaction is performed using a transition metallate reducing agent, the resulting transition metal complex contains a terminal multiple-bonded Ar–E ligand. These reactions are summarized in Scheme 14.[48,49]

Apart from the numerous Zintl ions, compounds containing zero-oxidation state group 14 atoms are rare because of the energetically favorable deposition of the element. Compounds (**10**)[50] and (**11**)[51] have been described as containing stabilized E atoms. Both of the compounds contain neutral ligands, bipy, and DAB, which are readily reduced to the corresponding

$$Ge_{(g)} + HBr_{(g)} \xrightarrow[-1/2\ H_2]{} 1/n\ [GeBr]_n \xrightarrow[\substack{-LiBr \\ \text{or} \\ -NaBr}]{\substack{+LiR \\ \text{or} \\ +NaR}} Ge_xR_y \text{ clusters}$$

Scheme 13

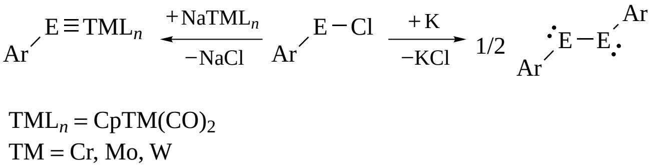

Scheme 14

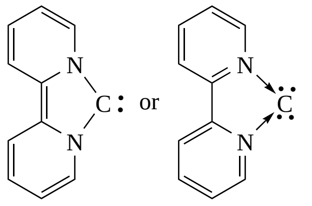

(**10**)

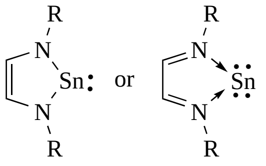

(**11**)

dianions, which also allows for the element to be described as being in the +2 oxidation state. The zero-valent description of the tin complex is supported by the observation of tin exchange from one DAB ligand to another neutral DAB ligand as shown in equation (5).[51]

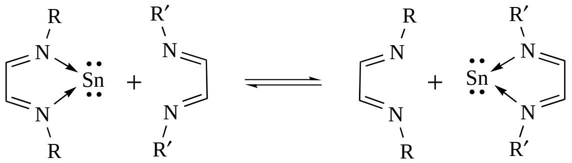

(5)

4 GROUP 15 ELEMENTS

In compounds, the elements of group 15 (pnictogens, Pn) are typically found in either the +3 or +5 oxidation state. Low oxidation state compounds are known for group 15 elements in the +2, +1, 0, −1, and −3 oxidation states; examples of compounds exhibiting common structural types are shown in Figure 6.

4.1 Oxidation State +2

The most common examples of pnictogens in the +2 oxidation state are the class of compounds of the general form $R_2Pn–PnR_2$ called ‘dipnictines’; a molecule of the type $R_2As–AsR_2$ is called a ‘diarsine’. Such compounds are typically prepared from the reduction of halopnictines by alkali metals, alkaline earth metals, or other reducing agents (equation 6). Alternatively, elimination of hydrogen from secondary pnictines and acid or salt elimination reactions have also been employed to synthesize dipnictines (equations 7 and 8). There are numerous examples of such compounds containing each of the group 15 elements (*see* ***Phosphorus: Organophosphorus Chemistry***; ***Arsenic: Organoarsenic Chemistry***; ***Antimony: Organometallic Chemistry***, and ***Bismuth: Organometallic Chemistry***), with the nitrogen analogs (hydrazines) being ubiquitous.

$$R_2PnX \xrightarrow[-NaX]{Na} R_2Pn–PnR_2 \qquad (6)$$

$$R_2PnH \xrightarrow[-H_2]{\Delta} R_2Pn–PnR_2 \qquad (7)$$

$$R_2PnX + R_2PnH \xrightarrow[-HX]{} R_2Pn–PnR_2 \qquad (8)$$

Although dipnictines formally contain +2 oxidation state pnictogens, most of their chemistry is similar to their +3 oxidation state PnR_3 analogs. In exceptional cases, unique behavior is observed. For example, when the R-groups are of sufficient steric bulk, the Pn–Pn bond in dipnictines can cleave homolytically to produce two PnR_2 radicals (equation 9) in either solution or the gas phase. The gas-phase structure of one such radical is depicted in Figure 7.[52] In addition, the metathesis reaction of diphosphines or diarsines with R′ChChR′, when R′ is sufficiently bulky, can also result in the generation of pnictinyl radicals (equation 10). Phosphinyl radicals can be generated by reduction under photolytic conditions in the presence of electron-rich olefins or by alkali metals (equation 11). In addition, both phosphinyl and arsinyl radicals have been obtained by the addition of excess aryllithium to the corresponding diarylchloropnictine (equation 12).[53]

$$R_2Pn–PnR_2 \xrightarrow{\Delta} :\dot{P}nR_2 \qquad (9)$$

$$RP{=}PR \xrightarrow[R' = t-\mathrm{Bu},\, n\text{-}\mathrm{Pr};\ \mathrm{Ch} = \mathrm{O,S}]{R'ChChR'} :\dot{P}n(R)(ChR') \qquad (10)$$

$$R_2PnX \xrightarrow[\text{or Na}]{h\nu + \text{olefin}} :\dot{P}nR_2 \qquad (11)$$

$$PnMes^*Cl_2 \xrightarrow[-LiCl]{\text{ex LiMes}^*} :\dot{P}nMes^*_2 \qquad (12)$$

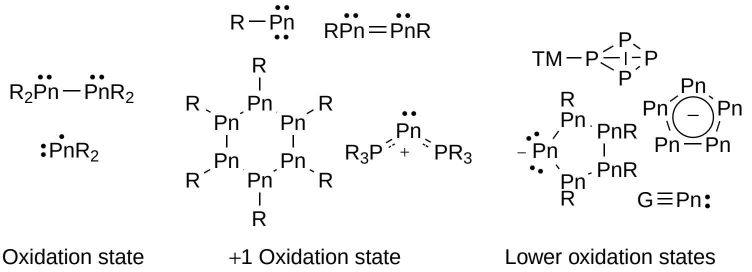

Figure 6 Common structural types of compounds containing low oxidation state group 15 elements

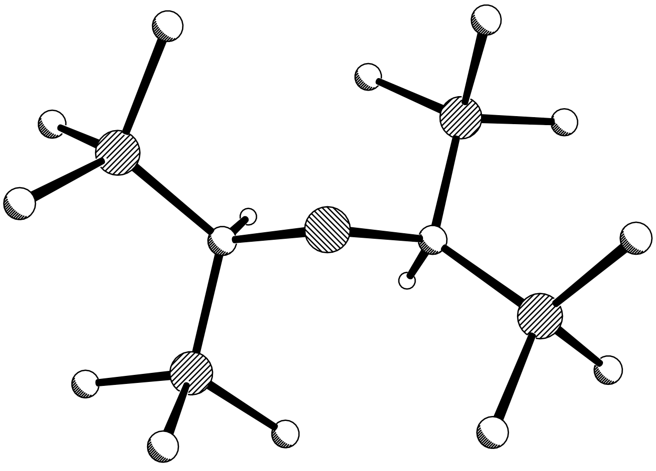

Figure 7 Gas-phase structure of a $\mathrm{Pn(CH(SiMe_3)_2)_2}$ radical

Cationic compounds that formally contain $\mathrm{P^{II}}$ are accessible through the reduction of phosphorus trihalides. $\mathrm{P_2X_5{}^+}$ can be synthesized by treating two equivalents of $\mathrm{PX_3}$ (X = Br, I) with a silver salt (equation 13).[54] Similarly, the addition of $\mathrm{PI_3}$ and $\mathrm{P_2I_4}$ to a silver salt produces salts containing the cation $\mathrm{P_3I_6{}^+}$ (equation 14).[55] Organophosphorus analogs of such salts can be synthesized by addition of phosphines to Lewis acidic phosphenium cations $\mathrm{R_2P^+}$ to produce $\mathrm{[R_2P\text{–}PR_3]^+}$; however, such compounds exhibit chemistry typical of $\mathrm{P^{III}}$ and are thus not generally considered in the context of containing phosphorus in a lower oxidation state.[56]

$$\mathrm{PX_3} \xrightarrow[-\mathrm{AgX}]{\mathrm{Ag[Al(OR)_4]}} \mathrm{X_2P\text{–}\overset{+}{P}X_3} \tag{13}$$

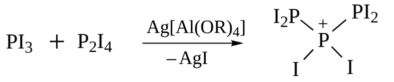

(14)

An alternate route to +2 oxidation state pnictogens is through the oxidation of the elemental form, which leads to compounds such as $\mathrm{Pn_2I_4}$ (Pn = P, As) (*see* ***Phosphorus: Inorganic Chemistry*** and ***Arsenic: Inorganic Chemistry***). Cationic $\mathrm{P^{II}}$ compounds can also be generated using this method, as exemplified by the addition of a silver salt to an equimolar mixture of $\mathrm{P_4}$ and $\mathrm{PX_3}$ (X = Br, I) to give $\mathrm{P_5I_2{}^+}$ (equation 15).[54]

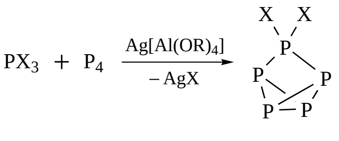

(15)

4.2 Oxidation State +1

The largest class of +1 oxidation state group 15 compounds are the 'pnictinidenes', R–Pn (e.g. a compound of the type R–P would be called a 'phosphinidene'), and their cyclic oligomers, which are known for all of the heavier pnictogens. Putative monomeric pnictinidenes are composed of a pnictogen atom with a single substituent and four nonbonding electrons. They may have either a singlet ground state with two lone pairs and an empty p orbital or a triplet ground state with one lone pair and two singly occupied p orbitals. Such highly reactive species are not able to be isolated under standard conditions and are generally used as intermediates that are generated in situ or as stabilized compounds such as those described below. Putative pnictinidenes are typically generated by either reduction of a dihalopnictine or photolytic release of either ethane from pnictiranes or CO from phosphaketenes. The nitrogen analogues, known as nitrenes, can form when azides are photolyzed (equation 16); however, the lack of appropriate starting materials prevents the use of such a method for the preparation of higher congeners.[57] Pnictinidenes are highly reactive and must be either trapped or stabilized (through cycloaddition with olefins, coordination to transition metal fragments, or donation from a Lewis base), otherwise they dimerize into multiply bonded dipnictines, RPn=PnR (*see* ***Main Group: Multiple Bonding***), oligomerize into rings (Scheme 15), or become oxidized.

Terminal phosphinidene-metal complexes, $\mathrm{L}_n\mathrm{TM{=}PR}$, readily add to double bonds (equation 17). Both metal-stabilized and phosphine-stabilized phosphinidenes, $\mathrm{R'P{=}PR_3}$, can act as phospha-Wittig reagents, which undergo metathesis reactions with carbonyl-containing compounds to generate carbon–phosphorus double bonds (equations 18 and 19).[58] Pnictinidenes and their complexes have been extensively reviewed in terms of both their syntheses and reactivities.[59–62]

$$\mathrm{R\text{–}N_3} \xrightarrow[-\mathrm{N_2}]{h\nu} \mathrm{R\text{–}N} \tag{16}$$

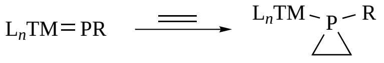

(17)

$$\mathrm{L}_n\mathrm{TM{=}PR} \xrightarrow{\mathrm{O{=}CR_2}} \mathrm{R_2C{=}PR} \tag{18}$$

$$\mathrm{R_3P{=}PR} \xrightarrow{\mathrm{O{=}CR_2}} \mathrm{R_2C{=}PR} \tag{19}$$

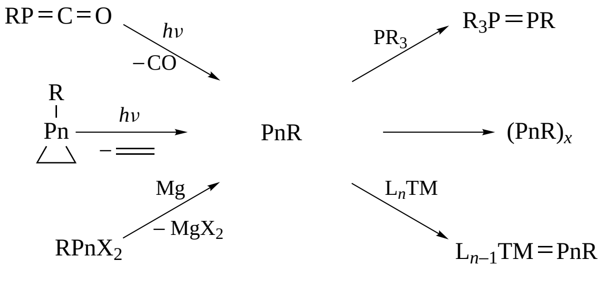

Scheme 15

Cyclic pnictinidenes, $(PnR)_n$, can coordinate to transition metal centers as monodentate or polydentate ligands. Alternatively, the homocycles can undergo ring opening and coordinate as chelating ligands or, in some cases, the compounds can liberate pnictinidene units that coordinate to metal centers. The actual mode of reactivity is dependent on the R-substituent and on the nature of the pnictogen atom.[63–66]

Stabilized pnictogen atoms in the +1 oxidation state are typically found in cations of the general formula $[R_3P–Pn–PR_3]^+$ (Pn = P, As). Cyclic and acyclic examples of such compounds have been synthesized by the reduction of PnX_3 in the presence of stabilizing phosphines (Scheme 16).[67–69] External reducing agents are not necessary in the case of PnI_3 (Pn = P, As), which disproportionates spontaneously in the presence of the phosphine ligands to form Pn^I salts.[70] The molecular structure of one such cation is depicted in Figure 8. Another route to related low oxidation state compounds is the reaction of lithium diphosphinoamides with pnictogen trihalides, which typically results in seven- or eight-membered ring compounds (equation 20).

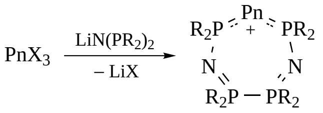
PnX3
LiN(PR2)2
– LiX
Pn
R2P + PR2
N N
R2P — PR2

(20)

A group of related zwitterionic (*see Zwitterion*) compounds is formed by the addition of lithium phosphinomethanides to either $PnCl_3$ or P_4, which result in four- or six-membered rings (equation 21).[71] It should be noted that the attempted reduction of Sb and Bi trihalides to form +1 oxidation state compounds typically results in the production of Sb^0 or Bi^0, which precipitates from solution.[72]

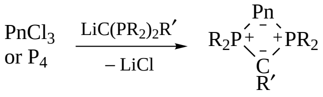
PnCl3
or P4
LiC(PR2)2R′
– LiCl
Pn
R2P+ – +PR2
C
R′

(21)

Several of the phosphine-stabilized P^I and As^I cations are air stable; the electronic structure of such compounds, as summarized by the various canonical forms shown in Figure 9, provides insight into the surprising stability. Pn → ligand back-bonding allows for the delocalization of electron density on Pn to the ligands, and reduces the reactivity of the cations.

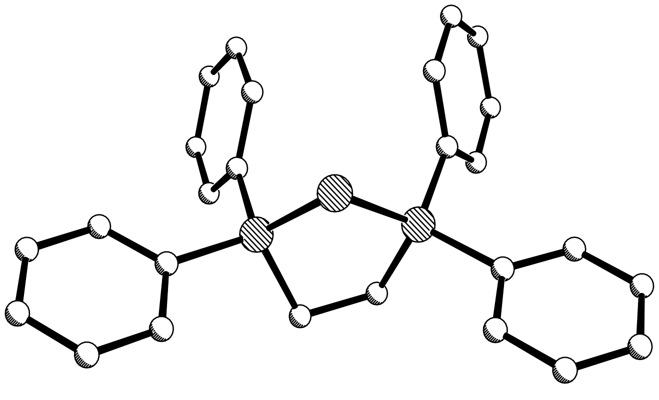

Figure 8 Molecular structure of a cation containing P^I, $[(dppe)P]^+$

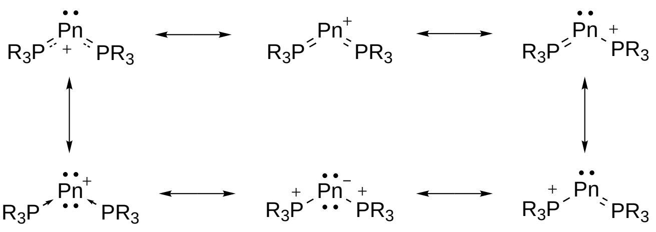
Pn
R3P + PR3
Pn+
R3P PR3
Pn +
R3P PR3
Pn+
R3P PR3
+ Pn– +
R3P PR3
+ Pn
R3P PR3

Figure 9 Canonical structures of stabilized P^I and As^I cations

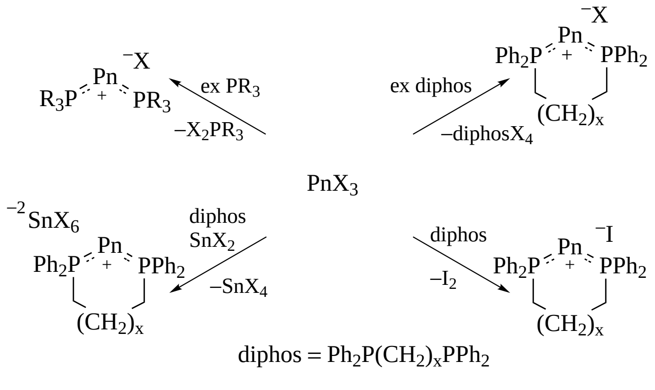
–X
Pn
R3P + PR3
ex PR3
–X2PR3
–X
Pn
Ph2P + PPh2
(CH2)x
ex diphos
–diphosX4
PnX3
–2SnX6
Pn
Ph2P + PPh2
(CH2)x
diphos
SnX2
–SnX4
diphos
–I2
–I
Pn
Ph2P + PPh2
(CH2)x
diphos = Ph2P(CH2)xPPh2

Scheme 16

Cationic P^I compounds exhibit several modes of reactivity, including: coordination to Lewis acids; oxidation by acids, water, and alkyl chlorides; and substitution of the stabilizing phosphine ligands by stronger donors (Scheme 17).[73–75] Some of these P^I and As^I cations have also been shown to be useful sources of P^I and As^I ions that provide zirconium complexes (**12**) containing unique square-planar Pn environments (equation 22).[76]

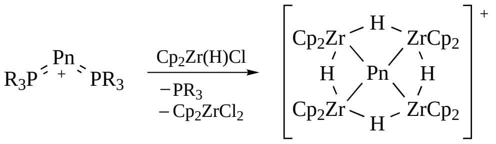
Pn
R3P + PR3
Cp2Zr(H)Cl
–PR3
–Cp2ZrCl2
Cp2Zr H ZrCp2
H Pn H
Cp2Zr H ZrCp2
+

(**12**)

(22)

4.3 Lower Oxidation States

There are a limited number of examples of white phosphorus, composed of P^0 atoms (equation 23), acting as a ligand to transition metals.[77–79] Lower oxidation state compounds of the pnictogens typically consist of oligomers

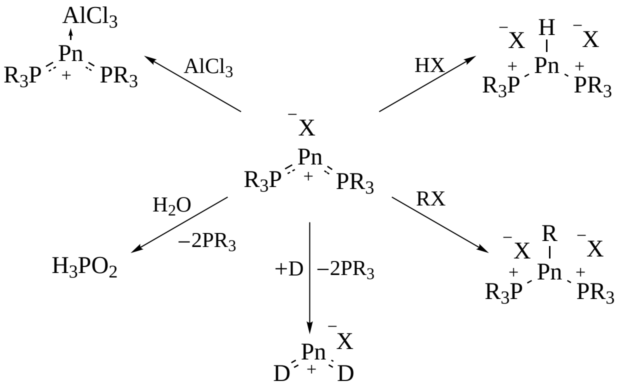

Scheme 17

of substituent-free pnictogen atoms. Phosphorus, arsenic, and antimony all form planar Pn_x, anionic rings that are analogous to Cp′, while bismuth can form a planar, dianionic four-membered ring.[80] These compounds can act either as terminal or bridging ligands for transition metal compounds. Other −1 oxidation state compounds include alkali metal salts of Pn clusters and various Zintl ions (*see* ***Zintl Compounds***), which are known for all the heavier pnictogens.

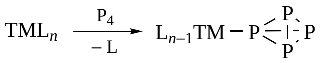

$$\mathrm{TML}_n \xrightarrow[-\,\mathrm{L}]{\mathrm{P}_4} \mathrm{L}_{n-1}\mathrm{TM}-\mathrm{P}\overset{\mathrm{P}}{\underset{\mathrm{P}}{<}}\mathrm{P} \tag{23}$$

The lowest oxidation state, −3, having a ns^2np^6 electron configuration, is found in transition metal complexes of ligand-free Pn anions. When a single Pn^{-3} ion is attached to a metal, they are collectively referred to as 'pnictido' ligands and form terminal metal–pnictogen triple bonds, which are known for all group 15 elements except bismuth.[81]

5 RELATED ARTICLES

Cluster Compounds: Inorganometallic Compounds Containing Transition Metal & Main Group Elements; Coordination Numbers & Geometries; Electronic Structure of Main-group Compounds; Inorganic Ring Systems; Main Group Carbenes; Main Group: Multiple Bonding; Subvalent Compounds.

6 REFERENCES

1. C. Janiak, *Coord. Chem. Rev.*, 1997, **163**, 107.
2. C. Dohmeier, D. Loos, and H. Schnockel, *Angew. Chem., Int. Ed. Engl.*, 1996, **35**, 129.
3. C. Dohmeier, E. Baum, A. Ecker, R. Koppe, and H. Schnockel, *Organometallics*, 1996, **15**, 4702.
4. T. H. Chan and Y. Yang, *J. Am. Chem. Soc.*, 1999, **121**, 3228.
5. D. G. Tuck, *Chem. Soc. Rev.*, 1993, **22**, 269.
6. M. Scheer, M. Kaupp, A. V. Virovets, and S. N. Konchenko, *Angew. Chem., Int. Ed. Engl.*, 2003, **42**, 5083.
7. S. T. Haubrich and P. P. Power, *J. Am. Chem. Soc.*, 1998, **120**, 2202.
8. H. Noth and H. Pommerening, *Angew. Chem., Int. Ed. Engl.*, 1980, **19**, 482.
9. H. Schmidbaur, *Angew. Chem., Int. Ed. Engl.*, 1985, **24**, 893.
10. G. Linti and H. Schnockel, *Coord. Chem. Rev.*, 2000, **206**, 285.
11. M. L. H. Green, P. Mountford, G. J. Smout, and S. R. Speel, *Polyhedron*, 1990, **9**, 2763.
12. M. Kehrwald, W. Kostler, A. Rodig, G. Linti, T. Blank, and N. Wiberg, *Organometallics*, 2001, **20**, 860.
13. L. O. Schebaum and P. Jutzi, Pentamethylcyclopentadienyl Complexes of the Monovalent Group 13 Elements, 'Group 13 Chemistry: From Fundamentals to Applications', ACS Symposium Series, American Chemical Society, Washington, DC, 2002, p. 16.
14. P. Jutzi and N. Burford, *Chem. Rev.*, 1999, **99**, 969.
15. C. L. B. Macdonald and A. H. Cowley, *J. Am. Chem. Soc.*, 1999, **121**, 12113.
16. J. D. Gorden, C. L. B. Macdonald, and A. H. Cowley, *Chem. Commun.*, 2001, 75.
17. C. L. B. Macdonald, A. M. Corrente, C. G. Andrews, A. Taylor, and B. D. Ellis, *Chem. Commun.*, 2004, 250.
18. C. M. Cui, H. W. Roesky, H. G. Schmidt, M. Noltemeyer, H. J. Hao, and F. Cimpoesu, *Angew. Chem., Int. Ed. Engl.*, 2000, **39**, 4274.
19. N. J. Hardman, B. E. Eichler, and P. P. Power, *Chem. Commun.*, 2000, 1991.
20. E. S. Schmidt, A. Jockisch, and H. Schmidbaur, *J. Am. Chem. Soc.*, 1999, **121**, 9758.
21. R. J. Baker, R. D. Farley, C. Jones, M. Kloth, and D. M. Murphy, *J. Chem. Soc., Dalton Trans.*, 2002, 3844.
22. M. Reiher and A. Sundermann, *Eur. J. Inorg. Chem.*, 2002, 1854.
23. M. N. S. Rao, H. W. Roesky, and G. Anantharaman, *J. Organomet. Chem.*, 2002, **646**, 4.
24. A. H. Cowley, V. Lomeli, and A. Voigt, *J. Am. Chem. Soc.*, 1998, **120**, 6401.
25. R. A. Fischer and J. Weiss, *Angew. Chem., Int. Ed. Engl.*, 1999, **38**, 2831.
26. C. Boehme, J. Uddin, and G. Frenking, *Coord. Chem. Rev.*, 2000, **197**, 249.
27. J. R. Su, X. W. Li, R. C. Crittendon, C. F. Campana, and G. H. Robinson, *Organometallics*, 1997, **16**, 4511.
28. J. D. Gorden, A. Voigt, C. L. B. Macdonald, J. S. Silverman, and A. H. Cowley, *J. Am. Chem. Soc.*, 2000, **122**, 950.

29. P. Jutzi, B. Neumann, G. Reumann, L. O. Schebaum, and H.-G. Stammler, *Organometallics*, 2001, **20**, 2854.
30. P. Greiwe, A. Bethauser, H. Pritzkow, T. Kuhler, P. Jutzi, and A. Siebert, *Eur. J. Inorg. Chem.*, 2000, 1927.
31. N. J. Hardman, P. P. Power, J. D. Gorden, C. L. B. Macdonald, and A. H. Cowley, *Chem. Commun.*, 2001, 1866.
32. H. W. Roesky, I. Haiduc, and N. S. Hosmane, *Chem. Rev.*, 2003, **103**, 2579.
33. N. J. Hardman, C. M. Cui, H. W. Roesky, W. H. Fink, and P. P. Power, *Angew. Chem., Int. Ed. Engl.*, 2001, **40**, 2172.
34. M. C. Kuchta and G. Parkin, *Coord. Chem. Rev.*, 1998, **176**, 323.
35. G. H. Robinson, Multiple Bonds Involving Aluminum and Gallium Atoms, ‘Advances in Organometallic Chemistry’, Elsevier, 2001, Vol. 47, p. 283.
36. G. H. Robinson, *Chem. Commun.*, 2000, 2175.
37. G. H. Robinson, *Acc. Chem. Res.*, 1999, **32**, 773.
38. K. Soulantica, A. Maisonnat, M. C. Fromen, M. J. Casanove, P. Lecante, and B. Chaudret, *Angew. Chem., Int. Ed. Engl.*, 2001, **40**, 448.
39. A. Schnepf and H. Schnockel, *Angew. Chem., Int. Ed. Engl.*, 2002, **41**, 3533.
40. W. Uhl, *Angew. Chem., Int. Ed. Engl.*, 1993, **32**, 1386.
41. W. Uhl, *Coord. Chem. Rev.*, 1997, **163**, 1.
42. W. Uhl, *Chem. Soc. Rev.*, 2000, **29**, 259.
43. H. Braunschweig and M. Colling, *Coord. Chem. Rev.*, 2001, **223**, 1.
44. H. Braunschweig and M. Colling, *Eur. J. Inorg. Chem.*, 2003, 393.
45. A. Schnepf and R. Koppe, *Z. Anorg. Allg. Chem.*, 2002, **628**, 2914.
46. A. Schnepf and R. Koppe, *Angew. Chem., Int. Ed. Engl.*, 2003, **42**, 911.
47. A. Schnepf, *Angew. Chem., Int. Ed. Engl.*, 2003, **42**, 2624.
48. P. P. Power, *Chem. Commun.*, 2003, 2091.
49. L. H. Pu, B. Twamley, S. T. Haubrich, M. M. Olmstead, B. V. Mork, R. S. Simons, and P. P. Power, *J. Am. Chem. Soc.*, 2000, **122**, 650.
50. R. Weiss, S. Reichel, M. Handke, and F. Hampel, *Angew. Chem., Int. Ed. Engl.*, 1998, **37**, 344.
51. T. Gans-Eichler, D. Gudat, and M. Nieger, *Angew. Chem., Int. Ed. Engl.*, 2002, **41**, 1888.
52. S. L. Hinchley, C. A. Morrison, D. W. H. Rankin, C. L. B. Macdonald, R. J. Wiacek, A. Voigt, A. H. Cowley, M. F. Lappert, G. Gundersen, J. A. C. Clyburne, and P. P. Power, *J. Am. Chem. Soc.*, 2001, **123**, 9045.
53. P. P. Power, *Chem. Rev.*, 2003, **103**, 789.
54. M. Gonsior, I. Krossing, L. Muller, I. Raabe, M. Jansen, and L. Van Wullen, *Chem. Eur. J.*, 2002, **8**, 4475.
55. I. Krossing, *J. Chem. Soc., Dalton Trans.*, 2002, 500.
56. N. Burford and P. J. Ragogna, *J. Chem. Soc., Dalton Trans.*, 2002, 4307.
57. P. N. D. Singh, S. M. Mandel, R. M. Robinson, Z. Zhu, R. Franz, B. S. Ault, and A. D. Gudmundsdottir, *J. Org. Chem.*, 2003, **68**, 7951.
58. S. Shah and J. D. Protasiewicz, *Coord. Chem. Rev.*, 2000, **210**, 181.
59. K. Lammertsma, *Top. Curr. Chem.*, 2003, **229**, 95.
60. A. H. Cowley, *Pure Appl. Chem.*, 1998, **70**, 765.
61. G. Huttner and K. Evertz, *Acc. Chem. Res.*, 1986, **19**, 406.
62. A. H. Cowley, *Acc. Chem. Res.*, 1997, **30**, 445.
63. R. M. De Silva, M. J. Mays, and G. A. Solan, *J. Organomet. Chem.*, 2002, **664**, 27.
64. R. M. De Silva, M. J. Mays, P. R. Raithby, and G. A. Solan, *J. Organomet. Chem.*, 2002, **642**, 237.
65. H. J. Breunig and L. Balazs, *Organometallics*, 2004, **23**, 304.
66. H. J. Breunig and R. Rosler, *Chem. Soc. Rev.*, 2000, **29**, 403.
67. A. Schmidpeter and S. Lochschmidt, *Inorg. Synth.*, 1990, **27**, 253.
68. J. A. Boon, H. L. Byers, K. B. Dillon, A. E. Goeta, and D. A. Longbottom, *Heteroatom Chem.*, 2000, **11**, 226.
69. R. J. Barnham, R. M. K. Deng, K. B. Dillon, A. E. Goeta, J. A. K. Howard, and H. Puschmann, *Heteroatom Chem.*, 2001, **12**, 501.
70. B. D. Ellis, M. Carlesimo, and C. L. B. Macdonald, *Chem. Commun.*, 2003, 1946.
71. H. H. Karsch and E. Witt, *J. Organomet. Chem.*, 1997, **529**, 151.
72. M. Dotzler, A. Schmidt, J. Ellermann, F. A. Knoch, M. Moll, and W. Bauer, *Polyhedron*, 1996, **15**, 4425.
73. A. Schmidpeter and S. Lochschmidt, *Angew. Chem., Int. Ed. Engl.*, 1986, **25**, 253.
74. S. Lochschmidt and A. Schmidpeter, *Z. Naturforsch., B: Chem. Sci.*, 1985, **40B**, 765.
75. A. Schmidpeter, S. Lochschmidt, K. Karaghiosoff, and W. S. Sheldrick, *J. Chem. Soc., Chem. Commun.*, 1985, 1447.
76. M. Driess, H. Ackermann, J. Aust, K. Merz, and C. Von Wullen, *Angew. Chem., Int. Ed. Engl.*, 2002, **41**, 450.
77. M. Di Vaira, M. P. Ehses, M. Peruzzini, and P. Stoppioni, *Eur. J. Inorg. Chem.*, 2000, 2193.
78. I. De los Rios, J.-R. Hamon, P. Hamon, C. Lapinte, L. Toupel, A. Romerosa, and M. Peruzzini, *Angew. Chem., Int. Ed. Engl.*, 2001, **40**, 3910.
79. I. Krossing and L. Van Wullen, *Chem. Eur. J.*, 2002, **8**, 700.
80. O. J. Scherer, *Acc. Chem. Res.*, 1999, **32**, 751.
81. M. Scheer, *Coord. Chem. Rev.*, 1997, **163**, 271.

Alkane Carbon–Hydrogen Bond Activation

Robert H. Crabtree
Yale University, New Haven, CT, USA

1	Introduction	1
2	Alkane Complexes	2
3	Shilov Chemistry and Alkane Oxidation Catalysis	2
4	Oxidative Addition and Related Alkane Conversion Catalysis	3
5	Sigma Bond Metathesis Pathways	5
6	Surface-bound Organometallics	5
7	Carbenes and CH Activation	5
8	Other Approaches	5
9	Conclusion and Future Challenges	6
10	References	6

1 INTRODUCTION

‘CH Activation’ is sometimes used rather too loosely to cover a wide variety of situations in which CH bonds are broken. As Sames has most recently pointed out,[1] the term was first adopted to make a distinction between organic reactions in which CH bonds are broken by classical mechanistic pathways, and the class of reactions involving transition metals that avoid these pathways and their consequences in terms of reaction selectivity. For example, radicals such as RO• and •OH readily abstract an H atom from alkanes, RH, to give the alkyl radical R•. Also in this class, are some of the metal catalyzed oxidations, such as the Gif reaction and Fenton chemistry (*see* ***Oxidation Catalysis by Transition Metal Complexes***). Since this reaction tends to occur at the weakest CH bond, the most highly substituted R• tends to be formed, for example, *i*Pr• and not *n*Pr• from propane. Likewise, electrophilic reagents such as superacids (*see Superacid*), readily abstract a H^- ion from an alkane. The selectivity is even more strongly in favor of the more substituted carbonium ion product such as $i\mathrm{Pr}^+$ and not $n\mathrm{Pr}^+$ from propane. The result is that in any subsequent functionalization, the branched product is obtained, for example, *i*PrX and not *n*PrX (Scheme 1).

In a broad class of reactions of CH bonds with low-valent transition metals, however, the metal inserts into a CH bond of the alkane to give an alkylmetal hydride in which there is often a preference for formation of the least substituted alkyl. In any subsequent functionalization, the linear (or least branched) product is obtained, for example, *n*PrX and not *i*PrX. Since the branched product can be obtained by classical organic procedures, CH activation is potentially important in providing a route to the linear compounds that are often more useful in many applications. Unfortunately, CH activation has not so far been made efficient enough for it to become commercially important. With the rise of methane as a feedstock for the twenty-first century, the need for alkane activation will become more acute. Methane is hard to transport and use, while its oxidation product, methanol (or a methanol derivative such as $MeOCH_2OMe$) would make a convenient fuel and carbon source.

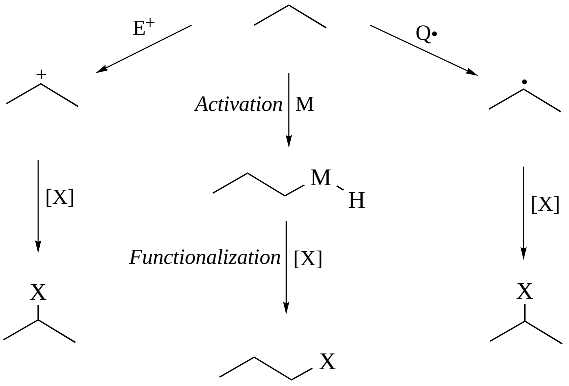

Scheme 1

The case of methane to methanol brings up a second important selectivity problem in the field: how to stop at the methanol oxidation level. Methanol is much more sensitive to oxidation than methane, so any classical oxidation procedure is likely to overoxidize the methanol to CH_2O, CO, and CO_2. The CH activation route has the advantage that the CH bond of methanol is not exceptionally reactive relative to that of methane, so the overoxidation problem, while not completely eliminated, is nevertheless reduced to manageable proportions.

The case of methane also raises the issue of enzymatic oxidation. This proceeds selectively to methanol with the methane monooxygenases (MMO, *see Monooxygenase*; ***Iron: Models of Proteins with Dinuclear Active Sites***; ***Iron Proteins with Dinuclear Active Sites***) but the selectivity is not a function of the chemistry employed, which appears to be H atom abstraction by a high-valent oxoiron cluster, but of the ‘chemical engineering’ of the site. The monooxygenase pathway automatically delivers only 2e of oxidation after which the hydrophobic site expels methanol before the site is reactivated for the next oxidation to occur. This step occurs by the provision of 2e of reducing power that serves to reduce one O atom of the O_2 substrate to water, leaving the remaining oxygen atom available for transfer to the substrate – hence the term monooxygenase.

Early work with transition metals, following Fenton-type chemistry (*see Fenton Chemistry*), employed the transition metal as a catalyst for the decomposition of a primary oxidant to yield radicals such as RO• and •OH that readily abstract an H atom from alkanes, RH, to give R•. These radicals can be functionalized, for example, by reaction with O_2 to give RO_2•, which in turn decompose under the conditions used to give a mixture of alcohol and ketone. This puts the chemistry within the realm of classical organic reactions, at least from a mechanistic perspective. Some high-valent oxometal intermediates may be able to oxidize alkanes without production of radicals but this area is controversial and we do no more than indicate a recent book.[2] Other early reactions, such as those of arenes with Hg^{2+}, led to electrophilic aromatic substitution, another well-recognized reaction of classical organic chemistry.

We restrict our attention to the reactions of CH bonds with low-valent transition metals that avoid radical or electrophilic selectivity patterns and are therefore considered CH activation in the sense considered at the outset of the review. A number of non-alkane CH activation reactions are included where they derive from concepts developed in alkane work and where they have proved particularly useful.

2 ALKANE COMPLEXES

Many CH activation pathways are thought to go via an intermediate in which the alkane is bound to the metal as a sigma complex. Sigma complexes[3,4] involve binding of a sigma bond to a metal without cleavage, of which the paradigmatic example is the Kubas[5] H_2 complex, $[W(H_2)(CO)_3(PCy_3)_2]$ (Scheme 2, *see* ***Hydride Complexes of the Transition Metals***). In such a case, the pair of electrons in the H–H bond acts as a 2e donor to the metal. Another important class of such complexes, agostic species, have a hemilabile ligand in which there is at least one normal metal–ligand bond and at least one C–H···M sigma bonded group, as first established by Trofimenko[6] and Cotton.[7] The alkyl CH bond is a poor ligand but as part of a chelate, it can readily form a sigma complex. Alkanes themselves can also form sigma complexes without the need for assistance from chelation, but these are rarely isolable. The first solid evidence for such species in the condensed phase came from $M(CO)_6$ photolysis in an alkane matrix where formation of $[M(CO)_5(\text{alkane})]$ (Scheme 2) was identified by Perutz and Turner in 1975.[8] Alkane complexes were proposed as intermediates to explain the scrambling and inverse kinetic isotope effects seen in a variety of reductive eliminations of alkylmetal hydride complexes.[9–12] A variety of studies has shown that alkane complexes are involved in the alkane reactions to be mentioned in later sections. $CpRe(CO)_2$(*n*-heptane) was detected by FTIR at room temperature in heptane,[13] and $CpRe(CO)_2$(cyclopentane) (Scheme 2) was detected by NMR.[14] Crystal structures have been obtained for a heptane complex of an iron porphyrin[15] and for a cyclohexane uranium complex.[16]

The key properties of a C–H sigma complex relevant to CH activation are: 1) the very large degree of acidification of the CH proton; 2) the ability of the adduct to undergo oxidative addition; and 3) the preference, probably of steric origin, for binding at the least-hindered CH bond. The first allows facile deprotonation or H/D exchange in an alkane complex. The second leads to alkylmetal hydrides that can evolve to give alkene or a functionalized product. The third may be a factor in the selectivity (primary > secondary > tertiary) shown by many of the systems described in this article, a selectivity that contrasts with that seen for conventional radical and electrophilic CH reactions (tertiary > secondary > primary).

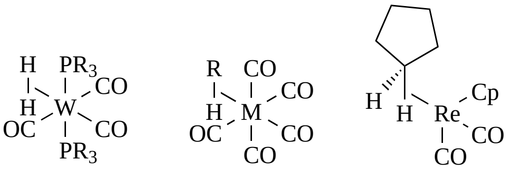

Scheme 2

3 SHILOV CHEMISTRY AND ALKANE OXIDATION CATALYSIS

In the late 1960s, Garnett and Hodges described the exchange of hydrogen for deuterium in polycyclic aromatic hydrocarbons and heterocycles, homogeneously catalyzed by platinum(II) salts in a deuterated aqueous acetic acid medium.[17–20] They noted that in alkylaromatics, the exchange also occurred in several carbons out along the alkyl chain. Noticing this point, Shilov[21] and coworkers took the critical step of extending the system to alkanes themselves. They noted slow but definite exchange at modest temperatures. More remarkable than the isotope exchange itself was the selectivity: activation of primary CH bonds in the terminal positions of long chain alkanes was preferred, in contrast with the preferential attack at secondary and tertiary positions by classical radical and electrophilic reagents.

$$CH_4 \xrightarrow{\text{DOAc, PtCl}_4^{2-}} CH_{(4-x)}D_x \tag{1}$$

Moving to a system having $[Pt(IV)Cl_6]^{2-}$ as primary oxidant and platinum(II) as catalyst, Shilov and coworkers saw alkane oxidation to ROH and RCl with the same nonstandard selectivity pattern they saw for the isotope exchange: terminal attack was preferred. The Pt(IV) was clearly intercepting the same intermediate alkyl that led to RD in the deuteriation experiments. In the case of methane as substrate, clinching evidence was obtained for a methylplatinum intermediate.[22,23] Through the 1970s, this work was met with reserve in the West and the field remained at a low level of activity at that time. The 1980s saw a growing number of CH activation systems, to be described in a later section, that led to a great increase in attention to the topic and a growing awareness of the true significance of the Shilov work. The state of Shilov chemistry and the field as a whole at this stage can be judged from Shilov's 1984 book**[23]** and the present author's 1985 review.**[24]**

$$\mathrm{PrH} \xrightarrow{\mathrm{PtCl_6}^{2-},\ \mathrm{PtCl_4}^{2-}} n\mathrm{PrCl} \tag{2}$$

From 1993, Bercaw and Labinger**[25]** examined the system in detail and employed a series of mechanistic probes that confirmed all the main points made by Shilov and helped refine the mechanistic picture. The current view of the mechanism is shown in Scheme. 3. An alkane complex either leads to oxidative addition of the alkane (i.e. metal insertion into the CH bond) and loss of a proton, or the alkane complex loses a proton directly. In the isotope exchange, the resulting alkyl is cleaved by D^+ to give RD. The selectivity for the terminal CH bond is either decided by the tendency for oxidative addition to occur at the terminal CH or by the tendency of alkane complexes to prefer binding and deprotonation at the terminal CH. In either case, the steric effect of the metal certainly contributes to this preference. The relatively low electronegativity of the metal may also have a role in analogy to the anti-Markownikov addition of a BH bond to an alkene in hydroboration, where a terminal C–B bond is preferred. In the alkane functionalization, the next step is oxidation of the Pt(II) alkyl by Pt(IV) to give a Pt(IV) alkyl; this occurs by electron transfer and not by alkyl transfer. The Pt(IV) now becomes a good leaving group, and Cl^- or OH^- can nucleophilically attack the R–Pt(IV) species with departure of Pt(II) to regenerate the catalyst. The origin of the unusual selectivity (methane $\sim$ MeOH) is not completely clear; it may be decided by the greater facility with which the sterically small methane, with its relatively basic CH bonds, is able to bind to Pt(II) or, more likely, it may be that CH_4 has more basic CH bonds that are better able to bind to the electrophilic Pt.

In an important development, Periana**[26]** made Shilov-like chemistry more practically useful with a series of methane conversion catalysts. The first such system involved Hg(II) salts in H_2SO_4 at 180°, the latter being both a solvent and a mild reoxidant (equation 3). Methane was converted to the methanol ester, methyl bisulfate, $MeOSO_3H$, in which the $-OSO_3H$ provides a powerful deactivating group to prevent overoxidation of the methanol. The reaction is efficient: at a methane conversion of 50%, 85% selectivity to methyl bisulfate (ca.43% yield) was achieved with the major side product being carbon dioxide. The molar productivity is $10^{-7}\,\mathrm{mole\,mL^{-1}\,s^{-1}}$ with a Hg(II) turnover frequency of $10^{-3}\,\mathrm{s^{-1}}$. $MeHg^+$ was detected as an intermediate by NMR spectroscopy, and a Shilov-like mechanism was proposed.

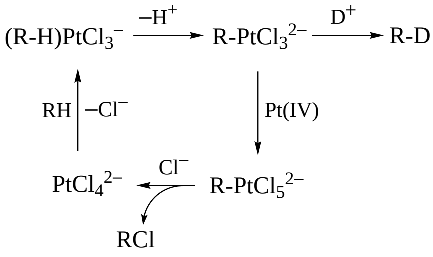

Scheme 3

$$\mathrm{CH_4} \xrightarrow{\mathrm{H_2SO_4,\ Hg(II)}} \mathrm{CH_3OSO_3H} \tag{3}$$

The next development**[27]** was a Pt(II) catalyzed process in H_2SO_4 at 180°, where the metal was stabilized with a 2,2′-bipyrimidine ligand or alternatively with two ammonias. The latter was more active but deactivated faster, while the diazene was more robust but less active.

The most spectacular system of this type, Periana**[28]** reported catalytic, oxidative condensation of CH_4 to CH_3COOH in one step. This direct, selective, oxidative condensation of two methane molecules to acetic acid took place at 180° in liquid sulfuric acid with Pd(II) salts as catalyst. C-13 isotopic labeling showed that both carbons of acetic acid originate from the methane. The results are consistent with the reaction occurring by tandem catalysis, involving methane C–H activation to generate Pd–CH_3 species, followed by efficient oxidative carbonylation with methanol, generated in situ from methane, to produce acetic acid. Sen**[29]** has reported an intriguing series of catalytic systems for conversion of methane and other alkanes that are probably similar in character.

Shilov-type chemistry has been extended to complex organic synthesis by Sames,**[30]** who finds that amino acids such as valine can be functionalized at their terminal $-CH_3$ groups by conversion to $-CH_2OH$ (equation 4). The preferred catalyst is the usual Pt(II) but the oxidant is not Pt(IV) but the much more convenient Cu(II). An aqueous medium is used and functional group protection is not needed, but 130° is required for catalytic turnover.

$$\mathrm{Me_2CHCH(COOH)NH_2} + [\mathrm{O}] = \mathrm{(HOCH_2)MeCHCH(COOH)NH_2} \tag{4}$$

4 OXIDATIVE ADDITION AND RELATED ALKANE CONVERSION CATALYSIS

Early efforts were directed at reversing the well-known transition metal catalyzed hydrogenation of alkenes to alkanes. In 1979, the stoichiometric dehydrogenation of alkanes was reported,**[31]** for example, of cyclopentane with $[IrH_2(Me_2CO)(PPh_3)_2]^+$ to $[CpIrH(PPh_3)_2]^+$, using tBuCH=CH_2 as mild oxidant, or 'hydrogen acceptor' (equation 5). Oxidative addition was proposed as the pathway.

$$[\mathrm{IrH_2(Me_2CO)(PPh_3)_2}]^+ \xrightarrow{\mathrm{C_5H_{10}},\ t\mathrm{BuCHCH_2}} [\mathrm{CpIrH(PPh_3)_2}]^+ \tag{5}$$

The key oxidative addition was directly observed in 1982, with the photogeneration of $Cp^*Ir(PMe_3)$ from the dihydride, followed by reaction with the alkane solvent, RH, to give a variety of $Cp^*Ir(R)(H)(PMe_3)$ species (equation 6).[32] The surprise was the high selectivity for attack at a terminal CH bond, contrary to typical organic reactivity, but analogous to Shilov chemistry. Strong CH bonds, as are present in the terminal CH bonds of linear alkanes or in cyclopropane or in benzene were cleaved in preference to weaker bonds, such as the internal CH bonds of linear alkanes, implying that the Ir–R bond strength tracked the H–C bond strength. Analogous iridium carbonyls and rhodium phosphine complexes gave similar chemistry.[33–35]

$$\mathrm{Cp^*Ir(PMe_3)H_2} \xrightarrow[-\mathrm{H_2}]{h\nu} \mathrm{Cp^*Ir(PMe_3)} \xrightarrow{\mathrm{PrH}} \mathrm{Cp^*Ir(PMe_3)}(n-\mathrm{Pr})\mathrm{H} \qquad (6)$$

Thermal reaction proved possible by starting from $Cp^*Ir(R)(H)(PMe_3)$ by thermally eliminating RH in the presence of methane to give the very thermodynamically and kinetically stable $Cp^*Ir(Me)(H)(PMe_3)$.[36] It had previously been thought that alkane activation of this sort was an unpromising prospect because *cis*-alkyl hydrides tended always to be unstable and eliminate RH. The key point in the Bergman system was the nonlability of the $Cp^*Ir(Me)(H)(PMe_3)$ complex. Reductive elimination, it was soon recognized, only becomes easy when a five-coordinate 16-electron intermediate is produced by ligand loss.

Reactions related to equation (6) are probably the most intensively studied in the whole field of organometallic chemistry. Ultrafast kinetics have given evidence for the formation of intermediates such as alkane and rare gas complexes in this system.[37]

A number of catalytic reactions have also been found that depend on oxidative addition as the first step. Felkin[38] described the selective catalytic conversion of a variety of cycloalkanes into cycloalkenes by using a soluble rhenium polyhydride system, $ReH_7(PR_3)_2$, and $t\mathrm{BuCH{=}CH_2}$ as hydrogen acceptor. The selective conversion of n-pentane into pent-1-ene also proved possible.[39] Other increasingly efficient alkane dehydrogenation (equation 7) catalysts were soon found,[40–42] although none has so far proved commercially useful. Alternatives to the use of $t\mathrm{BuCH{=}CH_2}$ were developed: the reaction can either be run photochemically or the H_2 removed by reflux.

$$\mathrm{RCH_2CH_3} + t\mathrm{BuCH{=}CH_2} \xrightarrow{\text{cata.}} \mathrm{RCH{=}CH_2} + t\mathrm{BuCH_2CH_3} \qquad (7)$$

Catalytic carbonylation of alkanes, RH, proved possible via CH activation catalyzed by $RhCl(CO)(PMe_3)_2$ under irradiation.[43] In this reaction, the alkyl hydride intermediate undergoes CO insertion, followed by reductive elimination of the aldehyde, RCHO.

Perhaps the most interesting development of these types of reactions, the formation of a single product from terminal borylation of linear alkanes by a transition metal catalyzed reaction, comes from Hartwig.[44] $Cp^*Rh(\eta^4\text{-}C_6Me_6)$ catalyzes the high-yield formation of linear alkylboranes from commercially available borane reagents under thermal conditions. Iridium catalysts are also effective.[45]

The Murai reaction (Scheme 4), the replacement of an ortho-CH on an aromatic ketone by an alkyl group derived from a substrate olefin, is catalyzed by a variety of Ru complexes. This C–C bond formation occurs via chelate directed C–H bond activation (cyclometalation) in the first step, followed by alkene insertion into RuH and reductive elimination of the alkylated ketone.[46] In a recent example of the use of a related cyclometalation in complex organic synthesis, Sames[47] reports catalytic arylation (Suzuki reaction) and alkenylation (Heck reaction) of alkyl segments of a synthetic intermediate mediated by Pd(II).

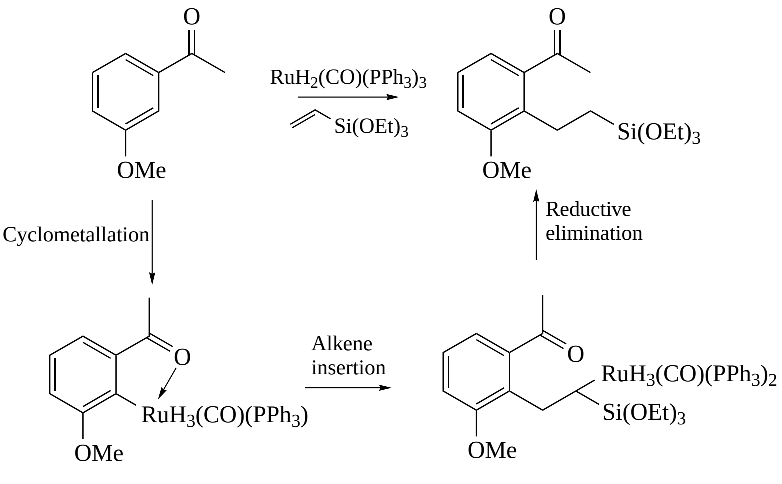

Scheme 4

Cyclometalation,[48] one of the earliest reactions involving CH oxidative addition, has been reviewed recently. Apart from the Murai reaction, cyclometalation has also been incorporated into a number of other catalytic reactions of interest in organic synthesis.[49,50]

5 SIGMA BOND METATHESIS PATHWAYS

Sigma complexes are particularly relevant to sigma bond metathesis pathways of alkane activation. Alkane binding induces a depletion of electron density on the CH bond that acidifies the CH proton. In the right situation, this can lead to exchange of the R group from the RH substrate with an M–R′ alkyl already present on the metal. The important early example of this process was Watson's[51] methane exchange, verified with C-13 methane (C^*H_4). The significance of this pathway is that the oxidation state of the metal does not change, so the route is available to metals that are redox-inactive like d^0 ions and the lanthanides. Indeed, the metalation of CH bonds with alkyllithiums, albeit only possible for substrates somewhat more activated than simple alkanes, is an example of the same general type of reaction. Marks[52] showed similar reactions with actinides.

Even the late metals can show this reaction, although in such cases it is hard to completely eliminate the possibility of oxidative addition/reductive elimination as an alternative redox pathway to the same products. Bergman[53] proposed a sigma bond metathesis pathway for the reaction of alkanes including methane with the dichloromethane complex, $[Cp^*IrR(PMe_3)(ClCH_2Cl)]^+$.

In a related type of reaction, an alkane RH is activated by addition across a metal-heteroatom bond, as in the Zr=N system of Wolczanski.[54] This could be considered a metathesis-like process where the RH proton is taken up by the basic heteroatom.

6 SURFACE-BOUND ORGANOMETALLICS

Marks[55] has reviewed this area. Basset[56] has bound organometallic species to a silica surface and seen interesting alkane reactions that go via initial CH bond activation; this step probably proceeds by a sigma bond metathesis pathway since the metals involved are d^0. Subsequent reactions include CC bond cleavage and carbon skeletal rearrangements.

7 CARBENES AND CH ACTIVATION

Diazo precursors to organic carbenes can be induced to insert into relatively unactivated CH bonds by transition metal catalysis, typically involving dirhodium(II) tetracarboxylates.[57] The Rh carbene complex that is proposed as an intermediate attacks the CH bond of a substrate, often with chelate control of the site of attack. Asymmetric ligands can provide good (enantiomeric excess) e.e.s in asymmetric synthesis. A recent example[58] is the asymmetric synthesis of (+)-indatraline using rhodium-catalyzed C–H activation. In all such cases, the CH bonds are activated by chelate control or by adjacent functionality, so the selectivity problem is simplified.

Carbene complexes have been synthesized by various CH activation routes. For example, amines and ethers can undergo double geminal CH activation to yield a Fischer-type (heteroatom substituted) carbene[59] and an imidazolium salt can yield *N*-heterocyclic carbenes directly in the same way.[60] In the latter case, abnormal binding via C-4 can occur as well as the usual C-2 binding.

8 OTHER APPROACHES

A whole range of reactions are known that do not fall within the categories above. The very long-established mercury photosensitized alkane reactions are radical in character,[61,62] but Schwarz[63,64] in particular has looked at other gas-phase reactions by metal ions. The vast metal oxo area is covered elsewhere (*see* ***Oxidation Catalysis by Transition Metal Complexes***) but two proposals that come from this work are worth mentioning because they may well relate to organometallic systems, too. The first is the two-state reactivity (TSR) model proposed[65,66] from theory for hydroxylation and epoxidation by cytochrome P-450. This postulates that when two different spin surfaces are accessible, both may contribute to reaction. TSR is used to reconcile the dilemma of the consensus 'rebound mechanism' of alkane hydroxylation, which came from experimental studies of ultrafast radical clocks. The dilemma is that radicals appear to be either present or absent depending on the experiment used to probe for them, so the standard rebound mechanism remained problematic. On TSR, this is simply understood on a two-state model, one low-spin (LS) the other high-spin (HS). In both states, CH bond activation proceeds in a manner akin to the rebound mechanism, but the LS mechanism is effectively concerted, whereas the HS is stepwise with the appearance of radical intermediates. In another proposal, Mayer[67] has shown how coupled proton/electron transfer can efficiently remove a hydrogen atom from a CH bond, a process that can readily occur in high-valent oxo species. The TSR proposal highlights the growing importance of computational chemistry in helping clarify difficult mechanistic problems in organometallic chemistry.

Finally, a number of useful recent books on[68] or including[69] the topic of CH activation have now appeared.

9 CONCLUSION AND FUTURE CHALLENGES

CH Activation and functionalization, once exotic, has now entered the mainstream. It is routinely used in synthesis even of complex organic molecules and is likely to greatly expand in future. In the inorganic realm, we still need a wider range of functionalization reactions to accompany the CH activation step. The latter provides a metal–alkyl bond, but these are often either inert or simply revert to alkane on attempted functionalization. Another problem is that functionalizing reagents tend not to be compatible with the alkane binding function of the catalyst – this is unsurprising since alkanes bind weakly and may be displaced by the functionalizing reagent. So far, it is hard to imagine how one could design a system capable of attacking not just a site along a linear alkyl chain of, say a carboxylic acid, but be tunable to attack at different specific sites as required. Such enzyme-like selectivity will no doubt need the introduction of molecular recognition at a very sophisticated level. In spite of the strong progress to date, much work therefore still remains.

10 REFERENCES

1. D. Sames, Personal communication, 2003.
2. B. Meunier ed., ‘Biomimetic Oxidations Catalysed by Transition Metal Complexes’, Imperial College Press, London, 2000.
3. M. Brookhart, M. L. H. Green, and L. L. Wong, *Prog. Inorg. Chem.*, 1988, **36**, 1.
4. R. H. Crabtree, *Angew. Chem., Int. Ed. Engl.*, 1993, **32**, 789.
5. G. J. Kubas, ‘Metal-dihydrogen and σ-bond Complexes’, Kluwer Academic, New York, 2001.
6. S. Trofimenko, *J. Am. Chem. Soc.*, 1968, **90**, 4754.
7. F. A. Cotton and A. G. Stanislowski, *J. Am. Chem. Soc.*, 1974, **96**, 5074.
8. R. N. Perutz and J. J. Turner, *J. Am. Chem. Soc.*, 1975, **97**, 4791.
9. R. M. Bullock, C. E. L. Headford, S. E. Kegley, and J. R. Norton, *J. Am. Chem. Soc.*, 1985, **107**, 727.
10. G. Parkin and J. E. Bercaw, *Organometallics*, 1989, **8**, 1172.
11. G. L. Gould and D. M. Heinekey, *J. Am. Chem. Soc.*, 1989, **111**, 5502.
12. W. D. Jones, *Acc. Chem. Res.*, 2003, **36**, 140.
13. G. I. Childs, D. C. Grills, X. Z. Sun, and M. W. George, *Pure Appl. Chem.*, 2001, **73**, 443.
14. S. Geftakis and G. E. Ball, *J. Am. Chem. Soc.*, 1998, **120**, 9953.
15. D. R. Evans, T. Drovetskaya, R. Bau, C. A. Reed, and P. D. W. Boyd, *J. Am. Chem. Soc.*, 1997, **119**, 3633.
16. D. W. Thompson, R. M. Kretzer, E. L. Lebeau, D. V. Scaltrito, R. A. Ghiladi, K. C. Lam, A. L. Rheingold, K. D. Karlin, and G. J. Meyer, *Inorg. Chem.*, 2003, **42**, 5211.
17. R. J. Hodges and J. L. Garnett, *J. Phys. Chem.*, 1969, **73**, 1525.
18. R. J. Hodges and J. L. Garnett, *J. Phys. Chem.*, 1968, **72**, 1673.
19. R. J. Hodges and J. L. Garnett, *J. Catal.*, 1969, **13**, 83.
20. J. L. Garnett, R. J. Hodges, and R. S. Kenyon, *J. Chem. Soc. Perkin Trans. 2*, 1979, 885.
21. N. F. Goldshleger, A. A. Shteinman, A. E. Shilov, and V. V. Eskova, *Zh. Fiz. Khim.*, 1972, **46**, 1353.
22. L. A. Kushch, V. V. Lavrushko, Y. S. Misharin, A. P. Moravsky, and A. E. Shilov, *New J. Chem.*, 1983, **7**, 729.
23. A. E. Shilov, ‘Activation of Saturated Hydrocarbons by Transition metal complexes’, Riedel, Dordrecht, 1984.
24. R. H. Crabtree, *Chem. Rev.*, 1985, **85**, 245.
25. J. A. Labinger and J. E. Bercaw, *Nature*, 2002, **417**, 507.
26. R. A. Periana, D. J. Taube, E. R. Evitt, D. G. Loffler, P. R. Wentrcek, G. Voss, and T. Masuda, *Science*, 1993, **259**, 340.
27. R. A. Periana, D. J. Taube, S. Gamble, H. Taube, T. Satoh, and H. Fujii, *Science*, 1998, **280**, 560.
28. R. A. Periana, O. Mironov, D. Taube, G. Bhalla, and C. J. Jones, *Science*, 2003, **301**, 814.
29. A. Sen, *Acc. Chem. Res.*, 1998, **31**, 550.
30. B. D. Dangel, J. A. Johnson, and D. Sames, *J. Am. Chem. Soc.*, 2001, **123**, 8149.
31. R. H. Crabtree, J. M. Mihelcic, and J. M. Quirk, *J. Am. Chem. Soc.*, 1979, **101**, 7738.
32. A. H. Janowicz and R. G. Bergman, *J. Am. Chem. Soc.*, 1982, **104**, 352; R. G. Bergman, *Science*, 1984, **223**, 902.
33. W. D. Jones and F. J. Feher, *J. Am. Chem. Soc.*, 1984, **106**, 1650.
34. J. K. Hoyano and W. A. G. Graham, *J. Am. Chem. Soc.*, 1982, **104**, 3723.
35. W. D. Jones and F. J. Feher, *Organometallics*, 1983, **2**, 562.
36. M. J. Wax, J. M. Stryker, J. M. Buchanan, C. A. Kovac, and R. G. Bergman, *J. Am. Chem. Soc.*, 1984, **106**, 1121.
37. A. A. Bengali, R. G. Bergman, and C. B. Moore, *J. Am. Chem. Soc.*, 1995, **117**, 3879.
38. D. Baudry, M. Ephritikhine, H. Felkin, and R. Holmes-Smith, *Chem. Commun.*, 1983, 788.
39. D. Baudry, M. Ephritikhine, H. Felkin, and J. Zakrzewski, *Chem. Commun.*, 1982, 1235.
40. M. J. Burk and R. H. Crabtree, *J. Am. Chem. Soc.*, 1987, **109**, 8025.
41. K. C. Shih and A. S. Goldman, *Organometallics*, 1993, **12**, 3390.
42. C. M. Jensen, *Chem. Commun.*, 1999, 2443.
43. T. Sakakura, T. Sodeyama, K. Sasaki, K. Wada, and M. Tanaka, *J. Am. Chem. Soc.*, 1990, **112**, 7221.

44. K. M. Waltz and J. F. Hartwig, *Science*, 1997, **277**, 211; H. Y. Chen, S. Schlecht, T. C. Semple, J. F. Hartwig *Science*, 2000, **287**, 1995.
45. J. Y. Cho, M. K. Tse, D. Holmes, R. E. Maleczka, and M. R. Smith, *Science*, 2002, **295**, 305.
46. F. Kakiuchi and S. Murai, *Acc. Chem. Res.*, 2002, **35**, 826.
47. B. Sezen, R. Franz, and D. Sames, *J. Am. Chem. Soc.*, 2002, **124**, 13372.
48. M. E. van der Boom and D. Milstein, *Chem. Rev.*, 2003, **103**, 1759.
49. M. Catellani, *Synlett*, 2003, 298.
50. A. M. Echavarren, B. Gomez-Lor, J. J. Gonzalez, and O. de Frutos, *Synlett*, 2003, 585.
51. P. L. Watson, *J. Am. Chem. Soc.*, 1983, **105**, 6491.
52. C. M. Fendrick and T. J. Marks, *J. Am. Chem. Soc.*, 1984, **106**, 2214.
53. B. A. Arndtsen and R. G. Bergman, *Science*, 1995, **270**, 1970.
54. C. P. Schaller, C. C. Cummins, and P. T. Wolczanski, *J. Am. Chem. Soc.*, 1996, **118**, 591.
55. T. J. Marks, *Acc. Chem. Res.*, 1992, **25**, 57.
56. C. Coperet, O. Maury, J. Thivolle-Cazat, and J. M. Basset, *Angew. Chem., Int. Ed. Engl.*, 2001, **40**, 2331.
57. M. P. Doyle, W. R. Winchester, J. A. A. Hoorn, V. Lynch, S. H. Simonsen, and R. Ghosh, *J. Am. Chem. Soc.*, 1993, **115**, 9968.
58. H. M. L. Davies and T. M. Gregg, *Tetrahedron Lett*, 2002, **43**, 4951.
59. G. Ferrando-Miguel, J. N. Coalter, H. Gerard, J. C. Huffman, O. Eisenstein, and K. G. Caulton, *New J. Chem.*, 2002, **26**, 687.
60. R. H. Crabtree, *Pure Appl. Chem.*, 2003, **75**, 435.
61. P. E. M. Siegbahn, M. Svensson, and R. H. Crabtree, *J. Am. Chem. Soc.*, 1995, **117**, 6758.
62. R. H. Crabtree, *Pure Appl. Chem.*, 1995, **67**, 39.
63. G. Hornung, D. Schroder, and H. Schwarz, *J. Am. Chem. Soc.*, 1997, **119**, 2273.
64. K. Eller and H. Schwarz, *Chem. Rev.*, 1991, **91**, 1121.
65. S. Shaik, S. P. de Visser, F. Ogliaro, H. Schwarz, and D. Schroder, *Curr. Opin. Chem. Biol.*, 2002, **6**, 556.
66. D. Schroder, S. Shaik, and H. Schwarz, *Acc. Chem. Res.*, 2000, **33**, 139.
67. J. R. Bryant and J. M. Mayer, *J. Am. Chem. Soc.*, 2003, **125**, 10351.
68. A. E. Shilov and G. B. Shul’pin eds, ‘Activation and Catalytic Reactions of Saturated Hydrocarbons in the Presence of Metal Complexes’, Kluwer, Dordrecht, 2000.
69. K. Kurosawa and A. Yamamoto eds, ‘Fundamentals of Molecular Catalysis’, Elsevier, Amsterdam, 2003.

Transition Metal Complexes with Bulky Allyl Ligands

Timothy P. Hanusa & Christin N. Carlson
Vanderbilt University, Nashville, TN, USA

1 Introduction 1
2 Substituted Allyl Ligands 1
3 Synthesis and Structures 2
4 Reactions and Applications 5
5 Related Articles 5
6 References 5

Abbreviations

dme = 1,2-dimethoxyethane; MAO = Methylaluminoxane; THF = tetrahydrofuran; OTf = Triflate $O_3SCF_3^-$; tmeda = Tetramethylethylenediamine $Me_2NCH_2CH_2NMe_2$.

1 INTRODUCTION

The allyl ion, $C_3H_5^-$, is a commonly encountered ligand (*see Ligand*) in organometallic chemistry. Transition metal-allyl complexes (*see Allyl Complexes*) have been known for over fifty years, and many varieties of homoleptic (*see Homoleptic Compound*) allyl compounds were prepared in the 1960s. Nevertheless, with a few important exceptions (e.g. the bis(allyl) complexes of Ni, Pd, and Pt, which are useful in organic synthesis (*see* ***Organic Synthesis using Transition Metal Complexes Containing π-Bonded Ligands***)), most $(C_3H_5)_nM$ compounds are poorly studied. A major reason for this is that metal centers in homoleptic allyl complexes are often coordinately unsaturated (*see Coordinative Saturation & Unsaturation*), and low-energy pathways for decomposition are available. Consequently, many of them are unstable and difficult to handle; for example, $(C_3H_5)_3V$ explodes above −30 °C, and $(C_3H_5)_4Zr$ decomposes at 0 °C (even $(C_3H_5)_2Ni$ decomposes within a day at room temperature). The early work in the area of homoleptic allyl complexes is summarized in a classic review by Wilke;[1] more recent specialized reviews are available.[2,3]

Sterically bulky cyclopentadienyl rings (*see Cyclopentadienyl*) (e.g. C_5Me_5, $C_5H_3(SiMe_3)_2$) are frequently used to synthesize compounds of greater diversity and stability than is possible with Cp alone, and a similar approach has recently been found effective with the allyl ligand. Some early research along these lines was conducted with methylated allyl ligands. For example, modest (30 °C) improvements in the thermal stability of iron complexes $(2\text{-Me-}C_3H_4)_2Fe(PR_3)_2$ were observed in solution when compared to the unsubstituted analogues $(C_3H_5)_2Fe(PR_3)_2$.[4] More recent research in the area has used larger substituents on the allyl groups, such as trimethylsilyl and dimethyl(*tert*-butyl)silyl, and compounds synthesized with these ligands not only are more stable than their unsubstituted analogues, but in many cases they also represent new classes of metal-allyl complexes.

2 SUBSTITUTED ALLYL LIGANDS

Although in principle a variety of substituents could be used to increase the steric bulk of the allyl ligand (e.g. *t*-Bu, Ph, $SiMe_2(t\text{-Bu})$), to date the most commonly used is the trimethylsilyl group. Fraenkel first reported the synthesis of $Li[(SiMe_3)_2C_3H_3]$ in 1990,[5] and allyl ligands with one to three trimethylsilyl substituents are now known. Space filling models of the parent allyl ligand (**1**), compared to the mono- (**2**), bi- (**3**), and tri-substituted (**4**) anions indicate how the steric profile of the anion is modified with successive substitution.

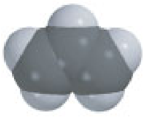

(**1**)

(**2**)

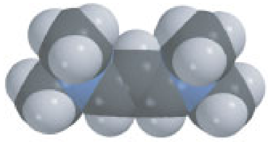

(**3**)

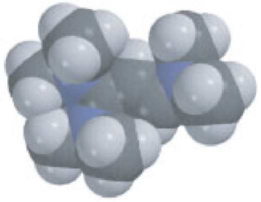

(**4**)

A silyl-bridged bis(allyl)ligand made from the bis(allyl) silane $Me_2Si(CH_2CHCHSiMe_3)_2$ can be converted into its dilithium or dipotassium salt (i.e. $K_2[3\text{-}(C_3H_3SiMe_3\text{-}1)_2SiMe_2])$ (equation 1); it has been used in the synthesis of *ansa*-bis(allyl) complexes.[6,7]

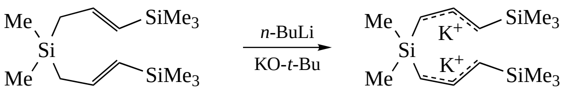

(1)

The terminal substituent in an allyl ligand can be found in a *syn* or *anti* position; the former conformation places the substituent on the same side of the ligand as the central hydrogen atom; in the *anti* form, the opposite arrangement occurs. To date, π-bound monosubstituted allyl ligands are found in *syn* orientations, and unless constrained by an *ansa*-bridge, 1,3-disubstituted allyl ligands have *syn*, *syn* configurations in complexes of highly electropositive metals (s- and f-block). Both *syn*, *syn* and *syn*, *anti* arrangements occur in allyl complexes of the d-block transition elements.

3 SYNTHESIS AND STRUCTURES

3.1 d-Block Complexes

Halide metathesis reactions such as that in equation (2) are commonly used as a route to bulky allyl metal complexes.

$$MX_n + nK[(SiMe_3)_mC_3H_{5-m}] \xrightarrow{THF} [(SiMe_3)_mC_3H_{5-m}]_nM + nKX\downarrow \qquad (2)$$

The 1,3-bis(trimethylsilyl)allyl anion, frequently in the form of its potassium salt, has been used extensively, and it reacts with $CrCl_2$,**[8]** $FeCl_2$,**[9]** $CoCl_2$,**[10]** or $NiBr_2$(dme)**[11]** in THF to produce the corresponding [1,3-$(SiMe_3)_2C_3H_3]_2M$ compounds in good yields.**[12]**

The first-row [1,3-$(SiMe_3)_2C_3H_3]_2M$ compounds are soluble in ethers and both aromatic and aliphatic hydrocarbons. The chromium, iron, and cobalt complexes are highly air-sensitive, but are indefinitely stable under a nitrogen atmosphere. The nickel compound is stable in water for several hours and in air for several days, unlike $(C_3H_5)_2Ni$, which inflames on contact with air. The thermal stability conferred on the complexes by the trimethylsilyl substituents is such that all have melting points above 50 °C, and can be sublimed under vacuum without decomposition. The Cr, Fe, Co, and Ni complexes have magnetic susceptibilities corresponding to 4, 2, 1, and 0 unpaired electrons, respectively. Calculations on the model compound $(C_3H_5)_2Cr$ have been used to rationalize the electronic structure (*see* ***Electronic Structure of Organometallic Compounds***) of [1,3-$(SiMe_3)_2C_3H_3]_2Cr$.**[8]** Evidently, the trimethylsilyl groups do not appreciably affect the ordering of the energy levels.

Some indication of the tunability of the molecular structures in response to the steric bulk of the allyl ligands is provided by the bis(allyl)chromium complexes. For example, the structure of dimeric {[1-$(SiMe_3)C_3H_4]_2Cr\}_2$ (**5**) is closely similar to that of the parent $[(C_3H_5)_2Cr]_2$ complex, including the length of the Cr–Cr bond (1.9784(7) Å and 1.97 Å, respectively).**[8]** With the bulkier [1,3-$(SiMe_3)_2C_3H_3$] anion, the monomeric 12-e^- complex is generated; the staggered ligands display *syn, anti* trimethylsilyl groups (**6**).

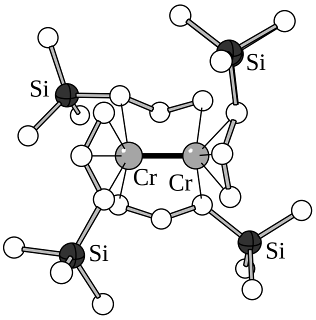

(**5**)

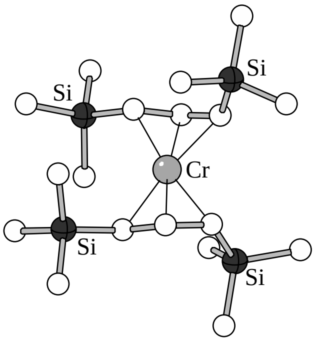

(**6**)

A staggered [π-$(SiMe_3)_2C_3H_3]_2M$ arrangement with *syn, anti* trimethylsilyl groups is also found for the cobalt analogue, although the iron complex is found with eclipsed allyl ligands, and both staggered and eclipsed forms occur for the nickel compound. Direct comparison of the staggered nickel complex [1,3-$(SiMe_3)_2C_3H_3]_2Ni$ with that of $(C_3H_5)_2Ni$**[13]** indicates that the core metal-allyl framework is essentially unaffected by the substituents (e.g. Ni–C bond lengths range from Ni–C = 1.970(3) – 2.064(3) Å in the substituted complex, compared to 1.980(1) – 2.031(1) Å in $(C_3H_5)_2Ni$).

The reaction of one equivalent of K[1,3-$(SiMe_3)_2C_3H_3$] with $NiBr_2$(dme) in toluene yields the mono(allyl)nickel species [1,3-$(SiMe_3)_2C_3H_3$]NiBr.**[11]** The same compound can be formed in THF from the reaction of $Ni(COD)_2$ with 1,3-$(SiMe_3)_2C_3H_3Br$ (equation 3). It forms a dimer in the solid state, with *syn, syn* allyl ligands and Ni–Br = 2.331(4) and 2.368(2) Å (**7**).

$$Ni(COD)_2 + 1,3\text{-}(SiMe_3)_3C_3H_3Br \xrightarrow{THF} \{[1,3\text{-}(SiMe_3)_2C_3H_3]NiBr\}_2 + 2COD \qquad (3)$$

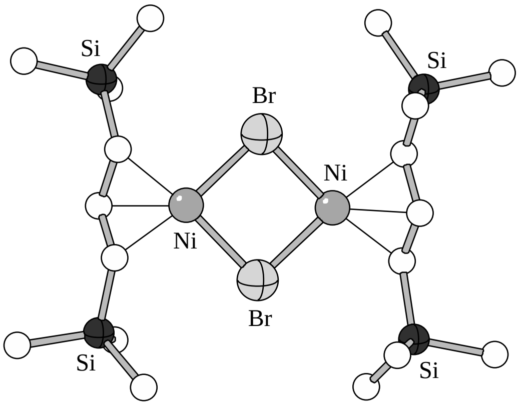

(**7**)

Reaction of $TiCl_4$ or $ZrCl_4$ with two equivalents of Li[1,3-$(Si(t\text{-}Bu)Me_2)_2C_3H_3$]•tmeda generates the trivalent complexes [1,3-$(Si(t\text{-}Bu)Me_2)_2C_3H_3]_2$(Ti,Zr)($\mu$-Cl$)_2$Li•tmeda, along with the coupled dimer of the allyl ligand, 1,3,4,6-tetrakis(tert-butyldimethylsilyl)-1,5-hexadiene.**[14]** In the solid-state structures of both compounds, the allyl ligands are slightly slipped to one side of the metal, suggesting a distortion toward a σ,π-(η^3) bonding arrangement. In the titanium complex (**8**), for example, the difference between the Ti–$C_{terminal}$ distances is ca. 0.2 Å. Both the titanium and zirconium complexes can be oxidized to form neutral tetravalent species [1,3-(Si(*t*-Bu)Me_2)$_2C_3H_3$]$_2$(Ti,Zr)Cl_2, which display $\eta^3 \rightleftharpoons \eta^1$ allyl ligand fluxionality (*see Fluxional Molecule*) on the ^{1}H NMR timescale.

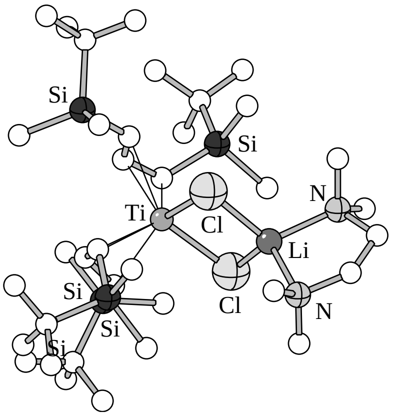

(**8**)

Hafnium tetrachloride reacts with [Li(tmeda)]$_2${3-($C_3H_3SiMe_3$-1)$_2SiMe_2$} to form the *ansa*-bis(allyl) complex [3-($C_3H_3SiMe_3$-1)$_2SiMe_2$]$_2$Hf, and zirconium tetrachloride reacts with the dipotassium derivative of the same allyl anion to produce [3-($C_3H_3SiMe_3$-1)$_2SiMe_2$]$_2$Zr (**9**).**6** The latter molecule lies on a crystallographic twofold axis, with the allyl ligands binding in a η^3-chelating manner; the Zr–C distances range from 2.46 to 2.59 Å.

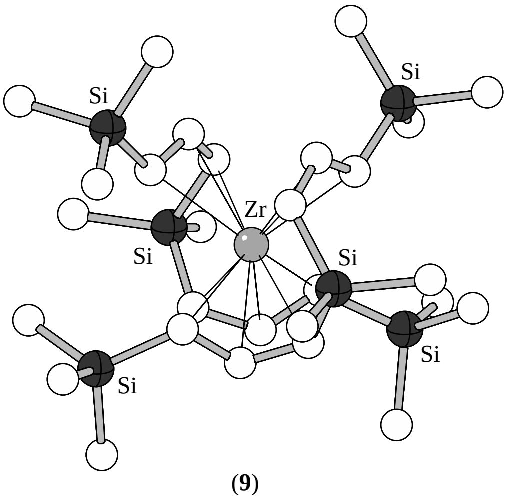

(**9**)

3.2 Scandium, Yttrium, and f-Block Metal Complexes

Reaction of $ScCl_3(thf)_3$ with two equivalents of Li[1,3-$(SiMe_3)_2C_3H_3$] in THF gives the heterometallic bis(π-allyl) complex [1,3-$(SiMe_3)_2C_3H_3$]$_2$Sc(μ-Cl)$_2$Li(thf)$_2$ (**10**).**15** The Sc–C distances range from 2.31–2.46 Å, and the Sc–Cl distances are nearly identical at 2.44 Å.

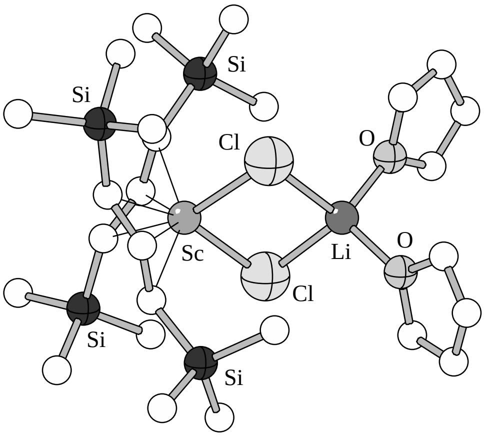

(**10**)

Yttrium trichloride is reported to react with two equivalents of K[1,3-$(SiMe_3)_2C_3H_3$] in THF to produce the bis(allyl) complex [1,3-$(SiMe_3)_2C_3H_3$]$_2$YCl. Reaction of three equivalents of K[1-$(SiMe_3)C_3H_4$] with YCl_3 in THF yields the expected tris(allyl) complex [1-$(SiMe_3)C_3H_4$]$_3$Y.**15**

Lanthanide(III) triflates (Ln(OTf)$_3$) react with three equivalents of the 1,3-bis(trimethylsilyl)allyl anion to produce neutral, solvated tris(allyl) species [1,3-$(SiMe_3)_2C_3H_3$]$_3$Ln(thf) (Ln = Ce, Nd, Tb).**16** The neodymium complex has three η^3-coordinated allyl ligands, with an approximate threefold axis through the Nd–O bond (**11**); Nd–C distances range from 2.64 to 2.78 Å.

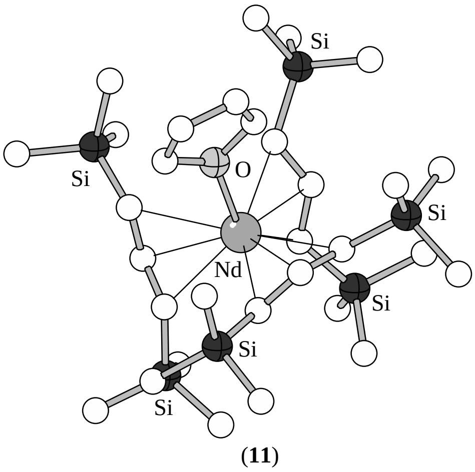

(**11**)

Consistent with the stability of the divalent oxidation states (*see Formal Oxidation State*) of ytterbium and europium, the triflates of Yb(III) and Eu(III) are reduced by the bis(trimethylsilyl)allyl anion, leading to Ln(II) species (equation 4).**12** The same compounds can be made in higher yield by starting with Yb(II) and Eu(II) triflates directly.

$$\begin{aligned} \mathrm{Ln(OTf)_3} + 3\mathrm{K[1,3\text{-}(SiMe_3)_2C_3H_3]} &\longrightarrow \mathrm{[1,3\text{-}(SiMe_3)_2C_3H_3]_2Ln(thf)_2} \\ &+ \tfrac{1}{2}\mathrm{[1,3\text{-}(SiMe_3)_2C_3H_3]_2} + 3\mathrm{K[OTf]}\downarrow \\ \mathrm{Ln} &= \mathrm{Yb, Eu} \end{aligned} \quad (4)$$

Reactions employing lanthanide triiodides do not always provide the anticipated products. For example, two equivalents of $K[1,3\text{-}(SiMe_3)_2C_3H_3]$ and $NdI_3(thf)_{3.5}$ produce a mixture of the mono(allyl) compound $[1,3\text{-}(SiMe_3)_2C_3H_3]NdI_2(thf)_{1.25}$[15] in addition to the expected bis(allyl) complex $[1,3\text{-}(SiMe_3)_2C_3H_3]_2NdI(thf)_2$.[17] The reaction of three equivalents of $K[1,3\text{-}(SiMe_3)_2C_3H_3]$ with LnI_3 (Ln = Ce, Pr, Nd, Gd, Tb, Dy, Er) in THF generates ion pairs of the general formula $\{K[thf]_4\}\{[1,3\text{-}(SiMe_3)_2C_3H_3]_3LnI\}$, as confirmed by X-ray structures of the Ce, Er, and Tb species (equation 5).[16]

$$LnI_3 + 3K[1,3\text{-}(SiMe_3)_2C_3H_3] \xrightarrow{\text{THF}} \{K[thf]_4\}\{[1,3\text{-}(SiMe_3)_2C_3H_3]_3LnI\} + 2KI\downarrow \qquad (5)$$

The erbium derivative (**12**) is typical for the class, with Er−I = 2.979(8) Å, and Er−C distances ranging from 2.61 to 2.64 Å.

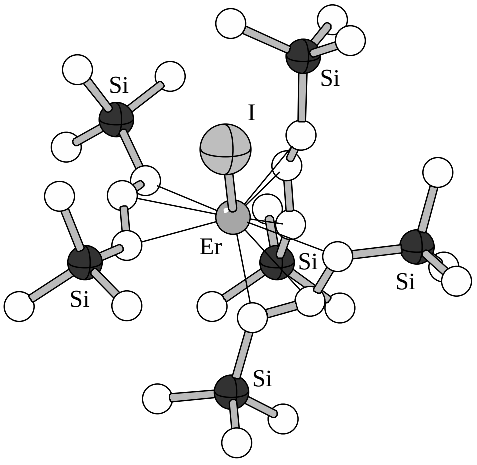

(**12**)

On reaction with two equivalents of the appropriately substituted allyl anions, the divalent $SmI_2(thf)_2$ forms the neutral bis(allyl)complexes $[1,3\text{-}(SiMe_3)_2C_3H_3]_2Sm(thf)_2$ and $[1,3\text{-}Ph_2C_3H_3]_2Sm(thf)_2$.[18] The use of three equivalents of the trimethylsilyl-substituted allyl with $SmI_2(thf)_2$ results in the tetrametallic salt $\{K(thf)_2Sm[1,3\text{-}(SiMe_3)_2C_3H_3]_3\}_2$, whose structure has been confirmed in the solid state (**13**).[17] The samarium and potassium ions are linked by four η^3-allyl ligands, and the potassium ions, which are in three separate coordination environments, display both π (*see* π-*Bond*) and agostic (*see Agostic Bonding*) interactions with the allyl ligands.

Various lanthanide halides ($ScCl_3$, YCl_3, $LaCl_3$, NdI_3) react with $K_2[3\text{-}(C_3H_3SiMe_3\text{-}1)_2SiMe_2]$ to form *ansa*-bis(allyl) complexes. The lanthanum derivative has been structurally authenticated as a coordination polymer (**14**), in which allyl anions interleave alternating lanthanum and potassium ions; the latter display K$\cdots$MeSi contacts of 2.79(3) and 2.96(4) Å.[7]

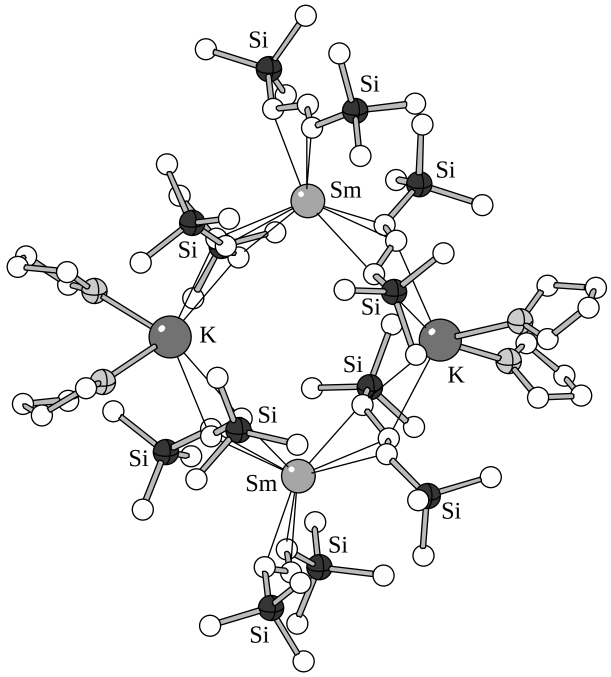

(**13**)

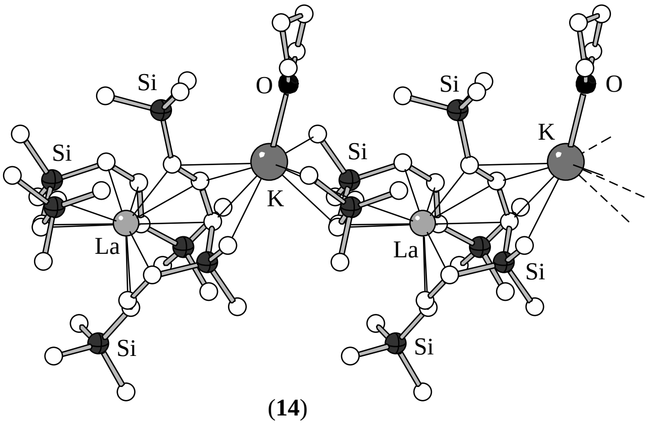

(**14**)

Curiously, when the divalent starting material $SmI_2(thf)_2$ reacts with a $Li_2[3\text{-}(C_3H_3SiMe_3\text{-}1)_2SiMe_2]$/KO-*t*-Bu mixture in light petroleum/Et_2O, the trivalent Sm(III) complex $[Li(OEt_2)_4][Sm\{(\eta^3\text{-}C_3H_3SiMe_3)_2SiMe_2\}_2]$ precipitates in low yield.[7] The anion is structurally similar to the zirconium analogue (**9**); Sm−C distances vary from 2.70−2.74 Å, and the trimethylsilyl substituents are in a *syn, anti* configuration.

$ThBr_4(thf)_4$ reacts with four equivalents of $K[1\text{-}(SiMe_3)C_3H_4]$ or $K[1,3\text{-}(SiMe_3)_2C_3H_3]$ in THF to form the homoleptic tetra(allyl)thorium complexes $[(SiMe_3)_nC_3H_{5-n}]_4Th$ (n = 1,2).[19] The compounds are stable up to 90 °C ($n = 1$) or 124 °C ($n = 2$) under an inert atmosphere, and $[1,3\text{-}(SiMe_3)_2C_3H_3]_4Th$ can tolerate brief (<5 min) exposure to air. The stability of these complexes contrasts strongly with $(C_3H_5)_4Th$, which decomposes at 0 °C.[1] Both molecules are fluxional (*see Fluxional Molecule*) on the ^1H NMR timescale,

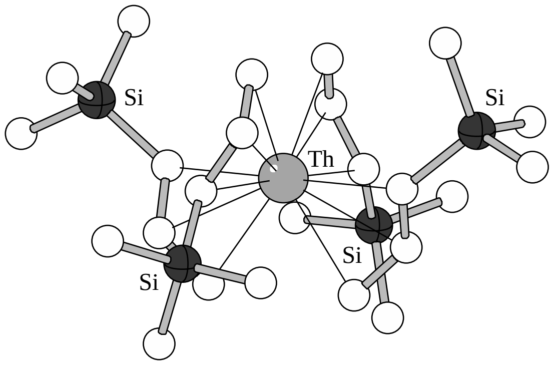

(**15**)

and $\eta^3 \rightleftharpoons \eta^1$ ligand rearrangements are involved in the interchange of their allylic protons. The thorium complexes contain four *syn* or *syn, syn* η^3-ligands; in the case of $[1\text{-}(SiMe_3)C_3H_4]_4Th$ (**15**), they are in a configuration with approximate S_4 symmetry.**[19]**

4 REACTIONS AND APPLICATIONS

Owing to the relative newness of the area, extensive studies of the reactions of complexes with bulky allyl ligands have yet to be made. In some cases, however, it seems that the ligands can block reactions with large substrates. For example, none of the $[1,3\text{-}(SiMe_3)_2C_3H_3]_2M$ (M = Cr, Fe, Co, Ni) compounds react with PPh_3, presumably because of steric interference; the smaller phosphine PMe_3, however, will react with the compounds. The tris(allyl) complex $[1\text{-}(SiMe_2\text{-}t\text{-}Bu)C_3H_4]_3Y(thf)_{1.5}$ evidently provides enough access to *tert*-butylnitrile that it can insert multiple times into the metal-allyl bonds, yielding a *sec*-amido species (equation 6).**[15]**

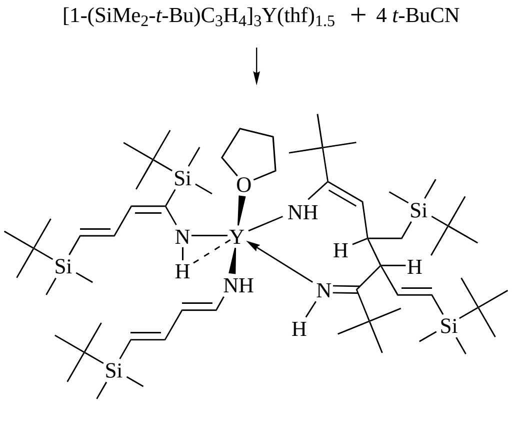

(6)

A variety of metal complexes with bulky allyl ligands function as polymerization catalysts; this may become a major area of application for these compounds. For example, $[1,3\text{-}C_3H_3(SiMe_3)_2]_2LaCl(thf)$, $[1,3\text{-}C_3H_3(SiMe_3)_2]_2YCl$ and $[1,3\text{-}C_3H_3(SiMe_3)_2]NdI_2(thf)_{1.25}$ have been examined with several activators, including methylaluminoxane (MAO), as catalysts for the polymerization of 1,3-butadiene.**[15]** When activated with MAO, $[1,3\text{-}(Si(t\text{-}Bu)Me_2)_2C_3H_3]_2(Ti,Zr)(\mu\text{-}Cl)_2Li{\bullet}tmeda$ and $[1,3\text{-}(Si(t\text{-}Bu)Me_2)_2C_3H_3]_2(Ti,Zr)Cl_2$ are polymerization catalysts for ethylene (forming high density polyethylene) and propylene (forming an elastomeric polypropylene with the Ti complexes and a stereoregular polymer with the Zr species).**[14]**

The cyclic $\{K(thf)_2Sm[1,3\text{-}(SiMe_3)_2C_3H_3]_3\}_2$ (**10**) is an effective single-component catalyst for the polymerization of methyl methacrylate and ε-caprolactone. $[1,3\text{-}(SiMe_3)_2C_3H_3]_3Nd(thf)$ (**9**), $[1,3\text{-}(SiMe_3)_2C_3H_3]_2Yb(thf)_2$,**[12]** $[Ln\{(\eta^3\text{-}C_3H_3SiMe_3)_2SiMe_2\}_2\{\mu\text{-}K(thf)\}(thf)]_\infty$ (Ln = Sc, Y, Nd) and $[Li(OEt_2)_4][Sm\{(\eta^3\text{-}C_3H_3SiMe_3)_2SiMe_2\}_2]$ polymerize methyl methacrylate without activation, and the yttrium compound displays turnover numbers (*see Turnover*) at 0 °C of over 86 000 per hour.**[7]**

5 RELATED ARTICLES

Scandium, Yttrium & the Lanthanides: Inorganic & Coordination Chemistry.

6 REFERENCES

1. G. Wilke, B. Bogdanovic, P. Hardt, P. Heimbach, W. Keim, M. Kroner, W. Oberkirch, K. Tanaka, and D. Walter, *Angew. Chem., Int. Ed. Engl.*, 1966, **5**, 151.
2. P. W. Jolly, *Angew. Chem.*, 1985, **97**, 279.
3. R. U. Kirss, *Appl. Organomet. Chem.*, 1992, **6**, 609.
4. J. M. Grosselin and P. H. Dixneuf, *J. Organomet. Chem.*, 1986, **314**, C76.
5. G. Fraenkel, A. Chow, and W. R. Winchester, *J. Am. Chem. Soc.*, 1990, **112**, 1382.
6. R. Fernandez-Galan, P. B. Hitchcock, M. F. Lappert, A. Antinolo, and A. M. Rodriguez, *Dalton Trans.*, 2000, 1743.
7. T. J. Woodman, M. Schormann, and M. Bochmann, *Organometallics*, 2003, **22**, 2938.
8. C. N. Carlson, J. D. Smith, T. P. Hanusa, W. W. Brennessel, and V. G. Young, Jr *J. Organomet. Chem.*, 2003, **683**, 191.
9. J. D. Smith and T. P. Hanusa, *J. Am. Chem. Soc.*, 2001, **123**, 6455.
10. J. D. Smith, K. T. Quisenberry, T. P. Hanusa, and W. W. Brennessel, *Acta Cryst.*, 2004, **C60**, m507.
11. K. T. Quisenberry, J. D. Smith, M. Voehler, D. F. Stec, T. P. Hanusa, and W. W. Brennessel, *J. Am. Chem. Soc.*, 2005, **127**(12), 4530.

12. C. K. Simpson, R. E. White, C. N. Carlson, D. A. Wrobleski, C. J. Kuehl, T. A. Croce, I. M. Steele, B. L. Scott, V. G. Young, Jr, T. P. Hanusa, A. P. Sattelberger, and K. D. John, submitted for publication.
13. R. Goddard, C. Krueger, F. Mark, R. Stansfield, and X. Zhang, *Organometallics*, 1985, **4**, 285.
14. B. Ray, T. G. Neyroud, M. Kapon, Y. Eichen, and M. S. Eisen, *Organometallics*, 2001, **20**, 3044.
15. T. J. Woodman, M. Schormann, and M. Bochmann, *Isr. J. Chem.*, 2003, **42**, 283.
16. C. J. Kuehl, C. K. Simpson, K. D. John, A. P. Sattelberger, C. N. Carlson, and T. P. Hanusa, *J. Organomet. Chem.*, 2003, **683**, 149.
17. T. J. Woodman, M. Schormann, D. L. Hughes, and M. Bochmann, *Organometallics*, 2003, **22**, 3028.
18. E. Ihara, K. Koyama, H. Yasuda, N. Kanehisa, and Y. Kai, *J. Organomet. Chem.*, 1999, **574**, 40.
19. C. N. Carlson, T. P. Hanusa, and W. W. Brennessel, *J. Am. Chem. Soc.*, 2004, **126**, 10550.

Subvalent Compounds

Penelope J. Brothers
The University of Auckland, Auckland, New Zealand

1	Introduction	1
2	Mononuclear Subvalent Compounds	2
3	Homonuclear Single-bonded Compounds	4
4	Electron-precise and Electron-rich Clusters	6
5	Electron-deficient Clusters	7
6	Metalloid Clusters	10
7	Multiple Bonding in Main Group Subvalent Compounds	12
8	Related Articles	16
9	References	16

Abbreviations

Cp = C_5H_5; Cp* = C_5Me_5; Mes = C_6H_2-2,4,6-Me_3; Dipp = C_6H_3-2,6-*i*-Pr_2; Trip = C_6H_2-2,4,6-*i*-Pr_3; Ar* = bulky terphenyl C_6H_3-2,6-Ar_2 where Ar = Mes, Dipp, or Trip; R* = $C(SiMe_3)_3$.

1 INTRODUCTION

Subvalent main group compounds can be broadly defined as compounds in which the mean oxidation state (N_{ox}) of the central element is lower than the normal oxidation state for elements in that group. In practical terms, this applies to group 13 compounds in which $N_{ox} < 3$ and group 14 compounds in which $N_{ox} < 4$, and, extending the concept more broadly, to group 15 compounds in which $N_{ox} < 3$ and group 16 compounds in which $N_{ox} < 4$. However, the range of such compounds is distinguished not by their adherence to a narrow definition, but by the diversity and richness of their structures and chemistry. More importantly, subvalent compounds present challenges to established ideas of 'normal' valence, chemical bonding, reactivity, and stability, and research directed towards meeting these challenges has extended the boundaries of our fundamental understanding of these concepts.

A predominant characteristic of subvalent compounds is the presence of homonuclear element–element bonds. As a very simple example, trialkylaluminium, AlR_3, contains Al(III), the normal oxidation state for this element. The dialane R_2Al-AlR_2 contains an Al–Al single bond between two Al(II) centres, and as such can be considered to be a subvalent aluminium compound. Indeed, the first example of a molecular aluminium compound containing a 2c,2e (2-centre, 2-electron) Al–Al bond was reported only as recently as 1988.[1] For other main group elements, however, simple 2c,2e homonuclear element–element bonding is well established in the chemistry of silicon, germanium, tin, phosphorus, arsenic, antimony, sulfur, and selenium.[2]

The challenges to our understanding of chemical bonding have arisen in examining subvalent compounds in which the bonding does not conform to simple classifications. These categories of compound fall into several classes. The first of these comprise the simple molecular compounds, which potentially contain element–element multiple bonds, for example, heavy element analogs of alkenes and alkynes. These have been extremely significant and, at times, highly controversial over the last two decades. Secondly, a wide variety of main group cluster molecules are known that contain element–element bonds, and these can be subdivided in a number of ways on the basis of electron counting, structural features, or bonding models.[3] Possibly the best known such class of main group cluster compounds are the polyhedral boranes and carboranes (neutral or anionic) for which electron-deficient, multicenter bonding described by Wade's rules has been established.[4] More recently it has been recognised that the bonding in a number of heavier group 13, 14, and 15 element clusters known as Zintl ions can also be described using Wade's rules. These clusters can occur within molecular compounds, but the same electron counting tools and electron-deficient, multicenter bonding can be attributed to clusters occurring within the solid state, known as Zintl phases. A further and different kind of cluster are those in which 'naked' metal atoms (not supported by ligands) occur, the largest of which are the $Al_{77}\{N(SiMe_3)_2\}_{20}{}^{2-}$ and $Ga_{84}\{N(SiMe_3)_2\}_{20}{}^{4-}$ clusters reported in 1997 and 2001.[5,6] Each cluster contains concentric shells of metal atoms whose arrangement has a close relationship with the structure of the pure element.

The most significant advances in the chemistry of subvalent compounds in the last decade arise in the synthesis of stable molecular compounds. One driver for this has been the development of elegant methods of synthesis, for example, the preparation of toluene solutions of metastable alumimum(I) halides, which in turn can be used to prepare molecular subhalides, metalloid cluster compounds and low-valent organometallic complexes.[7] Secondly, the development of sterically demanding ligands that impart kinetic stabilisation to otherwise reactive molecules has enabled further advances, particularly bulky substituted aryl groups, terphenyls, and bulky alkyl or silyl groups such as supersilyl, Si*t*-Bu_3 and hypersilyl, $Si(SiMe_3)_3$. Finally, electronic stabilisation has led to the isolation of stable low-valent compounds, for example, the N-heterocyclic carbenes and their heavier congeners.[8]

The scope of main group subvalent compounds is broad and this article does not attempt to be comprehensive. Areas have been identified in which there have been important developments within the last decade that have yielded significant new understanding. There is a focus on molecular compounds rather than the more traditional field where subvalent elements occur in solid-state compounds. This discussion include advances in both inorganic and organometallic chemistry. There is a greater focus on the chemistry of groups 13 and 14 where much of the significant development, particularly in cluster chemistry and multiple bonding, has occurred. For a useful, element-by-element description of the well-established chemistry of subvalent compounds the reader is referred to the individual element entries in this reference, or to a well-known text.[2]

Finally, in terms of oxidation state formalisms subvalent compounds are often considered to be those for which $0 < N_{\text{ox}} < m$ (where m is the group oxidation state), but in some cases it is also relevant to consider compounds for which $N_{\text{ox}} \leq 0$.

2 MONONUCLEAR SUBVALENT COMPOUNDS

A discussion of subvalent main group compounds should begin by first examining group trends. In group 14, for example, a stable carbon or silicon compound formally in the oxidation state II is a rarity worthy of comment, whereas for the heaviest congener lead, the oxidation state II is the most stable. This reflects the group trend, particularly pronounced for groups 13–15, whereby the heaviest element shows a stable oxidation state 2 units lower than the group oxidation state, giving Tl(I), Pb(II) and Bi(III). The oxidation state III is accessible for all the group 15 elements, unlike oxidation states I and II, which are much less prevalent for the lighter elements of groups 13 and 14. In(I) and Sn(II) compounds are fairly well known, and Ga(I) and Ge(II) species are relatively accessible.[2]

A number of matrix-isolation studies have investigated low-valent group 13 species and, in conjunction with computation, have given insights into their properties.[9,10] However, some important breakthroughs have occurred over the last two decades that have resulted in new classes of stable, isolable, low-valent compounds of the lighter elements, particularly of groups 13 and 14. For group 14, the preparation and chemistry of the N-heterocyclic carbenes has opened up a wide new field of chemistry.[8] In 1991, a straightforward synthetic route to an isolable N-heterocyclic carbene was published,[11] involving deprotonation of an imidazolium ion, and synthesis of the silicon[12] and germanium members of the family soon followed (Figure 1).[13–15] The parent carbene H_2C: has a triplet ground state, whereas the heteroatom-substituted carbenes are singlets, and are extremely strong electron-pair donors. Stabilization results from the π-donation by the two adjacent nitrogen atoms into the empty orbital on the singlet carbon, and indeed these heterocyclic carbenes can be considered to be 6π electron aromatic systems. The silylene and germylene analogs have some parallels in their electronic structure, but can also be considered to resemble Si or Ge with a chelating diazabutadiene ligand.[16] A range of other stable carbenes have been reported, in general stabilized by heteroatom substituents.[17]

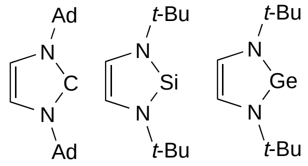

Figure 1 N-heterocyclic carbene, silylene, and germylene

Monoanionic ligands containing two or three nitrogen donors, for example, tris(pyrazolyl)hydroborate, aminotroponiminate, and β-diketiminate, have proved useful in isolating mononuclear, low-valent group 13 and 14 compounds (Figure 2). Aminotroponiminate ($L' = C_7H_5N_2i\text{-}Pr_2$) compounds of germanium, tin, and lead are known, with formulae $L'MCl$, $L'Ge^+$, $L'Sn^+$ and L'_2Sn.[18] The bulky β-diketiminate ligand ($L'' = HC(CMeNDipp)_2$) has been used

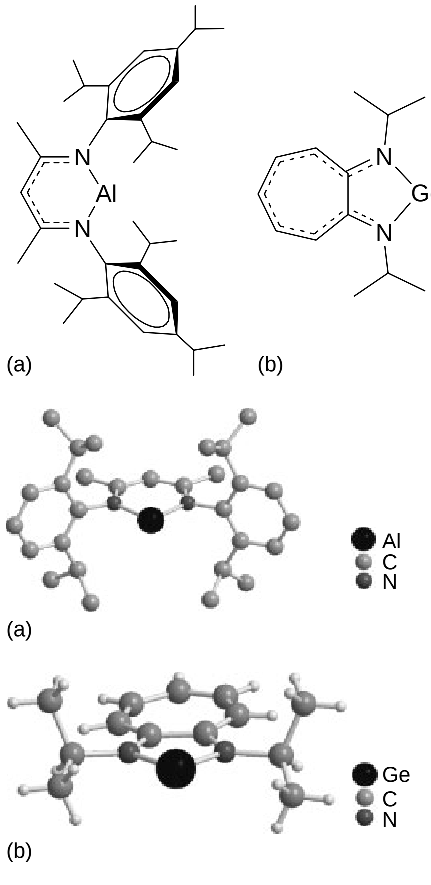

Figure 2 Sketches and molecular structures of (a) aluminum amidinate complex $Al\{HC(CMeNDipp)_2\}$ (H atoms removed for clarity) and (b) germanium aminotroponiminate cation $[Ge(C_7H_5N_2i\text{-}Pr_2)]^+$

to make the first stable mononuclear molecular aluminum complex, L″Al:[19,20] and also its gallium analog L″Ga:.[21] With two substitutents and a stereochemically active lone pair, these compounds can be considered to be group 13 analogs of carbenes, R_2C:.

Choice of appropriately bulky alkyl and aryl ligands has also allowed the isolation of stable, monomeric group 13 and 14 compounds.[22] The bulky terphenyl ligands ($Ar^* = C_6H_3$-2,6-Ar_2 where Ar = Mes, Dipp, or Trip) have been used to make one-coordinate InAr* (Figure 3) and TlAr* (Ar = Trip) and divalent germanium and tin compounds Ar^*_2E and $(Ar^*ECl)_2$ (Ar = Mes).[23] Other useful ligands are supersilyl Si*t*-Bu_3,[24] hypersilyl $Si(SiMe_3)_3$, and alkyls such as $CH(SiMe_3)_2$, $C(SiMe_3)_3$ and C*t*-Bu_3.

Particular ligand systems have proved to be especially amenable to stabilising low oxidation state species. The cyclopentadienyl family of ligands have a rich chemistry with main group elements.[25,26] The lower oxidation state compounds contain η^5-Cp ligands, compared to η^1-coordination in the higher oxidation state complexes. 'Slipped' complexes containing an η^2- or η^3-Cp ligand are also observed. For group 13, monomeric CpE molecules have been observed in the gas phase for all five group 13 elements. In the solid state, they occur as oligomers with an intriguing range of structures depending on the substitution pattern in the cyclopentadienyl ligand. $(Cp^*Al)_4$ exists as a tetrahedral cluster, while $(Cp^*Ga)_6$ and $(Cp^*In)_6$ are octahedral. The clusters contain a tetrahedral or octahedral core of metal atoms capped at the apexes by η^5-Cp* ligands. In contrast, the hexameric thallium complex $(Cp'Tl)_6$ ($Cp' = 1,2$-$C_5H_3(SiMe_3)_2$) is a cyclic cluster with the thallium atoms sandwiched between Cp′ units (Figure 4). Metal–metal interactions are observed in the dimers $(Cp'Tl)_2$ and $(Cp'In)_2$ ($Cp' = C_5(CH_2Ph)_5$), which have a trans-bent Cp′E···ECp′ arrangement, although the E···E interactions are long and relatively weak. The thallium compound is especially interesting as it represented an early example of a molecular compound with a rare Tl–Tl interaction. Thallium and indium compounds $(CpTl)_n$ and $(CpIn)_n$ containing unsubstituted Cp ligand form zig-zag polymers in the solid state.[27,28]

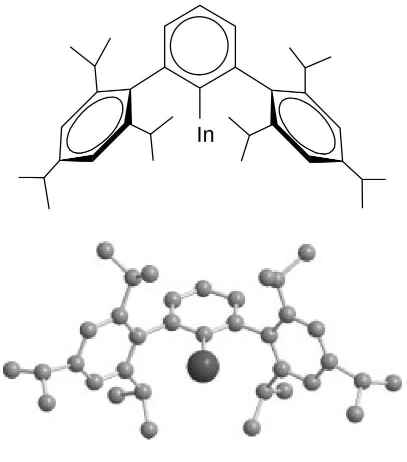

Figure 3 Sketch and molecular structure of InAr* (Ar = Trip)

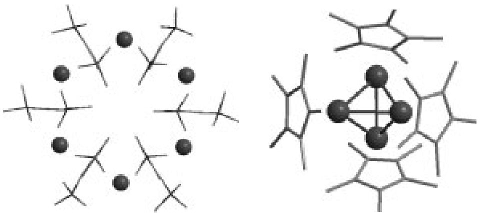

Figure 4 Molecular structures of $(Cp'Tl)_6$ ($Cp' = 1,2$-$C_5H_3(SiMe_3)_2$, viewed with Cp′ rings side-on) and $(Cp^*Al)_4$

Divalent group 14 cations $[Cp^*Ge]^+$ and $[Cp^*Sn]^+$ form crystalline salts containing isolated C_{5v} cations. The cations will coordinate neutral (pyridine) or anionic (halide) ligands to form 'slipped' η^3-Cp* complexes. Bis-cyclopentadienyl compounds Cp_2E are known for all five group 14 elements. Silicocene, Cp^*_2Si, is an important example of a stable divalent silicon compound, and crystallises in two forms within the same crystal, one with parallel (D_{5d}) and one with nonparallel (C_{2v}) Cp* rings.[29] Space-filling models of selected examples are shown in Figure 5. The bent (C_{2v}) structures observed for Cp^*_2E where E = Ge, Sn, and Pb have been the subject of intense theoretical study. In simple terms, the bending can be viewed as arising from the influence of a stereochemically active lone pair, although only very small energy differences ($<10\ kJ\ mol^{-1}$) separate the bent and parallel structures. Tin and lead can accommodate three Cp ligands, and a variety of oligomeric and lead anions such as $[Cp_5Pb_2]^-$ and $[Cp_9Pb_4]^-$ are known, which, along with polymeric $(CpPb)_n$, contain both bridging and terminal η^5-Cp ligands.[25,26]

Low-valent indium compounds have recently become important in mediating organic transformations in aqueous

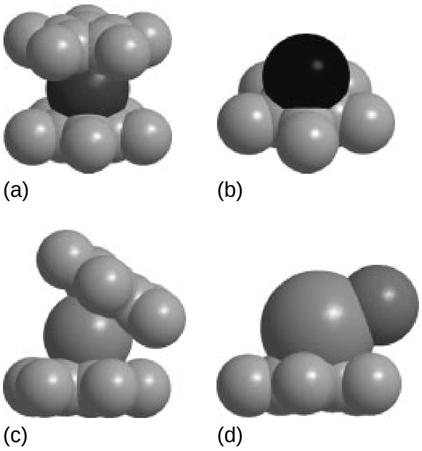

Figure 5 Molecular structures of (a) Cp^*_2Si (parallel Cp* rings), (b) the naked cation $[Cp^*Ge]^+$, (c) Cp^*_2Sn, and (d) the slipped structure Cp*SnCl

media. The nature of subvalent gallium and indium in aqueous media has been studied experimentally.[30]

3 HOMONUCLEAR SINGLE-BONDED COMPOUNDS

The focus of this section will be molecular subvalent dinuclear compounds, rings, and chains in which the composition and structure can be accounted for by localised electron-pair (2c,2e) bonds between adjacent atoms. Cluster compounds with a 3-dimensional architecture, some of which require a more delocalized bonding description, will be discussed in Sections 4 and 5.

Boron subhalides B_2X_4 ($X = F$, Cl, Br, I) of the form X_2BBX_2 are molecular compounds with localised B–B bonds. The gallium and indium analogs Ga_2X_4 and In_2X_4, despite having the same formulation, in fact exist as the mixed valence salts $M^+[MX_4]^-$. However, when a donor ligand is added, they form the genuinely divalent complexes $X_2M\text{-}MX_2{\cdot}L_n$ such as $Ga_2Br_4(\text{dioxane})_2$ and $InBr_4(\text{TMEDA})_2$.[31] The dialane $Al_2\{CH(SiMe_3)_2\}_4$ was prepared by reductive coupling of the dialkyl aluminium halide and represented the first example of a molecular aluminium compound to containing a 2c,2e (2-centre, 2-electron) Al–Al bond (Figure 6).[1] Organometallic digallane and diindane derivatives have also been prepared. The diborane(4) compounds can be reduced by two electrons, and the diborane(4), dialane(4), and digallane(4) compounds by one electron to give the radical anions $[E_2R_4]^{\cdot-}$, all of which display evidence for multiple bonding (see Section 7). Trigonal planar gallium and indium compounds $M(MR_2)_3$ contain three M–M bonds linking to a central unsubstituted metal atom (Figure 6), and a small number of dithallium(II) compounds bearing bulky silyl substituents are known.[32]

Diboron compounds (RXBBXR, R_2BBR_2) are extremely well known and are widely used in organic chemistry.[33] Heavier group 13 compounds containing localised M–M bonds and with a formal $N_{ox} = 2$ now represent a mature area of study. As well as halide and organic substituents, examples with heteroatom (Si, N, O, P) substitutents, and both coordinatively unsaturated (coordination number 3) and saturated (coordination number 4) are established giving a range of compounds of the forms $[X_3MMX_3]^{2-}$, LX_2MMX_2L, RXMMXR, and R_2MMR_2 (where X is a halide or anionic ligand, L a neutral donor, and R an alkyl or silyl group).[31,32]

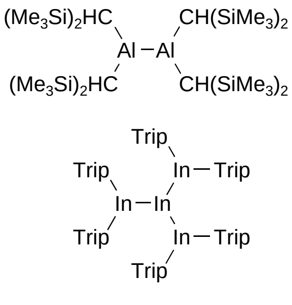

Figure 6 Dialane $Al_2\{CH(SiMe_3)_2\}_4$ and tetraindane $In(InTrip_2)_3$

An extraordinary experimental breakthrough occurred in 1989 when it was demonstrated that metastable solutions of the aluminium(I) and gallium(I) monohalides could be prepared in organic solvents.[7] The monohalides halides are prepared in a high-temperature reactor by the reaction of the molten metal with HX at around 1000 °C (equation 1). The monohalides are then cocondensed at −196 °C with toluene to which a donor solvent (NEt_3, Et_2O, THF) has been added. When the cocondensate is melted at around −100 °C, deep red solutions of the monohalide AlX or GaX are formed.[27,34]

$$\mathrm{Al_{(l)} + HCl \xrightarrow{1000\,^{\circ}C} AlCl_{(g)} + \tfrac{1}{2}H_2} \tag{1}$$

$$\mathrm{3AlCl \longrightarrow 2Al + AlCl_3} \tag{2}$$

Metastable solutions of the monohalides AlX and GaX ($X = Cl$, Br, I) have been prepared using this technique, and oligomeric species $(MX)_n{\cdot}L_m$ containing a variety of donors (L) have been crystallised. The solutions disproportionate to the trihalide and the metal (equation 2) when warmed to temperatures in the range −40 to +50 °C, depending on the halide, the donor, and the concentration. Species with oxidation states both higher and lower than +1 (i.e. on the path to both disproportionation products) have been isolated. The reduced species ($0 < N_{ox} < 1$) are discussed in the section on metalloid clusters, and the monohalides and more oxidized species ($1 \le N_{ox} < 3$) are discussed here. A sonochemical synthesis of a subvalent gallium species, possibly GaI, has also been developed.[27,34]

Examples of aluminium and gallium monohalides crystallised directly from metastable AlX or GaX solutions containing a suitable donor are $Al_4X_4{\cdot}4NH_3$ ($X = Cl$, Br) and $Ga_8I_8{\cdot}6PEt_3$ (Figure 7). The aluminium compounds comprise a planar Al_4 ring with each four-coordinate aluminium

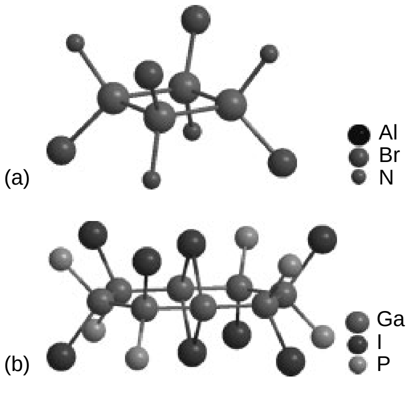

Figure 7 Molecular structures of $(AlBr)_4{\cdot}4NEt_3$ (a) and $(GaI)_8{\cdot}6PEt_3$ (b) (ethyl groups removed for clarity)

bearing a halide and NH_3 substituent. The gallium example comprises a Ga_8 ring with only 6 PEt_3 substituents, and cross-ring bridging iodo ligands complete the four-coordination at the remaining two gallium atoms. The M_2X_4 species, already described above, can also be prepared by the cocondensation technique, and a number of $Al_2X_4L_2$ and partially substituted $Al_2X_2R_2L_2$ examples have been characterised, and show staggered, ethane-like structures ($X = $ halide, $R = $ silyl, $L = $ neutral donor). The gallium compound $Ga_2X_2R_2L_2$ is bridged through the halide atoms and the donors are not coordinated directly to gallium. Other subhalide complexes isolated using this process are $Ga_3I_5 \cdot 3PEt_3$, $Ga_5Cl_7 \cdot 5Et_2O$, and $Al_5Br_7 \cdot 5Et_2O$. M_3X_5 and M_5X_7 species have average metal oxidation states (N_{ox}) 1.67 and 1.40. The two M_5X_7 compounds have different structures, although they both contain $M(M)_4$ units with an unsubstituted metal atom at the centre. The gallium example can be formulated as $Ga(GaCl \cdot 2Et_2O)(GaCl_2 \cdot Et_2O)_3$, while the aluminium compound exists as a mixed valence salt comprising $[Al_5Br_6 \cdot 6THF]^+$ cations and $[Al_5Br_8 \cdot 4THF]^-$ anions. The bonding in all these compounds can be described by localised 2c,2e bonds and coordinatively saturated metal centres. The tetrahedral aluminium cluster $(AlCp^*)_4$ was prepared by the cocondensation route, as were other Cp* clusters $SiAl_{14}Cp^*_6$ and $Al_5I_6Cp^*_3$. Further clusters derived from this route in which the number of direct metal–metal bonds exceeds the number of metal–ligand bonds are discussed in the section on metalloid clusters.[34]

Group 13 subhalide compounds have also been prepared by partial oxidation of tetrahedral $(MR)_4$ ($R = C(SiMe_3)_3$) or $(AlCp^*)_4$ clusters using organic halogen donors or AlX_3/X_2 mixtures. For example, $(In_2X_2R_2)_2$ can be prepared from $(InR)_4$ using hexachloroethene ($X = Cl$) or $AlBr_3/Br_2$ ($X = Br$). The structure of the cluster, which formally contains In(II), can be related to the tetrahedral In_4 precursor in which two of the edges remain in the product as localised In–In bonds and the remaining four edges are occupied by bridging halide atoms. Other indium subhalides prepared in a similar fashion are $In_4Br_2R_4$ and $In_3I_2R_3$ (Scheme 1). Gallium and aluminium compounds prepared by oxidation of tetrahedral clusters are limited to $Ga_2X_2R_2$ ($X = Br, I$), $Ga_3I_2R_3$ and $Cp^*_3Al_5I_6$. These compounds all have formal oxidation number N_{ox} between 1.5 and 2. Further synthetic routes to group 13 subhalides have been summarised recently.[32,35]

Two thallium subhalides have been reported, Tl_3ClR_4 and $Tl_6Cl_2R_6$ both containing the supersilyl ligand $R = Sit\text{Bu}_3$, and with $N_{ox} = 1.33$. The former contains a Tl_3Cl ring, the latter two Tl_3Cl rings linked through the central Tl atoms.[36]

One category of subvalent main group compounds that are difficult to classify are persistent main group radical species.[37] Most contain homonuclear element–element bonds, many have cluster frameworks and exhibit delocalized bonding and partial multiple bond character. Examples are reduced dimers or clusters such as $[Trip_2MMTrip_2]^-$ ($M = Al, Ga$), $[Al_6t\text{-Bu}_6]^-$, $[Ga_4R_4]^-$ ($R = C(SiMe_3)_3$) and $E_9{}^{3-}$ ($E = Ge, Sn, Pb$), and neutral compounds such as $R^*GaGaR^*_2$, $Ga_3R^*_4$ ($R^* = Sit\text{-Bu}_3$) and $(GeAr^*)_3$ ($Ar = $ Mes) (Figure 8).[13,37]

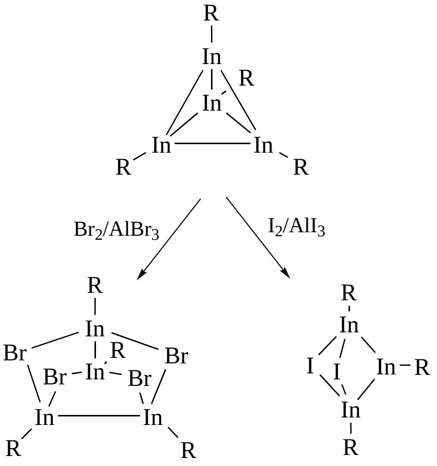

Scheme 1 Reactions of $(InR)_4$ to produce new indium clusters ($R = C(SiMe_3)_3$)

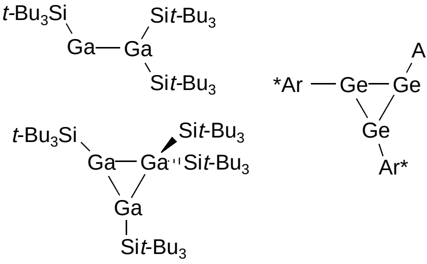

Figure 8 Sketches of radical species $R^*GaGaR^*_2$, $Ga_3R^*_4$ ($R^* = Sit\text{-Bu}_3$) and $(GeAr^*)_3$ ($Ar = $ Mes)

The remarkable ability of carbon to catenate means that carbon–carbon bonds form the basis of organic chemistry, and although they could strictly be classed as subvalent compounds we do not usually apply this formalism to carbon. Homonuclear element–element bonded compounds are also extensive for silicon (the polysilanes), which show some unusual materials properties and electronic features. Catenation is observed for the heavier elements germanium, tin, and lead, but these become progressively more labile with increasing atomic weight as the element–element bond strength decreases. Element–element bonding is also prevalent in groups 15, 16, and, to a lesser extent, group 17 (e.g. the polyiodide anions) but the well-established area of simple homonuclear bonding between subvalent elements from groups 14–17 will not be discussed here in further detail. Selected recent reviews describe advances in polysilane[38,39] and group 15[40,41] compounds.

4 ELECTRON-PRECISE AND ELECTRON-RICH CLUSTERS

Subvalent main group compounds can form clusters containing element–element bonds in which the electron count corresponds exactly to the total number of lone pairs and localised 2c,2e electron bonds between adjacent pairs of atoms. When these conditions are satisfied, the cluster can be described as electron-precise and each cluster atom bears an octet of electrons. This corresponds to a cluster electron count of $3n$, once electrons in lone pairs or in 2c,2e bonds to apical substituents have been accounted for. In electron-precise clusters each atom in the cluster framework is three-connected, in other words it is bonded to three other cluster atoms. Allowed geometries that meet these constraints are a tetrahedron, trigonal prism, cube, and pentagonal and higher prisms (Figure 9). The simplest such compound that can be described as an electron-precise cluster is P_4, with 12 ($3n$) electrons corresponding to 6 electron-pair P–P bonds along the edges, after allowing for the four lone pairs located one on each phosphorus atom.

Other examples are the group 14 compounds of formula $(ER)_n$, for which the simplest carbon examples are C_4H_4 tetrahedrane, C_6H_6 prismane, and C_8H_8 cubane. Although the electron count allows for 2c,2e pair bonds between adjacent pairs of atoms, in the tetrahedral, trigonal prismatic, and cubic clusters the bond angles (60° and/or 90°) do not accord with simple sp^3 hybridisation, and a delocalized molecular orbital bonding model might be more appropriate.[3] Selected compounds $(ER)_n$ of the heavier group 14 elements are known for $n = 2, 3, 4, 6, 8$, and 10. The compounds where $n = 2$ are the alkyne analogs REER and are discussed in the section on multiple bonding (Section 7). The $n = 3$ clusters exist only for germanium, as the radical $(GeAr^*)_3$ (Ar = Mes) and the cation $[GeR^*]_3^+$ ($R^* = Si\textit{t}\text{-}Bu_3$). Germanium and silicon exhibit tetrahedral clusters $(SiR^*)_4$ and $(GeR^*)_4$, while prismanes $(ER)_6$ and cubanes $(ER)_8$ occur for silicon, germanium, and tin, where R is a bulky aryl or alkyl group. The largest cluster $(SnAr)_{10}$ has a pentagonal prismatic structure. Representative structures are shown in Figure 10. The prismane C_6H_6 is an isomer of benzene, and for silicon $[SiDipp]_6$ has been isolated in the silicon form of Dewar benzene.[42,43]

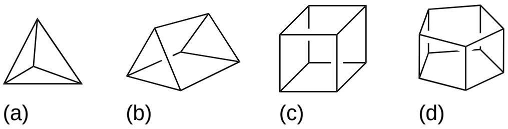

Figure 9 Geometries for electron-precise clusters: (a) tetrahedron, (b) trigonal prism, (c) cube, (d) pentagonal prism

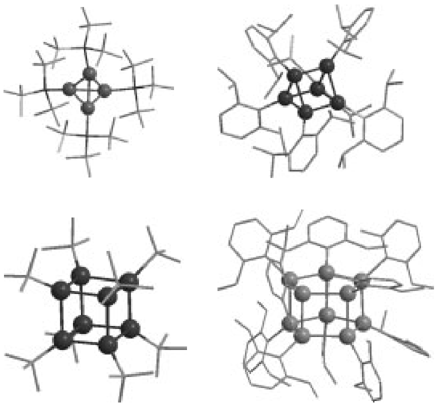

Figure 10 Group 14 clusters: tetrahedral $\{Ge(Si\textit{t}\text{-}Bu_3)\}_4$, trigonal prismatic $(SiDipp)_6$, cuboidal $(Si\textit{t}\text{-}Bu)_8$, and pentagonal prismatic $\{Sn(C_6H_3\text{-}2,6\text{-}Et_2)\}_{10}$

Electron-rich clusters can be considered to be based on electron-precise clusters for which each added pair of electrons results in the breaking of an element–element bond and formation of two new lone pairs. The limiting case is a cluster count of $4n$, which simply corresponds to a ring of atoms connected by 2c,2e bonds, of which the S_8 rings and Se_8 rings are simple examples. Subvalent polychalcogenide clusters (Table 1), by virtue of being in group 16, tend to fall into the electron-rich category, and show a variety of structural arrangements, some of which can be described by classical 2c,2e bonding and lone pairs, and others show delocalized, nonclassical bonding.[44,45]

The E_4^{2+} cations can also be considered as electron-deficient *arachno* clusters (see Section 5). The S_8^{2+} and Se_8^{2+} clusters are related to the neutral E_n rings by removal of two electrons and formation of transannular E–E bonds. The six-atom E_6^{2+} clusters illustrate nicely the contrast between classical and nonclassical bonding situations. The hypothetical electron-precise cluster ($3n$ electrons) would be trigonal prismatic E_6^{6+}. Addition of four electrons to give

Table 1 Subvalent polychalcogenide clusters[44]

n	4	6	8	10	>10	oligomeric
E_n^{2+}	S_4^{2+} Se_4^{2+} Te_4^{2+} $Te_2Se_2^{2+}$ Te_3Se^{2+}	$Te_3S_3^{2+}$ $Te_2Se_4^{2+}$ Te_6^{2+}	S_8^{2+} Se_8^{2+} $Te_4S_4^{2+}$ $Te_2Se_6^{2+}$ Te_8^{2+}	Se_{10}^{2+} $Te_2Se_8^{2+}$	S_{19}^{2+} Se_{17}^{2+}	$(Te_4^{2+})_n$ $(Te_3Se_4^{2+})_n$ $(Te_7^{2+})_n$ $(Te_8^{2+})_n$ $(Te_{10}^{2+})_n$
E_n^{4+}		Te_6^{4+}	Te_8^{4+}			

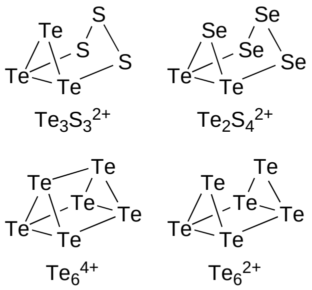

Figure 11 Classical ($Te_3S_3^{2+}$ and $Te_2Se_4^{2+}$) and nonclassical (Te_6^{4+} and Te_6^{2+}) group 16 clusters based on a trigonal prism

E_6^{2+} $(3n + 4)$ should result in a structure that is essentially a prism with two broken bonds, and indeed this is the case for $Te_3S_3^{2+}$ and $Te_2Se_4^{2+}$. On the other hand, Te_6^{2+} is a prism with only one broken bond, and Te_6^{4+} $(3n + 2)$ a closed prism, indicative of some delocalized bonding in these cations (Figure 11).[44]

Group 15 species also form a hugely varied range of structures which can be viewed as electron-rich clusters. P_7^{3-} can be described as a tetrahedral P_4 unit with a P^- fragment inserted in three of the edges, and a selection of formally isoelectronic analogs of these (e.g. where P^- has been replaced by As or S or Se,) have been reported. Although they are formally low-valent group 15 compounds, these and a wide range of related compounds are well known and will not be discussed further here.[3]

5 ELECTRON-DEFICIENT CLUSTERS

The quintessential class of subvalent main group compounds are the polyhedral neutral borane and anionic boron hydride cluster compounds. The bonding in the clusters can be described using delocalized molecular orbitals according to Wade's rules,[4] whereby the number of cluster-bonding electron pairs can be correlated with the structure. More generally, Wade's rules are also applicable to subvalent main group 'naked' anions and cations. The term 'naked' is used in this setting as the clusters bear lone pairs at each apical atom, rather than substituents (typically hydrogen in the boranes and carboranes).[46] The clusters are based on deltahedra (Figure 12), and may be closed (*closo*), or partially open with one (*nido*) or two (*arachno*) missing vertices. A *closo* cluster with n vertices has $2n + 2$ cluster-bonding electrons, a *nido* cluster has $2n + 4$ and an *arachno* cluster has $2n + 6$. As a result, the clusters become progressively more open as the number of electrons increases. The cluster-bonding electrons are those electrons not used in 2c,2e bonds to terminal substituents or as lone pairs at the apexes of 'naked' main group cluster atoms.

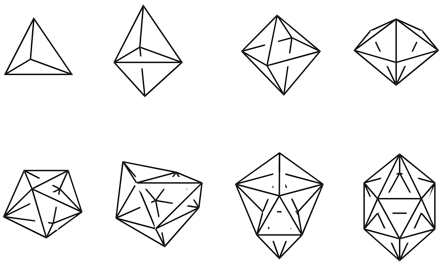

Figure 12 *Closo* polyhedra with n vertices: tetrahedron (4), trigonal bipyramid (5), octahedron (6), pentagonal bipyramid (7), dodecahedron (8), tricapped trigonal prism (9), bicapped square antiprism (10), and icosahedron (12)

Closo, nido, and *arachno* boranes form series with formulae $B_nH_n^{2-}$, B_nH_{2n+4}, and B_nH_{2n+6} confirming their status as formally subvalent compounds. Boranes and carboranes (in which one or more boron atoms in the cluster have been replaced by a carbon atom) have been extensively researched and described, and will not be discussed further here.[2,3] In an example of the application of Wade's rules to a heavier main group cluster, Sn_5^{2-} uses 10 of the total 22 valence electrons in 5 lone pairs. This allows 12 electrons, or $2n + 2$ for $n = 5$ for cluster bonding and specifies a *closo* structure, matching the observed D_{3h} trigonal bipyramidal structure.

A selection of 'naked' main group clusters whose structures can be described by Wade's rules are given in Table 2. Different strategies are required for the isolation of these. The polyanionic clusters (e.g. Sn_9^{4-} and Pb_5^{2-}) prepared by alkali metal reduction of the metals require effective chelating agents such as cryptands for the alkali metal countercations. This class of compounds are known as Zintl ions, named after Zintl's pioneering work on the composition of solutions of group 14 metals treated with sodium in liquid ammonia.[47] The stability of the cationic clusters (e.g. Bi_5^{3+}) is limited by their tendency to disproportionate to the metal and higher oxidation state (Bi^{3+}) species, but can be successfully isolated as the salts of weakly basic halo anions.[48,49] Finally, many of the clusters bearing higher net charges exist only the solid phase, stabilised by electrostatic interactions within the crystal.

Symmetries given in Table 2 are idealized (and refer to the symmetry of the cluster without taking into account heteroatoms) and many of the clusters show distortions from these ideal symmetries. For example, the group 14 clusters Ge_9^{4-}, Sn_9^{4-} and Pb_9^{4-} have $2n + 4$ cluster electrons and exist as the expected *nido* clusters with C_{4v} monocapped square antiprismatic geometry. On the other hand, the bismuth cluster Bi_9^{5+}, which also has a $2n + 4$ electron count, instead exists in the *closo* D_{3h} form with a tricapped trigonal prismatic structure. In fact, all these 9-atom clusters show some distortions from the idealised symmetry, and the energy differences between different geometries are small.[46,50] The *arachno* clusters Sb_4^{2-}, Bi_4^{2-}, Se_4^{2+} and Te_4^{2+} (square planar), and Sb_8^{2+} and Bi_8^{2+} (square antiprismatic) have

Table 2 Examples of *closo*, *nido*, and *arachno* Zintl ions

n	*Closo* ($2n+2$ cluster electrons)				*Nido* ($2n+4$ cluster electrons)				*Arachno* ($2n+6$ cluster electrons)			
4					In_4^{8-}, Tl_4^{8-}	[c]	T_d	Tetrahedral	Sb_4^{2-}, Bi_4^{2-}	[a]	D_{4h}	Square planar
					E_4^{4-} (Si–Pb)	[c]	T_d	Tetrahedral	Se_4^{2+}, Te_4^{2+}	[b]	D_{4h}	
					$Sn_2Bi_2^{2-}$, $Pb_2Sb_2^{2-}$	[a]	T_d	Tetrahedral				
					$TlSn_3^{5-}$	[c]	T_d	Tetrahedral				
					$InBi_3^{2-}$	[a]	T_d	Tetrahedral				
5	Tl_5^{7-}	[c]	D_{3h}	Trigonal bipyramid	In_5^{9-}	[c]	C_{4v}					
	Ge_5^{2-}, Sn_5^{2-}, Pb_5^{2-}	[a]	D_{3h}	Trigonal bipyramid								
	Bi_5^{3+}	[b]	D_{3h}	Trigonal bipyramid								
6	Ga_6^{8-}, Tl_6^{8-}	[c]	O_h	Octahedral								
8									Sb_8^{2+}, Bi_8^{2+}	[b]	D_{4d}	Square antiprism
9	Ge_9^{2-}	[a]	D_{3h}	Tricapped trigonal prism	Ge_9^{4-}, Sn_9^{4-}, Pb_9^{4-}	[a,c]	C_{4v}	Monocapped square antiprism				
					Bi_9^{5+}	[b]	D_{3h}	Tricapped trigonal prism[d]				
	$TlSn_8^{3-}$	[a]	D_{3h}	Tricapped trigonal prism	$In_4Bi_5^{3-}$	[a]	C_{4v}					
10	$TlSn_9^{3-}$	[a]	D_{4d}	Bicapped square antiprism								
	Ge_{10}^{2-}	[a]	D_{4d}	Bicapped square antiprism								

[a] Isolated as alkali metal cryptand salt. [b] Isolated as salt of a weakly basic halo anion. [c] Structure occurs within solid-state salt. [d] *Closo* structure observed.

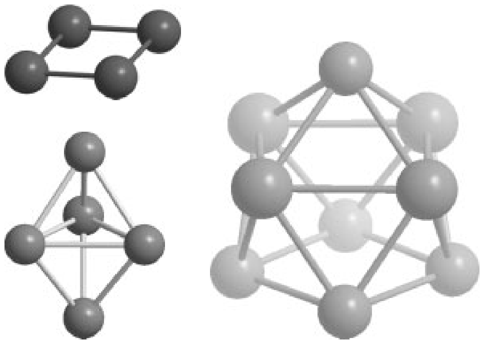

Figure 13 Naked Zintl ion clusters Sb_4^{2-} (*arachno*), Sn_5^{2-} (*closo*), and Sn_9^{4-} (*nido*)

each lost a pair of trans-related vertices from the *closo* parent clusters, rather than two adjacent vertices as occurs for the *arachno* borane clusters. The 14-electron clusters Sb_4^{2-}, Bi_4^{2-}, Se_4^{2+} and Te_4^{2+} can also be described as Hückel aromatic systems, comprising four element–element σ bonds and 6π electrons, and this might contribute to the stability of the square-planar arrangement. Selected clusters are shown in Figure 13.[51–53]

Further examples of formally subvalent main group compounds that contain element–element bonds but not necessarily clusters are the Zintl phases. The bonding in these has been described as the 'octet rule for all atoms'. The archetypal Zintl compound is NaTl, in which charges are assigned as Na^+ and Tl^-, representing a formal transfer of electrons from the more to the less electropositive element. The Tl^- ion can be considered to be a group 14 pseudoelement, and in fact exists in NaTl as a three-dimensional polyanionic diamond framework $(Tl^-)_n$ stuffed with Na^+ cations. The Zintl concept is extended more broadly to other binary and ternary solid-state compounds, whose structures show the formation of element–element bonds in one, two, or three dimensions.[47]

The clusters discussed above are described as 'naked', in other words without substituents at the apical atoms. This contrasts with the borane and carboranes, which bear hydride or other substituents at each apical atom. Extension of substituent-bearing borane-type clusters to heavier elements provides another category of electron-deficient subvalent clusters. Simple examples contain a single aluminium atom occupying one vertex in a borane or carborane cluster, for example, in the *closo* compounds $[MeAlB_{11}H_{11}]^{2-}$ and $EtAlB_9C_2H_{11}$.[54–56] However, the prime example is the aluminium cluster $[Al_{12}i\text{-}Bu_{12}]^{2-}$, which is an alkyl-substituted analog of the borane anion $B_{12}H_{12}^{2-}$, and has the expected *closo* icosahedral geometry in the solid state (Figure 14). The gallium anion $[Ga_8R_8]^{2-}$ (R = fluorenyl) has a $2n+2$ electron count, but exhibits square antiprismatic rather than the expected dodecahedral geometry (Figure 14), illustrating the same phenomenon observed for some of the heavier naked main group clusters for which different geometries have very similar energies. A number of carbaalanes comprising a carbon and aluminium framework have been reported, for example, $(AlMe)_8(CCH_2Ph)_5H$ and $(AlEt)_7(CCH_2Ph)_4(C{\equiv}CPh)H$, which have Al_8C_5 and Al_7C_4 cluster cores and electron counts corresponding to *arachno* and *closo* compounds.[54]

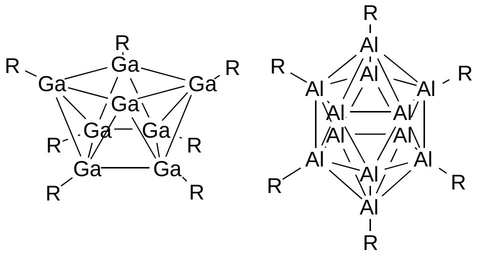

Figure 14 Substituted gallium and aluminium clusters $[Ga_8R_8]^{2-}$ (R = fluorenyl) and $[Al_{12}i\text{-}Bu_{12}]^{2-}$ (not all i-Bu groups shown)

Group 13 clusters with electron counts less than the $2n+2$ electrons corresponding to *closo* deltahedra have also been described. The classic examples of these are the boron subhalides, B_nCl_n where $n = 4$, 8–12 (and a more limited set of bromides and iodides), which have an electron count of $2n$ and are known as *hypercloso* clusters. These are based on the same *closo* structures expected for the $2n+2$ electron clusters, namely, tetrahedral, dodecahedral, and tricapped trigonal prismatic for $n = 4$, 8, and 9. The $2n+2$ dianions $B_nCl_n^{2-}$ also show the expected deltahedral structures. The stability of the B_nCl_n clusters has been attributed to a combination of the π-donor properties of the halides and steric effects.[2,57]

Of the heavier group 13 elements, a number of organoelement(I) compounds $(ER)_n$ with $2n$ cluster electron counts have been identified. Those with Cp* ligands, tetrahedral $(AlCp^*)_4$ and octahedral $(GaCp^*)_6$ and $(InCp^*)_6$ have already been discussed (Section 2).[27] The electron-rich and sterically shielding Cp* ligands contribute to their stability and the M–M interactions are long and weak. More generally, a range of tetrahedral M_4R_4 clusters for the four elements Al–Tl have been described, with t-Bu (Al), $C(SiMe_3)_3$, $Si(t\text{-}Bu)_3$ or $Si(SiMe_3)_3$ ligands. Delocalized bonding utilising the $2n$ cluster electrons is involved, and the clusters become progressively less stable with increasing atomic number. For example, the Tl–Tl interactions in $\{TlC(SiMe_3)_3\}_4$ are very long. The aluminium compounds exhibit a varied range of colors, for example, $(AlCp^*)_4$, $\{AlC(SiMe_3)_3\}_4$, and $(AlSiR_3)_4$ are yellow, orange, and violet, correlating with the Al–Al distances and the HOMO-LUMO gap. The largest of the $(ER)_n$ clusters are $(Ga\text{-}t\text{-}Bu)_9$ and its monoanion $[(Ga\text{-}t\text{-}Bu)_9]^-$, which both adopt the *closo*-type bicapped trigonal prism geometry, although with some differences in the Ga–Ga bond lengths for each.[35]

Hypoelectronic clusters have also been identified in solid phases. Hypoelectronic clusters have electron counts less than $2n + 2$, for example $2n$ in Tl_n^{n-} ($n = 6$, 7, 9) and $2n - 4$ in M_{11}^{7-} (M = Ga, In, Tl). A further new category of naked group 13 subvalent clusters are the centred clusters, for example, $Tl_{10}Zn^{8-}$, which contains a zinc atom in the centre of a bicapped square antiprism, giving an overall $2n - 2$ electron count.[53]

6 METALLOID CLUSTERS

The preparation of metastable solutions of the aluminium(I) and gallium(I) monohalides was outlined in Section 3.[7,28,34] These solutions disproportionate to the trihalide and the metal (equation 2) when warmed to temperatures in the range −40 to +50 °C, depending on the halide, the donor, and the concentration. Substitution of the halide by other suitable anionic ligands can also occur in the same temperature range, adding another variable to the conditions for the disproportionation reaction. The most effective group for these substitution reactions is the $N(SiMe_3)_2$ group, shown in equation (3).

$$AlCl + LiNR_2 \longrightarrow AlNR_2 + LiCl$$
$$(R = SiMe_3) \qquad (3)$$

Careful control of these conditions allowed the isolation of clusters that form on the path to the completed precipitation of the metal.[58–60] They have been termed 'metalloid' clusters, referring to the fact that the core arrangement of the cluster atoms resembles that in the bulk metals. (This use of the term 'metalloid' should not be confused with its use to refer to elements such as silicon, germanium, and arsenic, which lie on the metal/nonmetal border within the periodic table.) The clusters have the general formula $M_nR_m^{x-}$ where $n > m$, and thus the clusters comprise $m - n$ 'naked' metal atoms together with m MR fragments (M = Al, Ga; R = $N(SiMe_3)_2$) and the average $N_{ox} < 1$. Cluster size increases with increasing temperature, indicating that as the temperature increases the system has moved further along the path to complete disproportionation to the metal. For example, warming a solution of AlCl produces $[Al_7R_6]^-$ at −7 °C, $[Al_{12}R_6]^-$ at 25 °C, and $[Al_{69}R_{18}]^{3-}$ after warming briefly to 60 °C. A solution of the less reactive AlI produces $[Al_{14}R_6I_6]^{2-}$ at room temperature and $[Al_{77}R_{20}]^{2-}$ after brief warming to 60 °C. As the cluster size increases, the mean oxidation state (N_{ox}) of the metal decreases, again indicating further progress along the path to the metal. For example, N_{ox} values for the Al_7, Al_{12}, and Al_{69} clusters are 0.71, 0.42, and 0.22. Views of the Al_7 and Al_{12} clusters and the relationship of the clusters to the cubic close packing in aluminum metal are shown in Figures 15 and 16.

The structures of the clusters comprise inner 'naked' aluminium atoms, which for the larger clusters are layered in concentric shells with the substituted AlR groups occurring on the outside of the cluster.[59] The most significant feature of the clusters is that the aluminium cluster core resembles a distorted fragment of the structure of metallic aluminium and can be viewed as 'metalloid' fragments protected by a shell of AlR groups. In the largest cluster, $[Al_{77}R_{20}]^{2-}$, the structure comprises a single inner Al atom surrounded by a distorted icosahedral Al_{12} shell.[5] This, in turn, lies inside a shell of 44 Al atoms, and finally the outermost layer consists of 20 $AlN(SiMe_3)_2$ groups (Figure 17). On moving from the innermost, single Al atom to the fourth, outermost Al_{20} shell both the coordination number of the Al atoms and the mean Al–Al distances decrease, indicating that the Al–Al bonds become more localised and have more molecular character closer to the surface of the cluster. A comparison of the closely related $[Al_{69}R_{18}]^{3-}$ and $[Al_{77}R_{20}]^{2-}$ structures shows that despite overall broad similarities in their structures, there are significant differences in the packing of the aluminium atoms within each cluster, including the environment around

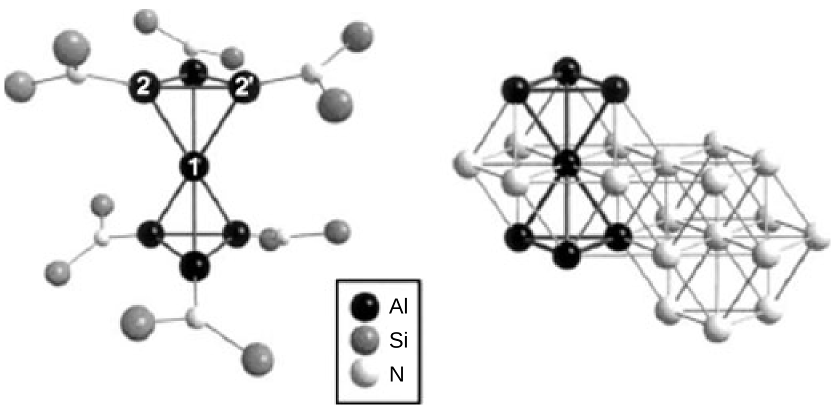

(a) (b)

Figure 15 (a) Molecular structure of $Al_7\{N(SiMe_3)_2\}_6^-$ (methyl groups omitted); (b) view showing the relationship of the Al_7 cluster to the cubic close packing in Al metal. (Reprinted from Ref. 59. © 2002, with permission from Elsevier)

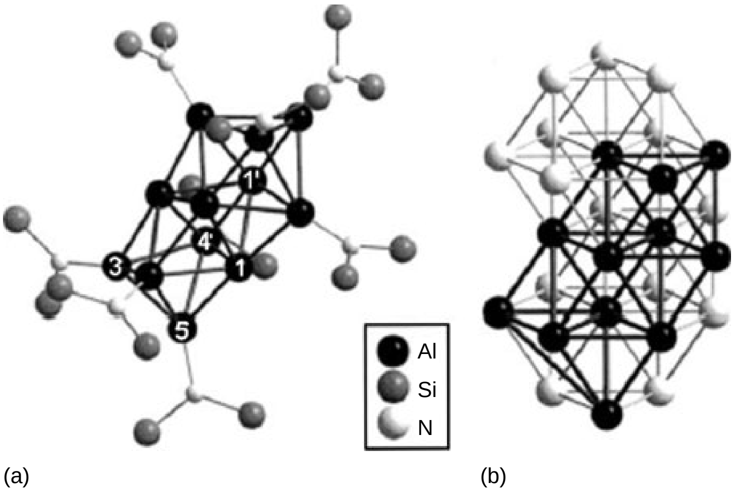

Figure 16 (a) Molecular structure of $Al_{12}\{N(SiMe_3)_2\}_8^-$ (methyl groups omitted); (b) view showing the relationship of the Al_{12} cluster to the cubic close packing in Al metal. (Reprinted from Ref. 59. © 2002, with permission from Elsevier)

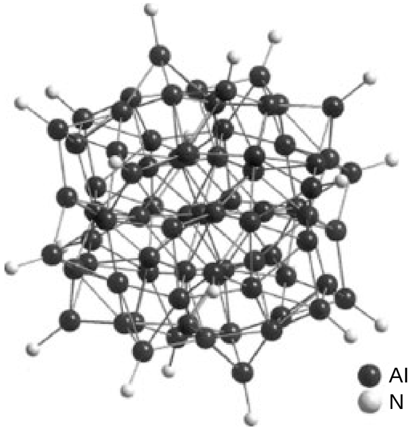

Figure 17 Molecular structure of the anion $Al_{77}\{N(SiMe_3)_2\}_{20}^{2-}$ ($SiMe_3$ groups omitted). (Reprinted from Ref. 28. © 2000, with permission from Elsevier)

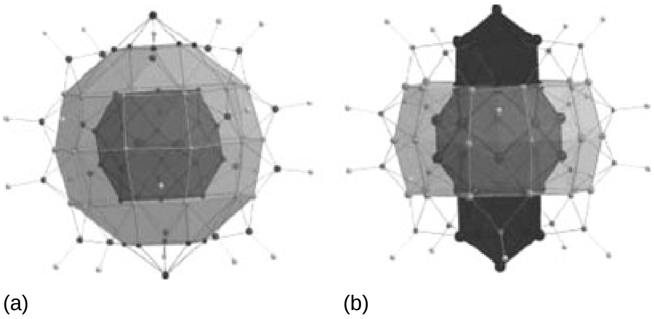

Figure 18 Molecular structure of the anion $Ga_{84}\{N(SiMe_3)_2\}_{20}^{4-}$ ($SiMe_3$ groups omitted): (a) layered representation showing shells of Ga atoms; (b) view showing relationship of the bond lengths within the Ga_{84} cluster. (Ref. 60. Reproduced by permission of Wiley-VCH)

the central aluminium atoms. This finding indicates that even slight variations on the surface of nanostructured materials can affect the arrangement of atoms for several layers towards the centre of the nanoparticle.

Only one solid-state structure is known for aluminium metal, contrasting with gallium metal, which can exist as a number of solid-state modifications. Starting with solutions of gallium halides GaX, a variety of clusters containing 6, 8, 12, 18, 19, 22, 26, or 84 gallium atoms can be prepared through the controlled disproportionation reactions.[61] These clusters show a variety of arrangements of gallium atoms in the cluster core, in parallel with the several modifications of gallium metal itself. The Ga_{84} cluster, $[Ga_{84}\{N(SiMe_3)_2\}_{20}]^{4-}$, is the largest metalloid cluster synthesised to date, and comprises 64 unsubstituted gallium atoms within a shell of 20 $GaN(SiMe_3)_2$ groups (Figure 18).[6] Like the Al_{77} cluster, the gallium cluster is comprised of successive concentric layers of gallium atoms. A remarkable feature is that a dumbell-shaped Ga_2 unit with a very short Ga–Ga distance of 2.34 Å lies at the centre of the cluster, surrounded by a rugby ball-shaped Ga_{32} shell. The next 30 gallium atoms form a cylinder around the widest part of the rugby ball, with the remaining 20 ligand-bearing $GaN(SiMe_3)_2$ groups distributed on the surface of the cluster.

Overall, the metalloid aluminium and gallium clusters bear some relationship to fragments of the bulk metals, protected and stabilised by the ligands on the surface, and as such can be considered intermediate between molecules and metals. They show a marked sensitivity to preparative conditions and the steric influence of the ligands on the surface. Spectroscopic studies and theoretical calculations on the clusters are not discussed here but are summarised in recent review articles, and these additional studies provide a greater depth of understanding of these unique molecules.[62] The Ga_{84} cluster has recently been demonstrated to become superconducting at ca. 7 K, indicating further unusual features and potential applications of these remarkable clusters.[63]

A small number of heavier group 13 clusters containing naked metal atoms are known, although nothing on the scale of the large aluminium clusters. In_4Ar_6, Ga_4Ar_6 and $[Ga_4Ar_6]^{2-}$ (Ar = Trip) each contain a trigonal planar unsubstituted metal bonded to three MAr_2 groups. $In_8Ar^*_4$ (Ar = Mes) comprises an In_8 cube with alternating substituted and naked indium atoms.[64] Ga_8R_6 ($R = C(SiMe_3)_3$) and $Ga_{10}R_6$ ($R = Si(SiMe_3)_3$) consist, respectively, of two tetrahedra linked by a Ga–Ga bond, and two octahedra sharing one edge.[60] The largest cluster, $In_{12}R_8$ ($R = Si(CMe_3)_3$) is an ellipsoidal polyhedron that can be loosely described as two In_6 octahedra linked through In–In interactions between the four naked indium atoms, the core of which has a structural relationship to elemental indium.[65]

Comparable metalloid clusters of the group 14 elements are much less well developed. The metastable subhalide route has just been established for germanium, with the preparation of GeCl.[66,67] A small number of examples are known of the type E_nR_m where $n >$ m and formal $N_{ox} < 1$. These clusters contain 2, 3, or 4 unsubstituted metal atoms, and can be considered to lie on the path approaching the metal, but not to the extent observed for the much larger group 13 clusters. The $Sn_8R^*_6$ ($R^* = Si\textit{t}\text{-}Bu3$) and Ge_8R_6 ($R = N(SiMe_3)_2$) clusters contain a cuboid E_8 core with six substituted and two unsubstituted atoms. The $M_4(GeAr^*)_2$ (M = Ge, Sn; Ar = Dipp) and $Sn_4(SnAr^*)_4$ (Ar = Mes) clusters have as a common structural element a square-planar unsubstituted M_4 core capped on the square faces by $GeAr'$ groups in the former case and Ar*SnSnAr* groups in the latter (Figure 19). The germanium cation $[Ge_{10}R^*_6I]^+$ contains a trigonal $Ge_3{}^+$ core capped above and below by Ge_4R_3I and Ge_3R_3 units. Two further tin clusters, Sn_5Ar_6 and Sn_7Ar_8 ($Ar = C_6H_3$-2,6-Et_2), although with a higher formal oxidation state, each contain two unsubstituted tin atoms in a propellane moiety.[42,43]

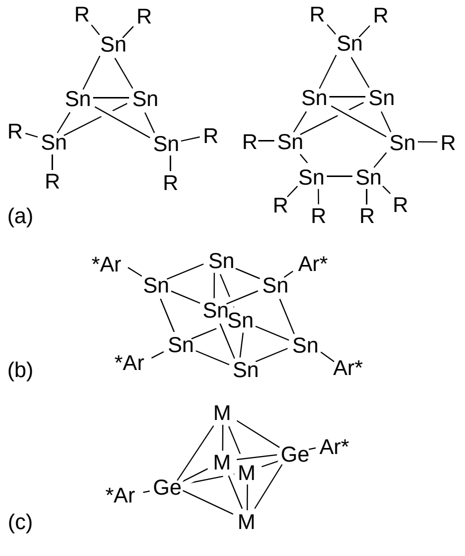

Figure 19 Group 14 clusters (a) Sn_5Ar_6, Sn_7Ar_8 ($R = C_6H_3$-2,6-Et_2), (b) $Sn_4(SnAr^*)_4$ (Ar = Mes), and (c) $M_4(GeAr^*)_2$ (M = Ge, Sn; Ar = Dipp)

7 MULTIPLE BONDING IN MAIN GROUP SUBVALENT COMPOUNDS

Until the early 1980s, the predominant view was expressed by the so-called ‘double bond rule’, which stated that elements with a principal quantum number greater than 2 do not form multiple bonds with themselves or with other elements.[68] Exciting events in 1981 saw this ‘rule’ overturned, with the announcement of the first silene Si=C[69] and disilene Si=Si[70] double bonds, followed not long after by a P=P double bond in Mes*P=PMes*.[71] In the 25 years since that time, a phenomenal advance in experimental results has taken place in this area, accompanied by a parallel advance, which has not been without controversy, in the understanding of the phenomenon of multiple bonding in the heavier main group elements.

A table of hypothetical multiply bonded main group compounds based on isoelectronic analogs of carbon can be easily drawn up. The challenge then arises in designing and synthesising target compounds. One of the keys to success in this area has been the use of bulky substituents to aid in kinetic stabilisation of very reactive molecules, and with each new generation of bulky ligands further advances have been made. For example, simple substituted arenes such as the mesityl group provide sufficient steric protection for alkene analogs containing boron and silicon, whereas bulkier arenes bearing isopropyl (Trip) and tertiary butyl (Mes*) substituents are required for aluminium, gallium, and phosphorus analogs. (Although phosphorus is smaller, its alkene analogs bear only one substituent at the main group atoms.) Alkyne analogs of the group 14 elements are stabilised using the new generation terphenyl ligands C_6H_3-2,6-Ar_2 in which the Ar groups are themselves bulky arenes such as Dipp, Trip, or Mes.[23] Sterically encumbering alkyl groups that have also proved useful are, for example, *t*-Bu, $CH(SiMe_3)_2$, Si*t*-Bu_3, and $Si(SiMe_3)_3$.

The target hypothetical multiple bonded main group compounds are shown in Table 3, in which the entries shown correspond to types for which at least one example has been prepared, and also show a selection of other analogs that differ from the simple target compounds by a one-electron redox change. The group 14 alkene analogs are simply the heavier element compounds R_2EER_2. Group 13 elements contain one electron less than their group 14 counterparts, so the isoelectronic boron analog of an alkene is $[R_2BBR_2]^{2-}$.

Table 3 Main group element compounds potentially containing multiple bonds

Alkene analogs			
Group 13 (and singly oxidized analogs)		Group 14	Group 15
N_{ox} +1	+1.5	+2	+1
$[R_2BBR_2]^{2-}$	$[R_2BBR_2]^{-}$	$R_2C{=}CR_2$	RN=NR
	$[R_2AlAlR_2]^{-}$	R_2SiSiR_2	RPPR
	$[R_2GaGaR_2]^{-}$	R_2GeGeR_2	RAsAsR
		R_2SnSnR_2	RSbSbR
		R_2PbPbR_2	RBiBiR

Alkyne analogs				
Group 13	Group 14 (and singly and doubly reduced analogs)			Group 15
N_{ox} 0	+1	+0.5	0	0
	RC≡CR			N≡N
$[RGaGaR]^{2-}$	RsiSiR			
	RGeGeR	$[RGeGeR]^{-}$	$[RGeGeR]^{2-}$	
	RSnSnR	$[RSnSnR]^{-}$	$[RSnSnR]^{2-}$	
	RPbPbR			

Group 15 elements each contain one more electron, giving the well-known imines RN=NR as the nitrogen examples but more exotic species RE=ER containing the heavier elements. Once the compounds have been successfully prepared the next challenge is to determine whether their structural, spectroscopic, and chemical properties are indeed in accord with the existence of a multiple bond.[72]

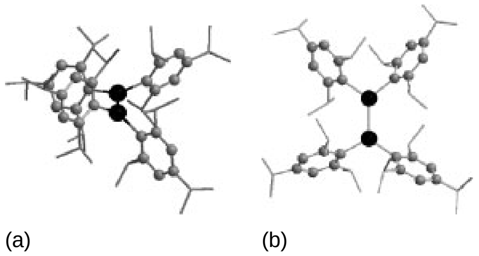

Figure 20 (a) Neutral $Trip_2AlAlTrip_2$ showing the torsion angle around the Al–Al bond and (b) the singly reduced anion $[Trip_2AlAlTrip_2]^-$ containing a partial Al–Al π bond

7.1 Alkene Analogs

The diboron dianion $[Mes_2BB(Mes)Ph]^{2-}$, prepared by lithium metal reduction of the neutral diborane precursor $Mes_2BB(Mes)Ph$, does indeed show a much reduced torsion angle about the B–B bond (the angle between the two C_2B planes) of 7°, relative to 79° in the neutral precursor, and a B–B bond length of 1.636 Å, some 7% shorter than the 1.706 Å distance in the neutral compound. Spectroscopic evidence (^{11}B NMR and observation of a π-π^* transition in the electronic spectrum) add further evidence for the existence of a B=B double bond in this compound with a π bond strength estimated to be around 40 kcal mol^{-1} (compared to 60 kcal mol^{-1}) in an alkene. The bond shortening is less than the 13% decrease observed for the C–C bond in an alkene relative to an alkane, but this is probably a result of electrostatic effects arising from the 2- charge. Support for this idea can be derived from the singly reduced compound $[Mes_2BB(Mes)Ph]^-$, which has only a half-occupied π orbital and a net B–B bond order of 1.5, yet has almost the same B–B bond length, 1.649 Å, as the doubly bonded dianion.[73] Only the singly reduced aluminium and gallium alkene analogs could be prepared, $[R_2AlAlR_2]^-$ and $[Trip_2AlAlTrip_2]^-$, but like their boron counterpart they show small torsion angles and E–E bonds some 7% shorter than the neutral precursors (Figure 20). EPR evidence indicates that the single electron occupies an orbital of π symmetry in each case, consistent with a partial π bond and E–E bond order of 1.5.[74–76]

The complete set of group 14 alkene analogs R_2EER_2 are known for carbon, silicon, germanium, tin, and lead. These include two landmark compounds, the disilene $Mes_2SiSiMes_2$ prepared in 1981,[70] and the tin compound $\{(Me_3Si)_2CH\}_2SnSn\{CH(SiMe_3)_2\}_2$ prepared in 1976[77] (Figure 21). The silicon compound was a breakthrough because its structural and spectroscopic characteristics were overwhelmingly in accord with its formulation as a Si=Si double-bonded compound, representing the first of its type. The tin compound, on the other hand, has the stoichiometry of an alkene analog, but its structural and chemical properties did not seem to be in accord with the presence of a double bond. The Sn–Sn bond (2.77 Å) is only marginally shorter than an Sn–Sn single bond (2.81 Å), the compound is not planar but rather the two C_2Sn planes are tilted 41° away from the Sn–Sn

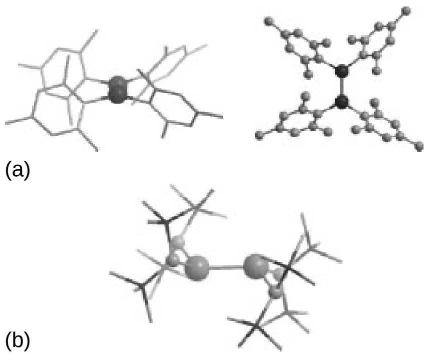

Figure 21 (a) Two views of the disilene $Mes_2Si{=}SiMes_2$, with the left view emphasising the planar geometry; (b) the trans-bent tin alkene analog $\{(Me_3Si)_2CH\}_2SnSn\{CH(SiMe_3)_2\}_2$

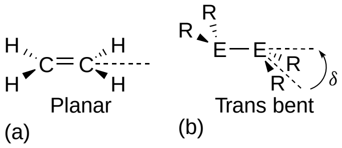

Figure 22 Geometry of alkene and alkene analogs: (a) planar geometry, angle between CH_2 plane and C–C bond = 0°; (b) trans-bent geometry, angle between ER_2 plane and E–E bond $> 0°$

axis, in a trans-bent geometry (Figure 22), and the compound dissociates into $(Me_3Si)_2CH\}_2Sn$ monomers in solution.

The characteristics observed for the group 14 alkene analogs are summarised in Table 4.[13,15,19,78–80] The extent of bond shortening (relative to an E–E single bond) decreases down the group – in fact some of the tin and lead 'double' bonds are *longer* than the corresponding single bonds. The occurrence of trans-bending increases down the group, and some of the germanium, and all of the tin and lead compounds are dissociated into monomers in solution. In fact, the enthalpy of association for the tin monomers ($2SnR_2$ forming R_2SnSnR_2) was calculated to be 10–12 kcal mol^{-1}, comparable to the energy of a hydrogen bond and much weaker than the value of 35 kcal mol^{-1} calculated for the energy of an Sn–Sn single bond. On the other hand, the disilene complexes can exist as *cis* and *trans* isomers with high barriers to rotation around the Si–Si bonds.[81] In summary, the group 14 compounds appear to range from true alkene-type compounds for the lighter elements carbon and silicon to compounds with quite different characteristics for tin and lead, which show chemistry consistent with a stannane- or plumbanediyl, $:ER_2$. The germanium examples are intermediate between silicon and tin: some behave more like a digermene, others more like a germanediyl. The challenge has been to derive an understanding of the bonding in these compounds that effectively rationalises these characteristics.

Table 4 Group 14 alkene analogs

	Number of compounds	E–E/Å	δ/°	E–E (single)	%^{a}
$R_2C{=}CR_2$	$>10^4$	1.34	0	1.54	13
$R_2Si{=}SiR_2$	12	2.138–2.251	0–18	2.34	4–9
R_2GeGeR_2	10	2.213–2.460	0–47	2.44	0–9
R_2SnSnR_2	5	2.768–3.639	28–46	2.76	0
R_2PbPbR_2	6	2.989–4.129	34–71	2.88	0

^{a}% shortening relative to single bond.

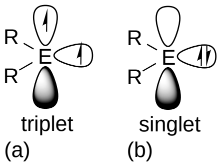

Figure 23 Group 14 diyl fragments: (a) triplet lower in energy for E = C; (b) singlet lower in energy for E = Si, Ge, Sn, Pb

Two electronic effects have been identified that can help account for the observed experimental results.[79] The first is the singlet-triplet energy gap in the sp^2–hybridised group 14 diyl fragments ER_2. For carbon (in other words a carbene), the triplet state is lower in energy, while for the heavier elements the singlet is the ground state (Figure 23). If the $\sigma + \pi$ bond combination in ethene is considered to arise from coupling of two triplet fragments, then the singlet to triplet promotion energy is an energy cost to forming an alkene-like double bond in the heavier elements. On descending the group, the energy gained from E–E bond formation is increasingly unable to offset the higher energy required for accessing the triplet state prior to forming the double bond. The chemistry of the double bond increasingly (especially for tin and lead) resembles that of two singlet monomers associated through dative bonding.

In molecular orbital terms, the C–C bonding in an alkene comprises one σ and one π bond. On descending the group 14 elements, the energy gap between the antibonding E–E σ^* orbital and the π orbital decreases, and mixing of these two orbitals ($\sigma^* + \pi$) increases in the order Si, Ge, Sn, Pb, with the mixing most marked for the heavier elements. This effect is related to the tendency for increased pyramidalization in the heavier main group elements. The $\sigma^* + \pi$ orbital mixing lowers the energy of the original π orbital, but at the same time increases its lone pair character and weakens the π bond. As a result of the bending and orbital mixing, it increasingly resembles a nonbonding, lone pair orbital rather than a π bonding orbital. The nonbonding orbital is distributed over the two E atoms but contains two electrons and can be described by the resonance forms shown in Figure 24. The E–E σ bond is also weakened as the orbital overlap is not as favourable in the bent geometry. The bonding in the tin and lead compounds is weakened to the extent that they dissociate to monomers in solution. Overall, the E–E bond orders are probably greater than one but less than two, and the correlation between bond

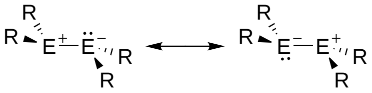

Figure 24 Resonance forms arising from $\sigma^* + \pi$ mixing in trans-bent group 14 alkene analogs

order and bond length is not as reliable as in the true alkene type ($\sigma + \pi$) double bonding.[79]

Isoelectronic analogs of alkenes containing group 15 elements contain one substituent (very bulky) and one lone pair at each E atom.[79,82–84] The homologous series shown in Table 5 (all containing the Ar* terphenyl ligand with Ar = Mes) gives a view of the trends down the group. Molecular structures of the phosphorus and bismuth compounds are shown in Figure 25. The % E–E bond shortening and C–E–E angles decrease. In orbital terms, the *s* character decreases in the E–E bond, and increases in the lone pair, so that for the bismuth examples, the C–Bi and Bi–Bi bonding is mainly *p* in character (as bond angles approach 90°) and the lone pair occupies a predominantly *s* orbital.

For the group 15 elements, both experimental and theoretical studies indicate that there is a double bond with both σ and π components. For example, both *cis* and *trans* isomers are isolable for the phosphorus compounds. The σ:π bond strength ratio for P (48:34 kcal mol^{-1}) is similar to that for C (81:62 kcal mol^{-1}). The ratio of σ:π bond strengths decreases down the group, but is still consistent with presence of both σ and π bonds for each compound. Overall, bonding in the group 15 analogs of alkenes can be described as full-fledged double (σ and π) bonds.[79]

Table 5 Group 15 alkene analogs Ar*EEAr* (Ar = Mes)

	E=E/Å	C–E–E/°	%
Ar*PPAr*	1.985(2)	103.7(av)	10.6
Ar*AsAsAr*	2.276(3)	98.5(4)	6.7
Ar*SbSbAr*	2.6558(5)	94.1(1)	6.5
Ar*BiBiAr*	2.8327(14)	92.5(4)	5.3

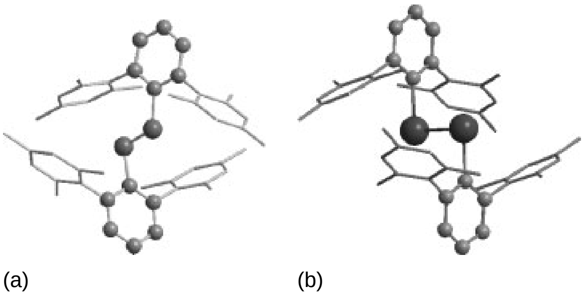

Figure 25 Group 15 alkene analogs (a) Ar*PPAr* and (b) Ar*BiBiAr* (Ar = Mes)

7.2 Alkyne Analogs

In 1997, a digallium dianion was reported that sparked off a controversy regarding the nature of the bonding between the two gallium atoms. The compound, Na_2[Ar*GaGaAr*] (Ar = Trip), was prepared by sodium metal reduction of Ar*$GaCl_2$. The compound is formally a triple bond (ethyne) analog, $[RM{\equiv}MR]^{2-}$. Although it has a short Ga–Ga bond of 2.319(3) Å, it is not significantly shorter than the shortest Ga–Ga single bond, and the molecule is not linear as might be expected, but has C–Ga–Ga angles of 131°. The two sodium cations are sandwiched between pairs of opposing phenyl rings from the terphenyl substituents, and theoretical studies indicate these interactions are significant in stabilising the molecule.[82,85,86]

Several isomeric forms can be written for group 13 'triple' bonds, shown in Figure 26. Bending of the C–Ga–Ga angle away from 180° is evidence for the presence of lone pairs, and calculations on a variety of model compounds are consistent with a Ga–Ga bond order of 2. The isomeric form with one π bond and one delocalized lone pair (as in the group 14 alkene analogs) is possibly the best description of this molecule.[76]

Neutral compounds of the form Ar*EEAr* are known for germanium, tin (Ar = Dipp), and lead (Ar = Trip) (Figure 27).[87,88] The lead compound Ar*PbPbAr* has a Pb–Pb bond length of 3.19 Å, even longer than a Pb–Pb single bond (2.88 Å). The C–Pb–Pb angles of 94° suggest that the orbitals involved in Pb–Pb and Pb–C bonding are almost pure *p* in character. A formulation with the Pb–Pb bond order close to 1 and a lone pair occupying a 6*s* orbital on each Pb atom is likely to be the most appropriate for the dilead compound (type c in Figure 26).

The germanium and tin compounds Ar*EEAr* have different characteristics, with C-E-E angles in the range 125–129°, and some bond shortening evidenced by the Ge–Ge and Sn–Sn bond lengths of 2.285 and 2.667 Å, compared to 2.44 and 2.81 Å for the corresponding single bonds, suggesting some multiple bond character. The trans-bending in these compounds can be explained using the same molecule orbital argument used for bending in the alkene analogs, based on mixing of the π and σ^* orbitals. In the linear, alkyne-like

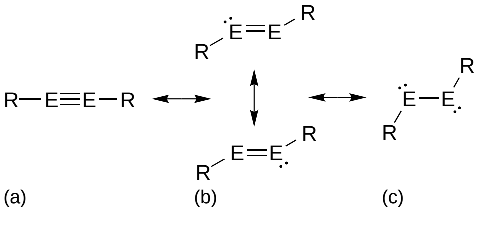

Figure 26 Resonance forms for E–E bonds in [REER]$^{n-}$ (E = group 13, $n = 2$; E = group 14, $n = 0$): (a) bond order 3; one σ bond, two π bonds; linear geometry; (b) bond order 2; one σ, one π bond, one lone pair; trans-bent geometry; (c) bond order 1; one σ bond, two lone pairs; strongly trans-bent geometry

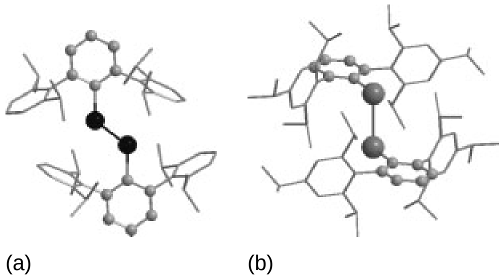

Figure 27 Group 14 alkyne analogs (a) Ar*GeGeAr* (Ar = Dipp) and (b) Ar*PbPbAr* (Ar = Trip)

form (type a in Figure 26), the bond order is three, with one σ and two π bonds. In the trans-bent form, one of the two π bonds has been converted into an essentially nonbonding orbital. Thus, the bond order is reduced from 3 to 2 (one σ and one π bond), or even less since the remaining σ and π bonds are weakened in the bent form (type b in Figure 27). The nonbonding orbital is distributed over the two atoms, and contains two electrons that from recent evidence might be formulated as a singlet diradicaloid.[87]

The lightest member of the series, containing silicon, has only just been reported in 2004.[89] The compound RSiSiR ($R = Si\textit{i}Pr(Si\textit{t}Bu_3)_2$) has an Si≡Si bond length of 2.06 Å, some 3.8% shorter than an Si=Si double bond, and 13.5% shorter than an Si–Si single bond. The compound is trans-bent with an Si–Si ≡Si angle of 137°.

The germanium and tin compounds can be further reduced to form mono- and dianions, $[ArEEAr]^-$ and $[ArEEAr]^{2-}$. In formulation c (Figure 26), each E atom bears an unused p orbital that can overlap to form a molecular orbital of π symmetry. For the reduced tin compounds, in particular, there is evidence that the additional electron(s) populate this π orbital, whereas for the germanium compounds, best described by b (Figure 26), the LUMO is nonbonding and the additional electron(s) have little direct effect on the Ge–Ge bonding.[90]

Multiple bonding in subvalent main group compounds has been discussed above primarily using examples of homonuclear element–element bonds. There are an increasing number of examples of heteronuclear pairs of elements for which there is evidence for multiple bonding. These will not be discussed here but some recent reviews are cited as follows: boron–carbon,[91] silicon–carbon,[92] silicon–nitrogen,[93] silicon–phosphorus and silicon–arsenic,[94,95] germanium and tin multiply bonded compounds,[96,97] group 14–group 16 compounds,[98,99] phosphorus,[100] and phosphorus-carbon.[101]

Finally, aromaticity is a hallmark of carbon chemistry that has received only limited attention among the heavier main group elements. Stable aromatic compounds containing the heavier group 14 elements[102] and also a small number of group 15 examples have been reported.[85]

8 RELATED ARTICLES

Boron: Polyhedral Carboranes; Group 14 Multiple Bonding; Low Oxidation State Main Group; Main Group Carbenes; Main Group: Multiple Bonding; Periodic Table: Trends in the Properties of the Elements; Polyhedra; Zintl Compounds.

9 REFERENCES

1. W. Uhl, *Z. Naturforsch.*, 1988, **43b**, 1113.
2. N. N. Greenwood and A. Earnshaw, 'Chemistry of the Elements', 2nd edn., Butterworth-Heinemann, Oxford, 1997.
3. C. E. Housecroft, 'Cluster Molecules of the p-Block Elements', Oxford University Press, Oxford, 1994.
4. K. Wade, *Adv. Inorg. Chem. Radiochem.*, 1976, **18**, 1.
5. A. Ecker, E. Weckert, and H. Schnöckel, *Nature*, 1997, **387**, 379.
6. A. Schnepf and H. Schnöckel, *Angew. Chem., Int. Ed. Engl.*, 2001, **40**, 711.
7. C. Dohmeier, D. Loos, and H. Schnöckel, *Angew. Chem., Int. Ed. Engl.*, 1996, **35**, 129.
8. W. A. Herrmann and C. Kocher, *Angew. Chem., Int. Ed. Engl.*, 1997, **36**, 2162.
9. A. J. Downs, H.-J. Himmel, and L. Manceron, *Polyhedron*, 2002, **21**, 473.
10. H.-J. Himmel, *Dalton Trans*, 2003, 3639.
11. A. J. Arduengo III, R. L. Harlow, and M. Kline, *J. Am. Chem. Soc.*, 1991, **113**, 361.
12. M. Haaf, T. A. Schmedake, and R. West, *Acc. Chem. Res.*, 2000, **33**, 704.
13. M. Driess and H. Grützmacher, *Angew. Chem., Int. Ed. Engl.*, 1996, **35**, 828.
14. M. Weidenbruch, *J. Organomet. Chem.*, 2002, **646**, 39.
15. M. Weidenbruch, *Eur. J. Inorg. Chem.*, 1999, 373.
16. P. P. Gaspar, M. Xiao, D. H. Pae, D. J. Berger, T. Haile, T. Chen, D. Lei, W. R. Winchester, and P. Jiang, *J. Organomet. Chem.*, 2002, **646**, 68.
17. D. Bourissou, O. Guerret, F. P. Gabbai, and G. Bertrand, *Chem. Rev.*, 2000, **100**, 39.
18. H. V. Rasika Dias, Z. Wang, and W. Jin, *Coord. Chem. Rev.*, 1998, **176**, 67.
19. M. N. Sudheendra Rao, H. W. Roesky, and G. Anantharaman, *J. Organomet. Chem.*, 2002, **646**, 4.
20. H. W. Roesky, *Inorg. Chem.*, 2004, **43**, 7284.
21. N. J. Hardman, A. D. Phillips, and P. P. Power, Bonding and Reactivity of a β-Diketiminate, Gallium(I), Carbene Analog, in 'Group 13 Chemistry. From Fundamentals to Applications', ACS Symposium Series 822, eds. P. J. Shapiro

and D. A. Atwood, American Chemical Society, Washington, DC, 2002, p. 2.

22. N. Tokitoh and R. Okazaki, *Coord. Chem. Rev.*, 2000, **210**, 251.
23. B. Twamley, S. T. Haubrich, and P. P. Power, *Adv. Organomet. Chem.*, 1999, **44**, 1.
24. N. Wiberg, *Coord. Chem. Rev.*, 1997, **163**, 217.
25. P. Jutzi and N. Burford, *Chem. Rev.*, 1999, **99**, 969.
26. P. Jutzi and G. Reumann, *J. Chem. Soc., Dalton Trans.*, 2000, 2237.
27. L. O. Schebaum and P. Jutzi, Pentamethylcyclopentadienyl Complexes of the Monovalent Group 13 Elements, in 'Group 13 Chemistry. From Fundamentals to Applications', ACS Symposium Series 822, eds. P. J. Shapiro and D. A. Atwood, American Chemical Society, Washington, DC, 2002, p. 16.
28. G. Linti and H. Schnöckel, *Coord. Chem. Rev.*, 2000, **206–207**, 285.
29. T. Kühler and P. Jutzi, *Adv. Organomet. Chem.*, 2003, **49**, 1.
30. L. Kloo, J. Rosdahl, and M. J. Taylor, *Polyhedron*, 2002, **21**, 519.
31. W. Uhl, *Coord. Chem. Rev.*, 1997, **163**, 1.
32. W. Uhl, *Adv. Organomet. Chem.*, 2004, **51**, 53.
33. V. M. Dembitsky, H. A. Al, and M. Srebnik, *Adv. Organomet. Chem.*, 2004, **51**, 193.
34. H. Schnöckel and C. Klemp, Molecular Aluminium and Gallium Subhalides, in 'Inorganic Chemistry Highlights', eds G. Meyer, D. Naumann, and L. Wesemann, Wiley, Weinheim, 2002, Chap. 15, p. 245.
35. W. Uhl, *Naturwissenschaften*, 2004, **91**, 305.
36. N. Wiberg, T. Blank, H.-W. Lerner, D. Fenske, and G. Linti, *Angew. Chem., Int. Ed. Engl.*, 2001, **40**, 1232.
37. P. P. Power, *Chem. Rev.*, 2003, **103**, 789.
38. S. Kyushin and H. Matsumoto, *Adv. Organomet. Chem.*, 2003, **49**, 133.
39. J. A. Corey, *Adv. Organomet. Chem.*, 2004, **51**, 1.
40. H. J. Breunig and R. Rösler, *Coord. Chem. Rev.*, 1997, **163**, 33.
41. H. J. Breunig and L. Balázs, *Organometallics*, 2004, **23**, 304.
42. A. Sekiguchi and H. Sakurai, *Adv. Organomet. Chem.*, 1995, **37**, 1.
43. N. Wiberg and P. P. Power, Molecular Cages and Clusters of the Heavier Group 14 Elements (E = Si, Ge, Sn or Pb) of Formula E_nR_m ($n \geq m$), in 'Molecular Clusters of the Main Group Elements', eds. M. Driess and H. Nöth, Wiley, Weinheim, 2004, Ch 2.5, p. 188.
44. J. Beck, *Coord. Chem. Rev.*, 1997, **163**, 55.
45. S. Brownridge, I. Krossing, J. Passmore, H. D. B. Jenkins, and H. K. Roobottom, *Coord. Chem. Rev.*, 2000, **197**, 397.
46. J. D. Corbett, *Struct. Bonding*, 1997, **87**, 157.
47. S. M. Kauzlarich ed., 'Chemistry, Structure and Bonding of Zintl Phases and Ions', VCH, New York, 1996.
48. A. N. Kuznetsov, L. Kloo, M. Lindsjö, J. Rosdahl, and H. Stoll, *Chem. – Eur. J.*, 2001, **7**, 2821.
49. M. Lindsjö, A. Fischer, and L. Kloo, *Angew. Chem., Int. Ed. Engl.*, 2004, **43**, 2540.
50. T. F. Fässler, *Coord. Chem. Rev.*, 2001, **215**, 347.
51. J. D. Corbett, *J. Chem. Soc., Dalton Trans.*, 1996, 575.
52. J. D. Corbett, *Inorg. Chem.*, 2000, **39**, 5178.
53. J. D. Corbett, *Angew. Chem., Int. Ed. Engl.*, 2000, **39**, 670.
54. W. Uhl and F. Breher, *Eur. J. Inorg. Chem.*, 2000, 1.
55. K. Vyakaranam, J. A. Maguire, and N. S. Hosmane, *J. Organomet. Chem.*, 2002, **646**, 21.
56. Y. Canac and G. Bertrand, *Angew. Chem., Int. Ed. Engl.*, 2003, **42**, 3578.
57. B. Speiser, C. Tittel, W. Einholz, and R. Schäfer, *J. Chem. Soc., Dalton Trans.*, 1999, 1741.
58. H. Schnöckel and A. Schnepf, *Adv. Organomet. Chem.*, 2001, **47**, 235.
59. H. Schnöckel and H. Köhnlein, *Polyhedron*, 2002, **21**, 489.
60. A. Schnepf and H. Schnöckel, *Angew. Chem., Int. Ed. Engl.*, 2002, **41**, 3532.
61. H. Schnöckel and A. Schnepf, Nanostructural Element Modifications: Synthesis and Structure of Elementoid Gallium Clusters, in 'Group 13 Chemistry. From Fundamentals to Applications', ACS Symposium Series 822, eds. P. J. Shapiro and D. A. Atwood, American Chemical Society, Washington, DC, 2002, p. 154.
62. W. H. Lam and Z. Lin, *Polyhedron*, 2002, **21**, 503.
63. J. Hagel, M. T. Kelemen, G. Fischer, B. Pilawa, J. Wosnita, E. Dormann, H. von Löhhneysen, A. Schnepf, H. Schnöckel, U. Neisel, and J. Beck, *J. Low Temp. Phys.*, 2002, **129**, 133.
64. B. E. Eichler, N. J. Hardman, and P. P. Power, *Angew. Chem., Int. Ed. Engl.*, 2000, **39**, 383.
65. N. Wiberg, T. Blank, H. Nöth, and W. Ponikwar, *Angew. Chem., Int. Ed. Engl.*, 1999, **38**, 839.
66. A. Schnepf and R. Köppe, *Angew. Chem., Int. Ed. Engl.*, 2003, **42**, 911.
67. A. Schnepf and R. Köppe, *Z. Anorg. Allg. Chem.*, 2002, **628**, 2914.
68. R. West, *Polyhedron*, 2002, **21**, 467.
69. A. G. Brook, S. C. Nyburg, F. Abdesaken, B. Gutekunst, G. Gutekunst, R. K. Kallury, Y. C. Poon, Y. M. Chang, and W. Wong-Ng, *J. Am. Chem. Soc.*, 1982, **104**, 5667.
70. R. West, M. J. Fink, and J. Michl, *Science*, 1981, **214**, 2343.
71. M. Yoshifuji, I. Shima, N. Inamoto, K. Hirotsu, and T. Higuchi, *J. Am. Chem. Soc.*, 1981, **103**, 4587.
72. H. Grützmacher and T. F. Fässler, *Chem. – Eur. J.*, 2000, **6**, 2317.
73. P. P. Power, *Inorg. Chim. Acta*, 1992, **198–200**, 443.
74. P. J. Brothers and P. P. Power, *Adv. Organomet. Chem.*, 1996, **39**, 1.

75. A. J. Bridgeman and N. A. Nielsen, *Inorg. Chim. Acta*, 2000, **303**, 107.
76. P. P. Power, *Struct. Bonding*, 2002, **103**, 57.
77. D. E. Goldberg, D. H. Harris, M. F. Lappert, and K. M. Thomas, *J. Chem. Soc., Chem. Commun.*, 1976, 261.
78. P. P. Power, *J. Chem. Soc., Dalton Trans.*, 1998, 2939.
79. P. P. Power, *Chem. Rev.*, 1999, **99**, 3463.
80. M. Weidenbruch, *Organometallics*, 2003, **22**, 4348.
81. R. Okazaki and R. West, *Adv. Organomet. Chem.*, 1996, **39**, 232.
82. G. H. Robinson, *Adv. Organomet. Chem.*, 2001, **47**, 283.
83. N. Tokitoh, *J. Organomet. Chem.*, 2000, **611**, 217.
84. C. Jones, *Coord. Chem. Rev.*, 2001, **215**, 151.
85. G. H. Robinson, *Acc. Chem. Res.*, 1999, **32**, 773.
86. G. H. Robinson, *Chem. Commun.*, 2000, 2175.
87. P. P. Power, *Chem. Commun.*, 2003, 2091.
88. A. J. Bridgeman and L. R. Ireland, *Polyhedron*, 2001, **20**, 2841.
89. A. Sekiguchi, R. Kinjo, and M. Ichinohe, *Science*, 2004, **305**, 1755.
90. L. Pu, A. D. Phillips, A. F. Richards, M. Stender, R. S. Simons, M. M. Olmstead, and P. P. Power, *J. Am. Chem. Soc.*, 2003, **125**, 11626.
91. J. J. Eisch, *Adv. Organomet. Chem.*, 1996, **39**, 355.
92. A. G. Brook and M. A. Brook, *Adv. Organomet. Chem.*, 1996, **39**, 71.
93. I. Hemme and U. Klingebeil, *Adv. Organomet. Chem.*, 1996, **39**, 159.
94. M. Driess, *Adv. Organomet. Chem.*, 1996, **39**, 193.
95. M. Driess, *Coord. Chem. Rev.*, 1995, **145**, 1.
96. K. M. Baines and W. G. Stibbs, *Adv. Organomet. Chem.*, 1996, **39**, 275.
97. J. Escudie and H. Ranaivonjatovo, *Adv. Organomet. Chem.*, 1999, **44**, 114.
98. N. Tokitoh and R. Okazaki, *Adv. Organomet. Chem.*, 2001, **47**, 121.
99. R. Okazaki and N. Tokitoh, *Acc. Chem. Res.*, 2000, **33**, 625.
100. M. Yoshifuji, *J. Organomet. Chem.*, 2000, **611**, 210.
101. F. Mathey, *Angew. Chem., Int. Ed. Engl.*, 2003, **42**, 1578.
102. V. Y. Lee, A. Sekiguchi, M. Ichinohe, and N. Fukaya, *J. Organomet. Chem.*, 2000, **611**, 228.

Group 14 Multiple Bonding

Takahiro Sasamori & Norihiro Tokitoh
Institute for Chemical Research, Kyoto University, Japan

1	Introduction	1
2	Theoretical Aspects	1
3	Double-Bond Compounds between Group 14 Elements	4
4	Double-Bond Compounds between Group 14–Group 15 Elements	15
5	Double-Bond Compounds between Group 14–Group 16 Elements	17
6	Triple-Bond Compounds between Group 14 Elements	21
7	Conjugated π Electron and Cumulative Systems of Heavier Group 14 Elements	24
8	Heavy Aromatic Systems	30
9	Concluding Remarks	36
10	References	37

Abbreviations

B3LYP = Becke's 3-parameter hybrid with Lee; Young and Parr's correlation functional; δ = Chemical shift of NMR signal in ppm; DBU = 1,8-diazabicyclo[5.4.0]-7-undecene; eq = Equivalent; NMR = Nuclear magnetic resonance; THF = Tetrahydrofuran.

1 INTRODUCTION

Since silicon represents the next homolog to carbon in the periodic table, the question about the analogy between carbon and silicon has existed for a long time, and many chemists have studied the chemical similarities and differences between them. Unsaturated species of the second row main group elements, such as olefins, carbonyl compounds (aldehydes, ketones, esters, amides, etc.), imines, aromatic compounds, azo compounds, carbenes, and so on, play very important roles in organic chemistry. On the other hand, the chemistry of heavier elements' homologs of these low-coordinated species has been undeveloped so far most probably owing to their extremely high reactivity and inherent instability under ambient conditions, while these unsaturated compounds have been postulated in many reactions only as reactive intermediates. Prior to the 1970s, all attempts at synthesizing the low-coordinated species of elements of the third period and downward (namely, heavier main group elements) proved unsuccessful, leading to the formation of cyclic oligomers or polymers containing only single covalent bonds even under the conditions without any oxygen and water. Therefore, it came to be believed that 'elements having a principal quantum number greater than two should not be able to form pπ–pπ bonds with themselves or with other elements', that is, the so-called 'double-bond rule'.[1] It should be most likely interpreted in terms of the poor overlap of p orbitals, owing to either a large distance between the two bonding atoms (e.g. Si–Si bond) or a poor size match (e.g. Si–C bond), precluding favorable bonding interactions. However, this rule came to be doubted during the 1970s with the reports on the preparations of such low-coordinated compounds of heavier main group elements in the gas phase and the trapping reactions of them at low temperature.[2] Then, the first phosphaalkene (P=C, in 1978),[3] diphosphene (P=P, in 1981),[4] silene (Si=C, in 1981),[5] and disilene (Si=Si, in 1981)[6] were successfully synthesized as stable compounds by taking advantage of steric protection, where the 'double-bond rule' was completely disproved. These compounds are significant landmarks in the chemistry of kinetically stabilized low-coordinated compounds of heavier main group elements, and many examples have been reported so far.[1,7]

For the stabilization of highly reactive compounds such as low-coordinated compounds of heavier main group elements, there are two conceivable methodologies, that is, thermodynamic and kinetic stabilization. The former is defined as stabilization of the ground state by the mesomeric effect of neighboring heteroatoms, that is, introduction of electron-donating or -withdrawing substituents, and/or complexation with transition metals. The latter is stabilization resulting from raising the transition state by taking advantage of steric protection using bulky groups, which suppress self-oligomerization and side-reactions with other reagents such as oxygen and water. Kinetic stabilization is obviously superior to thermodynamic stabilization, since the latter perturbs the intrinsic nature of the species to a greater extent than the former. Since some review articles are now available on the history of the synthesis of low-coordinated heavier main group elements,[8] the contents in this section will be restricted to deal with the synthesis and properties of unsaturated compounds of heavier group 14 elements. We delineate here especially the systematic comparison of their structures and properties from the viewpoint of elemental chemistry.

2 THEORETICAL ASPECTS

Theoretical calculations have played an important and/or crucial role in providing valuable information for establishing general concepts. Recent progress in theoretical methods, efficient computer programs, and powerful computers has greatly advanced the scope of applicability of ab initio and DFT calculations. Although large-scale calculations are generally required for systems of experimental interest, it is important to understand simple conceptual frameworks before extensive calculations. The concept of 'hybridization' is most helpful for an intuitive understanding of the essential difference in the chemical bondings between carbon and heavier group 14 elements.[9]

2.1 The Hybridization of Atomic Orbitals

The valence ns and np electrons play important roles in the chemistry of main group elements, in contrast to the d electrons in the chemistry of transition metals. In Figure 1 are shown the radii of atomic orbitals (maximal electron-density), which are calculated for group 14 elements.[10] It should be noted that the valence ns and np atomic orbitals show great difference in their sizes for the heavier atoms (Si, Ge, Sn, Pb), though the size of the 2s atomic orbital of carbon is almost equal to that of the 2p atomic orbitals. Therefore, the heavier atoms have a lower tendency to form s-p hybrid orbitals with high p character and they prefer to retain the ns^2np^3 valence electronic configuration, in contrast to the case of carbon.

In addition, it may be expected that the sizes of the ns and np orbitals increase monotonously going down the periodic table from C to Pb, since the principal quantum number (n) increases. Unexpectedly, however, one can see that the sizes of orbitals change irregularly. The irregularity in Si → Ge and Sn → Pb is most likely interpreted in terms of so-called 'd-block contraction' and 'relativistic effect'.[11,12] Anyway, one can see obviously two boundary lines drawn between carbon and silicon, and between germanium and tin. The first boundary line indicates the preference of heavier atoms for ns^2np^3 valence electronic configuration to the hybridization of s and p orbitals as described above. Taking into consideration the second boundary line, that is, the large difference of the orbital sizes between Ge and Sn, it should be expected that the properties of silicon and/or germanium compounds may differ from those of tin and/or lead compounds.

2.2 Doubly Bonded Systems Between Heavier Group 14 Elements

It is a well known fundamental property of the second row elements that they can form very stable double bonds, for example, ethylene ($H_2C{=}CH_2$). In addition, every chemist knows that ethylene has a planar D_{2h} structure. On the other hand, many chemists have desired synthesis of ethylene analogs of heavier group 14 elements, that is, disilenes, digermenes, distannenes, and diplumbenes (called as dimetallenes). However, no example of dimetallenes has been known until the first isolation of kinetically stabilized disilene ($Mes_2Si{=}SiMes_2$; Mes = mesityl) by West and coworkers.[6] The reason for difficulty in forming stable double bonds between heavier group 14 elements is most likely interpreted in terms of smaller π bond energy than the corresponding σ bond energy due to the long bond distance that leads to a small overlapping of p orbitals. Examples of calculated σ and π bond energies are shown in Table 1,[9] from which one can see the following points pertinent to the intrinsic character of the double bonds in dimetallenes. First, the π bond energies for homonuclear double bonds between carbon atoms are more than twice as large as those between the heavier atoms (Si and Ge). Second, the σ bond energies are significantly larger than the corresponding π bond energies in the case of heavier atoms. Here, somewhat exceptional is the C=C double bond, in which the s and p bond energies are of roughly the same magnitude. Therefore, the heavier double-bond compounds easily undergo oligomerization and/or addition reactions with oxygen, water, and so on, forming σ bonds at the expend of π bonds. It should be noted that the features of s and p bond energies of a disilene (Si=Si) and a digermene (Ge=Ge) show little difference from each other. The deduction that the properties of silicon and germanium compounds might be similar to each other, described in Section 2.1, is reasonably demonstrated here.

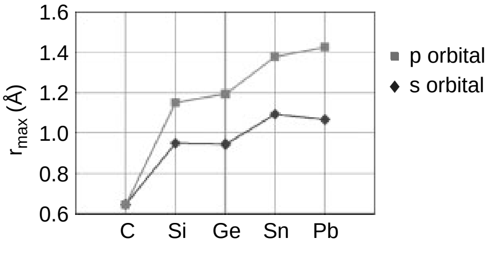

Figure 1 The sizes of valence ns and np orbitals of group 14 atoms

Much effort has been expended on the calculation of bonding properties of dimetallenes so far. Although several bonding models have been suggested,[13–15] it will be simply interpreted here for clarity. When the parent double-bond systems $H_2M{=}MH_2$ (M=Si, Ge, Sn, Pb) are homolytically cleaved, the resulting two H_2M: units may exist in a triplet or a singlet state. In contrast to the case of carbon atom, the heavier group 14 atoms have low ability to form hybrid orbitals; therefore, they prefer ns^2np^2 valence electronic configuration in their divalent species. Since two electrons remain to be as a singlet pair in the ns orbital, the ground state of H_2M: is singlet, unlike the case of H_2C:, the ground state of which is triplet.[16] As a result, severe repulsion between the closed-shell orbitals of two H_2M: units prevents dimerization, leading to $H_2M{=}MH_2$ in the planar form as shown in Figure 2. However, the two H_2M: units can form unique double bonds not only elongated to avoid the repulsion but also in trans-bent

Table 1 Bond energies of double bonds between group 14 elements (in kcal mol^{-1})

Bend energy (kcal mol^{-1})	C=C	Si=Si	Ge=Ge
σ	80	46	39
π	70	28	26

configuration,[17] where each of H_2M: units donates a lone pair of electrons to an empty p orbital of its bonding partner to form double donor-acceptor bonds as shown in Figure 2. These bond elongation and trans-bending properties increasingly appear as M becomes heavier from Si to Pb. Sn and Pb atoms are very reluctant to form the distinct double-bond structure, $H_2Sn{=}SnH_2$ and $H_2Pb{=}PbH_2$. The bridged dimer of H_2M: and 1,2-H-shifted isomer, $HM\text{-}MH_3$, are more stable in the case of Sn and Pb (Figure 3),[18] since at least one atom in these isomers can maintain ns^2np^2 valence electronic configuration as two valent species without hybridization of orbitals, leading to the formation of four valent species.

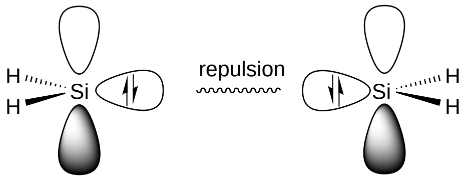

(a) In-plane structure of $H_2Si{=}SiH_2$

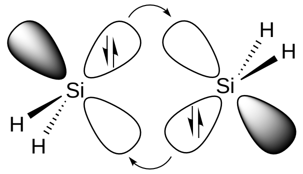

(b) Trans-bent structure of $H_2Si{=}SiH_2$

Figure 2 Interaction of singlet H_2Si

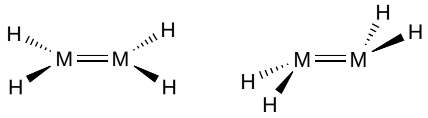

(a) in-plane (b) trans-bent

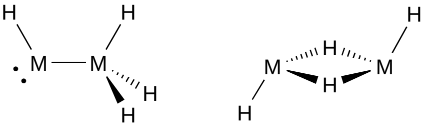

(c) 1,2-H-shifted (d) bridged dimer

M	enegry of isomers
C Si, Ge Sn, Pb	(a) (b) < (c) < (d) (d) < (c) < (b)

Figure 3 Isomers of $H_2M{=}MH_2$ (M = group 14 elements)

2.3 Triply Bonded Systems between Heavier Group 14 Elements

Recent remarkable progress in the theoretical calculations has revealed the bonding properties of heavier group 14 element analogs of acetylenes.[19–21] The understanding of triply bonded systems of heavier group 14 elements can be rationalized as that conceptually similar to the case of doubly bonded systems.[15]

It is most simple to view $HSi{\equiv}SiH$ as being composed of two SiH units. Similar to the case of a $H_2Si{=}SiH_2$ system, two interaction modes between SiH units are conceivable for $HSi{\equiv}SiH$ as shown in Figure 4.[22] The SiH unit has a doublet ground state more stable by $42.6\,\mathrm{kcal\,mol^{-1}}$ than the quartet state, since the quartet state unfavorably requires sp^3 hybridized orbitals in the Si atom.[22] That is, the more stable doublet states of the SiH unit originates from the strong tendency of heavier atoms to keep the valence electronic configuration of $ns^2np^1np^1$. This feature contrasts with the case of a CH unit, where the quartet state is less stable only by $17.9\,\mathrm{kcal\,mol^{-1}}$ than the doublet states.[23]

It should be noted that the trans-bent configuration of $HSi{\equiv}SiH$, in which two SiH units come up to each other in a way to form two donor-acceptor bonds together with a π bond using the singly occupied p orbital, is more stable than the linear configuration. In addition, the trans-bent disilyne ($HSi{\equiv}SiH$) was found by theoretical calculations to isomerize easily to a more stable 1,2-H-shifted isomer (:$Si{=}SiH_2$) (Figure 5), while the 1,2-H-shifted isomer of acetylene

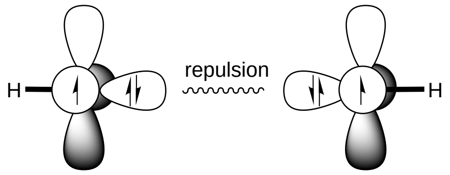

(a) Linear structure of $HSi{\equiv}SiH$

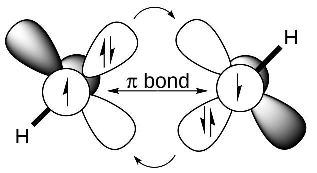

(b) Trans-bent structure of $HSi{\equiv}SiH$

Figure 4 Interaction of doublet HSi

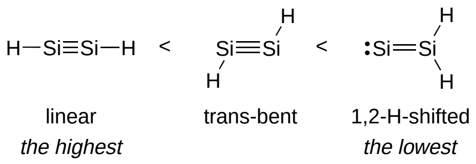

Figure 5 Relative energy of isomers of $HSi{\equiv}SiH$

(:$C{=}CH_2$) is very unstable and not a minima in calculations.[22] For the purpose of synthesis and isolation of these heavier triple-bond compounds, theoretical calculations suggest that bulky substituents should be necessary to prevent the 1,2-substituent-shift of the triply bonded heavier group 14 atoms.[24]

2.4 Concluding Remarks

Theoretical approach to multiple bonds between heavier group 14 elements revealed essential properties of their chemical bondings. Summarizing the theoretical findings leads to the following conclusion: The classical multiple bond indicators, that is, the shorter bond lengths and higher bonding energies, have almost no meaning for the multiple bonds between heavier atoms and they are valid for only an exceptional element, carbon. The bonding characters of the heavier multiple bonds described above are reasonably interpreted in terms of unfavorable s-p hybridization between the heavier atoms. The understanding of the feature of heavier atoms suggested that the electropositive and bulky substituents might be required in order to stabilize and isolate the heavier multiple bonds.[22,24,25] The advantage of electropositive substituents over electronegative ones is based on the fact that the increased negative charges on the low-valent heavier atoms decrease the size difference between s and p orbitals and make the s-p hybridization favorable. A merit of introducing bulky substituents is the kinetic stabilization of such highly reactive, unsaturated compounds. In addition, bulky substituents should prevent the 1,2-substituent-shift of $R_2M{=}MR_2$ and $RM{\equiv}MR$, leading to a more stable isomer, $R_3M{-}(R)M$: and $R_2M{=}M$:, respectively. Indeed, the concept of kinetic stabilization using bulky substituents led to the significant progress in the chemistry of unsaturated compounds with heavier main group elements.

3 DOUBLE-BOND COMPOUNDS BETWEEN GROUP 14 ELEMENTS

Problems for the synthesis of unsaturated compounds of group 14 elements due to their inherent instability and high reactivity have made many chemists to believe the 'classical double-bond rule'[1] described above. The first stable disilene, $Mes_2Si{=}SiMes_2$, which was prepared by West and coworkers in 1981,[6] opened the modern chemistry of doubly bonded systems of heavier group 14 elements, and it has been recognized that the concept of kinetic stabilization should certainly be of great use for the construction of these reactive, unprecedented chemical bondings without strong electronic perturbation. Since 1981, a great deal of M=M (M = Si, Ge, Sn, Pb) double-bond compounds have been synthesized by taking advantage of kinetic stabilization. Since several excellent reviews have been published covering a variety of aspects for these unsaturated compounds of heavier group 14 elements so far,[2,7,8,26–29] this review is intended to describe the synthesis and properties of kinetically stabilized double-bond compounds of heavier group 14 elements in this section.

3.1 Synthesis

3.1.1 *Synthesis of Stable Disilenes*

Previous studies on silicon chemistry show that the photolysis of poly- or oligosilanes or the reductive metalation of dihalosilanes are useful methods to generate oligosilanes, which might be formed by oligomerization of the transient silylenes (R_2Si:) or disilenes. However, the situation is drastically changed by the introduction of bulky substituents to the central silicon atom. As the size of substituents increases, the length of the silicon chain of the produced oligosilanes decreases. Based on this principle, West and coworkers have succeeded in the synthesis of $Mes_2Si{=}SiMes_2$, the first stable disilene, by the photolysis of linear trisilanes.[6]

Many stable disilenes have been prepared by the photolysis of linear trisilanes as well as the initiative work of West *et al.* (Scheme 1).[30,31] When trisilanes bearing two different substituents on the central silicon atom were photo-irradiated, a mixture of *E*- and *Z*-isomers of disilenes were obtained.[32,33] In addition, photolysis

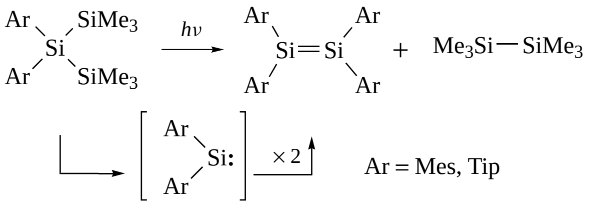

Ar = Mes, Tip

Scheme 1

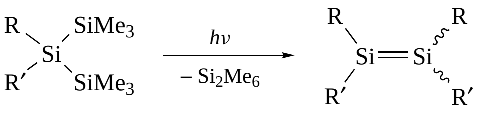

E/Z mixture

R = Mes, R′ = *t*-Bu
R = Mes, R′ = 1-Ad
R = Mes, R′ = Xyl
R = Mes, R′ = Dmt
R = Mes, R′ = $N(SiMe_3)_2$
R = Mes, R′ = Tip
R = Tip, R′ = $SiMe_3$
R = Tip, R′ = *t*-Bu

Scheme 2

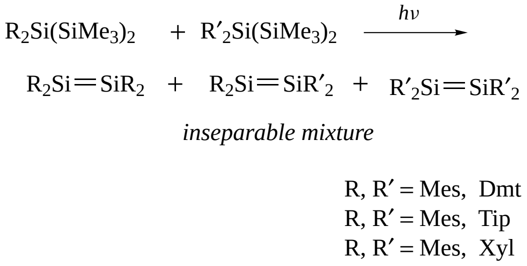
$R_2Si(SiMe_3)_2$ + $R'_2Si(SiMe_3)_2$
hν
$R_2Si{=}SiR_2$ + $R_2Si{=}SiR'_2$ + $R'_2Si{=}SiR'_2$
inseparable mixture
R, R′ = Mes, Dmt
R, R′ = Mes, Tip
R, R′ = Mes, Xyl

Scheme 3

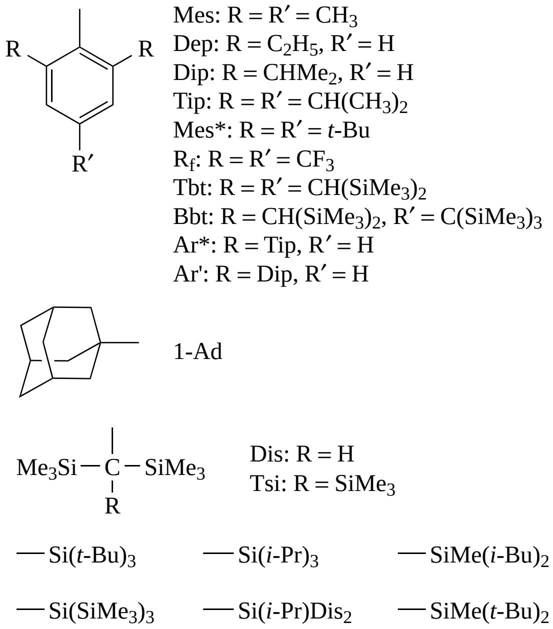
R
R
R′
Mes: R = R′ = CH_3
Dep: R = C_2H_5, R′ = H
Dip: R = $CHMe_2$, R′ = H
Tip: R = R′ = $CH(CH_3)_2$
Mes*: R = R′ = t-Bu
R_f: R = R′ = CF_3
Tbt: R = R′ = $CH(SiMe_3)_2$
Bbt: R = $CH(SiMe_3)_2$, R′ = $C(SiMe_3)_3$
Ar*: R = Tip, R′ = H
Ar': R = Dip, R′ = H
1-Ad
Me_3Si C $SiMe_3$
R
Dis: R = H
Tsi: R = $SiMe_3$
$Si(t\text{-}Bu)_3$
$Si(i\text{-}Pr)_3$
$SiMe(i\text{-}Bu)_2$
$Si(SiMe_3)_3$
$Si(i\text{-}Pr)Dis_2$
$SiMe(t\text{-}Bu)_2$

Scheme 4

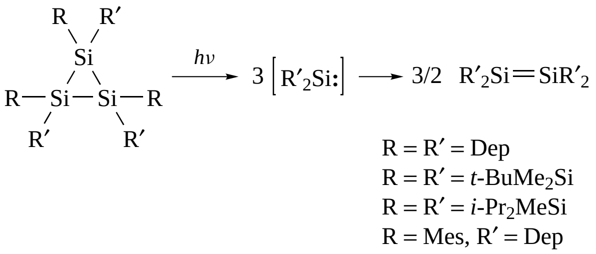
R R′
Si
R Si Si R
R′ R′
hν
3 $[R'_2Si:]$
3/2 $R'_2Si{=}SiR'_2$
R = R′ = Dep
R = R′ = t-$BuMe_2Si$
R = R′ = i-Pr_2MeSi
R = Mes, R′ = Dep

Scheme 5

of a mixture of two types of trisilanes, for example, $R_2Si(SiMe_3)_2$ and $R'_2Si(SiMe_3)_2$, afforded a mixture of disilenes, which contained unsymmetrically substituted disilene, $R_2Si{=}SiR'_2$,[2,34,35] together with symmetrically substituted disilenes (Schemes 2 and 3). The unsymmetrically substituted disilene was identified spectroscopically but was difficult to isolate under these conditions. The bulky substituents used for the synthesis of these disilenes include a variety of combinations of bulky aryl groups (e.g. mesityl, 2,4,6-triisopropylphenyl, etc.), bulky alkyl groups (*t*-Bu, 1-Ad, etc.), bulky silyl groups [Si(*i*-Pr)$_3$, Si(*t*-Bu)Me$_2$, etc.], N(SiMe$_3$)$_2$, and so on (depicted in Scheme 4).

Up-to-date, a variety of disilenes have been reported, owing to the improvement of several synthetic methods. For example, the photolysis of cyclic trisilanes[28,36] (Scheme 5) and the reduction of dihalosilanes[37] or 1,2-dihalodisilanes[38] (Scheme 6) were found to be useful approaches to the corresponding stable silylenes when the precursors are available as stable compounds.

Recently, an innovative synthetic method for disilenes using dilithiosilanes was reported. Dilithiosilanes were prepared by the exhaustive reduction of the corresponding dihalosilanes when it was well kinetically stabilized.[39,40] Since the dilithiosilanes have two nucleophilic Si–Li bonds on one silicon atom, it is thought to be a good building block for doubly bonded compounds of silicon (Scheme 7). Indeed, the reaction of a dilithiosilane with a dihalosilane reportedly resulted in the formation of the corresponding disilene.[41] This method is valid for not only the synthesis of unsymmetrically substituted disilenes but also the synthesis of several types of heteronuclear doubly bonded systems of heavier group 14 elements (vide infra).

3.1.2 Synthesis of Stable Digermenes

Digermenes,[42–45] the heavier analogs of disilenes, cannot exist as monomers under normal conditions owing to

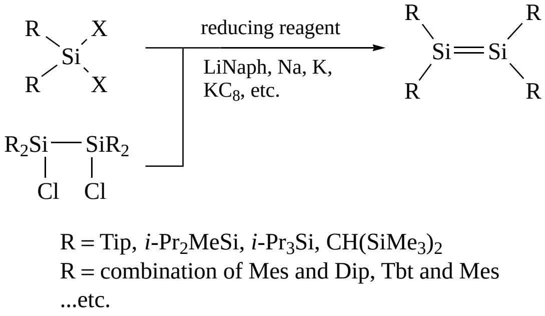
R X
Si
R X
R_2Si SiR_2
Cl Cl
reducing reagent
LiNaph, Na, K, KC_8, etc.
R R
Si=Si
R R
R = Tip, i-Pr_2MeSi, i-Pr_3Si, $CH(SiMe_3)_2$
R = combination of Mes and Dip, Tbt and Mes
...etc.

Scheme 6

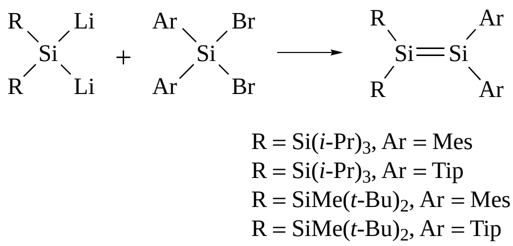
R Li
Si
R Li
+
Ar Br
Si
Ar Br
R Ar
Si=Si
R Ar
R = $Si(i\text{-}Pr)_3$, Ar = Mes
R = $Si(i\text{-}Pr)_3$, Ar = Tip
R = $SiMe(t\text{-}Bu)_2$, Ar = Mes
R = $SiMe(t\text{-}Bu)_2$, Ar = Tip

Scheme 7

their high reactivity as well as disilenes. Of course the introduction of bulky substituents into digermenes is effective for the stabilization of digermenes. It is certain that a digermene having small substituents undergoes immediate oligomerization or polymerization, whereas the introduction of too large substituents leads to the cleavage of a digermene giving two germylenes. In that case, the germylenes (σ^2, λ^2-species of germanium) are not only kinetically well-stabilized but also inherently stable because the germanium atom prefers an ns^2np^2 valence electronic configuration as silicon atom does (see Section 2). Therefore, only digermenes bearing moderately large substituents such as 2,6-diethylphenyl (Dep),**[46]** 2,6-diisopropylphenyl (Dip),**[47]** or bis(trimethylsilyl)methyl (Dis)**[48–50]** can exist as stable compounds with Ge=Ge double bonds. However, it should be noted that some digermenes feature their double-bond character only in the solid state, while they exist as equilibrium mixtures with the corresponding germylenes in solution. Delicate selection of the size of substituents on germanium atoms is very important for the synthesis of Ge=Ge double-bond compounds. For a typical example, a germylene having Mes and Tbt groups exists as an equilibrium mixture of germylenes and a digermene,**[51]** whereas that having Tip and Tbt groups completely behaves as a monomeric germylene in solution (Scheme 8).**[52]**

Most of the synthetic methods for disilenes are found to be applicable to digermenes (Scheme 9). For examples, the photolysis of cyclotrigermenes or bis(silyl)germanes bearing bulky substituents affords the corresponding digermenes. The reductive coupling reaction of dihalodigermenes is also an effective synthetic method for digermenes.

In the case of digermenes, there is another synthetic route, that is, the generation of digermenes from divalent germanium compounds. Contrary to the case of silicon analogs, stable divalent germanium species ($GeCl_2 \cdot$dioxane, $[(Me_3Si)_2N]_2Ge$:, GeI_2, etc.), which are potentially good precursors of digermenes, are available. Many digermenes are synthesized by the substitution reactions of such divalent species of germanium with a Grignard reagent or an organolithium reagent.

Recently, a new class of stable chlorogermylenes (ArGeCl) kinetically stabilized by a bulky *m*-terphenyl group such as 2,6-$Tip_2C_6H_3$, 2,6-$Mes_2C_6H_3$, and 2,6-$Dip_2C_6H_3$ were reported by Power and coworkers.**[53–55]** The ArGeCl species can exist as a chlorogermylene form in solution but as a dichlorodigermene form (or a chlorogermylene dimer) in the solid state. After that, digermenes bearing two 2,6-$Tip_2C_6H_3$ groups together with simple organic groups, that is, dimethyl-, diethyl-, diphenyl-substituted digermenes were synthesized by the nucleophilic substitution reactions of the chlorogermylene.**[56]** When ArGeCl (Ar = 2,6-$Dip_2C_6H_3$) was treated with Li[B(*s*-Bu)$_3$H] (L-selectride), a dihydrodigermene derivative, which is a more fundamental digermene system, was afforded (Scheme 10) as a stable crystalline compound.**[57]** Thus, chlorogermylene is a good precursor of several types of digermenes.

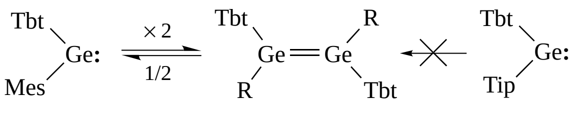

Scheme 8

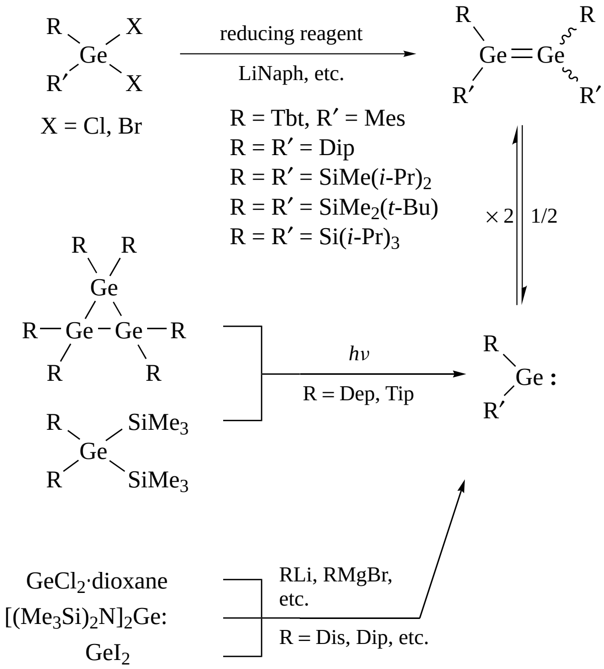

Scheme 9

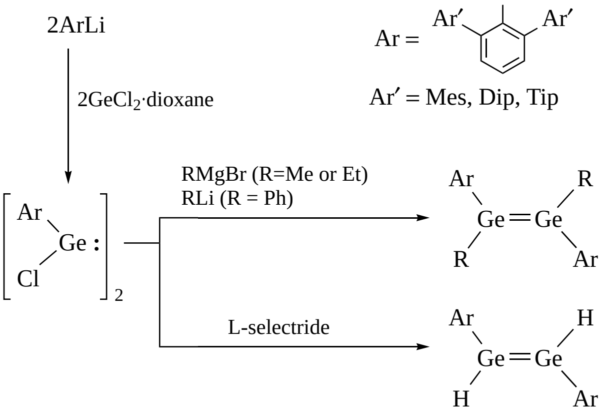

Scheme 10

A dilithiogermane**[58–60]** is known to be generated by the exhaustive reduction of an overcrowded dihalogermane as well as the case of dilithiosilanes. The dilithiogermane can also be a good precursor for a digermene via the reaction with a dihalogermane.**[60]**

3.1.3 Synthesis of Stable Distannenes and Diplumbenes

In contrast to the extensively studied doubly bonded systems of silicon and germanium, the corresponding chemistry of tin and lead compounds, that is, distannenes and diplumbenes, has not been fully disclosed probably owing to the much higher reactivity and instability of such low-coordinated organotin and organolead compounds. In addition, the situation in the cases of distannenes (Sn=Sn)[26–28,43,61] and diplumbenes (Pb=Pb)[8,43,61] differs from those of disilenes and digermenes. Divalent species of tin and lead, stannylenes, and plumbylenes, are more stable than the corresponding doubly bonded systems, which require s-p orbital hybridizations to some extent (see Section 2). Therefore, distannenes and diplumbenes tend to undergo dissociation into stannylenes and plumbylenes immediately in solution, and even in the solid state their two donor-accepter bonds are much weaker than those of disilenes and digermenes.

The synthesis of distannenes and diplumbenes are generally achieved by dimerization of stannylenes and plumbylenes (Scheme 11). Although most of them exist as divalent species in solution under equilibrium with the corresponding double-bond compounds, the equilibrium occasionally shifted to the corresponding dimer (double-bond compounds) by crystallization. It is essential to choose the proper size of steric protection groups for the synthesis of doubly bonded systems.

Stannylenes are prepared by the treatment of tin(II) chloride or bis(trimethylsilylamino)stannylene with organometallic compounds (organolithium compounds, Grignard reagents, silylpotassium reagents, etc.).[62,63] These methods are applicable in the case of lead as well, that is, using $PbCl_2$ or bis(trimethylsilylamino)plumbylenes instead of tin compounds leads to the formation of the corresponding plumbylenes. Alternatively, hexakis(2,4,6-triisopropylphenyl)tristannirane (cyclotristannane derivative) can afford the corresponding stannylenes by heating or photo-irradiation,[64] though triplumbirane (cyclotriplumbane) derivatives are very unstable to be isolated (the first stable cyclotriplumbane was reported very recently).[65] When a dihalostannane and a dihaloplumbane are stable enough to be treated and purified under ambient conditions, the corresponding stannylene and plumbylene can be generated via the reductive dehalogenation methods as in the case of germylenes. The only distannene, $Tip_2Sn{=}SnTip_2$, that features a double bond even in solution has been reported by Masamune and Sita.[64] On the other hand, no diplumbene stable in solution has been reported so far, while two diplumbenes stable in the solid states have been known.[66,67]

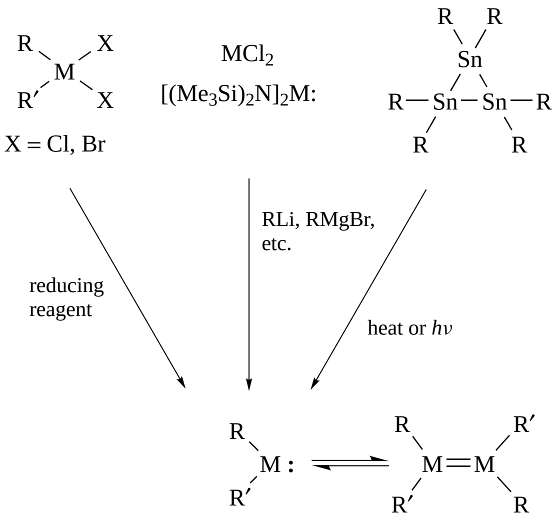

Distannenes and diplumbenes in the solid state

M	R	R′
Sn	Dis	Dis
Sn	Tip	Tip
Sn	Ar	Ar
Sn	$Si(SiMe_3)_3$	$Si(SiMe_3)_3$
Sn	2,4,6-$(F_3C)_3C_6H_2$	$Si(SiMe_3)_3$
Pb	Tip	Tip
Pb	Tip	$Si(SiMe_3)_3$

Ar = 2-*t*-Bu-4,5,6-Me_3C_6H

Scheme 11

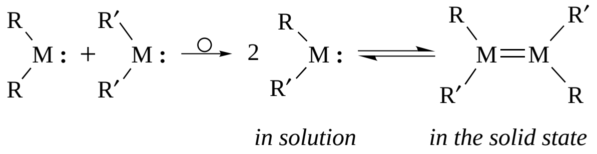

M = Sn, R = 2,4,6-$(F_3C)_3C_6H_2$, R′ = $Si(SiMe_3)_3$
M = Pb, R = Tip, R′ = $Si(SiMe_3)_3$

Scheme 12

The *E*-form diplumbene, R(Tip)Pb=Pb(Tip)R [R = $Si(SiMe_3)$], was formed by the treatment of Tip_2Pb: with R_2Pb: via an interesting substituent-scrambling (Scheme 12).[67] The similar phenomenon was observed in the case of a distannene.[68] When two different stannylenes, for example, bis[2,4,6-tris(trifluoromethyl)phenyl]stannylenes and bis[tris(trimethylsilyl)silyl]stannylenes, were mixed, the corresponding unsymmetric distannene, a naturally expected product, underwent a ready rearrangement of substituents upon crystallization, leading to the formation of a symmetric, *E*-form distannene. Owing to such ready substituent-scrambling in distannenes and diplumbenes, it should be very difficult to synthesize and isolate an unsymmetrically substituted distannene or diplumbene.

A stable chlorostannylene, which was prepared by Power and coworkers,[53,69,70] is potentially a good precursor of

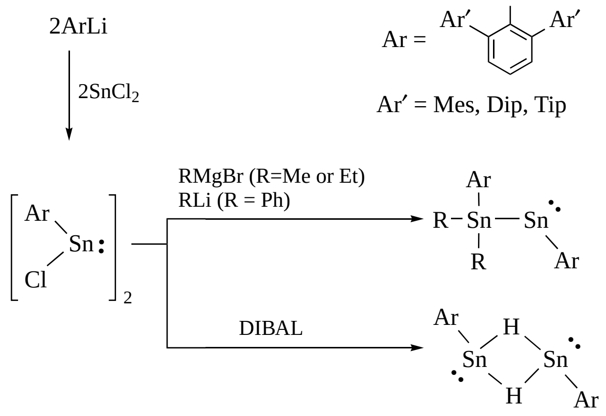

Scheme 13

several distannenes as well as the corresponding germanium congeners (vide supra). However, treatment of ArSnCl ($Ar = 2,6\text{-}Tip_2C_6H_3$) with MeMgBr or PhLi afforded no double-bond compounds but stannylene $ArMe_2Sn–Sn(II)Ar$ via the migration of a substituent, in contrast to the case of germanium congeners.[71–73] A similar rearrangement was observed for the lead systems. Thus, it was found that the divalent isomers, a stannylene and a plumbylene, were much more preferred than the corresponding double-bond isomers. In addition, the attempted synthesis of dihydrodistannene, that is, the reaction of chlorostannylene with DIBAL as a reducing reagent, resulted in the formation of a hydrostannylene dimer, in which the hydrogen atoms were found to make bridging bonds between the two tin atoms (Scheme 13).[74] It is interesting that the conformation of the hydrostannylene dimer differs from that of the dihydrodigermene, which features a Ge=Ge double-bond. These experimental results are most likely interpreted in terms of the difference between the inherent features of the elements (see Section 2).[57]

3.1.4 Synthesis of Heteronuclear Doubly Bonded Systems

Heteronuclear combination of double bonds, for example, Si=C, Ge=C, Si=Ge, and so on, are of particular interest, since they should provide a much greater variation in the bonding character than the homonuclear systems depending on the nature of the two low-coordinated elements. Whereas, they are more unstable than the homonuclear systems because they overlap p orbitals much less, owing to the difference of orbital size and their high reactivity toward head-to-tail dimerization promoted by their polar, twitterionic character ($M^{\delta+}{=}M'^{\delta-}$). In 1981, the preparation of the first stable silene $(Me_3Si)_2Si{=}C(OSiMe_3)(1\text{-}Ad)$ (1-Ad = 1-adamantyl) was reported by Brook and coworkers.[5] Since that time, much effort has been devoted to establish the chemistry of stable silenes and other low-coordinated species of group 14 elements, and some synthetic routes have now been established for several metallaalkenes (M=C, M = Si, Ge, Sn).[75–78] Although only one example has been reported for a plumbene (Pb=C), it is not a ‘plumbene’ in reality because it features a completely zwitterionic $Pb^+–C^-$ bond (Scheme 14).[79]

Many synthetic routes have been found for silenes and germenes as depicted in Scheme 15. The most frequent synthetic methods used to produce the sterically protected, stable metallaalkenes are the photochemical [1,3]-sigmatropic shift of a silyl group to an oxygen atom in acylsilanes [route (ii)] and the dehydrohalogenation reactions of the corresponding halometallanes [route (vii)].

Until quite recently, the compounds with a heteronuclear double bond between heavier group 14 elements, for example, Si=Ge, Ge=Sn, and so on, have been thought of as marginally stable or metastable species, because they are much more unstable than the C=M double-bond compounds. Indeed, tetramesitylsilagermene ($Mes_2Si{=}GeMes_2$), which was prepared by the photochemical reaction of a Ge–Ge–Si three-membered ring compound, was unstable under the reaction conditions and underwent immediate migration of the Mes group, leading to the formation of mesityl(trimesitylsilyl)germylene[$(Mes_3Si)(Mes)Ge$:].[80] However, a silagermene should be synthesized as a stable compound, if such a tendency to 1,2-migration was successfully suppressed. In 2000, the first stable silagermene, in which the Si=Ge double bond is incorporated in a unique three-membered ring system, was reported by Sekiguchi *et al.* (Scheme 16).[81] The strained silagermene moiety was preserved without the migration of substituents in a novel Si=Ge–C=C cyclic conjugated π system (see Section 7).[82]

One may simply think that a mixture of a pair of divalent species affords heteronuclear double-bond compounds because some germylenes, stannylenes, or plumbylenes are available as stable compounds. However, only homonuclear double-bond compounds were obtained by crystallization of a mixture of a pair of two different divalent species in many cases. Although one successful example, the synthesis of $Tip_2Ge{=}SnTip_2$ by the treatment of a mixture of $GeCl_2$·dioxane and $SnCl_2$ with TipMgBr, has been reported recently, the germastannene initially formed undergoes slow thermal decomposition, giving the corresponding tristannirane (cyclotristannane) and digermene (Scheme 17).[83] Thus, the divalent species of heavier group 14 elements are liable to associate with that of the same element to form homonuclear double-bond systems.

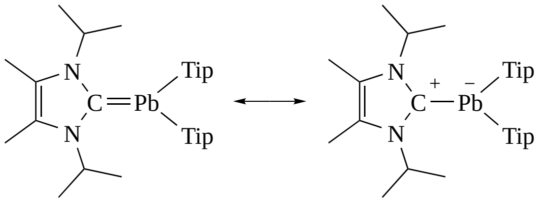

Scheme 14

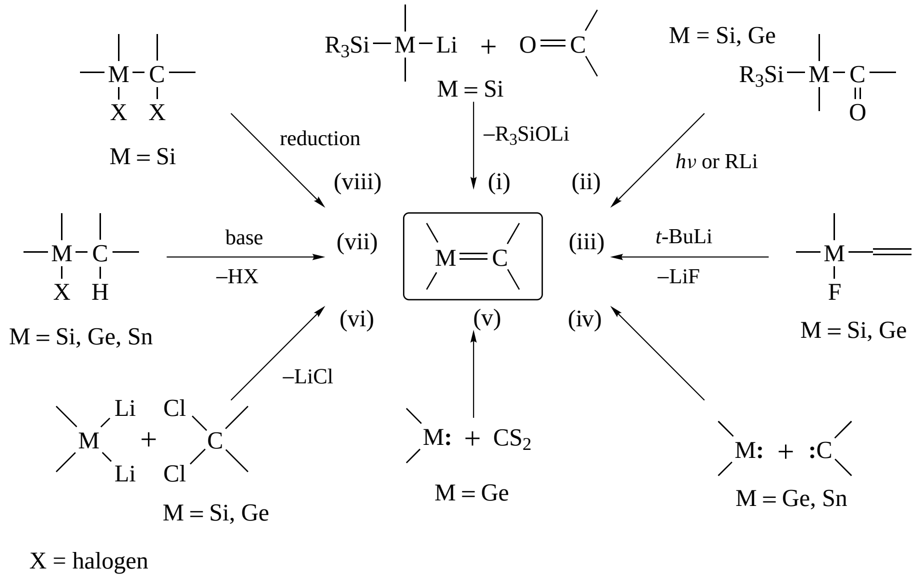
M = Si
reduction
(viii)
R3Si−M−Li + O=C
M = Si
−R3SiOLi
(i)
(ii)
M = Si, Ge
R3Si−M−C(=O)
hν or RLi
M = Si, Ge, Sn
base
−HX
(vii)
M=C
(iii)
t-BuLi
−LiF
M = Si, Ge
(vi)
(v)
(iv)
−LiCl
M = Si, Ge
M: + CS2
M = Ge
M: + :C
M = Ge, Sn
X = halogen

Scheme 15

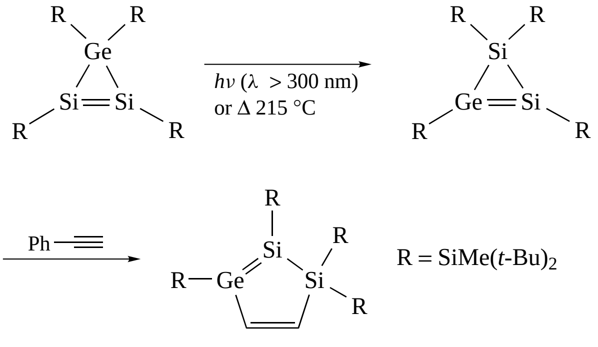
hν (λ > 300 nm)
or Δ 215 °C
Ph−≡

R = SiMe(t-Bu)$_2$

Scheme 16

Discovery of overcrowded dilithiometallane derivatives has opened the door leading to a novel synthetic method for the heteronuclear doubly bonded systems. Treatment of a dilithiometallane with a dihalometallane reasonably leads to the formation of the corresponding doubly bonded systems via the formal double nucleophilic substitution (Scheme 18).[78,84] Stable silagermene, silastannene, and germastannene were obtained by this method using a dilithiosilane and a dilithiogermane.[78,84] Interestingly, the germastannene R$_2$Ge=SnTip$_2$ [R=SiMe(t-Bu)$_2$] thus formed was found to undergo a ready isomerization into a symmetrically substituted germastannene R(Tip)Ge=Sn(Tip)R upon heating at 50 °C (Scheme 19).[84]

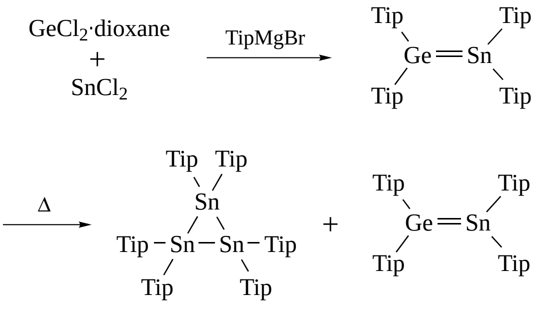
GeCl2·dioxane
+
SnCl2
TipMgBr
Δ
+

Scheme 17

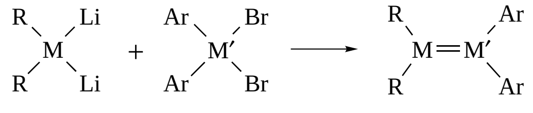

M = Si, M′ = Ge: R = SiMe(t-Bu)$_2$, Ar = Mes
M = Ge, M′ = Si: R = SiMe(t-Bu)$_2$, Ar = Mes
M = Si, M′ = Sn: R = SiMe(t-Bu)$_2$, Ar = Tip
M = Ge, M′ = Sn: R = SiMe(t-Bu)$_2$, Ar = Tip

Scheme 18

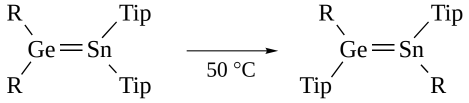

R = SiMe(t-Bu)$_2$

Scheme 19

3.2 Molecular Structures

X-Ray crystallographic analyses have revealed unique molecular structures of kinetically stabilized doubly bonded systems between heavier group 14 elements. The first example of the structural characterization of a dimetallene was that of Dis$_2$Sn=SnDis$_2$ reported in 1976.[85] It has a trans-bent geometry [out-of-plane angle (depicted in Figure 6) $\theta = 41^\circ$], which is now one of the characteristic features of dimetallenes (Section 2), and a slightly shortened Sn=Sn bond length [2.768(1) Å] as compared with the typical Sn–Sn single bond (Figure 7). As described in the previous section, it was found to dissociate into the corresponding stannylenes (Dis$_2$Sn:) in hydrocarbon solution. These features demonstrated the weak bonding of donor-acceptor interaction (see Section 2) in an Sn=Sn double bond. The next breakthrough was shown by the first stable Mes$_2$Si=SiMes$_2$ in 1981.[6] The X-ray crystallographic analysis (Figure 8) showed that the Si=Si double bond is ca. 0.2 Å shorter than a single bond and the out-of-plane angle (θ) is 0–18°, which is much smaller than those of the Sn=Sn double-bond compounds. In addition, it showed no tendency of dissociation into the corresponding silylenes in solution. When extremely bulky substituents are introduced into disilenes [Tbt(Mes)Si=Si(Mes)Tbt, E, Z-isomers] (Figure 9), they showed very long Si=Si double-bond lengths over 2.20 Å[37,86] and undergo ready dissociation ($\Delta H =$ ca.26 kcal^{-1} mol) into monomers in solution under very mild conditions (ca. 60 °C in benzene).[86,87]

Several dimetallenes have been structurally characterized so far,[8,28,29,44,45,88] and selected structural parameters of them are summarized in Table 2. Although the lengths of M=M

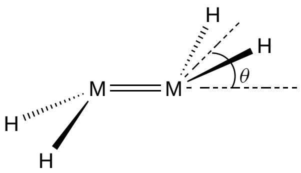

Figure 6 Out of plane angle (θ) of R$_2$M=MR$_2$ (M = group 14 elements)

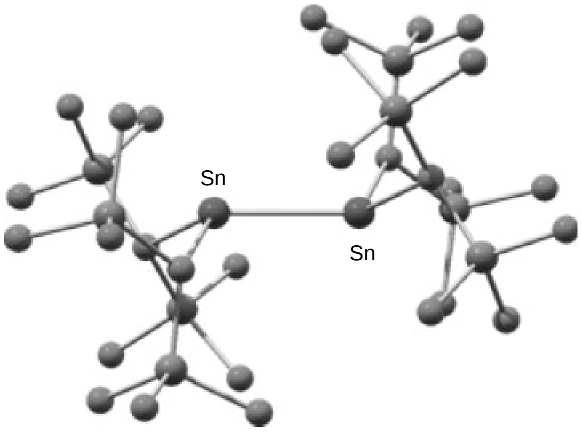

Figure 7 Molecular structure of Dis$_2$Sn=SnDis$_2$ illustrating its trans-bent configuration

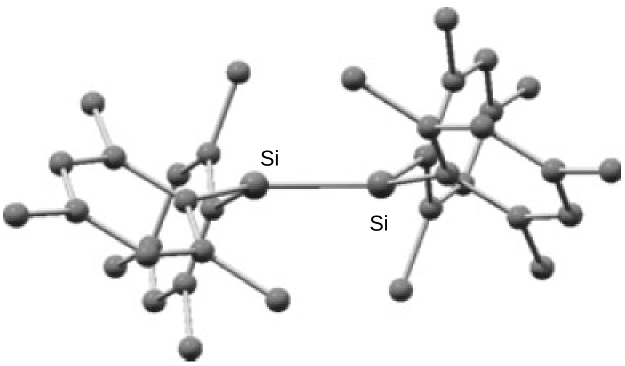

Figure 8 Molecular structure of Mes$_2$Si=SiMes$_2$

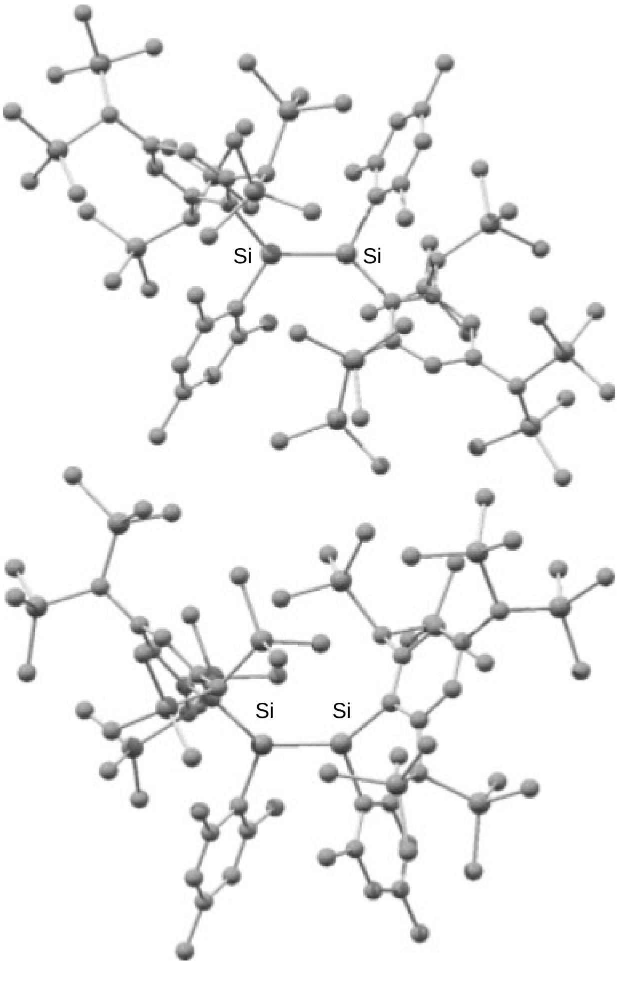

Figure 9 Structures of extremely hindered disilenes (a) E-Tbt(Mes)Si=Si(Mes)Tbt (b) Z-Tbt(Mes)Si=Si(Mes)Tbt

Table 2 Selected structural parameters for dimetallenes

$R_1R_2M{=}MR_3R_4$	M=M/Å	θ
$Mes_2Si{=}SiMes_2$	2.1433(2)	12
$Mes_2Si{=}SiMes_2$	2.160(1)	18
$Dep_2Si{=}SiDep_2$	2.140(3)	10
$Tip_2Si{=}SiTip_2$	2.145(6)	3
E-[Mes(1-Ad)Si]$_2$	2.138(2)	2.8
E-[Mes(t-Bu)Si]$_2$	2.143(1)	0
[{(t-Bu)Me$_2$Si}$_2$Si]$_2$	2.202(1)	0
[{(i-Pr)$_2$MeSi}$_2$Si]$_2$	2.228(2)	5.4
[{(i-Pr)$_3$Si}$_2$Si]$_2$	2.251(1)	10.2
E-[Tbt(Mes)Si]$_2$	2.228(3)	12
Z-[Tbt(Mes)Si]$_2$	2.195(4)	8.7
$Dep_2Ge{=}GeDep_2$	2.213(2)	12
$Tip_2Ge{=}GeTip_2$	2.213(1)	12.3
Z-[Dip(Mes)Ge]$_2$	2.301(1)	36
$Dis_2Ge{=}GeDis_2$	2.347(2)	32
[{(i-Pr)$_2$MeSi}$_2$Ge]$_2$	2.267(1)	0
[{(i-Pr)$_3$Si}$_2$Ge]$_2$	2.298(1)	0
[2,6-Mes$_2$C$_6$H$_3$(Cl)Ge]$_2$	2.443(2)	39
E-[Tbt(Mes)Ge]$_2$	2.416(2)	16,34
$Dis_2Sn{=}SnDis_2$	2.768(1)	41
[{(Me$_3$Si)$_3$Si}$_2$Sn]$_2$	2.8247(6)	28.6
[{(Me$_3$Si)$_3$Si}(Rf)Sn]$_2$	2.833(1)	41.5
$Ar_2Sn{=}SnAr_2$, Ar = 2, 3,4-Me$_3$-6-t-Bu-C$_6$H	2.910(1)	21.1
		64.4
$Rf_2Sn{=}SnRf_2$^{a}	3.639(1)	46
$Tip_2Pb{=}PbTip_2$	3.0515(3)	43.9
		51.2
[{(Me$_3$Si)$_3$Si}(Tip)Pb]$_2$	2.9899(5)	42.7
[{(Me$_3$Si)$_3$Si}(Rf)Pb]$_2$	3.537(1)	40.8
$Dis_2Pb{=}PbDis_2$^{a}	4.129	34.2

[a] They should not be referred to as double-bond compounds because their M=M bond lengths in the solid state are too long.

(M=Si, Ge, Sn, Pb) double bonds are variable, depending on their substituents to some extents, most of them are apparently shorter than the corresponding M–M single bonds in the cases of M = Si and Ge. The Si=Si and Ge=Ge double bonds show bond shortening in the range of circa. 7–9%, while the Sn=Sn double bonds show only circa. 3% bond shortening and the Pb=Pb double-bond lengths are almost the same as or slightly longer than the Pb–Pb single-bond lengths. The tendency of bond shortening reasonably explains the feature of π-bond strength.[87] The Si=Si π-bond energy was estimated to be ca. 25.4–30.3 kcal mol^{-1},[28,87] which is almost half of the C=C π-bond energy and is consistent with the theoretical data. The Ge=Ge π bonds may be similar in strength to those on their silicon analogs, though a variable-temperature electronic spectrum of the extremely hindered species [Tbt(Mes)Ge=Ge(Mes)Tbt] shows that it exists in a monomer-dimer equilibrium in hexane with $\Delta H =$ 14.7 kcal mol^{-1} for dissociation[51] ($\Delta H =$ ca. 26 kcal mol^{-1} for the corresponding silicon derivative as described above[87]). Based on the theoretical calculations, a sharp decrease in the π-bond energy is predicted for dimetallenes upon descending the group 14 elements from Ge to Sn. The Sn=Sn π-bond strength is estimated to be only 11 kcal mol^{-1} (Ge=Ge π-bond strength = 26 kcal mol^{-1}), whereas the strength of an Sn–Sn σ-bond (35 kcal mol^{-1}) is slightly less than that of a Ge–Ge σ-bond (39 kcal mol^{-1}).[44] Pb=Pb interaction in a Pb=Pb double-bond compound is very weak, and the Pb=Pb bond energy was predicted as circa. 23 kcal mol^{-1}, being much less than those of the corresponding tin analog (35 kcal mol^{-1}). Thus, it is found that the Pb–Pb single bond is stronger (33 kcal mol^{-1} in $Me_3Pb{-}PbMe_3$)[89] than the Pb=Pb double bond. This surprising result is consistent with the observation that the Pb=Pb double bonds (see Table 2) are longer than the Pb–Pb single bonds (ca. 2.9 Å).

The trans-bent structures are characteristic of double-bond systems between heavier group 14 elements. The out-of-plane angles (θ, shown in Figure 6) of disilenes (Si=Si) are ca. 0–18° and much less than those of the heavier analogs (Ge=Ge: ca. 0–40°, Sn=Sn: ca. 20–42°, Pb=Pb: ca. 35–70°), while ethylene has a completely planar structure. Since the values of θ in dimetallenes are variable depending on their substituents, it is difficult to compare them systematically from the viewpoint of the difference of elements. However, it may be roughly concluded that the out-of-plane angles of dimetallenes increase as the element raw descends from Si to Pb. That is, it was experimentally established that distannenes and diplumbenes clearly feature ‘donor-acceptor dimer of divalent species’ as predicted by theoretical calculations (see Section 2). In addition, the structural features in dimetallenes revealed the resemblance between Si=Si and Ge=Ge systems and that between Sn=Sn and Pb=Pb doubly bonded systems, and the great difference between Ge and Sn systems.

Some of the heteronuclear systems containing a double bond between group 14 elements have been structurally characterized so far.[27,78] The first silene, $(Me_3Si)_2Si{=}C(OSiMe_3)(1\text{-}Ad)$, showed a planar geometry at silicon and possesses a shorter Si=C bond (1.764 Å) than the typical Si–C single bond.[5] Not only the first stable silene, but most of other examples also feature Si=C double-bond character like disilenes, that is, shorter Si=C bond lengths, almost planar geometries at a silicon atom, and smaller bonding energies (ca. 35 kcal mol^{-1}) than those of C=C π bonds. The first stable germene, $Mes_2Ge{=}Flu$ (Flu = fluorenyl),[90] reported by Escudié and coworkers, has a Ge=C distance of 1.803(4) Å and almost planar geometry around the Ge=C bond. An extremely hindered germene shown in Scheme 20 possesses the shortest Ge=C bond length of 1.771(16) Å among all structurally characterized germenes.[91] Although the other germenes structurally characterized so far may have a formal Ge=C double bond, the perturbation caused by the heteroatom-substituents made most of them exhibit the properties of an ylide ($Ge^{-}{-}C^{+}$) or a germylene-carbene adduct ($>$Ge:$\leftarrow$:C$<$) species rather than the genuine Ge=C character.

Two types of boron-substituted stannenes[92,93] have been reported to show ca. 6% shortening in their Sn=C bonds

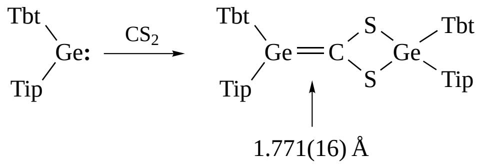

Scheme 20

(2.025 and 2.032 Å) compared with a typical Sn–C single bond. As for a stannene (Sn=C) bearing only hydrocarbon substituents around its central Sn=C double bond, one example (Tip$_2$Sn=Flu, Flu = fluorenyl) has been reported[94] though being structurally not characterized. As described in Section 3.1, the isolated plumbene (Pb=C) is not a genuine plumbene because it has a very long Pb–C bond length of 2.540(5) Å, indicating its completely zwitterionic character of Pb$^+$–C$^-$ bond.[79]

Molecular structures of heteronuclear dimetallenes, for example, Si=Ge, Si=Sn, Ge=Sn, and so on, have attracted the attention of many chemists.[78] Although several synthetic methodologies have been developed so far, only two examples have been reported with full structural characterization. One is a cyclic silagermene, 1,5-disila-2-germacyclopentadiene derivative,[81,82] in which the Si=Ge double bond is involved as a part of a cyclic conjugated system. The effect of conjugation should be negligible, since the Si=Ge bond length [2.250(1) Å] is in excellent agreement with the theoretically calculated value of the Si=Ge bond length (2.24 Å) in H$_2$Si=GeH$_2$. The other example is a silastannene (Si=Sn) derivative [Me(t-Bu)$_2$Si]$_2$Si=Sn(Tip)$_2$ (Figure 10).[78] The Si=Sn double-bond length of the silastannene was determined as 2.4188(14) Å, which is almost a middle value between the typical lengths of Si=Si (2.138–2.289 Å) and Sn=Sn (2.590–3.087 Å) double bonds. In addition, it should be noted that the sp^2 Sn atom of [Me(t-Bu)$_2$Si]$_2$Si=Sn(Tip)$_2$ is nearly planar, whereas the sp^2 Si atom is significantly pyramidalized. Taking the structural features into consideration, the silastannene [Me(t-Bu)$_2$Si]$_2$Si=Sn(Tip)$_2$ could be recognized as a representative of a new structural feature involving an unsymmetrical donor-acceptor interaction, resulting in the pyramidalization of the negatively charged Si atom and planarization of the positively polarized Sn atom (Figure 11).

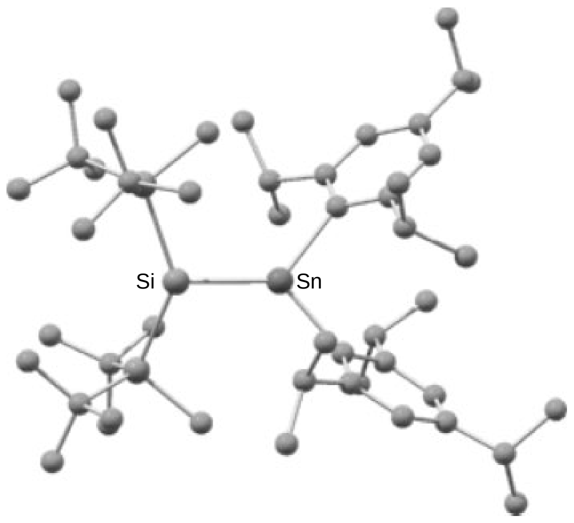

Figure 10 Molecular structure of {(t-Bu)$_2$MeSi}$_2$ Si=SnTip$_2$

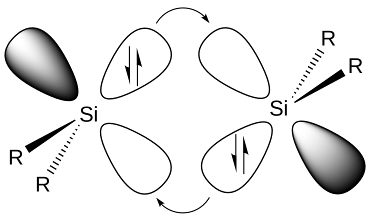

(a) Symmetrical donor-acceptor bond

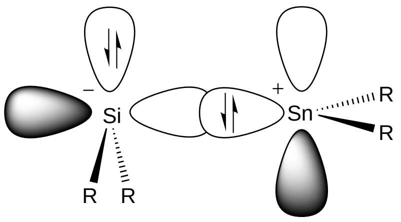

(b) Unsymmetrical donor-acceptor bond

Figure 11 Interaction of R$_2$Si: and R$_2$Sn

3.3 Spectroscopic Properties

UV–vis Spectra. Disilenes and digermenes showed colors of pale yellow to orange-red in solution and in the solid state. Their color arises from the M=M (M = Si, Ge) double-bond chromophore, which appears as an absorption maxima at wavelengths longer than 300 nm.[7,45,95] These absorption maxima observed in their electronic spectra can reasonably be assigned to those of the symmetry allowed $\pi \rightarrow \pi^*$ electron transitions. In general, tetraalkyldisilenes have absorption maxima at around 400 nm, whereas those for tetraaryldisilenes are red-shifted by 20–30 nm probably owing to a weak conjugation between the aryl groups with the Si=Si π bond. The absorptions of digermenes are nearly the same or slightly blue-shifted as compared to those of disilenes. Contrary to the case of disilenes, digermenes are occasionally demonstrated to undergo thermal dissociation into the corresponding germylenes. While digermenes are reported to show their $\pi \rightarrow \pi^*$ transitions in the range of circa. 400–440 nm, weak absorptions corresponding to the n → p electron transitions of germylenes are observed at characteristically longer wave lengths (ca. 460–580 nm). The experimental observation of an equilibrium between a digermene and germylenes has been accomplished in the case of an extremely hindered digermene, E-Tbt(Mes)Ge=Ge(Mes)Tbt.[51] It is difficult for distannenes and diplumbenes to maintain their double bond in solution. Distannene $Dis_2Sn{=}SnDis_2$ shows two characteristic absorption maxima at 332 and 495 nm, of which the extinction coefficients depend on the thermal conditions.[62] The former absorption presumably corresponds to the $\pi \rightarrow \pi^*$ transition of the distannene, and the latter to $n \rightarrow p$ transition of stannylene Dis_2Sn:. $Tip_2Sn{=}SnTip_2$,[64] which is an only example showing a double-bond character even in solution, reportedly showed a characteristic absorption maximum at 495 nm. All isolated diplumbenes (in the solid state) undergo immediate dissociation into plumbylenes in solution. For example, electronic spectra of $Tip_2Pb{=}PbTip_2$ showed three bands of $\lambda_{max} = 321$, 385, and 541 nm in hexane solution, which indicate the existence of an equilibrium between $Tip_2Pb{=}PbTip_2$ and Tip_2Pb: (the equilibrium might be largely shifted toward plumbylenes).[66] Thus, the intrinsic properties of Pb=Pb systems in solutions have not been fully disclosed yet.

NMR Spectra. In the Nuclear magnetic resonance (NMR) spectra of disilenes, the ^{29}Si resonances of the doubly bonded silicon atoms are of particular interest.[2,7] The fact that disilenes exhibit relatively low-field ^{29}Si chemical shifts (δ49–155) characteristic of low-coordinated silicon compounds is in good analogy to the behavior of doubly bonded carbon atom resonances in ^{13}C NMR. The large anisotropy of the ^{29}Si chemical shielding is quite similar to that found for the C=C double bonds. The unusually low-fielded ^{29}Si chemical shifts observed for tetrakis(trialkylsilyl)disilenes, for example, $[(i\text{-Pr})_3Si]_2Si{=}Si[(i\text{-Pr})_3Si]_2$ ($\delta_{Si} + 154.5$) and $[(t\text{-Bu})Me_2Si]_2Si{=}Si[(t\text{-Bu})Me_2Si]_2$ ($\delta_{Si} + 142.1$), are interesting,[29] while those for carbon-substituted disilenes are generally observed at ca. δ_{Si}55–65. The unusual low-field chemical shifts for the ^{29}Si atom of silyl-substituted disilenes should be compared with the corresponding ^{13}C resonances for silyl-substituted sp^2-carbon atoms, for example, $(Me_3Si)_2C{=}C(SiMe_3)_2$ (δ_C195.3), which are much lower than that of the parent ethylene (δ_C122.8). Additionally, the ^{29}Si NMR signals for $[(t\text{-Bu})Me_2Si]_2Si{=}SiMes_2$, which is an unsymmetrically substituted disilene having two silyl groups on one sp^2-silicon atom and two aryl groups on the other, are observed at 8.2, 24.1, and 148.6 ppm.[41] The signal at δ24.1 is assigned to that for the $(t\text{-Bu})Me_2Si$ group, and the other two signals at δ8.2 and 148.6 correspond to those for the two sp^2 silicon atoms. Contrary to expectations, NMR studies for the disilene using 2D NMR techniques revealed the assignment of the up-fielded signal at δ 8.2 to that of the silyl-substituted sp^2-silicon atom and the low-fielded signal at δ148.6 to that of the aryl-substituted one. Although similar assignment was established in the case of $[(i\text{-Pr})_3Si]_2Si_A{=}Si_BMes_2$ [−0.8 (Si_A) and 152.3 (Si_B) ppm], the reason for such unusual shifts of the sp^2 Si atoms is not clear at present.

The data of ^{29}Si and ^{13}C chemical shifts for silenes (Si=C) are available for limited examples of stable silenes.[96] $Mes_2Si{=}CHCH_2(t\text{-Bu})$ shows characteristic signals at relatively low fields in the ^{29}Si and ^{13}C NMR spectrum (δ_{Si}77.6 and δ_C110.4), indicating a little contribution of Si^+–C^- resonance structure. On the other hand, ^{29}Si and ^{13}C NMR signals of siloxysilenes $[(Me_3Si)_2Si{=}C(OSiMe_3)R]$ are usually found at characteristically low field in the range of 40–54 ppm (for ^{29}Si NMR) and 207–214 ppm (for ^{13}C NMR). These chemical shifts suggested the decreased Si^+–C^- polarization due to the contribution of Si^-–$C{=}O^+$ resonance structure.

Germenes have also been characterized by ^{13}C NMR, which shows chemical shifts between ca. 80 and 125 ppm for the sp^2 carbon doubly bonded to the germanium atom, indicating features similar to those of silenes.[95] However, it is not possible to characterize sp^2 germanium atoms by multinuclear NMR spectroscopy such as ^{73}Ge NMR, which is useful only for symmetrically substituted tetracoordinated germanium atoms. On the other hand, the structures of tin-containing double-bond compounds can be easily studied by the use of multinuclear NMR spectroscopy, since tin has two NMR active isotopes: ^{117}Sn and ^{119}Sn. The chemical shifts of sp^2-Sn atoms usually appeared in the low field region around 400 ppm or lower in ^{119}Sn NMR. However, the solvated stannene (Tip_2Sn=Fluorenyl)[94] showed a signal assignable to that of the sp^2-Sn atom at higher field (δ288) owing to the complexation of a solvent molecule toward the tin center. The ^{119}Sn NMR of $Tip_2Sn{=}SnTip_2$[64] showed a signal for its sp^2-Sn atom at low field (δ427) with ^{119}Sn–^{117}Sn coupling satellites of 2930 Hz, indicating that the Sn=Sn double bond remains even in solution. Although $Dis_2Sn{=}SnDis_2$ exists as the corresponding stannylene (Dis_2Sn:) in solution showing a very low-fielded signal at the chemical shift of 2325 ppm in ^{119}Sn NMR spectrum, the room temperature CPMAS spectrum of $Dis_2Sn{=}SnDis_2$ in the solid state gave an isotropic shift of 692 ppm, indicating that it undoubtedly preserves the Sn=Sn double bond in the solid state.[97]

Raman/IR Spectra. Vibrational spectroscopy should provide useful information on the nature of doubly bonded systems, but only a few reports using IR or resonance Raman spectroscopy are available for the vibrational spectra of the doubly bonded systems of heavier group 14 elements. The Raman lines observed at 539 cm^{-1} for $Mes_2Si{=}SiMes_2$ and 525 cm^{-1} for $Mes(t\text{-Bu})Si{=}Si(t\text{-Bu})Mes$ were assigned to the Si=Si vibrations.[88] These frequencies are about 30% higher than those for the Si–Si single-bond stretching vibrations. Although no vibrational data for stable digermenes have been reported so far, a transient digermene ($Me_2Ge{=}GeMe_2$) is reported to show the Ge=Ge stretching vibrations at 404 cm^{-1} in the Raman spectrum, the value of which is much higher than those of the Ge–Ge single bond and lower than those of the Si=Si double bond.[98] It was difficult to assign the Si=C vibrations in their IR spectra of stable silenes owing to a number of bands observed in the region of 1300–930 cm^{-1},[96] while Mes_2Ge=Flu (Flu = Fluorenyl) has

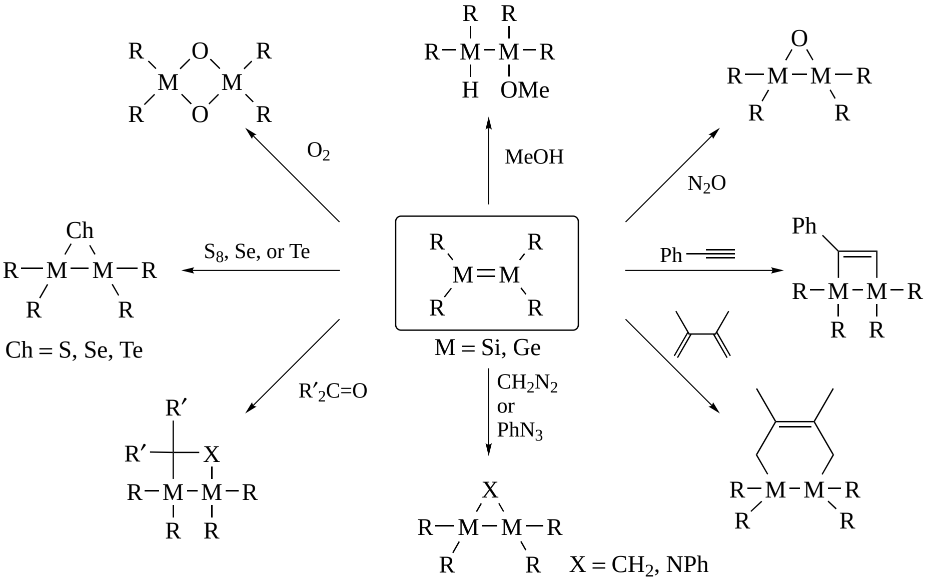

Scheme 21

a dominant vibration at 988 cm^{-1}, which can be assigned to the Ge=C double bond.[45]

3.4 Reactivities

A variety of fundamental reactions have been investigated for the M=C and M=M double-bond species of heavier group 14 elements. In spite of the steric protection by bulky substituents, stable unsaturated compounds of heavier group 14 elements described here are often the subject of many reactions such as oxidation reactions, addition reactions, and so on.

Stable disilenes and digermenes react with various reagents as shown in Scheme 21.[7,43,45,95,100] For example, the addition reaction of MeOH affords the corresponding methoxydimetallanes [$R_2M(OMe)–M(H)R_2$]. In the reactions with an appropriate chalcogen source, chalcogenadimetallиranes, which are [2 + 1]cycloadducts of the dimetallenes with chalcogen atoms, are obtained. Reactions with carbonyl compounds give the corresponding [2 + 2] cycloadducts. Reactions with diazomethane and phenyl azide afford the three-membered ring compounds provably via the initial [2 + 3] addition reactions followed by the extrusion of a nitrogen molecule. Thus, dimetallenes are useful building blocks for the synthesis of small-ring compounds containing an M–M bond.

In contrast to most alkenes, which do not react with triplet oxygen ($^3O_2$) under ambient conditions, $Mes_2Si{=}SiMes_2$ can be oxidized by atmospheric oxygen giving the corresponding 1,3,2,4-dioxadisiletane derivative.[101] Similar reactivity is reported for digermenes, $Dip_2Ge{=}GeDip_2$ and $Dep_2Ge{=}GeDep_2$, which eventually give 1,3,2,4-dioxadigermetane derivatives in the reactions with oxygen.[102] The mechanistic studies for the oxidation reaction of (*E*)-Mes(*t*-Bu)Si=Si(*t*-Bu)Mes[103] in solution have revealed that the corresponding [2 + 2] cycloadduct, that is, (*E*)-1,2,3,4-dioxadisiletane, was obtained stereospecifically at the initial stage of this reaction previous to the rearrangement giving the final product, (*E*)-1,3,2,4-dioxadisiletane (Scheme 22). Although the oxidation of disilenes is known to take place stereospecifically not only in the solid state but also in solution, there have been very few reports on the stereochemistry in the oxidation of a digermene probably owing to its immediate dissociation into two germylenes in solution. A unique result was reported in the oxidation reaction of (*E*)-Tbt(Mes)Ge=Ge(Mes)Tbt,[104] which undergoes dissociation in solution, giving germylenes as an equilibriated mixture (Scheme 23). The exposure of a finely powdered orange sample of (*E*)-Tbt(Mes)Ge=Ge(Mes)Tbt to atmospheric

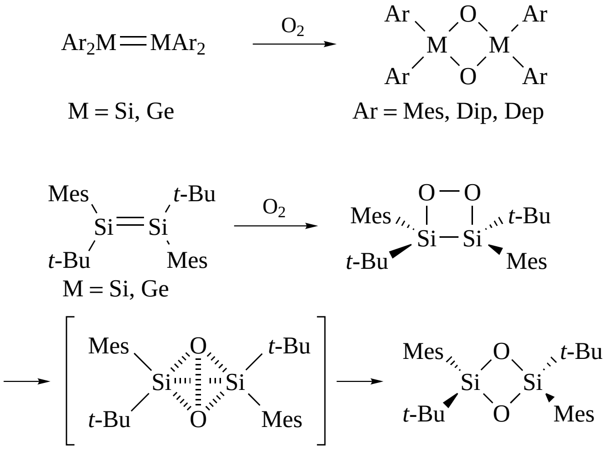

Scheme 22

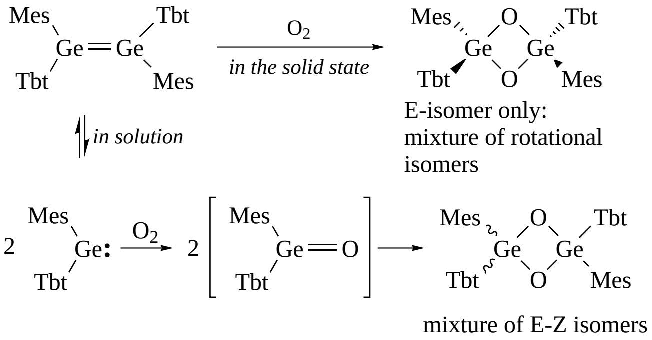

Scheme 23

oxygen affords (E)-1,3,2,4-dioxadigermetane exclusively, suggesting that the reaction of the digermene with oxygen in the solid state proceeds stereospecifically. On the other hand, the reaction of (E)-Tbt(Mes)Ge=Ge(Mes)Tbt with oxygen in solution gave (E)- and (Z)-1,3,2,4-dioxadigermetanes in 20 and 38% yields, respectively. The most plausible reaction mechanism is that the dissociation of the digermene into the corresponding germylene [Tbt(Mes)Ge:] in solution followed by the reaction of the germylene with molecular oxygen may give the germanone [Tbt(Mes)Ge=O], which readily undergoes dimerization to afford (E)- and (Z)-1,3,2,4-dioxadigermetanes nonstereospecifically.

Stable silenes and germenes also react with various reagents as shown in Scheme 24.[43,75,96,99,100] Addition reactions of metallenes with MeOH lead to the formation of $R_2M(OMe)–C(H)R_2$. The reactions of α,β-unsaturated carbonyl compounds afford the corresponding [4 + 2]cycloadducts regiospecifically, reflecting the $M^{\delta+}{=}C^{\delta-}$ polarity.

4 DOUBLE-BOND COMPOUNDS BETWEEN GROUP 14–GROUP 15 ELEMENTS

Azasilenes,[105] also called as iminosilanes, are one of the heavier analogs of imines. The difference in the electronegativity between Si (1.8) and N (3.0) gives azasilenes ylidic character ($Si^{\delta+}{=}N^{\delta-}$), which makes them susceptible to oligomerization and/or dimerization as in the case with silenes (Si=C).

4.1 Synthesis, Properties, and Structures

The first azasilene stable at room temperature was synthesized by taking advantage of kinetic stabilization in 1985.[106] The azasilene, $(t\text{-Bu})_2Si{=}NSi(t\text{-Bu})_3$, was formed in the reaction of $(t\text{-Bu})_2SiClN_3$ with $(t\text{-Bu})_3SiNa$ in $(n\text{-Bu})_2O$ at −78 °C (Scheme 25). The azasilene has a slightly yellow color and undergoes a melting decomposition at 85 °C. Its large down-field shift in the ^{29}Si NMR suggested that the azasilene features double-bond character as well as the case of Si=C or Si=Si double bonds. X-ray crystallographic analysis[107] of the azasilene revealed its monomeric structure (Figure 12) and nearly linear skeleton of Si=N–Si bond (177.8°). It was found that the Si=N bond length (1.568 Å) is apparently shorter than the N–Si bond (1.695 Å). The very wide angle

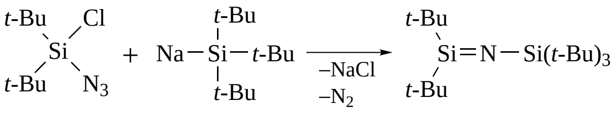

Scheme 25

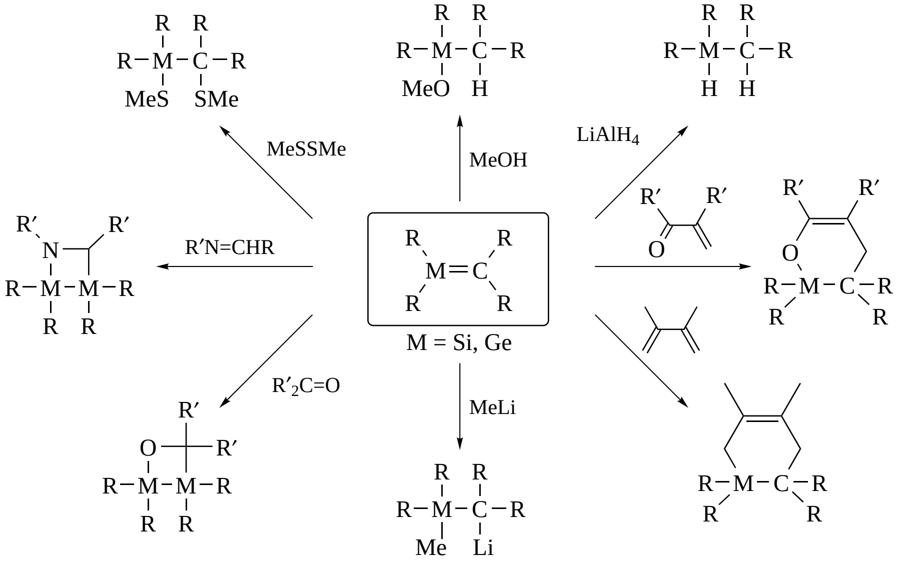

Scheme 24

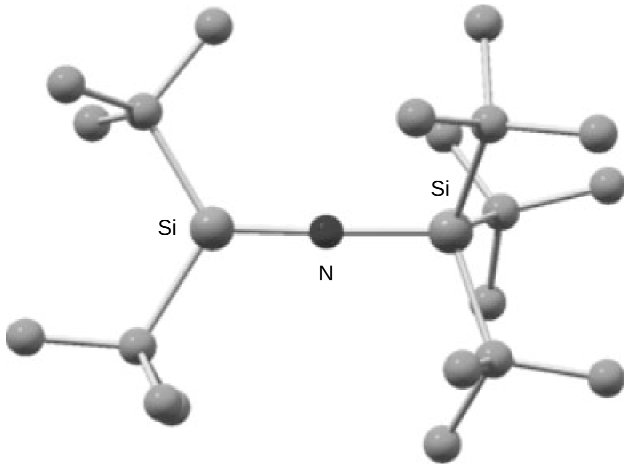

Figure 12 Molecular structure of $(t\text{-Bu})_2$ Si=NSi$(t\text{-Bu})_3$

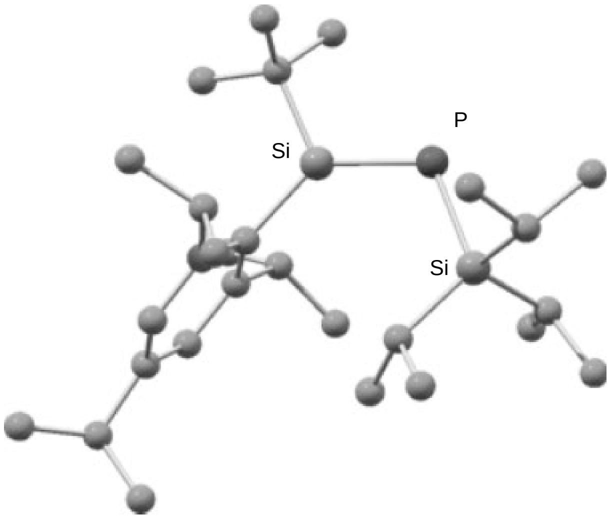

Figure 13 Molecular structure of Tip$(t\text{-Bu})$Si=PSi$(i\text{-Pr})_3$

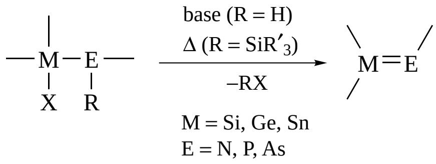

Scheme 26

at the nitrogen atom is due to electronic reasons rather than steric effect, since the relatively electropositive silyl substituents ensure a very low barrier to cis/trans isomerization via linear inversion process.**[108,109]** In the case of $H_2Si{=}NH$ (Si–N–H = 125.2°)**[110,111]** as a model compound, the cis/trans isomerization barrier is estimated as $5.6\,\text{kcal mol}^{-1}$ but the π bond strength, as measured by the rotational barrier, is $37.9\,\text{kcal mol}^{-1}$. Although carbon-substituted azasilenes are predicted by calculations to have smaller angles at the N atom and longer Si–N bond lengths, there have been no experimental data of such compounds obtained so far.

Stable azagermenes**[96]** and azastannenes**[96]** are obtained by the reactions of azides with a germylene or a stannylene as a precursor.**[45,75,76,100]** They feature planar geometries at the Ge and Sn atoms together with bent geometries at their N atoms. The Ge–N distances of the azagermenes lie in the range of 1.681–1.704 Å being in good agreement with the calculated values.**[112,113]** The observed structural parameters of azastannenes are also consistent with the features predicted by theoretical calculations.**[114]**

Furthermore, there are some reports on the synthesis of stable phosphasilenes and arsasilenes.**[115,116]** The structure of Tip$(t\text{-Bu})$Si=PSi$(i\text{-Pr}_3)$ showed shorter Si=P bond length (2.062 Å) and Si–P=Si bond angle of 112.79°, which is much smaller than the Si–N=Si bond angle of azasilenes (ca. 170°–178°) (Figure 13).**[117]** Theoretical calculations for $H_2Si{=}PH$ showed the Si=P bond length of 2.044 Å and the Si–P–H angle of 93°.**[118]** Other reports on the calculations for Si=P and Si=As doubly bonded species with silyl substituents at the pnictogen atoms predicted their molecular geometries with the Si=E (E = P, As) distances of 2.053 and 1.161 Å and the wide Si=E–Si angles near 100°.**[118]** Such relatively narrow angles compared with the Si=N–Si bond angles of azasilenes reflect the much larger barrier to linear inversion as a result of the increased s character of the phosphorus or arsenic lone pairs. The Si–E rotational barrier in $H_2Si{=}EH$ (E = P, As) are estimated as $34\,\text{kcal mol}^{-1}$ for E = P and $30\,\text{kcal mol}^{-1}$ for E = As.

Thus, several stable compounds featuring double bonds between heavier group 14 and 15 elements are now synthesized and well characterized.**[45,75,76,100,115,116]** In most cases, the aza-, phospha-, and arsametallanes were found to be synthesized via the dehydrohalogenation reactions of MX–EH precursors (M = Si, Ge, Sn, E = N, P, As, X = halogen) using a base or the thermal decomposition of MX–E(SiR_3) (Scheme 26). Structures of some stable azametallenes and phosphametallanes are summarized in Table 3. Although many stable examples have been reported for azametallenes, those for heavier analogs are very scarce. Indeed, there is no example of stiba- and bismametallenes (Sb=M, Bi=M), probably owing to the instability of precursors such as SiX–SbH derivatives. Dilithiophosphine derivatives $(ArPLi_2)$ are known to be applicable to the synthesis of low-coordinated phosphorus compounds, and the stable phosphagermene, $Mes_2Ge{=}PTip$, is reportedly formed by the reaction of Mes_2GeF_2 with $TipPLi_2$ directly.**[119]** Furthermore, the thermolysis of a linear (fluorostannyl)silylphosphine was reported to give the corresponding phosphastannene, though its structural parameters have not been determined so far.

Table 3 Selected structural parameters for $>M{=}E{-}$ ($M = Si, Ge, Sn$, $E = N, P, As$)

$R_1R_2M{=}ER_3$	M=E/Å	$M{-}E{-}R_3/°$
$(t\text{-Bu})_2Si{=}NSi(t\text{-Bu})_3$	1.568(3)	177.8(2)
$(t\text{-Bu})_2Si{=}NSiPh(t\text{-Bu})_2$	1.573(3)	170.1(18)
$(Dis_2Ge{=}N)_2SiMes_2$	1.681(8)	137.3(5)
$[Mes(Me_3Si)N]_2Ge{=}NMes$	1.688(9)	151.2(7)
$[Dip(Me_3Si)N]_2Ge{=}NDip$	1.703(2)	134.2(2)
$Dis_2Ge{=}NSi(t\text{-Bu})_2(N_3)$	1.704(5)	136.0(4)
$Dis_2Sn{=}NSi(t\text{-Bu})_2(N_3)$	1.905(5)	130.6(3)
$[(Me_3Si)_2N]_2Sn{=}NDip$	1.921(2)	120.6(2)
$Tip(t\text{-Bu})Si{=}PSi(i\text{-Pr})_3$	2.062(1)	112.79(2)
$Tip(t\text{-Bu})Si{=}AsSi(i\text{-Pr})_3$	2.164(1)	110.92(4)
$Mes_2Ge{=}PMes^*$	2.138(3)	112.9(4)
$Mes(t\text{-Bu})Ge{=}PMes^*$	2.144(3)	110.9(5)

4.2 Reactions

The addition of protic reagents such as an alcohol toward the double bond of unsaturated heavier group 14 elements is one of the most important reactions. The reaction usually occurs cleanly and in a high yield, and is taken as evidence for the existence of a doubly bonded compound.

The addition reactions of H_2O and MeOH (or EtOH) to azametallenes and phosphametallenes are completely regioselective with the formation of $>M(OR){-}E(H){-}$($M = Si$, Ge, $E = N$, P) compounds, indicating their ylidic character of $M^{\delta+}{=}E^{\delta-}$. Similarly, the addition of hydrogen halides is also regioselective, giving the corresponding halometallanes.

Unsaturated carbon compounds, such as acetone and 2,3-dimethyl-1,3-butadiene, having hydrogens in the α position prefer to undergo ene reactions with the M=N ($M = Si$, Ge, Sn) double-bond compounds, while benzaldehyde or benzophenone react with M=N double bonds to give the corresponding $[2+2]$ adducts regioselectively with the formation of M–O bonds. In addition, the $[4+2]$ cycloaddition reaction of azametallenes and phosphametallenes with α,β-unsaturated aldehydes and ketones have been reported to give the six-membered ring compounds. Other cycloaddition using 1,3-dipoles such as nitrileoxide and azide derivatives were reported. The reactivities of M=E double bond are summarized in Scheme 27.[45,75,76,100,115,116]

5 DOUBLE-BOND COMPOUNDS BETWEEN GROUP 14–GROUP 16 ELEMENTS

Heavier congeners of carbonyl compounds, one of the most important and fundamental functionalities in organic chemistry, have attracted a great deal of attention from the viewpoints of double bonds between a carbon atom and a heavier group 16 elements such as sulfur, selenium, and tellurium. Although no example of a stable telluroaldehyde has been reported yet, most of the structures and properties of C=Ch (Ch = S, Se, Te) double-bond compounds have been systematically elucidated so far.[120–122] In contrast to the chemistry of the C=Ch doubly bonded systems, that of heavier congeners of ketones containing a heavier group 14 element, which are called ‘heavy ketones’, have been much less explored until recently. Probably, this is due to the much greater difficulty in the stabilization of such extremely reactive species. Since the protecting group can be introduced only onto the group 14 elements and the terminal chalcogen

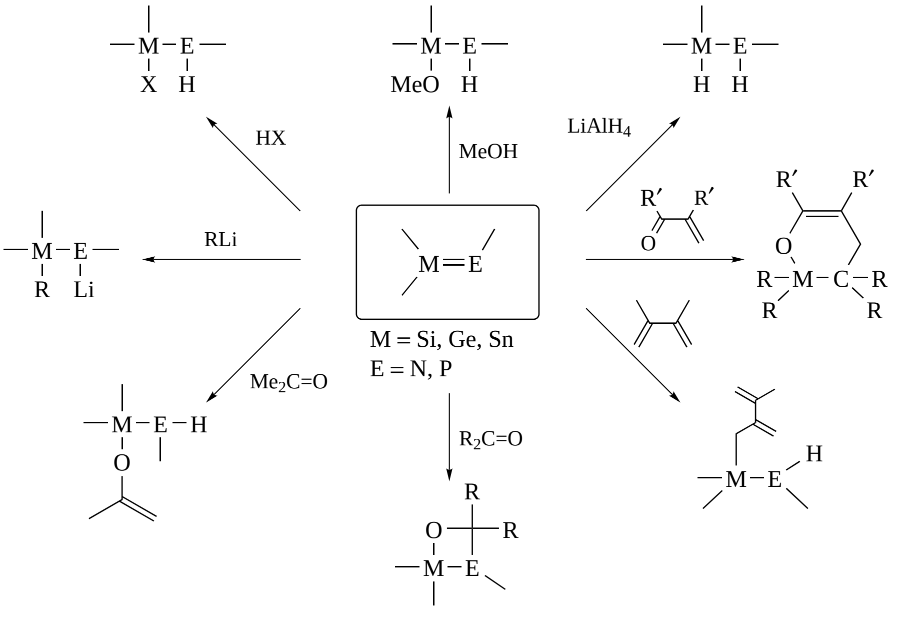

Scheme 27

atoms are unfortified, it is inherently difficult to stabilize the heavy ketones using the conventional steric protecting groups as described in previous sections. Although several examples of compounds having a formal M=Ch double bond, which are thermodynamically stabilized by the coordination of heteroatoms such as nitrogen or oxygen, are known,[123] they are considerably perturbed by the coordination and hence not suitable for a study on the intrinsic nature of the M=Ch double bonds. Tokitoh and Okazaki proved that the use of an effective protecting group such as a Tbt group is crucial for the isolation of heavy ketones without electronic perturbation, because they can be kinetically stabilized by only two substituents on the group 14 elements. The chemistry of kinetically stabilized 'heavy ketones' has been extensively developed by taking advantage of this new, effective steric protecting group.[124,125]

5.1 Synthesis

The extremely high reactivity of heavy ketones, RR′M=Ch (M = Si, Ge, Sn, Pb, Ch = O, S, Se, Te), obviously results from the fact that their M–Ch π-bond energies are much smaller than the corresponding M–Ch σ-bond energies, as one can see from Table 4.[124,125] Therefore, heavy ketones RR′M=Ch are difficult to generate by simple elimination of a leaving group (HX) from a precursor (or intermediate) of RR′M(ChH)(X), which is a commonly used method for the synthesis of ketones. In the case of M=O (M = Si, Ge, Sn, Pb) double bonds, the σ-bond energies are much larger than the corresponding π-bond energies, indicating their extremely high reactivity. Until now, no stable examples of M=O double-bond compounds have been isolated even by the method of thermodynamic or kinetic stabilization except for very few examples marginally stable in very low temperature matrices. Only kinetically stabilized heavy ketones are shown here, though several examples of marginally stable species and thermodynamically stabilized heavy ketones have been reported.

Table 4 Bond energies (kcal mol^{-1}) and lengths (Å) for $H_2M{=}Ch$ species calculated at the B3LYP/TZ(d,p) level. (σ: σ-bond energy, π: π-bond energy, d: lengths of an M=Ch double bond, Δ: percent reduction in a bond lengths defined as [(single-bond lengths – double-bond length)/single-bond lengths] ×100)

		Ch			
$H_2M{=}Ch$		O	S	Se	Te
$H_2C{=}Ch$	σ	93.6	73.0	65.1	57.5
	π	95.3	54.6	43.2	32.0
	d	1.200	1.617	1.758	1.949
	Δ	15.5	11.9	11.1	10.1
$H_2Si{=}Ch$	σ	119.7	81.6	73.7	63.2
	π	58.5	47.0	40.7	32.9
	d	1.514	1.945	2.082	2.288
	Δ	8.1	9.4	9.3	8.7
$H_2Ge{=}Ch$	σ	101.5	74.1	67.8	59.1
	π	45.9	41.1	36.3	30.3
	d	1.634	2.042	2.174	2.373
	Δ	8.6	9.5	9.2	8.6
$H_2Sn{=}Ch$	σ	94.8	69.3	64.3	56.4
	π	32.8	33.5	30.6	26.3
	d	1.802	2.222	2.346	2.543
$H_2Pb{=}Ch$	σ	80.9	60.9	57.0	50.3
	π	29.0	30.0	27.8	24.4
	d	1.853	2.273	2.394	2.590
	Δ	8.5	9.2	8.9	8.1

By trial and error for years, several approaches for the synthesis of heavy ketones have been developed (Scheme 28). In particular, dechalcogenation reaction of 1,2,3,4-tetrachalcogenametallolanes (RR′MCh_4) using phosphine reagents proved to be most useful for the isolation of heavy ketones in a pure form. Two other methods, the chalcogenation reactions of divalent species of heavier group 14 elements (metallylenes) and the reactions of dilithiometallanes (RR′MLi_2) with chalcogen dihalides, were found to be successful in some cases.

The synthetic strategy for the first stable silanethione, Tbt(Tip)Si=S, is based on a simple desulfurization of the corresponding 1,2,3,4-tetrachalcogenasilolane using a phosphine reagent.[126,127] Thus, a hexane solution of Tbt- and Tip-substituted tetrathiasilolane was refluxed in the presence of 3 molar equivalents of PPh_3 to produce the corresponding silanethione, Tbt(Tip)Si=S, as stable yellow crystals together with $Ph_3P{=}S$, which was easily separated from the reaction mixture by filtration. This dechalcogenation methodology was also successful in the synthesis of the stable germanethione, Tbt(Tip)Ge=S, and the germaneselone, Tbt(Tip)Ge=Se.[128–130] It should be noted that the combination of Tbt and Tip substituents is found to be indispensable for the stabilization of the reactive M=Ch double bond. However, it cannot prevent the dimerization of the Sn=X bond having much higher reactivity than the corresponding Si and Ge analogs. The bond lengths around the Sn atom become longer than those in the case of Si and Ge, and hence the steric protection of the tin center by the substituents become less effective.[131] Thus, desulfurization reactions of Tbt- and Tip-substituted tetrathiastannolane and tetraselenastannolane were reported to give the dimerized products of the intermediary stannanethione and stannaneselone.[131] However, the combination of Tbt with a newly developed bulky *m*-terphenyl type substituents (Ditp) led to the isolation of stable stannanethione and stannaneselone as red crystals.[124,125,131,132] Although desulfurization of Tbt- and Tip-substituted tetrathiaplumbolane [Tbt(Tip)PbS_4] with Ph_3P or $(Me_2N)_3P$ at −78 °C gave the corresponding plumbanethione [Tbt(Tip)Pb=S] as evidenced by the trapping experiments giving cycloadducts as in the cases of other heavy ketones,[133] the same reaction at 50 °C afforded an unexpected plumbylene and a 1,3,2,4-dithiaplumbetane derivative instead of the dimer (or oligomer) of the corresponding plumbanethione (Scheme 29).[134] The formation of the unexpected products was reasonably interpreted in terms of intermediacy of plumbylenes, Tbt–Pb–STip and Tip–Pb–STbt, which might

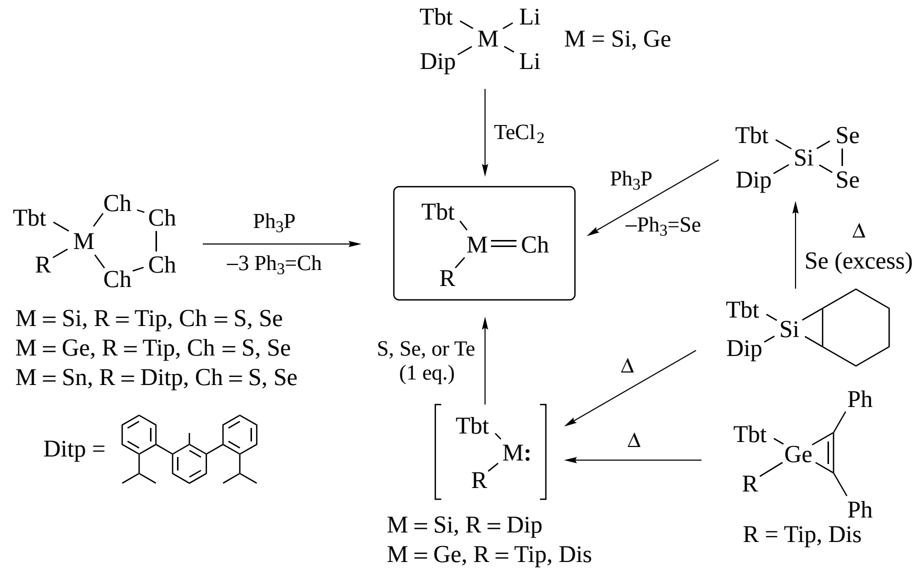

Scheme 28

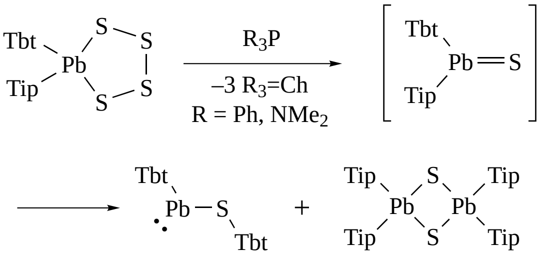

Scheme 29

be formed by the 1,2-aryl migration of the initially produced plumbanethione.[134]

The dechalcogenation reaction of tetrachalcogenametallolanes has proven to be an excellent synthetic approach to heavy ketones, but tetrachalcogenametallolanes are not always available. In such cases, the chalcogenation of divalent species can be an alternative method.

Although the tetrathiasilolane can be synthesized by the reaction of elemental sulfur (S_8) with the transient silylene Tbt(Tip)Si: (or its equivalent) prepared by the reduction of Tbt(Tip)$SiBr_2$ with lithium naphthalenide,[126] a similar reaction using selenium instead of S_8 did not afford the corresponding tetraselenide. However, the reaction of Tbt(Dip)Si:, generated by thermolysis of a silirane derivative, with 1 equivalent of selenium gave a silaneselone, Tbt(Dip)Si=Se, as a red solid.[59,124,125] The reaction of the thermally generated silylene Tbt(Dip)Si: with an excess amount of selenium resulted in the formation of a diselenasilirane derivative, Tbt(Dip)$SiSe_2$, deselenization of which with PPh_3 gave the silaneselone, Tbt(Dip)Si=Se.[59] Since the cyclic polytellurides, the expected precursors for metallanetellones, are generally unstable, the chalcogenation method of metallylenes is thought to be effective to synthesize the corresponding metallanetellones. Indeed, stable silanetellone [Tbt(Dip)Si=Te] and germanetellone [Tbt(R)Ge=Te (R = Tip, Dip)] were successfully synthesized by the reactions of the thermally generated silylene [Tbt(Dip)Si:] and germylene [Tbt(R)Ge:] with elemental tellurium, respectively.[59,135]

In addition to the tellurization of metallylenes, another unique synthetic route has been developed for the M=Te (M = Si, Ge) double bonds. It has been reported that the exhaustive reduction of an overcrowded dibromometallanes [Tbt(Dip)MBr_2] with an excess amount (more than 4 equiv.) of lithium naphthalenide leads to the generation of the corresponding diaryldilithiometallanes [Tbt(Dip)MLi_2] (see Section 3), which was found to be very useful for the synthesis of unprecedented organometallic compounds.[39,58,59] As one of the synthetic applications of the dilithiometallanes [Tbt(Dip)MLi_2], the reactions of Tbt(Dip)MLi_2 with $TeCl_2$ were examined in Tetrahydrofuran (THF) at −78 °C to give the expected metallanetellones [Tbt(Dip)M=Te (M = Si, Ge)].[59] Thus, the synthetic route via dilithiometallanes should be noted as an alternative synthetic approach to heavy ketones. The heavy ketones obtained here are very stable at ambient temperature not only in the solid state but also in solution of hydrocarbon solvents.

5.2 Structural and Spectroscopic Properties

X-ray Crystallographic Analysis. The most important structural feature of a carbonyl compound is its trigonal planar geometry, which results from the sp^2-hybridized carbon. Since it has been revealed experimentally and theoretically that dimetallenes have a trans-bent structure in contrast to alkenes with planar geometry (see Section 2 and 3), it is quite interesting to investigate the structural features of a series of heavy ketones. The results of X-ray crystallographic analysis of the kinetically stabilized heavy ketones are partially summarized in Table 5,**[124,125]** and the molecular structure of Tbt(Tip)Ge=Te**[135]** is shown in Figure 14 as a representative. All heavy ketones [Tbt(R)M=Ch (M = Si, Ge, Sn, Ch = S, Se, Te)] have an almost completely trigonal planar geometry and a distinct double-bond nature, as judged by the summation of bond angles around the M atom ($\Sigma\angle$M) and the bond shortening (%) compared to the corresponding single bonds (Δ_{obs}). The observed double-bond lengths and Δ_{obs} values are in good agreement with the calculated values for H_2M=Ch as listed in Table 4. These findings clearly indicate that heavy ketones have structural features similar to those of ketones, although their double-bond character is somewhat weaker than that of the corresponding carbon homologs judging from their Δ_{obs} (Table 5) as well as Δ (Table 4) values.

NMR Spectra. As in the case of ^{13}C NMR, the low-field chemical shifts are characteristic of the sp^2-hybridized nuclei of the heavy ketones. For example, the ^{29}Si NMR chemical shifts of the sp^2 silicon atoms Tbt(Tip)Si=S,**[126,127]** Tbt(Dip)Si=Se,**[59]** and Tbt(Dip)Si=Te**[59]** are 167, 174, and 171 ppm, respectively. This is the typical difference between kinetically stabilized Si=Ch double-bond compounds and thermodynamically stabilized ones, which showed their ^{29}Si NMR signals around 20–30 ppm, indicating the high sp^3 nature of the silicon centers.**[123]** The characteristic low-field ^{77}Se and ^{125}Te NMR chemical shifts of Tbt(Dip)Si=Ch (Ch = Se, Te; $\delta_{Se} = 635$ for Ch = Se, $\delta_{Te} = 731$ for Ch = Te) are also indicative of their sp^2 hybridized chalcogen atoms. Similarly, Tbt(Ditp)Sn=S and Tbt(Ditp)Sn=Se have shown their ^{119}Sn NMR signals at 531 and 440 ppm, respectively, while ^{119}Sn NMR of thermodynamically stabilized examples resonate at a much higher field in the range from −300 through −450 ppm.**[123]** Although such information is not available for Ge=Ch double-bond compounds because of the practical difficulty in observing ^{73}Ge NMR, the low-field resonating ^{77}Se and ^{125}Te NMR chemical shifts of Tbt(R)Ge=Se (941 ppm for R = Tip, 872 ppm for R = Dis) and Tbt(R)Ge=Te (1143 ppm for R = Tip, 1009 ppm for R = Dis) are in keeping with the sp^2 hybridization of these elements.**[128–130,135]**

Table 5 Structural parameters of heavy ketones Tbt(R)M=Ch. (*d*: lengths of an M=Ch double bond, $\Sigma\angle$M: summation of the bond angles around M atom, Δ_{obs}: percent reduction in bond lengths defined as [(single-bond lengths – double-bond length)/single-bond lengths] ×100)

Tbt(R)M=Ch					
R	M	Ch	*d*	$\Sigma\angle$M	Δ_{obs}
Tip	Si	S	1.948(4)	359.9	9
Tip	Ge	S	2.049(3)	359.4	9
Tip	Ge	Se	2.180(2)	359.3	9
Dis	Ge	Se	2.173(3)	360.0	8
Tip	Ge	Te	2.398(1)	359.5	9
Dis	Ge	Te	2.384(2)	360.0	8
Ditp	Sn	Se	2.375(3)	359.9	9

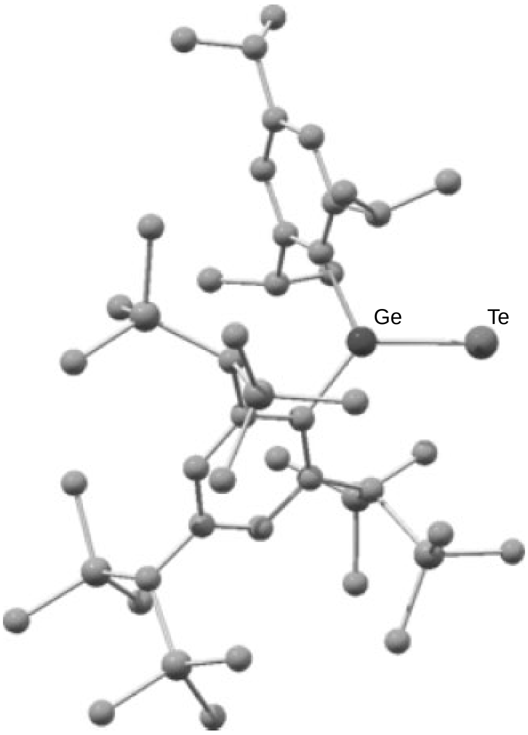

Figure 14 Molecular structure of Tbt(Tip)Ge=Te

UV–vis Spectra. In Table 6 are listed characteristic visible absorptions observed for the heavy ketones kinetically stabilized by a Tbt group. It is known that the absorption maxima attributable to the n-π^* electron transitions of a series of R_2C=Ch (Ch = O, S, Se, Te) undergo a systematic red-shift on going down the periodic table. A similar tendency is observed for the Si, Ge, and Sn series of Tbt(R)Si=Ch (Ch = S, Se, Te),**[59,126,127]** Tbt(R)Ge=Ch (Ch = S, Se, Te),**[128–130,135]** and Tbt(Ditp)Sn = Ch (Ch = S,

Table 6 Observed absorption maxima (λ_{max}/nm) in electronic spectra (n-p*) of M=Ch double-bond compounds (M = C, Si, Ge, Sn, Ch = S, Se, Te)

	Tbt(R)M=Ch		
M	Ch=S (R)	Ch=Se(R)	Ch=Te(R)
C	587 (H)	792 (H)	–
Si	396 (Tip)	456 (Dip)	593 (Dip)
Ge	450 (Tip)	519 (Tip)	640 (Tip)
Sn	491 (Ditp)	531 (Ditp)	–

Se).[131,132] One can see a very interesting trend in the absorption maxima of two series, Tbt(R)M=S and Tbt(R)M=Se (M = C, Si, Ge, Sn). In both series, their absorption maxima are greatly blue-shifted on going from C to Si congeners, whereas those of Si, Ge, and Sn congeners are red-shifted with increasing atomic number of the group 14 elements.

Raman Spectra. The stretching vibrations of the M=Ch bonds were measured using Raman spectroscopy: Silanethione Tbt(Tip)Si=S (724 cm^{-1}), germanethiones Tbt(R)Ge=S (521 cm^{-1} for R = Tip, 512 cm^{-1} for R = Dis), and germanetellones Tbt(R)Ge=Te (381 cm^{-1} for R = Tip, 386 cm^{-1} for R = Dis). These values are in good accordance with those calculated for $H_2M{=}Ch$ compounds [723 (Si=S), 553 (Ge=S), and 387 (Ge=Te) cm^{-1}].[126] It is noteworthy that the observed value of Tbt(Tip)Ge=S (521 cm^{-1}) is very close to that observed for $Me_2Ge{=}S$ (518 cm^{-1}) by IR spectroscopy in an argon matrix at 17–18 K,[136] indicating the similarity in the bond nature of both germanethiones in spite of the great difference in the size and nature of the substituents.

6 TRIPLE-BOND COMPOUNDS BETWEEN GROUP 14 ELEMENTS

Covalent triple bonds are common unsaturated species in carbon chemistry as well as double bonds, but are rare and unusual for heavier group 14 elements. Since the real existence of heavier doubly bonded systems have been experimentally demonstrated (see Section 2), triply bonded systems of heavier group 14 elements have been major target molecules of research for these several decades.[137] However, no experimental evidence for the isolation of triple-bond compounds of heavier group 14 elements has been achieved until very recently. One of the reasons for their absence was the greater steric requirements for their substituents. Another was the scarcity of suitable precursors that could be smoothly converted to a stable triply bonded compound. Recent theoretical calculations have suggested that it should be possible to stabilize Si≡Si and Si≡C triple bonds by the use of appropriate steric protection groups (see Section 2.3). In this section, recent experimental works on the synthesis of the triply bonded systems between heavier group 14 elements (containing 'formal' triple bonds) are presented.

6.1 Triply Bonded Systems of Germanium, Tin, and Lead

The first stable compound to feature triple bonding to a heavier group 14 elements was the molybdenum–germanium derivative, $(\eta^5\text{-}C_5H_5)(CO)_2Mo{\equiv}Ge\text{–}C_6H_3\text{-}2,6\text{-}Mes_2$.[138] After this sensational work, it was experimentally and theoretically demonstrated that a germanium atom can form stable triple bond with group 6 metals.[138–140] Details of such unique triply bonded systems between a transition metal and a germanium atom should be omitted here.

The isolation of transition metal complexes with the triple bonds to an almost linearly coordinated germanium atom and the isolation of R–M–X species (M = Ge, Sn, Pb, X = Cl, Br),[53–56,69,70,141,142] which should be good precursors for triple bonds, suggested that stable compounds of the general formula RM≡MR (M = Si, Ge, Sn, Pb) are synthesizable and isolable target molecules.

The reduction of a halometallylene having bulky *m*-terphenyl ligand, Ar*–M–X (Ar* = C_6H_3-2,6-Tip_2, M = Ge, Sn, Pb, X = Cl, Br), was found to afford the corresponding triply bonded systems, as evidenced by Power and coworkers (Scheme 30).[140] The Pb≡Pb triple-bond compound was reportedly characterized by X-ray crystallographic analysis as the first example of a stable heavier congener of an alkyne.[143] The diplumbyne, Ar*Pb≡PbAr*, was isolated as amber-green crystals in ca. 10% yield by the reduction of Ar*PbBr with $LiAlH_4$. The isolation of the diplumbyne is in contrast to the reduction of Ar*SnCl with $LiAlH_4$ leading

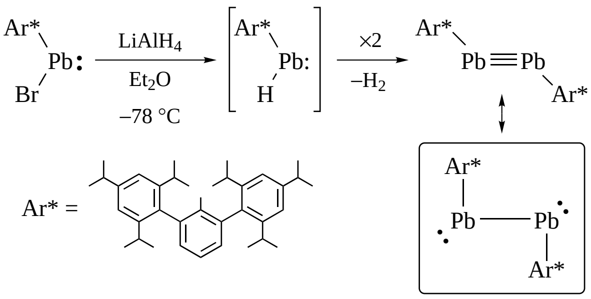

Scheme 30

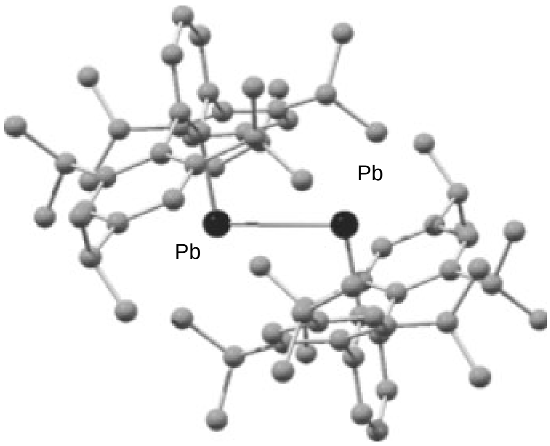

Figure 15 Molecular structure of Ar*Pb–PbAr* (Ar* = 2, 6-Tip_2-C_6H_3)

to the formation of a unusual hydride $[Sn(\mu\text{-}H)Ar^*]_2$.[74] The important structural features of Ar*Pb≡PbAr* are the Pb–Pb bond length [3.1881(1) Å], the planar, trans-bent C–Pb–Pb–C core arrangement, and the Pb–Pb–C angle [94.26(4)°] (Figure 15). That is, it was found that the Pb–Pb bond is much longer than those found in diplumbenes, which are usually in the range of 2.85–2.95 Å.[144] The Pb–C bond shows high p-orbital character because the Pb–Pb–C angle is nearly 90°. Thus, it can be concluded that the diplumbyne Ar*Pb≡PbAr* features a 'bis-plumbylene character', Ar*Pb–PbAr*, rather than a triple-bond character.

Power *et al.* have further reported the synthesis and structures of digermyne[145] (Figure 16) and distannyne[146] derivatives, Ar'M≡MAr' (M = Ge, Sn), using a modified *m*-terphenyl ligand of Ar', C_6H_3-2,6-Dip_2. As shown in Scheme 31, treatment of Ar'MCl (M = Ge, Sn) with potassium afforded Ar'M≡MAr' (M = Ge, Sn) in moderate yields. The main structural features of interest are obviously the planar, trans-bent CMMC core geometries, the M–M distances, and the M–M–C angles. It can be seen that the Ge≡Ge [2.2850(6) Å] and Sn≡Sn [2.6675(4) Å] bond lengths are much shorter than the distances expected for the corresponding dimetallanes [2.44 Å (Ge) and 2.81 (Sn)]. The M–M–C bond angles are much wider than the corresponding angles in Ar*Pb–PbAr*. These observed structural parameters suggest the considerable multiple bond character of Ar'M≡MAr' (M = Ge, Sn). The Ge–Ge distance and Ge–Ge–C bond angle may also be compared to the structural features [2.22 Å and 123.0° or 124.0°] calculated for parent *trans*-HGe≡GeH.[147] Similarly, calculations for the *trans*-HSn≡SnH revealed the Sn–Sn distance of 2.65 Å and the Sn–Sn–H bond angle of 122°, which agree more closely with those measured in Ar'Sn≡SnAr'.[147] In addition, calculations on much bulkier models Ar*M≡MAr* and TbtM≡MTbt (M = Ge, Sn) reportedly show good agreement in the structural parameters with experimental data and indicate that the triple-bond forms are much stable than $R_2M{=}M$: form owing to the steric reasons.[24]

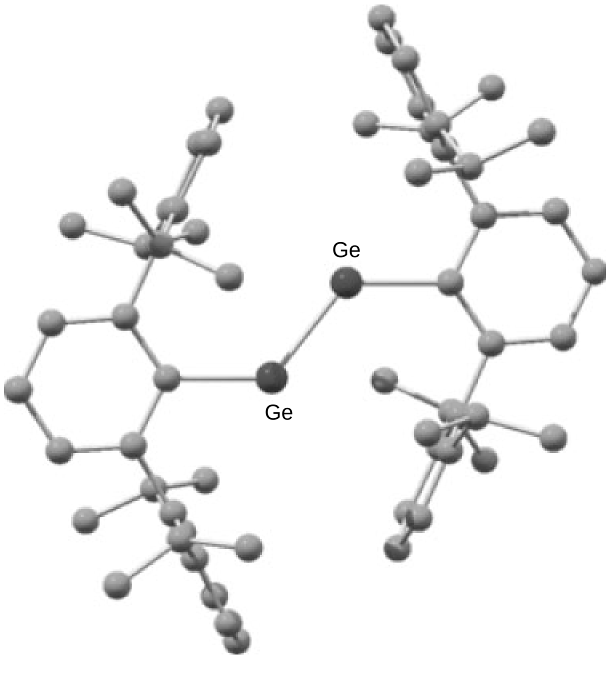

Figure 16 Molecular structure of Ar'Ge≡GeAr' (Ar' = 2, 6-Dip_2-C_6H_3)

Very recently, Tokitoh and coworkers demonstrated that a 2,6-bis[bis(trimethylsilyl)methyl]-4-[tris(trimethylsilyl) methyl]phenyl (Bbt) group, which is a ligand similar to the Tbt group, is well applicable to the synthesis of a stable digermyne, BbtGe≡GeBbt. The second example of an isolable digermyne, BbtGe≡GeBbt, was prepared by the reduction of 1,2-dibromo-1,2-digermene Bbt(Br)Ge=Ge(Br)Bbt in an almost quantitative yield (Scheme 32). Two nonidentical molecules of BbtGe≡GeBbt were observed in the unit cell by the X-ray crystallographic analysis. The Ge–Ge bond lengths in BbtGe≡GeBbt are the shortest [2.2059(8) and 2.2260(7) Å] among the previously reported Ge–Ge bonds, indicating its considerable triple-bond character.

It should be concluded that the M≡M bonds in the Ar'M≡MAr' (M = Ge, Sn) can be considered as a triple bond, which consists of two donor-acceptor bonds plus a π-bond owing to the coupling between the unpaired electrons in the p orbital on each element (see Section 2.3). However, the donor-acceptor bonds are unfavorable in the case of lead. Therefore, the bonding structure of diplumbyne is being interpreted in terms of a structure of Ar*Pb–PbAr* as shown in Figure 17, in which the Pb atoms are formally linked by a single bond with their p orbitals.

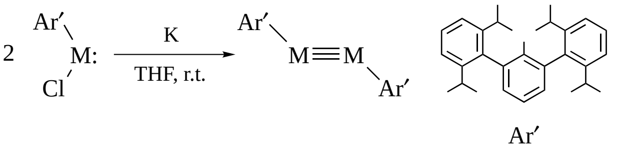

Scheme 31

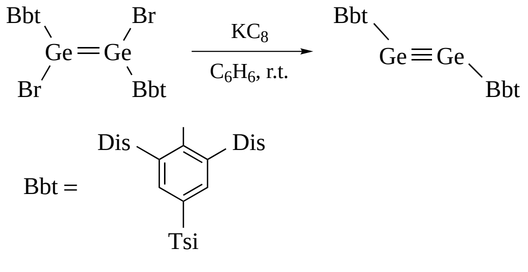

Scheme 32

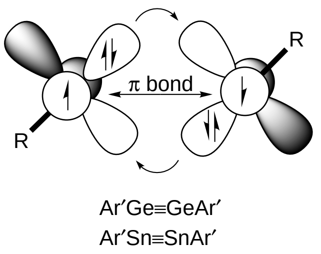

(a) Two-donor-acceptor bonds with a π-bond

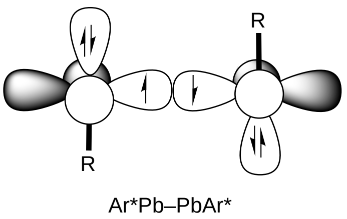

(b) Bis-metallylenes linked by a single bond

Figure 17 Bonding models of RM≡MR

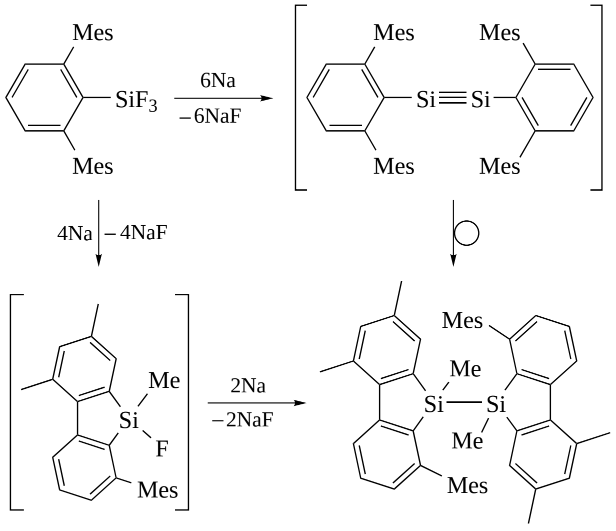

Scheme 33

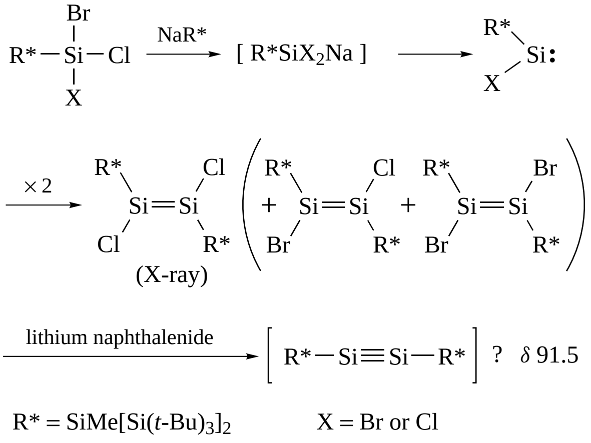

Scheme 34

6.2 A Stable Compound Containing A Silicon–Silicon Triple Bond

A triple-bond compound between a silicon atom has increasingly attracted many chemists after the successful isolation of its heavier analogs, ArM≡MAr (M = Ge, Sn, and Pb). Although the theoretical calculations predicted the experimental accessibility of a disilyne,[24] all attempts to isolate such triple-bond compounds have been unsuccessful.[148–150] Attempted synthesis of a disilyne using a bulky m-terphenyl ligand, C_6H_3-2,6-Mes_2, has been published.[149] Reduction of the corresponding trifluorosilane using sodium in THF afforded no disilyne but the decomposed compounds via the intramolecular cyclization (Scheme 33). On the other hand, Wiberg and coworkers have designed a new steric protection group R*, (SiMe[Si(t-Bu)$_3$]$_2$), which they call as a ‘megasilyl group’, for stabilizing a triple bond between silicon atoms.[150] They have succeeded in the synthesis of the first stable dichlorodisilene, R*(Cl)Si=Si(Cl)R*, of which the reduction with lithium naphthalenide in THF has been reported (Scheme 34). This reaction mixture contains an unstable product with a low-field ^{29}Si NMR signal at 91.5 ppm, which was ascribed to be a Si≡Si triple-bond resonance. However, the isolation and full-characterization of the compound have not been achieved yet.

Very recently, Sekiguchi and his coworkers have succeeded in the synthesis and isolation of the first stable disilyne finally.[151] The key to success is undoubtedly the design and choice of a substituent, and they chose the original bulky silyl substituents, Si(i-Pr)Dis$_2$ (R_{Si}). The disilyne R_{Si}Si≡SiR_{Si} is accessed by the reduction of the corresponding tetrabrominated precursor, ($R_{Si}SiBr_2)_2$, with potassium graphite (KC_8) (Scheme 35). The disilyne can be isolated as extremely air- and moisture-sensitive emerald green crystals in 73% isolated yield. No evidence for its isomerization to R_{Si2}Si=Si: or dissociation into the two R_{Si}Si fragments was observed, indicating that the two central silicon atoms are strongly bonded.

The most informative data should be its ^{29}Si NMR data for the central triply bonded Si atoms. The resonance of sp-hybridyzed Si atom in R_{Si}Si≡SiR_{Si} is observed at 89.9 ppm and is shifted upfield compared with those of the silyl-substituted disilenes (ca. 142–155 ppm).[152] Similar up-field shift is observed in the ^{13}C NMR chemical shifts of the silyl-substituted alkenes (ca. 188–197 ppm) and alkynes (112–114 ppm).[153] The molecular structure of the R_{Si}Si≡SiR_{Si} was revealed by X-ray crystallographic analysis (Figure 18). It has a trans-bent geometry [Si–Si–Si(R_{Si})

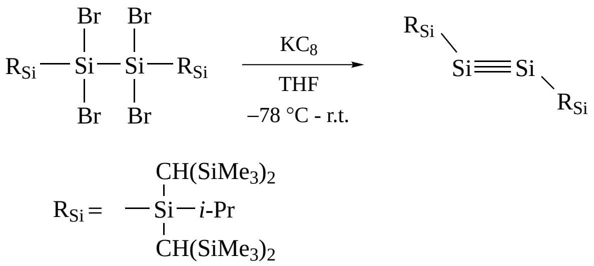

Scheme 35

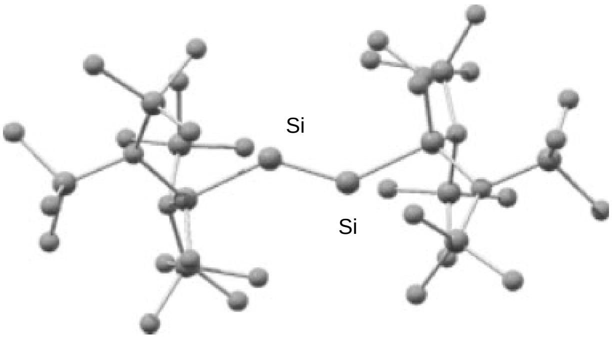

Figure 18 Molecular structure of $R_{Si}Si\equiv SiR_{Si}$ [$R_{Si} = Si(i\text{-}Pr)Dis_2$]

is 137.44(4)°] similar to that of Ar'Ge≡GeAr' with perfectly coplanar four silicon atoms of $Si(R_{Si})$–Si≡Si–$Si(R_{Si})$. The Si≡Si triple-bond length is 2.0622(9) Å, which is 3.8% shorter than the typical Si=Si double-bond lengths (ca. 2.14 Å) and 13.5% shorter than the typical Si–Si single bond lengths (ca. 2.34 Å). Thus, the disilyne $R_{Si}Si\equiv SiR_{Si}$ was characterized structurally and spectroscopically as a 'true' triply bonded compound between two silicon atoms.

7 CONJUGATED π ELECTRON AND CUMULATIVE SYSTEMS OF HEAVIER GROUP 14 ELEMENTS

A concept of 'conjugation of π electrons' plays an important role in the chemistry of hydrocarbons. One can easily hit upon butadienes (C=C–C=C) as typical conjugated π electron systems, and their unique properties are well known. Similarly, allenes (C=C=C) are also well studied in the chemistry of hydrocarbon systems. Since it is now concluded that the doubly bonded compounds between heavier group 14 elements can be isolated when they are well kinetically stabilized, a new and exciting challenge should be the synthesis and stabilization of the heavier congeners of another class of important low-coordinated organic molecules such as butadienes and allenes. In this chapter, recent works on the synthesis of stable conjugated-π-electron systems and allenes containing Si and Ge atom(s) will be described.**26,77,154** The chemistry of heavy aromatics, which is considered as one of the most important conjugated π electron systems, will be described in detail in the next section.

7.1 Stable Conjugated π Electron Systems Containing Heavier Group 14 Elements

7.1.1 Heavier analoges of a buta-1,3-diene

Synthesis and Properties. The first stable tetrasilabuta-1,3-diene derivative was synthesized by Weidenbruch *et al.* in 1997.**155** The synthetic route is unique as follows: the disilene $Tip_2Si{=}SiTip_2$**30** was treated with an excess amount of lithium to give the putative disilenyllithium compound. Then, mesityl bromide (MesBr) was added in the expectation that the bulk of this aryl group and the poor solubility of MesLi would favor halogenation over the competing transarylation. Thus, the intermediary bromodisilene $Tip_2Si{=}Si(Br)Tip$ was formed, and the intermolecular reaction of $Tip_2Si{=}Si(Br)Tip$ and $Tip_2Si{=}Si(Li)Tip$ with the elimination of LiBr furnished the tetrasilabutadiene $Tip_2Si{=}Si(Tip)\text{–}Si(Tip){=}SiTip_2$ in 60% yield (Scheme 36).

The reddish-brown crystals of $Tip_2Si{=}Si(Tip)\text{–}Si(Tip){=}SiTip_2$ are thermally very stable but extremely air-sensitive. The structure of $(Tip)_2Si{=}Si(Tip)\text{–}Si(Tip){=}Si(Tip)_2$ was revealed by X-ray crystallographic analysis, which showed the s-gauche configuration with a dihedral angle for the Si_4 framework of 51° in the solid state (Figure 19). The Si=Si double-bond lengths are slightly elongated [2.175(2) Å] as compared with those of the previously reported disilenes, while the central Si–Si bond lengths of 2.321(2) Å is remarkably short in view of its bulky substituents. The preference of the s-gauche form for $(Tip)_2Si{=}Si(Tip)\text{–}Si(Tip){=}Si(Tip)_2$ is in sharp contrast to that of the corresponding carbon compounds such as butadienes, which mostly prefer the s-trans configuration. Conjugation between the two Si=Si double bonds has been confirmed

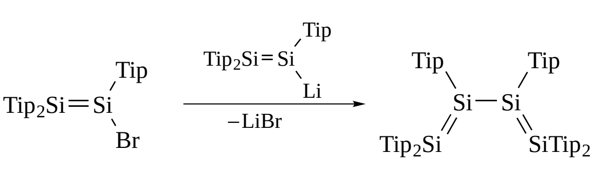

Scheme 36

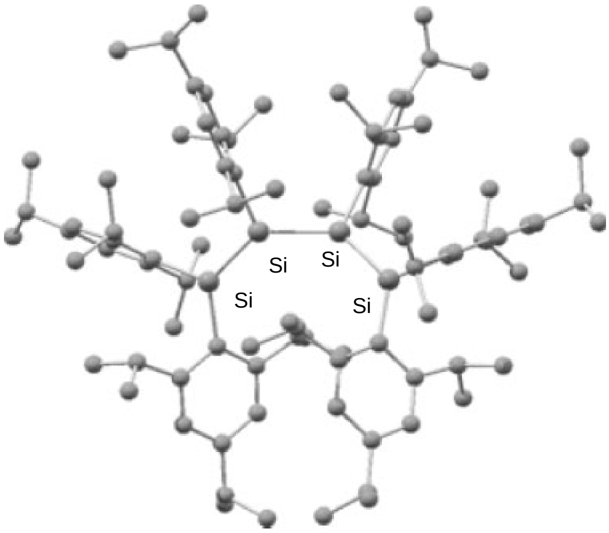

Figure 19 Molecular structure of Tip_2 Si=Si(Tip)–Si(Tip)=$SiTip_2$

by the electronic spectrum, where the band at the longest wavelength assignable to the corresponding π–π^* transitions showed a considerable bathochromic shift of more than 100 nm in comparison to those of diaryldisilenes.

In contrast to the case of silicon, treatment of $(Tip)_2Ge{=}Ge(Tip)_2$[47] with an excess amount of lithium afforded no tetragermabutadiene derivative, but dark-red crystals of anionic species, tetragermacyclobutenide derivative, which contains an allyl-like Ge_3 anion as a part of the four-membered ring.[156] Shortening the reaction time to such an extent that most of the digermenes had reacted before the formation of the tetragermacyclobutenide could make the main reaction to proceed more efficiently leading to the formation of $(Tip)_2Ge{=}Ge(Li)Tip$. Subsequent reaction with MesBr afforded the expected tetragermabutadiene, $(Tip)_2Ge{=}Ge(Tip){-}Ge(Tip){=}Ge(Tip)_2$, in ca. 10% yield (Scheme 37). An alternative synthetic method for the tetragermabutadiene has been developed. That is, the reaction of $GeCl_2$·dioxane with TipMgBr affords the tetragermabutadiene in one step and in a yield of more than 30% (Scheme 38).[157]

Similar to the case of the tetrasilabutadiene, the tetragermabutadiene adopts an s-gauche form with a dihedral angle of the Ge_4 framework of 22°. The Ge=Ge double bonds [2.3568(6) and 2.3439(5) Å] and the Ge–Ge single bond [2.4581(5) Å] are in the typical ranges for such bond lengths. Although the crystal structure of $(Tip)_2Ge{=}Ge(Tip){-}Ge(Tip){=}Ge(Tip)_2$ gave no distinct information about a possible conjugation between two Ge=Ge double bonds, the electronic spectrum revealed its conjugation. That is, the dark blue solution of the tetragermabutadiene showed the longest wavelength absorption at 560 nm in hexane. Compared with the yellow or orange color of digermenes, this absorption is bathochromically shifted by ca. 140 nm.

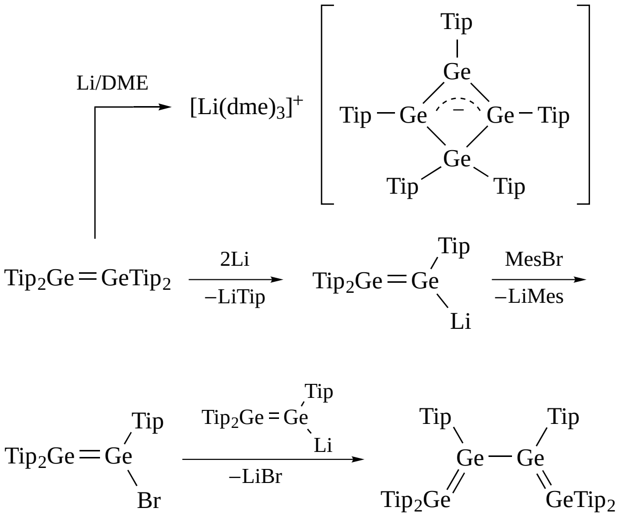

Scheme 37

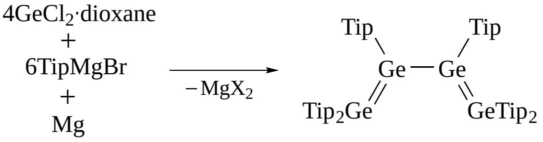

Scheme 38

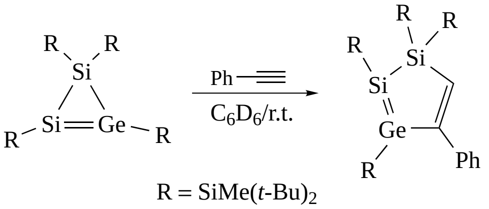

Scheme 39

Furthermore, a stable 1H-1,2,3-disilagermole system of Si–Si=Ge–C=C was synthesized as the first example of a structurally characterized silagermene (Scheme 39).[82] This is afforded by the reaction of a unique three-membered ring system, a 1*H*-disilagermirene derivative, with phenylacetylene via the initial [2 + 2] addition followed by the rearrangement. The length of the Si=Ge bond is 2.250(1) Å, which lies between the typical values of Si=Si and Ge=Ge bond lengths. The Ge–C and C=C bond lengths lie in the normal range of the corresponding single and double bonds. Thus, no structural evidence of conjugation between Si=Ge and C=C π bonds is obtained. However, the existence of the conjugation in the 1*H*-1,2,3-disilagermole was confirmed at least in solution by the result of its electronic spectrum in hexane.[82]

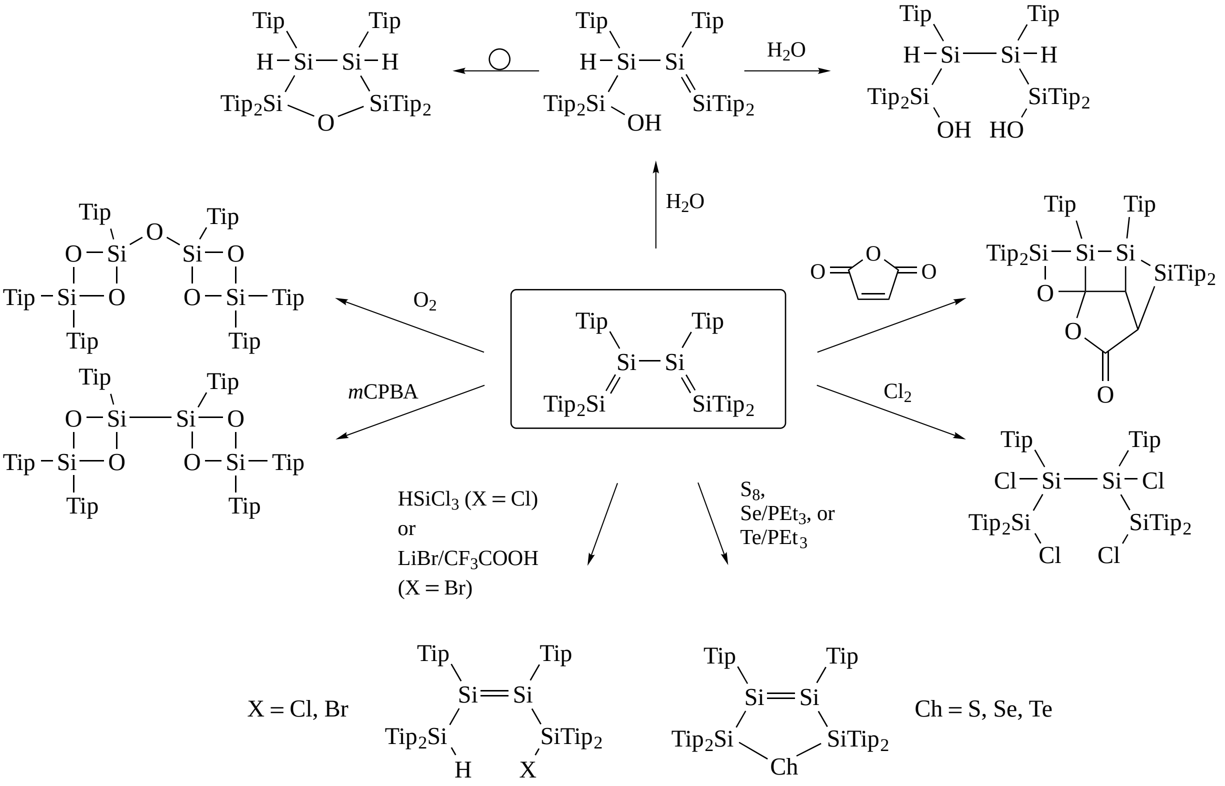

Scheme 40

Reactions. Experimental results of reactions of $(Tip)_2Si{=}Si(Tip){-}Si(Tip){=}Si(Tip)_2$ are summarized in Scheme 40. Treatment of the tetrasilabutadiene with a small amount of water gave an analog of tetrahydrofuran, an oxatetrasilolane derivative, probably via the 1,2-addition and the following rearrangement. Addition of an excess amount of water resulted in the formation of the tetrasila-1,4-diol derivative, which showed no tendency to eliminate water with the formation of the oxatetrasilolane derivative.[158]

Although the tetrasilabutadiene exists in the solid state as that with an s-gauche configuration, which should favor [4 + 2] cycloadditions, no successful reactions with alkenes, acetylenes, and carbonyl compounds have been reported so far, probably owing to the steric reason. It should be noted that the tetrasilabutadiene underwent a formal [4 + 4] cycloaddition with maleic anhydride leading to the formation of a tetracyclic compound.[159] In addition, the treatment of the tetrasilabutadiene with elemental sulfur afforded a five-membered ring compound, 2,5-dihydrothiatetrasilole derivative, via the formal [4 + 1] cycloaddition.[160] Upon the addition of a catalytic amount of PEt_3, elemental selenium and tellurium react with the tetrasilabutadiene to give the corresponding five-membered ring compounds.[160] Similarly, the reaction of the tetragermabutadiene with elemental sulfur reportedly gave the corresponding 2,5-dihydrothiatetragermole derivative.[157]

On the other hand, oxidation reaction of the tetrasilabutadiene with dry air was found to give a unique compound, which consists of two 1,3,2,4-dioxadisiletane rings linked by an oxygen atom. It is in a sharp contrast to the oxidation reaction using mCPBA, which gives an oxidation product consisting of two 1,3,2,4-dioxadisiletane rings connected with an Si–Si single bond.[158] Furthermore, the oxidation reaction of the tetragermabutadiene with dry air afforded a bicyclic compound depicted in Scheme 41.[157] Reaction mechanisms of such oxidation reactions have not been proven experimentally so far.

7.1.2 *Acetylene-Linked Bis(germenes)*

The reactions of the diarylgermylene Ar'_2Ge: ($Ar' = 2$-t-Bu-4,5,6-trimethylphenyl), which is generated from the corresponding digermene $Ar'_2Ge{=}GeAr'_2$ in solution, with 1,3-diynes $(R{-}C{\equiv}C{-})_2$ ($R = n$-Bu, Ph) gives the first molecules having conjugated Ge=C double bonds as depicted in Scheme 42.[161] The conjugation of the two Ge=C double bonds across the linking acetylene unit is reflected in the electronic spectra rather than in the bond lengths. Their λ_{max} values at the longest wavelengths are 518 ($R = n$-Bu) and 595 ($R = $ Ph) nm, and shifted bathochromically by ca. 100 nm compared with those for the previously reported germenes (see Section 3.1.4). The conjugation between the two double

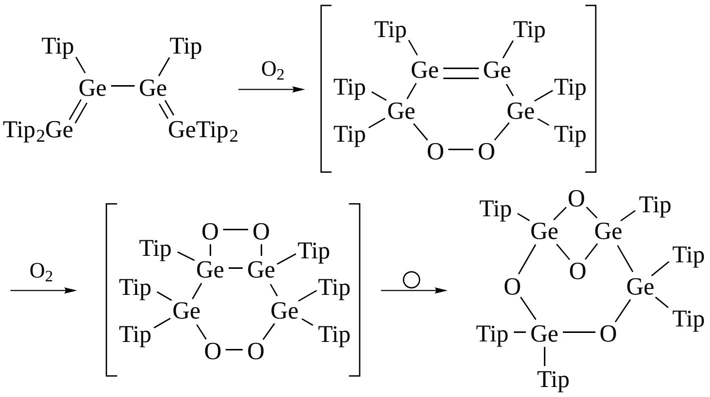

Scheme 41

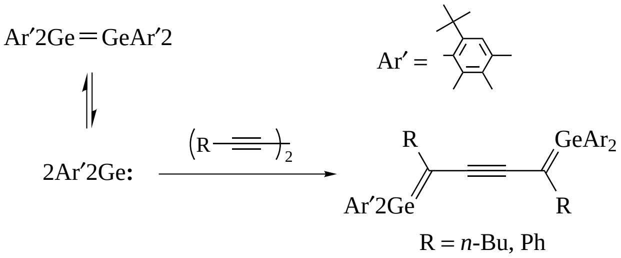

Scheme 42

bonds probably decreases their reactivity. For examples, these conjugated compounds cannot react with phosphaalkynes or dienes, whereas simple germenes form the corresponding addition products.[96] Addition reactions of conjugated Ge=C double bonds occur with only compounds containing electron poor multiple bonds.[162]

The successful synthesis of the acetylene-linked bis(germenes) posed a question whether analog compounds with conjugated Si=C double bonds could be isolated by the reaction of a silylene with 1,3-diynes. Although attempted reactions can postulate the existence of intermediary compounds consisting of bis(silenes) linked by an acetylene unit, no stable compounds having Si=C–C≡C–C=Si conjugated systems have been obtained by such a synthetic strategy.[163]

7.2 Stable Allenes Containing Heavier Group 14 Elements

Several kinds of cumulative double bonds containing heavier atoms such as Si=C=C, Si=C=C=C, N=C=Si (precisely, RN=C → SiR_2), Si=C=P, and so on, and their heavier congeners have been synthesized and reported as stable or marginally stable compounds.[154] Here, the main topic in this section is limited to the stable and isolable examples of allene derivatives containing heavier group 14 elements, that is, silaallenes, germaallenes, tristannaallene, and trisilaallene.

7.2.1 1-Silaallenes (Si=C=C) and 1-Germaallenes (Ge=C=C)

Since the first isolation of stable 1-silaallene synthesized by West and coworkers in 1993,[164] six stable examples of Si=C=C compounds have been reported.[154] Si=C=C compounds were mainly synthesized by two methods, that is, the dehalogenative intramolecular cabometalation-elmination method (route A) and the addition of an organolithium reagent at the triply bonded carbon atom of fluoroalkynylsilanes followed by the LiF elimination (route B) (Scheme 43).

The structures of some stable silaallenes have been revealed by X-ray crystallographic analysis (Figure 20).[164,165] The geometries of their Si=C=C skeletons are nearly the same with shorter Si=C double bonds (ca. 1.70 Å) than the typical Si=C bond lengths (see Section 3.2). Such a short distance is conceivable to be affected by the sp-hybridized central carbon atom. The C=C bond lengths (ca. 1.325 Å) in these Si=C=C allenes are in normal range of C=C double bonds. It is worthy of note that the Si=C=C bond angle is not completely 180°

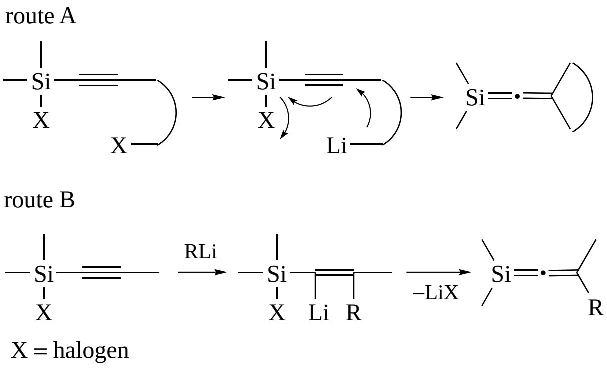

Scheme 43

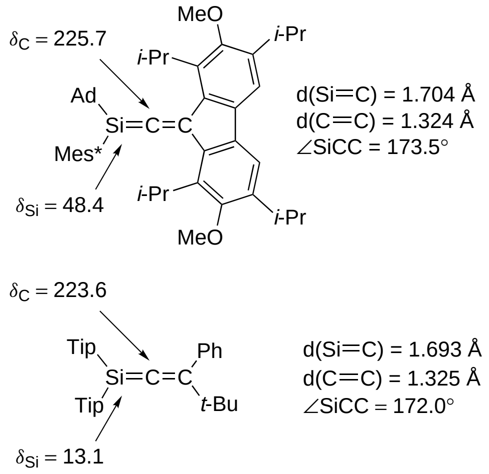

Figure 20 Properties of stable silaallenes

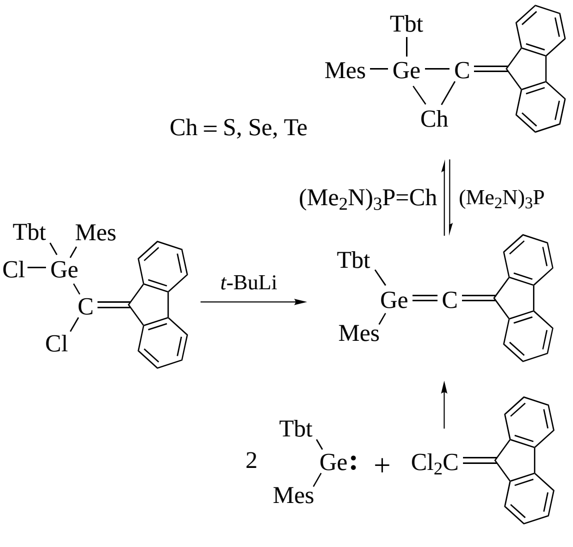

Scheme 45

but slightly bent (ca. 172–174°) unlike the case of C=C=C. In addition, the silicon atoms are slightly pyramidalized [the sum of angles around Si atoms are ca. 357°], whereas the terminal sp^2 carbons are essentially planar. Such structural features of Si=C=C compounds reflect the fundamental character of low-coordinated heavier group 14 elements (see Section 2).

In ^{13}C NMR of stable silaallenes are observed highly deshielded signals (216–237 ppm) assignable to their central sp-carbon atoms. ^{29}Si NMR chemical shifts of silaallenes vary in the range of 13.1–58.6 ppm, depending on the properties of substituents on the silicon atom as in the case of those of silenes (Si=C).

The first compounds with a Ge=C=C allene unit were reported by two groups, Tokitoh *et al.*[166] and R. West *et al.*[167] in 1998. Germaallene $Tip_2Ge{=}C{=}CPh$(*t*-Bu) was synthesized by the reaction of Tip_2GeF_2 with PhC≡CLi followed by the treatment of *t*-BuLi as a base (Scheme 44). This synthetic method is the same as that used for the preparation of silaallene $Tip_2Si{=}C{=}CPh$(*t*-Bu) (route B in Scheme 43). On the other hand, the stable germaallene Tbt(Mes)Ge=C=C(fluorenylidene) was obtained by the addition of an excess amount of $(Me_2N)_3P$ to the corresponding alkylidenetelluragermirane derivative[168] as an equilibrium mixture. Alternatively, the dechlorination of Tbt(Mes)Ge(Cl)–C(Cl)=C(fluorenylidene) with *t*-BuLi at −72 °C allowed the isolation of the germaallene as a stable crystalline compound (Scheme 45). The two examples of germaallenes have characteristic low-field chemical shifts for the central allenic carbons [235.1 pm for $Tip_2Si{=}C{=}CPh$(*t*-Bu) and 243.5 ppm for Tbt(Mes)Ge=C=C(fluorenylidene)] as in the case of silaallenes.

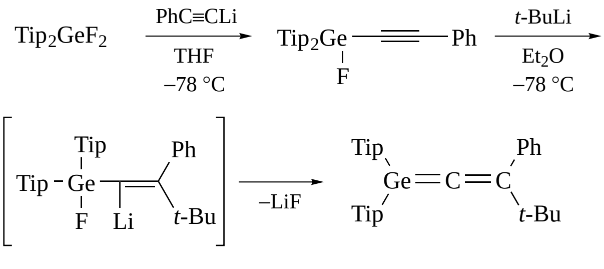

Scheme 44

The reactivities of sila- and germaallenes are summarized in Schemes 46 and 47,[154] respectively. Two silaallenes depicted in Figure 20 are stable for days under ambient conditions and in the presence of air, water, and even in refluxing ethanol. This is in striking contrast to all other multiply bonded silicon compounds, particularly silenes (see previous sections). Addition reactions of protic reagents or unsaturated compounds onto the M=C bond of sila- and germaallenes and their acid-catalyzed intramolecular cyclization have been reported. These reactivities reflect the properties of highly reactive M=C unsaturated bonds, therefore they showed reactivities similar to those of silenes and germenes.

7.2.2 *Tristannaallene (Sn=Sn=Sn) and Trisilaallene (Si=Si=Si)*

The successful isolation of 1-silaallenes and 1-germaallenes raises the expectation of synthesis of a novel class of allenic compounds having an sp-hybridized silicon unit, that is, 2-silaallene derivatives. Although the generation of 2-silaallene (*t*-Bu)–CH_2–CH=Si=CH–CH_2–(*t*-Bu) was postulated in the reaction of $(H_2C{=}CH)_2SiCl_2$ with 2-equivalent of *t*-BuLi,[169] no distinct evidence on the generation of such a compound has been obtained so far.

In the case of Sn, Wiberg *et al.* have reported the synthesis of a marginally stable tristannaallene, $R^*_2Sn{=}Sn{=}SnR^*_2$

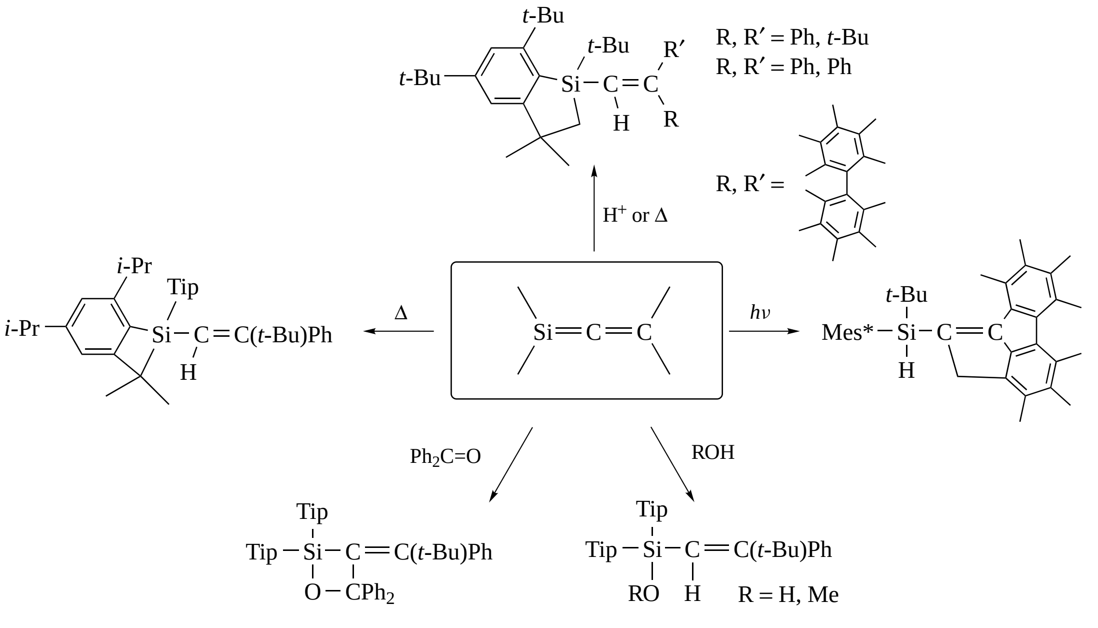
t-Bu
R, R′ = Ph, t-Bu
R, R′ = Ph, Ph
R, R′ =
H⁺ or Δ
Δ
hν
Ph₂C=O
ROH
Tip
Mes*
R = H, Me

Scheme 46

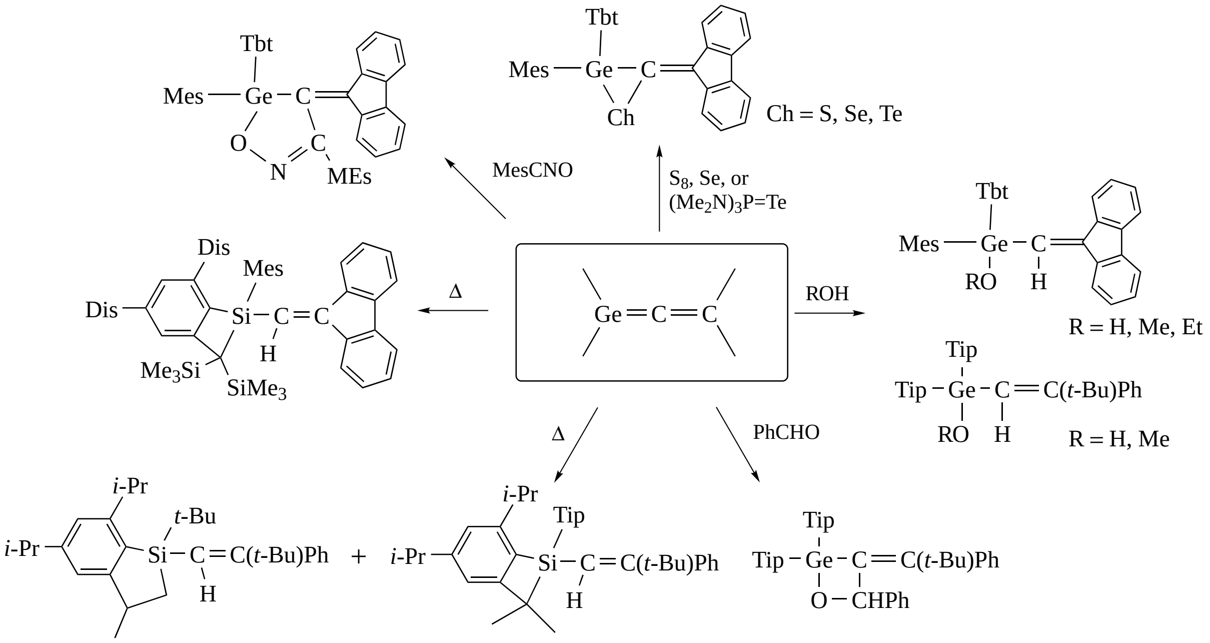
Tbt
Mes
Ch = S, Se, Te
MesCNO
S₈, Se, or (Me₂N)₃P=Te
Δ
ROH
R = H, Me, Et
Dis
Me₃Si
SiMe₃
PhCHO
R = H, Me
i-Pr
t-Bu
Tip

Scheme 47

[R* = Si(t-Bu)$_3$] (Scheme 48).[170] Treatment of diaminostannylene[$(Me_3Si)_2N]_2Sn$: with R*Na in pentane at −196 °C afforded the tristannaallene $R^*_2Sn{=}Sn{=}SnR^*_2$ together with disilane R^*_2. Unfortunately, the tristannaallene is too unstable at ambient temperature (the half-life period is 9.8 h at 25 °C in pentane) to undergo a rearrangement reaction giving the isomeric cyclotristannene. The structural feature of $R^*_2Sn{=}Sn{=}SnR^*_2$ was revealed by X-ray crystallographic analysis and NMR spectroscopy at −25 °C. The most striking structural features of the tristannaallene are the bent angle of Sn=Sn=Sn (155.9°) and the shorter Sn=Sn bond lengths (ca. 2.68 Å) than those observed in stable distannenes (see Section 3.2). The ^{119}Sn NMR spectrum showed two signals at 503 and 2233 ppm, which are attributed to the terminal and central tin atoms, respectively. Since stable stannylenes R_2Sn: are known to show their ^{119}Sn NMR chemical shifts in a range of ca. 2000–2300 ppm,[98,132,171] chemical shifts observed in the tristannaallene indicate the stannylene character of

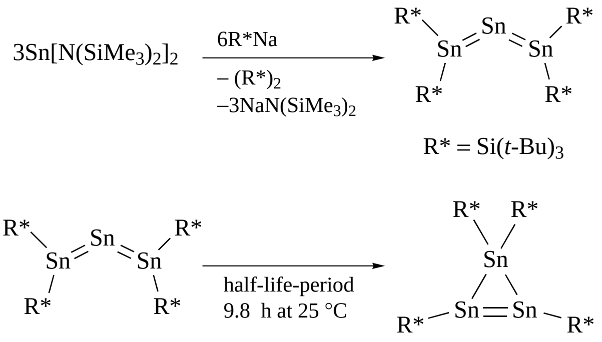

Scheme 48

its terminal tin atoms. Consequently, the tristannaallene should not be represented as ‘real’ homologs of an allene but understood in accordance with the resonance formulae depicted in Scheme 49.

The interesting structural feature of the tristannaallene prompted many chemists to take on the challenge of synthesizing stable trimetallaallenes. Finally, in 2003, Kira and his coworkers succeeded in the synthesis of the first stable trisilaallene with Si=Si=Si unit.**172** The trisilaallene, $R_2Si{=}Si{=}SiR_2$ (R_2 = -C(SiMe$_3$)$_2$–CH$_2$–CH$_2$–C(SiMe$_3$)$_2$-), was synthesized and isolated as a green solid via two-step reactions from the corresponding stable silylene R_2Si: in overall 42% yield as shown in Scheme 50.

X-Ray crystallographic analysis shows a quite unusual structural feature of the trisilaallene (Figure 21). In contrast to allenes, the trisilaallene skeleton is not linear but significantly bent with an Si=Si=Si bond angle of ca. 136°, indicating that the bonding property of the central =Si=atom cannot be interpreted in terms of simple sp-hybridization. The two Si=Si bond lengths [2.177(1) and 2.188(1) Å] are in the range of those for typical stable disilenes (2.14–2.29 Å, see Section 3.2). In addition, the geometry around the two terminal silicon atoms is not completely planar but slightly pyramidalized (the sums of the bond angles around terminal Si atoms are 354.1° and 354.9°). All these structural features indicate that trisilaallene $R_2Si{=}Si{=}SiR_2$ consists of two trans-bent Si=Si double bonds that share the central silicon atom. Additional information of theoretical calculations on trisilaallenes also supported such structural features.

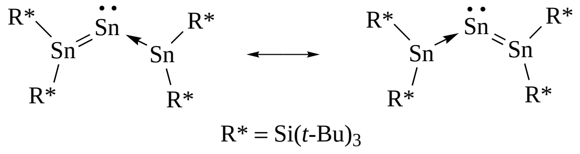

Scheme 49

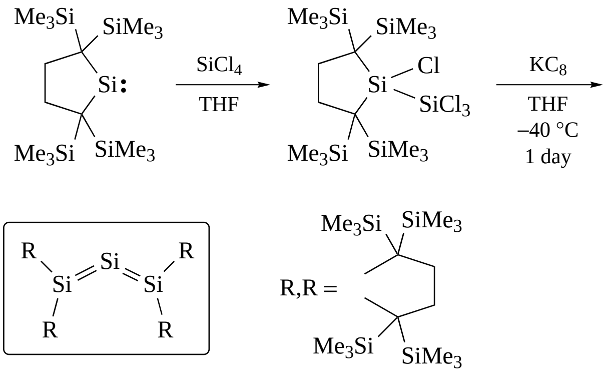

Scheme 50

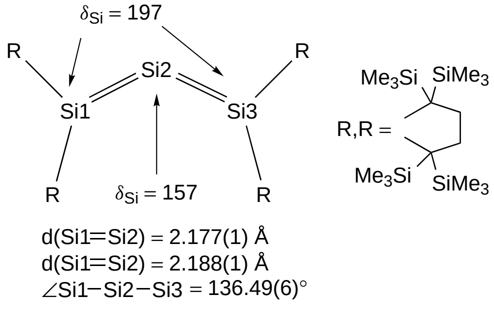

Figure 21 Properties of stable trisilaallenes $R_2Si{=}Si{=}SiR_2$. The central silicon atom (Si2) in the crystal was disordered at four positions. The structural parameters shown here are those of the major part of disordered atoms

The ^{29}Si NMR spectrum of the trisilaallene showed two signals at 157 and 197 ppm in C_6D_6, which are assigned to the central silicon atom (Si2) and the terminal silicon atoms (Si1, Si3), respectively. Such low-field shifted resonances indicate the sp^2-character of the three silicon atoms in the trisilaallene $R_2Si{=}Si{=}SiR_2$, though it shows a highly bent structure in the crystalline state.

The reaction of $R_2Si{=}Si{=}SiR_2$ with water gave the corresponding 1,3-dihydrotrisilane $R_2Si(OH)–SiH_2–(HO)SiR_2$ in an almost quantitative yield. This product reflects the intrinsic, bent allenic feature of the trisilaallene supported by the calculated electronic feature as $Si^{\delta+}{=}Si^{\delta-}{=}Si^{\delta+}$.

8 HEAVY AROMATIC SYSTEMS

Metallaaromatic compounds, that is, M-containing $[4n + 2]\pi$ ring systems (M = Si, Ge, Sn, Pb), have attracted much attention in recent decades, since they represent the heavier congeners of carbocyclic aromatic compounds, which play very important roles in organic chemistry. Although the aromatic character of silole anions and dianions**173** as well as that of cyclic diaminosilylene**174** (Scheme 51) was recently revealed from both experimental and theoretical standpoints, simple neutral silaaromatic compounds are known to be highly

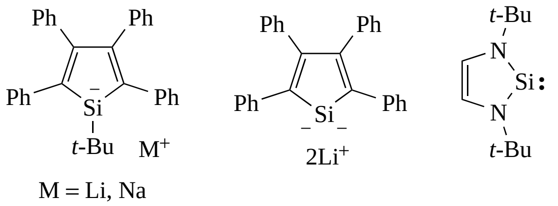

Scheme 51 Silaaromatic species of siloles and a silylene

reactive. Such silabenzenoids have only been characterized in low-temperature matrices or postulated as transient intermediates in some trapping reactions.[175] While nonconjugated, Si-containing doubly bonded compounds have already been synthesized as stable molecules by taking advantage of kinetic stabilization as described in the previous sections, no silabenzenoid compounds stable at ambient temperature have ever been reported until the first isolation of a stable 2-silanaphthalene derivative by Tokitoh *et al.* in 1997.[176] The situation for the chemistry of germaaromatics is almost the same as that of silaaromatics.[177–179] The syntheses of several examples of stable ionic species and the dimerization and intermolecular trapping of heavy aromatic systems have been reported (Scheme 52), while stable neutral metallaaromatics have been still elusive until quite recently.[178,179]

Meanwhile, many theoretical calculations have been reported for sila- and disilabenzenes,[180,181] and the recent study indicates that silabenzenes have a π-electron-delocalized structure and considerable aromaticity.[178,179,182] This implies that silaarenes might exist as stable molecules if their high reactivity could be suppressed by an appropriate protection. Since it has been fully demonstrated that Tbt group is very effective to stabilize the highly reactive, low-coordinated species of heavier main group elements (see previous sections), Tokitoh *et al.* applied the Tbt group to the kinetic stabilization of an unexplored class of low-coordinated species of heavier group 14 elements such as sila- and germaaromatic compounds.[178,179] Up to now, several kinds of silaaromatic compounds bearing a Tbt group on the sp^2-silicon atom such as silabenzene,[183,184] 1- and 2-silanaphthalenes,[176,185] 9-silaanthracene,[186,187] and 9-silaphenanthrene were successfully synthesized and isolated as stable compounds (Scheme 53). Furthermore, the first stable germabenzene[188] and 2-germanaphthalene[189] were also synthesized using a similar synthetic approach. The recent progress in the chemistry of stable metallaaromatic systems is outlined in this section.

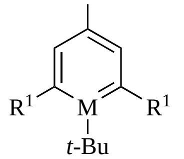

M = Si, R^1 = H, R^2 = t-Bu
M = Si, R^1 = $SiMe_3$, R^2 = t-Bu (δ_{Si} = 26.8)
M = Si, R^1 = $SiMe_2$(i-Pr), R^2 = $SiMe_3$
M = Ge, R^1 = H, R^2 = t-Bu

Scheme 52 Transient and metastable sila- and germabenzenes

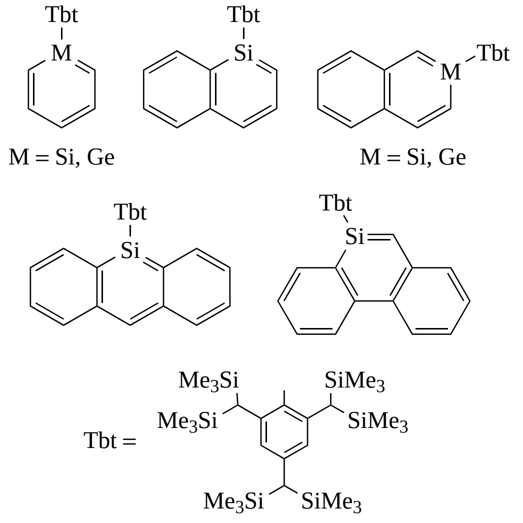

Scheme 53

8.1 Synthesis and Isolation

In view of the isolation of such a highly reactive species in a pure form, it is necessary to develop suitable synthetic methods (e.g. high yields and mild reaction conditions). Simple 1,2-dehydrohalogenation reactions of the corresponding cyclic halometallane precursors using an appropriate base (LDA was chosen in most cases) were proved to be effective for the synthesis and isolation of silabenzene, 1- and 2-silanaphthalenes, 9-silaphenanthrene, germabenzene, and 2-germanaphthalene. The synthetic route for the precursor of silabenzene is shown as a representative in Scheme 54.

In addition, in the case of 9-silaanthracene,[186] the leaving ability of the substituent on the silicon atom played a very crucial role. Although the use of the corresponding chloro- and bromosilanes as precursors resulted in very low yields of the 9-Tbt-9-silaanthracene as judged by the trapping experiments with MeOH, the treatment of the corresponding silyltriflate derivative with LDA in benzene gave the expected 9-silaanthracene quantitatively (Scheme 55).

Except for 1-Tbt-1-silanaphthalene,[185] which was found to undergo gradual dimerization in solution at room temperature, all other metallaaromatic compounds in Scheme 55 were isolated as stable crystalline compounds, indicating the high ability of the Tbt group as a steric protecting group. Recently, the matrix isolation and intermolecular trapping reactions have been described for the 9-silaanthracenes having a

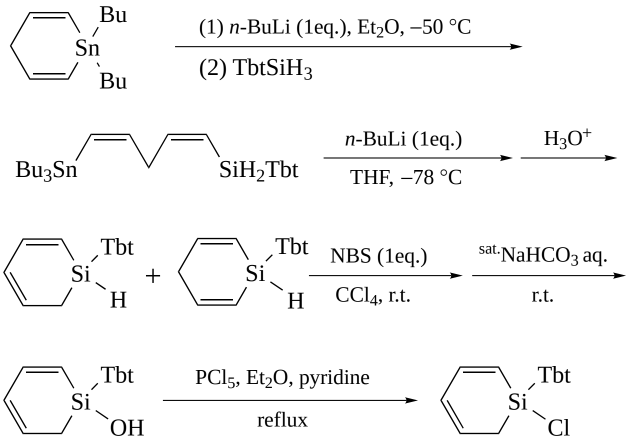

Scheme 54

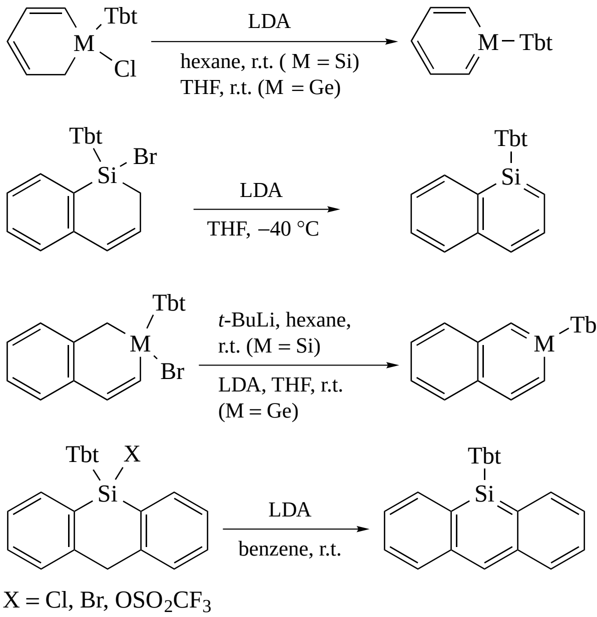

Scheme 55

2,4,6-triisopropylphenyl (Tip) or 2,4,6-tri-*t*-butylphenyl group (Mes*), but these species are reportedly not isolable.[190] This fact implies the indispensability of an extremely bulky substituent such as Tbt for the isolation of kinetically stabilized metallaaromatic compounds.

In contrast to the successful isolation and characterization of the kinetically stabilized sila- and germaaromatic compounds described here, their heavier congeners such as stannabenzene or plumbabenzene are still elusive and neither their isolation nor spectroscopic detection has been achieved. In addition, the synthesis of aromatic systems containing multiple heavier group 14 elements (polymetallabenzenes) still remain as the next target molecules in future. The concept of kinetic stabilization should certainly be of great use for the synthesis of these unprecedented heavy aromatic species.

8.2 Structures and Spectroscopic Properties

X-ray Crystallographic Analysis. The most important structural features of aromatic compounds are the planarity for their aromatic rings and the ring-bond lengths lying between those of the typical double and single bonds, which result from the delocalization of π-electrons of their aromatic rings. From the viewpoint of systematic comparison, it is of great significance to perform the X-ray crystallographic analysis of the stable metallaaromatic compounds obtained so far. Fortunately, most of them were isolated as stable crystalline compounds reflecting the high crystallinity of the Tbt-substituted compounds. The structural parameters of the analyzed metallaaromatics are summarized in Table 7 together with their atom-numbering schemes in Scheme 56. As a representative, the molecular structure for the silabenzene is shown in Figure 22, which clearly indicates the planar silabenzene ring nicely protected by the bulky Tbt group.

All metallaaromatic ring systems examined here have an almost planar aromatic ring, and the geometry around the central silicon or germanium atom is completely trigonal planar, suggesting the delocalization of π-electrons in these ring systems. Almost equal distances were observed for the group 14 metal−carbon bonds in both sila-[184] and germabenzenes,[188] while a small extent of bond alternation was recognized for 2-sila-[176] and 2-germanaphthalenes,[189] as in the case of parent naphthalene. Taking into account the fact that the C–C bond lengths in these metallaaromatic rings are comparable with those reported for parent benzene and naphthalene,[191] it should be concluded that replacement of one carbon with a heavier group 14 element such as a silicon or germanium atom does not disturb the delocalization of π-electrons in the monometallaaromatic ring systems. Furthermore, the crystallographically revealed structural features of these new metallaaromatic species are in good agreement with those obtained by the theoretical calculations with B3LYP/6-31G(d) level for some model compounds, suggesting the little steric and electronic influence of the Tbt group.

NMR Spectra. As for the silaaromatic compounds, ^{29}Si NMR spectroscopy gives useful information for the electronic and structural environments of their central silicon atom. All the stable silaaromatics showed characteristically low-fielded signals in the ^{29}Si NMR spectra [93.6 (silabenzene[183]), 91.7 (1-silanaphthalene[185]), 87.3 (2-silanaphthalene[176]), 87.2 (9-silaanthracene[186]), and 86.9 (9-silaphenanthrene) ppm in C_6D_6], suggesting the sp^2 character of their ring silicon atoms. These chemical shifts are more low-fielded than that for the previously reported marginally stable silabenzene of 1,4-di-*t*-butyl-2,6-bis(trimethylsilyl)silabenzene shown in Scheme 52

Table 7 Structural parameters of Tbt-substituted heavy aromatics. (ΣM: summation of the bond angles around the M atom, $\Sigma\angle MC_5$: summation of the internal angles of the MC_5 ring sketeton)

compounds		silabenzene	germabenzene	2-silanaphthalene	2-germanaphthalene	9-silaanthracene
bond lengths (Å)	M1–C2	1.765(4)	1.829(2)	1.800(3)	1.859(5)	1.787(3)
	M1–C6	1.770(4)	1.827(2)	1.728(3)	1.803(5)	1.784(3)
	C2–C3	1.391(6)	1.389(3)	1.359(3)	1.368(7)	1.442(4)
	C3–C4	1.399(6)	1.389(3)	1.438(3)	1.429(8)	1.398(4)
	C4–C5	1.381(6)	1.385(3)	1.431(3)	1.430(7)	1.399(4)
	C5–C6	1.394(7)	1.396(3)	1.433(3)	1.450(8)	1.446(4)
ΣM (deg)		359.8	360.0	360.0	360.0	360.0
$\Sigma\angle MC_5$ (deg)		720.0	720.0	720.0	720.0	720.0

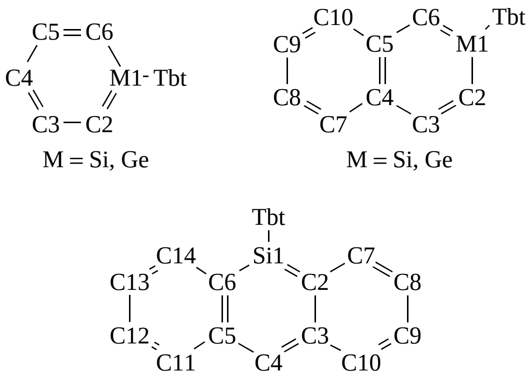

Scheme 56 Atom numbering schemes

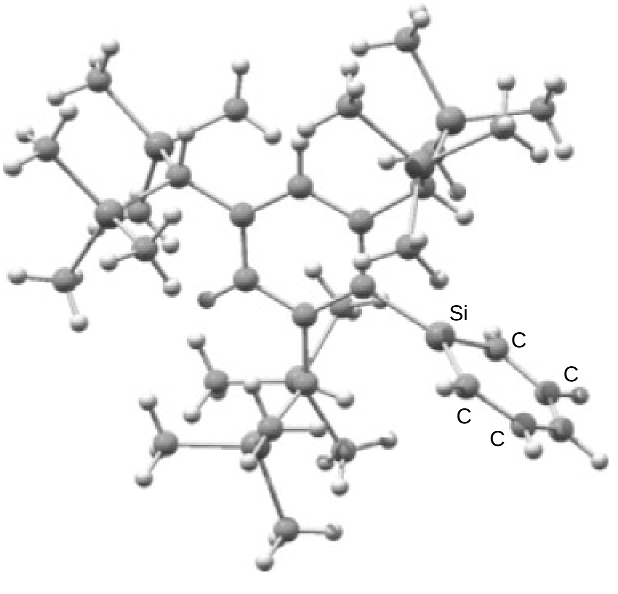

Figure 22 Molecular structure of 1-Tbt-silabenzene

(δSi = 26.8),[192] and almost no spectral change was observed even on measurement in the presence of an ethereal solvent such as that in THF:C_6D_6 = 6:1. These results strongly indicate not only the sp^2 character for their ring silicon atoms but also the effective steric protection afforded by the bulky Tbt group, which completely prevents their silicon atoms from coordination of the ethereal solvent. In other words, the marginally stable silabenzene reported by Märkl (Scheme 52) might be stabilized with the bulky substituents (*t*-Bu and Me_3Si groups) together with the coordination of Lewis-basic, ethereal solvents such as ether and/or THF.[192]

^{1}H and ^{13}C NMR spectral data of these stable metallaaromatics having a Tbt group also supported their molecular structures. The nice agreement of the observed chemical shifts with those obtained by theoretical calculations of several model compounds indicated that little perturbation with the aromatic Tbt group occurred on the central heavier atom. Of particular note among the ^{1}H NMR spectral data is that the chemical shifts for the ring protons of them are all shifted to lower field by ca. 0.5 to 1.0 ppm compared with those of precursors. This distinct low-field shift of the ring protons should be noted as one of the pieces of experimental evidence for the ring current effect of these metallaaromatic systems.

UV–vis and Raman Spectra. In order to examine the similarities and differences between metallaaromatic compounds and the parent aromatic hydrocarbons, the UV–vis and Ramam spectra of the stable metallaaromatics bearing a Tbt group were measured.[146,183–189] In the electronic spectra, all silaaromatic compounds showed a remarkable red-shift for their ^{1}B, ^1L_a, and ^1L_b bands as compared with those reported for the corresponding parent aromatic hydrocarbons. In Table 8 are summarized the experimentally observed absorption maxima at the longest wavelength for the metallaaromatics together with those for the carbon analogs. Interestingly, the absorption maxima of the germabenzene and the 2-germanaphthalene showed almost no shift compared with their silicon analogs though being clearly red-shifted in comparison with those of the parent aromatic hydrocarbons. These results indicate the $\pi-\pi^*$ energy gap of the cyclic $[4n+2]\pi$ electron systems containing a heavier group 14 element is much smaller than that of the corresponding hydrocarbons but almost similar to each other as for the silicon and germanium analogs. Although the silaaromatic species examined here have an extremely bulky Tbt group on the central silicon atom, their electronic spectra closely resembled

Table 8 Spectroscopic comparison between metallaaromatics and the corresponding aromatic hydrocarbons. ($\lambda_{\max}$: observed absorption maxima at the longest wavelengths, ν_{obsd}: observed wave numbers of the strongest Raman shift, ν_{calcd}: calculated wave number of the strongest Raman shift)

	benzene series	naphthalene series		anthracene series
C	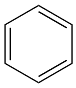	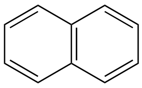		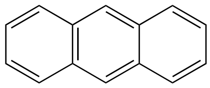
$\lambda_{\max}$/nm	256	312		375
ν_{obsd}/cm^{-1}	1600	1382		1401
ν_{calcd}/cm^{-1}	1590	1360		1387
Si	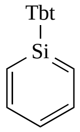	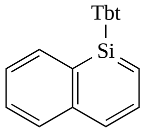	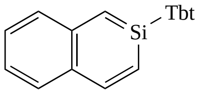	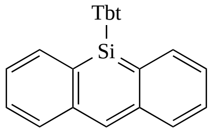
$\lambda_{\max}$/nm	331	378	387	503
ν_{obsd}/cm^{-1}	1530	1340	1368	1359
	1527	1330	1349	1338
Ge	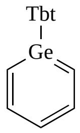		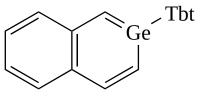	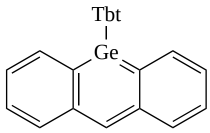
$\lambda_{\max}$/nm	326		386	535[a]
ν_{obsd}/cm^{-1}	1600		1363	–
ν_{calcd}/cm^{-1}	1590		1356	–

[a] N. Tokitoh, W. Hoshino, T. Sasamori, and N. Takeda, unpublished results.

those reported for the transient silaaromatics measured in the low-temperature matrices,[190,193] indicating the very little perturbation by the steric protection afforded by Tbt group.

The strongest Raman lines observed for them and the corresponding aromatic hydrocarbons are also summarized in Table 8. The experimentally observed Raman shifts for the metallaaromatic species and the parent hydrocarbons are reasonably reproduced by theoretical calculations. Although the vibrational frequencies for metallaaromatics were observed at somewhat smaller wave numbers than those of the carbon analogs, the similarity among their in-plane vibrational modes is clearly confirmed by calculations.

Consequently, it is experimentally evidenced again that the replacement of one of the ring carbons in the aromatic hydrocarbons with a heavier group 14 element does not have a big influence on the spectroscopic properties of the resulting $[4n + 2]\pi$ conjugated metallacycles as compared with the parent carbon analogs.

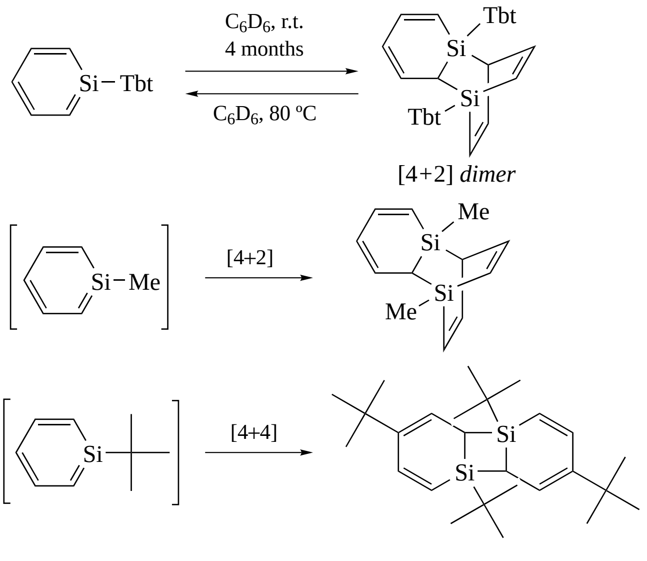

Scheme 57

8.3 Reactivities

Thermal and Photochemical Stability. Kinetically stabilized silaaromatic species shown in Scheme 53 showed some difference in their stability in solution (Schemes 57 and 58). Tbt-substituted silabenzene has high thermal stability in solution and no dimerization was observed on heating in hexane at 100 °C for a long time. However, standing its hexane solution in C_6D_6 for 4 months resulted in the formation

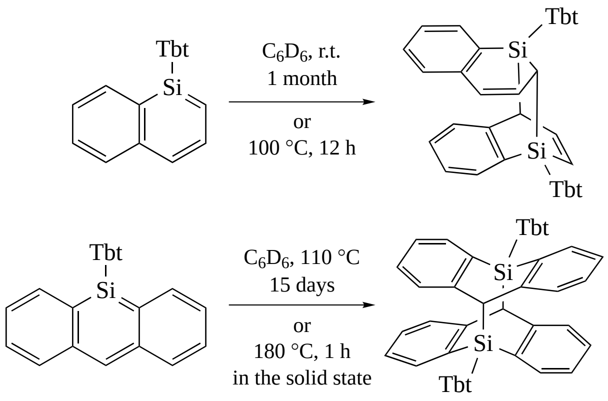

Scheme 58

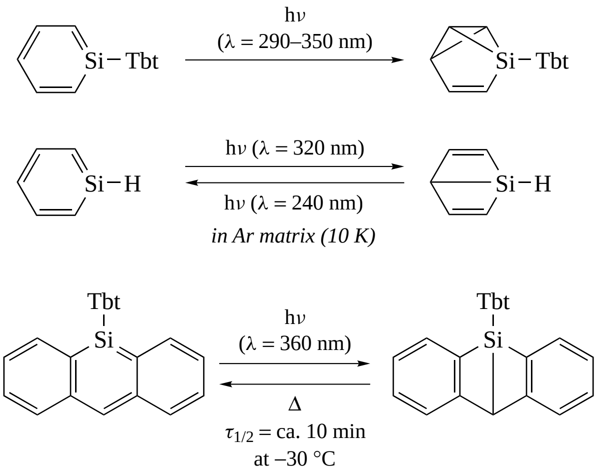

Scheme 59

(ca. 50%) of the corresponding [4 + 2] dimer, the structure of which was confirmed by X-ray crystallographic analysis (Scheme 57). The formation of the [4 + 2] dimer of 1-Tbt-silabenzene is interesting because the transient silatoluene reportedly undergo immediate dimerization to afford a [4 + 2] dimer**[194]** but the transient 1,4-di-*t*-butylsilabenzene is known to dimerize to give a [4 + 4] dimer.**[192]** Tbt-substituted 1-silanaphthalene also undergoes thermal dimerization in C_6D_6 to give the corresponding [4 + 2] dimer (at room temperature for 1 month in an almost quantitative yield or at 100 °C for 12 h in 49%), and the dimer is quite stable even on heating in C_6D_6 at 120 °C.**[185]** On the other hand, Tbt-substituted 2-silanaphthalene does not undergo any dimerization even on heating or standing.**[176]** Tbt-substituted 9-silaanthracene was found to be stable at room temperature either in solution or in the solid state, but it underwent thermal dimerization at higher temperatures (110 °C in C_6D_6 for 15 days or 180 °C in the solid state within 1 h) to give the [4 + 4] cycloaddition product quantitatively, and no thermal dissociation of the dimer to the initial 9-silaanthracene was observed even on heating at 300 °C.**[186]** It is very interesting that the thermal stability of the Tbt-substituted silaaromatics varies depending on the fused ring skeletons and/or the position of the silicon atom.

Photochemical isomerization was also examined for the kinetically stabilized silaaromatics (Scheme 59). When the silabenzene was irradiated with the light of $\lambda = 290-350$ nm in C_6D_6, a novel photochemical valence isomerization took place to give the corresponding silabenzvalene as a sole product. The highly shielded ^{29}Si chemical shift of −71.6 ppm observed for this silabenzvalene indicates the three-membered ring character of its central silicon atom.**[184]** This result is in sharp contrast to the photochemical valence isomerization of the matrix-isolated parent silabenzene into the Dewar-type silabenzene, the formation of which was only evidenced by the IR spectroscopic data indicative of sp ^{3}-SiH moiety.**[195]** Since DFT calculations (B3LYP/6-31G(d) level) on the relative stability of several valence isomers of silabenzene showed that the energy difference between the Dewar-type silabenzene and silabenzvalene is very small,**[184]** it is very difficult to assign the photo-isomerized product of the parent silabenzene as the Dewar-type silabenzene absolutely. On the other hand, the irradiation of 9-Tbt-9-silaanthracene in C_6D_6 with the light of $\lambda = 300-500$ nm resulted in the almost quantitative formation of 9-Tbt-9,10-Dewar-9-silaanthracene.**[187]** Its molecular structure was supported by the ^{1}H, ^{13}C, and ^{29}Si NMR data and chemically confirmed by the ready thermal interconversion to the initial 9-silaanthracene. 9-Tbt-9,10-Dewar-9-silaanthracene was found to be marginally stable at low temperature and the half-lifetime in hexane at −30 °C is estimated as about 10 min.

Addition Reactions. All the metallaaromatic species kinetically stabilized by a Tbt group showed considerably high reactivity toward the reagents such as water, methanol, styrene, phenyl acetylene, mesitonitrile oxide, benzophenone, and 2,3-dimethyl-1,3-butadiene. Some of them were allowed to react with elemental chalcogen such as sulfur and selenium to give several kinds of unique cyclic chalcogenides as the cycloadducts. In Scheme 60 were summarized the reactions of the sila- and germabenzenes as the representative.

Interestingly, Tbt-substitued metallabenzenes and 1-silanaphthalene were found to undergo 1,2- and/or 1,4-addition reactions depending on the character of the reactants, while Tbt-substituted 2-metallanaphthalenes afforded only 1,2-addition reaction products. The remarkable reactivity of the metallaaromatic species towards addition reactions implies that their aromatic stabilization energies are insufficient to suppress the inherent high reactivity of the M=C bonds (M = Si, Ge).

Transition Metal Complexation as an η^6-Arene Ligand. Unfortunately, owing to the instability of the substrates under the reaction conditions used, clear experimental evidence has

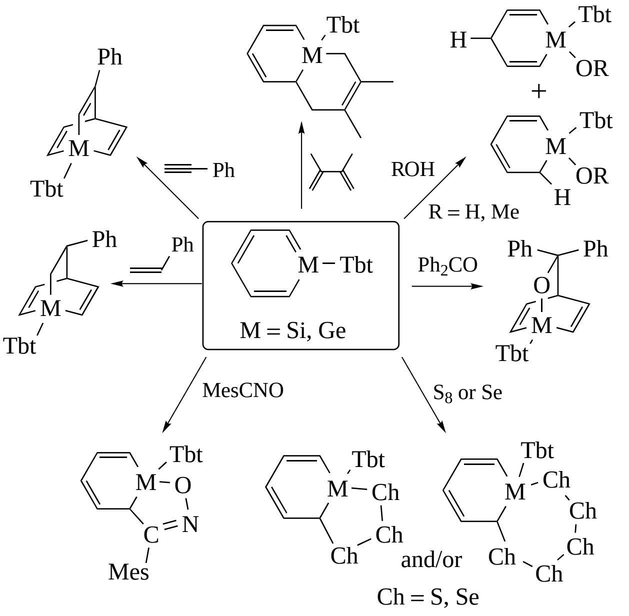

Scheme 60

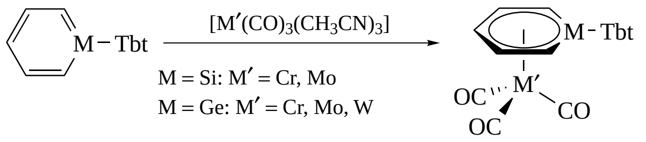

Scheme 61

not been obtained yet for the electrophilic substitution reactions of the metallaaromatic species, which may be the greatest point of interest among the reactivities of such novel aromatic systems. However, it was found that the complexation of the sila- and germabenzenes with some tricarbonyl complexes of group 6 metals resulted in the formation of the corresponding η^6-metallabenzene–transition metal complexes as stable crystalline compounds (Scheme 61).**[196]**

These metallabenzene complexes are thermally quite stable either in the solid state or in solution under argon atmosphere, and no detectable change was observed in the thermolysis in C_6D_6 at 120 °C in a sealed tube for a few days. These complexes were found to be more stable than the Tbt-substituted metallabenzenes toward air and moisture. However, they are still moisture-sensitive and undergo ready addition of water exclusively to their 1,2-positions to give the corresponding 1,2-adduct quantitatively in all cases in spite of the thermodynamic stabilization afforded by the coordination to the tricarbonyl metal center of group 6 metals. The high regioselectivity observed for the water addition to the metallabenzenes complexes is in sharp contrast to the competitive 1,2- and 1,4-addition of water to the Tbt-substituted free metallabenzenes.

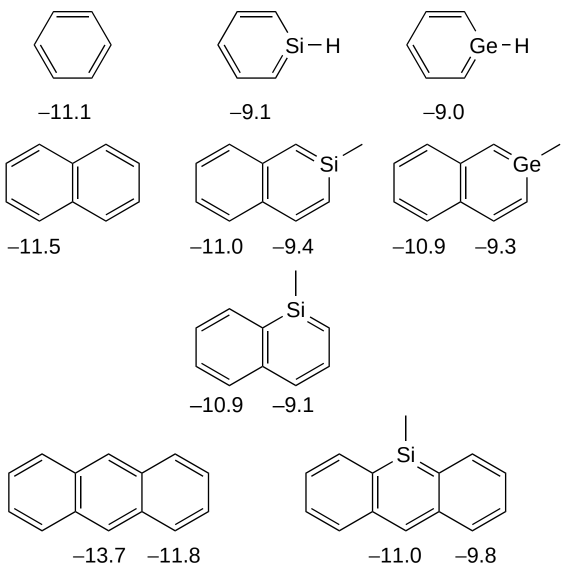

Figure 23 NICS(1) values (ppm) for aromatic systems and their heavier congeners calculated at the B3LYP/6-311G(d) (6-311G(3d) on Si, Ge)//B3LYP/6-31G(d) level

The successful complexation of the metallabenzenes with tricarbonyl transition metals of group 6 is of great importance from the viewpoint of the experimental evidence for the typical reactivity of aromatic compounds.

8.4 Nucleus Independent Chemical Shifts (NICSs)

As described above, the structural and spectroscopic features of the kinetically stabilized metallaaromatic species with Tbt group are in good agreement with those obtained for the less hindered model compounds by theoretical calculations, strongly suggesting that the bulky aromatic substituent (Tbt) does not perturb the intrinsic characters of the metallaaromatic species. As for their aromaticity, further theoretical calculations of NICS(1)s (Nucleus Independent Chemical Shifts)**[197]** were performed and it was found that monometallaaromatic species have considerably large absolute values as compared with the parent aromatic hydrocarbon systems (Figure 23). Despite the high aromaticity suggested by the NICS calculations, it should be noted again that the isolated metallaaromatics showed high reactivity toward a variety of addition reactions across the metal–carbon double bonds.

9 CONCLUDING REMARKS

Following the pioneering work on the first stable disilene, Mes_2 Si=SiMes_2, several kinds of multiply bonded compounds of heavier group 14 elements have been successfully synthesized by taking advantage of kinetic stabilization. Thus, the doubly bonded compounds and even triply bonded ones containing heavier group 14 elements are no more imaginary species but are those of real existence when they are appropriately protected by bulky substituents. The construction of a series of such multiply bonded systems of heavier group 14 elements revealed the feature of the core-like nature of the ns electron, namely, the so-called ‘inert s-pair effect’ or ‘nonhybridization effect’ of the heavier group 14 elements. With such novel π electron systems of heavier group 14 elements in hand, many chemists have a dream of finding unprecedented useful functions for them. Since all the properties of such attractive compounds have not been revealed satisfactorily, further studies from both experimental and theoretical standpoints should be performed on the chemistry of unsaturated bond species of heavier group 14 elements.

The concept of kinetic stabilization should certainly be of great use for the construction of these unprecedented chemical bondings. Also, cooperation of theoretical calculations with experiments has been shown to be very important to elucidate the intrinsic nature of new interelement linkages of heavier main group elements. We hope the recent remarkable progress in the chemistry of unsaturated heavier group 14 elements introduced here will lead to further progress in the isolation of a unique class of compounds having low-coordinated main group elements and the systematic elucidation of the intrinsic nature of chemical bondings of main group elements.

10 REFERENCES

1. K. S. Pitzer, *J. Am. Chem. Soc.*, 1948, **70**, 2140.
2. G. Raabe and J. Michl, *Chem. Rev.*, 1985, **85**, 419.
3. T. C. Klebach, R. Lourens, and F. Bickelhaupt, *J. Am. Chem. Soc.*, 1978, **100**, 4886.
4. M. Yoshifuji, I. Shima, N. Inamoto, K. Hirotsu, and T. Higuchi, *J. Am. Chem. Soc.*, 1981, **103**, 4587.
5. A. G. Brook, F. Abdesaken, B. Gutekunst, G. Gutekunst, and R. K. Kallury, *J. Chem. Soc., Chem. Commun.*, 1981, 191.
6. R. West, M. J. Fink, and J. Michl, *Science*, 1981, **214**, 1343.
7. R. Okazaki and R. West, *Adv. Organomet. Chem.*, 1996, **39**, 231.
8. P. P. Power, *Chem. Rev.*, 1999, **99**, 3463.
9. W. Kutzelnigg, *Angew. Chem., Int. Ed. Engl.*, 1984, **23**, 272.
10. J. P. Desclaux, *At. Data Nucl. Data Tables*, 1973, **12**, 311.
11. P. Pyykkö, *Chem. Rev.*, 1988, **88**, 563.
12. N. C. Norman, ‘Periodicity and the s- and p-Block Elements’, Oxford University Press, New York, 1997.
13. H. Jacobsen and T. Ziegler, *J. Am. Chem. Soc.*, 1994, **116**, 3667.
14. K. D. Dobbs and W. J. Hehre, *Organometallics*, 1986, **5**, 2057.
15. H. Grützmacher and T. F. Fässler, *Chem. – Eur. J.*, 2000, **6**, 2317.
16. Y. Apeloig, R. Pauncz, M. Karni, R. West, W. Steiner, and D. Chapman, *Organometallics*, 2003, **22**, 3250.
17. M. Karni and Y. Apeloig, *J. Am. Chem. Soc.*, 1990, **112**, 8589.
18. G. Trinquier, *J. Am. Chem. Soc.*, 1990, **112**, 2130.
19. D. Danovich, F. Ogliaro, M. Karni, Y. Apeloig, D. L. Cooper, and S. Shaik, *Angew. Chem. Int. Ed. Engl.*, 2001, **40**, 4023.
20. D. B. Chesnut, *Heteroat. Chem.*, 2002, **13**, 53.
21. M. Karni and Y. Apeloig, *Silicon Chem.*, 2002, **1**, 61.
22. K. Kobayashi and S. Nagase, *Organometallics*, 1997, **16**, 2489.
23. K. P. Huber and G. Herzberg, ‘Molecular Spectra and Molecular Structure’, Van Nostrand-Rheinhold, New York, 1979.
24. S. Nagase, K. Kobayashi, and N. Takagi, *J. Organomet. Chem.*, 2000, **611**, 264; N. Takagi and S. Nagase, *Organometallics*, 2001, **20**, 5498.
25. K. Krogh-Jespersen, *J. Am. Chem. Soc.*, 1985, **107**, 537.
26. M. Weidenbruch, *Organometallics*, 2003, **22**, 4348.
27. M. Driess and H. Grützmacher, *Angew. Chem., Int. Ed. Engl.*, 1996, **35**, 829.
28. T. Tsumuraya, S. A. Batcheller, and S. Masamune, *Angew. Chem., Int. Ed. Engl.*, 1991, **30**, 902.
29. M. Kira and T. Iwamoto, *J. Organomet. Chem.*, 2000, **611**, 236.
30. A. J. Millevolte, D. R. Powell, S. G. Johnson, and R. West, *Organometallics*, 1992, **11**, 1091.
31. R. S. Archibald, Y. Vandenwinkel, A. J. Millevolte, J. M. Desper, and R. West, *Organometallics*, 1992, **11**, 3276.
32. B. D. Shepherd, D. R. Powell, and R. West, *Organometallics*, 1989, **8**, 2664.
33. M. J. Michalczyk, R. West, and J. Michl, *Organometallics*, 1985, **4**, 826.
34. R. S. Archibald, Y. Vandenwinkel, D. R. Powell, and R. West, *J. Organomet. Chem.*, 1993, **446**, 67.
35. H. B. Yokelson, D. A. Siegel, A. J. Millevolte, J. Maxka, and R. West, *Organometallics*, 1990, **9**, 1005.
36. S. Masamune, Y. Hanzawa, S. Murakami, T. Bally, and J. F. Blount, *J. Am. Chem. Soc.*, 1982, **104**, 1150.
37. Many examples have been reported, see R. Okazaki and R. West, *Adv. Organomet. Chem.*, 1996, **39**, 231; For example; H. Suzuki, N. Tokitoh, R. Okazaki, J. Harada, K. Ogawa, S. Tomoda, and M. Goto, *Organometallics*, 1995, **14**, 1016.
38. H. Watanabe, K. Takeuchi, K. Nakajima, Y. Nagai, and M. Goto, *Chem. Lett.*, 1988, 1343.
39. N. Tokitoh, K. Hatano, T. Sadahiro, and R. Okazaki, *Chem. Lett.*, 1999, 931.
40. A. Sekiguchi, M. Ichinohe, and S. Yamaguchi, *J. Am. Chem. Soc.*, 1999, **121**, 10231.

41. M. Ichinohe, Y. Arai, A. Sekiguchi, N. Takagi, and S. Nagase, *Organometallics*, 2001, **20**, 4141.
42. N. Takeda and N. Tokitoh, Digermenes and Digermanes, in ‘Science of Synthesis, Houben-Weyl Methods of Molecular Transformations’, Vol. 5. Organometallics, Compounds of Group 14 (Ge, Sn, Pb) (Ed. M. G. Moloney), eds. D. Belllus, S. V. Ley, R. Noyori, M. Regitz, E. Schaumann, I. Shinkai, E. J. Thomas, and B. M. Trost, George Thieme Velag, Stuttgart, New York, 2003, p. 27.
43. N. Tokitoh and R. Okazaki, Multiply Bonded Germanium, Tin, and Lead Compounds, in ‘The Chemistry of Organic Germanium, Tin, and Lead Compounds’, ed. Z. Rappoport, John Wiley & Sons, New York, 2002, Chap. 13, p. 843.
44. P. P. Power, *J. Chem. Soc., Dalton Trans.*, 1998, 2939.
45. J. Escudié, C. Couret, H. Ranaivonjatovo, and J. Satgé, *Coord. Chem. Rev.*, 1994, **130**, 427.
46. J. T. Snow, S. Murakami, S. Masamune, and D. J. Williams, *Tetrahedron Lett.*, 1984, **25**, 4191.
47. J. Park, S. A. Batcheller, and S. Masamune, *J. Organomet. Chem.*, 1989, **367**, 39.
48. D. E. Goldberg, P. B. Hitchcock, M. F. Lappert, K. M. Thomas, A. J. Thorne, T. Fjeldberg, A. Haaland, and B. E. R. Schilling, *J. Chem. Soc., Dalton Trans.*, 1986, 2387.
49. T. Fjeldberg, A. Haaland, B. E. R. Schilling, M. F. Lappert, and A. J. Thorne, *J. Chem. Soc., Dalton Trans.*, 1986, 1551.
50. P. B. Hitchcock, M. F. Lappert, S. J. Miles, and A. J. Thorne, *J. Chem. Soc., Chem. Commun.*, 1984, 480.
51. K. Kishikawa, N. Tokitoh, and R. Okazaki, *Chem. Lett.*, 1998, 239.
52. N. Tokitoh, K. Manmaru, and R. Okazaki, *Organometallics*, 1994, **13**, 167.
53. R. S. Simons, L. H. Pu, M. M. Olmstead, and P. P. Power, *Organometallics*, 1997, **16**, 1920.
54. L. H. Pu, M. M. Olmstead, P. P. Power, and B. Schiemenz, *Organometallics*, 1998, **17**, 5602.
55. L. H. Pu, A. D. Phillips, A. F. Richards, M. Stender, R. S. Simons, M. M. Olmstead, and P. P. Power, *J. Am. Chem. Soc.*, 2003, **125**, 11626.
56. M. Stender, L. H. Pu, and P. P. Power, *Organometallics*, 2001, **20**, 1820.
57. A. F. Richards, A. D. Phillips, M. M. Olmstead, and P. P. Power, *J. Am. Chem. Soc.*, 2003, **125**, 3204.
58. N. Tokitoh, K. Hatano, T. Sasaki, T. Sasamori, N. Takeda, N. Takagi, and S. Nagase, *Organometallics*, 2002, **21**, 4309.
59. N. Tokitoh, T. Sadahiro, K. Hatano, T. Sasaki, N. Takeda, and R. Okazaki, *Chem. Lett.*, 2002, 34.
60. A. Sekiguchi, R. Izumi, S. Ihara, M. Ichinohe, and V. Y. Lee, *Angew. Chem. Int. Ed. Engl.*, 2002, **41**, 1598.
61. M. Weidenbruch, *Eur. J. Inorg. Chem.*, 1999, 373.
62. P. J. Davidson, D. H. Harris, and M. F. Lappert, *J. Chem. Soc., Dalton Trans.*, 1976, 2268.
63. M. Weidenbruch, H. Kilian, K. Peters, H. G. Vonschnering, and H. Marsmann, *Chem. Ber.*, 1995, **128**, 983.
64. S. Masamune and L. R. Sita, *J. Am. Chem. Soc.*, 1985, **107**, 6390.
65. F. Stabenow, W. Saak, H. Marsmann, and M. Weidenbruch, *J. Am. Chem. Soc.*, 2003, **125**, 10172.
66. M. Stürmann, W. G. Saak, H. Marsmann, and M. Weidenbruch, *Angew. Chem. Int. Ed. Engl.*, 1999, **38**, 187.
67. M. Stürmann, W. Saak, M. Weidenbruch, and K. W. Klinkhammer, *Eur. J. Inorg. Chem.*, 1999, 579.
68. K. W. Klinkhammer, T. F. Fässler, and H. Grutzmacher, *Angew. Chem. Int. Ed. Engl.*, 1998, **37**, 124.
69. L. H. Pu, M. O. Senge, M. M. Olmstead, and P. P. Power, *J. Am. Chem. Soc.*, 1998, **120**, 12682.
70. B. E. Eichler, L. H. Pu, M. Stender, and P. P. Power, *Polyhedron*, 2001, **20**, 551.
71. M. Stender, L. H. Pu, and P. P. Power, *Organometallics*, 2001, **20**, 1820.
72. A. D. Phillips, S. Hino, and P. P. Power, *J. Am. Chem. Soc.*, 2003, **125**, 7520.
73. B. E. Eichler and P. P. Power, *Inorg. Chem.*, 2000, **39**, 5444.
74. B. E. Eichler and P. P. Power, *J. Am. Chem. Soc.*, 2000, **122**, 8785.
75. J. Escudié, C. Couret, and H. Ranaivonjatovo, *Coord. Chem. Rev.*, 1998, **180**, 565.
76. J. Escudié and H. Ranaivonjatovo, *Adv. Organomet. Chem.*, 1999, **44**, 113.
77. M. Weidenbruch, *J. Organomet. Chem.*, 2002, **646**, 39.
78. V. Y. Lee and A. Sekiguchi, *Organometallics*, 2004, **23**, 2822; A. Sekiguchi, R. Izumi, V. Y. Lee, and M. Ichinohe, *J. Am. Chem. Soc.*, 2002, **124**, 14822.
79. F. Stabenow, W. Saak, and M. Weidenbruch, *Chem. Commun.*, 1999, 1131.
80. K. M. Baines and J. A. Cooke, *Organometallics*, 1992, **11**, 3487.
81. V. Y. Lee, M. Ichinohe, and A. Sekiguchi, *J. Am. Chem. Soc.*, 2000, **122**, 9034.
82. V. Y. Lee, M. Ichinohe, and A. Sekiguchi, *J. Organomet. Chem.*, 2001, **636**, 41.
83. A. Schäfer, W. Saak, and M. Weidenbruch, *Organometallics*, 2003, **22**, 215.
84. A. Sekiguchi, R. Izumi, V. Y. Lee, and M. Ichinohe, *Organometallics*, 2003, **22**, 1483.
85. D. E. Goldberg, D. H. Harris, M. F. Lappert, and K. M. Thomas, *J. Chem. Soc., Chem. Commun.*, 1976, 261.
86. N. Tokitoh, H. Suzuki, R. Okazaki, and K. Ogawa, *J. Am. Chem. Soc.*, 1993, **115**, 10428; H. Suzuki, N. Tokitoh, and R. Okazaki, *Bull. Chem. Soc. Jpn.*, 1995, **68**, 2471.
87. N. Tokitoh and R. Okazaki, *Coord. Chem. Rev.*, 2000, **210**, 251.

88. H. Suzuki, N. Tokitoh, and R. Okazaki, *Bull. Chem. Soc. Jpn.*, 1995, **68**, 2471.
89. R. West, *Angew. Chem., Int. Ed. Engl.*, 1987, **26**, 1201.
90. M. F. Lappert, J. B. Pedley, J. Simpson, and T. R. Spalding, *J. Organomet. Chem.*, 1971, **29**, 195.
91. M. Lazraq, J. Escudie, C. Couret, J. Satge, M. Drager, and R. Dammel, *Angew. Chem., Int. Ed. Engl.*, 1988, **27**, 828.
92. N. Tokitoh, K. Kishikawa, and R. Okazaki, *J. Chem. Soc., Chem. Commun.*, 1995, 1425.
93. A. Schäfer, M. Weidenbruch, W. Saak, and S. Pohl, *J. Chem. Soc., Chem. Commun.*, 1995, 1157.
94. N. Kuhn, T. Kratz, D. Bläser, and R. Boese, *Chem. Ber.*, 1995, **128**, 245.
95. G. Anselme, H. Ranaivonjatovo, J. Escudié, C. Couret, and J. Satgé, *Organometallics*, 1992, **11**, 2748.
96. K. M. Baines and W. G. Stibbs, *Adv. Organomet. Chem.*, 1996, **39**, 275.
97. A. G. Brook and M. A. Brook, *Adv. Organomet. Chem.*, 1996, **39**, 71.
98. K. W. Zilm, G. A. Lawless, R. M. Merrill, J. M. Millar, and G. G. Webb, *J. Am. Chem. Soc.*, 1987, **109**, 7236.
99. P. Bleckmann, R. Minkwitz, W. P. Neumann, M. Schriewer, M. Thibud, and B. Watta, *Tetrahedron Lett.*, 1984, **25**, 2467.
100. J. Barrau, J. Escudie, and J. Satge, *Chem. Rev.*, 1990, **90**, 283.
101. M. J. Fink, K. J. Haller, R. West, and J. Michl, *J. Am. Chem. Soc.*, 1984, **106**, 822.
102. S. Masamune, S. A. Batcheller, J. Park, W. M. Davis, O. Yamashita, Y. Ohta, and Y. Kabe, *J. Am. Chem. Soc.*, 1989, **111**, 1888.
103. M. J. Michalczyk, R. West, and J. Michl, *J. Chem. Soc., Chem. Commun.*, 1984, 1525; A. J. Millevolte, D. R. Powell, S. G. Johnson, and R. West, *Organometallics*, 1992, **11**, 1091; K. L. McKillop, G. R. Gillette, D. R. Powell, and R. West, *J. Am. Chem. Soc.*, 1992, **114**, 5203.
104. N. Tokitoh, K. Kishikawa, R. Okazaki, T. Sasamori, N. Nakata, and N. Takeda, *Polyhedron*, 2002, **21**, 563.
105. I. Hemme and U. Klingebiel, *Adv. Organomet. Chem.*, 1996, **39**, 159.
106. N. Wiberg, K. Schurz, and G. Fischer, *Angew. Chem., Int. Ed. Engl.*, 1985, **24**, 1053.
107. N. Wiberg, K. Schurz, G. Reber, and G. Muller, *J. Chem. Soc., Chem. Commun.*, 1986, 591.
108. P. v. R. Schleyer and D. Kost, *J. Am. Chem. Soc.*, 1988, **110**, 2105.
109. M. W. Schmidt, P. N. Truong, and M. S. Gordon, *J. Am. Chem. Soc.*, 1987, **109**, 5217.
110. P. v. R. Schleyer and P. D. Stout, *J. Chem. Soc., Chem. Commun.*, 1986, 1373.
111. T. N. Truong and M. S. Gordon, *J. Am. Chem. Soc.*, 1986, **108**, 1775.
112. G. Trinquier, J. C. Barthelat, and J. Satgé, *J. Am. Chem. Soc.*, 1982, **104**, 5931.
113. M. Veith and A. Rammo, *Z. Anorg. Allg. Chem.*, 1997, **623**, 861.
114. G. Ossig, A. Meller, S. Freitag, and R. Herbstirmer, *J. Chem. Soc., Chem. Commun.*, 1993, 497.
115. M. Driess, *Adv. Organomet. Chem.*, 1996, **39**, 193.
116. M. Driess, *Coord. Chem. Rev.*, 1995, **145**, 1.
117. M. Driess, S. Rell, and H. Pritzkow, *J. Chem. Soc., Chem. Commun.*, 1995, 253.
118. M. Driess and R. Janoschek, *J. Mol. Struct.*, 1994, **119**, 129.
119. H. Ranaivonjatovo, J. Escudié, C. Couret, and J. Satgé, *J. Organomet. Chem.*, 1991, **415**, 327.
120. R. Okazaki, in 'Organosulfur Chemistry', ed. P. D. Page, Academic Press, London, 1995, Chap. 5, p. 225.
121. N. Tokitoh and R. Okazaki, *Pol. J. Chem.*, 1998, **72**, 971.
122. M. Minoura, T. Kawashima, and R. Okazaki, *J. Am. Chem. Soc.*, 1993, **115**, 7019.
123. P. Arya, J. Boyer, F. Carré, R. Corriu, G. Lanneau, J. Lapasset, M. Perrot, and C. Priou, *Angew. Chem., Int. Ed. Engl.*, 1989, **28**, 1016; M. Veith, S. Becker, and V. Huch, *Angew. Chem., Int. Ed. Engl.*, 1989, **28**, 1237; M. Veith, A. Detemple, and V. Huch, *Chem. Ber.*, 1991, **124**, 1135; M. Veith and A. Detemple, *Phosphorus Sulfur Silicon*, 1992, **64–5**, 195; M. C. Kuchta and G. Parkin, *J. Am. Chem. Soc.*, 1994, **116**, 8372; M. C. Kuchta and G. Parkin, *J. Chem. Soc., Chem. Commun.*, 1994, 1351; W. P. Leung, W. H. Kwok, L. T. C. Law, Z. Y. Zhou, and T. C. W. Mak, *Chem. Commun.*, 1996, 505; Y. L. Zhou and D. S. Richeson, *J. Am. Chem. Soc.*, 1996, **118**, 10850; S. R. Foley, C. Bensimon, and D. S. Richeson, *J. Am. Chem. Soc.*, 1997, **119**, 10359.
124. R. Okazaki and N. Tokitoh, *Acc. Chem. Res.*, 2000, **33**, 625.
125. N. Tokitoh and R. Okazaki, *Adv. Organomet. Chem.*, 2001, **47**, 121.
126. H. Suzuki, N. Tokitoh, R. Okazaki, S. Nagase, and M. Goto, *J. Am. Chem. Soc.*, 1998, **120**, 11096.
127. H. Suzuki, N. Tokitoh, S. Nagase, and R. Okazaki, *J. Am. Chem. Soc.*, 1994, **116**, 11578.
128. N. Tokitoh, T. Matsumoto, K. Manmaru, and R. Okazaki, *J. Am. Chem. Soc.*, 1993, **115**, 8855.
129. T. Matsumoto, N. Tokitoh, and R. Okazaki, *Angew. Chem., Int. Ed. Engl.*, 1994, **33**, 2316.
130. T. Matsumoto, N. Tokitoh, and R. Okazaki, *J. Am. Chem. Soc.*, 1999, **121**, 8811.
131. M. Saito, N. Tokitoh, and R. Okazaki, *J. Am. Chem. Soc.*, 1997, **119**, 11124.
132. N. Tokitoh, M. Saito, and R. Okazaki, *J. Am. Chem. Soc.*, 1993, **115**, 2065; M. Saito, N. Tokitoh, and R. Okazaki, *J. Am. Chem. Soc.*, 2004, **126**, 15572.
133. N. Kano, N. Tokitoh, and R. Okazaki, *Chem. Lett.*, 1997, **26**, 277.
134. N. Kano, N. Tokitoh, and R. Okazaki, *Organometallics*, 1997, **16**, 4237.

135. N. Tokitoh, T. Matsumoto, and R. Okazaki, *J. Am. Chem. Soc.*, 1997, **119**, 2337.

136. V. N. Khabashesku, S. E. Boganov, P. S. Zuev, O. M. Nefedov, J. Tamas, A. Gomory, and I. Besenyei, *J. Organomet. Chem.*, 1991, **402**, 161.

137. P. Jutzi, *Angew. Chem. Int. Ed. Engl.*, 2000, **39**, 3797.

138. R. S. Simons and P. P. Power, *J. Am. Chem. Soc.*, 1996, **118**, 11966.

139. L. H. Pu, B. Twamley, S. T. Haubrich, M. M. Olmstead, B. V. Mork, R. S. Simons, and P. P. Power, *J. Am. Chem. Soc.*, 2000, **122**, 650.

140. P. P. Power, *Chem. Commun.*, 2003, 2091.

141. C. Eaborn, P. B. Hitchcock, J. D. Smith, and S. E. Sözerli, *Organometallics*, 1997, **16**, 5653.

142. L. H. Pu, B. Twamley, and P. P. Power, *Organometallics*, 2000, **19**, 2874.

143. L. H. Pu, B. Twamley, and P. P. Power, *J. Am. Chem. Soc.*, 2000, **122**, 3524.

144. A. F. Wells, ‘Structural Inorganic Chemistry’, 5th edn., Clarendon, Oxford, 1984, Chap. 26.

145. M. Stender, A. D. Phillips, R. J. Wright, and P. P. Power, *Angew. Chem. Int. Ed. Engl.*, 2002, **41**, 1785.

146. A. D. Phillips, R. J. Wright, M. M. Olmstead, and P. P. Power, *J. Am. Chem. Soc.*, 2002, **124**, 5930.

147. A. J. Bridgeman and L. R. Ireland, *Polyhedron*, 2001, **20**, 2841.

148. A. Sekiguchi, S. S. Zigler, R. West, and J. Michl, *J. Am. Chem. Soc.*, 1986, **108**, 4241.

149. R. Pietschnig, R. West, and D. R. Powell, *Organometallics*, 2000, **19**, 2724.

150. N. Wiberg, W. Niedermayer, G. Fischer, H. Nöth, and M. Suter, *Eur. J. Inorg. Chem.*, 2002, 1066.

151. A. Sekiguchi, R. Kinjyo, and M. Ichinohe, *Science*, 2004, **305**, 1755.

152. M. Kira, T. Maruyama, C. Kabuto, K. Ebata, and H. Sakurai, *Angew. Chem., Int. Ed. Engl.*, 1994, **33**, 1489.

153. H. Sakurai, H. Tobita, and Y. Nakadaira, *Chem. Lett.*, 1982, **11**, 1251.

154. J. Escudié, H. Ranaivonjatovo, and L. Rigon, *Chem. Rev.*, 2000, **100**, 3639.

155. M. Weidenbruch, S. Willms, W. Saak, and G. Henkel, *Angew. Chem., Int. Ed. Engl.*, 1997, **36**, 2503.

156. H. Schäfer, W. Saak, and M. Weidenbruch, *Angew. Chem. Int. Ed. Engl.*, 2000, **39**, 3703.

157. G. Ramaker, A. Schäfer, W. Saak, and M. Weidenbruch, *Organometallics*, 2003, **22**, 1302.

158. S. Willms, A. Grybat, W. Saak, M. Weidenbruch, and H. Marsmann, *Z. Anorg. Allg. Chem.*, 2000, **626**, 1148.

159. S. Boomgaarden, W. Saak, M. Weidenbruch, and H. Marsmann, *Organometallics*, 2001, **20**, 2451.

160. A. Grybat, S. Boomgaarden, W. Saak, H. Marsmann, and M. Weidenbruch, *Angew. Chem. Int. Ed. Engl.*, 1999, **38**, 2010.

161. F. Meiners, W. Saak, and M. Weidenbruch, *Organometallics*, 2000, **19**, 2835.

162. F. Meiners, D. Haase, R. Koch, W. Saak, and M. Weidenbruch, *Organometallics*, 2002, **21**, 3990.

163. D. Ostendorf, W. Saak, D. Haase, and M. Weidenbruch, *J. Organomet. Chem.*, 2001, **636**, 7.

164. G. E. Miracle, J. L. Ball, D. R. Powell, and R. West, *J. Am. Chem. Soc.*, 1993, **115**, 11598.

165. M. Trommer, G. E. Miracle, B. E. Eichler, D. R. Powell, and R. West, *Organometallics*, 1997, **16**, 5737.

166. N. Tokitoh, K. Kishikawa, and R. Okazaki, *Chem. Lett.*, 1998, **27**, 811.

167. B. E. Eichler, D. R. Powell, and R. West, *Organometallics*, 1998, **17**, 2147.

168. K. Kishikawa, N. Tokitoh, and R. Okazaki, *Organometallics*, 1997, **16**, 5127.

169. B. Goetze, B. Herrschaft, and N. Auner, *Chem. – Eur. J.*, 1997, **3**, 948.

170. N. Wiberg, H. W. Lerner, S. K. Vasisht, S. Wagner, K. Karaghiosoff, H. Noth, and W. Ponikwar, *Eur. J. Inorg. Chem.*, 1999, 1211.

171. M. Kira, R. Yauchibara, R. Hirano, C. Kabuto, and H. Sakurai, *J. Am. Chem. Soc.*, 1991, **113**, 7785.

172. S. Ishida, T. Iwamoto, C. Kabuto, and M. Kira, *Nature*, 2003, **421**, 725.

173. W. P. Freeman, T. D. Tilley, L. M. Liablesands, and A. L. Rheingold, *J. Am. Chem. Soc.*, 1996, **118**, 10457; W. P. Freeman, T. D. Tilley, G. P. A. Yap, and A. L. Rheingold, *Angew. Chem., Int. Ed. Engl.*, 1996, **35**, 882; B. Goldfuss, P. V. Schleyer, and F. Hampel, *Organometallics*, 1996, **15**, 1755; B. Goldfuss and P. V. Schleyer, *Organometallics*, 1997, **16**, 1543; S. B. Choi, P. Boudjouk, and P. R. Wei, *J. Am. Chem. Soc.*, 1998, **120**, 5814; J. M. Dysard and T. D. Tilley, *J. Am. Chem. Soc.*, 1998, **120**, 8245.

174. M. Denk, R. Lennon, R. Hayashi, R. West, A. V. Belyakov, H. P. Verne, A. Haaland, M. Wagner, and N. Metzler, *J. Am. Chem. Soc.*, 1994, **116**, 2691; C. Boehme and G. Frenking, *J. Am. Chem. Soc.*, 1996, **118**, 2039; C. Heinemann, T. Müller, Y. Apeloig, and H. Schwarz, *J. Am. Chem. Soc.*, 1996, **118**, 2023; R. West, J. J. Buffy, M. Haaf, T. Muller, B. Gehrhus, M. F. Lappert, and Y. Apeloig, *J. Am. Chem. Soc.*, 1998, **120**, 1639.

175. H. Hiratsuka, M. Tanaka, H. Horiuchi, Naris, T. Yoshinaga, M. Oba, and K. Nishiyama, *J. Organomet. Chem.*, 2000, **611**, 71; M. Oba, Y. Watanabe, and K. Nishiyama, *Organometallics*, 2002, **21**, 3667.

176. N. Tokitoh, K. Wakita, R. Okazaki, S. Nagase, P. v. R. Schleyer, and H. J. Jiao, *J. Am. Chem. Soc.*, 1997, **119**, 6951; K. Wakita, N. Tokitoh, and R. Okazaki, *Bull. Chem. Soc. Jpn.*, 2000, **73**, 2157; K. Wakita, N. Tokitoh, R.

Okazaki, S. Nagase, P. v. R. Schleyer, and H. J. Jiao, *J. Am. Chem. Soc.*, 1999, **121**, 11336.

177. G. Märkl and D. Rudnick, *Tetrahedron Lett.*, 1980, **21**, 1405; G. Märkl, D. Rudnick, R. Schulz, and A. Schweig, *Angew. Chem., Int. Ed. Engl.*, 1982, **21**, 221.
178. N. Tokitoh, *Acc. Chem. Res.*, 2004, **37**, 86.
179. N. Tokitoh, *Bull. Chem. Soc. Jpn.*, 2004, **77**, 429.
180. Y. Apeloig, Theoretical Aspects of Organosilicon Compounds, in 'The Chemistry of Organo Silicon Compounds', eds. S. Patai and Z. Rappoport, Wiley, New York, 1989, p. 151.
181. Y. Apeloig and M. Karni, Theoretical Aspects and Quantum Mechanical Calculations of Silaaromatic Compounds, in 'The Chemistry of Organo Silicon Compounds', eds. Z. Rappoport and Y. Apeloig, Wiley, New York, 1998, Vol. 2, Chap. 1.
182. H. B. Schegel, B. Coleman, and M. Jones Jr, *J. Am. Chem. Soc.*, 1978, **100**, 6499; P. H. Blustin, *J. Organomet. Chem.*, 1979, **166**, 21; U. D. Priyakumar and G. N. Sastry, *Organometallics*, 2002, **21**, 1493; A. Saieswari, U. D. Priyakumar, and G. N. Sastry, *J. Mol. Struct. (Theochem)*, 2003, **663**, 145.
183. K. Wakita, N. Tokitoh, R. Okazaki, and S. Nagase, *Angew. Chem. Int. Ed. Engl.*, 2000, **39**, 634.
184. K. Wakita, N. Tokitoh, R. Okazaki, N. Takagi, and S. Nagase, *J. Am. Chem. Soc.*, 2000, **122**, 5648.
185. N. Takeda, A. Shinohara, and N. Tokitoh, *Organometallics*, 2002, **21**, 4024.
186. N. Takeda, A. Shinohara, and N. Tokitoh, *Organometallics*, 2002, **21**, 256.
187. A. Shinohara, N. Takeda, and N. Tokitoh, *J. Am. Chem. Soc.*, 2003, **125**, 10804.
188. N. Nakata, N. Takeda, and N. Tokitoh, *J. Am. Chem. Soc.*, 2002, **124**, 6914.
189. N. Nakata, N. Takeda, and N. Tokitoh, *Organometallics*, 2001, **20**, 5507; N. Nakata, N. Takeda, and N. Tokitoh, *Organometallics*, 2003, **22**, 481.
190. K. Nishiyama, M. Oba, H. Takagi, I. Fujii, N. Hirayama, Narisu, H. Horiuchi, T. Okutsu, and H. Hiratsuka, *J. Organomet. Chem.*, 2000, **604**, 20.
191. V. J. Minkin, M. N. Glukhovtsev, and Y. B. Simkin, 'Aromaticity and Antiaromaticity; Electronic and Structural Aspects', Wiley, New York, 1994.
192. G. Märkl and W. Schlosser, *Angew. Chem., Int. Ed. Engl.*, 1988, **27**, 963.
193. P. Jutzi, M. Meyer, H. P. Reisenauer, and G. Maier, *Chem. Ber.*, 1989, **122**, 1227; B. Solouki, P. Rosmus, H. Bock, and G. Maier, *Angew. Chem., Int. Ed. Engl.*, 1980, **19**, 51; G. Maier, G. Mihm, and H. P. Reisenauer, *Angew. Chem., Int. Ed. Engl.*, 1980, **19**, 52.
194. C. L. Kreil, O. L. Chapman, G. T. Burns, and T. J. Barton, *J. Am. Chem. Soc.*, 1980, **102**, 841.
195. G. Maier, K. Schottler, and H. P. Reisenauer, *Tetrahedron Lett.*, 1985, **26**, 4079.
196. N. Nakata, N. Takeda, and N. Tokitoh, *Angew. Chem. Int. Ed. Engl.*, 2003, **42**, 115.
197. P. v. R. Schleyer, C. Maerker, A. Dransfeld, H. Jiao, J. R. Nicolaas, and v. E. Hommes, *J. Am. Chem. Soc.*, 1996, **118**, 6317; P. v. R. Schleyer, H. Jiao, J. R. Nicolaas, v. E. Hommes, V. G. Malkin, and O. L. Malkina, *J. Am. Chem. Soc.*, 1997, **119**, 12669.

Sol–Gel Encapsulation of Metal and Semiconductor Nanocrystals

Melissa A. Petruska & Victor I. Klimov
Los Alamos National Laboratory, Los Alamos, NM, USA

1 Introduction 1
2 Direct Growth Method for NC-Sol–Gel Composites 1
3 Encapsulation of Colloidal NCs in Sol–Gel Matrices 4
4 Conclusions 7
5 Related Articles 8
6 References 8

1 INTRODUCTION

Responsible for the deep reds and vibrant yellows found in the exquisite stained glasses that have adorned medieval cathedrals for more than half a century, Au and Ag nanocrystals (NCs) have experienced an illustrious history even before their unique spectroscopy was understood. NCs are the links that bridge individual molecules (<1 nm) and bulk materials (>100 nm), and their properties result from their finite sizes in this regime. In fact, Au and Ag NCs enjoy distinct optical characteristics *because* of their restricted dimensions, which lead to pronounced optical resonances associated with collective oscillations of surface charges (surface plasmons). While the NC-doped glasses of the Middle Ages can be appreciated for their splendor, the interesting optical properties of these materials have led to a resurgent interest in analogous glasses from a twenty-first century technological perspective, as they have found application in areas like nonlinear optics, sensing, and catalysis.

Methods for embedding metal NCs (*see* ***Metal Nanoparticles, Synthesis of*** and ***Metal Nanoparticles, Organization & Applications of***) and semiconductor NCs (*see* ***Semiconductor Nanocrystal Quantum Dots***) in glasses include such techniques as high-temperature precipitation in molten materials, sputtering, ion implantation, ion exchange, ion irradiation, laser ablation, and sol–gel processing.[1,2] Among the various routes to these composites, sol–gel processing has the distinction of being a 'wet chemistry' approach, and as such, it stands out as the method by which adverse side-effects, such as photodarkening in semiconductor-doped glasses, can be avoided.[2] Sol–gel syntheses have led to the fabrication of composites of better optical quality, smaller NC size dispersities, and larger NC volume loadings than alternative methods, and these improvements are important factors in NC-doped glass applications.

Sol–gel processing relies on the hydrolysis and condensation reactions of metal compounds to afford three-dimensional polymeric networks (*see* ***Sol–Gel Synthesis of Solids***).[3] In contrast to the more traditional ways of making glasses (i.e. from clays or sands at high temperatures), sol–gel syntheses are generally mild routes that employ high purity precursors, which are converted to inorganic oxides through a series of chemical reactions. Sol–gel reactants are typically metal alkoxides or metal salts, and the reactions proceed in organic or aqueous environments, respectively:[4]

$$\mathrm{Si(OR)_4} + 4\mathrm{H_2O} \xrightarrow[\text{catalyst}]{\text{MeOH}} 4\mathrm{ROH} + \mathrm{Si(OH)_4} \xrightarrow{-2\mathrm{H_2O}} \mathrm{SiO_2} \qquad (1)$$

At the sol stage, the solution can be spin-coated or dip-coated to make films. As the reaction progresses, the viscosity of the reaction mixture increases, and the sol solution eventually 'gels', assuming the shape of its containment vessel. Under normal drying conditions, the wet gel gives rise to a xerogel; a supercritical drying environment yields aerogels. This chemistry can be applied to a wide variety of metal precursors, including salts or alkoxides of silica, titania, zirconia, and alumina. Most importantly, the mild reaction conditions allow for the ready incorporation of assorted organic and inorganic molecules, affording the opportunity to fabricate a wide variety of glasses with tailored properties.

By employing these mild sol–gel routes for metal and semiconductor NC encapsulation, the prospect exists for producing NC-based glasses of high optical quality. While a general goal is to prepare optical quality, uniform NC-sol–gel composites with high NC volume loadings and narrow NC size dispersities, the specific requirements of the materials will vary from application to application. This article focuses on two main routes to noble metal and semiconductor NC-sol–gel composites. The first method involves the direct growth of the NCs within the host matrix, and this work has been extensively reviewed in recent articles.[2,4] The latter process concentrates on a decoupled procedure in which the synthesis of the NCs is independent of the fabrication of the composite material.

2 DIRECT GROWTH METHOD FOR NC-SOL–GEL COMPOSITES

Before mild chemical routes to high quality NCs were widely available, NCs were prepared in glasses by such strategies as precipitation, ion implantation, and laser ablation, which typically rely on high-temperature processing steps ($>500\,^\circ$C).[1,2] Glasses provide a durable, rigid, stable environment for the NCs, and their optical properties can be extensively explored in these transparent hosts. In fact, effects of quantum confinement in semiconductor NCs were first observed in such NC-doped glasses.[5] Despite some successes, drawbacks, including poor material reproducibility, broad NC size distributions (generally greater than 15%), and surface defects, which are particularly damaging for nanoscale semiconducting materials where poor surface quality leads to inferior optical properties, have hindered the wide use of these materials in applications.[2] More recently, the high-temperature routes to NCs have given way to an emphasis on moderate to low-temperature synthetic strategies, which afford colloidal NCs that can be purified and manipulated into larger arrays.

Glassy materials still present an attractive medium for encapsulating NCs because of the stability these environments provide. Direct syntheses of metal and semiconductor NCs in sol–gel glasses have been researched for more than a decade as low temperature, chemical routes to optical quality samples that provide an alternative to high-temperature paths and to the more involved processing that decoupled methods require, which use colloidal NCs as starting materials.[4] The resulting composites have been investigated for their unique catalytic,[4] magnetic,[4] and optical properties,[2,4] including enhanced optical nonlinearities that are important for, for example, all-optical switching. In fact, a significant amount of work on NC composites has been conducted in the context of their nonlinear optical applications. The performance of these materials can be characterized in terms of a resonant, Kerr-type, third-order nonlinear susceptibility that describes the changes in the absorption coefficient and refractive index of a material under the influence of intense light.[6] The changes in susceptibility, $\chi(\omega)$, induced by a monochromatic field at a frequency ω can be presented as $\Delta\chi = \chi^{(3)}(\omega)I(\omega) + \chi^{(5)}(\omega)I^2(\omega) + \cdots$, where $I(\omega)$ is the field intensity and $\chi^{(n)}$ is the nonlinear susceptibility of the nth order. Nonlinear optical properties of a material are often characterized by $\chi^{(3)}$, which describes the modifications in χ that are linear in field intensity.

2.1 Noble Metal NCs Grown in Sol–Gel Networks

The direct growth method of metal NC-sol–gel fabrication is the most straightforward approach to these materials. Many avenues have been explored in the context of this methodology, yielding a variety of NC-glass composites, including Cr, Fe, Os, Ni, Co, Pd, Pt, Cu, Rh, Ru, Au, and Ag NCs in silica, titania, zirconia, and alumina networks.[4] Refinements in some of the preparations have led to improvements in NC size dispersities, NC volume loadings, and sample homogeneity. Strict control over the size and stability of the resulting NCs within the transparent hosts is an advantage for the subsequent applicability of the composites.

Very simply, metal salts can be directly added to common sol–gel precursors like tetraethylorthosilicate (TEOS) in alcohol.[2,4] Polymerization reactions are initiated, and a porous gel forms in which the metal salt is embedded within the metal-oxide framework. Reduction reactions are then used to give the corresponding metal NCs, and these treatments can involve exposure to gases such as hydrogen at elevated temperatures (usually $>500\,^\circ$C, although lower temperatures have been reported),[4] interaction with chemical agents (e.g. borohydride or dextrose, which generates H_2 in situ following thermal decomposition),[7–9] or irradiation with UV light.[7] This approach has been successfully applied for the sol–gel synthesis of, for example, Co, Fe, Cu, Ni, Au, and Ag NCs,[4] and particle sizes can be tuned by changing hydrolysis conditions and reduction times and temperatures.

The drawbacks associated with this method of NC-sol–gel fabrication are broad NC size dispersities and sample inhomogeneities. Improvement in these features, particularly the latter, is critical for effective heterogeneous catalysis to be realized. Efforts in enhancing these important parameters have led to the design of new approaches, one of the more popular focusing on organically modified gels as depicted in the following equation:[10]

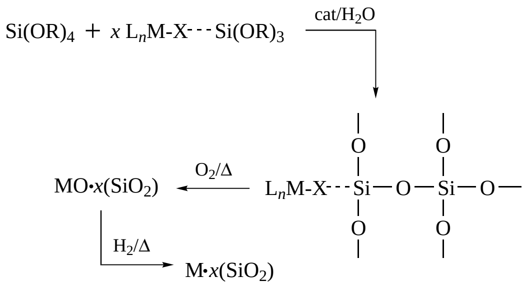

(2)

In this strategy, metal salts are tethered directly to the sol–gel matrix through bifunctional ligands of the type X···$Si(OR)_3$, where X is capable of coordinating to the metal center and the siloxy group co-condenses with silica precursors like TEOS or tetramethylorthosilicate (TMOS) to afford a composite in which the metal salt is intimately connected to the silicon-oxide network.[10] Under oxidative conditions, metal-oxide particles are formed and organic components are removed. These particles can then be reduced under a stream of hydrogen at elevated temperatures. Using this procedure, composites containing a uniform distribution of metal NCs throughout the sol-gel matrix are prepared. In addition, the particle size dispersity can be fairly narrow with limits dependent upon NC composition. For example, Pd NCs with a diameter range of 2.8–5.2 nm were synthesized using this approach (Figure 1). This chemistry has been applied to form NCs of Ag, Co, Cu, Ni, Pd, and Pt in silica networks using ligands of the type $X(CH_2)_3Si(OEt)_3$, in which X is NH_2, $NHCH_2CH_2\ NH_2$, or CN.[10] The effectiveness of this linking molecule at controlling particle size distribution was determined by performing a comparative study in which

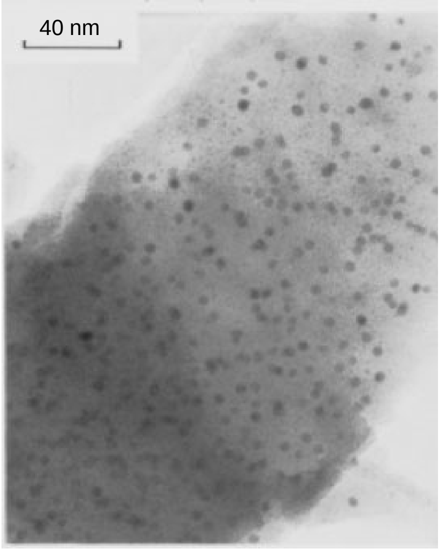

Figure 1 Scanning transmission electron micrograph of a Pd-silica composite formed via an organically modified gel. The average particle size is 3.8 nm, and the distribution range is 2.8–5.2 nm. (Reprinted with permission from Ref. 10. © 1991 American Chemical Society)

the bifunctional ligand was omitted from the reaction. In the latter case, the size distribution was significantly broadened.

This methodology has been increasingly employed for the synthesis of additional systems, thereby supplementing the results from the first investigations in the early 1990s. Single source precursors of Ag, Cu, Pd, Pt, Os, Re, Ru, and Au, whose ligands terminate in siloxy moieties, can be prepared, and these molecules then serve as the starting reagents that lead to the corresponding NC-doped sol–gel glasses.[11,12] An example of this reaction is shown in equation (3).[12] The Os-doped metal complexes were reduced directly with hydrogen, thereby avoiding oxidative treatments that would lead to the highly toxic, volatile intermediate OsO_4. By exploiting these reactions conditions, NC-silica composites were prepared in which the dopant was uniformly dispersed:

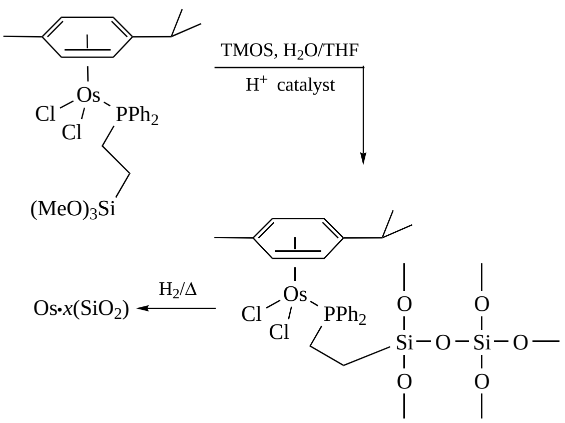

(3)

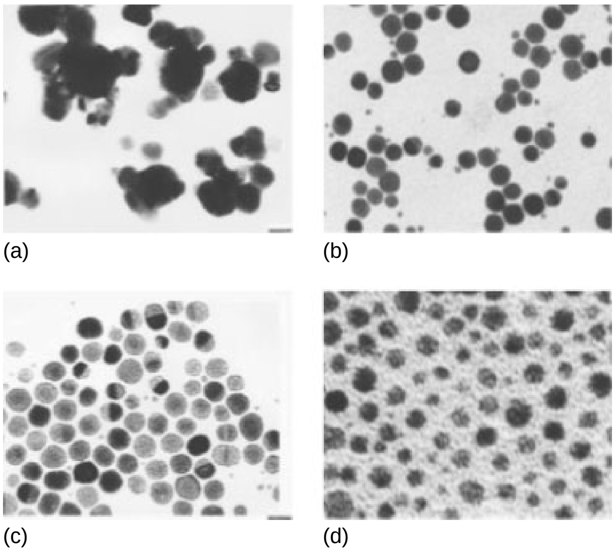

Figure 2 Transmission electron microscopy (TEM) images of EDAS-gold deposits from a sol containing EDAS:Au = 30:1 and Au = 1 mM at pH (a) 2, (b) 5, (c) 7, and (d) 9.5. At low pH, the particles are aggregated. The average particle size for (b), (c), and (d) is 5–6 nm. For pH = 5, a bimodal distribution is readily apparent. (Reprinted with permission from Ref. 8. © 1999 American Chemical Society)

A new take on this methodology omits the TEOS or TMOS precursor from sol–gel processing and relies purely on the hydrolysis and condensation reactions of the siloxy-functionalized metal complexes. In one example, an aqueous or methanolic solution of N-[3-(trimethoxysilyl)propyl]ethylenediamine (EDAS) and $HAuCl_4$ was prepared, and the polymerization reactions were initiated with water and varying amounts of HCl.[8] Chemical reduction of the gold salt using $NaBH_4$ gave rise to Au-doped silica sols that were either dip-coated or spin-coated into films or allowed to gel in their containers. The properties of the resulting gels were dependent on pH (Figure 2), and one set of conditions afforded a NC size range as narrow as 5–6 nm in a material that was stable with respect to NC aggregation for greater than four months. The results indicate that interaction of EDAS with the Au salt reduces the rate of reduction, and that once formed, coordination of the EDAS ligands to the Au NC surface slows down particle growth.[8] The siloxy groups also have the potential to form shells around the NCs, thereby stabilizing them during sol–gel processing. This method is generally applicable to other metal NCs including Ag, Pd, and Pt, although preliminary results with Ag NCs, which have a much lower affinity for amines, suggest a wide size distribution.

The pore doping approach has also been successful in maintaining small NC size dispersities.[2] Initially, porous dip-coated alumina and titania films were fabricated and then directly immersed into aqueous solutions of $NaAuCl_4 \cdot 2H_2O$ so that the $AuCl_4$ ions could be incorporated into the pores of the sol–gel films.[13] Following thermal treatment, Au NCs approximately 2 nm in diameter formed. These NCs are typically smaller than those particles grown in composites prepared via other routes, suggesting the size of the NCs is limited by the pore size in the dip-coated films.

2.2 Semiconductor NCs Grown in Sol–Gel Networks

The strategies for precipitating semiconductor NCs in sol–gel composites parallel those direct growth methods utilized to fabricate metal NC-doped sol–gels.[4] A general approach involves the addition of the metal salt to the sol solution and the subsequent exposure of the resulting gel to an atmosphere of H_2S.[2,4] In the final gel, CdS NCs are embedded throughout a silica matrix. CdS growth can also proceed through a CdO intermediate. In one procedure, cadmium acetate was added to the TEOS precursor.[14] Dip-coating gave rise to a film, which was then subjected to oxidative conditions to decompose organic matter. Exposure of the sample to an H_2S atmosphere at 200 °C yielded CdS NCs. Xerogels were also prepared in this study, and a maximum value of 2.1×10^{-7} esu for the third-order nonlinear susceptibility of the sample was reported and shown to be dependent on NC concentration within the sample.

Similar methods have been used to prepare CdS NCs in optical quality borosilicate glasses.[4] Nonlinear optical characterization of one composite sample with particle sizes ranging from ~2.5–5.5 nm yielded a range for $\chi^{(3)}$ of 10^{-7}–10^{-6} esu.[15] Optical gain measurements of a similar material afforded a value of 33 cm^{-1} at room temperature.[16] At 11 K, maximum gain values reached 200 cm^{-1}, and like the optical nonlinearities, these values were also dependent on NC concentration.[17]

Another possibility is to include both the metal salt and the chalcogenide precursor (e.g. thiourea) in the sol solution.[2,4] As an example, heat treatments of 350–400 °C for 10–15 h in air eliminated the residual organics and afforded the corresponding CdS NCs.[18] NC diameters could be tailored by controlling the ratio of Cd/Si, but size dispersities still remained large (>15%). A similar approach can be used to prepare PbS NCs in silica xerogels.[4] In one study, a mixture of TMOS, $Pb(NO_3)_2$, ammonium hydroxide, water, and thiourea in methanol was allowed to gel, during which time the PbS NCs formed.[19]

The direct growth of MSe or MTe (M is Cd, Zn, or Pb) NCs in sol–gel typically combines both the metal and chalcogenide sources in the sol solution.[2,4] Silica sol–gels prepared with cadmium acetate and H_2SeO_4 (or Se/HNO_3) yielded CdSe NC-silica composites after exposure to H_2/N_2 mixtures at temperatures from 300 to 900 °C. By controlling thermal parameters, the size of the NCs could be managed; however, the size dispersities remained broad.[20] Cadmium acetate and TeO_2 reagents added to zirconia tetrapropoxide afforded materials that upon reduction with hydrazine or stannous chloride under moderate temperatures gave CdTe.[21] Porous Cd-doped silica gels exposed to solutions of KSeCN or selenourea yielded embedded CdSe NCs with sizes tunable according to Se solution concentrations and immersion times.[18,22]

Organic ligands added to sol solutions can be used to control NC growth and size dispersities.[2,4] This approach, analogous to the method described for metal NCs in Section 2.1, employs bifunctional linkers to tether metal salts to the sol–gel network to improve the homogeneity of the sample. Silica precursors mixed with 3-aminopropyltriethoxysilane (APTES) and cadmium nitrate were allowed to gel.[23] Following oxidative treatments, the resulting CdO particles were converted to CdS upon exposure to H_2S, as shown in equation (4).[23] The size distribution of particles was much narrower under these conditions than when APTES was omitted from the reaction.

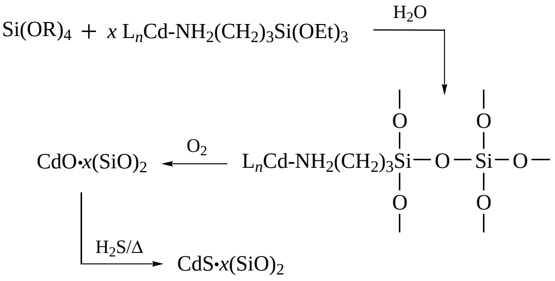

$Si(OR)_4 + x\,L_nCd\text{-}NH_2(CH_2)_3Si(OEt)_3$
H_2O
$CdO{\cdot}x(SiO)_2$
O_2
$L_nCd\text{-}NH_2(CH_2)_3Si-O-Si-O-$
O
O
O
O
H_2S/Δ
$CdS{\cdot}x(SiO)_2$

(4)

The pore doping approach has also been applied to the synthesis of semiconductor NCs in sol–gels in order to limit NC size and improve size dispersities.[2] This method, which relies on samples with well-defined pore structures, was used to fabricate waveguides.[24] Silica-titania films prepared from TEOS and tetrapropylorthotitanate were immersed in aqueous solutions of cadmium fluoride. After heating the film, the sample was exposed to H_2S gas, generating CdS NCs with maximum sizes of 2.6 nm. While small sized NCs were obtained, the major drawback to this approach was the difficulty in achieving a homogeneous dispersion of NCs throughout the sample.

3 ENCAPSULATION OF COLLOIDAL NCs IN SOL–GEL MATRICES

New routes to high quality colloidal NCs of varying compositions and shapes appear in the literature almost on a weekly basis. The most successful of these approaches to crystalline semiconductor NCs with excellent optical properties share the same basic premise of pyrolysis of metal-organic precursors in solutions of hot coordinating solvents.[25] In contrast, the syntheses of noble metal NCs typically rely on the reduction of metal salts in the presence of citrate ions (e.g. Au or Ag), in two-phase systems (e.g. Au or Ag), or under high-temperature conditions in the presence of stabilizing agents (e.g. Co and Ni).[25] In general, the best procedures afford colloidal NCs that are highly crystalline and highly monodisperse (size dispersities <10% are generally achieved from the reaction mixture or following post-preparative, size-selective precipitation of the NCs). A unique feature of the colloidal NCs is the chemical flexibility that stems from the stabilizing agents that cap the NCs during the course of the reaction. These ligands prevent the particles from aggregating, allow for NC solubility in a variety of organic solvents, and can be exchanged for ligands of varying functionalities. The surface capping groups also play an important role with regards to the photophysical properties of semiconducting NCs, as they passivate surface trapping states, allowing for highly efficient emission properties.

While many of the direct growth methods discussed in Section 2 are express routes to NC-doped gels and glasses, the resulting materials can have low volume loadings (<1%) and large size dispersities (>15%), which may adversely affect the application of these materials. In addition, the semiconductor NCs in these composites are often beset by poorly controlled surface properties, leading to low photoluminescence (PL) quantum yields (QYs). More recently, researchers have sought to decouple the synthesis of the NCs from the fabrication of the sol–gel matrix material,[2,26] thereby exploiting the synthetic procedures already available for making high quality, highly monodisperse NCs of specific sizes and relying on mild sol–gel processing conditions to preserve these properties. This approach also furnishes the opportunity to include core/shell NCs and NCs of modified shapes, such as rods, wires, or disks, into the glass matrices, which is an advantage over direct growth methods that are typically unable to achieve precise control over these parameters.[26]

3.1 Sol–Gel Matrices as Hosts for Colloidal Noble Metal NCs

Colloidal metal NCs can be directly introduced to the sol precursors to fashion metal NC-sol–gel composites. Silica glasses fabricated from TMOS with Au NCs as the dopant and ammonia as the catalyst contained NCs with diameters ranging from 10–20 nm uniformly distributed throughout the framework and exhibited measurable third-order nonlinear susceptibilities (2.2×10^{-9} esu).[27] Gold NC concentrations could be increased to 1 wt% with no evidence of particle aggregation, even in the absence of stabilizer.[28] Polymer-protected Au NCs with broad size dispersities were also incorporated into silica matrices using ammonia as a catalyst.[29] In the absence of polymer, extensive NC aggregation was observed.

Improvements in the stability of Au colloids should lead to composites of better quality. In one approach, 15 nm Au NCs with a 10% polydispersity were synthesized and overcoated with a silica shell.[30] The Au@SiO_2 NCs were added to a methanol solution of TMOS, and a gel formed. The silica-overcoated Au NCs were incorporated into the silica network homogeneously and without aggregation of the particles, as evidenced by the retention of optical properties following sol–gel processing, even at increasing concentrations (Figure 3). Third-order nonlinear susceptibility values of 7.5×10^{-10} esu were measured in gel samples with concentrations of 0.3 wt%. While the volume loading of NCs is still quite low, the success of this approach with Au NCs indicates the potential for extending this strategy to prepare silica-overcoated NC composites comprising a variety of metal and semiconductor materials.

3.2 Sol–Gel Matrices as Hosts for Colloidal Semiconductor NCs

Sol–gel matrices can also be employed to encapsulate colloidal semiconductor NCs. In one example, CdSe and CdSe/ZnS core/shell NCs were embedded in silica matrices using octylamine as a catalyst in solutions of butanol.[31] The octylamine reagent also displaced the existing surface cap of the NCs, leading to an enhanced PL QY (the resulting CdSe-silica composites exhibited QYs between 5 and 10%). At this stage, volume loadings were less than 0.1%. In general, the CdSe/ZnS core/shell NC heterostructures are more robust than their CdSe counterparts in this system and maintain luminescence for months. More recently, QYs and

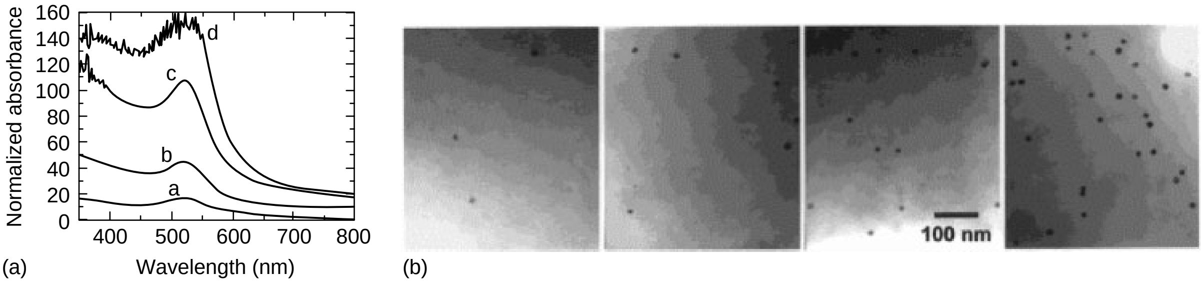

Figure 3 (a) Optical absorption spectra of thin xerogels containing Au@SiO_2 NCs at concentrations: a – 0.010, b – 0.019, c – 0.25, and d – 0.6 wt% Au. In each case, the surface plasmon resonance can be found at the same wavelength. (b) TEM images of xerogels containing Au@SiO_2 NCs at the same volume loadings as depicted in the optical absorption spectra. (Reprinted with permission from Ref. 30. © 2001 American Chemical Society)

volume fractions greater than 40% and 1%, respectively, were reported.[26]

In a similar approach, titania composites doped with CdSe and CdSe/ZnS NCs were prepared.[32] Here the NCs were mixed with titanium tetrabutoxide in a 2:1 THF/ethanol solvent system, and volume fractions as high as 13% were reported in films that were spin-coated from the sol solutions. While QYs for the CdSe/ZnS-titania sols remained near 10%, smaller values were reported for CdSe NCs that were not initially overcoated with ZnS. In addition, the samples were not very stable, as the PL intensity was observed to decrease in the films almost immediately following processing.

The surface chemistry of the as-synthesized NCs has been exploited in order to develop methods for anchoring the semiconductor NCs directly to the sol–gel network. The approaches investigated are analogous to methods discussed in Section 2 with respect to organically modified gels, with one major exception – the colloidal NC, and not just the starting metal salt, is directly tethered to the metal-oxide network:

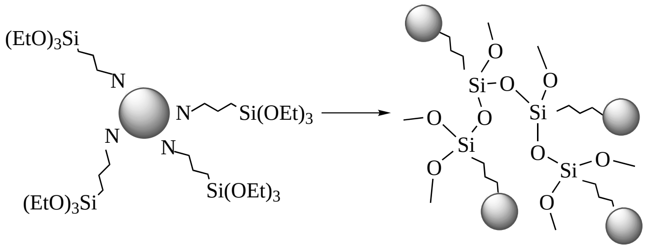

(5)

As an example, APTES-functionalized CdSe NCs were synthesized such that the triethoxysilane functionality was found of the periphery of the NCs.[33] Hydrolysis and condensation reactions of this moiety led to an extended metal-oxide network. Following thermal curing up to 350 °C, films with thicknesses near 10 µm were obtained. Comparison of this method to direct growth routes to CdSe-doped silica films suggests that the APTES-functionalized CdSe NC approach yields materials with better NC monodispersity and higher volume loadings (nearly 5%) than the alternative. The results indicate that doping silica composites with colloidal NCs has the advantage of using size-selective precipitation techniques to further improve the monodispersity of the NC sample.

Similarly, CdS NCs capped with mercaptopropyltrimethoxysilane (MPTMS) were added to alcoholic solutions of TEOS or TMOS and subsequently incorporated into silica matrices.[34] Pb and Hg-based NCs have also been synthesized with MPTMS as the capping agent, and the role of the pendant siloxy groups is again to anchor the NCs to the silica, silica-titania, or zirconia networks.[35–37] Zirconia films doped with PbS NCs were prepared with refractive indices up to 1.53 and a third-order susceptibility value of 1.3×10^{-7} esu.[37] Higher refractive index silica-titania sol–gel films doped with PbS ($n = 1.63$) were also fabricated.[36]

Hydroxy moieties have been explored as alternatives to siloxy groups for attaching the NCs to the sol–gel framework. In one example, the surface capping groups of high quality CdSe and CdSe/ZnS NCs were exchanged for tris(hydroxypropyl)phosphine ligands.[38] The resulting NCs have hydroxy groups on their surface, which allow them to be tethered to a sol–gel matrix. Titania is an attractive medium in this example because hydrolysis and condensation reactions do not normally require an acid or base catalyst to ensue, which can sometimes adversely affect the optical properties of the semiconductor NCs. The sols were spin-cast into thin films with a refractive index tunable from 1.61 to 1.82 and a 10–12% NC volume loading. Amplified spontaneous emission (ASE) was observed at liquid nitrogen and room temperatures in these materials, and NC-titania waveguide structures were developed into a distributed feedback laser.[39]

Higher volume loadings in NC-doped titania matrices were achieved with CdSe NCs overcoated with aminohexanol ligands.[40] The resulting nanocomposites exhibited a 20% volume loading of CdSe NCs (Figure 4a), spin-coated films had refractive indices tunable from 1.6 to 2.1, and the NCs could be incorporated into the titania matrix without

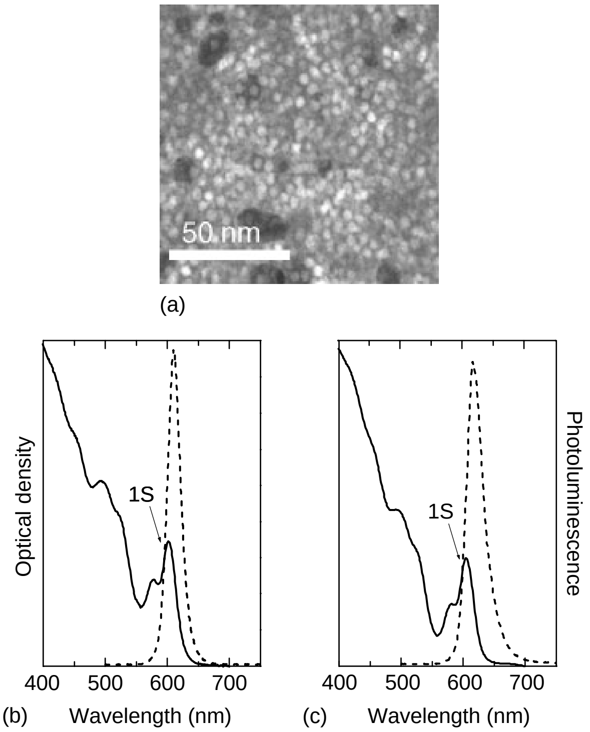

Figure 4 (a) Low-resolution scanning transmission electron microscopy (STEM) image of a thin sol–gel film (1–2 layers) containing 5 nm CdSe NCs. The NCs appear in white, and the dark areas are pores. (b) Linear absorption (solid line) and PL (dashed line) spectra of as-prepared CdSe NCs ($r = 2.5$ nm) in a hexane solution (the arrow marks the lowest 1S absorption resonance). (c) Absorption and PL spectra of the same NCs after their incorporation into titania

changes in their size or size dispersity (<7%) (Figure 4b and c). In addition, QYs as high as 15% were reported for the CdSe NCs in the titania sols. These waveguide structures demonstrated ASE at liquid nitrogen and room temperatures with optical gain values (100–200 cm^{-1} at room temperature) similar to values obtained for self-assembled films. A third-order nonlinear susceptibility of 1.5×10^{-4} esu was determined, which is comparable to results observed for bulk semiconductors (likely because of the high NC filling factors in the composite) and more than two orders of magnitude greater than $\chi^{(3)}$ values reported for composites prepared via the direct growth method discussed in Section 2. The titania composites prepared from colloidal CdSe NCs show improved photostability with regards to conventional, close-packed films of CdSe NCs and demonstrate consistent performance for several hours under continuous illumination.

While the ligand-exchange approach has been successful in generating functionalities on the NC periphery that allow them to be tethered to the metal-oxide sol–gel network, this exchange causes surface defects, which inevitably lead to a reduction in QY. In order to avoid deteriorating optical properties, new routes have been developed as a means of promoting higher QYs, which are important for light-emitting applications. CdTe NCs capped with thioglycolic acid were synthesized.[41] APTES was used as the sol–gel precursor, and the NCs were anchored to the resulting silica network through the ionic interactions between the COOH groups on the NC periphery and the amino groups of APTES. QYs in excess of 35% were reported, and the optical properties of the gel were stable for at least 6 months.

Polymer-NC adducts have been incorporated into titania and silica matrices via an amphiphilic approach that circumvents the need for ligand exchange.[32] Octylamine-modified poly(acrylic acid) complexes hydrophobically capped NCs as a result of the hydrophobic interactions between the ligands on the NCs and the hydrophobic portion of the amphiphilic polymer (Figure 5). The COOH groups remain on the NC periphery and can serve as the reactive sites through which the NCs are incorporated into the titania matrix. This general approach has been demonstrated for including CdSe and CdSe/ZnS NCs capped with a variety of ligands into titania and silica sol–gel networks. Volume fractions as high as 6% were obtained (these values are necessarily lower than those obtained for the ligand-exchange approach as a result of the added bulk of the polymer) with a refractive index tunable to 1.8 and QYs as high as 47%. ASE was also observed in these composites. This procedure is applicable to a wide variety of NCs and was successfully employed for incorporating PbSe NCs into titania matrices.[42] In this configuration, ASE was demonstrated, for the first time, from colloidal NCs emitting in the near infrared.

4 CONCLUSIONS

Sol–gel processing has been used to successfully encapsulate NCs in transparent host matrices, with the requirements of the resulting composite dictating the precise fabrication routes employed. By simply changing a few basic parameters, the properties of the materials can be easily and abruptly altered. Generally, the approach to these composites broadly diverges into two distinct paths. In

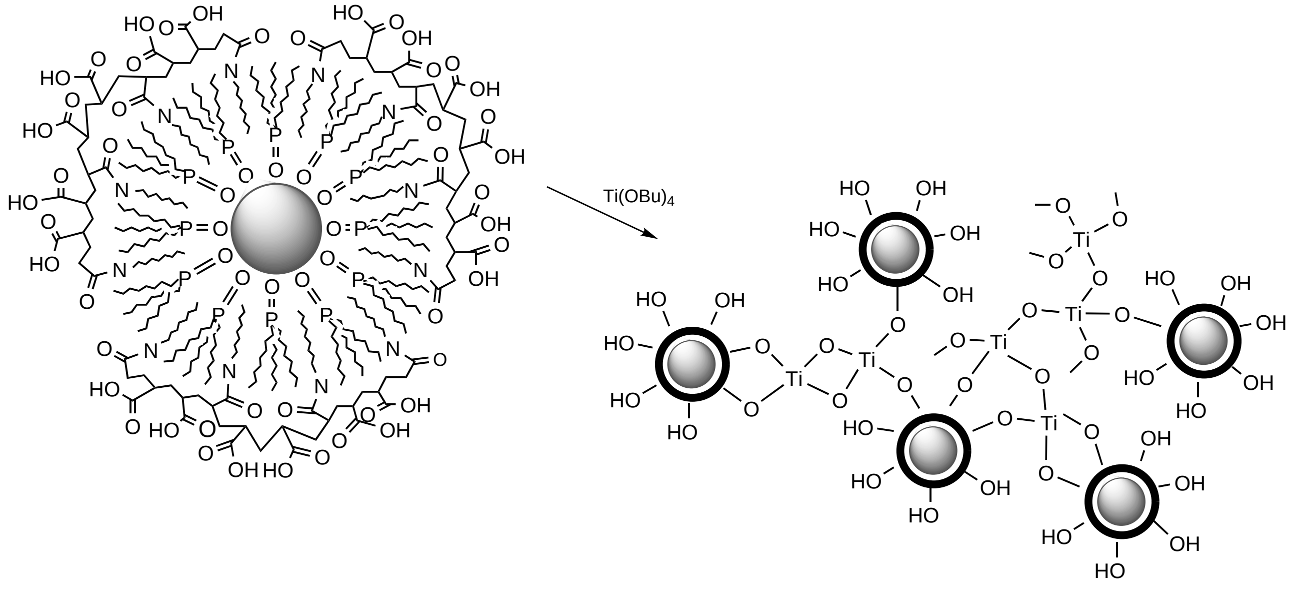

Figure 5 Polymer–NC complex showing an idealized micellar polymer shell (40% octylamine-modified poly(acrylic acid)). Upon addition of the titania precursor, the NC/polymer adducts are linked to each other through the titania network

one strategy, the synthesis of the NCs occurs during the fabrication of the host matrix. This direct growth method has been investigated as an express route to NC-doped glasses that usually involves the addition of metal salts to sol–gel precursors. Subsequent reduction or precipitation of the embedded metal salts, either with gases or other chemical reagents, leads to the formation of the desired NCs. The second approach focuses on a decoupled process in which the synthesis of the colloidal NCs is independent of the fabrication of the composite network. In this way, the size, shape, and composition of the NCs can be tailored for specific applications, promising a precise control over the dopant parameters that is unavailable in the direct growth method.

The flexibility of the methods described enables a variety of important materials properties, including NC volume loading and size dispersity, matrix pore size and chemical composition, and composite refractive index, to be customized by simply varying a few conditions. In addition, sol solutions are highly processible and are essentially unrestricted with regards to geometry, as they can be used to form films or fibers or incorporated into various cavities, where they can assume the shape of their containment vessels. The versatile features of this process provide a whole palette of options from which to choose, allowing for a wide assortment of tailored materials to be prepared while still relying on the same basic methodology for fabrication.

5 RELATED ARTICLES

Metal Nanoparticles, Organization & Applications of; Metal Nanoparticles, Synthesis of; Semiconductor Nanocrystal Quantum Dots; Sol–Gel Synthesis of Solids.

6 REFERENCES

1. F. Gonella and P. Mazzoldi, Metal Nanocluster Composite Glasses, in ‘Handbook of Nanostructured Materials and Nanotechnology’, ed. H. S. Nalwa, Academic Press, San Diego, 2000, p. 81.
2. J. Fick, Crystalline Nanoparticles in Glasses for Optical Applications, in ‘Handbook of Surfaces and Interfaces of Materials’, ed. H. S. Nalwa, Academic Press, San Diego, 2001, p. 311.
3. C. J. Brinker and G. W. Scherer, ‘Sol-Gel Science’, Academic Press, San Diego, 1990.
4. K. C. Kwiatkowski and C. M. Lukehart, Nanocomposites Prepared by Sol-gel Methods: Synthesis and Characterization, in ‘Handbook of Nanostructured Materials and Nanotechnology’, ed. H. S. Nalwa, Academic Press, San Diego, 2000, p. 57.
5. A. I. Ekimov and A. A. Onushchenko, *JETP Lett.*, 1981, **34**, 345.
6. V. I. Klimov, Linear and Nonlinear Optical Spectroscopy of Semiconductor Nanocrystals, in ‘Handbook of Nanostructured Materials and Nanotechnology’, ed. H. S. Nalwa, Academic Press, San Diego, 2000, p. 563.
7. S. Sakka and H. Kozuka, *J. Sol-Gel Sci. Tech.*, 1998, **13**, 701.
8. S. Bharathi, N. Fishelson, and O. Lev, *Langmuir*, 1999, **15**, 1929.
9. A. Basumallick, G. C. Das, and S. Mukherjee, *J. Mater. Res.*, 2000, **15**, 102.
10. B. Breitscheidel, J. Zieder, and U. Schubert, *Chem. Mater.*, 1991, **3**, 559.
11. J. P. Carpenter, C. M. Lukehart, S. B. Milne, D. O. Henderson, R. Mu, and S. R. Stock, *Chem. Mater.*, 1997, **9**, 3164.
12. J. P. Carpenter, C. M. Lukehart, S. B. Milne, S. R. Stock, J. E. Wittig, B. D. Jones, R. Glosser, and J. G. Zhu, *J. Organomet. Chem.*, 1998, **557**, 121.
13. J. Matsuoka, R. Naruse, H. Nasu, and K. Kamiya, *J. Non-Cryst. Solids*, 1997, **218**, 151.
14. A. Othmani, J. C. Plenet, E. Berstein, C. Bovier, J. Dumas, P. Riblet, P. Gilliot, R. Levy, and J. B. Grun, *J. Cryst. Growth*, 1994, **144**, 141.
15. T. Takada, J. D. Mackenzie, M. Yamane, K. Kang, N. Peyghambarian, R. J. Reeves, E. T. Knobbe, and R. C. Powell, *J. Mater. Sci.*, 1996, **31**, 423.
16. J. Butty, N. Peyghambarian, Y. H. Kao, and J. D. Mackenzie, *Appl. Phys. Lett.*, 1996, **69**, 3224.
17. J. Butty, Y. Z. Hu, N. Peyghambarian, Y. H. Kao, and J. D. Mackenzie, *Appl. Phys. Lett.*, 1995, **67**, 2672.
18. N. Tohge, M. Asuka, and T. Minami, *J. Non-Cryst. Solids*, 1992, **147–148**, 652.
19. N. N. Parvathy, G. M. Pajonk, and A. V. Rao, *Mater. Res. Bull.*, 1997, **32**, 397.
20. M. Nogami, S. Suzuki, and K. Nagasaka, *J. Non-Cryst. Solids*, 1991, **135**, 182.
21. M. Zelner, H. Minti, R. Reisfeld, H. Cohen, Y. Feldman, S. R. Cohen, and R. Tenne, *J. Sol-Gel Sci. Tech.*, 2001, **20**, 153.
22. D. A. Hummel, I. L. Torriani, A. F. Craievich, N. D. L. R. Fox, A. Y. Ramos, and O. Lyon, *J. Sol-Gel Sci. Tech.*, 1997, **8**, 285.
23. C.-Y. Li, Y.-H. Kao, K. Hayashi, T. Takada, J. D. Mackenzie, K.-I. Kang, S.-G. Lee, N. Peyghambarian, M. Yamane, G. Zhang, and S. I. Najafi, *Proc. SPIE*, 1994, **2288**, 151.
24. M. A. Fardad, E. M. Yeatman, E. J. C. Dawnay, M. Green, J. Fick, M. Guntau, and G. Vitrant, *IEE Proc. Optoelectron.*, 1996, **143**, 298.
25. C. B. Murray, C. R. Kagan, and M. G. Bawendi, *Annu. Rev. Mater. Sci.*, 2000, **30**, 545.
26. P. Mulvaney, *Glass Sci. Technol.*, 2002, **75**, 310.

27. S. T. Selvan, T. Hayakawa, M. Nogami, Y. Kobayashi, L. M. Liz-Marzan, Y. Hamanaka, and A. Nakamura, *J. Phys. Chem. B*, 2002, **106**, 10157.
28. S. T. Selvan, M. Nogami, A. Nakamura, and Y. Hamanaka, *J. Non-Cryst. Solids*, 1999, **255**, 254.
29. S. T. Selvan, Y. Ono, and M. Nogami, *Mater. Lett.*, 1998, **1998**, 156.
30. Y. Kobayashi, M. A. Correa-Duarte, and L. M. Liz-Marzan, *Langmuir*, 2001, **17**, 6375.
31. S. T. Selvan, C. Bullen, M. Ashokkumar, and P. Mulvaney, *Adv. Mater.*, 2001, **12**, 985.
32. M. A. Petruska, A. P. Bartko, and V. I. Klimov, *J. Am. Chem. Soc.*, 2004, **126**, 714.
33. V. Ptatschek, B. Schreder, K. Herz, U. Hilbert, W. Ossau, G. Schottner, O. Rahäuser, T. Bischof, G. Lermann, A. Materny, W. Kiefer, G. Bacher, A. Forchel, D. Su, M. Giersig, G. Müller, and L. Spanhel, *J. Phys. Chem. B*, 1997, **101**, 8898.
34. T. Hirai, H. Okubo, and I. Komasawa, *J. Mater. Chem.*, 2000, **10**, 2592.
35. M. Guglielmi, A. Martucci, J. Fick, and G. Vitrant, *J. Sol-Gel Sci. Tech.*, 1998, **11**, 229.
36. A. Martucci, J. Fick, J. Schell, G. Battaglin, and M. Guglielmi, *J. Appl. Phys.*, 1999, **86**, 79.
37. A. Martucci, P. Innocenzi, J. Fick, and J. D. Mackenzie, *J. Non-Cryst. Solids*, 1999, **244**, 55.
38. V. C. Sundar, H.-J. Eisler, and M. G. Bawendi, *Adv. Mater.*, 2002, **14**, 739.
39. H.-J. Eisler, V. C. Sundar, M. G. Bawendi, M. Walsh, H. I. Smith, and V. Klimov, *Appl. Phys. Lett.*, 2002, **80**, 4614.
40. M. A. Petruska, A. V. Malko, P. M. Voyles, and V. I. Klimov, *Adv. Mater.*, 2003, **15**, 610.
41. C. Li and N. Murase, *Langmuir*, 2004, **20**, 1.
42. R. D. Schaller, M. A. Petruska, and V. I. Klimov, *J. Phys. Chem. B*, 2003, **107**, 13765.

Metal Nanoparticles, Synthesis of

Günter Schmid
University of Duisburg-Essen, Essen, Germany

1	Introduction	1
2	Stabilization of Metal Nanoparticles	2
3	Syntheses of Noble Metal Nanoparticles	2
4	Synthesis of Magnetic Nanoparticles	7
5	Summary	10
6	Related Articles	10
7	Further Reading	10
8	References	10

1 INTRODUCTION

The term ‘nanoparticle’ is not properly defined. Roughly, one could say that any particle on the nanometer scale is to be called a nanoparticle. However, this would not express what ‘nanoparticle’ really means. The increasing interest in metal nanoparticles is based on their size-dependent properties placing them between molecules and bulk materials. Therefore, it is not very meaningful to define an exact size range for nanoparticles. Owing to their special properties, metal nanoparticles are contributing decisively to the expanding importance of nanosciences and in consequence of nanotechnology. Thus, the term ‘nanoparticle’ is inevitably linked with the definition of nanoscience and nanotechnology, respectively. What is nanoscience and nanotechnology? Among numerous definitions published in scientific papers as well as in secondary literature, one that has recently been defined seems to be the most comprehensive one and also the most suited one to define the term ‘metal nanoparticle’: *Nanotechnology comprises the emerging applications of nanoscience. Nanoscience is dealing with functional systems based on the use of subunits with specific size-dependent properties of the individual subunits or of a system of those*.[1]

A functional system is best described as a collection of a distinct number of interacting subunits forming a new entity with specific properties. The subunits are hierarchically organized on different levels of complexity, leading to new qualities of the functional system that cannot be achieved by uncontrolled combination of the subunits.

Specific size-dependent properties cover magnetic, mechanic, electronic, optical, thermodynamic, and thermal features as well as the abilities for self-assembly and recognition. The specific size-dependence of these properties becomes evident when they

- no longer follow classical physical laws but rather are described by quantum mechanical ones;
- are dominated by particular interface effects;
- exhibit properties due to a limited number of constituents, since the usual term ‘material’ refers to an almost infinite number of constituents (e.g. atoms, molecules) displaying an averaged statistical behavior.[1]

These three points comprehensively describe the conditions that convey the meaning of ‘nanoparticle’ much better than a simple section of a length scale. They exclude the huge number of oligo- and multinuclear cluster compounds, mainly of organometallic nature, that have become known in the course of the last 2–3 decades. Most of them exhibit typical molecular behavior, that is, they do not follow the rules described before. The term ‘cluster’ will therefore be avoided in the following in order to distinguish these molecular species from those being defined as nanoparticles.

This article on the synthesis of metal nanoparticles is divided into two parts. The first one deals mainly with nanoparticles consisting of noble metals, except for a few examples. The second one will describe synthetic strategies to generate magnetic nanoparticles that may also exist in metal combinations. Magnetic nanoparticles are attracting increasing attention owing to their promising properties with respect to novel magnetic devices.

There exists a huge number of synthetic procedures for metal nanoparticles, especially those consisting of noble metals because of the easy reducibility of noble metal salts. To discuss all the syntheses in detail would exceed the scope of this article by far. Rather, synthetic strategies, elucidated with the help of examples, will be discussed in the following.

Usually, syntheses of metal nanoparticles aim at the generation of monodisperse species. This is especially the case in more recent years, since the properties of interest become more expressed the more uniform the particles are. Metal nanoparticles with broad size-distributions have a long history in many technological applications, for instance, in heterogeneous catalysis, and so are not necessarily developed aiming at monodispersity. High-temperature reduction of metal salts on oxidic supports, a general industrial method to generate catalysts, are of course not very well suited to produce monodisperse particles. On the other hand, synthetic approaches to noble metal nanoparticles, traditionally called colloids, with rather narrow size distribution, originate already from Michael Faraday’s time, that is, the mid-nineteenth century.[2] Reduction of tetrachloroaurate $[AuCl_4]^-$ solutions with white phosphorus resulted in the formation of the known deep red solutions of gold nanoparticles (colloids) with surprisingly narrow size distributions. At the beginning of the twentieth century, Zsigmondy carefully studied the physical properties of colloidal solutions (metal sols) on a scientific

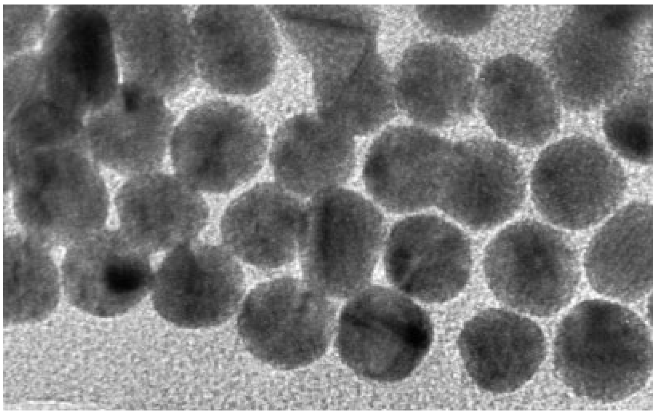

Figure 1 TEM image of 18 nm gold particles synthesized by the Turkevitch method

basis, especially the relation between preparative conditions and particle size using ultramicroscopy.[3] Numerous synthetic procedures have been developed over the years since the very first experiments. Later, Turkevitch *et al.* contributed considerably to synthetic aspects.

The knowledge at the end of the first half of the twentieth century has been summarized by Turkevitch, describing detailed synthesis conditions as well as first electron microscopic investigations.[4,5] He also contributed remarkably to the understanding of nucleation processes, particle growth, and agglomeration mechanisms. Turkevitch's preparative methods are partially used until today. Figure 1 shows a transmission electron microscopic (TEM) image of gold nanoparticles, synthesized by the Turkevitch method.

Nanoparticles in the size range of about 2–100 nm, depending on the experimental conditions and on the metal, became available.

The successful generation of metal nanoparticles is unavoidably linked with successful protection of the particles' surfaces, otherwise spontaneous aggregation with formation of metallic precipitates would happen. For that reason, some general and crucial aspects concerning stabilization of metal nanoparticles will be discussed before the description of synthetic strategies.

2 STABILIZATION OF METAL NANOPARTICLES

Metal nanoparticles are unstable with respect to agglomeration to the bulk. van der Waals forces between the particles attract them to such an extent that metal–metal bond formation occurs. The fact that nanoparticles can be kept in solution is due to either electrostatic or steric stabilization.[6] For instance, the ruby red gold sols, prepared from $[AuCl_4]^-$ and sodium citrate as reducing agent, are stabilized by an electrical double layer formed by adsorbed citrate and chloride ions and the corresponding cations. Thus, Coulombic repulsion between the particles happens, keeping them in solution. Figure 2 elucidates this electrostatic stabilization of metal nanoparticles.

At moderate interparticle distance, a weak minimum in potential energy guarantees stable arrangements of nanoparticles as long as the surface charge is not reduced, for instance, by displacement of adsorbed ions.

The second strategy by which metal nanoparticles can be stabilized is the fixation of molecules by the particles' surface atoms. The protecting molecules may consist of polymers, surfactants, or ligands, as they are known from traditional complex chemistry. The use of polymers is for their amphiphilic nature, that is, they have not only to coordinate to the metal particle, but must simultaneously be solvated by the surrounding fluid. Gelatin, agar, cyclodextrins, cellulose acetate, and cellulose nitrate are used as well as synthetic polymers. Poly(vinylpyrrolidone) (PVP) and poly(vinylalcohol) have turned out to work perfectly in this respect.

Surfactants tend to form micelles and so-called reverse micelles, depending on the solvent. Sphere-like holes are formed either by the hydrophobic tails or the hydrophilic heads of the surfactant molecules. Both are suited perfectly to encapsulating metal nanoparticles.

Small molecules such as phosphines and alkane thiols stabilize metal nanoparticles in a very effective manner. Very stable covalent metal-phosphorus or metal–sulfur bonds lead to such strong ligand shells that in some cases the protected particles can even be isolated in solid state, which can never be done with electrostatically stabilized particles. The chemical nature of the protecting ligand molecules is responsible for the solubility of the particles. Thus, the use of organic solvents has become very useful for several reasons. Figure 3 shows a sketch of the three types of steric stabilizations of metal nanoparticles.

3 SYNTHESES OF NOBLE METAL NANOPARTICLES

Chemical syntheses of metal nanoparticles are all based on the use of appropriate precursor complexes. Depending on the metal, its oxidation state, the desired type of nanoparticle, and so on, the methods applied vary in a wide range. Besides chemical syntheses, there exist also physical approaches. They usually start from bulk metals and use different kinds of energy to transfer them into the atomic state in the gas phase, where the atoms are allowed to condense to nanoparticles. From a preparative point of view, such physical methods are less important, since the resulting particles are bare. As has already been mentioned, unprotected metal nanoparticles cannot exist without aggregation except in the gas phase. That is why gaseous metal nanoparticles have been generated and used

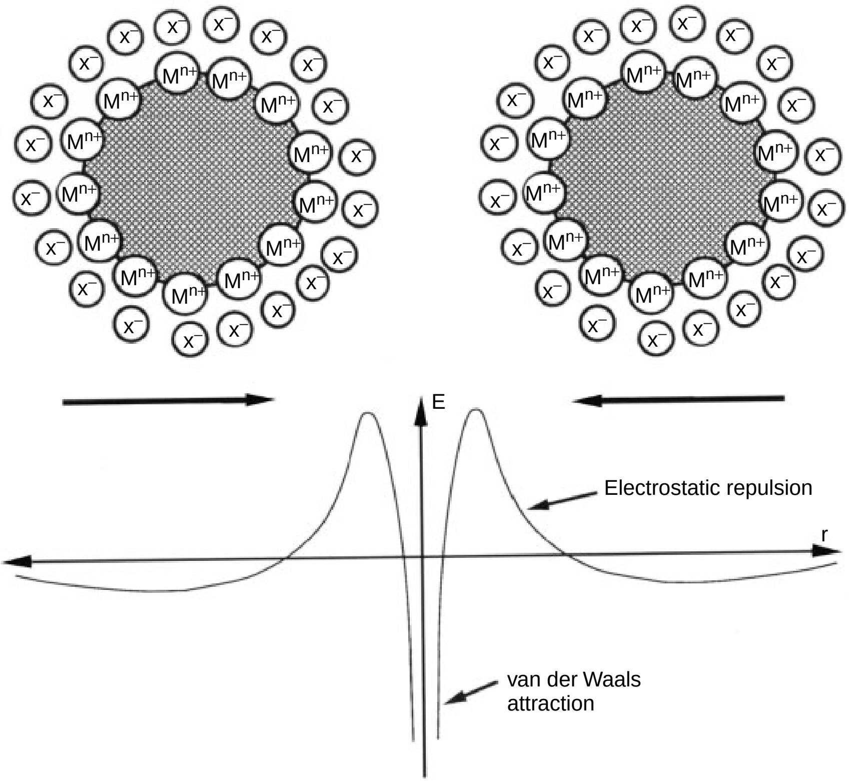

Figure 2 Electrostatic stabilization of metal nanoparticles. Repulsive electrostatic forces outweigh attractive van der Waals forces

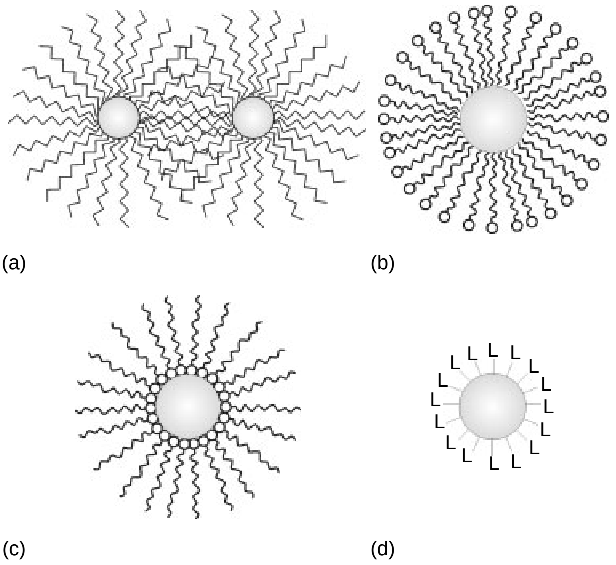

Figure 3 Different types of steric stabilization of metal nanoparticles. (a) polymer molecules on the particles' surface; (b) micelle; (c) inverse micelle; (d) ligand stabilized particle

mainly for spectroscopic investigations, and so on. However, there are some approaches to stabilize naked nanoparticles after their formation by interactions of the gas stream with suited molecules. Therefore, Section 3.1 will briefly deal with some physical methods, before chemical routes will be discussed in somewhat more detail.

3.1 Physical Methods

As already mentioned, the simplest way of generating metal nanoparticles in the gas phase is to produce atoms that are subsequently allowed to coalesce under controlled conditions. This so-called metal–vapour synthesis requires more or less expensive equipment. Numerous modifications of this well established technique have been successfully applied. However, a detailed description of all the devices would exceed the scope of this article. For a summarizing overview, see Reference 7. Some more recent and relevant results shall be mentioned here.

Laser ablation is one of the modern and frequently used methods.[8–12] The disadvantage of broad size distribution could be improved by the so-called 'laser-induced size reduction'. For instance, in the case of gold nanoparticles, their well expressed plasmon resonance around 520 nm can be used to influence the size and shape of the particles.[13–18] Thus, more or less monodisperse gold particles of 1.7 nm and 3.4 nm could be generated with a 532-nm pulsed laser irradiation of gold metal plates in diluted sodium dodecylsulfate solutions.[19]

The solvated metal-atom dispersion (SMAD) technique uses a traditional reactor to generate atoms from bulk gold.[20,21] The gold atoms are then frozen out at 77 K in acetone vapor. After warming up, acetone-stabilized gold nanoparticles are formed that can be further stabilized by dodecanethiol. Gram amounts of gold nanoparticles stabilized in such a manner can be produced. Digestive ripening of thiol stabilized particles in toluene at 120 °C results in 4–4.5 nm species, a remarkable narrow distribution obtained by combination of physical and chemical methods.

In spite of these promising advances based on evaporation methods, wet-chemical methods dominate clearly the field of metal nanoparticle syntheses. The following sections will deal with the most important routes.

3.2 Salt Reduction

Undoubtedly, salt reduction for generating metal nanoparticles is the most widespread chemical method. Aqueous solutions as well as organic solvents can be used to reduce metal salts and metal complexes. In some cases, the organic solvent and the reducing agent can be one and the same, for instance, alcohols. In some cases, even the reducing agent can in addition serve to protect the particles' surface. The so-called 'alcohol reduction process', developed by Hirai and Toshima,[22–28] is a very general process to fabricate metal nanoparticles.

The reduction of metal salts in nonreducing solvents by addition of reducing agents is the oldest and most established procedure for generating metal nanoparticle sols in water. It was especially Turkevitch who developed chemical routes that are still in use today. Sodium citrate is the best-known reducer. $[AuCl_4]^-$ in hot water is reduced to 15–20 nm gold particles.[4] The citrate itself as well as its oxidation products (e.g. acetone dicarboxylate) act, along with Cl^-, as protecting species. Figure 1 shows a selection of as-prepared gold nanoparticles. Besides gold, other noble metal salts, for instance, $[PtCl_4]^{2-}$, can be reduced successfully to metal sols.[29–31] Of course, Turkevitch's citrate is not the only reducing agent being used. Especially Glaunsinger and coworkers[32] have reported on the successful generation of Pt nanoparticles from $[PtCl_4]^{2-}$ and sodium borohydrate, hydroxylamine hydrochloride, dimethylamine borane, hydrazine hydrate, sodium formiate, formaldehyde, or sodium trimethoxyborohydride. Among these various reducing compounds, $[BH_4]^-$ is of paramount importance. Brust *et al.* used $[BH_4]^-$ successfully to fabricate 1–5 nm gold nanoparticles in the presence of alkanethiols.[33,34] Variations of the thiol concentrations allow satisfying control of size.

So-called seeding growth processes starting with 3.5 nm gold particles opened the door to a variety of further particle sizes.[35] Worth mentioning in this connection is the availability of bimetallic core-shell nanoparticles. Beginning with a seed of a distinct metal, a shell of a second metal can then be grown on this seed.[36,37] An example of a perfectly grown bimetallic core-shell particle consisting of a gold core and a palladium shell is shown in Figure 4.

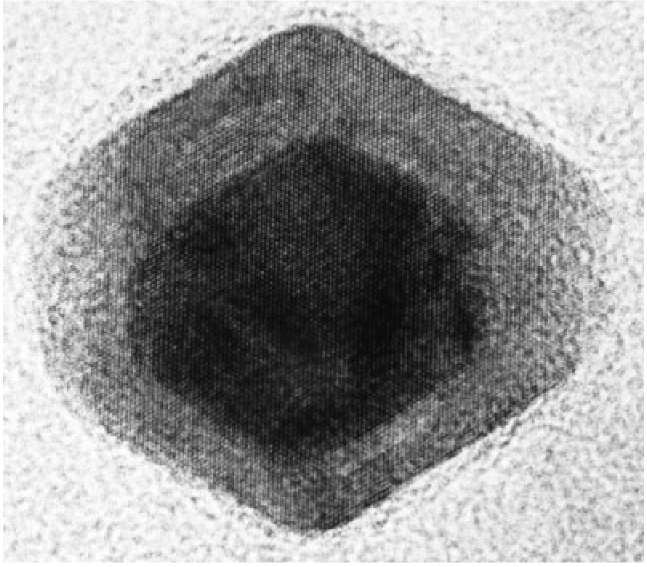

Figure 4 TEM image of a bimetallic core-shell nanoparticle, consisting of a gold core and a palladium shell

Reverse Pd/Au particles or those consisting of other metals become available using this method.

Gold nanoparticles between 10 and 30 nm can be produced by means of $[BH_4]^-$ as reducer and mercaptosuccinic acid as stabilizer. Very well defined sizes, for instance, of 10.2, 10.8, 12.8, 19.4, or 33.6 nm, become available with variation of the $[AuCl_4]^-$: succinic acid ratio.[38]

The number of reducing agents for gold compounds is enormous. In principle, any kind of organic compound having some reducing character can be applied under appropriate conditions to generate gold from a salt. Among those, the so-called 'green chemistry' is going to develop from an academic to a more practical technique.[39,40] Even living species like fungi have been found to transfer gold salts to elemental gold.[41]

Metal nanoparticles stabilized only electrostatically or by weakly binding molecules can be transferred into very stable species by the subsequent exchange of the weak by stronger ligand molecules. This has been successfully done in the case of gold nanoparticles by addition of water-soluble phosphines like $Ph_2PC_6H_4SO_3Na$, $P(C_6H_4SO_3Na)_3$ or by a series of thiols. Au–S bonds are of special strength and so give very well protected particles that can partially even be isolated in solid state, but keep redispersable.[42]

α-Hydrogen containing alcohols are effective reducing agents owing to their oxidizability to the corresponding carbonyl compounds (methanol gives formaldehyde, ethanol forms acetaldehyde, i-propanol gives acetone, etc.).[22–28] As an example, equation (1) describes the formation of rhodium nanoparticles, denoted as Rh(0):

$$RhCl_3 + \frac{3}{2}R_1R_2CHOH \longrightarrow Rh(0) + \frac{3}{2}R_1R_2C{=}O + 3HCl \quad (1)$$

Organosols of palladium nanoparticles become available by the reduction of palladium acetate with various alcohols in the presence of PVP. The boiling points of the alcohols influence the particles size.[43] Long-chain aliphatic alcohols like 1-decanol not only reduce palladium and platinum salts, but act as reasonable stabilizers for the resulting particles.[44] Pd particles in the size range of 1–4 nm can be prepared using C_1–C_5 aliphatic alcohols as solvents and as reducing compounds for palladium acetate, again in the presence of PVP.[45]

Tetraalkylammonium hydrotriorganoborates $[R_4N]^+$ $[BR'_3H]^-$ have become of interest in recent years for generating different metal nanoparticles, especially by numerous contributions of Bönnemann *et al.*[46–50] These salts not only are powerful reducers, but the ammonium cations stabilize the metal particles in a surprisingly good fashion. Equation (2) explains the reaction for $R' = Et$:

$$MX_n + n[R_4N][BEt_3H] \longrightarrow M(0) + n[R_4N]X + nBEt_3 + \frac{n}{2}H_2 \quad (2)$$
$$(X = Cl, Br;\ R = C_6\text{–}C_{20};\ M = \text{groups } 6\text{–}11 \text{ metals})$$

$[BEt_3H]^-$ not only reduces salts of the more noble metals, but even those of Ti, V, or Nb.[51] Aluminum alkyls have also turned out to act as reducing agents for groups 6–11 metals using halide or acetylacetonate salts.[52,53] Organoaluminum compounds seem to act as stabilizers of the 1–12 nm particles.

Nanoparticles of Ti, Fe, Co, Ni, Pd, Pt, Ag, and Au in preparative amounts became available by electrolytic methods.[54–60] The relevant metal in bulk form is used as anode where atoms from the surface become oxidized, whereas the cathode serves to reduce the cations to atoms and subsequently to nanoparticles. These can be protected, for instance, by tetraalkylammonium salts. A strategic advantage of this technique is the easy influence on the particle size by the current density. Increasing current density results in decreasing particle sizes.

Hydrogen is a reducing agent that has some special advantages. One is the low price, compared with some extraordinary chemical compounds. Without additional stabilizers, syntheses usually end up with only electrostatically stabilized nanoparticles. Hydrosols of Pd, Pt, Rh, and Ir can be yielded from the corresponding hydroxides.[61–65]

Hydrogen is also a successful reducing agent for polyoxoanion-iridium complexes. In rather complex reactions, salts such as $(Bu_4N)_5Na_3[(1,5\text{-COD})IrP_2W_{15}Nb_3O_{62}]$ are reduced in solution, ending up with polyoxoanions-protected nanoparticles containing 300–900 Ir atoms.[51,66,67]

In connection with the reductive element hydrogen, the synthesis of some special nanoparticles will be discussed because they have become known as those following rather discrete analytical composition that cannot be formulated for usual nanoparticles, owing to their size and shape deviations. Moiseev *et al.* reduced palladium acetate in the presence of phenanthroline or bipyridine in aqueous solution to yield nanoparticles of the composition $Pd_{561}L_{\approx 60}(OAc)_{\approx 180}$.[68–73] The number of exactly 561 Pd atoms results from the counting rules for so-called full-shell clusters. (Although the term 'cluster' is generally substituted in this article by 'nanoparticle', in the case of such molecularly precise particles, it will continue to be used.) Full-shell clusters are nanoparticles with hexagonally close-packed atoms, as is the case in most bulk transition metals. A central atom is surrounded by 12 densely packed others, resulting in a 13-atomic one-shell cluster. Two-shell particles consist of 55 and three-shell systems of 147 atoms. Generally, the nth layer consists of $10n^2 + 2$ atoms. Moiseev's 561 atomic Pd particle represents a five-shell cluster. In practice, the number of metal atoms as well as that of ligand molecules may deviate to some extent; however, compared with the usual nanoparticles, full-shell clusters of the above type are strictly monodisperse and deserves to be labelled with a chemical formula. Schmid *et al.* described some more Pd full-shell nanoparticles, namely, $Pd_{561}phen_{36}O_{\approx 200}$, $Pd_{1415}phen_{60}O_{\approx 1100}$, and $Pd_{2057}phen_{84}O_{\approx 1600}$ (phen = phenanthroline), representing another five-shell and a seven- and an eight-shell particle.[74–76] The seven- and the eight-shell clusters are formed simultaneously; however, they can be separated by careful chromatography. The most important tool to determine the exact size of such clusters is high-resolution transmission electron microscopy (HRTEM).

A full-shell cluster of a very special importance is $Au_{55}(PPh_3)_{12}Cl_6$ and some of its derivatives. It is probably the most frequently investigated cluster or nanoparticle owing to its unique electronic properties making it one of the most promising building blocks for future nanoelectronic devices. It can act as a single-electron switch even at room temperature and so follows strictly quantum mechanical rules instead of classical physical laws. It therefore is often called an artificial atom. A prerequisite for technical applications is the easy availability of this quantum dot. Ph_3PAuCl is reduced in benzene or toluene at 60 °C by gaseous diborane.[77,78] B_2H_6 not only reduces Au(I), but furthermore binds excessive PPh_3 as $H_3B\text{-}PPh_3$, an important fact in order to avoid formation of smaller clusters containing higher phosphine yields. The yield of $Au_{55}(PPh_3)_{12}Cl_6$ is about 30%. Bulk gold and larger particles are formed simultaneously. Pure cluster samples can be made by chromatography over Celite. In contrast to the larger gold nanoparticles, $Au_{55}(PPh_3)_{12}Cl_6$ is not red, but forms dark brown microcrystalline powders, best soluble in dichloromethane. Although stable in solid state at room temperature for a long time, the cluster starts decomposing in solution rather quick. This is due to partial dissociation of PPh_3 molecules leading to coalescence processes between clusters and finally to formation of precipitates. On the other hand, the easy dissociation of phosphines in solution can be used to substitute them by stronger ligands, as is usual

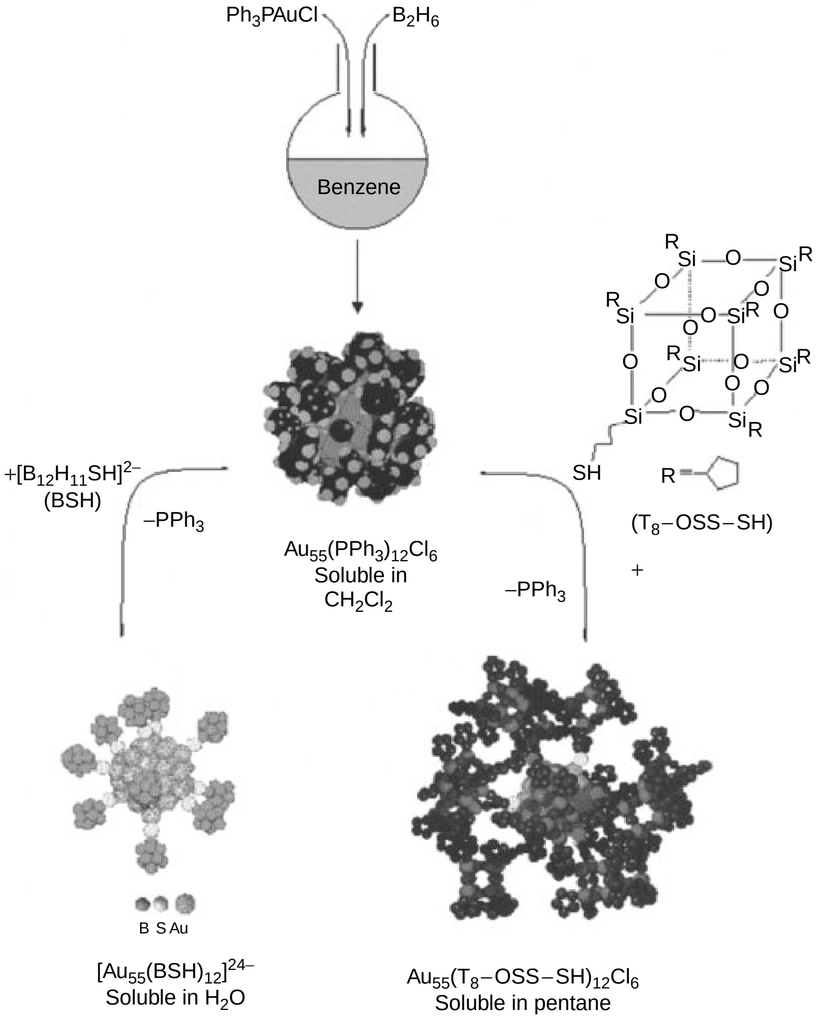

Figure 5 Synthesis of $Au_{55}(PPh_3)_{12}Cl_6$ and some ligand exchange reactions resulting in different solubilities. (Ref. 79. Reproduced by permission of Wiley-VCH)

in complex chemistry. Figure 5 summarizes some of the exchange reactions.

Such ligand exchange reactions lead to cluster derivatives that not only have changed their size, but also their solubility. The solubility of ligand stabilized nanoparticles depends exclusively on the nature of the protecting ligand shell. As can be seen from Figure 5, the solubility changes from dichloromethane for the PPh_3 containing starting compound to totally unpolar solvents like pentane or hexane if the alkyl-substituted silsesquioxane ligand T-OSS-SH is occupying the cluster surface.[80] Even water as solvent becomes possible when using the anionic ligand $[Ph_2C_6H_4SO_3]^-$[81] or $[B_{12}H_{11}SH]^{2-}$, making the Au_{55} cluster 24-fold negatively charged.[82]

The formation of full-shell clusters is a consequence of their thermodynamic stability. The ideal shape of such particles makes them unusually stable species with respect to chemical reactions. Thus, ligand-free Au_{55} clusters cannot be oxidized under oxygen plasma conditions where smaller and larger gold nanoparticles not possessing full-shell character are forming oxides.[83] Corresponding results are obtained from alloying experiments. Indium forms alloys of $AuIn_2$ type with all kinds of gold particles and with bulk gold, but not with Au_{55}.[84]

Some more special routes to metal nanoparticles shell complete this section on salt reductions.

Carbon monoxide/water reduces PtO_2 to nanoparticles based on the water–gas shift reaction providing electrons as is seen from equation (3).[85]

$$CO + H_2O \longrightarrow CO_2 + 2e + H_2 \qquad (3)$$

Alkalides and electrides allow homogenous reduction reactions for various transition metals, even for main group metals in aprotic solvents.[86,87] These reducers consist of alkali metal anions or electrons trapped in crown ethers.

3.3 Thermal Reactions

Thermally unstable metal complexes, particularly organometallic compounds, can be decomposed to liberating metal atoms forming nanoparticles. This widely applicable method is especially applicable for noble metals such as rhodium, iridium, ruthenium, osmium, palladium, and platinum. Particles of those elements in the size range of 1–10 nm are formed by decomposition of polymer-fixed organometallic species.[88–92] High boiling organic solvents are used to decompose complexes like palladium acetate, palladium, and platinum acetylacetonate.[93–98] Mixtures of acetates, for instance, of copper and palladium, are used to produce bimetallic nanoparticles in high boiling solvents. PVP has been used for stabilization.[99] In spite of this easy availability of nanoparticles, it must be stated that thermal decomposition of appropriate precursors often results in rather broad size distributions. This is probably why thermal routes have not been developed to such an extent as salt reduction methods.

3.4 Ligand Removal from Organometallics

A rather novel route to metal nanoparticles of increasing interest and relevance is the soft displacement of ligands from organometallic complexes with zero-valent metal atoms. An elegant way to do this is the decomposition of precursor molecules by CO and H_2.[100–117] A prominent example is the generation of Ru nanoparticles from Ru(COD)(COT) (COD = cyclooctadiene, COT = cyclooctatriene) in solution by hydrogen.[118,119] Scheme 1 elucidates the process.

Depending on the solvent, usually alcohols, the particle size can be astonishingly well controlled. Thus, nanoparticles in the range of about 3 up to more than 80 nm are made from the Ru(CO)(COT) compound at 3 bar of hydrogen at room temperature.

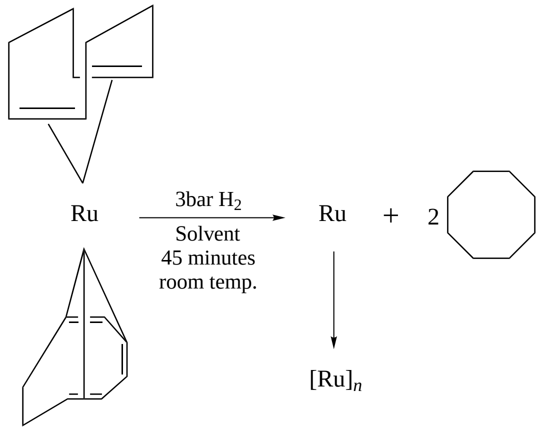

Scheme 1 Formation of Ru nanoparticles by removal of ligands from organometallic complex

Dibenzylideneacetone (dba) complexes of palladium and platinum serve as metal-atom source when they are treated with H_2 or CO under mild conditions.[120]

3.5 Photolysis and Radiolysis

Photolysis of metal compounds is a method of historical dimension as it has been used since the middle of the nineteenth century, when the light-sensitivity of silver salts was used for photographic purposes. Novel research, especially linked with the names Henglein and Belloni, led to a large extended field in the science of nanoparticles. UV-visible irradiation of Au, Ag, and Pt salts in surfactant or polymer solutions end up with nanoparticle formation.[121–136] Compared with hydrogen reduction, photolytic reactions usually give smaller particles with narrower size distribution.[137]

Radiolytic methods in the end result in salt reduction using electrons generated from irradiation with radioactive materials. The radiolysis of aqueous solutions of metal salts is based on formation of solvated electrons reacting with the metal ions or with other solutes to give secondary radicals, which then reduce the metal cations. The use of radioactive tools looks rather unattractive compared with usual chemical procedures; however, it may have advantages in special cases. For instance, radiolysis spontaneously produces many seeds leading to many small particles. Furthermore, radiolysis generates the reducing species in situ and so avoids side reactions of the chemical reducers and their oxidation products. However, all in all, radiolysis does not play a very important role in nanoparticle syntheses compared with other physical and chemical methods.

4 SYNTHESIS OF MAGNETIC NANOPARTICLES

4.1 Miscellaneous Routes

The applications of magnetic nanoparticles are manifold. Single-electron devices, ferrofluids, data storage, and catalyses are just a few examples indicating the importance of nanomagnets. Monodispersity is again a prerequisite in order to guarantee identical properties. Magnetic behavior of nanoparticles depends, except on the chemical composition, on their size and on their crystalline modification. It has been shown that magnetic nanoparticles of similar grain size differ in the magnetic properties when prepared by different methods.[138] Monodisperse magnetic nanoparticles are able to organize themselves to give highly ordered arrangements in two or even in three dimensions, a condition to align the electron spins in a certain direction by an external magnetic field. Sophisticated synthetic procedures are therefore a condition to reach that goal. Protection of magnetic nanoparticles by a shell of appropriate materials is usually even more important than for noble metal nanoparticles discussed in Section 3 for the easier oxidizability of the less noble magnetic metals. Several chemical and physical routes to magnetic nanoparticles are known. Nanoparticles of Fe, Co, and Ni are frequently generated by the inert gas condensation technique.[139,140] Metal atoms are produced from bulk material at high temperatures into an inert gas, for example, helium. Collisions with gas molecules reduce the kinetic energy of the atoms and allow condensation to nanoparticles. Arc discharges are also used to produce metal atoms that are channelled into a circulating gas mixture of H_2 and Ar. 20–30 nm Fe, Ni, and Fe–Ni alloy particles thus become available. Often, as-prepared nanoparticles are amorphous and partially oxidized, a problem always accompanying synthesis and use of less noble metal nanoparticles.

Among the synthetic methods, the reverse micelle technique shall only briefly be mentioned. It is based on the use of water droplets in an organic phase of a surfactant.[141,142] Metal salts, dissolved in the water droplets, are reduced inside the nanometer-sized water volume, to result in nanoparticles trapped in the micelles. Alloy-like particles as well as bimetallic core-shell particles thus become available. Size distributions up to over 20% have to be put up with this technique.[143] Another disadvantage of the reverse micelle procedure is the lack of crystallinity due to the low synthesis temperature ($<100\,°\text{C}$) requiring subsequent annealing at 200–300 °C.[144,145] Fe, Co, and Ni form carbonyl compounds that can be decomposed under elimination of gaseous CO and formation of magnetic nanoparticles of these most prominent metals. Decomposition can also be performed by ultrasonic irradiation of metal carbonyl solutions. The advantage of this method is, compared with heat treatment, the formation of acoustic cavitation, that is, formation and collapse of small bubbles within the liquid, resulting in local heats of some thousand K. Atoms and subsequently nanoparticles are formed that can be stabilized if necessary by suited molecules.[146,147] However, sonochemical generation of nanoparticles also yields amorphous and rather polydisperse species.

After these numerous methods, all linked with the one or the other disadvantage, some special routes shall be considered in the following sections, offering formation of monodisperse magnetic nanoparticles.

4.2 Reduction and Thermal Routes to Co and $CoPt_3$ Nanoparticles

High-quality magnetic nanoparticles become available taking routes via thermolysis or reduction of organometallic precursors containing appropriate metal atoms. If the original organic ligands do not act as protectors of the nanoparticles, other stabilizers have to be added during particle formation. Co and $CoPt_3$ nanoparticles will be the focus of this Section since they play an important role with respect to applications. Whereas cobalt nanoparticles can be called the most intensively investigated systems, $CoPt_3$ serves as prominent model for the study of magnetic alloy-like nanoparticles.

Owing to the easy oxidation of cobalt nanoparticles, all syntheses require rigorous exclusion of oxygen. As for other metal nanoparticles, the size distributions of magnetic particles depends on the kinetics of particle nucleation and growth.[148] The so-called ‘hot injection technique’ turned out to give really narrow size distributions. This procedure is based on the rapid injection of a precursor solution into a hot solvent containing the stabilizing molecules. Spontaneous nucleation happens, a prerequisite for uniform nuclei that then grow to nanoparticles by a controlled decrease of temperature.

In the case of less perfect monodispersity, later separation of particles of different size is possible either by differences in solubility or by the size-dependent magnetic interactions of the particles. The larger the particles, the stronger are the magnetic forces between them. This aggregation can be provoked by slow addition of a non-solvent to the particles’ solution. External magnetic fields can also be applied to separate larger from smaller particles with astonishingly good results.[149] Standard deviations below 5% can be reached by this primitive technique. One of the most frequently used organometallic precursors for cobalt nanoparticles is $Co_2(CO)_8$.

As is known, the magnetic properties not only depend on the kind of metal and the grain size, but also remarkably on the crystal modification. Cobalt nanoparticles are known to exist in three different modifications that can selectively be synthesized. Except the hexagonal close-packed (hcp) and the face-centered cubic (fcc) form, also known from bulk cobalt, nanoparticles form a third modification, the metastable ε-Co, which does not exist in the bulk state.[150] Surprisingly, ε-Co is the most frequently observed modification for nanoparticles.[151] Distorted fcc Co nanoparticles are usually generated if $Co_2(CO)_8$, dissolved in diphenylether, is injected into a 200 °C hot mixture of oleic acid and trioctylphosphine (TOP) or tributylphosphine (TBP) in diphenylether, followed by further heating at 200 °C for 15–20 min.[152] Monodisperse ε-Co nanoparticles are formed by reduction of $CoCl_2$ in hot dioctylether (200 °C) by $Li[BEt_3H]$ in the presence of oleic acid and TOP. Changing the amounts of stabilizing TOP varies the particle size from 2 to 6 nm. TBP instead of TOP causes formation of particles of 7–11 nm.[153,154] ε-Co nanoparticles are transferred into perfect hcp-structured particles when annealed at 300 °C.[154] hcp-Nanoparticles can alternatively be generated by reduction of cobalt acetate by 1,2-dodecanediol at 250 °C in diphenylether, again in the presence of oleic acid and TOP.[149,154]

The Co nanoparticles described up to here are more or less spherically shaped. Other geometries are available by selective adsorption of organic surfactants onto specific crystallographic faces, allowing crystal growth only in particular crystallographic direction.[155–157] For instance,

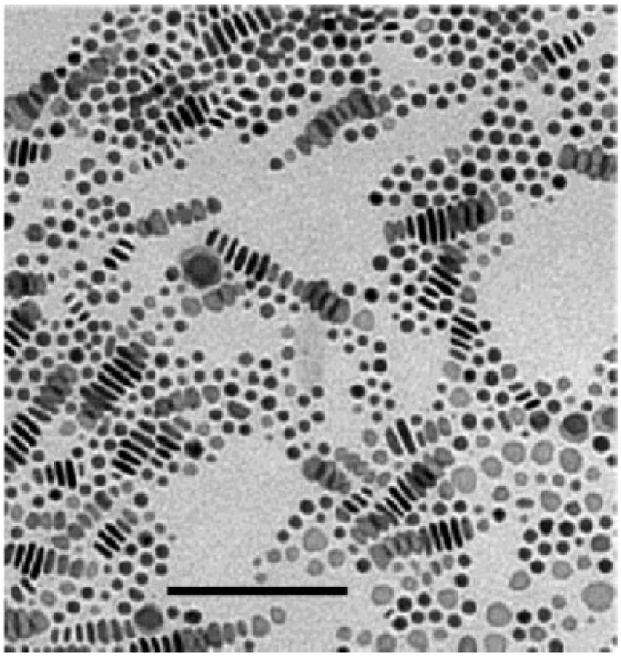

Figure 6 TEM image of partially self-assembled Co nanodisks. Bar = 100 nm. (Reprinted with permission from Ref. 157 © 2002 American Chemical Society)

thermolysis of $Co_2(CO)_8$ in the presence of octylamine together with trioctylphosphineoxide (TOPO) or oleic acid gives nanodisks of hcp cobalt,[156] as can be seen from Figure 6.

The geometry of the disks can be tailored by the reaction times or variation of the precursor:surfactant ratios. On the other hand, long-term annealing of nanodisks yields spherical nanoparticles of ε-Co. Owing to their ferromagnetic properties, Co nanodisks can arrange to give ribbons consisting of stacked nanodisks.

Nanorods and nanowires of hcp structure become available by thermolysis of the precursor $[Co(\eta^3\text{-}C_8H_{13})(\eta^4\text{-}C_8H_{12})]$ in oleic acid and oleylamine at 3 bar of H_2 pressure.[158] Variations in concentration and nature of stabilizing compounds result in changes of the aspect ratio of the nanorods.[158–164]

$CoPt_3$ nanoparticles earn interest as representatives of alloy-like species. Furthermore, they are less sensitive towards oxygen and so are somewhat easier to be prepared and to be handled. They become available by simultaneous reduction of platinum acetylacetonate and thermal decomposition of $Co_2(CO)_8$. As stabilizing agents, adamantanecarboxylic acid and hexadecylamine (HAD) are used.[165] Practically, the hot injection technique is applied. The recipient vessel contains the platinum salt, dissolved in 1,2-hexadecanediol, and the stabilizers, whereas $Co_2(CO)_8$ in 1,2-dichlorobenzene is injected into the hot stock solution. In order to obtain well crystallized nanoparticles, annealing of the reaction mixture at 275–285 °C for about an hour is necessary. The crystallinity can be checked by TEM and XRD. Figure 7 shows a TEM image of $CoPt_3$ nanoparticles, indicating excellent crystallinity.

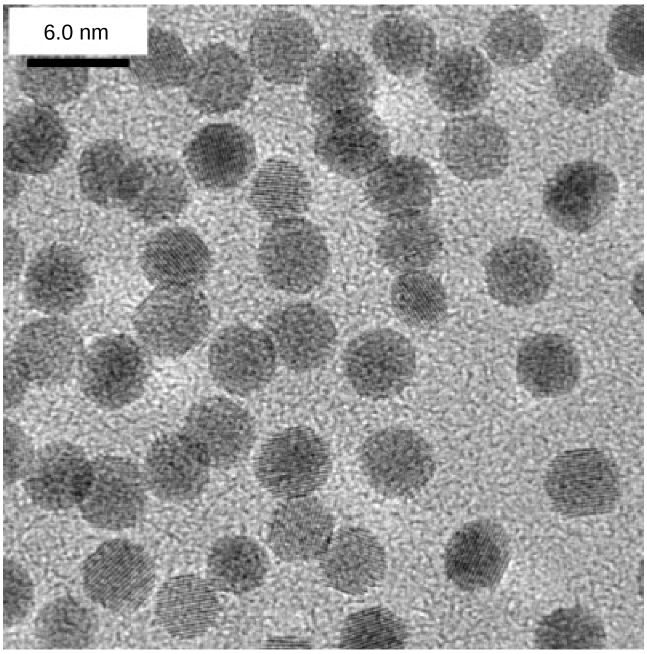

Figure 7 TEM image of $CoPt_3$ annealed nanoparticles. (Reprinted from D.V. Talapin, E.V. Shevchenko, H. Weller in ed. G. Schmid 'Nanoparticles. From Theory to Application', Wiley-VCH, Weinheim 2004, with permission of Wiley-VCH)

As in all cases of nanoparticle synthesis, controlling of particle size and distribution is the most important challenge. Like for monometallic nanoparticles, growth control can be tuned by nucleation and growth rates. Fast nucleation results in smaller particles, slow nucleation gives larger particles owing to the limited number of nuclei that grow as long as monomer is available.[148] The reaction temperature is the most important instrument to control the balance between nucleation and growth rates. Again, the concentration of the stabilizing compounds is an additional possibility to influence the particle size. As was shown for Co,[149] $CoPt_3$,[148] and Ni,[149] increasing concentrations of stabilizers result in decreasing particle sizes.

4.3 Other Magnetic Nanoparticles

Approximately 6 nm iron nanoparticles are formed if $Fe(CO)_5$ is thermally decomposed in the presence of oleic acid and TBP.[149] Their structure is bcc, like that of bulk iron. 2 nm Fe particles are generated if the decomposition of $Fe(CO)_5$ is performed in TOP at 320–340 °C.[157] They can be used to form rod-shaped species of 11–27 nm length by heating in pyridine in the presence of didodecyldimethylammonium bromide.[166]

Spherical nickel nanoparticles of 12–13 nm in diameter can be obtained by reduction of various nickel salts by polyalcohols in the presence of appropriate stabilizers such as

TBP or tributylamine (TBA).[149] Stabilizing molecules with longer alkyl chains like in trioctylamine (TOA) reduces the particle size to 8–10 nm.

Monodisperse 4 nm Ni particles are formed if nickel acetylacetonate is reduced by Et_2AlH in diethyl ether in the presence of PPh_3. As protecting shell on the particles' surface, PPh is observed, not the original PPh_3.[167] The PPh units are formed by hydrogen generated from the alane during the reduction process.

Iron–platinum alloy nanoparticles are very promising candidates for future data storage systems.[168] They become available by simultaneous reduction of platinum acetylacetonate and the decomposition of $Fe(CO)_5$ in oleic acid and oleyl amine.[169] The composition of Fe_xPt_{1-x} can be varied between $x = 0.48$ and $x = 0.7$. The particles exhibit disordered fcc structure. They are superparamagnetic at room temperature. Annealing at 550–600 °C transforms the fcc structure into a face-centered tetragonal (fct) one. These have been shown to be suited for storage devices owing to their room temperature coercivity.[169] The exact transition temperature depends on the stoichiometry.

Corresponding synthetic approaches are known for FePd[170] and MnPt[171] nanoparticles. Core-shell type bimetallic nanoparticles are also known.[172,173] They have to be prepared stepwise, starting with the generation of the core seed, which is then covered by a shell of the second metal as was already described above for nonmagnetic systems. For instance, reduction of platinum salts in the presence of cobalt nanoparticles gives air-stable CoPt nanoparticles with Co cores. AgCo nanoparticles are formed if $Co_2(CO)_8$ is decomposed in the presence of silver salts.[173]

5 SUMMARY

The generation of noble metal as well as of non-noble metal nanoparticles has meanwhile reached an enormous multiplicity. Apart from several somewhat sophisticated methods, most of the working and therefore frequently applied routes are based on traditional routes. First of all, it is the reduction of metal salts that brought big success. Decomposition of appropriate precursor molecules and complexes turned out to be another very successful way to metal nanoparticles. Different kinds of energies are available to evolve metal atoms from molecular compounds, forming nanoparticles in subsequent growth processes. Thus, it can be stated that chemistry offers enormous varieties of bottom-up techniques for generating metal nanoparticles. This fact opens doors for applications on numerous fields. These reach from using metal nanoparticles as quantum dots in single-electron switches and transistors up to the enormous potential of magnetic particles in storage systems. After a long period of inactivity after Ostwald's seminal works in the early nineteenth century, there was a second great development, mainly initiated by Turkevitch's pathbreaking preparative works from 1950 on, making metal nanoparticles meanwhile one of the pillars of modern nanoscience and nanotechnology.

6 RELATED ARTICLES

Biomimetic Synthesis of Nanoparticles; Carbonyl Complexes of the Transition Metals; Metallic Materials Deposition: Metal-organic Precursors; Polynuclear Organometallic Cluster Complexes; Porous Inorganic Materials; Self-assembled Inorganic Architectures; Semiconductor Nanocrystal Quantum Dots; Sol–Gel Encapsulation of Metal and Semiconductor Nanocrystals.

7 FURTHER READING

J. I. Park, N. J. Kang, Y. Jun, S. J. Oh, H. C. Ri, and J. Cheon, *Chem. Phys. Chem.*, 2002, **3**, 543.

8 REFERENCES

1. Europäische Akademie zur Erfoschung von Folgen wissenschaftlich-technischer Entwicklungen, Bad Neuenahr-Ahrweiler GmbH, to be published in 2005.
2. M. Faraday, *Phil. Trans. R. Soc.*, 1857, **147**, 145.
3. R. Zsigmondy, 'Colloids and the Ultramicroscope', English edn., Wiley, New York, 1909.
4. J. Turkevitch, P. C. Stevenson, and J. Hillier, *Discuss. Faraday Soc.*, 1951, **11**, 55.
5. J. Turkevitch, *Gold Bull.*, 1985, **18**, 86.
6. J. T. G. Overbeek, in 'Colloidal Dispersions', ed. J. W. Goodwin, Royal Society of Chemistry, London, 1981, p. 1.
7. J. S. Bradley, in 'Clusters and Colloids. From Theory to Applications', ed. G. Schmid, VCH Weinheim, 1994, p. 447.
8. A. Fojtik and A. Henglein, *Ber. Bunsen-Ges. Phys. Chem.*, 1993, **97**, 252.
9. M. S. Sibbald, G. Chumanov, and T. M. Cotton, *J. Phys. Chem.*, 1996, **100**, 4672.
10. M. S. Yeh, Y. S. Yang, Y. P. Lee, H. F. Lee, Y. H. Yeh, and C. S. Yeh, *J. Phys. Chem. B.*, 1999, **103**, 6851.
11. F. Mafuné, J. Kohno, Y. Takeda, and H. J. Sawabe, *J. Phys. Chem. B.*, 2000, **104**, 8333.
12. F. Mafuné, J. Kohno, Y. Takeda, T. Kondow, and H. J. Sawabe, *J. Phys. Chem. B.*, 2000, **104**, 9111.
13. H. Eckstein and U. Kreibig, *Z. Phys. D.*, 1993, **26**, 239.

14. Y. Niidome, A. Hori, T. Sato, and S. Yamada, *Chem. Lett.*, 2000, 310.
15. P. V. Kamat, M. Flumiani, and G. W. Hartland, *J. Phys. Chem. B*, 1998, **102**, 3123.
16. H. Kurita, A. Takami, and S. Koda, *Appl. Phys. Lett.*, 1998, **72**, 789.
17. A. Takami, H. Kurita, and S. Koda, *J. Phys. Chem. B*, 1999, **103**, 1226.
18. F. Mafuné, J. Kohno, Y. Takeda, and T. Kondow, *J. Phys. Chem. B*, 2001, **105**, 9050.
19. F. Mafuné, J. Kohno, Y. Takeda, and T. Kondow, *J. Phys. Chem. B*, 2002, **106**, 7575.
20. S. Stoeva, K. J. Klabunde, Ch. M. Sorensen, and I. Dragiera, *J. Am. Chem. Soc.*, 2002, **124**, 2305.
21. K. J. Klabunde, P. L. Timms, P. S. Shell, and S. Ittel, *Inorg. Synth.*, 1979, **19**, 59.
22. N. Toshima and T. Yonezawa, *New J. Chem.*, 1998, **22**, 1179.
23. H. Hirai, Y. Nakao, N. Toshima, and K. Adachi, *Chem. Lett.*, 1976, 905.
24. H. Hirai, Y. Nakao, and N. Toshima, *Chem. Lett.*, 1978, 545.
25. H. Hirai, Y. Nakao, and N. Toshima, *J. Macromol. Sci., Chem.*, 1978, **A 112**, 1117.
26. H. Hirai, Y. Nakao, and N. Toshima, *J. Macromol. Sci., Chem.*, 1979, **A 13**, 727.
27. N. Toshima and K. Hirakawa, *Polym. J.*, 1999, **31**, 1127.
28. P. Lu, T. Teramishi, K. Asakura, M. Miyake, and N. Toshima, *J. Phys. Chem. B.*, 1999, **103**, 9673.
29. D. N. Furlong, A. Launikonis, W. H. F. Sasse, and J. V. Saunders, *J. Chem. Soc., Faraday Trans.*, 1984, **80**, 571.
30. A. Harriman, G. R. Millward, P. Neta, M. C. Richoux, and J. M. Thomas, *J. Phys. Chem.*, 1988, **92**, 1286.
31. J. Turkevitch, R. S. J. Miner, I. Okura, and S. Namba, in Proc. Swedish Symp. Catal., 1981, 111.
32. P. R. van Rheenen, M. J. McKelvey, and W. S. Glaunsinger, *J. Solid State Chem.*, 1987, **67**, 151.
33. M. Brust, A. Walker, D. Bethell, D. J. Schiffrin, and R. Whyman, *Chem. Commun.*, 1994, 801.
34. M. J. Hostetler, J. E. Wingate, C. J. Zhong, J. E. Harris, R. W. Vachet, M. R. Clark, J. D. Londono, S. J. Green, J. J. Stokes, G. D. Wignale, G. L. Glish, M. D. Porter, N. D. Evans, and R. W. Muarry, *Langmuir*, 1998, **14**, 17.
35. N. R. Jana, L. Gearheart, and C. J. Murphy, *Langmuir*, 2001, **17**, 6782.
36. G. Schmid, A. Lehnert, J.-O. Malm, and J.-O. Bovin, *Angew. Chem., Int. Ed. Engl.*, 1991, **30**, 874.
37. Ch. J. Baddeley, D. A. Jefferson, R. M. Lambert, R. M. Ormerod, T. Rayment, G. Schmid, and A. P. Walker, 'Mat. Res. Soc. Symp. Proc.', Materials Research Society, 1992, Vol. 272.
38. S. Chen and K. Kimura, *Langmuir*, 1999, **15**, 1075.
39. J. W. Slot and H. J. Geuze, *Eur. J. Cell Biol.*, 1985, **38**, 87.
40. H. Mühlpfort, *Experimenta*, 1982, **38**, 1127.
41. P. Mukherjee, A. Ahmad, D. Mandal, S. Senapati, S. R. Sainkar, M. I. Khan, R. Ramans, R. Parisaka, P. V. Ajayakumar, M. Alam, M. Sastry, and R. Kumar, *Angew. Chem., Int. Ed. Engl.*, 2001, **40**, 3585.
42. G. Schmid and A. Lehnert, *Angew. Chem., Int. Ed. Engl.*, 1989, **28**, 780.
43. F. Porta, F. Ragaini, S. Cenini, and G. Scari, *Gazz. Chim. Ital.*, 1992, **122**, 361.
44. D. Mandler and I. Willner, *J. Phys. Chem.*, 1987, **91**, 3600.
45. K. Esumi, T. Itakura, and K. Torigoe, *Colloids Surf., A*, 1994, **82**, 111.
46. H. Bönnemann and R. M. Richards, *Eur. J. Inorg. Chem.*, 2001, 2455.
47. H. Bönnemann, W. Brijoux, R. Brinkmann, R. Fretzen, T. Joussen, R. Köppler, P. Neiteler, and J. Richter, *J. Mol. Catal.*, 1994, **86**, 129.
48. H. Bönnemann, G. Braun, W. Brijoux, R. Brinkmann, A. Schulze Tilling, K. Seevogel, and K. Siepen, *J. Organomet. Chem.*, 1996, **520**, 143.
49. H. Bönnemann and W. Brijoux, in 'Active Metals', ed. A. Fürstner, VCH, Weinheim, 1996, p. 339.
50. H. Bönnemann, W. Brijoux, R. Brinkmann, E. Dinjus, T. Joussen and B. Korall, *Angew. Chem.*, 1991, **103**, 1344; *Angew. Chem., Int. Ed. Engl.*, 1991, **30**, 1312.
51. J. D. Aiken III and R. G. Finke, *J. Mol. Catal. A*, 1999, **145**, 1.
52. H. Bönnemann, W. Brijoux, R. Brinkmann, U. Endruschat, W. Hofstadt, and K. Angermund, *Rev. Roum. Chim.*, 1999, **44**, 1003.
53. J. Sinzig, L. J. de Jongh, H. Bönnemann, W. Brijoux, and R. Köppler, *Appl. Organomet. Chem.*, 1998, **12**, 387.
54. M. T. Reetz, W. Helbig, and S. A. Quaiser, *Chem. Mater.*, 1995, **7**, 2227.
55. M. T. Reetz and W. Helbig, *J. Am. Chem. Soc.*, 1994, **116**, 7401.
56. M. T. Reetz, W. Helbig, and S. A. Quaiser, in 'Active Metals', ed. A. Fürstner, VCH, Weinheim, 1996, p. 279.
57. J. A. Becker, R. Schäfer, W. Festag, W. Ruland, J. H. Wendorf, J. Pebler, S. A. Quaiser, W. Helbig, and M. T. Reetz, *J. Chem. Phys.*, 1995, **103**, 2520.
58. M. T. Reetz, S. A. Quaiser, and C. Merk, *Chem. Ber.*, 1996, **129**, 741.
59. M. T. Reetz and S. A. Quaiser, *Angew. Chem., Int. Ed. Engl.*, 1995, **34**, 2240.
60. U. Kolb, S. A. Quaiser, M. Winter, and M. T. Reetz, *Chem. Mater.*, 1996, **8**, 1889.
61. L. D. Rampino and F. F. Nord, *J. Am. Chem. Soc.*, 1941, **63**, 2745.
62. L. D. Rampino and F. F. Nord, *J. Am. Chem. Soc.*, 1941, **63**, 3268.

63. K. E. Kavanagh and F. F. Nord, *J. Am. Chem. Soc.*, 1943, **65**, 2121.

64. L. Hernandez and F. F. Nord, *J. Colloid Sci.*, 1948, **3**, 363.

65. W. P. Dunsworth and F. F. Nord, *J. Am. Chem. Soc.*, 1950, **72**, 4197.

66. Y. Liu and R. G. Finke, *J. Am. Chem. Soc.*, 1994, **116**, 8335.

67. M. A. Watzky and R. G. Finke, *J. Am. Chem. Soc.*, 1997, **119**, 10382.

68. M. N. Vargaftik, V. P. Zargorodnikov, I. P. Stolarov, I. I. Moiseev, V. A. Likholobov, D. I. Kochubey, A. L. Chuvilin, V. I. Zaikovsky, K. I. Zamaraev, and G. I. Timofeeva, *J. Chem. Soc. Chem. Commun.*, 1985, 937.

69. M. N. Vargaftik, V. P. Zargorodnikov, I. P. Stolarov, I. I. Moiseev, D. I. Kochubey, V. A. Likholobov, A. L. Chuvilin, and K. I. Zamaraev, *J. Mol. Catal.*, 1989, **53**, 315.

70. V. V. Volkov, G. van Tendeloo, G. A. Tsirkov, N. V. Cherkashina, M. N. Vargaftik, I. I. Moiseev, V. M. Novotortsev, A. V. Krit, and A. L. Chuvilin, *J. Cryst. Growth*, 1996, **163**, 377.

71. I. I. Moiseev, M. N. Vargaftik, V. V. Volkov, G. A. Tsirkov, N. V. Cherkashina, V. M. Novotortsev, O. G. Ellett, I. A. Petrunenka, A. L. Chuvilin, and A. V. Krit, *Mendeleev Commun.*, 1995, 87.

72. V. Oleshko, V. Volkov, W. Jacob, M. Vargaftik, I. I. Moiseev, and G. van Tendeloo, *Z. Phys. D.*, 1995, **34**, 283.

73. I. I. Moiseev, M. N. Vargaftik, T. V. Chernysheva, T. A. Stromnova, A. E. Gekham, G. A. Tsirkov, and A. M. Makhlina, *J. Mol. Catal. A: Chem.*, 1996, **108**, 77.

74. G. Schmid, B. Morun, and J.-O. Malm, *Polyhedron*, 1988, **7**, 2321.

75. G. Schmid, *Mater. Chem. Phys.*, 1991, **29**, 133.

76. G. Schmid, M. Harms, J.-O. Malm, J.-O. Bovin, J. van Ruitenbeck, H. W. Zandbergen, and W. T. Fu, *J. Am. Chem. Soc.*, 1993, **115**, 2046.

77. G. Schmid, R. Boese, R. Pfeil, F. Bandermann, S. Meyer, G. H. M. Calis, and J. W. A. van der Velden, *Chem. Ber.*, 1981, **114**, 3634.

78. G. Schmid, *Inorg. Synth.*, 1990, **7**, 214.

79. G. Schmid and B. Corain, *Eur. J. Inorg. Chem.*, 2003, 3081.

80. G. Schmid, R. Pugin, J.-O. Malm, and J.-O. Bovin, *Eur. J. Inorg. Chem.*, 1998, 817.

81. A. H. A. Smit, R. C. Thiel, L. J. de Jongh, G. Schmid, and N. Klein, *Solid State Commun.*, 1988, **65**, 915.

82. G. Schmid, R. Pugin, W. Meyer-Zaika, and U. Simon, *Eur. J. Inorg. Chem.*, 1999, 2051.

83. H.-G. Boyen, G. Kästle, F. Weigl, B. Koslowski, C. Dietrich, P. Ziemann, J. P. Spatz, S. Riethmüller, C. Hartmann, M. Möller, G. Schmid, M. G. Garnier, and P. Oelhafen, *Science*, 2002, **297**, 1533.

84. H.-G. Boyen, A. Ethirajan, G. Kästle, F. Weigl, P. Ziemann, G. Schmid, M. G. Garnier, M. Büttner, and P. Oelhafen, *Phys. Rev. Lett.*, 2005, **94**, 016804-1.

85. M. R. Mucalo and R. P. Cooney, *J. Chem. Soc., Chem. Commun.*, 1989, 94.

86. J. L. Dye and K. L. Tsai, *Faraday Discuss. Chem. Soc.*, 1991, **92**, 45.

87. K.-L. Tsai and J. L. Dye, *Chem. Mater.*, 1993, **5**, 540.

88. T. W. Smith, US Patent 4252674, 1981.

89. T. W. Smith, US Patent 4252673, 1981.

90. T. W. Smith, US Patent 4252671, 1981.

91. T. W. Smith, US Patent 4252672, 1981.

92. T. W. Smith, US Patent 4252678, 1981.

93. T. Tano, K. Esumi, and K. Meguro, *J. Colloid Interface Sci.*, 1989, **133**, 530.

94. K. Esumi, T. Tano, and K. Meguro, *Langmuir*, 1989, **5**, 268.

95. K. Esumi, T. Tano, K. Torigoe, and K. Meguro, *Chem. Mater.*, 1990, **2**, 564.

96. K. Esumi, M. Suzuki, T. Tano, K. Torigoe, and K. Meguro, *Colloids Surf.*, 1991, **55**, 9.

97. K. Esumi, N. Sato, K. Torigoe, and K. Meguro, *J. Colloid Interface Sci.*, 1992, **149**, 295.

98. K. Esumi, O. Sadakane, K. Torigoe, and K. Meguro, *Colloids Surf.*, 1992, **62**, 255.

99. N. Toshima and Y. Wang, *Chem. Lett.*, 1993, 1611.

100. C. Amiens, D. de Caro, B. Chaudret, and J. S. Bradley, *J. Am. Chem. Soc.*, 1993, **115**, 11638.

101. D. de Caro, H. Wally, C. Amiens, and B. Chaudret, *J. Chem. Soc. Chem. Commun.*, 1994, 1891.

102. A. Rodriguez, C. Amiens, B. Chaudret, M.-J. Casanove, P. Lecante, and J. S. Bradley, *Chem. Mater.*, 1996, **8**, 1978.

103. M. Bardaji, O. Vidoni, A. Rodriguez, C. Amiens, B. Chaudret, M.-J. Casanove, and P. Lecante, *New J. Chem.*, 1997, **21**, 1243.

104. J. S. Bradley, E. W. Hill, S. Behal, C. Klein, B. Chaudret, and A. Duteil, *Chem. Mater.*, 1993, **4**, 1234.

105. A. Duteil, R. Quéau, B. Chaudret, R. Mazel, C. Roucau, and J. S. Bradley, *Chem. Mater.*, 1993, **5**, 341.

106. D. de Caro, V. Agelou, A. Duteil, B. Chaudret, R. Mazel, Ch. Roucau, and J. S. Bradley, *New J. Chem.*, 1995, **19**, 1265.

107. F. Dassenoy, K. Philippot, T. Ould Ely, C. Amiens, P. Lecante, E. Snoeck, A. Mosset, M.-J. Casanove, and B. Chaudret, *New J. Chem.*, 1998, **19**, 703.

108. J. Osuna, D. de Caro, C. Amiens, B. Chaudret, E. Snoeck, M. Respaud, J.-M. Broto, and A. Fert, *J. Phys. Chem.*, 1996, **100**, 14571.

109. T. Ould Ely, C. Amiens, B. Chaudret, E. Snoeck, M. Verelst, M. Respaud, and J. M. Broto, *Chem. Mater.*, 1999, **11**, 526.

110. J. S. Bradley, E. W. Hill, B. Chaudret, and A. Duteil, *Langmuir*, 1995, **11**, 693.

111. F. Dassenoy, M.-J. Casanove, P. Lecante, M. Verelst, E. Snoeck, A. Mosset, T. Ould Ely, C. Amiens, and B. Chaudret, *J. Chem. Phys.*, 2000, **112**, 8137.

112. M. Verelst, T. Ould Ely, C. Amiens, E. Snoeck, P. Lecante, A. Mosset, M. Respaud, J.-M. Broto, and B. Chaudret, *Chem. Mater.*, 1999, **11**, 2702.

113. K. Soulantica, A. Maisonnat, M. Fromen, M. Casanove, P. Lecante, and B. Chaudret, *Angew. Chem.* 2001, **113**, 462; *Angew. Chem., Int. Ed. Engl.*, 2001, **40**, 448.

114. C. Nayrak, E. Viala, P. Fau, F. Senocq, J. Jumas, A. Maisonnat, and B. Chaudret, *Chem. – Eur. J.*, 2000, **6**, 4082.

115. S. Gomez, K. Philippot, V. Colliere, B. Chaudret, F. Senocq, and P. Lecante, *Chem. Commun.*, 2000, **19**, 1945.

116. F. Fassenoy, M. Casanove, P. Lecante, M. Verelst, E. Snoeck, A. Mosset, T. Ould Ely, C. Amiens, and B. Chaudret, *J. Chem. Phys.*, 2000, **112**, 8137.

117. C. Pan, F. Dassenoy, M. Casanove, K. Philippot, C. Amiens, P. Lecante, A. Mosset, and B. Chaudret, *J. Phys. Chem. B*, 1999, **103**, 10098.

118. K. Pelzer, O. Vidoni, K. Philippot, and B. Chaudret, *Adv. Funct. Mater.*, 2003, **13**, 118.

119. K. Pelzer, K. Philippot, B. Chaudret, W. Meyer-Zaika, and G. Schmid, *Z. Anorg. Allg. Chem.*, 2003, **629**, 1217.

120. Y. Takahashi, T. Ito, S. Sakai, and Y. Ishii, *J. Chem. Soc. Chem. Commun.*, 1970, 1065.

121. A. Henglein, A. Holzwarth, and P. Mulvaney, *J. Phys. Chem.*, 1992, **96**, 8700.

122. A. Henglein and J. Lille, *J. Phys. Chem.*, 1981, **85**, 1246.

123. J. Butler and A. Henglein, *Radiat. Phys. Chem.*, 1980, **15**, 603.

124. B. G. Ershov and A. Henglein, *J. Phys. Chem.*, 1993, **97**, 3434.

125. A. Henglein, P. Mulvaney, A. Holzwarth, T. E. Sosebee, and A. Fojtik, *Ber. Bunsen-Ges. Phys. Chem.*, 1992, **96**, 754.

126. A. Henglein, *Ber. Bunsen-Ges. Phys. Chem.*, 1977, **81**, 556.

127. A. Henglein and R. Tausch-Treml, *J. Colloid Interface Sci.*, 1981, **80**, 84.

128. S. Mosseri, A. Henglein, and E. Janata, *J. Phys. Chem.*, 1989, **93**, 6791.

129. J. Belloni, M. D. Delcourt, and C. Leclerc, *Nouv. J. Chim.*, 1982, **6**, 507.

130. G. Mills and A. Henglein, *Radiat. Phys. Chem.*, 1984, **26**, 385.

131. M. O. Delcourt, N. Keghouche, and J. Belloni, *Nouv. J. Chim.*, 1983, **7**, 131.

132. M. O. Delcourt, J. Belloni, J.-L. Marignier, C. Mory, and C. Colliex, *Radiat. Phys. Chem.*, 1984, **23**, 485.

133. J. L. Marignier, J. Belloni, M. O. Delcourt, and J. P. Chevalier, *Nature*, 1985, **317**, 344.

134. B. G. Ershov, E. Janata, M. Michaelis, and A. Henglein, *J. Phys. Chem.*, 1991, **95**, 8996.

135. B. G. Ershov, E. Janata, and A. Henglein, *Radiat. Phys. Chem.*, 1992, **39**, 123.

136. A. Henglein, M. Guttierez, E. Janata, and B. G. Ershov, *J. Phys. Chem.*, 1992, **96**, 4598.

137. N. Toshima, T. Takahashi, and H. Hirai, *Chem. Lett.*, 1985, 1245.

138. D. L. Leslie-Pelecky and R. D. Rieke, *Chem. Mater.*, 1996, **8**, 1770.

139. J. F. Löffler, P. Scherrer, J. P. Meier, B. Doudin, J.-P. Ansermet, and W. Wagner, *Phys. Rev. B*, 1998, **57**, 2915.

140. C. Prados, M. Multigner, A. Hernando, J. C. Sánchez, A. Fernández, C. F. Conde, and A. Conde, *J. Appl. Phys.*, 1999, **85**, 6118.

141. J. Tanori, N. Duxin, C. Petit, P. Bonville, C. Colliex, and M. P. Pileni, *Colloid Polym. Sci.*, 1995, **273**, 886.

142. N. Duxin, O. Stephan, C. Petit, P. Bonville, C. Colliex, and M. P. Pileni, *Chem. Mater.*, 1997, **9**, 2096.

143. E. E. Carpenter, C. T. Seip, and C. J. O'Connor, *J. Appl. Phys.*, 1999, **85**, 5184.

144. C. B. Murray, C. R. Kagan, and M. G. Bawendi, *Annu. Rev. Mater. Sci.*, 2000, **30**, 545.

145. M. H. Yang and C. P. Flynn, *Phys. Rev. Lett.*, 1989, **62**, 2476.

146. K. Suslick, M. Fang, and T. Hyeon, *J. Am. Chem. Soc.*, 1996, **118**, 11960.

147. S. Ramesh, Y. Koltypin, R. Prozorov, and A. Gedanken, *Chem. Mater.*, 1997, **9**, 546.

148. E. V. Shevchenko, D. V. Talapin, H. Schnablegger, A. Kornowski, O. Festin, P. Svedlindh, M. Haase, and H. Weller, *J. Am. Chem. Soc.*, 2003, **125**, 9090.

149. C. B. Murray, S. Sun, H. Doyle, and T. Betley, *MRS Bull.*, 2001, **26**, 985.

150. D. P. Denega and M. G. Bawendi, *Angew. Chem., Int. Ed. Engl.*, 1999, **38**, 1788.

151. V. F. Puntes, K. M. Krishan, and A. P. Alivisatos, *Science*, 2001, **291**, 2115.

152. S. Sun and C. B. Murray, *J. Appl. Phys.*, 1999, **85**, 4325.

153. C. B. Murray, S. Sun, H. Doyle, and T. Betley, *MRS Bulletin*, 2001, **26**, 985.

154. S. Sun, C. B. Murray, and H. Doyle, *Mater. Res. Soc. Symp. Proc.*, 1999, **577**, 385.

155. V. F. Puntes, K. M. Krishan, and A. P. Alivisatos, *Science*, 2001, **291**, 2115.

156. V. F. Puntes, K. M. Krishan, and A. P. Alivisatos, *Topics in Catalysis*, 2002, **19**, 145.

157. V. F. Puntes, D. Zanchet, C. K. Erdonmez, and A. P. Alivisatos, *J. Am. Chem. Soc.*, 2002, **124**, 12874.

158. F. Dumestre, B. Chaudret, C. Amiens, M. C. Fromen, M.-J. Casanove, P. Renaud, and P. Zurcher, *Angew. Chem.*, 2002, **114**, 4462; *Angew. Chem., Int. Ed. Engl.*, 2002, **41**, 4286.

159. C. Pacholski, A. Kornowski, and H. Weller, *Angew. Chem., Int. Ed. Engl.*, 2002, **41**, 1188.

160. T. S. Ahmadi, Z. L. Wang, A. Henglein, and M. A. El-Sayed, *Chem. Mater.*, 1996, **8**, 1161.

161. N. R. Jana, L. Gearheart, and C. J. Murphy, *J. Phys. Chem. B*, 2001, **105**, 4065.

162. M. P. Pileni, *Nat. Mater.*, 2003, **2**, 145.

163. Z. Tang, N. A. Kotov, and M. Giersig, *Science*, 2002, **297**, 237.

164. X. Peng, L. Manna, W. Yang, J. Wickham, E. Scher, A. Kadavanich, and A. P. Alivisatos, *Nature*, 2000, **404**, 59.

165. E. V. Shevchenko, D. V. Talapin, A. L. Rogach, A. Kornowski, M. Haase, and H. Weller, *J. Am. Chem. Soc.*, 2002, **124**, 11480.

166. S. J. Park, S. Kim, S. Lee, Z. G. Khim, K. Char, and T. Hyeon, *J. Am. Chem. Soc.*, 2000, **122**, 8581.

167. A. Duteil, G. Schmid, and W. Meyer-Zaika, *Chem. Commun.*, 1994, 31.

168. R. F. Service, *Science*, 2000, **287**, 1902.

169. S. Sun, C. B. Murray, D. Weller, L. Folks, and A. Moser, *Science*, 2000, **287**, 1989.

170. M. Chen and D. E. Nikles, *Nano Lett.*, 2002, **91**, 8477.

171. K. Ono, R. Okuda, S. Kamimira, and M. Oshima, *J. Phys. Chem. B*, 2003, **107**, 1941.

172. J.-I. Park and J. Cheon, *J. Am. Chem. Soc.*, 2001, **123**, 5743.

173. N. Sobal, M. Hilgendorff, H. Möhwald, M. Giersig, M. Spasova, T. Radetic, and M. Farle, *Nano Lett.*, 2002, **2**, 621.

Metal Nanoparticles, Organization & Applications of

Günter Schmid
University of Duisburg-Essen, Essen, Germany

1 Introduction 1
2 Some Properties of Individual Metal Nanoparticles 1
3 Organization in Three Dimensions 4
4 Two- and One-dimensional Assemblies of Metal Nanoparticles 6
5 Summary 15
6 Related Articles 15
7 References 16

1 INTRODUCTION

The reasons for organizing metal nanoparticles in three (3D), two (2D), or in one dimension(s) (1D) are to be seen in the most attractive properties of those particles, namely, their size-dependent electronic behavior. In an ordered form, preferably in 2D, such particles are promising candidates as building blocks in future nanoelectronic devices. For instance, storage systems might contain metal nanoparticles of appropriate size as quantum dots working as single electron switches/transistors or as nanomagnets. Both possibilities look realistic since it was shown that Single Electron Tunneling (SET) processes can be realized at room temperature for metal particles in the 1–2 nm region and that nanoparticles of magnetic metals or of suited alloys can act as magnet storage units. Before describing principles of organization, the reasons for these unique properties shall briefly be discussed.

If a metal particle, independent of the element, is reduced in one, two, or in all three dimensions to such an extent that the mobility of the electrons is decisively restricted, one speaks of size quantization because the electrons no longer follow the laws of classical physics based on the statistics of an infinite assembly of atoms in three dimensions, but rather obey quantum mechanical rules as they are used to describe atoms or molecules. Figure 1 illustrates the formal transition from 3D to a 0D state, represented by a so-called quantum dot with three-dimensional quantum confinement.[1]

As can be seen, the density of electronic wave functions in a 3D system (I) changes in z-direction if the number of atoms is reduced to a few layers (II). Corresponding changes occur if restrictions happen in y (III) and x (IV) direction with the consequence of formation of discrete energy levels in z, y, and finally in all three directions. Situation IV corresponds principally with that in an atom. That is why quantum dots are often also called ‘artificial atoms’. In a more qualitative way, the transition from 3D to 0D can be illustrated as is done in Figure 2.[2]

A discrete molecule, for instance, consisting of 4 atoms, exhibits sharp energy levels (a), usually called bonding and antibonding molecular orbitals. Increasing the number of atoms to an up to here unknown value leads to a broadening of the energy levels (b) and is finally ending up in the well known band structure characterizing bulk metals (c). Following the process in the opposite direction, the question arises, how small a metal particle has to become to allow observation of an energy splitting indicating the existence of a quantum dot. In principle, there is a simple answer: if the diameter of the particle corresponds with the de Broglie wavelength of the electron. However, this wavelength is not a constant, but varies with the energetic conditions. So, the answer can only be given by the experiment.

From numerous experiments to get information on the electronic ‘inner life’ of metal nanoparticles only a few, but decisive ones shell be mentioned, explaining why predominantly the nanocluster compound $Au_{55}(PPh_3)_{12}Cl_6$ is in the focus of interest with respect to future applications. This precisely defined nanoparticle consists of a nucleus of 55 gold atoms in a hexagonal close-packed manner as is the case in bulk gold. It belongs to the special class of so-called full-shell clusters where a central atom is surrounded by a first shell of 12 atoms, resulting in the one-shell Au_{13} cluster. 42 atoms can be arranged on the first shell resulting in 55 atoms, and so on. Generally, the nth shell contains $10n^2 + 2$ atoms.

2 SOME PROPERTIES OF INDIVIDUAL METAL NANOPARTICLES

Full-shell clusters possess an unusual stable configuration, as has recently been demonstrated.[3] A series of smaller and larger gold nanoparticles have been oxidized in an oxygen plasma, demonstrated by X-ray photoelectron spectroscopy (XPS) spectra, except Au_{55}. Its oxidation would end up in a degradation of the full-shell constitution what obviously does not happen. A similar series of various gold nanoparticles has been alloyed with indium to $AuIn_2$ phases, but not Au_{55}.[4] The reasons for this surprising behavior are probably the same as in case of oxidation.

In one of several fundamental experiments, it has been demonstrated that Au_{55} in its ligand protected form behaves electronically like a metal in the ‘embryonic state’. Gold particles of 15 nm, 1.4 nm (Au_{55}) and 0.7 nm (Au_{13}) have been irradiated by femtosecond laser pulses, generating excited electrons.[5] Observation of the relaxation behavior is very

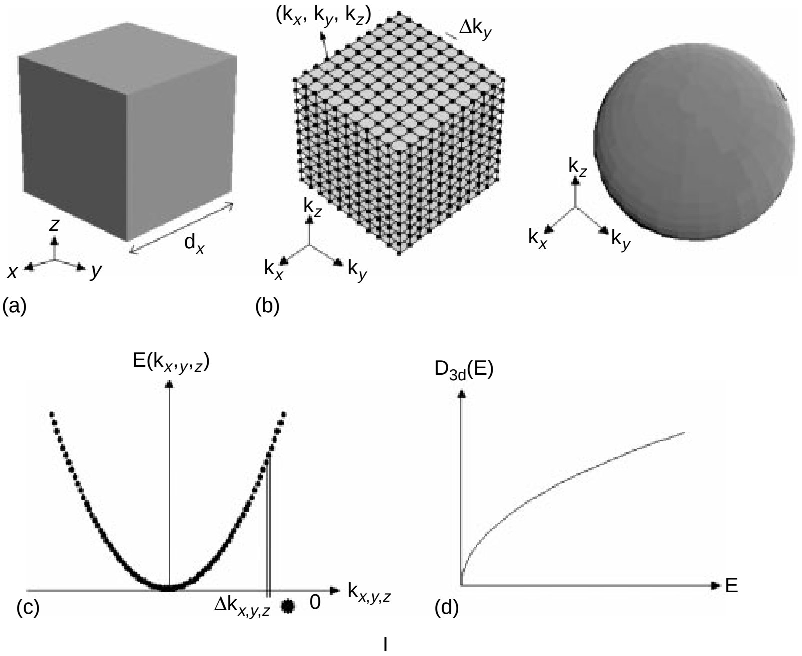

Figure 1 (I) Electronic behavior in a 3D system, infinitely extended in x, y, and z directions (a). The electronic states are symbolized by dots k_x, k_y, k_z (b). In a bulk particle the spacing $\Delta k_{x,y,z}$ between individual electronic states is so small that a quasi-continuous situation arises. The energy of the freely mobile electrons varies in the square of the wavenumber, resulting in the parabola (c). The density of states D_{3d} in a 3D system (d). The allowed energies are quasi-continuous. Their density varies with the square route of the energy $E^{1/2}$. (II) In a 2D system the extension in z-direction is limited to a few atomic layers. $\Delta k_{x,y}$ is still very small, but Δk_z is increased so that discrete values n_1, n_2 . . . exist (c), resulting in a so-called stair-case (d). (III) Situation in the 1D case. Only Δk_x is still small, whereas Δk_y and Δk_z are discrete, ending up in a density of states situation where each of the hyperbolas (d) corresponds to an individual k_y, k_z – state. (IV) In a zero-dimensional state (0D) of the extension of the de Broglie wavelength only discrete energy levels result (d). (Ref. 1. Reproduced by permission of Wiley-VCH)

much instructive. The relaxation time is controlled by two opposite effects: the electron-phonon coupling in the particle and the electronic collision rate on the particle's surface. As can be seen from Figure 3, the relaxation time in case of Au_{55} is much faster than for the 15 nm species because of a reduced electron-phonon coupling and an increased collision rate on the surface.

However, the relaxation behavior of Au_{13} is very much different. It behaves like a typical molecule without any freely mobile electrons so that collisions on the particle's surface cannot happen. $Au_{55}(PPh_3)_{12}Cl_6$ can therefore be considered as being positioned exactly at the borderline between bulk and molecule.

This interpretation agrees perfectly with results originating from Scanning Tunneling Spectroscopy (STS) investigations. An experimental setup as sketched in Figure 4 is used to study the current (I)-voltage (U) behavior of individual nanoparticles.

A single ligand protected particle is trapped between an Scanning Tunneling Microscopy (STM) tip and a conductive substrate. In case of having quantum size behavior, tunnelling of single electrons trough the insulating ligand shall into the cluster core should happen at an appropriate voltage. The presence of that electron blocks the transition of a next one until a voltage is reached overcoming this so-called Coulomb blockade (CB). In case of having a particle with bulk character, linear I-U behavior can be expected (Ohm behavior). However, SET can only be observed if the electrostatic energy $e^2/2C$ is very large compared with the thermal energy k_BT of the electron, in order to avoid uncontrolled thermal electron transitions. So, SET can indeed be observed in rather large particles if the temperature is low enough. A 15 nm Pd particle has been demonstrated to behave bulk-like at 295 K, but exhibits quantum size properties at 4.2 K.**[6]** However, $Au_{55}(PPh_3)_{12}Cl_6$ is small enough to reduce the capacity C to such an extent that $e^2/2C$ becomes large enough to allow SET at room temperature.**[7]** The corresponding Coulomb blockade is shown in Figure 5.

This is probably one of the most important results with respect to applications of metal nanoparticles in future electronic nanodevices: it impressively demonstrates $Au_{55}(PPh_3)_{12}Cl_6$ to work as single electron switch at room temperature. From this knowledge, a series of consequences are following with respect to future electronic applications of this quantum dot.

It should be mentioned that corresponding investigations of slightly larger particles, for instance, of a Pt_{309} four-shell cluster with a 1.8 nm metal core, clearly indicated

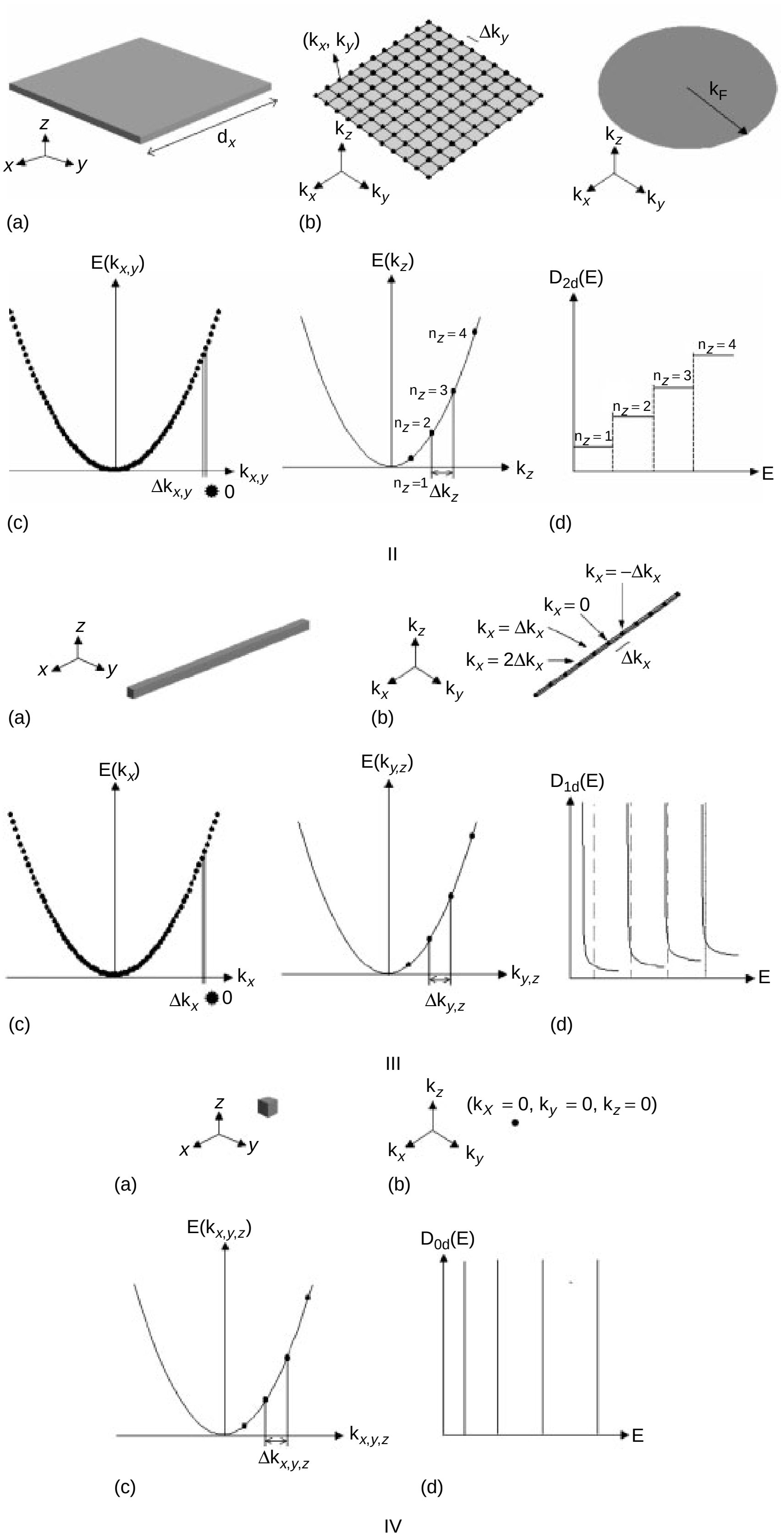
z
x
y
d_x
(k_x, k_y)
Δk_y
k_z
k_x
k_y
k_F
(a)
(b)
E(k_{x,y})
k_{x,y}
Δk_{x,y} → 0
E(k_z)
n_z = 4
n_z = 3
n_z = 2
n_z = 1
Δk_z
k_z
D_{2d}(E)
E
(c)
(d)
II
k_x = −Δk_x
k_x = 0
k_x = Δk_x
k_x = 2Δk_x
Δk_x
(a)
(b)
E(k_x)
k_x
Δk_x → 0
E(k_{y,z})
k_{y,z}
Δk_{y,z}
D_{1d}(E)
E
(c)
(d)
III
(k_x = 0, k_y = 0, k_z = 0)
(a)
(b)
E(k_{x,y,z})
k_{x,y,z}
Δk_{x,y,z}
D_{0d}(E)
E
(c)
(d)
IV

Figure 1 cont'd

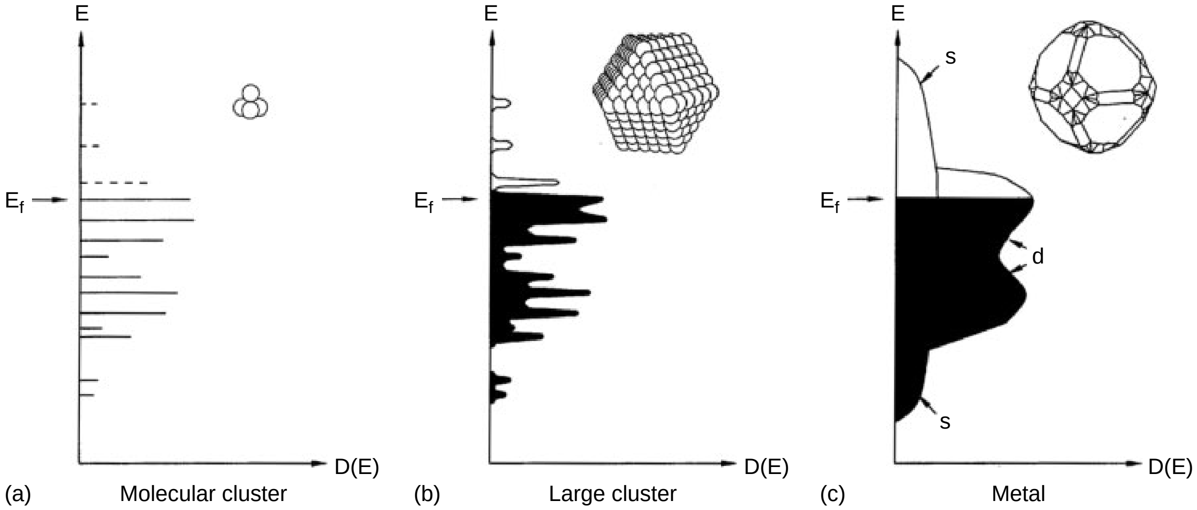

Figure 2 Simplified explanation of transition from a small molecule (a) via a nanoparticle (b) to the bulk (c) with respect to the electronic situation. Between states a and c there is a situation to be expected with broadened electronic levels (b)

bulk behavior at room temperature so that the discussion of electronic properties of even larger particles in this connection seems not necessary.

Magnetism is a result of moving charges. Magnetic properties arise mainly from moving electrons (orbital and spin motion). Since the electronic structure of a magnetic nanoparticle is characteristically dependent on the particle's size, monodispersity of the particles is therefore a condition to yield trustful results. Magnetic nanoparticles can be understood as single-domain magnets. The properties of individual particles can only be studied if they are separated from each other, for instance, in solution at low concentration.[8] Magnetic nanoparticles can exhibit unexpected properties. So, not only nanoparticulated iron, cobalt, or nickel, the only three metals that are ferromagnetic in the bulk state, are of interest, but, for instance, very small rhodium particles[9] that can be ferromagnetic as well as ferro- and ferrimagnetic alloy-like particles of manganese, chromium, cobalt, or platinum.[10] Monodisperse magnetic particles are able to organize themselves to build up highly ordered 2D and even 3D architectures. It can be expected that monodisperse magnetic nanoparticles can reach magnetic recording densities between 100 Gb/in^2 and 1 Tb/in^2.[11] Spin-dependent tunneling electron transport has been demonstrated in organized Co nanoparticles.[12] Unique magnetoresistive properties have been observed for magnetic nanoparticles embedded in matrices of nonmagnetic metals or dielectrics.[13–17] So-called ferrofluids develop rapidly to applicable materials.[18–23] These are magnetic nanoparticles having a shell of protecting molecules making them not only soluble in appropriate solvents, but prevent coagulation. In addition, a ligand shell can affect the magnetic properties.[24–26]

3 ORGANIZATION IN THREE DIMENSIONS

3D organization of metal nanoparticles is easy to be reached compared with 2D or even 1D, since nature tends to organize itself three-, but not two- or one-dimensionally. The most convenient way to get 3D assemblies of metal nanoparticles is to let them crystallize. Usually crystallization happens with identical molecules or with oppositely charged ions. Surprisingly, nanoparticles can form 3D crystals even if they are not identical in size and shape; however, it is obvious that deviations should be as small as possible.

So-called superlattices of 5 nm alkylthiolate protected silver particles having truncated octahedral shapes as well as thiol-stabilized 5–6 nm gold particles can be obtained from solution.[27–30] Fractional crystallization is a very usual method to separate chemical compounds from other compounds and impurities. Mixtures of thiolate stabilized gold nanoparticles between 1.5 and 3.5 nm could successfully be fractioned into real monodisperse species containing 140, 225, 314, and 459 atoms.[31] 2D assemblies have also become available of these fcc-structured nanoparticles. The decisive criterion to successfully fraction and crystallize metal nanoparticles is to protect them perfectly by strongly bound ligand molecules in order to avoid coalescence.

With respect to the mentioned conditions for nanoparticles, crystallization of the well defined nanocluster $Au_{55}(PPh_3)_{12}Cl_6$ and some of its derivatives are ideal candidates to form crystals. Indeed, $Au_{55}(PPh_3)_{12}Cl_6$ crystallizes spontaneously from dichloromethane solution as perfect, but small microcrystals. Macroscopic crystals, growing over longer periods of time, could not yet been gained owing to the continuous decomposition of the particles in solution. The reason for this decomposition must be traced back to the mobility of the ligand molecules, linked with partial dissociation. The

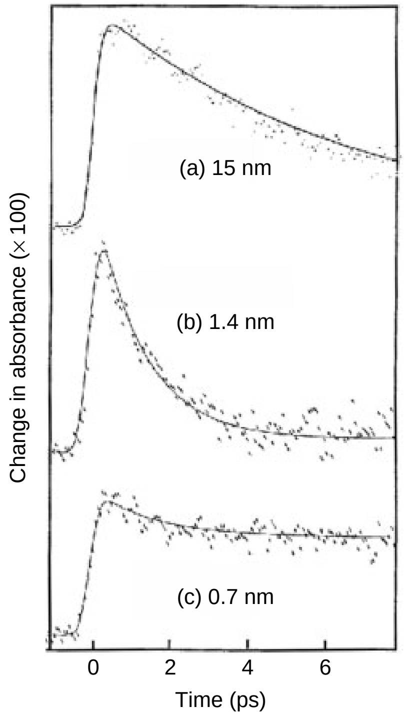

Figure 3 Electronic relaxation behavior of gold nanoparticles of different size after excitation with femtosecond laser pulses. The 1.4 nm particles (Au_{55}) represent a transition between bulk and molecule. (Reprinted from Ref. 5. © 1997, with permission of Elsevier)

high mobility of the PPh_3 ligands has been demonstrated by NMR experiments long time ago.[32] The loss of ligand molecules in solution provokes coalescence processes ending up in precipitates of agglomerated particles and sometimes even of gold mirrors. On the contrary, solid cluster samples are stable over long periods of time.

3D Au_{55} assemblies can also be generated, linking the particles by spacer molecules. This was done in order to vary the particle–particle distances aiming at systems with different conductivity properties. Two different types of spacers can be used: molecules that link the nanoparticles via contacts between ligand shell and spacer molecule and those that directly combine the metal nuclei via covalent bonds. Table 1 informs about the different ways to vary the distances. Except using spacers, variations of the ligand shells can also give samples of interest wherein the particles simply touch each other (Type I).

Type II consists of Au_{55} particles with a ligand shell consisting of sulfonated triphenylphosphine. The presence of SO_3H functions allows ionic interactions with diamines. Dithiols finally give type III systems. Here, part of the original PPh_3 molecules is substituted by thiol functions combining the metal particles directly via covalent bonds and not only by contact or by ionic interactions like in type II systems.

The electrical properties of such different 3D systems are quite interesting, since they show characteristic differences. They have been studied by dc and ac complex impedance measurements.[33,34] At temperatures several tens of Kelvin below room temperature, the temperature dependence of both conductivities follows the Arrhenius relation

$$\sigma(\mathrm{T}) = \sigma_o + \exp\frac{-E_A}{k_B T}$$
$$(E_A = \text{activation energy},\ k_B T = \text{thermal energy}) \qquad (1)$$

This behavior indicates hopping transport of individual charges between nearest neighboring particles (Nearest Neighbor Hopping). With decreasing measuring temperature, E_A becomes temperature dependent and so the conductivity follows the Variable Range Hopping (VRH) defined by Mott,[35] indicating a thermally activated stochastic multiple site hopping process, whereas at high temperatures around room temperature, nearest neighbor-hopping dominates.[36] This nearest neighbor-hopping around room temperature leads to the question if the charging energy of such metal nanoparticles can chemically be changed by varying the particle–particle distance as indicated in Table 1. Figure 6 summarizes the experimental results.

As long as the distance between the gold nanoparticles is based on noncovalent effects (type I and type II) an almost linear increase of activation energy in dependence of the particle spacing d can be observed.[37] This can be understood by a decrease of the junction capacitance scaling with 1/d. However, in case of covalent spacing (type III) with molecules having π-electrons, electrons use molecular orbitals for transport between the metal centres, resulting in characteristic energy drops, depending on the electronic structure of the spacer molecules and their respective length. These results remind the classical description of outer-sphere and inner-sphere mechanisms[38,39] of redox processes in aqueous systems.

3D assemblies of magnetic nanoparticles are formed if solutions of the corresponding particles are slowly reduced in volume or by careful destabilization of a solution by letting slowly diffuse a nonsolvent into the solution to get an oversaturation. Such procedures are in principle well known as crystallisation techniques also for nonmagnetic particles. 3D assemblies of up to several micrometers of cobalt,[40–43] nickel,[41] FePt,[44] or $CoPt_3$[45] have been generated by one of these traditional routes.

A method that can exclusively be applied for magnetic nanoparticles is the use of an external magnetic field that should not be too strong, otherwise glassy materials can be formed instead of 3D superstructures. The direction of the applied field influences the shape and structure of the resulting crystals.[41,46,47] For instance, a field applied in the plane of a substrate results in spindle-like aggregates of Co nanoparticles with their long axes aligned along the external magnetic field,[41,48] whereas $CoPt_3$ nanoparticles have been

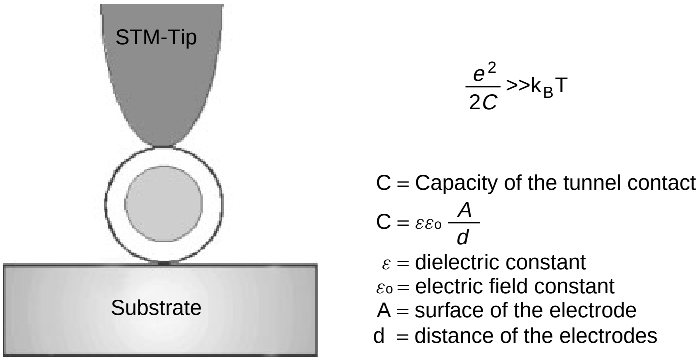
STM-Tip
Substrate
$\frac{e^2}{2C} >> k_B T$
C = Capacity of the tunnel contact
$C = \varepsilon\varepsilon_0 \frac{A}{d}$
ε = dielectric constant
ε_0 = electric field constant
A = surface of the electrode
d = distance of the electrodes

Figure 4 Sketch of an experimental setup to measure SET from a tip to a substrate and the conditions necessary to observe it

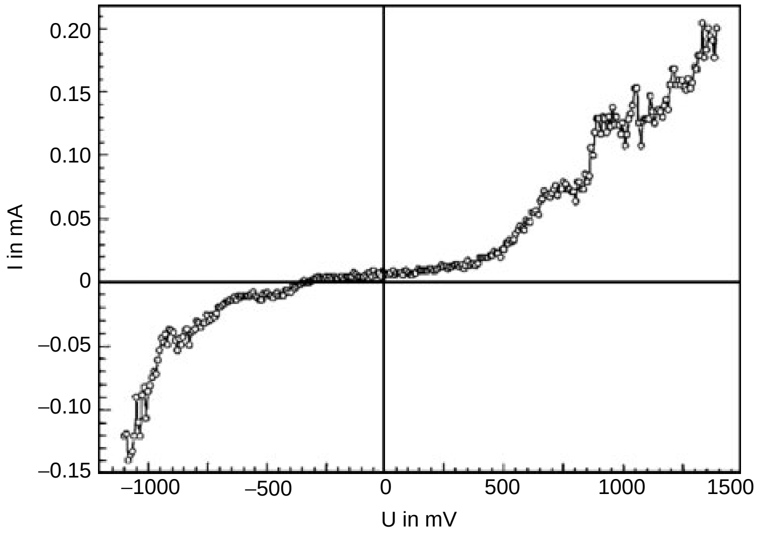

Figure 5 Current (I) voltage (U) characteristic of an individual $Au_{55}(PPh_3)_{12}Cl_6$ clusters at room temperature showing a well expressed Coulomb blockade between about -500 and $+500$ mV. (Ref. 7. Reproduced by permission of Springer Verlag)

ordered in parallel stripes if the field is directed parallel to the substrate. Needles of 4 nm $CoPt_3$ particles of up to 100 µm in length and 0.1–2 µm in diameter are formed in a magnetic field of 0.9 T applied perpendicularly to a substrate.[46]

There is still a lack of systematic investigations and also some contradictory results indicate that extended research is necessary to routinely generate superstructures of uniform magnetic nanoparticles.

4 TWO- AND ONE-DIMENSIONAL ASSEMBLIES OF METAL NANOPARTICLES

Compared with 3D organizations and with some respect also with 1D arrangements, ordered monolayers (2D) earn by far most interest owing to their potential applicability in future storage systems based on nanoparticulated building blocks. Like in case of 3D structures, identical size and shape of the nanoparticles help to start self-assembly processes; however, deviations from both properties are tolerated if they are not too large. 2D superlattices can even be generated if two very different species, each of distinct size, are combined. Generally, formation of 2D structures can be divided into processes where classical self-assembly is the dominating driving force, others that are called ‘guided self-assembly’ and finally formation of ‘aimed structures’ that are the most promising developments with respect to applications in nanoelectronics. Guided self-assembly of 2D structures is based on weak interactions between the particles and between the particles and appropriate surfaces, respectively. The various possibilities will be discussed in the following.

Self-assembled monolayers (SAMs) of organic molecules are known since decades. Self-organized metal nanoparticles have been observed for the first time only about 10 years ago.

Table 1 Noncovalently (I, II) and covalently (III) linked Au_{55} clusters with cluster–cluster distances and activation energies

Noncovalently linked			
Linking system	Type	Distance nm	E_a (eV)
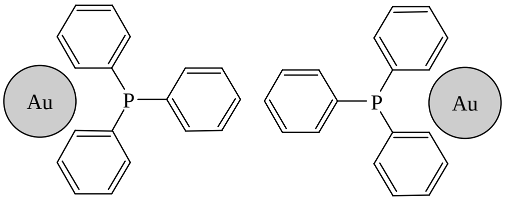	Ia	0.7	1.6
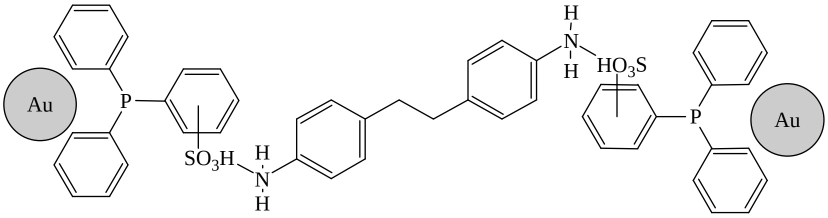	IIa	1.9	2.0
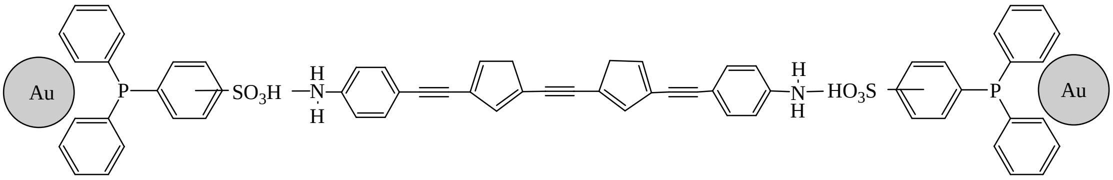	IIb	2.8	2.3
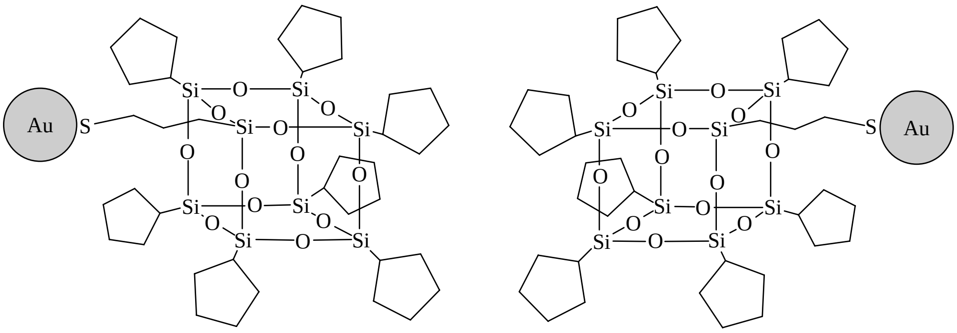	Ib	3.1	2.6
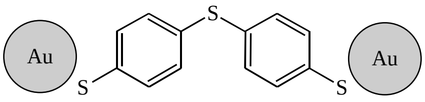	IIIa	1.1	0.095

(cont'd overleaf)

Schiffrin *et al.* generated SAMs of 8 nm gold particles at the phase boundary of a liquid–liquid system using dithiols to cross-link the particles.[49,50] From the same group, bimodal monolayers of AB_2 and AB type became known using silver and gold nanoparticles of different size[51,52] as is indicated in Figure 7.

For instance, ligand protected 8 nm Au and 5 nm Ag particles form perfect bimodal 2D arrays of the AB_2 type. Magnetic $CoPt_3$ nanoparticles of different size (4.5 and 2.6 nm) even form AB_5 structures,[53] whereas identical species spontaneously arrange to ordered monolayers when spread on a substrate, followed by slow evaporation of the solvent.[45,54] Depending on the experimental conditions, double and triplelayers are obtained that practically still can be considered to be two-dimensional.

Numerous examples of ordered 2D structures, especially of thiol-stabilized silver and gold nanoparticles, have become known in the course of the last few years.[27,31] They usually form spontaneously on Transmission Electron Microscopy (TEM) grids or other surfaces from solution and will not be

Table 1 cont'd

Covalently linked			
Linking system	Type	Distance nm	E_a (eV)
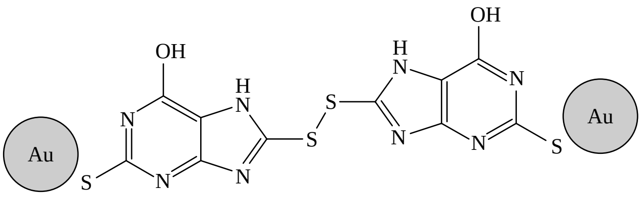	IIIb	1.6	0.11
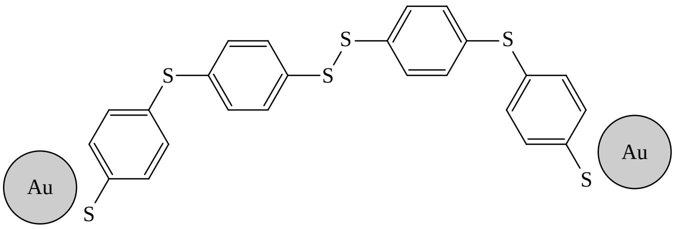	IIIc	2.3	0.12
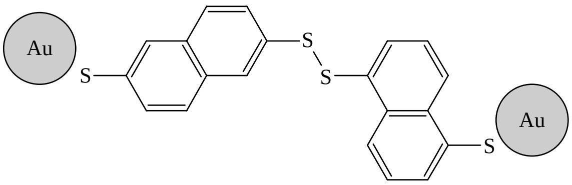	IIId	1.5	0.14

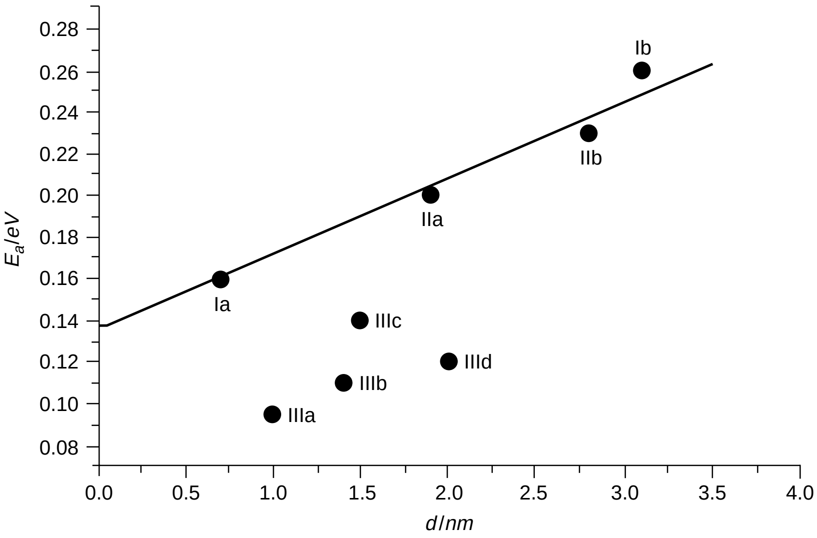

Figure 6 Dependence of activation energy and cluster–cluster distances in 3D arrangements of Au_{55} clusters. Systems I and II are noncovalently linked, system III are covalently interacting

discussed quantitatively. A decisive experimental prerequisite if ordered SAMs are formed or not is the hydrophobicity or hydrophilicity of the corresponding surface that has to fit to the nature of the solvent where the nanoparticles are dissolved in. On the one hand, particles that deposit from solution on a substrate must be freely mobile in order to organize themselves, usually in a dense packed manner. On the other hand, there should be some attraction between the particles and the substrate's surface, since otherwise there is no reason why to deposit from solution and in order to make the monolayers stable enough to survive drying or eventually transport to another surface. An illustrative example showing

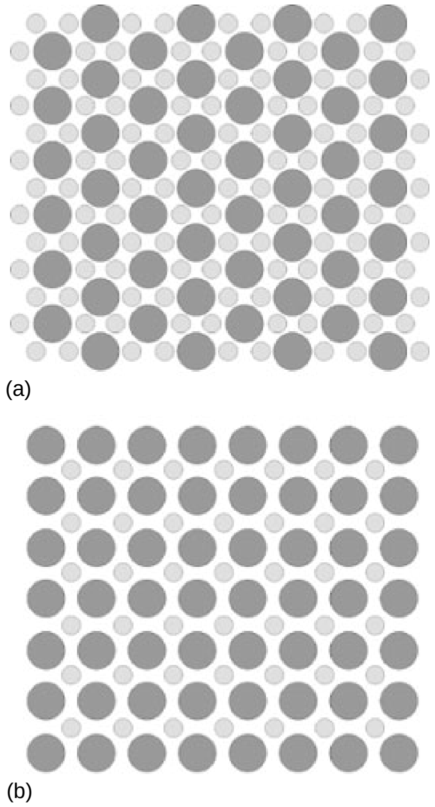

Figure 7 Sketch of monolayers of metal particles of different size. (a) represents an AB_2 system, (b) shows an AB superlattice

this sensitive interplay between particles in solution and surfaces is the 2D organization of $Au_{55}(PPh_3)_{12}Cl_6$ clusters. Dissolved in dichloromethane, they can be distributed on a water surface forming a thin film as is usually applied in Langmuir–Blodgett techniques. With proceeding evaporation the Au_{55} clusters organize with formation of small islands that are stable enough to be transferred to TEM grids for imaging, as can be seen from Figure 8.[55]

Partial overlap comes from the transfer process from the water surface onto the grid. Rather large extended ordered monolayers are formed if a thin film of appropriate polymer molecules is generated at the phase boundary between water and dichloromethane in advance.[56] Poly(vinylpyrrolidone) (PVP) or poly(*p*-phenyleneethynylene) (PPE) derivatives turned out to give best results. The reason for the formation of such largely extended 2D arrays is to be seen in weak interactions between the phenyl groups of the PPh_3 ligands and the chemically related polymers. Therefore, it can be understood that an alkyl terminated polymer film consisting of poly(methylmethacrylate) (PMMA) does not support formation of 2D films of comparable quality. Figure 9 shows a TEM image of a part of a perfectly ordered monolayer of $Au_{55}(PPh_3)_{12}Cl_6$ particles in a hexagonal arrangement, generated on a film of PPE at the phase boundary of water and dichloromethane.

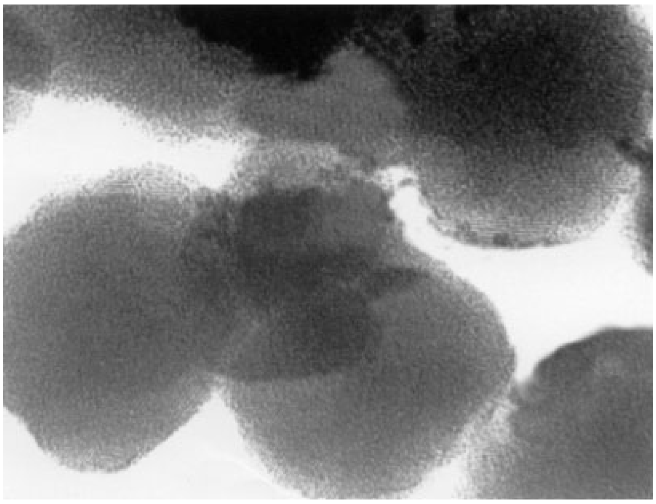

Figure 8 TEM image of self-assembled islands of $Au_{55}(PPh_3)_{12}Cl_6$ clusters on a water surface

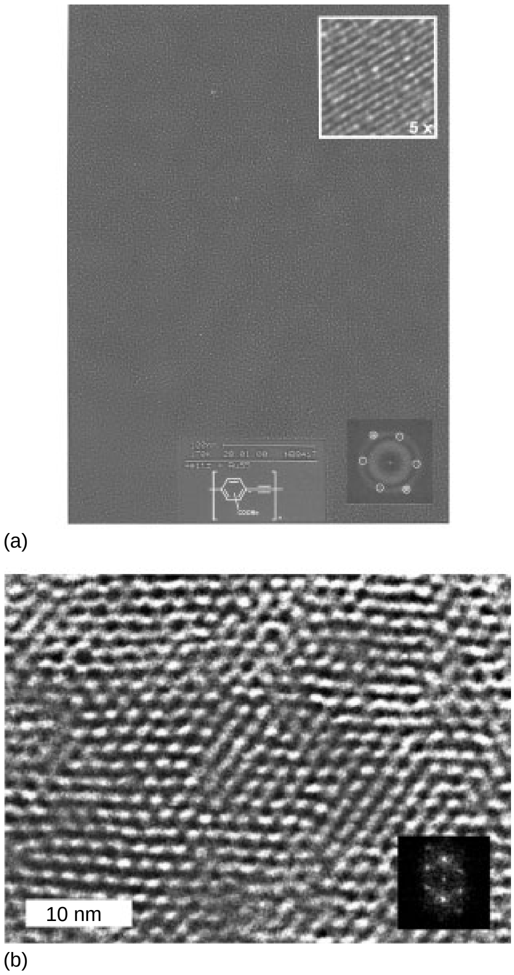

Figure 9 (a) TEM image of a cutout of hexagonally ordered $Au_{55}(PPh_3)_{12}Cl_6$ clusters, deposited on a polymer film. (Ref. 56. Reproduced by permission of Wiley-VCH). (b) Magnified cutout

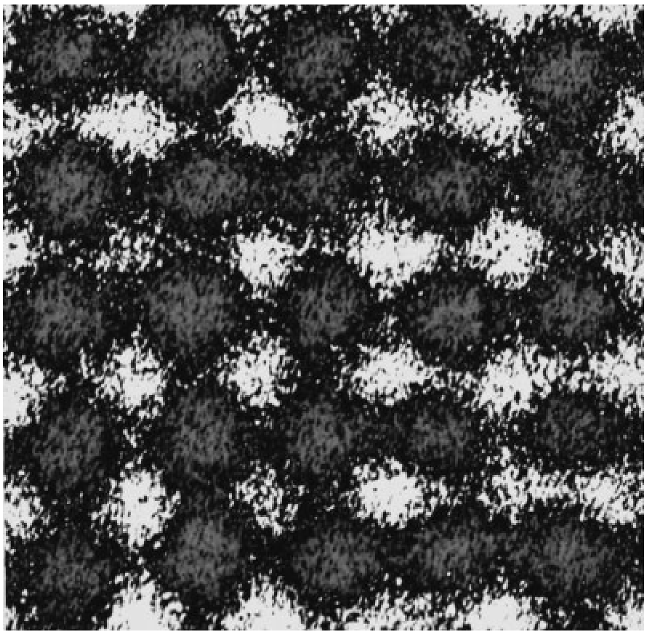

Figure 10 Cutout of orthogonally ordered Au_{55} clusters

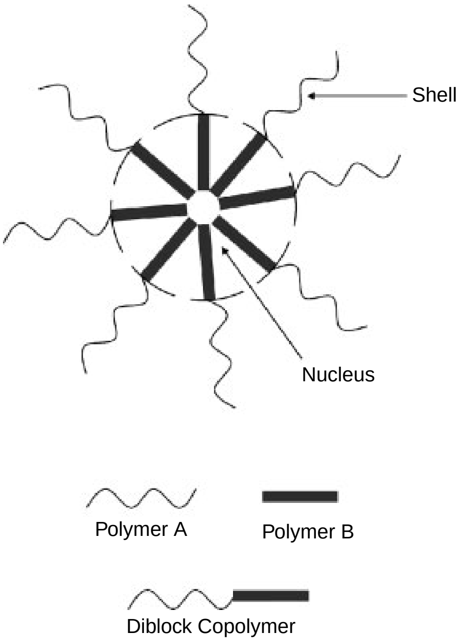

Figure 11 Sketch of the formation of micelles of diblock copolymers

The interaction between the nanoparticles and the polymer film is strong enough to survive the transfer onto a TEM grid. Simple square structured 2D organizations can also be found. If a hexagonal or a square architecture is generated may simply depend on the very first contacts between a few particles, serving as crystallization seeds. Figure 10 shows a small cutout of a monolayer with square-packed Au_{55} particles.[57]

Guided self-assembled monolayers are those where self-assembly is supported by means of experimental conditions that enforce the nanoparticles into distinct positions. Langmuir–Blodgett (LB) technique is one of the methods to organize molecules and also nanoparticles on a large scale. It is based on the spreading of solutions of the corresponding particles, dissolved in a suited organic solvent, on a water surface with subsequent compression of the thin film on the water surface. However, as it turned out, larger areas of nanoparticles generated by LB are usually not well ordered, but contain mostly randomly oriented nanoparticles. For some applications such monolayers may be suited, however, not with respect to the use of nanoparticles as individual species in nanoelectronics. Smaller areas with ordered metal nanoparticles could, however, be generated; for instance, alkanethiolate stabilized 3–5 nm gold metal particles[58] as well as ligand protected Au_{55} clusters.[59] Improvements were reached using amphiphilic particles and repeated compression resulting in areas of $0.25\,\mu m \times 0.35\,\mu m$.[60]

A guided self-assembly of gold nanoparticles succeeded also on patterned GaAs surfaces.[61] Structured Be-doped GaAs surfaces were first decorated with a monolayer of xylyl dithiol molecules. A uniform monolayer of dodecanethiol stabilized 5 nm Au particles, generated by spreading a hexane solution on a convex water surface (to be considered as a special kind of LB), is then transferred to the GaAs surface by gentle contacting this surface with the monolayer. It can be assumed that xylyl dithiols partially substitute dodecanethiol ligands. A remarkable development in making ordered metal nanoparticles arrangements is based on the use of so-called diblock copolymers. Polymer A and polymer B are first combined to the block copolymer A-B, which then forms micelles. Figure 11 illustrates the micelle formation.

Like other micelles, they represent perfect ‘nano reaction vessels’ that can be used to generate metal nanoparticles inside. The decisive point is that with the transfer onto smooth surfaces thin coherent films of ordered micelles become available.[62–68] Examples for A-B diblock copolymers are poly(styrene)-poly(ethylene oxide) or poly(styrene)-poly(2-vinylpyridine). Formation of metal nanoparticles inside of the micelles starts with loading of the hollow spheres with the corresponding metal salt, followed by the reduction step. For instance, gold nanoparticles are made from $HAuCl_4$ or $LiAuCl_4$. The tetrachloroaurates penetrate into the micelles in nonpolar solvents. Ultrasound supports the diffusion process. Subsequent reduction with hydrazine or $[BH_4]^-$ leads to gold nanoparticles. Usually, several nanoparticles are formed in each micelle in a first step. These can then be transferred into single particles by annealing. Gold particles of 2.5, 4, 6, or 12 nm have so been obtained. Figure 12 shows TEM images of ordered 2D gold nanoparticles of different size.

Except gold, several other metal nanoparticles, also those of less noble metals, could be prepared, for instance, of silver, palladium, and cobalt, as well as sulfidic species like CdS or PbS.[69]

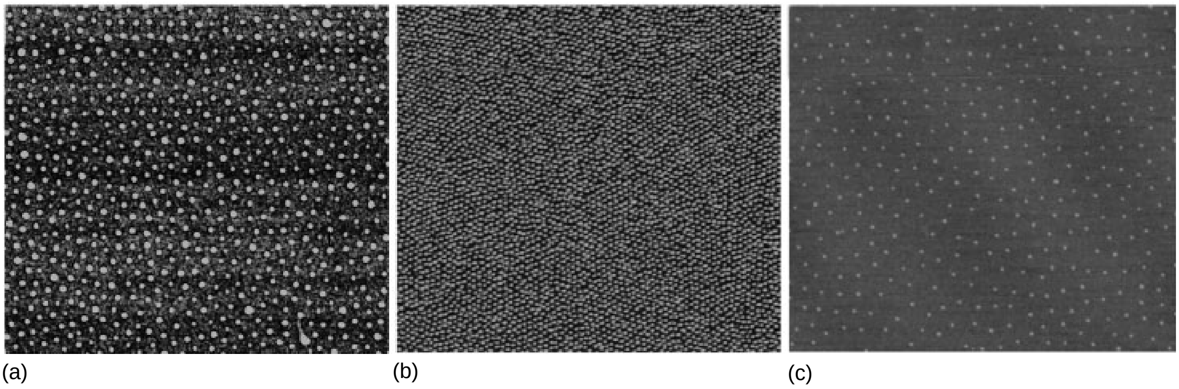

Figure 12 TEM images of gold nanoparticles of different size prepared in diblock copolymer micelles. (a) 6 nm, (b) 4 nm, (c) 2.5 nm. (Reprinted from G. Schmid, D.V. Talapin, E.V. Shevchenko in ed. G. Schmid Nanoparticles. From Theory to Application, Wiley-VCH, Weinheim 2004, with permission from Wiley-VCH)

The real value of this diblock copolymer technique is to be seen in the possibility to remove the organic matter without destroying the organization.[70–72] Ordered micellar films on glass or mica can be treated by an oxygen plasma leading to bare metal nanoparticles without loss of the original order. The metal particles are strongly fixed to the surfaces and cannot be removed by rinsing or even by rubbing with soft tissues. Furthermore, particle size, interparticle distances and herewith particle density can be varied by the composition of the micelles, the amount of metal salt, and so on. The use of diblock copolymers of different molecular weights determines decisively the interparticle distances. 1 nm Au particles with 140 nm distance from each other or 12 nm particles of 80 nm distance are available likewise.[70]

Ordered assemblies of gold nanoparticles generated by this micelle technique seem to become of importance on the rapidly developing field of nanobiotechnology. Regularly arranged spots of gold serve as anker places for biomaterials, as has impressively been demonstrated by Spatz *et al.*[73–75]

Finally, the so-called S-layers should be mentioned. They consist of 2D protein organizations, naturally formed as the outermost cell surface layer (S-layer) of prokaryotic organisms.[76] At liquid-surface interfaces of various lipid films or solid substrates such systems can form nanoporous monolayers that can be used for generating ordered arrays of, for example, 4–5 nm Au[77] or 1.9 nm Pt particles from salts.[78]

The 2D structures discussed up to here were all formed by self-assembly of particles or by self-assembly guided with the help of preformed surfaces, spheres, and so on. However, the highest goal of depositing metal nanoparticles on substrates is to create **aimed structures**, that is, those that are not influenced or even determined by any kind of a natural process, but instead are resulting in completely artificial architectures.

After having studied numerous templates for generating 1D assemblies of nonmagnetic metal nanoparticles, for instance, polymers,[79,80] nanopores[81–84] and even DNA,[85–87] it turned out that these approaches not really resulted in practicably applicable 1D systems. Therefore, they will not be discussed further. However, there are several other developments becoming visible that promise much better success with respect to aimed structures. They offer indeed chances to realize any kind of artificial architecture so that 2D or 1D structures can be designed likewise or combined with each other so that differentiation between both makes no longer sense from a technical point of view.

The so-called dip-pen nanolithography is one of these promising novel techniques. It has been developed by Ch. Mirkin *et al.* and is based on the use of Atomic Force Microscopy (AFM) tips to deposit functionalized molecules on appropriate surfaces.[88,89] The molecules are first deposited in solid state on the tip. The transport to the surface happens by means of the water meniscus between the tip and the surface that is present in air of usual humidity. Gold surfaces are preferably used to deposit thiol molecules forming strong Au–S bonds. The places were thiol molecules are deposited simply depend on the software moving the AFM tip on the surface. Figure 13 explains in a simplified manner the process.

Mirkin *et al.* used this method to even write down part of the famous lecture of R. Feynman given in 1960, predicting the future development of nanotechnology.[90]

Deposition of metal nanoparticles on molecularly patterned surfaces requires further functions. For instance, in case of using 16-thiohexadecanoic acid positively charged nanoparticles can be deposited at these positions. An impressive pattern of gold nanoparticles of two different sizes has been generated following several steps, elucidated in Figure 14.

Two interpenetrating orthogonal structures made of gold nanoparticles of different size can be generated following several steps: a first patterning of a gold surface is performed again with 16-thiohexadecanoic acid molecules. Unpatterned areas are then passivated with 1-octadecanethiol. The alkylamine-modified oligonucleotide *a* ($\mathrm{TCTCAACTCGTAA_{10}}$) can then be deposited exclusively on the positions exhibiting carboxylic functions. The second

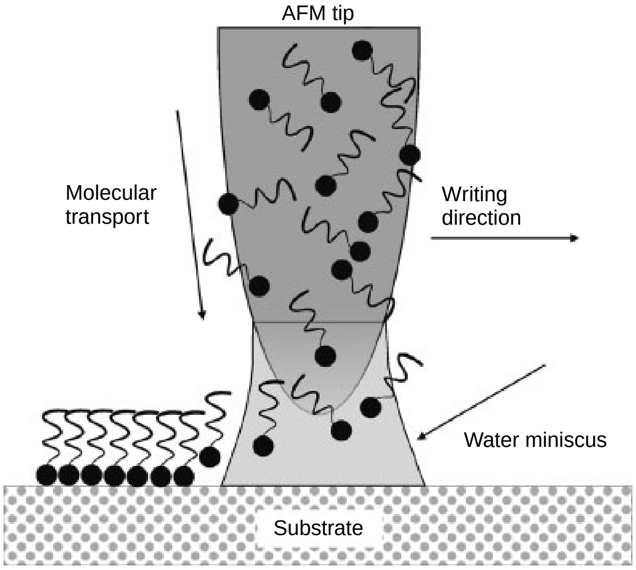

Figure 13 Dip-pen nanolithography. Sketch of the transport of molecules from the tip to a surface

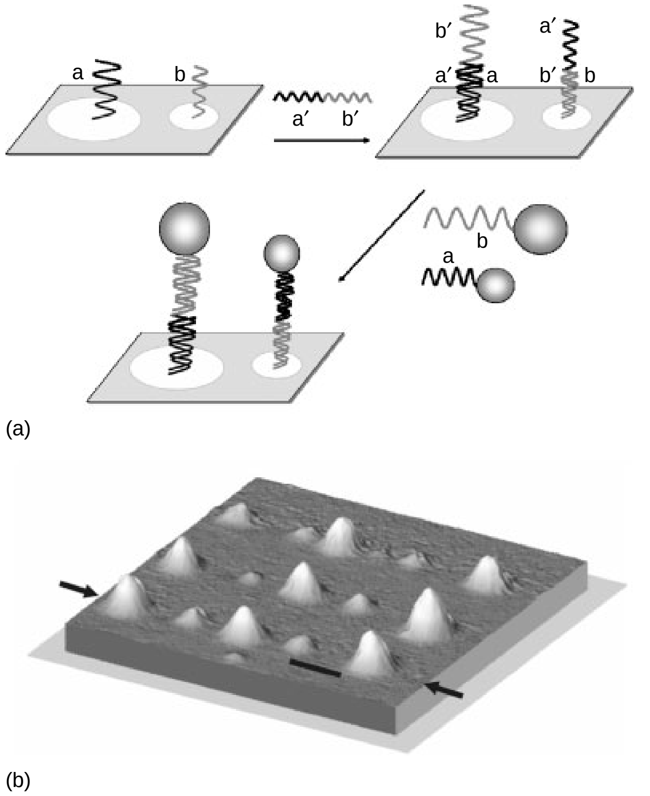

Figure 14 Formal illustration of the formation of a pattern of different gold nanoparticles via complementary oligonucleotides (a). (b): AFM image of an as-prepared arrangement

orthogonal structure is realized by replacing 1-octadecanethiol molecules by further 16-thiohexadecanoic acid molecules via the AFM tip at the relevant positions followed by derivatizing these places by another alkylamine-modified oligonucleotide *b* (A_{10}CGCATTCAGGAT). The as-prepared *ab*-modified surface is then combined with the complimentary *a*′*b*′-oligonucleotide. 13 and 30 nm gold nanoparticles, substituted with *a* and *b* oligonucleotides complete the structure. The impressive result is shown in 14b. No doubt that such structures earn highest interest in the field of future nanoelectronic devices.

A second developing technique also uses AFM tips to nanopattern surfaces. J. Sagiv uses conductive AFM tips to oxidize CH_3 end groups of (SAMs) to COOH functions by emitting electrical pulses.**[91,92]** Herewith, chemical information is written into an inert ‘methyl-surface’. Again, only the software moving the tip over the surface decides where to inscribe the information. However, similar like in the former case, there are further chemical steps necessary to finally end up with 2D or 1D patterns of metal particles. The chemical modifications used in this case are explained in Scheme 1.

The carboxylic groups are derivatized by alkene terminated silanes, followed by the photolytic addition of H_2S to the C=C double bond. Successive treatment with $BH_3\cdot THF$ is necessary to reopen S–S bonds that could have partially been formed during thiolization. In the last step gold nanoparticles can be attached to all positions with SH functions. Larger particles**[92]** can be used as well as the small Au_{55} clusters, here as the water-soluble derivative $Au_{55}(Ph_2PC_6H_4SO_3Na)_{12}Cl_6$.**[91]** In Figure 15, Picasso’s dove of peace, drawn from negatively charged 2–6 nm gold nanoparticles fixed at ammonium functions, is shown,**[92]** whereas Figure 16 shows a pattern

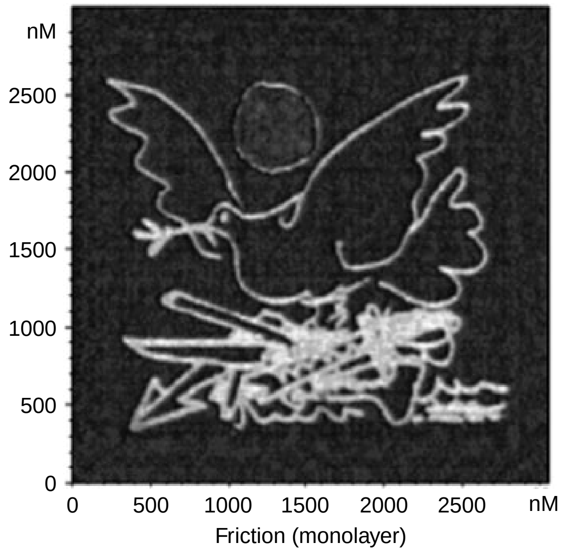

Figure 15 Picasso’s dove of peace, drawn by 2–6 nm gold nanoparticles by nanoelectrical surface patterning via ammonium functions. (Reprinted with permission from Ref. 92. © 2004 American Chemical Society)

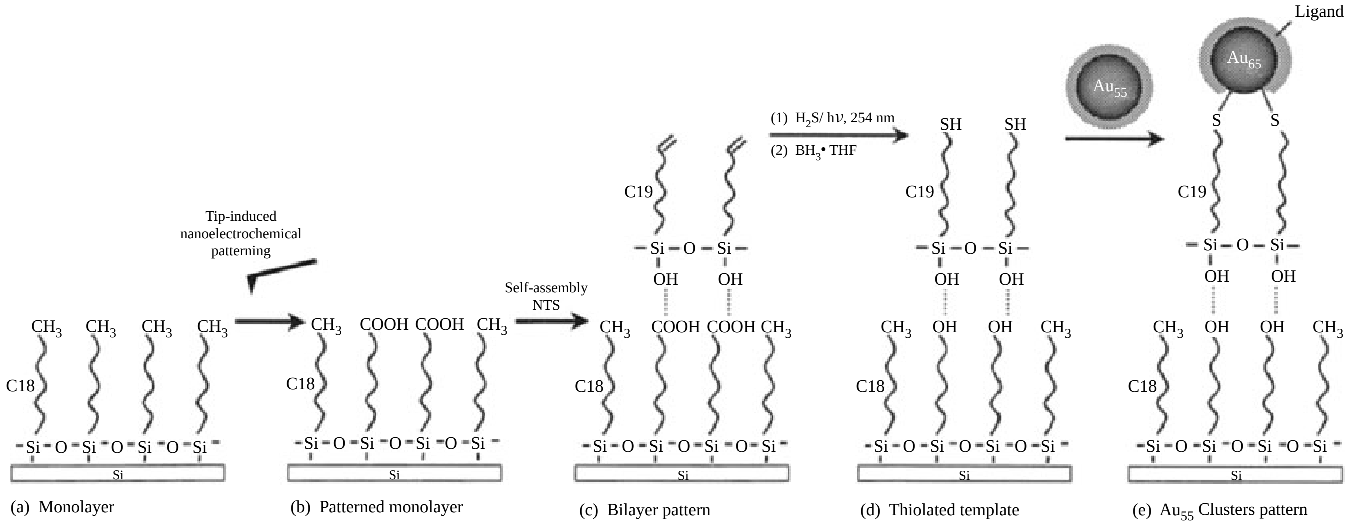
Ligand
Au55
Au65
Tip-induced nanoelectrochemical patterning
Self-assembly NTS
(1) H2S/ hν, 254 nm
(2) BH3• THF
CH3
COOH
OH
SH
S
C18
C19
Si
(a) Monolayer
(b) Patterned monolayer
(c) Bilayer pattern
(d) Thiolated template
(e) Au55 Clusters pattern

Scheme 1 Illustration of the nanoelectrical formation of SH functions in a CH_3 terminated monolayers surface with attached Au_{55} clusters

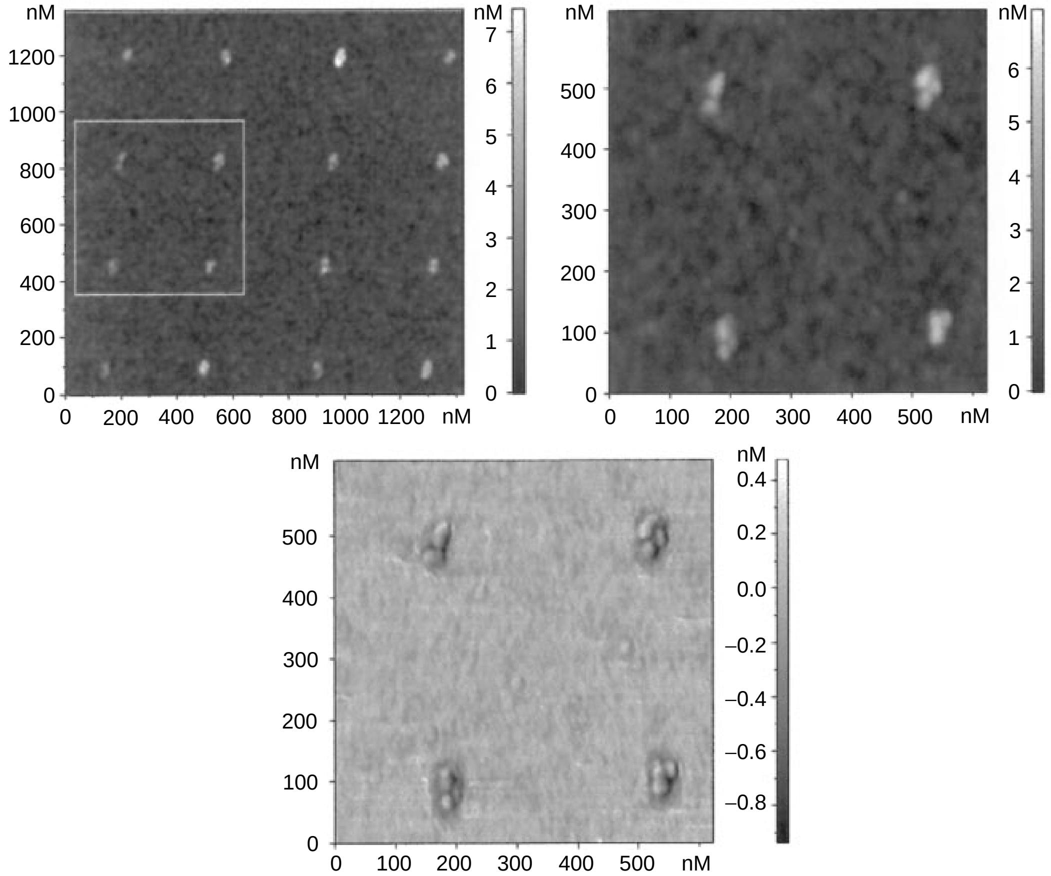
nM
1200
1000
800
600
400
200
0
0 200 400 600 800 1000 1200 nM
nM
7
6
5
4
3
2
1
0
nM
500
400
300
200
100
0
0 100 200 300 400 500 nM
nM
6
5
4
3
2
1
0
nM
500
400
300
200
100
0
0 100 200 300 400 500 nM
nM
0.4
0.2
0.0
−0.2
−0.4
−0.6
−0.8

Figure 16 Dots consisting of 3–4 $Au_{55}(Ph_2PC_6H_4SO_3Na)_{12}Cl_6$ clusters, generated by nanoelectrical surface pattering via SH functions. (Reprinted with permission from Ref. 91. © 2002 American Chemical Society)

of orthogonally positioned Au_{55} particles.[91] However, as can be recognized from the magnified part, each dot still consists of 3–4 clusters, but not of one. The reason for this is simply the quality of the AFM tip used for this experiment leading to too much extended functionalized areas.

With an improved AFM tip ideal one-dimensional wires of individual particles become available and as can also be seen from Figure 17, even individual Au_{55} particles are positioned in predefined intrawire gaps.[91]

This impressive example indicates possible routes to aimed structures of quantum dots that can be applied in future storage systems.

Magnetic metal nanoparticles tend to self-assemble not only for reasons known from nonmagnetic species, namely, van der Waals forces, but especially owing to their intrinsic magnetic nature. Solutions of 4.8 nm $CoPt_3$ particles, spread onto a substrate, organize spontaneously when the solvent is evaporated.[45,54] Higher concentrations of the solutions easily result in formation of double and triple layers as is indicated in Figure 18.[45]

The morphology of the self-assembled structures is strongly influenced by the shape of the individual nanoparticles.[93–95] Faceted and cubic nanoparticles organize in such a way that they all are oriented in the same direction. Such superstructures are promising candidates for generating materials of high magnetic anisotropy owing to the aligning of the axes of magnetization of the individual particles. This is especially valid for $CoPt_3$ particles for their high magnetic anisotropy.[96] Figure 19 shows a TEM image of self-assembled cubic $CoPt_3$ nanoparticles.

Starting from $Co(\eta_3\text{-}C_8H_{13})(\eta_4\text{-}C_8H_{12})$, which is decomposed in anisole at 150 °C in the presence of hexadecylamine and stearic acid under 3 bar of hydrogen pressure, spheric Co nanoparticles are formed that can be transferred to perfectly looking nanorods by successive aging.[97] These Co nanorods perfectly align as is seen from Figure 20.

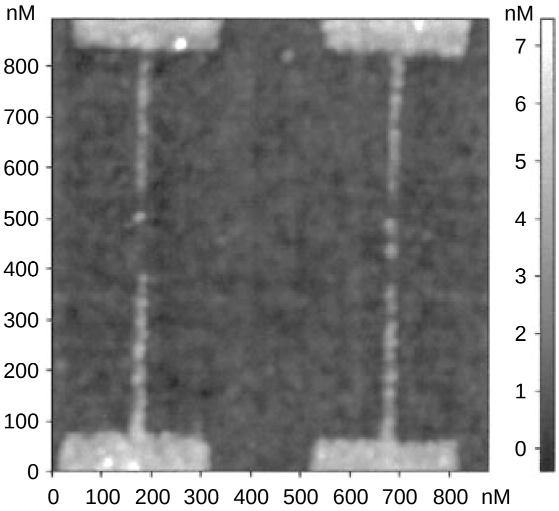

Figure 17 Optimized pattern of 1D lines of Au_{55} clusters and individual clusters at predefined intrawire gaps. (Reprinted with permission from Ref. 91. © 2002 American Chemical Society)

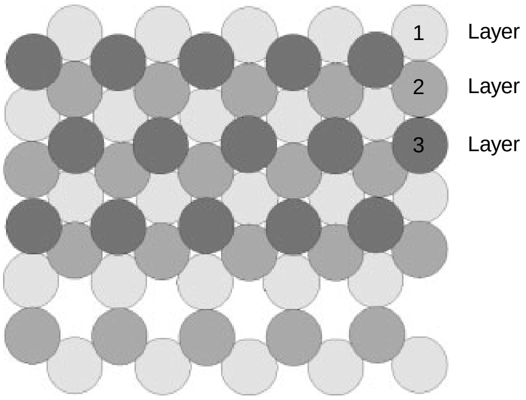

Figure 18 Illustration of a three-layer arrangement of $CoPt_3$ nanoparticles

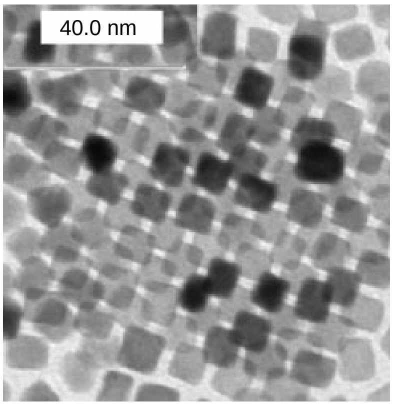

Figure 19 TEM image of a self-assembled structure of $CoPt_3$ nanoparticles. (Reprinted from G. Schmid, D.V. Talapin, E.V. Shevchenko in ed. G. Schmid Nanoparticles. From Theory to Application, Wiley-VCH, Weinheim 2004, with permission from Wiley-VCH)

Such organizations can be expected to exhibit high magnetic anisotropy and coercitivity, but have not yet been studied in this direction.

In contrast to nonmagnetic nanoparticles, 1D organization of magnetic nanoparticles is quite usual owing to their magnetic dipolar interactions. A magnetic single-domain nanoparticle of radius r has a magnetic dipole moment $\mu = 4\pi r^3 M_S/3$ (M_S = saturation magnetization of bulk). The dipole–dipole interaction between two contacting magnetic particles is proportional to $\mu^2/\sigma^3 \propto r^6/\sigma^3$ with σ = effective hard sphere diameter (magnetic core diameter and thickness of surfactant layer).[98] Anisotropic aggregation of magnetic nanoparticles are the consequence of those forces. Self-assembly of magnetic nanoparticles to flexible 1D chains

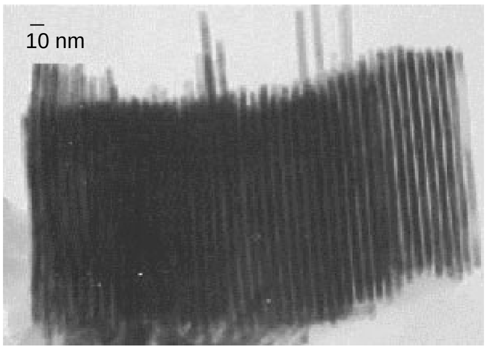

Figure 20 TEM image of cobalt nanorods. (Reprinted from G. Schmid, D.V. Talapin, E.V. Shevchenko in ed. G. Schmid Nanoparticles. From Theory to Application, Wiley-VCH, Weinheim 2004, with permission from Wiley-VCH)

has already been predicted in 1970 in order to minimize magnetostatic energy.[99] Figure 21 gives an impression of possible structure originating from such magnetic interactions.

Superparamagnetic nanoparticles can form chains even at zero field as has been demonstrated by simulations[100,101] and by experiment in a dispersion of iron nanoparticles at zero field.[102] Ring formation happens by unpaired dipoles at the ends of chains and have also been observed with 27 nm cobalt particles.[103] External magnetic fields can by applied in order to orient flexible chains in one direction enabling formation of superstructures.

Magnetic nanoparticles can be quasi or fully 1D organized by outer magnetic fields. Increasing magnetic fields lead to increasing widths of the lines, as has been shown by using cobalt nanoparticles.[48] Figure 22 shows TEM images of organized Co nanoparticles in dependence of the applied magnetic field.

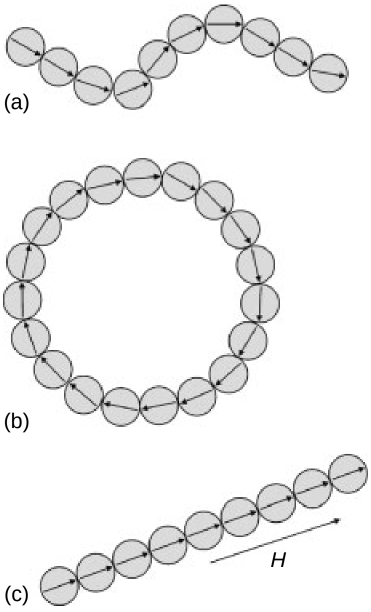

Figure 21 Various forms of chains of magnetic nanoparticles with head-to-tail organized paired dipoles

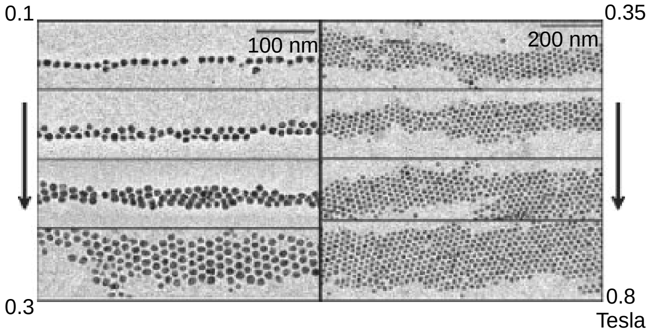

Figure 22 TEM images of 1 D formation of cobalt nanoparticles in dependence of the applied magnetic field. (Reprinted from Ref. 48. © 2002, with permission of Elsevier)

The progressive alignment is explained by the attractive chain–chain interactions.

5 SUMMARY

Summarizing the status quo of organization of metal nanoparticles, it can be stated that there exist several very promising procedures to especially generate 2D and also 1D arrangements. However, it has also to be recognized that we are still far from having techniques to routinely fabricate 2D and 1D structures. The final challenge to generate artificial instead of self-assembled structures seems indeed possible as is shown by the dip-pen lithography and the nanoelectrical surface patterning. Both allow construction of any kind of pattern of metal nanoparticles. Even if we would succeed in making aimed nanostructures routinely, there is still a long way to get working systems. These require techniques to individually address the quantum dots from outside. First steps to solve also these problems have been made; however, presently it is still too early to discuss them.

6 RELATED ARTICLES

Biomimetic Synthesis of Nanoparticles; Carbonyl Complexes of the Transition Metals; Metallic Materials Deposition: Metal-organic Precursors; Polynuclear Organometallic Cluster Complexes; Porous Inorganic Materials; Self-assembled Inorganic Architectures; Semiconductor Nanocrystal Quantum Dots; Sol–Gel Encapsulation of Metal and Semiconductor Nanocrystals.

7 REFERENCES

1. W. J. Parak, L. Manna, Ch. Rimmel, D. Gerion, and P. Alivisatos, in 'Nanoparticles. From Theory to Application', ed. G. Schmid, Wiley-VCH, Weinheim, 2004, p. 4.
2. L. J. de Jongh, in 'Physics and Chemistry of Metal Cluster Compounds', ed. L. J. de Jongh, Kluwer Academic Press, Dordrecht, Boston, London, 1994.
3. H.-G. Boyen, G. Kästle, F. Weigl, B. Koslowski, C. Dietrich, P. Ziemann, J. P. Spatz, S. Riethmüller, C. Hartmann, M. Möller, G. Schmid, M. G. Garnier, and P. Oelhafen, *Science*, 2002, **297**, 1533.
4. H.-G. Boyen, A. Ethirain, G. Kästle, F. Weigel, P. Ziemann, G. Schmid, M. G. Garnier, M. Büttner, and P. Oelhafen, *Phys. Rev. Lett.*, 2005, **94**, 016804-1.
5. B. A. Smith, J. Z. Zhang, U. Giebel, and G. Schmid, *Chem. Phys. Lett.*, 1997, **270**, 139.
6. A. Bezryadin, C. Dekker, and G. Schmid, *Appl. Phys. Lett.*, 1997, **71**, 1273.
7. L. F. Chi, M. Hartig, T. Drechsler, Th. Schwaack, C. Seidel, H. Fuchs, and G. Schmid, *Appl. Phys. A*, 1998, **66**, 187.
8. C. B. Murray, S. Sun, H. Doyle, and T. Betley, *MRS Bull.*, 2001, **26**, 985.
9. A. J. Cox, J. G. Louderback, and L. A. Bloomfield, *Phys. Rev. Lett.*, 1993, **71**, 923.
10. K. J. Klabunde, 'Nanoscale Materials in Chemistry', John Wiley & Sons, 2001, (Magnetism C.M. Sorensen 162).
11. S. Sun and C. B. Murray, *J. Appl. Phys.*, 1999, **85**, 4325.
12. C. T. Black, C. B. Murray, R. L. Sandstrom, and S. Sun, *Science*, 2000, **290**, 1131.
13. C. L. Chien, *J. Appl. Phys.*, 1991, **69**, 5267.
14. A. E. Berkowitz, J. R. Mitchell, M. J. Carey, A. P. Young, S. Zhang, F. E. Spada, F. T. Parker, A. Hutten, and G. Thomas, *Phys. Rev. Lett.*, 1992, **68**, 3745.
15. J. Q. Xiao, J. S. Jiang, and C. L. Chien, *Phys. Rev. Lett.*, 1992, **68**, 3749.
16. H. J. Lipkin, *Phys. Rev. Lett.*, 1987, **58**, 425.
17. S. Takahashi and S. Maekawa, *Phys. Rev. Lett.*, 1998, **80**, 1758.
18. S. A. Zahn and K. E. Shenton, *IEEE Trans. Magn.*, 1980, **16**, 387.
19. K. O'Grady and R. W. Chantrell, 'Magnetic Properties of Fine Particles', Elsevier, Amsterdam, 1992, p. 93.
20. A. Aharony, 'Introduction to the Theory of Ferromagnetism', Oxford University Press, New York, 1996, p. 133.
21. E. Blums, A. Cebers, and M. M. Maioriv, 'Magnetic Fluids', Walter de Gruyter, New York, 1997, p. 343.
22. R. E. Rosenwieg, 'Ferrohydrodynamics', Dover Publishing, New York, 1998.
23. B. M. Berkovskii and V. G. Bshtovio, 'Magnetic Fluids and Applications Handbook', Begell House, New York, 1996.
24. V. Russier, C. Petit, J. Legrand, and M. P. Pileni, *Phys. Rev. B*, 2000, **62**, 3910.
25. D. A. van Leeuwen, J. M. van Ruitenbeek, L. J. de Jongh, A. Cerotti, and G. Pacchioni, *Phys. Rev. Lett.*, 1994, **73**, 1432.
26. F. Bødker, S. Mørup, and S. Linderoth, *Phys. Rev. Lett.*, 1994, **72**, 282.
27. St. A. Harfenist, Z. L. Wang, M. M. Alvarez, I. Vezmar, and R. L. Whetten, *J. Phys. Chem.*, 1996, **100**, 13904.
28. St. A. Harfenist, Z. L. Wang, R. L. Whetten, I. Vezmar, and M. M. Alvarez, *Adv. Mater.*, 1997, **9**, 817.
29. Z. L. Wang, *Adv. Mater.*, 1998, **10**, 13.
30. J. E. Martin, J. P. Wilcoxon, J. Odinek, and P. Provencio, *J. Phys. Chem.*, 2000, **104**, 9475.
31. R. L. Whetten, J. T. Khoury, M. M. Alvarez, S. Murthy, I. Vezmar, Z. L. Wang, P. W. Stephens, C. L. Cleveland, W. D. Luedtke, and U. Landmann, *Adv. Mater.*, 1996, **8**, 428.
32. G. Schmid, U. Giebel, W. Huster, and A. Schwenk, *Inorg. Chim. Acta*, 1984, **85**, 97.
33. G. Schön and U. Simon, *Colloid Polym. Sci.*, 1995, **273**, 101.
34. G. Schön and U. Simon, *Colloid Polym. Sci.*, 1995, **273**, 202.
35. N. F. Mott, *Philos. Mag.*, 1969, **19**, 835.
36. M. P. J. van Staveren, H. B. Brom, and L. J. de Jongh, *Phys. Rep.*, 1991, **208**, 1.
37. V. Torma, O. Vidoni, U. Simon, and G. Schmid, *Eur. J. Inorg. Chem.*, 2003, 1121.
38. H. Taube, H. Myers, and R. L. Rich, *J. Am. Chem. Soc.*, 1953, **75**, 4118.
39. H. Taube, *Science*, 1984, **226**, 1028.
40. C. B. Murray, C. R. Kagan, and M. G. Bawendi, *Annu. Rev. Mater. Sci.*, 2000, **30**, 545.
41. C. B. Murray, S. Sun, H. Doyle, and T. Betley, *MRS Bull.*, 2001, 985.
42. S. Sun, C. B. Murray, and H. Doyle, *Mater. Res. Soc. Symp. Proc.*, 1999, **577**, 385.
43. S. Sun and C. B. Murray, *J. Appl. Phys.*, 1999, **85**, 4325.
44. E. V. Shevchenko, D. V. Talapin, A. Kornowski, F. Wiekhorst, J. Kötzler, M. Haase, A. L. Rogach, and H. Weller, *Adv. Mater.*, 2001, **14**, 287.
45. E. V. Shevchenko, D. V. Talapin, A. L. Rogach, A. Kornowski, M. Haase, and H. Weller, *J. Am. Chem. Soc.*, 2002, **124**, 11480.
46. M. P. Pileni, *J. Phys. Chem. B*, 2001, **105**, 3358.
47. A. T. Ngo and M. P. Pileni, *Adv. Mater.*, 2000, **12**, 276.
48. M. Giersig and M. Hilgendorff, *Colloids Surf., A*, 2002, **202**, 207.

49. M. Brust, D. Bethell, D. J. Shiffrin, and C. J. Kiely, *Adv. Mater.*, 1995, **7**, 795.
50. M. Brust, M. Walker, D. Bethell, D. J. Schiffrin, and R. Whyman, *J. Chem. Soc., Chem. Commun.*, 1994, 801.
51. C. J. Kiely, J. Fink, M. Brust, D. Bethell, and D. J. Schiffrin, *Nature*, 1998, **396**, 444.
52. C. J. Kiely, J. G. Zheng, J. Fink, M. Brust, D. Bethell, and D. J. Schiffrin, *Adv. Mater.*, 2000, **12**, 640.
53. W. B. Pearson, 'Crystal Chemistry and Physics of Metals and Alloys', Wiley-Interscience, London, 1972.
54. A. L. Rogach, D. V. Talapin, E. V. Shevchenko, A. Kornowski, M. Haase, and H. Weller, *Adv. Funct. Mater.*, 2002, **12**, 653.
55. G. Schmid, D. V. Talapin, and E. Shevchenko, in 'Nanoparticles: From Theory to Application', ed. G. Schmid, Wiley-VCH, Weinheim, 2004, p. 251.
56. G. Schmid and N. Beyer, *Eur. J. Inorg. Chem.*, 2000, 835.
57. G. Schmid, M. Bäumle, and N. Beyer, *Angew. Chem.*, 2000, **112**, 187; *Angew. Chem., Int. Ed. Engl.*, 2000, **39**, 181.
58. J. R. Heath, C. M. Knobler, and D. V. Leff, *J. Phys. Chem. B*, 1997, **101**, 189.
59. L. F. Chi, S. Rakers, M. Hartig, M. Gleiche, H. Fuchs, and G. Schmid, *Colloids Surf.*, 2000, **171**, 241.
60. J. J. Brown, J. A. Porter, C. P. Daghlian, and U. J. Gibson, *Langmuir*, 2001, **17**, 7966.
61. R. L. Whetten, M. N. Shafigullin, and J. T. Khoury, *Acc. Chem. Res.*, 1999, **32**, 397.
62. J. P. Spatz, A. Roescher, and M. Möller, *Polym. Reprints, Am. Chem. Soc.*, 1996, **36**, 409.
63. J. P. Spatz, S. Sheiko, and M. Möller, *Macromolecules*, 1996, **29**, 3220.
64. J. P. Spatz, A. Roescher, and M. Möller, *Adv. Mater.*, 1996, **8**, 337.
65. J. P. Spatz, S. Mößner, and M. Möller, *Angew. Chem., Int. Ed. Engl.*, 1996, **35**, 1510.
66. J. P. Spatz, S. Sheiko, and M. Möller, *Adv. Mater.*, 1996, **8**, 513.
67. J. P. Spatz, M. Möller, and P. Ziemann, *Phys. Blätter*, 1999, **55**, 1.
68. J. P. Spatz, P. Eibeck, S. Mößner, M. Möller, T. Herzog, and P. Ziemann, *Adv. Mater.*, 1998, **10**, 849.
69. J. P. Spatz, T. Herzog, S. Mößner, P. Ziemann, and M. Möller, *Adv. Mater.*, 1999, **11**, 149.
70. J. P. Spatz, T. Herzog, S. Mößner, P. Ziemann, and M. Möller, in 'ACS Symposium Serie, Micro- and Nanopattering Polymers', eds. H. Ito, E. Reichmanis, O. Nalamasu, and T. Ueno, American Chemical Society, 1997, Vol. 706, p. 12.
71. J. P. Spatz, S. Mößner, M. Möller, T. Herzog, A. Plettl, and P. Ziemann, *J. Lumin.*, 1998, **76,77**, 168.
72. J. P. Spatz, S. Mößner, C. Hartmann, M. Möller, T. Herzog, M. Krieger, H.-G. Boyen, P. Ziemann, and B. Kabius, *Langmuir*, 2000, **16**, 407.
73. M. Arnold, A. Cavalconti-Adam, R. Glass, J. Blümel, W. Eck, H. Kessler, and J. P. Spatz, *Chem. Phys. Chem.*, 2004, **3**, 383.
74. J. P. Spatz, in 'Cell – Nanostructure Interactions in Nanobiotechnology', eds. C. M. Niemeyer and C. A. Mirkin, Wiley-VCH, Weinheim, 2004, p. 53.
75. R. Glass, M. Arnold, J. Blümmel, A. Küller, M. Möller, and J. P. Spatz, *Adv. Funct. Mater.*, 2003, **14**, 569.
76. S. Dieluweit, D. Pum, and U. B. Sleytr, *Supramol. Sci.*, 1998, **5**, 15.
77. S. R. Hall, W. Shenton, H. Engelhardt, and S. Mann, *Chem. Phys. Chem.*, 2001, **2**, 194.
78. M. Mertig, R. Kirsch, W. Pompe, and H. Engelhardt, *Eur. Phys. J.*, 1999, **D9**, 45.
79. D. Wyrwa, N. Beyer, and G. Schmid, *Nano Lett.*, 2002, **2**, 419.
80. T. Reuter, O. Vidoni, V. Torma, G. Schmid, L. Nan, M. Gleiche, L. Chi, and H. Fuchs, *Nano Lett.*, 2002, **2**, 709.
81. G. Schmid, *J. Mater. Chem.*, 2002, **12**, 1231.
82. G. L. Hornyak, M. Kröll, R. Pugin, Th. Sawitowski, G. Schmid, J.-O. Bovin, G. Karsson, H. Hofmeister, and S. Hopfe, *Chem. – Eur. J.*, 1997, **3**, 1951.
83. T. Sawitowski, Y. Miquel, A. Heilmann, and G. Schmid, *Adv. Funct. Mater.*, 2001, **11**, 435.
84. P. Braunstein, H.-P. Kormann, W. Meyer-Zaika, R. Pugin, and G. Schmid, *Chem. – Eur. J.*, 2000, **6**, 4637.
85. Y. Liu, W. Meyer-Zaika, St. Franzka, G. Schmid, M. Leis, and H. Kuhn, *Angew. Chem., Int. Ed. Engl.*, 2003, **42**, 2853.
86. A. Kumar, M. Pattarkine, M. Bhadbhade, A. B. Mandale, K. N. Ganesh, S. S. Datar, C. V. Dharmadhikari, and M. Sastry, *Adv. Mater.*, 2002, **13**, 341.
87. M. G. Warner and J. E. Hutchison, *Nat. Mater.*, 2003, **2**, 272.
88. R. D. Piner, J. Zhu, F. Xu, S. Hong, and C. A. Mirkin, *Science*, 1999, **283**, 661.
89. S. Hong, J. Zhu, and C. A. Mirkin, *Science*, 1999, **286**, 523.
90. C. Mirkin, *Science*, 1996, **286**, 523.
91. S. Liu, R. Maoz, G. Schmid, and J. Sagiv, *Nano Lett.*, 2002, **2**, 1055.
92. S. Liu, R. Maoz, and J. Sagiv, *Nano Lett.*, 2004, **4**, 845.
93. Z. R. Dai, S. Sun, and Z. L. Wang, *Nano Lett.*, 2001, **1**, 443.
94. Z. L. Wang, *Adv. Mater.*, 1998, **10**, 13.
95. Z. L. Wang, Z. Dai, and S. Sun, *Adv. Mater.*, 2000, **12**, 1944.
96. F. Wiekhorst, E. V. Shevchenko, H. Weller, and J. Kötzler, *Phys. Rev. B*, 2003, **67**, 224416.
97. F. Dumestre, B. Chaudret, C. Amiens, M.-C. Fromen, M.-J. Casanove, P. Renaud, and P. Zurcher, *Angew. Chem., Int. Ed. Engl.*, 2002, **41**, 4286.

98. P. C. Scholten, in ‘Magnetic Properties of Fine Particles’, eds. J. L. Dortmann and D. Fiorani, Elsevier, Amsterdam, 1992.
99. P. G. de Gennes and P. A. Pincus, *Phys. Kondens. Mater.*, 1970, **11**, 189.
100. R. W. Chantrell, A. Bradbury, J. Popplewell, and S. W. Charles, *J. Appl. Phys.*, 1982, **53**, 2742.
101. J. M. Tavares, J. J. Weis, and M. M. Telo da Gama, *Phys. Rev. E*, 2002, **65**, 061201.
102. K. Butter, P. H. H. Bomans, P. M. Frederik, G. J. Vroege, and A. P. Philipse, *Nat. Mater.*, 2003, **2**, 8891.
103. S. L. Tripp, S. V. Pusztay, A. E. Ribbe, and A. Wei, *J. Am. Chem. Soc.*, 2002, **124**, 7914.

Carbon: Nanotubes

Durairaj Baskaran
University of Tennessee, Knoxville, TN, USA

1	Introduction	1
2	Structural Classification	2
3	Synthetic Techniques	3
4	Different Types of Carbon Nanotubes	10
5	Purification of Carbon Nanotubes	12
6	Properties of Carbon Nanotubes	15
7	Surface Modification of Carbon Nanotubes	22
8	Summary	28
9	Related Articles	28
10	References	28

Abbreviations

C_{60} = Fullerene; SWNTs = Single-walled carbon nanotubes; MWNTs = Multiwalled carbon nanotubes; DWNTs = Double-walled carbon nanotubes; CNTs = carbon nanotubes; TEM = Transmission electron microscopy; HRTEM = High-resolution transmission electron microscopy; SEM = Scanning electron microscopy; AFM = Atomic force microscopy; C_h = Chiral vector; CVD = Chemical vapor deposition; HiPco process = High-pressure disproportionation of CO; RBM = Radical breathing vibration modes; DOS = Electronic density of states.

1 INTRODUCTION

Carbon is the fundamental building block for life on earth. The ability of carbon to form covalent bonds with diverse elements is unique without which the basis for life would be impossible. There are more than 10 million carbon-compounds known so far and many of them are pivotal to sustain the cycle of life. Covalent bond formation between the carbon atoms with sp^2 or sp^3 hybridization in a two- or three-dimensional array produces different allotropes. Graphite and diamond are the two best-known examples with distinct chemical, physical, and mechanical properties. Another carbon allotrope, exhibiting a closed carbon cage-like structure, known as fullerene was recently discovered during laser-vaporization of graphite (Figure 1).[1] Fullerene (C_{60}) is a highly symmetrical and truncated iscosahedral molecule consisting of 60 carbons and resembling a soccer ball. Several larger fullerenes with a higher number of carbons were found in high yields along with C_{60} in arc-vaporization of graphite.[2,3] The formation of cage-like carbon structures with a positive curvature from planar fragments of hexagonal graphite lattice requires inclusion of a specific number of pentagons. According to Euler's principle of least action, the perfect closure of hexagonal lattices into fullerenes geometrically requires 12 pentagons.

The research on the chemistry of carbons has been rejuvenated by the discovery of fullerenes.[1–4] Although scientists have continued developing the chemistry of fullerenes, the formation and the stability of fullerenes induced speculation to yet another new carbon nanostructure of an elongated fullerene-like structure, with larger number of hexagons and closed through the incorporation of pentagons. It was Sumio Iijima, at the NEC Corporation Fundamental Research Laboratory, who first discovered the formation of needle-like carbon nanotubes on the surface of a graphite electrode in an electric arc-discharge experiment in 1991.[5] High-resolution transmission electron microscopy (HRTEM) images of the needles showed a unique arrangement of hexagonally packed graphene sheets, rolled into a number of coaxial cylindrical shells (Figure 2). Interestingly, these tubes had fullerene-like caps at the ends. These tubes have been named multiwalled carbon nanotubes (MWNTs). In 1992, Ebbesen and Ajayan achieved production of MWNTs in gram quantities using an arc-discharge method.[6] Single-walled carbon nanotubes (SWNTs) were synthesized in 1993 by Sumio Iijima[7] and Donald Bethune[8] using iron- or cobalt-catalyzed arc-discharge processes. Rick Smalley and coworkers produced bulk quantities of SWNTs using a laser-vaporization of graphite, in the presence of a nickel–cobalt mixture catalyst at 1200 °C.[9,10]

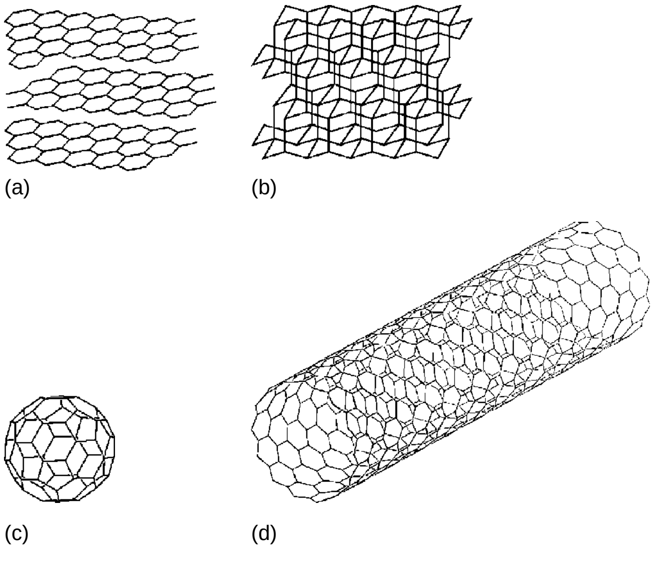

Figure 1 Different allotropic forms of carbon: (a) graphite, (b) diamond, (c) C_{60}, and (d) carbon nanotube

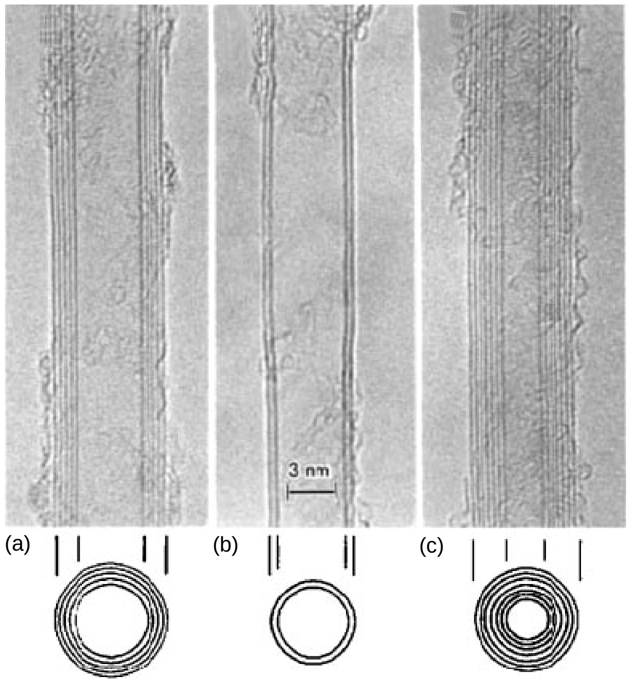

Figure 2 TEM images of multiwalled carbon nanotubes with different shells. (a) Tube with five cylindrical graphitic layers (6.7 nm diameter), (b) double-walled carbon nanotube (5.5 nm diameter), and (c) tube with seven cylindrical graphitic layers (6.5 nm diameter). (Reprinted with permission from Ref. 5. © 1991 Macmillan Magazines Ltd (www.nature.com))

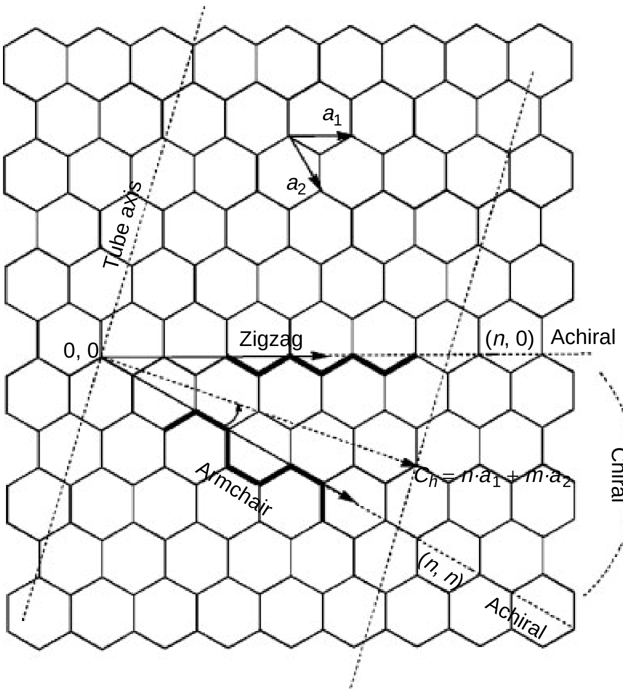

Figure 3 Illustration of chiral vector $C_h = n{\cdot}a_1 + m{\cdot}a_2$ using 2D graphene sheet with lattice vectors a_1 and a_2 and with limiting achiral cases of zigzag $(n, 0)$ and armchair (n, n) configuration

Carbon nanotubes, with one-dimensional 'honeycomb' sp^2 carbon structure, exhibit exotic electrical, optical, and mechanical properties. Defect-free carbon nanotubes are considered as prototype one-dimensional (1D) solid quantum wires. This article focuses on some of the fundamental developments in the area of synthesis, characterization, and modification of carbon nanotubes.

2 STRUCTURAL CLASSIFICATION

2.1 Achiral and Chiral Tubes

Different types of carbon nanotubes arise from the unique arrangement of the honeycomb hexagonal carbon lattice upon a cylindrical coordinate. The orientation of the honeycomb lattice with respect to the tube axis determines the chirality of the carbon nanotubes. The carbon nanotubes can be simply envisaged as folding a graphite sheet into a cylinder, with a perfect matching of the open edges to form a seamless shell. The folding of graphite can be expressed in terms of a chiral vector, $C_h = n{\cdot}a_1 + m{\cdot}a_2$ that connects two longitudinally equivalent sites specified by a pair of integers (n, m) (Figure 3).[11–14] Here, a_1 and a_2 are the unit vectors of the hexagonal lattice of the graphene sheet and n and m are the integers specifying the chiral vector.

There are different types of folding that can generate distinct structures depending on the specificity of the pair of integers n, m with respect to zigzag or armchair directions. The zigzag direction can be drawn from a carbon atom (0, 0) on the cylinder axis to the other side passing through similar carbon atoms of each hexagon (Figure 3). The armchair direction can be drawn from the same carbon and passing through each hexagon dividing them into two equal halves. The chiral vector starts from the same carbon atom on one side of the separation line in the cylinder axis to another carbon intersection on the other side closest to the armchair line. The chiral angle, θ, is the angle between the chiral vector (C_h) and the zigzag direction. If the chiral vector lies on the zigzag direction $(\theta = 0)$, then it is called a zigzag nanotube with the vector $m = 0$ $(n, 0)$ and if $\theta = 30°$, then it is called an armchair nanotube with the vector $n = m$ (n, n). These are two limiting cases called achiral nanotubes since they have a mirror plane. Nanotubes characterized by all other angles between 0° and 30° are chiral, with specific vectors $(n \neq m \neq 0)$. The different properties of carbon nanotubes arise from the variation in chiral angles and diameters. Atomically resolved images of SWNTs by scanning tunneling microscopy (STM) show clearly the honeycomb hexagonal lattice and orientation of different types of tubes (Figure 4).[15]

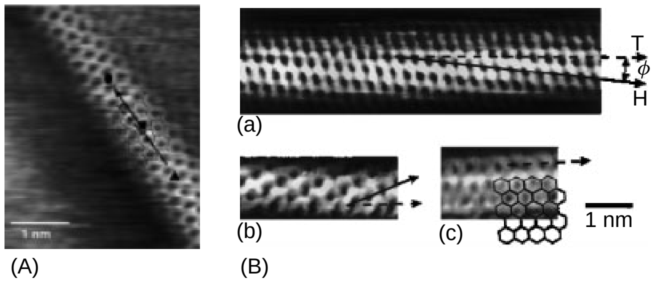

Figure 4 (A) Atomically resolved scanning tunneling microscopy (STM) of a SWNT in the surface of a rope revealing chiral-twist. (Reprinted with permission from Ref. 15. © 1998 Macmillan Magazines Ltd (www.nature.com).) (B) STM images of SWNTs produced by arc-discharge method; (a) chiral nanotube with angle 7°, (b) zigzag nanotube, and (c) armchair nanotube. The tube axis is shown with dashed arrows. (Reprinted with permission Ref. 16. © 1998 Macmillan Magazines Ltd)

2.2 Metallic and Semiconducting tubes

The properties of carbon nanotubes, in general, are strongly dependent on the orientation of their honeycomb lattice with respect to the tube axis.[11,13–15,17] The electronic band structure calculations show that the vectors (n, m) determine the conductance and other properties of carbon nanotubes.[18,19] It is known that the two dimensional graphite's valence and conductance bands touch and degenerate at six points (K_f) of the graphene layer, which define the corners of the first Brilluion zone (Figure 5a). For a one-dimensional (1D) tube generated by rolling a 2D graphite sheet, the periodic boundary condition imposed by C_h determines the allowed 1D subbands for the tubes. The conductance of nanotubes depends on how the graphene valence and conduction bands pass through their degeneration points with respect to C_h. The tubes become metallic when the subbands of the tubes depending on the vectors pass through the graphene's degeneration points. The quantized subbands of a zigzag tube (9, 0) touch the degeneration points unlike in a tube (10, 0) (Figure 5b and c). Those tubes whose subbands are not passing through degeneration points are called semiconducting nanotubes. The zigzag $(n, 0)$ and chiral (n, m) nanotubes can be either metallic or semiconducting depending on their pair of vectors. It is known that the zigzag $(n, 0)$ or chiral (n, m) SWNTs are metallic if the value $(n - m)/3$ becomes an integer and all other tubes are semiconducting. However, armchair (n, n) nanotubes are metallic as their subbands remain on the graphene's degeneration points.

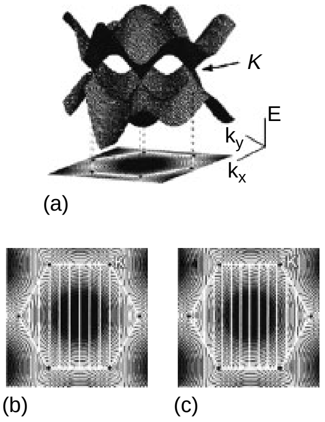

Figure 5 (a) Degeneration points (K) of a graphene's valence and conductance (π/π^*) bands in its three-dimensional projection. Black dots in the corners of white hexagon are the graphene K points. (b) The allowed 1D subbands passing through K for a metallic tube (9, 0). (c) The quantized 1D subbands deviating K for a semiconducting tube (10, 0). (Reprinted with permission from Ref. 14. © 2000 American Chemical Society)

3 SYNTHETIC TECHNIQUES

The synthesis of carbon nanotubes was first shown using an arc-discharge method.[5,7,8] The carbon nanotubes are generally synthesized by vaporization and condensation of carbon at high temperature in the presence or absence of a catalyst. The plume of carbon vapors reacts and rapidly assembles to form a tubular sp^2 network of various types. The synthesis can be classified, based on the source of carbon feedstock and the method of vaporization, into the following three basic techniques; 1) arc-discharge, 2) laser-vaporization, and 3) chemical vapor deposition (CVD). All of these techniques produce SWNTs or MWNTs under appropriate experimental conditions. Attempts have been made to optimize various factors influencing the growth processes to provide certain degree of control in the synthesis. However, the growth mechanism is very complex and not yet understood to the full extent needed to fine-tune these techniques to obtain selectively a particular type of carbon nanotubes. The task yet remains to produce exclusively semiconducting or metallic carbon nanotubes with uniform length and diameter distributions.

3.1 Arc-discharge Technique

The carbon arc-discharge method, also used for the mass production of C_{60}, under appropriate condition produces carbon nanotubes.[5,6] An arc is generated by applying a high dc/ac voltage between two graphite electrodes, placed end-to-end separated at 1 mm distance in a closed vessel under an inert atmosphere. Iijima accidentally discovered graphitic carbon needles deposited on the negative-end of the carbon electrode in arc-discharge evaporation of carbon at 100 torr argon pressure.[5] The analysis of the needles using transmission electron microscopy (TEM) showed graphite structure of lattices along the needle axis. The carbon needles exhibited the same number of lattice fringes from both sides of the needle with diameters of 4–30 nm and lengths up to

1 µm. The seamless and tubular carbon nanotubes consisted of several graphite sheets (Figure 2).

Under optimal conditions, the arc-discharge technique produces a large amount of MWNTs. It was found that increasing the pressure of inert gas during the arc-discharge increases the formation of tubes.[6] Later, the production of SWNTs was accomplished by using a small amount of iron as catalyst under an atmosphere of methane. The presence of metal catalyst in the vapor phase during arc-discharge favors selective growth of SWNTs against MWNTs. Metal catalyst mixed with graphite powder is filled into a drilled hole of the graphite electrode to selectively grow SWNTs. In the arc-discharge technique, the SWNTs are produced with an average diameter of 1 nm in large quantities.[7] The nature of the catalyst present in the arc-discharge technique controls the formation of SWNTs. The presence of cobalt in the absence of hydrogen also produces SWNTs along with fullerenes in the arc-discharge technique.[8] Several other bimetallic mixture catalysts such as Ni–Co, Co–Y, and Ni–Y in certain atomic percentages have been shown to be active in producing SWNTs with varying efficiency. For example, the mixture of 1 at.% of Y and 4.2 at.% of Ni under a helium atmosphere produced SWNTs in large scale (Figure 6a).[20] The electron diffraction pattern of the carbon nanotubes shows a slightly larger interlayer distance (0.344 ± 0.001 nm) than those found in bulk graphite (Figure 6b).[21]

The thermal conductivity and diffusion coefficient of the inert gas in the arc-discharge method have profound effects on the diameter of SWNTs. It was shown that an argon atmosphere produces smaller diameter SWNTs compared to helium and the average diameter of the tubes decreases ~0.2 nm per 10% increase of argon in the argon–helium ratio.[22] In situ observation of HRTEM of the growth process reveals that the micrographenes and disordered layers form at early stage and subsequently rearrange into highly ordered graphitic layer.[23] The growth occurs first by rapid formation of rod-like carbon, which slowly undergoes graphitization of its wall leaving a cavity inside.[24]

The arc-discharge technique has been used to produce both high quality MWNTs and SWNTs. The MWNTs have also been produced using an electric current passing between graphite electrodes in molten LiCl at 600 °C.[25,26] The MWNTs consisting of 5 to 20 concentric layers are produced at an optimum current (1–5 A) from the eroded surface of the graphite electrode and get dispersed in the LiCl melt. Only amorphous carbon was generated at a very low and a very high current, indicating the formation of carbon nanotubes is controlled by the kinetics of the diffusion of carbon. Arc-discharge of the graphite electrodes under liquid nitrogen also produces a highly crystalline MWNTs.[27] Simply annealing the carbon face of hexagonal silicon carbide (SiC) under vacuum without a metal catalyst produces carbon nanotubes.[28–30] However, the silicon face of the SiC gives only graphite-like structures. The MWNTs perpendicular to the surface have been grown when the carbon face of SiC is annealed at high temperature. When the annealing is done at temperatures above 1500 °C, the carbon face of the SiC forms ordered SWNTs with preferred atomic orientation of the surface morphology.[30]

The quality of carbon nanotubes depends on various parameters such as the nature and the concentration of metal catalyst, the kind of inert gas and its pressure, the applied voltage, and, most importantly, the vessel geometry.[20,22,31,32] Adjusting the anode to cathode distance, rotating one of the electrodes, or subjecting the arc under a strong magnetic field have significant effects on the quality of MWNTs.[33,34]

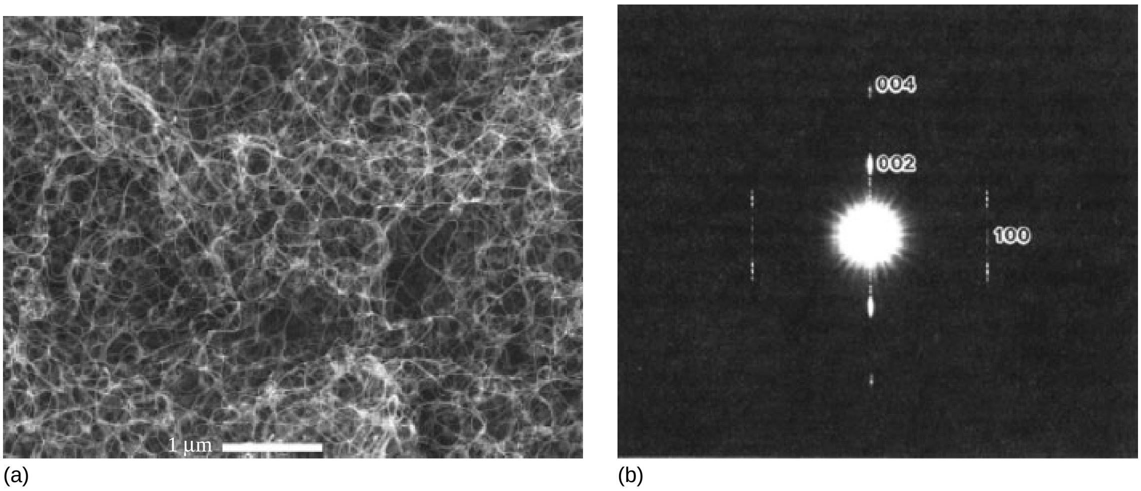

Figure 6 (a) SEM image of SWNTs produced by arc-discharge method using Ni:Y (4.2:1 at.%) catalyst (scale bar 1 µm). (Reprinted with permission from Ref. 20. © 1997 Macmillan Magazines Ltd.) (b) Electron diffraction pattern of carbon nanotubes produced by arc-discharge method. (Reprinted with permission from Y. Saito, T. Yoshikawa, S. Bandow, M. Tomita, and T. Hayashi, *Phys. Rev. B.*, 1993, **48**, 1907. © 1993 by the American Physical Society)

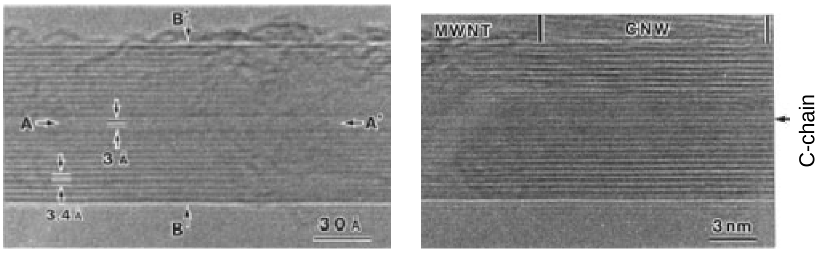

(a) (b)

Figure 7 (a) HRTEM image of carbon nanotube with 0.3 nm diameter inside the MWNT having 0.34 nm interlayer spacing. The ends of the smallest carbon nanotube is shown by two horizontal arrows, A, A′. (Reprinted with permission from X. Zhao, Y. Ando, Y. Liu, M. Jinno, and T. Suzuki, *Phys. Rev. Lett.*, 2003, **90**, 187401. © 2003 by the American Physical Society.) (b) HRTEM image of a MWNT having a carbon nanowire in the innermost tube. (Reprinted with permission from X. Zhao, Y. Ando, Y. Liu, M. Jinno, and T. Suzuki, *Phys. Rev. Lett.*, 2003, **90**, 187401. © 2003 by the American Physical Society)

Several catalysts have been used, and it has been learned that catalysts are technique specific (i.e. not all of the catalysts that work well in CVD method produce SWNTs in arc-discharge method). Under optimum conditions, the arc-discharge technique produces carbon nanotubes with diameters in the range of 0.3–1.4 nm. A very small diameter carbon nanotube has been found in the innermost shells of MWNTs in the arc-discharge method.[35–37] The use of hydrogen instead of helium in the absence of metals produced confined carbon nanotubes inside MWNTs with diameters of 0.3 and 0.4 nm (Figure 7a).[35,36] The presence of hydrogen atoms plays an important role in the formation of a small diameter tube. According to the density functional calculation, a tube with a diameter of 0.3 nm is probably an armchair (2, 2) with C_{12} end caps and would have severe steric distortion in the sp^2 bonds.[35] A smaller diameter carbon nanotube of 0.4 nm has been found inside MWNTs using a graphite anode filled with cobalt metal.[37] A type of one-dimensional carbon nanowire made of carbon atoms covalently connected with double bonds or alternatively connected with single and double bonds has also been found inside a MWNT produced by hydrogen arc-discharge (Figure 7b).[38]

A slight change in operating conditions leads to the formation CNTs with entirely different morphology in the arc-discharge technique. Using Ni/Y catalyst, selectively double-walled carbon nanotubes (DWNTs) can be produced at 1250 °C. However, the same catalyst system produces SWNTs at slightly lower temperatures. The Ni/Co catalyst also produces DWNTs over a wide temperature range from 1000 to 1400 °C.[39] A metal mixture catalyst consisting of Ni, Co, and Fe with elemental S selectively produces DWNTs in argon and H_2 (1:1 v/v) atmosphere.[40] The carbon nanotubes produced by the arc-discharge technique have several by-products as impurities such as fullerenes, graphitic carbons, enclosed metal nanoparticles, and amorphous carbon.[41] Special purification procedures have to be used to get pure carbon nanotubes.

3.2 Laser-ablation Technique

Smalley and coworkers at Rich University developed a new method for the synthesis of SWNTs using a laser impingement technique in 1995.[9] A laser was used to vaporize a graphite composite containing ~1 at.% transition metal in an oven filled with inert gas at 1200 °C.[9,42–44] In laser ablation, the target graphite surface absorbs the laser energy and raises its temperature to ~3000–4000 °C bringing the carbon and metal to a plume of vapors. Subsequent condensation of vapors and the chemisorption of metal atoms result in the formation of a fullerene precursor that nucleates the growth of graphitic sp^2 carbon network around the metal clusters.[9,45,46] The chemisorbed metal clusters migrate to the dangling bonds at the edges of the fullerene precursor preventing its closure (or termination). The carbon vapors quickly react with fullerene coordinated with metal and extend the growth. Insertion of new carbon linkages between the carbon edges and the metal particle occurs rapidly at high temperature leading to the formation of SWNTs. The yield of SWNTs increases with increasing the oven temperatures up to 1200 °C. A single metal or bimetal catalyst can be used in the synthesis in the laser-ablation technique. Continuous irradiation of graphite/bimetallic target (Ni:Y/2:0.5 at.%) using a 250 WCO_2 laser operated at 1074 nm produces SWNTs with average diameters of 1.4 nm (Figure 8).[47]

Recently, the mechanism of the growth process was probed by in situ imaging of the carbon/nickel/cobalt plume using Rayleigh scattering over different time and temperatures.[46] The results revealed that the metal evaporation occurs upon irradiation of the target and the plume stays in the vapor phase, which slowly grows nonuniformly for about 100 μs. At around 200 μs, the carbon vapor starts condensing and clustering well before the metal atoms condense. The size of carbon cluster is around 20 nm at 1100 °C. The nucleation of SWNTs growth occurs by condensation of all atoms and molecules into clusters and nanoparticles in 2 ms at the plume

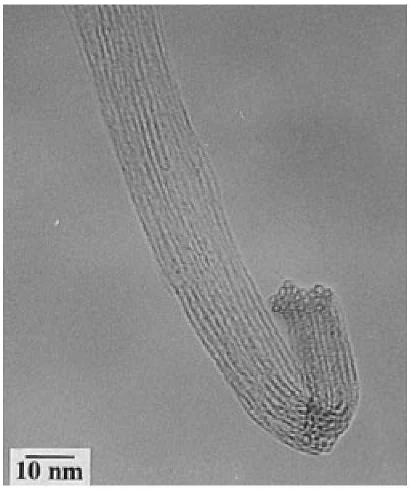

Figure 8 TEM of SWNTs bundle synthesized using Ni:Y (2:0.5 at.%) catalyst. (Reprinted from Ref. 47. © 1998, with permission from Elsevier)

temperature of ∼1400 °C just above the metal/C eutectic temperature (Figure 9).

The laser ablation of the graphite target produces high quality SWNTs with narrow size distribution in high yields. Among various catalysts studied, Ni, Co, and the mixture of Co/Ni and Ni/Y have produced higher yields of SWNTs.[45,47] A pulsed Nd:YAG laser beam has been used at 532 and 1064 nm to irradiate graphite-metal composites in many studies.[9,45,46,48,49] High efficiency laser-vaporization methods such as ultrafast pulses from a free electron laser and continuous wave laser have been used to grow SWNTs.[45,47] It was found that the growth and the nucleation of SWNTs are affected by the temperature and the laser-beam intensity respectively.[45] There is a direct correlation between the diameter and the low-frequency radial breathing modes of SWNTs in Raman spectroscopy. By optimizing the power of the laser pulse as well as the temperature, it is possible to obtain a certain degree of control over the diameter of SWNTs (Figure 10).[48,50] A single laser-beam pulse has also been used to produce SWNTs under specific conditions.[49]

Several factors affect the growth of SWNTs in the laser-ablation technique.[51,52] Extensive studies on the development of the laser-vaporization technique have optimized the process conditions such as laser parameters,[45,49] composition of graphite and metal,[45,47,52] carrier gas, pressure,[51] and temperature.[48,50] Through these studies, a significant understanding of the SWNT's growth and propagation under laser-vaporization condition is achieved.[42,43,46,53,54]

3.3 Chemical Vapor Deposition technique

A catalytic decomposition of carbon feedstock under a controlled environment at high temperature (>900 °C) produces carbon nanotubes. The CVD technique is one of the widely used techniques for the synthesis of both MWNTs and SWNTs. A hydrocarbon feedstock is used as the carbon source that is catalytically decomposed to form reactive carbon vapors. Ethylene and acetylene are used as carbon feedstocks at 550–750 °C in many CVD techniques. There are many different metals that can be used as catalysts to produce

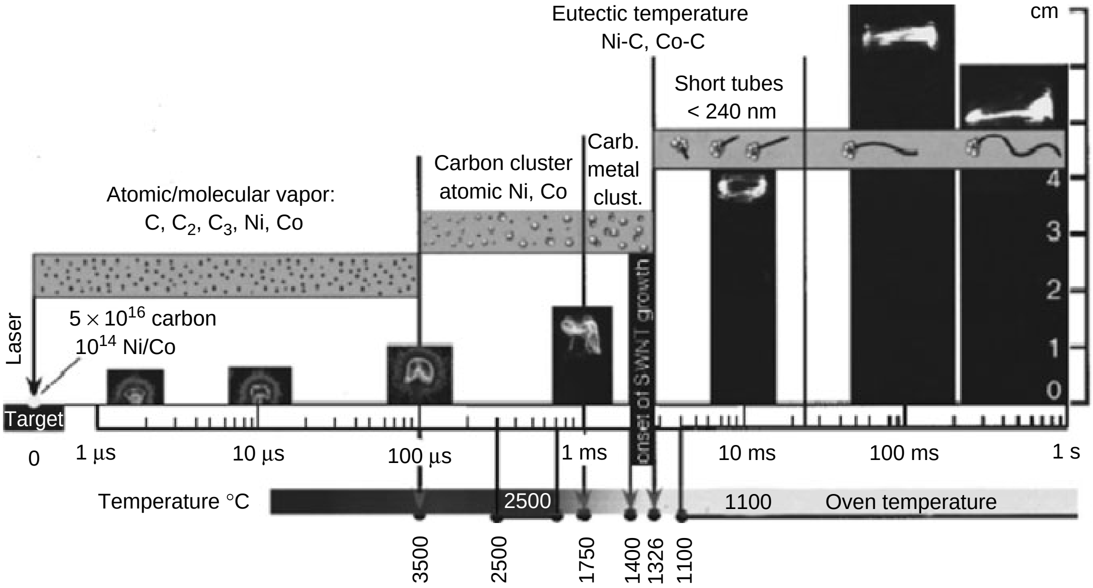
Eutectic temperature
Ni-C, Co-C
cm
Short tubes
< 240 nm
Carb.
metal
clust.
Carbon cluster
atomic Ni, Co
Atomic/molecular vapor:
C, C2, C3, Ni, Co
4
3
2
1
0
5 × 10^16 carbon
10^14 Ni/Co
Laser
Target
Onset of SWNT growth
0
1 μs
10 μs
100 μs
1 ms
10 ms
100 ms
1 s
Temperature °C
2500
1100
Oven temperature
3500
2500
1750
1400
1326
1100

Figure 9 Spectroscopic in situ imaging of the laser plasma ($t < 200\,\mu s$) and Rayleigh scattering images of the plume ($t > 200\,\mu s$) during the growth of SWNTs. (Reprinted with permission from A.A. Puretzky, H. Schittenhelm, X. Fan, M.J. Lance, L.F. Allard, and D.B. Geohegan, *Phys. Rev. B.*, 2002, **65**, 245425. © 2002 by the American Physical Society)

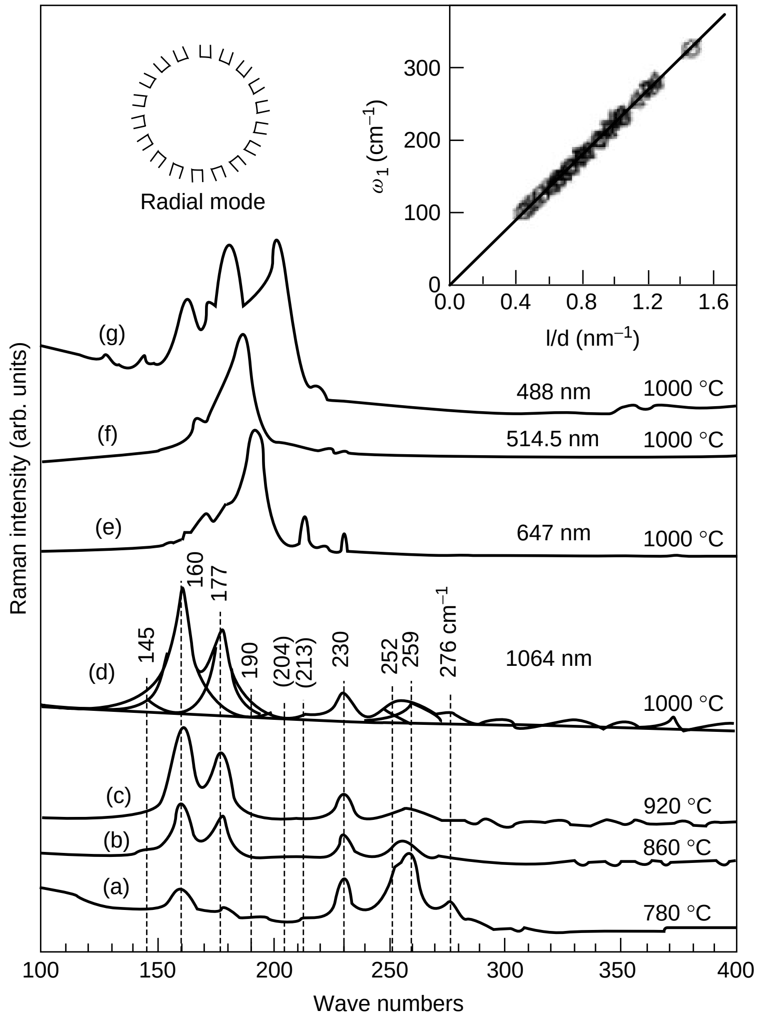

Figure 10 Low-frequency Raman spectra of SWTNs produced at different temperatures using Fe/Ni catalyst. The inset shows the dependency of radical frequency with tube diameter for armchair (○), zigzag (Δ), and chiral (∇) symmetry tubes. (Reprinted with permission from S. Bandow, S. Asaka, Y. Saito, A.M. Rao, L. Grigorian, E. Richter, and P.C. Eklund, *Phys. Rev. Lett.*, 1998, **80**, 3779. © 1998 by the American Physical Society)

MWNTs. However, only a few specific metal catalysts produce SWNTs in the CVD method.[7,55] The most effective catalysts used in the CVD method are iron, nickel, and cobalt. These metals have an ability to decompose hydrocarbons or other carbon sources to form metastable carbides at high temperature through a rapid diffusion mechanism. It has been proposed that the carbon vapors first deposit hemispherically on the exposed surface of the catalyst. A fast diffusion and deposition of carbon atoms occur around and below the bisecting diameter of the catalyst and the carbon atoms assemble into graphitic layers with an interlayer spacing of graphite. The deposition of carbon takes place in and around the hemisphere except for a small portion at the apex of the hemisphere leading to a hollow core while growing into carbon nanotubes. In the process, the catalyst particle is lifted upward, probably owing to a fast condensation of carbons at the bottom of the catalyst hemisphere. This leads to the formation of a cylindrical tube whose open-end carries a chemisorbed metal particle. Subsequently, a tubular growth occurs through the insertion of new carbons at the interface between the catalyst and the tube edge. This process is called a ‘tip-growth’ mechanism.[56–58] In some cases, the metal particles remain attached to the surface of the substrate and the carbon diffusion and deposition occur at the upper hemisphere of the metal particles. The carbon nanotube grows upward from the metal particles and this type of growth is called a ‘root-growth’ (extrusion) mechanism (Figure 11).[58–60] In situ observation of the state of the metal particle during the growth process is found to be fluidic and in some cases the upward pulling force of the carbon nanotube layers elongates and breaks the metal nanoparticles into two portions. One portion remains at the substrate surface and the other portion is active in the growth process.[56] The composition of chemicals that are used in the CVD technique is very important, as it has profound

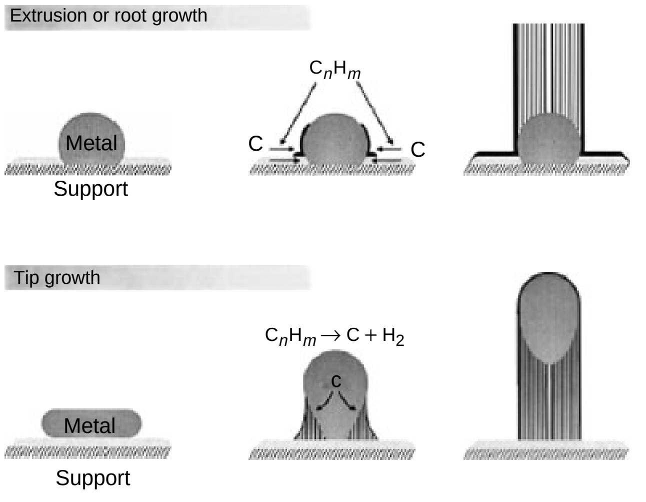

Figure 11 Tip-growth and extrusion mechanisms of carbon filament growth.[57,58] (Ref. 58. Reproduced by permission of Elsevier)

influence on the diffusion property of pyrolyzed carbon and its condensation.

3.3.1 HiPco Process

The formation of single- or multiwalled tubes depends primarily on the size and the nature of the catalyst. When the size of the catalyst becomes smaller comparable to C_{60}, it nucleates the growth of SWNTs. The Boudard reaction of catalytic disproportionation of CO into elemental carbon and CO_2 is well known and it has been used for the synthesis of SWNTs. It was found that a preformed iron cluster induces disproportionation of carbon monoxide at high pressure at 1200 °C and produces SWNTs in good yield.[55] This process of high-pressure disproportionation of CO at a high temperature to produce SWNTs is called the 'HiPco' process. Nanosized iron, molybdenum, and mixture of Ni/Co (1:1) were used as preformed catalysts in HiPco process. The gas-phase catalytic growth produces smaller diameters SWNTs (∼0.7–1.1 nm) with a metal particle cap. The diameter of the tubes correlated very well with the diameter of the metal particles. The growth of SWNTs stops only when the metal cluster size reaches a size that favors formation of a carbon shell around the cluster. The mechanism of growth was named 'yarmulke' or 'tip-nucleation' growth. One of the advantages of CO feedstock is that it decomposes in the vapor state at an optimum rate at 1200 °C. At this high temperature, the chances of formation of defects in the sp^2 network are minimized owing to annealing.

3.3.2 Hydrocarbons as Feedstock

Different types of hydrocarbons could be used in catalytic decomposition to produce SWNTs. It was shown that benzene could be used as a feedstock in the presence of a small amount thiophene as the catalyst precursor at 1200 °C.[61] High quality SWNTs with diameters ranging from 1.3 to 5 nm have been synthesized using methane in the presence of supported Fe_2O_3 at 1000 °C.[62] In the case of the production of MWNTs in the presence of a catalyst, a higher operating temperature significantly enhances the pyrolysis rate compared to the tube's growth rate leading to amorphous carbon deposition. However, the rate of decomposition of hydrocarbons could be controlled with an appropriate reactor design to minimize the amorphous carbon formation.

Long MWNTs of ∼2 mm lengths have been produced in the presence of iron/silica nanoparticles as catalyst using pyrolysis of acetylene at 600 °C.[63] Similarly, the SWNTs with large diameters in the range of 2–5.2 nm were prepared using benzene as feedstock with ferrocene as catalyst and thiophene as growth promoter.[64] The size of the catalyst and the nature of carbon feedstock have significant influence on the growth process. The catalyst size is closely related to the diameters of the CNTs formed in the CVD technique similar to the other techniques.[58–60] Nanoclusters consisting of Fe and Mo atoms with ∼1.3 nm in sizes produce SWNTs of similar diameter with narrow size distribution.[65] Synthesis of helically twisted MWNTs has been accomplished on a quartz plate by pyrolysis of $Fe(CO)_5$ and pyridine at 900–1100 °C under a flow of argon and hydrogen.[66] It is believed that a concomitant insertion of pentagon and heptagon pairs into the hexagonal sheet occurs during the growth that leads to a helical twisting.

It is possible to grow selectively DWNTs using molybdenum or by controlling the concentration of ferrocene in the decomposition of methane.[67,68] The mechanism associated with the selective growth of DWNTs by the CVD method is not well understood. A large amount of DWNTs was produced by pyrolysis of C_2H_4 at 900–1100 °C using iron in the presence of sulfur.[69] It was also noticed that the presence of sulfur is critical in promoting growth of DWNTs and the process gave only SWNTs in the absence of sulfur. This indicates that the chemical composition and the rate of pyrolysis are the important parameters that can be tuned to have certain control on the process. The diameters of DWNTs vary from ∼1 to 2.9 nm and the inner diameters from 0.4 to 2.0 nm. The DWNTs produced by the CVD method had varying inner layer spacing between 0.34 and 0.41 nm.[68]

Synthesis of MWNTs on a polymeric substrate at atmospheric pressure has been shown using microwave irradiation.[51] Enhanced selective heating of the catalyst particles occurs under microwave irradiation owing to the dielectric specific heating. This raises the temperature of the catalyst very high without raising the temperature of the substrate polymer. Polycarbonate and Teflon® have been used as substrates to produce MWNTs in the presence of cobalt with acetylene (C_2H_4) and hydrogen sulfide (H_2S) mixed gas as carbon feedstock.[70] One of the problems of the CVD process is that the carbon nanotubes have higher defect density compared to the arc- or laser- techniques. Low

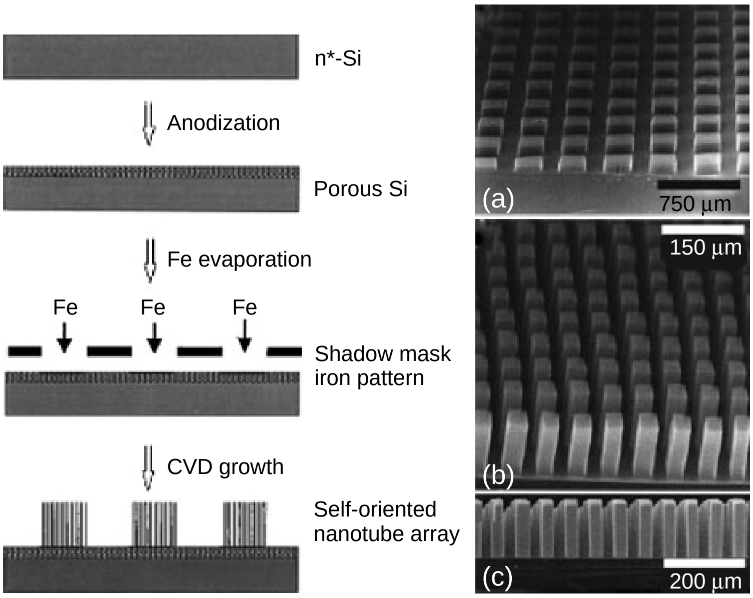

Figure 12 Schematic process flow-chart for the CVD synthesis of regular arrays of oriented nanotubes on a porous silicon through catalyst patterning; (a) SEM image of nanotube blocks synthesized on 250 μm by 250 μm catalyst pattern. The nanotubes are 80 μm long and oriented perpendicular to the substrate, (b) SEM image of nanotube towers synthesized on 38 μm by 38 μm catalyst pattern. The nanotubes are 130 μm long, and (c) side view of the nantube towers in (b). (Reprinted with permission from S. Fan, M.G. Chapline, N.R. Franklin, T.W. Tombler, A.M. Cassell, and H. Dai, *Science*, 1999, **283**, 512. © 1999 AAAS)

operating temperatures of the CVD process do not provide necessary thermal energy sufficient to anneal the nanotubes to form a perfect sp^2 network structure. However, the simplicity of the process makes it viable for a large-scale production of carbon nanotubes.

3.3.3 Aligned Carbon Nanotubes

One of the advantages of the CVD method is that well-aligned SWNTs and MWNTs perpendicular to the substrate could be grown from many substrates.[71,72] The specificity of the process is unique as the tubes grow only from the catalyst deposited regions of the substrate. The SWNTs have been grown from patterned silicon wafers using iron as the catalyst and methane as the feedstock at 1000 °C. The iron catalyzed methane decomposition produces pure SWNTs without any amorphous carbon coating for up to 10 min. However, a slow self-pyrolysis of methane produces amorphous carbon coating on the tubes if the process is continued over a period of time.[71] The end of SWNTs is closed and contains no catalyst, which indicates carbon nanotubes are formed by a ‘root-growth’ mechanism. When ethylene gas is used instead of methane, a regular array of MWNTs oriented perpendicular to the substrate is produced.[73]

A template assisted synthesis of MWNTs in an anoidic aluminum oxide (AAO) on metal surfaces has been shown to produce aligned MWNTs.[74] Well-aligned MWNTs have been grown perpendicular to the substrate from a quartz plate and it has been noticed that the length of the tube increases with time during synthesis. The tubes have a small amount of amorphous carbon deposited on the surface owing to a low temperature and a long reaction time.[75] By controlling the catalyst particle size and its patterned deposition, it is possible to grow MWNTs in a patterned orientation from the substrate (Figure 12). Aligned MWNTs have been grown on a quartz substrate and filled with polymer to form a nanotube membrane and used for transport studies.[76] Nickel catalyst deposited on a glass substrate in the presence of acetylene at 660 °C has been used for the production of MWNTs with diameters from 20 to 400 nm and lengths from 0.1 to 50 μm.[72,77] The MWNTs with a bamboo-like structure aligned perpendicular to nickel coated silicon substrate have been produced in the hot-filament CVD method using C_2H_4/NH_3 gas source at 600–800 °C.[56] Aligned CNTs have been grown in a pattern as ‘crop circles’ using iron(II) phthalocyanine at 1000 °C.[78]

Region-specific growth of CNTs has been achieved on a photolithographically patterned quartz surface or micro-molded surface with a micrometer resolution (Figure 13a).[79–81] The nanotubes can be grown in different directions perpendicular and tilted to the substrate simultaneously from a geometrically tailored catalyst deposited surface.[82] Multidirectional growth of MWNTs is achieved from a patterned SiO_2 template on silicon surface using xylene/ferrocene vapor at 800 °C (Figure 13b).[82,83] Aligned carbon nanotubes have been grown on a partially masked surface by pyrolysis of iron(II) phthalocyanine. Recently, a selective growth of semiconducting SWNTs was achieved by a plasma enhanced CVD method using Fe/CH_4 system on a SiO_2/Si wafer surface at 600 °C.[84]

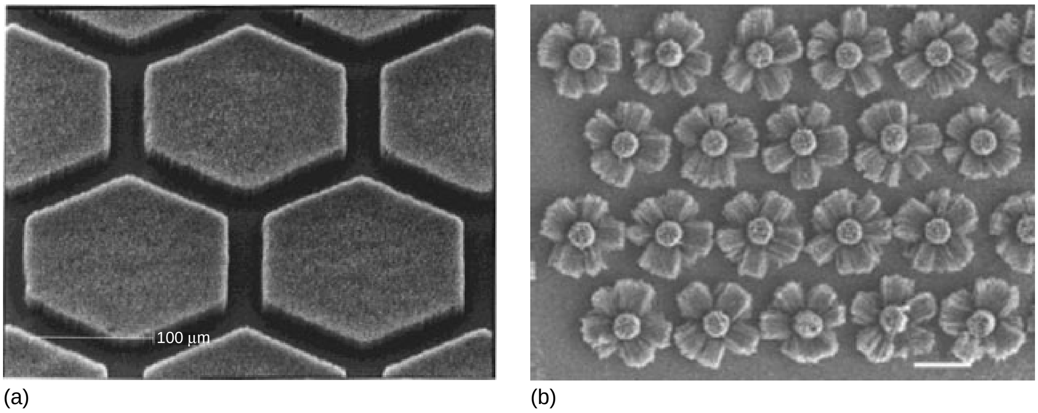

Figure 13 (a) SEM of the aligned carbon nanotubes micropatterns produced by contact photolithography with a TEM grid consisting of hexagonal windows as the mask (scale bar 100 µm). (Reprinted with permission from Ref. 82. © 1999 Macmillan Magazines Ltd.) (b) Repeating patterns containing mutually orthogonal nanotube arrays produced on deep (about 5 µm) silica features (circular cross section) machined on silicon substrates (scale bar, 50 µm). (Reprinted with permission from Ref. 79. © 1999 American Chemical Society)

The driving force for the growth of aligned carbon nanotubes is the presence of van der Waals interactions between the growing nanotubes.

3.3.4 Hydrothermal Synthesis

Hydrothermal pyrolysis is another approach used for the synthesis of MWNTs.[85,86] The MWNTs have been synthesized using amorphous carbon and water in an autoclave at 800 °C under 100 MPa. The MWNTs with diameters of 10–50 nm with graphitic nanoparticles were obtained in hydrothermal pyrolysis. The formation of CNTs in the absence of a metal catalyst under hydrothermal conditions involves rearrangement of bonds of amorphous carbon.[85] A simple procedure has been used to produce MWNTs by tipping a red-hot graphite rod into water at 0 °C.[87] The water turned black and particles slowly segregated, which were identified as MWNTs. It was explained that the temperature difference between inner and outer layers of the graphite rod while tipping into water produces necessary energy to crimp the graphitic layers and fuse the edges through covalent linkages in the presence of water. The actual mechanism of the formation of MWNTs by this procedure is not well understood. Nevertheless, the MWNTs produced by this method have defect-free lattices.

The hydrothermal synthesis of MWNTs can also be carried out in the presence of metal catalyst and other hydrocarbons as carbon feedstock. Nickel and high-density polyethylene or polyethylene glycol have been used as catalyst and carbon feedstock respectively to form MWNTs in the presence of water at 800 °C under 100 MPa.[86] The growth occurs in a high-density fluid phase and produces a large diameter MWNTs (50–150 nm). The process also produces some of the tubes partially filled with fluid in side the capped MWNTs. The presence of trapped fluid inside the cavity of MWNTs indicates a high perfection of the graphene layer.

4 DIFFERENT TYPES OF CARBON NANOTUBES

Topologically different types of carbon nanotubes can be synthesized using appropriate reagents and conditions. A structural deformation of a carbon nanotube leading to cross-linking, ring closing, and junction formation can also be accomplished using post chemical or physical treatment.[88–90] It is possible to weld the SWNTs at a desired location using electron beam irradiation at elevated temperatures.[88] A controlled irradiation at the cross section of two individual SWNTs can transform the junction geometry into ‘X’, ‘Y’, and ‘T’ shapes through welding depending on the point of irradiation (Figure 14A). The dynamic simulation studies indicate that the junction linkage occurs with the formation of seven or eight-membered carbon rings. However, the actual welded junctions are not showing such perfect rings and have defective atomic arrangements at the junctions. It is also possible to produce branched carbon nanotubes through the CVD process using appropriate precursor reagents. The pyrolysis of nickelocene along with thiophene at 1000 °C produces branched MWNTs with multiple ‘Y’ junctions (Figure 14B).[91] The MWNTs containing ‘Y’ junctions have been synthesized in a catalytic thermal decomposition process.[92] However, the mechanism of formation of branching during the synthesis is not well understood.

The formation of junctions in carbon nanotubes is important for use in electronic application. The SWNTs have been shown to react with silicon and transition metals and form metal carbide nanorods and nanoparticles at high temperature under high vacuum.[93] A heterojunction interface with metal carbide at the tips of SWNTs is possible. Silicon and metal substrates such as Ti and Nb have been used with SWNTs to form long SiC, TiC, and NbC nanorods respectively. A small number of SWNTs with partial reaction are found to have connected to SiC nanorods (Figure 15). The formation of such a carbide heterojunctions in carbon nanotubes with

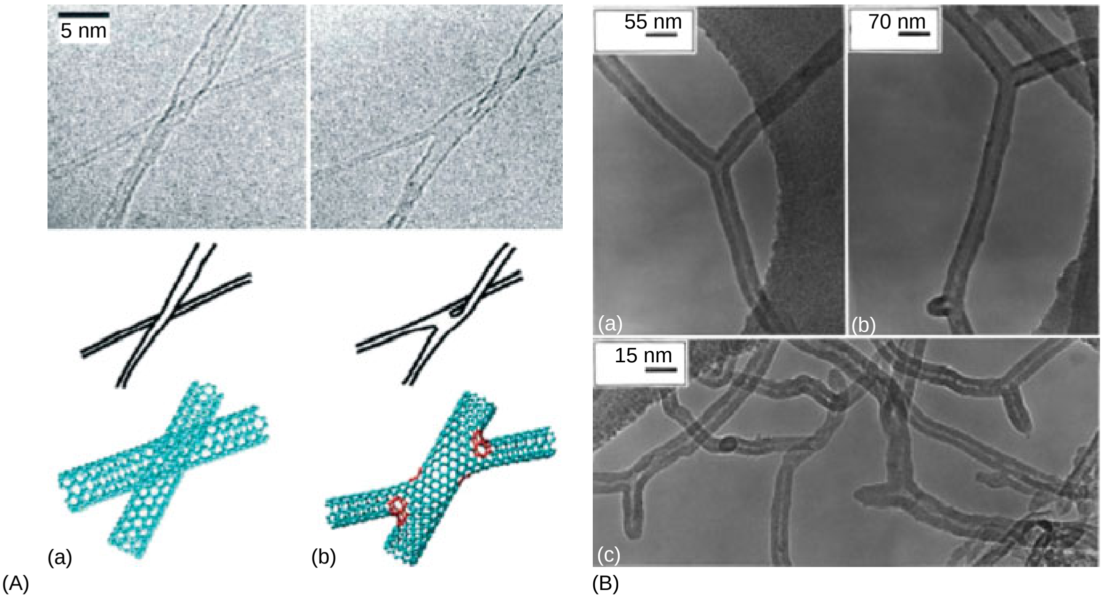
5 nm
(a)
(b)
(A)
55 nm
70 nm
(a)
(b)
15 nm
(c)
(B)

Figure 14 Different types of carbon nanotubes formed by irradiation (A) and CVD synthesis (B). (A) Cross-linking of SWNTs using 60 s electron irradiation (1.25 MeV with beam intensity ca. 10 A cm^{-2}) at 800 °C; (a) before irradiation and (b) after irradiation. (Reprinted with permission from M. Terrones, F. Banhart, N. Grobert, J.-C. Charlier, H. Terrones, and P.M. Ajayan, *Phys. Rev. Lett.*, 2002, **89**, 075505. © 2002 by the American Physical Society.) (B) 'Y'-Junction MWNTs synthesized using nickelocene with thiophene at 1000 °C. (Ref. 91. Reproduced by permission of American Institute of Physics)

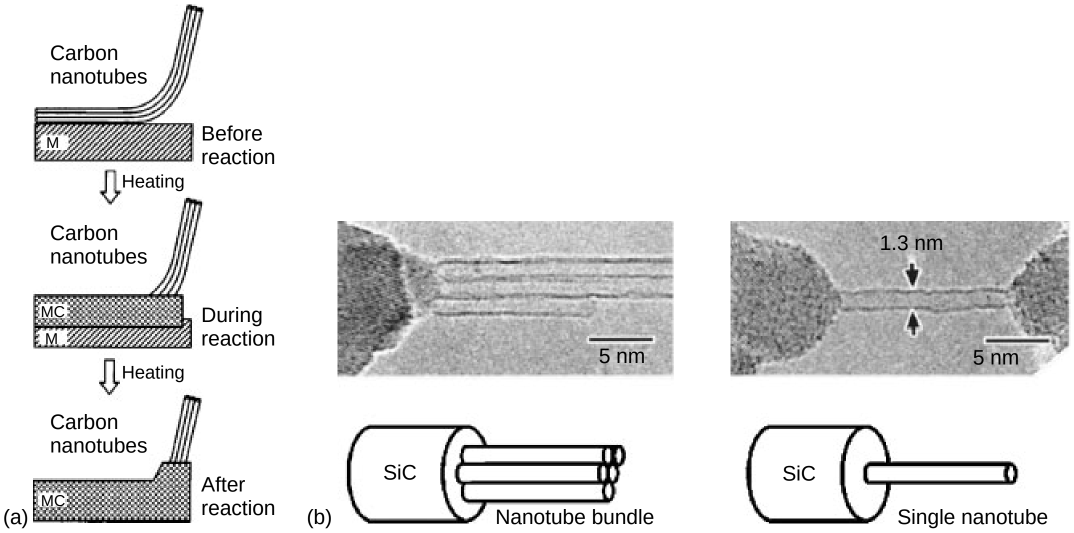
Carbon nanotubes
M
Before reaction
Heating
Carbon nanotubes
MC
M
During reaction
Heating
Carbon nanotubes
MC
After reaction
(a)
(b)
5 nm
1.3 nm
5 nm
SiC
Nanotube bundle
SiC
Single nanotube

Figure 15 (a) A schematic of the process for fabricating nanotube/carbide heterojunction by means of solid–solid reaction. M represents Si or Ti and MC represents formation of metal carbide. (b) TEM images showing SiC nanorods interfaced with SWNT bundles and a single SWNT. (Reprinted with permission from Y. Zhang, T. Ichihashi, E. Landree, F. Nihey, and S. Iijima, *Science*, 1999, **285**, 1719. © 1999 AAAS)

the properties of semiconducting or metallic is very important in the development of nanoelectronic devices.

Carbon nanobulbs have been formed in a process similar to the conventional 'glass' blowing.[89] Blowing carbon nanotubes requires a sudden formation of gas that should generate a sufficient pressure difference between the inside and outside of a closed tube. One of the synthetic procedures for MWNTs involves explosive decomposition of picric acid in the presence of nickel formate generating a high temperature (~1200 K) with a high pressure (~40 MPa). This gives a required pressure difference between the inside and outside of the tubes during the growth process until the end is capped by

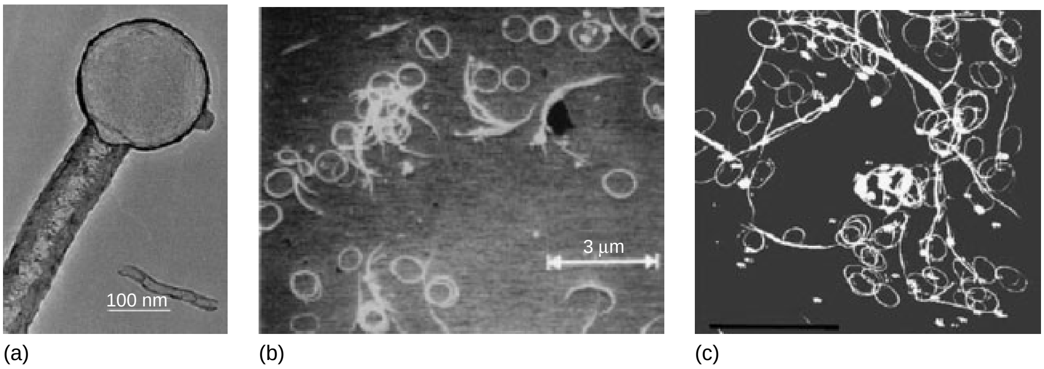

Figure 16 (a) TEM image of carbon bulb formed from tube blowing. The wall thickness is 25 nm for the parent tube and 9 nm for the blown blub. (Reproduced by permission from Ref. 89), (b) SEM of SWNTs rings formed by ultrasonication in the presence of H_2SO_4 and H_2O_2. (Reprinted with permission from Ref. 94. © 1999 Macmillan Magazines Ltd), and (c) AFM of SWNTs rings formed by intramolecular esterification in the presence of dicyclohexylcarbodiimide (DCC) (scale bar, 2 μm). (Reprinted with permission from M. Sano, A. Kamino, J. Okamura, and S. Shinkai, *Science*, 2001, **293**, 1299. © 2001 AAAS)

the termination. The end capping produces a temperature difference and the tubes expand in volume owing to the pressure difference into spherical bulbs at the tips as well as along the tube axis (Figure 16a). Up to 30% bulb formation has been reported.[89]

The carbon nanotubes are well known for their high flexural rigidity.[95] They can be mechanically or chemically forced to form nanorings and nanocoils.[90,94] A small percentage of rings of SWNTs with diameters ranging from 300 to 500 nm and rope widths of 5–15 nm have been found in some cases of laser-grown material.[96] It has been proposed that the rings are formed through 'intramolecular-growth' termination during the laser ablation. However, the formation of such rings is very low (0.1–1%). The ring formation of SWNTs occurs even under ultrasonication in a post treatment when long SWNTs are dispersed in a solvent and sonicated for 1–3 h at 40–50 °C. It is believed that a bubble formation during sonication around the hydrophobic nanotube forces the nanotube mechanically to bend at the bubble-liquid interface.[94] The ring formation occurs through van der Waals stabilization as the bubbles collapse leaving cavitation (Figure 16b). It is difficult to ascertain whether these rings are closed loops or open-ended coils. The acid and the hydroxyl groups generated during shortening or oxidative procedures are concentrated at the open ends of the SWNTs and they can be intramolecularly reacted to form rings.[90] The intramolecular ring closer of the oxidized SWNTs dispersed in N, N-dimethylformamide (DMF) using esterification in the presence of dicyclohexylcarbodiimide (DCC) produces a large amount of rings at room temperature (Figure 16c). This process shows the ability of SWNTs to bend and under go chemical reaction, intramolecularly, in solution like a semiflexible polymer. Theoretical studies show that the stability of SWNT rings is very high and the ring dissociation occurs only at high temperature.[97]

5 PURIFICATION OF CARBON NANOTUBES

The purity of carbon nanotubes mainly depends on the techniques used for the production. Unfortunately, none of the techniques, even after extensive optimization, produces pure carbon nanotubes that can be used directly for applications. In general, *as-synthesized* CNTs contain variable amounts of amorphous carbon, graphitic, and carbon coated metal nanoparticles, smaller fullerenes, and metal catalysts. The CNTs synthesized in the absence of metal catalyst contain largely amorphous and graphitic carbon impurities. The impurities vary widely in the range of 10–70% depending on the experimental conditions as well as the technique used for the synthesis. Several strategies have been developed for the purification of CNTs. Impurities are removed by subjecting CNTs to an appropriate repetitive dry or wet oxidation.[98–101] The amorphous carbon and the residual catalyst materials are removed first by oxidation with HNO_3, air-oxidation at high temperature, and subsequently the metal oxides are removed by dissolution in mineral acid.

It is difficult to remove the impurities by oxidation procedures without affecting the pristine CNTs since the carbon nanotubes and the impurities have only slight differences in their reactivity towards oxidation. The oxidative purification procedures are known to introduce defects, chemical functionality, doping, opening of caps, and shortening of lengths, and so on. Hence, the conditions for oxidation should be carefully chosen in order to minimize the damage to pristine CNTs. The reactivity of SWNTs varies depending on the diameter. The tubes with smaller diameters have higher reactivity then the larger ones. As different methods produce SWNTs with different average diameters, it is important to choose an appropriate oxidation procedure. The amount of impurity also differs from batch-to-batch since a slight variation in the experimental condition affects the growth significantly. Depending on the method of production and the level of impurities, the sequences of oxidation steps should be optimized for efficient purification of the carbon nanotubes.

5.1 Nitric Acid Reflux and Length Reduction

The SWNTs with larger diameters especially laser produced ones can be purified with the nitric acid reflux method. *As-prepared* SWNTs are treated with 3 M HNO_3 solution and refluxed for 48 h to remove a substantial amount of impurities.[101–106] The acid partially attacks the robust SWNTs network through intercalation of nanotube ropes and removes a considerable amount of exposed metal and nontubular carbons. The tubes are then thoroughly washed with water and dried. Further purification can be accomplished by treating the SWNTs in a mixture of sulfuric acid and nitric acid (3:1 v/v) at 70 °C for a short time followed by treating with a 4:1 (v/v) mixture of sulfuric acid and hydrogen peroxide (30%). This treatment shortens the SWNTs into smaller lengths (Figure 17). A longer duration in such a strong oxidizing agent is not advisable as it affects the sidewalls of SWNTs and cuts the tubes severely.[101,102,104,107–110]

The SWNTs have also been cut into smaller lengths using a simple grinding procedure with cyclodextrin.[111] The SWNTs composite mixed with cyclodextrin forms a colloidal suspension in water under sonication (10 min) and the TEM analysis shows that 70% of the nanotubes in the suspension have reduced in lengths between 100 and 600 nm from an average of 4 μm. Other reagents such as octadecylamine (ODA) when ground with SWNTs do not give a good dispersion. It is believed that the cyclodextrin is adsorbed noncovalently on the surface of SWNTs and the soft cutting occurs through mechanical force.

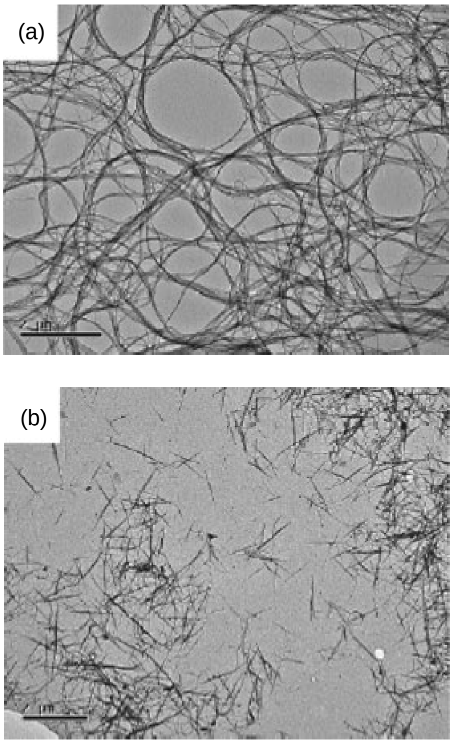

Figure 17 TEM images of (a) purified SWNTs and (b) after H_2SO_4/HNO_3 treatment (scale bar 2 μm). (Ref. 110. Reproduced by permission of Wiley-VCH)

5.2 Air-oxidation and Acid Treatment

One of the purification procedures involves air-oxidation followed by washing with HCl to remove metals. Metal nanoparticles that are covered with carbon coating are difficult to dissolve in an acid treatment. In order to break-up the carbon coating, air-oxidation is usually done at an optimal temperature for a specific duration. The presence of metal impurities enhances the oxidization of CNTs at higher temperatures and, hence, the oxidation is done by a step-by-step manner.[100,112,113] In this procedure, the sample is heated first in air at a moderate temperature ($T_1 \sim 225-300\,°C$) for a certain duration (t_1)

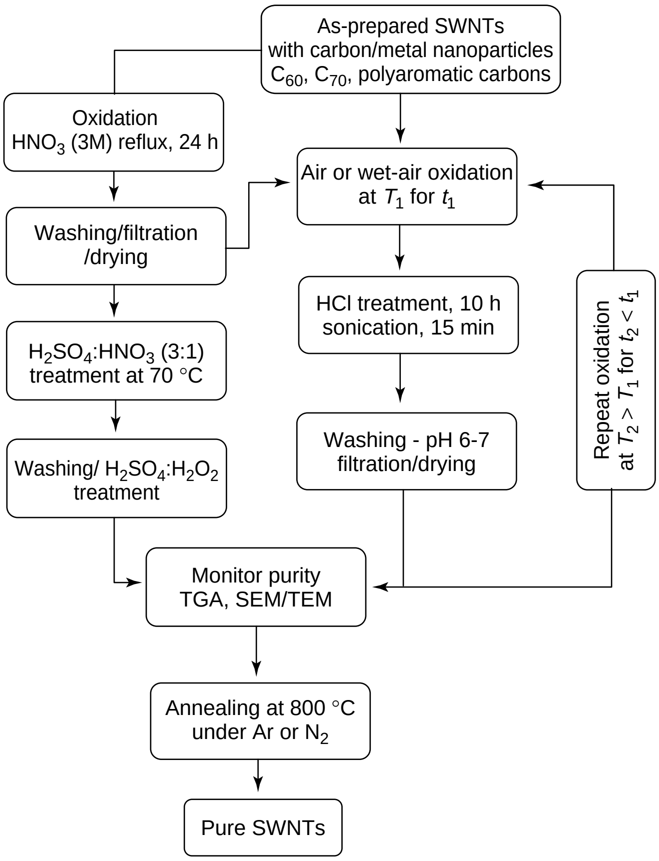
As-prepared SWNTs
with carbon/metal nanoparticles
C_{60}, C_{70}, polyaromatic carbons
Oxidation
HNO_3 (3M) reflux, 24 h
Washing/filtration
/drying
H_2SO_4:HNO_3 (3:1)
treatment at 70 °C
Washing/ H_2SO_4:H_2O_2
treatment
Air or wet-air oxidation
at T_1 for t_1
HCl treatment, 10 h
sonication, 15 min
Washing - pH 6-7
filtration/drying
Repeat oxidation
at $T_2 > T_1$ for $t_2 < t_1$
Monitor purity
TGA, SEM/TEM
Annealing at 800 °C
under Ar or N_2
Pure SWNTs

Figure 18 Schematic of the steps involved in different methods of oxidative purification of SWNTs. Oxidation is done at a particular temperature (T_1) for a certain period of time (t_1). Both the T_1 and t_1 are required to be determined for every sample batch with prior knowledge of decomposition rate using TGA

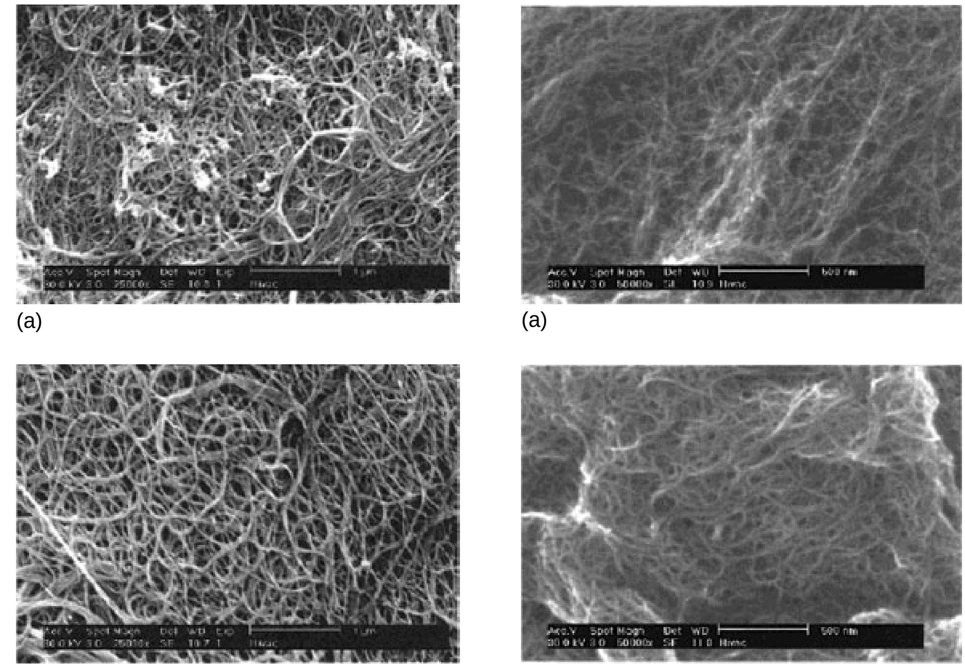

(a) (a)

(A) (b) (B) (b)

Figure 19 SEM images of purified SWNTs. (A) Laser-grown SWNTs subjected to two stage air oxidative purification (scale bar 1 μm); (a) before purification and (b) after purification. (Reprinted with permission from Ref. 100. © 2001 American Chemical Society.) (B) Raw HiPco SWNTs subjected to three stage wet-air oxidation (scale bar 500 nm); (a) before purification and (b) after purification. (Reprinted with permission from Ref. 109. © 2001 American Chemical Society)

and subsequently treated with HCl to remove dissolved metals and then washed with water to clean the CNTs.[99,109] The temperature (T_1) and the duration (t_1) are dependent on the amount of impurity present in the sample. On the basis of the decomposition rate of the carbon nanotubes, T and t can be estimated. The oxidation can be repeated at a slightly higher temperature ($T_2 > T_1$) for a shorter t_2 ($t_2 < t_1$). After every oxidation steps, the sample is treated with HCl to remove the metal oxides by dissolution and washing with water to neutral pH. The advantage of the step-by-step oxidation procedure is that it incrementally removes catalyst and improves the purification efficiency (Figures 18 and 19). The purification efficiency of every oxidation step can be monitored using thermogravimetric anaylsis (TGA), Raman and Near-IR spectroscopy, and SEM/TEM imaging. The oxidation and the cleaning steps are repeated until desired purity is achieved. The CNTs are finally annealed at a high temperature under vacuum or inert gas to get purified carbon nanotubes.

The SWNTs produced from the HiPco process exhibit a smaller average diameter and, hence, a mild wet-air oxidation is done to avoid damages to the tubes. The oxidation of SWNTs in the presence of wet-air is found to selectively oxidize the nontubular carbon impurities without affecting the small diameter tubes.[100,112] In this procedure, the oxidation is done in the presence of air saturated with water vapor at 225 °C for 24 h. This is followed by sonication for ~15 min or stirring 10–15 h in concentrated HCl. The tubes are washed with water and dried thoroughly. The TGA of purified tubes shows a considerable reduction in metal content and other impurities. The wet-air oxidation is continued in multiple steps at higher temperatures (325 °C for 1–2 h and 425 °C for 1 h) to remove catalysts and other nontubular impurities. The sample must undergo HCl treatment and water washing after each oxidation procedure. The purified carbon nanotubes are obtained after annealing in argon or under vacuum at 800 °C for 1 h.

The oxidation of CNTs has been done using microwave (2.5 GHz, 150 W) treatment at 500 °C.[114] Irradiation by microwaves raises the local temperature of the metal catalysts significantly and ruptures the carbon layer around the catalytic nanoparticles. Then, the exposed metal is removed by refluxing in 4 M HCl for 6 h. It has been reported that the amorphous carbon and the metal caps could be removed from aligned MWNTs using the radio frequency glow-discharge plasma etching technique.[98]

5.3 Sonication and Filtration

Ultrasonication has been used for the purification of CNTs.[115] The low-molecular weight impurities are removed from carbon nanotube dispersion in methanol by filtration under a continuous sonication. The carbon nanotubes are kept in dispersion in methanol through sonication during the filtration. Methanol is continuously supplied during the filtration to maintain a constant filtration volume and the filtered SWNTs are washed with H_2SO_4 to remove the residual metals. A microfiltration technique has also been used to separate C_{60}, C_{70}, and other polyaromatic carbons from the SWNTs dispersion in CS_2.[116] The chemical modification of SWNTs affects the solubility parameters of nontubular carbon impurities significantly. Nontubular carbon species in the 'as-prepared' SWNTs can be extracted in tetrahydrofuran (THF) and filtered using 0.2 µm Teflon® membrane after a simple fluorination procedure.[112]

5.4 Chromatographic Separation

The size of impurities such as fullerenes, metal nanoparticles, and polyaromatic carbons are much smaller than the carbon nanotubes. Such impurities can be separated using size exclusion chromatography (SEC).[105,117] The carbon nanotubes are first dispersed in organic solvent either by functionalization or using surfactants. The dispersed SWNTs in organic solvents at low concentration can be used to separate the impurities by SEC techniques.[105,118] The conventional styrene-divinylbenzene crosslinked column materials are used for the separation. The ODA functionalized SWNTs in THF can be separated into pure functionalized SWNTs, other nanoparticles, and amorphous carbon at different retention times. A similar procedure has been used to separate different lengths of zwitterion-functionalized SWNTs using SEC.[119]

5.5 Generation of Carboxylic Acid Functionality

The carbon nanotubes can be functionalized with carboxylic acid groups using several wet-oxidation procedures.[106–108,120–122] The carbon nanotubes undergo severe acid itching when subjected to oxidizing conditions such as refluxing with nitric acid, sonication in a mixture of sulfuric and nitric acids at moderate temperature, or treating with piranha solution (sulfuric acid-hydrogen peroxide). Acid treatment opens the caps and removes considerable amount of amorphous and nontubular carbons along with intense cutting of the tubes leading to a reduction in length distribution.[106,107,120,121] The open ends of the carbon nanotubes with reactive dangling carbons transform into an indefinite number of oxygenated functionalities under oxidative condition. The oxidative purification of carbon nanotubes generally introduces a large concentration of carboxylic acid groups at the ends of the tubes and also at the defective surfaces along the tube with a small amount of other functionalities such as anhydride, alcohol, quinines, and esters. The carbon nanotubes with smaller diameter are more reactive and get oxidized more readily. This leaves more defects generated all along the surface in smaller diameter tubes than larger diameter tubes. Hence the distribution of functional groups in the carbon nanotubes varies widely with length and diameter.

6 PROPERTIES OF CARBON NANOTUBES

6.1 Optical Properties

The properties of carbon nantotubes are strongly dependent on their symmetry and diameter.[13] The carbon nanotubes are considered as a one-dimensional quantum-wire, and the influence of the quantum-size effect on the physical properties is significant. Raman scattering of the crystalline ropes of SWNTs shows several vibration modes, which are dependent on the diameter of the carbon nanotubes.[123] The Raman spectrum of SWNTs have several radical breathing vibration modes (RBM) around 180 cm^{-1}, minor disorder-induced band (D-band) at around 1200–1400 cm^{-1}, and the first-order tangential vibration modes (G-band) between 1500 and 1600 cm^{-1} along with the second order mode at 2700 cm^{-1}.[13] The G-band corresponds to the stretching and bending vibrational movements of the C–C bond in the plane towards the tube axis and D-band corresponds to similar vibrational movements in the plane towards and away from the center of the hexagons. A typical Raman spectrum of the randomly oriented SWNTs at different excitation frequency is shown in Figure 20(a). Experimentally observed frequencies correlate very well with the theoretically calculated ones using the C–C force constant.[124] Raman frequency increases with decreasing diameter especially in the low-frequency region ($\omega \leq 500\,cm^{-1}$).[125] The vibration frequency and its intensity towards the low-frequency modes change with increasing laser wavelength. The electronic density state (DOS) calculation using the tight-binding model shows that the energy difference between the valance (v_1) and the conduction band (c_1), decreases with increasing diameter (Figure 20b). The optical symmetric transitions occur between the lowest subbands (mirror image spikes) in semiconducting and metallic tubes (v_1 to c_1 and v_2 to c_2, etc.).

The tangential modes of SWNTs show a distinct band broadening and shift to lower frequencies at a critically narrow range of laser energies ($1.7\text{ eV} \leq E_{\text{laser}} \leq 2.2\text{ eV}$).[126] This anomalous behavior is attributed to the presence of metallic nanotubes, which have a similar range of energy separation ($E_{11} = E_{c1} - E_{v1}$) in the one-dimensional density of electronic states. The differences in DOS for metallic and semiconducting SWNTs cause a distinct change in the tangential vibrational modes for Stokes and anti-Stokes Raman spectra.[127] The G-band frequencies determined for 62 isolated SWNTs show that they can be classified into two intense bands depending on the structure of the tubes.[128] The peak at 1591 cm^{-1} is found to be independent on diameter. The peaks at 1554–1575 cm^{-1} are dependent on diameter and shift to lower frequencies for both metallic and semiconducting tubes.

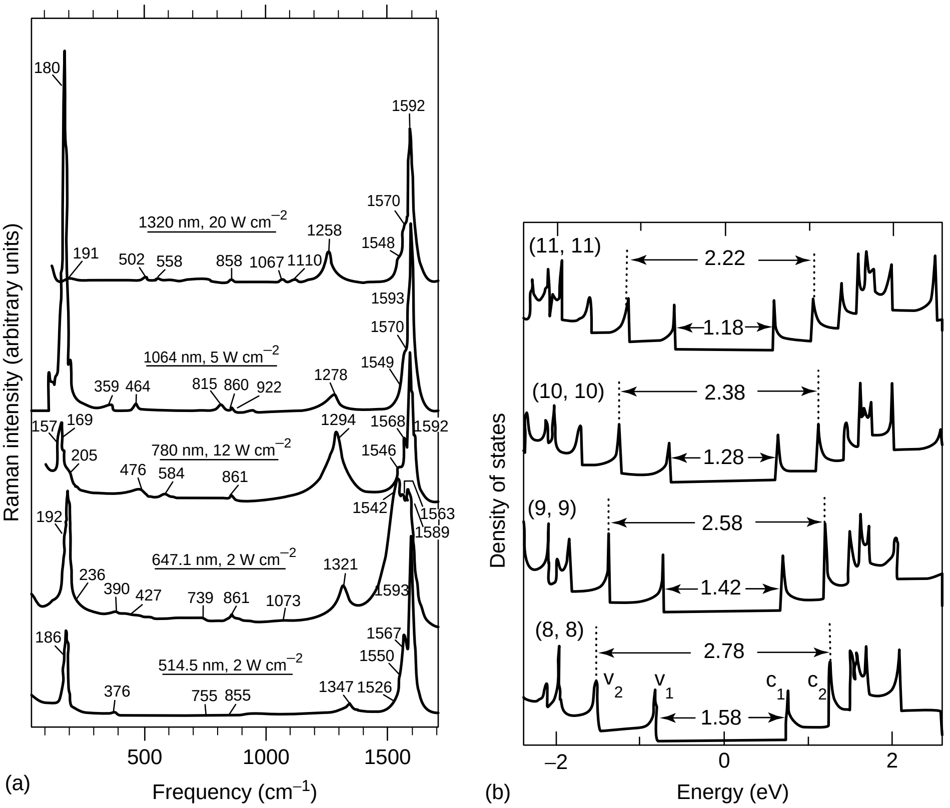

Figure 20 (a) Raman spectra of SWNTs excited at different laser frequencies and (b) Electronic density of states (DOS) calculated with the tight-binding model for the (8,8), (9,9), (10,10) and (11,11) arm chair nanotubes. (Reprinted with permission from A.M. Rao, E. Richter, S. Bandow, B. Chase, P.C. Eklund, K.A. Williams, S. Frang, K.R. Subbaswamy, M. Menon, A. Thess, R.E. Smalley, G. Dresselhaus, and M.S. Dresselhaus, *Science*, 1997, **275**, 187. © 1997 AAAS)

Unlike the SWNTs, the MWNTs do not show such well-defined vibrational frequencies owing to their larger diameter and broader distribution. The tangential vibrational and disorder mode for the MWNTs are very broad. The radical breathing modes of MWNTs in the region between 100 and 600 cm^{-1} are originating from the inner most tubes. Low-frequency RBM has been used to determine the diameter of the innermost tubes in MWNTs that agrees well with the high-resolution TEM results.[129] Raman scattering studies of DWNTs have shown that the RBM frequencies of the outer tube are not strongly influenced by the presence of an inner tube.[130] The tangential mode frequencies of the outer ($d \sim 1.3$–$1.6\,\text{nm}$) and inner ($d \sim 0.6$–$0.9\,\text{nm}$) semiconducting tubes are appearing distinctly at ~1590–1594 cm^{-1} and ~1584–1587 cm^{-1} respectively. The down field shift of the tangential mode frequencies of the inner tube is attributed to a wall-curvature.

The radical breathing, in-plane graphitic G-band and disorder-induced D-band frequencies of SWNTs have been found to be dependent on temperature. A linear decrease in frequency with respect to increasing temperature has been identified.[131] The temperature-dependent ω_D band for semiconducting tubes at 1565 cm^{-1} is $\sim -0.0226\,\text{cm}^{-1}\,\text{K}^{-1}$. However, experimental and molecular dynamic simulation studies have shown that the thermal expansion of the individual SWNTs in radical directions is extremely small and thus will have a minor effect in the frequencies of ω_RBM at various temperatures. The main reason for the dependence of ω_RBM is the temperature induced softening of the intratubular C–C bond strength and the intertubular van der Waals interactions.

It is known that the radical breathing mode has an inverse relation with respect to diameter $d = A/\omega_\text{RBM}$ where 'A' is a constant that can be obtained by theoretical models. A mean value of 'A' from many models appears to be $234\,\text{nm}\,\text{cm}^{-1}$. This correlation is consistent with the experimentally determined semiconducting tube diameter distribution.[132] The van dar Waals intertubular interaction between the individual tubes in a bundle also shifts RBM further to $\sim 14\,\text{cm}^{-1}$. Hence, the actual diameter is given by; $d = (A/\omega_\text{RBM}) + 14\,\text{cm}^{-1}$.

6.2 Absorption Spectroscopy

One-dimensionality of the carbon nanotubes transforms the DOS into several sharp van Hove singularities with distinct energy gaps. The energy differences in the electronic transition (E_{11}, E_{22}, etc.) of conduction and valence bands

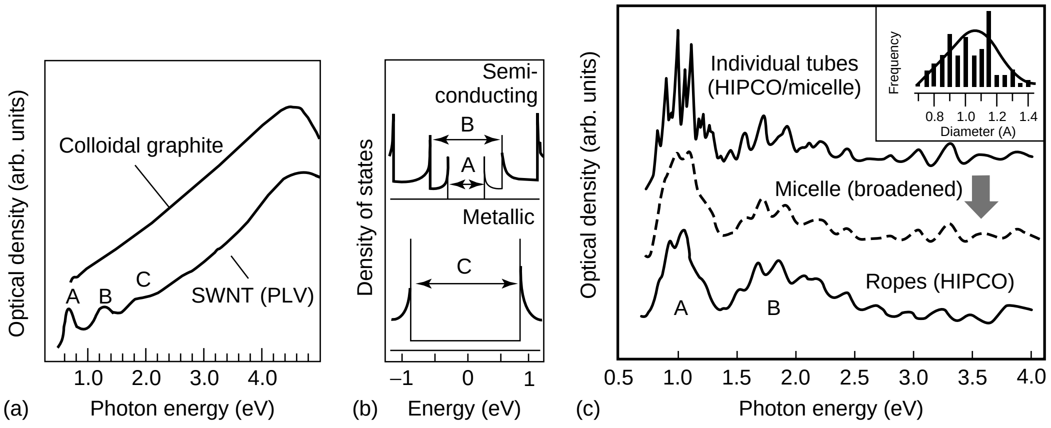

Figure 21 UV−vis-NIR spectra of different SWNTs. (a) Spectrum of SWNTs ropes produced by laser ablation in comparison with the colloidal graphite. (b) Symmetric transitions (DOS) between lowest subbands in the semiconducting (A, B) and the metallic (C) tubes. (c) HiPco samples in suspended sodium dodecyl sulfate (SDS) micelles. Individually suspended tubes shows 50 meV blue shit with respect to the rope material. (Reprinted with permission from Ref. 133. © 2003 American Chemical Society)

are dependent on the diameter, and the chirality of the carbon nanotubes. The existence of interband transitions between DOS singularities for various types of carbon nanotubes can be characterized using optical absorption spectroscopy. A typical optical absorption spectrum of SWNTs shows three broad peaks at energies between 0.65 and 2 eV that agree well with the theoretical calculations (Figure 21).[133–137] The peaks at ∼0.68−0.8 eV (1823−1549 nm) and ∼1.2−1.5 eV (1033−826 nm) (A and B) are related to interband transitions between the first and second subbands of semiconducting tubes and a peak at ∼1.8−2 eV (688−620 nm) is a second subband transition of metallic tubes (C) (Figure 21).

As the electronic transitions depend on the diameters of the carbon nanotubes, a smaller diameter SWNTs produced by the HiPco process (average $d \sim 1$ nm) shows fine structural details in the transition peaks. Any change in the electronic properties of the carbon nanotubes is reflected in these absorption peaks. The carbon nanotubes dopped with organic or inorganic materials have significant change in the electronic transition states. Doping SWNTs with electron acceptor (Br_2 or I_2) or donor (K, Cs) molecules makes the absorption peaks disappear owing to either electron depletion or addition of specific bands in the semiconducting or metallic tubes.[138]

It has been observed that the SWNTs suspended in a micellar solution exhibit a well-defined optical spectrum and show a bright photoluminescence in the near infrared region (Figure 22).[139] The individual SWNT suspended in air at room temperature also shows a bright photoluminescence.[140] The emission spectrum of the semiconducting SWNTs correlates well with the absorption spectrum in a micellar solution. The intensity of emission decreases dramatically when the isolated nanotubes start aggregating in a destabilized micellar solution. The decrease in the emission is attributed to the quenching of electrons by the metallic nanotubes when bundling occurs with the adjacent semiconducting tubes. On the basis of the lifetime and the quantum yield of luminescence, the photoluminescence has been characterized as fluorescence.[139]

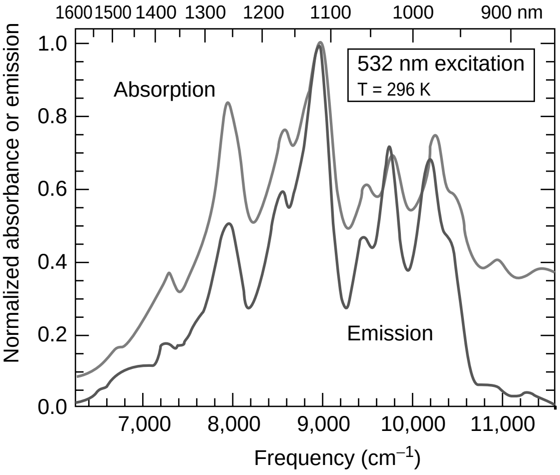

Figure 22 Absorption and emission spectrum of individual SWNTs in SDS micelles in D_2O excited by 8 ns with 532 nm laser pulses. (Reprinted with permission from M.J. O'Connell, S.M. Bachilo, C.B. Huffman, V.C. Moore, M.S. Strano, E.H. Haroz, K.L. Rialon, P.J. Boul, W.H. Noon, C. Kittrell, J. Ma, R.H. Hauge, R. Bruce Weisman, and R.E. Smalley, *Science*, 2002, **297**, 593. © 2002 AAAS)

6.3 Electrical and Thermal Properties

Electrical conductivity of the carbon nanotubes shows a quantized property of an extremely thin one-dimensional wire. As predicted by theory, the conductance of carbon nanotubes is found to be ballistic. The advantage in

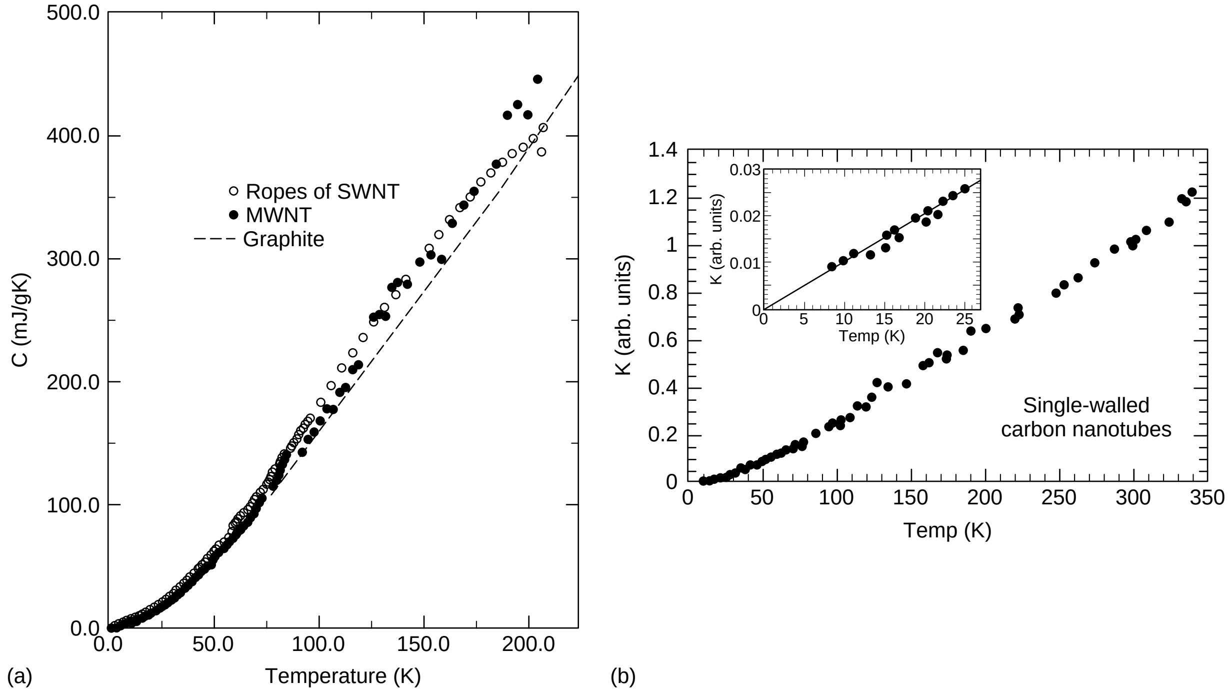

Figure 23 (a) Specific heat, C (T) versus T for SWNT ropes, MWNTs, and graphite. (Reprinted with permission from A. Mizel, L.X. Benedict, M.L. Cohen, S.G. Louie, A. Zettl, N.K. Budraa, and W.P. Beyermann, *Phys. Rev. B.*, 1999, **60**, 3264. © 1999 by the American Physical Society.) (b) Thermal conductivity of SWNTs (inlet shows expanded region of low-temperature behavior). (Reprinted with permission from J. Hone, M. Whitney, C. Piskoti, and A. Zettl, *Phys. Rev. B.*, 1999, **59**, R2514. © 1999 by the American Physical Society)

ballistic conductance is that the dissipation of heat energy is nearly absent during conduction.[141,142] The experiment carried out using MWNTs as a tip of a scanning probe microscope contacting a liquid metal to establish electrical contact shows a quantum conductance ($G_0 = 2e^2/h$ $\sim$12.9 kilo ohms^{-1}) without any heat dissipation.[143] The resistance of an individual SWNT and ropes of SWNTs decreases with the temperature and reaches superconductivity below 1 K.[75]

The electrical conductance of carbon nanotubes is sensitive to the chemical environment of the tubes. A large difference in the electrical conductance is observed for the carbon nanotubes in the presence of air and oxygen atmosphere.[144] It is possible to tune the electrical conductance of carbon nantubes reversibly using adsorbent gas molecules. The carbon nanotubes were also used to increase the conductance of a conjugated polymer for the development of electroluminescence polymer-nanocomposites.[145]

Thermal and thermal storage properties are very important and they determine the limitation of any applications such as molecular electronics, and conducting polymer composites, and so on. The carbon nanotubes have a higher specific heat and a higher thermal conductivity than any other known materials.[146–148] It is known that the heat transport in carbon nanotubes occurs through phonons.[149,150] The electronic and phonon spectra of carbon nanotubes are quantized owing to their smaller diameter. Low-energy phonons have a pronounce effect on the mechanical properties and thermal conductivity of carbon nanotubes. Similar to the one-dimensional electronic spectra of SWNTs, the low-energy phonon spectra also show a one-dimensional behavior.

The SWNTs have a larger specific heat at low temperature that follows a quadratic function (Figure 23a). The specific heat of the MWNTs determined in the temperature ranges from $1 < T < 200$ K is somewhat similar to that of the graphite. At temperatures, >50 K, the relationship between the specific heat and the temperature is linear up to 300 K. Thermal conductivity of SWNTs decreases gradually with decreasing temperature from 350 to 40 K, and the decrement is linear at <30 K up to zero K. The temperature-dependent thermal conductivity of SWNTs is very different from the graphite exhibiting a marked decrease of K with increasing temperature $>\sim150$ K (Figure 23b). However, it has been shown that the thermal conductivity of a single nanotube is comparable to that of diamond or in-plane graphite.[150] The thermal conductivity of MWNTs is independent of the tube length and smaller than diamond and in-plane graphite by a factor of 9 and 7.5 respectively.

6.4 X-ray Diffraction of Carbon Nanotubes

X-ray diffraction is used to characterize the structural parameters such as diameter distribution, intertube distances, and in-plane reflections of carbon nanotubes.[21,151,152] The powder X-ray diffraction plotted as a function of the wave vector θ is defined by $(4\pi Sin\theta)/\lambda$, where 2θ is the scattering angle and λ is the wavelength. A typical diffraction pattern for MWNTs plotted as a function of 2θ shows several Bragg peaks.[153] On the basis of the hexagonal graphite structure, the peaks can be indexed with (00*l*) and (*hk0*) relating to interplane layer stacking and in-plane reciprocal reflections respectively. The X-ray diffraction of MWNTs from 10 to 100°/2θ shows peaks for the layer stacking (00*l*) and reciprocal spacing (*hk0*). A strong Bragg peak centered around 26.1° in 2θ (3.4 Å) corresponds to the interlayer spacing (d_{002}) within the MWNTs. A similar diffraction pattern is observed for the SWNTs produced by the laser and the arc-discharge techniques indicating a unique growth mechanism involved in both of these techniques (Figure 24).

The interlayer distance between the coaxial tubes are slightly larger in MWNTs than in graphite and the determined mean value of the interlayer spacing is around 0.344 ± 0.0001 nm.[21,152,154–156] The electron diffraction pattern of the carbon nanotubes also confirms a slightly larger interlayer spacing.[21] The X-ray diffraction data show that the MWNTs have a nonuniform distribution of inner tube diameters. A high-resolution TEM image of the carbon nanotube shows that the d_{002} increases from 0.34 to 0.39 nm with decreasing inner tube diameter (Figure 25).[157] An empirical relation exists between the inner tube diameter and the layer spacing as given

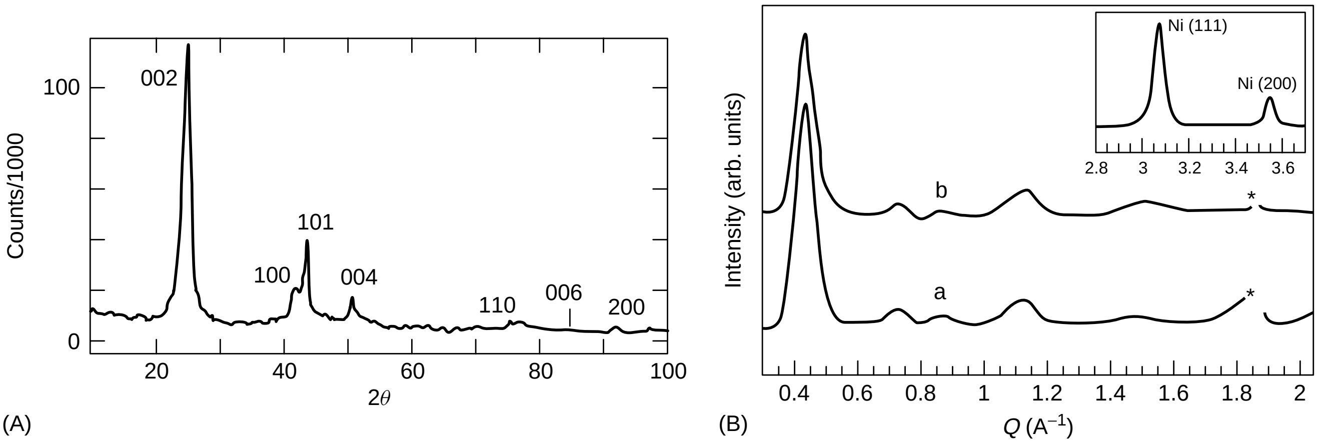

Figure 24 High-resolution X-ray diffraction of (A) MWNTs. (Ref. 153. Reproduced by permission of Wiley-VCH) and (B) SWNTs produced by (a) arc-discharge and (b) laser-ablation techniques. Asterisk marks are graphite peaks and removed for clarity. (Reprinted with permission from Ref. 20. © 1997 Macmillan Magazines Ltd)

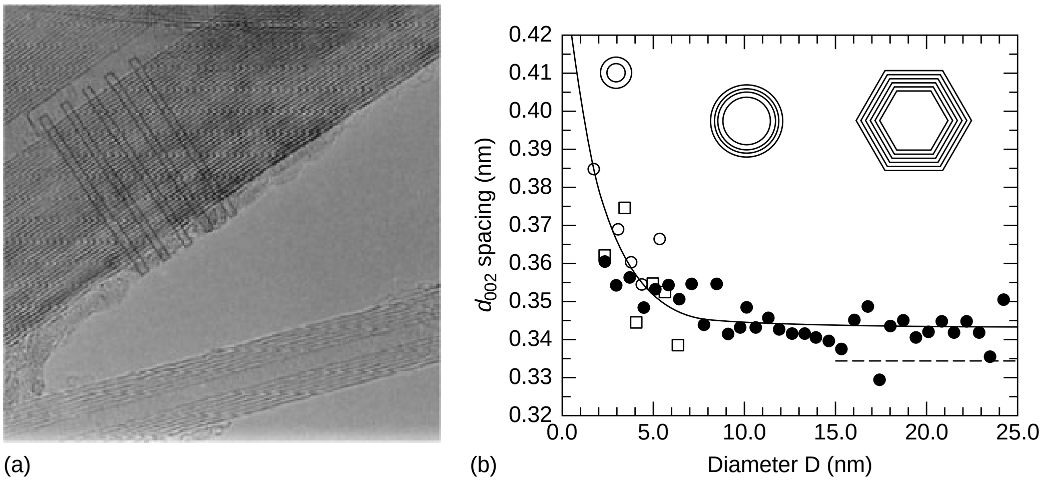

Figure 25 (a) The interlayer spacing (d_{002}) measurement using HRTEM images of MWNTs. (b) Relationship of d_{002} versus inner tube diameter for three different nanotubes; (○) 7 layer tube with $D_{\min} = 1.7$ nm, (●) 41 layer tube with $D_{\min} = 2.6$ nm, (□) 6 layer tube with $D_{\min} = 3.5$ nm. (Reprinted with permission from C.-H. Kiang, M. Endo, P.M. Ajayan, G. Dresselhaus, and M.S. Dresselhaus, *Phys. Rev. Lett.*, 1998, **81**, 1869. © 1998 by the American Physical Society)

below:

$$d_{002} = 0.344 + 0.1e^{-D/2} \text{ for } D \geq 0, \qquad (1)$$

where D is the inner tube diameter and d_{002} is the interlayer spacing and all the units are expressed in nm. It has been found that the interlayer spacing decreases exponentially and approaches 0.344 nm asymptotically at around $D \sim 10$ nm. The interlayer spacing in the MWNTs is strongly dependent on the intrinsic structure and on the basis of the method of production. The MWNTs produced in a H_2 atmosphere has a temperature-dependent shift of d_{002} reflection indicating the interlayers have varying thermal-expansion-coefficient along the radical direction of the MWNTs.[158]

The alignment of SWNTs can be determined in macroscopic quantities using a low θ X-ray diffraction pattern. A detailed study of the low θ X-ray diffraction on pellets of SWNTs (prepared by applying pressure of ~10 k bars) shows that the tubes axis are aligned in the plane of the pellets within an out-of-plane spread angle of ~4°.[151] The orientation and the degree of alignment of MWNTs in a stretched polymer composite material have been determined using the X-ray diffraction.[155]

6.5 Mechanical Properties

The structural perfection and the one-dimensional topology of the carbon nanotubes have predicted that they are the strongest material with high mechanical strength.[159–161] The carbon nanotubes with their high aspect ratio and low density are expected to be suited for the development of enhanced lightweight ultrastrong nanocomposites. Although theoretical calculations show that the Young's modulus of carbon nanotubes can reach up to 5.5 TPa,[159,160] various experimental results suggest that it is in the range of 1.2 to 1.8 TPa.[162–164] The experimentally determined Young's modulus for 27 individual SWNTs ($d \sim 1-1.5$ nm) using the room temperature vibrations method in a TEM has shown an average $\langle Y \rangle = 1.25$ Tpa, which is lower than a previous measurement using the thermal vibrations (1.8 ± 0.9 TPa) method. Nevertheless, the carbon nanotubes are the strongest known material with exceptional elongation and highest tensile strength around 100 GPa. It should be mentioned here that high strength steel has much lower Young's modulus and tensile strength of 200 GPa and 1–2 GPa respectively.

Atomic force microscopy (AFM) has been used to determine the bending force of suspended MWNTs pinned at one-end to a molybdenum disulfide surface.[95] The MWNTs with diameters from 26 to 76 nm show an average Young's modulus of 1.28 ± 0.59 TPa. The determined Young's modulus has no dependence on the diameter of MWNTs. The bending strength calculated for the MWNTs is around 28.5 GPa. Recently, a direct tensile-loading experiment using individual MWNT mounted between two opposing AFM tips that can be stress-loaded inside a scanning electron microscopy (SEM) has shown that the maximum Young's modulus and tensile strength are 950 and 63 GPa respectively (Figure 26 and 27b).[165] The mechanical response of 15 SWNTs ropes under tensile load using a similar experimental technique showed an average Young's modulus of 1.0 TPa (Figure 27a).

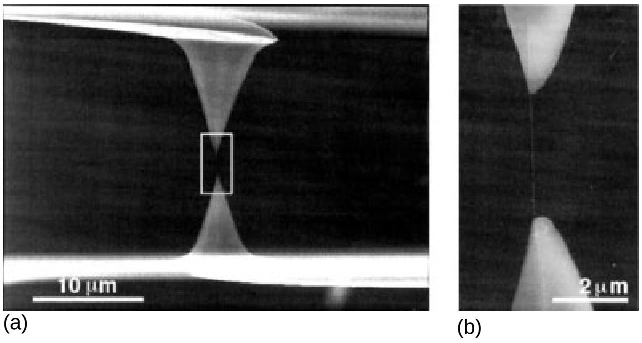

(a) (b)

Figure 26 (a) SEM image of AFM tips holding a MWNT. Attachment of MWNT to AFM silicon tip surface accomplished using electron beam deposition of carbonaceous material. The lower tip is attached to a soft cantilever and the deflection of which is imaged to determine the applied force, and (b) high-magnification of SEM image of the indicated region in (a). (Reprinted with permission from M.-F. Yu, O. Lourie, M.J. Dyer, K. Moloni, T.F. Kelly, and R.S. Ruoff, *Science*, 2000, **287**, 637. © 2000 AAAS)

The SWNTs under a hydrostatic pressure can undergo shape transitions gradually from a circle to an oval and to a peanut with a specific geometric constant.[166] The carbon nanotubes can undergo large deformations and can accommodate external forces without irreversible atomic rearrangements. The resilience of carbon nanotubes is remarkable as they can form kinks under compression and bending, ribbons under torsion, and are able to reversibly restore their original shape once the applied force is relieved. The presence of wear-free low interwall friction forces has been shown in MWNTs.[167] It has been also observed that a coalescence of SWNTs into MWNTs occurs at high temperatures (2200–2400 °C).[168] The molecular dynamic simulation indicates that this kind of transformation occurs through a 'patching and tearing' mechanism.

6.6 Alignment of Carbon Nanotubes

The carbon nanotubes are difficult to align or assemble owing to their broad size distribution along with overwhelming van der Waals interactions. The alignment and the control of the alignment process are important to realize the potential use of carbon nanotubes in applications such as conducting wires, electrodes, and nanocomposites. The carbon nanotubes have been aligned during synthesis in the CVD method.[169] The carbon nanotubes can also be aligned either in suspended or dispersed states.[110,170,171]

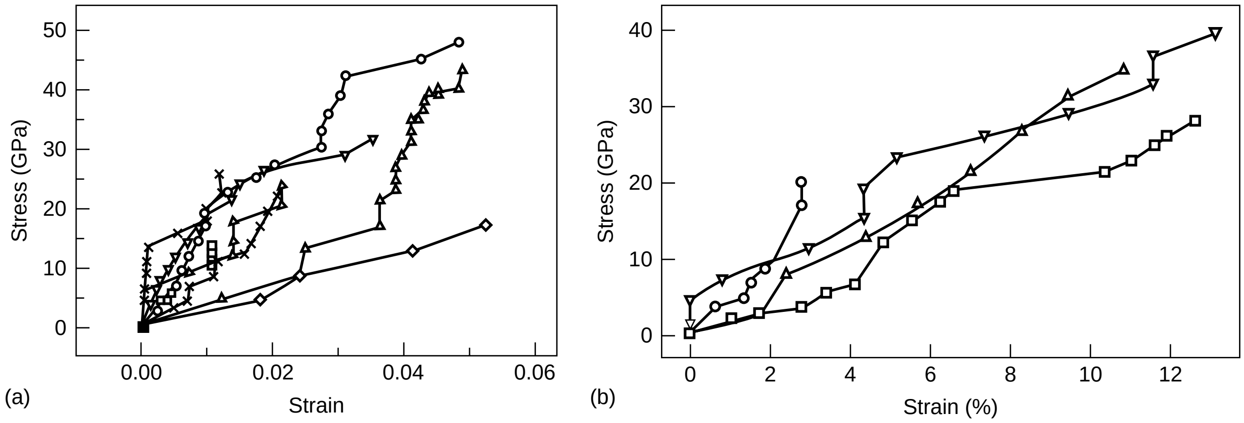

Figure 27 (a) Stress versus strain curves of different SWNTs ropes obtained in tensile-loading experiments carried out using AFM for eight ropes of SWNTs having diameter from 19 to 41 nm. (Reprinted with permission from M.-F. Yu, B.S. Files, S. Arepalli, and R.S. Ruoff, *Phys. Rev. Lett.*, 2000, **84**, 5552. © 2000 by the American Physical Society.) (b) Stress versus strain curves for individual MWNTs. (Reprinted with permission from M.-F. Yu, O. Lourie, M.J. Dyer, K. Moloni, T.F. Kelly, and R.S. Ruoff, *Science*, 2000, **287**, 637. © 2000 AAAS)

The SWNTs have been assembled into long macroscopic fibers and ribbons using a surfactant-dispersed nanotubes solution injected into a polymer solution with a continuous evaporation of solvent and recondensing the nanotubes in the flow of polymer solution to form an aligned fiber.[172] This procedure has been modified to produce SWNTs-polymer fibers composed of 60% SWNTs and 40% polymer exhibiting 1.8 GPa tensile strength similar to spider silk.[93] The SWNTs dispersed solution is injected into the center of a cylindrical pipe in which polyvinyl alcohol coagulation solution flows continuously. Upon contact with the coagulant, the SWNT solution collapses into a nanotube fiber associated with polyvinyl alcohol.[173] The SWNTs dispersed in water have been assembled in an electrode into a submicrometer diameter fibrils with lengths up to 1 cm under asymmetric electric field.[171] The individual tubes in such fibril bundles are aligned along the direction of the fibril axis. A continuous process of drawing carbon nanotubes into yarn by simply pulling a free-standing carbon nanotube array has been shown to produce 30 cm long yarns with 100 µm wide.[174] Similar to the Langmir-Blodgett film, the SWNTs suspended in solution can be used to form an aligned film on a substrate. A strong van der Waals interaction between the individual tubes at a critical concentration induces a self-assembly process at the air-liquid-substrate interface leading to the formation of an aligned SWNTs film on the substrate.[110] The alignment of SWNTs has been shown to occur in polymer composite under the influence of a magnetic field.[175]

6.7 Filling of Carbon Nanotubes

A large free volume is available inside the carbon nanotubes, which has been filled with various metals and gases. The filled carbon nanotubes have different physical and chemical properties that can be tailored to a specific application. The filling has been done using wet-chemistry in solution as well as in the molten state in the presence of chemical reagents.[120,176–179] The purification procedures such as acid treatment or refluxing in HNO_3 open the end caps and also fill partially ($<$20%) the inner volume of the carbon nanotubes. The presence of metal salts during acid reflux fills the tubes along with acid. The acid treated carbon nanotubes can also be filled in a post treatment with metal salts by using sonication.[120] The carbon nanotubes filled with metal salt are subjected to calcination to obtain the corresponding metal oxide filled carbon nanotubes.

Various metal oxides and metals from d-block and f-block transition metals have been used to fill partially the carbon nanotubes.[120,179] Metal salts such as KI, KCl, UCl_4, $CuCl_2$, $ZrCl_4$, $AuCl_3$, $AgNO_3$, $Pd(NO_3)_2$, $Cd(NO_3)_2$, CdO, and so on, have been used to fill the carbon nanotubes. Acid treated SWNTs have been filled using molten $AgNO_3$ at high temperature with filling efficiencies up to 3% (Figure 28A).[177] The filling occurs through a capillary action especially in a larger diameter tubes ($d \sim\geq 5$ nm). The filling of spherical or nonspherical organic gaseous molecules have been shown to diffuse through the interiors of carbon nanotubes.[178] Hydrothermally synthesized MWNTs are found to have an inner cavity partially filled with a dense aqueous fluid indicating that the filling can also occur during the formation of carbon nanotubes (Figure 28B).[180] The SWNTs filled with potassium iodide at a high temperature (~680 °C) show the metal salt trapped inside behaves distinctly.[181] The van der Waals force inside the tube surface have been found to affect the coordination of the surface atoms in the crystals of KI. This is supported by the fact that the filled KI inside the tubes had a distinct lattice spacing compared to normal KI.

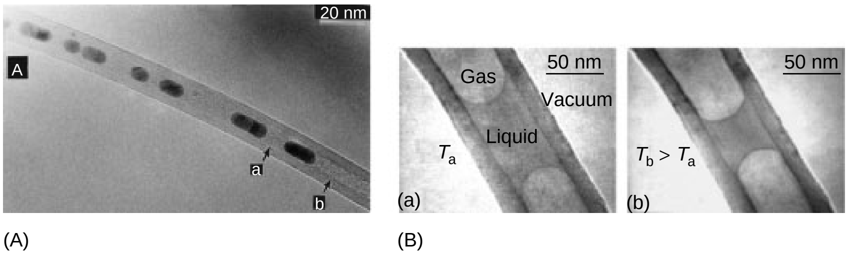

Figure 28 (A) High-resolution electron micrograph of a nanotube densely filled with silver particles. (Reprinted with permission from D. Ugarte, A. Chatelain, and W.A. de Heer, *Science*, 1996, **274**, 1897. © 1996 AAAS.) (B) TEM images of liquid trapped MWNTs portion showing reversible volume contraction/expansion of liquid upon heating/cooling using electron beam. (a) Initial shape of liquid at temperature T_a and (b) inclusion gets thinner upon heating at $T_b > T_a$. (Reprinted with permission from Y. Gogotsi, J.A. Libera, A.G. Yazicioglu, and C.M. Megaridis, *Appl. Phys. Lett.*, 2001, **79**, 1021. © 2001 by the American Physical Society)

7 SURFACE MODIFICATION OF CARBON NANOTUBES

The presence of an enhanced van der Waals interaction between individual carbon nanotubes makes them difficult to disperse and dissolve in an organic medium. The influence of van der Waals interaction with a high surface area and aspect ratio forces the carbon nanotubes to exist in an agglomerated bundle. Several potential applications of the carbon nanotubes require using them as an isolated material or integrated with other materials. Surface modification of the carbon nanotubes through chemical functionalization with organic substances is one of the strategies to break the overwhelming van der Waals interactions and use them either individually or disperse them homogeneously in a particular medium in many applications.

The problem associated with organic reactions of carbon nanotubes is the formation of multiple products with a different degree of functionality that renders functionalized carbon nanotubes with differing degree of solubility characteristics. There are basically three different types of distribution in the carbon nanotubes: 1) length, 2) diameter, and 3) functionality (Figure 29). It is very difficult to control the efficiency and the specificity of organic reactions in a heterogeneous reaction with respect to the placement of a functional group and the degree of functionalization.

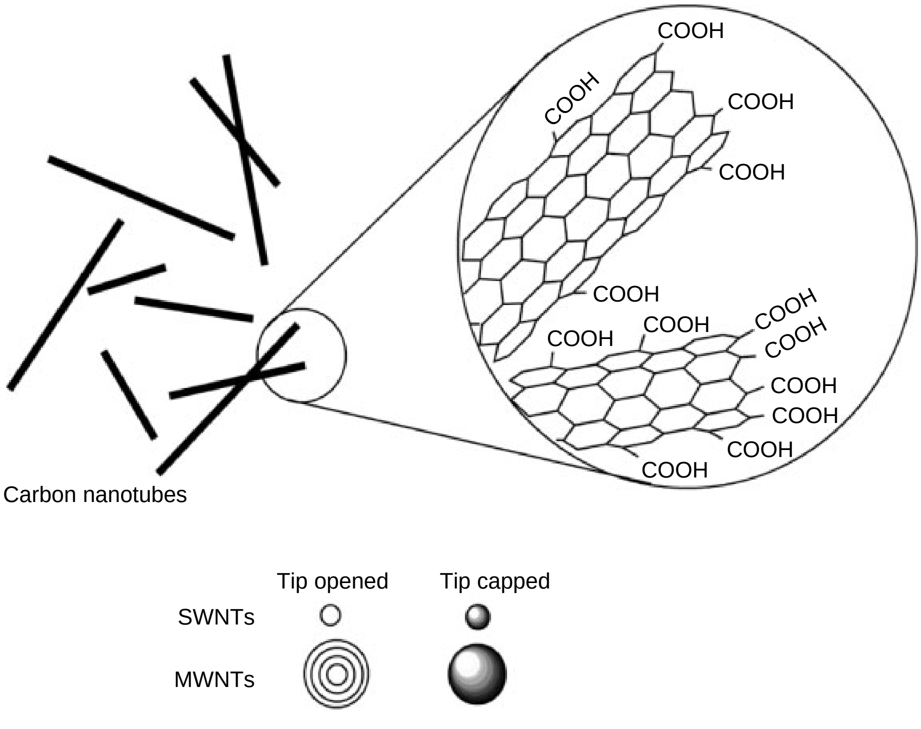

Figure 29 Distribution of the carbon nanotubes with their length, diameter, and functional groups

Moreover, some of the carbon nanotube's tips are either capped with a catalyst or opened. The amount of particular type of tubes present in a given sample also varies significantly depending on the method of production and, hence, every organic reaction performed with the carbon nanotubes would have, in principle, a multiple distribution of products.

The covalent attachment of organic moieties on carbon nanotubes would change the surface chemistry and help assembling them on a variety of substrates for electronic applications. The surface modified carbon nanotubes can be oriented conveniently in solution and in solid matrices. Controlled attachment of a specific functionality on the carbon nanotubes is essential in developing sensing nanodevices for biomedical and other applications. The surface modified carbon nanotubes can be used as nanofibers in novel ultrahigh-strength polymer composites that would have a low interfacial energy and a good load transfer efficiency. It is believed that the exotic mechanical and electrical properties of the carbon nanotubes will enhance the performance of polymer-carbon nanotube composites. Incorporation of carbon nanotubes in a polymer would produce electrically conductive composites with improved antistatic, electrostatic dissipation, electromagnetic interference shielding, and electroactive capabilities. Hence, the surface modification of carbon nanotubes through chemical reactions is very important to improve interaction with other materials and to realize the unique potentials of carbon nanotubes in many applications. Several strategies have been used for the functionalization of carbon nanotubes through post chemical reactions and noncovalent intermolecular weak-interactions $(\pi - \pi)$.[122,182–199]

7.1 Covalent Functionalization

The chemical modification through covalent functionalization of the carbon nanotubes can be classified broadly into two categories (Figure 30).[200] One of the methods involves the use of carboxylic acid groups that are formed in the carbon nanotubes during the purification processes. Another method involves a direct reaction with the sp^2 carbon network of the carbon nanotubes. The advantage of the covalent functionalization is that the surface modified carbon nanotubes are easily dispersible in organic/aqueous medium. However, the stability of the dispersion is highly dependent on the extent of modification. The attachment of organic moieties at the ends and at the surfaces even at a low concentration has improved significantly the dispersion of the carbon nanotubes in organic solvents.[200]

7.1.1 Reaction with Carboxylic Acid Groups

Various oxidative processes used for the purification of carbon nanotubes such as refluxing in acid, sonication in sulfuric and nitric acid (3:1) solution, and treatment with sulfuric acid and hydrogen peroxide solution introduce defects in the carbon nanotubes accompanied by the removal of amorphous and graphitic carbon.[41,120,122,201,202] Depending on the extent of oxidation, the carbon nanotubes are itched and shortened leaving the ends with large defects in the sp^2 network. The terminal carbons of the defective surface are converted into carboxylic acid groups along with small amounts of other oxygenated functionalities such as anhydride, quinine, alcohol, and ester. The carboxylic acid groups can also be introduced onto the carbon nanotubes using ozone treatment.[203,204] The amount of acid groups introduced during the purification steps varies between 1 and 5 mol% with respect to the total carbon depending on the procedure used for the purification. A high concentration of carboxylic acid groups is located at the open ends of the carbon nanotubes. The carbon nanotube bound carboxylic acids have been extensively used in amidation or esterification reactions with amine or hydroxyl containing organic molecules (Figure 31).

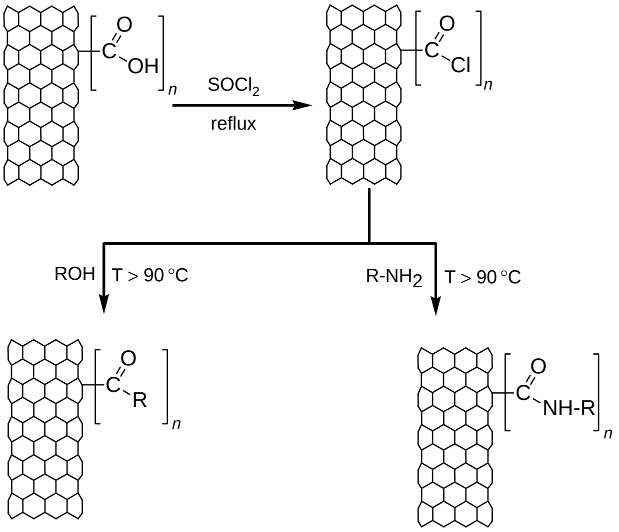

Figure 30 Use of carboxylic acid groups in postesterification and amidation reactions. The precursor acid functionality is distributed around the tubes and concentrated at the open ends. For clarity, one substitution with '*n*' multiples is illustrated

Haddon and coworkers have demonstrated the use of carboxylic acid groups of the SWNTs for attaching ODA.[122] The acid groups on the SWNTs are first converted in to acid chloride by refluxing with thionylchloride in the presence of a small amount of dimethylformamide at 70 °C for 24 h. The tubes are then reacted with excess ODA at 100 °C for 96 h to produce soluble surface modified SWNTs. The UV–vis spectrum of the soluble SWNTs shows a featureless absorption decreasing from 250 to 900 nm. The FT-IR spectrum showed a shift of carbonyl frequency of acid (1710 cm^{-1}, – COOH) to amide (1663 cm^{-1}, – CONH) indicating the presence of an octadecyl moiety on the SWNTs. Using a similar approach, the MWNTs have been solubilized and used for composite preparation.[205] A detailed end-group and defect analysis of

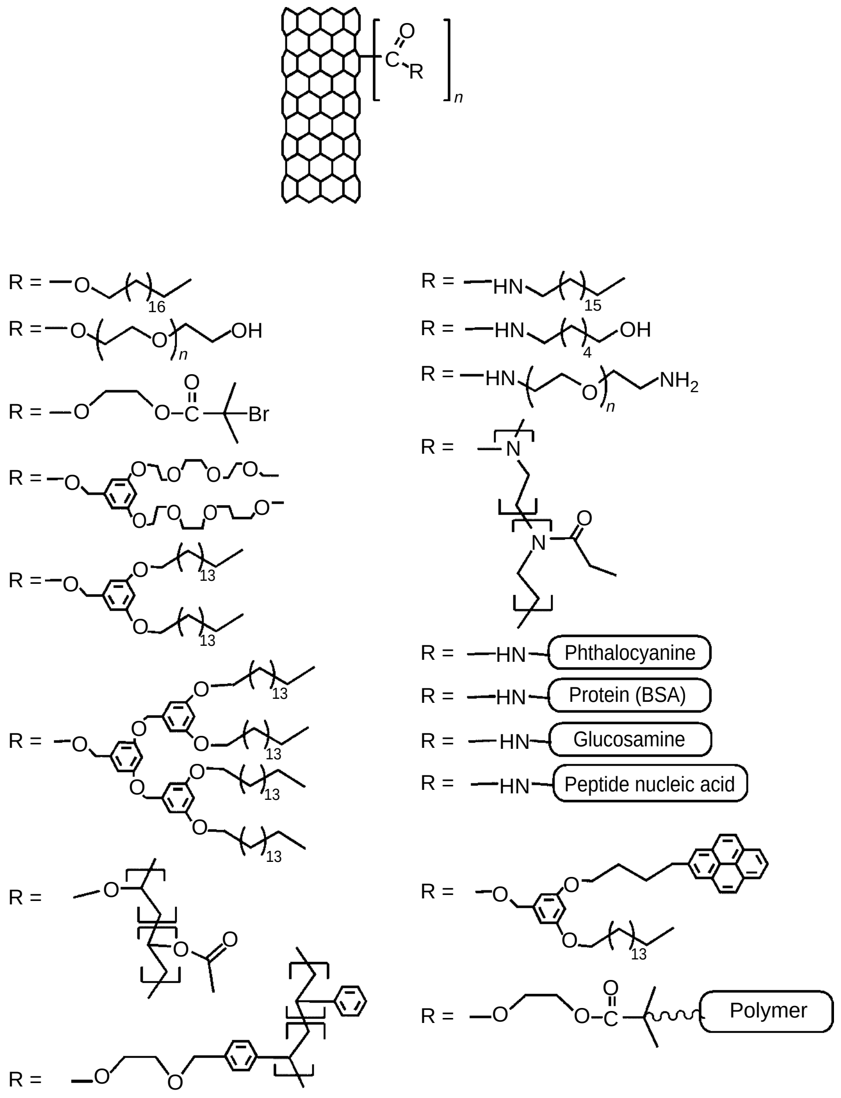

Figure 31 Representative reaction products obtained in the covalent functionalization of the carbon nanotubes. The precursor acid functionality is distributed all around the tubes and concentrated at the open ends (~1–3 mol%). For clarity, one substitution with '*n*' multiples is illustrated

ODA functionalized SWNTs has indicated that the affinity of the amine groups to the nanotubes is significant.[206] Hence, the dissolution of ODA functionalized SWNTs is not entirely due to the covalent grafting.

Amine containing phthalocyanines have been attached to SWNTs through an acyl chloride reaction.[207] A coordination of Wilkinson's complex with the oxidized SWNTs renders a high degree of solubility in organic solvents. The ^{1}H and ^{31}P NMRs of a saturated solution of SWNT-Winkinson's adduct show that the Rh in [RhCl(PPh$_3$)$_3$] coordinates strongly with the oxygen atoms of the tubes forming a hexacoordinate structure.[208,209] It is also possible to dissolve the SWNTs through a carboxylate-zwitterion association by simply heating carboxylic acid groups containing SWNTs with ODA at 130 °C for 4–8 days.[108] The zwitterion-functionalized SWNTs with lengths of several micrometers are soluble in organic solvent. Acid groups of the SWNTs are reacted with 2-aminomethyl-18-crown-6 ether under vigorous stirring to form zwitterions-functionalized SWNTs, which are soluble in water in high concentration (1 mg mL^{-1}).[210] The functionalization of carbon nanotubes is strongly dependent on the reaction conditions such as temperature and duration.[211] The reaction of diamine-terminated oligomeric poly (ethylene glycol) with SWNTs showed a different extent of functionalization depending on the temperature (100–140 °C) and the duration of the reaction (24 h to 6 days). The percentage of functionalized tubes was determined based on the weight difference between the starting and the residual weights of SWNTs after the extraction procedure, which varies from 28 to 70%.

The SWNTs have been rendered soluble by reacting with poly (propionylethylenimine-co-ethylenimine) ($M_w \sim 200\,000\,\mathrm{g\,mol^{-1}}$ and amine mole fraction ~15%) at 165 °C for 20 min. The SWNTs grafted with the copolymer were extracted in chloroform and it was found that the solubilized SWNTs solution exhibited a strong luminescence.[212] The MWNTs have also been functionalized using several aminopolymers to produce polymer attached-MWNTs that are soluble in many common organic solvents and in water.[183] Optical properties of the solubilized SWNTs and the grafted MWNTs with copolymer show a strong dependence on the concentration.[213] The STM of the high molecular weight copolymer attached SWNTs shows that the attached copolymers have some ordering depending on the chirality of the tubes.[214] The network formation owing to multiple hydroxyl or amine groups of a single copolymer chain reacting with different SWNTs is difficult to determine experimentally. Such a cross-linking has not been identified in these reactions. Fluorinated SWNTs have also been used for the functionalization with hexamethylenediamine.[215]

Protein attached SWNTs have been synthesized by reacting bovine serum albumin containing amino groups using a diimide-activated amidation reaction at room temperature.[216] The acid groups of the SWNTs have been converted into N-hydroxysuccinimide ester in the presence of 1-ethyl-3-(3-dimethyl-aminopropyl)carbodiimide hydrochloride and reacted with amine terminal peptide nucleic acid (PNA) in DMF to form a peptide attached SWNTs. The hybridization of a single-stranded DNA through a molecular recognition is performed in water with the peptide attached SWNTs. The attachment of DNA to the carbon nanotubes is evident clearly in the AFM of the DNA/PNA-SWNTs hybrids (Figure 32).[217]

A polystyrene copolymer containing *p*-4-(4′-vinylphenyl)-3-oxabutanol as comonomer has been reacted with SWNT-COCl in THF for 48 h. The resulting dark suspension is recovered by centrifugation at 7500 rpm. The copolymer attached SWNTs are soluble in organic solvent and the UV–vis absorption is shown to follow Lambert-Beer's Law.[184] Monohydroxyl functional dendrons consisting of long alkyl chains and oligomeric poly (ethylene glycol) have been used in the esterification reaction with acylchloride containing SWNT and MWNTs. The reactions are done in bulk at 75 °C for 48 h and the dendrons attached carbon nanotubes are extracted with chloroform.[182] The dendron attached carbon nanotubes are soluble in common organic solvents and the ones with oligomeric poly (ethylene glycol) attached tubes are soluble in water. Hydrolysis of ester linkages between the carbon nanotubes and the dendrons have resulted in the recovery of carbon nanotubes.[218] It has been observed that these functionalization reactions require high temperatures and longer reaction times to drive a heterogeneous reaction forward. In most of the reactions, the soluble portion of the reaction mixture has been recovered either by centrifugation or dialysis. These procedures, in general, do not separate carbon nanotubes that are adsorbed or coated with organic or polymeric reagents.

The surface initiated polymerization has been performed from the SWNTs and the MWNTs through a covalently attached atom transfer radical initiators.[186,188,190,219,220] Polymer grown MWNTs after a thorough washing and drying procedure show the characteristic vibration bands for the presence of polymer in the IR spectrum and the corresponding polymer decomposition in the thermogravimetic analysis. The surface initiated polymerization has been carried out either in bulk or at a high concentration of monomer. In some cases, the surface initiated polymerization has been performed in the presence of added free initiator to enhance the growth and to monitor the propagation kinetics.[188] The homo, block, and copolymers consisting of polystyrene and poly (methyl methacrylate) brushes chemically bound to the surfaces of MWNTs up to 70 wt% have been synthesized and characterized (Figure 33).[186] The polymer-*g*-nanotubes are soluble in organic solvent and have been characterized using ^{1}H NMR, UV, near-IR and Raman. The TEM and SEM

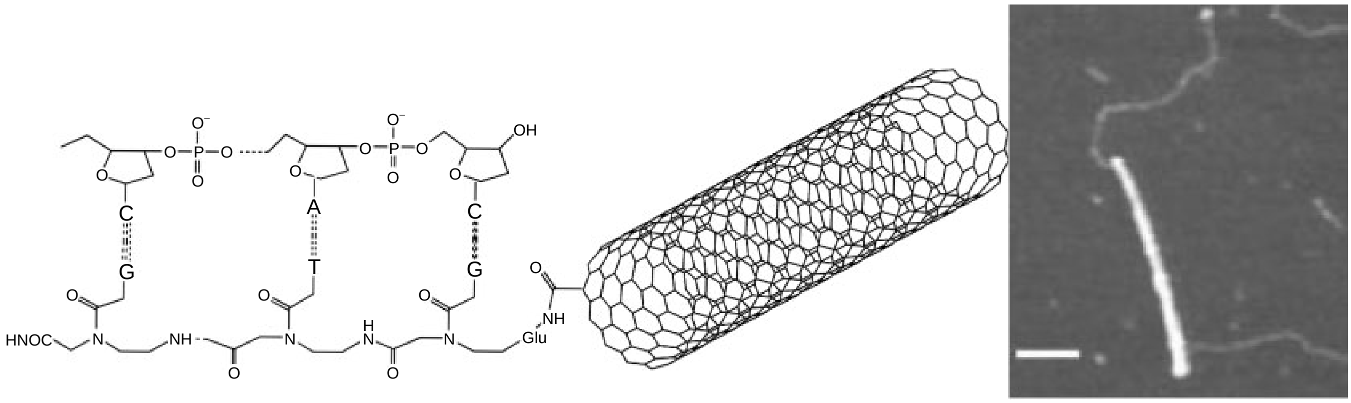

Figure 32 The structure and AFM image of a hybridized DNA on to peptide nucleic acid (PNA) attached SWNT. SWNT appear as bright light; the paler strands represent bound DNA. Scale bar = 100 nm. (Reprinted with permission from Ref. 217. © 2002 Macmillan Magazines Ltd)

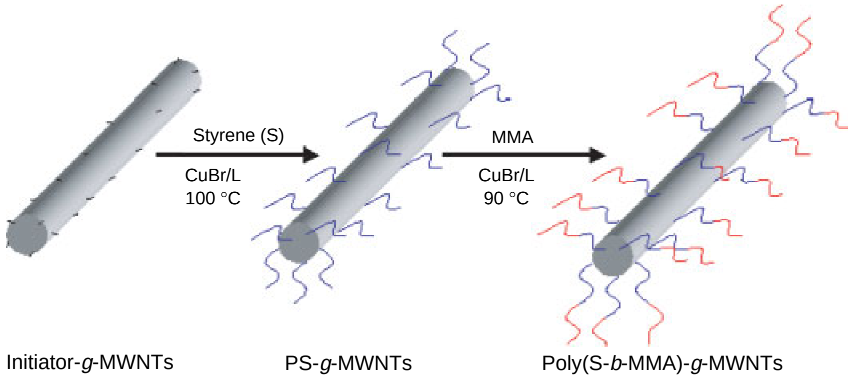

Figure 33 Surface initiated block copolymerization of styrene and methyl methacrylate through atom transfer radical polymerization[186]

of polymer-*g*-nanotubes show clearly the presence of a discontinuous amorphous layer on the surface of the nanotubes with layer thickness of around 2–8 nm. However, the overall percentage of polymer present on the surface of the tubes is very low on the basis of total monomer conversion. It is believed that a large amount of polymer forms from smaller tubes having a higher functionality. Owing to a broad functionality distribution within different size distributed carbon nanotubes, the polymer-*g*-carbon nanotubes contain multiple distributions of samples exhibiting different solubility characteristics.

7.1.2 Direct Reaction with the Surface

Covalent sidewall functionalization of SWNTs has been performed using several organic reactions such as cycloaddition of nitrenes[193] and bromomalonates,[221] addition of nucleophilic carbenes,[193] 1,3-dipolar cycloaddition of azomethine ylides,[189,192,222] reductive alkylation[223] ozonalyzes,[201,203,204] and carbanion addition[224,225] (Figure 34). The functional groups such as alkyl chains, aromatic groups, dendrimers, crown ethers, and oligoethylene glycol have been introduced by reacting such a functional group containing ($R-$) -oxycarbonyl nitrenes with SWNTs in 1,2-dichlorobenzene at 160 °C for 45 min.[226] The supernatant of the reaction mixture is decanted and the derivatized SWNTs are recovered by flocculation and centrifugation. Crown ether containing SWNTs are found to have a high solubility up to 1.2 mg mL^{-1}. Similarly, a different substituted azomethine ylides prepared by condensation of α-amino acid and an aldehyde have been used for the functionalization of SWNTs and MWNTs.[189,192,222] Ozone treatment of the carbon nanotubes introduces mainly oxygenated functionalities such as carboxylic acids, anhydrides, and alcohols. The main problem associated with the organic reactions performed directly on the sp^2 carbon network is the possibility of diminishing the integrity of CNTs. Introducing functional groups by cleaving the sp^2 carbon network would have a detrimental effect on the mechanical and electronic properties of the CNTs.

Alkyl halides have been attached radically to the sidewalls of SWNTs in liquid ammonia using lithium.[185,223] Addition of carbanion onto the double bonds of SWNTs using sec-butyllithium has been shown to generate anions on the surface of the SWNTs. The polymerization of styrene using the surface anions as the initiator has resulted in polystyrene grafted SWNTs with up to 15 wt% polymer.[224] Alkyl groups have been added to fluorinated SWNTs by reacting with alkyl magnesium bromide or alkyl lithium reagents. The alkylated SWNTs are found to be soluble in common organic solvents with 35 wt% functionalization.[225] Reaction of osmium tetroxide (OsO_4) with SWNTs in toluene in the presence of UV irradiation has produced nanotube bundles densely coated with OsO_4.[227] Detailed Raman studies reveal that the metallic SWNTs are more reactive toward osmylation than the semiconducting ones. Functionalization of SWNTs with various 4-substituted anilines has been performed in the absence of solvent and in the presence of isoamyl nitrile, sodium nitrile, and acid under a vigorous stirring condition.[228]

Free radicals have been used to introduce functional groups on the surface of carbon nanotubes (Figure 35).[193,229–233] Organic peroxides such as benzoyl, and lauroyl peroxides have been reacted with SWNTs.[230,233] The reactions are done generally for a longer reaction time (days) at a high temperature, though the half-lives of these free radicals are much shorter (hours). Introduction of acid functionality on the SWNTs has been achieved by reacting succinic or glutaric acid acylperoxides in *o*-dichlorobenzene at 90 °C.[232] The Raman, IR, and near-IR spectroscopy and TGA analyses of the functionalized SWNTs confirmed the attachment of radical groups. Aryl diazonium salts have been used to generate radicals for addition to SWNTs using electrochemical reduction.[196,197,229] Up to 49 wt% aryl functionality has been achieved and a stable homogeneous solution of aryl functionalized SWNT (50 mg L^{-1}) up to 36 h in chloroform is obtained after a 30 min sonication. Polymeric radical addition to SWNTs has been shown to occur during in situ free radical polymerization of styrene in toluene and sodium 4-styrenesulfonate in water.[231,234]

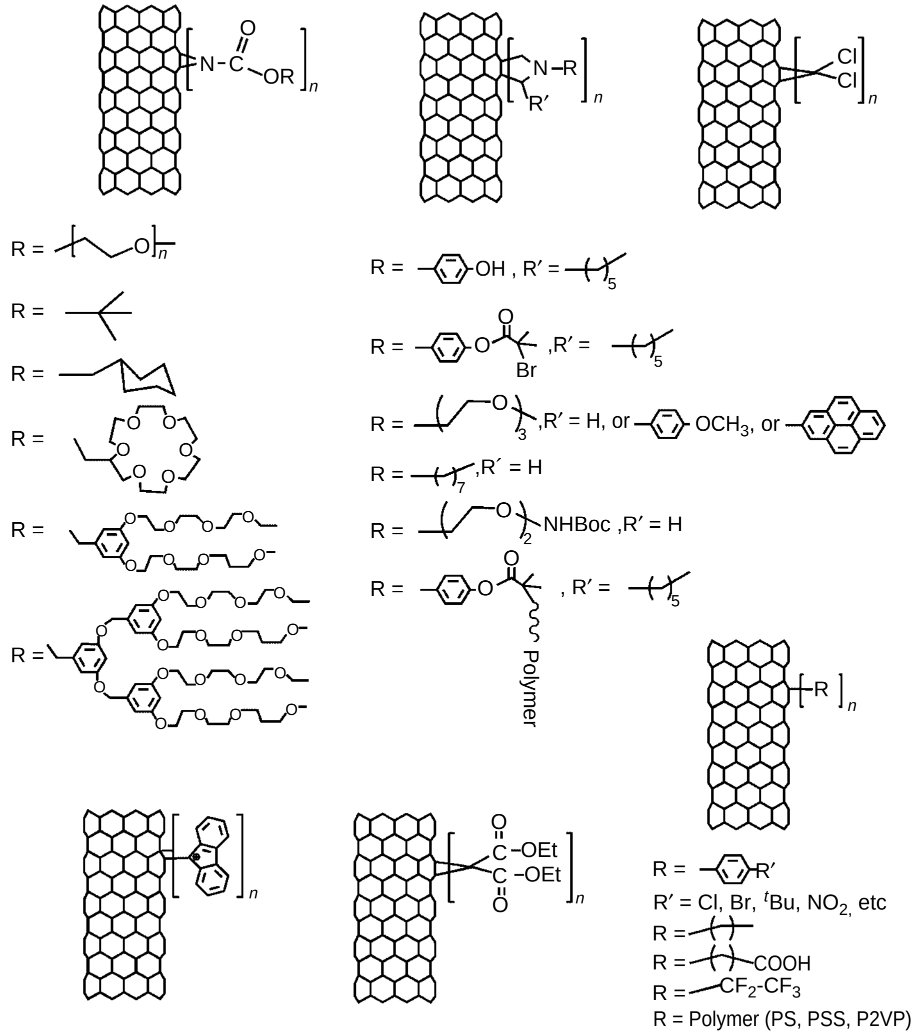

Figure 34 Surface modification of carbon nanotubes through chemical reactions with sp^2 network. For clarity, one substitution with '*n*' multiples is illustrated

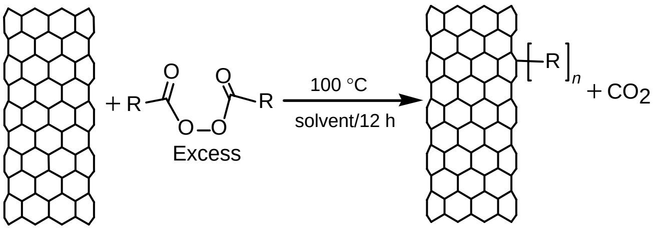

Figure 35 Radicals addition to carbon nanotubes. For clarity, one substitution with '*n*' multiples is illustrated

7.2 Noncovalent Functionalization

Noncovalent interactions of carbon nanotubes with polymers or organic molecules also provide a viable method for a dispersion of SWNTs, as reported by Stoddart,[235] Dai,[194] and coworkers, and others.[194,198,199,236–238] Nanotubes have been known to adsorb gas molecules (H_2, N_2, O_2, and H_2O) through adsorption.[236–240] Some polymers have strong noncovalent interactions with the carbon nanotubes. High molecular weight ionic or electron-rich polymers coat or wrap themselves around the carbon nanotubes. Polyvinyl pyrrolidone and polystyrene sulfonate and their copolymers, polyvinyl sulfate, and poly (metaphenylene vinylene) have been used to wrap around SWNTs.[198,235,241] The wrapping of polymer is accomplished by mixing solutions of purified SWNTs and polymer. The polymer wrapped SWNTs are soluble in organic solvents and in water depending on the solubility of the precursor polymer. It is not known whether these polymeric molecules wrap around or partially coat the surface of the SWNTs. It was proposed that the dissolution occurs in the case of water-soluble polymer wrapping or coating due to the thermodynamic driving force to eliminate the hydrophobic interface between the carbon nanotubes and aqueous medium and in the case of organic solvents, it is due to $\pi-\pi$ molecular interactions.[198,242]

Several surfactants and oligoethyleneoxides have been shown to disperse SWNTs through a nonspecific adsorption in water.[243,244] A natural polymer such as Gum Arabic is able to disperse SWNTs in water through a noncovalent adsorption.[245] However, the dissolution of carbon nanotubes using polymer wrapping has been shown to occur only with a few specific polymers. The mechanism of wrapping supposedly involves intermolecular noncovalent binding of polymers with SWNTs. Molecular interaction associated with this kind of adsorption can be characterized by a donor–acceptor complex formation through noncovalent interactions.

Rigid conjugated poly (aryleneethynylene)s have been shown to interact with SWNTs through $\pi-\pi$ stacking.[242] A significant up field shift of the substituent α-CH_2-signal of the poly (aryleneethynylene) with a signal broading has been noticed in the ^1H NMR indicating the presence of noncovalent interactions (Figure 36). Polyaromatic molecules such as pyrene and anthracene derivatives have been found to adsorb strongly onto SWNTs noncovalently through $\pi-\pi$ molecular interactions.[194,246] A substituted pyrene containing succinimidyl ester has been used to attach a protein on the surface of SWNTs through $\pi-\pi$ stacking.[194] Various copolymers containing pyrene pendant groups have been attached to the surface of MWNTs through $\pi-\pi$ interaction to render solubility in organic solvents.[247] The surface initiated polymerization has been performed using $\pi-\pi$ interaction with pyrene substituted with a metathesis polymerization initiator on the surface of SWNTs.[187] The polymerization of norbornene resulted in a homogeneous noncovalent coating (5–10 nm) of poly(norbornene) on the SWNTs. A dispersion of the SWNTs in aqueous solution is possible by mixing SWNTs and amphiphilic peptides using sonication.[248] It has been shown that a folding of certain peptides into amphiphilic α-helix in a segregated hydrophilic and hydrophobic faces enhances the formation of noncovalent interaction with the nanotubes. Porphyrin has been shown to interact noncovalently, specifically with semiconducting SWNTs in a mixture of semiconducting and metallic SWNTs.[249] The mechanism of such a selective interaction could be related to the differences in electronic structures associated with the nanotubes and the porphyrin. The porphyrin induced noncovalent solubilization and extraction in THF is a convenient method to separate the semiconducting SWNTs from the metallic SWNTs.

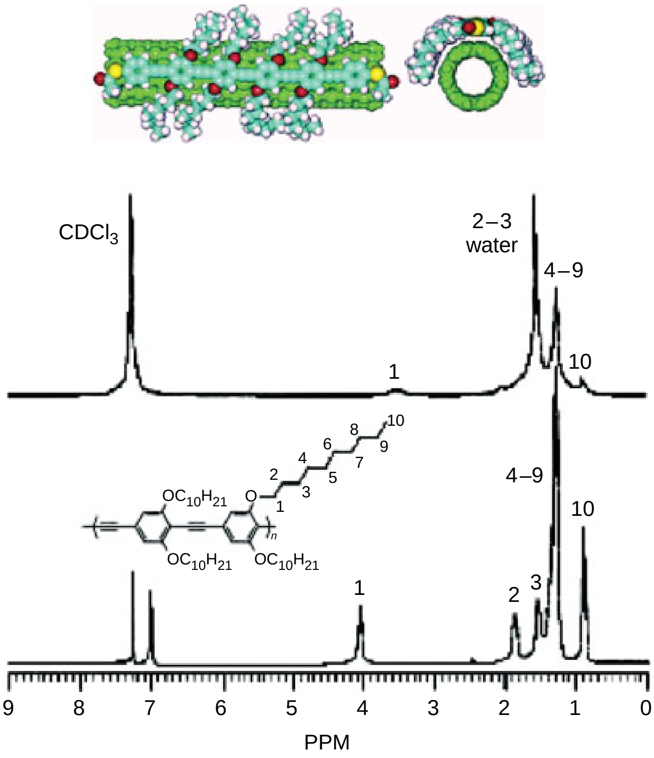

Figure 36 A molecular model of $\pi-\pi$ complex of a rigid conjugated poly(aryleneethynylene) with SWNT (6,6) and ^1H NMR spectra the complex with HiPco SWNT. (Reprinted with permission from Ref. 242. © 2002 American Chemical Society)

8 SUMMARY

An overview of the basic developments in the field of carbon nanotubes has been presented. The fundamental understanding of carbon nanotubes in terms of their synthesis, characterization, and structural manipulation has given a great impetus for the development of a multitude of applications exploiting their unique nanostructures. Research in the field of carbon nanotubes has seen a substantial amount of growth within a short span of time that simply reflects the enormous potential of carbon nanotubes in basic and applied science. Although the development is rapid, it is fair to say that the progress is continuing to gain control over the synthesis towards tailor-made carbon nanotubes with specific chirality and diameter. Revolutions in tailor-made and cast-effective carbon nanotube synthesis, separation, and controlled functionalization would undoubtedly bring closer to realization the forecasted opportunities in nanoscience and nanotechnology.

9 RELATED ARTICLES

Carbon: Fullerenes; Carbon: Inorganic Chemistry.

10 REFERENCES

1. H. W. Kroto, J. R. Health, S. C. O'Brien, R. F. Curl, and R. E. Smalley, *Nature*, 1985, **318**, 162.

2. W. Kratschmer, L. D. Lamb, K. Fostiropoulos, and D. R. Huffman, *Nature*, 1990, **347**, 354.
3. R. Taylor, J. P. Hare, A. K. Abdul-Sada, and H. W. Kroto, *J. Chem. Soc., Chem. Commun.*, 1990, 1423.
4. K. M. Kadish, R. S. Ruoff, eds, 'Fullerenes: Chemistry, physics and technology', John Wiley & Sons, New York, 2000.
5. S. Iijima, *Nature*, 1991, **354**, 56.
6. T. W. Ebbesen and P. M. Ajayan, *Nature*, 1992, **358**, 220.
7. S. Iijima and T. Ichihashi, *Nature*, 1993, **363**, 603.
8. D. S. Bethune, C. H. Klang, M. S. de Vrles, G. Gorman, R. Savoy, J. Vazquez, and R. Beyers, *Nature*, 1993, **363**, 605.
9. T. Guo, P. Nikolaev, A. Thess, D. T. Colbert, and R. E. Smalley, *Chem. Phys. Lett.*, 1995, **243**, 49.
10. A. Thess, R. Lee, P. Nikolaev, H. Dai, P. Petit, J. Robert, C. Xu, Y. H. Lee, S. G. Kim, A. G. Rinzler, D. T. Colbert, G. E. Scuseria, J. E. Fischer, and R. E. Smalley, *Science*, 1996, **273**, 483.
11. J. W. G. Wildoer, L. C. Venema, A. G. Rinzler, R. E. Smalley, and C. Dekker, *Nature*, 1998, **391**, 59.
12. M. S. Dresselhaus, G. Dresselhaus, and R. Saito, *Phys. Rev. B.*, 1992, **45**, 6234.
13. M. S. Dresselhaus, G. Dresselhaus, and P. C. Eklund, 'Science of fullerenes and carbon nanotubes', Academic Press, New York, 1996.
14. T. W. Odom, J. L. Huang, P. Kim, and C. M. Lieber, *J. Phys. Chem. B*, 2000, **104**, 2794.
15. T. W. Odom, J. L. Huang, P. Kim, and C. M. Lieber, *Nature*, 1998, **391**, 62.
16. J. W. G. Wiloder, L. C. Venema, A. G. Rinzler, R. E. Smalley, and C. Dekker, *Nature*, 1998, **391**, 59.
17. P. M. Ajayan and O. Z. Zhou, in 'Carbon Nanotubes, Topics Appl. Phys.', eds. M. S. Dresselhaus, G. Dresselhaus, and P. Avouris, Springer-Verlag, Berlin, Heidelberg, 2001, Vol. 80.
18. N. Hamada, S. Sawada, and A. Oshiyama, *Phys. Rev. Lett.*, 1992, **68**, 1579.
19. R. Saito, M. Fujita, G. Dresselhaus, and M. S. Dresselhaus, *Appl. Phys. Lett.*, 1992, **60**, 2204.
20. C. Journet, W. K. Maser, P. Bernier, A. Loiseau, M. Lamyde la Chapelle, S. Lefrant, P. Deniard, R. Lee, and J. E. Fischer, *Nature*, 1997, **388**, 756.
21. Y. Saito, T. Yoshikawa, S. Bandow, M. Tomita, and T. Hayashi, *Phys. Rev. B.*, 1993, **48**, 1907.
22. S. Farhat, L. M. La Chapelle, A. Loiseau, C. D. Scott, S. Lefrant, C. Journet, and P. Bernier, *J. Chem. Phys.*, 2001, **115**, 6752.
23. A. Yasuda, N. Kawase, F. Banhart, W. Mizutani, T. Shimizu, and H. Tokumoto, *J. Phys. Chem. B*, 2002, **106**, 1849.
24. A. Yasuda, N. Kawase, and W. Mizutani, *J. Phys. Chem. B*, 2002, **106**, 13294.
25. W. K. Hsu, J. P. Hare, M. Terrones, H. W. Kroto, D. R. M. Walton, and P. J. F. Harris, *Nature*, 1995, **377**, 687.
26. W. K. Hsu, M. Terrones, J. P. Hare, H. Terrones, H. W. Kroto, and D. R. M. Walton, *Chem. Phys. Lett.*, 1996, **262**, 161.
27. S. H. Jung, M. R. Kim, S. H. Jeong, S. U. Kim, O. J. Lee, K. H. Lee, J. H. Suh, and C. K. Park, *Appl. Phys. A*, 2003, **76**, 285.
28. M. Kusunoki, T. Suzuki, T. Hirayama, N. Shibata, and K. Kaneko, *Appl. Phys. Lett.*, 2000, **77**, 531.
29. H. Watanabe, Y. Hisada, S. Mukainakano, and N. Tanaka, *J. Microsc.*, 2001, **203**, 40.
30. V. Derycke, R. Martel, M. Radosavljevic, F. M. Ross, and P. Avouris, *Nano Lett.*, 2002, **2002**, 10.
31. H. Huang, J. Marie, H. Kajiura, and M. Ata, *Nano Lett.*, 2002, **2**, 1117.
32. C. Journet and P. Bernier, *Appl. Phys. A*, 1998, **67**, 1.
33. K. Anazawa, K. Shimotani, C. Manabe, H. Watanabe, and M. Shimizu, *Appl. Phys. Lett.*, 2002, **81**, 739.
34. S. J. Lee, H. K. Baik, J. Yoo, and J. H. Han, *Diamond Relat. Mater.*, 2002, **11**, 914.
35. X. Zhao, Y. Liu, S. Inoue, T. Suzuki, R. O. Jones, and Y. Ando, *Phys. Rev. Lett.*, 2004, **92**, 125502.
36. L. C. Qin, X. Zhao, K. Hirahara, Y. Miyamoto, Y. Ando, and S. Iijima, *Nature*, 2000, **408**, 50.
37. L. F. Sun, S. S. Xie, W. Liu, W. Y. Zhou, Z. Q. Liu, D. S. Tang, G. Wang, and L. X. Qian, *Nature*, 2000, **403**, 384.
38. X. Zhao, Y. Ando, Y. Liu, M. Jinno, and T. Suzuki, *Phys. Rev. Lett.*, 2003, **90**, 187401.
39. T. Sugai, H. Yoshida, T. Shimada, T. Okazaki, and H. Shinohara, *Nano Lett.*, 2003, **3**, 769.
40. J. L. Hutchison, N. A. Kiselev, E. P. Krinichnaya, A. V. Krestinin, R. O. Loutfy, A. P. Morawsky, V. E. Muradyan, E. D. Obraztsova, J. Sloan, S. V. Terekhov, and D. N. Zakharov, *Carbon*, 2001, **39**, 761.
41. O. Zhou, R. M. Fleming, D. W. Murphy, C. H. Chen, R. C. Haddon, A. P. Ramirez, and S. H. Glarum, *Science*, 1994, **263**, 1744.
42. G. De Boer, S. Arepalli, W. Holmes, P. Nikolaev, C. Range, and C. Scott, *J. Appl. Phys.*, 2001, **89**, 5760.
43. A. A. Puretzky, D. B. Geohegan, X. Fan, and S. J. Pennycook, *Appl. Phys. Lett.*, 2000, **76**, 182.
44. D. B. Geohegan, H. Schittenhelm, X. Fan, S. J. Pennycook, A. A. Puretzky, M. A. Guillorn, D. A. Blom, and D. C. Joy, *Appl. Phys. Lett.*, 2001, **78**, 3307.
45. M. Yudasaka, T. Ichihashi, and S. Iijima, *J. Phys. Chem. B*, 1998, **102**, 10201.
46. A. A. Puretzky, H. Schittenhelm, X. Fan, M. J. Lance, L. F. Allard, and D. B. Geohegan, *Phys. Rev. B.*, 2002, **65**, 245425.

47. W. K. Maser, E. Munoz, A. M. Benito, M. T. Martinez, G. F. de la Fuente, Y. Maniette, E. Anglaret, and J. L. Sauvajol, *Chem. Phys. Lett.*, 1998, **292**, 587.
48. A. C. Dillon, P. A. Parilla, J. L. Alleman, J. D. Perkins, and M. J. Heben, *Chem. Phys. Lett.*, 2000, **316**, 13.
49. M. Yudasaka, T. Ichihashi, T. Komatsu, and S. Iijima, *Chem. Phys. Lett.*, 1999, **299**, 91.
50. S. Bandow, S. Asaka, Y. Saito, A. M. Rao, L. Grigorian, E. Richter, and P. C. Eklund, *Phys. Rev. Lett.*, 1998, **80**, 3779.
51. M. Yudasaka, T. Komatsu, T. Ichihashi, Y. Achiba, and S. Iijima, *J. Phys. Chem. B*, 1998, **102**, 4892.
52. O. Jost, A. A. Gorbunov, J. Moller, W. Pompe, A. Graff, R. Friedlein, X. Liu, M. S. Golden, and J. Fink, *Chem. Phys. Lett.*, 2001, **339**, 297.
53. C. D. Scott, S. Arepalli, P. Nikolaev, and R. E. Smalley, *Appl. Phys. A: Mater. Sci. Process*, 2001, **72**, 573.
54. S. Arepalli, P. Nikolaev, W. Holmes, and B. S. Files, *Appl. Phys. Lett.*, 2001, **78**, 1610.
55. H. Dai, A. G. Rinzler, P. Nikolaev, A. Thess, D. T. Colbert, and R. E. Smalley, *Chem. Phys. Lett.*, 1996, **260**, 471.
56. X. Chen, R. Wang, J. Xu, and D. Yu, *Micron*, 2004, **35**, 455.
57. R. T. K. Baker and P. S. Harris, 'Formation of filamentous carbon in chemistry and physics of carbon', Marcel Dekker, New York, 1978, 14.
58. S. B. Sinnott, R. Andrews, D. Qian, A. M. Rao, Z. Mao, E. C. Dickey, and F. Derbyshire, *Chem. Phys. Lett.*, 1999, **315**, 25.
59. C. L. Cheung, A. Kurtz, H. Park, and C. M. Lieber, *J. Phys. Chem. B*, 2002, **106**, 2429.
60. Y. Li, W. Kim, Y. Zhang, M. Rolandi, D. Wang, and H. Dai, *J. Phys. Chem. B*, 2001, **105**, 11424.
61. H. M. Cheng, F. Li, G. Su, H. Y. Pan, L. L. He, X. Sun, and M. S. Dresselhaus, *Appl. Phys. Lett.*, 1998, **72**, 3282.
62. J. Kong, A. M. Cassell, and H. Dai, *Chem. Phys. Lett.*, 1998, **292**, 567.
63. Z. W. Pan, S. S. Xie, B. H. Chang, C. Y. Wang, L. Lu, W. Liu, W. Y. Zhou, W. Z. Li, and L. X. Qian, *Nature*, 1998, **394**, 631.
64. Q. H. Yang, S. Bai, J. L. Sauvajol, and J. B. Bai, *Adv. Mater.*, 2003, **15**, 792.
65. L. An, J. M. Owens, L. E. McNeil, and J. Liu, *J. Am. Chem. Soc.*, 2002, **124**, 13688.
66. V. Bajpai, L. Dai, and T. Ohashi, *J. Am. Chem. Soc.*, 2004, **126**, 5070.
67. E. Flahaut, R. Bacsa, A. Peigney, and C. Laurent, *Chem. Commun.*, 2003, 1442.
68. W. Ren, F. Li, J. Chen, S. Bai, and H. M. Cheng, *Chem. Phys. Lett.*, 2002, **359**, 196.
69. L. Ci, Z. Rao, Z. Zhou, D. Tang, X. Yan, Y. Liang, D. Liu, H. Yuan, W. Zhou, G. Wang, W. Liu, and S. Xie, *Chem. Phys. Lett.*, 2002, **359**, 63.
70. E. H. Hong, K. H. Lee, S. H. Oh, and C. G. Park, *Adv. Mater.*, 2002, **14**, 676.
71. J. Kong, H. T. Soh, A. M. Cassell, C. F. Quate, and H. Dai, *Nature*, 1998, **395**, 878.
72. Z. F. Ren, Z. P. Huang, J. W. Xu, J. H. Wang, P. Bush, M. P. Siegal, and P. N. Provencio, *Science*, 1998, **282**, 1105.
73. S. Fan, M. G. Chapline, N. R. Franklin, T. W. Tombler, A. M. Cassell, and H. Dai, *Science*, 1999, **283**, 512.
74. B. D. Yao and N. Wang, *J. Phys. Chem. B*, 2001, **105**, 11395.
75. A. Y. Kasumov, R. Deblock, M. Kociak, B. Reulet, H. Bouchiat, I. I. Khodos, Y. B. Gorbatov, V. T. Volkov, C. Journet, and M. Burghard, *Science*, 1999, **284**, 1508.
76. B. J. Hinds, N. Chopra, T. Rantell, R. Andrews, V. Gavalas, and L. G. bachas, *Science*, 2004, **303**, 62.
77. Y. C. Sui, D. R. Acosta, J. A. Gonzalez-Leon, A. Bermudez, J. Feuchtwanger, B. Z. Cui, J. O. Flores, and J. M. Saniger, *J. Phys. Chem. B*, 2001, **105**, 1523.
78. S. Huang, L. Dai, and A. W. H. Mau, *J. Mater. Chem.*, 1999, **9**, 1221.
79. Y. Yang, S. Huang, H. He, A. W. H. Mau, and H. Dai, *J. Am. Chem. Soc.*, 1999, **121**, 10832.
80. S. Huang, A. W. H. Mau, Tw. Turney, P. A. White, and H. Dai, *J. Phys. Chem. B*, 2000, **104**, 2193.
81. Q. Chen and L. Dai, *J. Nanosci. Nanotechnol.*, 2001, **1**, 43.
82. B. Q. Wei, R. Vajtai, Y. Yung, J. Ward, R. Zhang, G. Ramanath, and P. M. Ajayan, *Nature*, 2002, **416**, 495.
83. A. Cao, R. Baskaran, M. J. Frederick, K. Turner, P. M. Ajayan, and G. Ramanth, *Adv. Mater.*, 2003, **15**, 1105.
84. Y. Li, D. Mann, M. Rolandi, W. Kim, A. Ural, S. Hung, A. Javey, J. Cao, D. Wang, E. Yenilmez, Q. Wang, J. F. Gibbons, Y. Nishi, and H. Dai, *Nano Lett.*, 2004, **4**, 317.
85. J. M. Calderon Moreno and M. Yoshimura, *J. Am. Chem. Soc.*, 2001, **123**, 741.
86. J. Libera and Y. Gogotsi, *Carbon*, 2001, **39**, 1307.
87. Z. Kang, E. Wang, L. Gao, S. Lian, M. Jiang, C. Hu, and L. Xu, *J. Am. Chem. Soc.*, 2003, **125**, 13652.
88. M. Terrones, F. Banhart, N. Grobert, J. C. Charlier, H. Terrones, and P. M. Ajayan, *Phys. Rev. Lett.*, 2002, **89**, 075505.
89. Z. Zhu, D. Su, Y. Lu, R. Schlogl, G. Weinberg, and Z. Liu, *Adv. Mater.*, 2004, **16**, 443.
90. M. Sano, A. Kamino, J. Okamura, and S. Shinkai, *Science*, 2001, **293**, 1299.
91. B. C. Satishkumar, P. John Thomas, A. Govindaraj, and C. N. R. Rao, *Appl. Phys. Lett.*, 2000, **77**, 2530.
92. J. Liu, M. Shao, X. Chen, W. Yu, X. Liu, and Y. Qian, *J. Am. Chem. Soc.*, 2003, **125**, 8088.
93. Y. Zhang, T. Ichihashi, E. Landree, F. Nihey, and S. Iijima, *Science*, 1999, **285**, 1719.
94. R. Martel, H. R. Shea, and P. Avouris, *Nature*, 1999, **398**, 299.

95. E. W. Wong, P. E. Sheehan, and C. M. Lieber, *Science*, 1997, **277**, 1971.

96. J. Liu, H. Dai, J. H. Hafner, D. T. Colbert, and R. E. Smalley, *Nature*, 1997, **385**, 780.

97. O. Hod, E. Rabani, and R. Baer, *Phys. Rev. B.*, 2003, **67**, 195408.

98. S. Huang and L. Dai, *J. Phys. Chem. B*, 2002, **106**, 3543.

99. P. Hou, C. Liu, Y. Tong, S. Xu, M. Liu, and H. Cheng, *J. Mater. Res.*, 2001, **16**, 2526.

100. I. W. Chiang, B. E. Brinson, A. Y. Huang, P. A. Willis, M. J. Bronikowski, J. L. Margrave, R. E. Smalley, and R. H. Hauge, *J. Phys. Chem. B*, 2001, **105**, 8297.

101. M. T. Martinez, M. A. Callejas, A. M. Benito, M. Cochet, T. Seeger, A. Anson, J. Schreiber, C. Gordon, C. Marhic, O. Chauvet, and W. K. Maser, *Nanotechnology*, 2003, **14**, 691.

102. E. Borowiak-Palen, T. Pichler, X. Liu, M. Knupfer, A. Graff, O. Jost, W. Pompe, R. J. Kalenczuk, and J. Fink, *Chem. Phys. Lett.*, 2002, **363**, 567.

103. H. Kajiura, S. Tsutsui, H. Huang, and Y. Murakami, *Chem. Phys. Lett.*, 2002, **364**, 586.

104. J. M. Moon, K. H. An, Y. H. Lee, Y. S. ParK, D. J. Bae, and G. S. Park, *J. Phys. Chem. B*, 2001, **105**, 5677.

105. E. Farkas, M. E. Anderson, Z. Chen, and A. G. Rinzler, *Chem. Phys. Lett.*, 2002, **363**, 111.

106. A. G. Rinzler, J. Liu, H. Dai, P. Nikolaev, C. B. Huffman, F. J. Rodriguez-Macias, P. J. Boul, A. H. Lu, D. Heymann, D. T. Colbert, R. S. Lee, J. E. Fischer, A. M. Rao, P. C. Eklund, and R. E. Smalley, *Appl. Phys. A*, 1998, **67**, 29.

107. J. Liu, A. G. Rinzler, H. Dai, J. H. Hafner, R. K. Bradley, P. J. Boul, A. Lu, T. Iverson, K. Shelimov, C. B. Huffman, F. Rodriguez-Macias, Y. S. Shon, T. R. Lee, D. T. Colbert, and R. E. Smalley, *Science*, 1998, **280**, 1253.

108. J. Chen, A. M. Rao, S. Lyuksyutov, M. E. Itkis, M. A. Hamon, H. Hu, R. W. Cohn, P. C. Eklund, D. T. Colbert, R. E. Smalley, and R. C. Haddon, *J. Phys. Chem. B*, 2001, **105**, 2525.

109. I. W. Chiang, B. E. Brinson, R. E. Smalley, J. L. Margrave, and R. H. Hauge, *J. Phys. Chem. B*, 2001, **105**, 1157.

110. H. Shimoda, S. J. Oh, H. Z. Geng, R. J. Walker, X. B. Zhang, L. E. McNeil, and O. Zhou, *Adv. Mater.*, 2002, **14**, 899.

111. J. Chen, M. J. Dyer, and M. F. Yu, *J. Am. Chem. Soc.*, 2001, **123**, 6201.

112. R. Sivarajan, B. Brinson, M. P. Johnson, Z. Gu, R. K. Saini, P. Willis, T. Marriott, E. W. Billups, J. L. Margrave, R. H. Hauge, and R. E. Smalley, *J. Phys. Chem. B*, 2003, **107**, 1360.

113. S. R. C. Vivekchand and A. Govindaraj, *Proc. Indian Acad. Sci. (Chem. Sci.)*, 2003, **115**, 509.

114. A. R. Harutyunyan, B. K. Pradhan, J. Chang, G. Chen, and P. C. Eklund, *J. Phys. Chem. B*, 2002, **106**, 8671.

115. K. B. Shelimov, R. O. Esenaliev, A. G. Rinzler, C. B. Huffman, and R. E. Smalley, *Chem. Phys. Lett.*, 1998, **282**, 429.

116. S. Bandow, A. M. Rao, K. A. Williams, A. Thess, R. E. Smalley, and P. C. Eklund, *J. Phys. Chem. B*, 1997, **101**, 8839.

117. S. Niyogi, H. Hu, M. A. Hamon, P. Bhowmik, B. Zhao, S. M. Rozenzhak, J. Chen, M. E. Itkis, M. S. Meier, and R. C. Haddon, *J. Am. Chem. Soc.*, 2001, **123**, 733.

118. B. Zhao, H. Hu, S. Niyogi, M. E. Itkis, M. A. Hamon, P. Bhowmik, M. S. Meier, and R. C. Haddon, *J. Am. Chem. Soc.*, 2001, **123**, 11673.

119. D. Chattopadhyay, S. Lastella, S. Kim, and F. Papadimitrakopoulos, *J. Am. Chem. Soc.*, 2002, **124**, 728.

120. B. C. Satishkumar, A. Govindaraj, J. Mofokeng, G. N. Subbana, and C. N. R. Rao, *J. Phys. B: At. Mol. Opt. Phys.*, 1996, **29**, 4925.

121. M. A. Hamon, H. Hu, P. Bhowmik, S. Niyogi, B. Zhao, M. E. Itkis, and R. C. Haddon, *Chem. Phys. Lett.*, 2001, **347**, 8.

122. J. Chen, M. A. Hamon, H. Hu, Y. Chen, A. M. Rao, P. C. Eklund, and R. C. Haddon, *Science*, 1998, **282**, 95.

123. A. M. Rao, E. Richter, S. Bandow, B. Chase, P. C. Eklund, K. A. Williams, S. Frang, K. R. Subbaswamy, M. Menon, A. Thess, R. E. Smalley, G. Dresselhaus, and M. S. Dresselhaus, *Science*, 1997, **275**, 187.

124. R. A. Jishi, L. Venkataraman, M. S. Dresselhaus, and G. Dresselhaus, *Chem. Phys. Lett.*, 1993, **209**, 77.

125. G. Chen, G. U. Sumanasekera, B. K. Pradhan, R. Gupta, P. C. Eklund, M. J. Bronikowski, and R. E. Smalley, *J. Nanosci. Nanotechnol.*, 2002, **2**, 621.

126. M. A. Pimenta, A. Marucci, S. A. Empedocles, M. G. Bawendi, E. B. Hanlon, A. M. Rao, P. C. Eklund, R. E. Smalley, G. Dresselhaus, and M. S. Dresselhaus, *Phys. Rev. B.*, 1998, **58**, R16016.

127. S. D. M. Brown, P. Corio, M. S. Dresselhaus, M. A. Pimenta, and K. Kneipp, *Phys. Rev. B.*, 2000, **61**, R5137.

128. A. Jorio, A. G. Souza Filho, G. Dresselhaus, M. S. Dresselhaus, A. K. Swan, M. S. Unlu, B. B. Goldberg, M. A. Pimenta, J. H. Hafner, C. M. Lieber, and R. Saito, *Phys. Rev. B.*, 2002, **65**, 155412.

129. X. Zhao, Y. Ando, L. C. Qin, H. Kataura, Y. Maniwa, and R. Saito, *Chem. Phys. Lett.*, 2002, **361**, 196.

130. S. Bandow, G. Chen, G. U. Sumanasekera, R. Gupta, M. Yudasaka, S. Iijima, and P. C. Eklund, *Phys. Rev. B.*, 2002, **66**, 075416.

131. N. R. Raravikar, P. Keblinski, A. M. Rao, M. S. Dresselhaus, L. S. Schadler, and P. M. Ajayan, *Phys. Rev. B.*, 2002, **66**, 235424.

132. S. Bandow, S. Asaka, Y. Saito, A. M. Rao, L. Grigorian, E. Richter, and P. C. Eklund, *Phys. Rev. Lett.*, 1998, **80**, 3779.

133. A. Hagen and T. Hertel, *Nano Lett.*, 2003, **3**, 383.

134. O. Jost, A. A. Gorbunov, W. Pompe, T. Pichler, R. Friedlein, M. Knupfer, M. Reibold, H. D. Bauer, L. Dunsch, M. S. Golden, and J. Fink, *Appl. Phys. Lett.*, 1999, **75**, 2217.

135. T. Pichler, M. Knupfer, M. S. Golden, J. Fink, A. Rinzler, and R. E. Smalley, *Phys. Rev. Lett.*, 1998, **80**, 4729.
136. X. Wan, J. Dong, and D. Y. Xing, *Phys. Rev. B.*, 1998, **58**, 6756.
137. R. Saito, G. Dresselhaus, and M. S. Dresselhaus, *Phys. Rev. B.*, 2000, **61**, 2981.
138. S. Kazaoui, N. Minami, R. Jacquemin, H. Kataura, and Y. Achiba, *Phys. Rev. B.*, 1999, **60**, 13 339.
139. M. J. O'Connell, S. M. Bachilo, C. B. Huffman, V. C. Moore, M. S. Strano, E. H. Haroz, K. L. Rialon, P. J. Boul, W. H. Noon, C. Kittrell, J. Ma, R. H. Hauge, R. Bruce Weisman, and R. E. Smalley, *Science*, 2002, **297**, 593.
140. J. Lefebvre, Y. Homma, and P. Finnie, *Phys. Rev. Lett.*, 2003, **90**, 217401.
141. C. T. White and T. N. Todorov, *Nature*, 1998, **393**, 240.
142. T. Ando, H. Matsumura, and T. Nakanishi, *Physica B*, 2002, **323**, 44.
143. S. Frank, P. Poncharal, Z. L. WAng, and W. A. de Heer, *Science*, 1998, **280**, 1744.
144. P. G. Collins, K. Bradley, M. Ishigami, and A. Zettl, *Science*, 2000, **287**, 1801.
145. S. A. Curran, P. M. Ajayan, W. J. Blau, D. L. Carroll, J. N. Coleman, A. B. Dalton, A. P. Davey, A. Drury, B. McCarthy, S. Maier, and A. Strevens, *Adv. Mater.*, 1998, **10**, 1091.
146. S. Zhang, M. Xia, S. Zhao, T. Xu, and E. Zhang, *Phys. Rev. B.*, 2003, **68**, 075415.
147. A. Mizel, L. X. Benedict, M. L. Cohen, S. G. Louie, A. Zettl, N. K. Budraa, and W. P. Beyermann, *Phys. Rev. B.*, 1999, **60**, 3264.
148. J. Hone, B. Batlogg, Z. Benes, A. T. Johnson, and J. E. Fischer, *Science*, 2000, **289**, 1730.
149. D. J. Yang, Q. Zhang, G. Chen, S. F. Yoon, J. Ahn, S. G. Wang, Q. Zhou, Q. Wang, and J. Q. Li, *Phys. Rev. B.*, 2002, **66**, 165440.
150. J. Hone, M. Whitney, C. Piskoti, and A. Zettl, *Phys. Rev. B.*, 1999, **59**, R2514.
151. N. Bendiab, R. Almairac, J. L. Sauvajol, and S. Rols, *J. Appl. Phys.*, 2003, **93**, 1769.
152. J. T. Drotar, B. Q. Wei, Y. P. Zhao, G. Ramanath, P. M. Ajayan, T. M. Lu, and G. C. Wang, *Phys. Rev. B.*, 2001, **64**, 125417.
153. G. Xu, Z. c. Feng, Z. Popovic, J. y. Lin, and J. J. Vittal, *Adv. Mater.*, 2001, **13**, 264.
154. S. Iijima, *Nature*, 1991, **354**, 56.
155. L. Jin, C. Bower, and O. Zhou, *Appl. Phys. Lett.*, 1998, **73**, 1197.
156. D. Reznik, C. H. Olk, D. A. Neumann, and J. R. D. Copley, *Phys. Rev. B.*, 1995, **52**, 116.
157. C. H. Kiang, M. Endo, P. M. Ajayan, G. Dresselhaus, and M. S. Dresselhaus, *Phys. Rev. Lett.*, 1998, **81**, 1869.
158. Y. Maniwa, R. Fujiwara, H. Kira, H. Tou, E. Nishibori, M. Takata, M. Sakata, A. Fujiwara, X. Zhao, S. Iijima, and Y. Ando, *Phys. Rev. B.*, 2001, **64**, 073105.
159. D. H. Robertson, D. W. Brenner, and J. W. Mintmire, *Phys. Rev. Lett.*, 1992, **45**, 12592.
160. B. I. Yakobson, C. J. Brabec, and J. Bernholc, *Phys. Rev. Lett.*, 1996, **76**, 2511.
161. B. I. Yakobson and P. Avouris, in 'Carbon nanotubes', eds. M. S. Dresselhaus, G. Dresselhaus, and P. Avouris, Springer-Verlag, Berlin Heidelberg, 2001, Vol. 80.
162. A. Krishnan, E. Dujardin, T. W. Ebbesen, P. N. Yianilos, and M. M. J. Treacy, *Phys. Rev. B.*, 1998, **58**, 14013.
163. M. M. J. Treacy, T. W. Ebbesen, and J. M. Gibson, *Nature*, 1996, **381**, 678.
164. M. F. Yu, B. S. Files, S. Arepalli, and R. S. Ruoff, *Phys. Rev. Lett.*, 2000, **84**, 5552.
165. M. F. Yu, O. Lourie, M. J. Dyer, K. Moloni, T. F. Kelly, and R. S. Ruoff, *Science*, 2000, **287**, 637.
166. J. Zang, A. Treibergs, Y. Han, and F. Liu, *Phys. Rev. Lett.*, 2004, **92**, 105501.
167. J. Cumings and A. Zettl, *Science*, 2000, **289**, 602.
168. M. J. Lopez, A. Rubio, J. A. Alonso, S. Lefrant, K. Metenier, and S. Bonnamy, *Phys. Rev. Lett.*, 2002, **89**, 255501.
169. Y. Chen, L. Guo, S. Patel, and D. T. Shaw, *J. Mater. Sci.*, 2000, **35**, 5517.
170. H. Garmestani, M. S. Al-Haik, K. Dahmen, R. Tannenbaum, D. Li, S. S. Sablin, and M. Y. Hussaini, *Adv. Mater.*, 2003, **15**, 1918.
171. J. Tang, B. Gao, H. Geng, O. D. Velev, L. C. Qin, and O. Zhou, *Adv. Mater.*, 2003, **15**, 1352.
172. B. Vigolo, A. Penicaud, C. Coulon, C. Sauder, R. Pailler, C. Journet, P. Bernier, and P. Poulin, *Science*, 2000, **290**, 1331.
173. A. B. Dalton, S. Collins, E. Munoz, J. M. Razal, V. H. Ebron, J. P. Ferraris, J. N. Coleman, B. G. Kim, and R. H. Baughman, *Nature*, 2003, **423**, 703.
174. K. Jiang, Q. Li, and S. Fan, *Nature*, 2002, **419**, 801.
175. T. Kimura, H. Ago, M. Tobita, S. Ohshima, M. Kyotani, and M. Yumura, *Adv. Mater.*, 2002, **14**, 1380.
176. S. C. Tsang, Y. K. Chen, P. J. F. Harris, and M. L. H. Green, *Nature*, 1994, **372**, 159.
177. D. Ugarte, A. Chatelain, and W. A. de Heer, *Science*, 1996, **274**, 1897.
178. Z. Mao and S. B. Sinnott, *Phys. Rev. Lett.*, 2002, **89**, 278301.
179. Y. K. Chen, C. J. Cook, M. L. H. Green, P. J. F. Harris, R. Heesom, M. Humphries, J. Sloan, S. C. Tsang, and J. F. C. Turner, *J. Mater. Chem.*, 1997, **7**, 545.
180. Y. Gogotsi, J. A. Libera, A. G. Yazicioglu, and C. M. Megaridis, *Appl. Phys. Lett.*, 2001, **79**, 1021.
181. R. R. Meyer, J. Sloan, R. E. Dunin-Borkowski, A. I. Kirkland, M. C. Novotny, S. R. Bailey, J. L. Hutchison, and M. L. H. Green, *Science*, 2000, **289**, 1324.

182. Y. P. Sun, W. Huang, Y. Lin, K. Fu, A. Kitaygorodskiy, L. A. Riddle, J. Y. Yu, and D. L. Carroll, *Chem. Mater.*, 2001, **12**, 2864.

183. Y. Lin, A. M. Rao, B. Sadanadan, E. A. Kenik, and Y. P. Sun, *J. Phys. Chem. B*, 2002, **106**, 1294.

184. D. E. Hill, Y. Lin, A. M. Rao, L. F. Allard, and Y. P. Sun, *Macromolecules*, 2002, **35**, 9466.

185. Y. Chen, R. C. Haddon, S. Fang, A. M. Rao, P. C. Eklund, W. H. Lee, E. C. Dickey, E. A. Grulke, J. C. Pendergrass, A. Chavan, B. E. Haley, and R. E. Smalley, *J. Mater. Res.*, 1998, **13**, 2423.

186. D. Baskaran, J. W. Mays, and M. S. Bratcher, *Angew. Chem., Int. Ed. Engl.*, 2004, **43**, 2138.

187. F. J. Gomez, R. J. Chen, D. Wang, R. M. Waymouth, and H. Dai, *Chem. Commun.*, 2003, 190.

188. S. Qin, D. Qin, W. T. Ford, D. E. Resasco, and J. E. Herrera, *J. Am. Chem. Soc.*, 2004, **126**, 170.

189. Z. Yao, N. Braidy, G. A. Botton, and A. Adronov, *J. Am. Chem. Soc.*, 2003, **125**, 16015.

190. H. Kong, C. Gao, and D. Yan, *J. Am. Chem. Soc.*, 2004, **126**, 412.

191. R. K. Saini, I. W. Chiang, H. Peng, R. E. Smalley, W. E. Billups, R. H. Hauge, and J. L. Margrave, *J. Am. Chem. Soc.*, 2003, **125**, 3617.

192. V. Georgakilas, K. Kordatos, M. Prato, D. M. Guldi, M. Holzinger, and A. Hirsch, *J. Am. Chem. Soc.*, 2002, **124**, 2002.

193. M. Holzinger, O. Vostrowsky, A. Hirsch, F. Hennrich, M. Kappes, R. Weiss, and F. Jellen, *Angew. Chem., Int. Ed. Engl.*, 2001, **40**, 4002.

194. R. J. Chen, Y. Zhang, D. Wang, and H. Dai, *J. Am. Chem. Soc.*, 2001, **123**, 3838.

195. S. Pekker, J. P. Salvetat, E. Jakab, J. M. Bonard, and L. Forro, *J. Phys. Chem. B*, 2001, **105**, 7938.

196. J. L. Bahr and J. M. Tour, *Chem. Mater.*, 2001, **13**, 3823.

197. C. A. Dyke and J. M. Tour, *Nano Lett.*, 2003, **3**, 1215.

198. M. J. O'Connell, P. J. Boul, L. M. Ericson, C. B. Huffman, Y. Wang, E. H. Haroz, C. Kuper, J. M. Tour, K. D. Ausman, and R. E. Smalley, *Chem. Phys. Lett.*, 2001, **342**, 265.

199. W. Zhao, C. Song, and P. E. Pehrsson, *J. Am. Chem. Soc.*, 2002, **124**, 12418.

200. Y. P. Sun, K. Fu, Y. Lin, and W. Huang, *Acc. Chem. Res.*, 2002, **35**, 1096.

201. A. Kuznetsova, I. Popova, J. T. Yates, Jr, M. J. Bronikowski, C. B. Huffman, J. Liu, R. E. Smalley, H. H. Hwu, and J. G. Chen, *J. Am. Chem. Soc.*, 2001, **123**, 10699.

202. H. Hu, P. Bhowmik, B. Zhao, M. A. Hamon, M. E. Itkis, and R. C. Haddon, *Chem. Phys. Lett.*, 2001, **345**, 25.

203. D. B. Mawhinney, V. Naumenko, A. Kuznetsova, and J. T. Yates Jr, *J. Am. Chem. Soc.*, 2000, **122**, 2383.

204. D. B. Mawhinney, V. Naumenko, A. Kuznetsova, J. T. Yates Jr, J. Liu, and R. E. Smalley, *Chem. Phys. Lett.*, 2000, **324**, 213.

205. Y. Qin, L. Liu, J. Shi, W. Wu, J. Zhang, Z. X. Guo, Y. Li, and D. Zhu, *Chem. Mater.*, 2003, **15**, 3256.

206. D. Chattopadhyay, I. Galeska, and F. Papadimitrakopoulos, *J. Am. Chem. Soc.*, 2003, **125**, 3370.

207. Gdl. Torre, W. Blau, and T. Torres, *Nanotechnology*, 2003, **14**, 765.

208. S. Banerjee and S. S. Wong, *J. Am. Chem. Soc.*, 2002, **124**, 8940.

209. S. Banerjee, M. G. C. Kahn, and S. S. Wong, *Chem. – Eur. J.*, 2003, **9**, 1898.

210. M. G. C. Kahn, S. Banerjee, and S. S. Wong, *Nano Lett.*, 2002, **2**, 1215.

211. W. Huang, S. Fernando, L. F. Allard, and Y. P. Sun, *Nano Lett.*, 2003, **3**, 565.

212. J. E. Riggs, Z. Guo, D. L. Carroll, and Y. P. Sun, *J. Am. Chem. Soc.*, 2000, **122**, 5879.

213. J. E. Riggs, D. B. Walker, D. L. Carroll, and Y. P. Sun, *J. Phys. Chem. B*, 2000, **104**, 7071.

214. R. Czerw, Z. Guo, P. M. Ajayan, Y. P. Sun, and D. Carroll, *Nano Lett.*, 2001, **1**, 423.

215. J. L. Stevens, A. Y. Huang, H. Peng, I. W. Chiang, V. N. Khabashesku, and J. L. Margrave, *Nano Lett.*, 2003, **3**, 331.

216. W. Huang, S. Taylor, K. Fu, Y. Lin, D. Zhang, T. W. Hanks, A. M. Rao, and Y. Sun, *Nano Lett.*, 2002, **2**, 311.

217. K. A. Williams, P. T. M. Veenhuizen, B. G. de la Torre, R. Eritja, and C. Dekker, *Nature*, 2002, **420**, 761.

218. K. Fu, W. Huang, Y. Lin, L. A. Riddle, D. L. Carroll, and Y. P. Sun, *Nano Lett.*, 2001, **1**, 439.

219. H. Kong, C. Gao, and D. Yan, *Macromolecules*, 2004, **37**, 4022.

220. S. Qin, D. Qin, W. T. Ford, D. E. Resasco, and J. E. Herrera, *Macromolecules*, 2004, **37**, 752.

221. K. S. Coleman, S. R. Bailey, S. Fogden, and M. L. H. Green, *J. Am. Chem. Soc.*, 2003, **125**, 8722.

222. V. Georgakilas, N. Tagmatarchis, D. Pantarotto, A. Bianco, J. P. Briand, and M. Prato, *Chem. Commun.*, 2002, 3050.

223. F. Liang, A. K. Sadana, A. Peera, J. Chattopadhyay, Z. Gu, R. H. Hauge, and E. W. Billups, *Nano Lett.*, 2004, **4**, 1257.

224. G. Viswanathan, N. Chakrapani, H. Yang, B. Wei, H. Chung, K. Cho, C. Y. Ryu, and P. M. Ajayan, *J. Am. Chem. Soc.*, 2003, **125**, 9258.

225. P. J. Boul, J. Liu, E. T. Mickelson, C. B. Huffman, L. M. Ericson, I. W. Chiang, K. A. Smith, D. T. Colbert, R. H. Hauge, J. L. Margrave, and R. E. Smalley, *Chem. Phys. Lett.*, 1999, **310**, 367.

226. M. Holzinger, J. Abraham, P. Whelan, R. Graupner, L. Ley, F. Hennrich, M. Kappes, and A. Hirsch, *J. Am. Chem. Soc.*, 2003, **125**, 8566.

227. S. Banerjee and S. S. Wong, *J. Am. Chem. Soc.*, 2004, **126**, 2073.
228. C. A. Dyke and J. M. Tour, *J. Am. Chem. Soc.*, 2003, **125**, 1156.
229. J. L. Bahr, J. Yang, D. V. Kosynkin, M. J. Bronikowski, R. E. Smalley, and J. M. Tour, *J. Am. Chem. Soc.*, 2001, **123**, 6536.
230. H. Peng, P. Reverdy, V. N. Khabashesku, and J. L. Margrave, *Chem. Commun.*, 2003, 362.
231. M. S. P. Shaffer and K. Koziol, *Chem. Commun.*, 2002, 2074.
232. H. Peng, L. B. Alemany, J. L. Margrave, and V. N. Khabashesku, *J. Am. Chem. Soc.*, 2003, **125**, 15174.
233. P. Umek, J. W. Seo, K. Hernadi, A. Mrzel, P. Pechy, D. D. Mihailovic, and L. Forro, *Chem. Mater.*, 2003, **15**, 4751.
234. S. Qin, D. Qin, W. T. Ford, J. E. Herrera, D. E. Resasco, S. M. Bachilo, and R. B. Weisman, *Macromolecules*, 2004, **37**, 3965.
235. A. Star, J. F. Stoddart, D. Steuerman, M. Diehl, A. Boukai, E. W. Wong, X. Yang, S. W. Chung, H. Choi, and J. R. Health, *Angew. Chem., Int. Ed. Engl.*, 2001, **40**, 1721.
236. C. Kim, Y. S. Choi, S. M. Lee, J. T. Park, B. Kim, and Y. H. Lee, *J. Am. Chem. Soc.*, 2002, **124**, 9906.
237. V. Barone, J. Heyd, and G. E. Scuseria, *Chem. Phys. Lett.*, 2004, **389**, 289.
238. P. Kondratyuk and J. T. Yates Jr, *Chem. Phys. Lett.*, 2004, **383**, 314.
239. C. Liu, Y. Y. Fan, M. Liu, H. T. Cong, H. M. Cheng, and M. S. Dresselhaus, *Science*, 1999, **286**, 1127.
240. G. U. Sumanasekera, B. K. Pradhan, H. E. Romero, K. W. Adu, and P. C. Eklund, *Phys. Rev. Lett.*, 2002, **89**, 166801.
241. A. B. Dalton, B. McCarthy, J. N. Coleman, Mih. Panhuis, D. L. Carroll, R. Czerw, W. J. Blau, and H. J. Byrne, *Mater. Res. Soc. Symp. Proc.*, 2001, **675**, w4.5.1.
242. J. Chen, H. Liu, W. A. Weimer, M. D. Halls, D. H. Waldeck, and G. C. Walker, *J. Am. Chem. Soc.*, 2002, **124**, 9034.
243. M. F. Islam, E. Rojas, D. M. Bergey, A. T. Johnson, and A. G. Yodh, *Nano Lett.*, 2003, **3**, 269.
244. M. Shim, N. W. S. Kam, R. J. Chen, Y. Li, and H. Dai, *Nano Lett.*, 2002, **2**, 285.
245. R. Bandyopadhyaya, E. Nativ-Roth, O. Regev, and R. Yerushalmi-Rozen, *Nano Lett.*, 2002, **2**, 25.
246. J. B. Kim, M. L. Bruening, and G. L. Baker, *J. Am. Chem. Soc.*, 2000, **122**, 7616.
247. P. Petrov, F. Stassin, C. Pagnoulle, and R. Jerome, *Chem. Commun.*, 2003, 2904.
248. G. R. Dieckmann, A. B. Dalton, P. A. Johnson, J. Razal, J. Chen, G. M. Giordano, E. Munoz, I. H. Musselman, R. H. Baughman, and R. K. Draper, *J. Am. Chem. Soc.*, 2003, **125**, 1770.
249. H. Li, B. Zhou, Y. Lin, L. Gu, W. Wang, S. Fernando, S. Kumar, L. F. Allard, and Y. P. Sun, *J. Am. Chem. Soc.*, 2004, **126**, 1014.

Acknowledgments

I would like to thank Prof. David A. Atwood, Department of Chemistry, University of Kentucky for the invitation to write this article. I thank the U.S. Army for a grant in support of this work (DAAD19-01-2-002). I express my sincere gratitude to Prof. Jimmy W Mays and Mrs. Patricia Boyd for their constant support. I wish to deeply thank Mr. Tom Malmgren (UTK, US), Drs. C. Ramesh (NCL, India) and W. U. David (ORNL, US) for their help during the preparation of this article. I am thankful to my wife, Mrs. B. Meenakshi Sundari, and my kids for allowing me to undertake this task during the summer holidays.

Inorganic Ring Systems

Ionel Haiduc
Universitatea ‘‘Babes-Bolyai’’, Cluj-Napoca, Romania

1 Introduction 1
2 Defining the Inorganic Ring Concept 1
3 Types of Inorganic Cyclic Structures 3
4 Combining Building Blocks for Inorganic Ring Formation: A Chemical ‘Lego’ 15
5 References 20

1 INTRODUCTION

Cyclic compounds played an important role in organic chemistry from its very beginning. Both rings with carbon-only skeletons (cyclic hydrocarbons and their derivatives) and with heteroatom skeletons (an endless diversity of heterocycles) have been known for a long time. The discovery of the cyclic structure of benzene is a landmark in the history of chemistry, and it has been followed by a rapid progress in this branch of science, even in the nineteenth century, when elemental analysis and the chemist’s intuition and imagination were the most important research tools.

The development of inorganic chemistry followed a different path. Earlier attempts to apply the structural principles of organic chemistry to elements other than carbon almost ceased for a while after Werner introduced the coordination chemistry. It should be pointed out, however, that these early attempts led to correct assignments of cyclic structures to compounds such as metaphosphates,[1,2] cyclophosphazenes (‘phosphonitrile chlorides’),[3] and cyclosiloxanes.[4] The chemistry of inorganic rings continued its evolution in fragments, as chapters of the chemistry of individual elements or groups of related elements, with little emphasis on the ring concept. The discovery of borazine (initially called ‘borazole’ or ‘inorganic benzene’)[5] is another landmark in the development of modern chemistry and contributed much to focusing some attention upon inorganic cyclic structures. This era is reflected in some splendid monographs covering inorganic rings within the chemistries of sulfur,[6,7] phosphorus[8,9] and boron.[10]

The integrated approach to the chemistry of inorganic rings as *a self-consistent field of inorganic chemistry* across the periodic table has been promoted after 1960 by a series of other monographs.[11–18]

Now, the chemistry of inorganic ring compounds as an independent branch of chemistry is legitimized by the biannual International Symposia on Inorganic Ring Systems (IRIS).

The inorganic rings raise interesting questions of structure and bonding and quite often they challenge the theory. Thus, a subject of continuous interest is the stability and the possible aromaticity of inorganic rings.[19,20] The applicative interest for inorganic rings is related to their use as precursors for thermally stable polymers, ceramics, semiconductors, catalyst supports, or various other advanced materials.[21]

The nomenclature rules for inorganic rings are discussed in some publications.[22]

2 DEFINING THE INORGANIC RING CONCEPT

The organic cyclic structures are molecular constructions in which carbon atoms and possibly additional noncarbon atoms (heteroatoms) connected through covalent bonds form a closed ring. Consequently, inorganic rings could be simply defined as similar carbon-free molecular species. In fact, it is rather difficult to draw a separation line between organic and inorganic rings. Thus, in a five-membered ring series, the transition from cyclopentadiene (a purely organic C_5 homocycle) to cyclopentazadiene or pentazole (a purely inorganic N_5 ring)[23] occurs through the intermediacy of a series of organic heterocycles (pyrrole, pyrazole, imidazole, triazole, and tetrazole) (Scheme 1), all containing carbon and nitrogen heteroatoms.

Similarly, organic-inorganic ring transition series can be written as connecting a symmetric organic C_3N_3 heterocycle (triazine) with purely inorganic rings, for example, cyclotriphosphazene, P_3N_3, and cyclotrithiazene, S_3N_3 (Scheme 2).

The question is: which of these rings are ‘organic’ and which are ‘inorganic’? Sometimes organic chemists include pentazole in the family of heterocycles and refer to such species as ‘heteroatom-only’ rings. On the other hand, there is a tendency among inorganic chemists to consider a ring as ‘inorganic’ if the majority of ring atoms are different from carbon. If these two extremes are accepted, then it becomes impossible to draw a line between organic and inorganic rings. In a pragmatic approach, inorganic rings should be defined as ‘*carbon-free*’ rings, leaving to organic chemistry all rings that contain at least one carbon atom. Such a solution is adopted in this article.

Inorganic chemistry displays a rich diversity of ring structures, not limited to cyclic molecules formed through covalent bonds. Inorganic ring structures can be built by combining a number of various *building blocks* connected through covalent bonds (*synthons*) or by assembling supramolecular structures from molecular units (*tectons*) connected through noncovalent intermolecular forces (dative, secondary, ionic or hydrogen bonds).

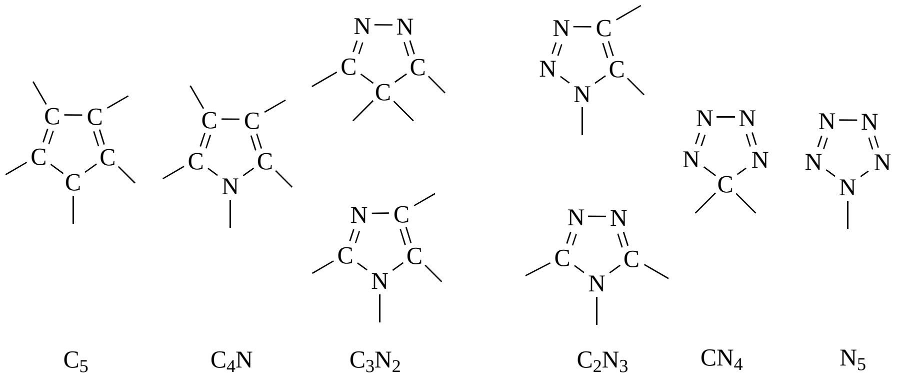

Scheme 1 The transition from an organic homocycle (cyclopentadiene) to an inorganic homocycle (pentazole) through intermediate heterocycles

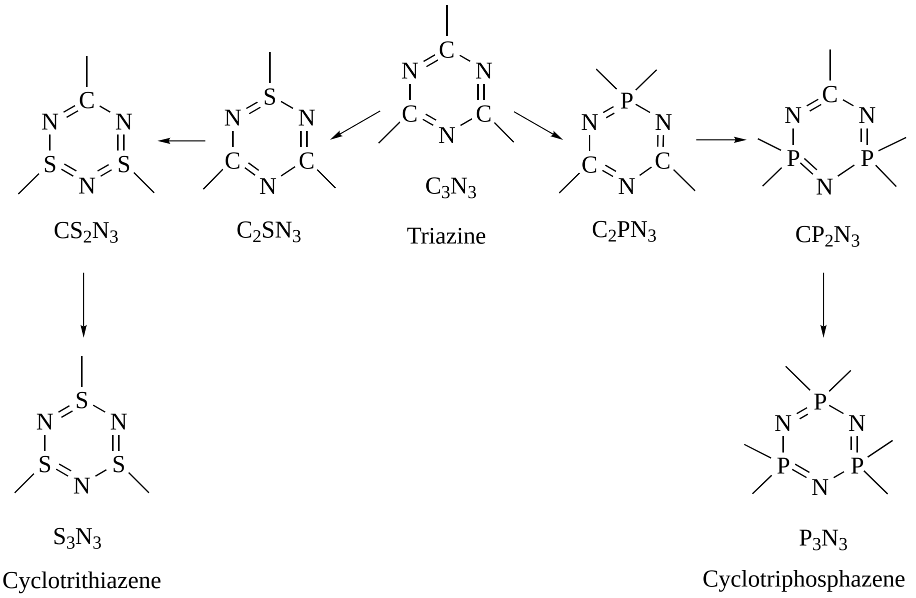

Scheme 2 The transition from organic heterocycles to inorganic analogs

The term *synthon* is more familiar to organic chemists and describes fragments from which various molecules can be built by synthetic procedures. Sometimes the term was also used to describe '*structural units within supermolecules which can be formed and/or assembled by known or conceivable synthetic operations involving intermolecular interactions*'.[24] To avoid confusion, the term *tecton* was introduced to describe the molecular units of supramolecular structures assembled through noncovalent forces. Thus, the *tecton* has been defined as '*any molecule whose interactions are dominated by particular associative forces that induce self-assembly of an organized network*'.[25,26] Here, we will use the term *synthon* for the fragments of covalent molecules and the term *tecton* for the molecular building blocks of supermolecules self-assembled through noncovalent interactions.

Since reference was made to supramolecular chemistry, perhaps it is useful to remember some definitions. Supramolecular chemistry is '*the chemistry of molecular assemblies and of the intermolecular bond*'. It is '*the chemistry beyond the molecule*' and deals with '*organized entities of higher complexity that result from the association of two or more chemical species held together by intermolecular forces*'.[27,28]

There are two types of subjects in supramolecular chemistry: (a) the *supramolecular assemblies* or systems, also called supramolecular arrays, that is, '*polymolecular entities that result from the spontaneous association of a large undefined number of components*', and (b) *supermolecules*, that is, '*well-defined discrete oligomolecular species that result from the intermolecular association of a few components*'.[29]

3 TYPES OF INORGANIC CYCLIC STRUCTURES

In the organic rings (homo- and heterocycles), the carbon atoms are constantly tetravalent and display sp^3 (tetrahedral), sp^2 (trigonal planar), or sp (linear) hybridizations with the corresponding bonding geometries. The most common heteroatoms are oxygen, sulfur, and nitrogen. Inorganic chemistry operates with all elements of the periodic table and consequently it has at its disposal a broader range of possibilities in terms of bond types, hybridizations of atomic orbitals, coordination geometries, and oxidation states within the building blocks (synthons). Thus, a much broader variety of structures can be expected for inorganic cyclic structures.

3.1 Covalent Rings (Homo- and Heterocycles)

The closest similarity between organic and inorganic cyclic structures is displayed by the *covalent rings.* These include both homo- and heterocycles. Homocycles contain identical atoms; in heterocycles the constituent atoms are different. Covalent inorganic rings are basically formed by nonmetals and Main Group metals, but transition metals are not excluded. To participate in ring formation, an atom should be able to form at least two covalent bonds, that is, to be at least a divalent element. This condition is satisfied by numerous elements of the periodic table and therefore a great *variety of compositions* can be expected.

The inorganic rings formed through covalent bonds are the real counterparts of organic cyclic molecules and illustrate the ability of other elements to imitate carbon. Although characteristic of elements close to carbon in the periodic table (in particular, boron, silicon, germanium, phosphorus, arsenic, antimony, sulfur, and selenium, alone or in association with oxygen, nitrogen, or sulfur), this ability is not restricted to nonmetals and covalent rings containing metals, for example, aluminum, gallium, tin, or lead, as well as transition metals are also well known.

There are two types of covalent inorganic rings:

1. *homocyclic ring systems* – consisting of catenated identical atoms, and
2. *heterocyclic ring systems* – containing different elements.

Inorganic homocycles containing three, four, five, six, seven, eight, or more identical atoms are known for various elements (Scheme 3).

Table 1 Inorganic (carbon-free) homocycles

–	Si_3	Ge_3	Sn_3	N_3	P_3	As_3	Sb_3	–	–	–
–	Si_4	Ge_4	Sn_4	N_4	P_4	As_4	Sb_4	–	–	–
B_4	Si_5	Ge_5	Sn_5	N_5	P_5	As_5	Sb_5	–	–	–
B_6	Si_6	Ge_6	Sn_6		P_6	As_6	Sb_6	S_6	Se_6	Te_6
								S_7	Se_7	–
								S_8	Se_8	Te_8
								S_n ($n > 8$)	Se_{12}	

A probably incomplete list includes the homocyclic rings E_n shown in (Table 1).

The homocycles are usually ‘saturated’ species, but occasionally double bonds may occur in silicon-based three-, four-, and five-membered rings with Si=Si double bonds[30,31] or in the cyclotrigallane anion $[Ga_3R_3]^{2-}$ (R = 2,6-$Mes_2C_6H_3$)[32] (Scheme 4).

The ability of chemical elements to form homocyclic rings depends upon their ability to concatenate. The propensity for catenation of chemical elements varies greatly and no other nonmetal can fully imitate carbon. Inorganic homoatomic rings usually need to be protected by organic groups and – unlike hydrocarbons – the kinetic stability of catenated hydrides of elements other than carbon is low. Therefore, cyclic polysilanes $(SiR_2)_n$, polygermanes $(GeR_2)_n$, and polystannanes $(SnR_2)_n$, are much more stable with R = alkyl or aryl instead of R = H.

Heterocycles can be formally generated in three different ways (Scheme 5):

1. by *insertion* of one or more heteroatoms in a parent homocycle and maintaining some E–E bonds (between identical atoms) to form rings of the type E_mY_n (m and n differing);
2. by *regular alternation* of two different elements E and Y that is, by combining a discrete number of *identical EY*

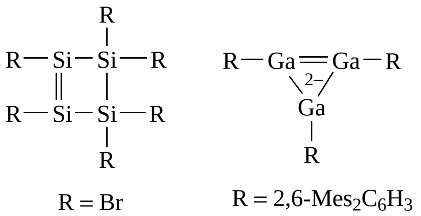

Scheme 4 Unsaturated homocyclic rings

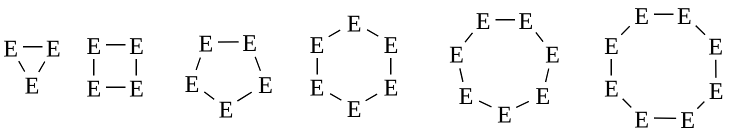

Scheme 3 Homocyclic systems

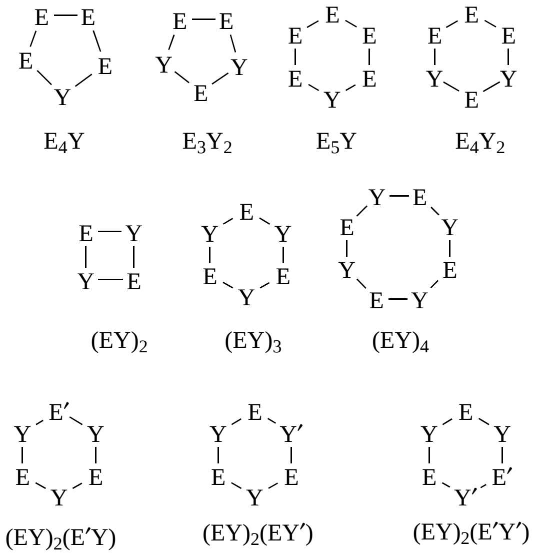

Scheme 5 Various types of inorganic heterocycles

repeating units to form rings of the type $(EY)_n$ ($n = 2, 3, 4, 5, 6 \ldots$);

3. by combining a number of *different repeating units* EY and E’Y or EY’, to form rings of the type $(EY)_m(E'Y)_n$ or $(EY)_m(EY')_n$ or even $(EY)_m(E'Y')_n$.

Usually, E and Y are elements of different electronegativities and the best combinations are obtained when E is less electronegative (i.e. more electropositive) than carbon (i.e. B, Al, Si, Ge, Sn, Pb, P, As, Sb, Se, Te) in association with an element Y that is more electronegative than carbon (O, N, S).

Inorganic rings can be treated as chemical graphs and an enumeration of all possible structures can be deduced using this approach.[33]

Almost all these cyclic graphs have correspondents in real inorganic covalent rings. The rarest are heterocycles containing bonds between identical atoms avoiding a regular alternation, but the sulfur–selenium pair offers beautiful examples (Scheme 6).[34,35]

There are several ways to combine rings into polycyclic and cage structures (e.g. spirocyclic systems and fused rings). These will not be discussed here. Theoretical speculations have been made about the possible existence of purely inorganic (carbon-free) fullerene-like polycyclic cages, for example, boron–nitrogen molecules[36–38] or silicon analogs.[39]

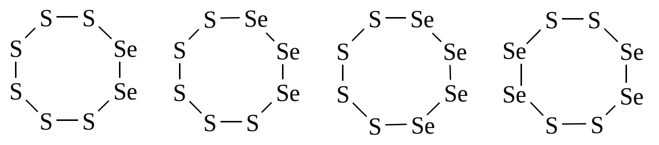

Scheme 6 Some mixed sulfur–selenium rings preserving bonds between identical atoms

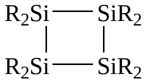

(1)

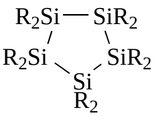

(2)

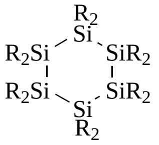

(3)

R = Me, Ph, etc.

3.1.1 Selected Homoatomic Inorganic Covalent Rings

Cyclosilanes. Cyclopolysilanes, (**1–3**) based upon silicon–silicon bond backbones, are known as stable compounds mainly as organosubstituted derivatives, $(SiR_2)_n$ but derivatives with R = H or Cl are also known.[40] The organocyclopolysilanes $(SiR_2)_n$ are usually prepared by dehalogenation of diorganodichlorosilanes, either with alkali metals (Wurtz coupling) or by electrochemical reduction. In most cases, the major product is the pentamer ($n = 5$) and/or hexamer ($n = 6$), but larger ring oligomers have been sometimes obtained, for example, with R = Me ($n = 9$, 1% yield; $n = 10–19$, 0.09–0.26% yield) in addition to the pentamer (12%), hexamer (59%), heptamer (3%) and octamer (1.8%). All members of the $(SiMe_2)_n$ series up to $n = 35$ have been separated by column chromatography and the members up to 19 silicon atoms have been isolated as individual compounds.[41] The nature of products formed depends greatly upon the solvent and the presence of complexing agents (e.g. crown ethers to solvate the alkali metal salt).[42]

The molecular structures of several cyclosilanes, for example, $(Me_2Si)_n$ ($n = 4$, 6 and 7)[43] and $(Ph_2Si)_n$ ($n = 4$, 5 and 6)[44] and also of the large ring compounds $(SiMe_2)_{13}$ (**4**) and $(SiMe_2)_{16}$ (**5**) have been established by single-crystal X-ray diffraction.[45]

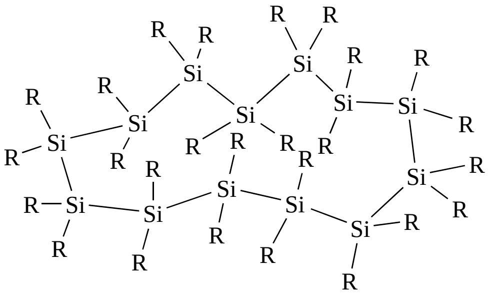

$(SiMe_2)_{13}$

(**4**)

In the case of $MePhSiCl_2$, the Wurtz coupling dehalogenation produces three fractions, containing low-molecular weight cyclics, intermediate molecular weight cyclic oligomers, and high polymeric materials.[46]

Anionic $[RSi]_4^{2-}$ (with R = Bu^t_2MeSi) has been reported recently and described as a sila analog of the cyclobutadiene dianion.[47]

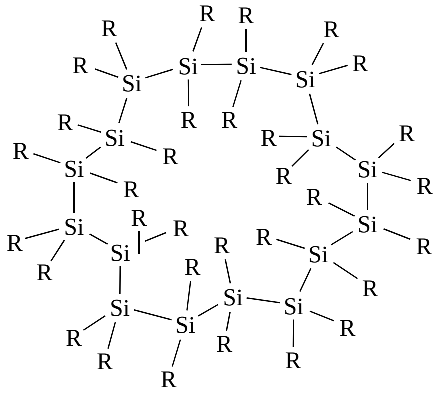

$(SiMe_2)_{16}$

(**5**)

Cyclogermanes. Cyclogermanes are prepared by methods similar to those used for polysilanes, for example, Wurtz dehalogenative coupling.[48] Cyclogermanes $(R_2Ge)_n$ with $n = 3$, 4, and 5 can be isolated.[49,50]

Cyclostannanes. Cyclostannanes, $(SnR_2)_n$, containing from 3 to 9 tin atoms,[51,52] are prepared from diorganotin dihalides with alkali metals (Wurtz coupling)[53] or from diorganotin hydrides by dehydrogenative coupling,[54] by coupling with diorganotin amides,[55] by electrochemical reduction of diorganotin dihalides,[56] or by reduction with samarium diiodide.[57] Cyclic polystannanes include dialkylstannanes $(R_2Sn)_n$ ($R = Et$, $n = 6–9$; $R = Cy$, $n = 5$; $R = Bu$, $n = 5$ and 6; $R = Bz$, $n = 4$ and 6)[58] and diarylstannanes, for example, $(Ph_2Sn)_6$.[59] Even three-membered ring cyclotristannanes (with bulky substituents) have been synthesized.[60]

Cyclophosphanes. Cyclophosphanes $(PR)_n$ ($n = 3–6$) (**6–8**) are well known with common organic substituents (alkyl, phenyl);[61] larger cyclic oligomers are stabilized only as transition metal complexes, for example, $[M_2(CO)_6(PMe)_9]$ (M = Cr, Mo, W) (**9**) and are formed in reactions involving ring expansion rearrangements.[62]

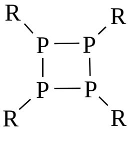

(**6**)

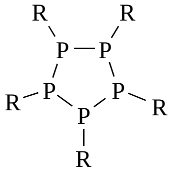

(**7**)

The cyclic P_5 anion can form ferrocene analog pi-complexes.[63]

Cycloarsanes and Cyclostibanes. Cyclopolyarsanes (**10**, **11**) of small and regular size, $(AsR)_n$ with $n = 3–6$, are well documented[64] and macrocyclic oligomers are formed in ring expansion reactions with metal carbonyls and stabilised as metal complexes. Thus, nine-membered rings $(AsR)_9$ (with R = Me or Ph) and ten-membered $(AsMe)_{10}$ (**12**) can be formed from the corresponding cyclic hexamers in reactions with chromium and molybdenum hexacarbonyls.[65]

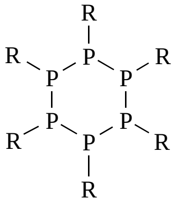

(**8**)

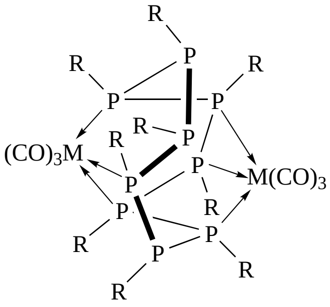

(**9**)

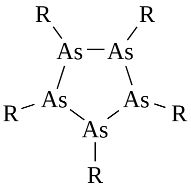

(**10**)

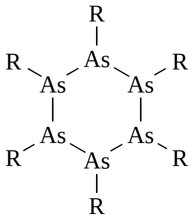

(**11**)

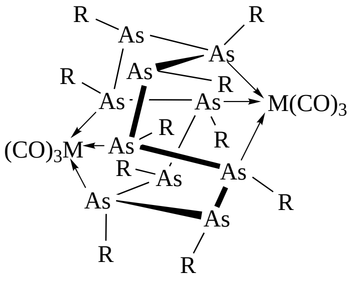

(**12**)

Related cyclostibanes and some cyclobismuthanes are well covered in the review literature.[66]

Cyclosulfanes (Elemental Sulfur Allotropes). Elemental sulfur displays a great propensity for catenation and polysulfur rings (cyclosulfanes) of various ring sizes (**13–22**) are known as allotropic forms of elemental sulfur.[67]

Currently all cyclic sulfur molecules S_n with $n = 6, 7, 8, 9, 10, 11, 12, 13, 14, 15, 18, 20, 25$ are known and single-crystal X-ray diffraction determinations of the molecular structure are available for S_6,[68] S_7,[69] S_8,[70] S_{10},[71] S_{11},[72] S_{12},[73] S_{13}, S_{14},[74] S_{18},[75] and S_{20}.[76] All these rings are puckered.

Most sulfur homocycles have been synthesized by reacting $(C_5H_5)_2TiS_5$ with appropriate open-chain polysulfur dichlorides (α, ω-dichloropolysulfanes); the various rings

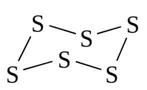

S_6

(13)

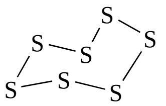

S_7

(14)

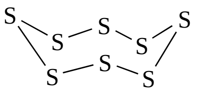

S_8

(15)

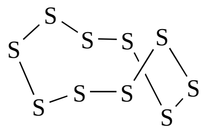

S_{10}

(16)

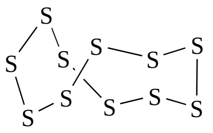

S_{11}

(17)

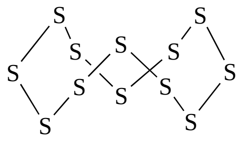

S_{12}

(18)

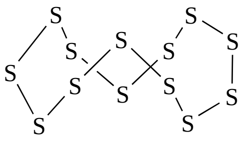

S_{13}

(19)

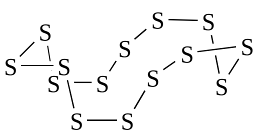

S_{14}

(20)

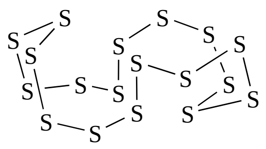

α–S_{18}

(21)

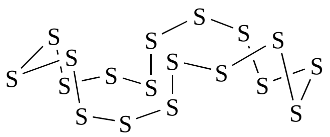

β–S_{18}

(22)

formed in a complex mixture can be separated with the aid of high-performance liquid chromatography.[77]

The eight-membered ring S_8 is the only thermodynamically stable form and all other rings undergo molecular rearrangements with formation of the octamer. Ring–ring and ring–chain thermal equilibria occur in sulfur melts, in variable concentrations.[78]

Similar, but less stable, selenium homocycles, as well as mixed sulfur–selenium related heterocycles formed by heteroatom replacement, are also well documented.[79] Cationic chalcogen homocycles are also known and have been reviewed.[80]

3.1.2 *Selected Heteroatomic Covalent Inorganic Rings*

Cycloborazanes, Cycloboroxanes, and Related Rings. In association with nitrogen, oxygen, sulphur, and selenium boron tends to form six-membered rings $(BY)_3$ ($Y = N$, O, S, Se), although some derivatives of the four- and eight-membered rings with the same synthons are known. Their chemistry has been reviewed.[81]

The boron–nitrogen rings (*see* ***Boron–Nitrogen Compounds***) are probably stabilized through some electron donation from nitrogen. Four-, six-, and eight-membered rings (**23–25**) consisting of RB-NR′ synthons have been described and some interconversions have been reported.[82]

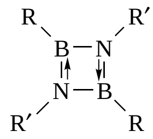

(23)

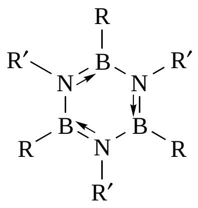

(24)

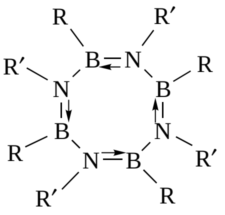

(25)

In the six-membered ring B_3N_3 of borazine, the electron delocalization leads to bond length equalization, but in the eight-membered ring the B–N bonds display differing bond lengths, which is reminiscent of the situation in the carbon isoelectronic rings (benzene and cyclooctatetraene).

The six-membered boron–oxygen ring, B_3O_3, is present intact as a building unit in numerous polymeric borates, which have been thoroughly reviewed in the Gmelin Handbook.[83] Organosubstituted cyclotriboroxanes (boroxines), $(RBO)_3$, are also well known.[84] Boron-sulfur[85] and boron-selenium[86] rings are also well documented.

Aluminum Heterocycles. A unique aluminum–nitrogen Al_3N_3 ring compound, $[MeAlN(2,6\text{-}Pr^i_2C_6H_3)]_3$, containing a planar Al_3N_3 heterocycle (**26,27**), can be regarded as a borazine analog.[87]

Most frequently, cubane or other aluminum–nitrogen cage supermolecules are formed through additional dative bonds (making the metal four-coordinate).[88]

Cyclosilazanes. The silicon–nitrogen pair displays a great tendency of ring formation and stable four-, six-,

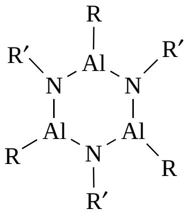
(**26**)

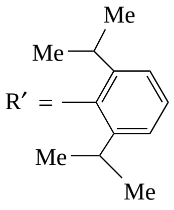
(**27**)

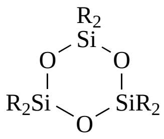
$(R_2SiO)_3$
(**31**)

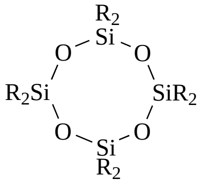
$(R_2SiO)_4$
(**32**)

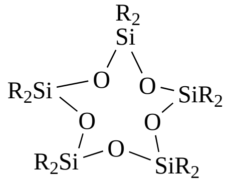
$(R_2SiO)_5$
(**33**)

and eight-membered rings are well known. Organocyclosilazanes can be readily obtained by ammonolysis of diorganodichlorosilanes, R_2SiCl_2, but the reaction produces only cyclotri- and cyclotetrasilazanes, $(R_2SiNH)_n$ ($n = 3$, 4).[89] Cyclodisilazanes are usually obtained by condensation or coupling reactions, with elimination of amines [from diorganodiaminosilanes, $R_2Si(NHR')_2$] or metal halides [from $R_2Si(NLiR')_2$ and R_2SiCl_2]. The best known are cyclodisilazanes (**28**), cyclotrisilazanes (**29**), and cyclotetrasilazanes (**30**).[90] Many have been structurally characterized, but we cite here only the methyl trimer $(Me_2SiNH)_3$ and tetramers $(Me_2SiNH)_4$ and $(Me_2SiNMe)_4$.[91,92] The ammonolysis of organotrichlorosilanes yields cage and polymeric (probably polycyclic) silazanes and one such structure (a SiN prismane $[Me_6Si_6(NH)_9]$) has been demonstrated by X-ray diffraction.[93]

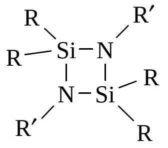
(**28**)

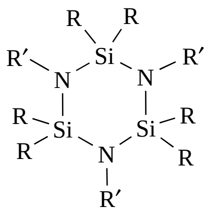
(**29**)

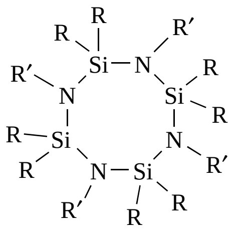
(**30**)

Silicon-phosphorus heterocyclic structures (rings, cages, polycyclic ladders) are also well investigated.[94]

Some germanium–nitrogen ring chemistry has been developed.[95]

Cyclosiloxanes and Cyclogermoxanes. Cyclosiloxanes (**31–35**) are among the most important inorganic rings. Organocyclosiloxanes $(R_2SiO)_n$ are formed in the hydrolysis of diorganodichlorosilanes. Catalytic molecular rearrangements of trimeric and tetrameric organocyclosiloxanes produce larger ring cyclosiloxanes. The most common and best studied are the poly(dimethylcyclosiloxanes), $(Me_2SiO)_n$, a family of compounds of great industrial importance as precursor of silicone materials (*see* ***Polysiloxanes & Polysilanes***).

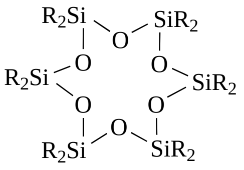
$(R_2SiO)_6$
(**34**)

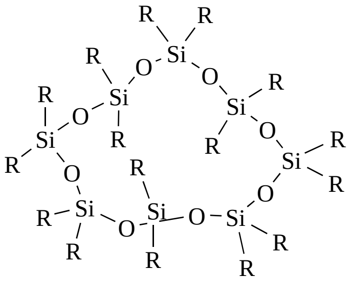
$(R_2SiO)_8$
(**35**)

R = Me

A careful study of the hydrolysis of H_2SiCl_2, $MeHSiCl_2$ and Me_2SiCl_2, using gas chromatography, mass spectrometry, and NMR spectroscopy, revealed that oligomeric cyclosiloxanes $(H_2SiO)_n$ (up to $n = 23$), $(MeHSiO)_n$ (up to $n = 19$) and $(Me_2SiO)_n$ (up to $n = 17$) can be detected in the hydrolysis product.[96] Rings containing from 5 to 8 Me_2SiO units have been separated from the hydrolysis product of Me_2SiCl_2 by traditional procedures of fractional distillation.[97]

Several organocyclosiloxanes have been structurally characterized by X-ray diffraction. Among these, hexamethylcyclotrisiloxane $(Me_2SiO)_3$ contains a planar six-membered ring Si_3O_3,[98] octamethylcyclotetrasiloxane $(Me_2SiO)_4$ contains a nonplanar eight-membered ring Si_4O_4,[99] and larger rings, for example, $(Me_2SiO)_5$,[100] $(Me_2SiO)_8$,[101] have also been analysed. Large stereoregular cyclosiloxanes $[Ph(Me_3SiO)SiO]_n$ ($n = 6$ and 12) have been synthesized by an indirect route and structurally characterized.[102] The lowest members of the series, cyclodisiloxanes (with bulky organic groups) have been obtained by oxidation of disilenes and characterized by X-ray diffraction.[103]

An interesting recent development is the synthesis and structural characterization of unusual cyclosiloxanolate metal complexes,[104] the crown ether-type complexation of potassium by a permethylcycloheptasiloxane[105] and the synthesis of dendrimers based upon mono- and polycyclic (cage) siloxanes.[106]

Catalytic equilibrations involving ring-opening molecular rearrangements of cyclosiloxanes, for example, of the tetramer $(Me_2SiO)_4$, produced mixtures containing cyclosiloxane oligomers and polymers $(Me_2SiO)_n$ with $n = 5-25$ (KOH used as catalyst)[107] and an extensive study of this type of reaction revealed that cyclic poly(dimethylsiloxanes) with up to $n = 1000$ can be thus obtained, by using a variety of basic or acidic catalysts.[108] The reaction has been extensively investigated and reviewed.[109] Silicon−oxygen rings are also present in numerous cyclosilicates and polycyclic silicates.

Germanium analogs of cyclosiloxanes reported to date include $(R_2GeO)_n$ trimers and tetramers (e.g. with R = Me, Et, Pr, Ph, etc.) but they did not attract as much interest as their silicon relatives.[110,111]

Cyclophosphazenes and Cyclophosphazanes. Cyclophosphazenes are an important class of inorganic rings, based upon an alternation of phosphorus(V) and nitrogen, that is, the –P=N–P=N– sequence. The general formula $(R_2PN)_n$ covers a large family in which R = halogen, functional group (alkoxo, amino, thiolato, etc.) or organic group (alkyl, aryl). The chemistry of cyclic and polymeric phosphazenes has been extensively covered in several reviews and books.[112] The six- and eight-membered rings (**36**, **37**) are the most important members of this class and their chemistry is quite comprehensive. Larger cyclic oligomers have also been investigated (*see* ***Phosphorus–Nitrogen Compounds***).

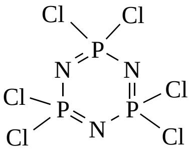
(**36**)

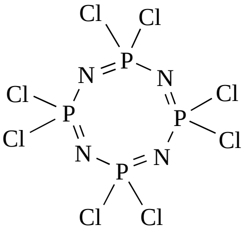
(**37**)

Usually the entry into phosphazene chemistry is based upon the formation of perchlorocyclophosphazenes, $(Cl_2PN)_n$, which are readily prepared by reacting phosphorus pentachloride with ammonium chloride in refluxing tetrachloroethane or other organic solvent. The major products are the trimer and the tetramer, but larger ring oligomers with $n = 5-8$ have also been isolated.[113]

The crude mixture also contains larger rings, as demonstrated by fluorination with potassium fluoride in liquid sulfur dioxide at 90−125° under pressure, producing cyclic oligomers $(F_2PN)_n$ with $n = 3-17$, which can be separated by a combination of fractional distillation and vapour-phase chromatography.[114] Cyclic bromophosphazenes $(Br_2PN)_n$ with $n = 3-6$ have also been obtained.[115]

The halogens can be readily replaced by various functional groups, for example, alkoxy and aroxy, to give $[(RO)_2PN]_n$ (R = Me, CH_2CF_3, Ph; $n = 3-8$) and dimethylamino groups to give $[(Me_2N)_2PN]_n$ ($n = 3-8$),[116] or with organic groups, to give $(Me_2PN)_n$ ($n = 3-10$) (**38–45**).[117]

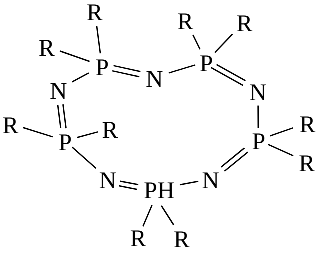
$(Me_2PN)_5$

(**38**)

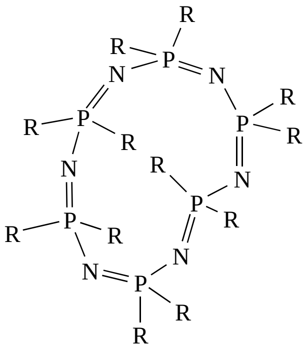
$(Me_2PN)_6$

(**39**)

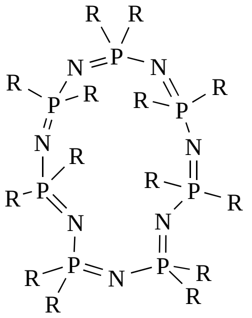
$(Me_2PN)_7$

(**40**)

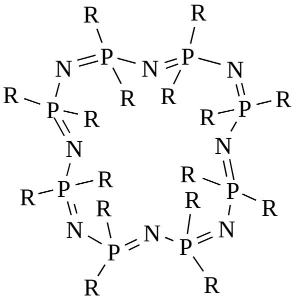
$(Me_2PN)_8$

(**41**)

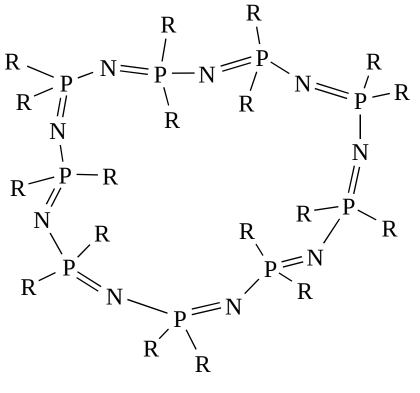
$(Me_2PN)_9$

(**42**)

Alkaline hydrolysis of perchlorocyclophosphazenes produces salts of cyclophosphazanic acid, $M^I_n[(O_2PNH)_n]$, $n = 3-8$, with preservation of the ring size and $(PN)_n$ cyclic

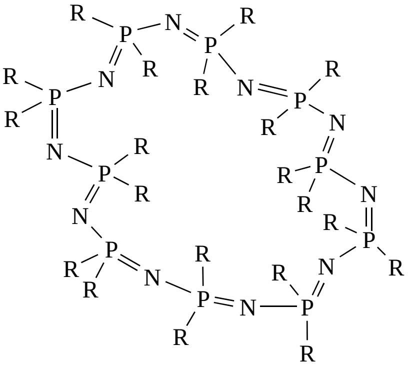

$(Me_2PN)_{10}$

(**43**)

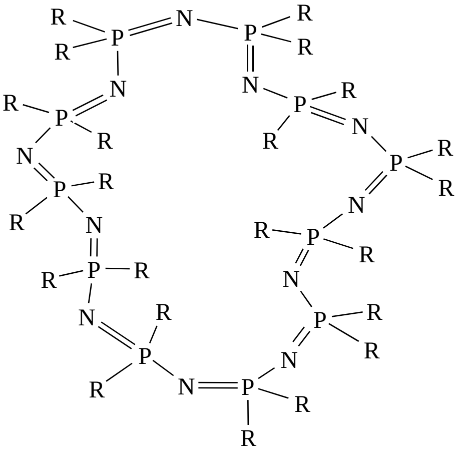

$(Me_2PN)_{11}$

(**44**)

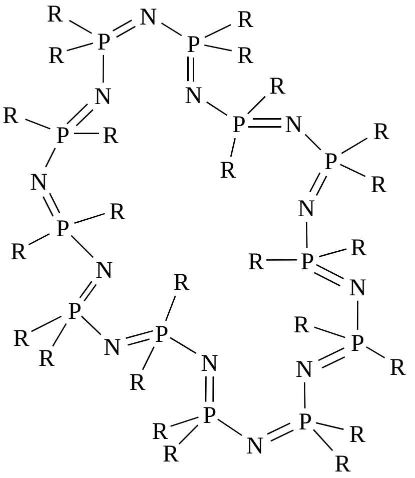

$(Me_2PN)_{12}$

(**45**)

skeleton, but involves an $[–(HO)_2P=N–]/[–(HO)(O)P–NH–]$ tautomerization.[118]

Numerous single-crystal X-ray diffraction studies confirmed the structures of cyclophosphazenes, for example, $(F_2PN)_3$,[119] $(Cl_2PN)_3$,[120] $(F_2PN)_4$,[121] $(Cl_2PN)_4$,[122] for example, $(F_2PN)_5$,[123] $(Cl_2PN)_5$,[124] $(Br_2PN)_5$,[125] $(Me_2PN)_5$,[126] $(Me_2PN)_6$,[127] $(Me_2PN)_7$, $(Me_2PN)_8$,[128] and $(Me_2PN)_n$ ($n = 9–12$).[129] The crystal and molecular structures of the hexamers $[(MeO)_2PN]_6$[130] and $[(Me_2N)_2PN]_6$[131] and octamers $[(MeO)_2PN]_8$[132] and $[(Me_2N)_2PN]_8$[133] have also been reported.

The conformations of these large rings are irregular and demonstrate the flexibility of the phosphazene chains, which allows the formation of phosphorus–nitrogen rings of practically any size.

Cyclophosphazenes (**46**) undergo both thermal ring-opening polymerization with formation of linear polymers (**47**) (*see* ***Polyphosphazenes***) and ring–ring equilibria (resulting in ring expansion).

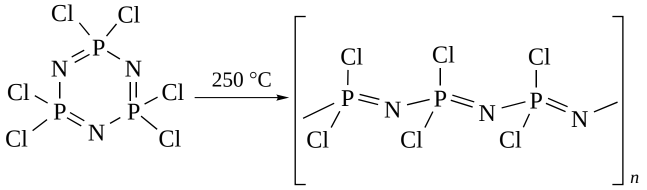

(**46**) (**47**)

The six-membered ring (**48**) can expand to 8-, 10-, and 12-membered rings (**49–51**) (and larger) and a mechanism has been suggested in which the first step is the conversion of the six-membered ring to a 12-membered ring.[134]

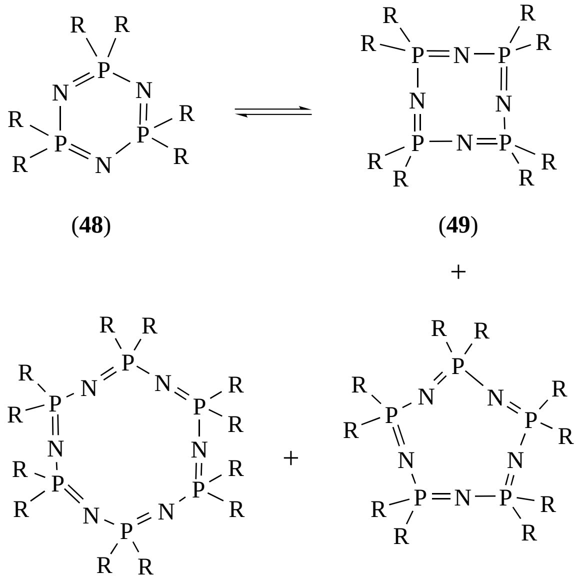

(**48**) (**49**)

(**51**) (**50**)

Anionic derivatives of cyclodiphosph(III)azanes and cyclodiphosph(V)azanes have emerged recently as versatile ligands.[135,136]

Partial replacement of phosphorus by other elements is possible leading to heterocyclophosphazenes. Among these, the P–N–B, P–N–As, P–N–Sb,[137] P–N–S[138–140] and group 13 heterocyclophosphazenes[141] are the most interesting. Several four-membered PN_2E rings with E = B, Al, Ga, In, Si, As, S have also been reported.[142]

Phosphorus-oxygen Rings. The most important cyclic compounds based upon phosphorus-oxygen backbones are the so-called metaphosphates or cyclophosphates (*see* ***Phosphates: Solid-state Chemistry***). They contain $[PO_3]_n^{n-}$ ring anions of various sizes, from $n = 3$ to $n = 12$ (isolated and structurally characterized).[143] The trimers and tetramers are readily obtained and have been thoroughly investigated, but it took considerable skill to isolate the higher members (**52**,**53**) of the series.

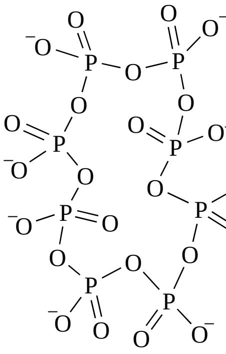

$(PO_3)_8^{8-}$

(**52**)

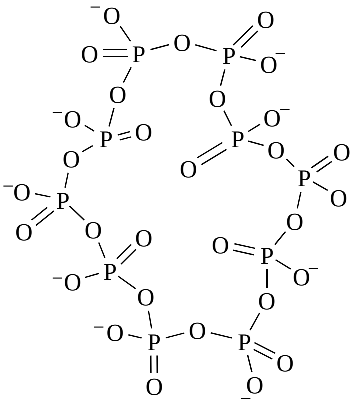

$(PO_3)_{10}^{10-}$

(**53**)

Cyclotri- and tetraphosphates have been known since the nineteenth century (see Ref. 144 for earlier literature). The cyclohexaphosphates have been isolated next, as sodium, potassium, and ammonium salts[145] and has been followed by isolation and characterization of cyclooctaphosphates,[146] cyclodecaphosphates,[147] and cyclododecaphosphates.[148] Cyclopenta- and cycloheptaphosphates are much more difficult to obtain.[149]

Phosphorus(III)-oxygen rings $(RPO)_n$ ($R = NPr^i_2$, $n = 4$ and 5) can be stabilized as metal complexes, but so far have not been isolated in free state.[150]

Cycloarsazanes, Cycloarsoxanes, Cycloarsathianes; Antimony Analogs. Cycloarsazene trimers and tetramers, $(R_2AsN)_n$ (R = Ph, $n = 3$ and 4), are well known.[151]

Cyclic organoarsenic oxides, $(RAsO)_n$, are readily interconvertible. According to ^{1}H NMR data, the methyl and ethyl arsoxanes (R = Me, Et) are mixtures of cyclic oligomers ($n = 2-5$) with the trimer (**54**) and tetramer (**55**) predominating.[152] Crystalline $(MeAsO)_4$ and $(MesAsO)_4$ have been structurally characterized by X-ray diffraction.[153] The cycloarsoxane rings are very labile. Ring expansion readily occurs and various ring sizes can be stabilised by complexation. Thus, crown ether-type complexation of sodium stabilizes the tetramer as $[Na(EtAsO)_4]^+$ whereas potassium and caesium stabilize the pentamer (**56**) as $[M(EtAsO)_5]^+$ (M = K, Cs).[154] Copper complexes of $(MeAsO)_4$ are also known.[155] Alkylcycloarsoxane hexamers $(RAsO)_6$ (R = Me, Et) have been stabilized as chromium, molybdenum,[156] rhenium, ruthenium, and copper[157] complexes, e.g. (**57**) and the methyl octamer $(MeAsO)_8$ as ruthenium or osmium complexes.[158]

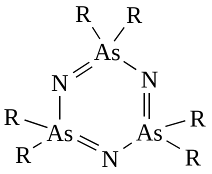

(**54**)

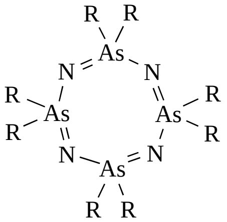

(**55**)

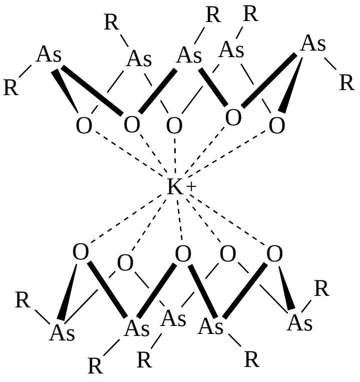

(**56**)

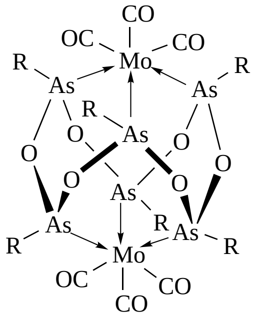

(**57**)

Only metal complexes of cycloarsathianes have been structurally characterized, and these include a tetramer $(EtAsS)_4$ (as ruthenium complex)[159] and the methyl cyclic oligomers $(MeAsS)_n$ with $n = 4$, 5, and 6 (as chromium and molybdenum complexes), e.g. (**58**) the later starting from a trimer-tetramer equilibrium mixture $(MeAsS)_n$, $n = 3$ and 4.[160] The structure of the pentamer complex is shown here.

The cycloarsoxanes and cycloarsathianes are versatile ligands owing to the presence of As(III) donor sites. Their coordination chemistry has been reviewed.[161]

These examples not only indicate an interesting chemistry of arsenic(III) rings but also illustrate their versatility as macrocyclic ligands. It is important to underscore that the coordinated ligand is formed in a metal induced ring

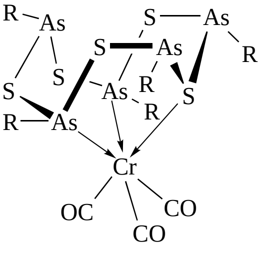

(**58**)

expansion of the smaller ring precursors. Surprisingly, no similar cycloarsazane chemistry has been reported so far.

Related antimony chemistry is less developed. A cyclic oligomer, a 'ring of rings' (**59**) containing six four-membered Sb_2N_2 synthons, has been formed in the reaction of 2-methoxyaniline with $Sb(NMe_2)_3$ and the compound was structurally charecterized.**162** Other Sb_2N_2 ring derivatives have also been reported recently.**163**

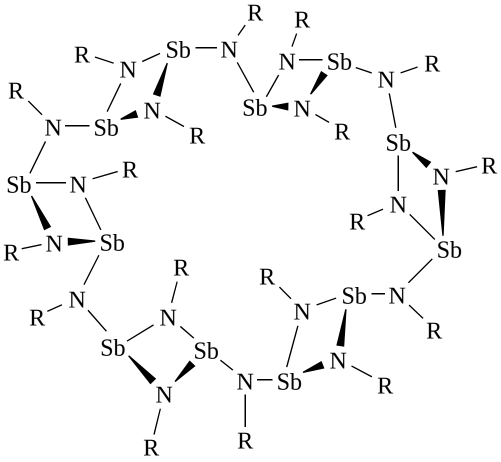

(**59**)

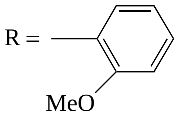

Trimeric and tetrameric organoantimony oxides $(RSbO)_n$ ($n = 3$ and 4) and sulfides $(RSbS)_n$ ($n = 2$, 3, and 4) have been prepared and some were structurally characterized.**164**

Sulphur-nitrogen and Related Selenium and Tellurium Rings. The unsubstituted sulphur-nitrogen pair forms a series of cyclic molecules (*see* ***Sulfur: Inorganic Chemistry***), which include the dimer S_2N_2 and the tetramer S_4N_4.**165** The pentamer is known only in cationic form $S_5N_5{}^{+}$**166** and no unsubstituted trimeric S_3N_3 ring compound is known.

In substituted form, sulphur(IV) forms a series of trimeric and tetrameric $[XSN]_n$ ($X = F$, Cl, etc.; $n = 3$ and 4) cyclic compounds, and similarly, sulphur(VI) forms trimeric and tetrameric $[X(O)SN]_n$ ($n = 3$ and 4). There is an extensive chemistry of these rings, which is well reviewed in some monographs.**167**

Selenium–nitrogen and tellurium–nitrogen heterocycles are less stable, but several are known.**168**

Other Covalent Rings. In addition to the inorganic heterocycles discussed, other element pairs form rings based upon the principle of repeating units. Among these there are inorganic rings containing germanium,**169** tin,**170** lead,**171** and antimony.**172** They are generally limited to a few regular size rings (four-, six-, or eight-membered, that is, made up of two, three, and four repeating units, respectively). Five- and six-membered nonalternating rings $Me_4Si_2E_2MR_2$ ($M = Si$, Ge, Sn, B; $R = Me$ or Ph), $E(SiMe_2SiMe_2)_2E$, and $[Me_4Si_2E_2SiMe\text{-}]_2$ ($E = S$, Se, Te) have been reported.**173** The literature before 1980 is covered in a monograph.**174**

Inorganic Covalent Heterocycles Containing Transition Metals. There are numerous inorganic (carbon-free) rings containing transition metal atoms. We will present only a few selected examples, to illustrate the principles of their structures and formation.

Transition metals can be incorporated in covalent rings, as components of repeating building units. There are three possible ways:

1. formation of rings from repeating units made up by association of a transition metal with an electronegative atom, for example, nitrogen, oxygen, sulfur, just as in the previous cases discussed above for nonmetals and main group metals;
2. incorporation of the transition metal as heteroatom into a nonmetal inorganic ring;
3. formation of covalent rings based upon metal–metal bonds, and containing only metal atoms in the ring.

Case (a) mentioned is illustrated by some rings in which the metal atoms alternate with oxygen. Thus, cyclopentadienyltitanium oxide trimers (**60**) and tetramers (**61**) e.g. $[Cp^*TiX(\mu\text{-O})]_n$ ($n = 3$ or 4, $X = F$, Cl, Br),**175** the vanadium analogs $[Cp^*VCl(\mu\text{-O})]_4$**176** or the organozirconium oxide $[Cp_2Zr(\mu\text{-O})]_3$**177** fit into this category. These cyclic and related polycyclic cage organometallic oxides have been reviewed.**178,179**

A second possibility, mentioned above, is the incorporation of the metal as heteroatom into covalent nonmetal rings, to give for example, metallacyclophosphazenes,**180** metallacyclosiloxanes,**181** metallacyclosilazoxanes,**182** metallaborazines,**183** and so on. Many such rings are known (for a review, see 184).

The third type of transition metal-containing rings is illustrated by a spectacular metal–metal bond, planar 12-membered ring (**62**) made of six $–Os(CO)_4–SnPh_2–$ repeating units (obtained from Ph_2SnCl_2 and the $[Os(CO)_4]^{2-}$ anion).**185**

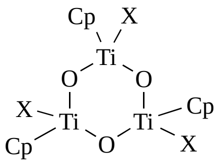

(60)

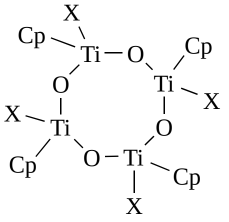

(61)

Cp = η^5-C_5H_5, η^5-C_5Me_5

X = Cl, etc.

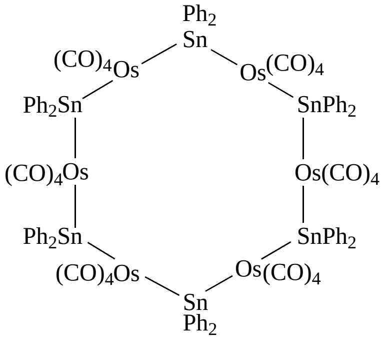

(62)

3.2 Inorganic Rings and Polycyclic Cages Self-assembled Through Dative Bonds

Chemical bonds in inorganic chemistry are not limited to covalency. Very important are the *dative* (*donor–acceptor*) *bonds*. Unlike normal covalent bonds, which are formed by pairing of electrons with a one-electron contribution from each atom, dative bonds are two-electron bonds formed by donation of an electron pair from one atom to another. There is a general tendency to assume that the two-electron bonds between a certain pair of atoms (*e.g.* boron and nitrogen in H_2B–NH_2 and $H_3B \leftarrow NH_3$) are identical, regardless of the origin of electrons (i.e. covalent and dative), but it has been pointed out that a distinction between the two types should be made.[186,187]

The normal covalent and dative bonds differ in several major aspects:

1. the nature of the fragments formed when the bonds are broken;
2. the nature of the bond rupture process;
3. the magnitude of the bond cleavage enthalpy.

Thus, if two isoelectronic molecules, ethane, H_3C–CH_3, and amine-borane, $H_3B \leftarrow NH_3$, are compared the distinction becomes obvious: the normal covalent C–C bond ruptures homolytically and the neutral species formed are $\cdot CH_3$ (paramagnetic) free radicals, with an energy of 89.8 kcal·mol^{-1} spent in the process. The dative $N \rightarrow B$ bond rupture proceeds heterolytically, with formation of neutral diamagnetic molecules, BH_3, and NH_3, and only 31.1 kcal·mol^{-1} are spent in the process. Note that the cleavage of the dative bond requires only about one-third of the energy needed for the cleavage of a normal covalent bond between the same atoms.

When an electron donor and an electron acceptor site are present in the same molecule, intermolecular association may occur with formation of cyclic species. This process is called *self-assembly*. Self-assembly is defined as *a spontaneous association of molecules under equilibrium conditions into stable aggregates held together by noncovalent forces*.[188] The resulting species is a *supermolecule* (see above).

Numerous monomeric molecules are able to self-assemble into cyclic supermolecules. One example is H_2Al–NMe_2, which self-assembles into dimeric $[H_2Al$–$NMe_2]_2$ and trimeric $[H_2Al$–$NMe_2]_3$ cyclic supermolecules, which undergo facile interconversion under equilibrium conditions (Scheme 7).[189] The isomeric Me_2Al–NH_2 also self-assembles into cyclic trimers $[Me_2Al$–$NH_2]_3$.[190] Numerous other dimeric and trimeric $[R_2Al$–$NR'_2]_2$ rings[191,192] are known, as well as aluminum-phosphorus polycyclic supermolecules[193] and gallium, indium, and thallium analogs with nitrogen, phosphorus, arsenic, and antimony donors.[194–197] Such compounds are attractive single-source precursors for metal nitrides and phosphide or arsenide semiconductors and other high-tech materials.[198] Self-assembled cyclic organoaluminum and -gallium hydroxylamides are interesting as they display different modes of association, to form four-, five-, or six-membered rings.[199]

The aminoboranes, R_2B–NR'_2, and phosphinoboranes, R_2B–PR'_2, can also exist in monomeric molecular form or as dimeric, trimeric or polymeric supermolecules (depending upon the nature of R and R′).[200] Dative bond self-assembly is not limited to amino derivatives. Halogen bridging can induce similar effects and numerous organometallic fluorides[201] and chalcogenolates[202] also form cyclic supermolecules.

Some large ring supermolecules are formed by dative bond self-assembly of monomers containing both donor and acceptor binding sites. Spectacular examples are the tetrameric trimethyltin diphenylphosphinate $[Me_3SnO_2PPh_2]_4$,[203] and cupferronate $[Me_3SnON(Ph)NO]_4$,[204] and hexameric $[Ph_3SnO_2P(OPh)_2]_6$[205] and $[Ph_3SnO_2P(OMe)Me]_6$,[206] (Scheme 8) whereas diorganoaluminum phosphinates and

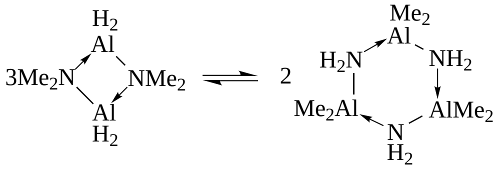

Scheme 7 Dimer-trimer equillibrium between two self-assembled cyclic supermolecules

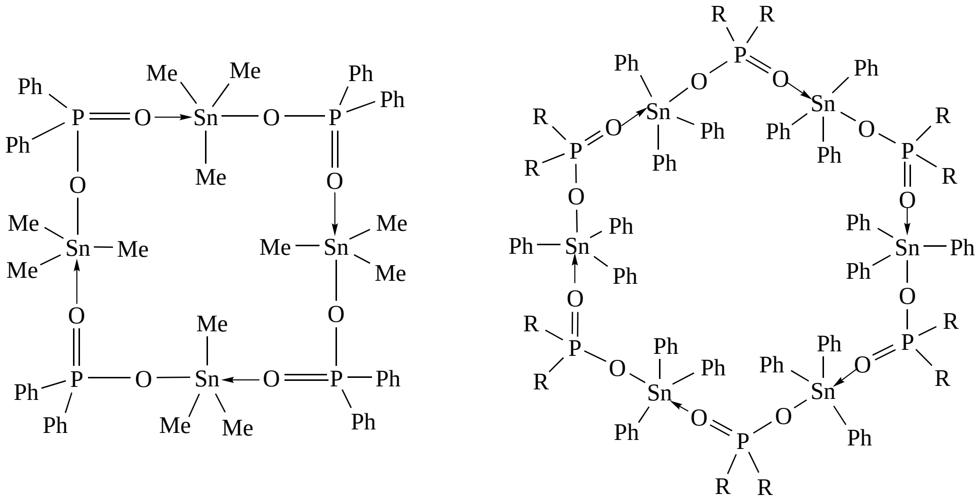

RR = $(OPh)_2$ or Me(OMe)

Scheme 8 Tetrameric and hexameric organotin self-assembled macrocyclic supermolecules

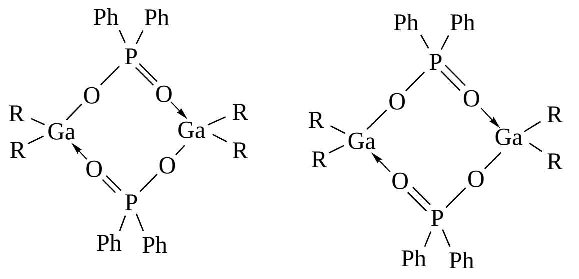

Scheme 9 Dimeric self-assembled eight-membered ring supermolecules

their organogallium analogs, are only dimers, *for example*, $[Me_2AlO_2PPh_2]_2$,[207] and $[Bu^t_2GaO_2PPh_2]_2$[208] (Scheme 9).

Dative bond self-assembly may also lead to polycyclic cage supermolecules, with cubane and prismane shapes, for example, in organoaluminum[209,210] and organogallium[211,212] phosphonates (Scheme 10).

There are numerous inorganic rings containing transition metals, self-assembled through dative bonds. Only a few illustrative examples are presented here.

Among the first to be named are the transition metal nitrido chlorides and alkoxides. Thus, nitride-chlorides $[Cl_3MN]_n$ (**63**), where M = Mo or W, are associated into cyclic trimers (**64**) or tetramers (**65**) and exhibit bond length alternation, owing to the alternation of triple and dative bonds.[213] Theoretical calculation on $[Cl_3MN]_n (n = 3, 4, 5,$ and 6) explains the formation of d^6 transition metal nitrido chlorides through weak donor–acceptor bonds between the lone pairs at nitrogen and the empty d orbitals at metal.[214] The theory predicts that chromium chloro-nitride Cl_3CrN will be stable as monomer and molybdenum chloro-nitride Cl_3MoN as tetramer. A bonding analogy between chlorophosphazenes and metal chloro-nitrides has also been analysed theoretically.[215]

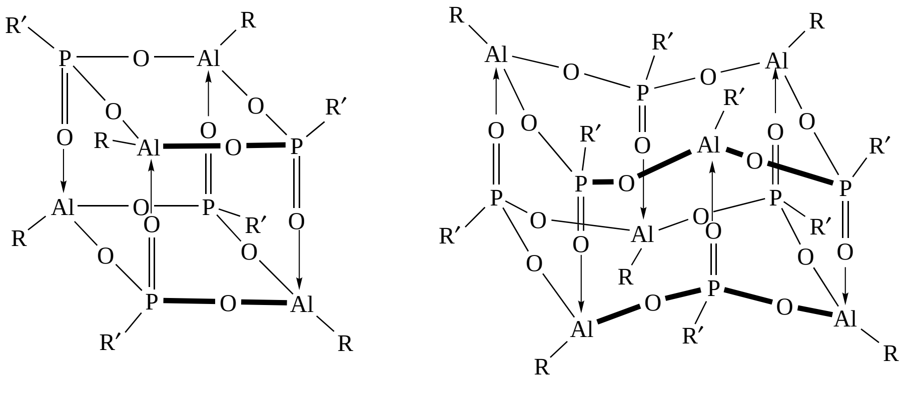

Scheme 10 Cubane and prismane cage-like supermolecules

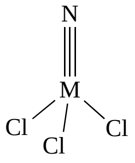

(63)

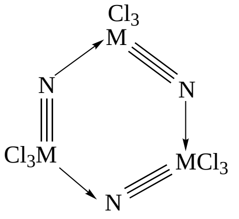

(64)

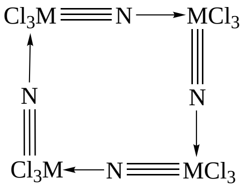

(65)

M = Mo, W

In the molybdenum–nitrogen four-membered ring, the metal-nitrogen bond lengths alternate (1.67 and 2.17 Å).

Good examples of cyclic (mostly polycyclic) structures are provided by metal alkoxides.[216] Some spectacular rings are the gold(I)-phosphido complexes of the type $[AuPR_2]_n$ ($n = 3$, 4 or 6).[217]

Incorporation of inorganic rings formed through dative bonds into wheel-shaped ‘metallacoronands’ is also worth mentioning. Examples include $[Fe_6Cl_6L_6]$ and $[In_6Cl_6L_6]$ macrocyclic compounds (L = substituted diethanolamines),[218] $[Fe_8(OH)_4(OPh)_8(O_2CBu^t)_{12}]$,[219] $[Fe_{12}(OMe)_{24}L_{12}]^{-12}$ (L = proline)[220] and $[(Bu^t_3SiS)_{12}M_{12}X_{12}]$ (M = Co, Ni, X = Cl or Br)[221] to cite only a few of the numerous examples known.

3.3 Inorganic (Carbon-free) Chelate Rings

Dative bonds can lead to ring closure with formation of inorganic (carbon-free) chelate rings, for example, dithiophosph(in,on)ates,[222] cupferronates,[223] dichalcogenoimidodiphosphinates,[224] and many others[225] (Scheme 11). This type of inorganic cyclic structures can involve all transition and nontransition metals in combinations with chelating ligands not containing carbon in their molecular skeleton. Therefore, the number of possible inorganic chelate rings is legion and are not discussed here in any detail.

Numerous chelate rings are formed with polychalcogenide ligands.[226]

An extensive class of inorganic chelate ring complexes is represented by pyrazolylborates and related ligands (‘scorpionates’).[227] Another group of versatile chelating ligands are the inorganic backbone di- and polyphosphines, that is, compounds containing phosphinyl groups (–PR$_2$) attached to inorganic divalent moieties such as – NR–(diphosphinoamines), –O–(diphosphoxanes), –S–(thiobis(phosphines)), –NR–NR–(bis(phosphinohydrazines)), –NR–PR–NR–(bis{phosphinoamino}phosphines), –R$_2$Si–(diphosphinylsilanes) and –O–SiR$_2$–O–(diphosphinylsiloxanes), –NR–SiR$_2$–NR–bis(phosphinoamino) silanes.[228,229] Other inorganic chelating ligands are di- and polysiloxanediolates,[230] sulfur diimido anions, $[S(NR)_2]^{-2}$.[231]

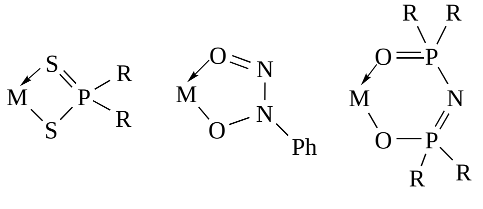

Scheme 11 Some inorganic (carbon-free) chelate rings

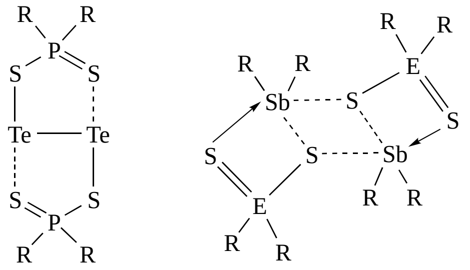

E = Sb, As

R = Ph

Scheme 12 Formation of quasi-cyclic structures through secondary bonds

3.4 Quasi-cyclic Molecules and Supermolecules Self-assembled Through Secondary Bonds

Another type of noncovalent forces which may lead to supramolecular self-assembly are the so-called *secondary bonds or soft–soft interactions.*[232–234] They are characterized by interatomic distances longer than covalent bonds but shorter than van der Waals interatomic distances. Such interactions are weaker than two-electron covalent or dative bonds, but are strong enough to influence the coordination geometry of the atoms involved and to hold together pairs of atoms, either to intramolecularly close a ring or to induce supramolecular self-assembly with formation of cyclic structures.[235] Rings formed by this route have been named *quasi-cyclic structures.*[236] As examples can be cited the formation of a tellurium quasi-bicylic system in $[Te_2(S_2PPh_2)_2]$[237] and the dimeric self-assembly of $[Ph_2SbS_2EPh_2]_2$ (E = P, As) into a quasi-tricyclic system[238] (Scheme 12).

3.5 Inorganic Ring Structures Self-assembled Through Ionic Interactions

Ionic (electrostatic) interaction may also lead to cyclic self-assembly. Numerous alkali metal and alkaline-earth molecular compounds fall into this category. These include three types of associated ring compounds:

1. alkali metal and alkaline earth alkyl and aryl derivatives, in which the metal-carbon is essentially ionic;
2. alkali and alkaline-earth metal amides, phosphides, arsenides, alkoxides, thiolates, and so on, that is, compounds not containing a direct metal–carbon bond; innumerable examples are known.[239–241]

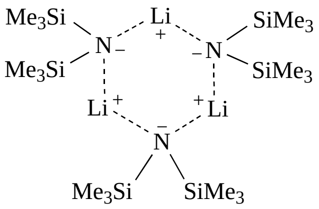

Scheme 13 Ring formation through ionic interactions

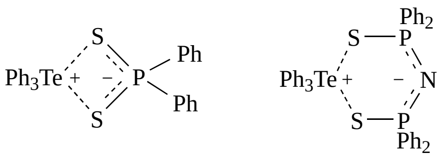

Scheme 14 Quasi-cyclic systems formed through ionic and secondary interactions

3. organometallic compounds which contain functional groups with mobile hydrogen, which can be readily displaced by an electropositive metal, to form cation-anion ion pairs (e.g. metal silanolates).

There are several relevant reviews covering the subject.[242]

Simple examples of cyclic oligomers formed through ionic interactions are the trimer of lithium bis(trimethylsilyl)amide, $[LiN(SiMe_3)_2]_3$ (Scheme 13),[243] and hexameric $[Li\{SC_6H_3(CH_2NMe_2)_2\text{-}2,6\}]_6$[244] More intricate cage, ladder, and other polycyclic structures are formed in various other compounds.[245]

The sodium analog, $[NaN(SiMe_3)_2]_3$ has a similar structure,[246] and the lithium phosphide, $[LiPBu^t_2(THF)]_4$ is a tetramer.[247] Cyclic alkoxides can be illustrated by trimeric $[Li\{OC_6H_2(CH_2NMe_2)_2\text{-}2,6\text{-}Me\text{-}4\}]_3$, hexameric $[NaOBu^t]_6$ and nonameric $[NaOBu^t]_9$.[248] Thiolates can be trimeric, for example, $[Li(SC_6H_2Bu^t_3\text{-}2,4,6)(THF)]_3$[249] and even hexameric $[LiSC_6H_3(CH_2NMe_2)_2\text{-}2,6]_6$.[250] Numerous other examples are cited in Ref. 251.

In triphenyltellurium diphenyldithiophosphinate, $[Ph_3Te]^+[S_2PPh_2]^-$ and triphenyltellurium tetraphenyldithioimidodiphosphinate, $[Ph_3Te]^+ [(SPPh_2)_2N]^-$, probably ionic interactions and Te···S secondary bonding are simultaneously acting to close a four- and a six-membered quasi-cycle, respectively (Scheme 14).[252]

3.6 Cyclic Supermolecules Self-assembled Through Hydrogen Bonds

Hydrogen-bond self-assembly may lead to formation of carbon-free cyclic structures containing oxygen and hydrogen in a ring, such as tetrameric $[Ph_3SiOH]_4$[253] or more complex cyclic structures such as dimeric diphenylarsinic-diphenylthioarsinic aggregate[254] (in solid state) or the anion-cation hydrogen-bond quasi-cyclic self-assembly in $[RNH–P–NH–R]^+ [AlCl_4]^-$ ($R = 2,4,6\text{-}Bu^t_3C_6H_2$)[255] (Scheme 15). The simplest examples are in fact some water cyclic supermolecules formed through hydrogen bonds, some of which have been found trapped in various crystal structures,[256] for example, the hexamer $(H_2O)_6$,[257] octamer $(H_2O)_8$,[258] decamer $(H_2O)_{10}$.[259] There is much interest for the cyclic water trimer $(H_2O)_3$.[260]

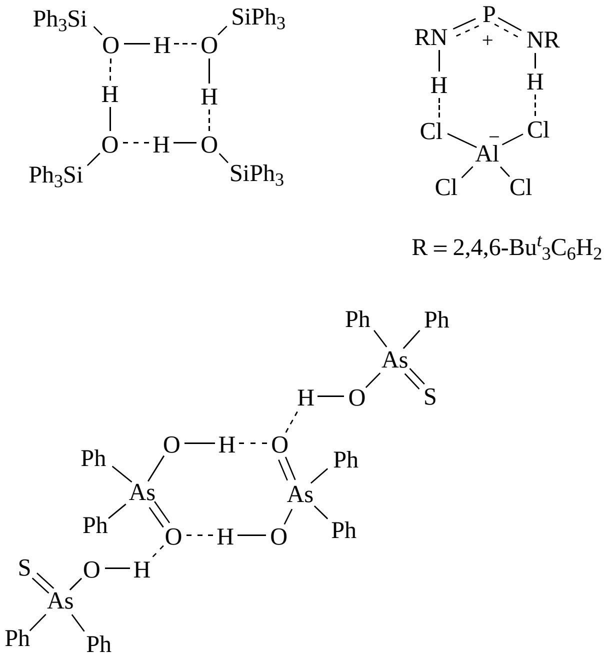

$R = 2,4,6\text{-}Bu^t_3C_6H_2$

Scheme 15 Cyclic supermolecules formed through hydrogen bonds

4 COMBINING BUILDING BLOCKS FOR INORGANIC RING FORMATION: A CHEMICAL 'LEGO'

It was shown above that inorganic ring structures can be built by combining a number of various building blocks (synthons). A building block or inorganic synthon consists of a *central element* surrounded by a number of *connecting atoms*, located at the corners of a regular or irregular polyhedron. The central atom is usually an element less electronegative than carbon (i.e. B, Si, Ge, P, As, Sb, S, Se, Te, or a metal) and the connecting atom is an electronegative elements (i.e. O, N, S^{II}, even halogen if the ring is formed by dative bond self-assembly).

Inorganic ring systems are formed through linkage of a discrete, small number of synthons by sharing corners, edges, or faces through common connecting atoms. The four-, six-, and eight-membered rings are most common. The synthons

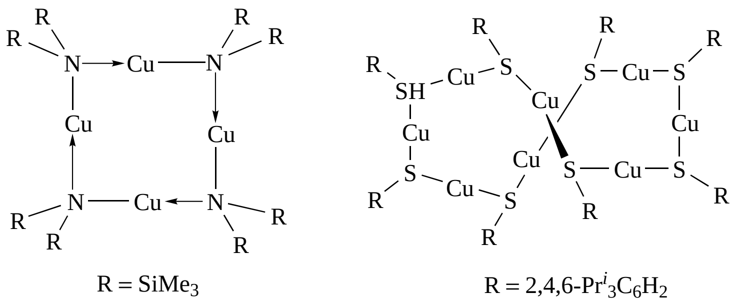

Scheme 16 Self-assembled cyclic supermolecules from linear copper(I) synthons

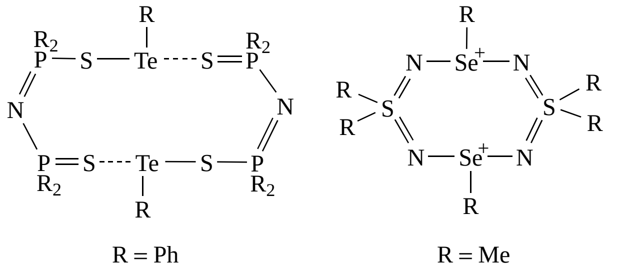

Scheme 17 T-shaped tellurium and selenium synthons in inorganic rings

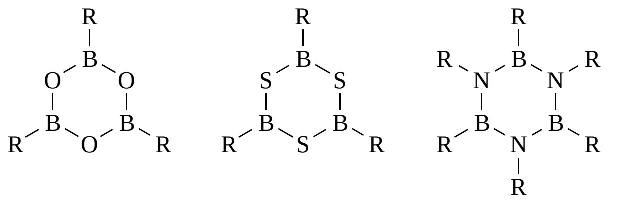

Scheme 18 Trigonal planar boron synthons in inorganic rings

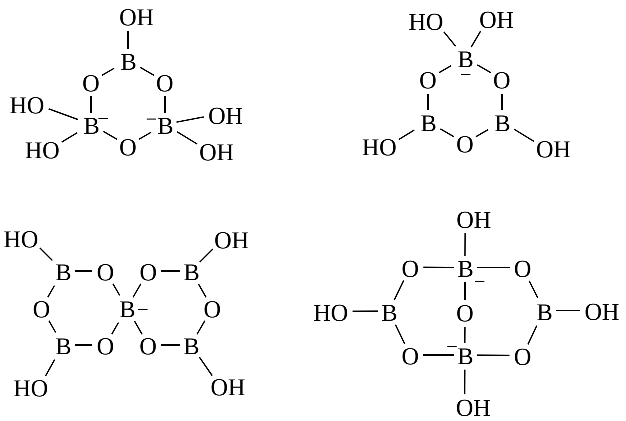

Scheme 19 Rings made from trigonal planar and tetrahedral boron synthons

available for building inorganic ring systems, with their coordination numbers and geometries, can be summarized as follows:

- dicoordinate: linear and bent (sp and ψ-sp^2 or ψ-sp^3 hybridization of the central atom);
- tricoordinate: trigonal planar (sp^2), trigonal pyramidal (ψ-sp^3), or T-shaped (ψ-sp^3d);
- tetracoordinate: tetrahedral (sp^3), square planar (spd^2), or ψ-trigonal bipyramidal;

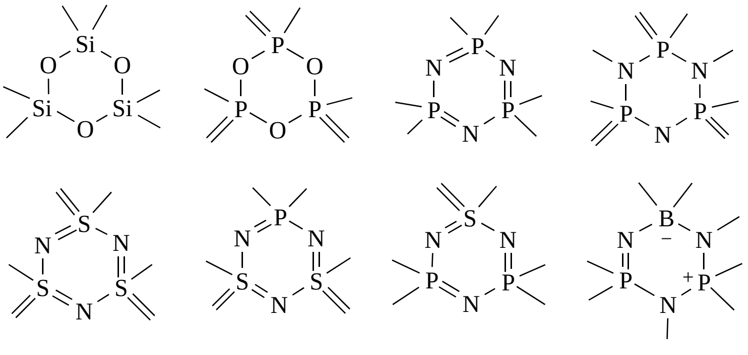

Scheme 20 Six-membered rings containing tetrahedral synthons

- five-coordinate: trigonal bipyramidal (sp^3d), rarely square pyramidal;
- six-coordinate: octahedral (sp^3d^2), rarely pentagonal bipyramidal.

Bent synthons are the sulfur atoms connected in homocyclic rings of various sizes cited above. Linear building blocks are illustrated by gold(I), silver(I), and copper(I) atoms bridged by nitrogen or sulfur in various self-assembled cyclic supermolecules, for example, Cu_4N_4 in $[CuN(SiMe_3)_2]_4$[261] or Cu_8S_8 in macrocyclic $[CuS(C_6H_2Pr^i_3$-2,4,6)]8 (Scheme 16).[262]

T-Shaped synthons are rare, but the RTe groups in some self-assembled quasicycles, for example, dithioimidodiphosphinates can be cited as examples.[263] The $MeSeN_2$ unit is trigonal pyramidal in $Me_2S(=N\text{-}SeMe\text{-}N=)_2SMe_2$ where the sulfur synthon is tetrahedral[264] (Scheme 17).

Examples of rings made up of planar triangles only are the boron heterocycles B_3O_3, B_3N_3, B_3S_3, and many others (Scheme 18). A combination of triangles with tetrahedra is illustrated by boron−oxygen rings present in various mono- and bicyclic borates[265] (Scheme 19).

Combinations of tetrahedra are numerous as four-, six-, and eight-membered rings and also as macrocyclic systems, for example, cyclosiloxanes, cyclophosphates, cyclophophosphazenes, cyclothiazenes, and the innumerable hybrid rings that may result by the intercombination of the large number of possible tetrahedral synthons. Only some six-membered rings are illustrated in Scheme 20.

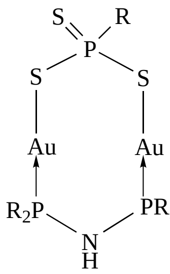

Scheme 21 An inorganic ring made up of linear and tetrahedral synthons

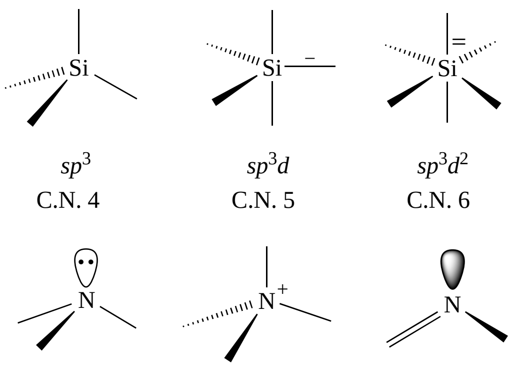

Scheme 22 Synthons of variable coordination numbers of silicon and nitrogen

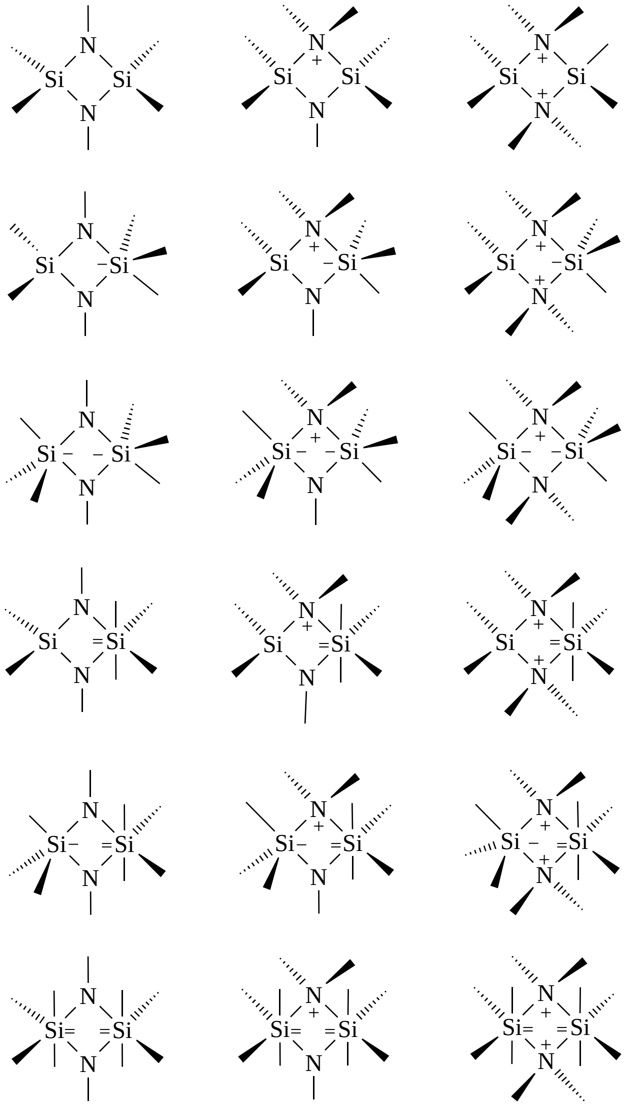

Scheme 23 Cyclodisilazane rings containing silicon synthons of different coordination numbers

Ring structures based upon tetrahedral building units connected through dative bonds can also be formed. Only a spectacular example is cited here as illustration: the Cu_nN_{2n} rings associated with Cu_nO_n rings in the pyrazolato cyclic complexes $[Cu(\mu\text{-OH})(\mu\text{-pz})]_n$ with $n = 6$, 8, 9, 12, and 14.[266]

An example of combining linear synthons with tetrahedral synthons in the same ring is provided by the gold(I) complexes of dithiophosphonates and a mixed ring consisting of linear, angular, and tetrahedral synthons is illustrated by the gold(I) complex[267] (Scheme 21).

For the same composition of the ring skeleton, owing to variations in the coordination numbers of the central elements in the building block (synthons), a large number of different ring systems may occur. Thus, for the Si_2N_2 composition by assuming four-, five-, and six-coordinate silicon, *that is*, tetrahedral, trigonal bipyramidal, and octahedral coordination geometries of the synthons and trigonal (planar or pyramidal) and tetrahedral for nitrogen (Scheme 22).

No less than 18 different cyclodisilazane ring systems can be formed from the synthons shown above, illustrated in Scheme 23.[268]

In these rings, silicon maintains a constant oxidation state IV and no Si=N double bond formation was considered, although some monomeric compounds containing such bonds are known. Some hypothetical cyclodisilazanes containing Si=N double bonds can be taken into consideration (Scheme 24).

If two additional sources of structural diversity, namely, variable oxidation state and double bond incorporation, in the ring are taken into account, the variety of four-membered ring systems increases greatly. This is illustrated by the phosphorus–nitrogen pair. In this case, the coordination number varies from two to three for phosphorus(III), from three to six for phosphorus(V) and two to four for nitrogen (Scheme 25).

Thus, four-membered P_2N_2 rings may occur as cyclodiphosphazanes and cyclodiphosphazenes, and the numerous possibilities are given in Schemes 26 and 27.[269]

When the substituents at phosphorus and nitrogen are also considered, geometrical isomerism adds to the structural diversity which can be expected. In addition, even four-membered rings can display various conformations (planar and bent) and this adds a new dimension to their diversity.[270,271]

Many of these ring systems are actually known (*see* ***Phosphorus–Nitrogen Compounds***). The phosphorus–nitrogen analog of cyclobutadiene deserves a special citation, because – unlike its organic (carbon) analog – it can be isolated as stable compound.

A selection of six-membered S_3N_3 rings containing sulfur–nitrogen synthons of various oxidation states and coordination numbers is illustrated in Scheme 28.

A particular case is the combination of octahedral synthons. If two octahedra share an edge the result is a four-membered ring. There are numerous examples, some being already shown above for P_2N_2 rings in the dimeric $[X_3PN–R]_2$ (*see* ***Phosphorus–Nitrogen Compounds***). Four octahedra are combined to form cyclic tetramers, for example, $[MF_5]_4$ (M = Mo, Nb, etc.) and six-octahedra form a larger ring known in some polyoxometallates.

The most spectacular was the discovery of large polyoxometallate rings containing as many as 154 molybdenum atoms in $[Mo_{154}O_{448}(NO)_{14}(H_2O)_{70}H_{28}]^{14-}$ anion[272] and 176 molybdenum atoms in $[(MoO_3)_{176}(H_2O)_{80}H_{32}]$ neutral species.[273,274] These contain octahedral and pentagonal bipyramidal building blocks. Other polyoxometallate macrocycles built from octahedral synthons are also known.[275–277] (*see* ***Polyoxometalates***).

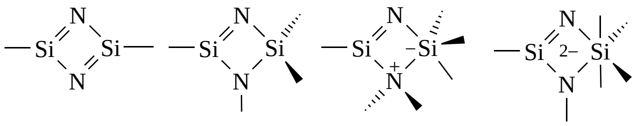

Scheme 24 Some hypothetical cyclodisilazanes containing double Si–N bonds

Bonding (valence) states of phosphorus:

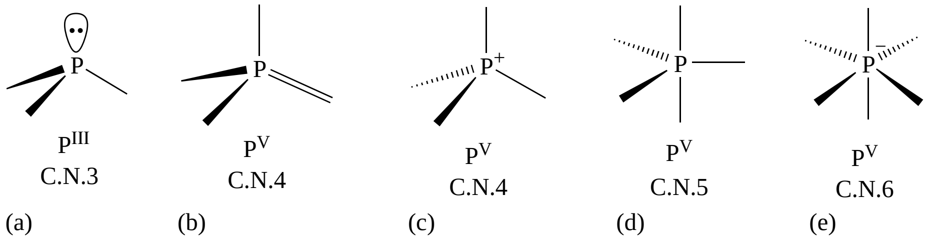

Bonding (valence) states of nitrogen:

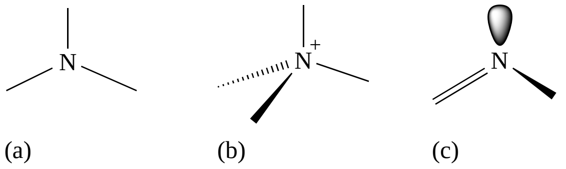

Scheme 25 Variable oxidation states and coordination numbers in phosphorus synthons to be combined with nitrogen in inorganic PN rings

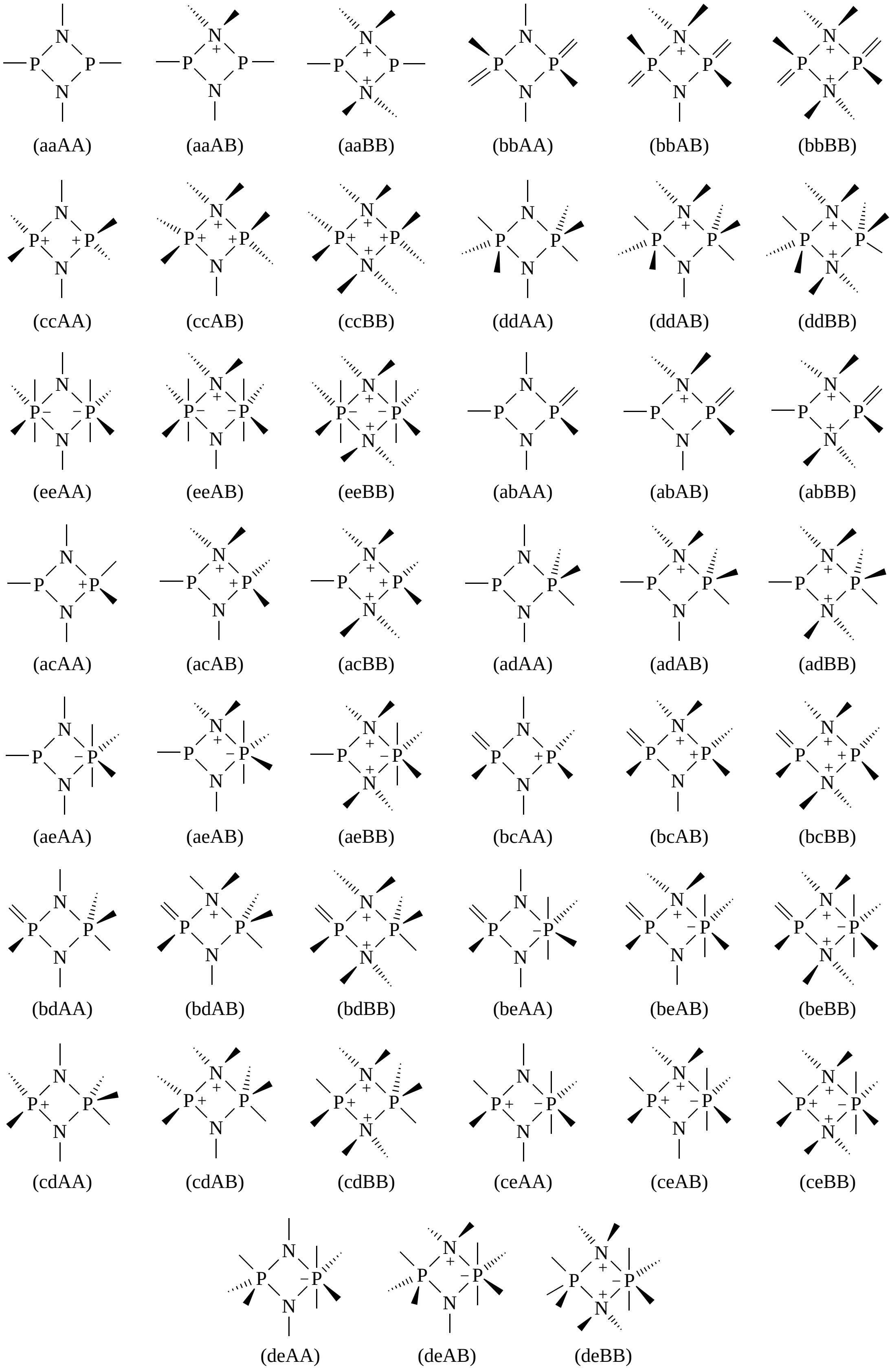
(aaAA)
(aaAB)
(aaBB)
(bbAA)
(bbAB)
(bbBB)
(ccAA)
(ccAB)
(ccBB)
(ddAA)
(ddAB)
(ddBB)
(eeAA)
(eeAB)
(eeBB)
(abAA)
(abAB)
(abBB)
(acAA)
(acAB)
(acBB)
(adAA)
(adAB)
(adBB)
(aeAA)
(aeAB)
(aeBB)
(bcAA)
(bcAB)
(bcBB)
(bdAA)
(bdAB)
(bdBB)
(beAA)
(beAB)
(beBB)
(cdAA)
(cdAB)
(cdBB)
(ceAA)
(ceAB)
(ceBB)
(deAA)
(deAB)
(deBB)

Scheme 26 Structural diversity of cyclodiphosphazane rings

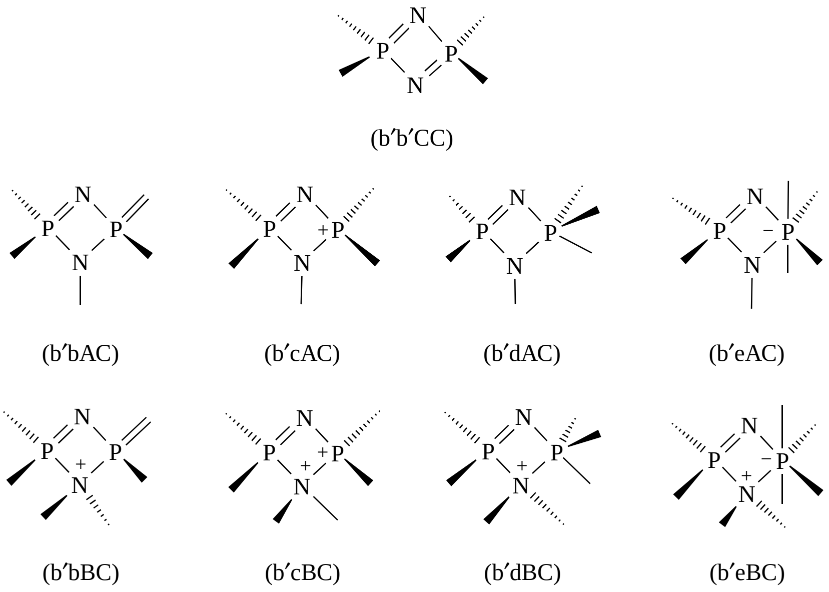
(b′b′CC)

(b′bAC) (b′cAC) (b′dAC) (b′eAC)

(b′bBC) (b′cBC) (b′dBC) (b′eBC)

Scheme 27 The structural diversity of cyclodiphosphazene rings

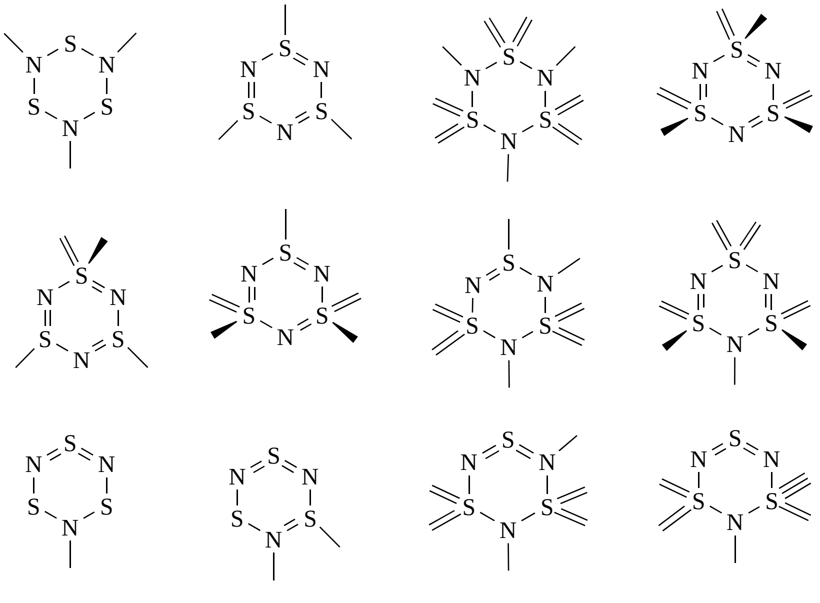

Scheme 28 A selection of known and hypothetical S_3N_3 rings

5 REFERENCES

1. C. G. Lindboom, *Ber. Dtsch. Chem. Ges.*, 1875, **8**, 122.
2. A. Glazel, Inaugural Discussion Würzburg, 1889, cited in Gmelin Handbuch, Band 1, Abt.3, 1911, 181.
3. (a) N. H. Stokes, *Am. Chem. J.*, 1895, **17**, 275; (b) N. H. Stokes, *Am. Chem. J.* 1896, **18**, 780.
4. W. Dilthey, *Ber. Dtsch. Chem. Ges.*, 1905, **38**, 4132.
5. A. Stock and E. Pohland, *Ber. Dtsch. Chem. Ges.*, 1926, **59**, 2215.
6. M. Goehring, ‘Ergenisse und Probleme der Chemie der Schwefelstickstoff-Verbindungen’, Akademie Verlag, Berlin, 1957.
7. H. G. Heal, ‘The Inorganic Heterocyclic Chemistry of Sulphur, Nitrogen and Phosphorus’, Academic Press, London, 1970.
8. S. Pantel and M. Becke-Goehring, ‘Sechs- und achtgliedrige Ringsysteme in der Phosphor-Stickstoff Chemie’, Springer Verlag, Berlin, 1969.

9. H. R. Allcock, ‘Phosphorus–Nitrogen Compounds. Cyclic, Linear and High-Polymeric Systems’, Academic Press, New York, 1972.

10. K. Niedenzu, ‘Boron-Nitrogen Compounds’, Academic Press, London, 1965.

11. (a) I. Haiduc, ‘Introducere in chimia ciclurilor anorganice’, Editura Academiei, Bucuresti, 1960, [Introduction to the chemistry of inorganic rings, in Roumanian]; (b) I. Haiduc, ‘Wstep do chemii nieorganicznych zwiazkow pierscienyowych’, PWN, Warszawa, 1964 [Introduction to the chemistry of inorganic ring compounds, in Polish].

12. (a) H. Garcia-Fernández, ‘Les hétérocycles en chimie minérale’, Hermann, Paris, 1964; (b) H. Garcia-Fernández, ‘Química heterociclica inorgánica’, Editorial Alhambra, Madrid, 1973.

13. H. R. Allcock, ‘Heteroatom Ring Systems and Polymers’, Academic Press, New York, 1967.

14. I. Haiduc, ‘The Chemistry of Inorganic Ring Systems’, Wiley-Interscience, London, 1970, Vol. 2.

15. D. A. Armitage, ‘Inorganic Rings and Cages’, E. Arnold, London, 1972.

16. I. Haiduc and D. B. Sowerby eds, ‘The Chemistry of Inorganic Homo- and Heterocycles’, Academic Press, London, 1987, Vol.2.

17. H. W. Roesky, ‘Rings, Clusters and Polymers of Main Group and Transition Elements’, Elsevier, Amsterdam, NY, 1989.

18. R. Steudel ed., ‘The Chemistry of Inorganic Ring Systems’, Elsevier Science Publishers, Amsterdam, NY, 1992.

19. B. J. Gimarc and M. Zhao, *Coord. Chem. Rev.*, 1997, **158**, 385.

20. (a) F. De Proft, P. W. Fowler, R. W. A. Havenith, Pv. R. Schleyer, G. Van Lier, and P. Geerlings, *Chem. Eur. J.*, 2004, **10**, 940; (b) M. Enlow, *Polyhedron*, 2003, **22**, 473; (c) A. Y. Timoshin and G. Frenking, *Inorg. Chem.*, 2003, **42**, 60; (d) B. Kiran, A. K. Phukan, and E. D. Jemmis, *Inorg. Chem.*, 2001, **40**, 3615; (e) R. Jaeger, M. Dembowski, I. Manners, and G. J. Vancso, *Inorg. Chem.*, 1999, **38**, 1153; (f) A. Sundermann and W. W. Schoeller, *Inorg. Chem.*, 1999, **38**, 6261.

21. (a) R. M. Laine and J. F. Harrod eds, ‘Inorganic and Organometallc Oligomers and Polymers’, Kluwer, Dordrecht, 1991; (b) J. E. Mark, H. R. Alcock and R. West eds, ‘Inorganic Polymers’, Prentice Hall, Englewood Cliffs, 1992; (c) I. Manners, *Angew. Chem., Int. Ed. Engl.*, 1996, **35**, 1602; (d) M. Zeldin, K. J. Wynne and H. R. Allcock eds, ‘Inorganic and Organometallic Polymers’ (ACS Symposium Series Nr. 360) American Chemical Society, Washington, DC, 1988; (e) ‘Inorganic and Organometallic Polymers II’ (ACS Symposium Series Nr. 572), American Chemical Society, Washington, DC 1994.

22. (a) I. Haiduc, in ‘The Chemistry of Inorganic Ring Systems’, ed. R. Steudel, Elsevier Science Publishers, Amsterdam, NY, 1992, p. 451; (b) W. H. Powell and T. E. Sloan, *Phosphorus, Sulfur Silicon*, 1989, **41**, 183; (c) I. Haiduc, *Rev. Inorg. Chem.*, 1980, **2**, 219.

23. M. T. Nguyen, *Coord. Chem. Rev.*, 2003, **244**, 93.

24. G. R. Desiraju, *Angew. Chem., Int. Ed. Engl.*, 1995, **34**, 2311.

25. S. Simard, D. Su, and J. D. Wuest, *J. Am. Chem. Soc.*, 1991, **113**, 4696.

26. M. C. T. Fyfe and J. F. Stoddart, *Acc. Chem. Res.*, 1997, **30**, 393.

27. J. M. Lehn, *Angew. Chem., Int. Ed. Engl.*, 1988, **27**, 89.

28. J. M. Lehn, ‘Supramolecular Chemistry. Concepts and Perspectives’, VCH, Weinheim, 1995.

29. J. M. Lehn, J. L. Atwood, J. E. D. Davies, D. D. MacNicol and F. Vögtle eds, ‘Comprehensive Supramolecular Chemistry’, Pergamon Press, Oxford, 1996.

30. M. Kira, T. Iwamoto, and C. Kabuto, *J. Am. Chem. Soc.*, 1996, **118**, 10303.

31. (a) A. Sekiguchi and V. Y. Lee, *Chem. Rev.*, 2003, **103**, 1429; (b) A. Grybat, S. Boomgaarden, W. Saale, H. Marsmann, and M. Weidenbruch, *Angew. Chem.*, 1999, **38**, 2010; (c) M. Weidenbruch, *Z. Anorg. Allg. Chem.*, 2000, **626**, 1148.

32. (a) X. W. Li, W. T. Pennington, and G. H. Robinson, *J. Am. Chem. Soc.*, 1995, **107**, 1122; (b) T. Iwamoto, C. Kabuto, and M. Kira, *J. Am. Chem. Soc.*, 1999, **121**, 886.

33. I. Haiduc, *Phosphorus, Sulfur Silicon*, 1992, **64**, 169.

34. J. Siivari, R. S. Laitinen, and Y. Hiltunen, *Phosphorus, Sulfur Silicon*, 1992, **65**, 177.

35. P. Pekonen, J. Taavitsainen and R. S. Laitinen, *Phosphorus, Sulfur Silicon* 1994, **93–94**, 467.

36. I. Silaghi-Dumitrescu, I. Haiduc, and D. B. Sowerby, *Inorg. Chem.*, 1993, **32**, 3755.

37. (a) I. Silaghi-Dumitrescu, F. Lara-Ochoa, and I. Haiduc, *J. Mol. Struct. (THEOCHEM)*, 1996, **370**, 17; (b) I. Silaghi-Dumitrescu, F. Lara-Ochoa, P. Bishof, and I. Haiduc, *J. Mol. Struct. (THEOCHEM)*, 1996, **367**, 47.

38. (a) D. L. Strout, *J. Phys. Chem. A*, 2001, **105**, 261; (b) D. L. Strout, *J. Phys. Chem. A*, 2000, **104**, 3364.

39. S. Nagase, *Acc. Chem. Res.*, 1995, **28**, 469.

40. (a) R. West, *J. Organomet. Chem.*, 1986, **300**, 327; (b) R. D. Miller and J. Michl, *Chem. Rev.*, 1989, **89**, 1359.

41. (a) K. Matsumura, L. F. Brough and R. West, *J. Chem. Soc., Chem. Commun.* 1978, 1092; (b) L. F. Brough, K. Matsumura, and R. West, *Angew. Chem., Int. Ed. Engl.*, 1979, **18**, 955; (c) L. F. Brough and R. West, *J. Organomet. Chem.*, 1980, **194**, 139; (d) L. F. Brough and R. West, *J. Am. Chem. Soc.*, 1981, **103**, 3049.

42. Z. Pawelec and W. Wojnowski, *J. Inorg. Organomet. Polym.*, 1995, **5**, 163.

43. (a) C. Kratky, H. G. Schuster, and E. Hengge, *J. Organomet. Chem.*, 1983, **247**, 253; (b) H. L. Carrell and J. D. Donohue, *Acta Crystallogr.*, 1972, **B 28**, 1566; (c) F. Shafiee, J. R. Damewood, K. J. Haller, and R. West, *J. Am. Chem. Soc.*, 1985, **107**, 6950.

44. (a) L. Párkányi, K. Sasvári, and J. Batha, *Acta Crystallogr.*, 1978, **B 34**, 883; (b) L. Párkányi, K. Sasvári, J. P. Declerc, and G. Germain, *Acta Crystallogr.*, 1978, **B 34**, 3678; (c) M. Dräger and K. G. Walker, *Z. Anorg. Allg. Chem.*, 1981, **479**, 65.
45. F. Shafiee, K. J. Haller, and R. West, *J. Am. Chem. Soc.*, 1986, **108**, 5478.
46. R. G. Jones, W. K. C. Wong, and S. J. Holder, *Organometallics*, 1998, **17**, 59.
47. V. Ya. Lee, K. Takanashi, T. Matsuno, M. Ichinobe, and A. Sekiguchi, *J. Am. Chem. Soc.*, 2004, **126**, 4758.
48. (a) P. Trefonas and R. West, *J. Polym. Sci., Polym. Chem. Ed.*, 1985, **23**, 2099; (b) R. D. Miller and R. Sooriyakumaran, *J. Polym. Sci., Polym. Chem. Ed.*, 1987, **25**, 111.
49. I. Haiduc and M. Dräger, in ‘The Chemistry of Inorganic Homo- and Heterocycles’, eds. I. Haiduc, and D. B. Sowerby, Academic Press, London, 1987, Vol. 1, p. 361.
50. K. M. Baines and W. G. Stibbs, *Coord. Chem. Rev.*, 1995, **145**, 157.
51. (a) W. P. Neumann and J. Pedain, *Liebigs Ann. Chem.*, 1964, **672**, 34; (b) R. Sommer, W. P. Neumann, and B. Schneider, *Tetrahedron Lett.*, 1964, 3875.
52. (a) L. R. Sita, *Adv. Organomet. Chem.*, 1995, **38**, 189; (b) L. R. Sita, *Acc. Chem. Res.*, 1994, **27**, 191; (c) A. Sekiguchi, *Chem. Rev.*, 2003, **103**, 1429.
53. N. Devilder, M. Hill, K. C. Molloy, and G. J. Price, *Chem. Commun.*, 1996, 711.
54. T. Imori, V. Lu, H. Cai, and T. D. Tilley, *J. Am. Chem. Soc.*, 1995, **117**, 9931.
55. B. Watta, W. P. Neumann, and J. Sauer, *Organometallics*, 1985, **4**, 1954.
56. M. Okano, N. Matsumoto, M. Arakawa, T. Tsuruta, and H. Hamano, *Chem. Commun.*, 1998, 1799.
57. K. Mochida, M. Hayakawa, T. Tsuchikawa, Y. Yokoyama, M. Wakase, and H. Hayashi, *Chem. Lett.*, 1998, 91.
58. (a) W. P. Neumann and K. König, *Liebigs Ann. Chem.*, 1964, **677**, 12; (b) W. P. Neumann and J. Pedain, *Liebigs Ann. Chem.*, 1964, **672**, 34; (c) W. P. Neumann, J. Pedain, and R. Sommer, *Liebigs Ann. Chem.*, 1966, **694**, 9; (d) B. Jausseaume, N. Noriet, M. Pereyre, A. Saux, and J. M. Frances, *Organometallics*, 1994, **13**, 1034; (e) H. Puff, C. Bach, H. Reuter, and W. Schuh, *J. Organomet. Chem.*, 1984, **277**, 17.
59. (a) W. P. Neumann and K. König, *Angew. Chem., Int. Ed. Engl.*, 1962, **1**, 212; (b) M. Dräger, B. Mathiasch, L. Ross, and M. Ross, *Z. Anorg. Allg. Chem.*, 1983, **506**, 99; (c) D. H. Olson and R. E. Rundle, *Inorg. Chem.*, 1963, **2**, 1310.
60. (a) S. Masamune and L. R. Sita, *J. Am. Chem. Soc.*, 1985, **107**, 6390; (b) L. R. Sita and R. D. Bickerstaff, *J. Am. Chem. Soc.*, 1989, **111**, 3769; (c) A. Schafer, M. Weidenbruch, W. Saak, S. Pohl, and H. Harsmann, *Angew. Chem., Int. Ed. Engl.*, 1991, **30**, 834; (d) F. J. Brady, C. J. Cardin, D. J. Cardin, M. A. Convey, M. M. Devereux, and G. A. Lawless, *J. Organomet. Chem.*, 1991, **241**, 199.
61. M. Baudler and M. Glinka, in ‘The Chemistry of Inorganic Homo- and Heterocycles’, eds. I. Haiduc, and D. B. Sowerby, Academic Press, London, 1987, Vol. 2, p. 423.
62. P. S. Elmes, B. M. Gatehouse, and B. O. West, *J. Organomet. Chem.*, 1974, **82**, 235.
63. (a) F. Mathey, *Coord. Chem. Rev.*, 1994, **137**, 1; (b) O. J. Scherer, *Angew. Chem., Int. Ed. Engl.*, 1990, **29**, 1104; (c) O. J. Scherer, *Acc. Chem. Res.*, 1999, **32**, 751.
64. (a) A. J. DiMaio and A. L. Rheingold, *Chem. Rev.*, 1990, **90**, 169; (b) I. Haiduc and D. B. Sowerby, in ‘The Chemistry of Inorganic Homo- and Heterocycles’, eds. I. Haiduc, and D. B. Sowerby, Academic Press, London, 1987, Vol. 2, p. 701.
65. (a) P. S. Elmes, B. M. Gatehouse, D. J. Lloyd, and B. O. West, *J. Chem. Soc., Chem. Commun.*, 1974, 953; (b) P. S. Elmes, B. M. Gatehouse, and B. O. West, *J. Organomet. Chem.*, 1974, **82**, 235; (c) A. L. Rheingold, M. L. Fountain, and A. J. Di Maio, *J. Am. Chem. Soc.*, 1987, **109**, 141.
66. (a) L. Balazs and H. J. Breunig, *Coord. Chem. Rev.*, 2004, **248**, 603; (b) H. J. Breunig and R. Rösler, *Coord. Chem. Rev.*, 1997, **163**, 33; (c) H. J. Breunig and R. Rösler, *Chem. Soc. Rev.*, 2000, **29**, 403.
67. (a) R. Steudel, in ‘Sulfur: Its Significance for Chemistry, for Geo-, Bio- and Cosmosphere and Technology’, eds. A. Müller and B. Krebs, Elsevier, Amsterdam, NY, 1984, p. 3; (b) R. Steudel, in ‘The Chemistry of Inorganic Homo- and Heterocycles’, eds. I. Haiduc and D. B. Sowerby, Academic Press, London, 1987, Vol. 2, p. 737; (c) R. Steudel, in ‘The Chemistry of Inorganic Ring Systems’, ed. R. Steudel, Elsevier, Amsterdam, NY, 1992, p. 233; (d) R. S. Laitinen, P. Pekonen, and R. J. Suontamo, *Coord. Chem. Rev.*, 1994, **130**, 1.
68. J. Steidel, J. Pickardt, and R. Steudel, *Z. Naturforsch.*, 1978, **33b**, 1554.
69. (a) R. Steudel, R. Reinhardt, and F. Schuster, *Angew. Chem., Int. Ed. Engl.*, 1977, **16**, 715; (b) R. Steudel, J. Steidel, J. Pickardt, F. Schuster, and R. Reinhardt, *Z. Naturforsch.*, 1980, **35b**, 1378.
70. (a) L. K. Templeton, D. H. Templeton, and A. Zalkin, *Inorg. Chem.*, 1976, **8**, 1999; (b) L. M. Goldschmidt and C. E. Strouse, *J. Am. Chem. Soc.*, 1977, **99**, 7580.
71. (a) R. Reinhardt, R. Steudel, and F. Schuster, *Angew. Chem., Int. Ed. Engl.*, 1978, **17**, 57; (b) R. Steudel, *Z. Naturfosch.*, 1983, **38b**, 543.
72. R. Steudel, J. Steidel, and T. Sandow, *Z. Naturforsch.*, 1986, **41b**, 958.
73. J. Steidel, R. Steudel, and R. Kutoglu, *Z. Anorg. Allg. Chem.*, 1981, **476**, 171.
74. R. Steudel, O. Schumann, J. Buschmann, and P. Luger, *Angew. Chem.*, 1988, **110**, 2502.
75. (a) T. Debaerdemaker, E. Hellner, and A. Kutoglu, *Z. Anorg. Allg. Chem.*, 1974, **405**, 153; (b) T. Debaerdemaker and A. Kutoglu, *Cryst. Struct. Commun.*, 1974, **3**, 611.
76. T. Debaerdemaker, E. Hellner, A. Kutoglu, M. Schmidt, and E. Wilhelm, *Naturwissenschaften*, 1973, **60**, 300.

77. (a) R. Steudel, H. J. Mausle, D. Rosenbauer, H. Mockel, and T. Freyholt, *Angew. Chem., Int. Ed. Engl.*, 1981, **20**, 394; (b) R. Steudel and R. Strauss, *Z. Naturforsch.*, 1982, **37b**, 1219; (c) F. N. Tebbe, E. Wasserman, W. G. Peet, A. Vatvars, and A. C. Hayman, *J. Am. Chem. Soc.*, 1982, **104**, 4971.

78. J. A. Semlyen, *Trans. Faraday Soc.*, 1968, **64**, 1396.

79. R. S. Laitinen, P. Pekonen, and R. J. Suontamo, *Coord. Chem. Rev.*, 1994, **130**, 1.

80. (a) J. Beck, *Coord. Chem. Rev.*, 1997, **163**, 55; (b) S. Brownridge, I. Krossing, J. Passmore, H. D. B. Jenkins, and H. K. Roobottom, *Coord. Chem. Rev.*, 2000, **197**, 397.

81. I. Haiduc and D. B. Sowerby eds, 'The Chemistry of Inorganic Homo- and Heterocycles', Academic Press, London, 1987, Vol. 1.

82. (a) P. Paetzold, *Adv. Inorg. Chem.*, 1987, **31**, 141; (b) W. Luthin, G. Elter, A. Heine, D. Stalke, G. M. Sheldrick, and A. Meller, *Z. Anorg. Allg. Chem.*, 1992, **608**, 147; (c) G. Elter, M. Geschwendter, and A. Meller, *Z. Anorg. Allg. Chem.*, 1993, **619**, 1474; (d) T. Albrecht, G. Elter, and A. Meller, *Chem. Commun.*, 1998, 2583.

83. 'Gmelin Handbook of Inorganic Chemistry, Boron Compounds', Springer Verlag, Berlin, 1983, Vol. 1, 2nd Suppl., p. 225.

84. I. Haiduc, in 'The Chemistry of Inorganic Homo- and Heterocycles', eds. I. Haiduc and D. B. Sowerby, Academic Press, London, 1987, Vol.1, p. 109.

85. W. Siebert, in 'The Chemistry of Inorganic Homo- and Heterocycles', eds. I. Haiduc and D. B. Sowerby, Academic Press, London, 1987, Vol.1, p. 143.

86. O. Conrad, C. Jansen, and B. Krebs, *Angew. Chem., Int. Ed. Engl.*, 1998, **37**, 3208.

87. K. M. Waggoner and P. P. Power, *J. Am. Chem. Soc.*, 1991, **113**, 3385.

88. M. Cesari and S. Cuccinela, in 'The Chemistry of Inorganic Homo- and Heterocycles', eds. I. Haiduc, and D. B. Sowerby, Academic Press, London, 1987, Vol.1, p. 167.

89. S. D. Brewer and C. P. Haber, *J. Am. Chem. Soc.*, 1948, **70**, 3888.

90. U. Klingebiel, in 'The Chemistry of Inorganic Ring Systems', eds. I. Haiduc and D. B. Sowerby, Academic Press, London, 1987, Vol.1, p. 221.

91. B. Rozsondai, I. Hargittai, A. V. Golubinskii, L. V. Vilkov, and V. S. Mastryukov, *J. Mol. Struct.*, 1975, **28**, 339.

92. (a) G. S. Smith and L. E. Alexander, *Acta Crystallogr.*, 1963, **16**, 1015; (b) B. P. E. Edwards, W. Harrison, I. W. Novell, M. L. Post, H. M. M. Shearer, and J. Trotter, *Acta Crystallogr.*, 1976, **B 32**, 648.

93. B. Rake, H. W. Roesky, I. Uson, and P. Müller, *Angew. Chem.*, 1998, **110**, 1508.

94. G. Fritz and P. Scheer, *Chem. Rev.*, 2000, **100**, 3341.

95. I. Haiduc, in 'The Chemistry of Inorganic Homo- and Heterocycles', eds. I. Haiduc and D. B. Sowerby, Academic Press, London, 1987, Vol. 1, p. 368.

96. D. Seyferth, C. Proud'home, and G. H. Wiseman, *Inorg. Chem.*, 1983, **22**, 2163.

97. (a) W. I. Patnode and D. F. Wilcock, *J. Am. Chem. Soc.*, 1946, **68**, 358; (b) R. O. Sauer and D. J. Mead, *J. Am. Chem. Soc.*, 1946, **68**, 1794.

98. G. Peyronel, *Atti Acad. Naz. dei Lincei, Rend. Cl. Fis. Mat. Nat.*, 1954, **16**, 231.

99. H. Steinfink, B. Post, and I. Fankuchen, *Acta Crystallogr.*, 1955, **8**, 420.

100. A. F. Skryshevskii, V. P. Klochkov, and Yu. V. Pasenchik, *Zh. Strukt. Khim.*, 1961, **2**, 140.

101. N. L. Paddock, S. J. Rettig, and J. Trotter, *Can. J. Chem.*, 1983, **61**, 541.

102. O. I. Shchegolikhina, V. A. Igonin, Yu. A. Molodtsova, Yu. A. Pozdniakova, A. A. Zhdanov, T. V. Strelkova, and S. V. Lindeman, *J. Organomet. Chem.*, 1998, **562**, 141.

103. M. Michalczuk, M. J. Fink, K. J. Haller, R. West, and J. Michl, *Organometallics*, 1986, **5**, 531.

104. (a) Yu. T. Struchkov and S. V. Lindeman, *J. Organomet. Chem.*, 1995, **488**, 9; (b) Yu. A. Pozdniakova, K. A. Lyssenko, A. A. Korlyukov, I. V. Blagodatskikh, N. Auner, D. Katsoulis, and O. I. Shchegolikhina, *Eur. J. Inorg. Chem.*, 2004, 1253; (c) O. I. Shchegolikhina, I. Blagodashkikh, and A. A. Zhdanov, in 'Tailor-made Silicon-Oxygen Compounds. From Molecules to Materials', eds. R. Corriu, and P. Jutzi, Vieweg Verlag, Braunschweig, 1996, p. 177; (d) A. Cornia, A. C. Fabreti, D. Gatteschi, G. Palyi, E. Reutschler, O. I. Shchegolikhina, and A. A. Zhdanov, *Inorg. Chem.*, 1995, **34**, 5383; (e) O. I. Shchegolikhina, Yu. A. Pozdniakova, S. V. Lindeman, A. A. Zhdanov, R. Psaro, R. Ugo, G. Gavioli, R. Battistuzzi, M. Borsari, T. Ruffer, C. Zucchi, and G. Pályi, *J. Organomet. Chem.*, 1996, **514**, 29; (f) C. Zucchi, M. Mattioli, G. Gavioli, M. Moret, A. Sironi, R. Ugo, M. Pizzotti, O. Shchegolokhina, and G. Pályi, *Eur. J. Inorg. Chem.*, 2000, 1327.

105. (a) M. R. Churchill, C. H. Lake, S. H. L. Chao and O. T. Beachley Jr, *J. Chem. Soc., Chem. Commun.* 1993, 1577; (b) C. Eaborn, P. P. Hitchcock, K. Izod, and J. D. Smith, *Angew. Chem., Int. Ed. Engl.*, 1995, **34**, 2679.

106. J. P. Majoral and A. M. Caminade, *Chem. Rev.*, 1999, **99**, 845.

107. J. F. Brown and G. M. J. Slusarczuk, *J. Am. Chem. Soc.*, 1965, **87**, 931.

108. (a) P. V. Wright and M. S. Beevers, in 'Cyclic Polymers', ed. J. A. Semlyen, Elsevier, London, 1986, Chap. 3; (b) J. A. Semlyen, *Pure Appl. Chem.*, 1981, **53**, 1797; (c) C. J. C. Edwards, S. Bantle, W. Burchard, R. F. T. Stepto, and J. A. Semlyen, *Polymer*, 1982, **23**, 873.

109. (a) S. Penczek and P. Kubisa, in 'Ring-Opening Polymerization. Mechanism, Catalysis, Structure, Utility', ed. D. J. Brunelle, Hansen Publishers, Munich, 1993, p. 72; (b) J. Chojnowski, *J. Inorg. Organomet. Polym.*, 1991, **1**, 299; (c) G. J. Out, A. A. Teretskii, M. Moller, and D. Oelfin, *Macromolecules*, 1994, **27**, 3310.

110. K. Moedritzer and J. R. Van Wazer, *Inorg. Chem.*, 1965, **4**, 1753.

111. (a) I. Ross and M. Dräger, *Z. Naturforsch.*, 1984, **39b**, 868; (b) K. Haeberle and M. Dräger, *Z. Anorg. Allg. Chem.*, 1987, **55**, 116.

112. (a) C. W. Allen, in 'The Chemistry of Inorganic Homo- and Heterocycles', eds. I. Haiduc and D. B. Sowerby, Academic Press, 1987, Vol. 2; (b) C. W. Allen, *Coord. Chem. Rev.*, 1994, **130**, 137; (c) H. R. Allcock, J. L. Desorcie, and G. H. Riding, *Polyhedron*, 1987, **6**, 119.

113. N. L. Paddock, T. N. Ranganathan, and J. N. Wingfield, *J. Chem. Soc., Dalton Trans.*, 1972, 1578.

114. A. C. Chapman, N. L. Paddock, D. H. Paine, H. T. Searle, and D. R. Smith, *J. Chem. Soc.*, 1960, 3608.

115. (a) G. E. Coxon, D. B. Sowerby, and G. C. Trauter, *J. Chem. Soc.*, 1965, 5679; (b) G. E. Coxon and D. B. Sowerby, *J. Chem. Soc. A*, 1967, 1566.

116. G. Allen, D. J. Oldfield, N. L. Paddock, F. Rallo, J. Serregi, and S. M. Todd, *Chem. Ind. (London)*, 1965, 1032.

117. (a) N. L. Paddock, T. N. Ranganathan, and S. M. Todd, *Can. J. Chem.*, 1971, **49**, 164; (b) K. D. Gallicano, R. T. Oakley, N. L. Paddock, S. J. Rettig, and J. Trotter, *Can. J. Chem.* 1977, **55**, 304.

118. (a) F. H. Pollard, G. Nickless, and R. W. Warrender, *J. Chromatogr.*, 1962, **9**, 513; (b) F. H. Pollard, G. Nickless, and R. W. Warrender, *J. Chromatogr.*, 1953, **10**, 78.

119. M. W. Dougill, *J. Chem. Soc.*, 1963, 3211.

120. G. J. Bullen, *J. Chem. Soc. A*, 1971, 1450.

121. H. Mc, M. Geachin, and F. R. Tromans, *J. Chem. Soc.*, 1961, 4777.

122. A. G. Wagner, A. Vos, J. L. De Boe, and T. Wichertjes, *Acta Crystallogr.*, 1963, **12**, 39A.

123. J. G. Hartsuiker and A. J. Wagner, *J. Chem. Soc., Dalton Trans.*, 1978, 1425.

124. A. W. Schlueter and R. A. Jacobson, *J. Chem. Soc. A*, 1968, 2317.

125. J. G. Hartsuiker and A. J. Wagner, *J. Chem. Soc., Dalton Trans.*, 1968, 1069.

126. M. W. Dougill and B. Sheldrick, *Acta Crystallogr.*, 1977, **B33**, 295.

127. R. T. Oakley, N. L. Paddock, S. J. Rettig, and J. Trotter, *Can. J. Chem.*, 1977, **55**, 3118.

128. R. T. Oakley, N. L. Paddock, S. J. Rettig, and J. Trotter, *Can. J. Chem.*, 1977, **55**, 2530.

129. R. T. Oakley, S. J. Rettig, N. L. Paddock, and J. Trotter, *J. Am. Chem. Soc.*, 1985, **107**, 6923.

130. M. W. Dougill and N. L. Paddock, *J. Chem. Soc.*, 1974, 1022.

131. A. J. Wagner and A. Vos, *Acta Crystallogr.*, 1968, **B24**, 1423.

132. N. L. Paddock, J. Trotter, and S. H. Whitlow, *J. Chem. Soc. A*, 1968, 2227.

133. H. P. Calhoun, N. L. Paddock, and J. Trotter, *J. Chem. Soc., Dalton Trans.*, 1976, 38.

134. H. R. Allcock, in 'The Chemistry of Inorganic Ring Systems', ed. R. Steudel, Elsevier, Amsterdam, NY, 1992, p. 145.

135. (a) T. Chivers, C. Fedorchuk, M. Krahn, M. Parvez, and G. Schatte, *Inorg. Chem.*, 2001, **40**, 1936; (b) G. G. Briand, T. Chivers, M. Krahn, and M. Parvez, *Inorg. Chem.*, 2002, **41**, 6808; (c) G. G. Briand, T. Chivers, M. Parvez, and G. Schatte, *Inorg. Chem.*, 2003, **42**, 525; (d) T. Chivers, M. Krahn, and M. Parvez, *Chem. Commun.*, 2000, 463; (e) G. G. Briand, T. Chivers, and M. Krahn, *Coord. Chem. Rev.*, 2002, **233–234**, 237.

136. (a) I. Schranz, L. P. Grocholl, L. Stahl, R. J. Staples, and A. Johnson, *Inorg. Chem.*, 2000, **39**, 3037; (b) D. F. Moser, I. Schranz, M. C. Gerrety, L. Stahl, and R. J. Staples, *J. Chem. Soc., Dalton Trans.*, 1999, 751.

137. (a) D. P. Gates, L. M. Liable-Sands, G. P. A. Yap, A. L. Rheingold, and I. Manners, *J. Am. Chem. Soc.*, 1997, **119**, 125; (b) A. R. McWilliams, D. P. Gates, M. Edwards, L. M. Liable-Sands, I. Guzei, A. L. Rheingold, and I. Manners, *J. Am. Chem. Soc.*, 2000, **122**, 8848.

138. I. Manners, *Coord. Chem. Rev.*, 1994, **137**, 109.

139. J. C. Van de Grampel, *Coord. Chem. Rev.*, 1992, **112**, 247.

140. T. Chivers and R. W. Hilts, *Coord. Chem. Rev.*, 1994, **137**, 201.

141. A. R. McWilliams, E. Rivard, A. J. Lough, and I. Manners, *Chem. Commun.*, 2002, 1102.

142. S. Schultz, T. Bauer, and M. Nieger, *Chem. Commun.*, 1999, 879.

143. (a) A. Durif, 'Crystal Chemistry of Condensed Phosphates', Plenum Press, New York, 1995; (b) A. Durif, in 'The Chemistry of Inorganic Homo- and Heterocycles', eds. I. Haiduc and D. B. Sowerby, Academic Press, London, 1987, Vol. 2, p. 659; (c) M. T. Averbuch-Pouchot and A. Durif, in 'Stereochemistry of Organometallic and Inorganic Compounds, Vol. 5, Chains, Clusters, Inclusion Compounds', ed. P. Zanello, Elsevier, Amsterdam, NY, 1994, p. 3.

144. I. Haiduc, 'The Chemistry of Inorganic Ring Systems', Wiley-Interscience, London, 1970, p. 819, Vol. 2.

145. (a) E. Thilo and U. Schülke, *Angew. Chem.*, 1963, **75**, 1175; (b) K. H. Jost, *Acta Crystallogr.*, 1965, **19**, 555; (c) E. J. Griffith and R. I. Buxton, *Inorg. Chem.*, 1965, **4**, 549.

146. U. Schülke, *Z. Anorg. Allg. Chem.*, 1968, **360**, 231.

147. (a) U. Schülke, M. T. Averbuch-Pouchot, and A. Durif, *Z. Anorg. Allg. Chem.*, 1994, **620**, 545; (b) M. T. Averbuch-Pouchot, A. Durif, and U. Schülke, *J. Solid State Chem.*, 1992, **97**, 299.

148. (a) A. V. Lavrov, M. Ya. Voitenkov, and E. G. Tselebrovskaya, *Izv. Akad. Nauk SSSR, Neorg. Mater.*, 1981, **17**, 99; (b) I. Grunze and N. N. Chudinova, *Izv. Akad. Nauk SSSR, Neorg. Mater.*, 1988, **24**, 988.

149. S. Ohashi, G. Kura, Y. Shimada, and M. Hara, *J. Inorg. Nucl. Chem.*, 1977, **39**, 1513.

150. (a) E. H. Wong, X. Y. Sun, E. J. Gabe, F. L. Lee, and J. P. Charland, *Organometallics*, 1991, **10**, 3010; (b) H. Yang,

E. H. Wong, A. L. Rheingold, B. E. Owens-Watermire, and B. S. Haggerty, *Organometallics*, 1994, **13**, 4825.

151. (a) H. H. Sisler and C. Stratton, *Inorg. Chem.*, 1966, **5**, 2003; (b) M. J. Begley, D. B. Sowerby, and R. J. Tillott, *J. Chem. Soc., Dalton Trans.*, 1974, 2527; (c) L. K. Krannick, H. Thewalt, W. J. Cook, S. R. Jain, and H. H. Sisler, *Inorg. Chem.*, 1973, **12**, 2304.

152. (a) H. C. Marsmann and J. R. Van Wazer, *J. Am. Chem. Soc.*, 1970, **92**, 3969; (b) M. Durand and J. P. Laurent, *J. Organomet. Chem.*, 1974, **77**, 225; (c) W. S. Sheldrick and T. Hausler, *Z. Naturforsch.*, 1993, **48b**, 1069.

153. (a) A. J. DiMaio and A. L. Rheingold, *Organometallics*, 1991, **10**, 3764; (b) A. M. Arif, A. H. Cowley, and M. Pakulski, *J. Chem. Soc., Chem. Commun.*, 1987, 165.

154. (a) W. S. Sheldrick and T. Hausler, *Z. Anorg. Allg. Chem.*, 1993, **619**, 1984; (b) T. Hausler and W. S. Sheldrick, *Chem. Ber.*, 1997, **130**, 371.

155. I. M. Miller and W. S. Sheldrick, *Z. Naturforsch.*, 1957, **52b**, 951.

156. A. L. Rheingold and A. J. DiMaio, *Organometallics*, 1986, **5**, 393.

157. T. Hausler and W. S. Sheldrick, *Z. Naturforsch.*, 1997, **52b**, 1997.

158. I. M. Miller and W. S. Sheldrick, *Eur. J. Inorg. Chem.*, 1998, 1999.

159. T. Hausler and W. S. Sheldrick, *Chem. Ber.*, 1996, **129**, 131.

160. O. M. Kekia and A. L. Rheingold, *Organometallics*, 1998, **17**, 726.

161. W. S. Sheldrick and I. M. Müller, *Coord. Chem. Rev.*, 1999, **182**, 125.

162. M. A. Beswick, M. K. Davies, M. A. Paver, P. R. Raitby, A. Steiner, and D. S. Wright, *Angew. Chem., Int. Ed. Engl.*, 1996, **35**, 1518.

163. D. C. Haagenson, L. Stahl, and R. J. Staples, *Inorg. Chem.*, 2001, **40**, 4491.

164. (a) H. J. Breunig, M. A. Mohamed, and K. H. Ebert, *Z. Naturforsch.*, 1994, **49b**, 877; (b) M. A. Mohamed, K. H. Ebert, and H. J. Breunig, *Z. Naturforsch.*, 1996, **51b**, 149.

165. M. M. Labes, P. Love, and L. F. Nichols, *Chem. Rev.*, 1979, **79**, 1.

166. A. J. Bannister, P. J. Dainty, A. C. Hazzell, and J. G. Lomberg, *Chem. Commun.*, 1969, 1187.

167. (a) T. Chivers, in 'The Chemistry of Inorganic Homo- and Heterocycles', eds. I. Haiduc and D. B. Sowerby, Academic Press, London, 1987, p. 793; (b) I. Haiduc, 'The Chemistry of Inorganic Ring Systems', Wiley-Interscience, London, 1970, Vol. 2, p. 913.

168. (a) A. Haas, J. Kasprowski, and M. Pryka, *Coord. Chem. Rev.*, 1994, **130**, 301; (b) R. Boese, A. Haas, E. Hoppmann, K. Merz, and A. Olteanu, *Z. Anorg. Allg. Chem.*, 2002, **628**, 673.

169. W. Ando, K. Tetsuji, and M. Ishii, *Angew. Chem., Int. Ed. Engl.*, 1992, **31**, 59.

170. (a) V. Chandrasekhar, S. Nagendran, and V. Baskar, *Coord. Chem. Rev.*, 2002, **235**, 1; (b) R. Okazaki, *Phosphorus, Sulfur Silicon*, 2001, **168**, 41; (c) J. Beckmann and K. Jurkschat, *Coord. Chem. Rev.*, 2001, **215**, 267; (d) H. Lange, U. Herzog, U. Bohme, and G. Rheinwald, *J. Organomet. Chem.*, 2002, **660**, 43; (e) U. Herzog and G. Rheinwald, *J. Organomet. Chem.*, 2001, **627**, 23; (f) U. Hermann, M. Schürmann, and F. Uhlig, *J. Organomet. Chem.*, 1999, **585**, 211; (g) U. Hermann, I. Prass, and F. Uhlig, *Phosphorus, Sulfur Silicon*, 2001, **168**, 145.

171. (a) N. Kano, K. Shibata, N. Tokitoh, and R. Okazaki, *Organometallics*, 1999, **18**, 2999; (b) N. Kano, N. Tokitoh, and R. Okazaki, *Organometallics*, 1997, **16**, 4237; (c) N. Tokitoh, N. Kano, K. Shibata, and R. Okazaki, *Organometallics*, 1995, **14**, 3121.

172. M. A. Beswick and D. S. Wright, *Coord. Chem. Rev.*, 1998, **176**, 373.

173. U. Herzog and G. Rheinwald, *J. Organomet. Chem.*, 2001, **627**, 23.

174. I. Haiduc and D. B. Sowerby eds, 'The Chemistry of Inorganic Homo- and Heterocycles', Academic Press, London, 1987.

175. (a) H. W. Roesky, I. Leichtweis, and M. Noltemeyer, *Inorg. Chem.*, 1993, **32**, 5102; (b) T. Carofiglio, C. Floriani, A. Sgamellotti, M. Rosi, A. Chiesi-Villa, and C. Rizzoli, *J. Chem. Soc., Dalton Trans.*, 1992, 1081; (c) S. Cirueles, T. Cuenca, J. C. Flores, R. Gomez, P. Gomez-Sal, and P. Royo, *Organometallics*, 1993, **12**, 944.

176. F. Bottomley, J. Darkwa, L. Sutin, and P. S. White, *Organometallics*, 1986, **5**, 2165.

177. G. Fachinetti, C. Floriani, A. Chiesi-Villa, and C. Guastini, *J. Am. Chem. Soc.*, 1979, **101**, 1767.

178. (a) F. Bottomley and L. Sutin, *Adv. Organomet. Chem.*, 1988, **28**, 339; (b) F. Bottomley, *Polyhedron*, 1992, **11**, 1707.

179. H. W. Roesky, I. Haiduc, and N. S. Hosmane, *Chem. Rev.*, 2003, **103**, 2579.

180. (a) H. W. Roesky, P. Olms, R. Hasselbring, N. Winkhofer, F. Q. Liu, and M. Noltemeyer, *Phosphorus, Sulfur Silicon*, 1993, **76**, 255; (b) S. K. Pandey, A. Steiner, H. W. Roesky, and D. Stalke, *Inorg. Chem.*, 1993, **32**, 5444; (c) H. J. Gosink, H. W. Roesky, H. G. Schmidt, M. Noltemeyer, E. Irmer, and R. Herbst-Irmer, *Organometallics*, 1994, **13**, 3420; (d) F. Q. Liu, I. Uson, and H. W. Roesky, *Z. Anorg. Allg. Chem.*, 1996, **622**, 819.

181. (a) H. W. Roesky, *Synlett*, 1990, 651; (b) T. Lubbeen, M. Witt, H. W. Roesky, M. Noltemeyer, and H. G. Schmidt, *Inorg. Chem.*, 1995, **34**, 4275; (c) F. Q. Liu, I. Uson, and H. W. Roesky, *J. Chem. Soc., Dalton Trans.*, 1995, 2453; (d) F. Q. Liu, I. Uson, and H. W. Roesky, *Z. Anorg Allg. Chem.*, 1996, **622**, 819.

182. (a) A. J. Elias, H. G. Schmidt, M. Noltemeyer, and H. W. Roesky, *Eur. J. Inorg. Solid State Chem.*, 1992, **29**,

23; (b) A. J. Elias, H. W. Roesky, W. T. Robinson, and G. M. Sheldrick, *J. Chem. Soc., Dalton Trans.*, 1993, 495.

183. H. J. Koch, H. W. Roesky, R. Bohra, M. Noltemeyer, and H. G. Schmidt, *Angew. Chem., Int. Ed. Engl.*, 1992, **31**, 598.
184. M. Witt and H. W. Roesky, *Chem. Rev.*, 1994, **94**, 1163.
185. W. K. Leong, R. K. Pomeroy, R. J. Batchelor, F. W. B. Einstein, and C. F. Campana, *Organometallics*, 1997, **16**, 1079.
186. A. Haaland, *Angew. Chem., Int. Ed. Engl.*, 1989, **28**, 992.
187. A. Haaland, in 'Coordination Chemistry of Aluminum', ed. G. H. Robinson, VCH Publishers, Weinheim, 1993, Chap. 1, p. 1.
188. B. König, *Eur. Chem. Chronicle*, 1998, **3**, 17.
189. F. C. Sauls, C. L. Czekaj, and L. V. Interrante, *Inorg. Chem.*, 1990, **29**, 4688.
190. K. Ouzounis, H. Riffel, H. Hess, U. Köhler, and J. Weidlein, *Z. Anorg. Allg. Chem.*, 1983, **504**, 67.
191. D. C. Bradley, I. S. Harding, I. A. Maia, and M. Motevalli, *J. Chem. Soc., Dalton Trans.*, 1997, 2969.
192. G. H. Robinson, in 'Coordination Chemistry of Aluminum', ed. G. H. Robinson, VCH Publishers, New York, 1993, Chap. 2, p. 57.
193. C. von Hanisch and F. Weigend, *Z. Anorg. Allg. Chem.*, 2002, **628**, 389.
194. (a) R. L. Wells, *Coord. Chem. Rev.*, 1992, **112**, 273; (b) S. Schultz, *Coord. Chem. Rev.*, 2001, **215**, 1.
195. J. Müller, *Coord. Chem. Rev.*, 2002, **235**, 105.
196. C. C. Chang and M. S. Ameerunisha, *Coord. Chem. Rev.*, 1999, **189**, 199.
197. (a) C. von Hanisch and B. Rolli, *Z. Anorg. Allg. Chem.*, 2002, **628**, 2255; (b) F. Thomas, S. Schultz, and M. Nieger, *Z. Anorg. Allg. Chem.*, 2002, **628**, 235.
198. (a) F. C. Sauls and L. V. Interrante, *Coord. Chem. Rev.*, 1993, **128**, 193; (b) J. A. Jegier and W. L. Gladfelter, *Coord. Chem. Rev.*, 2000, **206–207**, 631.
199. N. W. Mitzel, C. Lustig, and M. Woski, *J. Chem. Soc., Dalton Trans.*, 2004, 397; (b) B. Neumüller and E. Iravani, *Coord. Chem. Rev.*, 2004, **248**, 817.
200. (a) J. M. Brunel, B. Faure, and M. Maffei, *Coord. Chem. Rev.*, 1998, **178–180**, 1998; (b) H. Dorn, R. A. Singh, J. A. Massey, J. M. Nelson, C. A. Jaska, A. J. Lough, and I. Manners, *J. Am. Chem. Soc.*, 2000, **122**, 6669.
201. B. Neumüller, *Coord. Chem. Rev.*, 1997, **158**, 69.
202. J. P. Oliver, *J. Organomet. Chem.*, 1995, **500**, 269.
203. M. G. Newton, I. Haiduc, R. B. King, and C. Silvestru, *Chem. Commun.*, 1993, 1229.
204. A. Deák, I. Haiduc, L. Párkányi, M. Venter, and A. Kálmán, *Eur. J. Inorg. Chem.*, 1999, 1593.
205. K. C. Molloy, F. A. K. Nasser, C. L. Barnes, D. van der Helm, and J. J. Zukerman, *Inorg. Chem.*, 1982, **21**, 960.
206. J. G. Masters, F. A. K. Nasser, M. B. Hossain, A. P. Hagen, D. van der Helm, and J. J. Zukerman, *J. Organomet. Chem.*, 1990, **385**, 39.
207. J. M. Korker, D. J. Browning, and M. Webster, *Acta Crystallogr.*, 1996, **C52**, 583.
208. C. L. Landry, A. Hynes, A. R. Barron, I. Haiduc, and C. Silvestru, *Polyhedron*, 1996, **15**, 391.
209. M. G. Walawalkar, R. Murugavel, H. W. Roesky, and H. G. Schmidt, *Inorg. Chem.*, 1997, **36**, 4202.
210. Y. Yang, M. G. Walawalkar, J. Pinkas, H. W. Roesky, and H. G. Schmidt, *Angew. Chem., Int. Ed. Engl.*, 1998, **37**, 96.
211. M. G. Walawalkar, R. Murugavel, A. Voigt, H. W. Roesky, and H. G. Schmidt, *J. Am. Chem. Soc.*, 1997, **119**, 4656.
212. M. G. Walawalkar, R. Murugavel, H. Roesky, I. Uson, and R. Kraetzner, *Inorg. Chem.*, 1998, **37**, 473.
213. (a) M. R. Close and R. E. Mc Carley, *Inorg. Chem.*, 1994, **33**, 4198; (b) K. Dehnicke and J. Strähle, *Angew. Chem., Int. Ed. Engl.*, 1992, **31**, 955; (c) W. A. Hermann, S. Bogdanovich, T. Piermeier, R. Poli, and J. C. Fettinger, *Angew. Chem., Int. Ed. Engl.*, 1995, **34**, 112.
214. W. W. Schoeller and A. Sundermann, *Inorg. Chem.*, 1998, **37**, 3034.
215. R. A. Wheeler, R. Hoffmann, and J. Strähle, *J. Am. Chem. Soc.*, 1986, **108**, 5381.
216. (a) L. G. Hubert-Pfalzgraf, *Coord. Chem. Rev.*, 1998, **178–180**, 967; (b) M. A. Munoz-Hernandez, P. Wei, S. Liu, and D. A. Atwood, *Coord. Chem. Rev.*, 2000, **210**, 1; (c) B. Neumüller, *Chem. Soc. Rev.*, 2003, **32**, 50; (d) V. G. Kessler, *Chem. Commun.*, 2003, 1213.
217. D. M. Stefanescu, H. F. Yuen, D. S. Glueck, J. A. Golen, L. N. Zakharov, C. D. Incarvito, and A. L. Rheingold, *Inorg. Chem.*, 2003, **42**, 8891.
218. R. W. Saalfrank, C. Deutscher, H. Maid, A. M. Ako, S. Sperner, T. Nakajima, W. Bauer, F. Hampel, B. A. Hess, N. J. R. van Eikema Hommes, R. Puchta, and F. W. Heinemann, *Chem. Eur. J.*, 2004, **10**, 1899.
219. C. Canada-Vilalta, M. Pink, and G. Christou, *Chem. Commun.*, 2003, 1240.
220. A. A. H. Abu-Nawwas, J. Cano, P. Christian, T. Mallah, G. Rajaraman, S. J. Teat, R. E. P. Winpenny, and Y. Yukawa, *Chem. Commun.*, 2004, 314.
221. O. L. Sydora, P. T. Wolczanski, E. B. Lobkowski, E. Rumberger, and D. N. Hendrickson, *Chem. Commun.*, 2004, 650.
222. (a) I. Haiduc, D. B. Sowerby, and S. F. Lu, *Polyhedron*, 1995, **14**, 3389; (b) I. Haiduc and D. B. Sowerby, *Polyhedron*, 1996, **15**, 2469.; (c) I. Haiduc, in 'Comprehensive Coordination Chemistry-II, From Biology to Materials, Volume I', ed. A. B. P. Lever, Elsevier Pergamon, Amsterdam, NY, 2004, Chap. 1.15, p. 349; (d) V. K. Jain, *Coord. Chem. Rev.*, 1994, **135–136**, 809.
223. R. C. Mehrotra, in 'Comprehensive Coordination Chemistry', ed. G. Wilkinson, Pergamon Press, Oxford, 1987, Vol. 2, Chap. 15.9, p. 505.

224. (a) I. Haiduc, in ‘Comprehensive Coordination Chemistry-II, From Biology to Materials, Volume I’, ed. A. B. P. Lever, Elsevier Pergamon, Amsterdam, NY, 2004, Chap. 1.14, p. 323; (b) J. D. Woollins, *J. Chem. Soc., Dalton Trans.*, 1996, 2893; (c) C. Silvestru and J. E. Drake, *Coord. Chem. Rev.*, 2001, **223**, 117; (d) T. Q. Li and J. D. Woollins, *Coord. Chem. Rev.*, 1998, **176**, 451.

225. I. Haiduc and I. Silaghi-Dumitrescu, *Coord. Chem. Rev.*, 1986, **74**, 127.

226. (a) A. Müller and E. Diemann, *Adv. Inorg. Chem. Radiochem.*, 1987, **31**, 89; (b) M. Draganjac and T. B. Rauchfuss, *Angew. Chem., Int. Ed. Engl.*, 1985, **24**, 742; (c) M. G. Kanatzidis and S. P. Huang, *Coord. Chem. Rev.*, 1994, **130**, 509.

227. S. Trofimenko, ‘Scorpionates. The Coordination Chemistry of Polypyrazolylborate Ligands’, Imperial College Press, London, 1999.

228. M. M. S. Balakrishna, P. Chandrasekaran, and P. P. George, *Coord. Chem. Rev.*, 2003, **241**, 87.

229. T. Appleby and J. D. Woollins, *Coord. Chem. Rev.*, 2002, **235**, 121.

230. (a) V. Lorenz, A. Fischer, S. Giessmann, J. W. Gilje, Y. Gun’ko, K. Jacob, and F. T. Edelmann, *Coord. Chem. Rev.*, 2000, **206–207**, 321; (b) L. King and A. C. Sullivan, *Coord. Chem. Rev.*, 1999, **189**, 19.

231. R. Fleischer and D. Stalke, *Coord. Chem. Rev.*, 1998, **176**, 431.

232. N. W. Alcock, *Adv. Inorg. Chem. Radiochem.*, 1972, **15**, 1.

233. N. W. Alcock, ‘Bonding and Structure. Structural Principles in Inorganic and Organic Chemistry’, Ellis Horwood, London, 1993, p. 195.

234. P. Pyykkö, *Chem. Rev.*, 1997, **97**, 597.

235. I. Haiduc, *Coord. Chem. Rev.*, 1997, **158**, 325.

236. I. Haiduc, *Phosphorus, Sulphur Silicon*, 1994, **93–94**, 345.

237. M. G. Newton, R. B. King, I. Haiduc, and A. Silvestru, *Inorg. Chem.*, 1993, **32**, 3785.

238. C. Silvestru, L. Silaghi-Dumitrescu, I. Haiduc, M. J. Begley, M. Nunn, and D. B. Sowerby, *J. Chem. Soc., Dalton Trans.*, 1986, 1031.

239. E. Weiss, *Angew. Chem., Int. Ed. Engl.*, 1993, **32**, 1501.

240. M. Driess, *Adv. Organomet. Chem.*, 1996, **39**, 193.

241. U. Englich and K. Ruhland-Senge, *Coord. Chem. Rev.*, 2000, **210**, 135.

242. (a) E. Weiss, *Angew. Chem., Int. Ed. Engl*, 1993, **32**, 1501; (b) M. Driess, *Adv. Organomet. Chem.*, 1996, **39**, 193.

243. R. D. Rogers, J. L. Atwood, and R. Gruning, *J. Organomet. Chem.*, 1978, **157**, 229.

244. M. D. Janssen, E. Rijnberg, C. A. de Wolf, M. P. Hogerheide, D. Kruis, H. Kooijman, A. L. Spek, D. M. Grove, and G. van Koten, *Inorg. Chem.*, 1996, **35**, 6735.

245. (a) A. M. Sapse and P. von Rague-Schleyer eds, ‘Lithium Chemistry. A Theoretical and Experimental Overview’, J. Wiley and Sons, New York, 1995; (b) K. Gregory, P. von Rague-Schleyer, and R. Snaith, *Adv. Inorg. Chem.*, 1991, **37**, 48; (c) R. E. Mulvey, *Chem. Soc. Rev.*, 1998, **27**, 339; (d) F. Antolini, P. B. Hitchcock, A. V. Khvostov, and M. F. Lappert, *Eur. J. Inorg. Chem.*, 2003, 3391.

246. M. Driess, H. Pritzkow, M. Skipinski, and U. Winkler, *Organometallics*, 1997, **16**, 5108.

247. R. A. Jones, A. L. Stuart, and T. C. Wright, *J. Am. Chem. Soc.*, 1983, **105**, 7459.

248. (a) T. Greiser and E. Weiss, *Chem. Ber.*, 1977, **110**, 3388; (b) J. E. Davies, J. Köpf, and E. Weiss, *Acta Crystallogr.*, 1982, **B 38**, 2251.

249. K. Ruhland-Senge, U. Englich, M. O. Senge, S. O. Chadwick, and P. P. Power, *Inorg. Chem.*, 1996, **35**, 5820.

250. M. D. Janssen, E. Rijnberg, C. A. de Wolf, M. P. Hogerheide, D. Kruis, H. Kooijman, A. L. Spek, D. M. Grove, and G. van Koten, *Inorg. Chem.*, 1996, **35**, 6735.

251. I. Haiduc and F. T. Edelmann, ‘Supramolecular Organometallic Chemistry’, Wiley-VCH, Weinheim, 1999, Chap. 6.

252. A. Silvestru, I. Haiduc, R. Toscano, and H. J. Breunig, *Polyhedron*, 1995, **14**, 2047.

253. H. Puff, K. Braun, and H. Reuter, *J. Organomet. Chem.*, 1991, **409**, 119.

254. L. Silaghi-Dumitrescu, I. Silaghi-Dumitrescu, J. Zukerman-Schpector, I. Haiduc, and D. B. Sowerby, *J. Organomet. Chem.*, 1996, **517**, 101.

255. M. Nieger, E. Niecke, and R. Deutsch, *Z. Kristallogr.*, 1995, **210**, 971.

256. S. Supriya and S. K. Das, *J. Cluster Sci.*, 2003, **14**, 337.

257. (a) K. Nauta and R. E. Miller, *Science*, 2000, **287**, 292; (b) R. Custelcean, C. Afloroaiei, M. Vlassa, and M. Polverejan, *Angew. Chem., Int. Ed. Engl.*, 2000, **39**, 3094; (c) J. N. Moorthy, R. Natarajan, and P. Vegopalan, *Angew. Chem., Int. Ed. Engl.*, 2002, **41**, 3417; (d) A. Michaelides, S. Skoulika, E. G. Bakabassis, and J. Mrozinki, *Cryst. Growth Des.*, 2003, **3**, 487; (e) S. K. Ghosh and P. K. Bharadwaj, *Inorg. Chem.*, 2003, **42**, 8250; (f) I. Bernal and J. L. Bear, *J. Chem. Crystallogr.*, 2002, **32**, 485; (g) I. B. Rother, M. Willermann, and B. Lippert, *Supramol. Chem.*, 2002, **14**, 189.

258. (a) J. L. Atwood, L. J. Barbour, T. J. Ness, C. L. Raston, and P. L. Raston, *J. Am. Chem. Soc.*, 2001, **123**, 7192; (b) W. B. Blanton, S. W. Gordon-Wylie, G. R. Clark, K. D. Jordan, J. T. Wood, U. Geiser, and T. J. Collins, *J. Am. Chem. Soc.*, 1999, **121**, 3551.

259. (a) L. J. Barbour, G. W. Orr, and J. L. Atwood, *Chem. Commun.*, 2000, 859; (b) L. J. Barbour, G. W. Orr, and J. L. Atwood, *Nature*, 1998, **393**, 671.

260. F. N. Keutsch, J. D. Cruzan, and R. J. Saykally, *Chem. Rev.*, 2003, **103**, 2533.

261. A. M. James, R. K. Laxman, F. R. Fronczek, and A. W. Mawerick, *Inorg. Chem.*, 1998, **37**, 3785.

262. I. G. Dance, L. J. Fitzpatrick, D. C. Craig, and M. L. Scudder, *Inorg. Chem.*, 1989, **28**, 1853.

263. S. Husebye, K. Maartmann-Moe, and O. Mikalsen, *Acta Chem. Scand.*, 1990, **44**, 802.
264. D. Hänssgen, M. Kumpel, and M. Nieger, *Z. Anorg. Allg. Chem.*, 1996, **622**, 745.
265. I. Haiduc, in ‘The Chemistry of Inorganic Homo- and Heterocycles’, eds. I. Haiduc and D. B. Sowerby, Academic Press, London, 1987, Vol. 2, p. 109.
266. G. Mezei, P. Baran, and R. G. Raptis, *Angew. Chem., Int. Ed. Engl.*, 2004, **43**, 574.
267. W. E. van Zyl, R. J. Staples, and J. P. Fackler Jr, *Inorg. Chem. Comm.*, 1998, **1**, 51.
268. F. Lara-Ochoa, I. Silaghi-Dumitrescu, and I. Haiduc, *Main Group Chem.*, 1996, **1**, 387.
269. I. Haiduc and I. Silaghi-Dumitrescu, *Rev. Roum. Chim.*, 1991, **36**, 527; *Phosphorus, Sulfur Silicon*, 1992, **65**, 53.
270. I. Silaghi-Dumitrescu and I. Haiduc, *Studia Univ. Babes-Bolyai, Chemia*, 1993, **38**, 183.
271. I. Silaghi-Dumitrescu and I. Haiduc, *Phosphorus, Sulfur Silicon*, 1994, **91**, 21.
272. A. Müller, E. Krickemeyer, J. Meyer, H. Bögge, F. Peters, W. Plass, E. Diemann, S. Dillinger, F. Nonnenbruch, M. Randerath, and C. Menke, *Angew. Chem., Int. Ed. Engl.*, 1995, **34**, 2122.
273. A. Müller, E. Krickemeyer, H. Bögge, M. Schmidtmann, C. Beugholt, P. Kögerler, and C. H. Lu, *Angew. Chem., Int. Ed. Engl.*, 1998, **37**, 1220.
274. C. C. Jiang, Y. G. Wei, Q. Liu, S. W. Zhang, M. C. Shao, and Y. Q. Tang, *Chem. Commun.*, 1998, 1937.
275. A. Müller, E. Krickemeyer, H. Bögge, M. Schmidtmann, F. Peters, C. Menke, and J. Meyer, *Angew. Chem., Int. Ed. Engl.*, 1997, **36**, 484.
276. A. Müller, F. Peters, M. T. Pope, and D. Gatteschi, *Chem. Rev.*, 1998, **98**, 239.
277. P. Gouzerh and A. Proust, *Chem. Rev.*, 1998, **98**, 77.

High-Energy Electron Diffraction

Jian-Min Zuo

Materials Research Laboratory, University of Illinois, Urbana, IL, USA

	Method Summary	1
1	Introduction	2
2	Technical Background	3
3	Applications	13
4	Acknowledgement	24
5	Abbreviations and Acronyms	24
6	Further Reading	24
7	References	26

METHOD SUMMARY

Acronyms, Synonyms

- Transmission High Energy Electron Diffraction (THEED)
- Reflection High Energy Electron Diffraction (RHEED)
- Convergent Beam Electron Diffraction (CBED)
- Nanoarea (or Nanobeam) Electron Diffraction (NED)
- Large Angle Convergent Beam Electron Diffraction (LACBED)

Measured physical quantities

- diffraction pattern geometry
- diffraction intensity and its distribution
- temperature-dependent diffraction pattern geometry and intensity.

Information available

- d-spacings measured from the diffraction pattern geometry
- crystal orientations and interfacial relationships
- crystal unit cell and strain
- crystal symmetry
- atomic positions determined from diffraction intensities
- radial distribution function from diffraction ring patterns
- surface structure and the structure of surface adsorbates from RHEED
- crystal electron density distribution and bonding.

Information not available, limitations

- magnetic spins or isotopes
- study limited to thin foils of several hundreds of nanometers thick
- samples compatible with vacuum required for electron diffraction
- radiation damage for biological samples
- incompatible with high pressure.

Examples of questions that can be answered

- Is the material crystalline or amorphous?
- What is the crystal structure and where are the atoms?
- What is the interface between two crystals?
- What is the structure of a nanotube or nanoparticle?
- What is the surface structure and surface orientation?
- Where are the bonding electrons?

Major advantages

- It works with very small volumes, for example, a single nanoparticle or nanotube.
- It does not require single crystals.
- It can be combined with electron imaging for structural mapping.

Major disadvantages

- Samples must be electron transparent; destructive sample preparation is sometimes required.
- Dynamic diffraction effects must be considered for quantitative interpretation of diffraction intensities of thick crystals.
- Radiation damage can limit the type of structural information that can be extracted.

Sample constraints

- The sample must be electron transparent.
- It must be compatible with vacuum; observation of biological samples requires *cryo*-freezing.
- Air sensitive materials must be handled using a special sample transfer chamber.
- The sample must be free standing (like a thin disc) or supported on thin foils.

1 INTRODUCTION

Electron diffraction is a structural probe widely used for characterization of both inorganic and organic materials. The principle of electron diffraction is similar to that of X-ray diffraction. Both use atomic scattering and their interference to probe the atomic structure. The difference is that electrons are charged particles and electrons interact with both the electrons and nucleus of the atom (X rays only see the electrons). The electron elastic scattering cross section is also $\sim10^6$ times larger than that of X rays. Electron beams can also be shaped into small probes or used for imaging using electron magnetic lenses. The combination of the large scattering cross section and electron small probes makes electron diffraction very useful for studying ‘‘small’’ crystals, surfaces, or the microstructure of materials. The strong scattering can also lead to electron multiple scattering (EMS) in the case of a thick crystal, which complicates the interpretation of electron diffraction intensities for ab initio structure determination. For a known crystal, EMS effects can be taken into account by simulation. This is used for accurate measurement of lattice parameters and electron structure factors for electron density mapping.

There are several electron diffraction techniques based on (i) electron energy, (ii) the diffraction geometry, and (iii) the electron probe (Figure 1). Each has its own unique applications. High-energy electron diffraction (HEED) uses electrons with energy from tens of kilo electron volts (keV) to several millions of electron volts (MeV), while low-energy electron diffraction (LEED) uses the other end of the energy spectrum with electron energy ranging from few tens to hundreds of electrons volts. Electron diffraction patterns are recorded in either the transmission or reflection geometry. Transmission high-energy electron diffraction (THEED) is mainly a bulk structure characterization technique because of the electron penetration. The incident electron beam can be a focused probe with a convergent beam or spread out as a parallel illumination. A focused probe is used in convergent-beam electron diffraction (CBED) for parallel recording of diffraction intensities of different incident-beam directions. CBED is used for studying single crystals.**[1]** Parallel, or nearly parallel, beams are used in selected area electron diffraction (SAED) and nanoarea electron diffraction (NED). Both techniques can be used for studying crystalline or noncrystalline structures. Reflection high-energy electron diffraction (RHEED) and LEED are sensitive to surface structures. They are used primarily as surface characterization techniques. RHEED is performed in the glancing angle diffraction geometry which is very useful in a growth chamber for monitoring film growth. These two techniques are generally treated separately from transmission electron diffraction (TED). Readers interested in these two techniques are refered to the Ref. 3 and 2, respectively.

A closely related technique to electron diffraction is electron imaging where diffracted electrons are brought

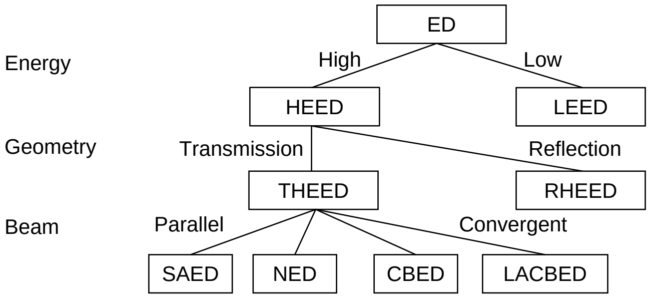

Figure 1 Classification of electron diffraction techniques

together to interfere and form atomic resolution images.[4] In modern transmission electron microscopes (TEM), electron diffraction patterns and images can be recorded from the same area to provide complementary information in real and reciprocal spaces. In scanning transmission electron microscopy (STEM), an angstrom-sized electron probe is scanned across the sample and the diffraction intensity is recorded by integrating over an area detector and displayed as a raster image.[5] The image, thus, can be viewed as a map of diffraction intensities. The commonly used detector for STEM has a hole in the middle (annular dark-field detector), which records electrons scattered into high angles. Electron diffraction is required for the interpretation of both TEM and STEM image contrast.

The study of electron diffraction dates back to 1927 when Davisson and Germer in USA, and Thompson and Reid in Scotland, reported electron scattering by a crystal and the formation of interference patterns by electrons similar to the pattern formed by light waves scattered by a diffraction grating. The Davisson and Germer's experiment used low-energy electrons, which was the start of LEED that is used today. Thompson and Reid used high-energy electrons in the transmission geometry. The first CBED pattern was recorded by Möllenstadt as early as 1939 using a two-magnetic lens setup.[6] MacGillavry first attempted structure factor measurement by using the two-beam theory of Blackman for dynamic electron diffraction.[7] The multi-beam theory of electron dynamic diffraction has its origin in the Bloch wave method originally formulated by Hans Bethe in his Ph.D. thesis. More recent developments of electron diffraction are entwined with the development of electron microscope technologies and the development of computer algorithms for data analysis. The development of field emission guns (FEG) in the 1970s and their adoption in conventional TEM brought high source brightness, small probe size, and improved coherence to electron diffraction. Electron energy filters, such as the in-column Ω-energy filter, allow the inelastic background from plasmon, or higher electron energy losses, to be removed from recorded diffraction patterns with an energy resolution of a few electron volts. The development of array detectors, such as crystal charge density (CCD) cameras, or imaging plates (IPs), enables parallel recording of diffraction patterns and quantification of diffraction intensities over a large dynamic range that was not available to electron microscopy before. These developments in the electron diffraction hardware were accompanied by the development of efficient and accurate algorithms to simulate electron diffraction patterns and modeling structures on a first-principle basis using fast computers, which has significantly improved our ability to interpret experimental electron diffraction patterns. The more recent developments are time-resolved electron diffraction at the time resolution approaching femtoseconds[8–11] and coherent NED for the study of individual nanostructures.[12] Further developments of these techniques will significantly improve our ability to interrogate structures at high spatial and time resolution that hitherto has not been available.

This chapter covers both the basics and the modern aspects of electron diffraction. The intention is to provide an integrated review that both the novice and the expert will find useful as a guide for modern electron diffraction. Some of the details that are not covered here can be found in monographs on electron diffraction.[1,13–15] The chapter is organized as follows. First, an introduction to different electron diffraction techniques is given. This is followed by background theories which are required for the interpretation of diffraction patterns. Experimental procedures are described after the technical background. The applications section has a large collection of examples from relatively straightforward tasks to more advanced ones that are under development for their promises. Experimental details are provided when it is appropriate to give some idea of what it takes to do electron diffraction.

2 TECHNICAL BACKGROUND

2.1 Electron Diffraction Techniques

The basic setup for electron diffraction is an electron gun, a sample, and an electron detector. The electron beam used for HEED is shaped using either magnetic or electrostatic lenses or both. A modern TEM uses at least three magnetic lenses for the illumination system, condenser I, II, and the objective prefield, which is a part of the objective lens magnetic field before the sample that also acts as a lens. Some of microscopes come with an additional condenser lens (condenser III, or condenser mini lens), which can be used for nanodiffraction. The high-energy electron gun used in RHEED typically comes with one or two magnetic or electrostatic lenses to produce a small electron beam. Figure 2 illustrates different electron illumination configurations for electron diffraction in a TEM using the combination of condenser II, III, and the objective prefield. The difference between different illuminations is the strength (or focal length) of the condenser II and III. The focal length of condenser II is varied continuously in electron microscopy. Condenser

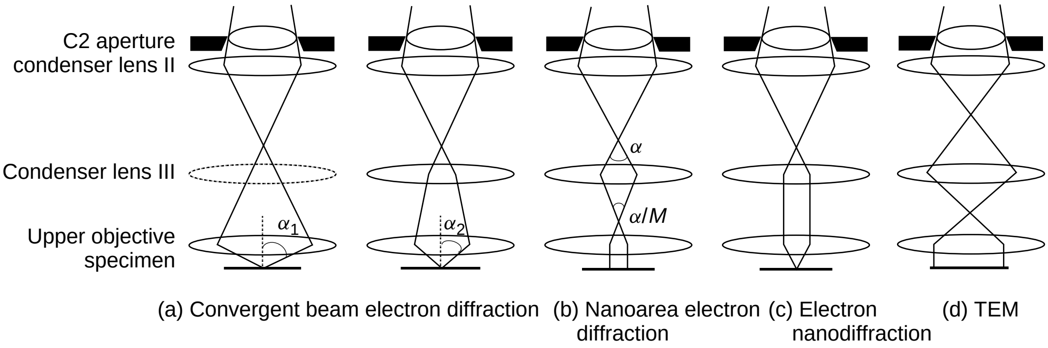

Figure 2 Electron illumination modes for transmission high-energy electron diffraction. The first two in (a) represent two different convergent beams used for convergent beam electron diffraction. The M in (b) is the magnification of the condenser III.

III has different settings for the focal length. Each of these illuminations is associated with a different electron diffraction technique.

2.1.1 Selected Area Electron Diffraction (SAED)

SAED is formed using the TEM illumination (Figure 2d), which is spread out over a large area of the specimen as a parallel beam. The diffraction pattern is recorded from an area of interest by placing an aperture in the imaging plane of the image forming objective lens. Only electron beams passing through this aperture contribute to the diffraction pattern. For a perfect lens without aberrations, electron beams recorded in the diffraction pattern come from an area that is defined by the image of the selected area aperture at the specimen. The aperture image is demagnified by the objective lens (a factor of ∼20). In a conventional electron microscope, rays at an angle to the optic axis are displaced away from the center because of the spherical aberration of the objective lens (C_s). The displacement is proportional to $C_s\alpha^3$, where α is twice the Bragg angle. The smallest area that can be selected in SAED is thus limited by the objective lens aberrations. This limitation is removed using an electron microscope equipped with a TEM aberration corrector placed after the objective lens.[16]

SAED is the most popular diffraction technique in TEM. The technique can be applied to study both crystalline and noncrystalline structures. The large area illumination is useful for recording diffraction patterns from polycrystalline samples or averaging over a large volume (e.g., a large number of nanoparticles). SAED can also be used for low-dose electron diffraction, which is required for studying radiation sensitive materials, such as organic molecules.

2.1.2 Nanoarea Electron Diffraction (NED)

NED uses a small (nanometer-sized) parallel illumination with the condenser/objective setup shown in Figure 2(b).[12] The small, parallel, beam is achieved by reducing the convergence angle of the condenser II crossover and placing it at the focal plane of the objective prefield, which then forms a parallel beam illumination on the sample. A third condenser lens, or a mini lens, is required for the formation of a nanometer-sized parallel beam. For a condenser aperture 10 micron in diameter, the probe diameter is ∼50 nm with an overall magnification factor of 1/200 in the JEOL 2010 electron microscopes (JEOL, USA). The beam size is much smaller than what can be achieved using a selected area aperture. The diffraction pattern recorded in this mode is similar to SAED. For crystals, the diffraction pattern consists of sharp diffraction spots. The major difference is that the diffraction volume is defined directly by the electron probe in NED. Since all electrons illuminating the sample are recorded in the diffraction pattern, NED in a FEG microscope also provides higher beam intensity than SAED (the probe current intensity using a 10 micron condenser II aperture in JEOL 2010F is $\sim10^5$ e/s-nm^2).[12]

The small probe size allows the selection of an individual nanostructure and reduction of the background in the electron diffraction pattern from the surrounding materials. An example is given in Section 3.5 for the structure characterization of individual carbon nanotubes (CNT) by electron diffraction.

The beam size in NED can be further reduced by weakening the condenser II and placing the crossover at the front focal plane of the condenser III lens. This results in a focused probe with the sample close to the back of the focal plane of the pre-objective lens. The probe size formed with coherent illumination can be as small as a few angstroms. The diffraction patterns recorded in this case consists of small disks, which are the same as those recorded in the nanodiffraction mode in STEM. This technique is useful for probing local structure variations.[17]

2.1.3 Convergent-Beam Electron Diffraction (CBED)

CBED is recorded using a focused electron probe at the specimen (see Figure 2a, c). Compared to SAED, CBED has two main advantages for studying crystals. First, the diffraction pattern is taken from a much smaller area using a focused probe. The smallest electron probe currently available in a high-resolution FEG-STEM is close to 1 Å. Thus, CBED patterns can be recorded from individual atomic columns. For crystallographic applications, CBED patterns are typically recorded with a probe of a few angstroms to hundreds of nanometers. The second advantage is that CBED patterns record diffraction intensities as a function of incident-beam directions. Such information is very useful for symmetry determination and quantitative analysis of electron diffraction patterns.

A comparison between the SAED and CBED is given in Figure 3. CBED patterns consist of disks. Each disk can be divided into pixels, each pixel approximately represents one incident-beam direction. For example, the beam P in Figure 3 gives one set of diffraction patterns shown in full lines. The geometry of the diffraction pattern by the incident-beam P is the same as the selected area diffraction pattern with a parallel illumination. For a second beam P′, which comes at a different angle compared to P, the diffraction pattern is displaced from that of P by α/λ with α as the angle between the two beams.

Experimentally, the size of the CBED disk is determined by the condenser aperture and the focal length of the probe-forming lenses. In modern microscopes with an additional mini lens placed in the objective prefield, it is also possible to vary the convergence angle by changing the strength of the mini lens. Underfocus of the electron beam also gives a smaller convergence angle; however, this leads to a bigger probe, which can be an issue for specimens with a large wedge angle.

The ability to record diffraction intensities over a range of incident-beam angles makes CBED readily accessible for quantitative comparison with simulations. In the past 15 years, CBED has evolved from a tool primarily for crystal symmetry analysis to the most accurate technique for strain and structure factor measurement.[18] For defects, large-angle CBED technique can characterize individual dislocations, stacking faults, and interfaces.[15] For applications to defect structures and structures without three-dimensional periodicity, parallel-beam illumination with a very small beam convergence is required.

2.1.4 *High-Resolution Electron Microscopy*

The power spectrum of high-resolution electron microscopy (HREM) images contains useful diffraction information, which can be used for studying defects, small particles or other local structures that are difficult to study by diffraction alone. For thin specimens below a certain thickness, the Fourier transform of the image intensity ($I(\vec{S})$) can be related to the Fourier transform of the potential ($F(\vec{S})$, the structure factor):

$$I_{\text{image}}(\vec{S}) = \delta(\vec{S}) + 2\sigma F(\vec{S})T(\vec{S}) \qquad (1)$$

where $T(\vec{S})$ is the contrast transfer function (CTF) of the objective lens and σ is electron interaction constant. As a diffraction technique, HREM is also limited by several factors. The CTF modifies the image spectrum; the function itself depends sensitively on the lens properties and the defocus. Electron images are also sensitive to noise introduced during image recording and inelastic scattering that reduce the image contrast. The largest diffraction angle obtainable in HREM is limited by the image resolution. Nonetheless, electron images contain useful phase information for structure determination. There are several successful cases using HREM to solve inorganic crystal structures using image processing techniques.[19–21]

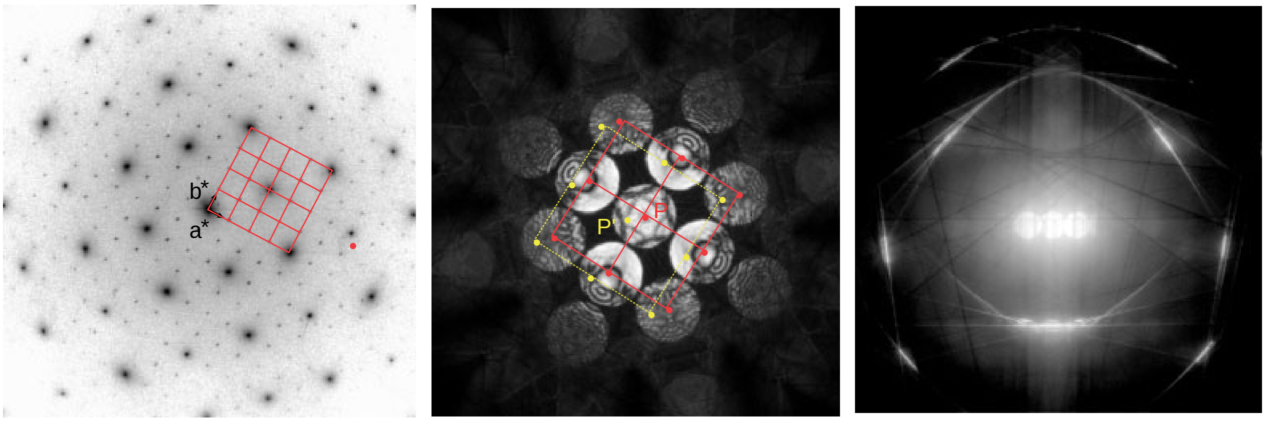

(a) (b) (c)

Figure 3 Examples of (a) selected area electron diffraction, (b) zone-axis CBED pattern, and (c) off-zone axis CBED pattern showing Kikuchi lines in the diffraction pattern

2.1.5 Hybrid Electron Diffraction and Imaging Techniques

There are several hybrid electron diffraction and imaging techniques that mix diffraction and imaging information. These techniques include large-angle convergent-beam electron diffraction (LACBED),[15,22] convergent-beam imaging (CBIM),[23] parallel recording of dark-field images (PARODI),[24,25] and fluctuation electron microscopy (FEM).[26,27] Both LACBED and PARODI use a focused probe that is placed above or below the specimen (Figure 4). Because of this, electron beams of different angles travel through different areas of the sample. The diffraction pattern recorded thus carries both reciprocal and real-space information. LACBED, as indicated by its name, is formed using electron beams with a large convergence angle (see Figure 4 for an example). The overlapping of diffraction disks resulting from the large convergence angle is removed by placing a small aperture around one of the diffraction spots that can be observed in the imaging plane of the objective lens because of the focused beam placed away from the sample. In comparison, PARODI uses a small convergence angle that avoids the overlapping of diffraction disks. LACBED is used for studying defects and crystal symmetry. PARODI, which is a relatively new technique, is useful for studying interfaces and crystals with large unit cells.[24]

FEM is another hybrid electron diffraction and imaging technique. In the original version of this technique, a hollow cone illumination was used for dark-field imaging, in which the electron beam is tilted away from the optical axis by an angle and rotated azimuthally. The image is formed by placing a small aperture at the center of the diffraction pattern (Figure 5).[26] Only electrons scattered with the selected angle are allowed for imaging. The variance of the image intensity is then calculated and tabulated as a function of the hollow cone illumination angle. The variance comes from the change in the scattering power of a projected sample volume. The area diameter is one over the aperture size in reciprocal space. A large image intensity variance is expected when the sample contains nano-crystallites and fluctuation in crystallite orientations leads to the variance. Theoretically, it has been shown that the calculated variance in the kinematical limit can be related to the many body correlation functions; a large variance is indicative of medium range ordering.[26] Applications of FEM to amorphous materials show that this technique is very sensitive to the structural differences in different amorphous materials.[27]

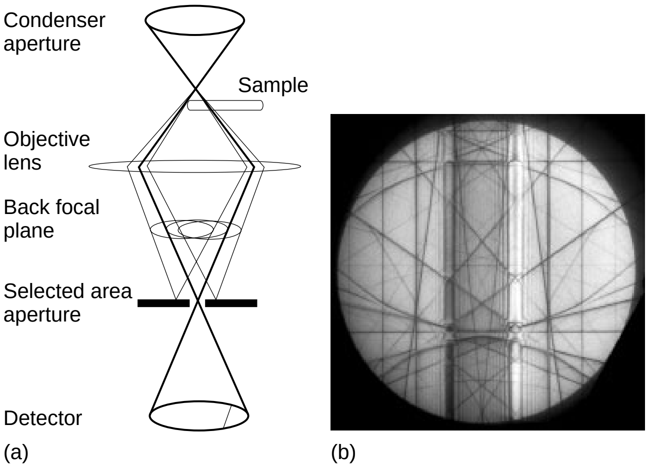

Figure 4 (a) Schematic illustration of large-angle CBED technique and (b) an example of LACBED pattern taken from Si near [113] zone axis showing high order Laue zone lines in the disk

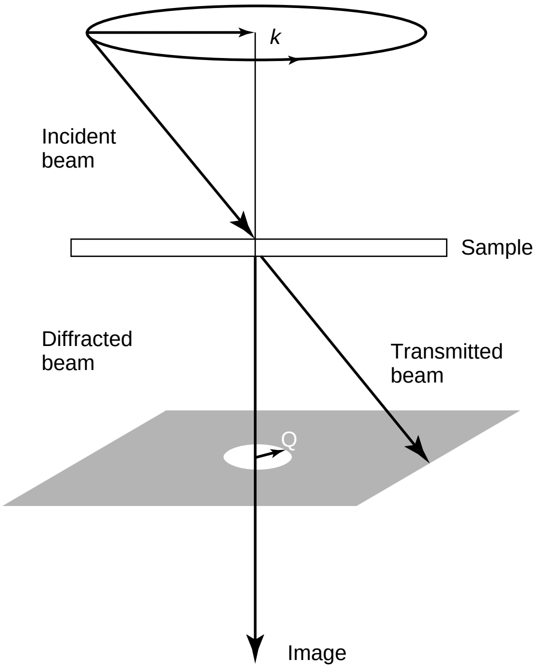

Figure 5 Schematic dark-field hollow cone imaging for fluctuation electron microscopy

2.2 Interpretation of Diffraction Pattern Geometry

Electron diffraction patterns in general appear as (i) broad halos for materials with amorphous structure, (ii) multiple concentric rings for powder samples, (iii) sharp diffraction spots (conventional diffraction pattern), and (iv) disks for CBED (see Figure 6). In the case of crystals, in addition to the diffraction spots, diffuse scattering or diffuse background may be observed including sharp lines for thick specimens. The lines, the so-called Kikuchi lines (see also Figure 3), are formed by Bragg diffraction of the diffuse background. Diffuse scattering comes from the perturbation of crystal lattices, which has its origin in composition, atomic displacements, or lattice terminations such as small particles or precipitates.

Structural information obtainable from electron diffraction patterns are lattice d-spacings, crystal unit cell

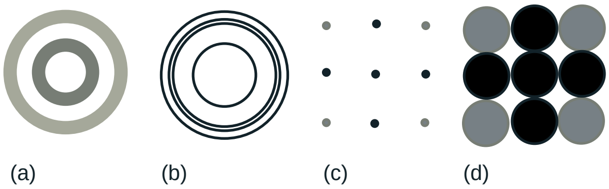

Figure 6 Schematic illustration of different types of electron diffraction patterns

symmetry, crystal orientations and texture, interatomic distances, atomic positions, atomic thermal vibrations, (the Debye–Waller factors), and crystal potential and charge density. A survey of procedures used to retrieve the structural information is given here. Some of the analyses involved are relatively straightforward and can be carried out by nonexperts without the requirement of extensive training. Others, involving quantitative analysis of diffraction intensities, require some expertise with electron diffraction.

2.2.1 The Geometry of Conventional Electron Diffraction Patterns

The diffraction spots are expected where transmitted and diffracted electron beams intersect with the detector. The basis for diffraction pattern geometry analysis, thus, is the crystal reciprocal lattice and the Laue diffraction condition, or the equivalent Bragg's law, for diffraction:

$$\vec{k} - \vec{k}_o = \vec{g} = h\vec{a}^* + k\vec{b}^* + l\vec{c}^* \tag{2}$$

where $\vec{k}_o$ and $\vec{k}$ are incident and diffracted electron wavevectors respectively and $\vec{g}$ is a reciprocal lattice vector. The lattice d-spacing is given by $d_{hkl} = 1/|\vec{g}| = 1/|h\vec{a}^* + k\vec{b}^* + l\vec{c}^*|$. The d-spacing can be obtained by measuring the length of $\vec{g}$ in the experimental diffraction pattern (D) using:

$$d = L\lambda/D \tag{3}$$

Where L is the experimental camera length (CL) and λ is the electron wavelength determined by the electron accelerating voltage, Φ, in volts:

$$\lambda = h/\sqrt{2me\Phi} \approx 1.226/\sqrt{\Phi}\sqrt{1 + 0.97845E - 6\Phi} \tag{4}$$

Experimentally, only the camera constant of the product of $L\lambda$ is needed, which can be calibrated using a sample with known d-spacings. For single crystals or polycrystals with grain size comparable to, or larger than, the selected area for diffraction, the lattice planes observed in the experimental diffraction patterns are nearly parallel to the electron beam. The wavelength of high-energy electrons is relatively short. For 200 kV electrons, the wavelength is 0.025 Å, the Bragg angle ($2d\sin\theta = \lambda$) is very small. For example, θ is 5 mrad for $d = 2.5$ Å.

The intersection of two sets of lattice planes defines a zone axis $[u,v,w]$. For a given zone axis, the reflections (h,k,l) that are allowed in the diffraction pattern must satisfy:

$$hu + kv + lw = n \tag{5}$$

Here n is an integer. Each n denotes a planar section of the reciprocal space, which is perpendicular to the zone axis. In diffraction, these planar sections are called the *Laue zones*. Zero order Laue zone (ZOLZ) refers to $n = 0$, while others are called *high order Laue zones* (HOLZs). An example of a single crystal electron diffraction pattern is shown in Figure 3(a). The lattice geometry of the ZOLZ is described by two, nonparallel, reflections $\vec{g}_1$ and $\vec{g}_2$, which are selected as the closest ones to the transmitted beam. The projected lattice of the HOLZs is the same as that of the ZOLZ, however, the lattice can be shifted relative to the ZOLZ. The offset of HOLZs is described by an additional reflection $\vec{g}_3$, which is independent of $\vec{g}_1$ and $\vec{g}_2$ and is also closest to the origin. Once these three reflections are identified, all reflections can be indexed using these three vectors as the basis:

$$\vec{g} = i\vec{g}_1 + j\vec{g}_2 + n\vec{g}_3 \tag{6}$$

Experimentally, for crystals of known structure, any two reflections in the ZOLZ can be used to identify the zone axis and the approximate crystal orientation using

$$\vec{Z} = \vec{g}_1 \times \vec{g}_2 = \begin{pmatrix} \vec{a} & \vec{b} & \vec{c} \\ h_1 & k_1 & l_1 \\ h_2 & k_2 & l_2 \end{pmatrix} \tag{7}$$

and reduce $\vec{Z}$ to the shortest lattice vector. Diffraction pattern indexing is performed by comparing the measured d-spacings referring to the powder diffraction files or a list of d-spacings generated using a crystallographic utility program. The angle between $\vec{g}_1$ and $\vec{g}_2$ is useful for indexing single crystal diffraction patterns, especially in case of a high index zone axis or a crystal with low symmetry. For crystals with unknown structure, the three dimensional unit cell can be reconstructed using two zone-axis diffraction patterns with a known rotation angle or from a single diffraction pattern with HOLZ reflections. A reduced unit cell can be identified from these diffractions which then can be converted to the Bravais lattice.**[28]**

The surface diffraction geometry of RHEED and LEED is determined by the intersection of the Ewald sphere with the 2-D reciprocal rods of the surface. The incidence for LEED is normal to the surface; the diffraction pattern is a projection of the positions of the rods. In RHEED, the incident beam is nearly normal to the surface reciprocal rods. The diffraction spots fall onto a semicircle, which is defined by the Ewald sphere. For more details on RHEED and LEED, refer to Ref. 3 and 2 respectively.

2.2.2 *The Geometry of CBED*

The diffraction pattern has the same geometry as the SAED pattern except that the sharp diffraction spots are replaced with disks. Within the disk, the intensity varies depending on the sample thickness. The variation comes from the change in diffraction condition for each point inside the CBED disk. This change can be seen in the Ewald sphere construction, which is illustrated in Figure 7. By the requirement of elastic scattering, all diffracted beams are on the Ewald sphere. Consider the incident-beam P, which satisfies the Bragg condition for the reflection of g, and an incident-beam P′ to the left of P; the diffracted beam of P′ also moves to the left. The deviation of the electron beam P′ from the Bragg condition is measured by the distance excitation error, which is defined by

$$S_g = (k_0^2 - |\vec{k} + \vec{g}|^2)/2|k_0| \tag{8}$$

The excitation error for g increases linearly away from the Bragg condition along the direction of g and stays constant, perpendicular to g. To see this, take $k_g = -g/2 + \Delta$ then

$$S_g = \lambda\left(\left(-\frac{g}{2} + \Delta\right)^2 - \left(\frac{g}{2} + \Delta\right)^2\right)\Big/ 2 = -\lambda g \Delta \approx -g\delta\theta \tag{9}$$

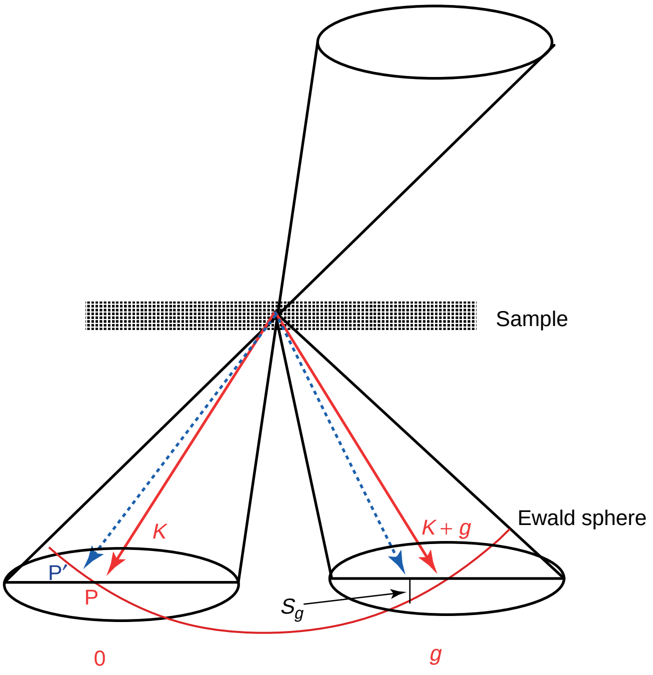

Figure 7 The schematic ray diagram of CBED. This figure demonstrates the variation of excitation errors at different positions of the CBED disk. The beam marked by the full line (P) is at Bragg condition, while the one marked by the dashed line is associated with a positive excitation error (S_g)

Here the positive Δ corresponds to a tilt towards g and $\delta\theta$ is the deviation angle from the Bragg condition. S_g is negative for positive Δ and positive for negative Δ. An incident beam moving to the left in the transmitted CBED disk gives a positive excitation error. Correspondingly, a beam, moving to the right of P, gives a negative excitation error. The range of excitation errors within each disk is proportional to the length of g and the convergence angle. Consequently, the excitation error of a HOLZ reflection changes much faster than that of a low-order reflection in the ZOLZ.

2.2.3 *Kikuchi Lines and HOLZ Lines*

Kikuchi lines are produced by Bragg diffraction of electron diffuse scattering produced by inelastic scattering, and appear as background intensities in the diffraction pattern (see Figure 3 for an example). The average electron energy loss is small, and the wavelength of the inelastic background is approximately the same as the incident electron beam. HOLZ lines are sharp lines observed in the CBED disks. They are produced by Bragg diffraction of lattice planes of high order reflections. The rapid increase in the excitation error of a high order reflection away from the Bragg condition results in a rapid decrease in the diffraction intensity. The maximum diffraction intensity occurs at the Bragg condition under the kinematic approximation, which appears as a straight line within the CBED disk. Since Kikuchi lines also mark the Bragg conditions, Kikuchi lines superimpose on HOLZ lines inside the disk and continue outside the disk. A major difference between the two is the contrast. Kikuchi lines are mostly observed for low and medium order reflections, while HOLZ lines can be observed for high order reflections.

The position of HOLZ lines is very sensitive to small changes in lattice parameters and the local strain. The sensitivity comes from the large scattering angle. This can be seen in the case of a cubic crystal for which $\theta \approx g\lambda/2 = \sqrt{h^2 + k^2 + l^2}\lambda/2a$. A small change in a gives $\delta\theta \approx 0.5g\lambda\delta a/a$. The amount change in the Bragg angle is proportional to the length of g. The positions of these lines move relative to each other when the lattice parameters change. This effect can be used for accurate measurement of lattice parameters.

The direction of a HOLZ line is normal to the reciprocal lattice vector and its position is decided by the Bragg condition. In diffraction analysis, it is useful to express HOLZ lines using line equations in an orthogonal zone-axis coordinate system (x, y, z), with z parallel to the zone-axis direction. The x direction can be taken along the horizontal direction of the experimental pattern and y is normal to x. The Bragg diffraction equation (2) expressed in this coordinate is given by

$$k_y = -\frac{g_x}{g_y}k_x + \frac{2g_z - g^2}{2g_y}|k_z| \tag{10}$$

Here

$$|k_z| = \sqrt{k_0^2 - k_x^2 - k_y^2} \approx k_0 = 1/\lambda \tag{11}$$

The approximation holds for high-energy electrons of small wavelengths and the typical acceptance angles in electron diffraction. Within this approximation, beams that satisfy the Bragg condition form straight lines.

2.3 Diffraction Pattern Symmetry and Crystal Space Group

The crystal symmetry is reflected in the diffraction patterns. For example, if the crystal has a rotation axis, two diffraction patterns related by rotation should be the same. The same is true for mirror symmetry. Additional symmetries are produced in electron diffraction because of (i) the principle of reciprocity and (ii) the projection along the zone axis for ZOLZ.[14] The principle of reciprocity states that the intensity of the diffracted beam (B) with a source (A) is the same as the intensity detected at A with the source at B by the same scatter. The projection of crystal structure along the zone-axis orientation used in the observation produces a mirror symmetry at the middle of the sample which may or may not exist in the crystal. The combination of reciprocity and projection with the crystal point groups produces 31 diffraction groups, whose relationships with the 32 point groups were tabulated by Buxton.[29] The correspondence is often not unique. The determination of crystal point groups comes down to elimination of multiple choices using the symmetry of diffraction patterns recorded along several major symmetric orientations and/or using information about the lattice determined from the diffraction pattern geometry. The diffraction pattern symmetries used in the determination are those of the whole pattern, the transmitted beam (Bright), the diffracted beams (dark-field), and the symmetry between $+g$ and $-g$ beam. It should be emphasized that the Friedel symmetry ($I_g = I_{-g}$) is absent in electron diffraction because of dynamic scattering. The point groups can be uniquely determined by electron diffraction.

The screw and glide axes present in the crystals can be determined by observing dynamic extinction in kinematical forbidden reflections (zero structure factor due to the glide or screw axes). These reflections generally show some intensities due to electron multiple scattering. The dynamic extinction is observed when the incident beam is in the glide plane in case of a glide; this was first reported by Gjonnes and Moodie (G-M lines) using CBED (the extinction appears as dark lines subsequently named as the *G-M lines*). The dynamic extinction of a screw axis is more complicated, and is described in detail in Ref. 29.

The combination of point group determination and identification of translation symmetry allows the unique identification of space groups.[30,31] Both CBED and LACBED techniques can be used for this purpose. Applications of symmetry determination by CBED include phase identification and determination of unknown structures.

2.4 Interpretation of Diffraction Pattern Intensity

The diffraction intensity of ultrathin films and small nanocrystals can be approximated by summing scattering from an assembly of atoms (kinematic approximation):

$$I(\vec{S}) \propto \left| \sum_i f_i T_i(\vec{S}) e^{2\pi i \vec{S}\cdot\vec{r}_i} \right|^2 \tag{12}$$

where the summation is over individual atoms i, $\vec{S} = \vec{k} - \vec{k}_o$ is the scattering vector, f_i and T_i are the atomic scattering and temperature factor, respectively, and $T(\vec{S}) = \exp(-B|\vec{S}|^2/4)$ in case of isotropic atomic vibrations. For a crystal, the sum is limited to atoms within the unit cell and $\vec{S} = \vec{k} - \vec{k}_o = \vec{g}$ and the intensity is proportional to the square of the crystal thickness and the structure factor $V_g = \sum_i f_i T_i(\vec{g}) e^{2\pi i \vec{g}\cdot\vec{r}_i}$. The kinematic approximation breaks down at a certain crystal thickness when the diffracted intensity approaches that of the incident beam. A useful criterion for kinematic approximation is $t \le \xi_g/4$, where ξ_g is the extinction distance of the strongest reflection in the diffraction pattern. The extinction distance is orientation dependent. In case only one set of lattice planes is strongly diffracting (the two-beam condition), the extinction distance is given by $\xi_g = h^2 2me\lambda V_g$.

For inorganic crystals, the typical extinction of a strong reflection is on the order of a few tens of nanometers. For a crystal of more than a few nanometers thick, multiple scattering must be taken into account for the interpretation of diffraction intensities. There are several approaches to EMS.[14] For perfect crystals, the Bloch wave approach is most useful, which is based on the Bloch wave method formulated by Hans Bethe in his thesis. The diffraction intensity in the Bloch wave theory is given by

$$I_g(x, y) = |\phi_g(x, y)|^2 = \left| \sum_i c_i(x, y) C_g^i(x, y) \exp[2\pi i \gamma^i(x, y) t] \right|^2 \tag{13}$$

Here the eigenvalue γ and eigenvector C_g are obtained from diagonalizing the equation:

$$2K S_g C_g + \sum_h U_{gh} C_h = 2K\gamma C_g \tag{14}$$

where

$$U_g = \frac{2me}{h^2} V_g = \frac{2me}{h^2} \sum_i (f_i + i f_i') T_i(\vec{g}) e^{2\pi i \vec{g}\cdot\vec{r}_i} \tag{15}$$

is the electron interaction structure factor. The imaginary term f_i' is included to describe the effect of inelastic scattering (absorption). Details on the evaluation of absorption potentials can be found in Refs. 32–34. S_g is the deviation from the Ewald sphere (excitation error) defined in Section 2.2.2. The c_i are obtained from the first column of the inverse eigenvector matrix as determined by the incident-beam boundary condition. The solution of equation (14) converges with the increasing number of beams included in the calculation. The strong beams are included in the diagonalization, while weak beams can be treated by perturbation. In practice, an initial list of beams is selected using the criteria of maximum g length, maximum excitation error, and their perturbational strength. Additional criteria are used for selecting strong beams.

Figure 8 shows an example of simulated CBED patterns using the Bloch wave method described here for the ZnO [10−10] zone axis and electron accelerating voltage of 200 kV. The simulation includes 99 beams in the ZOLZ. Standard numerical routines were used to diagonalize the complex general matrix. The whole pattern simulation on a modern PC only takes a few minutes.

Another method commonly used for dynamic electron diffraction simulation is the multislice method developed by Cowley and Moodie.[35] This method models electron wave propagation in the presence of a potential field by separating the potential into thin slices and then approximating wave propagation in each slice by introducing a phase change in the electron wave followed by wave propagation through the slice thickness. As a numerical method, multislice has the advantage that it can treat both crystals and nonperiodic structures such as defects. Because of this, the multislice method is used widely for high-resolution electron image simulation and also increasingly for simulation of diffraction of nanocrystals.

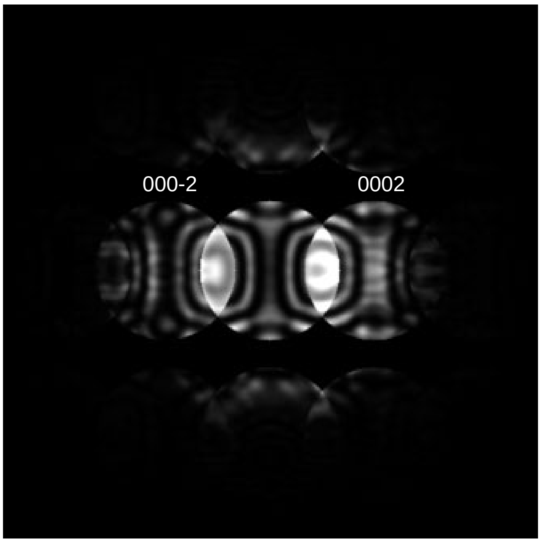

Figure 8 Simulated CBED pattern of hexagonal ZnO along [10−10] zone axis for crystal thickness of 165 nm and the electron voltage of 200 kV. The asymmetry between ±(0002) comes from the polarity of ZnO along the c-axis direction

2.4.1 *Ab initio Structure Determination*

Ab initio structure determination is based on the Fourier relationship between the diffraction intensity and the crystal potential for electron diffraction. In such cases, several crystallographic methods can be used to determine the atomic structure. The main advantage of using electron diffraction to determine structure is that it can be applied to nanocrystals, or 2-D membranes, or minor phases embedded in a matrix. Another advantage is that phase information can be obtained from HREM images which can help with structure determination, especially, noncentrosymmetric structures. This is important in a number of applications, for example, studying polymorphs in organic structures and determining the structure of precipitates in metals. Electrons also interact with both crystal electrons and nuclei so that electrons can see hydrogen atoms in organic molecules. This was the motivation behind the pioneering work of the Russian group led by Pinsker and Vainstein in the 1960s.[36]

The commonly used methods for solving the phase problem required for structure solutions are the direct methods[37,38] and Patterson maps.[39] Direct methods use relationships between phases such as triplets ($\theta = \phi_{\vec{h}} + \phi_{\vec{k}} + \phi_{-\vec{h}-\vec{k}} \approx 0$). The probability of $\theta \approx 0$ increases with the magnitude of the product of the normalized structure factors of the three reflections involved. Once these triplets associated with high certainty are identified based on diffraction intensities, they are used to assign new phases based on a set of known phases. Since the number of phase relationships is large the problem is over determined. Another approach is based on the Sayre equation, which is derived based on the relationship between the electron density and its square:

$$F_{\vec{h}} = \frac{\Theta}{V} \sum_{\vec{k}} F_{\vec{k}} F_{\vec{h}-\vec{k}} \tag{16}$$

where Θ is a constant and V the unit cell volume. The structure factor F is complex; thus, the relationship contains phase relationships. The Sayre equation was found useful in the limited data set situation which happens often in electron diffraction.[37]

Crucial to the success of ab initio structure determinations is the collection of 3-D diffraction data. The conventional TEM sample holders can handle limited rotation (up to ±35° e.g., in some HREM), which leaves a wedge-shaped gap in reciprocal space. Special holders used for tomography with a large rotation range can be used to address this problem. The diffraction patterns recorded at different rotations are merged to produce the 3-D data set. Special care must be taken to normalize the diffraction intensities because of the 3-D shape of the crystal and possible dynamic diffraction effects. In the absence of 3-D diffraction data set, diffraction patterns can be recorded along zone-axis orientations and reconstructed to obtain the projection maps. These maps then can be used to build a structural model or models of the crystal. The projection maps do not give 3-D atomic bond distances.

The number of structures solved using 3-D electron diffraction data sets is relatively small because of the experimental difficulties associated with the collection of 3-D diffraction data and dynamic scattering effects on diffraction intensities. A major development toward solving these difficulties is the precession electron diffraction technique, which allows a large number of reflections to be collected in a single orientation and averages over different beam directions to minimize dynamic effects. Progress is under way; for more information see Refs. 40 and 41.

2.4.2 *Refinement of Electron Diffraction Intensities*

Once an estimate of the structure is obtained, the structure or its parameters can be refined with high accuracy using the refinement method.**[18,42]** The refinement method works by comparing experimental and theoretical intensities and optimizing for the best fit. During optimization, parameters in the theoretical model are adjusted in search of the minimum difference between experiment and theory. Multiple scattering effects can be taken into consideration by using dynamical theory to calculate diffraction intensities during the refinement. Previously, strong EMS had made it difficult to use the kinematical approximation for electron structure determinations in the manner of X ray and neutron diffraction. In the case of accurate structure factor measurement, electron interference from multiple scattering actually enhances the electron diffraction sensitivity to crystal potential and thickness and improves the accuracy of electron diffraction measurements.

The refinement is automated by defining a goodness of fit (GOF) parameter and using a numerical optimization routine to do the search in a computer. One useful GOF parameter for a direct comparison between experimental and theoretical intensities is χ^2

$$\chi^2 = \frac{1}{n-p-1}\sum_{i,j}\frac{1}{\sigma_{i,j}^2}\left(I_{i,j}{}^{\mathrm{exp}} - cI_{i,j}{}^{\mathrm{Model}}(a_1, a_2, \ldots, a_p)\right)^2 \quad (17)$$

Here, $I_{i,j}^{\mathrm{exp}}$ is the experimental intensity (in units of counts) measured from an experimentally recorded diffraction pattern, $(i,\ j)$ is the pixel coordinate of the detector, and n is the total number of points. $I_{i,j}^{\mathrm{Model}}$ is the model intensity calculated with parameters a_1 to a_p and c is the normalization coefficient. χ^2 is best used when the differences between theory and experiment are normally distributed and when the variance σ is correctly estimated. The optimum χ^2 has a value close to unity.

To model diffraction intensities, both the detector response and background intensity from thermal diffuse scattering must be included. A general expression for the model intensity including both factors is

$$I_{i,j}^{\mathrm{Model}} = I^{\mathrm{Theory}}(i,\ j) \otimes H'(i,\ j) + B(i,\ j) \quad (18)$$

Here, the theoretical intensity I^{Theory} is convoluted with the detector response function H′ plus the background B. The detector response is a combination of the pixellated detector and the electron detector response function. The background intensity B, in general, is slowly varying, which can be modeled using a slowly varying function.

The structural parameters are the atomic positions, Debye–Waller factors, electron structure factors, and electron diffraction parameters, which include the absorption potential, sample thickness, and crystal orientation. Not all parameters can be refined together. Diffraction patterns that are sensitive to certain parameters are collected and they are often refined independently. Figure 9 shows an example of a structure factor measurement by fitting CBED intensities recorded in the systematic orientation where one row of reflections are set at or near the Bragg conditions. Details about this method and its applications for structure factor measurement and atomic structure refinement are given in Ref. 18 and 43.

2.4.3 *Radial Distribution Function Analysis*

Electron diffraction patterns of amorphous and nanocrystalline materials are analyzed to measure the radial distribution function (RDF) to provide interatomic distances and their distribution. The principle of RDF analysis using electron diffraction is similar to X ray diffraction with the

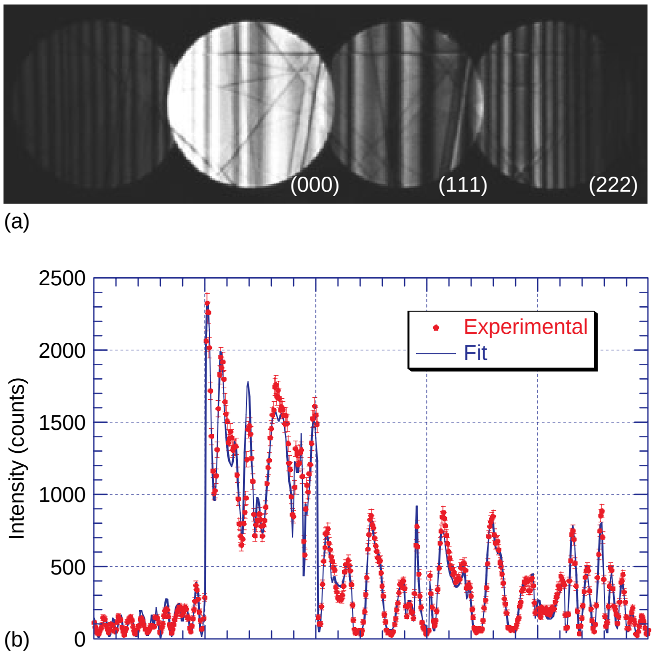

Figure 9 An example of the best fit obtained from an electron structure factor refinement. The experimental intensities are from a few selected line scans across the experimental pattern shown in (a). The fit was obtained using Si(111) and (222) structure factors as adjustable parameters together with parameters describing the electron diffraction geometry

exception of experimental procedures and the difference that electrons are scattered by strong Coulomb potentials.[44,45] The RDF gives the distance correlation between a pair of atoms. Following Warren,[46] the RDF is calculated by

$$rG(r) = 4\pi r^2[\rho(r) - \rho_o] = \frac{2r}{\pi}\int_0^\infty S\left[\frac{I(S)}{Nf^2} - 1\right]\sin rS\mathrm{d}S \qquad (19)$$

where $\rho(r)$ is the reduced density, which corresponds to the number of atoms per unit volume at a distance r from the reference atom, and $4\pi r^2\rho(r)\mathrm{d}r$ is the number of atoms contained in a spherical shell of radius r and thickness dr. Other quantities involved in equation (1) are ρ_o, which is the average density of atoms in the sample, $S = 4\pi\ \sin\theta/\lambda$, $I(S)$ the recorded electron diffraction intensity minus the inelastic background, N the normalization factor. The $\langle f\rangle$ is the averaged atomic scattering factor with $\langle f\rangle = \sum_i c_i K_i f$, the assumption made is that the atomic scattering is proportional to their atomic number. The f is determined from $\langle f^2\rangle = \sum_i c_i f_i^2 = \sum_i c_i K_i^2 f^2$ and $f_i = \sum_i c_i \int_0^\infty 4\pi r^2 V_i(r)(\sin Sr/Sr)\mathrm{d}r$ where V is the atomic potential and c the concentration. The RDF analysis can provide a general description of the degrees of order, the distribution of correlation distances, and the average nearest-neighbor coordination numbers. Orientation ordering or local geometrical packing of atoms cannot be retrieved from the one-dimensional RDF analysis, and we need to resort to other techniques like fluctuation microscopy.[47] The advantage of electron diffraction for RDF analysis is that it can be applied to thin films and small volumes because of the large electron elastic cross sections. For the same reason, electron diffraction must be limited to very thin films to avoid multiple scattering.

2.5 Experimental Procedures

The experimental procedures for electron diffractions involve: (i) the preparation of samples suitable for electron beam observation, (ii) selection of the instrument and the diffraction technique best suited for the sample, (iii) collection of diffraction data, and (iv) interpretation of diffraction patterns and data analysis. The sample must be compatible with the vacuum environment of the microscope or diffraction camera. In situ experiments are carried out using special holders for cooling, heating and cryogenic or environmental transfer. Special microscopes are also available to provide the gaseous or ultrahigh vacuum environment for investigating structures under gas or pressure environment or preparing samples in situ.

The samples used for RHEED and LEED are single crystals with carefully prepared flat surfaces. For THEED of thin films, the observed areas of the samples must be electron transparent with thickness less than or comparable to the inelastic mean free path of electrons. The inelastic mean free path increases with the electron voltage. The typical sample thickness ranges from tens to hundreds of nanometers for electrons of hundreds of kilo volts.

The preparation of samples is critical to the success of electron diffraction and its quantification. The same sample preparation techniques used for TEM are used for electron diffraction. The sample preparation techniques separate into two categories: (i) bulk-based and (ii) powder-based techniques. The bulk-based techniques involve mechanical cutting, thinning/polishing, and perforation. An ion beam is typically used in the last step of perforation to create a thin area around the edge of a hole for electron beam observation. Mechanical thinning and polishing are sometimes done with a wedge angle with the help of a tripod. The thin region around the edge only requires a brief ion beam bombardment to make it electron transparent. The powder-based techniques use dispersion of powders on thin supporting films placed on metal grids specially made for TEM observations. For micron or larger sized powders, additional grinding is done to produce smaller particles. The observation is performed on the edge of the powders. Typically used supporting films are continuous amorphous carbon films, holey carbon films, networked carbon fibers (lacey carbon), amorphous silicon nitride, and SiO_x. For amorphous carbon films, an ultrathin version is available which is useful for observing nanoparticles. Biological molecules are prepared by dispersing them with water onto holey carbon films then quenched into liquid methane to freeze the molecules together with water, which is then transferred to the electron microscope using a cryogenic transfer holder. The carbon film is treated by exposing it to a plasma which makes the film hydrophilic. Special instruments that help with the rapid freezing process are available from commercial suppliers. For organic molecules, some useful crystallization techniques for TEM are described in the book by Dorset.[37]

Instruments suitable for electron diffraction should have the sample rotation range that is required, the probe-forming capability for CBED or NED if needed, and a suitable detector such as a CCD camera or imaging plate. For quantification of electron diffraction intensities, an imaging electron energy filter is best to remove the inelastic scattering background. The different diffraction modes described in Section 2.1 can be achieved through a three condenser lens setup. There are two types of energy filters that are currently employed. One is the in-column Ω-energy filter[48] and the other is the post-column Gatan Imaging Filter (GIF).[49] Each has its own advantages. The in-column Ω-filter takes full advantage of the post-specimen lens of the electron microscope and can be used in combination with detectors such as film or IPs, in addition to the CCD camera. For electron diffraction, geometric distortion, isochromaticity, and angular acceptance are the important characteristics of filters.[48] Geometrical distortion complicates the comparison between experiment and theory and is best corrected by experiment. Isochromaticity defines the range of electron energies for each detector position. Ideally, this should be the same across the whole detector area. Angular acceptance defines the maximum range of diffraction angles that can be recorded on the detector without a significant loss of isochromaticity.

Another consideration is the choice of electron sources. The field emission electron guns provide better lateral coherence, smaller probes, and higher brightness in general than the thermionic source; they are more suitable for CBED and NED.

Electron diffraction data collection involves the required microscope optical alignment and special attention to the sample position, sample thickness and rotation, diffraction CL and diffraction lens focusing, and the detector used to record electron diffraction patterns. The CL is determined by the projection lenses in combination with the objective lens (the first lens after the specimen). To use the calibrated CL, the sample position and the objective lens setting must be the same setting between the calibration and experiment.

Current 2-D electron detectors include CCD cameras and IPs. The performance of the CCD camera and IP for electron recording has been measured.[50] Both are linear with large dynamic range. At low-dose range, the CCD camera is limited by the readout noise and dark current of CCD. The readout noise places a limit on what information can be recovered from recorded images if the CCD camera has a limited resolution. IP has a better performance at low-dose range due to the low dark current and readout noise of photomultiplier. For medium and high dose, the IP is limited by a linear noise due to the granular variation in the phosphor and instability in the readout system. The CCD camera is limited by the linear noise in the gain image, which can be made very small using averaging. There is an uncertainty in the uniformity of a CCD because its dependence on the gain image as prepared in the electron microscope. The performance of CCD also varies from one to another, which makes the individual characterization necessary.

The noise in the experimental data can be estimated using the measured detector quantum efficiency (DQE)

$$\mathrm{var}(I) = mgI/DQE(I) \tag{20}$$

Here I is the estimated experimental intensity, var denotes the variance, m is the mixing factor defined by the point spread function and g is the gain of the detector.[50] This expression allows an estimation of variance in experimental intensity once DQE is known, which is especially useful in the χ^2-fitting, where the variance is used as the weight. For the characterization of electron detectors, see Ref. 50.

3 APPLICATIONS

The main applications of electron diffraction are structure characterizations of inorganic and organic materials. Electron diffraction is also used for structure characterization of 2-D biological membranes.[51] The examples given here are limited to inorganic crystals. For electron diffraction study of organic molecules, see examples in Dorset's book.[37] The examples are used to demonstrate the materials problems that can be addressed by electron diffraction and the procedures involved in the analysis.

3.1 Phase Identification—CuO Nanowires

One of the common applications of HEED is phase identification. Figure 10 shows an example. The sample is copper oxide nanowires formed by heating a TEM Cu grid in air at temperatures ∼400 °C.[52] The wires are a few tens of nanometers wide (Figure 10a). To identify the structure of the nanowires, electron diffraction patterns were recorded on IPs in the SAED mode with a selected area of a few microns. The electron energy used is 200 kV and the diffraction pattern was recorded at the CL of 100 cm. The size of IPs is 94 × 75 mm. The largest diffraction angle recorded is about $s = \sin\theta/\lambda = 0.71\,\text{Å}^{-1}$. The diffraction pattern shows incomplete powder rings because of the preferred wire orientations that are seen in the electron image. To index the diffraction pattern, the diffraction intensities were projected onto a one-dimensional radial profile; this was achieved by first locating the center of the diffraction pattern using the powder rings and then averaging the intensity around the circle. The diffraction pattern radius was then converted into $s = \sin\theta/\lambda$ using equation (3). A search in the powder diffraction data base showed that all diffraction peaks can be indexed based on the monoclinic CuO structure with $a = 4.6927$, $b = 3.4283$, $c = 5.1370$ and $\beta = 99.546°$. The indices of the first few peaks are shown in Figure 10(c). Low-order Cu_2O reflections are absent in the diffraction pattern suggesting that the sample consists entirely of a single phase, CuO.

3.2 Crystal Orientation and Microstructure—the Structure of a CuO Nanowire

Electron diffraction can be used to identify the crystal orientation and orientation relationships between different crystals. In the case of the CuO nanowires discussed in the previous section, NED was used to characterize the structure of individual CuO nanowires. Diffraction patterns were recorded using a probe of 100 nm in diameter. The probe was placed on an isolated single wire (an image of the wire and probe is shown in Figure 11) for diffraction. The diffraction pattern shown consists of two set of diffraction spots; one belongs to the [101] zone axis and the other is from the [15−6] zone (Figure 11). The pattern was indexed using the length of g calculated based on the calibrated CL and the angle; both are measured directly from the experimental pattern. For the diffraction spots belonging to [101], the two shortest g-vectors have almost identical length (the experimental ratio is 1.017) and an angle of 83.8° between the two. The length

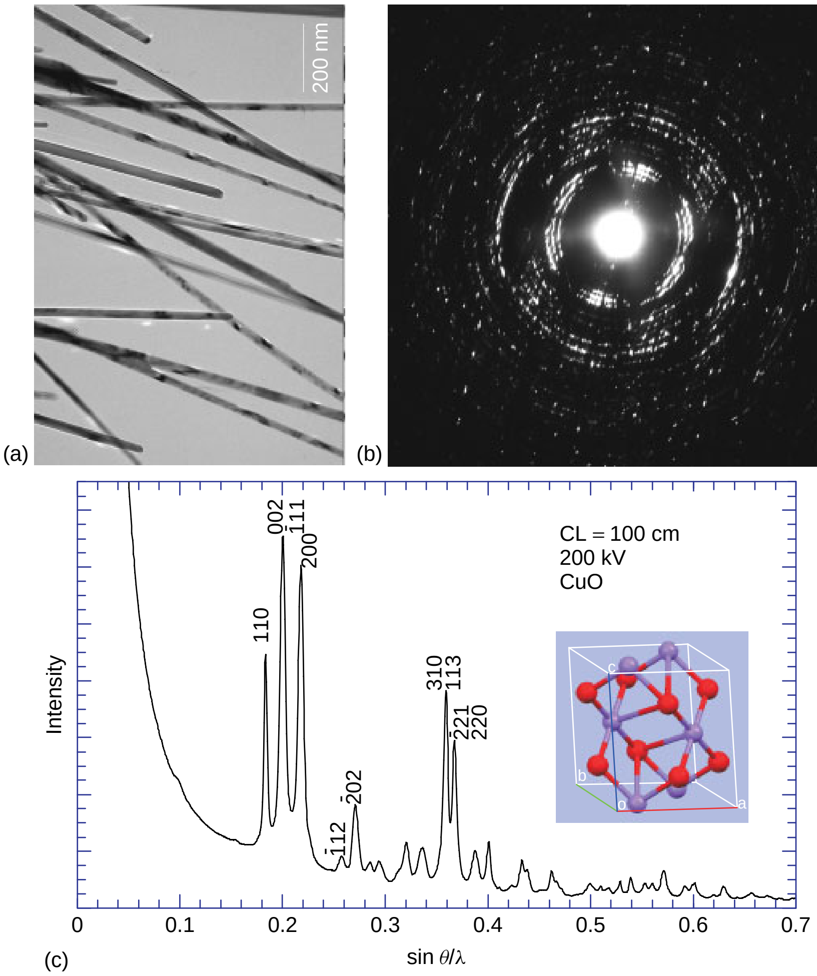

Figure 10 Phase identification of CuO nanowires. (a) An electron image of the wires, (b) the recorded diffraction pattern, (c) the diffraction intensity plotted as a function of sin θ/λ and indexing diffraction peaks based on CuO monoclinic structure

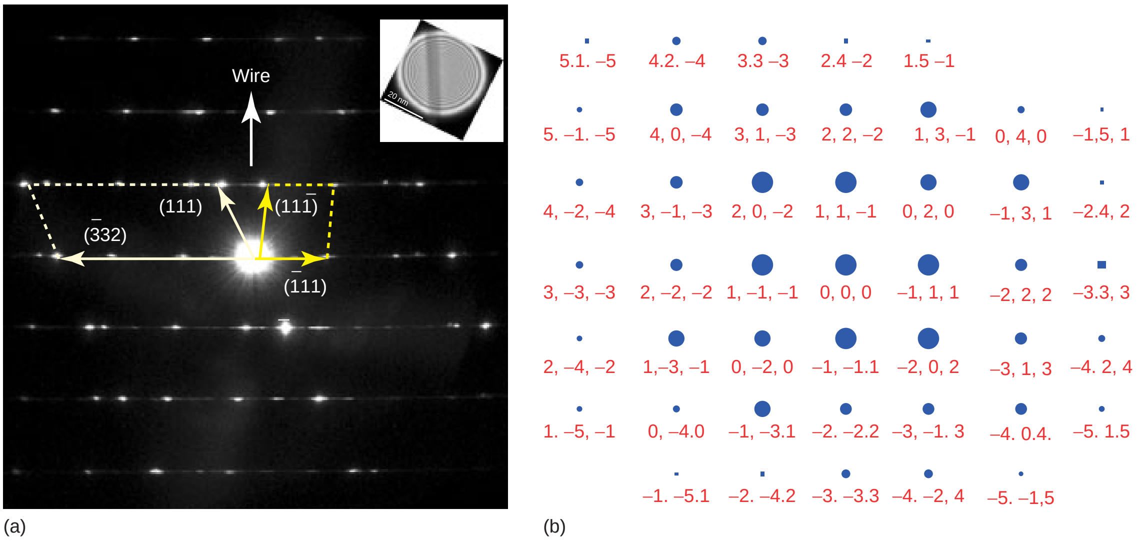
Wire
20 nm
(111)
(111̄)
(3̄32)
(1̄11)
(a)
5.1. –5
4.2. –4
3.3 –3
2.4 –2
1.5 –1
5. –1. –5
4, 0, –4
3, 1, –3
2, 2, –2
1, 3, –1
0, 4, 0
–1,5, 1
4, –2, –4
3, –1, –3
2, 0, –2
1, 1, –1
0, 2, 0
–1, 3, 1
–2.4, 2
3, –3, –3
2, –2, –2
1, –1, –1
0, 0, 0
–1, 1, 1
–2, 2, 2
–3.3, 3
2, –4, –2
1,–3, –1
0, –2, 0
–1, –1.1
–2, 0, 2
–3, 1, 3
–4. 2, 4
1. –5, –1
0, –4.0
–1, –3.1
–2. –2.2
–3, –1. 3
–4. 0.4.
–5. 1.5
–1. –5.1
–2. –4.2
–3. –3.3
–4. –2, 4
–5. –1,5
(b)

Figure 11 Electron diffraction pattern recorded from a single CuO nanowire and its indexing

of $0.394\,1\ \text{Å}^{-1}$ was obtained using the calibrated CL, which is very close to that of (−111) or (11−1) reflections. The calculated angle between (−111) or (11 − 1) is 85.03°, which is 1.2° higher than the experimental value. (The measurement accuracy is better than 1°.) The indexing is confirmed by simulation (see Figure 11b) using the WebEMAPS software (see the reference materials section for details). The diffraction pattern shows that the wire is twinned. The twin interface is parallel to the wire which can be seen in the electron image. The relationship between the two crystals is [101]||[15−6] and (−111)‖(−332).

3.3 Structure Characterization of Supported Nanoclusters and Epitaxy

The combination of electron imaging and electron diffraction is very useful for characterization of supported nanoclusters, or nanoparticles, and their orientation relationships with the substrate. The particles can be observed either in plane view or in cross section. The plane-view geometry is most suited for electron diffraction over many particles. The two examples shown in Figure 12 are from Ag nanoparticles supported on hydrogen-terminated Si(100) surfaces as deposited and after annealing.[53–55] The samples were prepared by first thinning the Si substrate followed by surface treatment and Ag deposition using an e-beam evaporation source.[55] The electron microscopy observation was performed using a JEOL2010F electron microscope at 200 kV. The diffraction patterns were taken at an orientation off the [001] zone axis to avoid strong multiple scattering in a zone-axis orientation. The diffraction pattern of the as-deposited sample consists of a strong and continuous Ag(111) ring, short Ag(200) arcs on a weak Ag(200) ring, short Ag(220) arcs on a weak Ag(220) ring and weak (311) rings. Upon annealing at 400 °C, Ag(020) and (200) reflection intensities increase significantly. Both have diffuse streaks along (110) and (1−10) directions. The Ag(020) and (200) are asymmetrical because of the off-zone axis orientation of the diffraction pattern. Meanwhile, the diffraction intensity in the continuous ring decreases significantly, but remains visible. Figure 12 shows high-resolution images of Ag clusters on H−Si(001). These images were taken at the Si[001] zone axis. At this orientation, the Si(220) and (2−20) planes are imaged. Most as-grown Ag clusters show no visible Moiré fringes, which is consistent with the diffraction pattern that is dominated by (111) ring. A few clusters with Moiré fringes are often defective. The clusters of dark contrast with no Moire fringes contribute to the strong (111) rings in the diffraction pattern. At first sight, orientation of these clusters appears to be random. However, a close inspection of the diffraction pattern shows a much weaker (200) ring than what it would be in a powder diffraction pattern of random polycrystalline Ag. For single crystals oriented with Ag[111]||Si[001] or Ag[001]||Si[001], strong Ag(220) is expected in both cases, while a strong Ag(200) is also expected in the case of Ag[001]||Si[001]. Both of these cases can be ruled out. In Figure 12(c), the Ag clusters show 2-D Moiré fringes (from interference between Ag and Si lattices[54]) perfectly parallel to Si(220) lattice planes. The corresponding electron diffraction pattern shows single crystal dominant diffraction of Ag[001] with Ag(220)||Si(220). At this stage, the transformation from random cluster orientation to epitaxial islands is not over, because we still see weak (111) diffraction rings from randomly oriented Ag clusters. The Ag(200) reflections have the shape of a plus-sign, centered at the Ag(200) position, which comes from the rectangular shapes of the epitaxial Ag islands. The edges of islands are along the Si(110) and (1−10) directions.

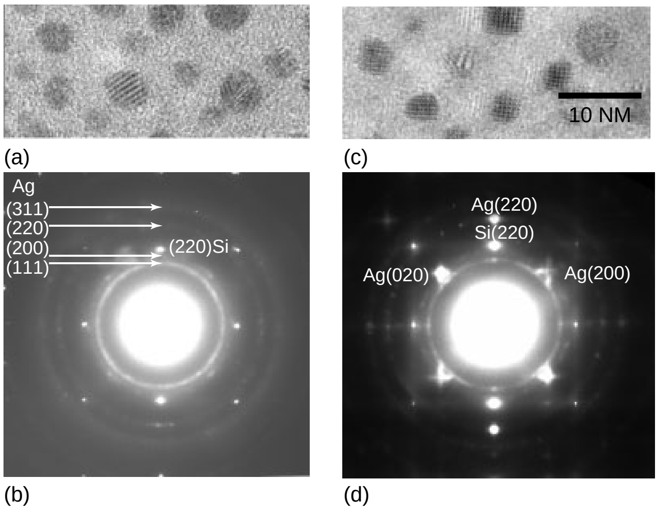

Figure 12 Combined electron diffraction and imaging characterization of supported Ag nanoclusters/nanocrystals on Si(100) substrate. (a) and (b) show randomly oriented nanoclusters. (c) and (d) show epitaxial nanocrystals after annealing

3.4 The Structure of Nanocrystalline Films — the Case of AgCu

For materials with nanocrystalline structure, RDF analysis is a powerful tool for structural analysis. The advantage of electron diffraction compared (DC) to X-ray/neutron diffraction is that it can be applied to technologically important thin films. The drawback is that electron diffraction averages overall atoms in the sample and consequently it cannot be used to study composition dependent local structures that is obtainable with extended X-ray absorption fine structures (EXAFS) (*see* ***X-Ray Absorption Spectroscopy***). The example shown in Figure 13 is a study of the structure of co-sputtered $Ag_{0.5}Cu_{0.5}$ films and its temperature-driven evolution. The eutectic Ag−Cu system is one of the glass-forming binary alloy systems with a positive heat of mixing in both solid and liquid states. Solid solution, amorphous or nanocrystalline, Ag−Cu alloys can be prepared by vacuum evaporation.[56–59] However, the solid solution of Ag and Cu alloy is unstable

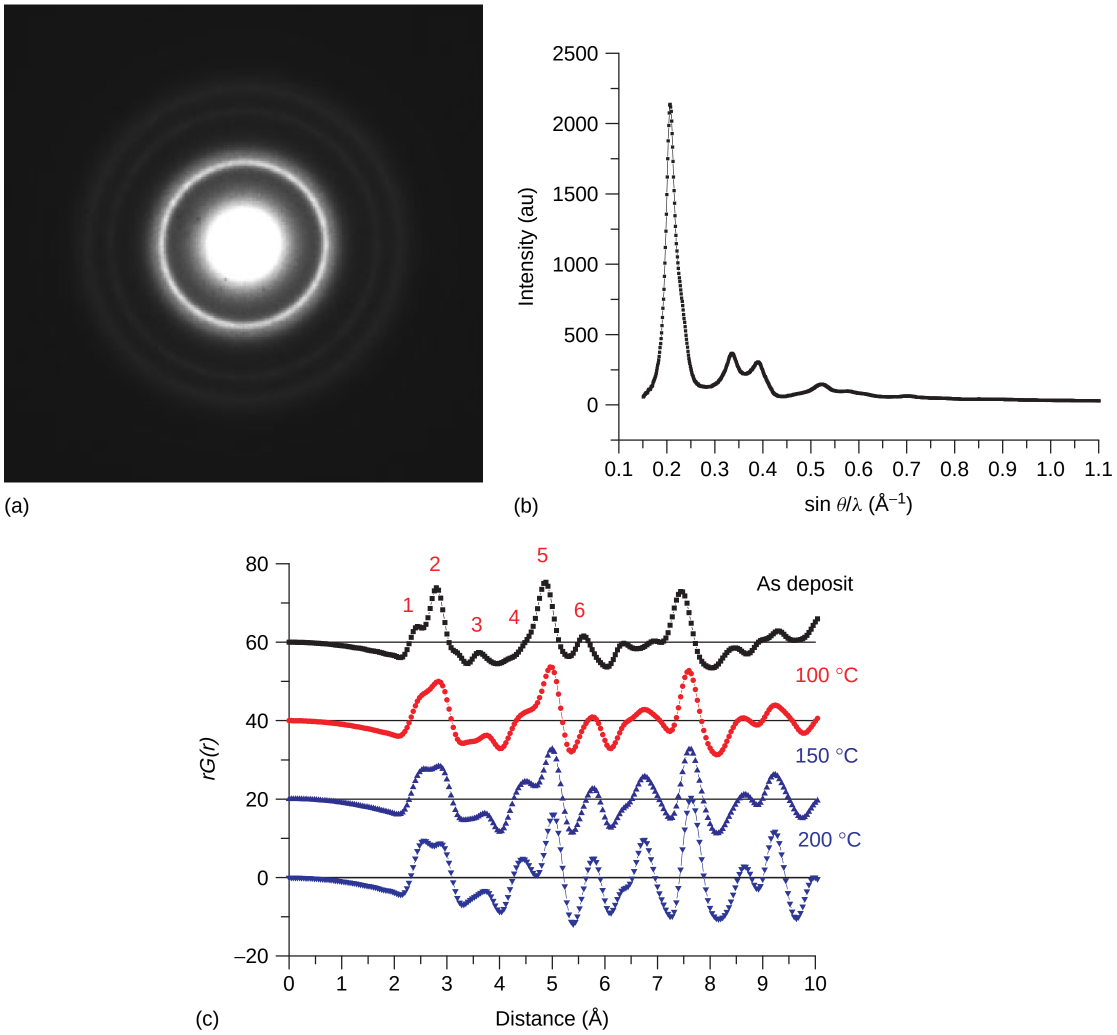

Figure 13 (a) An example of recorded electron diffraction pattern of as-deposited 28 Å $Ag_{50}Cu_{50}$ thin film sample. (b) The radial intensity profile of (a) obtained by averaging over the angle. (c) Radial distribution function (RDF) in the form of *rG(r)* obtained from the experimental diffraction patterns of $Ag_{50}Cu_{50}$28 Å samples at different annealing temperatures

since there is no barrier against decomposition. At higher cooling temperatures or upon reheating, Ag and Cu phase separate, or evolve, into crystalline structure from the initial amorphous or nanocrystalline state.[59] The Ag–Cu thin films (28 Å thick) studied in Figure 13 were deposited in a high-vacuum (HV) DC magnetron sputter deposition system by co-sputtering of high purity Ag and Cu targets onto amorphous carbon films at room temperature (RT). Quantitative structure analysis was carried out using the NED mode in the JEOL 2010F electron microscope with a highly parallel illumination of a submicron probe. Electron diffraction patterns were recorded from the samples at different annealing temperatures using image plates. The amorphous carbon background from the supported film was subtracted off using the diffraction intensity profiles recorded from amorphous carbon film alone. The diffraction intensity was used to investigate the structure and for RDF analysis.

The diffraction of as-deposited films gives diffuse ring patterns with a strong first peak at $\sin\theta/\lambda = 0.213\,\text{Å}^{-1}$ and a small shoulder at $\sin\theta/\lambda = 0.238\,\text{Å}^{-1}$, which indicates a good mixing of Ag and Cu atoms in the alloy thin films (Figure 13). The peak position is closer to that of Ag ($\sin\theta/\lambda = 0.212\,\text{Å}^{-1}$) than to Cu ($\sin\theta/\lambda = 0.240\,\text{Å}^{-1}$). As the sample is annealed to higher temperatures, the intensity of the Cu peak increases and it forms two distinct peaks at $T = 200\,°\text{C}$ with peak positions at $\sin\theta/\lambda = 0.212$ and $0.240\,\text{Å}^{-1}$, which is an indication of Cu–Ag phase separation. A comparison of the RDF of the $Ag_{50}Cu_{50}$ film at different annealing temperatures is shown in Figure 13(c). The RDF of the as-deposited $Ag_{50}Cu_{50}$ sample is in good agreement with that obtained by Wagner *et al.* using X-ray diffraction,[58] except the Cu peak is slightly more pronounced in our case. From the RDF plot, two separated nearest-neighbor peaks can be seen. The second peak corresponds to Ag–Ag distance, which shifts from 2.80 to 2.88 Å from the as-deposited sample to the sample annealed at 200 °C. The distance of 2.88 Å fits with the first nearest-neighbor peak of Ag crystal (2.875 Å) very well. At 200 °C, the first peak is situated at Cu−Cu atomic distance of 2.56 Å, which fit into the position of the first nearest-neighbor peak of Cu particles (2.55 Å) very well. Interestingly, for the as-deposited sample, the Cu−Cu peak is at 2.45 Å and is lower than the bulk Cu−Cu distance. A lower distance is expected for Ag with the doping of a smaller Cu atom, but not for Cu, for which we expected a large distance due to Ag doping. The reduced distance suggests that Cu is under compressive strain. The fourth and fifth peaks of RDF show splitting (Cu peak growing from Cu shoulder in Ag peak) and shifting during the annealing process, and this phase separation is due to Cu diffusing out of the Ag matrix. A detailed list of the position of the first 6 peaks in these RDF results is shown in Table 1. The peaks 1, 3 and 4 belong to Cu while 2, 5 and 6 belong to Ag. The ratio between the distances of peaks 5 and 2 is 1.74, which is close to $\sqrt{3}$ and the ratio between 6 and 2 is 2. The ratio of $\sqrt{3}$ comes from the third nearest neighbor, while 2 is from the fourth. Both are in agreement with a face-centered cubic cell. In the liquid, this ratio of 5 and 2 is 1.86 for close-packed liquid.[58] The ratios are temperature dependent. The ratio between peak 4 and 1 varies from 1.77 at 150 °C to 1.73 at 200 °C, while the ratio between peak 5 and 2 first increases to 1.76 with annealing temperature and then drops slightly to 1.75 at 200 °C. The same trend occurs for the ratio between peak 6 and 2. Thus, the early stage of phase separation appears to be associated with an initial increase in strain.

The experimental procedures used for RDF analysis are as follows. The electron diffraction patterns were recorded digitally using IPs. The CL of 600 mm was used to include $s = \sin\theta/\lambda$ up to 1.27 for rotation averaging. The recorded electron diffraction had a strong central peak that includes small angle inelastic scattering and the profile of the electron beam. This central peak was modeled by a pseudo-Voigt function and subtracted. The normalization coefficient, N, was found by fitting to large-angle scattering using the atomic scattering factors. Finally, the RDF was obtained by direct integration of equation (19).

Table 1 Peak positions in the radial distribution function of $Ag_{50}Cu_{50}$ as a function of the annealing temperature measured by electron diffraction (see Figure 13)

	Position of peaks in the radial distribution function (Å)					
	1	2	3	4	5	6
As-deposit	2.44	2.80	3.60	[a]	4.88	5.60
100 °C	[a]	2.84	3.76	4.56	4.96	5.76
150 °C	2.56	2.84	3.72	4.52	5.00	5.80
200 °C	2.56	2.88	3.72	4.44	5.04	5.80

[a] These peaks appear as a shoulder, whose position is difficult to measure.

The size of the nanocrystalline grains can be measured by taking the distance at which oscillation decreases to the noise level in the RDF spectrum. Using this, the size for the as-deposited film is estimated to be about 30 Å. Upon annealing, the strength of the first and fourth peaks increases which is a strong indication of the growth of a Cu-rich phase. The peak 2 decreases, which is associated with the decrease of nearest neighbors at that distance. This evidence can be taken as an indication of Cu separated out from the solutions. Substantial growth in overall crystal size is observed at 200 °C in the RDF.

3.5 In Situ Study of Phase Transformation—Charge Ordering in $La_{0.50}Ca_{0.50}MnO_3$

The doped manganite of $La_{0.50}Ca_{0.50}MnO_3$ (LCMO) undergoes a commensurate-incommensurate-commensurate phase transformation at low temperatures.[60,61] The LCMO belongs to a family of doped manganites $A_{1-x}B_xMnO_3$, where A-site atoms could be La, Pr, Nd, Bi, Sm, while B-site atoms are Ca, Sr, Ba, Pb. These materials have attracted considerable attention because of their interesting properties.[61] At high temperatures, the doped manganites have an ideal perovskite structure consisting of corner-shared MnO_6 octahedra. The A-site atoms fill in the holes of the MnO_6 octahedral network. At intermediate temperatures, the structure is distorted with an orthorhombic lattice (space group *Pnma*). The cell consists of $a_o \approx c_o \approx b_o/\sqrt{2} \approx \sqrt{2}a_c$, where a_c is the high-temperature cubic cell. In the case of LCMO, the commensurate-incommensurate-commensurate phase transformation is observed below 240 K. The transition is accompanied by a change in the transport property from conducting to insulating during cooling. The change in the transport property is believed to be caused by ordering of Mn^{4+} and Mn^{3+} ions, which is 50−50 LCMO. The nature of the charge ordering (CO) and its formation process has been a subject of considerable interest and debate.[62,63]

It is difficult to grow single crystals of LCMO and other compositions of this series except $LaMnO_3$. Electron diffraction (ED), because of its small probe size, can be used to study the phase transition within a single crystal grain. Figure 14 shows a single crystal ED pattern obtained from a polycrystalline grain of charge-ordered LCMO at the low temperature of 98 K recorded along the [010] zone axis. At the $x = 0.5$ Ca doping level, $La_{1-x}Ca_xMnO_3$ has an equal amount of Mn^{3+} and Mn^{4+} ions; the CO superlattice has a unit cell with $a_{co} = 2a_o$, where a_o is the orthorhombic cell constant at RT. Thus, the CO superlattice reflections (SRs) can be indexed as (h + 1/2, 0, l) in the units of the reciprocal lattice of the RT orthorhombic cell. In Figure 14, a pair of CO SRs around the $(00\bar{2})$ reflection are pointed out by arrows; they can be treated as the satellite reflections ($\pm q, q = 1/2$) of the fundamental reflection. The q is nearly commensurate ($q = 1/2$) at $T = 98$ K. As the temperature increases, q becomes incommensurate ($q = 1/2 - \varepsilon$) by moving toward

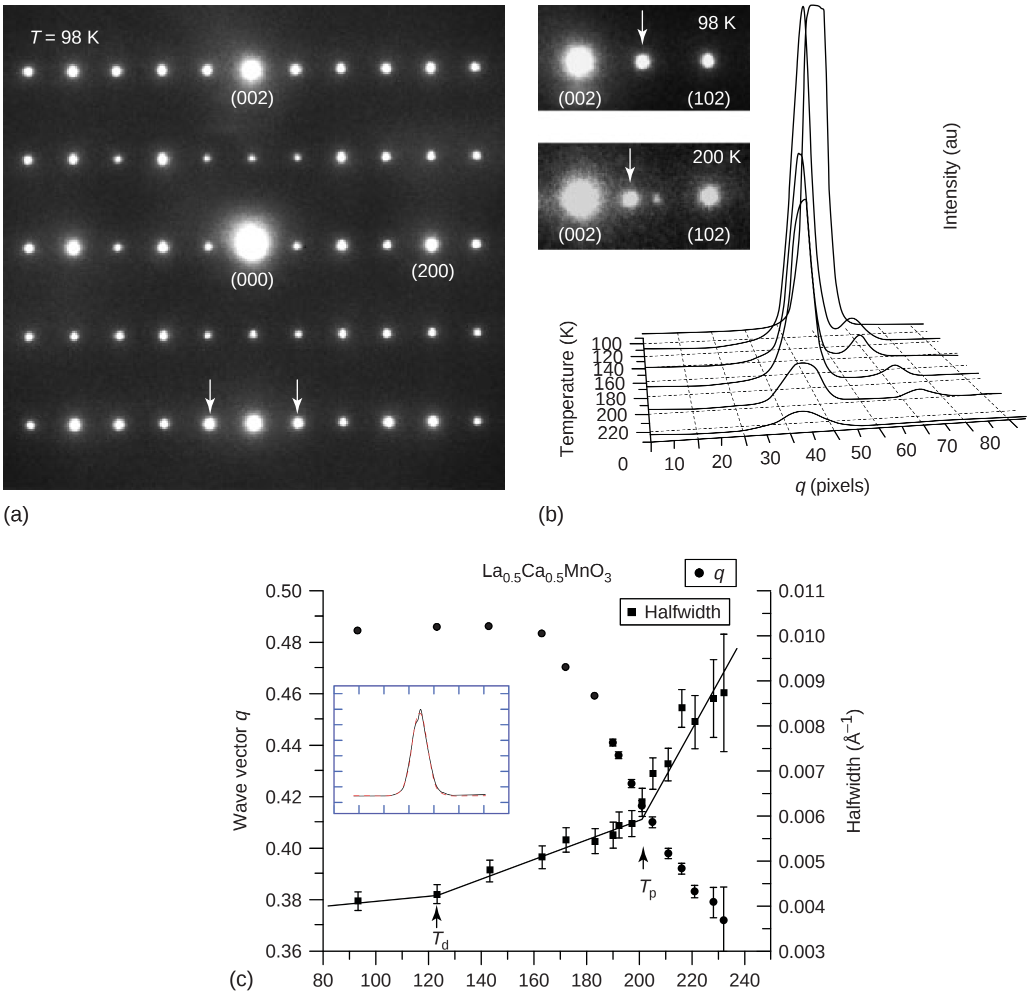

Figure 14 (a) An electron diffraction pattern obtained at 98 K in $La_{0.5}Ca_{0.5}MnO_3$ shows the CO ($h + 1/2$, 0, l) superreflections (CO SRs; indicated by arrows) at [010] zone axis. The profiles of the CO SRs between (002) and (102) reflections are plotted as a function of temperature in (b). The insets in (b) are the electron diffraction patterns at 98 and 200 K showing the movement of the CO SR superreflection. (c) Wave vector q (circles) and the Gaussian half width (squares) measured from the CO SRs in ED patterns are shown as a function of temperature. The half width was calculated by fitting the CO SRs in electron diffraction patterns using Gaussian functions (the fitting is shown in the inset). The half-width plot shows three linear relationships with the transition temperatures $T_o \sim 120$ K and $T_p \sim 200$ K

the fundamental reflections. The insets of Figure 14(b) are examples of the ED patterns at two different temperatures (98 and 200 K), showing the movement of CO SRs between the (002) and (102) reflections. The +q satellite reflection of (002) coincides with the $-q$ satellite SR of (102) at 98 K. The two SRs separate at $T = 200$ K. During the warming process, the SRs also become broadened and the intensities of the SRs change with temperature as well. Both can be seen from the intensity profile crossing the SR from the (002) to (102) reflections (see Figure 14b) as a function of the temperature.

To show the temperature dependence of the wave vector q and to characterize the CO structure, the position of q and the Gaussian half width (GHW) of the CO SRs were measured from the in situ recorded ED patterns during the warming process for LCMO. This is plotted in Figure 14(c). The GHW of the CO SRs was obtained by numerically fitting the intensity profile of the SRs[4] (an example is shown in the inset of Figure 14c). During warming, the wave vector q of the SR initially remains constant and then gradually decreases starting from ~160 K until the SR becomes difficult to measure at $T^* > \sim 230$ K. The change in the CO SR position (q) is contunous. In the same figure, the GHW plot has different features compared to q. Since the GHW is the inverse of real-space CO domain size, the different slopes in the GHW versus T plot indicate that the CO superstructure melts in stages: the GHW maintains the low value from low temperatures to $T_d \sim 120$ K; the GHW value starts to increase at a linear rate from T_d to $T_p \sim 200$ K; above T_p, the GHW increases at a higher rate until the SR disappears.

The GHW of the CO SR, measured from the ED patterns, reflects the coherent length of the CO superstructure.

Information obtained from the ED patterns about the CO phase transformation in LCMO is as follows. Commensurate CO exists at $T < T_d$ and becomes incommensurate by the appearance of CO defects above T_d during the warming process. The appearance of CO defects results in a melting of CO at a slow rate for $T_d < T < T_p$. Previously, synchrotron X ray and neutron powder diffraction (*see* ***Neutron Diffraction***) found that the lattice parameters change between T_d and T^*. There is hysteresis in the lattice parameters, the electrical transport property and the magnetism at $T_d < T < T_p$ in LCMO.[60,63] The appearance of CO defects can be considered as a first-order transition locally. Thus the pronounced hysteresis observed in the change of lattice parameters and resistivity in LCMO is strongly correlated with the generation and disappearance of CO defects between $T_d < T < T_p$. The change of CO from long-range order to short-range order has a significant influence on the transport property, for example, the resistivity has a steep drop at T_p.[5] At temperatures $T > T_p$, the CO superstructure, initially uniformly distributed in the entire single crystal domain, separates into isolated CO domains of the diameters of tens of nanometers (measured from the GHW). This percolation temperature T_p (transition from continuous to separate CO domains) of the CO phase transformation, was first found in the charge-ordered $La_{0.33}Ca_{0.67}MnO_3$,[63,64] which also has commensurate CO SRs at low temperatures. In this temperature range, the broadening of the GHW in Figure 14(c) comes mainly from the reducing size of the CO domains during the CO melting. At $T > T^*$ the CO superstructure completely melts away and the material reverts back to the RT paramagnetic phase. At this stage (RT), there is no visible CO SR in the recorded ED patterns.

3.6 Symmetry Determination — the Glide and Structural Models in $La_{0.33}Ca_{0.67}MnO_3$

The doped $La_{0.33}Ca_{0.67}MnO_3$ undergoes a similar commensurate-incommensurate-commensurate phase transformation as that of LCMO, but with a ratio of 1 Mn^{3+} to 2 Mn^{4+}.[62,63] The low-temperature commensurate structure is tripled along the a axis. Two different structural models have been proposed for this structure. One is the ‘‘Wigner-crystal’’ model proposed from the X ray and neutron powder diffraction study by Radaelli *et al.*[63] and the other is the ‘‘bi-stripe’’ model of Mori *et al.*[62] based on the high-resolution TEM images of the CO phase (Figure 15b). The two models are different in the crystal symmetry.[65] The space group of the ‘‘Wigner-crystal’’ model is *Pnma*, while the space group of the ‘‘Bi-stripe’’ model is *Pm*. The *Pnma* space group has an n-glide plane normal to the a axis and an a-glide plane normal to the c axis. The presence of the glide symmetry can be determined using G-M lines in CBED (see Section 2).

Figure 15(a) and (c) show the experimental CBED pattern from a single crystal domain in $La_{0.33}Ca_{0.67}MnO_3$ recorded at ~99 K and along the [010] zone axis. The indexing is based on the low-temperature structure at 99 K with a unit cell of $a \sim 1.6187$ nm, $b \sim 0.7499$ nm and $c \sim 0.5408$ nm.[63] The experimental CBED patterns were energy filtered via a GIF system. The thick sample required for CBED generates a certain amount of inelastic scattering and causes blurs in the experimental CBED patterns. A large portion of inelastic scattering has an energy loss of 10 eV or higher, which can be removed using the energy filter. Two types of extinction are observed. The dark lines crossing the four (303) type reflections are clearly visible; they are consistent with the n-glide of the *Pnma* space group. Figure 15(c) shows the line extinction across a series of odd-indexed reflections along the reciprocal $\vec{a}^*$ direction (the (3, 0, 0), (7, 0, 0), (9, 0, 0), (11, 0, 0), (13, 0, 0) and (15, 0, 0) reflections). The reflection (100) is overwhelmed by the direct beam (000) and the reflection (500) is too weak to identify its contrast. Among the reflections with the G–M lines, (700), (1100) and (1300) are from the low-temperature structure. Thus, the experimental CBED patterns clearly show that both the low-temperature modulated structure and the average structure in $La_{0.33}Ca_{0.67}MnO_3$ have a glide plane perpendicular to the c axis with the glide direction along the a axis of the crystal lattice and the n-glide normal to the b axis.

The symmetries revealed by the experimental CBED patterns are possessed by the structures described by the ‘‘Wigner-crystal’’ model but not by the ‘‘Bi-stripe’’ model. The ‘‘Wigner-crystal’’ model gives the CO structure a space group *Pnma* with a glide plane perpendicular to the c axis, while the ‘‘Bi-stripe’’ model does not have the glide plane symmetry (the space group is *Pm*). Therefore, the experimental CBED patterns with G–M lines can be considered as strong evidence against the structure described by the ‘‘Bi-stripe’’ model.

To verify the symmetry and identify the sensitivity of CBED to CO symmetry, dynamic simulations using the Bloch wave method were examined to see the difference between the two models. The atomic positions within the unit cells for the two models from Radaelli *et al.* are very close to each other.[63] To avoid the possible pseudo-symmetry generated in the ‘‘Bi-stripe’’ model, dynamic simulations from the CO structures described by the ‘‘Wigner-crystal’’ model and ‘‘Bi-stripe’’ model are calculated and compared for the thickness of 300 nm in Figure 15(d) and (e). The difference between the two simulations is that the G–M lines exist in four (303) reflections and $(2n + 1, 0, 0)$ reflections simulated by the ‘‘Wigner-crystal’’ model, as they are in the experimental CBED patterns, but do not show up in four (303) reflections simulated by the ‘‘Bi-stripe’’ model.

3.7 Polarity Determination

CBED can be used to determine the polarity of crystals without a center of symmetry. It can also be used for accurate determination of thickness. The principle of polarity determination is based on the difference between the

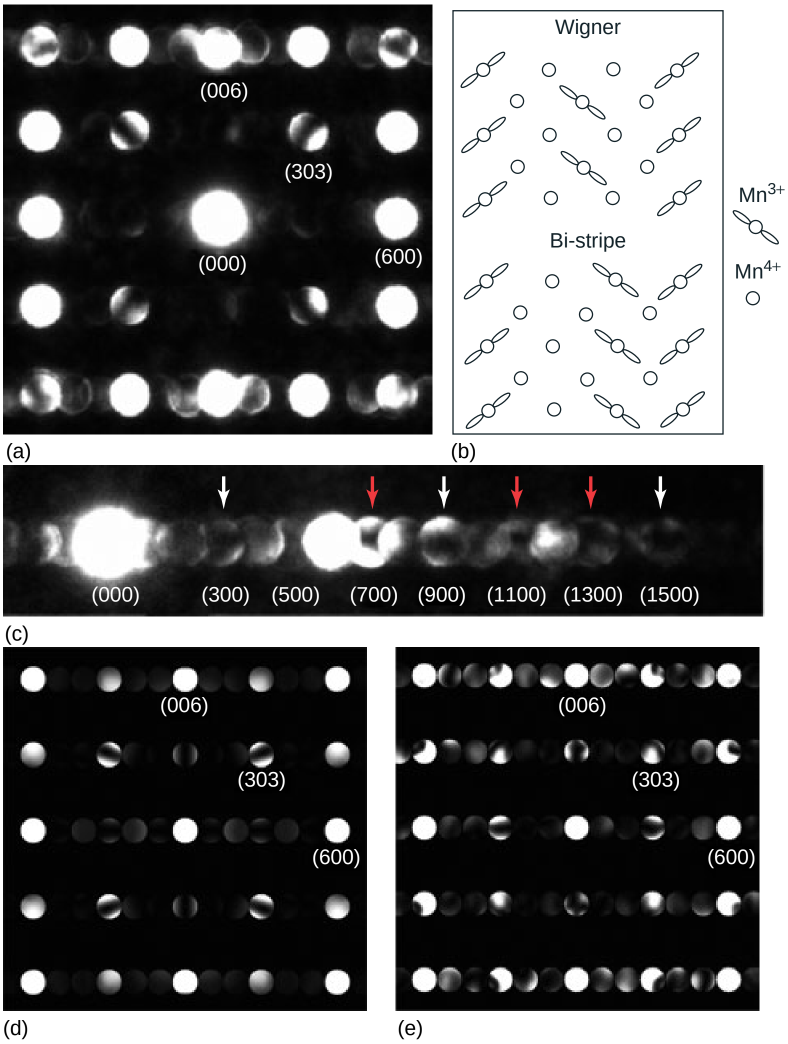

Figure 15 Symmetry identification of low-temperature charge-ordered La$_{0.33}$Ca$_{0.66}$MnO$_3$. (a) the experimental CBED pattern from a single crystal domain in La$_{0.33}$Ca$_{0.67}$MnO$_3$ recorded at $\sim$99 K and along the [010] zone axis. (b) schematic illustration of charge ordering models. (c) the line extinction across a series of odd-indexed reflections along the reciprocal $\vec{a}^*$ direction in the experimental pattern. (d) and (e) Simulated CBED patterns from the CO structures described by the ''Wigner-crystal'' and ''Bi-stripe'' models (b) for the thickness of 300 nm

intensity of $\pm g$ disks which comes from lack of Friedel's symmetry from dynamic scattering. The difference between $\pm g$ is first calculated based on the known structural model and atomic potentials including dynamic scattering, and is then compared with experiment for polarity determination. The comparison is usually performed for the whole diffraction pattern with crystal thickness determined simultaneously. Crystal thickness can be determined accurately using this method because the intensity pattern in CBED is very sensitive to thickness and the atomic potentials available in publication are good approximations of the real crystal potential.

An example of polarity determination and its application is the study of the growth mechanism of ZnO nanowires.[66] During ZnO growth, asymmetric side growth is often observed with one side showing finger-like structures and the other side tip-like structures. The difference was attributed to the surface termination; whether it is Zn- or O-terminated. To check this hypothesis, CBED electron diffraction was used to determine the wire polarity. The experimental diffraction pattern was first recorded from the wire (Figure 16). The orientation relationship between the wire direction and CBED was calibrated. The ±(0002) disks are asymmetric reflecting the lack of center of symmetry. To index the experimental diffraction, a Bloch simulation of the CBED pattern is performed for different thicknesses and compared with the experimental pattern. A best match is obtained (Figure 16). The determination was unique because of the complex intensity distribution in CBED and its sensitivity to the thickness.

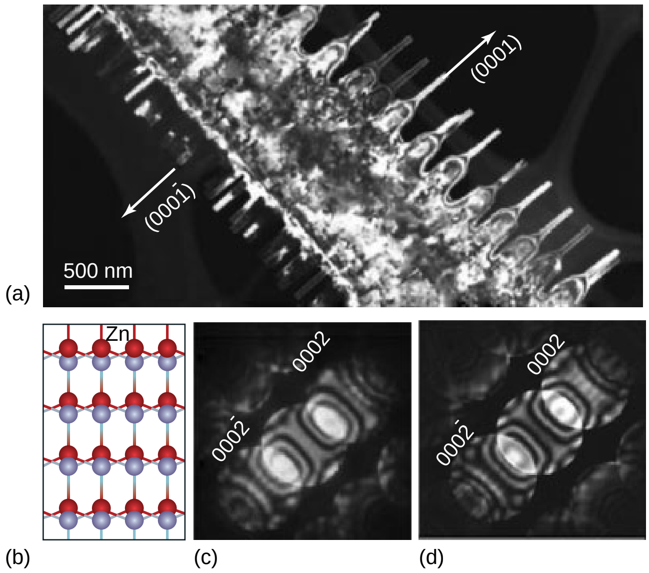

Figure 16 An example of polarity determination and application in the study of the growth mechanism of ZnO nanowires

3.8 Accurate Lattice Parameter Measurement and Strain Mapping

Measuring d-spacings from conventional spot diffraction patterns requires the calibration of the camera constant; the measurement accuracy is limited by errors in the calibration and the location of diffraction peak positions. An alternative is to measure lattice parameters from the HOLZ line positions. The advantages of using HOLZ lines are the high accuracy and high sensitivity to changes in lattice parameters. They have the advantage that (i) calibration is not required; the measurement relies on the relative positions of HOLZ lines, (ii) high order reflections are used in the measurement, which are sensitive to changes in lattice parameters, (iii) only the transmitted beam is used which is least affected by the lens distortion in the microscope. The strain is measured by fitting the position of HOLZ lines. There are two methods for fitting HOLZ lines; one is based on the kinematic approximation, in which HOLZ lines are approximated by straight lines.[67] The second is based on dynamic diffraction simulation. The fitting in this case is achieved by using pattern matching between the experimental and the simulated diffraction patterns.[68] Kinematic fitting is fast and involves several tasks, including measuring the experimental lines from the recorded CBED pattern, indexing the experimental lines and finally carrying out the fitting. These tasks are achieved through the following automated functions: (i) preprocessing of diffraction patterns for line detection; (ii) line detection using the Hough transformation; (iii) indexing the HOLZ lines; (iv) defining the fitting parameters; and (v) performing the fitting.

The most accurate measurement comes from dynamic fitting, which takes account of EMS effects. Using the Si crystal as a test, Kim *et al*. measured the Si lattice parameter at different orientations and sample positions. Their standard deviation is 0.0012 Å, which corresponds to 0.02% of the Si lattice parameter. The error bar of kinematic fitting includes a systematic error due to the neglect of the dynamic scattering. This error can be reduced by using the ‘‘so-called’’ kinematic orientations,[69,70] such as the [430] and [230] zone axes in Si.[71]

The spatial resolution depends on several factors: the electron probe size, the probe broadening in the sample due to diffraction, the beam direction relative to the strain axes. Theoretical consideration based on the column approximation suggests that the resolution in the zone-axis orientation can be as small as a few nanometers.[72] In the case of a thick sample, the resolution is limited by the probe broadening.[73]

3.9 Nanostructure Determination—the Case of Carbon Nanotubes

Nanostructure determination is a challenge in materials characterization. Many inorganic nanostructures lack the uniformity and symmetry of a single crystal or the monodispersity of some organic molecules. Their structure determination thus requires a high-resolution probe that can examine individual nanostructures. Electron diffraction has the resolution required; the nanoprobes used in CBED and NED are especially suited for studying nanomaterials. For structures like single-wall CNT, the structure can be determined directly from electron diffraction patterns.

A single-wall nanotube (SWNT) can be regarded as a single layer of graphite that has been rolled up into a cylindrical structure. In general, the tube is helical with the chiral vector (n, m) defined by $\vec{c} = n\vec{a} + m\vec{b}$, where $\vec{c}$ is the circumference of the tube, and $\vec{a}$ and $\vec{b}$ are the unit vectors of the graphite sheet. A striking feature is that tubes with $n - m = 3l$ (l is an integer) are metallic, while others are semiconductive. This unusual property, plus the apparent stability, has made CNTs an attractive material for constructing nanoscale electronic devices. As-grown SWNTs have a dispersion of chirality and diameters. Hence, a critical issue in CNT applications is the determination of the individual tube structure and its correlation to the properties of the tube. This requires a structural probe that can be applied to individual nanotubes.

Gao *et al*. have developed a quantitative structure determination technique of SWNT using NED.[74,75] This, coupled with improved electron diffraction pattern quality using NED, allows a determination of both the diameter and chiral angle, and thus the chiral vector (n, m), from individual SWNTs. The CNT they studied were grown by chemical vapor deposition (CVD). TEM observation was carried out in a JEOL2010F TEM with a high voltage of 200 keV.

Figure 17 shows the diffraction pattern from a SWNT. The main features of this pattern are as follows: (i) a relatively strong equatorial oscillation which is perpendicular to the tube direction; (ii) some very weak diffraction lines

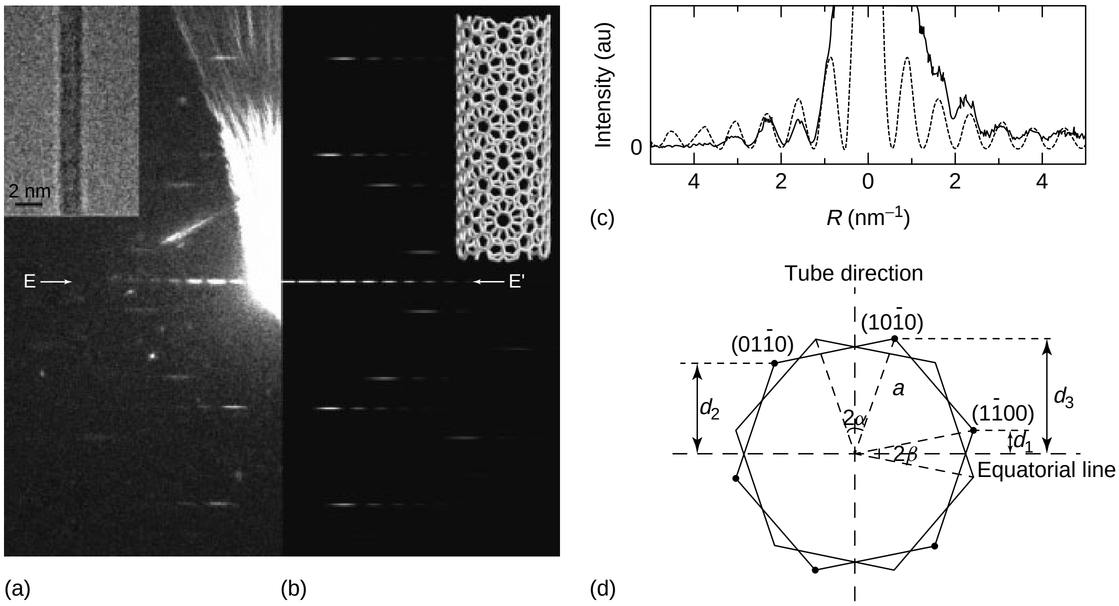

Figure 17 (a) A diffraction pattern from an individual SWNT of 1.4 nm in diameter. The inset is a TEM image. The radial scattering around the saturated (000) is an artifact from aperture scattering. (b) A simulated diffraction pattern of a (14,6) tube. The inset is the corresponding structure model. (c) Profiles of equatorial oscillation along EE′ from (a) and simulation for (14,6). d) A schematic diagram of electron diffraction from an individual SWNT. The two hexagons represent the first order graphite-like {100} diffraction spots from the top and bottom of the tube

from the graphite sheet, which are elongated in the direction normal to the tube direction.

The diameter of the tube is determined from the equatorial oscillation, while the chiral angle is determined by measuring the distances from the diffraction lines to the equatorial line. The details are as follows. The diffraction of SWNT is well described by kinematic diffraction theory (Section 3). The equatorial oscillation in the Fourier transformation of a helical structure like SWNT is a Bessel function with $n = 0$[76] which gives:

$$I_0(X) \propto J_0^2(X) \propto \left| \int_0^{2\pi} \cos^{X \cos\Omega} d\Omega \right|^2 \tag{21}$$

Here $X = 2\pi R r_0 = \pi R D_0$, R is the reciprocal vector, which can be measured from the diffraction pattern, and D_0 is the diameter of the SWNT. We use the position of $J_0^2(X)$ maxima $(X_n, n = 0, 1, 2, \ldots)$ to determine the tube diameter. With the first several maxima saturated and unaccessible, X_n/X_{n-1} can be used to determine the number N for each maximum in the equatorial oscillation. Thus, by comparing the experimental equatorial oscillation with values of X_n, the tube diameter can be uniquely determined.

To measure chirality from the diffraction pattern, Figure 17 is considered, which shows the geometry of the SWNT diffraction pattern based on the diffraction of the top-bottom graphite sheets. The distances d_1, d_2, d_3 relate to the chiral angle α by[74]:

$$\begin{gathered} d_1 + d_2 = d_3, \\ \alpha = \operatorname{atan}\left(\frac{1}{\sqrt{3}} \cdot \frac{d_2 - d_1}{d_3}\right) = \operatorname{atan}\left(\frac{1}{\sqrt{3}} \cdot \frac{2d_2 - d_3}{d_3}\right) \end{gathered} \tag{22}$$

These relationships are not affected by the tilting angle of the tube (see below). Because d_2 and d_3 correspond to the diffraction lines having relatively strong intensities and are further from the equatorial line, they are used in our study instead of d_1 to reduce the error. The distances can be measured precisely from the digitized patterns. The errors are estimated to be <1% for the diameter determination and <0.2° for the chiral angle.

Using the above methods, the SWNT giving the diffraction pattern shown in Figure 17 was determined to have a diameter of 1.40 nm (±0.02 nm) and a chiral angle of 16.9° (±0.2°). Among the possible chiral vectors, the best match is (20,6), which has a diameter and chiral angle of 1.39 nm and 17.0°, respectively. The closest alternative is (21,6), having a diameter of 1.46 nm and chiral angle of 16.1°, which is well beyond the experimental error. Figure 17(b) plots the simulated diffraction pattern of (20,6) SWNT from the structure model shown in the inset. Figure 17(c) compares the equatorial intensities of experiment and simulation. These results show excellent agreement.

The principles described are equally applicable for double-wall and multiwall nanotubes. For details, see Ref. 77 and 78.

3.10 Structure Factor Measurement and Charge Distribution

A major application of quantitative electron diffraction is the accurate determination of crystal charge density. The question here is how atoms bond to form crystals. This can be approached by accurate measurement of crystal structure factors (Fourier transform of charge density) and from these, electron distributions in crystals can be mapped. The full description is beyond the scope of this article. Here the results on the study of charge density in Cu_2O are summarized with an emphasis on the significance.

Cu_2O has a cubic structure with no free internal parameters (only Ag_2O is isostructural). The copper atoms are at the points of a face-centered cubic lattice with oxygen atoms in tetrahedral sites at (1/4,1/4,1/4) and (3/4,3/4,3/4) of the cubic cell. The resulting arrangement of Cu−O links is made up of two interpenetrating networks. The simplest description of Cu_2O using an ionic model with closed-shell Cu^+ and O^{2-} ions is known to be inadequate. It fails to explain the observed linear two-coordination of Cu.

Accurate measurements of the low-order structure factors were made with the quantitative CBED technique described in Section 4. Using the small electron probe, a region of perfect crystal was selected for study. The measurements are made by comparing experimental intensity profiles across CBED disks (rocking curves) with calculations, as illustrated in Figure 18. The intensity was calculated using the Bloch wave method, with structure factors, absorption coefficients, the beam direction, and thickness treated as refinable parameters. Structure factors for the (531) and higher-order reflections out to (14,4,2) were taken from X-ray measurements. Weak (ooe) (with o for odd and e for even) and very weak (eeo) reflections were also taken from X-ray work.[79]

There are two approaches to map crystal charge density from the measured structure factors; by inverse Fourier transform or by the multipole method.[80] Direct Fourier transformation of experimental structure factors was not useful due to the missing reflections in the collected data set, so a multipole refinement was used to map the charge density from the measured structure factors. In the multipole method, the crystal charge density is expanded as a sum of nonspherical pseudo-atomic densities. These consist of a spherical-atom (or -ion) charge density obtained from multi-configuration Dirac−Fock (MCDF) calculations[81] with variable orbital occupation factors to allow for charge transfer, and a small nonspherical part in which local symmetry-adapted spherical harmonic functions were used, which is expressed by:

$$\rho^a(r) = \rho^s(r) + \sum_{lm} P_{lm\pm} N_{lm\pm} R_l(r) y_{lm\pm}(\theta, \phi) \qquad (23)$$

here $\rho^s_{cu} = \rho^s_{Cu^+} + (1-q)(\rho^s_{Cu} - \rho^s_{Cu^+})$ and $\rho^s_O = \rho^s_O + q(\rho^s_{O^{2-}} - \rho^s_O)$ with q as the charge transfer from Cu to O; $R_l(r) = r^{n_l}\exp(-\alpha r)(n_3 = 3; n_4 = 4)$ is the radial function with population coefficient $P_{lm\pm}$; $N_{lm\pm}$ is the density-normalization coefficient. In addition atomic vibrations were accounted for using the Charlier−Gram expansion for the temperature factor. Refinements with and without anharmonic terms in the temperature factor clearly show the importance of an anharmonic term for Cu, especially for high order reflections with $s = \sin\theta/\lambda > 1.0$ ($Å^{-1}$). In either case the charge transfer from Cu to O is refined to 1.01(5) (i.e., Cu^+ and O^{2-}).

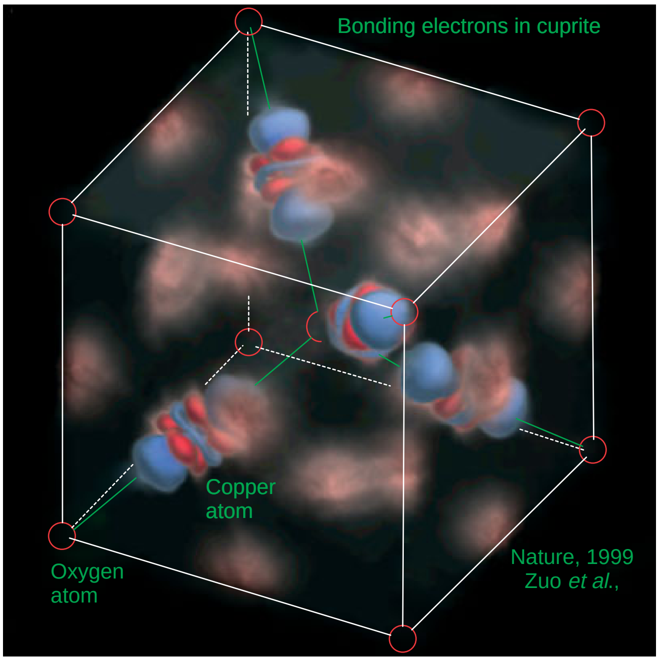

Figure 18 A 3-D rendering that reveals the details of chemical bonding and d_z^2 orbital-like holes in Cu_2O. The amount of charge redistribution is very small and its detection requires a high degree of experimental accuracy. In this picture, the small charge differences between the measured crystal charge density derived from CBED and that derived from superimposed spherical O^{2-} and Cu^+ ions are shown. The red and blue colors represent excess electrons and holes, respectively

Figure 18 shows a three-dimensional plot of the difference between the static crystal charge density obtained from the multipole fitting to experiment, and superimposed spherical O^{2-} and Cu^+ ions calculated by the MCDF method. The O^{2-} ion was calculated using a Watson sphere of 1.2 Å radius. The electron density difference shown in Figure 18 would be zero everywhere if cuprite were purely ionic (i.e., consisted of spherical ions). The difference, here seen unambiguously for the first time, confirms earlier theoretical speculation[82] that a covalent contribution exists. The correspondence between our *experimental* map and the classical diagrams of d_z^2 orbitals sketched in textbooks is striking. All our difference maps show strong nonspherical charge distortion around the copper atoms, with the characteristic shape of d orbitals, and excess charge in the interstitial region. There is little variation around oxygen in both the experimental and the theoretical results, which suggests that an O^{2-} anion description is valid. The most significant difference between experiment and theory is around Cu, and the charge in the interstitial region. The charge modification around Cu in the experiment is broader and larger than the theory. The experimental map also shows a large ($\sim$0.2e/Å^3) positive peak in the unoccupied tetrahedral interstitial region of the four neighboring Cu atoms, which suggests strong Cu^+-Cu^+ covalent bonding.

The nonspherical charge density around Cu+ can be interpreted as due to the hybridization of d electrons with higher-energy unoccupied s and p states. Among these states, hybridization is only allowed for d_z^2 and 4s by symmetry, and when this happens part of the d_z^2 state becomes unoccupied (''d hole''). These states are responsible for the spatial distribution of the deficiency in the map shown in Figure 18. The complementary empty states are important for electron energy loss spectroscopy (EELS) (*see* ***High Resolution Electron Energy-Loss Spectroscopy***) which probes empty states. The experimental studies reveal that the unoccupied states are predominately Cu-d character for the Cu $L_{2,3}$ edge; theory shows that they originate from hybridized d_z^2 orbitals. This theoretical interpretation, based on the calculated partial density of states (DOS) of the one-electron band structure, is supported by the generally good agreement with experimental spectroscopy of both occupied and unoccupied states.[83,84] From the charge density, we estimate the hybridization coefficient between d_z^2 and 4s, $|x| \sim 0.36$, so that about 0.22 electrons are removed from d_z^2 states.

4 ACKNOWLEDGEMENT

The author thanks DOE BES (DEFG02-01ER45923 and DEFG02-91ER45439) and NSF DMR Career 0449790, which provided several examples here, for supporting his research. The author also thanks Dr. Jing Tao for use of the examples of CuO and $LaCaMnO_3$, which came from her Ph.D. research and Prof. Spence for use of a part of his annotated book and web list for electron diffraction.

5 ABBREVIATIONS AND ACRONYMS

CBIM = convergent-beam imaging; CBED = convergent-beam electron diffraction; CCD = crystal charge density; CL = camera length; CNT = carbon nanotubes; CO = charge ordering; CTF = contrast transfer function; CVD = chemical vapor deposition; DC = diffraction compared; DQE = detector quantum efficiency; EELS = electron energy loss spectroscopy; EMS = electron multiple scattering; EXAFS = extended X-ray absorption fine structures; FEG = field emission guns; FEM = fluctuation electron microscopy; GHW = gaussian half width; GIF = gatan imaging filter; G−M = gjonnes and moodie; GOF = goodness of fit; HEED = high-energy electron diffraction; HOLZs = high order laue zones; HREM = high-resolution electron microscopy; HV = high-vacuum; IPs = imaging plates; LACBED = large-angle convergent-beam electron diffraction; LCMO = $La_{0.50}Ca_{0.50}MnO_3$; LEED = low-energy electron diffraction; MCDF = multi-configuration dirac−fock; NED = nanoarea electron diffraction; PARODI = parallel recording of dark-field images; RDF = radial distribution function; RHEED = reflection high-energy electron diffraction; RT = room temperature; SAED = selected area electron diffraction; SRs = superlattice reflections; STEM = scanning transmission electron microscopy; SWNT = single-wall nanotube; TED = transmission electron diffraction; TEM = transmission electron microscopes; THEED = transmission high-energy electron diffraction; ZOLZ = zero order laue zone.

6 FURTHER READING

6.1 Books on electron diffraction

P. E. Champness, 'Electron Diffraction in the Transmission Electron Microscope (Microscopy Handbooks)', Garland Science, 2001; an introductory text for graduate students and beginners of electron diffraction. The book includes examples useful for teaching and learning.

A. J. Schwartz, M. Kumar and B. L. Adams eds., 'Electron Backscattering Diffraction in Materials Science', Plenum Publishing, New York, 2000.

J. P. Morniroli, 'Large-Angle Convergent Beam Electron Diffraction', Society of French Microscopists, Paris, 2002. In English. A highly readable, detailed, description of large angle convergent beam electron diffraction and related techniques and applications to symmetry and defect analysis.

J. M. Cowley, 'Diffraction Physics', 3rd edition, North Holland, 1990. The book was written by a pioneer in electron diffraction for graduate students learning diffraction physics. It contains many insights of diffraction, including the author's unique approach to diffraction. The discussions, especially the treatment of diffuse scattering, are indispensable for practioners of diffraction.

E. J. Kirkland, 'Advanced Computing in Electron Microscopy', Plenum Publishing, New York, 1998. An excellent how to do book for electron diffraction and image simulations using the multiple slice method.

D. L. Dorset, 'Structural Electron Crystallography', Plenum Publishing/Kluwer Academic Publishers, 1997. Covers direct methods, electron diffraction of polymers and organic materials.

D. B. Williams and C. B. Carter, 'Transmission Electron Microscopy: A Textbook for Materials Science', Plenum Press, 1996. An introductory text to the instrumentation, electron microscopy and techniques, including a volume on electron diffraction.

J. C. H. Spence, ‘High Resolution Electron Microscopy’, 3rd edition, Oxford University Press, 2003. A how to do book on high-resolution electron microscopy and theory.

M. Tanaka, M. Terauchi, K. Tsuda and K. Saitoh, ‘Convergent Beam Electron Diffraction IV’, JEOL Ltd, Tokyo and earlier volumes. An outstanding collection of CBED patterns and application examples, including detailed description of the techniques used for analysis.

J. Spence and J. M. Zuo, ‘Electron Microdiffraction’, Plenum Publishing, 1992. An advanced text on quantitative analysis of CBED with useful examples, tables and computer simulation programs for electron diffraction analysis.

L. M. Peng, S. L. Dudarev and M. J. Whelan, ‘High-Energy Electron Diffraction and Microscopy’, Oxford University Press, Oxford, 2004. A systematic treatment of electron diffraction theory.

J. Cowley ed., ‘Electron Diffraction Techniques’, Oxford/IUCr Press, 1993. Vols 1 and 2. An edited book with contributions from practioners of the field.

P. B. Hirsch, A. Howie, R.B. Nicholson, D.W. Pashley, M. J. Whelan, ‘Electron Microscopy of Thin Crystals’, Krieger Publishing, New York, 1977. The reference book for theory of electron diffraction and image contrast. It also includes a useful list of recipes for thinning metal films.

B. B. Zvyagin, ‘Electron-Diffraction Analysis of Clay Mineral Structures’, Plenum Publishing, 1967.

B. K. Vainshtein, ‘Electron Diffraction Structure Analysis’, Pergamon Press, 1964.

K. Andrews, D. Dyson and S. Keown, ‘Interpretation of Electron Diffraction Patterns’, Plenum Publishing, New York, 1971. Has many examples for selected area electron diffraction.

L. J. Clarke, ‘Surface Crystallography: An Introduction to Low Energy Electron Diffraction’, John Wiley & Sons, Hoboken, 1985. A starter’s book for LEED.

A. Ichimiya and P. I. Cohen, ‘Reflection High-Energy Electron Diffraction’, Cambridge University Press, Cambridge, 2004. A comprehensive discussion of practice and theory of RHEED for surface studies.

P. W. Hawkes and J. C. H. Spence, ‘Science of Microscopy’, Springer, 2006. Vol. I. An outstanding new addition to electron microscopy. It describes techniques complementary to electron diffraction.

6.2 Software and websites for electron diffraction

The website of the International Union of Crystallographers has much useful information about diffraction and crystallography and related materials. The home page is http://www.iucr.org/. The Commission on Electron Diffraction under the link of ‘‘Commissions’’ has a list of techniques, websites, groups and books related to electron diffraction. Crystallographic software and programs are listed under the link of ‘‘Sincris’’.

WebEmaps (U of Illinois). General TED, Bloch wave simulation, CBED, X-ray structure factors, draw crrystal structures, etc. http://emaps.mrl.uiuc.edu/emaps.asp.

EMS. (Stadelman) General HREM, CBED multislice simulation, etc. http://cimesg1.epfl.ch/CIOL/summary.html.

Argonne National Lab software library for EM. Free programs for everything you need related to TEM and SEM. http://www.amc.anl.gov/ANLSoftwareLibrary/.

E.J. Kirkland, ‘Advanced Computing in Electron Microscopy’, Plenum, New York, 1998. This book contains a CD of software and source code. Multiple scattering calculations for STEM and TEM images, including phonon scattering. Excellent documentation.

Electron Microdiffraction. Spence and Zuo, 1992. Contains well-documented Fortran listings for programs to simulate CBED patterns by Bloch Wave method, and multislice. Indexed patterns shown with HOLZ to speed indexing.

IdealMicroscope. A Macintosh program helps index diffraction patterns, find excitation errors and structure factors, draw crystal structures, K-lines, stereograms, CBED geometry, etc. Contact sharon@emlabsoftware.com.

Berkeley USA NCEM Software. http://ncem.lbl.gov/frames/software.htm.

6.3 Commercial suppliers

Transmission electron microscope manufacturers:
JEOL USA, Inc.
11 Dearborn Road, Peabody, MA 01960
Tel. (978) 535-5900
Fax (978) 536-2205
http://www.jeolusa.com/

FEI Company Corporate Office
5350 NE Dawson Creek Drive
Hillsboro, OR
97124
Phone: +1 503 726 7500
Fax: +1 503 726 2615
http://www.fei.com/

Hitachi High Technologies America, Inc.
5100 Franklin Drive, Pleasanton, CA 94588
Phone: (800) 227-8877
Fax: (925) 218-3230
http://www.hitachi-hta.com/

Carl Zeiss NTS GmbH
A Carl Zeiss SMT AG Company
Carl-Zeiss-Str. 56
73447 Oberkochen
Germany
Tel. +49 73 64/20 44 88
Fax +49 73 64/20 43 43
http://www.smt.zeiss.com/nts

RHEED/LEED optics
Staib Instrumnets
http://www.rheed.net/

SPECS Scientific Instruments, Inc.
2055 Wood Street
Sarasota, FL 34237
Tel: (941) 362-4877

Fax: (941) 364-9706
http://www.specs.com/

Princeton Research Instruments, Inc.
PO Box 1174
Princeton, NJ 08542
Voice: 609-924-0570
Fax: 609-924-4970
www.prileeduhv.com

Kimball Physics
311 Kimball Hill Road
Wilton, New Hampshire 03086-9742 USA
Phone 1-603-878-1616 or 1-888-KIM-PHYS (1-888-546-7497)
Fax: 1-603-878-3700
www.kimballphysics.com

Omicron
NanoTechnology GmbH
Limburger Str. 75
65232 Taunusstein
Tel: 06128/987-0
Fax: 06128/987-185
www.omicron.de

Sample preparation/microscopy suppliers:
Structure Probe, Inc./SPI Supplies
P.O. Box 656
West Chester, PA 19381-0656, USA
Phone: 1-610-436-5400
FAX: 1-610-436-5755
http://www.2spi.com/

Electron Microscopy Sciences
P.O. Box 550
1560 Industry Road
Hatfield, PA 19440
Phone: 215-412-8400
Fax: 215 412-8450
http://www.emsdiasum.com/microscopy

Ted Pella Inc
P.O. Box 492477
Redding, CA 96049-2477
Telephone: 530-243-2200; 800-237-3526
Fax: 530-243-3761
http://www.tedpella.com/

7 REFERENCES

1. J. C. H. Spence and J. M. Zuo, ‘Electron Microdiffraction’, Plenum Publishing, New York, 1992.
2. L. J. Clarke, ‘Surface Crystallography: An Introduction to Low Energy Electron Diffraction’, John Wiley & Sons, Hoboken, 1985.
3. A. Ichimiya and P. I. Cohen, ‘Reflection High-Energy Electron Diffraction’, Cambridge University Press, Cambridge, 2004.
4. J. C. H. Spence, ‘High-Resolution Electron Microscopy’, Oxford University Press, Oxford, 2003.
5. P. W. Hawkes and J. C. H. Spence, ‘Science of Microscopy’, Springer, 2006, Vol. I.
6. G. Mollenstedt, *Phys. Status Solidi A: Appl. Res.*, 1989, **116**(1), 13.
7. C. H. MacGillavry, *Physica*, 1940, **7**, 329.
8. H. E. Elsayed-Ali and P. M. Weber, in ‘Time-Resolved Diffraction’, eds. J. R. Helliwell and P. M. Rentzepis, Oxford Science Publications, Oxford, 1997, p. 284.
9. W. E. King, G. H. Campbell, A. Frank, B. Reed, J. F. Schmerge, B. J. Siwick, B. C. Stuart and P. M. Weber, *J. Appl. Phys.*, 2005, **97**(11), 111101.
10. B. J. Siwick, J. R. Dwyer, R. E. Jordan and R. J. D. Miller, *Science*, 2003, **302**(5649), 1382.
11. C. Y. Ruan, F. Vigliotti, V. A. Lobastov, S. Chen and A. H. Zewail, *Proc. Natl. Acad. Sci. U.S.A.*, 2004, **101**(5), 1123.
12. J. M. Zuo, M. Gao, J. Tao, B. Q. Li, R. Twesten and I. Petrov, *Microsc. Res. Tech.*, 2004, **64**(5–6), 347.
13. J. M. Cowley, ‘Electron Diffraction Techniques’, Oxford University Press, Oxford, 1992, Vols. I, and II.
14. L. M. Peng, S. L. Dudarev and M. J. Whelan, ‘High-Energy Electron Diffraction and Microscopy’, Oxford University Press, Oxford, 2004.
15. J. P. Morniroli, ‘Large-Angle Convergent Beam Electron Diffraction, English Version’, Society of French Microscopists, Paris, 2002.
16. M. Haider, H. Rose, S. Uhlemann, E. Schwan, B. Kabius and K. Urban, *Ultramicroscopy*, 1998, **75**(1), 53.
17. J. M. Cowley, *Micron*, 2004, **35**(5), 345.
18. J. M. Zuo, *Mater. Trans., JIM*, 1998, **39**(9), 938.
19. S. Hovmoller, X. D. Zou and T. E. Weirich, *Adv. Imaging Electron Phys.*, 2002, **123**, 257.
20. F. H. Li, *Z. Kristallogr.*, 2003, **218**(4), 279.
21. J. J. Hu, F. H. Li and H. F. Fan, *Ultramicroscopy*, 1992, **41**(4), 387.
22. M. Tanaka, R. Saito, K. Ueno and Y. Harada, *J. Electron. Microsc.*, 1980, **29**(4), 408.
23. C. J. Humphreys, D. M. Maher, H. L. Fraser and D. J. Eaglesham, *Philos. Mag. A: Phys. Condens. Matter Structure Defects Mech. Prop.*, 1988, **58**(5), 787.
24. J. Tafto, Y. M. Zhu and L. J. Wu, *Acta Crystallogr., Sect. A*, 1998, **54**, 532.
25. Y. M. Zhu, L. J. Wu and J. Tafto, *J. Electron. Microsc.*, 2001, **50**(6), 465.
26. M. M. J. Treacy and J. M. Gibson, *Acta Crystallogr., Sect. A*, 1996, **52**, 212.
27. P. M. Voyles and J. R. Abelson, *Sol. Energy Mater. Sol. Cells*, 2003, **78**(1–4), 85.
28. J. M. Zuo, *Ultramicroscopy*, 1993, **52**(3–4), 459.
29. B. F. Buxton, *Philos. Trans. R. Soc. London, Ser. A: Math. Phys. Eng. Sci.*, 1976, **281**, 171.

30. M. Tanaka, H. Sekii and T. Nagasawa, *Acta Crystallogr., Sect. A*, 1983, **39**, 825.
31. M. Tanaka, R. Saito and H. Sekii, *Acta Crystallogr., Sect. A*, 1983, **39**, 357.
32. D. M. Bird and Q. A. King, *Acta Crystallogr., Sect. A*, 1990, **46**, 202.
33. A. Weickenmeier and H. Kohl, *Acta Crystallogr., Sect. A*, 1991, **47**, 590.
34. L. M. Peng, *Acta Crystallogr., Sect. A*, 1997, **53**, 663.
35. P. G. Self, M. A. Okeefe, P. R. Buseck and A. E. C. Spargo, *Ultramicroscopy*, 1983, **11**(1), 35.
36. Z. G. Pinsker, ‘Electron Diffraction’, Butterworths Scientific Publications, London, 1953.
37. D. L. Dorset, ‘Structural Electron Crystallography’, Springer, New York, 1995.
38. L. D. Marks, *Phys. Rev. B*, 1999, **60**(4), 2771.
39. R. Vincent and D. R. Exelby, *Philos. Mag. Lett.*, 1991, **63**(1), 31.
40. B. S. Berg, V. Hansen, P. A. Midgley and J. Gjonnes, *Ultramicroscopy*, 1998, **74**(3), 147.
41. R. Vincent and P. A. Midgley, *Ultramicroscopy*, 1994, **53**(3), 271.
42. J. M. Zuo and J. C. H. Spence, *Ultramicroscopy*, 1991, **35**(3–4), 185.
43. J. Jansen, D. Tang, H. W. Zandbergen and H. Schenk, *Acta Crystallogr., Sect. A*, 1998, **54**, 91.
44. D. J. H. Cockayne and D. R. Mckenzie, *Acta Crystallogr., Sect. A*, 1988, **44**, 870.
45. Y. Hirotsu, M. Ishimaru, T. Ohkubo, T. Hanada and M. Sugiyama, *J. Electron. Microsc.*, 2001, **50**(6), 435.
46. B. E. Warren, ‘X-Ray Diffraction’, Dover Publications, New York, 1969.
47. E. Ma, *Prog. Mater. Sci.*, 2005, **50**(4), 413.
48. L. Reimer, ‘Transmission Electron Microscopy’, Springer, New York, 1997.
49. O. L. Krivanek, S. L. Friedman, A. J. Gubbens and B. Kraus, *Ultramicroscopy*, 1995, **59**, 267.
50. J. M. Zuo, *Microsc. Res. Tech.*, 2000, **49**(3), 245.
51. Y. Fujiyoshi, *Adv. Biophys.*, 1998, **35**, 25.
52. X. C. Jiang, T. Herricks and Y. N. Xia, *Nano Lett.*, 2002, **2**(12), 1333.
53. B. Q. Li and J. M. Zuo, *Surf. Sci.*, 2002, **520**(1–2), 7.
54. B. Q. Li and J. M. Zuo, *J. Appl. Phys.*, 2003, **94**(1), 743.
55. B. Q. Li and J. M. Zuo, *Phys. Rev. B*, 2005, **72**(8), 085434.
56. J. H. He, H. W. Sheng, J. S. Lin, P. J. Schilling, R. C. Tittsworth and E. Ma, *Phys. Rev. Lett.*, 2002, **89**(12), 125507.
57. S. Mader and A. S. Nowich, *Acta Metall. Mater.*, 1967, **15**(2), 215.
58. C. N. J. Wagner, T. B. Light, N. C. Halder and W. E. Lukens, *J. Appl. Phys.*, 1968, **39**(8), 3690.
59. S. Mader, A. S. Nowich and H. Widmer, *Acta Metall. Mater.*, 1967, **15**(2), 203.
60. C. H. Chen and S. W. Cheong, *Phys. Rev. Lett.*, 1996, **76**(21), 4042.
61. M. B. Salamon and M. Jaime, *Rev. Mod. Phys.*, 2001, **73**(3), 583.
62. S. Mori, C. H. Chen and S. W. Cheong, *Nature*, 1998, **392**(6675), 473.
63. P. G. Radaelli, D. E. Cox, L. Capogna, S. W. Cheong and M. Marezio, *Phys. Rev. B*, 1999, **59**(22), 14440.
64. C. H. Chen, S. W. Cheong and H. Y. Hwang, *J. Appl. Phys.* **81**(8), 4326.
65. R. H. Wang, J. I. Gui, Y. M. Zhu and A. R. Moodenbaugh, *Phys. Rev. B*, 2001, **63**(14), 144106.
66. Z. L. Wang, X. Y. Kong and J. M. Zuo, *Phys. Rev. Lett.*, 2003, **91**(18), 185502.
67. J. M. Zuo, *Ultramicroscopy*, 1992, **41**(1–3), 211.
68. J. M. Zuo, M. Kim and R. Holmestad, *J. Electron. Microsc.*, 1998, **47**(2), 121.
69. B. F. Buxton, *Proc. R. Soc. London, Ser. A: Math. Phys. Eng. Sci.*, 1976, **350**, 335.
70. Y. P. Lin, D. M. Bird and R. Vincent, *Ultramicroscopy*, 1989, **27**(3), 233.
71. A. Armigliato, R. Balboni, G. P. Carnevale, G. Pavia, D. Piccolo, S. Frabboni, A. Benedetti and A. G. Cullis, *Appl. Phys. Lett.*, 2003, **82**(13), 2172.
72. J. M. Zuo and J. C. H. Spence, *Philos. Mag. A: Phys. Condens. Matter Structure Defects Mech. Prop.*, 1993, **68**(5), 1055.
73. A. Chuvilin and U. Kaiser, *Ultramicroscopy*, 2005, **104**(1), 73.
74. M. Gao, J. M. Zuo and R. D. Twesten, I. Petrov, L. A. Nagahara and R. Zhang, *Appl. Phys. Lett.*, 2003, **82**(16), 2703.
75. Z. J. Liu, Q. Zhang and L. C. Qin, *Phys. Rev. B*, 2005, **71**(24), 245413.
76. S. Amelinckx, A. Lucas and P. Lambin, *Rep. Prog. Phys.*, 1999, **62**(11), 1471.
77. M. Gao, J. M. Zuo, R. Zhang and L. A. Nagahara, *J. Mater. Sci.*, 2006, **41**(14), 4382.
78. Z. J. Liu, Q. Zhang and L. C. Qin, *Appl. Phys. Lett.*, 2005, **86**(19), 191903.
79. R. Restori and D. Schwarzenbach, *Acta Crystallogr., Sect. B: Struct. Sci.*, 1986, **42**, 201.
80. P. Coppens, ‘X-Ray Charge Densities and Chemical Bonding’, Oxford University Press, Oxford, 1997.
81. D. Rez, P. Rez and I. Grant, *Acta Crystallogr., Sect. A*, 1994, **50**, 481.
82. L. E. Orgel, *J. Chem. Soc.*, 1958, 4186.
83. J. Ghijsen, L. H. Tjeng, J. Vanelp, H. Eskes, J. Westrink, G. A. Sawatzky and M. T. Czyzyc, *Phys. Rev. B*, 1988, **38**(16), 11322.
84. J. M. Zuo, M. O’Keeffe, M. Kim and J. C. H. Spence, *Angew. Chem. Int. Ed.*, 2000, **39**(21), 3791.

High Resolution Electron Energy-Loss Spectroscopy

Manuel P. Soriaga, Xiaole Chen and Ding Li

Texas A&M University, College Station, TX, USA

John L. Stickney

University of Georgia, Athens, GA, USA

	Method Summary	1
1	Introduction	2
2	Technical Background	2
3	Selected Applications	4
4	Acknowledgments	14
5	Abbreviations and Acronyms	14
6	End Notes	14
7	Further Reading	15
8	References	15

METHOD SUMMARY

Acronyms, Synonyms
- High-resolution Electron Energy-Loss Spectroscopy
- Electron Energy-Loss Spectroscopy.

Measured physical quantities
- the number of counts (intensity) as a function of the energy loss of inelastically backscattered low-energy electrons.

Information available
- the vibrational modes, and the corresponding energies, of species at the interface: substrate, physisorbed adsorbate, chemisorbed adsorbate, adsorbate–adsorbate interactions.

Information not available, limitations
- The properties are not related to the vibrational modes of the interfacial species.

Examples of questions that can be answered
- What molecular species are present on the surface?
- What is the mode of bonding between the adsorbate and the substrate?
- How does the surface chemical bond influence the vibrational properties of the adsorbate?
- What is the surface coverage of the adsorbed species?

Major advantages
- extremely sensitive; limit of detection is ca .0.01% of a monolayer
- broad spectral range; typically, 50 (6.2 meV) to 4000 cm^{-1} (496 meV)

- impact-scattering mechanism not restricted by selection rules; in combination with dipole scattering, all vibrational modes may be discernible
- nondestructive.

Major disadvantages

- an ex situ method requiring an ultrahigh vacuum environment
- comparatively low resolution: typically, $30\,\mathrm{cm}^{-1}$ (3.7 meV); at best, $4\,\mathrm{cm}^{-1}$ (0.5 meV)
- backscattering may be inhibited by cationic species.

Sample constraints

- The sample surface must be conductive and relatively smooth.

---

1 INTRODUCTION

A vast amount is now known, at the atomic level, about heterogeneous processes at gas–solid interfaces. Yet, three decades ago, research in solid surface science was mired in traditional thermodynamic and kinetic experiments that were not able to yield molecular level information. Fundamental issues, such as the molecular structure and chemical composition of the surface complex, could not be adequately addressed by the data generated from the classical methods. It was not until the development of highly surface-specific empirical tools that tangible gains in the study of the gas–solid interface were achieved.

The main difficulty in surface characterization lies in the exceedingly low population of surface atoms (10^{15} atoms cm^{-2}) relative to that of bulk species (10^{23} atoms cm^{-3}). Experiments intended to examine the physical and chemical properties of surfaces must employ techniques that interact only with the outermost layers. For example, standard structural tools such as (nongrazing incidence) X-ray diffraction are not applicable to single-crystal surfaces since X rays penetrate deeply into the material and yield information on the bulk rather than the surface.

The majority of interfacial characterization techniques take advantage of the unique surface sensitivity of low-energy electrons. Such surface specificity arises because the mean free path of an electron through a solid is dependent upon its kinetic energy.[**1,2**] In particular, an electron whose kinetic energy is between 10 and 500 eV can traverse no more than 2 nm within the solid. Hence, the ‘‘interrogation’’ of low-energy electrons emergent from a sample will bear information that is specific only to the surface.

A solid subjected to a beam of electrons of primary (incident) energy E_p gives rise to backscattered (primary) and emitted (secondary) electrons. The energy distribution of these electrons can be divided into four regions based upon the origin of the scattered electrons. These regions correspond to the following: (i) True secondary electrons, are created from multiple inelastic interactions between the incident and bound electrons; these electrons give rise to an intense broad band at the lower end of the spectrum. (ii) Auger electrons which, along with primary electrons inelastically scattered by surface electronic states, are responsible for the small peaks in the medium-energy range. (iii) Primary electrons, which are inelastically scattered upon interactions with surface vibrational states; peaks associated with these electrons reside close to the elastic peak as their energy losses are comparatively small. (iv) Primary electrons, which are scattered elastically; such electrons, comprise only a small percent of the total incident electrons, and they generate the elastic peak at E_p. Regions (ii) to (iv) of the energy spectrum have been exploited in modern surface-structural and interfacial-elemental analysis. The elastic peak, for example, is used in diffraction experiments. The peaks in Region (iii) form the basis of high-resolution electron energy-loss spectroscopy (HREELS).

2 TECHNICAL BACKGROUND

2.1 Energy-Loss Mechanisms

Almost all of the electrons incident at a solid surface undergo inelastic events that cause them to be backscattered at energies lower than their initial or primary energy E_p. If E_l is the energy lost to the surface, peaks would appear in the spectrum at energies $\Delta E = E_p - E_l$. Such peaks, commonly referred to as energy-loss peaks, originate from core-level ionizations, valence-level excitations, plasmon losses, or vibrational excitations.[**1,2**] Since $E_{\mathrm{vibrational}} < 4000\,\mathrm{cm}^{-1}$ (0.50 eV)[a], the vibrational energy-loss peaks lie close to the elastic peak and can be observed only if electron-energy discrimination is carried out at high resolution.

Two mechanisms give rise to high-resolution electron energy-loss (HREEL) spectra[**1–8**]: dipole scattering and impact scattering. In dipole scattering, the incident electron may be treated similarly to an electromagnetic (infrared) wave that interacts, at long range, with oscillating dipoles created by the vibration of species at the surface. Dipole-scattering HREELS is thus governed by the well-known harmonic-oscillator[b] infrared selection rules: At ambient temperatures, (i) only fundamental transitions are allowed; and (ii) only vibrations accompanied by a change in dipole moment are observed.

On metal surfaces, two additional selection rules apply. The first is that only vibrations perpendicular to the surface are HREELS active. This rule follows from two phenomena unique at metal surfaces[3–8]: (i) Electromagnetic waves polarized perpendicularly to the plane of incidence (parallel to the plane of the surface) undergo a 180° phase shift upon reflection. That is, at the metal surface, the out-of-phase electric-field vectors of the incident and reflected waves cancel each other; as a result, no field exists that can couple with dipoles that oscillate parallel to the surface. (ii) The dynamic dipole moment generated by an oscillator that vibrates in the surface-parallel direction is cancelled by that of its image dipole (Figure 1); hence, there the net dynamic dipole moment is zero. On the other hand, if the real dipole is oriented perpendicularly to the surface, its dynamic dipole moment is reinforced by that of its image dipole. This selection rule is the same as that for infrared reflection-absorption spectroscopy (IRAS).[c]

The second dipole-scattering selection rule states that the intensity is at a maximum when the angle of collection is the same as the angle of (specular) reflection. This selection rule is illustrated in Figure 2; the intensity of the dipole-scattered peak at 130 meV (1050 cm^{-1}) falls precipitously as soon as the collection angle deviates from the specular angle. Figure 2 also shows that the angular dependence of the elastic peak is the same as that of the dipole-scattered peak.

The mechanism for impact scattering at solids is rather complex as it involves the penetration of the incident electron into the adsorbed molecule; the theoretical treatment requires a quantum mechanical formalism. The transfer of energy from the incident electron to a vibrational mode occurs, within a very short time, while the electron is inside the molecule. The dipole-scattering selection rules do not apply to impact scattering. Theoretical considerations have predicted, and experimental studies have confirmed, the following ‘‘propensity rules’’ for this mechanism[4]: (i) Impact scattering vanishes in the specular direction; that is, impact-scattered peaks can be observed only if detection is at angles removed from the specular direction. The dependence of impact scattering on the off-specular scattering angle (φ), where φ is the deviation of the collection angle from the angle of (specular) reflection, is shown in Figure 2.[4] Impact scattering (80 meV (645 cm^{-1})) is most prominent when $\varphi \sim 15°$. (ii) Impact scattering is more likely to be dominant, even at low off-specular angles, at higher vibrational energies. (iii) Strong dipole scatterers are weak impact scatterers; conversely, weak dipole scatterers are strong impact scatterers.[d]

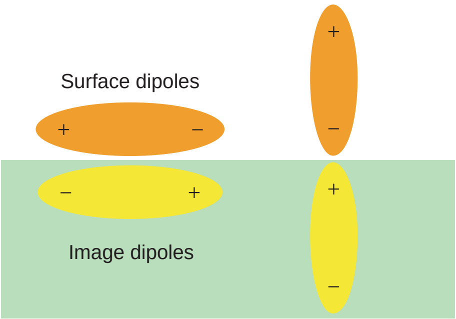

Figure 1 The dynamic electric moment of the dipole oriented parallel to the metal surface is cancelled by that of its image dipole. In the vertical orientation, the dynamic electric moments of the surface and image dipoles reinforce each other

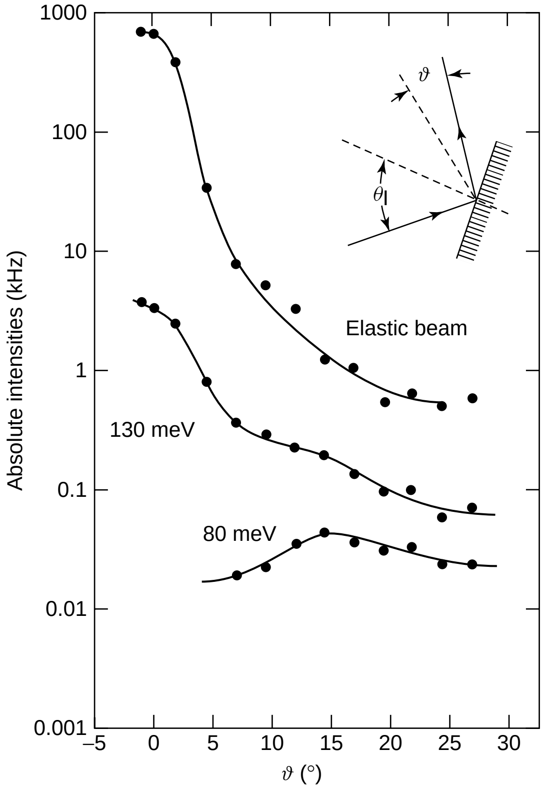

Figure 2 The influence of off-specular angle (φ) on the absolute peak intensities in dipole scattering (130 meV) and in impact scattering (80 meV). (Published in Electron Energy Loss Spectroscopy and Surface Vibrations, Ibach H & Mills D L, © Elsevier 1982)

It is clear that the combination of specular and off-specular HREELS provides a means for the complete identification of the normal modes of an adsorbed molecule; considerations based upon point-group and space-group theory would, of course, be required. HREELS is an extremely sensitive technique. The limit of detection for strong dipole scatterers such as CO can be as low as 0.0001 monolayer; for weak scatterers such as hydrogen, the limit is 0.01 monolayer. In comparison, IRAS for chemisorbed CO, a strong infrared absorber, is restricted to coverages above 0.1 monolayer. HREELS studies of non-CO organic molecules adsorbed at atomically smooth surfaces are abundant; similar experiments using IRAS are meager. The energy accessible to HREELS ranges from 50 (6.2 meV) to 4000 cm^{-1} (496 meV); common IRAS detectors are not useful below 600 cm^{-1} (74 meV). On the other hand, IRAS has higher-resolution (nominally 4 cm^{-1}) than HREELS (typically 30 cm^{-1} (3.7 meV)), although resolutions of up to 4 cm^{-1} (0.25 meV) have been claimed for the latest models of (Ultrahigh-resolution electron energy-loss spectroscopy (UHREELS)) instruments.[7] The primary limitation of HREELS is that the apparatus is quite specialized, rather delicate and requires an ultrahigh vacuum (UHV) environment; IRAS can be carried out under ambient conditions. It has recently been observed that countercations present in the adsorbed layer may block low-energy electron backscattering.[8]

2.2 Instrumentation

Figure 3(a) shows a schematic diagram of a first-generation HREEL spectrometer.[3] In this model, the energy of incident electrons can be varied from 1 to 10 eV. To afford high-resolution, energy monochromation and analysis are done either with a cylindrical mirror analyzer, cylindrical deflector, or spherical deflector analyzers in combination with retarding-field optics. Off-specular collection of the backscattered electrons is afforded by rotation of either the sample or the analyzer. Owing to extremely low signals (10^{-10} A), continuous dynode electron multiplier detectors are employed. Figure 3(b) is a photograph of an UHREELS spectrometer.[7] This model consists of an electron gun, a two-stage monochromator, a single-stage energy analyzer, and a channel electron multiplier detector. Both energy monochromation and energy analysis are carried out with 127° cylindrical deflection analyzers. The incident electrons have an initial energy spread of 0.3 eV. The two- stage monochromator serves to narrow the energy spread to <1 meV and generate a highly monoenergetic beam of low-energy electrons (typically 1 to 10 eV). A zoom lens system focuses and accelerates the electron beam onto the sample. The backscattered electrons are passed through a separate zoom lens for focusing and deceleration before they are sorted out by a single-stage energy analyzer into the detector. The signal is fed to a preamplifier as pulses for electron counting. The analyzer is designed to be rotatable from 0° to 78° for off-specular (impact-scattering) measurements.

3 SELECTED APPLICATIONS

3.1 Inorganic Molecules

3.1.1 Carbon Monoxide

Carbon monoxide is the most widely used molecular probe in the study of the coordination chemistry and catalytic reactivity of metal surfaces. The chemisorption of CO at transition-metal surfaces is similar to the coordinate-covalent bond formation in homogeneous metal–carbonyl complexes.[9–11] The interaction initially involves a σ bond formed by the electron-pair donation from a filled spσ ligand orbital to an unoccupied dσ metal orbital; this is followed by a π bond created by the electron-pair back-donation from a filled dπ (or dpπ) metal orbital to an empty $2\pi^*$ ligand orbital.[9,10] As a result of the surface coordination, the C≡O bond is weakened and ν_{CO}, the vibrational frequency of the C≡O stretch mode (2142 cm^{-1} (266 meV) in the gas phase) undergoes an appreciable redshift. The larger the extent of the back-donation, the stronger the metal–carbon (M–C) interaction, and the weaker the C≡O bond. The degree of π back-donation is also heightened by an increase in the number of surface atoms bridged by the CO ligand. In the latter case, multiple M–C bonds will be expected; for example, CO chemisorbed on a threefold hollow site will most likely be bonded to three different metal atoms. Consequently, ν_{CO} will display strong dependence on site geometry[11]: At ''atop'' (onefold) sites, ν_{CO} lies in the range from 2000 (248 meV) to 2130 cm^{-1} (264 meV); at twofold bridge sites, ν_{CO} falls between 1840 (228 meV) and 1960 cm^{-1} (242 meV); and for threefold bridge sites, ν_{CO} appears in the range from 1800 (223 meV) to 1920 cm^{-1} (238 meV). HREELS has been employed in the study of CO chemisorption on most transition metals.[12–26] Bimetallic[22] and oxide surfaces[23,24] relevant in catalytic oxidation have also been investigated.

Since the infrared absorptivity of the C≡O stretch mode is fairly large, IRAS has also enjoyed widespread use in the study of CO chemisorption. However, for the investigation of the metal–carbon vibrational mode, IRAS may not be the technique of choice since the frequency of this mode (ν_{M-CO}) lies below 400 cm^{-1} (50 meV), a region in which nonsynchrotron-based sources are quite weak and wide-range photoconductive detectors suffer degraded sensitivity. Studies on the metal–carbon stretch mode may be more reliably investigated by HREELS, although (infrared) sum-frequency generation also seems viable.[27] The expectation is that, since ν_{CO} is dependent upon adsorption-site geometry, ν_{M-CO} will likewise be influenced by it. For example, on Rh(111), it has been found that ν_{M-CO} was highest when the ligand was coordinated on a onefold site and lowest when located on a threefold site.[28] This observation may appear inconsistent with the fact that linearly bonded CO has the weakest metal–carbon bond. But it must be noted that an atop site attached CO has only one M–C bond, whereas a threefold-site-bonded CO would have three distinct bonds with three different metal atoms. While the combined strength of the three bonds would be greater than just one bond, the vibrational energy of each of the three (degenerate) bonds would, individually, not be as high. Of course, the role of dipole–dipole interactions in the observed frequency shift cannot be discounted since the shifts become pronounced at near-monolayer coverages where lateral interactions become significant.[28]

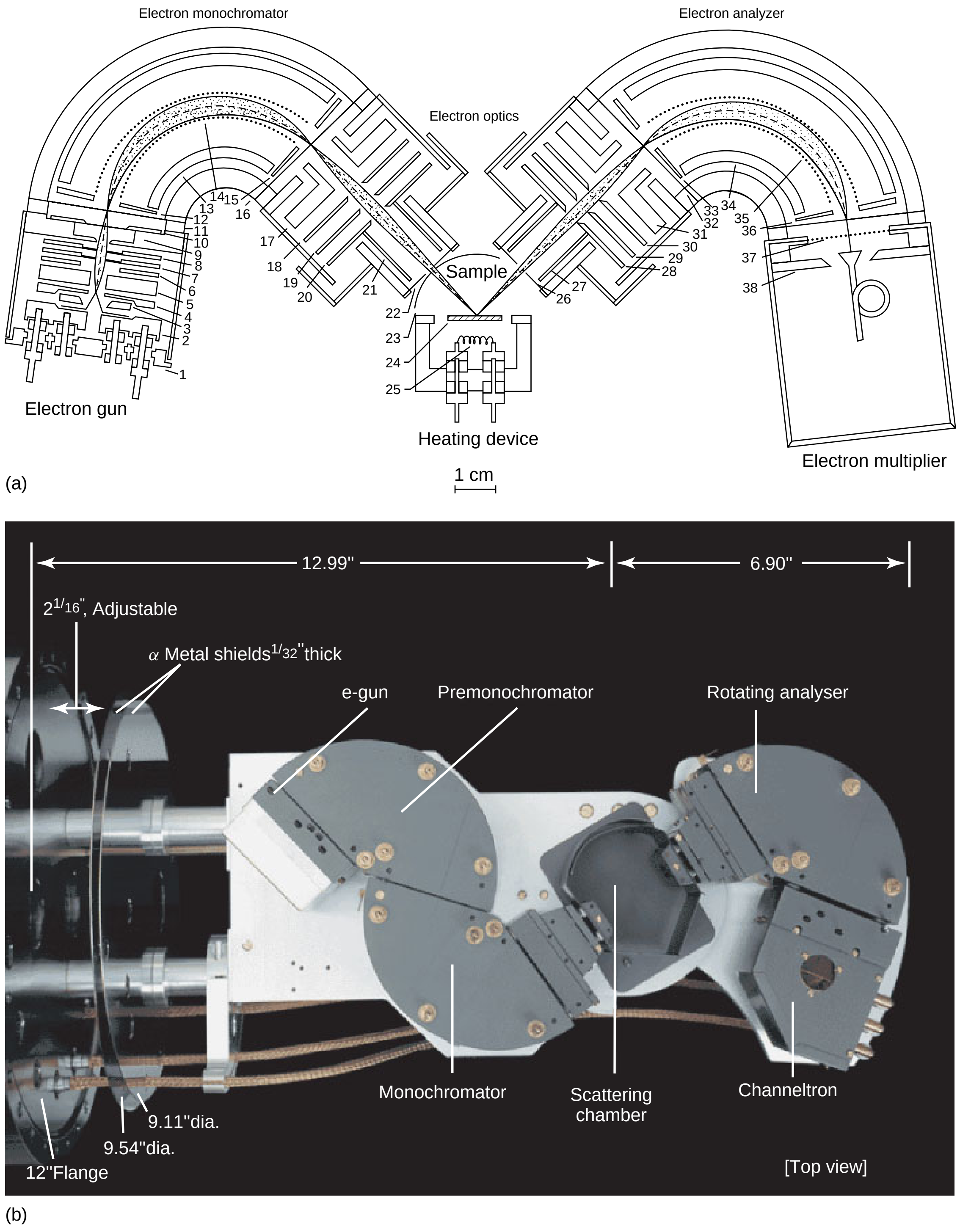
Electron monochromator
Electron optics
Electron analyzer
1
2
3
4
5
6
7
8
9
10
11
12
13
14
15
16
17
18
19
20
21
22
23
24
25
26
27
28
29
30
31
32
33
34
35
36
37
38
Sample
Electron gun
Heating device
Electron multiplier
1 cm
(a)
12.99"
6.90"
2 1/16", Adjustable
α Metal shields 1/32" thick
e-gun
Premonochromator
Rotating analyser
Monochromator
Scattering chamber
Channeltron
9.11"dia.
9.54"dia.
12"Flange
[Top view]
(b)

Figure 3 (a) Schematic diagram of first-generation HREEL spectrometer. (Reprinted from Froitzheim.[3] With kind permission of Springer Science & Business Media); (b) Photograph of a modern ultrahigh-resolution EEL spectrometer. (Reprinted from http://www.lktech.com/products/els5000.html, courtesy of LK Technologies, Inc)

Two other HREELS studies of dipole–dipole coupling will be mentioned. One focused on Ni(100) and involved the determination of the effect of temperature and coverage on ν_{CO}.[13] The results are displayed in Figure 4. The peak near 50 meV (400 cm^{-1}) was associated with $\nu_{\mathrm{M-CO}}$ and the peaks at 240 (1920 cm^{-1}) and 250 meV (2016 cm^{-1}) were assigned, respectively, to ν_{CO} at twofold and atop sites. At 150 K, only one peak, due to bridge-bonded CO, was observed

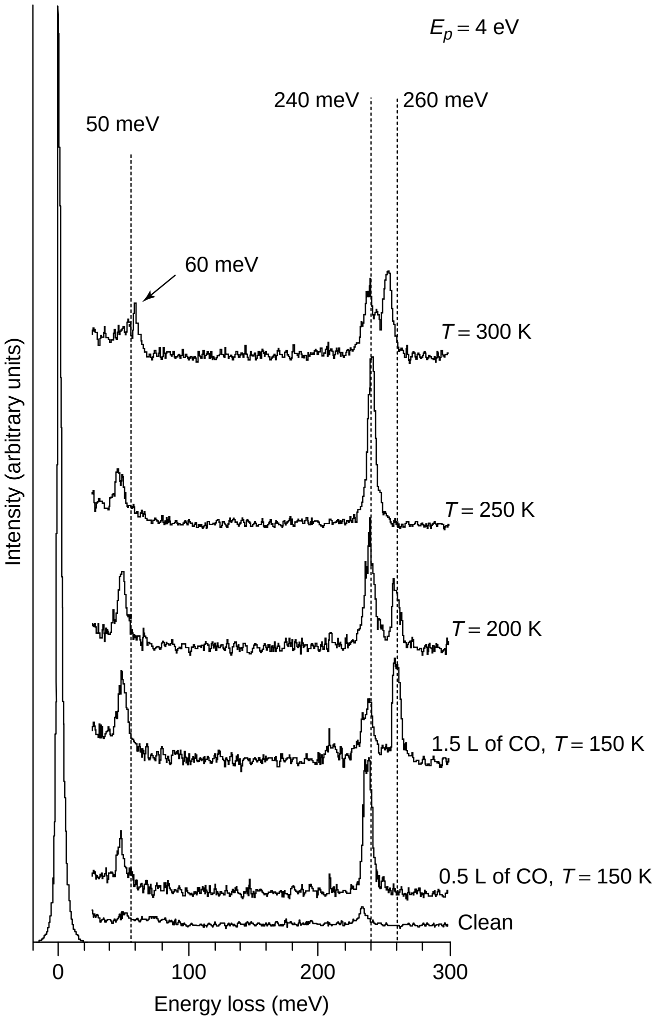

Figure 4 HREEL spectra of CO on Ni(100) for 0.5 L and 1.5 L of CO and thermal behavior of the 1.5 L CO in the 150–300 K range. (Reprinted from Formoso, Marino, Chiarello, Agostino, Caruso and Colavita,[13] © Elsevier 2006)

at submonolayer coverages. At near-monolayer coverage, a second prominent peak emerged at 260 meV (2097 cm^{-1}). The latter was not assigned to atop site-bonded CO since ν_{CO} for that is only 250 meV. A dipole–dipole interaction between adjacent CO molecules was thus postulated. It was thought that this type of coupling would weaken the metal–CO bond because of reduced π-back donation; the latter, in turn, would strengthen the C≡O bond and lead to the blueshift of ν_{CO}. Further evidence for the dipolar interactions was provided by the decrease in the intensity of the 260-meV peak as the temperature is raised; an increase in temperature tends to disrupt dipole–dipole coupling. At 300 K, CO coordinated at twofold and atop sites, devoid of dipole–dipole interactions, were indicated.

The other study examined the influence of Sn adatoms on the dipole–dipole interactions at Pt single-crystal surfaces.[22] On Pt(110), CO was bonded predominantly on atop sites at near-monolayer coverages. The same mode of coordination was found for the Pt(110)-(1 × 2)-Sn surface. When the CO coverage was further increased on the Sn-free surface, an upward shift to 260 meV was observed for ν_{CO},[22] a result that served as an indicator of the presence of dipole–dipole interactions. No similar blueshift in ν_{CO} was noted on Pt(110)-(1 × 2)-Sn, most likely because CO does not bind strongly on the interfacial Sn atoms; it was noted that the coverage of CO decreased when the amount of coadsorbed Sn was increased.

3.1.2 *Dioxygen*

When dioxygen is chemisorbed on a transition-metal surface, an electron pair is donated from a filled 2π orbital of O_2 to a vacant $d\sigma$ orbital on the metal, followed by back-donation from a filled $d\pi$ (or $dp\pi$) metal orbital to an empty $2\pi^*$ orbital on dioxygen. As a result, the O=O bond is weakened considerably.[29–40] For example, at 100 K, chemisorption of O_2 on most metals is molecular, but the vibrational frequency of the O–O stretch mode (ν_{OO}) is drastically redshifted, 630 cm^{-1} (78.1 meV) on Ag(110),[40] 870 cm^{-1} (108 meV) on Pt(111),[38] and 850 cm^{-1} (105 meV) on Cu(111),[33] relative to that in the gas phase 1580 cm^{-1} (196 meV). At room temperature, O_2 is dissociatively chemisorbed as oxygen atoms on the same metals.

While O_2 adsorption has been investigated for a variety of substrates,[29–40] Ag and Pt have received widest attention; Ag because of its superior selectivity toward ethylene epoxidation, and Pt for its singularly high catalytic efficiency in almost all types of exhaustive oxidation reactions. The interaction of O_2 with Ag(110) was found to yield four distinct adsorption states that depended upon the temperature: a physisorbed (condensed) layer at $T < 40$ K, two molecularly chemisorbed phases between 60 K and 180 K, and a dissociatively chemisorbed (atomic) state at $T > 180$ K.[41] The first molecularly chemisorbed species, labeled α-O_2,[37] may be generated from the physisorbed state by a temperature increase to 60 K; however, α-O_2 is not dissociated to atomic oxygen at higher temperatures. It was thought that lateral interactions within the preformed physisorbed layer induced a precursor orientation that enabled conversion to α-O_2. The other molecular species, tagged as β-O_2, was formed when the Ag surface was dosed directly from the gas phase at $T > 60$; evidently, under these conditions, the physisorbed layer that is favorably oriented toward α-O_2 formation is not the initial product. Above 180 K, β-O_2 undergoes dissociative chemisorption to oxygen adatoms.

Similar results were obtained for Pt(111): four temperature-dependent adsorption states of O_2 were also formed.[38,42,43] The two molecularly chemisorbed forms identified were (i) a superoxo-type (O_2^-) species bonded at twofold bridge sites and characterized by ν_{OO} of 870 cm^{-1} (108 meV), and (ii) a peroxolike (O_2^{2-}) species more strongly coordinated ($\nu_{OO} = 690$ cm^{-1} (86 meV)) at threefold

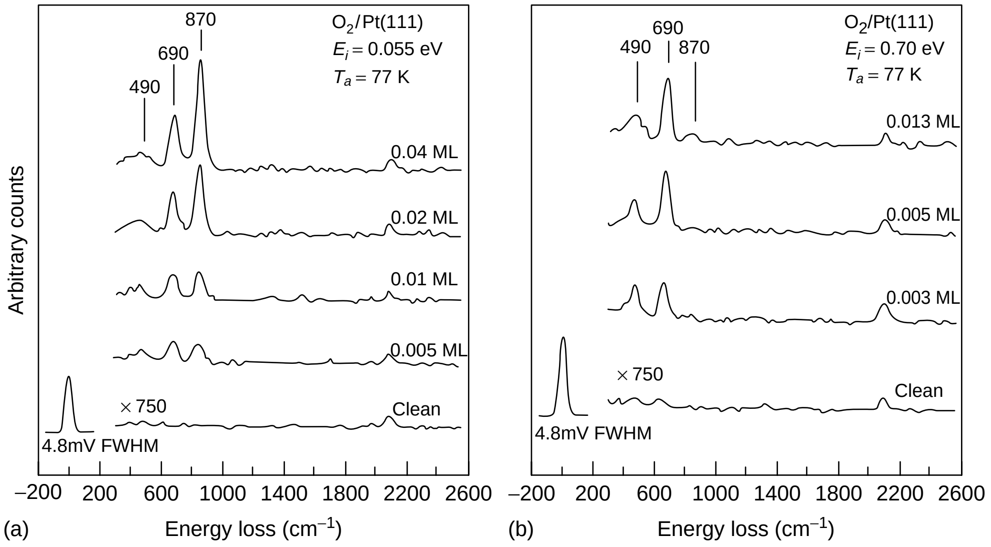

Figure 5 HREEL spectra of low-coverage doses of: (a) low incident energy (0.055 eV) oxygen, and (b) high incident energy (0.70 eV) oxygen on Pt(111) surfaces. (Reprinted with permission from P. D. Nolan, B. R. Lutz, P. L. Tanaka. J. E. Davis and C. B. Mullins. *J. Chem. Phys.* **111**:3696 (1999). © 1999 by the American Institute of Physics)

hollow sites. Experiments that combined HREELS with O_2-molecular-beam techniques indicated that high incident energies promoted the formation of the peroxo species (Figure 5a). At lower impact energies, both species were generated but the fraction of the superoxo species increased when the O_2 dosage was increased (Figure 5b). It was postulated that the O_2 molecules of higher energy are able to overcome the activation barrier for the two-electron metal-to-ligand charge transfer in the production of the peroxo species.

3.1.3 Water

As the most widely utilized solvent, studies of the adsorption of water at various surfaces abound. In such investigations, the emphasis has been on (i) its propensity toward dissociation, (ii) its structure in the adsorbed state, and (iii) its chemistry in the presence of other coadsorbed species. Although IRAS and HREELS have been employed in such studies, the former is limited to ultrathin films because of the strong infrared absorptivity of the O–H stretch mode; condensed multilayers can only be investigated by HREELS.[44]

The HREEL spectrum of water adsorbed on Pt(100) in multilayer amounts resembles that of ice. In submonolayer quantities, three ν_{OH} peaks were observed at 2850 (353 meV), 3380 (419 meV), and 3670 cm^{-1} (455 meV) respectively, these were assigned to O–H stretch modes in metal-bonded hydroxyls, hydrogen-bonded water, and water devoid of intermolecular interactions.[44] It is known that hydrogen bonding leads to a decrease in the O–H stretch frequency (ν_{OH}). When the oxygen is coordinated to the metal, the decrease in ν_{OH} is more profound. In fact, the presence of the lowest frequency ν_{OH} peak suggests that a fraction of the adsorbed water has undergone dissociation. On Ru(0001), three ν_{OH} peaks at 2935 (364 meV), 3290 (408 meV) and 3500 cm^{-1} (434 meV) were also observed at submonolayer coverages. Unexpectedly, however, the 408-meV peak was present even when the interfacial water existed as a bilayer.[45] This result prompted the conjecture that partial decomposition had likewise taken place within the bilayer. A subsequent theoretical investigation, however, showed that the 2935 cm^{-1} peak would still be possible in a bilayer that was completely molecular; as illustrated in Figure 6,[46] two structural types of hydrogen-bonded water are possible in the bilayer.

Interfacial water was studied on Pd(100) and on Pd(100)-(1 × 1)-O surfaces. At 10 K and submonolayer coverages, the interfacial water was found to exist as monomers[47] at both surfaces. When the temperature was increased to 110 K, hydrogen-bond formation between the water molecules transpired on the clean surface but not on the oxided metal. Evidently, oxygen coadsorbed on the metal disrupted hydrogen bonding between the water molecules. Such disruption, however, does not appear to occur when the surface oxygen is part of a nonmetallic species: When water was adsorbed on ultrathin SiO_2 films, hydrogen-bonded water was observed even at submonolayer coverages; evidently, the adsorbate–adsorbate hydrogen bonds are stronger than the substrate–adsorbate interactions.[48]

The adsorption of water on Ni(100) was compared with that on Pd(110) surfaces.[49] It was noted that the Pd–OH_2 bond is substantially weaker than the Ni–OH_2 bond, a result consistent with the fact that a molecular bilayer structure is formed on Pd(110) but not on Ni(100).

Work has also been published on other interfacial materials and structures that include (i) α-Cr_2O_3(001)/α–Fe_2

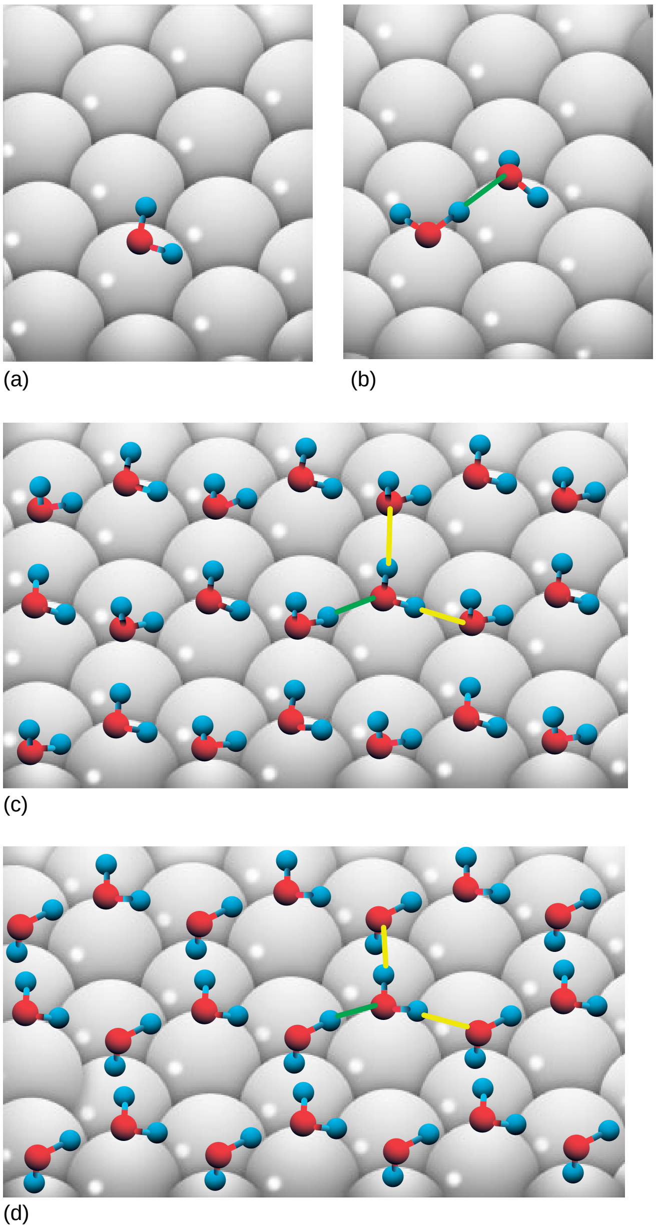

Figure 6 Equilibrium structure of (a) water monomer, (b) dimer, (c) H-up bilayer, and (d) H-down bilayer on the Pt(111) surface. (Reprinted with permission from M. Sock, A. Eichler, S. Surnev. J. N. Andersen, B. Klötzer, K. Hayek, M. G. Ramsey and F. P. Netzer. *Surf. Sci.* **545**:122 (2003). © 2003 by the American Physical Society)

$O_3/\alpha-Al_2O_3(001)$, a surface strained by the incorporation of Fe_2O_3;[50] (ii) ultrathin Pd films on MgO(100) substrates;[51] (iii) Si(100)-(2 × 1) and Si(111)-(7 × 7) single-crystal planes;[52] (iv) defect-free $SrTiO_3(100)$;[53] (v) Ag(011);[54] (vi) MgO(100) superlattices on Mo(100);[55] (vii) coadsorption of CO and water on Al(111);[56] (viii) oxygen-covered Pt group metals[57,58]; and (ix) hydrogen-pretreated Pt surfaces.[59]

3.1.4 *Organometallic Compounds*

Interest in the structure of adsorbed organometallic compounds stems from their capabilities as research-laboratory and industrial catalysts. In view of its inherent surface sensitivity and dramatically enhanced resolution, UHREELS has recently become a viable technique in the acquisition of fingerprint spectra[60,61] of adsorbed organometallic compounds such as the metallocenes.[62–65]

Ferrocene has recently been utilized in the synthesis of carbon nanotubes.[66] In this context, HREEL spectroscopic measurements have been carried out on the adsorption of ferrocene on graphite[67]; silver substrates have also been examined.[63,68,69] On Ag(100), ferrocene was found to exist as a weakly bound molecular entity at low temperatures.[68] Loss peaks at 60.4 (487 cm^{-1}) and 93.2 meV (752 cm^{-1}) that were prominent in the HREEL spectra collected at specular angles were not observed at off-specular angles (Figure 7), a result which strongly suggests that the two loss features are exclusively dipolar in character. The peak at 60.4 meV was assigned to the antisymmetric iron–cyclopentadienyl (Fe–Cp) stretch, and the peak at 90.3 meV was ascribed to the out-of-plane C–H bend frequency, γ_{CH}.[69] For the two modes to be dipole active, both must have a vibrational-mode component that is perpendicular to the silver surface; this can be satisfied only if the ferrocene molecule is adsorbed in an ''upright'' orientation in which both Cp rings are oriented parallel to the surface (Figure 7).[63,68,69] On graphite at 140 K, a similar orientation for adsorbed ferrocene was inferred from the HREEL spectra.[67] More importantly, the frequencies of the loss peaks were found to be nearly identical to those of the gas-phase absorption peaks; the absence of adsorption-induced frequency shifts provides ample evidence that ferrocene was only physisorbed on the graphite surface.

The adsorption of iron(0) pentacarbonyl was recently studied on a Si(111)-(7 × 7) surface.[70] The interest in $Fe(CO)_5$ lies in its availability as a source gas for the chemical vapor deposition of $FeSi_2$, a critical microelectronics material.[71] Even at temperatures as low as 100 K, $Fe(CO)_5$ already underwent dissociative adsorption to yield a linear iron monocarbonyl (FeCO) surface complex. The prominent loss peaks that appeared at 53 meV (428 cm^{-1}), 81 meV (653 cm^{-1}), and 255 meV (2056 cm^{-1}) were assigned to the Si–COFe, Fe–CO, and C≡O stretch modes, respectively. These peaks were shown to arise only via dipole scattering which, because of the dipole selection rule, indicates that the adsorbed FeCO is oriented vertically with the CO moiety bonded to the Si surface.

3.1.5 *Fullerene*

The growth and chemistry of C_{60}[72] films on transition metal[73,74] and semiconductor surfaces[75–77] has been extensively studied because of potential industrial applications. The surface coordination of fullerene with

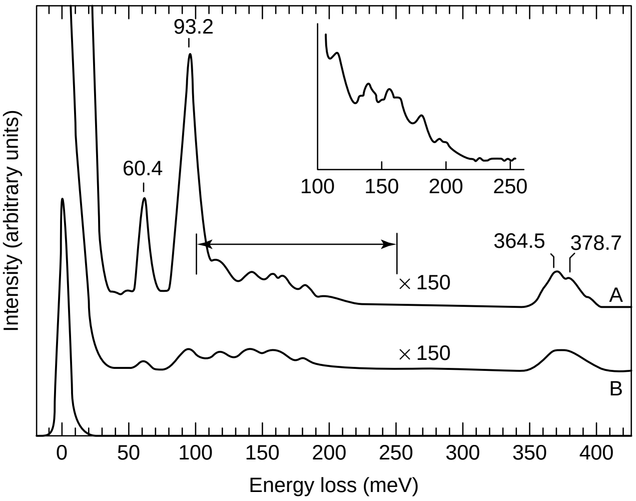

Figure 7 HREEL spectra for ferrocene adsorbed on Ag(100) at 110 K. A, specular spectrum; B, off-specular spectrum. (Reprinted with permission from Waldfried, Welipitiya, Hutchings, de Silva, Gallup, Dowben, Pai, Zhang, Wendelken and Boag.[69] © 1997 American Chemical Society)

transition-metal surfaces involves the donation of electrons from the π orbitals of the ligand to the d orbitals of the metal accompanied by the back-donation of electrons from a metal d orbital to the ligand π^* orbital. The π-electron back-donation significantly alters the chemical properties of the surface-attached C_{60}. Because of its high symmetry, there are more than just a few degenerate and IR-inactive vibrational modes.[78,79] However, most of these modes are observable in HREELS especially when detection is conducted at both specular and off-specular angles.[80]

Alkali-doped fullerides that exhibit superconductivity have received considerable attention. The spectral fingerprints of these materials show vibrational-mode-specific frequency shifts and intensity variations related to electron donation from the intercalated metal atoms to the C_{60} molecules (Figure 8a). HREELS of K-doped C_{60} thin films adsorbed on Ag(111) and Cu(111) showed loss peaks, barely visible for the undoped monolayer that increased when the dopant concentration was increased. This trend was thought to be a consequence of the charge transfer from the (electropositive) K atom to C_{60}.[81] The existence of positive K^+ ions and negative C_{60}^- ions may have been established by the appearance of a prominent optical-phonon loss peak brought about by the collective oscillations of the cations against the anions (Figure 8b).

Studies on fluoro–fullerenes ($C_{60}F_x$) were recently undertaken because of the interest in such materials as cathodes in Li batteries.[83] A recent HREELS-based work focused on the interaction between $C_{60}F_x$ and the silicon surface.[84,85] The spectrum of $C_{60}F_x$ thin layers deposited on Si(111)-(7 × 7) revealed a weak but well-defined loss feature at 107 meV. This peak was attributed to a Si–F stretch mode, which implied that the Si surface was able to defluorinate $C_{60}F_x$ and form a Si–F selvedge on the silicon substrate. The Si–F bond is rather strong and renders the substrate chemically inert toward further adsorption of $C_{60}F_x$.[84] The defluorination process is enhanced by an increase in temperature.[85]

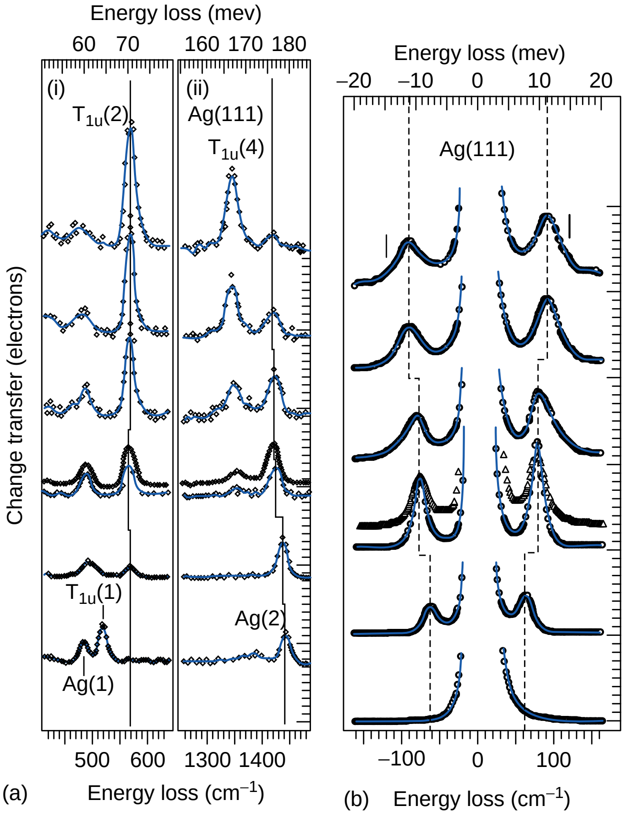

Figure 8 Evolutions of intramolecular vibrations (a) and extramolecular phonons, (b) of K-doped C_{60} on Ag(111) at different dopant concentrations. The lowest curves correspond to the undoped monolayers and the topmost ones to the saturated monolayers. (Reprinted from Silien, Thiry and Caudano,[82] © Elsevier 2004)

3.2 Organic Molecules

3.2.1 *Ethylene*

The structure and reactivity of ethylene chemisorbed on transition-metal surfaces are of fundamental importance in surface science and heterogeneous catalysis. HREELS has been foremost among the surface characterization techniques employed; in fact, the first vibrational spectroscopic study of ethylene chemisorbed on Pt(111) was carried out with electron energy-loss spectroscopy (EELS)[86] almost a decade before IRAS was employed.[87,88]

At temperatures below 200 K, two types of ethylene-derived surface species have been identified. One is a di-σ-bonded species that results when the C=C double bond is broken to form two C−metal bonds; the other is a π-bonded species in which the ethylene molecule remains intact. At higher temperatures, a third species, ethylidyne, may be generated on close packed face-centered cubic (111) surfaces.

The di-σ-bonded species has been observed on Pt(111),[89] Pt(100),[90] Fe(110),[91] Ru(001),[92] Si(100)[93,94] and Ni(*hkl*).[95–97] The HREEL spectrum of di-σ-bonded ethylene is characteristic of aliphatic (sp^3-hybridized) compounds with a C−H symmetrical stretch at ca. 3000 cm^{-1} (372 meV) and a CH_2 wag and C−C stretch in the region from 1170 cm^{-1} (145 meV) to 1830 cm^{-1} (227 meV); a peak near 450 cm^{-1} (55.8 meV) has been attributed to a metal−C stretch mode.[98] The π-bonded species has been found on Cu(100),[99] Pd(*hkl*)[100–103] as well as on hydrogen or oxygen pretreated surfaces.[104–107] The HREEL spectrum of the π-adsorbed species bears features reminiscent of the infrared spectrum of the ethylene ligand in Zeise's salt, $K[(C_2H_4)PtCl_3]$[108] with the C−H symmetric stretch at 3000 cm^{-1}, and a CH_2 wag and the C=C stretch in the region near 1530 cm^{-1} (190 meV); the metal−C stretch was found at 300 cm^{-1} (37 meV).[98]

When either the di-σ-bonded or the π-coordinated species is warmed to room temperature, ethylidyne ($\equiv C-CH_3$) is generated[89,109,110]; this surface compound is rather stable since the anchored carbon is bonded to three different metal atoms. The HREEL spectrum of chemisorbed ethylidyne is characterized by vibrational modes of C_{3v} symmetry; the C−H stretch is at 2900 cm^{-1} (360 meV), the CH_3 wag and C−C stretch within the 1400 (174 meV) to 1800 cm^{-1} (223 meV) interval, and the M−C stretch near 425 cm^{-1} (52.7 meV).[98] Although the complete mechanism of the ethylene to ethylidyne conversion is not known, it is thought to involve an initial dehydrogenation step followed by hydrogen migration; ethylidene ($=CH-CH_3$) was proposed as an intermediate in the transformation reaction at Pt(111).[111]

The adsorption of ethylene on clean and oxygen pretreated Pd(111) surfaces was recently studied[107]; the results in terms of HREEL spectra, are shown in Figure 9. As anticipated, ethylene was chemisorbed at 100 K as a di-σ-bonded species on the clean metal (Figure 9a). On the oxygen precoated surface, however, a π-coordinated complex was obtained (Figure 9b). At 300 K, ethylene chemisorption always resulted in an ethylidynic complex regardless of whether or not the surface was pretreated with oxygen (Figure 9c). When the di-σ-bonded or the π-attached species was warmed to 450 K, quantitative desorption of starting material (C_2H_4) occurred without dehydrogenation; no ethylidyne species was produced from either structure during the temperature increase.

Adsorption of ethylene on Rh(100) presaturated with hydrogen produced a π-bonded species at low temperatures.[105] The degree of sp^2-to-sp^3 rehybridization upon chemisorption was expressed in terms of a ''$\pi\sigma$ parameter'' derived from the HREEL spectrum via the mixing of the C−C (or C=C) stretch and the CH_2 scissor modes.[112] The $\pi\sigma$ parameter, which was normalized to zero for pure sp^2 hybridization (C_2H_4) and to unity for pure sp^3 hybridization ($C_2H_4Br_2$), was estimated to be 0.39 for chemisorbed C_2H_4; in comparison, a $\pi\sigma$ parameter of 0.38 was obtained for Zeise's salt. The close agreement

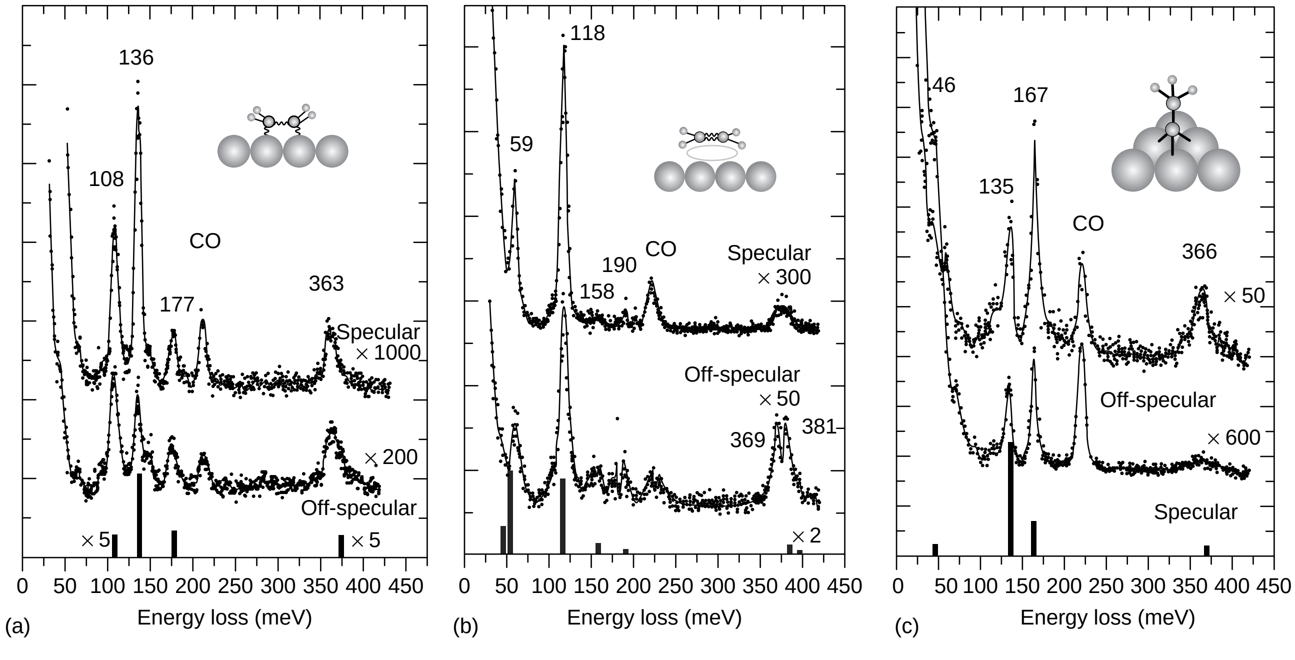

Figure 9 Specular and off-specular HREEL spectra of (a) Pd(111) surface exposed to C_2H_4 at 100 K; (b) Pd(111)-2 × 2-O surface exposed to C_2H_4 at 100 K; and (c) Pd(111) exposed to C_2H_4 at 300 K. The bars below the spectra indicate the calculated vibrations of each species in the inset. (Reprinted from Sock, Eichler, Surnev, Andersen, Klötzer, Hayek, Ramsey and Netzer,[107] © Elsevier 2003)

between the two $\pi\sigma$ parameters provides additional evidence that the ethylene molecule is bound to the surface as a π-bonded ligand. It was also reported in the same work that an ethyl intermediate was formed from π-bonded ethylene by insertion of preadsorbed H atoms, a process that is initiated even at temperatures below 110 K. At $110\,\mathrm{K} < T < 200\,\mathrm{K}$, evolution of gaseous ethane was observed, but further thermal treatment resulted in the rupture of the carbon–carbon bond.

3.2.2 *Methanol*

Research activity on methanol has been vigorous because of its commercial importance as an alternative feedstock in fuel cells. When CH_3OH is chemisorbed on a catalytic surface at ambient temperatures, it is usually present as a methoxy intermediate; the latter then undergoes extensive decomposition to yield a product distribution that depends upon the temperature. A tabulation of products generated under various experimental conditions such as metal catalyst and decomposition temperature is given in Table 1; HREELS and temperature programmed mass spectrometry were used to generate the data.

3.2.3 *Aromatic Compounds*

An immediate issue in the chemisorption of aromatic compounds is whether the phenyl ring is oriented parallel or perpendicular to the plane of the metal surface. In this regard, the intensity of the out-of-plane C–H bend (γ_{CH}) relative to the in-plane C–H stretch (ν_{CH}) provides a direct diagnostic indicator of adsorbed aromatic orientation.**[130–132]** At specular angles, the dipole selection rule states that ν_{CH} for a ring chemisorbed completely flat would be EELS-inactive; only the γ_{CH} mode would exhibit EELS activity. At off-specular angles, the impact-scattering selection rules are less restrictive and all modes would conceivably be EELS-active, although peaks obtained at specular angles would tend to vanish as the off-specular angle φ is increased.

Early studies with smooth polycrystalline Pt electrodes indicated that aromatic compounds such as *p*-diphenols

Table 1 Methanol decomposition on various metal surfaces

Surface	Temperature (K)	Decomposition/chemisorption products	References
V(110)	100	Methoxy ($-O-CH_3$)	113
C-modified V(110)	100	$-O-CH_3$	113
Ti(0001)	100	$-O-CH_3$	113
C-modified Ti(0001)	100	$-O-CH_3$	113
S-modified Fe(100)	150	CH_3O-(decreases if S is increased)	114
	450	CO (decreases if S is increased)	114
Fe(100)	110	CH_3O-	114
	450	H_2 and CO	114
O-modified Fe(100)	150	$-O-CH_3$	115
Pt(111)	200	CO and H	116
Pt(100)	200	H and CO	117
Pt(110)	140	$-CH_x$	118
	250	CH_4, H and C	118
Pt(110)-(2 × 1)	130	$-O-CH_3$	118
	250	CO and H	115
Rh(100)	250	$-O-CH_3$	119
	320	CO and H	119
Rh(111)	140	$-O-CH_3$	120
	210	CO and H_2	120
O-modified Rh(111)	140	$-O-CH_3$	120
Ni(110)	170	$-O-CH_3$	121
	270	CO and H	121
Ru(0001)	300	CO and H	122
Pd(111)	300	CO	123
Pd(100)	77	Methoxide (CH_3O^-)	124
	530	CO, H and H_2	124
Ge	300	$-CH_3$ and $-OH$	125
NiAl(100)	120	$-O-CH_3$	126
	400	H_2, CH_4, $-CH_3$ and C_2H_4	126
NiAl(110)	120	$-O-CH_3$	126
	400	H_2, CO, CH_4, $-CH_3$ and C_2H_4	114
NiAl(111)	200	$-O-CH_3$	127
	650	H_2, CO, CH_4, and CH_3	127
Cu(100)	370	Unidentified gaseous products	128
Co-modified Mo(110)	250	CH_3O^-	129

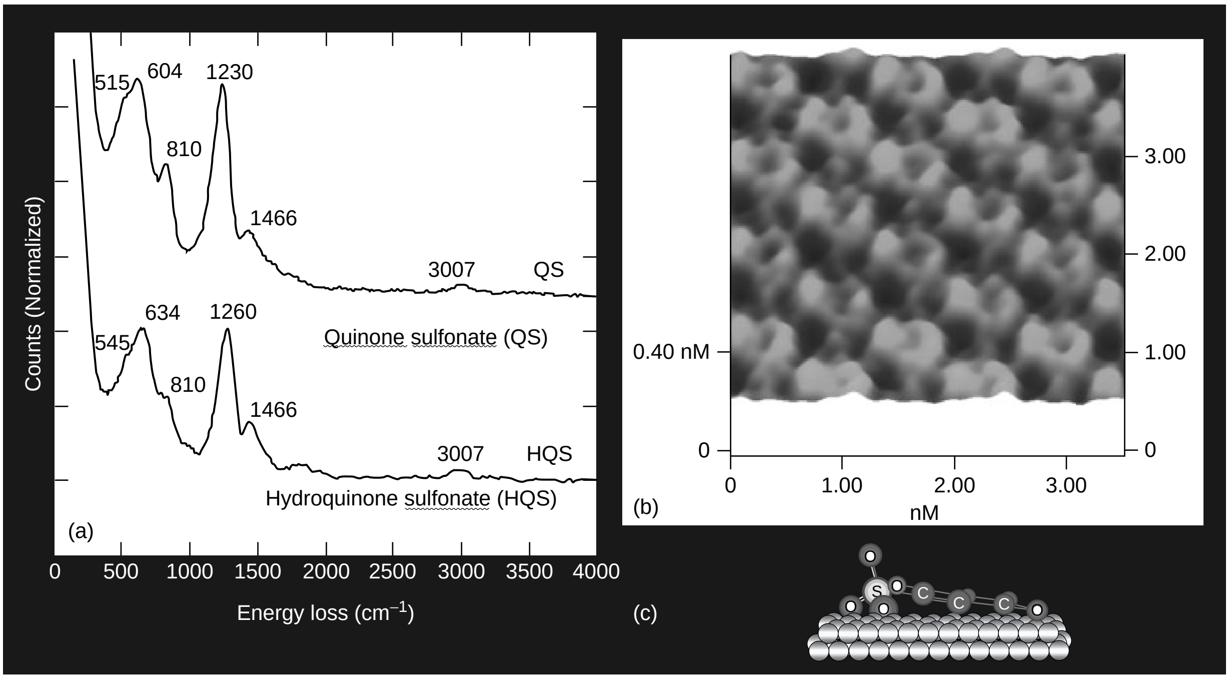

Figure 10 HREEL spectrum (a), in situ scanning tunneling microscope image (b), and molecular model (c) of quinone sulfonate chemisorbed on Pd(100)

are chemisorbed in discrete, nonrandom orientations that depend upon interfacial factors such as the solution concentration of the aromatic and the composition of the supporting electrolyte.[133–135] For example, when chemisorbed from dilute (0.1 mM) solutions, a molecular layer of horizontally oriented (η^6-coordinated) quinonoid species is formed; at higher concentrations (2 mM), a layer of vertically oriented (2,3-η^2-bound) aromatic molecules is generated. The orientational assignments made from measured adsorbed-molecule cross sections have since been verified by independent experiments foremost of which has been HREELS; work with the diphenols has been carried out with Pt and Pd single crystals.[136–139]

Figure 10 shows HREEL spectra of a Pd(111) electrode emersed[e] from aqueous solutions that contained either 0.1 mM hydroquinone sulfonate or 0.1 mM benzoquinone sulfonate.[132] Four features are most notable: (i) the spectra are identical whether the starting material is the diphenol or the quinone; (ii) there is a pronounced out-of-plane C–H bend (γ_{CH}) at 810 cm^{-1} (100 meV); (iii) no O–H stretch (ν_{OH}) is observed near 3600 cm^{-1} (446 meV); and (iv) there is a small but noticeable in-plane C–H stretch (ν_{CH}) at 3007 cm^{-1} (373 meV). These results indicate that, upon surface coordination, the diphenolic species undergoes a two-electron, two-proton oxidation to form essentially flat-chemisorbed benzoquinone; the small ν_{CH} peak, however, indicates that the aromatic ring is not completely flat, but is slightly tilted. The combination of HREELS and electrochemical (in situ) scanning tunneling microscopy[140] has been used to deduce the adsorbed–molecule orientation of the sulfonated quinone (Figure 10). Recent HREELS and thin-layer electrochemical measurements[141] have demonstrated that, at a tenfold increase in solution concentration, hydroquinone is chemisorbed on Pd(111) in an edgewise orientation reminiscent of an *o*-benzyne organometallic complex.[133–135]

The desorption and decomposition of benzene has been studied on Pt(111) and on Sn-modified Pt(111) for comparative purposes.[142] On the former surface, only a portion of the chemisorbed benzene desorbs upon heat treatment; the remainder is dehydrogenated to form a layer of carbon on the surface. On the Pt(111)-Sn alloys, only physisorption takes place.

The cyclization reaction of acetylene at ambient temperatures to form benzene on Pd(111) has recently been reinvestigated in an attempt to gain insights into its mechanism.[143] It has been claimed that, at low exposures of acetylene, only ethylidyne is formed. At higher exposures, benzene is formed, albeit at low coverages, as indicated by appearance of the ν_4 band of benzene at 720 cm^{-1}.

More recent work on the chemisorption of aromatic molecules has focused on new materials (e.g., Mo(112)-c(2 × 2)-SiO_2 and Mo_2C/Mo(100)) and with various benzene derivatives (e.g., C_6H_5I and C_5NH_5).[144–147]

3.2.4 Polymers

Only feeble attempts were initially made two decades ago in the application of HREELS to the study of polymer surfaces. The efforts did not become more earnest until a decade later. The use of HREELS has primarily been focused on the following aspects related to polymer films deposited on metals as well as to surfaces of the polymer films themselves: surface morphology, interfacial composition, the scattering mechanism, and the strength of the polymer−substrate bond. The utility of HREELS to probe polymer-surface morphology rests on the observation that elastic peaks due to electrons backscattered from hydrogen atoms can be correlated with the hydrogen content at smooth surfaces.[148]

Systems that employed HREELS for interfacial-composition determinations included: poly(ethylene oxide)-polystyrene diblock copolymer on Si wafers[149]; formaldehyde poly(oxymethylene) films on Cu(100)[150]; and Langmuir−Blodgett films of 4,4’-oxydianiline-pyromellitic dianhydride polyimide on Au and on highly ordered pyrolytic graphite.[151]

HREELS experiments with bisphenol-A polycarbonate, high-density polyethylene, and poly(2-vinylpyridine) suggested that, although dipole and impact scattering are prominent in polymer films, negative-ion resonance scattering cannot be discounted.[152] Investigations with highly oriented poly(tetrafluoroethylene) likewise indicated appreciable negative-ion resonance impact scattering with a maximum cross section at an incident electron energy of around 4 eV.[153]

The use of vibrational spectroscopy to monitor the strength of polymer adhesion on foreign substrates is based upon adsorption-induced frequency shifts and intensity changes in the free polymer modes and the emergence of new spectral peaks; the latter, due to metal−polymer bonds, generally appear at energies lower than 75 meV that can be accessed only by HREELS. It was found, for example, that Pd is inert toward polyimide, but Cr is quite reactive.[154] The interaction between aluminum deposited onto a polyimide film was also investigated by HREELS. When the Al coverage was $< 10^{14}$ atoms cm^{-2}, the reaction was limited to Al with the carbonyl group to form a C−O−metal complex. At a twofold increase in coverage, Al−O and Al−C bonds were formed; at intermediate coverages, no polymer−Al reactions transpired but bond breaking processes in the polymer occurred.[155]

3.2.5 Self-Assembled Monolayers

Technological and scientific interest in self-assembled monolayers (SAMs) lie in their applicability in many areas such as corrosion protection, biomimetic membranes, and chemical sensors.[156] The driving force in the facile formation of SAMs is the high affinity of an end group for the metal substrate. Organosulfur compounds such as alkanethiol and dialkyl disulfides have been widely studied because they spontaneously form highly ordered structures on transition-metal surfaces such as Au and Pt. IRAS, Raman scattering, sum-frequency generation and HREELS are among the vibrational spectroscopy techniques employed to probe the structure and organization of monolayer and bilayer SAMs.[157] HREELS has the unique advantage in that the metal−sulfur stretch mode occurs at low frequencies inaccessible by the other methods; hence, a determination of the adsorption sites of the organosulfur compounds is possible only with HREELS.[158,159] In addition, the degree of order in SAMs can be addressed uniquely by HREELS via a comparison of the specular and off-specular HREEL spectra.[160]

A vast majority of HREELS work has been focused on Au(111) and Au(100) surfaces.[161–163] The HREEL spectrum of alkanethiols surface coordinated on Au can be divided into the following group-frequency regions: 200 (24.8 meV) to 360 cm^{-1} (44.6 meV) for the Au−S stretch region; 620 (77 meV) to 740 cm^{-1} (91.7 meV) for the C−S stretch region; 1000 (124 meV) to 1100 cm^{-1} (136 meV) for the C−C stretch region; 1200 (149 meV) to 3000 cm^{-1} (372 meV) for the C−H stretch region; and 700 (86.9 meV) to 900 cm^{-1} (112 meV) for the C−H wag region). The absence of an S−H peak in the spectrum indicates that alkanethiol chemisorption involves the loss of an S−H bond to form an M−S bond accompanied by the evolution of H_2 gas.

The effect of alkyl chain length on the structure of alkanethiols on Au(111) was studied with $CH_3(CH_2)_{n-1}SH$, where $n = 2$, 4, 6, 8, 10, 11, 12, 14, 15, 16, and 18).[164] The results, in terms of HREEL spectra, are displayed in Figure 11. It is most interesting to note that the intensity of CH_3 σ-deformation mode at 1380 cm^{-1} (171 meV) is profoundly dependent on the number of carbons in the alkyl chain: It is present only when the number of carbon atoms is even (cf., the spectra labeled C_{10}, C_{12} and C_{16}); it is absent when the number is odd (cf., the spectra labeled C_{11} and C_{15}). This ‘‘odd−even’’ trend is caused by the fact that the orientation of the CH_3 head is parallel to the surface for odd number of carbon atoms but perpendicular when the number is even (cf., the inset in Figure 11). As dictated by the dipole selection rules, only the oscillator that has a component perpendicular to the surface (as in the even number chain) would show HREELS activity. It can also be seen in the frequency region below 220 cm^{-1} (27.3 meV) that more than one peak, separated by about 30 cm^{-1} (3.7 meV) are present; this indicates the existence of multiple adsorption sites for the subject alkanethiols on Au(111).

Octanethiol SAMs on Au(111) have been found to undergo an adlattice transition from a $c(4 \times 2)$ to a $(6 \times \sqrt{3})$ structure after long-term storage. HREELS was one of the techniques employed to examine the cause for the transitions.[165] It was established that the structural transitions were caused by the dynamic surface diffusion of the sulfur anchor group between multiple adsorption sites. The adsorption-site exchange also resulted in orientational changes in alkyl chains.[164]

The properties of octadecanethiol SAMs on three different gold substrates, Au on Si, Au(111), and Au(100), were studied by HREELS for comparative purposes.[132,140,141] The angular distribution of the elastic peak from the SAM on the Au on Si film was found to be at least 5 times broader than those on Au(111) and Au(100). This suggests

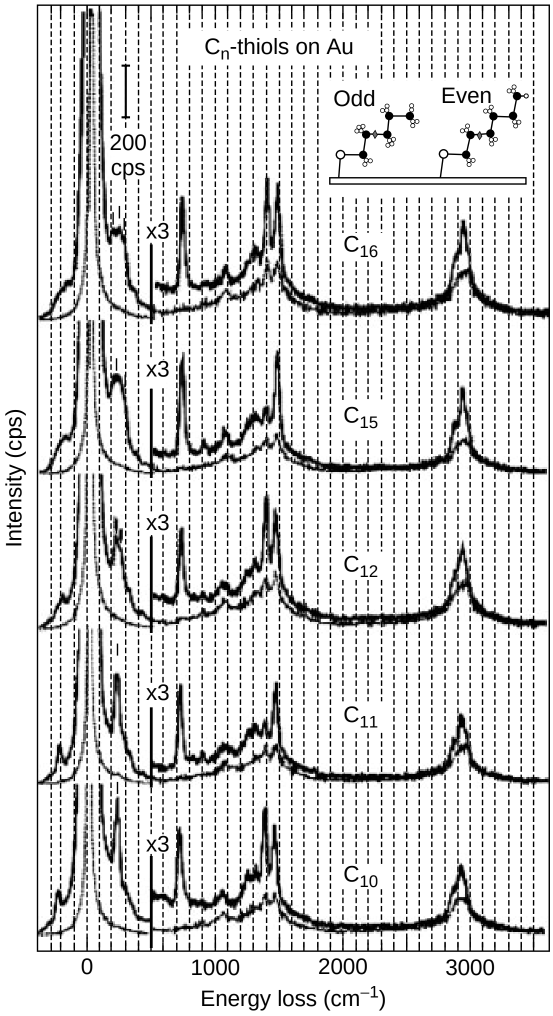

Figure 11 Odd–even effect on HREEL spectra of various alkanethiol SAMs on Au. The specular spectra and the off-specular spectra were plotted as solid and dotted lines, respectively. (Reprinted with permission from Kato, Noh, Hara and Kawai.[158] © 2002 American Chemical Society)

that the SAM on the Au film was far less ordered than on Au(111) and Au(100). An analysis of the dipole scattering and impact scattering contributions to the HREEL spectra provided evidence that the CH_2 (rocking and scissoring) and CH_3 (bending) modes are predominantly dipole scatterers, whereas the C–C and C–H stretching modes are primarily impact scatterers.[165]

Thiophenols and thiophenol derivatives chemisorbed on well-defined electrode surfaces have also been studied by HREELS.[2] The cyclic voltammetric peaks for the quinone/hydroquinone redox reaction of the 2,5-dihydroxythiophenol immobilized on the Pt surface was much broader than for the unadsorbed species; the broadening vanished when a methylene group was placed between the—SH group and the phenyl ring. These results indicated strong substrate mediated adsorbate–adsorbate interactions. Such interactions, however, were not manifested in the HREEL spectrum. This suggested that the adsorbate–adsorbate interactions were purely electronic in nature, devoid of vibrational (or vibronic) perturbations.

4 ACKNOWLEDGMENTS

Acknowledgment is made to the National Science Foundation by J. L. Stickney and M. P. Soriaga and to the Welch Foundation by MPS for support of their work cited in this article.

5 ABBREVIATIONS AND ACRONYMS

EELS = electron energy-loss spectroscopy; HREEL = high-resolution electron energy-loss; HREELS = high-resolution electron energy-loss spectroscopy; UHREELS = ultrahigh-resolution electron energy-loss spectroscopy; IRAS = infrared reflection-absorption spectroscopy; SAMs = self-assembled monolayers; UHV = ultrahigh vacuum; Cp = cyclopentadienyl group φ = off-specular scattering angle.

6 END NOTES

[a] $1\,eV = 8066\,cm^{-1} = 96.48\,kJ\,mol^{-1}$.

[b] HREELS generally does not possess enough sensitivity to detect higher-order effects due to mechanical and/or electrical anharmonicity.

[c] In IRAS, the surface is irradiated at near-grazing incidence and the quantity of absorption is obtained from the attenuation of the intensity of the reflected beam. Adsorbed molecule orientation can be determined directly from the spectrum since the metal–surface dipole selection rule states that only vibrations with components perpendicular to the surface are active.

[d] A third mechanism, first observed in gas-phase electron-impact scattering, has been referred to as negative-ion resonance. In this process, an electron is trapped, within 10^{-15} s, inside the molecule in a negative-ion state. For chemisorbed molecules, however, the adsorbate-substrate chemical bond and the electron–surface interactions can dramatically alter the resonance properties.[6] Hence, for HREELS at metal surfaces, this mechanism is quite rare; it will not be treated further in this article.

[e] In electrochemical surface science, emersion is a term used to indicate the removal of an electrode from solution under potential control.

7 FURTHER READING

F. Allegretti, V. De Renzi, R. Biagi, U. del Pennino, G. Contini, V. Di Castro, C. Mariani and C. Fontanesi, *Surf. Sci.*, 2003, **539**, 63.

J. M. Auerhammer, M. Knupfer, H. Peisert and J. Fink, *Surf. Sci.*, 2002, **506**, 333.

A. Bansal, Xiuling. Li, Sang. I. Yi, W. H. Weinberg and N. S. Lewis, *J. Phys. Chem.*, 2001, **105**, 10266.

W. Chen, I. Ermanoski, Q. Wu, T. E. Madey, H. H. Hwu and J. G. Chen, *J. Phys. Chem.*, 2003, **107**, 5231.

Y. Chen, R. E. Palmer and J. P. Wilcoxon, *Surf. Sci.*, 2000, **454–456**, 963.

M. S. Chen, A. K. Santra and D. W. Goodman, *J. Phys. Chem.*, 2004, **108**, 17940.

T. V. Choudhary and D. W. Goodman, *Top. Catal.*, 2002, **20**, 35.

V. De Renzi, R. Biagi and U. del Pennino, *Phys. Rev. B*, 2001, **64**, 1.

S. V. Didziulis, P. Frantz, L. C. Fernandez-Torres, R. L. Guenard and S. S. Perry, *J. Phys. Chem.*, 2001, **105**, 5196.

A. -S. Duwez, *J. Electron Spectrosc. Relat. Phenom.*, 2004, **134**, 97.

Y. Fukuda, T. Kobayashi, H. Yoshida, T. Sekizawa and N. Sanada, *Appl. Surf. Sci.*, 2002, **190**, 279.

V. V. Gorodetskii, M. Yu. Smirnov and A. R. Cholach, *Stud. Surf. Sci. Catal.*, 1993, **75**, 1587.

C. J. Hagedorn, M. J. Weiss and W. H. Weinberg, *J. Phys. Chem.*, 2001, **105**, 3838.

R. D. Haley, M. S. Tikhov and R. M. Lambert, *Catal. Lett.*, 2001, **76**, 125.

G. Hamm, T. Schmidt, J. Breitbach, D. Franke, C. Becker and K. Wandelt, *Surf. Sci.*, 2004, **562**, 170.

M. A. Henderson and S. A. Chambers, *Surf. Sci.*, 2000, **449**, 135.

G. Hess, Ch. Baumgartner and H. Froitzheim, *Phys. Rev. B*, 2001, **63**, 1.

T. Hoeche, F. Heyroth, M. Grodzicki and P. A. van Aken, *Phys. Status Solidi A*, 2005, **202**, 2355.

K. Jacobi, Y. Wang, C. Y. Fan and H. Dietrich, *J. Chem. Phys.*, 2001, **115**, 4306.

I. Jungwirthova and L. L. Kesmodel, *Surf. Sci.*, 2000, **470**, L39.

S. Katano, H. S. Kato, M. Kawai and K. Domen, *J. Phys. Chem.*, 2003, **107**, 3671.

K. A. Layman, M. M. Ivey and J. C. Hemminger, *J. Phys. Chem.*, 2003, **107**, 8538.

J. P. Lu, M. R. Albert and S. L. Bernasek, *Surf. Sci.*, 1991, **258**, 269.

K. K. Meagher, A. B. Bocarsly, S. L. Bernasek and T. A. Ramanarayanan, *J. Phys. Chem.*, 2000, **104**, 3320.

U. A. Paulus, Y. Wang, H. P. Bonzel, K. Jacobi and G. Ertl, *J. Phys. Chem.*, 2005, **109**, 2139.

V. M. Rei, P. Lang, G. Horowitz, C. Nogues, Y. Jugnet, O. Pellegrino and A. M. Botelho do Rego, *Langmuir*, 2003, **19**, 2649.

T. J. Rockey, M. Yang and H. L. Dai, *Surf. Sci.*, 2005, **589**, 42.

E. Salomon, T. Angot, N. Papageorgiou and J. -M. Layet, *Surf. Sci.*, 2005, **596**, 74.

C. Silien, Y. Caudano, A. Peremans and P. A. Thiry, *Appl. Surf. Sci.*, 2000, **162**, 445.

C. Silien, P. A. Thiry and Y. Caudano, *Phys. Rev. B*, 2003, **67**, 075412.

M. Sock, A. Eichler, S. Surnev, J. N. Andersen, B. Klotzer, K. Hayek, M. G. Ramsey and F. P. Netzer, *Surf. Sci.*, 2003, **545**, 122.

P. J. Unwin and T. S. Jones, *Surf. Sci.*, 2003, **532**, 1011.

J. Wang, C. Y. Fan, Q. Sun, K. Reuter, K. Jacobi, M. Scheffler and G. Ertl, *Angew. Chem.*, 2003, **42**, 2151.

C. M. Whelan, F. Cecchet, G. J. Clarkson, D. A. Leigh, R. Caudano and P. Rudolf, *Surf. Sci.*, 2001, **474**, 71.

X. Yang, Z. H. He, X. J. Zhou, S. H. Xu and K. T. Leung, *Appl. Surf. Sci.*, 2006, **252**, 3647.

H. Zhao, J. Kim and B. E. Koel, *Surf. Sci.*, 2003, **538**, 147.

8 REFERENCES

1. G. A. Somorjai, ‘Introduction to Surface Chemistry and Catalysis’, John Wiley & Sons, New York, 1994.
2. G. Ertl and J. Kuppers, ‘Low Energy Electrons and Surface Chemistry’, VCH Publishers, Weinheim, 1985.
3. H. Froitzheim, in ‘Topics in Current Physics’, ed. H. Ibach, Springer-Verlag, New York, 1977.
4. H. Ibach and D. L. Mills, ‘Electron Energy Loss Spectroscopy and Surface Vibrations’, Academic Press, New York, 1982.
5. N. R. Avery, in ‘Vibrational Spectroscopy of Molecules on Surfaces’, eds. J. T. Yates, Jr and T. E. Madey, Plenum Press, New York, 1987.
6. L. L. Kesmodel, in ‘Surface Imaging and Visualization’, ed. A. T. Hubbard, CRC Press, Boca Raton, 1995.
7. http://www.lktech.com/products/els5000.php, 2006.
8. J. E. Soto-Chevres, Molecular Adsorption at Well-Defined Palladium Electrode Surfaces, Ph. D. Dissertation, Texas A&M University, College Station, 2000.
9. F. A. Cotton and G. Wilkinson, ‘Advanced Inorganic Chemistry’, Wiley-Interscience, New York, 1988.
10. G. Blyholder, *J. Phys. Chem.*, 1964, **68**, 2772.
11. N. Sheppard and T. T. Nguyen, in ‘Advances in Infrared and Raman Scattering’, eds. R. E. Hester and R. J. H. Clark, Hayden and Son, London, 1978.
12. W. Erley, H. Wagner and H. Ibach, *Surf. Sci.*, 1979, **80**, 612.
13. V. Formoso, A. Marino, G. Chiarello, R. G. Agostino, T. Caruso and E. Colavita, *Surf. Sci.*, 2006, **600**, 1456.
14. H. S. Kato, H. Okuyama, J. Yoshinobu and M. Kawai, *Surf. Sci.*, 2002, **513**, 239.
15. H. Steininger, S. Lehwald and H. Ibach, *Surf. Sci.*, 1982, **123**, 264.

16. J. Wang, Y. Wang and K. Jacobi, *Surf. Sci.*, 2001, **482**, 153.
17. J. Radnik and H. J. Ernst, *J. Chem. Phys.*, 1999, **110**, 10522.
18. D. L. S. Nieskens, M. M. M. Jansen, A. P. Van Bavel, D. Curulla-Ferre and J. W. Niemantsverdriet, *Phys. Chem. Phys.*, 2006, **8**, 624.
19. A. G. Baca, L. E. Klebanoff, M. A. Schulz, D. Paparazzo and D. A. Shirley, *Surf. Sci.*, 1986, **173**, 215.
20. M. L. Colaianni, J. G. Chen, W. H. Weinberg and J. T. Yates, Jr, *J. Am. Chem. Soc.*, 1992, **114**, 3735.
21. C. M. Friend, J. G. Serafin, E. K. Baldwin, P. A. Stevens and R. J. Madix, *J. Chem. Phys.*, 1987, **87**, 1847.
22. H. Von Schenck, E. Janin, O. Tjernberg, M. Svensson and M. Gothelid, *Surf. Sci.*, 2003, **526**, 184.
23. C. Lemire, R. Meyer, V. E. Henrich and H. J. Freund, *Surf. Sci.*, 2004, **572**, 103.
24. S. H. Kim, U. A. Paulus, Y. Wang, J. Wintterlin, K. Jacobi and G. Ertl, *J. Chem. Phys.*, 2003, **119**, 9729.
25. H. Hopster and H. Ibach, *Surf. Sci.*, 1978, **77**, 109.
26. S. R. Bare, P. Hofmann and D. A. King, *Surf. Sci.*, 1984, **144**, 347.
27. Z. Chen, D. H. Gracias and G. A. Somorjai, *Appl. Phys. B*, 1999, **68**, 549.
28. R. Linke, D. Curulla, M. J. P. Hopstaken and J. W. Niemantsverdriet, *J. Chem. Phys.*, 2001, **115**, 8209.
29. Y. C. Lee and P. A. Montano, *Surf. Sci.*, 1985, **149**, 471.
30. T. S. Rahman, A. B. Anton, N. R. Avery and W. H. Weinberg, *Phys. Rev. Lett.*, 1983, **51**, 1979.
31. N. D. Shinn and T. E. Madey, *Surf. Sci.*, 1986, **173**, 379.
32. S. H. Kim and P. C. Stair, *Surf. Sci.*, 2000, **457**, L347.
33. T. Sueyoshi, T. Sasaki and Y. Iwasawa, *Surf. Sci.*, 1996, **365**, 310.
34. C. de Verdiere, J. Szeftel and P. Soukiassian, *Phys. Rev. B*, 1990, **42**, 7234.
35. F. P. Leisenberger, G. Koller, M. Sock, S. Surnev, M. G. Ramsey, F. P. Netzer, B. Klotzer and K. Hayek, *Surf. Sci.*, 2000, **445**, 380.
36. P. D. Nolan, B. R. Lutz, P. L. Tanaka, J. E. Davis and C. B. Mullins, *J. Chem. Phys.*, 1999, **111**, 3696.
37. F. Bartolucci, R. Franchy, J. C. Barnard and R. E. Palmer, *Phys. Rev. Lett.*, 1998, **80**, 5224.
38. J. L. Gland, B. A. Sexton and G. B. Fisher, *Surf. Sci.*, 1980, **95**, 587.
39. H. Steininger, S. Lehwald and H. Ibach, *Surf. Sci.*, 1982, **123**, 1.
40. C. Backx, C. P. M. De Groot and P. Biloen, *Surf. Sci.*, 1981, **104**, 300.
41. K. C. Prince, G. Paolucci and A. M. Bradshaw, *Surf. Sci.*, 1986, **175**, 101.
42. D. H. Parker, M. E. Bartram and B. E. Koel, *Surf. Sci.*, 1989, **217**, 489.
43. K. Gustafsson and S. Andersson, *J. Chem. Phys.*, 2004, **120**, 7750.
44. H. Ibach and S. Lehwald, *Surf. Sci.*, 1980, **91**, 187.
45. P. A. Thiel, R. A. Depaola and F. M. Hoffmann, *J. Chem. Phys.*, 1984, **80**, 5326.
46. S. Meng, L. F. Xu, E. G. Wang and S. Gao, *Phys. Rev. Lett.*, 2002, **89**, 176104.
47. C. T. Nyberg, C. G. Tengstal, P. Uvdal and S. Andersson, *J. Electron Spectrosc. Relat. Phenom.*, 1986, **38**, 299.
48. S. F. Wendt, T. Wei, M. S. Chen, V. Kempter and D. W. Goodman, *Surf. Sci.*, 2004, **565**, 107.
49. R. B. Rosseau and T. H. Ellis, *Surf. Sci.*, 1993, **280**, 23.
50. M. A. Henderson and S. A. Chambers, *Surf. Sci.*, 2000, **449**, 135.
51. F. Xu, Q. Guo and P. Moller, *J. Phys. Chem. B*, 2005, **109**, 9517.
52. H. W. Ibach, H. Wagner and D. Bruchmann, *Solid State Commun.*, 1982, **42**, 457.
53. P. A. E. Cox and P. D. Naylor, *J. Electron Spectrosc. Relat. Phenom.*, 1983, **29**, 247.
54. K. J. Wu, G. S. Elliott and S. D. Kevan, *J. Chem. Phys.*, 1989, **91**, 7964.
55. Y. Yu, Q. Guo, S. Liu, E. Wang and P. Moller, *Phys. Rev. B*, 2003, **68**, 115414.
56. K. B. Jacobi, P. Geng, W. Hansen, J. Schreiner and C. Astaldi, *Surf. Sci.*, 1991, **245**, 72.
57. E. Stuve and R. J. Madix, *Surf. Sci.*, 1984, **146**, 179.
58. M. S. Hock, I. Bassignana, K. Wagemann and J. Kueppers, *Surf. Sci.*, 1986, **177**, L978.
59. N. B. Chen and R. I. Masel, *Surf. Sci.*, 1999, **419**, 150.
60. G. Davidson, *Spectrosc. Prop. Inorg. Organomet. Compd.*, 1985, **18**, 220.
61. S. Cradock, *Spectrosc. Prop. Inorg. Organomet. Compd.*, 1985, **17**, 184.
62. D. L. Pugmire, C. M. Woodbridge, N. M. Boag and M. A. Langell, *Surf. Sci.*, 2001, **472**, 155.
63. C. M. Woodbridge, D. L. Pugmire, R. C. Johnson, N. M. Boag and M. A. Langell, *J. Phys. Chem. B*, 2000, **104**, 3085.
64. C. F. McConville and T. S. Jones, *Surf. Sci.*, 2002, **515**, 403.
65 Y. Fukuda, T. Kobayashi, H. Yoshida, T. Sekizawa and N. Sanada, *Appl. Surf. Sci.*, 2002, **190**, 279.
66. R. Sen, A. Govindaraj and C. N. R. Rao, *Chem. Phys. Lett.*, 1997, **267**, 276.
67. P. J. Durston and R. E. Palmer, *Surf. Sci.*, 1998, **400**, 277.
68. D. Welipitiya, P. A. Dowben, J. Zhang, W. W. Pai and J. F. Wendelken, *Surf. Sci.*, 1996, **367**, 20.
69. C. Waldfried, D. Welipitiya, C. W. Hutchings, H. S. V. de Silva, G. A. Gallup, P. A. Dowben, W. W. Pai, J. Zhang, J. F. Wendelken and N. M. Boag, *J. Phys. Chem. B*, 1997, **101**, 9782.

70. S. Mülbauer, A. Petkova and H. Froitzheim, *Surf. Sci.*, 2004, **562**, 195.
71. B. Rösen, H. Ch. Schäfer, Ch. Dieker, L. Lüth, A. Rizzi and D. Gerthsen, *J. Vac. Sci. Technol., B*, 1993, **11**, 1407.
72. H. W. Kroto, J. R. Heath, S. C. O'Brian, R. F. Curl and R. E. Smalley, *Nature*, 1985, **318**, 162.
73. A. Sellidj and B. E. Koel, *J. Phys. Chem.*, 1993, **97**, 10076.
74. C. Silien, I. Marenne, J. Auerhammer, N. Tagmatarchis, K. Prassides, P. A. Thiry and P. Rudolf, *Surf. Sci.*, 2001, **482**, 1.
75. G. Gensterblum, L. M. Yu, J. J. Pireaux, P. A. Thiry, R. Caudano, Ph. Lambin, A. A. Lucas, W. Krätschmer and J. E. Fischer, *J. Phys. Chem. Solids*, 1992, **53**, 1427.
76. P. Dumas, M. Gruyters, P. Rudolf, Y. He, L. -M. Yu, G. Gensterblum, R. Caudano and Y. J. Chabal, *Surf. Sci.*, 1996, **368**, 330.
77. S. Suto, K. Sakamoto, D. Kondo, T. Wakita, A. Kimura, A. Kakizaki, C. -W. Hu and A. Kasuya, *Surf. Sci.*, 1999, **438**, 242.
78. H. Kuzmany, R. Winkler and T. Pichler, *J. Phys.: Condens. Matter*, 1995, **7**, 6601.
79. H. Kuzmany, M. Matus, B. Burger and J. Winter, *Adv. Mater.*, 1994, **6**, 731.
80. G. Gensterblum, J. J. Pireaux, P. A. Thiry, R. Caudano, J. P. Vigneron, Ph. Lambin and A. A. Lucas, *Phys. Rev. Lett.*, 1991, **67**, 2171.
81. W. Andreoni, P. Giannozzi and M. Parrinello, *Phys. Rev. B*1995, **51**, 2087.
82. C. Silien, P. A. Thiry and Y. Caudano, *Surf. Sci.*, 2004, **558**, 174.
83. T. Nakajima, B. Zemva and A. Tressaud, 'Advanced Inorganic Fluorides: Synthesis, Characterization and Applications', Elsevier, St. Louis, 2000.
84. J. T. Sasowski, Y. Fujikawa, K. F. Kelly, K. Nakayama, T. Sakurai, E. T. Mickelson, R. H. Hauge and J. L. Margrave, *J. Cryst. Growth*, 2001, **229**, 580.
85. J. T. Sasowski, Y. Fujikawa, K. F. Kelly, K. Nakayama, T. Sakurai, E. T. Mickelson, R. H. Hauge and J. L. Margrave, *Mater. Charact.*, 2002, **48**, 127.
86. H. Ibach and S. Lehwald, *J. Vac. Sci. Technol.*, 1978, **15**, 407.
87. M. A. Chesters and E. M. McCash, *Surf. Sci.*, 1987, **187**, L639.
88. I. J. Malik, M. E. Brubaker, S. B. Mohsin and M. Trenary, *J. Chem. Phys.*, 1987, **87**, 5554.
89. H. Steininger, H. Ibach and S. Lehwald, *Surf. Sci.*, 1982, **117**, 685.
90. G. H. Hatzikos and R. I. Masel, *Surf. Sci.*, 1987, **185**, 479.
91. W. Erley, A. M. Baro and H. Ibach, *Surf. Sci.*, 1982, **120**, 273.
92. M. A. Barteau, J. Q. Broughton and D. Menzel, *Appl. Surf. Sci.*, 1984, **19**, 92.
93. J. Yoshinobu, H. Tsuda, M. Onchi and M. Nishijima, *Solid State Commun.*, 1986, **60**, 801.
94. C. Huang, W. Widdra and W. H. Weinberg, *Surf. Sci.*, 1994, **315**, L953.
95. L. Hammer, T. Hertlein and K. Müller, *Surf. Sci.*, 1986, **178**, 693.
96. S. Lehwald, H. Ibach and H. Steininger, *Surf. Sci.*1982, **117**, 342.
97. C. E. Anson, B. J. Bandy, M. A. Chesters, B. Keiller, I. A. Oxton and N. Sheppard, *J. Electron Spectrosc. Relat. Phenom.*, 1983, **29**, 315.
98. N. Sheppard, *Annu. Rev. Phys. Chem.*, 1988, **39**, 589.
99. C. Nyberg, C. G. Tengstål, S. Andersson and M. W. Holmes, *Chem. Phys. Lett.*, 1982, **87**, 87.
100. J. A. Gates and L. L. Kesmodel, *Surf. Sci.*, 1985, **120**, L461.
101. J. A. Gates and L. L. Kesmodel, *Surf. Sci.*, 1985, **124**, 68.
102. M. A. Chesters, G. S. McDougall, M. E. Pemble and N. Sheppard, *Appl. Surf. Sci.*, 1985, **22**, 369.
103. H. Okuyama, S. Ichihara, H. Ogasawara, H. Kato, T. Komeda, M. Kawai and J. Yoshinobu, *J. Chem. Phys.*, 2000, **112**, 5948.
104. S. Ichihara, H. Okuyama, H. Kato, M. Kawai and K. Domen, *Chem. Lett.*, 2000, **2**, 112.
105. C. Egawa, *Surf. Sci.*, 2000, **454**, 222.
106. E. M. Stuve and R. J. Madix, *Surf. Sci.*, 1985, **160**, 293.
107. M. Sock, A. Eichler, S. Surnev, J. N. Andersen, B. Klötzer, K. Hayek, M. G. Ramsey and F. P. Netzer, *Surf. Sci.*, 2003, **545**, 122.
108. M. J. Grogan and K. Nakamoto, *J. Am. Chem. Soc.*, 1966, **88**, 5454.
109. J. A. Gates and L. L. Kesmodel, *Surf. Sci.*, 1982, **120**, L461.
110. J. A. Gates and L. L. Kesmodel, *Surf. Sci.*, 1983, **124**, 68.
111. C. Hwang, C. Lee, H. Kang and C. Kim, *Surf. Sci.*, 2001, **490**, 144.
112. E. M. Stuve, R. J. Madix and C. R. Brundle, *Surf. Sci.*, 1985, **152**, 532.
113. M. B. Zellner, H. H. Hwu and J. G. Chen, *Surf. Sci.*, 2005, **598**, 185.
114. J. P. Lu, M. R. Albert and S. L. Bernasek, *Surf. Sci.*, 1991, **258**, 269.
115. J. P. Lu, M. Albert, S. L. Bernasek and D. Dwyer, *Surf. Sci.*, 1989, **218**, 1.
116. K. D. Gibson and L. H. Dubois, *Surf. Sci.*, 1990, **233**, 59.
117. N. Kizhakevariam and E. M. Stuve, *Surf. Sci.*, 1993, **286**, 246.
118. J. Wang and R. I. Masel, *J. Vac. Sci. Technol., A*, 1991, **9**, 1879.
119. J. E. Parmeter, X. Jiang and D. W. Goodman, *Surf. Sci.*, 1990, **240**, 85.
120. C. Houtman and M. Barteau, *Langmuir*, 1990, **6**, 1558.
121. L. J. Richter and W. Ho, *J. Chem. Phys.*, 1985, **83**, 2569.
122. J. Hrbek, R. A. DePaola and F. M. Hoffmann, *J. Chem. Phys.*, 1984, **81**, 2818.
123. J. A. Gates and L. L. Kesmodel, *J. Catal.*, 1983, **83**, 437.

124. K. Christmann and J. E. Demuth, *J. Chem. Phys.*, 1982, **76**, 6318.
125. C. W. Lim, J. M. Soon, N. L. Ma, W. Chen and K. P. Loh, *Surf. Sci.*, 2005, **575**, 51.
126. B. Sheu and D. R. Strongin, *J. Catal.*, 1995, **154**, 379.
127. S. Chaturvedi and D. R. Strongin, *J. Phys. Chem. B*, 1998, **102**, 2970.
128. B. A. Sexton, *Surf. Sci.*, 1979, **88**, 299.
129. N. F. Brown and M. A. Barteau, *J. Phys. Chem.*, 1996, **100**, 2269.
130. C. M. Whelan, F. Cecchet, R. Baxter, F. Zerbetto, G. Clarkson, D. Leigh and P. Rudolf, *J. Phys. Chem. B*, 2002, **106**, 8739.
131. C. M. Whelan, F. Cecchet, G. Clarkson, D. Leigh, R. Caudano and P. Rudolf, *Surf. Sci.*, 2001, **474**, 71.
132. J. E. Soto, Y. G. Kim, X. Chen, Y. S. Park and M. P. Soriaga, *J. Electroanal. Chem.*, 2001, **500**, 374.
133. M. P. Soriaga and A. T. Hubbard, *J. Am. Chem. Soc.*, 1982, **104**, 2735.
134. M. P. Soriaga, E. Binamira-Soriaga, A. T. Hubbard, J. B. Benziger and K. W. P. Pang, *Inorg. Chem.*, 1985, **24**, 65.
135. M. P. Soriaga, *Chem. Rev.*, 1990, **90**, 771.
136. F. Lu, G. N. Salaita, L. Laguren-Davidson, D. A. Stern, E. Wellner, D. G. Frank, N. Batina, D. C. Zapien, N. Walton and A. T. Hubbard, *Langmuir*, 1988, **4**, 637.
137. G. Salaita, L. Laguren-Davidson, F. Lu, N. Walton, E. Wellner, D. A. Stern, N. Batina, D. Frank, C. Lin and A. T. Hubbard, *J. Electroanal. Chem.*, 1988, **245**, 253.
138. J. E. Soto, Y. -G. Kim and M. P. Soriaga, *Electrochem. Commun.*, 1999, **1**, 135.
139. Y. -G. Kim, J. E. Soto, X. Chen, Y. -S. Park and M. P. Soriaga, *J. Electroanal. Chem.*, 2003, **554**, 167.
140. Y. -G. Kim and M. P. Soriaga, *Phys. Chem. Chem. Phys.*, 2001, **3**, 3303.
141. X. Chen, J. Sanabria-Chinchilla and M. P. Soriaga, *Electroanalysis*, 2005, **1**, 2121.
142. J. Breitbach, D. Franke, G. Hamm, C. Becker and K. Wandelt, *Surf. Sci.*, 2002, **507**, 18.
143. I. Jungwirthova and L. L. Kesmodel, *Surf. Sci.*, 2000, **470**, L39.
144. L. Bugyi, A. Oszko and F. Solymosi, *Surf. Sci.*, 2003, **539**, 1.
145. J. Eng, B. Bent, B. Fruhberger and J. G. Chen, *J. Phys. Chem. B*, 1997, **101**, 4044.
146. H. G. Huang, J. Y. Huang, Y. S. Ning and G. Q. Xu, *J. Chem. Phys.*, 2004, **121**, 4820.
147. M. Allan, *Chem. Phys.*, 1983, **81**, 235.
148. F. R. Yubero, J. P. Espinos, J. Cotrino and A. R. Gonzalez-Elipe, *Appl. Phys. Lett.*, 2005, **87**, 084101.
149. A. M. Botelho do Rego, O. Pellegrino, J. G. Martinho and J. Lopes da Silva, *Surf. Sci.*, 2001, **482**, 1228.
150. T. R. Bryden and J. Simon, *Langmuir*, 2001, **17**, 5850.
151. R. Becker, M. R. Ashton, T. S. Jones, N. V. Richardson and H. Sotobayashi, *J. Phys.: Condens. Matter*, 1991, **3**, S29.
152. W. P. McKenna and G. Apai, *J. Phys. Chem.*, 1992, **96**, 5902.
153. P. S. Dannetun and M. Rei Vilar, *Thin Solid Films*, 1996, **286**, 321.
154. N. J. Dinardo and T. C. Clarke, *Chem. Phys. Lett.*, 1985, **121**, 239.
155. J. -J. Pireaux, C. Gregoire, P. A. Thiry, R. Caudano and T. C. Clarke, *J. Chem. Phys.*, 1988, **88**, 3353.
156. A. Ulman, 'An Introduction to Ultrathin Organic Films: From Langmuir-Blodgett to Self-Assembly', Academic Press, New York, 1991.
157. A. Kudelski, *Vib. Spectrosc.*, 2005, **39**, 200.
158. H. S. Kato, J. Noh, M. Hara and M. Kawai, *J. Phys. Chem. B*, 2002, **106**, 9655.
159. J. Noh, H. S. Kato, M. Kawai and M. Hara, *J. Phys. Chem. B*, 2006, **110**, 2793.
160. A. S. Duwez, L. M. Yu, J. Riga, J. Delhalle and J. -J. Pireaux, *J. Phys. Chem. B*, 2000, **104**, 8830.
161. A. S. Duwez, L. M. Yu, J. Riga, J. -J. Pireaux and J. Delhalle, *Thin Solid Films*, 1998, **327**, 156.
162. A. S. Duwez, L. M. Yu, J. Riga, J. Delhalle and J. -J. Pireaux, *Langmuir*, 2000, **16**, 6569.
163. J. Noh, H. S. Kato, M. Kawai and M. Hara, *J. Phys. Chem. B*, 2002, **106**, 13268.
164. J. Gui, D. A. Stern, D. Frank, F. Lu, D. Zapien and A. T. Hubbard, *Langmuir*, 1991, **7**, 955.
165. B. G. Bravo, T. Mebrahtu and M. P. Soriaga, *Langmuir*, 1987, **3**, 595.

Magnetic Circular Dichroism (MCD) Spectroscopy

John Mack and Martin J. Stillman

University of Western Ontario, London, ON, Canada

	Method Summary	1
1	Introduction	2
2	Technical Background	2
3	Applications	5
4	Abbreviations and Acronyms	15
5	References	16

METHOD SUMMARY

Acronyms, Synonyms

- Magnetic Circular Dichroism
- Magnetic Optical Rotatory Dispersion

Measured physical quantities

- The difference in absorbance of left and right circularly polarized incident radiation (MCD), or the extent of the rotation of a beam of plane polarized light (MORD), with the sample located in a magnetic field aligned parallel to the axis of light propagation is observed.

Information available

- Ground and excited state orbital and spin degeneracies can be observed.
- Spectral band polarizations based on a qualitative analysis of the spectral bands can be determined in terms of the Faraday $\mathcal{A}_1$, $\mathcal{B}_0$ and $\mathcal{C}_0$ terms. The magnitudes of these Faraday terms have well defined theoretical interpretation.
- Identification of the individual split components due to the Zeeman splitting of the ground and excited states following absorption of lcp and rcp light.
- Spectral determination of the field-induced mixing of zero-field states and a ground state population adjustment as a result of Zeeman splitting.
- Quantitative analysis provides values for the ground and excited state magnetic dipole moments and the g-factors based on determination of the Faraday terms and the dipole strength of the corresponding electronic absorption band.
- Transition metal ion oxidation and spin states, and coordination environments from the geometry can be determined through prediction of expected MCD signals for each specific case.
- Axial and rhombic zero-field splitting parameters of Kramers doublet ground states and ligand field splitting parameters of non-Kramers doublet degenerate ground states can be determined from the variable temperature variable field data.

Information not available, limitations

- Spectra of lower symmetry species lacking a threefold or higher symmetry axis contain significantly less information.

Examples of questions that can be answered

- What are the symmetries of the ground and excited states?
- Do the experimentally derived state degeneracies and band polarizations match those predicted by theoretical calculations?

- What is the electronic structure of the atom, ion or complex?
- What is the oxidation state of the metal?
- Is the metal spin state high, intermediate or low?
- Is the ligand an anion or cation radical and/or is the metal paramagnetic?

Major advantages

- MCD spectroscopy provides key orbital and spin state degeneracy information that cannot be derived from electronic absorption and NMR spectroscopy.
- X-ray MCD spectroscopy based on L-edge absorption experiments can be used to analyze localized spin states at specific metal sites.

Major disadvantages

- The technique remains highly specialized due to the use of expensive electro- or superconducting magnets and cryogenic equipment.

Sample constraints

- The samples must be optically transparent and not cause depolarization of the incident light.

---

1 INTRODUCTION

Magnetic circular dichroism (MCD) spectroscopy provides information about the spin and orbital angular momenta associated with ground and excited electronic states. The MCD technique is complementary to electron paramagnetic resonance (EPR) spectroscopy (*see* ***Electron Paramagnetic Resonance (EPR) Spectroscopy***), which can provide key information about the electron spin state of paramagnetic complexes, and often provides the key to understanding the optical spectroscopy (*see* ***Electronic Spectroscopy***) of high symmetry ions and complexes. This, in turn, provides an important insight into the electronic structure. MCD spectroscopy is based on the Faraday effect in which a beam of plane polarized light is rotated either clockwise or counterclockwise during transmission through certain substances due to differences in the refractive indices for left circularly polarized (lcp) and right circularly polarized (rcp) light, when a magnetic field is aligned parallel to the axis of light propagation. Prior to the 1960s and the development of the photoelastic modulators required to create alternating beams of lcp and rcp from plane polarized light, magnetic optical rotatory dispersion (MORD) spectroscopy, which is based on the wavelength dependence of the Faraday effect experiment, was the primary electronic absorption-based technique used to study magnetic optical activity. However, a major restriction of MORD spectroscopy is that all components in the cuvette contribute significantly to the observed signal at any wavelength; this is particularly a problem with the signal from the solvent. In MCD spectroscopy, only the absorbing species contributes an MCD signal, dramatically simplifying the spectral data.

MCD spectra are recorded by mounting a magnet into the sample compartment of a circular dichroism (CD) (*see* ***Circular Dichroism (CD) Spectroscopy***) spectrometer, in the Faraday alignment with the applied field parallel to the axis of light propagation. A superconducting magnetic ($B \approx 0-11\,\mathrm{T}$) is required to perform the full range of spectral measurements associated with the technique at room and cryogenic temperatures, but less expensive electro- ($B \approx 0-1\,\mathrm{T}$) and permanent magnets can also be used in many instances particularly for measurements at room temperature.

2 TECHNICAL BACKGROUND

The major difference between MCD spectroscopy, and the nuclear magnetic resonance (NMR) (*see* ***Nuclear Magnetic Resonance (NMR) Spectroscopy of Inorganic/Organometallic Molecules***, ***Nuclear Magnetic Resonance (NMR) Spectroscopy of Metallobiomolecules***) and EPR techniques is that the MCD technique is not based on resonance between spin states, but is instead based on the wavelength dependent absorption of circularly polarized light into excited electronic states. MCD spectra are recorded by mounting a magnet into the sample compartment of a CD spectrometer. In contrast with natural CD, which requires a specific form of asymmetry, the Faraday effect is an intrinsic property of all matter. The UV-visible absorption and MCD spectra of a molecular complex contain the same set of spectral bands, but the band morphologies are different due to the effect of the applied magnetic field and the use of a differential absorbance intensity scale from the CD spectrometer used for the measurements.

2.1 Magnetism and Optical Spectroscopy

Predicting the optical spectrum requires the solution of the Schrödinger wave equation in terms of the states (Ψ_A) and energy levels (E_A) of the system and the Hamiltonian (H):

$$H\Psi_A = E_A\Psi_A \tag{1}$$

since this allows calculation of the observables in the spectrum, namely the transition energy and the oscillator strength of the transition dipole moment between states A and J:

$$M_{AJ} = \langle\Psi_A|m|\Psi_J\rangle \tag{2}$$

Analysis of the optical spectral data rests on the fact that absorption or emission of a photon of light with specific wavelength properties results in a redistribution of charge within a molecule based on a transition moment which couples the ground and excited electronic states, resulting in a new stationary electronic state. A linear displacement of charge induces an electric dipole transition moment, while a magnetic dipole transition moment is induced by any circular motion of electric charge. Electric dipole moments (m) are usually the dominant factor in the observed absorbance or oscillator strengths of bands in UV-visible absorption spectroscopy, because they tend to be ca. 5 orders of magnitude stronger than magnetic dipole moments (μ). In the case of chiral molecules, absorption of a photon results in both magnetic and electric dipoles, as there is a helical redistribution of electronic charge. Enantiomers preferentially absorb either lcp and rcp light based on the handedness of the helical redistribution of electronic charge. This differential absorbance of lcp or rcp forms the basis of CD spectroscopy.

The main selection rules for electronic absorption spectroscopy are based on whether a transition is spin ($\Delta S = 0$) allowed and/or Laporte ($\Delta l = \pm 1$) allowed. An additional selection rule based on the magnetic quantum number, which in simplistic terms can be stated as only $\Delta M_J = 0, \pm 1$ transitions are allowed, plays a major role in the case of MCD spectroscopy but is not such a significant factor in UV-visible absorption spectra in the absence of an applied field. An incident photon can provide a maximum of one quantum of orbital angular momentum ($J = 1$ and $\Delta M_J = \pm 1$), since the electric and magnetic vectors of the electromagnetic wave can rotate a maximum of once per wavelength, and the total angular momentum within an isolated system must be conserved in both magnitude and direction based on Newton's third law of motion. Absorption of a photon by an aromatic π system, for example, results in both a linear and a circular redistribution of charge within the xy plane. Although strong excited state magnetic dipoles are induced, there is no net CD signal since in the absence of a chiral center the absorbance of lcp and rcp light is equally likely. When a magnetic field is applied, however, the induced magnetic dipoles couple with and against the applied field, and a wavelength dependence is introduced.

2.2 Zeeman Splitting of States

Pieter Zeeman was the first to study the effect of an applied magnetic field on atomic emission spectra. Since a perpendicular applied field was subsequently typically used within Zeeman (excited state emission) spectroscopy the normal Zeeman effect is usually described in terms of parallel (‖) and perpendicular (⊥) plane polarized bands (Figure 1). It should be noted, however, that Zeeman also studied the parallel magnet alignment used within MCD spectroscopy. In Zeeman's words**[1]** during his Nobel prize lecture in 1902 describing results obtained for emission from the 5d orbital of Cd to the 5p orbital, ''. . . *But let us first consider the rays which run parallel with the lines of force . . . . The opposite circular oscillations of the electrons excite two circularly polarized rays rotating in opposite directions, one having a longer and the other a shorter period of oscillation than the original spectral line. The original spectral line splits up under the action of the magnetic field into two components which are circularly polarized in opposite directions. The light source emits two-color light*. . .''. The modern MCD experiment in many respects, then, is simply the reverse of Zeeman's emission spectroscopy experiment (Figure 1) in that differential absorbance of lcp and rcp photons is induced by the Zeeman splitting of states. When Zeeman studied metals with unpaired electrons he observed what is now referred to as the anomalous Zeeman effect with multiple emission lines appearing both in the presence and absence of an external magnetic field. This represented direct spectral evidence that spin and orbital angular momenta of the individual electrons couple to provide the total angular momentum quantum numbers, J and M_J, for the electronic state based on the L, M_L, S, and M_S quantum numbers and demonstrated that an applied magnetic field can be used to derive key quantitative information about state degeneracies.

In the case of the lighter atoms ($Z < 40$), spin-orbit coupling is relatively weak and the L and S quantum numbers can be combined according to the Russell–Saunders coupling scheme (as opposed to the strong-field $j - j$ coupling scheme observed in the case of heavier atoms where the spin-orbit coupling is stronger) to give the total angular momentum of the state $J(J = L + S)$. When a magnetic field is applied, there is a lifting of state degeneracies into $2J + 1$ microstates based on the M_J quantum number for orientation relative to the applied field. The Zeeman splitting of the states can then be defined:

$$\Delta E = \frac{e}{2m_e}(L_z + 2S_z)B = g_L\mu_B M_J B \tag{3}$$

The factor of 2 for S_z is related to the g-factor (g_L), which was demonstrated empirically during early

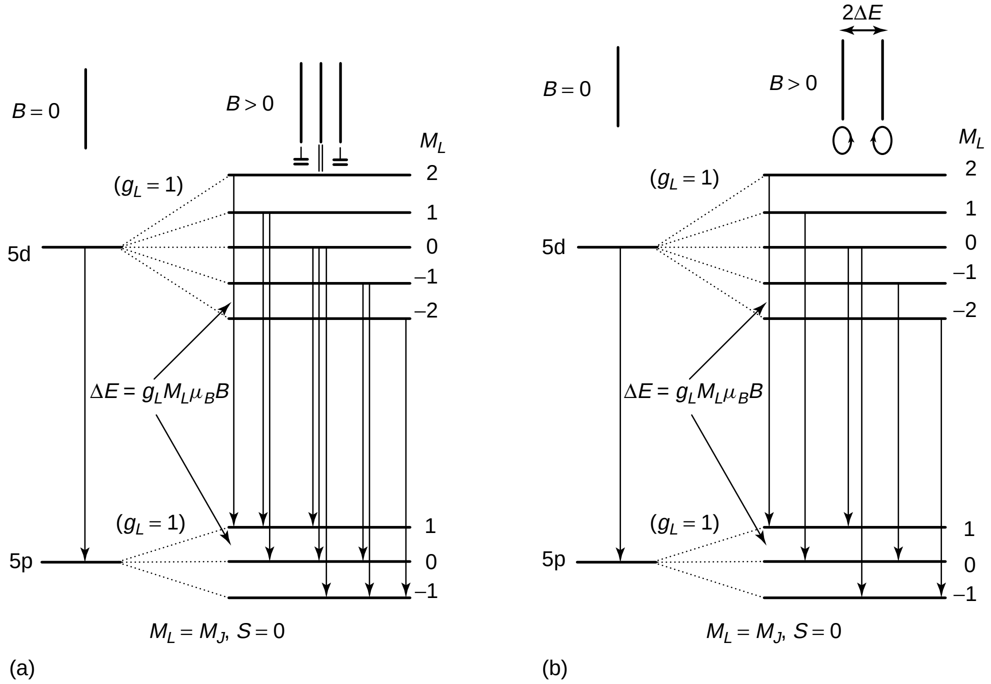

Figure 1 The normal Zeeman effect. The emission from an atomic lamp source placed within a magnet observed perpendicular (a) and parallel (b) to the lines of force. It should be noted that when $S = 0$ and the Russell–Saunders spin coupling mechanism is applicable, $J = L$, and $M_J = M_L$ as shown here. (Reprinted from Mack, Stillman and Kobayashi,^{2} © Elsevier 2007)

spectroscopic studies to be

$$g_L = \frac{1 + J(J+1) + S(S+1) - L(L+1)}{2J(J+1)} \tag{4}$$

Since the g-factor associated with orbital angular momentum has a value of 1 if $S = 0$, the factor does not always have to be included. The value for the z-component of the magnetic moment aligned with the axis of light propagation is defined as

$$\mu_z = -\mu_B(L_z + 2S_z) \tag{5}$$

In the case of cyclic aromatic molecules, absorption of an lcp or rcp photon results in either a left- or right-handed redistribution of charge within the π-system, since the total orbital angular momentum within the system must be conserved. The magnetic field lines induced by the circular redistribution of charge all point along the z-axis at the center of the ligand creating a magnetic dipole moment perpendicular to the plane of the π-system. Within the MCD experiment the splitting of the optically accessible microstates of an excited state is:

$$\Delta E = 2g_L\mu_B M_J B \tag{6}$$

The factor of two is based on the fact that the microstate accessed by a photon of one handedness will be stabilized due to an alignment of the magnetic dipole moment with the applied field, while that accessed by a photon of the opposing handedness will be destabilized since the magnetic dipole is aligned against the field (Figure 2).

2.3 CD and ORD Spectroscopy

Left handed photons were originally defined as positive within CD spectroscopy (Figure 3) since the electric vector rotates counterclockwise from the positive y-axis to the positive x-axis within a right-handed set of axes. Within the CD experiment, the incident plane polarized beam becomes elliptically polarized due to the differential absorbance of lcp and rcp light. While the ϕ unit for rotation of the plane polarized beam in optical rotatory dispersion (ORD) spectroscopy (Figure 3) is a measure of the rotation of the electric and magnetic vectors per unit field, concentration, and distance, the θ ellipicity unit in CD spectroscopy is defined in degrees based on the tangent of the ratio of the minor to major axis of the elliptical path followed by the electric vector within the xy plane when viewed toward the light source. Initially the θ unit was adopted by CD spectroscopists so that results could be readily compared to ORD data via Kramers–Kronig transformations. However, since θ is proportional to the differential absorbance of lcp and rcp light, differential absorbance (ΔA_{l-r}) has been increasingly adopted in CD spectroscopy in recent years.

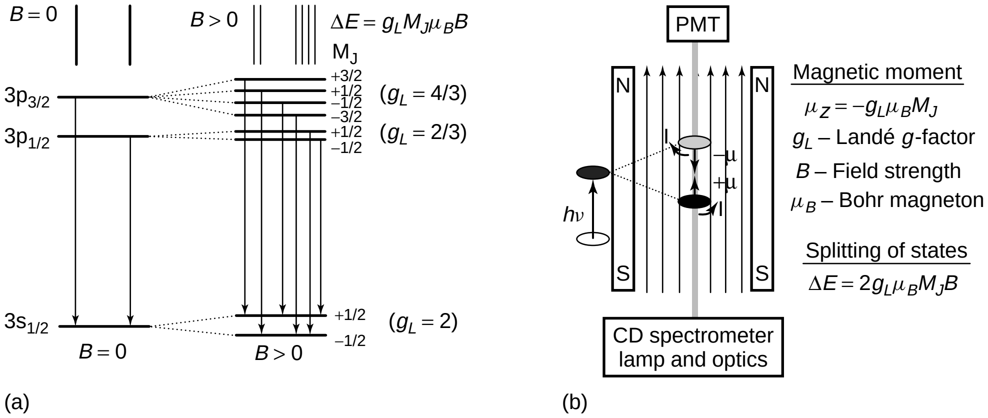

Figure 2 The direction of the induced magnetic moments within a cyclic polyene excited state can be derived from Ampere's Rule (right-hand rule) for a solenoid (i.e., for current in a loop). When the fingers of the right hand are curled in the flow direction for conventional current flow (i.e., for a positive charge carrier) the induced magnetic dipole moment is aligned in the direction the thumb is pointing. The MCD magnet's sample horizontal bore is surrounded by a solenoid to generate a high magnetic field, typically of 1–7 T, with field lines running from the south to north parallel to the axis of light propagation in the sample compartment of the CD spectrometer. (Reprinted from Mack, Stillman and Kobayashi,[2] © Elsevier 2007)

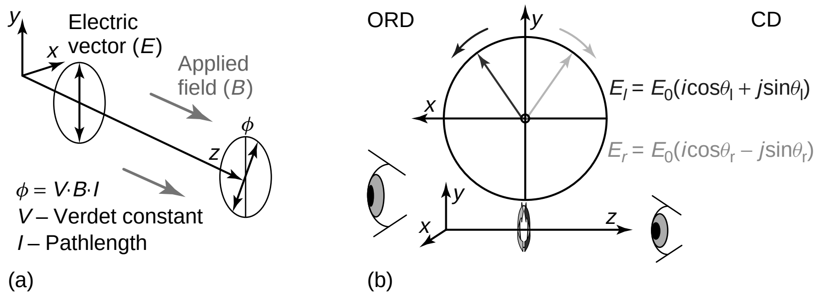

Figure 3 The Faraday Effect within magnetic optical rotatory dispersion (MORD) spectroscopy. A plane polarized beam is rotated by a magnetic field applied parallel to the axis of propagation. The rotation is defined as positive if the beam is rotated to the right in a clockwise direction when viewed toward the source (a). The original definition of lcp and rcp within CD spectroscopy—light plane polarized in the *yz*-plane can be described in mathematical terms as being comprised of left or right circularly polarized components of equal phase and amplitude (b). The perspective is depicted schematically toward the source. (Reprinted from Mack, Stillman and Kobayashi,[2] © Elsevier 2007)

3 APPLICATIONS

3.1 Measuring MCD Spectra

The recommended unit for MCD spectroscopy, $\Delta\varepsilon_M$, is based on the extinction coefficient for differential absorbance of a 1 M solution of the solute at a field strength of 1 T. The original θ ellipicity unit is still sometimes used. The conversion factors are $\theta = 32.98\Delta A$, where θ is expressed in units of mdeg or $[\theta]_M = 3298\Delta\varepsilon_M$ where, $[\theta]_M$ is expressed in units of deg·cm^2·dmol^{-1}. Room temperature spectral measurements are usually measured in solution, ideally in a solvent which is optically transparent in the 280–1000 nm region.

More highly resolved data can be obtained by measuring samples in the vapor phase either at room temperature in the case of volatile compounds or at temperatures as high as 500 °C in the case of thermally stable complexes like metallophthalocyanines. The absence of an organic solvent allows spectral bands to be measured to the UV cut-off of the spectrometer, near 200 nm.

Spectral measurements at cryogenic temperatures are often obtained from vitreous solvent mixtures in which the solute is randomly oriented with respect to the axis of light propagation. The level of depolarization of the frozen MCD samples can be determined by comparing the CD spectra of a standard CD active solution, for example, a nickel (+)-tartrate solution placed before and after the sample. The natural CD and zero-field baseline effects due to the optical quality of the frozen sample can be corrected by subtracting the corresponding zero-field scan at each temperature. Cryogenic temperature spectra have also been recorded using Shpol'skii (shock-frozen *n*-alkane solutions) and argon matrices. Narrow bandwidths are achieved, making the resolution of vibrational bands much easier than in vitreous solutions but the analysis is complicated by the fact that, unlike in vitreous solutions, the alignment of the sample is usually not random. Multiple sites can exist, each with a different overall energy, resulting in a series of overlapping spectral bands, one for each site.

Solid state spectra from thin films on quartz disks are relatively easy to measure at all temperatures but the spectral data are complicated by the broadening that arises due to the Davydov effect. While this enables spectra to be recorded over a wavelength range down to 200 nm, the spectral envelopes are not at all similar to the spectral bands observed in either the vapor or solution phases. An alternative technique that mixes the matrix isolation and thin film advantages is to dissolve the solute into polymers. The subsequent cast film may allow distortion-free and solvent-reduced spectral measurements at a range of temperatures.

3.2 Analysis of the Three Faraday Terms

The modern theoretical background to MCD spectroscopy is based on the earlier research on MORD spectroscopy, which involved an estimation of the magnitudes of the three so-called Faraday terms, $\mathcal{A}$, $\mathcal{B}$, and $\mathcal{C}$, used to quantify the effect of the applied field on the Zeeman splitting of the absorption bands for lcp and rcp light, the field-induced mixing of zero-field states, and the Zeeman splitting-based ground state population adjustment, respectively. Although MORD spectroscopy was developed first, MCD spectroscopy became the dominant technique after photoelastic modulators became available because there is greater resolution of the component spectral bands within the MCD experiment and there is typically no signal due to the solvent and cell, a significant factor that had to be compensated for in MORD experiments. In MORD spectroscopy, a positive ϕ value denotes rotation of a plane polarized beam in a clockwise or right-handed direction when viewed toward the source, while in contrast absorption of incident lcp light results in a positive signal within the MCD intensity definition. When the existing MORD conventions were initially adopted in MCD spectroscopy this led to negative MCD ΔA_{l-r} intensity being associated with positive Faraday term values so Stephens and Schatz later modified the intensity equations to better fit MCD spectroscopy. In any review of the MCD literature the conventions used by different authors need to be carefully checked.[2]

In the case of MCD spectroscopy, for a fully allowed electronic transition based on the rigid shift, Born–Oppenheimer, and Franck–Condon approximations, the intensity equation, according to the modified conventions recommended by Stephens, Piepho and Schatz,[3,4] is

$$\frac{\Delta A_{l-r}}{E} = 152.5Bcl\left[\mathcal{A}_{\mathbf{1}}\left(-\frac{\mathrm{df}}{\mathrm{dE}}\right) + \left(\mathcal{B}_{\mathbf{0}} + \frac{\mathcal{C}_{\mathbf{0}}}{\mathrm{kT}}\right)f\right] \tag{7}$$

ΔA_{l-r} is the differential absorbance of lcp and rcp light, B is the field strength, cl is the product of the concentration (mol.L^{-1}) and pathlength (cm), E represents the energy coordinate in cm^{-1} and is used here to signify that the expression is for the entire spectral band rather than for just one wavelength, while f is a normalized band shape function (normally a Gaussian-shaped curve).

The dipole strength of the absorption intensity in the absence of an applied field is

$$\mathcal{D}_{\mathbf{0}} = \frac{3.062\times 10^{-3}}{\nu_{\max}}\int \varepsilon\, \mathrm{d}\nu \approx \frac{\langle A\rangle_0}{326.6cl} = \frac{\langle \varepsilon\rangle_0}{326.6} \tag{8}$$

where $\mathcal{D}_{\mathbf{0}}$ is expressed in (debye)^2 units (D^2), $\nu_{\max}$ is the band center energy in cm^{-1} and $\langle A\rangle_0$ is the zeroth moment of the intensity for the entire absorption band. The right-hand side of the equation is valid for any symmetrical band shape. It is important to note that throughout this section energies are in cm^{-1} and field strengths are in tesla (T). In practical terms absorption and MCD spectra are normally reported in terms of extinction coefficients ε (M^{-1} cm^{-1}) and $\Delta\varepsilon_{\mathrm{M}}$ (M^{-1} cm^{-1} T^{-1}) based on Beer's Law.

3.3 Identification and Analysis of Faraday A Terms in the Spectra of Porphyrins with Excited State Degeneracy and Near Degeneracy

The $\mathcal{A}_{\mathbf{1}}$ term arises from the Zeeman splitting of an orbitally degenerate excited state (Figure 4). There is a highly distinctive first derivative band shape due to the separation of the individual band centers of the lcp and rcp light absorbing bands. A consideration of equation (5) makes it clear that the $\mathcal{A}_{\mathbf{1}}$ term intensity is based on the relative magnitudes of the combined orbital (L_z) and spin (S_z) angular momenta of electrons within the ground and excited states, labeled as A and J, respectively:

$$\mathcal{A}_{\mathbf{1}} = -\frac{1}{d_A}\sum \langle \mathrm{J}|\mu_{\mathrm{z}}|J\rangle - \langle \mathrm{A}|\mu_{\mathrm{z}}|A\rangle \left(\left[m_{-1}^{\mathrm{AJ}}\right]^2 - \left[m_{+1}^{\mathrm{AJ}}\right]^2\right) \tag{9}$$

where $\left[m_{-1}^{\mathrm{AJ}}\right]$ and $\left[m_{+1}^{\mathrm{AJ}}\right]$ are the electric dipole matrix elements associated with the absorption of rcp and lcp light, respectively, while d_A relates to the degree of degeneracy of the excited states. The sign convention for handedness used in the subscripts of the matrix elements is the opposite of that used in ΔA_{l-r}. The literature for MCD spectroscopy can be somewhat confusing unless the reader is aware that the classical optics definition used within CD and MCD spectroscopy is based on a perspective toward the light source, while physicists usually favor a perspective along the axis of light propagation. When describing an MCD spectrum use the style, ''positive $\mathcal{A}_{\mathbf{1}}$ term'' for a derivative-shaped signal that is positive to high energy of the cross-over point. For example, the MCD spectrum of zinc octaethylporphyrin (ZnOEP) contains two intense xy-polarized positive $\mathcal{A}_{\mathbf{1}}$ terms at 401 and 564 nm (Figure 4).

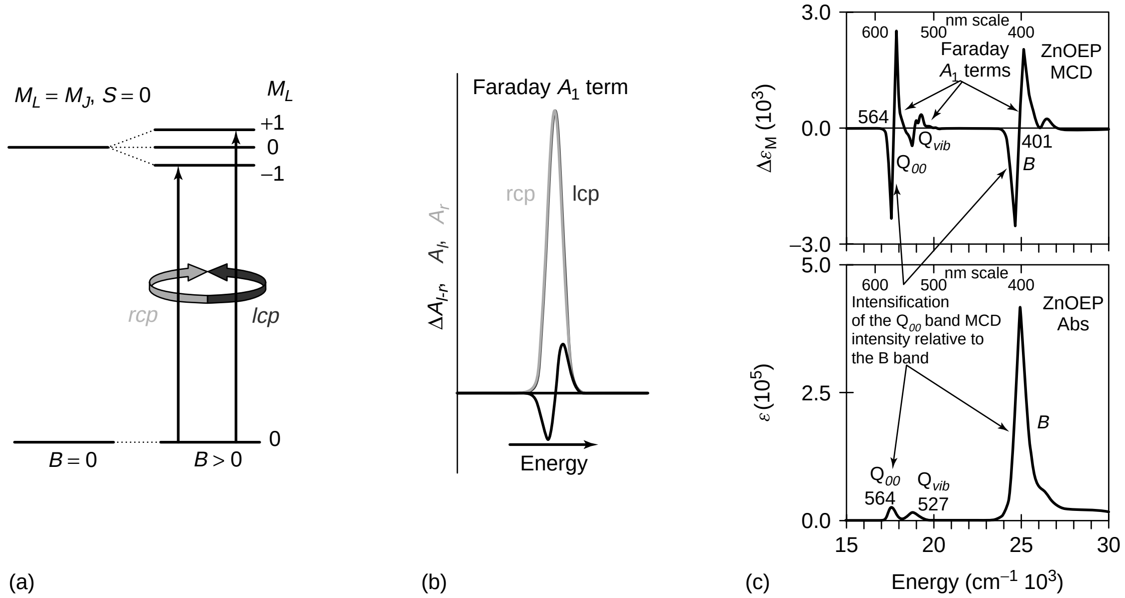

Figure 4 Selection rules for the absorption of lcp and rcp light based on a transition between an orbitally nondegenerate ground state and an orbitally degenerate excited state within a magnetic field applied parallel to the axis of light propagation (a). A derivative-shaped Faraday $\mathcal{A}_1$ term is observed due to the Zeeman splitting of states and the associated energy separation of bands based on the $\Delta M_L = \pm 1$ selection rule (b). (Reprinted from Mack, Stillman and Kobayashi,[2] © Elsevier 2007.) We note that in this example, since $S = 0$ for closed shell atoms or molecules, $J = L$, and $M_J = M_L$. Absorption and MCD spectra of zinc octaethylporphyrin (ZnOEP) in $CHCl_3$ (c). The MCD spectrum is dominated by derivative-shaped $\mathcal{A}_1$ terms. (Reproduced with permission from J. Mack, Y. Asano, N. Kobayashi, M. J. Stillman, *J. Am. Chem. Soc.*, 2005, **127**, 17697–17711. © 2005 American Chemical Society)

The Gaussian-shaped $\mathcal{B}_0$ term arises from second order effects based on the field-induced mixing of the zero-field states via magnetic dipole transition moments (Figure 5). $\mathcal{B}_0$ terms completely dominate the MCD spectrum when there is no threefold or higher rotation axis, since there are no orbitally degenerate states that can be split due to the Zeeman effect. $\mathcal{B}_0$ terms are also present in the spectra of high symmetry complexes but tend to be significantly less intense than the $\mathcal{A}_1$ and $\mathcal{C}_0$ terms, since there is a dependence on the energy separation of states J and K (ΔE_{KJ}) mixed by the field. $\mathcal{B}_0$ term intensity, in the absence of significant field-induced mixing between the ground and excited states, is:

$$B_0 = \frac{2}{d_A}\Re e \sum \frac{\langle \mathrm{J}|\mu_z|K\rangle}{\Delta E_{KJ}} \left(\left[m_{-1}^{\mathrm{AJ}}\right]\left[m_{+1}^{KA}\right] - \left[m_{+1}^{\mathrm{AJ}}\right]\left[m_{-1}^{KA}\right] \right) \qquad (10)$$

When a structural modification results in a small (relative to the spectral bandwidth) zero-field splitting of what would otherwise be an orbitally degenerate $\pi\pi^*$ excited state, the resulting derivative-shaped signal is often referred to as a pseudo-$\mathcal{A}_1$ term (Figure 5). The MCD spectrum of tetrabenzotetraazachlorin contains both a pseudo-$\mathcal{A}_1$ term at 341 nm and a coupled pair of oppositely signed $\mathcal{B}_0$ terms at 605 and 749 nm, due to the differing effects of the symmetry lowering structural changes on the major electronic transitions, relative to the spectrum of ZnOEP (Figures 4 and 5). In the absence of the band polarization information that can be derived from the MCD spectrum, the assignment of the 605 nm band as the high energy component of a pair of symmetry-split x- and y-polarized bands would be much more problematic.

3.4 Identification and Analysis of Faraday *C* Terms in the Spectra of Phthalocyanines with Ground State Degeneracy

The $\mathcal{C}_0$ term (Figure 6) arises from the Boltzmann population distribution across a degenerate ground state and, therefore, shows a strong $1/kT$ temperature dependence (equation 7). In many cases, $\mathcal{C}_0$ terms are associated with the presence of an open-shell transition metal. When the splitting of the microstates is small relative to the spectral bandwidths of the lcp and rcp light-specific absorption bands the $\mathcal{C}_0$ term is essentially Gaussian-shaped. $\mathcal{B}_0$ terms can be readily distinguished from $\mathcal{C}_0$ terms by measuring spectra at both room and cryogenic temperatures since they lack a $1/kT$ temperature dependence.

$$\mathcal{C}_0 = -\frac{1}{d_A}\sum \langle \mathrm{A}|\mu_z|A\rangle \left(\left[m_{-1}^{\mathrm{AJ}}\right]^2 - \left[m_{+1}^{\mathrm{AJ}}\right]^2 \right) \qquad (11)$$

The temperature dependence of the MCD spectrum of $Na[(CN^-)_2Fe^{III}Pc(-2)]$ (Figure 6) is due to the Faraday $\mathcal{C}_0$ terms associated with the ^2E_g ground state. The signal saturates at low temperature and/or high field when the lowest energy microstate is preferentially populated.

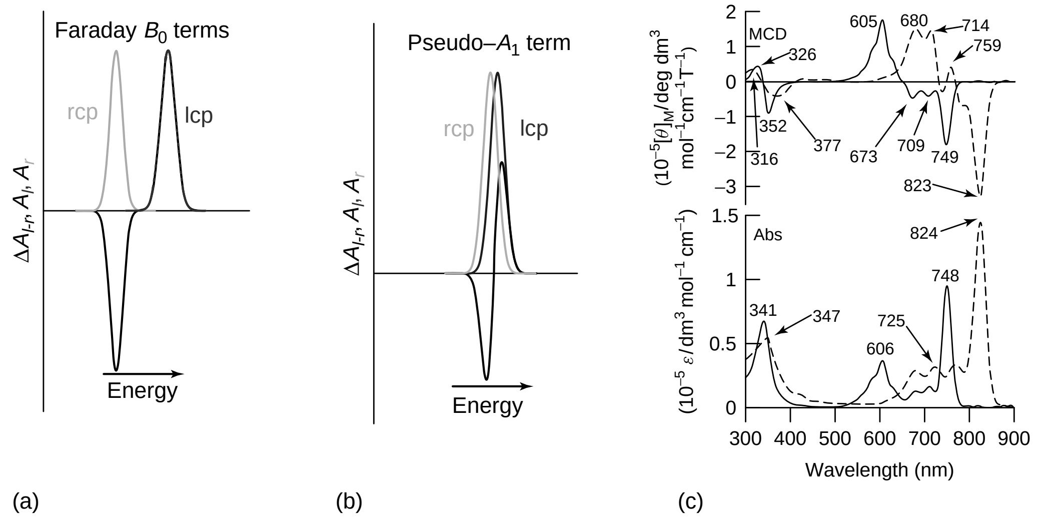

Figure 5 The appearance and the intensity of coupled Faraday $\mathcal{B}_0$ terms (a) depends upon the extent of the zero-field splitting (ZFS) of states relative to the bandwidth. The splitting of the +ve and −ve Gaussian-shaped MCD signals (black) is determined by the energy separation of the lcp and rcp light absorption bands (dark and light gray) that arise within the applied field due to field-induced mixing of states via a magnetic dipole transition moment. When it is relatively minor the two coupled Faraday $\mathcal{B}_0$ terms form a pseudo $\mathcal{A}_1$ term (b). (Reprinted from Mack, Stillman and Kobayashi,[2] © Elsevier 2007.) The MCD and absorption spectra of tetrabenzotetraazachlorin (c, solid lines) and tetranaphthotetraazachlorin (c, broken lines) in chlorobenzene. (Reproduced from Fukuda *et al. Chem. Eur. J.* (2004) **10**, with permission of Wiley-VCH)

Comparison of equations (8), (10), and (11) for $\mathcal{A}_1$, $\mathcal{B}_0$, $\mathcal{C}_0$ with equation (12) for the dipole strength of the absorption band, $\mathcal{D}_0$, demonstrates that the electric dipole contribution is cancelled out within $\mathcal{A}_1/\mathcal{D}_0$, $\mathcal{B}_0/\mathcal{D}_0$ and $\mathcal{C}_0/\mathcal{D}_0$ ratios:

$$\mathcal{D}_0 = \frac{1}{d_A}\sum\left[m^{\mathrm{AJ}}_{\pm 1}\right]^2 \tag{12}$$

Since $\mathcal{D}_0$ can be derived from the corresponding UV-visible absorption spectra, the MCD technique can be used to directly quantify the magnetic moments associated with the ground and excited states. In instances where $S = 0$ and $g_L = 1$, the z-component of the magnetic dipole moments for the ground and excited states can be derived directly from the $\mathcal{A}_1/\mathcal{D}_0$ and $\mathcal{C}_0/\mathcal{D}_0$ ratio:

$$\mu_z(\text{excited state}) = -\frac{\mathcal{A}_1}{\mathcal{D}_0} \qquad \mu_z(\text{ground state}) = \frac{\mathcal{C}_0}{\mathcal{D}_0} \tag{13}$$

The method of moments analysis has since been used extensively to derive the magnetic moments of the ground and/or excited states from MCD spectral data by determining the intensity of the MCD and UV-visible absorption bands. In instances where the bands overlap extensively, spectral band deconvolution techniques have also been used.

3.5 MCD Spectroscopy of Inorganic Ions

MORD and MCD spectroscopy have both been used to answer key questions about the electronic structure of inorganic ions, testing the validity of molecular orbital (MO) models of the electronic structure based on the ground and excited state degeneracy information that can be derived from the Faraday $\mathcal{A}_1$ and $\mathcal{C}_0$ terms. Since the MCD experiment usually entails the use of an expensive superconducting cryomagnet, cooled with liquid helium to keep the magnet coil operational and to obtain the cryogenic temperature measurements required in the sample compartment to analyze Faraday $\mathcal{C}_0$ terms, the MCD technique is generally not available in many laboratories around the world and is not a standard spectroscopic technique performed regularly at most university chemistry departments. In recent decades most of the work on inorganic ions has been carried out in the North American context by Prof. W. Roy Mason at Northern Illinois University. For example, in recent years, he has used MCD spectroscopy to assign the spectral bands within the optical spectra of a variety of centered gold cluster complexes, including $\mathrm{M(AuPPh_3)_8^{2+}}$, $M = \mathrm{Pd}$ or Pt (D_{4d} centered crown structure), and $\mathrm{Au(AuPPh_3)_8^{3+}}$ (D_{2h} centered icosahedral fragment structure).[5,6] Spectra were measured from acetonitrile solutions at room temperatures and from nitrate salts in thin films made by casting poly(methylmethacrylate) dissolved in $\mathrm{CH_2Cl_2}$ and then making measurements at cryogenic temperatures. These films, which could be cooled reversibly to 10 K with no cracking, showed no sign of excessive strain or birefringence. The presence of Faraday $\mathcal{A}_1$ terms enabled spectral features to be assigned, which could not be resolved from the absorption spectrum alone and detailed models of the electronic structure to be formulated for the first time.

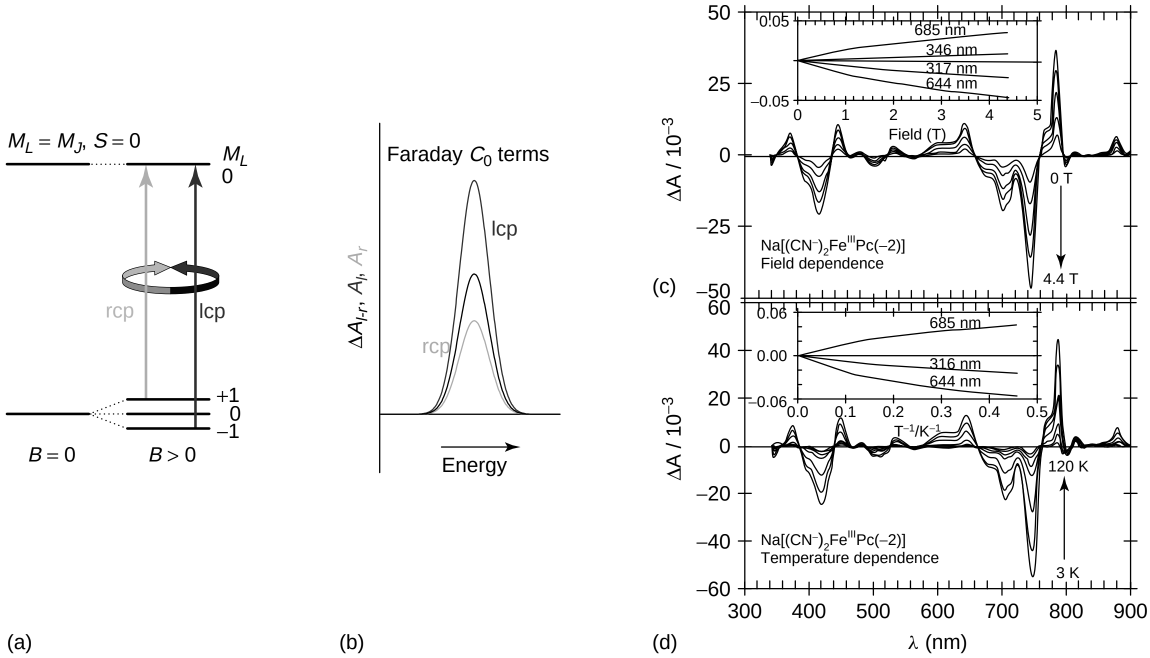

Figure 6 Selection rules (a) for the absorption of circularly polarized light based on a transition between an orbitally degenerate ground state and an orbitally nondegenerate excited state within a magnetic field applied parallel to the axis of light propagation. $\mathcal{C}_0$ terms are extremely temperature sensitive. The $\mathcal{C}_0$ term has a $1/kT$ temperature dependence since the ground state microstates are populated according to a Boltzmann distribution. At very low temperatures, a symmetric Gaussian-shaped Faraday $\mathcal{C}_0$ term (b) is observed because only the lowest split state contributes to the MCD. Understandably, the intensity of this $\mathcal{C}_0$ term dominates the MCD spectrum at low temperatures. At temperatures above the temperature that the lowest state exists with 100% of the population, the measured $\mathcal{C}_0$ term shape begins to become asymmetric due to the separation of the band centers of transitions absorbing lcp and rcp light, until both states are equally populated at very high temperatures at which point an $\mathcal{A}_1$-term-like derivative band will be observed. In this example $S = 0$ so $M_L = M_J$. (Reprinted from Mack, Stillman and Kobayashi,[2] © Elsevier 2007.) MCD changes observed for a 1 mm glass of Na[(CN$^-$)$_2$Fe^{III}Pc(−2)] (c) when the temperature is held constant at 3.8 K and the magnetic field is varied between 0 and 4.4 T (the inset displays the change in MCD intensity versus magnetic field at four wavelengths) and (d) when the temperature is varied between 3 and 120 K under a constant 3.92 T magnetic field (the inset displays the change in MCD intensity versus temperature at three wavelengths). (Reproduced with permission from J. Mack, Y. Asano, N. Kobayashi, M. J. Stillman (2005) *J. Am. Chem. Soc.* **127**:17697−17711. © 1995 American Chemical Society)

3.6 MCD Spectroscopy and Perimeter Molecular Orbital (MO) Models for Heteroaromatic π-Systems and Metal Complexes

One of the most active areas of MCD research in the past few decades has been the study of the electronic structure of aromatic and heteroaromatic π-systems both within molecules in proteins and as ligands in inorganic and bioinorganic metal complexes. In the late 1940s, Platt[7] proposed a free electron model for describing the π-system perimeter MOs of benzene based on the M_L quantum number and a $M_L = 0$, ± 1, ± 2, 3 sequence in terms of ascending energy. The highest occupied molecular orbital (HOMO) and lowest unoccupied molecular orbital (LUMO) of benzene have $M_L = \pm 1$ and ± 2 nodal properties and can be linked by an allowed $\Delta M_L = \pm 1$ and a forbidden $\Delta M_L = \pm 3$ transition, referred to these as the B and L bands, respectively. The L band lies at lower energy based on Hund's second rule. Moffitt[8,9] subsequently developed a linear combination of atomic orbitals (LCAO)-based cyclic perimeter model of a wide range of aromatic cyclic polyenes and noted that in the case of heteroaromatic polyenes the nodal patterns of structural homologs derived from the same charged or uncharged parent C$_n$H$_n$ perimeter are consistently retained and demonstrated that MO model-based methods for predicting the energies and relative intensities of the major spectral bands can be simplified on this basis. Michl[10,11] later developed a qualitative and quantitative perimeter model for predicting the signs of the Q and L bands within the MCD spectra of a wide range of aromatic and heteroaromatic π-systems and demonstrated that this could be used to derive key information about geometry and electronic structure even in the case of low symmetry molecules and complexes. It is important to note that Michl used the original MORD spectroscopy based definitions for the three Faraday terms.[2]

In the case of metal porphyrin complexes, $C_{16}H_{16}^{2-}$ can be viewed as the parent perimeter based on a 16-atom 18 π-electron system with an $M_L = 0$, ± 1, ± 2, ± 3, ± 4, ± 5, ± 6, ± 7, 8 MO sequence in ascending energy based on the inner ligand perimeter. In the 1960s, Gouterman[12] developed a 4-orbital LCAO model for metal porphyrin complexes with the

HOMOs and LUMO having $M_L = \pm 4, \pm 5$ nodal properties resulting in a forbidden Q transition ($\Delta M_L = \pm 9$) at lower energy and an allowed B transition ($\Delta M_L = \pm 9$) at higher energy. On this basis, MCD spectroscopy provided conclusive evidence that the Q bands were of $\pi\pi^*$ rather than $n\pi^*$ origins based on the ratio of the observed $\mathcal{A}_1/\mathcal{D}_0$ ratios (Figure 4) and that the π-system HOMOs are accidentally nearly degenerate, resulting in a π-system with ideal D_{16h} properties despite the D_{4h} symmetry of the porphyrin ligand.

3.7 Band Deconvolution as a Tool in the Quantitative Analysis of MCD Spectral Data-Application to the Spectra of Porphyrins and Phthalocyanines

The Stillman group[13–15] has used MCD spectroscopy to fully assign the optical spectra of both main group and transition metal phthalocyanines (tetraazatetrabenzoporphyrins) and their anion and cation radical species to resolve the component spectral bands within broad spectral envelopes. The requirement that the same band widths and band centers be used to fit the bands which comprise both the UV-visible absorption and MCD spectra removes much of the ambiguity normally associated with band deconvolution techniques (Figure 7). This approach helped to identify the presence of two overlapping Faraday $\mathcal{A}_1$ terms in the 300–400 nm region of the spectra of metal phthalocyanines based on a study involving a wide range of different axial ligands. Structural modifications result in a substantial separation of the $1a_{1u}$ and $1a_{2u}$ HOMOs so that the π-system no longer has ideal D_{16h} symmetry properties. The band nomenclature for phthalocyanines was modified to include B1 and B2 bands. In the case of π-anion radical species such as $[\mathrm{MgPc}(-3)]^-$ and $[\mathrm{ZnPc}(-3)]^-$, a partially filled $1e_g^*$ LUMO would be expected to have a partially occupied orbitally degenerate ground state. When MCD spectra were recorded at room and cryogenic temperatures, there was no significant temperature dependence observed beyond some band sharpening due to the presence of hot bands (Figure 8).

Since a $1/kT$ temperature dependence is expected in the case of Faraday $\mathcal{C}_0$ terms this represented definitive evidence that the MCD spectrum is completely dominated by Faraday $\mathcal{B}_0$ terms and that the ground state is subject to a substantial static Jahn–Teller effect. The intense pairs of oppositely signed coupled Faraday $\mathcal{B}_0$ terms identified the major electronic bands within the spectrum and enabled a detailed band assignment. The presence of negative $\mathcal{A}_1$ terms in the spectrum of zinc tetraphenyltetraacenaphthoporphyrin (Figure 8), provided direct spectral evidence that steric hindrance between the peripheral substituents results in a reversal of the alignment of the excited state magnetic

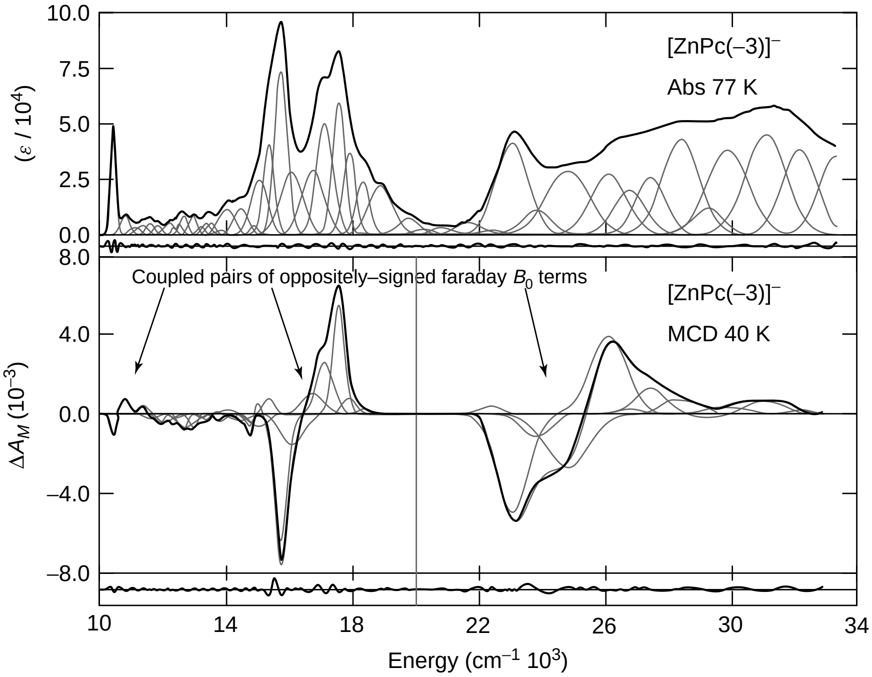

Figure 7 Complete set of 45 bands required to fill the absorption and MCD band envelopes of the phthalocyanine-ring-reduced radical anion species $[\mathrm{ZnPc}(-3)]^-$. The absorption spectrum was recorded at 77 K, and the MCD spectrum at 40 K. The bands were fitted using Gaussian-shaped bands with the identical band centers and bandwidths for pairs of absorption and MCD bands. A weak, Faraday $\mathcal{A}_1$ term located at 14 860 cm^{-1} is due to a residual 1% impurity of neutral ZnPc(−2). Experimental data (solid line); fitted data (broken line). (Reproduced with permission from J. Mack, Y. Asano, N. Kobayashi, M. J. Stillman (2005) *J. Am. Chem. Soc.* **127**:17697–17711. © 2005 American Chemical Society)

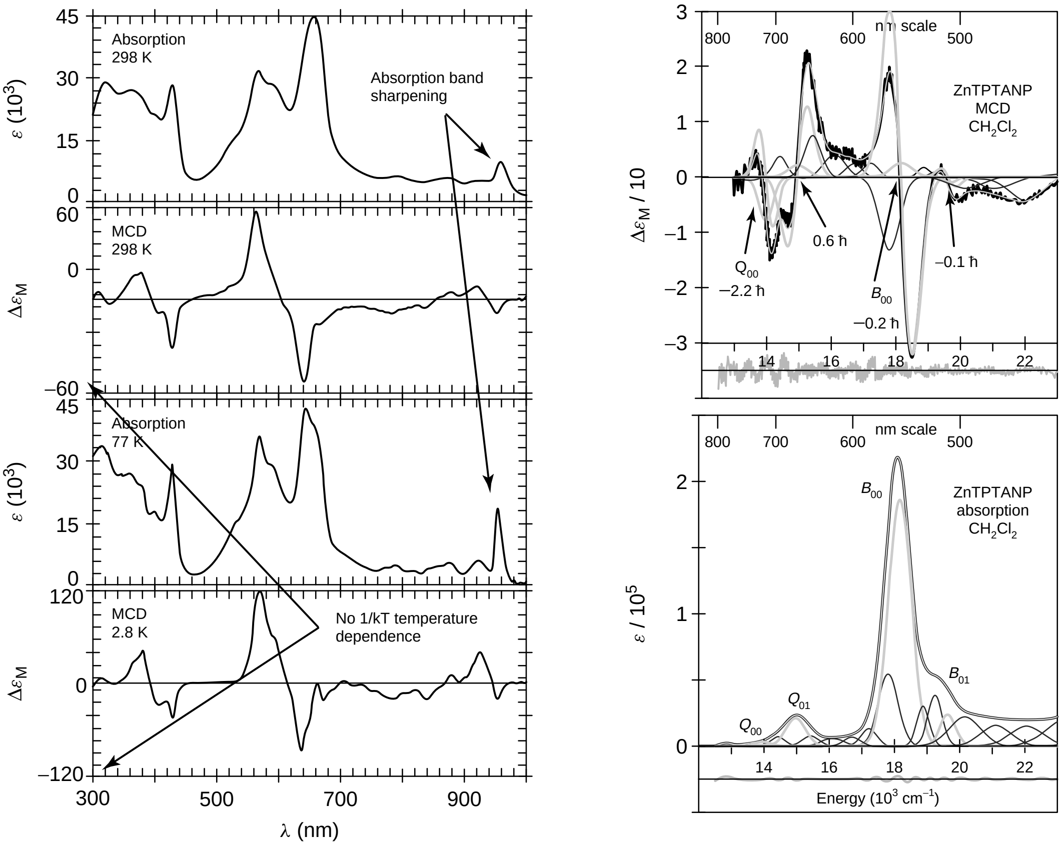

Figure 8 The absorption and MCD spectra of the phthalocyanine-ring-reduced radical anion species $[\text{MgPc}(-3)]^-$ prepared electrochemically at room temperature and recorded at room and cryogenic temperatures (a). (Reproduced with permission from J. Mack, Ph.D. Thesis, University of Western Ontario 1994.) Spectral deconvolution analyses of the absorption and MCD spectra of ZnTPTANP recorded in CH_2Cl_2 (b). (Reproduced with permission from J. Mack, Y. Asano, N. Kobayashi, M. J. Stillman (2005), *J. Am. Chem. Soc.* **127**:17697–17711. © 2005 American Chemical Society)

moments relative to planar metal porphyrins such as ZnOEP. Spectral band deconvolution analysis was used to quantify the magnitude of the magnetic moments based on the $\mathcal{A}_1/\mathcal{D}_0$ ratios.

3.8 MCD Spectroscopy of Heme Proteins

Since the mid-1960s, MCD spectroscopy has found considerable use in biochemistry for studying heme proteins, such as myoglobin and hemoglobin, and other biologically significant transition metal complexes. MCD spectroscopy has consistently provided key ground and excited state degeneracy information that cannot easily be derived from an analysis of UV-visible absorption spectra and theoretical calculations alone. The complex band morphologies arising from the three Faraday terms result in major changes within the overall MCD spectrum. In contrast, only relatively minor changes in band centers and intensities are typically observed in the UV-visible absorption spectra.[16–19] Since there is a partially filled set of d orbitals, ligand-to-metal charge transfer (LMCT), and metal-to-ligand charge transfer (MLCT) bands are observed in both the absorption and MCD spectra in addition to the $\pi \to \pi^*$ bands. The ligand field splitting of the d orbitals in metal porphyrinoid complexes tends to be essentially tetragonal based on the tetradentate nature of the porphyrin ligand and some form of axial ligation from above and below the ring. In an O_h symmetry environment the ligand field splitting (Δ_{OCT}) is typically of the order of $10\,000\,\text{cm}^{-1}$. Most six coordinate D_{4h} symmetry porphyrinoid complexes are axially distorted ($x = y \neq z$) so that the degeneracy of the e_g and t_{2g} levels is lifted, while lower symmetry porphyrinoids contain a rhombic distortion ($x \neq y \neq z$) in which there is a complete lifting of d orbital degeneracy. In the case of Fe^{II} and Fe^{III} complexes, the spin state of the central metal is determined by the nature of axial ligation from above and below the ring. Strong ligands such as CO and CN^-, which act as π-acceptors based on back bonding, result in low-spin complexes by increasing the separation of the e_g and t_{2g} orbitals, while weak ligands, which act as π-donors, such as F^-, reduce the separation and result in a high-spin state with $S > 1/2$. In the case of Fe^{III} hemes, ligation with azide (N_3^-) can also result in an intermediate spin state with $S = 3/2$. In complexes where there are unpaired electrons so that $S > 0$, spin-orbit coupling (Figure 9) results

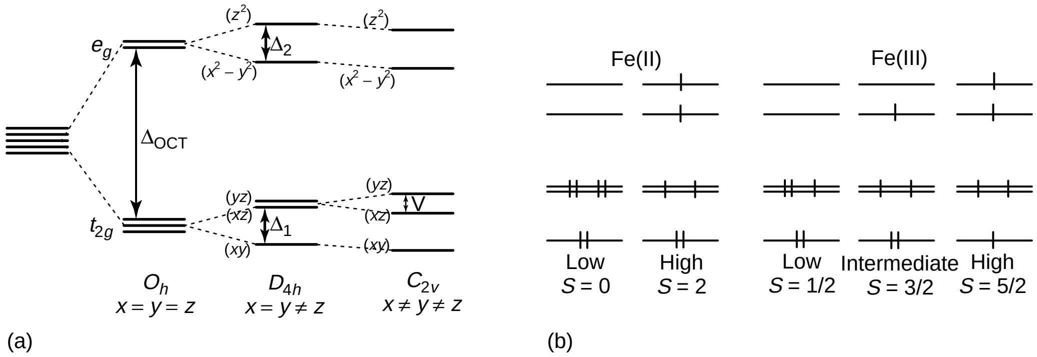

Figure 9 The crystal field splitting of Fe^{II} and Fe^{III} d orbitals in cubic O_h, tetragonal D_{4h} and rhombic C_{2v} environments (a). Only the latter two are typically observed for metal porphyrinoid complexes. The axial and rhombic ligand field parameters are denoted as Δ and V. The low-, intermediate- and high-spin states for Fe^{II} and Fe^{III} based on a tetragonal environment (b). (Reprinted from Mack, Stillman and Kobayashi,[2] © Elsevier 2007)

in zero-field splitting (ZFS) of state degeneracies in addition to the ligand field effects on orbital degeneracy, which are related to the axial and rhombic distortions to the coordination sphere of the central metal.

The spectra arising from the low, intermediate, and high-spin states of Fe^{II} and Fe^{III} porphyrin complexes (e.g., in heme proteins) depend on the nature of axial ligation from above and below the ring as well as the configuration interaction between the main $\pi \rightarrow \pi^*$ and charge transfer states. This results in characteristic ''fingerprint patterns'' that can be used to derive information,[16–19] which can help to provide answers to questions such as: (i) How many ligands are attached to the iron and what is the nature of these coordinating ligands (for example, in the case of a protein, nitrogen from a histidine, or a sulfur from a cysteine)? (ii) Is the spin state of the iron, which relates to the binding strength of the axial ligand present, high, intermediate, or low? (iii) What is the oxidation state of the central iron? (iv) Can the heme iron be readily oxidized or reduced? (v) And finally, can axial ligands approach and bind to the iron?

Key information about the ground state degeneracy can be derived by determining whether the MCD spectrum contains Faraday $\mathcal{C}_0$ terms with a $1/kT$ temperature dependence (Figure 10). For example, in the case of Fe^{II} and Ru^{II} porphyrinoid MCD spectra, the absence of temperature dependence is consistent with the presence of a low-spin d^6 central metal configuration with $S = 0$. For heme proteins, this configuration can normally be obtained through reduction with $Na_2S_2O_4$ and the addition of a strong axial ligand. The MCD spectra of low-spin d^6 porphyrinoid complexes, such as $Fe^{II}Pc$ and $Ru^{II}Pc$, are dominated by Faraday $\mathcal{A}_1$ terms and are typically similar to those of the main group metal and closed shell d^{10} Pc complexes, complicated somewhat by the presence of MLCT and LMCT in addition to the main $\pi \rightarrow \pi^*$ transition observed for main group metal complexes.

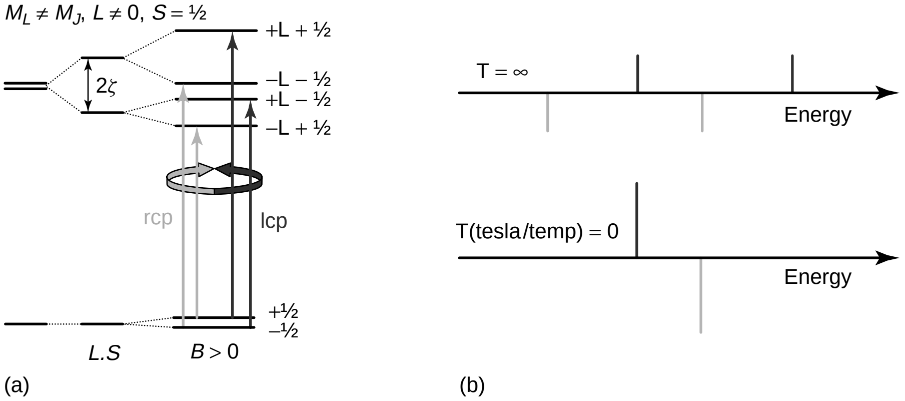

Figure 10 The origin of the Faraday $\mathcal{C}_0$ term from Kramers doublets for the ground and excited states of a paramagnetic complex with $S = 1/2$, a nonorbitally degenerate ground state and orbitally degenerate excited state (a). Temperature dependent, derivative-shaped signals can result when the ground state is orbitally nondegenerate and the excited state is orbitally degenerate (b). (Reprinted from Mack, Stillman and Kobayashi,[2] © Elsevier 2007)

In the case of Fe^{III} hemes with d^5 central metal configurations, LMCT bands in the near infra red (IR) (1000 to 2000 nm) are an ideal probe for determining the extent of rhombic splitting of the $d_{(yz)}$ and $d_{(xz)}$ orbitals (Figure 9). Thomson[20,21] has reported combined EPR, MCD and UV-visible absorption spectroscopic studies which demonstrate that the near IR region LMCT bands for a series of low-spin Fe^{III} hemes can be used to determine the nature of the axial ligands. Because $S = 1/2$, the ground and excited states of low-spin d^5 complexes will split into Kramers doublets within an applied magnetic field with $M_S = -1/2$ and $M_S = +1/2$. At high temperature and low field, the lcp and rcp bands tend to cancel, resulting in a weak MCD signal (Figure 10). As the temperature is lowered or the applied field is increased, the Boltzmann population of the higher sublevel decreases and the $\mathcal{C}_0$ term, therefore, increases in intensity. During measurement of vitreous solutions at cryogenic temperatures (1–4 K) and high field strengths (4–7 K), the lowest component of the ground state will often be populated and the MCD signal will saturate.

Although it is possible in principle to derive the ground state g-factor value by measuring the $\mathcal{C}_0/\mathcal{D}_0$ ratio from the Method of Moments analysis, this is usually not practical, as the absorption bands lack a baseline-to-baseline band envelope or due to overlap with bands associated with other metal centers or chromophores. It should be noted that in some instances, excited state parameters also have to be carefully considered. For example, when ground state degeneracy (and the associated Boltzmann distribution of population across microstates within an applied magnetic field) is introduced by spin degeneracy into what would otherwise be a Faraday $\mathcal{A}_1$ term (Figure 11) a temperature dependent, derivative-shaped signal is observed for $\mathcal{C}_0$ term intensity.

The intensity mechanism for a single isotropic Kramers doublet ground state is

$$\Delta A = 152.5 \tanh\left(\frac{g_L \mu_B B}{kT}\right) \times \left(\left[m^{AJ}_{-1}\right]^2 - \left[m^{AJ}_{+1}\right]^2\right) \tag{14}$$

The analysis is complicated by the fact that, in the case of porphyrinoids, the molecular symmetry is usually axial rather than isotropic. The g-factor values are therefore different, parallel ($g_{\|}$), and perpendicular ($g_{\perp}$), to the applied field, but are averaged (g_{av}) out in solution due to random orientation.

Schatz *et al.*[22] demonstrated that for a D_{4h} symmetry complex with $S = 1/2$ Kramers doublet ground states such as those associated with low-spin Fe^{III} porphyrinoids, the zeroth moment of $\mathcal{C}_0$ term intensity for an axial complex with $g_x \approx g_y$ in the linear limit is given by

$$\langle \Delta\varepsilon \rangle_0 = \frac{K\mu_B B}{3kT} \times \frac{g_{\|}[m^{AJ}_{+}]^2}{2} \tag{15}$$

where $m^{AJ}_{+} \equiv 1/\sqrt{2(m_x + i m_y)}$.

At saturation:

$$\langle \Delta\varepsilon \rangle_0 = \left(K\left[m^{AJ}_{+}\right]^2\right) \frac{\cosh(\alpha)}{\sinh^3(a)} \times \left(\frac{\sinh(2\alpha)}{4} - \frac{\alpha}{2}\right) \tag{16}$$

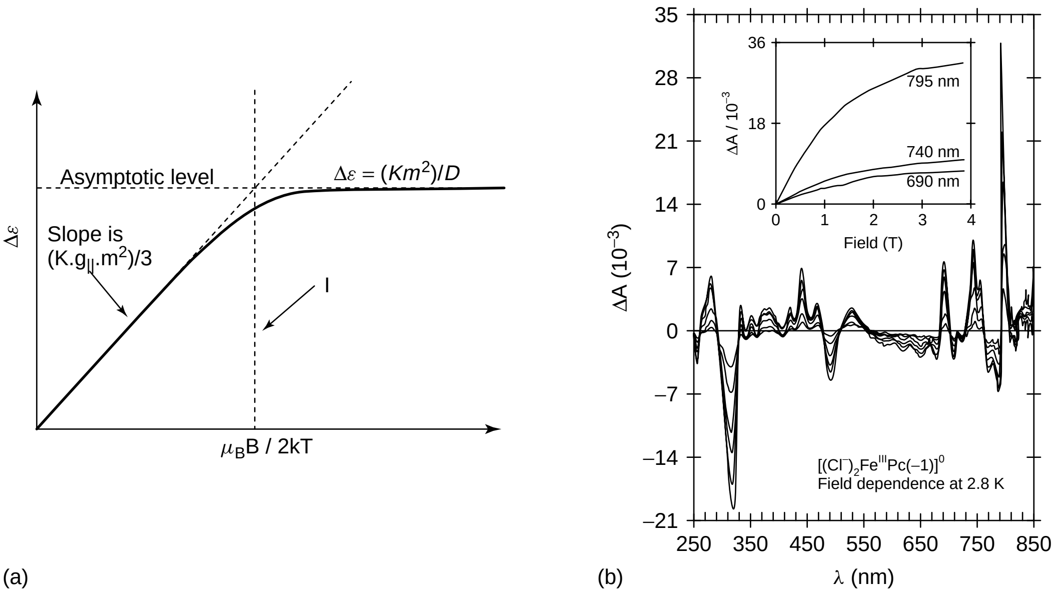

(a) (b)

Figure 11 Analysis of an MCD magnetization curve based on equations (15)–(19) (a). (Reprinted from Mack, Stillman and Kobayashi,[2] © Elsevier 2007.) Field dependence of the MCD spectra recorded at 2.8 K from a 1 mm pathlength frozen CH_2Cl_2/C_4H_8Cl solution of $(Cl^-)_2Fe^{III}Pc(-1)$ as the magnetic field strength was varied from 0 to 4 T (b). The inset displays the change in MCD spectral intensity at three wavelengths (690, 740, 795 nm). The spectrum contains Kramers doublet based signals since both the metal and the ligand contain unpaired electrons. (Reproduced with permission from E. A. Ough, Ph.D. Thesis, University of Western Ontario 1994)

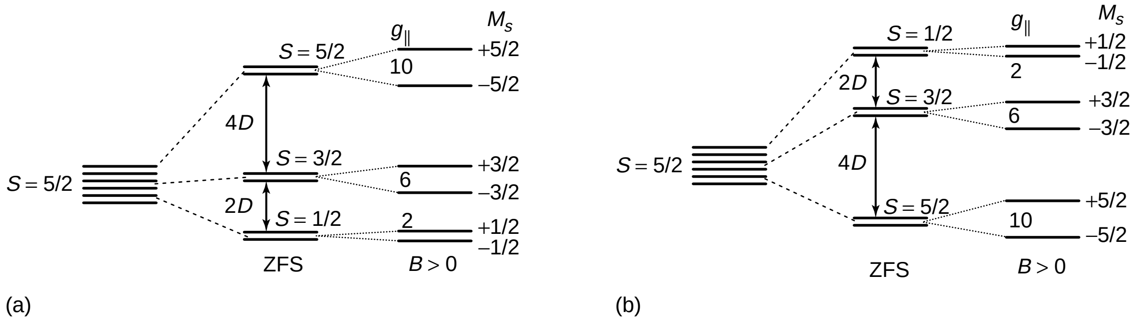

Figure 12 The ZFS of the ground state of a D_{4h} symmetry metal porphyrinoid complex with $S = 5/2$ based on the axial parameter, D. When D is positive, the $S = 1/2$ microstates are stabilized (a), while if D is negative, the $S = 5/2$ microstates are stabilized (b). (Reprinted from Mack, Stillman and Kobayashi,[2] © Elsevier 2007)

where K is a proportionality factor, and α is related to the degree of anisotropy in the g-factor values:

$$\frac{\mathrm{g}_{\|}}{\mathrm{g}} = \sigma = \cosh(\alpha) \tag{17}$$

$$\frac{1}{L} = \frac{\cosh(\alpha)}{\sinh^3(\alpha)} \times \left(\left(\frac{\sinh(2\alpha)}{4} - \frac{\alpha}{2}\right) - \left(\frac{\alpha}{2}\right)\right) \tag{18}$$

The ratio of the slope to the MCD intensity at saturation defined by an intercept value, I, can be used to derive the expression:

$$g_{\|} = \frac{3\mathrm{I}}{\mathrm{L}} \tag{19}$$

Thomson[23] demonstrated that is possible to use magnetization curves of $\Delta\varepsilon$ plotted against $\mu_{\mathrm{B}}B/2\ kT$ (Figure 12) based on $\mathcal{C}_0$ term temperature dependence studies at cryogenic temperatures (typically 2 to 50 K) and applied field strengths of 1 to 6 T, to derive values for $g_{\|}$ and $g_{\perp}$ based on the expressions:

$$g_{\|} = \frac{1}{\sqrt{3}}\sqrt{\mathrm{g}_{\mathrm{x}}^2 + \mathrm{g}_{\mathrm{y}}^2 + \mathrm{g}_{\mathrm{z}}^2} \tag{20}$$

$$g_{\perp} = \frac{1}{\sqrt{2}}\sqrt{\mathrm{g}_{\mathrm{x}}^2 + \mathrm{g}_{\mathrm{y}}^2} \tag{21}$$

Band polarization information can also be derived since the slope of the magnetization curves should be the same for all x/y- or z-polarized transitions.

In the case of the $S = 5/2$ ground states of high-spin $\mathrm{Fe^{III}}$ complexes, there is a ZFS of the $M_S = \pm 1/2, \pm 3/2, \pm 5/2$ microstates due to spin-orbit coupling based on the axial (D) and rhombic (E) ZFS parameters within the spin Hamiltonian, H, with the central metal (Figure 13) and equation (22):

$$H = D\left(\mathrm{S}_{\mathrm{z}}^2 - \frac{1}{3}\mathrm{S}^2\right) + E\left(\mathrm{S}_{\mathrm{x}}^2 - \mathrm{S}_{\mathrm{y}}^2\right) \tag{22}$$

In the early 1980s, Stephens *et al.*,[24] demonstrated that the magnitude of D could be derived by fitting a plot of $\Delta\varepsilon$ against T^{-1} from cryogenic temperature MCD spectral data of a high-spin $\mathrm{Fe^{III}}$ tetraphenylporphyrin with a set of quadratic equations based on a least squares fitting approach, since the MCD signal is the sum of the MCD signals of the three sets of Kramers doublets which are populated according to a Boltzmann distribution based on the magnitude and sign of D. An analysis of the temperature dependence over a temperature range in which kT is comparable to the magnitude of the ZFS (typically $<20\ \mathrm{cm}^{-1}$) enables D to be calculated.

Analysis of $S = 2$ ground states associated with high-spin d^6 configurations of $\mathrm{Fe^{II}}$ are considerably more challenging than the Kramers doublet based systems which arise from d^5 configurations, since the even spin ground states are EPR silent. In 1980, Thomson and Johnson[23] reported multiple nested magnetization curves (Figure 13) for the ground state of high-spin $\mathrm{Fe^{II}}$ myoglobin but did not attempt a detailed analysis due to the complexity of the field-induced mixing of the ZFS components. During the 1990s, Solomon[25,26] developed techniques for analyzing variable temperature variable field (VTVF) MCD spectra for non-Kramers doublet ground states as part of a wide-ranging study of nonheme iron enzymes. Solomon has demonstrated that it is possible to calculate values for the ligand field splitting properties, Δ and V (Figure 9) of the t_{2g} set of orbitals of high-spin $S = 2$ $\mathrm{Fe^{II}}$ complexes derived from analysis of nested magnetization curves (Figure 13) based on experimentally obtained values of the zero-field rhombic splitting (δ) of the $M_S = \pm 2$ level and $g_{\|}$.

In addition, work by Solomon's group at Stanford University on copper binding active sites has been particularly significant in terms of establishing the power of variable temperature and field studies.[27] The unique spectral and structural features of the copper–protein active sites and their intermediates have been studied in depth based on a wide range of different spectroscopic techniques. This has provided detailed insights into the nature of these sites that

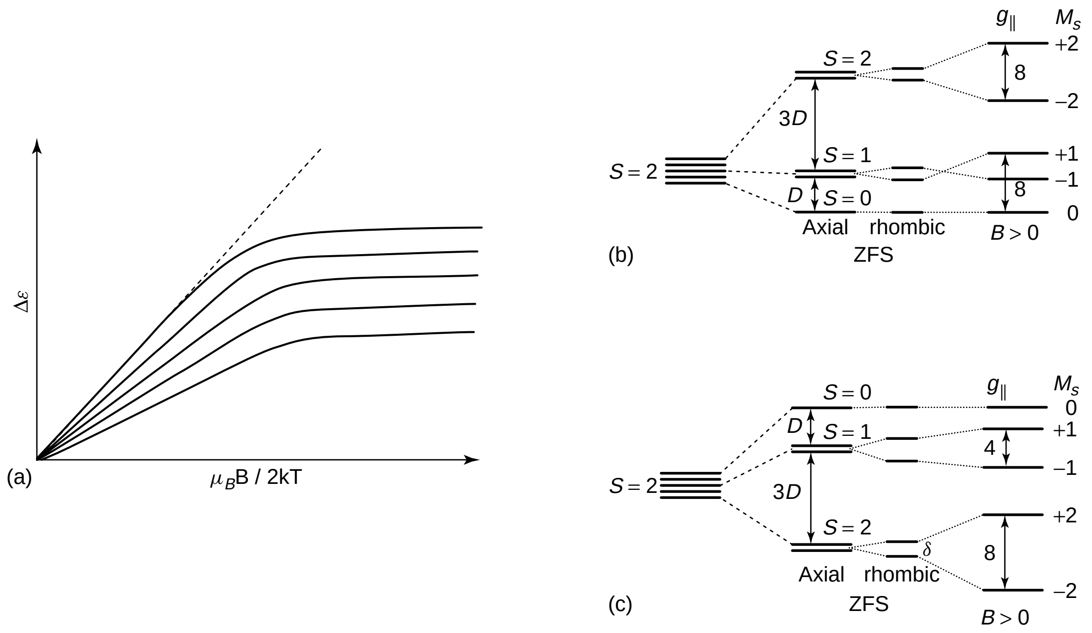

Figure 13 When there is a non-Kramers doublet ground state, complex nested magnetizations are observed at different temperatures (a). The ZFS of the ground state of a D_{4h} symmetry metal porphyrinoid complex with $S = 2$ based on positive (b) and negative (c) values for the axial parameter, D. (Reprinted from Mack, Stillman and Kobayashi,[2] © Elsevier 2007)

has enhanced the understanding of their contributions to the unique catalytic functions in biology.

Although the focus of this section has primarily been on iron and copper complexes, probably the most important transition metals biologically studied by the MCD technique, variable temperature and field dependence studies have also been carried out for complexes of other transition metals such as cobalt and manganese and the techniques described for iron and copper can easily be applied to other metals based on the nature of the ground state. MCD spectroscopy has the key advantage, over other techniques used to study bulk magnetic properties of an entire sample, that spectral bands associated with specific metal centers can be studied in isolation.

3.9 X-ray MCD Spectroscopy

In recent years the use of MCD spectroscopy has been extended beyond the UV-visible-near IR region to synchrotron-based L-edge absorption experiments. Initially X-ray MCD was only used to investigate ferromagnetic systems, because paramagnetic systems required very high fields and/or very low temperatures to saturate the magnetization properties of the sample. In 2001, Cramer[28] successfully extended this earlier work to the Ni center of Fe–Ni hydrogenase in *Desulfovibrio desulfuricans* by utilizing temperatures <1 K and a 2 T magnetic field as a new approach to determining localized spin states at specific metal sites within the proteins. Since then a number of similar studies have been reported.

3.10 Key Features in Selecting MCD Spectroscopy as a Technique with which to Probe the Electronic Structure of Atoms, Ions and Molecules

MCD spectroscopy is and will continue to be a valuable spectroscopic probe for molecules and metal complexes of high symmetry. The technique is complementary to EPR spectroscopy and provides key ground and excited state degeneracy information that is required to fully understand the electronic structure and assign the associated optical properties. Even when the symmetry is lowered substantially, Michl's perimeter model approach can be used in the case of aromatic and heteroaromatic molecules, to analyze the optical properties in the readily accessible UV-visible-near IR regions based on the orbital angular momentum properties associated with the ring current of the heteroaromatic π-system. Since the same spectral bands are also observed in the UV-visible absorption spectrum, MCD spectroscopy can be used to derive quantitative values for the magnetic moments associated with the ground and/or excited states.

4 ABBREVIATIONS AND ACRONYMS

CD = circular dichroism; EPR = electron paramagnetic resonance; HOMO = highest occupied molecular orbita; IR = infra red; LCAO = linear combination of atomic orbitals; LUMO = lowest unoccupied molecular orbital; lcp = left circularly polarized; LMCT =

ligand-to-metal charge transfer; MLCT = metal-to-ligand charge transfer; MCD = magnetic circular dichroism; MO = molecular orbital; MORD = magnetic optical rotatory dispersion; NMR = nuclear magnetic resonance; OEP = octaethylporphyrin; ORD = optical rotatory dispersion; Pc = phthalocyanine; rcp = right circularly polarized; TPP = tetraphenylporphyrin; VTVF = variable temperature variable field; ZFS = zero-field splitting; ZnOEP = zinc octaethylporphyrin.

5 REFERENCES

1. P. Zeeman, ‘Nobel Lectures, Physics 1901–1921’, Elsevier Publishing, Amsterdam, 1967.
2. J. Mack, M. J. Stillman and N. Kobayashi, *Coord. Chem. Rev.*, 2007, **251**, 429.
3. P. J. Stephens, *Adv. Chem. Phys.*, 1976, **35**, 197.
4. S. B. Piepho and P. N. Schatz, ‘Group Theory in Spectroscopy with Applications to Magnetic Circular Dichroism’, John Wiley & Sons, New York, 1983.
5. M. J. Androwski and W. R. Mason, *Inorg. Chem.*, 1997, **36**, 1443.
6. W. R. Mason, *Inorg. Chem.*, 2000, **39**, 370.
7. J. R. Platt, *J. Chem. Phys.*, 1949, **17**, 484.
8. W. Moffitt, *J. Chem. Phys.*, 1954, **22**, 320.
9. W. Moffitt, *J. Chem. Phys.*, 1954, **22**, 1820.
10. J. Michl, *J. Am. Chem. Soc.*, 1978, **100**, 6801, and the other 16 articles within the same issue.
11. J. Michl, *Pure Appl. Chem.*, 1980, **52**, 1549.
12. M. Gouterman, in ‘The Porphyrins’, ed. D. Dolphin, Academic Press, New York, 1978, Vol. III, Part A, p. 1.
13. M. J. Stillman and T. Nyokong, in ‘Phthalocyanine. Principles and Properties’, eds. C. C. Leznoff and A. B. P. Lever, VCH Publications, New York, 1989, Vol. 1, p. 133.
14. M. J. Stillman, in ‘Phthalocyanine. Principles and Properties’, eds. C. C. Leznoff and A. B. P. Lever, VCH Publications, New York, 1993, Vol. 3, p. 227.
15. J. Mack and M. J. Stillman, in ‘Handbook of Porphyrins and Related Macrocycles’, eds. K. M. Kadish, K. M. Smith and R. Guilard, Academic Press, New York, 2003, Vol. 16, p. 43.
16. J. H. Dawson and D. M. Dooley, in ‘Iron Porphyrins’, eds. A. B. P. Lever and H. B. Gray, VCH, London, 1989, Vol. 4.
17. J. Cheek and J. Dawson, in ‘The Porphyrin Handbook’, eds. K. M. Kadish, K. M. Smith and R. Guilard, Academic Press, New York, 2000, Vol. 7, p. 339.
18. M. L. Kirk and K. Peariso, *Curr. Opin. Chem. Biol.*, 2003, **7**, 220.
19. E. I. Solomon, E. G. Pavel, K. E. Loeb and C. Campochiaro, *Coord. Chem. Rev.*, 1995, **144**, 369.
20. A. J. Thomson and P. M. A. Gadsby, *J. Chem. Soc., Dalton Trans.*, 1990, 1921.
21. P. M. A. Gadsby and A. J. Thomson, *J. Am. Chem. Soc.*, 1990, **112**, 5003.
22. P. N. Schatz, R. L. Mowery and E. R. Krausz, *Mol. Phys.*, 1978, **35**, 1537.
23. A. J. Thomson and M. K. Johnson, *Biochem. J.*, 1980, **191**, 411.
24. W. R. Browett, A. F. Fucalaro, T. V. Morgan and P. J. Stephens, *J. Am. Chem. Soc.*, 1983, **105**, 1868.
25. E. I. Solomon, *Chem. Rev.*, 2000, **100**, 235.
26. M. L. Neidig, M. Kavana, G. R. Moran and E. I. Solomon, *J. Am. Chem. Soc.*, 2004, **126**, 4486.
27. E. I. Solomon, *Inorg. Chem.*, 2006, **45**, 8012.
28. H. Wang, D. S. Patil, C. Y. Ralston, C. Bryant and S. P. Cramer, *J. Electron Spectrosc. Relat. Phenom.*, 2001, **114–116**, 865.

Metal Analysis

Katarzyna Wrobel and Kazimierz Wrobel

Instituto de Investigaciones Cientificas, Universidad de Guanajuato, Guanajuato, Mexico and
University of Cincinnati/Agilent Technologies Metallomics Center of the Americas, Cincinnati, OH, USA

Joseph A. Caruso

University of Cincinnati, Cincinnati, OH, USA and
University of Cincinnati/Agilent Technologies Metallomics Center of the Americas, Cincinnati, OH, USA

	Method Summary	1
1	Introduction	2
2	Technical Background	3
3	Applications	9
4	Abbreviations and Acronyms	18
5	Further Reading	18
6	References	18

METHOD SUMMARY

Acronyms, Synonyms

- Inductively coupled plasma mass spectrometry (ICP-MS)
- Inductively coupled plasma optical emission spectrometry (ICP-OES)

Measured physical quantities

- ICP-OES: emission spectra of atoms and ions in the gas phase; wavelengths (λ, nm) and peak intensity as output current of the transducer (I, nA);
- ICP-MS: atomic mass spectra of the generated ions: accurate mass measurement based on m/z values, and peak intensity as counts per second (cps).

Information available

- ICP-OES: quantification of more than 70 elements present at the concentration levels from part-per-billion up to weight percent in a single run after calibration (2 min);
- ICP-MS: quantification of more than 70 elements present at the concentration levels from part-per-trillion up to part-per-million in a single run after calibration in time comparable to that in ICP-OES.

Information not available, limitations

- This is a destructive analysis and structural information is lost.
- There are troublesome spectral interferences, spectral line overlapping in ICP-OES, and polyatomic interferences in ICP-MS.
- ICP-OES: atomic/ionic spectral lines must be within the range 160–800 nm. Gaseous elements, halogens, and carbon are not determined. There are poor detection limits for biologically important elements (As, Se, Pb, Th, etc.) in the radial viewing spectrometers.
- ICP-MS: ionization energy of elements must be lower than that for Ar (15.8 eV). The determination of nonmetals is possible only with modern instruments and detector lifetime is limited.

Examples of questions that can be answered

- What is the element profile in a given material?
- Is this environment (air, water, soil, living organisms) contaminated with metals?
- Are people living in this area exposed to metals in air, water, and/or food?
- Is this dairy product a good source of essential elements?
- What is the pharmacokinetics of metal or metal-tagged drug in the living organism?
- Is this plant a good candidate for phytoremediation of heavy metals and or metalloids?
- Are the levels of wear metals in the motor oil from this airplane acceptable?
- What are the trace impurities in semiconductor materials (ICP-MS)?
- What are the chromatographic elution profiles of the elements in the sample?

Major advantages

- ICP-OES: this is a well-established technique, easily adopted for routine determinations of metals in geochemical, environmental, biological samples and in the preventive maintenance of aircraft and vehicle lubricants. The quantitative information on major, minor, and trace elements is obtained with high-speed, good accuracy, and precision.
- ICP-MS: this is the primary detection technique in the determination and speciation of trace elements. It has excellent selectivity, sensitivity, multielement and isotopic capability and easy coupling with different separation techniques (especially low-flow and low-volume chromatographic methods). Modern instruments enable practically interference-free response over the wide range of element concentrations in a variety of samples and quantification of metalloids and nonmetals.

Major disadvantages

- ICP: elevated cost, low efficiency of sample introduction via pneumatic nebulization, poor tolerance of plasma to organic solvents, and high salt contents;
- ICP-MS: elevated cost (although less than most molecular MS instrumentation), possibly troublesome polyatomic interferences, low ionization efficiency for biologically important elements (Se, S, P, halogens), and, in most commercially available instruments, sequentially scanning nature of mass analyzer and detection system.
- ICP-OES: elevated, but lower cost with respect to ICP-MS; common interferences caused by the overlapping of spectral lines; detection limits that are 2 to 3 orders of magnitude higher with respect to ICP-MS.

Sample constraints

- Liquid samples are typically analyzed, gaseous phase from hydride generation is easily accepted, and solids can be introduced as slurries or after appropriate pretreatment procedure aimed at solubilization and/or preconcentration of the analytes. However, laser ablation techniques continue to increase in popularity.
- When the liquid sample is directly introduced to ICP, about 2–3 mL is needed to complete the measurement.

1 INTRODUCTION

Optical emission spectrometry (OES) is the oldest multielemental atomic spectrometric technique. The analytical applications are based on the spontaneous emission of photons from gaseous atoms and ions that have been generated from the sample and then thermally excited. Because the excited atom or ion only emits light of certain wavelengths, specific atomic or ionic spectra are produced, enabling qualitative evaluation of elements in the sample. A calibration curve relating the intensity of spectral line with the concentration can be used for the quantification of a given element. In principle, the emission source should provide a high rate of atomization and excitation of as many elements as possible, including those with low and high excitation energy. It should also assure reproducible atomization and excitation to yield good accuracy and precision in single-element and multielement analyses. Furthermore, it is desired that atomization and excitation occur in an inert chemical environment to minimize possible interferences. Different flame, spark, and arc sources have been used as the excitation sources since the beginning of the twentieth century; however, none of these approximates the full list of conditions listed above. It was not until mid-1960s when the analytically useful plasma sources were developed, substantially improving the capabilities of OES. The first commercially available inductively coupled plasma optical emission spectrometry (ICP-OES) was introduced in 1974 and since then the revival of OES can be noted.

Inductively coupled plasma (ICP) is an electrically neutral, highly ionized gas composed of ions, electrons, and neutral species. Typically, it is sustained by a stream of argon, which is energized with a radiofrequency (RF) electromagnetic field. Owing to the high temperature in the observation zone (6000–7000 K), efficient and reproducible atomization, excitation, and ionization occur for a variety of elements in different chemical matrices. The high temperature avoids chemical interferences, and the ICP presents high stability and less noise than other excitation sources. ICP-OES is characterized by complex spectra. For example, the 70 elements typically determined give rise to at least 70 000 emission lines in the 160–800 nm wavelength range. A consequence of this high density of spectral information is the need for high resolving power (bandpass at least 0.01 nm, or $\lambda/\Delta\lambda \geq 100\,000$). Optical spectrometers are typically equipped with grating monochromators and can operate in sequential or simultaneous multichannel mode.

Since high ionization is achieved in the ICP, it has also been explored as the ionization source for atomic mass spectrometry. The first inductively coupled plasma mass spectrometry (ICP-MS) publication was by Houk *et al.* in 1980.[1] Similar to ICP-OES, in most applications, the liquid sample is introduced into the plasma as an aerosol. This aerosol is carried by the stream of argon, which punctures the plasma, forming a central channel where atomization and ionization take place. In contrast to typical optical instruments, with the mass spectrometer the plasma torch is mounted horizontally, enabling the extraction of ions into a vacuum system. In the mass analyzer, fast moving ions are separated according to their mass-to-charge ratio (m/z). Consequently, mass spectra obtained are much simpler and easier to interpret as compared to optical emission spectra and isotope-specific detection becomes possible. In a relatively short time, ICP-MS has become recognized as a powerful tool and primary detection technique for element determination and speciation.[2–5]

In Table 1, the principle features of ICP-OES and ICP-MS techniques are presented. As can be observed, each technique presents specific capabilities and limitations, which determine their applications in the analysis of real-world samples. In the following sections, the basic principles of ICP-OES and ICP-MS are described with a special focus on the recent technological and methodological developments. An overview of their applications in inorganic and organometallic analysis is also presented.

2 TECHNICAL BACKGROUND

Even though the physicochemical backgrounds of ICP-OES and ICP-MS are substantially different, in both techniques the ICP serves as the analytical cell. Consequently, the same introduction systems can be used, yet some differences should be noted owing to specific selectivity and sensitivity of each technique. In this section, basic aspects of ICP-OES and ICP-MS are introduced.

2.1 Inductively Coupled Plasma

In Figure 1, the scheme of ICP assembly is presented. The plasma is formed within a quartz torch, which consists of three concentric tubes through which argon gas is introduced at different flow rates. A RF electromagnetic field (27.12 or 40.68 MHz) is generated at the top of the torch using a ‘‘load coil’’.

When the argon stream enters through the outer tube of the torch (10–16 L min^{-1}) the plasma is ignited by a spark discharge and the charged particles are forced to flow in a closed annular path. These fast moving ions and electrons collide with other atoms of argon to produce further ionization. High thermal energy results from the resistance of charged particles to their flow and the plasma becomes self-sustained. The argon stream flowing by the external tube is used to cool the torch as well and also helps to center and stabilize the plasma because of the helical gas flow. The liquid or gaseous sample is introduced into plasma through the inner torch tube (argon flow 0.5–1.5 L min^{-1}) and the thermal energy causes sample atomization, excitation, and ionization. The intermediate argon flow (auxiliary gas, 0–1.5 L min^{-1}) is optional and it is recommended for high organic solvent content. The plasma contains various ‘‘regions’’ where different steps of the excitation/ionization process are carried out. The region at the base of the plasma, closest to the nebulizer flow, is called the *preheating zone* (PHZ). This region is involved in desolvation of the aerosol, leaving the salt form of the analyte. Subsequent vaporization of the salt

Table 1 Comparison of the ICP-OES and ICP-MS techniques

	ICP-OES	ICP-MS
ICP function	Excitation source (mounted vertically or horizontally)	Ionization source (mounted horizontally)
Interface ICP spectrometer	Radial or axial view of spontaneous emission occurring in ICP	Ion extraction from ICP
Spectrum type	Electromagnetic: atomic/ionic emission lines *complicated*	Mass spectra: m/z of ions *simple*
Resolution	Grating monochromator	Mass analyzer
Common detectors	Photomultiplier tubes, photodiode array	Electron multipliers, Faraday cup
Analytical information	Multielemental	Multielemental
Qualitative analysis	Wavelength	m/z value
Quantitative analysis	Peak intensity at specific (λ photocurrent)	Peak intensity at specific m/z (counts per second)
Isotope capabilities	No	Yes
Detection limits	Part-per-billion levels	Part-per-trillion levels
Linear dynamic range	Up to 6 orders of magnitude	Up to 9 orders of magnitude
Interferences	Chemical–no Spectral–yes	Chemical–no Spectral–yes

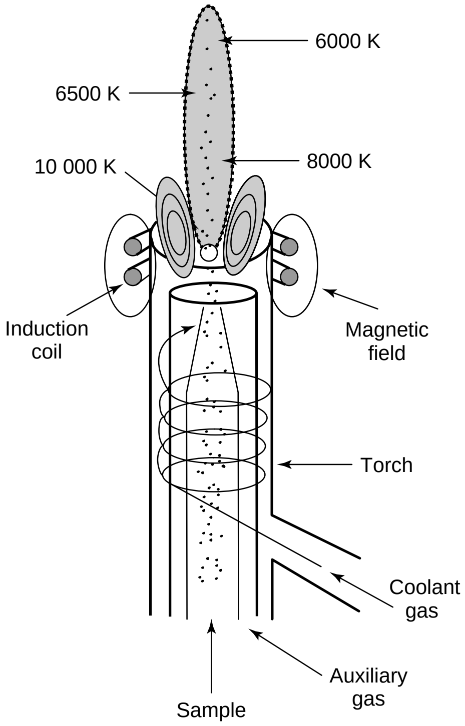

Figure 1 Inductively coupled plasma

produces a gas phase, which is then atomized. The initial radiation zone (IRZ) and the normal analytical zone (NAZ) are involved in the excitation and radiation of the sample. A toroidal region at the base of the plasma is formed by the puncture of nebulized sample, called the *inductive region* (IR).

The advantages of ICP as an ionization/excitation source include high temperatures, relatively long analyte residence times, high electron density, efficient ionization (for most elements), good stability, and a relatively inert environment. In addition, singly charged positive element ions are primarily generated (with the exception of those with low second ionization energy, like barium), so the mass spectra obtained are simple. Assuming an electron density of $10^{15}\,\mathrm{cm}^{-3}$ and a source temperature of 7500 K, Houk calculated that more than 50 elements (mainly metals) form singly charged positive ions to an extent $>90\%$.[2] For metalloids and some nonmetals, good ionization yields were also obtained. Thus, the calculated ionization yields for As, Se, P, S, and Br, whose first ionization potentials are 9.81, 9.75, 10.49, 10.36, and 11.81 eV (15.8 eV for Ar), were 52, 33, 33, 14, and 5% respectively.[2] Most of the elements have second ionization energies higher that 15 eV (except Ba and light rare earths), so the atomic doubly charged ions are not abundant in the plasma. It should be noted that the emission lines of singly charged ions are often the most useful analytical lines in ICP-OES.

In contrast to the numerous advantages, high solvent and/or salt loads considerably alter the stability of the plasma and its excitation/ionization characteristics, which imposes more rigorous requirements for sample composition.

The most obvious difference in ICP assembly in OES and MS is its vertical or horizontal mounting, respectively. A larger diameter plasma torch (9–27 mm) is typically used in OES in order to increase the residence time of analytes in the plasma. On the other hand, a long residence time is not convenient for ICP-MS, because it favors the formation of doubly charged ions.

2.2 Sample Introduction

The vast majority of ICP-based analyzes are performed on liquid samples that are introduced to the plasma in the form of an aerosol. In this case, sample introduction system consists of four parts: (i) a nebulizer, which generates an aerosol; (ii) a spray chamber, which filters the aerosol and transports it to the plasma; (iii) a desolvation system to reduce the mass of solvent reaching the plasma; (iv) an injector tube to introduce the aerosol into the plasma base.

Different types of nebulizers are commercially available and their detailed descriptions can be found elsewhere.[6–8] In Figure 2, general schemes of pneumatic and ultrasonic nebulizers are presented. In the concentric pneumatic nebulizer, both the gas stream and the liquid flow in the same direction (Figure 2a), while in the cross flow and Babington nebulizers, the two streams are at right angles to each other (Figure 2b,c). When the gas travels at a high flow rate, it creates a drop in pressure near the tip, which draws the liquid through the inner tube and a sample emerges as an aerosol. In the ultrasonic nebulizer (USN, Figure 2d), a thin film of the solution flows over the surface of a piezoelectric transducer and is converted to the aerosol by the high-frequency vibrations from the transducer. The common shortcoming of the above nebulizers is low transport efficiency. This important parameter depends primarily on the mean droplet size of the aerosol and on the distribution of the droplet size. It should also be noted that the ionization capabilities of the plasma depend inversely on the particle size of the aerosol. In a conventional concentric nebulizer at typical solution uptake rates ($1-2\,\mathrm{mL\,min^{-1}}$), only 1–2% of the solution aspirated makes its way to the plasma. In the USNs, the transport efficiency is usually higher (10–30%). To improve the ‘‘quality’’ of the aerosol traveling to the plasma, different designs of spray chamber have been developed. The most common are double-pass or Scott-type, cyclonic, and single-pass chambers (Figure 3).[8]

Finally, several desolvation systems have been proposed to reduce the solvent loading to the plasma, thus improving its performance and avoiding interferences. Most desolvation systems comprise two steps: (i) heating, in which the solvent is totally or partially evaporated from the aerosol droplets; and (ii) removal of solvent vapor from the aerosol stream. More detailed information can be found elsewhere.[8]

The analysis of microsamples and coupling ICP with different liquid separation techniques require low-consumption introduction systems. In principle, for standard-sized analytical columns, the flow rate in liquid

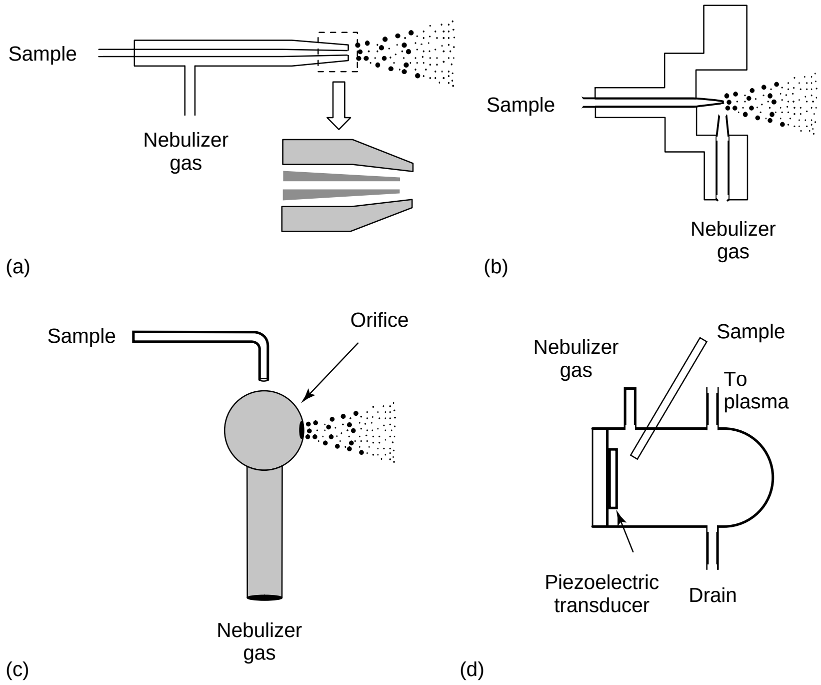

Figure 2 Different types of nebulizers. (Reprinted from Kannamkumarath, Wrobel, B'Hymer and Caruso[9] © 2002, with permission from Elsevier)

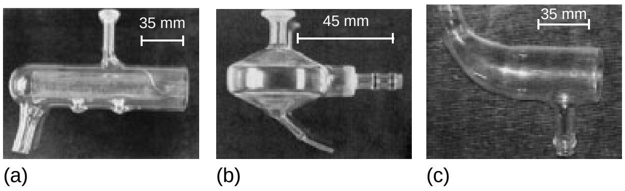

Figure 3 Different designs of spray chamber: (a) double pass; (b) cyclonic; (c) single pass. (Reproduced with permission Mora, Maestre, Hernandis and Todoli[8] © 2003, Elsevier)

chromatographic separation (0.5–1.2 mL min^{-1}) is compatible with the aspiration rate of traditional pneumatic nebulizers, so the column outlet can be connected directly with the liquid inlet of the nebulizer using polymeric or stainless steel tubing. However, low transport efficiency of traditional pneumatic nebulizers is an important limiting factor. Furthermore, in such coupling the composition of the column effluent can affect the performance of the plasma.[10–12] The increased efficiency of sample introduction to ICP can be achieved by using microconcentric nebulizer (MCN), hydraulic high pressure nebulizer (HHPN), direct injection nebulizer (DIN), high-efficiency nebulizer (HEN) or direct injection high-efficiency nebulizer (DIHEN).[6,7,9] These are low-flow devices and are particularly well suited for microbore and capillary liquid chromatography (LC). The commercially available MCNs operate at flow rates of 10–100 µL min^{-1}, yielding a transport efficiency close to 50%.[13–16] The DIN was developed by Shum *et al.*[17]; this nebulizer is positioned inside the ICP torch and its nozzle is placed only a few millimeters from the base of the plasma. The sample uptake requires a flow rate in the range 30–150 µL min^{-1} at relatively high gas flow rate (1 L min^{-1}). The DIN does not use a spray chamber and thus offers 100% analyte transport efficiency, low dead volume (<2 µL), rapid wash-in and wash-out times, low memory effects, enhanced sensitivity, and improved precision as compared to nebulizer–spray chamber arrangements. However, easy clogging of the DIN capillary hinders the introduction of elevated salt/buffer concentrations. Plasma cooling has also been observed.[18] An alternative low-flow design is the HEN, which is composed of a small capillary and a spray chamber. The efficient formation of uniform fine droplets is achieved at 40–100 µL min^{-1} sample flow rate (gas flow rate 1 L min^{-1}, as in the DIN). The designs of HEN and DIN have been combined and modified to produce a simple and low-cost DIHEN. The DIHEN offers optimal sensitivity at 1–100 µL min^{-1} sample flow rate and significantly lower injector gas flow rates (0.25 L min^{-1}). It should be stressed that, in spite of higher transport efficiency, the analyte(s) mass introduced to plasma through the low-consumption devices is generally low, so they are more frequently used in ICP-MS rather than in ICP-OES applications.

The introduction of gaseous samples is another possibility in ICP-based spectrometric techniques. The clear advantage is excellent transport efficiency; however, the applications are limited to the volatile forms of elements. There are several reviews available on gas chromatography

(GC) coupling to ICP,[19,20] and on the applications of hydride generation,[21,22] electrothermal vaporization (ETV),[23] and laser ablation techniques.[24,25] Finally, the introduction of slurries in the analysis of different solid samples should be mentioned.[26]

2.3 Inductively Coupled Plasma Optical Emission Spectrometry

The emission spectra produced in a plasma can be observed using radial, axial, or dual-view configurations. In most commercial instruments, the plasma torch is in a vertical position and spectral data are collected using the side view of the analytical zone (Figure 4). Since only this plasma region is observed, the contribution of spectral and background interferences is generally low, but the sensitivity is relatively poor.

For axial configuration, the torch is moved to the horizontal position and spectral information is collected from the central channel of the plasma. The viewing path is longer with respect to the radial configuration, so the detection limits are improved, typically by a factor of 5–10. However, spectral and matrix-induced interferences are more severe in the axial view. In particular, high concentrations of easily ionized elements (EIE) affect the ionization of other elements in the plasma, causing considerable suppression of the ionic emission lines. Another possible interference is due to the self-absorption effects occurring in the cooler tail plume of the plasma. As a consequence, the axial configuration is not recommended for the analysis of samples containing a wide range of elements at different concentrations. Some commercial instruments have a dual-view system, which enables one to select the configuration according to the sample composition.[27]

As already mentioned, the emission spectra generated in ICP-OES are remarkably rich. Thus, high resolving power is required in order to minimize spectral interferences. Optical spectrometers are typically equipped with grating monochromators based on conventional or echelle-type gratings. In brief, conventional plane grating has a high groove density (up to 3600 grooves mm^{-1}), the radiation strikes the broad faces of the grooves, the diffraction angle is low (10° 22′) and the first-order spectral line typically is used. The required spectral bandwidth (0.01 nm) is achieved by using a large number of grooves and large focal length ($\geq$0.5 m). With the echelle grating, high resolution is achieved by using low groove density (70 grooves/mm) and larger blaze angle ($>$45°), so the constructive interference is more intense at higher spectral orders (usually 10–1000). The overlapping orders are separated with the use of an auxiliary dispersing element (prism or low-dispersion grating), yielding a two-dimensional, high-resolution spectrum. The focal plane has wavelengths dispersed in the horizontal direction and ordersorted in the vertical direction. An echelle monochromator often provides a spectral bandpass nearly 10 times smaller (higher resolution of about 1 order of magnitude) than that of a conventional plane grating with a similar focal length.[28] The additional advantage here is that ultimately a line spectrum is replaced with a series of stacked broken lines resulting in a two-dimensional array eliminating the need for long focal lengths as well as allowing an easy focus onto 2D-array detectors.

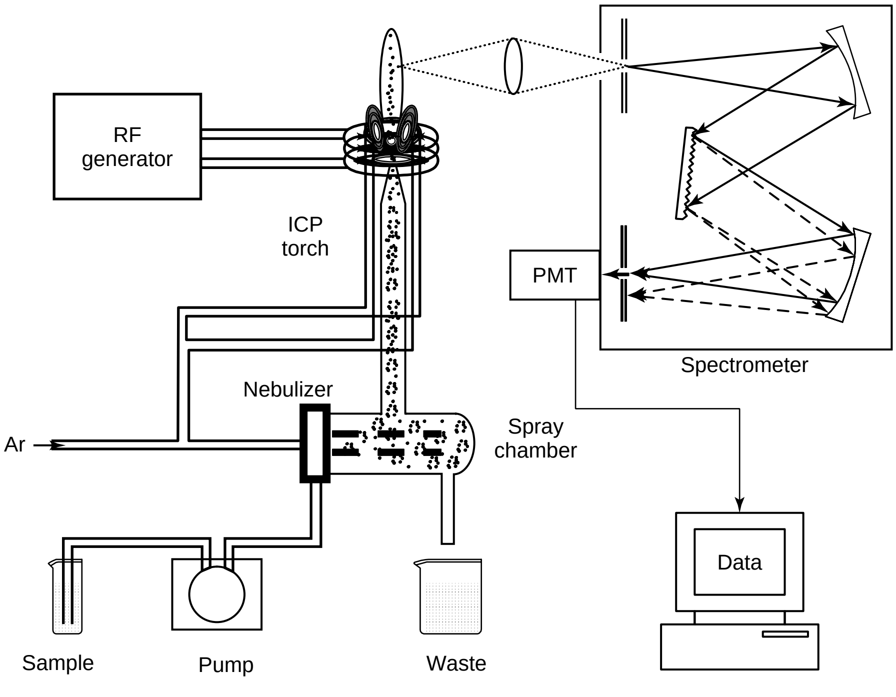

Figure 4 Schematic diagram of ICP-OES instrument

The ICP-OES spectrometers can be adapted either for sequential or simultaneous multielement measurements. In most sequential instruments, one or a few photomultiplier tubes (PMT) are used for detection. Scanning can be accomplished by changing the grating angle at the fixed position of the PMT. In another design, the PMT is rapidly moved along the focal curve of the Rowland circle. The strong point of sequential instruments is high sensitivity of the PMT and the flexibility for measuring the signal at any wavelength. However, only one element is measured at a time, so multielement analysis requires a longer observation time, and thus a larger sample volume. The analytical performance is compromised at high sample throughput and special care is needed to assure good reproducibility of wavelength selection.

In simultaneous spectrometers, the grating, the entrance, and the exit slits are typically fixed on the Rowland circle (Paschen–Runge mount). The detectors and gratings are stationary and the slit positions are tuned for preselected wavelengths. The number of lines is limited by the size of PMTs and the polychromator geometry (up to 60 PMTs). Since all target elements are detected simultaneously, such instruments are faster and more accurate, but only for a predictable set of analytes and potential interferences. The development of solid-state detectors has overcome the limitations of sequential and PMT-based polychromators. Thus, simultaneous spectrometers equipped with charge-coupled or charge injection devices have essentially unlimited possibilities for elemental analysis with better detection limits, precision, and higher throughput than sequential instruments.

In spite of high temperatures in the ICP, several interferences occur in OES. The recombination of argon ions with electrons results in continuum background emission, which becomes important at low analyte concentrations and hence, needs to be corrected. In addition, owing to the complexity of emission spectra, line overlapping is frequently observed. The simplest way to circumvent this problem is to select different analytical line(s) at a wavelength(s) with no background interference. A more efficient solution to the problem of spectral interferences is in the use of high-resolution instruments and/or advanced background correction systems. A common chemical interference is the effect of EIE. These elements have low ionization potentials (e.g., alkaline and alkaline earth elements) and, if present at high concentrations, they may suppress or enhance the emission signal of the target element. The effect of EIEs can be reduced by sample dilution, appropriate selection of instrumental conditions (forward power, viewing height, etc.), and/or mathematical correction.[29]

2.4 Inductively Coupled Plasma Mass Spectrometry

For mass spectrometric measurements, the ions must be extracted from the ICP, which operates at atmospheric pressure, into a vacuum system. A cooled nickel or platinum sampler cone (1 mm diameter), mounted at the entrance to the spectrometer, is used for this approach. In the low-pressure region behind the cone, gas expansion occurs and a fraction of the ions pass through another cone (skimmer), while the majority of the argon is pumped away. Finally, the ions are focused into a more direct path to the mass analyzer using a series of ion ''lenses'', which are simply a series of electrodes, held at variable dc voltages. After separation of ions according to their mass-to-charge ratio (m/z) in the mass analyzer, the detector (channel electron multiplier, Faraday cup, or discrete dynode electron multiplier) converts the ion stream into an electrical signal, which can be correlated through the calibration procedure to the concentration of targeted elements within the sample.[30,31] The most popular mass filter in ICP-MS instruments is the quadrupole analyzer, which gives better than unit mass resolution over a mass range up to $m/z = 300$. A schematic of a quadrupole-based ICP-MS instrument is shown in Figure 5.[9]

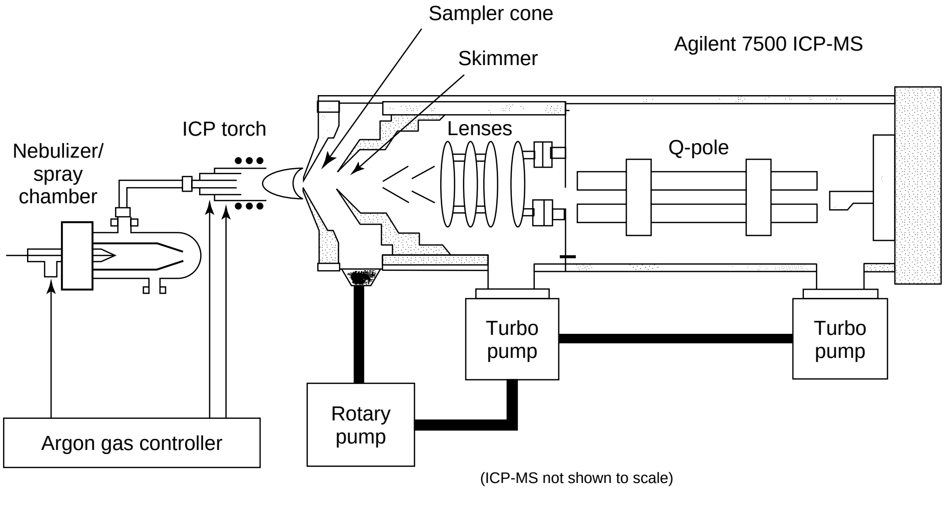

Figure 5 Schematic diagram of a quadrupole-based ICP-MS instrument. (Reprinted from Kannamkumarath, Wrobel, B'Hymer and Caruso[9] © 2002, with permission from Elsevier)

Typical shortcomings of ICP-MS, especially in the early applications, were due to severe polyatomic interferences, low ionization efficiency for biologically important elements (Se, S, P, halogens), and the sequentially scanning nature of the mass analyzer and detection system. When aqueous solutions are aspirated into the ICP, typical background spectra contain signals of several ions such as $OH^+ (m/z = 17)$, $OH_2^+ (m/z = 18)$, $OH_3^+ (m/z = 19)$, $O_2^+ (m/z = 32)$; $ArH^+ (m/z = 41)$, $ArO^+ (m/z = 56)$, $Ar_2^+ (m/z = 80)$ and those formed by less abundant isotopes of Ar, O, and H. Additionally, depending on the plasma operating conditions and also on the composition of sample, different charged species originating from plasma argon, air, and/or sample may be generated with possible isobaric overlap between their m/z values and those of the target ions. In Table 2, common polyatomic interferences observed for some elements are listed.[4,32]

The need for reliable results of total element determinations and, in particular, increasing research interest in speciation analysis have spurred instrumental and methodological development, thus considerably extending the scope and capabilities of ICP-MS. Actual strategies used to enhance the performance of ICP-MS include the following: (i) optimization of plasma operating conditions, (ii) high-resolution instruments, (iii) collision/reaction cell technology, and (iv) isotope analysis. With regard to plasma operating conditions, using reduced RF forward power (500–800 W) and increased nebulizer Ar flow rates (1.5–1.8 L min^{-1}), the plasma becomes ''cooler'', hindering generation of interfering Ar-based ions.[33,34] The weak point of the cold-plasma strategy is the increased contribution of polyatomic charged species originating from the sample matrix. Such interference can be avoided by separating the analyte from the potentially interfering sample components, prior to its introduction to ICP-MS.[35] Thus, different chromatographic, extraction, and dialysis procedures have been reported for the elimination of chloride ions prior to As determination/speciation.[36]

Table 2 Typical isobaric interferences in ICP-MS elemental analysis

Element	The most abundant isotopes	Interfering species
Arsenic	^{75}As (100%)	$^{40}Ar^{35}Cl^+$
Chromium	^{52}Cr (83.79%)	$^{40}Ar^{12}C^+$
Cobalt	^{59}Co (100%)	$^{42}Ca^{16}O^1H^+$, $^{43}Ca^{16}O^+$
Copper	^{63}Cu (69.17%)	$^{46}Ca^{16}O^1H^+$
Iron	^{56}Fe (91.75%)	$^{40}Ar^{16}O^+$, $^{40}Ca^{16}O^+$, $^{23}Na^{35}Cl^+$
Nickel	^{58}Ni (68.08%)	$^{42}Ca^{16}O^+$
Phosphorus	^{31}P (100%)	$^{15}N^{16}O^+$, $^{14}N^{16}OH^+$, $^{12}CH_3{}^{16o+}$, $^{62}Ni^{2+}$
Sulfur	^{32}S (95.02%)	$^{16o_2}+$, $^{14}N^{18}O^+$, $^{15}N^{16}OH^+$
Selenium	^{78} Se (23.77)	$^{40}Ar^{38}Ar^+$, $^{31}P_2^{16o+}$
	^{80} Se (49.61)	$^{40}Ar_2{}^+$, $^{79}BrH^+$
	^{82} Se (8.73)	$^{40}Ar_2H_2{}^+$, $^{12}C^{35}Cl_2{}^+$, $^{34}S^{16}O_3{}^+$, $^{82}Kr^+$, $^{81}BrH^+$, $^{65}Cu^{17}O^+$, $^{64}Zn^{18}O^+$, $^{68}Zn^{14}N^+$

The commercial availability of high-resolution ICP-MS (inductively coupled plasma high-resolution mass spectrometry (ICP-HRMS)) instruments has enabled a significant advance in the analysis/speciation of nonmetal elements. Mass analyzers typically used are composed of either magnetic sector or double-focusing sector device.[37,38] In the magnetic sector, a field is perpendicular to the ion beam from the plasma. The trajectory of the ions in a circular path depends on mass-to-charge ratio, permitting the separation of different elements and isotopes. In double-focusing sector mass analyzers, the ions are additionally subjected to an electrostatic field with the resultant trajectory being dependent on the energy of the ion. The resolving power ($R = m/\Delta m$) of ICP-HRMS can be changed (between 300 and 10 000), as compared to the range of 300–400 typically offered by traditional quadrupole mass analyzers.[39] The desired resolution is achieved by selecting different entrance and exit slit widths. The narrower slit widths used to yield higher resolution also limit the number of ions transmitted to the detector, subsequently reducing sensitivity. An important benefit from sector field instruments is a high signal-to-noise ratio, as a result of very good ion transmission (high sensitivity at low R) and low background (<0.2 ions$^-$/s). As a consequence, detection limits in the range of picogram per liter are typically obtained in the low resolution mode.[40,41] Finally, the excellent precision (0.1–0.5% RSD) of ICP-HRMS should be mentioned. These instruments have dramatically enhanced the analytical capabilities of ICP-MS by increasing the number of elements that can be effectively measured.[3,36,42] In particular, ICP-HRMS technology has been used to mitigate polyatomic interferences in the determination of biologically important As, Fe, P, S, and Se.

The common limitation of the quadrupole and sector field analyzers for multielemental and liquid separation ICP-MS applications is their sequentially scanning character. When the instrument is operated in such noncontinuous manner, the duty cycle is reduced, producing lower signal-to-noise ratio, poorer precision, and also lower mass resolution for the increasing number of elements/isotopes monitored.[43] Logically, longer observation time can be used to circumvent this problem. However, when ICP-MS is used as an element-specific detector for LC, ions are generated from relatively fast transient events and the observation time is restricted by chromatographic peak width. Recently available ICP-time of flight (TOF) mass spectrometers with scan rates up to 20 000 spectra/s can overcome this drawback, because, rather than time-consuming scanning from one mass to the other, the mass filter distinguishes the different isotopes by their individual (m/z-dependent) time of flight to the detector.[35,44] For simultaneous detection of an entire atomic mass range, ICP has also been used with the quadrupole ion traps (QIT), Fourier transform ion cyclotron resonance mass spectrometers (FTICR), and multichannel mass spectrometers.[22,40,45]

Over the past decade, the development of quadrupole ICP-MS instruments equipped with collision/reaction cells inserted between the ion optics and the mass filter has offered an interesting alternative to high-resolution systems for the removal of polyatomic interferences.[46] Conceptually, a collision/reaction cell for ICP-MS provides adequate conditions for controlled reaction or conversion of the interfering species or the analyte itself, which results in a change of their m/z and thereby enables determination of the element at quadrupole resolution.[43] A collision/reaction cell instrument essentially resembles the configuration of a traditional ICP-MS except that a collision/reaction cell with gas inlet is positioned just before the quadrupole mass analyzer. The cell consists of another quadrupole, hexapole, or octopole to which only RF-voltages are applied. When subjected to this field, incoming ions are focused and collide or react with the collision/reaction gas that is admitted through the cell gas inlet. The collisions and reactions that occur between the analyte ions and the gas molecules can eliminate problematic interferences as follows: (i) collisional deactivation where the energy of the collision gas exceeds the bond energy of the interfering polyatomic; (ii) the analyte reacts with the cell gas shifting its m/z; or (iii) energy discrimination by preferentially reducing the polyatomic ion energy over the analyte ion energy (because the polyatomic has a larger collision cross-section), followed by carefully adjusting the quadrupole bias voltage to admit only the more energetic analyte ions. Unfortunately, under these conditions rather complex secondary collisions and reactions can occur within the cell, leading to the generation of other interfering species. Such secondary interferences are rejected in different ways, depending on the multipole of the cell. Quadrupoles act through mass discrimination, whereas higher-order multipoles, such as hexapoles and octopoles, can discriminate analytes from interferences based on kinetic energy.[3] In particular, the concept of dynamic reaction cell (DRC) technology is based on the use of highly reactive gases (e.g., ammonia or methane) acting as catalysts for ion-molecule chemistry and the ions generated are discriminated in quadrupole.[43,47] Since hexapoles do not function as mass filters, only low reactivity gases (He, H_2, Xe) are used, thus limiting the formation of new ions. In this case, analyte ions can be distinguished from other ions by allowing the cell bias to be slightly less positive than the mass filter bias. This causes ions with the same energy as the cell bias to be rejected, whereas the analyte ions, which have energy higher than the cell bias, can be transmitted. Octopoles operate in a similar manner, but offer higher transmission characteristics, particularly at the lower end of the mass range.[3,46]

One of the main characteristics of mass spectrometry is the possibility of precise and accurate isotope ratio measurements. The isotopic dilution technique is based on the principle that most elements in nature possess fixed isotopic ratios. This natural ratio can be altered by spiking a sample with an analyte standard consisting of a different isotopic abundance. The change in the measured isotopic ratio can then be used to elucidate the original elemental composition of the sample. The only real requirements of this technique are that the analyte of interest has more than one stable isotope and that the spike standards are isotopically pure. Furthermore, isotope dilution has become widely recognized as a definitive technique that can be used to overcome many of the problems associated with instrumental drift and incomplete extraction of analyte from the sample.[48] In the same manner, isotope dilution can also be used to compensate for the poor ionization efficiency exhibited by a number of nonmetal elements. Over the past 40 years, isotope dilution mass spectrometry (IDMS) has proved to be a very effective method for the measurement of total element concentration and as applied to elemental speciation studies.[35,45] In particular, the quadrupole-based spectrometers with collision/reaction cells, high-resolution instruments, and those offering simultaneous monitoring of different ions are well suited for isotopic analysis. If the sector field mass analyzer is operated at low resolution ($R \sim 300$), the isotope ratios can be measured with a precision as high as 0.02% (RSD) and the detection limits are in the picograms per liter range.[35]

3 APPLICATIONS

Historically, most analytical applications of ICP-OES and ICP-MS have addressed total concentrations of elements in real-world matrices. It is now common knowledge that the mobility, bioavailability, retention, and specific biological function of an individual element depend on its physicochemical form. As approved by respective international union of pure and applied chemistry (IUPAC) commissions, ‘‘chemical species’’ is a specific and unique molecular, electronic, or nuclear structure of an element. The term ‘‘speciation analysis’’ refers to the measurement of the quantities of one or more individual chemical species in a sample.[49] Analytical results are helpful in studies on the mechanisms of element transport and/or degradation in the environment and also on the element pathways in living organisms. Other relevant topics include more efficient elimination and/or recovery of elements from industrial and mining effluents (Hg, As, Cd, etc.), refining of certain industrial processes (tanning with chromium salts, metal-based catalytic mixtures, etc.), development of new metal drugs (Pt, Ru, Ti), as well as promotion of necessary regulations for the commercial use of metal/metalloid based biocides (As, Sn). Different classifications have been proposed for possible elemental forms, depending on the selectivity of measurement (specific compounds versus operationally separated forms), the type of element bonding (chemical bonds versus weak interactions, covalent versus coordination bonds, etc.), molecular structure (inorganic salts, organic and biometals, or biometalloid compounds), and also molecular size (small molecules vs biomolecules).[50–53] A consensus seems to exist in regarding ‘‘large molecules’’ as those with molecular weight >5 kDa. In this section, ‘‘small molecules’’ are limited to inorganic salts, organometals, and organometalloids with molecular weights <5 kDa.

3.1 Total Concentrations of Elements

The primary application field of ICP-MS and ICP-OES in routine analysis is semiquantitative and quantitative determination of metals and metalloids in a wide range of materials that can be of either natural or anthropogenic origin.

As already discussed, the detection limits of ICP-OES are generally poorer than those of ICP-MS (Table 1), which limits specific applications of this technique. Generally speaking, it can be used for practically all metallic elements in liquid, dissolved, or suspended samples. It is an important tool in geochemistry, providing precise and accurate results for trace, minor, and major elements. This technique is also suitable for the analysis of biological materials, natural, and waste waters, fuels, and lubricating fluids. The industrial applications include process control, evaluation, and quality control of final products in metallurgy, refinery, ceramics, glass, polymer production, as well as catalyst evaluation. The detailed information on these applications can be found in atomic spectrometry updates on environmental, industrial, food, and beverage analysis, which are published annually in the *Journal of Analytical Atomic Spectrometry*.

In principle, the applications of ICP-MS resemble those listed for OES. This technique however is required for samples containing sub-part per billion concentrations of elements. Quantitative information of nonmetals such as P, S, I, B, Br can be obtained. Since atomic mass spectra are much simpler and easier to interpret compared to optical emission spectra, ICP-MS affords superior resolution in the determination of rare earth elements. It is widely used for the control of high-purity materials in semiconductor and electronics industries. The applications also cover the analysis of clinical samples, the use of stable isotopes for metabolic studies, and the determination of radioactive and transuranic elements. In addition to outstanding analytical features for one or a few elements, this technique provides quantitative information on more than 70 elements present from low part-per-trillion to part-per-million concentration range in a single run and within less than 3 min (after sample preparation and calibration). Comprehensive reviews on ICP-MS applications in total element determinations are available.[54–59]

3.2 Speciation of Small Molecules

Speciation studies have been focused on relatively few elements, mainly aluminum, antimony, arsenic, chromium, lead, mercury, selenium, and tin.[60,61] The primary species of these elements studied with ICP-MS detection are presented in Table 3 and they include different oxidation states, alkylated metal and/or metalloid compounds, selenoaminoacids, and selenopeptides. In addition, applications in studies of the pharmacokinetics of metal-based drugs (Pt, V, Au), metalloporphyrins (Ni, V, Fe, etc.), heavy metals in phytochelatins (Cd, Cu, Zn, Hg, etc.) and in humic substances should be mentioned.

A common speciation scheme after sample preparation involves a fractionation step followed by the quantification of element in the obtained fractions. A clear trend exists toward using the techniques that combine separation and detection steps into one operating online system. In these procedures, the selectivity is achieved by application of powerful separation modes (different chromatographic or electrophoretic methods), while the use of atomic spectrometric techniques assures high sensitivity of detection. The number and variety of combinations have been continuously increasing and almost every possible instrumental coupling has been examined. Among element-specific detectors, ICP-MS has become a primary tool in speciation analysis because of its unique features such as (i) monitoring effluents for their elemental composition with high sensitivity, (ii) determination of the target element with the selectivity over coeluting elements, (iii) compensation of incomplete chromatographic resolution from complex matrices, isotope ratio, and isotope dilution capabilities, and (iv) detection of a number of elements virtually simultaneously.[60] On the other hand it should be stressed that hyphenated techniques with atomic spectrometry detection do not provide structural information for the species. If the appropriate standards are available, the assignation of chromatographic peaks can be accomplished by spiking experiments. On the other hand, the identification of unknown forms and/or ultimate confirmation of unexpected compounds observed in the sample require the use of complementary techniques (molecular mass spectrometry or NMR (*see* ***Nuclear Magnetic Resonance (NMR) Spectroscopy of Inorganic/Organometallic Molecules***)).

The selection of a suitable separation technique is always dictated by the analyte(s) properties (volatility, stability, polarity, electrical charge, etc.) as well as the sample composition. In speciation of small molecules, different chromatographic and electrophoretic modes have been explored. It should be stressed that, owing to high sensitivity, ICP-MS is especially suitable for low-flow and low-volume chromatographic methods (microbore LC columns or capillary electrophoresis (CE)). The advantages of such coupling include outstanding resolution power, low sample loading, minute amount of column effluent entering plasma, and hence better transport efficiency and enhanced analytical performance of the plasma.

The great majority of small elemental forms are polar or ionic compounds, and thus the first separation technique of choice to address speciation analysis is LC. Of special importance for small molecules are reversed phase, ion-pairing, micellar, and ion exchange techniques that have been reviewed elsewhere.[11,12,18] The optimum separation conditions may not always be used in speciation studies. Compromises are sometimes necessary to avoid possible changes in natural species distribution due to their interaction with stationary and mobile phases (pH conditions, complexing agents, organic modifiers).[61]

Table 3 Elements and their species of low molecular mass analyzed with ICP-OES and ICP-AES detection

Element	‘‘Small molecules’’ of interest	Importance	Typical samples
Al	Organic complexes with citric, lactic, malonic acids, etc., Al-desferroxiamine	Studies on Al toxicity and detoxification routes	Clinical materials
As	Stable oxidation states: As(III) and As(V)	Higher toxicity of As(III) vs As(V), detoxification routes	Environmental, biological, and clinical samples
	Monomethylarsonic acid (MMAs(V)) Monomethylarsonous acid (MMAs(III)) Dimethylarsinic acid (DMAs(V)) Dimethylarsinous acid (DMAs(III)) Trimethilarsineoxide (TMAsO) Tetramethylarsonium ion (TETRA) Arsenocholine (AsC) Arsenobetaine (AsB) Arsenosugars (AsS)	Biomethylation pathways	
Cr	Stable oxidation states: Cr(III) and Cr(VI)	Toxicity of Cr(VI) versus essentiality of Cr(III)	Natural and waste waters, biological fluids
Hg	Inorganic (Hg(II))	Biomethylation with formation of toxic organomercuric compounds	Sea water, natural and waste waters, sediments, food products, fish tissues, biological fluids
	Mono- and dimethylmercury (MMHg, DMHg) Mono- and diethylmercury (MEHg, DEHg) Monophenylmercury (MPhHg)		
Pb	Inorganic and alkyllead:	Toxicity and persistence of lead species in the environment	Air, sea water, natural waters, biological materials
	$R'_nR''_mPb^{(4-m-n)+}$ (R′-methyl, R″-ethyl)		
Pt	Anticancer drugs and their metabolites:	Pharmacokinetics and toxicological studies	Drug formulations,
	Cisplatin, carboplatin, oxaplatin, lobaplatin, nedaplatin, JM216		Clinical materials
Sb	Oxidation states: Sb(III) and Sb(V)	Higher toxicity of Sb(III) vs Sb(V), possible biomethylation processes	Different types of water, fermentation gases, headspace over microorganism cultures
	Mono-, di- and trimethylated Sb compounds		
Se	Stable oxidation states: Se(IV) and Se(VI)	Elucidation of biological pathways and specific role of Se species, phytoremediation	Environmental samples, yeast, plants from allium family and Se-accumulating plants, clinical samples
	Organic selenium species: Mono- and dimethylselenide (MMSe; DMSe) Mono- and diethylselenide (MESe, DESe) Trimethylselonium ion (TMSe) Selenomethionine (Se-Met) Methylselenomethionine (Me-Se-Met) Selenocysteine (Se-Cys or oxidized Se-Cis) Methylselenocysteine (Me-Se-Cys) Selenohomocystine (Se-Hcy) Selenoethionine (Se-Et) Adenosylselenomethionine (AdoSe-Met) Adenosylselenohomocysteine (AdoSe-Hcy) γ-Glutamyl-methylselenocysteine		
Sn	Inorganic forms (Sn(IV)/Sn(II))	Harmful effects of organotin pesticides, antifouling paints, and their degradation products	Sea water, natural waters, sediments, soils, marine organisms
	Organotin compounds: $R_nSn^{(4-n)+}$ ($1 < n < 4$; R-methyl, ethyl, butyl or phenyl)		

Volatile compounds that present thermal stability, monomeric form, neutrality, relatively low molecular weight, coordinative saturation, and shielding of the metal/metalloid atom by bulky and inert organic functional groups can be separated by GC.[51] The direct applications of GC with ICP-MS detection in speciation analysis are limited to relatively few volatile organometals (Hg, Pb, Sn, Bi) and organometalloid compounds (Se, As). Different precolumn derivatizations can be used to improve and/or expand GC potential. The most common procedures include (i) conversion of inorganic and small organometallic ions into volatile covalent compounds (hydrides, fully ethylated or propylated species) in aqueous media, (ii) conversion of larger alkylated cations with Grignard reagents to saturated nonpolar species, and (iii) conversion of ionic species to volatile chelates (dithiocarbamate, trifluoroacetone, etc.).[62,63] In the separation of small elemental species, low-temperature GC should also be mentioned. In this mode, the gaseous species are cryogenically trapped on the column (Pb, Sb, Hg, As) and then separated during the controlled column heating, according to their boiling points.[64,65] Owing to the sharpness of chromatographic peaks, the speed of data acquisition by the mass analyzer is of vital importance. Within this context, the time of flight analyzer offers better detection conditions with respect to the quadrupole.[66] Virtually simultaneous extraction of all m/z ions in time of flight mass spectrometry (TOFMS) enables the measurements of multiple isotopic ratios (species-specific isotope dilution and multielemental speciation); however the loss of sensitivity in the single ion mode is still a limitation.

Supercritical fluid chromatography (SFC) combines the high diffusion coefficient of GC and the solubility properties of LC and this separation mode has also been coupled with atomic spectrometric detection.[67–69]

Performing electrophoretic separations in capillaries allowed the possibility of automated analytical equipment, fast analysis times, and online detection of the separated peaks. The separation of species in CE is controlled by two phenomena: the electrophoretic mobility and the electroosmotic flow. With careful selection of separation conditions (type and concentration of the electrolyte solution, complexing reagents, pH, etc.), the combined effect of these two forces can be controlled, resulting in the high-speed resolution of a large number of cations, anions, small metal ions, metal–organic ligand complexes, and organometallic molecules in a single run. Moreover, the technique has been successfully used for the separation of relatively labile complexes and to study the kinetics of complex formation. Owing to the small sample volume (in the range of nanoliter) introduced to a narrow capillary (internal diameter 20–100 µm), the lack of sensitivity is a general limitation, almost independent of the detection systems used. One approach for improving the detection limits is to increase loading of the CE system. This can be achieved by preseparation cleanup or preconcentration procedures, electrokinetic sample introduction, application of electrostacking effect, or isotachophoresis. On the other hand, coupling of CE to highly sensitive and specific ICP-MS detection seems to be an attractive speciation tool.[9,70] As the amount of capillary effluent entering the plasma is very low, its chemical composition does not affect the performance of the plasma and the optimum separation conditions can be used. However, the applications of CE in real-world samples have been limited, because the effect of sample matrix and/or chemical conditions applied during separation on the speciation results is difficult to control. CE-ICP-MS has been used in the analysis of stable oxidation states (As, Cr, Se), metal complexes (Au, Cd, Co, Pt, Sb), and small organic compounds (As, Se, Hg).

3.2.1 *Aluminum and Antimony*

These two elements have a variety of important chemical forms and provide a number of very interesting speciation applications, but to discuss these here would exceed the limitations of this article. The reader is referred to Table 3 and selected references.[64,69,71]

3.2.2 *Arsenic*

In addition to the natural abundance of arsenic forms, various compounds have been extensively used in processes, such as arsenic-based pigments, biocides, and so on. The arsenicals emitted into the environment can be degraded and/or biotransformed, resulting in a variety of chemical forms (Table 3). Owing to the species-dependent toxicity, the environmental materials, foods, and biological and clinical samples have been analyzed.[12,61,72] In particular, elemental speciation in marine organisms that accumulate and metabolize arsenic have often been addressed. LC hyphenated with ICP-MS is suitable for the common small molecules (As(III), As(V), MMAs(V), DMAs(V), and arsenobetaine (AsB)). Depending on the pH conditions, these species can be cationic, anionic, or uncharged (pK_{a1} respectively, 9.3, 2.3, 2.6, 6.2, and 2.2),[72] which makes the separation by anion exchange, ion-pairing, and, to a lesser extent, cation-exchange chromatographic modes possible. In the applications of anion-exchange LC, good resolution has been achieved at pH ranges from 5 to 11, usually with the elution order AsB, As(III), DMAs(V), MMAs(V), As(V) and separation times between 7 and 30 min. Cation-exchange separations, requiring lower pH values ($pH < 4$) have been preferred for the analysis of AsC, tetramethylarsonium ion (TETRA), and/or trimethylarsineoxide (TMAsO).[73] Several applications of ion-pairing separation have been proposed, based on the use of tetrabutylammonium ion (pH 6–11) and different alkylsulfonates (pH 2.7–4.5).[10] The separation of larger amount of species has been addressed. For more detailed information, recent reviews can be consulted.[12,36,74,75] The particular interest in the intermediate products of arsenic methylation (MMAs(III) and DMAs(III)) is worth mentioning. As these species are highly toxic, the detoxification effectiveness of arsenic biomethylation is uncertain. Pergantis *et al*. reported the speciation procedure of As(III), DMAs(V), MMAs(III), and MMAs(V) by anion-exchange LC coupled with ICP-MS, which was applied to study the mechanism of nonenzymatic methylation of arsenic.[76]

The separation of As species (As(III), As(V), MMAs(V), DMAs(V), AsB, AsC) has also been accomplished by CE (electrolyte in the pH range 5.6–11.2; phosphate, triethanolamine or borate buffers), but only in simple aqueous matrices.[9] Online hydride generation in capillary effluent has been proposed to increase transport efficiency.[77] SFC has been used only for nonpolar As compounds, like trimethyl-, triphenylarsine, and triphenylarsine oxide.[69]

3.2.3 Chromium

Various industrial processes, like plating, tanning, paint, and pigment production, and so on, involve the use of chromium. The hexavalent form of this element represents a considerable health hazard, related to the easy permeation through biological membranes and high oxidation potential. The challenge for analytical speciation is to discriminate between two stable oxidation states and to perform their quantification in environmental and clinical materials. The difficulty is increased, because the Cr(III)/Cr(VI) equilibria are highly pH dependent, the two forms have opposite electrical charge and different Cr(III) species can be formed in the aqueous medium (mono- and polynuclear complexes presenting different electrical charge and considerable lability). A great number of speciation schemes and procedures have been described, both for the specific determination of one form and for simultaneous speciation of the two forms.[78] The most common hyphenated techniques involve liquid chromatographic separation; ethylenediaminetetraacetic acid (EDTA) has often been used for stabilization of Cr(III) and the separation was accomplished on anion-exchange columns.[75] Increased detection power was obtained with the use of a microbore column and DIN (detection limit (DL) 3 pg for each species, as compared to 44 pg with the application of conventional analytical column).[79] The application of ion-pairing LC with tetrabutylammonium ion has also been reported.[68] In addition to the valence states, hydrolytic polymerization products of Cr(III) were investigated by CE.[9,80] Several organic complexes of Cr(III) were analyzed by SFC–ICP-MS.[69]

3.2.4 Lead

The main anthropogenic sources of lead include lead-based paints, solder, and metallurgy. Even though utilization of the alkyllead compounds such as gasoline additives has already been regulated, the persistence of various lead forms in the environment is still an issue (Table 3). ICP-MS detection of lead has been used in hyphenation of GC, ion exchange, ion-pairing LC, and, to a lesser extent, SFC.[69,75] The gas chromatographic approach usually involves the extraction with diethyldithiocarbamate (DDTC) followed by the reaction with Grignard reagent (butylmagnesium chloride) to form volatile butylated organolead species. Alternatively, tetraalkylborates (ethyl- or propyl-) have been used, allowing for the derivatization of lead species directly in aqueous solutions. Different mono- to trimethylated and ethylated lead species have been analyzed in water samples, airborne particles, fuel, and naphtha.[12,81] Capillary columns have been preferentially used because of better resolution and lower plasma loading with solvents, as compared to the packed columns. Owing to the reduced sample volume, the high sensitivity of ICP-MS detection becomes essential.[20,75] The detection limits for organolead species obtained with a quadrupole mass analyzer were around 50 and 500 pg L^{-1} in ICP-TOFMS.[82,83] In the latter case, substantial improvement (DL 3 pg L^{-1}) has been achieved after preconcentration of trimethyllead, dimethyllead, and triethyllead complexes with DDTC on C_{60} (fullerene).[81] In liquid chromatographic separations, different alkylsulfonate ion-pairing reagents have been used for inorganic lead and the charged alkyllead compounds in aquatic and urine samples. Even though gradient elution enhances the speed of separation, isocratic conditions have been preferred to maintain the same sensitivity of ICP-MS quantification over the whole chromatogram.[68,84]

3.2.5 Mercury

Mercury has been extensively used in different anthropogenic activities and the forms released to the environment include elemental Hg, inorganic salts, as well as organic species. Furthermore, naturally occurring biomethylation processes contribute in species interconversion. The accumulation of toxic methylmercury in different living organisms (in particular aquatic) is well documented. Other forms of organomercury are listed in Table 3. For risk assessment, accurate speciation analysis is needed with emphasis on natural and sea water, marine organisms (fish and mussels), soils, sediments, and biological fluids. The important part of the analytical procedure is the efficient extraction of different mercury species from the original sample. According to a recent review, distillation of methylmercury from soils and microwave-assisted alkaline digestion of fish tissue with tetramethylammonium hydroxide assured recoveries in the range 95–105%.[85] Practically every possible hyphenation technique with ICP-MS detection has been explored for mercury. In GC, the reactions with Grignard reagents or with tetraalkylborates yield volatile, thermally stable covalent derivatives.[20] Purge and trap, cryogenic trapping, and solid phase microextraction techniques for the recovery and/or preconcentration of these compounds have been used.[20,86] Relatively poor resolution on the packed columns was observed (undesirable interaction of mercury species with packing material) and capillary columns have been used in the majority of applications. Absolute detection limits reported recently in the analysis of biological tissues ranged between 100 and 200 fg (as Hg mass) for methylmercury and between 500 and 600 fg for inorganic mercury using a 1 μL injection.[87] Isotopically enriched inorganic mercury and methylmercury have been used for species-specific isotope dilution.[20,54,88] A detailed review on mercury speciation by high performance LC is available.[85] In brief, the majority of procedures reported involve reversed phase columns (silica-bonded phases) and the mobile phases containing a chelating (sodium pyrrolidinedithiocarbamate, cysteine, 2-mercaptoethanol) or ion-pairing (ammonium pentanesulfonate or acetate) reagent. ICP-MS detection has gained popularity relatively recently. With the use of HHPN or DIN, the detection limits for monomethyl-, monoethyl-, and monophenylmercury (MMHg, MEHg and MPhHg, respectively) were in the range of a few picograms (as Hg). Similar results were reported with online cold-vapor generation prior to ICP-MS detection.[85,86] There have been several reports on CE–ICP-MS for mercury speciation; cysteine was used for species chelation and separation carried out with borate or carbonate buffers.[9] Typical detection limits for MMHg, MEHg, and MPhHg were in the range of a few picograms (as Hg).[77] Similar absolute detection limits have been reported for diethylmercury (DEHg) and inorganic mercury by SFC.[69]

3.2.6 Platinum

Cisplatin has become one of the most widely used chemotherapy drugs. The mechanism of action relies on the ability of the drug to modify the DNA structure in cancer cells, hence causing their apoptosis. However, it presents severe toxicity and its anticancer activity is limited to a small group of tumor cell types. In further development, several other platinum complexes (mainly oxaliplatin, carboplatin, satraplatin, JM-216, ZD0473) have been synthesized and tested for their possible anticancer activity.[89–93] The challenge is to obtain drugs active against a broad spectrum of tumor cells, to minimize their toxicity and to avoid development of resistance mechanisms in target cells.[94]

After intravenous or oral administration of the drug, it undergoes several biotransformations that activate its toxicity (tumor cells as well as nephro- and neurotoxicity). A number of speciation studies that focused on characterization and quantification of parent drug and its possible metabolites in vitro and in vivo have been reported. Element-specific ICP-MS detection has been applied after LC separation of platinum compounds.[89,91,92,95–101] In Figure 6, the LC–ICP-MS chromatogram is presented, and this was obtained for the mixture of cancerostatic platinum compounds.[91]

3.2.7 Selenium

The growing interest in selenium speciation is due to its toxic and/or essential properties that depend on the actual physicochemical form of the element. Strong evidence exists on the adverse health effects related to selenium deficiency. It was also demonstrated that supplementation with different selenium forms might help to remove the symptoms of deficit.[102] Selenium has been found in the active site of different antioxidant enzymes, protecting cells against the action of free radicals. The species-dependent cancer-preventive properties are well documented, yet the specific biological functions have not been ultimately elucidated. The list of small selenium compounds includes inorganic forms (two stable valence states), volatile alkylated species, and

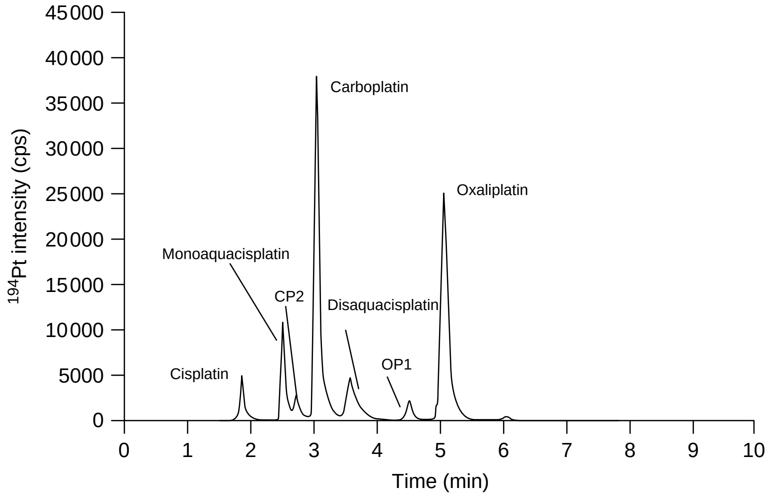

Figure 6 LC–ICP-MS chromatogram obtained from a 24-h mixture of cisplatin ($Rt = 1.9$ min), carboplatin ($Rt = 3.1$ min), and oxaliplatin ($Rt = 5.1$ min) in subboiled water using pentafluorophenylpropyl-functionalized silica as stationary phase. In addition to the parent drugs, the chromatogram shows the major degradation products of cisplatin (monoaquacisplatin, $Rt = 2.5$ min; diaquacisplatin ($Rt = 3.6$ min)), the product of carboplatin (CP2, $Rt = 2.7$ min) and the product of oxaliplatin (OP1, $Rt = 4.5$ min). (Reproduced with permission Hann, Stefanka, Lenz and Stingeder[91] © 2005, Springer Science & Business Media)

nonvolatile organoselenium compounds (Table 3). Speciation studies focus on the analysis of environmental materials, food (vegetables from the Allium family, wheat sprouts, crops and nuts), nutritional supplements (Se-enriched yeast), as well as clinical samples (serum, urine). Element speciation in selenium-accumulating plants (*Brassica juncea*, *Astragalus praleongus*) has also been addressed.[103] The reliability of speciation results in biological materials strongly depends on sample pretreatment. The homogenization of the initial material (for yeast–the rupture of cell walls), fractionation protocol to separate large molecules from low molecular weight compounds, extraction of lipids, and protein hydrolysis yielding selenoaminoacids are key steps in any speciation procedure.[61,104–106] For urine analysis, the cleanup and preconcentration steps are important.[104,107]

LC coupled to ICP-MS is preferentially used for nonvolatile species. Two inorganic forms (Se(IV) and Se(VI)) predominating in aquatic samples, are usually separated on strong anion-exchange columns. Anion-exchange separations have also been performed on mixtures of inorganic and organic compounds (Se-Met, Me-Se-Cys, Se-Cis, TMSe); however poor resolution has often been observed.[108] The applications to real-world samples include vegetable and yeast extracts, bacteria, as well as urine samples.[61,104,109] Different organic selenium compounds (selenoaminoacids, peptides, TMSe, etc.) are cations, or can be easily converted to cationic species by lowering the pH of the solution, thus enabling separation by a cation-exchange mechanism. Up to eight selenium compounds (Se(IV), Se(VI), Se-Cys, Se-Hcy, Se-Met, Se-Et, TMSe, dimethyl selenium propionate) have been resolved with different mobile phases at pH 2–5.7 (pyridine, ammonium formate, etc.).[10,110] Cation-exchange columns have been used for selenium speciation in urine.[104] Ion-pairing LC is a common separation technique in the analysis of yeast, garlic, onion extracts, and urine. Different perfluorinated carboxylic acids have been examined and the feasibility for separation of a large number of species demonstrated (pH 2.5–4.5).[12,111] The alkylsulfonic acids have been successfully used as counterions in the speciation analysis carried out on nuts, yeast, and urine.[10] The identification of selenium-containing compounds observed by LC–ICP-MS is not always straightforward. The lack of commercially available standards and often unknown selenium pathways in the studied system are the main problems. The characterization of a number of species (AdoSe-Hcy in yeast, γ-glutamyl-methylselenocysteine in garlic, Se-methyl-N-acetylselenohexosamine in rat urine, etc.) has been obtained by complementary electrospray ionization mass spectrometry experiments.[12]

Owing to the different biological activities of D and L enantiomers of selenoaminoacids, chiral separation of these compounds has been undertaken. Both, chiral stationary phase (crown ether) and chiral derivatization prior to reversed phase LC were used.[10]

GC–ICP-MS is suitable for the determination of volatile selenium species. Figure 7 shows the chromatogram obtained by GC–ICP-MS measuring Se and S (m/z 77 and 33, respectively) from the *Brassica juncea* seedlings grown in the presence of sodium selenate. The main Se species found were dimethylselenide and dimethyldiselenide as labeled in the chromatogram.[103] GC separation of volatile, chiral derivatives of Se-Met enantiomers has also been reported.[10]

The applications of CE–ICP-MS to selenium speciation has been reviewed.[9] This technique allows the separation of two inorganic forms of the element and several organic compounds in a short time. Different alkaline electrolytes have been reported in the pH range 9–11.5. Detection limits of 10 to 50 µg L^{-1} have often been obtained. The majority of studies have dealt with standard mixture

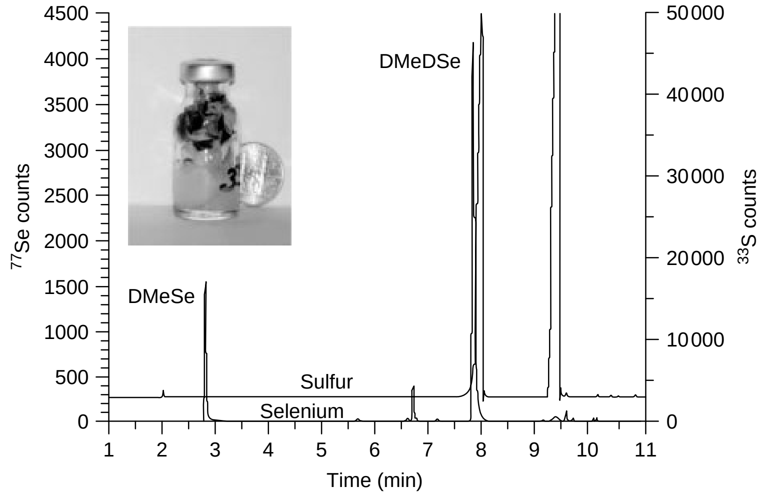

Figure 7 GC - ICP-MS chromatogram of Se and S in Brassica juncea headspace after solid phase microextraction. The photograph shows Brassica plant grown for the experiments. (Montes-Bayon, Grant, Meija and Caruso.[103] Reproduced by permission of The Royal Society of Chemistry)

solutions, and the analysis of milk and serum samples was reported only by Michalke *et al*.[112]

3.2.8 Tin

The main toxicological and ecotoxicological aspects of tin are related to the extensive use of organotin antifouling boat bottom paints. There is a need for speciation analysis in sea water, natural waters, soils, sediments, and marine organisms. The efficient extraction of tin compounds from solid matrices is a challenge. Certain complexing agents (tropolone or DDTC) were shown to favor the extraction of monobutyltin and, to a lesser extent, other cationic species. On the other hand, accelerated solvent extraction, supercritical fluid extraction, and microwave-assisted leaching techniques have been explored.[12,113] The small tin molecules of interest are summarized in Table 3; among them, tributyltin and triphenyltin have received major attention, followed by mono- and disubstituted species and inorganic forms. GC is the most common approach; it allows the separation of many different groups of organotin compounds in a single analysis. The derivatization of mono-, di-, and triorganotins to form thermally stable volatile species is necessary. This has been achieved with Grignard reagents and also by ethylation or propylation in an aqueous medium.[20,63] Conventional solvent extraction, solid phase microextraction, stir bar sorptive extraction (SBSE), and cryotrapping prior to capillary GC have been used. The majority of detection limits have been in the range of parts per trillion (picogram per liter); however with the preconcentration approach (SBSE, capillary cryofocusing) these values could be lowered by about 1 order of magnitude.[20] Multicapillary technology is a recent addition to the well-established GC, aiming for miniaturization of the GC unit and solute resolution in short time.[20]

Liquid chromatographic methods and detection techniques have been reviewed.[113,114] Elimination of the need for derivatization is a strong point for LC; however, the number of Sn species that can be analyzed in a single run is generally lower, the resolution poorer, and the transport to plasma less efficient than in GC. The separation of cationic butylated species has been achieved on cation-exchange columns using methanol–water mobile phases containing ammonium acetate or citrate. Ion-pairing chromatography with ammonium heptanesulfonate enabled the separation of cationic butylated, phenylated, propylated, ethylated, and methylated species. The capability of reversed phase LC for separation of butyltin and phenyltin species has been demonstrated with the addition of complexing agent tropolone to aqueous methanol or acetonitrile mobile phase. In a few studies, micellar mobile phases have been used with the aim of improving the separation.[113] The resolution of six species was reported (di- and trimethylated, -butylated and -phenylated Sn); however the elevated concentrations of surfactants increased the clogging of plasma torch. Similar absolute detection limits have been obtained for different separation modes; however, the lower values were reported with the use of DIN (1.8–2.5 pg of Sn in mono-, di-, and tributyltin). Post-column hydride generation has also been proposed.[113]

Isotopically labeled mono-, di-, and tributyltin have been obtained, allowing the use of species-specific isotope dilution techniques both in GC and LC separations. A comparative study revealed that the separation mode had no significant effect on mass fractions determined in the sediment sample; however GC–ICP-MS analysis yielded about 2 orders of magnitude better absolute detection limit (0.03 pg Sn as tributyltin) with respect to reversed phase LC–ICP-MS.[115]

Several applications of SFC–ICP-MS in organotin have been reported. The SFC mode is particularly suitable for tri- and tetraorganotin species and this technique enables better sensitivity when compared with LC (better transport efficiency to plasma). A comprehensive review is available.[69]

3.3 Element-Specific Detection in Metallobiomolecules

Different metals and/or metalloids, while present at low concentrations, play an important role in the biological activity of ‘‘large’’ molecules. It has been estimated that around 40% of all proteins and enzymes contain metal ions in their structures. Metal-binding proteins and metalloproteins are responsible for many metabolic processes, such as biological energy conversion in photosynthesis and respiration, as well as for signaling processes, which govern gene expression and regulation. Metal sites in protein structures also command other processes such as catalysts action, substrate binding and activation, transportation, and storage.[41,116] Atomic spectrometry techniques have been introduced in studies of metallobiomolecules relatively recently. In particular, ICP-MS and, to a lesser extent, ICP-OES are used as element-specific detectors in chromatographic and electrophoretic separations.[117–120] To assess the patterns of element distributions in molecular mass fractions, size exclusion chromatography is typically used.[3,41,121–123] As an example, the elution profiles of Fe, S, P in protein liver extract was obtained and polyatomic interferences typically observed on most abundant isotopes, were removed using a magnetic sector mass analyzer at medium spectral resolution.[124] In other work, the speciation of zinc and copper binding with proteins in human serum was studied.[125] The concentrations of α2-macroglobulin-zinc, ceruloplasmin-copper, and the element species with albumin were estimated. Metal binding to proteins has also been investigated in cancerous and healthy human thyroid samples.[126] For the protein extract of Brazil nuts, SEC–ICP-MS was carried out in the presence and in the absence of reducing agent (β-mercaptoethanol) to distinguish between selenium firmly and weakly bound to proteins.[106] This technique has also been used for studying the distribution of metals and metalloids in molecular mass fractions of different mushrooms.[127,128]

Another separation technique suitable in nondenaturing conditions is ion exchange chromatography and it has been frequently coupled with ICP-MS. A post-column isotope dilution analysis was used for the quantitative speciation of Fe, Cu, and Zn in human serum.[129] A similar separation system with high-resolution ICP-MS was applied to multielemental speciation.[130] The use of variable resolution allowed the detection of Ca, Sr, Fe, Cu, Zn, Se, Mn, Cr, Pb, Al, and Sn in different serum samples.

A common practice in the fractionation of proteins is the use of sodium dodecylsulfate polyacrylamide gel electrophoresis (SDS-PAGE). The feasibility of ICP-MS as a detection tool in the measurements of heteroatom stoichiometry in a biomolecule isolated as a spot in two-dimensional gel electrophoresis has been demonstrated.[41,118,131] As an example, ETV–ICP-MS was applied for the detection and quantification of selenium in proteins directly from the bands of a stained gel.[132] The method was optimized by using glutathione peroxidase and then applied to the determination of selenium in proteins fractionated from a selenium–yeast candidate reference material. In another study, Lustig *et al.* used two-dimensional electrophoretic separation (isoelectric focusing and native PAGE) combined with sector field ICP-MS for the speciation of Cr, Ga, In, Pt, and V in human and rabbit sera.[133] Laser ablation of PAGE gels for sample introduction to ICP-MS has become a fast growing application area in the analysis of biomolecules.[41,118,134]

3.3.1 Metallothioneins

Element-specific detection by ICP-MS has been widely used in the characterization of metallothioneins (MTs). The biological importance of these proteins is due to their role in homeostatic regulation of essential heavy metals like Cu and Zn. On the other hand, MT protects the cells from harmful chemicals, like nonessential and excessive essential heavy metals, reactive oxygen species, radicals, and alkylating agents.[135] Fararello *et al.*[136] reviewed different chromatographic approaches with ICP-MS detection for the multielemental speciation in MTs and MT-like proteins.

3.3.2 Metal binding to transferrin

Several papers have focused on elements binding to transferrin (Tf). As to the possible biological significance, the identification of this iron-transporting glycoprotein as a target for other elements could contribute to better understanding the pharmacokinetics of these elements in the human body. It should be stressed that the application of a highly sensitive ICP-MS detection system allowed the determination of element speciation in unspiked clinical samples.[137] The chemical forms of Al and Fe bound to human serum Tf were investigated by anion-exchange HPLC coupled to high-resolution (HR) ICP-MS.[138] The levels of ^{27}Al, ^{56}Fe, and ^{32}S, which are interfered with by polyatomic ions such as $^{13}C^{14}N^+$, $^{12}C^{15}N^+$ and $^{12}C^{14}N^1H^+$, $^{40}Ar^{16}O^+$ and $^{40}Ca^{16}O^+$, and $^{16}O_2{}^+$, when using a quadrupole mass analyzer, were monitored simultaneously by HR-ICP-MS at a resolution of $m/\Delta m = 3000$. Monitoring ^{32}S helped to assess the protein levels in the HPLC eluate. In the following study, the same analytical system was used to investigate the effect of structural changes in Tf on the affinity of Al and Fe to this protein.[139] The binding patterns of V(III), V(IV), and V(V) to human serum Tf were also investigated.[140] The observed affinity decreased from the lowest to the highest oxidation state of the element in the presence of bicarbonate. This order was altered in the absence of bicarbonate, which is generally required for metal binding to Tf. Another element of interest is bismuth, which is widely used in clinical treatment of different gastrointestinal ulcers. Fast protein LC–ICP-MS was the analytical tool for studying competitive binding of Bi to human albumin and transferrin.[141] It was found that over 70% of bismuth binds to Tf even in the presence of a large excess of albumin (albumin/transferrin = 13:1).

3.3.3 Metalloenzymes

A few reports on metal ion characterization in metalloenzymes by hyphenated techniques with ICP-MS detection should also be mentioned. Inhibition, reactivation, and determination of metal ions in membrane metalloproteases of bacterial origin was studied by Leopold *et al.*[142] The results obtained by SEC–ICP-MS and the results of enzymological methods indicated that two different membrane proteases from *Bacillus cereus* and *Pseudomonas aeruginosa* were zinc metalloproteases. In another study, ICP-MS measurements helped in the characterization of a fibrinolytic metalloprotease from the fruiting bodies of an edible mushroom.[143] Using HPLC–ICP-MS, Suzuki *et al.* detected a zinc-binding protein present specifically in the livers of male adult rats.[135]

3.4 Metallomics Approach

Metallomics is emerging as an important application area of ICP-based atomic spectrometries. While there is no IUPAC definition of metallomics yet, the metallome has been defined as the complete complement of metals and metal moieties in a biological cell, tissue, or system. This definition is analogous to that of the genome (genes), proteome (proteins), and metabolome (metabolites). Metallomics, accordingly, is the study of metals and metal species, and their interactions, transformations, and functions in biological systems.[144–146] Metallomics differs from speciation and other related terms in that it considers the global role of all metals/metalloids in a given system.[145] Thus, multielement capabilities of ICP-MS and ICP-OES make these techniques especially well suited to meet present and future challenges of metallomics in different research fields.[119,147,148] Several papers reporting specific applications are available.[127,149–153]

4 ABBREVIATIONS AND ACRONYMS

AdoSe-Hcy = adenosylselenohomocysteine; AdoSe-Met = adenosylselenomethionine; AsB = Arsenobetaine; AsC = arsenocholine; CE = capillary electrophoresis; DDTC = diethyldithiocarbamate; DEHg = diethylmercury; DESe = diethylselenide; DIHEN = direct injection high-efficiency nebulizer; DIN = direct injection nebulizer; DL = detection limit; DMAs(III) = dimethylarsinous acid; DMAs(V) = dimethylarsinic acid; DMHg = dimethylmercury; DMSe = dimethylselenide; DPhHg = diphenylmercury; EDTA = ethylenediaminetetraacetic acid; EIE = Easily ionized elements; ETV = electrothermal vaporization; GC = gas chromatography; HEN = high-efficiency nebulizer; HHPN = hydraulic high pressure nebulizer; ICP = inductively coupled plasma; ICP-HRMS = inductively coupled plasma high-resolution mass spectrometry; ICP-MS = inductively coupled plasma mass spectrometry; ICP-OES = inductively coupled plasma optical emission spectrometry; IDMS = isotope dilution mass spectrometry; LC = liquid chromatography; MCN = microconcentric nebulizer; MEHg = monoethylmercury; MESe = monoethylselenide; Me-Se-Cys = methylselenocysteine; Me-Se-Met = methylselenomethionine; MMSe = monomethylselenide; MMHg = monomethylmercury; MPhHg = monophenylmercury; MTs = metallothioneins; NMR = nuclear magnetic resonance; pKa = negative logarithm of acid dissociation constant; PMT = photomultiplier tube; QITMS = quadrupole ion trap mass spectrometry; SBSE = stir bar sorptive extraction; SDS-PAGE = sodium dodecylsulfate polyacrylamide gel electrophoresis; Se-Cis = selenocystine; Se-Cys = selenocysteine; Se-Et = selenoethionine; Se-Hcy = selenohomocysteine; Se-Met = selenomethionine; SFC = supercritical fluid chromatography; TBT = tributyltin; TETRA = tetramethylarsonium ion; Tf = transferrin; TMAsO = trimethylarsineoxide; TMSe = trimethylselonium ion; TOFMS = time of flight mass spectrometry; USN = ultrasonic nebulizer.

5 FURTHER READING

P. W. J. M. Boumans ed., 'Inductively Coupled Plasma Emission Spectroscopy', John Wiley & Sons, New York, 1987—basic source book on ICP-OES.

J. A. Caruso, K. L. Sutton and K. L. Ackley eds., 'Elemental Speciation. New Approaches for Trace Element Speciation Analysis', 1st edition, Elsevier, Amsterdam, 2000—a comprehensive view of the analytical speciation and the hyphenated techniques with atomic spectrometry detection.

R. Cornelis, J. A. Caruso, H. Crews and K. G. Heumann eds., 'Handbook of Elemental Speciation: Techniques and Methodology', 1st edition, John Wiley & Sons, 2003.

R. Cornelis, J. A. Caruso, H. Crews and K. G. Heumann eds., 'Handbook of Elemental Speciation II: Species in the Environment, Food, Medicine and Occupational Health', 1st edition, John Wiley & Sons, 2005.

A. Montaser, 'Inductively Coupled Plasma Mass Spectrometry', 1st edition, Wiley-VCH, Weinheim, 1998—source of information on ICP-MS spectrometry.

A. Montaser and D. W. Golightly eds., 'Inductively Coupled Plasmas in Analytical Atomic Spectrometry', 2nd edition, VCH Publishers, New York, 1992—technical background and application fields of plasma based atomic spectrometries.

J. Nölte, 'ICP Emission Spectrometry. A Practical Guide', 1st edition, Wiley-VCH, Weinheim, 2002—the essential information needed for successful ICP OES analyses.

H. Taylor, 'Inductively Coupled Plasma Mass Spectrometry—Practices and Techniques', 1st edition, Elsevier, 2000—covers both theory and applications in a concise, informative and readable form.

C. Vandecasteele and C. B. Block, 'Modern Methods for Trace Element Determination', 1st edition, John Wiley &Sons, Chichester, 1993—very good source book on the principles of ICP-OES and ICP-MS.

6 REFERENCES

1. R. S. Houk, V. A. Fassel, G. D. Flesch, H. J. Svec, A. L. Gray and C. E. Taylor, *Anal. Chem.*, 1980, **52**, 2283.
2. R. S. Houk, *Anal. Chem.*, 1986, **58**, 97A.
3. K. Wrobel, K. DeNicola, K. Wrobel and J. A. Caruso, in 'Advances in Mass Spectrometry', ed. J. J. Monaghan, Elsevier Science, Amsterdam, 2004, Vol. 16, Chap. 4.
4. S. J. Ray, F. Andrade, G. Gamez, D. McClenathan, D. Rogers, G. Schilling, W. Wetzel and G. M. Hieftje, *J. Chromatogr. A*, 2004, **1050**, 3.
5. A. L. Rosen and G. M. Hieftje, *Spectrochim. Acta, Part A*, 2004, **59**, 135.
6. C. B'Hymer and J. A. Caruso, in 'Comprehensive Analytical Chemistry', eds. J. A. S. Caruso and K. L. Ackley, Elsevier Science B.V., Amsterdam, 2000, p. 213, Vol. 33.
7. J. L. Todoli and J. M. Mermet, *Spectrochim. Acta, Part A*, 2006, **61**, 239.
8. J. Mora, S. Maestre, V. Hernandis and J. L. Todoli, *Trends Anal. Chem.*, 2003, **22**, 123.
9. S. S. Kannamkumarath, K. Wrobel, C. B'Hymer and J. A. Caruso, *J. Chromatogr. A*, 2002, **975**, 245.
10. J. A. Caruso and M. Montes-Bayon, *Ecotoxicol. Environ. Saf.*, 2003, **56**, 148.
11. B. Michalke, *Trends Anal. Chem.*, 2002, **21**, 154.
12. M. Montes-Bayon, K. DeNicola and J. A. Caruso, *J. Chromatogr. A*, 2003, **1000**, 457.
13. A. A. Ammann, *Anal. Bioanal. Chem.*, 2002, **372**, 448.

14. S. Karthikeyan and S. Hirata, *Appl. Organomet. Chem.*, 2004, **18**, 3232.
15. I. Pizarro, M. Gomez, M. A. Palacios and C. Camara, *Anal. Bioanal. Chem.*, 2003, **376**, 102.
16. M. Kovacevic, L. Leber, S. D. Kohlwein and W. Goessler, *J. Anal. At. Spectrom.*, 2004, **19**, 80.
17. S. C. Shum, R. Neddersen and R. S. Houk, *Analyst*, 1992, **117**, 577.
18. B. Michalke, *Trends Anal. Chem.*, 2002, **21**, 142.
19. J. C. A. Wuilloud, R. G. Wuilloud, A. P. Vonderheide and J. A. Caruso, *Spectrochim. Acta, Part A*, 2004, **59B**, 755.
20. B. Bouyssiere, J. Szpunar and R. Lobinski, *Spectrochim. Acta, Part A*, 2002, **57**, 805.
21. I. Rojas, M. Murillo, N. Carrion and J. Chirinos, *Anal. Bioanal. Chem.*, 2003, **376**, 110.
22. J. A. Broekaert, *Fresenius J. Anal. Chem.*, 2000, **368**, 15.
23. J. D. Venable, D. Langer and J. A. Holcombe, *Anal. Chem.*, 2002, **74**, 3744.
24. R. Hergenroeder, *Spectrochim. Acta, Part A*, 2006, **61B**, 284.
25. R. E. Russo, X. Mao, H. Liu, J. Gonzalez and S. S. Mao, *Talanta*, 2002, **57**, 425.
26. M. C. Santos and J. A. Nobrega, *Appl. Spectrosc. Rev.*, 2006, **41**, 427.
27. I. B. Brenner and A. T. Zander, *Spectrochim. Acta, Part A*, 1999, **55**, 1195.
28. T. W. Barnard, M. I. Crockett, J. C. Ivaldi and P. L. Lundberg, *Anal. Chem.*, 1993, **65**, 1225.
29. D. C. Gregoire, *Spectrochim. Acta, Part A*, 1987, **42**, 895.
30. R. Thomas, *Spectroscopy*, 2001, **16**, 38.
31. A. Taylor, S. Branch, A. Fisher, D. Halls and M. White, *J. Anal. At. Spectrom.*, 2000, **16**, 421.
32. T. W. May and R. H. Wiedmeyer, *At. Spectrosc.*, 1998, **19**, 150.
33. C. B'Hymer and J. A. Caruso, *J. Chromatogr. A*, 2004, **1045**, 1.
34. B. Fairman, M. W. Hinds, S. M. Nelms, D. M. Pennyd and P. Goodal, *J. Anal. At. Spectrom.*, 2000, **15**, 1606.
35. J. S. Becker, *J. Anal. At. Spectrom.*, 2005, **20**, 1173.
36. K. A. Francesconi and D. Kuehnelt, *Analyst*, 2004, **129**, 373.
37. K. L. Ackley, K. L. Sutton and J. A. Caruso, in 'Comprehensive Analytical Chemistry', ed. D. Barcelo, Elsevier, Amsterdam, 2000, Vol. XXXIII, p. 249.
38. G. O'Connor and E. H. Evans, in 'Inductively Coupled Plasma Spectrometry and Its Applications', ed. S. J. Hill, Sheffield Academic Press, Sheffield, 1999, p. 370.
39. F. Adams, R. Gijbels and R. Van Grieken, 'Inorganic Mass Spectrometry', John Wiley & Sons, New York, 1988.
40. M. Moldovan, E. M. Krupp, A. E. Holliday and O. F. X. Donard, *J. Anal. At. Spectrom.*, 2004, **19**, 815.
41. J. Szpunar, *Analyst*, 2005, **130**, 442.
42. M. Shah and J. A. Caruso, *J. Sep. Sci.*, 2005, **28**, 1969.
43. S. Mazan, N. Gilon, G. Crétier, J. L. Rocca and J. M. Mermet, *J. Anal. At. Spectrom.*, 2002, **17**, 366.
44. M. Balcerzak, *Anal. Sci.*, 2003, **19**, 979.
45. J. S. Becker and H. J. Dietze, *Fresenius J. Anal. Chem.*, 2000, **368**, 23.
46. S. D. Tanner, V. I. Baranov and D. R. Bandura, *Spectrochim. Acta, Part A*, 2002, **57**, 1361.
47. V. I. Baranov and S. D. Tanner, *J. Anal. At. Spectrom.*, 1999, **14**, 1133.
48. S. J. Hill, L. J. Pitts and A. S. Fisher, *Trends Anal. Chem.*, 2000, **19**, 120.
49. P. Quevauviller, in 'Elemental Speciation. New Approaches for Trace Element Analysis', ed. K. L. Ackley, Elsevier Science, Amsterdam, 2000, p. 531.
50. R. Lobinski and J. Szpunar, *Anal. Chim. Acta*, 1999, **400**, 321.
51. P. C. Uden, in 'Encyclopedia of Separation Science', ed. C. F. Poole, Academic Press, San Diego, 2000, p. 3347.
52. A. Sanz-Medel, *Analyst*, 1995, **120**, 799.
53. R. Cornelis, J. De Kimpe and X. Zhang, *Spectrochim. Acta, Part A*, 1998, **53**, 187.
54. K. G. Heumann, *Anal. Bioanal. Chem.*, 2004, **378**, 318.
55. F. Cubadda, *J. AOAC Int.*, 2004, **87**, 173.
56. H. Haraguchi, *Bull. Chem. Soc. Jpn.*, 1999, **72**, 1163.
57. L. Bencs, K. Ravindra and R. Van Grieken, *Spectrochim. Acta, Part A*, 2003, **58**, 1723.
58. D. Lariviere, V. F. Taylor, R. D. Evans and J. Cornett, *Spectrochim. Acta, Part A*, 2006, **61**, 877.
59. R. Nageswara Rao and M. V. N. Kumar Talluri, *J. Pharm. Biomed. Anal.*, 2007, **43**, 1.
60. J. A. Caruso, B. Klaue, B. Michalke and D. M. Rocke, *Ecotoxicol. Environ. Saf.*, 2003, **56**, 32.
61. B. Michalke, *Ecotoxicol. Environ. Saf.*, 2003, **56**, 122.
62. J. Szpunar, B. Bouyssiere and R. Lobinski, in 'Element Speciation: New Approaches for Trace Element Analysis', ed. K. L. Ackley, Elsevier Science, Amsterdam, 2000, p. 7.
63. W. Liu and H. K. Lee, *J. Chromatogr. A*, 1999, **834**, 45.
64. M. Krachler, H. Emons and J. Zheng, *Trends Anal. Chem.*, 2001, **20**, 79.
65. C. M. Tseng, D. Amouroux, I. D. Brindle and O. F. Donard, *J. Environ. Monit.*, 2000, **2**, 603.
66. A. M. Leach, F. C. Heisterkamp, F. C. Adams and G. M. Hieftje, *J. Anal. At. Spectrom.*, 2000, **15**, 151.
67. M. J. Tomlinson, L. Lin and J. A. Caruso, *Analyst*, 1995, **120**, 583.
68. K. L. Sutton, R. M. C. Sutton and J. A. Caruso, *J. Chromatogr. A*, 1997, **789**, 85.
69. N. P. Vela and J. A. Caruso, *J. Biochem. Biophys. Methods*, 2000, **43**, 45.
70. B. Michalke, *Electrophoresis*, 2005, **26**, 1584.

71. S. P. Bi, X. D. Yang, F. P. Zhang, X. L. Wang and G. W. Zou, *Fresenius J. Anal. Chem.*, 2001, **370**, 984.
72. M. Bissen and F. H. Frimmel, *Acta Hydroch. Hydrob.*, 2003, **31**, 9.
73. K. Wrobel, K. Wrobel, B. Parker, S. S. Kannamkumarath and J. A. Caruso, *Talanta*, 2002, **58**, 899.
74. C. A. Ponce de Leon, M. Montes-Bayon and J. A. Caruso, *J. Chromatogr. A*, 2002, **974**, 1.
75. G. K. Zoorob, J. W. McKiernan and J. A. Caruso, *Mikrochim. Acta*, 1998, **128**, 145.
76. S. A. Pergantis, M. Miguens-Rodriguez, N. P. Vela and D. Heitkemper, *J. Anal. At. Spectrom.*, 2004, **19**, advanced article.
77. J. M. Liu and J. K. Cheng, *Electrophoresis*, 2003, **24**, 1993.
78. M. J. Marqués, A. Salvador, A. Morales-Rubio and M. de la Guardia, *Fresenius J. Anal. Chem.*, 2000, **367**, 601.
79. M. J. Tomlinson, J. A. Wang and J. A. ACaruso, *J. Anal. At. Spectrom.*, 1994, **9**, 957.
80. I. I. Stewart and J. W. Olesik, *J. Chromatogr. A*, 2000, **872**, 227.
81. J. R. Baena, M. Gallego, M. Valcarcel, J. Leenaers and F. C. Adams, *Anal. Chem.*, 2001, **73**, 3927.
82. M. Heisterkamp and F. C. Adams, *Fresenius J. Anal. Chem.*, 2001, **370**, 597.
83. F. C. Heisterkamp, T. De Smaele, L. Candelone, L. Moens, R. Dams and F. C. Adams, *J. Anal. At. Spectrom.*, 1997, **12**, 1077.
84. K. L. Sutton and J. A. Caruso, *J. Chromatogr. A*, 1999, **856**, 243.
85. C. F. Harrington, *Trends Anal. Chem.*, 2000, **19**, 167.
86. A. M. Carro and M. C. Mejuto, *J. Chromatogr. A*, 2000, **882**, 283.
87. R. Garcia Fernandez, M. Montes-Bayon, J. I. Garcia Alonso and A. Sanz-Medel, *J. Mass Spectrom.*, 2000, **35**, 639.
88. R. C. Rodriguez Martin-Doimeadios, M. Monperrus, E. Krupp, D. Amouroux and O. F. Donard, *Anal. Chem.*, 2003, **75**, 3202.
89. T. Oe, Y. Tian, P. J. O'Dwyer, I. A. Blair, D. W. Roberts and C. J. Bailey, *J. Chromatogr. B Analyt. Technol. Biomed. Life Sci.*, 2003, **792**, 217.
90. R. Falter and R. D. Wilken, *Sci. Total Environ.*, 1999, **225**, 167.
91. S. Hann, Z. Stefanka, K. Lenz and G. Stingeder, *Anal. Bioanal. Chem.*, 2005, **381**, 405.
92. J. L. Carr, M. D. Tingle and M. J. McKeage, *Cancer Chemother. Pharmacol.*, 2002, **50**, 9.
93. F. Levi, G. Metzger, C. Massari and G. Milano, *Clin. Pharmacokinet.*, 2000, **38**, 1.
94. P. Zöllner, A. Zenker, M. Galanski, B. K. Keppler and W. Lindner, *J. Mass Spectrom.*, 2001, **36**, 742.
95. Z. Zhao, K. Tepperman, J. G. Dorsey and R. C. Elder, *J. Chromatogr.*, 1993, **615**, 83.
96. P. F. Smith, B. M. Booker, P. Creaven, R. Perez and L. Pendyala, *J. Clin. Pharmacol.*, 2003, **43**, 1324.
97. W. R. Cairns, L. Ebdon and S. J. Hill, *Anal. Bioanal. Chem.*, 1996, **355**, 202.
98. P. Galettis, J. L. Carr, J. W. Paxton and M. J. McKeage, *J. Anal. At. Spectrom.*, 1999, **14**, 953.
99. J. Szpunar, A. Makarov, R. Lobinski, T. Pieper and B. K. Keppler, *Anal. Chim. Acta*, 1999, **387**, 135.
100. S. Hann, A. Zenker, M. Galanski, T. L. Bereuter, G. Stingeder and B. K. Keppler, *Fresenius J. Anal. Chem.*, 2001, **370**, 581.
101. S. Hann, G. Koellensperger, G. Stingeder, Z. Stefánka, M. Fürhacker, W. Buchberger and R. M. Mader, *J. Anal. At. Spectrom.*, 2003, **18**, 1391.
102. L. C. Clark, B. W. Turnball, E. H. Slate, D. K. Chalker, J. Chow, L. S. Davis, R. A. Glover, D. K. Graham, E. G. Gross, A. Krongrad, J. L. Lesher, H. K. Park, B. B. Sanders, C. L. Smith, J. R. Taylor, D. S. Alberts, R. J. Allison, J. C. Bradshaw, D. Curtus, D. R. Deal, M. Dellasega, J. D. Hendrix, J. H. Herlong, L. J. Hixon, J. Knight, J. Moore, J. S. Rice, A. I. Rogers, B. Schuman, E. H. Smith and J. C. Woodward, *J. Am. Med. Assoc.*, 1996, **276**, 1957.
103. M. Montes-Bayon, T. D. Grant, J. Meija and J. A. Caruso, *J. Anal. At. Spectrom.*, 2002, **17**, 1015.
104. B. Gammelgaard, O. Jons and L. Bendahl, *J. Anal. At. Spectrom.*, 2001, **16**, 339.
105. B. Michalke, H. Witte and P. Schramel, *Anal. Bioanal. Chem.*, 2002, **372**, 444.
106. S. S. Kannamkumarath, K. Wrobel, A. Vonderheide and J. A. Caruso, *Anal. Bioanal. Chem.*, 2002, **373**, 454.
107. K. Wrobel, S. S. Kannamkumarath, K. Wrobel and J. A. Caruso, *Anal. Bioanal. Chem.*, 2003, **377**, 670.
108. S. M. Bird, H. Ge, P. C. Uden, J. F. Tyson, E. Block and E. Denoyer, *J. Chromatogr. A*, 1997, **789**, 349.
109. V. Díaz Huerta, L. Hinojosa Reyes, J. M. Marchante-Gayón, M. L. Fernández Sánchez and A. Sanz-Medel, *J. Anal. At. Spectrom.*, 2003, **18**, 1243.
110. W. Goessler, D. Kuehnelt, C. Schagenhaufen, K. Kachler, M. Abegaz and K. J. Irgolic, *J. Chromatogr. A*, 1997, **789**, 233.
111. M. Kotrebai, J. F. Tyson, E. Block and P. C. Uden, *J. Chromatogr. A*, 2000, **866**, 51.
112. B. Michalke and P. Schramel, *J. Chromatogr. A*, 1998, **807**, 71.
113. L. Ebdon, S. J. Hill and C. Rivas, *Trends Anal. Chem.*, 1998, **17**, 277.
114. E. González-Toledo, R. Compaño, M. Granados and M. D. Prat, *Trends Anal. Chem.*, 2003, **22**, 26.
115. R. Wahlen and C. Wolff-Briche, *Anal. Bioanal. Chem.*, 2003, **377**, 140.
116. J. S. Garcia, C. Schmidt de Magalhaes and M. A. Zezzi Arruda, *Talanta*, 2006, **69**, 1.

117. A. Sanz-Medel, M. Montes-Bayon and M. Luisa Fernandez Sanchez, *Anal. Bioanal. Chem.*, 2003, **377**, 236.

118. N. Jakubowski, R. Lobinski and L. Moens, *J. Anal. At. Spectrom.*, 2004, **19**, 1.

119. R. Lobinski, C. Moulin and R. Ortega, *Biochimie*, 2006, **88**, 1591.

120. L. Ebdon and A. Fisher, in 'Comprehensive Analytical Chemistry', eds. J. A. Caruso, K. L. Sutton and K. L. Ackley, Elsevier Science B.V., Amsterdam, 2000, Vol. 33, p. 227.

121. C. N. Ferrarello, M. D. R. Fernández De La Campa, A. Sanz-Medel and J. F. Carrasco, *Anal. Chem.*, 2000, **72**, 5874.

122. R. Koplik, H. Pavelkova, J. Cincibuchova, O. Mestek, F. Kvasnicka and M. Suchanek, *J. Chromatogr. B Analyt. Technol. Biomed. Life Sci.*, 2002, **770**, 261.

123. I. Pizarro, M. Gomez, C. Camara, M. A. Palacios and D. A. Roman-Silva, *J. Anal. At. Spectrom.*, 2004, **19**, 292.

124. J. Wang, D. D. D. R. Wiederin and R. S. Houk, *Anal. Biochem.*, 2001, **288**, 89.

125. K. Inagaki, N. Mikuriya, S. Morita, H. Haraguchi, Y. Nakahara, M. Hattori, T. Kinosita and H. Saito, *Analyst*, 2000, **125**, 197.

126. S. F. Boulyga, V. Loreti, J. Bettmer and K. G. Heumann, *Anal. Bioanal. Chem.*, 2004, **380**, 198.

127. A. H. Serafin Muñoz, K. Kubachka, K. Wrobel, S. K. V. Yathavakilla, F. Gutierrez Corona, J. A. Caruso and K. Wrobel, *J. Agric. Food Chem.*, 2005, **53**, 5138.

128. R. G. Wuilloud, S. S. Kannamkumarath and J. A. Caruso, *J. Agric. Food Chem.*, 2004, **52**, 1315.

129. C. Sariego Muñiz, J. M. Marchante Gayón, J. I. García Alonso and A. Sanz-Medel, *J. Anal. At. Spectrom.*, 2001, **16**, 587.

130. M. Bayón Montes, A. B. Cabezuelo Soldado, E. González Blanco and A. Sanz-Medel, *J. Anal. At. Spectrom.*, 1999, **14**, 947.

131. A. Prange and D. Profrock, *Anal. Bioanal. Chem.*, 2005, **383**, 372.

132. C. C. Chery, H. Chassaigne, L. Verbeeck, R. Cornelis, F. Vanhaecke and L. Moens, *J. Anal. At. Spectrom.*, 2002, **17**, 576.

133. S. Lustig, J. De Kimpe, R. Cornelis, P. Schramel and B. Michalke, *Electrophoresis*, 1999, **20**, 1627.

134. M. Wind, I. Feldmann, N. Jakubowski and W. D. Lehmann, *Electrophoresis*, 2003, **24**, 1276.

135. Y. Ogra and K. T. Suzuki, *J. Chromatogr. B Biomed. Sci. Appl.*, 1999, **735**, 17.

136. C. N. Ferrarello, M. R. Fernández de la Campa, J. F. Carrasco and A. Sanz-Medel, *Spectrochim. Acta, Part B At. Spectrosc.*, 2002, **57**, 439.

137. A. Belen Soldado Cabezuelo, M. Montes-Bayon, E. Blanco Gonzalez, J. I. Garcia Alonso and A. Sanz-Medel, *Analyst*, 1998, **123**, 865.

138. M. H. Nagaoka and T. Maitani, *Analyst*, 2000, **125**, 1962.

139. M. H. Nagaoka and T. Maitani, *Biochim. Biophys. Acta*, 2001, **1526**, 175.

140. M. Nagaoka, T. Yamazaki and T. Maitani, *Biochem. Biophys. Res. Commun.*, 2002, **296**, 1207.

141. H. Sun and K. Y. Szeto, *J. Inorg. Biochem.*, 2003, **94**, 114.

142. I. Leopold and B. Fricke, *Anal. Biochem.*, 1997, **252**, 277.

143. J. H. Kim and Y. S. Kim, *Biosci. Biotechnol. Biochem.*, 1999, **63**, 2130.

144. H. Haraguchi, *J. Anal. At. Spectrom.*, 2004, **19**, 5.14.

145. D. W. Koppenaal and G. M. Hieftje, *J. Anal. At. Spectrom.*, 2007, **22**, 111.

146. J. Szpunar, *Anal. Bioanal. Chem.*, 2004, **378**, 54.

147. M. N. V. Prasad, 'Trace Elements in the Environment, Biogeochemistry, Biotechnology, and Bioremediation', CRC/Taylor & Francis, 2006.

148. Lopez-Barea, J.; Gomez-Ariza, J. L. *Proteomics* 2006, **6**(Suppl. 1), S51.

149. J. L. Gomez-Ariza, T. Garcia-Barrera, F. Lorenzo and A. Arias, *Int. J. Environ. Anal. Chem.*, 2005, **85**, 255.

150. J. L. Gómez-Ariza, T. García-Barrera, F. Lorenzo, V. Bernal, M. J. Villegas and V. Olivera, *Anal. Chim. Acta*, 2005, **524**, 15.

151. T. Hasegawa, M. Asano, K. Takatani, H. Matsuura and T. H. H. Umemura, *Talanta*, 2005, **68**, 465.

152. H. Haraguchi, *Biomed. Res. Trace Elem.*, 2005, **16**, 217.

153. A. Sussulini, J. S. Garcia and M. A. Z. Arruda, *Anal. Biochem.*, 2007, **361**, 146.

Microwave Rotational Spectroscopy

Yunjie Xu and Wolfgang Jäger

University of Alberta, Edmonton, AB, Canada

Method Summary 1
1 Introduction 2
2 Technical Background 3
3 Measured Quantities and Derived Information 4
4 Case Studies 6
5 Abbreviations and Acronyms 14
6 References 14

METHOD SUMMARY

Acronyms, Synonyms

- Fourier Transform Microwave Spectroscopy.
- Microwave Spectroscopy.
- Rotational Spectroscopy.

Measured physical quantities

- rotational transition frequencies; fine and hyperfine structure splittings.

Information available

- rotational constants, A, B, C
- centrifugal distortion constants, for example, Δ_{J}, Δ_{JK}, Δ_{K}, δ_{J}, δ_{K}
- nuclear quadrupole coupling constants, χ
- nuclear spin rotation (C) and nuclear spin−spin interaction (S) constants
- electron spin rotation and electron spin−spin interaction constants
- tunneling splittings
- electric dipole moment components, μ.

Information not available, limitations

- The molecule needs to have nonzero electric dipole moment.

Examples of questions that can be answered

- What are the symmetry, geometry, and structure of the molecule?
- How high is the inversion or internal rotation barrier?
- What is the nature of the bond of this atom with a quadrupolar nucleus?
- What are the (approximate) relative stabilities of the different conformers?

Major advantages

- accurate determination of bond lengths (±0.01 Å or better) and bond angles (±0.1° or better)
- exquisitely sensitive to small structural changes and small mass changes
- unambiguous identification of structural isomers and conformers
- applicable to the study of neutral molecules, ions, radicals, and noncovalently bound complexes and clusters.

Major disadvantages

- Complete structure determination requires investigation of several isotopically labelled compounds.
- Spectroscopic analysis and interpretation can be complex.
- Instrumentation is not commercially available.

Sample constraints

- The sample must be brought into the gas phase.

---

1 INTRODUCTION

Microwave spectroscopy in general is a method to investigate rotational transitions or low energy ro-vibrational transitions of small (two atoms) to medium sized (∼40 atoms) molecules. For the purpose of this article, we can define the microwave wavelength range rather narrowly to be between 300 and 10 mm, corresponding to frequencies between 1 and 30 GHz. This region is bordered by the radio frequency range at lower, and the millimeter range at higher frequencies. The standard reference books for the area of microwave molecular spectroscopy are those by Gordy and Cook[1] and Townes and Schawlow.[2]

The molecules under investigation must possess a nonvanishing electric dipole moment to exhibit a (dipole-allowed) microwave rotational spectrum. Normally, the species of interest must be brought into the gas phase, at pressures of a few mTorr or in a molecular beam, for the spectroscopic investigation. The primary data obtained are rotational transition frequencies that correspond to energy differences between rotational energy levels. The observed rotational lines may be split into fine and hyperfine components as a result of large amplitude tunneling motions (e.g., the inversion splitting due to the umbrella motion in ammonia) and magnetic or electric interactions (e.g., nuclear quadrupole hyperfine structure due to the interaction of a nuclear electric quadrupole moment with the molecular electric field gradient at the site of the nucleus). Analyses of the spectra can then yield the corresponding spectroscopic constants, for example, rotational constants, which are inversely proportional to the molecular moments of inertia; centrifugal distortion constants, which are a measure of the change of moment of inertia due to centrifugal effects as the molecule rotates; barriers to internal motions; and nuclear quadrupole coupling constants, which are a measure of the molecular electric field gradient. The interpretation of these spectroscopic parameters can yield some of the most accurate structural information about gas phase molecules, and a detailed description of the electronic character of the molecular bonds.

From its inception, microwave rotational spectroscopy has contributed greatly to our knowledge about classical inorganic compounds. It all began with a low resolution recording of the ammonia inversion spectrum in 1934.[3] The first high resolution microwave spectra were recorded after the Second World War and resolved rotational structure of the ammonia inversion spectrum and later nitrogen nuclear quadrupole hyperfine structure. An account by Gordy of the early history of microwave spectroscopy can be found in Ref. 4. Since then, a myriad of small inorganic compounds has been studied and their structures and bonding characterized by rotational spectroscopy. This includes gas phase diatomic molecules, such as alkaline and alkaline earth halides and chalcogenides, essentially all diatomics involving C, Si, N, O, boron family (I) halides, basically any imaginable linear molecule, transition metal compounds, interhalogen compounds, species of atmospheric importance, including halogen-containing molecules, and reactive intermediates, and other types of molecules too many to be listed here. In most of these cases structural parameters of the highest accuracy were determined, and in many cases it was possible to extract information about the bonding character of these compounds.

Much of the microwave work up to the 70s or 80s had been done with waveguide based absorption spectrometers. Waveguides are round or rectangular metal tubes up to several meters in length that serve both to propagate the microwave radiation and as sample cell. The cross-sectional inside area of a waveguide depends on the wavelength and is, for example, $0.900'' \times 0.400''$ for a so-called X-band waveguide with frequency range from 8.2 to 12.2 GHz (*see* ***Electron Paramagnetic Resonance (EPR) Spectroscopy***). For a 2 m cell, this corresponds to a sample volume of not quite 0.5 L. These spectrometers typically employ a modulation scheme for sensitivity enhancement. In the case of Stark modulation, the molecular absorption is modulated by a square wave electric field that is introduced using an electrode that runs through the entire length of the waveguide. The detected signal is then processed with a phase sensitive detector. Flygare introduced Fourier transform techniques into microwave spectroscopy,[5,6] analogously to pulsed nuclear magnetic resonance (NMR) spectroscopy (*see* ***Nuclear Magnetic Resonance (NMR) Spectroscopy of Inorganic/Organometallic Molecules***). Here, a relatively high power (up to 20 W) microwave pulse is used to excite the molecular sample. After the excitation pulse has dissipated, the subsequent molecular emission signal is detected, digitized in the time domain, averaged, and finally Fourier transformed to obtain the spectrum in the frequency domain. This technique has been used in the Dreizler[7,8] laboratory in Kiel, Germany, and in the Bauder[9] laboratory at the eidgenössische technische hochschule (ETH) in Zürich, Switzerland. In combination with waveguides and static gas samples, this technique was used to characterize many molecular systems. Numerous technical improvements were implemented by these research groups. The Fourier transform microwave (FTMW) technique is now most commonly used in combination with a molecular beam and a microwave resonator, or cavity, as a sample cell designed originally by Flygare.[10] Since, in our opinion, pulsed molecular beam cavity FTMW spectroscopy is the most sensitive and most versatile method, we will restrict our discussions from now on mainly to this technique.

The pulsed molecular beam technique provides a wide open playing field for sample preparation. The pulsed nozzle can be combined with an electric discharge or a laser ablation source to generate and to stabilize reactive species, weakly bound complexes and clusters,[11] and compounds that cannot be made otherwise. The molecular beam technique allows us to ‘‘synthesize’’ inorganic and organometallic compounds that are of interest to modern inorganic chemistry and to bring them into the gas phase for high resolution spectroscopic investigation and characterization. Very recent examples include the discovery of the long elusive molecule AuF,[12] detection of covalent bonding involving the noble gas argon,[13] and structure elucidation of organometallic compounds.

2 TECHNICAL BACKGROUND

In the 1970s, a commercial microwave spectrometer employing Stark modulation and a waveguide sample cell was developed and sold by Hewlett Packard[14] and used in a number of research laboratories. Twenty years later, there were a number of attempts to commercialize a trace gas sensor based on a cavity FTMW spectrometer. It turned out that the complexity of the rotational spectra, the difficulties associated with the spectroscopic analyses, and the problems with intensity calibration, amongst other issues, foiled these attempts to transform microwave spectroscopy into a routine analytical tool. However, microwave Fourier transform spectroscopy as a research tool continues to contribute significantly to our understanding of geometry, electronic structure, and dynamics of small to medium sized molecules and molecular associations. We estimate that there are today about 25 to 30 research groups worldwide that operate cavity FTMW spectrometers, and essentially all are in use for research applications. Since this type of instrument is not commercially available, it is appropriate to give a brief overview of instrument design and operation. More details about the instrument design and literature references can be found in a recent review on rotational spectra of weakly bound complexes.[11] We also note the recent development of a broadband FTMW spectrometer[15] that overcomes the narrow bandwidth problems of the current general design (see succeeding text).

2.1 Instrument Design and Operation

A schematic diagram of a typical FTMW spectrometer is given in Figure 1. The heart of the instrument is a microwave cavity which serves as the sample cell. In our case, the cavity consists of two aluminum mirrors each with a diameter of 25 cm and radius of curvature of 30 cm. This microwave cavity is housed in a vacuum chamber which is evacuated by a diffusion pump/forepump combination to reach background pressures in the sub-mTorr range. The gaseous sample is introduced into the microwave cavity as a pulsed molecular expansion that is generated using a pulsed nozzle mounted near the center of one of the cavity mirrors. A microwave synthesizer serves as the radiation source. The microwave single sideband modulator generates a frequency sideband, for example, 20 MHz above the original frequency, to simplify detection of the molecular signal. A pin diode switch can generate microwave pulses of a few microseconds duration and this excitation pulse is fed into the microwave cavity through a simple wire-hook antenna. The molecular signal is picked up by an antenna in the other mirror and fed into the detection microwave circuit. This consists of a low-noise microwave amplifier, followed by an image rejection mixer which is used to down-convert the molecular emission signal from the microwave range to frequencies around 20 MHz. Signals in this radio frequency regime can be conveniently amplified, filtered, and finally sampled and analog-to-digital converted.

In general it is necessary to average the time domain signals of successive experiments to increase the signal-to-noise ratio of the observed transitions. To

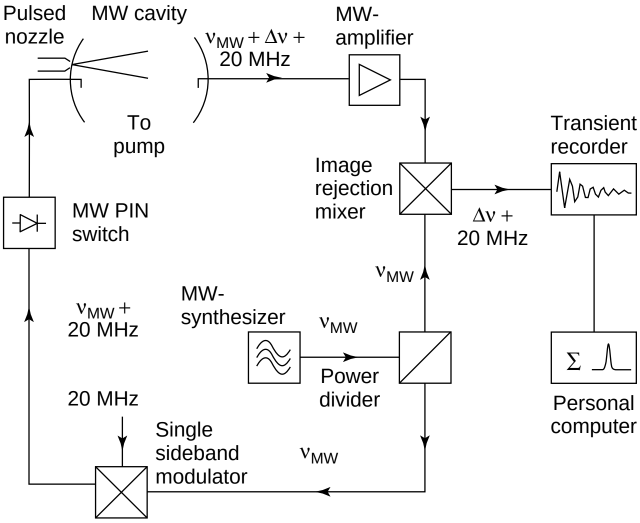

Figure 1 Simplified block diagram of a FTMW spectrometer

achieve this, it is essential to ensure phase coherent coaddition of the time domain signals, which is achieved by deriving mixing and sampling frequencies from a 10 MHz frequency standard and by tying all timing pulses to this standard.

The useful bandwidth of a single FTMW experiment is limited by both the length of the microwave excitation pulse (several μs) and by the quality factor of the microwave cavity ($Q \approx 10\,000-100\,000$). Useful ranges are typically 100 to 500 kHz in a single experiment. It is often necessary to conduct relatively wide frequency range searches for transitions of new compounds. FTMW spectrometers have therefore been automated and frequency stepping, tuning of the cavity into resonance with the external microwave radiation, and data accumulation can be done intervention-free over GHz ranges.

The molecular expansion travels parallel to the microwave cavity axis and, as a result, the observed transitions are split into Doppler doublets at sufficient resolution. Typical linewidths are 10 kHz and depend on the observation time, that is, the time required for the beam to travel from the nozzle to the opposite mirror. This in turn depends on the mirror separation and the backing gas (typically He, Ne, or Ar) used.

2.2 Sample Preparation

The molecular beam expansion into the microwave cavity is formed using a pulsed nozzle with circular orifice. The nozzle sample system by itself can be used to bring any compound with sufficient vapor pressure into the molecular expansion and also to synthesize complexes and clusters for spectroscopic study. The sample mixture typically consists of a few percent of sample molecules in a backing gas, often helium, neon, or argon, at pressures from 1 to 100 atmospheres. The combination of the pulsed nozzle with an electric discharge, a laser ablation source, or a miniature heating element extends its use significantly to bring low vapor pressure substances into the gas phase or to produce highly labile species that can further react with other precursors that are entrained in the backing gas or can be investigated directly. A typical laser ablation setup has a rod of the material to be evaporated mounted near the nozzle orifice. In some of the studies described in Section 3.1, for example, a copper rod was used to produce Cu atoms that then react with Cl_2 molecules in the expanding sample gas to form CuCl. CuCl can then react further with argon in the sample gas to form ArCuCl, a compound with significant covalent Ar–Cu bond character. Similarly, an electric discharge through the sample gas within the nozzle orifice can be used to generate, for example, fluorine atoms from SF_6 for further reaction with an additional precursor molecule in the sample gas.

3 MEASURED QUANTITIES AND DERIVED INFORMATION

The primary measured quantities are the frequencies of the recorded spectroscopic transitions of the species under investigation. Often, these frequencies correspond to energy differences between rotational energy levels or between fine or hyperfine components of the rotational levels. Typically, a good number of transitions need to be measured to assign their quantum numbers confidently. The frequencies can then be used in a fitting procedure to determine the spectroscopic parameters of a model effective Hamiltonian, such as rotational constants, centrifugal distortion constants, nuclear quadrupole coupling constants, spin rotation coupling constants, spin–spin coupling constants, and barriers to internal motions. Although rotational transitions within excited vibrational states have been recorded in many instances, we restrict our discussions to the measurement and analyses of rotational transitions within the vibrational and electronic ground state. We discuss selected spectroscopic parameters below, which we feel are of most importance for the purpose of extracting information about the molecular system. For example, we neglect completely the interactions of molecules with external magnetic fields.

3.1 Mechanical Parameters: Rotational and Centrifugal Distortion Constants

The rotational constants are inversely proportional to the moments of inertia of the molecule in its principal inertial axis system, that is, the axis system in which the moment of inertia tensor is diagonal. They are thus a measure of the mass distribution within the molecule and can be used to derive structural information, that is, bond lengths and bond angles. For an asymmetric top molecule there are three rotational constants, A, B, and C, which can be used to determine at most three structural parameters. If more structural parameters are required, it is necessary to investigate the spectra of isotopically labeled species which can often be achieved using their natural abundances. All rotational constants can then be used to directly fit the structural parameters to obtain a so-called effective or r_o-structure, where r_o refers to the vibrational ground state. The r_o-structure differs from the equilibrium, r_e-structure because of the zero-point vibrational motions, and r_o-values are typically larger than r_e-values, depending on the ‘‘floppiness’’ of the bending or stretching vibration. The effects of the zero-point motions can partly be corrected for by the evaluation of a substitution, r_s-, structure using Kraitchman’s equations.[1] This procedure allows determining the position of an atom in the principal inertial axis system using the rotational constants of the parent molecule and of the species that is isotopically substituted at the atom in question. For a complete structure determination of a molecule with N atoms it is necessary to know the rotational constants of $(N-2)$ singly substituted species in the case of a planar asymmetric top, and $(N-3)$ for a nonplanar asymmetric top. The remaining coordinates can be obtained using the moment of inertia equations and center of mass relations. A word of caution regarding the accuracy of derived structural parameters is warranted. Experimental rotational constants can be determined with sub-kHz accuracy at values of several GHz. A straightforward fitting procedure often results in very precise structural parameters, for example, bond lengths with errors in the 0.0001 Å range. These errors, however, do not take into account model inadequacies of the effective Hamiltonian or that the structural parameters represent some kind of average over zero-point motions that may be quite large in amplitude. Realistic errors are therefore often probably in the 0.001 to 0.01 Å range.

The centrifugal forces that occur during the rotation of a molecule lead to a slight deformation of the molecular structure and thus a slight change in molecular moments of inertia. The degree of bond stretching depends on the particular rotational state of the molecule. The centrifugal distortion constants are corrections to the rotational constants and account for this dependence. It is, therefore, possible to extract information about bond strengths, that is, force constants and vibrational frequencies from the centrifugal distortion constants. In a harmonic force field analysis, the force constants corresponding to, for example, the normal modes of vibration, are determined by fitting to the centrifugal distortion constants of one or more isotopomers. The vibrational frequencies can then be extracted using Wilson's GF matrix method.[16]

3.2 Nuclear Quadrupole Coupling Constants, Nuclear Spin-Rotation Constants, Nuclear Spin–Spin Interaction Constants

Some nuclei have a nonzero spin angular momentum **I** which can couple to the overall rotation of the molecule or to another spinning nucleus. If the nuclear spin quantum number $I > 1/2$, the nucleus has a nonzero electric quadrupole moment, Q, that can interact with the electric molecular field gradient, $q_{zz} = \delta^2 V/\delta z^2$, at the location of the nucleus to mediate the coupling between nuclear spin and molecular rotation (*see* ***Nuclear Quadrupole Resonance (NQR) Spectroscopy***). The result is a splitting of the rotational energy levels and the occurrence of a nuclear quadrupole hyperfine structure in the spectrum, where the number of hyperfine components depends on I and the rotational angular momentum quantum number J. The magnitude of the splitting depends on the nuclear quadrupole moment and the field gradient and can range from a few kHz for deuterium to several hundred MHz for iodine hyperfine structures. The analyses of the hyperfine structure yields the nuclear quadrupole coupling constants $\chi_{ij} = eQq_{ij}, (i, j = a, b, c)$, which are components of the nuclear quadrupole coupling tensor in the principal inertial axis frame of the molecule. Typically, the χ_{aa}, χ_{bb}, and χ_{cc} constants can be determined; sometimes one can obtain values for an off-diagonal constant, for example, χ_{ab}. In some cases, it is clear from the molecular symmetry that the principal axes of the quadrupole coupling tensor and of the inertial tensor coincide; in other cases, their relative orientation may be inferred from the geometry of the molecule or from χ_{ab}.

Since the electric quadrupole moments of many important nuclei are known, it is then possible to determine the electric field gradient tensor at the site of the nucleus, in particular, the field gradient components along the directions of the bonds involving the quadrupolar nucleus. Some of the dominant contributors to the field gradient are the electronic structure of the atom itself, the degree of hybridization of the bonding orbitals, the ionic character of the bond, π electron participation in the bond, and orbital overlap with the bonded atom. Townes and Daily[17] developed a method for the interpretation of nuclear quadrupole coupling constants in terms of the ionic character of the bond and hybridization, which takes into account only the valence electrons of the participating atoms. Consider the Cl nuclear quadrupole coupling constants in the cases of NaCl, with a rather ionic bond, and of ICl which has a substantial covalent bonding character. The Cl^- in NaCl has an essentially closed third electron shell and thus an essentially zero field gradient at the nucleus; the nuclear quadrupole coupling constant is therefore rather small, less than 1 MHz. In ICl, however, the singly occupied 3p orbital of Cl points along the bond axis, causing a substantial field gradient at the nucleus. The coupling constant χ_{Cl} is -82.5 MHz, whereas χ_{Cl} of the free Cl atom is -109.6 MHz. The discrepancy between χ_{Cl} in ICl and the Cl atom can be attributed to hybridization in ICl. Mixing of the doubly occupied 3s orbital with the bonding 3p orbital would reduce the electron deficiency along the bond axis and the magnitude of the nuclear quadrupole coupling constant decreases. In practice, one cannot differentiate between the effects of ionic bond character and hybridization, and one needs to, for example, estimate the ionic bond character based on electronegativity differences. A more detailed account regarding the interpretation of nuclear quadrupole coupling constants can be found in ***Nuclear Quadrupole Resonance (NQR) Spectroscopy***. Today, wavefunction-based and density functional ab initio methods are capable of calculating field gradients of at least second row elements and the Gaussian 03 program can calculate the actual nuclear quadrupole coupling constants.

Nuclei with nuclear spin quantum number $I \geq 1/2$ possess a nuclear magnetic moment that can interact with the magnetic field generated by the molecular rotation (spin rotation coupling) or with the magnetic field generated by another spinning nucleus (dipole–dipole or spin–spin interaction). The interpretation of spin rotation coupling constants, C, in terms of molecular properties is not straightforward. Bryce and Wasylishen have reviewed the relationships between microwave and NMR parameters involving spinning nuclei,[18] and point out the connection between spin rotation tensor and the chemical shift tensor, δ, an NMR observable (*see* ***Nuclear Magnetic Resonance (NMR) Spectroscopy of Inorganic/Organometallic Molecules***). The spin–spin interaction is described by two parameters, a second rank tensor parameter, S, and a scalar spin–spin constant. Their connection to the corresponding NMR parameters, that is, the direct dipolar coupling constant, R_{DD}, and the scalar coupling constant, J_{iso}, is also given in Ref. 18. The tensor spin–spin constant, S, provides information about the distance, r, between the interacting nuclei, and is proportional to $\langle 1/r^3 \rangle$, where the brackets indicate averaging over the corresponding wavefunction.

3.3 Electron Spin and Electron Orbital Angular Momentum Interactions

Electronic spin and orbital angular momenta in radicals and ions result in large magnetic moments that can interact with each other and with the rotational motion of the molecule.[19] The most important interactions are spin orbit coupling, spin–spin coupling, and spin rotation interaction. For molecules in Π electronic states, Λ-doubling effects are important. Nuclei with $I \geq 1/2$ possess a magnetic moment that leads to additional hyperfine structure through the interaction with the electronic angular momenta. These are the Fermi contact interaction and the dipole–dipole coupling term. The resulting spectroscopic parameters can be interpreted in terms of the molecular distribution of the electrons with nonzero angular momentum (see Section 4.3). However, the vast majority of microwave investigations involve molecules in $^1\Sigma$ states, and the reader is referred to Ref. 19 for a detailed description for the case of diatomic molecules.

3.4 Barriers to Internal Motions

Some molecules undergo large amplitude internal motions that interconvert equivalent configurations. Examples are the inversion umbrella motion in ammonia and methyl group internal rotations. These tunneling motions lead to splittings of the rotational energy levels that can manifest themselves as tunneling splittings in the observed spectra. In general, the higher the barrier to the internal motion, the smaller the tunneling splitting is. The splittings can be analyzed with an appropriate effective Hamiltonian to give parameters, such as the tunneling barrier, moment of inertia of the internal rotor, and orientation of the internal rotor axis within the molecular inertial axis frame.

3.5 Dipole Moments

The $(2J + 1)$-fold degeneracy of an energy level with rotational quantum number J can be partially lifted by placing the molecule in a static electric field. This so-called Stark effect can be utilized to measure the magnitudes of the dipole moment components, μ_a, μ_b, μ_c, in the principal inertial axis system of the molecule. For this purpose, Stark electrodes can be mounted outside the microwave cavity to generate a reasonably homogeneous electric field in the region of the molecular expansion. The observed rotational transition will split into several Stark components and the splittings can be used to fit values for the dipole moment components. It turns out that the splittings depend only on the magnitude of μ; the direction of the dipole moment must therefore be inferred from structural considerations or ab initio calculations.

3.6 Effects of Spin Statistics

If there are equivalent nuclei in the molecule, effects of spin statistics have to be taken into account.[20] In the case of two equivalent nuclei, such as for example, the two hydrogen nuclei in the water molecule, the total molecular wavefunction has to be antisymmetric under exchange of equivalent fermions (nuclei with half integer spin, e.g., the proton with $I = 1/2$) and symmetric under exchange of equivalent bosons (integer spin nuclei, e.g., the deuteron with $I = 1$). As a consequence, energy levels of different symmetries may have different spin statistical weights and certain levels may be completely missing. The observation of characteristic intensity ratios or the failure to observe transitions involving rotational levels of particular symmetry are thus good evidence for the existence of particular molecular symmetry elements.

4 CASE STUDIES

The following case studies are not meant to represent a comprehensive review, but are rather our narrow selection of some interesting cases that illustrate, in our view, the power and versatility of FTMW spectroscopy for the discovery and investigation of compounds that are of interest to inorganic and organometallic chemists.

4.1 Noble Gas–Metal Bonding in, and Structures of, Noble Gas–Noble Metal Halides

The first noble gas–metal halide investigated with the method of FTMW spectroscopy is Ar–NaCl.[21] The ^{23}Na and ^{35,37}Cl nuclear quadrupole coupling constants are changed by 1.3% to 17.3% from the respective NaCl monomer values. This is indicative of a slight change of the electronic structure of NaCl upon complex formation, although some of this effect must be attributed to vibrational averaging. The Ar–Na bond length ($r = 2.887$ Å) determined from the rotational constants and the relatively large centrifugal distortion constants are indicative of a true van der Waals bond in this linear complex. The small dissociation energy (660 cm^{-1}) and the low Ar–Na stretching frequency (76 cm^{-1}) obtained from ab initio calculations further support the notion of a true van der Waals bond. Some of the relevant parameters are listed in Table 1. Also given in Table 1 are columns with ‘‘covalent’’

Table 1 Derived spectroscopic and ab initio parameters of noble gas–metal halide systems(a)

	r_o/Å(b)	r_{vdW}/Å(c)	r_{cov}/Å(d)	D_o/ kHz	ω_e/cm^{-1}(e)	E_e/cm^{-1}(f)	ΔeQq/%(g)
Ar–NaCl	2.887	2.67		9.0874(59)	21	670	+1.8% (^{23}Na), −14.8% (^{35}Cl)
Ar–AgF	2.558			0.9533(15)	141	1470	N/A
Ar–AgCl	2.597	2.69	2.26	0.34651(49)	135	1360	−5.4% (^{35}Cl)
Ar–AgBr	2.639			0.11069(23)	124		−6.1% (^{79}Br)
Ar–CuF	2.219			0.9416(24)	224	3080	+73.3% (^{63}Cu)
Ar–CuCl	2.258	2.48	2.04	0.3435(14)	197	2300	+105.2% (^{63}Cu); −12.7% (^{35}Cl)
Ar–CuBr	2.296			0.12085(40)	170		+132.9% (^{63}Cu); −13.6% (^{79}Br)
Ar–AuF	2.391			0.5075(14)	221	4200	+507% (^{197}Au)
Ar–AuCl	2.469	2.65	2.25		198	3150	+2690% (^{197}Au), −12.8% (^{35}Cl)
Ar–AuBr	2.502			0.06506(39)	178		+582% (^{197}Au), −13.0% (^{79}Br)
Xe–AuF	2.548	2.95	2.57	0.06753(14)	169	8150	+891% (^{197}Au)

(a) Data for most abundant isotopomer, except for r_o.

(b) r_o-separation between noble gas and metal atom, averaged over all available isotopomers.

(c) r_{vdW} = van der Waals reference bond length = noble gas van der Waals radius + M^+ ionic radius.

(d) r_{cov} = covalent reference bond length = covalent noble gas radius + covalent M(I) radius.

(e) noble gas–metal stretching frequencies were obtained from the experimental rotational and centrifugal distortion constants (see the text).

(f) ab initio dissociation energies are from Ref. 22.

(g) magnitude of the changes in nuclear quadrupole coupling constants in going from metal halide to noble gas–metal halide.

and ''van der Waals'' noble gas–metal bond lengths, which were obtained from the covalent noble gas and metal radii and from the van der Waals noble gas radius and ionic metal radius, respectively. Note that the Ar–NaCl bond length is actually larger than the ''van der Waals'' reference bond length.

The Gerry group began then to investigate coinage metal-containing systems, starting with ArAgX (X = F, Cl, Br).[23] Here, the Ar metal bond lengths range from 2.56 Å in ArAgF to 2.64 Å in ArAgBr, and are somewhat shorter than the reference van der Waals separation, r_{vdW} (see Table 1). Similarly, the centrifugal distortion constants, D_o, range from 0.9533 kHz in ArAgF to 0.11069 kHz in ArAgBr and are at least an order of magnitude smaller than those of typical van der Waals complexes. This implies that the ArAgX are more tightly bound than typical van der Waals complexes and that the Ar–Ag bonds may be classified as borderline between van der Waals and covalent bonds. It should be noted that the $^{35/37}$Cl and $^{79/81}$Br nuclear quadrupole coupling constants in the complexes are changed by only 5.3% to 6.1% from the monomer values. However, these coupling constants of the terminal halogen atoms are not very sensitive to the charge rearrangement upon complex formation that would involve mainly the Ar–Ag subunit. Unfortunately, there is no stable silver isotope with a nuclear quadrupole moment to probe this charge rearrangement more directly. Van der Waals stretching frequencies were determined from the rotational and centrifugal distortion constants, using $\omega_e = \left(4B_e^3/D_{J_e}\right)^{1/2}$ and approximating B_e and D_{Je} with the effective ground state constants B_o and D_o, respectively. Relatively large values of 141 cm^{-1} and 135 cm^{-1} were obtained for ArAgF and ArAgCl, respectively. For ArAgF and ArAgCl, ab initio dissociation energies of 1470 cm^{-1} (ArAgF) and 1360 cm^{-1} (ArAgCl) were determined.[22] These results are also supportive of some covalent bonding character of the Ar–Ag bond, as is the comparison of centrifugal distortion constant, Ar metal stretching frequency, and dissociation energy with the corresponding values of Ar–NaCl (see preceding text and Table 1).

Copper-containing noble gas–metal halides are predicted to have stronger noble gas–metal bonds compared to the silver analogues. Analyses of the microwave spectra of the ArCuX (X = F, Cl, Br) complexes[13] support this. The Ar–Cu bond lengths are rather short, ranging from 2.22 Å in ArCuF to 2.30 Å in ArCuBr. In fact the Ar–Cu bond lengths are about halfway between the reference van der Waals, r_{vdW}, and covalent, r_{cov}, bond distances in Ar–Cu (see Table 1). The centrifugal distortion constants are small, implying that the Ar–Cu bond is relatively rigid and can be classified as ''weakly covalent''. There is strong support for this view from the experimental nuclear quadrupole coupling constants, in particular, those of ^{63}Cu. The absolute values of these constants increase by 73% for ArCuF to 133% for ArCuBr compared to the respective copper halide monomers. This is a result of a significant charge redistribution upon complex formation. Second order Møller-Plesset calculations show significant overlap between the Cu 3d$_\sigma$ and Ar 3p$_\sigma$ orbitals in ArCuF, consistent with the large change in Cu nuclear quadrupole coupling constants.

The investigations continued with ArAuX (X = F,[24] Cl,[25] Br). In all instances, the Ar metal distances are now about halfway between the reference van der Waals, r_{vdW}, and covalent, r_{cov}, bond lengths (see Table 1). This is accompanied by dramatic changes in the ^{197}Au nuclear quadrupole coupling constants and large ab initio dissociation energies. Further evidence for real chemical bonds between Ar and Au comes from molecular orbital ab initio calculations on the MP2 level of theory. In the cases of ArAuF and ArAuCl, there is significant overlap of Ar and Au orbitals in the 9σ, 6π and 11σ, 8π orbitals, respectively.

Gerry and co-workers have also investigated the corresponding compounds with krypton and xenon as noble gas atoms.**[26–29]** An example spectrum of the $J = 8-7$ rotational transition of XeCuCl is shown in Figure 2 to demonstrate the sensitivity and resolution that can be achieved with a FTMW spectrometer, and also indicates the complexity of the spectra if, for example, two quadrupolar nuclei are involved (^{65}Cu, $I = 3/2$; ^{35}Cl, $I = 3/2$) (J. M. Michaud, Private Communication). As expected, the degree of covalent bonding increases in going from argon to krypton to xenon. Of particular interest is that there are krypton and xenon isotopes with a nuclear quadrupole moment, that is, ^{83}Kr, $I = 9/2$ and ^{131}Xe, $I = 3/2$. In an isolated noble gas atom, the electric field gradient at the site of its nucleus is zero because of the spherical electronic charge distribution of the atom. The result is a nuclear quadrupole coupling constant of zero. There have been many cases reported of weakly bound complexes involving krypton and xenon atoms.**[11]** In all these cases, small, but nonzero, ^{83}Kr or ^{131}Xe nuclear quadrupole coupling constants provided evidence for a nonzero field gradient. This was attributed to the electric multipole moments (electric dipole moment, electric quadrupole moment) of the binding partners (a few MHz contribution to the nuclear quadrupole coupling constant at most) and to dispersion interactions (less than a MHz contribution). The ^{83}Kr and ^{131}Xe nuclear quadrupole coupling constants in Kr-, Xe-noble metal halide molecules are on the order of 100 MHz. These large values cannot be explained by the effect of charges external to the noble gas atom and with dispersion effects, but rather point to a significant participation of noble gas orbitals in a noble gas-noble metal chemical bond. It appears that the strongest such bond has been found in XeAuF (see Ref. 30, see Table 1). Note that the Xe–Au bond length in this compound is actually shorter than the reference covalent bond distance, r_{cov}. Most significant, however, remains the fact that this series of investigations provided some of the first evidence for covalent character of bonds involving the noble gas atom argon.

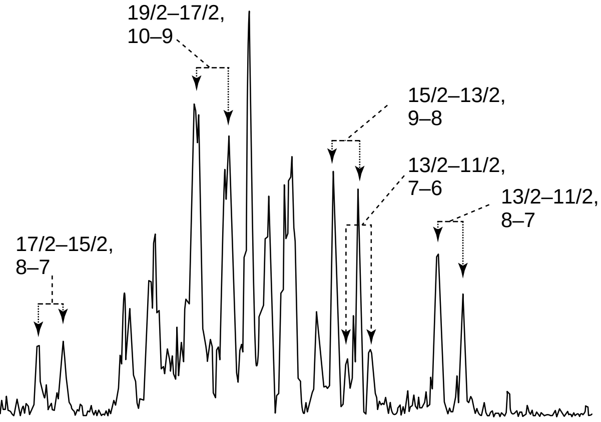

Figure 2 Spectrum of the $J = 8-7$ rotational transition of ^{132}Xe^{65}Cu^{35}Cl. The complicated hyperfine structure arises from nuclear quadrupole interactions of ^{65}Cu ($I_{Cu} = 3/2$) and ^{35}Cl ($I_{Cl} = 3/2$). All transitions are split into Doppler doublets as a result of the molecular expansion traveling parallel to the microwave cavity axis. For clarity of the picture, the quantum number assignments of only a few hyperfine components are given as $F_1'-F_1''$, $F'-F''$. The angular momentum coupling scheme $\mathbf{F}_1 = \mathbf{I}_{Cu} + \mathbf{J}$; $\mathbf{F} = \mathbf{F}_1 + \mathbf{I}_{Cl}$ was used. The compound was produced using laser ablation of a copper rod in a molecular expansion of a mixture of 0.1% Cl_2, 15% Xe, and 85% Ar. The particular isotopomer was measured in its natural abundance of 6.3%. This spectrum was recorded using 15 000 averaging cycles with a total accumulation time of about 3.5 h

High resolution spectroscopic measurements of the type described above often go hand in hand with highest level ab initio electronic structure calculations, to provide either help with the spectroscopic searches and quantum number assignments, or to aid in the interpretation of the spectroscopic information obtained. In the case of the larger noble gas atoms, xenon in particular, and the transition metals, ab initio calculations are still far away from even approaching spectroscopic accuracy. This has to do with the larger number of electrons involved and with the difficulties to account for relativistic effects. The ab initio computation of field gradients for atoms beyond the second row, for example, is exceedingly difficult.

4.2 Organometallic Compounds

Microwave spectroscopic studies of organometallic complexes began in the mid 90s, pioneered by the Kukolich group at the University of Arizona. One emphasis of these studies is to understand the relation between structure and reactivity of transition metal complexes. Very often the structures of these complexes were determined using X-ray diffraction in the solid state where ‘‘crystal packing’’ effects are present. These effects can distort the ‘‘true structure’’ of the molecule, and it is desirable to investigate these systems in the gas phase where these effects are absent. Using FTMW spectroscopy, the Kukolich group has measured rotational transitions of several transition metal complexes and determined the corresponding rotational constants, which have been utilized to derive structural information about these compounds. The transition metal complexes studied so far can loosely be grouped into four different types and some examples are discussed below.

4.2.1 Transition Metal Hydrides

One group of complexes studied are transition metal monohydrides such as the $C_5H_5Mo(CO)_3H$ and $C_5H_5W(CO)_3H$ complexes.**[31]** Transition metal monohydride complexes can serve as catalysts in acid–base synthetic reactions. Some of their molecular derivatives have been explored as selective catalysts for hydrogenation reactions and protonation of aldehydes and ketones. Central to their catalytic activities is the metal hydrogen bond, which can function as a proton, hydrogen, and hydride donor under different conditions. Information about bonding and stability of the metal hydrogen bond is therefore essential in these studies. In general, X-ray diffraction experiments are the most common routes applied to probe the overall geometry of large organometallic complexes. However, the uncertainties in the hydrogen atom coordinates from X-ray data are very large. It has been recognized that the X−H distances thus obtained are often significantly shorter than the true X−H distances. This is because the X-ray measurements show electron density, and the density around hydrogen atoms is aspherically displaced toward the bonded atom. Neutron diffraction can help, but this is not always feasible (*see* ***Neutron Diffraction***). Microwave spectroscopic measurements, on the other hand, can overcome this limitation. The rotational spectra of both the naturally occurring isotopes of tungsten: ^{186}W, ^{184}W, ^{183}W, and ^{182}W, and the corresponding isotopically enriched deuterium isotopomers were measured and assigned. The W−H bond length was obtained using a Kraitchman analysis by comparing the sets of rotational constants for the isotopomers substituted at tungsten and hydrogen atoms. The W−H bond distance thus obtained is 1.79(4) Å. A similar analysis was also reported for the Mo−H bond distance in $C_5H_5Mo(CO)_3H$ and the value obtained is 1.80(1) Å. By studying species that are isotopically substituted at different atoms, a nearly complete gas phase structure of $C_5H_5W(CO)_3H$ was obtained from the microwave data and a slightly improved W−H bond distance of 1.79(2) Å was determined.

Microwave spectroscopy has also been applied to studies of transition metal complexes containing two hydrogen atoms. The unexpected discovery of the existence of dihydrogen complexes has attracted considerable attention. In these dihydrogen complexes, the H−H bond remains intact and the bond length is very similar to that of a free hydrogen molecule. Two systems studied so far are tetracarbonyldihydroosmium[32] and tetracarbonyldihydroiron.[33] Through the analyses of the microwave isotopoic data, important structural parameters were determined, for example, $r_{HH} = 2.40(2)$ Å, $r_{OsH} = 1.72(1)$ Å, $r_{OsC1} = 1.96(1)$ Å, and $r_{OsC3} = 1.97(2)$ Å. The H−H bond distance clearly indicates that tetracarbonyldihydroosmium is a classical ‘‘dihydride’’ rather than a ‘‘dihydrogen’’ complex. An analogous analysis was performed for tetracarbonyldihydroiron, showing a H−H bond distance of 2.2 Å, also indicating that this is also a dihydride complex.

4.2.2 Ferrocenes and Their Derivatives

The most extensively studied group of transition metal complexes using microwave spectroscopy are ferrocene-based systems[34–39]: the π bonding of the cyclopentadienyl (cp) radical to metals results in surprisingly stable complexes and many examples have been reported since the earliest discovery in the 1950s. A series of microwave spectroscopic studies were carried out with emphasis on providing ‘‘true structures’’ of these ferrocenes without the interference of, for example, crystal packing effects that are present in the solid phase. A complete set of gas phase structural parameters of ethynylferrocene was determined using rotational constants of eight isotopomers.[38] Both direct least squares fitting and Kraitchman analyses were performed and the structure parameters obtained with these two methods agree within their quoted uncertainties. Because of the extremely high resolution nature of pulsed molecular beam FTMW spectroscopy, it was also possible to detect the hyperfine splittings due to quadrupolar nuclei such as ^{35}Cl, ^{37}Cl, ^{79}Br, and ^{81}Br. The corresponding nuclear quadrupole coupling constants determined provide information about the electric field gradient at the particular nucleus and therefore the associated chemical bonding character.

One very exciting result obtained using microwave spectroscopy is the experimental discovery of the existence of two different structural isomers of 1,1′-dimethylferrocene (Figure 3). With the help of density functional theory (DFT) calculations, energies of five different geometries (Figure 4) were evaluated. These are associated with different dihedral angles ϕ between the two methyl groups on the cyclopentadienyl ligands, with ϕ fixed at 0° and four multiples of 36°. Three structures E0, E72 and E144 were identified theoretically as true minima, while S108 and S180 were identified as saddle points, that is, transition states. Other ϕ values were tried, but no new isomers could be located. Experimentally, only E0, an eclipsed synperiplanar isomer, and E72, an eclipsed synclinal

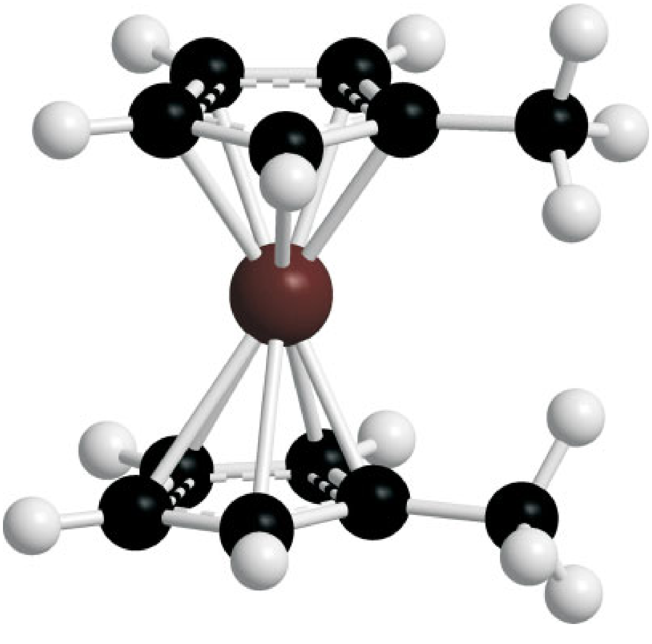

Figure 3 Structure of the eclipsed, synperiplanar (E0) conformer of 1,1′ -dimethylferrocene

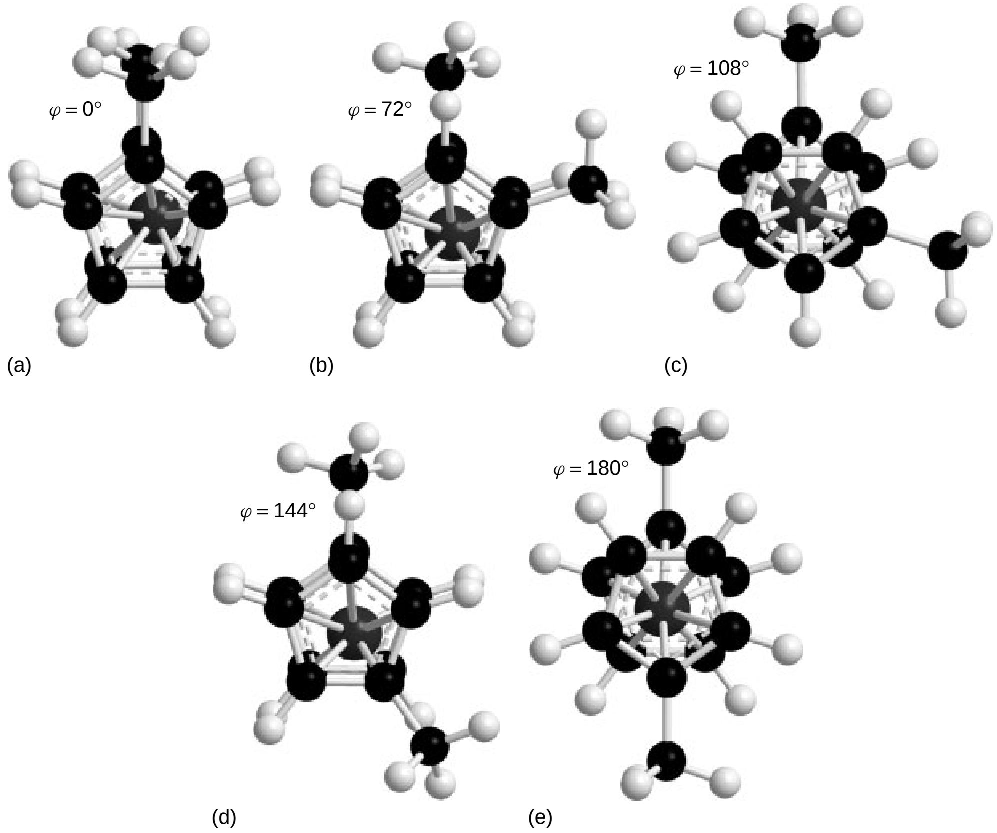

Figure 4 Five distinct structural conformers of 1,1′-dimethylferrocene: (a) eclipsed synperiplanar conformer E0 with $\phi = 0°$; (b) eclipsed synperiplanar conformer E72 with $\phi = 72°$; (c) staggered anticlinal conformer S108 with $\phi = 108°$; (d) eclipsed anticlinal conformer E144 with $\phi = 144°$; (e) staggered antiperiplanar conformer S180 with $\phi = 180°$

isomer, were detected. The assignment of the observed sets of rotational constants to these two isomers was achieved by comparing the experimental and the DFT rotational constants. The magnitudes of the centrifugal distortion constants indicate that E0 isomer is nearly rigid, while the E72 isomer exhibits fluxional behavior. For E72, the eclipsed synclinal isomer, some additional splittings were detected, providing further evidence of an internal tunneling motion. The E144 isomer could not be observed experimentally and this was attributed to the fairly small electric dipole moment predicted. The previous X-ray diffraction experiment showed only one isomer, E0, in the solid phase. The rotational constants determined from the X-ray structural parameters are somewhat larger than the experimental constants, evidence for possible effects of crystal packing forces.

From the microwave studies of different substituted ferrocene compounds, correlations between properties of the substituents and structural changes were established. It was noted that the carbon-iron bond distance in $\eta 5$ C_5H_5-Fe is much more sensitive to substitution on the cyclopentadienyl ligand than the C–C bond distances of the C_5H_5 ring. This is summarized in Table 2. A linear correlation of the gas phase structural parameter r(Fe–Cp) and the electronegativity of the substituent group, represented by the Hammett substituent constant, $\sum \sigma_1$,[40] was established. In addition, a linear correlation was established between the r(Fe–Cp) structural parameter and the ferrocene/ferrocenium redox potential, $\Delta E°$,[41,42] at ambient temperatures relative to the ferrocene standard. The results of linear regression analyses are plotted in Figure 5. From the graphs, one can predict, for example, the r(Fe–Cp) gas phase value for unsubstituted ferrocene[43] to be 1.65(1) Å.

4.2.3 Dinuclear Metal–Metal Carbonyl Complexes

Metal–metal bonded dinuclear transition metal complexes are an important group of inorganic compounds and the research in this area has been reviewed recently.[44] Metal–metal carbonyl complexes are considered as building blocks for more specialized biological models and catalysts. One example of these simple metal–metal carbonyl complexes studied using the FTMW technique is $MnRe(CO)_{10}$. The Mn–Re bond distance obtained is 2.99 Å, in good agreement with the earlier solid phase value of 2.96 Å by Nesmeyanov *et al.*[45] but considerably longer than the 2.906 Å reported by Ridge *et al.*[46] Of interest is the determination of nuclear

Table 2 Structural parameters of different ferrocene compounds, (C_5H_4-Y)-Fe-(C_5H_4-X), relative oxidation potentials at ambient temperatures, and Hammett substituent constants ($\sum \sigma_1$) for cp ligands

Compound	X	Y	r(C−C)	r(Fe−Cp)	$\Delta E^{\circ(a)}$	$\sum \sigma_1{}^{(b)}$	References
Chloroferrocene	Cl	H	1.433(2)	1.610(5)	0.195	0.47	35
Bromoferrocene	Br	H	1.433(1)	1.630(2)	0.165	0.44	34
Methylferrocene	CH_3	H	1.4289(2)	1.6528(3)	−0.06	−0.04	36
Dimethylferrocene	CH_3	CH_3	1.434(5)	1.670(2)	−0.115	−0.08	37
Ethynylferrocene	C≡CH	H	1.432(2)	1.6464(1)	0.110	0.21	38
Ferrocene	H	H	1.440(2)	1.661(2)	0.0	0	38

(a)The values of ΔE° are from Ref. 41, 42.
(b)The values for $\sum \sigma_1$ are from Ref. 40.

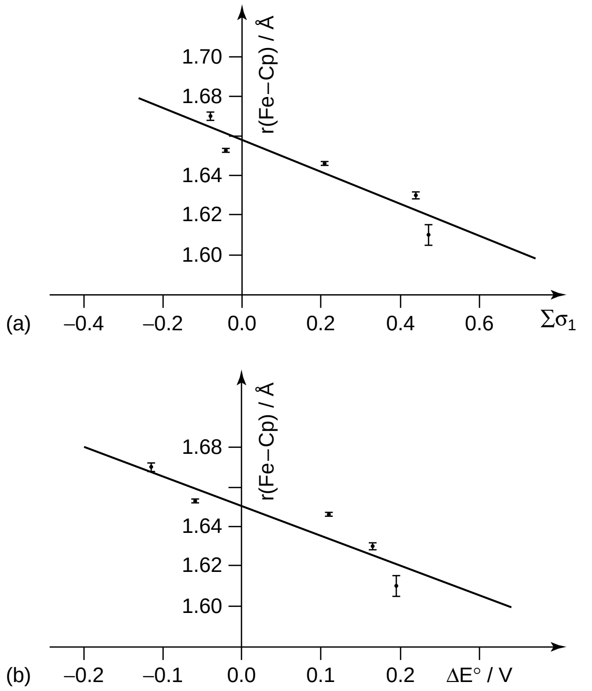

Figure 5 (a) The result of a linear regression analysis correlating the r(Fe−Cp) distance and $\Sigma\sigma_1$ of the substituent. This plot is governed by the equation r(Fe−Cp) $= -0.0821\Sigma\sigma_1 + 1.6585$ with a value of $r = 0.93$; (b) the result of a linear regression analysis between the r(Fe−Cp) distance and ΔE° of the substituent: r(Fe−Cp) $= -01499\Delta E^\circ + 1.6509$, with a value of $r = 0.91$

quadrupole coupling constants for ^{55}Mn, ^{185}Re, and ^{187}Re. The corresponding calculated ab initio values show very strong basis set dependent behavior and sometimes even the signs cannot be unambiguously determined. The experimental data here will be useful to guide and to test further theoretical developments in this respect.

4.3 Diatomic Transition Metal-containing Compounds

High resolution spectroscopic investigations of rotational spectra of transition metal compounds can contribute significantly to the characterization of the electronic structures of these compounds, which can often have high electronic spin and orbital angular momenta. The results are particularly important as a gauge for ab initio electronic structure calculations, which are still difficult for such heavy systems, partly because of the large number of low-lying electronic states. The method of FTMW spectroscopy in combination with a laser ablation/pulsed molecular expansion system is particularly suited for such investigations because of the high sensitivity and the high resolution achieved.

The National Institute of Standards and Technology (NIST) laboratory has studied rotational spectra of transition metal oxides, that is, YO, LaO, ZrO, and HfO.**47** Metal oxide molecules were entrained into the Ne backing gas expansion by laser ablation of the corresponding metal oxide rods near the nozzle orifice. ZrO and HfO have $^1\Sigma^+$ ground electronic states and their spectra are complicated by several naturally occurring isotopes of Zr and Hf, respectively. In addition, Hf has two nuclei with electric quadrupole moments (^{177}Hf, $I = 7/2$; ^{179}Hf, $I = 9/2$) leading to hyperfine structure in the spectra of the corresponding oxides. In both instances, the $J = 1–0$ rotational transitions were measured. The Stark effect of the $J = 1 - 0$ transitions was also investigated and dipole moments of 2.551 (11) D for ZrO and 3.431 (5) D for HfO could be determined. YO and LaO both have $^2\Sigma^+$ electronic ground states and both occur as only one naturally occurring isotopomer (^{89}Y, $I = 1/2$; ^{139}La, $I = 7/2$). The nuclear spins are coupled to the electron spin by a Fermi-contact interaction and there is additional nuclear quadrupole hyperfine structure in the spectra of LaO. The effect of Earth's magnetic field was canceled by the use of Helmholtz coils. Stark investigations gave dipole moments of 4.45 (8) D for YO and 3.207 (11) D for LaO. The dipole moment is a direct measure of the ionic character of the bond and the determined values agree with the expected trends. In general, the ionic bond character decreases in a row with increasing atomic number; an exception occurs between La and Hf, where the 4f shell is being filled.

Rotational spectra of copper iodide and silver iodide were investigated by the Legon group with a FTMW spectrometer.**48** The species were generated in a pulsed supersonic expansion in combination with a laser ablation source. Cu or Ag atoms were produced by laser ablation of the corresponding metal rod. The metal atoms then reacted with methyl iodide contained in a pulse of argon backing gas, to abstract the iodine atom and to form the respective metal iodides. The hyperfine splittings of the rotational transitions were analyzed to give ^{107,109}Ag ($I = 1/2$), ^{63,65}Cu ($I = 3/2$), and ^{127}I ($I = 5/2$) nuclear quadrupole coupling constants. These constants were interpreted using the Townes-Daily model to evaluate the fractional ionic character, i_c, of the metal halide bonds to be 0.59 and 0.54 for CuI and AgI, respectively. The fractional ionic character of AgI can also be evaluated from its known dipole moment to be 0.53, in agreement with the value from the nuclear quadrupole coupling constants.

The FTMW spectrometer at the University of Tokyo was used to investigate rotational spectra of CrF and CrCl. Cr atoms were generated in a laser ablation source and reacted subsequently with chlorine or fluorine gas mixed into argon backing gas in the supersonic expansion to form the chromium halides. Both species have a $^6\Sigma^+$ electronic ground state. The electronic and nuclear spin angular momenta give rise to complex fine and hyperfine structures of the rotational transitions. Analyses of the spectra gave rotational and centrifugal distortion constants, electron spin–spin coupling parameters, λ, electron spin rotation coupling parameters, γ, magnetic hyperfine coupling constants that describe coupling of electron spin and nuclear spin of F or Cl, and, in the case of CrCl, a Cl nuclear quadrupole coupling constant. The electron configuration of CrF is (core) $(9\sigma)^1$ $(1\delta)^2$ $(4\pi)^2$. The magnetic hyperfine coupling constants are a measure of the contributions of the fluorine 2s orbital to the 9σ molecular orbitals and of the 2p (F) orbital to the 9σ and 4π orbitals. The former contribution was determined to be 0.19% and the latter to be 4.9%, implying that the 9σ and 4π molecular orbitals are mainly localized on the Cr atom. The 1δ orbital can be identified mainly with the 3d (Cr) orbital. The unpaired electrons are thus located at the Cr atom and the fluorine atom is essentially a closed shell F^- anion. The corresponding analysis of CrCl was complicated by effects of spin polarization. However, the ^{35}Cl nuclear quadrupole coupling constant $\chi = -17.4$ MHz allowed qualitative evaluation of the ionic character of the CrCl bond. If the bond is nearly ionic, such as in KCl, the Cl^- ion has a nearly spherically symmetric charge distribution and the value of the quadrupole coupling constant will be close to zero. In case of a nearly covalent bond, such as BrCl, the coupling constant is close to the atomic value, -109.74 MHz. A quantitative interpretation of χ will require support from high level ab initio calculations.

4.4 Species of Atmospheric and Astrophysical Interest

Microwave spectroscopy has been widely used to study small inorganic molecules and radicals that are of importance in atmospheric chemistry and astrophysics. One main driving force is the establishment of a spectroscopic database in the laboratory to aid the search and measurements of these species in the atmosphere and in interstellar and circumstellar environments.

Müller and Cohen have published a number of rotational spectroscopic studies on several important atmospheric molecules, such as $ClClO_2$,[49,50] which participate in catalytic ozone destruction. $ClClO_2$ was generated in situ by reacting $FClO_2$ with a volatile chloride. The products were then flowed through the absorption cell for spectroscopic investigation. The $ClClO_2$ molecule is an asymmetric prolate top and has four naturally occurring isotopomers due to the ^{35}Cl and ^{37}Cl isotopes. Extensive rotational data with quantum numbers $10 \leq J \leq 77$ and $0 \leq K_a \leq 34$ were collected in selected regions between 10 and 417 GHz, using a Stark-modulated absorption spectrometer. Analyses of the transition frequencies yielded rotational and centrifugal distortion constants with very high accuracy and the uncertainties of the fits are of a few kHz. It is therefore now possible to predict the frequencies of rotational transitions for future atmospheric measurements with very high confidence. The obtained rotational and centrifugal distortion constants were then used to derive the structural parameters and to refine the molecular harmonic force field. The quadrupole coupling constants for both Cl nuclei were determined and the molecular dipole moment was derived from low field Stark effect measurements. The experimental results were compared to theoretical predictions using ab initio and DFT methods with different levels of theory and basis sets. Such comparisons show that even with a fairly large basis set such as TZ2Pf at the MP2 level of theory, the dipole moment of the molecule is overestimated by 40%, while coupled cluster and density functional theories show good agreement for the dipole moment and its components in the principal inertial axis system.

Microwave spectra of small sulfur clusters and silicon clusters were reported by McCarthy, Thaddeus and co-workers.[51,52] Sulfur is one of the most cosmically abundant second row elements and 14 sulfur-containing molecules have been detected in a variety of galactic sources,[53] such as cold dense clouds and hot molecular cores, and some of them have been found in external galaxies. Despite extensive previous astronomical detection of small sulfur molecules, sulfur chemistry in space is still not well understood. In one of the laboratory studies, S_3 and S_4 were generated using a low-current DC discharge through argon flowing over a sulfur sample that was heated to 70 °C. Rotational transition lines of S_3 are typically four to five times more intense than those of S_4. These laboratory measurements of S_3 and S_4 provided accurate spectroscopic constants and relevant line frequencies to aid radio-astronomical searches for these new species in molecular clouds, circumstellar shells, Io, and comets. The ultimate aim is to identify the major sulfur reservoir in dense molecular clouds. A wide range of silicon bearing molecules has been observed in circumstellar envelopes, for example, SiO, SiS, SiC_2, SiC, SiC_4. This is in part due to extensive previous laboratory spectroscopic investigations which have provided accurate rest frequencies for these compounds. More recently, pure silicon clusters, such as Si_3, were detected using a sensitive FTMW spectrometer.[52] Si_3 in its electronic ground state has an isosceles triangular structure with a dipole moment of 0.3 D.[54,55] Rotational transition frequencies of the main isotopomer, $^{28}Si_3$, and several of its rare isotopomeric species were measured to an accuracy of a few parts in 10^7. The frequencies of the most intense radio lines were calculated from the derived spectroscopic constants with an uncertainty of better than $3\,\text{km s}^{-1}$ in equivalent radial velocity up to frequencies of 50 GHz. This is good enough for a search in the most promising astronomical sources for such species.

Small inorganic radicals have also been studied quite extensively in the microwave region. Some examples are metal-containing radicals such as $MgNH_2$,[56] $LiNH_2$,[57] and linear carbon chain radicals such as C_5H_2, C_6H_2,[58] C_5H, C_6H, and C_8H.[59] $LiNH_2$ can be used to deprotonate ketones, aldehydes, and other structurally related organic molecules and play an important role in organic synthesis. One challenge in carrying out gas phase measurements of alkali metal amides is that they tend to aggregate in the condensed phase and even in the gas phase. Rather than vaporizing monomeric $LiNH_2$ from a solid phase sample, Ziurys *et al.* produced it directly in the gas phase by the reaction of gaseous NH_3 and lithium vapor. In this way, they were able to generate enough monomeric $LiNH_2$ in the gas phase to study its rotational spectrum. From the microwave data, it was found that the molecule is planar with an Li–N distance of 1.736(3) Å, an N–H distance of 1.022(3) Å and an H–N–H angle of 106.9(1)°. Although there had been over 20 theoretical calculations reported for $LiNH_2$ and a substantial amount of experimental data for oligomeric solid phase samples, the question whether monomeric $LiNH_2$ is planar or not was not resolved before this study. These microwave results have provided the first direct experimental evidence for the planar structure of $LiNH_2$.

Linear hydrocarbon radicals have been the subject of intensive laboratory spectroscopic and radio-astronomical research since the early 1980s. In recent years, a considerable number of rotational spectroscopic studies of medium to longer hydrocarbon chains such as C_5H, C_6H, C_8H,[59] and $C_{14}H$[60] have been carried out using a pulsed molecular beam FTMW spectrometer. The high resolution offered by such a spectrometer allowed the detection of the hyperfine splitting of rotational transitions. These measurements improved fine and hyperfine coupling constants and provided rest frequencies with accuracies better than $0.30\,\text{km s}^{-1}$ in equivalent radial velocity up to 50 GHz. Indeed, some of the small C_nH radicals with $n < 9$ have subsequently been detected in space, in molecular cloud cores, and in certain circumstellar shells. These hydrocarbon chains are among the most abundant reactive space molecules known.

An exciting recent development is the work by Endo *et al.* who reported the detection and analyses of the rotational spectrum of the water-hydroperoxy radical complex.[61] The self reaction of the hydroperoxy radical is a primary source of atmospheric hydrogen peroxide: $HO_2 + HO_2 \rightarrow H_2O_2 + O_2$.[62,63] This reaction is catalyzed by water. The $H_2O{-}HO_2$ radical complex was proposed to be the intermediate generated in the process.[62,63] The binding energy of the complex is fairly large, about $9.4\,\text{kcal mol}^{-1}$. It was hypothesized that this complex could act as a sink for the atmospheric HO_2 radical. Endo *et al.* produced the HO_2 radical by applying a high voltage electric discharge (1.5 kV) in a gas mixture of O_2 and Ar inside a pulse discharge nozzle. The radical entrained in the Ar flow was subsequently passed through a reservoir filled with pure water and then expanded into a vacuum chamber through the pulsed nozzle. The targeted radical complex was generated in the supersonic expansion. Pure rotational transitions with hyperfine splittings were measured and the frequencies were fitted to yield spectroscopic parameters. In addition to the rotational spectroscopic constants, the Fermi coupling constant, a_F, was also determined. This parameter is a direct measure of the unpaired electron density at each hydrogen nucleus and provides information about the unpaired electron distribution upon complex formation. In particular, this study shows that the a_F value for the HO_2 proton is −27.511(21) MHz, almost identical to that of free HO_2, while that of the H_2O protons is much smaller at −0.0395(62) MHz. This indicates that only a very small portion of the unpaired electron density is delocalized over the H_2O part. This result is somewhat surprising since substantial delocalization of the unpaired electrons was detected in other radical molecule complexes such as $H_2O{-}OH$[64] and NO–HF.[65] This is despite the fact that $H_2O{-}HO_2$ is much more strongly bound than $H_2O{-}OH$. The rotational spectroscopic study also shows that the radical complex forms a nearly planar five-membered ring with HO_2 acting as a proton donor and one hydrogen atom of water sticking out from the ring plane. The accurate transition frequencies obtained provide the data needed for remote sensing of this complex. Such work may further elucidate the potential roles of the water-hydroperoxy radical complex in atmospheric chemistry and provide a conclusive answer to the proposed hypothesis.

4.5 Weakly Bound Complexes

The method of FTMW spectroscopy has been used to study a large number of weakly bound complexes and clusters.[11,66] One main goal in these studies is to determine the structure and the intermolecular dynamics, that is, the degree of large amplitude vibrational motions, in these systems, and ultimately to characterize the intermolecular interaction potential as a function of separation and orientation. These are aspects of these studies that are of interest to the inorganic chemist.

As mentioned before, a nonzero electric molecular dipole moment is necessary for the observation of (dipole-allowed) rotational microwave transitions. That makes it impossible to study the rotational spectra of substances such as dinitrogen, N_2. Note, however, that microwave studies were reported for isotopically labeled carbondioxide, $^{16}OC^{18}O$,[67] and for higher J transitions of methane[68] with a centrifugally induced dipole moment. Another possibility is to use a rare gas atom as a structureless probe to enable the spectroscopic investigation of otherwise nonpolar molecules. A molecular expansion of N_2 in neon backing gas can be used to produce Ne–N_2 van der Waals complexes. The binding energy is provided primarily by dispersion interactions, which also lead to a small, but nonvanishing, electric dipole moment. The rotational spectrum of the Ne–N_2 complex can then be investigated with a FTMW spectrometer.[69] This work has resulted in an accurate experimental determination of the ^{14}N nuclear quadrupole coupling constant in dinitrogen [$\chi = 5.372(2)$ MHz], which had thus far been unavailable. This procedure was validated by the microwave investigation of the Ar–CO_2 van der Waals complex.[70] In this case, the ^{17}O nuclear quadrupole coupling constant of the complexes could be determined. This constant was used to determine the corresponding constant in the carbon dioxide monomer, and was found to agree with the value obtained from the isotopic study.[67]

Another interesting aspect of the spectroscopy of van der Waals complexes is the investigation of species containing xenon atom. Hyperpolarized xenon is used in magnetic resonance imaging experiments to characterize void spaces, such as, for example, micropores in zeolites.[71] An interpretation of the measured chemical shifts in terms of the microscopic, molecular environment will require the availability of accurate Xe-surroundings interaction potentials and shielding surfaces. The microwave investigations of Xe-molecule systems are a first step to achieve this goal. Recent studies of the Xe–H_2O and Xe–$(H_2O)_2$ complexes,[72,73] for example, can help to determine the effect of crystal water in zeolites on magnetic resonance parameters. It was possible in these studies to determine the ^{131}Xe nuclear quadrupole coupling constants. Their interpretation in terms of the electric multipole moments of water, together with ab initio calculations on the MP2 level, revealed that the two water molecules in Xe–$(H_2O)_2$ assume distinctly different orientations with respect to the xenon atom (Figure 6).

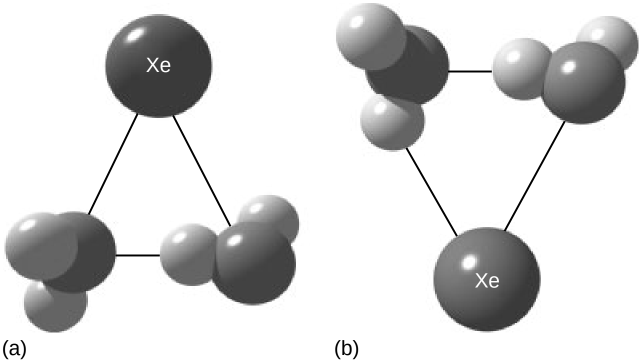

Figure 6 These two structures of the Xe–$(H_2O)_2$ complex correspond to the two minima found in ab initio calculations on the MP2 level for this system. An interpretation of the ^{131}Xe nuclear quadrupole coupling constants and comparison with the corresponding constant in Xe–H_2O reveal that the structure in (a) is consistent with the data from the microwave spectrum

The xenon atom can therefore be used as a delicate probe to determine the number of surrounding water molecules and their orientations. These results demonstrate the sensitivity of the easily polarizable xenon electronic structure to the electrostatic properties of its surrounding and the great potential for achieving accurate interpretations of magnetic resonance parameters from imaging experiments with hyperpolarized xenon.

5 ABBREVIATIONS AND ACRONYMS

cp = cyclopentadienyl; DFT = density functional theory; ETH = eidgenössische technische hochschule; FTMW = Fourier transform microwave; NMR = nuclear magnetic resonance; NIST = National Institute of Standards and Technology.

6 REFERENCES

1. W. Gordy and R. L. Cook, ‘Microwave Molecular Spectra’, 3rd edition, John Wiley & Sons, New York, 1984, Vol. XVIII.
2. C. H. Townes and A. L. Schawlow, ‘Microwave Spectroscopy’, Dover Publications, New York, 1975.
3. C. E. Cleeton and N. B. Williams, *Phys. Rev.*, 1934, **45**, 234.
4. W. Gordy, *J. Mol. Spectrosc.*, 1983, **97**, 17.
5. J. Ekkers and W. H. Flygare, *Rev. Sci. Instrum.*, 1976, **47**, 448.
6. W. H. Flygare, in ‘Laser and Coherence Spectroscopy’, ed. J. I. Steinfeld, Plenum Press, New York, 1978, p. 125.
7. H. Dreizler, *Z. Naturforsch.*, 1992, **47a**, 342.
8. H. Dreizler, *Ber. Bunsen-Ges. Phys. Chem.*, 1995, **99**, 1451.
9. A. Bauder, in ‘Vibrational Spectra and Structure’, ed. J. R. Durig, Elsevier, New York, 1993, Vol. 20, p. 157.
10. T. J. Balle and W. H. Flygare, *Rev. Sci. Instrum.*, 1981, **52**, 33.
11. Y. Xu, J. van Wijngaarden and W. Jäger, *Int. Rev. Phys. Chem.*, 2005, **24**, 301.
12. C. J. Evans and M. C. L. Gerry, *J. Am. Chem. Soc.*, 2000, **122**, 1560.
13. C. J. Evans and M. C. L. Gerry, *J. Chem. Phys.*, 2000, **112**, 9363.
14. H. W. Harrington, J. R. Hearn, and R. F. Rauskolb, *Hewlett-Packard J.*, 1971, **22**, (http://www.hparchive.com/Journals/Low-Resolution/HPJ-1971-06-Low-Resolution.pdf).
15. G. G. Brown, B. C. Dian, K. O. Douglass, S. M. Geyer and B. H. Pate, *J. Mol. Spectrosc.*, 2006, **238**, 200.

16. E. B. Wilson, J. C. Decius and P. C. Cross, ‘Molecular Vibrations’, Dover Publications, New York, 1980.
17. C. H. Townes and B. P. Daily, *J. Chem. Phys.*, 1955, **23**, 118.
18. D. L. Bryce and R. E. Wasylishen, *Acc. Chem. Res.*, 2003, **36**, 327.
19. J. Brown and A. Carrington, ‘Rotational Spectroscopy of Diatomic Molecules’, Cambridge University Press, Cambridge, 2003.
20. P. R. Bunker and P. Jensen, ‘Molecular Symmetry and Spectroscopy’, 2nd edition, NRC Research Press, Ottawa, 1998.
21. A. Mizoguchi, Y. Endo and Y. Ohshima, *J. Chem. Phys.*, 1998, **109**, 10539.
22. C. C. Lovallo and M. Klobukowski, *Chem. Phys. Lett.*, 2003, **368**, 589.
23. C. J. Evans and M. C. L. Gerry, *J. Chem. Phys.*, 2000, **112**, 1321.
24. C. J. Evans, D. S. Rubinoff and M. C. L. Gerry, *Phys. Chem. Chem. Phys.*, 2000, **2**, 3943.
25. C. J. Evans, A. Lesarri and M. C. L. Gerry, *J. Am. Chem. Soc.*, 2000, **122**, 6100.
26. J. M. Michaud, S. A. Cooke and M. C. L. Gerry, *Inorg. Chem.*, 2004, **43**, 3871.
27. J. M. Thomas, N. R. Walker, S. A. Cooke and M. C. L. Gerry, *J. Am. Chem. Soc.*, 2004, **126**, 1235.
28. J. M. Michaud and M. C. L. Gerry, *J. Am. Chem. Soc.*, 2006, **128**, 7613.
29. S. A. Cooke and M. C. L. Gerry, *Phys. Chem. Chem. Phys.*, 2004, **6**, 3248.
30. S. Cooke and M. C. L. Gerry, *J. Am. Chem. Soc.*, 2004, **126**, 12000.
31. C. Tanjaroon, K. S. Keck, M. M. Sebonia, C. Karunatilaka and S. G. Kukolich, *J. Chem. Phys.*, 2004, **121**, 1449.
32. S. G. Kukolich, S. M. Sickafoose and S. M. Breckenridge, *J. Am. Chem. Soc.*, 1996, **118**, 205.
33. B. J. Drouin, *J. Am. Chem. Soc.*, 1998, **120**, 6774.
34. B. J. Drouin, T. G. Lavaty, P. A. Casak and S. G. Kukolich, *J. Chem. Phys.*, 1997, **107**, 6541.
35. B. J. Drouin, J. J. Dannemiller and S. G. Kukolich, *J. Chem. Phys.*, 2000, **112**, 747.
36. D. S. Margolis, C. Tanjaroon and S. G. Kukolich, *J. Chem. Phys.*, 2002, **117**, 3741.
37. C. Tanjaroon, K. S. Keck and S. G. Kukolich, *J. Am. Chem. Soc.*, 2004, **126**, 844.
38. R. Subramanian, C. Karunatilaka, K. S. Keck and S. G. Kukolich, *Inorg. Chem.*, 2005, **44**, 3137.
39. R. Subramanian, C. Karunatilaka, R. O. Schock, B. J. Drouin, P. A. Cassak and S. G. Kukolich, *J. Chem. Phys.*, 2005, **123**, 054317.
40. R. M. G. Roberts and J. Silver, *J. Organomet. Chem.*, 1984, **263**, 235.
41. W. F. Little, C. N. Reilley, J. D. Johnson, K. N. Lynn and A. P. Sanders, *J. Am. Chem. Soc.*, 1964, **86**, 1376.
42. W. E. Britton, R. Kashyap, M. El-Hashash, M. El-Kady and M. Herberhold, *Organometallics*, 1986, **5**, 1029.
43. A. Haaland and J. E. Nilsson, *Acta Chem. Scand.*, 1968, **22**, 2653.
44. T. E. Concolino and J. L. Eglin, *J. Cluster Sci.*, 1997, **8**, 461.
45. Y. T. Struchkov, K. N. Anisimov, O. P. Osipova, N. E. Kalobava and A. N. Nesmeyanov, *Dokl. Akad. Nauk SSSR, Ser. A*, 1967, **172**, 107.
46. A. L. Rheingold, W. K. Meckstroth and D. P. Ridge, *Inorg. Chem.*, 1986, **25**, 3706.
47. R. D. Suenram, F. J. Lovas, G. T. Fraser and K. Matsumura, *J. Chem. Phys.*, 1990, **92**, 4724.
48. S. G. Batten, A. G. Ward and A. C. Legon, *J. Mol. Struct.*, 2006, **780–781**, 300.
49. H. S. P. Müller and E. A. Cohen, *J. Phys. Chem. A*, 1997, **101**, 3049.
50. H. S. P. Müller, E. A. Cohen and D. Christen, *J. Chem. Phys.*, 1999, **110**, 11865.
51. C. A. Gottlieb, S. Thorwirth, M. C. McCarthy and P. Thaddeus, *Astrophys. J.*, 2005, **619**, 939.
52. M. C. McCarthy and P. Thaddeus, *Astrophys. J.*, 2003, **592**, L91.
53. P. Thaddeus and M. C. McCarthy, *Spectrochim. Acta, Part A*, 2001, **57**, 757.
54. C. M. Rohlfing and K. Raghavachari, *J. Chem. Phys.*, 1992, **96**, 2114.
55. I. Vasiliev, S. Öğüt and J. R. Chelikowsky, *Phys. Rev. Lett.*, 1997, **78**, 4805.
56. P. M. Sheridan and L. M. Ziurys, *Astrophys. J.*, 2000, **540**, L61.
57. D. B. Grotjahn, P. M. Sheridan, I. Al Jihad and L. M. Ziurys, *J. Am. Chem. Soc.*, 2001, **123**, 5489.
58. M. C. McCarthy, M. J. Travers, A. Kovács, W. Chen, S. E. Novick, C. A. Gottlieb and P. Thaddeus, *Science*, 1997, **275**, 518.
59. M. C. McCarthy, W. Chen, A. J. Apponi, C. A. Gottlieb and P. Thaddeus, *Astrophys. J.*, 1999, **520**, 158.
60. C. A. Gottlieb, M. C. McCarthy, M. J. Travers, J.-U. Grabow and P. Thaddeus, *J. Chem. Phys.*, 1998, **109**, 5433.
61. K. Suma, Y. Sumiyoshi and Y. Endo, *Science*, 2006, **311**, 1278.
62. E. J. Hamilton, Jr, *J. Chem. Phys.*, 1975, **63**, 3682.
63. E. J. Hamilton, Jr and R.-R. Lii, *Int. J. Chem. Kinet.*, 1977, **9**, 875.
64. Y. Ohshima, K. Sato, Y. Sumiyoshi and Y. Endo, *J. Am. Chem. Soc.*, 2005, **127**, 1108.
65. C. R. Dennis, C. J. Whitham and B. J. Howard, *J. Chem. Phys.*, 2001, **115**, 1367.
66. S. Novick, Bibliography of Rotational Spectra of Weakly Bound Complexes, http://www.wesleyan.edu/chem/faculty/novick/vdw.html, 2007.

67. J. Gripp, H. Mäder, H. Dreizler and J. L. Teffo, *J. Mol. Spectrosc.*, 1995, **172**, 430.
68. C. W. Holt, M. C. L. Gerry and I. Ozier, *Phys. Rev. Lett.*, 1973, **31**, 1033.
69. W. Jäger, Y. Xu, G. Armstrong, M. C. L. Gerry, F. Y. Naumkin, F. Wang and F. R. W. McCourt, *J. Chem. Phys.*, 1998, **109**, 5420.
70. H. Mäder, N. Heineking, W. Stahl, W. Jäger and Y. Xu, *J. Chem. Soc., Faraday Trans.*, 1996, **92**, 901.
71. I. L. Moudrakovski, S. Lang, C. I. Ratcliffe, B. Simard, G. Santyr and J. A. Ripmeester, *J. Magn. Reson.*, 2000, **144**, 372.
72. Q. Wen and W. Jäger, *J. Phys. Chem. A*, 2006, **110**, 7560.
73. Q. Wen and W. Jäger, *J. Phys. Chem. A*, 2007, **111**, 2093.

Neutron Diffraction

Muhammed Yousufuddin

University of Maryland, College Park, MD, USA and NIST Center for Neutron Research,
National Institute of Standards and Technology, Gaithersburg, MD, USA

Robert Bau

University of Southern California, Los Angeles, CA, USA

Method Summary 1
1 Introduction 2
2 Some Basic Facts of Neutron Diffraction 2
3 Disadvantages of Neutron Scattering 3
4 Neutron Facilities (Reactor Sources and Spallation Sources) 3
5 Neutron Instruments (Diffractometers) 4
6 Powder Diffraction 5
7 Magnetic Studies 6
8 Location of Hydrogen Atoms 6
9 Oxidative Addition to a H–H Bond 6
10 Hydrogen Atoms in Metal Clusters 8
11 Agostic Interactions 10
12 Absolute Configuration of Chiral Molecules of the Type CHDRR* 10
13 Neutron Diffraction Studies on Proteins 12
14 Conclusion 15
15 Acknowledgments 15
16 End Notes 16
17 Abbreviations and Acronyms 16
18 Further Reading 16
19 References 16

METHOD SUMMARY

Acronyms, Synonyms

- Neutron Radiation
- Crystallography
- Single-Crystal Neutron Diffraction.

Measured physical quantities

- diffraction of neutrons by the nuclei of atoms in a crystal.

Information available

- structural information including geometry and bond lengths, especially those involving light atoms like hydrogen;
- isotopic discrimination (most notably, distinguishing H from D).

Information not available, limitations

- not suitable for materials with a high content of neutron-absorbing elements such as boron or cadmium;
- heavy atom coordinates are usually required from an X-ray experiment to phase the single-crystal neutron diffraction data.

Examples of questions that can be answered

- What is the location of chemically interesting hydrogen atoms?
- What is the magnetic structure of the sample?
- Where has (H/D) isotopic exchange occurred?

Major advantages

- Hydrogen atoms can be located in a single crystal diffraction experiment.
- Information regarding magnetic structure can be obtained.
- The sample does not usually suffer any radiation damage.
- Metal–hydrogen and hydrogen–hydrogen distances can sometimes be measured to accuracies of ±0.005 Å or more in a single-crystal diffraction experiment.

Major disadvantages

- Neutron sources (a nuclear reactor or spallation source) are very limited in number.
- Large crystals (typically 1–5 mm^3) are required because neutron radiation is relatively weak (as compared to X-ray intensities).
- For single-crystal experiments, data collection times (1 day to 2 weeks) are several orders of magnitude longer than X-ray data collection times.
- Powder experiments are usually limited to compounds with smaller unit cells.

Sample constraints

- Large crystals in the range of 1 mm^3 or bigger are required for single-crystal neutron diffraction experiment.
- The sample must not contain, high amount of neutron absorbing element.

---

1 INTRODUCTION

Neutron diffraction is, for most practicing chemists, an underutilized and underappreciated tool. Nevertheless, it is rapidly gaining in popularity as newer (and more effective) instruments, as well as more intense neutron sources become available in the future. Thus, the main point of this article is to provide examples to show that neutron diffraction can offer additional valuable information in certain areas of chemistry where X-ray diffraction is either inadequate or inapplicable. As the focus of this article is on applications, the theory of neutron diffraction will not be discussed in detail, although we do refer the reader to a number of texts that cover this topic.[a][1,2] Nevertheless, to give the reader a ‘‘flavor’’ of what is ‘‘usually expected’’ in a neutron diffraction study, we will briefly describe the features of a few selected existing neutron facilities and instruments.

First of all, one should realize that, although the main focus of this article will be on *single-crystal* neutron diffraction,[3–7] it should be kept in mind that this only represents a small slice of all neutron scattering experiments. First and foremost, there is powder neutron scattering,[8–10] a field in which there are far more publications than those that feature single-crystal neutron studies. Then there are innumerable other applications that do not require the availability of crystalline samples, such as small-angle neutron scattering (SANS), inelastic neutron scattering (INS),[11] to name a few. Secondly *within single-crystal neutron diffraction itself* there are a number of subfields, such as (i) the location of small atoms (usually H or D) under conditions in which X-ray diffraction cannot provide an unambiguous answer, (ii) isotopic discrimination (usually experiments designed to tell the difference between H and D positions), (iii) studies of magnetic structure,[12,13] which take advantage of the fact that the neutron has a spin (unlike X rays, which as photons have no spin),[b] (iv) diffuse scattering,[14] in which the nature of *disorder* in a structure is studied, and (v) high-pressure studies in which the structure of crystalline materials when subjected to enormous pressures are probed. In this article we will mainly be focusing on topic (i), (also reviewed in references Refs. 3–7) which is starting to expand from the realm of small-molecule structure determination to the determination of H and D positions in macromolecules (proteins and oligonucleotides).[15–25]

2 SOME BASIC FACTS OF NEUTRON DIFFRACTION

In contrast to X rays, the scattering factors for neutrons are not proportional to atomic number. Whereas X rays

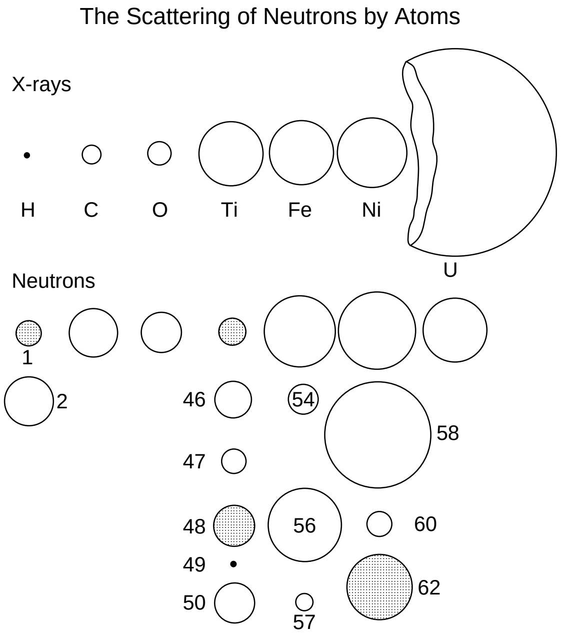

Figure 1 A comparison between the scattering of X rays and neutrons by the same seven atoms (H, C, O, Ti, Fe, Ni, and U). The numbers given in the bottom half of the figure are atomic weights, not atomic numbers. Shaded circles represent isotopes which appear as negative peaks in a neutron Fourier map. (From Bacon.[1] Permission of Oxford University Press)

are scattered from electrons, the point of diffraction for neutrons is the nucleus of an atom. Figure 1 schematically compares the scattering factors of some atoms for both X rays and neutrons. One can immediately notice that for the small atoms, like H and D, neutrons are scattered significantly better than X rays, while the opposite is true for heavier atoms. A second feature to note from Figure 1 is that neutrons have the ability to distinguish between some isotopes (notably H from D) since the scattering factor for hydrogen is negative (shaded in Figure 1). (Note: a positive scattering factor indicates that the neutron wave undergoes a phase inversion upon scattering, whereas a negative scattering factor corresponds to no phase change. This peculiar ‘‘inverted’’ convention was adopted deliberately in order to ensure that most nuclei would have positive scattering values.[1] In practice, this means that H appears as a negative peak in a neutron difference Fourier map, whereas a D-atom appears as a positive peak.)

To summarize what was pointed out earlier, this makes neutron diffraction invaluable for studies of metal hydrides, agostic interactions, and H/D exchange. Furthermore, since neutrons have an intrinsic spin (unlike X rays which are massless photons) they can interact with the electronic spin of the atoms in a sample and thereby provide information concerning the magnetic properties of the sample under study. Data collection at high scattering angles (backscattering reflections) are often possible since the level of falloff of neutron intensity at high resolution is much less than that of X rays.[1] In addition, neutron radiation is nondestructive in nature which allows for the study of most materials that are sensitive to radiation damage.

3 DISADVANTAGES OF NEUTRON SCATTERING

The major disadvantages of neutron diffraction, from the viewpoint of most practicing chemists, are twofold: the requirement of a large crystal, and the limited availability of neutron sources. (i) Since the neutron flux from most existing neutron sources are several orders of magnitude weaker than photon fluxes from a typical X-ray tube, much larger crystals (originally in the range of 5–20 mm^3, more recently, vide infra, in the range of 1–2 mm^3) are needed for a neutron diffraction experiment. Any chemist who has gone through the trouble of growing diffraction-quality crystals for an X-ray study can appreciate the difficulty involved in growing ‘‘neutron-sized’’ crystals: that is, samples with 10–100 times the volume of ‘‘X-ray-sized’’ crystals. (ii) Another consequence of low neutron flux is data collection time: while modern X-ray diffractometers equipped with efficient charge-coupled device (CCD) detectors can typically collect a data set in several hours (and in tens of minutes or less in the case of X-ray synchrotron sources), most of the older ‘‘traditional’’ neutron diffractometers require data collection times of a week or so. Currently there are newer instruments[26,27] that can cut neutron data collection times to a day or two, and these will be discussed later in this article. The second disadvantage mentioned earlier is the fact that neutron *sources* are not as widely available as X-ray sources, with only a handful of facilities in the world capable of conducting neutron experiments. In the next section, we will give a little more background information and briefly describe the two major types of neutron sources that are used around the world today.

4 NEUTRON FACILITIES (REACTOR SOURCES AND SPALLATION SOURCES)

Neutron ‘‘user’’ facilities are scattered throughout the world. These neutron sources are of two types, (i) nuclear reactors which provide a steady beam of neutrons[1] and (ii) spallation sources which offer pulsed neutron beams.[2] Each type of facility offers its own advantages and a reader interested in pursuing this topic is referred to the description of each individual site[28–33] for further details. Reactor sources are based on the conventional ^{235}U fission process and therefore, are somewhat similar to conventional nuclear-powered electricity generators, with the major exception that the ^{235}U enrichment level of the nuclear fuel in a research reactor is much higher than that in a conventional electricity-generating nuclear power plant. Existing neutron sources of this type include the HFIR reactor in Oak Ridge,

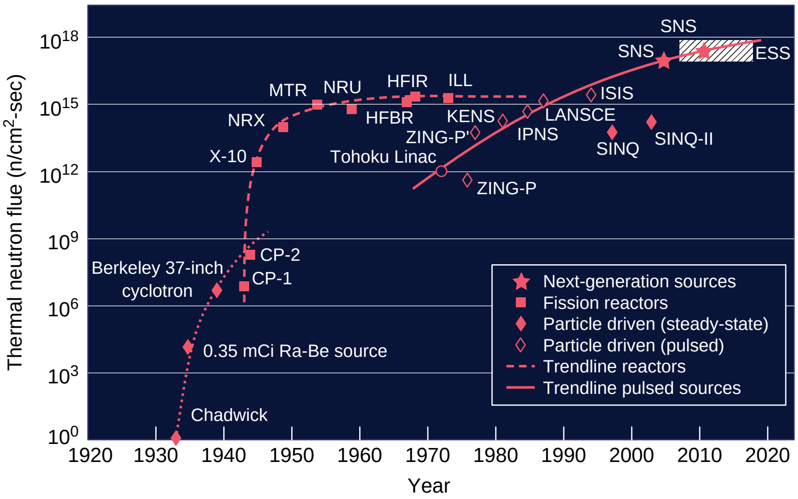

Figure 2 Improvement in Neutron Fluxes (vertical axis) over time (horizontal axis). Note the predominance of fission reactor sources from 1945 to 1980 (dashed line in the middle) and the steady drift toward more intense spallation sources in more recent years (solid line to the right). (Drawn from data in Skold & Price, 1986)

Tennessee,[28] the JRR-3 reactor in Tokai (Japan),[29] the Institut Laue-Langevin (ILL) reactor in Grenoble, France,[30] and, two more recent facilities, the new Opal reactor in Lucas Heights, Australia[31] and the FRM-II Reactor in Munich, Germany.[32] There are countless other less intense sources too numerous to mention in this brief review.[33] It is generally acknowledged that the ILL reactor currently has the highest flux of conventional nuclear sources (Figure 2).

Pulsed sources[2,34,35] operate under a completely different principle and basically are meant to produce neutrons without the use of a nuclear reactor. In brief, hydride ions (H^-) are accelerated down a linear accelerator (LINAC) to velocities approaching the speed of light. Then their electrons are stripped off, converting the H^- ions into H^+ (protons) which are then diverted into an accumulator ring in most sources, whose main function is to accumulate protons to produce short-, high-intensity pulses. Several times a second (typically, 10–60 s), these protons are directed onto a target (usually made of a high-melting, heavy-atom target such as tungsten, tantalum, or uranium), where they collide with the nuclei of the target and produce large amounts of neutrons through a process known as spallation.[2,34,35] Each collision of a proton with a heavy-atom nucleus produces between 10 and 30 neutrons. The main advantage of a pulsed source is that, in principle, all the thermal neutrons from each pulse are useful in a diffraction experiment (as opposed to those from a monochromatized steady-state nuclear reactor source, most of which are wasted). At a pulsed source, the more energetic neutrons arrive at the sample and the detector *earlier* than the slower and less energetic neutrons such that time-of-flight techniques are utilized to determine the wavelength of each detected neutron. Thus, one needs ‘‘three-dimensional’’ detectors (recording two spatial coordinates, x, y, and time), coupled to computers able to acquire and process enormous amounts of data. The first spallation source was ZING-P constructed by Jack Carpenter and his group at Argonne Laboratory,[34,35] subsequently replaced by ZING-P’ and now the intense pulsed neutron source (IPNS)[36] at Argonne. Other pulsed sources included the LANSCE spallation source at Los Alamos, New Mexico[37] and ISIS in Didcot, England.[38] Currently under construction are much more powerful spallation sources: spallation neutron source (SNS) in Oak Ridge, Tennessee[39] and J-PARC in Tokai, Japan.[40] The latter two facilities, whose single-crystal instruments will gradually become available in the years between 2008 and 2010, are expected to have neutron beams about 50–100 times more intense than those of existing spallation sources because of their intended use of liquid mercury as a heavy-metal target.[39,40] When operational, it is expected that they should cut down crystal-size requirements by at least an order of magnitude compared to current ‘‘neutron-sized’’ crystals, which should clearly be an advantage for practicing chemists (and biologists).

Figure 2 summarizes the historical development of neutron sources and the gradual drift toward spallation sources (and a concomitant increase in neutron flux) with the progress of time.

5 NEUTRON INSTRUMENTS (DIFFRACTOMETERS)

Historically, all the early neutron sources were of the conventional reactor type, and a large monochromating crystal was commonly employed (for single-crystal diffraction experiments) to select neutrons with a small wavelength spread in order to produce a monochromatic neutron beam.[1] The rest of the neutrons (of different wavelengths) were discarded and hence the use of a monochromatic beam was intrinsically a wasteful process (in that only a small fraction of the neutrons was used in a diffraction experiment). In addition, the earliest single-crystal instruments were modeled after existing X ray diffractometers, meaning that in those early days reflections were collected one at a time, another inefficient technique by today's standards. During that period (from the 1950s to the 1970s), crystal size requirements were typically in the volume range 5–20 mm^3.

With time, improvements in instrumentation[26,27,33,41–45] were made which resulted in reduced sample size and/or data collection time. An especially significant step (following developments in X-ray data collection) involved the use of area detectors to collect dozens to hundreds or thousands of reflections simultaneously. The details of various area detectors used are too varied to warrant a detailed discussion here, and may not be of interest to many readers of this article. Suffice it to say that most detectors rely on efficient neutron-absorbing components (such as ^{3}He, ^{6}Li, ^{10}B, or ^{157}Gd), which then produce other particles (typically, photons or electrons) that are actually counted.

One noteworthy (relatively recent) event is the development of neutron-sensitive image plates that are relatively inexpensive and capable of high spatial resolution. A particularly successful example of this is a plastic film containing atoms of Gd, which act as neutron-capturing centers that subsequently emit detectable radiation.[41,42] The flexibility of this plastic-supported detector allows it to be fashioned into a cylindrical shape, which results in a much larger solid angle of reflections that can be collected, as compared to a flat detector. Examples of such cylindrical detectors include those presently used in the BIX-3 and BIX-4 diffractometers at JAEA in Tokai, Japan,[43] the LADI[44] and VIVALDI[26,27] diffractometers at ILL in Grenoble, France, and the soon-to-be-operational quasi-Laue diffractometer (KOALA) diffractometer at the open pool Australian light-water reactor (OPAL) reactor in Lucas Heights, Australia, which has a design similar to VIVALDI. Some of the above-mentioned instruments further take advantage of data collection using the quasi-Laue technique[46–48] (which employs a broader range of neutron wavelengths and allows for a greater neutron flux).[46–48] VIVALDI, in particular, is capable of handling samples as small as 0.5–1.0 mm^3, and with (in favorable cases) data collection times as short as 24 h.[26,27]

But arguably, the most exciting future development is the SNS, which is currently being built in Oak Ridge, Tennessee.[39] When fully completed (scheduled to take place around 2007–2008), this facility is estimated to provide neutron beams between 50 and 100 times the intensity of current pulsed neutron sources. As far as single-crystal neutron diffraction experiments are concerned, the instrument currently being built for medium-sized unit cells is TOPAZ[49] (Figure 3), which is scheduled to be available to users some time in 2009 and is planned to handle crystals having volumes as small as 0.1 mm^3 (i.e., ''X-ray-sized'' crystals) and/or data collection times as short as 6–12 h. Also in the planning stage is an instrument at SNS designed to handle protein crystals called *macromolecular neutron diffractometer* (MaNDi),[50] which should be ready about a year or so after TOPAZ. It should also be pointed out that, additionally, another instrument called BIX-P1[51] is also being planned for macromolecular crystallography in the analogous spallation source J-PARC[40] under construction in Tokai, Japan and an instrument called LMX[52] (large molecule crystal diffractometer) designed for crystals with large unit cells is planned for a second target station at ISIS[38] in Didcot, England.

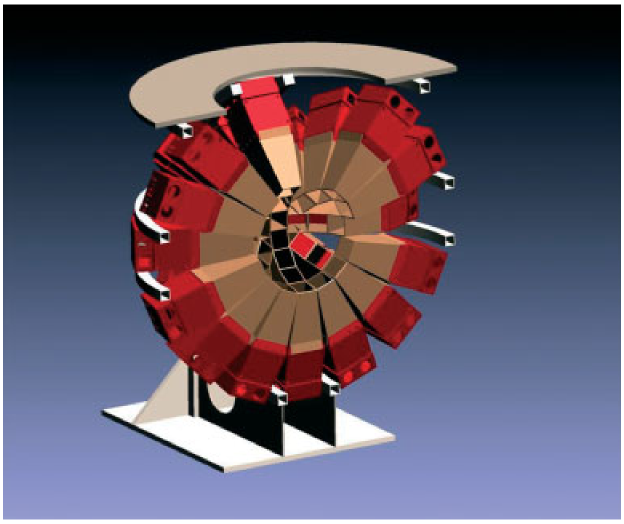

Figure 3 Schematic diagram of the TOPAZ single-crystal diffractometer to be completed at the SNS (spallation neutron source, Oak Ridge, Tennessee) by 2009. (Image downloaded in 2006 from http://neutrons.ornl.gov/instrument_systems/beamline_12_topaz/index.shtml. © US Government)

6 POWDER DIFFRACTION

In cases where it is difficult to obtain large crystals, chemists may logically conclude that powder diffraction experiments offer a suitable alternative. However, powder diffraction experiments[8–10] are usually restricted to large samples of smaller unit cells than those commonly involved in a typical organometallic structure. In addition, because the nature of the diffraction data is one-dimensional (rather than three-dimensional in a single-crystal experiment), peak overlap is a serious problem. This difficulty is largely alleviated by the use of the Rietveld method,[53–57] in which the overall *profile* of the diffraction pattern is essentially scanned stepwise to yield hundreds of individual intensity measurements. Furthermore, deuteration is almost always necessary in a powder diffraction experiment because, otherwise, background problems (arising from the incoherent scattering[1] from hydrogen atoms) would seriously compromise the results of the structural analysis. Finally, combined X-ray/neutron refinement, in which both X-ray and neutron data[58] are used in least-squares refinement of a structure, is much more commonly used in powder diffraction studies (*see* ***X-Ray Powder Diffraction***). Despite all these limitations, publications involving powder neutron studies far outnumber those involving single-crystal neutron investigations largely because of the previously mentioned difficulties in growing large single crystals.

7 MAGNETIC STUDIES

Another widely used application of neutron diffraction is in the study of magnetic structure.[59–61] We will not say much in this article because of space limitations, but in essence the technique takes advantage of the fact that neutrons, being intrinsic particles, have spins, while X rays do not. The *nuclear* spin of the neutrons can interact with the *electronic* spins in a magnetically active sample and, for example, can distinguish between parallel and antiparallel spins of pairs of atoms in a ferromagnetic or antiferromagnetic sample (e.g., Figure 4).

In favorable cases, even the spin density of a paramagnetic molecule can, in principle, be mapped out.[62–66] In some cases, polarized neutrons[67–70] are necessary in a magnetic structural study, in other cases, an unpolarized neutron beam is adequate. The subject matter of magnetic structure is discussed in Ref. 61 but for a more detailed discussion the reader is encouraged to consult more specialized texts regarding this subject.[59,60]

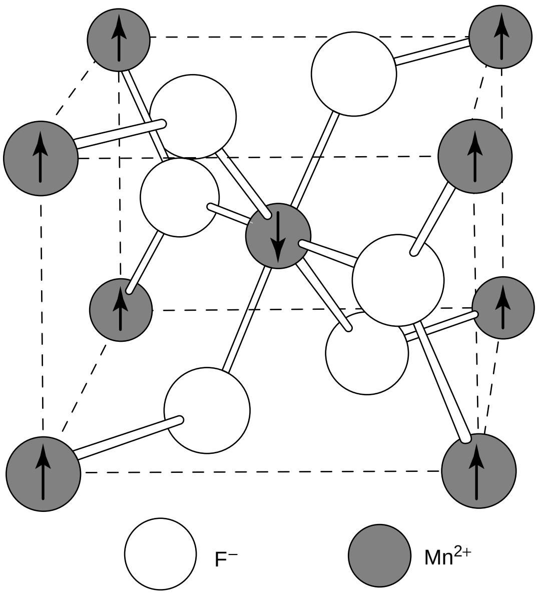

Figure 4 The magnetic structure of MnF_2 from a neutron diffraction study.[1] Note that the central Mn atom has its spin opposite to those at the corners in this antiferromagnetic arrangement. (From Bacon.[1] Permission of Oxford University Press)

8 LOCATION OF HYDROGEN ATOMS

We now come to the main theme of the article, the part that is perhaps the most interesting to the average chemist (and biologist), and that is the accurate location of hydrogen atoms in a molecule. While it is true that the data from current CCD-based X ray diffractometers are good enough to enable the investigator to find most hydrogens (certainly hydrogens bonded to the light elements, or at times to a single atom of a first-row transition metal), there remain several areas in which neutron diffraction data can make a difference: (i) when ultra-accurate H atom positions are needed (e.g., in distinguishing between a symmetric and an almost-symmetric hydrogen bond);[71] (ii) when H atoms are bonded to extremely large atoms like Th or U,[72] or when H atoms are surrounded by several metal atoms in a cluster[73–76]; (iii) when H. . .H distances, such as those in nonclassical dihydrogen complexes[77–81] or ‘‘stretched’’ dihydrides,[82–89] need to be measured to a high-level of precision (vide infra); (iv) when H atoms are involved in agostic[90] interactions (again, this involves measuring C–H distances and M–C-H angles to a high-degree of accuracy); and finally (v) last but rapidly gaining in scientific interest, the location of H atoms near the active site of an enzyme.[15–25] Owing to limited space, we will not attempt to cover all of these areas but will selectively discuss a few.

The general strategy for a single-crystal neutron diffraction study is to first solve the crystal structure using X-ray diffraction, in order to acquire the coordinates of all the nonhydrogen atoms. Then, after a sample suitable for neutron diffraction has been grown and data collected, the atomic positions obtained from the earlier X-ray study are used to phase the neutron data. At this point, location of H atoms is done merely by searching for negative neutron peaks in the density map (or positive peaks in the case of D atoms). (The separate subject matter of H/D discrimination will be discussed later in this article.)

9 OXIDATIVE ADDITION TO A H–H BOND

Oxidative addition of H_2 to a metal has been well characterized only in recent years from a structural point of view using single-crystal neutron diffraction. Back in the mid-1980s, Kubas *et al.* made a landmark discovery when they first reported that H_2 can exist as a discrete ligand in the stable organometallic complex molecule $W(CO)_3(H_2)(P^iPr_3)_3$.[91] Subsequent structural characterization (using neutron diffraction)[92] showed that the H_2 ligand was bound to

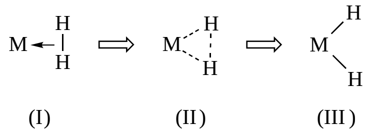

Scheme 1 Oxidative addition of H_2 to a metal center

the metal in a sideways fashion (structure I in Scheme 1). If enough complexes could be analyzed similarly,[93] the process of oxidative addition of H_2 to a metal could be captured structurally in a series of ''stop-action'' photographs and characterized as a series of interactions (see Scheme 1 above).

We start from the first interaction (I in Scheme 1) in which the H_2 ligand (now called the nonclassical dihydrogen[77,78] ligand) is only loosely bound to the metal atom. Further insertion of the metal into the H_2 ligand activates the H–H bond (II) until it is cleaved, forming two terminal metal-hydride bonds (III). Many classical complexes of type (III) were already well known[94,95] and thoroughly characterized before Kubas made his seminal discovery, and similar ''reaction profiles'' of the type represented by Scheme 1 had already been well studied in organic systems (using X-ray structural results) by Bürgi and Dunitz.[96]

Figure 5 shows the results of a neutron diffraction study[91] of the original Kubas complex, which unambiguously showed that the hydrogen molecule interacts with the metal in a side-on fashion, a fact that had not been previously anticipated. But the H...H distance in that compound was very short [0.82(1) Å], almost as short as that of molecular H_2 itself (0.74 Å).[97] Subsequent papers published in following years, by Koetzle, Morris, Heinekey, Jensen, *et al.*,[79–81] all seemed to indicate H...H distances in the 0.8–0.9 Å range (top portion of Table 1). So for a while, it seemed like the process of oxidative addition of a M atom to a H–H bond, like that to a C–H bond (see Figure 5 in Ref. 98), was an ''all or nothing'' process as far as structural studies were concerned: in other words, either (I) or (III) (in Scheme 1) could be observed, with nothing in between.

The situation changed dramatically some years later in 1991, when Brammer, Koetzle, Howard, Spencer *et al.*[82] reported an unusual H...H distance of 1.357(7) Å amongst the seven hydrogens in the complex $ReH_7[P(p\text{-tolyl})_3]_2$ (Figure 6), which fit neither (I) nor (III). In other words, here was a H...H interaction which was neither ''single-bond-like'' (I) nor ''zero-bond-like'' (III). The authors rationalized from this study that they had discovered the first example of the intermediate state (II) between the nonclassical dihydrogen ligand and the classical hydride.

Since then, other complexes with intermediate H...H distances (now called ''stretched'' dihydrogen ligands) have been located[83–89] whose bond order seems ambiguous. They are listed in the middle two blocks of Table 1 and numerous theoretical studies have been published to explain their existence.[102–110] The results of experimental studies in this area, collected in Table 1, have allowed for a crude approximation of a ''reaction profile,'' the process of oxidative addition of a metal atom to an H–H bond (a unique analysis that could not have been achieved using X-ray diffraction, given the low precision of measuring a distance between *two* weakly scattering atoms). In this table, an attempt has been made to include all the available neutron diffraction data on H–H complexes, with the exception of the last category at the bottom of the table (''classical'' hydride complexes in which there are no H...H bonding interactions), for which neutron diffraction results are too numerous to be listed in full.

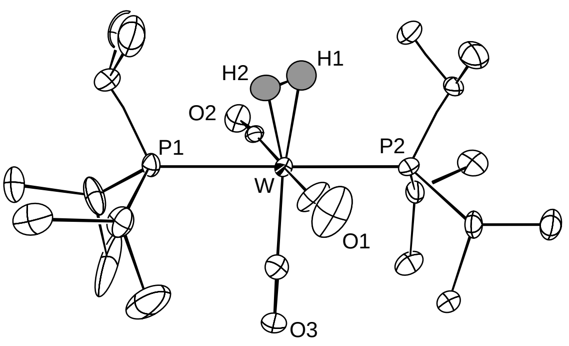

Figure 5 Molecular structure of $W(CO)_3(H_2)(P^iPr_3)_3$ from a neutron study. (Reprinted with permission from Kubas, Ryan, Swanson, Vergamini and Wasserman[91] © 1984 American Chemical Society)

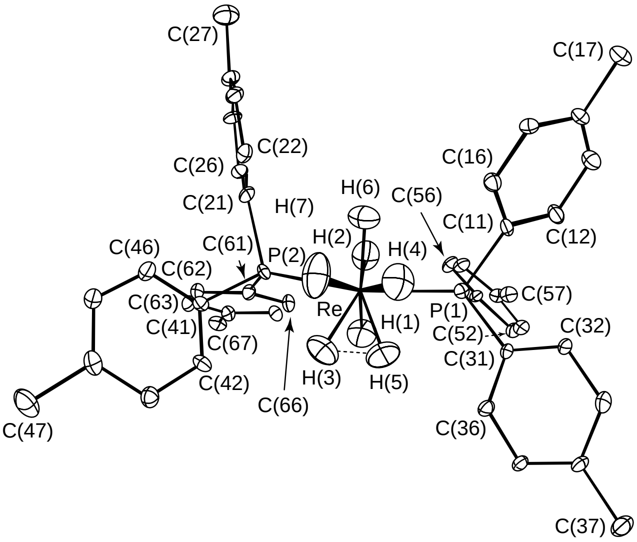

Figure 6 Structure of $ReH_7[P(p\text{-tolyl})_3]_2$ showing the ''stretched'' dihydrogen ligand [H(3)...H(5) = 1.357(7) Å]. (Brammer, Howard, Johnson, Koetzle, Spencer and Stringer[82] — Reproduced by permission of The Royal Society of Chemistry)

In Table 1, the first three columns, (i), (ii), and (iii), list the experimental H–H distances, H–M–H angles and M–H distances respectively, sorted in the order of increasing H–H distance. One can discern a very crude general trend of longer

Table 1 A selection of H. . .H distances in dihydrogen (η^2-H_2) and polyhydride $(H)_n$ complexes determined by neutron diffraction

	Compound	(i) H–H distance(a) (Å)	(ii) H–M–H angle (deg)	(iii) Avg M–H distance (Å)	(iv) ‘‘Adjusted’’ avg. M–H distance(a) (Å)	(v) M–X distance(b) (Å)	(vi) ‘‘Adjusted’’ M–X distance(a,b) (Å)
Nonclassical complexes (with ‘‘almost unstretched’’ H. . .H distances)	$Mo(\eta^2\text{-}H_2)(CO)(dppe)_2$	0.80–0.85[81]	24.0–25.6	1.922(15)	1.79	1.886(15)	1.76
	$[Fe(\eta^2\text{-}H_2)(H)(dppe)_2]^+$	0.816(16)[79]	29.3(5)	1.616(10)	1.62	1.616(10)	1.62
	$W(\eta^2\text{-}H_2)(CO)_3(P^iPr_3)_2$	0.82(1)[91]	25.1	1.89(1)	1.76	1.89(1)	1.76
	$[Fe(\eta^2\text{-}H_2)H_2(PPh_2Et)_3$	0.821(10)[92]	29.9(4)	1.592(8)	1.59	1.538(8)	1.54
	$Ir(\eta^2\text{-}H_2)(H)_2(I)(P^iPr_3)_2$	0.856(9)[80]	28.2(3)	1.756(7)	1.66	1.703(7)	1.60
Slightly stretched H. . .H distances	$[(C_5Me_5)Os(\eta^2\text{-}H_2)H_2(PPh_3)]^+$	1.014(11)[88]	35.4(4)	1.669(9)	1.58	1.589(9)	1.50
	$[Cp^*OsH_4(AsPh_3)][BF_4]$	1.075(13)[93]	37.5(5)	1.669(9)	1.579	1.580(9)	1.49
	$[(C_5Me_5)Ru(\eta^2\text{-}H_2)(dppm)]^+$	1.10(2)[85]	38(1)	1.67(2)	1.59	1.58(2)	1.50
	$IrHCl_2(\eta^2\text{-}H_2)(P^iPr_3)_2$	1.11(3)[86]	42.3(9)	1.444(18)	1.34	1.347(14)	1.25
Significantly stretched H. . .H distances	$[Os(dppe)_2Cl(\eta^2\text{-}H_2)]^+$	1.22(3)[84]	42.6(12)	1.58(2)	1.49	1.47(2)	1.38
	$[Cp^*OsH_4(PCy_3)][BF_4]$	1.306(25)[93]	47.8(7)	1.613(20)	1.523	1.475(20)	1.39
	$[Os(en)_2(\eta^2\text{-}H_2)CH_3CO_2]^+$	1.34(2)[83]	49.6(6)	1.60(1)	1.51	1.45(1)	1.36
	$ReH_7[P(p\text{-tolyl})_3]_2$	1.357(7)[82]	47.6(2)	1.681(4)	1.57	1.538(4)	1.43
	$OsH_3Cl(PPh_3)_3$	1.48(2)[89]	55.1(8)	1.60(2)	1.51	1.42(2)	1.33
	$[OsH_5(PMe_2Ph)_3]^+$	1.49(4)[87]	54.1(1)	1.64(2)	1.55	1.46(2)	1.37
Classical complexes (with no H. . .H bonding interactions)	$OsH_4(PMe_2Ph)_3$	1.840(6)[99]	67.9(2)	1.646(3)	1.56	NA(c)	NA(c)
	$ReH_5(PMePh_2)_3$	1.845(7)[100]	66.8(3)	1.677(5)	1.57	NA(c)	NA(c)
	$FeH_2(CO)_2[P(OPh)_3]_2$	2.011(3)[101]	82.5(1)	1.525(2)	1.53	NA(c)	NA(c)

(a)The ‘‘adjusted’’ M–H and M–X distances were corrected for the differences in the atomic radii of the metal atoms, relative to the Fe radius as the ‘‘standard’’ (that is, the ‘‘correction term’’ for Fe was arbitrarily set to be zero) (atomic radii data from J. McMurray, R. C. Fay, *Chemistry 2nd Edition*, Prentice Hall, New Jersey, (1998)).

(b)M–X distances involved with the H_2 ligand where *X is the center of the H. . .H bond*.

(c) NA = not applicable. The position of ‘‘*X*’’ (the midpoint of the H. . .H bond) is not meaningful for classical hydrides, in which there are no H. . .H interactions.

(d) Please note that some H. . .H distances are corrected for libration (rotational effects) and some have not been corrected. Please refer to original publications for details.

H–H distances coupled with shorter M–H distances. However, one has to account for differences in metallic radii, and so in column (iv) the ‘‘adjusted’’ M–H distances are listed in which the differences in atomic radii are used as ‘‘correction factors’’, with the atomic radius of iron selected arbitrarily as a ‘‘standard’’. One can see that column (iv) is somewhat ‘‘smoother’’ than column (iii). Finally, recognizing that one should perhaps consider metal–*ligand* distances instead of metal–*hydrogen* distances, two extra columns have been included in which M–X distances are tabulated, where X is the midpoint of the H–H bond. Once again, the ‘‘unadjusted’’ and ‘‘adjusted’’ values [columns (v) and (vi) respectively] are listed, in which column (vi) contains the values ‘‘corrected’’ for differences in atomic radii.

Perhaps the most meaningful comparison in Table 1 is between column (i) [or column (ii)] and column (vi). Although there is obviously some scatter in the data, one can discern a definite trend, in which an increasing H–H distance appears to be correlated with decreasing metal–ligand distance: in other words, experimental evidence for the ‘‘reaction profile’’ depicted in Scheme 1. Schultz *et al.* have also recently written an authoritative article about this subject.[93]

10 HYDROGEN ATOMS IN METAL CLUSTERS

Hydrogen atoms can often occupy the interstitial sites of metal lattices. These materials are of potential use in areas of hydrogen storage applications, but normally they are not available in single-crystal form.[111,112] A somewhat related area is the chemisorption of hydrogen atoms on metal surfaces, which again often involve H atoms located on the surface as well as in interstitial sites. These can be studied with surface diffraction techniques,[113–116] but this work is usually carried out with X rays (*see* ***X-Ray Powder Diffraction***) and gives only limited information as far as truly embedded bulk interstitial H atoms are concerned. Perhaps, the best way to study the geometry of interstitial hydrides is to examine the structures of *molecular* metal cluster complexes, with their covalent-like behavior (such as solubility in organic solvents). Covalent ligand-surrounded metal clusters are often obtainable as single crystals.**[117–120]** This is precisely one of the cases discussed in the introduction in which the *accurate* location of hydrogen atoms with X-rays diffraction is difficult because of the large number of metals involved (in other words, the signal-to-noise problem of finding one electron in the presence of three or more metals is a difficult problem with X rays). The tendency for H atoms to occupy vacant sites in metal clusters has led to unusually high coordination numbers (e.g., 4, 5, and 6) of hydrogen in these compounds. The method of choice to study these interactions is obviously neutron diffraction.

The existence of six-coordinate hydrogen (μ^6-H) in the metal cluster anions $[HCo_6(CO)_{15}]^-$ and $[HRu_6(CO)_{18}]^-$ was established**[121–123]** using neutron diffraction. The results from this neutron diffraction study were analyzed along with several other neutron studies involving cobalt clusters and there appears to be a relationship between the number of metal atoms surrounding a hydrogen atom and its corresponding M–H distance. In a series of cobalt compounds containing the following bonds: Co–H (terminal), $Co_2(\mu_2$-H), $Co_3(\mu_3$-H), $Co_6(\mu_6$-H), one can observe a gradual increase in Co–H distance (1.56, 1.64, 1.73, and 1.82 Å) along the above series.**[121,122,124]** This may reflect a decrease in Co–H bond order as the coordination number of hydrogen increases (Table 2).

Neutron analysis of a five-coordinate H (μ^5-H) atom has also been reported, located in two square pyramidal positions of the $[H_2Rh_{13}(CO)_{24}]^{3-}$ metal cluster anion.**[124]** As in the case of the Co–H series, a similar trend was noticed in Rh–H distances increasing as a function of the number of metal atoms around the H atom.

Recently, a four-coordinate H atom**[125,126]** has been unambiguously located by single-crystal neutron diffraction in the center of the tetrahedral metal complex $Y_4H_8(Cp'')_4$(THF) [$Cp'' = C_5Me_4(SiMe_3)$]. The core of the molecule consists of a tetranuclear cluster with one interstitial, one face-bridging, and six edge-bridging hydride ligands (Figure 7). The four individual Y–H distances to the unique interstitial hydride ligand are 2.184(16), 2.189(16), 2.221(13), and 2.168(12) Å.

The existence of four-coordinate hydrogen completed the series of high-connectivity hydride ligands (e.g., four, five, and six) located in the interstitial cavities of molecular cluster complexes. Other features that exist (more commonly than interstitial hydrides) in metal clusters include edge-bridging (two-coordinate H) and face-bridging hydride ligands (three-coordinate H).**[94,95,127]**

Table 2 Variation of Co–H distance with H coordination number

Compound	H coord no	Co–H dist(Å)
$CoH(CO)_4$	1	1.558(18)
$Co_2(\mu_2\text{-}H)_3(\eta^5\text{-}Cp^{(a)})_2$	2	1.641(6)
$Co_3Fe(\mu_3\text{-}H)(CO)_9[P(OMe)_3]_3$	3	1.734(4)
$[Co_6(\mu_6\text{-}H)(CO)_{15}]^-$	6	1.823(13)

(a) For the original version of this table, complete with literature citations. (Data from Ref. 124)

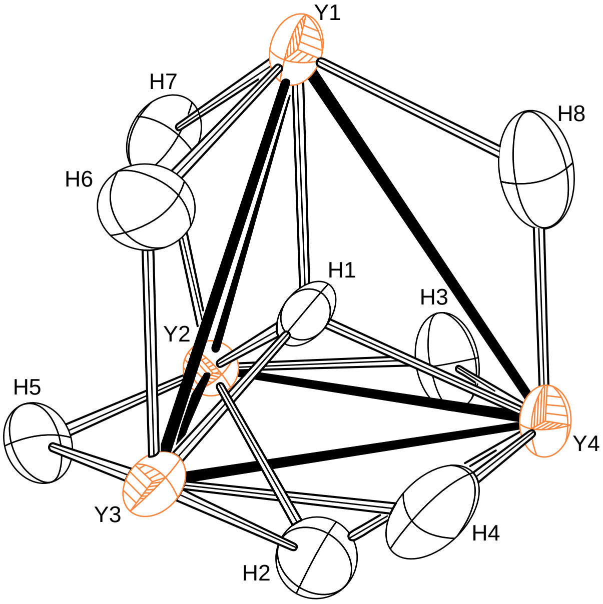

Figure 7 ORTEP plot of core of $[Cp''YH_2]_4$(THF). (Published in Yousufuddin, Baldamus, Tardif, Hou, Mason, McIntyre and Bau,**[126]** © Elsevier 2006)

The structure of $Y_4H_8(Cp'')_4$(THF) (Figure 7) [$Cp'' = C_5Me_4(SiMe_3)$] allows us (uniquely) to compare the three different types of linkages *in the same compound*: (μ_2-H), (μ_3-H), and (μ_4-H) metal–hydrogen bonds. Curiously, one does not observe exactly the same trends as those featured for Co–H bonds in Table 2. Although there is the usual (expected) increase as one goes from $Y_2(\mu_2$-H) [2.171(11) Å], to $Y_3(\mu_3$-H) [2.350(11) Å], the Y–H distance actually decreases in the next step, from $Y_3(\mu_3$-H) [(2.350(11) Å] to $Y_4(\mu_4$-H) [2.200(10) Å]. The relative shortness of the $Y_4(\mu_4$-H) distance probably reflects the tightness of a tetrahedral cavity, and the ability of the H atom to be four-coordinate may be attributed to the stabilizing effect of the other H atoms in the cluster.

In contrast, for an octahedral interstitial site it is well known that there is more than enough space to allow the H atom to ‘‘rattle around’’ inside the cavity. In $[HCo_6(CO)_{15}]^-$**[121,122]** and $[HRu_6(CO)_{18}]^-$**[123]** the H atom is in the center of the octahedron, while in $[HNi_{12}(CO)_{21}]^{3-}$ and $[H_2Ni_{12}(CO)_{21}]^{2-}$**[128]** the H atoms are significantly off-centered (by 0.48 Å in the case of $[HNi_{12}(CO)_{21}]^{3-}$).**[128]** Additionally, inelastic neutron scattering**[129,130]** and low-temperature vibrational studies**[131]** on the Cs^+, K^+, and $[(Ph_3P)_2N]^+$ salts of $[HCo_6(CO)_{15}]^-$ suggest that, for *octahedral* interstitial cavities, there could be enough room for the H atom to ‘‘rattle around’’ inside the octahedral cage.

Some solid-state metal hydrides are commercially (and in some cases potentially) very important because they are a safe and efficient way to store highly flammable hydrogen gas (for example, in nickel-metal hydride (NiMH) batteries). However, from a structural and theoretical point of view many aspects of metal–hydrogen bonding are still not well understood, and it is hoped that the accurate analysis of H positions in the various interstitial sites of the previously described *covalent, molecular* metal hydride cluster complexes will serve as models for H atoms in binary or more complex solid state hydride systems. For example, we can speculate that the octahedral cavities are more spacious in which H atoms can ‘‘rattle around’’, while tetrahedral sites have less space and may even have to experience some ‘‘expansion’’ to accommodate a H atom.

11 AGOSTIC INTERACTIONS

In cases where a metal center is electron deficient, C–H bonds from a coordinated ligand can, in some cases, interact with the metal forming an agostic[90] C–H...M interaction. Structural studies of agostic interactions contribute to our understanding of the role of a metal atom in oxidative addition or reductive elimination processes involving a C–H bond (Scheme 2), in an obvious analogy with our earlier discussion of metal insertion into an H–H bond (Scheme 1).

Originally suspected to exist in certain molecules via X-ray studies,[132,133] agostic interactions are characterized structurally (as depicted in the left portion of Scheme 2) either (i) by a significantly shorter H...M distance[93,134–136] than those predicted by the van der Waals' radii of the M and H atoms, or (ii) by unusual distortions of M–C–H angles (i.e., smaller than expected M–C–H angles that suggest significant M...H attractive interactions that ‘‘pull’’ the H and M closer together than normal).[137,138] The former is represented by the neutron diffraction analysis of $\{Fe[P(OCH_3)_3]_3(\eta^3\text{-}C_8H_{13})\}^+[BF_4]^-$ (Figure 8), by Brown, Williams, Ittel *et al.*,[134,135] as well as by Williams, Schultz, Brookhart *et al.* on $Mn(CO)_3(C_7H_{11})$.[136] The agostic interaction in $\{Fe[P(OCH_3)_3]_3(\eta^3\text{-}C_8H_{13})\}^+[BF_4]^-$ (Figure 8) is characterized by an extra-short Fe–H(1A) distance of 1.879(9) Å, which is well below the sum of the covalent radii of H and Fe.

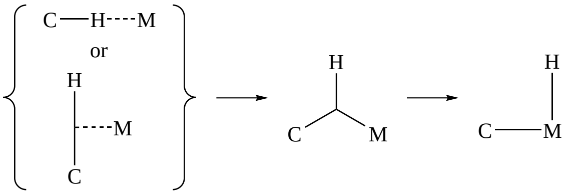

Scheme 2 Oxidative addition of a metal atom (M) to a C–H bond

The second characteristic of an agostic C–H...M interaction, as discussed before, is the existence of an unnaturally distorted C–H–M bond angle. An example is given by the alkylidene complex $t\text{-Bu–CH} = TaCl_4(PMe_3)$ (Figure 9), in which the normally sp^2 hybridized middle atom, C(1) of the C–CH = Ta linkage shows a significant compression from the normal sp^2 value of 120 degrees to the actually observed H(1)–C(1)–Ta value of 84.8 degrees shown in the figure.

A more recent example is represented by $Zr(9\text{-BBN})_4$ [$9\text{-BBN} = (\mu\text{-H})_2BC_8H_{14}$] (Figure 10), in which *three* different C–H...Zr agostic interactions were found associated with the electron-deficient zirconium atom.[139]

In the case of the analogous Si–H...M systems, the only two *bona fide* cases of known agostic interactions are neutron structure determinations carried out by Schubert *et al.* in 1982,[140] and by Mork *et al.* in 2004.[141] However, in recent years Nikonov *et al.* have been introducing an alternative concept, that of interligand hypervalent interactions (IHIs), to describe related systems.[142]

12 ABSOLUTE CONFIGURATION OF CHIRAL MOLECULES OF THE TYPE CHDRR*

The difference in scattering amplitudes between hydrogen (−3.74 fm) and deuterium (+6.67 fm) allows these atoms to be distinguished in a neutron diffraction study. In practice, as pointed out earlier in this article, this makes H atoms appear as negative peaks in a neutron Fourier map, while D atoms (like most other atoms) appear as positive peaks. Therefore, molecules that are chiral by virtue of a stereospecific isotopic substitution (such as molecules of the type CHDRR*) can have, in principle, their absolute configurations determined by neutron diffraction. This fact was first exploited in 1965 by C.K. Johnson *et al.*[143] for determining the absolute configuration of a deuterated glycolate ion $[(OH)\text{–}(CHD)\text{–}(COO)]^-$. In that experiment, the fact that the neutron scattering of ^6Li is anomalous[1] was used to determine the absolute stereochemistry of enzymatically produced $^6Li^+[(OH)\text{–}(CHD)\text{–}(COO)]^-$. However, this particular approach has a severe disadvantage due to the fact that anomalously scattering isotopes (^6Li, ^{10}B, ^{113}Cd, ^{149}Sm, ^{151}Eu, and ^{157}Gd) are also, by definition, efficient absorbers of neutrons, making a neutron diffraction study involving these atoms somewhat problematic (in other words, one needs a big crystal for a neutron-scattering experiment, but if the target molecule contains too much of a neutron absorber, then one runs into substantial absorption problems that make the measurement of neutron diffraction intensities difficult). To our knowledge, the only successful *single-crystal* neutron analysis of a boron compound with a high-boron content, is a $B_{10}D_{14}$ sample in which the B atoms were almost entirely replaced by the weakly neutron-absorbing isotope ^{11}B.[144]

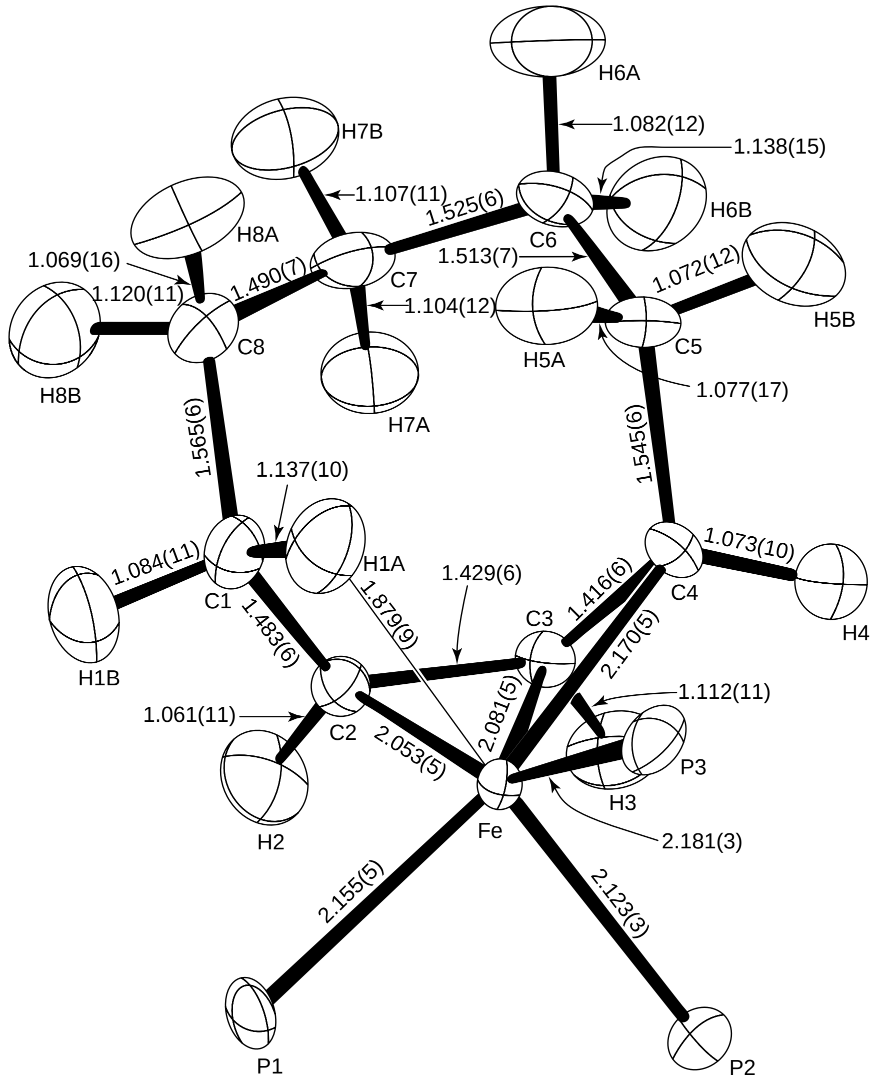
H6A
1.082(12)
1.138(15)
H7B
1.107(11)
1.525(6)
H6B
C6
H8A
1.069(16)
1.490(7)
1.513(7)
1.072(12)
C7
1.120(11)
1.104(12)
H5B
C8
C5
H5A
H8B
1.077(17)
H7A
1.565(6)
1.545(6)
1.137(10)
H1A
1.429(6)
1.073(10)
1.084(11)
1.416(6)
C4
H4
C1
1.879(9)
C3
1.483(6)
2.170(5)
H1B
1.112(11)
1.061(11)
C2
2.081(5)
2.053(5)
P3
H3
H2
Fe
2.181(3)
2.155(5)
2.123(3)
P1
P2

Figure 8 Neutron structure of $\{Fe[P(OCH_3)_3]_3(\eta^3\text{-}C_8H_{13})\}^+[BF_4]^-$. (Reprinted with permission from Williams, Brown, Schultz, Stucky and Ittel.[134] © 1978 American Chemical Society)

A more practical way to get around the problem of absorption is to incorporate into the target crystal a reference fragment having a known absolute configuration. This reference group can either be covalently attached to the chiral CHD group being studied, or be in the form of a counterion. To our knowledge, there are only a handful of studies[145–150] that make use of this approach. Two of these will be discussed here. One simple example (Scheme 3) is the study of the absolute stereochemistry of the addition of D_2O across the double bond of fumaric acid (I) to form malic acid (II), a process carried out naturally by the enzyme fumarase.

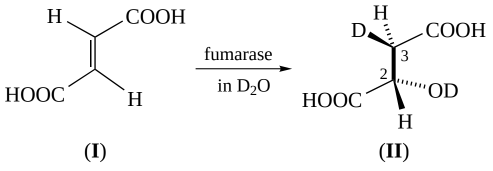
H
COOH
HOOC
H
fumarase
in D2O
H
D
COOH
3
2
OD
HOOC
H
(I)
(II)

Scheme 3 Addition of D_2O to fumaric acid to form malic acid

In principle the reaction could conceivably proceed four ways: two different ways of cis addition of D and OD, and two ways of transaddition, leading to four potential products. The results of our neutron analysis, which was carried out using the known absolute configuration of the chiral cation [(+)](R) phenylethylammonium as a reference, is that the enzymatic reaction only produces the one product[145] shown in Figure 11, corresponding to a stereospecific transaddition of D_2O.

Another pair of studies involved investigating the absolute stereochemistry of the conversion of aldehydes

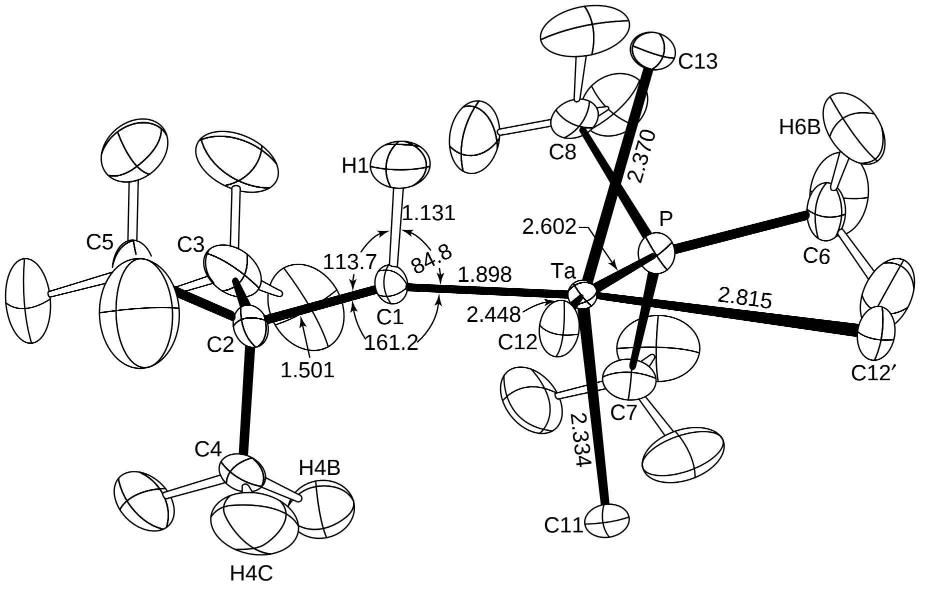
C13
H6B
C8
2.370
H1
1.131
C5
C3
113.7
84.8
2.602
P
C6
1.898
Ta
C1
2.448
2.815
C2
161.2
C12
C12′
1.501
C7
2.334
C4
H4B
C11
H4C

Figure 9 Neutron structure of t-Bu–CH=TaCl$_4$(PMe$_3$). (Reprinted with permission from Schultz, Williams, Schrock, Rupprecht and Fellmann.[137] © 1979 American Chemical Society)

to alcohols by the enzyme yeast alcohol dehydrogenase (Scheme 4), carried out in collaboration with Prof. Harry Mosher of Stanford University.

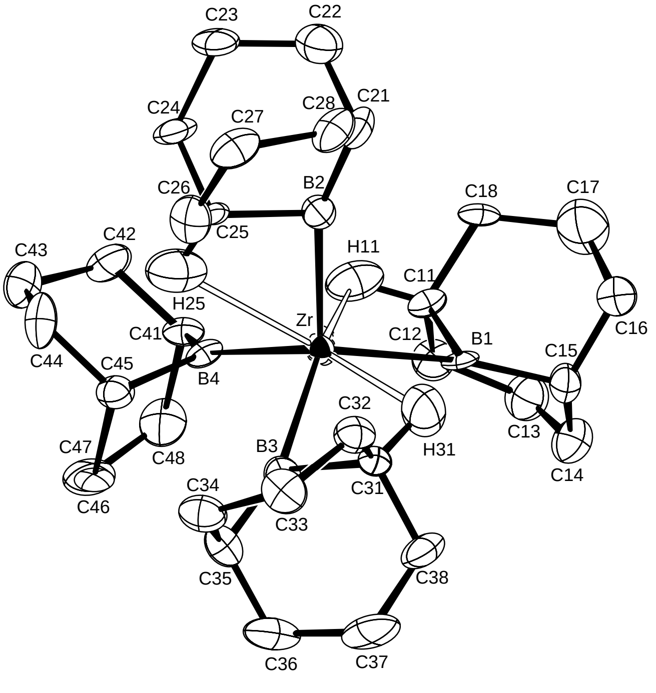
C23
C22
C21
C24
C28
C27
C26
B2
C25
C18
C17
C43
C42
H11
C11
C16
H25
C41
Zr
C12
B1
C15
C44
C45
B4
C32
C13
C47
C48
B3
H31
C14
C34
C31
C46
C33
C35
C38
C36
C37

Figure 10 Neutron structure of Zr(9-BBN)$_4$ [9-BBN = (μ-H)$_2$BC$_8$H$_{14}$]. The three Zr...H agostic interactions are indicated by hollow bonds. (Reprinted with permission from Ding, Du, Meyers, Shore, Yousufuddin, Bau and McIntyre.[139] © 2005 American Chemical Society)

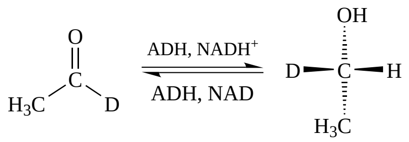
O
C
H3C
D
ADH, NADH+
ADH, NAD
OH
D
C
H
H3C

Scheme 4 Conversion of aldehyde to alcohol

Studies were carried out both with chiral ethanol[146] and chiral neopentanol.[147] Figure 12 shows the anionic phthalate half-ester of (+)-neopentyl-1-*d* alcohol crystallized as its strychnine salt. In this study the absolute configuration of the –O–CHD–C(CH$_3$)$_3$ group was determined to be (S) (Figure 12).

These studies, in particular the one concerning chiral ethanol,[146] are completely consistent with the protein crystallographic results showing the active site of the zinc metalloenzyme alcohol dehydrogenase.[151]

13 NEUTRON DIFFRACTION STUDIES ON PROTEINS

Publications of single-crystal neutron studies of macromolecules are comparatively underrepresented, but activity in this area has been increasing significantly in recent years. A survey of the Protein Data Bank[152] at the time this article was written reveals only 19 protein structures determined by neutron diffraction. However, the technique has actually been available for decades: in fact, two books have been published highlighting achievements in this area.[15,16]

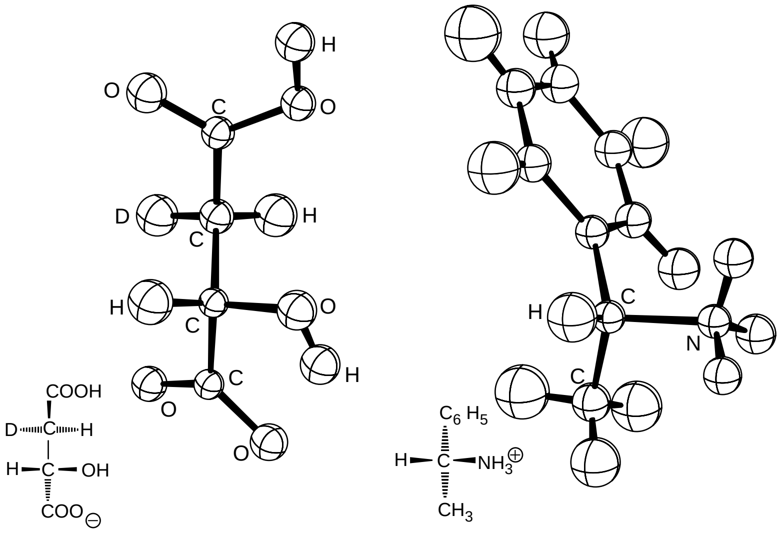

Figure 11 The neutron diffraction results of the enzymatic reaction of Scheme 3. The known absolute configuration of the (+)(R)α-phenylethylammonium cation (a) showed that the product malate anion, produced enzymatically by the enzyme fumarase (b), had the absolute configuration (−)(2S,3R), meaning that the enzymatic addition of D_2O was stereospecifically trans. (Published in Bau, Brewer, Chiang, Fujita, Hoffman, Watkins and Koetzle,[145] © Elsevier 1983)

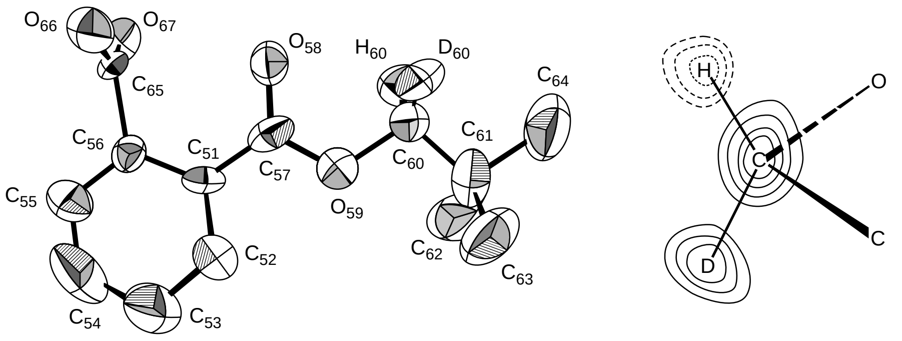

Figure 12 Neutron structure of the phthalate anion of (+)-neopentyl-1-*d* alcohol (a) crystallized with a strychnine cation (not shown). The corresponding neutron Fourier map of the key portion (b) shows the absolute configuration at the chiral CHD center. Dashed lines indicate the negative H peak and positive contours indicate the position of the D atom. (H.S.H. Yuan, R.C. Stevens, S.Fujita, R. Bau, H.S. Mosher and T.F. Koetzle (1994) *Proc. Nat. Acad. Sci. USA.*, **91**: 12872)

Lately, improvements in neutron sources and (especially) in instrumentation have led to dramatic changes, and these have been reflected in more recent review articles.[19–25] A description of current and future neutron *instruments* capable of studying macromolecules was discussed earlier in this article (end of Section 5) and described in Refs. 49–52. In this section we will simply discuss a few representative experimental results.

In proteins, neutrons can offer a wealth of scientific information often not obtainable from X rays alone. The principal applications of neutron studies, besides the location of H atoms near the active site of a protein, are the study of (i) the protonation sites of particular residues like glutamate (Glu), apartate (Asp), histidine (His), and lysine (Lys) residues; (ii) the O–H bonds in tyrosine (Tyr), serine (Ser), and threonine (Thr) residues; (iii) the orientation of amide groups in glutamine (Gln) and aparagine (Asn); (iv) the conformation of methyl groups in hydrophobic residues; (v) the H-bonding patterns in the core of a protein; and (vi) the detailed water structure inside and outside a protein molecule.

An early example of a neutron study of a protein is represented by a 1981 study of oxymyoglobin by Phillips and Schoenborn[153] in which the authors were able to show the existence of a rather unusual hydrogen bond involving the N–D group of a histidine residue and a coordinated O_2 ligand (Figure 13).

Another notable early example involves the investigation of the digestive enzyme trypsin (a member of the serine protease family) by Kossiakoff and Spencer in 1980.[154,155] This class of enzymes contains an Asp–His–Ser triad essential

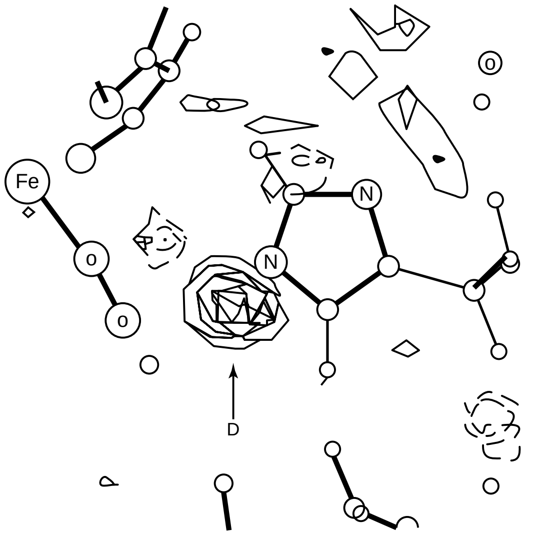

Figure 13 Neutron diffraction map of oxymyoglobin showing the presence of an unusual N–D. . .O_2 hydrogen bond involving the deuterated N(ε) atom (left) of a histidine group and the coordinated dioxygen ligand. Note that the other nitrogen atom of the imidazole ring, N(δ) (right), is seen to be unprotonated. (Reprinted by permission from Macmillan Publishers Ltd: Phillips and Schoenborn.[153] © 1981)

for catalytic activity. The mechanism of this class of proteases is generally acknowledged to involve a base-catalyzed nucleophilic attack, in which the O–H group of serine is deprotonated by the imidazole ring of the histidine residue (Scheme 5). As a result, the level of activity of the Ser residue is dramatically increased with the presence of the newly generated alkoxide-like transient O^- atom now available for nucleophilic attack of a carbonyl group of the target peptide bond. The central issue left unresolved was whether the histidine residue acts as an intermediate (Step 1 in Scheme 5) or rather as the actual base in the hydrolysis reaction (Step 2 in Scheme 5).

Kossiakoff and Spencer (Figure 14) unambiguously showed the histidine residue in its diprotonated form, consistent with mechanism 2 of Scheme 5.

A more recent example is represented by endothiapepsin, a member of the aspartate protease family of protein-cleaving enzymes. A neutron diffraction study by Cooper, Myles *et al.*[156,157] on this protein complexed with a transition state analog conclusively showed that the two catalytic aspartate residues are in different protonation states in the active enzyme. The results demonstrated that Asp215 crystallized in the neutral (protonated) state unlike Asp32 (Figure 15). This finding supported a proposed mechanism involving a tetrahedral intermediate stabilized by neutral and negatively charge Asp residues.

Oligonucletides have also been studied by neutron diffraction lately. The structure of large single crystals of

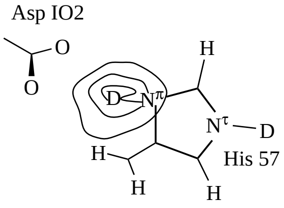

Figure 14 The result of the neutron diffraction experiment by Kossiakoff and Spencer, showing unambiguously that the central His-57 residue is in its diprotonated form. (Reprinted by permission from Macmillan Publishers Ltd: Kossiakoff and Spencer.[155] © 1980)

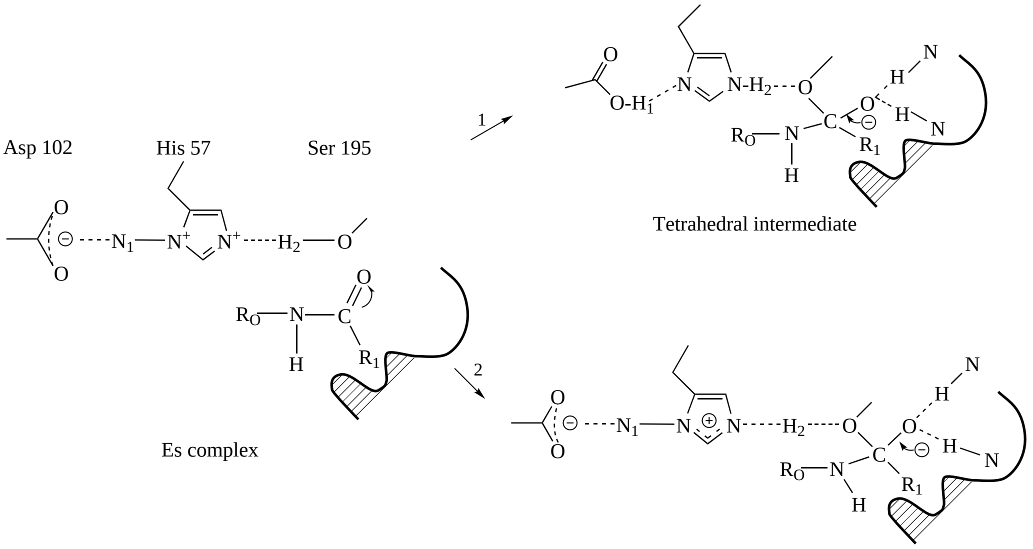

Scheme 5 Two proposed mechanisms for the mode of action of serine proteases, which differ mainly in the degree of protonation of the central imidazole ring. (Reprinted with permission from Kossiakoff and Spencer.[154] © 1981 American Chemical Society)

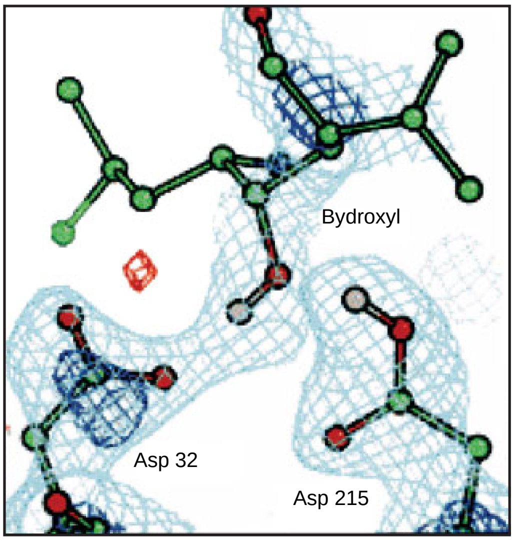

Figure 15 Neutron difference map showing the active site region of endothiapepsin (an aspartate protease) complexed with a transition state analogue. In this 2.1 Å resolution neutron study by Myles *et al*., Asp32 was found to be in its deprotonated state, while Asp215 is protonated. (Reprinted with permission from Coates, Erskine, Wood, Myles and Cooper.[157] © 2001 American Chemical Society)

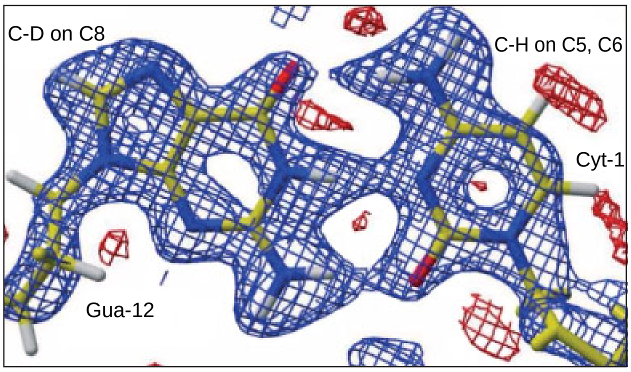

Figure 16 A view of one of the C–G base pairs of the hexameric Z-DNA oligomeric duplex, showing the C–H group at the #8 position of guanine12 (the yellow-to-white bond labeled ‘‘C–D on C8’’) being deuterated [blue (positive) contours], while the other C–H groups (the two yellow-to-white bonds of cytosine-1 labeled ‘‘C–H on C5, C6’’) are undeuterated [red (negative) contours, indicating the presence of unexchanged hydrogens]. (From Chatake, Tanaka, Umino, Arai and Niimura.[159] Reproduced by permission of International Union of Crystallography)

a double-stranded B-DNA decamer, d(CCATTAATGG)$_2$,[158] and a Z-DNA hexamer, d(CGCGCG)$_2$,[159] have been reported by the Niimura group. In the case of d(CCATTAATGG)$_2$, it was found that the ‘‘spine’’ of water molecules of hydration in the minor groove of this DNA oligomeric duplex were largely ordered but arranged in a complicated H-bonding pattern, while most of the water molecules in the major groove were less ordered and mostly ill-defined. Another interesting result is that in the case of d(CGCGCG)$_2$, it was found that the C–H groups of guanine, unlike virtually all other C–H groups in proteins and oligonucleotides, are kinetically labile and participate in H/D exchange (Figure 16). The only other example of a kinetically labile C–H bond in macromolecules that participates in H/D exchange is the central C–H group of the five-membered ring of histidine, an exchange which was shown to take place by the neutron analysis of insulin.[160] In both the imidazole case in proteins and the guanine case in nucleic acids, the common feature is that both kinetically labile C–H groups are in a five-membered ring situated between two N atoms.

Finally, one important development is the demonstration of the usefulness of complete deuteration of a protein for a neutron study, first demonstrated by Schoenborn *et al*.[161] and further developed recently by Podjarny *et al*.,[162] who were able to carry out a single-crystal neutron diffraction study of aldose reductase on a crystal as small as 0.15 mm^3, which is an order of magnitude smaller than a typical ‘‘neutron-sized’’ crystal. Deuteration is particularly advantageous because (as was pointed out earlier) hydrogen has a large incoherent scattering component, which gives rise to an undesirably high background level. A sample in which all H atoms have been replaced by D produces much better data (i.e., a much higher signal-to-noise ratio), and thus several laboratories[163] (D. Myles and F. Meilleur, Private Communication; B. Schoenborn and P. Langan, Private Communication; N. Niimura, Private Communication) have invested a significant amount of effort in developing complete deuteration facilities for single crystal protein crystallographic analysis, or are in the process of doing so.

14 CONCLUSION

Neutron diffraction has been shown to provide essential chemical information in a wide range of systems. We have selected a number of examples for which the technique is particularly well suited. Modern techniques have enabled improvements in instrumentation and data collection that allow for lower sample requirements and more sophisticated sample environments. In particular, the high-intensity spallation sources[39,40] currently under construction should be especially appealing not only to chemists,[49] but also biologists,[50–52] for which shorter data collection times and (more importantly) smaller crystal sizes are of paramount importance.

15 ACKNOWLEDGMENTS

We would like to thank many of my neutron diffraction colleagues who have collaborated with me and my group in the many decades of this work, in particular Tom Koetzle *et al*., the late Dick McMullan and Wim Klooster. More recently, we have benefited greatly through interactions with Art Schultz, Sax Mason, Garry McIntyre, Nobuo Niimura, and his group, Benno Schoenborn, Paul Langan, Dean Myles, and their colleagues, and most recently Matthias Gutmann. Without their ability, expertise, and help, much of the work described in this article would not have taken place. This work was largely supported over the years by the US National Science Foundation, the American Chemical Society and the US Department of Energy.

16 END NOTES

[a] Although virtually all spallation sources (described in the text) are pulsed sources, one exception is SINQ in Switzerland, which is almost a continuous spallation source.

[b] Although technically photons have no spin, there is a very small magnetic scattering cross section for X rays, which has been exploited in magnetic X-ray scattering experiments at synchrotron sources. Some investigators believe the effect can be enhanced by working near an absorption edge, e.g., for lanthanides.

17 ABBREVIATIONS AND ACRONYMS

CCD = charge-coupled device; IHIs = interligand hypervalent interactions; ILL = Institut Laue-Langevin; INS = inelastic neutron scattering; IPNS = intense pulsed neutron source; LINAC = linear accelerator; MaNDi = macromolecular neutron diffractometer; NiMH = nickel-metal; OPAL = open pool Australian light-water reactor; hydride; SANS = small-angle neutron scattering; SNS = spallation neutron source.

18 FURTHER READING

R. Bau, S. A. Mason, B. O. Patrick, C. S. Adams, W. B. Sharp and P. Legzdins, *Organometallics*, 2001, **20**, 4492.

D. W. Hart, R. Bau and T. F. Koetzle, *J. Am. Chem. Soc.*, 1977, **99**, 7557.

19 REFERENCES

1. G. E. Bacon, ‘Neutron Diffraction’, 3rd edition, Clarendon Press, Oxford, 1975.
2. C. G. Windsor, ‘Pulsed Neutron Scattering’, Taylor and Francis, London, 1981.
3. C. C. Wilson, ‘Single Crystal Neutron Diffraction from Molecular Materials’, World Scientific Press, Singapore, 2000.
4. T. F. Koetzle, *Trans. Am. Crystallogr. Assoc.*, 1995, **31**, 57.
5. A. J. Schultz, *Trans. Am. Crystallogr. Assoc.*, 1993, **29**, 29.
6. J. B. Parise, in ‘Reviews in Mineralogy and Geochemistry’, ed. H. R. Wenk, Mineralogical Society of America, 2006, Vol. 63, Chap. 1 p. 1.
7. N. L. Ross and C. Hoffmann, in ‘Reviews in Mineralogy and Geochemistry’, ed. H. R. Wenk, Mineralogical Society of America, 2006, Vol. 63, Chap. 3, p. 59.
8. J. D. Jorgensen and J. M. Newsam, *MRS Bull.*, 1990, **15**, 49.
9. A. N. Fitch, *Mater. Sci. Forum*, 1986, **7**, 45.
10. R. M. Ibberson and W. I. F. David, in ‘Structure Determination from Powder Diffraction Data’, ’International Union of Crystallography Monographs on Crystallography, Vol. 13’, eds. W. I. F. David, K. Shankland, L. B. McCusker and Ch. Baerlocher, Oxford University Press, 2002, Chap. 5.
11. P. Mitchell, S. Parker, A. Ramirez-Cuesta and J. Tomkinson, ‘Vibrational Spectroscopy With Neutrons With Applications in Chemistry, Biology, Materials Science and Catalysis’, World Scientific Publishing, June 2005, Vol. 3.
12. R. J. Harrison, in ‘Reviews in Mineralogy and Geochemistry’, ed. H. R. Wenk, Mineralogical Society of America, 2006, Vol. 63, Chap. 6, p. 113.
13. G. L. Jones, J. Baker, W. C. Chen, B. Collett, J. A. Cowan, M. F. Dias, T. R. Gentile, C. Hoffmann, T. Koetzle, W. T. Lee, K. Littrell, M. Miller, A. J. Schultz, W. M. Snow, X. Tong, H. Yan and A. Yu, *Physica B*, 2005, **356**, 86.
14. V. M. Nield and D. A. Keen, ‘Diffuse Neutron Scattering from Crystalline Materials’, Oxford University Press, 2000.
15. B. P. Schoenborn, ‘Nature in Biology, Basic Life Sciences’, Plenum Press, New York, 1984, Vol. 27.
16. B. P. Schoenborn and R. B. Knott, ‘Neutrons in Biology, Basic Life Sciences’, Plenum Press, New York, 1996, Vol. 64.
17. A. A. Kossiakoff, *Annu. Rev. Biochem.*, 1985, **54**, 1195.
18. A. Wlodawer, *Prog. Biophys. Mol. Biol.*, 1982, **40**, 115.
19. J. R. Helliwell, *Nat. Struct. Biol.*, 1997, **4**, 874.
20. E. Pebay-Peyroula and D. Myles, *J. Struct. Dyn. Biomol.*, 2000, **18**, 102.
21. T. Gutberlet, U. Heinemann and M. Steiner, *Acta Crystallogr.*, 2001, **D57**, 349.
22. I. Tsyba and R. Bau, *Chemtracts*, 2002, **15**, 233.
23. N. Niimura, S. Arai, K. Kurihara, T. Chatake, I. Tanaka and R. Bau, *Cell. Mol. Life Sci.*, 2006, **63**, 285.
24. F. Meilleur, D. A. A. Myles and M. P. Blakeley, *Eur. Biophys. J.*, 2006, **35**, 611.
25. M. P. Blakeley, M. Cianci, J. R. Helliwell and P. J. Rizkallah, *Chem. Soc. Rev.*, 2004, **33**, 548.
26. C. Wilkinson, J. A. Cowan, D. A. A. Myles, F. Cipriani and G. J. McIntyre, *Neutron News*, 2002, **13**, 37.
27. G. J. McIntyre, M. H. Lemée-Cailleau and C. Wilkinson, *Physica B*, 2006, **1052**, 385.
28. http://neutrons.ornl.gov/, 2007.

29. Y. Morii, *Neutron News*, 1990, **1**, 14 (http://www.issp.u-tokyo.ac.jp/labs/neutron/jrr3/).
30. http://www.ill.fr/, 2007.
31. http://www.anawa.org.au/nsw/lucas-heights.html.
32. http://wwwnew.frm2.tum.de/en.html/.
33. For a listing of existing single-crystal neutron instruments and their locations, refer to a compilation assembled by A.J. Schultz of Argonne National Laboratory: http.//www.pns.anl.gov/instruments/scd/subscd/htm_files/single_xtal.htm, 2007.
34. J. M. Carpenter, *Nucl. Instrum. Methods*, 1979, **145**, 91.
35. J. M. Carpenter, G. H. Lander and C. G. Windsor, *Rev. Sci. Instrum.*, 1984, **55**, 1019.
36. A. J. Schultz, K. Srinivasan, R. G. Teller, J. M. Williams and C. M. Lukehart, *J. Am. Chem. Soc.*, 1984, **106**, 999 (http://www.pns.anl.gov/).
37. http://lansce.lanl.gov/, 2007.
38. http://www.isis.rl.ac.uk/, 2007.
39. T. E. Mason, D. Abernathy, J. Ankner, A. Ekkebus, G. Granroth, M. Hagen, K. Herwig, C. Hoffmann, C. Horak, F. Klose, S. Miller, J. Neuefeind, C. Tulk and X.-L. Wang, *Phys. Rev. B: Condens. Matter*, 2006, **385–386**, 955 (http://www.sns.gov/).
40. S. Nagamiya, *J. Neutron Res.*, 2005, **13**, 7 (http://j-parc.jp/index-e.html).
41. N. Niimura, Y. Minezaki, T. Nonaka, J. C. Castagna, F. Cipriani, P. Hoghoj, M. S. Lehmann and C. Wilkinson, *Nat. Struct. Biol.*, 1997, **4**, 909.
42. N. Niimura, Y. Karasawa, I. Tanaka, J. Miyahara, K. Takahashi, H. Saito, S. Koizumim and M. Hidaka, *Nucl. Instrum. Methods*, 1994, **A349**, 521.
43. I. Tanaka, K. Kurihara, T. Chatake and N. Niimura, *J. Appl. Crystallogr.*, 2002, **35**, 34.
44. D. A. A. Myles, C. Bon, P. Langan, F. Cipriani, J. C. Castagna, M. S. Lehmann and C. Wilkinson, *Physica B*, 1998, **241–243**, 1122.
45. P. Langan, G. Greene and B. P. Schoenborn, *J. Appl. Crystallogr.*, 2004, **37**, 24.
46. D. W. J. Cruickshank, J. R. Helliwell and L. N. Johnson eds., 'Time-Resolved Macromolecular Crystallography', Oxford University Press, 1992, (ISBN 0-19-855781-7).
47. G. J. McIntyre, M.-H. Lemée-Cailleau and C. Wilkinson, *Physica B*, 2006, **385–386**, 1055.
48. H. Lemée-Cailleau, G. J. McIntyre and C. Wilkinson, *J. Phys. IV (France)*, 2005, **131**, 33531.
49. http://neutrons.ornl.gov/instrument_systems/beamline_12_topaz/index.shtml, 2007.
50. http://www.pns.anl.gov/instruments/mandi/pdf_files/2003 LOI-MaNDi.pdf, 2007.
51. I. Tanaka, T. Ozeki, T. Ohhara, K. Kurihara and N. Niimura, *J. Neutron Res.*, 2005, **15**, 49.
52. http://ts-2.isis.rl.ac.uk/instruments/phase2/lmx2005Web.pdf, 2007.
53. R. A. Young ed., 'The Rietveld Method' (in: International Union of Crystallography Monographs on Crystallography 5), Oxford University Press, 1993, p. 298.
54. H. M. Rietveld, *Acta Crystallogr.*, 1966, **20**, 508.
55. H. M. Rietveld, *Acta Crystallogr.*, 1966, **21**, A228.
56. H. M. Rietveld, *Acta Crystallogr.*, 1967, **22**, 151.
57. A. Albinati and B. T. M. Willis, *J. Appl. Crystallogr.*, 1982, **15**(4), 361.
58. A. C. Larson and R. B. Von Dreele, 'GSAS-General Structure Analysis System', Los Alamos National Laboratory, Los Alamos, 1994.
59. J. W. Lynn, *J. Appl. Phys.*, 1994, **75**(Pt. 2B), 6806.
60. R. J. Harrison, in 'Reviews in Mineralogy and Geochemistry', ed. H. R. Wenk, Mineralogical Society of America, 2006, Vol. 63, Chap. 6, p. 113.
61. G. E. Bacon, 'Neutron Diffraction', 3rd edition, Clarendon Press, Oxford, 1975. (See Chapters 6,7 and 8).
62. B. N. Figgis, J. B. Forsyth, E. S. Kucharski, P. A. Reynolds and F. Tasset, *Proc. R. Soc. London, Ser. A*, 1990, **328**, 113.
63. B. N. Figgis, P. A. Reynolds and J. W. Cable, *Mol. Phys.*, 1993, **80**, 1377.
64. S. P. Best, B. N. Figgis, J. B. Forsyth, P. A. Reynolds and P. L. W. Tregenna-Piggott, *Inorg. Chem.*, 1995, **34**, 4605.
65. P. Cassam-Chenai, S. K. Wolff, G. S. Chandler and B. N. Figgis, *Int. J. Quantum Chem.*, 1996, **60**, 667.
66. N. S. S. Murthy and S. K. Paranjpe, *Indian J. Pure Appl. Phys.*, 1981, **19**, 863.
67. G. L. Jones, J. Baker, W. C. Chen, B. Collett, J. A. Cowan, M. F. Dias, T. R. Gentile, C. Hoffmann, T. Koetzle, W. T. Lee, K. Littrell, M. Miller, A. J. Schultz, W. M. Snow, X. Tong, H. Yan and A. Yu, *Physica B*, 2005, **356**, 86.
68. I. S. Anderson, J. Cook, G. Felcher, T. Gentile, G. Greene, F. Klose, T. Koetzle, E. Lelievre-Berna, A. Parizzi, R. Pynn and J. Zhao, *J. Neutron Res.*, 2005, **13**, 193.
69. H. Glattli, *Physica B*, 2001, **297**, 273.
70. G. P. Felcher, S. G. E. te Velthuis, A. Ruhm and W. Donner, *Physica B*, 2001, **297**, 87.
71. W. C. Hamilton and J. A. Ibers, 'Hydrogen Bonding in Solids', W. A. Benjamin, New York, 1968.
72. R. W. Broach, A. J. Schultz, J. M. Williams, G. M. Brown, J. M. Manriquez, P. J. Fagan and T. J. Marks, *Science*, 1979, **203**, 172.
73. R. G. Teller, R. D. Wilson, R. K. McMullan, T. F. Koetzle and R. Bau, *J. Am. Chem. Soc.*, 1978, **100**, 3071.
74. T. F. Koetzle, J. Müller, D. L. Tipton, D. W. Hart and R. Bau, *J. Am. Chem. Soc.*, 1979, **101**, 5631.
75. R. Bau, N. N. Ho, J. J. Schneider, S. A. Mason and G. J. McIntyre, *Inorg. Chem.*, 2004, **43**, 555.
76. R. A. Heintz, T. F. Koetzle, R. L. Ostrander, A. L. Rheingold, K. H. Theopold and P. Wu, *Nature*, 1995, **378**, 359.

77. G. Kubas, ‘Metal Dihydrogen and s-Bond Complexes: Structure, Theory, and Reactivity’, Kluwer Academic/Plenum Publishers, New York, 2001.
78. R. H. Crabtree, *Acc. Chem. Res.*, 1990, **23**, 95.
79. J. S. Ricci, T. F. Koetzle, M. T. Bautista, T. M. Hofstede, R. H. Morris and J. F. Sawyer, *J. Am. Chem. Soc.*, 1989, **111**, 8823.
80. J. Eckert, C. M. Jensen, T. F. Koetzle, T. L. Husebo, J. Nicol and P. Wu, *J. Am. Chem. Soc.*, 1995, **117** 7271.
81. G. J. Kubas, C. J. Burns, J. Eckert, S. W. Johnson, A. C. Larson, P. J. Vergamini, C. J. Unkefer, G. R. K. Khalsa, S. A. Jackson and O. Eisenstein, *J. Am. Chem. Soc.*, 1993, **115**, 569.
82. L. Brammer, J. A. K. Howard, O. Johnson, T. F. Koetzle, J. L. Spencer and A. M. Stringer, *Chem. Commun.*, 1991, 241.
83. T. Hasegawa, Z. Li, S. Parkin, H. Hope, R. K. McMullan, T. F. Koetzle and H. Taube, *J. Am. Chem. Soc.*, 1994, **116**, 4352.
84. P. A. Maltby, M. Schlaf, M. Steinbeck, A. J. Lough, R. H. Morris, W. T. Klooster, T. F. Koetzle and R. C. Srivastava, *J. Am. Chem. Soc.*, 1996, **118**, 5396.
85. W. T. Klooster, T. F. Koetzle, G. Jia, T. P. Fong, R. H. Morris and A. Albinati, *J. Am. Chem. Soc.*, 1994, **116**, 7677.
86. A. Albinati, V. I. Bakhmutov, K. G. Caulton, E. Clot, J. Eckert, O. Eisenstein, D. G. Gusev, V. V. Grushin, B. E. Hauger, W. T. Klooster, T. F. Koetzle, R. K. McMullan, T. J. O’Loughlin, M. Pelissier, J. S. Ricci, M. P. Sigalas and A. B. Vymenits, *J. Am. Chem. Soc.*, 1993, **115**, 7300.
87. T. J. Johnson, A. Albinati, T. F. Koetzle, J. Ricci, O. Eisenstein, J. C. Huffman and K. G. Caulton, *Inorg. Chem.*, 1994, **33**, 4966.
88. C. L. Gross, D. M. Young, A. J. Schultz and G. S. Girolami, *J. Chem. Soc., Dalton Trans.*, 1997, 3081.
89. M. Yousufuddin, T. B. Wen, S. A. Mason, G. J. McIntyre, G. Jia and R. Bau, *Angew. Chem., Int. Ed. Engl.*, 2005, **44**, 7227.
90. M. Brookhart, M. L. H. Green and L. Wong, *Prog. Inorg. Chem.*, 1988, **36**, 1.
91. G. J. Kubas, R. R. Ryan, B. I. Swanson, P. J. Vergamini and H. J. Wasserman, *J. Am. Chem. Soc.*, 1984, **106**, 451.
92. L. S. Van der Sluys, J. Eckert, O. Eisenstein, J. H. Hall, J. C. Huffman, S. A. Jackson, T. F. Koetzle, G. J. Kubas, P. J. Vergamini and K. G. Caulton, *J. Am. Chem. Soc.*, 1990, **112**, 4831.
93. C. E. Webster, C. L. Gross, D. M. Young, G. S. Girolami, A. J. Schultz, M. B. Hall and J. Eckert, *J. Am. Chem. Soc.*, 2005, **127**, 15091.
94. R. Bau, R. G. Teller, S. W. Kirtley and T. F. Koetzle, *Acc. Chem. Res.*, 1979, **12**, 176.
95. R. G. Teller and R. Bau, *Struct. Bonding*, 1981, **44**, 1.
96. H. B. Bürgi and J. D. Dunitz, *Acc. Chem. Res.*, 1983, **16**, 153.
97. D. R. Lide ed., ‘CRC Handbook of Chemistry and Physics’, 75th edition, CRC Press, 1994.
98. R. H. Crabtree, E. M. Holt, M. Lavin and S. M. Morehouse, *Inorg. Chem.*, 1985, **24**, 1986.
99. D. W. Hart, R. Bau and T. F. Koetzle, *J. Am. Chem. Soc.*, 1977, **99**, 7557.
100. T. J. Emge, T. F. Koetzle, J. W. Bruno and K. G. Caulton, *Inorg. Chem.*, 1984, **23**, 4012.
101. N. N. Ho, R. Bau and S. A. Mason, *J. Organomet. Chem.*, 2003, **85**, 676.
102. D. M. Heinekey, A. Lledos and J. M. Lluch, *Chem. Soc. Rev.*, 2004, **33**, 175.
103. D. G. Gusev, *J. Am. Chem. Soc.*, 2004, **126**, 14249.
104. R. Gelabert, M. Moreno, J. M. Lluch, A. Lledos, V. Pons and D. M. Heinekey, *J. Am. Chem. Soc.*, 2004, **126**, 8813.
105. P. Barrio, M. A. Esteruelas, A. Lledos, E. Onate and J. Tomas, *Organometallics*, 2004, **23**, 3008.
106. B. Eguillor, M. A. Esteruelas, M. Olivan and E. Onate, *Organometallics*, 2005, **24**, 1428.
107. M. Vogt, V. Pons and D. M. Heinekey, *Organometallics*, 2005, **24**, 1832.
108. R. Gelabert, M. Moreno, J. M. Lluch, A. Lledos and D. M. Heinekey, *J. Am. Chem. Soc.*, 2005, **127**, 5632.
109. G. Barea, M. A. Esteruelas, A. Lledos, A. M. Lopez, E. Onate and J. I. Tolosa, *Organometallics*, 1998, **17**, 4065.
110. F. Maseras, A. Lledos, E. Clot and O. Eisenstein, *Chem. Rev.*, 2000, **100**, 601.
111. W. M. Mueller, J. P. Blackledge and G. G. Libowitz eds., ‘Metal Hydrides’, Academic Press, New York, 1968.
112. G. Auffermann, P. Muller and W. Bronger, *Z. Anorg. Allg. Chem.*, 2004, **630**, 2113.
113. K. Christmann, *Surf. Sci. Rep.*, 1988, **9**, 1.
114. H. Okuyama, T. Ueda, C. M. Mate and G. A. Somorjai, *Phys. Rev. B*, 1986, **34**, 7414.
115. G. A. Somorjai and L. L. Kesmodel, *Trans. Am. Crystallogr. Assoc.*, 1977, **13**, 67.
116. L. L. Kesmodel and Gabor. A. Somorjai, *Acc. Chem. Res.*, 1976, **9**, 392.
117. P. Chini, *J. Organomet. Chem.*, 1980, **200**, 37.
118. P. Chini, G. Longoni and V. G. Albano, *Adv. Organomet. Chem.*, 1976, **14**, 285.
119. P. Chini, *Inorg. Chim. Acta*, 1968, **2**, 30.
120. M. Tachikawa and E. L. Muetterties, *Prog. Inorg. Chem.*, 1981, **28**, 203.
121. D. W. Hart, R. G. Teller, C. Y. Wei, R. Bau, G. Longoni, S. Campanella, P. Chini and T. F. Koetzle, *Angew. Chem. Int. Ed. Engl.*, 1979, **18**, 80.
122. D. W. Hart, R. G. Teller, C. Y. Wei, R. Bau, G. Longoni, S. Campanella, P. Chini and T. F. Koetzle, *J. Am. Chem. Soc.*, 1981, **103**, 1458.
123. P. F. Jackson, B. F. G. Johnson, J. Lewis, P. R. Raithby, M. McPartlin, W. J. H. Nelson, K. D. Rouse, J. Allibon and S. A. Mason, *Chem. Commun.*, 1980, 295.

124. R. Bau, M. H. Drabnis, L. Garlaschelli, W. T. Klooster, Z. Xie, T. F. Koetzle and S. Martinengo, *Science*, 1997, **275**, 1099.

125. M. Yousufuddin, M. J. Gutmann, J. Baldamus, O. Tardif, Z. Hou, S. A. Mason, G. J. McIntyre and R. Bau, submitted for publication 2007.

126. M. Yousufuddin, J. Baldamus, O. Tardif, Z. Hou, S. A. Mason, G. J. McIntyre and R. Bau, *Physica B*, 2006, **385–386**, 231.

127. R. Bau and M. Drabnis, *Inorg. Chim. Acta.*, 1997, **259**, 27.

128. R. W. Broach, L. F. Dahl, G. Longoni, P. Chini, A. J. Schultz and J. M. Williams, *Adv. Chem. Ser.*, 1979, **167**, 93.

129. D. Graham, J. Howard, T. C. Waddington and J. Tomkinson, *J. Chem. Soc., Faraday Trans. 2*, 1983, **79**, 1713.

130. J. Eckert, A. Albinati and G. Longoni, *Inorg. Chem.*, 1989, **28**, 4055.

131. P. L. Stanghellini and G. Longoni, *J. Chem. Soc., Dalton Trans.*, 1987, 685.

132. F. A. Cotton, T. LaCour and A. G. Stanislowski, *J. Am. Chem. Soc.*, 1974, **96**, 754.

133. Y. W. Yared, S. L. Miles, R. Bau and C. A. Reed, *J. Am. Chem. Soc.*, 1977, **99**, 7076.

134. J. M. Williams, R. K. Brown, A. J. Schultz, G. D. Stucky and S. D. Ittel, *J. Am. Chem. Soc.*, 1978, **100**, 7407.

135. R. K. Brown, J. M. Williams, A. J. Schultz, G. D. Stucky, S. D. Ittel and R. L. Harlow, *J. Am. Chem. Soc.*, 1980, **102**, 981.

136. A. J. Schultz, R. G. Teller, M. A. Beno, J. M. Williams, M. Brookhart, W. Lamanna and M. B. Humphrey, *Science*, 1983, **220**, 197.

137. A. J. Schultz, J. M. Williams, R. R. Schrock, G. A. Rupprecht and J. D. Fellmann, *J. Am. Chem. Soc.*, 1979, **101**, 1593.

138. M. A. Beno, J. M. Williams, M. Tachikawa and E. L. Muetterties, *J. Am. Chem. Soc.*, 1980, **102**, 4542.

139. E. Ding, B. Du, E. A. Meyers, S. G. Shore, M. Yousufuddin, R. Bau and G. J. McIntyre, *Inorg. Chem.*, 2005, **44**, 2459.

140. U. Schubert, K. Ackermann and B. Woerle, *J. Am. Chem. Soc.*, 1982, **104**, 7378.

141. B. V. Mork, T. D. Tilley, A. J. Schultz and J. A. Cowan, *J. Am. Chem. Soc.*, 2004, **126**, 10428.

142. G. I. Nikonov, P. Mountford, J. C. Green, P. A. Cooke, M. A. Leech, A. J. Blake and J. A. K. Howard, *Eur. J. Inorg. Chem.*, 2000, **9**, 1917.

143. C. K. Johnson, E. J. Gabe, M. R. Taylor and I. A. Rose, *J. Am. Chem. Soc.*, 1965, **87**, 1802.

144. R. Brill, H. Dietrich and H. Dierks, *Acta Crystallogr.*, 1971, **B27**, 2003.

145. R. Bau, I. Brewer, M. Y. Chiang, S. Fujita, J. Hoffman, M. I. Watkins and T. F. Koetzle, *Biochem. Biophys. Res. Commun.*, 1983, **115**, 1048.

146. T. Metzenthin, A. Schreiber, R. K. McMullan, T. F. Koetzle, H. S. Mosher and R. Bau, *J. Org. Chem.*, 1997, **62**, 5017.

147. H. S. H. Yuan, R. C. Stevens, S. Fujita, R. Bau, H. S. Mosher and T. F. Koetzle, *Proc. Natl. Acad. Sci. U.S.A.*, 1994, **91**, 12872.

148. H. S. H. Yuan, R. C. Stevens, S. Fujita, M. I. Watkins, T. F. Koetzle and R. Bau, *Proc. Natl. Acad. Sci. U.S.A.*, 1988, **85**, 2889.

149. R. Bau, A. Schreiber, T. Metzenthin, R. S. Lu, F. Lutz, W. T. Klooster, T. F. Koetzle, H. Seim, H. P. Kleber, F. Brewer and S. Englard, *J. Am. Chem. Soc.*, 1997, **119**, 12055.

150. R. K. McMullan, T. F. Koetzle and M. D. Fronckowiak, *Acta Crystallogr.*, 1992, **C48**, 1509.

151. H. Eklund, J.-P. Samama, L. Wallen, C. Branden, A. Akeson and T. A. Jones, *J. Mol. Biol.*, 1981, **146**, 561.

152. H. M. Berman, J. Westbrook, Z. Feng, G. Gilliland, T. N. Bhat, H. Weissig, I. N. Shindyalov and P. E. Bourne, *Nucleic Acids Res.*, 2000, **28**, 235.

153. S. E. V. Phillips and B. P. Schoenborn, *Nature (London)*, 1981, **292**, 81.

154. A. A. Kossiakoff and S. A. Spencer, *Biochemistry*, 1981, **20**, 6462.

155. A. A. Kossiakoff and S. A. Spencer, *Nature*, 1980, **288**, 414.

156. J. B. Cooper and D. A. A. Myles, *Acta Crystallogr.*, 2000, **D56**, 246.

157. L. Coates, P. T. Erskine, S. P. Wood, D. A. A. Myles and J. B. Cooper, *Biochemistry*, 2001, **40**, 13149.

158. S. Arai, T. Chatake, T. Ohhara, K. Kurihara, I. Tanaka, N. Suzuki, Z. Fujimoto, H. Mizuno and N. Niimura, *Nucleic Acids Res.*, 2005, **33**, 3017.

159. T. Chatake, I. Tanaka, H. Umino, S. Arai and N. Niimura, *Acta Crystallogr.*, 2005, **D61**, 1088.

160. N. Niimura, *et al.*, 2008, submitted for publication.

161. F. Shu, V. Ramakrishnan and B. P. Schoenborn, *Proc. Natl. Acad. Sci. U.S.A.*, 2000, **97**, 3872.

162. I. Hazemann, M. T. Dauvergne, M. P. Blakeley, F. Meilleur, M. Haertlein, A. Van Dorsselaer, A. Mitschler, D. A. A. Myles and A. Podjarny, *Acta Crystallogr.*, 2005, **D61**, 1413.

163. V. T. Forsyth, D. A. A. Myles, P. A. Timmins and M. Hartlein, in ‘Opportunities for Neutron Scattering in the 3rd Millennium’, ed. J. Dianoux, Institut Laue Langevin publication, 2002 p. 47 (http://www.ill.fr/YellowBook/deuteration/index.htm).

Neutron Scattering

J. Z. Larese

University of Tennessee, Knoxville, TN, USA and Oak Ridge National Laboratory, Oak Ridge, TN, USA

	Method Summary	1
1	Introduction	2
2	Technical Background	2
3	Applications	19
4	Abbreviations and Acronyms	21
5	Further Reading	21
6	References	21

METHOD SUMMARY

Acronyms, Synonyms

- Neutron Diffraction
- Elastic Neutron Scattering
- Inelastic Neutron Scattering
- Inelastic Neutron Spectroscopy
- Neutron Spectroscopy
- Neutron Vibrational/Rotational Spectroscopy
- Quasi-elastic Neutron Scattering

Measured physical quantities

- Elastic Scattering (Diffraction)
- number of scattered neutrons of a particular wavelength (monochromatic) or by time-of-flight (white beam)
- Inelastic Scattering
- change (either gain or loss) in energy/momentum by incident neutron beam (of known energy)
- Quasi-elastic Scattering
- broadening of an elastic scattered neutron peak.

Information available

- characterize the atomic arrangement in crystalline and amorphous solids and liquids (magnetic materials in particular) via diffraction;
- microscopic dynamics: lattice vibrations, molecular motion and diffusion (both rotational and translational).

Information not available, limitations

- Some elements do not scatter well or have large neutron capture cross sections making them hard to study.
- The intensity of neutron beams are of orders of magnitude lower than X rays — structural determination is generally not as accurate for heavy — element containing materials.

Examples of questions that can be answered

- What is the structure of this material? In particular, what is the structure of light element-containing materials and magnetic materials?

- What are the vibrational/rotational modes of the material?
- What type of diffusion takes place within the system (rotational, translation, or both)?

Major advantages

- wavelengths and energies comparable to interatomic spacings and fluctuations within most condensed matter
- does not induce chemistry or physical change
- can vary sample environments greatly (high or low pressure, temperature)
- sees light elements well and has no selection rules for vibrational states
- highly penetrative; samples may be held in metal cans
- weak interactions with matter; pointlike scattering facilitates data analysis
- isotopic sensitivity enables contrast variation
- neutron magnetic moment couples to magnetic fields; unpaired electron spins characterized
- nonionizing radiation.

Major disadvantages

- measurements can take days for statistics
- low flux of neutrons on sample; which means low signals and large amounts of sample needed
- weak interaction with matter
- some elements (e.g., boron, rare earths, cadmium) absorb strongly
- limited number of worldwide neutron sources; hence production costly.

Sample constraints

- temperatures between $\sim$25 mK and 2000 K
- pressures between 10^{-5} Pa and 25 GPa
- magnetic fields below 30 T
- large sample (size depends on elemental content).

1 INTRODUCTION

The enormous opportunities that neutron scattering studies provide for probing the structure and dynamics of condensed matter have been the driving force behind continued interest in the development of new sources around the world. In fact, a soon to be released report from a workshop, ‘‘X-Rays and Neutrons: Essential Tools for Nanoscience Research’’ as part of the National Nanotechnology Initiative, indicates that ‘‘*for more than 50 years, x-ray- and neutron-based tools have opened new vistas at the (often intersecting) frontiers of materials science, biology, medicine, physics, chemistry, engineering, and geology.*’’ The initiation of operations at the Spallation Neutron Source (SNS) on the Oak Ridge National Laboratory facility, and recent operations in Germany and Australia, as well as plans in Japan, China, and Europe to develop new, more powerful sources clearly underscores how valuable these sources are. In this section, the two main methods of generating thermal neutrons for research purposes will be discussed in brief, namely, nuclear fission and spallation. While details concerning power level, core configuration for the fission sources, and accelerator design for the specific sources may vary, the production in generic terms will be discussed, and then, when specific examples are necessary, the Institute Laue Langevin (ILL) and the ISIS spallation sources will be used as the typical ‘‘best in class’’ examples of a reactor and accelerator source, respectively.

2 TECHNICAL BACKGROUND

2.1 Neutron Sources

2.1.1 Reactor-Based Sources

The very first nuclear reactor built, where the main objective was to perform condensed matter research, was the High Flux Beam Reactor (HFBR) at Brookhaven National Laboratory, Upton, NY. The first self-sustaining chain reaction at the HFBR took place on Halloween, 1965. For over 30 years, the HFBR was one of the premier beam reactors in the world, matched only by the ILL reactor in Grenoble, France. These reactor-based sources have been a continuous and reliable source of thermal neutrons for research in a wide range of different scientific fields from physics, chemistry, materials science, and biology to engineering and isotope enrichment. The instrumentation that is in place at these sources has seen steady improvement from the days when Nobel laureates, Brockhouse and Shull, performed their pioneering work at these facilities.

Nuclear reactors operate using the fission chain reaction process wherein heavy nuclei like uranium are used, for which the number of neutrons exceeds the number of protons by a large fraction. In the case of ^{235}U, when a neutron is absorbed, a significant amount of energy is transferred into the system, and an excited ^{236}U nucleus is created. As more energy is absorbed, this excited ^{236}U nucleus oscillates with increasingly larger amplitude until the repelling Coulomb force drives it into separation. Each of these fission reaction steps liberates two or three free neutrons leading to the ‘‘chain’’ reaction. A free neutron is necessary to sustain the chain reaction, that is, to trigger the generation of additional free neutrons. The energy of the fissioning nucleus is about 200 MeV, hence the quantity of neutrons produced in a nuclear reactor scales with the thermal energy produced. For a 60 Mwatt reactor like High Flux Reactor (HFR) at the ILL there are $\sim 1.8 \times 10^{18}$ fission events per second which results in about 7.5×10^{16} neutrons produced per MW. The research reactor is designed to generate as many neutrons as possible for use in research purposes; hence the reactor core design and the HFBR tangential beam tube concept, along with sophisticated neutron optical design components, are arranged to maximize the flux of neutrons at the sample position of the specific instrument. The main requirement is a high power density at the neutron core along with attendant reflectors to minimize the number of escaping neutrons at the core.

The most common configurations of research reactor vessels are the pool and tank coretypes (see Figure 1). Within the core of such reactors is an assembly composed of an organized collection of U fuel elements or rods (the collection known as *the core*), suspended in a large pool of light (H_2O) or heavy ($D_2O = {}^2H_2O$) water. In order to ‘‘control’’ the fission process, moveable rods of neutron-absorbing material like boron or cadmium are distributed among the fuel rods in such a way that they can be raised or lowered into the fuel element package in order to slow down or quench the reaction rate. The *water* moderates (or decelerates) the neutrons and cools the reactor core, while reflector materials like graphite or beryllium are used to bounce the neutrons back into the core region. As noted above, beam tubes (Figure 1) are inserted from the wall of the pool or tank vessel and are used to extract the neutrons from the core region to the instrumental research area (Figure 2).

Neutrons generated within the reactor have a broad energy distribution, ranging from below 1 meV to above 10 MeV. They can be subdivided into three subgroups, those with energies >500 keV or *fast neutrons* with a spectral distribution $N(E)$ given approximately by $N(E) \sim \mathrm{e}^{-E} \sinh \sqrt{(2E)}$; those whose energies lie between 200 meV and 500 keV called *epithermal neutrons* (where the neutron spectrum is largely determined by the collisions they make with nuclei in the moderators)—here the spectral distribution, $N(E) \sim 1/N$; and thirdly, the *thermal neutrons* whose energies lie below 200 meV, whose spectral range looks like that of a gas in thermal equilibrium with the moderator nuclei (i.e., Maxwellian) or such that $N(E) \sim E/(kT)\mathrm{e}^{-E/kT}$ where k is Boltzmann’s constant. These thermal neutrons resulting from the interaction with a water moderator at room temperature have an average energy of about 25 meV or a wavelength of about 0.18 nm. The absolute flux within these three ranges depends on the reactor design, the reactor power level, and the location and type of moderator. Even

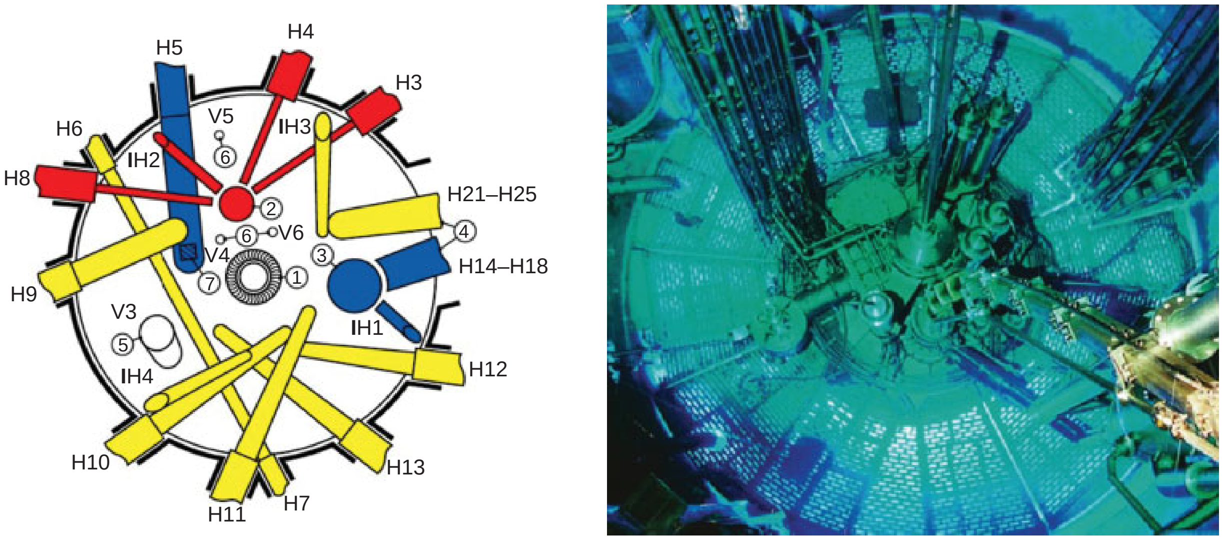

(a) (b)

Figure 1 The figure (a) shows the beam tube arrangement for the High Flux Reactor at the ILL. The figure (b) is a photograph of the reactor core at the ILL. The blue glow is an excellent example of the Cherenkov radiation (i.e., electromagnetic radiation emitted when a charged particle passes through an insulator at a speed greater than the speed of light in that medium)

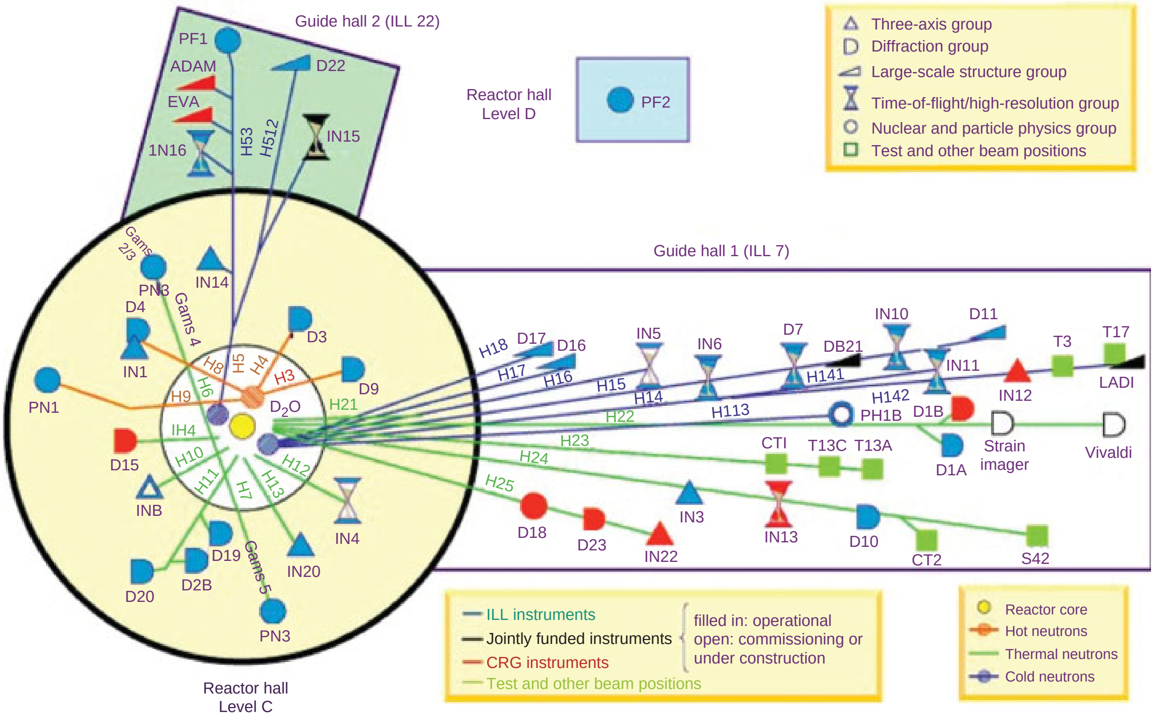
Guide hall 2 (ILL 22)
PF1
ADAM
EVA
1N16
H53
H512
D22
IN15
Reactor hall
Level D
PF2
Three-axis group
Diffraction group
Large-scale structure group
Time-of-flight/high-resolution group
Nuclear and particle physics group
Test and other beam positions
Guide hall 1 (ILL 7)
Gams 2/3
PN3
IN14
D4
Gams 4
IN1
PN1
H8
H5
H4
H3
D3
D9
H9
H6
D$_2$O
H21
IH4
D15
H10
H11
H7
H13
H12
INB
IN4
D19
D2B
Gams 5
IN20
D20
PN3
H18
D17
D16
H17
H16
H15
IN5
IN6
H14
H22
D7
DB21
H141
H113
IN10
D11
IN11
H142
PH1B
D1B
T3
T17
LADI
IN12
H23
H24
H25
CTI
T13C
T13A
D1A
Strain imager
Vivaldi
D18
D23
IN22
IN3
IN13
D10
CT2
S42
ILL instruments
Jointly funded instruments
CRG instruments
Test and other beam positions
filled in: operational
open: commissioning or under construction
Reactor core
Hot neutrons
Thermal neutrons
Cold neutrons
Reactor hall
Level C

Figure 2 Layout of the Institute Laue Langevin (Grenoble, France) Research Reactor Instrumentation including two cold neutron guide halls

longer wavelength, or lower energy, neutrons are desired at times for examining large scale structures or probing slow motions. The lowest energy thermal neutrons (typically of wavelengths 0.5 nm or longer) are often called ‘‘cold’’ neutrons and are generated by using moderators filled with liquid cryogens (usually hydrogen or methane). Since neutrons are such a unique tool to study the microscopic structure and dynamics of condensed matter, it is not surprising that neutron scattering plays a major role in the experimental methods used at research reactors. Neutrons are electrically neutral and therefore don’t scatter from the electron clouds but penetrate deep within matter (i.e., scatter from the nucleus). Furthermore, neutrons can be used to study bulk materials or those contained within pressure vessels, high or low temperature equipment or within magnetic fields (Table 1). Figure 2 shows the multitude of different instruments available for use at the ILL in Grenoble. An excellent description of the capabilities and applicability of each of these instruments at the ILL can be found in the ILL ‘‘*Yellow Book*’’,[1] located at http://www.ill.fr/YellowBookCDrom/index.htm.

2.1.2 *Spallation Sources*

As opposed to the nuclear reactor-based production of neutrons, the SNS is usually accelerator based. Hydrogen ions, either H^+ or H^-, are produced by an ion source, accelerated in vacuum to speeds that exceed 80% of the speed of light, then directed at a heavy metal, for example, uranium (ISIS); tungsten (Los Alamos Neutron Science Center (LANSCE)); or mercury (Spallation Neutron Source (SNS)) target. A linear accelerator raises the velocity of the ions in stages by using a standing electric wave radiofrequency (RF) cavity. The nodes of the electric field are positioned such that the ions don’t change their location (or decelerate) in these ‘‘drift tubes’’. In the region between these drift tubes, the ions gain energy and increase their velocity such that the gaps between and the drift tubes themselves increase in length. The efficiency of operation is increased because when the RF field reverses,

Table 1 Physical properties of a neutron[2]

Particle and wave properties of neutrons

Mass: $m_n = 1.675 \times 10^{-27}$ kg
Charge $= 0$
Spin $= 1/2$
Nuclear magneton: $\mu_N = 5.051 \times 10^{-27}\ \mathrm{J\,T^{-1}}$
Magnetic dipole moment: $\mu_n = 1.913\,\mu_N$

Approximate values for ranges of energy

	Energy (E/meV)	Temp (T/K)	Wavelength (λ/Å)
Cold	0.1–10	1–120	30–3
Thermal	5–100	60–1000	4–1
Hot	100–500	1000–6000	1–0.4

Relationships between neutron properties

$$E = 1/2 m_n v^2 = k_b T = (h\mathbf{k}/2\pi)^2/(2m_n) = (h^2k^2)(2m_n)$$
$$\text{Wavevector } \mathbf{k} = 2\pi/\lambda = m_n v/(h/2\pi) = m_n v/h$$
Units: E(meV); $\mathbf{k}$(Å^{-1}); λ(Å); v(m sec^{-1}); T(K)

ions of opposite charge are accelerated in the gap. Magnetic fields serve to bunch and focus the ions at the ends of the drift tubes. Another type of accelerator is the synchrotron. Both of these types may be used in combination. Stripper foils are used to remove the electrons from the H^- ions. In most cases, once the ions are stripped of their negative charge, they are injected into a storage ring which converts the pulse of H^- ions that was $\sim$650 µs long and accumulates the protons into a short $\sim$100 ns bunch of protons that is then directed onto the spallation target. Proton currents are on the order of $\sim$125 µA at LANSCE and $\sim$300 µA at ISIS (after 2007 upgrade); these are two of the brightest spallation sources currently operating. Hence bursts of protons are released to the targets once every 1/20 of a second at LANSCE or once every 1/50 of a second at ISIS. When the protons hit the target nuclei, neutrons are spalled (knocked out) of the target. For example, when a pulse of energetic protons hits a tungsten target, each proton that collides with a tungsten nucleus causes the nucleus to release $\sim$20 neutrons with different energies. These spalled neutrons, after passing through a moderator, travel along a beam line. The resulting pulse of neutrons is very short, but as the pulse travels down the beam line, neutrons with the higher energy travel down the beam pipe faster, and hence the pulse stretches out in space, much like cars that start out in a small group but are traveling at slightly different speeds; as they travel down the highway they start to move apart in space. In fact, the arrival times of the neutrons serve to identify their energies and wavelengths (by a time-of-flight (TOF) method). Neutrons generated by spallation in the targets are adjusted by the moderator-reflector configuration. For example, beryllium has a large neutron scattering cross section with negligible absorption and is used as a neutron reflector. Moderators slow down the spallation neutrons and can take various shapes and configurations. These moderators are typically filled with ambient temperature water, liquid methane or liquid parahydrogen, and are used to adjust the mean energy of the neutrons within the individual pulse (Figure 3). The sources at ISIS (Figure 4) and LANSCE produce neutron fluxes on the order of 10^{16} neutrons $\text{cm}^{-2}\,\text{s}^{-1}$.

When compared to reactor-based sources, SNSs appear to have the advantage that the proton current is virtually unlimited and thus the neutron flux could increase without physical limit. Naturally, this is not the case, since dissipation of heat and recrystallization of the heavy metal target and shock wave issues associated with the huge energy density of the beam ultimately constrain the designs. At reactor-based sources, it is not possible to increase the power without bounds due to reactor safety. Furthermore, SNSs are, due to the time structure of the neutron flux, ideal for TOF measurements. The SNS at Oak Ridge National Laboratory (Figure 5) is designed for proton currents of 2 mA at 1 GeV proton energy directed toward a liquid mercury target at a repetition rate of 60 Hz, resulting in a peak neutron flux on the order of 10^{17} neutrons $\text{cm}^{-2}\,\text{s}^{-1}$.**[3]** The KENS SNS**[4]** under construction at Tokai, Japan, is designed for a 333 µA current of 3 GeV proton energy, using a liquid mercury target and generating a peak neutron flux on the order of 10^{17} neutrons $\text{cm}^{-2}\,\text{s}^{-1}$. The US and Japanese SNSs are scheduled to become available to users in late 2007.

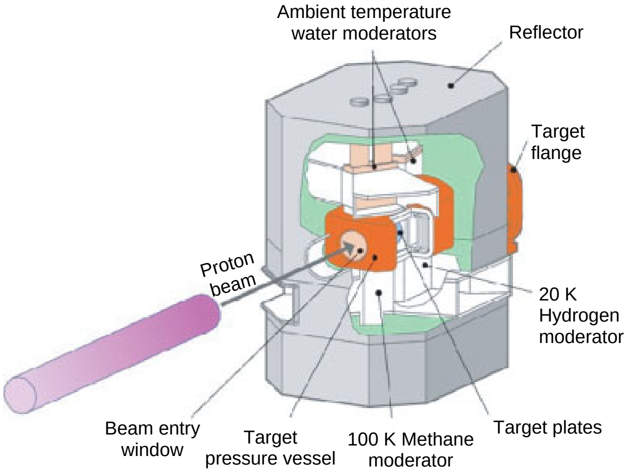

Figure 3 Schematic layout of the ISIS target-moderator region

2.2 General Remarks

At any finite temperature, all matter is composed of atoms that are in constant motion, not just sitting in a fixed position in a crystal lattice. For example, at the atomic level, molecular solids exhibit vibrational, oscillatory and small excursions around their equilibrium position, as a result of thermal energy, even at low temperatures. In a crystalline solid, these movements are centered on the lattice position in the crystal and from the standpoint of diffraction, Bragg, or elastic scattering (*see* ***Neutron Diffraction***), these atoms (or scattering centers) contribute constructively to the diffraction signal only when they are at the *exact* lattice point. The more time that the atoms spend away from this lattice position, the smaller the diffraction signal becomes. If the diffraction signal is used to determine the arrangement of atoms in the crystal structure, the magnitude of these thermal departures can be determined from the distribution of the scattering. In many systems, these departures from the equilibrium lattice position are not uniform in every direction in the crystal. This anisotropy of the motion is signaled by a nonuniform distribution of the elastically scattered intensity. This can signal the onset of a phase transformation or the anisotropy of the elastic response of a system to some physical parameter (i.e., uniaxial pressure). In addition to the observation that the elastic (or Bragg) scattering has decreased thanks to thermal motion, other neutron scattering methods can be effectively used to identify the dynamics of these atoms. So-called *inelastic neutron scattering* (INS) techniques can be effectively used to monitor and quantify these atomic

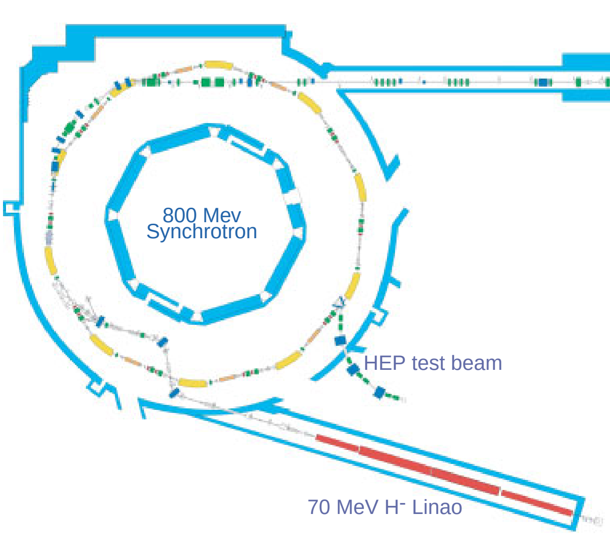

Figure 4 Layout of the ISIS Spallation Neutron facility in Chilton England including linear accelerator, 800 MeV synchrotron, target and instrument hall

Figure 5 Aerial view of the SNS on the Chestnut ridge site at the Oak Ridge National Laboratory operated by the University of Tennessee–Battelle

movements within the solid. As noted in the introduction, neutrons can be used to determine the thermal motion of the atoms that compose molecules or crystalline lattices and this property underlies the other great strengths of using neutrons to study condensed matter and inorganic systems. These motions or response to thermal (or other) forms of energy can be realized by monitoring the changes in the neutron energy after the neutron scatters off of the system. A net increase (or decrease) in the neutron energy can take place when the neutron interacts with the system under study and thus the neutron moves away at a faster (or slower) speed. This is analogous to the Doppler effect that causes the stationary listener to hear the whistle on an approaching and passing train to first raise and then lower in pitch. These changes in neutron energy can either be transferred to or from a crystal lattice, or to or from molecules in a liquid, or at an interface.

The dynamics of the sample can either be of a random nature, like translational or rotational diffusion, or of a collective type that has a propagating wavelike property. The latter collective type wave propagation in the crystal lattice is known as a *phonon* and these coordinated thermal motions of the crystal take place at discrete quantized phonon frequencies (hence energies) given by $h\nu$. These frequencies are usually dependent on the propagation direction in the crystal, the specific crystal structure, and its atomic composition. Rotational, vibrational, and librational motions can also be effectively studied with neutrons. Finally, using high surface-to-volume materials, neutrons can be employed to investigate surface phenomena. In the following sections, some of the mathematical formalism of the neutron scattering technique will be used and several examples that are aimed at illustrating the power of the technique, with the goal of stimulating additional interest and further reading in more advanced and specialized monographs and journals.

2.3 Neutron Scattering Formalism

In a typical neutron scattering experiment, the intensity of the neutrons scattered from a beam incident on a sample is recorded. Usually, the scattering process will involve a deflection of the incident neutrons identified by a change in the wave vector, $\boldsymbol{k}$, of the beam, and denoted by the scattering vector $\mathbf{Q} = \boldsymbol{k}_i - \boldsymbol{k}_f$, where the subscripts i and f denote the incident and final directions, respectively. In addition to the change in wave vector, the scattering can also involve a change in the energy, E, of the neutrons. The magnitude of this energy change is usually associated with some dynamic process in the sample and hence we can represent that as an angular frequency, ω, such that $E = h\omega$. The scattered intensity measured in a neutron experiment is proportional to the dynamical structure factor, $S(\mathbf{Q}, \omega)$ and hence is a function of both $\mathbf{Q}$ and ω. $S(\mathbf{Q}, \omega)$ represents the Fourier transform of the temporal and spatial fluctuations of the atomic (spin) density in a normal (magnetic) neutron scattering process. There are many comprehensive discussions of neutron scattering formalism and the reader is directed to such monographs written by Marshall and Lovesey,[5] Lovesey,[6] Bacon[7] and Squires[8] for a much more thorough treatment.

What appears below is a brief discussion of neutron scattering formalism (for an in depth exposition see, for example, the classic paper by van Hove).[9] We assume the scattering is from point particles, which is reasonable, because thermal neutron scattering involves wavelengths on the order of 1 Å and the length scale of the interaction between an atomic nucleus and the neutron is around five orders of magnitude smaller. If we consider an individual particle j at position $\mathbf{r}_j$ at time t, the number density can be expressed as

$$r_j(\mathbf{r}, t) = \delta(\mathbf{r} - r_j(t)) \tag{1}$$

where δ is the Dirac delta function. The Fourier transform of the spatial component of the number density is given by

$$\rho_j(\mathbf{Q}, t) = \int \rho_j \mathrm{e}^{i\mathbf{Q}\bullet r}\, \mathrm{d}r = \mathrm{e}^{i\mathbf{Q}\bullet r_j(t)} \tag{2}$$

We can now express fluctuations in time by using the cross-correlation function.

$$f_{jk}(\mathbf{Q}, t) = \langle \rho_j(\mathbf{Q}, t)\rho_k(-\mathbf{Q}, 0)\rangle \tag{3}$$

The angular brackets denote an average over all initial times. Because most materials are composed of a collection of different elements, the neutron scattering process represents the contribution of each atomic nucleus to the scattering process, weighted by the scattering length, b_j, of the individual nucleus j. The scattering length corresponds to the strength of the interaction between the jth nucleus and the neutron. As a result, each contribution to the scattering must be weighted accordingly, and taking into consideration the fluctuations of the whole sample, we can express the neutron scattering for N atoms in the form:

$$\begin{aligned} F(\mathbf{Q}, t) &= \frac{1}{N}\sum_{j,k} \langle b_j b_k \rho_j(\mathbf{Q}, t)\rho_k(-\mathbf{Q}, 0)\rangle \\ &= \frac{1}{N}\sum_{j,k} \overline{b_j b_k}\langle \rho_j(\mathbf{Q}, t)\rho_k(-\mathbf{Q}, 0)\rangle \end{aligned} \tag{4}$$

$F(\mathbf{Q}, t)$ is referred to as the *intermediate scattering function*, and the bars placed above the scattering length variables b_j and b_k in equation (4) represent the time average of the cross-correlation functions. These scattering lengths are time independent and thus can be separated out from the time variations in the nuclear density. With this in mind, the dynamical structure factor can be derived using the time Fourier transform of $F(\mathbf{Q}, t)$ as

$$\begin{aligned} S(\mathbf{Q}, \omega) &= \int f(\mathbf{Q}, t)\mathrm{e}^{i\omega t}\, \mathrm{d}t \\ &= \frac{1}{N}\int \sum_{j,k} \overline{b_j b_k}\langle \rho_j(\mathbf{Q}, t)\rho_k(-\mathbf{Q}, 0)\rangle \mathrm{e}^{i\omega t}\, \mathrm{d}t \end{aligned} \tag{5}$$

In terms of energy, this expression can be cast in the following form

$$S(\mathbf{Q}, E) = \frac{1}{N}\int \sum_{j,k} \overline{b_j b_k}\langle \rho_j(\mathbf{Q}, t)\rho_k(-\mathbf{Q}, 0)\rangle \mathrm{e}^{i2\pi Et/h}\, \mathrm{d}t \tag{6}$$

While the treatment appears to be mathematically complicated, it is instructive to consider several special cases that lead to some special methods for extracting unique information about the system under investigation. For example, we can separate the elastic from the inelastic scattering, as well as the coherent from the incoherent scattering. Furthermore, we can use methods to integrate over either energy or scattering vector. The fact that we are able to carry out the separation of different scattering processes leads to the versatility and the application of neutron scattering methods to a wide variety of topics as suggested in the introduction.

Having introduced the neutron scattering length, b, above it has been assumed that the scattering length is the same for all of the atoms of a particular element in the sample. This presumes that the scattering length is independent of the isotope number and nuclear spin state, but what this assumption effectively does is average out the variation of the scattering length with isotope and spin number. No significant error results for many elements since only one isotope occurs naturally in significant quantities. In the case of the isotopes of oxygen, the relative abundances for ^{16}O, ^{17}O and ^{18}O are 99.76%, 0.04%, and 0.2%, respectively, and the variation in scattering length is small (5.803, 5.78 and 5.84 fm, respectively); hence, assuming that the scattering length is constant has negligible consequences. There are of course important exceptions. For example, the two most abundant isotopes of nickel are ^{58}Ni and ^{60}Ni with relative abundance of 68.27% and 26.1% and scattering lengths of 14.4 and 2.8 fm respectively. Neither of these two nuclei has a nonzero value of the spin. As noted above, the effects of nuclear spin can also be important. In the case of hydrogen (^{1}H) the spin dependence of the nucleus–neutron interaction is extremely important. The natural abundance of ^{1}H isotope is more than 99.9%. When the quantum mechanical interaction of the spin 1/2 entities (i.e., the neutron and the ^{1}H, nuclear proton) is taken into account, four different arrangements of the spins need to be considered. Three of these configurations yield a total spin of $S = 1$ with z components -1, 0 or $+1$ (i.e., parallel alignment), whereas the fourth is the antiparallel alignment and total spin of $S = 0$. Many elements exhibit a nuclear spin of zero where the spin-dependent components of the nucleus–neutron interaction are not present, and in most cases the nuclear spin effects are often relatively weak. The scattering lengths for parallel and antiparallel alignment are 10.4 and -47.4 fm, respectively, giving an average value of only -3.74 fm. Sodium is another nucleus with an incoherent scattering cross section that arises from the spin states; the incoherent scattering length, 3.59 fm, is close to the coherent scattering length, 3.63 fm. Vanadium is unusual in that the sum of the coherent contributions is almost zero, with only a significant incoherent cross section. We therefore need to consider how the neutron scattering function can be modified to account for these effects, and it will be found that there are considerable applications from this extended approach. The comparisons between values of the coherent and incoherent scattering cross sections are illustrated in Table 2. A compilation of scattering lengths and cross sections can be found on the National Institute of Standards and Technology (NIST) website at http://www.ncnr.nist.gov/resources/n-lengths/,**[10]** or the monographs noted above.

In order to account for different scattering lengths for atoms of the same type, we can separate the intermediate scattering factor described above into two components:

$F(\mathbf{Q}, t) = F_{\mathrm{coh}}(\mathbf{Q}, t) + F_{\mathrm{inc}}(\mathbf{Q}, t)$ where the *coherent* term can be expressed as

$$F_{\mathrm{coh}}(\mathbf{Q}, t) = \frac{1}{N} \int \sum_{j,k} \overline{b_j}\;\overline{b_k} \langle \rho_j(\mathbf{Q}, t) \rho_k(-\mathbf{Q}, 0) \rangle \qquad (7)$$

and the *incoherent* term as

$$F_{\mathrm{inc}}(\mathbf{Q}, t) = \frac{1}{N} \int \sum_{j,k} \left(\overline{b_j b_k} - \overline{b_j}\;\overline{b_k} \right) \langle \rho_j(\mathbf{Q}, t) \rho_k(-\mathbf{Q}, 0) \rangle \qquad (8)$$

The coherent term has an average value for the scattering length and involves correlations between the position of an

Table 2 Bound scattering lengths, b(fm) and cross section for selected isotopes and for selected naturally occurring isotopic mixtures of the elements; σ (barns, 1 barn $= 100\,\mathrm{fm}^2$). Z, atomic number; A, mass number; I, spin of the nuclear ground state; $b_{\mathrm{coh}}, b_{\mathrm{inc}}$, coherent and incoherent scattering lengths; σ_a, σ_{coh}, coherent and incoherent cross sections; σ_a, absorption cross section for 2.2 km s^{-1} neutrons[a]

Element	Z	M	I	C (%)	b_{coh}	b_{inc}	σ_{coh}	σ_{inc}	σ_a
H	1				−3.74		1.76	79.9	0.33
		1	1/2	99.98	−3.74	25.22	1.76	79.9	0.33
		2	1	0.02	6.67	4.03	5.59	2.04	0.00
Li	3				−1.9		0.45	0.83	70.5
		6	1	7.5	$2-0.3i$	$-1.9+0.3i$	0.51	0.46	940
		7	3/2	92.5	−2.22	−2.32	0.62	0.68	0.05
C	6				6.64		5.55	0	0.00
O	8				5.803		4.23	0.0008	0.0002
Mg	12				5.375		3.63	1.62	0.06
Al	13				3.449	0.256	1.49	0.008	0.23
Si	14				4.149		2.16	0.004	0.17
Ca	20				4.70		2.78	0.05	0.43
Ti	22				−3.44	1.49	2.76		6.1
Mn	25	55	5/2	100	−3.73	1.79	1.75	0.4	13.3
Fe	26				9.54		11.44	0.39	2.56
Ni	28				10.3		13.3	5.2	4.49
		58	0		14.4	0	26.1	0	4.6
		62	0		−8.7	0	9.5	0	14.5
Zr	40				7.16		6.44	0.16	0.19
Cd	48				$5.1-0.7i$		3.3	2.4	2520
Au	79	197	3/2	100	7.63	−1.84	7.32	0.43	98.65
Pb	82				9.40		11.11	0.00	0.17
U	92				8.42		8.9	0.00	7.57

[a] In the *free state* nuclei upon neutron impact; cross sections related to atomic mass number (M) by $\sigma_{\mathrm{free}} = (A/A+1)^2\sigma_{\mathrm{bound}}$. For H, $\sigma_{\mathrm{free}} = 1/4\sigma_{\mathrm{bound}}$, with the difference between the two cross sections decreasing rapidly for heavier nuclei.

atom j at time zero and the position of a second atom k at time t. Although j and k can be the same atom, in general they are not the same because most samples contain a large number of nuclei, N. Coherent scattering, in essence, describes the interference of waves produced by the scattering of a single neutron from all the nuclei in a sample. The intensity for this type of scattering varies strongly with the scattering angle and contains the information about coherent (i.e., correlated) processes, such as Bragg (diffraction) and phonon scattering. In most cases, $F_{\text{coh}}(\mathbf{Q}, t)$ is expanded in terms of the instantaneous displacements of the atoms from their mean positions, which makes it easier to apply the formalism to the study of phonon dispersion curves and other dynamical processes that will be discussed below.

Some expansion and development of the incoherent term will help us cast it in a more useful form. It is important to note that it has been assumed that there is no correlation between the particular value of the neutron scattering length and the location of the scatterer within the sample. We can use this to write $\overline{b_j b_k} = \overline{b_j}\ \overline{b_k}$ for $j \neq k$ so that in equation (8) above, only the terms where $j = k$ survive leaving:

$$F_{\text{inc}}(\mathbf{Q}, t) = \frac{1}{N} \int \sum_{j,k} \left(\overline{b_j^2} - \overline{b_j}^2\right) \langle \rho_j(\mathbf{Q}, t) \rho_j(-\mathbf{Q}, 0) \rangle \tag{9}$$

It is convenient to define two scattering cross sections:

$$\begin{aligned} \sigma_j^{\text{coh}} &= 4\pi \overline{b_j}^2 \\ \sigma_j^{\text{inc}} &= 4\pi \left(\overline{b_j^2} - \overline{b_j}^2\right) \end{aligned} \tag{10}$$

Then the incoherent structure factor can be expanded as:

$$F_{\text{inc}}(\mathbf{Q}, t) = \frac{1}{4\pi N} \sum_j \sigma_j^{\text{inc}} \left\langle e^{i\mathbf{Q}\bullet[\mathbf{r}_j(t) - \mathbf{r}_j(0)]} \right\rangle \tag{11}$$

Because incoherent scattering involves correlations between the position of an atom j at time zero and the position of the *same* atom at time t, the scattered waves from different nuclei do not interfere with one another. In light of this, it is useful to introduce a probability distribution function, $G(\mathbf{r}(t), \mathbf{r}(0))$, which gives the probability of finding a particle at a position $\mathbf{r}(t)$ at time t if it had a position $\mathbf{r}(0)$ at time 0. Thus we can cast equation (11) in a new form:

$$F_{\text{inc}}(\mathbf{Q}, t) = \frac{1}{4\pi N} \sum_j \sigma_j^{\text{inc}} \int e^{i\mathbf{Q}\bullet[r_j(t) - r_j(0)]} G(\mathbf{r}(t), \mathbf{r}(0))\, p(\mathbf{r})\, \mathrm{d}r(t)\, \mathrm{d}\mathbf{r}(0) \tag{12}$$

where $p(\mathbf{r})$ is the probability of finding the atom at position $\mathbf{r}$ at time $t = 0$. Writing the intermediate scattering function in this way makes it easy to express the time dependence of the atomic motions using rate equations that will govern the time dependence of $G(\mathbf{r}(t), \mathbf{r}(0))$. For this reason, incoherent scattering provides a good method of examining processes in which atoms diffuse. In most situations, the incoherently scattered intensity is isotropic, that is, independent of scattering angle. Hence it is often possible to ignore this incoherent contribution during studies of coherent scattering processes, because the incoherent effects just add intensity as a featureless background.

Having discussed how the coherent and incoherent components of the scattered neutrons can be treated, it is extremely important to extend the mathematical discussion to include the formalism used to separate the elastic and inelastic scattering processes. Elastic scattering arises from the time-independent (static) component of a sample. This sample could be a crystalline or amorphous solid (i.e., a glass), but not a fluid (which exhibits molecular diffusive motions), because we are considering the case where $\omega = 0$. However, the elastic scattering is not identical with $S(\mathbf{Q}, \omega = 0)$, as discussed below. The function $S(\mathbf{Q}, \omega = 0)$ can be written as $S(\mathbf{Q}, \omega = 0) = \int F(\mathbf{Q}, r)\, \mathrm{d}r$. We can use this to separate $F(\mathbf{Q}, t)$ into two components, a constant term and one that depends on time (the temporal behavior is such that it either tends to zero as $t \to \infty$ or oscillates about zero at large t). We can then write $F(\mathbf{Q}, t) = F(\mathbf{Q}, \infty) + F'(\mathbf{Q}, t)$, where the first term is the time-independent (constant) term while the second term contains all of the time dependence. Naturally, this is written in such a way that the Fourier transform of the constant term yields a delta function for $\omega = 0$ (i.e., $F(\mathbf{Q}, \infty)\delta(\omega) = \int F(\mathbf{Q}, \infty) e^{i\omega t}\, \mathrm{d}t$), and the Fourier transform of the time-dependent term produces the same energy spectrum as the full $F(\mathbf{Q}, t)$ when $\omega \neq 0$.

Using equation (4) above, the function $F(\mathbf{Q}, \infty)$ can be written as:

$$\begin{aligned} F(\mathbf{Q}, \infty) &= \frac{1}{N} \sum_{j,k} \left\langle b_j b_k \rho_j(\mathbf{Q}, \infty) \rho_k(-\mathbf{Q}, 0) \right\rangle \\ &= \frac{1}{N} \sum_{j,k} \overline{b_j b_k} \langle \rho_j(\mathbf{Q}) \rangle \langle \rho_k(-\mathbf{Q}) \rangle \end{aligned} \tag{13}$$

which includes the situation that at infinite times the random fluctuations in the density function are totally uncorrelated. Consideration of the coherent scattering leads to a simplification of equation (7) to the form:

$$F_{\text{coh}}(\mathbf{Q}, \infty) = \frac{1}{N} \left| \sum_j \overline{b_j} \langle \rho_j(\mathbf{Q}) \rangle \right|^2 \tag{14}$$

What has been presented here underscores the fact that the elastic scattering is the Fourier transform of the time-independent component of the intermediate scattering function. Naturally, the Fourier transform of a constant function produces a δ-function at $\omega = 0$, which is the elastic scattering, but this is not the same as the zero frequency component of the scattered intensity. If the time correlation function has a component that exhibits some time decay or relaxation, then the integral of the time dependant part of

$F(\mathbf{Q}, t)$ will have a contribution to $S(\mathbf{Q}, \omega)$ at zero frequency that is nonzero. This makes an additional contribution to $S(\mathbf{Q}, \omega)$ as part of a continuous function separate from and in addition to the δ-function (from the elastic scattering) discussed above.

2.3.1 Inelastic Scattering

The formalism can now be developed for the neutron scattering function in the case when atoms vibrate about their mean positions, as in a crystalline solid, in order to examine the mathematical treatment of inelastic coherent scattering (once again treatments described in the monographs above give a much more detailed mathematical account of this). Consider a sample consisting of N atoms where the instantaneous position of atom j is identified by $\mathbf{r}_j(t) = \mathbf{R}_j + \mathbf{u}_j(t)$ where $\mathbf{R}_j$ is the average position of the atom, and $\mathbf{u}_j(t)$ is the instantaneous displacement of the atom from its average position. The intermediate scattering function, equation (7), can then be expressed as:

$$F(\mathbf{Q}, t) = \frac{1}{N}\sum_{j,k} \overline{b}_j \overline{b}_k \mathrm{e}^{i\mathbf{Q}\bullet[\mathbf{R}_j - \mathbf{R}_k]} \left\langle \mathrm{e}^{i\mathbf{Q}\bullet[u_j(t) - u_k(0)]} \right\rangle \tag{15}$$

If the motion of the atom about its equilibrium position is harmonic, then one can find, in numerous places (including the monographs identified above) that the time average of the exponential function with the main displacements in the argument is

$$\begin{aligned} \left\langle \mathrm{e}^{i\mathbf{Q}\bullet[u_j(t) - u_k(0)]} \right\rangle &= \mathrm{e}^{-\frac{1}{2}\langle \mathbf{Q}\bullet[u_j(t) - u_k(0)]^2 \rangle} \\ &= \mathrm{e}^{-\frac{1}{2}\left(\left\langle [\mathbf{Q}\bullet u_j(t)]^2 \right\rangle - \langle [\mathbf{Q}\bullet u_k(0)]^2 \rangle + 2\langle [\mathbf{Q}\bullet u_j(t)][\mathbf{Q}\bullet u_k(0)] \rangle \right)} \end{aligned} \tag{16}$$

The first two terms in the exponential argument correspond to the normal thermal factors $\mathrm{e}^{-\frac{1}{2}([\mathbf{Q}\bullet u_j(0)]^2)} = \mathrm{e}^{-W_j}$ and $\mathrm{e}^{-\frac{1}{2}([\mathbf{Q}\bullet u_k(0)]^2)} = \mathrm{e}^{-W_k}$. The third term can be expanded in a power series as:

$$\mathrm{e}^{-(\langle [\mathbf{Q}\bullet u_j(t)][\mathbf{Q}\bullet u_k(0)] \rangle)} = \sum_{l=0}^{\infty} \frac{1}{m!} \left\langle [\mathbf{Q}\bullet u_j(t)]\, [\mathbf{Q}\bullet u_k(0)] \right\rangle^m \tag{17}$$

The $m = 0$ term in the series corresponds to elastic scattering, while the $m = 1$ term can be examined within the harmonic approximation of the lattice dynamics; the instantaneous displacement can be written as:

$$u_j(t) = \frac{1}{\sqrt{N m_j}} \sum_{k,\nu} \mathrm{e}_j(\mathbf{k}, \nu) \mathrm{e}^{i(\mathbf{k}\cdot\mathbf{r}_j) Q(\mathbf{k},\nu)} \tag{18}$$

where the term $\mathbf{Q}(\mathbf{k}, \nu)$ is the normal mode coordinate for a phonon of wave vector $\mathbf{k}$ and branch n, and $\mathbf{e}_j(\mathbf{k}, \nu)$ is the normalized vector that gives the relative displacements of each atom. Treating the normal mode coordinate as a quantum operator, it can be shown that the $m = 1$ term contributes the following term to the dynamical scattering factor:

$$\begin{aligned} S_1(\mathbf{Q}, \omega) &= \frac{1}{N} \sum_{j,k} \overline{b}_j \overline{b}_k \mathrm{e}^{i(\mathbf{Q}\cdot[\mathbf{R}_j - \mathbf{R}_k])} \mathrm{e}^{-(W_j - W_k)} \\ &\quad \times \int \langle [\mathbf{Q}\cdot u_j(t)][\mathbf{Q}\cdot u_k(0)] \rangle \mathrm{e}^{-i\omega t}\, \mathrm{d}t \\ &= \frac{1}{N} \sum_{\nu} \frac{\hbar}{2\,\omega(\mathbf{k}, \nu)} |F_\nu(\mathbf{Q})|^2 \\ &\quad \times ([1 + n(\omega)]\delta\,(\omega + \omega(\mathbf{k}, \nu) + n(\omega)\delta(\omega - \omega(\mathbf{k}, \nu)))) \end{aligned} \tag{19}$$

where the phonon structure factor component is given as:

$$F_\nu(\mathbf{Q}) = \sum_j \frac{\overline{b}_j}{m_j} \mathrm{e}^{-W_j} \mathrm{e}^{i\mathbf{Q}\cdot R_j} Q \cdot \mathrm{e}(\mathbf{k}, \nu) \tag{20}$$

This expression for the single-phonon dynamical scattering factor has to be examined in a little more detail. Because we consider only the creation or annihilation of a single phonon, the δ functions identify that scattering from a phonon of angular frequency $\omega(\mathbf{k}, n)$ takes place such that changes in the energy of the neutron beam take place only at $\pm\omega(\mathbf{k}, n)$. The likelihood that phonon scattering occurs is determined by the thermal distribution of phonons, which were described using Bose–Einstein statistics such that distribution $n(\omega) = 1/(\mathrm{e}^{\hbar\omega/k_B T} - 1)$ where $n(\omega)$ is the number of phonons of frequency ω for a given temperature, T. In the case where there has been a loss of neutron energy, the situation corresponds to a scattering event that has taken place following the creation of a phonon, and this process occurs with probability $[1 + n(\omega)]$. If the scattering event takes place such that there is a gain in energy of the scattered neutron beam, this corresponds to situation where the neutron absorbs a phonon; here the probability of this process is given by the number of phonons $n(\omega)$. At sufficiently high temperatures, the intensity from a single phonon is proportional to:

$$S_1(\mathbf{Q}, \omega) \propto \frac{k_B T}{\omega^2} \delta(\omega \pm \omega(\mathbf{k}, \nu)) \tag{21}$$

In both cases, the intensity of scattering is determined by the phonon structure factor that takes into account the relative positions of atoms, the relative orientation of the scattering vector $\mathbf{Q}$, and the displacement of the atoms. These factors determine the so-called selection rules for the one phonon neutron scattering process. It should be noted that the restrictions associated with the one phonon scattering event described here are certainly not as restrictive as the selection rules associated with the optical equivalent analogs of Raman or infrared spectroscopy (*see* ***Vibrational Spectroscopy***). This property of the nuclear scattering can be useful in separating measurements for which there are a large number of phonons for any wave vector $\mathbf{k}$. The terms in the expansion for $m > 1$

involve *multiphonon* processes. However, these processes prove to be much less informative because these processes do not yield enough structure in measured spectra to be useful, and understanding the behavior of these processes is mostly motivated by the need to subtract them from absolute measurements of intensities in both inelastic and total scattering measurements.

The single-phonon coherent inelastic processes described above are often used for measurements of phonon dispersion curves with single crystal samples[11,12] (Figure 6). These studies are not trivial, and as a result, it is often the case that measurements will only focus on a small subset of all phonon modes (particularly the lower energy modes). Examples of measurements of relatively complete sets of dispersion curves of minerals include calcite,[13] sapphire,[14] and quartz.[15] It should be appreciated that the measurements of the high frequency modes are particularly difficult. It can be seen from equation (21) that the one phonon intensity scales as ω^{-2}. Because other spectroscopic probes can access these phonon modes more readily, and their variation across a range of wave vectors is often slight, it is often not worth attempting to measure complete sets of dispersion curves. Moreover, the experimental difficulties increase with more complex minerals. Examples of partial sets of dispersion curves include the olivines—forsterite[16] and fayalite,[17] pyrope,[18] andalusite,[19] and zircon.[20]

Inelastic coherent scattering measurements using single crystals may focus on selected modes. For triple-axis spectroscopy, the work of Shirane *et al*. sets the standard by which most other studies can be gauged (Figures 7 and 8). For additional examples, see the monograph by Shirane, Shapiro and Transquada.[21] Measured phonon densities of

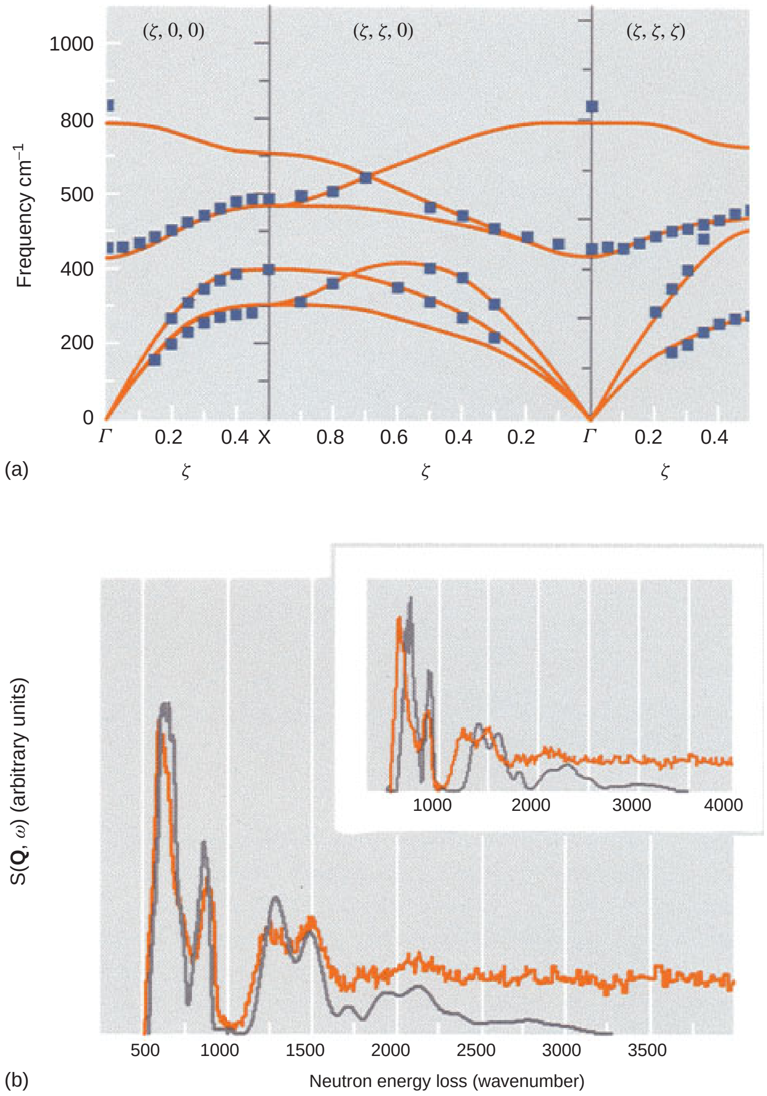

Figure 6 (a) Phonon dispersion curves for LiD; squares represent data, lines represent calculation (b). (Reproduced with permission Colognesi, Ramirez-Cuesta, Zoppi, Senesi and Abdul-Redah[12] © 2004, Elsevier)

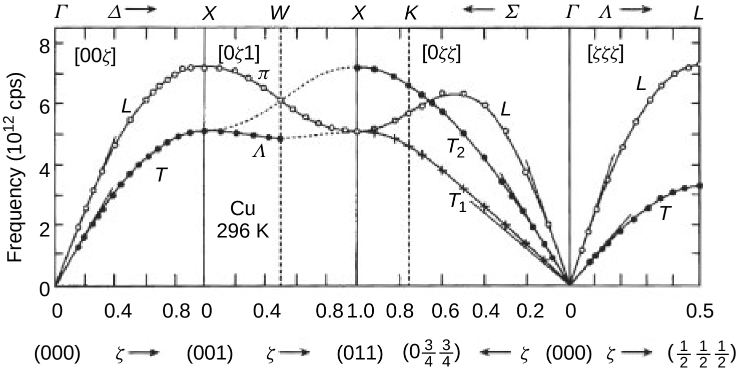

Figure 7 Phonon dispersion curves for face-centered cubic Cu at 296 K. (Reproduced with permission Svensson, Brockhouse and Rowe[28] © 1967, American Physical Society)

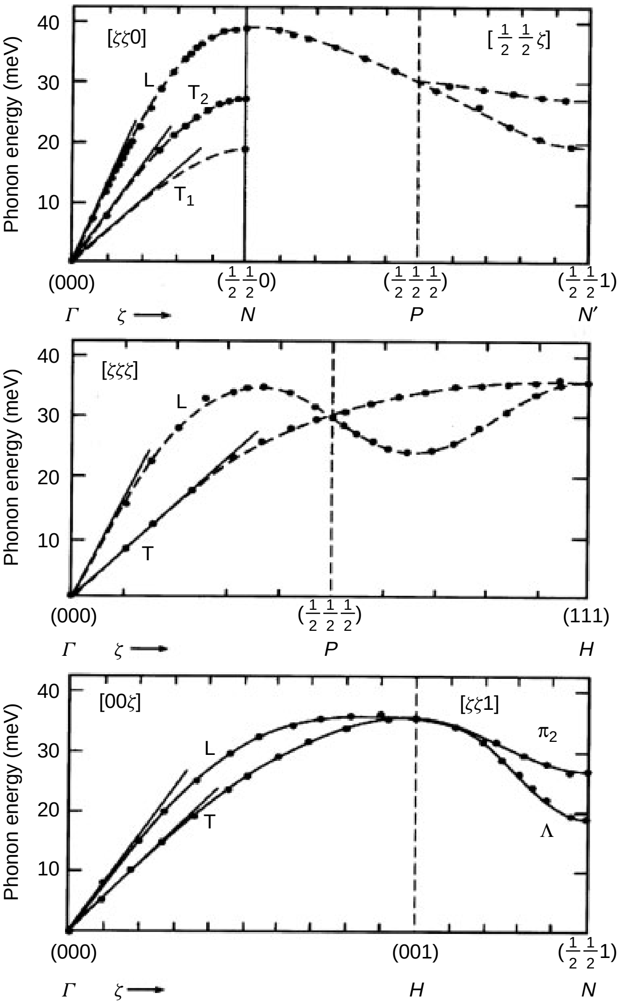

Figure 8 Phonon dispersion curve in body-centered cubic Fe at room temperature. (Reprinted with permission Minkiewicz and Nathans,[29] © 1967, American Physical Society)

states have been reported for complex minerals such as almandine,[22] pyrope,[23] sillimanite, kyanite,[24] orthoenstatite,[25] and fayalite.[26] With spectrometers such as the MARI instrument at ISIS, it is now possible to perform inelastic scattering measurements from powdered samples as functions of **Q**. The value of these types of measurements is that they enable comparisons to be made between the excitation spectra of different phases. It has been shown by these measurements using INS that spectra of silica glass are closely related to the spectra of the two phases of cristobalite.[27]

There has been a considerable effort in the physics and chemistry communities to use INS methods to study magnetic dynamics, which can often be described as *spin waves*. Measurements of spin wave dispersion curves can provide information about the interactions between atomic magnetic moments, the so-called *exchange interactions*. There have been comparatively few INS measurements on magnetic minerals. INS methods have been used to produce spin wave dispersion curves for hematite.[30] Crystal field magnetic transitions in cobalt bearing cordierite, and spinel phases have also been studied by INS.[31]

2.3.2 Formalism for Incoherent Scattering

General Considerations. Hydrogen is the ideal atom for investigating the incoherent scattering of neutrons, since the cross section for incoherent scattering is large relative to its own coherent scattering cross section and the cross sections of most atoms likely to be encountered in natural materials. This is true when hydrogen is a constituent part of a molecule, such as water or methane. Hence, consider a single hydrogen atom in a molecule, its position at time t being given by $\mathbf{r}(t)$, where $\mathbf{r}(t) = \mathbf{R}(t) + \mathbf{d}(t) + \mathbf{u}(t)$, and $\mathbf{R}(t)$ is the position of the center of mass of the molecule and $\mathbf{d}(t)$ is the position of the hydrogen atom relative to the molecular center of mass, assumed to have constant magnitude but variable direction, and $\mathbf{u}(t)$ is the vibrational motion of the atom about its ‘‘average’’ position (where $|d| \gg |u|$). The vibrational motions associated with $\mathbf{u}(t)$ are much faster than the rotational motion of the molecule, which is why we can treat the behavior of the bond vector $\mathbf{d}(t)$ separately from the vibrational displacement $\mathbf{u}(t)$. We are interested in evaluating the quantity $\langle \mathrm{e}^{iQ^o - [\mathbf{r}(t) - \mathbf{r}(0)]} \rangle$. This can be written as

$$\langle \mathrm{e}^{iQ^o - [\mathbf{r}(t) - \mathbf{r}(0)]} \rangle = \langle \mathrm{e}^{iQ^o - [\mathbf{R}(t) - \mathbf{R}(0)]} \mathrm{e}^{iQ^o - [\mathbf{d}(t) - \mathbf{d}(0)]} \mathrm{e}^{iQ^o - [\mathbf{u}(t) - \mathbf{u}(0)]} \rangle \quad (22)$$

If the translational, rotational, and vibrational motions are not coupled, we can perform the averages on the three exponential terms separately, obtaining the total function (with self-explanatory notation), $F_{\mathrm{inc}}^{\mathrm{tot}}(\mathbf{Q}, t) = F_{\mathrm{inc}}^{\mathrm{trans}}(\mathbf{Q}, t) \times F_{\mathrm{inc}}^{\mathrm{rot}}(\mathbf{Q}, t) \times F_{\mathrm{inc}}^{\mathrm{vib}}(\mathbf{Q}, t)$. When we take the Fourier transforms, we have the convolution of the incoherent inelastic scattering functions for the three types of motion:

$$S_{\mathrm{inc}}^{\mathrm{tot}}(\mathbf{Q}, \omega) = S_{\mathrm{inc}}^{\mathrm{trans}}(\mathbf{Q}, \omega) \otimes S_{\mathrm{inc}}^{\mathrm{rot}}(\mathbf{Q}, \omega) \otimes S_{\mathrm{inc}}^{\mathrm{vib}}(\mathbf{Q}, \omega)$$

In practice the various types of motion within materials occur on sufficiently different time scales and so the effects of the convolution do not cause any major problems in the analysis of incoherent neutron scattering data; these problems mostly occur in the study of molecular fluids.

Incoherent neutron scattering is an excellent tool for characterizing the motion of individual molecules on the atomic level as they diffuse through a crystalline or liquid medium, or at the interface of a bulk solid, or within a porous media. This can be followed by examining the time dependence of $\mathbf{R}$. One example that has been exhaustively studied is the diffusion of hydrogen atoms in metals such as palladium. In these systems, atomic hydrogen enters the metal via interstitial sites, and then ''hops'' from site to site rapidly. Diffusion within molecular fluids or within surface-adsorbed molecular films on the surface of graphite or MgO are other examples. In these studies, incoherent neutron scattering provides direct information about the time constants for the diffusion, the temperature dependence, and some information of the diffusion mechanism. *Isotropic diffusion* might occur, for example, in a simple liquid. In this situation it can be assumed that there is no potential to be concerned with, hence we can use a standard rate equation for molecular diffusion (i.e. Fick's second law):

$$\frac{\partial G}{\partial t} = D \nabla^2 G \quad (23)$$

Where G is the probability distribution function $G(\mathbf{r}(t), \mathbf{r}(0))$ first introduced in equation (13), which we rewrite as $G(\mathbf{r}, t), \mathbf{r} = \mathbf{r}(t) - \mathbf{r}(0)$, and D is the diffusion constant consistent with the *Fickian* diffusion.

This standard expression for the diffusion with boundary conditions, $G(\mathbf{r}, 0) = d(\mathbf{r})$ and $\int G(\mathbf{r}, t) d\mathbf{r} = 1$ for all t has the solution:

$$G(\mathbf{r}, t) = (4\pi D t)^{-3/2} \mathrm{e}^{-r^2/4Dt} \quad (24)$$

where r is the modulus of $\mathbf{r}$. Inserting this solution into the equation for the intermediate scattering function (noting that for the present case the probability $p(\mathbf{r})$ is constant for all values of $\mathbf{r}$), leads to the result $F_{\mathrm{inc}}(\mathbf{Q}, t) = \exp(-DQ^2 t)$, where Q is the modulus of $\mathbf{Q}$, and N is the number of atoms. Fourier transformation of this expression gives the final incoherent scattering function for the Fickian diffusion:

$$S_{\mathrm{inc}}(\mathbf{Q}, \omega) = \frac{1}{\pi} \frac{DQ^2}{(DQ^2)^2 + \omega^2} \quad (25)$$

Notice that the final scattering function for the case of isotropic diffusion is just a Lorentzian function centered at $\omega = 0$ with a frequency width that varies with Q^2 and an amplitude that varies as Q^{-2}. Further inspection of this expression shows us that the width varies directly with the diffusion constant D, and thus the time constant associated with the diffusion. Normally, the energy width associated with the diffusion is significantly narrower than the phonon frequencies, usually by several orders of magnitude when compared to phonon frequencies, and hence this scattering is often referred to as *quasi-elastic scattering*. In fact, the motion and time scales associated with diffusion are so slow that special instruments have been designed and built for *incoherent* quasi-elastic neutron scattering (QENS) studies. The typical resolution of a QENS instrument will range from 10^8 to 10^{10} Hz, which is much finer than the typical value of 10^{11} Hz for a triple-axis spectrometer.

What has just been outlined is a simple introduction to diffusion in fluids and model studies; however, when considering crystalline materials, this very elementary model needs to be modified in order to address a position-dependent potential. The diffusion constant is generally a tensor rather than a scalar quantity, a reflection of the fact that the motion will be easier in some directions than in others. While the more realistic case is obviously more difficult to analyze, the general form of the Q^2-dependent Lorentzian term is usually retained, even if the solution involves the superposition of several Lorentzian functions. However, significant insight and progress can be made in these more realistic and complicated situations. Restricting our attention to large length scales, or small $\mathbf{Q}$, allows for the individual components of the motion (particularly the lowest order component) to be extracted. Working with powders, and therefore imposing an average over all orientations of the crystalline lattice, reduces the difficulties associated with the tensor nature of the diffusion (i.e., that it is anisotropic) and may not be a significant limitation on accuracy if the diffusion is only significant along one direction in the crystal. If diffusion is limited to primarily lattice sites such that the motion is one of ''hopping'' from lattice site to lattice site due to the periodic potential of the crystal, then there will be an *elastic incoherent scattering signal* when $\mathbf{Q}$ is equal to a reciprocal lattice vector. This elastic scattering contains information about the strength of the periodic potential. In the limit where the jump is instantaneous, that is, much less than the average time that an atom dwells at the lattice site, then standard jump diffusion models can be used in the interpretation of the quasi-elastic scattering. The monographs by Bee[32] and Hempelmann[33] are two excellent resources in that they discuss many experimental and theoretical examples, including the development of the mathematical formalism.

Neutron Characterization of Vibrational Motions. As noted above, the time scales for phonon motion get significantly longer for translational diffusion, but within the formalism described, both the positional terms **R** and **u** contain a time dependence. An accurate, but somewhat simplified view of the temporal behavior would allow us to assign the low frequency lattice vibrations (phonons) where the molecules move as rigid bodies to the **R** term, while **u** could be assigned to the internal vibrational motions of the molecules (i.e., high frequency). This decoupled view is generally a reasonable assumption and can be characterized if the incoherent response is measured over the proper range. The so-called phonon density of states is the form of $S_{\text{inc}}(\omega)$ if the result is averaged over all **Q** and weighted by the appropriate incoherent neutron cross sections. If hydrogen is present in the sample, the motions of the hydrogen atoms will dominate the recorded spectrum because hydrogen has a large incoherent scattering cross section, making it ideally suited to perform vibrational spectroscopy on such systems. Coupled with the fact that the high frequency modes have only a weak dependence of wave vector density of state, measurements typically exhibit sharp phonon peaks. Furthermore, incoherent neutron scattering can be used as an effective tool for vibrational spectroscopy because there are no symmetry related selection rules (as there are in optical scattering techniques like IR and Raman) which make certain transitions unobservable. Despite the phonon spectrum being at a much higher frequency than the translational and rotational motions, the QENS is convoluted with the vibrational spectrum. This convolution gives rise to a Debye–Waller prefactor to the proper QENS intensity in the same way as in the case of coherent neutron scattering. There are numerous examples of using neutrons to characterize the vibrational spectrum of a sample, but one of the more effective illustrations of this for inorganic systems involves hydrated crystalline systems like the zeolites, or minerals like gypsum, or metal oxides containing tetrahedrons of aluminum (AlO_4) or silicon (SiO_4), like analcime or leutice. An excellent recent monograph that addresses the use of neutrons in vibrational spectroscopy has recently been published by Mitchell, Parker, Ramirez–Cuesta, and Tomkinson.[34] An example of the vibrational spectrum of a C_{60} fullerene is shown in Figure 9.

Rotational Motions. In addition to molecular vibrational motions, one can use neutrons to characterize the rotation of a molecule about its center of mass. If the position of the hydrogen atoms in a molecule rotates as a function of time in such a way that the relative positions of the atoms move with a *constant radius* **d**, but the motion is such that the terminus of the vector **d** moves randomly or ergotically on the surface of the sphere; this motion is referred to as *rotational diffusion*. This motion can also provide insight into the nuclear density. An example of this is shown in Figure 10.

It is instructive to first consider isotropic rotational diffusion of an atom, which is a simple but somewhat accurate description of a molecular liquid like liquid methane just below $\boldsymbol{T}_{\text{melting}}$, a situation wherein the centers of mass of the molecules remain stationary, but the molecules rotate freely about their centers of mass. If we use the polar angle $\boldsymbol{\Omega} = (\theta, \phi)$ to define the orientation of the vector **d**, the probability distribution function, **G** (see equation 12), which

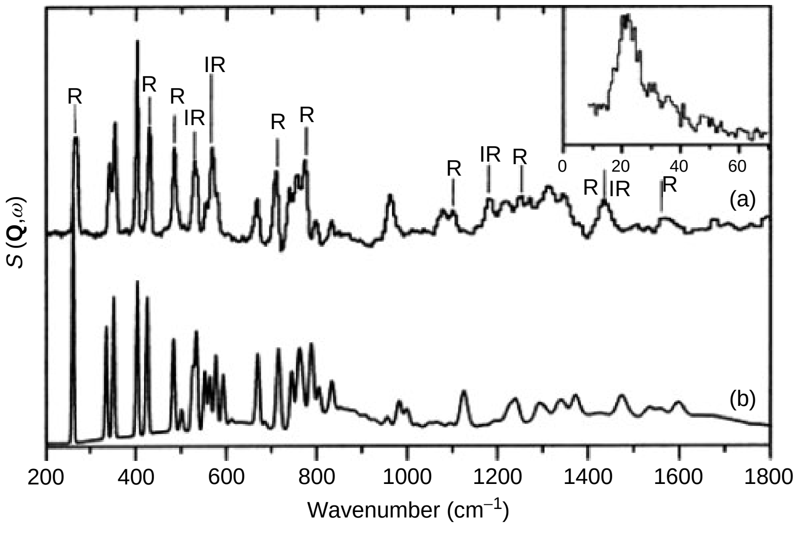

Figure 9 (a) Inelastic neutron scattering spectrum of C_{60}, buckyballs recorded at 20 K and (b) calculated spectrum using Density Functional Theory (DFT) methods from Parker and co-workers (Mitchell *et al.*[34] © World Scientific Publishing Company). R and IR indicate Raman and IR active modes, respectively; all other modes are optically forbidden. The lattice (phonon) modes are shown in the inset

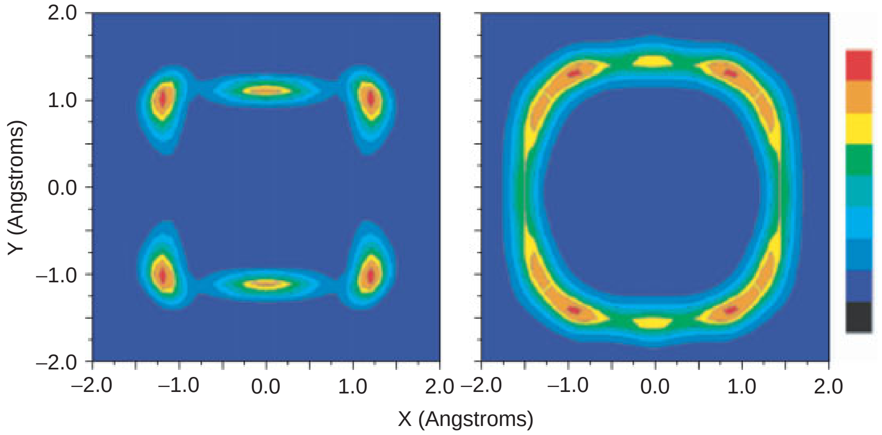

Figure 10 Contour plots of calculated (a) and measured (b) nuclear density for the methyl group in lithium acetate dihydrate. In both cases, four peaks of strong intensity are found at the corners of the square, and weaker peaks are observed at the middle of the upper and lower sides

is a function of $\mathbf{\Omega}(t)$ and $\mathbf{\Omega}(0)$, $\mathbf{G}(\mathbf{\Omega}(t), B(0))$ becomes the probability of finding the vector $\mathbf{d}$ at the orientation $\mathbf{\Omega}(t)$ when the orientation at $t = 0$ was $\mathbf{\Omega}(0)$. The similarity to the translational diffusion case can be made apparent by considering that the rotational rate law is expressed as: $\partial\mathbf{G}/\partial t = D_R\nabla^2_\Omega G$, where D_R is the *rotational diffusion constant.* The time constant for the rotational motion is found by taking the inverse of D_R; as with most problems involving spherical motion some simplification of this expression can be realized by using spherical coordinates for the operator, ∇^2_Ω. However, this is where the simplicity ends. A full treatment of the solution can be found in many places; the monograph by Bee[32] is still the best exposition of the mathematics involving rotational diffusion. The solution is given by

$$G(\mathbf{\Omega}(t), \mathbf{\Omega}(0)) = 4\pi \sum_{l=0}^{\infty} e^{(-D_R l(l+1)t)} \sum_{m=-l}^{+l} Y_m^l(\mathbf{\Omega}(t)) Y_m^{l*}(\mathbf{\Omega}(0)) \qquad (26)$$

As usual, there are the spherical harmonics or the complex conjugates (identified by the *). This expression can be inserted into the intermediate scattering function where one gets the following expression containing the regular Bessel functions j_l:

$$F_{\text{inc}}(\mathbf{Q}, t) \propto j_0^2(Qd) + \frac{1}{\pi}\sum_{l=1}^{\infty}(2l+1)j_l^2(Qd)e^{(-D_R l(l+1))t} \qquad (27)$$

The more useful form of this expression is found by considering the incoherent scattering function obtained by taking the Fourier transform to get

$$S_{\text{inc}}(\mathbf{Q}, \omega) \propto j_0^2(Qd)\delta(\omega) + \frac{1}{\pi}\sum_{l=1}^{\infty}(2l+1)j_l^2(Qd)\frac{D_R l(l+1)}{(D_R l(l+1))^2 + \omega^2} \qquad (28)$$

where $\delta(\omega)$ is the Dirac delta function. The two terms in the above expression warrant some discussion. The first term is the elastic peak centered at $\omega = 0$ and is dependent on $\boldsymbol{Q}$, while the second term (often referred to as a *quasi-elastic* component) is a summation of Lorenztian peaks. The Lorenzian *linewidths* depend on D_R and increase with l, but are independent of $\boldsymbol{Q}$. For example, the $l = 1$ term has a linewidth equal to $2D_R$. It is noted that the *quasi-elastic* component *amplitude* depends on $\boldsymbol{Q}$ because it appears in the argument of the Bessel functions. This is an elementary description of the rotational behavior without considering the contribution due to the so-called crystal field effects that result in a much more complicated expression for the incoherent scattering function (see Ref. 32 for more details). Nonetheless, the essential features have been included, namely, an elastic and quai-elastic component of the behavior here. The barrier to rotational motion can be quantified using the temperature dependence of the quasi-elastic linewidth. It is often found that the rotational reorientation rate follows an Arrhenius behavior given by $(1/\tau) = D = D_0 e^{-(E_R/RT)}$, where E_R is the activation energy associated with the rotational motion.

2.3.3 *Bragg Diffraction and Coherent Elastic Scattering*

There have been some excellent encyclopedic contributions in the past by Cheetham[35] and Vogt[36] on crystallography and structure determinations using neutrons so, the formalism of the topic will be briefly touched on, for completeness (*see* ***Neutron Diffraction***). Equation (19) above can be written for $m = 0$ term as:

$$F_0(\mathbf{Q}, t) = \frac{1}{N}\sum_{j,k}\bar{b}_j\bar{b}_k e^{i\mathbf{Q}\cdot[\mathbf{R}_j - \mathbf{R}_k]} e^{-(W_j - W_k)} = \frac{1}{N}\left|\sum_j \bar{b}_j e^{i\mathbf{Q}\cdot\mathbf{R}_j} e^{-W_j}\right|^2 \qquad (29)$$

which is time independent. The Fourier transform of this term introduces a delta function into the scattering function which takes the form: $S_0(\mathbf{Q}, \omega) = (1/N)|\sum_j \bar{b}_j e^{i\mathbf{Q}\cdot\mathbf{R}_j} e^{-W_j}|^2\delta(\omega)$, which is equivalent to the elastic form ($\omega \to 0$ limit of $S(\mathbf{Q}, \omega)$) of the scattering function discussed earlier. The usual form of the structure factor for Bragg diffraction can be arrived at by starting with the intermediate scattering function for coherent scattering and noting that $\sum_j \overline{b_j}\langle \mathrm{e}^{i(\mathbf{Q}\cdot\mathbf{R}_j)}\rangle = \sum_j \overline{b_j}\mathrm{e}^{i(\mathbf{Q}\cdot\mathbf{R}_j)}\langle \mathrm{e}^{i(\mathbf{Q}\cdot\mathbf{u}_j)}\rangle = \sum_j \overline{b_j}\mathrm{e}^{i(\mathbf{Q}\cdot\mathbf{R}_j)}\mathrm{e}^{-\langle[\mathbf{Q}\cdot\mathbf{u}_j]^2\rangle}$. Bragg diffraction is naturally used to determine the structures of crystalline solids, but the expression can be used for systems like glasses as long as there is no diffusion and the atoms vibrate about their equilibrium positions. This expression would not be useful for a liquid since, by their very nature, the atoms diffuse in a liquid. Bragg diffraction studies can be performed on powders, where Rietveld refinements are the method of choice for data analysis. The advent of high intensity TOF powder diffractometers like General Materials Diffractometer (GEM) at ISIS have enabled structural refinements with exquisite accuracy for a wide range of materials. Figure 11 is one of numerous examples of the high quality of the diffraction pattern and an illustration of the attendant crystal structure. There are numerous monographs dedicated to the Rietveld method for extraction of detailed crystal structural information. The one by Young[37] is especially comprehensive. Bragg diffraction using neutrons can also be performed using single crystals; the review by Artioli in 2002[38] is a nice presentation. While diffraction using single crystals yields structural information with higher precision than powder diffraction, one pays the price of the increased time necessary for a single measurement which sometimes limits the studies to a few temperatures or pressures. A new generation single crystal TOF diffractometer is being constructed at the SNS where the emphasis will be on investigating a new generation of novel materials with unique properties, biomimetics, magnetic structures, soft matter, nanomaterials, thermoelectrics, and so on.

Neutron Diffraction from Layered and Two-Dimensional Systems. While single crystal surfaces and interfaces are readily studied using X-ray and electron diffraction techniques, neutrons can only be applied to such interfacial studies if high surface to volume materials can be used, or where large beam footprints are employed such as in reflectometry studies. As noted above, these studies typically involve materials like clays, mica, graphite, and silica. One of the earliest studies relevant to the discussion here is that of Warren[40] who explained how the diffraction from crystalline powders of random layer materials (like graphite and carbon blacks) exhibit diffraction patterns with characteristic lineshapes that are shaped like a sawtooth. Warren considered a model system composed of a random layer lattice structure arranged parallel and equidistant from one another, but a random translation parallel to a layer and rotation about the normal. Warren explained his results by noting that the calculated lineshape was a direct result of the powder averaging of a perfect two-dimensional (2D) reciprocal lattice of rods that correspond to the real space ''sheets'' of carbon that form the basal plane of graphite. Figure 12 shows schematically how the asymmetric sawtooth line shape arises, while Figure 13 is a plot of the diffraction pattern from a randomly oriented material that is a collection of 2D planes. This diffraction profile is often referred to as the ''Warren'' lineshape. His argument holds true for other lamellar materials as well, so it is relevant to our discussion here.

Since we are considering a 2D system, we note that this is a monomolecular system and all of the centers of mass of the molecules are in the same plane (even if individual nuclei in the molecule are not). $S(\mathbf{Q})$, introduced earlier in this chapter, therefore only depends on the component of $\mathbf{Q}$ projected onto the scattering plane, $\mathbf{Q}_{\mathrm{parallel}}$. Just as Warren did, the case of lamellar systems like graphite and mica can now be considered, assuming that the scattering system has random orientations of the crystallites about an axis normal to the basal (or 2D) plane. Because the magnitude of the parallel component of the structure factor $S(\mathbf{Q})$ is the relevant quantity

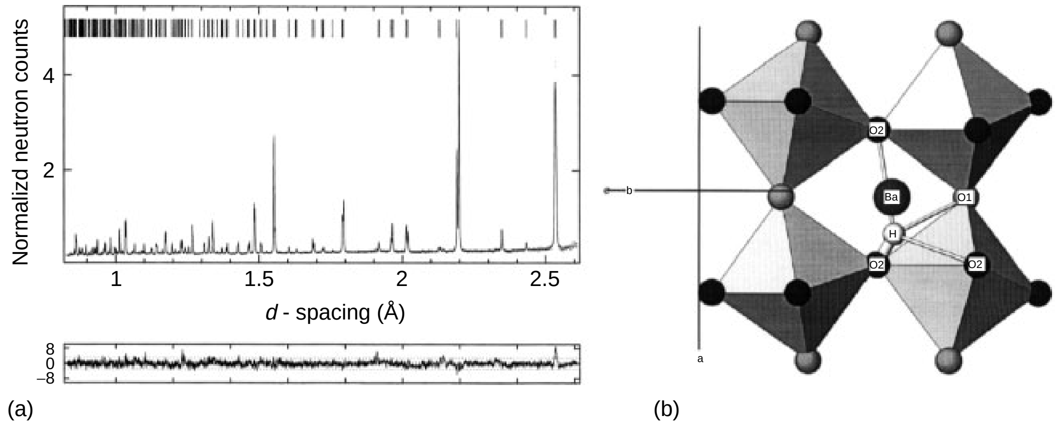

Figure 11 (a) Rietveld refinement of $BaCe_{0.9}Y_{0.1}O_{2.95}$ at 4.2 K. Observed data: dots; calculated profile: full line and difference/Estimated Standard Deviation (ESD) plot. (b) The refined structural site for the proton in $BaCe_{0.9}Y_{0.1}O_{2.95}$ at 4.2 K. (Reproduced with permission Knight[39] © 2000, Elsevier)

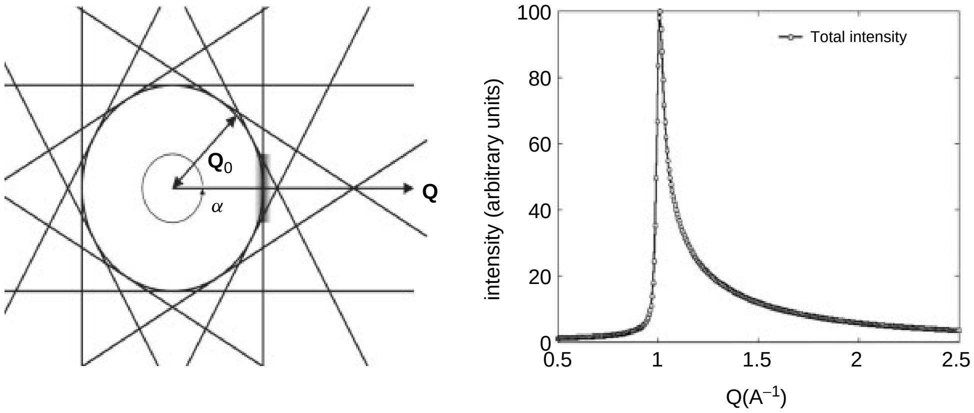

Figure 12 (a) Schematic representation of how the projection of Bragg rods leads to the asymmetric shape shown in the Warren lineshape figure illustrated in panel (b). The origin of this asymmetry is discussed in the text. This diffraction pattern uses a Lorentzian profile for the structure factor of the Bragg rod. (Reprinted with permission Arnold, Chanaa, Clarke, Cook and Larese[41] © 2006, American Physical Society)

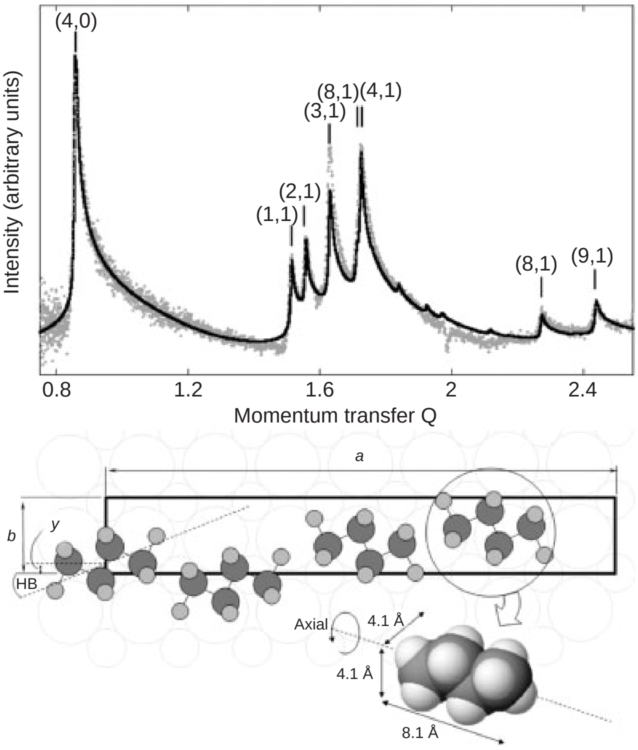

Figure 13 (a) Neutron diffraction study of the structure of a single layer of butane adsorbed to a MgO(100) surface. The sawtooth shaped peaks in the diffraction pattern indicate that the molecular film is two-dimensional. Panel (b) illustrates how the four molecules in the unit cell ($a = 29.5$ Å; $b = 4.21$ Å) are arranged. The molecules are found to ‘‘register’’ with the MgO lattice with cell a $2\sqrt{2} \times 7\sqrt{2}$ configuration[41]

we note that:

$$\mathrm{S}(\mathrm{Q}_{\text{parallel}}) = \frac{1}{2\pi}\int_0^{2\pi} S(\mathrm{Q}_{\text{parallel}},\xi)\,\mathrm{d}\xi \qquad (30)$$

where ξ is the angle made by $\mathbf{Q}_{\text{parallel}}$ with respect to an arbitrary reference direction in the scattering plane. Finally, an average must be made over the distribution of the surface normal to the individual crystallites that make up the powdered sample. Figure 14 illustrates the geometry for a single crystallite. This figure shows a crystallite (labeled as the primed coordinate system), where the surface normal (z' axis) is oriented at an angle θ with respect to the unprimed laboratory frame. The primed frame is chosen so that both the primed and unprimed y axes lie in the same plane and the z' axis lies in the *yz* plane of the lab frame. For this illustration let us chose the $\boldsymbol{Q}$ vector to be along the y axis. Hence $\mathbf{Q}_{\text{parallel}}$ can be given by:

$$Q_{\text{parallel}} = |Q\hat{y} - (Q\bullet\hat{z}')\hat{z}| = Q(1-\sin^2\theta\sin^2\phi)^{1/2} \qquad (31)$$

where $\mathbf{y}$, $\hat{z}$ and $\hat{z}'$ are unit vectors pointing along the respective primed and unprimed axes, some straightforward vector

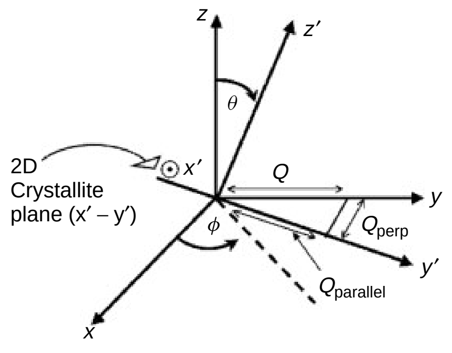

Figure 14 Scattering geometry for a 2D crystallite with the surface normal (z') tilted with respect to the fixed laboratory z axis. Note that the x' axis comes out of the plane of the paper. (Reprinted with permission Larese, Harada, Passell, Krim and Satija[45] © 1988, American Physical Society)

geometry can be used to express the unit vector $\hat{z}'$ in terms of the laboratory (unprimed) frame. If the probability distribution of the crystallite plane normals per unit solid angle is $P(\theta)$, then the fraction of plane normals within the solid angle $\sin\theta\,\mathrm{d}\theta\,\mathrm{d}\phi$ is given by their product $(P(\theta)\sin\theta\,\mathrm{d}\theta\,\mathrm{d}\phi)$ by combining our results from above and assuming that $F(\mathbf{Q})$ only depends on the magnitude of $\mathbf{Q}$, we find that the cross section can be written as:

$$\frac{\mathrm{d}\sigma}{\mathrm{d}\Omega} = B^2|F(Q)|^2 \int_0^{2\pi} \mathrm{d}\phi \int_0^{\pi} \mathrm{d}\theta \sin\theta\, P(\theta) S[Q(1 - \sin^2\theta \sin^2\phi)^{1/2}] \tag{32}$$

While this is the essence of what is required to calculate the cross section, it is noteworthy to indicate that Warren deduced that in the neighborhood of the two-dimensional reciprocal lattice vector τ_{hk} for a finite-sized 2D crystallite of coherence length, L, the structure factor can be approximated by:

$$S(\mathbf{Q}) = \rho_0 (L/a)^2 \mathrm{e}^{-[|\mathbf{Q}_{\mathrm{parallel}} - \tau_{hk}|^2 L^2/4\pi]} \tag{33}$$

Numerous authors have more recently expanded the expression for the cross section given by equation (32) in various ways. Most of this work is for determining the structure of adsorbed films on solid substrates in particular graphite. The details of these expansions can be found in Stephens *et al.*,[42] Dutta *et al.*[43] and Dimon *et al.*[44] The work of Dimon *et al.*[44] is particularly noteworthy in that it finds that a Lorentzian distribution gives a more satisfactory fit to the lineshape. Our recent experimental evidence suggests that the Lorentzian lineshape can be successfully used to describe the scattering profile of adsorbed molecular films on substrates like graphite foam and MgO where a truly random distribution of the crystallites seems to be realized. Figure 13 illustrates the overall quality of the Lorenztian lineshape description for a monolayer butane film adsorbed on MgO(100) surfaces. So far, the focus has been on describing the lineshape for 2D solid systems; however, in cases where the range of spatial correlations is restricted to near neighbor and next near neighbor coordination rings, and where translational mobility also is present (i.e., 2D liquid/fluids), these lineshapes would broaden in response to the decay of the spatial correlations. This discussion, will later indicate how inelastic and quasi-elastic scattering can be used in conjunction with diffraction to gain further microscopic information about the details of the dynamics in interfacial solids and fluids.

It is of some interest to consider the situation where one of the idealized 2D systems that have been addressed can be followed in a layer-by-layer growth mode from a strictly 2D plane to one that is more 3D like. Such is the situation in the formation of multilayer molecular films adsorbed to uniform substrates or where epitaxial metal or soft matter growth is realized in chemical vapor deposition, molecular beam epitaxy or polymeric deposition systems. The ‘‘lineshape’’ discussion above has to be modified to account for the development of the third dimension of order in the system. Conceptually this is rather straightforward. Instead of considering, as Warren[40] did, an ideal 2D reciprocal lattice composed of an ordered array of uniform rods, the reciprocal lattice for an idealized multilayer (e.g., two to five individual layers) system is characterized by

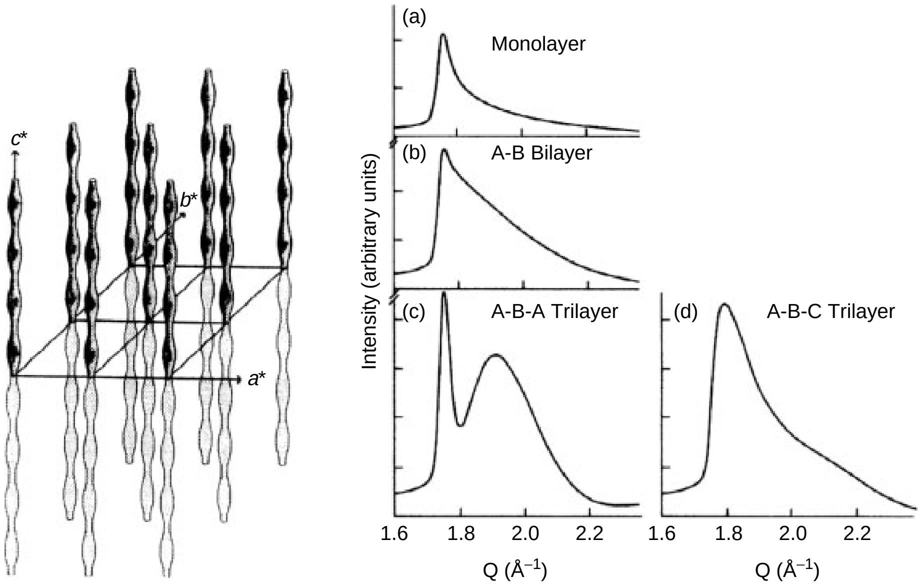

Figure 15 (left) Schematic view of a modulated lattice of rods characteristic of a spatially finite bilayer structure. (right) Model lineshape calculations for a powder-averaged diffraction profile resulting from an A-B stacking sequence for (a) monolayer, (b) bilayer, (c) trilayer thick film, (d) illustrates the diffraction profile for an A-B-C trilayer. A triangular, commensurate, close-packed structure was used in each case. The in-plane lattice spacing was the same in all cases. The interplane distance was held fixed between all layers[45]

an array of modulated rods, where the functional form of the modulation of those rods represents the details of the spatial distribution of the scatters in the direction perpendicular to the original 2D plane. Stephens *et al.*[42] considered the multilayer diffraction situation in X-ray scattering studies, while Larese and his collaborators considered how neutron scattering could be used to follow the growth and melting of atomic and molecular systems on graphite. Figure 15 illustrates how neutron diffraction (ND) patterns evolve with film thickness for the growth of ideal two- and three-layer close-packed films on the graphite basal plane.

2.3.4 Magnetic Scattering with Neutrons

The treatment presented here could be extended to address magnetic materials as well. For the sake of completeness and as an illustration, the magnetic scattering of a neutron beam (unpolarized) can be written equivalently to equation 4 presented earlier as:

$$F_{\text{magnetic}}(\mathbf{Q},\infty)=\frac{1}{N}\left|\sum_{j}\mathbf{q}_j\,p_j\,\langle \mathrm{e}^{i\mathbf{Q}\cdot r_j}\rangle\right|^2 \tag{34}$$

The vector **q** is the magnetic interaction vector given by $\mathbf{q}=\mathbf{m}/m-\mathbf{Q}(\mathbf{Q}\cdot\mathbf{m})/Q^2\mathrm{m}$, where **m** is the magnetic moment of an atom or ion. If we express the angle between the magnetic moment and the magnetic vector as α then we can write $q=|\mathbf{q}|=sin\alpha$. The magnetic scattering amplitude p is given by:

$$p=\frac{\mathrm{e}^2\gamma}{2mc^2}gJf \tag{35}$$

where γ is the magnetic moment of the neutron, e is the electronic charge, m is the neutron mass, c is the speed of light, g is the *Landé factor*, J is the total orbital angular momentum and f is the form factor (which depends on Q and has similar behavior to the X-ray atomic form factor). The product gJ is the magnetic moment of the atom. p has numerical values that are very similar to the neutron nuclear scattering length, b. While this is an extremely important field in neutron scattering, a complete discussion would be the topic for an entire article in this compendium. The formalism for magnetic scattering can be developed in a manner that parallels what has been presented here for the elastic and inelastic scattering, so that a characterization of the structure and dynamics of magnetic material could be described. Furthermore, all of the standard monographs listed at the beginning of this article provide excellent descriptions of magnetic scattering.

3 APPLICATIONS

Neutron scattering has been vital in a multitude of applications, especially as more and more scientists discover its usefulness. Traditionally, neutrons have been primarily used in inorganic chemistry as a probe for magnetic properties. Neutron sources and instrumentation continue to improve, and the impact on neutron scattering continues to broaden. As already mentioned in the text, neutron scattering has been utilized for inorganic studies in geology, magnetic ordering, hydrate and hydride compounds, and confined systems. The following briefly overviews a cross section of interesting applications of neutron scattering related to inorganic chemistry. Due to the large number of techniques and instruments that are employed around the world under the label ‘‘neutron scattering’’, this set of examples is in no way an exhaustive list, but it is intended to be a very small sample for illustrative purposes. It is therefore broken into several categories: bioinorganic, anthropological, electrochemical, engineering (stress and strain), geological, magnetic, catalysis, and rotational motion.

3.1 Bioinorganic Applications

To study complex bioinorganic systems, researchers must use a large number of complementary techniques. Neutron scattering, particularly diffraction, has been used because of the neutron's unique sensitivity to the hydrogen/deuterium element. Neutrons provide information, not only about the bioinorganic molecule, but also information about the solvation shell (water around the bioinorganic molecule). Since biological samples can be difficult to prepare, the nondestructive nature of neutron scattering has a particular appeal.

In particular, Sukumar *et al.*[46] used the Protein Crystallography Station (PCS) at LANSCE to investigate the structure of amicyanin, a Type I blue copper protein. The study was used to identify the positions of key hydrogens within the protein, something that even high resolution and high intensity studies using X rays cannot properly determine.

3.2 Anthropological Applications

An interesting application of neutron scattering techniques is the use of neutrons to determine the validity of artifacts. Because neutron scattering (specifically using thermal to cold neutrons) is a nondestructive technique, it can be utilized to probe sensitive, priceless artifacts. Leever *et al.*[47] used the GEM neutron diffractometer at ISIS to do a comparative, structural analysis of two harquebusier breastplates. In the study, it was determined that the structural makeup of the two breastplates was different; hence one was verified to date around 1600–1650 A.D., while the other was a replica from the late 19th century.

3.3 Applications Involving Electrochemical Processes

Neutron scattering experiments allow a large degree of freedom in the sample environment, since materials such as Al and V are used as windows and sample cans. This allows neutrons to be used as a probe *in situ* during chemical processes. Vivet *et al.*[48] have used ND to study the hydrogen cycle within $AB_{5+x}Ni-MH$ negative electrode materials. The hydrogen cycle is vital to the long-term performance of the electrode, hence the life of the electrochemical cell. The study shows that Fe- and Mn-substituted electrodes exhibit a three-phase process and cycle life comparable to commercial electrodes that use the more costly Co as the substitute.

3.4 Applications Involving Stress Determination in Materials

Neutrons provide a unique, nondestructive probe for determining residual stress in materials. Traditionally, laboratory-based X-ray generators were used, but because of the generally small penetration depth, only limited information is available nondestructively. Bruno *et al.*[49] have used the D1A two-axis diffractometer at the ILL to analyze the interface residual stress in Mo-coated steel gear wheels. This work was used to develop a new experimental method for similar studies.

3.5 Geological Applications

The geosciences have recently started to take advantage of neutron spectroscopy. This technique can be used to study the structure and dynamics of various complex minerals that have subtle phase transitions. Neutrons are particularly useful in studying the diffusion of hydrogen in minerals, especially the motion/dynamics of water molecules in small cavities found in various zeolites. Cole *et al.*[50] cite an example of using vibrational incoherent neutron spectroscopy. These authors display spectra of analcime in various states of hydration with a comparison to the similarly structured leuctite. These spectra show the coupling of the water molecules to the vibrations of the network of silica and alumina tetrahedra. They also show an example of a quasi-elastic spectrum that can be obtained from the rotations of water molecules in analcime. This is an example of the high resolution needed in QENS experiments.

3.6 Applications Involving Magnetic Materials

Neutron scattering is a powerful method for studying the spin structure and spin excitations of magnetic materials. Mirbeau *et al.*[51] utilized the TOF spectrometer, IN5, at the ILL to study the energy sublevels, spin structure, and spin excitations of Mn_{12}-acetate magnetic nanoclusters. Determination of energy level spacing allowed for the identification of higher order terms in the spin Hamiltonian. The relative intensity of low energy peaks can be used to determine the zero field coefficient of the Hamiltonian.

Polarized neutrons may be utilized to measure magnetic ordering. Mook *et al.*[52] investigated magnetic ordering of $YBa_2Cu_3O_{6.45}$ using the SPINS spectrometer at NCNR (NIST Center for Neutron Research), the IN20 spectrometer at ILL, and Oak Ridge National Laboratory's HB-1 spectrometer. Researchers obtained results which indicate that a small magnetic moment is present, primarily in the *c*-axis direction, at a temperature less than 200 K.

3.7 Applications Involving Catalysis

Various types of neutron scattering can be utilized to extract data on structure and dynamics for novel catalytic materials. By selectively deuterating an SSZ-13 zeolite, Cheetham and others[41] used ND performed on the Dual Beam Neutron Spectrometer (DUALSPEC) diffractometer at the Chalk River Laboratories and found that two acid sites are present in the unit cell of the zeolite. INS can be used to probe the mechanism of the catalytic reaction by looking at the change in the vibrational modes of the adsorbed molecules on the surface. Lennon *et al.*[53] found that the interaction of HCl with a η-alumina catalyst results in the dissociative adsorption of HCl, in which the hydroxyl groups terminally bound to Al are replaced by chlorine. INS spectra reveal an in-plane deformation mode, δ (OH), that can be resolved into two bands located at 990 and 1050 cm^{-1}.

3.8 Applications Involving Rotational Tunneling

Quantum rotational tunneling can be observed in thin adsorbed films using INS. Larese *et al.*[45,54] have used INS to probe the free rotor line of methane for an adsorbed methane film on MgO(100) nanocubes. At monolayer coverage of methane, the MgO substrate restricts the free rotation of the molecules; hence there are no free rotation signals. Formation of a second layer causes the first layer of molecules to move slightly further away from the surface, effectively lowering the overall interaction of the first layer molecules with the surface. This reduces the overall attractive hold the substrate has on the near-surface molecules. Molecules in the second layer are further from the surface, and thereby naturally experience a lower attraction to the surface and a lower barrier to rotation. The origin of the two signals in the neutron spectrum are likely due to hindered rotations of molecules in the near-surface layer (peak near 0.9 meV) and the molecules in the second layer (peak near 1 meV). Methane molecules in the first layer, not covered by molecules in the second layer, still experience a large barrier to rotation. Finally, the bulklike neutron signals near 1.1 meV, that appear with the addition of third layer of molecules, can be traced to the basic building block of the face centered cubic (fcc) solid (i.e., the three-layer A-B-C stacking arrangement). It is not surprising that this is the thinnest film where an interaction potential for a *fcc* solid could be realized. These results represent the first direct evidence of how combined adsorption studies and neutron measurements of the rotational dynamics can be used to examine the thickness dependence of the intermolecular and the molecule–substrate interaction potentials.

4 ABBREVIATIONS AND ACRONYMS

DFT = density functional theory; DUALSPEC = dual beam neutron spectrometer; ESD = estimated standard deviation; fcc = face centered cubic; GEM = general materials diffractometer; HFBR = high flux beam reactor; HFR = high flux reactor; ILL = institute laue langevin; *INS = inelastic neutron scattering*; KENS = KEK neutron source; LANSCE = los alamos neutron science center; NIST = National institute of standards and technology; RF = radiofrequency; QENS = quasi-elastic neutron scattering; SNS = spallation neutron source; TOF = time-of-flight; $N(E)$ = spectral distribution; E = energy; N = number; k = Boltzmann's constant; T = temperature; $\boldsymbol{k}$ = wave vector; $\boldsymbol{Q}$ = scattering vector; $\boldsymbol{k}_i$, $\boldsymbol{k}_f$ = incident, final wave vector; ω = angular frequency; $S(\boldsymbol{Q}, \omega)$ = dynamical structure scattering factor; $\mathbf{r}_j$ = jth particle positon; t = time; $\rho_j(\mathbf{Q}, t)$ = Fourier transform of the spatial component of the number density; δ = Dirac delta function; $f_{jk}(Q, t)$ = cross-correlation function; b_j = scattering length of nucleus j; $F(\mathbf{Q}, t)$ = intermediate scattering function or structure factor; $F_{\mathrm{coh}}(\mathbf{Q}, t)$ = coherent term of intermediate scattering function; $F_{\mathrm{inc}}(\mathbf{Q}, t)$ = incoherent term of intermediate scattering function; σ_j^{inc} = incoherent scattering cross section of jth nucleus; σ_j^{coh} = coherent scattering cross section of jth nucleus; $G(\mathbf{r}(t), \mathbf{r}(0))$ or G = probability distribution function; $\mathbf{r}(t)$ = position at time t; $\mathbf{r}(0)$ = position at time 0; $p(\mathbf{r})$ = probability of finding the atom at position, $\mathbf{r}$, at time, $t = 0$; $\mathbf{R}_j$ = average position of atom j; $\mathbf{u}_j(t)$ = instantaneous displacement of atom j from its average position; $\mathbf{e}^{-\mathrm{Wj}}$ = normal thermal factor; $Q(\boldsymbol{k}, \nu)$ = normal mode coordinate for a phonon of wave vector $\boldsymbol{k}$ and branch n; $\mathbf{e}_j(\boldsymbol{k}, \nu)$ = normalized vector representing relative displacements of each atom; $\mathrm{F}_\nu(\mathbf{Q})$ = phonon structure factor component; $\omega(\boldsymbol{k}, n)$ = angular frequency as a function of wave vector; $\mathrm{n}(\omega)$ = number of phonons of frequency ω; $\mathbf{R}(t)$ = position of the center of mass of H_2; $\mathbf{d}(t)$ = position of the hydrogen atom relative to the molecular center of mass; $\mathbf{u}(t)$ = vibrational motion of the atom about its ''average'' position; D = diffusion constant consistent with the *Fickian* diffusion; r = modulus of $\mathbf{r}$; d = constant radius; $\boldsymbol{\Omega} = (\theta, \phi)$ = polar angle; $\mathbf{G}(\Omega(t), B(0))$ = probability of finding the vector $\mathbf{d}$ at the orientation $\Omega(t)$ when the orientation at $t = 0$ was $\Omega(0)$; $\partial\mathbf{G}/\partial t$ = rotational rate law; D_R = rotational diffusion constant; τ = time constant; $\mathrm{E_R}$ = activation energy associated with rotational motion; μ = magnetic moment; $\mathrm{m_n}$ = mass of a neutron; MeV = megaelectron volt.

5 FURTHER READING

G. E. Bacon, 'Neutron Diffraction', Oxford University Press, 1962; and G. E. Bacon, 'Neutron Diffraction', Clurendon Press, 1975, Gives an overview of neutron scattering methods from both pulsed and reactor sources. Also provides some experimental examples.

R. Pynn, The Mathematical Foundations of Neutron Scattering, 1990, http://www./as.org/sgp/othergov/&e/lanVplits/00326652.pdf. A beginners text on the mathematical foundations of neutron scattering primarily from pulsed sources.

G. Shirane, S. M. Shapiro and J. M. Transquada, 'Neutron Scattering with a Triple-Axis Spectrometer', Cambridge University Press, 2002. A through text on neutron scattering with a triple-axis spectrometer.

G. L. Squires, 'Introduction to the Theory of Thermal Neutron Scattering', Dover Press, 1996. A more advanced treatise on the mathematical foundations of thermal neutron scattering.

R. Wenk, *Rev. Mineral. Geochem.*, 2006, **63**, 313. An excellent volume that addresses the current use of neutron scattering techniques in the field of geochemistry and mineralogy, used as the textbook for a weeklong student tutorial.

C. Windsor, 'Pulsed Neutron Scattering', Halsted Press, 1981. An excellent text on all aspects of pulsed neutron scattering, including applications.

6 REFERENCES

1. H. G. Buettner, E. Lelievre-Berna and F. Pinet 'The Yellow Book', Institute Laue Langevin, 2005.
2. G. Squires, 'Introduction to the Theory of Thermal Neutron Scattering', Dover Press, 1996.
3. T. E. Mason, T. E. Mason1, R. K. Crawford1, G. J. Bunick1, A. E. Ekkebus1 and D. Belanger, *Appl. Phys. A: Mater. Sci. Process.*, 2002, **74**(Suppl., Pt. 1), S11.
4. S. Ikeda, Present status of KENS, 'JAERI-Conference', Tsukuba, Japan, 2001–2002, p. 93 (International Collaboration on Advanced Neutron Sources, 2000, Volume 1).
5. W. G. Marshall and S. W. Lovesey, in 'Theory of Thermal Neutron Scattering: The Use of Neutrons for the Investigation of Condensed Matter', '*The International Series of Monographs on Physics*', ed. W. G. Marshall and D. H. Wilkinson, Clarendon Press, Oxford, 1971.
6. S. W. Lovesey, 'Theory of Neutron Scattering from Condensed Matter', '*The International Series of Monographs on Physics*', Vol. 1, Clarendon Press, Oxford, 1984.
7. G. E. Bacon, 'Monographs on the Physics and Chemistry of Materials: Neutron Diffraction', Oxford University Press, 1975, p. 650.
8. G. L. Squires, 'Introduction to the Theory of Thermal Neutron Scattering', Cambridge University Press, 1978, p. 260.
9. L. van Hove, *Phys. Rev.*, 1954, **95**, 249.
10. V. F. Sears, *Neutron News*, 1992, **3**(3), 26.
11. S. L. Chaplot, N. Choudhury, S. Ghose, M. N. Rao, R. Mittal and P. Goel, *Eur. J. Mineral.*, 2002, **14**(2), 291.

12. D. Colognesi, A. J. Ramirez-Cuesta, M. Zoppi, R. Senesi and T. Abdul-Redah, *Physica B: Condens. Matter(Amsterdam, Netherlands)*, 2004, **350**(1–3, Suppl. 1), e983.
13. E. R. Cowley and A. K. Pant, *Acta Crystallogr., Sect. A: Cryst. Phys. Diffr. Theor. Gen. Crystallogr.*, 1970, **26**(Pt. 4), 439.
14. H. Schober, D. Strauch and B. Dorner, *Z. Phys. B: Condens. Matter*, 1993, **92**(3), 273.
15. D. Strauch and B. Dorner, *J. Phys.: Condens. Matter*, 1993, **5**(34), 6149.
16. K. R. Rao, S. L. Chaplot, N. Choudhury, S. Ghose, J. M. Hastings, L. M. Corliss and D. L. Price, *Phys. Chem. Miner.*, 1988, **16**(1), 83.
17. S. Ghose, J. M. Hastings, N. Choudhury, S. L. Chaplot and K. R. Rao, *Physica B: Condens. Matter(Amsterdam, Netherlands)*, 1991, **174**(1–4), 83.
18. G. Artioli, A. Pavese and O. Moze, *Am. Mineral.*, 1996, **81**(1–2), 19.
19. B. Winkler and W. Buehrer, *Phys. Chem. Miner.*, 1990, **17**(5), 453.
20. R. Mittal, S. L. Chaplot, R. Parthasarathy, M. J. Bull and M. J. Harris, *Phys. Rev. B: Condens. Matter Mater. Phys.*, 2000, **62**(18), 12089.
21. G. Shirane, S. M. Shapiro and J. M. Transquada, 'Neutron Scattering with a Triple-Axis Spectrometer: Basic Techniques', Cambridge University Press, 2002, p. 273.
22. R. Mittal, S. L. Chaplot, N. Choudrury, C. K. Loong, *Phys. Rev. B: Condens. Matter Mater. Phys.*, 2000, **61**(6), 3983.
23. A. Pavese, G. Artioli and O. Moze, *Eur. J. Mineral.*, 1998, **10**(1), 59.
24. M. N. Rao, S. L. CHaplot, R. T. Azuah, W. T. Montfrooij, N. Choudhury, K. R. Rao and S. M. Bennington, *Phys. Rev. B*, 1999, **60**(17), 12061.
25. N. Choudhury, S. Ghose, C. Pal Chowdhury, C. K. Long and S. L. Chaplot, *Phys. Rev. B*, 1998, **58**(2), 756.
26. D. L. Price, S. Ghose, N. Choudhury, S. L. Chaplot and K. R. Rao *Physica B: Condens. Matter(Amsterdam, Netherlands)*, 1991, **174**(1–4), 87.
27. M. T. Dove, M. S. Craig, D. A. Keen, W. G. Marshall, S. A. T. Redfern, K. O. Trachenko and M. G. Tucker, *Mineral. Mag.*, 2000, **64**(3), 569.
28. E. C. Svensson, B. N. Brockhouse and J. M. Rowe, *Phys. Rev.*, 1967, **155**(3), 619.
29. V. J. G. S. Minkiewicz and R. Nathans, *Phys. Rev.*, 1967, **162**, 528.
30. E. J. Samuelsen and G. Shirane, *Phys. Status Solidi*, 1970, **42**(1), 241.
31. B. Winkler, M. J. Harris, R. S. Eccleston, K. Knorr and B. Hennion, *Phys. Chem. Miner.*, 1997, **25**(1), 79.
32. M. Bee, ''Quasielectric Neutron Scattering. Principles and Applications in Solid State Chemistry, Biology, and Materials Science'', Adam Hilger, 1988, p. 437.
33. R. Hempelmann, ''Quasielastic Neutron Scattering and Solid State Diffusion'', '*Oxford Series on Neutron Scattering in Condensed Matter*', Vol. 13, Oxford University Press, Oxford, 2000.
34. P. C. H. Mitchell, S. F. Parker, J. Tomkinson and A. J. Ramirez-Cuesta in ''Vibrational Spectroscopy with Neutrons with Applications in Chemistry, Biology, Materials Science and Catalysis'', '*Series on Neutron Techniques and Applications*', Vol. 3, eds. J. L. Finney and D. L. Worcester, World Scientific, 2005.
35. A. K. Cheetham, in ''The Encyclopedia of Inorganic Chemistry'', ed. R. B. King, Wiley, 1994.
36. T. Vogt, in ''The Encyclopedia of Inorganic Chemistry'', 2nd edition, ed. R. B. King, John Wiley & Sons, 2005.
37. R. A. Young, in ''The Rietveld Method'', '*International Union of Crystallography: Monographs on Crystallography*', ed. R. A. Young, Oxford University Press, 1993.
38. G. Artioli, *Eur. J. Mineral.*, 2002, **14**(2), 233.
39. K. S. Knight, *Solid State Ionics*, 2000, **127**, 43.
40. B. E. Warren, *Phys. Rev.*, 1941, **59**, 693.
41. T. Arnold, S. Chanaa, S. M. Clarke, R. E. Cook and J. Z. Larese, *Phys. Rev. B*, 2006, **74**, 085421.
42. P. W. Stephens, P. A. Heiney, R. J. Birgeneau, P. M. Horn, D. E. Moncton and G. S. Brown, *Phys. Rev. B: Condens. Matter Mater. Phys.*, 1984, **29**(6), 3512.
43. P. Dutta and S. K. Sinha, *Phys. Rev. Lett.*, 1981, **47**(1), 50.
44. P. Dimon, P. M. Horn, M. Sutton, R. J. Birgeneau and D. E. Moncton, *Phys. Rev. B: Condens. Matter Mater. Phys.*, 1985, **31**(1), 437.
45. J. Z. Larese, M. Harada, L. Passell, J. Krim and S. Satija, *Phys. Rev. B: Condens. Matter Mater. Phys.*, 1988, **37**(9), 4735.
46. N. Sukumar, P. Langan, F. S. Mathews, L. H. Jones, P. Thiyagarajan, B. P. Schoenborn and V. L. Davidson, *Acta Crystallogr., Sect. D: Biol. Crystallogr.*, 2005, **D61**(5), 640.
47. S. Leever, D. Visser, W. Kockelmann and J. Dik, *Physica B: Condens. Matter(Amsterdam, Netherlands)*, 2006, **385**, 542.
48. S. Vivet, M. Latroche, Y. Chabre, J.-M. Joubert, B. Knosp and A. Percheron-Guegan, *Physica B: Condens. Matter(Amsterdam, Netherlands)*, 2005, **362**(1–4), 199.
49. G. Bruno, C. Fanara, D. J. Hughes and N. Ratel, *Nucl. Instrum. Methods Phys. Res. Sect. B: Beam Interact. Mater. At. B*, 2006, **246**, 425.
50. D. R. Cole, K. W. Herwig, E. Mamontov and J. Z. Larese *Rev. Mineral. Geochem.*, 2006, **63**, 313.
51. I. Mirebeau, M. Hennion, H. Casalta, H. Andres, H. U. Gudel, A. V. Irodova and A. Caneschi, *Phys. Rev. Lett.*, 1999, **83**(3), 628.

52. H. A. Mook, P. Dai, S. M. Hayden, A. Hiess, S.-H. Lee and F. Dogan, *Phys. Rev. B*, 2004, **69**, 134509.
53. A. R. McInroy, D. T. Lundie, J. M. Winfield, C. C. Dudman, P. Jones, S. F. Parker and D. Lennon, *Catal. Today*, 2006, **114**(4), 403.
54. J. Z. Larese, Neutron Scattering Investigations of the Dynamics of Thin Films Adsorbed on Solid Surfaces, 'Materials Research Using Cold Neutrons at Pulsed Neutron Sources, [Proceedings]', Argonne, Aug. 25–26, 1997, 1999, p. 57.

Nuclear Magnetic Resonance (NMR) Spectroscopy of Inorganic/Organometallic Molecules

Jonathan A. Iggo, Jianke Liu and Yaroslav Z. Khimyak

University of Liverpool, Liverpool, UK

Method Summary 1
1 Introduction 3
2 Technical Background 4
3 Applications 8
4 End Note 38
5 Abbreviations and Acronyms 38
6 Further Reading 38
7 References 39

METHOD SUMMARY

Acronyms, Synonyms

- PMR (Proton Magnetic Resonance) — obsolete.

Measured physical quantities

- Transitions between nuclear spin energy levels are modulated by:
  - chemical shift and chemical shift anisotropy
  - scalar and quadrupolar coupling between spins
  - exchange between spins
  - relaxation times (T_1, T_2, $T_{1\rho}$).

Information available

- number of *types* and number of *each type* of NMR active nuclide present
- relative *disposition* of NMR active groups
- *exchange rates* and *pathways* between sites
- *distance* between NMR active nuclei
- *reaction pathways*
- *ion pairing* and *ion contacts*
- spectra can be *quantitative*
- mobility and molecular dynamics both in solution and in solids
- long and short range order in crystalline, amorphous, multiphase and micro-heterogeneous materials
- imaging of flow and diffusion in catalytic pellets and reactors
- diffusion coefficients, dispersion and flow hydrodynamics.

Information not available, limitations

- useful NMR active nuclei not available for all important transition metals and ligand donors
- relatively low sensitivity
- relatively long NMR timescale, ca 10^{-7} s, limiting routine detection to long-lived species and slow-exchange rates

- quadrupolar nuclei giving broad lines and paramagnetism causing extreme line broadening
- very broad ^{1}H lines in solid-state NMR due to very strong (ca. 100 kHz) homonuclear dipolar interactions
- very long T_1 relaxation times for rare (^{13}C, ^{29}Si) and ''large'' (^{207}Pb, ^{112}Cd, etc.) spin-1/2 nuclei in solid-state NMR
- only first-order quadrupolar interactions for $I = (2n + 1)/2$ quadrupolar nuclei (i.e., ^{27}Al, ^{23}Na, ^{51}V, ^{11}B) efficiently eliminated by MAS.

Examples of questions that can be answered

- What is the chemical environment of the nuclide (via the chemical shift)?
- What neighbours does the nuclide have (via the scalar coupling)?
- What is the topology of the molecule (via scalar couplings and correlation spectroscopy)?
- Is chemical exchange or ligand dynamics occurring (via variable temperature or saturation transfer measurements)?
- Are these groups proximal in space (via Overhauser spectroscopy)?
- Is a reaction occurring (via e.g., in situ methods, isotopic labelling, *para*-hydrogen)?
- How many crystallographically nonequivalent sites (with similar chemical environment) are present in the structure?
- What is the content of the amorphous phase in the material?
- What is the distance between different nuclei in a solid (via measurements of heteronuclear dipolar coupling constants)?
- Are any domains present in a solid and what are their sizes?
- What are the transport properties of a porous catalyst and its structure?

Major advantages

- NMR can obtain direct structural information on solution, semiliquid, gel, crystalline and amorphous samples.
- The technique is multinuclear and nuclide-selective; no resonances from other nuclides appear in the spectra.
- Topology of the NMR active parts of the molecule can be obtained directly from the spectra.
- Structure of (the NMR active parts of) molecules can be deduced with confidence.
- Topology of the exchange and reaction pathways of the NMR active parts of the molecule can be obtained directly from the spectra.
- The through-space interactions can be probed via Overhauser spectroscopy.
- Instantaneous excitation of spins is possible, allowing complex systems to be simplified using two-dimensional techniques.
- Presence of protons in solid materials can be useful for the enhancement of the signal of rare spins via cross-polarisation.

Major disadvantages

- The low sensitivity requires (relatively) high concentration samples and (relatively) long acquisition times for most *inorganic* samples.
- The spectra of paramagnetic samples are not easily obtainable.
- Little or no direct information about NMR inactive sites, for example, (effectively) all halides except ^{19}F, is available.
- A *unique* determination of metal environment may depend on inductive effects and experience.
- High-resolution spectra, in which all sites are resolved, are only obtained
  - in solution or in the gas phase,
  - for spin 1/2 nuclides,
  - in the slow-exchange limit.

Sample/Instrument constraints

- Depending on spectrometer field and the nuclide under study, sample concentrations, in solution, of $0.1 \sim 400$ mM are typically required to give spectra of good quality in reasonable ($2 \sim 300$ min) time; two-dimensional spectra do not require higher sample concentrations.
- For solid-state NMR measurements at least ca. 80 mg (4 mm rotor) or ca 25 mg (2.5 mm rotor) of sample is needed.
- Signal-to-noise improves linearly with sample strength and as the square of number of transients recorded.
- Degassed samples are usually preferred for experiments studying relaxation phenomena.
- Degassed samples may require inconveniently long recovery delays in two-dimensional experiments.
- Most inorganic samples can be successfully studied at moderate strengths of magnetic field (9.4 T; $^{1}\text{H} = 400$ MHz). Higher field spectrometers may cause chemical shift anisotropy broadening with some nuclei (e.g., ^{31}P).
- Field gradient techniques are not always preferred for 2D spectra of inorganic samples (e.g., HMQC).
- Good shimming is essential.

- Vibration may destroy the desired signal in 2D experiments.
- Magic-angle spinning is essential for practically all solid-state NMR experiments implying:
  - very fast spinning rates are needed to significantly improve ^{1}H resolution,
  - static NMR is very useful for spin-1 quadrupolar nuclei.
- High-power *rf* fields (ca. 100 kHz) are essential both for the observing and decoupling channels.

1 INTRODUCTION

NMR spectroscopy is today perhaps the most widely used spectroscopic tool in inorganic chemistry for the characterization of inorganic compounds. The power of NMR spectroscopy in the characterization of unknown compounds follows from the sensitivity of the chemical shift to the chemical environment and the presence of scalar couplings between spins that allow the topology of the spin system to be mapped. Recently solid-state NMR has grown into an indispensable method for the determination of the structure and dynamics of organic solids, inorganic materials, and composites. In addition to information on the molecular structure (similar to the high-resolution NMR), solid-state NMR can probe the organization of a material in the solid state without any need for its dissolution. The initial solid-state NMR methodology[1,2] aspired to acquire spectra with resolution, comparable to that in the solution high-resolution NMR spectra, by the elimination of a significant line broadening due to the presence of anisotropic magnetic interactions (using magic-angle spinning (MAS), high-power heteronuclear decoupling etc.). These interactions (i.e., dipolar couplings, chemical shift anisotropy (CSA), quadrupolar coupling) are averaged out in liquids due to the rapid molecular tumbling.[3,4] Modern solid-state NMR methods employ these interactions to derive structural information about a solid under study, often not available from other characterization techniques. Applications of solid-state NMR in catalysis range from the determination of the structure of heterogeneous catalysts,[5] understanding of the interactions between the surface of the pores and guests,[6] and also monitoring catalytic transformations in situ.[7,8]

A description of the theoretical basis of solid-state NMR spectroscopy is beyond the scope of this article. Nevertheless, such knowledge is essential for the understanding the main concepts of solid-state NMR and is extensively covered by recent reviews and books.[4,9,10] The anisotropic magnetic interactions, responsible for the significant broadening of the lines, can be described by the respective Hamiltonians. Generally, both the geometric and spin parts in these Hamiltonians can be used to eliminate their effects on the overall appearance of the spectra or reintroduce specific interactions via the manipulation of a pulse program. For instance, in the heteronuclear dipolar coupling Hamiltonian for the $I-S$ spin pair (equation 1, Figure 1):

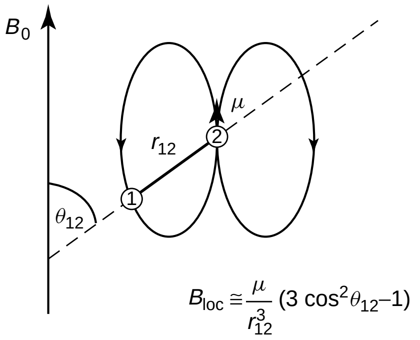
B_0
μ
r_{12}
②
①
θ_{12}
$B_{\mathrm{loc}} \cong \frac{\mu}{r_{12}^3}(3\cos^2\theta_{12}-1)$

Figure 1 Heteronuclear dipolar interactions

$$\hat{H}_D^{hetero} = -\mathrm{d}_{IS}(3\cos^2\theta - 1)\hat{I}_Z\hat{S}_Z,\ \mathrm{d}_{IS} = \frac{\mu_0}{4\pi}\frac{\hbar^2\gamma_I\gamma_S}{r_{IS}^3} \qquad (1)$$

d_{IS} is the dipolar coupling constant depending on the $I-S$ distance r_{IS} and gyromagnetic ratios (γ); $\hat{I}_z$ and $\hat{S}_z$ are the projections of spin operators for I and S spins on the z-axis.

The geometric part of the heteronuclear dipolar coupling Hamiltonian is as follows:

$$H_{D(geom)}^{hetero} = -\mathrm{d}_{IS}(3\cos^2\theta - 1) \qquad (2)$$

and includes both the $I-S$ intermolecular distance and the part depending on the orientation of the intermolecular vector with respect to the external magnetic field B_0. The term $(3\cos^2\theta - 1)$ is also present in the Hamiltonians describing chemical shift anisotropy, homonuclear dipolar interactions and first-order quadrupolar interactions.

The aim of this applications article is not to review the spectroscopic information in the literature—such a task is clearly beyond the scope of any review—but rather to guide the reader through the application of multipulse and two-dimensional techniques both in solution and the solid state that the author have found particularly useful in studying inorganic systems. The goal is to provide enough background to allow the reader to determine the applicability of NMR to new inorganic research problems and enough technical advice to get started on the right experimental path. Readers interested in application of NMR to biological inorganic chemical problems should *see* ***Nuclear Magnetic Resonance (NMR) Spectroscopy of Metallobiomolecules***.

2 TECHNICAL BACKGROUND

2.1 Acquisition of the NMR Spectrum of an ‘‘Inorganic’’ Nuclide

Setting up an NMR spectrometer to observe an ‘‘inorganic’’ nuclide, X, is little different from setting up for observation of carbon-13; a known sample, giving a ‘‘strong’’ signal should be selected and a trial spectrum recorded. The 90° transmitter and decoupler pulses are then measured. There are, however, a few wrinkles. Although IUPAC have issued recommended reference *frequencies* for all nuclei, these are not in universal use, so the chemical shift given in the literature for the selected test compound may be on a ‘‘different’’ ppm scale and hence not appear at the ‘‘expected’’ position (or, indeed, at all) in the spectrum. Furthermore, the receptivity of the desired nucleus may be so low that a suitable test sample for direct observation and measurement of the 90° pulse simply does not exist. This section seeks to offer guidance on what to do in these situations.

2.1.1 The Spectrometer

- Is the spectrometer capable of measuring nuclide X, or is it ^{1}H and ^{13}C only? Ask *and* check the hardware yourself.
- Has anyone measured nuclide X on this spectrometer before? It might seem obvious, but ask!
- Can the probe be tuned to the nuclide of interest?
- Is the probe direct, or inverse? The former is good for direct observation with or without INEPT enhancement. The latter will give poor signal-to-noise in direct experiments since the sample does not fill the coil space, but is much preferred for indirect detection via, for example, a heteronuclear multiple quantum coherence (HMQC) or heteronuclear single quantum coherence (HSQC) experiment.
- Is the spectrometer/probe capable of variable temperature operation? Dynamic samples need to be measured at low temperatures to freeze out the dynamic processes. Quadrupolar nuclei are often best observed at high temperatures; the increased molecular tumbling rates help to average out the quadrupolar line-broadening interaction.
- Finally, what is the ^{1}H frequency? In common parlance spectrometers are referred to as a ‘‘400’’, or ‘‘360’’, or ‘‘500’’. However, this does not usually correspond to the actual spectrometer ^{1}H frequency. For example, the default frequency of a Bruker spectrometer is 0.13 MHz above this, that is, 400.13 MHz, etc. Furthermore, the frequency may have been shifted ±0.07 MHz from the default value during installation to prevent interference with another, nearby spectrometer of the same nominal ^{1}H frequency.
    - It is very unlikely that the protons of tetramethylsilane (TMS) will resonate at exactly the notional spectrometer frequency. *Measure* a proton spectrum of a standard sample containing TMS and note the absolute TMS frequency. Compare this with the spectrometer’s base ^{1}H frequency.
    - Use the *measured value* (in the appropriate lock solvent) in calculating the observation frequency for other nuclides on the IUPAC scale. Best of all, add TMS to the sample of interest (if it’s compatible) and record a ^{1}H NMR spectrum as well.

2.1.2 The Test Sample

- Always use a test sample of known chemical shift. It is usually unwise to attempt the first observation on the ‘‘real’’ sample of interest. If no suitable test sample exists because of low sensitivity, see the section on determining pulse lengths in adverse situations in the subsequent text.
- Was the chemical shift in the literature measured on the IUPAC scale or some other scale?
- Calculate the expected absolute frequency on the IUPAC scale for the test sample *versus* the *measured* absolute frequency of TMS on your spectrometer.
- Use a short pulse length and moderate power hard pulse—check what has been used before for nuclides of similar γ. Once you have found the signal of interest, measure the 90° transmitter pulse. Measure several pulses of different length; you should observe a sinusoidal variation in the intensity of the NMR resonance (Figure 2).
    - If the intensity reaches a plateau as the pulse length increases, or varies randomly, then the probe is ‘‘breaking down’’. Reduce the pulse power and try again.
    - If the intensity initially varies sinusoidally but then the sinusoidal envelope ‘‘stretches’’ as the pulse length

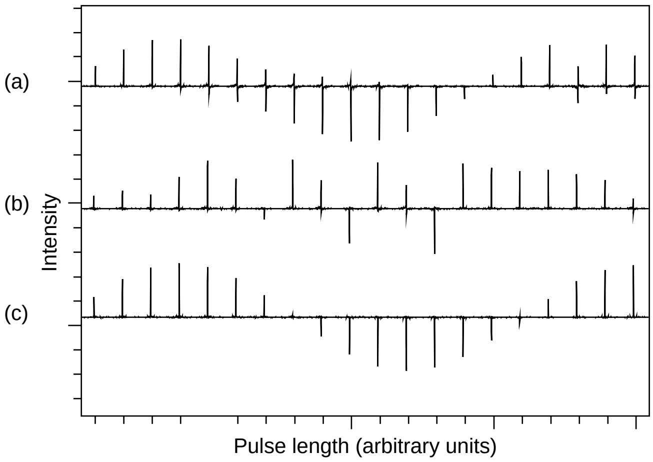

Figure 2 ^{119}Sn 90° transmitter pulse measurement. SnMe$_4$ in CDCl$_3$. (a) Signal 100 ppm off-resonance gives phase distortion, which can be severe, as pulse length varies. (b) Probe breakdown gives random intensity variations. (c) Correct

increases, you are not allowing a sufficient recovery delay between measurements. Increase the recovery delay or add a relaxation agent such as $Cr(acac)_3$.

2.1.3 The 90° Decoupler Pulse

Two situations now confront the inorganic chemist—interest in $^1H\{X\}$ direct and ^1H,X indirect spectroscopy; in these cases the X decoupler pulses will be on the first decoupler channel; or interest in samples where neither nuclide is proton? In this case, the X decoupler pulses will be on the second decoupler channel, variously denoted, ''second decoupler channel'', ''Y channel'', ''f3'', etc. *Consult* the manufacturer's applications department for advice if you are not sure.

$^1H\{X\}$ Direct and ^1H, X Indirect Spectroscopy. This is no different from setting up the decoupler pulses for $^1H\{^{13}C\}$—you will need a sample in which ^1H couples to X.

- Use the appropriate pulse sequence provided by the manufacturer (DECP90 on Bruker machines).
- Tune the probe to the correct frequencies. For low γ nuclei, or nuclei with very large chemical shift ranges, make sure the probe is tuned for the resonance frequency of the sample you are using, for example, the chemical shift range of ^{103}Rh can exceed the width of the probe resonance.
- Position the relevant resonances of ^1H in the center of the spectrum (to avoid phase shifts as the pulse length increases) and set the decoupler frequency so that X is on-resonance. Make sure you are using a ^1H 90° pulse and that the mixing delay is set to $1/2J_{HX}$. Start with the X pulse power determined above and a *shorter* X pulse length. Increase the X pulse length and look for the *zero* crossing. This corresponds to the decoupler 90° *pulse*, NB *not* the 180° pulse.
- Check the probe is not mismatching on the X channel.
- Make sure that the phase of the lines of the multiplet inverts as you go through the zero crossing point (Figure 3). If the phase does not invert, then you are probably far off-resonance for nucleus X. Double check the X channel is on-resonance—is your test sample's chemical shift on the IUPAC scale or some other? Is the manufacturer's default X frequency on the IUPAC scale or some other? Has someone changed the default X frequency on your spectrometer? Start again.

X, Y Indirect Spectroscopy. The easiest way to measure the 90° pulse on the second decoupler channel is to use the same sample as above, but switch the X nucleus from the first to the second decoupler channel. Load the appropriate, manufacturer supplied pulse program; on Bruker machines this is DECP90F3. Proceed as above.

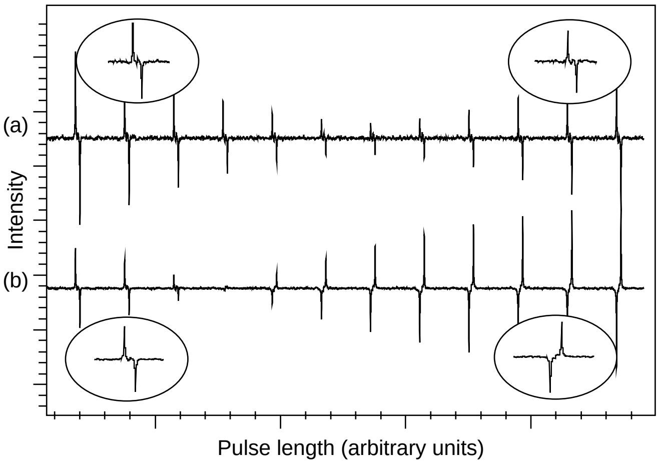

Figure 3 ^{15}N 90° decoupler pulse measurement via ^{31}P, using Bruker pulse program DECP90F3, sample $[Pt(C_5H_5{}^{15}N)(PPh_3)Cl_2]$ in d_8-THF. (a) decoupler off-resonance—antiphase doublet does not invert, gives a false result. (b) decoupler on-resonance, correct

If no suitable sample is available to measure the decoupler pulse via ^1H, then use a sample containing an XY spin pair, where X gives a strong signal showing coupling to Y. Observe X and decouple Y. Centre the resonances of X in the observation window. Use an X 90° transmitter pulse and set the mixing delay to $1/2J_{XY}$. Use DECP90F3 or the equivalent, manufacturer supplied pulse program. Proceed as above.

2.1.4 Determining Pulse Lengths in Adverse Situations

If the nuclide is of very low receptivity and/or low natural abundance, is there a nuclide of approximately the same γ and of reasonable receptivity that will allow pulse lengths that are ''good enough'' to be measured? For example, $GeMe_4$ is a good substitute to measure the 90° transmitter pulse for nuclides with resonance frequencies in the range ^{57}Fe to ^{187}Os, which includes ^{103}Rh.

Are you ever going to measure X directly? If not, then you only need the decoupler 90° pulse length; proceed as above.

2.1.5 Pulse Sequence

A brief outline of the pulse program for each experiment is given in the following sections. Where phase cycling is necessary, this is noted in the accompanying text. This is intended to help the reader follow what is going on at each stage of the experiment; it is not intended as an explanation of the workings of the pulse program, references are given for the interested reader.

2.2 Acquisition of the NMR Spectrum of a Solid or Semi-Solid Sample

2.2.1 Magic-Angle Spinning

MAS is routinely used in solid-state NMR spectroscopy for eliminating the effects of chemical shift anisotropy, heteronuclear dipolar interactions and first-order quadrupolar interactions. In this method the sample is rotated about the axis inclined at 54.74° with respect to the external magnetic field B_0, so that the average of the geometric term in nuclear spin interactions $(3\cos^2\theta - 1) = 0$.[11,12] Except for some specific applications of static wide-line solid-state NMR spectroscopy (i.e., for ^{2}H or for the determination of CSA patterns), the MAS is an essential feature of solid-state NMR spectroscopy and can also be used in variable temperature mode. The MAS methodology can also be used for high-resolution studies of viscous liquids and soft solids.[13,14]

The rate of MAS needed for the elimination/reduction of the effect of anisotropic magnetic interactions depends on the nuclei under observation and the strength of the interactions present. If the rate of rotation is comparable to the strength of an anisotropy, then in addition to the main isotropic chemical shifts the spectrum will contain a set of spinning sidebands separated from the main peak by $n\omega_r$ (ω_r is the MAS rate) (Figure 4). The sidebands can be used for the estimation of the size of CSA (Herzfeld–Berger method[15]). However, in the case of a complex spectrum these lines can obscure main resonances. Therefore the MAS rate should be carefully optimized. One can also apply sideband elimination methods described in the subsequent text (total supression of spinning side bands (TOSS) pulse sequence[16]).

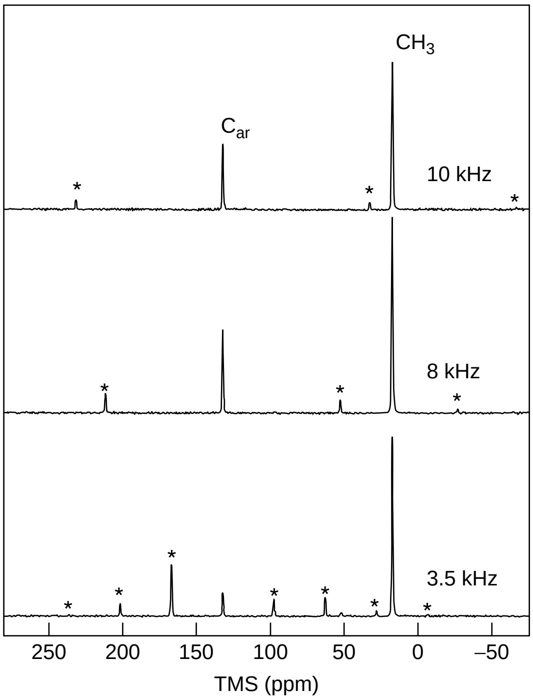

Figure 4 ^{1}H–^{13}C CP/MAS NMR spectra of hexamethylbenzene recorded at different MAS rates (* spinning sidebands corresponding to the aromatic peak at 132.2 ppm)

The probe heads supplied with modern solid-state NMR spectrometers vary in the diameters of the coils and, therefore, in the maximum MAS rate achievable. Recent developments in MAS technology led to the first commercial ultrafast MAS probe heads with MAS rate up to 65 kHz employing rotors with 1.2 mm diameter.[17] When selecting an appropriate probe head, one should take into account the sensitivity of a nucleus under study. The faster the MAS rate, the smaller the amount of the sample required. Typically, one employs MAS rates of 4–15 kHz. The lower end of these rates is covered by the probe heads with large MAS rotors (ca. 7 mm in diameter) suitable for nuclei with very low natural abundance and long relaxation times (^{29}Si, ^{15}N etc.). The fast and ultrafast MAS probe heads are particularly suitable for ^{1}H and ^{19}F nuclei.

MAS is ensured by the supply of compressed gases and can be performed at different temperatures. Spinning in boil-off N_2 is preferable to dried air. Spinning in nitrogen enables a wide temperature range of solid-state NMR experiments (from 173 to 423 K using an ordinary MAS probe head). The temperature range of experiments in dried air is significantly narrower due to both possible oxidation of the probe components at high temperatures and the presence of traces of water even at moderately low temperatures (253–283 K). The MAS results in increased temperature of the rotor due to friction, even in compressed gases. This effect is particularly noticeable at fast MAS rates and low temperatures when the temperature of a spinning gas measured at the entrance point to the probe head can be significantly different from the real temperature of the sample. The correct temperature of the MAS experiments should be derived from the calibration of a probe head using the temperature dependence of chemical shifts. $Pb(NO_3)_2$ is the most widely used standard for such calibrations,[18] although other standards (^{13}C NMR in d-camphor or pivalic acid,[19] ^{7}Li NMR of $Li_{0.24}La_{0.54}TiO_3$ for very high temperature MAS,[20] ^{119}Sn NMR of $Sm_2Sn_2O_7$ for fast MAS[21]) have been proposed.

2.2.2 Setting up MAS

Correct setting of the magic angle is essential in solid-state NMR spectroscopy. The most commonly used method relies on the ^{79}Br resonance in solid KBr. ^{79}Br is a quadrupolar nucleus (spin 3/2) ensuring a short relaxation time. The ^{79}Br first-order quadrupole coupling on the satellite transition ($\pm 3/2 \leftrightarrow \pm 1/2$) produces a set of distinct spinning sidebands. When the magic angle is set correctly, one should be able to identify at least 10 pairs of spinning sidebands. The setting of the magic angle can be performed using the ^{79}Br free-induction decay (FID) via the observation of rotational echoes. The correct MAS corresponds to the FID with the largest number of rotational echoes.

Some solid-state NMR experiments require significantly more accurate setting of the magic angle (satellite transition magic-angle spinning (STMAS)**[22]**). The setting of the magic angle can be checked conveniently using the secondary standard for ^{13}C spectra hexamethylbenzene (HMB). The position of the methyl resonance can be used for setting the ^{13}C chemical shift, while the aromatic peak should be observed at (132.2 ± 0.2) ppm provided that the magic angle is set correctly. The HMB is a convenient standard for setting the conditions for $^{1}H-^{13}C$ cross-polarization (CP) experiment (see below).

2.2.3 *High-Resolution Magic-Angle Spinning method (HR-MAS)*

High-resolution magic-angle spinning (HR-MAS) NMR spectroscopy is a new method aimed at bridging the gap between the high resolution and solid-state NMR methodologies. This method relies on the MAS of ''semi''-liquids/solids so that the anisotropic magnetic interactions resulting in a significant broadening of spectral lines can be removed and typical high-resolution NMR experiments (described earlier) can be applied.**[13]** The HR-MAS NMR has been applied successfully for a variety of biomedical systems including drug-delivery materials, cells, and biological tissues.**[13,23,24]** The HR-MAS NMR probe heads can be used with conventional high-resolution spectrometers supplied with the MAS units.

2.2.4 *Heteronuclear Decoupling*

The broadening due to heteronuclear dipolar coupling is a serious problem for the observation of a spectrum even when MAS is applied. The effect of heteronuclear dipolar coupling can be removed by *rf* irradiation of the ^{1}H channel.

Heteronuclear decoupling can be achieved using different methods. The easiest pulse sequence involves *high-power irradiation of the* ^{1}H *channel* during the acquisition of ^{13}C. Although this pulse sequence is very straightforward to setup, the power level on the ^{1}H channel is often very high as it should be set at least three times as high as the strongest heteronuclear dipolar coupling in the system (since the directly bonded $^{1}H-^{13}C$ dipolar coupling is about 22 kHz, the ^{1}H power should be set to ca. 70 kHz). This is easily achievable using medium or fast MAS rate probe heads, but can be problematic for larger sample volumes (ca. 7 mm rotor diameters). The high-power decoupling should be applied for the whole length of the FID which can cause further complications due to arcing and overheating of the sample which might be detrimental for sensitive biological samples. Typically, the ^{1}H pulse is set on-resonance. The presence of the efficient $^{1}H-^{1}H$ dipolar coupling network ensures the efficient transmission of the ^{1}H pulse between different protons. These disadvantages of high-power decoupling can be eliminated using multiple-pulse decoupling sequences which can also be applied with fast MAS. The Two Pulse Phase Modulated (TPPM) decoupling**[25]** uses continuous irradiation with two pulses of flip angle θ_p and phases that differ by $\Delta\phi$. Both θ_p and $\Delta\phi$ depend on the spinning rate and the sample and need to be optimized. Since the optimization on the sample is not always feasible, the best standard for the optimization is glycine (methylene resonance). Usually the TPPM sequence achieves better decoupling than high-power decoupling at the same *rf* power. Other methods which found numerous applications in other pulse sequences include small phase incremental alteration decoupling (SPINAL),**[26]** amplitude-modulated TPPM and XiX.**[27]**

2.3 Referencing

Referencing of heteronuclear NMR spectra can be a source of confusion. In an effort to establish universal NMR standards, and hence chemical shift scales, IUPAC have recently adopted a procedure in which *all* NMR spectra are, effectively, referenced to the ^{1}H signal of TMS.**[28]**

The procedure can be summarized thus:

1. Record a ^{1}H NMR spectrum of TMS in the same solvent as that used for the real sample. If TMS is compatible with the sample under study, then simply add TMS to the sample and record the ^{1}H NMR spectrum.
2. Note the *absolute* frequency of TMS $= \Theta_{TMS}$.
3. Look up the reference frequency, Ξ_X, (against TMS $=$ 100 MHz exactly) for the nuclide of interest (X) in Table 1 or 2.
4. The zero of the ppm scale for the nuclide X is then $\Xi_{X*}\Theta_{TMS}/100$ MHz, exactly.
5. Enter this value into the appropriate parameter on the spectrometer, for example, SF1 on a Bruker Avance spectrometer.
6. Record the NMR spectrum of the sample of interest.

Tables 1 and 2 also give the reference compound on which each chemical shift is based. It should be noted that:

1. Under the IUPAC scheme, these compounds act as *secondary* references.
2. Some of the reference compounds chosen by IUPAC differ from common practice, for example, many (most) workers reference ^{103}Rh to $\Theta_{Rh} = 3.16$ MHz when $\Theta_{TMS} = 100$ MHz.
3. Some reference compounds are extremely hazardous, for example, $Fe(CO)_5$, $HgMe_2$, OsO_4, $PbMe_4$. In these cases the IUPAC scheme should be followed.
4. For ^{15}N, the chemists' preferred reference, $MeNO_2$, differs from that chosen by structural biologists, NH_3. Some manufacturers (e.g. Bruker) use the structural biologists reference as the default. Shifts on the IUPAC scale are approximately 380.5 ppm less positive than on the NH_3 scale, for example, on the IUPAC scale, $\delta(^{15}NH_3) = -380.4$ ppm. The exact correction required depends on the resonance frequency of the sample.

Table 1 The spin properties of selected spin-1/2 nuclei. (Adapted from R. Harris *et al.*[28] © IUPAC)

Isotope	Natural abundance ($\chi/\%$)	Magnetic moment (μ/μ_N)	Magnetogyric ratio ($\gamma/10^7$ rad s^{-1} T^{-1})	Frequency ratio[(a)] ($\Xi\%$)	Reference compound	Sample conditions[(b)]	Relative receptivity[(c)] D^C
^{1}H	99.9885	4.837 353 570	26.752 2128	100.000 000[(d)]	Me_4Si	$CDCl_3$, $\varphi = 1\%$	5.87×10^3
^{13}C	1.07	1.216 613	6.728 284	25.145 020	Me_4Si	$CDCl_3$, $\varphi = 1\%$	1.00
^{15}N	0.368	−0.490 497 46	−2.712 618 04	10.136 767	$MeNO_2$	Neat/$CDCl_3$	2.25×10^{-2}
^{19}F	100.0	4.553 333	25.181 48	94.094 011	CCl_3F		4.90×10^3
^{29}Si	4.6832	−0.961 79	−5.3190	19.867 187	Me_4Si	$CDCl_3$, $\varphi = 1\%$	2.16
^{31}P	100	1.959 99	10.8394	40.480 742	80% H_3PO_4		3.91×10^2
^{57}Fe	2.119	0.156 9636	0.868 0624	3.237 778	$Fe(CO)_5$	80% in C_6D_6	4.25×10^{-3}
^{77}Se	7.63	0.926 775 77	5.125 3857	19.071 513	Me_2Se	Neat/C_6D_6	3.15
^{89}Y	100	−0.238 010 49	−1.316 2791	4.900 198	$Y(NO_3)_3$	H_2O/D_2O	0.700
^{103}Rh	100	−0.1531	−0.8468	3.186 447[(e),(f)]	$Rh(acac)_3$	$CDCl_3$, sat.[(f)]	0.186
^{109}Ag	48.161	−0.226 362 79	−1.251 8634	4.653 533	$AgNO_3$	D_2O, sat.[(f)]	0.290
^{113}Cd[(g)]	12.22	−1.077 8568	−5.960 9155	22.193 175	Me_2Cd	Neat	7.94
^{119}Sn	8.59	−1.813 94	−10.0317	37.290 632	Me_4Sn	Neat/C_6D_6	26.6
^{125}Te	7.07	−1.538 9360	−8.510 8404	31.549 769	Me_2Te	Neat/C_6D_6	13.4
^{129}Xe	26.44	−1.347 494	−7.452 103	27.810 186	$XeOF_4$	Neat	33.6
^{171}Yb	14.28	0.85506	4.7288	17.499306	$Yb(C_5Me_5).THF_2$	THF, 0.171 M	4.63
^{183}W	14.31	0.204 009 19	1.128 2403	4.166 387	Na_2WO_4	D_2O, 1 M	6.31×10^{-2}
^{187}Os	1.96	0.111 9804	0.619 2895	2.282 331	OsO_4	CCl_4, 0.98 M	1.43×10^{-3}
^{195}Pt	33.832	1.0557	5.8385	21.496 784[(e)]	Na_2PtCl_6	D_2O, 1.2 M	20.7
^{199}Hg	16.87	0.876 219 37	4.845 7916	17.910 822	Me_2Hg[(h)]	Neat	5.89
^{205}T1	70.476	2.837 470 94	15.692 1808	57.683 838	$T1(NO_3)_3$	H_2O, extrapolated to infinite dilution	8.36×10^2
^{207}Pb	22.1	1.009 06	5.580 46	20.920 599	Me_4Pb	Neat/C_6D_6	11.8

[(a)] Ratio, expressed as a percentage, of the resonance frequency of the reference to that of the protons of TMS at infinite dilution (in practice at $\varphi = 1\%$) in $CDCl_3$.

[(b)] M, molarity in mol dm^3 (solution); m, molality in mol kg^{-1} (solvent). See Ref. 28 for further details.

[(c)] D^C is the receptivity relative to that of ^{13}C, see *NMR and the Periodic Table,* R. K. Harris and B. E. Mann (Eds.), Academic Press (1978).

[(d)] By defnition.

[(e)] The precise values 3.160 000 MHz and 21.400 000 have also been suggested as the references for ^{103}Rh and ^{195}Pt, respectively.[29,30]

[(f)] Subject to considerable variation with temperature.

[(g)] Long-lived radioactive isotope.

[(h)] The high toxicity of this compound means its use should be discouraged.

5. The chemical shifts of many nuclides of interest to the inorganic chemist, for example, ^{31}P, ^{103}Rh, and ^{195}Pt, show large temperature, concentration and/or solvent shifts; referencing to an absolute frequency, rather than a compound makes good sense.
6. Given the above, the temperature, and concentration, as well the solvent, need to be given in reporting data.

3 APPLICATIONS

3.1 INEPT Sensitivity Enhancement

The guidance given in the previous section should allow the acquisition of a simple 1D NMR spectrum from appropriate inorganic NMR samples. However, the signal-to-noise ratio may be very low, either because of low natural abundance, or low inherent sensitivity. If the nucleus of interest (S, the *indirectly detected* spin), couples to a higher γ nucleus (I, the *detector* spin), sensitivity enhancement should be considered. The best 1D method for inorganic samples is INEPT since the sensitivity enhancement is greater than that of DEPT (distortionless enhancement by polarization transfer) and the spectral editing features of DEPT are not usually required.[31] In the authors' experience, refocussed INEPT, with or without decoupling, is the best choice, since this yields spectra similar in appearance to normal 1D spectra, although there is some slight loss of signal intensity due to the longer pulse sequence (Figure 5).[32,33] Note that integrals in polarization transfer experiments are dependent on factors such as the efficiency of polarization transfer and the number of I spins to which the insensitive nuclide S couples. Thus, integrals are *not* a good measure of the number of nuclei present.

3.1.1 *Pulse Sequence*

Figure 6 illustrates the pulse sequence for INEPTRD. p1 excites the I spin magnetization, d2, p2, d2, and p5 create

Table 2 The spin properties of selected quadrupolar nuclei. (Adapted from R. Harris *et al.*[28] © IUPAC)

Isotope	Spin	Natural abundance (χ/%)	Magnetic moment (μ/μ_N)	Magnetogyric ratio ($\gamma/10^7$ rad s^{-1} T^{-1})	Quadrupole moment (Q/fm^2)	Frequency ratio[(a)] (Ξ %)	Reference sample	Sample conditions[(b)]	Line width factor[(c)] (λ/fm^4)	Relative receptivity[(d)] D^C
^{2}H	1	0.0115	1.212 600 77	4.106 627 91	0.2860	15.350 609	$(CD_3)_4Si$	$CDCl_3$ $\phi = 1\%$	0.41	6.52×10^{-3}
^{6}Li	1	7.59	1.162 5637	3.937 1709	−0.0808	14.716 086	LiCl	D_2O, 9.7 m	0.033	3.79
^{7}Li	3/2	92.41	4.204 075 05	10.397 7013	−4.01	38.863 797	LiCl	D_2O, 9.7 m	21	1.59×10^{3}
^{9}Be	3/2	100	−1.520 136	−3.759 666	5.288	14.051 813	$BeSO_4$	D_2O, 0.43 m	37	81.5
^{10}B	3	19.9	2.079 2055	2.874 6786	8.459	10.743 658	$BF_3.Et_2O$	$CDCl_3$	14	23.2
^{11}B	3/2	80.1	3.471 0308	8.584 7044	4.059	32.083 974	$BF_3.Et_2O$	$CDCl_3$	22	7.77×10^{2}
^{14}N	1	99.632	0.571 004 28	1.933 7792	2.044	7.226 317	CH_3NO_2	Neat/$CDCl_3$	21	5.90
^{17}O	5/2	0.038	−2.240 77	−3.628 08	−2.558	13.556 457	D_2O	Neat	2.1	6.50×10^{-2}
^{21}Ne	3/2	0.27	−0.854 376	−2.113 08	10.155	7.894 296	Ne	Gas, 1.1 MPa	140	3.91×10^{-2}
^{23}Na	3/2	100	2.862 9811	7.080 8493	10.4	26.451 900	NaCl	D_2O, 0.1 M	140	5.45×10^{2}
^{25}Mg	5/2	10.00	−1.012 20	−1.638 87	19.94	6.121 635	$MgCl_2$	D_2O, 11 M	130	1.58
^{27}Al	5/2	100	4.308 6865	6.976 2715	14.66	26.056 859	$Al(NO_3)_3$	D_2O, 1.1 m	69	1.22×10^{3}
^{33}S	3/2	0.76	0.831 1696	2.055 685	−6.78	7.676 000	$(NH_4)_2SO_4$	D_2O, sat.[(f)]	61	0.101
^{35}Cl	3/2	75.78	1.061 035	2.624 198	−8.165	9.797 909	NaCl	D_2O, 0.1 M	89	21.0
^{37}Cl	3/2	24.22	0.883 1998	2.184 368	−6.435	8.155 725	NaCl	D_2O, 0.1 M	55	3.87
^{39}K	3/2	93.2581	0.505 433 76	1.250 0608	5.85	4.666 373	KCl	D_2O, 0.1 M	46	2.79
^{43}Ca	7/2	0.135	−1.494 067	−1.803 069	−4.08	6.730 029	$CaCl_2$	D_2O, 0.1 M	2.3	5.10×10^{-2}
^{45}Sc	7/2	100	5.393 3489	6.508 7973	−22.0	24.291 747	$Sc(NO_3)_3$	D_2O, 0.06 M	66	1.78×10^{3}
^{47}Ti	5/2	7.44	−0.932 94	−1.5105	30.2	5.637 534	$TiCl_4$	Neat	290	0.918
^{49}Ti	7/2	5.41	−1.252 01	−1.510 95	24.7	5.639 037	$TiCl_4$	Neat	83	1.20
^{51}V	7/2	99.750	5.838 0835	7.045 5117	−5.2	26.302 948	$VOCl_3$	Neat/C_6D_6	3.7	2.25×10^{3}
^{53}Cr	3/2	9.501	−0.612 63	−1.5152	−15.0	5.652 496	K_2CrO_4	D_2O, sat.[(f)]	300	0.507
^{55}Mn	5/2	100	4.104 2437	6.645 2546	33.0	24.789 218	$KMnO_4$	D_2O, 0.82 m	350	1.05×10^{3}
^{59}Co	7/2	100	5.247	6.332	42.0	23.727 074	$K_3[Co(CN)_6]$	D_2O, 0.56 m	240	1.64×10^{3}
^{61}Ni	3/2	1.1399	−0.968 27	−2.3948	16.2	8.936 051	$Ni(CO)_4$	Neat/C_6D_6	350	0.240
^{63}Cu	3/2	69.17	2.875 4908	7.111 7890	−22.0	26.515 473	$[Cu(CH_3CN)_4][ClO_4]$	CH_3CN, sat.[(f)]	650	3.82×10^{2}
^{65}Cu	3/2	30.83	3.074 65	7.604 35	−20.4	28.403 693	$[Cu(CH_3CN)_4][ClO_4]$	CH_3CN, sat.[(f)]	550	2.08×10^{2}
^{67}Zn	5/2	4.10	1.035 556	1.676 688	15.0	6.256 803	$Zn(NO_3)_2$	D_2O, sat.[(f)]	72	0.692
^{71}Ga	3/2	39.892	3.307 871	8.181 171	10.7	30.496 704	$Ga(NO_3)_3$	D_2O, 1.1 m	150	3.35×10^{2}
^{73}Ge	9/2	7.73	−0.972 2881	−0.936 0303	−19.6	3.488 315	$(CH_3)_4Ge$	Neat	28	0.642
^{75}As	3/2	100	1.858 354	4.596 163	31.4	17.122 614	$NaAsF_6$	CD_3CN, 0.5 M	1300	1.49×10^{2}

(*continued overleaf*)

Table 2 *Continued*

Isotope	Spin	Natural abundance (χ/%)	Magnetic moment (μ/μ_N)	Magnetogyric ratio ($\gamma/10^7$ rad s^{-1} T^{-1})	Quadrupole moment (Q/fm^2)	Frequency ratio[(a)] (Ξ %)	Reference sample	Sample conditions[(b)]	Line width factor[(c)] (λ/fm^4)	Relative receptivity[(d)] D^C
^{81}Br	3/2	49.31	2.931 283	7.249 776	26.2	27.006 518	NaBr	D_2O, 0.01 M	920	2.88×10^2
^{83}Kr	9/2	11.49	−1.073 11	−1.033 10	25.9	3.847 600	Kr	Gas	50	1.28
^{87}Rb^f	3/2	27.83	3.552 582	8.786 400	13.35	32.720 454	RbCl	D_2O, 0.01 M	240	2.90×10^2
^{87}Sr	9/2	7.00	−1.209 0236	−1.163 9376	33.5	4.333 822	$SrCl_2$	D_2O, 0.5 M	83	1.12
^{91}Zr	5/2	11.22	−1.542 46	−2.497 43	−17.6	9.296 298	$Zr(C_5H_5)_2Cl_2$	CH_2Cl_2, sat.[(f)]	99	6.26
^{93}Nb	9/2	100	6.8217	6.5674	−32.0	24.476 170	$K[NbCl_6]$	CH_3CN, sat.[(f)]	76	2.87×10^3
^{95}Mo	5/2	15.92	−1.082	−1.751	−2.2	6.516 926	Na_2MoO_4	D_2O, 2 M	1.5	3.06
^{99}Tc^f	9/2	–	6.281	6.046	−12.9	22.508 326	NH_4TcO_4	D_2O	12	–
^{99}Ru	5/2	12.76	−0.7588	−1.229	7.9	4.605 151	$K_4[Ru(CN)_6]$	D_2O, 0.3 M	20	0.848
^{101}Ru	5/2	17.06	−0.8505	−1.377	45.7	5.161 369	$K_4[Ru(CN)_6]$	D_2O, 0.3 M	670	1.59
^{115}In$^{(e)}$	9/2	95.71	6.1256	5.8972	81.0	21.912 629	$In(NO_3)_3$	D_2O, 0.1 M	490	1.98×10^3
^{121}Sb	5/2	57.21	3.9796	6.4435	−36.0	23.930 577	$KSbCl_6$	CH_3CN, sat	410	5.48×10^2
^{127}I	5/2	100	3.328 710	5.389 573	−71.0	20.007 486	KI	D_2O, 0.01 M	1600	5.60×10^2
^{131}Xe	3/2	21.18	0.893 1899	2.209 076	−11.4	8.243 921	$XeOF_4$	Neat	170	3.50
^{133}Cs	7/2	100	2.927 7407	3.533 2539	−0.343	13.116 142	$CsNO_3$	D_2O, 0.1 M	0.016	2.84×10^2
^{137}Ba	3/2	11.232	1.210 13	2.992 95	24.5	11.112 928	$BaCl_2$	D_2O, 0.5 M	800	4.62
^{139}La	7/2	99.910	3.155 6770	3.808 3318	20.0	14.125 641	$LaCl_3$	D_2O, 0.01 M	54	3.56×10^2
^{181}Ta	7/2	99.988	2.6879	3.2438	317.0	11.989 600	$KTaCl_6$	CH_3CN, sat.[(f)]	1.4×10^4	2.20×10^2
^{187}Re^f	5/2	62.60	3.8096	6.1682	207.0	22.751 600	$KReO_4$	D_2O, 0.1 M	1.4×10^4	5.26×10^2
^{209}Bi	9/2	100	4.5444	4.3750	−51.6	16.069 288	$Bi(NO_3)_2$	$HNO_3/D_2O/H_2O$	200	8.48×10^2

(a) Ratio of the resonance frequency of the reference to that of the protons of TMS at infinite dilution (in practice at $\varphi = 1\%$) in $CDCl_3$.

(b) M, molarity in mol dm^3 (solution); m, molality in mol kg^{-1} (solvent). See Ref. 28 for further details.

(c) $l = (2I + 3)Q^2/I^2(2I - 1)$. The values are quoted, arbitrarily, to 2 significant figures.

(d) $D^C$is the receptivity relative to that of ^{13}C.

(e) Radioactive, with a long half-life.

(f) saturated.

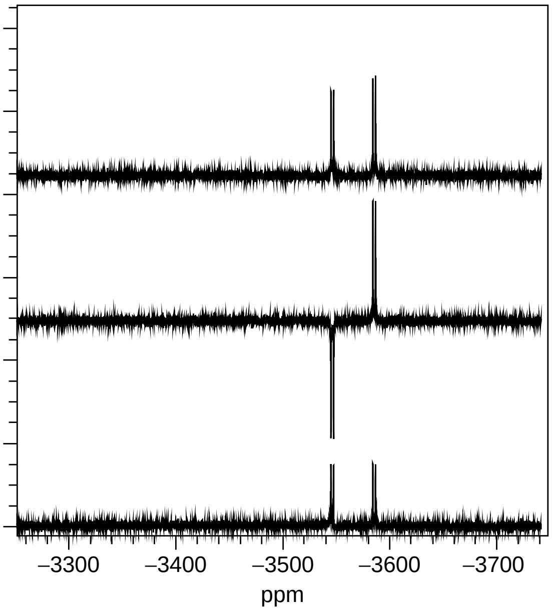

Figure 5 $^{195}Pt\{^1H\}$ NMR spectra of $[Pt(C_5H_5{}^{15}N)(PPh_3)Cl_2]$ recorded in THF: (bottom) normal spectrum; (middle) with INEPT enhancement from ^{31}P, $\gamma_I/\gamma_S = 40.48/21.50 \sim 2$, note the antiphase multiplet; (top) with refocused INEPT enhancement from ^{31}P, note slight loss of intensity due to signal dephasing during the longer pulse sequence

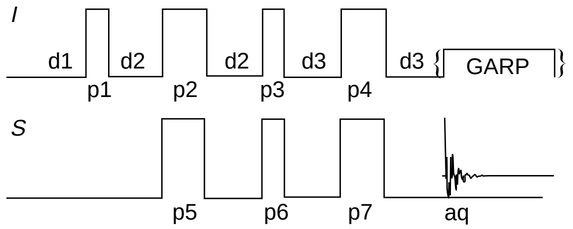

Figure 6 INEPTRD pulse sequence

a spin echo after the second d2. p3 and p6 transfer this I spin magnetization to S. If $d2 = 1/4J$ then antiphase S spin magnetization results and is enhanced by the ratio γ_I/γ_S. In addition, the ''normal'' S spin magnetization contributes a ''normal'' spectrum to the signal, hence the intensities *within* the multiplets are distorted. d3, p4, and p7 remove this distortion and correct the phase within the multiplets giving a spectrum that looks ''normal'' but is enhanced by γ_I/γ_S. $d3 = 1/(\pi J.\surd\ \arcsin(n))$, where n is the number of coupled I spins. GARP (globally optimized alternating-phase rectangular pulses), rather than WALTZ, decoupling is normally used to decouple heteronuclei and is optional.

Advantages

- It is simple to implement, little can go wrong provided pulses and delays are set accurately.
- It gives the strongest signal.
- The enhancement is greatest if $\gamma_I \gg \gamma_S$ and is independent of the sign of γ.
- The number of coupled I nuclei can be determined directly from the multiplicity if decoupling is *not* used; cf indirect methods where this information is not routinely available.
- The pulse sequence repetition rate is determined by relaxation of the I spins which is often faster than that of the S spins.

Disadvantages

- The enhancement is sensitive to accurate setting of the coupling constant $J(IS)$.
- The enhancement is sensitive to the value chosen for d3. Incorrect setting of d3 can severely degrade the spectrum.
- Greater enhancement, giving a spectrum in less time, might be available by an indirect method such as HMQC.
- If I is not ^1H, then a three-channel machine, and triple resonance probe are required.

Acquisition tips

- Use the pulse program, and phase cycling sequences supplied with your instrument. Make sure all necessary experimental parameters are set as described by the manufacturer. The manufacturer should provide sequences with and without I decoupling.
- The *minimum* number of scans is defined by the phase cycle. The total number of scans must be an integral multiple of this.
- Inspect your spectrum after a few scans have been recorded to see all is well.
- Make sure that d3 is set correctly.

Processing tips

- Process normally.

3.2 Selective Observation of *S* Spin Satellites

It is frequently necessary to detect the signals arising from only those spins of nuclide 1 (I) that are coupled to nuclide 2 (S). For example, it may be necessary for chemical reasons to record the ^1H NMR spectrum of a metal–hydride in protio-, rather than deutero-solvent (Figure 7), or it may be that the exact value of the coupling $J(IS)$ is required for a polarization transfer experiment, but cannot be measured directly from the spectrum of I due, for example, to a low natural abundance of S (Figure 8). There are many ways that this can be achieved, the most popular of which is the 1D

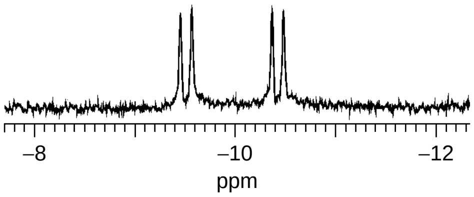

Figure 7 $^1H,^{31}P$ 1D HMQC phase cycle selected NMR spectrum of $[PdH(LL)(solv)]^+$, (LL = 1, 2-bis((di-tert-butylphosphino)methyl) benzene) recorded in MeOH at 295 K. Note: resonances not coupled to ^{31}P are suppressed, allowing the metal–hydride resonance to be seen clearly in protio solvent

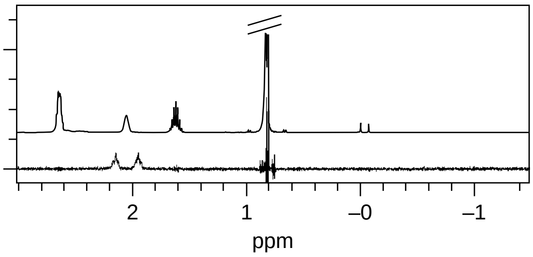

Figure 8 ^1H NMR spectrum of $[(N_3(P(Bu^i)_2)_3]$ in $CDCl_3$ at 295 K: (top) normal 1D spectrum; (bottom) $^1H,^{15}N$ 1D HMQC gradient-selected spectrum. Note ^{15}N satellites are readily observed at natural abundance

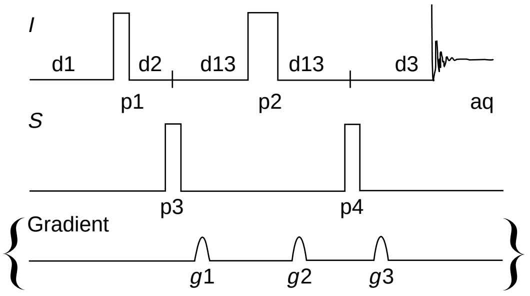

Figure 9 Gradient-accelerated 1D HMQC pulse sequence

HMQC experiment which can be run either as a gradient or nongradient experiment (Figure 9).[34]

3.2.1 Pulse Sequence

The I spins are first excited by p1 = 90° (Figure 9) and IS coupling allowed to develop during d2. p3 creates multiple quantum coherence. d13–p2–d13 allows a short delay for evolution and refocuses the I chemical shifts. The magnetization is converted back into observable magnetization by p4. Either phase cycling, or gradient selection can be used to cancel signals arising from molecules containing NMR silent ‘‘S’’ nuclei. d2 is set to select the desired IS spin coherences, normally $d2 = 1/2J$, however, in systems in which I couples to more than one S spin this will result in distortions due to multiple S spin flips. The spin system should first be simulated to determine the optimum value of d2.[35] d3 is omitted in the nongradient version, and should be calculated by the pulse program in the gradient version. The recycle delay d1, is a compromise between relaxation of the I spin and experimental time.

Advantages

- It is straightforward to setup.
- Gradient selection or phase cycling removes signals from isolated I spins allowing the satellites resulting from coupling to S to be clearly seen in the spectrum of I.
- Multiplets are correctly phased.
- In principle only one scan is required although more scans may be necessary for weak samples.

Disadvantages

- The effect depends on $J(IS)$; it cannot preserve magnetization from all IS spin pairs if $J(IS)$ varies widely.
- The success of the experiment depends on reasonably accurate setting of d2, that is, $J(IS)$ must be known with reasonable accuracy.
- The signal intensity is modulated with offset, so in an extreme case, if more than one S spin is present, an unfortunate choice of offset may give zero intensity. This problem can be minimized by including a 180° S pulse to refocus S spin chemical shifts.[36]

Acquisition tips

- Use the pulse program, and phase cycling sequences supplied with your instrument. Make sure all necessary experimental parameters are set as described by the manufacturer.
- $d2 = 1/2J(IS)$, if the I spin couples more or less equivalently to more than one S spin, try $d2 = 1/4J(IS)$.
- Centre the resonances of interest in both spectral windows.
- Set the gradient ratios to obey.

$$g1(\gamma_I + \gamma_S) + g2(-\gamma_I + \gamma_S) + g3(-\gamma_I) = 0$$

Processing tips

- Process normally.

3.3 Selective Observation of Selected Spectral Regions

An alternative solution to the problem of selectively observing, for example, the ^1H NMR spectrum of a metal–hydride in protio-, rather than deutero-solvent is to excite just that region of the NMR spectrum that contains signals of interest. This can be done using a shaped soft pulse, using a DANTE (delays alternating with nutation for tailored excitation) type sequence or, on a modern

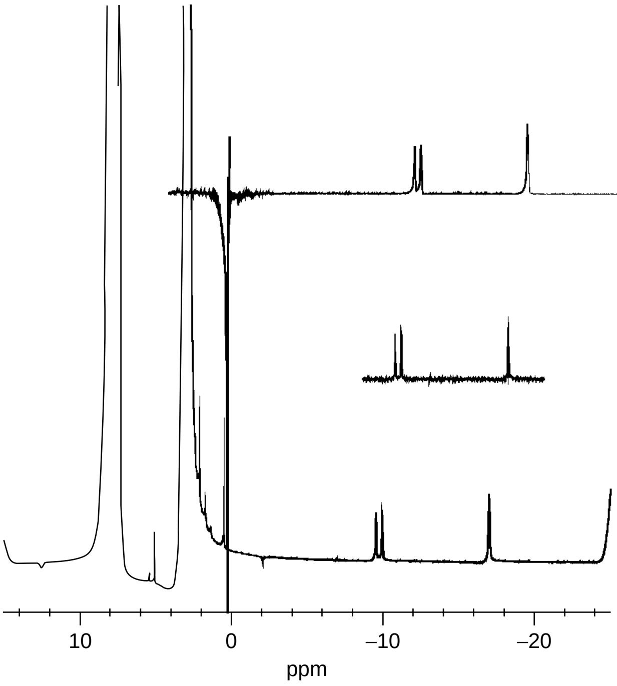

Figure 10 ^1H NMR spectrum of Wilkinson's hydride, $[Rh(H)_2(PPh_3)_3Cl]$, recorded in C_7H_8:CD_2Cl_2 (1:1) with: (bottom) no filtering, (middle) digital filtering, and (top) using a DANTE-Z pulse. Note the suppression of the solvent resonances. The distortions at the edges of the bottom spectrum are artefacts from digital filtration

spectrometer equipped with a digital filter, simply by selecting the region of interest. None of these methods use spin–spin coupling to edit the spectrum; this has the advantage that these methods can be applied to any resonance; the disadvantage is that they are not applicable to the selective observation of spin satellites. Figure 10 compares the ^1H NMR spectra of Wilkinson's hydride, $[Rh(H)_2(PPh_3)_3Cl]$, recorded with no filtering, with digital filtering and using a DANTE-Z pulse to excite selectively the hydride region of the spectrum.[37]

3.3.1 Pulse Sequence

The DANTE-Z excitation sequence $(\theta_{\phi 1} - \tau - \theta_{\phi 2} - \tau)_n$ uses a train of hard pulses and phase cycling to align the excited magnetisation along z, cf DANTE which aligns the magnetization at the selected tip angle (Figure 11). DANTE-Z, therefore, requires an additional read pulse. Do not use DANTE-Z in a saturation transfer experiment, Section 3.5.1, use the simple DANTE sequence.

Advantages

- It is straightforward to setup.
- The DANTE-Z sequence effectively suppresses the sinc oscillations that occur using the simple DANTE sequence or Gaussian pulses.

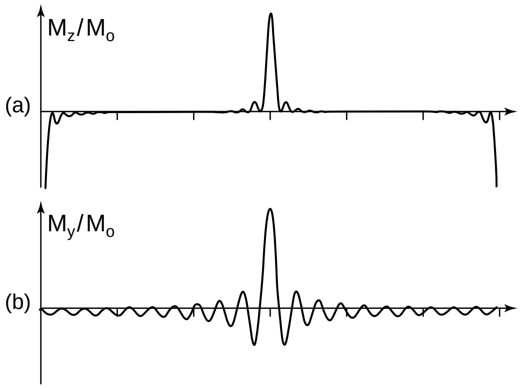

Figure 11 Excitation profiles for the DANTE-Z (top) and DANTE (bottom) pulse sequences. Note the almost complete suppression of the sinc oscillation using DANTE-Z excitation. (Reprinted from *J. Magn. Reson.*, **83**, Boudot, D.; Canet, D.; Brondeau, J.; Boubel, J. C., 'DANTE-Z—A New Approach for Accurate Frequency-Selectivity using Hard Pulses', 428–439. © 1989, with permission from Elsevier)

- DANTE pulse sequences do not require spectrometers equipped with shaped pulses.
- DANTE pulse sequences do not require spectrometers equipped with digital filtering.
- Spin–spin couplings are not used/required to select resonances.

Disadvantages

- It cannot be used to observe spin satellites selectively.

Acquisition tips

- Use the pulse program, and phase cycling sequences supplied with your instrument. Make sure all necessary experimental parameters are set as described by the manufacturer.
- Centre the resonances of interest in the spectral window.

Processing tips

- Process normally.

3.4 Indirect Detection of Insensitive Nuclei and Heteronuclear Correlation Spectroscopies in Solution

In many cases the inorganic chemist will be interested in the NMR spectrum of a nuclide of low sensitivity (denoted *S* or *indirectly detected* spin) in a compound containing a high-sensitivity nucleus (denoted *I* or *detector* spin). If scalar coupling exists between the two nuclides, then the 2D HMQC and HSQC techniques offer an alternative to direct observation.[34,38,39] The distinction between HMQC and HSQC is that *IS*-magnetization is stored as either multiple

(HMQC) or single (HSQC) quantum coherence during the t_1 evolution period. The sensitivity of any NMR experiment is proportional to the gyromagnetic ratios of the starting and the detected spins as $\gamma_{\text{start}}\gamma_{\text{detect}}{}^{3/2}$. For HMQC and HSQC-type experiments, $\gamma_{\text{start}} = \gamma_I$, $\gamma_{\text{detect}} = \gamma_I$, hence the sensitivity $\sim \gamma_I^{5/2}$ (*cf* a direct, polarization transfer experiment such as INEPT, $\gamma_{\text{start}} = \gamma_I$, $\gamma_{\text{detect}} = \gamma_S$, sensitivity $\sim \gamma_I\gamma_S^{3/2}$). Additionally, HSQC and HMQC provide a correlation map linking coupled sensitive and insensitive spins. However, the number of coupled sensitive spins is not directly available from the multiplicity patterns in the HSQC and HMQC spectra.

Notes:

1. The normal convention places the I spin on the x-axis and the indirectly detected S nucleus on the y-axis. The I dimension is referred to as $F2$, the S dimension as $F1$. This does not correspond to the channel labelling on Bruker spectrometers, f1 (observe channel), f2 (1st decoupler), f3 (2nd decoupler), etc.
2. Use of HMQC and HSQC for sensitivity enhancement is most appropriate where the detector has a high γ *relative to* the insensitive nuclide. HMQC/HSQC cannot compensate for low natural abundance of the insensitive spin since only the satellites from coupling to S are detected.
3. Isotopic enrichment can be used where a suitable detector has low natural abundance but is readily available in enriched form, for example, ^{13}CO in metal carbonyl clusters, or to boost the number of insensitivie spins, for example, ^{15}N.
4. The HSQC pulse sequence is longer than that of HMQC, thus is more affected by pulse errors and relaxation during the pulse sequence; HMQC is thus inherently more sensitive. However, passive coupling between detector spins is not present in F1 in HSQC spectra but is in HMQC. Therefore, if *II* coupling is present (e.g., coupling between protons, or ^{13}C, or ^{31}P being used as detector spins), the collapse of these multiplets into a singlet will compensate for the intrinsically lower sensitivity of the HSQC sequence.
5. The relaxation time of the I spins affects the signal intensity as $[1-\exp(-D1/T_{1I}.)]$, where $D1$ is the recycle time. If the I spin has a very long T_1, for example, ^{13}C in a degassed sample, it has been suggested that addition of a relaxation agent may be beneficial. However, the presence of the relaxation agent will also increase dephasing of the desired multiple-quantum coherence during the pulse sequence. Care should therefore be taken when employing a relaxation agent.
6. Particular problems are encountered where the detector I couples to more than one S spin since the assembly of S spins can act as a unit. The result is false coherences relating the I spin to the sums or differences of the frequencies of the S spins and intensity distortions. In the worst case this can result in an HMQC spectrum in which only coherences resulting from ''multiple S spin transitions'' are seen. *None* of these transitions occur at the chemical shift of the S spin (Figure 12).**35**

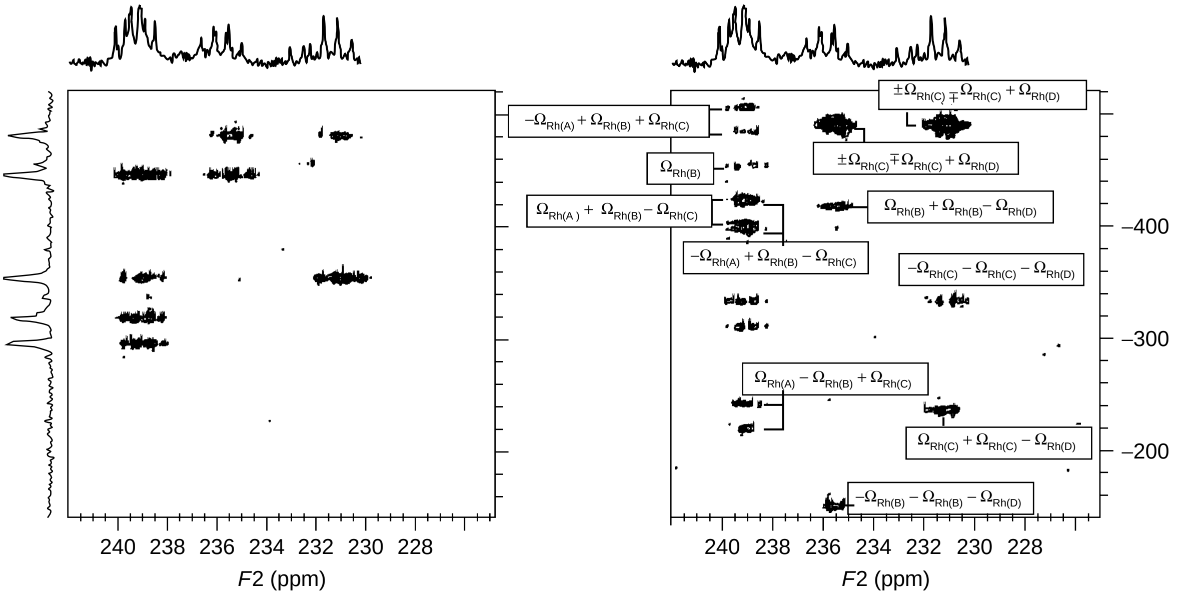

Figure 12 Using the conventional delay $d2 = 1/2J$ results in false coherences relating the I spin to the sums or differences of the frequencies of the S spins, and intensity distortions. In the worst case this can result in an HMQC spectrum in which only coherences resulting from ''multiple S spin transitions'' are seen. Inverse detected HMQC ^{13}C{^{103}Rh} NMR spectrum of [$Rh_6(CO)_{15}\{P(C_6H_4F)_3\}$]; left ''unconventional'' mixing time = $1/(5J)$ gives ''single spin'' Rh transitions only, correlations appear at the correct δ_{Rh}; right, ''conventional'' mixing time = $1/(2J)$, gives ''multiple Rh spin transitions''. Only ONE of these transitions occurs at a Rh chemical shift

Gradient Acceleration

It is debatable whether gradient acceleration offers any advantage in HMQC/HSQC spectroscopy.**[40]** The situation will be different for different S spins depending on the natural abundance. The decision to use gradient acceleration depends on sample concentration and may even be influenced by environmental factors. The final decision will depend on the following considerations:

1. In gradient-accelerated HMQC only one coherence pathway is selected, that is, *half* the signal intensity is *discarded*.
2. However, suppression of T_1 noise is much better in gradient spectroscopy.
3. Where the S nuclide is less than 100% abundant, breakthrough of signals from molecules containing NMR silent ''S'' nuclei is better suppressed by gradient selection.
4. Sensitivity improved gradient experiments are available, however, the increased length of the pulse sequences allows for dephasing of the desired magnetization. Therefore, the theoretical sensitivity enhancement is not always obtained. Furthermore, the sensitivity improvement is often restricted to a particular spin system (usually one I spin and one S).
5. T_1 noise problems are exacerbated by environmental factors such as sample vibration, sample spinning, building vibrations and temperature variations. Gradient selection seems better able to cope in such adverse situations—although the real solution is better control of the environmental disturbance.

Thus overall S/N may be better in the gradient-accelerated experiment, even though the signal is weaker. Paradoxically, therefore, it may be useful to use gradient acceleration to suppress the noise in the spectra if the indirectly observed spin has low natural abundance. Gradient acceleration also offers the possibility of acquiring HXQC spectra using a single scan per $F1$ increment on strong samples. Thus, for example, in favourable cases, ^{1}H-detected ^{15}N HMQC spectra, at natural abundance, can be recorded in ca. 15 min. In unfavourable cases, ^{31}P-detected, ^{195}Pt HMQC spectra can be markedly inferior to the nongradient spectrum.

The case for using phase cycle, rather than gradient, selection is:

1. In phase cycle selection both coherence pathways are selected, that is the signal intensity is *doubled.*
2. Many S nuclides have high natural abundance (^{89}Yb, ^{103}Rh, ^{109}Ag, etc.); suppression of signals from molecules containing NMR silent ''S'' nuclei is not an issue.
3. If the *intensity* of the desired signal is the limiting factor, then phase cycle selection is preferred. A phase cycle selection version of HMQC that uses a spin-lock to purge signals from molecules containing NMR silent ''S'' nuclei has been developed—poor man's gradient-heteronuclear multiple quantum coherence (PMG-HMQC). This allows acquisition of an HMQC spectrum of a strong sample using 1 or 2 scans per increment, that is, the same time saving as gradient selection.

Instrumental Considerations

HMQC spectra using ^{1}H as the detector (I) spin can be recorded on a conventional two-channel NMR spectrometer with a ''normal'' broad band, or selective dual, probe head. However, better signal-to-noise will be achieved using an inverse probe head due to the better filling factor.

For HMQC spectroscopy in which both the detector I and indirect S nuclei are ''heteronuclei'', a third spectrometer channel is required. An inverse broadband, triple resonance probe head in which the inner coil is tuned to ^{1}H, I and ^{2}D lock, and the outer coil is broadbanded is then the best option, particularly where a single I nuclide or ^{1}H will be used for detection. Such probe heads are ''stock items'' for some manufacturers (Bruker). Although it may be possible to build probe heads in which two channels are broadbanded, the lead time on such a probe head is likely to be long, and the performance markedly inferior due to the technical difficulties involved.

If gradient acceleration is to be used, a gradient unit in the spectrometer and gradient coils in the probe head are also necessary.

Phase Sensitive Detection

Phase-sensitive versions of the experiments below are available and afford Lorentzian lineshapes from which coupling constants can be determined reliably after phase correction.

Suggested HMQC Experiments

1. The Basic HMQC Experiment
   This is recommended for the inexperienced user—all that is needed if the insensitive nucleus has high abundance.
2. PMG-HMQC
   This is highly recommended by Berger and Braun for nongradient HMQC and is useful when large (kHz) coupling constants result in ''negative'' gradient delays.
3. Gradient-selected HMQC/HSQC with GARP decoupling, see discussion earlier.

3.4.1 The Basic HMQC Experiment

The basic HMQC pulse sequence (Figure 13) is the shortest, simplest HMQC experiment and gives the best sensitivity. It is used both to determine the chemical shifts of an insensitive nuclide (spin S) coupled to a nuclide of higher sensitivity (spin I) and to correlate the coupled pairs of I and S spins. The experiment is not phase sensitive hence lineshapes are not Lorentzian and coupling constants cannot

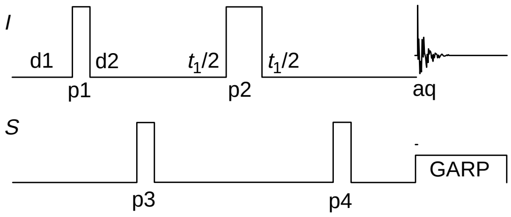

Figure 13 Basic HMQC pulse sequence

be measured accurately. Use this for samples in which the insensitive nuclide S has *high* natural abundance.

Pulse Sequence. The I spins are first excited by $\text{p1} = 90°$ (Figure 13) and IS coupling allowed to develop during d2. The magnetization is then converted to multiple-quantum coherences by p3 and stored while the $t_1/2$ incrementing delays create the second dimension. The magnetization is converted back into observable magnetization by p4; p2 refocuses the I chemical shifts removing them from the second dimension. Phase cycling is used to cancel signals arising from molecules containing NMR silent ‘‘S’’ nuclei. d2 is set to select the desired IS spin coherences, normally $\text{d2} = 1/2J$. However, in systems in which I couples to more than one S spin, this will result in distortions due to multiple S spin flips. The spin system should first be simulated to determine the optimum value of d2.[35] The recycle delay d1, is a compromise between relaxation of the I spins and experimental time.

Advantages

- The sequence is simple to implement, little can go wrong.
- The short pulse sequence minimizes relaxation during the active part of the sequence.
- The sequence gives the strongest signal.
- Couplings to third nuclei appear in both dimensions and couplings between I and S spins occur only in $F2$.
- The correlations of interest flank the T_1 noise and breakthrough signals.

Disadvantages

- T_1 noise and breakthrough of signals from molecules containing NMR silent ‘‘S’’ nuclei can be problematic.

Acquisition tips

- Use the pulse program, and phase cycling sequences supplied with your instrument. Make sure all necessary experimental parameters, for example, number of transients per increment, number of variable delays in the pulse sequence, are set as described by the manufacturer.
- Measure J(IS) via the 1D HMQC experiment in Section 3.4.1 given earlier.
- The *minimum* number of transients per increment is defined by the phase cycle. The total number of transients per scan must be an integral multiple of this.
- You can inspect your spectrum at any time after two increments have been recorded; there is no need to acquire all increments before transforming the data. Thus a quick check to see all is well is recommended. Note, however, that resolution and S/N improve dramatically as more increments are completed.
- Run a quick series of experiments to locate the resonances of interest, then reduce the sweep width in $F1$. It may be quicker to record several spectra, with narrow sweep width, than attempt to include several resonances with widely varying chemical shifts in a single experiment.
- It is always better to record more data points in $F2$ than to zero-fill this dimension afterwards during processing.
- For samples containing more than one S spin, first simulate the spectrum to determine if multiple S spin transitions need to be eliminated (Figure 14).[35]
- If decoupling of S is needed in $F2$ then add a delay d2 after p4 and use GARP decoupling. A filter to block the $F1$ decoupling irradiation is essential in the lock channel.
- If I is not ^{1}H, then ^{1}H decoupling can be applied either throughout the pulse sequence or just during acquisition.
- A BIRD filter (bilinear rotation decoupling) can be used to suppress signals from molecules containing NMR silent ‘‘S’’ nuclei when the insensitive nuclide S has *low* natural abundance.

The BIRD Filter.

Pulse Sequence

The BIRD filter[41] is a selective T_1 filter, removing signals from molecules containing NMR silent ‘‘S’’ nuclei (Figure 15). I spin magnetization from molecules containing I coupled to S evolves under scalar coupling and experiences both 180° pulses p2 and p6. p2 refocuses the chemical shifts and p6 interchanges the S spin labels in the I multiplets. Thus, when $\text{d2} = 1/2J$, magnetisation from IS coupled spins is refocused along $-y$. p3 rotates this magnetization to $+z$. I spin magnetization from molecules containing NMR *silent* ‘‘S’’ nuclei does not evolve under IS coupling and does not experience p6. As a result, it is refocused along $+y$ by the 180° pulse p2. p3 rotates this magnetization to the $-z$ axis. During d3, T_1 relaxation of the $-z$ magnetization occurs, d3 is set so that this magnetization is at the zero crossing point before proceeding to the HMQC sequence. p7 removes artefacts.

The HMQC Sequence

This is as in the previous experiment, but an additional delay d2 is included after the last S spin pulse (p9) to refocus IS spin coupling and allow GARP decoupling.[42]

Advantages

- BIRD filter helps to remove signals from molecules containing NMR silent ‘‘S’’ nuclei, essential if decoupling

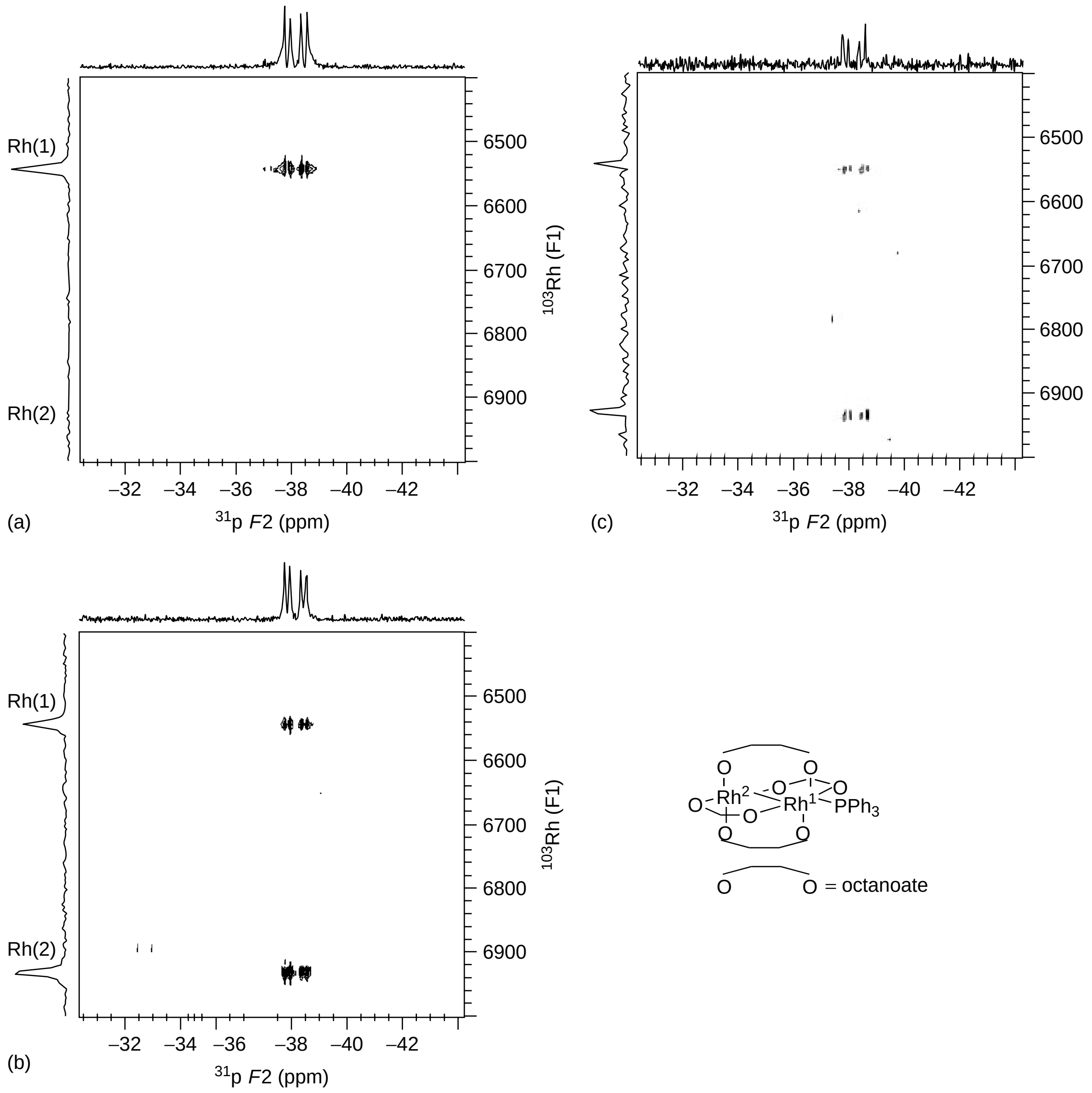

Figure 14 ^{31}P,^{103}Rh HMQC spectrum of [Rh$_2$(μ-octanoate)$_4$(PPh$_3$)] in CDCl$_3$ at 295 K recorded with (a) d2 $= 1/(2.^2J(\mathrm{RhP}) = 5.2$ ms, note the *absence* of a correlation between P and Rh(2) and the *presence* of a correlation between P and Rh(1); (b) d2 $= 7.7$ msec a delay calculated to optimize the experiment to observe correlations to *both* Rh(1) and Rh(2); (c) d2 $= 1/2.^2J(\mathrm{RhP}) = 14.7$ ms, the conventional delay to optimize correlations to Rh(2). Contours in each spectrum drawn at the same levels

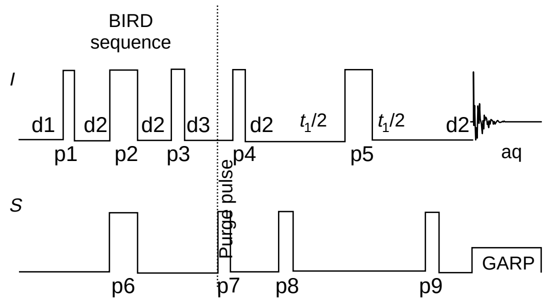

Figure 15 HMQC pulse sequence incorporating a BIRD filter to suppress magnetization from molecules containing NMR *silent* ‘‘*S*’’ nuclei

is to be applied in $F2$ since the desired signals would otherwise be overlaid by breakthrough signals.

Disadvantages

- Setup is more complex.
- Longer pulse sequence results in increased relaxation during the active part of the sequence.
- T_1 noise is not suppressed and suppression of breakthrough signals is not 100% effective.
- Very long relaxation delays can be required to achieve good results with inorganic samples having long T_1s—in which case consider the poor man’s gradient (PMG) experiment in Section 3.4.2, instead.

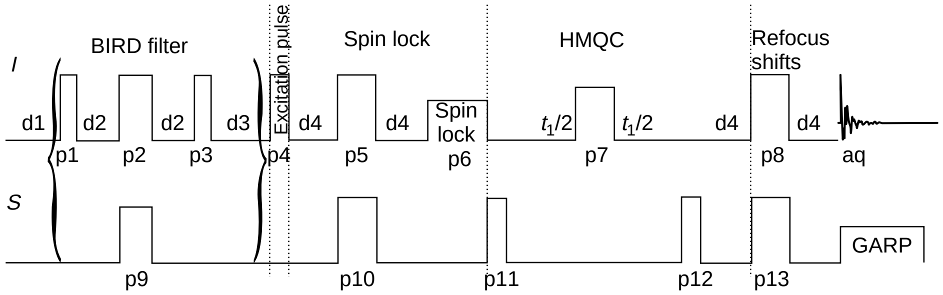

Figure 16 ‘‘Poor Man’s Gradient’’ version of the HMQC sequence

Acquisition and processing tips

- d3 is most easily set using a simple 1D inversion recovery experiment. Usually the sample will be strong enough to observe a spectrum with a single scan. Inspect the spectrum and vary d3 until the intensity is *minimized*.

Processing tips

- Zero-fill in $F1$, truncate in $F2$.
- Exponentially multiply in $F2$, use a shifted sine bell in $F1$.
- Forward linear prediction can be applied in $F1$ but may give artefacts and degrades the signal-to-noise.
- Spectra are not phase sensitive, transform in magnitude mode, do not phase correct.
- Passive, I spin homonuclear couplings appear in $F1$.
- The behaviour of foldback in $F1$ is not easily predicted.

3.4.2 *Phase-Sensitive PMG-HMQC*

This variant uses a spin-locking pulse to suppress signals from molecules containing NMR silent ‘‘S’’ nuclei. A BIRD filter can be added to achieve excellent suppression of these unwanted signals. GARP decoupling of S and WALTZ decoupling of ^{1}H (if $I \neq {}^1$H) can be added to improve signal-to-noise by removing IS and $I-{}^1$H couplings.[43,44] This type of spin-lock sequence has been dubbed the PMG since it gives almost as good suppression, from almost as few scans, as gradient selection but without the need for a gradient equipped spectrometer. However, the full benefit is rarely obtained since the pulse sequence is longer, so more dephasing of the desired magnetization during the pulse sequence occurs (Figure 16). HMQC sequences with the BIRD filter but without the spin lock are available, see Experiment 3.4.1. Phase-sensitive acquisition gives Lorentzian lineshapes allowing coupling constants to be measured accurately. Use this for samples in which the insensitive nuclide S has *low* natural abundance, or for very strong samples when 2 transients per increment will give a good spectrum. Do not use if relaxation times are short.

Pulse Sequence. Figure 16 illustrates the pulse sequence for PMG-HMQC.

The BIRD Filter. The BIRD filter is optional (see Experiment 3.4.1). If used, d3 is set so that the undesired magnetization from molecules containing NMR silent ‘‘S’’ is at the zero crossing point before proceeding to the spin-lock sequence. $d2 = 1/2J(IS)$ (Figure 16).

The Spin Lock. p4 excites the I spin magnetization that survives the BIRD filter. I spin magnetization from molecules containing NMR *silent* ‘‘S’’ nuclei does *not* evolve under IS coupling and does *not* experience p10, so is refocused along $+y$ by the 180° pulse p5. I spin magnetization from molecules containing I coupled to S *does* evolve under scalar coupling and so experiences both 180° pulses p5 and p10. p5 refocuses the chemical shifts and p10 interchanges the S spin labels in the I multiplets. Thus, when $d4 = 1/4J$, magnetization from IS coupled spins is aligned along $+/-x$. A spin-lock pulse (with phase x) preserves this magnetization while that of isolated I spins is dephased. Two types of spin-locking pulse have been advocated in the literature, a soft long pulse, p3 around 10 ms at 20 dB attenuation or a hard pulse, p3 = 2 ms, at 3 dB attenuation. p4, d4 p5, d4 p6 and p10 replace p1, d2 in Experiment 3.4.1, thus, $d4 = d2/2 = 1/4J$, but see comment on multiple S spin systems above.

The HMQC sequence is as in the previous experiments but is extended with 180° pulses and delays to refocus the chemical shifts.

Advantages

- The spin lock removes signals from isolated I spins. Suppression of unwanted signals can approach that of gradient selection.
- GARP decoupling can be used to improve the signal-to-noise ratio by collapsing $J(IS)$ in $F2$.
- Only two scans per transient are required (Figure 17).

Disadvantages

- This is a more complex setup.
- Much longer pulse sequence results in increased relaxation during the active part of the sequence.

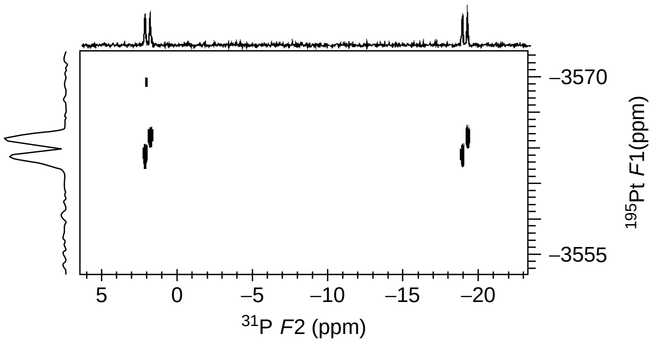

Figure 17 Phase sensitive ^{31}P,^{195}Pt{^{1}H} PMG-HMQC spectrum of [Pt($C_5H_5{}^{15}N$)(PPh_3) Cl_2] in THF at 295 K. A standard gradient experiment could not be used due to the large ^1J(P–Pt). NS = 2, spin-lock pulse duration 5900 µs, 14 dB attenuation, total acquisition time 15 min. Further reductions in experiment time, or improved resolution in $F1$ could be achieved by using a smaller spectral width in the ^{195}Pt dimension. SW = 125 ppm, with 128 increments was used here. Compare the signal-to-noise achieved in the ^{195}Pt spectrum with that in Section 3.1

Acquisition tips

- See Basic HMQC sequence (Experiment in Section 3.4.1).
- A filter to block the $F1$ decoupling irradiation is essential in the lock channel.
- d3 is most easily set using a simple 1D inversion recovery experiment (Experiment in Section 3.4.1).
- Use the pulse program, and phase cycling sequences supplied with your instrument. Make sure all necessary experimental parameters are set as described by the manufacturer.
- Make sure the correct phase sensitive type is selected as indicated in the manufacturers documentation (time proportional phase increment (TPPI)).
- The spin-locking pulse is traditionally set at 10 ms with typically 20 dB attenuation; more recently 2 ms at 3 dB attenuation has been used. The best values will be spectrometer, probe, and nucleus dependent and must be found by experiment. Be careful not to use so much power that the probe breaks down.

Processing tips

- See Basic HMQC sequence (Experiment in Section 3.4.1).
- The spectra are phase sensitive; use the transformation protocol recommended by the instrument manufacturer. Do not use magnitude calculation.
- Spectra must be phase corrected in both dimensions—all peaks positive.
- Passive, I spin homonuclear couplings appear in $F1$.

3.4.3 Gradient-Accelerated HMQC and HSQC

Gradient acceleration of HMQC and HSQC sequences reduces the sensitivity but can be advantageous if strong samples are used.

Pulse Sequences. The HMQC sequence is the same as the basic experiment but includes an additional delay (d3) after the last S spin pulse (p4) for refocusing of IS spin coupling to allow GARP decoupling (Figure 18). Gradients, not phase cycling, are used to select the desired coherences so a single transient per increment can be used.

The HSQC sequence (Figure 18) is built around two INEPT transfers (Experiment in Section. 2.1). The first generates a single-quantum coherence $-2I_{Iz}I_{Sy}$. During t_1, which creates the second time dimension, the S chemical shifts evolve. The second INEPT sequence transfers the magnetization back to I. During d2, observable proton magnetization modulated by the S chemical shifts develops. The 180° I pulse p4 eliminates $I-S$ couplings in $F1$.

Choice of Pulse Sequence. Many variants of these basic pulse sequences exist. HMQC sequences are often preferred in studies of low-γ metal nuclei, while HSQC sequences are preferred by authors interested in ^{15}N. The present authors' experience is in line with these ''prejudices''. We have found versions incorporating adiabatic decoupling of third nuclei (e.g., ^{1}H,^{15}N HSQC with adiabatic decoupling of ^{31}P) particularly useful (Figure 19).

Advantages

- Gradient selection removes signals from isolated I spins and $T1$ noise from the spectra.

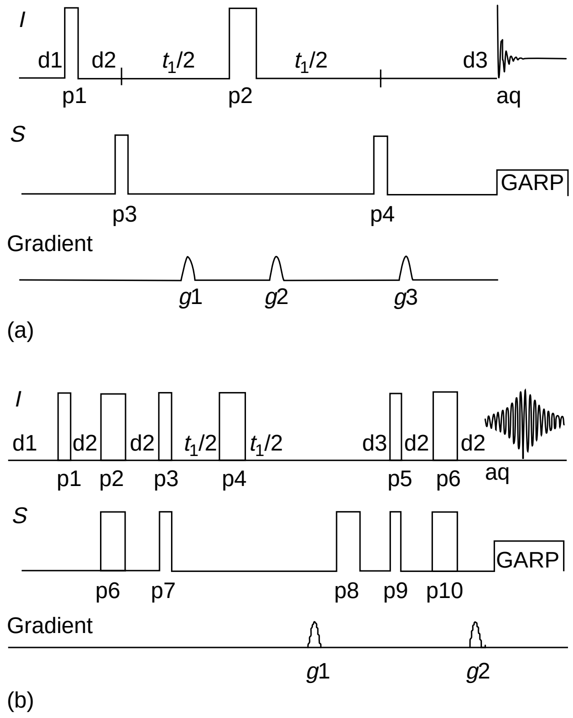

Figure 18 Gradient-accelerated HMQC (a) and HSQC (b) pulse sequences

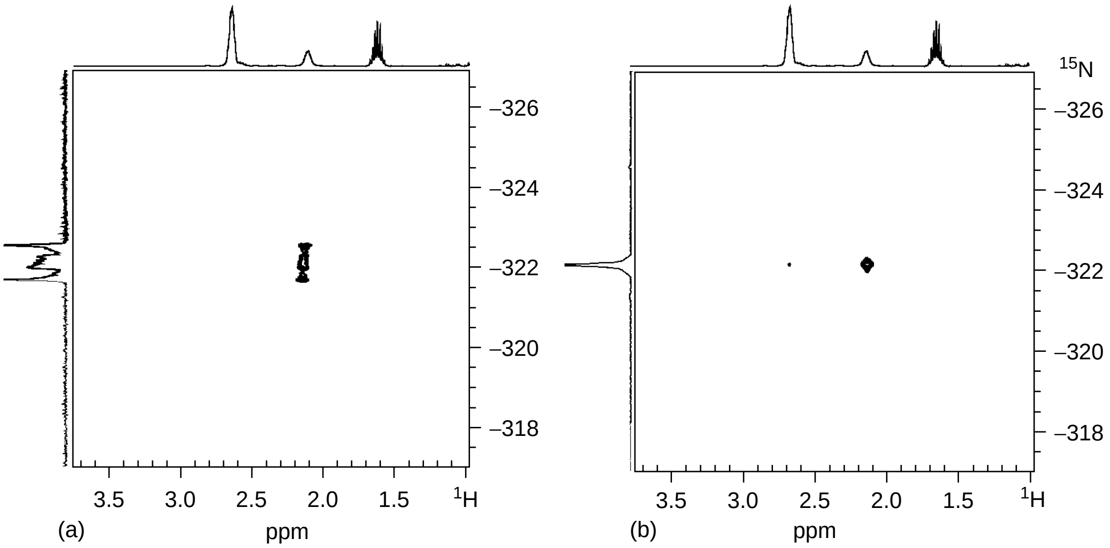

Figure 19 ^{1}H,^{15}N{^{15}N} HSQC spectra of $[(N_3(P(Bu^i)_2)_3]$ in $CDCl_3$ at 295 K recorded without (a) and with (b) CHIRP60 adiabatic ^{31}P decoupling pulse. Bruker pulse program hsqcetf3gpsi2

- GARP decoupling improves the signal-to-noise ratio.
- Only two scans per transient are required for phase-sensitive spectra, one for magnitude data.
- Passive couplings are not present in HSQC.

Disadvantages

- Only one coherence pathway is selected resulting in a 50% loss of signal intensity. Sensitivity improved versions restore some of this loss at the expense of a longer pulse sequence.

Acquisition tips

- Use HSQC if passive coupling between I spins is present.
- Use the pulse program, and phase cycling sequences supplied with your instrument. Make sure all necessary experimental parameters are set as described by the manufacturer.
- Modern spectrometers should have routines for calculating the gradient ratios correctly.

  For HMQC set $g1$, $g2$, and $g3$ to satisfy

$$g1(\gamma_I + \gamma_S) + g2(-\gamma_I + \gamma_S) + g3(-\gamma_I) = 0$$

  For HSQC set $g1$ and $g2$ to satisfy

$$g1(\gamma_S) - g2(\gamma_I) = 0$$

- For HMQC the number of scans per increment must be a multiple of 2.
- For HSQC use at least 16 dummy scans, some authors additionally recommend DS = 2* NS.
- For HMQC, $d2 = 1/(2J)$, for HSQC, $d2 = 1/(4J)$. d3 positions the pulses following the gradient pulse correctly and is normally calculated by the pulse program.

Processing tips

- See Basic HMQC sequence (Experiment in Section 3.4.1).
- If phase-sensitive acquisition is used, phase all peaks positive.

3.5 Dynamic NMR Spectroscopy

The use of variable temperature to study dynamic systems is well documented, however, a few comments on the accuracy, or not, of temperature calibration, and some guidance on simulation of variable temperature (VT) spectra might be helpful.

Calibration of the VT unit

1. If the probe thermocouple is intended to be user removable, first check that it reports the correct temperature by removing the thermocouple from the probe and recording the temperatures reported for liquid nitrogen, melting ice, and boiling water.
2. Next check the temperature reported for a sample in the probe; two strategies are possible:
   (a) Prepare a dummy sample containing some suitable solvent. Push a *calibrated*, nonmagnetic thermocouple through the NMR tube cap. Place the sample/thermocouple assembly into the magnet and record the sample temperature reported by the spectrometer VT unit and the calibration thermocouple.

Plot a temperature correction graph. Your spectrometer may have routines to make this correction in the spectrometer's software.

(b) The temperature dependence of the chemical shift difference $\Delta\delta$ between the CH_3 and OH protons of anhydrous methanol is known. Thus, by recording the ^{1}H NMR spectrum of anhydrous methanol at several temperatures a calibration curve can be plotted. Berger and Braun (see Section 5) give the following relations:

$$T[\mathrm{K}] = -114.83\Delta\delta + 471.85 \quad 1.4965 < \Delta\delta < 1.75999$$

$$T[\mathrm{K}] = -125\Delta\delta + 490 \quad 1.76 < \Delta\delta < 2.07999$$

$$T[\mathrm{K}] = -140\Delta\delta + 521.33 \quad 2.08 < \Delta\delta < 2.43$$

The recorded and actual temperatures of the sample should be within 1–2 K. This systematic error should be borne in mind when reporting, for example, reactions rates, and thermodynamic parameters.

For high temperature calibrations, Berger and Braun recommend 1,2-ethanediol.

Simulation of spectra

Band-shape analysis can be a powerful mechanistic tool, affording exchange rates, from which activation parameters can be derived via Arrhenius and/or Eyring plots. Thus, possible exchange/reaction mechanisms can be distinguished. Care, however, is needed since:

- Near the slow- and fast-exchange limits, other factors will contribute significantly to the line width; rate constants determined near these limits will be inaccurate.
- Chemical shifts can be temperature dependent. Although it is possible to fit both the chemical shifts and the rate constants simultaneously, the two will be correlated.
- Coupling constants are less temperature dependent and should be fixed at the values measured from the slow-exchange limiting spectrum.
- Small amounts of impurities may have a large effect on reaction rates and may provide additional exchange pathways.
- Minor species which cannot be directly observed due to their low concentration may affect the behaviour of the major species, resulting in spectra that are difficult to interpret.
- Band-shape analysis gives ‘‘pseudo-first-order rate constants’’; a good kinetic model for the proposed dynamic processes is also required to relate these ‘‘pseudo-first-order rate constants’’ to what is happening chemically.
- The presence of more than one dynamic process can only be proved by a difference in computed rate constants. However, the errors in the rate constants are always large. NB: It is important to realize that a difference in coalescence temperatures does not imply a difference in rate constants.

Several packages are available in addition to the instrument manufacturer offerings, for example, gNMR, http://home.cc.umanitoba.ca/~budzelaa/gNMR/gNMR.html. Follow the instructions and remember that sample concentration is important. Once the rate constants have been extracted, the thermodynamic parameters of activation can be obtained via an Eyring plot.

3.5.1 Saturation Transfer Exchange Spectroscopy

If the dynamic process is too slow to allow study by conventional variable temperature methods, then saturation transfer can be used to study the exchange.**[45]** Two selective, 1D strategies are useful:

Selective Inversion Using a DANTE Pulse.

Pulse sequences

The DANTE pulse sequence is shown in Figure 20b. A peak that is exactly on-resonance or an integral multiple of 1/d2 Hz off-resonance, experiences the cumulative effect of the n p1 pulses. Other resonances see a random excitation that effectively sums to zero. In exchange experiments, a variable delay (vd) is inserted between the end of the DANTE pulse train and the read pulse, p2. During vd, magnetization is transferred between exchanging sites.

Acquisition tips

- Use the DANTE sequence provided by your instrument manufacturer.
- Choose d2 such that sideband excitation (which occurs at integral multiples of 1/d2), does not interfere with other resonances in the spectrum. When the variable delay is very short, the inverted resonance appears in emission and all other signals should be in absorption.
- Choose n and p1 such that $n^*\mathrm{p1} = 90°$ pulse. The selectivity is approximately $1/(n^*\mathrm{d2})$.
- p1 is typically 1 μs, attenuate the pulse power if necessary.
- Set the peak to be inverted exactly on-resonance.

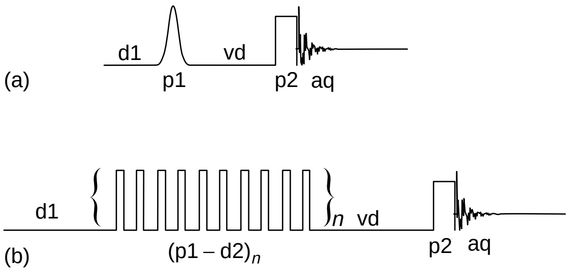

Figure 20 Saturation transfer experiment using: (a) Selective inversion by a shaped pulse; or (b) a DANTE pulse sequence. Do not use the DANTE-Z sequence, Section 3.3, in saturation transfer experiments

- d1, the recovery delay, must be ca. 5–10 T_1. An inadequate relaxation delay will give spurious results.
- p2 is a 90° read pulse.
- vd is a variable delay during which exchange can occur. By acquiring spectra with different values of vd, the exchange rate can be obtained.

Advantages

- DANTE is highly selective; it can be used in crowded regions of the spectrum.
- Appropriate for instruments that do not have shaped pulses.

Disadvantages

- Care must be taken in setup—watch out for excitation side bands.
- Quantitative treatment requires knowledge of the T_1 relaxation times.

Selective Inversion Using a Shaped Pulse. Gaussian shaped pulses[46] are designed to excite only a narrow frequency range. Various shaped pulses intended for refocusing, inversion or 90° excitation are now available as routine experiments on modern spectrometers. The width of the excited region is set by the pulse length and the pulse power adjusted to achieve the desired flip angle.

Pulse sequence and acquisition tips

- p1 (Figure 20a) is typically a 50 ms, Gaussian inversion pulse. It is usually sufficient to use the routines supplied with the spectrometer to calculate the required attenuation. (Choose the pulse length to achieve the desired selectivity, for Gaussian pulses *longer* pulses are *more* selective, and adjust the pulse power to suit.)
- d1 must be ca. 5–10 T_1· An inadequate relaxation delay will give spurious results.
- p2 is the read pulse.
- vd is a variable delay during which exchange can occur. By acquiring spectra with different values of vd, the exchange rate can be obtained.

Advantages and disadvantages

- Not as selective inversion as using DANTE.
- Appropriate for instruments that have shaped pulses.

Processing tips

- Use ca. 2 Hz exponential multiplication.
- For accurate integrations, zero-fill the FIDs, baseline correct the spectra, and correct the slope and bias of the integrals individually.
- When the vd is very short, the inverted resonance appears in emission and all other signals in absorption (Figure 21). As the vd increases, chemical exchange leads to the inverted magnetisation being partially transferred to other sites. At the same time spin-lattice relaxation is taking place. Therefore, a biexponential recovery is observed; for the inverted resonance the two exponentials have the same sign, while the exponentials have opposite signs for resonances involved in exchange with the inverted site. For simple two-site exchanges, a quasi spin-lattice relaxation time, T_1, is obtained by plotting $\ln(\Sigma(I_o) - \Sigma(I_{vd}))$ *versus* vd, the vd time, where $\Sigma(I_o)$ is the summed equilibrium intensity of the irradiated resonance and its exchange partner and $\Sigma(I_{vd})$ the summed intensity at time vd. T_1 is the inverse of the slope of the line. The rate constant for exchange is then obtained by plotting $\ln(I_{Ir} - I_{Ex})$ *versus* vd, where I_{Ir} is the intensity of the irradiated resonance and I_{Ex} that of the resonance of the exchanging site at time vd. The slope of the line is $(2k + 1/T_1)$. The procedure assumes that the spin-lattice relaxation time is identical at the two sites. See Akitt and Mann for more details.[47]

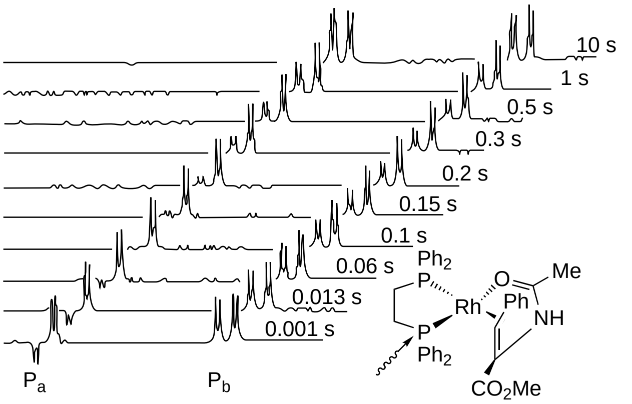

Figure 21 Saturation transfer experiment; the downfield branch of the P_a doublet of 1 was inverted using a DANTE selective excitation pulse. The exchange of the magnetization was followed as a function of mixing time. T_1 was found to be 1.26 s and $k_{exchange} = 2.85\,s^{-1}$ at 300 K. (From J. M. Brown, and P. A. Chaloner and G. A. Morris (1987) *J. Chem. Soc. Perkin Trans. 2*, 1583. Reproduced by permission of The Royal Society of Chemistry)

3.5.2 *EXSY Spectroscopy*

Exchange spectroscopy (EXSY) is a two-dimensional method that can detect chemical exchange and fluxional processes *before* line broadening occurs (Figure 22).[49,50]

Pulse Sequence. The pulse sequence (Figure 23) is identical to that for phase sensitive, nuclear overhauser effect spectroscopy NOESY). The first pulse tips the magentization into the *xy* plane. This is coded with the chemical shift information during the incrementing delay t_1. The second pulse tips the coded magnetization into the $-z$ direction. Exchange occurs during the delay d2. p3 is a read pulse. Phase cycling is used to suppress unwanted COSY signals and the axial peaks.

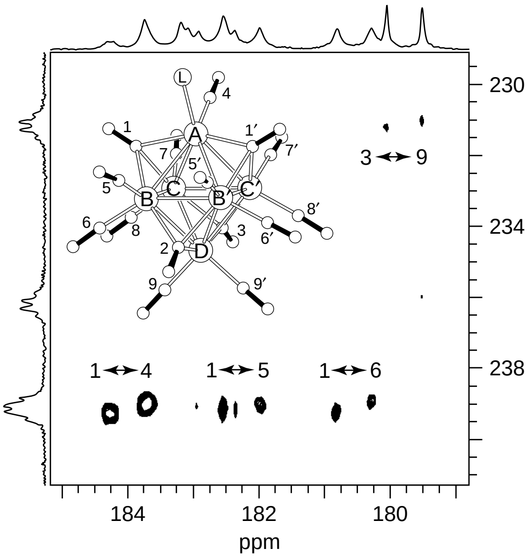

Figure 22 ^{13}C EXSY spectrum showing stereospecific exchange correlations between bridging and terminal carbonyls in $[Rh_6(CO)_{15}\{P(4\text{-}(MeO)C_6H_4)_3\}]$, in $CDCl_3$ at 274 K; $\tau_{mix} = 0.02$ s

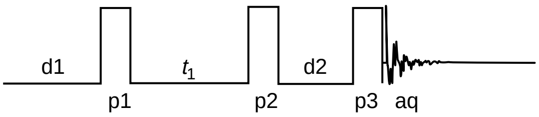

Figure 23 EXSY pulse sequence

Advantages

- Complex exchange networks, for example, CO fluxionality in a metal carbonyl cluster, can be readily mapped.
- EXSY peaks are very strong, and are unlikely to be confused with NOESY peaks.
- A gradient version is available. EXSY and diagonal peaks are positive, NOESY peaks negative—use the gradient-accelerated NOESY sequence supplied with your instrument.

Disadvantages

- Rates are not readily extracted from the spectra.[51]
- A zero result may reflect the experimental conditions chosen, rather than no exchange.
- The nongradient version is relatively time consuming due to the need for phase cycling.

Acquisition tips

- Use the pulse program, and phase cycling sequences supplied with your instrument. Make sure all necessary experimental parameters are set as described by the manufacturer.
- Record the spectrum in phase sensitive mode using TPPI.
- d2 is mixing time, ideally.

$$d2 = \frac{1}{(T_1^{-1} + k_{AB} + k_{BA})}$$

However, since the rates are usually not known, d2 must be set by trial and error; try 0.5–1 s.

- If several exchange processes, with different rates, are occurring, several values of d2 will be needed.

Processing tips

- Zero-fill in $F1$, truncate in $F2$ to obtain a (roughly) square matrix.
- Exponentially multiply in $F2$, use a shifted sine bell in $F1$.
- The spectra are phase sensitive, so apply real Fourier Transformation with TPPI.

3.5.3 Gradient Accelerated HOESY Spectroscopy

Heteronuclear overhauser effect spectroscopy (HOESY) is the heteronuclear equivalent of NOESY. It is useful when scalar coupling information is unhelpful or not available.[52] It is also useful in determining the relative dispositions of the cation and anion in solutions of organometallic salts, where the anion is fluorinated. Several excellent reviews have appeared recently.[53–56] HOESY can provide valuable information about cation–anion interactions, especially in systems for which both the anion and cation contain NMR-active nuclei of high receptivity (e.g., ^1H or ^{19}F), and several magnetically distinct nuclei are present in each ion, so that different anion–cation orientations can be distinguished (Figure 24). Overhauser enhancements decrease rapidly with increasing separation of the nuclei, however, this is not usually a limitation since, most often, we are interested in studying systems in which ion pairing affects the reactivity. For this to be the case, a proportion of intimate ion pairs, albeit transient in nature, must be present. Quantitative analysis requires a reference distance. Inevitably, this will be an *intra*molecula*r* distance in the anion or cation, however, the contacts we want to measure will be *inter*ionic distances, between sites on the cation and anion. The reference nuclei should have the same correlation time as the pair of nuclei of interest, thus, if accurate interionic distances are to be obtained, the correlation times must also be checked. The anion–cation distances obtained will be average values reflecting the transient nature of an ion pair, rotation of, or within, the ion pair, and internal motions. In practice, the distances obtained are usually accurate to about 10%.[57] Both gradient and nongradient versions are useful. Here the gradient-accelerated version is described (Figure 25).

Pulse Sequence. The S spins are excited by p3 and evolve under the chemical shift during t_1. p1 refocuses IS coupling and creates $-I_z$ magnetization. p4 flips the

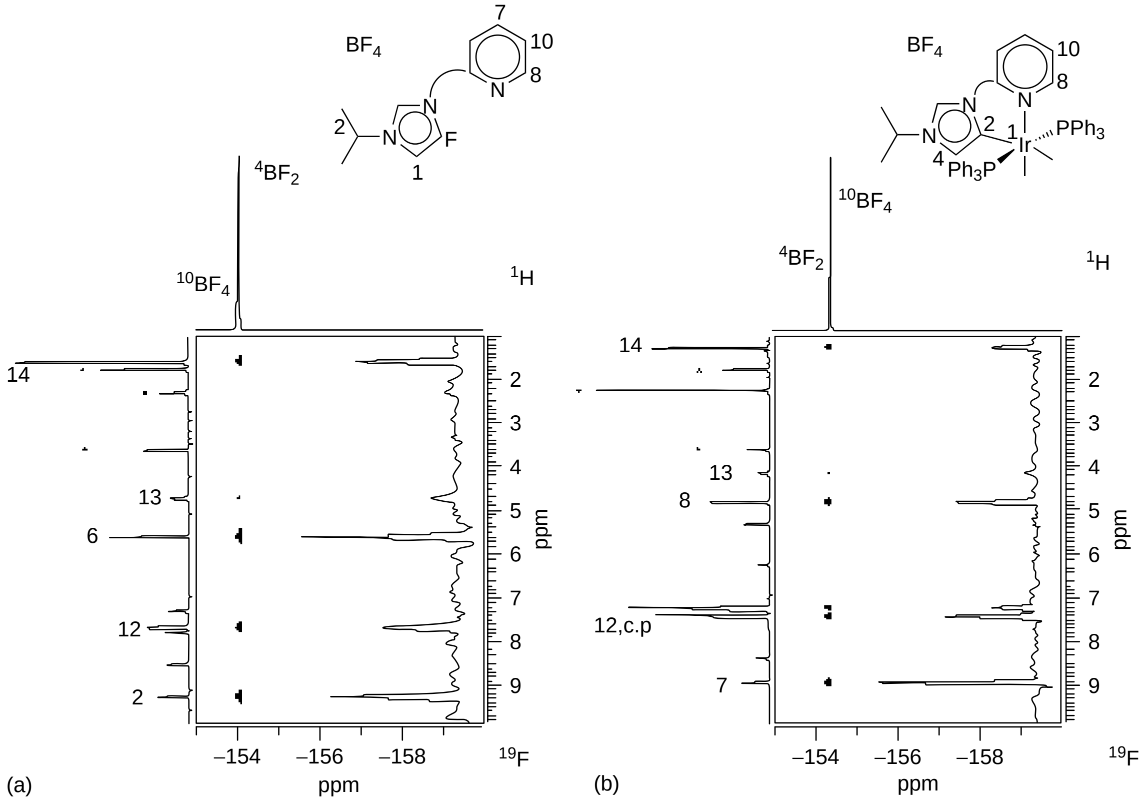

Figure 24 $^{19}F,^{1}H$-HOESY NMR spectra (376.65 MHz, 323 K, THF-d_8) of (a) and (b) showing the selective interactions of the anion with the indicated protons. ''*'' THF and water resonances. (Reprinted with permission from L. N. Appelhans, *et al.* (2005) *J. Amer. Chem. Soc.* **127**: 16299–16311. © 2005 American Chemical Society)

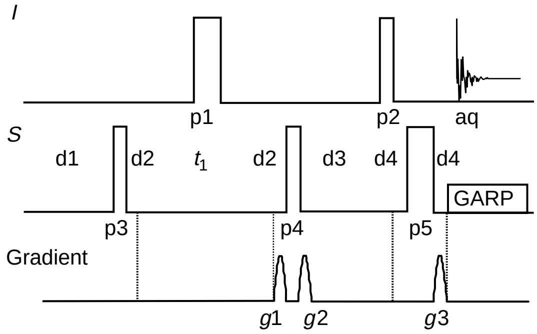

Figure 25 Pulse sequence for gradient-accelerated version HOESY

S magnetization, which now contains its chemical shift information, to $-z$ as well. Cross relaxation occurs during d3 + d4 giving a heteronuclear nOe. Gradient $g1$ causes dephasing during t_1, with the factor $g1\gamma_S$. p2 generates $-I_y$ magnetization which is refocused by $g3$ when $g1\gamma_S = g3\gamma_I$. $g2$ dephases any ''left-over'' transfer magnetization.

Advantages

- Considerable time savings result from inverse detection and gradient selection.
- Only one scan per transient is required.

Disadvantages

- Problems have been reported if the indirectly detected S nucleus has a long relaxation time.
- Like NOESY, HOESY is a dynamic, not equilibrium, measurement. A zero result may reflect the experimental conditions chosen, rather than no nOe.

Acquisition tips

- Use the pulse program, and phase cycling sequences supplied with your instrument. Make sure all necessary experimental parameters are set as described by the manufacturer.
- Set $g1$ and $g3$ to satisfy

  $$g1\gamma_S = g3\gamma_I$$

  $g2$ is a homospoil gradient pulse, its duration is not critical.
- d2 and d4 equal $g1$ and $g3$ gradient durations, typically 1 ms.
- d3 is the mixing time.

Processing tips

- Zero-fill once in $F1$, apply exponential multiplication in $F2$ and a shifted sine bell squared in $F1$.
- The spectra are not phase sensitive, use magnitude calculation.

3.5.4 *Pulsed Field Gradient—Spin Echo (PGSE) Diffusion Spectroscopy*

Pulsed gradient spin-echo (PGSE) NMR diffusion methods were first introduced ca. 40 years ago by Stejskal and Tanner, and are now enjoying renewed interest from inorganic NMR spectroscopists since they provide a reliable method of studying phenomena such as the relative volume of a compound, hydrogen bonding, host/guest encapsulation, and ion pairing. The technique can be used either in 1D, or as a 2D experiment with chemical shift in one dimension and the diffusion coefficient in the other—diffusion ordered spectroscopy (DOSY) (Figure 26). DOSY can also be used to aid the resolution and assignment of complex mixtures especially where the molecules are relatively large and thus give complicated NMR spectra. Although potentially quantitative, integrating DOSY cross peaks is not straightforward. On the other hand PGSE routinely gives diffusion constants that are accurate to ∼2%.[52,53]

Pulse Sequence. The stimulated echo experiment (Figure 27) with p1 = p2 = p3 = 90°, is recommended by Pregosin since, in this version, T_1, rather than T_2, is the effective relaxation path during time Δ. Since T_2 must be shorter than T_1, a better signal-to-noise ratio is obtained. The effect of the two gradient pulses is to defocus, and then refocus, the magnetization. If, during the time Δ, the molecules diffuse from their positions after the first gradient pulse, the effective magnetic field experienced by the spins of those molecules will be different during both gradient pulses. This results in incomplete refocusing of the spins and a consequent decrease in the intensity of the corresponding NMR signal. By recording a series of spectra, varying one of the following; gradient strength G, length δ, or the delay Δ, the diffusion coefficient, D (often called a ‘‘*self-diffusion constant*’’), can be obtained (equation 3).

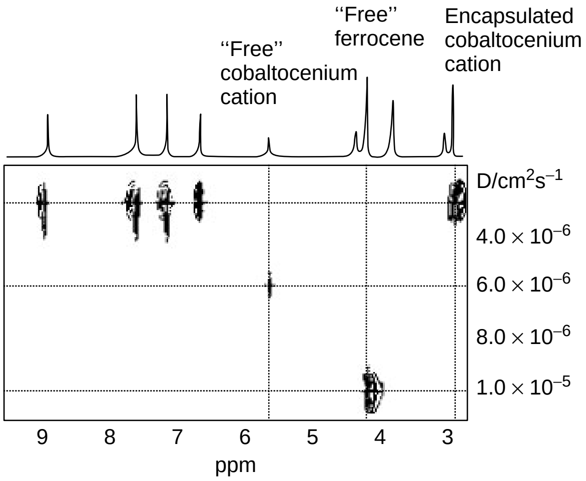

Figure 26 The DOSY spectrum of a solution containing a tetraureacalix[4]arene host, ferrocene, and cobaltocenium cation in $C_2D_4Cl_2$, recorded at 400 MHz, 298 K. The signal at $\delta = 2.72$ ppm has the same D as all the signals of the calixarene indicating encapsulation. The signals of the free ferrocene and cobaltocenium cation at $\delta = 4.06$ and 5.61 ppm, respectively, have much higher diffusion coefficients. (Adapted with permission from Cohen, Y.; Avram, L.; Frish, L. (2005) *Angew. Chem., Int. Ed.,* **44**:520. © 2005 Wiley-VCH)

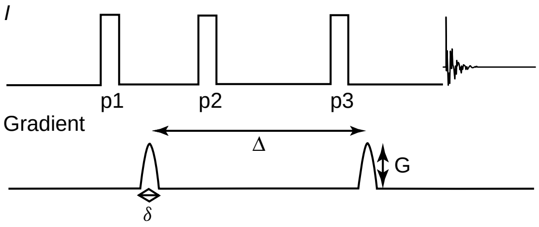

Figure 27 Pulse sequence for stimulated echo PGSE diffusion spectroscopy

$$\ln\left(\frac{I}{I_0}\right) = -(\gamma_X \delta)^2 G^2 \left(\Delta - \frac{\delta}{3}\right) D \qquad (3)$$

Advantages

- The results can be accurate to ±2%.
- The diffusion constants for each chemical shift can be determined simultaneously (for a given nuclide).
- For ^{1}H and ^{19}F, PGSE measurements can be recorded in 1 ∼ 2 h.
- Only small quantities of material (usually 1–2 mM solutions) are required.
- The components of a mixture can be measured simultaneously (as long as they give resolvable NMR resonances).
- The complexes do not need to be isolable; thus measurements can be made on several species in equilibrium.

Disadvantages

- Great care in setting up the experiment is required if reliable results are to be obtained.
- The gradient strength (G) must be known accurately.
- Temperature control of the sample must be precise; the experiment is sensitive to thermal convection currents within the sample.
- If ion pairing is being studied, both anion and cation must have a suitable NMR label.

Acquisition tips

- Use the pulse program, and phase cycling sequences supplied with your instrument. Make sure all necessary experimental parameters are set as described by the manufacturer.
- Normally the gradient strength is varied.
- Use rectangular gradient pulses, ca. 0–8 ms duration, strength 0–0.2 $\mathrm{T m^{-1}}$, 0–0.02 s. The exact values will be sample dependent and depend on which parameter is chosen to be varied.
- Do not spin the sample.

Processing tips

- Process all spectra identically.
- For accurate integrations zero fill the FIDs, baseline-correct the spectra, and correct the slope and bias of the integrals individually.
- Use a solvent resonance to normalize the integrals.
- Plot $\ln(I_g/I_0)$ against Δ, $\delta^2(\Delta-\delta/3)$, or G^2, depending on which parameter was varied. D is obtained from the gradient of the line (Figure 28).
- The hydrodynamic radius can be obtained from D by substitution in the Stoke–Einstein equation (4)

$$D = k_B T/n.\pi\eta.r \tag{4}$$

where η is the viscosity and r the hydrodynamic radius n is usually taken to be 6; however, a value of 4 has also been used when solute and solvent have similar molecular size.

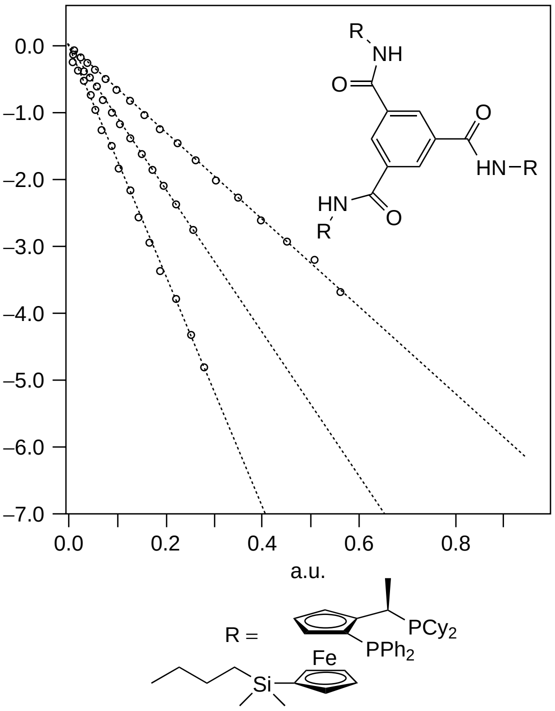

Figure 28 Plot of $\ln(I/I0)$ *versus* G^2 (in arbitrary units) for the first, second, and third generation ferrocene dendrimers based on **A**. The largest compound shows the smallest slope $\propto D$. (Reprinted with permission from D. Valentini, M.; Pregosin, P. S.; Ruegger, H (2000) *Organometallics* **19**: 2551. © 2000 American Chemical Society)

3.6 High Pressure NMR Spectroscopy

High pressure NMR techniques find application in inorganic chemistry in studies of reaction mechanisms in coordination chemistry, where they are used to determine, for example, volumes of activation,[61,62] and in in situ studies of homogeneous catalysis.[63–72] High pressure NMR cells for imaging studies have also been described.[73,74] The equipment required is often highly specialized, pressures in the kilobar range being required for studies of volumes of activation. In studies of reacting homogeneous catalysts, where it is self-evident that it is the concentration of dissolved gas, rather than simply the gas overpressure that is of critical importance (Figure 29),[71,75] some method of gas–liquid mixing that breaks the gas–liquid interface is essential.[76–78] Some workers have suggested that, with care, and suitable protection, and at low pressure, this can be achieved simply by shaking the Roe sapphire tube.[66] This is not to be recommended and is expressly forbidden in some laboratories. The simplest alternative is a dip tube that bubbles gas through the solution,[79] however, such a system still requires ca. 3 min to achieve

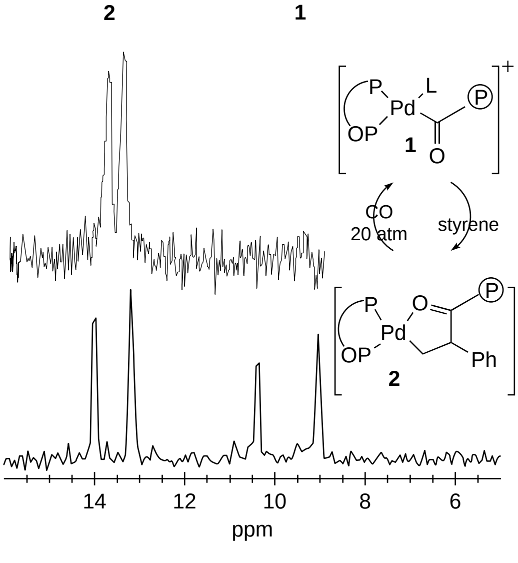

Figure 29 In situ $^{31}P\{^1H\}$ HPNMR spectra (phosphine region) of the co-polymerisation of CO with styrene catalysed by Rh-BINAPHOS: (a) in a zirconia NMR tube, recorded at 202.5 MHz; (b) in a bubble column reactor, recorded at 81.0 MHz. Note only the alkyl intermediate **2** is observed in the unmixed HPNMR tube due to inefficient mass transfer of CO into solution. In the bubble column, delivery of CO to the catalyst is efficient, and so the acyl intermediate **1** is also observed[71]

saturation of the liquid with gas.[80] More complex designs include those of Merbach[81] and Jonas[82] which use mechanical stirrers, that of Bargon and Woelk,[63] which sparges gas through the solution, and the author's bubble column reactor.[78] Yet another alternative is to recirculate the reaction solution between a conventional stirred reactor and the spectroscopic cell;[65] however, care must be taken to ensure gas depletion does not occur while the reaction solution is in the transfer lines/spectroscopic cell. These designs can all achieve efficient mixing of gas with liquid but are more complex to operate.

The Sapphire HPNMR Tube. First introduced by Roe in the 1980s, these have become popular and are in widespread use. More recently, a variant using PEEK tubes has appeared.[83]

Advantages

- The tube can be used in the pressure range 1 to >200 bar.
- It can be used in conventional NMR systems.
- Tubes can be purchased from commercial suppliers.

Disadvantages

- Sapphire tubes are susceptible to unpredictable, catastrophic failure.
- Sapphire tubes require protection from chips and scratches.
- Dissolved gas is rapidly depleted from *reacting* systems.
- Batch operation; experiments requiring changes in gas composition must be performed as a series of separate experiments.

Acquisition tips

- Take great care handling the tubes, make sure the surfaces of the tube are not chipped or scratched.
- Always use a blast shield around pressurized tubes to protect the operator (also applies to PEEK tubes).
- Use a fishing line and (nonmagnetic) hook to insert the sample into the magnet.
- Do not use the lift gas to insert the tube into the magnet; chipping of the base of the tube will almost certainly result. The face of the air bearing may also be damaged by the tube.
- Do not quench tubes, thermal or pressure shock will stress the sapphire and may lead to catastrophic failure.

Autoclave Cells. The NMR probe is constructed inside a high pressure autoclave.[61,62,84] Autoclave cells are principally used for volume of activation studies.[61,62] Toroid cells have been used for studies of organometallic reactions.[64]

Advantages

- can be used from vacuum to >5 kbar
- are extremely robust
- It is possible to incorporate efficient gas-solution mixing.

Disadvantages

- extremely complex
- expensive.

Acquisition tips

- Unless a long-term interest in such measurements exists, the sensible course is to seek a collaboration with a group that specializes in such measurements.

Gas-Liquid Mixing Cells. The simplest approach is to use a dip tube in conjunction with Roe's sapphire tube.[79] More complex designs include bubble columns,[78] and recirculating cells.[65,85] The most complex use mechanical stirring.[81,82]

Advantages

- Such cells can be used in the pressure range 1 to >200 bar.
- Designs using metal vessels are robust.
- Gas concentrations in solution are maintained.
- Experiments requiring changes in gas composition are easily performed.

Disadvantages

- Sapphire tubes require protection from chips and scratches.
- Such cells are more expensive than conventional NMR probes.

Acquisition tips

- All require specialized equipment; unless a long-term interest in such measurements exists, the sensible course is to seek a collaboration with a group that specializes in such measurements.

NMR in Supercritical/Pressurized Fluids. Any of the above systems can be easily modified to record NMR spectra of samples in supercritical/pressurized fluids (within the pressure range of the chosen device).[65,69]

3.7 *para*-Hydrogen NMR spectroscopy[a]

The inherent low sensitivity of NMR spectroscopy makes the detection and characterisation of reaction intermediates, which might be present in low concentration, difficult. One technique that can circumvent this problem is the use of *para*-enriched hydrogen.[86] Any molecule of high symmetry that contains coupled, equivalent, magnetically active nuclei can exist in isomeric forms that differ only in their nuclear spin arrangements. Thus, dihydrogen has two isomers, *ortho*-hydrogen, in which the nuclear spin wavefuntions correspond to the combinations $\alpha\alpha$, $\beta\beta$, or the linear combination $\alpha\beta + \beta\alpha$, and *para*-hydrogen ($p$-$H_2$), which exists as the antisymmetric linear combination

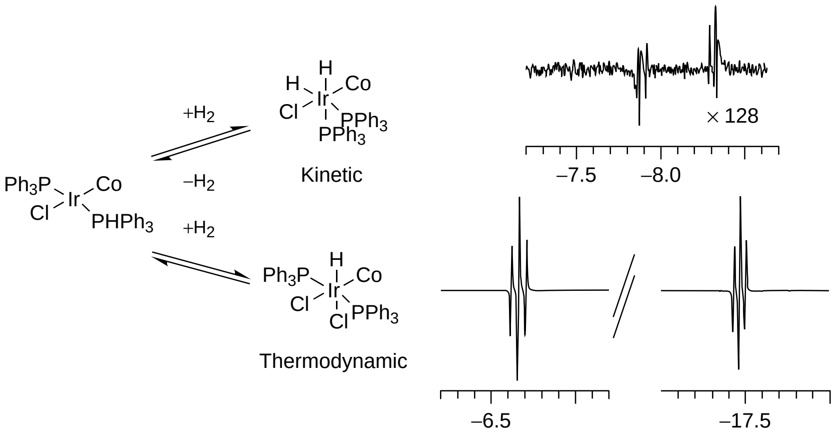

Figure 30 Hydride region of the ^{1}H NMR spectra for the addition of *para*-H_2 to $[Ir(PPh_3)_2(CO)Cl]$ at 295 K, showing the weak second-order resonance from *cis*-*cis*-$[Ir(CO)(PPh_3)_2(Cl)(H)_2]$ and the strong signal due to *trans*-*cis*-$[Ir(CO)(PPh_3)_2(Cl)(H)_2]$. (Figure courtesy of Prof. S. Duckett)

$(\alpha\beta - \beta\alpha)$. Enhanced ^{1}H NMR signals are observed on addition of H_2 in the *para* spin-state to a molecule. In the absence of an applied magnetic field this is the PASADENA (para-hydrogen and synthesis allow dramatically enhanced nuclear alignment) or PHIP (para-hydrogen induced polarization) effect. For example, on oxidative addition of p-H_2 to Vaska's complex, $[IrCl(CO)(PPh_3)_2]$, the metal dihydride complex $[IrCl(CO)(H)_2(PPh_3)_2]$, that contains two magnetically distinct hydride ligands, is obtained in which only the $\alpha\beta$ and $\beta\alpha$ spin states of the product are populated. Large population differences will exist across transitions that involve these hydride ligands, and hence signal intensities will be large. The resonances of the hydride ligands will also appear in antiphase with respect to J(HH) (Figure 30). If the reaction involving p-H_2 occurs in a weak magnetic field, a different effect, dubbed ALTADENA (adiabatic longitudinal transport after dissociation engenders net alignment), is observed. This arises because under these conditions the coupling between the nuclei is large compared to their frequency difference and hence the lower energy $\alpha\beta$ or $\beta\alpha$ level is populated. In the corresponding ^{1}H NMR spectrum, only two enhanced transitions are observed. When a reaction does not go to completion before the sample is placed in the NMR spectrometer both ALTADENA**[87]** and PASADENA**[88,89]** effects are observed simultaneously.

3.7.1 *para-Hydrogen Enhanced HMQC*

With suitable modification of the pulse sequences the *para*-hydrogen effect can be used to enhance the signals in many NMR experiments, for example, COSY, HMQC, HSQC, EXSY and Overhauser spectroscopy.**[86]**

Example Pulse Sequence

The HMQC sequence can be modified by replacing the initial 90° proton excitation pulse, p1, with a 45° pulse (Figures 31 and 32). The proton magnetisation must then evolve with respect to heteronuclear couplings prior to magnetisation transfer to heteronuclei. As in the normal HMQC experiment, this is achieved by the fixed delays d2 which must be optimised for heteronuclear magnetisation transfer. During d2 the proton spins evolve with both J(HH) and J(HX). In organometallic complexes J(HH) is typically small, corresponding to a slow evolution time; the effect of this evolution can therefore be neglected. A purge pulse p5 completes the modified HMQC sequence.

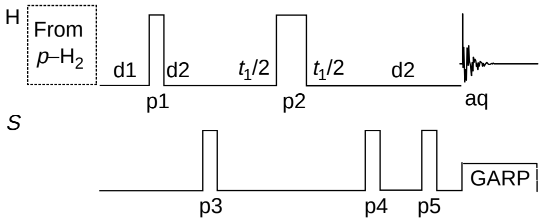

Figure 31 Modified HMQC sequence using *para*-hydrogen

Advantages

- strong enhancement (ca 15 000 times) of NMR signals
- observation of intermediates present in low concentrations
- evidence for pairwise hydrogen transfer
- polarization transfer to hetero nuclides (^{13}C, ^{31}P, etc.).

Disadvantages

- No enhancement is observed if the hydrogen nuclei are transferred to equivalent sites.
- Enhanced signals due to minor species will dominate the spectrum at the expense of signals due to major species that are not enhanced.

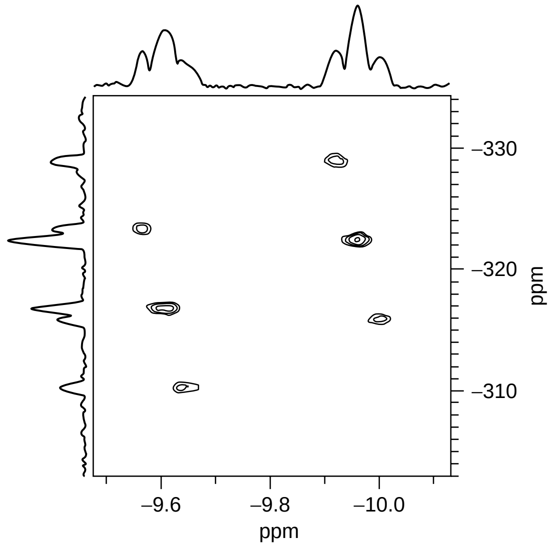

Figure 32 Selected cross peaks and projections from the $^{1}H,^{103}Rh$ HMQC spectrum of $Rh(PMe_3)_3Cl(H)_2$ obtained with *para*-H_2. (Figure courtesy of Prof. S. Duckett)

Acquisition tips

- Use a 45° excitation pulse for maximum signal intensity.

3.7.2 *Preparation of para-Hydrogen*

Often a sufficient enrichment in *para-hydrogen* can be achieved simply by storing the NMR sample, containing the complex to be studied and hydrogen gas, in liquid nitrogen for a few hours. If higher enrichment is required, *para-hydrogen* can be readily prepared by cooling hydrogen gas in the presence of a paramagnetic catalyst such as $FeCl_3$. On separation of the gas from the catalyst *at low temperature,* re-establishment of the thermodynamic equilibrium is very slow. A sample containing *para*-enriched hydrogen, in a suitable container, and in the absence of a catalyst, can be stored for several hours prior to use—remember the walls of a lecture bottle will also catalyse equilibration. A device that can produce essentially pure p-H_2 (>99.8%) by cooling H_2 to 18 K is available form Prof S. B. Duckett.

3.8 Solid-State NMR Spectroscopy

3.8.1 *Cross-Polarization*

The transfer of magnetization from an abundant spin (I), to a dilute one (S), by CP[90] is widely used in numerous pulse sequences in solid-state NMR. The process of CP occurs through the tendency of the magnetization to flow from highly polarized nuclei to nuclei with lower polarizations when the two are brought into contact. CP improves the signal-to-noise ratio due to the transfer of magnetization from abundant ^{1}H spins and significantly reduces recycling delays between the pulses (the relaxation is governed by the ^{1}H system with much shorter relaxation times compared to S spins). The CP relies on the heteronuclear dipolar couplings and the efficiency of CP depends on the strength of the $^{1}H-S$ dipolar couplings governed by the $^{1}H-S$ distance and mobility of the S-containing groups. This explains the non-quantitative character of CP. The application of the cross-polarization extends beyond the systems where ^{1}H act as source spins. Recent advances in the development of triple resonance probe heads enable the X $\rightarrow$ S in which protons are used to either generate X-magnetization (especially for source spins with low natural abundance) or provide $^{1}H-X$ or $^{1}H-S$ heteronuclear decoupling. Examples of such experiments include $^{31}P-^{27}Al$, $^{31}P-^{29}Si$, $^{51}V-^{31}P$, $^{13}C-^{15}N$ pairs.[91–93]

Pulse Sequence. The initial ^{1}H $(\pi/2)_x$ pulse creates ^{1}H magnetization along the $-y$ axis (Figure 33). During the following on-resonance $-y$ pulse (contact pulse) applied at the spin-lock field $B_1(^{1}H)$ the ^{1}H magnetization is kept in the rotating frame of reference. This pulse is applied simultaneously with the S pulse with amplitude $B_1(S)$ (Figure 33). The transfer of magnetization from ^{1}H to S occurs when the amplitudes of the two contact pulses are set to achieve the Hartmann–Hahn matching condition (equation 5).

$$\gamma_{^1H} B_1(^{1}H) = \gamma_S B_1(S) \qquad (5)$$

This condition corresponds to the situation when the energy gaps in the rotating frames of S and ^{1}H spins are equal.

Setting up the CP Experiment. CP can be used for the acquisition of the spectra of both dilute and abundant nuclei. While setting up the CP experiments for spin-1/2 nuclei is relatively straightforward, several difficulties exist for quadrupolar nuclei related to both the presence of several transitions for the quadupolar spins and usually short relaxation times, making it difficult to maintain sufficient magnetization for the time required for the transfer of magnetization. In addition, in rotating samples, strong quadrupolar interaction also

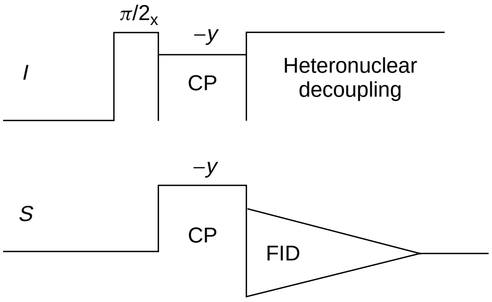

Figure 33 Pulse sequence for CP experiment

becomes time dependent and severely affects the spin-locking efficiency.[92,94,95] The crucial step in setting up the CP experiments is the optimization of the Hartmann–Hahn matching conditions. One should take into account the effect of MAS on the Hartmann–Hahn matching condition. While at relatively slow MAS rates this effect can be neglected, it should be taken into account even at moderate spinning rates. At the high MAS rates, the application of CP is particularly sensitive to the instabilities of the spinning and *rf* power since sidebands of the Hartmann–Hahn match are particularly sharp.

The usual procedure for setting up the CP is:

- Set ^{1}H offset on-resonance via recording a ^{1}H spectrum;
- Determine the ^{1}H ($\pi/2$) pulse (this is also important from the point of view of not overpowering the NMR probe);
- The Hartmann–Hahn match can be found by varying the $B_1(S)$ power level so that maximum intensity is observed. It is important to ensure that the observed spectrum results from the CP (the best indication of this is the absence of the signal after increase of the power beyond the H–H matching condition).
- The CP can be used with different decoupling sequences during the acquisition (these should also be optimized).

The cross-polarization spectra can be acquired using single or RAMP amplitude of B_1^H during the contact time. By using the RAMP amplitude CP (RAMP-CP, Figure 34), one can recover the broad Hartmann–Hahn matching profile even at fast spinning speeds.[96–99] An increase in the intensity of peaks is observed compared to both conventional CP and the originally proposed variable amplitude cross-polarization (VA-CP) pulse sequence since the inhomogeneous Hartman–Hahn conditions are matched over the whole sample volume,[97] making the quantification of the measurements much easier.

The CP step is an essential building block for pulse sequences in solid-state NMR. The easiest 1D experiments that are routinely used for characterization of organic, organometallic and hybrid solids are total suppression of spinning sidebands (TOSS), nonquaternary suppression, and so on.

Cross-Polarization Kinetics. Knowledge of the CP kinetics (dependence of the intensity of the peaks versus contact time) is essential for quantification of the CP-spectra. The CP-kinetics parameters can also provide information on the dynamic properties of the materials under study. A typical CP-kinetics curve consists of two distinct parts: at short contact times the magnetization is increased followed by the decrease

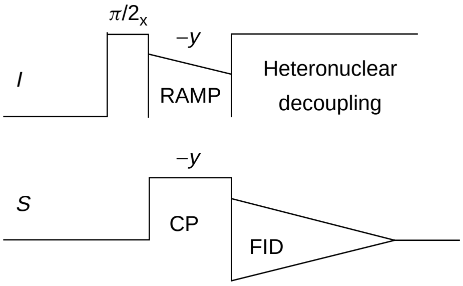

Figure 34 Pulse sequence for RAMP-CP experiment

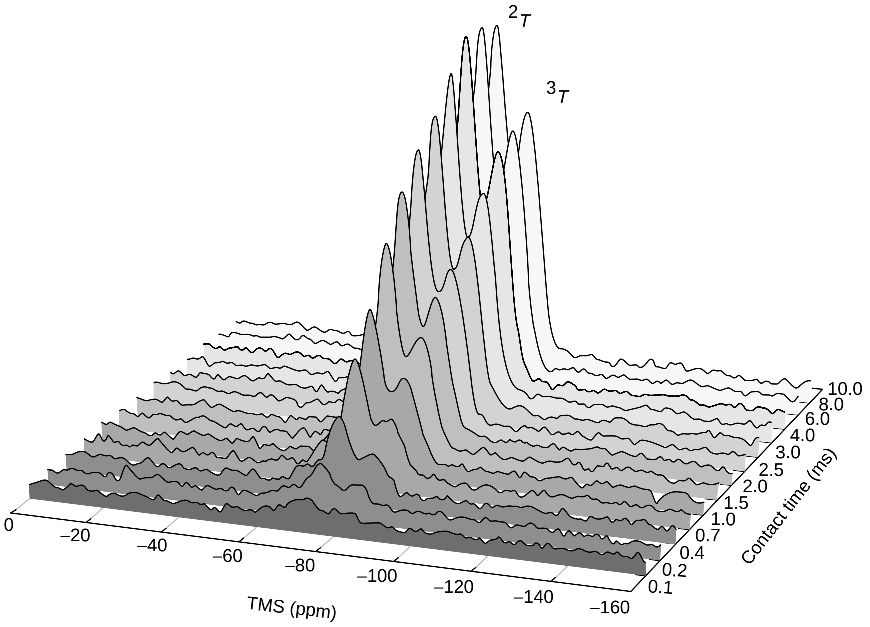

Figure 35 ^{1}H–^{29}Si CP/MAS NMR spectra of –CH=CH– SiO$_2$ hybrids measured with different contact times. ^{2}T sites denote –CH=CH– Si(OSi)$_2$OH units and ^{3}T sites denote the –CH=CH– Si(OSi)$_3$ units

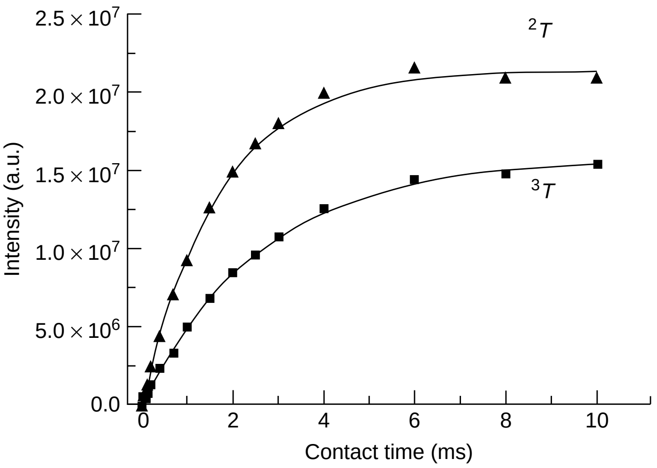

Figure 36 ^{1}H–^{29}Si CP/MAS kinetics curves of ^{2}T and ^{3}T sites in the –CH=CH– SiO$_2$ hybrids

of the intensity (due to the ^{1}H relaxation in the rotating frame) or a plateau (Figures 35 and 36).

Different models of CP kinetics have been developed.[100] The simplest model of CP dynamics (I–S) was derived for homogeneous solids where the I–S heteronuclear interactions are relatively weak and the I–I homonuclear dipolar interactions are sufficiently strong to provide efficient spin diffusion. For the abundant-dilute spin system, the CP dynamics can be described by equation (6):

$$I(t) = I_0\left(1-\frac{T_{\mathrm{IS}}}{T^{I}_{1\rho}}\right)^{-1}\left[\exp\left(-\frac{t}{T^{I}_{1\rho}}\right)-\exp\left(-\frac{t}{T_{IS}}\right)\right] \qquad (6)$$

Since CP is governed by the heteronuclear dipolar interactions, the T_{IS} time constant is related to the internuclear distances and molecular mobility. The $T^{\mathrm{I}}_{1\rho}$ relaxation time describes the decay of intensity for longer contact times. Relaxation is mostly ensured by the ^{1}H–^{1}H homonuclear dipolar interactions. In contrast to the T_{IS} time characteristic of the chemical group under study, $T^{\mathrm{I}}_{1\rho}$ relaxation time is a volume property averaged over the distance of ca. 2 nm.[100,101]

Whereas the I–S model is simple to understand and is widely applied, it is not sufficient to describe the CP kinetics for solids with heterogeneous populations of the source spins. The I–I^*–S model[100] takes into account the efficiency of spin diffusion, which relies on homonuclear dipolar interactions and proceeds through flip–flop spin transitions. The I–I^*–S model relies on the existence of different proton populations, denoted I^* for the protons directly bound to an S spin under study and I for the rest of the proton network. The CP proceeds in two steps. A fast rise of the intensity is observed initially due to the transfer of the magnetization to a dilute spin (I^*–S) by the abundant spins in close proximity followed by a slow rise of the intensity or damped oscillation. Several equations have been proposed to describe the CP kinetics; the simplest is shown below (equation 7).[100]

$$I(t) = I_0\exp\left(-\frac{t}{T^{I}_{1\rho}}\right)\left[1-\lambda\exp\left(-\frac{t}{T_{df}}\right)\right.$$
$$\left.-(1-\lambda)\exp\left(-\frac{3}{2}\frac{t}{T_{df}}\right)\exp\left(-\frac{1}{2}\frac{t^2}{T_2{}^2}\right)\right] \qquad (7)$$

where $T^{\mathrm{I}}_{1\rho}$ is the I spin-lattice relaxation time in the rotating frame; T_{df} is the ^{1}H spin-diffusion time constant describing the strength of the homonuclear dipolar interactions and the homogeneity of the I spin pool; λ is defined by the number n of I spins attached to the S spin under study ($\lambda = 1(n+1)$); T_2 is the spin–spin relaxation time. The values of absolute intensity I_0 derived from either the I–S or I–I^*–S models can be used for the quantification of the ^{1}H–^{13}C CP/MAS spectra.

3.8.2 Total Suppression of Spinning Sidebands (TOSS)

The spectra of organic and organometallic compounds, especially ones bearing aromatic rings in their structure, recorded at low or moderate MAS rates often display a series of spinning sidebands in addition to the isotropic peaks. While such sidebands can be used to derive important structural information (via the knowledge of CSA), they often mask other lines in the spectra which makes the assignment of the spectrum a considerable challenge. The TOSS pulse sequence[16] (Figure 37) has been designed to obtain the spectra in which the sidebands have significantly reduced intensity (Figure 38). This is particularly important for low MAS rates.

Pulse Sequence. In the TOSS pulse sequence a series of usually four (π) pulses are applied in precisely placed points with respect to the rotor cycle prior to acquisition. The TOSS experiments are designed for MAS rates below 8 kHz. The setup of this experiment is identical to the one for the CP apart from the need for an accurate determination of the S (π)-pulse. This can be difficult as a standard with relatively short T_1 relaxation time is required. The S (π)-pulse can also be set using the TOSS pulse sequence indicated by the lowest intensity of spinning sidebands.

The most significant disadvantage of this experiment is the fact that eliminated sidebands do not necessarily contribute to the central band, thus making the quantification of the spectra less reliable than a CP spectrum. The

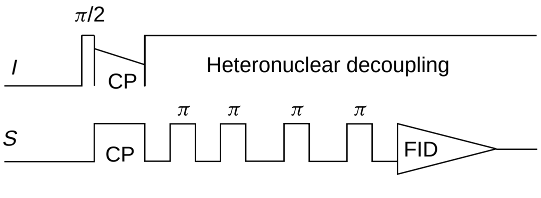

Figure 37 TOSS pulse sequence

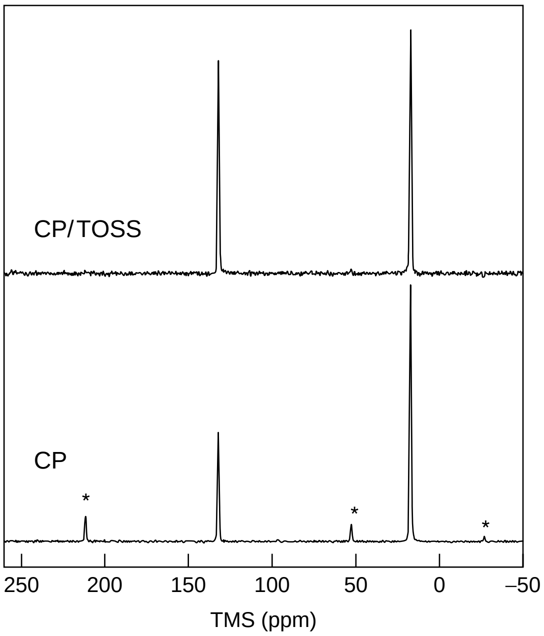

Figure 38 $^1H-^{13}C$ CP/MAS and $^1H-^{13}C$ CP/TOSS/MAS NMR spectra of hexamethylbenzene measured using MAS rate of 8.0 kHz

pulse sequence was designed for samples with cylindrical symmetry. The large number of spinning sidebands hampers the performance of the sequence. In addition, the sequence might suffer from the problems of setting up the S (π)-pulse.

3.8.3 *Nonquaternary Suppression (Dipolar Dephasing)*

The assignment of the $^1H-^{13}C$ CP/MAS spectra can be assisted using a simple pulse sequence which differs from the traditional CP pulse sequence only by the delay between the contact pulse and proton decoupling.**102** Such delay results in a rapid decay of transverse magnetization for carbon sites with very strong $^1H-^{13}C$ heteronuclear dipolar interactions. As a result, the magnetization of the protonated carbons (except CH_3 groups) decays, while that of the quaternary carbons remains in the spectra.

Pulse Sequence. The setup for this experiment is very similar to the conventional CP experiment (Figure 39). The delay times can be set in the range 10–100 μs. The dependence of the signal intensity *versus* the delay time can be used for the estimation of the strength of heteronuclear dipolar coupling and can provide information on mobility.

3.8.4 *Homonuclear Decoupling*

Elimination of homonuclear dipolar coupling is a significant challenge in solid-state NMR of nuclei with high natural abundance and large γ (particularly ^1H and ^{19}F) and can be achieved using multiple-pulse sequences (i.e., WAHUHA, Mansfield, Rhim, Elleman and Vaughan homonuclear decoupling pulse (MREV-8)).**3,4** Most of these pulse sequences are designed in such a way that at certain points in the pulse sequences the effect of the homonuclear dipolar Hamiltonian on the nuclear magnetization is zero. By recording the signal at these specific points, the effect of homonuclear dipolar coupling vanishes. These pulse sequences are far from trivial to implement. Firstly, the FID points need to be collected at a particular point between cycles of pulses. Secondly, high-power pulses are required as the pulse length must be short relative to the cycle time. Moreover, the spectral width of the resulting spectrum is the inverse of the cycle time and it must be large enough to contain all the signals; as a result, short cycle times are preferable. Finally, MAS can interfere with the decoupling sequence so that the decoupling sequence and sample spinning should be accurately synchronized. To avoid these problems, one often relies on two-dimensional (2D) experiments; the homonuclear decoupling being implemented in the indirect dimension. This has been used to generate high-resolution ^1H spectra from 2D experiments.**103** The main advantage of this approach over the implementation of one-dimensional (1D) homonuclear decoupling is that the homonuclear decoupling does not need to be rotor synchronized.

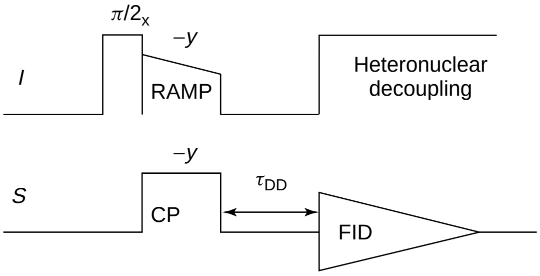

Figure 39 NQS pulse sequence

Frequency-Switched Lee–Goldburg Decoupling (FSLG). The frequency-switched Lee–Goldburg decoupling (FSLG) decoupling**104,105** has found numerous applications in solid-state NMR pulse sequences. The Lee–Goldburg (LG) decoupling employs off-resonance (2π) pulses (Figure 40). If the offset frequency, $\Delta\omega$, is chosen as $\Delta\omega = \omega_{RF}\sqrt{2}$, ω_{RF} corresponding to the on-resonance *rf* pulse, the effective field that the spins experience in the rotating frame is oriented at magic angle with respect to $\vec{B}_0$. Thus a (2π) pulse with such offset causes the net magnetization to precess by one turn around this effective field leading to averaging out the homonuclear dipolar coupling between the spins. To compensate errors in the averaging of the dipolar Hamiltonian, the offset is switched between $+\Delta\omega$ and $-\Delta\omega$ and its phase simultaneously changed by (π).

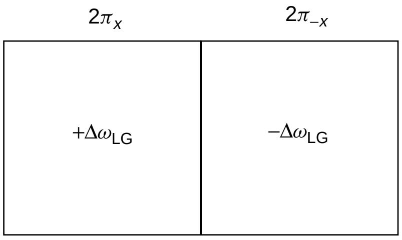

Figure 40 FS-LG Homonuclear decoupling

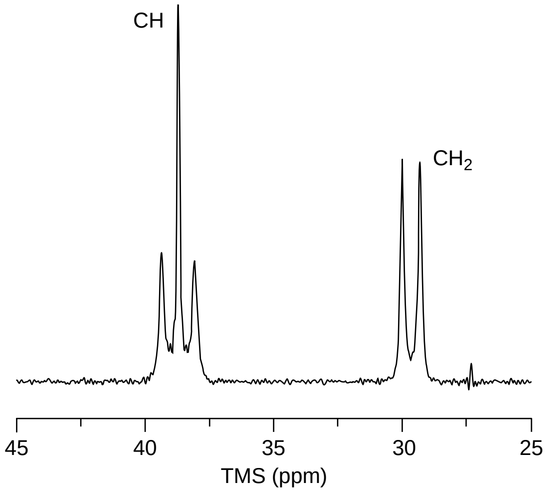

Figure 41 $^1H-^{13}C$ CP/MAS NMR spectrum of adamantane recorded using FSLG decoupling. Note the splitting of lines: the triplet corresponds to CH sites, the doublet corresponds to CH_2 sites

Setting up the FSLG is not straightforward. The pulse sequence is rotor synchronized and particular consideration should be taken when setting the ^1H offset. The FSLG decoupling can be setup using the $^1H-^{13}C$ CP/MAS spectrum of adamantane recorded at the conditions of the homonuclear decoupling (Figure 41). FSLG decoupling is correctly setup when the spectrum shows a well defined triplet and doublet corresponding to the CH and CH_2 sites respectively. The presented pulse sequence requires well set up CP and TPPM decoupling steps. The FSLG is frequently used as a building block for the pulse sequences employing homonuclear decoupling. Other recently developed pulse sequences for homonuclear decoupling include decoupling using mind-boggling optimization (DUMBO) and phase-modulated Lee–Goldburg experiment.**[106]**

3.9 Correlation Experiments in Solid-State NMR

3.9.1 Homonuclear Correlation

Most homonuclear correlation experiments rely on the homonuclear dipolar couplings to provide information on the spatial proximity of nuclei. Such experiments utilize the possibility of excitation of multiple-quantum transitions in the dipolar-coupled systems. The high-resolution type experiments relying on the J-couplings (i.e., incredible natural abundance double-quantum transfer experiment (INADEQUATE)) can be used. All these experiments are performed under MAS to meet the requirements of the resolution.

2D CRAMPS Spectroscopy. The measurement of ^1H solid-state NMR spectra for organic compounds is a significant challenge due to the presence of very strong homonuclear coupling. Combined rotation and multiple pulse spectroscopy (CRAMPS)**[107]** provides a significant improvement in the resolution of the spectra. Despite the obvious advantages, wider application of this method has been hampered by the very difficult setup procedure and its high sensitivity to the instabilities of *rf* power and MAS. Unlike its predecessor, the 2D CRAMPS method is much easier to setup due to the recent development of homonuclear decoupling sequences (i.e., FSLG or DUMBO).**[103,108]**

Pulse Sequence. The first $(\pi/2)$ pulse creates the proton magnetization in a plane perpendicular to the direction of the effective field present during the application of the multiple-pulse homonuclear decoupling sequence (Figure 42). During t_1, the proton magnetization evolves in this tilted transverse plane under homonuclear decoupling. At the end of the evolution time t_1 a pre-pulse of flip-angle θ is applied. This rotates the proton magnetization from the tilted transverse plane to the (x, y) plane of the rotating frame. A z-filter is then applied to allow phase-sensitive detection in t_1, before direct signal detection in t_2. As a result, a two-dimensional correlation between a high-resolution proton CRAMPS spectrum in ω_1 and the MAS spectrum in ω_2 can be observed (Figure 43). The one-dimensional CRAMPS spectrum is obtained by simply summing the ω_1 traces extracted at the various proton frequencies. This method of indirect detection of the high-resolution proton spectrum is particularly convenient since it allows the use of windowless multiple-pulse sequences which currently have a far superior performance to sequences allowing direct acquisition of the signal. The method is also less prone to artefacts.

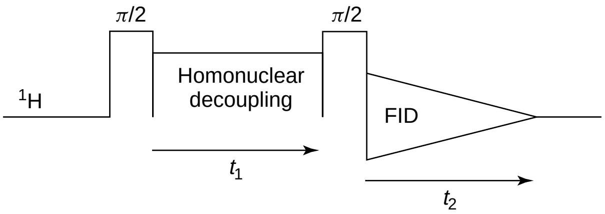

Figure 42 2D CRAMPS pulse sequence

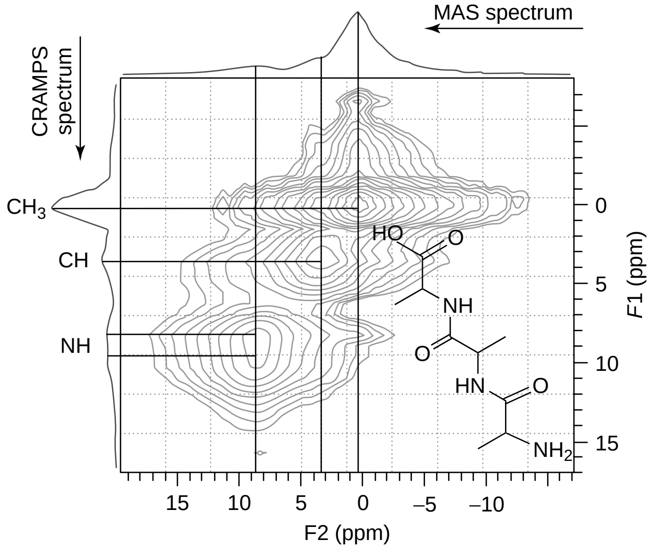

Figure 43 $^1H-^1H$ correlation spectrum of tri-L-alanine recorded using FSLG decoupling in t_1, MAS = 15 kHz

Experimental Setup. The setup of the experiment is determined by a homonuclear decoupling sequence used during t_1. For FSLG decoupling the spectra can be recorded with MAS rate up to 15 kHz (both 4 mm and 2.5 mm rotors can be used). The resolution of the spectra can be improved by using the rotors with reduced sample volume (CRAMPS rotor). FSLG decoupling needs to be optimized prior to the experiment. The performance of the pulse program can be improved by the careful optimization of the pre-pulse. Since the FSLG is used during the acquisition, the chemical shift in ω_2 is altered by a factor of $3^{-1/2}$ and rescaling of the ω_2 is required during the processing step.

Double-Quantum. (DQ) Proton Spectroscopy. Multiple-quantum (MQ) coherences are routinely used in high-resolution solution-state NMR spectroscopy. The MQ coherences cannot be observed directly and the application of two-dimensional methodology is required. The Double-Quantum (DQ) methodology is particularly useful to derive the information on the spatial proximity of different spins on the basis of the homonuclear dipolar couplings.**[106]**

Pulse Sequence. A typical pulse sequence for DQ experiments consists of several blocks (Figure 44). One also needs to consider the effect of MAS. The commonly used pulse sequences are designed in such a way that the excitation time is synchronized with the rotor period. The excitation of DQ coherence can be achieved by using different recoupling sequences (i.e., back-to-back recoupling sequence (BABA),**[109]** dipolar recovery at the magic angle (DRAMA), C7 recoupling pulse sequence (C7), homonuclear rotary resonance (HORROR)). The DQ coherence evolves subsequently during t_1. In the following step, the DQ coherence needs to be converted back into observable, single-quantum coherence which is detected during t_2.

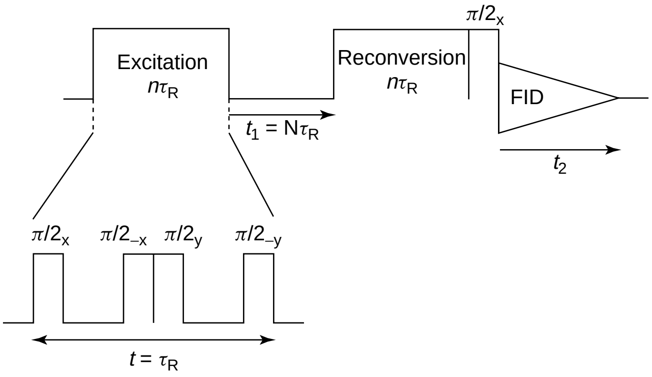

Figure 44 Double-quantum pulse program

In the case of very strong dipolar couplings ($^1H-^1H$) the experiment is performed using fast MAS rates (ca. 30 kHz) so that spectra with sufficient resolution can be recorded. The performance of this pulse sequence is very sensitive to the instabilities of MAS. The rotor synchronised 2D DQ NMR spectrum (the increment in t_1 set to one rotor period) provides information on the spatial proximity of different protons based on the presence of peaks in the ω_2 dimension. If the spins A (ν_A) and B (ν_B) are close in space, the peaks at $((\nu_A + \nu_B), \nu_A)$ and $((\nu_A + \nu_B), \nu_B)$ will appear in the 2Q spectrum (Figure 45). This provides semi-quantitative

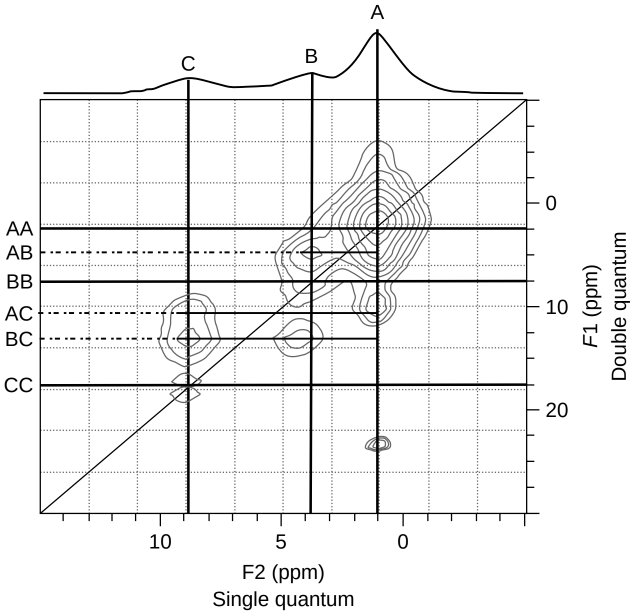

Figure 45 Rotor synchronised $^1H-^1H$ double-quantum MAS spectrum of tri-L-alanine using 1 rotor period BABA for excitation and reconversion, MAS = 30 kHz

assignment of the structures. If the increment in t_1 is reduced and a suitable recoupling sequence is used (BABA or DRAMA), the DQ MAS sideband pattern is generated from which the ^{1}H−^{1}H dipolar coupling constant and, hence, the ^{1}H−^{1}H distances can be determined.**[106]**

DQ spectroscopy is not limited just to ^{1}H−^{1}H pairs and has been applied to determine proximities between ^{13}C nuclei (in isotopically enriched systems). Recently, Levitt *et al.* developed a new SR26_4 homonuclear recoupling pulse sequence which was used for the determination of ^{29}Si−^{29}Si correlations in zeolites.**[110,111]** One should be aware of the important difference between the DQ and INADEQUATE experiments. While the former is based on the homonuclear dipolar couplings, the INADEQUATE relies on the J-couplings to create the DQ coherence. The DQ coherences build up much faster using the dipolar recoupling sequence in comparison with INADEQUATE experiments due to much higher ^{29}Si–O–^{29}Si dipolar couplings compared with the ^{29}Si–O–^{29}Si J-couplings.

3.9.2 Heteronuclear Correlation Methods

HETCOR. Heteronuclear correlation (HETCOR) experiments are very important in solution-state NMR spectroscopy and are used for the assignment of structure of complex organic molecules. While in high-resolution NMR spectroscopy the inverse detection (HSQC or HMQC) is a method of choice, the presence of strong ^{1}H–X (X = ^{13}C, ^{15}N, ^{29}Si etc.) heteronuclear dipolar couplings, which can be used for the ^{1}H → X transfer of magnetization in CP, is exploited further to determine the ^{1}H–X connectivities in the solid.**[112]** The ^{1}H–X HETCOR experiment enables the increased resolution of ^{1}H peaks due to the usually much higher resolution of the spectra for the heteronucleus. The HETCOR method has been applied to the determination of the structure of porous heterogeneous catalysts with limited long−range order.**[6,113]**

Pulse Sequence. The basic pulse sequence for the HETCOR experiment can be considered as a derivative of the pulse sequence used for the CP experiments (Figure 46). The main difference between the CP and HETCOR pulse sequences lies in the presence of the homonuclear decoupling step before the ^{1}H ($\pi/2$) pulse. The experiment starts with the excitation of the single-quantum coherence of the ^{1}H spins and its evolution during t_1. In the case of FSLG-HETCOR the ^{1}H magnetization is to be brought to the *xy* plane by an additional θ_m pulse (in the FSLG pulse sequence the ^{1}H magnetization is kept at θ_m). This is followed by the usual CP transfer of magnetization and detection of X FID in t_2 (under the heteronuclear decoupling, i.e., TPPM). In the basic HETCOR experiment it is important to use a very short contact time in the CP step to ensure the detection of the X peaks with ^{1}H in close proximity. This problem can be eliminated by the application of Lee−Goldburg CP ensuring the transfer of magnetization from directly bound protons (Figure 47).**[112]** It is important to note that due to the use of FSLG, the scale of the ^{1}H dimension in the resulting spectrum is modified by the factor $(1/3)^{1/2}$.

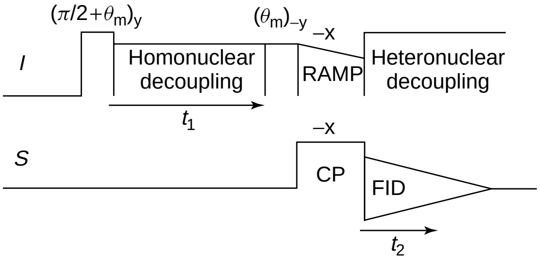

Figure 46 HETCOR pulse sequence

Since its introduction, several other coherence transfer pathways have been employed. The described FSLG-HETCOR and recently proposed MAS-J-HMQC pulse sequence**[114]** uses heteronuclear dipolar couplings, while the REPT-HMQC employs the rotational-echo double resonance (REDOR)**[115]** recoupling pulse sequence.

Wide Line Separation Spectroscopy (WISE). Wide line separation spectroscopy (WISE) has been applied to correlate the molecular structure and mobility based on the linewidths of static ^{1}H lines (Figure 48). In this experiment ^{1}H lines are separated by virtue of a much better resolved chemical shift of ^{13}C sites in their close proximity.**[9,116]** The linewidths of ^{1}H peaks provide a qualitative estimation of mobility (the wider the peak, the stronger the ^{1}H−^{1}H coupling and, hence, a reduced mobility), while the well-resolved ^{13}C sites provide the information on molecular structure.

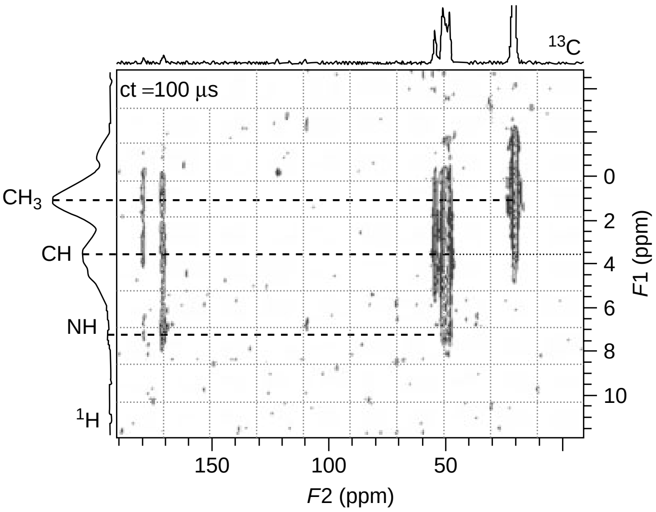

Figure 47 ^{1}H−^{13}C HETCOR spectrum of tri-L-alanine, 100 µs contact time was used, the MAS rate was 10 kHz

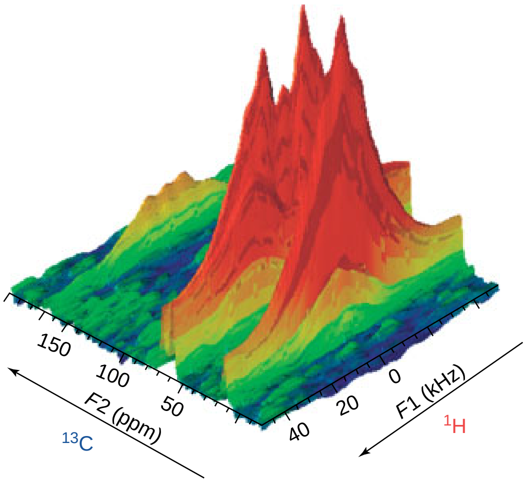

Figure 48 $^{1}H-^{13}C$ WISE NMR spectrum of poly-lactide/glycolide. The projection in F_2 corresponds to $^{1}H-^{13}C$ CP/MAS NMR spectrum ensuring site resolution; the projections in F_1 corresponds to ^{1}H wide lines: the linewidth can be correlated with molecular mobility of a particular ^{13}C site

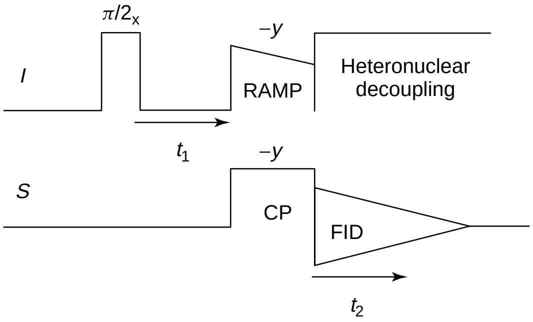

Figure 49 Pulse sequence for WISE

Pulse Sequence. The pulse sequence for WISE experiments can be considered as a derivative of the CP pulse sequence (Figure 49). After the initial ($\pi/2$) pulse, the ^{1}H magnetization is allowed to evolve during t_1. Subsequently, the remaining ^{1}H magnetization is transferred via CP to ^{13}C. The resulting ^{13}C magnetization is then recorded in t_2. The very short CP step (50–150 μs) is essential to prevent ^{1}H spin diffusion.

3.10 Measurement of Dipolar Couplings in Solid-State NMR

Measurement of the heteronuclear dipolar couplings defines the use of solid-state NMR spectroscopy for determination of internuclear distances. The main part of such experiments involves refocusing of the heteronuclear dipolar couplings. The REDOR experiment has been used extensively to determine the internuclear distances ($^{13}C-^{15}N$, $^{13}C-^{31}P$ etc.).[112,115,117]

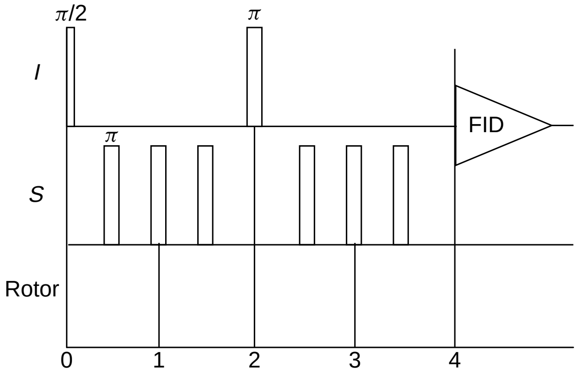

Figure 50 Pulse sequence for REDOR experiment

3.10.1 Pulse Sequence

The measurement of the heteronuclear dipolar coupling constant is achieved via a rotor synchronized pulse sequence in which the transverse magnetization dephases under the $I-S$ heteronuclear dipolar coupling during the first half of the rotor period and is subsequently refocused during the second half of the rotor period via the application of $S\pi$ pulse (Figure 50). The difference of spectra recorded with and without the application of $S\pi$ pulses depends on the strength of dipolar coupling. An I π pulse applied at the halfway point of dephasing period ensures refocusing of any I spin chemical shift offset.[118]

The magnitude of the $I-S$ dipolar coupling can be derived from the plot of intensity of difference spectra versus number of rotor periods. This is easily achievable for $I-S$ isolated spin pairs. Such analysis becomes significantly more difficult when I spin is coupled to several S spins so that several dipolar coupling constants are present. The dephasing effect in REDOR depends on the strength of dipolar coupling (for very strong couplings the magnetization will be totally dephased after only one or two rotor periods). The setup of the experiment depends on the rotor speed and accuracy of the used π pulses.

The REDOR experiment has been proposed for spin-1/2 pairs. For quadrupolar nuclei-spin-1/2 pairs, the use of this experiment is limited. The main reason behind this is the fact that a significant quadrupolar broadening (in order of several MHz) makes the $S\pi$ pulses inefficient for the inversion of S populations. For such systems REDOR experiments can be applied if the π pulses are applied to the spin-1/2 nucleus and only central transition is observed for a half-integer spin. The transfer of population in double resonance (TRAPDOR)[119] or rotational-echo adiabatic passage double resonance (REAPDOR)[120] experiment offer a much better choice for the measurement of quadrupolar nuclei-spin-1/2 pair dipolar couplings.

3.11 Quadrupolar Nuclei

Quadrupolar nuclei present several challenges in solid-state NMR. While for spin-1 (^{2}H, ^{6}Li) nuclei most of the solid-state NMR experiments rely on the wide lines and measurement of quadrupolar coupling constants (though significant progress in MAS methodology for ^{2}H has been reported recently), for half-integer quadrupolar nuclei it is possible to record high-resolution spectra. The central transition of the latter is not broadened by the first-order quadrupolar interactions ensuring its much easier detection relative to the satellite transitions. MAS can provide a significant narrowing of the lines of quadrupolar nuclei for solids. MAS will average out the first-order quadrupolar broadening of satellite transitions (in most cases not completely, due to the rate of spinning not being large enough relative to the size of the anisotropy). It is important to note that the central transition is still affected by the second-order quadrupolar interactions. Therefore, MAS does not succeed in a complete removal of anisotropic quadrupolar effects.

The theoretical background of solid-state NMR spectroscopy of quadrupolar nuclei can be found in excellent recent reviews.[4,22] In this section only the main techniques will be highlighted. Such methods achieve the averaging out of the quadrupolar anisotropy by using either a purely geometric part of the Hamiltonian (i.e., double-rotation or dynamic-angle spinning methods) or combine multiple-pulse methodology with MAS (Multiple-quantum magnetic angle spinning (MQMAS) or Satellite Transition MAS methods).

The double-rotation (DOR) method[121,122] leads to high-resolution NMR spectra of quadrupolar nuclei by spinning the sample at two different angles: the first angle is set at the magic angle, thus ensuring averaging out of the first-order quadrupolar effects; the second angle is set at either 30.6 or 70.1° so that the second-order effects are averaged out (Figure 51). Practical implementation of this method requires the use of the specifically designed NMR probe heads capable of ensuring the stable MAS of a complex sample holder consisting of two rotors spun simultaneously (much lower rate of rotation of the outer rotor results in generation of numerous sidebands). The dynamic-angle spinning (DAS) method[121,123] results in a two-dimensional spectrum, separating isotropic chemical shift and quadrupolar powder patterns. This is achieved by rotor synchronized refocusing of the quadrupolar broadening. The transition frequency is changed by the alteration of the sample spinning angle (usually, the combination of spinning angles of 37.38° and 79.19° is used). Since only rotation about one axis is required at any time in the pulse sequence, this method can employ relatively fast spinning rates. However, the need to change the spinning angle during the acquisition can only be achieved with specially designed probe heads. In addition, the DAS method does not use rotation about the magic angle. Therefore other anisotropic magnetic interactions are not averaged out.

Unlike DAS or DOR methods, the MQMAS method achieves high resolution for half-integer spins under the conditions of MAS and therefore can be used on any conventional solid-state NMR spectrometer. The resulting two-dimensional spectra correlate isotropic chemical shifts in t_1 with a quadrupolar coupling pattern in t_2. Whereas in DAS method the refocusing of the evolution period is carried out via the change of spinning angle, in MQMAS the same is achieved by changing the order of the evolving coherence. The theoretical background of MQMAS spectroscopy can be found in an excellent book by M. J. Duer.[4] Considering the practical aspects of this method, the pulse sequence consists of three main parts: excitation of the multiple-quantum coherence, transfer of multiplequantum into the single-quantum coherence, and detection during t_2 (Figure 52). The excitation of multiple-quantum coherence can be achieved by $(\pi/2) - \tau - (\pi/2)$ sequence (used in high-resolution NMR

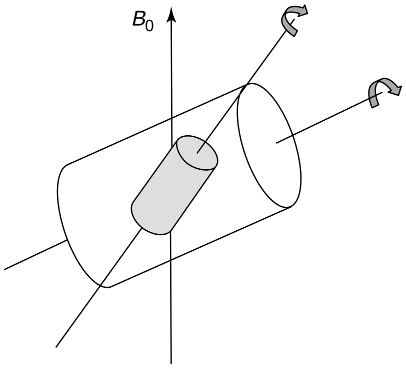

Figure 51 Set-up for double-Rotation NMR

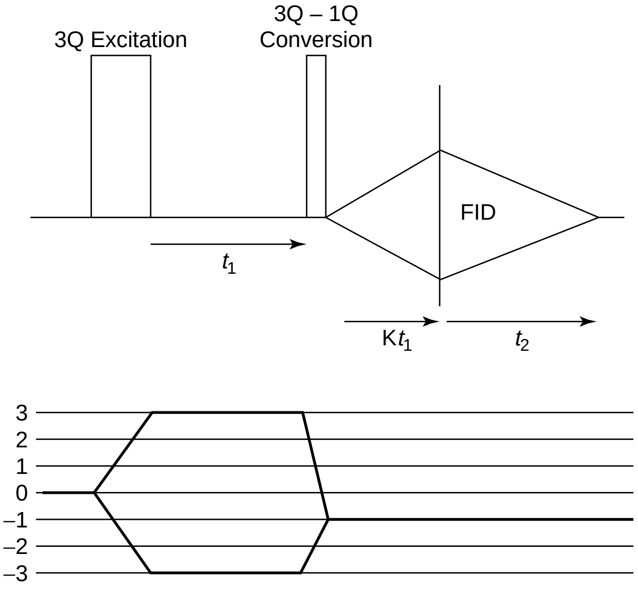

Figure 52 MQMAS pulse sequence

spectroscopy) and its selection is ensured by the specific phase cycling. The high-power of the pulse is needed for effective excitation. It is important to note that the efficiency of this step depends on the magnitude of quadrupolar coupling constant. The MQ-SQ transfer is also dependent on the quadrupolar coupling constant and, hence, on the pulse power.

The MQMAS has now become the most widespread method for the acquisition of high-resolution solid-state NMR spectra of quadrupolar nuclei. The MQMAS step has been incorporated into the other pulse sequences focusing on achieving the correlation between the quadrupolar and spin-1/2 nuclei (i.e., HETCOR-MQMAS).[124]

The recently proposed Satellite Transition Magic-Angle Spinning (ST-MAS)[22] is similar to the MQMAS, apart from the fact that the central transition is correlated with satellite transition rather than MQ transitions. The use of only single-quantum coherences in ST-MAS is advantageous (compared with the MQMAS method where MQ coherences are used) from the point of view of better signal-to-noise. The satellite transitions show a much weaker dependence on the quadrupolar coupling constant in comparison with the MQ coherences. The main disadvantage of ST-MAS method is in its very high sensitivity to the setting of the magic angle to prevent the reintroduction of first- and second-order quadrupolar couplings into the satellite transition coherence. The very accurate setting of magic angle can be achieved using the Rb NMR and ensures a satisfactory resolution of the resulting 2D spectrum.

4 END NOTE

[a] The authors thank Prof. S. Duckett for providing the following information.

5 ABBREVIATIONS AND ACRONYMS

ALTADENA = adiabatic longitudinal transport after dissociation engenders net alignment; aq = acquire; BABA = back-to-back recoupling sequence; BIRD = bilinear rotation decoupling; C7 = C7 recoupling pulse sequence; CHIRP = a quick, frequency modulated ‘‘chirp’’ pulse used for broadband decoupling; CP = cross-polarization; CRAMPS = combined rotation and multiple-pulse spectroscopy; CSA = chemical shift anisotropy; DANTE = delays alternating with nutation for tailored excitation; DEPT = distortionless enhancement by polarization transfer; DOR = double-rotation method; DOSY = diffusion ordered spectroscopy; DRAMA = dipolar recovery at the magic angle; DUMBO = decoupling using mind-boggling optimization; EXSY = exchange spectroscopy; FID = free-induction decay; FSLG = frequency-switched Lee–Goldburg decoupling; GARP = globally optimized alternating-phase rectangular pulses; HETCOR = heteronuclear correlation; HMB = hexamethylbenzene; HMQC = heteronuclear multiple quantum coherence; HOESY = heteronuclear overhauser effect spectroscopy; HORROR = homonuclear rotary resonance; HSQC = heteronuclear single quantun coherence; INADEQUATE = incredible natural abundance double quantum transfer experiment; IUPAC = International union of pure and applied chemistry; MAS = magic-angle spinning; MQMAS = multiple-quantum magic-angle spinning; MREV-8 = Mansfield, Rhim, Elleman and Vaughan homonuclear decoupling pulse sequence; NOESY = nuclear overhauser effect spectroscopy; PASADENA = para-hydrogen and synthesis allow dramatically enhanced nuclear alignment; PGSE = pulsed gradient spin echo; PHIP = para-hydrogen induced polarization; PMG-HMQC = poor man’s gradient-heteronuclear multiple quantum coherence; RAMP = cross-polarisation with ramped amplitude during the contact time; REAPDOR = rotational-echo adiabatic passage double resonance; REDOR = rotational-echo double resonance; SPINAL = small phase incremental alteration decoupling; ST-MAS = satellite transition magic-angle spinning; TMS = tetramethylsilane; TOSS = total suppression of spinning sidebands; TPPI = time proportional phase increment; TPPM = two pulse phase modulation; TRAPDOR = transfer of population in double resonance; WAHUHA = Waugh, Huber and Haeberlen pulse sequence; WALTZ = A composite pulse decoupling sequence named for the succession of pulses of varying lengths ($1 \times \pi/2$, $2 \times \pi/2$, $3 \times \pi/2$, etc.); WISE = wide-line separation spectroscopy; XiX = A heteronuclear decoupling pulse sequence.

6 FURTHER READING

J. W. Akitt and B. E. Mann, ‘NMR and Chemistry’, Stanley Thornes, Cheltenham, 2000—an excellent, example led text on the applications of NMR spectroscopy in chemistry.

S. Berger and S. Braun, ‘200 and More NMR Experiments—A Practical Course’, Wiley-VCH, Weinheim, 2004, p. 405. An excellent practical manual covering all NMR spectroscopy.

A. E. Derome, ‘Modern NMR Techniques for Chemistry Research’, Pergamon Press, Oxford, 1987. An excellent book giving practical advice covering all NMR spectroscopy.

R. Freeman ‘Spin Choreography: Basic Steps in High Resolution NMR’, Oxford University Press, Oxford, 1998. An excellent text covering multipulse NMR spectroscopy.

gNMR, http://home.cc.umanitoba.ca/~budzelaa/gNMR/gNMR.html An excellent (presently free) NMR simulation program.

R. K. Harris, E. D. Becker, S. M. Cabral de Menezes, R. Goodfellow, and P. Granger, *Pure Appl. Chem.* 2001, **73**, 1795; http://www.

iupac.org/publications/pac/2001/7311/7311x1795.html IUPAC guidance on referencing NMR spectra.

R. K. Harris and B. E. Mann eds., 'N.M.R. and the Periodic Table', Academic Press, London, 1979.

7 REFERENCES

1. J. Klinowski, *Chem. Rev.*, 1991, **91**, 1459.
2. G. Engelhardt and D. Michel, 'High Resolution Solid-State NMR of Silicates and Zeolites', John Wiley & Sons, Chichester, 1987.
3. R. K. Harris, 'Nuclear Magnetic Resonance Spectroscopy: A Physicochemical View', Longman Group, Harlow, 1994.
4. M. J. Duer, 'Introduction to Solid-State NMR Spectroscopy', Blackwell Science, Oxford, 2004.
5. M. L. Occelli, U. Voigt and H. Eckert, *Appl. Catal., A: Gen.*, 2004, **259**, 245.
6. M. D. Jones, M. J. Duer, S. Hermans, Y. Z. Khimyak, B. F. G. Johnson and J. M. Thomas, *Angew. Chem., Int. Ed. Engl.*, 2002, **41**, 4726.
7. M. Hunger and J. Weitkamp, *Angew. Chem., Int. Ed. Engl.*, 2001, **40**, 2954.
8. I. I. Ivanova, N. S. Nesterenko and C. Fernandez, *Catal. Today*, 2006, **113**, 115.
9. K. Schmidt-Rohr and H. W. Spiess, 'Multidimensional Solid-State NMR and Polymers', Academic Press, London, 1994.
10. D. D. Laws, H. M. L. Bitter and A. Jerschow, *Angew. Chem., Int. Ed. Engl.*, 2002, **41**, 3096.
11. E. R. Andrew, A. Bradbury and R. G. Eades, *Nature*, 1958, **182**, 1659.
12. E. R. Andrew, A. Bradbury and R. G. Eades, *Nature*, 1959, **183**, 1802.
13. R. Warrass, J. M. Wieruszeski, C. Boutillon and G. Lippens, *J. Am. Chem. Soc.*, 2000, **122**, 1789.
14. T. Posset, F. Rominger and J. Blumel, *Chem. Mater.*, 2005, **17**, 586.
15. J. Herzfeld and A. E. Berger, *J. Chem. Phys.*, 1980, **73**, 6021.
16. W. T. Dixon, *J. Chem. Phys.*, 1982, **77**, 1800.
17. J. W. Traer, E. Montoneri, A. Samoson, J. Past, T. Tuherm and G. R. Goward, *Chem. Mater.*, 2006, **18**, 4747.
18. A. Bielecki and D. P. Burum, *J. Magn. Reson., Ser. A*, 1995, **116**, 215.
19. F. G. Riddell, R. A. Spark and G. V. Gunther, *Magn. Reson. Chem.*, 1996, **34**, 824.
20. L. van Wullen, G. Schwering, E. Naumann and M. Jansen, *Solid State Nucl. Magn. Reson.*, 2004, **26**, 84.
21. B. Langer, L. Schnell, H. W. Spiess and A. R. Grimmer, *J. Magn. Reson.*, 1999, **138**, 182.
22. S. E. Ashbrook and S. Wimperis, *Prog. Nucl. Magn. Reson. Spectrosc.*, 2004, **45**, 53.
23. C. P. Jaroniec, C. E. MacPhee, V. S. Bajaj, M. T. McMahon, C. M. Dobson and R. G. Griffin, *Proc. Natl. Acad. Sci. U.S.A.*, 2004, **101**, 711.
24. T. Asakura, K. Ohgo, T. Ishida, P. Taddei, P. Monti and R. Kishore, *Biomacromolecules*, 2005, **6**, 468.
25. A. E. Bennett, C. M. Rienstra, M. Auger, K. V. Lakshmi and R. G. Griffin, *J. Chem. Phys.*, 1995, **103**, 6951.
26. B. M. Fung, A. K. Khitrin and K. Ermolaev, *J. Magn. Reson.*, 2000, **142**, 97.
27. A. Detken, E. H. Hardy, M. Ernst and B. H. Meier, *Chem. Phys. Lett.*, 2002, **356**, 298.
28. R. K. Harris, E. D. Becker, S. M. C. De Menezes, R. Goodfellow and P. Granger, *Pure Appl. Chem.*, 2001, **73**, 1795.
29. S. J. Anderson, J. R. Barnes, P. L. Goggin and R. J. Goodfellow, *J. Chem. Res., Miniprint*, 1978, 3601.
30. P. L. Goggin, R. J. Goodfell and F. J. S. Reed, *J. Chem. Soc., Dalton Trans.*, 1974, 576.
31. G. A. Morris and R. Freeman, *J. Am. Chem. Soc.*, 1979, **101**, 760.
32. O. W. Sorensen and R. R. Ernst, *J. Magn. Reson.*, 1983, **51**, 477.
33. D. P. Burum and R. R. Ernst, *J. Magn. Reson.*, 1980, **39**, 163.
34. A. Bax, R. H. Griffey and B. L. Hawkins, *J. Magn. Reson.*, 1983, **55**, 301.
35. B. T. Heaton, J. A. Iggo, I. S. Podkorytov and S. P. Tunik, *Magn. Reson. Chem.*, 2004, **42**, 769.
36. F. Du, M. L. Liu, X. J. Miao, X. A. Mao and L. C. Song, *Meas. Sci. Technol.*, 1999, **10**, 170.
37. D. Boudot, D. Canet, J. Brondeau and J. C. Boubel, *J. Magn. Reson.*, 1989, **83**, 428.
38. A. Bax and S. Subramanian, *J. Magn. Reson.*, 1986, **67**, 565.
39. http://www.pitt.edu/∼pkm9/pravat.pdf.
40. W. F. Reynolds and R. G. Enriquez, *Magn. Reson. Chem.*, 2001, **39**, 531.
41. J. R. Garbow, D. P. Weitekamp and A. Pines, *Chem. Phys. Lett.*, 1982, **93**, 504.
42. A. J. Shaka, P. B. Barker and R. Freeman, *J. Magn. Reson.*, 1985, **64**, 547.
43. G. Otting and K. Wuthrich, *J. Magn. Reson.*, 1988, **76**, 569.
44. J. M. Nuzillard, G. Gasmi and J. M. Bernassau, *J. Magn. Reson., Ser. A*, 1993, **104**, 83.
45. L. A. Bengtsson, B. T. Heaton, J. A. Iggo, C. Jacob, G. L. Monks, J. Ratnam and A. K. Smith, *J. Chem. Soc., Dalton Trans.*, 1994, 1857.
46. C. Bauer, R. Freeman, T. Frenkiel, J. Keeler and A. J. Shaka, *J. Magn. Reson.*, 1984, **58**, 442.
47. J. W. Akitt and B. E. Mann, 'NMR and Chemistry', 4th edition, Stanley Thornes, Cheltenham, 2000, p. 198.
48. J. M. Brown, P. A. Chaloner and G. A. Morris, *J. Chem. Soc. Perkin Trans. 2*, 1987, 1583.

49. J. Jeener, B. H. Meier, P. Bachmann and R. R. Ernst, *J. Chem. Phys.*, 1979, **71**, 4546.
50. C. L. Perrin and T. J. Dwyer, *Chem. Rev.*, 1990, **90**, 935.
51. E. W. Abel, T. P. J. Coston, K. G. Orrell, V. Sik and D. Stephenson, *J. Magn. Reson.*, 1986, **70**, 34.
52. W. Bauer, *Magn. Reson. Chem.*, 1996, **34**, 532.
53. P. S. Pregosin, P. G. A. Kumar and I. Fernandez, *Chem. Rev.*, 2005, **105**, 2977.
54. A. Macchioni, *Chem. Rev.*, 2005, **105**, 2039.
55. B. Binotti, G. Bellachioma, G. Cardaci, A. Macchioni, C. Zuccaccia, E. Foresti and P. Sabatino, *Organometallics*, 2002, **21**, 346.
56. B. Binotti, A. Macchioni, C. Zuccaccia and D. Zuccaccia, *Comments Inorg. Chem.*, 2002, **23**, 417.
57. D. Neuhaus and M. Williamson, ‘The Nuclear Overhauser Effect in Structural and Conformational Analysis’, VCH Publishers, Weinheim, 1989.
58. L. N. Appelhans, D. Zuccaccia, A. Kovacevic, A. R. Chianese, J. R. Miecznikowski, A. Macchioni, E. Clot, O. Eisenstein and R. H. Crabtree, *J. Am. Chem. Soc.*, 2005, **127**, 16299.
59. Y. Cohen, L. Avram and L. Frish, *Angew. Chem., Int. Ed.*, 2005, **44**, 520.
60. M. Valentini, P. S. Pregosin and H. Ruegger, *Organometallics*, 2000, **19**, 2551.
61. C. D. Hubbard and R. Van Eldik, *J. Coord. Chem.*, 2007, **60**, 1.
62. L. Helm and A. E. Merbach, *Chem. Rev.*, 2005, **105**, 1923.
63. H. G. Niessen, P. Trautner, S. Wiemann, J. Bargon and K. Woelk, *Rev. Sci. Instrum.*, 2002, **73**, 1259.
64. M. J. Chen, R. J. Klingler, J. W. Rathke and K. W. Kramarz, *Organometallics*, 2004, **23**, 2701.
65. C. R. Yonker and J. C. Linehan, *Prog. Nucl. Magn. Reson. Spectrosc.*, 2005, **47**, 95.
66. D. C. Roe, P. M. Kating, P. J. Krusic and B. E. Smart, *Top. Catal*, 1998, **5**, 133.
67. D. C. Roe, *Adv. Chem. Ser.*, 1992, **230**, 33.
68. J. W. Sprengers, A. M. Kluwer, S. Gaemers and C. J. Elsevier, ‘High Pressure Effects in Chemistry, Biology and Materials Science’, 2002, Vol. 208–2, p. 283.
69. S. Gaemers, H. Luyten, J. M. Ernsting and C. J. Elsevier, *Magn. Reson. Chem.*, 1999, **37**, 25.
70. I. T. Horvath and J. M. Millar, *Chem. Rev.*, 1991, **91**, 1339.
71. J. A. Iggo, Y. Kawashima, J. Liu, T. Hiyama and K. Nozaki, *Organometallics*, 2003, **22**, 5418.
72. S. M. Silva, R. P. J. Bronger, Z. Freixa, J. Dupont and P. van Leeuwen, *New J. Chem.*, 2003, **27**, 1294.
73. W. Behr, A. Haase, G. Reichenauer and J. Fricke, *Rev. Sci. Instrum.*, 1999, **70**, 2448.
74. S. Hirai, K. Kuwano, K. Ogawa, N. Iriguchi and K. Okazaki, *Magn. Reson. Imaging*, 2000, **18**, 221.
75. R. J. Hamilton, C. G. Leong, G. Bigam, M. Miskolzie and S. H. Bergens, *J. Am. Chem. Soc.*, 2005, **127**, 4152.
76. R. Whyman, *Adv. Chem. Ser.*, 1992, **230**, 19.
77. M. Garland, in ‘The Encyclopedia of Catalysis’, ed. I. T. Horvath, Wiley-Interscience, Hoboken, 2002.
78. J. A. Iggo, D. Shirley and N. C. Tong, *New J. Chem.*, 1998, **22**, 1043.
79. D. Selent, W. Baumann and A. Börner, German Patent, DE 10333143, 2003, Gaseinleitungs- und zirkulationsvorrichtung zur Verfolgung von Reaktionen in flüssiger Phase unter Beteiligung gasförmiger Reaktanden unter Normal- und Hochdruck mittels Kernresonanzspektroskopie (Druck-NMR-Spektroskopie) unter stationären Bedingungen.
80. D. Selent, Easy access to high pressure NMR data of homogeneous catalysts. ’XXI International Conference on Organometallic Chemistry, ICOMC’, Vancouver, 2004.
81. A. Cusanelli, U. Frey, D. Marek and A. E. Merbach, *Spectrosc. Eur.*, 1997, **9**, 22.
82. D. G. Vandervelde and J. Jonas, *J. Magn. Reson.*, 1987, **71**, 480.
83. S. L. Wallen, L. K. Schoenbachler, E. D. Dawson and M. A. Blatchford, *Anal. Chem.*, 2000, **72**, 4230.
84. D. T. Brown, T. Eguchi, B. T. Heaton, J. A. Iggo and R. Whyman, *J. Chem. Soc., Dalton Trans.*, 1991, 677.
85. C. R. Yonker, T. S. Zemanian, S. L. Wallen, J. C. Linehan and J. A. Franz, *J. Magn. Reson., Ser. A*, 1995, **113**, 102.
86. D. Blazina, S. B. Duckett, J. P. Dunne and C. Godard, *Dalton Trans.*, 2004, 2601.
87. M. G. Pravica and D. P. Weitekamp, *Chem. Phys. Lett.*, 1988, **145**, 255.
88. C. R. Bowers and D. P. Weitekamp, *J. Am. Chem. Soc.*, 1987, **109**, 5541.
89. T. C. Eisenschmid, R. U. Kirss, P. P. Deutsch, S. I. Hommeltoft, R. Eisenberg, J. Bargon, R. G. Lawler and A. L. Balch, *J. Am. Chem. Soc.*, 1987, **109**, 8089.
90. A. Pines, M. G. Gibby and J. S. Waugh, *J. Chem. Phys.*, 1973, **59**, 569.
91. C. Bonhomme, C. Coelho, T. Azais, L. Bonhomme-Coury, F. Babonneau, J. Maquet and R. Thouvenot, *C. R. Chim.*, 2006, **9**, 466.
92. M. Eden, J. Grins, Z. J. Shen and Z. Weng, *J. Magn. Reson.*, 2004, **169**, 279.
93. R. D. Gougeon, E. B. Brouwer, P. R. Bodart, L. Delmotte, C. Marichal, J. M. Chezeau and R. K. Harris, *J. Phys. Chem. B*, 2001, **105**, 12249.
94. G. Mali and V. Kaucic, *J. Chem. Phys.*, 2002, **117**, 3327.
95. A. S. Lipton, J. A. Sears and P. D. Ellis, *J. Magn. Reson.*, 2001, **151**, 48.
96. G. Metz, X. L. Wu and S. O. Smith, *J. Magn. Reson., Ser. A*, 1994, **110**, 219.
97. G. Metz, M. Ziliox and S. O. Smith, *Solid State Nucl. Magn. Reson.*, 1996, **7**, 155.

98. O. B. Peersen, X. L. Wu, I. Kustanovich and S. O. Smith, *J. Magn. Reson., Ser. A*, 1993, **104**, 334.
99. O. B. Peersen, X. L. Wu and S. O. Smith, *J. Magn. Reson., Ser. A*, 1994, **106**, 127.
100. W. Kolodziejski and J. Klinowski, *Chem. Rev.*, 2002, **102**, 613.
101. R. Voelkel, *Angew. Chem., Int. Ed. Engl.*, 1988, **27**, 1468.
102. S. J. Opela and M. H. Frey, *J. Am. Chem. Soc.*, 1979, **101**, 5854.
103. A. Lesage, D. Sakellariou, S. Hediger, B. Elena, P. Charmont, S. Steuernagel and L. Emsley, *J. Magn. Reson.*, 2003, **163**, 105.
104. M. H. Levitt, A. C. Kolbert, A. Bielecki and D. J. Ruben, *Solid State Nucl. Magn. Reson.*, 1993, **2**, 151.
105. A. Bielecki, A. C. Kolbert and M. H. Levitt, *Chem. Phys. Lett.*, 1989, **155**, 341.
106. S. P. Brown and H. W. Spiess, *Chem. Rev.*, 2001, **101**, 4125.
107. C. E. Bronnimann, B. L. Hawkins, M. Zhang and G. E. Maciel, *Anal. Chem.*, 1988, **60**, 1743.
108. A. Lesage, L. Duma, D. Sakellariou and L. Emsley, *J. Am. Chem. Soc.*, 2001, **123**, 5747.
109. M. Feike, D. E. Demco, R. Graf, J. Gottwald, S. Hafner and H. W. Spiess, *J. Magn. Reson., Ser. A*, 1996, **122**, 214.
110. D. H. Brouwer, R. J. Darton, R. E. Morris and M. H. Levitt, *J. Am. Chem. Soc.*, 2005, **127**, 10365.
111. D. H. Brouwer, P. E. Kristiansen, C. A. Fyfe and M. H. Levitt, *J. Am. Chem. Soc.*, 2005, **127**, 542.
112. S. S. Hou, F. L. Beyer and K. Schmidt-Rohr, *Solid State Nucl. Magn. Reson.*, 2002, **22**, 110.
113. F. Blanc, C. Coperet, J. Thivolle-Cazat, J. M. Basset, A. Lesage, L. Emsley, A. Sinha and R. R. Schrock, *Angew. Chem., Int. Ed. Engl.*, 2006, **45**, 1216.
114. A. Lesage, D. Sakellariou, S. Steuernagel and L. Emsley, *J. Am. Chem. Soc.*, 1998, **120**, 13194.
115. M. Hong and R. G. Griffin, *J. Am. Chem. Soc.*, 1998, **120**, 7113.
116. Y. Z. Khimyak and J. Klinowski, *Phys. Chem. Chem. Phys.*, 2001, **3**, 616.
117. K. Saalwachter and I. Schnell, *Solid State Nucl. Magn. Reson.*, 2002, **22**, 154.
118. T. Gullion, *Concepts Magn. Reson.*, 1998, **10**(5), 277.
119. C. P. Grey and A. J. Vega, *J. Am. Chem. Soc.*, 1995, **117**, 8232.
120. T. Gullion, *Chem. Phys. Lett.*, 1995, **246**, 325.
121. B. F. Chmelka, K. T. Mueller, A. Pines, J. Stebbins, Y. Wu and J. W. Zwanziger, *Nature*, 1989, **339**, 42.
122. A. Samoson, E. Lippmaa and A. Pines, *Mol. Phys.*, 1988, **65**, 1013.
123. K. T. Mueller, B. Q. Sun, G. C. Chingas, J. W. Zwanziger, T. Terao and A. Pines, *J. Magn. Reson.*, 1990, **86**, 470.
124. C. Fernandez, C. Morais, J. Rocha and M. Pruski, *Solid State Nucl. Magn. Reson.*, 2002, **21**, 61.

Nuclear Magnetic Resonance (NMR) Spectroscopy of Metallobiomolecules

Kara L. Bren

University of Rochester, Rochester, NY, USA

Method Summary 1
1 Introduction 2
2 Technical Background 4
3 Application to Metalloprotein Structure Determination 10
4 Application to Characterization of Metal Sites in Metalloproteins 16
5 Application to Characterization of Internal Metalloprotein Dynamics 18
6 Application to Analysis of Intermolecular Interactions 20
7 Application to Quadrupolar Metal Nuclei 23
8 Application to Nucleic Acids 24
9 Acknowledgments 26
10 Related Articles 26
11 Abbreviations and Acronyms 26
12 Further Reading 26
13 References 27

METHOD SUMMARY

Acronyms, Synonyms

- Nuclear Magnetic Resonance

Measured physical quantities

- nuclear spin transition frequency (chemical shift, ppm)
- relative numbers of equivalent spins (signal area)
- nuclear relaxation rates (R_1, R_2, s^{-1})
- dipole−dipole and scalar couplings (Hz).

Information available

- high-resolution three-dimensional solution structure (in favorable cases)
- dipolar and scalar couplings between nuclei, and between unpaired electrons and nuclei
- rates of conformational and chemical exchange processes
- magnetic anisotropy and orientation of magnetic axes in paramagnetic molecules.

Information not available, limitations

- Only nuclei with spin $I \neq 0$ can be observed.
- Detailed information is difficult to obtain on molecules that are insoluble, very large, or highly disordered.

Examples of questions that can be answered

- Is this protein or RNA folded?
- What amino acid residues bind the cofactor?
- What is this paramagnetic transition metal oxidation and spin state?
- Does ligand or cofactor binding to this biomolecule induce a change in conformation or in dynamics?

Major advantages

- Spatially resolved high-resolution information on structure and dynamics across the entire molecule may be discerned in favorable cases.
- Effects of ligand binding, pH, temperature, denaturant, and so on, are readily studied.
- For molecules that bind paramagnetic metals, spectra contain information on metal electronic structure.

Major disadvantages

- Low sensitivity is a major disadvantage and requires relatively large amounts of sample.
- Spectral crowding decreases resolution for larger biomolecules.
- Isotopic labeling of sample may be required.
- Linebroadening resulting from paramagnetism, nuclear spin $>1/2$, or large molecular weight (MW) decreases resolution and may severely limit analysis.
- Specialized approaches are required for molecules of high molecular weight or low solubility.

Sample constraints

- The volume of sample is restricted to 300–500 μL (using a conventional 5 mm probe), or a few microliters (using a microprobe).
- Liquid sample is preferred for high-resolution studies; nuclear magnetic resonance (NMR) of solids requires specialized methodologies.
- Concentration should optimally be at or above 1 mM; considerably lower values are possible with state-of-the art probes and/or experiments.
- High sample purity is needed if a detailed study is to be undertaken.

1 INTRODUCTION

Life has evolved making use of a wide range of elements, including metals.[1] It is estimated that ∼25% of known proteins bind one or more metal ions,[2] and the majority of catalytic nucleic acids require divalent metal ions for function.[3] As metal ions play key functional or structural roles in biological systems, the metals and the portions of the biomolecule with which they interact are a natural focus of structural and spectroscopic studies. In the application of nuclear magnetic resonance (NMR) spectroscopy, the presence of metal ions in biomolecules raises both opportunities and challenges. In paramagnetic biomolecules, the interaction of unpaired electron spins with nuclear spins perturbs both chemical shifts and line widths in NMR spectra. These effects complicate the interpretation of spectra, but in favorable cases they allow the metal to act as a ‘‘beacon’’ to light up the metal-binding site, which is frequently the biomolecule active site. Because the perturbations to NMR spectra by paramagnetic ions depend on the metal spin state and coordination geometry, the NMR spectra provide a means by which the metal coordination environment and electronic structure may be characterized. Even for metals typically thought of as spectroscopically silent, the changes in biomolecule chemical shifts upon metal binding provide a probe of the active site.

The application of NMR to metallobiomolecules, and metalloproteins in particular, has a long history. In fact, paramagnetic cytochrome *c* is among the first proteins for which multiple well-resolved NMR signals were observed (in 1962).[4] The field of biological NMR has developed rapidly since that time; the first solution structure of a protein was reported in 1985,[5] and the first NMR structure of a paramagnetic protein was reported only nine years later.[6] Soon thereafter, it was demonstrated that the effect of the paramagnetic center on proton chemical shifts can be utilized to refine metalloprotein solution structures[7,8]; such restraints are now included in standard software packages for biomolecule structure refinement. The utility of paramagnetic restraints is such that extrinsic paramagnetic centers are being introduced to allow the spectroscopist to take advantage of paramagnetic effects on NMR spectra for characterizing biomolecules that do not bind metals.[9]

Among the metallobiomolecules, small (MW $<$ 30 kDa), soluble metalloproteins are the most amenable to study by NMR, and thus many studies of soluble heme proteins

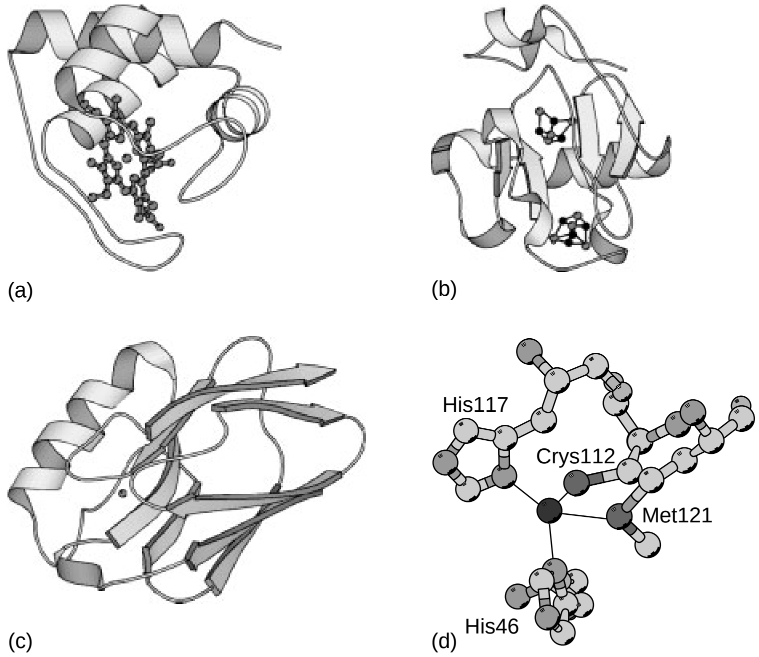

Figure 1 Three-dimensional structures of metalloproteins illustrating examples of metal-binding sites probed in NMR studies. (a) *Hydrogenobacter thermophilus* cytochrome c_{552} (PDB:1YNR), a heme protein. (b) *Azotobacter vinelandii* ferredoxin (PDB:1FDA), an iron–sulfur cluster protein (with one Fe_3S_4 and one Fe_4S_4 cluster). (c) *Pseudomonas aeruginosa* azurin (PDB:1AZU), a blue copper protein. The Cu ion is shown as a sphere in (c), and the copper-binding residues in azurin are enlarged in (d). Biomolecule figures prepared using Molscript[13]

(cytochromes, globins),[10] iron–sulfur proteins (ferredoxins, high-potential iron proteins (HiPIPs)),[11] and copper proteins (cupredoxins)[12] have been reported (Figure 1). As many small, soluble metalloproteins are electron transfer proteins, our understanding of biological electron transfer has benefited greatly from NMR. Metalloenzymes tend to have larger molecular masses and thus have been studied less by NMR, although enzymes such as peroxidases and superoxide dismutases have been studied extensively, whereas larger enzymes such as cytochrome P-450 are being tackled in detail only recently. Whereas most NMR studies in the area of metallobiomolecule NMR have focused on metalloproteins, NMR also has provided vital information on binding of metals to RNAs. As our understanding of the varied activities and roles of RNA in biology continues to grow, so will the interest in obtaining detailed information on metal sites in RNA.

Advances in NMR spectrometer and probe technology and in solid-state NMR methods, along with development of new pulse sequences have opened up the biomolecular NMR field to the study of membrane-bound proteins and large molecular weight (MW > 50 kDa) systems. In addition, studies of low-sensitivity nuclei are expected to gain in popularity as the appropriate technical and experimental expertise is developed and refined. Another important area concerns developments in protein engineering that allow preparation of biomolecules isotopically labeled either uniformly or at particular sites. The rapid and continuing development of these methodologies suggests that the footprint of NMR on the metallobiomolecule field will continue to grow into the future.

This article will concentrate on topics most likely to be of interest to inorganic and bioinorganic chemists, and not requiring highly specialized equipment or training. Thus, the focus will be on NMR of soluble metallobiomolecules, as studies of biomolecules in the solid-state and/or bound to membranes are typically reserved for specialists. One exception is that solid-state NMR studies that allow interpretation of data on low-sensitivity quadrupolar metal nuclei (^{25}Mg, ^{67}Zn) will be described briefly because of the direct relevance to inorganic chemistry and the difficulty in characterizing such sites using other spectroscopic methods. Most of the examples and applications will utilize metalloproteins, as the preponderance of NMR studies on metallobiomolecules is on proteins. The application of NMR to metal-binding RNAs will be described in a separate Section 8 as metal binding to nucleic acids is addressed using approaches that are distinct from those usually applied to proteins. In summary, NMR encompasses a broad range of approaches to characterize not only structure but also dynamics and reactivity of metallobiomolecules. Technical developments in the NMR field have been exceedingly rapid, resulting in its application to biomolecules that were considered as recently as the year 2000 to be inaccessible to detailed NMR study. NMR is expected to grow in its importance in the metallobiomolecule field for years to come.

2 TECHNICAL BACKGROUND

NMR spectroscopy probes transitions between nuclear spin states. The transition frequencies and relaxation times contain a wealth of information related to molecular structure and dynamics. Transition frequencies also reveal couplings between nuclear spins, and between electron and nuclear spins. The primary experimental observables in NMR are the chemical shift, which is related to the transition frequency, and the line width, which is related to the relaxation time. In paramagnetic systems, both of these parameters have the potential to be affected significantly by the unpaired electron, requiring special interpretation of data but also revealing information on the nature of the metal site. To make full use of NMR to study complex systems such as metallobiomolecules, it is important to understand the factors that influence observables in NMR.

2.1 The NMR Transition

Nuclei of certain isotopes possess angular momentum, or spin, with an associated quantum number, I. Nuclei with $I \neq 0$ have a nonzero magnetic moment, μ. In the presence of a magnetic field, there are $2I + 1$ possible orientations for the nucleus relative to the applied field, each associated with a different energy described by

$$E_\mathrm{m} = \frac{-m\mu B_0}{I} \tag{1}$$

where B_0 is the magnetic field strength and m is a quantum number, which can take on the values of $I, I-1, I-2, \ldots, -I$. In the most familiar case, a nucleus with $I = 1/2$ has m values of $+1/2$ and $-1/2$ and thus two possible energies E_m. NMR probes transitions between these states (Figure 2), which are governed by the selection rule $\Delta m = \pm 1$, giving the expression for transition energy

$$\Delta E = \frac{\mu B_0}{I} \tag{2}$$

This expression is often written in terms of the magnetogyric ratio, which is the ratio of the magnetic moment (μ) and the maximum value of the spin angular momentum ($hI/2\pi$):

$$\gamma = \frac{2\pi\mu}{hI} \tag{3}$$

Substituting into equation (2) yields

$$\Delta E = \frac{h\gamma B_0}{2\pi} \tag{4}$$

As $\Delta E = h\nu$, the frequency of the associated electromagnetic radiation is given by the Larmor equation

$$2\pi\nu_0 = \omega_0 = \gamma B_0 \tag{5}$$

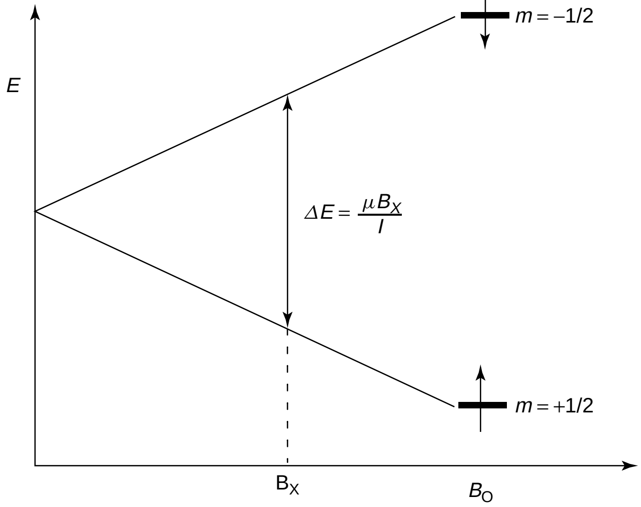

Figure 2 Illustration of the splitting of the $m = +1/2$ and $m = -1/2$ states for a spin-1/2 nucleus by applied magnetic field with strength B_x. The ΔE between these states increases in proportion to field strength

Thus, the frequency of the nuclear spin transition depends on the strength of the applied magnetic field and magnitude of γ for the nucleus. The transition frequency of a particular nucleus is one of the important parameters in NMR and is related to the chemical shift as explained in the next section. The value of γ also determines sensitivity of a given isotope, as ΔE (equation 4) determines the ratio of the number of spins in the upper (n_1) and lower (n_2) energy levels according to the Boltzmann relationship:

$$\frac{n_1}{n_2} = \exp\left(\frac{-\Delta E}{k_\mathrm{b}T}\right) \tag{6}$$

Because ΔE is small in NMR compared to many other spectroscopic methods, there exists only a small excess of spins in the lower energy state, giving rise to low sensitivity. This becomes a greater problem for nuclei with low γ values including many that are of interest to bioinorganic chemists (Table 1).

2.2 The Chemical Shift in Diamagnetic Molecules

NMR is a powerful technique for probing the chemical environments of nuclei. Even in large molecules such as metallobiomolecules, signals from individual nuclei can be distinguished from each other as a result of differences in transition frequency. This is expressed as the chemical shift (δ), which relates the transition frequency of the nucleus being examined (ω) to that of a reference nucleus (ω_ref):

$$\delta(\mathrm{ppm}) = \frac{10^6(\omega - \omega_\mathrm{ref})}{\omega_\mathrm{ref}} \tag{7}$$

Table 1 Properties of selected NMR-active nuclei

Nucleus	Spin (I)	γ (10^7 rad s^{-1} T^{-1})	Natural abundance (%)	Larmor frequency at 11.744 T (MHz)	Q (10^{-28} m^2)	Chemical shift range (ppm)$^{(a)}$
^{1}H	1/2	26.7519	99.98	500	0	50$^{(b)}$
^{2}H	1	4.1066	1.5×10^{-2}	76.75	2.8×10^{-3}	50$^{(b)}$
^{13}C	1/2	6.7283	1.108	125.721	0	250
^{14}N	1	1.9338	99.653	36.118	1.99×10^{-2}	1100
^{15}N	1/2	−2.712	0.365	50.664	0	1100
^{17}O	5/2	−3.6279	3.7×10^{-2}	67.784	-2.6×10^{-2}	1650
^{19}F	1/2	25.181	100	470.385	0	1300
^{31}P	1/2	10.841	100	202.404	0	1900
^{25}Mg	5/2	−1.639	10.13	30.597	0.22	70
^{57}Fe	1/2	0.8661	2.19	16.156	0	9000
^{67}Zn	5/2	1.6768	4.11	31.271	0.16	2700
^{205}Tl	1/2	15.589	70.5	288.54	0	7000

(a) In the absence of unpaired electrons.
(b) Including metal hydrides.

The interpretation of the chemical shift depends on the identity of the nucleus and whether it interacts with unpaired electrons. In general, the immediate chemical environment plays a central role in determining chemical shift. This is a result of the fact that the electrons near the nucleus affect the local magnetic field such that the magnetic field at a nucleus, B_{eff}, is slightly different from the applied magnetic field, B_0. This effect is known as *screening* and is described by a proportionality constant σ:

$$B_{\mathrm{eff}} = B_0(1 - \sigma) \tag{8}$$

As a result, a particular nucleus experiences a transition frequency ω determined by B_{eff} that is slightly different from the Larmor frequency (equation 5), giving rise to chemical shift.

$$\omega = \gamma B_{\mathrm{eff}} \tag{9}$$

The screening constant σ is the trace of a second-rank tensor, the components of which can be observed in solid-state NMR. In high-resolution solution NMR, however, an average value, σ, is measured as a result of rapid reorientation of the molecule in the magnetic field. The screening constant has two components, diamagnetic (σ_{d}) and paramagnetic (σ_{p}):

$$\sigma = \sigma_{\mathrm{d}} + \sigma_{\mathrm{p}} \tag{10}$$

The diamagnetic screening constant describes the circulation of electrons around the nucleus, whereas the paramagnetic screening constant is related to bond orders, internuclear distances, and the energy difference between filled and empty orbitals. For ^{1}H, σ_{d} dominates, but for heavier atoms, σ_{p} becomes the dominant factor. Thus, ^{1}H has a small chemical shift range relative to heavier atoms, but ^{1}H shifts are straightforward to interpret in terms of chemical environment. The complexity of factors contributing to σ_{p} means that, unlike for ^{1}H, heavy atom chemical shifts cannot be interpreted using concepts of local electron density, and chemical shifts for different heavy elements are interpreted differently from each other with significant reliance on comparison to known compounds.

In biomolecular NMR, the nuclei most often utilized are ^{1}H, ^{13}C, and ^{15}N. Each of these nuclei has distinct factors determining chemical shift values. Chemical shifts of ^{1}H can be interpreted in a straightforward manner in the context of local chemical environment, ^{13}C shifts (particularly of backbone Cα nuclei) are an indicator of protein secondary structure, and ^{15}N shifts are determined largely by local bonding interactions. ^{13}C and ^{15}N show greater dispersion than ^{1}H, greatly aiding the obtainment of assignments in biomolecules of larger molecular weight, or that show disorder or poor dispersion in ^{1}H resonances. Factors determining ^{1}H, ^{13}C, and ^{15}N chemical shifts in proteins have been analyzed in detail.**[14,15]**

2.3 The Chemical Shift in Paramagnetic Molecules

Paramagnetic centers can exert dramatic effects on the chemical shifts of nuclei with which they interact. The observed shift of a nucleus in a paramagnetic molecule is the sum of its hypothetical shift in an isostructural diamagnetic molecule (δ_{dia}) and its shift due to the electron–nucleus (hyperfine) interaction (δ_{hf}), which in turn has dipolar (pseudocontact, δ_{pc}) and scalar (contact, δ_{con}) contributions**[16,17]**:

$$\delta_{\mathrm{obs}} = \delta_{\mathrm{dia}} + \delta_{\mathrm{hf}} \tag{11}$$

$$\delta_{\mathrm{hf}} = \delta_{\mathrm{pc}} + \delta_{\mathrm{con}} \tag{12}$$

The contributions of δ_{hf} and δ_{dia} to δ_{obs} can be estimated by comparing the chemical shift of a nucleus in the paramagnetic molecule to its shift in a structurally homologous diamagnetic form. This is most commonly achieved by utilizing a different metal oxidation state within the molecule (i.e., reducing Cu^{II} to Cu^{I}), or substituting with a diamagnetic metal (i.e., Zn^{II} or low-spin Co^{III}). Alternatively, the δ_{dia} values may be estimated using chemical shift prediction programs.

2.3.1 The Fermi Contact Shift

The Fermi contact shift describes the influence of the unpaired electron spin on nuclear chemical shifts as a result of through-bond hyperfine coupling. The contact shift is caused by the presence of unpaired electron spin density at the observed nucleus.[18,19] Thus, spin density must be transferred to an s orbital of the nucleus of interest, which is typically achieved through spin polarization. In the case of a single, isolated spin state for a molecule in solution, contact shift can be described by

$$\delta_{con} = \left(\frac{2\pi A}{h}\right)\left[\frac{(g\mu_B S(S+1))}{3\gamma k_B T}\right] \quad (13)$$

where $2\pi A/h$ is the coupling constant for the scalar interaction between the unpaired electron and nucleus, g is the average g value, μ_B is the Bohr magneton, and S is the total electron spin. The $1/T$ temperature dependence of δ_{con}, known as *Curie behavior*, may be utilized to identify contact-shifted nuclei, although deviations from Curie behavior are common. Note that a dependence on magnetogyric ratio is not observed as γ cancels out with a component of A. The hyperfine coupling constant is the key variable determining δ_{con}, and falls off rapidly as the number of bonds between the paramagnetic metal and the nucleus being examined increases. The magnitude of δ_{con} may be assumed to be negligible if the number of bonds between the paramagnetic metal and the nucleus is greater than four, and there are no π bonds. For nuclei in π-bonded systems such as substituents on hemes, δ_{con} can be substantial four or more bonds from the metal.

2.3.2 The Pseudocontact (Dipolar) Shift

The pseudocontact shift results from a through-space interaction between the magnetic moments of the unpaired electron and nucleus as modulated by molecular rotation.[20,21] It is described by

$$\delta_{pc} = (24\pi r^3)^{-1}\left[2\Delta\chi_{ax}(3\cos^2\theta - 1) + 3\Delta\chi_{rh}\sin^2\theta\cos 2\phi\right] \quad (14)$$

where $\Delta\chi_{ax}$ and $\Delta\chi_{rh}$ are the axial and rhombic components of the paramagnetic susceptibility tensor χ^{para}, and r, θ, ϕ are the polar coordinates of the nucleus in the metal-centered reference frame of χ^{para}. Thus, δ_{pc} requires an anisotropic magnetic susceptibility tensor, and can be positive, negative, or zero depending on the angular position of the nucleus within this reference frame (Figure 3). Pseudocontact shifts are largest in magnitude for nuclei in molecules with highly anisotropic χ^{para}, such as low-spin Fe^{III} and some of the trivalent lanthanides (Table 2). The dependence of δ_{pc} on the position of the nucleus within χ^{para} makes it a valuable parameter in structure determination and refinement for paramagnetic biomolecules.

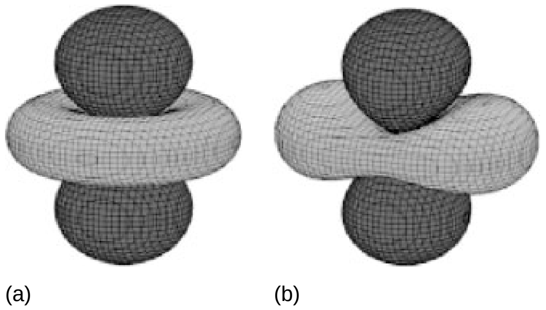

Figure 3 Isopseudocontact shift surfaces calculated from equation (14) with $\Delta\chi_{rh} = 0$ (a) and $\Delta\chi_{rh} = 1/3\Delta\chi_{ax}$ (b). Positive shifts are in dark gray, negative in light gray. (Adapted from Bertini, Luchinat, Parigi and Pierattelli.[22] © 2005 Wiley-VCH)

2.4 Nuclear Relaxation

Relaxation is the establishment of the equilibrium distribution of spins after perturbation. For nuclear spins, relaxation is induced by coupling to fluctuating magnetic fields, described by rate constants ($R_1 = 1/T_1$) and ($R_2 = 1/T_2$). T_1 is the spin-lattice relaxation time and is modulated by high-frequency fluctuations, whereas T_2 describes spin–spin relaxation, which in addition to high-frequency fluctuations is also modulated by low-frequency processes such as chemical exchange. T_2 determines line widths according to

Table 2 Magnetic susceptibility anisotropies of selected paramagnetic metal ions[(a)]

Metal ion	S or J	$\Delta\chi_{ax}$ (10^{-32} m^3)[(b)]	δ_{pc} (ppm) $r = 7$ Å[(c)]
Fe^{II}	2	2.1	1.1
Fe^{III} (LS)	1/2	2.4	1.3
Fe^{III} (HS)	5/2	3.0	1.6
Co^{II} (HS, 5–6 coordinate)	3/2	7	3.7
Co^{II} (HS, 4 coordinate)	3/2	3	1.6
Cu^{II}	1/2	0.6	0.3
Gd^{III}	7/2	0.2	0.1
Ce^{III}	5/2	2	1.0
Tb^{III}	6	35	19

(a) Data from Ref. 22.
(b) Measured at 21.1 T.
(c) Assuming $\Delta\chi_{rh} = 0$ and nucleus in axial position relative to χ tensor ($\theta = 0°$).

the following:

$$W_0 = (\pi T_2)^{-1} \tag{15}$$

where W_0 is the homogeneous line width in hertz. The coupling of the nuclear spin to fluctuating magnetic fields is characterized by a correlation time, τ_c, which has contributions from time constants for molecular tumbling (τ_r) and chemical exchange (τ_m) if present, and electron relaxation in paramagnetic systems (τ_s):

$$\tau_c^{-1} = \tau_s^{-1} + \tau_r^{-1} + \tau_m^{-1} \tag{16}$$

Values for τ_s for paramagnetic metals range from 10^{-13} to 10^{-8} s (Table 3), and values for τ_r depend on the size of the molecule and can be roughly approximated by equating τ_r in picoseconds to the molecular weight. Thus τ_r is $\sim 10^{-11}$ s for small molecules, and 10^{-8} to 10^{-7} s for most proteins. In paramagnetic metalloproteins, τ_c is typically determined by τ_s as this is usually the fastest among these three processes in equation (16).**[23]** The value of τ_c along with transition frequency ω (equation 5) determines the spectral density function $J(\omega)$, which describes the frequencies sampled by a system described by τ_c (Figure 4). This function in turn relates to T_1 and T_2 as shown in Figure 5.

Table 3 Relaxation properties of selected paramagnetic metal ions[(a)]

Metal ion	S	τ_s (s)[(b)]	Line width (Hz)[(c)]
Mn^{II}	5/2	10^{-8}	100 000
Mn^{III}	2	$10^{-10} - 10^{-11}$	150–1500
Fe^{II} (HS, 5–6 coordinate)	2	$10^{-12} - 10^{-13}$	5–20
Fe^{II} (HS, 4 coordinate)	2	$\sim 10^{-11}$	150
Fe^{III} (LS)	1/2	$10^{-11} - 10^{-13}$	0.5–20
Fe^{III} (HS)	5/2	$10^{-9} - 10^{-11}$	200–12 000
Co^{II} (HS, 5–6 coordinate)	3/2	$5 \times 10^{-12} - 10^{-13}$	2–50
Co^{II} (HS, 4 coordinate)	3/2	10^{-11}	100
Co^{II} (LS)	1/2	$10^{-9} - 10^{-10}$	500
Ni^{II} (5–6 coordinate)	1	10^{-10}	500
Ni^{II} (4 coordinate)	1	10^{-12}	5
Cu^{II}	1/2	10^{-9}	1000–5000
Gd^{III}	7/2	$10^{-8} - 10^{-9}$	20 000–200 000
Ln^{III}		$10^{-12} - 10^{-13}$	1–100

(a) Data from Refs. 17 and 24.
(b) Measured at 11.7 T.
(c) Contribution of dipolar relaxation line width of a ^1H resonance 5 Å from metal center.

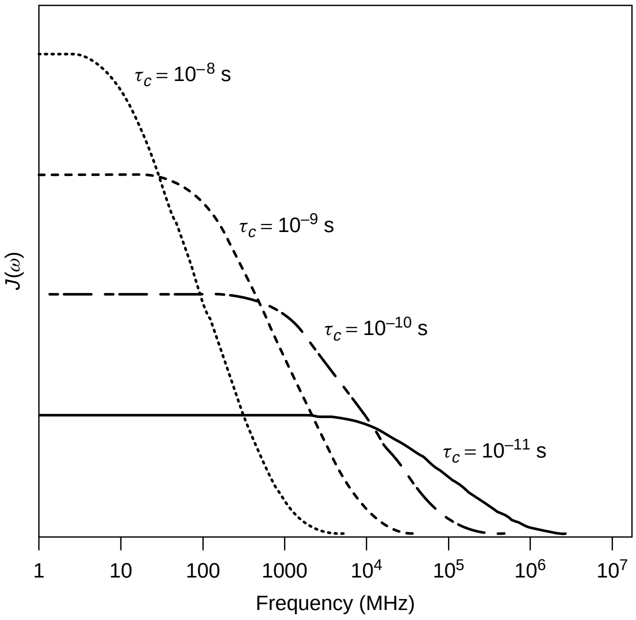

Figure 4 Spectral density function $J(\omega)$ as a function of frequency on a log scale. The functions are calculated for the different τ_c values indicated on the plot. The inflection points occur at $\omega\tau_c = 1$. Note that the vertical scale is not the same for the four curves

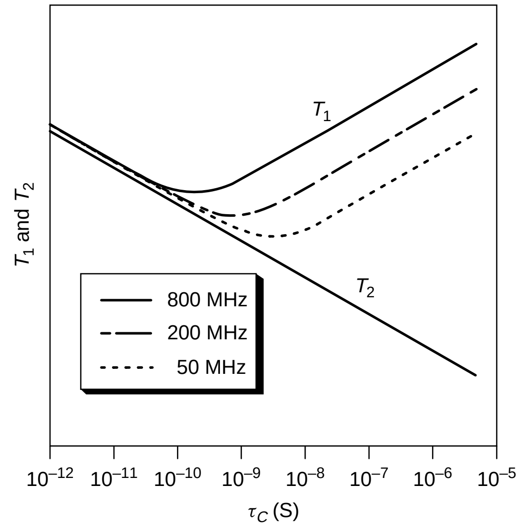

Figure 5 Plot of T_1 and T_2 as a function of τ_c at three different Larmor frequencies. The region where T_1 and T_2 diverge is the slow-motion regime and characterizes relaxation properties of most biomolecules

As in the case of the hyperfine shift, both contact and dipolar contributions to nuclear relaxation induced by the unpaired electron are present. In paramagnetic metalloproteins, the primary contribution to relaxation induced by the unpaired electron for most nuclei is the dipolar term, which is described in the fast motion limit ($\omega^2\tau_c^2 \ll 1$) by**[23,25]**

$$R_{1p,2p} = \frac{4}{3}\left(\frac{\mu_0}{4\pi}\right)^2 \gamma^2 g_e^2 \mu_B^2 S(S+1) r^{-6} \tau_c \tag{17}$$

where the subscript p indicates paramagnetic contribution to relaxation. Although the fast motion limit does not apply to molecules the size of biomolecules (Figure 5), equation (17) provides an approximation of behavior that is helpful for understanding how the properties of the paramagnetic center impact relaxation rates and thus line widths. Relaxation enhancement increases with τ_c, which is usually equal to τ_s in paramagnetic macromolecules. Values for τ_s range over many orders of magnitude (Table 3) and therefore τ_s is key for determining the extent of linebroadening induced by the paramagnetic center. For example, obtaining high-resolution NMR spectra of molecules containing low-spin Fe^{III} is straightforward, as it has a short τ_s and thus induces minimal linebroadening. In contrast, Cu^{II}-containing molecules generally display severe linebroadening as a result of the long τ_s. The dependence of relaxation enhancement on r^{-6} means that information on electron–nucleus distance can be obtained from relaxation measurements, as described in Section 3.4.3.

For macromolecules, the fast motion limit does not apply and T_1 and T_2 diverge (Figure 5). The decreasing value of T_2 with τ_c is the reason large proteins exhibit broad lines (equation 15). Studies of large proteins (MW > 50 kDa) by NMR is thus assisted by transverse relaxation-optimized NMR spectroscopy (TROSY) experiments that yield narrower resonances by optimizing transverse relaxation.[26,27] The increase in T_1 at long τ_c values results in efficient nuclear cross-relaxation, which allows, for example, observation of transfer nuclear Overhauser effects (NOEs) in studies of intermolecular interactions (see Section 6).

An additional relaxation mechanism, Curie relaxation, can become a significant contributor to R_2 and thus line widths when $\tau_s \ll \tau_r$, in other words, for large paramagnetic molecules. Curie relaxation increases with B_0^2 and T^{-2} and thus its presence can be deduced by identifying this magnetic field and temperature dependence.[23,28] Curie relaxation can be a limiting factor in obtaining high-resolution spectra of large paramagnetic biomolecules.

The quadrupole moment (Q) exhibited by nuclei with $I > 1/2$ (Table 1) is an efficient source of nuclear relaxation and depends on the quadrupole coupling constant Cq, which contains nuclear quadrupole moment Q and the electric field gradient at the nucleus. As a result of the dependence on electric field gradient, quadrupole relaxation is highly sensitive to the symmetry of the nuclear environment, making it a valuable observable when it can be determined and interpreted (see Section 7). Quadrupole relaxation can lead to significant linebroadening that makes signal detection difficult, but depends on the nucleus and its environment. For example, Cq of ^{14}N is usually a few megahertz and T_1 values are ~10 to 20 ms, giving quite broad lines. The situation is more severe for Cl and Br in asymmetric bonds for which Cq may be 100 MHz, giving T_1 values of microseconds. In contrast, Cq is typically small for ^2H such that it displays relatively narrow lines.

2.5 Dynamics and Exchange Phenomena

NMR is a powerful tool for the characterization of chemical exchange phenomena and has been widely used for monitoring reactions of metallobiomolecules such as ligand binding and electron transfer. When two or more species interchange to perturb the magnetic environment of one or more nuclei, this process will impact chemical shifts and/or line widths in NMR spectra provided that the process occurs on a timescale to which the experiment is sensitive. The exquisite sensitivity of chemical shifts to environment means that even subtle changes in conformation may be detected. A variety of experiments probing a range of timescales are available; for example, kinetics ranging from $\sim 10^{-2}$ to 10^8 s^{-1} may be probed by ^1H NMR. Importantly, timescales directly relevant to chemical reactivity (microseconds to milliseconds) are often accessible.

Depending on the timescale of the process, exchange rates can be measured or estimated, and characteristics of the species in exchange may be discerned. The timescale regime of the process is defined by comparing the time constant for exchange ($\tau_{ex} = 1/k_{ex}$) to the reciprocal of the difference in frequency for the nucleus observed in the two forms A and B in exchange ($|\nu_A - \nu_B| = \Delta\nu$). It is important to consider the rate of the process relative to the experimental timescale in order to select informative experiments and interpret data correctly. The exchange process is commonly described as slow, intermediate, or fast on the NMR timescale (Figure 6). For very slow exchange, the lifetime at each site is long such

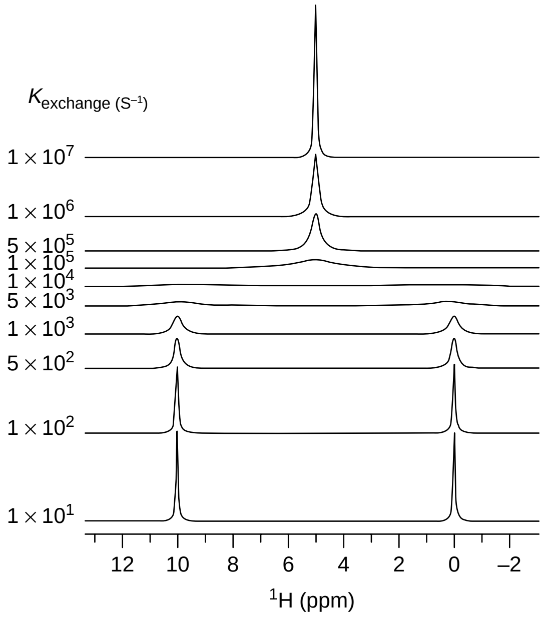

Figure 6 Simulation of ^1H NMR spectrum for exchange of a nucleus with $\Delta\nu = 5000$ Hz (10 ppm at 500 MHz) at different exchange rates, showing exchange rates slow, intermediate, and fast on the experimental timescale. Simulation performed using WinDNMR[29]

that sharp lines at ν_A and ν_B are observed, as if no exchange was occurring. For slow exchange causing linebroadening but not coalescence, the first-order rate constant can be related to the observed line width at half height ($W_{1/2}$) according to

$$W_{1/2} = \frac{k_{ex}}{\pi} + \frac{1}{\pi T_2} \tag{18}$$

provided there is minimal overlap between the two peaks. T_2 may be estimated from the line width W_0 in the absence of exchange (equation 15). In the intermediate exchange regime, a highly broadened resonance is observed and if the natural line width is small compared to the observed line ($W_0 \ll W_{1/2}$) the exchange rate can be determined from the following expression:

$$k_{ex} = \left[\frac{\pi(\Delta\nu)}{2}\right]\left[\left(\frac{\Delta\nu}{W_{1/2}}\right)^2 - \left(\frac{W_{1/2}}{\Delta\nu}\right)^2 + 2\right]^{1/2} \tag{19}$$

Under fast exchange ($W_{1/2}/\Delta\nu \ll 1$), a Lorentzian line is observed at the population-weighted mean of ν_A and ν_B, and an approximate expression for the rate constant based on the observed line width can be used:

$$k_{ex} = \frac{\pi(\Delta\nu)^2}{[2(W_{1/2} - W_0)]} \tag{20}$$

In addition to evaluation of line widths and peak separations, analysis of T_1 values and spin saturation transfer can be performed to access a wide range of timescales. Under conditions of slow exchange between forms A and B and upon irradiation at ν_B, the time constant associated with state A (τ_A) can be determined from the measured T_1 of nucleus A in the presence of exchange and the T_1 of nucleus A in the absence of exchange:

$$(T_{1,A}^{app})^{-1} = (T_{1,A})^{-1} + \tau_A^{-1} \tag{21}$$

Equation (21) is applicable in the slow-exchange regime provided resonances A and B do not overlap.

Saturation transfer experiments are useful in the slow-exchange case in which resolved resonances of the two states can be observed simultaneously and the exchange rate is on the same order as the relaxation rates. In this experiment, a resolved resonance at ν_B is saturated, and a change in the corresponding resonance at ν_A is observed. If ν_B is saturated for a period long enough to reach steady state, the ratio of the signal intensity of signal A upon saturation of B (I_{on}) and in the absence of saturation (I_{off}) is related to lifetime τ_A according to

$$\frac{I_{on}}{I_{off}} = \frac{\tau_A}{(\tau_A + T_{1A})} \tag{22}$$

In addition to providing exchange rates, saturation transfer experiments have been useful for assigning resonances in one form of a metalloprotein by obtaining correlations with previously assigned resonances of another form with which it is in exchange. An example of this application is shown in Figure 7.

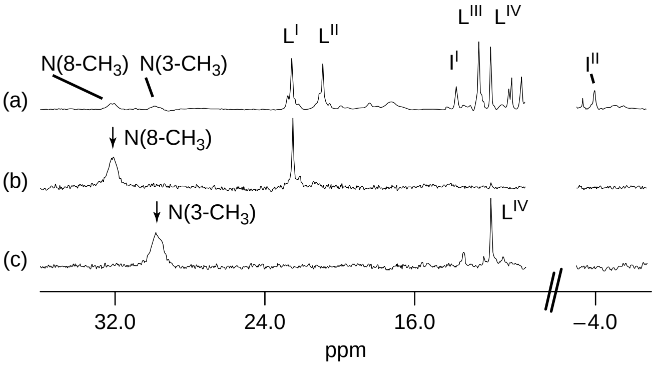

Figure 7 Illustration of the use of saturation transfer to assign ^{1}H NMR resonances of one form of a metalloprotein based on known assignments of another form of the protein. Here, heme methyl ^{1}H NMR resonances of a folding intermediate of horse ferricytochrome *c* in exchange with the native form are assigned. (a) Reference 500-MHz ^{1}H NMR spectrum, 90% H_2O:10% D_2O, 55 °C, 5.4 M urea. (b, c) Difference spectra showing saturation transfer observed (90% H_2O:10% D_2O, 55 °C, 5.4 M urea) upon irradiating the native protein resonances at (b) 32.1 ppm (native 8-CH_3) and (c) 29.8 ppm (native 3-CH_3), allowing assignment of L^I and L^{IV} in species L to heme 8-CH_3 and 3-CH_3, respectively. (Adapted from Russell, Melenkivitz and Bren**[30]**)

2-D exchange spectroscopy (EXSY) is a convenient method for correlating resonances for two species in slow exchange. In theory, the integrations of the cross peaks can be related to the exchange rate; however, 1-D methods provide more precise rate determinations. In the case of paramagnetic proteins, 1-D methods are preferred as the resonance with the shorter T_1, which is often well resolved, can be saturated selectively, in which case the magnetization transfer is under the control of the species with the longer T_1.

Another means by which chemical exchange can be monitored is through isotope exchange. This is most commonly done to determine rates of exchange with solvent for exchangeable protons in biomolecules by transferring the molecule into deuterated buffer and observing the decrease in exchangeable ^{1}H signal intensity with time. Relatively slowly exchanging protons ($k_{obs} < 5 \times 10^{-2}\ s^{-1}$) can be monitored this way. These experiments provide site-specific information on conformational fluctuations in proteins that control local solvent exposure and also probe hydrogen bonding interactions. The application of hydrogen exchange (HX) methods to metalloproteins is discussed further in Section 5.2.

The reader is referred to the monograph by Sandström for a detailed treatment of the subject of dynamic NMR.**[31]** A helpful tool in evaluating NMR spectra of species in chemical exchange is to perform simulations of spectra, which can be assisted by the available software.[29] The application of dynamic NMR techniques to study chemical exchange and intermolecular interactions involving metalloproteins is described in Sections 5 and 6.

2.6 Residual Dipolar Couplings

Dipolar couplings result from the dipole moment of one nucleus affecting the dipole moment of another. Dipolar couplings depend on the distance between the spins and the orientation of the vector between the spins with respect to the external magnetic field B_0. In isotropic solution, this effect averages to zero because the molecular reorientation in the magnetic field is fast relative to the reciprocal of the dipolar interaction (i.e., <ms for a ^{1}H and a ^{15}N nucleus separated by 1 Å). In a solid sample, in contrast, coupling of each nucleus to many other nuclei is observed, but the result is a spectrum showing severe overlap. The most useful case for obtaining information related to structure is an intermediate case in which partial alignment of a sample relative to B_0 is achieved. In other words, the sample is prepared in such a way that not all orientations of the molecules have equal probabilities. In this case, residual dipolar couplings (RDCs) that provide angular restraints for internuclear vectors (usually bond vectors) relative to the orientation of the applied field can be observed. RDCs (D^{res}, Hz) between nuclei i and j separated by distance r_{ij} are given by[32,33]

$$D^{\text{res}} = -\left[\frac{\left(B_0^2\gamma_i\gamma_j h\right)}{\left(240 k_{\text{B}} T \pi^3 r_{ij}^3\right)}\right]\left[\Delta\chi_{\text{ax}}^{\text{mol}}(3\cos^2\theta - 1) + 1.5\Delta\chi_{\text{rh}}^{\text{mol}}\sin^2\theta\cos 2\phi\right] \qquad (23)$$

where θ is the angle between the vector connecting i and j (usually bonded ^{15}N$-^1$H) and the z axis of the χ^{mol} tensor, and ϕ is the angle describing the projection of the internuclear vector on the xy plane of the χ^{mol} tensor axes, relative to the x axis. Note that the molecular magnetic anisotropy $\Delta\chi^{\text{mol}}$ has two components, magnetic anisotropy arising from the paramagnetic center, which also gives rise to pseudocontact shifts (equation 14), and the magnetic anisotropy of the diamagnetic protein frame. Such bond orientation restrictions have become important restraints in determinations of biomolecule structure in solution.[34] RDCs are useful for defining long-range order within a molecule because they constrain bond orientations within the frame of the applied field. Because the restraints most used in structure determination by NMR (NOEs, which are usually observed for internuclear distances <5 Å, and J couplings, which are observed only through a few bonds) are local in nature, dipolar couplings provide an important complementary restraint for structure determination. This information is particularly valuable for elongated molecules, and for molecules with multiple domains. Experiments making use of RDCs also can provide insight into biomolecule motions on timescales from picoseconds to milliseconds.[35]

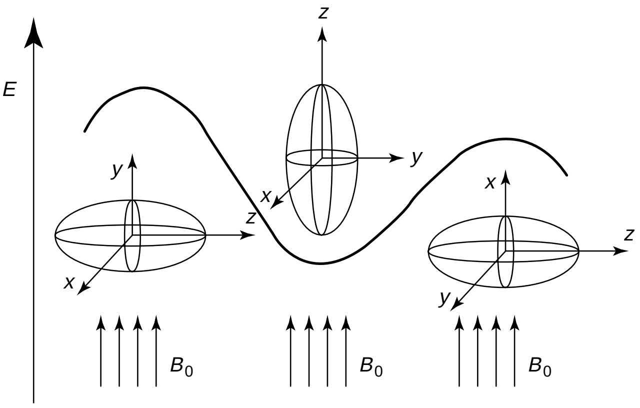

Figure 8 Illustration of a magnetically anisotropic molecule. Its energy depends on its orientation relative to the applied magnetic field, B_0. Thus, it will preferentially adapt orientations with lower energies. (Adapted from Bertini, Luchinat, Parigi and Pierattelli.[22] © 2005 Wiley-VCH)

Metalloproteins have played an important role in the development of RDCs as a tool for structure determination. Pioneering work on RDCs was performed by Prestegard, who showed RDCs could be measured in paramagnetic cyanometmyoglobin.[32] Partial alignment yielding observable RDCs resulted from the interaction of the highly anisotropic paramagnetic susceptibility tensor of cyanometmyoglobin with a strong applied magnetic field (Figure 8). Partial alignment also can be achieved by obtaining NMR data in the presence of a medium that imposes a weak degree of order on the molecule. Bicelles, bacteriophage, and anisotropic gels have been commonly used for this purpose.[34] There has been increased interest in taking advantage of the interaction between an anisotropic paramagnetic metal and B_0 to induce partial alignment, which can be employed on paramagnetic metallobiomolecules or on biomolecules tagged with paramagnetic moieties.[9] The ability of paramagnetic samples to achieve partial alignment is a valuable tool available to the bioinorganic chemist interested in characterizing metallobiomolecule structure and dynamics.

3 APPLICATION TO METALLOPROTEIN STRUCTURE DETERMINATION

NMR has become an important tool for determination of high-resolution three-dimensional structures of biomolecules. As of the end of 2006, over 14% of all structures deposited in the protein data bank (PDB) were determined using NMR,[36] a trend showing tremendous growth since the first NMR structure of a protein was reported in

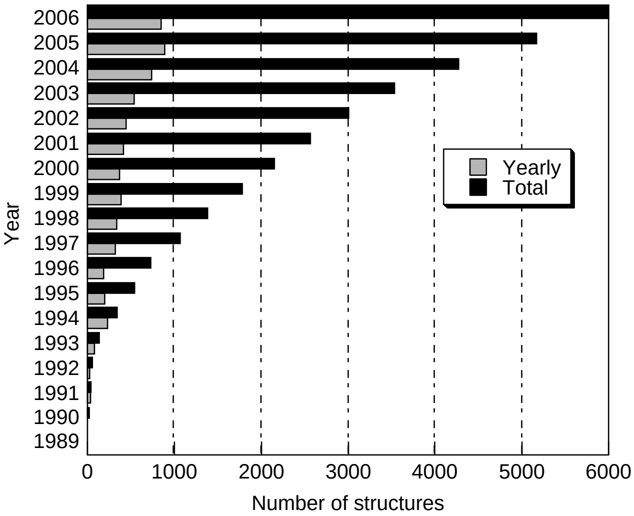

Figure 9 Growth in the number of biomolecule (protein and RNA) structures solved by NMR by year. Data from the Protein Data Bank[36]

1985 (Figure 9).[5] Initially, paramagnetic proteins were considered intractable targets for structure determination because of the challenge of making assignments and identifying NOEs involving nuclei experiencing paramagnetic relaxation enhancement. Today, not only are solution structures of paramagnetic metalloproteins being determined by NMR on a routine basis, but employing paramagnetism-based restraints in structure determinations has been shown to improve structure quality.[8,24,37] The utility of paramagnetic restraints is such that efforts are being put forth to devise paramagnetic tags for nonmetalloproteins for this purpose.[9]

NMR analysis of metalloprotein structure does not necessarily mean performing a complete structure determination, as in some cases this effort is not required to answer the salient questions. Many of the observables in NMR experiments (chemical shifts, NOEs, coupling constants) can be related to specific structural properties of a particular site within a biomolecule. Thus, NMR can provide an efficient means to answer a specific question requiring structural data without performing a complete structure determination. This focused approach is particularly attractive in paramagnetic metalloproteins, as the paramagnetic center endows characteristic properties on nuclei with which it interacts that can allow resonances from these nuclei to be observed and analyzed selectively. Paramagnetic effects on NMR spectra also make it possible to study metal sites in proteins for which a full structure determination is problematic because of size or disorder. Paramagnetic metalloproteins thus have moved beyond being just tractable to being attractive targets for NMR studies. Meeting the challenges of characterizing paramagnetic biomolecule structure has provided new tools useful for NMR studies of all biomolecules.

3.1 Protein Sample Preparation

As a result of the small energies involved in nuclear spin transitions, sensitivity of NMR is inherently low (equation 6), and relatively large amounts of sample are needed, with a typical sample having a minimum of 1 mM biomolecule in 300–500 µL volume. Whereas this amount of sample is usually not limiting in studies of small molecules, it can present a significant impediment to studies of biological samples. If this amount of sample is not available, obtaining a greater number of scans can compensate for low signal-to-noise, but only to a point, as signal-to-noise increases by a factor of $N^{1/2}$ where N is the factor by which the number of scans is increased. Advances in pulse sequences and in probe technology have significantly eased sample requirements. The availability of cryoprobes and microprobes has made NMR studies on significantly lower concentrations and volumes of biomolecule possible; however, these technologies are not always available to the routine user.

The need for large amounts of sample for NMR often requires that the protein be overexpressed, although in some cases sufficient amounts of sample are available from the native source. Overexpression is most conveniently done using *Escherichia coli* as a host. A major advantage of expressing the target protein in *E. coli* is that this often provides a means to prepare isotopically labeled protein. Uniformly labeled (^{15}N and/or ^{13}C) protein can be prepared by growth of *E. coli* containing the appropriate expression plasmid on medium in which the sole source of nitrogen or carbon is labeled with the desired isotope. Minimal medium containing $^{15}NH_4^+$ and/or ^{13}C-glucose is typically used for this purpose, although rich media are available commercially for producing labeled proteins.

Metalloproteins that have been overexpressed may need to be reconstituted with their native metal(s). For example, overexpression of the blue copper protein azurin results in a mixture of apo- and Zn^{II} forms. When a gene of an uncharacterized metalloprotein is expressed, care must be taken to assure that the identity of the native metal is determined through studies of native protein. Overexpression of heme proteins typically requires reconstitution with hemin. In the case of *c*-type heme, the heme must be attached covalently to the polypeptide with the assistance of cellular machinery. Wide success in expressing a range of *c*-heme containing proteins has been achieved by expression of both the structural cytochrome gene and the apparatus for protein maturation.[38,39]

Solution conditions (buffer, ionic strength, pH, and temperature) of the NMR sample should be optimized by monitoring 1-D ^{1}H or 2-D ^{1}H–^{15}N heteronuclear single quantum correlation (HSQC) spectra as a function of conditions to assure the protein is folded as seen by the expected peak dispersion (Figure 10). HSQC data correlate ^{15}N with directly bound ^{1}H and thus provide a probe of each nonproline amino acid. Because pH has a significant effect on exchange rates of exchangeable protons, slightly acidic

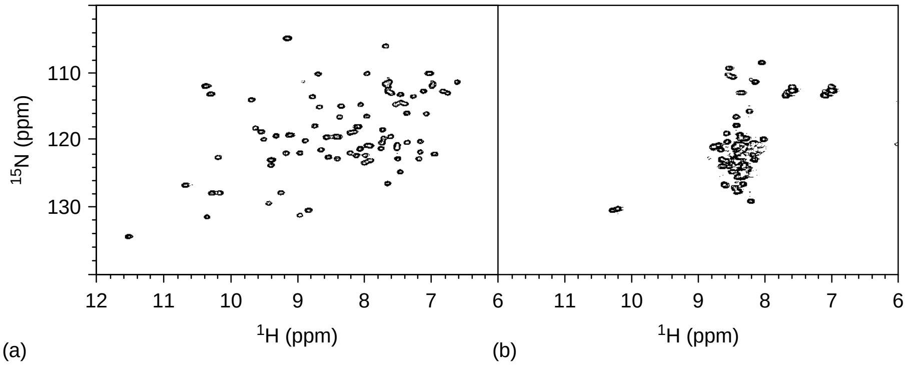

Figure 10 ^{1}H$-$^{15}N HSQC spectra of 0.5 mM ^{15}N-labeled *Pseudomonas aeruginosa* ferricytochrome c_{551} illustrating effect of protein unfolding on spectral dispersion. (a) Folded protein; note excellent dispersion in both the ^{1}H and ^{15}N dimensions. (b) Unfolded protein (in 8 M urea); note loss of dispersion particularly in the ^{1}H dimension. Proteins displaying partial unfolding or disordered regions will show spectra with properties between these extreme cases

pH values (pH 4 to 6) are often preferred as amide proton exchange rates are minimized at lower pH values, enhancing their detection.

3.2 Data Collection and Analysis for Protein Structure Determination

The experiments required to do a detailed analysis of protein structure are now standard in the case of well-behaved proteins (i.e., well structured, soluble, and relatively small size). What is required are enough experimental restraints (in addition to ''intrinsic'' restraints on bond lengths and angles, van der Waals distances, etc.) to allow a calculation of the structure. Experimental restraints include internuclear distances, dihedral angles, and positions of nuclei or angles of bond vectors within some reference frame. For small proteins (MW $<$ 10 kDa), 2-D homonuclear data alone are often enough to yield assignments of ^{1}H chemical shifts throughout the protein. The most useful experiments for this purpose are nuclear overhauser effect spectroscopy (NOESY), which provides information on through-space connectivities, and total correlated spectroscopy (TOCSY), which provides through-bond correlations over many bonds and thus aids in identification of amino acid side chain spin systems. The key experimental input for 3-D structure determination is the NOE, which scales with internuclear distance in a r^{-6} fashion and thus provides distances between protons relatively close in space (usually $<$5 Å). Coupling constants and, in partially ordered systems, RDCs provide additional restraints. Larger proteins require ^{15}N and/or ^{13}C labeling and use of a suite of multidimensional experiments to obtain sufficient chemical shift assignments and structural restraints because of increased spectral crowding, which is a particular problem for ^{1}H resonances. Compounding this problem for larger proteins is the increase in line widths resulting from efficient R_2 relaxation at long τ_c (Figure 5). The introduction of TROSY methods that optimize transverse relaxation has been a breakthrough for obtaining high-quality spectra of large proteins and has opened up the possibility of determining high-resolution structures of larger proteins, up to 100 kDa.[26,27]

Significant structural information can also be obtained without performing a full structure calculation. For example, chemical shifts of backbone nuclei are sensitive to secondary structure and can be utilized to determine locations of α and β structures within a polypeptide.[14] It also is possible to use protein engineering to incorporate specific amino acid probes, for example, ^{13}C$-$Leu, or a fluorinated amino acid, for a targeted study. In the case of paramagnetic metalloproteins, the hyperfine interaction allows for application of methods that enhance detection of nuclei in the vicinity of the paramagnetic metal, as explained in more detail in the following sections. This allows detailed information on metalloprotein active site structure to be obtained without determining a full three-dimensional structure.

3.3 Experiments Optimized for Paramagnetic Systems

NMR analysis of a paramagnetic biomolecule may require modifications to the standard experiments. In some cases, this is to compensate for deleterious line broadening caused by unpaired electrons, which interferes with detection of resonances and NOEs. In other cases, modifications are made to take advantage of the effects of unpaired electrons to selectively observe nuclei in the vicinity of the paramagnetic metal. The effects of the metal on the NMR spectrum depend largely on the τ_s value, which determines amount of linebroadening (equations 16 and 17). For systems with relatively short τ_s, few, if any, modifications need to be made, whereas study of systems with long τ_s require specially tailored experiments to obtain any information on nuclei in the vicinity of the metal site.[40]

Enhanced nuclear relaxation leads not only to broad lines, but also to less efficient magnetization and coherence transfer. This has an important impact on the NOE since this

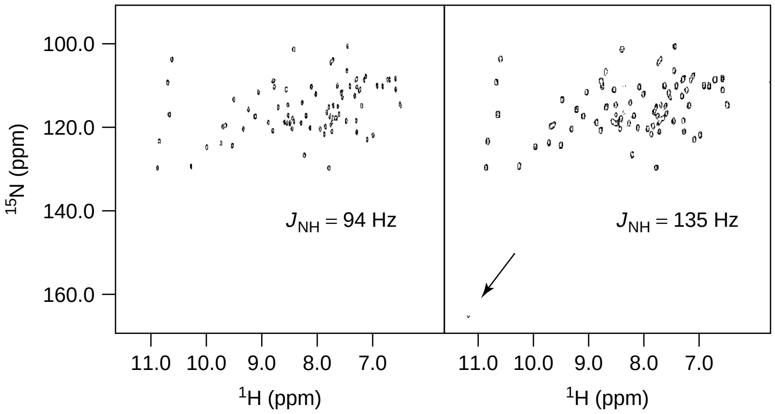

Figure 11 ^{1}H–^{15}N HSQC spectra of 1 mM ^{15}N-labeled *Hydrogenobacter thermophilus* ferricytochrome c_{552} showing the effect of a decreased INEPT delay on intensity of the peak correlating the heme axial His δHN nuclei. The input J_{NH} value is 94 Hz in (a), and 135 Hz in (b). The axial His δHN is readily observed in spectrum (b) (indicated with arrow), but is not detected under conditions used in (a)

effect is dependent on dipole–dipole relaxation. For nuclei with short T_1 values, detection of NOEs is aided by using a 1-D steady state NOE experiment rather than a transient NOE experiment (including the 2-D NOESY). In the steady state 1-D NOE, if the rapidly relaxing nucleus is saturated, the observation of the NOE depends only on the T_1 of the more slowly relaxing nucleus, aiding NOE detection. In 2-D NOESY and TOCSY experiments, mixing and spin-lock times may need to be adjusted to account for these effects. Often, collection of a spectrum with a shorter mixing or spin-lock time relative to standard values will reveal cross peaks involving rapidly relaxing nuclei. Similarly, decreasing the insensitive nuclei enhanced by polarization transfer (INEPT) delay times in an HSQC experiment will enhance peaks for nuclei with short T_1 values (Figure 11). Applying these methods can afford the advantage of identifying resonances from nuclei near the metal, even if they do not have unusual chemical shifts. In addition, experiments optimized to detect nuclei with short T_1 values can be performed with significantly faster repetition rates, thus allowing more scans to be acquired in a given amount of time. A detailed account of optimization of NMR data collection and processes for paramagnetic biomolecules has been provided by La Mar.[40]

Nuclei with low magnetogyric ratios experience weaker dipolar coupling with unpaired electrons because the coupling energy depends on γ^2. For example, for ^{13}C the line width enhancement from dipolar relaxation will be 1/16 of that seen for ^{1}H (equation 17). Thus for heteronuclei hyperfine coupling information is lost far from the paramagnetic center, but the decreased paramagnetic linebroadening may allow detection of residues not observable in ^{1}H NMR experiments. Detailed studies of nuclei near metal sites with long τ_s values thus benefit from detection of heteronuclei. ^{13}C is attractive as it provides a balance between a γ that is smaller than that of ^{1}H to decrease relaxation enhancement, but not so small that sensitivity becomes a limiting factor. A number of experiments have been designed to take advantage of this effect (e.g., see Figure 12).[41]

3.4 Characterization and Refinement of Metalloprotein Structure Using Paramagnetic Effects

The effects of the hyperfine interaction on NMR properties of nuclei can be exploited to obtain information on molecular structure beyond what is available using ‘‘traditional’’ restraints such as NOEs and coupling constants.

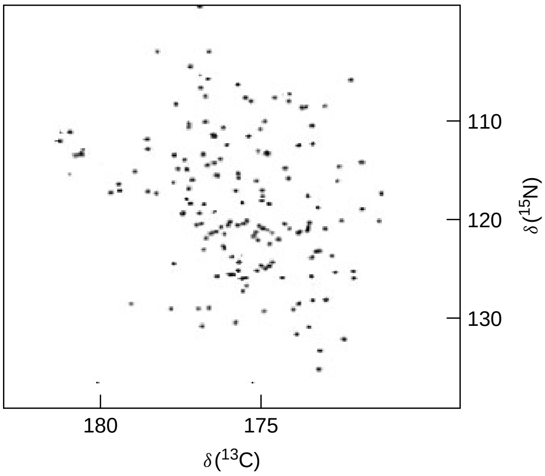

Figure 12 2-D in-phase–antiphase spectrum correlating backbone ^{13}C and ^{15}N nuclei, with detection of ^{13}C (CON-in-phase-antiphase (CON-IPAP) experiment). Data were acquired on a 1.5 mM sample of ^{13}C, ^{15}N labeled reduced monomeric superoxide dismutase with a 14.1 T Bruker Avance spectrometer equipped with a cryogenically cooled probehead optimized for ^{13}C detection at 298 K. (Reprinted from Bermel, Bertini, Felli, Piccioli and Pierattelli.[42] © 2006, with permission from Elsevier)

Through-space (dipolar) and through-bond (contact) interactions can be employed to perform a focused study of the structure of a paramagnetic metal-binding site in a protein, or to obtain additional structural restraints for determination of a full solution structure. This section is dedicated to the analysis of global molecular structure. Examples of focused studies of metal site structure are given in Section 4.

3.4.1 *Pseudocontact (Dipolar) Shifts*

Metal sites with anisotropic paramagnetic susceptibility tensors (χ^{para}) will induce pseudocontact shifts, δ_{pc}, on nuclei. The magnitude and sign of δ_{pc} are determined by the position of the nucleus relative to the principal axes of χ^{para}, centered at the metal, according to equation (14). The pseudocontact shift has both a distance and angular dependence, making it a valuable structural restraint for molecules in which the orientation of χ^{para} can be defined relative to the molecular frame. The value of δ_{pc} for a nucleus may be estimated experimentally by comparing the observed chemical shift in a paramagnetic system δ_{obs} with the chemical shift of the same nucleus in a diamagnetic reference system (which gives an estimate of δ_{dia}, equations (11), (12), and (14)). For example, a reduced, low-spin Fe^{II} heme protein may be used as a diamagnetic reference for the paramagnetic oxidized form, provided no significant structure change occurs with redox state change. The δ_{pc} values may then be obtained by subtraction ($\delta_{obs} - \delta_{dia}$), provided there is no contact contribution to the shifts, which will be the case for any nuclei not on moieties bound directly to the paramagnetic metal. The values defining the magnetic axes may then be calculated using equation (14) as was originally described by La Mar.[43] If one knows the axes and anisotropy of χ^{para}, a δ_{pc} value for a nucleus restrains its position within that frame of reference.

Pseudocontact shifts serve as a link between molecular and electronic structure, allowing the magnetic axes to be defined relative to the molecular frame. This interrelationship has been put to use in an iterative procedure for calculating χ^{para} tensor axes and anisotropies and refining molecular structure based on initial input data (Figure 13).[8] In addition, the pseudocontact shifts can be related to the heme axial ligand orientations as illustrated in Figure 14. Most pseudocontact shift refinements of structure have been on low-spin Fe^{III} heme proteins, although trivalent lanthanides also have been used for this purpose. Because the δ_{pc} values are greatest near the metal center, the additional structural restraints are identified in a region of the protein that frequently lacks restraints due to loss of NOE intensities. By including pseudocontact shift restraints, the structure near the paramagnetic center can be much more well defined than when solely traditional restraints are relied upon. Standard structure calculation programs now routinely provide means to incorporate pseudocontact shift restraints.[44]

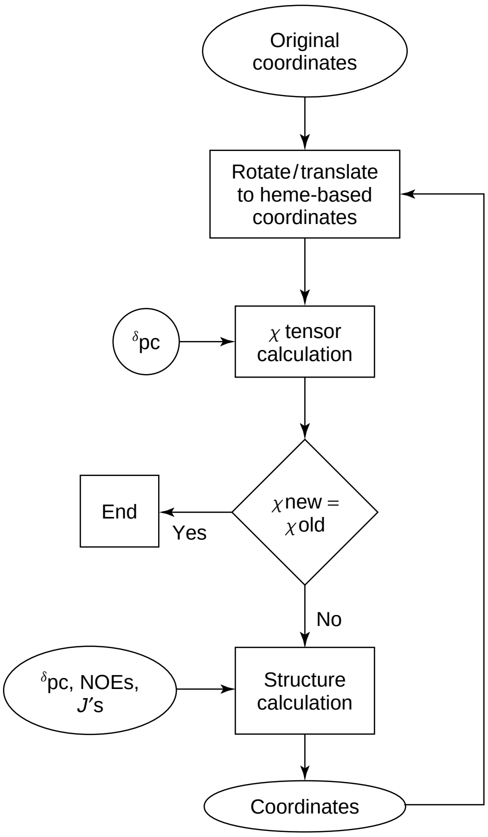

Figure 13 Flowchart for refinement of NMR solution structures and the parameters defining χ[8]

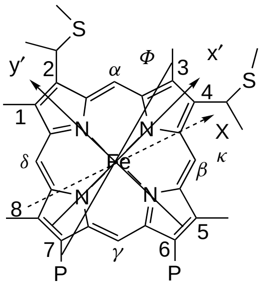

Figure 14 Relationship between orientation of magnetic axes and heme ligand orientation. The coordinates x and x' indicate the x axis in the magnetic and molecular coordinate systems, respectively. The solid line indicates the axial ligand orientation angle Φ (i.e., the plane of an imidazole ring), and the dashed line indicates κ, which is the orientation of χ_{xx}. The ligand orientation determines magnetic axes orientation according to $\kappa = -\Phi$. The orientation of axial ligands to the heme also determine contact shifts, as the ligand orientation determines which heme π orbital contains the largest unpaired electron spin density

3.4.2 *Contact Shifts*

Contact shifts are determined by unpaired electron spin density at the nucleus being observed (equation 13) and provide structural restraints for a limited number of nuclei as this effect becomes minimal more than a few bonds from the metal in most cases. Nevertheless, nuclei connected to a paramagnetic metal through bonds may lack observable NOEs such that obtaining a few contact shift restraints on their positions may provide a significant improvement on structure of the metal coordination environment. Contact shifts can be determined by subtracting the reference diamagnetic shift from the observed shift in the paramagnetic system, provided the pseudocontact shift does not contribute, or the pseudocontact shift contribution is determined and subtracted (equations 11, 12 and 14).

Contact shifts for nuclei three bonds from the metal are dependent on dihedral angle θ through a Karplus-type relationship:

$$\delta_{\text{con}} = a\cos^2\theta + b\cos\theta + c \tag{24}$$

where the coefficients depend on the nature of the bonds and atoms between the metal and nucleus in question and have been determined heuristically.[45] This analysis has been applied to the definition of dihedral angles between iron and βCH_2 protons of coordinated Cys residues in iron–sulfur proteins. Nuclei near iron–sulfur sites typically exhibit severe linebroadening, and incorporating these restraints can play an important role in defining metal site structure.

There have been extensive studies relating heme substituent shifts, some of which are dominated by the contact contribution, to the type and orientation of the heme ligands.[46] Thus, the chemical shifts for the heme substituents provide information on heme ligand type and orientation.

3.4.3 Dipolar Relaxation Enhancement

Paramagnetic enhancement of R_1 in macromolecules ($R_{1\text{p}}$) primarily depends on dipolar coupling between the electron and nuclei and is proportional to r^{-6} (equation 17). Thus, relaxation enhancement contains electron–nucleus distance information, although the enhancement diminishes sharply as distance increases. The metal-centered sphere in which this effect can be measured depends on the molecule studied and the properties of the metal, especially the τ_s; metals with longer τ_s will exert greater effects on relaxation. To use relaxation enhancement as a restraint on structure, a reference R_1 value from a diamagnetic system is needed. This may be determined on a diamagnetic homolog, or estimated from R_1 values of nuclei within the molecule at a distance far from the paramagnetic center. $R_{1\text{p}}$ is taken as the difference between the observed and reference R_1 values. This approach has been used, for example, to refine the structure of a Fe_4S_4 ferredoxin. Inclusion of relaxation constraints led to a substantial improvement of the structure near the iron–sulfur cluster relative to the structure obtained using conventional constraints in particular, because of the difficulty of observing NOEs near the cluster.[22] Caution is called for in interpretation as nonlinear dependence on r^{-6} has been observed at longer distances, which may result from effects of spin delocalization.[41] Similarly, $R_{2\text{p}}$ values, which contribute to R_2 and thus line widths, may be employed as constraints. When interpreting R_2 values, contributions from Curie spin relaxation and chemical exchange must be considered. Relaxation enhancement has also been applied to NMR studies of RNAs as described in Section 8.

3.4.4 Residual Dipolar Couplings

RDCs provide information on angular orientations of bond vectors relative to the applied magnetic field (Section 2.6). For measurement of RDCs it is required that the molecule take a preferred orientation relative to the external magnetic field, which is usually achieved by including an alignment medium in the sample.[34] In principle, all biomolecules in solution will take on a preferred orientation relative to B_0 as a result of magnetic susceptibility anisotropy, but in practice RDCs will be observable only at high B_0 and highly anisotropic $\Delta\chi^{para}$. Prestegard's seminal study on cyanometmyoglobin demonstrated paramagnetic-induced alignment and also the ability to determine relative orientations of helices within the protein through analysis of RDCs.[32]

With their typically high magnetic anisotropies, low-spin ferric heme proteins are attractive candidates for structure analysis using RDCs, as they may achieve a degree of orientational preference within the applied field significant enough to allow observation of RDCs. Low-spin ferric heme proteins that have been analyzed in this way include the alkaline form of a cytochrome *c* mutant, cytochrome b_5, and *E. coli* cytochrome b_{562}.[37,47,48] Proteins that bind the paramagnetic lanthanide ions with high magnetic anisotropies are also attractive candidates for self-orientation (Table 2). Substitution of trivalent lanthanides for calcium in calcium-binding proteins has been a useful approach as the lanthanides are known to substitute for Ca^{II} and typically maintain a nativelike coordination environment. For example, the calcium-binding protein calbindin D_{9k} substituted with trivalent lanthanides was shown to self-orient to yield observable dipolar couplings to aid solution structure determination.[49] A means of preparing self-orienting samples of diamagnetic proteins and even proteins that do not bind metals is to attach a lanthanide-binding tag or to prepare a fusion protein with a lanthanide-binding domain such as an EF-hand.[9]

RDC restraints can be incorporated into structure calculations using modules available in standard structure determination software as well as programs developed specifically for RDC analysis.[37,50] They are expected to be particularly helpful for determining structures of large proteins or any system for which obtaining sufficient restraints is difficult. RDCs also are valuable for characterizing elongated, multidomain, or other nonglobular proteins as they define relative orientations of distant bond vectors. For example, in a two-domain protein, few NOEs may be observed between the domains, making the determination of their relative

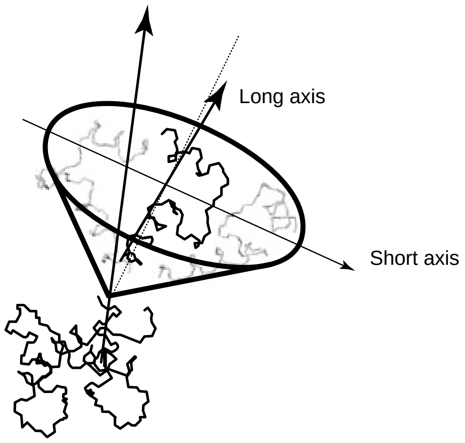

Figure 15 Cone containing three conformations of the C-terminal domain of calmodulin providing pseudocontact shifts and residual dipolar couplings consistent with experimental data. (Adapted from I. Bertini *et al.* (2004) *Proc. Natl. Acad. Sci. U. S. A.*, **101**:6841–6846. © 2004 National Academy of Sciences, USA)

orientations difficult. Measuring RDCs for the two domains however, allows the definition of the orientation of each domain relative to a common external frame of reference, and thus relative to each other (Figure 15). The increased availability of high-field spectrometers and methods for creating self-aligning samples, coupled with ongoing efforts to push the size limit of biomolecules for which NMR structures can be determined, is expected to result in increased use of RDCs in the future.

4 APPLICATION TO CHARACTERIZATION OF METAL SITES IN METALLOPROTEINS

The goal of many biomolecular NMR studies is characterization of global molecular structure. In metallobiomolecules, and in particular, for paramagnetic species, it is sometimes preferable to use NMR to perform a more focused study of the metal ion coordination environment and the metal electronic structure. Metal sites show great variation in the effects on chemical shifts and line widths and thus often call for tailored approaches. In this section, characteristics of some of the metalloproteins metal sites most frequently studied by NMR are summarized. Examples have been selected to illustrate approaches described in this chapter such as metal substitution, use of pseudocontact shifts, RDCs, relaxation enhancement, and detection of nuclei other than ^{1}H.

4.1 Heme

Heme is found in proteins and enzymes and performs a wide range of biological functions. Heme also exhibits a range of oxidation and spin states, with the ferric and ferrous states usually being the most stable. Low-spin Fe^{II} heme has filled t_{2g} orbitals and is diamagnetic, whereas high-spin Fe^{II} heme has spin state $S = 2$. Ferric heme is paramagnetic but can be found in low- ($S = 1/2$), intermediate- ($S = 3/2$), or high-spin ($S = 5/2$) states, depending on heme ligation (Figure 16).

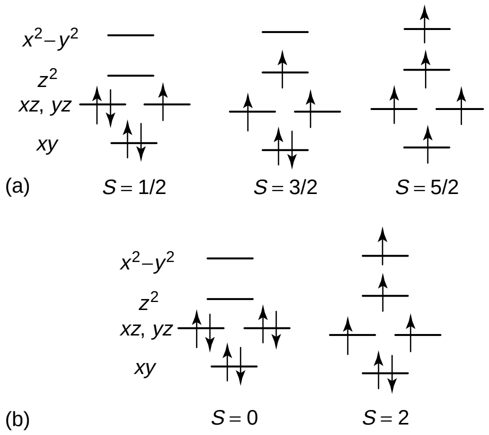

Figure 16 Spin states displayed by ferric (a) and ferrous (b) heme

Heme proteins containing low-spin Fe^{III} have played important roles in the development of NMR techniques for paramagnetic proteins. Low-spin ferric heme proteins are popular targets for NMR study because they display minimal linebroadening (due to short τ_s) and large pseudocontact shifts (due to large χ anisotropy). Other than using a larger than usual spectral width, few accommodations need to be made for the paramagnetism to obtain high-resolution spectra, and in fact the large chemical shift range increases dispersion, in particular, for ^{1}H. Early studies related chemical shifts of heme substituents of paramagnetic cytochromes *c* to the heme axial methionine orientation; this has evolved to a detailed understanding of how heme axial ligand orientations determine contact and pseudocontact shifts of heme substituents.**[43,46]** Cyanometmyoglobin was the first protein for which magnetic axes were calculated on the basis of pseudocontact shifts,**[43]** and was the subject of an early study of RDCs.**[32]** The favorable properties of low-spin ferric heme also allows direct analysis of axial ligand resonances, providing vital information on how hydrogen bonding to axial ligands tunes heme electronic structure and redox potential.**[10]**

High-spin ferrous heme has functional importance as an intermediate of several heme enzymes. Deoxy-hemoglobin and deoxy-myoglobin also have high-spin ferrous heme. Nevertheless, there are relatively few NMR studies of $S = 2$ heme because of the high amount of linebroadening exacerbated by Curie spin relaxation, which results in poorer resolution at high magnetic fields. High-spin ferric heme is the resting state of many heme enzymes. Linebroadening is less severe than for high-spin ferrous heme as a result of a faster electron spin relaxation time. Despite the ^6A symmetry of the high-spin heme ground state, zero field splitting introduces anisotropy that induces pseudocontact shifts; this is also the mechanism through which electronic relaxation is made relatively efficient. Proteins containing high-spin ferric heme nevertheless, display a substantial amount of linebroadening that often calls for specially tailored experiments. An example is the study of the hemophore HasA (proposed to exhibit a mixture of $S = 5/2$ and $S = 1/2$ states) using ^{13}C- and ^{15}N-detection, including specially tailored 2-D experiments in which ^{13}C is detected. Ferric HasA (His/Tyr$^-$ axial ligation) has extremely short T_1 values for residues near the heme, hindering ^1H NMR approaches. ^{15}N and ^{13}C-detected experiments, however, yielded assignments for heme axial ligands, which in turn allowed characterization of a functionally relevant hydrogen bond to the axial Tyr ligand.[51] Another important development has been preparation of selectively labeled hemes by Rivera and coworkers. Chemical shifts of ^{13}C resonances of high- and intermediate-spin ferric hemes have been related to porphyrin conformations relevant to the function of the heme-degrading enzyme heme oxygenase.[52]

4.2 Iron–sulfur centers

Iron–sulfur proteins are challenging targets for NMR because of the significant linebroadening they typically display. At the same time, NMR is a valuable approach for the study of iron–sulfur proteins as it provides a way to probe properties of the ligands to the individual iron ions within the cluster, thus allowing the electronic coupling among the iron ions to be examined in detail. Mononuclear iron protons such as rubredoxin display extremely broad lines, especially in the ferric state. Many NMR studies have thus utilized proteins substituted with diamagnetic metals (Zn^{II} or Ga^{III}). Detection of low-γ nuclei, however, has provided a means to directly study mononuclear Fe^{II} and Fe^{III} sites. For example, in *Clostridium pasteurianum* rubredoxin containing a single Fe^{II} or Fe^{III} ion, ^{15}N hyperfine shifts of amide ^{15}NH groups that hydrogen bond with Cys γS ligands to iron (Fe–S–H–N) in a series of mutants have been analyzed to determine electron spin density delocalized to the ^{15}N, which in turn was related to redox potential tuning.[53] Iron–sulfur cluster proteins (Figure 17) are more tractable for NMR than the mononuclear systems because coupling between the iron ions enhances electron relaxation. The Fe_4S_4 and Fe_3S_4 proteins in particular display narrower lines than the mono and dinuclear iron–sulfur proteins and can be studied directly using ^1H NMR methods.

4.3 Copper

Copper ions are found in electron transfer proteins such as the cupredoxins and in enzymes such as Cu–Zn superoxide dismutase. Cu^{II} has a long τ_s and is thus effective in enhancing nuclear relaxation. As a result, ^1H resonances of ligands to Cu^{II} are typically broadened beyond detection. NMR studies of mononuclear Cu^{II} proteins such as the cupredoxins have usually made use of variants substituted with diamagnetic Zn^{II}, or paramagnetic ions with shorter τ_s values such as Co^{II} or Ni^{II}. New methodologies have now provided means to directly study mononuclear Cu^{II} proteins. An example is the use of specialized experiments to observe the extremely broad ^1H resonances for Cu^{II} ligands in *Anabaena variabilis* plastocyanin. Relaxation rates of rapidly relaxing contact-shifted signals have been measured using the signal eliminating relaxation filter (SERF) experiment. This experiment involves substituting the 180° inversion pulse of the conventional inversion-recovery sequence with a SERF consisting of three 180° pulses separated by two variable delays. The SERF experiment allows a selective suppression of signals with relaxation rates below a given limit while monitoring the relaxation of faster relaxing signals. Secondly, a saturation transfer experiment was used to detect broadened signals not actually observed in the NMR spectrum. Employing these methods allowed the measurement of paramagnetic relaxation enhancement of protons close to the metal site and the distribution of the unpaired electron spin onto the ligand atoms. These paramagnetic restraints supplemented conventional restraints to allow determination of geometric metal site structure directly on the Cu^{II} protein.[54]

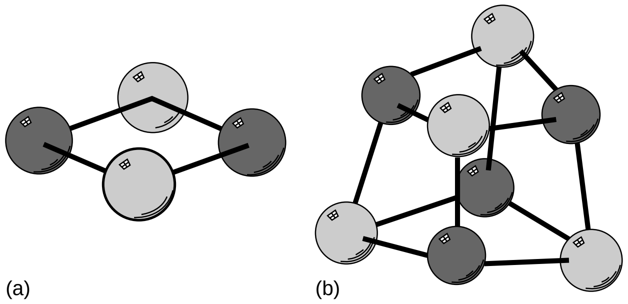

Figure 17 Structure of a Fe_2S_2 (a) and Fe_4S_4 (b) cluster, with the Fe atoms in dark gray. Cys are the most common ligands to Fe, but other amino acids such as Asp and His also bind Fe in clusters

As with iron-containing systems, coupling between copper ions results in longer electron spin relaxation times and thus narrower NMR lines. This was first demonstrated in a protein in the study of the soluble Cu$_A$ fragment of cytochrome *c* oxidase (Figure 18).[55] Whereas ligand ^1H nuclei are not directly observable in mononuclear Cu^{II} systems, in oxidized (Cu^{II}–Cu^{I}) Cu$_A$, many ligand ^1H resonances are readily assignable. Strong Cu–Cu coupling is evident both in the relatively long nuclear T_1 values (reflecting a short τ_s) and in the similar hyperfine shifts of the ligands to the two coppers, indicating that the Cu^{II}–Cu^{I} site behaves as a Cu$^{+1.5}$–Cu$^{+1.5}$ site. In addition, the high (100–300 ppm) chemical shifts of βH_2 protons of the bridging Cys residues, dominated by the contact shift, reveal a high amount of electron spin delocalization onto the ligands. It is suggested that this delocalized nature enhances electron transfer by reducing reorganization energy and increasing electronic coupling.

4.4 Zinc

Zinc plays an essential role as a cofactor in many metalloproteins and as a regulatory agent in cell homeostasis.[1] Zn^{II} has a preference for tetrahedral geometry and can thus serve a structural role, for example, templating the folding of ubiquitous zinc finger domains.[56] Zn^{II} also plays catalytic roles, for example, activating water through polarization or ionization in hydrolytic enzymes.[57] Although Zn^{II} displays a wide range of functions in nature, it has been subjected to fewer spectroscopic studies than many other metals because its closed-shell nature makes its direct study difficult. One approach is to perform ^{67}Zn NMR using solid-state NMR experiments, described in Section 7, although this is a highly specialized approach. Other NMR studies of Zn^{II} proteins performed to probe active site properties have made use of variants substituted with paramagnetic metals. Co^{II} exhibits coordination properties similar to Zn^{II}, and also has properties favorable for NMR as it induces hyperfine shifts on active site nuclei and does not induce excessive broadening. NMR studies of Zn^{II} proteins substituted with Co^{II} have been performed on Zn^{II} enzymes as well as on zinc finger proteins.

4.5 Calcium

Ca^{II} plays diverse roles in biology, displaying structural, catalytic, and regulatory functions. The importance of Ca^{II} in signal transduction has piqued great interest in its interactions with proteins. NMR has been extremely valuable for probing the effects of Ca^{II} binding on protein structure and dynamics, providing vital information on the regulatory role of calcium. A large superfamily of calcium-binding proteins, the EF-hand proteins, have been most studied by NMR. The EF-hand motif itself is small, and may be studied in isolation from other EF-hand domains as these domains are often connected by flexible linkers. However, the flexibility of such linkers introduces challenges in NMR study of multidomain EF-hand proteins as it reduces interdomain NOEs, making it difficult to determine relative orientations of the domains.

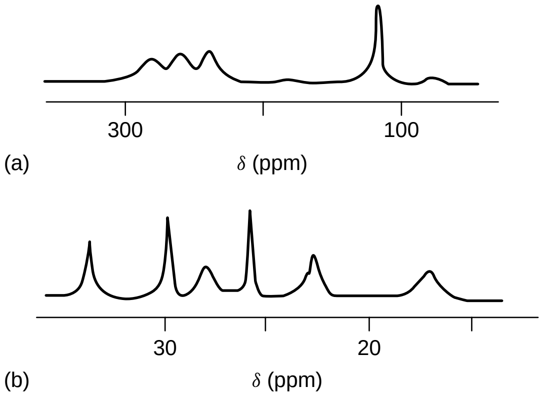

Figure 18 A 600-MHz ^1H NMR spectrum of the Cu_A domain of *Thermus thermophilus* cytochrome *c* oxidase at pH 8 and 278 K (b). The top spectrum (a) shows the far-downfield region of the spectrum recorded in D_2O at 298 K. (Adapted from Bertini, Bren, Clemente, Fee, Gray, Luchinat, Malmstrom, Richards, Sanders and Slutter.[55] © 1996 American Chemical Society)

As Ca^{II} is diamagnetic, substitution is necessary to take advantage of paramagnetic effects on NMR spectra. Trivalent lanthanides have been shown to substitute for Ca^{II} without significantly altering protein structure, and are an attractive paramagnetic probe because of their short τ_s values and large paramagnetic anisotropies (Table 2). Thus, they do not cause significant linebroadening, but do induce pseudocontact shifts. In addition, they may be used to achieve partial alignment in the magnetic field so that RDCs may be observed. This approach is particularly helpful for obtaining restraints of EF-hand domains relative to each other. An example of the use of lanthanide substitution is di-Ce^{III} substituted calmodulin, a protein with two EF-hand motifs. The addition of T_1 and pseudocontact shift restraints was shown to significantly improve the solution structure.[58] In another example, the ability to observe RDCs in calbindin D_{9k} substituted with a range of lanthanide ions was also reported. In addition to characterizing structure, it is possible to assess mobility of domains through RDC analysis.[49]

5 APPLICATION TO CHARACTERIZATION OF INTERNAL METALLOPROTEIN DYNAMICS

It is now appreciated that a full description of the physicochemical basis for biomolecular function must consider the thermally accessible motions of the biomolecule in addition to the average structure. Protein flexibility has been invoked in a wide range of biological processes including folding and assembly, ligand binding and catalysis, and regulation and signal transduction.[59–61] NMR has proved to be a particularly powerful tool for analysis of biomolecule motions, as it provides probes of motions in solution occurring on timescales ranging from picoseconds to milliseconds and longer. In addition, NMR provides site-specific information on polypeptide motion, aiding elucidation of the relationship between dynamics and function.[62,63]

5.1 Nuclear Relaxation Studies of Backbone Dynamics

Molecular motions modulate fluctuating magnetic fields that induce nuclear spin relaxation. Nuclear relaxation properties thus contain information on these motions. A majority of relaxation studies of protein dynamics have

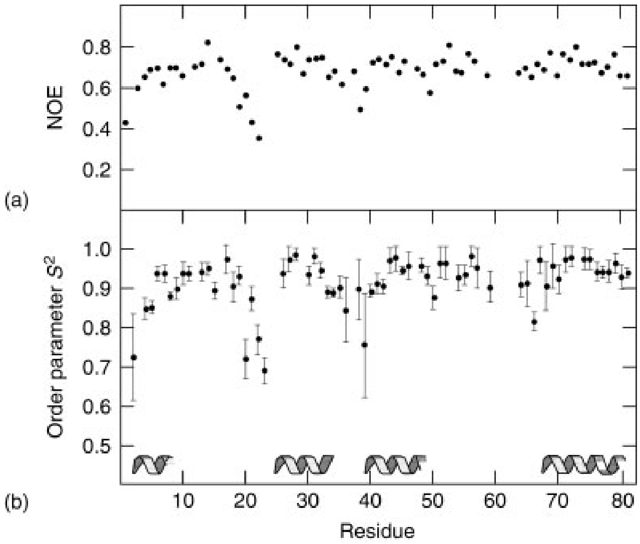

Figure 19 Results of ^{15}N relaxation experiments on *Pseudomonas aeruginosa* ferricytochrome c_{551}, collected at 298 K on a 500-MHz spectrometer. Values for (a) $\{^1H\}-^{15}N$ NOE and (b) order parameter S^2 are shown. Order parameters are calculated from relaxation data and reflect the magnitude of picosecond–nanosecond timescale motions of backbone N–H bond vectors. S^2 ranges from 0 to 1 with 1 indicating a rigid bond vector in the molecular frame. Helices at the bottom of the figure indicate α-helical regions of the protein; the helices are connected by loops. (Figure prepared from data published in Russell, Zhong, Bigotti, Cutruzzolà and Bren[65])

focused on the polypeptide backbone ^{15}N nuclei. One reason for this is convenience; ^{15}N labeling of metalloproteins is economical and also provides one probe of backbone motion per amino acid residue. Methods for collecting and analyzing ^{15}N relaxation data are well established.[62] Analyzing backbone amide ^{15}N relaxation properties also yields a general picture of dynamics, as backbone conformation defines secondary structure and the overall fold. Relaxation of protonated nitrogen nuclei is typically described by their R_1 and R_2 values as well as the heteronuclear $\{^1H\}-^{15}N$ NOE, measured using standard $^1H-^{15}N$ correlation spectra.[64] Of these parameters, the heteronuclear NOE is the most straightforward to interpret directly; its magnitude is determined by rapid ($\tau < \tau_r$) internal motions. R_1 and R_2 are also influenced by rapid motions, but slower motions provide an additional contribution to R_2. Other relaxation parameters also may be measured, in particular, to characterize slower motions (microseconds). The R_1, R_2, and NOE may be interpreted using the Lipari–Szabo model-free treatment, which yields magnitudes of N–H bond vector motions (order parameters, S^2) from relaxation data. An example of these results is shown in Figure 19. In nuclear relaxation studies of paramagnetic metalloproteins, care needs to be taken to account for enhanced relaxation imparted by the paramagnetic center, as otherwise interpretation of data cannot be made simply on the basis of dynamics. This is not a significant problem for ^{15}N nuclei because the effect is attenuated 100-fold in comparison with ^{1}H nuclei, according to equation (17), as $(\gamma_H/\gamma_N)^2 \sim 100$.

Relaxation studies of metalloproteins have revealed effects of metal binding and metal redox state on backbone dynamics.[66] Calcium-binding proteins have been a favorite subject of dynamics studies and show significant changes in flexibility induced by metal binding. For example, backbone dynamics changes upon metal binding have been correlated with cooperativity of Ca^{II}-binding in EF-hand proteins. Dynamics of electron transfer proteins have also been characterized, although the direct functional significance is less clear. Some electron transfer proteins have been shown to display enhanced mobility in regions of the protein proposed to interact with redox partners. For example, a surface hydrophobic patch of *Pseudomonas aeruginosa* cytochrome c_{551} with particularly high mobility is the site of interaction with its physiological electron acceptor, nitrite reductase.[65] Similarly, in the blue copper protein azurin, the hydrophobic patch proposed to be the port of entry for electrons is characterized by large magnitude nanosecond timescale mobility. In addition, longer timescale motions of active site residues are proposed to play a role in a gated electron transfer mechanism.[67]

5.2 Hydrogen Exchange Experiments

Whereas relaxation experiments to probe biomolecule dynamics have become popular only within the past 10 years, HX experiments have been performed on proteins for many decades. Provided that the experiment is carried out under conditions favoring the native protein state, thermodynamics of conformational fluctuations that lead to exchange of protons with solvent (ΔG_{HX}) can be determined using the following expression:

$$\Delta G_{HX} = RT \log\left(\frac{k_{int}}{k_{obs}}\right) \qquad (25)$$

where k_{obs} is the observed exchange rate and k_{int} is the intrinsic chemical exchange rate, which is sequence-dependent.[68–70] The values of ΔG_{HX} obtained provide site-specific information on thermodynamics of conformational fluctuations leading to exchange, and modeling studies suggest these energies of structural fluctuations reflect magnitude of motions on the micro to millisecond timescale.[71] HX experiments are best performed on ^{15}N-labeled proteins in which HX can be followed by the decrease in HSQC peak intensity as a function of time after exchange of the protein into D_2O, as HSQC spectra yield one peak for each $^1H-^{15}N$ bond and can be collected in a period of minutes. An example is shown in Figure 20. HX rates are dependent on the oxidation state of metalloproteins and in some cases this dependence has been subscribed functional significance. An interesting example is in putidaredoxin, a Fe_2S_2 protein that is the

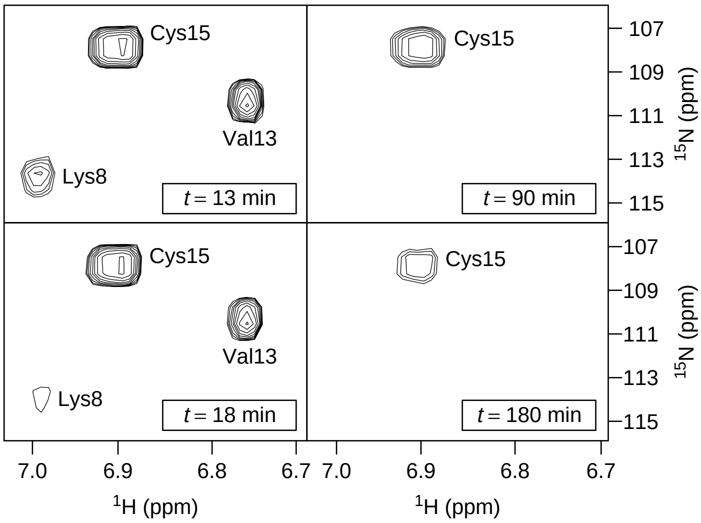

Figure 20 Example of hydrogen–deuterium exchange experiment monitored by HSQC. A portion of the $^{1}H-^{15}N$ HSQC spectrum of *Pseudomonas aeruginosa* ferricytochrome c_{551} is shown with time after exchange into D_2O indicated. Note the different rates of change in NH peak intensity for the residues shown

electron donor to *Pseudomonas putida* cytochrome P-450. Redox-dependent dynamics in putidaredoxin are inferred from differential HX rates, with the largest differences being near the metal center. This change is proposed to play a role in controlling redox-dependent affinity of putidaredoxin for cytochrome P-450.[72]

5.3 Side Chain Dynamics

Relaxation studies can be performed to analyze side chain dynamics, usually using ^{13}C or ^{2}H nuclei. Whereas analysis of backbone relaxation relies on a limited number of bond vectors to sample the protein, side chains present a wider array of possible probes of dynamics. Relaxation studies of amino acid side chains require specialized isotope enrichment schemes to yield interpretable relaxation behavior.[73] An example of an application to a metalloprotein is the study of *Rhodobacter capsulatus* cytochrome c_2 in the reduced (diamagnetic) state in which ^{2}H relaxation of amino acid side chain methyl groups was analyzed. Relative to other proteins, methyl side chains were found to have very limited mobility, which was attributed to interactions with the hydrophobic heme group for many of the hydrophobic amino acids. This high rigidity is proposed to enhance electron transfer by minimizing reorganization energy.[74]

Line shape analysis has been utilized to detect and elucidate dynamics of ligands bound to metals. For iron porphyrin models of metalloproteins, axial imidazole ligands may rotate relative to the heme axes; linebroadening of heme substituents resulting from this process can be observed at low temperature.[75] Such ligand motion is not commonly observed within metalloproteins because of constraints of the protein structure and metal–ligand bonding. NMR studies of some metalloproteins, however, have revealed linebroadening of active site nuclei interpreted to indicate amino acid side chain dynamics.[67] For example, in some cytochromes *c*, the heme axial methionine ligand has been shown to undergo inversion at sulfur on the microsecond time scale. This process results in averaging of the heme methyl proton chemical shifts of the two conformations in exchange. Heme methyl resonance linebroadening is evident as the exchange process approaches the intermediate timescale regime at low temperatures (Figure 21).[76]

6 APPLICATION TO ANALYSIS OF INTERMOLECULAR INTERACTIONS

NMR is a powerful tool for characterizing intermolecular interactions such as ligand binding to proteins, or protein–protein interactions. Under favorable conditions, dissociation constants (K_d) and dissociation rates (k_{off}) can be determined, as can the binding site(s) on the protein. In addition, changes in protein structure and dynamics resulting from protein or ligand binding may be determined. The utility of NMR for characterizing in detail even weak ($K_d \sim$ mM) intermolecular complexes sets it apart from other methods used to analyze intermolecular interactions involving biomolecules.

When characterizing an intermolecular interaction by NMR, the experimenter is examining a system in dynamic exchange. Considering this to be a simple two-state process exchanging the two unbound molecules (A and B) with the complex (AB),

$$A + B = AB \tag{26}$$

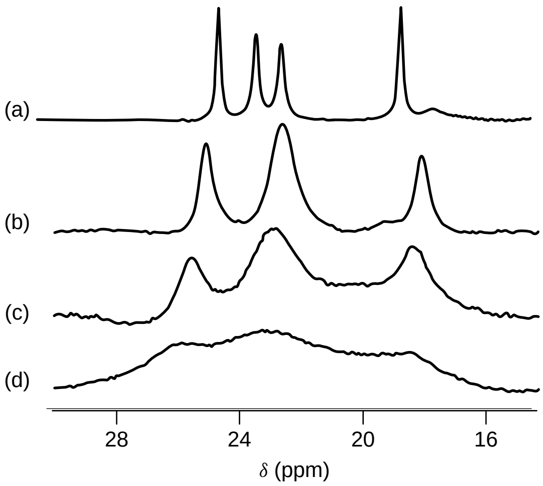

Figure 21 ^{1}H resonances of heme methyl groups of *Hydrogenobacter thermophilus* ferricytochrome c_{552} at (a) 26, (b), 11 (c) 1, (d) −6 °C. The chemical shifts observed are an average of shifts for two different axial methionine orientations in fast exchange on the NMR timescale. Upon lowering the temperature, the exchange process is slowed so that resonance broadening is evident as the process approaches the intermediate exchange regime. Samples for (b)–(d) are in 20% methanol

the dissociation constant (K_d, M^{-1}) is described by the ratio of the rate constants for binding (k_{on}, $M^{-1}\,s^{-1}$) and dissociation (k_{off}, s^{-1}):

$$K_d = \frac{k_{on}}{k_{off}} \tag{27}$$

Thus, it becomes important to consider the rate-limiting process (k_{off}) when designing experiments to characterize the complex, as dissociation may be slow, intermediate, or fast relative to the NMR time scale. The reader is referred to Section 2.5 for a summary of dynamic NMR methods. This section will present an application of these methods to study binding of molecules to metalloproteins.

6.1 Ligand Binding to Metalloproteins

Small molecules that bind to biological macromolecules are referred to as *ligands*. In bioinorganic chemistry, the term ligand also has the more specific meaning of a small molecule, ion or other moiety that binds to a metal site to form a coordination complex. NMR is readily employed to characterize both kinds of ligand binding to metalloproteins. A simple and effective general approach to studying ligand–protein interactions is to monitor chemical shift changes in the ^{15}N–^{1}H HSQC spectrum of the target protein as a function of added ligand. This is effective for proteins with molecular weights up to about 40 kDa. For larger proteins, protein deuteration and use of TROSY is needed to obtain sufficient resolution. In addition, ^{13}C-methyl labeling of specific residues (i.e., Ile, Leu, and Val) may help in studying larger proteins. An alternative method for monitoring protein–ligand binding is saturation transfer. If the ligand's off rate is fast relative to T_1, its signal will be reduced in the unbound form upon saturation of the bound form. This method is particularly useful when applied to a large biomolecule because of effective spin diffusion. Also useful for detecting binding to relatively large proteins (>50 kDa) is the transfer NOE, which can reveal the bound-state conformation of the ligand. These and other methods for NMR characterization of protein–ligand interactions have been reviewed recently.**[77]**

The above methods may be applied to binding of ligands either at or away from a metal site in a metalloprotein. In the case that a ligand binds a metal site, particularly when that metal is paramagnetic, significant changes in chemical shifts and/or line widths of the ligand and metal often result. The spectral changes observed depend on the differences in the electronic structure of the metal caused by binding and are particularly dramatic when ligand binding induces a spin-state change, as commonly occurs in heme proteins, for example.**[10]** As large shift differences between bound and unbound forms may be seen, application of 1-D methods to monitor ligand binding are greatly facilitated.

6.2 Protein–Protein Interactions

Protein–protein interactions play key roles in all areas of biology. The dissociation constant (K_d) for these interactions ranges over many orders of magnitude, from subpicomolar to millimolar. For weakly associating complexes ($K_d > \mu$M) in particular, structural information on complexes between proteins is scarce. This lack of structural information results from the difficulty of crystallizing these complexes, which by nature are transient and not characterized by a single specific set of interactions. Rather, weak protein–protein complexes may be considered a collection of complexes with a fluctuating interface. The topic of weak protein–protein complexes is of particular relevance in bioinorganic chemistry as metalloproteins that function in electron transfer tend to bind weakly to their redox partners, with K_d values ranging from millimolar to micromolar. Association rates (k_{on}) for electron transfer partners are usually high (10^7 to $10^9\,M^{-1}\,s^{-1}$),**[78]** and dissociation rates often fall in the range of 10^3 to $10^6\,s^{-1}$. Thus, from the NMR perspective, interactions between redox proteins are dynamic phenomena spanning multiple rate regimes on the experimental timescale. There are a number of recent reviews on the topic of NMR characterization of redox protein complexes providing excellent summaries of recent work in this active field.**[78–81]**

The most straightforward means to characterize binding of redox partner proteins is by monitoring chemical shift changes upon complex formation. This is most conveniently performed by observing ^{1}H–^{15}N HSQC resonances of a uniformly ^{15}N-labeled protein as a function of added concentration of the partner protein. Complex formation causes changes in chemical shifts, which are expected to be largest at the protein–protein interface. Under the typical case of fast exchange, a change in chemical shift between the values characteristic of the unbound and bound forms of the protein is observed. Plotting the change in chemical shift as a function of ratio of the partner proteins yields binding curves that may be fitted to obtain a K_d value. In addition, the resonances showing the largest chemical shift changes provide a ‘‘chemical shift map’’ of the binding interface. Chemical shift changes are not confined to binding interface residues. Binding may cause alterations in structure reflected by changes in chemical shifts, although this is not commonly seen in the case of weak complexes. Detecting structural changes remote from the binding interface is facilitated in paramagnetic proteins because of the higher sensitivity of chemical shifts to structure.

Chemical shift mapping is the most common method of analyzing interactions between metalloproteins, but other approaches similar to those outlined above for ligand binding (Section 6.1) can be applied. The most relevant methods for studying weak protein–protein interactions are transferred NOEs that may be observed in protein–protein complexes in the case that one of the target proteins has a large molecular weight (>50 kDa) and the complex is under fast exchange. In addition, RDCs can aid in characterization of weak protein–protein complexes, for which relative orientations of the two proteins may be discerned.

Utilizing these methods, the past decade has seen an explosion of structural information on weak complexes of metalloproteins that have revealed important fundamental information relevant to understanding biological electron transfer. For one, the typically weak and transient nature of binding of redox partner proteins is a substantial deviation from the ‘‘lock and key’’ hypothesis of biomolecular recognition. At the same time, the binding interface arranges the protein partners so as to minimize separation of the redox metal sites. The interface may be hydrophobic in nature, or electrostatic, with one partner having a positive and the other a negative electrostatic potential at the binding site. The experimental determination that interfaces between electron transfer partners are fluctuating and mobile has provided information vital to the advancement of experimental and theoretical studies of biological electron transfer.

6.3 Self-exchange Electron Transfer

The electron self-exchange (ESE) reaction is the interconversion of oxidized and reduced forms of a redox-active molecule, with a rate described by a second-order rate constant (k_{11}):

$$A_{ox} + A'_{red} = A_{red} + A'_{ox} \tag{28}$$

The ESE reaction is both convenient and informative to study because it has a driving force of 0, such that the Marcus equation describing electron transfer rates takes the simple form

$$k_{11} = \nu_n \kappa S \exp\left(\frac{\lambda}{4RT}\right) \tag{29}$$

where the nuclear factor ν_n is 10^{13} s^{-1}, κ is the transmission coefficient (=1 when the donor and acceptor are in close contact), S is a steric factor reflecting the fraction of complexes formed that are competent for electron transfer, and λ is reorganization energy.**[82]** If the ESE rates for two redox partners (k_{11}, k_{22}) are known, the rate for the cross-reaction (k_{12}) can be estimated using the Marcus cross-relation:

$$k_{12} = (k_{11} k_{22} K_{12} f_{12})^{1/2} \tag{30}$$

where f_{12} is ~1 and K_{12} is the equilibrium binding constant.**[82]**

The ESE rate is conventionally used as an indication of intrinsic electron transfer reactivity. In the case of a strongly coupled system (close contact between partners), this rate reflects reorganization energy and the formation of the productive complex for electron transfer. NMR has proven convenient for analyzing ESE as measurements can be made on a system at equilibrium through a range of temperature and solution conditions. ESE rates for metalloproteins range from ~10^2 to 10^8 M^{-1}s^{-1}, and in some cases depend strongly on solution conditions. Thus ESE can be slow or fast on the NMR timescale. For slow exchange, saturation transfer and T_1 methods can be used to determine k_{11}, whereas for fast exchange, line width analysis can be utilized (see Section 2.5) (Figure 22). ESE experiments not only provide information on electron transfer rates, but can also be used to obtain assignments of one oxidation state of a protein based on known assignments of the other oxidation state. This method was used to determine the first assignments of hyperfine-shifted resonances of paramagnetic horse ferricytochrome *c*.**[83]**

Information on the nature of the binding site for the ESE reaction can be obtained by varying solution conditions, in particular, ionic strength. If the binding interface

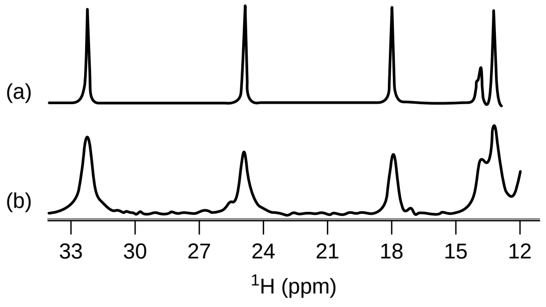

Figure 22 Effect of electron self-exchange reaction (Fe^{II}/Fe^{III}) on oxidized heme methyl resonance line widths of *Pseudomonas aeruginosa* ferricytochrome c_{551}, 25 °C. (a) 100% Fe^{III}, (b) 98% Fe^{III}. This ESE reaction is fast on the NMR timescale (~10^7 s^{-1})

is hydrophobic, little dependence on ionic strength will be observed, whereas protein complexes binding through a charged interface will display marked ionic strength dependence. Another approach to characterizing the binding interface in an ESE reaction is to observe effects on ESE rates of mutations targeting residues proposed to be involved in protein–protein binding.

7 APPLICATION TO QUADRUPOLAR METAL NUCLEI

Despite their abundance in nature and varied roles in biology, Zn^{II} and Mg^{II} have received less attention from spectroscopists in the bioinorganic field than most other metals. This is a result of these ions having closed-shell configurations, which renders them silent to conventional spectroscopic methods. Studies of the effects of Zn^{II} or Mg^{II} binding on protein structure and dynamics can be accomplished by titrations of the metal ion monitored by the protein resonances; however, such studies do not provide direct information on the nature of the metal ion itself. Substitutions of Zn^{II} by similar ions as spectroscopic probes have been informative, but again fail to provide direct information on the Zn^{II} ion. Mg^{II} is even more difficult to probe; its electron density is similar to that of water, making its identification in X-ray crystal structures problematic. In addition, Mg^{II} tends to bind weakly to proteins, so that Mg^{II} enzymes may not be isolated as an active holo-enzyme. As a result, the role of Mg^{II} in bioinorganic chemistry of proteins is underappreciated. For example, Mg^{II} plays an important role in many metabolic enzymes in mammals, but Mg^{II} binding to these enzymes is not well characterized.**84** Directly probing Mg^{II} and Zn^{II} sites remains a major challenge in bioinorganic chemistry.

A method of directly probing Zn^{II} and Mg^{II} sites in enzymes is by the use of ^{67}Zn and ^{25}Mg NMR. These nuclei are demanding targets for NMR, as both have low values of γ and thus low sensitivities. In addition, both nuclei have large quadrupole moments, which can lead to extremely broad NMR lineshapes (Table 1). An approach for directly studying these nuclei, put forth by Ellis and coworkers,**85** is to detect ^{67}Zn and ^{25}Mg in the solid-state at low temperature (~10 to 25 K) and high magnetic field (i.e., 18.8 T). The low temperature provides the important advantage needed for detecting these low-sensitivity nuclei of enhancing signal-to-noise ratio via the Boltzmann distribution (equation 6), and also providing for lower noise of the receiver coil. A challenge with solid-state NMR is that orientation-dependent phenomena that in liquid samples are averaged out by molecular tumbling remain in place, yielding extreme resonance overlap. In these experiments, a pulse sequence that transforms the powder lineshape into a manifold of side bands, and also utilizes cross-polarization to reduce consequences of long T_1 values, is employed to yield a detectable signal retaining valuable lineshape information. Comparison of experimental data to calculated spectra allows extraction of the key observable in the experiments, which is the quadrupole coupling constant, Cq:

$$\mathrm{Cq} = q_{zz}\left[\frac{e^2}{a_0^3 h}\right] Q \tag{31}$$

where Q is the quadrupole moment of the nucleus and q_{zz} is the zz element of the field gradient tensor. Cq is thus directly proportional to the electric field gradient at the nucleus, which in turn is determined by the details of the metal coordination environment. Because Cq depends on charges of ligands, water versus anionic hydroxide ligation is readily distinguished. This provides a route to answer questions about Zn^{II} and Mg^{II} enzyme active site structure and mechanism that are extremely difficult to answer using other methods.

An example of the application of this method is a study of human carbonic anhydrase (CAII), a zinc enzyme that catalyzes the reaction

$$CO_2 + H_2O = HCO_3{}^- + H^+ \tag{32}$$

which, despite extensive study, remains poorly characterized from a mechanistic standpoint. CAII contains Zn^{II} coordinated by three His residues and a fourth ligand presumed to be water, which undergoes deprotonation with a pK_a near 7. The measured values of Cq for CAII, however, fit a model with a hydroxide fourth ligand present at pH values ranging from 5 to 8.5, calling for reconsideration of the previously accepted mechanism (Figure 23).**86** Although low-temperature solid-state NMR is not a technique accessible to many bioinorganic chemists, it holds the potential to fill a significant gap in our knowledge about the biology of Zn^{II} and Mg^{II}.

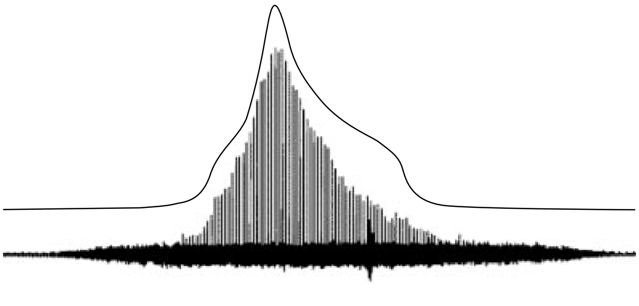

Figure 23 Low-temperature (10 K) solid-state ^{67}Zn NMR spectrum of CAII at pH 5. Above the experimental spectrum is a simulation of the spikelet envelope. The extracted value of Cq is 9.6 MHz, whereas at pH 8.5 the value is 10 MHz; the results are consistent with hydroxide ligation to Zn^{II} at both pH values. (Adapted from Lipton, Heck and Ellis.**86** © 2004 American Chemical Society)

8 APPLICATION TO NUCLEIC ACIDS

NMR has been a crucial tool for structural characterization of small nucleic acids, including both DNAs and RNAs. RNAs have been of particular interest since the discovery of catalytically active RNAs (ribozymes) in the 1980s. In the intervening decades, our understanding of the rich and versatile reactivity of nucleic acids has continued to grow, with the development if in vitro selection methodology for RNA engineering, and the discoveries of new RNA functions such as RNA interference. The expansion of the nucleic acid field has thus called for studies relating high-resolution structure to function, including understanding of the role of metal ions in stability and reactivity. Metal ions frequently play important roles in ribozyme function; RNA will thus be the focus of this section because of the particular interest the bioinorganic chemist has in it.[3,87]

The growth of available high-resolution structures of nucleic acids has relied largely on NMR. In contrast with proteins for which X-ray crystallography is the dominant method for structure determination, NMR is the leading technique for solving RNA structures,[36] in part because of the difficulty of obtaining suitable crystals. As a result of the polyanionic nature of nucleic acids, metal ion binding is ubiquitous, although often less specific than is metal binding to proteins. Detection of the binding of the metals to nucleic acids is complicated by the fact that the metal ions most often found associated with nucleic acids (Na^{I}, K^{I}, Mg^{II}) are extremely difficult to detect directly by NMR, and do not exert characteristic paramagnetic effects on NMR spectra. For these reasons, NMR studies of metal sites in nucleic acids are limited in comparison with the number and variety of studies on metalloproteins. Here, a brief overview of the methods used to address the challenges of NMR studies of metallo-nucleic acids, with a focus on RNAs, is presented.

8.1 Sample Preparation

Despite the considerable success in using NMR to determine nucleic acid structure, these biopolymers offer particular challenges to the NMR spectroscopist. The building blocks of nucleic acids are larger than those of proteins, and as a result one encounters the complications that arise with performing NMR on high molecular mass molecules for relatively short nucleic acids. Compounding this difficulty is the inherent heavy resonance overlap in ^{1}H NMR spectra even for small nucleic acids, a problem particularly severe for ribose protons. In addition, nucleic acids do not display as many NOEs between nucleotide units as do proteins between amino acid units, as most proteins are more globular in structure than RNAs, and there are fewer protons in RNA per mass unit. Thus, only small RNAs (less than ∼20 nucleotides) can be studied with routine homonuclear (^{1}H) methods, with larger molecules requiring isotopic (^{13}C and/or ^{15}N) labeling. As a result of severe chemical shift degeneracy and linebroadening, studies of RNAs ∼ 50–60 nucleotides and larger are extremely challenging and reserved for the specialist.

In contrast with proteins, suitable amounts of RNA are rarely available from a native source. Thus, expression or synthesis is necessary to obtain amounts appropriate for NMR studies. Mitigating some of the challenges of NMR of RNA is that large RNAs can often be divided into functionally significant segments that fold independently. This allows the researcher to prepare and study relatively small RNAs and obtain information relevant to understanding structure and function of the larger RNA. In addition, the ability to chemically synthesize small nucleic acids for specific labeling, or to insert labeled segments into larger RNAs, allows one to readily obtain samples tractable for NMR study. The key to preparation of isotopically labeled RNA samples is availability of labeled nucleotide triphosphates (NTPs), which have typically been prepared from ribosomal RNA of bacterial cells grown on ^{13}C and/or ^{15}N-labeled media. The reader is referred to the literature for details on preparation of nucleic acid samples for NMR using chemical and molecular biological techniques.[88]

8.2 Data Collection for Structure Determination

NMR spectra of RNAs are quite sensitive to solution conditions, and thus pH, temperature, and type and concentration of cations in RNA samples should be optimized to obtain optimal signal detection and dispersion. Sequential ^{1}H assignments for small RNAs are obtained through 2-D NOESY spectra for through-space $^{1}H-^{1}H$ correlation. Use of NOESY spectra is particularly useful not only for assigning imino and amino protons, but also for ribose 2′-OH protons in some cases. A double quantum filtered-correlation spectroscopy (DQF-COSY) spectrum is typically used to identify through-bond correlations and in combination with NOESY aids with assignments of base protons. In ^{15}N-labeled nucleic acids, imino proton assignments are assisted by $^{1}H-^{15}N$ HSQC or heteronuclear multiple quantum correlation (HMQC) data. Multidimensional experiments on ^{13}C labeled samples are helpful with making assignments of ribose ^{1}H and ^{13}C resonances. ^{31}P chemical shifts are poorly dispersed, but correlations with ribose nuclei can be used to assist assignments. As with proteins, the key parameter input for structure calculation is the $^{1}H-^{1}H$ NOE. In addition, coupling constants (i.e., $^{3}J_{HH}$ in ribose sugars) can reveal torsion angles. RDCs that reveal angular restraints for bond vector orientations in weakly aligned samples are also useful.

8.3 Studies of Native Metal Sites

The metal ions that most commonly bind nucleic acids, Na^{I}, K^{I}, and Mg^{II}, have closed-shell configuration and do not impart the broadening or shifting caused by paramagnetic ions that can serve as clear signs of binding. None of these metal nuclei has a spin-1/2 isotope, and thus direct NMR measurements are challenging. In addition, these metals tend to bind nonspecifically as they have poorly defined coordination environments and high lability. Nevertheless, NMR has an important role to play in identifying metal-binding sites in nucleic acids. In particular, detection of Na^I and Mg^{II} binding by X-ray crystallography is complicated by the similarity of the electron density of these cations to that of water. Another concern is that the particular conditions (pH, salt, etc.) required to crystallize a nucleic acid may alter cation binding relative to what is seen in solution or in the cell.

A simple means to discern binding sites for cations is by monitoring chemical shift and/or line width changes of nucleic acid nuclei as a function of metal ion concentration. Interpretation does require that changes detected are not a result of nucleic acid conformational changes caused by altered ionic strength. Metal ion titration data can often be obtained using 1-D NMR spectra. Generally, in titrations with diamagnetic metal ions, chemical shift and line width changes will be small. The magnitude of any changes observed will depend on the change in the environment of the nucleus being observed upon metal binding including any metal-binding-induced conformational changes, and the exchange regime of binding (the off rate) relative to the NMR timescale (see Section 2.5). Metal binding to RNA is typically weak, so that the exchange rate is in the fast exchange regime. In this case, the rate of exchange and the residence lifetime cannot be calculated, although the equilibrium binding constant may be determined by monitoring the change in chemical shift as a function of added metal.

8.4 Metal Substitutions

Monitoring chemical shift changes as a function of added diamagnetic metal, such as Mg^{II}, may not reveal weak binding sites or any sites that show a very small chemical shift change upon metal binding. Mimics that bind in a similar manner but more strongly than native metals, however, may be used as probes of native metal-binding sites. Some such probes can themselves be detected directly by NMR, or they may induce nucleic acid resonance shifting or linebroadening. Monitoring binding of nonnative metals can also be used to confirm results obtained on native metals.

8.4.1 Diamagnetic metal probes

Monovalent ions (K^I, Na^I) tend to bind weakly and are particularly difficult to probe. Thus, mimics have been an important tool for probing monovalent ion binding sites. Ammonium ion has an ionic radius similar to K^I, and is a useful NMR probe as its protons can give rise to NOEs to nucleic acid protons. In addition, the nitrogen of $^{15}NH_4^+$ may be detected directly. An example is the detection of $^{15}NH_4^+$ binding to the DNA quadruple $[d(G_4T_4G_4)]_2$; use of ^{15}N filtering aids in identification of $^{15}NH_4^+$ ions.**[89]** A drawback to use of NH_4^+ is that it is most effective at low pH values at which its resonances are relatively narrow.

Divalent metals bind more strongly to nucleic acids but also may not bind strongly enough to be readily detectable, in particular, when binding through an outer-sphere mechanism. A useful mimic of $[Mg(H_2O)_6]^{2+}$ is $[Co(NH_3)_6]^{3+}$, as it has a comparable ionic radius and contains protons from which NOEs may be observed. $[Co(NH_3)_6]^{3+}$ typically binds $\sim 10\times$ more tightly to nucleic acids as a result of its higher charge, which may aid in detection of weak binding sites. As a substitution-inert complex, $[Co(NH_3)_6]^{3+}$ will specifically probe binding sites for hydrated $[Mg(H_2O)_6]^{2+}$ (outer-sphere binding) over sites requiring loss of ligands (inner-sphere binding). An example of the use of $[Co(NH_3)_6]^{3+}$ as a probe of metal-binding sites to an RNA is shown in Figure 24.

Metal ions that can be observed directly by NMR also are attractive probes of metal-binding sites in RNA. For example, direct ^{113}Cd NMR has been used to demonstrate Cd^{II} binding to a small ribozyme.**[91]** With an ionic radius similar to K^I and a nuclear spin of 1/2, $^{205}Tl^I$ is an attractive probe of K^I binding sites.**[89]** The NMR signal of $^{205}Tl^I$ bound to the G-quadruple, $d(G_4T_4G_4)_2$ from the telomeric sequence of *Oxytricha nova* has been detected to demonstrate monovalent ion binding to this structure. In addition, the exchange rate of $^{205}Tl^I$ was determined using magnetization transfer experiments.**[92]**

8.4.2 Paramagnetic metal probes

The dramatic effects paramagnetic centers may have on NMR spectra can aid in observing metal-binding sites that are difficult to detect otherwise. In studies of RNA, the most commonly used paramagnetic metal ion for this purpose is Mn^{II}, which provides highly efficient pathways for nuclear relaxation enhancement, causing significant linebroadening

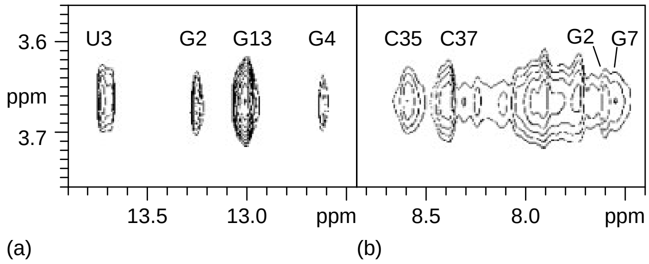

Figure 24 Portion of a 500-MHz 2-D NOESY spectrum in 90% H_2O/10% D_2O, 10 °C, of the hairpin ribozyme B domain in the presence of 1 mM cobalt hexamine, which resonates at 3.65 ppm. NOEs could be unambiguously assigned to the imino protons of nucleotides G2, U3, and G4 (a) and the amino protons of C35 and C37 and the H8 protons of G2 and G7 (b). NOEs with imino (a) and amino (b) protons are shown. (Adapted from Butcher, Allain and Feigon.**[90]** © 2000 American Chemical Society)

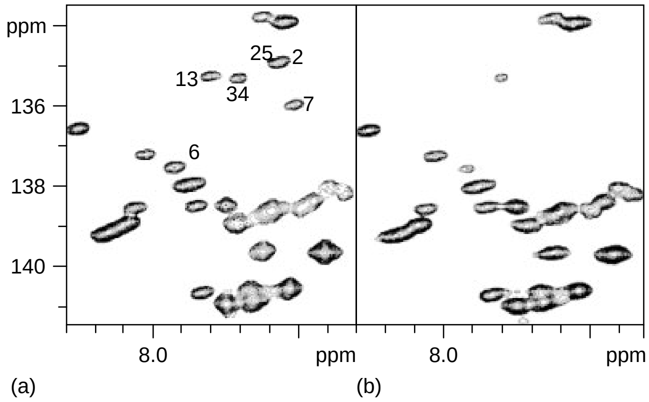

Figure 25 Five hundred megahertz ^1H, ^{13}C ct-HSQC spectra (aromatic region) of the hairpin ribozyme B domain, 30 °C, without (a) and with (b) the addition of 20 µM $MnCl_2$. Resonances that are broadened as a result of Mn^{2+} binding are labeled with their corresponding numbers in the spectrum without Mn^{2+}. (Adapted from Butcher, Allain and Feigon.[90] © 2000 American Chemical Society)

for nuclei in its vicinity (within about 10 Å) in a distance-dependent (r^{-6}) manner (equation 17). As it has an ionic radius similar to Mg^{II}, Mn^{II} is a reasonable probe of magnesium binding sites, which is achieved by titration of low (micromolar) concentrations of $MnCl_2$ into millimolar RNA samples. Using substoichiometric Mn^{II} will lead to significant linebroadening of nucleic acid nuclei in the vicinity of specific binding sites; higher amounts will begin to broaden resonances in a nonspecific manner. An example is the use of Mn^{II}-induced linebroadening to identify Mg^{II} binding sites in B domain RNA of the hairpin ribozyme (Figure 25).[89] Notably, the paramagnetic linebroadening data are in agreement with results obtained by diamagnetic ion titrations. Electron paramagnetic resonance (EPR) is used to identify Mn^{II} binding sites in RNA, and is in more common use for this purpose than NMR.[93]

In principle, paramagnetic ions also may be used to induce hyperfine shifts in nucleic acids to aid detection of binding sites. Ions with high relative magnetic anisotropy and short unpaired electron relaxation times (i.e., Co^{II}, Fe^{II}, and trivalent lanthanide ions except for Gd^{III}) are candidates for such studies. Indeed, Tb^{III} and Eu^{III} ions have been used as fluorescent probes of nucleic acid structures; it is expected that NMR studies also would be informative.[94]

9 ACKNOWLEDGMENTS

Dr. Lea R. Vacca is gratefully acknowledged for assistance with the manuscript. Data collected in the author's laboratory is under support of a grant from the NIH (GM63170).

10 RELATED ARTICLES

Electron Paramagnetic Resonance (EPR) Spectroscopy; ***Electron Spin Echo Envelope Modulation (ESEEM) Spectroscopy***; ***Electron-Nuclear Double Resonance (ENDOR) Spectroscopy***; ***Nuclear Magnetic Resonance (NMR) Spectroscopy of Inorganic/Organometallic Molecules***.

11 ABBREVIATIONS AND ACRONYMS

CON-IPAP = CON-in-phase-antiphase; DQF-COSY = double quantum filtered-correlation spectroscopy; EPR = electron paramagnetic resonance; ESE = electron self-exchange; EXSY = exchange spectroscopy; HiPIPs = high-potential iron proteins; HMQC = heteronuclear multiple quantum correlation; HSQC = heteronuclear single quantum correlation; HX = hydrogen exchange; INEPT = insensitive nuclei enhanced by polarization transfer; MW = molecular weight; NMR = nuclear magnetic resonance; NOEs = nuclear overhauser effects; NOESY = nuclear overhauser effect spectroscopy; NTPs = nucleotide triphosphates; PDB = protein data bank; RDCs = residual dipolar couplings; SERF = signal eliminating relaxation filter; TOCSY = total correlated spectroscopy; TROSY = transverse relaxation-optimized NMR Spectroscopy.

12 FURTHER READING

I. Bertini, C. Del Bianco, I. Gelis, N. Katsaros, C. Luchinat, G. Parigi, M. Peana, A. Provenzani and M. A. Zoroddu, *Proc. Natl. Acad. Sci. U.S.A.*, 2004, **101**, 6841.

I. Bertini and C. Luchinat, 'NMR of Paramagnetic Molecules in Biological Systems'. Benjamin Cummings, Menlo Park, 1986, A classic text describing effects of paramagnetism on chemical shifts and line widths. Many examples of data are included.

I. Bertini and C. Luchinat, *Coord. Chem. Rev.*, 1996, **150**, 1. An update of the above text, with an emphasis on description of physical aspects of the electron-nuclear interaction.

I. Bertini, C. Luchinat, G. Parigi and R. Pierattelli, *ChemBioChem.*, 2005, **6**, 1536. A clear account of methods for structure determination of paramagnetic metalloproteins with a focus on recent developments in the field.

J. Flinders and T. Dieckmann, *Prog. Nucl. Magn. Reson. Spectrosc.*, 2006, **48**, 137. Methods for structure determination, study of dynamics, and analysis of metal binding are described.

G. N. La Mar and J. S. de Ropp, in 'Biological Magnetic Resonance: NMR of Paramagnetic Molecules', eds. L. J. Berliner, J. Reuben, Plenum Press, New York, 1993, Vol. 12, p. 1. A detailed description of experimental approaches to detecting NMR resonances in paramagnetic molecules.

G. N. La Mar, J. D. Satterlee and J. S. de Ropp, in ‘The Porphyrin Handbook’, eds. K. M. Kadish, K. M. Smith and R. Ruilard, Academic Press, New York, 2000, , Vol. 5, p. 185. A thorough account of NMR of heme-containing proteins including useful background information on heme electronic structure.

G. Simonneaux and A. Bondon, *Chem. Rev.*, 2005, **105**, 2627. Experimental results and approaches are covered in this review.

13 REFERENCES

1. I. Bertini, H. B. Gray, E. I. Steifel and J. S. Valentine, ‘Biological Inorganic Chemistry: Structure and Reactivity’, University Science Books, Sausalito, 2007.
2. C. Andreini, I. Bertini and A. Rosato, *Bioinformatics*, 2004, **20**, 1373.
3. V. J. DeRose, S. Burns, N.-K. Kim and M. Vogt, in ‘Bio-coordination Chemistry’, J. A. McCleverty and T. J. Meyer eds. Elsevier, 2004, Vol. 8, p. 787.
4. A. Kowalsky, *J. Biol. Chem.*, 1962, **237**, 1807.
5. M. P. Williamson, T. F. Havel and K. Wüthrich, *J. Mol. Biol.*, 1985, **182**, 295.
6. L. Banci, I. Bertini, L. D. Eltis, I. C. Felli, D. H. W. Kastrau, C. Luchinat, M. Piccioli, R. Pierattelli and M. Smith, *Eur. J. Biochem.*, 1994, **225**, 715.
7. M. Gochin and H. Roder, *Protein Sci.*, 1995, **4**, 296.
8. L. Banci, I. Bertini, K. L. Bren, M. A. Cremonini, H. B. Gray, C. Luchinat and P. Turano, *J. Biol. Inorg. Chem.*, 1996, **1**, 117.
9. F. Rodriguez-Castaneda, P. Haberz, A. Leonov and C. Griesinger, *Magn. Reson. Chem.*, 2006, **44**, S10.
10. G. N. La Mar, J. D. Satterlee and J. S. de Ropp, in ‘The Porphyrin Handbook’, eds. K. M. Kadish, K. M. Smith and R. Ruilard, Academic Press, New York, 2000, Vol. 5, p. 185.
11. I. Bertini, C. Luchinat and A. Rosato, *Adv. Inorg. Chem.*, 1999, **47**, 251.
12. C. O. Fernandez and A. J. Vila, in ‘Paramagnetic Resonance of Metallobiomolecules’, Joshua Telser eds., American Chemical Society (ACS Symposium Series; distributor is Oxford University Press), 2003, Vol. 858, p. 287.
13. P. J. Kraulis, *J. Appl. Crystallogr.*, 1991, **24**, 946.
14. D. S. Wishart and B. D. Sykes, *Methods Enzymol.*, 1994, **239**, 363.
15. S. Schwarzinger, G. J. A. Kroon, T. R. Foss, J. Chung, P. E. Wright and H. J. Dyson, *J. Am. Chem. Soc.*, 2001, **123**, 2970.
16. G. N. La Mar, W. D. Horrocks, Jr and R. H. Holm, in ‘NMR of Paramagnetic Molecules: Principles and Applications’, La Mar, Horrocks and Holm ed., Academic Press, New York, 1973.
17. I. Bertini and C. Luchinat, ‘NMR of Paramagnetic Molecules in Biological Systems’, Benjamin Cummings, Menlo Park, 1986.
18. H. M. McConnell, *J. Chem. Phys.*, 1956, **24**, 764.
19. H. M. McConnell and D. B. Chesnut, *J. Chem. Phys.*, 1958, **28**, 107.
20. R. J. Kurland and B. R. J. McGarvey, *J. Magn. Reson.*, 1970, **2**, 286.
21. H. M. McConnell and H. E. Robertson, *J. Chem. Phys.*, 1958, **29**, 1361.
22. I. Bertini, C. Luchinat, G. Parigi and R. Pierattelli, *ChemBioChem.*, 2005, **6**, 1536.
23. L. Banci, I. Bertini and C. Luchinat, ‘Nuclear and Electron Relaxation. The Magnetic Nucleus-Unpaired Electron Coupling in Solution’, VCH, Weinheim, 1991.
24. F. Arnesano, L. Banci and M. Piccioli, *Q. Rev. Biophys.*, 2005, **38**, 167.
25. A. Abragam, ‘The Principles of Nuclear Magnetism’, Oxford University Press, Oxford, 1961.
26. A. G. Tzakos, C. R. R. Grace, P. J. Lukavsky and R. Riek, *Annu. Rev. Biophys. Biomol. Struct.*, 2006, **35**, 319.
27. V. Tugarinov, P. M. Hwang and L. E. Kay, *Annu. Rev. Biochem.*, 2004, **73**, 107.
28. A. J. Vega and D. Fiat, *Mol. Phys.*, 1976, **31**, 347.
29. H. J. Reich, *J. Chem. Educ.*, 1995, **72**, 1086.
30. B. S. Russell, R. Melenkivitz and K. L. Bren, *Proc. Natl. Acad. Sci. U.S.A.*, 2000, **97**, 8312.
31. J. Sandström, ‘Dynamic NMR Spectroscopy’, Academic Press, London, 1982.
32. J. R. Tolman, J. M. Flanagan, M. A. Kennedy and J. H. Prestegard, *Proc. Natl. Acad. Sci. U.S.A.*, 1995, **92**, 9279.
33. N. Tjandra, J. G. Omichinski, A. M. Gronenborn, G. M. Clore and A. Bax, *Nat. Struct. Biol.*, 1997, **4**, 732.
34. J. H. Prestegard, C. M. Bougault and A. I. Kishore, *Chem. Rev.*, 2004, **104**, 3519.
35. J. R. Tolman and K. Ruan, *Chem. Rev.*, 2006, **106**, 1720.
36. The Protein Data Bank. http://www.pdb.org. 2007.
37. I. Bertini, C. Luchinat and G. Parigi, *Concepts Magn. Reson.*, 2002, **14**, 259.
38. E. Arslan, H. Schulz, R. Zufferey, P. Kunzler and L. Thöny-Meyer, *Biochem. Biophys. Res. Commun.*, 1998, **251**, 744.
39. J. A. Fee, Y. Chen, T. R. Todaro, K. L. Bren, K. M. Patel, M. G. Hill, E. Gomez-Moran, T. M. Loehr, J. Y. Ai, L. Thöny-Meyer, P. A. Williams, E. Stura, V. Sridhar and D. E. McRee, *Protein Sci.*, 2000, **9**, 2074.
40. G. N. La Mar and J. S. de Ropp, in ‘Biological Magnetic Resonance: NMR of Paramagnetic Molecules’, eds. L. J. Berliner and J. Reuben, Plenum Press, New York, 1993, Vol. 12, p. 1.
41. F. Arnesano, L. Banci and M. Piccioli, *Q. Rev. Biophys.*, 2005, **38**, 167.
42. W. Bermel, I. Bertini, I. C. Felli, M. Piccioli and R. Pierattelli, *Prog. Nucl. Magn. Reson. Spectrosc.*, 2006, **48**, 25.
43. S. D. Emerson and G. N. La Mar, *Biochemistry*, 1990, **29**, 1556.

44. L. Banci, I. Bertini, G. Cavallaro, A. Giachetti, C. Luchinat and G. Parigi, *J. Biomol. NMR*, 2004, **28**, 249.
45. R. J. Fitzgerald and R. S. Drago, *J. Am. Chem. Soc.*, 1967, **89**, 2879.
46. N. V. Shokhirev and F. A. Walker, *J. Biol. Inorg. Chem.*, 1998, **3**, 581.
47. J. H. Prestegard, K. L. Mayer, H. Valafar and G. C. Benison, *Methods Enzymol.*, 2005, **394**, 175.
48. P. Turano, *Inorg. Chem.*, 2004, **43**, 7945.
49. R. Barbieri, I. Bertini, G. Cavallaro, Y. M. Lee, C. Luchinat and A. Rosato, *J. Am. Chem. Soc.*, 2002, **124**, 5581.
50. C. Schmitz, M. John, A. Y. Park, N. E. Dixon, G. Otting, G. Pintacuda and T. Huber, *J. Biomol. NMR*, 2006, **35**, 79.
51. C. Caillet-Saguy, M. Delepierre, A. Lecroisey, I. Bertini, M. Picciolo and P. Turano, *J. Am. Chem. Soc.*, 2006, **128**, 150.
52. M. Rivera and G. A. Caignan, *Anal. Bioanal. Chem.*, 2004, **378**, 1464.
53. I. J. Lin, E. B. Gebel, T. E. Machonkin, W. M. Westler and J. L. Markley, *Proc. Natl. Acad. Sci. U.S.A.*, 2005, **102**, 14581.
54. D. F. Hansen and J. J. Led, *Proc. Natl. Acad. Sci. U.S.A.*, 2006, **103**, 1738.
55. I. Bertini, K. L. Bren, A. Clemente, J. A. Fee, H. B. Gray, C. Luchinat, B. G. Malmstrom, J. H. Richards, D. Sanders and C. E. Slutter, *J. Am. Chem. Soc.*, 1996, **118**, 11658.
56. J. M. Berg, *Annu. Rev. Biophys. Biophys. Chem.*, 1990, **19**, 405.
57. D. S. Auld, *Biometals*, 2001, **14**, 271.
58. F. Capozzi, F. Casadei and C. Luchinat, *J. Biol. Inorg. Chem.*, 2006, **11**, 949.
59. R. M. Daniel, R. V. Dunn, J. L. Finney and J. C. Smith, *Annu. Rev. Biophys. Biomol. Struct.*, 2003, **32**, 69.
60. A. J. Wand, *Nat. Struct. Biol.*, 2001, **8**, 926.
61. M. J. Stone, *Acc. Chem. Res.*, 2001, **34**, 379.
62. A. G. Palmer, *Chem. Rev.*, 2004, **104**, 3623.
63. A. Mittermaier and L. E. Kay, *Science*, 2006, **312**, 224.
64. N. A. Farrow, R. Muhandiram, A. U. Singer, S. M. Pascal, C. M. Kay, G. Gish, S. E. Shoelson, T. Pawson, J. D. Formankay and L. E. Kay, *Biochemistry*, 1994, **33**, 5984.
65. B. S. Russell, L. Zhong, M. G. Bigotti, F. Cutruzzolà and K. L. Bren, *J. Biol. Inorg. Chem.*, 2003, **8**, 156.
66. V. A. Jarymowycz and M. J. Stone, *Chem. Rev.*, 2006, **106**, 1624.
67. A. V. Zhuravleva, D. M. Korzhnev, E. Kupce, A. S. Arseniev, M. Billeter and V. Y. Orekhov, *J. Mol. Biol.*, 2004, **342**, 1599.
68. A. Hvidt and S. O. Nielsen, *Adv. Protein Chem.*, 1966, **21**, 287.
69. S. W. Englander and N. R. Kallenbach, *Q. Rev. Biophys.*, 1983, **16**, 521.
70. Y. W. Bai, J. S. Milne, L. Mayne and S. W. Englander, *Proteins*, 1993, **17**, 75.
71. I. Bahar, A. Wallqvist, D. G. Covell and R. L. Jernigan, *Biochemistry*, 1998, **37**, 1067.
72. T. A. Lyons, G. Ratnaswamy and T. C. Pochapsky, *Protein Sci.*, 1996, **5**, 627.
73. T. I. Igumenova, K. K. Frederick and A. J. Wand, *Chem. Rev.*, 2006, **106**, 1672.
74. P. F. Flynn, R. J. B. Urbauer, H. Zhang, A. L. Lee and A. J. Wand, *Biochemistry*, 2001, **40**, 6559.
75. F. A. Walker, *Chem. Rev.*, 2004, **104**, 589.
76. L. Zhong, X. Wen, T. M. Rabinowitz, B. S. Russell, E. F. Karan and K. L. Bren, *Proc. Natl. Acad. Sci. U.S.A.*, 2004, **101**, 8637.
77. K. Takeuchi and G. Wagner, *Curr. Opin. Struct. Biol.*, 2006, **16**, 109.
78. P. B. Crowley and M. Ubbink, *Acc. Chem. Res.*, 2003, **36**, 723.
79. J. Qin, O. Vinogradova and A. M. Gronenborn, *Methods Enzymol.*, 2001, **339**, 377.
80. J. Vaynberg and J. Qin, *Trends Biotechnol.*, 2006, **24**, 22.
81. G. Simonneaux and A. Bondon, *Chem. Rev.*, 2005, **105**, 2627.
82. R. A. Marcus and N. Sutin, *Biochim. Biophys. Acta*, 1985, **811**, 265.
83. A. G. Redfield and R. K. Gupta, *Cold Spring Harb. Symp. Quant. Biol.*, 1972, **36**, 405.
84. F. W. Heaton, *Met. Ions Biol. Syst.*, 1990, **26**, 119.
85. A. S. Lipton, J. A. Sears and P. D. Ellis, *J. Magn. Reson.*, 2001, **151**, 48.
86. A. S. Lipton, R. W. Heck and P. D. Ellis, *J. Am. Chem. Soc.*, 2004, **126**, 4735.
87. V. J. DeRose, *Curr. Opin. Struct. Biol.*, 2003, **13**, 317.
88. J. Flinders and T. Dieckmann, *Prog. Nucl. Magn. Reson. Spectrosc.*, 2006, **48**, 137.
89. J. Feigon, S. E. Butcher, L. D. Finger and N. V. Hud, *Methods Enzymol.*, 2001, **338**, 400.
90. S. E. Butcher, F. H. T. Allain and J. Feigon, *Biochemistry*, 2000, **39**, 2174.
91. M. Vogtherr and S. Limmer, *FEBS Lett.*, 1998, **433**, 301.
92. M. L. Gill, S. A. Strobel and J. P. Loria, *J. Am. Chem. Soc.*, 2005, **127**, 16723.
93. P. Z. Qin and T. Dieckmann, *Curr. Opin. Struct. Biol.*, 2004, **14**, 350.
94. R. L. Gonzalez and I. Tinoco, *Methods Enzymol.*, 2001, **338**, 421.

Nuclear Quadrupole Resonance (NQR) Spectroscopy

Gary P. Wulfsberg

Middle Tennessee State University, Murfreesboro, TN, USA

Method Summary 1
1 Introduction 2
2 Technical Background 3
3 Applications 6
4 Abbreviations and Acronyms 14
5 Further Reading 14
6 References 14

METHOD SUMMARY

Acronyms, Synonyms

- Nuclear Quadrupole Resonance Spectroscopy
- Quadrupole Resonance
- Zero-Field Nuclear Magnetic Resonance Spectroscopy.

Measured physical quantities

- NQR Frequency(ies) (ν) of quadrupolar nucleus ($I \geq 1$)
- temperature dependence of NQR frequency
- linewidths and relaxation times for NQR signals.

Information available

- *nuclear quadrupole coupling constant* (e^2Qq_{zz}) of the quadrupolar nucleus, which reflects the deviation of the electron distribution around quadrupolar nucleus from spherical symmetry, but includes the asymmetry of the nucleus itself;
- *asymmetry parameter* ($\eta = e^2Q_{xx} - e^2Qq_{yy})/(e^2Qq_{zz})$ of the quadrupolar nucleus, which reflects the deviation of the electron distribution from axial symmetry;
- *electric field gradient* (*EFG*, q_{zz}) of the electron distribution around an atom, which measures its deviation from spherical symmetry, and does not include any asymmetry of the nucleus;
- approximate *populations of valence orbitals* of quadrupolar atom;
- approximate fractional *covalent* (σ) versus *ionic* (i) *character* of a bond, or multiple bond order, of bond(s) to quadrupolar atom; *number of electrons transferred* to or from quadrupolar atom; *partial charge* δ of the quadrupolar atom;
- number of chemically and crystallographically distinct quadrupolar nuclei in asymmetric unit of unit cell;
- presence of *weak* (*secondary*, *noncovalent*) *bonding interactions* to quadrupolar atom.

Information not available, limitations

- Very large frequency ranges may need to be searched (*see* Table 1, Column E), which may exceed the capabilities of a given NQR spectrometer.
- Unfavorable relaxation times, disorder, and paramagnetism at or near quadrupolar nucleus may cause the spectrum to be unobservable.
- Radio waves used for detection cannot penetrate deep within a metallic sample.

Examples of questions that can be answered

- Is there really a covalent bond of this quadrupolar atom to a nearby atom, even one in a neighboring molecule?
- What is the energy barrier to hindered rotation or fluxional behavior of a functional group bearing a quadrupolar atom?
- Is there a bomb in this suitcase?
- Is there a bomb under the clothing of, or inside the body of this passenger?
- Is there a landmine buried in this field?
- Does this package contain a significant amount of an illicit drug?
- Do we have the right crystalline modification of this compound?
- Is strain building up in this material?

Major advantages

- a nondestructive technique: all of the sample can be recovered
- extremely sensitive to weak (noncovalent, secondary) bonding interactions, which cause easily measured chemical shifts.

Major disadvantages

- Very large chemical shifts are possible, which require long times to scan (hours to days), and may require retuning circuitry or changing radio-frequency coils.

Sample constraints

- Usually the sample must be a microcrystalline solid, without any major disorder.
- The sample size requirements are large: at least about 0.5 g for heavy nuclei with high frequencies (100–1000 MHz, such as ^{79,81}Br and ^{127}I), but as much as 25 g for light nuclei with low frequencies (1–5 MHz, such as ^{14}N).

1 INTRODUCTION

Nuclear quadrupole resonance (NQR) spectroscopy is a method of sensitively characterizing the electronic environment of nuclei with nuclear spins $I \geq 1$. Such nuclei are nonspherical in shape and have electric quadrupole moments; commonly studied nuclei are confined to odd-numbered groups of the periodic table (Table 1). NQR spectra, unlike nuclear magnetic resonance (NMR) spectra (*see* ***Nuclear Magnetic Resonance (NMR) Spectroscopy of Inorganic/Organometallic Molecules***), are measured without external magnetic fields (hence its synonym of zero-field NMR), because the energy levels of quadrupolar nuclei are principally determined not by their magnetic environments, but by their electronic environments. Samples are studied, not in solution, but mainly in the form of microcrystalline solids.

Since more nuclei have spins $I \geq 1$ than have $I = 1/2$ (all but 17 of the naturally occurring elements through uranium have at least one such isotope), and since inorganic chemists commonly are more interested in the electronic rather than the magnetic environment of a nucleus, the technique of NQR became popular soon after its discovery around 1950. Continuous-wave (CW) superregenerative NQR spectrometers (analogous to older NMR spectrometers) were used, which could search fairly wide frequency ranges automatically.

During the 1950s through 1970s many inorganic chemists used the technique to characterize the structure and bonding in polar covalent and covalent molecules and network solids, coordination compounds, and organometallic compounds. Many types of bonding were studied: ionic, covalent, coordinate covalent, and weaker interactions such as hydrogen bonding and lattice forces. NQR proved much more sensitive to weak bonding interactions than did NMR or infrared (IR) spectroscopy, for example, although NQR required much larger samples.

NQR also offered another way of determining elements of crystal structure, such as the presence of bridging versus terminal atoms, number of crystallographically inequivalent molecules in the unit cell, and so on. However, X-ray crystallography subsequently improved vastly in quickness and ease of use, and supplanted this use of NQR.

NQR has its drawbacks. One fails to observe expected NQR signals much more frequently than expected NMR signals, since NQR relaxation times can be either too long or too short for effective detection of signals, especially using CW-NQR spectrometers, and especially for transition-metal nuclei and nuclei in ionic compounds. The search for an unknown NQR signal can take much longer than the search for an NMR signal: in NMR, one deals with chemical shifts and coupling constants of hertz, while in NQR, the frequency ranges (shifts) one needs to scan for a given nucleus may be many *megahertz*. Thus it is easy to see why NQR is much less frequently used than NMR.

Now pulse-Fourier Transform (pulse-FT) NQR instruments are commercially available, which allow signal averaging and improved sensitivity. They strongly resemble

Table 1 Abundant nuclei most commonly studied by NQR spectroscopy[(a)]

A Group.	B Element	C Isotope	D Abund.	E ν range MHz	F Spin	G High e^2Qq_{zz} MHz	H η	I Substance	J e^2Qq_0 MHz	K for orbital
3	La	139	100	6–26	7/2	121.8	0.000	La_2NiO_4		
3	Lu	175	97	17–195	7/2	691.5	0.615	$Lu_z(SO_4)_3 \cdot 8H_2O$		
5	Nb	93	100	1–21	9/2	117.29	0.190	NbF_5		
	Ta	181	100	50–240	7/2	1796.5		Ta_2Cl_{10}		
7	Mn	55	100	9–24	5/2	78.92	0.061	$C_5Cl_5Mn(CO)_3$		
	Re	187	63	27–300	5/2	833.555	0.143	$Re(CO)_5I$		
	Re	185	37		5/2					
9	Co	59	100	8–36	7/2	171.5	0.000	$(C_5H_5)_2Co(ClO_4)$		
11	Cu	63	69	8–62	3/2	117.0	0.028	$Cu_2(C_2H_3O_2)_4 \cdot 2H_2O$		
	Cu	65	31		3/2					
13	B	11	81	0.7–2.7	3/2	10.216	0.000	$B(CD_3)_3$	−11.83	2p
	B	10	19		3				−5.390	2p
	Al	27	100	0.1–13	5/2	45.41	0.070	$Al(t\text{-}C_4H_9)_3$	−37.52	3p
	Ga	69	60	7–81	3/2	Ca. 162		$Ga(CH_3)_3$	−125.045	4p
	Ga	71	40		3/2				−78.80	4p
	In	115	96	7–212	9/2	1115.1	0.140	$In(CH_3)_3$	−899.105	5p
15	N	14	100	0.1–6.0	1	6.333	0.788	$(CH_3)_2NCl$	-10 ± 4	2p
	As	75	100	15–170	3/2			$(CH_3)AsCl_2$	−400	4p
	Sb	121	57	7–254	5/2				+650	5p
		123	43		7/2	884.43	0.000	$(C_6H_5)_3SbCl_2$	+830	5p
	Bi	209	100	14–178	9/2	1069.9	0.020	$(C_6H_5)_3BiCl_2$	+1500	6p
17	Cl	35	75	0–75	3/2	−108.95	0.20	Cl_2	+109.746	3p
	Cl	37	25		3/2				+86.510	3p
	Br	79	51	0–445	3/2	765.85	0.20	Br_2	−769.762	4p
		81	49		3/2				−643.032	4p
	I	127	100	0–940	5/2	−2156	0.175	I_2	+2292.712	5p

[(a)] Column headings: A = Group of periodic table; D = Percent abundance; E = NQR frequency(ν) ranges (MHz); G = One of highest observed quadrupole coupling constants (MHz); H = Asymmetry parameter corresponding to value in column G; I = Substance to which data in columns G and H apply; J = Quadrupole coupling constant for one valence electron in isotope in column C; K = Orbital occupied by valence electron in column J.

pulse-FT NMR spectrometers without the magnets, so they are much less expensive than modern NMR spectrometers. Indeed, some pulse-FT NMR spectrometers can be used as pulse-FT NQR spectrometers by disconnecting the magnets and making other adjustments. But pulse-FT NQR spectrometers (the only kind currently available) have some disadvantages as well as advantages as compared to continuous wave NQR (CW-NQR) spectrometers. Because of the large range of chemical shifts found in NQR, single pulses cannot be wide enough to cover the entire frequency range that needs to be scanned, so the circuit must then be retuned (normally manually) and run again in the new frequency range; CW-NQR spectrometer can cover broader frequency ranges without adjustments. Thus pulse-FT NQR spectrometers, which can accumulate spectra far more easily, in the end, may not give spectra any more quickly.

However, only pulse instruments can deal with the aforementioned difficulties associated with broad signals and unfavorable relaxation times. Therefore, some of the problems that inorganic chemists gave up on using CW-NQR to solve after the 1970s could now be solved with FT-NQR, especially using its new pulse sequences and enhanced data acquisition ability. Modern applications of pulse-FT NQR include studies of glasses, nondestructive characterization of materials, studies of host-guest interactions and probes of host cavity symmetry and size in supramolecular chemistry,[1] and (using the great temperature sensitivity of NQR frequencies and linewidths) the studies of activation energies for hindered rotations and fluxional behavior of NQR-active groups such as *monohapto*-C_5Cl_5.[2] In certain situations NQR can provide information not easily obtained by other methods. In this review we try to highlight opportunities of this type, particularly for research problems for which one needs sensitive information on weak bonding or even noncovalent interactions involving quadrupolar nuclei.

2 TECHNICAL BACKGROUND

2.1 Direct Uses of NQR Frequencies

Like NMR, NQR spectra[3,4] are detected by flipping nuclei using MHz-range radio-frequency waves; NQR frequencies can readily be measured to within a few kHz. Since NQR frequencies are *extremely* sensitive to small changes in the electronic environment of quadrupolar nuclei, they are shifted by their environment over a range of a few or many MHz (Table 1, Column E). Thus virtually every compound has a unique set of NQR frequencies.

NQR frequencies are so sensitive to electronic environments that they are affected by charges in neighboring functional groups, neighboring molecules, and (especially) neighboring ions. Therefore, different polymorphs of compounds have different NQR frequencies, and phase transitions between polymorphs can be detected. Within a given crystalline modification of a compound, NQR spectra include distinct frequencies for each crystallographically distinct atom: as an extreme example, CCl_4(s) adopts a complex lattice with 16 crystallographically inequivalent chlorine sites. CCl_4(s) has 16 ^{35}Cl NQR frequencies averaging 40.64 MHz, with a *spectral width* between the highest and lowest frequency of 0.351 MHz. Spectral widths in covalent organochlorine compounds normally are limited to about 0.8 MHz. However, in a study of 11 clathrate compounds in which CCl_4 is the guest, the spectral widths exceeded this amount in three, being as large as 1.3 MHz in one case.**[5]** Quadrupolar nuclei are very sensitive both to their electronic environments and to the polarizing effects of lattice ionic charges, so spectral widths can be larger in ionic compounds: we estimate up to at least 1.4 MHz in salts of chlorinated organic anions.**[6]** These differences have historically been termed ‘‘crystal field effects’’,**[7]** although they have nothing to do with the crystal field theory in inorganic chemistry.

Consequently, NQR frequencies are useful for detecting and quantifying extremely weak noncovalent (secondary-bonding) interactions between molecules or ions (such as the host-guest interactions in CCl_4 clathrates). These weak secondary interactions will be a main emphasis of this article. However, since mere crystallographic inequivalence produces quite substantial spectral widths, one must use caution in concluding that small frequency shifts are due to what one chooses to call ‘‘noncovalent’’ or ‘‘secondary-bonding’’ interactions. (One might argue that NQR frequencies are too sensitive to their environment for their own good!)

2.2 Quantities Derived from NQR Frequencies

The number of NQR frequencies observed per crystallographically and chemically inequivalent atom depends on the spin I of the nucleus: each inequivalent $I = 3/2$ nucleus gives only one NQR frequency, while each $I = 1$ or $I > 3/2$ nucleus gives two or more frequencies. With two or more NQR frequencies, it is possible to calculate the two intermediate physical properties of interest. One is the *nuclear quadrupole coupling constant* e^2Qq_{zz} (or, removing the effect of the *quadrupole moment* Q of the nucleus, the *electric field gradient EFG or* eq_{zz}) which measures the deviation of the electronic environment from *spherical* (in practice, from a higher-order point group) symmetry. This depends on the *number of unbalanced electrons* around the nucleus (the number of electrons in the z direction minus the average of the numbers in the x and y directions). (Thus, e^2Qq_{zz} for a chloride ion in an octahedral environment in the NaCl lattice is zero.) The other is the *asymmetry parameter* η, which falls between zero and one, and measures the deviation of the electronic environment from *axial* symmetry (in practice, threefold or higher symmetry), and relates to the difference in the numbers of electrons in the x and in the y directions. For the many spin-3/2 nuclei (Table 1, Column F) calculating these quantities requires additional data from single-crystal or other specialized measurements, or requires certainty that η is close to zero, as is normally found to be the case in covalent compounds in which the quadrupolar atom is a terminal atom, singly bonded to one other atom. Values of the e^2Qq_{zz} and η can also be determined experimentally in appropriate cases using microwave (*see* ***Microwave Rotational Spectroscopy***), EPR (*see* ***Electron Paramagnetic Resonance (EPR) Spectroscopy***), NMR (*see* ***Nuclear Magnetic Resonance (NMR) Spectroscopy of Inorganic/Organometallic Molecules***), and Mössbauer (*see* ***Mössbauer Spectroscopy***) spectroscopy, and using the perturbed angular correlation (PAC) method (*see* ***Perturbed Angular Correlations of γ-rays (PAC) Spectroscopy***).

From atomic spectral or atomic beam measurements it is possible, in favorable cases, to measure the quadrupole coupling constants e^2Qq_0 of atoms in which there is one valence electron, or one hole in the valence-electron shell (Column J of Table 1). From this one can obtain the number of unbalanced electrons, and ultimately, the *populations of the valence orbitals* of the quadrupolar atom and its *partial charge,* δ.

Therefore, there is a more direct connection between valence orbital populations and NQR frequencies than there is with NMR frequencies, and indeed the Gaussian computational program allows for straightforward calculations of the electric field gradient.**[8]** However, the *EFG* is especially sensitive to any nonsphericity of the core electrons (or inner lobes of the valence orbitals), which normal molecular-orbital computations tend to neglect or approximate, so that such computations seriously miss producing the experimental *EFG* values. More successful calculations have been obtained by using density functional theory (DFT) and by avoiding the pseudopotential method, which simplifies the core electron wave functions.**[9]** These calculations give values of the *EFG* that correlate very well with the experimental ones for nitrogen and halogen atoms in a variety of bonding situations.

Often the Townes–Dailey approximation**[10]** is used rather successfully. This approximation assumes that contributions to the *EFG* from nonsphericity of core electron and from lattice charge distributions offset each other. Then the *EFG* results from imbalances in valence electron populations. The calculations also show that the errors introduced by the approximations of the Townes–Dailey theory do not exceed 5%. Thus Townes–Dailey calculations generally do well in showing *trends* in quadrupole coupling constants or NQR frequencies.

Using the Townes–Dailey theory, a relationship of the NQR frequency of a single-bonded terminal unhybridized ^{35}Cl atom can be derived to the ionic character, i, of the bond to the chlorine atom, or to the partial charge of the chlorine atom, δ_{Cl}.

$$\nu(^{35}\mathrm{Cl}) = -\frac{1}{2}(1-i)e^2Qq_o = -\frac{1}{2}(1-i)(109.746\,\mathrm{MHz}) = 54.873(1+\delta_{\mathrm{Cl}}) \quad (1)$$

$$\delta_{\mathrm{Cl}} = -1 + \frac{\nu(^{35}\mathrm{Cl})}{54.873} \quad (2)$$

Hence the chlorine NQR frequency is very sensitive to the ionic character of its single bond. In close agreement with the prediction from equation (1), the NQR frequency of Cl_2(s) is 54.247 MHz, while NQR frequencies for solid Group I halides are zero, expected both from their virtually complete ionic character and their high solid-state symmetry.

In Gordy's approach[11] the ionic character of a single bond to chlorine equals one-half of the difference in electronegativities of the chlorine, 3.16, and the atom to which it is bonded. Thus the NQR frequency of this chlorine atom is a strong function of the Pauling electronegativity, X_P, of the atom M bonded to chlorine:

$$\text{Theoretical } \nu(^{35}\mathrm{Cl}) = 27.436\ (X_P - 1.16) \quad (3)$$

$$\text{Empirical best fit } \nu(^{35}\mathrm{Cl}) = 24.500\ (X_P - 1.07) \quad (4)$$

Figure 1 shows the fit of predicted and observed NQR frequencies for other solid binary chlorides in which the chlorine is terminal and singly bonded; similar results can be obtained for bromine and iodine. For chlorine bonded to carbon ($X_P = 2.55$) these equations predict a frequency of 38.14 or 36.26 MHz, respectively. The observed NQR frequencies of $R_1R_2R_3C$–Cl compounds span a wider range of about 33–42 MHz: they are strongly influenced by the inductive (electron-withdrawing) effects of the R groups and on any other interactions that may be present with those groups.

If the terminal atom is multiply bonded to its neighbor, slightly different equations result. The π bonding results in a reduction of population(s) of the chlorine p_π orbitals below 2.00 electrons, to a value closer to the population of the chlorine p_σ orbital. Therefore the quadrupole coupling constant and the NQR frequency of the chlorine atom are reduced.

If the atom is doubly bonded, a nonzero asymmetry parameter η also results; if the atom is triply bonded, there is axial symmetry and η returns to zero. For the case of doubly bonding the π bond order can be calculated if η can be determined:

$$\pi = \left(\frac{2}{3}\right)\eta\left(\frac{e^2Qq_{zz}}{e^2Qq_0}\right) \quad (5)$$

In practice double bonding is appreciable for chlorines bonded to aromatic rings ($\eta > 0$), and partial triple bonding is quite substantial for the chlorides of early transition metals having vacant d orbitals to which the p_π electrons are donated.[12] Thus such chlorides have been deleted from the correlation of Figure 1. For example, the electronegativity of Ti, 1.54, leads us to expect a ^{35}Cl NQR frequency of 10.42 MHz (equation 3) or 11.51 MHz (equation 4). In practice, the average frequency for $TiCl_4$ is 6.052 MHz. The cyclopentadienide anion, $C_5H_5^-$, is a much better π-donor than chloride, however, so that when it is substituted for Cl^- the π-donating ability of Cl^- is suppressed. Consequently the average frequencies[13] grow closer to the predicted values: $(C_5H_5)TiCl_3$, 8.076 MHz, and $(C_5H_5)_2TiCl_2$, 11.971 MHz.

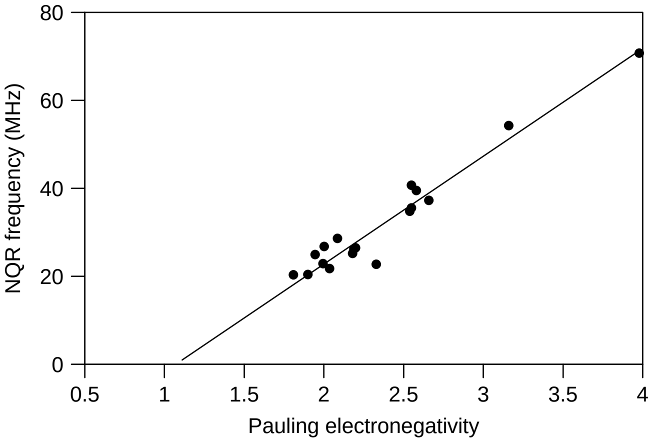

Figure 1 Average ^{35}Cl NQR frequencies (MHz) of terminal singly bonded binary element chlorides, measured in the solid state at 77 K, as a function of the Pauling electronegativity of the element

If the quadrupolar atom is bonded to more than one other atom (i.e., it is bridging or even central to the complex), the Townes–Dailey theory can be applied to give a different equation for each geometry at the bridging or central atom; a nonzero η generally results. We will consider in detail only two-coordinate bridging quadrupolar atoms. In this case, the two bonds to the bridge can be equivalent (symmetrical bridging): the NQR frequency then depends sensitively on the interbond angle at the quadrupolar atom.

Or (in the case we will emphasize), one of the two bonds may be a normal covalent bond (with a high covalent bond order) and the other ''bond'' is a weak (secondary) Lewis base donation of an electron pair to a nearby Lewis acid. Then NQR can be used to estimate the number of electrons that are transferred from the halogen lone pair in the valence p_y orbital to (or polarized toward) the site of Lewis acidity; we can also refer to this quantity as the secondary covalent bond order σ_{B2}. If the asymmetry parameter η is known, σ_{B2} can be calculated from it using an equation analogous to equation (5):

$$\sigma_{B2} = \left(\frac{2}{3}\right)\eta\left(\frac{e^2Qq_{zz}}{e^2Qq_0}\right) \quad (6)$$

More frequently η is not known. However, it is still possible to proceed if the NQR frequency of the donor atom is known both for the terminal halogen in the free ligand and for the otherwise-equivalent bridged halogen atom in the complexed ligand. For the terminal (one-coordinate) halogen atom we designate its NQR frequency as ν_T and its covalent bond order as σ_T; for the bridged halogen atom we designate its NQR frequency as ν_B and its primary covalent bond order as σ_{B1}. For ^{35}Cl the approximate Townes–Dailey equation that results is:

$$\frac{(\nu_T - \nu_B)}{54.873} = (\sigma_T - \sigma_{B1}) + \frac{1}{2}\sigma_{B2} \qquad (7)$$

To solve this equation for σ_{B2} we need to know the relationship of σ_T and σ_{B1}, that is, whether the primary covalent bond order is altered upon coordination. For halocarbons as ligands there is generally no detectable lengthening of the bond noted by X-ray crystallography, which might justify the conclusion that $\sigma_T \approx \sigma_{B1}$. If so, we have:

$$\sigma_{B2} = \frac{2(\nu_T - \nu_B)}{54.873} \qquad (8)$$

In some secondary-bonding situations the primary bond is lengthened and therefore, σ_T and σ_{B1} are presumably not equal. This case will be considered in Section 3.2.

3 APPLICATIONS

There have been several modern developments in pulse-FT NQR spectrometry dealing with important practical applications which are not necessarily considered to be inorganic:

1. ^{63,65}Cu and ^{139}La NQR have been extensively used to study high-temperature superconductors while they are in the superconducting state, and the magnetic fields needed for NMR are being excluded.[14]
2. ^{14}N NQR is used to detect, identify, and quantify amounts of illicit drugs hidden in suitcases, packages, or the body, without having to open the container.
3. ^{14}N NQR is used to detect, identify, and quantify amounts of explosives hidden in suitcases, packages, on the body, or in buried landmines, without having to put the sample inside the instrument.[15]
4. NQR (a proprietary type) is being investigated for use to detect strains that may develop in aerospace composite structures before these structures can fail and lead to crashes.
5. ^{14}N and ^{35}Cl NQR are being investigated for uses in the pharmaceutical industry for measuring quantities of medicines in containers without opening them, and for determining whether, during the manufacturing process, the proper polymorph of the pharmaceutical is being produced.[16] (Different polymorphs of drugs can have different stabilities and bioavailabilities.)

In this article we emphasize modern uses of NQR spectroscopy in inorganic chemistry, particularly those involved with characterizing relatively weak bonding and noncovalent interactions. We divide them according to the bonding situation in which the quadrupolar nucleus is found, beginning with terminal (one-coordinate) atoms, for which Townes–Dailey equations (1) through (5) apply, followed by bridging (two-coordinate) atoms, for which equations (6) through (8) apply, followed by brief mention of some cases of central (three-coordinate or higher) atoms, for which a variety of Townes–Dailey equations can be derived but will not be described.

3.1 Applications Involving Terminally Single-bonded Halogen Complexes and Organometallic Compounds

3.1.1 *Relativistic Effects*

The s and p orbitals of heavy atoms undergo relativistic contraction: an electron in such an orbital is accelerated to a speed near that of light.[17] The electron increases in mass, and consequently is pulled closer to the nucleus: the electronegativity of the atom therefore increases. This effect reaches a maximum in elements close to gold, which therefore is predicted to show an unusually high electronegativity. The Pauling electronegativity of Au is the highest of any metal, 2.54, and is close to that of iodine, 2.66. Correspondingly, the terminal chlorines of Au_2Cl_6 have the highest ^{35}Cl NQR frequencies found in any metal chlorides, 36.094, and 33.401 MHz[18]; these values are similar to those found in I_2Cl_6, 35.680, and 33.916 MHz. (Much lower NQR frequencies would be predicted using the Allred-Rochow electronegativity of Au, 1.42, which is derived from the nonrelativistic approximations of Slater's rules.[17]) The chemistry of gold indeed shows remarkable similarities to that of iodine (e.g., Au forms Au^-). Relativistic effects on *EFG*s for elements through Np have been calculated.[19]

3.1.2 *Effects of Nearby Charges in Haloacetate Salts*

The properties of the familiar chloroacetate ion, $ClCH_2COO^-$, are surprisingly cation dependent: among group 1 chloroacetates in the solid state, thermal decomposition to metal chloride and the polymer poly(glycolide), $(CH_2CO_2)_n$,[20] does not occur in the lithium salt, but occurs at progressively lower temperatures with larger cations; the cesium salt decomposes at room temperature (Table 2). As noted earlier by Guibé,[21] the ^{35}Cl NQR frequencies in group 1 chloroacetates decrease for larger cations–for example, by 3.46% from the Li^+ salt to the K^+ salt. Ab initio calculations[6]

Table 2 NQR frequencies and decomposition temperatures of group 1 chloroacetates and hexachlorostannates

Cation	Chloroacetates $M^+ClCH_2CO_2{}^-$ Layer lattice type NQR ν MHz at 77 K[(a)]	Decomp. Temperature (K)[(b)]	Cation	Hexachlorostannates $(M^+)_2SnCl_6{}^{2-}$ Cubic antifluorite lattice NQR ν MHz at 298 K[(c)]	Decomp. Temperature (K)[(d)]
Li^+	35.254	484	Li^+		415
Na^+	34.794	471	Na^+		457
K^+	34.11	430	K^+	15.064	729
Rb^+	33.82	393	Rb^+	15.60	760
Cs^+		<298	Cs^+	16.05	785
Me_4N^+			Me_4N^+	16.663	
			Et_3NMe^+	16.844	

(a) Source: Ref. 21.
(b) Source: Ref. 20.
(c) Sources: T. B. Brill, Z. Z. Hugus, Jr., and A. F. Schreiner, *J. Phys. Chem.*, 1970, **74**, 2999–3002; D. Borchers and A. Weiss, *Ber. Bunsen-Ges. Phys. Chem.*, 1989, **93**, 559–568.
(d) Source: T. Janiak, I. Nikel, and J. Blazejowski, *J. Therm. Anal.*, 1990, **36**, 2205–2210.

on symmetrically chelated $ClCH_2COO$-M systems predict a 3.24% drop in electric field gradients (hence NQR frequencies) from the Li^+ salt to the K^+ salt. These calculations and the NQR data suggest that the Cl atom in the chloroacetate ion carries substantially more negative charge in salts of larger, less polarizing cations, and hence, is more readily lost as chloride ion. It should be noted that haloacetate salts typically have layer structures, in which the nearest neighbors of the halogen ends of the anions include no metal cations to attract neighboring layers of anions close together.

3.1.3 *Effects of Nearby Charges in Halometallate Salts*

In contrast, the thermal stability and NQR frequencies *increase* in hexahalometallate salts of larger group 1 cations (Table 2).[22] The trend in stability limits the usefulness of hexahalometallate ions as weakly coordinating anions, since they are easily broken down into MX_4, and so on, and group I MX by typical small or more highly charged cations. Hexahalometallate salts have typical ionic structures, in which anions and cations alternate, and halogen atoms have group 1 cations and chlorines of neighboring anions as neighbors. Due to the large numbers of electrons, the theoretical analyses of these trends have involved point-sphere and soft-sphere[23] along with MS-Xα[24] calculations. The latter two types of calculations successfully give the trend of increasing *EFG*s with increasing cation radius, and indicate that the gradient due to the lattice is responsible (the lattice gradient partially opposes the *EFG* due to the Sn–Cl bond). There is a good correlation of ^{35}Cl NQR frequencies with interionic chlorine–chlorine distances and with Born repulsive potentials $e^{-r/\rho}$ (r is the Cl–Cl interionic distance) in hexachlorostannates.[25] The calculations are consistent with the changes in the lattice *EFG*s due to changing polarization of the chlorine $p_{x,y}$ orbitals as they are drawn into closer contact with chlorine atoms in adjacent ions in salts of smaller group 1 cations. The calculations tend to refute another possible explanation: that smaller cations may polarize the Sn–Cl σ bond more toward chlorine.

3.1.4 *Effects of Nearby Charges in Organosilicon Compounds*

The electronegativity of silicon is well below that of carbon; consequently organosilyl chlorides R_3SiCl have lower ^{35}Cl NQR frequencies (16–20 MHz) than corresponding organic halides R_3CCl (33–42 MHz). We might expect the same trend if a $-CH_2-$ group were to be inserted in the element–chlorine bond. But the opposite is, in fact, observed:[26] $(CH_3)_3\mathbf{Si}CH_2Cl$ (34.320 MHz) > $(CH_3)_3\mathbf{C}CH_2Cl$ (33.015 MHz); $H_3\mathbf{Si}CH_2Cl$ (34.3 MHz) > $H_3\mathbf{C}CH_2Cl$ (32.646 and 32.759 MHz); $Cl_3\mathbf{Si}CH_2Cl$ (36.786 MHz) > $Cl_3\mathbf{C}CH_2Cl$ (36.40 MHz). Computations suggest that the chlorine $3p_z$ orbital population in $(CH_3)_3\mathbf{C}CH_2Cl$ is anomalously higher (0.960 e^-) than the chlorine $3p_z$ population in $(CH_3)_3\mathbf{Si}CH_2Cl$ (0.948 e^-), while the corresponding chlorine $3p_{x,y}$ populations are virtually identical. It was concluded[27] that the direct cause of the anomalous frequency raising is due to the polarizing effect of the nearby partially positive $(CH_3)_3Si$ (and H_3Si) groups, which polarize the CH_2–Cl bond electrons toward CH_2. Measurements of η for some compounds of this type give values near zero. This and the calculations are inconsistent with earlier suggestions that this ''alpha effect''[28] is due to electron donation from the Cl $3p_x$ orbital to a vacant Si 3d orbital, creating some Si=Cl double bond character.

3.1.5 *Cis and Trans Influences in Substituted Halometallate Anions*

Ligands in octahedral complexes alter the bonding to ligands that are trans- to them in ways that are different

Table 3 NQR data illustrating *cis* and *trans* influences in halo complexes

a. Halogens *trans* to the Substituent (Distances, NQR Frequencies, Charges)

Halo Anion	d(M–Cl), pm *trans*-Cl	d(M–Br), pm *trans*-Br	NQR υ *trans*-Cl	NQR υ *trans*-Br	Charge per *trans*-Cl	Charge per *trans*-Br
OsX_6^{2-}	240.0		16.84	111.80	−0.57	−0.53
$Os(NO)X_5^{2-}$	238.6	252.1	14.10	91.08		
$OsNX_5^{2-}$	260.5		7.00	44.95	−0.87	−0.86
$OsNX_4^{-}$						
SnX_6^{2-}	242.2	260.5	16.68	115.07	−0.70	−0.64
$Sn(Alk)X_5^{2-}$	241.0	256.6	18.04	130.79	−0.67	−0.58

b. Halogens *cis* to the Substituent (Distances, NQR Frequencies, Charges)

Halo Anion	d(M–Cl), pm *cis*-Cl_4	d(M–Br), pm *cis*-Br_4	NQR υ *cis*-Cl_4	NQR υ *cis*-Br_4	Charge per *cis*-Cl_4	Charge per *cis*-Br_4
OsX_6^{2-}	240.0		16.84	111.80	−0.57	−0.53
$Os(NO)X_5^{2-}$	238.0	251.9	18.15	122.10		
$OsNX_5^{2-}$	236.2		20.40	140.50	−0.62	−0.56
$OsNX_4^{-}$	231.0	245.7	22.26	149.50	−0.59	−0.53
SnX_6^{2-}	242.2	260.5	16.68	115.07	−0.70	−0.64
$Sn(Alk)X_5^{2-}$	251.6	269.9	12.30	80.55	−0.77	−0.73

c. Iodides *cis* and *trans* to the Substituent (Distances, NQR Quadrupole Coupling Constants)

	d(M–I), pm *cis*-I_4	d(M–I), pm *trans*-I	NQR e^2Qq_{zz} *cis*-I_4	NQR e^2Qq_{zz} *trans*-I
OsX_6^{2-}			942.33	942.33
$Os(NO)X_5^{2-}$	271.9	274.0	1033.50	782.20
$OsNX_5^{2-}$				
$OsNX_4^{-}$			1366.50	

Source: Ref. 29.

from the effects on ligands that are cis- to them.[29] This effect shows up through changes in bond lengths, but even more sensitively through changes in NQR frequencies. Alkyl groups are more strongly electron donating than halo groups due to electronegativity effects, while nitrido ions ($\equiv N^{3-}$) donate electrons not only via σ bonds, but also via two π bonds, so are also more strongly electron donating than halo groups. The nitrosyl ligand ($N\equiv O$) falls between nitrido and halo ligands in this respect.

The effects on halo groups depend, however, on whether the central metal ion of the complex is from the d block or the p block. In complexes of the type $[OsLX_5]^{2-}$, when L is changed from being another X^- to being NO and then to being N^{3-}, the effects on bond lengths and especially NQR frequencies are dramatically different for the four halogens cis to L as compared to the unique halogen that is trans to L. Data are shown in Table 3 for osmium chloro and bromo complexes of these ligands (it must be noted that the oxidation state of Os also changes during these substitutions). The chloro- or bromo-ligand trans to the new nitrido experiences an 8.5% increase in bond length, a 60% decrease in NQR frequency, and a 53% increase in partial charge δ (as computed from NQR frequencies). The effects on the four cis ligands are much more modest: a 1.6% decrease in bond length, a 21–26% increase in NQR frequency, and a 6–9% increase in δ. We note that these cis and trans effects manifest themselves both in NQR and in X-ray crystallographic data, but more dramatically in the NQR data.

Table 3 also shows data for $[SnLX_5]^{2-}$ complexes, in which L is changed from being another X^- to being a much more electron-donating alkyl group (ethyl or butyl). The effects in these p-block complexes are opposite to those seen above for the d-block element Os: when the alkyl ligand is introduced, the trans-halogen atom experiences a 0.5–1.5% *decrease* in bond length, an 8–14% *increase* in NQR frequency, and a 4–9% *decrease* in δ. Clearly the trans bond is strengthened in tin complexes but weakened in osmium complexes. In the tin complexes the cis ligands experience the largest, not the smallest effects: a 4% *increase* in bond length, a 27–30% *decrease* in NQR frequency, and a 10–14% *increase* in δ.

3.1.6 Trihalide Ions

Bromine and iodine atoms can be at the center of linear (two-coordinate) complexes when in the familiar trihalide ions, Br_3^- and I_3^-. NQR data are then available on all atoms in the complex,[30,31] and can be analyzed to show the charge distribution within the ion using equations corresponding to equation (2) and a related equation for the central halogen atom. When these simple Townes–Dailey equations presume neither the involvement of halogen s nor halogen d orbitals, it is found that the totals of the three charges in all cases add up to sums (in practice, from -0.94 to $-1.06\,e^-$) close to the actual -1 charge on the trihalide ion. Although this could be due to fortuitous cancellation of the opposing effects of s and d hybridization, this seems unlikely since the conclusion holds for all 13 salts studied. In all cases the central halogen atom is computed to have a small *positive* partial charge of $+0.04 - +0.08$, while the terminal halogen charges average close to -0.50. This is consistent with three-centered, four-electron bonding, with the highest occupied molecular orbital being localized on the two outer (terminal) halogens.

However, the negative charge is not always equal on the two terminal halogen atoms. With very large cations (tetramethylammonium through tetrabutylammonium), each terminal bromine or iodine atom carries the same, or nearly the same charge of $-0.50\,e^-$ each. But with the smaller Tl^+, Cs^+, Rb^+, and $NH_4{}^+$ cations, one halogen atom carries most of the negative charge. For the extreme case, NH_4Br_3, one bromine atom has only a -0.18 charge while the opposite bromine atom bears a large -0.87 charge. The bond distances are all long, since the covalent bond orders are less than one: in $CsBr_3$ the shorter Br–Br bond distance is 244 pm and the longer 270 pm, as compared to the sum of Br covalent radii, 228 pm. Clearly, in such a case the two Br–Br bonds are unequal in covalent bond order: in this case it seems to be appropriate to call the bond to the second Br atom a *secondary bond*, and one might represent the bonding as $Br–Br\cdots Br^-$.

3.2 Applications Involving Secondary Bonding of Halogens to Metal Ions

Weak (‘‘noncovalent’’) interactions between molecules are currently of great interest in chemistry, not only in biochemistry (e.g., the study of enzyme-substrate bonding) but in the study of—host–guest interactions and crystal engineering, for example. (The very important phenomenon of hydrogen bonding falls in this category, but will not be considered here.) In the chemistry of halocarbons, metal halides, and even the halogens themselves, such bonding (to metal atoms or ions, or even other molecules of the same type) was originally overlooked, but is increasingly being found to be of interest. The earliest focus on it was perhaps in the review of Allcock, who termed such interactions *secondary bonding*.[32]

Secondary bonds are characterized crystallographically by bond lengths that are longer than the sums of covalent radii of the atoms involved, but are shorter than the sums of van der Waals radii. However, van der Waals radii are difficult to determine, since one must first be assured that there is, in fact, no bonding in the direction in which the nonbonded distances are measured.

For example, solid halocarbons commonly pack with halogen–halogen distances that are less than the sums of their van der Waals radii. This raises questions as to whether the van der Waals radii are incorrect, or differ in different directions around an organohalogen atom, or whether the radii are correct, and the halocarbon molecules are in fact bonding to each other via *halophilic* interactions.[33]

Furthermore, secondary bond distances vary widely, even among chemically equivalent bonds in the same complex (e.g., from 264.0 pm to 292.6 pm for $Ag\cdots Cl$ contacts in $Ag[CB_{11}H_6Cl_6]$[34]). One wonders whether these differences signify any difference in secondary bond strength or bond order, or whether secondary bonding involves such a shallow potential well that the differences merely represent variations in what is needed to achieve optimal solid-state packing.

Hence confirmation by another method is very helpful in determining whether a long metal-donor atom contact actually signifies secondary bonding and involves coordinate covalent bond formation. Most spectroscopic methods cannot reliably detect or interpret such subtle bonding interactions, but halogen NQR spectroscopy offers great promise here.

Even in the solid halogens themselves, halophilic secondary interactions (donation from a lone pair of electrons on one X_2 molecule to the empty σ^* orbital of another) occur between diatomic molecules in the same layers, giving interatomic distances much shorter within layers than between layers, and a lengthened σ bond in the case of I_2. This destroys the axial symmetry of the X_2 molecule, so that they have nonzero asymmetry parameters (Table 1, Column H): $\eta = 0.20$ for Cl_2 and for Br_2; $\eta = 0.175$ for I_2.

Secondary bonding of halogens in one molecule to metal or metalloid atoms in a neighboring molecule is a common feature in the chemistry of the halides of the heavier elements of the p- and late d blocks. With such weak interactions, the angle between the shorter primary bond in the molecule and the secondary bond to the metal center in the next molecule is normally in the range of $90° - 109°$. If there is one secondary interaction per halogen atom, and if the bond angle is taken as 90°, as discussed in Section 2.2 the situation from the halogen atom's point of view is similar to that in a double bond to the halogen, which involves a stronger (primary) σ bond using the p_z orbital and a weaker (secondary) π bond involving the p_y orbital. The consequence of such bonding is also similar: there is a nonzero asymmetry parameter, and a lowering of the quadrupole coupling constant and NQR frequency of the halogen atom (as suggested by equation (8)).

An analysis was made of 15 such cases of secondary bridging halogen atoms, primarily among adducts of HgI_2 and $SbCl_3$.[35] Values of η for these adducts ranged from 0.057 in $SbCl_3$ to 0.18 in $BiCl_3$ and AsI_3; the resulting secondary bond orders σ_{B2} computed using equation (6) ranged from 0.041 in $SbCl_3$ to 0.071 in AsI_3. For these adducts the Sb-halogen and Hg-halogen bonds do lengthen slightly upon coordination, so that the approximation of equation (8) is not justified. For seven of these adducts for which η, ν_T, and ν_B were all known, it was found that typically, about one-third of the electronic effect of secondary bonding is compensated by an alteration of the primary bonding. This gives a moderate alteration of equation (8).

$$\sigma_{B2} = \frac{2.4(\nu_T - \nu_B)}{54.873} \tag{9}$$

These calculations, of course, are subject to the usual limitations of Townes–Dailey theory, as well as the assumption that the bond angle is effectively 90°. So they are most likely useful to show, not absolute values of σ_{B2}, but periodic trends in those values.

3.2.1 Halocarbons as Ligands

For decades inorganic chemists assumed that chlorocarbons could safely be used as noncoordinating solvents for reactions of metal ions and complexes, but this view is no longer tenable,[36] particularly since the work of Strauss and others on Ag^I complexes of dichloromethane and related halocarbons.[37] As an example, they prepared the complex $[Ag(1,2\text{-}C_2H_4Cl_2)(OTeF_5)]_2$, with chelating chlorocarbons ligands having Ag···Cl secondary bond distances of 262.4–300.0 pm, longer than the sums of Ag and Cl covalent radii, 251 pm, but well within the sums of van der Waals radii, 340–350 pm. In this complex the ^{35}Cl NQR frequency of $1,2\text{-}C_2H_4Cl_2$, 34.361 MHz, is replaced by four frequencies between 31.700 and 32.036 MHz. The average $(\nu_T - \nu_B)$ is 2.513 MHz, so that σ_{B2} is 0.19 according to equation (8) or 0.22 according to equation (9). If these numbers are not too far off due to the approximations in the theory, the secondary bond order is about 20% that of a full covalent bond (as in Cl_2); qualitatively this seems plausible since the Ag···Cl distance is not so much longer than that expected for a covalent Ag–Cl bond. No value of η was obtained for these complexes.

The asymmetry parameter was measured for the intramolecularly coordinated organochlorine atom in the compound $ClCH_2CH_2CH_2SnCl_3$,[38] which has a five-coordinate tin atom with the organochlorine atom in an axial position, showing an Sn···Cl distance of 327.9 pm, intermediate between the 239-pm sum of covalent radii and the 400-pm sum of van der Waals radii. The ^{35}Cl NQR frequency for the organochlorine is 31.750 MHz, considerably below the value typical for longer-chain $Cl(CH_2)_nX$ compounds with $n \geq 3$, 33.1 MHz. The application of equations (8) and (9) gives values for σ_{B2} between 0.049 and 0.059. The value measured for η for this chlorine was 0.087 ± 0.020, which when used with equation (6) gives us $\sigma_{B2} = 0.034 \pm 0.008$, in rough agreement with the values obtained using equations (8) and (9).

Iodocarbons are expected to be softer bases than chlorocarbons, so should complex more strongly to the soft Ag^+ cation; Powell and others have found the synthesis of iodocarbon complexes of Ag^+ to be more facile and commonly achieved than the syntheses of chlorocarbon complexes; the iodocarbon ligands in these complexes tend to be bridging rather than chelating. For example, in $[Ag(I_2CH_2)_2](PF_6)$ the average Ag···I distance is 285.9 pm, only 0.9 pm longer than the sum of covalent radii, while the C–I bond lengths in such complexes is 211 pm, very slightly longer than the normal C–I bond length, 210 pm. The average C–I–Ag bond angle is 101.5°. For purposes of comparison, in diphenyliodonium salts (in which iodine is symmetrically bridging) the C–I bond lengths are 207–210 pm, and the C–I–C bond angles are 91.8°–93.2°.[39]

For $[Ag(I_2CH_2)_2](PF_6)$ the average e^2Qq_{zz} was 1744 MHz, below the 1897 MHz found in the free ligand, and η for iodine in the silver complex was quite substantial, 0.32. For diphenyliodonium salts e^2Qq_{zz} values range from 1944 to 1970 MHz, above the 1822 MHz average for C_6H_5I, and η for iodine in the iodonium salts is also quite substantial, 0.369–0.395.[40] (The values of η in these two free ligands are much smaller, 0.027 and 0.069, respectively.)

If one assumes that the Ag···I bond in $[Ag(I_2CH_2)_2](PF_6)$ is secondary, with no sp hybridization, substitution of the observed η in equation (6) gives a value for σ_{B2} of 0.162; this corresponds to the donation of the slight δ found in neutral CH_2I_2, 0.15 e^-, to Ag^+ to give a neutral iodine atom in the complex. However, use of the quadrupole coupling constants of the free and complexed ligand in equations analogous to equations (8) or (9) give significantly different σ_{B2} values of 0.067 and 0.080.

Because the Ag···I distance is so close to the sum of covalent radii, one may alternately assume that the Ag···I bond is a full covalent bond, not a secondary bond. If we then call the C–I–Ag bridging interaction ''symmetrical'', the covalent Ag–I bond order can be computed from the equation

$$\sigma_{B2} = \left(1 + \frac{\eta}{3}\right)\left(\frac{e^2Qq_{zz}}{e^2Qq_0}\right) \tag{10}$$

and the value of σ_{B2} is computed to be 0.84, which is virtually identical to the C–I covalent bond order in the free CH_2I_2 ligand, 0.85. This then puts a large δ of +0.68 on the iodine atom, which is broadly comparable to the δ values found in iodonium ions (+0.78 – +0.81).[41] (However, contributions to *EFG* and η from the ionic lattice forces have not been taken into account; these could be significant.) With the assumption that the iodine atom in this complex undergoes sp hybridization that is set by the bond angle θ, the Townes–Dailey theory predicts:

$$\eta = -3\cos\theta \tag{11}$$

From the observed asymmetry parameter $\eta = 0.32$, one calculates an interbond angle $\theta = 96°$, which is in the vicinity but not identical to the observed internuclear angle of 101.5°. It is unfortunate that the atoms involved are so heavy, as more detailed molecular-orbital calculations would help clarify whether the Ag–I interaction is secondary, fully covalent, or somewhere in between.

3.2.2 *Chloroacetates and Chlorophenolates as Cl-Donor Ligands*

Weak Cl···M secondary bonding is likely to be stabilized if the secondary bond completes the formation of a chelate ring, as in the case of $ClCH_2CH_2CH_2SnCl_3$ discussed previously. The crystal structure of calcium chloroacetate,**42** $Ca(ClCH_2CO_2)_2 \cdot H_2O$, involves one of the two chlorines in a chelate ring with a $Cl\cdots Ca^{2+}$ contact of 320.6 pm, which is long compared to the $Cl^{-}\cdots Ca^{2+}$ distance of 274.1 pm in $CaCl_2 \cdot 4H_2O$ (the van der Waals radius of Ca is unavailable for computing that sum). Because of the large difference in electronegativities and hard–soft properties, the $Cl^{-}\cdots Ca^{2+}$ secondary interaction is not expected to be coordinate covalent, but is more likely to be of an ion–dipole type. The crystal structure of dimeric silver chloroacetate,**43** $Ag_2(ClCH_2CO_2)_2$, shows interdimer coordination of all chlorines to silver at a distance of 290.3 pm, which exceeds the sum of Ag and Cl covalent radii, 251 pm, but is well under the 340–350 pm sum of van der Waals radii; covalent secondary bonding of soft Ag and Cl is considerably more likely here. The ^{35}Cl NQR spectrum**21** of $Ca(ClCH_2CO_2)_2 \cdot H_2O$ shows no significant difference between the free and coordinated chlorines: 34.49 and 34.77 MHz. The spectrum of $Ag_2(ClCH_2CO_2)_2$ shows four closely spaced NQR frequencies**6** averaging 33.671 MHz, which is much lower than found in covalent chloroacetates, but is in the range found for some ionic chloroacetates. Since no reference NQR frequency for a noncoordinated Cl in silver chloroacetate is available, a measurement of η would be useful.

The 2,6-dichlorophenoxide ion can readily form chelate complexes with a number of metal ions, in which coordination is through the oxygen and the 2-chlorine atoms, while the 6-chlorine remains noncoordinated (and thus provides the reference NQR frequency ν_T for a terminal atom). There is some π-bond character to the Cl-aromatic C bond (η values of several percent are found). In principle these alter the usefulness of equations (8) and (9)—in practice, insignificantly so—but the usefulness of equation (6) is significantly compromised by this π bonding.

We first consider complexes of some d^{10} metal ions. Substituted phenyl mercury chlorophenolates gave frequency differences ($\nu_T - \nu_B$) between the 2- and 6-chlorines in the range 0.88—1.25 MHz,**44,45** which is barely outside of the 0.8-MHz spectral width expected for molecular compounds. The crystal structure of phenylmercury 2-chloro-4-bromophenolate shows a Cl···Hg intramolecular bond distance of 303 pm, which is well over the sum of covalent radii, 247 pm, but which is still under the sum of van der Waals radii, 330 pm. The d^{10} ions Ag^+ and Cu^+ gave larger frequency differences of 1.675 MHz and 1.88–2.05 MHz in the compounds $(Ph_3P)_2Ag(OC_6H_3Cl_2-2,6)$ and $(Ph_3P)_2Cu(OC_6H_3Cl_2-2,6)$, respectively, and 1.50 MHz in $(Ph_3P)_2Ag(OC_6H_2Cl_3-2,4,6)$.**46** The crystal structure of the latter compound showed a Cl···Ag intramolecular bond distance of 316 pm, which is 65 pm over the sum of covalent radii, 251 pm. A very acute O–Ag–Cl bond angle of 64.5° is found, which was attributed to strain in the nonplanar chelate ring. Finally, NQR data were obtained for two Zn^{II} 2,6-dichlorophenolates,**47** one containing two pyridine (py) ligands and the other containing one tetramethylethylenediamine (TMED) ligand. The frequency differences averaged 1.191 MHz and 1.116 MHz, respectively, and thus were similar to those found in Hg^{II} derivatives.

The study was then extended leftward in the periodic table to incorporate the 2,6-dichloro-, 2,4,6-trichloro-, and 4-bromo-2,6-dichlorophenolates of the d^7 through d^9 ions Co^{2+}, Ni^{2+}, and Cu^{2+}, with (mainly) the coligands py, TMED, and N-methylimidazole.**47–49** Crystal structures of several complexes of these metals and ligands (generally involving 2,4,6-trichlorophenolato groups) are also available. Figure 2 shows that there is a good (though nonlinear) correlation of the NQR frequency differences between the 2-chlorine and the 6-chlorine, and the excess M···Cl bond distance (the observed M···Cl distance minus the normal single M···Cl bond distance). (It should be noted that this correlation is for chlorophenolates, and does *not* apply to silver-chlorocarbon complexes.)

Finally, it was determined that the NQR frequency difference depended strongly on the identity (d^n electron configuration) of the metal ion, as would be expected from the (inorganic) crystal field theory. With complexes of M^{II} 2,6-dichlorophenolates and common coligands (TMED or two py), if the 2-chlorine is coordinated to the metal and is acting as a classical ligand, one has octahedral complexes; if the chlorines are not coordinated, one has tetrahedral complexes. The octahedral site stabilization energy (OSSE) (energy preference for octahedral over tetrahedral coordination) depends on the

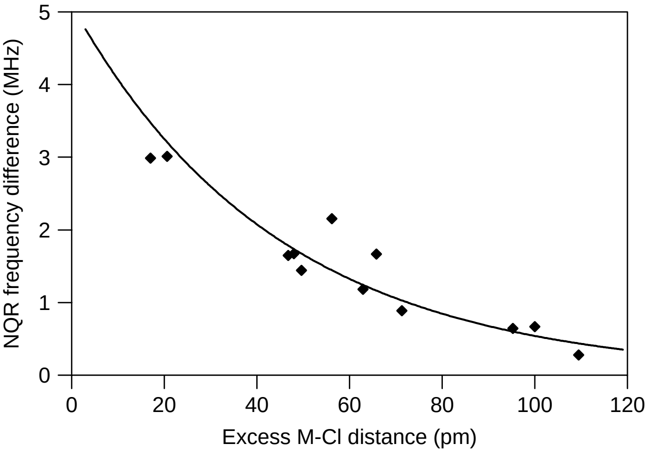

Figure 2 Average ^{35}Cl NQR frequency difference of coordinated ortho-chlorine and noncoordinated (free) ortho-chlorine atoms in 2,6-dichlorophenolato(*O,Cl*) complexes of metals, as a function of the excess M–Cl distance, defined as the average observed M–Cl distance minus the normal M–Cl single bond distance in octahedral complexes, from A. G. Orpen, L. Branner, F. H. Allen, O. Kennard, D. G. Watson, and R. Taylor, *J. Chem. Soc., Dalton Trans.* 1989, S1–S83

Table 4 Effects of OSSE on average ^{35}Cl NQR frequency differences of coordinated and free *ortho* chlorines 2,6-dichlorophenolato(*O,Cl*) complexes of late transition metals (as compared to zinc complexes)

Complex Type$^{(a)}$	M = Co vs. Zn$^{(b)}$	M = Ni vs. Zn$^{(b)}$	M = Cu vs. Zn$^{(b)}$
OSSE (Δ_{oct})	$0.267\Delta_{oct}$	$0.845\Delta_{oct}$	$0.422\Delta_{oct}$
M(TMED)(OPhH)$_2$	0.559 MHz	1.450 MHz	0.118 MHz
Mpy$_2$(OPhH)$_2$	0.226 MHz	1.577 MHz	0.132 MHz
M(TMED)(OPhCl)$_2$	0.373 MHz	1.704 MHz	−0.340 MHz
Mpy$_2$(OPhCl)$_2$	0.554 MHz	1.713 MHz	1.590 MHz
Mean	0.428 MHz	1.611 MHz	0.375 MHz
Standard deviation	±0.160 MHz	±0.124 MHz	±0.839 MHz

$^{(a)}$Ligand abbreviations: TMED = tetramethylethylenediamine; py = pyridine; OPhH = 2,6-dichlorophenolato(*O,Cl*); OPhCl = 2,4,6-trichlorophenolato(*O,Cl*).
$^{(b)}$NQR frequencies shown are the average differences of the 2- and 6-chlorine NQR frequencies in a given metal complex minus the corresponding average difference in the zinc complex.
Sources: Refs. 47–49.

d^n electron configuration, and is zero for the d^{10} ion Zn^{2+}. As indicated in the first row of Table 4, the d^7 and d^9 ions Co^{2+} and Cu^{2+} ions have intermediate OSSE (for weak-field ligands such as in these complexes), and the largest stabilization energy is expected for the d^8 Ni^{2+} ion. As shown in the remainder of Table 4, nickel chlorophenolates indeed give significantly the largest frequency differences between free and coordinated ortho chlorines of any of these metals (in Table 4, these are compared to the frequency differences of the zinc chlorophenolates). It may be noted that there is a great deal of variability for the Cu^{II} complexes: the chlorines in these octahedral complexes occupy sites showing quite variable Jahn-Teller elongation.

Another example not involving 4th-period d-block ions or chlorophenolates has been studied. The Schiff base formed from 2-chloroaniline and 2,6-dichlorobenzaldehyde undergoes oxidative addition to $Mo(CO)_6$ to give a d^4 molybdenum tricarbonyl complex with a Mo···Cl–(aniline) distance of 262.4 pm, only a little longer than the single inorganic Cl–Mo bond distance of 247.3 pm in the same compound.**[50]** The ^{35}Cl NQR frequency of the complexed Schiff base is 3.685 MHz lower than the free Schiff base. Applying equations (8) and (9) allows us to estimate $\sigma_{B2} = 0.134–0.161$. This large value can be justified by noting that Period 5 metal ions give larger crystal field stabilization energies than do Period 4 metal ions, especially when strong-field ligands such as CO are present.

3.2.3 *Weakly Coordinating Anions*

Chemists working in catalysis need weakly coordinating anions**[51]** as counterions to serve as good leaving groups from complexes of very reactive cations such as silylium ions, R_3Si^+, porphyrinatometal cations, (porphyrinato)Fe$^+$, and various catalytically active transition-metal organometallic cations, most importantly the zirconocene catalysts that are used in the industrial polymerization of alkenes.**[52]** Almost all anions will bond to such cations in preference to the neutral substrates (e.g., alkenes) required for the catalytic process involved. Therefore, one seeks very weakly coordinating anions that would be bound to the reactive cation only by very weak secondary bonding or even only by weak (since long-range) electrostatic (ion–ion or ion-induced dipole) interactions.

In order to be weakly attracted electrostatically to the cation, a weakly coordinating anion should have a low charge and a large size over which the charge can be dispersed: it should be as nonbasic**[17]** as possible. The weakly basic and poorly coordinating properties of anions such as methanesulfonate ($CH_3SO_3^-$), tetraphenylborate, $[B(C_6H_5)_4]^-$, and 1-carba-*closo*-dodecaborate, $(CB_{11}H_{12})^-$ can be further reduced by extensively substituting them with very electronegative atoms such as halogens, to give anions such as $CF_3SO_3^-$ and $[B(C_6F_5)_4]^-$.

However, such fluorine atoms are hard bases, and have been shown to coordinate to the (presumably) hard zirconium cation.**[53]** It is worth investigating whether the secondary bonding would be weaker if the fluorine atoms on typical nonbasic anions were replaced with softer chlorine, bromine, or iodine atoms. Perhaps, in this light, it may be significant that zirconocene catalysis is especially efficient when the anion is $(CB_{11}H_6X_6)^-$ (X = Cl, Br, or I).

Since the oxygen atoms of carboxylate anions or even sulfonate ions are hard bases, they coordinate readily to zirconium, as indicated by the infrared spectra of zirconocene and hafnocene bis(chloroacetates) and by X-ray crystallography for titanocene bis(trifluoromethanesulfonate).**[54]** Thus we envision the design of a large, low-charged, nonbasic anion that might be very weakly coordinating to hard acids such as the zirconocene cation having *no* hard-base atoms on its surface, yet having electronegative atoms (hence Cl, Br, or I). Oxygen atoms would either have to be absent from this anion, or would have to be confined to its interior. An example of the former might be a C_{60}^{-} anion which had been thoroughly chlorinated, so that no double bonds were available to coordinate to Zr; an example of the latter might be the perchloro analogue of the well-known weakly coordinating anion $[Al(O\text{-}tert\text{-}C_4F_9)]^-$, in which the oxygen atoms are inaccessible.

We might be able to use chlorine NQR to identify whether such an anion showed secondary bonding interactions with catalyst cations, or whether it interacted with them only by long-range (and therefore weak) interionic attractions. Such an anion probably *would* show secondary interactions with soft cations such as Ag^+, which would result in low halogen NQR frequencies for the coordinated chlorines (and, if measurable, high asymmetry parameters). However, we would hope for no such results for hard-acid cations that are similar in charge and size to Ag^+ (e.g., Na^+ or K^+).

However, there *would* be significant ''crystal field effects'' from nearby ions. As we discussed earlier, these are significant, and differ in how they depend on cation size. If our salts adopted typical ionic lattices as found in the hexahalometallate salts discussed earlier, we might again see *increases* in NQR frequencies with increasing group 1 cation radius. Since we hope that our anion would be less polarizable (and less easy to dismember) than $SnCl_6^{2-}$, we would then look for *smaller* increases with increasing cation size. On the other hand, the zirconocene cation itself is only open to coordinate anions on one side, so that its salts might adopt layer type lattices (or even be present as discrete ion pairs). In this case we might see *decreases* in NQR frequencies with increasing cation size, but they would hopefully be less than is the case in chloroacetates. And in such a case, the chlorines on one side of the large perchlorinated anion would not be close to a cation at all, so their NQR frequencies might be independent of cation size. Regardless of whether the salts adopted typical ionic lattices or layer lattices, we would look for an anion in which the effect of the hard-acid cation on the NQR frequency was notably small.

3.3 Applications Involving Multivalent Central Atoms

The Townes–Dailey approach to interpreting NQR spectra of atoms at the center of polyatomic ions or complexes depends in its details on the geometry and bond angles of the central atom, so no attempt will be given here to summarize the equations; we will only mention a few examples to illustrate the availability and use of the data.

High-temperature superconductors are based on copper, which has NQR-active nuclei, and NQR spectra can be obtained on these superconductors while they are in the superconducting state, which excludes magnetic fields. For the classic superconductor $YBa_2Cu_3O_{6.9}$, two ^{63}Cu NQR signals can be obtained. The square-planar-coordinated Cu(1) gives an NQR signal at 22.05 MHz, for which $e^2Qq_{zz} = 38.9$ MHz and $\eta = 0.95$; the square-pyramidal-coordinated Cu(2) gives an NQR signal at 31.5 MHz, for which $e^2Qq_{zz} = 63.08$ MHz and $\eta = 0.04$.**[14,55]** Data have also been obtained using the medium-abundance isotope ^{133}Ba, as well as ^{139}La in the La_2CuO_4–related superconductors. We also mention a review of Cu NQR spectroscopy in Cu^I complexes.**[56]**

There have been reviews of NQR spectroscopic studies of central-atom nuclei in complexes**[57,58]** and in organometallic compounds.**[59]** The interpretation of the e^2Qq_{zz} and η values of these nuclei depends on the coordination number of the atom, the bond angles, the covalency of the bonds to the central atom, and lattice effects, so it is not practical to summarize the field. We illustrate with a ^{59}Co NQR and NMR spectroscopy study**[60]** of a series of cobaloxime (bis-dimethylglyoximato)cobalt(III), $[XCo(dmg)_2L]$ complexes, in which dmg is the dimethylglyoximato monoanion, L is a Lewis base such as methanol, pyridine, trimethylamine, halide ion, and triphenylphosphine, and X is an anion such as CH_3^-, $CHCl_2^-$, Cl^-, and Br^-. (These complexes are of interest as bioinorganic models for Vitamin B_{12} (cobalamin).) A ''partial field gradient'' model was developed for the bonding, composed of contributions from the equatorial (dimethylglyoximato) and the axial (X and L) ligands. It proved to be less appropriate to derive fixed partial field gradients for each ligand, than to assume that the sums of all partial field gradients were constant in this set of complexes (changing the axial ligand also changed the partial field gradient due to the equatorial bis(dimethylglyoximato) ligand). Then it was possible to order the axial ligands in terms of the ratios of the axial and equatorial partial field gradients: for example, methanol > trimethylamine > pyridine > triphenylphosphine.

Studies have also been made of complexes from the point of view of the nitrogen atom in the ligand. Because of the low NQR frequencies of ^{14}N, these have often been done using NMR–NQR double resonance techniques. Again we cite only one example, a series of studies of pyridine (C_5H_5N) ligands coordinated to different diamagnetic metal**[61]** (and even nonmetal)**[62]** atoms. Through another adaptation of the Townes–Dailey method, the electron populations of the σ-donating orbital of the pyridine nitrogen atom were deduced, and showed reasonable trends: free pyridine (2.00 e^-) > $Cdpy_2Cl_2$ (1.87 e^-) > $Znpy_2Cl_2$ (1.79 e^-) > $py \cdot I_2$ (1.74 e^-) > $Fepy(CO)_4$ (1.72 e^-) > $[Ipy_2]ClO_4$ (1.64 e^-) > $[pyH]NO_3$ (1.38 e^-). In this series, the coordinate covalent bond order would then proceed in the other direction, from 0.00 in free pyridine to 0.62 in the $[pyH]^+$ cation.

The usefulness of NQR spectroscopy is thus not confined to the study of weak secondary bonds, but can be applied to ordinary covalent or coordinate covalent bonding as well. Hopefully with the advent of modern pulse-FT NQR methods, easier structural determination by X-ray crystallography, and more powerful computational methods to handle the many bonds in complex ions, NQR can resume its contribution in this area of inorganic chemistry as well.

4 ABBREVIATIONS AND ACRONYMS

CW = continuous-wave; CW-NQR = continuous wave NQR; DFT = density functional theory; EFG = electric field gradient; IR = infrared; NMR = nuclear magnetic resonance; NQR = nuclear quadrupole resonance; OSSE = octahedral site stabilization energy; PAC = perturbed angular correlation; pulse-FT = pulse-fourier transform; TMED = tetramethylethylenediamine.

5 FURTHER READING

I. P. Biryukov, M. G. Voronkov and I. A. Safin, 'Tables of Nuclear Quadrupole Resonance Frequencies', Israel Program for Scientific Translation, Jersalem, 1969, Includes frequencies measured at different temperatures (commonly 77 K, 195 K, and 273 K or 298 K): temperature effects in NQR are quite substantial and have not been reviewed here.

T. B. Brill, *Adv. Nucl. Quadrupole Reson.*, 1977, **3**, 131. Good compilation of principles and data.

Yu. A. Buslaev, E. A. Kravchenko and L. Kolditz, Special issue of *Coord. Chem. Rev.*, 1987, **82**, 1.

H. Chihara and N. Nakamura, in 'Landolt-Börnstein Numerical Data and Functional Relationships in Science and Technology', 'New Series: Group III, Crystal and Solid State Physics, Vols. 20a, 20b, 20c, 31a, 31b, and 39', eds. K.-H. Hellwege and A. M. Hellwege, Springer-Verlag, Berlin, 1989, 1993, 1997, Critical compilations of NQR frequencies, quadrupole coupling constants, and asymmetry parameters.

T. P. Das and E. L. Hahn, 'Nuclear Quadrupole Resonance Spectroscopy' (Supplement 1 in the series *Solid State Physics*) Academic Press, New York, 1958, The classic early work on NQR theory.

K. B. Dillon, Annual chapters in *Spectrosc. Prop. Inorg. Organomet. Compd*.

Fortschr.Chem. Forsch: Top. Curr. Chem., 1972, **30**, 1. Special issue on NQR spectroscopy, with useful article on crystal field effects in NQR.

E. A. C. Lucken, 'Nuclear Quadrupole Coupling Constants', Academic Press, London, 1969, A good summary of NQR theory and applications to different bonding situations, with selected NQR data.

'Nuclear Quadrupole Resonance Spectra Database', Japan Association for International Chemical Information, Tokyo. Updated twice yearly.

G. K. Semin, T. A. Babushkina and G. G. Yakobson, 'Nuclear Quadrupole Resonance in Chemistry', John Wiley & Sons, New York, 1975, A good catalog of NQR frequencies, e^2Qq_{zz} values, and η values as well as a summary of NQR theory and applications.

6 REFERENCES

1. E. A. C. Lucken, F. Grandjean and G. J. Long, *Compr. Supramol. Chem.*, 1996, **8**, 225.
2. N. Weiden, A. Weiss, G. Wulfsberg, W. Ilsley, K. Benner and W. Wourster, *Z. Naturforsch., A: Phys. Sci.*, 1990, **45a**, 503.
3. E. A. C. Lucken, 'Nuclear Quadrupole Coupling Constants', Academic Press, London, 1969, Chap. 7.
4. G. K. Semin, T. A. Babushkina and G. G. Yakobson, 'Nuclear Quadrupole Resonance in Chemistry', John Wiley & Sons, New York, 1975.
5. L. Pang, E. A. C. Lucken and G. Bernardinelli, *J. Am. Chem. Soc.*, 1990, **112**, 8754.
6. G. Wulfsberg, M. Cochran, J. Wilcox, T. Koritsanszky, D. J. Jackson and J. C. Howard, *Inorg. Chem.*, 2004, **43**, 2031.
7. A. Weiss, *Top. Curr. Chem.*, 1972, **30**, 1.
8. O. Kh. Poleshchuk, J. N. Latosińska and B. Nogaj, *Z. Naturforsch., A: Phys. Sci.*, 2000, **55a**, 271.
9. J. N. Latosińska, *Int. J. Quantum Chem.*, 2003, **91**, 284.
10. C. H. Townes and B. P. Dailey, *J. Chem. Phys.*, 1949, **17**, 782.
11. W. Gordy, *J. Chem. Phys.*, 1951, **19**, 792.
12. D. Nakamura, R. Ikeda and M. Kubo, *Coord. Chem. Rev.*, 1975, **17**, 281.
13. E. V. Bryukhova, G. K. Semin, I. M. Alimov, A. N. Nesmeyanov, O. V. Nogina, V. A. Dubovitsky and S. I. Kuznetsov, *J. Organomet. Chem.*, 1974, **81**, 195.
14. D. Brinkmann, *Z. Naturforsch., A: Phys. Sci.*, 1990, **45a**, 393.
15. J. B. Miller and G. A. Barrall, *Am. Sci.*, 2005, **93**, 50.
16. E. Balchin, D. J. Malcolme-Lawes, I. J. F. Poplett, M. D. Rowe, J. A. S. Smith, G. E. S. Pearce and S. A. C. Wren, *Anal. Chem.*, 2005, **77**, 3925.
17. G. Wulfsberg, 'Inorganic Chemistry', University Science Books, Sausalito, 2000.
18. R. Lenk and E. A. C. Lucken, *Chem. Phys. Lett.*, 1973, **21**, 552.
19. P. Pyykkö and M. Seth, *Theor. Chem. Acc.*, 1997, **96**, 92.
20. M. Epple and O. Herzberg, *J. Mater. Chem.*, 1997, **7**, 1037.
21. S. David, L. Guibé and M. Gourdji, *New J. Chem.*, 1995, **19**, 37.
22. Yu. A. Buslaev, E. A. Kravchenko and L. Kolditz, *Coord. Chem. Rev.*, 1987, **82**, 1 (specifically, pages 53–62).
23. D. H. Current, *J. Magn. Reson.*, 1975, **20**, 259.
24. D. Borchers, P. C. Schmidt and A. Weiss, *Z. Naturforsch., A: Phys. Sci.*, 1988, **43**, 643.
25. T. B. Brill, R. C. Gearhart and W. A. Welsh, *J. Magn. Reson.*, 1974, **13**, 27.
26. M. G. Voronkov, V. P. Feshin, V. F. Mironov, S. A. Mikhailyants and T. K. Gar, *J. Gen. Chem. USSR*, 1971, **41**, 2237.
27. V. P. Feshin, *Main Group Met. Chem.*, 1997, **20**, 669.
28. V. P. Feshin, L. S. Romanenko and M. G. Voronkov, *Russ. Chem. Rev. (Engl. Transl.)*, 1981, **50**, 248.

29. E. A. Kravchenko and M. Yu. Burtzev, *Z. Naturforsch., A: Phys. Sci.*, 1992, **47a**, 134.

30. A. Sasane, D. Nakamura and M. Kubo, *J. Phys. Chem.*, 1967, **71**, 3249.

31. H. Harada, D. Nakamura and M. Kubo, *J. Magn. Reson.*, 1974, **13**, 56.

32. N. W. Alcock, *Adv. Inorg. Chem. Radiochem.*, 1972, **15**, 1.

33. G. R. Desiraju and R. Parthasarathy, *J. Am. Chem. Soc.*, 1989, **111**, 8725.

34. Z. Xie, B.-M. Wu, T. C. W. Mak, J. Manning and C. A. Reed, *J. Chem. Soc., Dalton Trans.*, 1997, 1213.

35. G. Wulfsberg and A. Weiss, *Ber. Bunsen-Ges. Phys. Chem.*, 1980, **84**, 474.

36. R. J. Kulawiec and R. H. Crabtree, *Coord. Chem. Rev.*, 1990, **99**, 89.

37. M. R. Colsman, T. D. Newbound, L. J. Marshall, M. D. Noirot, M. M. Miller, G. P. Wulfsberg, J. S. Frye, O. P. Anderson and S. H. Strauss, *J. Am. Chem. Soc.*, 1990, **112**, 2349.

38. V. P. Feshin, G. V. Dolgushin, M. G. Voronkov, Ju. E. Sapozhnikov, Ja. B. Jasman and V. I. Shirjaev, *J. Organomet. Chem.*, 1985, **295**, 15.

39. N. W. Alcock and R. M. Countryman, *J. Chem. Soc., Dalton Trans.*, 1977, 217.

40. G. K. Semin, T. L. Khotsyanova, S. I. Gushin and S. A. Petukhov, *Chem. Phys. Lett.*, 1985, **114**, 147.

41. H. Ikezwa, M. Takahashi, M. Takeda and Y. Ito, *Bull. Chem. Soc. Jpn.*, 1993, **66**, 1959.

42. A. Karipides and K. Peiffer, *Inorg. Chem.*, 1988, **27**, 3255.

43. M. Epple and H. Kirschnick, *Chem. Ber. Recl.*, 1997, **130**, 291.

44. D. N. Kravtsov, A. P. Zhukov, B. A. Faingor, El. M. Rokhlina, G. K. Semin and A. N. Nesmeyanov, *Bull. Acad. Sci. USSR, Div. Chem. Sci.*, 1968, 1611.

45. G. Wulfsberg, R. J. C. Brown, J. Graves, D. Essig, T. Bonner and M. Lorber, *Inorg. Chem.*, 1978, **17**, 3426.

46. G. Wulfsberg, D. Jackson, W. Ilsley, S.-Q. Dou, A. Weiss and J. Gagliardi, Jr, *Z. Naturforsch., A: Phys. Sci.*, 1992, **47a**, 75.

47. M. F. Richardson, G. Wulfsberg, R. Marlow, S. Zaghonni, D. McCorkle, K. Shadid, J. Gagliardi, Jr and B. Farris, *Inorg. Chem.*, 1993, **32**, 1913.

48. R. Meyer, J. Gagliardi, Jr and G. Wulfsberg, *J. Mol. Struct.*, 1983, **111**, 311.

49. G. Wulfsberg, J. Yanisch, R. Meyer, J. Bowers and M. Essig, *Inorg. Chem.*, 1984, **23**, 715.

50. R. Harrison, A. M. Arif, G. Wulfsberg, R. Lang, T. Ju, G. Kiss, C. D. Hoff and T. G. Richmond, *J. Chem. Soc., Chem. Commun.*, 1992, 1374.

51. S. H. Strauss, *Chem. Rev.*, 1993, **93**, 927.

52. R. F. Jordan, *Adv. Organomet. Chem.*, 1991, **32**, 325.

53. Y. Sun, R. Ev. H. Spence, W. E. Peirs, M. Parvez and G. P. A. Yap, *J. Am. Chem. Soc.*, 1997, **119**, 5132.

54. U. Thewalt and H.-P. Klein, *Z. Kristallogr.*, 1980, **153**, 307.

55. D. Brinkmann, *Physica C*, 1988, **153–155**, 75.

56. E. A. C. Lucken, *Z. Naturforsch., A: Phys. Sci.*, 1994, **49a**, 155.

57. L. Ramakrishnan, S. Soundararajan, V. S. S. Sastry and J. Ramakrishna, *Coord. Chem. Rev.*, 1977, **22**, 123.

58. T. L. Brown, *J. Mol. Struct.*, 1980, **58**, 293.

59. T. B. Brill, *Adv. Nucl. Quadrupole Reson.*, 1977, **3**, 131.

60. R. A. LaRossa and T. L. Brown, *J. Am. Chem. Soc.*, 1974, **96**, 2072.

61. Y.-N. Hsieh, G. V. Rubenacker, C. P. Cheng and T. L. Brown, *J. Am. Chem. Soc.*, 1977, **99**, 1384.

62. G. V. Rubenacker and T. L. Brown, *Inorg. Chem.*, 1980, **19**, 398.

Nuclear Resonance Vibrational Spectroscopy (NRVS)

Weiqiao Zeng, Nathan J. Silvernail, W. Robert Scheidt and J. Timothy Sage

Northeastern University, Boston, MA, USA and University of Notre Dame, Notre Dame, IN, USA

Method Summary 1
1 Introduction 2
2 Technical Background 2
3 Applications: Heme Proteins/Porphyrins 10
4 Acknowledgments 19
5 End Notes 19
6 Abbreviations and Acronyms 19
7 Further Reading 19
8 References 19

METHOD SUMMARY

Acronyms, Synonyms

- Nuclear Resonance Vibrational Spectroscopy (NRVS)
- Nuclear Resonant Inelastic X-ray Scattering (NRIXS)
- Nuclear Inelastic Scattering (NIS)
- Phonon-assisted Mössbauer effect

Measured physical quantities

- Simultaneous excitation of Mössbauer nucleus and vibrational quanta; vibrational features appear as sidebands on recoilless resonance.

Information available

- Complete vibrational spectrum of probe nucleus.
- isotope-specific; access to individually labelled metal sites.

Information not available, limitations

- no direct sensitivity to vibrations of other atoms;
- resolution slightly lower than Raman or infrared (IR).

Examples of questions that can be addressed

- Strength of metal coordination
- Energetic cost of probe displacement
- Distinguish metal-ligand vibrations from cofactor or peptide vibrations
- Local versus global character of active site vibrations

Major advantages

- selective to vibrations of Mössbauer isotope;
- quantitative information on vibrational amplitudes, as well as frequencies;
- single crystal measurements selective for motion along X-ray beam;
- applicable to photolabile samples;

- equally applicable to all ligation and oxidation states;
- direct comparison to predicted vibrational frequencies, amplitudes, and directions.

Major disadvantages

- Low count rate experiments; limited to highly specialized synchrotron beam lines.
- Limited range of accessible nuclei with current technology; primarily ^{57}Fe for bioinorganic applications.

Sample constraints

- requires isotopic enrichment with Mössbauer isotope;
- high concentrations (5–10 mM) of probe nucleus required;
- volume approximately 100 µL (depending on beam size);
- detailed interpretation requires cryogenic temperature.

1 INTRODUCTION

Mössbauer experiments (*see* ***Mössbauer Spectroscopy***) rely on constraining the probe nucleus in a solid in order to enable the recoilless absorption of incident γ rays.[1] However, this does not stop the probe nucleus from undergoing vibrational motions. Soon after the Mössbauer effect was discovered, it was suggested that it could be extended to measure the vibrational spectrum of the Mössbauer nucleus in the solids by tuning the photon energy to excite vibrational energy levels coincident with the nuclear excitation.[2,3] This suggestion is the genesis of nuclear resonance vibrational spectroscopy (NRVS).

Typical vibrational quanta lie in the order of tens of meV ($1\,\text{MeV} \approx 8\,\text{cm}^{-1}$); however they correspond to inconveniently large Doppler velocities on the order of hundreds of meters per second. As a result, practical experimental realization of this idea required the development of appropriate technology at brilliant third-generation synchrotron radiation facilities, where X-rays can be generated and tuned over the range needed to excite vibrational quanta. This was first accomplished only about a decade ago.[4–6] NRVS has become the most common terminology for applications of this method to inorganic and bioinorganic systems.[7,8] However, the same technique is described in the literature using alternate names, including nuclear resonant inelastic X-ray scattering (NRIXS),[9] nuclear inelastic scattering (NIS),[10] and the phonon-assisted Mössbauer effect.[11]

In traditional vibrational methods such as Raman or IR spectroscopy (*see* ***Vibrational Spectroscopy***), only vibrational modes allowed by selection rules will appear in the spectra. To help assign the modes, isotope difference spectra are used. But owing to selection rules, some modes do not appear in the spectrum. Spectral congestion also raises difficulty in resolving modes with close frequencies, particularly for macromolecules containing thousands of atoms.

NRVS is both more selective and more comprehensive than Raman or IR. NRVS reveals all vibrations of the probe nucleus, ignoring motions of all other atoms. ^{57}Fe, with a nuclear resonance energy $E_0 = 14.4125\,\text{kev}$, is a Mössbauer isotope with favorable properties for currently available sources. Moreover, iron plays important roles in many proteins, including heme proteins and iron–sulfur proteins.[12]

Synchrotron-based nuclear resonance methods have revealed the vibrational dynamics of the iron atom in numerous systems, including alloys, amorphous materials, nanomaterials, and materials under high pressure.[9,13–15] The above-mentioned selectivity for the probe nucleus is particularly valuable for biological macromolecules, which may contain many thousands of atoms, but a localized active site is often the true center of interest. Since its availability,[4–6] NRVS has been applied to study the vibrational dynamics of Fe in proteins,[7,11,16–19] porphyrin model compounds,[8,20–26] and iron–sulfur clusters.[27–29] It is shown that NRVS can provide frequencies, amplitudes, and directions for Fe vibrations in the samples. It helps to clarify mode assignments in vibrational spectra and reveals many important vibrational modes of Fe that cannot be seen by other methods. In particular, NRVS reveals low-frequency motions of the Fe down to below $100\,\text{cm}^{-1}$ that control biological reactions. The applications presented here use ^{57}Fe as the probe nucleus, but the principle applies to other Mössbauer isotopes such as ^{119}Sn, ^{83}Kr, ^{61}Ni, and ^{67}Zn if appropriate sources are available.

2 TECHNICAL BACKGROUND

2.1 Overview of Experiment

NRVS is related to Mössbauer spectroscopy (*see* ***Mössbauer Spectroscopy***), but it cannot be easily realized using conventional Mössbauer equipment. Practical NRVS experiments target the sample containing the probe nucleus (^{57}Fe, for example) with X-rays generated by a synchrotron radiation facility. The incident photon energy varies around the nuclear resonance energy $E_0 = 14.4125$ kev with a typical resolution of about $1\,\text{meV} \approx 8\,\text{cm}^{-1}$ sufficient to provide vibrational resolution. It can be tuned to more than 100 meV from E_0 to explore sidebands that result from excitation of vibrations consistent with population of the nuclear excited state. The energy range must be large enough to include all vibrations with significant Fe amplitude, with a resolution sufficient to resolve individual vibrational modes. The energy bandwidth is much larger than the hyperfine splittings detected in conventional Mössbauer measurements (*see* ***Mössbauer Spectroscopy***), and all of the nuclear sublevels are excited in these synchrotron-based experiments.

Figure 1 depicts a typical sequence of events started by absorption of an incident photon with an energy near the nuclear excited state energy E_0. The ^{57}Fe nucleus has an excited state lifetime of 141 ns, and excited nuclei have two decay channels. About 10% of them reemit a 14.4 kev photon. For recoilless absorption, where no vibrational levels are excited, time-resolved measurements of 14.4 kev photons scattered in the forward direction reveal information on hyperfine interactions comparable to conventional Mössbauer spectroscopy (*see* ***Mössbauer Spectroscopy***). The remaining nuclei expel electrons from the atomic K shell, followed by 6.4 kev atomic fluorescence when an electron drops from a higher level to fill this hole. These delayed signals at 6.4 and 14.4 kev indicate nuclear resonance absorption of the X-ray and constitute the NRVS signal. The relative contribution of 6.4 and 14.4 kev photons will depend on sample thickness and detection efficiency.

2.2 Source Characteristics and Detection

Because of the extremely narrow energy window selected, practical NRVS measurements require the highest X-ray brilliance currently available at third-generation light sources. At present, there are three major synchrotron radiation sources for nuclear resonance experiments: beam line 3ID at the Advanced Photon Source (APS) at Argonne National Lab, in the USA,**[30]** beam lines ID18 and ID22N at the European Synchrotron Radiation Facility (ESRF) in France,**[31]** and beam line BL09XU at SPring8 in Japan.**[32]** These are public beam lines and users can submit research proposals to apply for beam time for experiments.

Figure 2 illustrates the experimental setup at the APS. Separated electron bunches circulate at a speed very close to the speed of light in the storage ring, which is 1100 m in circumference. X-rays are generated over a broad bandwidth when the electrons pass through the undulator. Diffraction from perfect single crystals selects a narrow range of energies that meet the Bragg diffraction condition.

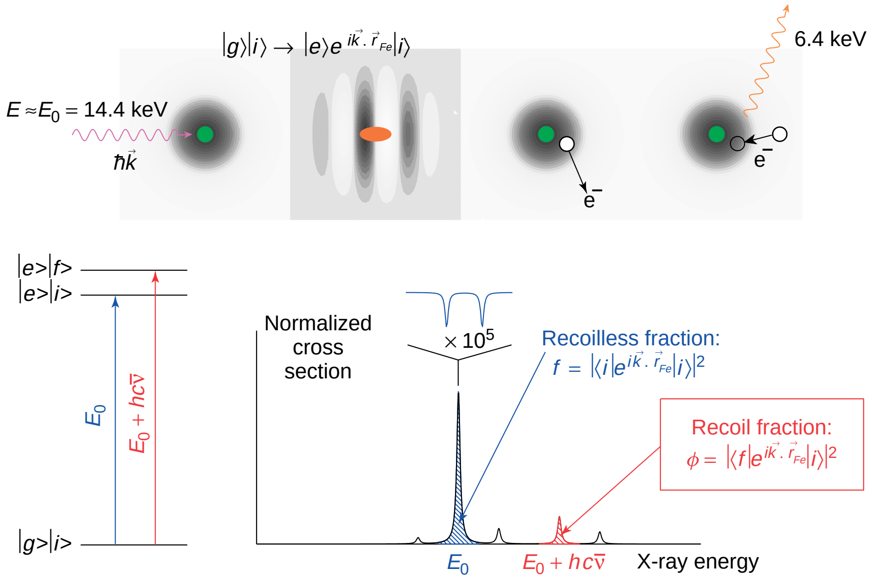
$|g\rangle|i\rangle \rightarrow |e\rangle e^{i\vec{k}\cdot\vec{r}_{Fe}}|i\rangle$
6.4 keV
$E \approx E_0 = 14.4$ keV
$\hbar\vec{k}$
e$^-$
e$^-$
$|e>|f>$
$|e>|i>$
$|g>|i>$
E_0
$E_0 + hc\bar{\nu}$
Normalized cross section
$\times 10^5$
Recoilless fraction:
$f = |\langle i|e^{i\vec{k}\cdot\vec{r}_{Fe}}|i\rangle|^2$
Recoil fraction:
$\phi = |\langle f|e^{i\vec{k}\cdot\vec{r}_{Fe}}|i\rangle|^2$
E_0
$E_0 + hc\bar{\nu}$
X-ray energy

Figure 1 Excitation of the ^{57}Fe resonance at $E_0 = 14.4125$ kev. Absorption of a 14.4 kev photon by a hypothetical free nucleus (top) in an initial state $|i\rangle$ would leave it in a final state $|f\rangle = \exp(i\vec{k}\cdot\vec{r}_{\text{Fe}})\,|i\rangle$, in order to conserve momentum. The primary decay channel for the nuclear excited state is to expel one electron from the atomic K shell, which is followed by 6.4 kev fluorescence when an electron drops from a higher energy level to fill the resulting vacancy. Emitted 6.4 kev photons, together with 14.4 kev photons emitted from the nuclear excited state, are delayed with respect to the excitation by a time on the order of the 141 ns nuclear excited state lifetime, and constitute the detected nuclear resonance signal. In a realistic experimental situation (bottom), the nucleus is bound to neighboring atoms, final states are quantized, and a series of vibrational sidebands appear, corresponding to transitions to a final vibrational state $|f\rangle$ with energy $hc\bar{\nu}$ coincident with the nuclear excitation. Each transition appears at an energy $E_0 + hc\bar{\nu}$ with a relative area $|\langle f|\exp(i\vec{k}\cdot\vec{r}_{\text{Fe}})|i\rangle|^2$. Unlike conventional Mössbauer measurements, synchrotron-based measurements do not directly resolve hyperfine splittings of the recoilless resonance ($|f\rangle = |i\rangle$) at $E = E_0$

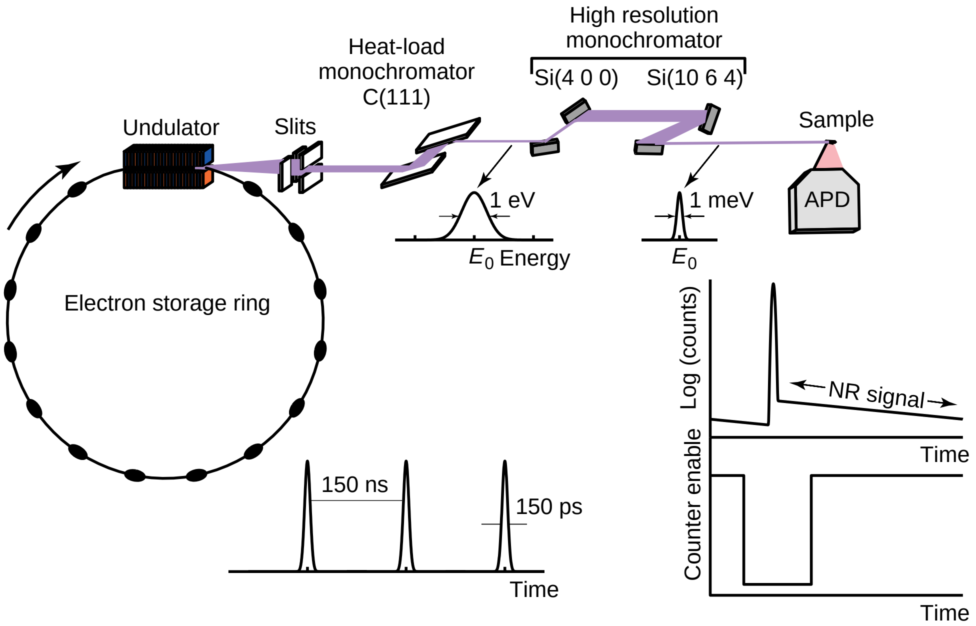

Figure 2 Experimental arrangement for measurements of the ^{57}Fe nuclear resonance at the Advanced Photon Source (APS). In the standard fill pattern, electron bunches with a duration of 100 ps are separated by 153 ns. X-ray pulses are generated when alternating magnetic fields in the undulator accelerate these electron bunches. The spectral bandwidth of the X-rays is reduced to ~1 eV by the heat-load monochromator and to ~1 meV by the high-resolution monochromator. At the sample, the flux of the beam is about 10^9 photons/s. APD indicates the avalanche photodiode used to detect emitted X-rays. The lower right inset illustrates that counting is enabled only for times well-separated from the X-ray pulse, so that only delayed photon emission resulting from decay of the nuclear excited state contributes to the experimental signal

Following the heat-load monochromator, the X-ray bandwidth is narrowed to approximately 1 eV and centered on the nuclear resonance energy (14.4 kev for ^{57}Fe). The high-resolution monochromator[33] further reduces the X-ray bandwidth to about 1 meV and motorized scanning of this monochromator tunes the energy over a range (typically within 100 meV of the resonance) adequate to explore excitation or annihilation of vibrational quanta. The X-ray flux at the sample is about 10^9 photons/s (~10 μW), which is very low compared to typical milliwatt beam powers in laser-based Raman experiments (*see* ***Vibrational Spectroscopy***). Additional X-ray optics may reduce the beam size. The cross section of the beam at the sample point is currently about $0.5 \times 0.5\,\text{mm}^2$ at station D of beam line 3ID at APS.

Detection of nuclear resonance signals exploits the time structure of the electron bunches circulating in the storage ring. The standard fill pattern at the APS, with bunches separated by 153 ns, is favorable for ^{57}Fe measurements. Ideally, each bunch is about 100 ps in length. When the resulting X-ray pulse hits the sample, it interacts with the ^{57}Fe nuclei, as well as with electrons. Strong prompt signals as high as 6 MHz result from electronic scattering coincident with the X-ray pulse. This signal is not related to the nuclear resonance at all, and the counting electronics are gated off during a time interval surrounding the arrival time of the X-ray pulse (see inset in Figure 2). The X-ray photon can be absorbed by the ^{57}Fe nucleus only when its energy matches the nuclear resonance transition energy (with or without excitation or annihilation of vibrational quanta). Photons emitted as a result of nuclear excitation arrive with a delay on the order of the lifetime of the nuclear excited state (141 ns for ^{57}Fe). The maximum delayed count rate near E_0 is typically on the order of 100 Hz for protein samples and 1000 Hz for model compounds with appropriate concentrations described in the next section. The vibrational signal is substantially weaker.

The avalanche photodiode detector (APD) has nanosecond time resolution and is controlled by timing circuits so that only delayed signals are counted to give a NRVS spectrum. Under favorable operating conditions, electronic noise is the main source of background. The APD is designed to work at room temperature, and care must be taken to avoid unwanted noise generated by cold air from a nearby cryostat. Electronic timing errors or beam fill errors may also contribute to background noise by causing electronically scattered photons to register as delayed counts. An acceptable noise level of 0.03 Hz or less can usually be achieved with an X-ray flux of 10^9 photons/s.

2.3 Sample Characteristics

Several factors have to be considered when preparing samples for NRVS measurements.

First, the sample must be isotopically enriched with ^{57}Fe or other Mössbauer nucleus of interest. Small molecule samples such as porphyrins enriched with up to 95% ^{57}Fe are prepared according to the small scale metalation procedure of Landergen and Baltzer.[34] Proteins are usually enriched with ^{57}Fe through reconstitution. For many heme proteins, the Fe protoporphyrin [Fe(PPIX)] can be extracted using Teale's method[35] and then replaced with commercially available [^{57}Fe(PPIX)].[7,18] Harsher procedures are required to extract and replace the Fe from the covalently bonded heme in cytochrome *c*.[36] Proteins can also be expressed, for example in *Escherichia coli*, with ^{57}Fe supplied in the culture medium. In favorable cases, reconstitution may provide an opportunity to selectively label one of multiple distinct Fe sites, a feature often exploited in Mössbauer spectroscopy (*see* ***Mössbauer Spectroscopy***).

Another important factor is the sample concentration or, more specifically, the ^{57}Fe concentration, which must be high enough to yield reasonable signal strength. Solutions of protein enriched with ^{57}Fe at a single site and which are of concentration 5–10 mM yield interpretable NRVS data at $8\,\mathrm{cm}^{-1}$ resolution within 20–30 hours of beam time at the APS.[18] The small size of molecules designed to mimic protein-active sites allows significantly higher concentrations, often reducing measurement times to a few hours. For porphyrin samples, using a $1 \times 2 \times 10\,\mathrm{mm}^3$ sample holder, a sample of up to ∼26 mg can be used, corresponding to $1–2 \times 10^{19}$ ^{57}Fe nuclei.

Sample purity is a key concern. The NRVS experiment is a bulk technique sampling all ^{57}Fe nuclei, and impurities that also contain the probe nucleus may confound quantitative data interpretation. Impurities may be introduced during sample preparation or may result from sample instability during measurement. Because of this, care must be taken to ensure purity and reproducibility as judged by Mössbauer (*see* ***Mössbauer Spectroscopy***), single-crystal X-ray diffraction, electronic absorption spectroscopy (*see* ***Electronic Spectroscopy***), Raman spectroscopy or other qualitative techniques.

To make full use of the incident beam, the sample volume should be large enough to fill the beam. Single crystals should ideally exceed the area of the beam ($0.5 \times 0.5\,\mathrm{mm}^2$) to maximize signal. Single crystals are aligned using a four-circle diffractometer, which adds the additional degree of freedom (χ) needed for single-crystal alignments. Careful observation of crystal morphology along with molecular packing acquired on natural abundance iron samples may allow an approximate alignment. In the ideal crystalline case, the porphyrins are all coplanar. It is beneficial to place the porphyrin plane, or plane normal to the porphyrin plane, along the goniometer arcs. Use of an eucentric goniometer head for all alignments allows for fine orientation adjustment without significant recentering.

Sample holders for powders and solutions consist of a high-density polyethylene (HDPE) block with a $1 \times 2 \times 10\,\mathrm{mm}^3$ milled well. The sample is placed into the well, a small Teflon seal is placed on the block, and a sapphire window is placed over the seal. Brass screws attach the HDPE block to a round copper block to facilitate heat transfer to the cold finger of a helium-flow cryostat. Some practice may be needed to avoid bubbles created when the Teflon seal or sapphire wicks viscous protein solutions out of the well. If possible, it may be helpful to freeze the solution in the cell before placing the sapphire window. Isolated polycrystalline samples are mulled with a minimal amount of Apiezon M vacuum grease on a microscope slide using a *non*-metallic instrument and placed in the sample holder.

In the experiment, the high-resolution monochromator tunes the incident X-ray energy through the recoilless nuclear transition energy E_0. The energy range must include all vibrational signals for accurate normalization. A typical range around E_0 is $[-30, 80]$ meV for heme proteins or porphyrins at $T < 30\,\mathrm{K}$, but larger ranges may be required at higher temperature or for certain samples to enable data normalization, at the cost of increased measurement time. The energy sampling interval should be less than the resolution of the monochromator. A step size of 0.25 meV is typical for 1 meV energy resolution, with an accumulation interval of 5 s/point, allowing completion of one full energy scan within 1 h. Typically, multiple scans are averaged to improve signal-to-noise ratios, and to identify possible scan-to-scan variations resulting from instrumental artifacts or from sample instability. For porphyrin model compound samples, either in the form of crystal or powder, three to four scans may be enough to obtain acceptable data quality. Satisfactory results on concentrated protein samples may require more than 20 scans (about 1 d).

Unless there is specific interest in temperature dependence, data interpretation is simplest at the lowest temperatures that are conveniently achievable. Crystal samples can be placed in a cold nitrogen gas stream and powder or solution samples can be mounted on a helium-cooled cryostat. Figure 3 shows NRVS data recorded for an Fe(TPP)(1-MeIm)(NO) crystal at two different temperatures with the heme plane lying nearly parallel to the X-ray beam. Differences between the two spectra are apparent both for the central line (Figure 3 inset) and for the higher frequency signals. Thermal excitation of low-frequency vibrations with increasing temperature leads to the appearance of unresolved shoulders on all bands, including the recoilless line (inset), reducing the effective experimental resolution. Substantial ''anti-Stokes'' signals resulting from vibrational deexcitation also appear at energies below E_o as the temperature increases, necessitating measurement over a larger frequency range to ensure spectral normalization. However, the relative intensities of these ''anti-Stokes'' signals provide a useful measure of sample temperature (see next section).

Figure 4 shows a typical design of a helium-cooled cryostat, which balances the competing requirements for X-ray detection and temperature control. Samples are loaded in the

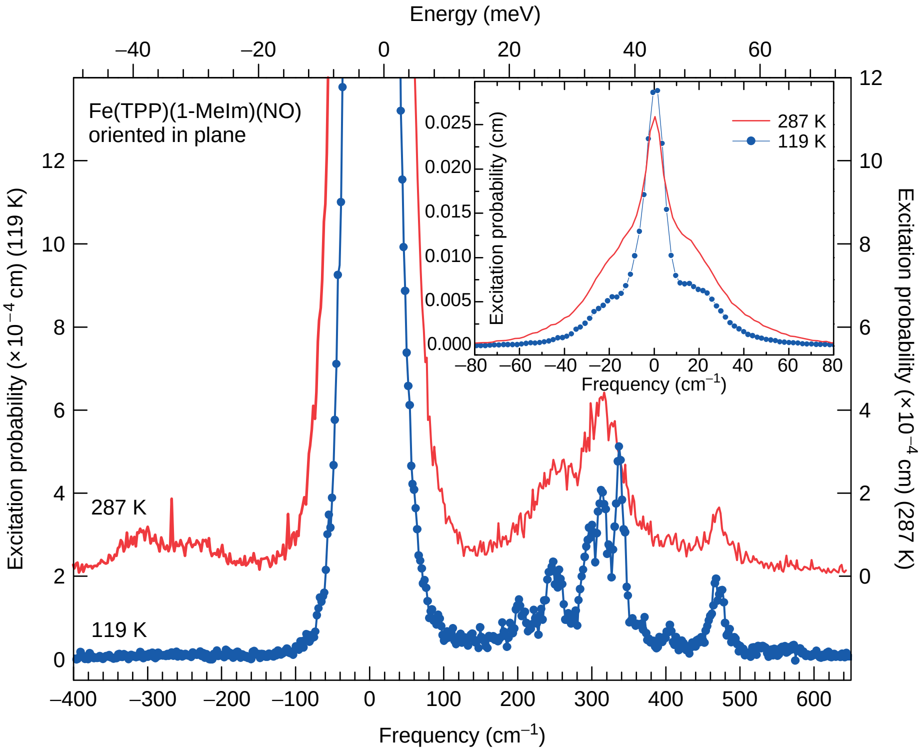

Figure 3 NRVS data recorded on a single crystal of Fe(TPP)(1-MeIm)(NO), oriented with the X-ray beam 13.8° from the planes of all porphyrin molecules, at two different temperatures, 119 K (blue) and 287 K (red). The two curves in the main panel are normalized according to Lipkin's first moment sum rule (equation 2) and scaled up by 200 times. It is apparent that increasing temperature leads to effective line broadening and to signals at negative energy resulting from vibrational deexcitations. The inset shows an expanded view of the recoilless line, with shoulders due to low-frequency lattice vibrations

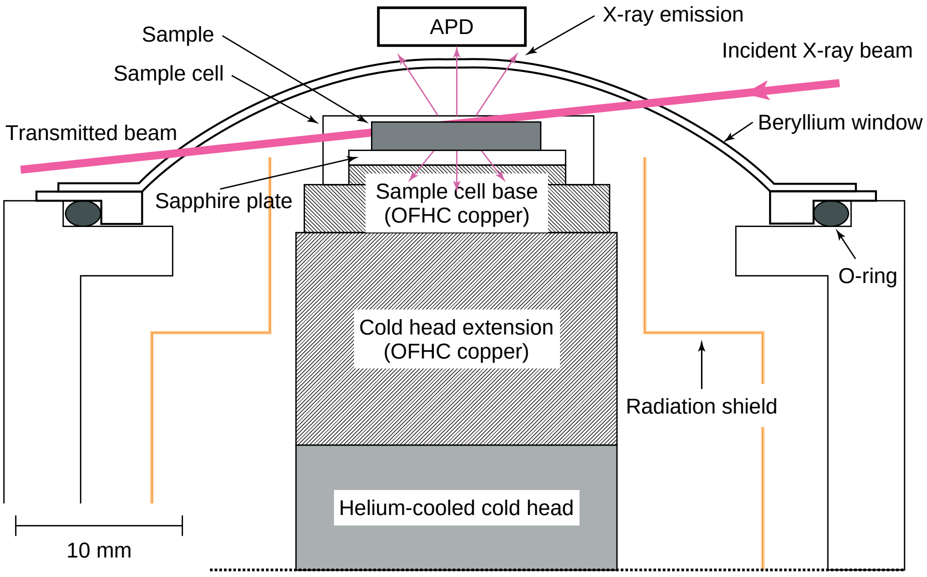
APD
X-ray emission
Sample
Sample cell
Incident X-ray beam
Transmitted beam
Beryllium window
Sapphire plate
Sample cell base
(OFHC copper)
O-ring
Cold head extension
(OFHC copper)
Radiation shield
Helium-cooled cold head
10 mm

Figure 4 Typical cryostat design for solution and powder samples. This design features an expanded beryllium dome, which allows detection of the transmitted beam as well as the emitted X-rays that contribute to the NRVS signal. The Be dome and a thin polyethylene window on the front face of the sample cell minimize the absorption at 6.4 and 14.4 kev. A sapphire plate provides excellent thermal contact between the sample cell and the cryostat cold head, as well as allowing optical access for off-line Raman measurements to monitor sample integrity. Sample temperatures in the 20–30 K range are typically achieved for both solutions and powders

cup, which has good thermal contact with the cold head. The cryostat chamber is kept in a vacuum state of 10^{-5} mbar during experiments. The beryllium dome is transparent to X-rays. The APD detector is placed as close as possible to the sample to maximize the solid angle over which X-rays are collected. If desired, a second APD can be used to detect the forward scattering beam.

2.4 Data Collection

As with all beam line experiments, advance planning is essential. The availability of beam time is not entirely predictable, may be awarded with relatively short notice, and cannot be rescheduled because of the large number of users affected. Facilities for preparing or modifying samples will be very limited or nonexistent. Moreover, the round-the-clock attention required for successful NRVS data collection, particularly on samples with low count rates, provides little opportunity for sample modification.

If a previous user has performed measurements using the same nuclear resonance, data collection may commence near the start of the assigned beam time. Otherwise, time must be invested in adjusting the undulator, aligning the monochromator, finding the resonance, optimizing energy resolution and throughput, and establishing appropriate voltage thresholds and timing for detection of delayed counts. These are specialized operations that are usually performed by trained beam line personnel, who may also handle certain local arrangements such as the availability of cryogens.

Users take primary responsibility for all other aspects of data collection and analysis, although further guidance from beam line personnel may be required if problems arise. Because experimental problems occur, data are nearly always recorded as multiple energy scans, which are subsequently summed. The energy sampling interval is usually chosen to be smaller than the energy resolution (typical values are 0.25 and 1 meV), so that scans containing unphysical features narrower than the experimental resolution can be excluded. Other reasons for excluding individual scans include high background count rate and interruptions in the X-ray beam. Excluded scans may indicate a problem that will compromise further data collection, and such problems should be identified and addressed before continuing.

The actual beam energy typically deviates slightly from the value selected by the nominal monochromator position, because the lattice constants of the crystals respond to temperature variations. Small energy corrections are automatically determined at each monochromator setting from temperature sensors in thermal contact with the crystals. Data summation software must account for the resulting small scan-to-scan variations in energy values. Crystal temperatures should be continually monitored for changes larger than this level, and the start of new scans is usually delayed to allow reestablishment of equilibrium following any event that substantially alters crystal temperature, such as an interruption in the X-ray beam. Ideally, the monochromator is housed in a separate enclosure upstream from the experimental station containing sample and detector, in order to keep temperature variations below 10 mK over the course of an energy scan.

Energies should be reproducible from scan to scan, with the exception of the small variations just described. However, it is customary to obtain data on a standard sample to verify the accuracy of the overall energy scale. This may be a sample whose vibrational frequencies have been well established in the scientific literature, or a sample measured at a previous data collection run. An alternative procedure involves measuring a concentrated sample, such as an ^{57}Fe foil whose temperature can be accurately measured, and adjusting the energy scale to ensure that $S(E)/S(-E) = \exp(E/k_B T)$. Such overall energy scale corrections may be on the order of 1%.

Data analysis usually involves subtraction of the recoilless absorption line at $E = E_0$, which has the shape of the monochromator energy resolution function, because the fundamental linewidth is orders of magnitude smaller than the experimental resolution. Delayed 14.4 kev photons scattered in the forward direction from a ^{57}Fe foil carry no vibrational signal and provide a straightforward experimental determination of the resolution function. Appropriate experimental design may allow this measurement in parallel with the NRVS measurement, using the X-ray beam transmitted through the sample (Figure 4). However, if the monochromator is stable, it may be sufficient to average two to three scans of the delayed forward scattering measured over a limited energy range (typically ±10 meV) at occasional intervals during the data collection period.

Continuous monitoring of experimental performance is essential in order to minimize the number of scans that ultimately need to be excluded because of experimental problems, and thus to ensure optimal use of limited beam time. Individual scans should be compared periodically to monitor sample stability, although experience to date has revealed no evidence of radiation damage resulting from exposure of cryogenic samples to the low X-ray flux in NRVS measurements. Sample temperature must also be monitored because averaging of scans at different temperatures may interfere with accurate data analysis.

Monochromator throughput should be recorded at the beginning of each scan, along with user-determined experimental parameters such as energy sampling interval and dwell time. Efficient use of measurement time requires maintaining the incident X-ray flux, and may necessitate occasional adjustments to monochromator alignment to maximize throughput, with guidance from beam line personnel if needed. Depending on monochromator design and on which crystal is adjusted, this may require redetermination of the experimental resolution function.

It is especially important to systematically monitor the level of background noise from the detector, because apparently unobtrusive increases in background noise may degrade the experimental signal-to-noise ratio as badly as decreases in X-ray flux. A straightforward noise check is to monitor the detector signal after setting the energy 200 meV below the recoilless resonance energy E_0, where delayed counts cannot be attributed to genuine nuclear resonance signal. Under favorable operating conditions at the APS, the count rate may be 0.02–0.03 counts/s. Action must be taken if the background count rate rises significantly above this level, particularly for low count rate samples such as protein solutions.

The most common reasons for elevated background levels are electronic detector noise and timing problems. Sources of electronic noise, particularly machinery such as vacuum pumps, must be placed outside the experimental station and the detector must be protected from possible temperature variations resulting from proximity to cryogenically cooled samples. Users can exercise limited control over noise levels by setting the voltage threshold of a discriminator to exclude low amplitude voltage pulses while registering larger pulses due to genuine photon detection events.

Beam fill errors can create stray electrons that are temporally separated from the main bunch, leading to detection of electronically scattered photons within the time interval where delayed emission from the nuclear excitation is expected. This signal will vary weakly across the narrow energy window of a NRVS scan, and thus contribute to a uniform background. In many cases, adjustments to the width and delay time of the gate signal can eliminate this contribution to background.

Software available at the beam line allows individual energy scans to be selected and added, and the summed scans should be periodically examined during data collection in order to identify any unanticipated experimental problems. The software calculates each experimental energy from the monochromator position, with correction for temperature variations of the monochromator crystals if needed. A fit in the region of the intense recoilless absorption line determines zero energy precisely. Measured counts are then binned according to the calculated energies and added. Variations of the incident X-ray flux during each energy scan are usually small, but are ordinarily measured and used to normalize the measured counts energy by energy in individual scans before summing. An optional input scale factor allows rescaling of the energy axis, if needed, to agree with energy calibration measurements. The data in Figure 3 are a sum of three to four scans, followed by an overall normalization as described in the following section.

2.5 Data Analysis

The measured NRVS signal is proportional to the number of resonant ^{57}Fe nuclei in the effective sample volume and to an excitation probability**[2]**

$$S(\bar{\nu}) = \sum_{if} p_i \left|\left\langle f|e^{i\vec{k}\cdot\vec{r}_{\mathrm{Fe}}}|i\right\rangle\right|^2 \mathcal{L}(\bar{\nu} - \bar{\nu}_{if}) \tag{1}$$

measured as a function of the energy separation $hc\bar{\nu} = E - E_0$ from the resonance energy E_0. Here, $|i\rangle$ and $|f\rangle$ represent the initial and final states of the nuclear center of mass. In thermal equilibrium, the occupation probabilities $p_i = \exp(-E_i/k_BT)/\sum_i \exp(-E_i/k_BT)$ weight the relative contribution of each initial state to the sum in equation (1), while the matrix element $\langle f|e^{i\vec{k}\cdot\vec{r}_{\mathrm{Fe}}}|i\rangle$ determines the contribution of the final states.

In the hypothetical scenario of absorption by a free nucleus (Figure 1, top), initial and final states both correspond to free translation of the nucleus and the only allowed final state $|f\rangle = e^{i\vec{k}\cdot\vec{r}_{\mathrm{Fe}}}|i\rangle$ corresponds to the absorbing nucleus recoiling with the momentum $\hbar\vec{k}$ of the incident photon. In this hypothetical situation, the excitation probability would consist of a single feature at an energy $E_0 + hc\bar{\nu}_R$ exceeding the nominal resonance energy E_0 by the amount of the nuclear recoil energy $hc\bar{\nu}_R = \hbar^2k^2/2m_{\mathrm{Fe}}$. This feature would have unit area, since the line shapes and the initial state probabilities are both normalized, $\int\mathcal{L}(\bar{\nu})\,\mathrm{d}\bar{\nu} = 1$ and $\sum_i p_i = 1$.

However, this freely recoiling state is not a stationary state of the Hamiltonian in relevant experimental situations, where the ^{57}Fe nucleus is bound to other atoms in a condensed phase. In general, a series of discrete lines appear in the spectrum (Figure 1, bottom), corresponding to a range of possible final states. Conventional Mössbauer spectroscopy relies on the presence of a narrow line ($f = i$) at E_0, with an area proportional to the recoilless fraction

$$f = \sum_i p_i \left|\left\langle i|e^{i\vec{k}\cdot\vec{r}_{\mathrm{Fe}}}|i\right\rangle\right|^2$$

to perform extremely high-resolution measurements of hyperfine interactions (*see* ***Mössbauer Spectroscopy***). In contrast, NRVS measurements exploit the appearance of a number of sidebands at energies separated from the resonance energy E_0 by the energy difference $hc\bar{\nu}_{if} = E_f - E_i$ between initial and final energy levels. Each sideband has an area

$$\phi = \sum_{if} p_i \left|\left\langle f|e^{i\vec{k}\cdot\vec{r}_{\mathrm{Fe}}}|i\right\rangle\right|^2$$

that can be considered a ‘‘recoil fraction’’. (Here, the sum over f is restricted to final states with a constant energy separation with respect to the initial state.)

The total spectral area is normalized, $\int S(\bar{\nu})\,\mathrm{d}\bar{\nu} = 1$, independent of the nuclear environment, since $\int\mathcal{L}(\bar{\nu})\,\mathrm{d}\bar{\nu} = 1$, and a simple closure argument ensures that $\sum_f \left|\left\langle f|e^{i\vec{k}\cdot\vec{r}_{\mathrm{Fe}}}|i\right\rangle\right|^2 = 1$. As a result, $f + \sum\phi = 1$, and situations that reduce the Mössbauer signal correspondingly strengthen the integrated NRVS signal. Lipkin**[37]** has shown that the first moment

$$\int_{-\infty}^{\infty} \bar{\nu}S(\bar{\nu})\mathrm{d}\bar{\nu} = \bar{\nu}_R \tag{2}$$

of the excitation probability yields the recoil energy. Since the recoil energy has a precisely determined value ($\bar{\nu}_R = 15.8\,\mathrm{cm}^{-1}$ for ^{57}Fe), equation (2) provides a practical recipe for normalizing the experimental data to obtain a signal proportional to the excitation probability.

NRVS data are commonly interpreted within a harmonic approximation,**[8,38]** which describes molecular vibrations in terms of independent oscillations along a set of normal coordinates $Q_a = \sum_j \vec{e}_{j\alpha} \cdot \vec{r}_j m_j^{1/2}$ related through a linear transformation to the Cartesian coordinates $\vec{r}_j$ of atoms j weighted by their masses m_j. Molecular rotation and translation lead to six modes having zero frequency. Projection of the transformation coefficients $\vec{e}_{j\alpha}$ onto the direction $\hat{k}$ of the X-ray wave vector $\vec{k} = (E_0/\hbar c)\,\hat{k}$ determines the recoil fraction

$$\phi_\alpha = \frac{\bar{\nu}_R}{\bar{\nu}_\alpha} f\,(\bar{n}_\alpha + 1)\,(\hat{k} \cdot \vec{e}_{j\alpha})^2, \tag{3}$$

which is the fractional contribution of a feature appearing at frequency $\bar{\nu}_\alpha$ to the area of the excitation probability $S_j\,(\bar{\nu})$ of atom j, resulting from a single excitation of vibrational mode α. These fundamental transitions ($n_\alpha \longrightarrow n_\alpha + 1$) dominate the observed data at high frequencies and low temperatures, but weak vibrational overtones and combinations can be resolved under favorable conditions.**[39]** Spectral features corresponding to deexcitation of mode α appear at frequency $-\bar{\nu}_\alpha$, with an area given by an expression identical to equation (3) but with the factor $\bar{n}_\alpha + 1$ replaced by $\bar{n}_\alpha$.[a] The latter features become significant at temperatures high enough (or frequencies low enough) that the mean occupation number $\bar{n}_\alpha = [\exp\,(hc\bar{\nu}_\alpha/k_B T) - 1]^{-1}$ of mode α becomes significant (e.g., Figure 3).

The spectral area provides quantitative information on the amplitude and direction of motion of the probe nucleus through the final factor $(\hat{k} \cdot \vec{e}_{j\alpha})^2$ in equation (3). This information can be determined for each mode using equation (3). Alternatively, further analysis of the data can yield an estimated vibrational density of states (VDOS)

$$D_{\hat{k}}\,(\bar{\nu}) = \sum_\alpha (\hat{k} \cdot \vec{e}_{j\alpha})^2 \mathcal{L}(\bar{\nu} - \bar{\nu}_\alpha) \tag{4}$$

for the probe atom. $D_{\hat{k}}\,(\bar{\nu})$ is normalized such that $\int D_{\hat{k}}\,(\bar{\nu})\,\mathrm{d}\bar{\nu} = 1$ and represents the contribution of motion of the probe atom along $\hat{k}$ to the total vibrational density of states $D\,(\bar{\nu}) = \sum_\alpha \mathcal{L}(\bar{\nu} - \bar{\nu}_\alpha)$, with $\int D\,(\bar{\nu})\,\mathrm{d}\bar{\nu} = 3N$.

Practical measurements involve averaging over a large ensemble of molecules. For randomly oriented molecules, as in a solution or a polycrystalline powder, $\langle(\hat{k} \cdot \vec{e}_{j\alpha})^2\rangle = \frac{1}{3}e_{j\alpha}^2$, the recoil fraction becomes

$$\phi_\alpha = \frac{1}{3}\frac{\bar{\nu}_R}{\bar{\nu}_\alpha} f\,(\bar{n}_\alpha + 1)\,e_{j\alpha}^2 \tag{5}$$

and the partial VDOS

$$D\,(\bar{\nu}) = \sum_\alpha e_{j\alpha}^2 \mathcal{L}(\bar{\nu} - \bar{\nu}_\alpha) \tag{6}$$

represents the contributions from probe motion in all three directions. (Note that $\int D\,(\bar{\nu})\,\mathrm{d}\bar{\nu} = 3$.) However, the directional information implicit in equations (3) and (4) is partially or completely retained in measurements on oriented single crystals (e.g., Figure 3), where the crystal structure restricts molecular averaging to a discrete set of orientations.

Figure 5 presents an example of the excitation probability $S\,(\bar{\nu})$ and the VDOS $D\,(\bar{\nu})$ for the iron atom in the molecule Fe(TPP)(1-MeIm)(CO), as determined from measurements on a polycrystalline sample. Sharp features in both representations of the experimental data clearly identify vibrational frequencies above $100\,\mathrm{cm}^{-1}$, although low-frequency vibrational features are more apparent in the VDOS representation. The VDOS also provides the most convenient estimate of the mode composition factor $e_{j\alpha}^2$, since the area of each feature directly yields the sum of $e_{j\alpha}^2$ values for all contributing vibrations. This avoids the need to remove the additional factors in equation (5) that contribute to the area of a feature in $S\,(\bar{\nu})$, with the subtleties associated with determining an appropriate value for the recoilless fraction f.**[8,39]** However, calculation of $D\,(\bar{\nu})$ from $S\,(\bar{\nu})$ involves implicit assumptions that may not be valid in some situations, for example, when more than one molecular species contributes to the experimental signal or when vibrational anisotropy is significant.

The program PHOENIX**[40]** implements the calculation of $D\,(\bar{\nu})$ from $S\,(\bar{\nu})$, using the Fourier-log deconvolution method.**[41]** This program reads two input data files containing the summed sample data and the experimental resolution function, and two input parameters, background and temperature, are specified. The background is typically estimated from the counts in the high or low energy limit of the sample data, where no genuine vibrational signal is expected. The initial temperature can be estimated from a temperature reading or from the relative size of features at negative frequency, but is usually iterated to obtain a consistent analysis. Most protein solutions and polycrystalline porphyrin samples are measured in a helium-flow cryostat at 20–30 K, while the single crystals are typically measured in a cold gas stream near 100 K. After subtraction of the background, the data are normalized to satisfy equation (2), thus providing the excitation probability $S\,(\bar{\nu})$.

Subtraction of the resolution function reveals the vibrational contribution $S'\,(\bar{\nu})$ to the excitation probability. PHOENIX adjusts the subtraction weight to achieve the best match to the one-phonon contribution to the vibrational signal near E_0 expected for a Debye frequency distribution $\left(D\,(\bar{\nu}) \propto \bar{\nu}^2\right)$. The Fourier-log algorithm**[5,41]** then yields the dominant first-order vibrational contribution

$$S_1\,(\bar{\nu}) = \frac{1}{3}\frac{\bar{\nu}_R}{\bar{\nu}_\alpha}\,(\bar{n}_\alpha + 1)\,D\,(\bar{\nu})$$

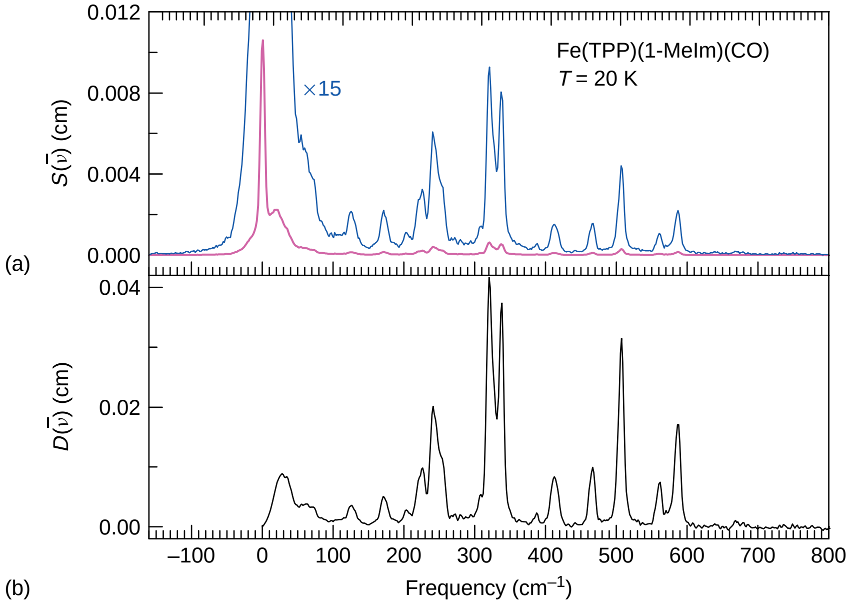

Figure 5 The excitation probability $S\,(\bar{\nu})$ (a) and corresponding Fe vibrational density of states $D\,(\bar{\nu})$ (b) of polycrystalline Fe(TPP)(1-MeIm)(CO). $S\,(\bar{\nu})$ results from normalization of summed experimental scans according to equation (2), and $D\,(\bar{\nu})$ results from Fourier-log deconvolution as implemented by the program PHOENIX[40]

to the excitation probability, from which the VDOS $D\,(\bar{\nu})$ is readily calculated.

Output results include a quantitative indication of how consistent the input temperature value is with the detailed balance condition $S'\,(\bar{\nu})\,/S'\,(-\bar{\nu}) = \exp\,(hc\bar{\nu}/kT)$. The recoilless fraction f and other vibrational properties that can be calculated from moments of $S'\,(\bar{\nu})$ according to sum rules given by Lipkin[37] are compared with values calculated directly from $D\,(\bar{\nu})$ as further consistency checks. Small adjustments in the values input for temperature and background are typically needed to achieve self-consistent results. In our experience, the resulting estimate of the sample temperature may be 10 K or more higher than the reading of a nearby sensor because of temperature gradients. Output spectral files include first-, second-, and higher-order contributions $S_1\,(\bar{\nu})$, $S_2\,(\bar{\nu})$, and $\sum_{n>2} S_n\,(\bar{\nu})$, to the excitation probability as well as the total vibrational contribution $S'\,(\bar{\nu}) = \sum_{n\geq 1} S_n\,(\bar{\nu})$ and the VDOS $D\,(\bar{\nu})$.

As noted above, the area of a peak in the VDOS provides a straightforward measure of the mode composition factor $e_{j\alpha}^2$ according to equation (6) (possibly summed over a number of unresolved modes). However, there are nontrivial approximations implicit in the calculation. In addition to the Debye approximation used to subtract the recoilless contribution, the Fourier-log algorithm assumes a unique environment for the probe atom and neglects vibrational anisotropy. The resulting errors are often smaller than the experimental uncertainty, particularly for protein samples. However, there may be situations where these assumptions are questionable, for example, if the probe nucleus occupies more than one distinct site. If there is reason to believe that this is not adequate, careful analysis of the recoil fraction according to equation (5) provides an independent estimate of $e_{j\alpha}^2$.

3 APPLICATIONS: HEME PROTEINS/ PORPHYRINS

3.1 Heme Proteins

NRVS represents the ultimate limit in vibrational selectivity, because it reveals the vibrational spectrum of an individual probe atom even when embedded in a complex environment such as a biomolecule containing thousands of other atoms. ^{57}Fe NRVS is thus an exquisite probe for the structure and dynamics of the immediate coordination sphere of the iron, which is the heart of the reactivity of numerous important proteins.

The earliest protein applications have involved myoglobin (Mb)[16,7,11], which can be reconstituted with ^{57}Fe and prepared at concentrations exceeding 10 mM. Early measurements required days of data collection, but continual experimental improvements now allow collection of interpretable data from 5–10 mM solutions in 20–30 h of beam time, as illustrated by the data shown for nitrosylmyoglobin (MbNO) in Figure 6.[18]

Fe–ligand vibrations dominate the NRVS signal. In this section, we survey the character of the observed modes for heme proteins, and briefly consider their importance for future

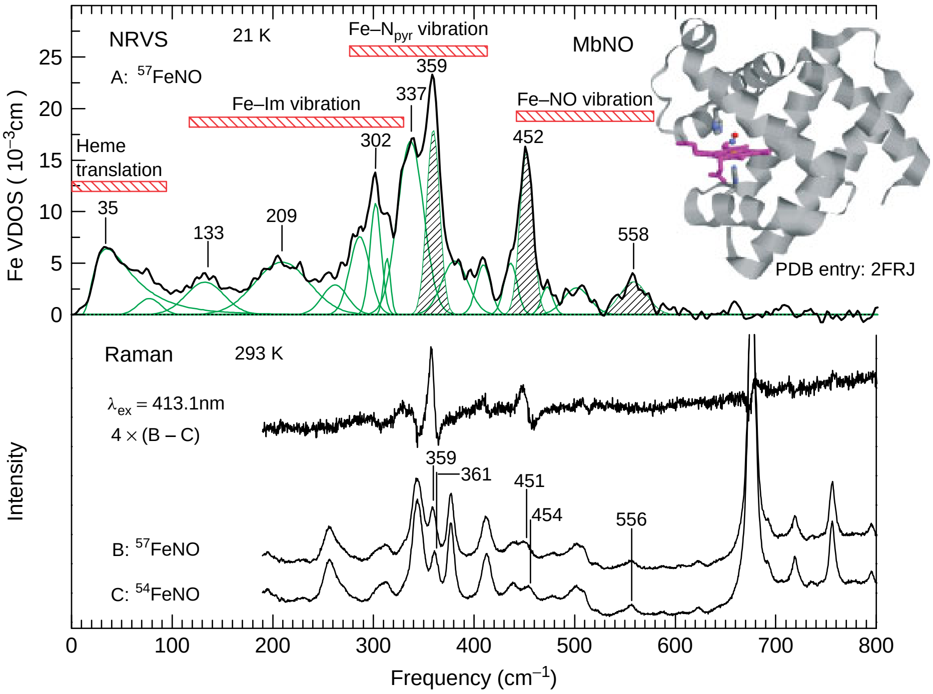

Figure 6 Comparison of NRVS and resonance Raman data on nitrosyl myoglobin (MbNO). (A) Fe VDOS determined from experimental NRVS data at 21 K. The peaks fit to the curve are also shown. Cross-hatched horizontal red bars indicate frequency ranges for Fe–ligand vibrations and for low-frequency vibrations attributed to translation of the entire heme. (B, C) Resonance Raman spectra of MbNO labeled with ^{57}Fe and ^{54}Fe, respectively, recorded at ambient temperature. The difference between these two spectra is expanded by a factor of 4. Raman-active vibrations that are sensitive to Fe mass also contribute strongly to the NRVS signal

applications. Subsequent sections will describe in greater detail the identification of these modes through comparison with data on single crystals of iron porphyrins and with the results of calculations.

The vibrational characteristics of MbNO are likely to be characteristic of other six-coordinate heme proteins having NO and histidine as axial ligands to the heme iron (Figure 6). Vibrations involving the FeNO fragment appear above 400 cm^{-1}. Simplified vibrational models have suggested that the nonlinear FeNO geometry leads to significant mixing of Fe–NO stretching and FeNO bending contributions to these modes.**[42]** Isotope substitution allows identification of the same vibrations in the Raman spectrum of MbNO in resonance with the heme Soret band.**[18]**

Quantitative comparison of isotopic frequency shifts with NRVS data suggests that motion of the nitrosyl N atom accounts for 80% of the mode energy for the higher frequency mode near 560 cm^{-1}.**[18]** The Fe amplitude, and consequently the NRVS signal, is thus relatively low. Although several modes contribute to this region of the Raman spectrum, the FeNO vibration is clearly identified by subtracting spectra of samples labeled with ^{14}NO and ^{15}NO.**[43,44]**

The FeNO vibration near 450 cm^{-1} is easily identified in both NRVS and Raman data for MbNO. Although FeNO bending and porphyrin vibrations also contribute to this mode, measurements on oriented single crystals of [Fe(TPP)(1-MeIm)(NO)] reveal that the Fe motion is primarily perpendicular to the plane of the porphyrin, as expected for stretching of the Fe–NO bond. We attributed the large frequency decrease relative to the approximately 530 cm^{-1} Fe–NO stretching frequency measured for five-coordinate NO derivatives of heme proteins and iron porphyrins to a significant weakening of the Fe–NO bond in the presence of the histidine ligand.**[18]**

NRVS measurements on MbCO**[7]** revealed the Fe–CO stretching and FeCO bending modes that have been extensively characterized using Raman measurements. The linear FeCO geometry allows observation of a pure Fe–CO stretching mode well described as a two-body Fe–CO oscillator.**[25]** Extensive studies have established a linear correlation between the Fe–CO and C–O stretching frequencies that is attributed to varying backbonding between Fe d_π and CO π^* orbitals controlled by the local electrostatic field.**[45–47]** As a result, this vibration is a well-calibrated probe of the local electrostatic environment.**[48]** In contrast, the mode mixing described above has complicated the establishment of such a correlation involving N–O stretching and Fe–NO vibrations.**[44,49–51]**

Each of these features contributes an area e_{Fe}^2 to the VDOS[b] that can be compared quantitatively with the frequency shift between ^{57}Fe and ^{54}Fe-labeled molecules observed using resonance Raman spectroscopy. For MbNO, the fitted area of the 452 cm^{-1} feature in the NRVS VDOS is 0.25, in reasonable agreement with the value $e^2_{\mathrm{Fe}} = 0.29$, obtained from the Raman isotope shift.[18] (see equation (7) below)

Although useful, practical Raman measurements on proteins are restricted to modes that couple to an electronic excitation such as the heme Soret transitions. A great advantage of NRVS is that it reveals the complete spectrum of ^{57}Fe vibrational dynamics even for nonheme centers that do not display Raman activity, such as the ferrous state of the iron–sulfur center in rubredoxin[52,17] or the FeMoCo cluster in nitrogenase.[53] Vibrations of the remaining heme Fe–ligand vibrations must also contribute to the VDOS derived from NRVS measurements, although none have been conclusively identified in extensive Raman investigations of six-coordinate diatomic ligand adducts of heme proteins.

The Fe–His bond holds particular interest as a probe of the covalent connection with the protein.[54,55] Calculations and single-crystal NRVS data on NO and CO derivatives of imidazole-ligated iron porphyrins identify multiple modes with Fe–Im stretching character.[25,26] Many of the frequencies are considerably lower than the 200–230 cm^{-1} range observed in NRVS data for five-coordinate deoxyMb[7] and for the Fe(TPP)(2-MeHIm) mimic for the deoxyMb active site.[21] This again suggests that NO binding weakens the *trans* Fe–Im bond, consistent with indirect indications from measurements of the Fe–NO stretch (above)[18] as well as with the increased bond length observed in structural studies[56] and mechanisms proposed for NO activation of heme proteins such as soluble guanylate cyclase (sGC).[57,58]

Numerous investigations have used the Raman-active Fe–His vibration to probe heme–protein interactions and protein structural dynamics for five-coordinate heme proteins. Identification of a similar vibrational probe for six-coordinate heme proteins would be valuable. Comparison with results on iron porphyrins suggests that the feature near 130 cm^{-1} in the MbNO data (Figure 6) is a potential candidate for probing the Fe–His bond. We note the absence of this feature in the five-coordinate [Fe(PPIXDME)(NO)].[23] Further studies, including density functional theory (DFT) calculations, will clarify the character of this mode. However, the relatively small Fe amplitude with respect to the Fe–His mode in deoxyMb[7] indicates an altered mode character.

Fe motion along the two in-plane directions constitutes two thirds of the VDOS, and vibrations of the in-plane bonds to the pyrrole nitrogens appear to dominate the VDOS reported for heme proteins and iron porphyrins.[7,18,59] NRVS data on deoxyMb allowed the first identification of the Fe–N_{pyr} vibrations for a heme protein.[7] The appearance of two resolved features at 251 and 267 cm^{-1} for deoxyMb (Figure 7) indicates that deviations from fourfold symmetry are sufficient to remove the nominal equivalence between the two in-plane directions. Comparison of experimental and computational results on iron porphyrins indicates additional structure that is not resolved experimentally. The in-plane vibrations apparently have little Raman activity, although they have been identified in IR data on ferric halide octaethylporphyrin (OEP) compounds.[60]

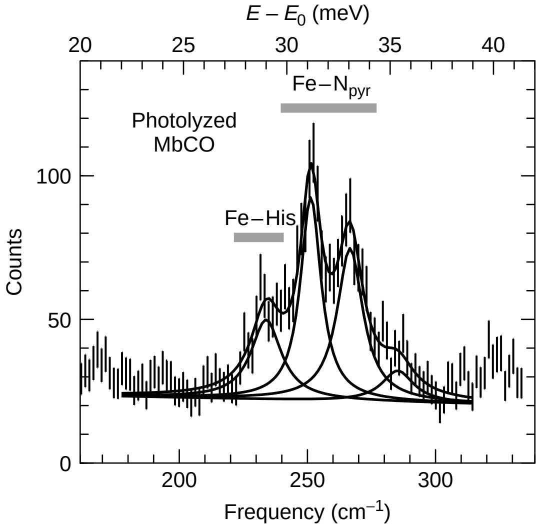

Figure 7 Experimental signal recorded for photolyzed MbCO. Fe–ligand vibrations dominate the cluster of modes observed in the 230–270 cm^{-1} region. The clearly resolved frequency separation between the in-plane Fe–N_{pyr} frequencies at 251 and 267 cm^{-1} reflects the asymmetric interactions with the histidine ligand. The Fe–histidine stretching frequency appears at 234 cm^{-1}. Data were recorded under continuous illumination by a 15 mW helium neon laser with $\lambda = 633$ nm. The temperature of a sensor mounted in the sapphire sample block was 15 K

NRVS measurements unambiguously identified in-plane motion as the primary contribution to the NRVS signal between 30.2–36.5 meV (244–294 cm^{-1}) for an oriented single crystal of metMb,[59] which contains a high-spin ferric heme with a solvent water molecule bound as a sixth Fe ligand.

We suggest identification of the complex feature in the 340–360 cm^{-1} region of the MbNO VDOS (Figure 6) with Fe–N_{pyr} vibrations, based on comparison with iron porphyrins with NO and 1-MeIm as axial ligands to the iron, although calculations on a computational model for MbNO or measurements on oriented MbNO crystals will be needed to confirm this. Similar comparisons with NRVS measurements on CO derivatives of imidazole-ligated iron porphyrins[25] suggest that in-plane vibrations dominate the 320–360 cm^{-1} region of the VDOS reported for MbCO.[7,25,11]

The increase of approximately 90 cm^{-1} with respect to the in-plane frequencies reported for deoxyMb (Figure 7)[7] indicates a strong sensitivity to the decrease in average Fe–N_{pyr} bond length from 206 pm in the high-spin deoxyMb[61] to 200 pm in the low-spin MbNO.[62] Once assignments are firmly established, these frequencies should provide a reliable vibrational marker for Fe spin state in heme proteins.

Data on all proteins examined to date includes significant signal below 100 cm^{-1} (Figure 8) that is not attributable to the vibrational dynamics of the immediate

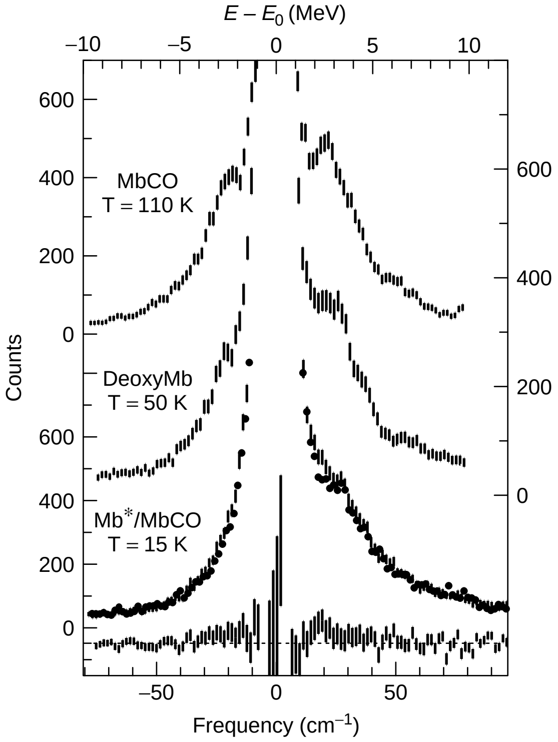

Figure 8 Low-frequency spectra of MbCO, deoxyMb, and photolyzed MbCO (Mb*). Shoulders on the recoilless absorption line are attributed to translational motion of the heme in response to global oscillations of the surrounding protein matrix, and become more prominent with increasing temperature. Filled circles overlaid on the photolyzed MbCO spectrum represent the spectrum of unphotolyzed MbCO. Subtraction of the latter two spectra reveals no measurable influence of ligand binding on these vibrations

Fe coordination sphere. For myoglobin, the Fe-weighted density of states peaks near $30\,\mathrm{cm}^{-1}$,[7] and qualitatively resembles the hydrogen-weighted density of states determined using inelastic neutron scattering (INS)[63–65] (*see* ***Neutron Scattering***). We proposed that translation of the entire heme in response to the same global protein vibrations responsible for the neutron signal dominates the NRVS signal in this frequency region.[7] No changes in this frequency region were detected following CO photolysis from MbCO (Figure 8), consistent with the attribution to global modes and in contrast with the large changes observed in all Fe–ligand vibrations.[7] This contribution dominates the raw experimental signal (Figure 8) because of the inverse dependence on frequency.

Careful investigations revealed that the VDOS varies as the square of the frequency below $10\,\mathrm{cm}^{-1}$ for deoxyMb solutions, as predicted from a Debye model, but reveal significant deviations from Debye behavior at higher frequencies,[11] reminiscent of the ‘‘boson peak’’ observed in amorphous solids.[13] Interestingly, these deviations were not observed for deoxyMb crystals.[11]

The area expected for heme motion can be estimated from the area $3m_{\mathrm{Fe}}/M$ of the total density of states that can be attributed to pure translation of a molecule of mass M. However, there is some ambiguity regarding the number of atoms included in the effective translational mass M. Taking the mass $M = 357$ of the Fe and the 24 atom porphyrin core leads to the prediction that translational degrees of freedom contribute 15% of the total VDOS.

This estimate may be questioned, especially in situations where the heme has several covalent attachments to the proteins, as for cytochrome c[36] and cytochrome f.[19] It will be of some interest to observe how NRVS data reflect such factors.

3.2 Studies of Small Molecule Systems

As established in earlier sections, the measured NRVS spectral intensities determine the VDOS for the Mössbauer active nucleus. The VDOS includes all modes that involve motion of the Mössbauer active nucleus, which in our current discussion is limited to iron. The richness of the observation of all vibrational modes is a case of a ‘‘good news–bad news’’ situation. A major concern is how to manage the assignment of vibrational modes to the observed NRVS frequencies. Two complementary approaches, one experimental and the other computational, show substantial utility for the challenge of making assignments and understanding the vibrational complexity of the systems. It is important to recognize that NRVS provides information on modes that are not observable, or at least not easily observable, by any of the commonly used vibrational methods (*see* ***Vibrational Spectroscopy***).

The geometry of planar heme derivatives naturally provides for an important partitioning of the vibrations: those that are in-plane with iron motion parallel to the porphyrin plane and those that are out-of-plane with iron motion perpendicular to the porphyrin plane. The NRVS experiment can easily distinguish between the two cases whenever an appropriately aligned sample can be measured. Whether these heme plane orientations are accessible in an appropriately aligned single crystal depends on the crystallographic characteristics of the sample. Both in-plane and out-of-plane orientations are accessible in single crystalline materials belonging to the triclinic system; an in-plane orientation can always be measured for monoclinic system crystals.

The NRVS spectra obtained for the (triclinic) crystalline species [Fe(TPP)(2-MeHIm)] in the two orientations are compared in Figure 9. These spectra are also compared to the powder spectrum obtained. The differences in the two orientations are clearly apparent and the utility of such measurements for spectral assignments is clear. In this figure, the signal intensities have been scaled to the approximate relation $D_{tot}(\bar{\nu}) = D_z(\bar{\nu}) + 2D_x(\bar{\nu})$ that results from assuming $D_x(\bar{\nu}) = D_y(\bar{\nu})$. Although most of the observed frequencies in the in-plane and out-of-plane oriented crystal measurement are resolved, some spectral overlap (at $200–220\,\mathrm{cm}^{-1}$) is

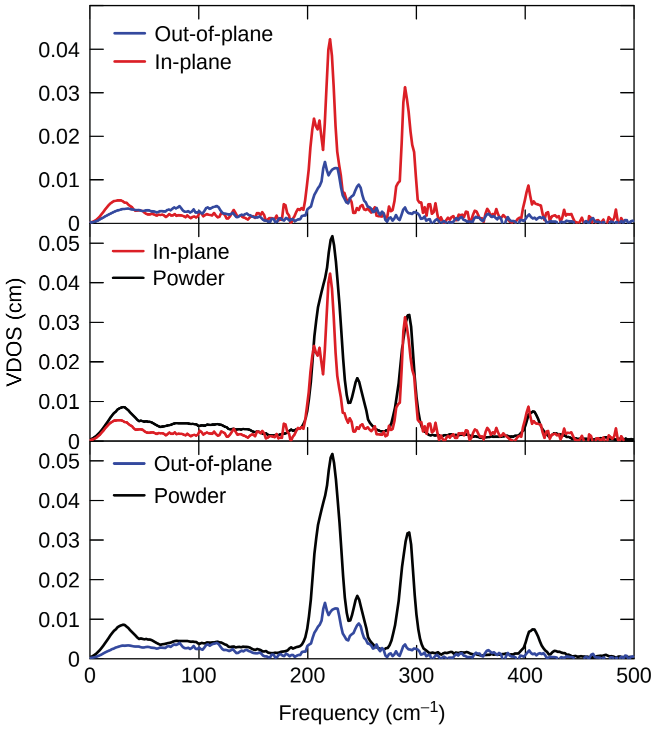

Figure 9 Experimental NRVS spectra of polycrystalline (powder, $D(\bar{\nu})$) and single-crystal (in-plane, $D_x(\bar{\nu})$ and out-of-plane, $D_z(\bar{\nu})$) [Fe(TPP)(2-MeHIm)]. Crystals are oriented with porphyrin planes parallel (in-plane) and perpendicular (out-of-plane)

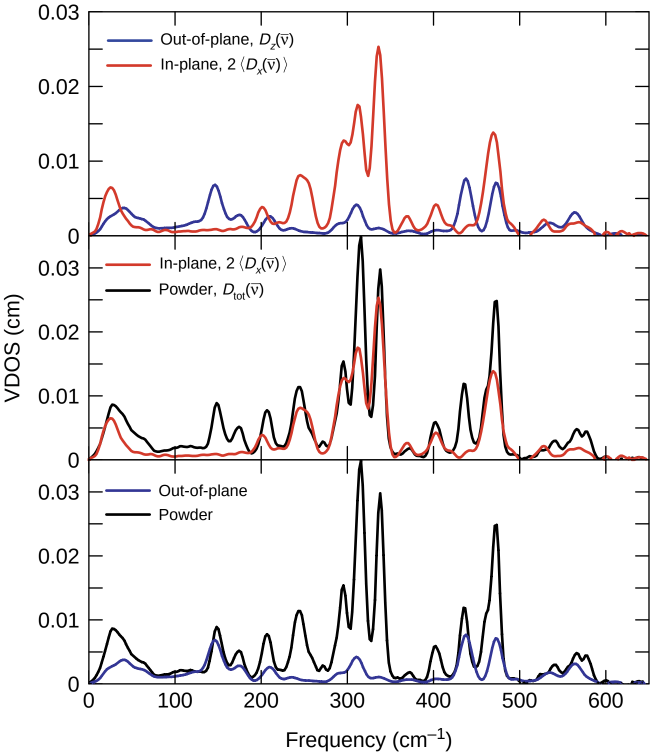

Figure 10 Experimental NRVS spectra of polycrystalline (powder, $D(\bar{\nu})$) and single crystal (in-plane, $D_x(\bar{\nu})$ and out-of-plane, $D_z(\bar{\nu})$) [Fe(TPP)(1-MeIm)(NO)]. Due to porphyrin packing in the $P2_12_12_1$ space group, the ''in-plane'' orientation orients all porphyrin planes 13.8° from the incident beam. The ''out-of-plane'' orientation obtained by rotation of the crystal by 90° orients all porphyrin normals to within 13.8°

observed. This appears to be a general feature of the oriented crystal heme spectra in that, in every case studied to date, at least one modest out-of-plane feature is in the same frequency range as a set of more dominant in-plane features.

Despite the fact that the triclinic system is the only crystallographic system that unequivocally allows single-crystal orientations to provide both enhanced in-plane and out-of-plane NRVS spectra, many other crystalline heme derivatives fortunately have all porphyrin planes close to being parallel to a common crystallographic plane. For example, [Fe(TPP)(1-MeIm)(NO)] has four independent porphyrin plane orientations, but all planes are within 13.8° of a common plane in the crystal. Data were collected using this common plane as the crystal-orienting plane to obtain an ''in-plane'' and an ''out-of-plane'' spectrum. As shown in Figure 10, a comparison of the ''in-plane'', ''out-of-plane'', and powder spectra show that useful intensity enhancements are still evident. Moreover, and fortunately, this situation of nearly coincident planes appears to be moderately frequently observed.

While the qualitative partitioning of in-plane and out-of-plane character is a powerful tool in spectral assignments, the quantitative features of NRVS spectra are also of significant assistance in making assignments (see following section). The most complete use of the frequency and amplitude (e^2_{Fe} values) comes from the use of DFT calculations to obtain predicted frequencies and e^2_{Fe} values. In the two published studies where comparisons between the DFT-predicted and the NRVS-obtained values have been made in the greatest detail, there has been good overall agreement between the predicted and observed general character, frequencies and e^2_{Fe} values.[23,25] The e^2_{Fe} values in particular are a quantitative measure of the agreement between the calculated and observed spectra. Our experiences to date lead us to believe that DFT calculations provide useful descriptions of detailed mode compositions, especially in conjunction with oriented crystal measurements. As described in the next paragraph, an important proviso must be attached to the use of DFT for mode calculations.

The use of DFT calculations for mode assignments requires the determination of an energy-minimized structure of the molecule in question. Theoretical calculations on porphyrin systems have been traditionally simplified by truncating the porphyrin skeleton; DFT calculations have typically used the porphine core, deleting all peripheral group atoms other than hydrogen atoms. However, it has become clear that many features of the vibrational spectrum depend strongly on peripheral groups of the porphyrin moiety.

The importance of the peripheral groups on the vibrational spectrum leads to the necessity of including the complete molecule in the DFT calculation and thereby substantially increasing the computational time required. Accordingly, the required DFT calculations for mode assignments are near the current practical limit. The importance of the peripheral groups on the vibrational spectroscopy of the iron atom can be readily seen from Figure 11, which displays the experimental NRVS spectra observed for five different five-coordinate nitrosyl complexes. What remains to be ascertained is whether there are systematic differences in the effects of meso-substituents versus β-pyrrole substituents. This issue is important in assaying how results from the small molecule studies may be related to those of the proteins.

The most prominent features in NRVS spectra are the strong set of peaks in the middle portion of the spectrum, which are principally from the in-plane motion of iron. At this time, a complete general analysis of the in-plane modes is not possible. However this is probably not a final state. A relationship between the frequencies of the in-plane modes, iron spin state, and coordination state can be reasonably expected and is qualitatively observed. The increasing database of NRVS measurements on oriented single crystals of iron porphyrins should enable a more quantitative approach to understanding the relation between the set of iron in-plane modes and the Fe–N_p bond lengths.

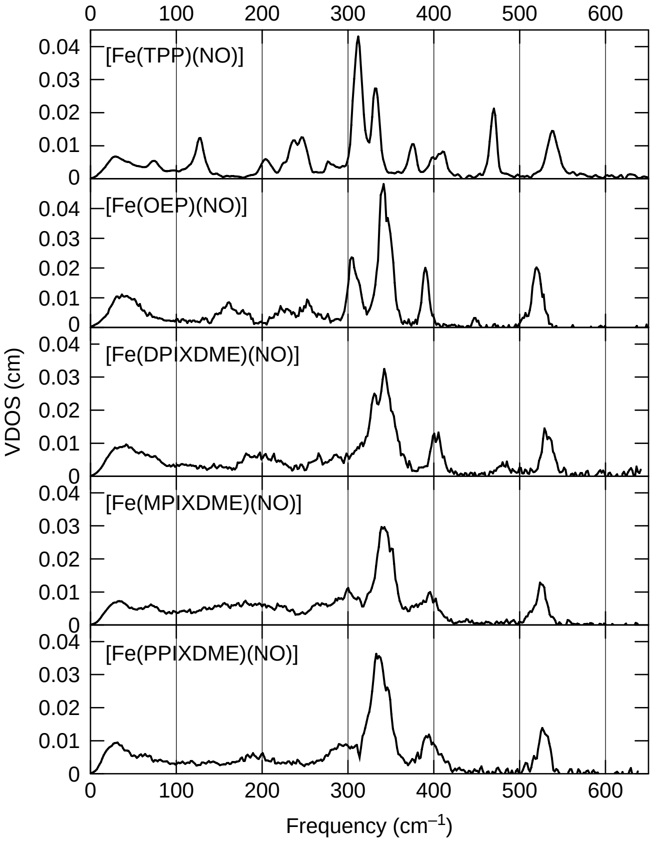

Figure 11 Diagram illustrating the experimental NRVS spectra of five different [Fe(Porph)(NO)] derivatives, each with varying substitution patterns on its periphery

The in-plane modes for [Fe(TPP)(NO)] were the first to be studied and have been predicted in detail from DFT studies.[23] Near-degenerate pairs of Fe–N_p in-plane modes are expected for this five-coordinate species. Pairs of bands with in-plane iron motion along with larger contributions to the total kinetic energy from porphyrin motion are observed (predicted) at 236, 248 (241, 253) cm^{-1}, 410 (410, 413) cm^{-1}, and 470 (474, 476) cm^{-1}. Not surprisingly, in all of these in-plane modes the iron motion is in the direction of the Fe–N_p bond. The description of the most intense set of in-plane modes (observed at 313 and 333 cm^{-1}) is more complex. The intensities of this pair are not equal, but both are clearly in-plane modes with a substantial iron contribution. The DFT calculations suggest that there are two near-degenerate pairs of in-plane modes with three of the four predicted at 308, 317, and 318 cm^{-1}, all within the resolution of the experiment and are thus seen as a single NRVS peak. The fourth band, with a predicted frequency of 334 cm^{-1} is distinct. This leads to the difference in intensities of the observed ''pair''. These in-plane modes are vibrationally mixed with FeNO bending and Fe–NO bending modes. In two of these strong in-plane modes, predicted at 308 and 334 cm^{-1}, the iron motion is approximately parallel to the FeNO plane and has some out-of-plane motion of the iron as well. The other two modes, predicted at 317 and 318 cm^{-1}, have the iron motion approximately perpendicular to the FeNO plane.

Investigations of six-coordinate derivatives [Fe(Porph)(XO)(1-MeIm)] with the diatomic ligands NO or CO have been carried out on both powder and oriented single-crystal samples.[25,26] The oriented crystal data have allowed clear assignments of the in-plane and out-of-plane modes. The most intense in-plane modes in the two distinct [Fe(TpFPP)(NO)(1-MeIm)] derivatives (predicted frequencies at 339 and 321 cm^{-1}) have the iron motion directed perpendicular and parallel to the FeNO plane and not along the Fe–N_p directions. The motion of the 321 cm^{-1} band is complex with iron having both in-plane and out-of-plane components. This is distinctly different from the analogous carbonyl derivatives where the principal predicted modes with in-plane motion are more complex (at 318, 321, 323, and 329 cm^{-1}), but are along the Fe–N_p bond directions. The CO and NO systems suggest that orientation of the imidazole ligand has little effect on the in-plane iron motion. In addition, a mode at 320 cm^{-1} in the CO complex is an out-of-plane mode in which the iron and the axial diatomic CO move together perpendicular to the porphyrin core. It is important to note that the complexity of the predicted spectra are verified by the mode-specific single-crystal measurements of both the nitrosyl and carbonyl complexes.

The information available thus far on the iron in-plane motion direction shows that there are substantial possible effects from the axial ligand. More generally the measurements raise the possibility that the environment could have significant effects on the directions of the in-plane iron motions.

As outlined below, NRVS studies have provided information on iron out-of-plane modes that was previously unavailable. For five-coordinate nitrosyl complexes, classical theory predicts that the three-atom FeNO grouping should have three modes: the N–O stretch, the Fe–N stretch, and the FeNO bend, with the latter two expected to be found in the region below 600 cm^{-1}. In a detailed analysis of [Fe(TPP)(NO)] provided by a series of DFT calculations, the predicted frequency of the stretch was overestimated when the calculation used the BP86[66,67] functional and underestimated when the B3LYP[68,69] functional was employed.[23] The reasons for the difficulties in this prediction appear to arise from the unusual nature of the unpaired electron in the compound that is significantly delocalized over the NO ligand as well as the metal.[50] In this case, the Fe–N stretch was actually observed at 540 cm^{-1} for [Fe(TPP)(NO)] powder at 80 K.[8,20,23] This vibration is also seen at similar frequencies in several other five-coordinate nitrosyls (see Figure 11). What is not identified in the VDOS for [Fe(TPP)(NO)] is a frequency in which the principal contributor is the FeNO bend. Rather this mode is distributed over a number of frequencies. This illustrates what has become an important general feature of the NRVS-revealed VDOS, namely that the total spectral features that involve iron motion involve many mixed modes.

NRVS studies have illuminated the nature of the axial modes involving the diatomic ligand in [Fe(Porph)(XO)(1-MeIm)] (NO or CO) derivatives. In MbNO, NRVS has clarified the assignment of the frequency with predominant Fe–NO stretch character.[18] Although a band at 558 cm^{-1} shows a substantial shift on ^{15}NO substitution, the NRVS studies show that it has only a small iron contribution to its kinetic energy distribution (KED). Rather, the band at 452 cm^{-1} has motions that are more characteristic of the Fe–NO stretch. However, both bands do have some contributions from the FeNO bend, smaller in the 452 cm^{-1} band and larger in the 558 cm^{-1} band. Finally, a band similar to the ~470 cm^{-1} band originally found in [Fe(TPP)(NO)] and assigned as an FeNO bend by empirical methods[20] is also seen in the six-coordinate systems. NRVS spectra/DFT calculations show that the iron contribution is small and it is principally a porphyrin-phenyl mode.

However, FeCO bending modes are clearly seen in the six-coordinate carbonyl complexes. In [Fe(TPP)(1-MeIm)(CO)], two bands are observed at 561 and 586 (predicted at 560, 566, 580 and 583) cm^{-1} corresponding to two distinct FeCO bending modes as shown in Figure 12. The two observed modes are predicted by DFT to be degenerate x, y pairs with separations less than the resolution of the experiment. The sets of modes correspond to differing coupling of the porphyrin motions, especially the phenyl ring motions, with the FeCO bend. The bending modes in [Fe(OEP)(1-MeIm)(CO)] appear to be somewhat less complicated owing to a reduction in mode mixing with porphyrin core distortions, attributed to the different peripheral substituent pattern observed in the β-substituted porphyrinates.[25]

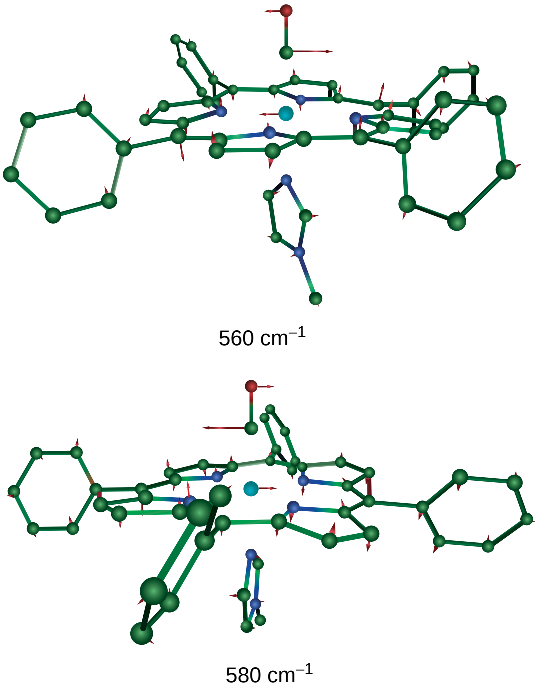

Figure 12 FeCO bending modes predicted by DFT. The relative phase of the FeCO bending and porphyrin motions reverses between 560 and 580 cm^{-1}

An important point found from the measurements is that the NRVS-observed kinetic energy contribution of iron to the bending modes is much larger than the predicted value from a classical treatment of an FeCO group. This is not the case for the Fe–CO stretch that is observed at 507 cm^{-1} in [Fe(TPP)(1-MeIm)(CO)]. The classical model prediction for the iron kinetic energy contribution to this mode and the NRVS-observed value are in much closer agreement. The difference between the classical theory prediction and experiment are likely related to the suggestion that a combined Fe–CO tilt and FeCO bend is a low-energy mode in carbonyl complexes. The softness of this mode is consistent with an FeCO group that is readily deformable from linearity.[70] The in-phase component will occur at low frequency (70–80 cm^{-1}), but the out-of-phase component of this mode is suggested as an explanation of the unusually high frequency the FeCO bending mode, consistent with the NRVS observations. This issue has been dealt with in an earlier publication that should be consulted for additional detail.[25]

An especially interesting mode in six-coordinate hemes with a diatomic axial ligand and a trans-imidazole is the identification is the Fe–Im stretch.[25] This band has never been identified in the resonance Raman spectra of such species. NRVS data on six-coordinate NO and CO derivatives allow the identification of several frequencies that involve significant simultaneous motion of the iron and the imidazole. For the carbonyl complex, [Fe(TPP)(1-MeIm)(CO)], a total of four bands have been predicted at 157, 182, 214, and 320 (observed at 172, 225 and 321) cm^{-1}. One of these, the vibration at a frequency of 214 cm^{-1}, has motion that qualitatively resembles a classical Fe–Im stretch, although none of the four modes can be described quantitatively as a simple two-body oscillator. The modes with predicted frequencies of 157 and 182 cm^{-1} have motions that change the Fe–Im distance but the relative motions of the Fe and Im are complex. Although the iron motion in these two is perpendicular to the porphyrin plane, the motion of the imidazole is much more a torsional motion with respect to the porphyrin plane. Finally the band at 320 cm^{-1}, which is in the middle of the in-plane motions, but has been experimentally found in oriented single crystal measurements to be an out-of-plane contributor, has translational motion of the FeCO group. All of these bands display some sensitivity to the Fe–Im distance.[25] The character of the modes, as predicted by the DFT results, are shown in Figure 13. In the analogous nitrosyl complexes with a longer Fe–Im bond distance, these bands are predicted to appear at 146, 164.5/169, 195, and 323 cm^{-1}. Moreover, the observed counterparts in two crystalline modifications of [Fe(TpFPP)(1-MeIm)(NO)] with a small (0.038 Å) difference in Fe–N_{Im} show a systematic shift to lower frequency for the form with the longer Fe–Im distance.[26]

The possible mechanistic importance of the Fe–imidazole(histidine) bond, especially in various models for hemoglobin cooperativity, has been recognized for some time.[71–73] NRVS clearly provides the first experimental method for systematic studies of how the Fe–Im bond strength can be modulated in six-coordinate hemes, both by protein environmental effects as well as by the consequences of systematic ligand change.

The very low frequency bands also provide information on the doming mode, which has proved to be very difficult to observe. The doming mode describes the motion of the iron perpendicular to the porphyrin plane with the iron motion opposed by motion of the core atoms. This mode is expected to be of substantial utility in understanding the reactivity of heme derivatives that are involved in the association/dissociation of small ligands. In the complex [Fe(TPP)(NO)] there are two low-frequency modes at 74 and 128 cm^{-1} that are the prime candidates for assignment as the doming mode. Perhaps surprisingly, the predicted mode corresponding to the higher frequency more closely resembles a doming mode , while the lower frequency mode primarily involves motion of the NO oxygen. However, we suggested significant mixing of the character of the observed modes.[23] Similar complexities are seen in the motions of six-coordinate carbonyls. Modulation of these motions by the protein environment may have important implications that affect mechanism and biological function in heme proteins.

The combination of experimental and theoretical data based on the technique of NRVS has shown that the vibrational spectral features of the iron-containing hemes are quite complex. NRVS experiments and calculations have clearly demonstrated that the expectations from simple models, for example, the three-atom model for FeCO, are inadequate. Other iron-containing systems are undoubtedly equally complex and present challenges in the spectral assignments. We are still in the early stage of understanding the complexities of the vibrational motions of hemes. Nonetheless, the power of the method in understanding the dynamics of iron-containing systems, biomolecules and others, should be evident. It is to be hoped that a coherent view of the Fe–ligand modes, which are clearly very mixed, will allow, inter alia, an understanding of how the iron dynamics can be modulated by the protein environment.

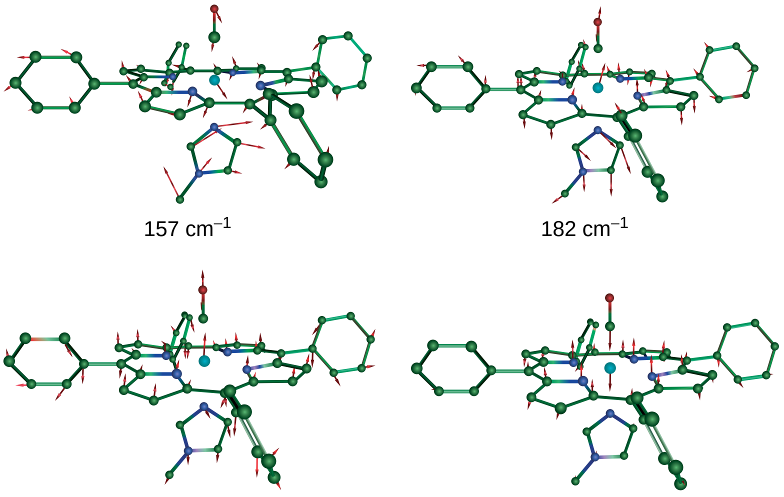

157 cm^{-1}

182 cm^{-1}

214 cm^{-1}

320 cm^{-1}

Figure 13 Predicted vibrational modes of [Fe(TPP)(1-MeIm)(CO)] with frequencies 157, 182, 214, and 320 cm^{-1} involve Fe–Im motion

3.3 Description of Mode Character: Quantitative Vibrational Dynamics

The coefficients $\vec{e}_{j\alpha}$ governing the mathematical transformation from normal coordinates Q_α to atomic Cartesian coordinates $\vec{r}_j$ provide a transparent description of mode character. The vector $\vec{e}_{j\alpha}$ parallels the motion of atom j in normal mode α, while the squared magnitude $e^2_{j\alpha}$ describes its relative mean squared amplitude. Normalization, according to $\sum_j e^2_{j\alpha} = 1$, then ensures that the mode composition factor $e^2_{j\alpha}$ is equal to the fraction of mode energy associated with motion of atom j. The resulting KED, together with the directional information, facilitates model-independent comparison of experiments with each other and with computational predictions.

NRVS directly samples the KED because the spectral area contributed by mode α directly yields the mode composition factor e^2_{Fe} for the ^{57}Fe probe atom, according to equations (3–6). Using more traditional vibrational methods, frequency shifts resulting from isotope substitution of atom j can yield an estimate[8]

$$e^2_{j\alpha} = -2\frac{d(\ln\bar{\nu}_\alpha)}{d(\ln m_j)} \approx -2\frac{\Delta\bar{\nu}_a/\bar{\nu}_a}{\Delta m_j/m_j} \tag{7}$$

of its mode composition factor. Although the implicit assumption that the mode character is unaltered by the isotope substitution may not always be valid, this expression establishes an approximate quantitative correspondence between NRVS and other vibrational methods such as Raman, and also extends the description of the KED to include atoms other than the NRVS isotope.

Investigation of MbNO has illustrated the value of quantitative comparisons between NRVS and Raman isotope shift measurements.[18] For a mode at 556 cm^{-1}, the KED indicated 80–90% of mode energy localized on FeNO with primary involvement of the nitrosyl N atom $\left(e^2_N = 0.8\right)$, while Fe motion dominated the KED of a second FeNO vibration at 451 cm^{-1}. These results supported the attribution of Fe–NO stretching character to the 451 cm^{-1} mode, with consequent sensitivity to the Fe–NO bond strength. For a Raman peak near 360 cm^{-1}, NRVS signal in excess of that expected on the basis of the e^2_{Fe} value estimated from isotope shift measurements was rationalized in terms of unresolved contributions from two in-plane modes. This conclusion would not be possible on the basis of either NRVS nor Raman measurements individually.

The wealth of quantitative vibrational information available from NRVS also facilitates unusually detailed and quantitative comparison with theoretical predictions. NRVS data on model compounds[20–22,28,29,74,75] and on proteins[17,76,77] have been successfully reproduced by adjusting force constants in empirical potentials. Moreover, NRVS provides a particularly rigorous test of vibrational predictions from quantum chemical models, which may otherwise be difficult to test for transition metal systems. DFT methods have now reproduced vibrational frequencies, amplitudes, and directions for several iron porphyrins with sufficient fidelity that quantum chemical methods are emerging as the most effective methods to understand the character of modes that contribute to the NRVS signal.[23,25,26,29,39]

In contrast with empirical models, quantum chemical methods do not provide adjustable force constants. It is therefore not unexpected that quantitative discrepancies appear when quantum chemical predictions are compared in detail with the results of NRVS measurements.[23,25] NRVS results thus provide a benchmark for development of quantum chemical methods for transition metal systems. Using quantum chemical results as starting input in empirical calculations may be a valuable approach for future work. Meanwhile, however, reproduction is sufficiently accurate to guide the understanding of observed vibrational features. Mode descriptions given in the previous section largely rely on comparison with quantum chemical predictions.

The quantitative information derived from measurements of spectral areas is a characteristic strength of NRVS measurements, but imposes certain requirements that must be borne in mind during sample preparation and data collection. Accurate interpretation of peak areas relies on having a pure sample or at least knowing the fraction of molecules that contribute to an individual spectral feature. In addition, measurements must be conducted over an energy range sufficient to encompass all significant vibrational signals in order to ensure accurate normalization according to equation (2).

3.4 Summary and Prospects

Although NRVS measurements are restricted to molecules that can be labeled with an appropriate isotope such as ^{57}Fe, they provide important advantages over established vibrational spectroscopies. NRVS is a uniquely quantitative and informative probe of vibrational dynamics, yielding not only the frequency but also the amplitude and direction of motion for all vibrational modes involving the probe nucleus. IR and Raman spectroscopies (*see* ***Vibrational Spectroscopy***) have been the favored techniques for biomolecular applications, partly because appropriate techniques provide selectivity for active sites. However, information on individual atomic motions must be obtained indirectly through isotope editing. For INS measurements (*see* ***Neutron Scattering***), the experimental signal is proportional to the atomic amplitude but represents an average over all atoms (weighted by scattering length). As a result, INS applications to biological macromolecules have been most effective as probes of global dynamics, and indeed provide an important quantitative test for molecular mechanics potentials, but lack selectivity to local sites. In many ways, NRVS combines the advantages of existing techniques, extending selectivity to the ultimate limit of a single atom among thousands while revealing detailed *quantitative* information on vibrational dynamics.

The future appears bright for NRVS applications to protein active sites, and a number of promising ideas remain to be fully exploited. As experimental count rates improve, results on more complex molecules with multiple metal sites are beginning to appear,[27,53] and selective isotope labeling of distinct Fe sites should be particularly illuminating for proteins. Light-driven reactions have been successfully monitored using NRVS,[7] setting the stage for using NRVS to monitor reaction-induced changes in structure and dynamics. Single crystals have been crucial for establishing vibrational mode descriptions in iron porphyrins,[20,21,23,25,26] and analogous experiments on proteins only require ^{57}Fe-enriched crystals of sufficient size, since the ^{57}Fe concentration will exceed that in solution samples. Among the more intriguing observations to date is the experimental and theoretical identification of low-frequency modes involving Fe displacement out of the porphyrin plane, resembling the heme doming motion long hypothesized to control heme reactivity.[20,21,23,25,26] NRVS measurements may allow quantitative estimates of the contribution of reactive modes to the energy of transition states.

The growing NRVS database also exposes unanticipated interpretational challenges. Simulation of a restricted set of atoms has been a cornerstone of the traditional approach to understanding the properties of protein-active sites. However, NRVS measurements on proteins lend credence to expectations that vibrations may involve protein regions distant from the active site.[7,77] The frequency range over which vibrations remain localized is not only a challenge to accurate modeling of observations but may also conceivably influence active site functionality, if reactive vibrations involve large regions of the protein.[7] Even for small molecule models, NRVS measurements and quantum chemical modeling are revealing unanticipated vibrational complexities, which are not fully resolved experimentally. In some cases, the extraction of effective force constants directly from experimental data may provide valuable model-free information on proteins.[37,78,19]

4 ACKNOWLEDGMENTS

We acknowledge financial support from the National Science Foundation (PHY-0545787 to J.T.S.) and the National Institutes of Health (GM-38401 to W.R.S.). Use of the Advanced Photon Source was supported by the U.S. Department of Energy, Basic Energy Sciences, Office of Science, under Contract No. DE-AC02-06CH11357.

5 END NOTES

[a] This statement is actually implicit in equation (3) because $\bar{n}_\alpha(\bar{\nu})/\bar{\nu} = (\bar{n}_\alpha(-\bar{\nu})+1)/-\bar{\nu}$.

[b] Here and in the remainder of the chapter, we express the mode composition factor $e^2_{j\alpha}$ as e^2_{Fe}, setting $j = \mathrm{Fe}$ and suppressing the mode index α.

6 ABBREVIATIONS AND ACRONYMS

APD = avalanche photodiode detector; APS = advanced photon source; DFT = density functional theory; ESRF = European synchrotron radiation facility; HDPE = high-density polyethylene; IR = infrared; INS = inelastic neutron scattering; KED = kinetic energy distribution; Mb = myoglobin; NIS = nuclear inelastic scattering; NRVS = nuclear resonance vibrational spectroscopy; NRIXS = nuclear resonant inelastic X-ray scattering; OEP = octaethylporphyrin; sGC = soluble guanylate cyclase; VDOS = vibrational density of states.

7 FURTHER READING

early theory:

K. S. Singwi and A. Sjölander, *Phys. Rev.*, 1960, **120**, 1093.

W. M. Visscher, *Ann. Phys.*, 1960, **9**, 194.

early experiments

M. Seto, Y. Yoda, S. Kikuta, X. W. Zhang and M. Ando, *Phys. Rev. Lett*, 1995, **74**, 3828.

W. Sturhahn, T. S. Toellner, E. E. Alp, X. W. Zhang, M. Ando, Y. Yoda, S. Kikuta, M. Seto, C. W. Kimball and B. Dabrowski, *Phys. Rev. Lett.*, 1995, **74**, 3832.

data analysis

M. Y. Hu, W. Sturhahn, T. S. Toellner, P. Hession, J. Sutter, E. E. Alp, *Nucl. Instr. and Meth. Phys. Res. A.*, 1999, **428**, 551.

H. J. Lipkin, *Phys. Rev. B*, 1995, **52**, 10073.

J. T. Sage, C. Paxson, G. R. A. Wyllie, W. Sturhahn, S. M. Durbin, P. M. Champion, E. E. Alp and W. R. Scheidt, *J. Phys.: Condens. Matter*, 2001, **13**, 7707.

W. Sturhahn, *Hyperfine Interact.*, 2000, **125**, 149.

8 REFERENCES

1. R. L. Mössbauer, *Z. Physik.*, 1958, **151**, 124.
2. K. S. Singwi and A. Sjölander, *Phys. Rev.*, 1960, **120**, 1093.
3. W. M. Visscher, *Ann. Phys.*, 1960, **9**, 194.

4. M. Seto, Y. Yoda, S. Kikuta, X. W. Zhang and M. Ando, *Phys. Rev. Lett.*, 1995, **74**, 3828.
5. W. Sturhahn, T. S. Toellner, E. E. Alp, X. Zhang, M. Ando, Y. Yoda, S. Kikuta, M. Seto, C. W. Kimball and B. Dabrowski, *Phys. Rev. Lett.*, 1995, **74**, 3832.
6. A. I. Chumakov, R. Rüffer, H. Grünsteudel, H. F. Grünsteudel, G. Grübel, J. Metge and H. A. Goodwin, *Europhys. Lett.*, 1995, **30**, 427.
7. J. T. Sage, S. M. Durbin, W. Sturhahn, D. C. Wharton, P. M. Champion, P. Hession, J. Sutter and E. E. Alp, *Phys. Rev. Lett.*, 2001, **86**, 4966.
8. J. T. Sage, C. Paxson, G. R. A. Wyllie, W. Sturhahn, S. M. Durbin, P. M. Champion, E. E. Alp and W. R. Scheidt, *J. Phys.: Condens. Matter*, 2001, **13**, 7707.
9. W. Keune, T. Ruckert, B. Sahoo, W. Sturhahn, T. S. Toellner, E. E. Alp and R. Röhlsberger, *J. Phys.: Condens. Matter*, 2004, **16**, S379.
10. H. Paulsen, R. Benda, C. Herta, V. Schünemann, A. I. Chumakov, L. Duelund, H. Winkler, H. Toftlund and A. X. Trautwein, *Phys. Rev. Lett.*, 2001, **86**, 1351.
11. K. Achterhold, C. Keppler, A. Ostermann, U. van Bürck, W. Sturhahn, E. E. Alp and F. G. Parak, *Phys. Rev. E*, 2002, **65**, 051916.
12. P. F. Lindley, *Rep. Prog. Phys.*, 1996, **59**, 867.
13. A. I. Chumakov, I. Sergueev, U. van Bürck, W. Schirmacher, T. Asthalter, R. Rüffer, O. Leupold and W. Petry, *Phys. Rev. Lett.*, 2004, **92**, 245508.
14. A. B. Papandrew, A. F. Yue, B. Fultz, I. Halevy, W. Sturhahn, T. S. Toellner, E. E. Alp and H. -K. Mao, *Phys. Rev. B*, 2004, **69**, 144301.
15. J. -F. Lin, W. Sturhahn, J. Zhao, G. Shen, H. -K. Mao and R. J. Hemley, *Science*, 2005, **308**, 1892.
16. C. Keppler, K. Achterhold, A. Ostermann, U. van Bürck, W. Potzel, A. I. Chumakov, A. Q. Baron, R. Rüffer and F. Parak, *Eur. Biophys. J.*, 1997, **25**, 221.
17. Y. Xiao, H. Wang, S. J. George, M. C. Smith, M. W. W. Adams, Jr, F. E. Jenney, W. Sturhahn, E. E. Alp, J. Zhao, Y. Yoda, A. Dey, E. I. Solomon and S. P. Cramer.. *J. Am. Chem. Soc.*, 2005, **127**, 14596.
18. W. Zeng, N. J. Silvernail, D. C. Wharton, G. Y. Georgiev, B. M. Leu, W. R. Scheidt, J. Zhao, W. Sturhahn, E. E. Alp and J. T. Sage, *J. Am. Chem. Soc.*, 2005, **127**, 11200.
19. K. L. Adams, S. Tsoi, J. Yan, S. M. Durbin, A. K. Ramdas, W. A. Cramer, W. Sturhahn, E. E. Alp and C. Schulz, *J. Phys. Chem. B*, 2006, **110**, 530.
20. B. K. Rai, S. M. Durbin, E. W. Prohofsky, J. T. Sage, G. R. A. Wyllie, W. R. Scheidt, W. Sturhahn and E. E. Alp, *Biophys. J.*, 2002, **82**, 2951.
21. B. K. Rai, S. M. Durbin, E. W. Prohofsky, J. T. Sage, M. K. Ellison, W. R. Scheidt, W. Sturhahn and E. E. Alp, *Phys. Rev. E*, 2002, **66**, 051904.
22. B. K. Rai, S. M. Durbin, E. W. Prohofsky, J. T. Sage, M. K. Ellison, A. Roth, W. R. Scheidt, W. Sturhahn and E. Ercan Alp, *J. Am. Chem. Soc.*, 2003, **125**, 6927..
23. B. M. Leu, M. Z. Zgierski, G. R. A. Wyllie, W. R. Scheidt, W. Sturhahn, E. E. Alp, S. M. Durbin and J. T. Sage, *J. Am. Chem. Soc.*, 2004, **126**, 4211.
24. W. R. Scheidt, S. M. Durbin and J. T. Sage, *J. Inorg. Biochem.*, 2006, **99**, 60.
25. B. M. Leu, N. J. Silvernail, M. Z. Zgierski, G. R. A. Wyllie, M. K. Ellison, W. R. Scheidt, J. Zhao, W. Sturhahn, E. E. Alp and J. T. Sage, *Biophys. J.*, 2007, **92**, 3764.
26. N. J. Silvernail, A. Barabanschikov, J. W. Pavlik, B. C. Noll, J. Zhao, E. E. Alp, W. Sturhahn, J. T. Sage and W. R. Scheidt, *J. Am. Chem. Soc.*, 2007, **129**, 2200.
27. V. S. Oganesyan, J. E. Barclay, S. M. Hardy, D. J. Evans, C. J. Pickett and U. A. Jayasooriya, *Chem. Commun.*, 2004, 214.
28. M. C. Smith, Y. Xiao, H. Wang, S. J. George, D. Coucouvanis, M. Koutmos, W. Sturhahn, E. E. Alp, J. Zhao and S. P. Cramer, *Inorg. Chem.*, 2005, **44**, 5562.
29. Y. Xiao, M. Koutmos, D. A. Case, D. Coucouvanis, H. Wang and S. P. Cramer, *Dalton Trans.*, 2006, 2192.
30. E. E. Alp, T. Mooney, T. Toellner and W. Sturhahn, *Hyp. Interact.*, 1994, **90**, 323.
31. R Rüffer and A. I. Chumakov, *Hyp. Interact.*, 1996, **97/98**, 589.
32. Y. Yoda, M. Yabashi, K. Izumi, X. W. Zhang, S. Kishimoto, S. Kitao, M. Seto, T. Mitsui, T. Harami, Y. Imai and S. Kikuta, *Nucl. Instrum. Methods Phys. Res., Sect. A*, 2001, **467**, 715, July.
33. T. S. Toellner, *Hyperfine Interact.*, 2000, **125**, 3.
34. M. Landergen and L. Baltzer, *Inorg. Chem.*, 1990, **29**, 556.
35. F. W. J. Teale, *Biochim. Biophys. Acta*, 1959, **35**, 543.
36. Bogdan. M. Leu. *Nuclear Resonance Vibrational Spectroscopy: A Quantitative Picture of Iron Dynamics in Heme Proteins and Model Compounds*. Ph. D. dissertation, Northeastern University, Department of Physics, 2006.
37. H. J. Lipkin, *Phys. Rev. B*, 1995, **52**, 10073.
38. W. Sturhahn, *J. Phys.: Condens. Matter*, 2004, **16**, S497.
39. B. M. Leu, M. Z. Zgierski, G. R. A. Wyllie, M. K. Ellison, W. R. Scheidt, W. Sturhahn, E. E. Alp, S. M. Durbin and J. T. Sage, *J. Phys. Chem. Solids*, 2005, **99**, 2250.
40. W. Sturhahn, *Hyperfine Interact.*, 2000, **125**, 149.
41. D. W. Johnson and J. C. H. Spence, *J. Phys. D*, 1974, **7**, 771.
42. S. Hu and J. Kincaid, *J. Am. Chem. Soc.*, 1991, **113**, 9760.
43. T. Tomita, S. Hirota, T. Ogura, J. S. Olson and T. Kitagawa, *J. Phys. Chem. B*, 1999, **103**, 7044.
44. C. M. Coyle, K. M. Vogel, T. S. Rush, III, P. M. Kozlowski, R. Williams, T. G. Spiro, Y. Dou, M. Ikeda-Saito, J. S. Olson and M. Z. Zgierski, *Biochemistry*, 2003, **42**, 4896.
45. G. B. Ray, X.-Y. Li, J. A. Ibers, J. L. Sessler and T. G. Spiro, *J. Am. Chem. Soc.*, 1994, **116**, 162.
46. T. Li, M. L. Quillin, G. N. Phillips, Jr and J. S. Olson, *Biochemistry*, 1994, **33**, 1433.

47. E. S. Park, S. S. Andrews, R. B. Hu and S. G. Boxer, *J. Phys. Chem. B*, 1999, **103**, 9813.
48. T. G. Spiro and I. H. Wasbotten, *J. Inorg. Biochem.*, 2005, **99**, 34.
49. M. R. Thomas, D. Brown, S. Franzen and S. G. Boxer, *Biochemistry*, 2001, **40**, 15047.
50. V. K. K. Praneeth, C. Näther, G. Peters and N. Lehnert, *Inorg. Chem.*, 2006, **45**, 2795.
51. M. Ibrahim, C. Xu and T. G. Spiro, *J. Am. Chem. Soc.*, 2006, **51**, 16834.
52. U. Bergmann, W. Sturhahn, D. E. Linn, Jr, F. E. Jenney, Jr, M. W. Adams, K. Rupnik, B. J. Hales, E. E. Alp, A. Mayse and S. P. Cramer, *J. Am. Chem. Soc.*, 2003, **125**, 4016.
53. Y. Xiao, K. Fisher, M. C. Smith, W. E. Newton, D. A. Case, S. J. George, H. Wang, W. Sturhahn, E. E. Alp, J. Zhao, Y. Yoda and S. P. Cramer, *J. Am. Chem. Soc.*, 2006, **128**, 7608.
54. D. L. Rousseau and J. M. Friedman, ‘Transient and Cryogenic Studies of Photodissociated Hemoglobin and Myoglobin’, ‘Volume 3 of Biological Applications of Raman Spectroscopy’, Wiley-Interscience, New York, 1988, Chap. 4, p. 133.
55. A Bitler and S. S. Solomon, *Biophys. J.*, 1999, **77**, 2764.
56. G. R. A. Wyllie, C. E. Schulz and W. R. Scheidt, *Inorg. Chem.*, 2003, **42**, 5722.
57. E. M. Boon and M. A. Marletta, *J. Inorg. Biochem.*, 2005, **99**, 892.
58. B. Pal and T. Kitagawa, *J. Inorg. Biochem.*, 2005, **99**, 267.
59. K. Achterhold and F. G. Parak, *J. Phys.: Condens. Matter*, 2003, **15**, S1683.
60. H. Ogoshi, E. Watanabe, Z. Yoshida, J. Kincaid and K. Nakamoto, *J. Am. Chem. Soc.*, 1973, **95**, 2845.
61. A. M. Rich, R. S. Armstrong, P. J. Ellis, H. C. Freeman and P. A. Lay, *Inorg. Chem.*, 1998, **37**, 5743.
62. A. M. Rich, R. S. Armstrong, P. J. Ellis and P. A. Lay, *J. Am. Chem. Soc.*, 1998, **120**, 10827.
63. W. Doster, S. Cusack and W. Petry, *Nature*, 1989, **337**, 754.
64. J. C. Smith, *Q. Rev. Biophys.*, 1991, **24**, 227.
65. M. Diehle, W. Doster, W. Petry and H. Schober, *Biophys. J.*, 1997, **73**, 2726.
66. A. D. Becke, *Phys. Rev. A*, 1988, **38**, 3098.
67. J. P. Perdew, *Phys. Rev. B*, 1986, **33**, 8822.
68. A. D. Becke, *J. Chem. Phys.*, 1993, **98**, 5648.
69. C. Lee, W. Yang and R. G. Parr, *Phys. Rev. B*, 1988, **37**, 785.
70. A. Ghosh and D. F. Bocian, *J. Phys. Chem.*, 1996, **100**, 6363.
71. M. F. Perutz, *Nature*, 1970, **228**, 726.
72. J. L. Hoard and W. R. Scheidt, *Proc. Natl. Acad. Sci. U.S.A.*, 1973, **70**, 3919.
73. J. J. Hopfield, *J. Mol. Biol.*, 1973, **77**, 207.
74. T. E. Budarz, E. W. Prohofsky, S. M. Durbin, T. A. Sjodin, J. T. Sage, W. Sturhahn and E. E. Alp, *J. Phys. Chem.*, 2003, **107**, 11170.
75. V. Starovoitova, T. E. Budarz, G. R. A. Wyllie, W. R. Scheidt, W. Sturhahn, E. E. Alp, E. W. Prohofsky and S. M. Durbin, *J. Phys. Chem. B*, 2006, **110**, 13277.
76. B. K. Rai, E. W. Prohofsky and S. M. Durbin, *J. Phys. Chem. B*, 2005, **109**, 18983.
77. M.-L. Tan, A. R. Bizzarri, Y. Xiao, S. Cannistraro, T. Ichiye, C. Manzoni, G. Cerullo, M. W. W. Adams, F. E. Jenney, Jr and S. P. Cramer, *J. Inorg. Biochem.*, 2007, **101**, 375.
78. G. Zaccai, *Science*, 2000, **288**, 1604.

Perturbed Angular Correlations of γ-rays (PAC) Spectroscopy

Lars Hemmingsen

University of Copenhagen, Frederiksberg, Denmark

Tilman Butz

University of Leipzig, Leipzig, Germany

Method Summary 1
1 Introduction 2
2 Technical Background 3
3 Applications 6
4 Abbreviations and Acronyms 14
5 Further Reading 14
6 References 15

METHOD SUMMARY

Acronyms, Synonyms

- Time Differential Perturbed Angular Correlation (TDPAC)
- Perturbed Angular Correlation (PAC).

Measured physical quantity

- Hyperfine interactions, that is the interaction of a nuclear magnetic moment with extranuclear magnetic fields and the interaction of a nuclear quadrupole moment with electric field gradients from extranuclear charge distributions, are measured via time differential perturbed angular correlation (TDPAC) of γ-rays emitted from radioisotopes.

Information available

- Probe site coordination geometry (types, number, and geometric arrangement of coordinating atoms) is available.
- If several probe sites are present, the signals can often be resolved and the relative population determined.
- Probe site dynamics on a time scale dictated by properties of the nucleus in question–typically nanoseconds (exchange dynamics, molecular reorientational correlation times) is available.

Information not available, limitations

- Full structural information on coordination geometry is not available.
- The structural information is limited to a radius of 3–5 Å from the probe site.

Examples of questions that can be answered

- What is the coordination geometry at a probe site?
- How does the probe site coordination geometry change, for example, during a metalloenzyme-catalyzed reaction or a pH titration?

- Does a molecule labeled with a PAC isotope bind to proteins, DNA, membranes, or other macromolecular partners (via determination of rotational correlation times) in solution?
- Is local dynamics, for example, ligand exchange, occurring at the PAC probe site (provided it occurs in the time window ‘‘visible’’ to PAC spectroscopy)?

Major advantages

- Very small amounts of sample are required ($\sim 10^{10}$ probe atoms)
- The signal is very sensitive to structural changes–often a change of a few degrees in a ligand-probe-ligand angle significantly changes the signal.
- Measurements can be carried out over a broad temperature and pressure range because the anisotropy is essentially determined by nuclear properties.
- In most cases the γ rays emitted in the nuclear decay have sufficiently high energy such that there are basically no constraints for sample containers.
- All inequivalent probe sites yield a signal, that is, there is no ‘‘missing fraction’’.
- Samples can be solid, liquid, immobilized on a surface, or in many other physical states—even in vivo experiments are possible.

Major disadvantages

- Only PAC isotopes with appropriate nuclear properties can be used (*see* the list in the text); most of them are metals.
- A radiochemistry laboratory is required; some of the probe isotopes have short half-lives (∼minutes–hours) and thus they require relatively fast sample preparation.
- For biological samples, for example, metal ion binding proteins, the native metal ion must be exchanged with a suitable PAC isotope.
- So-called after effects from the decay of the mother isotope can give rise to difficult and even incorrect interpretation of the data. This is often the case for electron capture but not for isomeric transitions.

Sample constraints

- Typical sample volumes are 0.05–1.0 mL, but in principle, they are not limited to this range.

1 INTRODUCTION

Perturbed Angular Correlations (PAC) spectroscopy belongs to the family of techniques monitoring hyperfine interactions, such as nuclear magnetic resonance (NMR) (*see* ***Nuclear Magnetic Resonance (NMR) Spectroscopy of Inorganic/Organometallic Molecules***, ***Nuclear Magnetic Resonance (NMR) Spectroscopy of Metallobiomolecules***), nuclear quadrupole resonance (NQR) (*see* ***Nuclear Quadrupole Resonance (NQR) Spectroscopy***), electron paramagnetic resonance (EPR) (*see* ***Electron Paramagnetic Resonance (EPR) Spectroscopy***), and Mössbauer spectroscopy (*see* ***Mössbauer Spectroscopy***). In inorganic and bioinorganic chemistry, the most common applications of PAC spectroscopy provide information on the local electronic and molecular structure and dynamics at the site of the PAC probe via the electric interaction between the nuclear charge distribution and the surrounding charge distribution (the nuclear quadrupole interaction (NQI)). Thus, the technique provides a spectroscopic fingerprint of the local molecular and electronic structure at the site of the PAC probe. The focus of this work is on the NQI, although magnetic interactions have also been studied in magnetically ordered inorganic materials. Dynamics may also be monitored if it occurs within the time window ‘‘visible’’ by PAC spectroscopy (vide infra).

The PAC technique relies on the fact that particles emitted in cascades in nuclear decays are not detected in random directions with respect to each other, due to the conservation of angular momentum. For example, in a nuclear decay where two γ rays are emitted in succession, the first γ ray may be detected in a certain direction. The second γ ray is then in general emitted anisotropically with respect to the first. For ^{111m}Cd, a commonly used PAC isotope, the second γ ray is most likely emitted in the same direction as or opposite direction of the first, and least likely at right angles to the first. This so-called angular correlation, representing the last two letters in the PAC acronym, was first described theoretically by Hamilton in 1940[1] and confirmed experimentally in 1947 by Brady and Deutsch.[2–4] In itself this is entirely uninteresting from the point of view of chemistry, although of great interest in nuclear physics. However, if the nucleus interacts with extranuclear fields, for example, from the surrounding charge distribution in an inorganic or bioinorganic complex, the angular correlation is perturbed, as described theoretically in 1946 by Goertzel[5] and demonstrated experimentally five years later by Frauenfelder *et al.*[6,7] The first application of such perturbations was the determination of nuclear magnetic moments (or g-factors) by applying external magnetic fields to a sample containing a suitable probe nucleus. A breakthrough was the introduction of time differential measurements of the angular correlation, that is, the angular correlation was recorded as a function of the time between the first γ-quantum populating the intermediate nuclear state and the second γ-quantum which depopulates it. In this way, perturbation functions could be determined as a function of time, and it is for this reason that the term ''time differential perturbed angular correlation'' or ''TDPAC'' was coined. Frequently, the abbreviation ''PAC'' is used synonymously because time integral measurements are no longer performed whenever possible.

A pioneering effort dealing mainly with inorganic chemistry was conducted by Haas and Shirley in 1973[8] and the first bioinorganic application was an investigation of serum albumin carried out in 1968 using ^{111}In as PAC probe.[9] Since these groundbreaking achievements, PAC spectroscopy has been applied in a variety of inorganic and bioinorganic investigations. In 1987, a comprehensive table of NQI-data in compounds obtained by PAC spectroscopy was compiled.[10] In bioinorganic chemistry many fundamental problems have been addressed, most notably structure, function, and nanosecond dynamics of metal ion binding sites in proteins and protein–protein interactions.[11] The latter is possible as the PAC signal is affected by the rotational diffusion (Brownian tumbling) of the macromolecule to which the PAC isotope is bound, and this tumbling depends on—apart from viscosity and temperature—the size of the molecule or molecular complex. Most bioinorganic applications have focused on the function of zinc, copper, or iron binding proteins using ^{99}Mo,^{111m}Cd, ^{111}Ag, ^{111}In, ^{181}Hf, and ^{199m}Hg as PAC probes. Peptides, DNA, and proteins with a function in heavy metal detoxification have also been studied, and even whole cell and in vivo experiments have been carried out on bacteria and mice.

Several technical improvements have appeared over the past 10–20 years. Efficient spectrometers such as the six-detector TDPAC-camera,[12] and progress in γ-ray scintillation detector performance with respect to timing and energy resolution (BaF_2, and recently, $LaBr_3$(Ce)) have allowed for considerable improvement in signal-to-noise ratio, and thus reduced the time required to record a PAC spectrum to minutes in favorable cases. New spectrometers with ultrafast digitizers may further advance this trend. Rapid freeze quench technology (*see* ***Freeze-Quench Kinetics***) combined with PAC spectroscopy appears to be a promising approach for studies of chemical and biochemical reactions or molecular dynamics on the millisecond time scale (or slower), allowing for trapping of intermediates in enzyme catalysis and protein folding. Facilities such as CERN(www.cern.ch), providing beams of radioactive PAC isotopes, have promoted the field, especially for the production of high purity trace amounts of short-lived isotopes. This allows for PAC studies at very low concentrations of biomolecules in solution, including normal physiological conditions. PAC spectroscopy has traditionally been limited to elements of the periodic table for which radioactive nuclei with appropriate properties exist. Synchrotron-based PAC spectroscopy, in which the angular correlation between an incoming high energy photon that excites the nucleus and the photon emitted as the nucleus decays, may extend the range of accessible elements considerably.[13] Synchrotron-based PAC spectroscopy has been successfully applied to iron in ferrocene, and this technique holds promise to foster further applications in inorganic and bioinorganic chemistry. Finally, the recent advancement of first principle quantum mechanical calculations of electron densities and electric field gradients (EFGs) in molecules, periodic lattices, and of surface species, including lattice relaxations around the probe atom, has become a central element in the identification of probe geometries.

Reviews on PAC theory,[14–16] applications of TDPAC in materials science and chemistry,[17] in the border region between physics, chemistry, and biology,[18] and in biology[11,19] as well as a comprehensive compilation of NQI-data obtained by TDPAC[10] can be found under References.

2 TECHNICAL BACKGROUND

2.1 What is Measured in PAC Spectroscopy?

Using PAC spectroscopy, the NQI can be measured. The NQI is the electric interaction between the nuclear charge distribution and the surrounding charge distribution. At the risk of offending the knowledgeable reader we proceed via a very figurative and qualitative description of NQIs and PAC, in order to highlight the basic principles of the spectroscopy. We strongly recommend that the reader consults relevant references where a more thorough treatment of the theory and instrumentation is presented.[11,12,14–19] In Figure 1, a simplified classical (i.e., nonquantum mechanical) picture of a nucleus in the external electric field gradient from two negative point charges is presented, followed by a discussion on the corresponding NQI between the nuclear charge distribution and the surrounding charge distribution.

In state (c) the energy is lowest because the electrostatic interaction between the positively charged nucleus and the external negative point charges is largest; state (a) is intermediate, and in state (b) the energy is highest. We include this simple picture because it illustrates that in order to measure an NQI, (i) the nucleus must be nonspherical, and the measure of this is the nuclear electric quadrupole moment Q; and (ii) the surrounding charge distribution must deviate from spherical or cubic symmetry. For example, highly symmetric structures such as a perfect tetrahedral or octahedral coordination geometry with four or six identical ligands will not give rise to a measurable NQI. The relevant property of the charge distribution surrounding the nucleus is the EFG tensor at the position of the nucleus, which reflects the deviation

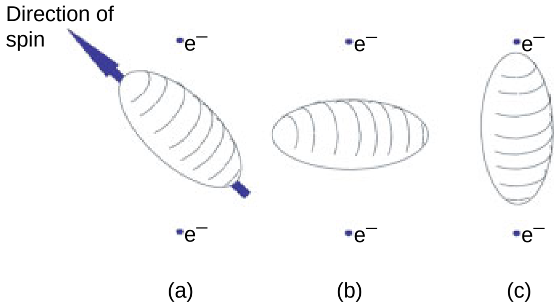

Figure 1 Nucleus in external electric field gradient—a classical picture. The nuclear quadrupole interaction (NQI) between the positive nuclear charge distribution and the surrounding charge distribution (in this case two negative point charges) leads to the energy being lowest in (c), intermediate in (a), and highest in (b). Similarly in a quantum mechanical picture the NQI leads to a splitting of a nuclear energy level into a number of sublevels, depending on the spin, I, of the nucleus ($I + 1/2$ sublevels for half-integer spin and $2I + 1$ for integer spin). In PAC spectroscopy this hyperfine splitting is measured, providing a ‘‘fingerprint’’ of the local charge distribution. (Reprinted with permission from E. Danielsen’s lecture notes on PAC spectroscopy (http://www.matfys.kvl.dk/biophys/notes.pdf))

from spherical symmetry. Finally, the figure illustrates that if the nuclear spin direction is inverted is not affected the NQI (in an axially symmetric EFG). These qualitative arguments imply that, contrary to NMR, for example, the $m = +3/2$ and the $m = -3/2$ states of spin $I = 3/2$ nucleus are degenerate, as the geometric arrangement between nucleus and external charges is the same in these two cases. Thus, the NQI leads to a splitting of the nuclear energy levels for nuclei with $I \geq 1$. In the general case where the EFG is not axially symmetric, the m-states are no longer eigenstates of the Hamiltonian, but the same number of substates appear for half-integer spins because the ±degeneracy is not lifted. For integer spins, this is not the case and thus $2I + 1$ sublevels appear. *The energy differences between these sublevels are dictated by the NQI, and thus by the local electronic and molecular structure around the PAC probe, and this ‘‘fingerprint’’ of the local structure is measured in PAC spectroscopy.*

2.2 How are These Energy Differences Measured?

As briefly touched upon in the introduction, there is an angular correlation between particles emitted in succession in a nuclear decay. They are not emitted in random directions with respect to each other, due to the conservation of angular momentum in the nuclear decay. In Figure 2, the properties of the nuclear decay of $^{111\mathrm{m}}$Cd, a commonly used PAC isotope, are presented.

Two γ-rays are emitted (γ_1 and γ_2) in succession, and the angular correlation between them inherent in the nuclear decay is depicted in Figure 2(b). This angular correlation is perturbed by the NQI that the nucleus experiences in the time between emission of γ_1 and γ_2, that is, while it is in its intermediate state (the $I = 5/2$ state for $^{111\mathrm{m}}$Cd, Figure 2(a)). It turns out that the effect of the NQI is that the probability of detecting γ_2 at a given angle with respect to γ_1 changes in a periodic manner with time. For example, for $^{111\mathrm{m}}$Cd the probability of detecting γ_2 at 180° with respect to the first γ ray is maximal at time = 0 ns (Figure 2b) but after a certain time it will fall to a minimum, then increases to the maximum again, and so on, in an oscillatory manner, similar to watching a lighthouse, where the probability of seeing a photon also varies periodically. This so-called perturbation function is, however, in most cases more complicated than just a single cosine; it is a linear combination of cosines. The frequencies (ω_i) in this periodic function are those corresponding to transitions between the nuclear energy sublevels ($\hbar\omega_\mathrm{i}$) described above; this is the essence of PAC spectroscopy, because it allows for measurement of these energy differences. For a spin 5/2 intermediate nuclear state, which splits into three sublevels (Figure 2(a)), transitions may occur between sublevel 1 and 2, 1 and 3, or 2 and 3, leading to three frequencies (ω_1, ω_2, and ω_3). Notice that $\omega_1 + \omega_2 = \omega_3$, so only two independent parameters are determined (for PAC measurements on randomly oriented samples). In a single crystal experiment, it is, in addition, possible to determine the orientation of the principal coordinate system of the EFG tensor, that is, to record five independent parameters. *In PAC spectroscopy the NQI is measured through the time dependent change of the angular correlation between γ-rays emitted in succession in nuclear decays.*

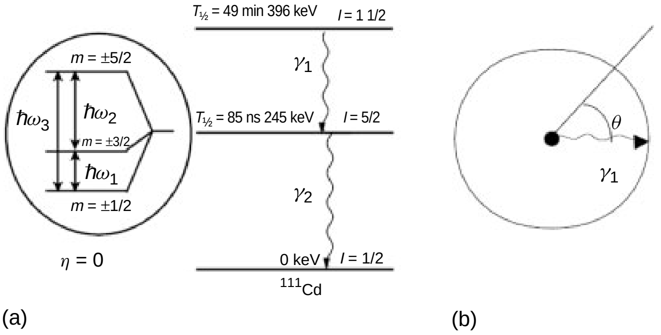

Figure 2 The decay of $^{111\mathrm{m}}$Cd–a commonly used PAC isotope (a) $^{111\mathrm{m}}$Cd decays by the successive emission of two γ rays, and in PAC spectroscopy the hyperfine splitting of the intermediate nuclear level ($I = 5/2$) is measured. The hyperfine splitting is shown magnified by about a factor of 10^{12} in the circle to the left for the case of an axially symmetric EFG from the surrounding charge distribution ($\eta = 0$, see the text). (b) The angular correlation between γ_1 and γ_2 is shown; the distance from the center to the curve is proportional to the probability of detecting γ_2 at a given angle, θ, with respect to γ_1

If the EFG changes in the time between the emission of the first and second γ ray, that is, while the nucleus is in the intermediate state, the PAC signal is affected. Such dynamic features may originate from Brownian tumbling of the molecules in solution or from dynamics at the site of the PAC probe. Consequently PAC spectroscopy can provide information on dynamics if it occurs on the timescale of the lifetime of the intermediate level (or faster[20–24]) of the PAC probe.

As α- and β-particles will not escape the sample (e.g., a solution or crystals) and a test tube to any significant degree, only $\gamma-\gamma$ PAC spectroscopy has been applied in chemistry.

In Table 1, relevant data for selected PAC isotopes are presented. Several other PAC isotopes exist, for example (mother/daughter nucleus): ^{115}Cd/^{115}In, ^{117}Cd/^{117}In, $^{118\mathrm{m}}$Sb/^{118}Sn, $^{129\mathrm{m}}$Te/^{129}I, ^{140}La/^{140}Ce, ^{172}Lu/^{172}Yb, and we refer the reader to the bibliography for details on these.[25–27] The three nuclei decaying via isomeric transitions ($^{111\mathrm{m}}$Cd, $^{199\mathrm{m}}$Hg, and $^{204\mathrm{m}}$Pb) are attractive because no change of element accompanies the nuclear decay. So-called after effects of the nuclear decay can cause serious complications in the interpretation of the experimental data, a problem that is particularly pronounced for electron capture (EC) processes.

2.3 How are the Data Extracted in an Experiment?

The six-detector PAC instrument[12] has γ-ray detectors positioned at either 90° or 180° with respect to each other (Figure 3).

When a γ_1 is detected in one detector a clock is started. If a γ_2 is detected in one of the remaining five detectors within 5–10 times the lifetime of the intermediate level (85 ns for $^{111\mathrm{m}}$Cd) the time and angle (90° or 180°) between γ_1 and γ_2 is recorded. In a PAC measurement a large number of such $\gamma_1-\gamma_2$ coincidences are recorded, and the data are transformed into the so-called perturbation function, that is, the periodic function containing the transition frequencies described above. That is, the perturbation function holds the information about the NQI and therefore, about the local electronic and molecular structure that can be determined in a PAC experiment. The perturbation function is subsequently Fourier (or cosine-) transformed, and this gives a spectrum with a number of peaks depending on the nuclear spin; in the case of $I = 5/2$ three peaks at ω_1, ω_2, and ω_3 are found (Figure 4).

Table 1 Properties of selected PAC isotopes[25]

Parent	Half-life	Decay	Daughter	Intermediate state half-life (ns), spin	E(γ_1) keV	E(γ_2) keV
^{44}Ti	47 years	EC	^{44}Sc	153, 1	78	68
^{57}Co	271 days	EC	^{57}Fe	98.5, 3/2	122	14.4
^{99}Mo	66 h	β^-	^{99}Tc	3.61, 5/2	740	181
^{99}Mo	66 h	β^-	^{99}Tc	3.61, 5/2	740	141
^{99}Rh	4.7 h	EC	^{99}Ru	20.5, 3/2	527	89
$^{111\mathrm{m}}$Cd	49 min	IT	^{111}Cd	85.0, 5/2	151	245
^{100}Pd	3.6 days	EC	^{100}Rh	214.5, 2	84	75
^{111}In	2.8 days	EC	^{111}Cd	85.0, 5/2	171	245
^{111}Ag	7.5 days	β^-	^{111}Cd	85.0, 5/2	97	245
^{133}Ba	11 years	EC	^{133}Cs	6.27, 5/2	356	81
^{181}Hf	42 days	β^-	^{181}Ta	10.8, 5/2	133	482
^{187}W	23.9 h	β^-	^{188}Re	555, 9/2	479	72
$^{199\mathrm{m}}$Hg	42.6 min	IT	^{199}Hg	2.45, 5/2	374	158
$^{204\mathrm{m}}$Pb	67.2 min	IT	^{204}Pb	265, 4	912	375

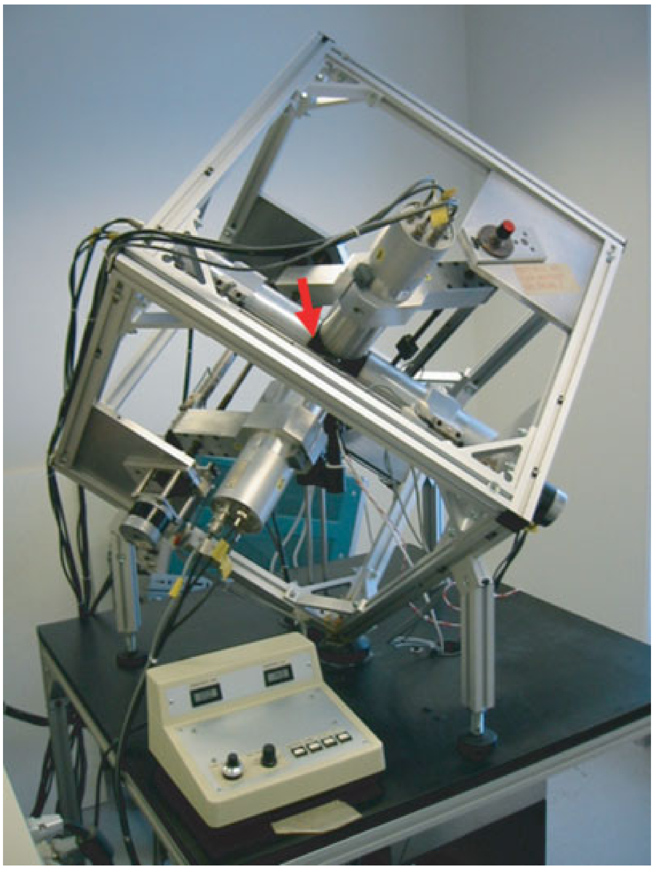

Figure 3 Six-detector PAC instrument. The arrow indicates the position of the sample, which in this setup is a regular test tube. The six detectors face the sample (two of the detectors are not visible; they are hidden behind the other detectors)

2.4 Parameters Determined in a PAC Experiment

The analytical expression for the perturbation function is known, and this is fitted to the experimentally determined perturbation function. This leads to the determination of not only the transition frequencies described above, but also of other parameters related to amplitude and lineshape of the signal, as described in the following text. For a spin 5/2 intermediate nuclear state, the data analysis leads to the determination of ω_1, ω_2, and ω_3. Usually ω_1, ω_2, and ω_3 are not reported in themselves, but transformed into two other independent parameters (recall that only two of these frequencies are independent). There are various traditions in terms of which parameters to report, but qualitatively one refers to the NQI strength $\nu_\mathrm{Q} = eq_{zz}Q/h$ (or $\omega_\mathrm{Q} = \omega_\mathrm{E} = 2\pi/(4I(2I-1))\nu_\mathrm{Q}$),

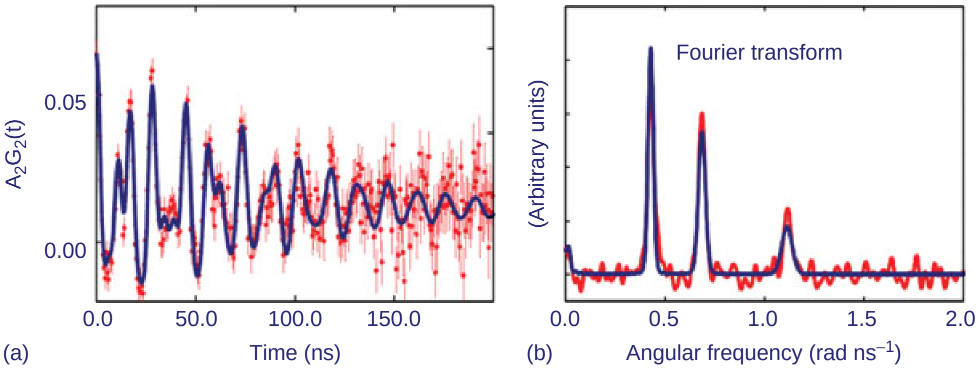

Figure 4 ^{111m}Cd PAC data—example. (a) Experimentally determined perturbation function that contains the information on the local structure and dynamics at the PAC probe site (data points with error bars and fit (full line)).(b) Fourier transform of the experimental data (red) and of the fit (blue). This dataset was recorded for the cadmium-substituted blue copper protein azurin.[28] (After Figure 6 in[11])

where q_{zz} is the numerically largest eigenvalue of the EFG tensor, and Q is the electric quadrupole moment of the nucleus in the intermediate state with nuclear spin I ($\omega_0 = (3\pi/10)\nu_Q$ is used for ^{111m}Cd and ^{111}Ag). The other refers to the asymmetry parameter ($\eta = (q_{xx} - q_{yy})/q_{zz}$, where eq$_{ii}$ are the eigenvalues of the EFG tensor ordered such that $|q_{zz}| \geq |q_{yy}| \geq |q_{xx}|$) and thus to the asymmetry of the structure at the site of the PAC probe. In an axially symmetric structure η is 0, and the largest value of this parameter, namely 1, is found, for example, in a tetrahedral complex with 2A and 2B ligands. η and ν_Q can be calculated for a given molecular structure using first principles quantum mechanical methods.[29–36] For cadmium a semiempirical method has been developed[37] based on complexes of relevance in bioinorganic chemistry.

The amplitude of the signal, A, is also determined. It depends on spins, multipolarities, and eventually on mixing ratios of the transitions involved, that is, entirely on nuclear parameters, and thus is a well-known quantity; in practice, it is further reduced by solid angle correction factors. If more than one structure at the site of the PAC probe is present in the sample, the relative amplitudes will, in general, directly reflect the relative population of the different sites.

The lineshape of the Fourier transformed data can be affected by structural variations at the site of the PAC probe from one molecule to the next, reflected in the relative peak width δ. Thus, δ qualitatively reflects the structural flexibility at the site of the PAC probe. Dynamics similarly affects the PAC signal, and is reflected in the parameter τ_c. An important difference between static inhomogeneous linebroadening and dynamic linebroadening is given by the fact that in the former case a time-independent fraction (1/5 for half-integer spins) of the anisotropy remains whereas in the latter case the angular correlation is completely lost for sufficiently long times.

To summarize, five parameters (A, η, ν_Q (or ω_0), δ and τ_c) are determined for each structure present at the site of the PAC probe in the sample.

3 APPLICATIONS

3.1 Bioinorganic Chemistry

In this section we illustrate the problems that may be addressed using PAC spectroscopy by a variety of examples from the literature. We aim to cover the central aspects of application of PAC spectroscopy in bioinorganic chemistry using these selected examples, rather than to provide a description of all papers published in this field.

It is well-known that the key processes of life, including enzyme catalysis, biochemical signalling via protein–protein interactions and protein structure, dynamics, and folding require the presence of metal ions in many cases. In PAC spectroscopy the native metal ion has to be replaced with a radioactive element with appropriate nuclear properties, and the most commonly used isotopes in bioinorganic applications are ^{99}Mo,^{111m}Cd, ^{111}Ag, ^{111}In, ^{181}Hf, ^{199m}Hg, and very recently, also ^{204m}Pb. Cd(II) is a useful substitute for Zn(II) in biochemistry because it holds the same formal charge and is a closed shell ion, and usually Cd(II)-substituted zinc ion containing enzymes are still active. Ag(I) is similarly a useful substitute for Cu(I), and several copper ion binding proteins have been investigated using PAC spectroscopy. Both Zn(II) and Cu(I) are silent in most other spectroscopic (except X-ray and nuclear) techniques, and PAC spectroscopy offers a unique approach to study zinc[38–62] and copper ion[28,47,48,53,58,59,63–74] containing proteins. ^{181}Hf, ^{111}In, and ^{99}Mo have been applied to study iron ion and molybdenum ion containing proteins, respectively.[75–92] Finally, ^{111m}Cd and ^{199m}Hg have been used in studies of de novo designed heavy metal ion binding proteins and proteins involved in bacterial heavy metal resistance.[71,93–97] Other applications include cadmium and indium binding to bovine serum albumin and DNA, as well as in vivo experiments on bacteria.[84–87,94,98–115]

3.1.1 Structure at the Site of the PAC Probe

The most common application of PAC spectroscopy in bioinorganic chemistry is the elucidation of the local structure at the PAC probe site. Selected examples of this type of application are covered in the following paragraphs.

Certain bacteria have developed resistance toward heavy metals such as mercury, and a well characterized system is that of the MerR and MerA proteins. MerA is an enzyme that reduces Hg(II) to the less toxic Hg, and MerR is a DNA-binding protein that regulates the expression of MerA. If Hg(II) is present at concentrations above about 10 nM in the cell, the MerR mercury biosensor binds the Hg(II) and consequently MerA is expressed. The high affinity and high selectivity for Hg(II) at the binding site in MerR has led to considerable effort to uncover how this binding site is designed, that is, what is the coordination geometry of the bound Hg(II). Initially, this was studied using ^{199}Hg NMR leading to the conclusion that Hg(II) is bound in a planar trigonal structure with three cysteines coordinating in both the free and the DNA-bound protein.**[116]** The free protein was studied a few years later by $^{199\mathrm{m}}$Hg PAC spectroscopy. In order to interpret the PAC spectrum recorded for MerR a variety of small Hg(II) complexes with known structure were investigated with $^{199\mathrm{m}}$Hg PAC spectroscopy. Using this reference data set the $^{199\mathrm{m}}$Hg PAC data for MerR was assigned to an almost perfect trigonal planar coordination geometry in agreement with the NMR data.**[117]** Similarly, the Hg(II) coordination geometry was studied for the MerA enzyme.**[65,117]** The interpretation of the PAC data was also carried out using a theoretical approach, and it was demonstrated that using first principles density functional calculations on selected thiol containing Hg(II) complexes, agreement with experimental data within about 20% was obtained.**[36]** In the investigation of the MerR and MerA proteins PAC spectroscopy is particularly useful, as a PAC probe ($^{199\mathrm{m}}$Hg) exists for the biochemically relevant element (Hg(II)), and no potential artifacts occur due to the replacement of the native metal ion with a different probe.

In an effort to uncover the basic chemistry of heavy metal–protein interactions, the group led by Pecoraro carried out de novo design of a variety of thiol-rich heavy metal ion binding peptides, and characterized the metal site structure using (extended X-ray absorption fine structure, *see* ***X-Ray Absorption Spectroscopy***) EXAFS, UV-Vis absorption spectroscopy (of the sulfur-to-metal charge transfer bands), electronic circular dichroism (CD), and NMR spectroscopy. In the first $^{111\mathrm{m}}$Cd PAC study of these peptides, it immediately became clear that PAC spectroscopic data contributed unique information on the Cd(II) coordination geometry:**[95]** Only one ^{113}Cd NMR signal was observed, but surprisingly two $^{111\mathrm{m}}$Cd PAC signals were observed for several of the peptides. The explanation for this apparent discrepancy is found in the time scales on which the two techniques monitor the sample. In the PAC experiment the two NQIs recorded correspond to two coordination geometries in slow exchange, which are stable on a timescale of nanoseconds (this timescale is dictated by the lifetime of the intermediate level in the nuclear decay; 85 ns for $^{111\mathrm{m}}$Cd). One NQI was unambiguously assigned to a trigonal planar structure with three coordinating cysteines, while the other was tentatively assigned to a tetrahedral structure with an additional coordinating water molecule. The NMR signal is in fast exchange, that is, the water molecule jumps on and off on a timescale faster than milliseconds. The group led by Pecoraro then redesigned the peptides, and managed to construct peptides which displayed exclusively one or the other of the two coordination geometries, as supported by both NMR and PAC data recorded for these species.**[96]** In Figure 5,

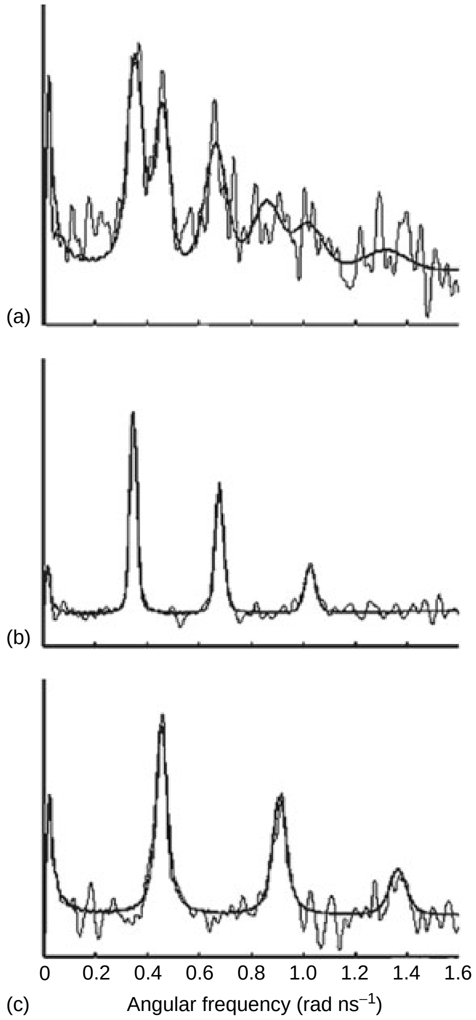

Figure 5 $^{111\mathrm{m}}$Cd PAC spectra for de novo designed peptides. Fourier transform of the experimental data (thin line) and Fourier transform of the fit (bold line). (a) Two coexisting coordination geometries in slow exchange in $[\mathrm{Cd(II)(TRI\ L16C)_3}]^-$, (b) the signal interpreted as a tetrahedral structure with three cysteines and one water molecule coordinating in $[\mathrm{Cd(II)(TRI\ L12A/L16C)_3}]^-$, and (c) the signal from a trigonal planar structure with three cysteines coordinating in $[\mathrm{Cd(II)(TRI\ L16Pen)_3}]^-$. Note that adding spectrum (b) and (c) gives spectrum (a). (Reprinted with permission from Lee, Cabello, Hemmingsen, Neil, Marsh and Pecoraro.**[96]** © 2006 Wiley-VCH)

the PAC spectra are shown for the peptide with a pure trigonal Cd(II) coordination geometry (c), a pure tetrahedral coordination geometry (b) and the more complex spectrum of the peptide with the two coordination geometries coexisting in slow exchange (a). Recently, ^{199m}Hg PAC spectroscopic studies of Hg(II) binding to de novo designed peptides has been undertaken. The results indicate that the fundamental chemistry, for example, affinity and selectivity, of Hg(II) binding to proteins can be explored successfully.**[118]**

A particular advantage of PAC spectroscopy is the extreme sensitivity to changes in the first coordination sphere of the PAC probe. Examples of such changes include titration of a metal ion-bound water molecule in the enzyme alcohol dehydrogenase, binding of inhibitors to the blood pressure regulating enzyme angiotensin converting enzyme (ACE), and metallo β-lactamases, structural changes at the metal site of carboxypeptidase during catalysis, and several others. As an example, Figure 6 shows the ^{111m}Cd PAC spectra recorded for horse liver alcohol dehydrogenase at different pH values.**[38]** The spectra clearly change with pH. At pH 7.9, only one NQI is found, giving rise to a broad peak at about 450 Mrad s^{-1}. In principle, three peaks should be observed, but in this case the line broadening of the two first peaks, which are close to each other, is so large that they coalesce into one, and the third peak (at about 900 Mrad s^{-1}) is so broad that it vanishes in the noise. (There is an additional small signal at low frequency that originates from cadmium that has migrated to the so-called structural site of the enzyme.) On increasing the pH, a new signal at about 250 Mrad s^{-1} appears, whereas the signal at 450 Mrad/s^{-1} decreases, and a pK$_a$ of 11.0 can be fitted to the data. In the resting state, the enzyme supplies three ligands to the metal ion binding site, two cysteines and a histidine, and the fourth ligand position is occupied by a water molecule. The pK$_a$ of this water molecule is of considerable interest as it may affect the function of the enzyme. In the native enzyme a Zn(II) ion essential for the function of the enzyme is bound at the active site. The Cd(II)-substituted species is still catalytically active, although with a lower specific activity than the native enzyme at the pH of the standard assay. Kvassman and Pettersson**[119]** carried out a careful analysis of the pH dependence of the association of the oxidized and reduced coenzyme (nicotinamide adenine dinucleotide (NAD$^+$) and reduced nicotinamide adenine dinucleotide (NADH)), and found a pK$_a$ of 9.2, regulating the association but the coenzyme binding probes a large part of the active site, and the pK$_a$ might originate from other titrating groups than the metal ion-bound water molecule. The PAC data are specific for the very local surroundings of the metal ion, and spectral changes as large as those reported in Figure 6 indicate that the titrating group is in the first coordination sphere. It can be observed that the NQI falls off rapidly with the distance from the cadmium nucleus (roughly as r^{-3}),**[29]** and typically changes within the first 3–5 Å can be abserved. The fact that the pK$_a$ observed for the Cd(II) substituted enzyme is higher than that observed for the native Zn(II) containing enzyme is expected, as the ionic radius of Cd(II) is larger than that of Zn(II), and thus Cd(II) is less potent at polarizing the metal ion-bound water molecule. Thus the two sets of experiments indicate that the pK$_a$ of the metal ion-bound water molecule is 9.2 for the native free enzyme. Similarly, a pK$_a$ of 9.6 was determined in ^{111m}Cd PAC studies of the binary complex between enzyme and NAD$^+$, whereas no pK$_a$ was observed for the binary complex between enzyme and NADH, probably because it lies above the pH range covered. The quantitative structural analysis in Ref. 38 was based on the Bauer's axially symmetric independent ligands model (BASIL) (previously denoted the angular overlap model (AOM) for PAC spectroscopy),**[37]** and a few years later a comprehensive analysis using a combined quantum mechanical and molecular mechanical (QM/MM) method was preserved.**[32]**

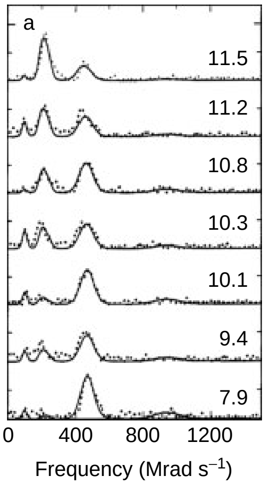

Figure 6 ^{111m}Cd PAC spectra for horse liver alcohol dehydrogenase at different pH values. Fourier transform of the experimental data (dotted line) and Fourier transform of the fit (bold line). The spectrum changes with pH (indicated for each spectrum), and this is interpreted as the titration of a metal ion-bound water molecule with a pK$_a$ of 11.0. (Reprinted with permission from Hemmingsen, Bauer, Bjerrum, Zeppezauer, Adolph, Formicka and Cedergren-Zeppezauer.**[38]** © 1995 American Chemical Society)

The linebroadening of the PAC signal offers information on the structural flexibility and dynamics at the site of the PAC probe. Qualitatively, a structurally flexible site will result in slightly different structures from one molecule to the next, giving rise to a distribution of NQIs, typically observed as a relatively broad signal. In this paragraph we will focus on structural flexibility, returning to dynamics later (*see* Section 3.1.2). One example of this is the signal recorded for carboxypeptidase A under different physical conditions (Figure 7). In the crystalline state, the lines in the Fourier transform of the perturbation function are narrow, indicating that the structure at the metal ion binding site is relatively rigid, as expected. In solution the signal is very similar, but the lines are broadened, indicating that the metal site structure is more flexible than in the crystalline state, at least for the

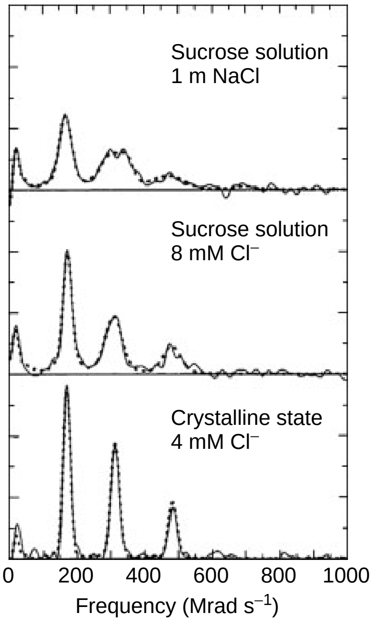

Figure 7 ^{111m}Cd PAC spectra for carboxypeptidase A under different physical conditions. Fourier transform of the experimental data (dotted line) and Fourier transform of the fit (bold line). The line broadening found in solution as compared to the crystalline state indicates that the metal ion binding site is structurally more flexible in solution. (Reprinted with permission from Bauer, Danielsen, Hemmingsen, Sørensen, Ulstrup, Friis, Auld and Bjerrum.[42] © 1997 American Chemical Society)

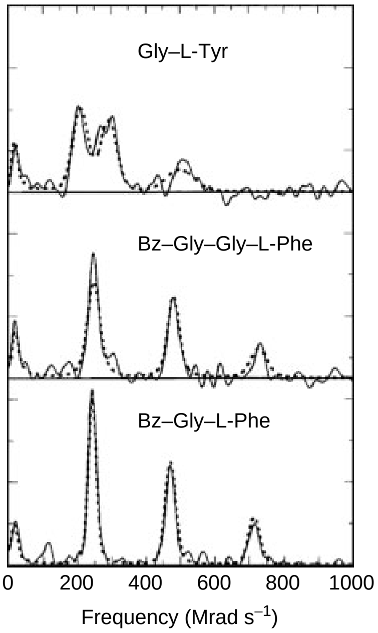

Figure 8 ^{111m}Cd PAC spectra for Carboxypeptidase A under steady state hydrolysis of small peptides. Fourier transform of the experimental data (dotted line) and Fourier transform of the fit (bold line). The lines are relatively narrow for the two ‘‘good’’ substrates Bz–Gly–L-Phe and Bz–Gly–Gly–L-Phe, but relatively broad for the ‘‘poor’’ substrate Gly–L-Tyr, indicating that the active site structure is more rigid for the ‘‘good’’ substrates, possibly because it is optimized for catalysis. (Reprinted with permission from Bauer, Danielsen, Hemmingsen, Sørensen, Ulstrup, Friis, Auld and Bjerrum.[42] © 1997 American Chemical Society)

enzyme in the resting state. In a 1M NaCl solution the signal is also broadened, and different from the signal with low chloride concentration, indicating that chloride affects the coordination geometry. This example also illustrates that PAC spectroscopy can be applied to different physical states, for example, in addressing the question whether the structure in the crystalline state (used in X-ray diffraction based protein structure determination) represents that found in solution. In several PAC studies on enzymes it has been observed that the metal site structure is flexible in the free enzyme, but rigid in complexes with substrate or inhibitors.

PAC spectroscopic studies may be carried out during catalysis, as has been demonstrated under steady state conditions for the hydrolysis of peptides by cadmium-substituted carboxypeptidase A[42] (Figure 8). The ^{111m}Cd PAC spectra reflect the structure(s) present at the rate determining step of the reaction. The two substrates Bz–Gly–L-Phe and Bz–Gly–Gly–L-Phe are hydrolyzed relatively fast by the enzyme, that is, they are ‘‘good’’ substrates, whereas Gly–L-Tyr is hydrolyzed relatively slowly. The line width for the two ‘‘good’’ substrates is relatively small, indicating that the metal site coordination geometry is very well defined, probably optimized for catalysis. In contrast, there is considerable line broadening for Gly–L-Tyr, possibly reflecting the suboptimal structure for catalysis in this case. An interesting new approach to the study of enzyme catalysis is the combination of PAC spectroscopy with rapid freeze quench equipment (*see* ***Freeze-Quench Kinetics***).[120] The enzyme and substrate are simply mixed and frozen rapidly (on the time scale of milliseconds or slower), and the freeze quenched samples then placed in the PAC spectrometer. Rapid freeze quenching has been successfully combined with several other spectroscopic techniques such as electron nuclear double resonance (ENDOR) (*see* ***Electron-Nuclear Double Resonance (ENDOR) Spectroscopy***), EPR (*see* ***Electron Paramagnetic Resonance (EPR) Spectroscopy***), EXAFS (*see* ***X-Ray Absorption Spectroscopy***) and Mössbauer spectroscopy (*see* ***Mössbauer Spectroscopy***). This, in principle, allows for real time recording of spectroscopic snapshots of structures evolving and decaying during the reaction, in analogy to stopped flow UV-Vis absorption (*see* ***Rapid Scan, Stopped-Flow Kinetics***) spectroscopy.

As indicated in the introduction, it is possible to carry out PAC experiments under physiological conditions, and even in vivo experiments are possible. One example of the latter is the study of the fast inhibition of photosynthesis in cyanobacteria.[98] Photosynthesis in cyanobacteria is inhibited within about 15 min after exposure to Cd(II). Exposing the cyanobacteria to ^{111m}Cd it was possible to follow the fate of Cd(II) in terms of binding to biomolecules, as the biological material is almost transparent to the γ-rays. Combining the PAC spectroscopic data with other spectroscopic data, SDS PAGE, and bioinformatics analysis of potential metal ion binding proteins in the genome of the bacteria, it was concluded that there may be a variety of biomolecules binding the Cd(II) ions, but that carbonic anhydrase is a probable candidate in the context of inhibition of photosynthesis. Similar investigations have been carried out with ^{99}Mo PAC on Fe/Mo-nitrogenases in *Azotobacter vinelandii*.[**84–87**]

A final but exclusive advantage of PAC spectroscopy is the possibility to work at extremely low probe concentrations. In principle, only of the order of 10^{10} probe nuclei are necessary for an experiment, corresponding to a concentration of about 10 pM in a 1 mL sample. However, the presence of other metal ions, even in well prepared samples where the concentration of such pollution is minimized, may interfere with the binding of the PAC probe to the biomolecule of interest. To avoid this problem, the PAC probe concentration is often kept above 1–10 μM. In addition, working with very low concentrations there is a risk that the PAC probe will be lost, for example, due to adsorption to the surface of the glassware or test tube. Nonetheless, several examples of successful PAC experiments carried out under such (so-called carrier-free) conditions exist in the literature. One particularly interesting application which can only be carried out with PAC spectroscopy, is the titration of PAC probe into a solution of a protein with two or more metal ion binding sites, starting from carrier-free conditions and ending with fully loaded protein. The final data point may be studied with most techniques, but the initial data point in this titration requires extremely low probe concentration. This has been done in a ^{111m}Cd PAC spectroscopic study of metallo β-lactamases.[**40**] Metallo β-lactamases are bacterial enzymes that hydrolyze penicillin and similar β-lactam based antibiotics, as a defense mechanism against these drugs. This leads to resistance against these drugs, and is currently a serious threat to public health. These enzymes have two metal ion binding sites, and the PAC spectra display two NQIs at carrier-free conditions. On increasing the Cd(II) concentration to fully load the two metal ion binding sites in the enzyme, the two NQIs change into two new NQIs. Thus, the metal ion binding site structure changes for both sites when the enzyme is fully loaded. The most straightforward explanation of this is that (i) at carrier-free conditions either site may be occupied, one in some enzymes, and the other site in others, and (ii) the two binding sites are positioned relatively close to each other, so the PAC signal in one site depends on whether the other site is occupied or not. Interestingly, the titration of Cd(II) into the protein solution allows for investigation of whether the binding of the two metal ions is cooperative (the signal from the binuclear site appears already at low Cd(II) to protein stoichiometry) or not. Such studies have been carried out both with and without the presence of inhibitors of the metallo β-lactamases.

3.1.2 Dynamics at the Site of the PAC Probe

Dynamics at a metal ion binding site in a protein may originate from qualitatively different sources, for example rotational diffusion (Brownian tumbling) of the molecules, conformational dynamics, or ligand exchange. In this section we illustrate how dynamics affects the PAC signal and how this may be used to derive information on protein–protein interactions, dynamics of protein folding, and metal site exchange dynamics.

In a dynamic situation where the EFG changes during the time the nucleus spends in the intermediate state, the NQI also changes, and this can lead to linebroadening or even total loss of anisotropy in the perturbation function and thus, to the loss of the PAC signal, or it can lead to motional narrowing in analogy to NMR in the case of fast exchange between two structures, a description of which follows. The dynamics is reflected in the rotational correlation time, τ_c, fitted to the PAC data, as indicated in the section on technical background. It is, in principle, possible to discriminate between structural flexibility (vide supra) and dynamics in PAC spectroscopy.

For the small blue copper protein plastocyanin the pH dependence of the metal site structure of the Cd(II)-substituted species has been investigated by ^{111m}Cd PAC. Plastocyanin is an electron transfer protein involved in photosynthesis.[**74**] For all these experiments 55% w/w sucrose was added to the solution to slow the Brownian tumbling of the molecules, an approach used routinely in biological applications of PAC spectroscopy. At pH 7.5 one dominating metal site coordination geometry is detected (see Figure 9, top panel), and as the pH is lowered to 4.4, the metal ion dissociates from the protein, giving a characteristic signal from Cd(II) in 55% w/w sucrose solution at 1 °C. Upon subsequent increase of the pH to 7.5 the original signal is recovered, but surprisingly, a new signal is also present (indicated by an arrow in Figure 9(b), lower panel). The relative population of the two signals changed on a timescale of hours, increasing the fraction of the signal originally recorded at pH 7.5, indicating that a slow structural relaxation occurred to the coordination geometry originally found at pH 7.5. As the second signal is not observed in the initial experiment at pH 7.5, where the apoprotein was incubated with cadmium for about 15 min before carrying out the experiment, the structural relaxation is not related directly to the association of the metal ion at this pH. The fact that the two signals are quite similar, indicates that the same ligands are coordinating to the metal ion. Thus, the relaxation may reflect structural changes further away from the metal ion binding site, possibly slow refolding of the protein from a local energy minimum to the native state, with a barrier large enough that this refolding intermediate exists for hours.

For rotational diffusion of the protein molecules two extreme situations can be described analytically: in the case of slow reorientation of the EFG, the amplitude of the perturbation function is damped exponentially, but oscillations are still present, and in the other extreme of fast reorientation of the EFG, the oscillations in the perturbation

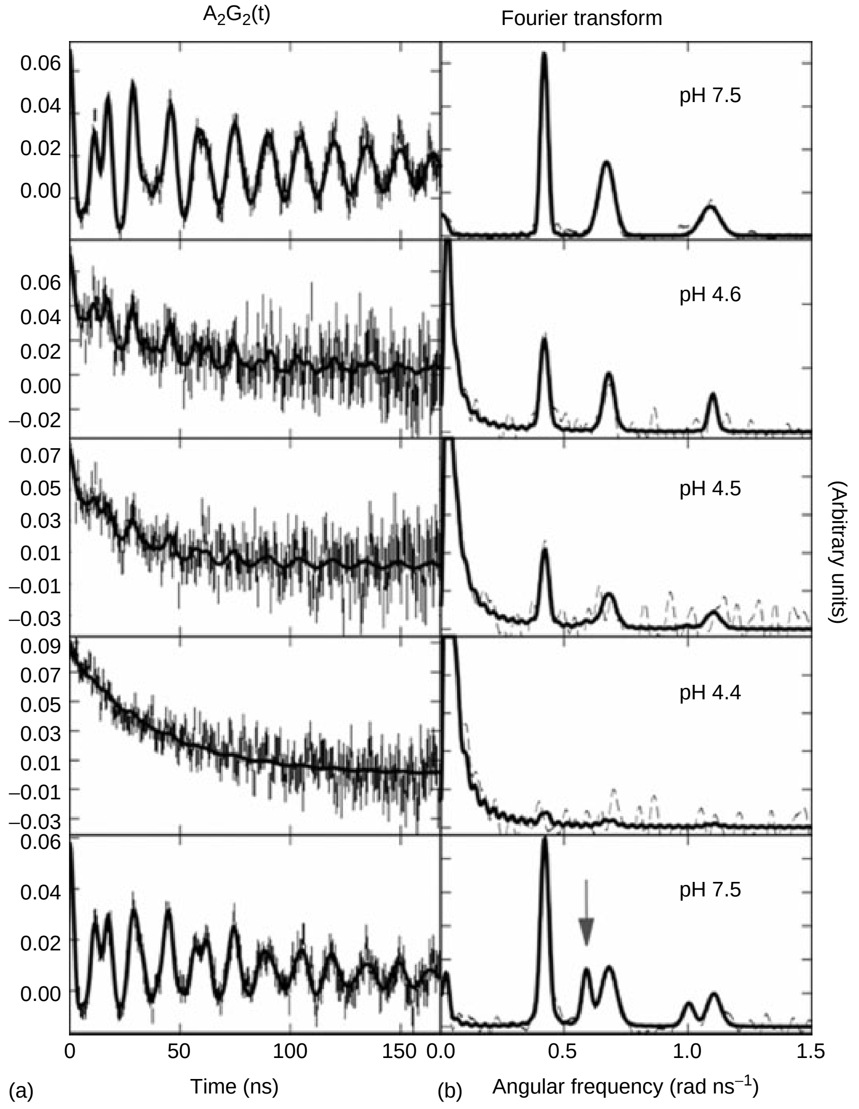

Figure 9 ^{111m}Cd PAC spectra for plastocyanin at different pH values. (a) Perturbation function (fit indicated by full line); (b) Fourier transform of the perturbation function (dotted line) and Fourier transform of the fit (bold line). On decreasing pH from 7.5, the signal from Cd(II) at the metal ion binding site is lost because it dissociates from the protein. Subsequently, on increasing pH the original signal at pH 7.5 is recovered, but surprisingly, an additional signal is present for hours (indicated by the arrow). (Reprinted with permission of Federation of the European Biochemical Societies from Sas, Hemmingsen and Danielsen[74])

function are completely lost and the perturbation function is simply described by an exponential decay. In the intermediate range it is also possible to calculate the perturbation function, although no analytical expression exists.[11,20,21] In order to limit the loss of signal due to rotational diffusion sucrose is often added to the sample (e.g., 55% w/w) to make it very viscous, and the experiments are carried out at 1 °C, or the proteins are immobilized by other means. However, in the first demonstration of the use of PAC spectroscopy to monitor protein–protein interactions, the immobilization was intentionally excluded. Two different PAC probes, ^{111}Ag and ^{111m}Cd were bound to plastocyanin, see top panels of Figure 10, in an attempt to model the two oxidation states of the copper ion bound in the native protein. The recorded perturbation function contained almost no periodic signal, indicating that the plastocyanin molecules were tumbling at a rate that obscured the signal that was observed in a quasi-static case (*see* Figure 9(a) for cadmium-substituted plastocyanin). Photosystem I (PSI) is the electron accepting physiological partner of plastocyanin. Adding PSI to the solution had practically no effect for the Cd(II)-substituted plastocyanin, but significantly affected the signal from Ag(I)-substituted plastocyanin. This indicates that the rotational diffusion of Ag(I) plastocyanin is significantly reduced and the periodic signal in the perturbation function is recovered because Ag(I) plastocyanin binds to photosystem I, whereas

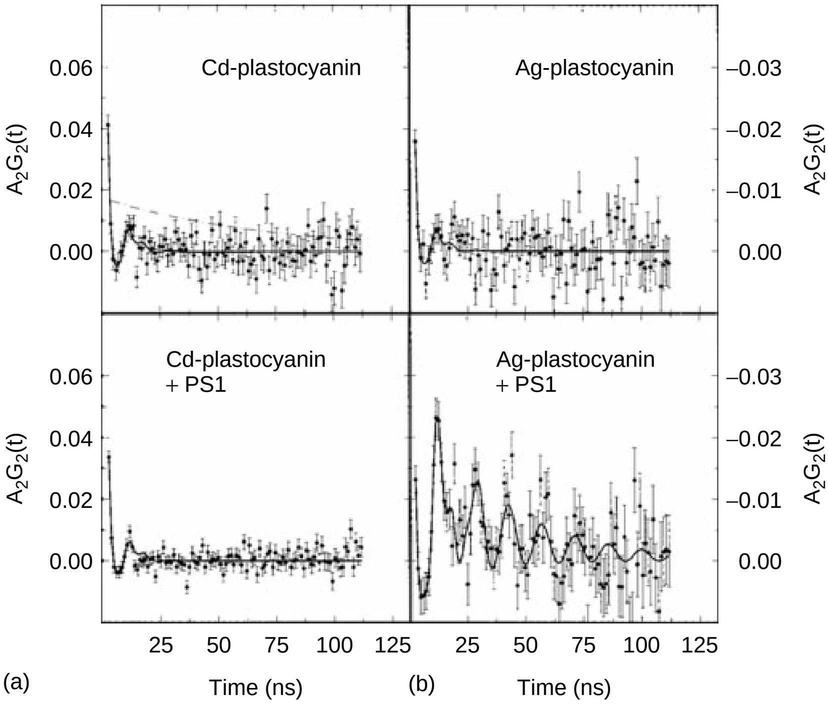

Figure 10 PAC perturbation functions for Cd(II)- and Ag(I)-substituted plastocyanin in the absence and presence of photosystem I. Experimental data with error bars and fit (full line). (a) For Cd(II)-substituted plastocyanin, there is no significant change upon addition of photosystem I (PSI), whereas for (b) Ag(I)-substituted plastocyanin the perturbation function changes dramatically. This indicates that Ag(I)-substituted plastocyanin binds to the large protein complex photosystem I, significantly reducing the rotational diffusion of plastocyanin, and thus shows that the association of these two physiological partners is regulated by the charge state of the metal ion in the manner expected. (Reprinted with permission from Danielsen, Scheller, Bauer, Hemmingsen, Bjerrum and Hansson.[28] © 1999 American Chemical Society)

Cd(II) plastocyanin does not, under the given experimental conditions. This is an illustration of an application of PAC spectroscopy to the study of protein–protein interactions, and it is even possible to estimate the dissociation constant directly from the spectroscopic data. Note that in this example the perturbation function and not the Fourier transformed data, is displayed in the figure, as the perturbation function illustrates the effect of dynamics more clearly. Note that the data analysis is almost always carried out on the perturbation function.

It has been known for decades that it should be possible to detect exchange dynamics at the site of the PAC probe in analogy to NMR, but at shorter timescales.[22,23] The timescale on which exchange dynamics can be observed is dictated by the lifetime of the intermediate nuclear level of the PAC probe. Two coordination geometries in slow exchange will give two NQIs; in intermediate exchange a damped signal will be observed, and in fast exchange, one sharp weighted average signal (of the two NQIs) will be observed. Exchange dynamics has been suggested as the most plausible explanation of experimental data in a limited number of publications (Ref. 11 and references therein). Only recently, a temperature series on Cd(II) binding to de novo designed peptides has provided data which probably constitute the first clearcut observation of exchange dynamics with PAC spectroscopy on biological samples.[121]

The final example in this section describes global rotational diffusion, as well as internal dynamics in transferrins, in what is probably the most comprehensive study of a protein family carried out with PAC spectroscopy.[75–83] Transferrins are iron transporters, with two metal ion binding sites, one in the so-called N-terminal lobe and one in the C-terminal lobe. Using ^{181}Hf as PAC probe and varying the temperature from 0 to 45 °C, the dynamics was investigated for ovotransferrin and serum transferrin.[78] It was demonstrated that slow reorientation was a valid approximation in this study, and thus that the dynamics could be represented by an exponential damping of the perturbation function for the static case. Obviously, the rotational diffusion is temperature and viscosity dependent, and in a simple model $1/\tau_c$ is proportional to T/η (where T is the absolute temperature and η the viscosity of the liquid sample–not to be confused with the asymmetry parameter). Plotting $1/\tau_c$ against T/η, the slope provides information on the hydrodynamic volume of the molecule, a property that may also be determined by neutron scattering (*see* ***Neutron Scattering***). In addition, and perhaps more interestingly, on extrapolating the fit to $T/\eta = 0$, there was a residual value for $1/\tau_c$ indicating that internal dynamics on the nano- to microsecond timescale of the proteins plays a significant role for these systems.

3.2 Inorganic Chemistry and Solid State Physics

In this section we focus on applications which provide information different from that illustrated by the examples in the section on bioinorganic chemistry. Thus the coverage of inorganic chemistry and solid state physics is not intended to be exhaustive, but to highlight the information that can be derived in addition to the local structure and dynamics at the PAC probe site (vide supra).

A seminal paper dealt with NQIs in metals and compounds for the purpose of the determination of nuclear quadrupole moments using reference moments.[8]

In the field of nuclear solid state physics the technique of TDPAC was first applied to the study of internal magnetic fields in ferromagnets and other magnetically ordered systems. The magnetic hyperfine field followed closely—but not exactly—the macroscopically determined magnetization. The deviations are likely due to the fact that the magnetic hyperfine field is determined at the site of an impurity atom where lattice relaxations and local modifications of the spin-polarized charge density play a role. Nevertheless, systematic studies of hyperfine fields in ferromagnets like iron and nickel for a large series of impurity probes gave a rather complete picture. Several studies were devoted to the determination of critical exponents near the Curie temperature.[122]

The study of NQI's on a large scale started with metals, especially defects trapped at the impurity probe atom like vacancies or other impurity atoms.[123,124] In cubic metals, the EFG at the nuclear site vanishes due to symmetry. This even holds for cases where the local lattice relaxation around an impurity atom is large, as long as the point symmetry remains cubic. As soon as there is a near-neighbor defect, the symmetry is broken locally and a finite EFG acts on the probe nucleus. In many cases, the impurity probe attracts defects or other foreign atoms—at least after annealing—such that extremely low concentrations become detectable. Of particular interest was radiation damage in cubic metals.[125] Temperature[126] and pressure[127] dependencies of EFG's were investigated. In many metals a $T^{3/2}$ temperature dependence was observed, which was related to the mean square lattice displacements due to vibrations. However, it turned out that the lattice expansion alone cannot explain the observed temperature dependence, but a local repopulation of conduction electron states is required. It should be mentioned that in a point-charge plus uniform background (of electrons) model, that is, representing the neighboring ion cores by point charges which produce the EFG via unscreened Coulomb potentials, lattice vibrations would not lead to a temperature dependence of the EFG at all. Thus far, no general theory on the temperature dependence of NQIs in metals is available.

Similarly, an attempt to separate the observed pressure dependence of the NQI in noncubic metals (mainly hexagonal closed packed) into a contribution due to the pressure dependence of the lattice constant ratio c/a and the volume V yielded an as yet unexplained $V^{-\alpha}$ dependence with α being more like three rather than one, as would be expected in a point-charge model.

Amorphous metals,[128] alloys,[128] and internal oxidation[129,130] have also been investigated. In amorphous systems, very broad frequency distributions, or in other words, heavily damped TDPAC spectra prevail, which do not readily yield more information other than that the local environment consists of a multitude of inequivalent geometries. The situation in alloys is more interesting as soon as local ordering occurs and intermetallic phases are formed. Here, TDPAC offers complementary information to X-ray diffraction because short-range order would clearly show up in the TDPAC spectra, whereas the phase analysis via X-ray diffraction requires long-range order. The same arguments apply to the case of internal oxidation. Due to the short-range nature of the NQI, molecule formation at a very early stage can be detected.

Of particular interest is the study of metal surfaces.[131,132] Probe atoms can reside on terraces or in the first surface layer or they can reside at steps, kinks, and so on. All these sites can be readily distinguished via their EFG strength, symmetry, and orientation. The deposition of probe atoms at low temperatures preferentially produces adatoms which, upon subsequent isochronous annealing, migrate to other sites. With the invention of surface techniques with atomic resolution like scanning tunneling microscopy or variants thereof, the TDPAC studies of surfaces got a strong competitor. Therefore, modern applications of TDPAC deal with magnetism on surfaces and at interfaces[133] where information with atomic resolution can be obtained, which is not accessible otherwise. It appears that the magnetic hyperfine field acting on the probe nucleus depends essentially on the coordination number of the magnetic neighbors rather than on the geometrical details.

After the ‘‘metal era’’ the studies of defects at impurity probe atoms were extended to semiconductors,[134] a field which is still active due to the relevance for applications. Doping of semiconductors is achieved by introducing donor or acceptor atoms, usually at extremely low concentrations. Frequently, the number of mobile charge carriers (electrons or holes) is much lower than expectations based on the doping levels. Here, the dopants can be passivated by impurities, for example, hydrogen or copper atoms. In addition, the dopant could reside on an interstitial or even bond-center site instead of being substitutional. In all these cases, TDPAC can be of valuable help due to its extreme sensitivity. The strength, symmetry, and orientation of the EFG tensor yields detailed information on the probe atom geometry on an atomic level. Again, interactions of the impurity atom with defects play a crucial role. The situation becomes particularly complicated in binary or ternary systems.

Further investigations dealt with structural phase transitions. In general, structural phase transitions are easily detected in diffraction studies or by differential thermal calorimetry. However, frequently such transitions are accompanied by local dynamics of atoms on sublattices prior to the transition which are not readily observed by diffraction techniques. Here, the lattice dynamics which shows up in the TDPAC spectra are of particular value in understanding the origin of the phase transition.

Particularly interesting cases are charge density wave (CDW) transitions in transition metal dichalcogenides.[135] In the commensurate CDW state, a superlattice is formed whose size and symmetry is given by diffraction studies. What is less obvious is the determination of the phase of the CDW with respect to the underlying lattice, that is, is the charge density maximum (or minimum) located on an atomic site or not. This has immediate consequences for the number of inequivalent lattice sites with certain populations. These are easily detected by TDPAC. Thus, in 1T-TaS_2 with octahedral metal coordination, a $\sqrt{13} \times \sqrt{13}$ superstructure is formed with the charge density maximum located on an atom site, thus forming a star-of-David structure with three inequivalent lattice sites with populations of 1:6:6 and axial symmetry at the central site (the strong coupling between adjacent layers leads to further small distortions; the undistorted 1:6:6 pattern is best observed in the 6R-modification where the CDW is formed in every second layer with octahedral coordination). On the contrary, in 2H-TaS_2 with trigonal prismatic metal coordination, a 3×3 superlattice is formed with the charge density maximum between three Ta-atoms. Hence, a sort of ‘‘snow-flake’’ with three inequivalent lattice sites and 3:3:3 populations, none of which exhibit axial symmetry, is formed (again, the coupling between neighboring layers leads to a further small distortion). A rather interesting situation is observed when the CDW is incommensurate with the underlying lattice. In this situation, there is no repeat period any more, that is, there is no unit cell. All metal atoms are subjected to slightly different EFGs due to slightly different charge densities, and line shapes characteristic of 1- or 2-dimensional incommensurate CDWs are observed. They manifest themselves in streaks in electron diffraction patterns. Hyperfine spectroscopies, in general, have elucidated this field of CDWs.[135]

TDPAC turned out to be ideally suited for the in situ study of intercalation reactions in 2H-TaS_2 and other host materials.[136,137] Metal ions, hydrated or solvated ions, as well as molecules can be intercalated between the layers which are held together with weak van der Waals forces only. These guest species can enter the host lattice only via the prism surfaces, that is, parallel to the layers. Upon intercalation, the lattice expands perpendicularly to the layers in order to accommodate the guest species. In the initial stage, strong elastic lattice deformations occur. The driving force which actually overcomes the energy barrier due to elastic lattice deformation is the charge transferred from the guest to the host. This has an immediate effect on the NQI at the host metal site (and also on the chalcogen site). It turned out that the NQI is a reliable measure of the charge transfer and also of the fraction of intercalated phase during the reaction. Electrochemical control of the reaction allows to keep the average prism current density constant, contrary to chemical reactions. In the latter case, nonequilibrium phases were observed when a critical current density was exceeded. This could be verified by electrochemical intercalation at high current densities.

Structure and bonding have been explored using the EFG as an experimental anchor that must be reproduced in theoretical studies of the electronic structure. For Cd(II), it has been demonstrated that both charge transfer from the ligands into the unfilled 5p cadmium orbitals and back-bonding involving the filled 4d cadmium orbitals, play a significant role in determination of the EFG at the site of the cadmium nucleus.[34] The contribution from the 5p electrons is dominating, and this forms the basis of the semiempirical BASIL model for calculations of NQIs in cadmium complexes.[29,35,37] A ‘‘calculator’’ for this model is available at http://www.matfys.kvl.dk/~eva/aom.html (we acknowledge Eva Danielsen for providing the code for this program).

Finally, in a single crystal experiment it is possible to extract all five independent elements of the traceless NQI tensor, usually chosen to be the orientation of the EFG principal axis system, in addition to the two parameters accessible for randomly oriented samples (η and ν_Q). This, of course, requires that it is possible to make a single crystal incorporating the radioactive mother nucleus, and is therefore limited to cases where the preparation can be completed within roughly the lifetime of the mother nucleus, for example, see Ref. 138.

4 ABBREVIATIONS AND ACRONYMS

ACE = angiotensin converting enzyme; AOM = angular overlap model; BASIL = Bauer's axially symmetric independent ligands model; CD = circular dichroism; CDW = charge density wave; EC = electron capture; EFG = electric field gradient; ENDOR = electron nuclear double resonance; EPR = electron paramagnetic resonance; EXAFS = extended X-ray absorption fine structure; NAD^+ = nicotinamide adenine dinucleotide; NADH = reduced nicotinamide adenine dinucleotide; NMR = nuclear magnetic resonance; NQI = nuclear quadrupole interaction; NQR = nuclear quadrupole resonance; PAC = perturbed angular correlation; PSI = photosystem i; SDS-PAGE = sodium dodecyl sulfate-polyacrylamide gel electrophoresis; TDPAC = time differential perturbed angular correlation.

5 FURTHER READING

C. Hohenemser, G. S. Collins, R. M. Suter and L. Chow, *Phys. Rev. Lett.*, 1983, **50**, 1877.

T. Butz, *Phys. Scr.*, 1978, **17**, 445.

6 REFERENCES

1. D. R. Hamilton, *Phys. Rev.*, 1940, **58**, 122.
2. E. L. Brady and M. Deutsch, *Phys. Rev.*, 1947, **72**, 870.
3. E. L. Brady and M. Deutsch, *Phys. Rev.*, 1948, **74**, 1541.
4. E. L. Brady and M. Deutsch, *Phys. Rev.*, 1950, **78**, 559.
5. G. Goerzel, *Phys. Rev.*, 1946, **70**, 897.
6. H. Frauenfelder, *Phys. Rev.*, 1951, **82**, 549.
7. H. Aeppli, A. S. Bishop, H. Frauenfelder, M. Walter and W. Zünti, *Phys. Rev.* 1951, **82**, 550.
8. H. Haas and D. Shirley, *J. Chem. Phys.*, 1973, **58**, 3339.
9. T. K. Leipert, J. D. Baldeschwieler and D. A. Shirley, *Nature*, 1968, **220**, 907.
10. A. Lerf and T. Butz, *Hyperfine Interact.*, 1987, **36**, 275.
11. L. Hemmingsen, K. N. Sas and E. Danielsen, *Chem. Rev.*, 2004, **104**, 4027.
12. T. Butz, S. Saibene, T. Fraenzke and M. Weber, *Nucl. Instrum. Methods Phys. Res., Sect. A- Accel. Spectromet. Detect. Assoc. Equip.*, 1989, **284**, 417.
13. I. Sergueev, U. van Bürck, A. I. Chumakov, T. Asthalter, G. V. Smirnov, H. Franz, R. Rüffer and W. Petry, *Phys. Rev. B.*, 2006, **73**, 24203.
14. H. Frauenfelder and R. M. Steffen, ‘Alpha-, Beta and Gamma-Ray Spectroscopy’, North Holland, Amsterdam, 1965, p. 997.
15. T. Butz, *Hyperfine Interact.*, 1989, **52**, 189.
16. T. Butz, *Hyperfine Interact.*, 1992, **73**, 387.
17. H. H. Rinneberg, *At. Energ. Rev.*, 1979, **172**, 477.
18. A. Lerf and T. Butz, *Angew. Chem. Int. Ed.*, 1987, **26**, 110.
19. R. Bauer, *Q. Rev. Biophys.*, 1985, **18**, 1.
20. E. Danielsen and R. Bauer, *Hyperfine Interact.*, 1990, **62**, 311.
21. E. Danielsen, L. E. Jørgensen and P. Sestoft, *Hyperfine Interact.*, 2002, **142**, 607.
22. R. Bauer, ‘Carbonic anhydrase studied by perturbed angular correlation of gamma rays’ Thesis/Dissertation, University of Copenhagen, Niels Bohr Institute, 1976.
23. H. Winkler and E. Gerdau, *Z. Phys.*, 1973, **262**, 363.
24. M. J. Clauser, *Phys. Rev. B.*, 1971, **3**, 3748.
25. R. B. Firestone, V. S. Shirley, C. M. Baglin and S. Y. F. Chu, ‘Table of Isotopes’, John Wiley & Sons, Chichester, 1996.
26. C. M. Lederer and V. S. Shirley, ‘Table of Isotopes’, 7th edition, John Wiley & Sons, 1978.
27. T. Butz, *Z. Naturforsch.*, 1996, **51a**, 396.
28. E. Danielsen, H. V. Scheller, R. Bauer, L. Hemmingsen, M. J. Bjerrum and O. Hansson, *Biochemistry*, 1999, **38**, 11531.
29. L. Hemmingsen and U. Ryde, *J. Phys. Chem.*, 1996, **100**, 4803.
30. P. Pyykkö, *Z. Naturforsch. A*, 1992, **47**, 189.
31. J. Antony, B. Hansen, L. Hemmingsen and R. Bauer, *J. Phys. Chem. A*, 2000, **104**, 6047.
32. U. Ryde and L. Hemmingsen, *J. Biol. Inorg. Chem.*, 1997, **2**, 567.
33. P. Dufek, P. Blaha and K. Schwarz, *Phys. Rev. Lett.*, 1995, **75**, 3545.
34. L. Hemmingsen, R. Bauer, M. J. Bjerrum, K. Schwarz, P. Blaha and P. Andersen, *Inorg. Chem.*, 1999, **38**, 2860.
35. L. Hemmingsen, U. Ryde and R. Bauer, *Z. Naturforsch. A*, 1999, **54**, 422.
36. T. Soldner, W. Tröger, T. Butz, P. Blaha, K. Schwarz and The ISOLDE-Collaboration, *Z. Naturforsch. A*, 1998, **53**, 404.
37. R. Bauer, S. J. Jensen and B. Schmidt-Nielsen, *Hyperfine Interact.*, 1988, **39**, 203.
38. L. Hemmingsen, R. Bauer, M. J. Bjerrum, M. Zeppezauer, H. W. Adolph, G. Formicka and E. Cedergren-Zeppezauer, *Biochemistry*, 1995, **34**, 7145.
39. L. Hemmingsen, C. Damblon, J. Antony, M. Jensen, H. W. Adolph, S. Wommer, G. C. K. Roberts and R. Bauer, *J. Am. Chem. Soc.*, 2001, **123**, 10329.
40. R. Paul-Soto, M. Zeppezauer, H. W. Adolph, M. Galleni, J. M. Frere, A. Carfi, O. Dideberg, J. Wouters, L. Hemmingsen and R. Bauer, *Biochemistry*, 1999, **38**, 16500.
41. C. Damblon, M. Jensen, A. Ababou, I. Barsukov, C. Papamicael, C. J. Schofield, L. Olsen, R. Bauer and G. C. K. Roberts, *J. Biol. Chem.*, 2003, **278**, 29240.
42. R. Bauer, E. Danielsen, L. Hemmingsen, M. V. Sørensen, J. Ulstrup, E. P. Friis, D. S. Auld and M. J. Bjerrum, *Biochemistry*, 1997, **36**, 11514.
43. R. Bauer, H. W. Adolph, I. Andersson, E. Danielsen, G. Formicka and M. Zeppezauer, *Eur. Biophys. J.*, 1991, **20**, 215.
44. L. Hemmingsen, R. Bauer, M. J. Bjerrum, H. W. Adolph, M. Zeppezauer and E. Cedergren-Zeppezauer, *Eur. J. Biochem.*, 1996, **241**, 546.
45. E. Carvalho, P. O. Gothe, R. Bauer, E. Danielsen and L. Hemmingsen, *Eur. J. Biochem.*, 1995, **234**, 780.
46. U. Heinz, R. Bauer, S. Wommer, W. Meyer-Klaucke, C. Papamichael, J. Bateson and H. W. Adolph, *J. Biol. Chem.*, 2003, **278**, 20659.
47. R. Bauer, M. J. Bjerrum, E. Danielsen and P. Kofod, *Acta Chem. Scand.*, 1991, **45**, 593.
48. E. Danielsen and R. Bauer, *Hyperfine Interact.*, 1990, **62**, 311.
49. R. Paul-Soto, M. Zeppezauer, H. W. Adolph, M. Galleni, J. M. Frere, A. Carfi, O. Dideberg, J. Wouters, L. Hemmingsen and R. Bauer, *Biochemistry*, 1999, **38**, 16500.
50. R. Bauer, P. Limkilde and J. T. Johansen, *Biochemistry*, 1976, **15**, 334.
51. R. Bauer, J. Johansen and P. Limkilde, *Hyperfine Interact.*, 1978, **4**, 906.
52. R. Bauer, P. Limkilde and J. T. Johansen, *Carlberg Res. Commun.*, 1977, **42**, 325.
53. M. J. Bjerrum, R. Bauer, E. Danielsen and P. Kofod, *Free Radical Res. Commun.*, 1991, **12-3**, 297.

54. R. Bauer, P. Limkilde and O. Glomset, *Phys. Rev. Lett.*, 1974, **32**, 340.
55. G. R. Demille, K. Larlee, D. L. Livesley and K. Mailer, *Chem. Phys. Lett.*, 1979, **64**, 534.
56. R. Bauer, C. Christensen, J. T. Johansen, J. L. Bethune, B. L. Vallee, *Biochem. Biophys. Res. Commun.*, 1979, **90**, 679.
57. R. Bauer, M. Bjerrum, E. Danielsen, E. Friis, J. M. Hammerstad, L. Hemmingsen, M. V. Pedersen and J. Ulstrup, ‘Protein Folds: A Distance Based Approach’, CRC Press, 1996.
58. R. Bauer, I. Demeter, V. Hasemann and J. T. Johansen, *Biochem. Biophys. Res. Commun.*, 1980, **94**, 1296.
59. R. Bauer, M. Bjerrum, E. Danielsen and P. Kofod, *Hyperfine Interact.*, 1990, **61**, 1201.
60. F. A. Smith, P. W. Martin and A. Shukri, *Hyperfine Interact.*, 1985, **23**, 375.
61. W. Tröger, B. Ctortecka, P. Faller and M. Vasak, *J. Inorg. Biochem.*, 2001, **86**, 460.
62. M. Vasak and R. Bauer, *J. Am. Chem. Soc.*, 1981, **104**, 3226.
63. E. Danielsen, R. Bauer, L. Hemmingsen, M. L. Andersen, M. J. Bjerrum, T. Butz, W. Tröger, G. W. Canters, C. W. G. Hoitink, G. Karlsson, O. Hansson and A. Messerschmidt, *J. Biol. Chem.*, 1995, **270**, 573.
64. R. Bauer, E. Danielsen, L. Hemmingsen, M. J. Bjerrum, O. Hansson and K. Singh, *J. Am. Chem. Soc.*, 1997, **119**, 157.
65. W. Tröger and T. Butz, *Hyperfine Interact.*, 2000, **129**, 511.
66. T. Butz and W. Tröger, ‘Bioinorganic Chemistry, Transition Metals in Biology and their Coordination Chemistry’, John Wiley & Sons, Weinheim, 1997.
67. W. Tröger, C. Lippert, T. Butz, K. Sigfridsson, O. Hansson, E. McLaughlin, R. Bauer, E. Danielsen, L. Hemmingsen and M. J. Bjerrum, *Z. Naturforsch., A: Phys. Sci.*, 1996, **51**, 431.
68. T. Butz, W. Tröger, A. Messerschmidt, U. Thoenes and R. Huber, *Hyperfine Interact.*, 1993, **80**, 1127.
69. T. Butz, *Hyperfine Interact.*, 1993, **80**, 1079.
70. W. Tröger, T. Butz, E. Danielsen, R. Bauer, U. Thoenes, A. Messerschmidt, R. Huber, G. W. Canters and T. den Blaauwen, *Hyperfine Interact.*, 1993, **80**, 1133.
71. B. Ctorecka, V. Hartmann, W. Tröger, M. Lösche, and T. Butz, in ‘Condensed Matter Studies by Nuclear Methods, Proceedings of the XXXII. Zakopane School of Physics 1997’, eds. K. Tomala and E. A. Görlich, Institute of Physics, Jagiellonian University and Niewodniczanski Institute of Nuclear Physics, Krakow, 1997, p. 137.
72. E. Danielsen, R. Bauer, L. Hemmingsen, M. J. Bjerrum, T. Butz, W. Tröger, G. W. Canters, T. den Blaauwen and G. van Pouderoyen, *Eur. J. Biochem.*, 1995, **233**, 554.
73. K. N. Sas, A. Haldrup, L. Hemmingsen, E. Danielsen and L. H. Øgendal, *J. Biol. Inorg. Chem.*, 2006, **11**, 409.
74. K. N. Sas, L. Hemmingsen and E. Danielsen, *FEBS Lett.*, 2006, **580**, 6861.
75. H. Appel, J. Duffield, D. M. Taylor, G. M. Then and W. G. Thies, *Hyperfine Interact.*, 1987, **35**, 957.
76. H. Appel, A. Brownmason, M. Neumüller, F. Schwab, D. M. Taylor and W. G. Thies, *Hyperfine Interact.*, 1990, **61**, 1223.
77. F. J. Schwab, H. Appel, M. Neu and W. G. Thies, *Eur. Biophys. J. Biophys Lett.*, 1992, **21**, 147.
78. F. J. Schwab, H. Appel, M. Neu and W. G. Thies, *Hyperfine Interact.*, 1993, **80**, 1155.
79. F. J. Schwab, H. Appel, A. B. Mason, M. Neu and W. G. Thies, *Biometals*, 1993, **6**, 193.
80. H. Appel, J. Duffield, D. M. Taylor, G. M. Then and W. G. Thies, *J. Inorg. Biochem.*, 1987, **31**, 229.
81. H. Appel, M. Neumüller, F. Schwab, D. M. Taylor and W. G. Thies, *Hyperfine Interact.*, 1990, **61**, 1219.
82. G. M. Then, H. Appel, J. Duffield, D. M. Taylor and W. G. Thies, *J. Inorg. Biochem.*, 1986, **27**, 255.
83. G. Becker, H. Appel, M. Neu, F. J. Schwab and W. G. Thies, *Hyperfine Interact.*, 1993, **80**, 1161.
84. M. L. Dong, J. F. Huang, H. S. Du, J. H. Li, S. B. Du, A. L. Luo, Y. Jiang and C. H. Zhang, *J. Radioanal. Nucl. Chem.*, 1996, **205**, 261.
85. P. Mottner, T. Butz, A. Lerf, J. Erfkamp, K. Schneider and A. Müller, *Biochim. Biophys. Acta*, 1993, **1164**, 311.
86. A. Müller, W. Suer, C. Pohlmann, K. Schneider, W. G. Thies and H. Appel, *Eur. J. Biochem.*, 1997, **246**, 311.
87. C. Pohlmann, H. Appel, W. G. Thies, A. Müller, K. Schneider and W. Suer, *Hyperfine Interact.*, 1999, **121**, 731.
88. O. C. Mullins and M. Kaplan, *J. Chem. Phys.*, 1983, **79**, 4475.
89. Y. X. Wang, X. B. Ni, W. B. Chen, J. L. Xu, C. W. Sun, D. Z. Yin and S. Ding, *Biol. Trace Elem. Res.*, 1989, **22**, 1.
90. P. J. Marsden, F. A. Smith and R. W. Evans, *Appl. Radiat. Isot.*, 1989, **40**, 715.
91. P. Faller, B. Ctortecka, W. Tröger, T. Butz and M. Vasak, *J. Biol. Inorg. Chem.*, 2000, **5**, 393.
92. W. Tröger, B. Ctortecka, P. Faller, T. Butz and M. Vasak, *J. Inorg. Biochem.*, 1999, **74**, 318.
93. W. Tröger, *Hyperfine Interact.*, 1999, **120/121**, 117.
94. T. Butz, A. Lerf and R. Huber, *Phys. Rev. Lett.*, 1982, **48**, 890.
95. M. Matzapetakis, B. T. Farrer, T. C. Weng, L. Hemmingsen, J. E. Penner-Hahn and V. L. Pecoraro, *J. Am. Chem. Soc.*, 2002, **124**, 8042.
96. K.-H. Lee, C. Cabello, L. Hemmingsen, E. Neil, G. Marsh and V. L. Pecoraro, *Angew. Chem. Int. Ed.*, 2006, **45**, 2864.
97. Y. Wang, L. Hemmingsen and D. P. Giedroc, *Biochemistry*, 2005, **44**, 8976.
98. K. N. Sas, L. Kovács, O. Zsíros, Z. Gombos, G. Garab, L. Hemmingsen and E. Danielsen, *J. Biol. Inorg. Chem.*, 2006, **11**, 725.
99. R. Bauer, A. Atke, E. Danielsen, J. Marcussen, C. E. Olsen, J. Rehfeld, T. Saermark, D. Schneider, H. Vilhardt and M. Zeppezauer, *Appl. Radiat. Isot.*, 1991, **42**, 1015.

100. R. D. Vis, A. J. J. Bos, S. Idzenga and H. Verheul, *Nucl. Instrum. Methods*, 1979, **163**, 265.
101. C. A. Kalfas, E. G. Sideris, S. El-kateb, P. W. Martin and U. Kuhnlein, *Chem. Phys. Lett.*, 1980, **73**, 311.
102. C. A. Kalfas, E. G. Sideris, G. K. Loukakis and A. Anagnostopouloukonsta, *J. Non-Cryst. Solids*, 1994, **172**, 1121.
103. E. Tsoulou, C. A. Kalfas and E. G. Sideris, *Radiat. Res.*, 2001, **156**, 181.
104. E. Tsoulou, C. A. Kalfas and E. G. Sideris, *Radiat. Res.*, 2003, **159**, 33.
105. J. D. Baldeschwieler and P. G. Schmidt, *Chem. Tech.*, 1997, **27**, 34.
106. P. W. Martin, C. A. Kalfas and K. Skov, *Chem. Phys. Lett.*, 1978, **57**, 279.
107. E. Danielsen, R. Bauer and D. Schneider, *Eur. Biophys. J.*, 1991, **20**, 193.
108. C. A. Kalfas, E. G. Sideris and P. W. Martin, *J. Appl. Radiat. Isot.*, 1984, **35**, 889.
109. Y. F. Liu, T. Qu and X. Y. Wang, *Pure Appl. Chem.*, 1991, **63**, 1298.
110. P. W. Martin, S. El-kateb and U. Kuhnlein, *J. Chem. Phys.*, 1992, **76**, 3819.
111. E. G. Sideris, C. A. Kalfas and N. Katsaros, *Inorg. Chim. Acta-Bioinorg. Chem.*, 1986, **123**, 1.
112. P. W. Martin and C. A. Kalfas, *Nucl. Instrum. Methods*, 1980, **171**, 603.
113. M. Ceolín, J. A. Martinez and M. R. Ermacora, *J. Biochem. Bioph. Methods*, 1997, **35**, 135.
114. M. Ceolín, *J. Biochem. Bioph. Methods*, 2000, **45**, 117.
115. C. F. Meares and D. G. Westmoreland, *Cold Spring Harbor Symp. Quant. Biol*, 1971, **36**, 511.
116. L. Utschig, J. Bryson and T. O'Halloran, *Science*, 1995, **268**, 380.
117. C. Lippert, W. Tröger and T. Butz, in 'Condensed Matter Studies by Nuclear Methods, Proceedings of the XXX. Zakopane School of Physics 1995', eds. K. Tomala and E. A. Görlich, Institute of physics, Jagiellonian University and H. Niewodniczanski Institute of Nuclear Physics, Krakow, 1995.
118. O. Iranzo, L. Hemmingsen, P. W. Thulstrup, S.-B. Ryu, V. L. Pecoraro. (In preparation).
119. J. Kvassman and G. Pettersson, *Eur. J. Biochem.*, 1979, **100**, 115.
120. U. Heinz, H. W. Adolph, and L. Hemmingsen. (Unpublished data).
121. L. Hemmingsen, N. J. Christensen, L. Olsen, E. Danielsen, K.-H. Lee, M. Matzapetakis, and V. L. Pecoraro, Book of Abstracts, p. 210, Metal ion binding site dynamics on the nanosecond time scale: A ^{111m}Cd-PAC spectroscopic study, Aveiro, 2006.
122. C. Hohenemser, L. Chow and R. M. Suter, *Phys. Rev. B.*, 1982, **26**, 5056.
123. E. N. Kaufmann and R. Vianden, *Rev. Mod. Phys.*, 1979, **51**, 161.
124. R. Vianden, *Hyperfine Interact.*, 1983, **15/16**, 1081.
125. E. Recknagel, G. Schatz and T. Wichert, in 'Hyperfine Interactions of Radioactive Nuclei', ed. J. Christiansen, Springer-Verlag New York, Berlin, 1983, p. 133.
126. W. Witthuhn and W. Engel, in 'Hyperfine Interactions of Radioactive Nuclei', ed. J. Christiansen, Springer-Verlag New York, Berlin, 1983, p. 205.
127. T. Butz, *Phys. Scr.*, 1978, **17**, 87.
128. P. Heubes, D. Korn, G. Schatz and G. Zibold, in 'Nuclear and Electron Resonance Spectroscopies Applied to Material Science', eds. E. N. Kaufmann and G. K. Shenoy, Elsevier Science, North Holland, New York, 1981, p. 385.
129. A. F. Pasquevitch, F. H. Sanchez, A. G. Bibiloni, J. Desimoni and A. Lopez-Garcia, *Phys. Rev. B.*, 1983, **27**, 963.
130. M. Uhrmacher and W. Bolse, *Hyperfine Interact.*, 1983, **15/16**, 445.
131. W. Körner, W. Keppner, B. Lehndorff-Junges and G. Schatz, *Phys. Rev. Lett.*, 1982, **49**, 1735.
132. W. Körner, W. Keppner, T. Klas, B. Lehndorff-Junges and G. Schatz, *Hyperfine Interact.*, 1983, **15/16**, 993.
133. K. Potzger, A. Weber, H. H. Bertschat, W.-D. Zeitz and M. Dietrich, *Phys. Rev. Lett.*, 2002, **88**, 247201.
134. Th. Wichert, *Semicond. Semimet.*, 1999, **51B**, 297.
135. M. Naito, H. Nishihara and T. Butz, in 'Nuclear Spectroscopy on Charge Density Wave Systems', ed. T. Butz, Kluwer Academic Publishers, 1992, p. 35.
136. T. Butz and A. Lerf, *Rev. Chim. Miner.*, 1982, **19**, 496.
137. T. Butz, A. Lerf and J. O. Besenhard, *Rev. Chim. Miner.*, 1984, **21**, 556.
138. B. Hansen, J. T. Bukrinsky, L. Hemmingsen, M. J. Bjerrum, K. Singh and R. Bauer, *Phys. Rev. B.*, 1999, **59**, 14182.

Photoelectron Spectroscopy

Nadine E. Gruhn and Dennis L. Lichtenberger

University of Arizona, Tucson, AZ, USA

	Method Summary	1
1	Introduction	2
2	Technical Background	3
3	Applications	7
4	Conclusion	16
5	Acknowledgement	17
6	Abbreviations and Acronyms	17
7	Further Reading	17
8	References	17

METHOD SUMMARY

Acronyms, Synonyms

- Photoelectron Spectroscopy, PES
- Photoemission Spectroscopy, PES
- Ultraviolet Photoelectron Spectroscopy, UPS
- X-ray Photoelectron Spectroscopy, XPS
- Electron Spectroscopy for Chemical Analysis, ESCA
- Multiphoton Ionization Spectroscopy, MPI
- Resonantly enhanced Multiphoton Ionization Spectroscopy, REMPI
- Zero Electron Kinetic Energy Spectroscopy, ZEKE
- Auger Electron Spectroscopy, AES
- Penning Ionization Electron Spectroscopy, PIES

Measured physical quantities

- kinetic energy of electrons ejected from molecules or materials through excitation by one or more photons.

Information available

Depending on the photoelectron method and the particular sample:

- ionization energies to states related to ejection of core and/or valence electrons from neutral molecules or materials
- Koopmans' theorem, ionization energies related to the energy of core and/or valence orbitals
- electron configurations
- vibrational and rotational energies from fine structure on ionization bands
- spin-orbit coupling energies
- electron exchange energies
- charge distributions and bonding interactions
- substituent electronic effects
- information on the atomic character of molecular orbitals by analyses of photoionization cross sections
- information on geometry changes and reorganization energies associated with ionizations
- quantitative determination of elements present within about 10 nm of a sample surface

- electron affinity and related one-electron excited electronic states of the neutral molecule
- oxidation states of the elements present.

Information not available, limitations

- difficulty in resolving vibrational and/or rotational fine structure for gas-phase molecules larger than about 10 atoms without jet cooling
- possibility of contamination in the gas phase for neutral molecules
- solid-phase XPS detection limits in parts-per-thousand
- PES of solid materials surface sensitive, only probes about 10 nm deep
- must be performed in vacuum ($<10^{-5}$ torr for gas-phase studies, $<10^{-9}$ torr for solid-phase studies).

Examples of questions that can be answered

- What is the ionization energy of a molecule?
- What is the electron affinity of a molecule (negative-ion PES)?
- How much is the ionization energy of a molecule stabilized or destabilized by addition of substituents?
- What are the charge and orbital overlap interactions in a molecule?
- What is the inner-sphere reorganization energy of a molecule upon ionization?
- What is the oxidation state of the metal in a molecule?
- How ‘‘electron rich’’ is the metal in the molecule?
- How strong an electron donor or electron acceptor is a ligand?
- What is the exchange coupling in a bimetallic system?

Major advantages

- All one-electron ionizations are observed.
- Clearly defined measurement is a major contributor to thermodynamic relationships.
- An energy measure of electronic interactions can be obtained.
- The technique can be performed in some manner on essentially any molecule, in any phase.
- The lack of solvation effects in gas-phase spectroscopy makes the measurements amenable to theoretical calculations and provides solid benchmarks.
- Photoelectron spectroscopy is directly correlated to molecular orbital models via Koopmans’ theorem.

Major disadvantages

- All ionizations are observed; limited selection rules are present to help in assignments.
- The technique is not useful for cations (except in condensed phase).
- Valence photoelectron spectra are often very convoluted; individual ionizations are not resolved for large, low-symmetry molecules.
- Data collection requires substantial expertise and time.
- General access is limited.
- Commercial instruments are not available for gas-phase studies.
- Surface XPS instruments are expensive.
- Instrument maintenance is high.

Sample constraints

- For gas-phase studies of neutral molecules, samples must be sufficiently volatile.
- The technique is generally destructive of samples.
- The quantity of sample required is of the order of 10 mg or more.
- Valence photoelectron spectroscopy of solid molecular materials requires highly ordered thin films, typically prepared by epitaxial film deposition.

1 INTRODUCTION

Photoelectron spectroscopy is based on Einstein’s photoelectric effect.[1] A photon can remove an electron from a molecule or material if the photon has an energy greater than the electron binding energy, and any photon energy in excess of the electron binding energy is carried by the outgoing electron in the form of kinetic energy. The kinetic energy of the ejected photoelectron is measured by a photoelectron spectrometer. In the case of a neutral molecule, ejection of the electron results in ionization of the molecule, and the difference between the photon energy ($h\nu$), which is known, and the electron kinetic energy (*KE*), which is measured, is the ionization energy (*IE*).

$$IE = \mathrm{E}(h\nu) - KE(e^-) \tag{1}$$

Ionization is explicitly defined in terms of transitions between the ground state of a molecule and ion states as shown in equation (2).

$$\mathrm{M} + \mathrm{photon}(h\nu) \longrightarrow \mathrm{M_i}^+ + e^- \tag{2}$$

The information obtained from photoelectron spectroscopy is typically discussed in terms of the electronic structure and bonding in the ground states of molecules, with ionization of electrons occurring from bonding molecular orbitals, lone pairs, antibonding molecular orbitals, or atomic cores. These descriptions reflect the relationship of ionization energies to the molecular orbital model of electronic structure. The ionization energies are directly related to the energies of molecular orbitals by Koopmans' Theorem,[2] which states that the negative of the eigenvalue of an occupied orbital from the Hartree–Fock model of the electronic structure is equal to the vertical ionization energy to the ion state formed by removal of an electron from that orbital, provided the distributions of the remaining electrons do not change. While there are limitations to the applicability of Koopmans' theorem[3] in a first order approximation, each ionization of a molecule can be described as removal of an electron from an individual orbital. The ionization energies can then be considered as measures of orbital stabilities, and shifts can be interpreted in terms of orbital stabilizations or destabilizations due to changes in electron distributions and bonding.

Photoelectron spectroscopy remains among the most direct and comprehensive experimental probes of electronic structure. Photoelectron spectroscopy of neutral molecules in the gas phase has served as a particularly important basis for the bonding models used to describe inorganic molecules because the energetics of ion formation from the neutral ground state are directly related to the orbital electron configurations, oxidation states, charge distributions, and covalency. Photoelectron spectroscopy has become an established field over the last 40 years, with several books available on the subject.[4–6] There are also review articles on gas-phase photoelectron spectroscopy of neutral transition metal molecules,[3,7–9] which include case studies based on several well-characterized molecular systems. In addition to conventional photoelectron spectroscopy, additional photoionization spectroscopic techniques continue to be developed, which give additional types of experimental information and have different sample constraints. Examples include gas-phase photoelectron spectroscopy of anions and a variety of techniques using multiphoton ionization. This article considers examples of applications of photoelectron spectroscopy in bioinorganic chemistry and applications of newer photoelectron techniques to inorganic molecules.

2 TECHNICAL BACKGROUND

2.1 Photoionization

Considering the photoionization process in more detail for a neutral molecule in the gas phase, the photon ionizes the molecule (M) and leaves the molecule in a positively charged ion state ($\mathrm{M_i^+}$) according to equation (2). Rearranging equation (2) and considering the energy components of the process as in equation (3), shows that a measure of the ionization energy is also a measure of the difference in energy between the positive ion state $\mathrm{M_i^+}$ and the initial state of the molecule M.

$$\mathrm{E}(\mathrm{M_i}^+) - \mathrm{E(M)} = \mathrm{E}(h\nu) - KE(e^-) = IE \tag{3}$$

Thus photoelectron spectroscopy measures the relative energies of the ground and excited positive ion states that are obtained by removal of single electrons from the neutral molecule.

The direct ionization transition is not restricted by any symmetry selection rules because the ejected electron can carry any necessary angular momentum to make the process electric dipole allowed, so ionization to any excited positive ion state obtained by removal of a single electron and within range of the photon energy can be observed. That is, ionizations that correspond to removal of electrons from any of the occupied orbitals can be observed. Additional states of these ions may also be observed, most commonly for core electron ionizations of metal complexes, corresponding to additional ''shake up'' of remaining electrons from occupied orbitals to virtual orbitals accompanying the ionization process. This lack of selection rules results in the photoelectron spectra of large molecules becoming congested and more difficult to analyze.

2.2 Ionization Band Shape

Photoionization is an electronic process that occurs on a timescale much faster than molecular vibrations, and therefore for each discrete ionization band the band maximum corresponds to the Franck–Condon vertical ionization energy. The ionization can be illustrated, as shown in Figure 1 for the hydrogen molecule, as the transition between the potential energy well of the initial state and the potential energy well of the state formed by removal of an electron. Removal of an electron changes the overall bonding in the molecule and results in a shift of the equilibrium internuclear separations. If the geometry changes are sufficiently great, the most probable transitions from the neutral ground state are to excited vibrational levels of the final ion state, and the adiabatic ionization will be at some lower energy than the vertical ionization. When the vibrational levels are resolved, as shown for the photoelectron spectrum of hydrogen compared to the potential energy surface in Figure 1, the change in vibrational spacing from the initial state to the final state gives a measure of the change in vibrational frequencies and force constants associated with the excitation, while the intensity pattern (Franck–Condon factors) of the transitions to the excited vibrational levels gives a measure of the change in equilibrium bond distances. This information can also be used to give a measure of the inner-sphere reorganization energy of electron transfer, which is discussed in more detail in the applications section.

For large molecules the individual vibrational levels of the ionizations will typically not be resolved, but the overall shape of an ionization band is still governed by the difference in equilibrium geometry between the initial and ionized states. For example, if the vibrational levels for the ionization of hydrogen in Figure 1 were not resolved, the overall band shape would resemble the asymmetric Gaussian shown with a dotted line. The energy width and shape of the band will still be dependent upon the Franck–Condon factors of the unresolved vibrational structure. For large molecules with unresolved vibrational structure, it is often impossible to exactly measure an adiabatic ionization energy. Measurement of adiabatic ionization energies is further complicated by the fact that excited vibrational levels may be occupied in the neutral ground state of the molecules, resulting in the presence of hot bands in the spectra. Vertical ionization energies are of most interest in the molecular orbital description of electronic structure as they are directly related to orbital energies by Koopmans' theorem.

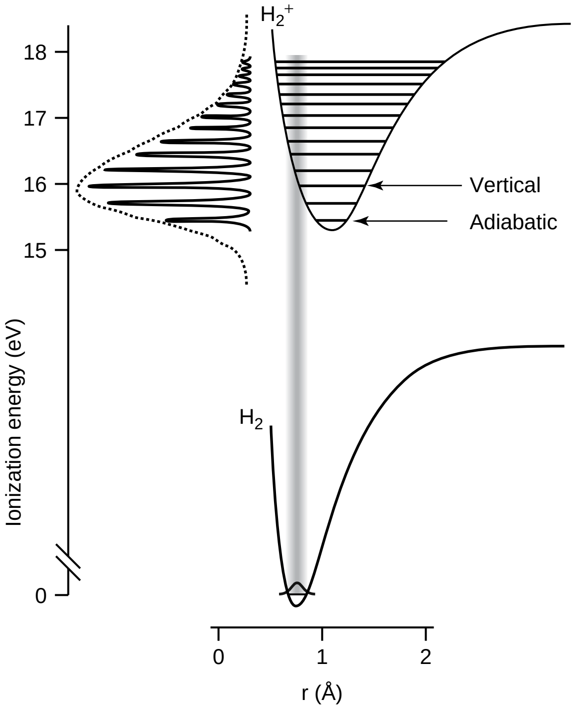

Figure 1 Transition between potential energy surfaces that describe the ionization of the hydrogen molecule

2.3 Photoionization Cross Sections

In addition to the energy information that is contained in a photoelectron spectrum, the intensities of ionizations also give valuable information regarding electronic structure and the orbital origin of ionizations. The probability of ionization is dependent upon the energy of the ionizing photon and the character of the orbitals. The probability is also dependent upon the angle at which photoelectrons are collected and the polarized nature of the photons. These probabilities of photoionization are understood in terms of photoionization cross sections.

The dependence of photoionization cross sections upon the energy of the ionization photon and the character of the molecular orbital has been particularly useful in the assignments of the spectra of inorganic and organometallic molecules. The general trends that have been observed for photoionization behavior often lead to a clear and convenient differentiation between ionization from metal-based and ligand-based orbitals. Variable energy photon studies have become increasingly common since the advent of high intensity, tuneable synchrotron radiation sources. Synchrotron studies have led to a better understanding of the influences to cross-section behavior as photon energy changes.[10]

2.4 Core Ionization

Photons with energies in the kilo-electron volt (X-ray) range are able to ionize down to the core electrons of atoms and molecules. Core ionizations of molecules are associated with the individual atoms present and fall in characteristic energy ranges related to the specific elements. Core-ionization spectroscopy, most commonly carried out on solids, is therefore useful as an analytical tool, and Siegbahn coined the name *electron spectroscopy for chemical analysis* (ESCA) for the technique,[11,12] although X-ray photoelectron spectroscopy (XPS) is more commonly used today.[12,13] The exact ionization energy of a core level is influenced by the charge potential around the atom, and is useful for distinguishing between atoms in different chemical environments. The sensitivity for XPS is on the order of parts-per-thousand, so while XPS is the premier technique for analyzing oxidation states of transition metals in many systems, its use is limited by the concentration of the atom of interest. For example, XPS has not proven useful for the analysis for transition metal active sites in enzymes due to the low concentration of transition metal atoms present, but is often used for analyzing active-site models.

The influences of bonding/overlap and charge potential contributions to ionization energies also can be differentiated through use of the gas-phase core-valence ionization correlation approach of Jolly.[14,15] Core ionization energies are dependent on the charge distribution at atomic positions in a molecule, as well as relaxation effects. Valence ionization energies also respond to these factors, but in addition, are sensitive to bonding. The principle of core-valence ionization correlation states that, when comparing ionization spectra for two related molecules, the binding energy shift of a nonbonding valence orbital localized on an atom present in both molecules should be eight-tenths of the core binding energy shift for that atom between the two molecules.[16] A valence/core shift ratio differing from the benchmark 0.8 value indicates the contribution of bonding/overlap interactions to the valence shift.

2.5 Photoionization in the Solid Phase

Photoelectron spectroscopy of valence and core electrons in solids has been useful in the study of the surface properties of transition metals and other solid-phase materials.[12] When photoelectron spectroscopy is performed on a solid sample, an additional step that must be considered is the escape of the resultant photoelectron from the bulk. The analysis can only be performed as deep as the electrons can escape from the bulk and then be detected. The escape depth is dependent upon the inelastic mean free path of the electrons, determined by electron–electron and electron–phonon collisions, which varies with photoelectron kinetic energy. The depth that can be probed is on the order of about 5–50 Å, which makes this spectroscopy actually a surface-sensitive technique rather than a probe of the bulk properties of a material. Because photoelectron spectroscopy only probes such a thin layer, analysis of bulk materials, absorbed molecules, or thin films must be performed in ultrahigh vacuum ($<10^{-9}$ torr) to prevent interference from contaminants that may adhere to the surface.

2.6 Auger Electron Spectroscopy

Auger electron spectroscopy (pronounced ‘‘O-Jay’’ but with the softer J associated with French pronunciation) has similarities to photoelectron spectroscopy and is one of the most commonly used tools for probing the elemental composition of surfaces[13] because the energies of Auger transitions are also dependent on the characteristic atomic core level energies. The initial state in an Auger process is a core hole, which can be generated by photoionization, but is usually produced experimentally by impact from an electron beam to overcome the intensity limitations caused by the cross-section of photoionization. The core hole state produced then decays via an electronic transition from a higher lying orbital to the core orbital, with release of the resultant energy of relaxation by the ejection and kinetic energy of a secondary electron, referred to as an Auger electron. If the core hole was created in a K (1s) shell, and if the relaxing electron and ejected Auger electron are from valence orbitals, the overall process is referred to as producing a KV_1V_2 Auger electron, where V_1 and V_2 are the valence levels. In the photoelectron process, the energy for the ejection and kinetic energy of the electron is provided by the photon, which is an essentially monoenergetic source. In the Auger process, the energy for ejection and kinetic energy of the electron comes from relaxation of a valence electron into the core hole. Because there are many different valence electron energy levels in the molecule, the source of energy for production of the Auger electrons is not monoenergetic.

Auger spectroscopy is also capable of probing the valence electronic structure of molecules and solids,[17–19] because the lineshapes of Auger transitions are dependent on the energies of the valence levels. The Auger lineshape can be considered as a superposition of a series of overlapping photoelectron spectra for the molecule, where each spectrum is shifted according to the energy of relaxation from the particular valence level V_1. A Koopmans' approximation for the energy of a particular transition, ignoring the ‘‘repulsion’’ between the two valence holes in the final state, is given by equation (4), where the ε values are the orbital eigenvalues of the valence and core levels.

$$KE\ (\text{Auger electron}) = \varepsilon(V_1) + \varepsilon(V_2) - \varepsilon(\text{K}) \tag{4}$$

In the low kinetic energy region of the Auger line shape, there are many overlapping transitions, because electrons with high binding energies (high ε) that are ejected by relaxation of an electron from the highest occupied valence levels (low ε) have kinetic energies similar to electrons with low binding energies (low ε) that are ejected by relaxation of an electron from more stable valence levels (high ε). The ionizations on the leading edge of the Auger band at high kinetic energy correspond to ejection of electrons with the lowest binding energies (lowest ε) by relaxation of electrons from the highest occupied valence levels (lowest ε) to the core level. This leading edge of the Auger band provides the most useful electronic structure and bonding information.

Additional useful information is provided as a consequence of the way Auger spectroscopy couples the core levels and the valence levels. In simple terms, the intensity of a KVV Auger transition is a measure of the valence charge available for decay into the core hole. Because a core hole is localized on a particular atom, this can give an indication of the amount of electron density in a particular valence orbital around the atom where the core hole was made.

2.7 Penning Ionization

Penning ionization electron spectroscopy (PIES), also referred to as *metastable atom electron spectroscopy*

(MAES) or *metastable ionization electron spectroscopy* (MIES), is another spectroscopy related and complementary to photoelectron spectroscopy that has been used for the study of inorganic molecules.[20] In Penning ionization, electrons are ejected by collisions between target molecules and a beam of metastable atoms (atoms in an excited electronic state that have a long lifetime) such as He* atoms in the (2^3S) excited state, which have an energy of 19.82 eV above the ground state of He. The Penning ionization process shown in equation (5) is interpreted in terms of an electron exchange, in which an electron of the target molecule transfers to a hole of the metastable atom and the excited-state electron from the metastable atom is ejected simultaneously.

$$\mathrm{M} + \mathrm{He}^* \longrightarrow \mathrm{M}^+ + \mathrm{He} + e^- \qquad (5)$$

The energy source for the ejection and kinetic energy of the electron is the energy of the metastable atom, which is essentially monoenergetic. The transition probability for the electron transfer depends largely on the spatial overlap of the relevant orbital of the sample molecule and the vacant orbital of the excited state, metastable atom. In other words, the intensity of a transition will be greater if the occupied orbital of the sample molecule has electron density on the periphery of the molecule, in contrast to photoelectron spectroscopy, where the intensity of an ionization is governed by the photoionization cross section. Comparison of the intensity of Penning ionization transitions to the intensities observed for the corresponding ionization bands in the photoelectron spectrum of the sample allows study of the spatial electron distribution of individual molecular orbitals, and is often also used to analyze solid materials.[21]

2.8 Photoionization of Anions

Gas-phase studies of neutral molecules are limited to molecules that can be sublimed in vacuo without decomposition, and therefore the majority of photoelectron spectroscopic studies of inorganic molecules have focused on organometallic molecules, many of which are reasonably volatile. Gas-phase photoelectron spectroscopy on negatively charged atoms or small ($<$10 atom) molecules has also been performed for many years.[22] Recent advances in instrumentation and sample introduction have opened these types of experiments to anionic species of interest to inorganic chemists.[23] The ionization energy of an anion is the electron affinity of the neutral molecule. This means that the ionization transitions observed when photoelectron spectroscopy is performed on anions, which are from the ground state of the anion to states of the neutral species, now give electron affinities and other information on the neutral molecule. Anion photoelectron spectroscopy has proven particularly useful in giving information on excited electronic states of neutral molecules that cannot be accessed by other spectroscopic techniques.

Neutral inorganic molecules have first ionization energies in the range of about 5–15 eV, meaning that photons in the vacuum UV range must be used to observe the ionizations of these molecules. The vacuum UV is a difficult energy region photons with usable intensity for experimentally producing, and the only practical laboratory sources use emission from noble gas discharge lamps; increasingly synchrotron radiation is used as a photoionization source for these experiments. In contrast to neutral molecules, the ionization energies of many anions are sufficiently low that ionization can be achieved using visible photons, which opens the use of commercially available, intense laser sources for performing photoelectron spectroscopy on these species. Anions can be introduced into the gas phase by techniques such as electrospray, or reactive anionic molecules such as clusters or molecular ions can be generated by pyrolysis, photolysis, or some other means. The anions can first be mass selected before being introduced into the photoelectron ionization area.

2.9 Multiphoton Ionizations

The cross sections for photoionization caused by simultaneous interaction with two or more photons are much lower than those for one-photon ionization, and consequently multiphoton ionization is not observed with the moderate intensity vacuum UV or soft X-ray sources used in conventional photoelectron spectroscopy. However, the availability of high-power tuneable laser sources has made the development of spectroscopic techniques associated with multiphoton ionization possible.[22] The use of two or more photons to reach an ionization threshold means that low energy lasers can be used to provide the excitation energy for multiphoton ionization of neutral molecules. The overall cross section of multiple photon events can be increased by using one photon that is in resonance with the transition energy to an excited state that effectively acts as an intermediate state; this intermediate transition will occur with the higher probabilities associated with normal photon absorption and increases the overall cross section of ionization. This technique, which typically uses two photons of different energy to cause ionization, is referred to as *resonantly enhanced multiphoton ionization* (REMPI) spectroscopy. The final ionization event gives information about the intermediate excited state.

Zero electron kinetic energy (ZEKE) spectroscopy was first introduced in 1984.[24] It is a subset of multiphoton spectroscopy, where the molecules are photoexcited to an ionization energy threshold level, from which electrons with very low or effectively zero kinetic energy will be produced. ZEKE spectroscopy combines the use of pulsed lasers and a delayed pulsed electrical field used for detecting the ZEKE electrons. The advantage of this technique is that extremely good resolution can be achieved, on the order of 1 cm^{-1} or greater, so vibrationally and rotationally resolved structure can be observed, and accurate adiabatic ionization energies can be obtained,[25,26] but to date this technique has only been applied to the analysis of relatively small molecular systems. A variant of this technique uses the pulsed field to actually cause the ionization, and is referred to as ZEKE-PFI (pulsed field ionization) spectroscopy.

2.10 Additional Experimental Considerations

To summarize, photoelectron spectroscopy is a large field of study that has many subfields, and new techniques continue to be introduced. These different subfields all have different instrumental and sample constraints, but taken as a whole, photoelectron spectroscopic experiments can be performed on almost any system of interest in inorganic chemistry. The main physical constraints limiting the usage of different photoelectron techniques to different chemical problems have been summarized above.

One additional constraint to the widespread application of these techniques is the availability of spectrometers. Surface spectrometers are commercially available, although due to the need for ultrahigh vacuum technology, the purchase price and upkeep costs can be appreciable. Gas-phase spectrometers are not currently commercially available and must be custom built with the specific design dependent upon the type of samples and experimental information of interest. The most important components that control the key features of any photoelectron spectrometer are the sample handling and entry area, the photon source, and the electron kinetic energy analyzer. Ancillary components for vacuum production, vacuum measurement, and electron measurement are also required. Samples for gas-phase spectroscopy are typically introduced as a constant flow, with neutral molecules requiring heating to a sufficient vapor pressure; once in the gas-phase samples may be cooled by jet expansion to decrease thermal broadening of signals.

3 APPLICATIONS

The following section includes discussion of several applications of photoelectron spectroscopy to the study of bioinorganic model complexes. The ‘‘Further Reading’’ section at the end of this article lists previous reviews and articles and other applications in inorganic and organometallic chemistry that can be consulted for areas not covered here.

3.1 Metal–Sulfur Interactions in $CpFe(CO)_2(SPh)$

An important contribution of photoelectron spectroscopy to inorganic chemistry has been the use of this technique to understand the bonding capabilities of different ligands to metal centers.[27] If the bonding for a series of ligands is to be compared, the metal fragment to which those ligands are bound must be similar. The d^6 piano-stool complexes of the general form $CpM(CO)_2L$ have been useful for the comparison of a wide variety of metal–ligand interactions. The general electronic structure of the $CpM(CO)_2$ fragment is well understood,[28] and the large number of complexes of this general geometry available for study has allowed systematic characterization of the relative bonding capabilities of many ligands. While these molecules are of low molecular symmetry, the relatively high local electronic symmetry at the metal makes evaluation of the photoelectron spectra (PES) of these complexes straightforward. As one example, this molecular framework has been used to study iron–thiolate bonding, which is an important interaction present in many bioinorganic systems. The pseudo-octahedral geometry of $CpFe(CO)_2(SPh)$ and its formal d^6 electron configuration provide ideal molecular and electronic characteristics to observe the effect of filled–filled $d\pi-p\pi$ antibonding interactions between formally occupied metal orbitals and the thiolate ligand lone pair that is principally sulfur 3p in character.[29]

The gas-phase photoelectron spectra of piano-stool molecules shown in Figure 2 illustrate how information on metal–ligand bonding can be gained through application of this technique. The three occupied metal d orbitals of formal d^6 piano-stool complexes are closely related to the t_{2g} set for an octahedral molecule, and the relative energy of these three orbitals are related to the relative π interactions that the metal orbitals have with the CO and L ligands.[27] For example, the spectrum in Figure 2(a) is that of $CpMn(CO)_3$.[30] For this compound, each of the three metal-based orbitals are stabilized by back-bonding to two COs and the three resultant ionizations are grouped together at around 8 eV. The near-degeneracy of the ionizations reflects the pseudo-octahedral symmetry at the metal center. This spectrum also shows the Cp e_1''-symmetry, π-based ionization at about 10 eV.

The spectrum shown in Figure 2(b) is that of $CpFe(CO)_2H$.[27] For this compound, the H^- ligand now has no capability of undergoing π-interaction with the metal, and the metal ionizations split into a two-above-one pattern as two of the metal ionizations are destabilized away from the third due to loss of π-back-bonding to the third ligand (now the hydride). The energy splitting of the metal ionizations therefore acts as a benchmark for metal splitting in the absence of a π-interactive ligand.

The spectrum shown in Figure 2(c) is that of $CpFe(CO)_2(SPh)$.[29] This photoelectron spectrum is more complicated due to the presence of the additional ionizations from the Ph π and S 3p lone pair. The electronic structure of $CpFe(CO)_2(SPh)$ can be considered as the combination of the $[CpFe(CO)_2]^+$ and $[SPh]^-$ fragments, and the photoelectron spectrum of the $CpFe(CO)_2H$ and thiophenol (HSPh, shown in Figure 2d) can be used to model the ionizations of these fragments. The three lowest energy ionizations of thiophenol correspond to a mixture of sulfur lone pair and aryl π character, with the lowest energy (highest occupied molecular orbitals (HOMO)) ionization attributed to the orbital with the most sulfur lone pair character. For $CpFe(CO)_2(SPh)$,

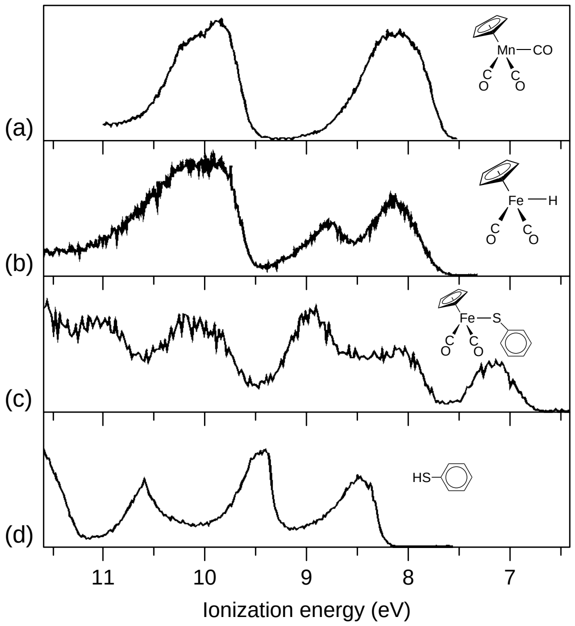

Figure 2 Valence photoelectron spectra of (a) CpMn(CO)$_3$, (b) CpFe(CO)$_2$H, (c) CpFe(CO)$_2$(SPh), and (d) HSPh

the predominantly metal ionizations should occur in the region of 8–9 eV in analogy with the ionizations of other CpFe(CO)$_2$X complexes.[30] The Cp π and aryl π orbitals give rise to additional ionization features at greater than 9 eV. The lowest energy ionization of CpFe(CO)$_2$(SPh) at about 7 eV is metal–sulfur antibonding and principally sulfur in character, which would indicate that the thiolate lone pair orbital has been destabilized relative to thiophenol by about 1.3 eV. This destabilization is the result of two cooperating effects, the charge difference between H$^+$ and the [CpFe(CO)$_2$]$^+$ fragment and filled–filled interactions between the sulfur 3p lone pair and the occupied iron dπ orbitals.

3.2 Photoelectron Spectroscopy of Models for Active Sites in Molybdenum Enzymes

Molybdenum–sulfur bonding is also important in biology due to the large group of molybdenum-containing enzymes that catalyze a wide range of oxidation/reduction reactions in carbon, sulfur, and nitrogen metabolism. A common structural feature of the active sites of these molybdenum-containing enzymes is coordination by the sulfur atoms of one (or two) unique ene-dithiolate ligands derived from the side chain of a novel substituted pterin. Complexes with sulfur ligation of Mo centers often exhibit different spectroscopic behavior from those with alkoxide donors, and it is believed that the role of the ene-dithiolate coordination in molybdoenzymes is to buffer the influences of molybdenum oxidation state changes and the presence of strong π ligands.[31]

3.2.1 The ‘‘Electronic Buffering’’ Effect

The photoelectron spectra of model complexes for these molybdenum enzyme active sites have been investigated to gain a better understanding of their basic electronic structure and the role of the ene-dithiolate ligand.[31–33] For example, the metal coordination of model complexes such as Tp*MoO(tdt) are similar to the molybdenum center of sulfite oxidase, which possesses the basic structural core of a terminal oxo group cis to a 1,2-dithiolate.

The lower energy portion of the HeI photoelectron spectrum of Tp*MoO(tdt) is shown in Figure 3(a). The ionizations located from about 8 to 10.5 eV arise from the removal of electrons from orbitals primarily associated with the Tp* and oxo ligands. The large number of individual ionizations and the overlapping nature of these bands make it difficult to unambiguously assign any feature in this region to a particular ionization. The ionization band located at about 6.8 eV and labeled M$_{\text{ip}}$ can be attributed to the ionization of the Mo d^1 electron from this formally Mo(V) complex; this

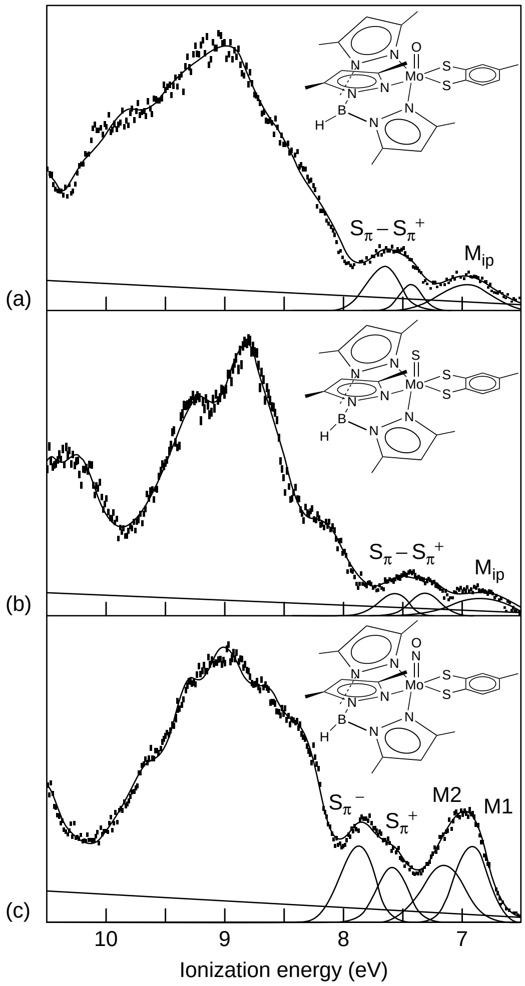

Figure 3 Valence photoelectron spectra of (a) Tp*MoO(tdt), (b) Tp*MoS(tdt), and (c) Tp*Mo(NO)(tdt)

electron resides in a Mo d orbital in the plane of the two sulfurs of the ene-dithiolate. The ionization bands located between about 7.25 and 8 eV are assigned to ionizations associated with symmetric ($S_\pi{}^+$) and antisymmetric ($S_\pi{}^-$) combinations of S 3p orbitals. The spectrum of Tp*MoS(tdt) is shown in Figure 3(b), and is very similar to that of the oxo complex. The spectrum of the nitrosyl complex Tp*Mo(NO)(tdt) is shown in Figure 3(c), with the first ionization feature fit with two Guassians labeled M1 and M2 assigned to ionization from the two nearly degenerate, primarily metal-based orbitals of the formally Mo(II) d^4 center.

The first ionization energies measured for these ene-dithiolate complexes, as well as those for analogous alkoxide complexes, are listed in Table 1. The first ionization energies of the Tp*MoE(tdt) complexes (E = O, S, or NO) are essentially independent of the E ligand present, even though the formal oxidation state of the Mo center in these complexes ranges from +2 to +5. In contrast, for analogous alkoxide complexes such as TpMoE(OEt)$_2$,**[34]** the formally Mo(II) nitrosyl complex was found to be almost 0.8 eV more difficult to ionize than the formally Mo(V) oxo analog. This counterintuitive behavior for the alkoxide complex is attributed to the strong π-accepting ability of the NO ligand.

The control that the ene-dithiolate ligand has upon the first ionization energy of these complexes illustrates the importance of this ligation to the reactivity found for molybdoenzymes. The ene-dithiolate ligand acts as an ‘‘electronic buffer’’, effectively dampening the harsh electronic changes that would otherwise be expected to take place with changes in the metal formal oxidation states and atom transfer reactions at the active site in these enzymes.

3.2.2 *Ene-Dithiolate Ligand Folding and Covalency*

The spectra discussed above indicate the presence of the ene-dithiolate electronic buffering effect, but not its cause. Insight into this cause can be gained by comparing spectra of a compound that have been collected with different photon energies to evaluate the photoionization cross sections. From previous experimental studies and calculations of atomic photoionization cross sections,**[35,36]** it is expected that ionizations from orbitals with significant Mo 4d contributions will increase in intensity compared to ionizations of primarily S 3p character when data collected with a HeII photon source are compared to data collected with a HeI photon source. Mixing of metal and sulfur character in orbitals will result in smaller changes in relative intensities of ionizations being observed.

Table 1 Comparison of first ionization energies for ene-dithiolate and alkoxide molybdenum complexes

Complex	First ionization energy (eV)	References
Tp*MoO(OEt)$_2$	6.57	34
Tp*Mo(NO)(OEt)$_2$	7.40	34
Tp*MoO(tdt)	6.95	32
Tp*MoS(tdt)	6.88	32
Tp*Mo(NO)(tdt)	6.90	32

The spectra of Tp*MoO(bdt) collected with HeI and HeII photons are compared in Figure 4.**[37]** The initial three ionizations in the spectra of Tp*MoO(bdt) are assigned as in the spectrum of Tp*MoO(tdt). Observation of only small changes in the relative intensities of the first three bands with different ionization source energy is evidence of substantial mixing of metal and sulfur character in these three orbitals.

The bent-metallocene ene-dithiolate compound Cp$_2$Mo(bdt) provides access to the Mo d^2 electron configuration, with the added benefit that the sulfur ionizations can be more clearly observed because the Cp ionizations are more stable than Tp* ionizations. The spectra of Cp$_2$Mo(bdt) in Figure 4 also show three low energy ionizations,**[37]** with the HeII data clearly showing an increase in the intensity of the middle band, and perhaps a slight decrease in intensity of the highest energy band. These results imply that the middle band is mainly metal-based, the lowest energy band is primarily $S_\pi{}^+$ with some additional Mo 4d or C 2p character, and the highest energy band is $S_\pi{}^-$. While the spectra of Tp*MoO(bdt) indicate large amounts of covalency between the Mo and S orbital interactions, the spectra of Cp$_2$Mo(bdt) indicate essentially none.

An explanation for this difference in covalency between the d^1 and d^2 systems lies in previous structural studies of molybdenum complexes, which have shown that the fold angle of the dithiolate metallocycle along the S$\cdots$S vector varies in a way that is dependent upon the occupation of the d orbital that is in the equatorial plane. A larger fold angle is observed as the occupation of the metal orbital decreases, which can be ascribed to a stabilizing interaction of the filled p orbitals on sulfur with the metal orbital in the equatorial plane upon bending, as illustrated schematically in Figure 5. Folding of the dithiolate ligand enables the S electron density

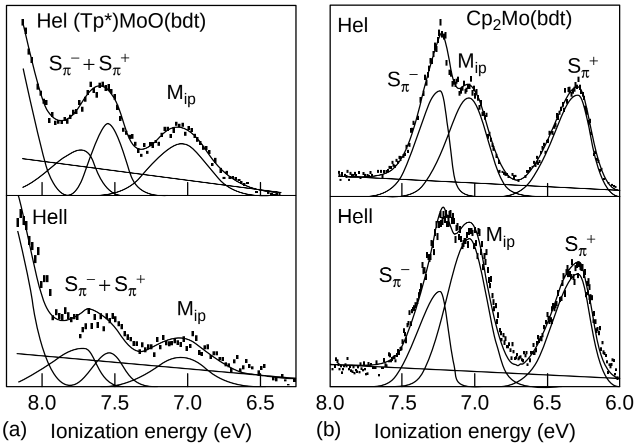

Figure 4 Comparison of the valence photoelectron spectra of (a) Tp*MoO(bdt) and (b) Cp$_2$Mo(bdt) collected with HeI and HeII photon sources

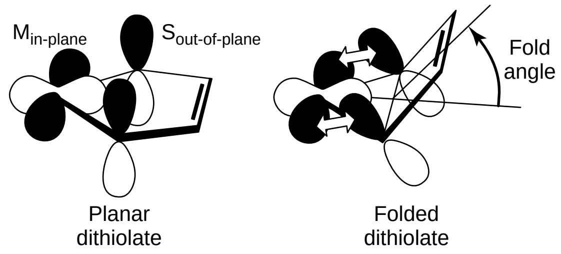
$\mathrm{M_{in\text{-}plane}}$
$\mathrm{S_{out\text{-}of\text{-}plane}}$
Fold angle
Planar dithiolate
Folded dithiolate

Figure 5 Schematic of metal–sulfur covalency that can occur upon dithiolate folding

to modulate the electron density in the equatorial plane of the metal and thus can play a very significant role in metal–sulfur anisotropic bonding. For the d^2 metal system $Cp_2Mo(bdt)$, the metal d orbital in the equatorial plane is fully occupied and the dithiolate metallocycle is essentially planar to avoid the filled–filled orbital interaction, with a fold angle in the solid state of 9.0°. For $(Tp^*)MoO(bdt)$, which has a formal d^1 electron configuration, the fold angle is intermediate at 21.3°, while for $(Tp^*)Mo(NO)(bdt)$, the fold angle is 41.1°. Although the metal center of $(Tp^*)Mo(NO)(bdt)$ is formally d^4, the strong π-acceptor character of the NO ligand results in an electron configuration in which the d orbital in the equatorial plane is empty.

The symmetric $S_{\pi}{}^{+}$ orbital has the right symmetry and energy to match the metal in-plane orbital upon folding of the dithiolate unit, and the substantial mixing of the out-of-plane $S_{\pi}{}^{+}$ orbitals and metal in-plane orbital upon folding is shown experimentally by the intensity changes observed in the HeI and HeII spectra of $(Tp^*)MoO(bdt)$. The S orbitals of dithiolate can therefore serve as an effective mechanism for the buffering of electron density at the metal center by either involving themselves in strong mixing with an empty metal orbital, or by localization of electron density on the S orbitals in the presence of a filled metal orbital. This ''dithiolate-folding-effect'' may be important in stabilizing the multiple oxidation states that result from the electron transfer or equatorial oxygen atom transfer (OAT) in pyranopterin Mo/W enzymes.

3.3 Photoelectron Spectroscopy of Porphyrins, Metalloporphyrins and Phthalocyanines

Porphyrins and metalloporphyrins have been studied extensively due to their importance in biology. The related phthalocyanine macrocycles are often considered for comparison to porphyrins and are also of interest because of their increased use in molecular electronic devices.[38] Much attention has been given to electronic structure calculations on porphyrins and metalloporphyrins,[39–41] and as discussed earlier, the quality of a computational method for describing the electronic wavefunction of any system can be judged by the method's ability to calculate accurate ionizations energies. Here we will specifically consider the experimental results that are referenced for theoretical calibration.

3.3.1 Analysis of Porphyrin and Metalloporphyrin Charge Potentials by XPS

XPS has been used extensively to analyze the donor ability of porphyrins and the charge potentials present throughout a metalloporphyrin molecule, particularly with regard to the electronic effects of substituents and changes at the central core. In a typical study, XPS is performed on a solid-phase sample of the molecule of interest that has been thinly distributed on a conductive substrate. The conductive substrate guarantees that the sample does not build up positive charge from the loss of photoelectrons, which can create difficulties with calibration. For XPS analysis, the sample can be deposited on the substrate by vacuum deposition to create a thin film, or can be simply spread and ground into a relatively soft substrate such as a gold foil. The core-ionization energies of the analyte are then internally calibrated to a core ionization of either the substrate or of a separate atom in the analyte.

The nitrogen 1s ionization energies that have been reported for tetraphenylporphyrin and various first row transition metal complexes of tetraphenylporphyrin are listed in Table 2. As can be seen, the values reported from different references for some of these molecules vary much more than the precision of ±0.1 eV that is typically reported for these measurements, so some care must be taken in comparing values from different papers. The overall shifts between molecules of these ligand-based core ionizations are also on the order of the precision of the measurements, so some caution must also be taken in their interpretation.

Table 2 Nitrogen core (1s) ionization energies for tpp complexes

Compound	N 1s (eV)	References
$tppH_2$	397.2, 399.1	42
$tppH_2$	398.2, 400.2	43
$tppH_2$	397.2, 399.1	44
$tppH_2$	397.2, 399.2	45
$tppH_2$	398.5, 400.3	46
$tppH_2$	397.4, 399.5	47
$tppH_2$	398.2, 400.1	48
Zn(tpp)	397.2	42
Zn(tpp)	397.2	44
Zn(tpp)	397.8	45
Zn(tpp)	398.7	48
Cu(tpp)	398.9	43
Cu(tpp)	398.2	45
Ni(tpp)	398.5	45
Co(tpp)	397.2	42
Co(tpp)	398.1	45
Co(tpp)NO	397.7	42
Fe(tpp)Cl	398.6	42
$Fe(tpp)(pip)_2$	397.7	42
Mg(tpp)	397.8	45

There are two distinct N 1s ionizations observed for free-base $tppH_2$, with the peak at lower ionization energy assigned to the two iminic (unprotonated) nitrogens and the peak at higher ionization energy assigned to the two pyrrolic (protonated) nitrogens. These two peaks are separated by about 2 eV, which indicates the lower charge potential at the pyrrolic nitrogens due to the presence of the protons. When the porphyrin is metallated the four nitrogens become equivalent, and the N 1s ionization energy is approximately the same as was observed for the iminic nitrogens in the free-base porphyrin. The N 1s ionization energy shifts when the central metal is varied, and this shift has been used as an indication that the charge potential at nitrogen is changing as the electronegativity of the metal varies. For example, the N 1s energies of M(tpp) are stabilized by 0.7 eV from Zn(II) to Ni(II).[45]

Core ionizations have also been used to analyze the electronic influence that substituents on the periphery of the porphyrin macrocycle have upon the donor ability of the central nitrogen atoms. Table 3 lists the N 1s ionization energies that have been reported for a series of substituted porphyrins, with the core levels of the unsubstituted porphine used for comparison.[47] The core ionizations of $oepH_2$ and $tppH_2$ are both destabilized from those of porphine, indicating the electron-donating nature of the ethyl and phenyl substituents in these common porphyrin ligands; the core ionizations indicate that tpp^{2-} should be a better donor than oep^{2-}. The core ionizations of tetraphenylporphyrins bearing electron withdrawing substituents on the phenyl rings, which have been of interest as a way of designing electron-poor porphyrins with bulky steric properties, are stabilized from those of $tppH_2$ to an extent that they are now similar to those of unsubstituted porphine.

The shifts of core ionization energies in bulk samples such as these just presented are typically interpreted in terms only of the molecular changes that influence the shifts. However, solid-state effects could also contribute to the experimental trends, particularly for molecules that have very strong intramolecular interactions in the solid phase. A recent paper[49] has addressed the possibility that the shifts that have been observed in the bulk phase XPS of porphyrins are actually due to solid-state packing effects rather than the inherent molecular electronic structure.

Table 3 Nitrogen core (1s) ionization energies for substituted porphyrins

Porphyrin	N 1s (eV)
porphine	398.1, 400.1
$oepH_2$	397.7, 399.8
$tppH_2$	397.4, 399.5
$TMeOPPH_2$	397.6, 399.7
TCl_2PPH_2	398.0, 400.05
$TCNPPH_2$	398.1, 400.2
TCF_3PPH_2	398.1, 400.2
TNO_2PPH_2	398.1, 400.2
TF_5PPH_2	398.2, 400.4

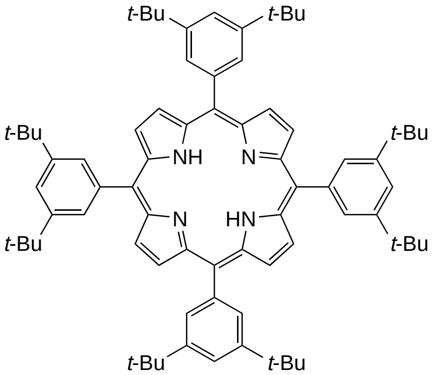

This study looked at the XPS of a series of metalloporphyrins for the sterically bulky phenyl-substituted porphyrin shown. The addition of the *tert*-butyl groups to the phenyl rings leads to large interplane distances between the porphyrin rings of about 7 Å in the crystal structures, meaning that there will be little electronic communication between neighboring molecules. The N 1s ionization energies of this free-base porphyrin were measured at 398.2 and 400.1 eV, essentially the same as those measured for $tppH_2$, although they would be expected to be destabilized by the addition of eight electron-donating *tert*-butyl substituents. When the N 1s energies are compared for different metal complexes of this bulky porphyrin, they are found to be effectively identical; that for the Zn(II) complex is 389.9 eV, for Cu(II) complex it is 399.0 eV, and for Ni(II) complex it is 399.0 eV. In comparison, the N 1s energies of M(tpp) have been reported to shift by 0.7 eV from Zn(II) to Ni(II) as mentioned above.[45] These results indicate that the degree of aggregation may have significant control over the relative core ionization energies of metalloporphyrins in the solid phase.

3.3.2 Gas-phase Photoelectron Spectroscopy of Neutral Porphyrins

Very few studies have been reported on the gas-phase photoelectron spectra of porphyrins, not due to lack of interest, but rather because acquisition of the spectra of these molecules is nontrivial with most spectrometers used for study of neutral molecules.

A molecular orbital treatment of the valence electronic structure of porphyrins indicates that the HOMO are two π orbitals that are close in energy to each other, but well separated in energy from all other occupied orbitals. The relative energy of these two orbitals is predicted to be dependent upon the substituents present. For metalloporphyrins, which are discussed in the next section, occupied metal orbitals may be in the same energy region as these ligand-based orbitals, and the specific metal or ancilliary ligands will control exactly where the metal-based ionizations fall relative to the two porphyrin-based HOMOs.

As examples of the type of valence photoelectron spectra that are typical for these molecules, the gas-phase valence photoelectron spectra of oepH$_2$ and tppH$_2$ from 5 to 15 eV ionization energy are shown in Figure 6.[50] The ionizations located above about 10 eV for each compound arise from the removal of electrons from orbitals primarily associated with σ bonds and the most stable π bonds. The rather intense ionization at about 9 eV in the spectrum of tppH$_2$ is due to the π orbitals of the phenyl substituents that derive from the e$_{1u}$ orbitals of benzene. The lowest energy set of ionizations, located between 6 and 7 eV for each of these molecules, has two distinct features that are characteristically a sharp first ionization, followed closely by a broad nondistinct ionization. As in the spectrum of simple pyrrole, the shape and intensity of the second ionization feature is dictated by vibronic coupling.[51] As mentioned, it is expected that two porphyrin π orbitals, which have labels a$_u$ and b$_{1u}$ in D_{2h} symmetry (a$_{1u}$ and a$_{2u}$, respectively, in D_{4h} symmetry), should be separated from all of the other filled orbitals and close to each other in energy, giving rise to ^{2}A$_u$ and ^{2}B$_{1u}$ ion states that are also close to each other in energy. For comparison, the photoelectron spectrum of unsubstituted porphine has an ionization band at 6.9 eV that does not show two clear ionization features, because for porphine the ^{2}A$_u$ and ^{2}B$_{1u}$ ion states are essentially degenerate.[52] Addition of eight ethyl substituents in the β positions of the porphyrin pyrroles slightly separates the ^{2}A$_u$ and ^{2}B$_{1u}$ ion states due to hyperconjugative π interaction of the alkyl substituents. The a$_u$ orbital has more electron density at the substituted sites than the b$_{1u}$ orbital does, and the a$_u$ orbital is therefore destabilized away from the b$_{1u}$ orbital, causing the energy splitting seen in the photoelectron spectrum of oepH$_2$. The total destabilization of the ^{2}A$_u$ state of oepH$_2$ from its position in unsubstituted porphine is about 0.7 eV.

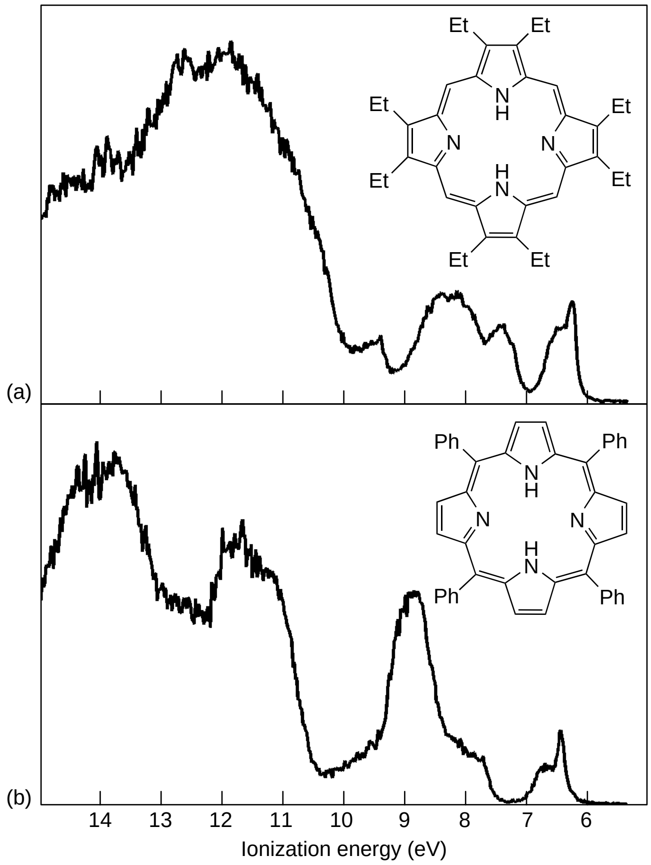

Figure 6 Valence photoelectron spectra of (a) oepH$_2$ and (b) tppH$_2$

The substituents in tppH$_2$ affect the relative energies of the ^{2}A$_u$ and ^{2}B$_{1u}$ ionizations in the opposite trend as the substituents in oepH$_2$. In tppH$_2$, the four electron-donating phenyl substituents are in the meso positions of the porphyrin; the a$_u$ orbital has nodes passing through these positions, while the b$_{1u}$ orbital has significant electron density at these positions and is destabilized relative to the a$_u$ orbital. For tppH$_2$ the first ionization is then due to the ^{2}B$_{1u}$ ionization, the opposite ordering observed for oepH$_2$. This assignment is also supported by the cross-sectional behavior of the ionizations with changing photon energy.[50]

A comparison of all of the ionization energies that have been reported for the ^{2}A$_u$ and ^{2}B$_{1u}$ ion states of oepH$_2$ and tppH$_2$ are listed in the Table 4. The two reports of tppH$_2$ are in good agreement, but the two studies of oepH$_2$ have given greatly different results. The paper that first reported a spectrum of oepH$_2$ also includes essentially identical spectra of several metalloporphyrins, raising the possibility of contamination of the samples during or between data collections. Cross contamination of samples in the vacuum chamber or decomposition are major concerns with gas-phase spectroscopy of neutral molecules. The latter report of the photoelectron spectrum of oepH$_2$ gives results that are fairly similar to spectra of etioporphyrin-I, -II, and -III, as would be expected for these similar octaalkylporphyrins.[52]

3.3.3 *Photoelectron Spectroscopy of Metalloporphyrins*

A question that is central to the chemistry of metalloporphyrin complexes concerns the energy of the metal-based ionizations and their relationship with respect to the porphyrin-based π ionizations. One example that

Table 4 Valence ionization energies for porphyrins

	Ionization energy (eV)		
Molecule	^{2}A$_u$ (^{2}A$_{1u}$)	^{2}B$_{1u}$ (^{2}A$_{2u}$)	References
porphine	6.55		52
oepH$_2$	6.24	6.49	50
	6.39	6.83	53
tppH$_2$	6.70	6.43	50
	6.72	6.39	54

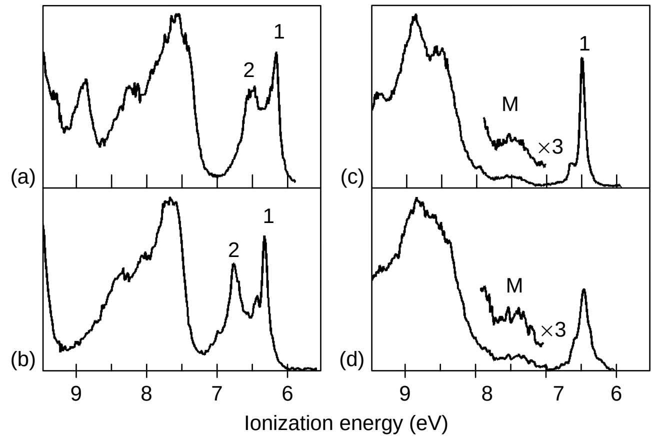

Figure 7 Valence photoelectron spectra of (a) Mg(oep), (b) VO(oep), (c) VO(pc) collected with HeI photons, and (d) VO(pc) collected with HeII photons. (Reprinted with permission from Westcott, Gruhn, Michelsen, Lichtenberger.[55] © 2000 American Chemical Society)

has been studied is VO(oep),[55] which is of interest due to its relationship to the reactive oxoiron(IV) porphyrinate intermediates in OAT. The spectrum of VO(oep) is compared to that of Mg(oep) in Figure 7. The assignment of the initial (6−7 eV) ionizations is straightforward for Mg(oep) because the porphyrin π electrons are the only low-valence electrons in this molecule. These ionizations shift slightly from 6.24 and 6.47 eV for oepH$_2$ to 6.16 and 6.52 eV for Mg(oep). For VO(oep), which should include an additional low energy ionization from the lone electron of the d^1 V(IV) metal center, the characteristic shapes of the two porphyrin-based ionizations are again observed. The similar relative intensities show that the two porphyrin π orbitals retain occupations of two electrons in the neutral molecule. The porphyrin-based ionizations of VO(oep) will be split into singlet and triplet states because of the unpaired V d electron, but the similar shapes of the ionizations in both spectra show that the spin-state splitting is less than the width of the ionizations and is not resolved in these spectra. Comparison of the ionizations of VO(oep) with those of oepH$_2$ and Mg(oep) show that the initial ionizations of VO(oep) do not correspond to removal of the single vanadium d electron from the d_{xy} orbital, and the specific location of this metal ionization is not apparent because of the porphyrin-based ionizations in this region.

To aid in locating the vanadyl d_{xy} ionization, the spectra of the related phthalocyanine complexes were also examined. Gas-phase spectra of Mg(pc) and other metallophthalocyanines have been reported.[56] The ionization of Mg(pc) that corresponds to band 2 of Mg(oep) is stabilized because of the extra nitrogen atoms of phthalocyanine, which opens a window of ionization energy to allow observation of other ionizations. The spectrum of VO(pc) is similar to that of Mg(pc), with band 1 located at 6.49 eV. Most significantly, the VO(pc) spectrum contains a broad ionization at 7.59 eV that is not seen in the spectrum of Mg(pc). The area of this ionization increases by 80% with respect to ionization 1 with HeII excitation, similar to the behavior observed for the vanadium-based ionizations of other vanadyl complexes. The band labeled M is therefore identified as the metal d_{xy} ionization. The HeII spectrum of VO(oep) suggests that the d_{xy} ionization of this molecule also is between 7.3 and 8 eV. However, because of the relatively low intensity of the d_{xy} ionization as seen for VO(pc) and because of the presence of other porphyrin π ionizations in this region, the d_{xy} ionization of VO(oep) cannot be clearly observed.

The observation that considerably less energy is required to remove electrons from filled orbitals than to remove an electron from a singly-occupied orbital indicates that the Aufbau Principle is being violated in these systems. Similar behavior has been observed for cobalt(II) and copper(II) phthalocyanines[56] and other metalloporphyrins with unpaired metal electrons.[53,54] Non-Aufbau electron configurations are occasionally invoked in theoretical calculations, but experimental observation of non-Aufbau behavior for transition metal molecules has been limited to the cases of porphyrins and phthalocyanines.

3.3.4 Multicharged Phthalocyanine Anions with Negative Ionization Energies

Only within the last few years has gas-phase photoelectron spectroscopy of multicharged anions been reported.[57] Electrons are bound in neutral molecules or stable anions by a coulombic potential, and due to coulombic repulsions few species with multiple negative charges are stable in the gas phase. Some of the first examples observed and studied by photoelectron spectroscopy were copper phthalocyanines that contain three or four negatively charged sulfonate ($-SO_3^-$) substituents.[58] Gas-phase ions of the molecules of interest were generated using electrospray from solutions of sodium salts of the anions; the gas-phase anions produced were then accumulated and stored in a quadrupole ion trap, separated by mass/charge ratio by a time-of-flight mass spectrometer, and then analyzed by photoelectron spectroscopy using photons of either 6.424 eV (193 nm wavelength) or 4.661 eV (266 nm wavelength).

The photoelectron spectra of $[CuPc(SO_3)_4]^{4-}$ (a, b) and $[CuPc(SO_3)_4]^{3-}$ (c, d) are shown in Figure 8. The negative charge of the molecules leads to a substantial decrease of ionization energy as compared to the neutral porphyrin and pthalocyanine molecules discussed in the previous section. Also, there is a further destabilization of the first ionization energy of $[CuPc(SO_3)_4]^{4-}$ as compared to $[CuPc(SO_3)_4]^{3-}$ as the negative charge on the anion increases. Most surprisingly, the spectrum of $[CuPc(SO_3)_4]^{4-}$ shows that the lowest energy ionization band has a threshold energy of *−0.9 eV*, indicating that in the gas phase the tetra-anion is actually unstable with respect to loss of an electron. The fact that this species can indeed be isolated is due to a coulombic barrier. This barrier,

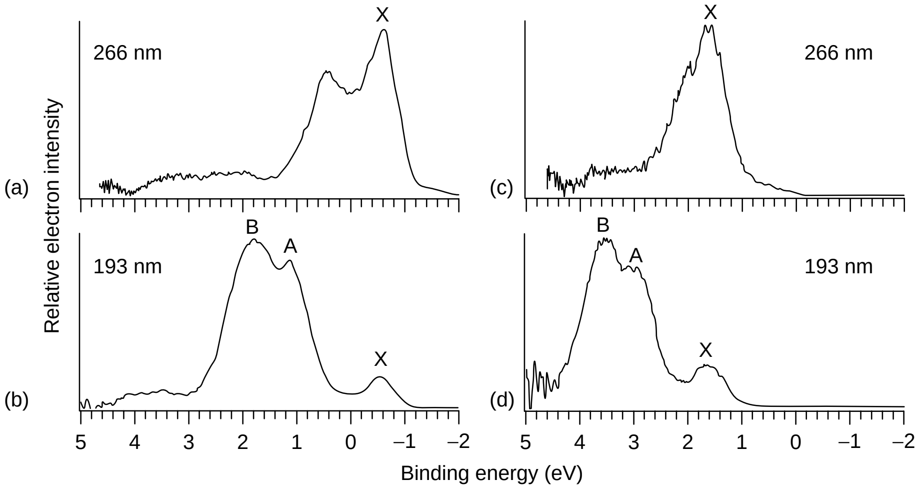

Figure 8 Photodetachment spectra of $[CuPc(SO_3)_4]^{4-}$ at (a) 266 nm and (b) 193 nm and of $[CuPc(SO_3)_4]^{3-}$ at (c) 266 nm and (d) 193 nm. (Reprinted by permission from Macmillan Publishers Ltd: *Nature*, Wang and Wang,[58] © 1999)

estimated to be 2.5 eV for the tri-anion and 3.5 eV for the tetra-anion species, is caused by long-range repulsive forces located at the exterior of the molecule that the electrons, even though energetically unstable for binding, must overcome if they are to be removed from the molecule. The unstable electron is essentially held in an electrostatic ''corral'' by the negative charges by which it is surrounded, until the photon provides the energy to overcome the barrier. If energy is not put into the system, this barrier is not overcome and the tetra-anion exists as a metastable species. The lifetime of this metastable species is at least as long as the 400 s for which the anions were stored in the quadrupole during the process of the experiment.

3.4 Measures of Inner-Sphere Reorganization Energies

Electron-transfer processes are key steps in a vast array of chemical and biological transformations. Ionization itself is an electron-transfer process. According to semiclassical theory, the rates of these reactions in solution are governed by three fundamental parameters: the reorganization energy, λ (where $\lambda = \lambda_i + \lambda_o$, the inner-sphere and outer-sphere contributions); the electronic coupling matrix element, H_{AB}; and the standard free energy change, ΔG^0. Both theoretical and experimental investigations suggest that the solvent contribution λ_o to the reorganization energy is much larger in most cases than the inner-sphere contribution (λ_i). It also has been shown that the ratio λ_o/λ_i decreases with decreasing solvent polarity. The limiting case is a reaction in the absence of bulk solvent, as occurs in the gas phase. Several recent papers have demonstrated that it is possible to obtain inner-sphere reorganization energies of isolated molecules from band-shape analyses of ionizations obtained by gas-phase photoelectron spectroscopy.[59–61] Compared to other experimental methods used to analyze reorganization energies, gas-phase photoelectron spectroscopy has the advantage of allowing direct measure of λ_i without contribution from λ_o.

The total inner-sphere self-exchange λ_i for a neutral molecule is the sum of the reorganization energy of the initial neutral molecule, λ^0, and the reorganization energy of the radical cation, $\lambda^{\bullet +}$. These energies are illustrated in Figure 9 in terms of a general distortion coordinate that prepares a molecule for electron transfer. If the distortions are sufficiently small that the transitions occur near the bottom of the potential wells, where the wells are essentially harmonic, λ^0 and $\lambda^{\bullet +}$ are similar in magnitude. Photoelectron spectroscopy of a neutral molecule directly measures the transition from state 1 to state 2 as the vertical ionization energy, and the width, vibrational structure, and contour of the ionization band give information on the distortion energy $\lambda^{\bullet +}$.[59]

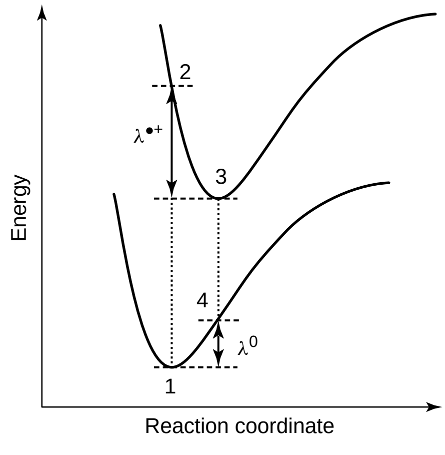

Figure 9 Potential energy surfaces for neutral and cation states that define λ^0 and $\lambda^{\bullet +}$

3.4.1 Reorganization Energies of Metalloporphyrins

As previously discussed, the first two ionizations of free-base porphyrins correspond to the two highest occupied π orbitals and are close in energy. If the second ionization is too close in energy to the first, it can obscure the profile associated with the lowest positive ion state. However, with the proper choice of porphyrin substituents and metal, these two ionizations are separated appropriately for band-shape analysis of the first ionization.

As an example, the portion of the photoelectron spectrum of Zn(oep) that contains the first two ionization bands is shown in Figure 10.**[61]** The Gaussian labeled A on the low binding energy side of the first main ionization is due to a hot band. The intensity of this Gaussian is consistent with the relative intensity expected from population of excited vibrational levels in the ground state of the molecule at the temperature at which the data were collected (280–320 °C). The vertical ionizations of the two π ionizations are associated with the two maxima on the overlapping band structure, which are modeled with the Guassians labeled 1 and 5. There is a splitting of about 0.4 eV between these two maxima, which leaves room for observation of the ionization intensity on the high binding energy side of the first ionization due to a partially resolved vibrational progression. This structure is modeled with the Gaussians labeled 2 and 3. The spacing of these Guassians is about 0.11 eV ($\approx 900\,\text{cm}^{-1}$), which is in the energy region expected for vibrational modes associated with the C−C and C−N bonds of the porphyrin ring. Of course, this vibrational structure is most likely the result of many vibrational modes rather than one particular mode, but the regular spacing of the Guassians can be used to represent an average of many vibrational contributions by mode averaging.

The experimentally measured reorganization energy for formation of a radical cation, $\lambda^{\bullet+}$,

$$\lambda^{\text{QM}} = \sum_{\text{k}} h\upsilon_{\text{k}}\text{S}_{\text{k}} \tag{6}$$

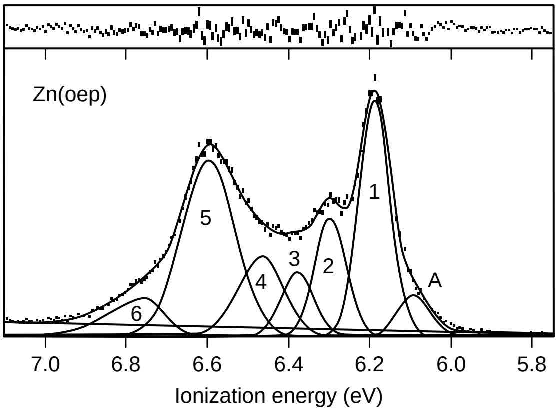

Figure 10 Photoelectron spectrum of Zn(oep) and residual of fit. (Reprinted with permission from Amashukeli, Gruhn, Lichtenberger, Winkler, Gray.**[61]** © 2004 American Chemical Society)

can be considered as the sum of λ^{QM} and λ^{SC}, the reorganization energies obtained from quantum-mechanical (QM) and semiclassical (SC) band-shape analyses of photoelectron data for the first ionization of a molecule.**[59]** QM analysis of any resolved vibrational fine structure in the ionization band yields distortion parameters (S), which are related to λ^{QM} according to equation (6) (h is Planck's constant and υ_{k} is the vibrational frequency of mode k). With the assumption that the geometry changes upon ionization are small enough that a harmonic oscillator model is appropriate, the intensities of the individual symmetric Gaussian bands in the vibrational progression can be considered to follow a Poisson distribution (where I_n is the intensity of the nth vibrational band) as shown in equation (7). For Zn(ppix) and Zn(oep),

$$I_n = \frac{\text{S}_n}{n!}e^{-\text{S}} \tag{7}$$

only the first two vibrational bands are well resolved, and the values of S are extracted from the ratio of I_1 to I_0. The fit of the data for Zn(oep) gives a value for λ^{QM} of 55 ± 3 meV.

Distortions along low-frequency modes and small frequency changes between the neutral and cation states, if present, contribute to the width of the vibrational lines in the photoelectron spectra after taking into account instrumental line broadening. Such band profiles can be treated semiclassically using equation (8), where IE is the ionization energy and D is related to the transition moment. The Gaussian functions used to fit the experimental spectra can be described

$$G = |D|^2 \exp \frac{-(hv - IE)^2}{4\text{k}_{\text{b}}\text{t}\lambda^{\text{SC}}} \tag{8}$$

as a convolution of G and another function defined by the resolution of the instrument. The Guassians used to model the band shape of Zn(oep) are quite narrow, and the value of λ^{SC} is fairly negligible (3 ± 2 meV) compared to the λ^{QM} value, showing that very low-frequency modes contribute very little to $\lambda^{\bullet+}$. Taken together, λ^{QM} and λ^{SC} indicate an overall $\lambda^{\bullet+}$ for Zn(oep) of 58 ± 3 meV, while the $\lambda^{\bullet+}$ reorganization energy for Zn(ppix) is about 10 meV greater.

The small values of $\lambda^{\bullet+}$ obtained for Zn(oep) and Zn(ppix) indicate that the assumption that λ^0 is approximately the same as $\lambda^{\bullet+}$ should be reasonably valid for these molecules. The self-exchange λ_i in the gas phase can then be experimentally estimated to be about 120 meV (Zn(oep)) to 140 meV (Zn(ppix)). For comparison to studies by other methods, an analysis of electron-transfer kinetics in Ru-Zn-cytochrome produced an estimated upper limit of 300 meV for the innter-sphere contribution to the Zn-porphyrin self-exchange reorganization energy. These photoelectron spectroscopy measurements indicate that this quantity is likely to be $\leq$ 120 meV, and that the outer-sphere contribution to the total reorganization energy in Ru-Zn-cytochrome is some 90 meV greater than the earlier estimate.

3.4.2 Reorganization Energy of the Fe^{+2}–Fe^{+3} Redox Couple in Rebredoxin

Negative-ion gas-phase photoelectron spectroscopy has also recently been used to evaluate the reorganization energies of tetrahedrally coordinated Fe^{+2} anions that serve as models for the active sites of mononuclear iron–sulfur proteins such as rubredoxin that cycles between high spin Fe^{+2} and high spin Fe^{+3}.**[62,63]**

The electronic structure of several model complexes for mononuclear iron proteins has been evaluated by gas-phase photodetachment photoelectron spectroscopy. Molecules of interest are negatively charged, such as $Fe(SCN)_3^-$, $Fe(SCN)_4^-$, and $Fe(SCN)_4^{2-}$. The anions were transported into the gas phase by electrospray ionization; isolated $Fe(SCN)_4^{2-}$ was not detected in the gas phase, but rather was trapped as the stabilized ion pair $Na^+[Fe(SCN)_4^{2-}]$.

The spectra of some of these molecules are shown in Figure 11. The spectra of each of these molecules shows a broad feature centered at around 6 eV, which for the Fe^{+3} and Sc^{+3} molecules is the lowest energy ionization feature. The spectrum of the d^0 Sc^{+3} complex serves as a reference to assign the Fe 3d and ligand ionizations in the spectra of the corresponding Fe complexes, and corroborates that the lowest energy ionizations for $Fe(SCN)_4^-$ are from ligand-based ionizations. For the Fe^{+2} molecules $Fe(SCN)_3^-$ and $Na^+[Fe(SCN)_4^{2-}]$, the spectra each contain a weak low ionization energy feature near 5 eV that is assigned to the Fe d ionization.

The lowest energy iron-based ionization of these and similar Fe^{+2} complexes are clearly observed in the photoelectron spectra, but the lack of distinct vibrational structure means that the quantum-mechanical method used to analyze reorganization energies for the porphyrins described earlier cannot be used. However, the difference between the vertical detachment energies (VDE) and adiabatic detachment energies (ADE) ionization energy can also be taken as an estimation of λ_{ox}. The VDE is measured directly from the peak maximum, while the ADE can be estimated by drawing a straight line along the leading edge of the threshold band and then adding a constant to the intersection with the energy axis to correct for experimental resolution and thermal broadening. In the case of large geometry changes (large reorganization energies), the adiabatic transition may not actually be observed in the photoelectron spectra, so the adiabatic values obtained by this method are upper limits.

The reorganization energies measured for Fe(II) molecules are shown in Table 5. There is a clear trend that λ_{ox} increases as the size of the molecule and number of vibrational modes increases. It is interesting to note that λ_{ox} for Na^+ $[Fe(S_2\text{-o-xyl})_2^{2-}]$ is significantly smaller than λ_{ox} for Na^+ $[Fe(SCN)_4^{2-}]$, most likely because the chelated ligands of $Fe(S_2\text{-o-xyl})_2^{2-}$ make the molecule more rigid. Also note that these reorganization energy values are significantly larger than those measured for Zn(oep) and Zn(ppix).

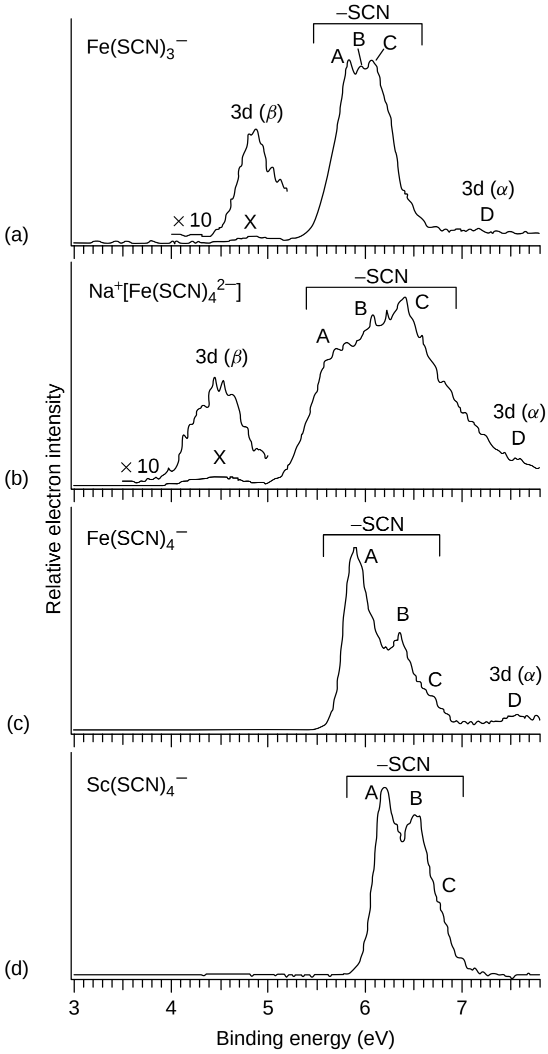

Figure 11 Photoelectron spectra of (a) $Fe(SCN)_3^-$, (b) $Na^+[Fe(SCN)_4^{2-}]$, (c) $Fe(SCN)_4^-$, and (d) $Sc(SCN)_4^-$ collected with a 157 nm laser. Note that the energy scale is reversed compared to all other spectra shown here. (Reprinted with permission from Yang, Wang, Fu, Wang.**[62]** © 2003 American Chemical Society)

4 CONCLUSION

Development of new photoionization methods and instrumentation, along with advances in supporting electronic structure calculations, have allowed photoelectron spectroscopy to be progressively applied to larger and more complicated chemical systems. The applications presented here are just a few examples of the uses of photoelectron spectroscopy to the study bioinorganic model complexes. Studies to this point have provided many unique and in several cases surprising insights into the electronic structure properties of metal active sites in biology. There is much promise for the future in a wide array of applications of photoelectron spectroscopy in this area.

Table 5 Adiabatic detachment energies (ADE), vertical detachment energies (VDE), and reorganization energies of Fe^{+2} complexes

Molecule	ADE (eV)	VDE (eV)	λ_{ox} (eV)
$FeCl_3^-$	4.10(6)	4.36(6)	0.26
$Fe(SCN)_3^-$	4.64(5)	4.96(8)	0.32
$Na^+ [Fe(SCN)_4^{2-}]$	4.12(5)	4.56(8)	0.44
$Fe(SCH_3)_3^-$	2.80(6)	3.08(5)	0.28
$Na^+ [Fe(S_2\text{-o-xyl})_2^{2-}]$	2.30(5)	2.60(5)	0.30

5 ACKNOWLEDGEMENT

Photoelectron spectroscopy research is funded in our laboratories by the National Science Foundation.

6 ABBREVIATIONS AND ACRONYMS

ADE = adiabatic detachment energies; ESCA = electron spectroscopy for chemical analysis; HOMO = highest occupied molecular orbitals; MAES = metastable atom electron spectroscopy; MIES = metastable ionization electron spectroscopy; OAT = oxygen atom transfer; PES = photoelectron spectra; PFI = pulsed field ionization; PIES = Penning ionization electron spectroscopy; QM = quantum-mechanical; REMPI = resonantly enhanced multiphoton ionization; SC = semiclassical; VDE = vertical detachment energies; XPS = x-ray photoelectron spectroscopy; ZEKE = zero electron kinetic energy; Cp = cyclopentadienyl, η^5-$C_5H_5^-$; Ph = phenyl, $C_6H_5^-$; Tp* = hydrotris(3,5-dimethyl-1-pyrazolyl) borate; tdt = toluene-3,4-dithiolate; bdt = benzenedithiolate; tpp = 5,10,15,20-tetraphenylporphyrin dianion; oep = 2,3,7,8,12,13,17,18-octaethylporphyrin dianion; pip = piperidine; $TMeOPPH_2$ = 5,10,15,20-tetra(4-methoxyphenyl)porphyrin; TCl_2PPH_2 = 5,10,15,20-tetra(3,5-dichlorophenyl)porphyrin; $TCNPPH_2$ = 5,10,15,20-tetra(4-cyanophenyl)porphyrin; TCF_3PPH_2 = 5, 10,15,20-tetra(4-trifluoromethylphenyl)porphyrin; TNO_2PPH_2 = 5,10,15,20-tetra(4-nitrophenyl)porphyrin; TF_5PPH_2 = 5,10,15,20-tetra(2,3,4,5,6-pentafluorophenyl)porphyrin; pc = phthalocyanine dianion; ppix = protoporphyrin IX dianion.

7 FURTHER READING

A. Ellis, M. Feher and T. Wright, 'Electronic and Photoelectron Spectroscopy: Fundamentals and Case Studies', Cambridge University Press, Cambridge, 2005. A good introduction to the fundamentals of photoelectron spectroscopy that includes case studies on several small molecules and clusters.

J. C. Green and P. Decleva, *Coord. Chem. Rev.*, 2005, **249**, 209. Discusses the use of synchrotron radiation in photoelectron spectroscopy of transition metal molecules, with case studies taken from organometallic carbonyls and metallocenes.

N. E. Gruhn and D. L. Lichtenberger, in 'Encyclopedia of Mass Spectrometry', ed. P. Armentrout, Volume Editor, eds. M. L. Gross and R. Caprioli, Editors-in-Chief, Elsevier, 2003, Vol. 1, p. 818. Discusses the use of photoelectron spectroscopy to analyze ion states of inorganic molecules, specifically considering the influences of spin-orbit, Jahn-Teller, and exchange splitting.

S. Hüfner, 'Photoelectron Spectroscopy: Principles and Applications', 3rd edition, Spring-Verlag, Berlin, 2003. In-depth discussion of photoemission in solid materials.

NIST Chemistry Webbook: http://www.webbook.nist.gov/chemistry/. 2007. Exhaustive database of all first ionization energies reported in the primary literature. Free access.

NIST X-ray Photoelectron Spectroscopy Database: http://srdata.nist.gov/xps/. 2007. Database of many core photoelectron and Auger-electron spectral lines, currently containing over 22,000 entries. Free access.

D. W. Turner, C. Baker, A. D. Baker and C. R. Brundle, 'Molecular Photoelectron Spectroscopy', Wiley-Interscience, London, 1970. Classic book, with many examples of organic molecules.

D.-S. Yang, *Coord. Chem. Rev.*, 2001, **214**, 187. Describes the application of ZEKE photoelectron techniques to metal-containing molecules. Examples include metal dimer and trimer oxides, carbides, and nitrides.

T. Waters, X.-B. Wang and L.-S. Wang, *Coord. Chem. Rev.*, 2007, **251**, 474. Review describing the use of electrospray to transfer negatively charged transition metal complexes to the gas phase for photoelectron spectroscopy. Examples discussed include square planar and octahedral halide complexes, metal-metal bonded species, transition metal bis(dithiolene) complexes, and mononuclear and polynuclear iron-sulfur clusters.

8 REFERENCES

1. A. Einstein, *Ann. Phys.*, 1905, **17**, 549.
2. T. Koopmans, *Physica (The Hague)*, 1933, **1**, 104.
3. N. E. Gruhn and D. L. Lichtenberger, in 'Encyclopedia of Mass Spectrometry', ed. P. Armentrout, Elsevier, 2003, Vol. 1, p. 818.
4. D. W. Turner, C. Baker, A. D. Baker and C. R. Brundle, 'Molecular Photoelectron Spectroscopy', Wiley-Interscience, London, 1970.
5. D. Turner, C. Baker, A. Baker and C. R. Brundle, 'Molecular Photoelectron Spectroscopy', John Wiley & Sons, New York, 1983.
6. J. H. D. Eland, 'Photoelectron Spectroscopy: An Introduction to Ultraviolet Photoelectron Spectroscopy in the Gas Phase', Butterworths, London, New York, 1984.
7. J. C. Green, *Acc. Chem. Res.*, 1994, **27**(5), 131.

8. G. M. Bancroft and Y. F. Hu, *Inorg. Electron. Struct. Spectrosc.*, 1999, **1**, 443.
9. X. Li, G. M. Bancroft and R. J. Puddephatt, *Acc. Chem. Res.*, 1997, **30**(5), 213.
10. J. C. Green and P. Decleva, *Coord. Chem. Rev.*, 2005, **249**(1–2), 209.
11. K. Siegbahn, C. Nordling, A. Fahlman, R. Nordberg, K. Hamrin, J. Hedman, G. Johansson, T. Bergmark, S.-E. Karlsson, I. Lindgren and B. Lindberg, *Nova Acta Regiae Soc. Sci. Ups.*, 1967, **20**, 282.
12. S. Hufner, 'Photoelectron Spectroscopy: Principles and Applications', Springer-Verlag, Berlin, 2003.
13 J. F. Watts and J. Wolstenholme, 'An Introduction to Surface Analysis by XPS and AES', John Wiley & Sons, Chichester, England, 2003.
14. W. L. Jolly, *J. Phys. Chem.*, 1981, **85**(25), 3792.
15. W. L. Jolly, *Acc. Chem. Res.*, 1983, **16**(10), 370.
16. W. L. Jolly and C. J. Eyermann, *J. Phys. Chem.*, 1982, **86**(24), 4834.
17. R. R. Rye and J. E. Houston, *Acc. Chem. Res.*, 1984, **17**(1), 41.
18. D. E. Ramaker, *Appl. Surf. Sci.*, 1985, **21**(1–4), 243.
19. D. E. Ramaker, 'Surface Analysis by Auger and X-Ray Photoelectron Spectroscopy', IM Publications, Chichester, England, 2003, p. 465.
20. K. Ohno, *Bull. Chem. Soc. Jpn.*, 2004, **77**(5), 887.
21. Y. Harada, S. Masuda and H. Ozaki, *Chem. Rev.*, 1997, **97**(6), 1897.
22. A. Ellis, M. Feher and T. Wright, 'Electronic and Photoelectron Spectroscopy: Fundamentals and Case Studies', Cambridge Press, Cambridge, 2005.
23. X. Wang, X. Yang and L. Wang, *Int. Rev. Phys. Chem.*, 2002, **21**(3), 473.
24. A. Held and E. W. Schlag, *Acc. Chem. Res.*, 1998, **31**, 467.
25. D. S. Yang, *Coord. Chem. Rev.*, 2001, **214**, 187.
26. C. Ng, *Annu. Rev. Phys. Chem.*, 2002, **53**, 101.
27. D. L. Lichtenberger, N. E. Gruhn and S. K. Renshaw, *J. Mol. Struct.*, 1997, **405**, 79.
28. B. E. R. Schilling, R. Hoffmann and D. L. Lichtenberger, *J. Am. Chem. Soc.*, 1979, **101**, 585.
29. M. T. Ashby, J. H. Enemark and D. L. Lichtenberger, *Inorg. Chem.*, 1988, **27**, 191.
30. D. L. Lichtenberger and R. F. Fenske, *J. Am. Chem. Soc.*, 1976, **98**, 50.
31. J. H. Enemark, J. J. A. Cooney, J. Wang and R. H. Holm, *Chem. Rev. (Washington, D.C.)*, 2004, **104**(2), 1175.
32. B. L. Westcott, N. E. Gruhn and J. H. Enemark, *J. Am. Chem. Soc.*, 1998, **120**, 3382.
33. H. K. Joshi, J. A. Cooney, F. E. Inscore, N. E. Gruhn, D. L. Lichtenberger and J. H. Enemark, *Proc. Natl. Acad. Sci. U.S.A.*, 2003, **100**, 3719.
34. B. L. Westcott and J. H. Enemark, *Inorg. Chem.*, 1997, **36**(23), 5404.
35. J. J. Yeh and I. Lindau, *Atom. Data Nucl. Data Tables*, 1985, **32**, 1.
36. J. J. Yeh, 'Atomic Calculation of Photoionization Cross Sections and Asymmetry Parameters', Gordon and Breach Science Publishers, Langhorne, 1993.
37. H. K. Joshi, J. J. A. Cooney, F. E. Inscore, N. E. Gruhn, D. L. Lichtenberger and J. H. Enemark, *Proc. Natl. Acad. Sci. U.S.A.*, 2003, **100**, 3719.
38. N. R. Armstrong, *J. Porphyrins Phthalocyanines*, 2000, **4**, 414.
39. A. Ghosh and E. Steene, *J. Biol. Inorg. Chem.*, 2001, **6**(7), 739.
40. A. Ghosh, 'Porphyrin Handbook', Academic Press, London, 2000, Vol. 7, p. 1.
41. A. Ghosh, *J. Porphyrins Phthalocyanines*, 2000, **4**(4), 380.
42. M. V. Zeller and R. G. Hayes, *J. Am. Chem. Soc.*, 1973, **95**(12), 3855.
43. Y. Niwa, H. Kobayashi and T. Tsuchiya, *J. Chem. Phys.*, 1974, **60**(3), 799.
44. A. J. Signorelli and R. G. Hayes, *J. Chem. Phys.*, 1976, **64**(11), 4517.
45. D. H. Karweik and N. Winograd, *Inorg. Chem.*, 1976, **15**(10), 2336.
46. J. P. Macquet, M. M. Millard and T. Theophanides, *J. Am. Chem. Soc.*, 1978, **100**(15), 4741.
47. P. G. Gassman, A. Ghosh and J. Almlof, *J. Am. Chem. Soc.*, 1992, **114**(25), 9990.
48. A. Kretschmann, M. Walz, K. Flechtner, H. Steinrueck and J. M. Gottfried, *Chem. Commun.*, 2007, (6), 568.
49. K. Sugiura, K. Iwasaki, K. Umishita, S. Hino, H. Ogata, S. Miyajima and Y. Sakata, *Chem. Lett.*, 1999, (8), 841.
50. N. E. Gruhn, D. L. Lichtenberger, H. Ogura and F. A. Walker, *Inorg. Chem.*, 1999, **38**, 4023.
51. A. B. Trofimov, H. Koppel and J. Schirmer, *J. Chem. Phys.*, 1998, **109**, 1025, references therein.
52. P. Dupuis, R. Roberge and C. Sandorfy, *Chem. Phys. Lett.*, 1980, **75**(3), 434.
53. S. Kitagawa, I. Morishima, T. Yonezawa and N. Sato, *Inorg. Chem.*, 1979, **18**, 1345.
54. S. C. Khandelwal and J. L. Roebber, *Chem. Phys. Lett.*, 1975, **34**, 355.
55. B. L. Westcott, N. E. Gruhn, L. J. Michelsen and D. L. Lichtenberger, *J. Am. Chem. Soc.*, 2000, **122**, 8083.
56. J. Berkowitz, *J. Chem. Phys.*, 1979, **70**(6), 2819.
57. T. Waters, X. Wang and L. Wang, *Coord. Chem. Rev.*, 2007, **251**(3–4), 474.
58. X. Wang and L. Wang, *Nature (London)*, 1999, **400**(6741), 245.
59. X. Amashukeli, J. R. Winkler, H. B. Gray, N. E. Gruhn and D. L. Lichtenberger, *J. Phys. Chem. A*, 2002, **106**, 7593.

60. N. E. Gruhn, D. A. da Silva Filho, T. G. Bill, M. Malagoli, V. Coropceanu, A. Kahn and J. Bredas, *J. Am. Chem. Soc.*, 2002, **124**(27), 7918.
61. X. Amashukeli, N. E. Gruhn, D. L. Lichtenberger, J. R. Winkler and H. B. Gray, *J. Am. Chem. Soc.*, 2004, **126**(47), 15566.
62. X. Yang, X. Wang, Y. Fu and L. Wang, *J. Phys. Chem. A*, 2003, **107**(11), 1703.
63. X. Wang and L. Wang, *J. Chem. Phys.*, 2000, **112**(16), 6959.

Photoluminescence and Electroluminescence, Solid State

Joel R. Deye and Keith A. Walters

Northern Kentucky University, Highland Heights, KY, USA

	Method Summary	1
1	Introduction	2
2	Technical Background	2
3	Applications	5
4	Abbreviations and Acronyms	8
5	Further Reading	8
6	References	8

METHOD SUMMARY

Acronyms, Synonyms

- Solid-State luminescence, fluorescence, or phosphorescence.
- Electrogenerated chemiluminescence.

Measured physical quantities

- Photons of light emitted by the solid sample following creation of an excited state via irradiation (photoluminescence) or application of a potential (electroluminescence).

Information available

- direct measurement of bandgap energy
- presence of excitons, dopants, or point defects in the sample material
- indirect measurement of excited state lifetime.

Information not available, limitations

- The sample must be inherently luminescent to successfully utilize the technique.
- Sample morphology (differences in crystal structure between samples) is not provided.
- No structural information is provided.
- The exact nature of excitons, dopants, or point defects in the sample material may not be determined without additional techniques.

Examples of questions that can be answered

- What is the bandgap energy of this material?
- Does the addition of a dopant or introduction of point defects in the material alter the bandgap energy?
- What is the threshold voltage needed to produce luminescence?
- Will this material be suitable for the development of a photonic device (e.g., solid-state laser, light emitting diode, photovoltaic cell)?

Major advantages

- very sensitive when compared to other analytical methods
- large linear concentration range
- more selective when compared to other molecular spectroscopic methods.

Major disadvantages

- less applicable than other molecular spectroscopic methods since not all samples are inherently luminescent (or require extreme conditions to be luminescent);
- instrumentation more complicated than molecular absorption spectroscopy.

Sample constraints

- Luminescence may be quenched by other nonradiative processes, which can be minimized by cooling the sample.
- The irradiation angle and sample geometry can have a large effect on the observed spectrum.
- The application and conduction of voltage through the sample can have unanticipated effects.

1 INTRODUCTION

Emission spectroscopy has been used to study both atomic and molecular systems for the last 75 years. However, with the rise of materials science and surface chemistry there has been interest in studying the luminescent properties of such solid-state systems, as evidenced by the large number of publications in the 1960s and 1970s focusing on semiconductor luminescence. Recent interest in solid-state luminescence focuses on the usage of semiconductors for light sources and active lasing materials in solid-state lasers. When considering luminescence in semiconducting materials (a major focus of this article), many radiative transitions can be observed, as shown in Figure 1. These transitions focus on (i) direct band-band recombination of the electron and hole, (ii) luminescence from an exciton as described below, (iii) luminescence from a donor (identical to ii) or to an acceptor impurity, and (iv) direct donor-acceptor interaction.

The information obtained from solid-state luminescence is electronic in nature. The most common information available from such measurements revolves around excited-state energy levels. This parameter is particularly important in considering semiconductor materials, as this technique provides a direct measurement of the material bandgap energy (E_g). Furthermore, the presence of defects and/or dopants in the material can be observed through the presence of additional emission peaks. Excitation of the material into its excited state can be achieved via photolytic or electrolytic stimulation, thus providing ‘‘real world’’ conditions for the material, depending on its ultimate application (e.g. photodiode, light-emitting diode, etc.). Stability of the system in its excited state can also be indirectly assessed through the measurement of the emission lifetime (which directly relates to the lifetime of the excited state).

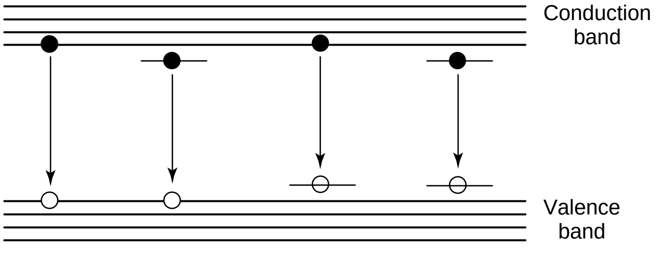

Figure 1 Typical transitions in semiconductors that produce luminescence (see text for details)

Since only the electronic levels of the sample are probed with this technique, many parameters of interest to the material cannot be directly assessed. For example, morphology or structural information of the material cannot be determined through luminescence measurements. In addition, the specific nature and location of the observed defects described above cannot be determined without more sophisticated luminescence microscopy measurements. Also, the material must be inherently luminescent to provide any useful information from this technique. This luminescence may not be visible at ambient temperatures, however; some sample cooling might be required to obtain usable data. With these limitations in mind, however, the solid-state luminescence technique has many benefits. Many of these advantages are also commonly profiled in molecular or atomic emission spectroscopy treatments.[1] Luminescence is one of the most sensitive of analytical techniques, with a large linear concentration range and very low limits of detection.

2 TECHNICAL BACKGROUND

2.1 Luminescence Instrumentation

If the researcher has commercial molecular luminescence instrumentation (e.g., a spectrofluorometer) available, then solid-state luminescence data should not be difficult to obtain. Many good references are available discussing the basic theory of luminescence,[1–3] so the focus herein will be on its use in solid-state applications. Instrumentation normally consists of an excitation source, excitation wavelength selector, sample compartment, emission wavelength selector, and detector. The largest issue for conducting measurements on solid-state samples involves the sample presentation. While molecular luminescence spectrometers are typically designed with perpendicular excitation and emission beam paths to minimize light scatter at the detector, this geometry presents problems for a solid-state sample. Since the excitation source cannot pass through the sample (indeed, many such materials are opaque to light and perform such emission processes at or near the surface), it must be positioned at an angle to the excitation and emission light paths. As the obtained emission intensity is geometry dependent, care must be taken to utilize the same angle for all samples, should quantitative data be necessary (e.g., quantum yields). Alternately, the sample compartments of some commercial spectrophotometers already contain additional optics to allow the researcher to select an emission beampath either perpendicular (''right angle'') or only 10 to 15° offset (''front face'') from the excitation beampath. Any emission geometry, other than perpendicular, greatly increases the chance of excitation light reaching the detector. Therefore, judicious filtering is normally necessary to obtain relevant data.

Another issue to consider with sample presentation is temperature. Many materials are not luminescent at room temperature, due to other nonradiative processes precluding the luminescent radiative energy deactivation pathway. Since the population of energy levels that lead to nonradiative pathways is normally thermally dependent, lowering the sample temperature can eliminate these pathways and, in essence, ''turn-on'' sample luminescence. Sample cooling is typically conducted in commercial optical cryostats that provide transparent windows to the observed luminescence, either to liquid nitrogen (77 K) or helium (4 K) temperatures. Such cryostats can be wired with electrical pass-through leads to facilitate electro-generated luminescence as well. Furthermore, studies can be performed on samples under the influence of a magnetic field. This experiment will allow the degeneracy of any electronic levels involved in the emission to be lifted (the Zeeman effect), thus altering the observed spectrum.**[4–6]** For materials studies, this measurement can provide some structural information with respect to the presence of defect centers. Cooling can be performed through immersion in or evaporation of the cryogen. The former method provides better electrical insulation, should high voltages be needed for the experiment, but cavitation from the cryogen can lead to poor spectral resolution.

2.2 Luminescence Measurements

As with other molecular luminescence measurements, three methods of recording spectra are normally used. In *emission spectra*, the excitation wavelength is held constant while the emission wavelength is swept during data acquisition. This spectrum shows the wavelengths where the sample emits light, and is commonly reported in the chemical literature when luminescence is reported. However, to obtain the complete spectral waveform *excitation spectra* are also recorded. In these measurements, the emission wavelength is held constant while the excitation wavelength is swept during data acquisition. The resulting spectrum shows what wavelengths of light produce the emission observed in the first measurement. Normally, this spectrum will correspond to any available absorption spectrum of the material, after taking instrumentation differences into account. Agreement of these two spectra can confirm that the absorption and emission transitions are directly related. The presence of additional bands in the excitation spectrum indicates the presence of some mediary in the energy manifold between excitation and emission (e.g., a defect in the material).**[3]** Lastly, *synchronous spectra* scan both the excitation and emission wavelengths (normally with a small offset to prevent significant scattering interference) during data acquisition. This technique is utilized more for the measurement of scattering phenomena, although the presence of significant peaks can indicate extreme heterogeneity in the material sample (e.g., presence of aggregated clumps of material on the surface). This technique is also referred to as *resonance light scattering*.**[7–9]** Commercial spectrophotometers typically have instrumentation profiles to perform all three experiments.

Luminescence of materials can normally be considered under two broad categories: semiconductor materials and point defects in insulating materials. Examination of the latter can be analyzed and interpreted using methodologies adopted for solution-based molecular luminescence.**[1]** For semiconducting materials (the major focus of this discussion), the groundbreaking work of Van Roosebroek and Shockley**[10]** determined that band–band recombination (path 1 in Figure 1) can be described based on its lifetime (τ_{BB}) and spectral bandshape ($I(\omega)$), as shown in equations (1) and (2):

$$\tau_{BB} = C\mathrm{e}^{\frac{E_g}{k_B T}} \tag{1}$$

$$I(\omega) = C'\alpha(\omega)\mathrm{e}^{\frac{\hbar\omega}{k_B T}} \tag{2}$$

where ω is angular frequency and T is the temperature. The presence of the absorption constant $\alpha(\omega)$ indicates the direct connection between the absorptive and emissive properties of the material of interest. Also, the lifetime of the emission is directly tied to the magnitude of the bandgap.

Another common parameter measured in luminescence spectroscopy is the *quantum yield*. This value indicates the efficiency of the system to radiative decay and typically is the ratio of the emitted energy to the total energy imparted upon the system. There are various mathematical treatments to determine this value, many utilizing actinometer references.**[1]** However, a recent study by Palsson and Monkman**[11]** provides a methodology where the film is excited both directly and through the use of a integrating sphere. Comparing the integration of these two spectra can provide a direct measurement of the quantum yield.

2.3 Observation of Excitons

As noted above, a primary piece of data obtained from solid-state luminescence spectra is the bandgap energy, observed as a single peak. However, a simple bandgap measurement can only occur if the material sample is relatively defect free and in a single phase. Should multiple phases or defects occur, isolated electronic states, or *excitons*, are likely to be observed. Exciton formation has been theorized and interpreted since the 1930s and is particularly common when mixed semiconductors or multiple-domain materials are examined. The presence of excitons in a sample produces a series of quantized emission peaks. The observed energies (E_n) based on quantum number n can be explained using effective mass theory, as shown in equations (3) and (4):

$$E_n = E_g - \frac{\mu^* e^4}{2\varepsilon^2 h^2}\frac{1}{n^2} + \frac{\hbar^2 k_B^2}{2(m_e^* + m_h^*)} \tag{3}$$

$$\frac{1}{\mu^*} = \frac{1}{m_e^*} + \frac{1}{m_h^*} \tag{4}$$

where m_e^* is effective mass of electron, m_h^* is effective mass of electron hole, ε is the dielectric constant of sample, e is elementary charge, k_B is the Boltzmann constant, h is the Planck constant and $\hbar$ is the Planck constant/2π. Based on the composition of the material, several emission progressions can be observed in a single measurement. In addition, should the defect concentration or illumination intensity become high, *excitons* can interact and form biexcitons, which readily lead to the observance of nonlinear optical properties.[12,13]

Should a system contain donor and acceptor moieties, an exciton like behavior can be observed when the charges recombine. Again, effective mass theory can present us with the energy of the observed transition, as shown in equation (5):

$$h\upsilon = E_g - (E_D + E_A) + \frac{e^2}{\varepsilon R} \tag{5}$$

where E_D is ionization energy of donor in semiconductor, E_A is ionization energy of acceptor in semiconductor and R is distance between donor and acceptor in semiconductor. Application of this equation can produce distances between donor and acceptor sites within the material lattice (R). Indeed, energy transfer can commonly be observed between donor and acceptor moieties. Parameters controlling the observation of such transfer include the separation in space of the involved centers and the energetic separation of their energy levels. Since the probability of energy transfer decreases with the sixth power of the distance between the two centers (Förster energy transfer), the distribution of the donor and acceptor defects in the material is crucial.

2.4 Deep Level Centers and Site-Selection Spectroscopy

In addition to excitons, ‘‘deep level’’ centers can be observed in the system, especially if lanthanide or transition metal ions are present in the material. These centers occur at a localized state removed from the fundamental band gap of the material. Observation of these centers can provide information pertaining to the electronic structure of defects present in the material, vibronic states associated with the ion in question, and/or the existence of energy transfer within the material. Observation of these centers can be obtained with *site-selection spectroscopy*, where only a specific moiety of the material is probed. This technique is particularly useful if the deep center has a particularly weak emission that is normally overpowered by the bulk material. A system that takes advantage of this process needs a defect center with excitation and emission energies slightly lower than the corresponding bulk material energies. Assuming that the excitation waveform is sufficiently narrow, the bulk and defect can be selectively probed, producing emission spectra exclusively exhibiting the system components in question. This technique has been successfully utilized to probe Mn^{2+} defect sites in ZnS semiconductor crystals.[14,15]

2.5 Electroluminescence Measurements

As noted previously, electroluminescence can be performed using commercial spectrophotometers provided the researcher has the necessary instrumentation to provide an electric bias to the material sample. The most reliable means for obtaining these data is through thin film electroluminescence, where the material is placed between two electrodes. This sample geometry reduces problems caused by electrical diffusivity in the material. At least one of these electrodes must be optically transparent to provide for the emission of visible light (typically indium tin oxide, ITO). The layering of multiple materials with varying electrical properties will ultimately lead to increased luminescence intensity and duration (*vide infra*). The electric bias can be either constant or pulsed, with each producing different electronic effects and light intensities. In addition to the spectra measured previously, the major parameter of interest is the *turn-on voltage*, or the bias necessary to obtain an observable emission. Typically materials exhibit a reasonably linear voltage/emission intensity relation. However, extremely high biases will lead to dielectric breakdown between the electrodes and deformation of the material. Also commonly reported is the effective lifetime of the observed emission at a given bias. Naturally, the observed emission lifetime exhibits an inverse relation to the applied bias, so a balance between emission intensity, lifetime, and applied bias must be determined.

3 APPLICATIONS

3.1 Temperature Dependence of Emission

One study performed by Omary and Patterson**[16]** observed luminescence as a function of temperature. The particular system is a thallium–silver complex, Tl[Ag(CN)$_2$], that demonstrates interesting behavior over a range of temperatures. Upon heating, the wavelength of maximum emission undergoes a slight redshift as the temperature is raised. This is not surprising, but the intensity of the luminescence is. As the temperature is raised from 10 to 76 K, the band intensity increases (Figure 2a). However, as the system is heated from 76 to 195 K, the intensity drops dramatically, with no observable luminescence at room temperature (Figure 2b). By utilizing site selection spectroscopy (*vide supra*), the authors successfully probed the different transitions associated with the thallium centers.

Another study relating emission intensity to temperature was performed by Assefa *et al.***[17]** The system under examination involves Eu^{3+} and gold and silver cyanide complexes. This study is similar to that of Omary**[16]** in that the intensity of the emission from [EuAu] decreases as temperature increases from 10 to 150 K. In contrast, the opposite is observed with [EuAg]; the intensity increases as temperature increases from 78 to 200 K. This study also demonstrates the excited state energy transfer from donor Au(CN)$_2{}^-$ and Ag(CN)$_2{}^-$ to acceptor Eu^{3+} ions.

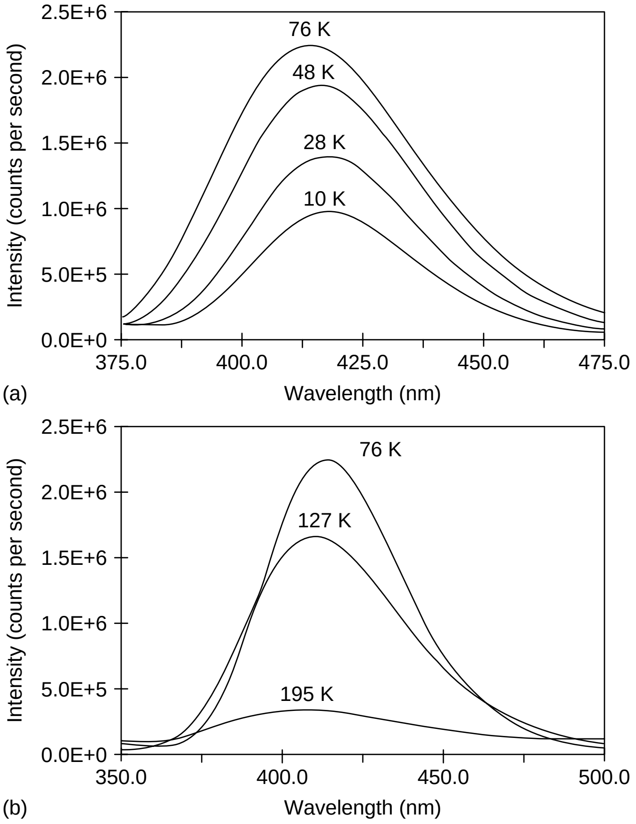

Figure 2 Variable temperature photoluminescence of Tl[Ag(CN)$_2$], (Adapted with permission from Omary and Patterson**[16]** © 1998 American Chemical Society)

3.2 Light-Emitting Diodes

Perhaps the most promising application of solid-state luminescence, and certainly recognizable by the general public, is the area of light emitting diodes (LEDs). Numerous articles are available regarding this application, depending on the specific type or function of concern. DenBaars**[18]** provides a detailed review of LED materials and their general emission properties. Table 1 summarizes various properties of some commercially available inorganic LED materials. The review also provides information on data calculation and manipulation, describing equations for radiative and nonradiative recombination rates, internal quantum efficiencies, and electron-to-hole injection ratios. The author also explains various methods to construct the material and device of choice, and gives a description of the process of injection luminescence and other physical properties of LEDs.

Thin film electroluminescent (TFEL) materials are similar to LEDs, in that they are completely solid-state materials. The difference lies in the application of charge and a higher level of defects. Therefore, TFEL devices require a much higher electrical field than the injection electroluminescence observed in LEDs. However, devices in this category typically possess the possibility of multicolor emission. Mach**[19]** provides a review similar to that of DenBaars**[18]** on the application, construction, and properties of various materials in this application.

A good example of the concomitant study of photoluminescence and electroluminescence in a materials study involves the blue emission observed from siloles as reported by Tang *et al.***[20]** The photoluminescence (Figure 3) and electroluminescence (Figure 4) of the thin films were compared, and similar emission profiles were noted. Current-voltage-brightness curves are presented, illustrating the typical correlation between the current density and brightness. Band gaps of these materials were determined using the luminescence data to be around 3 eV, slightly lower than their acyclic cousin.

Composite materials have been examined for LED work with the intention of producing dual emission as described above. A recent study by Ding *et al.***[21]** blended a violet–blue emitting polymer with a green emitting polymer in a single device. A comparison of the absorption and emission of the blends both in solution and in the solid-state was presented. Although the weight ratios of the blends were varied, the authors noticed only the green emission of the blends. Their conclusion was that this suggested a Förster energy transfer in the double layer LEDs instead of their independent operation. They also noted a decrease in

Table 1 Standard LED materials. (Adapted from DenBaars.[18] With kind permission of Springer Science & Business Media)

Material	Color range	Peak emission (nm)	Luminous efficiency (lm W^{-1})	External quantum efficiency (%)	Growth technique	Device type
AlGaInP	Red–green	585	12.0	2.2	MOCVD	DH
AlGaAs	Red	660	9.0	20.0	LPE	DH
GaP	Pure green	555	1.4	0.2	LPE	H
GaP:N	Yellow–green	565	1.8	0.3	LPE	H
GaP:NN	Yellow	590	1.0	0.2	LPE	H
GaP:Zn–O	Red	650	4.0	5.0	LPE	H
$GaAs_{0.15}P_{0.85}$:N	Yellow	590	1.0	0.3	VPE	H
$GaAs_{0.35}P_{0.65}$	Orange–red	630	0.7	0.3	VPE	H
$GaAs_{0.40}P_{0.60}$	Red	650	0.15	0.2	VPE	H
SiC	Blue	470	–	0.02	LPE, CVD, MBE	H
ZnSe	Blue	470	–	–		DH
					MOCVD	
GaN	Blue	465	–	0.03	MOCVD	DH

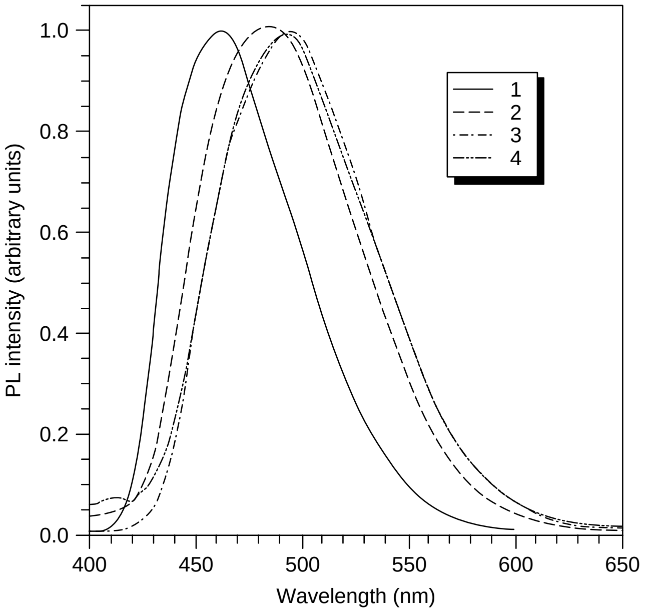

Figure 3 Photoluminescence of representative siloles. (Adapted from Tang, Zhan, Yu, Lee, Liu and Zhu.[20] Reproduced by permission of The Royal Society of Chemistry)

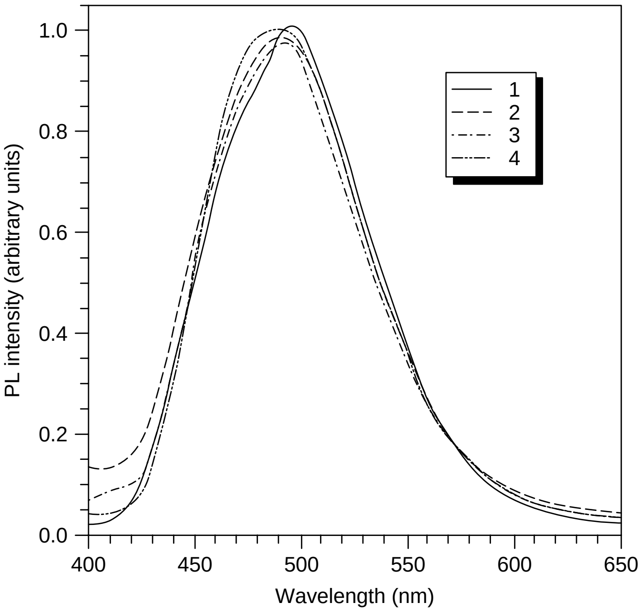

Figure 4 Electroluminesence of representative siloles. (Adapted from Tang, Zhan, Yu, Lee, Liu and Zhu.[20] Reproduced by permission of The Royal Society of Chemistry)

the turn-on voltage and an increase in efficiency when p-phenylenevinylene (PPV) and polyethylene dioxythiophene (PEDOT) were used as hole-transport layers (common materials utilized in multilayer devices to improve electron and hole mobility).

3.3 Other Luminescence Application Examples

Many materials are designed to luminesce when exposed to relatively low-energy radiation, such as visible, ultraviolet, or possibly infrared light. A recent report by Issler and Torardi[22] focuses on inorganic phosphors specifically designed to luminesce when exposed to higher energy X-ray radiation (in particular, X-rays in the 15–100 keV range). These measurements obviously require certain instrumental precautions beyond those necessary for typical luminescence measurements. The films studied show strong absorption in the X-ray region and high emission efficiency in the visible region. These materials will likely play an important role in medical imaging.

Up-conversion and down-conversion luminescence, scintillator materials, and photonic crystals are other topics of recent interest.[23] Up-conversion is the ability of a material to convert low-energy excitation light into higher energy emission light due to multiple energy transfer processes (as shown in Figure 5).[24] One necessary characteristic of these materials is the existence of multiple long-lived ($>10^{-6}$ s) excited states. Previous systems focused on trivalent lanthanide systems due to their multiple long-lived excited states. However, several instances involving transition metal systems have been reported. One such system incorporates Re^{4+} into a Cs_2ZrCl_6 matrix to convert near-IR radiation into intense visible light.[24] Another up-conversion example uses Yb^{3+} doped $RbMnCl_3$ to obtain orange luminescence upon excitation with near-IR radiation.[25] The system is not ideal, however, as the up-conversion is only viable at low (10 K) temperatures. The system utilizes Yb^{3+} to absorb radiation in the near-infrared region to ultimately produce Mn^{2+} emission in the visible region.

Down-conversion is another useful technique that has applications in lighting and plasma flat panel displays. The process involves the input of a vacuum ultraviolet photon and the output of multiple visible photons. This down-conversion was recently reported with Eu^{3+} doped $LiGdF_4$.[26] Upon absorption of a high-energy photon by Gd^{3+}, two visible photons were emitted through an energy transfer between Eu^{3+} and Gd^{3+} with a quantum efficiency near 200%. This research has an environmentally interesting application as an alternative to mercury-vapor lamps.

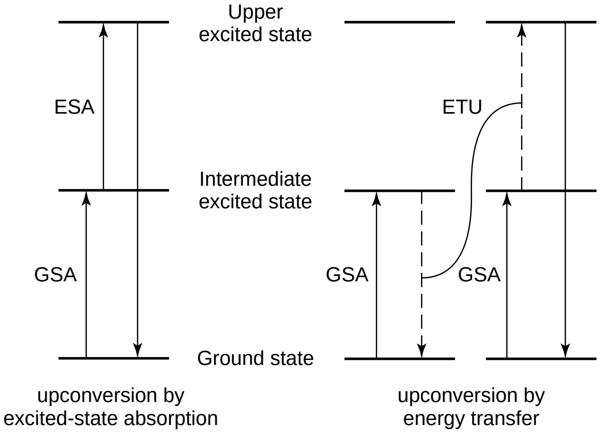
Upper excited state
ESA
ETU
Intermediate excited state
GSA
GSA
GSA
Ground state
upconversion by excited-state absorption
upconversion by energy transfer

Figure 5 Up-conversion in materials. (Adapted from Gamelin and Gudel.[24] Reprinted with permission, © 1999 American Chemical Society)

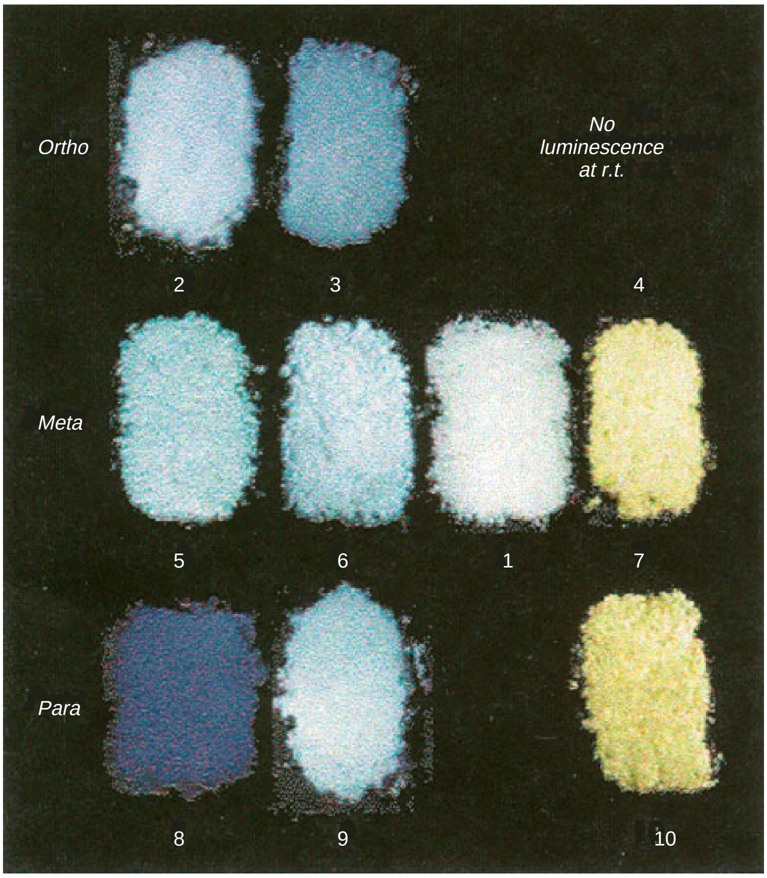
Ortho
No luminescence at r.t.
2
3
4
Meta
5
6
1
7
Para
8
9
10

Figure 6 Gold(I) benzenethiolate complexes exhibiting room temperature luminescence. (Adapted from Watase, Nakamota, Kitamura, Kanehisa, Kai and Yanagida.[28] Reproduced by permission of The Royal Society of Chemistry)

Scintillator materials have been used for many years as a way to detect high-energy radiation (X- and γ-rays). Due to the nature of the application of these materials, the selection criteria are very strict, requiring high conversion efficiencies. These systems have historically been limited to Tl^+-doped NaI and CsI, until recent advances using Ce^{3+}-doped chloride and bromide systems.[23] As with the previously mentioned Issler study,[22] high-energy radiation is converted to visible light. However, instead of using phosphors, $LaBr_3$ is doped with a small percent (0.5%) of Ce^{3+}.[27]

Although many solid-state systems require cooling to make luminescence feasible (*vide supra*), Watase *et al.*[28] provide an example of a system that exhibits luminescence at room temperature. The system is a series of gold(I) benzenethiolate complexes that reportedly emit light from 450 to 530 nm. The excited states that produce the luminescence are suggested to be caused by metal-to-ligand charge-transfer or ligand-centered transitions. Figure 6 is a photograph of the complexes studied when excited by a xenon lamp.

4 ABBREVIATIONS AND ACRONYMS

CVD = chemical vapor deposition; DH = double heterostructure; H = homojunction device; ITO = indium tin oxide; LEDs = light emitting diodes; LPE = liquid phase epitaxy; MBE = molecular beam epitaxy; MOCVD = metal organic chemical vapor deposition; PPV = p-phenylenevinylene; PEDOT = polyethylene dioxythiophene; TFEL = Thin film electroluminescent; VPE = vapor phase epitaxy.

5 FURTHER READING

J. D. Ingle and S. R. Crouch, 'Spectrochemical Analysis', Prentice Hall, Englewood Cliffs, 1988.

A. H. Kitai ed., 'Solid State Luminescence', Chapman & Hall, London, 1993.

H. Kuzmany, 'Solid-State Spectroscopy: An Introduction', Springer-Verlag, Berlin, 1998.

J. R. Lakowicz, 'Principles of Fluorescence Spectroscopy', Springer, New York, 2006, Considered by many the seminal reference material on luminescence instrumentation and basic measurements, although solid-state measurements are not directly addressed.

6 REFERENCES

1. J. D. Ingle and S. R. Crouch, 'Spectrochemical Analysis', Prentice Hall, Englewood Cliffs, 1988.
2. U. W. Pohl and H.-E. Gumlich, in 'Solid State Luminescence', ed. A. H. Katai, Chapman & Hall, London, 1993, p. 53.
3. J. R. Lakowicz, 'Principles of Fluorescence Spectroscopy', Springer, New York, 2006.
4. U. W. Pohl and H. E. Gumlich, *J. Cryst. Growth*, 1990, **101**, 521.
5. B. Litzenburger, U. W. Pohl and H. E. Gumlich, *J. Lumin.*, 1994, **60–61**, 44.
6. A. Hoffmann, R. Heitz and I. Broser, *Phys. Rev. B: Condens. Matter Mater. Phys.*, 1990, **41**, 5806.
7. R. F. Pasternack and P. J. Collings, *Science (Washington, D.C.)*, 1995, **269**, 935.
8. R. F. Pasternack, K. F. Schaefer and P. Hambright, *Inorg. Chem.*, 1994, **33**, 2062.
9. R. F. Pasternack, C. Bustamante, P. J. Collings, A. Giannetto and E. J. Gibbs, *J. Am. Chem. Soc.*, 1993, **115**, 5393.
10. W. Van Roosbroeck and W. Shockley, *Phys. Rev.*, 1954, **94**, 1558.
11. L.-O. Palsson and A. P. Monkman, *Adv. Mater.*, 2002, **14**, 757.
12. S. W. Koch, H. Haug and M. Lindberg, *J. Phys. Colloq.*, 1988, **49**, 179.
13. C. Klingshirn, *Semicond. Sci. Technol.*, 1990, **5**, 457.
14. D. Langer and S. Ibuki, *Phys. Rev.*, 1965, **138**, 809.
15. W. Busse, H. E. Gumlich, E. Neumann and D. Theis, *J. Lumin.*, 1971, **3**, 351.
16. M. A. Omary and H. H. Patterson, *Inorg. Chem.*, 1998, **37**, 1060.
17. Z. Assefa, G. Shankle, H. H. Patterson and R. Reynolds, *Inorg. Chem.*, 1994, **33**, 2187.
18. S. P. DenBaars, in 'Solid State Luminescence', ed. A. H. Katai, Chapman & Hall, London, 1993.
19. R. Mach, in 'Solid State Luminescence', ed. A. H. Katai, Chapman & Hall, London, 1993.
20. B. Z. Tang, X. Zhan, G. Yu, P. P. S. Lee, Y. Liu and D. Zhu, *J. Mater. Chem.*, 2001, **11**, 2974.
21. L. Ding, F. E. Karasz, Z. Lin, M. Zheng, L. Liao and Y. Pang, *Macromolecules*, 2001, **34**, 9183.
22. S. L. Issler and C. C. Torardi, *J. Alloys Compd.*, 1995, **229**, 54.
23. G. M. Salley, O. S. Wenger, K. W. Kramer and H. U. Gudel, *Curr. Opin. Solid State Mater. Sci.*, 2002, **6**, 487.
24. D. R. Gamelin and H. U. Gudel, *Inorg. Chem.*, 1999, **38**, 5154.
25. R. Valiente, O. S. Wenger and H. U. Gudel, *Phys. Rev. B*, 2001, **63**, 165102.
26. R. T. Wegh, H. Donker, K. D. Oskam and A. Meijerink, *Science*, 1999, **283**, 663.
27. E. V. D. van Loef, P. Dorenbos, C. W. E. van Eijk, K. W. Kramer and H. U. Gudel, *Appl. Phys. Lett.*, 2001, **79**, 1573.
28. S. Watase, M. Nakamoto, T. Kitamura, N. Kanehisa, Y. Kai and S. Yanagida, *J. Chem. Soc., Dalton Trans.*, 2000, **20**, 3585.

Rapid Scan, Stopped-Flow Kinetics

Rui-Yong Wang

Zhengzhou University, Zhengzhou, China

	Method Summary	1
1	Introduction	2
2	Technical Background	3
3	Applications	4
4	Abbreviations and Acronyms	18
5	Further Reading	18
6	References	18

METHOD SUMMARY

Acronyms, Synonyms

- Rapid-Scan Stopped-Flow Kinetics
- Rapid-Mixing
- Stopped-Flow

Measured physical quantities

- Changes in absorbance, fluorescence, circular dichroism, light scattering, or luminescence, as a function of time after mixing

Information available

- Time course at a single wavelength and time-resolved spectra
- Kinetic parameters (e.g. the observed rate constants (k_{obs}))
- Activation parameters (e.g. the activation enthalpies and entropies)
- The possible pathway of reactions.

Information not available, limitations

- It is difficult to obtain the true spectra of the isolated intermediate.

Examples of questions that can be answered

- What are the values of rate constants for ligand binding and ligand dissociation?
- Are there any intermediates formed during a reaction?
- How do factors such as temperature, pH, or concentration affect the rate constant?
- Does the binding reaction constitute a one- or two-step mechanism?

Major advantages

- Obtains the kinetics of fast reactions (e.g. k_{on} and k_{off} for ligand substitution)
- Detects and characterizes reaction intermediates
- Defines reaction pathways and proposes a kinetic model
- Provides thermodynamic insight into rapid reactions
- Has lower sample consumption compared with continuous-flow techniques
- Is able to couple with a wide range of detection modes.

Major disadvantages

- Reactions completed within the dead time of stopped-flow instruments cannot be measured; dead times are on the order of milliseconds for conventional instruments but can be somewhat shorter if special mixers are used.
- It requires the availability of optical signals to monitor changes (in conventional instruments).

Sample constraints

- Samples must be in solution
- Reactions must produce detectable signal changes.

1 INTRODUCTION

In order to elucidate the mechanism of any reaction, be it chemical or biochemical, a binding process, or a macromolecular conformational change, we need to determine the time-dependent evolution of the molecular species involved. Kinetic techniques fall into two broad categories, equilibrium, and relaxation methods. Equilibrium methods extract rate information without physically or chemically perturbing a system, for example, by measuring dynamic effects on the spectral line shape (optical, electron paramagnetic resonance (EPR) or nuclear magnetic resonance (NMR)), or by observing molecular fluctuations. Relaxation techniques generally rely on a rapid change of an extrinsic variable (e.g. temperature, pressure or solvent composition) to perturb the system and follow its response as it evolves toward a new equilibrium position. Rapid mixing of two (or more) solutions is an example of a relaxation method.

Rapid-mixing techniques play a particularly prominent role in kinetic studies of fast reactions. In 1923, Hartridge and Roughton developed the first rapid-mixing kinetic techniques to follow chemical and biochemical reactions.[1] Chance introduced the stopped-flow (SF) modification in 1940.[2] Since then it has undergone extensive modification by Chance, Gibson, and others. Occasionally stopped-flow has been used to follow anaerobic reactions. This necessitates the development of deoxygenating systems that are suited to adaptation to rapid-mixing techniques.

In the past, mainly as a consequence of the advances in computer technology, instrumentation for kinetic investigations has improved dramatically. For example, a stopped-flow unit in the late eighties consisted of a large number of different parts, which included the syringe system, a lamp together with a monochromator, an oscilloscope for viewing the data, and a transient recorder for collecting the data and for their transfer to a computer for data fitting. Many problems occurred during these measurements and they were time consuming because programs for analyzing the data were still slow once absorbance versus time traces that could not be fitted to a single exponential function were observed. Furthermore, only measurements at single wavelengths were possible, therefore making it often necessary to repeat the analysis at different wavelengths.

Today a stopped-flow instrument consists of only the unit itself combined with a diode array detector and a computer allowing fast kinetic measurements of time-resolved UV–vis spectra under anaerobic, high pressure and/or low temperature conditions. Improvements have been made as well, for example, syringes are installed vertically instead of horizontally (to avoid problems with gas bubbles) and polyetheretherketone (PEEK) is used instead of Teflon for valves and flow tubes to improve the anaerobic capabilities of the instrument. Further, the syringe drives setup was optimized. Application of ‘‘rapid-scan’’ devices (usually, but not exclusively, diode arrays) allows complete spectra to be collected at very short time intervals during a reaction.

Extreme experimental conditions (low temperature and high pressure) have been successfully applied to rapid kinetic analysis. High-pressure techniques have been recognized to be very important for the elucidation of chemical reaction mechanisms. Since a high-pressure stopped-flow apparatus was first reported in the 1980s, a slightly modified apparatus was constructed by several researchers. Low-temperature stopped-flow methods together with diode array instrumentation have become extremely useful for studying reactions that are too fast at ambient temperatures and/or for detecting reactive intermediates that can only be observed at low temperatures. For example, the low-temperature stopped-flow kinetic method is an approach used successfully in copper-dioxygen chemistry.[3,4]

Stopped-flow, one of the most frequently used rapid kinetics techniques, is a simple and elegant technique for monitoring reaction kinetics in solution. Examples include ligand substitution, binding reactions, organic and inorganic oxidation and reduction reactions, proton exchange, metal–ligand complex formation, and surfactant aggregation to form micelles.

In general, stopped-flow methods provide a reasonably inexpensive means of determining a large number of fairly fast reactions. Stopped-flow mixing is usually coupled with real-time optical observation using absorbance (UV through IR; *see*, ***Vibrational Spectroscopy***), fluorescence emission, or circular dichroism (CD) spectroscopy. In addition, the stopped-flow technique has been implemented in conjunction with many other biophysical techniques, such as EPR, NMR (*see* ***Nuclear Magnetic Resonance (NMR) Spectroscopy***

of Inorganic/Organometallic Molecules, ***Nuclear Magnetic Resonance (NMR) Spectroscopy of Metallobiomolecules***), and small-angle X-ray scattering. A number of commercial stopped-flow instruments are now available that provide fast reaction analysis capability. Examples include instruments from Applied Photophysics Ltd. (Leatherhead, UK), Bio-Logic-Science Instruments SA (Claix, France), Hi-Tech Scientific (Salisbury, UK), and Olis Incorporated (Bogart, GA, USA).

2 TECHNICAL BACKGROUND

2.1 Features of the Basic Instrument

Stopped-flow methods constitute commonly used tools for investigation of mechanisms of molecular kinetic processes in the time range from milliseconds to hundreds of seconds. In stopped-flow experiments, two or more reactants are expelled from a set of pneumatically or stepper motor-driven syringes. The reactant solutions meet in a mixer where the reaction is initiated. The fresh reaction mixture is rapidly transferred into an observation cell while the previous contents of the cell are flushed out. Then the liquid flow is stopped by a stopping syringe or a valve at the exit of the cell. The kinetics are monitored by recording an optical signal (e.g. absorbance, fluorescence, or CD) as a function of time. The most common mixing options for stopped-flow include single mixing and multi mixing (also known as *double mixing* or *sequential mixing*) where more than two solutions are mixed together. This is schematically illustrated in Figure 1.

2.2 Data Collection by Stopped-flow Methods

Data acquisition in the stopped-flow mode requires rapid sampling of the signal at intervals shorter than the dead time. Data associated with monitoring a molecular process to completion comprise a progress curve. An analysis of the progress curves for a second-order reaction, in terms of rate constants of the underlying molecular processes, is generally not simple because usually the observed reaction starts far from the final equilibrium state and the kinetic equations cannot be linearized. Therefore the solution is not just a simple exponential function (or a sum of such functions) except under special conditions called pseudo-first-order reactions, when one reactant is greatly in excess over the other reactant. Therefore kinetic studies are most commonly carried out under pseudo-first-order conditions.

Kinetic traces acquired under pseudo-first-order conditions can be fitted to exponential functions, and the observed rate constants, k_{obs}, can be calculated. The second-order rate constants can be obtained from the slopes of the linear plots of k_{obs} versus [ligand] (e.g. the ligand-binding reactions). The activation parameters can be determined through a systematic variation of temperature and pressure. The activation enthalpies and entropies, $\Delta H^{\neq}$ and $\Delta S^{\neq}$, are calculated using the Eyring equation (1), and the volumes of activation, $\Delta V^{\neq}$, calculated from the slope of $\ln k_{\mathrm{obs}}$ versus pressure (under certain conditions).

The Eyring equation is

$$k = \frac{k_{\mathrm{B}}T}{h} \exp\left(\frac{-\Delta G^{\neq}}{RT}\right) \tag{1}$$

where R is the gas constant, k_{B} is the Boltzmann constant, h is the Planck's constant, k is rate constant, and T is absolute temperature.

For the stopped-flow spectroscopy method, one can monitor the kinetics of a reaction by capturing and analyzing time courses at a single wavelength using a photomultiplier as detector. In contrast to this a diode array detector can register simultaneously absorbance changes at a large number of wavelengths. This feature is valuable when a complex

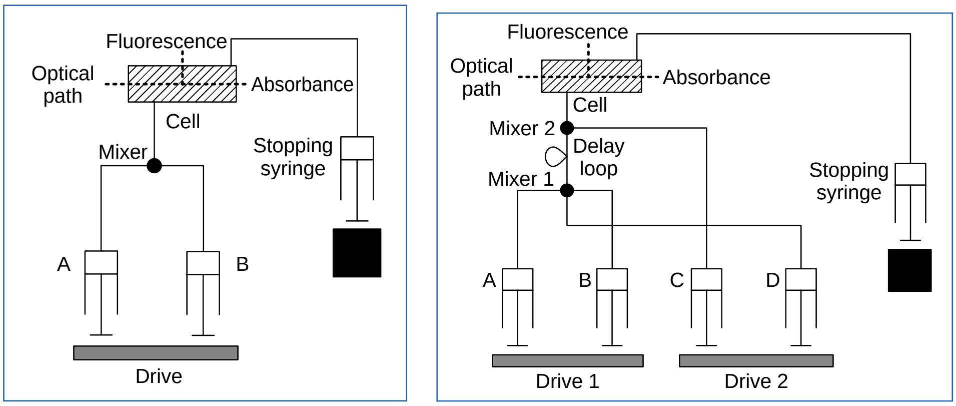

Single-mixing stopped–flow

Double-mixing stopped–flow

Figure 1 Schematic diagram of stopped-flow single-mixing (a) and double mixing (b). (Adapted from a diagram downloaded from http://www.hitech-inc.com)

reaction, involving a number of spectral species, is to be analyzed. The data set generated by a single rapid-scan experiment is large. Analysis of these data uses matrix algebra methods to filter signal from noise and to assess the number of linearly independent spectral components, which contribute to the total spectral change accompanying the reaction, and to extract the spectra and their time courses. Inherent to these methods is great data compression, thus permitting economic and efficient data storage. Once the number of components and their time courses are known, global analysis of the data allows one to fit the kinetic process to a chemical model by solving the differential equations which describe it. By so doing, not only can the rate constants be extracted but also the spectra of any intermediates (model-dependent) on the reaction pathway. These analytical techniques are powerful and easy to implement. However, they can mislead and it is important to retain one's chemical/biochemical common sense when examining the output.

2.3 Dead Time of a Stopped-flow Instrument

The interpretation of stopped-flow data requires a careful calibration of the instrumental dead time by measuring a pseudo-first-order reaction tuned to the time scale of interest (i.e. a single-exponential process with a rate constant approaching the expected dead time) and an optical signal matching the application. The dead time of a stopped-flow instrument is the time that elapses between mixing and observation, and is usually determined by employing a pseudo first-order reaction of 2,6-dichlorophenolindophenol (DCPIP) with ascorbic acid. Commercial instruments can routinely reach dead times of a few milliseconds. Recent improvements in mixer and flow-cell design by several manufacturers of stopped-flow instruments resulted in dead times well under 1 ms. The upper end of the time scale that can be reliably measured in a stopped-flow experiment is determined by the stability of the mixture in the flow cell, which is limited by convective flow or diffusion of reagents in and out of the observation volume.

2.4 Samples for a Conventional Stopped-flow Instrument

Because stopped-flow techniques are widely used with optical detection, samples should be prepared in solution and produce detectable signal changes after mixing into the cell. In some situations, if the reaction of some samples is very rapid and complete within the dead time of the stopped-flow instruments, the majority and indeed the entire kinetic time course may be lost. Selected adjustment of concentration, solution conditions, temperature, and so on, may be able to slow the reaction into an accessible time range, but this is not always possible or desirable. Such systems are not amenable to the stopped-flow technique. In general, other techniques will have to be used, and these will be dependent on the availability of a signal for monitoring of the reaction.

3 APPLICATIONS

The goal of a comprehensive kinetic analysis is to identify each step in the reaction pathway, define the rate and equilibrium constants for each step, identify all conformational and chemical intermediates, identify the rate-limiting steps, and ultimately establish the basis for mechanisms. Various techniques are needed to attain this goal. In this section, applications of stopped-flow techniques in contributing to this goal in the fields of inorganic and bioinorganic chemistry are presented. The most common detection methods for following the kinetics are absorbance or fluorescence spectrometry, which are mainly described in this part.

3.1 General Procedures

In order to provide kinetic and thermodynamic insight into new reaction systems, the following steps are frequently followed in applications of stopped-flow techniques.

1. Spectra or rapid-scan spectra are obtained by the stopped-flow method establishing also a suitable wavelength at which kinetic measurements could be performed.
2. Progress curves at a single wavelength are monitored. The time courses are the average of several independent kinetic runs. Usually these studies are performed under pseudo-first-order conditions that allow the experimenter to analyze the kinetic time courses as a sum of exponential functions. The single wavelength can be chosen from the time-resolved spectra, and is always selected close to the absorbance maximum (or fluorescence emission maximum) of reactant, intermediate, or product.
3. The observed rate constants (k_{obs}) and second-order rate constants (if possible) are calculated. The traces are fitted to a single-exponential or to a sum of exponentials model. The validity of the fitting is evaluated by an inspection of residuals and normalized variation parameters. The software that runs stopped-flow spectrophotometers provides fitting programs to extract rate constants. Other commercial software is also available. The operator must decide the likely form of the curve and the time range over which the curves should be fitted. Reactions are generally monitored for at least several half-lives ($6 \sim 9$ is common in the literature). In practice, the time is decided by the experimental conditions. It is often the case that time courses are not simple but comprise more than one exponential phase. The trace is easily fitted, but in order to do so the user must select the time range over which the fitting should take place. This selection should be made to

ensure that approximately equal numbers of data points representing the kinetic process are collected. It is best to be aware that rather different values for rate constants may be obtained depending on the ‘‘fit-range’’ one chooses.

4. The influence of variables such as pH, concentration, buffer, solvents, and different reactants on the observed rate constants or rapid-scan spectra is examined.
5. The influence of temperature can be studied, and the activation parameters (e.g. the activation enthalpies and entropies) can be calculated. If necessary, the high-pressure stopped-flow technique can be used to study the pressure dependence of reactions, and the corresponding volumes of activation may be calculated.
6. On the basis of multiple experimental results (kinetic and steady-state) and the kinetics analysis, a global analysis or singular value decomposition (SVD) can be used to extract spectra for species (intermediates and product) and a possible reaction mechanism can be proposed.

It is good practice to check from time to time that the stability of the instrument is within the manufacturer’s specification. It is necessary to test the reliability of the stopped-flow instrument using control experiments that test a range of parameters such as the dead time, mixing efficiency and signal output. In general, these tests will be the same for the instrument in the configuration for fluorescence studies as that for absorbance studies.

3.2 Ligand Substitution

3.2.1 *Substitution Reaction of Fe(III) Complexes with Thiocyanate*

Seven-coordinate three-dimensional metal complexes are considered to be quite unstable and kinetically labile species, and their solution chemistry is largely undefined. Over the last few years it was shown that these species exhibit extremely interesting chemical properties and catalytic activity. They can catalyze disproportionation of deleterious superoxide radicals, even faster than natural enzymes, and therefore this became a challenging research area. Recently, Rudi van Eldik[5] reported a detailed rapid-scan stopped-flow kinetic study of the substitution behavior of the seven-coordinate $[Fe(dapsox)(L)_2]ClO_4$ complex with thiocyanate as a function of the thiocyanate concentration, temperature, and pressure in protic and aprotic organic solvents.

Kinetic data were obtained by recording time-resolved UV–vis spectra using a stopped-flow instrument combined with a thermostat and equipped with a high-speed diode array spectrometer. At least 10 kinetic runs were recorded under all conditions, and the reported rate constants represent the mean values. All kinetic measurements were carried out under pseudo-first-order conditions; that is. the ligand concentration was in large excess (complex concentration 5×10^{-5} M).

Kinetic traces in ethanol clearly showed two subsequent reaction steps over the whole SCN^- concentration range (Figure 2), similar to that observed in MeOH solution,

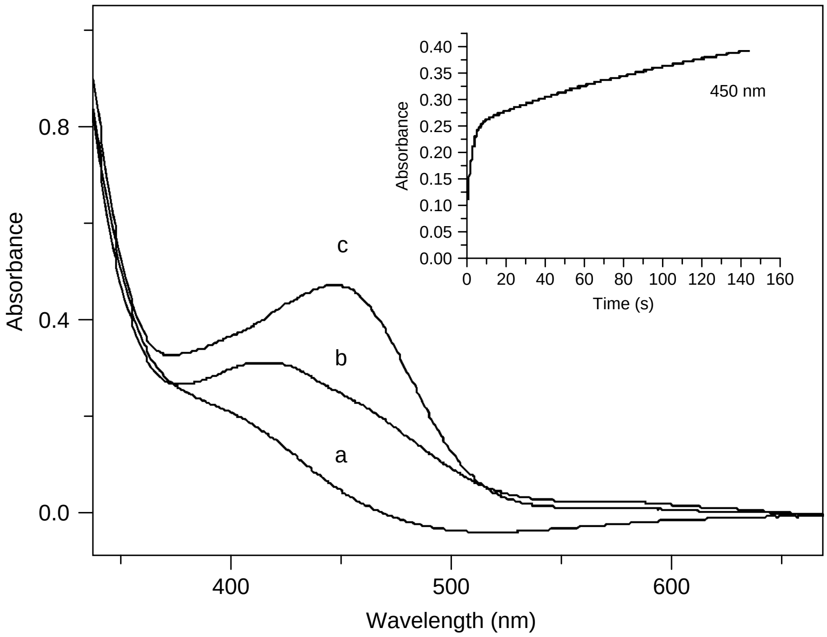

Figure 2 UV–vis spectra obtained from the time-resolved spectra of the reaction in nonacidified MeOH at −50 °C of [Fe(dapsox)(OMe)(MeOH)] (a), intermediate [Fe(dapsox)(NCS)(MeOH)] (b) and $[Fe(dapsox)(NCS)_2]^-$ (c). Experimental conditions: $[Fe(III)] = 5 \times 10^{-5}$ M, $[SCN^-] = 0.3$ M. Inset: corresponding kinetic trace fitted to a double-exponential function

and they were fitted to a double-exponential function that resulted in k_{obs} values for the first and second reaction steps. Plots of k_{obs} versus $[\mathrm{SCN}^-]$ for both reaction steps at 5 °C show a linear increase in k_{obs} with increasing $[\mathrm{SCN}^-]$ over the whole concentration range without a significant intercept, indicating that there is no reverse solvolysis or parallel reaction. From the slopes of the linear plots of k_{obs} versus $[\mathrm{SCN}^-]$ the second-order rate constants can be calculated. Measurements under high pressure were carried out using a homemade high-pressure stopped-flow instrument. Values of $\Delta H^{\neq}$ and $\Delta S^{\neq}$ were calculated from the slopes and intercepts of plots of $\ln(k/T)$ versus $1/T$, respectively, and values of $\Delta V^{\neq}$ were calculated from the slope of plots of $\ln k$ versus pressure in the usual manner.

On the basis of the reported activation parameters, a dissociative mechanism for the first substitution step and a dissociative or dissociative interchange (I_d) mechanism for the second substitution step are suggested for the reaction in MeOH and EtOH.

3.2.2 Substitution Reaction of Fe(III) Complexes with Hydrogen Peroxide

A detailed kinetic investigation of the reaction between $[\mathrm{Fe^{III}(edta)H_2O}]^-$ and H_2O_2 has been reported.**[6]** The reaction was found to consist of two steps and resulted in the formation of the already characterized high-spin Fe(III) side-on bound peroxo complex.

For the investigation of the first reaction step, the kinetics of this reaction was studied by stopped-flow spectrometry. The effect of five different buffers on k_{obs1} was investigated. Kinetic data were obtained under pseudo-first-order conditions, $[H_2O_2] \gg [\mathrm{Fe(edta)}^-]$. Kinetic traces recorded in the presence of an excess of H_2O_2 showed a two-step behavior that could be fitted by two exponential functions. The time scales of the two steps were different enough for the reaction to be separated into two steps by selecting different time scales and fitting each step to a single-exponential function. Typical kinetic traces and the corresponding fits for the two reaction steps are shown in Figure 3. Plots of k_{obs1} versus the H_2O_2 concentration at different buffer concentrations were found to be linear with a significant intercept. The rate law for this reaction based on the first reaction step is $k_{\mathrm{obs1}} = k_{-1} + k_1[H_2O_2]$. The overall spectral changes increased significantly with increasing hydrogen peroxide concentration, from which it followed that coordination of hydrogen peroxide is a reversible process. Under conditions where the dead time of the stopped-flow instrument (ca. 4 ms) does not interfere with the spectral changes observed during the kinetic traces, an apparent thermodynamic equilibrium constant of $38 \pm 3\,\mathrm{M}^{-1}$ was calculated from the spectral changes observed for the first step in this reaction. The temperature dependence of k_{obs1} as a function of $[H_2O_2]$ at selected pH values was used to construct Eyring plots for k_1 and k_{-1}, from which the activation parameters $\Delta H^{\neq}$ and $\Delta S^{\neq}$ were determined. The volume of activation, $\Delta V^{\neq}$, was determined from the slope of a plot of $\ln k_{\mathrm{obs}}$ versus pressure.

For the second reaction step, the observed rate constant of this reaction (k_{obs2}) was independent of the hydrogen peroxide concentration. As described above, the temperature dependence of k_{obs2} was used to construct a linear Eyring plot from which $\Delta H^{\neq}$ and $\Delta S^{\neq}$ were obtained. The volume of activation was derived from the slope of the linear plot of $\ln k_{\mathrm{obs2}}$ versus pressure at 25 °C in the pressure range 10–170 MPa. The reported volumes of activation can be used to construct a volume profile for the overall reaction. The positive activation volume, $\Delta V^{\neq} = +6.8 \pm 0.4\,\mathrm{cm^3\,mol^{-1}}$, suggests a dissociative interchange (I_d) mechanism for the ligand substitution reaction on $[\mathrm{Fe(edta)OH}]^-$ with hydrogen peroxide.

The results clearly indicate that the reaction of Na[Fe(edta)] with hydrogen peroxide occurs in a two-step process. In combination with all the other kinetic data available, a detailed reaction mechanism could be presented.

3.2.3 Substitution Reaction of Pt(II) complexes with Nucleophiles

Kinetic studies on reactions of Pt(II) complexes with biologically relevant nucleophiles have been reported.**[7]** The substitution of both coordinated water molecules by a series of nucleophiles (namely, thiourea (tu), L-methionine (L-Met), and guanosine-5′-monophosphate (5′-GMP)) was investigated as a function of concentration, temperature, and pressure using stopped-flow techniques and was found to occur in two subsequent reaction steps. The activation parameters for all reactions suggest an associative substitution mechanism.

The spectral changes of the reactions were first recorded over the wavelength range of 190–500 nm to establish a suitable wavelength at which the kinetic trace could be followed. The ligand substitution reactions were studied under pseudo-first-order conditions with respect to either the Pt(II) complex or the nucleophile to force the reactions to go to completion. This was achieved by using at least a 10-fold (1:1 complex formation) or 20-fold (1:2 complex formation) excess of the nucleophile or the complex. All reported rate constants represented an average value of at least three to five independent kinetic runs for each experimental condition.

A linear dependence of the observed rate constants on the tu concentration was found for the Pt(amp) complex. k_{obs1} and k_{obs2} can be expressed by equations (2) and (3). All of the reactions studied do show a zero intercept; therefore, the reactions are irreversible, and k_{-1} and k_{-2} are zero.

$$k_{\mathrm{obs1}} = k_1[\mathrm{Nu}] + k_{-1} \approx k_1[\mathrm{Nu}], \quad \mathrm{Nu} = \text{L-Met, tu, 5}'\text{-GMP} \tag{2}$$

$$k_{\mathrm{obs2}} = k_2[\mathrm{Nu}] + k_{-2} \approx k_2[\mathrm{Nu}], \quad \mathrm{Nu} = \text{tu, 5}'\text{-GMP} \tag{3}$$

Kinetic traces for reactions with L-Met gave excellent fits to a double-exponential function. The obtained constants, k_{obs1} and k_{obs2}, were plotted against the concentration of the entering L-Met molecule. In the case of k_{obs1}, a linear

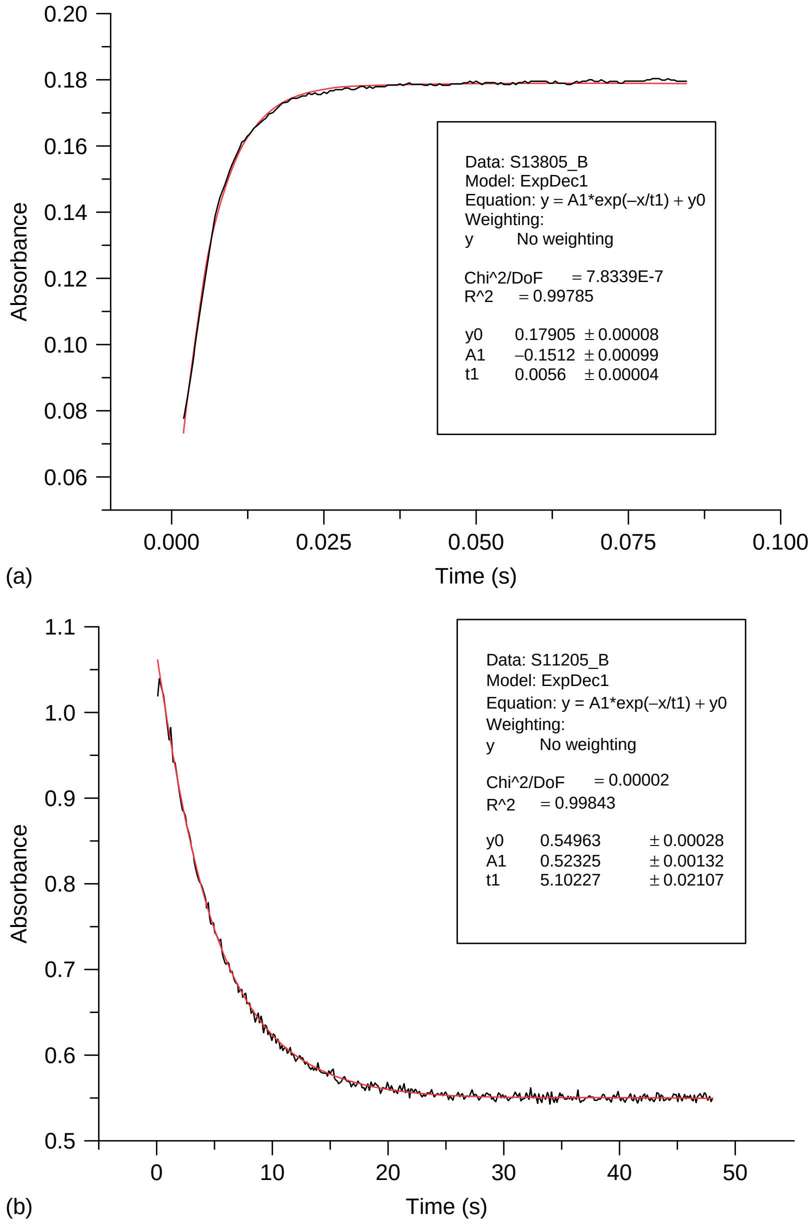

Figure 3 (a) Typical absorbance-time trace for the first reaction step in TAPS as buffer. Experimental conditions: $[\mathrm{Fe(edta)}^-] = 0.001\,\mathrm{M}$, $[H_2O_2] = 0.020\,\mathrm{M}$, I = 0.5 M, pH = 9.1 (b)Typical absorbance-time trace for the second reaction step in glycine as buffer. Experimental conditions: $[\mathrm{Fe(edta)}^-] = 0.001\,\mathrm{M}$, $[H_2O_2] = 0.020\,\mathrm{M}$, I = 0.5 M, pH = 10.75, T = 25 °C

dependence on the nucleophile concentration was observed for all the complexes studied; k_{obs2} was found to be independent of the L-Met concentration, suggesting a chelate formation process. The results for the reactions with L-Met imply that k_{obs1} and k_{obs2} can be expressed by equations (2) and (4).

$$k_{\mathrm{obs2}} = k_2, \quad \mathrm{Nu} = \text{L-Met} \tag{4}$$

The k_{obs} values for all reactions increased with increasing pressure and showed a linear dependence. The acceleration of the reactions by pressure indicates an activation process that is consistent with an associative substitution mechanism and is dominated by bond making. This is also supported by the negative $\Delta S^{\neq}$ values calculated from the temperature dependence of the reactions. The values for the activation entropy, $\Delta S^{\neq}$, and the activation volume, $\Delta V^{\neq}$, are significantly negative for all reactions studied. The second substitution step in the reaction with L-Met, which involves chelate formation, shows a more negative activation entropy and activation volume compared to the first step.

3.3 Complex Formation

3.3.1 *Nitric Oxide Binding and Dissociation with Iron(III) Porphyrin Complex*

The rates of ligand binding and ligand dissociation (k_{on} and k_{off}) can be determined by stopped-flow methods. For example, the kinetics of the binding and release of NO with an iron(III) porphyrin complex was studied as a function of pH, temperature, and pressure by stopped-flow and laser flash photolysis techniques.**[8]** The diaqua-ligated form of the porphyrin complex binds and releases NO according to a dissociative interchange mechanism based on the positive values of the activation parameters $\Delta S^{\neq}$ and $\Delta V^{\neq}$ for the ''on'' and ''off'' reactions.

The kinetics of the reaction was followed at 427 nm (pH 7) or 432 nm (pH 11) under pseudo-first-order conditions with at least a 10-fold excess of NO. The k_{obs} values determined under such conditions by fitting the kinetic traces to a single-exponential function depend linearly on [NO] according to equation (5). The rates of NO binding and release (k_{on} and k_{off}) were determined from slopes and intercepts of linear plots of k_{obs} versus [NO], respectively. The overall equilibrium constant calculated from the kinetic data, $K_{\text{NO}} = k_{\text{on}}/k_{\text{off}}$, was in reasonable agreement with the corresponding thermodynamic value of K_{eq} determined from a combination of UV–vis and electrochemical measurements. In general, the values of k_{on} and k_{off} can be checked against the value of the equilibrium constant (K) if it is known.

$$k_{\text{obs}} = k_{\text{on}}[\text{NO}] + k_{\text{off}} \tag{5}$$

To determine the activation parameters $\Delta H^{\neq}$, $\Delta S^{\neq}$, and $\Delta V^{\neq}$ for the binding and release of NO, the kinetics was studied at different temperatures (6–30 °C) and hydrostatic pressures (0.1–170 MPa). The k_{on} and k_{off} values determined from linear dependences of k_{obs} versus [NO] at each temperature and pressure allowed the construction of Eyring plots for the ''on'' and ''off'' reaction. Activation parameters can be calculated from the plots. Because of the small intercepts in the plots of k_{obs} versus [NO] in the pressure-dependent study, the activation volume for the ''off'' reaction could not be determined accurately in this way. This value, however, could be measured in a stopped-flow experiment using the NO-trapping method.

Activation volumes determined in these studies enabled the construction of volume profiles for the binding of NO to the diaqua and monohydroxo forms of the complex, respectively. On the basis of these data, a feasible explanation for the significant kinetic and mechanistic differences observed in the reactivity of these two species was offered.

3.3.2 *Kinetics of the Formation of Lead(II) Complexes*

For new compounds, the stopped-flow method is one important approach to study kinetics. For example, three lead(II) complexes were synthesized, and stopped-flow kinetic measurements enabled the unraveling of the formation process of the three lead(II) complexes on the basis of thermodynamic and kinetic studies.**[9]**

Formation and proton-assisted dissociation kinetic studies were performed under pseudo-first-order conditions. The kinetic traces, recorded at the maximum of the UV absorption band assigned to the lead complexes (274 nm) by single-wavelength stopped-flow spectrophotometry, were averaged from at least six replicates and then processed on-line with the fitting routine software. This program fits up to three-exponential functions to the experimental curves by the Marquardt nonlinear least-squares algorithm. The goodness of fit was judged in terms of the statistical parameter χ^2 (in general, values less than 0.1 were obtained) and by visual inspection of the residual plots. The pseudo-first-order rate constants were thus derived. Linear regression and nonlinear least-squares calculations were performed with Origin 6.0 (Microcal Software, Inc., Northampton, MA USA).

The time course of the complex formation was studied under pseudo-first-order conditions with excess ligand. Concentrations after mixing were at least 10 times larger than those of lead(II). Under such conditions the reaction proceeded to completion in a single rate-limiting step with no more initial loss of spectrophotometric amplitude than that expected from the dead time of the employed instrument. The process was found to be of first order with respect to lead(II). Indeed, the recorded signal could be fitted with excellent statistical confidence to a single-exponential function by nonlinear least squares.

A combination of potentiometric and absorption spectroscopic data allowed the authors to characterize the formation and the dissociation mechanism of octacoordinated lead(II) complexes of primary and tertiary tetrakiscarbamoylmethyl cyclam derivatives.

3.4 Redox Reactions

Noncomplementary redox reactions between halogen and oxyhalogen species often exhibit complex kinetic patterns which can be understood in terms of multistep kinetic models. The corresponding mechanisms are centered on the formation and subsequent reactions of reactive intermediates such as XO_2 (X = halogen) and related compounds. Stopped-flow techniques can be used to provide insights into the redox reactions. Several examples of redox reaction are also described in Section 3.5.

Stopped-flow spectroscopy was used to relate the rate constants, activation parameters, and mechanisms of the oxidation of ClO_2^- and BrO_2^- by O_3.**[10]** Ozone reactions with XO_2^- (X = Cl or Br) are studied under pseudo-first-order conditions with excess XO_2^-. The kinetic traces were obtained observing the loss of O_3 at 260 nm and fitted to an exponential equation to give the pseudo-first-order rate constants. The O_3/XO_2^- reactions are first order in $[O_3]$ and

$[XO_2^-]$. The proposed rate-determining step is an electron transfer from XO_2^- to O_3 to form XO_2 and O_3^-. Subsequent rapid reactions of O_3^- with general acids produce O_2 and OH. The OH radical reacts rapidly with XO_2^- to form a second XO_2 and OH^-. However, for $X = Br$, kinetic spectra show that small but observable concentrations of BrO_2 form within the dead time of the stopped-flow instrument. Bromine dioxide is a transitory intermediate, and its observed rate of decay is equal to half the rate of the O_3/BrO_2^- reaction. Variation of rate constant values with temperature gives $\Delta H^{\neq}$ and $\Delta S^{\neq}$. The positive $\Delta S^{\neq}_{Br}$ value is attributed to the loss of coordinated H_2O from BrO_2^- upon formation of an $[O_3BrO_2^-]^{\neq}$ activated complex.

3.5 Observation of Intermediates

3.5.1 *Methods for Collecting Spectral Data*

The spectra of reaction intermediates may be reconstructed either by collecting a series of single-wavelength kinetic traces over the wavelength range of interest, or by rapidly collecting individual spectra during the course of a single reaction. The method used depends primarily on the capabilities of the available instruments, and also on the chemical properties of the system being investigated.

Absorbance stopped-flow data are most commonly collected at a single wavelength with a monochromator and photomultiplier or photo-diode detector. By repeating a reaction across the wavelength range of interest, data for spectral analysis can be collected. Spectrophotometers capable of acquiring hundreds (or more) of spectra each second are available in commercial stopped-flow systems. These are most often based on an array of photodiodes. An alternative method for rapid scanning uses a subtractive double grating monochromator with intermediate slits that are mounted on a rapidly spinning disk. This initial technology contributed the name ''rapid-scan'' kinetics, even though kinetic spectra are more often now collected with no spectral scanning at all by photo-diode arrays.

An isosbestic point is a wavelength where the absorbances of two light-absorbing forms are equal. The isosbestic point is useful in both quantitative and qualitative work. Where a clear isosbestic point occurs during the course of a reaction, it is often taken as evidence that only two species are involved, since it is considered unlikely that a third absorbing species would also have an identical absorbance at the same wavelength. It is more likely that a third species may simply have no absorbance at this wavelength.

3.5.2 *Example of a Two-step Reaction Mechanism*

The observation of intermediates is important because it can help to provide useful information to describe a detailed reaction pathway for the reaction. Rapid-scan experiments can directly show whether the change in absorbance at all wavelengths is monotonic or not, and how many well-defined isosbestic points are observed in this process.

The intermediate formed may or may not show a UV–vis spectrum. If it does, it is easy to make a decision that an intermediate is formed. For example, Stanbury *et al.*[11] found that the aqueous reaction of acidic Cl_2 with excess SCN^- rapidly generates a UV-absorbing intermediate. Sometimes, the reaction investigated proceeds rapidly, generating an unstable intermediate within the dead time of all stopped-flow instruments used for kinetic analysis. In order to obtain confirmative evidence on the structure of the intermediate, additional approaches are required to provide evidence. Researchers can gain significant insight into the reaction mechanism through combined stopped-flow kinetics and UV–vis, EPR, and resonance Raman spectroscopic studies, etc., as well as information about the structures of intermediates.

In our previous work,[12] it was found that an absorbance peak at 526 nm appeared within the first seconds, then decreased slowly, upon mixing of perphenazine with potassium persulphate (Figure 4). Both perphenazine and potassium persulphate have no absorbance peak in the range between 390 and 700 nm (spectrum not shown), so their spectral changes do not interfere with the spectrum of intermediate. Therefore time-resolved spectra in Figure 4 provided clear evidence for the formation and decay of an intermediate, the visible spectrum of which was characterized by an absorbance maximum at 526 nm.

The spectra (recorded between 280 and 705 nm and between 1.3 ms and 16.4 s) were analyzed by Pro-Kineticist global analysis/simulation software (Applied Photophysics Ltd., Leatherhead, UK). Singular values, which are a measure of the contribution of the corresponding basis spectra to the observed spectra, indicated that the number of colored components present in this system was three. Before simulating with Pro-Kineticist global simulation software program, a possible model was entered in the form of two-step reaction mechanism ($A \rightarrow B \rightarrow C$). Global analysis of the spectrum (Figure 5a) indicated the presence of three species assigned as perphenazine (A), the intermediate (B), and the final oxidized product of perphenazine (C). The concentration changes of the compounds A, B, and C with time are displayed in Figure 5(b), the curve for B possesses a typical characteristic of successive reaction and is similar to the time course at 526 nm in the experimental results. We also tried other possible models, such as $A + B \rightarrow C \rightarrow D$, or $A \rightarrow B \rightarrow C \rightarrow D$; the synthesized spectra and concentration-time curves were not consistent with the experimental results. These results calculated by the software in Figure 5(a) and (b) were consistent with the experimental data, proving that the two-step reaction model ($A \rightarrow B \rightarrow C$) was the most reasonable mechanism. The chemical identity of this intermediate is still under investigation.

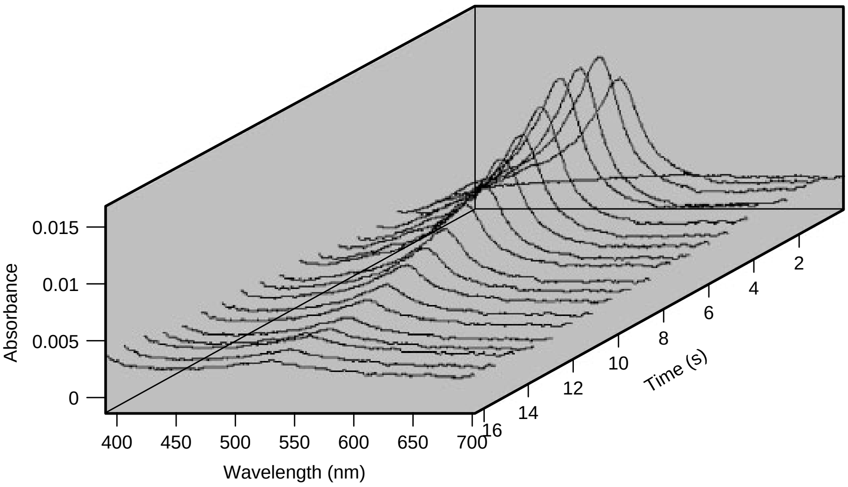

Figure 4 Time-resolved spectra (800 spectra are acquired in the 390–705 nm range per shot. Only 19 spectra are present for clear observation.) of 6.0×10^{-5} M perphenazine mixed with 2.0×10^{-2} M $K_2S_2O_8$ in 0.3 M H_2SO_4 buffer at 25.0 °C The reaction was monitored by photodiode array detector (PDA) attached to the stopped-flow instrument

3.5.3 Example of a Three-step Reaction Mechanism

Rapid-scan UV-vis spectra of the nitrite-catalyzed reaction between HbFe(II)NO (Hb = hemoglobin) and peroxynitrite were obtained.[13] The analysis of the spectra with singular-value decomposition/global analysis demonstrated that the spectral changes follow a three-exponential process ($A \rightarrow B \rightarrow C \rightarrow D$) and are indicative of the formation of HbFe(III)NO and HbFe(III)NO_2 as intermediates. The observed rate constants for the first two reaction steps were determined by global analysis of the rapid-scan stopped-flow spectrophotometric data. The calculated spectra of three species were obtained from singular-value decomposition and global analysis of the rapid-scan data as shown in Figure 6. The rate-determining step was determined from kinetic data, and the step changed depending on the conditions.

3.6 Double-mixing Stopped-flow

The double-mixing stopped-flow method is a convenient and powerful tool to generate a labile component transiently, for example avoiding anaerobic conditions for investigating interprotein electron transfer. Studies of interprotein electron transfer require the rapid mixing of a reduced (donor) and oxidised (acceptor) protein. A requirement of single-mixing approaches is that the donor protein is pre-reduced (e.g. with a reducing substrate or artificial reductant) before being introduced into the stopped-flow analyser. Reduced enzymes are often sensitive to oxidation by O_2, making the approach technically demanding since anaerobic conditions are often required to prevent reoxidation of the protein. However, double mixing can be used to reduce transiently the donor protein prior to mixing with the acceptor. The following two examples show the applications of double-mixing mode, as well as the disadvantages of double mixing.

Lippard *et al.*[14] presented the results of detailed double-mixing stopped-flow kinetic studies of the reaction of diiron(II) compounds ($Fe_2(\mu\text{-}O_2CAr^{Tol})_4(4\text{-CNPy})_2$) with water and the subsequent interaction of the aqua species with dioxygen.

This reaction $Fe_2(\mu\text{-}O_2CAr^{Tol})_4(4\text{-CNPy})_2$ with water was investigated at −60 °C with different excess amounts of water. A plot of $\ln k_{obs}$ versus $\ln[H_2O]$ was fitted to a linear equation, which had a slope of 0.99, indicating a first-order dependence on water. The pseudo-first-order rate constant is also linearly dependent on the concentration of water, with an intercept, which corresponds to the reverse reaction rate constant, near zero. This result indicates the reaction to be irreversible under these conditions.

After $Fe_2(\mu\text{-}O_2CAr^{Tol})_4(4\text{-CNPy})_2$ was mixed with water, the solution was further allowed to react with excess dioxygen in a second push using the double-mixing stopped-flow apparatus (Figure 1). The 460 nm absorbance arising from the aqua adduct decreased with time, a change that could be nicely fitted to a pseudo-first-order expression. The derived rate constants are comparable to those obtained from a previous competition experiment, which indicates that aquation was completed prior to oxygenation.

The second example is the measurement of the kinetics of a substrate binding to extracted FeMo-cofactor of nitrogenase by a double-mixing stopped-flow approach.[15] In a typical experiment, solutions of FeMoco-L and CN^- are rapidly mixed and held together for a known length of time. Subsequently, this solution is mixed with a solution of $[NEt_4]SPh$ whereupon the thiolate reacts with the cofactor.

In principle, the double-mixing approach can be used to monitor the binding of any substrate to extracted

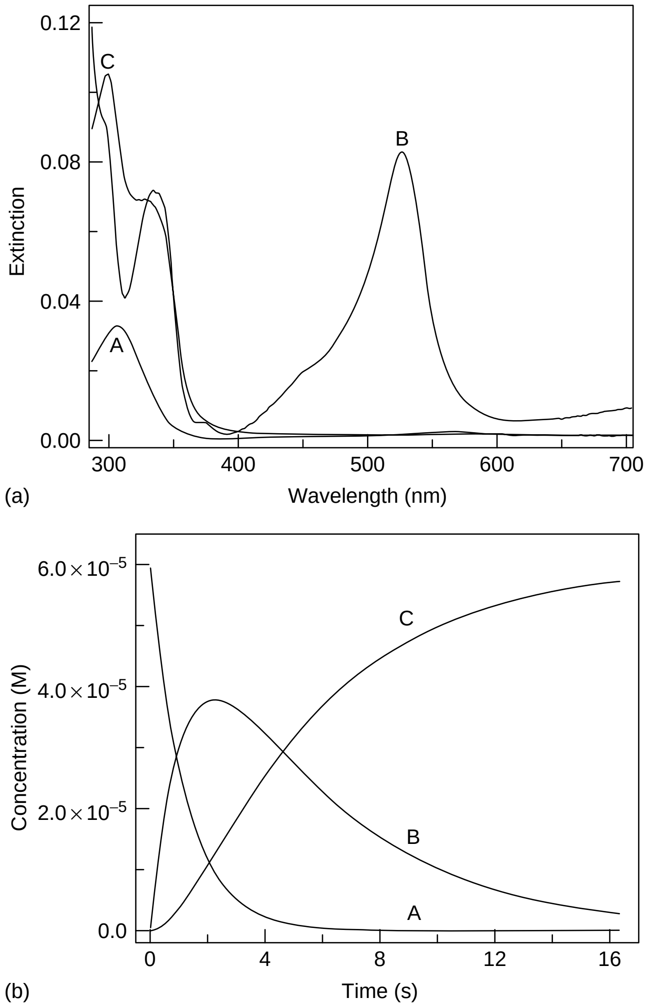

Figure 5 (a) Calculated spectra of the perphenazine (A), intermediate (B) and product (C); (b) Change of concentrations of different substances in the course of reaction. Results in (a) and (b) were calculated by Pro-Kineticist global simulation program, which was used for spectral analysis of intermediates using a set of spectral data from the reaction of 2.0×10^{-2} M $K_2S_2O_8$ with 6.0×10^{-5} M perphenazine in 0.3 M H_2SO_4 buffer at 25.0 °C obtained by PDA

FeMo-cofactor; in practice, its application is limited. During the double-mixing experiments, the cofactor solution is diluted fourfold before it is analyzed; initial equivolume mixing with the solution of CN^- is followed by equivolume mixing with the PhS^- solution. Consequently, the solution of the cofactor being analyzed is only half the concentration of a conventional stopped-flow experiment, and thus, the absorbance-time curves are only half the magnitude. (This can be somewhat improved by using syringes of different volume.) In addition, when configured in the double-mixing mode, the dead time of the apparatus is about 3–4 ms, which is more than double that of the stopped-flow configuration and leads to loss of some of the absorbance change for more rapid reactions. The consequence of both these limitations is that (compared to conventional stopped-flow spectrophotometry) the data from double-mixing stopped-flow experiments are associated with a poorer signal-to-noise ratio.

3.7 Low-temperature Stopped-flow

Low-temperature stopped-flow methods have become extremely useful for studying reactions that are too fast at ambient temperatures and/or for detecting reactive intermediates that can only be observed at low temperatures. The low-temperature stopped-flow technique has been well documented as a useful tool for the detection of unstable copper-dioxygen intermediates. The kinetic and thermodynamic behavior of O_2-binding to Cu(I) complexes can provide fundamental understanding of copper(I)/dioxygen chemistry, which is of interest in chemical and biological systems. As an illustration of low-temperature stopped-flow in inorganic chemistry, the reaction of dioxygen with the tripodal copper(I) complex was studied by Siegfried *et al.*[16] For example, low-temperature stopped-flow studies of the least oxidizing copper(II) complexes reacting with $O_2^{\bullet-}$ provided evidence of a CuO_2 intermediate.[3] The low-temperature technique was applied to study the reactions between copper(II) complexes and H_2O_2, which enabled the researcher to detect a mononuclear Cu^{II}-peroxo complex.[4]

Zuberbühler *et al.* reported stopped-flow kinetic investigations of the oxygenation reactions of a series of tetradentate copper(I) complexes in propionitrile, tetrahydrofuran, and acetone.[17] The formation of $[(L^{MeO})Cu^{II}(O_2^-)]^+$ can only be followed below 203 K because at a higher temperature it occurs faster than the stopped-flow instrumental limit. On the basis of experimental results, the authors proposed a reaction mechanism, which involved four steps, at least three intermediates. On the basis of the kinetics analysis, spectra for species (intermediates and product) could be calculated.

3.8 High-pressure Stopped-flow

Chemical reactions are often highly pressure-dependent. As a matter of fact, high pressure is an elegant way to perturb reversibly chemical equilibria and reactions. Another advantage of using the pressure parameter is that reactions are slowed or accelerated depending on the type of chemical interaction involved. For instance, pressure weakens electrostatic interactions, but stimulates some hydrophobic interactions, such as stacking between aromatic residues. Similarly to the activation enthalpy, $\Delta H^{\neq}$, obtained from kinetics as a function of temperature, experiments under pressure yield an activation volume, $\Delta V^{\neq}$. When the activation volume is positive, the reaction is slowed, and when it is negative, the velocity is increased by pressure. From the pressure-dependent kinetic constants (k_{obs}) the activation volumes ($\Delta V^{\neq}$) were determined according to $(\mathrm{d}\ln k_{obs}/\mathrm{d}P)_T = -\Delta V^{\neq}/RT$ where P is the hydrostatic pressure, T the absolute temperature and R the gas constant.

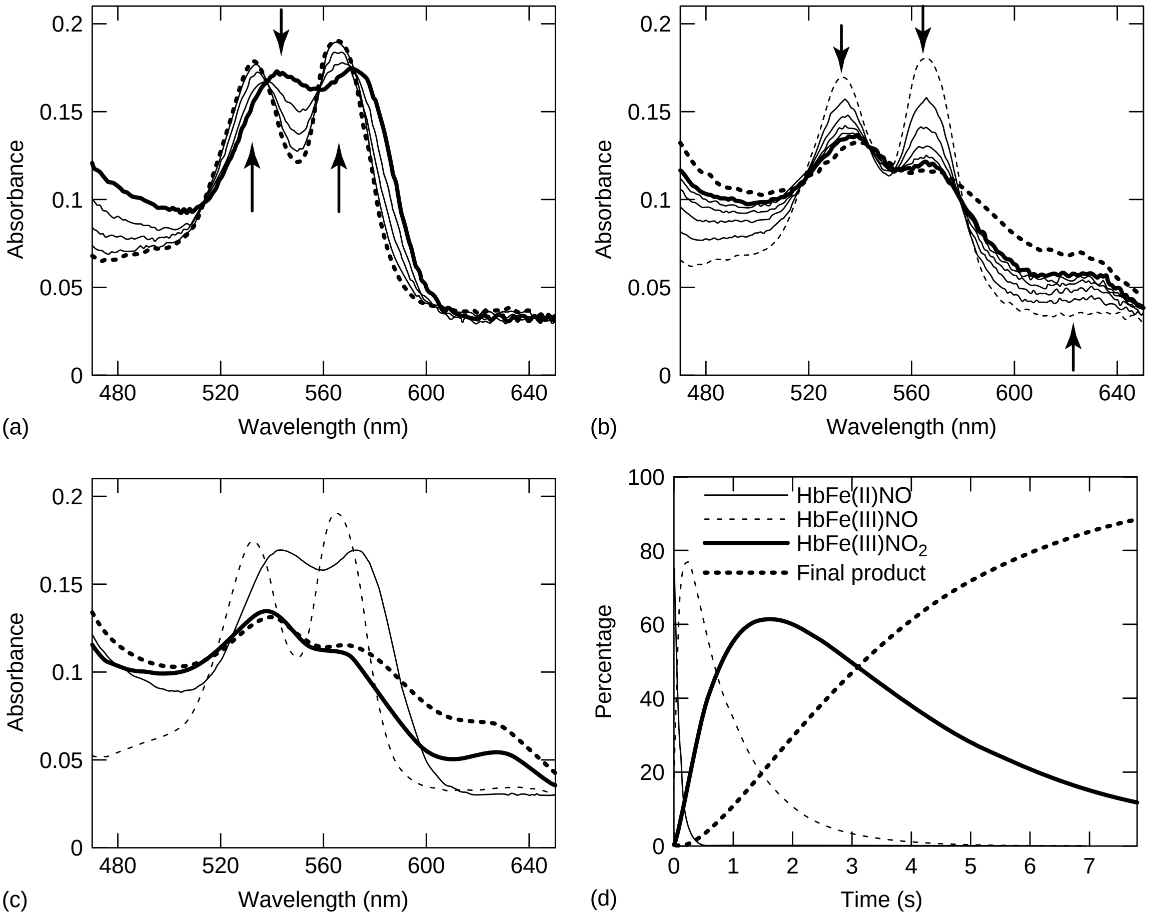

Figure 6 Rapid-scan UV–vis spectra of the nitrite-catalyzed reaction between HbFe(II)NO (14 μM) and peroxynitrite (400 μM) in a 0.05 M phosphate buffer at pH 7.0 and 20 °C, $[NO_2{}^-] = 175$ mM. Absorbance spectra were collected every millisecond, but to improve the signal-to-noise ratio, each curve shown represents the average of two measured curves. (a) Oxidation of HbFe(II)NO (bold line) to HbFe(III)NO (bold dotted line): the traces depicted were recorded every 40 ms up to 160 ms. (b) The dissociation of $NO^{\bullet}$ from HbFe(III)NO (dotted line) and the binding of nitrite to metHb generates $HbFe(III)NO_2$ (bold line, ~2.2 s). The traces depicted were recorded every 400 ms. The dotted bold line represents the final spectrum after a total of 7.8 s. (c) The three species obtained from singular-value decomposition and global analysis of the data from parts (a) and (b). The data were fitted to a three-exponential expression (A → B → C → D), and the values of the three observed rate constants obtained are $11.6 \pm 0.2\,s^{-1}$, $1.2 \pm 0.1\,s^{-1}$, and $0.31 \pm 0.06\,s^{-1}$, respectively. (d) Time courses for the four species involved (see legend, which also applies to c) obtained from singular-value decomposition and global analysis of the data from parts (a) and (b)

High-pressure stopped-flow techniques were also widely used to monitor fast reactions with gaseous fluid as reactants. For example, Bailey *et al.*[18] developed a high-pressure stopped-flow apparatus in their laboratories and used this apparatus to follow the reaction of dioxygen with bovine cytochrome *c* oxidase. This technique was also applied to study the reaction of nitric oxide synthase with oxygen, which is fast and takes place within several steps, separated by ephemeral intermediates. These experiments under high pressure indicated that oxygen binding occurred in more than one step.[19] The use of extreme experimental conditions, such as low temperature and high pressure, associated with rapid kinetic analysis, has proven to be a convenient tool to study complex reactions.

3.9 pH-jump Stopped-flow

The pH-jump technique can be used in the conventional stopped-flow mode in order to elucidate the kinetics of the reaction at different pH. In such experiments, a pH-dependent equilibrium is perturbed by mixing the system equilibrated at one pH in a weak buffer with a strong buffer at a different pH.

For example, the kinetics of Fe dissociation from Fe^{3+}nFbp(X) (nFbp = recombinant ferric binding protein from *Neisseria meningitides*, $X = PO_4{}^{3-}$, citrate) driven by H^+ were studied by pH-jump stopped-flow methods. Researchers used this technique to induce Fe^{3+} dissociation from Fe^{3+} nFbp(X) ($X = PO_4{}^{3-}$, citrate), which enabled researchers to study the mechanism in the absence of a competing chelator.[20] A low buffer concentration was maintained to enable a pH jump during the stopped-flow experiment. The kinetics of Fe^{3+} release from Fe^{3+} nFbp(X) via a pH jump were investigated by fast mixing of the Fe^{3+}-loaded protein at near neutral pH (6.65) with $HClO_4$ of the desired concentration (0.001–0.05 M). The rapid pH jump results in successive dechelation events and complete dissociation of Fe^{3+} from the protein.

3.10 Analysis of Stopped-flow Data

Kinetic data in most cases are complex and hence best analyzed by computational methods that make no assumptions in fitting the data, except for the model chosen by the investigator. Comprehensive data treatments are often required for kinetic studies, and finally kinetic models are proposed based on these results.

The kinetic traces are obtained from stopped-flow experiments and fit to a single-exponential or to a sum-of-exponentials model. Strictly speaking, one does not know beforehand how many exponentials will be required to describe adequately a particular kinetic curve, so that one has to perform several separate fits, each using a different number of such terms. We therefore need criteria to use in choosing which model best describes the data. The standard ones are the form of: (i) the residuals; (ii) the autocorrelation function values; and (iii) the χ^2 value (statistical goodness-of-fit parameter).

3.10.1 Ligand–Binding Reaction; Data Analysis

The observed rate constant, k_{obs}, can be determined from the exponential function. When the plots follow a linear dependence of k_{obs} against initial concentration of ligand, equation (6) is adopted:

$$C + L \underset{k_{-1}}{\overset{k_{+1}}{\rightleftarrows}} C - L \tag{6}$$

where C is the compound, L is the ligand, $C - L$ is the compound-ligand complex, and k_{+1}, k_{-1} are the transient-phase kinetic rate constants. If the initial concentration of ligand, $[L]$, is greater than $[C]$, k_{obs} is then expressed as equation (7):

$$k_{\mathrm{obs}} = k_{+1}[L] + k_{-1} \tag{7}$$

The values of k_{+1} and k_{-1} are determined from the slope and the intercept of the plot of $[L]$ versus k_{obs}, respectively. The dissociation constant of $C - L$, K_{-1}, can be calculated from equation (8):

$$K_{-1} = \frac{k_{-1}}{k_{+1}} \tag{8}$$

In contrast, when the plots of $[L]$ versus k_{obs} are nonlinear, equation (9) is applied:

$$C + L \underset{k_{-1}}{\overset{k_{+1}}{\rightleftarrows}} C - L \underset{k_{-2}}{\overset{k_{+2}}{\rightleftarrows}} C^* - L \tag{9}$$

where $C - L$ is an intermediate (loosely bound) form and $C^* - L$ is a more tightly bound isomerized form, and k_{+1}, k_{-1}, k_{+2} and k_{-2} are the transient-phase kinetic rate constants. In this mechanism, the reciprocal of the slower relaxation time, k_{obs}, is expressed as equation (10) when $[L] \gg [C]$

$$k_{\mathrm{obs}} = \frac{k_{+2}[L]}{K_{-1} + [L]} + k_{-2} \tag{10}$$

where $K_{-1}(= k_{-1}/k_{+1})$ is the dissociation constant for the intermediate $C - L$ complex. The k_{-2} value can be estimated by linear extrapolation in the low $[L]$ region of k_{obs} versus $[L]$ plot. The k_{+2} and K_{-1} values are obtained with the k_{-2} value determined above, by the reciprocal of the intercept and the slope/intercept of the secondary plot of $1/(k_{\mathrm{obs}} - k_{-2})$ versus $1/[L]$, respectively. In the two-step mechanism, the overall dissociation constant, K_{d}, for the $C - L$ complex can be calculated from equation (11).

$$K_{\mathrm{d}} = \frac{K_{-1}}{[1 + (k_{+2}/k_{-2})]} \tag{11}$$

3.10.2 Calculating Spectra

Two approaches may be used to extract the spectra of species (as well as the kinetics of the reaction scheme) from data collected by stopped-flow experiments: SVD and global analysis. For SVD, the data set is reduced to a matrix representation that allows the spectral and kinetic parameters to be calculated. For global analysis, each absorbance trace is fit to an equation to obtain rate constants and extinction coefficients. For example, SVD results provide information on the number of reaction components and hence the minimum reaction complexity. The interested reader is directed to more thorough reviews listed at the end of this chapter (Section 5 Further Reading).

3.10.3 Examples of Analysis and Simulation

Transient-state kinetic data are typically fit with multiple exponentials and not with analytically derived equations. This procedure yields observed rate constants and amplitudes, each of which is typically assigned to one process. These amplitudes can be complex functions of rate constants, extinction coefficients, and intermediate concentrations. It can be difficult to extract meaningful parameters from them without the use of a full model for the reaction and corresponding mathematical analysis.

The next example shows how to choose a kinetic model. The unusual kinetic curves observed by stopped-flow spectrophotometry have been successfully simulated for all levels of iron loading of human H-chain ferritin. The presence of an additional intermediate, postulated to be a hydroperoxo diFe(III) complex, was suggested by a detailed analysis of the kinetic data of 48Fe/protein samples. A mathematical model for catalysis was developed that explains the observed kinetics. The model consists of two sequential mechanisms.[21]

When 48 equiv Fe(II) was mixed with the apoprotein in a multiwavelength stopped-flow experiment, a family of UV–vis reaction spectra was obtained. Absorbance maxima occur at ∼305 and ∼650 nm. The result shows the series of spectra for the first 50 ms of the reaction where the concentration of the peroxo intermediate ($\lambda_{max} \sim 650$ nm) increases and reaches a maximum; the series of spectra for the decay of the intermediate occupy the time interval of 50 ms to 14 s. A pure isosbestic point is not obtained in the spectra, indicating the presence of more than one decay product of the peroxo intermediate. After the authors tried several kinetic models, the 650 nm data for the 48Fe(II)/protein sample were best fitted according to a sequential reaction of the type

$$A \rightarrow B \rightarrow B' \rightarrow C$$

At least two intermediates, B and B′ can be consistently resolved in the rate data. A significantly poorer fit to the data and a correspondingly large residual were obtained with the simpler scheme, $A \rightarrow B \rightarrow C$. Similarly, the reaction scheme $A \rightarrow B$ plus $B \rightarrow C$ and $B \rightarrow C'$ or $A \rightarrow B \rightarrow C$ plus $A \rightarrow B' \rightarrow C'$ was found to either give poorer fits to the kinetic data or resulted in physically meaningless values of the rate constants with 10- to 1000-fold errors and negative molar absorptivities for some species with similarly large errors, indicating strong correlation between the fitting parameters and inappropriateness of these models. Nevertheless, the fitting results reported here do not preclude the possibility that the data, while appearing to conform to $A \rightarrow B \rightarrow B' \rightarrow C$ very well, are in fact due to another kinetic process not yet considered. The model fits the observed kinetics very well, and good correspondence is obtained between the rate constants from the data for the two wavelengths.

If the wrong kinetic model is used in analysis, the spectra obtained may not be meaningful. Indeed, one possible use for spectral analysis is to assist in deciding between rival mechanisms; if the spectra generated for one mechanism are unlike anything ever observed for the prosthetic group, while the alternate mechanism gives known spectra, the latter mechanism should be preferred. Statistical criteria are not adequate to distinguish between some rival mechanisms.

In another example, the kinetics of the protonation of Re(O)I(2,7-nonadiyne) by CF_3SO_3H in CH_3CN were monitored by visible spectroscopy. Two second-order rate constants and presumably successive protonations were observed.[22] Global fits gave calculated spectra for the starting material, the intermediate, and the product that best fits the observed stopped-flow traces in an $A \rightarrow B \rightarrow C$ sequence.

3.10.4 Examples of Computer Fitting Programs

The kinetics of most reactions is studied under pseudo-first-order conditions. However, large excess of one of the reactants might result in association processes too fast for this technique, because stopped-flow measurements are capable of following processes with observed rate constants, k_{obs}, not exceeding 1000–1500 s^{-1}. All these make numerical methods of analysis of the progress curves potentially very useful because they are not limited by any assumptions. A promising numerical integration approach to analyze progress curves obtained in stopped-flow experiments was described by Frieden and Dang.[23] Their programs KINSIM and FITSIM are applicable for any reaction mechanism and can treat simultaneously up to 20 real data files and mechanisms with up to 100 species and 100 reaction steps. One must keep in mind that a given experiment may only be sensitive to a small subset of the kinetic parameters; this situation is handled by varying only the kinetic parameters that are sensitively defined by a given experiment, while holding all others fixed.

A method for extracting kinetic and optical parameters from progress curves for protein–ligand association, obtained by stopped-flow experiments, was described by Antosiewicz *et al.*[24] The method is limited to one-step and two-step association kinetics, but it allows concentration of protein and offset of the signals to be adjustable parameters during an interactive nonlinear least-squares fitting procedure. The method was tested on simulated pseudo-experimental data and applied to progress curves obtained in a stopped-flow spectrofluorimeter.

A multitude of mathematical software is available that can simultaneously fit several traces to a single set of rate constants. Data fitting can be performed using the software supplied for the operation of the stopped-flow apparatus, the integrated J&M software Kinspec, Origin (OriginLab Corporation, Northampton, MA) or Igor (WaveMetrics, Inc., Lake Oswego, OR) for simple exponential functions. Several commercial and homemade software are frequently used for stopped-flow data analysis, such as, Specfit (Spectrum Software Ass.), Globfit (MATLAB), and Pro-Kineticist global simulation program (Global Analysis for Spectra, Kinetic Data) from Applied Photophysics.

3.11 Stopped-flow Fluorescence Spectroscopy

For fast reactions with observed fluorescence signal changes, stopped-flow fluorescence spectroscopy is a better choice for kinetic investigation. Stopped-flow fluorometry measurements have been widely employed to study the kinetics of protein interactions. A typical stopped-flow system is assembled from modular components of a conventional spectrophotometer/fluorimeter, a device permitting rapid mixing of the components of a reaction and a data recording system with fast response. Commercially available instruments offer facilities for the observation of changes in absorbance and/or fluorenscence emission after rapid mixing of the reagents. These measurements can be made simultaneously due to the different optical requirements of the two spectroscopic techniques as illustrated in Figure 1. The change in light absorption at a certain wavelength is detected at 180° relative to the light beam. Changes in fluorescence intensity are detected at 90 degree relative to the excitation light beam via a second monochromator, a narrow bandpass filter or a cut-off filter to select the emission wavelength.

3.11.1 Example of Nucleotide Binding to 3α-Hydroxysteroid Dehydrogenase

This example shows how to determine whether a binding reaction constitutes a one- or two-step mechanism. Transient-phase kinetic studies using the fluorescence stopped-flow method were conducted with 3α-hydroxysteroid dehydrogenase (3α-HSD) to characterize the nucleotide binding mechanism.**25** The time course for oxidized nucleotide binding demonstrated that binding of not only NAD$^+$ but also NADP$^+$ was apparent by the fluorescence kinetic transients. From the relationship of k_{obs} against the respective initial concentrations of NAD$^+$ and NADP$^+$, the linear dependence of k_{obs} against both [NAD$^+$] and [NADP$^+$] indicated that the oxidized nucleotide cofactor binding is in accordance with a simple one-step mechanism. The nicotinic acid adenine dinucleotide (NAAD$^+$) binding also showed a one-step mechanism (equation 6).

In the case of reduced nucleotide binding, the dependence of k_{obs} on the initial concentration of NADH showed a hyperbolic curve. Different from oxidized nucleotides, the kinetic feature of the NADH binding was consistent with a two-step mechanism, which involves a fast bimolecular association process followed by a slow unimolecular isomerization process (equation 9). In conclusion, the binding of oxidized nucleotides, NAD$^+$, NADP$^+$ and NAAD$^+$, agreed well with a one-step mechanism, while that of reduced nucleotide, NADH, showed a two-step mechanism as described in Section 3.10.1.

3.11.2 Example of Fluoride Binding to Tyrosinase

Stopped-flow fluorescence spectroscopy was used to obtain insight into the interaction of fluoride with tyrosinase (Ty) under pseudo-first-order conditions, as well as to validate the use of fluorescence quenching in studying ligand-binding kinetics.**26**

Ty fluorescence was detected using a photomultiplier tube equipped with an optical cut-off filter of 320 nm supplied with the stopped-flow system, thus resulting in the detection of all emitted light above 320 nm. Fluoride binding traces were fitted to a single-exponential decay function of the form $F_t = F_\infty + A\,\exp(-k_{\mathrm{obs}}t)$, where F_t denotes the fluorescence at time t; F_∞ is the fluorescence level at completion of the binding reaction; A is the signal amplitude. The fitting was performed using the least-squares fitting algorithm implemented in the stopped-flow software.

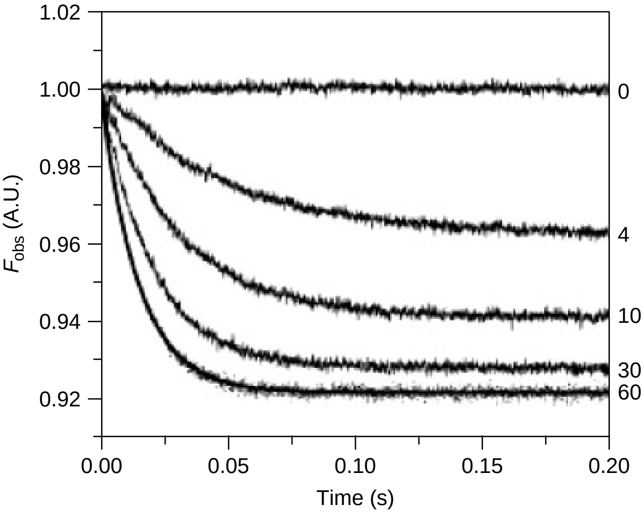

Figure 7 The kinetics of fluoride binding to Ty$_{\mathrm{met}}$. Stopped-flow fluorescence traces of fluoride binding obtained by mixing 2.5 μM resting Ty in air-saturated 100 mM Pi at pH 6.80 with solutions containing various concentrations of fluoride made up in the same buffer. The fluoride concentrations (in millimolar) indicated with each trace represent end concentrations in the observation cell. Data could be fitted to single-exponential decay functions (as indicated for the trace with [F$^-$] = 60 mM) yielding values for the observed binding rate k_{obs} and the fractional fluorescence quenching amplitude F_∞/F_0 at each [F$^-$]

Representative fluoride binding traces obtained by mixing 2.5 μM resting Ty with various [F$^-$] (0–120 mM) at pH 6.80 in 1:1 volume ratio at 21 °C are represented in Figure 7, where a decrease in fluorescence is observed upon binding of F$^-$. The plots of k_{obs} versus [F$^-$] at a given pH are linear in all cases, in agreement with a two-state binding scheme where a single fluoride ion binds to the enzyme. The apparent first-order fluoride binding rate (k_{on}) and the Ty$_{\mathrm{met}}$F fluoride dissociation rate constant (k_{off}) can be determined from the slope and intercept of k_{obs} versus [F$^-$], according to $k_{\mathrm{obs}} = k_{\mathrm{on}}[\mathrm{F}^-] + k_{\mathrm{off}}$.

The use of Ty fluorescence quenching as a probe provides a direct spectroscopic probe of fluoride binding to Ty$_{\mathrm{met}}$. Stopped-flow fluorimetric experiments can be performed with high sensitivity and speed, thereby avoiding the need for large amounts of protein and the experimental difficulties arising from the intrinsic instability of the enzyme, the latter being important especially at the lower pH values.

In addition, many examples of binding systems were investigated by stopped-flow fluorescence spectroscopy, such as the binding of calmodulin to calcineurin, the binding of guanine to calf spleen purine nucleoside phosphorylase, the nucleotide cofactor binding to the *Escherichia coli* PriA Helicase, etc.

3.12 Stopped-flow Circular Dichroism

If some or all of the reactants or products of chemical and biological processes are chiral, then circular dichrosim (CD) detection may be the ideal tool for monitoring the kinetics of a reaction, and if the half-life of the reaction is of the order of milliseconds to seconds or even minutes then stopped-flow mixing of the reagents will almost certainly be the appropriate choice of sample handling method.

CD is very commonly used method for studying protein conformational change. The combination of stopped-flow mixing and CD provides an important tool for protein investigation. The advantage of CD measurements over the other optical methods is that the far-UV signals monitor changes over the entire protein (i.e. its secondary structure). A disadvantage is that CD instruments are moderately expensive and less available than absorbance and fluorescence detectors. As one of the main applications of stopped-flow CD is in the study of protein folding and unfolding, samples are often viscous, have significant absorbance due to buffers, and the experiments often require wide and variable mixing ratios. For further information and examples the reader may consult references.[27]

3.13 Other Stopped-flow Detection Methods

It is a serious limitation that all these optical techniques can only be used for reactions that are accompanied by significant chromophoric changes. It is an additional limitation of all these techniques that optical spectra tend to be broad and often show considerable overlap. Therefore reactive species can often not be monitored individually, even in cases where all of them have distinct spectral properties. Optical methods also provide little structural information about the various species in the mixture. The use of traditional stopped-flow is dependent upon the availability of optical signals to monitor change in fluorescence, absorbance or CD that occur upon binding or chemical conversion of substrate to product. In order to overcome these limitations of traditional stopped-flow optical techniques, various detection methods have been developed, such as stopped-flow mass spectrometry (MS), stopped-flow NMR, and stopped-flow EPR.

3.13.1 Stopped-flow EPR

Stopped-flow instruments with optical detection have been established since 1952, and stopped-flow techniques with EPR detection were first introduced in 1960. Stopped-flow EPR accessories with improved driving systems have been available since 1980. A stopped-flow experiment with EPR detection allows the observation of a time-dependent change of the amplitude of an EPR signal at a distinct field value (usually at the maximum of first derivative) during the reaction of two reactants in the liquid state by time-sweep acquisition (kinetic display). The result of such a measurement is a rate constant for formation, decay, or conversion of a paramagnetic species, for example a radical occurring in the reaction mixture. The procedure is analogous to the well-established case of stopped-flow operation with optical detection in which a time dependence of the optical absorption at a distinct wavelength is observed.

Typical applications of stopped-flow EPR instruments have been reported in chemistry and biochemistry, and the kinetics of transient radicals occurring in typical redox reactions with life-times down to milliseconds have been published. Examples are the decay of stable nitroxide radicals during reduction by ascorbate[28] or dithionite,[29] and formation and decay of semi-dehydro ascorbate radicals during the oxidation of ascorbate by Ce^{4+}.[30] Recently, a novel EPR stopped-flow accessory was described which allows time-dependent cw-EPR measurements of rate constants of reactions involving paramagnetic species after rapid mixing of two liquid reagents. This EPR stopped-flow design represents a state-of-the-art, computer controlled fluid driving system, a miniresonant EPR structure with an integrated small ball mixer, and a stopping valve.[31]

3.13.2 Stopped-flow Fourier Transform Infrared Spectroscopy

Stopped-flow mixing coupled with time-resolved Fourier transform infrared (FTIR) spectroscopy (*see* ***Vibrational Spectroscopy***) represents a new experimental approach to explore kinetic events, which has become possible only recently with the development of appropriate techniques. Thorneley *et al*. developed stopped-flow FTIR as a probe of the dynamics of metalloenzyme-substrate interactions, such as the binding of CO to molybdenum nitrogenase,[32] the binding chemistry of NO to cytochrome c' from *Alcaligenes xylosoxidans*., the hydroxylation of a substrate by diiron-(IV) intermediate, and the reaction between hydrogen and the [NiFe]-hydrogenase from *Allochromatium Vinosum*.[33]

The strongest advantage of the FTIR approach as a structure-specific probe is that a complete spectrum is available for each time point of measurement. Methods to study protein folding by stopped-flow FTIR have been reviewed.[34] In this way, several spectral windows are accessible simultaneously for the observation of the formation of different secondary structure elements and also events that can be attributed to changes in tertiary structure. One specific advantage of the infrared technique is the ability to monitor directly the kinetics of processes involving β-sheet structures, which is exceptionally difficult to do with other techniques.

3.13.3 Stopped-flow Conductivity

Many fast reactions do not result in measurable changes in absorbance or fluorescence. A large number, however, do exhibit a change in conductivity as the reaction progresses. The use of a stopped-flow system equipped with conductivity measurement facilities can, therefore, considerably extend the scope of this already powerful technique. Conductivity measurements offer greater signal-to-noise and a much better dynamic range than spectrophotometric measurements. Reactions are generally characterised before the kinetic study is carried out to ensure that conductivity changes are due solely to the reaction of interest. Conductivity measurements can be made in the presence of a large, but constant background signal, so it is possible to work with comparatively large buffer concentrations and to use nonaqueous ionising solvents such as ethanol and acetone. One example involves the oxidation of ferrocyanide by birnessite studied by stopped-flow conductivity measurements. Two processes were detected by the stopped-flow experiments.[35]

3.13.4 *Stopped-flow Light Scattering*

Kinetic recordings of light scattering can be obtained in a conventional stopped-flow spectrometer. For example, the kinetics of the interaction between DNA and cationic vesicles were followed using stopped-flow light scattering techniques.[36] Stopped-flow scattering was used as a tool for the characterization of solution structures of DNA-cationic vesicle complexes. The combination of light scattering, fluorescence and small-angle neutron scattering measurements provided information about the minimum number of stages and time scales for the formation of DNA-cationic vesicle complexes, as well as information about the structures of intermediates.

3.13.5 *Additional Modes*

A highly useful application of fluorescence spectroscopy is the technique known as fluorescence resonant energy transfer (FRET). The basic principle is to have a pair of chromophores attached to a molecule. One chromophore, the donor, absorbs the excitation energy and transfers this excitation energy to the second chromophore, the acceptor, through a dipole–dipole interaction mechanism. FRET can potentially give more specific information on the changes in average distance between fluorescence donors and acceptors. For example, the combination of stopped-flow and FRET is available for kinetic investigation of GAAA tetraloop-receptor docking and monitoring the rate of DNA bending.[37,38]

Luminescence measurements can also be carried out by using a conventional stopped-flow apparatus. In additional, stopped-flow techniques are used in conjunction with NMR (*see* ***Nuclear Magnetic Resonance (NMR) Spectroscopy of Inorganic/Organometallic Molecules***), MS, and electrospray ionization mass spectrometry (ESI-MS).

3.14 Additional Considerations

3.14.1 *Limitations of Stopped-flow Techniques*

Transient-state kinetic analysis is most commonly based upon stopped-flow methods where an optical signal is used to follow the time dependence of a reaction; however, it is often difficult or impossible to rigorously interpret the optical signal. For example, if the absolute extinction coefficients and concentrations of species contributing to the optical signal are not known, then the reaction pathway cannot be determined unambiguously. Some fast reactions do not result in measurable changes in absorbance or fluorescence. These problems can also be solved by use of chemical quench-flow methods. Quench-flow methods do not require a chromophore and is a complementary alternative technique for traditional stopped-flow. In these experiments a reaction is initiated by rapid mixing of two or more reactants, followed by mixing with a quenching reactant (e.g. acid, base, or liquid nitrogen) after a specified period of time. This step abruptly stops the reaction. Subsequently the reaction mixture is analyzed off-line using methods such as chromatography, NMR, or MS. Quench-flow experiments require that the quenched reaction mixture be stable during the off-line analysis, which often presents a problem. The difference between these approaches is that in stopped-flow, an optical signal is produced and observed during a reaction, while in quench flow, the reaction is stopped by a quenching solution and the reaction mixture is analyzed by chemical methods.

The time resolution in optical stopped-flow experiments is typically in the millisecond time range; sub-millisecond resolution can be achieved by using specially designed mixers. In optical experiments using pulsed-flow or continuous-flow methods a time resolution in the microsecond range can be achieved. Continuous-flow measurements can achieve shorter dead times compared to stopped-flow, but this comes at the expense of sample economy. For a very rapid reaction that is complete within the mixing time of the stopped-flow instrument, the majority and indeed the entire kinetic time course may be lost. Some rapid reactions can be followed at lower temperature, lower concentration, or different pH. For example, if the reactions are too rapid to allow measurement of rate constants under pseudo-first-order conditions using the stopped-flow technique, the rate constants can be measured under second-order conditions; in order to measure such high rate constants on the stopped-flow instrument, second-order reaction conditions and low concentrations of both reaction partners may be selected to obtain conditions where the reaction is slower than the dead time of the stopped-flow instrument. Obviously, lower concentrations also reduce the signal intensity.

3.14.2 *Sample Preparation*

Sample preparation is critical to the success of any spectrophotometric experiment whether using absorbance or fluorescence detection systems. Even the rapid mixing of two samples of buffer in a sensitive instrument can result in what appears to be a reaction curve. This may be caused by simple effects such as the rapid compression and decompression of an air bubble in the flow path, the mixing of two solutions at different temperatures or the effect of the stopping process upon small dust particles present in the solution. Therefore it is essential that solutions be prepared thoroughly before use. Sometimes it is necessary to degas buffers to remove dissolved air that may otherwise come out of solution following rapid decompression of the reaction solutions. In practice, it is important to ensure that there are no air bubbles observed in the drive syringes before triggering, as these bubbles lead to optical artefacts. If the air bubbles produce meaningless data, it is wasteful for small or expensive samples.

3.14.3 *Selecting the Wavelength*

If one is to use the stopped-flow apparatus in the absorbance mode it is important to know the spectra of the starting reactants and of the final products in order to select the best wavelength at which to collect kinetic data. This wavelength is generally the one where the absorbance change is greatest on going from reactants to products. This may not always be the case, and one must sometimes be prepared to work at wavelengths away from the peak in the difference spectrum in order to work in regions of the spectrum where the apparatus is more sensitive.

3.14.4 *Anaerobic Experiments*

For oxygen-sensitive systems, anaerobic stopped-flow techniques are required. The anaerobic kit is available from some stopped-flow companies. Two principal strategies are commonly used: either solutions and instruments are cleansed of oxygen and manipulated in a way that excludes oxygen from the experiment, or the instrument and all solutions are kept in an anaerobic chamber.

3.15 Conclusions

In summary, the simple but versatile stopped-flow technique, coupled with optical detection (typically absorbance, fluorescence, or CD), has long been the primary source of kinetic insight into fast reactions. A major strength of stopped-flow methods is that they can be readily combined with a wide range of detection methods. As the need to understand molecular mechanisms increases, stopped-flow methods will continue to play an important role.

4 ABBREVIATIONS AND ACRONYMS

CD = circular dichroism; DCPIP = 2, 6-dichlorophenolindophenol; EPR = electron paramagnetic resonance; ESI-MS = electrospray ionization mass spectrometry; FTIR = Fourier transform infrared; FRET = fluorescence resonant energy transfer; 5′-GMP = guanosine-5′-monophosphate; L-Met = L-methionine; NAAD = nicotinic acid adenine dinucleotide; MS = mass spectrometry; NMR = nuclear magnetic resonance; PEEK = polyetheretherketone; SF = stopped-flow; SVD = singular value decomposition; tu = thiourea.

5 FURTHER READING

C. J. Bernasconi, ‘Relaxation Kinetics’, Academic Press, New York, 1976. Information on pseudo-first-order conditions and analysis with exponential functions.

G. Golub and C. Vanloan, ‘Matrix computations’, John Hopkins University Press, Baltimore, 1983.

M. G. Gore, ‘Spectrophotometry and Spectrofluorimetry: A Practical Approach’, Oxford University Press, Oxford, New York, 2000. Basic information on spectrophotometry, spectrofluorimetry, and circular dichrosim.

E. R. Henry and J. Hofrichter, *Meth. Enzymol.*, 1992, **210**, 129. Information and examples for singular value decomposition and global analysis.

K. A. Johnson, ‘Kinetic Analysis of Macromolecules’, Oxford University Press, Oxford, New York, 2003.

M. Maeder and A. D. Zuberbuhler, *Anal. Chem.*, 1990, **62**, 2220.

R. I. Shrager and R. W. Hendler, *Anal. Chem.*, 1982, **54**, 1147.

Z. G. Szabó, in ‘The Theory of Kinetics’, eds. C. H. Bamford and C. F. H. Tipper, Elsevier, New York, 1969. Basic information about kinetics.

M. L. Tobe and J. Burgess, ‘Inorganic Reaction Mechanisms’, Addison-Wesley-Longman Inc., Essex, 1999. How do you calculate kinetic parameters? How do activation parameters support the operation of an associative mechanism? The answers are in this article. Information about activation parameters is provided.

6 REFERENCES

1. H. Hartridge and F. J. W. Roughton, *Proc. R. Soc. London*, 1923, **A104**, 376.
2. B. Chance, E. N. Harvey, F. Johnson and G. Millikan, *J. Cell. Comp. Physiol.*, 1940, **15**, 195.
3. V. V. Smirnov and J. P. Roth, *J. Am. Chem. Soc.*, 2006, **128**, 3683.
4. T. Osako, S. Nagatomo, Y. Tachi, T. Kitagawa and S. Itoh, *Angew. Chem., Int. Ed. Engl.*, 2002, **41**, 4325.
5. I. Ivanović-Burmazović, M. S. A. Hamza and R. van Eldik, *Inorg. Chem.*, 2006, **45**, 1575.
6. A. Brausam and R. van Eldik, *Inorg. Chem.*, 2004, **43**, 5351.
7. N. Summa, W. Schiessl, R. Puchta, N. van Eikema Hommes and R. van Eldik, *Inorg. Chem.*, 2006, **45**, 2948.
8. J. Jee, S. Eigler, F. Hampel, N. Jux, M. Wolak, A. Zahl, G. Stochel and R. van Eldik, *Inorg. Chem.*, 2005, **44**, 7717.
9. F. Cuenot, M. Meyer, E. Espinosa and R. Guilard, *Inorg. Chem.*, 2005, **44**, 7895.
10. J. S. Nicoson, L. Wang, R. H. Becker, K. E. Huff Hartz, C. E. Muller and D. W. Margerum, *Inorg. Chem.*, 2002, **41**, 2975.
11. J. J. Barnett, M. L. McKee and D. M. Stanbury, *Inorg. Chem.*, 2004, **43**, 5021.

12. R. Y. Wang and Y. T. Lu, *Spectrochim. Acta, Part A*, 2005, **61**, 791.
13. S. Herold and F. Boccini, *Inorg. Chem.*, 2006, **45**, 6933.
14. M. Zhao, D. Song and S. J. Lippard, *Inorg. Chem.*, 2006, **45**, 6323.
15. Z. Cui, A. J. Dunford, M. C. Durrant, R. A. Henderson and B. E. Smith, *Inorg. Chem.*, 2003, **42**, 6252.
16. M. Weitzer, M. Schatz, F. Hampel, F. W. Heinemann and S. Schindler, *J. Chem. Soc., Dalton Trans.*, 2002, **5**, 686.
17. C. X. Zhang, S. Kaderli, M. Costas, E. Kim, Y. Neuhold, K. D. Karlin and A. D. Zuberbühler, *Inorg. Chem.*, 2003, **42**, 1807.
18. J. A. Bailey, C. A. James and W. H. Woodruff, *Biochem. Biophys. Res. Commun.*, 1996, **220**, 1055.
19. S. Marchal, A. C. F. Gorren, K. K. Andersson and R. Lange, *Biochem. Biophys. Res. Commun.*, 2005, **338**, 529.
20. H. Boukhalfa, D. S. Anderson, T. A. Mietzner and A. L. Crumbliss, *J. Biol. Inorg. Chem.*, 2003, **8**, 881.
21. F. Bou-Abdallah, G. Zhao, H. R. Mayne, P. Arosio and N. D. Chasteen, *J. Am. Chem. Soc.*, 2005, **127**, 3885.
22. Y. Han, C. Harlan, P. Stoessel, B. J. Frost, J. R. Norton, S. Miller, B. Bridgewater and Q. Xu, *Inorg. Chem.*, 2001, **40**, 2942.
23. Q. Dang and C. Frieden, *Trends Biochem. Sci.*, 1997, **22**, 317.
24. M. Dlugosz, E. Bojarska and J. M. Antosiewicz, *J. Biochem. Biophys. Methods*, 2002, **51**, 179.
25. S. Ueda, M. Oda, S. Imamura and M. Ohnishi, *Eur. J. Biochem.*, 2004, **271**, 1774.
26. A. Tepper, L. Bubacco and G. W. Canters, *J. Biol. Chem.*, 2004, **279**, 13425.
27. M. Nakao, K. Maki, M. Arai, T. Koshiba, K. Nitta and K. Kuwajima, *Biochemistry*, 2005, **44**, 6685.
28. A. Sienkiewicz, A. daCosta Ferreira, B. Danner and C. P. Scholes, *J. Magn. Reson.*, 1999, **136**, 137.
29. V. M. Grigoryants, A. V. Veselov and C. P. Scholes, *Biophys. J.*, 2000, **78**, 2702.
30. N. Klimes, G. Lassmann and B. Ebert, *J. Magn. Reson.*, 1980, **37**, 53.
31. G. Lassmann, P. P. Schmidt and W. Lubitz, *J. Magn. Reson.*, 2005, **172**, 312.
32. S. J. George, G. A. Ashby, C. Wharton and R. N. F. Thorneley, *J. Am. Chem. Soc.*, 1997, **119**, 6450.
33. S. Kurkin, S. J. George, R. N. F. Thorneley and S. P. J. Albracht, *Biochemistry*, 2004, **43**, 6820.
34. H. Fabian and D. Naumann, *Methods*, 2004, **34**, 28.
35. T. Rennert, A. Pohlmeier and T. Mansfeldt, *Environ. Sci. Technol.*, 2005, **39**, 821.
36. P. C. A. Barreleiro, R. P. May and B. Lindman, *Faraday Discuss.*, 2002, **122**, 191.
37. C. D. Downey, J. L. Fiore, C. D. Stoddard, J. H. Hodak, D. J. Nesbitt and A. Pardi, *Biochemistry*, 2006, **45**, 3664.
38. D. A. Hiller, A. M. Rodriguez and J. J. Perona, *J. Mol. Biol.*, 2005, **354**, 121.

Resonance Raman Spectroscopy

Roman S. Czernuszewicz & Marzena B. Zaczek
University of Houston, Houston, TX, USA

Method Summary	1
1 Introduction	1
2 Technical Background	2
3 Applications	15
4 Further Reading	33
5 References	34

METHOD SUMMARY

Acronyms, synonyms

- Resonance Raman (RR)
- Resonance Raman effect (RRE)
- Resonance Raman scattering (RRS)

Measured physical quantities

- Intensity of inelastically (Raman) scattered photons (i) as a function of the wavenumber separation (Raman shift) from the elastically (Rayleigh) scattered photons and (ii) as a function of the exciting radiation wavelengths (three-dimensional spectrum).

Information available

- Vibrational frequencies of the chromophore in resonance with incident frequency.
- Metal coordination geometry and ligand environment via analysis of vibrational frequencies.
- Metal−ligand bond strengths via analysis of vibrational frequencies.
- Electronic assignments via resonance excitation profiles (REPs).

Information NOT available, limitations

- Not useful for nonchromophoric metal sites.
- Insensitive to magnetic properties for metal centers, e.g., Zn^{2+}.
- Cannot be used for absolute quantitation of metal centers.

Examples of questions that can be answered

- What are the spin state, oxidation state, and axial ligation of this heme?
- What is the effect of this substrate/inhibitor/mutation on this metal coordination sphere?
- What type of Fe–S cluster is this?
- What is the Fe–O–Fe bond angle in this diiron center?

Major advantages

- Extremely sensitive to minor structural and electronic changes at the active site.
- Selective determination of the vibrational properties of individual chromophores possible in proteins with multiple chromophoric prosthetic groups.
- Can monitor kinetics of changes at the metal site down to the femtosecond timescale using time-resolved techniques.
- Requires minuscule amount of material for low-temperature studies (∼10 µl).
- Can be used at room temperature or low temperature with (frozen) solutions, solids, or single crystals.

Major disadvantages

- Fluorescence or traces of fluorescent impurities can prevent acquisition of RR spectra.
- Meaningful vibrational analysis requires extensive isotope substitution data.
- The factors controlling the extent of resonance enhancement of discrete vibrational modes are generally not well understood.

Sample constraints

- Requires at least 10 µl of pure protein (∼1 mM).

1 INTRODUCTION

Resonance Raman (RR) spectroscopy is a powerful and versatile technique for the study of both vibrational and electronic structures of chromophoric molecular systems. RR spectra are obtained by irradiation of the sample with a monochromatic light source whose energy is close to that of an electric-dipole-allowed electronic absorption band. Most of the Raman bands are attenuated by the absorption, but some bands may be greatly enhanced. This effect arises from a coupling of the electronic and vibrational transitions, and the vibrational modes that do show enhancement are localized on the chromophore, that is, on the group of atoms that give rise to the electronic transition.

Early RR spectra[1,2] indicated that only one allowed electronic transition (the resonant one) was responsible for the strongly enhanced intensity of the Raman scattering with excitation lines in the visible or near-ultraviolet region. Classical examples of these are the RR spectra of such inorganic species as MnO_4^-, CrO_4^{2-}, TiI_4, SnI_4, $Mo_2Cl_8^{4-}$, etc.[1] All of the above are characterized by an enormous enhancement of the intensity of one or more totally symmetric vibrational modes, together with an appearance of a long series of overtone bands (usually only one of the totally symmetric modes). The RR spectroscopic studies of the $Mo_2Cl_8^{4-}$ ion[3,4] had verified the close relationship between the electronic transition and the vibrational mode to be resonance enhanced.

This ion exhibits an intense absorption band at ∼525 nm, which arises from the allowed $\delta \rightarrow \delta^*$ charge-transfer (CT) transition involving excitation of a δ-electron of the quadruple Mo–Mo bond.[5] Thus, it is not surprising that of the three totally symmetric fundamentals, ν(MoMo), ν(MoCl), and δ(ClMoCl), it was only the ν(MoMo) stretch that showed strong RR activity in the spectrum taken with excitation corresponding to the $\delta \rightarrow \delta^*$ CT transition. Similar RR spectra obtained from other metal–metal bonded $M_2X_8{}^{n-}$ ions[6] have led to the correction of their electronic spectra assignments in the visible region.

The advantage of selective enhancement has quickly made RR spectroscopy a favorite method for the study of relatively large molecules such as heme proteins,[7–14] whose chromophoric center is an iron porphyrin complex (*see* ***Iron Porphyrin Chemistry***). Excitations in the visible and near-ultraviolet region have produced relatively simple Raman spectra, because only the vibrations associated with the heme chromophore are resonance enhanced, but the vibrations of the surrounding polypeptide chains are not. Among those enhanced, the in-plane stretching vibrations of the porphyrin ring (1000–1700 cm^{-1}) showed the largest increase in intensity due to interactions with the $\pi \rightarrow \pi^*$ allowed electronic transitions (400–600 nm), which are also polarized in the porphyrin plane. There was further differentiation of this set, with bands enhanced depending upon whether the excitation wavelength was tuned to the near-UV (Soret) or visible bands (α and β). The RR spectra obtained by using excitation lines with $\lambda_{ex} < 500$ nm, i.e., with lines approaching the energy of the Soret band, were dominated by bands attributable to totally symmetric vibrations. On the other hand, such vibrations were not observed when $\lambda_{ex} > 500$ nm were used (α–β region). Instead, bands attributable to nontotally symmetric vibrations were strongly enhanced. This differential enhancement of the Raman bands in different scattering regimes of heme proteins is the first reported example of more complex resonance behavior under multiple resonant state conditions.[7–10] It attracted the attention of theorists and inspired the development of the vibronic theory of RR scattering (*vide infra*).

Progress in the field of Raman and RR spectroscopy has been heavily dependent on laser technology. The advent of accessible and relatively inexpensive laser sources in the early 1960s has caused a revolution in Raman techniques, by largely displacing the traditional mercury discharge lamp as a Raman excitation source. Before lasers were available, the process of obtaining a good quality Raman spectrum of anything but the most straightforward molecular systems involved as much art as science, required about 10–20 ml of sample, and was often a very time-consuming operation. While important early investigations of resonance enhancement were carried out,[15] highly colored materials could not be studied. The laser has changed this situation dramatically by providing an intense directional line source. In fact, the laser is almost ideal as a Raman excitation source; it gives a very narrow, highly monochromatic beam of intense radiation, which can be focused very precisely into a small sample under a variety of flexible sampling geometries.[16–18] The sample can be moved rapidly through the laser beam to minimize complications due to local heating or photochemistry. In addition to the development of laser technology, the introduction of extremely sensitive phototubes and later diode array transducers enabled Raman and RR spectra to be recorded photoelectrically rather than photographically, with consequent enormous saving in recording time. Further, high-quality double and triple monochromators, spectrographs, cutoff filters, and Fourier-transform Raman interferometers of high efficiency have been developed,[19] so that it is now possible to scan to within a few wavenumbers of the exciting laser line and acquire excellent quality Raman and RR spectra of any material in any physical state.

Technical advances continue to grow, and applications will certainly multiply. The purpose of this article is to lay out the principles behind RR spectroscopy and to illustrate them with examples from recent research, especially in the context of bioinorganic chemistry.

2 TECHNICAL BACKGROUND

2.1 IR and Raman Basics

Molecular vibrational frequencies (10^{-13}–10^{-14} Hz) lie in the infrared (IR) region of the electromagnetic spectrum. Transitions to vibrationally excited states can therefore be probed by direct absorption of IR photons (IR spectroscopy) (*see* ***Vibrational Spectroscopy***).[20–22] All molecules except homonuclear diatomic molecules (e.g., H_2, O_2, N_2, and the halogens) absorb IR light. In IR spectroscopy the vibrational frequency is observed as a peak in the absorption spectrum at the absolute frequency of the absorbed IR radiation. Alternatively, inelastic collisions of the sample molecules with the quanta of light in the ultraviolet, visible, or near-infrared regions can induce the same vibrational transition via an inelastic light scattering process. This Raman process is shown diagrammatically in relation to IR absorption in Figure 1. All molecules including the homonuclear diatomics are Raman scatterers. In Raman spectroscopy, the exciting photon has much higher frequency and energy than the molecular vibration. As a result of the inelastic collision, part of the incident photon energy $h\nu_0$, equal to the vibrational quantum, $\upsilon \rightarrow \upsilon'$, is retained by the vibrating molecule, while the scattered photon emerges with lower frequency, $\nu_0 - \nu_{\upsilon,\upsilon'}$, and energy $h(\nu_0 - \nu_{\upsilon,\upsilon'})$ (Stokes scattered radiation). The molecular vibration is therefore encoded in the Raman spectrum as the frequency separation between the incident photon (or the elastic scattering Rayleigh peak) and the scattered photon (Figure 2). A Raman experiment requires illuminating the sample with *monochromatic* radiation and

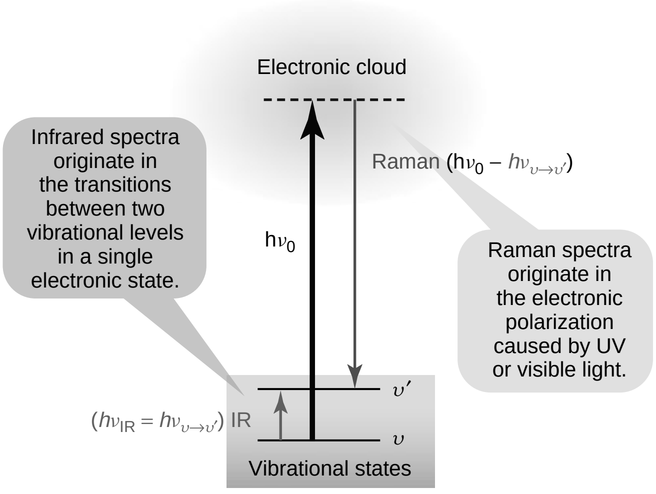
Electronic cloud
Infrared spectra originate in the transitions between two vibrational levels in a single electronic state.
Raman ($h\nu_0 - h\nu_{\upsilon\rightarrow\upsilon'}$)
$h\nu_0$
Raman spectra originate in the electronic polarization caused by UV or visible light.
υ'
($h\nu_{IR} = h\nu_{\upsilon\rightarrow\upsilon'}$) IR
υ
Vibrational states

Figure 1 Origin of infrared (IR) absorption and Raman scattering spectra

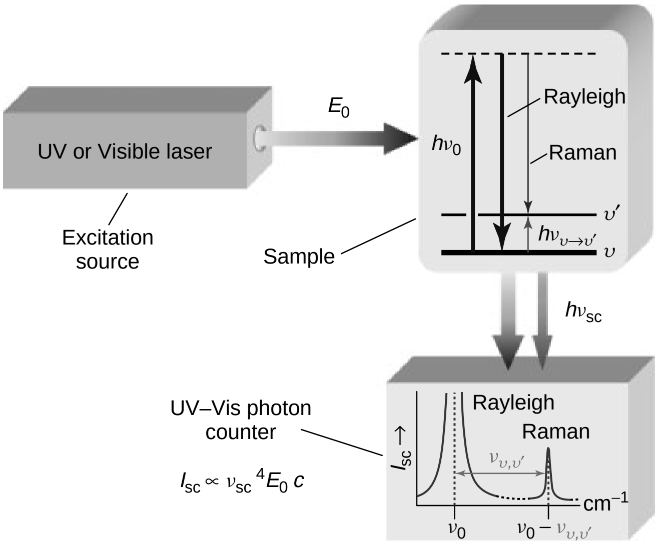
UV or Visible laser
E_0
$h\nu_0$
Rayleigh
Raman
υ'
$h\nu_{\upsilon\rightarrow\upsilon'}$
υ
Excitation source
Sample
$h\nu_{sc}$
UV–Vis photon counter
$I_{sc} \propto \nu_{sc}{}^4 E_0\, c$
Rayleigh
Raman
$I_{sc} \rightarrow$
$\nu_{\upsilon,\upsilon'}$
cm^{-1}
ν_0
$\nu_0 - \nu_{\upsilon,\upsilon'}$

Figure 2 Measurement of scattered light at 90°: The excitation radiation for the Raman experiment must be monochromatic. Scattering of UV or visible photons produces an intense Rayleigh peak and weaker Raman peaks, displaced from the Rayleigh by $\nu_{\upsilon,\upsilon'}$. These arise because of energy transfer from the incident photon $h\nu_0$ to the molecule, which is raised to an excited vibrational level. The readout signal is proportional to the flux of the scattered light (I_{sc}), which is directly related to the fourth power of the scattered frequency (ν_{sc}), irradiance of the source (E_0), and the concentration of scattering molecules

analyzing the polychromatic radiation scattered by the sample. In practice, a monochromatic radiation of any convenient frequency from the laser is shone on to the sample and the absolute radiant power of scattering can be measured at any convenient angle with respect to the excitation beam; 90° collection geometry is shown in Figure 2.

If the incident frequency is offset to zero, then Raman peaks occur at the same frequencies as peaks in the IR spectrum. Different selection rules, however, govern the intensity of the IR- and Raman-active vibrational modes. Absorption of IR photons requires a change in the dipole moment during molecular vibration, and IR band intensity $I_{IR} \propto (\partial\mu/\partial Q_k)^2$, where μ is the dipole moment and Q_k is the vibrational coordinate. Raman scattering, on the other hand, depends on the variation of the polarizability (or induced dipole moment) of the molecule, α, during vibration, and Raman band intensity $I_R \propto (\partial\alpha/\partial Q_k)^2$. Hence, the vibrations of polar bonds such as O–H, N–H, S–H, and C=O are more readily observed in the IR spectrum, while vibrations of less polar bonds are better seen in the Raman spectrum (C≡C, C=C, P=S, S–S, and C–S). Moreover, totally symmetric bond stretching vibrations, which preserve the symmetry of the molecule and produce large polarizability changes, usually dominate the Raman spectra, whereas antisymmetric stretching and deformation modes, which distort the molecule and involve large dipole moment changes, tend to be more intense in IR spectra. This makes Raman spectroscopy more favorable for the study of biological materials, because there is considerably less spectral interference from the deformation modes associated with the H-bond network of water molecules; these are often dominant features in the IR spectra of aqueous samples.[20] The IR spectra of liquid H_2O and D_2O are shown in Figure 3. The Raman spectra of liquid and frozen water (H_2O, D_2O) are shown in Figure 4.

For highly symmetrical molecules and ions such as $TiCl_4$ (T_d), C_6H_6 (D_{6h}), and $PtCl_4{}^{2-}$ (D_{4h}), both IR and Raman spectroscopies are required to obtain the full set of vibrational frequencies. If a molecule or an ion possesses a center of inversion, there is a *rule of mutual exclusion*; no fundamental vibration that is active in the IR absorption can be active in the Raman scattering, and no fundamental vibration that is active

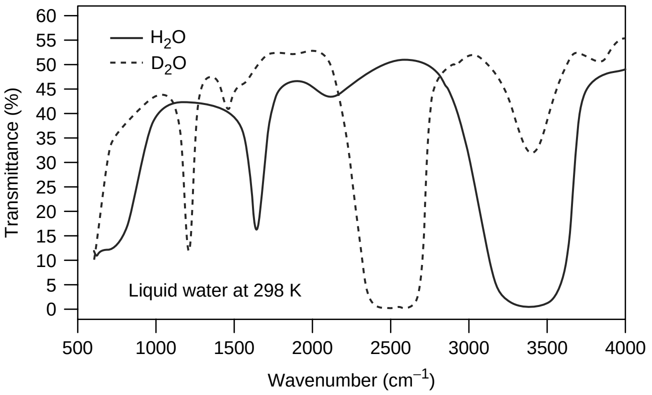

Figure 3 Infrared spectra of neat liquid H_2O (solid line) and D_2O (dashed line)

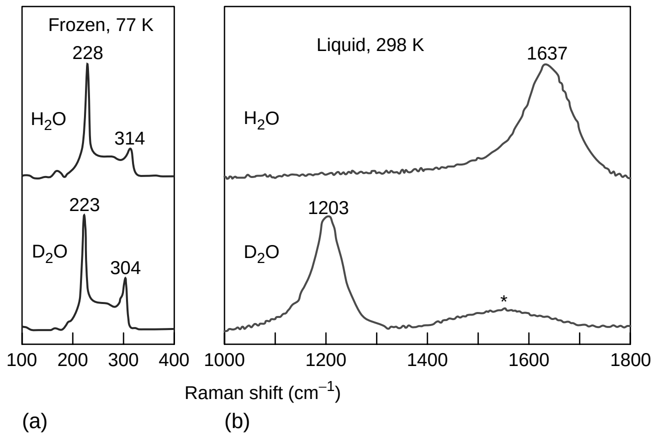

Figure 4 Raman spectra of H_2O and D_2O: (a) as ice at 77 K and (b) as neat liquid at 298 K

in the Raman scattering can be active in the IR absorption. Thus, IR absorption and Raman scattering are complementary and overlapping methods for investigating the vibrations of molecules. Table 1 summarizes the basic aspects of IR and Raman spectroscopy.

2.2 The Raman Effect

The Raman effect – first predicted from theoretical considerations by A. Smekal (1923) and H. A. Kramers and W. Heisenberg (1924) – is a *light scattering* phenomenon with a change of frequency.[23,24] When monochromatic light of frequency ν_0 passes through molecular matter, much of the light continues in its original direction, but a small fraction ($\sim 10^{-3}$) is scattered in other directions (Figure 5). Most of the scattered light emerges at the same frequency as the incident light; this is *elastic* or *Rayleigh scattering*; except for being deflected, the photons neither lose nor gain energy in their collisions with molecules. Rayleigh scattering carries no information about molecular vibrational transitions. A few collisions, however, are *inelastic*. A net transfer of quantized energy ($\Delta E = h\nu_k$) occurs and some scattered light ($\sim 10^{-6}$) obtains new modified frequencies ($\nu_0 \pm \nu_k$). The frequency changes are equal to the frequencies associated with transitions between vibrational (υ_k) or, less frequently, rotational or electronic levels of the system. These two forms of light scattering with change of frequency were first observed by C. V. Raman and K. S. Krishnan in liquids,[25,26] and independently by G. Landsberg and L. Mandelstam in

Table 1 Basic characteristics of infrared (IR) and Raman spectroscopy[a]

Parameter	Infrared spectroscopy	Raman spectroscopy
Spectroscopic phenomenon	Absorption of light: $h\nu_{\mathrm{IR}} = \Delta E_{\mathrm{vibr}}$	Inelastic scattering of light: $h\nu_{\mathrm{ex}} - h\nu_{\mathrm{sc}} = \Delta E_{\mathrm{vibr}}$
Allowed transition	$\Delta\upsilon = +1, +2, +3, \ldots$	$\Delta\upsilon = \pm 1, \pm 2, \pm 3, \ldots$ (transitions for $\Delta\upsilon = +2, +3, \ldots$, i.e., overtones are considerably less conspicuous than in IR)
Excitation	Polychromatic IR radiation	Monochromatic radiation (ν_{ex}) in the UV, visible, or near IR
Molecular origin	Dipole moment: $\mu = q\boldsymbol{r}$	Induced dipole moment: $\boldsymbol{P} = \alpha\boldsymbol{E}$
Requirement for vibrational activity	Change in dipole moment during vibration: $(\partial\mu/\partial Q_k)0 \neq 0$	Change in polarizability during vibration: $(\partial\alpha/\partial Q_k)0 \neq 0$
Band intensity	${I_{\mathrm{IR}}}^{1/2} \propto (\partial\mu/\partial Q_k)0$	${I_{\mathrm{R}}}^{1/2} \propto (\partial\alpha/\partial Q_k)_0$
Frequency measurement	Absolute: $\nu_{\mathrm{vibr}} = \nu_{\mathrm{IR}}$	Relative to the excitation frequency: $\nu_{\mathrm{vibr}} = \nu_{\mathrm{ex}} - \nu_{\mathrm{sc}}$
Readout signal	Comparative: transmittance: ($T = \Phi_{\mathrm{s}}/\Phi_{\mathrm{r}}$) or absorbance ($A = -\log T$)	Absolute: radiant power or intensity of scattered radiation
Spectral plot	Linear in %T or logarithmic in A versus wavenumber (cm^{-1})	Linear: Raman intensity versus wavenumber shift (cm^{-1})
Dominant spectral feature	Vibrations destroying molecular symmetry: antisymmetric stretching and deformation modes	Vibrations preserving molecular symmetry: symmetric stretching modes
Inactive molecule	Homonuclear diatomics	None
Centrosymmetric molecule	Only ‘‘*u*’’-symmetry modes active	Only ‘‘*g*’’-symmetry modes active
Medium	Water is a strong absorber and is a poor solvent for IR studies	Water is a weak scatterer and is a good solvent for Raman studies

[a] h, Planck's constant; ΔE_{vibr}, energy difference of vibrational levels; ν, photon frequency; $\Delta\upsilon$, change in vibrational quantum number; q, charge; $\boldsymbol{r}$, charge spacing; α, molecular polarizability; $\boldsymbol{E}$, electric field; Φ_{s} and Φ_{s}, radiant powers transmitted by the sample and reference cells, respectively; Q_k, vibrational normal coordinate ($k \leqslant 3N - 6$); ‘‘*g*’’ and ‘‘*u*’’, normal modes of vibration symmetric (*gerade*) and antisymmetric (*ungerade*) with respect to the molecular center of inversion.

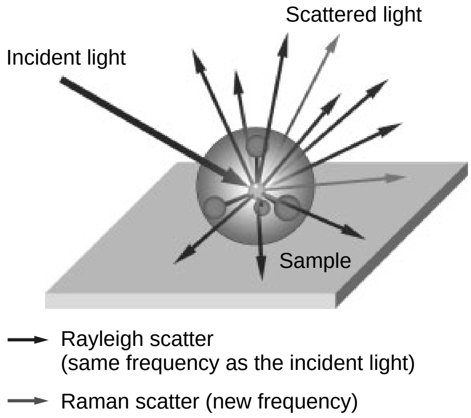
Scattered light
Incident light
Sample
Rayleigh scatter
(same frequency as the incident light)
Raman scatter (new frequency)

Figure 5 Principle of Rayleigh (elastic) and Raman (inelastic) scattering

quartz**[27]** in 1928, and are now called *Raman scattering*. C. V. Raman received the Nobel Prize in 1930 for his work on the scattering of light. In 1998, the Raman effect was designated an ACS National Historical Chemical Landmark in recognition of its significance as a tool for analyzing the composition of liquids, gases, and solids. Radiation scattered with a frequency lower than that of the incident light (i.e., $\nu_0 - \nu_k$) is referred to as *Stokes Raman scattering*, while that at the higher frequency (i.e., $\nu_0 + \nu_k$) is called *anti-Stokes Raman scattering*. The magnitude of the frequency shift from the incident radiation provides a measure of the vibrational energy level spacing. In practice, the former spectral region is used for this purpose because the Stokes Raman scattering is *always* more intense than the anti-Stokes Raman at normal temperatures.

The transfer of energy results from the perturbation of the electronic wavefunction of the molecule by the rapidly changing electric field of the photon. The wavefunction of the perturbed system can be expressed as a linear combination of all possible wavefunctions of the unperturbed molecule, with time-dependent coefficients. For a very short time interval ($<10^{-14}$ s), the photon loses identity and becomes indistinguishable from the kinetic and potential energy of the perturbed electrons. Formally, the molecule is regarded as having attained a higher nonstationary energy level (*virtual state*); it returns to a stationary (typically vibrational) state by reemitting (scattering) a photon (Figure 6). If the molecule returns to its original stationary state, the reemitted photon has the same frequency as the incident photon (Rayleigh scattering, $\nu_{sc} = \nu_0$). However, if the final state differs from the initial state by a vibrational quantum ($h\nu_k$), the photon is reemitted with shifted frequencies (Raman scattering, $\nu_{sc} = \nu_0 \pm \nu_k$). At temperatures normally used, a decrease

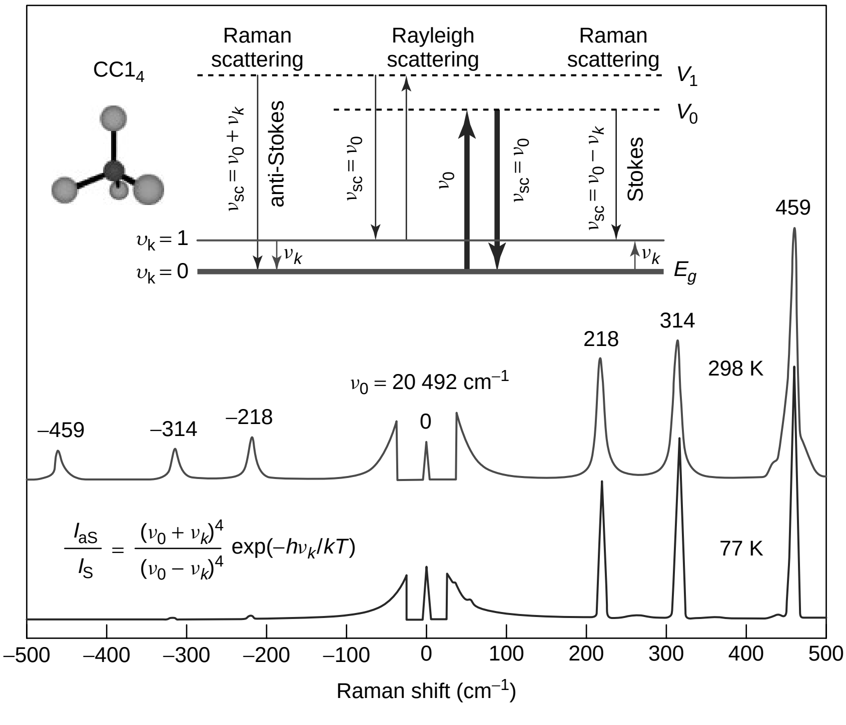

Figure 6 Energy transfer diagram illustrating Rayleigh and Raman scattering (*top*), and Raman spectra for CCl_4 excited at room (298 K) and liquid-N_2 (77 K) temperatures by Ar^+ ion laser radiation of $\lambda_0 = 488.0$ nm or $\nu_0 = 20\,492\ \mathrm{cm}^{-1}$ (*bottom*). The number above the peaks is the Raman shift, $\Delta\tilde{\nu} = \tilde{\nu}_0 - \tilde{\nu}_{sc}\ \mathrm{cm}^{-1}$. Since the fraction of molecules occupying excited states depends on the Boltzmann factor ($kT = 207\ \mathrm{cm}^{-1}$ at 298 K), the intensities of anti-Stokes bands fall off rapidly with decreasing temperature ($kT = 54\ \mathrm{cm}^{-1}$ at 77 K) and increasing vibrational frequency ν_k

in frequency (Stokes emission) is more probable because there are few thermally excited molecules. Although we can speak of a sequence of events in which the emission of a photon from the virtual state follows an absorption process, it is important to appreciate that these processes are actually simultaneous and cannot be separated in time. This means that the Rayleigh and Raman scattering are two-photon processes in which one photon is destroyed and one created at the same time (*induced secondary emission processes*).

The scattered radiation has a spectrum characteristic of the given substance, with an intense band at the incident frequency, ν_0, resulting from Rayleigh scattering, and fainter Raman bands on both sides of ν_0 at distances corresponding to the molecular vibrational frequencies, ν_k. Typical examples of such bands are seen in Figure 6, which displays the Raman spectra obtained on pure carbon tetrachloride, CCl_4, at 298 K (liquid) and 77 K (frozen liquid) upon excitation with an Ar^+ ion laser line at 488.0 nm (20 492 cm^{-1}).[28,29] The measured spectral frequencies are expressed in wavenumber shifts $\Delta\tilde{\nu}$, or *Raman shifts*, which are defined as the *difference in wavenumbers* (cm^{-1}) between the incident and scattered rays, $\Delta\tilde{\nu} = \tilde{\nu}_0 - \tilde{\nu}_{sc}$. Hence, $\Delta\tilde{\nu} = \tilde{\nu}_0 - \tilde{\nu}_0 = 0\,cm^{-1}$ for the Rayleigh peak and $\Delta\tilde{\nu} = \tilde{\nu}_0 - (\tilde{\nu}_0 \pm \tilde{\nu}_k) = \pm\tilde{\nu}_k\,cm^{-1}$ for the Raman peaks. Since Stokes transitions occur at wavenumbers $\tilde{\nu}_0 - \tilde{\nu}_k$, they exhibit *positive* Raman shifts (an *increase* of energy by the scattering system); anti-Stokes transitions occur at $\tilde{\nu}_0 + \tilde{\nu}_k$, and exhibit *negative* Raman shifts (a *decrease* of energy by the scattering system). That is, Stokes bands of CCl_4 are found at 218, 314, and 459 cm^{-1} while their anti-Stokes counterparts occur at −218, −314, and −459 cm^{-1}, regardless of the wavelength of excitation. In general, only the *fundamental* vibrational modes show up in the Raman spectrum because of the much greater probability of transitions involving the two lowest energy vibrational states ($\upsilon_k = 0$, $\upsilon'_k = 1$) of a molecule.

2.3 Requirements for Raman Scattering

In Rayleigh scattering, the sample particles, like molecules, scatter radiation *elastically* by removing radiant energy from the incident beam of (usually) UV−visible photons and instantly reemitting that energy in all directions as the molecules return to their unperturbed forms.[21] Except for undergoing a brief polarization, i.e., momentary distortions on irradiation, the scattering molecules neither gain nor lose energy in their collisions with photons. The Rayleigh light intensity increases with the size of scattering particles; it has a symmetrical and uniform angular distribution, and varies directly with the fourth power of the frequency. For a substance to Rayleigh scatter radiation, it must possess polarizable molecules or aggregates of polarizable molecules with dimensions significantly smaller ($d_m < 0.05\lambda_0$) than the wavelength of the incident radiation (λ_0). (Scattering of radiation by larger particles ($0.05\lambda_0 < d_m < \lambda_0$) is often called *Debye scattering*, while that by still larger particles ($d_m > \lambda_0$) is often termed *Mie scattering*.) Since typical molecular dimensions are on the order of nanometers, the UV−visible photons (∼200−680 nm) readily satisfy this criterion and Rayleigh scattering will always be observed in the Raman spectrum, unless it is suppressed with bandpass filters.

The Raman effect differs from Rayleigh scattering in that the molecules scatter part of the incident radiation energy *inelastically* by increasing (Stokes) or decreasing (anti-Stokes) their own (usually) vibrational energy. For a molecular vibration to Raman scatter radiation, it must (i) have a frequency considerably lower than that of the incident radiation and (ii) change the magnitude and/or direction of the *induced electric dipole moment*, or of the molecular polarizability. Excitation (for a spontaneous Raman effect) must be carried out by radiation having a frequency that is well away from any electronic absorption transitions. These criteria are easy to describe physically when we remember that light can be considered as having oscillating electric and magnetic fields and that a molecule has an electron cloud of negatively charged orbitals. *A molecule scatters electromagnetic radiation because it is polarizable*. When a fluctuating electric field $\boldsymbol{E}$ of frequency ν_0 (laser beam) $\gg \nu_k$ (vibrational frequency) strikes a molecule, it sets the electron cloud around heavy and fixed nuclei of the molecule into oscillatory motion. In its distorted form, the molecule is temporarily *polarized*, that is, it undergoes a momentary charge displacement, forming an *induced electric dipole moment* $\boldsymbol{P}$, which oscillates at the frequency, ν_0, of the incoming laser beam. However, if the oscillating dipole induced by light activates (excites) or deactivates (relaxes) a molecular vibration of frequency ν_k, the frequency of the electron cloud oscillation will change correspondingly to $\nu_0 - \nu_k$ or $\nu_0 + \nu_k$. Thus, the polarized molecule becomes an instant source of its own radiation (vibrating electrons emit radiation in all directions) by reemitting excitation energy as light of frequency $\nu_{sc} = \nu_0$ on immediately relaxing to its original stationary energy state (Rayleigh scattering) or at frequencies $\nu_{sc} = \nu_0 \pm \nu_k$ on returning to its stationary states other than the original one (Raman scattering).

The scattered intensity varies directly with the square of the induced dipole moment $\boldsymbol{P} = \alpha\boldsymbol{E}$, where α is the polarizability of the molecule, a volumetric measure of its electron cloud distortion in the path of an incident light, relative to the nuclear framework. The polarizability α is closely related to the structure and bonding properties of the molecule and is *always* nonzero; it increases with decreasing electron density, decreasing bond strength, and increasing bond length. The probability of transition for fundamentals in the Raman spectrum is proportional to the square of the polarizability gradient along the normal coordinate of the vibration, $(\partial\alpha/\partial Q_k)_0$. Accordingly, if there is no net change in polarizability when the vibration occurs, i.e., $(\partial\alpha/\partial Q_k)_0 = 0$, the intensity of a band in the Raman spectrum equals zero and the vibration is said to be Raman inactive. In contrast, the probability of transition of fundamentals in IR absorption is proportional to the square of the dipole moment gradient along the normal coordinate of the vibration, $(\partial\mu/\partial Q_k)_0$. Accordingly, if there is no change in dipole moment when the vibration occurs, i.e., $(\partial\mu/\partial Q_k)_0 = 0$, the intensity of a vibrational band in the IR spectrum equals zero and the vibration is said to be IR inactive.

2.4 Molecular Symmetry and Vibrational Activity

For a molecule that has little or no symmetry, it is usually correct to assume that all its vibrational modes are both IR and Raman active.[20,21] However, when the molecule has considerable symmetry, it is not always easy to picture whether the molecular dipole moment and polarizability will change during the vibration, especially for large and complex molecules. Fortunately, we can easily solve this problem by resorting to simple symmetry selection rules. The molecular vibration is active in IR absorption if it belongs to the same representation as at least one of the dipole moment components (μ_x, μ_y, μ_z) or, since the dipole moment is a vector, as one of the Cartesian coordinates (x, y, z). In contrast, the molecular vibration is active in Raman scattering if it belongs to the same representation as at least one of the polarizability components (α_{xx}, α_{xy}, etc.) or, since the polarizability is a tensor, as one of the binary products of Cartesian coordinates (x^2, xy, etc.) or their linear combinations ($x^2 + y^2$, $x^2 - y^2$, etc.). The symmetry species of the Cartesian coordinates and their binary products are customarily given in the point group *character tables*. IR and Raman activities for vibrational modes of any symmetry species can therefore be simply read off from these tables. Figure 7 is an example of a character table for the point group C_{4v}. It follows from that table that the symmetry species (irreducible representations) $\Gamma(z) = A_1$ and $\Gamma(x, y) = E$, and hence fundamental vibrations of type A_1 and E are *allowed* and of type A_2, B_1, and B_2 are *forbidden* in the IR spectrum for any molecule that belongs to the C_{4v} point group. The vibrations of type A_2 are also *forbidden* in the Raman spectrum of C_{4v} molecules but those of type A_1, B_1, B_2, and E are all Raman *allowed* because $\Gamma(x^2 + y^2, x^2) = A_1$, $\Gamma(x^2 - y^2) = B_1$, $\Gamma(xy) = B_2$, and $\Gamma(xz, yz) = E$ in C_{4v} point group.

2.5 Depolarization Ratios and Symmetry of Vibrations

Useful information on the scattering process and on the symmetry of the vibration involved can be obtained by measuring the depolarization ratio, ρ, of a Raman band.[1,21,24,30] The incident and scattered photons in Raman scattering both involve a polarization (plane in which the radiation vibrates), and the polarization of the scattered light is related to but not necessarily the same as that of the incident light, even if the sample molecules are randomly oriented. If the incident radiation is linearly (or plane) polarized, as it is with a laser source, the Raman scattered light can be polarized to various degrees that depend on the nature of the active vibration. The depolarization ratio is given by $\rho = I_\perp/I_\parallel$, where $I_\perp$ and $I_\parallel$ are the intensities of Raman light that is linearly polarized perpendicular and parallel, respectively, to the polarization of the excitation radiation. Experimentally, it is obtained by inserting a polarization analyzer between the sample and the monochromator, which upon rotation by 90° passes $I_\perp$ or $I_\parallel$ (Figure 8). For totally symmetric vibrations, which by nature do preserve molecular symmetry during the motion of the nuclei, the incident beam polarization is largely maintained in the scattered light leading to small ρ values ($0 \leqslant \rho < 3/4$,

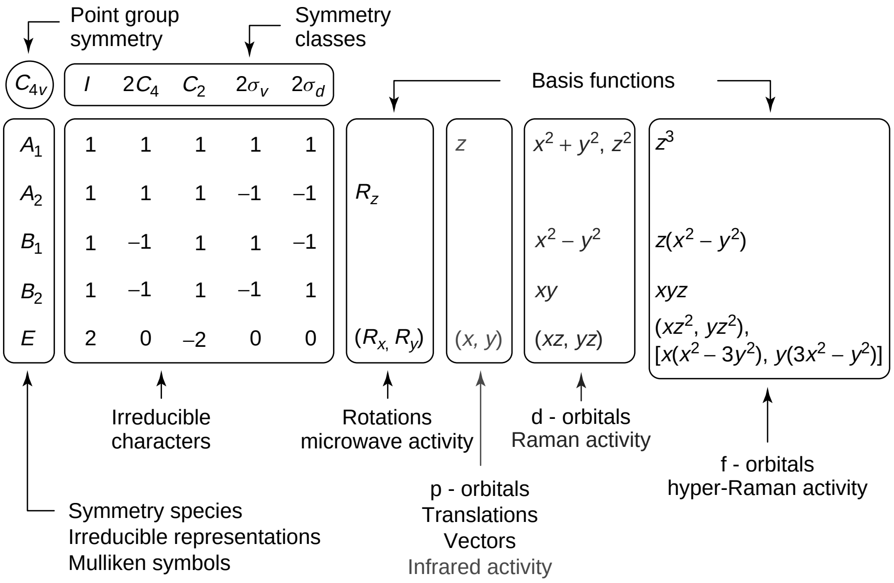

C_{4v}	I	$2C_4$	C_2	$2\sigma_v$	$2\sigma_d$				
A_1	1	1	1	1	1		z	$x^2 + y^2$, z^2	z^3
A_2	1	1	1	−1	−1	R_z			
B_1	1	−1	1	1	−1			$x^2 - y^2$	$z(x^2 - y^2)$
B_2	1	−1	1	−1	1			xy	xyz
E	2	0	−2	0	0	(R_x, R_y)	(x, y)	(xz, yz)	(xz^2, yz^2), $[x(x^2 - 3y^2), y(3x^2 - y^2)]$

Point group symmetry
Symmetry classes
Basis functions
Irreducible characters
Rotations microwave activity
d - orbitals Raman activity
f - orbitals hyper-Raman activity
p - orbitals Translations Vectors Infrared activity
Symmetry species Irreducible representations Mulliken symbols

Figure 7 The structure of the character table for the symmetry point group C_{4v}

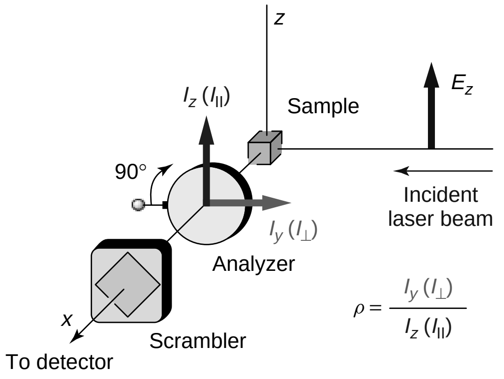

Figure 8 Schematic layout of a typical 90° Raman depolarization experiment showing the positions of the polarization analyzer and the scrambler. The analyzer may simply be a polaroid sheet, which can be rotated by 90° to allow the parallel ($\|$) and perpendicular ($\perp$) components of the scattered light to pass through to the detector. The function of a scrambler is to change linear into circular polarization of the light entering the Raman spectrometer slit in order to avoid measurement errors due to the variable spectrometer transmittance of the light polarized in different directions

polarized Raman bands). The higher the symmetry of a molecule, the closer to zero is the value of ρ. It should also be pointed out that the polarized bands are (usually) the strongest features in the Raman spectrum. On the other hand, if the vibrational motion distorts the symmetry (nontotally symmetric vibrations), a significant depolarization can occur producing depolarized Raman bands. From scattering theory, it is predicted that for such vibrations $\rho = 3/4$. In the Raman spectrum of CCl_4, shown in Figure 9, the dominant band at 459 cm^{-1} loses nearly all intensity in the perpendicular scattering ($\rho = 0.006$) and a number of weaker bands at 217, 314, 759, and 788 cm^{-1} are only slightly weakened ($\rho = 0.75$). The band at 459 cm^{-1} is therefore immediately assignable to a totally symmetric vibration of the molecule and the ones at 217, 314, 759, and 788 cm^{-1} cannot arise from totally symmetric modes.

Under resonance or near-resonance excitation conditions, however, certain nontotally symmetric modes can also give rise to anomalously ($\rho > 3/4$) or even inversely ($\rho = \infty$) polarized Raman bands.**[9]** Figure 10 depicts RR spectra of nickel(II) porphine (NiP) and indeed the strongest bands show exactly the opposite of what is observed for CCl_4 (Figure 9), i.e., the perpendicular scattered radiation ($\perp$) is dramatically more intense than that with parallel radiation ($\|$). NiP has a D_{4h} symmetry and these bands arise from the A_{2g} vibrational modes that have rotational symmetry themselves ($\Gamma(R_z) = A_{2g}$ in D_{4h} point group). Modes of this type are normally Raman forbidden, but can be activated under certain resonant excitations in the RR spectrum by vibronic mixing of excited electronic states (*vide infra*). Table 2 summarizes the ranges of values expected for the depolarization ratio for bands arising from modes of various symmetries in the off-resonance and RR spectra.**[1,30]**

The depolarization ratio in Raman scattering has no true counterpart in IR absorption. However, the dipole moment is

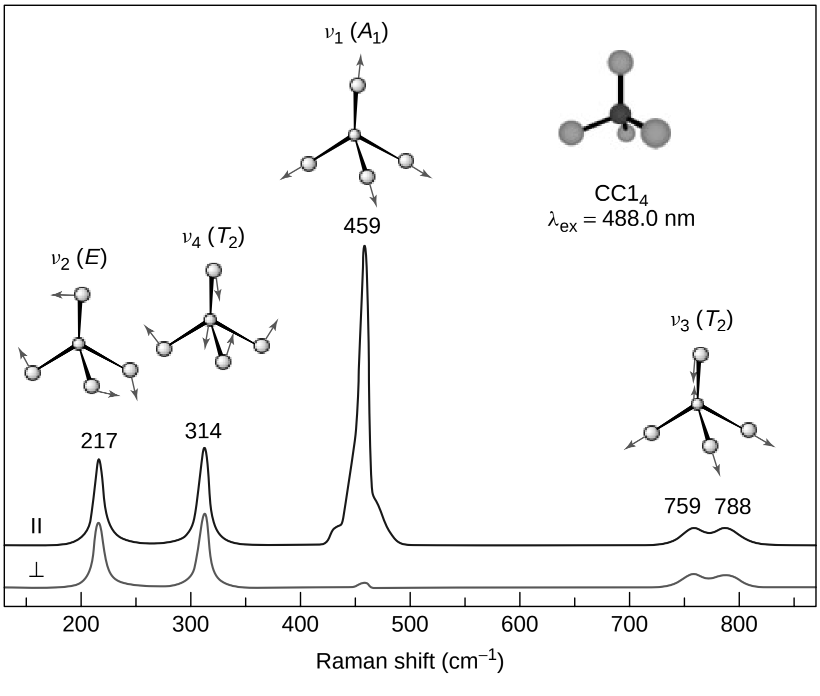

Figure 9 Parallel ($\|$) and perpendicular ($\perp$) scattered Raman spectra from liquid CCl_4 showing the polarized (ν_1) and depolarized (ν_2, ν_3, and ν_4) bands associated with totally symmetric (A_1) and nontotally symmetric (E, T_2) vibrations, respectively

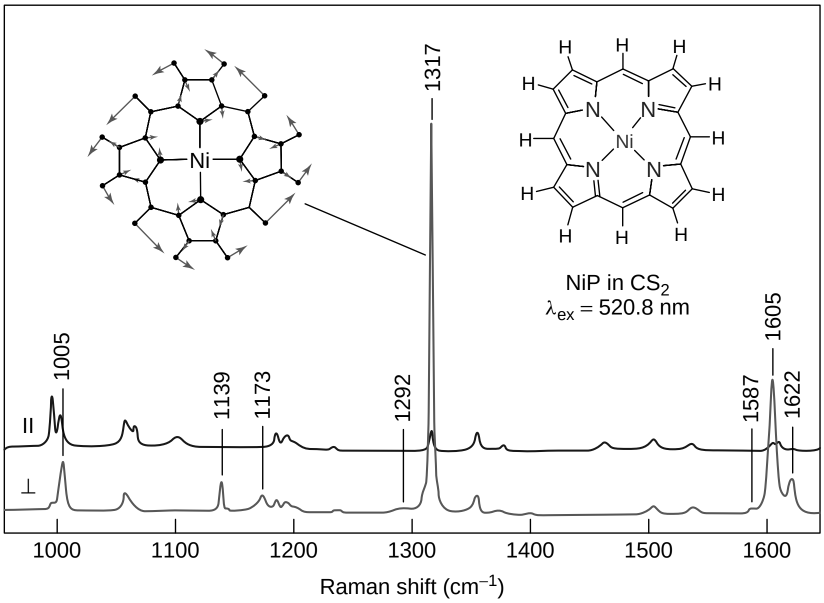

Figure 10 Parallel (||) and perpendicular (⊥) scattered resonance Raman spectra from NiP in CS_2 showing the anomalously polarized bands (labeled) associated with the ring A_{2g} vibrations

Table 2 Values of depolarization ratio for vibrational Raman bands observed in normal Raman and resonance Raman spectra

Type of Raman scattering	Vibrational band character	Polarizability tensor symmetry	Depolarization ratio
Off-resonance (all cases) and resonance (most cases)	Polarized (totally symmetric modes)	Symmetric, $\alpha_{\rho\sigma} = \alpha_{\sigma\rho}$	$0 < \rho < 3/4$
	Depolarized (nontotally symmetric modes)	Symmetric, $\alpha_{\rho\sigma} = \alpha_{\sigma\rho}$	$\rho = 3/4$
Resonance (special cases)	Anomalously polarized (nontotally symmetric modes, normally Raman forbidden)	Nonsymmetric, $\alpha_{\rho\sigma} \neq \alpha_{\sigma\rho}$	$\rho > 3/4$
	Inversely polarized (nontotally symmetric modes, normally Raman forbidden)	Antisymmetric, $\alpha_{\rho\sigma} = -\alpha_{\sigma\rho}$	$\rho = \infty$

a vector quantity, and the absorption of IR light depends on the relative orientation of the molecule and the photon electric vector. If all the molecules are aligned, as in a crystal or a stretched film, and the photon vector points along a molecular axis, e.g., z, then absorption occurs for those vibrations that displace the dipole along z. Vibrations that are purely x or y polarized would be absent. Thus, extra information about the character of the vibration is available from IR absorption spectra for oriented samples.

2.6 Enhancement of Raman Scattering

The intensity of Raman scattering depends strongly on the excitation frequency.[21,22] Figure 11 illustrates what happens if, for a given molecular system, we change excitation frequency so that it moves from the transparent region (a) to the vicinity of an allowed electronic absorption band (b)–(e). As discussed before, excitation in the transparent region of a scattering system leads to a normal (or off-resonance) Raman effect. Under this circumstance, the intensity of Raman bands is described by a ν^4 law (Figure 2), and some advantage can be taken of this dependence by using the higher frequency irradiation (e.g., the blue and green lines of the argon laser, rather than the red line of the helium–neon laser). However, when the frequency of the exciting laser line is close to (preresonance) or equal to (resonance) the frequency of an allowed electronic absorption of a molecule, as in (b) and (c), the intensities of certain Raman bands are greatly increased (up to 10^6-fold) above their off-resonance values. This happens because the polarizability, and its dependence on the molecular motions, is enhanced via the electronic transition. Not all Raman bands intensify,

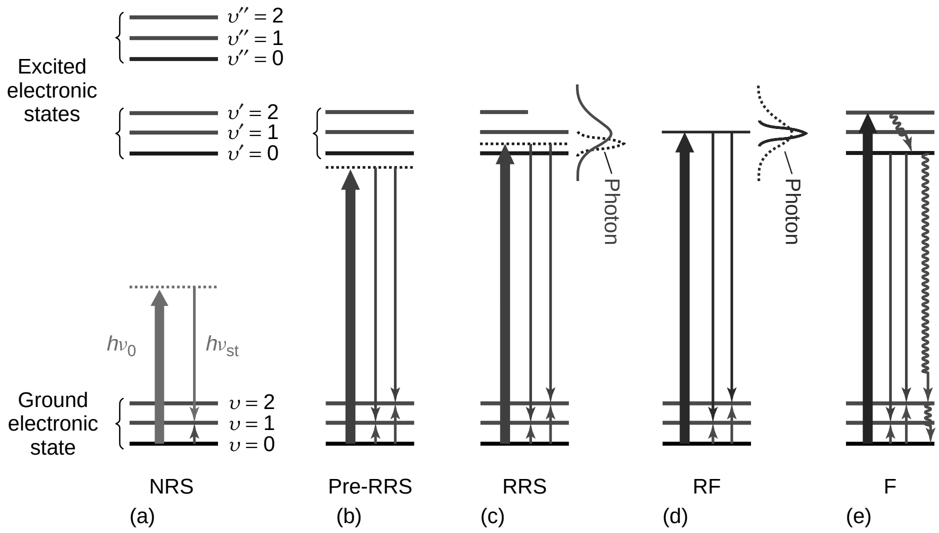

Figure 11 Diagram of Stokes transitions ($h\nu_{St}$) of Raman scattering (a)–(c) and fluorescent emission (d), (e) as a function of excitation energy ($h\nu_0$). (a) Normal Raman scattering occurs upon excitation in the transparent region of the molecule. The molecular polarizability creates a nonstationary (virtual) state to interact with $h\nu_0$, which does not resemble any particular molecular state. Many excited electronic states contribute to this state and the scattering process is nonselective in that all vibrations (usually fundamental) that can change the polarizability may be observed. (b) Preresonance Raman scattering in which $h\nu_0$ approaches the energy of an electronic transition. The interacting state is then dominated by this electronic state, which produces some enhancement of Raman scattering (10–100-fold) and possible appearance of overtones. (c) Resonance Raman scattering, in which the interacting state is dominated by a few vibronic levels in the interior of the excited electronic state. Many Raman bands are then attenuated by the absorption, but those associated with normal coordinates that can carry the molecule into its excited-state geometry may be greatly enhanced (10^3–10^6 times). (d) Resonance fluorescence occurs when $h\nu_0$ coincides with a single sharp level of the electronic manifold (small molecules in gas phase). The distinction between RRS and RF is that the RF involves actual population of the upper state (its width is smaller than that of the $h\nu_0$ pulse), the emission decaying with the excited-state lifetime, whereas RRS process is simultaneous (actually $<10^{-14}$ s) with the excitation pulse. If not in exact resonance with the upper state, only RR scattering occurs. (e) Relaxed fluorescence, in which radiational relaxation to the ground state is preceded by prior radiationless relaxation to the lowest vibrational level of the excited electronic state. This produces a red-shifted broad envelope of emission on the 10^{-6}–10^{-8} timescale

however, but only those due to vibrational transitions that couple with the electronic transition. This is illustrated in Figure 12 which shows a dramatic increase in intensity of the Cu–S(Cys) vibrational modes near 400 cm^{-1} as the excitation wavelength (647.1 nm) approaches that of the (Cys)S → Cu(II) CT electronic transition (~600 nm) in the blue copper protein, azurin (*see* ***Copper Proteins with Type 1 Sites***).**[16]** Another example of RR scattering was seen in Figure 10, where stretching modes of the porphyrin π bonds are enhanced because of their coupling with the $\pi-\pi^*$ resonant transitions of NiP.**[31–33]** Thus, the correct identification of the vibrational modes showing RR enhancement will aid in the assignment of the resonant electronic transition and vice versa.

The laser frequency is an important consideration in Raman applications because resonance enhancement greatly increases both the sensitivity and the selectivity of the technique. Nonresonance Raman scattering is weak enough that sample concentrations in the molar range are often required to obtain good quality spectra, but resonance enhancement can lower the required concentration to the millimolar to micromolar ranges. Selectivity is an equally important feature since vibrational spectroscopy frequently suffers from crowding and overlap of bands when complex molecules or mixtures are investigated. Since only Raman modes associated with the excited-state distortion are enhanced, the RR spectrum is simplified and one can be sure that the enhanced bands are associated with the chromophore; interferences from other parts of the molecule or other constituents of the mixture are eliminated. Of course, this selectivity means a loss of information if the nonchromophoric parts of the sample are of interest. Wide tunability of the laser source is desirable so that different chromophores in the sample (or different excited states of the same chromophore, which may enhance different Raman bands) can be accessed. The main differences between Raman and RR scattering are summarized in Table 3.

2.7 Electronic Structure and RR Scattering Mechanisms

The vibronic theory of the RR effect distinguishes two major intensity enhancement mechanisms that play a dominant role in the RR spectra: (i) *Franck–Condon* (*FC*) *principle* and (ii) *Herzberg–Teller* (*HT*) *vibronic coupling*, which have quite different properties.**[21,33–35]** The FC scattering mechanism involves displacement of the potential minima of the ground and excited electronic states along a vibrational normal

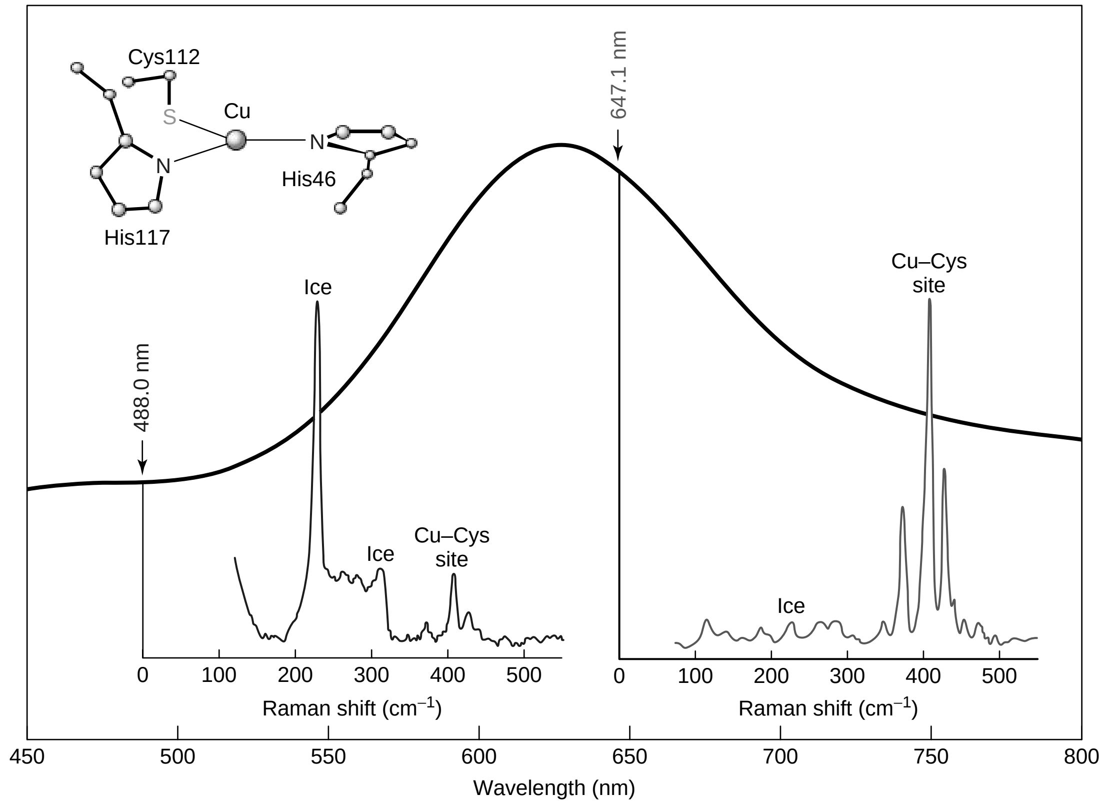

Figure 12 Vibrational enhancement selectivity available from resonance Raman spectroscopy. The UV–visible spectrum of a *P. aeruginosa* azurin is shown together with two different Raman spectra (frozen solution at 77 K) that derive from laser excitation within the S(Cys) → Cu(II) charge-transfer absorption band at 625 nm (647.1 nm) and away from the absorption (488.0 nm). Excitation within resonance leads to dramatically increased Raman scattering from the Cu active site, whereas off-resonance excitation produces a spectrum dominated by bands of nonchromophoric ice

Table 3 Main differences between Raman and resonance Raman scattering

Raman scattering	Resonance Raman scattering
B-term effective (any Raman allowed mode)	A-term (totally symmetric modes), B-term (nontotally symmetric modes), and C-term (first overtones and binary combinations of vibronically active modes) effective
Polarized (p) and depolarized (dp) bands only	Anomalously polarized (ap) and inversely polarized (ip) bands attainable as well
Overtones and combination bands very weak and seldom observable	Overtones and combination bands common
More vibrations observed in the spectrum	Some vibrations selectively enhanced
No electronic information	Electronic information present
Inherently weak scattering (10^6-10^9 times weaker than Rayleigh scattering)	Much stronger scattering (10^3-10^6 times greater than normal Raman scattering)
Intensity arises from the dependence of the ground-state polarizability on molecular vibrations only	Ground-state polarizability and its dependence on molecular vibrations is enhanced via electronic transition(s)

coordinate, whereas the HT scattering mechanism involves a transfer of the transition moment between different excited electronic states induced by a vibrational excitation. This means that by moving into the resonance region, the vibrational modes that reflect the change in geometry when converting the molecule from its ground to excited state (FC allowed) or those that are able to vibronically couple the resonant excited state to some other electronic state with different transition moments (HT allowed) will be strongly enhanced. In general, the former effect is most pronounced for *totally symmetric modes* and *allowed resonant electronic transitions*, whereas the latter is pronounced for *nontotally symmetric modes* and *weakly allowed or forbidden resonant electronic transitions*. This selective enhancement is one of the most important and valuable aspects of RR spectroscopy, since it leads to a considerable simplification of the observed spectra; the RR spectra consist primarily of bands arising from either totally or nontotally symmetric vibrations depending upon the nature of the resonant electronic transitions.

To determine the scattered radiation spectrum of an oscillating molecule under conditions of resonance excitation, we must consider how the polarizability α varies not only with normal modes of vibration but also with frequency of the incident radiation that excites them. For a molecule in a molecular state $|g\rangle$ (initial) perturbed by the electromagnetic wave of frequency ν_0 so that it passes into a molecular state $|f\rangle$ (final) while scattering light of frequency $\nu_0 \pm \nu_k$ ($\nu_k = \nu_f - \nu_g$), the matrix elements of α for the vibrational transition k, $[\alpha_{\rho\sigma}]_k$, are given by the Kramers–Heisenberg–Dirac (KHD) dispersion equation[36,37]:

$$[\alpha_{\rho\sigma}]_k = \frac{1}{h}\sum_e \left(\frac{\langle f|M_\rho|e\rangle\langle e|M_\sigma|g\rangle}{\nu_{eg} - \nu_0 + i\Gamma_e} + \frac{\langle f|M_\sigma|e\rangle\langle e|M_\rho|g\rangle}{\nu_{eg} + \nu_0 + i\Gamma_e} \right) \quad (1)$$

where $\rho,\ \sigma = x, y, z$, which independently refer to the molecule-fixed nonrotating Cartesian coordinate system and represent the polarizations of the incident (σ) and scattered light (ρ), $|g\rangle$ and $|f\rangle$ are the initial and final states of the molecule, and the summation is over all the excited electronic states $|e\rangle$. The integrals $\langle f|M_\sigma|e\rangle$ and $\langle e|M_\rho|g\rangle$ are the electric dipole transition moments along the ρ and σ directions; M is the electron position operator; $h\nu_0$ is the energy of the incident radiation; and Γ_e is a damping factor (which prevents the denominator at resonance from reaching zero), reflecting the finite natural lifetime and sharpness of the excited state, $|e\rangle$.

Far from resonance ($\nu_0 \ll \nu_{eg}$), the magnitude of $[\alpha_{\rho\sigma}]_k$ is independent of ν_0; the number of excited electronic states contributing to the polarizability is large. In this case, all the energy denominators in the KHD equation become large and the scattering tensor $[\alpha_{\rho\sigma}]_k$ correspondingly small, leading to very weak scattering (normal Raman or Raman scattering). As the excitation frequency, ν_0, is tuned to the frequency of an electronic transition, ν_{eg}, the first (resonance) term of the KHD equation will become dominant and large because $\nu_{eg} - \nu_0 \approx 0$ in its denominator, and the second (nonresonance) term will become negligible. As a result, the scattered intensity is expected to increase drastically (but not to infinity owing to the Γ_e term) when ν_0 is in resonance region, provided the resonant state $|e\rangle$ has a large enough transition dipole moment from the ground state. The summation over all the electronic states can be relaxed except for the electronic state in resonance, and by applying (following Albrecht[36]) the adiabatic Born–Oppenheimer approximation of separability of electronic and vibrational wavefunctions for $|g\rangle$, $|e\rangle$, and $|f\rangle$ states, the KHD equation can be rewritten as

$$[\alpha_{\rho\sigma}]_k = \frac{1}{h}\sum_\upsilon \frac{\langle j|(\mu_\rho)_e|\upsilon\rangle\langle \upsilon|(\mu_\sigma)_e|i\rangle}{\nu_{\upsilon i} - \nu_0 + i\Gamma_\upsilon} \quad (2)$$

where $(\mu_\rho)_e = \langle g|(\mu_\rho)_e|e\rangle$ and $(\mu_\sigma)_e = \langle e|(\mu_\sigma)_e|g\rangle$ are the pure electronic transition moments, along ρ and σ directions, for the resonant excited state e; of which υ is a particular vibrational level of bandwidth Γ_υ; $\nu_{\upsilon i}$ is the transition frequency from the ground vibrational level i to the level υ; $|i\rangle$, $|j\rangle$, and $|\upsilon\rangle$ represent vibrational states of a given normal coordinate, Q_k; and the summation is over all excited-state vibrational levels, υ. The dependence of $(\mu_{\rho,\sigma})_e$ on Q_k is small if the Born–Oppenheimer approximation is valid and therefore it can be expanded as a Taylor series:

$$\mu_e = \mu_e^0 + \sum_k \mu_e' Q_k + \ldots \quad (3)$$

where $\mu_e' = (\partial\mu_e/\partial Q_k)_0$. (In writing equation (3), we have dropped the polarization subscripts.) When the electronic resonant transition is weakly allowed, μ_e' can be of the same magnitude as μ_e^0, or even exceed it, if the excited-state $|e\rangle$ can gain absorption strength from other excited states by vibronic mixing via the coordinate Q_k (called *vibronic coupling*). In the HT formalism for the vibronic coupling,[36–38]

$$\mu_e' = \mu_s^0 \frac{\langle s|(\partial H_e/\partial Q_k)_0|e\rangle}{\nu_s - \nu_e} \quad (4)$$

where $|s\rangle$ is another excited state that can be mixed in to $|e\rangle$ by Q_k; ν_s and μ_s are the frequency and transition dipole moment of the mixing electronic state, $|s\rangle$; and $(\partial H_e/\partial Q_k)_0$ is the vibronic coupling operator that connects two excited states $|e\rangle$ and $|s\rangle$, with H_e being the Hamiltonian for the total electronic energy of the molecule. Thus, the stronger the transition to the state $|s\rangle$, and the closer it is in energy to $|e\rangle$, the larger the μ_e' will be.

Substitution of equations (4) and (3) into equation (2) yields an expression with many terms, of which the first three terms, called *A*-, *B*-, *and C-terms*, are the dominant mechanisms in RR scattering.

$$[\alpha]_k = \mathbf{A} + \mathbf{B} + \mathbf{C} + \cdots \quad (5)$$

where

$$\mathbf{A} = (\mu_e^0)^2 h^{-1} \sum_\upsilon \frac{\langle j|\upsilon\rangle\langle \upsilon|i\rangle}{\nu_{\upsilon i} - \nu_0 + i\Gamma_\upsilon} \quad (6)$$

$$\mathbf{B} = \mu_e^0 \mu_e' h^{-1} \sum_\upsilon \frac{\langle j|Q_k|\upsilon\rangle\langle \upsilon|i\rangle + \langle j|\upsilon\rangle\langle \upsilon|Q_k|i\rangle}{\nu_{\upsilon i} - \nu_0 + i\Gamma_\upsilon} \quad (7)$$

$$\mathbf{C} = (\mu_e')^2 h^{-1} \sum_\upsilon \frac{\langle j|Q_k|\upsilon\rangle\langle \upsilon|Q_k|i\rangle}{\nu_{\upsilon i} - \nu_0 + i\Gamma_\upsilon} \quad (8)$$

Each term of equations (6)–(8) is factorized into parts that can be related to the electronic and vibrational wavefunctions and excitation frequency. The electronic contribution (matrix elements of μ_e^0 and μ_e'), weighted with the differential energy denominators ($\nu_{\upsilon i} - \nu_0 + i\Gamma_\upsilon$), determines the *total* enhancement of all the normal vibrations for a given electronic transition and a given ν_0. Since μ_e^0 and μ_e' in $[\alpha]_k$ also determine the optical absorption spectrum, structural information often emerges from the interpretation of both the RR and UV–visible spectra. The vibrational part described by FC factors and $(\partial H_e/\partial Q_k)_0$ (vibronic coupling operator) governs the intensity distribution among the enhanced modes, and is therefore responsible for the selectivity of the vibrational mode enhancement, the enhanced modes containing information about the vibronic nature of the electronic transitions as well as the molecular distortion and dynamics at the electronic excited state(s).

2.7.1 A-term RR Scattering

The A-term is the leading RR scattering mechanism encountered in practice and involves vibrational interactions with a single excited electronic state, $|e\rangle$, by way of FC overlap integrals, $\langle j|\upsilon\rangle$ and $\langle \upsilon|i\rangle$ (FC scattering), as illustrated in Figure 13. This term is nonzero only if $\mu_e^0 > 0$ and $\langle\upsilon|i\rangle\langle j|\upsilon\rangle \neq 0$. Consequently, the A-term is most pronounced for strongly allowed electronic transitions, with large values of $(\mu_e)^2$ and substantial nonorthogonalities of the FC factors $\langle\upsilon|i\rangle$ and $\langle j|\upsilon\rangle$ upon electronic excitation, such as electric-dipole-allowed $\sigma-\sigma^*$, $\pi-\pi^*$, and CT transitions. Excitations into weak electronic transitions, such as forbidden $\pi-\pi^*$, ligand field d–d, and spin forbidden transitions, will not produce significant FC scattering.[16,21,22] The relative enhancements for different vibrational modes are determined by the values of the FC factors, which are nonzero, and may become large if there is a substantial shift of the excited-state potential, Δ_k^e, along the vibrational coordinate Q_k. Only totally symmetric modes are subject to A-term enhancement, because they can satisfy the latter condition ($\Delta_k^e \neq 0$) by symmetry. Frequently, Δ_k^e in the excited electronic state is large enough to give appreciable magnitudes of $\langle\upsilon|i\rangle\langle j|\upsilon\rangle$ products for up to several quanta of vibrational energy. Intense overtone progression $n_k\nu_k$ of totally symmetric modes ν_k can then be observed in the RR spectrum, making it possible to determine their harmonic frequencies and anharmonicity constants. Clark and coworkers have carried out extensive work in this area on coordination compounds.[1,39] The longest progressions observed thus far

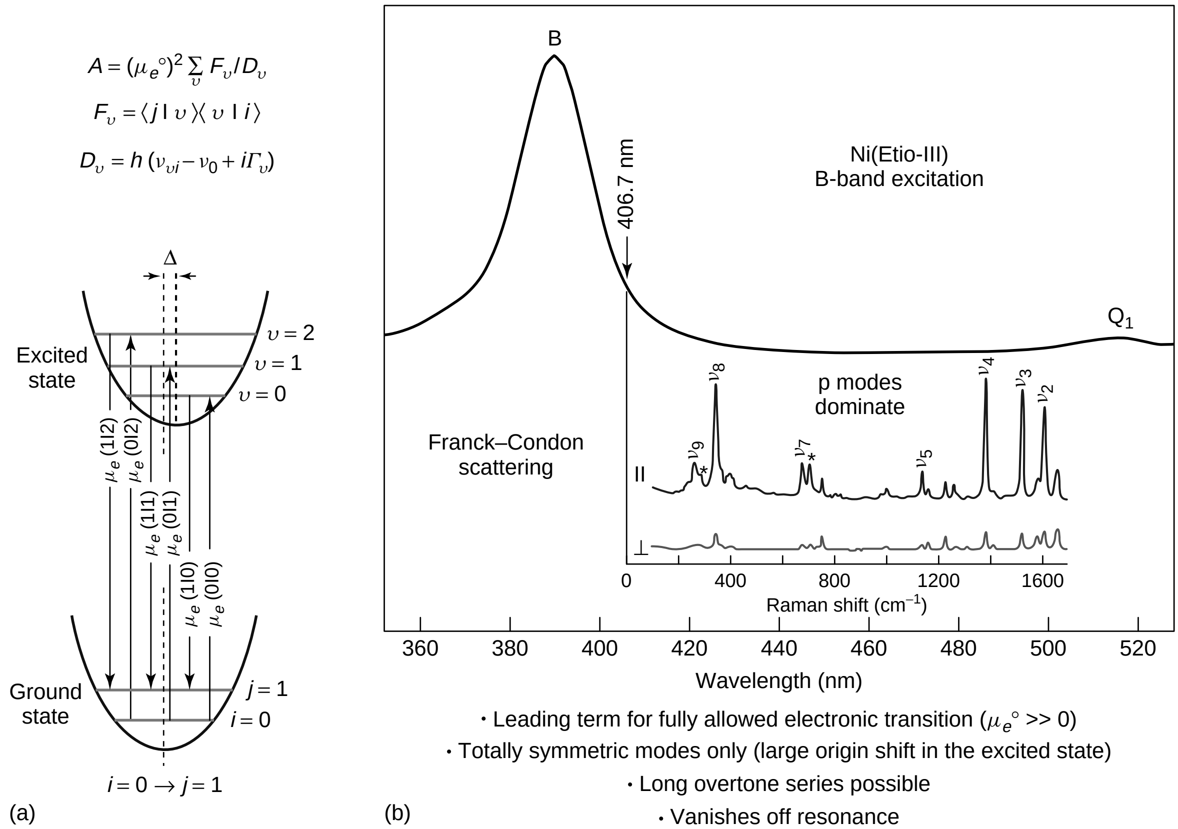

- Leading term for fully allowed electronic transition ($\mu_e°$ >> 0)
- Totally symmetric modes only (large origin shift in the excited state)
- Long overtone series possible
- Vanishes off resonance

Figure 13 (a) Diagrammatic representation of Raman process responsible for A-term resonance scattering. The applicable electronic transition moment and vibrational overlap integral is indicated for each contributing transitions for $\upsilon = 0$, 1, and 2 intermediate levels of the resonant excited state. (b) Soret electronic transition excitation and Franck–Condon (A-term) scattering in metalloporphyrins. Soret absorption band (B) is shown for Ni(Etio-III) together with the RR spectra in parallel (∥) and perpendicular (⊥) scattering excited at 406.7 nm. Resonance with the Soret absorption band enhances mainly polarized bands (p), arising from totally symmetric modes, A_{1g}. The asterisks indicate solvent bands (CH_2Cl_2)

are for the diatomic I_2 (up to $n_1 = 25$), the linear-chain ($[Pt(tn)_2][Pt(tn)_2Br_2])^{4-}$ (up to $n_1 = 18$), tetrahedral SnI_4 (up to $n_1 = 15$), and μ-oxo-bridged $[Ru_2OCl_{10}]^{4-}$ (up to $n_2 = 12$) for which the respective $\nu_2 < 400\,cm^{-1}$.**1,39**

2.7.2 *B-term RR Scattering*

The B-term scattering arises from the vibronic coupling of the resonant state, $|e\rangle$, to another excited state, $|s\rangle$ (HT scattering). Since the magnitude of μ'_e increases with the oscillator strength of μ_s and decreasing frequency separation between the $|e\rangle$ and $|s\rangle$ states, the B-term scattering is most pronounced when the exciting frequency is tuned to a weakly allowed electronic transition that is mixed vibronically with a nearby strong one ($\mu'e > \mu_e^0$ under this circumstance). The B-term denominator is the same as for the A-term, but its numerator contains the Q_k-dependent vibrational overlap integrals $\langle \upsilon|Q_k|i\rangle$ and $\langle j|Q_k|\upsilon\rangle$. These integrals connect ground- and excited-state vibrational levels that differ by one quantum (Figure 14). When they are multiplied by FC factors $\langle j|\upsilon\rangle$ or $\langle \upsilon|i\rangle$, having the same quantum numbers in the ground and excited states (e.g., $\langle 1|1\rangle$ and $\langle 0|0\rangle$) , the numerator does not vanish even if there is no excited-state shift of the potential upon electronic excitation. Thus, B-term scattering is exhibited only by fundamental vibrational modes and the vibrations enhanced may have any symmetry that is contained in the direct product of the two electronic transition representations, $(\Gamma|e\rangle \times \Gamma|s\rangle)$. The relative enhancement factors for different mode symmetries depend on the effectiveness of the vibration in coupling the excited states $|e\rangle$ and $|s\rangle$. Consequently, B-term scattering provides a primary mechanism for RR activity of nontotally symmetric modes, which can be, and usually are, enhanced. The more efficient the vibronic coupling of the two excited electronic states, the more effective B-term enhancement can be observed. Moreover, under nonresonance

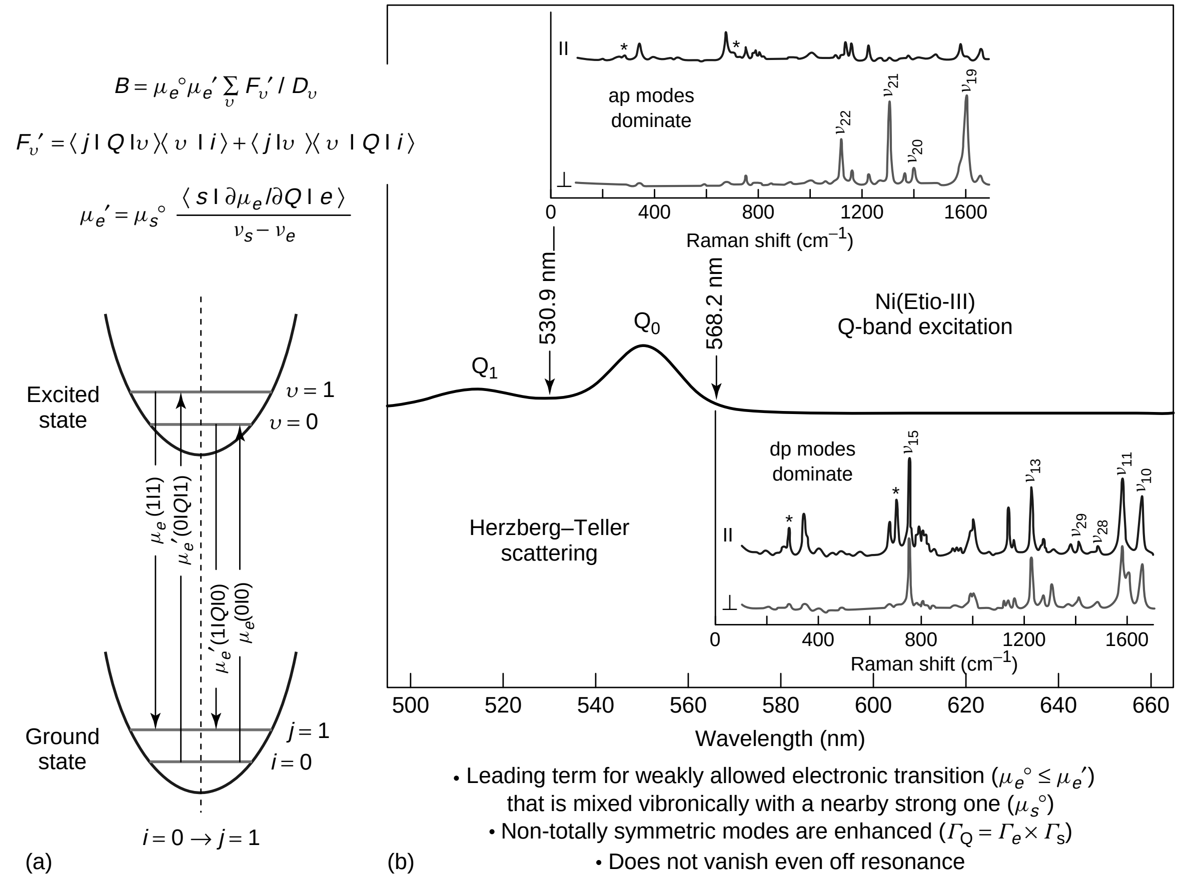
$B = \mu_e^\circ \mu_e' \sum_\upsilon F_\upsilon' / D_\upsilon$
$F_\upsilon' = \langle j | Q | \upsilon \rangle \langle \upsilon | i \rangle + \langle j | \upsilon \rangle \langle \upsilon | Q | i \rangle$
$\mu_e' = \mu_s^\circ \frac{\langle s | \partial\mu_e/\partial Q | e \rangle}{\nu_s - \nu_e}$
Excited state
$\upsilon = 1$
$\upsilon = 0$
$\mu_e(1|1)$
$\mu_e'(0|Q|1)$
$\mu_e'(1|Q|0)$
$\mu_e(0|0)$
Ground state
$j = 1$
$i = 0$
$i = 0 \to j = 1$
(a)
∥
*
*
ap modes dominate
ν_{22}
ν_{21}
ν_{20}
ν_{19}
⊥
0
400
800
1200
1600
Raman shift (cm^{-1})
530.9 nm
568.2 nm
Q$_1$
Q$_0$
Ni(Etio-III)
Q-band excitation
Herzberg–Teller scattering
dp modes dominate
ν_{15}
ν_{13}
ν_{11}
ν_{10}
ν_{29}
ν_{28}
*
*
∥
⊥
0
400
800
1200
1600
Raman shift (cm^{-1})
500
520
540
560
580
600
620
640
660
Wavelength (nm)
(b)

- Leading term for weakly allowed electronic transition ($\mu_e^\circ \le \mu_e'$) that is mixed vibronically with a nearby strong one (μ_s°)
- Non-totally symmetric modes are enhanced ($\Gamma_Q = \Gamma_e \times \Gamma_s$)
- Does not vanish even off resonance

Figure 14 (Left) Diagrammatic representation of Raman process responsible for B-term resonance scattering. The applicable electronic transition moment and vibrational overlap integral is indicated for each contributing transition for $\upsilon = 0$, 1, and 2 intermediate levels of the resonant excited state. (Right) Q-electronic transition excitation and Herzberg–Teller (B-term) scattering in metalloporphyrins. Q absorption band (Q_0 and Q_1) are shown for NiEtio-III together with the RR spectra in parallel (∥) and perpendicular (⊥) scattering excited at 530.9 (top) and 568.2 nm (bottom). Resonance in the Q-band region enhances depolarized (B_{1g}, B_{2g}) and anomalously polarized (A_{2g}) modes that are effective in vibronic mixing of the Q and Soret electronic transitions. Owing to interference effects, the A_{2g} modes are brought out most strongly via excitation between Q_0 and Q_1 (530.9 nm), while the B_{1g} and B_{2g} modes are brought out more strongly with excitation outside the Q bands (568.2 nm). The asterisks indicate solvent bands (CH_2Cl_2)

conditions, when the energy denominator $(v_{vi} - v_0 + \mathrm{i}\Gamma_v)$ can be factored out, the sum over all excited states in the numerator of equation (7) reduces to $\langle j|Q_k|i\rangle$, which is nonzero for $j = i + 1$, i.e., fundamental modes. Thus, off-resonance Raman scattering is preserved by the B-term (although under these conditions any specific resonance effects are lost in the sum over all excited states of equation (7)).

2.7.3 A- and B-term RR Scattering Illustrated

RR scattering by heme proteins and metalloporphyrins (*see* ***Iron Porphyrin Chemistry***-)[14,31–33] provides a classical example of the differential A- and B-term vibrational enhancement pattern, as shown in Figures 13 and 14 for nickel(II) etioporphyrin-III, Ni(Etio-III),[40] which occurs naturally in crude oils and marine sediments. The electronic absorption spectrum of Ni(Etio-III) is due to two allowed in-plane π–π^* transitions, $a_{1u} \to e_g{}^*$ and $a_{2u} \to e_g{}^*$, which have the same $a_{1u} \times e_g = a_{2u} \times e_g = E_u$ symmetry in the idealized $D_{4\mathrm{h}}$ point group of the porphyrin chromophore.[40,41] The in-phase mixing of these π–π^* transitions gives rise to very intense absorption in the violet region at 391 nm, known as the *B or Soret band* (Figure 13), whereas their out-of-phase combination produces much weaker absorption in the yellow region at 551 nm, known as the *Q_0 or α band* (Figure 14). There is also a composite side band in the green region at 515 nm that results from vibronic coupling between the Q_0 and B transitions, referred to as the *Q_1 or β band*. As expected, laser irradiation of Ni(Etio-III) near the Soret absorption band (406.7-nm excitation, Figure 13) leads to RR spectra that are dominated by the polarized peaks (p, $\rho = I_\perp/I_\parallel \approx 1/8$) arising from the totally symmetric vibrations of the porphyrin skeleton, $A_{1\mathrm{g}}$.[40] This dominance reflects that only totally symmetric vibrations, that is, those capable of shifting the excited-state potential surface, are subject to the FC (A-term) enhancement mechanism for allowed electronic transitions (equation 6). Porphyrin structure-sensitive modes ν_2, ν_3, ν_4, and ν_8 are especially strong, indicating large geometric displacements in the excited state along these vibrational coordinates.

Laser irradiation of Ni(Etio-III) near the α (568.2-nm excitation) and β bands (530.9-nm excitation) also produces strong resonance enhancement, as shown in Figure 14. In contrast to Soret-band excitation, it is the depolarized (dp, $\rho \approx 3/4$) and anomalously polarized (ap, $\rho \gg 3/4$) Raman peaks from the nontotally symmetric vibrations that are dominant.[40] These vibrations derive their intensity from the B-term (HT scattering) involving a vibronic coupling of the two excited states of the α and Soret electronic transitions (which is also responsible for the β absorption side band). Since both the Soret and α excited states are of E_u symmetry, the allowed symmetries of the mixing vibrations are $E_u \times E_u = A_{1\mathrm{g}} + A_{2\mathrm{g}} + B_{1\mathrm{g}} + B_{2\mathrm{g}}$. The $A_{1\mathrm{g}}$ modes are, however, not efficient in vibronic coupling. The $B_{1\mathrm{g}}$ and $B_{2\mathrm{g}}$ modes both give depolarized bands, while the $A_{2\mathrm{g}}$ modes give anomalously polarized bands. The Q-band resonance is also subject to an interference effect between 0–0 and 0–1 components, which produces an additional RR selectivity among the mixing nontotally symmetric modes.[31] It selects for $A_{2\mathrm{g}}$ modes at excitation wavelengths falling in between α and β bands, while excitation on either side selects for $B_{1\mathrm{g}}$ and $B_{2\mathrm{g}}$ modes.[35] This is the reason that ap bands are dominant with 530.9-nm excitation, whereas dp bands dominate the 568.2-nm excited spectrum (Figure 14).

2.7.4 C-term RR Scattering

The C-term RR scattering is a dominant mechanism when the exciting frequency is in resonance with a vibronic side band of a forbidden or weakly allowed 0–0 electronic transition, where the side band is allowed ($\mu_s^0 \neq 0$) due to the vibronic coupling between the 0–0 transition and another strongly allowed transition ($|g\rangle \to |s\rangle$). Under such conditions, the vibronic transition moment μ_e' described by equation (4) is much greater than μ_e^0 and since the electronic factor is $(\mu_e')^2$ in equation (8), the C-term can outweigh the B-term. The special feature of the C-term RR scattering is that it gives rise to first overtones ($k = l$) and binary combination tones ($k \neq l$) of those vibrational modes that are effective in coupling the two electronic states, instead of the fundamentals. This is because the numerator of the C-term equation (8) contains products of two Q-dependent integrals, $\langle j|Q_k|v\rangle$ and $\langle v|Q_l|i\rangle$. Since each of these connects vibrational states differing by one quantum, the final state, $|j\rangle$, must differ from $|i\rangle$ by two quanta, i.e., $j = i \pm 2$, as diagrammatically shown in Figure 15. Consequently, only first overtones ($k = l$) and binary combinations ($k \neq l$) are enhanced by the C-term. An example is shown in Figure 15(a), where overtone and combination bands involving the high-frequency ap and dp modes $\nu_{19}(A_{2\mathrm{g}})$, $\nu_{10}(B_{1\mathrm{g}})$, $\nu_{11}(B_{1\mathrm{g}})$, $\nu_{20}(A_{2\mathrm{g}})$, and $\nu_{29}(B_{2\mathrm{g}})$ in the β-resonant spectrum of vanadyl tetraphenylporphyrin, VO(TPP), are seen to be dramatically stronger than the fundamentals.[32,42] The α absorption band shows no discernible intensity in this case (Figure 15(b)), indicating accidental degeneracy of the a_{1u} and a_{2u} porphyrin π orbitals, while the β band retains ≈10% of the intensity of the Soret band. As a result, $\mu_e^0 \approx 0$ but $\mu_e' \neq 0$ and $B \ll C$.

3 APPLICATIONS

3.1 The Mononuclear Type-1 Cu Site in Cupredoxins

The mononuclear blue (or type 1) copper proteins (cupredoxins) (*see* ***Copper Proteins with Type 1 Sites***), involved in biological electron transport, share a common structural motif, in which the single Cu(II) ion is tightly bound (~1.9–2.2 Å) to two histidine and one cysteine ligand

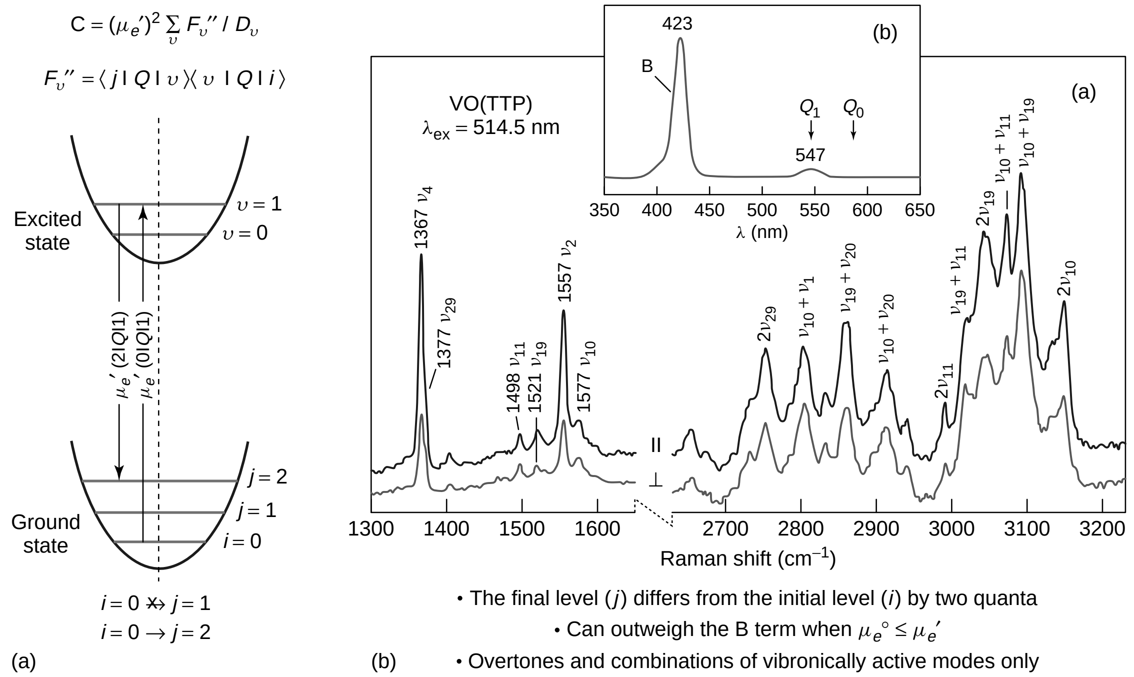

- The final level (*j*) differs from the initial level (*i*) by two quanta
- Can outweigh the B term when $\mu_e^{\circ} \leq \mu_e'$
- Overtones and combinations of vibronically active modes only

Figure 15 (A) Diagrammatic representation of Raman process responsible for C-term resonance scattering. The applicable electronic transition moment and vibrational overlap integral is indicated for each contributing transition for $\upsilon = 0$ and 1 intermediate levels of the resonant excited state. (B) The RR spectra (a) in parallel (‖) and perpendicular (⊥) scattering of solid (VO)TPP (rotating KCl pellet) excited at 514.5 nm showing strong enhancement of overtone and combination modes involving vibronically active ν_{19}, ν_{10}, ν_{11}, and ν_{29}, which themselves are very weak. The Q_0 absorption band (b) is virtually invisible in this case, giving very large overtone/fundamental ratios via the much larger C-term than B-term scattering

in a distorted trigonal CuN_2S planar geometry.[43–47] These three residues are conserved in all cupredoxins. A methionine thioether sulfur atom or, in some cases, a glutamine amide oxygen atom is present above the trigonal plane at a long distance (~2.6–3.1 Å). The azurin structure is different in that it has a fifth distant (~2.8–3.2 Å) ligand to copper, the peptide carbonyl oxygen from glycine (Gly45) across the N_2S plane (His46, His117, Cys112) from the methionine residue (Met121).[48–50] The trigonal bonding arrangement lowers the energy of the half-occupied copper $d_{x^2-y^2}$ orbital, relative to its energy in the usual tetragonal complexes of Cu(II), and in addition orients $d_{x^2-y^2}$ for optimal overlap with the π, instead of the σ filled orbital on the cysteine sulfur atom. Both factors lead to an unusually low energy (Cys)S → Cu(II) CT transition, ~625 nm, which accounts for the intense blue color of these proteins.

The main effect of CT excitation should be to weaken the Cu(II)–S(Cys) bond, and RR enhancement of the Cu(II)–S(Cys) stretching mode, $\nu(\mathrm{CuS})_{\mathrm{Cys}}$, is therefore expected. This is a FC overlap argument, based upon equation (6). The Cu(II)–S(Cys) bond is short (~2.1–2.2 Å)[51] and a high stretching frequency is expected, ~400 cm^{-1}. The other Cu(II)–ligand stretches should be at much lower frequencies, because of the very long bonds for the methionine and peptide ligands, and because of the high effective mass of the rigid imidazole rings. Hence, a single dominant RR band might be expected, near 400 cm^{-1}. This is, in fact, what is observed[52] for a set of model compounds, LCu(II)–SR, where L = hydrotris(3,5-diisopropyl-1-pyrazolyl)borate (Figure 16).[53] When R is varied from *t*-butyl to triphenylmethyl to pentafluorophenyl, the frequency of this band decreases from 437 to 422 to 409 cm^{-1}, consistent with the expected weakening of the Cu–S bond due to increasing electron withdrawal. For the blue copper proteins, however, laser excitation within a (Cys)S → Cu(II) CT band results in a group of four or more strong RR fundamental bands near 400 cm^{-1}, as well as a series of weak-to-moderate bands below 300 cm^{-1} and groups of weaker features in the first (~800 cm^{-1}) and second (~1200 cm^{-1}) overtone regions of the ~400 cm^{-1} fundamentals.[43–47] The 647.1-nm excitation spectrum of azurin from *Pseudomonas aeruginosa*,[43] shown in Figure 17, exemplifies the unusual but characteristic richness of the type-1 copper RR scattering. Another property is the species dependence of RR scattering from proteins that have ostensibly the same active site structure. Despite homologous structures, different families of blue copper proteins, as well as individual members of the same family, exhibit considerable dissimilarities regarding the number of RR modes observed, their frequencies, and relative intensities (Figure 18).

The source of this band multiplicity and spectral differences has been a matter of considerable speculation.[45,47]

What is expected from Raman excitation into a (thiolate) S → Cu(II) CT transition?

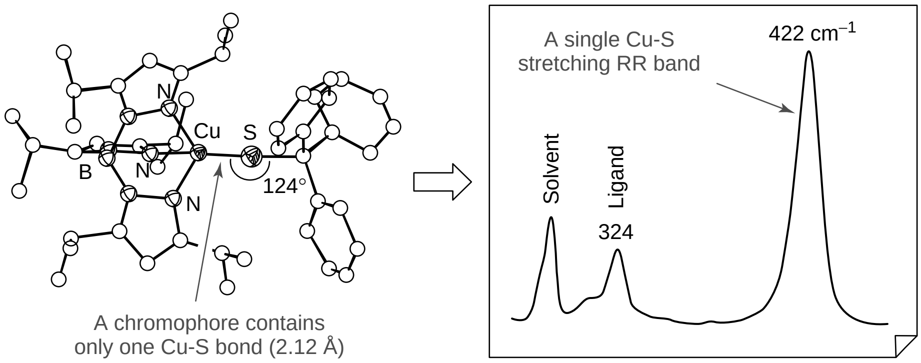

Figure 16 Structural diagram and 647.1-nm excitation RR spectrum of the blue copper site analog complex, LCu(II)–SR (L = hydrotris(3,5-diisopropyl-1-pyrazolyl)borate).[53] A single Cu–S stretching mode is seen in the RR spectrum,[52] as expected from excitation into RS → Cu CT transition of a chromophore containing only one terminal Cu–S bond

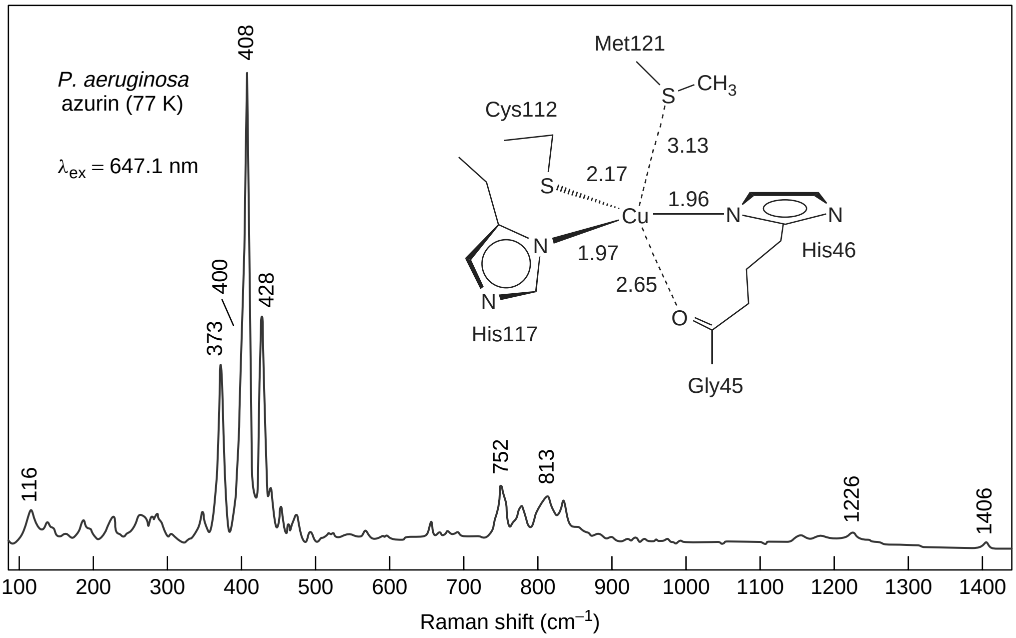

Figure 17 Low-temperature (77 K) RR spectrum of *P. aeruginosa* azurin obtained with 647.1-nm excitation wavelength and structural drawing of the active site showing distances (Å) to the three strong (Cys112, His46, His117) and two weak ligands (Met121, Gly45)

Significantly, the LCu–SR model compound gives three RR bands of nearly equal intensities near 400 cm^{-1} when R = *s*-butyl. Normal coordinate analysis (NCA) calculations indicate that the simple interchange of a methyl group and a hydrogen atom, between R = *t*-butyl and *s*-butyl, is sufficient to induce significant mixing of the C–C–C bending coordinates, δ(CCC), with the Cu–S(thiolate) stretching coordinate, ν(CuS), thereby accounting for the three strong bands.[52] No doubt mixing of ν(CuS) with heavy atom bending coordinates of the cysteine ligand produces some complexity seen in the cupredoxin spectra. Such mixing was anticipated in an early study of stellacyanin,[54] in which the two main RR bands were each found to shift upon $^{65\rightarrow 63}$Cu substitution, by half the amount expected for an isolated Cu–S oscillator, implying nearly equal contributions from ν(CuS) and another coordinate. Further insight into the coordinate mixing phenomenon has been obtained by $^{34\rightarrow 32}$S substitution in *P. aeruginosa* azurin and site-specific mutants,[44,55,56] *A. lcaligenes denitrificans* azurin,[57] *Cucumber sativus* stellacyanin,[58] and *Populus nigra* plastocyanin,[59] carried out by bacterial expression of the respective protein gene.

Figure 19 presents the 350–450 cm^{-1} RR spectra for the natural abundance wild-type (WT) *P. aeruginosa* azurin and its M121G (Met121 replaced with glycine) and H46D

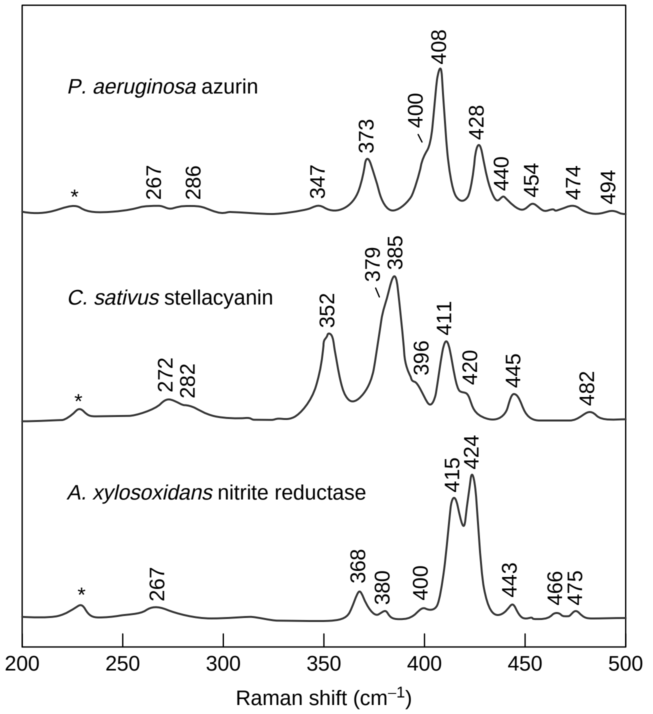

Figure 18 Low-temperature (77 K) RR spectra in the 200–500 cm^{-1} region of indicated blue Cu proteins excited at 568.2 (stellacyanin, NiR) and 647.1 nm (azurin). Asterisks denote ice band

(His46 replaced with aspartate) Cu site mutants, and their corresponding [^{34}S]Cys112-substituted proteins.**[55]** Each spectrum shows four dominant RR peaks in this region (~370, ~400, 408, and ~427 cm^{-1}) that are characteristic for the type-1 Cu structure of the Cu(II)–Cys chromophores. Among these, the bands showing the greatest intensity and [^{34}S]Cys isotope shift, 408 (WT) and ~400 cm^{-1} (mutants), are identified with the vibrational mode involving primarily stretching of the Cu(II)–S(Cys) bond. This assignment is also corroborated by the $^{63/65}$Cu isotope shifts, as shown in Table 4.**[44]** A shift of the ν(CuS)$_{\text{Cys}}$ character from the 408 cm^{-1} peak of WT to the ~400 cm^{-1} peaks in H46D and M121G indicates a decrease of the Cu(II)–S(Cys) interaction in both mutants as their Cu sites adopt more tetrahedral character relative to the WT site.**[44,55,60]**

There are far too many strong bands (up to nine) in the cupredoxin RR spectra near 400 cm^{-1} to be entirely due to the metal–ligand stretches, and attention must turn to other vibrational modes of the active site. Toward this end, site-selective isotopomers of azurin**[61]** and plastocyanin**[62]** were genetically produced with ^{2}H and ^{15}N labels in the cysteine C$_\beta$ hydrogen and amide nitrogen atom positions, respectively, and their high-resolution RR spectra were recorded and analyzed.**[43,61–63]** Figure 20 shows the effects on the RR spectrum in the 350–450 (fundamental) and 650–850 cm^{-1} (first overtone) regions of selective deuterium labeling of the Cys112 β-hydrogen atoms in *P. aeruginosa* azurin, carried out by bacterial expression of the azurin gene using a Cys

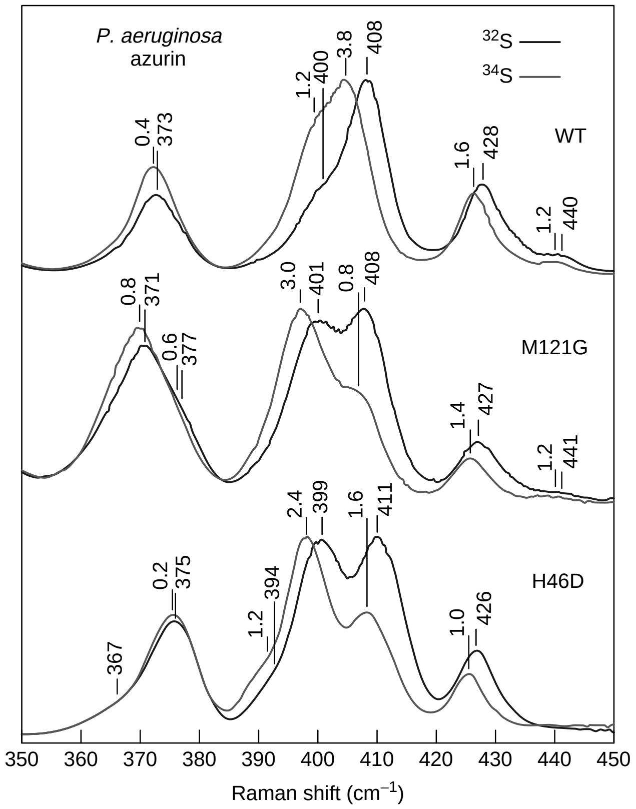

Figure 19 Low-temperature (77 K) RR spectra of *P. aeruginosa* azurins from cells grown on [^{32}S]- or [^{34}S]sulfate, excited at 647.1 (WT) and 568.2 nm (mutants). Italic numbers show the [$\nu(^{32}$S) $-$ $\nu(^{34}$S)] band shifts

auxotrophic *E. coli* strain and cysteine(3,3-D$_2$).**[61]** Three of the four RR bands with ν(CuS)$_{\text{Cys}}$ character are markedly affected by [C$_\beta$D$_2$]Cys112 incorporation; the 408 and 373 cm^{-1} bands undergo shifts of -6 and -4 cm^{-1}, respectively, while a shoulder near 400 cm^{-1} loses most of its intensity and drops ~3 cm^{-1} in frequency. The fourth S-dependent band at 428 cm^{-1} is much less sensitive to C$_\beta$D$_2$ labeling, shifting approximately -1.5 cm^{-1}. These shifts are further emphasized by the first overtone and combination bands as indicated in the figure. On the other hand, selective labeling of the nitrogen atom in the azurin Cys112 residue causes only small changes in the [^{15}N]Cys112 RR spectrum.**[61]** Three shoulders at 264, 400, and 377 cm^{-1} all shift downward by ~1 cm^{-1}, while the ^{34}S-sensitive peaks at 408 and 428 cm^{-1} shift less than 0.5 cm^{-1}, indicating only a small contribution from the amide group of the cysteinate ligand. Hence, the [C$_\beta$D$_2$]Cys and [^{15}N]Cys RR data**[43,61–63]** unambiguously establish that the multiple S-dependent bands of cupredoxins contain contributions mainly from CH$_2$ group-dependent deformations of Cu-bound cysteine,**[43,56]** as predicted by RR studies on model compounds**[52]** and ^{34}S- and $^{63/65}$Cu-substituted proteins.**[54,55,59]**

However, growth of azurins,**[45,56,60,61]** stellacyanin,**[58]** and plastocyanin**[59]** on ^{15}NH$_4$Cl(aq), which completely labels

Table 4 Effects of ^{34}S, ^{65}Cu, and D_2O substitutions on frequencies of the 370–430 cm^{-1} RR bands for type-1 Cu sites in azurins

Azurin	RR frequency and isotope shift (cm^{-1})				Total shift
Wild type	373	400	408	428	
$^{32}S \rightarrow {}^{34}S$	−0.4	−1.2	−3.8	−1.6	−7.0
$^{63}Cu \rightarrow {}^{65}Cu$	−0.6	−1.0	−0.4	−0.4	−2.4
$H_2O \rightarrow D_2O$	−0.5	−1.0	−0.5	−1.5	−3.5
M121L[a]	372	400	405	427	
$^{63}Cu \rightarrow {}^{65}Cu$	−0.8	−0.6	−0.7	−0.4	−2.5
$H_2O \rightarrow D_2O$	−0.5	−1.0	−0.5	−2.0	−4.0
M121G[b]	371	401	408	427	
$^{32}S \rightarrow {}^{34}S$	−0.8	−3.0	−0.8	−1.4	−6.4
$^{63}Cu \rightarrow {}^{65}Cu$	−0.6	−0.8	−0.6	−0.4	−2.4
$H_2O \rightarrow D_2O$	−2.5	−1.5	−2.0	−2.0	−7.0
H46D[c]	375	399	411	426	
$^{32}S \rightarrow {}^{34}S$	−0.2	−2.4	−1.6	−1.0	−5.2
$^{63}Cu \rightarrow {}^{65}Cu$	−0.6	−0.6	−0.5	−0.2	−1.9
$H_2O \rightarrow D_2O$	−1.5	−3.5	−3.0	−4.5	−12.5

[a] ^{34}S data not available for M121L azurin.
[b] M121G azurin shows a shoulder at 377 cm^{-1}, which downshifts ~0.6 and ~0.3 cm^{-1} on ^{34}S and ^{65}Cu substitutions, respectively.
[c] H46D azurin shows a shoulder at 394 cm^{-1}, which downshifts ~1.2 cm^{-1} on ^{34}S substitution. All data are from Czernuszewicz *et al.*[44]

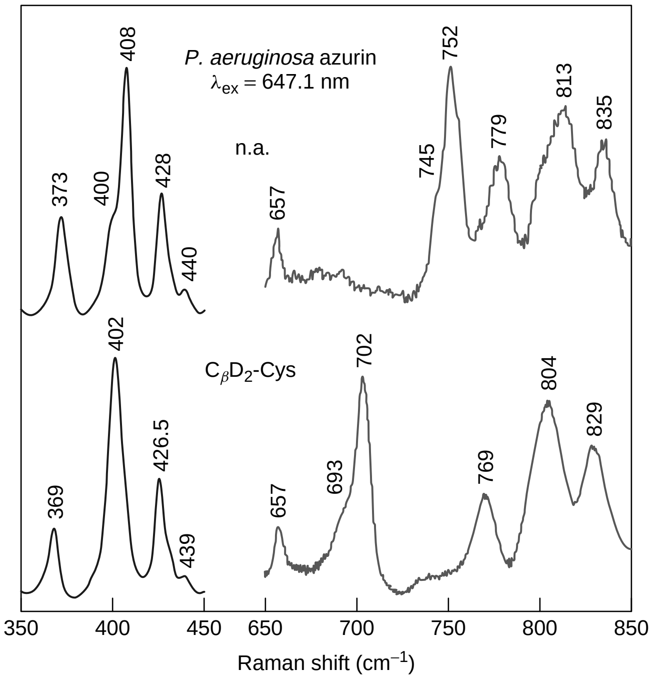

Figure 20 RR spectra of *P. aeruginosa* azurin and its [CβD2] Cys112-labeled protein obtained at 77 K with 647.1-nm excitation

all nitrogen atoms in the protein with ^{15}N, leads to the RR spectra that exhibit relatively large (1.0–4.2 cm^{-1} for *P. aeruginosa* azurin[56]) shifts to lower frequencies for nearly all the fundamental Raman bands in the 100–500 cm^{-1} region. Even the ^{34}S-sensitive strongest Raman bands in the 400 cm^{-1} region showed these downshifts.[56] At first, these results seem to support an earlier suggestion[54,64] that the deformation coordinates of Cu-bound histidine residues could also be good candidates for kinematic mixing with $\nu(CuS)_{Cys}$. Selective isotope labeling of the histidine imidazole ring has become possible through the availability of the azurin ligand mutants (H46G and H117G).[65–67] These mutants bind exogenous imidazole to generate blue copper sites almost indistinguishable from those of the WT proteins. Incorporation of [^{15}N] imidazole into either the H46G or H117G mutant gives no ^{15}N-sensitive RR bands other than a ~285 cm^{-1} band assigned to $\nu(CuN_{Im})$ (~1 cm^{-1} downshift).[68] Clearly, the substantially larger ^{15}N shifts observed for cupredoxins grown in the $^{15}NH_4Cl$ media are due to contributions from vibrations of the backbone amides rather than the histidine ligands. It is also apparent from the [^{15}N]Cys-dependent RR experiments that coupling of $\nu(CuS)$ to cysteine amide coordinates alone is not sufficient to explain the observed [^{15}N] protein shifts. That a single $\nu(CuS)$ stretch of cupredoxins undergoes extensive kinematic coupling with internal vibrational coordinates of not just one (cysteine) but several side chain residues has been obtained from NCA calculations of azurin[43] and plastocyanin.[63] The multiple vibrational features in the azurin RR spectrum arise from kinematic coupling between $\nu(CuS)$ and the internal ligand deformation modes of the coordinated Cys112 and at least three other residues (Thr113, Phe111, and Phe110) linked to Cys112 in the polypeptide chain.

3.2 Effects of Met121 Mutation on the Azurin Active Site

Substitution of amino acid residues at the metal center by site-directed mutagenesis can alter the geometry and properties of the active site, thus allowing elucidation of the minimal requirements for the proper functioning of the metalloprotein.[44,60] As an example, Figure 21 and Table 5 show the results of RR scattering from a series of *P. aeruginosa* azurins in which the active site Met121 has

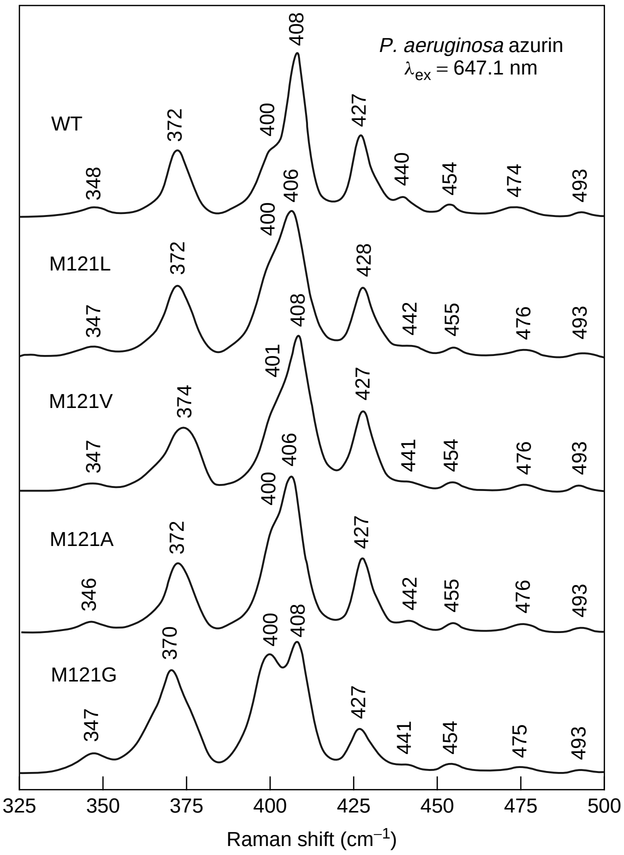

Figure 21 Low-temperature (77 K) RR spectra of *P. aeruginosa* azurin and indicated mutants (M121X, X = glycine, alanine, valine, and leucine) obtained in the 320–500 $\mathrm{cm^{-1}}$ region with 647.1- and 568.2-nm (M121G) excitations

Table 5 Optical spectral parameters and Cu–$\mathrm{S_{Cys}}$ RR stretching frequencies for *P. aeruginosa* azurins and their complexes with exogenous ligands[a]

Protein[b]	$\lambda_1(\varepsilon_1)$[c]	$\lambda_2(\varepsilon_2)$[c]	$\nu(\mathrm{CuS})_{\mathrm{Cys}}$[d]
WT	**628** (5.5)	480 (0.04)	372, 400, **408**, 427
Met121Gly	**612** (4.9)	453 (0.8)	370, **400**, 408, 427
Azido	550 (1.9)	**422** (3.2)	300, 342, **357**, 391
Thiocyanato	550 (1.4)	**415** (3.5)	300, 318, **344, 353**, 392
Cyano	550 (0.9)	**432** (3.4)	300, 329, **338**, 352, 390
Met121Ala	**625** (5.6)	463 (0.5)	372, 400, **406**, 427
Azido	520 (2.7)	**409** (5.2)	299, **339**, 353, 363, 389
Thiocyanato	530 (1.7)	**409** (4.6)	300, **339**, 353, 389
Cyano	520 (1.1)	**413** (5.1)	298, **329, 338**, 351, 390
Met121Val	**626** (5.2)	460 (0.8)	374, 400, **408**, 428
Azido	520 (1.8)	**416** (5.5)	300, 345, **355**, 392
Thiocyanato	550 (1.1)	**416** (3.5)	300, **342**, 350, 393
Cyano	550 (1.0)	**420** (3.7)	300, 329, **337**, 352, 390
Met121Leu	**630** (6.0)	480 (0.1)	372, 400, **406**, 428
Azido	350 (1.2)	**412** (3.0)	300, 343, **358**, 391
Thiocyanato	–	–	301, **342**, 354, 391
Cyano	550 (1.1)	**416** (3.7)	300, 329, **337**, 354, 391

[a] $\lambda_{\max}$ are given in nm, $\varepsilon_{\max}$ in $\mathrm{mM^{-1}\,cm^{-1}}$, and $\nu(\mathrm{CuS})_{\mathrm{Cys}}$ in $\mathrm{cm^{-1}}$; absorption and the RR bands with the highest intensity are indicated by bold numbers.
[b] All samples in pH 7 solutions.
[c] Values from Bonander *et al.*[69]
[d] Values from Franczkiewicz *et al.*[60]

been replaced by smaller hydrophobic amino acids: glycine (M121G), alanine (M121A), valine (M121V), and leucine (M121L).[60] The data emphasize that azurin RR spectra contain precise structural information regarding the nature of extremely subtle and minor variations in copper–amino acid interactions caused by Met121 replacements. Among the four most prominent peaks seen at 373, 400(sh), 408, and 427 $\mathrm{cm^{-1}}$ for WT azurin (Figure 21, top spectrum), the strongest one at 408 $\mathrm{cm^{-1}}$ bears the highest $\nu(\mathrm{CuS})_{\mathrm{Cys}}$ character,[55] because it shifts the most to lower frequency (~4 $\mathrm{cm^{-1}}$) upon ^{34}S substitution (Figure 19); the other three peaks shift appreciably less (~1.0–2.5 $\mathrm{cm^{-1}}$). Thus, to a first approximation, the position of the most intense azurin fundamental peak reflects the strength of the Cu(II)–S(Cys) interaction. The RR spectral patterns of M121A, M121V, and M121L closely resemble that of the WT azurin; there are only small differences (±0.5 to ±2 $\mathrm{cm^{-1}}$) in the positions of the bands (Table 5) and slight changes in the relative intensities, which indicate that a trigonal $\mathrm{N_2S}$ bonding arrangement about Cu(II) of the WT azurin has not been altered much by mutations of Met121 to alanine, valine, and leucine.[60] That M121A, M121V, and M121L retain trigonal character of the Cu is also highlighted by the axiality of the electron paramagnetic resonance (EPR) signals[69] and small ratios of the molar absorptivities for electronic transitions in the violet (λ_2, ~460 nm) and red regions (λ_1, ~620 nm), $R_{\mathrm{f}} = \varepsilon(\lambda_2)/\varepsilon(\lambda_1)$[45,68] (Table 5).

In contrast, the M121G mutant displays the most pronounced changes in the RR spectrum near 400 $\mathrm{cm^{-1}}$ (Figure 21, bottom) relative to those of the WT and the other three Met121 mutants under study. It would seem from a comparison of the spectra of all five proteins that the frequencies of the M121G bands are not as changed as their intensities, including the major peaks at 370, 400, 408, and 427 $\mathrm{cm^{-1}}$. However, as we have demonstrated above, through ^{34}S-isotope labeling of the Cys112 ligand,[44,55] the predominantly $\nu(\mathrm{CuS})_{\mathrm{Cys}}$ band downshifted from 408 $\mathrm{cm^{-1}}$ (WT) to 400 $\mathrm{cm^{-1}}$ upon mutation of Met121 to glycine (Figure 19). Since there are still at least four major bands between 360 and 430 $\mathrm{cm^{-1}}$, this implies an increase in frequency for the shoulder at 400 $\mathrm{cm^{-1}}$ observed in WT that now has moved to higher energy (408 $\mathrm{cm^{-1}}$) in M121G. Such a frequency crossover indicates differences in kinematic coupling between vibrations of the Cu–Cys moiety because of ground-state alteration. A shift of the $\nu(\mathrm{CuS})_{\mathrm{Cys}}$ character from the 408 $\mathrm{cm^{-1}}$ band of the WT to the 400 $\mathrm{cm^{-1}}$ band in M121G indicates that the Met121 $\rightarrow$ glycine substitution causes the Cu–$\mathrm{S_{Cys}}$ interaction to weaken, as the Cu site adopts more tetrahedral character relative to the WT site. Consistent with the weaker Cu–$\mathrm{S_{Cys}}$ interaction is the higher cysteine C_β–S stretching mode frequency (760 $\mathrm{cm^{-1}}$ in M121G versus 751 $\mathrm{cm^{-1}}$ in WT),[44] whereas the enhanced

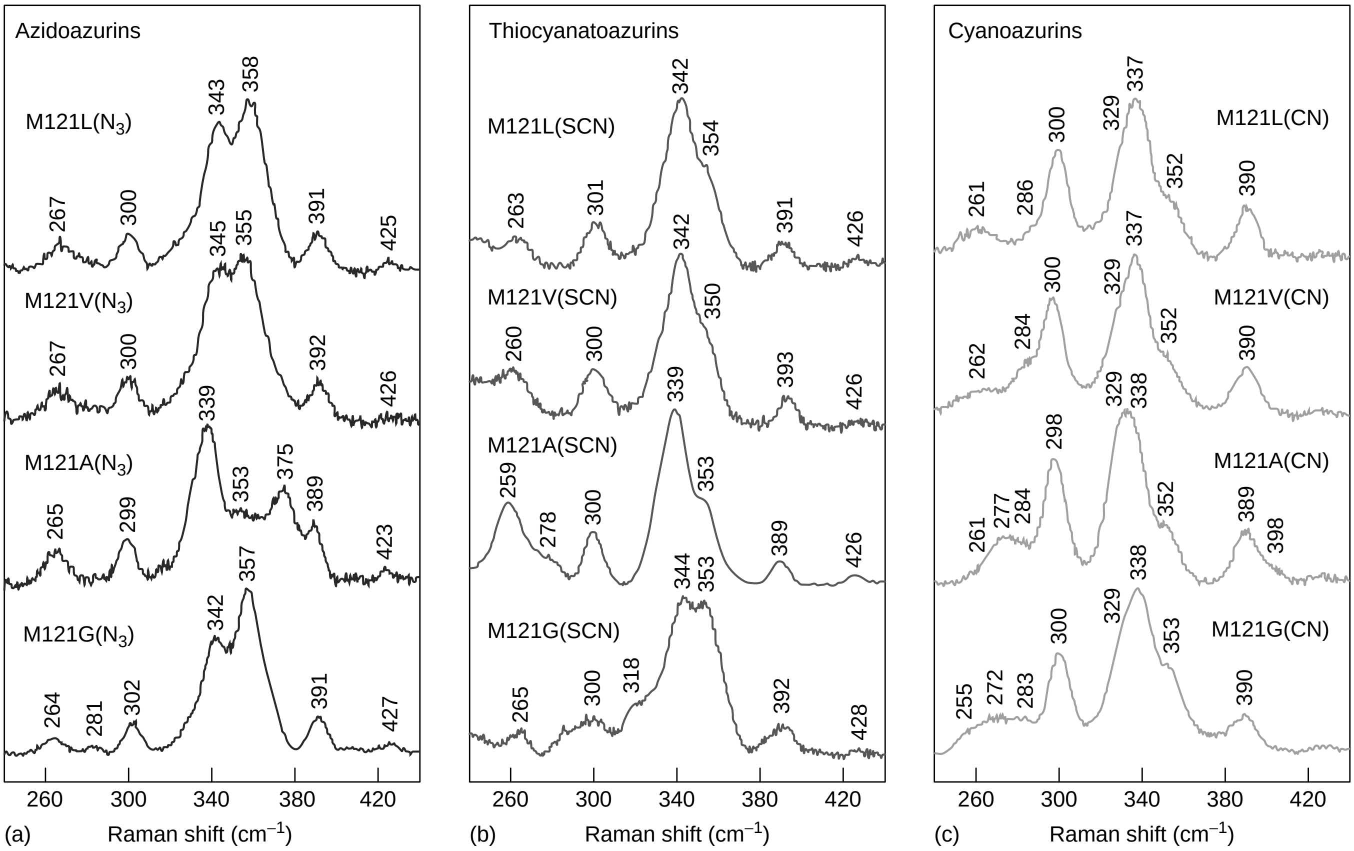

Figure 22 Low-temperature (77 K) RR spectra of indicated (a) azido, (b) thiocyanato, and (c) cyanoazurins obtained in the 240–440 cm^{-1} region with 406.7-nm excitation wavelength

tetrahedral character of the Cu in M121G is emphasized by increased absorption in the violet region (Table 5) and rhombicity of the EPR signal.[69]

3.3 Effects of Exogenous Ligand Coordination on Type-1 Cu Site

Figure 22 compares the RR spectra below 500 cm^{-1} for the azurin Met121X mutants (M121L, M121V, M121A, and M121G) treated with azide, thiocyanate, or cyanide, where most of the copper–ligand vibrations are expected to occur.[44,60] All spectra were obtained on frozen solutions (77 K) using a Kr^{+} ion laser excitation at 406.7 nm. This excitation is in close resonance with an intense absorption band of the adducts in the violet region (Table 5), which arises from a hypsochromic shift of the ~620 nm (Cys)S $\rightarrow$ Cu(II) CT transition due to a strong apical interaction provided by exogenous ligand binding. The optical parameters and the vibrational frequencies of the dominant RR peaks are summarized in Table 5, and one example of the optical absorption of complexes is given in Figure 23. While the Met121X azurins exhibit the most strongly enhanced vibrational modes in the ~400 cm^{-1} region, assigned to the

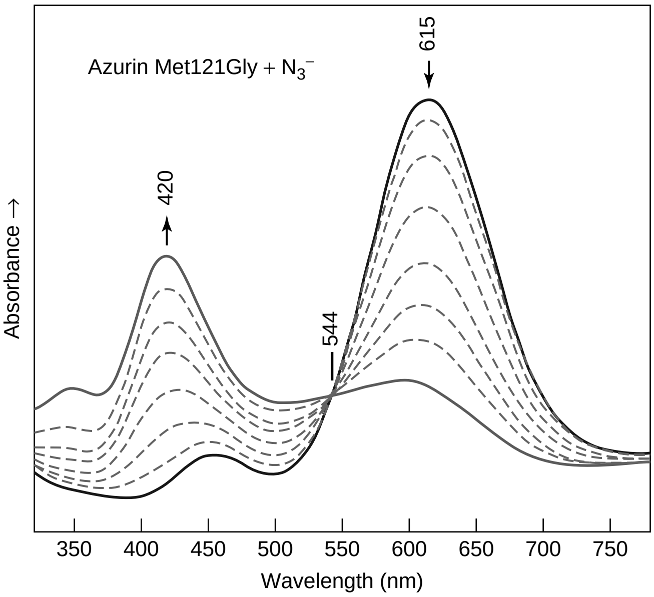

Figure 23 Changes in the UV–visible absorption spectrum of *P. aeruginosa* M121G azurin on sequential addition of aqueous sodium azide

Cu–S(Cys) vibrations, the strongest bands in their azido, thiocyanato, and cyano adducts occur in the ~350 cm^{-1} region. Such behavior is characteristic of a structural rearrangement of the metal center to a distorted tetrahedron with a markedly weakened Cu(II)–S(Cys) bond caused by strong coordination of an exogenous anion. To investigate the origin of these new sets of bands, the RR spectrum (413.1-nm excitation) was obtained on the ^{34}S-labeled M121G azurin mixed with aqueous NaN$_3$, focusing on the 280–450 cm^{-1} spectral region.**[44,55]** The greatest influence of ^{34}S-mass incorporation occurs with the most intense peak at 357 cm^{-1}, which shifts 3.0 cm^{-1} to lower frequency (Figure 24, bottom). This substantial isotope shift identifies the 357 cm^{-1} mode of M121G–azide as predominantly due to stretching of the Cu(II)–S(Cys) bond, analogous to the 401 cm^{-1} mode of M121G that also shifts 3.0 cm^{-1} upon ^{34}S substitution (Figure 24, top). Meanwhile, the frequency of the β-carbon–sulfur(Cys) stretch, $\nu(\mathrm{CS})_{\mathrm{Cys}}$, increased from 758 cm^{-1} in M121G to 773 cm^{-1} in the M121G–azide complex (Table 5). These vibrational results indicate a substantially weaker Cu(II)–S(Cys) interaction in the M121G–azide complex and, by extension, in all other adducts.

The most remarkable feature of Figure 24 is that at least four more bands around the dominant 357 cm^{-1} vibration also display isotope sensitivity (^{34}S minus ^{32}S): one strong peak at 342 (−1.6) and three weaker peaks at 302 (−1.2), 391 (−2.6), and 427 (−1.2) cm^{-1}. Thus, these bands must also arise from the vibrational modes that involve some motion of the cysteinyl sulfur atom. This finding is extraordinary in that the extensive kinematic coupling between the $\nu(\mathrm{CuS})_{\mathrm{Cys}}$ stretch and internal vibrational modes of the protein matrix exhibited by cupredoxins is evidently independent of their Cu(II)–S(Cys) bond strength.

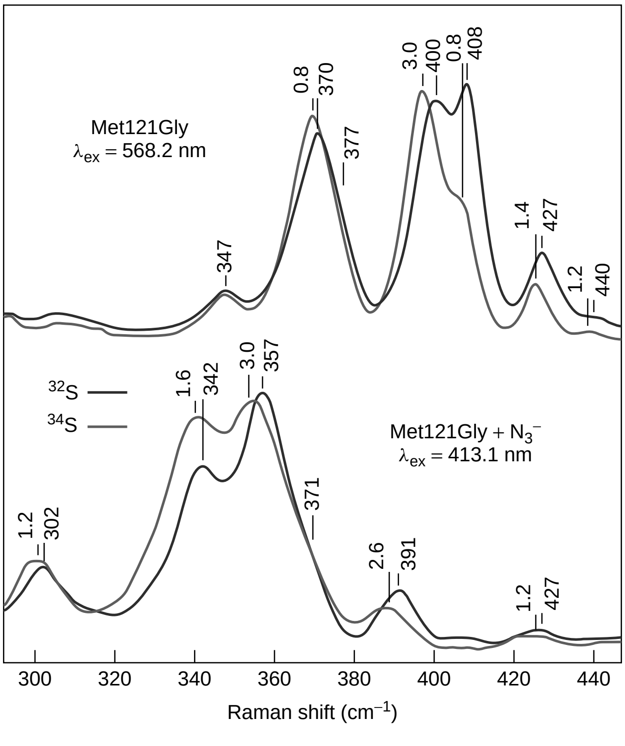

Figure 24 Low-temperature (77 K) RR spectra of *P. aeruginosa* M121G azurin and its azide adduct in the natural abundance and ^{34}S-labeled excited at 568.2 (M121G) and 413.1 nm (M121G–azide) Italic numbers show the $[\nu(^{32}\mathrm{S}) - \nu(^{34}\mathrm{S})]$ band shifts

Two azide-related vibrational modes in the M121A–N$_3{}^-$ adduct were found at 375 and 2024 cm^{-1} and assigned as the $\nu(\mathrm{Cu{-}N_3})$ and $\nu_{\mathrm{as}}(\mathrm{N_3})$ stretching modes based on $^{15}\mathrm{N}_3/^{14}\mathrm{N}_3$ isotopic shifts, −8 and −67 cm^{-1}, respectively, as shown in Figure 25.**[60]** Their counterparts in the glycine, valine, and leucine variants occur near 371 and 2045 cm^{-1} (Table 6), suggesting a weaker azide interaction with the Cu site than in the alanine variant. A nearly complete set of the thiocyanato-bound vibrational frequencies afforded by RR spectra of M121V–SCN$^-$ has permitted accurate band assignments based on the observed S^{13}CN$^-$ and SC^{15}N$^-$ isotope shifts (Figure 26) and the results of NCA calculations.**[60]** In particular, the characteristic $\nu(\mathrm{S{-}CN})$ (~720 cm^{-1}) and $\nu(\mathrm{C{\equiv}N})$ (~2100 cm^{-1}) stretching frequencies established that SCN$^-$ binds to the metal via the S atom to give a planar Cu–S–C≡N moiety. The CN$^-$ ligand coordinates to the copper via its carbon atom giving rise to two ^{13}CN-sensitive weak bands at approximately 277 and 398 cm^{-1}, assigned as the $\nu(\mathrm{Cu{-}CN})$ stretch and the $\delta(\mathrm{Cu{-}C{\equiv}N})$ bend, respectively (Table 6).

3.4 Metal Substitution in Cupredoxins

Replacement of the Cu(II) ion in native and site-directed mutants of cupredoxins with other divalent metal ions such as Mn(II), Zn(II), Ni(II), Co(II), Ru(II), or Cd(II) proved useful in structural and spectroscopic characterization of type-1 copper sites by a number of different techniques.**[70]** Single crystal structures of several Zn(II)-, Cd(II)-, Ni(II)-, and Co(II)-substituted azurins showed the metal center that is better described as a distorted tetrahedron, instead of trigonal bipyramidal as in the Cu(II) azurin, because the metal ion is shifted away from the Met121 sulfur toward the carbonyl O-ligand of Gly45.**[49,71]** Figure 27 shows a comparison of the electronic absorption spectra obtained at room temperature from solutions of WT (Cu-containing) *P. aeruginosa* azurin and its Ni(II)- and Co(II)-substituted metalloderivatives.**[70]** Addition of Ni(II) or Co(II) to apoazurin causes the major cysteine-to-metal CT electronic transition to blue shift from 627 nm (Cu azurin) to 440 (Ni azurin) and 330 nm (Co azurin). As a result, pronounced changes are also observed in the RR scattering of Ni(II) and Co(II) azurins when the laser excitation is tuned through their absorption bands at 440 and 330 nm, respectively.This is shown in Figure 28, which reports the RR spectra taken in the 100–500 cm^{-1} region from a frozen (77 K) solution of *P. aeruginosa* Ni(II)-substituted azurin upon excitation with laser radiation at 406.7,

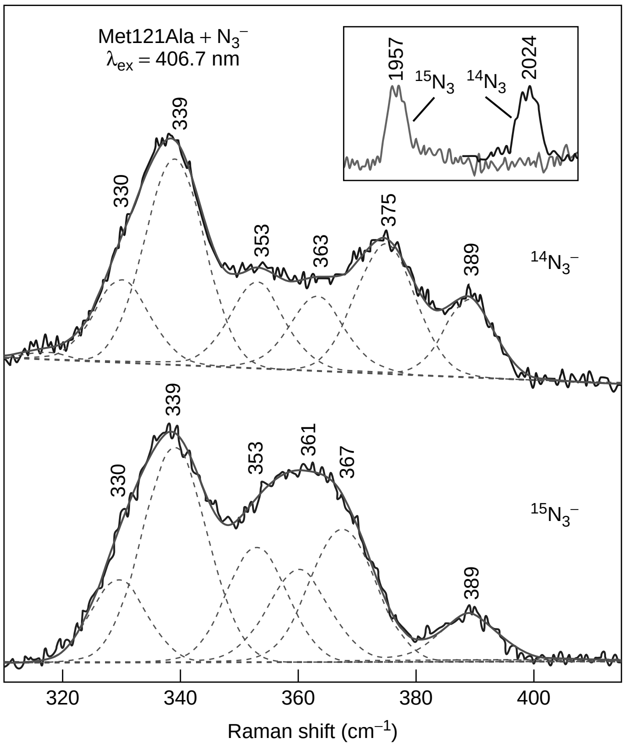

Figure 25 Curve-fitting analyses of the 310–415 cm^{-1} RR spectra of natural abundance and $^{15}N_3$-labeled azido-M121A azurins (77 K)

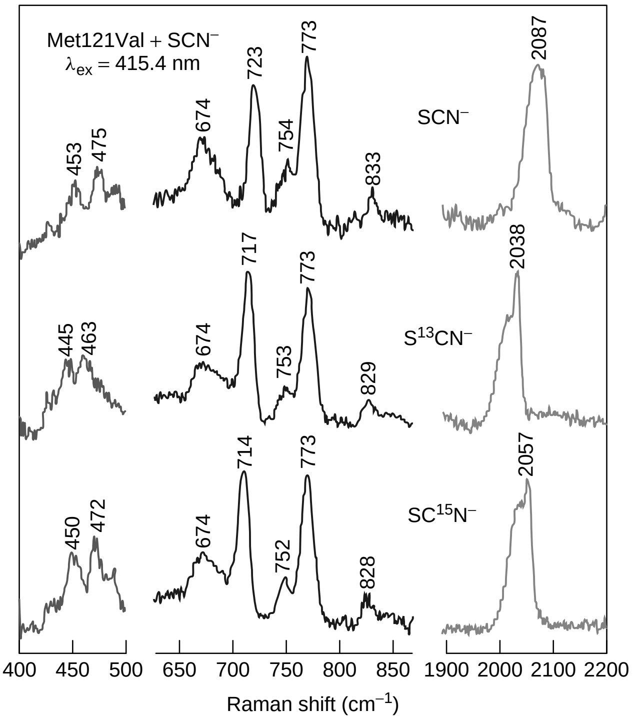

Figure 26 Low-temperature (77 K) RR spectra of thiocyanato-M121V azurin and its $S^{13}CN$ and $SC^{15}N$ isotopomers excited at 415.4-nm wavelength

Table 6 Ligand vibrations of *P. aeruginosa* azurin derivatives[a]

Vibration[b]	M121G	M121A	M121V	M121L
$\nu(C\text{–}S)_{Cys}$[c]	758	753	758	751
	Azidoazurins			
$\nu(C\text{–}S)_{Cys}$[c]	773	771	772	773
$\nu(Cu\text{–}N_3)$	∼371sh	∼375sh	∼370sh	∼370sh
$\nu_{as}(N_3)$	2042, 2051sh	2024	2048	2044
	Thiocyanatoazurins			
$\nu(C\text{–}S)_{Cys}$[c]	768	766	773	768
$\nu(Cu\text{–}SCN)$	242	237	240	244
$\delta(S\text{–}C{\equiv}N)_{oop}$	454	446	453	450
$\delta(S\text{–}C{\equiv}N)_{ip}$	470	457	475	472
$\nu(C\text{–}S)$	–	712	723	–
$\nu(C{\equiv}N)$	2072	2103	2087	2070
	Cyanoazurins			
$\nu(C\text{–}S)_{Cys}$[c]	770	767	770	771
$\nu(Cu\text{–}CN)$	–	277	–	–
$\delta(Cu\text{–}C{\equiv}N)$	–	398	–	–

[a] Values for frequencies reported in cm^{-1} from RR spectra; sh = shoulder. [b] Cu–L and internal ligand vibrations of exogenous ligand (ν = stretching, δ = bending, as = antisymmetric, ip = in-plane, and oop = out-of-plane), except where noted. [c] C–S stretch of endogenous cysteine ligands; $\nu(C\text{–}S)_{Cys}$ = 751 cm^{-1} for WT azurin.

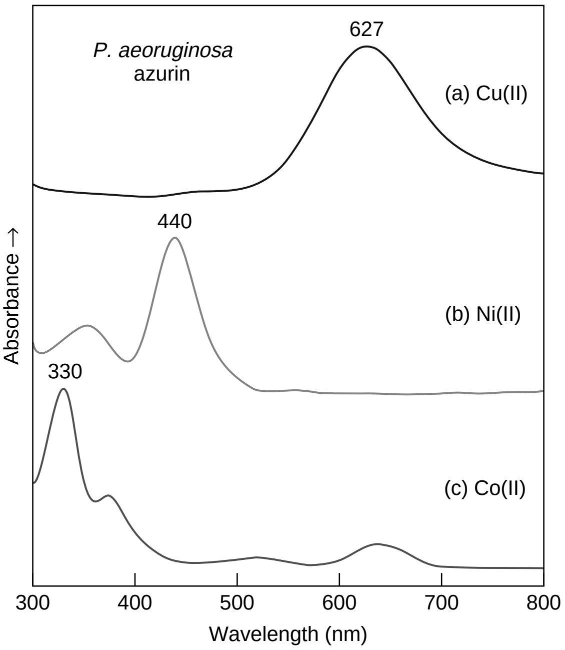

Figure 27 Room temperature UV–visible spectra of (a) native *P. aeruginosa* azurin and its (b) Ni(II)-, and (c) Co(II)-substituted derivatives

413.1, 441.6, 457.9, and 488.0 nm, and in Figure 29 where its 413.1-nm excitation spectrum is compared to that of the WT protein excited at 647.1 nm. Table 7 lists the observed RR

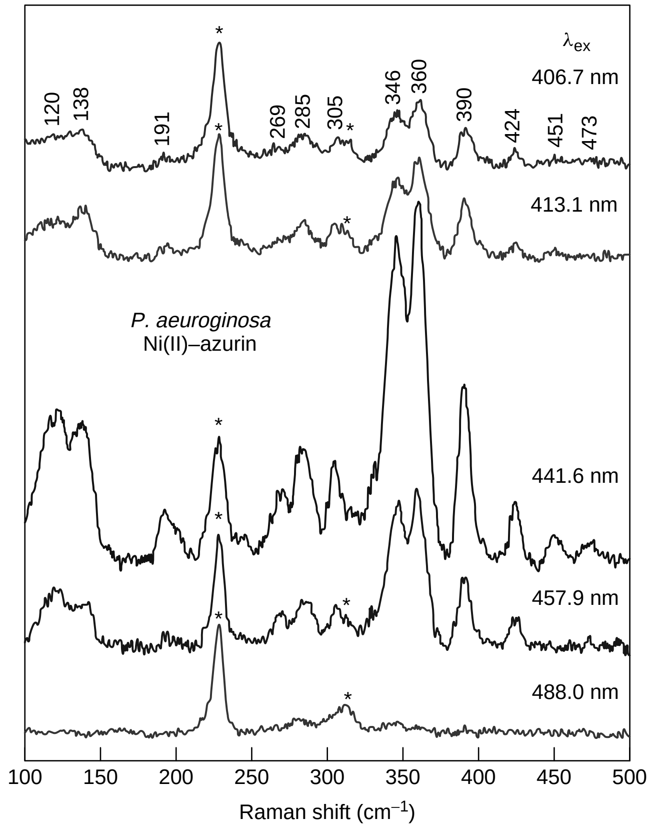

Figure 28 RR spectra (77 K) of Ni(II)-substituted *P. aeruginosa* azurin obtained with indicated excitation wavelengths. Asterisks indicate ice Raman bands

frequencies for the fundamental vibrations (100–1750 cm^{-1}) of both native *P. aeruginosa* azurin and its Ni(II) derivative,**[70]** together with those reported for Cu(II) and Ni(II) derivatives of *Alcaligenes xylosoxidans* azurin II**[72]** and *R. vernicifera* stellacyanin.**[73]**

Ni(II)-substituted azurin gives numerous vibrational bands in the 100–500 cm^{-1} range, which are maximally resonance enhanced with exciting radiation at 441.6 nm (as judged by the intensity of the protein Raman peaks relative to the ice band) (Figure 28), and which uniformly correspond to the vibrational modes of native azurin (Figure 29). Essentially, all of the 100–500 cm^{-1} vibrational modes that are observed for the native Cu(II) azurin are also detected in its Ni(II) derivative. The major vibrations that are observed for the Ni(II)-substituted azurin include a group of three intense RR peaks at 346, 360, and 391 cm^{-1} (Figure 29a), which clearly correspond to the strongest RR peaks at 373, 401(sh), 408, and 428 cm^{-1} of the native Cu(II) azurin (Figure 29b). Similarly, Co(II)-substituted azurin also gives three bands at 345, 360, and 390 cm^{-1} upon preresonant excitation at 354.2 nm (spectrum not shown).**[70]** Although [^{34}S]Cys isotopic shifts are not available for Ni(II)- and Co(II)-substituted derivatives, the apoprotein samples of *P. aeruginosa* azurin were reconstituted with different Ni isotopes (^{58}Ni or ^{62}Ni) and their high-resolution RR spectra were recorded to provide evidence for the Ni(II)–ligand vibrations. Figure 30 shows that upon substitution of ^{62}Ni for ^{58}Ni, the peaks at 424, 390, 360, 346, 285, and 269 cm^{-1} undergo shifts of −0.4, −1.0, −2.0, −0.8, −1.6, and −1.4 cm^{-1}, respectively. Thus, all of these RR bands must arise from vibrational motions that have nickel–ligand oscillatory character. The strongest Ni(II)-azurin band at 360 cm^{-1}, which exhibits the largest isotope shift (−2 cm^{-1}) upon substitution of ^{58}Ni for ^{62}Ni is ascribed to the predominantly Ni(II)–S(Cys) stretching mode, $\nu(\mathrm{NiS})_{\mathrm{Cys}}$, analogous to the dominant 408 cm^{-1} $\nu(\mathrm{CuS})_{\mathrm{Cys}}$ mode in WT azurin. The $\nu(\mathrm{NiS})_{\mathrm{Cys}}$ character is also detected for the bands at 346 and 390 cm^{-1} from their $^{62/58}$Ni isotope shifts (−0.8 and −1.0 cm^{-1}), which is consistent with kinematic coupling of the metal–thiolate stretch with internal vibrations of the cysteine ligand side chain observed in the RR spectra of cupredoxins. Meanwhile, the frequency of the β-carbon–sulfur(Cys) stretching vibration, $\nu(\mathrm{CS})_{\mathrm{Cys}}$, increased from 751 cm^{-1} in Cu(II) azurin to 763 cm^{-1} in Ni(II) azurin (Table 7, Figure 29). Taken together, these vibrational results indicate that Ni(II) substitution causes a significant weakening of the metal–S(Cys) bond as the metal coordination changes from trigonal bipyramidal of Cu(II) azurin to tetrahedral in Ni(II)-modified protein. This bond weakening is supported by the trend found in X-ray crystallographic studies of *P. aeruginosa* azurin and its Ni(II) derivative, which showed a much longer Ni–S(Cys) bond distance (2.39 Å) in Ni(II) azurin than in the WT protein (2.25 Å).**[49,71]**

The excitation wavelength-dependent RR spectra (Figure 28) also provided unambiguous evidence for the nature of the CT electronic transition at 440 nm as due to (Cys)S → Ni(II). Figure 31 compares the Ni(II)-azurin optical absorption spectrum with excitation profiles for the three most intense $^{58/62}$Ni-sensitive RR bands at 346, 360, and 390 cm^{-1}. The profiles are quite similar and closely track the absorption band in the violet region.

3.5 Substrate Binding to Type-2 Cu Site in Blue Nitrite Reductase

Copper-containing nitrite reductases (NiRs) (*see* ***Copper Enzymes in Denitrification***), involved in the anaerobic respiratory pathway as a part of the denitrification process, utilize two types of metal centers, type-1 copper (T1Cu) and type-2 copper (T2Cu), to transfer electrons in the reduction of $\mathrm{NO_2}^-$ to NO and further to $\mathrm{N_2O}$ and $\mathrm{N_2}$.**[74]** X-ray crystal structure determinations of several Cu-containing NiRs showed that these enzymes are trimers constituted of three identical monomers, each monomer containing two Cu sites.**[75–78]** The coordination environment of the T1Cu is consistent with all other blue copper electron-transfer proteins. The T1Cu of *A. xylosoxidans* NiR is coordinated by two histidines, one methionine, and one cysteine in a distorted tetrahedral arrangement, while the T2Cu is ligated by two histidines from one monomer and by one histidine form a

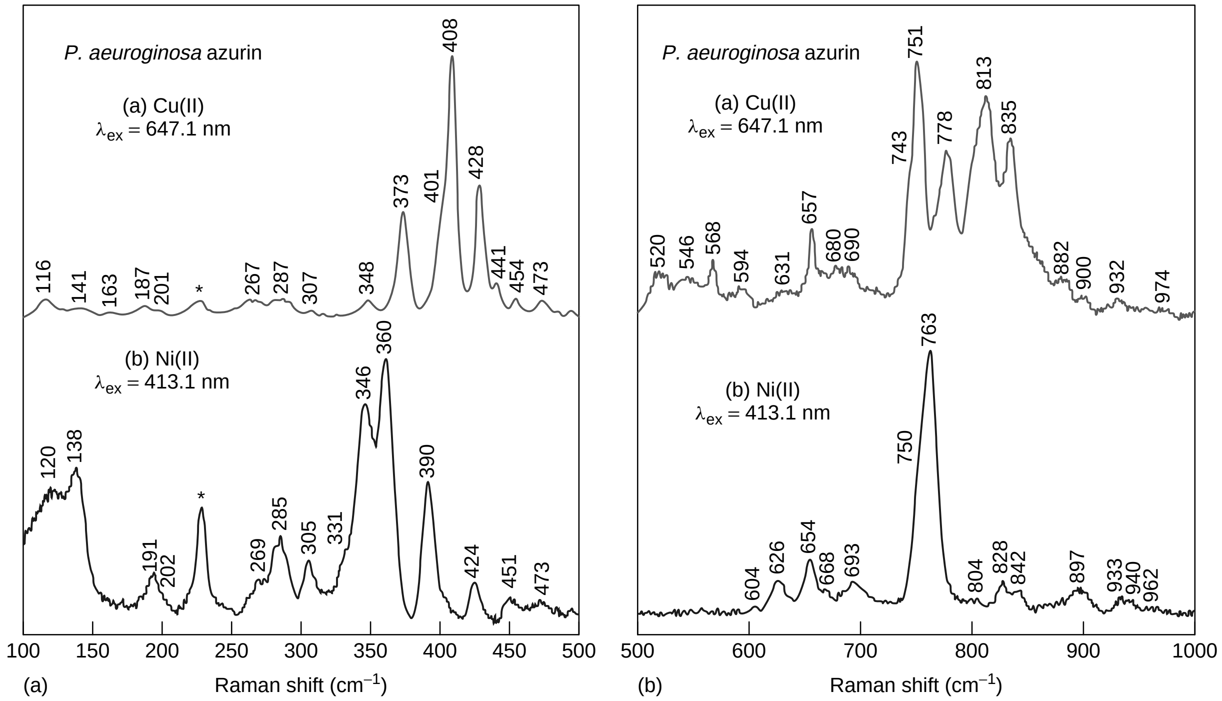

Figure 29 Low-temperature (77 K) RR spectra of *P. aeruginosa* azurin obtained in the(A) 100–500 cm^{-1} and (B) 500–1000 cm^{-1} regions on (a) native Cu(II) protein (647.1-nm excitation) and (b) its Ni(II)-substituted derivative (413.1-nm excitation). Asterisks indicate ice Raman bands

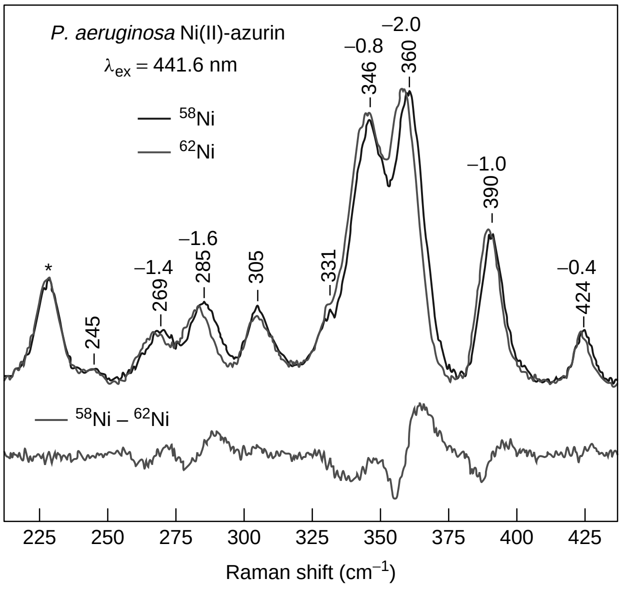

Figure 30 Effects of Ni-isotope substitution on the 200–430 cm^{-1} RR spectrum of *P. aeruginosa* azurin Italic numbers show the [$\nu(^{58}\mathrm{Ni}) - \nu(^{62}\mathrm{Ni})$] band shifts

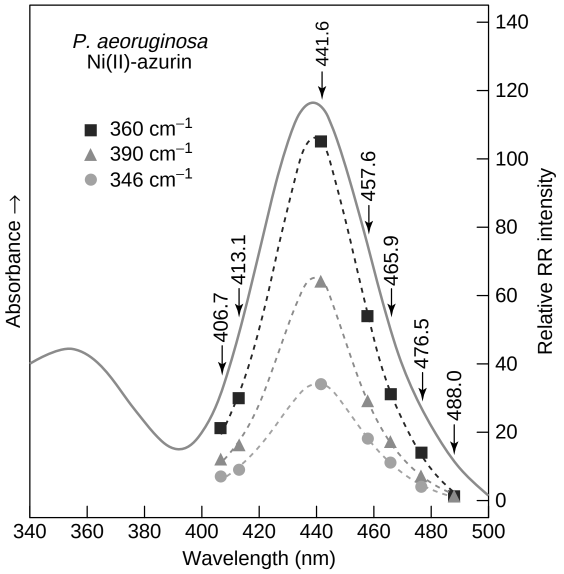

Figure 31 Excitation profiles of *P. aeruginosa* Ni(II) azurin (77 K) superimposed on the electronic absorption spectrum (298 K)

second monomer. The two copper sites of *A. xylosoxidans* NiR are directly connected through adjacent residues Cys130 and His129 that are coordinated to the T1Cu and T2Cu centers, respectively. This linkage provides a 12.5 Å pathway for efficient electron transfer from the T1Cu to T2Cu site.[78] X-ray crystallographic studies on the NO_2^--soaked NiR crystals have revealed that the T2Cu is the substrate-binding site, with an asymmetric coordination of NO_2^- to the Cu.[76–78]

Table 7 Observed resonance Raman frequencies (cm^{-1}) for fundamental vibrational modes of native Cu(II) and Ni(II)-substituted cupredoxins

Azurin[a] *P. aeruginosa*		Azurin II[b] *A. xylosoxidans*		Stellacyanin[c] *R. vernicifera*		
Cu(II)	Ni(II)	Cu(II)	Ni(II)	Cu(II)	Ni(II)	Assignment[d]
116	120					δ(NMS)
141	138					τ(CC)
187	191					δ(CCC) + δ(OCC)
267[e]	269	259		273	275	δ(CCN) + $\nu(MN)_{sym}$
287[e]	285	273		285		$\nu(MN)_{sym}$
307	305			315		$\nu(MN)_{asym}$
348	331sh	332sh		349		$\delta(CO)_{ip}$ + δ(CCN)
373	346[g]	375	331sh	360		δ(CCN) + δ(CCC)
401sh	**346**[g]	**400**		**376**	**350**	ν(MS) + δ(CCN)
408[f]	**360**	**412**	**349**	**387**	**376**	ν(MS) + δ(SCC)
428	390	426	366	418		δ(CCC) + ν(MS)
440	424			423		δ(OCC) + δ(CCC)
454	451	463		447	454	δ(OCC) + δ(CCC)
474	473			463	467	δ(CCN)
494	493			488		δ(CCN)
631	626					Amide IV
657	654	654				Amide VI
690	693					Amide IV + VI
743sh	750sh					$\delta(CO)_{wag}$ + ν(CS)
751	**763**	**750**	**755**		**762**	ν(CS)
846sh	842					Amide V
900	897					Amide V
932	933					Amide V
1001	1000					$\nu(C_\alpha C_\beta)$
1033	1045[g]					$\nu(C_\alpha C_\beta)$
1067	1068					$\nu(C_\alpha C_\beta) + \nu(C_\alpha N)$
1150sh	1147					$\nu(C_\alpha N)$
1193sh	1198					Amide III
1224	**1229**					Amide III + CH bend
1243sh	1252					Amide III
1272sh	1275					CH_2 twist
1300	1301					CH bend
1313	1312					CH bend + CH_2 wag
1344	1350					CH bend + CH_2 wag
1406	**1417**					CH_2 scissor
1433	1432					Amide II
1450	1449					Amide II
1504	1510					Amide II
1589	1588					Amide I
1631	1622					Amide I
1650	1643					Amide I
1678	1682					Amide I

[a] Native and Ni(II) azurin data from Czernuszewicz *et al.*[70] [b] Native and Ni(II) azurin II data from Hannan *et al.*[72] [c] Native and Ni(II) stellacyanin data from Musci *et al.*[73] [d] Assignments based on NCA calculations of *P. aeruginosa* azurin.[44] [e] Contain contributions from peaks at 262/268 and 280/286 cm^{-1}, respectively. [f] Boldface numbers indicate the RR peaks with the greatest intensity; sh = shoulder. [g] Possibly overlapping bands.

The RR spectroscopic investigation of blue Cu-containing *A. xylosoxidans* NiR (*Ax*NiR) has recently been carried out,[74] and the structural rearrangements at the electron-transfer site of T1Cu caused by substrate binding (NO_2^-) and the depletion of T2Cu, are briefly presented in this section. The electronic absorption spectrum of the *A. xylosoxidans* NiR exhibits the intense absorption band due to T1Cu (Cys)S → Cu(II) CT transition at 597 nm. The T2Cu site does not contribute to the visible spectrum. Trace (a) in Figure 32(A) shows the RR spectrum of the enzyme obtained at room temperature by excitation at 647.1 nm.[74] The *A. xylosoxidans* NiR has its own unique T1Cu spectrum in the $\nu(CuS)_{Cys}$ region, with one strong peak at 412 cm^{-1}, a prominent shoulder at ~420 cm^{-1}, and additional small features at 364 and 376 cm^{-1}.

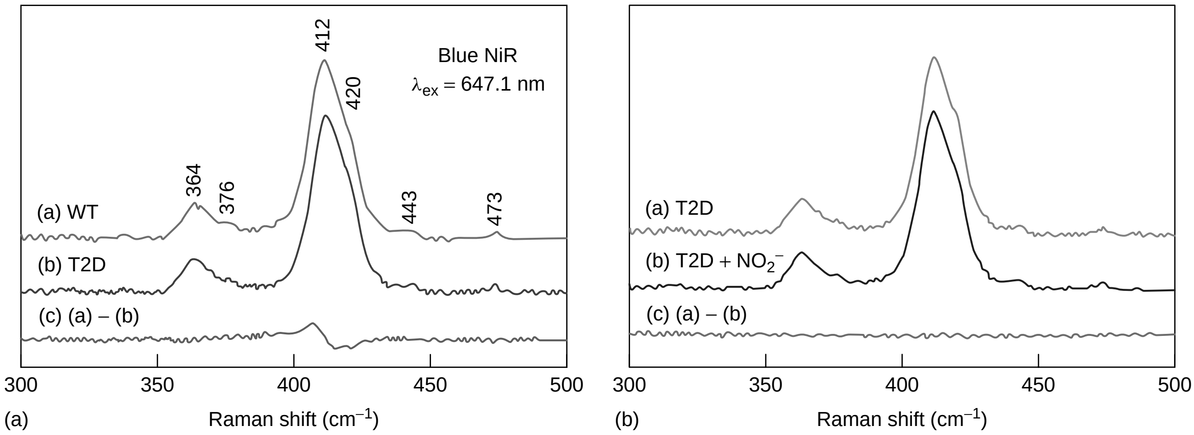

Figure 32 (A) RR spectra of (a) holo-*Ax*NiR (WT) and (b) its T2Cu-depleted protein (T2D) in 20 mM phosphate buffer (pH 7.0), and (c) their difference spectrum. (B) RR spectra of T2D *Ax*NiR in the absence (a) and presence (b) of nitrite and their difference spectrum (c)

To investigate the spectral contribution of the T2Cu, the RR spectra of type-2-copper-depleted (T2D) *A. xylosoxidans* NiR were measured. Trace b in Figure 32(A) shows that the T2D enzyme gave a spectrum almost identical to that of the holoenzyme (trace a in Figure 32A). The difference spectrum (trace c in Figure 32A) between T2D and holoenzyme revealed that the Raman bands associated with stretching the Cu(II)–S(Cys) bond, particularly those at 412 and 420 cm^{-1}, are slightly shifted to higher frequencies upon removal of the T2Cu ion, because of the subtle rearrangement of the T1Cu–Cys130–His129–T2Cu intersite structure.

By the sensitive RR difference spectroscopic technique, *A. xylosoxidans* NiR in the presence of various nitrite concentrations has been probed (Figure 33). The RR spectra of blue NiR recorded in the presence and absence of nitrite do not show significant changes (Figure 33a and b), but their difference spectra (Figure 33i) clearly show that the substrate binding alters the structure of the T1Cu site in NiR. The Raman bands of $\nu(\mathrm{CuS})_{\mathrm{Cys}}$ at 412, 420, and 364 cm^{-1} all shift to higher energies in the presence of nitrite, and the intensity of the difference spectra depends on the concentration of nitrite (Figure 33c–i). These spectral changes, upon treatment of the enzyme with aliquots of increasing NO$_2^-$ concentration, imply that nitrite does not enter the coordination sphere of the T1Cu center in NiR but rather binds to its T2Cu ion, as had been previously established by X-ray crystallography.[76–78] The increased frequencies of the Raman bands at 412, 420, and 364 cm^{-1} in nitrite-bound enzyme suggest that there could be a stronger Cu(II)–S(Cys) bonding than that in the absence of substrate, or a weakened hydrogen bonding to the coordinated sulfur ligand of cysteine, as a result of the T1Cu–T2Cu intersite structural rearrangement. That substrate binding occurs at the T2Cu site has been supported by the RR spectra of T2D *A. xylosoxidans* NiR measured in the presence and absence of nitrite. The results are presented in Figure 32(B), where it can be seen that the spectrum of T2D enzyme does not show any changes in the $\nu(\mathrm{CuS})_{\mathrm{Cys}}$ bands by the addition of nitrite, as evident from the nitrite-treated T2D minus untreated T2D difference spectrum (trace c in Figure 32B).

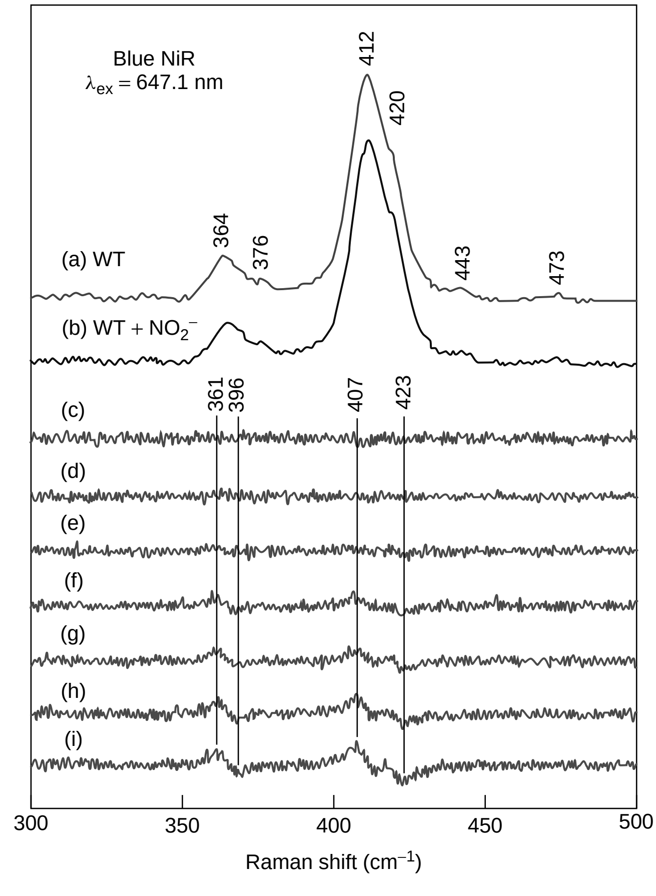

Figure 33 RR spectra of (a) holo-*Ax*NiR (0.5 mM) and (b) its complex with nitrite (10 mM). Traces (c–i) are difference RR spectra between those in the absence and presence of nitrite: (c) none; (d) 0.5 mM; (e) 1.25 mM; (f) 2.5 mM; (g) 4.0 mM; (h) 5.0 mM; (i) 10 mM

3.6 The Mononuclear FeS_4 Site in Rubredoxins

Iron–sulfur clusters (*see* ***Iron–Sulfur Proteins***), involved in a variety of biological redox processes, photosynthesis, nitrogen fixation, and respiration, have a common building block with Fe tetrahedrally coordinated to four S-donor ligands.[16,22,79] In 1-Fe rubredoxins, in which the building block itself constitutes their active site, the sulfur atoms belong to four cysteine amino acids of the protein backbone. In [2Fe–2S] ferredoxins, the iron ions are bridged by inorganic μ_2-sulfides and bound to two sulfur atoms of cysteine residues. In cuboidal [3Fe–4S] clusters, each iron is ligated to three of the four acid-labile sulfur atoms and to one additional cysteinyl sulfur. The most prevalent cluster type is found in [4Fe–4S] proteins, the bacterial ferredoxins, and high-potential iron–sulfur proteins, in which each iron interacts with three inorganic μ_3-sulfides and sulfur atom of cysteine, forming a cubane shape with iron and sulfur atoms in alternation.[79] The Fe–S proteins are brown in color, owing to visible absorption bands that are associated with CT transitions from sulfur (both bridging and terminal) to Fe(III). Consequently, the structurally diverse 1-Fe, 2-Fe, 3-Fe, and 4-Fe centers of Fe–S proteins have been probed extensively with room- and cryogenic-temperature RR spectroscopy, using isotope labeling to identify the Fe–S cluster vibrational modes in the RR spectra.[22,79–85] As expected, the RR spectra show selective enhancement of Fe–S vibrations, due to the extension of the Fe–S bonds in the CT-excited states. The spectral patterns are unique and distinctive for different structural types and several detailed reviews on this subject have been published.[16,22,79]

Rubredoxin was the very first metalloprotein to which RR spectroscopy was applied. In 1970 and 1971, Long and coworkers found four bands in the metal–ligand stretching and bending region in the 488.0-nm excitation RR spectra of rubredoxin from *Clostridium pasteurianum*,[86,87] just the number of normal modes expected for a tetrahedral FeS_4 complex. A strong polarized band at $314\,cm^{-1}$ was assigned to the totally symmetric breathing mode $\nu_1(A_1)$, involving the in-phase stretching of all four Fe(III)–S(Cys) bonds. The other three stretches (there must be four altogether, one for each bond) were assigned to the triply degenerate out-of-phase mode $\nu_3(T_2)$, observed weakly as a depolarized band at $368\,cm^{-1}$. The remaining two bands at 126 and $150\,cm^{-1}$ were identified with the S–Fe–S bending modes, $\nu_2(E)$ (doubly degenerate) and $\nu_4(T_2)$ (triply degenerate), respectively. These four bands are close in frequency to the modes of the isoelectronic complex $[FeCl_4]^- = 385$ (ν_3), 330 (ν_1), 133 (ν_4), and $108\,cm^{-1}$ (ν_2).[88] Thus, the analysis of the protein RR spectrum was satisfyingly straightforward.

Subsequent RR studies,[89] with better spectral quality and with isotope shift data, have shown the situation to be more complex, however. Figure 34 shows an interesting variation

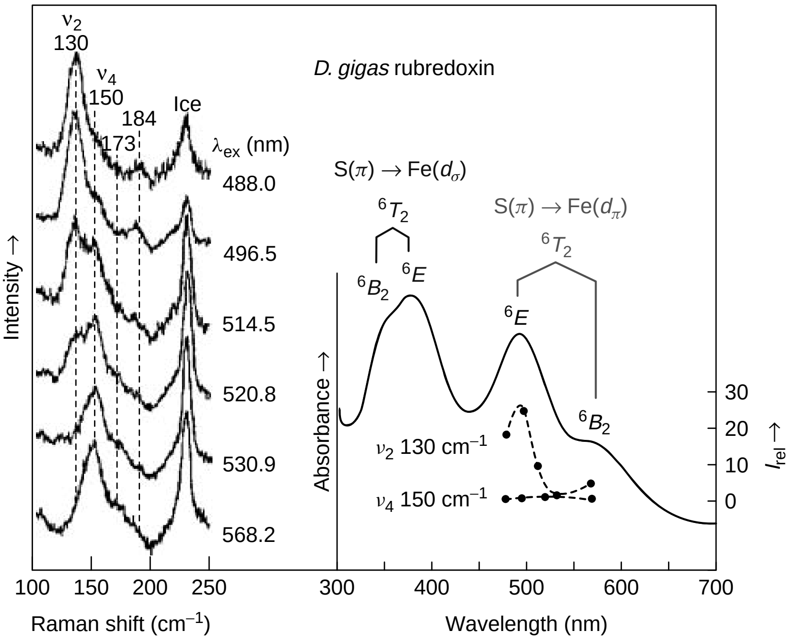

Figure 34 Variable wavelength RR spectra of a frozen *D. gigas* rubredoxin solution in the bending-mode region. The intensities of ν_2 and ν_4 were determined by ratioing them with the $227\,cm^{-1}$ ice band (marked with an asterisk) intensity. The resulting excitation profiles are compared with the absorption spectrum, showing that ν_2 is strongly resonant with the 495-nm absorption band, while ν_4 is weakly resonant with the 565-nm shoulder. These transitions are assigned respectively to the ^6E and $^6B_2$ components of the $S(\pi) \rightarrow Fe(d\pi)$) charge-transfer transition, split by symmetry lowering from T_d to D_{2d}. The former electronic component provides A-term enhancement of the A_1 vibrational component of the E bending mode (ν_2), while the latter provides B-term enhancement to the E component of the T_2 mode (ν_4), via vibronic coupling with the nearby ^6E electronic transition

with laser wavelength of the $\nu_2(E)$ and $\nu_4(T_2)$ bending modes of rubredoxin from *Desulfovibrio gigas*. The excitation profiles, constructed by ratioing the band intensities of the frozen protein sample to the intensity of the nearby ice band at 227 cm^{-1}, showed $\nu_2(E)$ to be strongly resonant with the strong absorption band at 495 nm, while $\nu_4(T_2)$ is weakly resonant with the 565-nm shoulder. These results were interpreted on the basis of a previous electronic assignment by Eaton and Lovenberg,**[90]** also shown in Figure 34. Two CT transitions are expected in the visible region, from the sulfur π to the Fe d_π and d_σ orbitals, but these are split by a lowering of the effective symmetry of the chromophore, from T_d to at least D_{2d}, because of an elongation of the tetrahedron along the S_4 symmetry axis. The 495-nm band and its 565-nm shoulder were assigned respectively to the ^6E and $^6B_2$ components of the $\text{Fe}(d_\pi) \leftarrow \text{S}(\pi)$ transition. These components can be coupled vibronically via a mode of $B_2 \times E = E$ symmetry. The T_2 vibrational modes also have E and B_2 components in D_{2d} symmetry. Therefore, the E component of the T_2 mode can couple the weak 565-nm transition with the strong nearby 495-nm transition, thereby accounting for the ν_4 enhancement via the B-term scattering mechanism. On the other hand, the ν_2 enhancement in resonance with the strong 495-nm transition can be attributed to FC scattering, since the E (T_d) mode has A_1 and B_1 components in D_{2d} symmetry, and the A_1 component is subject to A-term enhancement. The second components of each mode, B_2 of ν_4 and B_1 of ν_2, are not observed because they lack effective enhancement mechanisms.

Further complexity was discovered when the Fe–S stretching region was reexamined at higher resolution in frozen protein solution at 77 K.**[89]** When the low-temperature spectrum was recorded with 568.2-nm excitation (Figure 35), three bands were now seen at 376, 363, and 348 cm^{-1}, not one, in the $\nu_3(\text{T}_2)$ region, implying the degeneracy being completely lifted. In addition, a prominent shoulder at 324 cm^{-1} became apparent on the ν_1 band. The assignment of the bands at 376, 363, and 348 cm^{-1} to ν_3 components was established by examining their isotope shifts in ^{54}Fe-reconstituted protein via RR difference spectroscopy, as shown in Figure 36. All three bands showed clear ^{54}Fe-isotope shifts to higher frequency, as expected for antisymmetric Fe–S stretching vibrations. The dominant RR band at 314 cm^{-1} did not shift on ^{54}Fe substitution, confirming its assignment to the FeS$_4$ breathing mode, ν_1 (the Fe atom does not move in such a mode). Likewise, a side band at 324 cm^{-1} showed no discernible ^{54}Fe shift; the intensity is canceled in the difference spectrum over the 314–324 cm^{-1} band envelope (Figure 36). This band was therefore assigned to a cysteine SCC bending mode, δ(SCC).**[89]**

To account for the main features of the rubredoxin RR spectrum, vibrational modes of a series of small molecule analogs, $[\text{Fe}^{\text{III}}(\text{SMe})_4]^-$, $[\text{Fe}^{\text{III}}(\text{SEt})_4]^-$, and $[\text{Fe}^{\text{III}}(\text{S}_2\text{-}o\text{-xyl})_2]^-$ (SMe = methylthiolate, SEt = ethylthiolate, and S$_2$-o-xyl = o-xylene-α,α'-dithiolate), have been analyzed using RR and IR spectra of isotopomers (^{54}Fe, ^{34}S, and ^{2}H).**[91]** The vibrational spectra of analog complexes revealed that the splitting of the triply degenerate ν_3Fe–S stretching mode is mainly due to (i) nontetrahedral S–Fe–S angles, (ii) out-of-plane rotation of the S–C bonds, and (iii) kinematic coupling between Fe–S stretching and S–C–C bending modes, which is greatly dependent on the FeS–CC dihedral angles. Using a consistent force field for all three complexes, NCA calculations provided a good match to the observed values of ν_1, ν_2, ν_{3a-c}, and ν_4, and their respective isotope shifts.

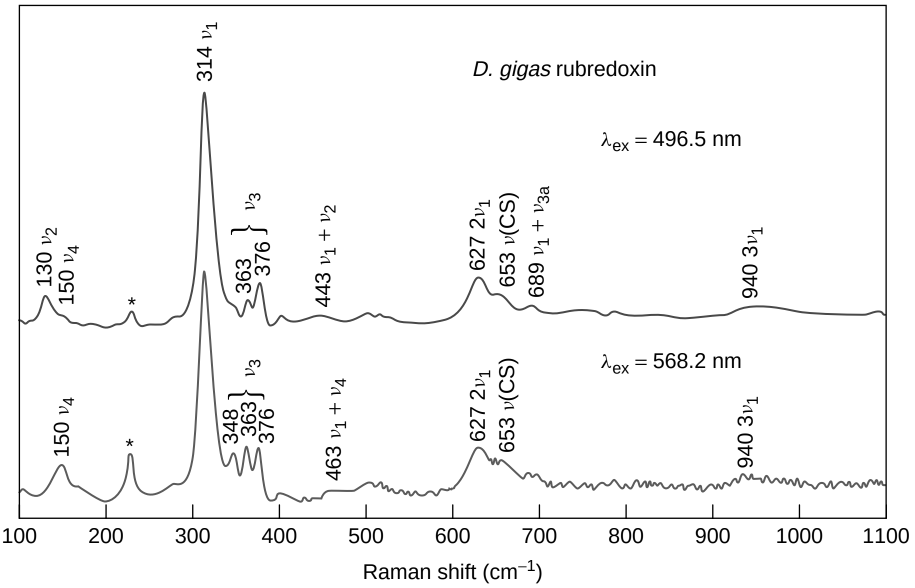

Figure 35 Low-temperature (77 K) RR spectra of *D. gigas* rubredoxin obtained in the 100–1100 cm^{-1} region using 496.5- and 568.2-nm excitations

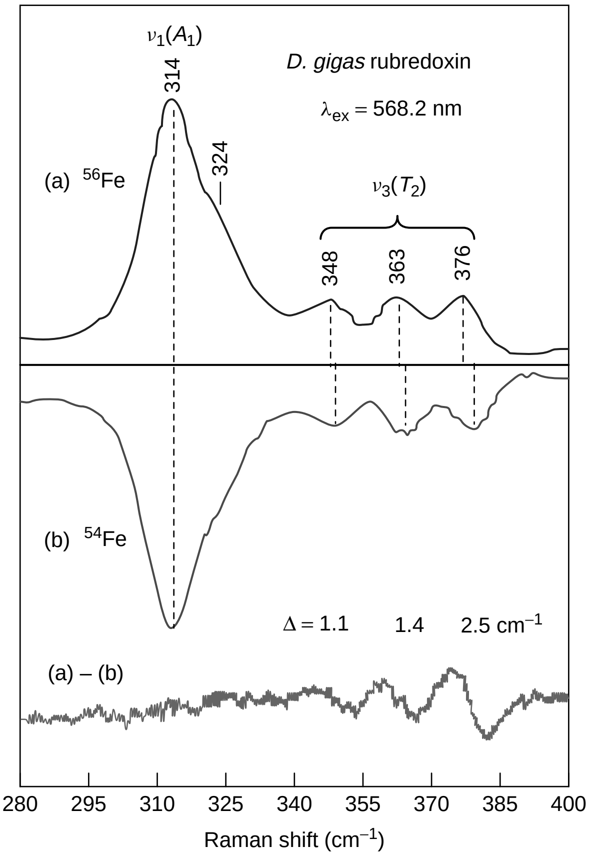

Figure 36 568.2-nm excited RR spectrum in the Fe–S stretching region for (a) natural abundance *D. gigas* rubredoxin and (b) of the protein reconstituted with ^{54}Fe

The rubredoxin RR bands and ^{54}Fe isotope shifts were also modeled with the same force field, which revealed a dominant influence of ν(FeS)/δ(SCC) mixing due to 180° FeS–CC dihedral angles for two of the cysteine ligands at the rubredoxin active site. However, proper calculation of the ν_1 frequency of rubredoxin required a significant reduction of the Fe–S stretching force constant (1.27 mdyn/Å), relative to that of the analog complexes (1.34 mdyn Å^{-1}). The lower force constant implies weaker Fe(III)–S(Cys) bonds. This reduction was proposed to reflect the influence of H bonding to the cysteinate S atom in the protein.**[89]** The H bonds reduce the negative charge on the S atoms and reduce their donor strength, i.e., weaken the Fe–S(Cys) bonds in the protein.

3.7 The FeS$_4$ and Fe–O–Fe Sites in Rubrerythrin

This intriguing nonheme homodimeric protein (*see* ***Iron Proteins with Dinuclear Active Sites***), originally isolated from the anaerobic sulfate-reducing bacterium *Desulfovibrio vulgaris*,**[92]** contains a unique combination of two types of chromophoric iron(III) sites in each subunit: one rubredoxin-like Fe(S-Cys)$_4$ center in the C-terminal domain and one nonsulfur, (μ-oxo)*bis*(μ-carboxylato)-triply bridged binuclear Fe(III) cluster in the N-terminal domain.**[93,94]** The initial spectroscopic indications of these sites have been confirmed by protein X-ray crystallography structural studies**[95–97]** (Figure 37), but the first evidence for the Fe–O–Fe structural unit in rubrerythrin came from RR spectroscopy.**[92]** Figure 37 shows low-temperature (77 K) RR spectra of as-isolated *D. vulgaris* rubrerythrin in a liquid N$_2$ cell with excitation at 496.5 and 406.7 nm.**[92]** These excitation wavelengths are in resonance with the well-separated (Cys)S $\rightarrow$ Fe(III) (~492 nm) and μ-oxo $\rightarrow$ Fe(III) (~370 nm) CT electronic absorption bands, respectively, of rubrerythrin. Figure 38 compares RR spectra obtained with 406.7-nm excitation for the protein contained in H$_2$O and the recrystallized protein dissolved in H$_2{}^{18}$O, D$_2$O, and D$_2{}^{18}$O. Band frequencies, isotope shifts, and assignments are listed in Table 8. The 496.5-nm excitation spectrum in Figure 37 (upper trace) is overwhelmingly dominated by the vibrational modes characteristic of rubredoxin-like Fe(Cys)$_4$ sites: a strong band at 314 cm^{-1}, assigned to the cluster breathing ν_1 mode; a set of widely spaced weaker bands at 340, 355, and 374 cm^{-1}, assigned to three components of the ν_3 antisymmetric Fe–S(Cys) stretch; weak bands at 128 and 156 cm^{-1}, assigned to ν_2 and ν_4 S–Fe–S bending modes; and numerous overtone and combination bands of the Fe–S(Cys) stretches in the 450–800 cm^{-1} region. Indeed, the number, positions, and intensities of these resonance-enhanced Raman bands closely match those observed for frozen solutions of rubredoxins from *D. gigas* (Figure 35, Table 8)**[89]** and *Pyrococcus furiosus*.**[98]**

In contrast, the RR spectrum of *D. vulgaris* rubrerythrin excited at 406.7 nm shows dramatically diminished intensities of the FeS$_4$ bands with concomitant enhancement of a band at 514 cm^{-1} (Figure 37, bottom trace). This band shifts 18 cm^{-1} to lower frequency (496 cm^{-1}) when the protein is dissolved in H$_2{}^{18}$O (Figure 38). Therefore, the 514-cm^{-1} band must involve vibrational motion of a water-exchangeable oxygen atom. The frequency of this band and the ^{18}O isotope shift are those expected for the symmetric Fe–O–Fe stretch, ν_s(FeOFe), of a bent μ-oxo-bridged diiron(III) cluster that has one or two additional cobridging carboxylate ligands.**[92]** From the observed ν_s(FeOFe) frequency (514 cm^{-1}) and its ^{18}O isotope shift (-18 cm^{-1}), an Fe–O–Fe angle of 124° was calculated for the diferric cluster in rubrerythrin by solving a simple X–Y–X three-body vibrational problem.**[21]** The bridge substitution experiments also revealed a small but reproducible shift (+2 cm^{-1}) to higher frequency for the ν_s(FeOFe) stretch when the rubrerythrin crystals are dissolved in D$_2$O and D$_2{}^{18}$O (Figure 38), implying involvement of hydrogen bonding to the oxo group at the Fe–O–Fe site. All these RR inferences have later been confirmed by protein X-ray crystallography performed on single crystals of all-ferric recombinant *D. vulgaris* rubrerythrin.**[95,96]** As shown in Figure 37, its Fe^{3+} ions are both pseudo-octahedrally coordinated; one Fe^{3+} ion is ligated terminally by one bidentate glutamate and one histidine, the other Fe^{3+} ion

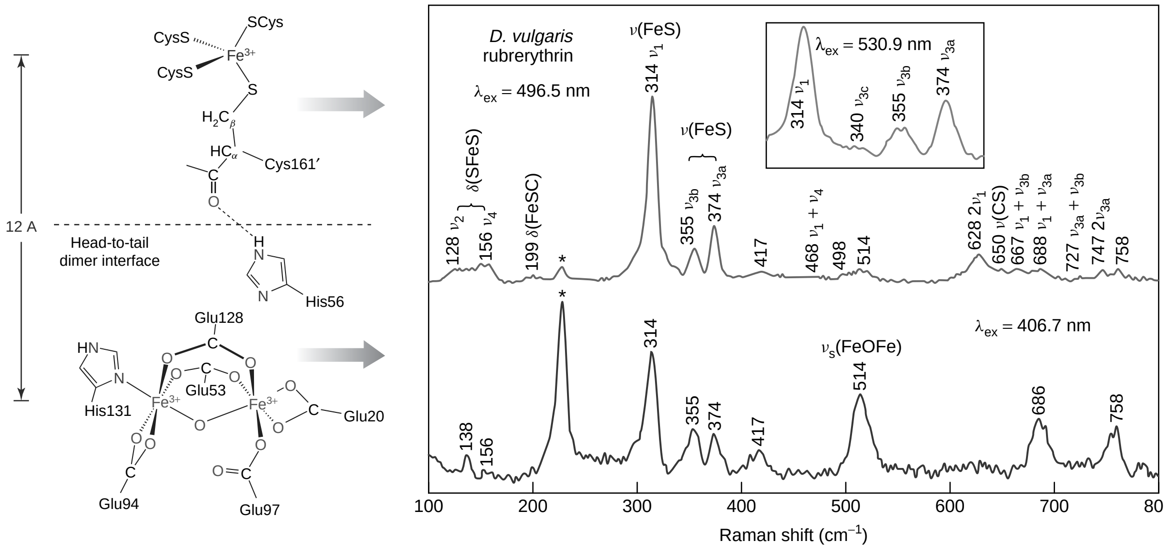

Figure 37 Low-temperature (77 K) RR spectra of *D. vulgaris* rubrerythrin obtained in the 100–800 cm^{-1} region with 496.5- (upper trace) and 406.7-nm (lower trace) excitation wavelengths. The spectrum excited at 496.5 nm is totally dominated by the bands arising from the Fe(S-Cys)_4 cluster, whereas that excited at 406.7 nm shows dramatically diminished intensities of the Fe–S bands with a concomitant enhancement of the band at 514 cm^{-1} assigned to ν_s(FeOFe) mode of a bent Fe–O–Fe cluster. Asterisks indicate the 228 cm^{-1} ice band

Table 8 Observed RR frequencies (cm^{-1}) and assignments for *D. gigas* rubredoxin and *D. vulgaris* rubrerythrin[a]

D. gigas rubredoxin	*D. vulgaris* rubrerythrin	Assignment
130	128	δ(SFeS),[b] ν_2,[c] $A_1(E)$[d]
150	156	δ(SFeS), ν_4, $E(T_2)$
174		δ(FeSC)
184	199	δ(FeSC)
314	314	ν(FeS), ν_1, $A_1(A_1)$
324		δ(SCC)
348	340	ν(FeS), ν_{3c}, $E(T_2)$
363	355	ν(FeS), ν_{3b}, $E(T_2)$
376	374	ν(FeS), ν_{3a}, $B_2(T_2)$
403	417	?
443	442	$\nu_1 + \nu_2$
463	468	$\nu_1 + \nu_4$
502	498	?
518	514	?
	514(−18)[+2][e]	ν_s(FeOFe)[f]
627	628	$2\nu_1$
653	650	ν(CS)
	667	$\nu_1 + \nu_{3b}$
	686[−1]	?
689	688	$\nu_1 + \nu_{3a}$
733	727	$\nu_{3a} + \nu_{3b}$
751	747	$2\nu_{3a}$
	758[−17]	?
757	759	$2\nu_1 + \nu_2$
777		$2\nu_1 + \nu_4$

[a] Rubredoxin data and assignments from Czernuszewicz *et al.*[89] Rubrerythrin data from Dave *et al.*[92]. ? = Indeterminate assignment. [b] δ(XYZ) and ν(XY) are bending and stretching coordinates involving the indicated atoms. [c] ν_{1-4} are normal modes of a XY_4 tetrahedron. [d] Symmetry designation for the $D_{2d}(T_d)$ point groups. [e] The numbers in () and [] indicate the frequency shifts in $\text{H}_2{}^{18}\text{O}$ and D_2O, respectively. [f] ν_s is the symmetric (in-phase) Fe–O–Fe stretching coordinate.

is ligated terminally by two glutamates, and the two Fe^{3+} ions are bridged by two bidentate glutamate ligands and an oxo (O^{2-}) group derived from the solvent. From the Fe···Fe (3.33 Å) and Fe–O (average 1.93 Å) distances,[96] the Fe–O–Fe angle of ∼120° can be calculated for the binuclear Fe(III) structure in rubrerythrin, which compares well with the bridge angle of 124° derived from RR spectroscopy. The Fe–O–Fe site is located close to the protein surface such that the μ-oxo-bridge is accessible to bulk solvent through a crevice formed between two α-helices (A and C).[91] Thus, intramolecular hydrogen bonding between the bridging μ-oxo group and H_2O can be anticipated and is responsible for the deuterium isotope effects on the ν_s(FeOFe) stretch in the RR spectrum of rubrerythrin (Figure 38).[92]

3.8 Cysteine Ligand Substitution in Rubredoxin

Systematic replacement of cysteine ligands at the Fe(S-Cys)_4 active site of rubredoxin[99,100] by site-directed mutagenesis has proven useful in probing many fundamental properties of iron–sulfur proteins.[99–104] For example, mutant forms of rubredoxin from *C. pasteurianum* (Rd*Cp*) in which each of its four cysteine ligands was replaced, in turn, with serine (C6S, C9S, C39S, and C42S)[99,101] constitute a set of four geometric isomers that have differently oriented Fe(S-Cys)_3(O-Ser) centers within the same protein chain. Their properties fall into two pairs, depending upon whether a surface (C9, C42) or an interior (C6, C39) ligand is substituted (Figure 39). A comparison of the solution optical spectra of the WT protein and its surface ligand cysteine-to-serine mutants (C9S, C42S, and C9S/C42S) showed blue shifts of the absorption bands arising from (Cys)S → Fe(III)

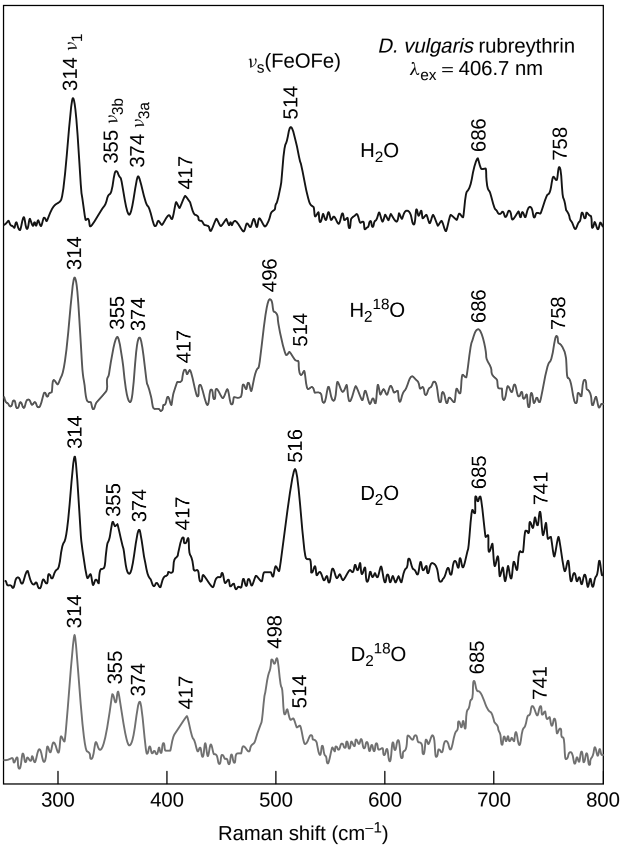

Figure 38 406.7-nm excited RR spectra of *D. vulgaris* rubrerythrin contained in H_2O, $H_2{}^{18}O$, D_2O, and $D_2{}^{18}O$ (frozen protein solutions at 77 K), showing the effects of $^{16/18}O$ and H/D exchange on the resonance-enhanced vibrational modes

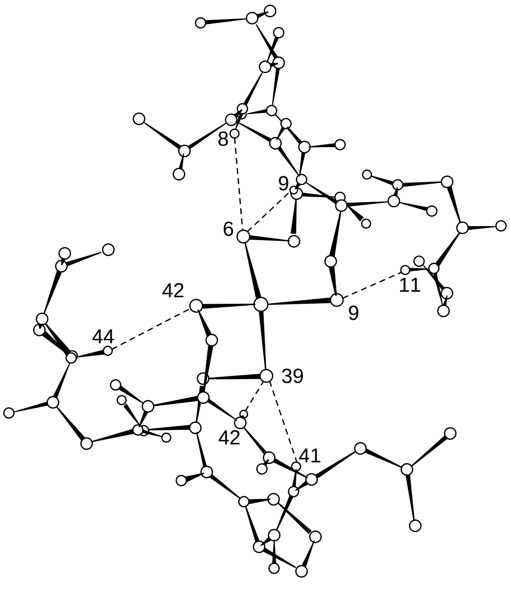

Figure 39 NH· · ·S interactions (- - - -) around the Fe(S-Cys)$_4$ center in Rd*Cp* (pdb5rxn.ent).[105] A pseudo-2-fold axis is perpendicular to the page, passing through the Fe atom

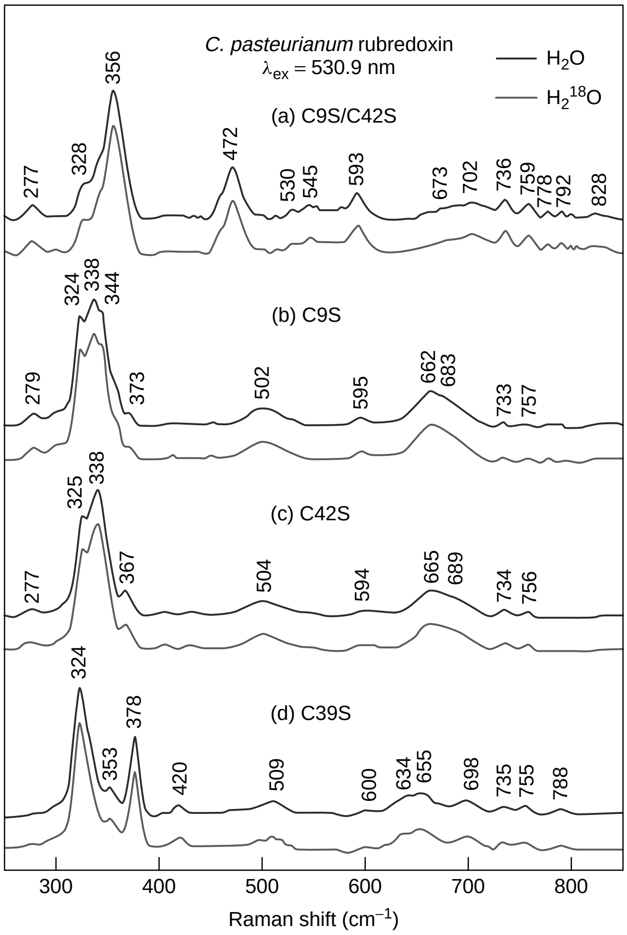

Figure 40 Low-temperature (77 K) RR spectra (530.9-nm excitation) of oxidized Rd*Cp* proteins: (a) C9S/C42S, (b) C9S, (c) C42S, and (d) C39S mutants in H_2O and $H_2{}^{18}O$

CT, consistent with the number of oxygen atoms increasing in the order FeS_4, FeS_3O, FeS_2O_2.[101] Figure 40 compares RR spectra for the C9S/C42S doubly mutated protein in H_2O and $H_2{}^{18}O$ with those of single mutants C9S, C42S, and C39S, using an excitation wavelength of 530.9 nm.[99] Each protein exhibits strong $\nu(FeS_{2,3})$ stretching modes of vibration in the range 325–475 cm^{-1} and a cluster of weaker overtone and combination bands associated with $\nu(FeS_{2,3})$ in the range 650–850 cm^{-1}, as expected for Raman scattering excited in resonance with the rubredoxin (Cys)S → Fe(III) CT transitions.[22,43,89,98] In addition, each gives a band at 597 ± 4 cm^{-1} that is not present in the WT protein spectrum. These frequencies (i) shift by 1.5–3.0 cm^{-1} to higher frequency in ^{54}Fe-reconstituted protein samples; (ii) do not shift in samples that have been freeze-dried and redissolved in $H_2{}^{18}O$ (compare with the C6S protein discussed later); and (iii) are independent of pH in the range pH 6–10. The new band at 597 ± 4 cm^{-1}, which exhibited a ca. +3 cm^{-1} ^{54}Fe isotope upshift, may be assigned to $\nu(FeO_x)$ ($x = 1, 2$) vibrational modes, consistent with the presence of ferric Fe(S-Cys)$_3$(O-Ser) and Fe(S-Cys)$_2$(O-Ser)$_2$ centers in the single and double mutants, respectively.**[99]** An enhancement of the Fe–O(Ser) stretching vibration is possible via kinematic coupling with the intense ν(FeS$_{2,3}$) modes.

RR spectra of the interior ligand C6S mutant dissolved in H_2O and in isotopically labeled waters, $H_2{}^{18}O$ and D_2O, are presented in Figure 41.**[99,100]** Also shown there is the spectrum of C6S reconstituted with ^{54}Fe. The C6S spectra are independent of pH in the range 6–10, but in contrast to those of the other cysteine-to-serine mutants (Figure 40), it is sensitive to $H_2{}^{18}O$. A band at ~617 cm^{-1} in H_2O (Figure 41a), which occurs at ~620 cm^{-1} for the ^{54}Fe-reconstituted C6S protein (Figure 41b), and shifts down by ~25 cm^{-1} on $H_2{}^{18}O$ exchange (Figure 41c). This band must involve vibrational motion of an iron atom and a water-exchangeable oxygen atom and is attributed to a ν(FeOH) vibration of an Fe–OH fragment. Evidence that the 617 cm^{-1} band is associated with a hydroxyl group is provided by its 13 cm^{-1} *increase* in frequency in D_2O (Figure 41d), resulting from differential coupling of the stretching ν(FeOH) coordinate with the bending δ(FeOH) coordinate involving H or D atoms.**[106]** The frequencies of the δ(FeOH) bending modes are variable but can be close to 700 cm^{-1} for strongly H-bonded hydroxyl groups. The interaction between ν(FeOH) at 617 cm^{-1} and δ(FeOH) near 700 cm^{-1} would be relieved in D_2O because of the large drop in the δ(FeOD) frequency. This would result in the observed *increase* of the ν(FeOD) stretching frequency. The observed upshift of 13 cm^{-1}, upon dissolution of C6S in D_2O, has been reproduced by a simplified NCA calculation with a three-atom Fe–O–H model using reasonable force constants and structure parameters.**[99]** The RR spectra of the C6S and C39S proteins are very similar, indicating the presence of a similar Fe^{III}S$_3$O center in each protein. Thus, while an [Fe^{III}(S-Cys)$_3$(O-Ser)]$^-$ center is maintained in C39S, the weakness of a longer Fe(III)–O(Ser) bond in C6S has led to its hydrolysis and the presence of an [Fe^{III}(S-Cys)$_3$(OH)]$^-$ center and an unligated HO-Ser-6 residue. The [Fe^{III}(S-Cys)$_3$(OH)]$^-$ center in the C6S protein is a promising model system for a number of M(S-Cys)$_3$ sites, including the mononuclear iron sites in NifU and IscU proteins involved in the iron–sulfur cluster assembly.**[103,104]** The RR spectrum reported for the monomeric iron-binding site in NifU**[103]** is very similar to that of the C6S mutant of *C. pasteurianum* rubredoxin.**[107]**

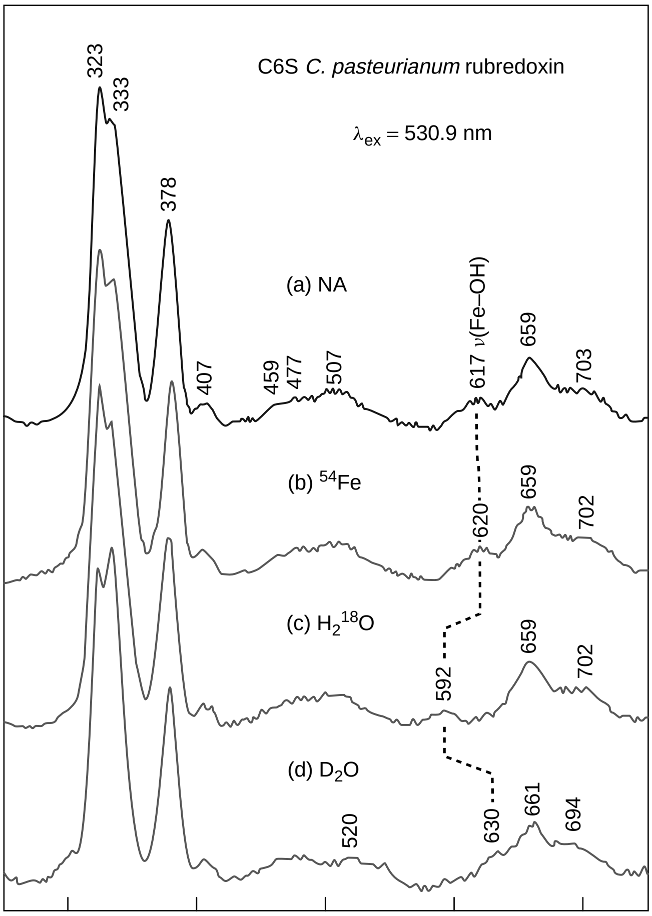

Figure 41 530.9-nm excited (77 K) RR spectra of C6S Rd*Cp* mutant: (a) in natural abundance, (b) ^{54}Fe-reconstituted protein, (c) in $H_2{}^{18}O$, and (d) in D_2O

4 FURTHER READING

R. S. Czernuszewicz, E. M. Maes, and J. G. Rankin, *Resonance Raman Spectroscopy of Petroporphyrins*, in eds. K. M. Kadish, K. M. Smith and R. Guilard, ‘The Porphyrin Handbook’, Academic Press, 2000, Vol. 7. Metalloporphyrins have provided a particularly rich opportunity for resonance Raman studies and this book chapter discusses various aspects of pioneering work in the area of geological metalloporphyrins.

R. S. Czernuszewicz and T. G. Spiro, *IR, Raman and Resonance Raman Spectroscopy* in eds. E. I. Solomon and A. B. P. Lever, ‘Inorganic Electronic Structure and Spectroscopy’, John Wiley & Sons, New York, 1999, Vol. I, Methodology. A detailed compilation of the principles of IR, Raman, and resonance Raman spectroscopies and their applications in bioinorganic chemistry.

M. Diem, ‘Introduction to Modern Vibrational Spectroscopy’, John Wiley & Sons, New York, 1993. This easy to read book features detailed discussion of the theoretical and experimental aspects of IR and Raman spectroscopy and provides many examples for the interpretation of vibrational spectra.

J. R. Ferraro and K. Nakamoto, ‘Introductory Raman Spectroscopy’, Academic Press, New York, 1994. A well-balanced Raman text on an introductory level that explains basic theory, instrumentation and experimental techniques (including special techniques), and a wide variety of applications in structural chemistry, biochemistry, biology and medicine, solid-state chemistry and industry will serve well as a guide for beginners.

D. C. Harris and M. D. Bertolucci, 'Symmetry and Spectroscopy: An Introduction to Vibrational and Electronic Spectroscopy', Oxford University Press, New York, 1979. Easy-to-follow, instructive textbook on vibrational and electronic spectroscopy with numerous helpful figures, line drawings, and exercises illustrating important concepts. Excellent choice for anyone teaching or studying molecular spectroscopy at junior to beginning graduate level. Also available in paperback from Dover, New York.

J. R. Kincaid, *Resonance Raman Spectra of Heme Proteins and Model Compounds*, in eds. K. M. Kadish, K. M. Smith and R. Guilard, 'The Porphyrin Handbook', Academic Press, New York, 2000, Vol. 7. An excellent review that summarizes and clearly illustrates the power of RR spectroscopy in probing structure–function relationships for a wide variety of heme proteins.

I. R. Lewis and H. G. M. Edwards eds, 'Handbook of Raman Spectroscopy', Marcell Dekker Inc, New York, 2001. This comprehensive handbook lays out the richness and technical details of Raman techniques, instrumentation and measurements now employed in a variety of industrial and academic research fields.

D. A. Long, 'Raman Spectroscopy', McGraw-Hill, New York, 1977. The most comprehensive, unified and fully illustrated treatment of the basic theory and physical principles of Raman, resonance Raman and nonlinear Raman scattering. Readers will be inspired by the elegance and information content of the technique to delve further into the book.

K. Nakamoto, 'Infrared and Raman Spectra of Inorganic and Coordination Compounds', Wiley-Interscience, New York, 1997. Unsurpassed resource textbook available for researchers and graduate students in the field of vibrational spectroscopy, inorganic chemistry, organometallic chemistry, and bioinorganic chemistry.

E. Smith and G. Dent, 'Modern Raman Spectroscopy', John Wiley & Sons, New York, 2005. A practical approach to modern Raman spectroscopy that provides the information necessary to enable new users to understand and apply the technique correctly, including descriptions of the many pitfalls that can be encountered.

T. G. Spiro ed, 'Biological Applications of Raman Spectroscopy', Wiley-Interscience, 1988, Vol. 1–3. Through summaries of representative areas by authorities in biological Raman applications, this set of three volumes provides in-depth coverage of the theoretical and experimental aspects of modern bio-Raman spectroscopy.

E. B. Wilson Jr, J. C. Decius, and P. C. Cross, 'Molecular Vibrations: The Theory of Infrared and Raman Vibrational Spectra', McGraw-Hill, New York, 1955. Classic graduate text; contains rigorous yet easily followed exposition of mathematics involved in detailed vibrational analyses of polyatomic molecules. Also available in paperback from Dover, New York.

5 REFERENCES

1. R. J. H. Clark and B. Stewart, *Struct. Bond.*, 1979, **36**, 1.
2. R. J. H. Clark, *Resonance Raman Spectra of Inorganic Molecules and Ions*, in 'Advances in IR and Raman Spectroscopy', eds. R. J. H. Clark and R. E. Hester, John Wiley & Sons, New York, 1975, Vol. 1, p. 143.
3. C. L. Angel, F. A. Cotton, B. A. Frenz, and T. A. Webb, *Chem. Commun.*, 1973, 399.
4. R. J. H. Clark and M. L. Franks, *J. Am. Chem. Soc.*, 1975, **97**, 2691.
5. C. D. Cowman and H. B. Gray, *J. Am. Chem. Soc.*, 1973, **95**, 8177.
6. F. A. Cotton, *Chem. Soc. Rev.*, 1975, **4**, 27.
7. T. C. Strekas and T. G. Spiro, *Biophys. Biochim. Acta*, 1972, **263**, 830.
8. T. C. Strekas and T. G. Spiro, *Biophys. Biochim. Acta*, 1972, **278**, 188.
9. T. G. Spiro and T. C. Streaks, *Proc. Natl. Acad. Sci.*, 1972, **69**, 2622.
10. T. G. Spiro and T. C. Strekas, *Acc. Chem. Res.*, 1974, **7**, 339.
11. T. G. Spiro and T. M. Loehr, *Resonance Raman Spectra of Heme Proteins and Other Biological Systems*, in 'Advances in IR and Raman Spectroscopy', eds. R. J. H. Clark and R. E. Hester, John Wiley & Sons, New York, 1975, Vol. 1, p. 98.
12. T. G. Spiro, *The Resonance Raman Spectroscopy of Metalloporphyrins and Heme Proteins*, in 'Iron Porphyrins', eds. A. B. P. Lever and H. B. Gray, Addison-Wesley, Reading, MA, 1983, p. 89.
13. T. G. Spiro, ed, 'Biological Applications of Raman Spectroscopy: Resonance Raman Spectra of Heme and Metalloproteins', John Wiley & Sons, New York, 1987, Vol. 3.
14. J. R. Kincaid, *Resonance Raman Spectra of Heme Proteins and Model Compounds*, in 'The Porphyrin Handbook', eds. K. M. Kadish, K. M. Smith, and R. Guilard, Academic Press, San Diego, 2000, Vol. 7, p. 225.
15. J. Behringer, *Observed Resonance Raman Spectra*, in 'Raman Spectroscopy. Theory and Practice', ed. H. A. Szymanski, Plenum Press, New York, 1967, Vol. 1, p. 168.
16. T. G. Spiro and R. S. Czernuszewicz, *Meth. Enzym.*, 1995, **246**, 416.
17. Y. Wang and H. E. Van Wart, *Meth. Enzym.*, 1993, **226**, 319.
18. T. M. Loehr and J. Sanders-Loehr, *Meth. Enzym.*, 1993, **226**, 431.
19. I. R. Lewis and H. G. M. Edwards, eds, 'Handbook of Raman Spectroscopy', Marcel Dekker, Inc., New York, 2001.
20. K. Nakamoto and R. S. Czernuszewicz, *Meth. Enzym.*, 1993, **226**, 259.
21. R. S. Czernuszewicz and T. G. Spiro, *IR, Raman and Resonance Raman Spectroscopy*, in 'Inorganic Electronic Structure and Spectroscopy', eds. E. I. Solomon and A. B. P. Lever, John Wiley & Sons, New York, 1999, p. 353.
22. T. G. Spiro and R. S. Czernuszewicz, *Resonance Raman Spectroscopy*, in 'Physical Methods in Bioinorganic Chemistry', ed L. Que Jr, University Science Books, Sausalito, CA, 2000, p. 59.

23. J. A. Koningsten, 'Introduction to the Theory of the Raman Effect', Reidel, Dordrecht, The Netherlands, 1973.
24. D. A. Long, 'Raman Spectroscopy', McGraw-Hill, New York, 1977.
25. C. V. Raman and K. S. Krishnam, *Nature*, 1928, **121**, 501.
26. C. V. Raman and K. S. Krishnam, *Nature*, 1928, **121**, 619.
27. G. S. Landsberg and L. J. Mandelstam, *Naturwissenschaften*, 1928, **16**, 557.
28. R. S. Czernuszewicz and M. K. Johnsson, *Appl. Spectrosc.*, 1983, **37**, 297.
29. R. S. Czernuszewicz, *Appl. Spectrosc.*, 1983, **40**, 571.
30. D. P. Strommen and K. Nakamoto, 'Laboratory Raman Spectroscopy', John Wiley & Sons, New York, 1984.
31. T. G. Spiro and H.-Y. Li, *Resonance Raman Spectroscopy of Metalloporphyrins*, in 'Biological Applications of Raman Spectroscopy', ed. T. G. Spiro, John Wiley & Sons, New York, 1988, Vol. 3, p. 1.
32. T. G. Spiro, R. S. Czernuszewicz, and X.-Y. Li, *Coord. Chem. Rev.*, 1990, **100**, 541.
33. R. S. Czernuszewicz, E. M. Maes, and J. G. Rankin, *Resonance Raman Spectroscopy of Petroporphyrins*, in 'The Porphyrin Handbook', eds. K. M. Kadish, K. M. Smith, and R. Guilard, Academic Press, San Diego, 2000, Vol. 7, p. 293.
34. W. Siebrand and M. Z. Zgierski, *Resonance Raman Spectra–A Key to Vibronic Coupling*, in 'Excited States', ed. E. C. Lim, Academic Press, New York, 1979, Vol. 4, p. 1.
35. T. G. Spiro and P. Stein, *Ann. Rev. Phys. Chem.*, 1977, **28**, 501.
36. A. C. Albrecht, *J. Chem. Phys.*, 1961, **34**, 1476.
37. J. Tang and A. C. Albrecht, *J. Chem. Phys.*, 1968, **49**, 1144.
38. A. C. Albrecht, *J. Chem. Phys.*, 1960, **33**, 937.
39. R. J. H. Clark and T. J. D. Dines, *Angew. Chem. Int. Ed. Engl.*, 1986, **25**, 131.
40. J. G. Rankin and R. S. Czernuszewicz, *Org. Geochem.*, 1993, **20**, 521.
41. M. Gouterman, *Optical Spectra and Electronic Structure of Porphyrin and Related Rings*, in 'The Porphyrins', ed. D. Dolphin, Academic Press, New York, 1979, Vol. 3, p. 1.
42. Q. Yan, '*Applications of Resonance Raman Spectroscopy to Complexes of Biological and Clinical Significance: I. High-Valent Oxo- and Nitridometalloporphyrins; II. μ-Oxo Vanadium(III) Dimers; III. Antitumor Drug-DNA Intercalators*,' PhD. Dissertation, University of Houston, 1996.
43. R. S. Czernuszewicz and E. M. Maes, *Biological Applications of Resonance Raman Spectroscopy: Copper-Cysteinate Active Sites*, in 'Education in Advanced Chemistry', eds. A. M. Trzeciak, P. Sobota, and J. J. Ziolkowski, Wydawnictwo Poznanskie, Poznan-Wroclaw, Poland, 2000, Vol. 7, p. 67.
44. R. S. Czernuszewicz, B. C. Dave, and J. P. Germanas, *A Probe of Metal-Ligand Interactions in Cupredoxin by Active Site Redesign and Resonance Raman Spectroscopy*, in 'Spectroscopic Methods in Bioinorganic Chemistry', eds. E. I. Solomon and K. O. Hodgson, American Chemical Society, Washington, DC, 1997, Vol. 692, p. 220.
45. J. Sanders-Loehr, 'Bioinorganic Chemistry of Copper', eds. K. D. Karlin and Z. Tyeklar, Chapmaan & Hall, New York, 1993, p. 51.
46. C. R. Andrew and J. Sanders-Loehr, *Acc. Chem. Res.*, 1996, **29**, 365.
47. W. H. Woodruff, R. B. Dyer, and J. R. Schoonover, *Resonance Raman Spectroscopy of Blue Copper Proteins*, in 'Biological Applications of Raman Spectroscopy', eds. T. G. Spiro and X.-Y. Li, John Wiley & Sons, New York, 1988, Vol. 3, p. 413.
48. E. N. Baker, *J. Mol. Biol.*, 1988, **203**, 1071.
49. H. Nar, A. Messerschmidt, and R. Huber, *J. Mol. Biol.*, 1991, **221**, 765.
50. B. R. Crane, A. J. Di Bilio, J. R. Winkler, and H. B. Gray, *J. Am. Chem. Soc.*, 2001, **123**, 11623.
51. E. T. Adman, *Copper Protein Structures*, in 'Advances in Protein Chemistry', eds. C. B. Anifsen, J. T. Edsall, F. M. Richards, and D. S. Eisenberg, Academic Press, New York, 1991, Vol. 42, p. 45.
52. D. Qiu, L. Kilpatrick, N. Kitajima, and T. G. Spiro, *J. Am. Chem. Soc.*, 1994, **116**, 2585.
53. N. Kitajima, F. Kiyoshi, and M. Yoshihiko, *J. Am. Chem. Soc.*, 1990, **112**, 3210.
54. L. Nestor, J. A. Larrabee, G. Woolery, B. Reinhammer, and T. G. Spiro, *Biochemistry*, 1984, **23**, 1084.
55. B. C. Dave, J. P. Germanas, and R. S. Czernuszewicz, *J. Am. Chem. Soc.*, 1993, **115**, 12175.
56. R. S. Czernuszewicz, G. Fraczkiewicz, R. Fraczkiewicz, B. C. Dave, and J. P. Germanas, *Ground and Excited State Dynamics of Blue Copper Active Site from Resonance Raman Spectroscopy of Azurin*, in 'Spectroscopy of Biological Molecules', eds. J. C. Merlin, S. Turrel, and J. P. Huvenne, Kluwer Academic Publishers, Dordrecht, The Netherlands, 1995, p. 273.
57. C. R. Andrew, H. Yeom, J. S. Valentine, B. G. Karlsson, N. Bonander, G. van Pouderoyen, G. Centers, T. M. Loehr, and J. Sanders-Loehr, *J. Am. Chem. Soc.*, 1994, **116**, 11489.
58. A. M. Nersissian, Z. B. Mehrabian, R. M. Nalbandyan, P. J. Hart, G. Fraczkiewicz, R. S. Czernuszewicz, C. J. Bender, J. Peisach, R. G. Herrmann, and J. S. Valentine, *Protein Sci.*, 1996, **5**, 2184.
59. D. Qiu, S. Dong, J. A. Ybe, M. H. Hecht, and T. G. Spiro, *J. Am. Chem. Soc.*, 1995, **117**, 6443.
60. G. Fraczkiewicz, N. Bonander, and R. S. Czernuszewicz, *J. Raman Spectrosc.*, 1998, **29**, 983.
61. G. Franczkiewicz, R. Franczkiewicz, J. P. Germanas, and R. S. Czernuszewicz, 'Proceedings of the XVth International Conference on Raman Spectroscopy', John Wiley & Sons, New York, 1996, p. 408.

62. S. Dong and T. G. Spiro, *J. Am. Chem. Soc.*, 1998, **120**, 10434.
63. D. Qiu, S. Dasgupta, P. M. Kozlowski, and T. G. Spiro, *J. Am. Chem. Soc.*, 1998, **120**, 12791.
64. D. F. Blair, G. W. Campbell, J. R. Schoonover, S. I. Chan, H. B. Gray, B. G. Malmstrom, I. Pecht, B. I. Swanson, W. H. Woodruff, W. K. Cho, A. M. English, H. A. Fry, V. Lum, and K. A. Norton, *J. Am. Chem. Soc.*, 1985, **107**, 5755.
65. G. van Pouderoyen, C. R. Andrew, T. M. Loehr, J. Sanders-Loehr, S. Mazamudar, H. A. O. Hill, and G. W. Canters, *Biochemistry*, 1996, **35**, 1397.
66. T. den Blaauwen and G. W. Canters, *J. Am. Chem. Soc.*, 1993, **115**, 1121.
67. C. R. Andrew, J. Han, T. den Blaauwen, G. van Pouderoyen, E. Vijgenboom, G. W. Canters, T. M. Loehr, and J. Sanders-Loehr, *J. Bioinorg. Chem.*, 1997, **2**, 98.
68. J. Han, T. M. Loehr, Y. Lu, J. S. Valentine, B. A. Averill, and J. Sanders-Loehr, *J. Am. Chem. Soc.*, 1993, **115**, 4256.
69. N. Bonander, B. G. Karlsson, and T. Vanngard, *Biochemistry*, 1996, **35**, 2429.
70. R. S. Czernuszewicz, G. Fraczkiewicz, and A. A. Zareba, *Inorg. Chem.*, 2005, **44**, 5745.
71. J. M. Moratal, A. Romero, J. Salgado, A. Perales-Alarcon, and H. R. Jimenez, *Eur. J. Biochem.*, 1995, **228**, 653.
72. J. P. Hannan, S. L. Davy, R. R. Eady, and C. R. Andrew, *J. Biol. Inorg. Chem.*, 1998, **3**, 282.
73. G. Musci, A. Desideri, L. Morpurgo, and L. Tosi, *J. Inorg. Biochem.*, 1985, **23**, 93.
74. T. Kohzuma, M. Kikuchi, N. Horikoshi, S. Nagatomo, T. Kitagawa, and R. S. Czernuszewicz, *Inorg. Chem.*, 2006, **45**, 8474.
75. J. G. Grossmann, Z. H. L. Abraham, E. T. Adman, M. Neu, R. R. Eady, B. E. Smith, and S. S. Hasnain, *Biochemistry*, 1993, **32**, 7360.
76. M. Kukimoto, M. Nishiyama, M. E. Murphy, S. Turly, E. T. Adman, S. Horinouchi, and T. Beppu, *Biochemistry*, 1994, **33**, 5246.
77. S. V. Antonyuk, R. W. Strange, G. Sawers, R. R. Eady, and S. S. Hasnain, *Proc. Natl. Acad. Sci.*, 2005, **102**, 12041.
78. M. A. Hough, M. J. Ellis, S. V. Antonyuk, R. W. Strange, G. Sawers, R. R. Eady, and S. S. Hasnain, *J. Mol. Biol.*, 2005, **350**, 300.
79. T. G. Spiro, R. S. Czernuszewicz, and S. Han, *Iron-Sulfur Proteins and Analog Complexes*, in ‘Biological Applications of Raman Spectroscopy’, ed. T. G. Spiro, John Wiley & Sons, New York, 1988, Vol. 3, p. 523.
80. S. Han, R. S. Czernuszewicz, T. Kimura, M. W. W. Adams, and T. G. Spiro, *J. Am. Chem. Soc.*, 1989, **111**, 3505.
81. S. Han, R. S. Czernuszewicz, and T. G. Spiro, *J. Am. Chem. Soc.*, 1989, **111**, 3496.
82. M. K. Johnson, R. S. Czernuszewicz, T. G. Spiro, J. A. Fee, and W. V. Sweeney, *J. Am. Chem. Soc.*, 1983, **115**, 6671.
83. M. K. Johnson, R. S. Czernuszewicz, T. G. Spiro, R. R. Ramsay, and T. P. Singer, *J. Biol. Chem.*, 1983, **258**, 12771.
84. R. S. Czernuszewicz, K. A. Macor, M. K. Johnson, A. Gewirth, and T. G. Spiro, *J. Am. Chem. Soc.*, 1987, **109**, 7178.
85. E. M. Walters, R. Garcia-Serres, G. N. L. Jameson, D. A. Glauser, F. Bourquin, W. Manieri, P. Schurmann, M. K. Johnson, and B. H. Huynh, *J. Am. Chem. Soc.*, 2005, **127**, 9612.
86. T. V. Long and T. M. Loehr, *J. Am. Chem. Soc.*, 1970, **92**, 6384.
87. T. V. Long, T. M. Loehr, J. R. Alkins, and W. Lovenberg, *J. Am. Chem. Soc.*, 1971, **93**, 1809.
88. L. A. Woodward and M. J. Taylor, *J. Chem. Soc.*, 1960, 4473.
89. R. S. Czernuszewicz, J. LeGall, I. Moura, and T. G. Spiro, *Inorg. Chem.*, 1986, **25**, 696.
90. W. A. Eaton and W. Lovenberg, *The Iron-Sulfur Complex in Rubredoxin*, in ‘Iron Sulfur Proteins’, ed. W. Lovenberg, Academic Press, New York, 1973, Vol. 12, p. 131.
91. R. S. Czernuszewicz, L. K. Kilpatrick, S. A. Koch, and T. G. Spiro, *J. Am. Chem. Soc.*, 1994, **116**, 7134.
92. B. C. Dave, R. S. Czernuszewicz, B. C. Prickril, and D. M. Kurtz Jr, *Biochemistry*, 1994, **33**, 3572.
93. J. LeGall, B. C. Prickril, I. Moura, A. V. Xavier, J. J. G. Moura, and B. Huynh, *Biochemistry*, 1988, **27**, 1636.
94. I. Moura, P. Tavares, and N. Ravi, *Meth. Enzym.*, 1993, **243**, 216.
95. F. deMare, D. M. Kurtz Jr, and P. Nordlund, *Nat. Struct. Biol.*, 1996, **3**, 539.
96. S. Jin, D. M. Kurtz Jr, Z.-J. Liu, J. Rose, and B.-C. Wang, *J. Am. Chem. Soc.*, 2002, **124**, 9845.
97. M. Li, M. Liu, L. Gall, L. Gui, J. Liao, T. Jiang, J. Zhang, D. Liang, and W. Chang, *J. Biol. Inorg. Chem.*, 2003, **8**, 146.
98. Y. Xiao, H. Wang, S. J. George, M. C. Smith, M. W. W. Adams, F. E. Jenney, Jr., W. Sturhahn, E. E. Alp, J. Zhao, Y. Yoda, A. Dey, E. I. Solomon, and S. P. Cramer, *J. Am. Chem. Soc.*, 2005, **127**, 14596.
99. Z. Xiao, A. R. Gardner, M. Cross, E. M. Maes, R. S. Czernuszewicz, M. Sola, and A. G. Wedd, *J. Biol. Inorg. Chem.*, 2001, **6**, 638.
100. M. Cross, Z. Xiao, E. M. Maes, R. S. Czernuszewicz, S. C. Drew, J. R. Pilbrow, G. N. George, and A. G. Wedd, *J. Biol. Inorg. Chem.*, 2002, **7**, 781.
101. Z. Xiao, M. J. Lavery, M. Ayhan, S. D. B. Scrofani, M. C. J. Wilce, J. M. Guss, P. A. Tregloan, G. N. George, and A. G. Wedd, *J. Am. Chem. Soc.*, 1998, **120**, 4135.
102. J. Meyer, J. Gaillard, and M. Lutz, *Biochem. Biophys. Res. Commun.*, 1995, **212**, 827.
103. J. N. Agar, P. Yuvanyiama, R. F. Jack, V. L. Cash, D. R. Smith, D. R. Dean, and M. K. Johnson, *J. Biol. Inorg. Chem.*, 2000, **5**, 167.

104. J. N. Agar, L. Zheng, V. L. Cash, D. R. Dean, and M. K. Johnson, *J. Am. Chem. Soc.*, 2000, **122**, 2136.

105. K. D. Watenpaugh, L. C. Sieker, and L. H. Jensen, *J. Mol. Biol.*, 1980, **138**, 615.

106. R. S. Czernuszewicz, Y. O. Su, M. K. Stern, K. A. Macor, D. Kim, J. T. Groves, and T. G. Spiro, *J. Am. Chem. Soc.*, 1988, **110**, 4158.

107. E. M. Maes, '*Structural Characterization of Iron and Copper Active Sites by Resonance Raman Spectroscopy: Nitrophorin, Nitrite Reductase, and Iron-Sulfur Proteins,*' PhD. Dissertation, University of Houston, 2000.

Vibrational Spectroscopy

R. Brian Dyer and William H. Woodruff

Los Alamos National Laboratory, Los Alamos, NM, USA

	Method Summary	1
1	Introduction	2
2	Technical Background	4
3	Applications	9
4	Acknowledgments	22
5	Abbreviations and Acronyms	22
6	Further Reading	22
7	References	22

METHOD SUMMARY

Acronyms, Synonyms

- InfraRed
- Fourier Transform InfraRed
- Resonance Raman
- Time Resolved

Measured physical quantities

- absorption spectrum of IR light
- inelastic scattering spectrum of incident monochromatic (laser) light (Raman)
- intensities, widths, and shapes of IR and Raman peaks
- polarization and anisotropy (IR and Raman)
- in the TR case, kinetics and dynamics (IR and Raman).

Information available

- structure: force constants of bonds; masses and spatial disposition of atoms
- structure: molecular symmetry and symmetries of vibrations
- coupling between vibrational and electronic transitions (RR)
- temporal evolution of structure; excited-state information (TR)

Information not available, limitations

- Specific vibrational assignments often require isotope or (in proteins) mutant studies.

Examples of questions that can be answered

- Is a carboxylic acid or tyrosine sidechain in a protein protonated or not?
- What are the effective oxidation states of metals and organic groups?
- What structural and electronic changes occur in reaction transients and excited states?
- What changes in secondary structure occur due to perturbations of proteins?

Major advantages

- All molecules have vibrational spectra: nearly all vibrations are IR or Raman active.
- Exceptionally small structural changes are observable by difference techniques.

- This method is applicable to all phases of matter and all levels of organization–diatoms to in vivo.
- This method is applicable to all relevant timescales–femtoseconds to months or longer.

Major disadvantages

- Photochemical damage is an issue (Raman, especially RR, TR).
- Structural interpretations are indicative but frequently not unique.
- The more complex the molecule, the more congested the spectrum (e.g. protein IR).

Sample constraints

- Relatively high concentrations (100 μM or higher) may be required (except RR).
- Sample volumes can be very small–typically 1 fl (Raman) to 1 ml (IR).
- Medium (e.g., solvent) interferences are avoided or mitigated by different techniques.

---

1 INTRODUCTION

Vibrational spectroscopy is defined for the purposes of this article as the measurement of the interaction of electromagnetic radiation with molecular vibrations (this terse definition is expanded in the next section). Modern vibrational spectroscopy comprises a multitude of specialized techniques, in many cases for very sophisticated purposes. However, by far the most common vibrational methods exploit the direct absorption of infrared (IR) light (infrared spectroscopy) or the inelastic scattering of monochromatic light of either near IR, visible, or near ultraviolet wavelengths (spontaneous Raman spectroscopy, or simply Raman). In both IR and Raman the observables include the vibrational frequencies of molecules (see next section), intensities of spectral peaks, peak widths, and polarizations. More sophisticated versions of either technique may measure time-dependent spectral changes, quantum lifetimes, phase relationships, etc. The two most common applications of IR and Raman are (i) to act as analytical ‘‘fingerprint’’ methods to identify specific molecular species or functional groups having known spectral signatures, and (ii) to infer unknown molecular structures or structural changes. A brief historical survey of the development of IR and Raman spectroscopies is in order.

The initial discovery of IR radiation is attributed to William Herschel in 1800.[1] Herschel noticed that, when visible light was dispersed through a prism, invisible radiation beyond the red end of the dispersed visible spectrum caused heating, and could be measured using a thermometer. He called this radiation ‘‘*calorific rays*’’—the term ‘‘*infrared*’’ came into use later in the 19th century. Over more than a century following Herschel's discovery, it came to be recognized that the IR region of the electromagnetic spectrum lies between the shortest-wavelength radio waves (microwave radiation, wavelength longer than one, or a few, millimeters) and visible light (approximately 700 nm). It was also known by the end of the 19th century that spectral features in the IR region were predominately due to the characteristic vibrational motions of molecules.[2]

The first IR *spectra* were reported in 1882 by Abney and Festing who measured the near-IR spectra of some 50 liquids.[3] Because they used a conventional spectrograph and photographic plates, their spectral coverage was limited to wavelengths shorter than approximately 1.2 μm (micrometers, microns), which we would call today the near IR. Further innovations followed quickly in the hands of Ångström,[4] Julius,[5] and others, who used bolometer detectors and rock-salt optics to measure IR spectra to 10 μm and beyond (roughly, the mid-IR region lies at wavelengths between 2.5 and 25 μm). While the collection of IR spectra at this time was an extremely laborious point-by-point exercise, the state of the art by the beginning of the 20th century was such that a major book on IR spectroscopy was authored by William Coblentz.[6] This landmark work (and subsequent books by Coblentz), which among other notable advances established the idea of characteristic vibrational ‘‘group frequencies,’’ is still useful a century later.

The inelastic light scattering effect that we commonly know as *Raman scattering* was discovered concurrently and independently by Raman and Krishnan[7] and by Landsberg and Mandelstam,[8] and reported in papers published in 1928. Raman's observation was highly qualitative, reporting that sunlight extinguished by a set of two complementary colored filters was made visible again when certain liquids were placed between the filters. We now understand this to be due to light shifted some 3000 cm^{-1} (wavenumbers, reciprocal wavelength) to the red by the C–H stretching vibrations of the liquids (see following section). Landsberg and Mandelstam, on the other hand, used a monochromatic light source (a mercury arc lamp), a dispersive spectrograph, and photographic detection to record actual *spectra* of crystals. The experimental setup invented by Landsberg and Mandelstam in the 1920s became essentially the exclusive technique for ‘‘Raman’’ spectroscopy until the advent of scanning multiple monochromators and lasers in the 1960s.

During the first 60 years or so of the 20th century many technical developments occurred that profoundly advanced both IR and Raman spectroscopy. Some of these developments had immediate effects, and others were integrated in combination, over decades. Examples include the advent of electrical detectors for both IR and visible/ultraviolet light, electronic devices, optical technology, digital computation, and new computer algorithms. The first detectors based on the photoelectric effect[9] were applied to visible spectroscopy early in the century.[10] IR detectors based on thallous sulfide were used to detect aircraft during World War I, followed between the wars by lead chalcogenide and pyroelectric detectors. All of these were used in IR spectroscopy. The development of photomultiplier tubes offered a quantum detector that approached single-photon sensitivity, and one of the first application of the photomultiplier was as a detector for Raman spectroscopy[11]; thus the combination of a scanning monochromator with a photomultiplier detector began to supplant the spectrograph with photographic detection developed by Landsberg and Mandelstam decades earlier.

The vacuum tube was developed between 1904 and 1916 by researchers including Fleming, de Forrest, and Langmuir. The whole field of electronics followed with a multitude of very important applications, many of them essential to modern spectroscopy, culminating in the solid-state revolution that began in the 1950s and continues today. One of the most significant results was the digital computer, a development with a long nonelectronic history transformed by the exigencies of World War II into its modern form, an electronic device with the stored-program architecture pioneered by von Neumann.[12] By the 1960s the digital revolution had advanced to the point where small computers suitable for dedicated laboratory applications appeared. These found immediate application in the chemical laboratory, for automation of data collection and analysis in spectroscopy and many other areas.

The first practical optical interferometer was designed and reported by Michelson in 1881,[13] but the potential applicability of this development to spectroscopy was not realized for some time. The first interferogram (light intensity as a function of the difference in pathlength through the two arms of the interferometer) was reported by Rubens *et al.*[14] beginning in 1910. It was not until 1951 that it was recognized that the interferogram and the spectrum were related by a Fourier transform, and the first numerical Fourier transform spectrum was calculated by Fellgett,[15] who also realized the advantage in sensitivity offered by the interferometer because of its ability to simultaneously detect the entire spectrum as a single, time-varying signal (the multiplex or Fellgett advantage). Jacquinot discovered an additional advantage of the optical interferometer over dispersive systems, namely, its greater optical throughput due to its large aperture (lacking the slits required by a dispersive spectrometer). This throughput advantage is now termed the Jacquinot advantage.[16] Early applications of Fourier transform spectroscopy to IR (Fourier transform infrared (FTIR))—in fact, for technical reasons, to spectroscopy in general—were largely limited to the far IR (wavelengths from roughly 1 mm to 25 μm) where dispersive prism or grating instruments had great difficulties. Advances in detectors, including pyroelectric devices such as deuterated triglycine sulfate (DTGS) and quantum-sensitive semiconductors such as indium antimonide (InSb) and mercury cadmium telluride (MCT) aided both dispersive IR and FTIR during this period. Still, the manual acquisition of an interferogram and computation of a spectrum were very tedious and time-consuming in the absence of appropriate computers. This began to change with the development of the ‘‘minicomputer’’ in the early 1960s, and with the development of the fast Fourier transform algorithm by Cooley and Tukey in 1965.[17] In the early 1960s a number of commercial FTIR instruments were marketed with mixed degrees of success. The first modern FTIR instrument incorporating solid-state electronics, a dedicated minicomputer, and the Cooley–Tukey algorithm were introduced by Block Engineering (Digilab or Bio-Rad) in 1969. A very extensive literature is available on the development and applications of FTIR spectroscopy.[18,19]

Of the many significant developments in spectroscopy during the 20th century, arguably the most revolutionary was the advent of the laser (the word laser is an acronym for light amplification by stimulated emission of radiation). The first laser was a pulsed ruby laser invented by Maiman at Hughes Aircraft in 1960.[20] This was quickly followed by the first continuous-wave (CW) gas laser, the helium–neon (He–Ne) laser reported by Javan *et al.* in 1961.[21] Like the photomultiplier tube, the laser found immediate application to Raman; the extremely bright monochromatic source was a natural for Raman purposes. The first laser Raman spectra were reported by Porto and Wood in 1962,[22] using a Ruby excitation source. However, laser use for Raman created several instrumental problems, a major one being that the laser’s great brightness along with increasing demands for high sensitivity and measurement of low vibrational frequencies made stray light levels within a single monochromator an unacceptable interference in the detection of weak spectra. To solve this problem Landon and Porto devised a laser Raman spectrometer based on a double monochromator.[23] This, with various modifications and advances, became the standard type of instrument for Raman spectroscopy for many years, and as lasers became readily available the mercury arc as a Raman excitation source became obsolete in a very short time.

Another advance in detector technology that has been very important in spectroscopy is the development of multichannel detectors, either one-dimensional (e.g., diode arrays) or two-dimensional (e.g., television detectors such as vidicon tubes and, more recently, charge coupled device (CCD) chips). In concept, detectors of this class are similar to the photographic plates that had largely been supplanted by electronic detectors, in that they detect an ‘‘entire’’ spectrum (or a significant part of a spectrum) all at once without the need for scanning dispersed light past the slit of a monochromator to be detected, in essence, point by point. Thus the use of an array or image detector yields a *spectral* *multiplex advantage*, meaning that the time to achieve a spectrum of a given signal-to-noise ratio (S/N) is related to the square root of the number of spectral resolution elements that can be detected simultaneously. (In Fourier transform spectroscopy this is known as the *Fellgett advantage*,[15] and this term is sometimes applied to dispersive multichannel spectrography. For FTIR, the Jacquinot advantage and the Fellgett advantage are multiplicative.) Aside from intrinsically better sensitivity (given equivalent detector performance), the multiplex advantage allows spectra to be detected in short times (because no scanning of a monochromator is required), thus enabling time-resolved vibrational spectroscopy (TRVS), especially time-resolved Raman and resonance Raman (RR) (TR^3). This principle was first demonstrated, using image-intensified vidicon detectors, by Delhaye *et al.* at Lille[24] and later for the RR case in our laboratories.[25] This is now routinely done using CCD image detectors for Raman. For IR, InSb image detectors have been available for some time for near-IR imaging and MCT image detectors are now available for the mid-IR. Apart from the multiplex advantage and time resolution, these devices offer the possibility of *hyperspectral imaging*,[26] that is, obtaining Raman or IR images wherein each pixel (the word ‘‘pixel’’ is a contraction of ‘‘picture element’’) of a two-dimensional spatial image carries a third, spectral dimension. Hyperspectral imaging techniques have very promising potential applications in bioinorganic spectroscopy and materials characterization.

We mentioned earlier that vibrational spectroscopy is a very innovative and rapidly developing field with many very sophisticated and highly specialized applications. In general these are too numerous and specialized to include in this article, but one of the advanced techniques has such profound potential importance as to demand mention. Multidimensional, coherent nuclear magnetic resonance (NMR) spectroscopy (*see* ***Nuclear Magnetic Resonance (NMR) Spectroscopy of Metallobiomolecules***) is able to determine molecular structures in solution or other random phases, in short, under realistic chemical conditions without requiring crystals. In principle, all the capabilities of this radio-frequency spectroscopy can be implemented in vibrational spectroscopies, given the right coherent light sources (lasers) and their appropriate manipulation. If this can be accomplished, the possibility will be opened to determine actual time-resolved molecular structures of all sorts (electronically excited molecules, reaction intermediates, transient protein structures, etc.) at very short timescales (picoseconds, or less). The potential of this approach has been demonstrated in the IR.[27]

Inorganic and bioinorganic applications of IR and Raman spectroscopies are covered in some detail in subsequent sections. General types of information that can be obtained include analytical identification, structure and symmetry, ligand and functional group identification, metal–ligand and metal–metal bonding potentials and force constants, structural kinetics and dynamics, excited-state properties, vibronic coupling, etc. Extensive literature on inorganic applications can be found in numerous reference works (Section 4).

2 TECHNICAL BACKGROUND

2.1 General Concepts

Molecular vibrations and vibrational spectroscopies are among the simplest quantum phenomena to understand at an intuitive level via classical concepts. A molecule can be viewed as a system of masses (atoms) held together by springs (chemical bonds). Like a mass-and-spring system in classical physics, each chemical bond is characterized by a *force constant*, k, that reflects the stiffness of the bonding ‘‘spring,’’ that is, the force necessary to displace the bonded masses a given distance from equilibrium (k is in units of force per distance, e.g., newtons per meter or millidynes per angström unit). Figure 1 shows this for a diatomic molecule. The equilibrium bond distance is r_{eq}, ‘‘equilibrium’’ meaning that at the interatomic distance r_{eq}, no force is exerted on the spring representing the bond. In order to displace the atoms such that the new interatomic distance is $r_{\mathrm{eq}} \pm \Delta\mathrm{r}$, a force $f = k(\Delta r)$ has to be exerted. The potential energy (force times distance), U, that is stored in the spring system as a result of the Δr displacement is $f(\Delta r)$, thus $U = k(\Delta r)^2$. This leads to the familiar *harmonic potential*, illustrated in Figure 2, where potential energy is quadratic in bond displacement (here it is assumed that there is no anharmonicity, that is that k is independent of Δr, thus that $U = k(\Delta r)^2$ for all Δr. In real molecules the bonding potential is always expected to be anharmonic to some degree, but anharmonic effects are negligible for many purposes and anharmonicity is beyond the scope of this discussion).

If a classical mass-and-spring system is displaced by Δr and then released, it will oscillate around $r = r_{\mathrm{eq}}$ (Figure 2). The total energy of the system E will be constant, equal to the potential energy U originally supplied, but divided between potential energy U_r and kinetic energy V_r, both functions of the time-dependent distance r between the centers of mass, such that $E = U_r + V_r$. The maximum

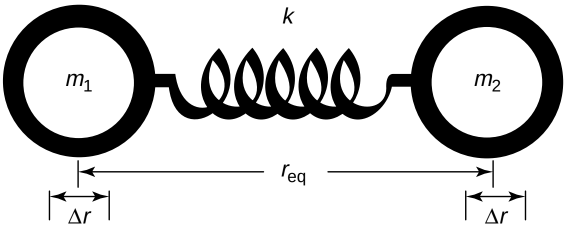

Figure 1 Classical mass-and-spring representation of a vibrating diatomic molecule

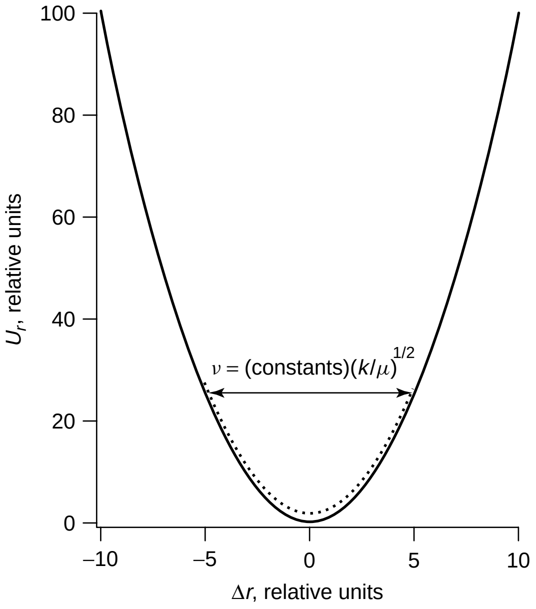

Figure 2 Energy and vibrational frequency of a classical harmonic oscillator. The solid line is the harmonic potential function. The dashed line represents the motion of the mass-and-spring system, displaced by $\Delta r = \pm 5$ units then released

vibrational amplitude is Δr, which is constant with time in a loss-free system. At this extreme, $r = r_{\mathrm{eq}} \pm \Delta r$, $V_r = 0$ and $U_r = U$. At $r = r_{\mathrm{eq}}$, $U_r = 0$ and $V_r = U$. At intermediate values of r, U_r and V_r will both be nonzero and E will be partitioned between potential and kinetic energy depending on the oscillating masses and their velocity, v. This brings in the concept of *reduced mass*, μ, the effective mass of the oscillating system. For the diatomic system in Figure 1, $\mu = (m_1)(m_2)/(m_1 + m_2)$ and the kinetic energy of the system $V = 1/2\mu v^2$. Without going further with the derivation (see Nakamoto[28] and references therein), the *period* of the oscillations of this system will be proportional to $(\mu/k)^{1/2}$, and the *vibrational frequency*, ν (in Hertz, $1\,\mathrm{Hz} = 1\,\mathrm{s}^{-1}$), is the inverse of the period; $\nu = (\text{constants}) \cdot (k/\mu)^{1/2}$.

2.2 Molecular Vibrations and Quantization

The fact that molecular vibrations are actually quantized alters the foregoing classically based discussion. In the classical case the vibrating system can have any amount of total energy, depending only upon the maximum vibrational amplitude, and the system can be at rest, not vibrating at all. In the quantum case the system can only have energies that are integral multiples of $h\nu$, where h is Planck's constant (e.g., h in erg · s and ν in s^{-1}). Furthermore, in the vibrational *ground state* the system is still in motion, retaining its *zero-point vibrational energy*. This modifies the classical energy diagram in Figure 2 as shown in Figure 3, where only discrete vibrational energy levels are allowed and the energy of the lowest level is nonzero. Thus absorption of IR light occurs when light quanta having $E = h\nu$ are incident on the system; these IR quanta excite the molecule directly from one vibrational *energy level* to another (Figure 3a) and in the process are absorbed. If the molecule is a harmonic oscillator as discussed above, all of the vibrational energy levels are equally spaced. Anharmonicity will cause the higher energy levels to be successively more closely spaced than the lower levels. To summarize the relationships that arise from quantization, $E = h\nu = hc/\lambda$ (c is the velocity of light, $3 \times 10^{10}\,\mathrm{cm\,s}^{-1}$, and λ is the wavelength of the light; $\nu = c/\lambda$) and, as in the classical case, $\nu = (\text{constants}) \cdot (k/\mu)^{1/2}$.

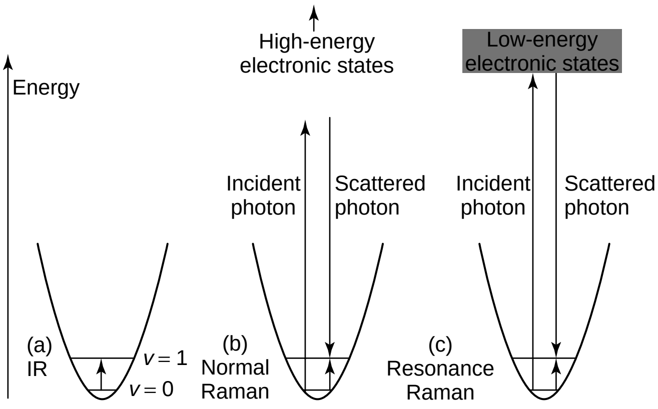

Figure 3 Schematic quantum representation of (a) IR absorption, (b) normal Raman scattering, and (c) RR scattering (see text). The parabolas represent harmonic potentials in the ground electronic states. The two energy levels shown in the harmonic ground-state (GS) potentials are quantum vibrational states; $v = 0$ is the zero-point vibrational energy, and $v = 1$ is the first excited vibrational state

In contrast to IR absorption, the Raman effect is a fundamentally different way of measuring molecular vibrational frequencies. Light can be scattered by matter in many ways; at the molecular level, scattering occurs because the electric field of light *polarizes*, and induces a dipole in the electron cloud of the molecule. Since the electric field of light is oscillating (at frequency ν), the induced dipole also oscillates and, as an oscillating dipole, radiates light. Most of the incident light is *elastically scattered*, that is, scattered without any change in energy or, equivalently, frequency or wavelength. Elastic scattering is known as *Rayleigh* scattering.[29] The Raman effect is also light scattering by a mechanism similar to Rayleigh scattering, but Raman scattering is inelastic rather that elastic. In the classical sense[30] this occurs because the polarizability of a molecule is not constant, but is modulated by the vibrations of the molecule (the vibrations, in effect, make the molecule larger or smaller at the extremes of displacement, thus making the molecule more or less polarizable). Viewed classically, this in turn results in amplitude modulation of the induced dipole due to the incident light, and in *sidebands* (as in radio technology) in the scattered light, displaced in frequency from the incident by an amount equal to the vibrational frequencies. In quantum terms, the incident photon exchanges a vibrational quantum with the molecule (Figure 3b). In either case, if the incident light is monochromatic (in the past, an emission line of a mercury arc; at present, a laser line) the vibrational frequencies can be measured by spectroscopically resolving the difference in frequency between the incident and Raman scattered light.

If the frequency of the incident light is remote from any electronic transitions of the illuminated molecules (Figure 3b), the intensity of both Rayleigh and Raman scattering is simply proportional to the fourth power of the scattered frequency, ν^4; that is, blue light is scattered more efficiently than red. This is, in fact, the reason that the sky appears blue. Furthermore, Raman scattering in this case (*normal Raman scattering*) is many orders of magnitude weaker than Rayleigh. Thus a central experimental problem in Raman spectroscopy is the detection of small amounts of inelastically scattered light at frequencies that are close to the Rayleigh (elastic scattering) frequency. Approaches to this challenge have been discussed elsewhere.[31] Despite the ‘‘insensitivity’’ of normal Raman scattering, this way of measuring vibrational frequencies has certain advantages over IR (e.g., because the method uses visible light it is easily applied to aqueous solutions, where IR requires special approaches or is simply inapplicable). Moreover, modern techniques give normal Raman adequate sensitivity for reasonably low concentrations (millimolar or lower).

When Raman scattering is excited by light within or near an electronic transition (*see* ***Electronic Spectroscopy***) as illustrated in Figure 3(c), the intensity of Raman scattering may be enhanced by orders of magnitude over the normal Raman case. This is known as the *resonance Raman effect*, which arises from the interactions of molecular vibrations with electronic transitions of the molecule. A detailed discussion of RR is beyond the scope of this article, but in brief, resonance enhancement may arise from two main vibronic mechanisms: a *Franck–Condon effect* where the enhanced vibration distorts the ground electronic state of the molecule to resemble the resonant excited electronic state; and *Herzberg–Teller coupling* wherein the vibration resembles the distortion that couples two different electronically excited states (ES). The RR effect and its consequences are perhaps best understood via the semiclassical wavepacket dynamics approaches pioneered by Heller *et al.*[32]

2.3 Normal Modes, Selection Rules, and Symmetry

The foregoing discussion has used as an example an oversimplified system, a diatomic molecule with just one vibrational *mode*. For more complicated molecules, in fact for arbitrarily complicated ones, the same mass-and-spring model applies — there are just more masses and more springs. Each local vibrational oscillator behaves as we have already discussed, but in a polyatomic molecule local vibrations will interact (couple) with one another — in principle, over the entire molecule. This can occur because local oscillators are not greatly dissimilar in energy and are geometrically arranged so that they interact. This possibility exists for either a classical mass-and-spring system or a real molecule. In molecules there is the additional possibility that displacement of one of the local coordinates (bonds) may actually change the force constant of another, via electronic interactions. Either classical or electronic interactions require us to develop concepts that are applicable to the molecular system as a whole. These are discussed in exhaustive detail elsewhere,[33] leading us to the idea of *normal vibrational modes*. These are a representation of how the local vibrational oscillators couple to produce the ‘‘actual’’ molecular vibrations. The normal modes constitute a set of $(3N - 6)$ molecular motions, where N is the number of atoms (this expression becomes $3N - 5$ if the molecule is linear, e.g., the diatom in Figure 1). These motions must be orthogonal to one another, and they must preserve the center of mass of the molecule. The normal modes of the carbon dioxide molecule are shown in Figure 4 (adapted from Tobias[34]).

Not all normal modes of a molecule will necessarily be observed in the IR spectrum, nor in the Raman. The *selection rules* for the two processes are different. The term ‘‘*selection rules*’’ refers to the combined properties of light and matter that are required for a quantum transition to occur.

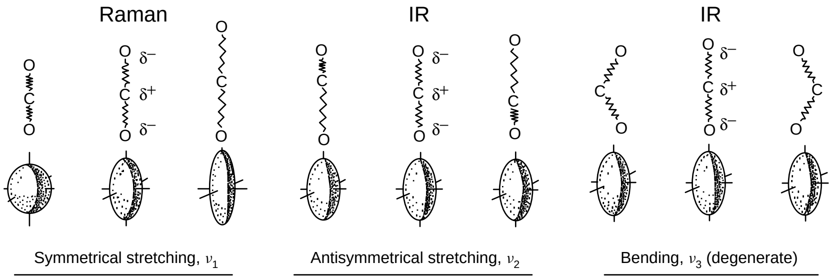
Raman
IR
IR
O
C
O
δ−
δ+
δ−
Symmetrical stretching, ν_1
Antisymmetrical stretching, ν_2
Bending, ν_3 (degenerate)

Figure 4 Schematic representation of the normal vibrational modes of the CO_2 molecule (Adapted from Cotton[35]). The molecular schematics show the atomic displacements that occur during each normal mode. The partial charges shown indicate the bond dipoles, and the ellipsoids represent the molecular polarizabilities. Note that only ν_1 results in a change in polarizability but no change in molecular dipole moment (thus is Raman active), while ν_2 and ν_3 result in changes in molecular dipole moment but not polarizability (thus are IR active)

The absorption of IR light by a vibrating molecule follows *dipolar selection rules*. This means that, to interact with the electric field of an incident photon so as to excite a normal mode of a molecule, absorb the photon, and be observed in the IR spectrum, a given normal mode must distort the molecule such that it alters the molecule's *dipole moment*. On the other hand Raman scattering, which is a two-photon process (the two being the incident and scattered photons), follows *quadrupolar selection rules*. This means that, to interact with an incident photon so as to result in the excitation of the normal mode of a molecule and the scattering of a Raman-shifted photon, the mode must distort the molecule such that it alters the molecule's *polarizability*.

The consequences of these differing selection rules can be seen qualitatively in Figure 4, showing the normal modes of the CO_2 molecule: ν_1, the symmetric C–O stretching vibration (''symmetric'' meaning that the vibration preserves the symmetry of the molecule); ν_2, the asymmetric C–O stretching vibration; and ν_3, the degenerate O–C–O angle bending vibrations (''degenerate'' meaning that there are two energetically equivalent but symmetrically distinct bending modes, the in-plane bend shown, and the out-of-plane bend 90° to the plane). Note that CO_2, a linear molecule, has $3N - 5 = 4$ normal modes, three of which are shown in Figure 4. CO_2 has no permanent dipole moment, but the individual C–O bonds are polar in opposite directions as shown in Figure 4. Thus ν_1, which stretches or compresses both C–O bonds equally, results in no transient, oscillating dipole moment and cannot be observed in the IR. However, the symmetric shortening and lengthening of the C–O bonds compresses or expands the electron cloud of the molecule, leading to an oscillatory polarizability change, therefore this mode is observed in Raman scattering. Conversely ν_2, the asymmetric C–O stretching vibration, shortens one of the C–O bonds and lengthens the other during its period, leading to a transient dipole moment that oscillates around zero. This mode is observed in the IR spectrum. However, ν_2 does not alter the size (polarizability) of the molecule's electron cloud, and thus cannot be observed by Raman. Likewise the degenerate ν_3 pair of modes result in an oscillating dipole moment perpendicular to the O–C–O axis but no change in polarizability, and thus are seen in the IR spectrum but not in the Raman.

The preceding paragraph illustrates two points about Raman and IR spectroscopies. First, the two techniques are complementary—information obtained by one or the other alone is generally incomplete. For example, for a molecule that is *centrosymmetric* (possesses an inversion center, like CO_2) IR-active normal modes are forbidden in the Raman, and vice versa. Second, it is implicit that molecular symmetry matters—if CO_2 were a bent molecule instead of linear, the conclusions about IR and Raman activity of the modes (indeed, the number of modes) would not be the same.[30,34] The determination of molecular symmetry groups and how molecular symmetry in turn determines spectroscopic and other properties is the realm of *group theory*.[35] Vibrational spectroscopy is one of the most important applications of group theory, but treatment of this subject is beyond the scope of this article. The reader is referred to any of several excellent texts on the subject (Section 4). For the present purposes it is enough to realize that molecular symmetry, along with number of atoms, determines the number of vibrations of various symmetry types and, in turn, the identity and spectroscopic activity (IR, Raman, both, or neither) of the normal modes.

2.4 Force Constants and Bond Distances

We mentioned earlier that the harmonic potentials depicted in Figures 2 and 3 are only approximations to real chemical bonding potentials. The harmonic approximation is very useful and works well in many cases for the first few quanta of excitation of a strong bond (low in the potential well). The obviously absurd extrapolation of the harmonic potential, however, is that a chemical bond can be stretched or compressed arbitrarily without changing its force constant. In reality a bond will ultimately dissociate (its force constant will go to zero) when stretched to many times its equilibrium length, and its force constant will approach infinity when the bond is compressed to the point that electrostatic repulsion of core electrons becomes very large. This is illustrated by the more realistic potential diagram in Figure 5, where bonding potential energy U is plotted versus internuclear distance r. Here the force constant k is the second derivative of the potential function, d^2U/dr^2, evaluated at the potential minimum (r_{eq}) where the first derivative $dU/dr = 0$ (both dU/dr and d^2U/dr^2 approach zero as r approaches infinity, i.e., at the dissociation limit).

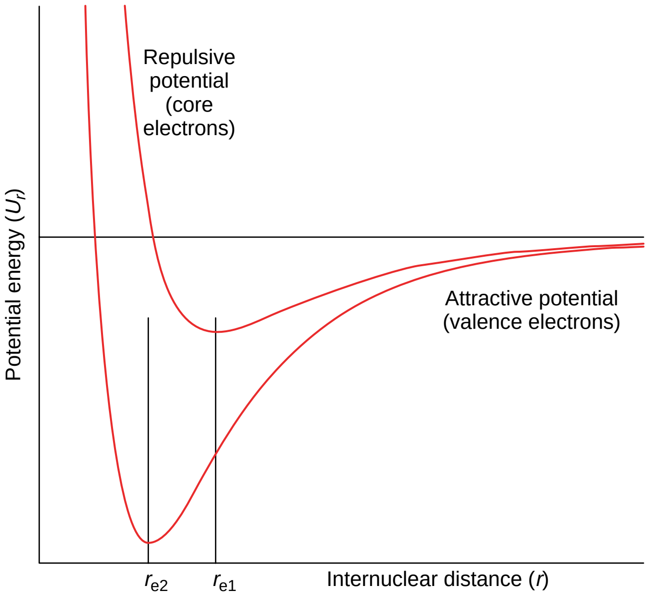

Figure 5 Simulated molecular potential functions

The potential function $U_{(r)}$ has at least two terms, an attractive term U_+ reflecting valence interactions, and a repulsive term U_- due to core electrostatic repulsions (Figure 5). Thus

$$U_r = U_+ + U_-$$

The attractive term dominates at longer distances and the repulsive term at shorter. The point at which $U_{(r)}$ is a minimum and $r = r_{\text{eq}}$ requires that

$$\frac{dU_r}{dr} = 0, \text{ thus } \frac{dU_-}{dr} = -\frac{dU_+}{dr}$$

In other words, whatever the functional form of U_+ and U_-, the slope of the repulsive term at r_{eq} must be equal and opposite to the slope of the attractive term. Since the units of dU/dr are force, this means that at $r = r_{\text{eq}}$ the forces due to the attractive and repulsive potentials are equal and opposite, that is, there is no net force acting on the bonded atoms, a trivial observation implicit in the definition of ''equilibrium internuclear distance.''

The conclusions regarding the force constant, $k = d^2U/dr^2$, are nontrivial and counter to intuitive expectations. First of all, unlike the harmonic case discussed previously, d^2U/dr^2 is a function of position (value of r) on the potential curve; the force ''constant'' k is evaluated at a specific point, namely, where $r = r_{\text{eq}}$. In fact, d^2U/dr^2 is *negative* over a very large range of the attractive part of the potential (negative curvature, see Figure 5). Furthermore, the point at which $d^2U/dr^2 = 0$ is at the *inflection point* of the potential curve, which is at a considerably greater value of r than r_{eq} (Figure 5); at that point $d^2U_-/dr^2 = d^2U_+/dr^2$. At any value of r shorter than that at the inflection point, approaching r_{eq}, the repulsive contribution to the curvature of the potential, d^2U_-/dr^2, is greater than the attractive contribution d^2U_+/dr^2, becoming increasingly greater as r becomes shorter, through r_{eq} and beyond. Thus, at r_{eq}, $d^2U_-/dr^2 \gg d^2U_+/dr^2$, and

$$k = \frac{d^2U_{(\text{req})}}{dr^2} = \frac{d^2U_-}{dr^2} + \frac{d^2U_+}{dr^2} \sim \frac{d^2U_-}{dr^2}$$

Thus, depending upon the validity of the assumptions that we have made about the form of the potential function, *the force constant of a chemical bond is primarily due to the repulsive, not the attractive, part of the potential*! This conclusion will be used quantitatively in a later subsection of this article.

The foregoing gives quantitative insight into the relationship expected between force constants and bond distances. Because k is determined largely by U_-, and because the curvature (second derivative) of U_- is a function of internuclear distance r (positive curvature increasing with decreasing r, at least over normal bonding distances), then a functional relationship between r_{eq} and k is expected, wherein shorter bond distances require larger force constants as the attractive part of U_r forces the potential function against the ''repulsive wall'' determined by U_-. Furthermore, if a valid functional relationship between r_{eq} and k is established, and there have been numerous efforts to do so beginning with Badger and Pauling in the 1930s,[36–42] the repulsive component of a potential function can be approximated by integration of $k \sim d^2U_-/dr^2$. We will undertake this exercise in Section 3.2.

2.5 Group Frequencies in Inorganic Compounds

The concept of vibrational *group frequencies*, frequencies at which particular molecular substructures typically exhibit IR or Raman transitions, dates back to the 19th century.[6] This concept has been of immense value in interpreting vibrational spectra. While group frequencies in organic compounds are relatively well defined, inorganic compounds present significant additional complexities.[28] Many inorganic compounds contain organic functionalities, and these can be expected to obey the basic ''organic'' group frequency behavior, although this may be altered by any number of effects unique to inorganic chemistry, including symmetry-breaking interactions (e.g., monodentate coordination of a carboxylate to a metal ion) or by electronic interactions that change force constants and thus vibrational frequencies from their ''expected'' values (e.g., coordination of CO, NO, or isocyanide to a metal). In general, effects like this depend on the valence electronic configuration of the inorganic species, its position in the periodic table, oxidation state, etc. In addition there are myriad chemical options in inorganic chemistry that do not exist in organic chemistry and that have their own vibrational manifestations, for example, the entire field of coordination chemistry and metal–ligand binding, modes of isomerization unique to inorganic systems, etc. Actual enumeration of group frequencies is beyond the scope of this chapter, but comprehensive works on this topic are available (Section 4) and commercial databases also exist.

2.6 Units

SI units are the proper units for vibrational spectroscopy. In practice, however, chemists have been slow to convert to SI in many areas, vibrational spectroscopy among them. In the following, both the SI units and the common-usage units will be given.

2.6.1 Wavelength

Many optical devices, in particular spectrometers, fundamentally work in wavelength (λ), not frequency. For this reason it is common to see vibration (especially IR) displayed as a function of wavelength, although this has become less common in recent decades as the conversion from wavelength to frequency has become a routine feature of instrumentation. Wavelength is in fact length, and the SI unit of length is the meter (m). The most common wavelength unit used in vibrational spectroscopy is the micrometer or micron, (μm or simply μ) $1\,\mu\text{m} = 10^{-6}\,\text{m}$. So, vibrational spectroscopy is on firm SI ground with regard to wavelength. The entire wavelength range of vibrational fundamentals is from approximately 1000 μm (1 millimeter, $\text{mm} = 10^{-3}\,\text{m}$; longer wavelengths are more properly radio) to a little shorter than 2.5 μm, the vibrational wavelength of the H_2 molecule. Vibrational overtones and combinations may appear at shorter wavelengths.

2.6.2 *Frequency*

It is convenient to use frequency units in any spectroscopy because frequency is directly proportional to energy ($E = h\nu$). Frequency units are related to wavelength by the familiar equation $\nu = c/\lambda$ (c is the velocity of light, $3 \times 10^8\,\text{m}\,\text{s}^{-1}$). The SI unit for frequency is the hertz (Hz, $1\,\text{Hz} = 1\,\text{s}^{-1}$). This unit is inconvenient for most vibrational spectroscopy because vibrational frequencies in hertz are very large (3×10^9 to greater than $1 \times 10^{14}\,\text{Hz}$). Instead it is common to express vibrational frequencies in wavenumber, the number of wavefronts per unit length ($\nu = 1/\lambda$). The most common unit for wavenumber is reciprocal centimeters, (cm^{-1}) ($1\,\text{cm} = 10^{-2}\,\text{m}$). In wavenumber units of cm^{-1} the vibrational spectral range is from approximately $10\,\text{cm}^{-1}$ to greater than $4000\,\text{cm}^{-1}$.

2.6.3 *Bond Length*

Chemists are accustomed to expressing bond lengths in angström units, $1\,\text{Å} = 10^{-10}\,\text{m}$. This is not, however, an SI unit. The accepted SI unit for bond length is the picometer (pm) ($1\,\text{pm} = 10^{-12}\,\text{m} = 0.01\,\text{Å}$). Distances in macromolecular assemblies and biomolecules may be expressed in nanometers (nm) ($1\,\text{nm} = 10^{-9}\,\text{m} = 10\,\text{Å}$).

2.6.4 *Force Constant*

Force is mass times acceleration, in SI units newtons, $1\,\text{N} = 1\,\text{kg} \cdot \text{m}\,\text{s}^{-2}$. Thus the proper SI unit for force constant, k, is newtons per meter ($\text{N}\,\text{m}^{-1}$). The units of force constants typically used by chemical spectroscopists are millidynes per angström, ($\text{mdyn}\,\text{Å}^{-1}$) ($1\,\text{dyne} = 1\,\text{g} \cdot \text{cm}\,\text{s}^{-2} = 10^{-5}\,\text{N}$, $1\,\text{mdyne} = 10^{-3}\,\text{dyn}$). Thus $1\,\text{N/m} = 0.01\,\text{mdyn}\,\text{Å}^{-1}$.

2.6.5 *Vibrational Frequencies from Masses and Force Constants*

The relationship between frequency, force constant, and the mass of bound atoms is $\nu = (\text{constants}) \cdot (k/\mu)^{1/2}$ (in this case μ is reduced mass, see earlier). The constant multiplier depends on the units of ν, k, and μ. If ν in cm^{-1} is the desired quantity, k is expressed in millidynes per angstrom, and μ is in atomic mass units (amu), then $\nu = (1302) \cdot (k/\mu)^{1/2}\,\text{cm}^{-1}$. The constants that constitute this factor are given elsewhere (Nakamoto**[28]** p. 10 ff.).

3 APPLICATIONS

Applications of vibrational spectroscopy in inorganic chemistry range from the characterization of inorganic materials and coordination complexes of transition metals to determining bonding and nonbonding interactions in the active sites of metalloproteins. Vibrational methods have proved particularly useful for characterizing the structures and dynamics of bioinorganic systems, which are difficult to handle with conventional structural tools such as NMR (*see* ***Nuclear Magnetic Resonance (NMR) Spectroscopy of Metallobiomolecules***) and X-ray crystallography. Many excellent reviews and books have been written on this subject (Section 4). More recently, advances in vibrational spectroscopy techniques have significantly increased the usefulness of these methods by improving both the structural specificity and the time resolution. In this chapter we emphasize applications of these modern vibrational spectroscopy methods to the analysis of the structures and dynamics of inorganic and bioinorganic systems.

3.1 Difference Vibrational Spectroscopy

In principle, vibrational spectroscopy can probe any portion of a large, complex protein, including an embedded metal active site. Information on the local structure and interactions of the metal is obtained through analysis of the frequencies and intensities of the observed spectral lines. However, because every bond or molecular interaction in the protein can contribute to the vibrational spectrum, the spectral features are so highly congested and overlapping in a directly measured vibrational spectrum that their detailed analysis is at best difficult, and often impossible. Thus, the development of experimental methods that reduce spectral congestion has been essential for the application of vibrational spectroscopy methods in bioinorganic systems.

There are two general approaches to reducing spectral congestion in vibrational spectroscopy. The first, which has found wide use in bioinorganic chemistry, takes advantage of the resonance enhancement of Raman scattering cross sections obtained when the excitation wavelength is tuned into an electronic absorption. The large enhancement of Raman scattering for those vibrations coupled to the electronic transition, which is generally spatially localized on the metal chromophore, provides extreme discrimination against all other nonresonant Raman signals. Thereby the study of the local structure of the metal active site within a much larger and complex protein system is possible. Because the metal center is usually functionally important, RR techniques provide a powerful approach to study the structures and dynamics important to protein function. Selected examples (and related reviews) include the study of photosynthetic proteins,[43] heme proteins[44] blue-copper proteins,[45] and heme-copper oxidases.[46] A more in-depth review of the use of RR spectroscopy in inorganic chemistry is provided in a separate chapter.

The second approach to reducing the spectral complexity of bioinorganic systems is difference vibrational spectroscopy. In this approach, vibrational spectra are recorded before and after some chemical, or physical perturbation is applied. Thus the difference spectrum reflects only the vibrational features that respond to the perturbation and many of the complex, overlapping features of the raw spectra simply cancel. The difference features that remain are observable with much greater sensitivity than in the raw spectra. If the perturbation is specific to the metal active site, then the difference spectrum will reflect the changes to this site and the nearby protein structure. For example, it is often possible to perturb the redox or ligation state of the metal center, both of which lead to changes in the vibrational spectrum. Temperature, pressure and pH are also excellent variables for inducing changes to the spectra, although these changes may be more broadly distributed throughout the protein structure. All of these perturbation methods have been used in conjunction with IR and Raman spectroscopies to probe the active sites of proteins. A few illustrative examples follow.

3.1.1 *Photochemical Difference FTIR Spectroscopy*

Probably the most common approach to generating difference IR spectra of metalloproteins is to use a photochemically induced change of the metal active site to probe its structure and dynamics. This method has been widely used to study ligand binding to the Fe center of heme proteins. An example from our work on heme-copper oxidases illustrates this method.[47] The heme-copper oxidases have a binuclear active site (heme a_3 or o_3 and Cu_B) that is the site of O_2 binding and reduction. Figure 6 shows the raw (unsubtracted) FTIR spectrum of the carbon monoxide complex of the heme-copper terminal oxidase cytochrome bo_3, the quinol oxidase of *Escherichia coli*. The FTIR spectrum was obtained with 300 µM enzyme in a 50 µm pathlength cell with CaF_2 windows. The observed IR absorbance bands represent the superposition of contributions from three polypeptide subunits comprising more than 1000 amino acid residues and having a molecular weight of approximately 250 kDa. The spectrum is dominated by the amide absorbances of the polypeptide (amide I peak O. D. approximately 0.5) and individual features cannot be discerned except for a very weak peak at 1963 cm^{-1} which is the C≡O stretching mode of heme-bound CO. Figure 6 also shows the difference spectrum

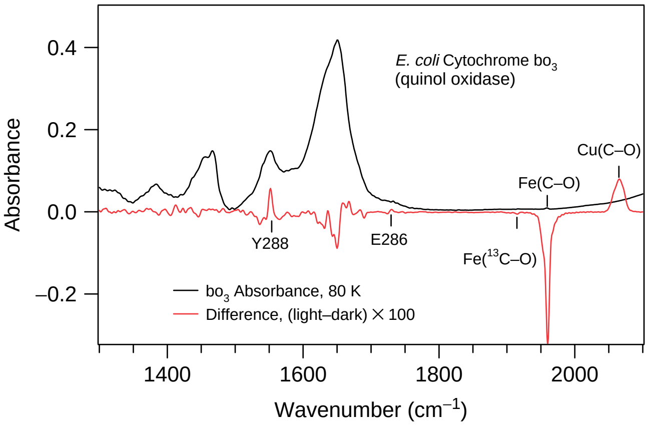

Figure 6 The FTIR absorbance spectrum (black) and the light minus dark difference absorbance spectrum (red) of carbonmonoxy *E. coli* cytochrome bo_3

(×100 relative to the raw absorbance spectrum) obtained at a temperature of 80 K by subtracting the spectrum taken in the dark from the spectrum taken after the sample is irradiated for a few seconds with a CW Ar ion laser at 514.5 nm. In the dark, the CO is bound to the heme to form a six-coordinate, low-spin Fe^{2+} complex. When CO is photodissociated from the heme at 80 K, the Fe^{2+} becomes high spin five-coordinate and the CO does not immediately recombine, but rather is transferred to the nearby $Cu_B{}^+$. All these changes are reflected in the FTIR difference spectrum. The loss of CO from the heme produces a negative peak at 1963 cm^{-1}, corresponding to the CO stretch when bound to Fe^{2+}. When CO binds to the nearby copper site, a new positive peak at 2063 cm^{-1} is observed. The large increase (100 cm^{-1}) in CO-stretching frequency reflects the different mode of CO binding to the different metals. When bound to the heme, there is significant π-back-bonding from the Fe^{2+} to the CO, resulting in a weakening of the CO bond and concomitant reduction in its stretching frequency (see Section 2.4). The higher frequency of the CO stretch when bound to Cu_B reflects the absence of significant π-back-bonding on this metal.

Obviously, the Fe(C–O) and Cu(C–O) absorbances are detected with excellent signal-to-noise. In fact, the ^{13}CO satellite on the 1963 cm^{-1} peak, due to 1.1% of the total enzyme-CO complexes, is seen at 1941 cm^{-1} with S/N approximately 10. About 10 000 scans were averaged to obtain this quality of data, requiring about 30 min of acquisition time. Other single-residue features in the difference spectrum include the frequency shift (derivative-shaped feature at 1740 cm^{-1}) of the COOH sidechain of glutamic acid 286 and the peak at 1510 cm^{-1} belonging to a ring mode of tyrosine 288, both in subunit 1. In addition, there are difference features due to the heme and the protein amide I backbone vibrations in the 1600–1700 cm^{-1} range. The amide I band (roughly, the collective carbonyl stretch of the peptide bonds) is sensitive to polypeptide secondary and tertiary structures in ways that are well established by a large body of empirical evidence.[48] Note that most of these features would not be visible in the raw absorbance spectra as they are smaller than the width of the trace as drawn in Figure 6. Clearly, FTIR difference spectroscopy is both structurally and functionally informative and sufficiently sensitive to observe specific features in very complex metalloproteins.

3.1.2 Electrochemical Difference FTIR Spectroscopy

Most metalloproteins are stable in more than one oxidation state, meaning that oxidation or reduction is another perturbation method that can be employed to generate vibrational difference spectra. A change in the oxidation state of a metalloprotein can be achieved chemically, electrochemically or in some cases photochemically. The FTIR spectrum is obtained in each oxidation state, and the difference spectrum contains only those vibrations that respond to the change. Care must be exercised to avoid spectral interference from chemical or photochemical oxidants or reductants. In this sense, the electrochemical approach is the cleanest, although it is still important to obtain an accurate subtraction of the solvent contribution with electrochemical methods. Additional technical difficulties arise from the need to use very thin pathlength cells (required because of the large solvent absorptions) in an electrochemical apparatus that allows controlling the redox potential. In laboratories that have implemented this technique, approaches have included the use of a very small pathlength cell in which the probing beam is reflected off one of the electrodes,[49] or the use of a thin pathlength transmission cell in which the electrode is a partially transmitting grid.[50] In addition, for protein studies, the use of electrochemical mediators is typically required to provide a sufficiently rapid response to changes in applied potential.[51]

The approach developed in our laboratory for electrochemical difference FTIR spectroscopy uses a reflectance cell having a thin film electrode that also serves as an IR reflector. The IR probe beam enters through an IR transparent window (ZnSe or CaF_2), passes through the sample and then is reflected off the electrode back through the sample and out the same window. Such an arrangement is easily adapted to a standard commercial FTIR sample compartment. An example of an electrochemical difference FTIR spectrum is shown in Figure 7 for the heme protein myoglobin. The absorbance spectra of the oxidized (Fe^{3+}) and reduced (Fe^{2+}) forms of the protein are also shown for comparison. Electrochemical mediators have been added to the solution in catalytically small concentrations to accelerate the electrochemical processes in a manner similar to that used by Mantele *et al.*[50] Under these experimental conditions, no spectral changes due to the low-concentration mediators are observed in the difference FTIR spectrum (lower trace). The features in the difference spectrum are primarily due to the changes of the heme and the surrounding protein residues that accompany the oxidation state change of the iron. The porphyrin ring modes in the 1600–1700 cm^{-1} range are shifted to lower frequency upon reduction, reflecting the change in electron density on the metal and in the π-system of the porphyrin.

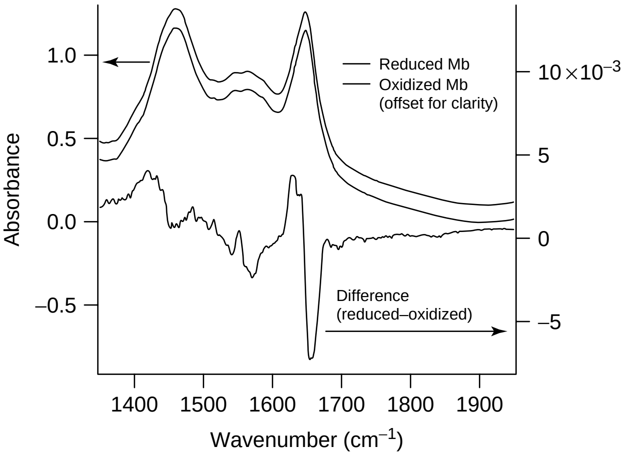

Figure 7 Electrochemical FTIR absorbance spectra (top) and difference spectrum (reduced–oxidized, bottom) of horse heart myoglobin

Proton transfer reactions often accompany electron transfers to or from the active sites of metalloproteins, termed *proton coupled electron transfer* (PCET). Since movement of electrons through the low dielectric medium of a protein is energetically unfavorable, simultaneous or coupled movement of a proton to balance the charge may reduce the energetic cost. IR spectroscopy is ideally suited to detect changes in the protonation state of ligands bound to a metal, or nearby protein sidechains. The acid dissociation constants of ligands can be modified by several orders of magnitude due to metal binding, or due to the change in the oxidation state of the metal. For example, the carboxylic acid sidechain of Asp or Glu may be deprotonated in the oxidized form of the metal center, but become protonated when the metal center is reduced. This change is readily detected in the IR spectrum from the large shift in the carboxylate mode, the asymmetric COO^- stretch between 1560 and 1590 cm^{-1}, and to the carboxylic acid C=O stretch between 1710 and 1740 cm^{-1}. An example of this behavior is Glu242 in cytochrome *c* oxidase, which serves as a proton gate between the proton channels from the inside of the membrane (the D-channel) to the binuclear active site. Using FTIR spectroscopy we have demonstrated that this residue is protonated in response to the reduction of the binuclear center.

3.1.3 Isotope-Edited Difference Vibrational Spectroscopy

Similar difference measurements can be made using resonance-enhanced or spontaneous Raman spectroscopy.[52] In Raman spectroscopy, in general, the signal from an aqueous solvent is not large (water is a very weak Raman scatterer), which makes the solvent subtractions much easier or even unnecessary. However, Raman scattering is an experiment with a very low signal rate, so long accumulation times are often required in order to obtain spectra from which good difference data can be generated. In turn, there is a requirement for very high stability in both the laser excitation sources and in the detectors that are used. Obviously, in both techniques, an additional requirement is that the samples being studied must be stable under the experimental conditions for the length of time required for data accumulation.

Figure 8 shows the raw, unsubtracted normal (nonresonant) Raman spectrum of phosphoglucomutase (PGM) which catalyzes the interconversion of glucose 1-phosphate and glucose 6-phosphate. PGM is an approximately 60 kDa protein. Panel (a) shows the Raman spectrum for PGM complexed with [^{16}O]glucose 1-phosphate while panel (b) shows the spectrum for PGM complexed with [^{18}O]glucose 1-phosphate. The differences between these two spectra involve only the phosphate group of bound glucose 1-phosphate, and it is not possible to observe by eye any changes due to the labeling of the phosphate group. The *isotopically-edited* difference spectrum is shown in panel (c), where the intensity scale is about 100 times that of panels (a) and (b). The spectral changes brought about by isotopic labeling are now evident. The positive peak at 977 cm^{-1} in the difference spectrum is the $\mathrm{P}\underline{\cdot\cdot}{}^{16}\mathrm{O}$ symmetric stretch of bound glucose 1-phosphate, and the negative peak, shifted down by 42 cm^{-1}, the $\mathrm{P}\underline{\cdot\cdot}{}^{18}\mathrm{O}$ stretch. The background noise is simple shot noise (at a level of about 0.1% of the main bands of PGM). Hence, the spectrum of a *single* and *specific* phosphate group is determined within a 60 kDa macromolecule.

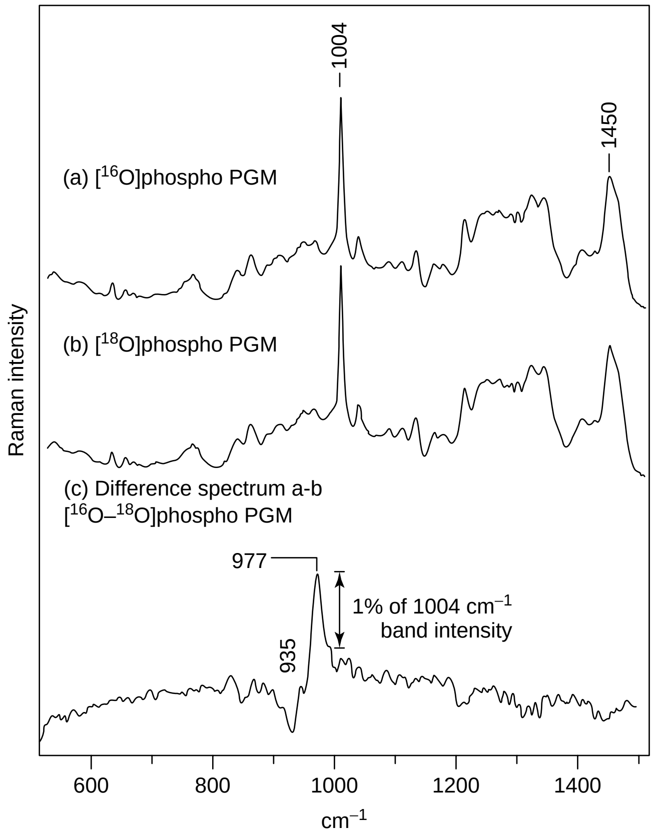

Figure 8 Raman spectra of phosphoglucomutase (PGM) at pH = 7.4 and 4 °C. Approximate data accumulation time was 2 h using 514.5 nm laser excitation. (a) The spectrum of PGM complexed with [^{16}O]glucose 1-phosphate. (b) The spectrum of PGM complexed with [^{18}O]glucose 1-phosphate. (c) The difference spectrum between (a) and (b), ×100

3.2 Quantitative Relationships between Force Constants and Bond Distances

We observed in Section 2.4 that we expect there to be some relationship between force constants and bond distances, that is, bonds with greater force constants should be shorter. Furthermore, because the force constant (given our previous assumptions) is dominated by the repulsive part of the potential function, and the repulsions are primarily due to nonbonding core electrons which are more numerous row by row down the periodic table, we expect that the ‘‘repulsive wall’’ of the core is further from the nucleus in each successive row (i.e., increasing principal quantum number). So if a functional relationship between force constants and bond distances exists, we expect that the parameters of the relationship, whatever its functional form, will depend on which row(s) of the periodic table the bonded atoms occupy.

The first empirical relationship between force constants and bond distances was ‘‘Badger’s Rule,’’ developed by Richard Badger in the 1930s.**[36–38]** Badger’s Rule has had impressive staying power and is still used (and useful) today. In the ensuing decades this general idea has been extended (e.g., to solid metals by Pauling**[41]**) and new functional forms have been proposed, most prominently by Herschbach and Laurie in the 1960s**[40]** and in the ‘‘complete neglect of practically everything (CNPE)’’ formulation of Burgi and Dunitz.**[39]** These relationships have been very useful over their applicable ranges of force constants and bond distances, namely, for single and some double bonds, and relatively strong fractional-order bonding (Figure 9a). There are some obviously unrealistic aspects to these empirical functions, however, if they are extrapolated outside their intended bounds. In general they allow arbitrarily long bonding distances when force constants approach zero; the actual expectation is that bonding distances approach a definite value as k approaches zero, and that distance is equal to or less than the van der Waals distance. Furthermore, this kind of function should approach a nonzero asymptote in bond distance as k becomes large, representing the distance at which the repulsive electrostatic forces of core nonbonding electrons overwhelm any possible valence attractions. Some of the earlier empirical functions approach an asymptote at large k, some do not.

Inorganic chemists by definition are interested in bonding of all types, energies, strengths, and formal orders,

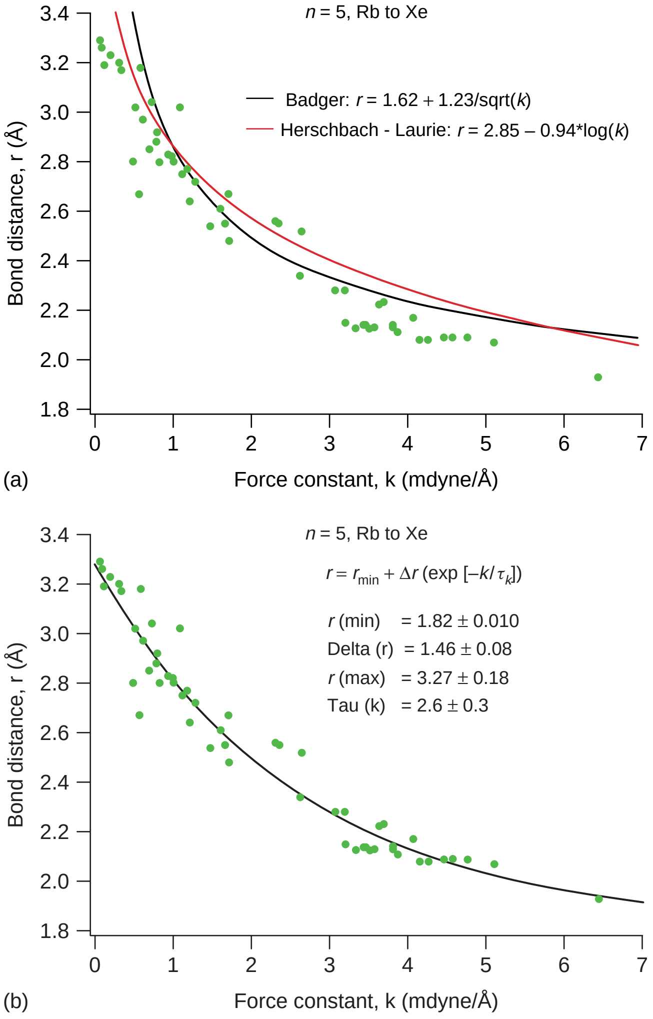

Figure 9 Bond distance versus force constant data for intra-row bonding in the row of the periodic table containing the second transition series ($n = 5$, Rb to Xe): (a) data fit to empirical force constant-bond distance functions (see text); (b) same data fit to the exponential decay function that we have proposed. Identity of the points is given in Ref. 42

in all states of matter. If there are empirical functions that describe bond distances and force constants for all these situations, their significance in inorganic and bioinorganic chemistry could be considerable. First of all, bond distances could be inferred and structural information gained in situations where vibrational frequencies can be measured but direct structure determinations are not possible, for instance, in reaction transients or electronically excited molecules. Secondly, the multitude of inorganic molecular structures that have been determined, plus the large and increasing number of metalloprotein structures, would allow one to infer approximate force constants that could be used to parameterize or verify force fields and theoretical calculations. Thirdly, examination of these relationships over large ranges of force constant and bond distance, and over the periodic table, may lead to general insights into chemical bonding. Finally, a truly valid functional relationship between force constants and bond distances provides a mathematical constraint on the form of the repulsive contribution to bonding potential functions via the relationship between the force constant and the potential function discussed in Section 2.4, $k \sim d^2U_{-}/dr^2$.

We became involved in force constant-bond distance relationships through our interest in the photochemistry of complexes containing metal–metal bonds at either extreme of the scale; formal zero-order bonds in d^8 dimers,[53] and quadruple bonds in d^4 dimers.[54] We were interested in inferring excited-state structures from vibrational data and we turned to Badger's Rule and other relationships to infer bond distances from vibrational frequencies. We found that, for the weak bonding in d^8 dimers, excited-state displacements calculated from frequency shifts were greatly overestimated (compared to calculations from vibronic data[55]), and that in the quadruple bond regime even ground-state bond distances were overestimated. Figure 9(a) (adapted from Miskowski[42]) shows how both these errors occurred. The data points in Figure 9(a) represent force constants and bond distances of compounds in the row of the periodic table containing the second transition series (Rb to Xe), including Rh and Mo, the subjects of our early studies of metal–metal bonding.[53,54] Both of the empirical relationships plotted in Figure 9(a) (lines) fit the data well in the middle range, but fail badly at small k (predicting unrealistically large r values and having slopes that are much too great) and are systematically above the data at large k. Clearly, a new empirical relationship was needed if we were to fit the whole range of data.

We found that the function that fit the data best (see Figure 9b) is a simple exponential decay ''rule'' having the form:

$$r = r_{\min} + \Delta r \left(\exp\left[\frac{-k}{\tau_k} \right] \right) \tag{1}$$

where r is internuclear distance, $r_{\min}$ is the minimum r at infinite k, Δr is the total range of r from $k = 0$ to $r_{\min}$, k is the force constant, and τ_k is the exponential 1/e decay constant for k. We found that equations of this form can be fit to force constant and bond distance data within any row of the periodic table, and between one row and another, regardless of the state of matter, formal bonding mode (e.g., ionic or covalent), bond order, spin multiplicity, electronic excitation, symmetry, etc., vide infra. The adjustable parameters in equation (1) (the values of which are dependent on which row(s) of the periodic table is/are involved) are $r_{\min}$, Δr, and τ_k. At first glance this may seem to be an unsatisfactorily large number of parameters, but if data are available over a sufficiently large range of r (and they generally are, see Figure 9b), $r_{\min}$ and Δr are very tightly constrained and only τ_k is really a free-floating adjustable parameter. Moreover, this relationship has satisfying functional properties: r reaches a definite, finite value at $k = 0$ ($r = r_{\max} = r_{\min} + \Delta r$); r approaches an asymptote at large k ($r \rightarrow r_{\min}$); and, the entire expression can be integrated to establish constraints on acceptable potential functions. All the parameters are expected to depend on which row(s) of the periodic table the bonded atoms occupy (i.e., principle quantum numbers or core electron population). There is a tradition of eponymy in this field that we have attempted to follow,[56] and we gratefully acknowledge the contributions of the late Vinny Miskowski.

Having established the exponential decay function equation (1) as a good descriptor of the force constant-bond distance relationship for bonding between elements both of which are in the row of the periodic table containing the second transition series (Figure 9), we test the generality of this functional form for the other rows of the periodic table, and for bonding between elements in different rows (data primarily from[28,57–60]). Figure 10 shows the relationships, and the exponential fits, for intra-row bonding between elements in rows 1–6. Figure 11 shows the data and fits for row 1 (H–He) bonding to rows 1–6 (Figure 11a) and for row 2 (Li–Ne) bonding to rows 2–6 (Figure 11b). Data for rows 3 and 4 bonding to subsequent rows are not shown, and interrow data involving row 6 are too sparse to be statistically significant. The exponential decay function gives satisfactory fits to the data in all cases, and the fit parameters are given in Table 1.

These relationships have been tested independently of our work and found to be quite accurate in determining bond distances in systems where crystallography is inapplicable (e.g., ES[55]) or estimating force constants where bond distances are known.[61] What other insights may be gained?

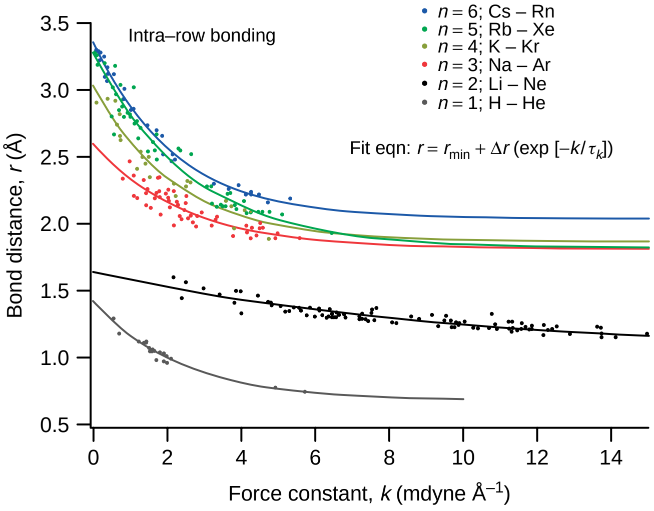

Figure 10 Bond distance versus force constant data for intra-row bonding in all rows ($n = 1$–6) of the periodic table preceding the actinoids. The solid lines show the fits to an exponential decay function (see text)

Table 1 Parameters for homonuclear and heteronuclear bonding of elements in the same (intra-row) and subsequent (interrow) rows of the periodic table (n = principal quantum number; r in angstrom; k in millidyne per angstrom; standard deviations in parentheses)

Parameters fit to equation (1): $r = r_{min} + \Delta r(\exp[-k/\tau_k])$; $r_{max} = r_{min} + \Delta r$
Parameters for intra-row bonding (n = 1,1 to 6,6):

n = 1,1; H–He to H–He	$r_{min} = 0.68(0.04)$	$r_{max} = 1.42(0.05)$	$\tau_k = 2.34(0.29)$
n = 2,2; Li–Ne to Li–Ne;	$r_{min} = 1.05(0.01)$	$r_{max} = 1.65(0.02)$	$\tau_k = 9.20(0.09)$
n = 3,3; Na–Ar to Na–Ar;	$r_{min} = 1.81(0.09)$	$r_{max} = 2.59(0.12)$	$\tau_k = 2.45(0.84)$
n = 4,4; K–Kr to K–Kr;	$r_{min} = 1.87(0.12)$	$r_{max} = 3.03(0.13)$	$\tau_k = 2.23(0.56)$
n = 5,5; Rb–Xe to Rb–Xe;	$r_{min} = 1.82(0.10)$	$r_{max} = 3.28(0.10)$	$\tau_k = 2.61(0.52)$
n = 6,6; Cs–Rn to Cs–Rn;	$r_{min} = 2.04(0.04)$	$r_{max} = 3.36(0.06)$	$\tau_k = 2.17(0.44)$
Parameters for elements in row 1 (n = 1, H–He) to elements in subsequent rows:			
n = 1,2; H–He to Li–Ne	$r_{min} = 0.90(0.03)$	$r_{max} = 1.93(0.07)$	$\tau_k = 2.70(0.29)$
n = 1,3; H–He to Na–Ar	$r_{min} = 1.20(0.05)$	$r_{max} = 2.17(0.07)$	$\tau_k = 2.07(0.32)$
n = 1,4; H–He to K–Kr	$r_{min} = 1.42(0.03)$	$r_{max} = 3.22(0.04)$	$\tau_k = 0.74(0.08)$
n = 1,5; H–He to Rb–Xe	$r_{min} = 1.52(0.09)$	$r_{max} = 3.41(0.11)$	$\tau_k = 0.68(0.17)$
n = 1,6; H–He to Cs–Rn	$r_{min} = 1.54(0.11)$	$r_{max} = 3.33(0.70)$	$\tau_k = 0.68(0.28)$
Parameters for elements in row 2 (n = 2, Li–Ne) to elements in subsequent rows:			
N = 2,3; Li–Ne to Na–Ar;	$r_{min} = 1.44(0.02)$	$r_{max} = 2.32(0.05)$	$\tau_k = 3.13(0.31)$
N = 2,4; Li–Ne to K–Kr;	$r_{min} = 1.57(0.02)$	$r_{max} = 2.56(0.05)$	$\tau_k = 2.52(0.52)$
N = 2,5; Li–Ne to Rb–Xe;	$r_{min} = 1.62(0.05)$	$r_{max} = 2.66(0.08)$	$\tau_k = 2.81(0.56)$
N = 2,6; Li–Ne to Cs–Rn;	$r_{min} = 1.59(0.05)$	$r_{max} = 2.54(0.07)$	$\tau_k = 3.68(0.72)$
Parameters for elements in row 3 (n = 3, Na–Ar) to elements in subsequent rows:			
N = 3,4; Na–Ar to K–Kr;	$r_{min} = 1.94(0.05)$	$r_{max} = 3.04(0.12)$	$\tau_k = 1.67(0.27)$
N = 3,5; Na–Ar to Rb–Xe;	$r_{min} = 2.17(0.10)$	$r_{max} = 3.00(0.14)$	$\tau_k = 1.28(0.42)$
Parameters for elements in row 4 (n = 4, K–Kr) to elements in subsequent rows:			
N = 4,5; K–Kr to Rb–Xe;	$r_{min} = 2.30(0.04)$	$r_{max} = 3.31(0.10)$	$\tau_k = 0.96(0.15)$

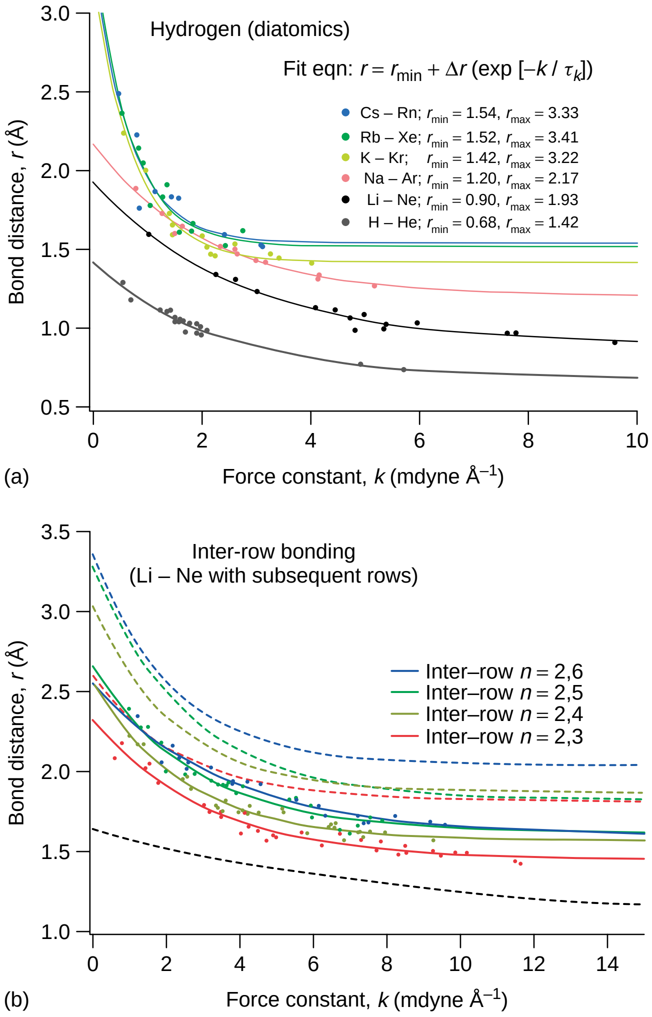

Figure 11 Bond distance versus force constant data for interrow bonding: (a) for hydrogen ($n = 1$) bonding to all rows ($n = 1-6$) of the periodic table preceding the actinoids; and (b) for second-row elements ($n = 2$) bonding to all subsequent rows ($n = 3-6$) of the periodic table preceding the actinoids. The solid lines show the fits to the exponential decay function that we have proposed. The dashed lines in (b) are the fits to the intra-row bonding shown in Figure 10

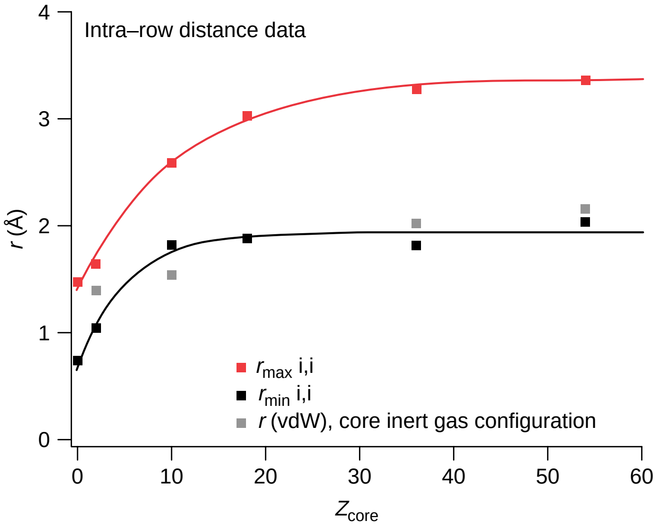

Figure 12 Maximum and minimum bond distances for intra-row bonding within various rows of the periodic table, taken from the intra-row exponential fits shown in Figure 10 and plotted versus the atomic numbers of the core inert gas electronic configurations of the various rows ($n = 1-6$)

3.2.1 *Maximum and Minimum Bond Lengths, Core Repulsions and Inert Gas Configurations*

Figure 12 plots the intra-row r_{max} and r_{min} values, row by row, versus the core inert gas atomic number for each row (i.e., zero for row 1, [He] for row 2, [Ne] for row 3, etc.). Both r_{max} and r_{min} increase as expected with Z_{core}, and both seem to approach constant maxima at large Z_{core} (approximately 3.4 Å for r_{max} and 1.9 Å for r_{min}; the solid lines in Figure 12 are exponentials but their physical significance if any is unclear). All of the interrow data follow the same general behavior; in fact, most of the interrow data can be directly superimposed on the plot in Figure 12, with two exceptions. Both the row 1 (H–He) and row 2 (Li–Ne) interrow r_{min} data are similar, systematically below the r_{min} data for the other rows, approaching a maximum of approximately 1.6 Å. Similarly, the r_{max} values for row 2 (but not row 1) fall below the interrow line, approaching a maximum of only approximately 2.7 Å. Part of this behavior can be ascribed to the unique ability of row 2 elements to form exceptionally strong bonds of all orders at short distances (see Figures 10 and 11) using only their 2s and 2p orbitals, at least in their ground electronic states. Similarly, H is unique in having only its 1s orbital available for GS bonding. Given that we ascribe r_{min} values to core electronic repulsions that overcome attractive bonding forces, we expect there to be some correspondence between minimum bonding distances and the sizes of the corresponding inert gases that are isoelectronic with the respective cores. The van der Waals radii of the inert gases are also plotted in Figure 12, and they qualitatively correspond to the behavior of r_{min}.

3.2.2 *The Lanthanoid Contraction and the Lanthanoid Expansion*

The lanthanoid contraction—the similarity in size of elements in row 5 and row 6 due to the filling of 4f orbitals between Ba and Lu—is an established paradigm that accounts for many chemical similarities between elements in the same groups of these two rows. These similarities are largely properties of the valence electrons, which are incompletely shielded from increasing nuclear charge by the 4f electrons and thus have similar spatial extension in rows 5 and 6 despite increasing atomic number. The lanthanoid contraction is very evident in interrow bonding, for example, Figure 11, where the entire bond distance and force constant ranges are indistinguishable for rows 5 and 6 bonding to H and to Li–Ne. In a sense this is unexpected, however, because despite the valence similarities between rows 5 and 6, core repulsive forces ultimately must exert their effects at greater distances for row 6 simply because its elements have more core electrons than row 5. One might expect this to manifest itself in a ''lanthanoid expansion'' of $r_{\min}$ under certain bonding circumstances. This is actually seen in the intra-row binding within rows 5 and 6 (see Figure 10). While the force constants and bond distances for rows 5 and 6 are virtually indistinguishable for force constants less than approximately 2 mdyne $Å^{-1}$, at greater values of k the r values begin to diverge, eventually reaching $r_{\min}$ values that differ by some 0.2 Å. This novel observation of a lanthanoid expansion is important in understanding very strong bonding regimes and their differences between rows 5 and 6, for example, the chemistry of compounds having intra-row bond orders of 3 or higher.

3.2.3 Bonds, Nonbonds, and Bond Order

The $r_{\max}$ values from the exponential decay fits to the bond distance-force constant data set maximum distances for ''real'' bonding (but not, for example, van der Waals interactions, vide infra). Longer distances would generally be considered nonbonding. The converse of this statement is that interatomic distances shorter than $r_{\max}$ must be considered to be bonding distances. Nobody would argue, for example, that the internuclear distances between 2.7 and 3.0 Å in the unsupported metal–metal bonds of $Co_2(CN–CH_3)_{10}$ and $Mn_2(CO)_{10}$ in row 4, or those between 3.0 and 3.3 Å in $Tc_2(CO)_{10}$ and $Rh_2(CN–C_6H_5)_8$ in row 5, constitute nonbonding interactions. Yet there are many cases where internuclear distances considerably shorter than $r_{\max}$ are generally thought to be nonbonding. This is particularly prevalent in cluster chemistry, in compounds with bridging groups, and in multimetal sites in proteins, in all of which cases ambiguities may exist and direct measurements may be difficult. It is possible that revised thinking is in order in these cases. For example, we used these arguments along with evidence from model compounds to argue that the dimeric Cu_A site in cytochrome oxidases exhibited a Cu–Cu bond in its Cu(I)–Cu(II) state,**[62]** and this suggestion has subsequently been verified.**[63]** Another insight forthcoming from these relationships is that formal bond order is at best only a qualitative indicator of where a particular bond will reside in force constant-bond distance space. There is considerable overlap among all of the formal bond orders of compounds in these correlations.

3.2.4 Exceptions

Pathological potentials, for example, those with double minima, will not adhere to these rules. Very weak interatomic and intermolecular interactions, for example, van der Waals interactions and weak metallic bonding (e.g., Hg and alkali metals) do not fit the relationships given here. Instead they follow their own exponential decay functions at longer distances and smaller force constants. In general the rules given are valid for electronically excited molecules, and are independent of spin state, term symbol, parity, symmetry, and so on. An exception to this, however, is bonding involving heteronuclear compounds of hydrogen in electronically ES. Bonds of this type generally have shorter internuclear distances than the GS H–X distances given in Table 1 and Figure 11. This may be because hydrogen is able to use orbitals other than 1s in these electronically excited species.

3.3 Time-Resolved Vibrational Spectroscopy

TRVS is ideally suited to probe the dynamics of inorganic and bioinorganic systems, including GS reactions (mechanisms of electron transfer, ligand exchange, oxidative addition, etc.) and excited-state photochemistry and photophysics. TRVS methods provide high structural specificity and time resolution. The molecular vibrations are sensitive to changes in charge, symmetry, bond lengths, bond angles, and energy content, any or all of which can be used to follow the molecular dynamics of interest. Furthermore, changes in the vibrational spectrum track molecular dynamics down to ultrashort time scales because vibrational transitions respond to changes in structure or environment on time scales as short as the 10–100 fs periods of molecular vibrations. TRVS can be regarded as a special case of vibrational difference spectroscopy, where the perturbation is generally a laser pump pulse and the time-resolved spectrum is differenced with the equilibrium spectrum. Only the structures that respond to the transient perturbation give rise to features in the difference spectrum. The transient perturbation can be direct excitation of a chromophore of the inorganic complex being probed, or a more indirect perturbation, such as a laser-induced pH-jump. It is now possible to make such measurements on all relevant time scales, from femtoseconds to kiloseconds.

The application of TRVS methods to the study of the dynamics of inorganic and bioinorganic systems has two main challenges. The first is how to initiate the dynamics of interest. Ideally the dynamics are initiated with a pulsed laser, for example, by direct excitation of a metal-to-ligand charge transfer transition. In cases where direct excitation is not possible, other approaches have been developed to rapidly initiate a chemical reaction. Examples of some important new approaches to the initiation problem are given below. The second challenge is the measurement of the vibrational spectrum on the relevant timescale. Despite major advances in methodology in the past decade, TRVS methods remain technologically difficult and require expensive equipment. Ultrafast IR and Raman measurements, for example, require sophisticated lasers and instrumentation that are generally only present in highly specialized laboratories. Even measurements on the nanosecond timescale and slower, that are possible to make in real-time (direct resolution of the transient signals with fast detectors) are not trivial. A revealing example is time-resolved step-scan Fourier transform infrared (SS-FTIR) spectroscopy. SS-FTIR spectrometers are commercially available from several manufacturers (Bruker, DigiLab, Nicolet). Nevertheless, there are only a handful of groups that have published results using SS-FTIR to study molecular dynamics of inorganic and bioinorganic systems.[64,65] Nevertheless, these studies have demonstrated the power of TRVS methods and their use is becoming more widespread.

3.3.1 Fast Initiation Methods

Direct pulsed-laser excitation is the most commonly employed approach to pump-probe time-resolved IR or Raman measurements. For example, studies of bioinorganic systems have focused on proteins with an absorbing metal active site such as heme or chlorophyll, because the chromophore provides a convenient means to both initiate and probe the dynamics. Generally, these experiments pump an electronic state of the chromophore, leading to photochemistry (ligand photodissociation), conformational changes (cis-trans isomerization) or electron transfer; the response of the chromophore is probed using TRVS. Other rapid initiation methods have been developed that do not rely on direct excitation of a metal center, including laser-induced temperature-jump (T-jump),[66] laser initiated electron transfer,[67] photolytic release of caged reagents such as Ca^{2+},[68] and submillisecond rapid mixing techniques.[69] In contrast to the optical trigger approaches, these techniques are much more generally applicable to the study of the dynamics of inorganic and bioinorganic systems that lack a readily accessible chromophore, or to the study of reactions that cannot be directly initiated with light. The fast mixing techniques, for example, are completely general and have a long history of successful application to the study of inorganic reactions (*see* ***Rapid Scan, Stopped-Flow Kinetics***).[70] The sample is probed downstream of mixing. Since the volume of this continuous flow system is kept small to minimize the sample solution volume required and to improve time resolution, laser-based probes that can be tightly focused are used, especially RR spectroscopy. The best demonstrated dead time to date is ca. 10 µs, an improvement of 2 orders of magnitude over most commercial stopped-flow instruments. Disadvantages are that physical limitations of mixing place a lower limit on the time resolution of the technique (1–10 ms), and that the large shear forces produced by turbulent flow in the mixing volume may affect the dynamics themselves as well as degrade the optical quality needed for some probes. Since all these methods are well developed and described in the literature, we focus here on two new approaches developed in our laboratories: the laser-induced pH-jump and photolysis of caged metals.

Laser-Induced pH-Jump. A macroscopic change in pH can be used to initiate many reactions of inorganic and bioinorganic systems, or at least to shift the equilibrium sufficiently to measure the relaxation dynamics. A persistent laser-induced pH-jump can be produced using a pH-jump reagent such as *o*-nitrobenzaldehyde (*o*-NBA) that acts as an excited-state proton emitter.[71] UV photolysis of *o*-NBA results in an intramolecular redox reaction yielding *o*-nitrosobenzoic acid plus a free proton. The redox reaction occurs with an efficiency of 50% and with a rate constant of $2 \times 10^9\,s^{-1}$. Rapid H_2O addition to the aci-ketene intermediate yields the benzoic acid. Thus, the photochemistry is irreversible and produces a rapid decrease in the pH of the solution. We have demonstrated the efficacy of this approach for initiating protein dynamics by initiating the folding of a helical peptide model, polyglutamic acid. Polyglutamic acid forms a random coil at neutral pH due to the repulsive forces of the ionized carboxylate side chains. However, at low pH ($pK_a \sim 3.4$) the peptide forms an α-helix, as the carboxylate sidechains become protonated. This transition can be induced on a short time scale using a laser-induced pH-jump with *o*-NBA. The steady state difference FTIR spectrum following 266 nm laser excitation (7 ns, 1 mJ) is shown in Figure 13. The short laser pulse generates a 2 pH unit change (from 6.0 to 4.0) within 100 ns. The steady state difference FTIR spectra in Figure 13 were obtained by subtracting the spectrum before excitation from the spectrum after the flash. The *o*-NBA difference spectrum (without polyglutamic acid) is shown for reference. Clearly, the pH-jump initiates two major changes in the polyglutamic acid spectrum: first, the side chains become protonated, as evidenced by the disappearance of the glutamate COO^- bands ($1410\,cm^{-1}$, sym and $1555\,cm^{-1}$, asym stretches) and appearance of the corresponding COOH band at $1715\,cm^{-1}$. Second, the polyglutamic acid becomes helical, as evidenced by the shift in the amide I absorbance.

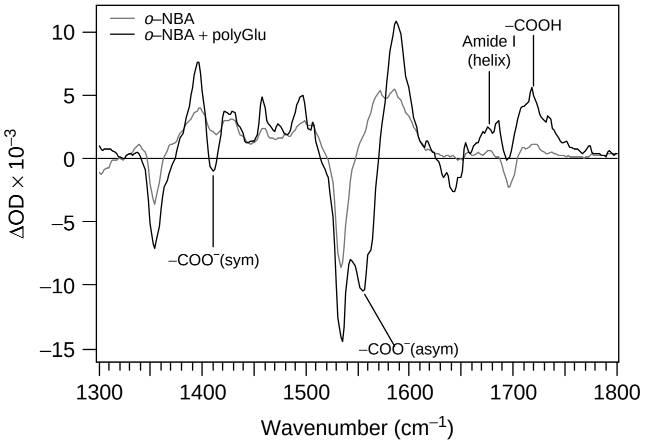

Figure 13 Rapid-scan FTIR difference spectra of an *o*-NBA + polyglutamic acid mixture following a single 266 nm laser pulse, which induces a pH-jump from 6.0 to 4.0, triggering the folding of the polyglutamic acid

Furthermore, a kinetics trace obtained at the helix wavelength indicates that the helix is completely formed within the time resolution of the pH-jump measurement (100 ns).[71] This result not only demonstrates the efficacy of the laser-induced pH-jump but also has important implications for the dynamics of helix formation. The polyglutamic acid refolds from a highly disordered state and hence must cross the helix nucleation barrier, which it does on a very short timescale (<100 ns).

Photolysis of Caged Reagents. Photolysis of caged reagents is a general approach to the study of binding and reaction of substrates and metal ions with proteins. An example of this approach is the photorelease of caged Ca^{2+} to study its binding dynamics to Ca^{2+} binding proteins such as calmodulin. Fundamental unresolved issues related to the dynamics of Ca^{2+} binding to calmodulin include the rates of binding to individual sites, the role of dynamics in cooperativity and the protein dynamics coupled to Ca^{2+} binding. Experimental approaches to these issues must overcome two problems: how to rapidly (impulsively) initiate Ca^{2+} binding and how to probe the binding and coupled protein dynamics on the relevant time scales. Rapid initiation of Ca^{2+} binding has been achieved in our laboratory using a laser-induced release of caged Ca^{2+} thereby allowing the binding dynamics to be observed using time-resolved infrared (TRIR) spectroscopy. Several caged calcium complexes that rapidly release calcium upon photoexcitation have been developed and are commercially available. One of the most promising candidates is nitrophenyl-EGTA (Figure 14 inset), which releases Ca^{2+} when excited at 355 nm through benzylic proton abstraction and subsequent rupture of the cage.[68] The rate of Ca^{2+} release is greater than 100 000 s^{-1}, with 14–20% photolytic yield. Thus a 1 mM solution of nitrophenyl-EGTA: Ca will produce a maximum concentration of 200 µM Ca within a few microseconds of a short (10 ns) laser pulse at 355 nm.

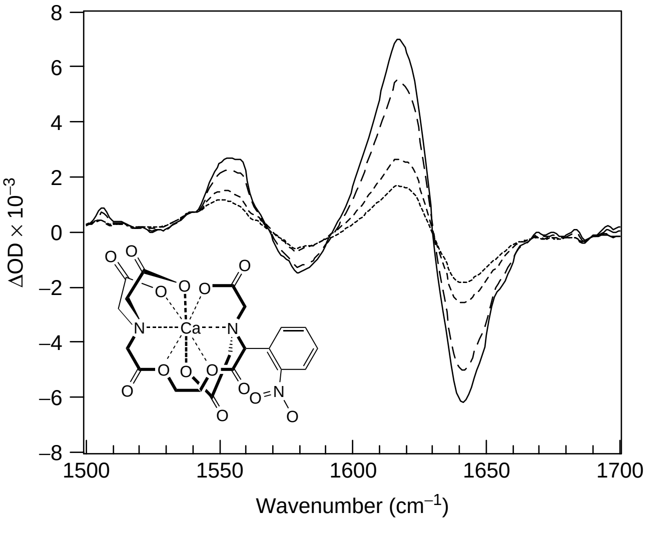

Figure 14 Ca^{2+} titration of calmodulin by photolysis of caged Ca^{2+}. The structure of the cage is shown in the inset. The difference FTIR spectra correspond to the addition of 4, 3, 2, and 1 equivalent(s) of Ca^{2+}, from top to bottom, respectively

The equilibrium difference FTIR spectra of calmodulin following titration with Ca^{2+} generated by photolysis of nitrophenyl-EGTA are shown in Figure 14. A solution of the apoprotein plus caged Ca^{2+} was irradiated with 355 nm light to photolytically produce 1, 2, 3 and 4 equivalents of free Ca^{2+}, which was then taken up by the protein. The difference spectra are computed as the spectrum after photolysis minus the spectrum before. In addition, the difference spectrum of the cage has been subtracted, to yield the difference spectrum of the protein alone. These spectra are identical to those produced from a chemical titration of Ca^{2+}, thereby demonstrating that the cage does not interfere with the Ca^{2+} binding, nor does it perturb the calmodulin structure. The difference FTIR spectra are dominated by changes in carboxylate modes that act as ligands to the Ca^{2+}. For example the asymmetric stretch of a COO−group is shifted from 1578 to 1550 cm^{-1}, characteristic of bidentate binding to the metal. In order to study the dynamics of Ca^{2+} binding using this approach, the FTIR acquisition must be time-resolved with respect to the cage photolysis. This was accomplished using a flow-flash scheme coupled with rapid-scan acquisition of the FTIR spectra as a function of time after the flash. Since the photolytic release of Ca^{2+} from the cage is irreversible, this scheme also enables repetitive signal averaging by constantly replenishing the sample in the flowing stream. Using this approach the binding kinetics for the individual Ca^{2+} binding events were resolved directly for the first time.[72]

3.3.2 *Time-Resolved Resonance Raman (TR^3) Spectroscopy*

TR^3 methods were originally developed in our laboratories to study excited-state structures and dynamics of transition metal complexes such as $Ru^{3+}(bpy)_3$ and metalloproteins.[73–75] TR^3 measurements rely on a pump-probe approach in which two separate laser pulses are used, one to excite the system and the other to probe the transient Raman spectrum. The time resolution of the experiment is determined by the width of the laser pulses (typically 7 ns for a Q-switched laser or as short as 1 ps for a mode-locked laser). The pulses are variably delayed with respect to one another to achieve time resolution, either by optically delaying the probe pulse with respect to the pump pulse or by electronically delaying two independently tunable lasers. Thus, two different approaches are required depending on the time scale of interest. The fastest timescale (from 10^{-12} to 10^{-8} s) requires optical delay to achieve sufficiently short separation between the pump and probe pulses. In such a scheme, the probe pulse is sent through a fixed path, but the pump pulse is sent through a variable path that can be scanned. Since light travels about 1 ft per ns, a difference in pathlength of a few feet is sufficient. The second approach typically uses two Q-switched Nd:YAG lasers that are electronically delayed with respect to one another, to access time scales from 10^{-8} to 10^{-1} s. In both these approaches, the detection of the Raman scattering is accomplished using a spectrograph and multichannel CCD detector. The detector does not need to be gated in this scheme since it relies on the delay of the probe pulse relative to the pump pulse to achieve time resolution.

An important example of the application of TR^3 spectroscopy to the study of metalloproteins has been its use to study the functional dynamics of the terminal oxidase of cellular respiration, cytochrome *c* oxidase (C*c*O).[46,76] TR^3 spectroscopy was first used to identify the reaction intermediates in the reduction of O_2 by C*c*O.[76] More recently, TR^3 spectroscopy has been used to study the dynamics of ligand binding to the binuclear center in greater detail.[46] Figure 15 shows TR^3 spectra for photodissociated carbonmonoxy C*c*O, obtained at pulse-probe time delay of 200 ns; the high- and low-frequency regions are both shown. The upper traces employ relatively high probe laser pulse energy (1 mJ) and the lower traces employ low-energy probe pulses (ca. 10 µJ). In the high-frequency region some diminution in intensity of the high-spin indicator band (1572 cm^{-1}) may occur at low probe pulse energy. At the same time, the oxidation state marker peak appears unchanged in frequency and lineshape at 1356 cm^{-1} in the two traces. This demonstrates that the spectrum in the low-power trace is not due to the CO complex, which would show an oxidation state marker peak at ca. 1372 cm^{-1}. In the low-frequency region the high-power trace clearly shows the Fe–N(Im) stretch of 5-coordinate high-spin cytochrome a_3 at 223 cm^{-1}, as in an earlier TR^3 study. However, this peak is greatly reduced in the low-power trace.

There are two tenable interpretations of the TR^3 results. First, the low-power TR^3 spectrum may be due to a six-coordinate low-spin species with both an unknown ligand L and imidazole as axial ligands. In general, the Fe–N(Im) stretching peak is missing from the RR spectra of six-coordinate low-spin heme complexes. In this interpretation the photolability of the Fe–L bond accounts for the typical 5-coordinate high-spin spectrum observed at high laser pulse energies; L may be imidazole itself or other ligands which are relatively poor π-acids. Alternatively, the low-power TR^3 spectrum may be due to a five-coordinate high-spin cytochrome a_3-L complex wherein L is not imidazole and has properties that induce cleavage of the Fe_{a3}–N(proximal histidine) bond. In this interpretation the disappearance of the 223 cm^{-1} peak occurs simply because the axial ligand L is not imidazole. Photodissociation of L by the probe laser pulse allows photostationary rebinding of the proximal histidine and regeneration of an essentially normal high-spin Raman spectrum. These ligation dynamics may all involve protonation and deprotonation reactions that play a crucial role in the proton pumping mechanism of the protein.

3.3.3 Time-Resolved Infrared (TRIR) Spectroscopy

The application of TRIR spectroscopy to study the dynamics of inorganic and bioinorganic systems has come more slowly than its Raman counterpart. This lag has been due in part to technical difficulties in developing IR sources with sufficient spectral brightness and detectors with sufficient sensitivity required for making fast TRIR measurements. Recent advances in laser technology, including femtosecond lasers and solid-state lasers, have provided the means to generate very bright and tunable sources throughout the midIR. Fast and sensitive IR detectors, optimized for detection of transients in real-time (10^{-9}–10^{-1} s) are now commercially available. In addition, advances in FTIR spectrometers and

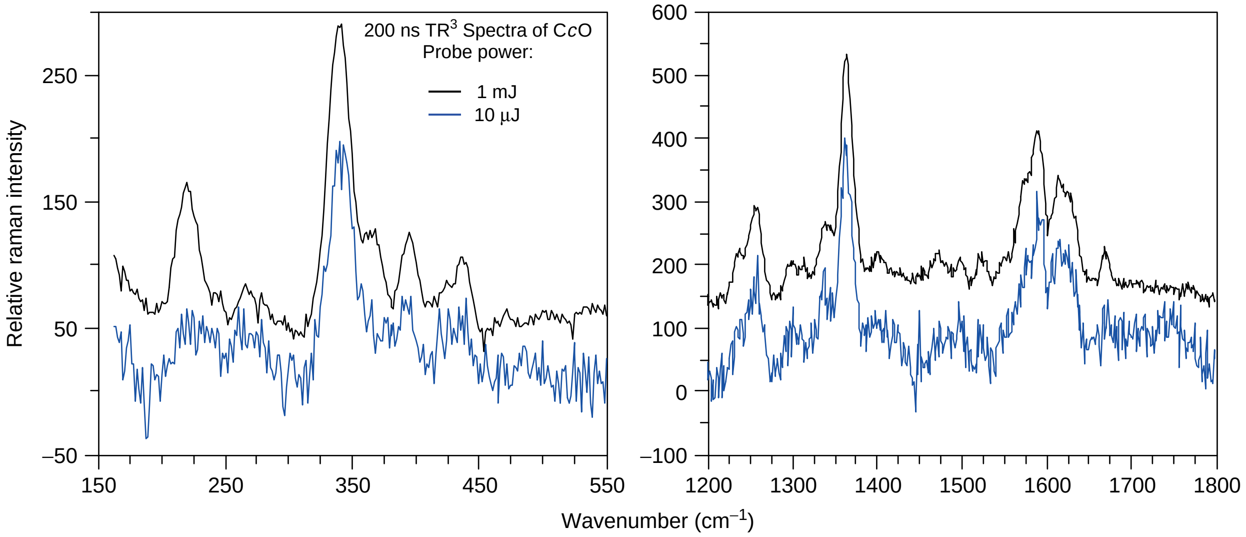

Figure 15 Time-resolved RR spectra obtained 200 ns after photodissociation of CO from fully reduced C*c*O with both high power (1 mJ, upper trace) and low power (10 µJ, lower trace) probe excitation

multichannel IR detectors (focal plane arrays) have improved the ability to measure transient IR spectra. As a consequence of these improvements, the application of TRIR spectroscopy to inorganic and bioinorganic problems has begun to flourish. Here we describe two of the most important examples, time-resolved step-scan FTIR and ultrafast TRIR spectroscopy.

Time-Resolved Step-Scan FTIR Spectroscopy (SS-FTIR). There are two approaches to obtaining time-resolved IR spectra of transient species on the $10^{-9}-10^{-1}$ s timescale.**[77,78]** The first employs a monochromatic IR source such as a CW lead–salt diode laser to measure the time course of the transient IR absorbance at a single wavelength. The transient transmission of this probe through the sample in response to a pump laser pulse is measured with a fast IR detector (usually a photovoltaic HgCdTe detector). The IR source is then scanned in a point-by-point manner, until IR transients are obtained throughout the spectral region of interest. Time-resolved spectra can then be generated by plotting the transient absorbance at each wavelength for a specific time following the excitation. While this approach is tedious, it does map the time course of the absorbance changes with high sensitivity. The alternative approach is to use time-resolved FTIR approaches that allow the entire IR spectrum to be obtained with good spectral and temporal resolution. Several specific approaches to time-resolved FTIR have appeared within the last decade, the most useful being time-resolved step-scan FTIR. A step-scan interferometer allows the moving mirror to be held at a fixed position while a transient is repetitively produced in the sample, for example, with a laser excitation. A temporally digitized reaction transient is obtained at each discrete mirror position. The temporal resolution is determined by the detector response and the digitization process. The spectral resolution and free spectral range are determined by the number and interval of interferometer mirror steps. These data are then reorganized by the FTIR control computer to yield a series of interferograms at a sequence of times. These are Fourier transformed into the time-resolved IR spectra. The critical value of this approach is that it allows a rapid survey of where in the IR spectrum the phenomena of interest appear. In this regard the rich detail of IR spectra can be a liability; if one tries to locate the dynamical phenomena of interest using the real-time point-by-point approach described above, the exercise is extremely tedious or else one trusts to luck in finding the right observation wavelength. Once these spectral signatures are identified, however, their temporal evolution can be monitored with greater sensitivity and simplicity using the single wavelength TRIR approach.

Step-scan FTIR systems are available commercially from several vendors. Unfortunately, they are (despite manufacturer's claims) unsuitable for time-resolved measurements without extensive system modifications. Typically, the illumination optics must be modified to permit a tighter focus of the probe beam and overlap of the laser excitation source. Wide-band photovoltaic HgCdTe detectors with high sensitivity are available with response times approaching 10 ns. For optimum time response of the system, the signal processing electronics must be replaced with boxcar integrators and averagers to extend the time resolution down to 10 ns. Finally, appropriate timing circuitry is required to synchronize the laser excitation with the mirror stepping.

Figure 16 shows time-resolved SS-FTIR results for the inorganic complex [*fac*$(CO)_3$(phen)Re(I)-CN-Ru(II)$(bpy)_2$CN]$^+$ (phen = 1,10-phenanthroline, bpy = 2,2′-bipyridine). Photoexcitation of this molecule produces the Ru-based metal-to-ligand charge transfer (MLCT) ES best characterized as [*fac*$(CO)_3$(phen)Re(I)-CN-Ru(III)(bpy$^-$)(bpy)CN]$^+$, which has a lifetime of several microseconds.**[79]** The frequencies of the C≡O and C≡N stretches are sensitive to the charge redistribution in the ES; the solid trace and the (+) symbols are the 100 ns SS-FTIR and point-by-point TRIR difference spectra, respectively. There are two Re–CO GS bands due to the approximate C_{3v} symmetry at 1920 and 2030 cm^{-1} and two CN bands at 2080 and 2097 cm^{-1} (bridging and terminal, respectively). There are four ES bands and four corresponding ground-state bleaches, the positions of which clearly indicate that the ES is a Ru^{III}-bpy MLCT state. It is important to realize the extreme differences in data acquisition effort required to get the step-scan compared to the point-by-point spectrum. The point-by-point transient difference spectrum represents a heroic effort consisting of separate kinetic measurements at some 70 different wavelengths. Each measurement represents approximately an hour of signal accumulation time, plus setup and alignment, etc. The investment in such a transient spectrum is obvious. The

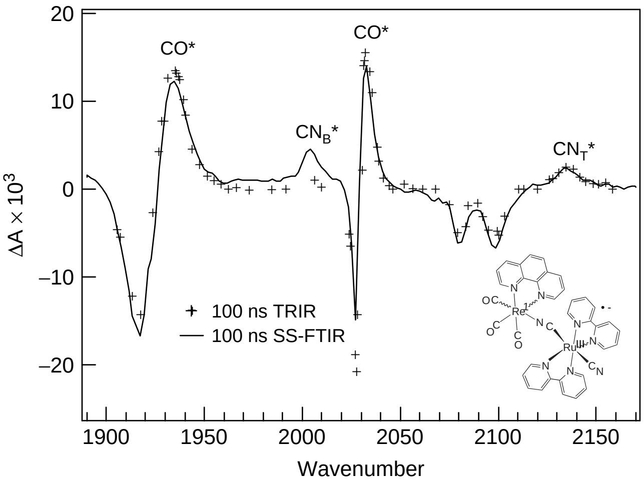

Figure 16 Comparison of the 100 ns TRIR spectrum obtained point-by-point from individual kinetics transients to the 100 ns SS-FTIR spectrum of the MLCT excited state of [*fac*$(CO)_3$(phen)Re(I)–CN–Ru(II)$(bpy)_2$CN]$^+$

step-scan spectrum, on the other hand, requires 60 min of signal acquisition time. Note also the resolution required to get complete information. The sharp C–O stretch at 2030 cm^{-1} shifts only 2 cm^{-1} in the transient spectrum. In the point-by-point spectrum 13 points are necessary over a range of less than 15 cm^{-1} to record this shift. Modest resolution (say, 10 points over the 250 cm^{-1} range instead of 70) might have missed this feature entirely. Furthermore, the ES bridging cyanide band at 2002 cm^{-1} is largely missing in the TRIR spectrum due to incomplete sampling in this spectral region, but is clearly visible in the SS-FTIR spectrum. The advantages of the step-scan approach are obvious. The example also illustrates the utility of the TRIR approach in following the movement of energy and electrons in transition metal complexes. The intense and sharp absorbance bands of the CO and CN ligands act as sensitive reporters of transient changes in the electron density at the metal centers. Similarly, the polypyridyl vibrations in the fingerprint region are sensitive to the localization of charge on the ligand in an MLCT state. Such information is difficult to obtain by any other method. Transient UV-visible absorbance, for example, is ambiguous in such systems because the electronic absorbance bands are broad and overlapping.

Dynamics of Ligation and Electron-Transfer Reactions in Terminal Oxidases. An example of time resolved, step-scan FTIR of a metalloprotein is shown in Figure 17. The spectra in Figure 17 are the time-resolved analog of Figure 6, the FTIR difference spectra observed upon photodissociation of CO from the heme of wild-type cytochrome *bo*$_3$, a terminal oxidase of respiration from *E. coli*. Upon photodissociation from the heme, CO rapidly binds to $\mathrm{Cu_B}$. The spectra show both the bleaching of the Fe(C–O) stretch (1961 cm^{-1}) and the appearance of the Cu(C–O) stretch (2062 cm^{-1}). In addition, changes in the amide and sidechain regions related to protein conformational changes are seen in the region below 1800 cm^{-1}, and these are quite similar among the WT protein and various mutants thereof. The mutants involve a particular sidechain, residue 286, which is glutamic acid (E) in WT and is mutated for aspartic acid (D) and cysteine (C), respectively. The identification of the E286 and D286 absorbances near 1750 cm^{-1}, and their absence in the E286C mutant, are apparent in low-temperature static difference FTIR spectra. The high sensitivity of these measurements is also clear. The absorbances of the 286 residue are in the order of 10^{-5} OD units, while the maximum OD's (corresponding to the amide I' absorbance) in the raw spectra from which the difference spectra are extracted are approximately 1. The transient IR absorbance of the 286 residue represents the time-resolved detection and positive identification of *one specific chemical bond*, the C=O of the carboxylic acid sidechain, in a protein having molecular weight of approximately 250 000. Finally, we can clearly follow the dynamics of the specific chemical processes involved. The photodissociated CO, bound to $\mathrm{Cu_B}$, rapidly equilibrates with solution between 5 and 23 µs, and does not return to the $\mathrm{Fe_{a3}}$ for several ms. The E286 carboxylic acid peak shifts in concert with CO binding to $\mathrm{Cu_B}$, and the intensity of the difference feature tracks the $\mathrm{Cu_B}$–CO feature in time. These dynamics are important features of the ligand shuttle and coupled proton pumping functions of the binuclear center of oxidases. This work clearly demonstrates the capability of time resolved, SS-FTIR for following metalloprotein dynamics with high structural specificity and time resolution.

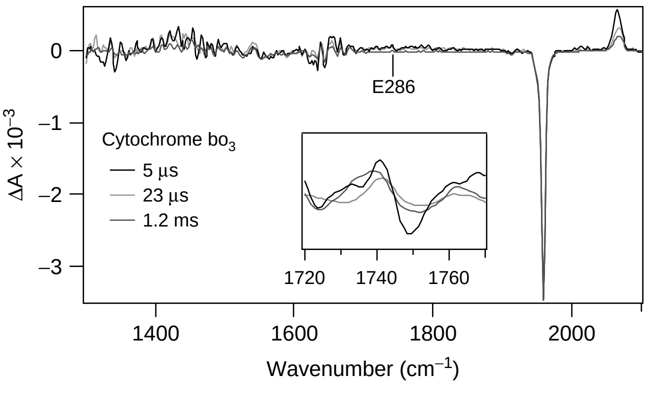

Figure 17 Time-resolved SS-FTIR spectra of photodissociated CO Cytochrome *bo*$_3$ from *E. coli*. The inset shows the evolution of the glutamic acid 286 difference feature. The noise level in the spectrum is indicated by the flat region between 1800 and 1900 cm^{-1}

Ultrafast TRIR. The most fundamental processes of bond making, bond breaking and electron transfer have ultrafast dynamics. Access to these ultrafast time scales by TRIR requires a different approach from real-time measurements. Instead, pulsed-laser techniques based upon optical delay for measurement of time must be used. There are several approaches to measuring TRIR on the $10^{-13} - 10^{-8}$ s time scale.[80] These include upconversion of a CW IR laser into the visible by sum frequency generation with picosecond (or shorter) visible pulses, use of an amplified optical parametric oscillator (OPO), and production of femtoseconds or picoseconds IR pulses by difference frequency generation. Probably the most versatile approach is the use of an OPO to generate a spectrally broad IR pulse (usually about 300 cm^{-1} with a 100 fs pulse). Ultrafast IR spectra are obtained by interrogating the sample with this broadband pulse, which is then dispersed in a spectrograph and detected with a multichannel detector (e.g., a focal plane array MCT detector). Alternatively, the ultrafast IR absorbance is measured at a single wavelength and the pump-probe delay is scanned to obtain the complete temporal response of the sample. An example of this approach is the resolution of the ultrafast ligand transfer from the heme to the $\mathrm{Cu_B}$ of cytochrome oxidase. Application of ultrafast IR to this reaction showed that CO photodissociated from the heme appears on $\mathrm{Cu_B}$ in an astonishingly short time, less than 1 ps.[81,82] Considering the energetics and geometry of the problem, the photochemical transfer half-life of CO from the heme to $\mathrm{Cu_B}$ is essentially as fast as it can physically be (although the thermal transfer lifetime almost certainly is slower). It is possible that nuclear tunneling is a factor in this extremely fast reaction. In any case, the ps TRIR result shows us that the binuclear site is elegantly arranged for facile transfer of ligands between the metal centers. This reaction is also of interest from a fundamental standpoint in understanding the elementary steps involved in atom transfer, bond formation and energy relaxation dynamics.

4 ACKNOWLEDGMENTS

The authors acknowledge support for this work from National Institute of Health grants DK36265 (WHW) and GM68036 (RBD).

5 ABBREVIATIONS AND ACRONYMS

CCD = charge coupled device; CNPE = complete neglect of practically everything; CW = continuous wave; DTGS = deuterated triglycine sulfate; ES = excited states; FTIR = fourier transform infrared; GS = ground-state; IR = infrared; MCT = mercury–cadmium–telluride (HgCdTe); MLCT = metal-to-ligand charge transfer; NMR = nuclear magnetic resonance; OPO = optical parametric oscillator; PCET = proton coupled electron transfer; PGM = phosphoglucomutase; RR = resonance Raman; SS-FTIR = step-scan fourier transform infrared; TRVS = time-resolved vibrational spectroscopy; TRIR = time-resolved infrared; TR^3 = time-resolved resonance Raman.

6 FURTHER READING

Inorganic Applications of Vibrational Spectroscopy

R. J. H. Clark and T. J. Dines, *Angew. Chem. Int. Ed.*, 1986, **25**, 131.

R. J. H. Clark and R. E. Hester, ‘Spectroscopy of Inorganic-Based Materials’, John Wiley & Sons, New York, 1987.

P. R. Griffiths, ‘Chemical Infrared Fourier Transform Spectroscopy’, John Wiley & Sons, New York, 1975.

K. Nakamoto, ‘Infrared and Raman Spectra of Inorganic and Coordination Compounds’, 5th edition, John Wiley & Sons, New York, 1997.

T. G. Spiro and R. S. Czernuszewicz, in ‘Physical Methods in Bioinorganic Chemistry’, L. Que, Editor, University Science Books, Savsalito, CA, 2000, p. 59.

Group Theory

F. A. Cotton, ‘Chemical Applications of Group Theory’, 2nd edition, John Wiley & Sons, New York, 1971.

K. Nakamoto, ‘Infrared and Raman Spectra of Inorganic and Coordination Compounds’, 5th edition, John Wiley & Sons, New York, 1997.

Collections of Reference Spectra

W. W. Coblentz, ‘Investigations of Infra-Red Spectra’, Carnegie Institution of Washington, Washington, DC, 1905.

F. R. Dollish, W. G. Fateley and F. F. Bentley, ‘Characteristic Raman Frequencies of Organic Compounds’, Wiley-Interscience, Chichester, 1974, p. 443.

7 REFERENCES

1. W. Herschel, *Philos. Trans. R. Soc. London*, 1800, **90**, 284.
2. W. W. Coblentz, *Phys. Rev.*, 1905, **20**, 273.
3. W. Abney and E. R. Festing, *Philos. Trans. R. Soc. London*, 1881, **172**, 887.
4. K. Ångström, *Ofversigt Kongl. Vet. Adad. Stockholm*, 1889, **46**, 549.
5. W. H. Julius, *Verhandl. Koninkl. Akad. Wetensch. Amsterdam*, 1892, **1**, 1.
6. W. W. Coblentz, ‘Investigations of Infra-Red Spectra’, Carnegie Institution of Washington, Washington, DC, 1905.
7. C. V. Raman and K. S. Krishnan, *Nature*, 1928, **121**, 501.
8. G. Landsberg and L. Mandelstam, *Naturwissenschaften*, 1928, **16**, 557.
9. A. Einstein, *Ann. Phys.*, 1905, **17**, 132.
10. E. L. Nichols and E. Merritt, *Phys. Rev.*, 1912, **34**, 475.
11. D. H. Rank, R. J. Pfister and P. D. Coleman, *J. Opt. Soc. Am.*, 1942, **32**, 390.
12. J. von Neumann, ‘First Draft of a Report on the Edvac’, Contract No. W-670-ORD-4926 between the U. S. Army Ordnance Department and the University of Pennsylvania Moore School of Electrical Engineering, University of Pensylvania, 1945.
13. A. A. Michelson, *Am. J. Sci.*, 1881, **3**, 120.
14. H. Rubens and H. Hollnagel, *Sitz. Preuss. Akad. Wissen. Berlin*, 1910, **4**, 26.
15. P. B. Fellgett, Theory of Infra-Red Sensitivities and Its Application to Investigations of Stellar Radiation in the near Infra-Red, Unpublished Ph.D. Thesis, Cambridge University, 1951.
16. P. Jacquinot, *Rep. Prog. Phys.*, 1960, **23**, 267.
17. J. W. Cooley and J. W. Tukey, *Math. Comput.*, 1965, **19**, 297.

18. J. R. Ferraro, ‘Low-Frequency Vibrations of Inorganic and Coordination Compounds’, Plenum Publishing, New York, 1999.
19. P. R. Griffiths, ‘Chemical Infrared Fourier Transform Spectroscopy’, John Wiley & Sons, New York, 1975.
20. T. H. Maiman, *Nature*, 1960, **187**, 493.
21. A. Javan, W. R. Bennett and D. R. Herriott, *Phys. Rev. Lett.*, 1961, **6**, 106.
22. S. P. S. Porto and D. L. Wood, *J. Opt. Soc. Am.*, 1962, **52**, 251.
23. D. Landon and S. P. S. Porto, *Appl. Opt.*, 1965, **4**, 762.
24. M. Bridoux and M. Delhaye, *Nouv. Rev. Opt. Appl.*, 1970, **1**, 23.
25. W. H. Woodruff and G. H. Atkinson, *Anal. Chem.*, 1976, **48**, 186.
26. G. J. Puppels, F. F. M. Demul, C. Otto, J. Greve, M. Robert-nicoud, D. J. Arndtjovin and T. M. Jovin, *Nature*, 1990, **347**, 301.
27. M. C. Asplund, M. T. Zanni and R. M. Hochstrasser, *Proc. Natl. Acad. Sci. U.S.A.*, 2000, **97**, 8219.
28. K. Nakamoto, ‘Infrared and Raman Spectra of Inorganic and Coordination Compounds’, 5th edition, John Wiley & Sons, New York, 1997.
29. J. W. Strutt (Lord Rayleigh), ‘Encyclopedia Britannica’, 9th edition, Henry C. Allen Publisher, New York, 1890, Vol. XXIV, p. 421.
30. R. S. Tobias, *J. Chem. Educ.*, 1967, **44**, 2.
31. A. Campion and W. H. Woodruff, *Anal. Chem.*, 1987, **59**, 1299A.
32. E. J. Heller, *Acc. Chem. Res.*, 1981, **14**, 368.
33. E. B. Wilson, J. C. Decius and P. C. Cross, ‘Molecular Vibrations: The Theory of Infrared and Raman Vibrational Spectra’, McGraw-Hill, New York, 1955.
34. R. S. Tobias, *J. Chem. Educ.*, 1967, **44**, 70.
35. F. A. Cotton, ‘Chemical Applications of Group Theory’, 2nd edition, John Wiley & Sons, New York, 1971.
36. R. M. Badger, *J. Chem. Phys.*, 1934, **2**, 128.
37. R. M. Badger, *Phys. Rev.*, 1935, **48**, 284.
38. R. M. Badger, *J. Chem. Phys.*, 1935, **3**, 710.
39. H. B. Burgi and J. D. Dunitz, *J. Am. Chem. Soc.*, 1987, **109**, 2924.
40. D. Herschbach and V. W. Laurie, *J. Chem. Phys.*, 1961, **35**, 458.
41. L. Pauling, *Phys. Rev.*, 1938, **54**, 899.
42. V. M. Miskowski, R. F. Dallinger, G. G. Christoph, D. E. Morris, G. H. Spies and W. H. Woodruff, *Inorg. Chem.*, 1987, **26**, 2127.
43. R. J. Donohoe, R. B. Dyer, B. I. Swanson, C. A. Violette, H. A. Frank and D. F. Bocian, *J. Am. Chem. Soc.*, 1990, **112**, 6716.
44. M. R. Chance, *Meth. Enzymol.*, 1993, **226**, 97.
45. W. H. Woodruff, R. B. Dyer and J. R. Schoonover, in ‘Biological Applications of Raman Spectroscopy’, ed. T. G. Spiro, John Wiley & Sons, New York, 1988, Vol. III, p. 413.
46. W. H. Woodruff, O. Einarsdottir, R. B. Dyer, K. A. Bagley, G. Palmer, S. J. Atherton, R. A. Goldbeck, T. D. Dawes and D. S. Kliger, *Proc. Natl. Acad. Sci. U.S.A.*, 1991, **88**, 2588.
47. A. Puustinen, J. A. Bailey, R. B. Dyer, S. L. Mecklenburg, M. Wikstrom and W. H. Woodruff, *Biochemistry*, 1997, **36**, 13195.
48. H. Susi and D. M. Byler, *Meth. Enzymol.*, 1986, **130**, 291.
49. R. E. Wittrig and C. P. Kubiak, *J. Electroanal. Chem.*, 1995, **393**, 75.
50. D. Moss, E. Nabedryk, J. Breton and W. Mantele, *Eur. J. Biochem.*, 1990, **187**, 565.
51. P. Hellwig, C. Ostermeier, H. Michel, B. Ludwig and W. Mantele, *Biochim. Biophys. Acta Bioener.*, 1998, **1409**, 107.
52. H. Deng, J. H. Wang, R. Callender and W. J. Ray, *J. Phys. Chem. B*, 1998, **102**, 3617.
53. C. M. Che, L. G. Butler, H. B. Gray, R. M. Crooks and W. H. Woodruff, *J. Am. Chem. Soc.*, 1983, **105**, 5492.
54. M. D. Hopkins, W. P. Schaefer, M. J. Bronikowski, W. H. Woodruff, V. M. Miskowski, R. F. Dallinger and H. B. Gray, *J. Am. Chem. Soc.*, 1987, **109**, 408.
55. S. F. Rice, V. M. Miskowski and H. B. Gray, *Inorg. Chem.*, 1988, **27**, 4704.
56. W. H. Woodruff, *Abs. Pap. Am. Chem. Soc.*, 2005, **229**, U960.
57. C. P. Horwitz and D. F. Shriver, *Adv. Organomet. Chem.*, 1984, **23**, 219.
58. K. P. Huber and G. Herzberg, ‘Molecular Spectra and Molecular Structure, 4: Constants of Diatomic Molecules’, Van Nostrand Reinhold, New York, 1979.
59. M. D. Morse and R. E. Smalley, *Ber. Bunsen-Ges. Phys. Chem.*, 1984, **88**, 228.
60. D. F. Shriver and C. B. Cooper, *Adv. Inf. Raman Spectrosc.*, 1980, **6**, 127.
61. J. Manna, R. F. Dallinger, V. M. Miskowski and M. D. Hopkins, *J. Phys. Chem. B*, 2000, **104**, 10928.
62. N. J. Blackburn, M. E. Barr, W. H. Woodruff, J. Vanderooost and S. Devries, *Biochemistry*, 1994, **33**, 10401.
63. K. R. Williams, D. R. Gamelin, L. B. LaCroix, R. P. Houser, W. B. Tolman, T. C. Mulder, S. deVries, B. Hedman, K. O. Hodgson and E. I. Solomon, *J. Am. Chem. Soc.*, 1997, **119**, 613.
64. K. Gerwert, *Biol. Chem.*, 1999, **380**, 931.
65. J. R. Schoonover, G. F. Strouse, R. B. Dyer, W. D. Bates, P. Y. Chen and T. J. Meyer, *Inorg. Chem.*, 1996, **35**, 273.
66. R. Callender and R. B. Dyer, *Curr. Opin. Struct. Biol.*, 2002, **12**, 628.
67. T. Pasher, J. P. Chesick, J. R. Winkler and H. B. Gray, *Science*, 1996, **271**, 1558.
68. G. C. R. EllisDavies, J. H. Kaplan and R. J. Barsotti, *Biophys. J.*, 1996, **70**, 1006.
69. S. Takahashi, S. R. Yeh, T. K. Das, C. K. Chan, D. S. Gottfried and D. L. Rousseau, *Nat. Struct. Biol.*, 1997, **4**, 44.

70. C. P. Bowers, K. D. Fogelman, J. C. Nagy, T. Y. Ridley, Y. L. Wang, S. W. Evetts and D. W. Margerum, *Anal. Chem.*, 1997, **69**, 431.
71. T. P. Causgrove and R. B. Dyer, *Chem. Phys.*, 2006, **323**, 2.
72. S. C. Gallagher, Z. H. Gao, S. P. Li, B. Dyer, J. Trewhella and C. B. Klee, *Biochemistry*, 2001, **40**, 12094.
73. R. F. Dallinger, W. H. Woodruff and M. A. J. Rodgers, *Appl. Spect.*, 1979, **33**, 522.
74. W. H. Woodruff, *Proc. Soc. Phot. Opt. Inst. Eng.*, 1983, **426**, 121.
75. W. H. Woodruff and S. Farquharson, *Anal. Chem.*, 1978, **50**, 1389.
76. G. T. Babcock, J. M. Jean, L. N. Johnston, G. Palmer and W. H. Woodruff, *J. Am. Chem. Soc.*, 1984, **106**, 8305.
77. J. A. Bailey, F. L. Tomson, S. L. Mecklenburg, G. M. MacDonald, A. Katsonouri, A. Puustinen, R. B. Gennis, W. H. Woodruff and R. B. Dyer, *Biochemistry*, 2002, **41**, 2675.
78. J. R. Schoonover, G. F. Strouse, K. M. Omberg and R. B. Dyer, *Comments Inorg. Chem.*, 1996, **18**, 165.
79. J. R. Schoonover, K. C. Gordon, R. Argazzi, W. H. Woodruff, K. A. Peterson, C. A. Bignozzi, R. B. Dyer and T. J. Meyer, *J. Am. Chem. Soc.*, 1993, **115**, 10996.
80. P. O. Stoutland, R. B. Dyer and W. H. Woodruff, *Science*, 1992, **257**, 1913.
81. R. B. Dyer, K. A. Peterson, P. O. Stoutland and W. H. Woodruff, *J. Am. Chem. Soc.*, 1991, **113**, 6276.
82. U. Liebl, G. Lipowski, M. Negrerie, J. C. Lambry, J. L. Martin and M. H. Vos, *Nature*, 1999, **401**, 181.

X-Ray Absorption Spectroscopy

Krisztina Z. Bencze, Kalyan C. Kondapalli and Timothy L. Stemmler

Wayne State University, Detroit, MI, USA

Method Summary 1
1 Introduction 2
2 Technical Background 3
3 Applications 5
4 Reference Material 11
5 Abbreviations and Acronyms 14
6 References 14

METHOD SUMMARY

Acronyms, Synonyms

- X-ray Absorption Fine Structure (XAFS)
- X-ray Absorption Near Edge Structure (XANES)
- Extended X-ray Absorption Fine Structure (EXAFS)

Measured physical quantities (initial/final states and selection rules)

- core electron excitation energies of absorbing atom
- scattering of X-ray photoelectron by electron density around neighboring atoms

Information available (strengths of technique)

- average oxidation state of redox active metals — XANES
- metal–ligand coordination geometry/symmetry for selected metals (Mn, Fe, Cu, etc.) — XANES
- highly accurate metal–ligand bond distances (±0.02 Å) — EXAFS
- metal–ligand coordination numbers — EXAFS
- types of coordinating atoms — EXAFS

Information not available (limitations)

- cannot directly distinguish type of scattering from adjacent elements in same periodic table row
- high error in accuracy of coordination numbers (error bars of at least ±0.5)
- precise coordination geometry is not available; only radial distances are determined
- structural information is constrained to within approximately a 5 Å radius from the absorbing atom
- insensitive to magnetic or isotopic properties of metal sites

Major advantages of technique

- can obtain highly accurate metal–ligand bond lengths
- can obtain structural information from samples in either the frozen solution or solid state
- technique is element selective; no interference from other types of metals

Major disadvantages of technique

- if the sample is heterogeneous, the scattering signal is the average of all sites of the same element; it is impossible to deconvolute scattering from these sites
- technique requires high intensity X rays from a synchrotron light source
- technique often does not give a unique determination of ligand environment; it depends on simulation/curve fitting

Questions that can be addressed using technique

- What is the oxidation state of the metal in the sample?
- Is the metal site affected by the presence of substances like substrate, inhibitors, and redox agents?
- What is the ligand environment around the metal site in the sample?
- Is the metal part of a multinuclear cluster?

Sample constraints

- sample concentration of at least 0.3 mM in excited element (typically the higher the better) is required
- sample volume should generally be between 50 and 140 μL (microliter volumes are required only in special cases)
- solution samples must be frozen quickly, typically with adition of glassing agents (glycerol, etc.)
- sample cells must fit cryostat being used
- atomic number of excited elements must be >19; lower values require special handling

1 INTRODUCTION

X-ray absorption spectroscopy (XAS) is quickly emerging as a premier tool for investigating the structure and redox properties of molecules. Utilizing the high-flux and broad energy range of X rays supplied by synchrotron sources, one can selectively excite core electron transitions for specific atoms in a molecule using XAS. Spectroscopic signals from these electronic transitions can be used to dissect the chemical architecture of molecules, providing a better understanding of their functionality. With the achievement of brighter energy sources, the field of XAS has grown as an application that can be utilized to solve more complex issues regarding the structure of molecules. Coupled to the growth of this technique is the push from many laboratories toward developing hardware and software to expand the utility of XAS. As this technique continues to grow in its capability and general ease of use, so does the demand for its application by chemists and biochemists alike.

XAS has historically been utilized to provide structural details of molecules, predominantly at metal centers in inorganic and bioinorganic systems. The ability to selectively excite electrons in specific atoms allows for the identification of metal–ligand coordination details at distinct positions in molecules. An inherent strength of the technique is that it provides highly accurate metal–ligand bond lengths for a molecule. In addition, information from the excitation edges provides an additional wealth of information regarding the electronic environment, the coordination geometry, and even ligand identity of specific atoms in molecules. This technique is generally easier to apply than other structural techniques, given one can characterize a molecule in the gaseous, solution, or solid state. Limitations of the technique (i.e., spectra are the average of all same element sites, etc.), however can hinder the unique identification of the metal environment particularly within a multinuclear complex.

When coupled with other techniques, XAS can often provide the additional key information required to decipher the chemical properties of a molecule. The high resolution and accuracy of structural details provided by this technique are perfectly suited when one is interested in solving structurally related questions. Highly accurate bond lengths derived from XAS can easily serve as metrical constraints when refining molecular structures by nuclear magnetic resonance (NMR) spectroscopy (*see* ***Nuclear Magnetic Resonance (NMR) Spectroscopy of Metallobiomolecules***) or X-ray crystallography. XAS excitation edges can provide complementary electronic detail for electrochemical and electron paramagnetic resonance (EPR) studies if there is interest in understanding the electronic properties of metals in a molecule. The specificity of signals from different atoms can be used to complement metal analysis from techniques like atomic absorption or inductively coupled plasma-mass spectroscopy (ICP-MS) (*see* ***Metal Analysis***). Whether being used as a ‘‘stand-alone’’ technique or in combination with other methods, XAS can provide the unique structural and electronic details required to understand the chemical framework of many important molecules.

This article is directed toward providing the reader with a general understanding of the technique and to describe how it can be utilized to address specific questions. Numerous published reviews describe the physics behind the technique, therefore only a general overview of these physical principles is provided in this article. Numerous examples illustrating how XAS was used to address specific questions are provided to help the reader gauge the utility of the technique regarding their research. Finally a summary of practical descriptions and important reference material regarding XAS are provided to assist the reader in applying this technique.

2 TECHNICAL BACKGROUND

XAS utilizes high intensity X rays provided by synchrotron radiation sources to excite core electrons in specific atoms within a molecule. By drawing X rays tangential to the circular electron path within a synchrotron, focused high intensity X-ray photons can be delivered over a broad energy range at a flux orders of magnitude higher than those provided by standard X-ray generators. Energies required to excite electronic transitions are atom specific, so the technique is selective for the element of interest. Energies below the absorption edge, too low to promote electron excitation, result in baseline noise within the low energy region of an XAS spectrum (Figure 1). When the X-ray energy matches the excitation energy of a core electron for the element of interest, this electron is promoted to unpopulated energy levels or dissociated, accounting for the large absorption edge seen in an XAS spectrum. The energy range immediately before and after the excitation edge is referred to as the *X-ray absorption near edge structure* (XANES) region of the XAS spectrum. At energies above the excitation edge, the electron is ejected to the continuum where it behaves as a photoelectron wave following a sinusoidal variation. This high-energy region of the XAS spectrum, covering the spectral oscillations, is defined as the *extended X-ray absorption fine structure* (EXAFS) spectral region.

The excitation edge in a typical XAS spectrum contains a wealth of information regarding different electron excitation events. The K-absorption edge, driven from the excitation of 1s core electrons, is often utilized to investigate elements ranging from sulfur to cadmium, since X rays required to induce these transitions often fall within the energy range provided by XAS monochromators. To characterize elements with atomic numbers above 48, one typically utilizes a lower energy L-absorption edge, where electron excitation for the L_{I} edge comes from a 2s electron and L_{II} and L_{III} edges come from exciting 2p orbital electrons. XANES spectra span the photon energy range immediately below and going about 40 eV above the excitation edge (Figure 2). The excitation edge in a XANES spectrum can provide information regarding the redox state of the excited element and the identity of ligand atoms around the excited element. Low intensity transitions, sometimes seen in a K-edge spectrum at photon energies below the large excitation edge, arise from the excitation of 1s electrons to vacant 3d or 4p (for first-row transition elements) energy levels. These excitation signals, often referred to as pre-edge transitions (Figure 2, inset), can be utilized to determine the geometrical arrangement of the atoms surrounding the absorbing element. When applied to molecules on a surface, the *near edge X-ray absorption fine structure* (NEXAFS) provides additional information regarding the orientation of the molecule based on the polarization dependence of the signal. Direct structural detail from the technique comes, however, from the EXAFS region of the XAS spectrum.

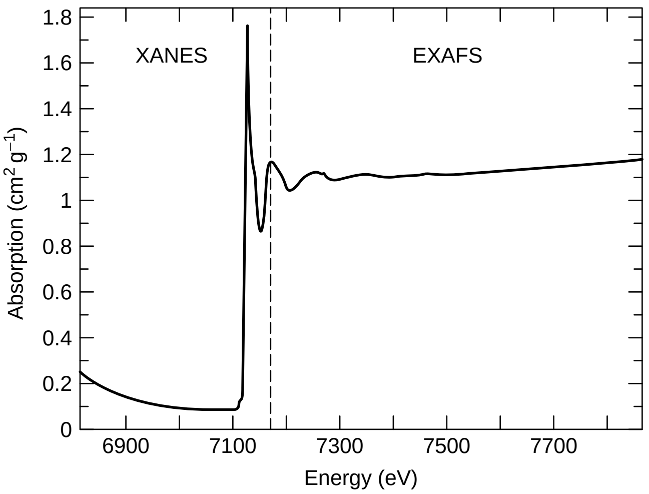

Figure 1 XAS spectrum for the Fe(II)-metal chaperone protein yeast frataxin with spectral regions labeled for clarity. Dashed line separates the regions

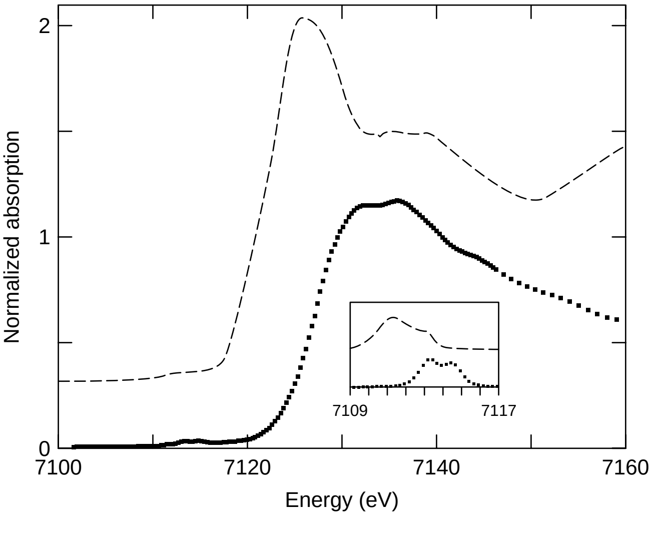

Figure 2 XANES comparison of Fe(II) (dashed line) and Fe(III) (dotted line) ammonium sulphate, offset vertically for clarity. First inflection energies for edges occur at about 7123 and 7127 eV, respectively. Inset: 1s → 3d transitions expanded and offset for clarity

The EXAFS spectral region is dominated by the damped sinusoidal oscillations in the absorption spectrum and generally refers to the energy region 40–1000 eV above the absorption edge (Figure 3). In this energy range, the photon energy is much higher than the core electron binding energy, resulting in substantial kinetic energy for the excited photoelectron. Following excitation and ejection of the core electron, the resulting signal can be viewed as an outwardly propagating wave traveling away from the absorbing atom. When neighboring atoms surround the absorbing element, the photoelectron wave will be backscattered by each neighboring atom, producing an inwardly propagating wave for each backscattering atom (Figure 3, inset). The outgoing and incoming waves can constructively or destructively interfere, perturbing the apparent absorption. The constructive and destructive overlap of waves gives rise to maxima (E_1) and minima (E_2) in the absorption cross-section (μ), hence producing the sinusoidal variations in μ versus individual photon energy value (E) that are known as EXAFS (χ). EXAFS data are converted from X-ray photon energy to photoelectron wave vector (k) values during quantitative analysis, according to equation (1):

$$k = \left[\frac{2m_e(E - E_0)}{\hbar^2}\right]^{1/2} \tag{1}$$

where E_0 is the threshold energy for excitation of the core electron, m_e is the mass of the electron and $\hbar$ is Planck's constant over 2π.

The overall EXAFS of a system can be broken down to the individual wave properties of each resolvable absorber–scatterer (as) interaction. The frequency of each EXAFS wave depends on the distance between the absorber and scatterer. During the forward and backscattering process, the photoelectron wave encounters a phase shift (Coulombic interaction) twice with the absorbing atom (i.e., once going out and once coming back) and once with the scattering atom. The amplitude of each EXAFS wave depends upon the number and backscattering strength of the scattering atom, as well as the bonding mode and distance between the absorber and scatterer. One can describe in k space the total EXAFS (χ_{Total}) for a multicomponent scattering system (equation 2) as the sum of the individual EXAFS ($\chi_i(k)$) observed when the photoelectron interacts with a unique scattering atom before returning to the absorbing atom (equation 3):

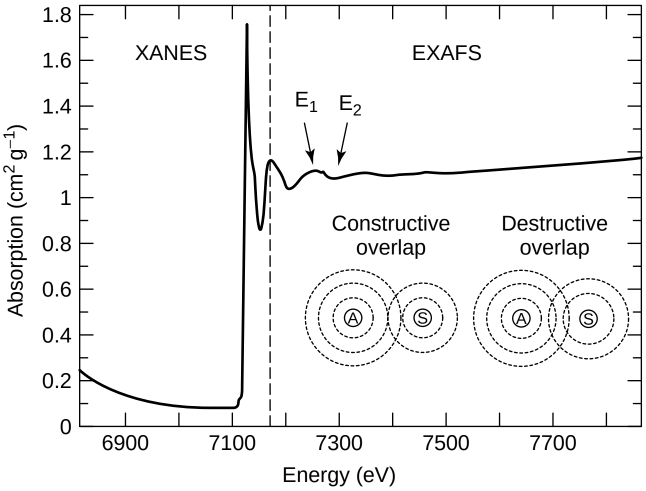

Figure 3 XAS spectrum with absorption maxima (E_1) and minima (E_2) in the EXAFS. Inset: constructive and destructive overlap of photoelectron wave

$$\chi_{\text{Total}}(k) = \sum_i \chi_i(k) \tag{2}$$

$$\chi_i(k) = \frac{N_s S_0^2 A_s(k)}{kR_{\text{as}}^2} \exp\left(-2k^2\sigma_{\text{as}}^2\right) \times \exp\left(\frac{-2R_{\text{as}}}{\lambda}\right) \cdot \sin(2kR_{\text{as}} + \phi_{\text{as}}(k)) \tag{3}$$

In equation (3), N_s is the number of scattering atoms at the bond distance (R_{as}) from the absorbing atom. The factor $A_s(k)$ is the backscattering strength of the scattering atom and S_0 is a passive electron reduction factor in the interaction. Within the two exponential components, σ_{as}^2 is the mean free deviation in R_{as}, often referred to as the Debye–Waller factor, and λ is the mean-free-path of the photoelectron. Finally, $\phi_{\text{as}}(k)$ is the phase shift the photoelectron wave undergoes when passing through the potentials of the absorbing and the scattering atoms. The Debye–Waller factor accounts for the reduction in scattering intensity due to thermal motion or static disorder of atoms about their equilibrium positions.[1] Data are often collected at low temperatures to reduce the vibrational component of this disorder.

While the amplitude of a scattering interaction can be difficult to accurately determine by EXAFS, the strength of this technique lies in the fact that the frequency components of the EXAFS wave are extremely well defined. Simulating the frequency component in EXAFS can therefore lead to highly accurate measurements in absorber–scatterer bond lengths (R_{as} uncertainty of ±0.02 Å). Bond length determination is partially complicated by the uncertainty in E_0 for a specific system; however, methodologies for addressing this in a sample-specific manner (outlined in Section 4) increase the accuracy in this measurement. Imprecision in EXAFS amplitude measurements, often resulting from data analysis methodologies and the large number of parameters affecting scattering signal intensity, lead to a generally accepted accuracy in coordination number measurement of ±0.5 for this technique. The EXAFS phase factor, which is strongly affected by uncertainty in E_0, complicates the specific identification of the scattering ligand, and this leads to a generally accepted accuracy in scattering element to only within the row of the periodic table (e.g., one can directly distinguish between oxygen and sulfur scattering but not between oxygen and nitrogen scattering).

3 APPLICATIONS

Owing to its unique advantages, XAS has been successfully applied in numerous situations to address structure and reactivity related questions regarding a variety of molecules. The deconvolution and characterization of overlapping XANES features has helped provide direct insight into the ligand coordination geometry and redox state of absorbing atoms in many relevant molecules. Since this technique can be applied in the solid, liquid, or gaseous state, XAS has had a selective advantage for structural characterization compared to other techniques. While practical limitations reduce the utility of this technique for only probing local structural environments in molecules, the high accuracy and resolution provided by XAS has been utilized to obtain precise structural details of molecules in their resting or under turnover conditions. Below we list a series of examples in which XAS was successfully applied to answer specific scientific questions. Each example illustrates a different aspect of the technique.

3.1 Coordination Geometry from XANES Pre-Edge Analysis

Analysis of many XANES spectra show sharp pre-edge features immediately prior to the general excitation edge arising from electron excitation to unoccupied low energy orbitals.**[2]** This region in the XANES spectrum often provides a sensitive probe for the electronic environment and structural geometry of the absorbing atom.**[3]** A careful, mechanistic, and quantitative evaluation of spectral patterns for these pre-edge transitions has proved useful when determining the coordination number and symmetry of metal centers at active sites in numerous metalloprotein and metal-containing compounds.**[4–6]**

For the first-row transition metals, this weak pre-edge transition originates from a 1s → 3d electron transition, observed for metals with open 3d orbital energy shells (see Figure 2, inset). In centrosymmetric structural environments, this transition is electric dipole forbidden, however electric quadrupolar coupling or mixing of the 4p and 3d orbitals distorts the centrosymmetric environment and provides 1s → 4p character, which in turn makes the transition more dipole allowed.**[7]** The intensity of the pre-edge feature provides a measurement of the metal site symmetry, with intensity increasing by almost two orders of magnitude as one proceeds from a centrosymmetric environment (e.g., octahedral, square planar, etc.) to a non-centrosymmetric environment.**[8]** An extensive study on the vanadium compounds by Lytle *et al.* in the 80's indicated that integrated intensity ''A'' of the 1s → 3d transition varies with the coordination geometry according to equation (4)

$$A \propto \left[\sum C_i R_i^2 \exp\left(-\alpha_i R_i^2\right)\right]^2 \qquad (4)$$

where C_i is the linear combination of atomic orbital (LCAO) coefficients of the final state molecular orbital, R_i is the bond distance and α_i is the orbital exponents of the i^{th} type ligand.**[9]** In addition, two other factors that provide geometry and spin-state information are: (i) the energy splitting and (ii) the intensity distribution along the pre-edge.**[6]** These factors have been characterized in great detail for high and low spin inorganic iron (ferrous and ferric) model complexes in various structural symmetries.**[4,6]** Using ligand field theory, the authors calculated the allowable multielectron excited states and the energies of these excited states were compared to the energy splitting of the 1s → 3d pre-edge features for the model compounds. The intensity distribution pattern of the pre-edge feature was also compared with the relative intensity for the transitions; the effect of distortion of symmetry and contribution of the electric dipole and quadrupole mechanisms to the intensity of the pre-edge feature were also analyzed. This detailed study helped establish a general trend for various geometries of iron complexes.**[6]** An additional piece of information obtained from the quantitative estimation of the intensity of the pre-edge transition is the coordination number. By comparing the area and shape of the pre-edge feature with iron model compounds of varied coordination numbers, the authors were able to estimate the iron-ligand coordination number. This approach was utilized when analyzing nonheme iron active sites where a change in the coordination number is reflected in the intensity of the 1s → 3d pre-edge feature, as a result of a change in the symmetry at the metal site.**[5]** Selective transition energy features between the ferric and ferrous high and low spin systems provided a qualitative measure of the spin-state for iron in these systems.**[6,10]** Although numerous studies exist, one excellent example for how pre-edge analysis was utilized to characterize structural and electronic properties of protein bound iron was in the published XAS characterization of the hydroxylase of methane monooxygenase.**[11]**

Additional intense pre-edge features can be observed for other first-row transition metals. In cuprous containing systems, this feature arises from the 1s → 4p transition. As with the 1s → 3d transition, the intensity of the 1s → 4p transition depends on the coordination number and symmetry of the cuprous metal site.**[12–14]** A weak 1s → 3d transition can also be observed for cupric systems. Our laboratory has successfully applied the methodology of quantitating both 1s → 3d and the 1s → 4p transition areas to elucidate the complex mixed valence copper environment in the multicopper active sites in particulate methane monooxygenase.**[15]**

For second row transition metals, the corresponding 1s → 4d transition requires very high energies. Low monochromator resolution and short core-hole lifetimes hinder the ability to detect this transition in many cases.**[8]** Other options to obtain information for these metals rely on intensity estimations of the 2p → 4d (allowed) transitions at the $L_{(\text{II,III})}$ edges.**[8]** Another promising approach, mentioned in

Section 3.6, is the use of ligand XANES.[16] Covalency in the interaction of a ligand 3p and metal 3d orbitals, for example, is reflected in the intensity of a pre-edge transition arising due to a ligand 3p hole character, produced as a result of the mixing of orbitals during bond formation.[16] Furthermore, changes in the ligand field and coordination number affect the 3d orbital energies, which, along with the ligand 1s core energy, affect the pre-edge transition energy, providing electronic structural information. Ligand XANES has been successfully used in many studies, particularly for Cl or S ligands.[16]

3.2 Oxidation State of Absorbing Atom from XANES

The dependence of electron excitation edge energies relative to the excited atom's valence state makes XANES a powerful tool for elucidating the average oxidation state in redox active elements. From XANES edge-energy analysis, one can gain a semi-quantitative understanding of the oxidation state of the averaged metal site. General trends show a shift to higher edge energies coupled to an increase in the element's oxidation state, based on the principle that it takes a higher energy to excite core electrons as the valence state of the element increases.[17] XANES can also be used as a tool to monitor changes in oxidation state coupled with substrate/ligand binding and/or catalysis. This principle is illustrated for iron in Figure 2, which showed the K-edge XANES spectra for hydrated iron at two oxidation states. Edge inflection energies for hydrated Fe(II) and Fe(III) occur at about 7123 and 7127 eV, respectively. In addition to oxidation state, ligands bound to the absorbing element also contribute to the general shape of the edge and apparent edge energy for the metal.[18,19] Hence, a robust methodology for characterizing the oxidation state of metal using XANES must include analysis of the edge shape and not just the inflection energy. As a result, relating edge energy to a metal's formal oxidation state is purely empirical.[7] Though it has been successfully used in many cases, unequivocal results are not always obtained from this analysis. This is particularly true in multinuclear complexes where edge shifts due to the oxidation of a single metal may be small and outside the resolution limit of the data. Furthermore, the XANES edge reflects the element's, averaged oxidation state in a multinuclear complex, so clarification of the specific oxidation state of a metal at each site is complicated. A classic example for how these obstacles were overcome in a multinuclear complex can be seen in the XAS studies of the multinuclear Mn center in the oxygen evolving complex (OEC) in photosystem II.

The OEC, along with several other proteins, comprise photosystem II (PSII) the reaction center involved in photosynthetic charge separation. Light energy absorbed from antenna systems (chlorophyll molecules) is initially transferred to the primary electron donor P680. Electrons released from P680 are transferred through an electron transfer chain and bring about the reduction of plastoquinone. Electrons from the OEC re-reduce P680. In the OEC, electrons are generated by a unique photo induced oxidation of water ($2H_2O \xrightarrow{4h\nu} O_2 + 4e + 4H^+$). The electrons are transferred to P680 through a redox active tyrosine residue, protons are ejected into the luminal space, and molecular oxygen is released into the atmosphere. Protons and electrons are ultimately used to convert carbon dioxide to organic molecules that constitute the biosphere and the oxygen released supports most life on earth.[20,21]

A tetranuclear manganese complex, along with two additional but essential inorganic cofactors (Ca^{2+} and Cl^-) form the catalytic center of the OEC.[20] The four-electron driven process of molecular oxygen formation presumably takes place as an independent event, where each photon absorption and charge separation provides a single oxidizing equivalent to the Mn center in the OEC. The intermediate oxidation states of OEC, known as S_n states ($n =$ number of oxidizing equivalents stored), accumulate these oxidizing equivalents and oxidize water only when $n = 4$. These oxidizing equivalents were proposed to be stored on the tetranuclear Mn cluster in the OEC.[21–23] A detailed understanding of the oxidation states of Mn is therefore crucial to gain an understanding of the mechanism of water oxidation as the OEC advances through the S states. Given that XAS can selectively probe each metal type within a complex system, the use of XANES was perfectly suited to help characterize the valence state changes in Mn within the OEC during molecular oxygen production. As a result, multiple groups applied this technique to characterize the Mn center in the OEC, often coupled with additional complementary electronic techniques like EPR. Three factors had to be accounted for in the XANES analysis when estimating changes in the Mn oxidation state during O_2 production. These factors were: (i) the position of the edge inflection energy, (ii) the shape of the edge, and (iii) the comparison of protein data to appropriate inorganic model complexes. A summary of these analyses is provided below.

Mn edge studies in the early 1980's indicated that a shift to higher energy is observed in the K-edge spectrum of the S_2 state relative to the S_1 state.[24] For the $S_0 \rightarrow S_1$ and $S_1 \rightarrow S_2$ transitions in the OEC, a 2.1 eV and 1.1 eV increase in edge inflection energies were observed indicating that Mn is oxidized during these transitions.[22] As previously stated, the method employed to quantify the edge energy affects the oxidation-state estimation to a great extent. Therefore, each of the three different approaches were tested to quantify the edge position to a single energy value. These approaches included: (i) utilizing only the inflection point energy (i.e., edge energy = inflection point energy), (ii) utilizing the edge half-height (i.e., the edge energy = energy corresponding to the normalized absorption (y-axis of XANES) value of 0.5), and (iii) the integral method (i.e., the edge energy = mean energy value of the edge region).[25] In one study, the K-edge energies of various mixtures of Mn(III)O–Mn(IV)O_2 inorganic compounds was determined by all the three methods mentioned above.[25] It was shown that the edge energy remains constant at the Mn(III) value until the mixing ratio of Mn(III) and Mn(IV) reaches 50%; it then jumps to the Mn(IV) value. Though the additional two approaches showed a comparatively better linear progression, no method was strictly linear. This clearly illustrates that no single method is unambiguously applicable to all systems. Smoothing of XANES spectra is required in most cases, as noise contributions cannot be completely avoided. Hence the method of choice for edge-energy determination must take into account the sensitivity of the approach to extensive smoothing and the experimenter should be cautious when employing only a single method for oxidation-state analysis. This study also highlights the usefulness of calibrating complex protein data with well-characterized inorganic model compound simulations.

Comparisons of the different S states with Mn model XANES spectra was a useful method to help clarify the oxidation state differences that occur during the OEC's calalytic cycle. Mn K-edge spectrum of the OEC in the S_{-1} state, produced by a two-electron reduction from S_1, was best fit with Mn(II_2,IV_2) oxidation states for the four Mn atoms.[26] The second derivative of the S_0 XANES spectrum is again not only different from the S_1 state, but also shows distinct spectral features at 6548 eV, similar to the second derivative XANES spectrum of Mn(II)-containing model compounds. As model complex comparison and other data indicated the presence of Mn(II) in the S_0 state, Mn(II,III,IV_2) was also proposed for the S_0 state.[22,23] Studies on model compounds showed inflection point energy shifts for Mn(II) → Mn(III) were greater than those for Mn(III) → Mn(IV), indicating that application of this methodology toward characterizing the higher states would be less direct.[22] XANES studies, coupled with other spectroscopic techniques, indicated the possibility of Mn(III_2,IV_2) oxidation states in S_1.[22,27] Mn is oxidized in the transition from S_1 to S_2 in a single electron event, so a global oxidation state of Mn(III,IV_3) would be plausible. The $S_2 \rightarrow S_3$ state transition is more ambiguous and hence controversial, placing it beyond the scope of discussion in this report. Thus XANES studies on the multinuclear Mn center in the OEC show this is a valuable technique for identification of metal oxidation states, even though a final consensus on Mn oxidation states in OEC has not been reached.

3.3 Ligand Identity from EXAFS

Practical limitations discussed earlier reduce the ability of EXAFS to directly determine the identity of scattering atoms between elements within the same row of the periodic table. Ligand scattering from oxygen and nitrogen atoms are nearly indistinguishable in their phase and amplitude, making direct identification impossible. In addition, metal–ligand environments are often constructed by a combination of similar elements, often at nonresolvable bond distances, further complicating their identification. Direct ligand identification is therefore constrained to the row of the periodic table. However, in some cases, even these criteria cannot be achieved. Under cases where the k space for the data is limited, and interference from multiple ligand environments exists,[22] distinguishing a metal–metal interaction from a metal–sulfur interaction can also be complicated. In many cases, it is impossible to determine a unique identification of the ligand environment, so extreme caution should be taken to verify ligand identification without over-interpreting the data. In many cases, having an understanding of the general coordination chemistry for model systems has led to the selective identification of ligand environments within systems with similar ligand types.

An emerging occurrence in metalloproteins is the presence of dinuclear metal centers, with dimetal centers constructed by μ-oxygen bridged ligands anchored to the protein using carboxylate oxygens and imidazole nitrogens from Asp/Glu and His residues, respectively. The short metal–oxygen distance is often (but not always) distinguishable from carboxylate ligation, as illustrated in the oxidized forms of the dinuclear iron proteins hemerythrin and ribonucleotide reductase.[28] Under ideal conditions, identification of the progressive protonation of the oxo-bridge can also be monitored, as illustrated in a series of dinuclear Mn model compounds with unique bridging schemes.[29] In the case of the dinuclear iron protein methane monooxygenase, distinguishing between ligand environments constructed of carboxylate oxygens and imidazole nitrogens was possible, given the generally long Fe–N imidazole bond distance relative to the shorter Fe–O carboxylate ligation in the protein.[30] Correct identification of the independent but similar scattering atoms in these cases was accomplished in part because data were collected over a large k range (hence very high resolution). Ligand identification was additionally confirmed by coupling XAS studies with additional complementary techniques like Mössbauer and ESEEM.

3.4 Multiple Scattering

Further clarification between nearest-neighbor oxygen and nitrogen scattering can be obtained when a subset of these atoms are structurally restricted within a rigid ligand cage. Nitrogen atoms, constrained in an imidazole ring or as part of a porphyrin ring, often serve as direct ligands to metals. Unlike normal single scattering signals (i.e., absorber → scatterer 1 → absorber) generally observed for nearest-neighbor ligands, scattering from rigid ligand cages is much more complex and generally involves multiple scattering events. In this case, EXAFS oscillations from a multiple scattering pathway (i.e., absorber → scatterer 1 → scatterer 2 → absorber) can be as much as an order of magnitude more intense than single scattering. Overlap of multiple scattering pathway signals often results in a distinct fingerprint of a group of resolvable signals in the overall EXAFS, especially in the case of metals bound to imidazoles or porphyrin rings.[31] These linked scattering signals can often be directly simulated for the entire rigid ligand unit, and upon removing this scattering contribution, it is often possible to deconvolute scattering signals from additional similar atoms. As an example, in biological samples, EXAFS scattering from water oxygens and imidazole nitrogens are virtually identical, as they occur at similar bond lengths, and phase differences between O and N are minimal. Classic examples where a multiple scattering deconvolution methodology was successfully applied to isolate metal–histidine imidazole ligation were in characterizing the Ni site structure of urease[32] and in Cu site structure of the peptidylglycine alpha-amidating enzyme.[33]

Multiple scattering will also significantly enhance observable metal···metal scattering in systems that contain structurally rigid multinuclear metal centers that are indirectly coordinated. As discussed previously, two metals constrained in dinuclear metal compounds are often structurally linked by bridging atoms (often μ-oxo, μ-hydroxo or carboxylato bridging ligands); in the case of iron–sulfur clusters, the two iron are linked by bridging sulfur atoms. A general property of EXAFS multiple scattering is that it is extremely angle dependent. When scattering angles between the absorber → scatterer 1 → scatterer 2 atoms are less than 150°, multiple scattering is generally weak and can be neglected. In this scenario, if the absorber and scatterer atoms are the two metals in a dinuclear metal complex, direct simulation of the metal···metal interaction using a single scattering approximation would provide accurate structural characteristics of the molecule. If the multiple scattering angle is between 150° and 180°, multiple scattering interactions are more prevalent, and a consequence of direct simulation of the dinuclear center using single scattering models would result in distorted metal···metal bond lengths and coordination numbers. Hence multiple scattering modeling in this system would be required for an accurate fit. Although there are many, one example where multiple scattering was required to simulate a metal···metal interaction in a dinuclear protein is in the iron center of the hydroxylase of methane monooxygenase.[11]

3.5 Mixed Metal Compound

In cases where molecules contain multinuclear metal centers, XAS can be used to probe the unique structural and oxidation-state properties of each site independently. These conditions were successfully achieved in characterizing Cu/Zn superoxide dismutase, although the close proximity of the Zn excitation energy to the Cu edge limited the ability to extend the copper data to high resolution (Cu and Zn K-edge excitation energies occur at 8980 and 9659 eV, respectively). The Zn K-excitation edge limits the resolution of the copper data by introducing a severe distortion in the Cu EXAFS at k of ca. $13\,\text{Å}^{-1}$. Practical use of the Cu EXAFS was therefore limited to a k limit below $13\,\text{Å}^{-1}$. As zinc is a ubiquitous metal found in numerous metal amalgams, very low-level Zn contamination is often an issue when collecting Cu EXAFS. In spite of these difficulties, the identification of the Cu/Zn center in bovine superoxide dismutase proved to be somewhat straightforward.[34,35] XAS studies aided in the identification of Cu and Zn ligands, the exact coordination number of each, and the symmetry of the metal center. Additional X-ray crystallographic studies combined with a series of spectroscopic techniques (EPR, ENDOR, NMR *see* ***Nuclear Magnetic Resonance (NMR) Spectroscopy of Metallobiomolecules***) helped confirm the identity of the exact coordination environment of the copper atom.[36,37] The identity and position of the zinc atom was further identified on the basis of X-ray structure of heavy metal replaced protein (i.e., Hg for Zn).[38] The nearest-neighbor environment (i.e., presence of histidine and oxygen ligations for both atoms) were identified from the high resolution X-ray structure (*see* ***Electron Paramagnetic Resonance (EPR) Spectroscopy*** and ***Electron-Nuclear Double Resonance (ENDOR) Spectroscopy***).[36]

3.6 Sulfur XAS

Although complicated in experimental setup, sulfur XAS is emerging as a powerful tool for characterizing oxidation state and structure of sulfur atoms in molecules. Sulfur is often a ligand to a metal, so these analyzes provide a complementary analysis to metal–ligand XAS in an appropriate system. Experimental hardware requirements include a low energy monochromator and a beamline path entirely under vacuum to reduce absorption of soft X rays from the air. Distinct differences in the shape and first inflection energies for multiple reduced and oxidized sulfur compounds proved early on that sulfur K-edge can be used to identify the oxidation state and structural environment of sulfur in molecules.[39,40] Sulfur K-edge EXAFS has also been used to elucidate the structure and ligand coordination in numerous model compounds and metalloprotein active sites, especially regarding metal–thiolate interactions from the viewpoint of the thiol.[41]

3.7 Heavy Metal Site Structure

Although core electron binding energies for K-edge transitions occur at energies up to 115 606 eV (uranium), hardware limitations reduce the range of achievable high-energy values for XAS studies. Many XAS experimental stations have hardware with upper energy limits of roughly 40 000 eV. In addition, insertion devices used to increase the spectral brightness of the beamlines, often decay dramatically at intensities above 50 000 eV, further restricting the achievable K-edge excitation range to elements within the second row of the transition elements in the periodic table. However, L-edge excitation energies for the third row transition elements and higher are within the achievable range for current hardware; these edges yield strong signals and as a result have been utilized in several studies to characterize heavy elements (i.e., Hg, Pb, Gd, etc.).[42–44] A good example of one such study includes the mercury-binding metalloregulatory protein MerR.[45,46] L-edge XAS studies provided evidence for a novel tridentate Hg-cysteine receptor complex at the protein's active site that helped address the protein's selectivity for mercury over the other metals of group IIB, since Hg prefers tetrahedral cysteine coordination.[46]

In addition to providing direct structural information at the metal, XAS can be used to derive anomalous scattering parameters during structure determination by multiwavelength anomalous diffraction (MAD) for heavy element systems. Anomalous scattering is a manifestation of the X-ray diffraction in specific electron resonant frequencies. As incident photon energies approach an L-absorption edge, electrons bound in atomic orbitals exhibit resonant frequencies corresponding to dipole allowed transitions. Anomalous scattering breaks down the equation for X-ray diffraction as follows:

$$\boldsymbol{F} = \mathbf{F}_p + \mathbf{f}_h + f' + f'' \tag{5}$$

where $\boldsymbol{F} =$ total scattering vector, $\mathbf{F}_p =$ sum of scattering from light atoms, $\mathbf{f}_h =$ normal scattering from heavy atom, $f' =$ real component of anomalous scattering, and $f'' =$ imaginary component of anomalous scattering. Components $\mathbf{F}_p$ and f_h remain constant while f' and f'' change, as the X-ray radiation scans across a heavy atom's absorption edge. MAD takes advantage of these differences in scattering across the absorption edge. The imaginary component of anomalous scattering is a source of phase information in macromolecular crystallography and is proportional to the atomic absorption coefficient. Anomalous dispersion factors are sensitive to the chemical environment of an atom and can be extracted from the oscillations of an XAS spectrum. The MAD signal can therefore be estimated from these dispersion factors.[47]

A specific case where XAS was utilized to determine anomalous scattering factors from a MAD signal was in the structural characterization of guanosine monophosphate synthetase (GMPS).[48] GMPS belongs to a family of glutamine amido-transferases and catalyzes the final step of the *de novo* guanine nucleotide biosynthesis. GMPS uses ATP to catalyze the amination of xanthosine-5′-ribonucleotide. Free thiol groups of GMPS cysteine residues were labeled with mercury. X-ray absorption data were measured as fluorescence excitation through the L_{III} edge of mercury at 12 284 eV (the K-edge occurs at over 83 000 eV). The L_{III} energy made this experiment feasible using synchrotron radiation; furthermore L-edge anomalous scattering is stronger, making it applicable for large protein structures. In the case of GMPS, an average spectrum was constructed from fluorescence spectra and after subtracting the background, the experimental spectrum was fit to the theoretical absorption spectrum of mercury. As mentioned earlier, the imaginary component (f″) is directly proportional to the atomic absorption coefficient and Kramers-Kronig transformation was applied to the hybrid f″ spectrum to get the real component f′ of the anomalous scattering factors. Structure determinations are more direct and rapid in this way as compared to isomorphous replacement, where data are collected from multiple heavy atom derivatives.

3.8 XAS Applied with Additional Structural Techniques

Although structural details provided by XAS are localized to a narrow region of a molecule (ca. <5 Å from the absorbing atom) with limited information regarding metal–ligand geometry, the high accuracy in bond lengths obtained can be used to construct an overall 3D structure of a molecule in combination with other structural techniques. This is especially true in cases for which the metal is generally considered to be spectroscopically silent (e.g., Zn). In the case of GMPS,[48] metal–ligand bond lengths obtained from XAS provided extremely high resolution structural detail of the mercury–sulfur center in the crystal. During NMR structural characterization, when an active site contains an element with a non spin-active nucleus, XAS bond lengths can be utilized to provide the structural constraints in this local region of the molecule.[49] The paramagnetic behavior of many metals often complicates the identification and structural characterization of even commonly detectable spin-active nuclei surrounding the metal (at ca. <10 Å), due to significant line broadening effects. XAS can be used to significantly enhance the structural detail of a molecule's solution structure by providing metrical details of the metal site. This was true in the example of the ubiquitin binding motif protein Npl4 zinc finger (NZF). Zinc–sulfur bond lengths determined by XAS for the Zinc–(Cys)$_4$ zinc finger site provided interatomic distance constraints for solving the solution structure of this protein domain.[50]

3.9 Structural Changes Coupled to Molecular Reactivity

Metalloproteins exploit the redox and coordination chemical properties of metals to catalyze reactions. With bond-length resolution capabilities of ±0.02 Å,[51] XAS is ideal for monitoring subtle changes at metal centers during catalysis. Interrogating the oxidation state and coordination environment of active site metals using XAS can provide a mechanistic picture of the system being studied. An excellent example of this was in the characterization of nickel containing superoxide dismutase (SOD). SODs are widely distributed in prokaryotic and eukaryotic cells[52] and catalyze the breakdown of superoxide. These proteins contain metal ions at their catalytic centers which are usually constructed of Mn, Fe, Ni, Cu, and/or Zn metals.[53] In many cases, the active site metal is maintained in the oxidized form during the enzyme's resting state. The metal binds superoxide and, following a subsequent proton transfer event, molecular oxygen is released leaving the metal in the reduced state. This reduced form of the enzyme will bind a second superoxide anion and a proton to release peroxide, hence returning back to its resting state (i.e., the oxidized form).

Ni-SODs are a novel group of SODs in that they share a much lower sequence homology to other metal-containing SODs, even though they have similar catalytic rates.[53] In order to elucidate the mechanism of this enzyme, the nickel site was examined using XAS. Ni K-edge XAS data were collected on the as-isolated and dithionite-reduced enzyme.[54] XANES data indicated the metal–ligand site changes from a four-/five-coordinate square-pyramidal environment to a planar environment as the metal goes from an oxidized Ni(III) to a reduced Ni(II) state.[54] Subsequent crystallographic studies confirmed this structural change.[55] EXAFS analysis suggested a unique five-coordinate site with three sulfur donors, one nitrogen donor, and one O/N-donor in the oxidized state. Sulfur ligation was unexpected due to its susceptibility to oxidant dependent modification and the fact that none of the other previously studied SODs had sulfur ligation. Recent additional studies, using complementary techniques, have further expanded the understanding of the structure and mechanism of NiSOD.[55]

3.10 Time-resolved X-ray Absorption Spectroscopy

The ability to collect electronic snapshots on subsecond timescales is a currently expanding branch of XAS being used to probe dynamic chemical systems. XAS studies covering timescales in the millisecond to seconds range are becoming routine.[56] Time-resolved XAS is currently being applied for elucidating ‘‘in situ’’ the chemistry of dynamic systems and the structural characterization of reaction intermediates. Application of this technique to metalloproteins is still in early stages, although it has been successfully applied to study slower reactions.[8,56,57] Several approaches to utilizing XAS to address time resolution studies include the following techniques: quick-extended X-ray absorption fine structure (QEXAFS), dispersive-energy extended X-ray absorption fine structure (DE-EXAFS), turbo-EXAFS, piezo-XAFS, and laser-initiated time-resolved XAS.[56,58,59] In general, these techniques have been developed but are surprisingly under-utilized, a fact that will certainly change as exposure to these techniques becomes more publicized.

QEXAFS samples a single energy at a time and hence retains the point-by-point mode of data acquisition; however, a double crystal monochromator utilizes a high-geared stepper motor with encoder that continuously moves to complete an entire scan in a matter of seconds.[56] The time resolution is generally in the range of about 30–60 s. This approach has been predominantly utilized to study catalysis, solid and liquid phase chemistry, and surface-mediated electrochemical processes.[56] A good example of a homogenous liquid phase system where QEXAFS was used to obtain quantitative kinetic data of halogen exchange in 2-bromopropane with sodium iodide.[60] Using highly concentrated samples, accurate kinetic data were derived from the structural data obtained in these studies.[60] The QEXAFS approach can yield high quality data often in all modes of detection (transmission, fluorescence, etc), however, this technique does have temporal limitations.[56] DE-EXAFS on the other hand uses dispersive geometry and focuses a polychromatic X-ray beam on the sample using a curved crystal, which allows for sub-millisecond time resolution as the effective time for single point accumulation.[8,56] Detection is only possible in the transmission mode, thus limiting the applicability of the technique to highly concentrated samples.[56] Turbo-EXAFS is a hybrid approach that retains the positive features of Q- and DE-EXAFS. Sequential energy scanning is made available by incorporating a slit that scans across the wide spectral energy range provided by a dispersive monochromator. Hence, all modes of detection are possible and good quality data can be collected.[56,61] Piezo-XAFS makes use of piezo tilt tables mounted below crystals that provide for fast XANES data collection, where a large eV range can be scanned with repetition frequencies of 10 Hz; in this case, EXAFS data can be collected in the millisecond time scale.[58] Laser-initiated time-resolved XAS uses a laser pulse to initiate a physical or chemical process, while X-ray pulses probe the structural response.[59] All the above-mentioned techniques have been successfully applied, mostly in the areas of materials science, and detailed reviews for each technique are available.[56,58,59]

In addition to applications in materials sciences and catalysis, time-resolved XAS is making steady inroads into metalloprotein research. The potential of time-resolved XAS for characterizing changes occurring at catalytic sites in metalloenzymes, especially for generally spectroscopically silent metals like zinc, is bright.[8] In one such laudable study, the evolution of catalytic intermediate states during enzyme turnover were characterized for the zinc metalloenzyme alcohol dehydrogenase.[62] Alcohol dehydrogenase, from *Thermoanerobacter brockii*, catalyzes the conversion of secondary alcohol to a corresponding ketone using nicotinamide adenine dinucleotide phosphate ($NADP^+$) as a cofactor.[62] Two mechanisms were proposed for catalysis at the zinc site based on numerous previous studies. In one mechanism, the zinc-bound water plays a catalytic role by serving as a transient proton transfer site. In this case, zinc coordination changes from four to five upon substrate binding. According to the other mechanism, water is displaced upon substrate binding and hence coordination of zinc would not change. Enzyme–substrate complexes were rapidly frozen using isopentane at different intervals of time ranging from ~2 ms to 110 ms following mixing. Using high intensity single-wavelength beam, they observed two pentacoordinate intermediate states in the first 70 ms, one of which had a very short lifetime, supporting the mechanism in which water plays a catalytic role.[57,62]

3.11 Surface Electronic Structure

With the emergence of the new generation synchrotrons and the extremely high flux they provide, new techniques that utilize X rays for structural studies are just beginning to flourish. One such technique, resonant inelastic X-ray scattering (RIXS), can utilize either soft or hard X rays to investigate low energy electronic and magnetic excitations in metal-containing compounds.[63] In the soft X-ray regime, this technique often operates at the L_{II} and L_{III} absorption edges for 3d transition metals in compounds, as these resonant excitation and de-excitation events allow one to measure the energy of excited states that are unreachable by direct electric dipole transitions. In the hard X-ray regime, this technique can be applied to the *K*-absorption edge of elements. RIXS has been used to study the momentum dependence of various electronic excitations in strongly correlated electron systems. This technique shares the chemical specificity and sensitivity of X-ray absorption spectroscopy although it requires an extremely high-flux beam.

4 REFERENCE MATERIAL

4.1 Data Collection and Analysis

The availability of experimental stations at many major synchrotrons provides an opportunity for users to apply XAS to study more sophisticated problems. The knowledge and experience in the field accumulated over the past approximately 40 years has resulted in well-developed methodologies and technical resources geared for obtaining optimal XAS data at these sites in very little time. Today, more than 65 radiation facilities around the world utilize electron beams at energies up to 7 GeV, and these can provide a large range of both soft (<2000 eV) and hard (>2000 eV) X rays. Radiation facilities continue to be upgraded and grow as the demand for beam brilliance and experimenter time rises. The general design of XAS experimental stations (or beamlines) has, however, remained fairly constant.

4.1.1 Generation, Storage and Delivery of High Intensity X Rays

The schematics of the different synchrotrons may be different, but the components are usually the same. The general schematic of an XAS beamline from the storage ring into the hutch is shown in Figure 4. A heated cathode emits electrons and these electrons are often accelerated in the direction of the storage ring utilizing a linear accelerator. Booster rings further contribute to the acceleration and focusing of the electrons; however, these electrons are eventually dumped into the storage ring (the synchrotron). X rays are drawn tangentially from the synchrotron electron path at beamline stations to allow for the attainment of extremely high intensity X rays. X rays, depending on the demands of the different beamlines, are further collimated and focused through a series of slits, mirrors, and monochromators until they enter the corresponding experimental stations (hutches). Mirrors are often placed before or after the monochromator to focus the X-ray beam or to reject monochromator harmonics. Mono or multicrystal monochromators are used to sort the energy of the incoming X rays. Slits are used to adjust beam size and provide energy resolution. In the physical experimental station (usually a Pb-lined hutch), the exposed beam travels first through a series of slits to define the final beam size. The beam then proceeds through an ionization detector (I_0), which measures the intensity of the incident X-ray beam. Immediately downstream of I_0 is the sample cryostat. The cryostat is usually under constant liquid helium flow to ensure low temperature; lower temperatures reduce thermal disorder and help prevent sample degradation. Two additional ionization detectors are placed in series downstream of the cryostat, the first (I_1) can be used to measure absorption spectra of the sample, when coupled with the signal in I_0, or when a metal foil is placed between I_1 and I_2, to provide a standardized internal reference spectrum. Fluorescence spectra can be obtained by placing a fluorescence detector perpendicular in position to the beam path, but directly adjacent to the cryostat. Fluorescence detectors range from simple photomultiplier tubes, to fluorescent ion chamber detectors like those designed by Dr. Farrell W. Lytle, to complex multielement Ge detectors. When using fluorescence detectors, samples are positioned such that the angle of incidence and exit are 45° to minimize elastic scattering into the detector and maximize fluorescent signals.

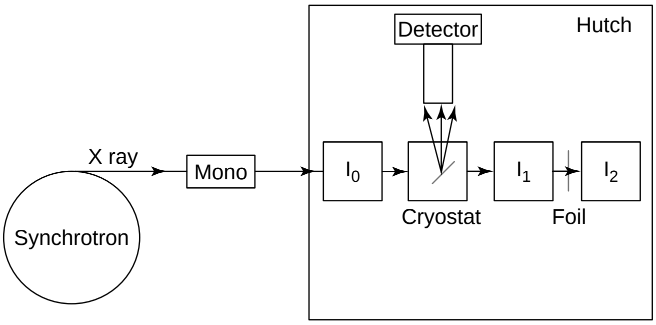

Figure 4 Schematic of an XAS beamline. Cryostat is placed between I_0 and I_1 ionization detectors to allow for absorption measurements. In the cryostat, samples can be place at a variety of angles to allow for absorption or fluorescence measurements. A fluorescence detector is placed tangential to the X-ray path. A metal foil is placed between I_1 and I_2 for energy calibration

4.1.2 Applications to Obtain Access to the Radiation Laboratories

Requesting time at the different synchrotrons requires careful planning and thorough implementation. A comprehensive list of the different XAS beamlines available in the U.S. and Europe is included on the following website: http://www.df.unibo.it/iucr/beamlines.htm. In the case of most national laboratories, applications can be submitted twice a year and require three to six months of processing before time is allotted. Proposals are scored using a peer review panel and time allocation depends on the relevance and score of proposed projects. Hardware and energy capabilities of each beamline are unique, and since proposals request time on specific beamlines, one should confirm the capabilities of the requested beamline match one's desired need. Training courses are available (Section 4.2.2).

4.1.3 Sample Preparation

As with all techniques, proper sample preparation is essential for collecting high quality data. XAS samples can be prepared in solid, liquid, or gaseous form. Signals are the average of all forms of the excited element present, so special care should be taken to remove adventitious forms of the element under investigation. For optimal data collection, samples should be between 0.5 and 1 mM in metal concentration, often prepared with about 30% (v/v) glycerol as a glassing agent. Sample cells are typically constructed from metal free material (i.e., Lucite) and wrapped with a transparent tape (i.e., Kapton, Mylar tape). The size of the sample cell is specific to the sample holder in the beamline cryostat. Small molecule samples are often collected in transmission/absorption mode utilizing a rectangular sample cell with a rectangular hole bored in the middle similar to the Lucite holder in Figure 5(a). Solid inorganic samples are also often diluted with inert boron nitride to ensure that sufficient photon flux travels through the sample so that a reference spectrum can also be collected. Solution sample cells are also often rectangular with a long bore in the face that resembles a trough. A solution sample cell (shown in the Figure 5(b)) made of Lucite, has a hole drilled in one side for sample injection and has an active volume of around 80 μL. This cell was designed with no top for easy cleaning and to allow almost direct access of the incident beam to the sample, so it must be wrapped with tape to prevent sample loss, should thawing occur. Liquid sample cells are immediately frozen in liquid nitrogen or an isopentane (2-methylbutane)–liquid nitrogen mixture. Given the variability of sample holders for different cryostats at each beamline, the reader is suggested that as much information as possible be gathered about the beamline setup, before the samples are prepared.

4.1.4 Data Reduction and Analysis

Programs for XAS data reduction, analysis and presentation are plentiful and available on all computer platforms. Software packages Athena/Artemis, EXAFSPAK and numerous others are well documented and guide experimenters through the process of data reduction and simulation. A summary of these programs and where they can be located is given in Section 4.2. Data processing and reduction proceeds along the following strategy: calibrating spectral energies and averaging blocks of spectra, fitting and subtracting a background from the pre-edge region of the averaged file, fitting and subtracting a spline from the EXAFS region of the averaged spectrum, converting the χ data from energy to k space, and calculating a Fourier transform (FT) for visualization. Spectral energy calibration links the inflection edge of the internal reference foil to a standard edge foil energy value for each element. Pre-edge fitting assures removal of any background noise. Removal of the low frequency components in the EXAFS involves fitting a spline function such that the EXAFS itself won't be removed. EXAFS is converted from energy to k space using equation (1), and k^3 weighted to enhance the high k components, allowing for better FT visualization. A Fourier transform is often applied to the EXAFS data to provide a radial distribution function of the ligand environments surrounding the absorbing atom for easy visualization of the different ligand environments.

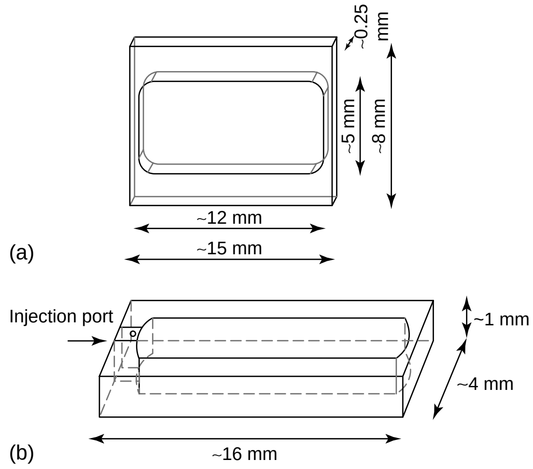

Figure 5 Common dimensions and design of transmission (a) and fluorescence (b) XAS sample cells

4.1.5 Data Simulations

EXAFS simulations can provide accurate structural parameters (N_s, σ_{as}, and R_{as}) for the metal–ligand system under investigation, assuming proper measures have been taken to calibrate the parameters that define the scattering in equation (3) ($A_s(k)$, S_0^2, $\phi_{\text{as}}(k)$, and $\lambda(k)$). Calibration of these parameters is greatly assisted by supplementation from data collected on crystallographically characterized model compounds; calibrated spectra from model compounds can therefore be used to simulate EXAFS for uncharacterized systems. However, advances in theoretical methods for quickly and accurately calculating these structural parameters have improved dramatically in recent years, thus providing a second, and currently the standard, approach for simulating EXAFS for uncharacterized systems. Ab initio calculations that provide the structural parameters required for accurately simulating EXAFS data typically come from three main programs, each involving different approaches: FEFF, EXCURVE, and GNXAS. Regardless of the theoretical approach, it is extremely beneficial to still calibrate theoretical parameters by first fitting data for well-defined crystallographically characterized model compounds.

Current data analysis protocols consist of fitting experimental data according to equations (2) and (3) using theoretical amplitude and phase functions for different atoms and appropriately calibrated values for S_0^2 and often E_0. The simulation procedure involves performing a nonlinear least-square fit in which (a subset of) typically three parameters N_s, $\sigma_{as,}$ and R_{as} (and in some cases, E_0) are varied. While general approaches involve simulating the global EXAFS data, it is often useful to apply the Fourier transform to the data and filter the EXAFS for a specific ligand environment by back-transforming the data within selected bond-length regions in the Fourier transform spectrum. Fourier transforms are however often misleading, given the prevalence of destructive scattering between nonresolvable ligand environments and complications due to nonlinear, multiple scattering systems; so, when published, data should only include fit results from simulating raw data.

Fitting strategies vary from laboratory to laboratory; however, a general standard approach involves initially simulating the scattering from atoms directly coordinated to the absorbing atom (i.e., the nearest-neighbor environment). Although typical coordination complexes can have numerous independent nearest-neighbor atoms, these atoms are often similar in nature (same row in the periodic table) and in absorber–scatterer bond distance. Spectral resolution (ΔR) is a direct consequence of the energy range for which the data are collected (equation 6).[7,8]

$$\Delta R = \frac{\pi}{2\Delta k}; \quad (\Delta k \text{ is the } k \text{ range of the data used during the simulation}) \tag{6}$$

For example, if fitting data between $k = 2\text{–}12\,\text{Å}^{-1}$, $\Delta R \approx 0.15\,\text{Å}$. So in many cases, it is often impossible to distinguish between scattering from atoms within this local environment. Therefore, initial simulations involve fitting all nearest-neighbor ligands as a single environment shell at approximately the same distance to obtain an averaged coordination number and bond length for this environment. Given the phase differences between ligand atom types within the different rows of the periodic table, is it usually very straightforward to distinguish between an average ligand environment constructed predominantly of oxygen versus sulfur atoms, and this should be taken into account during the simulation. Additional fitting shells are then progressively added to the simulation to account for resolvable independent ligand environments. Each simulation is scored by a ‘‘goodness of fit’’ parameter that measures the mean-square deviation between empirical and theoretical data. Since data are available over a finite k range, and since there is always inherent noise in the data, especially at high k, it is often difficult to distinguish if there is a general improvement in the quality of the fit upon adding additional ligand shells. This is especially true because there will be an inherent direct improvement in the fit in any case, on account of additional variables being added in the simulation. It is therefore useful to measure the fit quality using a reduced chi-squared statistic (ξ^2) that weights the quality of the fit relative to the number of degrees of freedom in the data, as outlined in equation (7).[28]

$$\xi^2 = \frac{(N_{idp}/\nu)\sum_{i=1}^{N}(\chi_{\mathrm{obs}}(k_i) - \chi_{\mathrm{calc}}(k_1))^2/\varepsilon_i^2}{N} \tag{7}$$

In equation (7), ν is the number of degrees of freedom calculated according to equation (8), using N_{idp} as the number of independent data points and N_{var} as the number of refined variables.

$$\nu = N_{idp} - N_{\mathrm{var}} \tag{8}$$

The sum in equation (7) is calculated over all measured data points, N, and the deviation at each point is weighted by $1/\varepsilon_i^2$, where ε_i is the root-mean-square uncertainty in the observed EXAFS (χ_{obs}). The $1/\nu$ weighting introduces a penalty for adding additional, unnecessary, scattering shells. A complete description of ξ^2 and how it is applied can be found elsewhere.[8] By building upon the progressive addition of independent but justifiably included ligand shells, keeping in mind the resolution limit of the data, one can develop a detailed description of the average ligand environments surrounding the scattering atom out to a generally reliable radius of 5 Å. Results from EXAFS simulations can be presented during publication with a table of fitting results, and with the corresponding raw and simulated k^3-weighted EXAFS and their corresponding Fourier transforms.

4.2 Resource Material

Prospective XAS users have numerous excellent resources available that provide a more detailed description of the technique and which will assist them in their training. There is a wealth of information available through books, websites, and summer courses, some of which are described below. In addition, each beamline has support staff that can provide specific information regarding the beamline and regarding the technique in general. It is beneficial to have a good understanding of the physics driving the technique, and to gain experience preparing samples, collecting data, and operating one of the multiple analysis and simulation programs under the direction of a trained user or at a hands-on workshop. The following text directs potential users to this information.

4.2.1 Description of the Technique

New XAS users will likely want to gain an advanced understanding of the physics behind the technique. Numerous excellent books and reviews are available.[64–68]

In addition, multiple web pages are available that compile extremely valuable information. A few are:

- http://xafs.org/ (XAFS Organization)
- http://www.i-x-s.org/ (International XAFS Society)

4.2.2 Training Courses Offered

Many synchrotrons offer XAS training courses. These are typically summer workshops that train students in the theoretical and practical use of the technique. Information regarding these can be gained at the following web pages:

- http://lightsources.org/cms/?pid=1000510
- http://xafs.org/Workshops
- http://smb.slac.stanford.edu/public/news/summer_school/

4.2.3 Data Collection/Analysis Protocols and Analysis Software

Numerous reviews are available that provide a detailed description of data collection/analysis protocols.[8,69]

Data analysis software packages are available on all platforms. The two most widely used are Artemis/Athena and EXAFSPAK. Both software packages were written to utilize the theoretical code FEFF. Excellent manuals are available for both, significantly helping shorten the learning curve. Artemis/Athena were developed by Dr. M. Newville and Dr. B. Ravel (2005). EXAFSPAK was developed by G. George (2001). These programs can be found at:

- http://cars9.uchicago.edu/~ravel/software/ (Artemis/Athena)
- http://www-ssrl.slac.stanford.edu/~george/exafspak/exafs.htm (EXAFSPAK)

5 ABBREVIATIONS AND ACRONYMS

DE-EXAFS = dispersive-energy extended X-ray absorption fine structure; EPR = electron paramagnetic resonance; EXAFS = extended X-Ray absorption fine structure; FT = Fourier transform; GMPS = guanosine monophosphate synthetase; ICP-MS = inductively coupled plasma-mass spectroscopy; LCAO = linear combination of atomic orbital; NEXAFS = near edge X-Ray absorption fine structure; NMR = nuclear magnetic resonance; NZF = Npl4 zinc finger; OEC = oxygen evolving complex; PSII = photosystem II; QEXAFS = quick-extended X-ray absorption fine structure; RIXS = resonant inelastic X-ray scattering; SOD = superoxide dismutase; XAS = X-Ray absorption spectroscopy; XAFS = X-Ray absorption fine structure; XANES = X-Ray absorption near edge structure.

6 REFERENCES

1. C. G. Scherk, A. Ostermann, K. Achterhold, O. Iakovleva, C. Nazikkol, B. Krebs, E. W. Knapp, W. Meyer-Klaucke and F. G. Parak, *Eur. Biophys. J.*, 2001, **30**(6), 393.
2. D. C. Koningsberger and P. Prins, ‘X-ray Absorption: Principles, Applications, Techniques of EXAFS, SEXAFS and XANES’, John Wiley & Sons, New York, Chichester, Brisbane, Toronto, Singapore, 1988, Vol. 92.
3. R. G. Shulman, Y. Yafet, P. Eisenberger and W. E. Blumberg, *Proc. Natl. Acad. Sci. U.S.A.*, 1976, **73**(5), 1384.
4. A. L. Roe, D. J. Schneider, R. L. Mayer, J. W. Pyrz, J. Widon and L. Que, Jr, *J. Am. Chem. Soc.*, 1984, **106**, 1676.
5. M. A. Pavlosky, Y. Zhang, T. E. Westre, Q. Gan, E. G. Pavel, C. Campochiaro, B. Hedman, K. O. Hodgson and E. I. Solomon, *J. Am. Chem. Soc.*, 1995, **117**(15), 4316.
6. T. E. Westre, P. Kennepohl, J. G. DeWitt, B. Hedman, K. O. Hodgson and E. I. Solomon, *J. Am. Chem. Soc.*, 1997, **119**, 6297.
7. J. E. Penner-Hahn, ‘X-ray Absorption-Spectroscopy for Characterizing Metal-Clusters in Proteins—Possibilities and Limitations’, ACS Symposium Series, L. Que, Jr (Ed), 1988, Vol. 272, p. 24.
8. J. E. Penner-Hahn, ‘Comprehensive Coordination Chemistry II—From Biology to Nanotechnology’, 2nd edition, eds. J. A. McCleverty and T. J. Meyer, Elsevier, 2004, Vol. 2, p. 8400.
9. J. Wong, R. P. Messmer, D. H. Maylotte and F. W. Lytle, *Phys. Rev. B*, 1984, **30**(10), 5596.
10. C. R. Randall, L. Shu, Y.-M. Chiou, K. S. Hagen, M. Ito, N. Kitajima, R. J. Lachicotte, Y. Zang and L. Que, Jr, *Inorg. Chem.*, 1995, **34**, 1036.
11. D. J. Rudd, M. H. Sazinsky, M. Merkx, S. J. Lippard, B. Hedman and K. O. Hodgson, *Inorg. Chem.*, 2004, **43**(15), 4579.
12. T. A. Smith, J. E. Penner-Hahn, M. A. Berding, S. Doniach and K. O. Hodgson, *J. Am. Chem. Soc.*, 1985, **107**(21), 5945.
13. L.-S. Kau, D. J. Spira-Solomon, J. E. Penner-Hahn, K. O. Hodgson and E. I. Solomon, *J. Am. Chem. Soc.*, 1987, **109**, 6433.
14. G. J. Colpas, M. J. Maroney, C. Bagyinka, M. Kumar, W. S. Willis, S. L. Suib, K. Pradip, N. Baidya and P. K. Mascharek, *Inorg. Chem.*, 1991, **30**(5), 920.
15. R. L. Lieberman, K. C. Kondapalli, D. B. Shrestha, A. S. Hakemian, S. M. Smith, J. Telser, J. Kuzelka, R. Gupta, A. S. Borovik, S. J. Lippard, B. M. Hoffman, A. C. Rosenzweig and T. L. Stemmler, *Inorg. Chem.*, 2006, **45**(20), 8372.
16. E. I. Solomon, B. Hedman, K. O. Hodgson, A. Dey and R. K. Szilagyi, *Coord. Chem. Rev.*, 2005, **249**(1–2), 97.
17. V. Kunzl, *Collect. Czech. Chem. Commun.*, 1932, **4**, 213.
18. J. A. Kirby, D. B. Goodin, T. Wydrzynski, A. S. Robertson and M. P. Klein, *J. Am. Chem. Soc.*, 1981, **103**(18), 5537.

19. J. E. Penner-Hahn, R. M. Fronko, V. L. Pecoraro, C. F. Yocum, S. D. Betts and N. R. Bowlby, *J. Am. Chem. Soc.*, 1990, **112**(7), 2549.
20. C. W. Hoganson and G. T. Babcock, *Science*, 1997, **277**(5334), 1953.
21. P. J. Riggs-Gelasco, R. Mei, C. F. Yocum and J. E. Penner-Hahn, *J. Am. Chem. Soc.*, 1996, **118**, 2387.
22. J. Messinger, J. H. Robblee, U. Bergmann, C. Fernandez, P. Glatzel, H. Visser, R. M. Cinco, K. L. McFarlane, E. Bellacchio, S. A. Pizarro, S. P. Cramer, K. Sauer, M. P. Klein and V. K. Yachandra, *J. Am. Chem. Soc.*, 2001, **123**(32), 7804.
23. W. Y. Hsieh, K. A. Campbell, W. Gregor, R. David Britt, D. W. Yoder, J. E. Penner-Hahn and V. L. Pecoraro, *Biochim. Biophys. Acta*, 2004, **1655**(1–3), 149.
24. D. B. Goodin, V. K. Yachandra, R. D. Britt, K. Sauer and M. P. Klein, *Biochim. Biophys. Acta*, 1984, **767**(2), 209.
25. H. Dau, P. Liebisch and M. Haumann, *Anal. Bioanal. Chem.*, 2003, **376**(5), 562.
26. P. J. Riggs, C. F. Yocum, J. E. Penner-Hahn and R. Mei, *J. Am. Chem. Soc.*, 1992, **114**(26), 10650.
27. J. M. Peloquin, K. A. Campbell, D. W. Randall, M. A. Evanchik, V. L. Pecoraro, W. H. Armstrong and R. David Britt, *J. Am. Chem. Soc.*, 2000, **122**(44), 10926.
28. P. J. Riggs-Gelasco, T. L. Stemmler, J. E. Penner-Hahn, *Coord. Chem. Rev.*, 1995, **144**, 245.
29. M. J. Baldwin, T. L. Stemmler, P. J. Riggs-Gelasco, M. L. Kirk, J. E. Penner-Hahn and V. L. Pecoraro, *J. Am. Chem. Soc.*, 1994, **116**, 11349.
30. A. Ericson, B. Hedman, K. O. Hodgson, J. Green, H. Dalton, J. G. Bentsen, R. H. Beer, S. J. Lippard, *J. Am. Chem. Soc.*, 1988, **110**, 2330.
31. R. W. Strange, N. J. Blackburn, P. F. Knowles and S. S. Hasnain, *J. Am. Chem. Soc.*, 1987, **109**, 7157.
32. S. Wang, M. H. Lee, R. P. Hausinger, P. A. Clark, D. E. Wilcox and R. A. Scott, *Inorg. Chem.*, 1994, **33**, 1589.
33. J. S. Boswell, B. J. Reedy, R. Kulathila, D. Merkler and N. J. Blackburn, *Biochemistry*, 1996, **35**(38), 12241.
34. W. E. Blumberg, J. Peisach, P. Eisenberger and J. A. Fee, *Biochemistry*, 1978, **17**(10), 1842.
35. N. J. Blackburn, S. S. Hasnain, N. Binsted, G. P. Diakun, C. D. Garner and P. F. Knowles, *Biochem. J.*, 1984, **219**(3), 985.
36. J. A. Tainer, E. D. Getzoff, K. M. Beem, J. S. Richardson and D. C. Richardson, *J. Mol. Biol.*, 1982, **160**(2), 181.
37. J. S. Valentine and M. W. Pantoliano, ‘Copper Proteins’, ed. T. G. Spiro, John Wiley & Sons, New York, 1981, Vol. 3, p. 292.
38. J. Richardson, K. A. Thomas, B. H. Rubin and D. C. Richardson, *Proc. Natl. Acad. Sci. U.S.A.*, 1975, **72**(4), 1349.
39. I. J. Pickering, R. C. Princeb, T. Diversc and G. N. George, *FEBS Lett.*, 1998, **441**, 11.
40. A. Rompel, R. M. Cinco, M. J. Latimer, A. E. McDermott, R. D. Guiles, A. Quintanilha, R. M. Krauss, K. Sauer, V. K. Yachandra and M. P. Klein, *Proc. Natl. Acad. Sci. U.S.A.*, 1998, **95**, 6122.
41. Z. Gui, A. R. Green, M. Kasrai, G. M. Bancroft and M. J. Stillman, *Inorg. Chem.*, 1996, **35**, 6520.
42. L. S. Busenlehner, T. C. Weng, J. E. Penner-Hahn and D. P. Giedroc, *J. Mol. Biol.*, 2002, **319**, 685.
43. Q. Zeng, C. Stalhandske, M. C. Anderson, R. A. Scott and A. O. Summers, *Biochemistry*, 1998, **37**(45), 15885.
44. M. C. Corbett, F. A. Tezcan, O. Einsle, M. Y. Walton, D. C. Rees, M. J. Latimer, B. Hedman and K. O. Hodgson, *J. Synchrotron Radiat.*, 2005, **12**(Pt 1), 28.
45. J. D. Helmann, B. T. Ballard and C. T. Walsh, *Science*, 1990, **247**(4945), 946.
46. J. G. Wright, H. Tsang, J. E. Penner-Hahn and T. V. O’Halloran, *J. Am. Chem. Soc.*, 1990, **112**(6), 2434.
47. R. C. Lye, J. C. Phillips, D. Kaplan, S. Doniach and K. O. Hodgson, *Proc. Natl. Acad. Sci. U.S.A.*, 1980, **77**(10), 5884.
48. J. J. Tesmer, T. L. Stemmler, J. E. Penner-Hahn, V. J. Davisson and J. L. Smith, *Proteins*, 1994, **18**(4), 394.
49. A. S. Lipton, R. W. Heck and P. D. Ellis, *J. Am. Chem. Soc.*, 2004, **126**(14), 4735.
50. B. Wang, S. L. Alam, H. H. Meyer, M. Payne, T. L. Stemmler, D. R. Davis and W. I. Sundquist, *J. Biol. Chem.*, 2003, **278**(22), 20225.
51. G. N. George, B. Hedman and K. O. Hodgson, *Nat. Struct. Biol.*, 1998, **5**, 645.
52. I. Fridovich, *Annu. Rev. Biochem.*, 1995, **64**, 97.
53. F. Johnson and C. Giulivi, *Mol. Aspects Med.*, 2005, **26**(4–5), 340.
54. S. B. Choudhury, J. W. Lee, G. Davidson, Y. I. Yim, K. Bose, M. L. Sharma, S. O. Kang, D. E. Cabelli and M. J. Maroney, *Biochemistry*, 1999, **38**(12), 3744.
55. A. T. Fiedler, P. A. Bryngelson, M. J. Maroney and T. C. Brunold, *J. Am. Chem. Soc.*, 2005, **127**(15), 5449.
56. M. A. Newton, A. J. Dent and J. Evans, *Chem. Soc. Rev.*, 2002, **31**(2), 83.
57. J. E. Penner-Hahn, *Nat. Struct. Biol.*, 2003, **10**(2), 75.
58. M. Richwin, R. Zaeper, D. Lutzenkirchen-Hecht and R. Frahm, *Rev. Sci. Instrum.*, 2002, **73**(3), 1668.
59. L. X. Chen, *Annu. Rev. Phys. Chem.*, 2005, **56**, 221.
60. M. Epple, L. Tröger and N. Hilbrandt, *J. Chem. Soc., Faraday Trans.*, 1997, **17**, 3035.
61. S. Pascarelli, S. De Panfilis and T. Neisius, *Phys. Rev. B*, 2000, **62**(6), 3717.
62. O. Kleifeld, A. Frenkel, J. M. Martin and I. Sagi, *Nat. Struct. Biol.*, 2003, **10**(2), 98.
63. V. K. Yachandra, *Philos. Trans. R. Soc. London, Ser. B, Biol. Sci.*, 2002, **357**(1426), 1347.

64. B. K. Teo, ‘EXAFS: Basic Principles and Data Analysis’, Inorganic Chemistry Concepts, Springer-Verlag, Berlin, 1986.
65. D. C. Koningsberger and R. Prins eds., ‘X-ray Absorption: Principles, Applications, Techniques of EXAFS, SEXAFS, and XANES’, Chemical Analysis Vol. 92, John Wiley & Sons, 1988.
66. E. A. Stern and S. M. Heald, ‘Handbook of Synchrotron Radiation’, ed. E. E. Koch, North Holland, 1983, p. 995.
67. J. Als-Nielsen and D. McMorrow, ‘Elements of Modern X-ray Analysis’, John Wiley & Sons, 2001.
68. J. J. Rehr and R. C. Albers, *Rev. Mod. Phys.*, 2000, **72**, 621.
69. R. A. Scott, *Methods Enzymol.*, 1985, **117**, 414.

X-Ray Powder Diffraction

Abraham Clearfield and Nattamai Bhuvanesh

Texas A&M University, College Station, TX, USA

Method Summary 1
1 Introduction 2
2 Applications 3
3 Technical Background 4
4 Phase Identification 10
5 Solid Solutions 18
6 Crystallite Size Determination and Lattice Strain 19
7 Quantitative Analysis 21
8 High and Low Temperature Powder Patterns 23
9 Ab initio Structure Determination from Powder Diffraction Data 26
10 End Notes 30
11 Abbreviations and Acronyms 30
12 Further Reading 30
13 References 30

METHOD SUMMARY

Acronyms, Synonyms

- X-Ray Diffraction (XRD)
- Powder X-Ray diffraction (PXRD)
- X-Ray Powder Diffraction (XRPD) pattern.

Measured physical quantities

- angular values of XRD peaks
- X-ray peak profiles
- intensities as areas under peak profiles
- X-ray peak heights.

Information available

- identification of crystalline phases from the X-ray peak angular positions and intensities
- unit cell dimensions from peak angular positions
- density of crystals if formula is known
- quantitative analysis of phase mixtures
- crystallite size from peak broadening
- lattice strain
- type of solid solution
- coefficients of thermal expansion
- crystal structure as positions of atoms within the unit cell, bond distances and bond angles.

Information not available, limitations

- elemental analysis
- limited information from poorly crystalline materials
- PO may limit information obtainable from X-ray pattern
- complex structures may prove difficult to solve by powder methods.

Examples of questions that can be answered

- Is this a crystalline substance?
- What compound is this?
- Is this a mixture of compounds?
- What are the compounds in this mixture?
- How much of each compound is in this mixture?
- Is this polymer crystalline?
- Is this polymer isotactic or syndiotactic?
- Will this compound change structure upon heating?
- Does this material have a large, small or zero coefficient of thermal expansion?
- Does this metal or ceramic suffer from strain?
- Does this catalyst contain small crystallites?
- What is the structure of this compound?
- Have we synthesized the right crystalline phase of this compound?

Major advantages

- nondestructive technique—sample can be recovered
- small samples may be used
- large databases available for phase identification.

Major disadvantages

- The method yields very limited information from amorphous or poorly crystalline materials.

Sample constraints

- The samples must be finely ground and packed properly in holder.
- Some samples may be air sensitive and require encapsulation in argon or nitrogen.
- Layered compounds may suffer from PO.

Related techniques

- X-ray crystallography
- Neutron diffraction.

---

1 INTRODUCTION

The term Powder X-ray Diffraction (PXRD),[1] as the name implies, is a diffraction pattern obtained by the interaction of X-rays (usually monochromatic) from a collection of crystallites (powder), which are statistically oriented in all possible crystallographic directions satisfying the Bragg condition:

$$n\lambda = 2d \sin\theta \qquad (1)$$

The sample usually is in the form of finely divided polycrystalline powder, but depending on the nature of the application, the sample also can be a thin film or bulk material.

1.1 Brief History

XRD was first observed by Max von Laue in 1912. Von Laue, in a discussion with Paul Ewald, a Ph.D. candidate in physics, concerning the interaction of light with crystals, realized that if X-ray wavelengths were of the order of the distances between atoms in the crystal, then diffraction should occur. The effect is similar to that of a ruled grating where light passing through the slits in the grating forms a series of bright and dark lines. The separation of the lines depends upon the wavelength (λ) of the radiation and the spacing (d) between the slits. If two slits are placed at right angles to each other, the pattern takes the form of a spot pattern. The distances between the spots are now two-dimensional and reflect the distances between the ruled lines on both diffraction gratings. Crystals are three-dimensional in nature and therefore behave as a three-dimensional grating.

X-rays were discovered by Wilhelm Conrad Röntgen in 1895. He observed a green glow on the glass envelope of a cathode ray tube, which he surmised, darkened the film enclosed in its protective wrapping. Subsequently, Röntgen showed that a hand placed in front of the film in a darkened room produced a picture of the bone structure of the hand. He understood that the X-rays must be very penetrating and therefore possess small wavelengths. However, there was no way to measure these wavelengths until von Laue's discovery.

In 1914 the father and son team, William Henry Bragg and William Laurence Bragg, simplified the three-dimensional theory of diffraction developed by von Laue, by considering the diffracted radiation as being reflected by sets of parallel planes of atoms. The condition for diffraction from a set of parallel planes of interlayer spacing d is described by equation (1), where θ is the angle of incidence of the X-rays to the planes and λ is the X-ray wavelength (Figure 1). When the wavelets of the X-ray beam leave the source all the wavelets are in phase. As the wavelets enter the crystal, they travel longer distances than the wavelet reflected from the surface. These distances are dependent on the interlayer spacing, d. The wavelets are in phase at the line BJL drawn parallel to ADG (Figure 1). The pathlength difference between the wavelets ABC and DEF is JE + EK and for the wavelet GHI, LH + HM. The condition for diffraction is that the wavelets be in phase at BKM. This requires that the distance JE + EK = nλ, that is, the path difference is an integral number of wavelengths. If JE + EK = λ, then LH + HM = 2λ, etc. and all the layers in the stack scatter in phase and intensity of diffracted photons is recorded by the detector. If the wavelets are slightly out of phase, destructive interference occurs because there are hundreds of layers with the out of phaseness increasing by degrees.

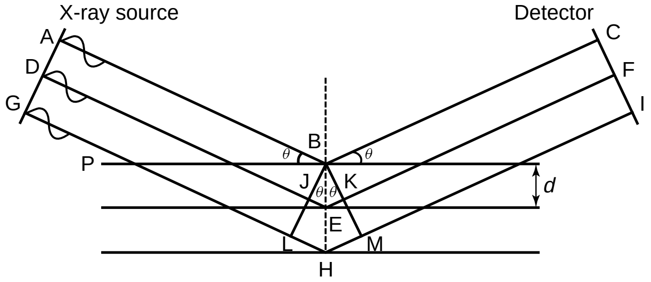

$$n\lambda = JE + EK$$

$$\sin\theta = \frac{JE}{BE} = \frac{EK}{BE}$$

$$BE = d$$

$$2\sin\theta = \frac{JE + EK}{d}$$

$$n\lambda = 2d\sin\theta$$

d = distance between planes, waves are in phase at BJL ($\parallel ADG$), Path length diference = $JE + EK$

Figure 1 Illustration of Bragg reflection from a set of parallel planes

Applying this equation, the Braggs were able to solve the crystal structures of NaCl and KCl. Subsequently, the structures of many simple inorganic compounds were solved. Single crystals are largely used for structure determination. However, upon consideration of equation (1), it was realized that powdered solids may also be used to provide diffraction data. In a finely divided powder containing millions of particles their orientation is normally chaotic. That is, they will statistically have large numbers of crystallites in every possible orientation to the X-ray beam. Placing such a sample in the X-ray beam generates diffraction from all the sets of planes simultaneously but at angles that depend upon the values of d. Application of the powder technique has tremendous value, as not all solids can be obtained as large enough (order of tenths of millimeters) single crystals.

Powder diffraction is widely used throughout industry, academia, or wherever a knowledge of solids is required. With the great advances in electronics, computers, and software, the accuracy of the data, the ease of obtaining it, and data interpretation have progressed accordingly. In the last two decades, a large effort has been put forward to determine crystal structures from X-ray powder data. This effort has been largely successful to the point where a great deal of information on structure may be obtained even from solids as complex as crystalline proteins.

2 APPLICATIONS

Powder diffraction, although used by most as a tool for identification (or finger printing), remains a powerful technique, which can be used for a range of applications to obtain a great deal of information.[1] From the chemists' point of view, qualitative phase identification, quantitative phase analysis (for samples containing more than one phase), structure solution, and structure refinement (popularly known as Rietveld refinement) are considered. For materials scientists and engineers, in addition to the above, crystallinity studies, particle size, strain and texture analysis in thin films and bulk materials are some of the objectives. In situ diffraction under forced conditions such as temperature, pressure, humidity, etc., gives powder diffraction a strong advantage. The information for the various applications is extracted from different types of details in the powder diffraction pattern: As given in the table below, the quantity measured is given in the first row and the applications derived from that quantity are presented in their respective columns[2]

Peak position	Peak intensity	Peak shape/width
Phases present	Unit cell contents	Size of crystallites
Unit cell	Point symmetry	Microstrain
Crystal system	Quantity of various phases present	Extended defects

3 TECHNICAL BACKGROUND

3.1 Generation of X-rays

X-rays are most often generated by means of cathode ray tubes of the type shown in Figure 2. The cathode consists of a tungsten filament through which a current is passed to excite electrons in the filament. The electrons are accelerated by a high potential between the filament acting as cathode and a metal anode. When the electrons strike the target, they are rapidly decelerated by multiple collisions. Most of the energy of deceleration is evolved as heat, but a small amount is converted into radiation. To prevent meltdown, cold water is run across the target. The smallest wavelength possible, at a given voltage, would be obtained when an electron is brought to a complete stop by one encounter. However, interactions of the high speed electrons with the electromagnetic field of the target atoms can lead to their gradual deceleration with transfer of energy to the target. Some of this energy is reemitted as X-ray photons and since all quantities of energy less than the single encounter maximum are allowed, a continuum of radiation is obtained (Figure 3).

Obviously, the intensity-wavelength curves depend upon the kinetic energy of the electrons, which is given by the relationship

$$\tfrac{1}{2}\,\mathrm{mv}^2 = \mathrm{eV} \tag{2}$$

where e = the charge of an electron and V = the applied voltage. The smallest wavelength obtainable at a particular voltage is known as the short-wavelength-limit (SWL) and can be calculated by recognizing that:

$$\mathrm{E} = h\upsilon = \mathrm{eV} \tag{3}$$

Since $\upsilon = c/\lambda$ and h = Planck's constant, the SWL is

$$\lambda_{\mathrm{SWL}} = \frac{hc}{eV} \tag{4}$$

Substituting the values of the constants to yield the answer in angstrom units, this equation takes the form

$$\lambda_{\mathrm{SWL}} = \frac{12\,400}{V} \tag{5}$$

At a voltage of 40 000 V, $\lambda_{\mathrm{SWL}} = 0.310$ Å. Figure 3 illustrates how the intensity and wavelength range of the general radiation varies with the applied voltage. The intensity also depends upon the tube current in milliamperes (mA) and the target atomic number.[3,4]

In addition to the general or white radiation, X-ray spectra show a number of intense lines whose wavelengths are fixed and characteristic of the target material (Figure 3). Their origin lies in the ejection of electrons from the ground state orbitals of the target atoms by the bombarding cathode electrons. Electrons from upper orbitals then fall into the vacancies created, and in the process, radiation of energy equal to the difference in orbital energies are emitted. This effect is the basis for determination of elemental composition by X-ray fluorescence analysis. Each element has a unique spectrum of characteristic lines.

We wish to use the Kα radiation (Figure 3) because it is the most intense of all the spectral lines. In addition, Bragg's law was derived based on use of monochromatic radiation. For most purposes Kα, which consists of two lines: Kα_1, and Kα_2, is sufficiently accurate. However, for the most exacting procedures Kα_2 needs to be removed to have truly monochromatic radiation.

Kα, Kβ radiation arises from ejection of electrons from the K-shell of the target atoms by impact with the bombarding electrons. Electrons from the L-shell then replace

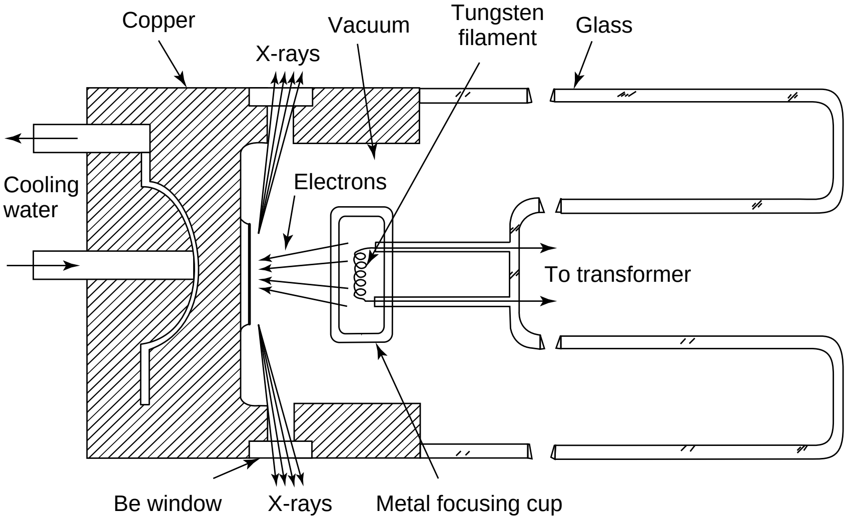

Figure 2 Cross section of a sealed X-ray tube (schematic)

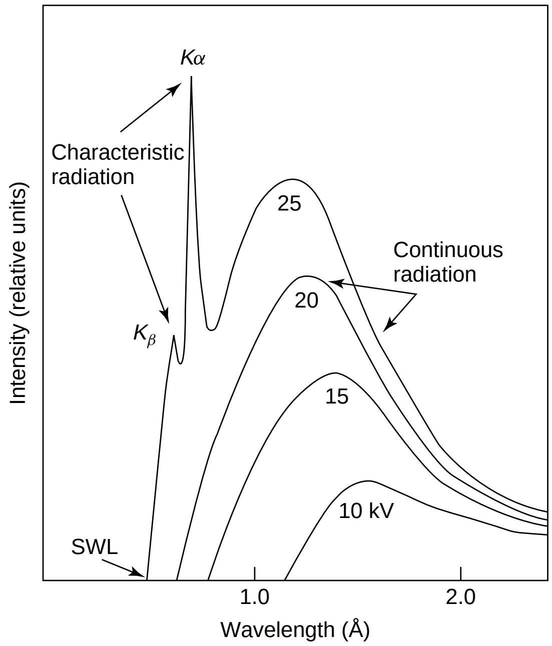

Figure 3 Schematic Mo X-ray spectrum as a function of applied voltage. Line widths are not to scale

the lost electrons, emitting radiation specific to the energy of the electronic transitions. The electrons in the L-shell are arranged into three energy states according to their total angular momentum or J states. The situation is treated as a one-electron problem. For the 2s electrons, $\ell = 0$, $s = 1/2$, $\mathrm{J} = \ell + s = 1/2$. Similarly, for the 2$p$ electrons, $\ell = 1$ and we have two J states, $\mathrm{J} = 1/2$, $\mathrm{J} = 3/2$. These states are identified in the energy level diagram as $\mathrm{L_I}$, $\mathrm{L_{II}}$, and $\mathrm{L_{III}}$ respectively. The allowed transitions are $\mathrm{L_{II}}$ and $\mathrm{L_{III}}$ to K (see Figures 3, 4, and 5). There are two electrons in the $\mathrm{L_{II}}$ state but four electrons in the $\mathrm{L_{III}}$ state so that Kα_1 is always twice as intense as Kα_2. Note that the $\mathrm{L_{III}} \rightarrow \mathrm{K}$ transition is the more energetic one so its accompanying wavelength is always slightly shorter than that of Kα_2. Kβ arises from similar transitions from the M shell to K.

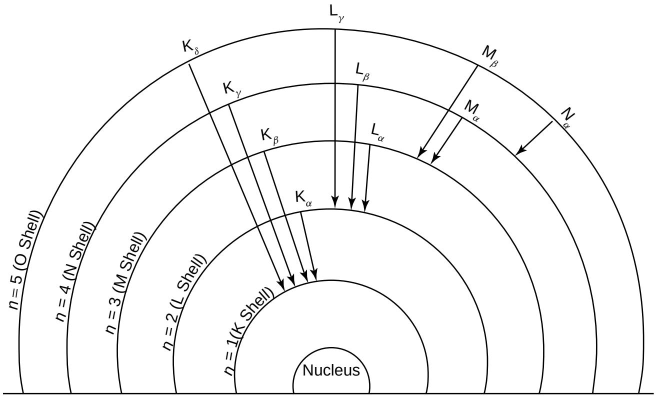

Figure 4 Electron energy transitions giving rise to X-radiation

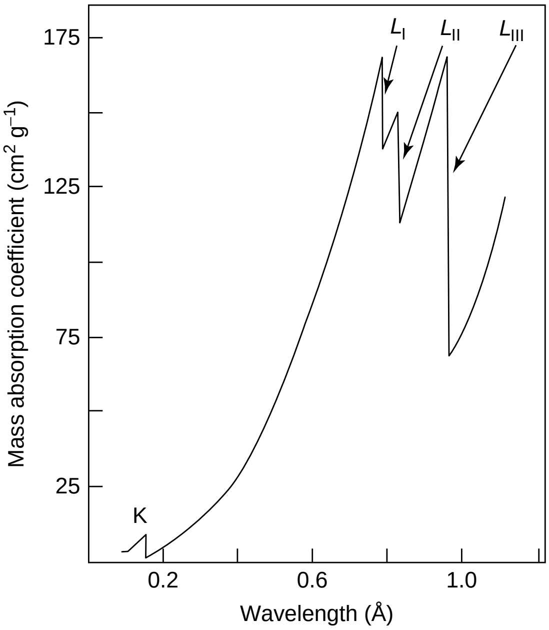

Figure 5 Variation of mass absorption coefficient with wavelength for Pb

3.2 Monochromatic X-rays

For modern crystal diffraction studies, a nearly monochromatic beam of X-rays is required. This may be achieved by using a crystal monochromator. The direct beam from the X-ray tube is reflected from a large crystal in such a way as to give a very narrow (almost monochromatic) beam. This technique will become easier to explain after we have discussed diffraction procedures. Another method in common use is that of filtering. We wish to use only the Kα wavelengths in a diffraction experiment because they are the most intense. A metal absorber is placed in front of the beam which absorbs the unwanted radiation. Absorption of X-rays follows the equation:[4]

$$\frac{I}{I_0} = e^{-\mu_l X} \tag{6}$$

where μ_ℓ = linear absorption coefficient, in units of cm^{-1}, X = path length of X-rays in the absorber, and I_0 = initial intensity. In equation (6), it is understood that the particular value of μ depends upon the wavelength of the incident radiation. Therefore, it is necessary to determine μ as a function of λ. For a given element, this dependence follows a curve such as that shown in Figure 5. At high energies absorption is low, but increases in a nonlinear way with increasing wavelength (decreasing energy). The sharp breaks in the curve are called absorption edges. These discontinuities occur at the wavelength at which an incident X-ray photon is just energetic enough to knock an electron out of an atomic orbital. For example, at very high energies, photons readily pass through the absorber since the probability of their interaction with electrons in the absorber is small. However, increased attenuation occurs as the wavelength of the photons increase. Maximum absorption is achieved when this wavelength is equal to the energy required to just dislodge a K electron. This energy is equal to the transition K → ∞ and is therefore larger than that of any of the characteristic X-ray lines of the absorber. At slightly higher wavelengths, or lower energy, a large drop in the value of μ occurs because the photons are now unaffected by the K electrons. Once again, μ increases as λ decreases until at the L absorption edge, three discontinuities are observed. These result from electrons in the L_I, L_{II} and L_{III} energy levels being dislodged, respectively.

A suitable filter is one whose K absorption edge falls between the Kβ and Kα wavelengths of the X-ray target. Usually, an element of atomic number Z-1 or Z-2 satisfies this condition, Z being the atomic number of the tube target. For example, nickel foil is used to filter copper radiation. The proper thickness can be calculated from equation (4). Not all of the white and Kβ radiation is eliminated (Figure 6), so filtered radiation is not strictly monochromatic.

3.3 Recording an XRPD Pattern

Consider a set of parallel atomic planes within the crystal to be oriented to the incident X-ray beam as in Figure 7(a). The incident beam is at an angle θ to the set of planes. The incident beam passes through the sample and strikes the detector at $\theta = 0°$. It is immediately apparent that the reflected beam is at angle 2θ to the zero point. If the detector were placed at the angle of reflection 2θ, it would record the diffracted intensity for this set of planes. Imagine that the set of crystal planes precesses around the incident beam while always maintaining an angle θ to it. The diffracted radiation then forms a cone of radiation about the incident beam as cone axis (Figure 7b). If a film is placed at the bottom of the cone, the radiation would form a black circle on the film. Since many sets of parallel planes with different d-spacings are present in the sample, a set of concentric circles would be recorded simultaneously on the film. A moment's reflection should convince you that only those cones whose base is less than the film length would be recorded. Debye and Scherrer independently developed a simple camera that would record all the data. They chose a steel hollow cylinder into which a strip of film is placed around the inside periphery. The sample is held in the center of the cylinder and is rapidly rotated to ensure uniformity of distribution of the crystallites. All the concentric circles of diffracted radiation are now recorded on the 360° strip of film. The developed film appears as shown in Figure 7(c). Portions of the base of each cone are recorded on the film as pairs of arcs that are proportional to 4θ the circle diameter. More properly we know that the angle subtended in radians is given by the arc divided by the camera radius. Cleverly the radius of the camera was made to be 57.3 mm, so that one mm in arc measured linearly is 1° in θ. From the measured θ values, Bragg's equation allows us to determine all the recorded d-spacings. In its simplest use the list of d-spacings serves as a fingerprint to identify the crystalline phase.

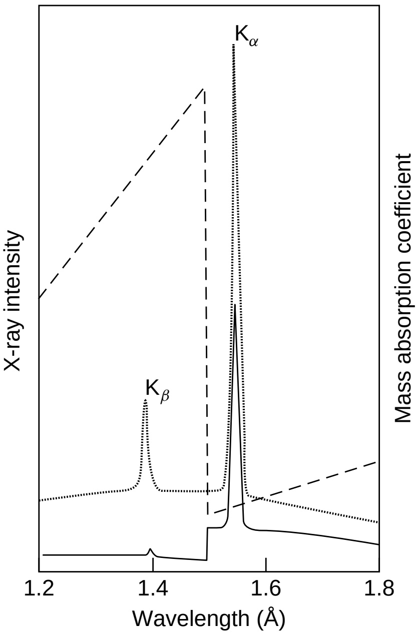

Figure 6 Comparison of the spectra of Cu-radiation before (dotted line) and after (continuous line) passage through a Ni-filter (schematic). The dashed line indicates the mass absorption coefficient of Ni

Film methods are tedious to apply. Careful measurements of all the arc-pairs may take several hours, in addition to development of the film, drying, and correcting for film shrinkage. Fortunately, automated diffractometers were developed that obviate the use of film. Such instruments are able to move the detector around the focusing circle recording the X-ray intensities one at a time. One can think of it as photometering the film pattern from 0 to 90° in θ to produce a pattern as shown in Figure 8. This powder pattern is a one-dimensional recording of the intensity of diffracted radiation from all the sets of parallel planes as a function of the angle 2θ within the angular range measured. We shall show later that from knowledge of the θ values we can derive the interplanar spacings of the individual set of planes. For example, the first peak in the pattern shown in Figure 8 is at $2\theta = 10.467°$. Theta is therefore 5.2335° and the radiation used was Cu Kα_1 for which $\lambda = 1.54056$ Å. Rearranging Bragg's equation to solve for the interlayer spacing gives

$$d = \frac{n\lambda}{2\sin\theta} = \frac{1.54056}{2\sin 5.2335} = 8.4451\,\text{Å}$$

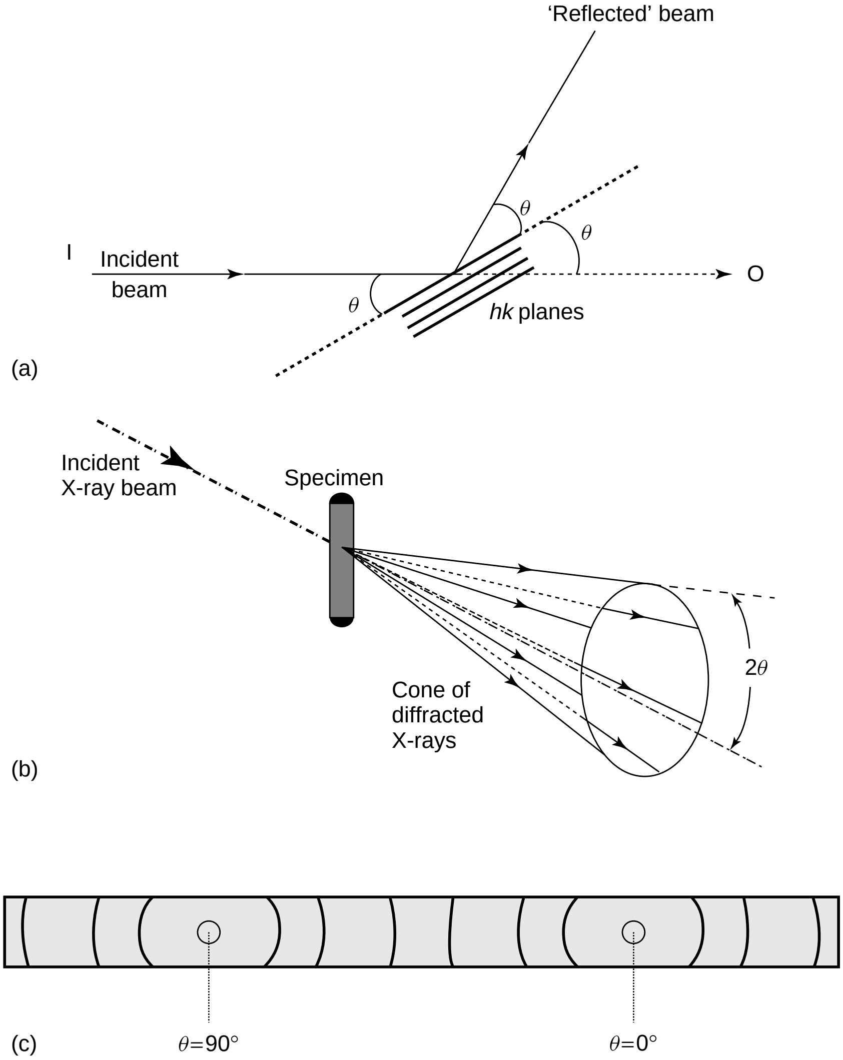

Figure 7 (a) Bragg reflection from a set of lattice planes. (b) The cone of diffracted X-rays from a powder specimen. The cone contains all X-rays reflected from one particular family of lattice planes in all crystals which are correctly oriented. (c) The form of a powder pattern (asymmetric film mounting)

The next peak is at 14.066° and $d = 6.2911$ Å. Note that as θ increases, d decreases, a result of the inverse relationship of these quantities in Bragg’s equation.

3.4 The Diffractometer

The basic components of an X-ray diffractometer are

(i) The X-ray source or generator
(ii) The specimen holder
(iii) The detector

There is a specific arrangement of these three components as shown in Figure 9. The specimen for which the pattern is recorded is held at the center of a circle termed the diffractometer circle. The X-ray source is fixed at the circumference of the circle. The X-ray detector is also on the circumference of the circle. When the detector is at zero, the source, the specimen, and the detector are in the same plane with the angle between source and detector 180°. In a typical run, the specimen rotates at an angle θ while the detector rotates an angle 2θ and so is always in position to record the diffracted beam. This is popularly termed the “$\theta - 2\theta$” method. In a second type of diffractometer the X-ray source moves as well as the detector, but in opposite directions toward each other. In this case the specimen does not move, so the powder pattern is recorded as a function of θ. In both diffractometers the focusing circle changes in diameter as the moving parts change position.[3,4]

3.5 Instrument Optics

The optical components of the diffractometer are shown in Figure 10. A line source of the X-ray tube is used

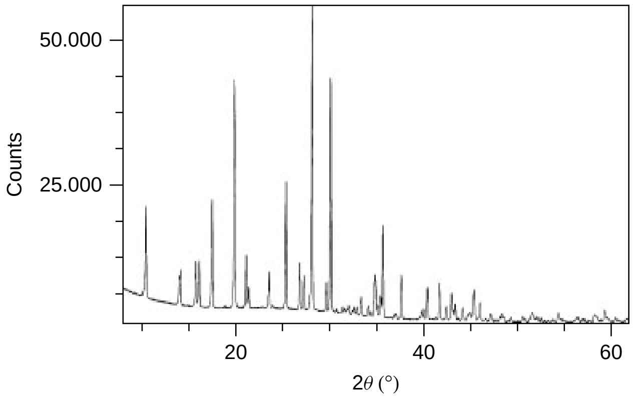

Figure 8 Plot of 2θ vs. X-ray intensity

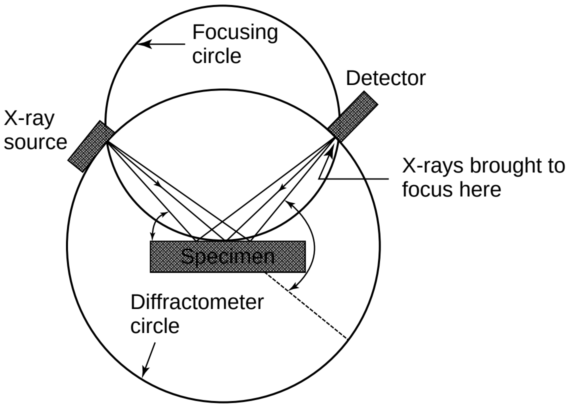

Figure 9 Schematic representation of the geometry of an X-ray diffractometer

for most powder work. As soon as the X-ray beam exits from the tube, it begins to diverge. Bragg's Law requires that a parallel beam strike the sample. Therefore, the line source is passed through a system of slits. Soller slits are a series of closely spaced parallel metal plates that collimate the incident beam. The Soller slits prevent in-plane or lateral divergence and a second slit termed *the divergence slit* defines the width of the incident beam. The diffracted beam is then subjected to another series of slits. The antiscatter slit reduces the background radiation by eliminating stray radiation and any radiation scattered outside the specimen. The receiving slit defines the width of the beam admitted to the detector. An increase in slit width increases the intensity, but at a loss of some resolution.[3,4]

3.6 Preparing the specimen

The first step toward powder diffraction (assuming a goal of ab initio structure determination) is making a pure phase. There is no clear and definite way to define a phase as pure unless proven otherwise. A good starting step would be to look at the sample under the microscope before any processing (e.g. grinding, washing, etc.) has been done. This serves two useful purposes: first, if there is any obvious impurity, based on color or morphology, it will give a lead to look for impurities. The second is to look for any possibility to find a single crystal. Though the powder diffraction analysis methods are advancing rapidly, even a small inferior quality crystal would give a great deal of information on unit cell parameters, possible space groups, and perhaps a good starting structural model. Any knowledge known or gained about the sample would help further analysis a great deal.[4–6]

For data collection the specimen should be ground, using an agate mortar and pestle to reduce the particle size to 10–50 µm. This is a requirement to ensure sufficient particles will occupy each of the many possible orientations equally. In the case of a mixture, it is necessary to ensure that the phases are uniformly distributed throughout. The simplest procedure is to grind about 50 mg of sample in ethyl acetate to which a small amount of cellulose acetate has been added. The fluid

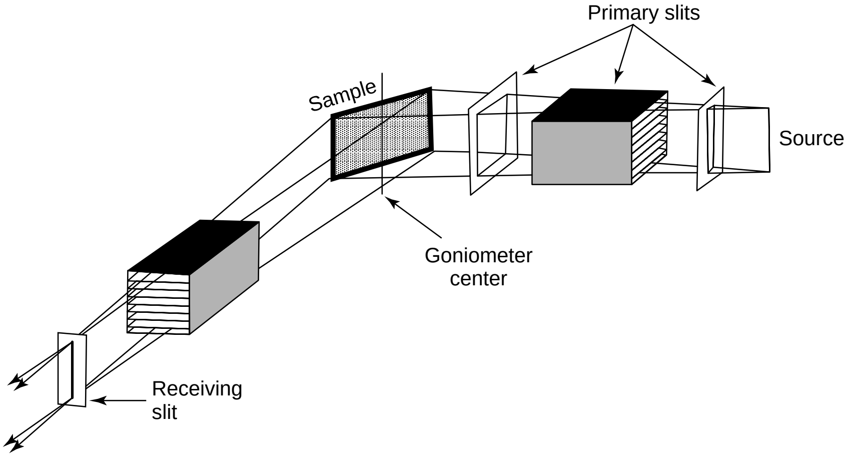

Figure 10 Arrangement of slits in a powder diffractometer

mix is then cast out on a glass slide and dried slowly, a little above room temperature. The idea is to have a small, flat layer of sample. Reference to Figure 9 shows that the X-rays at the surface of the sample are focused to the detector. The thinner the layer, the more accurately the position of the peaks recorded. However, it should be recognized that this technique does not yield accurate values of the peak intensities because such a thin sample layer will allow the X-ray beam through to the glass. The more common specimen holder will contain a well a few mm thick as shown in Figure 11. The well must be filled flush to the top. This assures that the sample is in the plane of the source and detector. Otherwise an error in the peak position or 2θ will be incurred.

Usually a 3 mm-deep well is sufficient to keep the X-rays from passing through to strike the bottom of the well. However, when the sample consists of elements of low atomic number such penetration will occur and scattering from the sample holder will increase the background. However, it is also not good practice to have a deep well sample holder. X-rays that penetrate deeply into the sample will be focused slightly behind those at the surface causing broadening of the peak and a slight displacement of the 2θ angles. However, because diffraction is occurring from a larger portion of sample the intensities will be increased.

To avoid scattering from the bottom of the sample one may use a procedure called back-loading. The holder is prepared with the bottom of the well cut away. A glass slide is taped to the top of the holder, turned upside down and loaded from the bottom pressing the sample against the glass. The glass is then carefully removed to leave a smooth surface. Any radiation passing through the sample is not scattered back. However, some samples have a tendency to fall out of the holder if some binder is not added to the sample.

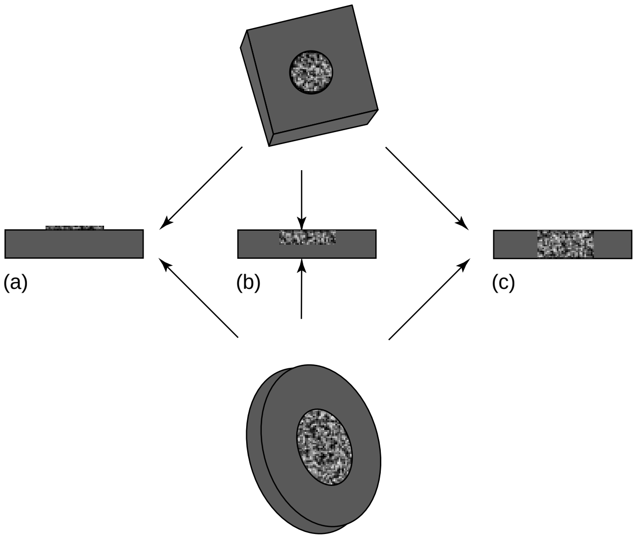

Figure 11 Common types of rectangular and circular specimen holders: (a) zero background, (b) top-loaded, and (c) back-loaded configurations

Some diffractometers can accommodate samples held in capillary tubes usually made of glass or quartz. Only a few milligrams of sample are required. The capillary is rapidly rotated to help insure the distribution of the particles in all possible crystallite orientations. The X-ray beam is perpendicular to the sample and passes through it (transmission method). Some discretion must be used, as the presence of heavy elements in the sample will increase the absorption.

3.7 The Detector

Detectors in use today are of three types: proportional, scintillation, and solid state. The proportional counter consists of a tube filled with a noble gas such as xenon. A thin tungsten wire runs down the center of the tube and is positively charged. A thin window of low-absorbing glass allows the X-ray photons to enter the tube. The photons displace electrons from the xenon atoms. Each such photoelectron loses its energy by ionizing other xenon atoms causing a cascade of electrons. The released electrons are drawn to the positively charged wire giving rise to a charge pulse. The size of the pulse is proportional to the energy of the incident photon, which allows X-rays of different wavelengths to be distinguished.[3,4,6]

Scintillation counters usually consist of a sodium iodide crystal doped with 1% thallium. The incident X-ray photons cause the crystal to fluoresce producing a flash of light for every photon absorbed. The size of the light pulse is proportional to the energy of the photon and is measured by a photomultiplier. A deficiency associated with scintillation counters is that they do not provide as good energy resolution as proportional or solid state detectors.

Solid state detectors consist of three layers, a layer of pure silicon sandwiched between a p-type and an n-type conductor. We recall that an example of an n-type conductor is germanium to which is added P or As, an impurity. The extra electron in the phosphorus or arsenic atoms is thought of as being in an energy level close to the conduction band. These electrons are readily thermally excited into the conduction band increasing the conductivity. A p-type semiconductor may be silicon to which a trivalent element such as boron or aluminum is added as an impurity. This creates holes close to the valence band. Electrons are readily promoted to these holes leaving positive holes in the valence band that provide for a conduction pathway.

The p- and n-type conductors are necessary in the solid state detector because silicon crystals are very difficult to obtain pure. Usually they contain impurities such as boron, which would make it a p-type semiconductor. This situation would allow thermal electrons to cross the silicon energy gap to the low lying hole state. However, we want only electrons that are excited by X-ray photons to act as conductors. Interference of thermal electrons is avoided by a process called drifting in which a small amount of lithium is added, usually by thermal diffusion, to one side of the Si crystal and a larger amount to the opposite side. The lithium ionizes within the silicon crystal neutralizing the holes that were present. The high concentration lithium side is the n-type conductor and the low concentration side the p-type conductor, because not all the holes were neutralized. The center of the crystal behaves as pure silicon.

The incoming X-ray photons excite electrons into the valence band creating an electron-hole pair. A negative charge is applied to the p-type part of the crystal and a positive charge to the n-type side. This creates a charge pulse of electrons. The number of electron-hole pairs is given by equation (7)

$$n = \frac{\text{photon energy}}{\text{energy of electron—hole pair formation}} \tag{7}$$

Because the numerator is large (e.g. Cu Kα is 8.04 keV) and the denominator small, that is, of the order of electron volts, a large number of electron-hole pairs are produced by each photon. The Si(Li) detectors must be kept at liquid nitrogen temperature at all times in order to minimize thermal excitation of electrons and to prevent lithium thermal diffusion. Either a Dewar vessel or a Peltier thermoelectric device is used in conjunction with the solid state detector.

Two new detectors marketed by the Bruker Corporation provide sensitivities much greater than the detectors already described. The Lynx Eye is a linear silicon strip detector that is claimed to have sensitivity 200 times that of the standard scintillation detector. The Vantec is a linear microgap/wire detector. It is an ultra-low noise detector and is about 100 times more sensitive than the scintillation detector.

3.8 Monochromators and focusing devices

We have already discussed the use of filters to achieve a monochromatic X-ray beam. Filters do not remove all of the white radiation and sometimes a small amount of β-radiation leaks through. This extraneous radiation may result in the presence of extra weak peaks or higher background radiation. For strictly monochromatic radiation a high quality single crystal is used. The crystal is usually placed behind the sample at a specific angle θ so as to diffract the X-ray beam from the sample into the detector (Figure 12a). This angle depends upon the d-spacing of the crystal plane chosen to allow only a specific wavelength such as Cu Kα_1 to diffract. The crystal angle may be reset for other wavelengths. If the crystal is curved as shown in Figure 12(b), the focusing of the beam is much better producing a gain in intensity. With a back end monochromator there is no need for a metal filter so the beam striking the sample is very intense. The loss of intensity from the monochromator may not be as great as from the filter. Another advantage of the back end monochromator is that it eliminates fluorescent radiation and Compton or incoherent radiation resulting in a very low background. Fluorescent radiation arises from excitation of sample electrons by the X-ray beam. For example, first row transition elements strongly fluoresce, especially Fe and Co, when the radiation is Cu Kα.[4,6]

A disadvantage of the back end monochromator is its inability to separate Kα_2 from Kα_1. For very precise unit cell determinations this separation is desirable. For this purpose a front end or primary beam monochromator is used (Figure 12c). This monochromator is the only type that can be used with area detectors. Their disadvantages include a high intensity loss, the need for precise alignment and nonremoval of fluorescent radiation.

A number of new optical devices that increase the intensity of the X-ray beam are worth mentioning. The use of slits eliminates a large portion of the X-ray beam before it strikes the sample. However a much larger proportion of the incident beam may be delivered to the sample by the use of optical fibers. Each optical fiber consists of a large number of tiny hollow glass capillaries. These capillaries act as wave guides in which the X-rays undergo total reflection from the capillary surfaces and are led to the sample with very little loss of intensity.

Unlike optical light, X-rays cannot be reflected or deflected easily by mirrors. But specially deposited multilayers of low-Z and high-Z materials can be used to reflect and monochromatize the X-rays based on Bragg's condition. Typically combinations of W-B_4C, W-Si, Ni-C and combination of such layers are used. By using Göbel mirrors, the diverging X-ray beam from conventional sources could be made into parallel or focused. The major advantage of Göbel mirrors is the near removal of sample displacement error ($\sim \pm 200\,\mu$m). Besides, removal of the K_β component, increased intensity, removal of fluorescent radiation (when used in the diffracted beam side) are some of the benefits. These mirrors are extensively used in thin film studies, and in stress/strain analysis.

4 PHASE IDENTIFICATION

The simplest application of powder diffraction is to identify a crystalline phase. One merely runs the powder pattern of the solid and records either 2θ values or d-spacings or both. This information is given by the program and can be printed directly on the pattern. Then one may consult a database such as the JCPDS file. These initials refer to the JCPDS. As a result of the complexity of keeping pace with the ever growing list of known phases, the operation grew and was renamed the International Centre for Diffraction Data (ICDD), headquartered in Newton Square, Pennsylvania.

The database was formerly a card file on which the data for each phase was printed on $3'' \times 5''$ cards, but now this information is available on CD-ROM. A typical data card is shown in Figure 13. Each card is identified by a number such as 25–1495. A search manual is provided in which the d-spacings of eight peaks for each compound are listed in order of decreasing intensity with the most intense peak in the pattern listed first. The cards are listed in groups of d-spacings such as 7.99–7.00. There are 40 such groups from very high to very low d-spacings. One searches through the proper group

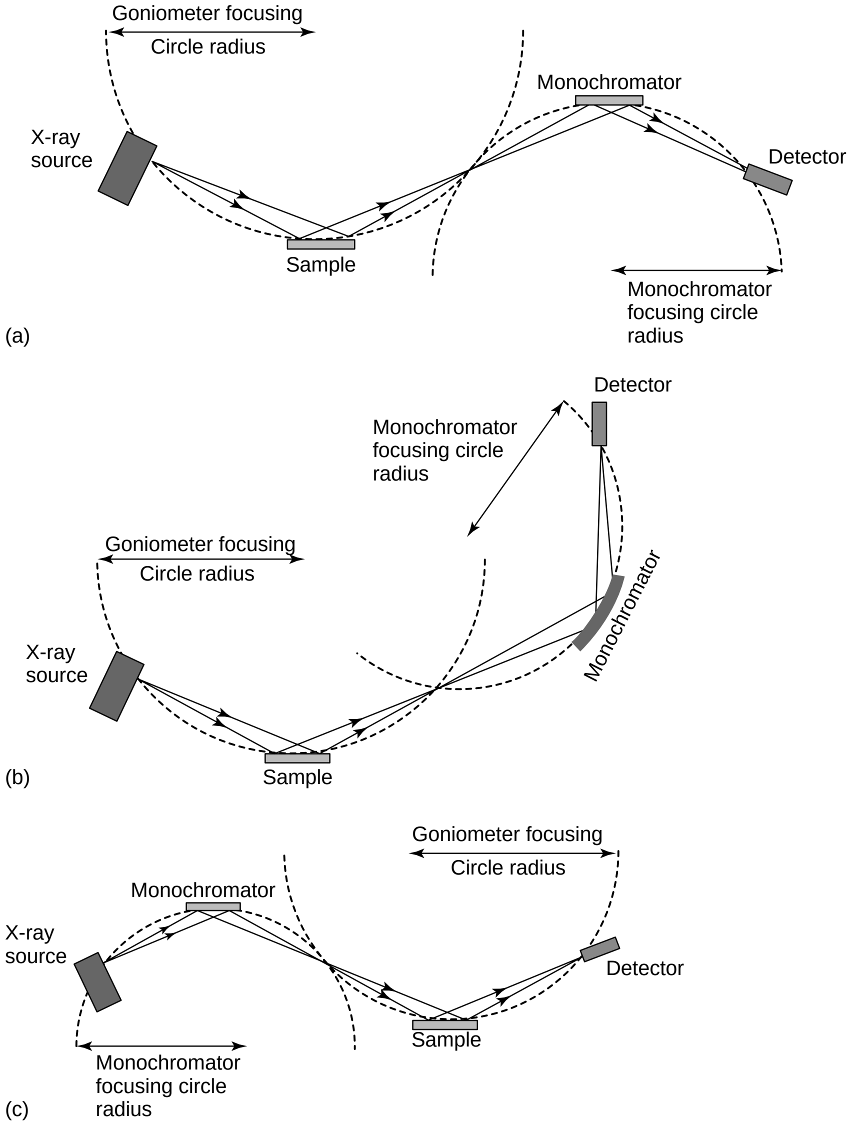
Goniometer focusing
Circle radius
Monochromator
X-ray source
Detector
Sample
Monochromator focusing circle radius
(a)
Detector
Monochromator focusing circle radius
Goniometer focusing
Circle radius
X-ray source
Monochromator
Sample
(b)
Goniometer focusing
Circle radius
Monochromator
X-ray source
Detector
Sample
Monochromator focusing circle radius
(c)

Figure 12 Three different monochromator/sample geometries used in powder diffraction: (a) flat diffracted beam monochromator, parallel arrangement, (b) curved diffracted beam monochromator, angular arrangement, and (c) flat primary beam monochromator, parallel arrangement

for a match. When one is found, then the remaining peaks are compared. Relative intensities are listed with the largest represented as 100 and the others as a percent, in comparison with the most intense peak. A total match is sufficient to have identified the phase. If the data are available on CD-ROM, the observed d-spacings, already on a computer may be utilized in a search−match procedure. Inclusion of some or all of the chemical elements in the sample, if known, speeds up the search. Books listing all the phases in alphabetical order are also available. If, for example, elemental analysis indicates that you are dealing with a calcium phosphate you can check your X-ray pattern with the many listings of all the calcium phosphates in the volume. For information on purchase of the various databases available from ICDD, refer to www.icdd.com. The databases are categorized as inorganic (with some organic), organic and organometallic (with some inorganic) and minerals. In all, more than 500 000 entries are listed. The entire file is automated. A great deal of information is listed for each phase. For example, many entries include unit cell dimensions, and atomic coordinates. These can be used in Rietveld techniques (to be described in a later section) to carry out a quantitative assessment of the phases present in a mixture. It is perhaps wise at this stage to describe problems that may arise leading to difficulty of identification.

4.1 Preferred Orientation

A major problem in dealing with powder patterns is PO. Crystals with texture may prefer to orient in favored

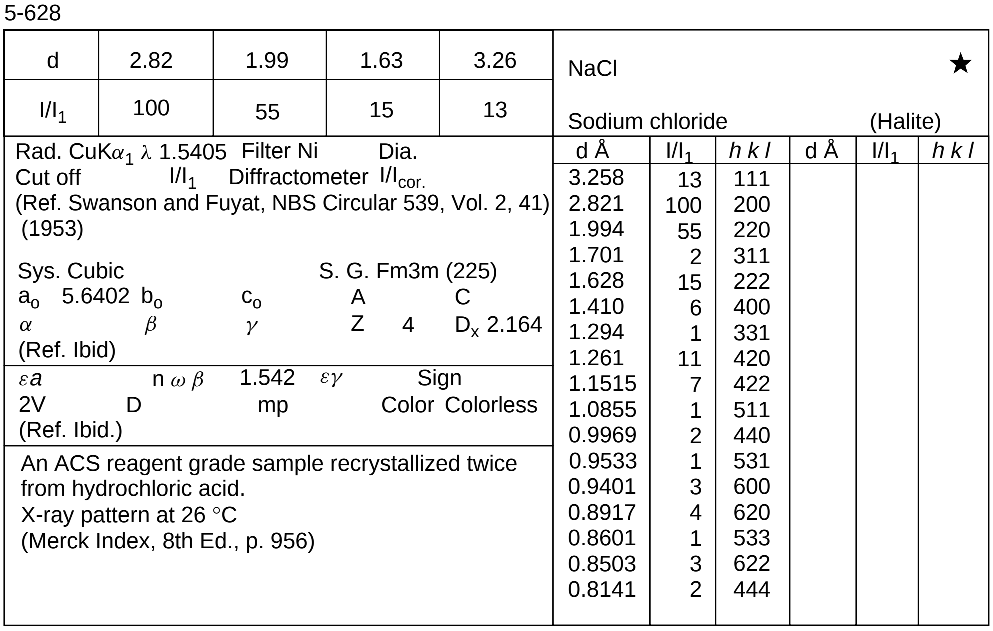

5-628

d	2.82	1.99	1.63	3.26
I/I_1	100	55	15	13

NaCl ★

Sodium chloride (Halite)

Rad. Cu$K\alpha_1$ λ 1.5405 Filter Ni Dia.
Cut off I/I_1 Diffractometer $I/I_{cor.}$
(Ref. Swanson and Fuyat, NBS Circular 539, Vol. 2, 41) (1953)

Sys. Cubic S. G. Fm3m (225)
a_o 5.6402 b_o c_o A C
α β γ Z 4 D_x 2.164
(Ref. Ibid)

εa n ω β 1.542 $\varepsilon\gamma$ Sign
2V D mp Color Colorless
(Ref. Ibid.)

An ACS reagent grade sample recrystallized twice from hydrochloric acid.
X-ray pattern at 26 °C
(Merck Index, 8th Ed., p. 956)

d Å	I/I_1	*h k l*	d Å	I/I_1	*h k l*
3.258	13	111			
2.821	100	200			
1.994	55	220			
1.701	2	311			
1.628	15	222			
1.410	6	400			
1.294	1	331			
1.261	11	420			
1.1515	7	422			
1.0855	1	511			
0.9969	2	440			
0.9533	1	531			
0.9401	3	600			
0.8917	4	620			
0.8601	1	533			
0.8503	3	622			
0.8141	2	444			

Figure 13 Standard ICDD diffraction data card for sodium chloride

ways, instead of randomly. This feature increases the intensity of diffracted radiation from certain planes and reduces it from others. The most egregious examples are layered compounds that tend to lay flat, thin films and cold-worked metals. Even compounds that are not layered may exhibit some PO due to their odd shape. In such cases side loading of the sample may be sufficient. Side loading coupled with rotation of the sample in the plane is better and may produce satisfactory results. A more effective technique is to fill a capillary with the sample and rotate the sample rapidly. The beam is passed through the sample in transmission mode. Not every diffractometer has this option. Additions of fine grains of starch are also somewhat effective. The best way to eliminate PO is to use a vacuum chamber.[7] It consists of a glass container filled with small glass beads to which the sample is added. By mixing the two thoroughly the sample particles cling to the glass spheres. The layers are tangent to the spheres and thus take every possible orientation over the sphere surfaces. A vacuum is then applied and the solid sample is pulled into a chamber containing a filter paper that catches the particles. Happily, the particles maintain the orientation they took on the glass surface, producing a sample free of PO Software is available to correct for PO mathematically, but this is best done on samples treated by one of the above-mentioned methods to remove the bulk of the PO.

4.2 Indexing the Powder Pattern

The determination of previously unknown unit cell constants (*viz.*, a, b, c, α, β, γ) from the various interlayer spacing values obtained from the powder diffraction profile and assigning each peak with a certain set of Miller indices (hkl) is known as indexing. The most general equation for the lowest symmetry triclinic system is given by:

$$\frac{1}{d^2} = \frac{1}{V^2}[h^2b^2c^2\sin^2\alpha + k^2a^2c^2\sin^2\beta + l^2a^2b^2\sin^2\gamma + 2hkabc^2(\cos\alpha\cos\beta - \cos\gamma) + 2kla^2bc(\cos\beta\cos\gamma - \cos\alpha) + 2hlab^2c(\cos\alpha\cos\gamma - \cos\beta)]$$

where, d is the interplanar spacing, and V is the volume of the unit cell. When considering higher symmetry systems, some of the angles are constrained to 90° and the equation simplifies. Although, every step in powder diffraction is crucial and important, the process of indexing is generally accepted as the bottleneck toward structure determination from powder diffraction data.

The ICDD cards or data sheets contain a column with a heading *hkl*. This column contains three integers associated with each d-spacing. These trios of integers are termed Miller indices and reveal the positioning of the different sets of planes within the crystal. Indexing the crystal planes is important from several points of view. If you indeed are dealing with a single phase, then every reflection or peak in the powder pattern should be assignable to a Miller index. The indices are assigned on the basis of a unit cell which is also listed on the ICDD sheet.

4.2.1 *Bravais Lattices and Unit Cell Axes*

You will recall that in solids the atoms have fixed positions about which they vibrate. If the atoms are replaced by points, a point lattice results. In Figure 14, we show such a

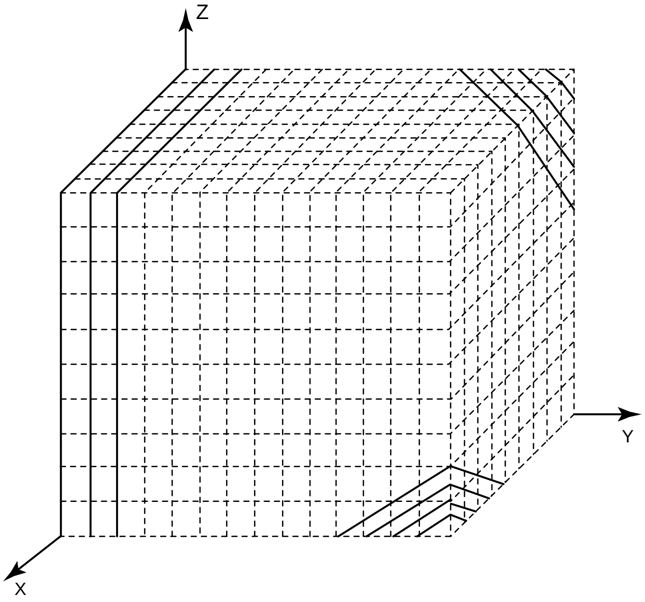

Figure 14 A three-dimensional point lattice and some examples of set of parallel planes of points

point lattice with sets of planes drawn through the points. It is evident that a large number of such sets are possible. In order to be able to identify the individual planes, each of which will give rise to a peak in the powder pattern, we require an axial system. The choice of axial system depends upon the symmetry of the crystal. The allowed symmetry elements are axes, mirror planes and an inversion center. Fortunately, the only axes that need be considered are 1-, 2-, 3-, 4-, and 6-fold. This limitation arises from the condition that the crystal must fill the space it occupies. The combination of all these symmetry elements leads to six axial systems as listed in Table 1.

Table 1 Crystal axis systems

System	Minimal symmetry	Axial conditions
Triclinic	1 or $\bar{1}$	$a \neq b \neq c$, $\alpha \neq \beta \neq \gamma$
Monoclinic	2 or $\bar{2}$	$a \neq b \neq c, \alpha = \gamma = 90° \neq \beta$
Orthorhombic	222	$a \neq b \neq c, \alpha = \beta = \gamma = 90°$
Tetragonal	4 or $\bar{4}$	$a = b \neq c, \alpha = \beta = \gamma = 90°$
Cubic	Four 3s or $\bar{3}$s	$a = b = c, \alpha = \beta = \gamma = 90°$
Hexagonal	3 or 6 ($\bar{3}$ or $\bar{6}$)	
(a) Rhombohedral	3	$a = b = c, \alpha = \beta = \gamma \neq 90°$
(b) Hexagonal	6	$a = b \neq c$, $\alpha = \beta = 90°$, $\gamma = 120°$

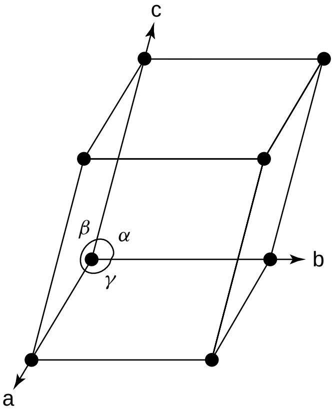

Figure 15 Representation of a unit cell indicating the correct positioning of the axes and angles

The axes may be designated by X, Y, and Z, that are infinite in length in both the positive and negative directions. a, b, c in Table 1 are listed unit lengths along X, Y, Z, respectively and α, β, γ, the angles between the axes as shown in Figure 15. These unit lengths and angles define a unit cell. The unit cell contains a portion of the crystal that is unique and when the unit cell is repeated by the vectors $\vec{a}$, $\vec{b}$, $\vec{c}$, they reproduce the crystal. The point lattices we mentioned earlier must be compatible with the symmetry of the axial systems and this gives rise to 14 lattices termed Bravais lattices (Figure 16). The positioning of the points in the lattice is constrained by the requirements that each point have the same environment. Consider the triclinic unit cell. Reference to Table 1 indicates that the symmetry elements are a one-fold axis, that is, rotation by 360° which brings the point acted upon back to itself, and a center of symmetry designated as one bar, $\bar{1}$. Thus all the axes are of different length and none of the angles are equal. The only arrangement of points possible is a set occupying the corners of the unit cell. Because each point is equally shared by eight unit cells and there are eight such points, there is only one point contained in the unit cell. Such a cell is termed primitive, designation P. Consider the orthorhombic unit cell. It has three mutually perpendicular two-fold axes (222 in Table 1) so that all the angles are 90°. There is no restriction on the length of the axes therefore they are all of unequal length. The simplest unit cell is primitive but more complex cells, termed *centered cells* are possible. One such cell has a point in the body center or at 1/2a, 1/2b, 1/2c in addition to those at the corners. This cell is termed body-centered with symbol I. Similarly, a face centered cell has a point in the center of each face. Note that the body-centered cell has a total of two points, one represented by those points at the corners and one in the center. Similarly, the face-centered cell has four points. Each point in the face is shared with another unit cell so the six faces produce three points in addition to the one at the corners. Finally we have a side centered cell. In the figure the points are in the ab

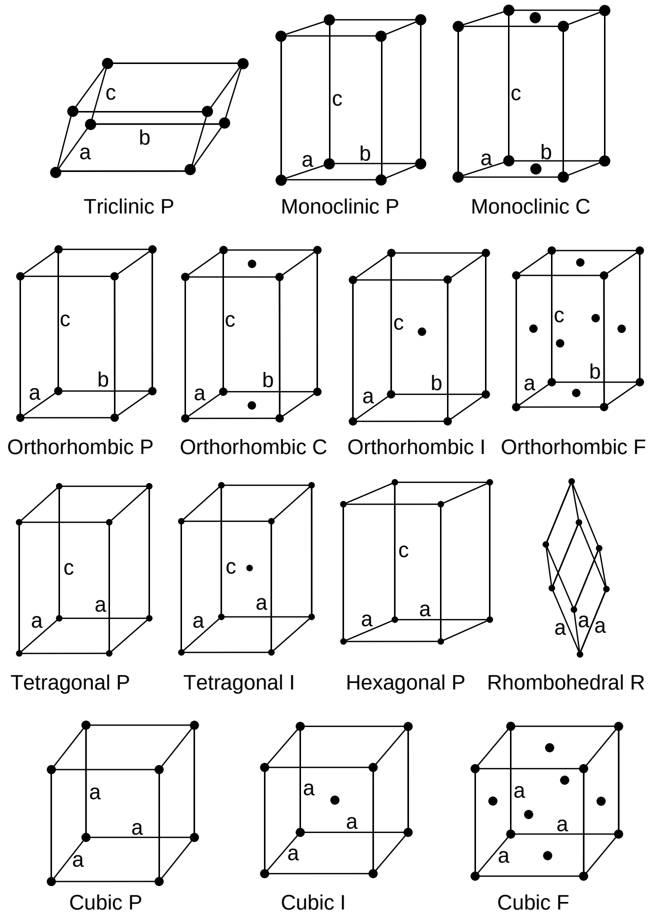

Figure 16 Representation of the 14 Bravais lattices of three-dimensional space

plane and so it is designated as C-centered. A more complete treatment of Bravais lattices can be found in many texts.

4.2.2 Relationship between Miller Indices and Interplanar Spacings

In order to index the powder pattern we need to show the relationship between the axial system and the individual planes. Consider a plane oriented as shown along the X, Y, Z-axes (Figure 17). The perpendicular to the plane from the origin O is the d-spacing because a parallel plane touches the origin. Another way to define the plane is by its intercepts along the three axes. If h is three, then the intercept along the X-axis is 1/3a. Similarly if k is 1, then the plane cuts the Y-axis at b. The intercepts are given as fractions of the unit cell but the Miller indices are reciprocals of the intercepts that the first plane of the set makes with the axes. This is illustrated by the following example. Suppose the plane cuts the axes at 2a, 1/2b, 1/3c. These are the intercepts but the Miller indices are the reciprocals 1/2, 2, 3 respectively. We clear fractions so the Miller indices are 1, 4, 6. This designation tells us that the first plane from the origin was not chosen initially. The first plane cuts the axes at a, 1/4b, 1/6c and would have half the d-spacing as the initially chosen plane. One other point, if the plane is parallel to an axis it cuts the plane at infinity and the reciprocal is zero. 200 cuts the X-axis at 1/2a and is parallel to the bc plane.[3,4,6]

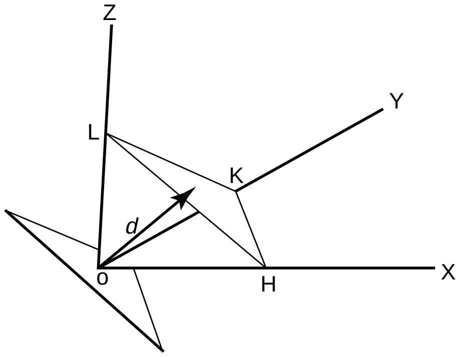

Figure 17 The plane cuts the crystallographic axes at H, K, L giving rise to the normal to the plane ON. A parallel plane passes through the origin illustrating that ON $= d$, the interlayer spacing

There is a direct relationship between the d-spacing of a set of planes and its intercepts. It is beyond the scope of this article to derive such an expression. However, the simplest relationship is for a cubic unit cell that can be simply stated as

$$d_{hkl} = \frac{a_0}{[h^2 + k^2 + l^2]^{\frac{1}{2}}} \tag{8}$$

Similarly for the orthorhombic system we have

$$d_{hkl} = \left[\frac{h^2}{a^2} + \frac{k^2}{b^2} + \frac{l^2}{c^2}\right]^{-\frac{1}{2}} \tag{9}$$

Table 2 contains the relationships for all the axial systems.

What these equations tell us is that if we know the value of a_0 for a cubic unit cell, we can determine indices for all the reflections. For example, if $a_0 = 8.00$ Å, then for the 111 plane $d_{111} = 8.00/\sqrt{3} = 4.62$ Å (equation 8) and from Bragg's law

$$\sin\theta = \frac{n\lambda}{2d} = \frac{1.542\,\text{Å}}{2 \times 4.62\,\text{Å}} = 0.1669$$
$$\theta = 9.60^\circ,\ 2\theta = 19.2^\circ$$

The peak at 19.2 in 2θ is labeled 111. However, what we have to work with is the powder pattern from which we wish to determine a_0. Most laboratories have programs that automatically determine the unit cell dimensions from the powder pattern. To avoid mistakes some fundamentals that help the experimenter to judge the correctness of the result is in order. Consider the pattern of aluminum in Figure 18. We notice that there are very few peaks compared to the powder pattern in Figure 8 even though the pattern was recorded out to very high $2 - \theta$. Also we note that the first and strongest peak is at a high value of $2\theta = 38.52^\circ$, $d = 2.337$ Å. The prognosis

Table 2 Values of the interplanar spacing (d_{hkl}) in the six crystal systems

System	d_{hkl}
Cubic	$\left[\frac{1}{a^2}(h^2+k^2+l^2)\right]^{-1/2}$
Tetragonal	$\left[\frac{h^2+k^2}{a^2}+\frac{l^2}{c^2}\right]^{-1/2}$
Orthorhombic	$\left[\frac{h^2}{a^2}+\frac{k^2}{b^2}+\frac{l^2}{c^2}\right]^{-1/2}$
Hexagonal	$\left[\frac{4}{3a^2}(h^2+hk+k^2)+\frac{l^2}{c^2}\right]^{-1/2}$
	$\left[\frac{1}{a^2}\frac{(h^2+k^2+l^2)\sin^2\alpha+2(hk+kl+lh)(\cos^2\alpha-\cos\alpha)}{1-2\cos^3\alpha+3\cos^2\alpha}\right]$
Monoclinic	$\left[\frac{\frac{h^2}{a^2}+\frac{l^2}{c^2}-\frac{2hl\cos\beta}{ac}}{\sin^2\beta}+\frac{k^2}{b^2}\right]^{-1/2}$
Triclinic	$\left[\frac{\frac{h^2}{a^2}\sin^2\alpha+\frac{k^2}{b^2}\sin^2\beta+\frac{l^2}{c^2}\sin^2\gamma+\frac{2hk}{ab}(\cos\alpha\cos\beta-\cos\gamma)+\frac{2kl}{bc}(\cos\beta\cos\gamma-\cos\alpha)+\frac{2lh}{ca}(\cos\gamma\cos\alpha-\cos\beta)}{1-\cos^2\alpha-\cos^2\beta-\cos^2\gamma+2\cos\alpha\cos\beta\cos\gamma}\right]^{-1/2}$

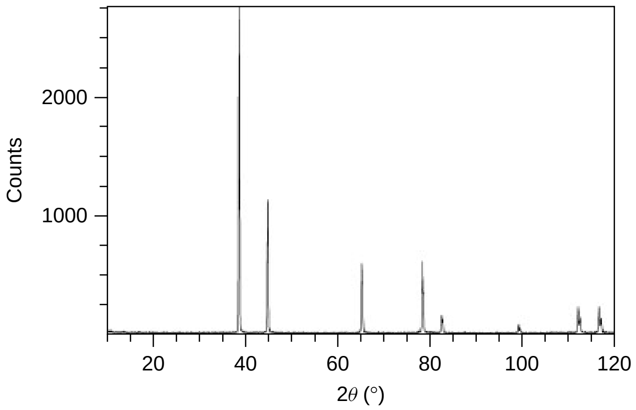

Figure 18 XRD pattern of aluminum metal. (From *X Ray Diffraction, A Practical Approach*, 1998, C Suryanarayana & M Grant Norton. With kind permission of Springer Science & Business Media)

is that we are dealing with a very small cell, probably cubic, because of the small number of peaks. The more complex the relationship between d and *hkl*, the more complex is the powder pattern. For example, in the cubic system 100, 010, 001 occurs at the same 2θ value but in the orthorhombic system these indices would each yield separate peaks.

4.2.3 *Procedure for Indexing a Cubic Unit Cell*

We will illustrate how a_0 for a cubic system may be determined that will lead to further information concerning powder patterns. From equation (8) we can determine the allowed values of $h^2+k^2+l^2$. Let $\mathrm{N}=h^2+k^2+l^2$, then the allowed values of N are given in Table 3. We note that no combination of *hkl* gives 7 or 15 as the sum of their squares.[8]

However, this numbering sequence only holds for primitive cubic unit cells. Certain systematic absences occur for centered cells of which we need consider only I and F in the cubic system (the allowed Bravais Lattices). These absences arise in the following way. Let us assume that we have a cubic unit cell with $a = 5.00$ Å. Normally we expect the 100 reflection to have $d_{100} = 5.00$ Å for which $2\theta = 17.74°$. The angle of incidence of the X-ray beam for this plane is θ, 8.87°. However, there is an exactly similar plane of atoms 200 at $(5.00\,\text{Å}/2) = 2.50$ Å. When the angle of incidence is 8.87°

Table 3 Values of N as derived from the sum of the squares of the Miller indices

hkl	$h^2+k^2+l^2$
100	1
110	2
111	3
200	4
210	5
211	6
220	8
221	9
300	
310	10
311	11
222	12
320	13
321	14
400	16

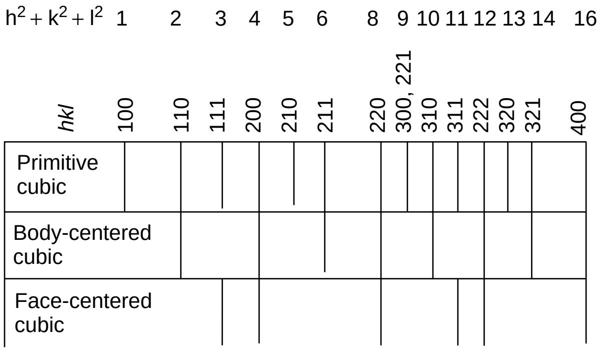

Figure 19 Systematic absences arising for centered cubic unit cells. (From *X Ray Diffraction, A Practical Approach,* 1998, C Suryanarayana & M Grant Norton. With kind permission of Springer Science & Business Media)

for Cu Kα radiation, the pathlength difference between any two such planes d_{100} with 5-Å spacings, is one wavelength. But the exactly similar plane at $d_{200} = 2.50$ Å has a pathlength difference of one-half wavelength and is exactly out of phase with the 100 plane. This is true for all the planes in the (100) set of parallel planes. However, for d_{200} the angle of diffraction is (from Bragg's law) 17.96° and the peak is at 35.93°. Now the pathlength difference for the plane at 2.50 Å to the one passing through the origin is one wavelength, etc., so all the planes are in phase and a strong reflection is observed.

The rule for body centering is that the sum of the indices must be even to appear and are absent if the sum is odd. For face-centering the rule is the *hkl* values must all be even or all odd to appear, those with mixed indices are absent. A useful summary of the nature of the several types of cubic X-ray patterns is given in Figure 19. Similar absences appear for any body and face-centered unit cell so that by indexing any powder pattern one may be able to tell the lattice type.

4.2.4 Deriving the Unit Cell Dimension

We are now in a position to determine the value of a_0 for a cubic unit cell. By now the observant reader should have noted that the d-spacings decrease with increasing values of θ. This feature of the powder pattern is a direct result of Bragg's law, $\sin\theta$ and d have a reciprocal relationship. For the calculation it is convenient to use Bragg's law in the form of its square

$$\sin^2\theta = \frac{\lambda^2}{4d^2} \tag{10}$$

From the equation for d as a function of h, k, l we see that

$$\frac{1}{d^2} = \frac{h^2 + k^2 + l^2}{a_o^2} \tag{11}$$

substituting this result into equation (10) yields

$$\sin^2\theta = \frac{\lambda^2}{4a_o^2}(h^2 + k^2 + l^2) \tag{12}$$

Because h, k, l must be integers we may substitute $N = h^2 + k^2 + l^2$ into equation (12). Let $K = \lambda^2/4a_0^2$ so that equation (12) may be rewritten as

$$\frac{\sin^2\theta}{N} = \frac{\lambda^2}{4a_o^2} = K \tag{13}$$

A table is prepared by dividing the measured $\sin^2\theta$ values by allowed values of N. There should then arise a recurring value of K from which a_0 may be derived. Such a table for aluminum is provided as Table 4 from which it is shown that K is 0.0363. The derived value of a_0 is then

$$a_o = \frac{1.54056}{2\sqrt{K}} = 4.049\ \text{Å}$$

4.2.5 Indexing Procedure for Tetragonal Unit Cell

Although indexing powder patterns for crystals with more unit cell parameters than cubic may be carried out by similar procedures as just described, the task increases in difficulty with the number of parameters to be determined. For example, in the case of tetragonal crystals, we have

$$\sin^2\theta = \mathrm{A}(h^2 + k^2) + \mathrm{C}l^2 \tag{14}$$

Where A and C are constants involving the a and c unit cell dimensions. The permissible values of $(h^2 + k^2)$ are 1, 2, 4,

Table 4 Calculation of the common quotient for Aluminum (Cu Kα radiation; $\lambda_{K\alpha 1} = 1.54056$ Å). (From *X Ray Diffraction, A Practical Approach,* 1998, C Suryanarayana & M Grant Norton. With kind permission of Springer Science & Business Media)

Peak #	2θ (°)	$\sin^2\theta$	$(\sin^2\theta)/2$	$(\sin^2\theta)/3$	$(\sin^2\theta)/4$	$(\sin^2\theta)/5$	$(\sin^2\theta)/6$	$(\sin^2\theta)/8$
1	38.534	0.1089	0.0544	**0.0363**	0.0272	0.0218	0.0181	0.01361
2	44.774	0.1451	0.0725	0.0484	**0.0363**	0.0290	0.0242	0.01813
3	65.124	0.2897	0.1448	0.0966	0.0724	0.0579	0.0483	**0.03621**
4	78.244	0.3981	0.1991	0.1327	0.0995	0.0796	0.0664	0.04977
5	82.438	0.4342	0.2171	0.1447	0.1086	0.0868	0.0724	0.05428
6	99.085	0.5789	0.2895	0.1930	0.1447	0.1158	0.0965	0.07237
7	112.008	0.6874	0.3437	0.2291	0.1718	0.1375	0.1146	0.08592
8	116.560	0.7236	0.3618	0.2412	0.1809	0.1447	0.1206	0.09045

5, 8 etc. Therefore $\sin^2\theta$ values are divided by these integers until a match is found. To obtain C a search for 00l reflections may be tried which are in the ratio of 1, 4, 9, 16 etc. for $l = 1$, 2, 3, 4, respectively. Alternatively we use the differences

$$\sin^2\theta - \mathrm{A}(h^2 + k^2) = \mathrm{C}l^2 \tag{15}$$

to find a consistent set of $\mathrm{C}l^2$ values in the above ratio. Today, sophisticated softwares are available for determining unit cell dimensions for all crystal systems. Usually about twenty prominent reflections obtained over a range of 2θ values are used as input to the program. The correct unit cell should have reasonable values of the parameters in conformity with the symmetry of the crystals.

4.2.6 Automated Indexing Procedures

With the computing abilities of modern day computers increasing rapidly, indexing by manual means is almost not necessary even for the simplest systems.[9] However, the user is left with a large set of possible unit cells and corresponding Miller indices for them to decide which one to choose based on the a priori knowledge of the system in question. Information on the purity of the sample and acquiring best possible data are very essential to succeed using auto-indexing programs. Also, the figures of merit usually given by M_{20} and F_{20} help the user to choose between the various possible resulting unit cells.

Some of the common programs used are TREOR,[10] DICVOL,[11] and ITO.[12] TREOR is one of the fastest indexing programs and is based on trial-and-error methods. The program examines the data from higher to lower symmetry lattice, proceeding in steps. Trial parameters for various lattice constants are obtained from a set of baselines with standard Miller indices. DICVOL uses successive dichotomy approach for indexing. This program is usually more accurate and exhaustive but takes a lot of computing time. It is also very sensitive to systematic errors. ITO is a method based on reciprocal lattice zones. This program has been successfully used even for low-symmetry systems including triclinic unit cells. All three programs along with other indexing programs have been conveniently employed as subroutines in CRYSFIRE; thus having one input file for all the indexing programs is a major advantage. Newer software such as McMaille,[13] and EFLECH,[14] have also been used successfully in some difficult problems.

Recent software, taking advantage of fast computing, directly use the powder diffraction profiles instead of peak positions for indexing. Softwares such as X-Cell[15] (based on successive dichotomy approach similar to DICVOL) and TOPAS-I[16] (based on Monte Carlo methods) are examples.

The success rates of the modern indexing programs are very encouraging and provide the users with the ability to work even on lower symmetry systems.

4.3 Accurate Unit Cell Determination

Many applications require accurate unit cell determinations such as solid solutions studies and thermal expansion coefficients. We discuss the case of cubic crystals first. Precision in a_0, the unit cell parameter, depends upon accurate values of d. The key in this determination is to have accurate values of $\sin\theta$. Fortunately, $\sin\theta$ varies very slowly for θ angles near 90°. For example, an error of 1° in θ leads to an error in $\sin\theta$ of about 0.3% at 80° but to a 1.0% error at 60°. Therefore the approach is to measure the high angle reflections very accurately and carry out a linear extrapolation of a_0 as a function of θ.[6]

The proper extrapolation function depends on the type of diffractometer used for the measurements. Generally such functions are provided in the software provided with the instrument. Several sources of error need to be taken into account to insure that they are dealt with before undertaking the measurements.

1. Misalignment of the instrument. Proper alignment of the instrument is detailed in the company literature. An experienced operator should align the instrument and check to see that the incident beam intersects the diffractometer axis and the 0° position of the detector slit.
2. Displacement of the sample from the diffractometer axis. This is usually the largest error so care must be taken to properly place the sample.
3. Use of a flat specimen rather than a curved one to conform to the focusing circle. This error can be minimized by decreasing the irradiated width of the sample by decreasing horizontal divergence of the incident beam.
4. Vertical divergence error—may be decreased by decreasing the vertical opening of the detector slit.

With proper technique, and use of high angle data extrapolated to $\theta = 90°$ a precision of 0.001 Å in cell dimensions is possible. Use of a modern Guinier camera is advisable when the highest accuracy is required. This camera makes use of a focusing monochromator and a back reflection technique that is able to focus the reflected beam to a narrow line. This focusing results in excellent resolution and high accuracy. The data are recorded rapidly in digital form. Proper extrapolation of the data to $\theta = 90°$ removes systematic errors inherent in the data. However, extrapolation of the lattice parameter versus θ is not linear. Therefore, a function is required that can result in a linear extrapolation and the exact nature of such a function depends on the kind of equipment used to record the diffraction data. In most cases one of two extrapolation functions[17] may be used. They are as follows:

1. Bradley–Jay function, $\cos^2\theta$.
2. Nelson–Riley function $\dfrac{\cos^2\theta}{\sin\theta} + \dfrac{\cos^2\theta}{\theta}$.

The Nelson–Riley function has a greater range of linearity than the Bradley–Jay function. It is appropriate to use a least squares procedure to obtain the best straight line through the data.

The extrapolation function $\cos^2\theta$ is best if the flat sample effect is the principal error, while $\cos^2\theta/\sin\theta$ for specimen displacement error. Using this latter function, it can be shown that

$$a = a_0 + a_0\mathrm{k}\frac{\cos^2\theta}{\sin\theta} \tag{16}$$

where k is a proportionality constant. A plot of a values, determined at each measured θ as a function of $\cos^2\theta/\sin\theta$, yields a straight line. Extrapolation by a least squares procedure to $\theta = 90°$ provides the desired a_0 value. Similarly, if a Nelson–Riley function is used the corresponding equation is

$$a = a_o - a_o k\left[\frac{\cos^2\theta}{\sin\theta} + \frac{\cos^2\theta}{\theta}\right] \tag{17}$$

In this case values of a are plotted as a function of the term in brackets. Extrapolation to 90° yields $a = a_0$, the desired value. Examples of extrapolations as a function of $\cos^2\theta$ and $\cos^2\theta/\sin\theta$ are given in Figure 20.

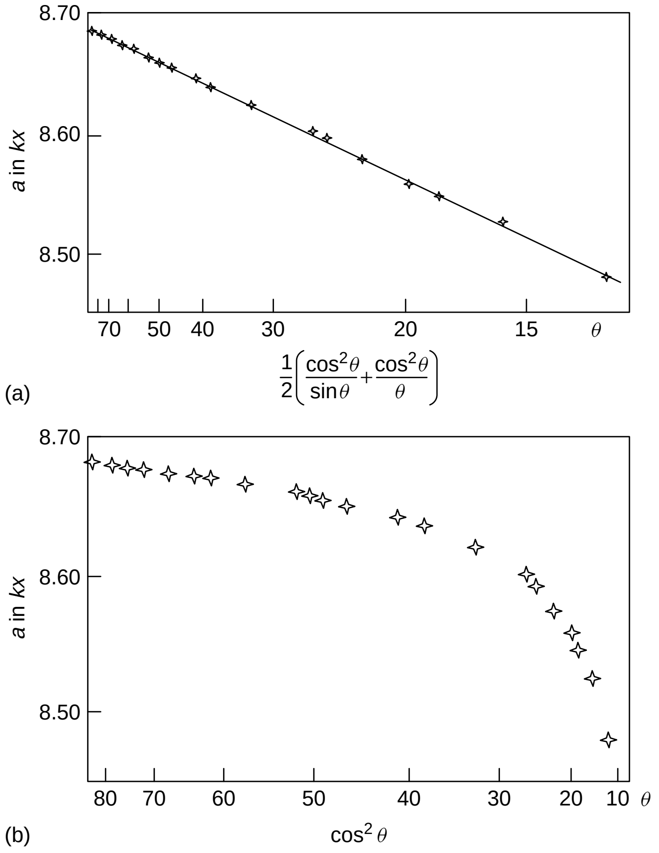

Figure 20 Plots of unit cell dimension a as a function of two different extrapolation functions. (Reprinted from Nuffield.[17] © John Wiley & Sons, Inc)

The Nelson–Riley function is linear over a broad range of θ angles, whereas the Bradley–Jay plot is linear only above about $\theta = 60°$. The B-J function is best when absorption is the largest error but where observational errors are large it is recommended that extrapolation as a function of $\cot^2\theta$ be used.[17]

4.3.1 General Procedure for Noncubic Unit Cells

As we have indicated the data with the lowest error in angle values is obtained at high θ, 50 to 80° in θ. Data at higher angles are not available so for the best accuracy an extrapolation must be made. For tetragonal and hexagonal systems hk0 data are required for the a-axis and 00l for the c-axis parameters. There may be very few such data at high angles leading to poor extrapolations. The procedure here is to use all the data and carry out a linear least squares procedure to obtain the best values. First the powder pattern must be indexed. If there is a set of unit cell dimensions in the ICDD file or in the literature, start with those values. The powder pattern should be run on a well ground pure sample, making sure to properly place the sample and calibrate the instrument with standard samples of Si or quartz. One of several programs may be used to index the powder pattern assigning *hkl* values to each peak. High resolution of the peaks is necessary. Use a step size of 0.02° or less and a count time of 10 s or more. Several iterations of the refinement may be necessary to obtain the best agreement between θ_{obs} and θ_{calc}. The least squares procedure is then applied to the data to obtain the best unit cell parameters.[3,6,8]

5 SOLID SOLUTIONS

5.1 Interstitial Solid Solutions

Solid solutions are classified as either interstitial or substitutional. Interstitial solid solutions occur when one of the components is very small and can fit into the interstices of the larger component. These are commonly formed between metals and carbon, nitrogen, hydrogen or boron. These solid solutions are always accompanied by an increase in volume of the unit cell. If the larger sized component A is cubic, then the value of a_0, its unit cell size must increase as the smaller component B is added. If a standard curve of a_0 as a function of the weight percent of its B content is prepared, this curve can be used to determine the level of B in any other sample of the solid solution. An example of such a solid solution is austenite, an interstitial solid solution[18] of carbon in face-centered γ-iron. A standard solid solution curve is shown in Figure 21 where it is seen that the increase in a_0 is a straight line function of the amount of carbon in the solid phase. If the solid solution is not cubic, one cell length may decrease while

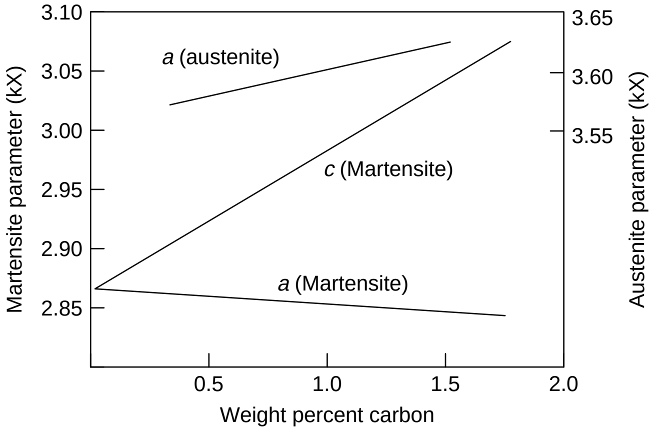

Figure 21 Variation of cubic austenite unit cell dimension a as a function of carbon content and that of tetragonal martensite in which the a-axis decreases as the c-axis increases with carbon loading

another increases, but the volume must always increase. This fact is illustrated for martensite, an interstitial solid solution of carbon in α-iron. α-iron is body centered tetragonal and as shown in Figure 21, the a-axis unit cell parameter decreases as the carbon content increases whereas the c-axis parameter increases.[3]

5.2 Substitutional Solid Solutions

Far more numerous are the substitutional solid solutions. They may be random or ordered. In the case of a random solid solution of B substituting for A there is a linear increase or decrease in volume depending on whether the B atom is larger or smaller than the A atom. This is Vegards Law, which in most cases is only approximate. For cubic unit cells, a plot of a_0 versus the percent B may be prepared over the solid solution range and used as a standard curve. The unit cell parameters need to be measured to four significant figures or at least three decimal places, as the increases in a_0 may be very small. For noncubic crystals one may plot the dimension of the axis that changes the most or unit cell volumes versus the atomic percent of B. The same parameter, cell dimension or volume may be used to determine the composition of the unknown sample.

It often occurs that the disordered or random solid solution has a limited composition range. This is heralded by the appearance of a new phase of $A + B$ by a change in slope of the plot. Alternatively a solid solution of B in A is accompanied by the appearance in the X-ray pattern of pure B, marking the limit of solubility of B in A. Another phenomenon that the reader should be aware of is ordering of a disordered structure. This usually occurs when a rational stoichiometry is reached such as AB_2 or AB_3. A classic case is the copper-gold alloy $AuCu_3$. In the disordered state the gold and copper atoms are randomly distributed so that on average each atomic position scatters as though it were occupied by a portion of a gold atom and a portion of copper atom (Figure 22a). In this disordered state the crystals are face-centered cubic and thus there are four total atoms within the unit cell. The gold atoms provide 1/4 Au at each site and Cu supplies 1/4 Cu, but there are three coppers; so each site has a contribution of 3/4 Cu. Each site has the same occupancy and the X-ray pattern exhibits the systematic absences of a face centered cubic (FCC) lattice. In the ordered state the Au atoms occupy the corners of the unit cell, whereas the Cu atoms occupy the face centers. Now the pattern resembles that of a primitive unit cell with reflections at 2θ values at the angles of previously absent ones. These reflections are weak for the following reason. The arrangement of atoms is as shown in Figure 22(b). The 100 reflection will appear because the plane halfway between the gold and Cu atoms in the (100) planes are all copper atoms. Thus the scattering power of the two atomic planes is not equal and the reflection will not be extinguished. The (200) planes will be strong as in a true FCC unit cell because all the planes will now be in phase. However, in this primitive unit cell all the reflections normally absent in a face-centered cell will be weak, revealing the nature of the structure.

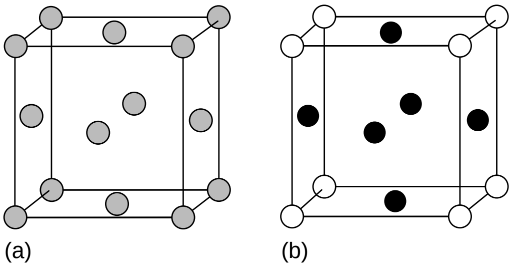

Figure 22 Depiction of the arrangements of metal atoms in solid solutions of gold copper alloys: (a) disordered structure in which the metal atoms are statistically distributed and (b) the ordered structure with copper atoms (filled circles) are in the face centers and gold atoms (open circles) at the cube corners

6 CRYSTALLITE SIZE DETERMINATION AND LATTICE STRAIN

6.1 Crystallite Size Determination

When the crystallites within a sample are smaller than 100 nm (0.1 μm) the X-ray reflections are broadened. Diffraction theory indicates that the diffraction peaks should be extremely thin, just a few seconds of a degree. However, all diffraction peaks have a measurable width, as illustrated in Figure 23. This width arises from the divergence of the incident beam and the width of the X-ray source. These factors are termed instrumental broadening and depend upon the instrument used. There is another factor that influences the peak width known as domain size. Even highly ordered crystals are thought to consist of small domains that are

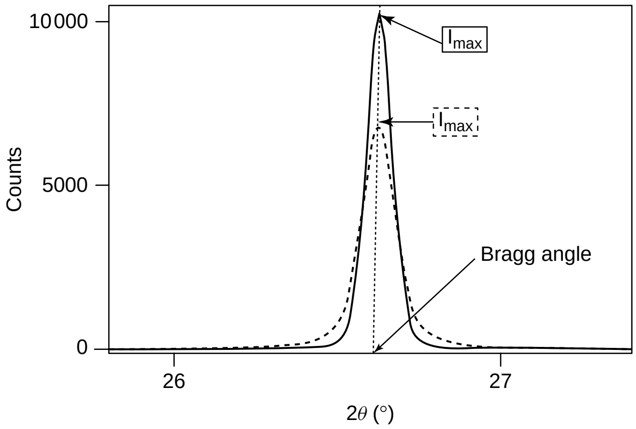

Figure 23 The relative broadness of powder diffraction peaks based upon theory (dotted line) and instrumental broadening (continuous line). The effect of reduced crystallite size in lowering I$_{max}$ and widening of the peak (increasing FWHM) is shown with dashed line

slightly disoriented relative to each other. Some domains are in a position to diffract slightly before the Bragg angle and the others slightly behind. This has the effect of broadening the peak over that predicted by diffraction theory. However, the effect of small crystallite size is not detectable if it is below about 200 nm. Figure 23 shows the effect of peak broadening due to small crystallite size. The peak height is reduced, but the FWHM is increased. Sherrer provided an equation for the crystallite size in terms of peak broadening.[3,8]

$$t = \frac{0.9\lambda}{B\cos\theta} \tag{18}$$

where, θ is the Bragg angle, λ is the wavelength, B is the FWHM, and t is the crystallite size.

For more precise values, especially for crystallites larger than 500 Å, the instrumental broadening should be subtracted. The value of B is measured in degrees, but the equation requires that it be given in radians.

Example: Suppose a peak at $\theta = 10°$ gave a measured B value of 0.20°. Dividing by 57.3°/radian yields 3.49×10^{-3} radians with $\lambda = 1.542$ Å for Cu Kα.

$$t = \frac{0.9 \times 1.542\ \text{Å}}{3.49 \times 10^{-3} \times \cos 10°} = 404\ \text{Å}$$

The size of the crystallite perpendicular to the planes indexed at $2\theta = 20°$ is 404 Å. If the indices are known, say the peak was the 111 reflection, the perpendicular is along the unit cell diagonal.

Let us now see what the effect of subtracting the instrumental broadening has on the calculation of the crystallite size. The best procedure, if it is possible to do so, is to anneal the compound of interest at elevated temperature so that the peaks no longer show a broadening effect. The FWHM of the 111 peak is then used as the value of B_{inst}. Barring this, a compound such as ceramic alumina may be used, choosing a peak near the same 2θ value as for the compound under investigation. For Lorentzian-shaped peaks the subtraction is straightforward,

$$B = B_{\text{meas}} - B_{\text{inst}}$$

The measured B_{inst} was 0.03°, yielding $B = 0.20 - 0.03° = 0.17°$ and $t = 484$ Å. Similarly, for Gaussian shaped peaks the correction is

$$B^2 = B^2_{\text{meas}} - B^2_{\text{inst}}$$

For the same measurements we have

$$B^2 = (0.2)^2 - (0.03)^2 = 0.04 - 9 \times 10^{-4} = 0.0391$$
$$B = 0.1977 \text{ and } t = 408\ \text{Å}$$

It is seen that the correction for Gaussian peaks is small. However, most peaks have contributions from both Gaussian and Lorentzian shaped peaks. Programs are available to map the shape of X-ray reflections as a combination of the two shape functions. Suppose we find that the peak shape is two-thirds Lorentzian and one-third Gaussian. Multiplying the results for each type by their respective fractions give a value of 459 Å. The larger B_{meas} is, the less the influence of the instrumental correction because we are subtracting a small width from a much larger one.

To obtain a more complete picture of the crystallite size it is good to measure about three peaks with indices that place the plane normals in different directions, for example 111, 200, 220, or 202. The value of the cosine function does not change much at low values of θ, but changes more rapidly above $2\theta = 40°$.

It should be remembered that the accuracy with which the crystallite size may be determined decreases with increasing crystallite size. The limit is about 2000 Å with careful and accurate measurement of the peak profile, the FWHM and the instrumental broadening. Furthermore, the result is an average over all the crystallite sizes, as the method does not provide the distribution of sizes in the sample.[19]

6.2 Determination of Strain

There is another factor affecting peak broadening that should be considered, lattice strain.[20] Strain may result from ball milling, compression of small particles into larger aggregates for use as catalysts, and plastic deformation of metals. Strain may be either uniform or nonuniform in the direction of a set of parallel planes. If the grain is then given a uniform tensile strain at right angles to the set of parallel planes, the interlayer spacings of this set of planes will increase slightly. This increase has the effect of shifting the peak to a lower two θ value. If the strain is nonuniform, the grain bends and the set of parallel planes will have a nonuniform change of d-spacing. On one side the d-spacing will increase, in the middle it will be the same as the nonstandard state, and on the bottom the planes will have a smaller d-spacing. The net effect is a broadened X-ray peak. The relationship between the broadening, b, and the nonuniformity of the strain is obtained by differentiating Bragg's equation

$$b = -2\frac{\Delta d}{d}\tan\theta \tag{19}$$

The total broadening is a combination of equation (19) and equation (18), broadening by crystallite size and by strain

$$B_{\text{Total}} = B_{\text{Crystallite}} + b_{\text{Strain}} \tag{20}$$

The left hand side of equation (20) is the same as $B\cos\theta$ in the Sherrer equation (18). If the peak broadening is only due to particle size, then the value of $B\cos\theta$ should be constant with variation of θ. If strain broadening is important, then $B\cos\theta$ should change as a function $\sin\theta$. Measurement of the FWHM over a range of θ values is required. A plot of $B\cos\theta/\lambda$ versus $\sin\theta/\lambda$ is shown in Figure 24. Extrapolation to $\sin\theta = 0$, yields the value of $B\cos\theta$ due to particle size only. Dividing by λ makes the curve independent of wavelength. The slope of the line is $-2(\Delta d/d)$ that provides the broadening resulting from strain.

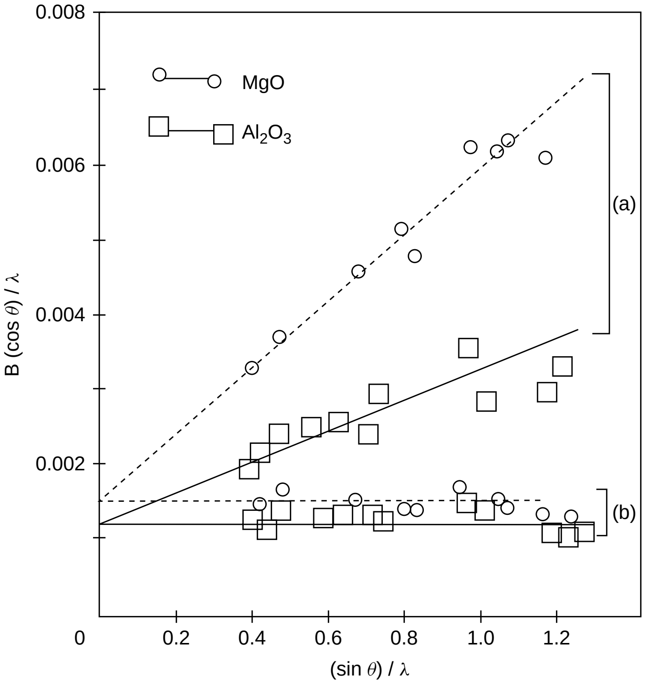

Figure 24 Plot of B $(\cos\theta)/\lambda$ as a function of $(\sin\theta)/\lambda$ for (a) oxides ball milled to introduce strain and (b) the same oxides heated to 1350 °C to remove the effects of strain. (Reprinted from Langford and Louer.[2] © Pearson Prentice Hall)

7 QUANTITATIVE ANALYSIS

7.1 Background Theory

The central problem in carrying out quantitative analysis of a mixture of phases by X-ray powder diffractometry is that the intensity of the peaks is not linear with concentration. For quantitative analysis of binary solid solutions, see the section on solid solutions. Here we concern ourselves with mixtures of two or more phases. In such cases the intensity depends upon the absorption of the sample. We assume that the two phases have already been identified from prior knowledge or from the powder pattern. The expression for the intensity of a reflection from a set of parallel planes hkl, I_{hkl} is a very complex equation. For our purpose we will use a simplified form.[3,4,21]

$$I_a = \frac{K_a V_a}{\mu_\ell^m} \tag{21}$$

where K is a constant, V_a is the volume fraction of phase a in the mixture, and μ_ℓ^m is the linear absorption coefficient of the mixture. Each element in the mixture has its own value of μ_ℓ. We recall from equation (6) that passage of an X-ray beam through a slab of an element of thickness x reduces the intensity of the initial beam I_o as $e^{-\mu_\ell x}$, where μ_ℓ is the linear absorption coefficient. The absorption coefficient depends upon the number of atoms in the path of the beam because it is the electrons that scatter the X-rays out of the path of the incident beam. Therefore we may rewrite equation (21) as

$$I_a = \frac{V_a}{\sum_1^n V_n \mu_\ell^n} \tag{22}$$

The denominator is the sum of the volume fraction of each element, V_n, multiplied by its respective linear absorption coefficient μ_ℓ^n. To facilitate calculations based upon absorption coefficients, a second coefficient was defined as

$$\mu_m = \frac{\mu_\ell}{\rho} \tag{23}$$

where, μ_m is the mass absorption coefficient and ρ is the density of the absorber.

Tables of μ_m values, based upon measured μ_ℓ for each element divided by their respective densities, are collected in the International Tables for Crystallography Vol. C. The variation of μ_m with wavelength has the general form shown in Figure 5. Because volume times density equals weight we may rewrite equation (21) in terms of weight fraction

$$I_a = \frac{K_a W_a/\rho_a}{\sum_1^n (W_n/\rho_n)\mu_\ell^n} \tag{24}$$

applying equation (23), equation (24) may be rewritten as

$$I_a = \frac{K_a W_a/\rho_a}{\sum W_n \mu_m^n} \tag{25}$$

However, our aim is to determine the weight fraction of a phase in a two-component mixture. Therefore, in terms of two phases 1 and 2 the intensity due to phase 1 is

$$I_a = K_a \frac{W_a/\rho_a}{W_a\mu_m^a + W_b\mu_m^b} \tag{26}$$

where μ_m^a, μ_m^b are the mass absorption coefficients of the two phases, respectively and W_a, W_b are their weight fractions. Mass absorption coefficients need to be calculated for each phase. In general, for a compound the mass absorption coefficient is given by summing up the individual mass absorption coefficients of each component multiplied by their respective weight fractions

$$\mu_m^{cp} = W_a\mu_m^a + W_b\mu_m^b + W_c\mu_m^c \cdots \tag{27}$$

Example: What is the mass absorption coefficient of LiCl for Cu Kα radiation? According to equation (27),

$$\mu_m^{LiCl} = W_{Li}(\mu_m^{Li}) + W_{Cl}(\mu_m^{Cl}) \tag{28}$$

The necessary mass absorption coefficients for the elements are taken from the tables for the particular wavelength used in the analysis; in this case Cu Kα.

$$\mu_m^{Li} = \frac{1.10\,\text{cm}^2}{\text{g}}, \quad \mu_m^{Cl} = \frac{109.3\,\text{cm}^2}{\text{g}}$$

These units arise from the fact that the linear absorption coefficient has the units of cm^{-1}. Therefore,

$$\mu_m = \frac{\mu_\ell}{\rho} = \frac{\text{cm}^{-1}}{\text{g/cm}^3} = \frac{\text{cm}^2}{\text{g}} \tag{29}$$

The formula weight for LiCl is 42.392 g, therefore

$$\mu_m^{LiCl} = \frac{6.939\,\text{g}}{42.392\,\text{g}}(1.10) + \frac{35.453\,\text{g}}{42.392\,\text{g}}(109.3) = \frac{91.40\,\text{cm}^2}{\text{g}}$$

7.2 External Standard Method

If the phases within the mixture are known or were identified from the powder pattern of the mixture, we can calculate the mass absorption coefficients in equation (26). The most common method of determining W_a is to compare a peak in the mixture with the same peak in the pure phase. For a pure phase we may write from equation (21)

$$I_a^p = \frac{K_a}{\rho_a\mu_m^a} \tag{30}$$

Dividing equation (30) into equation (26) gives

$$\frac{I_a}{I_a^p} = \frac{W_a\mu_m^a}{W_a\mu_m^a + W_b\mu_m^b} \tag{31}$$

To eliminate W_b, we use the fact that $W_b = 1 - W_a$, from which we derive our required equation by making this substitution

$$\frac{I_a}{I_a^p} = \frac{W_a}{W_a(\mu_m^a - \mu_m^b) + \mu_m^b} \tag{32}$$

The meaning of equation (32) is that the intensity of any peak hkl in the mixture I_a divided by the intensity of the same peak in the pure sample of phase a, I_a^p is given by the right hand side of the equation. The mixture and the pure phase measurements are carried out exactly in the same way. It is assumed that the phases have been identified prior to the intensity measurements, so their mass absorption coefficients may be calculated. As an example we will consider a mixture of LiCl and $CaSO_4$. The mass absorption coefficient of calcium sulfate is 77.37 cm^2/g. Let us assume that the mixture contains 10 weight percent $CaSO_4$. The mass absorption coefficient of the mixture is then

$$\mu_m^m = 0.1 \times \frac{77.37\,\text{cm}^2}{\text{g}} + 0.9 \times \frac{91.40\,\text{cm}^2}{\text{g}}$$

$$\mu_m^m = \frac{7.737\,\text{cm}^2}{\text{g}} + \frac{82.26\,\text{cm}^2}{\text{g}} = \frac{89.997\,\text{cm}^2}{\text{g}}$$

The ratio of the observed peak in the mixture to that peak in pure $CaSO_4$ is

$$\frac{I_a}{I_a^p} = \frac{0.1 \times 77.37\,\text{cm}^2/\text{g}}{89.997\,\text{cm}^2/\text{g}} = 0.0859$$

By calculating this ratio over a range of weight fractions of phase 1, a standard curve is obtained. The best fit of the experimental ratios for several reflections fixes the actual percentage of phase 1. In Table 5 we have tabulated the intensity ratios for increasing ratios of $CaSO_4$ to LiCl in a mixture of the two compounds. The results are plotted in Figure 25.

We note in Figure 25 that the intensity ratios for $CaSO_4$ are slightly below the line for pure $CaSO_4$. This is a common effect. When the absorption coefficient of the compound in question is lower than that of the other member of the binary mixture, the curve dips below the line. The phase with the larger μ_m value will produce a curve that falls above the line (Figure 26).

The method just described suffers from the disadvantage that two separate XRPD patterns must be

Table 5 Cumulated standard curve for intensity ratios of increased ratio of $CaSO_4$ in a mixture of Calcium Sulphate and Lithium Chloride ($\mu_m^{LiCl} = 91.4$, $\mu_m^{CaSO_4} = 77.37\,\text{cm}^2/g$)

Wt % $CaSO_4$	$CaSO_4$ $W_a\mu_m$	LiCl W_b (μm)	$\frac{I^m_{CaSO_4}}{I^p}$
10	7.737	82.26	0.086
20	15.474	73.12	0.175
30	23.21	63.98	0.266
40	30.95	54.84	0.361
50	38.68	45.70	0.458
60	46.42	36.56	0.559
70	54.16	27.42	0.664
80	61.90	18.28	0.772
90	69.63	9.14	0.884
100	77.37	0	1

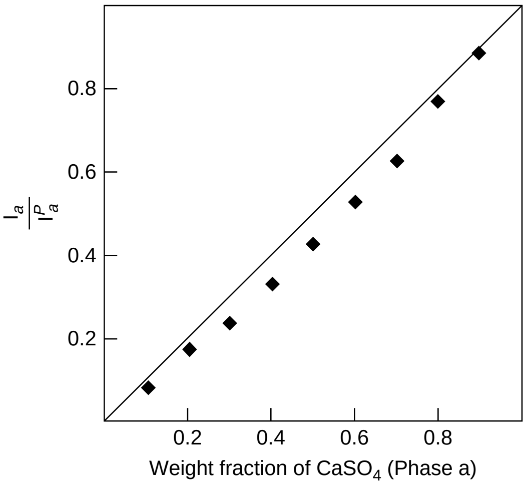

Figure 25 Standard curve for quantitative determination of $CaSO_4$ in a mixture with LiCl. The straight line represents the result for a mixture with equal mass absorption coefficients for the components

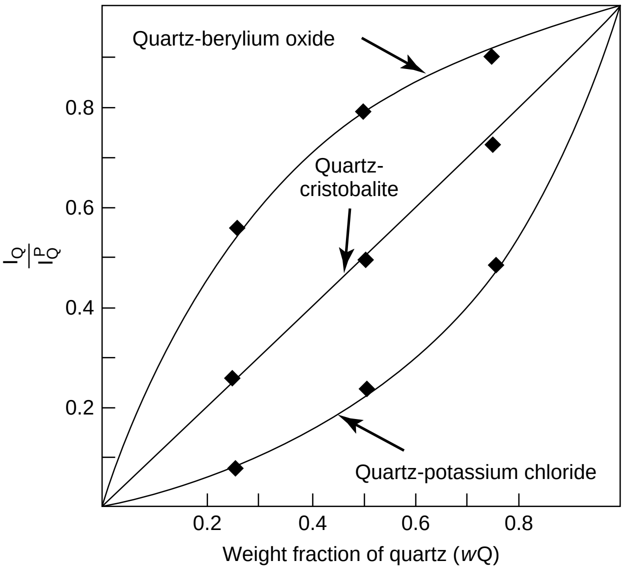

Figure 26 A plot of the intensity of quartz in three binary mixtures compared to the intensity of the same plane in pure quartz as a function of the weight fraction of quartz in the mixtures. Conditions: Cu Kα, $d = 3.34$ Å, mass absorption coefficients, BeO 8.6; SiO_2 34.9; KCl 124 cm^2/g. (Reprinted from Nuffield.[17] © John Wiley & Sons, Inc)

recorded, one for the mixture and another for the pure phase. Both patterns must be taken under identical conditions requiring a certain amount of operator care. However, the use of an internal standard avoids this problem.

7.3 Internal Standard Method

Suppose we wish to determine the weight fraction of a phase A in a mixture of phases A, B, C, D, ... This can be done by mixing a weighed amount of a standard compound with a known amount of the sample. While the absorption coefficient for the entire mixture may be unknown, if we consider the ratio of the intensity of a peak from phase A, I_A, to that of a peak from the standard, I_s, the μ_m drops out of the equation because it is the same for both peaks. Physically, this means that variations in absorption due to variations in the sample have no effect on the ratio I_A/I_s. In other words, the total absorption affects both intensities equally. The working equation is then a simple one

$$\frac{I_A}{I_s} = KW_A \quad W_A = \text{weight fraction of phase } A \tag{33}$$

Equation (33) states that the ratio of intensities from a peak from phase A and one from the standard is a linear function of the weight fraction of phase A. A calibration curve can be set up containing known concentrations of A and a constant concentration of a suitable standard phase. Then the concentration of phase A in the unknown is obtained by measuring I_A/I_s in which the same amount of the standard was added to the unknown as was used to prepare the standard curve. Good standards to use are α-Al_2O_3, a synthetic corundum marketed as Linde A and CaF_2, fluorite.

7.4 Practical Difficulties

In dealing with powders, accurate sampling and homogeneous mixing is necessary to obtain accurate results. Examination of the sample for homogeneity may be effected with a low power binocular microscope. Further grinding the sample with an agate mortar and pestle is recommended to achieve a fine textured uniformity. If the sample was taken from a larger prepared quantity then good sampling techniques are in order.[4] PO will result in some peaks being inordinately intense and others being weak. Rotation of the sample in a capillary tube improves the situation by presenting more crystal orientations.

8 HIGH AND LOW TEMPERATURE POWDER PATTERNS

Temperature controlled powder patterns at higher or lower temperatures than room temperature are useful for tracking phase changes, obtaining improved intensity data, measuring coefficients of expansion, tracking dehydration, etc.

8.1 Background and Theory

There are many factors that determine the intensity of a diffracted beam. For simplicity we shall indicate the equation as

$$I = k|F^2|(LP)\frac{T}{A} \tag{34}$$

where k is a constant containing many terms, F is the structure factor, *Lorentz and polarization* (*LP*) is the LP factors, T is the temperature factor and A is the absorption factor. We have already seen that the absorption effects are quite profound and need to be considered when dealing with intensities. The structure factor is the only term that arises from the positions of all the atoms in the unit cell. It shall be dealt with in detail in the next section. L (for Lorentz) is a geometric factor that depends upon the way in which the data are obtained, and P stands for the polarization effect. When X-rays are diffracted, partial polarization of the beam takes place. If a monochromator is used, the beam is polarized twice, once from the monochromator crystal and once from the sample. However, in this section we are interested in T the temperature factor. In its simplest form

$$T = \exp\left[-B\left(\frac{\sin^2\theta}{\lambda^2}\right)\right] \tag{35}$$

where B is a temperature coefficient. It is related to the mean square amplitude of vibration ($\bar{u}^2$) as

$$B = 8\Pi^2\bar{u}^2 \tag{36}$$

The atoms within a solid vibrate as a function of temperature. The greater the vibration the larger is B and the greater is the reduction of the intensity. The decrease in intensity is also angle dependent. This contribution is attributable to the finite size of the electron clouds of the atoms. The larger this cloud, for a given number of electrons, the greater the decrease in the atoms scattering effectiveness. Units of Å^2 are assigned to B so that the exponent in equation (35) is unitless. B has values between 2 and $5\,\text{Å}^2$ for most atoms at room temperature. As an example, suppose we determine that an overall temperature factor, B, for a compound is $3\,\text{Å}$ and that the (111) reflection occurs at $\theta = 15°$. Then for Cu Kα using equation (35)

$$T = \exp\left[-3\,\text{Å}^2\left(\frac{0.2588}{1.542\,\text{Å}}\right)^2\right] = \exp(-0.08452) = 0.919$$

Thus, the intensity is reduced by this amount. At higher angle of 60° for the (824) reflection $T = 0.388$, a significantly larger reduction of the intensity. As the temperature is reduced, B reduces proportionately because the atoms vibrate less energetically and the intensities correspondingly increase. Conversely, as the temperature is raised the atoms vibrate more vigorously, increasing $\bar{u}^2$ and the intensities are lowered.

8.2 Thermodiffraction

We shall illustrate the use of recording XRD patterns at elevated temperatures with some practical examples. The diffractometer was a Siemens D-5000 fitted with a special goniometer permanently equipped with an HTK 10 heating chamber. The samples were mounted directly on Pt foil, which is both the heater and the sample holder. The patterns were scanned over the angular range of 3 to 38° in 2θ with a step size of 0.05° and counting for 15 s per step.

The sample studied was a cobalt bis(phosphonate) of composition $Co_2(O_3PC_6H_4OC_6H_4PO_3)\cdot 2H_2O$. It is one of the series of first row transition element compounds with the same general formula, but different water contents.[22] The Cu(II) compound structure was solved from its powder pattern, unit cell dimensions $a = 8{:}1012(5)$, $b = 5.3109(3)$, $c = 29.2595(5)\,\text{Å}$. It has a layered structure in which the layers are spaced at half the c-axis dimension. The reason for the doubling of the c-axis is that in one layer the rings are tilted around the ether oxygen to the left and in the next layer to the right. The Cu atoms are 5-coordinate with square pyramidal structure.

The unit cell dimensions for the Co derivative could not be determined because of the poor quality of the powder pattern (Figure 27, RT). The first diffraction peak is at $2\theta = 6°$, $d_{001} = 14.73\,\text{Å}$, a value that is very close to half the c-axis of the copper compound. Thermal analysis showed that two moles of water are lost at 160 °C. The thermodiffraction patterns in Figure 27 are similar from room temperature to 120 °C. The pattern taken at 160 °C is characterized by a reduction in intensity of all the peaks, a small shift in the position of the first peak to higher 2θ indicative of a small decrease in the interlayer spacing. The sample color changes from purple to blue. The same X-ray pattern persisted to 240 °C. Upon cooling to room temperature the original color was restored and the original X-ray pattern restored but with lower intensities. These changes indicate that the original coordination of the Co was octahedral and became tetrahedral upon loss of the two water molecules at 160 °C. Diffuse reflectance measurements confirmed this coordination transition. It was then possible to construct a model structure for the cobalt compound.[22]

A second example involves an aluminum phenylphosphonate whose composition was found to be $Al_2(O_3PC_6H_5)_3\cdot 2H_2O$.[23] A combined thermogravametric analysis (TGA) and differential thermal analysis (DTA) gave an endothermic event at ~80 °C and three exotherms centered at 600, 840 and 950 °C. The X-ray thermodiffractometric powder patterns are presented in Figure 28. The equilibration time at each temperature was 15 min before obtaining the pattern. The highest d-spacing recorded at room temperature is very weak with $d_{001} = 26.1\,\text{Å}$ and the second very intense peak is at 13.2 Å and very likely the 002 reflection. A phase change begins at ~45 °C and both phase I and II coexist to 60 °C, whereupon only phase II remains. In phase II, the dehydrated phase, the d_{001} and d_{002} peaks shift to 23.2 and 11.7 Å. Once again, we expect that the layer separation in both cases is half d_{001}, but the unit cell dimension is doubled. This is apparently due to a large difference in arrangement of two contiguous layers such that they largely diffract out of phase, but at half the distance all the layers diffract in phase, accounting for the weak–strong effect. Exposure of the dehydrated phase at room temperature results in rehydration.

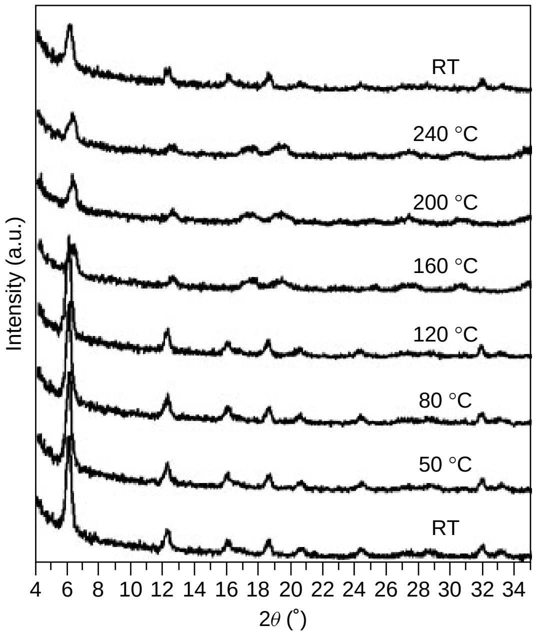

Figure 27 X-ray thermodiffraction powder patterns for $Co_2(O_3PC_6H_4OC_6H_4PO_3)·2H_2O$ showing dehydration takes place between 120 °C and 160 °C and rehydration at room temperature

Upon heating the sample above 500 °C, combustion of the organic phase occurs, accounting for the large exotherm. The X-ray pattern is amorphous above this temperature. Crystallization to a mixture of $AlPO_3 + AlPO_4$ occurs at 950 °C. The overall reaction is

$$2Al_2(O_3PC_6H_5)_3 \cdot 2H_2O + 45O_2 \longrightarrow Al(PO_3)_3 + 3Al\,PO_4 + 36CO_2 + 19H_2O$$

A knowledge of the end products obtained at 950 °C allows confirmation from the total weight loss of the formula of the synthesized compound.

8.3 Determination of Thermal Expansion Coefficients

Thermal expansion studies are not frequently pursued, but can give valuable insight into the behavior of solids. Because the increases in unit cell dimensions over a range of temperatures are very small the data must be extremely accurate. This requires that the furnace have a constant temperature zone surrounding the sample with thermocouples touching the sample holder. Because of the possible movement of the sample during heating, it is advisable to have an internal standard such as α-Al_2O_3 or TiO_2,[24,25] whose peak positions can be used to correct the 2θ values. A back reflection digital Guinier camera is recommended for the measurements. However, it is convenient to do the measurements at a synchrotron such as NSLS at Brookhaven National Laboratory. There is a current interest in low and negative thermal expansion coefficients.[24–26] Figure 29 presents some data for cubic low expansion behavior by $TaOF_2$ and normal expansion behavior by NbO_2F. The expansion data for NbO_2F were measured from 20 K to 300 K. The total expansion over this temperature range was 0.0113225 Å and the initial unit cell dimension was 3.888226 Å. The linear expansion coefficient is the observed expansion value divided by the initial unit cell dimension divided by ΔT, 280 K. The value obtained for NbO_2F is 104×10^{-7}/K. We note that for TaO_2F there is almost no change in cell dimension even over a very large temperature range. The three data sets give values of $1 - 6 \times 10^{-7}$/K. Sleight has discussed mechanisms of low and negative thermal expansion coefficients involving movement or rocking of metal oxygen polyhedra which reduces the space between the polyhedra (Figure 30).

For noncubic unit cells, the expansion or change of each cell dimension is required. The coefficients may be presented as linear for each cell dimension or as volume expansion coefficients, in which case the total volume change is divided by the initial volume. Division by the temperature

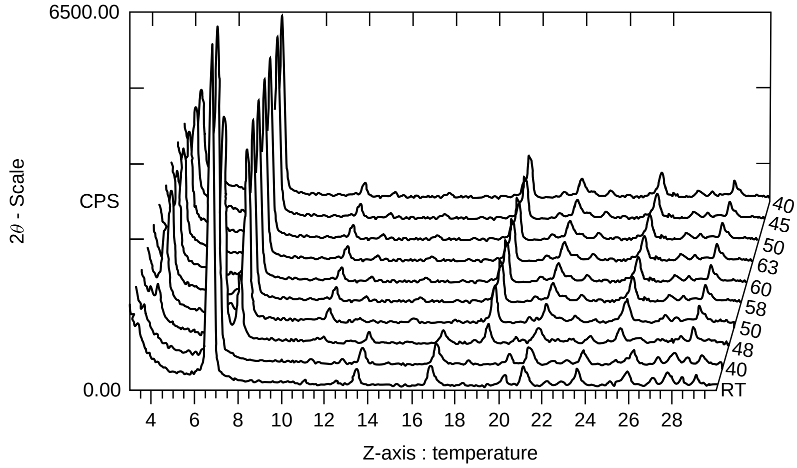

Figure 28 X-ray Thermodiffraction patterns for $Al_2(O_3PC_6H_5)_3.2H_2O$ showing a phase change occurring between 40 °C and 50 °C

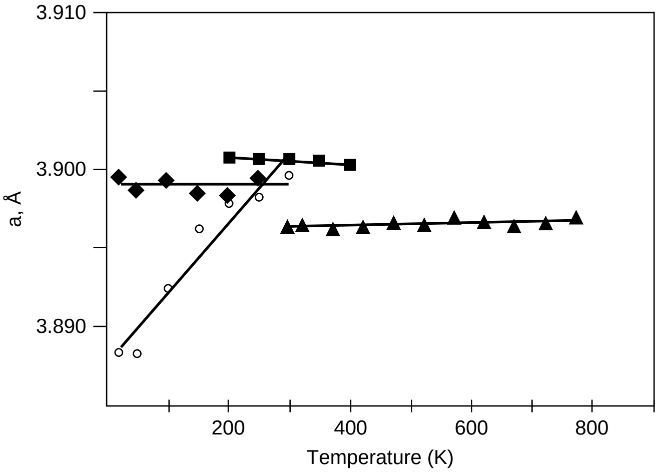

Figure 29 Changes in cubic unit cell dimensions for a phase, NbO_2F, with positive cell expansion and TaO_2F showing near zero expansion. (Reprinted from Tao and Sleight[24] © Elsevier 2003)

over which the measurements were made yields the desired volume expansion coefficients.

9 AB INITIO STRUCTURE DETERMINATION FROM POWDER DIFFRACTION DATA

With the advancement in many facets of powder diffraction including sources, sampling techniques, detectors and software, in particular, with the availability of high speed computing, ab initio structure determination from PXRD data has become increasingly feasible even for systems of reasonable complexity.[6,27] Also, the structure determination is becoming progressively automated starting from the raw powder data all the way to the structure refinement, with minimum assistance from the user, for at least simple structures. Complexity of the structures that can be solved with the availability of synchrotron X-ray sources is also ever increasing. We discuss below some of the fundamental aspects of ab initio structure determination. A flow chart on the different steps involved in ab initio structure determination is given in Figure 31.

9.1 Software Available for Different Steps Toward ab initio Structure Determination

Data collection software is generally supplied by the instrument manufacturers. This data collection software would also normally be equipped to perform preliminary analysis including peak finding routines and search/match of powder diffraction patterns from a database. The most popular database for powder diffraction data is maintained by the International Centre for Diffraction Data.[28]

Although approximate peak positions could be obtained from many different types of software, programs which use peak shape functions to fit the powder diffraction peak profiles are more appropriate to determine the peak position more precisely. Some of the common programs are XFIT,[29] TOPAS,[30] etc.

For autoindexing software, see Section 4.2.5 for details.

Space group possibilities based on systematic absences can be obtained from the International Tables for X-ray Crystallography, or can also be determined using CHEKCELL.[a]

For structure solution software, see Section 9.3 for details.

A number of software programs are known for structure refinement. The most common programs used are FULLPROF,[b] GSAS,[c] RIETAN,[31] and TOPAS.[30]

Some of the software can perform several steps toward structure determination, for example, DASH,[32] TOPAS,[30] POWDERSOLVE,[33] etc.

Various programs have specific advantages and limitations. The website www.ccp14.ac.uk maintains a list of public domain software and their details. It also gives the most recent advancements in current and new software.

9.2 Profile Fitting

There are a multitude of applications for profile fitting: accurate peak position determination, stress and strain

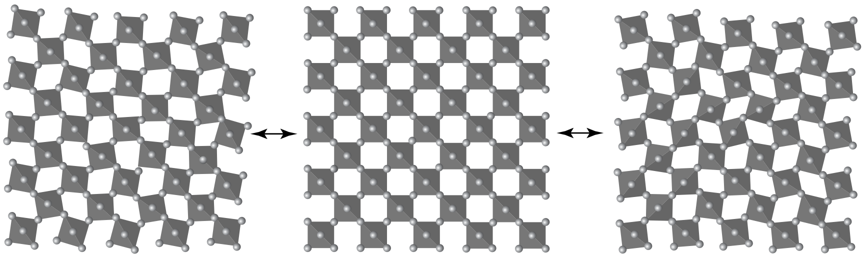

Figure 30 Rocking of the ReO_3 structure indicating possible correlation of the transverse thermal motions of the oxygen atoms. The octahedra do not change volume on rocking, but the distance between the octahedra decreases as they rock away from the structure in the middle producing negative thermal expansion. (Reprinted from Tao and Sleight[24] © Elsevier 2003)

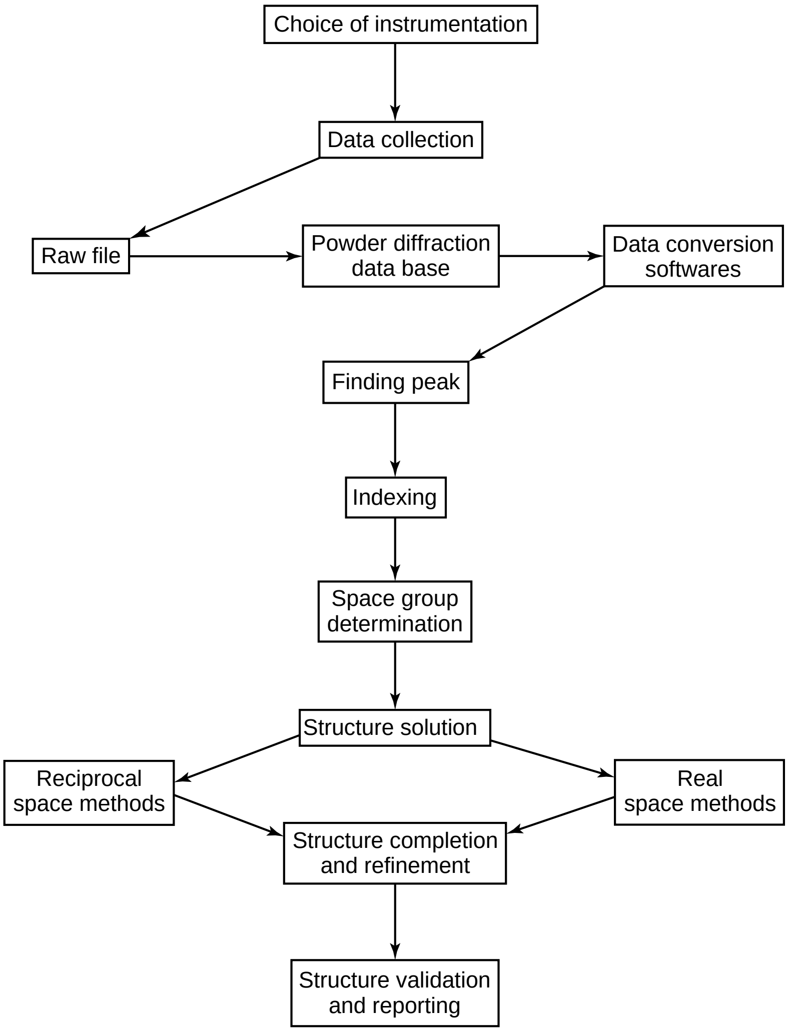
Choice of instrumentation
Data collection
Raw file
Powder diffraction data base
Data conversion softwares
Finding peak
Indexing
Space group determination
Structure solution
Reciprocal space methods
Real space methods
Structure completion and refinement
Structure validation and reporting

Figure 31 Various steps involved in ab initio structure determination from PXRD

analysis, intensity extraction for ab initio structure solution, etc.[6,34]

9.2.1 *Peak Position determination*

Accurate peak position is very important for determining the unit cell constants using various autoindexing programs. The peak position obtained by visual judgment of the peak height maximum suffers in samples showing (i) pronounced asymmetry, (ii) significant transparency, (iii) considerable peak overlap, etc. Under such circumstances, profile fitting individual or overlapping peaks using one of the common peak profile functions, namely, Gaussian, Lorentzian, Pseudo-voigt, or Pearson-VII provides improved peak position for indexing. Also, use of the fundamental parameter approach, implemented in some of the programs such as TOPAS, in addition to giving more accurate peak positions, can also give a rough estimate of particle sizes.

9.2.2 *Full-Profile Fitting*

As the name indicates, fitting the complete powder diffraction profile as a function of intensities, background and a peak shape function is full-profile fitting.[34]

In addition to extracting the integrated intensities, full-profile fitting provides a useful means to establish the truthfulness of the unit cell constants, and the choice of space group of a powder pattern. Although space group determination can be done by the examination of the systematic absences, in PXRD, due to exact and accidental overlap of the peaks, a knowledge of systematic absences would lead only to the extinction symbol. More recently, methods based upon Bayesian probability theory have been successfully used to estimate the most probable space groups, by using integrated intensity covariance matrix obtained by profile fitting using one of the profile fitting methods.

There are three common methods used for full-profile fitting, namely, Le Bail method,[35] Pawley method,[36] and fundamental parameter approach for extraction of integrated intensity data from powder diffraction patterns. These methods are also often called pattern decomposition methods.

The Pawley method is a method of least squares analysis where parameters that depend on the intensities, namely, atomic coordinates, displacement parameters, etc., are ignored and refinement is against the intensities themselves.

The Le Bail method is a clever extension of the original work of Rietveld. The key difference between the two methods is that the Le Bail method uses iteratively the values of intensities obtained from the previous least squares cycle, and assumes unit values for all the peaks to initiate the refinement. Rietveld's method, on the other hand, uses the intensities calculated based on an initial model for the structure.

Both the Pawley and Le Bail methods of intensity extraction or pattern decomposition have their own benefits and shortcomings.

The fundamental parameters approach[37] has been recently implemented in some of the current programs. It gives, to a certain extent, physical meaning to the parameters involved in pattern decomposition. This method attempts to model the contributions from various instrumental components (such as monochromators, slits) and geometry to the observed peak profile shapes. Since this is done considering the relevant physics involved from the generation, diffraction, and detection of PXRD, it leads to more physical meaning than the two methods described earlier. This method can be used not only to perform full pattern decomposition, but also effectively to do a standardless refinement of the sample effects such as crystallite size and microstrain.

9.3 Structure Solution

Structure solution in powder diffraction[27] is approached by two different methodologies. One is using the conventional reciprocal space methods. The second is by real space methods where all the known details about the sample (say, molecular details such as bond distances, angles, etc., for an organic molecule, and coordination spheres such as octahedral, tetrahedral etc., in case of inorganic compounds) in question are exploited to solve the structure.

9.3.1 *Reciprocal Space Methods*

In theory single crystal methods can be effectively used for structure solution from powder diffraction X-ray data. However, in powder diffraction the number of peaks involved are limited, and hence the data-to-parameter ratio is very small, due to the transfer of the three-dimensional data to one dimension, namely, 2θ. In spite of the inherent shortcomings, conventional crystallographic methods such as Direct, Patterson and maximum entropy methods have been successfully applied to powder diffraction data. The most popular program, which uses reciprocal space methods for structure solution is EXPO.[38]

In Direct methods, the intensities are extracted from an indexed powder diffraction pattern by profile fitting procedures such as the Le Bail method and Pawley method. Then the integrated intensities obtained are corrected for Lorentz polarization and normalized. These corrected intensity values are then subjected to routine Direct-method procedures. The structural model obtained is completed using difference Fourier maps. This method works successfully when a sufficient number of intensities could be extracted from the powder diffraction pattern.

Patterson methods have also been successfully used for structure solution from powder diffraction data. By taking advantage of the Patterson function $|F_{\vec{h}}|$, useful information about the crystal structure can be deduced. Compared to Direct methods, Patterson techniques are more suitable for powder diffraction data with lower resolution, and peak overlap causing significant difficulties. The Patterson function can be calculated by using the equation

$$P(\vec{u}) = \frac{1}{V^2}\sum_{\vec{h}} |F_{\vec{h}}|^2 \exp(2\pi i\vec{h}\cdot\vec{u}) \qquad (37)$$

where, $|F_{\vec{h}}|^2$ are the extracted intensity structure factors at the reciprocal point $\vec{h}$. The vector $\vec{u}_{ij}$ from the origin to a peak in the Patterson map corresponds to a vector $\vec{x}_i - \vec{x}_j$ between two atoms at positions $\vec{x}_i$ and $\vec{x}_j$ in the real space lattice. By this approach, usually the heavy atoms in the unit cell are located. Then by incorporating these atoms and doing several least squares cycles, and by analyzing the difference Fourier map the structural model is completed.

Modifications of the original Patterson methods have been designed to improve on the success rates for powder diffraction applications. Maximum entropy methods based on Patterson maps have also been developed.[27]

9.3.2 *Real Space Methods*

The real space methods have become possible with ever increasing computational power. In real space methods, all the known information about the compound in question is input into the unit cell. Based on the supplied information, a powder pattern is calculated. An agreement factor between the observed and the calculated pattern is estimated. Then the structural model is tuned based on the agreement factor. One of the real space methods, namely, simulated annealing (SA), which is based on a Monte Carlo approach, can be related to the physical crystallization from a melt, where at high temperatures the molecules/atoms are at higher energy and hence higher randomness. As the temperature decreases the energy of the system decreases and crystallizes into the thermodynamically stable crystal. In a similar process, several thousands of molecular configurations are tested. At higher temperatures of simulation, jumping between different configurations with larger residual differences are accepted, and as the temperature decreases the perturbations in the configurations are decreased. With every change in the arrangement of the molecule in question, the agreement factor between the observed powder pattern and the pattern generated based on the model is calculated; in the process the configuration with lowest reliability factor is saved in. This process works well with organic, and pharmaceutical compounds. As the whole hypersurface is not examined in this process, it is possible that the SA process would end in a false minimum. For this reason, more than one SA process is carried out to confirm the minimum. In a related process, parallel tempering (PT), instead of using one SA chain with decreasing temperature, several parallel optimizations are run simultaneously, each with a different temperature. After regular intervals, exchange of configurations is allowed between the parallel chains, with the same rules of probability within a single chain. This allows any configuration caught in a local minimum to come out of it to a higher temperature and hence increases the possibility of finding the true minimum. Although PT needs exhaustive computational power compared to SA, with modern computers this becomes absolutely feasible. DASH[32] and FOX[39,40] are two programs that have implemented SA and PT, respectively. These programs have been successfully used to solve several crystal structures from powder diffraction patterns. FOX, in particular, is friendly for solving both molecular and nonmolecular structures.

Other methods such as Genetic Algorithm based on evolution principles, maximum entropy method based on Bayesian theory, and maximum likelihood methods have also been developed.[27]

The choice of whether to use the conventional reciprocal space approach or the modern real space method depends on the quality of the powder diffraction and the complexity of the problem in hand.

9.4 Structure Refinement or Rietveld Refinement

A structural model obtained either from a database (such as ICSD, CCDC, etc.) or from the ab initio structure solution method is refined with the observed powder pattern by a nonlinear least squares method to obtain accurate values of various parameters involved.[6,41] The residual, S_y, is minimized:

$$S_y = \sum_i w_i (y_{io} - y_{ic})^2 \tag{38}$$

where, $w_i = 1/y_{io}$, y_{io} is the observed intensity at the ith step, and y_{ic} is the corresponding calculated intensity. This procedure is popularly known as *Rietveld-Refinement* (also known as Rietveld-method or Rietveld-analysis). Although the method was initially developed for constant wavelength neutron diffraction data, it has been widely extended to accommodate PXRD data, and time of flight data as well.

The powder pattern (i.e. the intensity at the ith step, y_i) is calculated from the structural model by including the structure factor contributions from the Bragg reflections (taking into account the neighboring reflections, if necessary), and various factors that influence the intensity including Lorentz, polarization, and multiplicity factors, a function to define the profile, PO, absorption effects, and the background.

Several reliability factors are defined to compare the observed pattern *vs.* the pattern calculated based on the model. Most common are the weighted profile R-factor (R_{wp}), profile R-factor (R_p), Bragg R-factor (R_B), and goodness of fit (S) or its square (χ^2). These are defined as follows:

$$R_{wp} = \left\{ \frac{\sum w_i (y_{io} - y_{ic})^2}{\sum w_i (y_{io})^2} \right\}^{1/2} \tag{39}$$

$$R_p = \frac{\sum |y_{io} - y_{ic}|}{\sum y_{io}} \tag{40}$$

$$R_B = \frac{\sum |I_{Ko} - I_{Kc}|}{\sum I_{Ko}} \tag{41}$$

$$\chi^2 = \left(\frac{R_{wp}}{R_{\text{exp}}} \right)^2 \tag{42}$$

where, I_{Ko} and I_{Kc} are the observed and calculated intensity of the Kth Bragg reflection at the end of refinement cycles. $R_{\text{exp}} = \left[(N - P)/\sum w_i y_{io}\right]^{1/2}$ (N and P represent the number of data points and number of refined parameters, respectively).

In the presence of several minima close to the true one, it is often possible to get trapped into local false minima. This is more true when restraints and/or constraints are used in the refinement. There is no foolproof procedure that will lead to a global (true) minimum instead of a false minimum. A practical way is to test the minimization by varying the starting model and verifying that the same minimum is reached on refinement. When Rietveld refinement is carried out, it is important to understand the sequence in which the parameters could be ‘‘turned on’’ for refinement. Although, there is no simple rule for this, from experience, some of the parameters, which are known beforehand and dependent on the instrument, for example zero shift (known from instrument alignment), peak shape functions, etc., can be fixed to their known values. If accurate lattice parameters were known from a full-profile fitting, by the Pawley or Le Bail method, it can be fixed until near the end of refinement. It is also important to understand the parameters that correlate with each other, say zero shift and sample displacement errors, occupancy and thermal parameters, etc. If possible these correlating parameters should not be allowed to vary simultaneously until a stable refinement is reached.

There will always be a question of when to stop carrying out the refinement cycles. Perhaps the best way to decide on this is to make sure the variations in the parameters involved in the refinement change the model within acceptable standard deviations. Also, the model, in addition to explaining the observed powder pattern, must also make absolute chemical sense (*e.g.* bond distances, angles, torsions) and should justify other properties observed for the sample in question.

Rietveld-analysis can be used to handle more than one phase. This ability has been exploited to perform accurate quantitative analysis. The results obtained are reasonably precise and have been used extensively, for example, in the cement industry.

10 END NOTES

[a] CHEKCELL, by J. Laugier & B. Bochu [E' cole Nationale Supe' rieure de Physique de Grenoble (INPG), Saint Martin d'He‘ res, France], is a modified version of Celref (http://www.ccp14.ac.uk/tutorial/lmgp).

[b] FullProf.98 and WinPLOTR: by J. Rodriguez-Carvajal, and T. Roisnel, New Windows 95/NT Applications for Diffraction Commission For Powder Diffraction, International Union for Crystallography, Newletter N°20 (May-August) 1998.

[c] GSAS. General Structure Analysis System. by Larson, A. C. & Von Dreele, R. B. Los Alamos National Laboratory, NM, USA. 1995.

11 ABBREVIATIONS AND ACRONYMS

DTA = differential thermal analysis; FCC = face centered cubic; FWHM = full width at half maximum; ICDD = international center for diffraction data; JCPDS = joint committee on powder diffraction standards; LP = Lorentz and polarization; PO = Preferred orientation. PT = parallel tempering; PXRD = powder X-ray diffraction; SA = simulated annealing; SWL = short-wavelength-limit; TGA = thermogravametric analysis; XRPD = X-ray powder diffraction; XRD = X-ray diffraction;

12 FURTHER READING

B. O. Cullity and S. R. Stock, 'Elements of X-Ray Diffraction', 3rd Edition, Prentice Hall, Upper Saddle River, 2001, Excellent treatment of powder methods in general. Includes phase-diagram determination, polycrystalline aggregates, polymers, quantitative analysis and stress analysis.

J. Faber and T. Fawcett, *Acta Crystallogr.*, 2002, **B58**, 325.

T. Hahn ed., 'International Tables for Crystallography', 5th revised edition, International Union of Crystallography by Kluwer Academic Publishers, Boston/Dordrecht/London, 2002, Vol. A.

R. Jenkins and R. L. Snyder, 'Introduction to X-Ray Powder Diffractometry', John Wiley & Sons, New York, 1996, Excellent introductory material, diffraction theory, instrumentation, and data acquisition and treatment.

S. N. Kahekkodu, J. Faber and T. Fawcett, *Acta Crystallogr.*, 2002, **B58**, 333.

H. P. Klug and L. E. Alexander, 'X-Ray Diffraction Procedures', 2nd edition, John & Wiley Sons, New York, 1974, A very comprehensive treatment. X-ray powder methods including line-broadening analysis, texture determination, stress measurement and studies of amorphous materials.

V. Pecharsky and P. Zavalij, 'Fundamentals of Powder Diffraction and Structural Characterization of Materials', Springer, Berlin, 2005, Comprehensive treatment of all aspects of powder diffractometry and determination of crystal structures from powder data. Contains up to date information on software for X-ray powder studies. Also contains an extensive list of additional texts and key journal articles.

U. Shmueli ed., 'International Tables for Crystallography', International Union of Crystallography by Kluwer Academic Publishers, Boston/Dordrecht/London, 2001, Vol. B.

C. Suryanarayana and M. G. Norton, 'X-Ray Diffraction, A. Practical Approach', Plenum Press, New York, 1998, An excellent elementary introduction to powder methods with worked examples and exercises that allow the reader to work through determination of unit cell dimensions, crystallite size, strain and quantitative phase analysis. Highly recommended for the novice.

A. J. C. Wilson and E. Prince eds., 'International Tables for Crystallography', International Union of Crystallography by Kluwer Academic Publishers, Boston/Dordrecht/London, 1999, Vol. C.

L. S. Zevin and G. Kimmel, in 'Quantitative X-Ray Diffractometry', ed. I. Mureinik, Springer, New York, 1995, More mathematical in nature with rigorous treatment of quantitative phase analysis. Contains a chapter on industrial applications.

13 REFERENCES

1. D. Louer and E. J. Mittemeijer, 'Powder Diffraction in Materials Science', European Powder Diffraction Conference, Barcelona, Trans Tech Publications, 2001, p. 5.
2. J. I. Langford and D. Louer, *Rep. Prog. Phys.*, 1996, **59**, 131.
3. B. D. Cullity and S. R. Stock, 'Elements of X-Ray Diffraction', 3rd edition, Prentice Hall, Upper Saddle River, 2001.
4. R. Jenkins and R. L. Snyder, in 'Chemical Analysis, A Series of Monographs on Analytical Chemistry and its Applications', ed. J. D. Winefordner, John Wiley & Sons, New York, 1996.
5. V. E. Buhrke, R. Jenkins and D. K. Smith, 'A Practical Guide for the Preparation of Specimens for X-Ray Fluorescence and X-Ray Diffraction Analysis', Wiley-VCH, New York, 1998.
6. V. Pecharsky and P. Zavalij, 'Fundamentals of Powder Diffraction and Structural Characterization of Materials', Springer, Berlin, 2005.
7. J. P. Cline and R. L. Snyder, in 'Advances in Materials Characterization II', eds. R. L. Snyder, R. A. Condrate and P. F. Johnson, Plenum Press, New York, 1985, p. 131.

8. C. Suryanarayana and M. G. Norton, ‘X-Ray Diffraction, A Practical Approach’, Plenum Press, New York, 1998, p. 153.
9. P.-E. Werner, in ‘Structure Determination from Powder Diffraction Data’, eds. W. I. F. David, K. Shankland, L. B. McCusker and C. Baerlocher, Oxford University Press, New York, 2002, p. 118.
10. P.-E. Werner, L. Eriksson and M. Westdahl, *J. Appl. Crystallogr.*, 1985, **18**, 367.
11. A. Boultif and D. Louer, *J. Appl. Crystallogr.*, 1991, **24**, 987.
12. J. W. Visser, *J. Appl. Crystallogr.*, 1969, **2**, 89.
13. A. L. Bail, *Powder Diffr.*, 2004, **19**, 249.
14. J. Bergmann and R. Kleeberg, *IUCr CPD Newslett.*, 1999, **21**, 5.
15. M. A. Neuman, *J. Appl. Crystallogr.*, 2003, **36**, 356.
16. A. A. Coelho, *J. Appl. Crystallogr.*, 2003, **36**, 86.
17. E. W. Nuffield, ‘X-Ray Diffraction Methods’, John Wiley & Sons, 1966, p. 155.
18. W. N. Schreiner, C. Surdukowski and R. Jenkins, *J. Appl. Crystallogr.*, 1982, **15**, 605.
19. J. Gubicza, J. Szépvölgyi, I. Mohai, L. Zsoldos and T. Ungár, *Mater. Sci. Eng.*, 2000, **A280**, 263.
20. D. Balzar, N. Audedrand, M. R. Daymond, A. Fitch, A. Hewat, J. I. Langford, A. L. Bail, D. Louer, O. Masson, C. N. McCowan, N. C. Popa, P. W. Stephens and B. H. Toby, *J. Appl. Crystallogr.*, 2004, **37**, 911.
21. L. S. Zevin and G. Kimmel, ‘Quantitative X-Ray Diffractometry’, Springer, New York, 1995.
22. M. M. Gomez-Alcantara, A. Cabeza, M. Martinez-Lara, M. A. G. Aranda, R. Suau, N. Bhuvanesh and A. Clearfield, *Inorg. Chem.*, 2004, **43**, 5283.
23. A. Cabeza, M. A. G. Aranda, S. Bruque, D. M. Poojary, A. Clearfield and J. Sanz, *Inorg. Chem.*, 1998, **37**, 4168.
24. J. Z. Tao and A. W. Sleight, *J. Solid State Chem.*, 2003, **173**, 45.
25. T. G. Fawcett, P. M. Kirchhoff and R. A. Newman, in ‘Advances in X-Ray Analysis’, eds. C. R. Hubbard, C. S. Barrett, P. K. Predecki and D. E. Leydon, Plenum Press, New York, 1983, p. 171.
26. A. W. Sleight, *Inorg. Chem.*, 1998, **37**, 2854.
27. W. I. F. David, K. Shankland, L. B. McCusker and C. Baerlocher eds., ‘Structure Determination from Powder Diffraction Data’, Oxford University Press, New York, 2002.
28. J. Faber and T. G. Fawcett, *Acta Crystallogr.*, 2002, **B58**, 325.
29. R. W. Cheary and A. A. Coelho, ‘Programs XFIT and Fourya’, CCP14 Powder diffraction library — Daresbury Laboratory, Warrington, 1996.
30. A. A. Coelho, ‘TOPAS User Manual’, Version 3.1, Bruker AXS GmbH, Karlsruhe, 2003.
31. F. Izumi and T. Ikeda, ‘A Rietveld-Analysis Program RIETAN-98 and Its Applications to Zeolites’, EPDIC 6, Sixth European Powder Diffraction Conference, R. Delhez and E. J. Mittemeijer (ed.) Trans Tech Publications, 2000, p. 198.
32. W. I. F. David, K. Shankland and N. Shankland, *Chem. Commun.*, 1998, 931.
33. G. E. Engel, S. Wilke, O. Donig, K. D. M. Harris and F. J. J. Leusen, *J. Appl. Crystallogr.*, 1999, **32**, 1169.
34. W. I. F. David and D. S. Sivia, in ‘Structure Determination from Powder Diffraction Data’, eds. W. I. F. David, K. Shankland, L. B. McCusker and C. Baerlocher, Oxford University Press, New York, 2002, p. 136.
35. A. Lebail, H. Duroy and J. L. Fourquet, *Mater. Res. Bull.*, 1988, **23**, 447.
36. G. S. Pawley, *J. Appl. Crystallogr.*, 1981, **14**, 357.
37. R. W. Cheary and A. A. Coelho, *J. Appl. Crystallogr.*, 1992, **25**, 109.
38. A. Altomare, C. Giacovazzo, A. Grazia, G. Moliterni and R. Rizzi, *J. Res. Natl. Inst. Stand. Technol.*, 2004, **109**, 125.
39. R. Çerný and V. Favre-Nicolin, *Powder Diffr.*, 2005, **20**, 359.
40. V. Favre-Nicolin and R. Çerný, *Z. Kristallogr.*, 2004, **219**, 847.
41. R. A. Young ed. ‘The Rietveld Method’, Oxford University Press, New York, 1993.

Circular Dichroism (CD) Spectroscopy

P. Anthony Presta and Martin J. Stillman

University of Western Ontario, London, ON, Canada

	Method Summary	1
1	Introduction	2
2	Technical Background	2
3	Applications	3
4	Acknowledgments	15
5	Abbreviations and Acronyms	15
6	References	15

METHOD SUMMARY

Acronyms, Synonyms

- Circular Dichroism (CD)
- Optical Rotatory Dispersion (ORD).

Measured physical quantities

- CD spectroscopy measures the difference in absorbance between left- and right-circularly polarized incident radiation, in the near ultraviolet to visible and infrared regions of the spectrum.
- ORD uses plane polarized light and provides the degree of rotation of plane polarized light as an angle.

Information available

When ORD can specifically provide information it is mentioned, otherwise the following information is for CD primarily:

- presence of chiral chromophores (both CD and ORD)
- relative amounts of α-helix and β-sheet secondary structure in protein molecules
- changes in all degrees of structure in biological molecules
- denaturation as a function of structure, readily determined using CD spectral data as a function of a physical (e.g., temperature) or chemical (e.g., pH, denaturant) change
- monitoring of structural and metal ion-ligand changes in metalloprotein complexes by titration experiments
- metal-ligand stoichiometry
- metal-ligand coordination geometry.

Information not available, limitations

- Chromophore must be chiral for any information to be obtained.
- Metal-ligand binding information is inferred from changes in spectral titrations, but specific bonds between a metal atom and its ligating atoms cannot be assigned.
- Metal atoms with high energy absorbance bands (that absorb in the far ultraviolet) cannot be directly probed; these include the alkali metals and alkaline earth metals.

Examples of questions that can be answered

- What are the stoichiometries of the major complexes between a metal ion M^{n+} and a protein ligand?
- How does metal substitution occur when a different metal ion with higher binding affinity to the protein is added to a solution of an existing metal-protein ligand complex?

- How does the protein morphology or secondary structure change upon metal binding?
- What are the identities of the protein atoms that bind to the metal ion (e.g., Cotton effect question, especially for Fe binding)?
- Is the compound analytically pure?
- Is the chirality opposite that of the enantiomer?

Major advantages

- The method obtains highly reproducible information on metal-ligand changes as the titration experiment proceeds.
- CD signals can be compared to the analogous absorbance spectra for distinguishing metal binding.
- Chiral chromophores are discernible in samples with multiple overlapping absorbance bands.
- Sample can be combined with other spectroscopic techniques in ‘‘real time’’.
- CD spectra in particular are immune to solvent effects and therefore can provide exceptionally good data on the chirality of a molecule with absorption bands distributed throughout the optical spectrum.

Major disadvantages

- Much of the structural information for metal-ligand binding (coordination number, stoichiometry) is inferred by the titration; confirmation of structural information is required by other techniques.
- Analytical uses cannot be estimated prior to use of a pure sample. Estimation of the rotation (in ORD) and the signal intensity (in CD) cannot be carried out.
- The absolute sign of the rotation or the CD signal cannot be calculated (+ or −) currently.

Sample constraints

- Soluble samples are the easiest.
- Scatter from frozen samples can cause significant baseline deviations in CD experiments.
- Samples must contain a chiral chromophore that absorbs in the near ultraviolet to infrared region.

1 INTRODUCTION

Circular dichroism (CD) spectroscopy is a method that measures the difference in the absorbance of left- and right-circularly polarized light as a function of the energy of the radiation (but usually reported as the wavelength of the light) by chiral chromophores. The absorbing chromophore may be a chiral center due to asymmetric coordination chemistry, as in the example of the chiral Cotton effect due to the asymmetric coordination chemistry of iron complexes. Alternatively, the chromophore may display an induced chirality brought about by the formation of three-dimensional bonding structures. This is the case in chiral structures such as the α-helix or β-sheet conformations found in peptide chains, and commonly referred to as the secondary structures of proteins and polypeptides. Similar delocalized chiral chromophores resulting from induction of the specific three-dimensional structure are also observed in metal-ligand clusters. These structures are commonly found in proteins chelating a variety of metal ions. Moreover, the variety of possible metal-binding side-chain functionalities in the amino acids within the protein chain, the changes in metal-ligand stoichiometry, variable metal coordination chemistry, and the possibility of intermolecular cross-linking all can result in changes to the three-dimensional structure of the chromophore, with concomitant profound changes in the resultant CD spectrum of the sample. These specific changes in the CD spectrum allow detailed study of metal-binding properties.

There is a formidable and varied array of metal ions that participate in biological systems, both as essential cofactors within the cells and organs of the living organism or as toxic elements deleterious to the organism. Metal ions in vivo are principally found chelated to proteins and polypeptides, owing to the wide variety of negative dipole functional groups (usually with oxygen, nitrogen, or sulfur as the ligating atom from the amino acid side chains of the protein) attracted to the positive metal ions. A great deal of research has been conducted and remains ongoing to define and elucidate the roles and unique chemistry that the various metal ions play in biological systems, specifically as metal-protein complexes.

In general, the type of information that is of greatest interest when discussing metal-protein chemistry include the following: (1) changes in stability of the protein resulting from changes in protein secondary structure; (2) identification of the ligating functional group of the protein; (3) the oxidation state of the metal ion; (4) the coordination number of the metal ion; (5) the metal-to-ligand stoichiometry; and (6) changes in metal-protein reactivity.

2 TECHNICAL BACKGROUND

2.1 Measuring CD Spectra

The easiest way to obtain a CD spectrum is to use a spectropolarimeter. In these instruments the signal is plotted as the ellipticity of the emerging radiation after passage through a sample, $\theta = (2.303/4)(A_l - A_r)$ with units of radians as a function of the wavelength of the light, θ vs. λ in units of nm usually.

When reduced to units of degrees, $\theta = 2.303(A_l - A_r)(180/4\pi) = 32.98\Delta A_{L-R}$

The molar quantity is given by: $[\theta] = 3298(\varepsilon_L - \varepsilon_R) = 3298\Delta\varepsilon_{L-R}$, where the 3298 converts the L M^{-1} cm^{-1} unit of molar absorptivity (ε) to the 0.1 L M^{-1} cm^{-1} units of molar ellipticity.

It is easier, and to some extent more useful, to quote CD spectral data in terms of ΔA_{L-R} for solutions without known concentrations and $\Delta\varepsilon_{L-R}$ when concentrations are known. This then can match data from the associated magnetic CD spectroscopy (*see* ***Magnetic Circular Dichroism (MCD) Spectroscopy***).

Reporting CD spectral data as $\Delta\varepsilon_{L-R}$ vs. λ in nm is good practice.

Most CD spectropolarimeters must be calibrated. A common way is to compare the absorption and CD spectra of ammonium (+)-d10-camphorsulfonate (ACS) using a solution nominally 1 mg mL^{-1} in a 1 mm cell. Using the absorption at 285 nm ($\varepsilon_{285\,\text{nm}} = 34.5$ M^{-1} cm^{-1}) to determine the concentration, the positive CD band at 290 nm may be used for calibration $\Delta\varepsilon_{291\,\text{nm}} = 2.36$. A negative band at 190 nm can be used as well to extend the calibration into the UV region.

Of major concern in measuring CD spectra, is the absorbance of the solvent. Whereas in the electronic absorption spectrum (*see* ***Electronic Spectroscopy***) all components can be measured if the blank is simply set to be the empty cuvette or air in the double beam instrument, in the CD experiment, the nonchiral components are not ‘‘seen’’ or recorded in the CD spectrum yet they absorb light and can easily reduce the CD spectral data to useless lines. In reality, this only becomes a major problem when solvents and buffers begin to absorb below about 300 nm. Although, we should note that great care should be taken to keep the absorption low (may be less than 0.6) for the CD spectra of porphyrinoids, especially in the Q−band region from 580 to 800 nm. However, the problem is insidious in that after the measurement has been made, it is not possible to determine if the background absorbance precluded accurate measurement.

What goes wrong? The CD intensities start being nonlinear with respect to concentration of the absorbing species when the background absorbance (and instrument insensitivity) results in the controlled DC voltage of the photomultiplier tube losing its lock. Most instruments maintain this DC voltage by changing the applied dynode volts of the photomultiplier tube within its working range. The gain on the photomultiplier tube is increased by increasing the dynode voltage, which concomitantly increases the noise of the measurement. As the light striking the photomultiplier tube decreases (because of increased background absorbance), so the dynode voltage increases. When no more gain can be obtained, the signal starts being nonlinear and eventually the photomultiplier reports totally erroneous CD signals. Remembering that an absorbance of 1 allows transmission of only 10% of the incident light, and an absorbance of 2 allows transmittance of just 1% of the incident light, it is easy to see that with solvent or buffer, most of the light may be absorbed. CD spectrometers typically do not measure linearly for total sample absorbance above 1.0.

2.2 Choice of Cuvettes

Continuing with the theme of obtaining CD spectral data unaffected by the nonchiral components, including the solvent, leads us to consider the cuvette. As described above, one must be very careful to check that the cuvette, solvent, and all other components do not absorb significantly in the region of interest. This becomes a concern in the UV- and IR-regions of the spectrum. As an example, for spectra below 190 nm, fused silica windows are beneficial and the sample compartment must be purged of O_2 with N_2 gas, because O_2 has absorption lines near 178 nm (O_2 must also be purged from the lamp and monochromator to reduce the build up of O_3). Because the concentration of the solvent (including all components, notably buffers) is so high, cells with pathlengths down to 0.01 cm should be used. For all measurements below 200 nm, it would be wise to use a series of cuvettes, with pathlengths of 0.05, 0.1 and 0.2 cm to confirm linearity of the CD signal.

Strain in the cuvette (from the windows themselves, from misalignment, etc.) can result in significant distortions in the CD spectrum recorded. It is essential that a solvent blank be measured with the cuvette in *exactly* the same orientation to be used with the sample. It is good practice to mark the cuvette so it is placed with the same window facing the lamp. Many other factors can contribute to depolarizing distortion that will result in incorrect spectral data; it is wise to be very careful with cuvette choice and testing, especially below 200 nm and below room temperature.

A final word of caution extends to the quality of the lamp. Xe lamps darken quite quickly with age, so long before the lamp should be replaced (say at 1000 h), the far-UV output will have diminished. This makes the head-room for absorbing species much less. Opening the slits can help, but then spectral resolution is lost. Always using two or three cuvettes for setting up these measurements will provide confirming evidence that the measurements are real.

3 APPLICATIONS

3.1 Identification of Protein Secondary Structure

CD spectroscopy has long been used as a simple and direct technique to assess the extent of folding within the protein structure, as well as the type of secondary structure adopted by the protein.[1] In general, proteins with α-helical structure display negative CD signals in the far-UV region at 208 and 222 nm. The second signal is typically used to estimate the α-helix content of a protein. Comparatively, the β-sheet conformation within the protein is characterized by a signal at 215 nm, which may be sinusoidal in nature.

The simplicity of performing this protein secondary structure analysis makes CD spectroscopy useful in monitoring protein conformational changes between wild-type and mutant proteins, as well as in identifying changes in the protein secondary structure upon addition of a bound cofactor such as a metal ion. Several recent examples of applying CD spectroscopy for these purposes are now described.

Yamniuk *et al.* report the use of CD spectroscopy to measure the structural changes in calcium- and integrin-binding protein upon addition of the divalent metal ions Ca^{2+} and Mg^{2+} to the metal-free apoprotein.[2] They found increases in the α-helical content of the protein of over 30% when either of the metal ions was added to the protein. Futaki *et al.* showed that the α-helical character of a model peptide could be destabilized by the addition of ferric ion.[3] This destabilization of the secondary structure was indicated by suppression of the 222 nm signal upon addition of Fe^{3+}. The authors concluded a possible ferric/ferrous redox control of the helical structure of the peptide.

Dai *et al.* reported that intermolecular associations within the γ-carboxyglutamate-rich neuroactive peptide conantokin-G could be promoted specifically by the binding of Ca^{2+} ions to the protein.[4] The binding of Ca^{2+} was found to favor an α-helical structure important for intermolecular cysteine–cysteine cross-linking. Interestingly, other divalent metal ions (Mg^{2+}, Zn^{2+}, and Mn^{2+}) bound to the protein with greater increase in α-helical content of the protein as observed in their respective CD spectra as compared to Ca^{2+} binding, but did not promote the intermolecular cross-linking.

Murphy *et al.* used CD spectroscopy to monitor the secondary structure of a novel human-derived apyrase (human soluble calcium-activated nucleotidase-1 (hSCAN)) in the presence and absence of calcium ion binding.[5] Their study indicated that although Ca^{2+} was essential for enzymatic activity, the binding of Ca^{2+} was not accompanied by any observable changes in the secondary structure, as the calcium-free protein displayed a β-sheet conformation that was not altered upon Ca^{2+} addition. By comparison, in a study by Tickler *et al.*,[6] CD spectroscopy was used to monitor changes in secondary structure of wild-type amyloid-β peptide (Aβ40) and its methylated histidine imidazole equivalents [Aβ40(HisτMe)] and [Aβ40(HisπMe)].[6] This study demonstrated that the binding of Cu^{2+} to the wild-type peptide and to the π-nitrogen methylated imidazole peptide was accompanied by a conformational shift from random coil to predominantly β-sheet structure.

The increase in β-sheet content in the peptide accelerates the peptides susceptibility to form aggregates.[7] The further indication that the modified peptide analog methylated at the τ histidine imidazole nitrogen did not change conformation upon Cu^{2+} binding supports the idea that it is these imidazole nitrogens within the amyloid-β peptide that form bridging structures leading to the oligomerization of the peptide.

The finding that metal binding by a peptide leads to preferred α-helix structure within the peptide was also indicated in a study by Wang *et al.* using CD spectroscopy to monitor the metal-peptide structure[8] (Figure 1). The authors prepared a five-residue peptide that models the metal-binding site of the olfactory receptor protein. They found that upon addition of up to one Cu^{2+} equivalent, the CD signal changes from one characteristic of a random peptide structure to one with the double minima at 209 and 222 nm characteristic of α-helix peptide structure.

Interestingly, α-helicity is very uncommon for a peptide of less than 15 residues, suggesting that binding to the metal ion is essential for creating and maintaining the peptide structure. This structure is thought to require a tetrahedrally coordinated metal ion such as Cu^{2+}, Zn^{2+}, or Ni^{2+}. Using the spectroscopic and structural data for the metal-bound peptide, the authors indicated that the ligation of the metal ion occurs with coordination to one histidinyl nitrogen atom, a cysteinyl sulfur atom, a glutamate oxygen atom, and one solvent molecule that can be replaced by an odorant molecule. This binding is consistent with the 1:1 metal ion:peptide binding ratio observed spectroscopically.

The ability of CD spectroscopy to monitor changes in protein secondary structure is also used to assess the stability

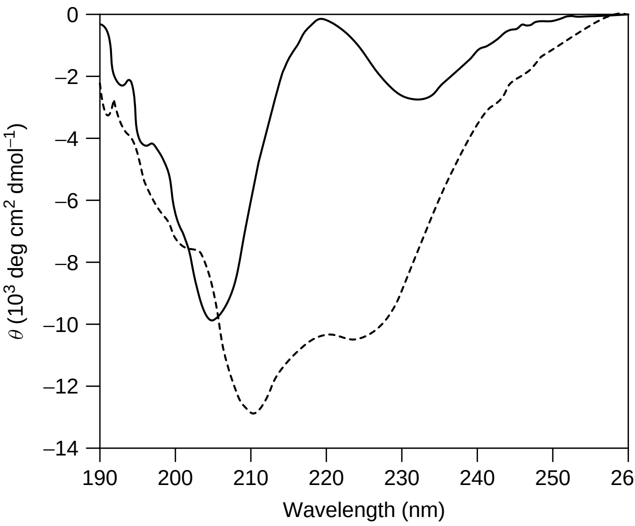

Figure 1 Far-UV CD spectrum of HAKCE peptide, in the absence of metal ions (solid line) and in the presence of 1.0 equivalent of Cu(II) added (dotted line); 20 mM peptide, pH 7.4 potassium phosphate buffer, 298 K. (Wang, J., Luthey-Schulten, Z. A., Suslick, K. S. (2003) *Proc. Natl. Acad. Sci.* USA **100**:3035–3039. © 2003 National Academy of Sciences, USA)

of the protein toward thermal or chemical denaturation. This is especially applicable when comparing the structural stability of the protein in the absence and presence of bound metal ions. A number of recent studies have employed CD spectroscopy for this purpose.

Golynskiy *et al.* used the CD signal at 222 nm characteristic of the α-helical protein conformation to monitor the thermal denaturation of the metalloregulatory protein MntR, a manganese(II)-responsive transcription factor in *Bacillus subtilis*[9] (Figure 2). In the metal-free form, the protein displayed a melting temperature of about 67 °C. Addition of Mg^{2+} or Ca^{2+} had no effect on the melting temperature of the protein. However, the *d*-group divalent metal ions Mn^{2+}, Co^{2+}, Ni^{2+}, and Cd^{2+} increased the thermal stability of the protein such that the melting temperature increased by 15 to 30 °C upon addition of these metals (Figure 2).

The thermal stability of wild-type peptides and modified analogs in the absence and presence of bound metal ions was also measured using CD spectroscopy in studies by Sissi *et al.*[10] and by Cox *et al.*[11]

In a separate study by Kovári *et al.*, the authors report the use of CD spectroscopy to study the binding of Mg^{2+} to the DNA repair enzyme dUTPase.[12] This enzyme catalyzes the hydrolysis of uracil triphosphate (UTP) to uracil monophosphate and inorganic pyrophosphate, leading to removal of excess uracil. The Mg^{2+} ion is an essential cofactor for enzyme activity. CD spectroscopy indicated that Mg^{2+} binding modulates the conformation of the enzyme allowing for enhanced formation of the enzyme-substrate complex. Binding of the Mg^{2+} ion and the subsequent binding of the UTP substrate also lead to increased stability of the enzyme toward proteolytic digestion by trypsin.

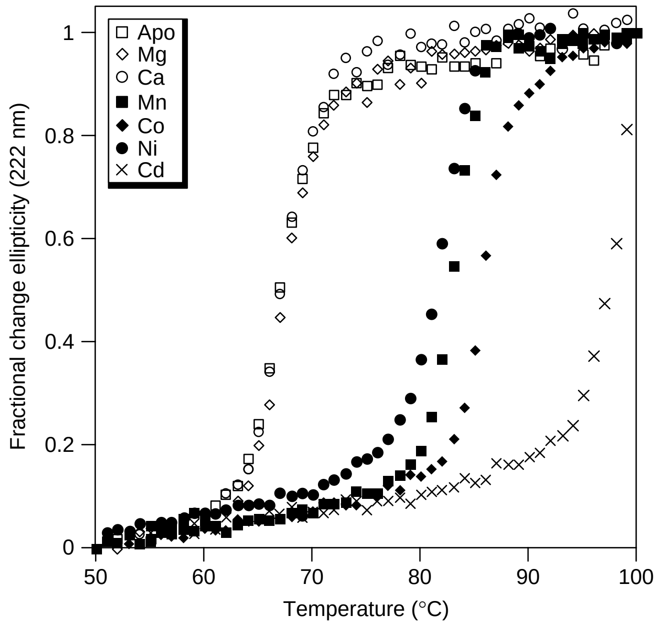

Figure 2 Thermal denaturation curves for wild-type MntR (8 µM) monitored by CD spectroscopy at 222 nm: unfolding of apo MntR (open squares) and of MntR in the presence of 1.0 mM Mg^{2+}, Ca^{2+}, Mn^{2+}, Co^{2+}, Ni^{2+}, and Cd^{2+}. Buffer 20 mM HEPES, pH 7.2 at 4 °C, 200 mM NaCl, 5% (v/v) glycerol. Pathlength 2 mm. (Reprinted with permission from Golynskiy, Davis, Helmann and Cohen.[9] © 2005 American Chemical Society)

CD spectroscopy has also provided valuable insight into the chemical stability and chemical denaturation of proteins. A recent study by Rumfeldt *et al.*[13] examines the guanidinium-chloride induced denaturation of mutant copper-zinc superoxide dismutases (SODs).[13] These mutant forms of the Cu, Zn-SOD enzyme are associated with toxic protein aggregation responsible for the pathology of amyotrophic lateral sclerosis. In this study, CD spectroscopy was used in conjunction with tryptophan fluorescence, enzyme activity, and sedimentation experiments to study the mechanism by which the mutated enzyme undergoes chemical denaturation. The authors found that the mutations in the enzyme structure increased the susceptibility of the enzyme to form partially unfolded destabilized monomers, rather than the stable metallated monomer intermediate or native metallated dimer.

Ghosh *et al.* also used CD spectroscopy to assess the association affinities of peptide coils in the absence and presence of bound Hg^{2+} or Cd^{2+}.[14] These authors constructed a family of peptides having secondary structures that bind metal ions in a trigonal thiolate coordination environment, even metal ions like Hg^{2+} and Cd^{2+} that prefer tetrahedral coordination geometries. Their results indicate increased stability of coiled-coil peptide structures upon addition and binding of the metal ions, and support the hypothesis that favorable tertiary interactions within the protein systems allow for stabilizing the non-preferred coordination geometry of the bound metal ions.

While the study by Ghosh *et al.*[14] examined the use of CD spectroscopy to elucidate metal ion coordination chemistry as a result of the stabilization of specific secondary structures within the peptide, CD spectroscopy can also directly probe the binding environment and coordination chemistry of metal ions bound to protein ligands. This is the case when functional groups on the peptide chain bind metal ions with the formation of asymmetric metal-ligand clusters due to bond constraints within the peptide structure. This asymmetry in the metal ion environment leads to chiral chromophores centered at the metal ion. This is especially the case when clusters of metal ions are bound within a protein structure by bridging peptide ligands between the metal ions. The chiral electronic transitions that are most often observed in these instances are ligand-to-metal charge transfer (LMCT) transitions most common with *d*-shell metal ions.

Many *d*-block metals (Groups 3–12) have important roles in biological systems, both as essential cofactors within a variety of cellular processes, and as interfering species that are toxic to the cell and organism. These metals exist in biological systems as ions that are often bound to proteins and peptides with the exhibition of unique coordination geometries, such that these species become of interest to the inorganic chemist as well as the biological scientist. Because of the ubiquitous nature of the interaction of *d*-shell metal ions with biological molecules and the inherent sophistication of the metal ion chemistry when bound to the biological molecules, tools that have sought to explain the character of metal-protein binding, including CD spectroscopy, have mainly been applied to the binding of the following metal ions by protein or peptide ligands: Fe^{2+} and Fe^{3+}, Cu^{+} and Cu^{2+}, and the Group 12 triad of Zn^{2+}, Cd^{2+}, and Hg^{2+}. The applications of CD spectroscopy to the understanding of metal-protein binding, structure, and reactivity are herein presented with focus on these metal ions, followed by brief descriptions of CD spectral studies of protein molecules binding other metal ions less common to biological environments. Finally, we highlight the use of CD spectroscopy in the determination of speciation in the protein metallothionein.

3.2 CD Spectra of: Complexes of the Group 8–10 Transition Metals

The formation of metal-protein complexes of the transition metals has been an area of intense research, with CD spectroscopy providing essential insights into the structural, electronic and stoichiometric properties of the complexes. The binding of iron ions to proteins has provided the greatest amount of results. As with copper ions, iron complexation with biological ligands is of interest due to iron being both an essential element and a potentially toxic element, as well as the wide range of complexes that iron ions form because of two different stable oxidation states (Fe^{2+} and Fe^{3+}) and the variety of protein ligands and structural motifs that the iron cations may adopt.

The binding of iron to a model miniaturized protein has been reported by Lombardi *et al.*[15] The miniaturized protein was constructed based on the tetrahedral tetrathiolate $[S\text{-}Cys]_4$ iron-binding site of the rubredoxin protein, and named miniaturized electron transfer protein (METP). The far-UV CD spectrum of the apoprotein and of the Fe^{3+} complex indicate that the protein structure changes from an unordered peptide chain in the metal-free state to an ordered α-helical structure with negative CD bands at 204 nm and 222 nm upon addition of Fe^{3+}. In the near-UV and visible regions of the spectrum, the Fe^{3+}-METP complex displays a strong Cotton effect with signals at 580 nm (+), 500 nm (−), 440 nm (+), 370 nm (+), and 315 nm (−). In the metal-reduced complex of Fe^{2+}-METP, CD signals are observed at 280 nm (+), 305 nm (−), and 320 nm (+). These spectral characteristics, as well as those for the Co^{2+}-METP complex, are similar to the CD spectra of natural and reconstituted rubredoxin, confirming that the same metal-binding environment was maintained in the model system relative to the natural protein.

Multi-thiolate iron-protein clusters are also found in the ferredoxin family of electron transport proteins. In particular, the interconversion between ferredoxin clusters containing three iron atoms and other clusters containing four iron atoms was the subject of research by Jung *et al.*[16] It was found that the replacement of one cysteine residue central to the metal-binding site with an aspartate residue allowed for the conversion of the redox active site from $[4Fe\text{-}4S]^{2+/+}$ to the $[3Fe\text{-}4S]^{+/0}$ cluster. CD spectroscopy is very sensitive to the type of iron-sulfur cluster that is formed within the protein. Native ferredoxin has CD spectra with signals at 310 nm (+), 395 nm (+), 470 nm (+), and 580 nm (+) for the ferric protein, and 360 nm (+), 405 nm (+), 450 nm (−), 510 nm (+), and 580 nm (+) for the ferrous protein. The mutated protein with substitution of a central cysteine → aspartate displayed CD spectra for both the oxidized and reduced forms that were very similar to those for the native ferredoxin protein. This indicates that the mutated protein has iron atoms ligated by only three thiolate cysteine residues, without a distant cysteine providing a fourth thiolate ligand to the cluster. Supporting crystallography data indicate that the aspartate residue itself provides the fourth ligand to the Fe-S cluster through a carboxyl oxygen atom.

CD spectroscopy has also been used to study the metal-binding and reactivity properties of iron- and manganese-containing SODs. These enzymes metabolize the superoxide ion radical $O_2^{\bullet-}$ into molecular oxygen and hydrogen peroxide. The Fe- and Mn-SOD enzymes are strictly metal specific. Jackson and Brunold[17] show that, despite the fact that Fe replacement of Mn in the Mn-SOD enzyme [(Mn → Fe)-SOD] results in an inactive enzyme, the CD spectrum of wild-type Fe-SOD and (Mn → Fe)-SOD are remarkably similar. This suggests that the destroyed enzyme activity, upon replacement of the metal, does not occur via distortion of the enzyme active site.

CD spectroscopy of the Fe-heme binding site of a protein has also been used to monitor the binding of other metal ions to a protein. Hemopexin is a plasma protein that binds free heme, reducing the extent of iron loss and preventing possible oxidative damage that would be catalyzed by free heme. Hemopexin has also been shown to bind other metal ions. Mauk *et al*. indirectly studied the binding of Cu^{2+} and Zn^{2+} to hemopexin by monitoring the CD Soret signal of the heme iron group within this protein[18] (Figure 3). Addition of up to 18 equivalents of either Cu^{2+} or Zn^{2+} altered the CD signal from a bisignate Soret with maximum at 415 nm and minimum at 430 nm, to a positive Cotton signal centered at 420 nm.

These changes were reversed upon addition of excess EDTA. The changes in the CD spectrum caused by Cu^{2+} or Zn^{2+} addition to hemopexin suggest structural or electrostatic perturbations in the vicinity of the heme group by the added metal ions. The authors indicate that binding of Cu^{2+} or Zn^{2+} to hemopexin may play a role in exchanging ligands to the bound heme group, possibly leading to dissociation of the heme complex from the protein.

In comparison to the large amount of research that has been conducted on copper and iron complexes of biological

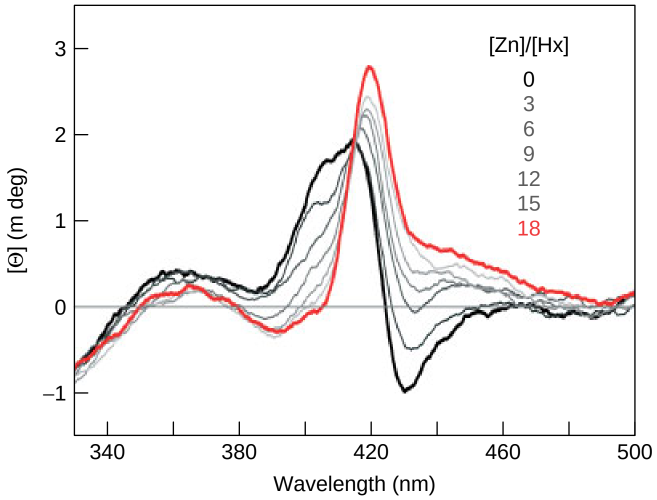

Figure 3 Effect of Zn^{2+} binding on the CD spectrum of the hemopexin (Hx)-heme complex: the Hx-heme complex (thick black curve), additions of 3–15 equiv of Zn^{2+} (thin black curve), and addition of 18 equiv of Zn^{2+} (red curve). The Hx-heme concentration is 8 µM, with 50 mM bisTris buffer and 50 mM sodium chloride (pH 7.0, 25 °C). (Reprinted with permission from Mauk, Rosell, Lelj-Garolla, Moore and Mauk.[18] © 2005 American Chemical Society)

ligands, similar information with other metal ions is relatively sparse. Vanadium is an essential trace element with a very complex inorganic chemistry, owing to its multiple stable oxidation states and its chelation by a variety of ligand donors. Tasiopolous *et al*. synthesized and characterized dipeptide complexes of V^{3+} and oxovanadium(IV) (VO^{2+}) as possible models of vanadium-protein interactions.[19] The dipeptides used in this study all contained glycine as one residue, with alanine, valine, or phenylalanine as the second amino acid. 1,10–phenanthroline was also present as an additional ligand. Part of the characterization of these complexes included CD spectroscopic analysis of the complexes in solution and in the solid state. The authors report that the V^{3+}–dipeptide complexes with phenanthroline had CD spectral signals that were too weak to be measured in solution. However, in the solid state the V^{3+} complexes displayed visible CD signals at about 740 to 780 nm (+), 480 to 550 nm (−), and 420 to 490 nm (+). By contrast, the VO^{2+} analogues of these dipeptide complexes had much stronger CD spectral signals that could be measured in solution. CD signals were observed at 725 to 735 nm (+), 470 to 480 nm (−), and 395 to 410 nm (+). In the solid state, the VO^{2+}-dipeptide phenanthroline complexes were characterized by strong signals at 770 to 800 nm (+), 550 to 570 nm (+), and 465 to 485 nm (−). The two lower wavelength signals are inverted in sign relative to the V^{3+} complexes. These CD signals may be used as a spectral fingerprint of octahedral VO^{2+} complexes with $N_{amine}–N_{peptide}–O_{carboxylate}$ ligation.

The chemistry of cobalt with biological ligands has been an area of increasing research owing to the role of this metal as an essential trace element, for example, as a cofactor in the vitamin B_{12} molecule, and as a possible mimic of the biological chemistry of other metal ions. Cobalt binds to biological ligands predominantly as the divalent ion, such that its bioinorganic chemistry is expected to be similar to other d-shell divalent metal ions like Zn^{2+}, Cu^{2+}, or Fe^{2+}. The Co^{2+} ion also displays d–d electronic transitions in the visible region of the spectrum which can be easily monitored by CD spectroscopy during a binding experiment.

Zhu *et al*. studied the metal-binding properties of copper chaperone proteins using CD spectroscopy by addition of Co^{2+} as a mimic of copper binding.[20] The authors of this study compared the binding of Co^{2+} to two different copper chaperone proteins, from Tomato copper chaperone for superoxide dismutase (tCCS) and human copper chaperone for superoxide dismutase (hCCS) sources. Both of these proteins are comprised of three structural domains. The tomato protein sequence includes four cysteine residues, two cysteines in each of domains 1 and 3, which were expected to be responsible for metal ion ligation. The human protein has nine cysteine residues with 3, 4, and 2 cysteines in the three respective domains of the protein. The main structural difference between the copper chaperone homologs is that the tomato protein has no cysteine residues in its second domain while the human protein has four cysteines in this domain. Moreover, this domain in hCCS has a great extent of sequence homology with the Zn^{2+} binding site of Cu,Zn-superoxide dismutases. Thus it is expected that divalent metal ions bind to domain 2 of hCCS with high affinity in a tetrahedral M^{2+}-$Scys_4$ geometry.

Addition of Co^{2+} to metal-free hCCS initially leads to minimal changes in the CD spectrum, up to addition of one equivalent of the metal ion. Further, addition of a second equivalent of Co^{2+} results in significant alterations to the CD spectrum, with strong signals appearing at 380 nm (+), 505 nm (−), and 610 nm (+). From these results the authors conclude that the binding of Co^{2+} to hCCS occurs first with one equivalent binding to the tetra-cysteinyl domain 2 with a symmetric tetrahedral binding geometry, followed by the binding of a second Co^{2+} to four of the remaining cysteine residues of domains 1 and 3 in a chiral distorted tetrahedral structure.[20]

Addition of Co^{2+} to tomato CCS resulted in the immediate formation of strong CD signals at 395 nm (+), 520 nm (−), and 620 nm (+). The spectrum reached saturation after addition of one Co^{2+} equivalent, at which point the spectrum was almost superimposable to the CD spectrum resulting from addition of two Co^{2+} equivalents to hCCS. Removal of the domain 1 cysteine residues resulted in much weaker CD signals. These data further indicate that the binding of Co^{2+} to cysteine residues across domains 1 and 3 of the CCS proteins results in a highly optically active distorted tetrahedral structure with Co^{2+} bound to four cysteine ligands.

3.3 CD Spectra of Group 11 Metals

Most of the research that has examined the binding of Group 11 metal ions to biological molecules has focused on the binding of copper ions. There are a number of reasons for this, including the range of biological molecules that bind copper ions, the fact that copper is both an essential element acting as a cofactor in numerous enzymatic processes while being potentially toxic at elevated concentrations, the various coordination geometries that copper can adopt, and different binding characteristics between the monovalent and divalent oxidation states of copper ions.

As a general rule, monovalent copper ions bind exclusively to cysteine thiolate ligands of proteins and peptides. The bound Cu$^+$ ions usually adopt the trigonal planar coordination geometry, although digonal binding geometries are sometimes observed, especially with bridging thiolate ligands. As with the Group 12 metal ions, the use of CD spectroscopy to probe the binding of Cu$^+$ to metallothioneins has been a very rich area of research in terms of the biological and inorganic chemistry of the Cu$^+$-thiolate cluster formation. Studies that have examined Cu$^+$ binding to metallothioneins using CD spectroscopy are also discussed within the separate Section (3.6) on metal binding to the metallothioneins.

CD spectroscopy has also been used to monitor Cu$^+$ binding to a copper-transporting protein, the P-type ATPase ATP7B found to be involved in Wilson's disease, a disorder characterized by over-accumulation of copper in liver cells and other sites[21] (Figure 4). It was found that the addition of Cu$^+$ (by reduction of added Cu^{2+} with dithiothreitol) had the most dramatic effect on a peptide derived from the ATPase that contained three cysteine residues, two of which were separated by a single proline residue to give a –CPC–motif. Moreover, the authors of this study examined the nature of the CD spectral bands in order to formulate a hypothesis regarding the speciation of the Cu$^+$-peptide complexes. In this study, four well-resolved signals were detected including a maximum at 270 nm, a double minimum at 290 nm and 320 nm, and another maximum signal centered at 354 nm.

The CD signals in the near-UV to visible region are typically LMCT transitions. The authors also suggest that the higher wavelength signal at 354 nm may be assigned to a spin-forbidden $3d \rightarrow 4s$ metal cluster-centered transition that is favored by d^{10}–d^{10} interactions of adjacent Cu$^+$ ions. These transitions would require multiple Cu$^+$ ions binding in close proximity to each other, with bridging thiolate ligation necessary for the assembly of these clusters. The presence of these bridged Cu$^+$-thiolate clusters is also associated

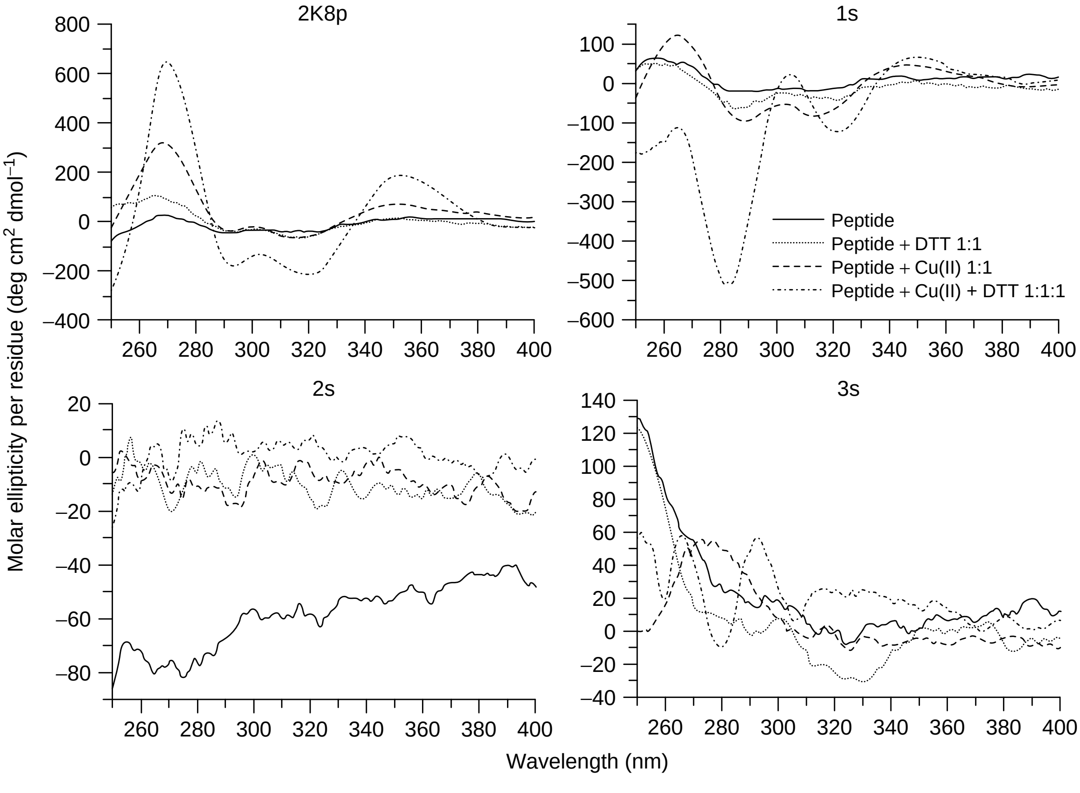

Figure 4 Changes in the CD spectra of variants of ATP7B, 2K8p and the mutants 1s, 2s and 3s in the region 250–400 nm induced by the addition of Cu(II) and DTT (peptide, solid line; peptide + DTT, dot; peptide + Cu(II) 1:1, dash; peptide + Cu(II) + DTT, dash dot). (Reprinted from Myari, Hadjiliadis, Fatemi and Sarkar.[21] © Elsevier 2004)

with the formation of oligomeric species. The equilibrium between the formation of the monomeric Cu^+-thiolate species with only terminal thiolate ligation and formation of the oligomeric bridged Cu^+-thiolate clusters is dependent on the stoichiometric ratio of added Cu^+ to peptide concentration.

Another class of copper transport proteins that have been studied using CD spectroscopy are the copper chaperone proteins. Two copper chaperones, one from *B. subtilis*[22] and another from *Enterococcus hirae*,[22] have recently been examined. The work of Kihlken *et al*. demonstrated that Cu^+ binds to the *B. subtilis* chaperone protein CopZ in three phases.[21] The first phase lasts up to a Cu^+: protein ratio of 0.5:1, and is characterized by the growth of CD signals at 265 nm (+) and 287 nm (−). The second phase of Cu^+ binding to the CopZ protein extends from 0.5 up to 1.0 Cu^+ equivalent per protein. This second phase is characterized by a shift and weakening of the 265 nm signal to about 275 nm, and the growth of a broad negative band that is centered at about 335 nm. The final phase of Cu^+ binding to the CopZ protein lasts up to a Cu^+: protein ratio of 1.5:1. This final phase is characterized by the formation of a derivative-shaped CD signal with a minimum at 265 nm, a maximum at 287 nm, and a sharp isodichroic point at 280 nm. Carrying out the titration in the presence of dithiothreitol, a small molecule-reducing agent that may also act as a sulfur donor ligand, limits the Cu^+-CopZ binding mechanism to the first phase only. Along with results from analytical ultracentrifugation and gel-filtration experiments, this CD study for Cu^+ binding to CopZ concluded that the binding of Cu^+ initially results in the assembly of a dimeric complex with a single metal center. Further addition of Cu^+ leads to formation of a second dimeric species with two Cu^+ ions bound by four cysteine thiolate sulfur atoms. In this species, two of the cysteine sulfur ligands (one from each peptide subunit) are bridging ligands, leading to closer Cu^+-Cu^+ interactions. These metal-centered interactions may be responsible for the higher wavelength CD signal that is observed during the second phase of the Cu^+ titration. In the third phase of the titration, the dimeric structure is thought to be conserved with an additional Cu^+ center within the metal-thiolate cluster.

For Cu^+ binding to the CopZ protein from *E. hirae*, Urvoas *et al*. also observed the formation of a dimeric species with a stoichiometric ratio of two protein subunits to one Cu^+ ion.[23] These authors also report that the dimeric species can be changed to a monomeric complex by the addition of the copper-coordinating molecule glutathione.

As we have seen, the electronic spectra of Cu^+ complexes are dominated by LMCT and metal-ligand charge transfer (MLCT) transitions in the near-UV and UV regions only under specific conditions of metal loading and bridging ligation within the metal-protein cluster. No $d-d$ transitions are possible. By comparison, the loss of a d-shell electron to give the Cu^{2+} ion results in the formation of complexes in which the electronic spectra are dominated by transitions in the visible region.

Ganadu *et al*. have presented CD spectroscopic evidence for complex formation between Cu^{2+} and the $\alpha\beta$-crystallin protein.[24] This protein is a structural protein of the eye lens that functions as a stress response protein, presumably as a molecular chaperone involved in protecting denatured proteins from aggregation. The chaperone-like activity of $\alpha\beta$-crystallin is enhanced in the presence of the Cu^{2+} ion, indicating that the protein contains a binding site for this metal ion. The CD spectrum of the $\alpha\beta$-crystallin protein with Cu^{2+} added is composed of a band at 343 nm, which becomes more enhanced with increased pH. This signal is ascribed to an imidazole $N \rightarrow Cu$ charge transfer (CT) transition, suggesting that a histidine residue is one of the ligands of the Cu^{2+} ion. The CD spectrum of the Cu^{2+}-protein complex also shows a strong derivative-shaped signal in the visible region, with a negative band at 550 nm and positive band at about 650 nm. This signal is consistent with a Cotton effect typical for the chiral $d-d$ electronic transitions of optically active Cu^{2+} complexes.

A further example of the use of CD spectroscopy to monitor Cu^{2+}-protein complex formation is the binding of this ion to the amyloid β-peptide. This peptide is composed of 40 to 43 amino acids residues and is the principal component of the aggregates or plaques associated with neurodegenerative disorders such as Alzheimer's disease. The ability of this peptide to bind metal ions has been well documented. In fact, it has been shown that Cu^{2+} and Fe^{3+} induce the formation of β-amyloid aggregates.[25] A study by Kowalik-Jankoska *et al*.[26] sought to elucidate the binding of Cu^{2+} to the amyloid β-peptide from human and mouse sources. The authors used CD spectroscopy and EPR spectroscopy (*see* ***Electron Paramagnetic Resonance (EPR) Spectroscopy***) to elucidate Cu^{2+}-peptide complex formation with different fragments of the peptide under a variety of solution conditions. The authors showed that in all cases of Cu^{2+} binding to the various peptide fragments, the CD spectrum is composed of $d-d$ transitions in the visible region from 480 nm to 670 nm, and LMCT transitions assigned to (i) imidazole $N \rightarrow Cu$ transitions in the near-UV region from 320 nm to 370 nm, (ii) amide $N \rightarrow Cu$ transitions at wavelengths from 310 nm to 320 nm, and (iii) amino $N \rightarrow Cu$ transitions in the region below 300 nm. The intensities and signs of the CD bands, along with complementary data from EPR spectroscopic experiments, are used to arrive at a distribution of Cu^{2+}-amyloid β-peptide species under different conditions of pH and Cu^{2+} loading.

In a similar way, the binding of Cu^{2+} to another protein involved in neurodegenerative disease has also been studied using CD spectroscopy. The prion protein is a membrane-associated glycoprotein that undergoes an alteration from a monomeric form to an oligomeric protease-resistant form leading to its toxic effects. It has been suggested that the prion protein plays a role in copper metabolism.[27,28] The amino-terminal end of the prion protein is rich in histidine and glycine residues, and is believed to be the metal-binding site of the protein. Specifically, the mammalian prion protein contains a highly conserved region of four repeats of the eight residue sequence –PHGGGWGQ–, the so-called octarepeat sequence. Separate studies by Aronoff-Spencer *et al.*[29] and La Mendola *et al.*[30] have examined the speciation of Cu^{2+}-prion protein complexes using CD spectroscopy, in addition to other spectroscopic techniques. The CD spectra demonstrate the visible region d–d transitions and imidazole N → Cu CT transitions observed in other Cu^{2+}-protein complexes with imidazole and amide ligation. Specifically, in the study by Aronoff-Spencer *et al.*, the data are indicative of a 1:1 stoichiometry between Cu^{2+} and the aforementioned octarepeat, such that the histidine imidazole provides one ligand to the Cu^{2+} ion and glycine amide groups provide additional ligation of the metal ion.[29]

In addition to studying the binding of Cu^{2+} to known metal-binding proteins, CD spectroscopy has also been used to characterize a novel putative metal-binding protein. Barney *et al.* report on the isolation of a small (9.9 kiloDalton) protein (SmbP) from the periplasm of the ammonia-oxidizing bacterium *Nitrosomonas europaea*[31] (Figure 5). The authors found that this protein was expressed in the bacterium in response to Cu^{2+} addition to the growth medium, suggesting that this novel protein plays a role in cellular copper metabolism. To characterize the protein, they prepared the metal-free protein and titrated with increasing equivalents of Cu^{2+}.

In the far-UV region, the apoprotein displayed the CD signal characteristic of α-helix secondary structure with double minima at 209 nm and 222 nm. This region of the CD spectrum was unchanged with addition of Cu^{2+}. However, the visible region of the CD spectrum showed dramatic changes during titration of the protein with Cu^{2+}. A positive band was observed at about 490 nm with addition of the first equivalent of the Cu^{2+} ion, which remained unchanged with further Cu^{2+} addition. This band is ascribed to a histidine imidazole N → Cu CT transition. Further addition of Cu^{2+} was accompanied by the formation of a derivative-shaped CD signal with minimum at 580 nm and maximum at 760 nm. These transitions are Cu^{2+}-centered d–d transitions, and their relative energies are suggestive of mixed ligation by nitrogen and oxygen donor ligands. The sequence of this novel protein indicates the absence of any cysteine residues and a large proportion of histidine, aspartate, and glutamate residues, consistent with the suggested ligation of the Cu^{2+} ions. With further addition of Cu^{2+} equivalents, the visible region CD signals increase in intensity in a relatively linear manner up to 5 to 6 equivalents of Cu^{2+} being added. This stoichiometry is further supported by comparable titration experiments monitored by absorbance spectroscopy and EPR spectroscopy. Moreover, a similar titration of the protein with Fe^{3+} revealed absorbance and CD spectral changes up to a stoichiometry of six Fe^{3+} equivalents per protein molecule. From these experiments, the authors propose that the novel protein isolated from *Nitrosomonas europaea* in response to Cu^{2+} is a metal ion scavenger induced to sequester high concentrations of free Cu^{2+}, and possibly other free metal ions as well.

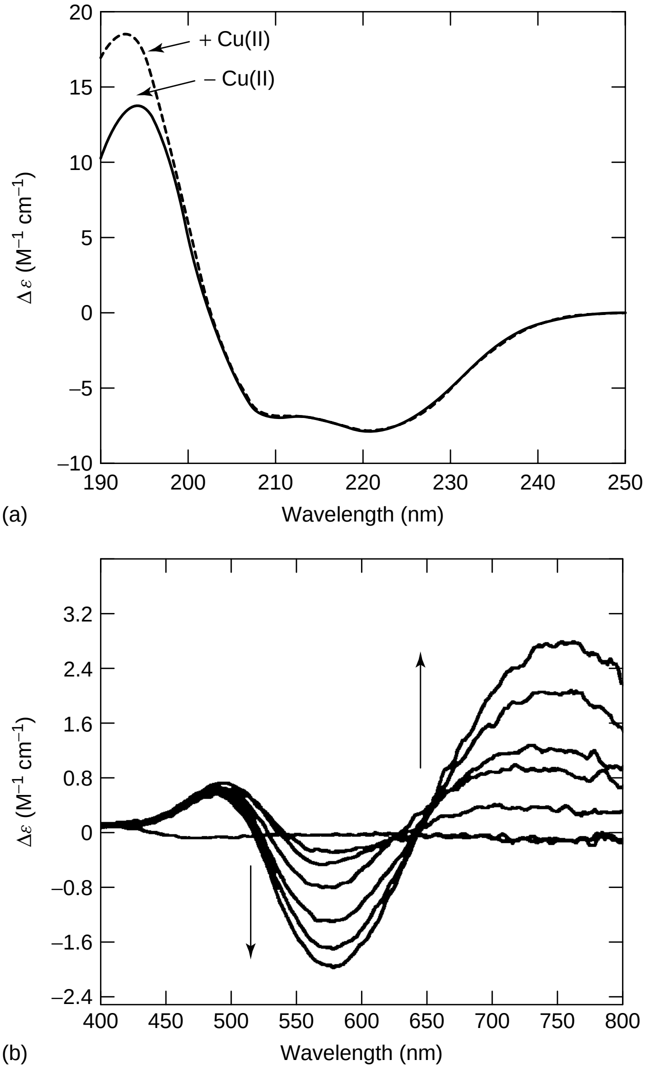

Figure 5 Panel (a) shows the UV CD spectra (190–250 nm) of apo-SmbP and SmbP (25 μM, pH 7.5, no buffer) with 1 equiv of Cu(II) bound. Spectra for 2 and 5 mol equiv of Cu(II) are not shown because they are virtually identical to the 1 mol equiv of Cu(II). Panel (b) shows the visible CD spectra (400–800 nm) of SmbP (250 μM, pH 7.5, no buffer) titrated with increasing equivalents of Cu(II) (0, 0.8, 1.4, 2.7, 3.7, 4.6, and 5.3) from an aqueous solution of $CuCl_2$. Additional mole equivalents of Cu(II) did not result in further changes in the CD spectra. (Reprinted with permission from Barney, LoBrutto and Francisco.[31] © 2004 American Chemical Society)

In addition to the protein complexes of copper ions, CD spectroscopy has also been used to study metal-protein complex formation of the other Group 11 metals, silver, and gold. The Ag^+ ion has been used extensively in metal-protein experiments to act as an analog of Cu^+ complex formation. Ag^+ is comparable to Cu^+ in oxidation state, the types of ligands to which it binds, and often displays equivalent binding geometries to these ligands. Moreover, Ag^+ is easier to work with because of its oxidative stability, as it does not have a higher stable oxidation state to which it can be oxidized, as is the case with Cu^+. However, the structural properties of Ag^+ complexes are not identical to those of Cu^+, likely due to the larger ionic radius of Ag^+ leading to other preferred binding geometries under certain ligand and stoichiometric conditions. For example, the binding of Ag^+ to the metallothioneins results in both similarities and differences in comparison to Cu^+ binding to this family of proteins. These specific results will be discussed in the section on applications of CD spectroscopy with metallothioneins (Section 3.6).

Gold complexes with biological ligands present further structural possibilities because of a different preferred oxidation state, the +3 oxidation state. Marcon *et al.* have employed CD spectroscopy to study complex formation between Au^{3+} and the abundant serum protein albumin.[32] This protein is believed to play a role in extracellular metal ion transport, and may be involved in the exhibited anticancer activity of Au^{3+}-based drugs. The authors determined that bovine serum albumin (BSA) forms very stable complexes with the Au^{3+} compounds $[Au(diethylenetriamine)Cl]^{2+}$ and $[Au(6\text{-}(1,1\text{-dimethylbenzyl})\text{-}2,2'\text{-bipyridine})OH]^+$, such that the metal ion could only be removed from the protein complex by treatment with excess potassium cyanide. The CD spectrum of the BSA complex with the latter of the two Au^{3+} compounds results in the appearance of visible spectrum signals characteristic of Au^{3+} complexes bound within a chiral protein environment. These signals include two negative bands, a strong signal at 405 nm and a weaker band at about 340 nm.

3.4 CD Spectra of Complexes involving Group 12 metals

This group consists of the elements zinc, cadmium, and mercury. Each of these metals binds to ligands as divalent metal ions, and usually adopt the tetrahedral binding geometry. These metal ions often bind to thiolate ligands, such as the cysteine sulfur atoms of proteins and polypeptides, although Zn^{2+} may also bind to the imidazole nitrogen atom of histidine residues. These metal ions are also known to form clusters of multiple metal ions within one protein unit through the chelation by both bridging and terminal peptide residue ligands.

The spectral characteristics of the Group 12 metal ions binding to biological ligands are dominated by the LMCT transitions from the electron-donating ligand atom to the *d*-shell of the metal atom. These transitions occur in the near-UV region of the spectrum, from 230 nm to 360 nm.

We have previously mentioned that Ghosh *et al.* have examined the binding of Cd^{2+} and Hg^{2+} to peptide coils[14] (Figure 6). They found that the metal ions adopted the unusual trigonal planar binding geometry in order to stabilize the coiled-coil structure of the peptides. This group had previously elucidated the binding geometry of the metal ions to these peptides.[33] In this earlier study, the authors found that the placement of the cysteine ligand along the peptide chain had a profound effect on the metal-protein structure as evidenced by complete inversions of the CD spectra.

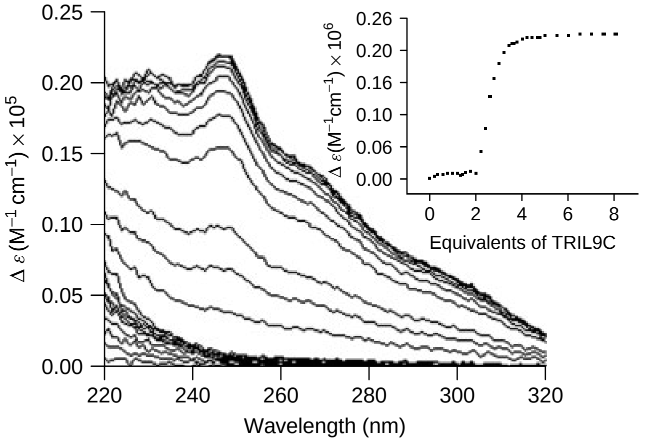

Figure 6 UV-visible titration of TRI L9C into a solution of $Hg^{II}Cl_2$ at pH 8.5. The data are plotted versus wavelength. The inset shows the titration curve following $\Delta\varepsilon$ at 247 nm plotted versus equivalents of peptide added at 247 nm. (Reprinted with permission from Ghosh, Lee, Demeler and Pecoraro.[14] © 2005 American Chemical Society)

The identical energies of the electronic transitions indicate that the coordination geometry of the metal ions, essentially trigonal planar with some trigonal pyramidal character in the Cd^{2+}-bound peptide structure, remained the same regardless of the position of the cysteine ligand. However, the peptide folding around the metal ion was drastically altered upon changing the placement of the cysteine residue, resulting in significant modifications in the constraints placed on the metal-thiolate cluster and different interaction of the chiral center with polarized light accompanied by inversion of the CD spectrum.

The formation of cadmium-protein complexes has also been observed in a protein model of the metal-binding domain of rubredoxin.[34] This protein model contains one Cys–X–X–Cys metal-binding motif. CD spectroscopy indicated that addition of the Cd^{2+} ion to the metal-free protein model resulted in binding of the metal ion with assembly of the protein into a coiled-coil secondary structure. The CD spectrum of the apoprotein model indicated a disordered random structure in the absence of bound metal ions, as evidenced by a major signal at 205 nm and a weak broad band centered at about 220 nm. Binding of Cd^{2+} led to a far-UV CD signal representative of a coiled α-helix structure in the protein model, with strong negative bands centered at 209 nm and 222 nm, and a thiolate $S \rightarrow Cd$ charge transfer transition at about 240 nm. Both the LMCT signal and the CD bands representing the α-helix structure of the protein were destroyed upon oxidation of the cysteine thiolate residues, indicating that the reduced thiolate was required to bind the Cd^{2+} ion leading to stabilization of the α-helix secondary structure of the protein model surrounding the Cd^{2+}-thiolate cluster. Moreover, both CD spectroscopy and UV-visible absorbance spectroscopy were used to monitor the titration of the protein model with increasing relative amounts of Cd^{2+} ions. It was found that the respective changes in the spectral signals occurred up to a Cd^{2+}: protein stoichiometry of 1:2, suggesting that four chelating cysteine thiolates are required to bind one Cd^{2+} ion having a tetrahedral binding geometry, such that the Cd^{2+} ion acts as a bridging atom between two α-helix coiled protein ligands.

Like cadmium, mercury is the subject of significant research owing to its toxicity to living things. Bacterial resistance to mercury poisoning involves a specific periplasmic mercury-binding protein, MerP, and the mercuric reductase enzyme, MerA. Rossy *et al*. have studied the amino-terminal extension of a mercuric reductase that resembles the Hg^{2+}-binding motif of a MerP protein.**[35]** Using CD spectroscopy to monitor Hg^{2+} addition to the MerA amino-terminal extension, the authors noted that Hg^{2+} ion binding occurs with three main characteristics: an increased intensity and blue-shifting of a signal at 265 nm in the metal-free peptide to about 260 nm upon Hg^{2+} addition, the development of a negative CD signal centered at about 290 nm, and a sharp isodichroic point at 270 nm. Changes in the CD spectrum were observed for Hg^{2+} addition up to one mole equivalent with respect to the MerA amino-terminal model peptide, indicating only one metal-binding site within the peptide. The isodichroic point indicates the existence of only two possible states for the peptide, these being the metal-free and Hg^{2+}-bound forms. Moreover, the authors report that the far-UV CD signal did not change upon Hg^{2+} addition, indicating no change in the secondary structure of the peptide with metal binding. The authors propose that the metal-free peptide adopts a structure such that it is poised to bind the metal ion. This may be a critical property of a protein conferring mercury resistance to an organism.

Modeling of the metal-binding characteristics of the mercury-resistance proteins was also the subject of a study by DeSilva *et al*.**[36]** The authors constructed 18-residue peptides with metal-binding sites consisting of two cysteine residues and two alanine residues, with metal-binding site sequences as –CCAA–, –CACA–, or –CAAC–. The binding of each of the Group 12 metal ions, as well as Group 11 metal ions Cu^+ and Ag^+, were monitored by CD spectroscopy. The authors found that Hg^{2+} bound the strongest of any of the metal ions to the peptide containing the –CAAC–motif, and was the only metal ion to bind to the –CCAA–containing peptide. It is thought that the fact that Hg^{2+} can adopt a range of geometries, specifically the linear digonal coordination, allows it to bind to the peptide with the neighboring cysteine residues.

Similar metal-binding motifs are common in various proteins and peptides with metal-binding capabilities. Suzuki *et al*. examined the metal-binding characteristics of one such protein, the heavy metal-binding protein Cdl19 from *Arabidopsis*.**[37]** The authors prepared the 225 amino acid residue amino-terminal peptide containing the –CXXC–metal-binding motif. Addition of Cd^{2+} to the cysteine-containing peptide was accompanied by significant changes in the CD spectrum. These changes were not observed if the cysteine residues were replaced with glycine. Similar spectral changes were also observed upon addition of Cu^{2+} and Hg^{2+}, consistent with chelation of the metal ions by the cysteine thiolate groups of the peptide, but not upon addition of Mn^{2+}, Co^{2+}, or Ca^{2+}.

The formation of metal-protein complexes and clusters containing Group 12 metal ions is further exemplified in the metallothionein class of proteins. Metallothioneins are a ubiquitous class of cysteine-rich polypeptides (approximately one-third of the residues are cysteines) that are known to bind a variety of metal ions as poly-metal thiolate clusters, containing both bridging and terminal thiolate ligation. The binding of the Group 12 metal ions to metallothioneins is discussed in a separate section devoted to the use of CD spectroscopy in monitoring metal-binding within this class of proteins (Section 3.6).

3.5 CD Spectral Data from other Metal Complexes

As we have seen, CD spectroscopy is uniquely sensitive in its ability to monitor both the binding environment of a metal ion within a biological molecule and the structural environment of the entire biological molecule. Determining the predominant secondary structure motifs of a protein or polypeptide is achieved by measuring far-UV CD signals that are characteristic of α-helix or β-sheet conformations. By comparison, the environment of a bound metal ion is monitored through visible to near-UV signals that may originate either from d–d, MLCT or LMCT electronic transitions. For this reason the binding of transition metal ions or of the Group 12 metal ions to protein ligands are most applicably studied by CD spectroscopy via the electronic transitions to their d-shells of specific LMCT bands. Only a few of the heavier main group metal ions display electronic transitions in a range applicable for CD spectroscopy, and of these Pb^{2+} is of significant biological significance due to its known toxicity.

In many ways, metal-ligand complexes containing Pb^{2+} are very similar to the analogous complexes of Hg^{2+}. Both of these ions are large, predominantly divalent, and can adopt a range of binding geometries with various donor ligands, although Hg^{2+} typically binds with higher affinity than Pb^{2+}. Mehra *et al*. used CD spectroscopy to study the binding of Pb^{2+} to the phytochelatins,**[38]** a glutathione-derived class of polypeptides commonly found in plants. These polypeptides have the general structure $(\gamma\text{-Glu–Cys})_n$–Gly, in which n determines the length of the polypeptide chain. As with many of the cysteine-containing polypeptides and proteins that have been discussed, metal ligation by the phytochelatins is almost exclusively via the cysteine S atoms either as terminal or bridging ligands.

Addition of Pb^{2+} to the $n = 2$ phytochelatin (containing two cysteine residues) induced changes in the

CD spectrum including formation of a band at 255 nm (+), a shoulder at about 270 nm (+), a weaker signal at 300 nm (−), and a broad signal centered at 330 nm (+). The CD spectrum became saturated after addition of one equivalent of Pb^{2+} per phytochelatin molecule. The authors concluded from these spectral data that the bound Pb^{2+} adopts a two-coordinate binding geometry when bound to this phytochelatin.[38]

For the $n = 3$ phytochelatin, Pb^{2+} addition resulted in a CD spectrum very different from that for the $n = 2$ phytochelatin. A CD spectrum was formed comprised of a peak at 225 nm (+), a shoulder at 255 nm (+), a broad negative signal in the 270 to 310 nm region, and a slight positive signal at 335 nm. This CD spectrum was again saturated with addition of one Pb^{2+} equivalent to the polypeptide. The spectroscopic and stoichiometric evidences indicate a distinct binding geometry for Pb^{2+} with this phytochelatin, either in a three-coordinate geometry or possibly adopting a distorted tetrahedral geometry with bridging cysteine thiolate ligands to form a multi-metal thiolate cluster.

Titration of the $n = 4$ phytochelatin with Pb^{2+} produced even more interesting results. Up to the addition of 0.75 equivalents of Pb^{2+}, CD bands were formed at 250 nm (+), 300 nm (−), and 325 nm (+). Further addition of Pb^{2+} up to two equivalents resulted in a new CD signal developing at 360 nm (+) and a red-shift of the main positive CD signal from 250 nm to 260 nm. These CD results indicate a shift in the binding geometry adopted by Pb^{2+} bound to the longer phytochelatin. Up to about the first equivalent, the Pb^{2+} binds in a three-coordinate or four-coordinate geometry comparable to that observed with the $n = 3$ phytochelatin. With further Pb^{2+} addition, the binding geometry shifts to two-coordinate. These results are very similar to the binding pattern of Hg^{2+} to the metallothioneins, with lowering of the metal ion coordination number, as more equivalents of the metal ion are added to the polypeptide ligands.

3.6 Metallothioneins: a Special Case of a Metalloprotein with Highly Sensitive Metal-dependent CD Spectral Properties

The protein metallothionein provides an example of a very special metal-induced CD spectrum. The spectrum to the red of 220 nm is entirely due to the presence of LMCT bands. These bands are measured at a range of wavelengths depending on the metal ion bound to the protein.[39] Metallothioneins have been isolated from an extremely wide range of organisms, suggesting that this protein exists throughout biology. Quite a remarkable range of elements bind to the protein both in vivo and in vitro, with As(III) being a recent addition to the list of those elements with detailed stoichiometric data available.[40] Key to the mammalian proteins is a high fraction of cysteines (up to 20 out of approximately 60 residues in total), a lack of aromatic amino acids, a two-domain metal-binding structure, the formation of clustered metal-cysteine binding sites and a metal-to-protein stoichiometry of 7 for divalent metals, 12 for monovalent metals and up to 18 for Hg(II) and Ag(I). The metal-binding properties have been very well studied using UV-visible absorption and CD spectroscopies,[39–47] with confirmation of the metal speciation available recently from electrospray ionization mass spectrometry. The typical divalent metal-binding structure for the α and β domains involves the peptide wrapping around both metal-binding sites providing the thiolate sulfurs from the cysteine residues (Figure 7).[41] This wrapping generates the chiral field that results in distinctive CD spectral patterns under the LMCT absorption due to the Cys → M.

The CD spectrum of rabbit liver Cd_7-MT 2a shows a characteristic spectrum of mammalian metallothioneins, with a derivative band centered at 250 nm (cross-over), positive at 260 nm, and a negative at 240 nm.[43–45] This band envelope was first characterized as due mainly to the filled α domain, arising from exciton splitting of pairs of Cd(II) atoms in this domain. The CD spectrum of the isolated Cd_3-β domain is weak and broad.[39] While the CD spectrum of Cd(II)-containing proteins has been used as a marker for cadmium binding detailed information can be obtained by titrating out the Cd(II) with metals of higher binding affinity. Metal binding to the cysteinyl sulfurs in metallothioneins follows the same trend as to organic thiolates: K_B Zn(II) < Cd(II) < Cu(I) < Hg(II). The changes in the CD spectrum as an incoming metal binds follow the trends: (i) the band maxima are dependent solely on the LMCT energies, so as the metal changes, so the band maxima change, (ii) LMCT energies are dependent on the coordination geometry, so as the geometry changes from tetrahedral, to trigonal to digonal, so the band maxima changes, and, finally, (iii) the CD spectral envelope measured is determined directly by the route the peptide chain takes in wrapping the 20 cysteine residues around the metal ions.

In total then, the CD spectrum provides a direct view of the changes in the coordination geometry in the

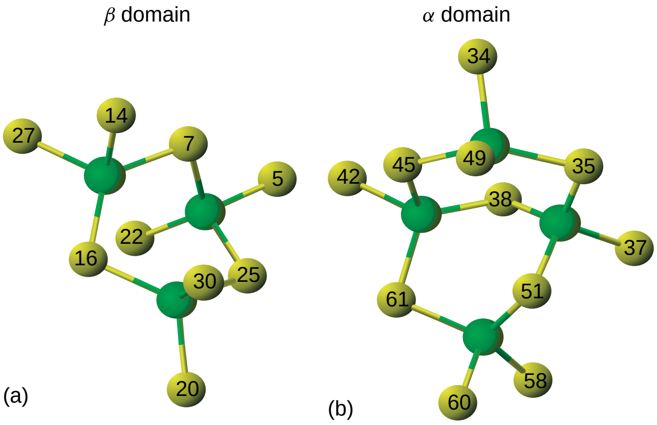

Figure 7 The β (a) and α (b) cadmium-thiolate domain structures in mammalian metallothionein. Yellow spheres represent Cys-sulfurs and Green spheres represent Cd(II) atoms. Based on models developed in our laboratory, for example, Ref. 41

metal-binding site, unobscured by the usual, strong chiral signals of aromatic amino acids. We illustrate this with the spectral changes when Cu(I) is added in mole equivalent aliquots to Zn_7-MT 2a[45] (Figure 8). At the elevated 52 °C temperature used in this experiment, the peptide chain is able to realign to accommodate the trigonally directing Cu(I).[45] Interestingly, because the folding is metal-directed, there is no ''melting'' or other typical denaturing effects observed. The 3D-representation in Figure 8 clearly shows a number of steps. Initially, the bands from the S $\rightarrow$ Zn(II) CT are replaced by new bands arising from the Cu(I). The maximum at Cu_9Zn_2-MT can be seen to exist in the same or similar peptide wrapping because the CD spectral intensities do not change between the Zn_7 and this species. However, immediately after this, a new species dominates the spectrum. Cu_{15}-MT exhibits bands at 340 nm—very much red-shifted. We interpret this as being due to a change to digonal $Cu(S^-)_2$ geometry.

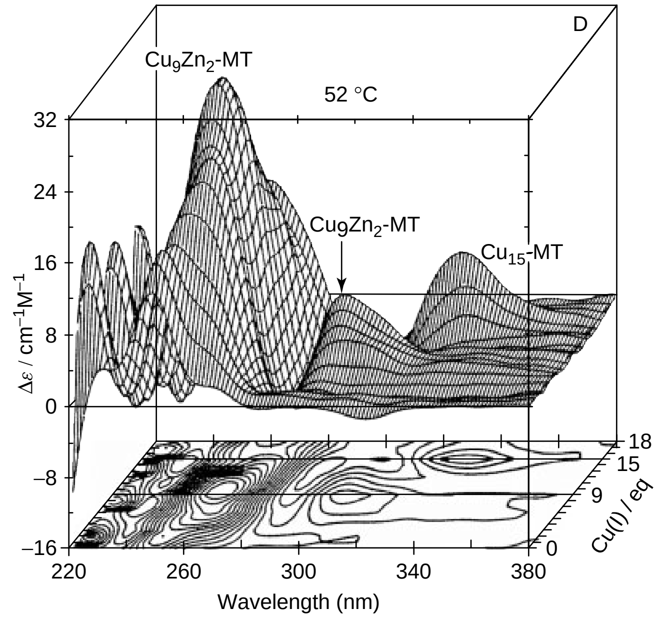

Figure 8 CD spectral changes as Cu(I) is added stepwise to Zn_2-MT 2A. (Reprinted with permission from Presta, Green, Zelazowski and Stillman.[45] © 1995 Wiley-Blackwell)

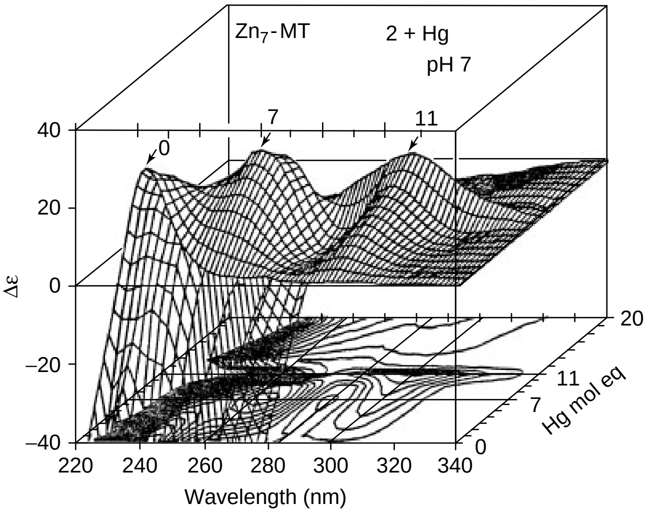

Figure 9 CD spectral changes recorded as Hg(II) was added to rabbit liver Zn_7-MT 2A at pH 7. Hg-dependent species form at the 7 and 11 Hg:MT points. (Reprinted with permission from Lu and Stillman.[46] © 1993 American Chemical Society)

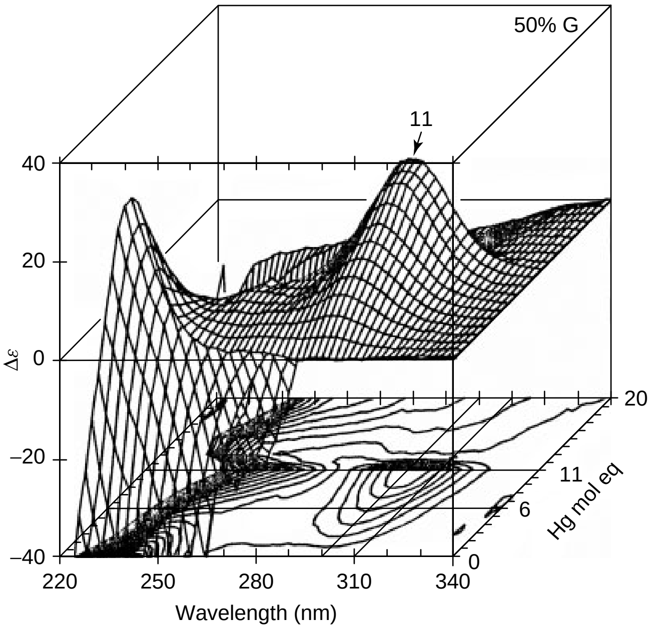

Figure 10 CD spectral changes recorded as Hg(II) was added in mole equivalent aliquots to a solution of rabbit liver Zn_7-MT 2A in a solution 50% v/v ethylene glycol showing the formation of Hg_{11}-MT as the major species. (Reprinted with permission from Lu and Stillman.[46] © 1993 American Chemical Society)

It may be expected that Hg(II) would replace other group 12 metals isomorphously in a tetrahedral geometry. The CD spectral changes measured during a titration of Zn_7-MT with Hg(II) shown in Figures 9 and 10 provide evidence once again that, in fact, the geometry changes from the initial tetrahedral coordination to trigonal coordination.[46] The tetrahedral geometry adopted at 7 Hg(II) gives way to a possible trigonal geometry at 11 Hg(II), which collapses at >11 Hg(II), presumably because the Hg-S_n clusters are too large to sustain with the restrictive core size offered by the 11 cysteines in the α domain and the 9 cysteines in the β domain. Further support that the 11 Hg(II):20 cys represents a specific and well-defined structure is obtained from a titration in which the solvent includes 50% by volume of ethylene glycol.[46] Now only the Hg_{11}-MT forms (Figure 10); that more Hg(II) can bind is evident in the spectral changes when Hg(II) is added at low pH (pH $<$ 5 in the presence of Cl^-). Figure 11 shows the development of a signal at 18 Hg:20 cys.[44] The strong

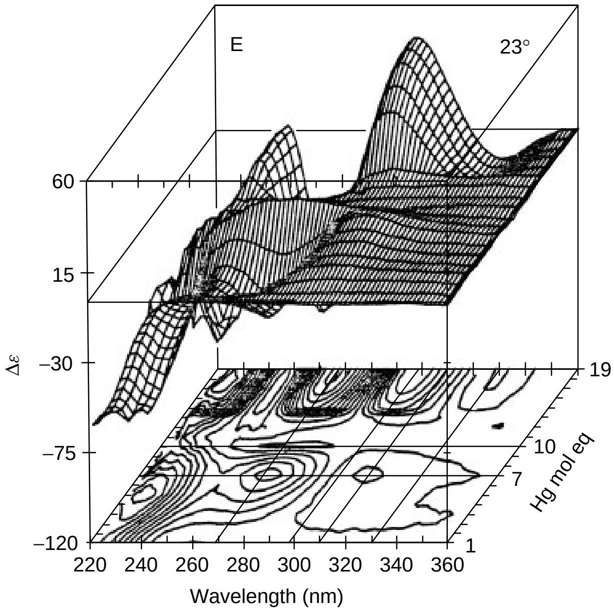

Figure 11 CD spectral changes as Hg(II) was added stepwise to a solution of rabbit liver metallothionein at pH 2. The z-axis shows the mole equivalents of Hg(II) added. (Reprinted with permission from Cai and Stillman.[44] © 1998 American Chemical Society)

CD spectrum is indicative of a chiral structure involving all 18 Hg(II) ions.

4 ACKNOWLEDGMENTS

We wish to acknowledge the assistance of Dr. Sharbari Lahiri in writing this chapter. Research described from our laboratory was supported by NSERC of Canada.

5 ABBREVIATIONS AND ACRONYMS

ACS = ammonium (+)-D10-camphorsulfonate; BSA = bovine serum albumin; CD = circular dichroism; CT = charge transfer; hCCS = human copper chaperone for superoxide dismutase; hSCAN = human soluble calcium-activated nucleotidase-1; LMCT = ligand-to-metal charge transfer; METP = miniaturized electron transfer protein; MLCT = metal-ligand charge transfer; ORD = optical rotatory dispersion; SODs = superoxide dismutases; tCCS = tomato copper chaperone for superoxide dismutase; UTP = uracil triphosphate.

6 REFERENCES

1. R. W. Woody, *Methods Enzymol.*, 1995, **246**, 34.
2. A. P. Yamniuk, L. T. Nguyen, T. T. Hoang and H. J. Vogel, *Biochemistry*, 2004, **43**, 2558.
3. S. Futaki, T. Kiwada and Y. Sugiura, *J. Am. Chem. Soc.*, 2004, **126**, 15762.
4. Q. Dai, M. Prorok and F. J. Castellino, *J. Mol. Biol.*, 2004, **336**, 731.
5. D. M. Murphy, V. V. Ivanenkov and T. L. Kirley, *Biochemistry*, 2003, **42**, 2412.
6. A. K. Tickler, D. G. Smith, G. D. Ciccotosto, D. J. Tew, C. C. Curtain, D. Carrington, C. L. Masters, A. I. Bush, R. A. Cherny, R. Cappai, J. D. Wade and K. J. Barnham, *J. Biol. Chem.*, 2005, **280**, 13355.
7. A. I. Bush, *Trends Neurosci.*, 2003, **26**, 207.
8. J. Wang, Z. A. Luthey-Schulten and K. S. Suslick, *Proc. Natl. Acad. Sci. U.S.A.*, 2003, **100**, 3035.
9. M. V. Golynskiy, T. C. Davis, J. D. Helmann and S. M. Cohen, *Biochemistry*, 2005, **44**, 3380.
10. C. Sissi, E. Marangon, A. Chemello, C. G. Noble, A. Maxwell and M. Palumbo, *J. Mol. Biol.*, 2005, **353**, 1152.
11. J. A. Cox, F. Tirone, I. Durussel, C. Firanescu, Y. Blouquit, P. Duchambon and C. T. Craescu, *Biochemistry*, 2005, **44**, 840.
12. J. Kovári, O. Barabás, E. Takács, A. Békési, Z. Dubrovay, V. Pongrácz, I. Zagyva, P. Szabó and B. G. Vértessy, *J. Biol. Chem.*, 2004, **279**, 17932.
13. J. A. O. Rumfeldt, P. B. Stathopulos, A. Chakrabarrty, J. R. Lepock and E. M. Meiering, *J. Mol. Biol.*, 2006, **355**, 106.
14. D. Ghosh, K.-H. Lee, B. Demeler and V. L. Pecoraro, *Biochemistry*, 2005, **44**, 10732.
15. A. Lombardi, D. Marasco, O. Maglio, L. Di Costanzo, F. Nastri and V. Pavone, *Proc. Natl. Acad. Sci. U.S.A.*, 2000, **97**, 11922.
16. Y. S. Jung, C. A. Bonagura, G. J. Tilley, H. S. Gao-Sheridan, F. A. Armstrong, C. D. Stout and B. K. Burgess, *J. Biol. Chem.*, 2000, **275**, 36974.
17. T. A. Jackson and T. C. Brunold, *Acc. Chem. Res.*, 2004, **37**, 461.
18. M. R. Mauk, F. I. Rosell, B. Lelj-Garolla, G. R. Moore and A. G. Mauk, *Biochemistry*, 2005, **44**, 1864.
19. A. J. Tasiopolous, E. J. Tolis, J. M. Tsangaris, A. Evangelou, J. D. Woollins, A. M. Z. Slawin, J. Costa Pssoa, I. Correia and T. A. Kabanos, *J. Biol. Inorg. Chem.*, 2002, **7**, 363.
20. H. Zhu, E. Shipp, R. J. Sanchez, A. Liba, J. E. Stine, P. J. Hart, E. B. Gralla, A. M. Nersissian and J. S. Valentine, *Biochemistry*, 2000, **39**, 5413.
21. A. Myari, N. Hadjiliadis, N. Fatemi and B. Sarkar, *J. Inorg. Biochem.*, 2004, **98**, 1483.
22. M. A. Kihlken, A. P. Leech and N. E. Le Brun, *Biochem. J.*, 2002, **368**, 729.
23. A. Urvoas, M. Moutiez, C. Estienne, J. Couprie, E. Mintz and L. Le Clainche, *Eur. J. Biochem.*, 2004, **271**, 993.
24. M. L. Ganadu, M. Aru, G. M. Mura, A. Coi, P. Mlynarz and H. Kozlowski, *J. Inorg. Biochem.*, 2004, **98**, 1103.
25. C. S. Atwood, R. D. Moir, X. Huang, N. M. E. Bacarra, R. C. Scarpa, D. M. Romano, M. A. Hartshorn, R. E. Tanzi and A. I. Bush, *J. Biol. Chem.*, 1998, **273**, 12817.

26. T. Kowalik-Jankowska, M. Ruta-Dolejsz, K. Wioniewska and L. Œankiewicz, *J. Inorg. Biochem.*, 2001, **86**, 535.
27. D. R. Brown, K. F. Qin, J. W. Herms, A. Madlung, J. Manson, R. Strome, P. E. Fraser, T. Kruck, A. Vonbohlen, W. Schulzschaeffer, A. Giese, D. Westaway and H. Kretzschmar, *Nature*, 1997, **390**, 684.
28. S. Lehmann, *Curr. Opin. Chem. Biol.*, 2002, **6**, 187.
29. E. Aronoff-Spencer, C. S. Burns, N. I. Avdievich, G. J. Gerfen, J. Peisach, W. E. Antholine, H. L. Ball, F. E. Cohen, S. B. Prusiner and G. L. Millhauser, *Biochemistry*, 2000, **39**, 13760.
30. D. La Mendola, R. P. Bonomo, G. Impellizzeri, G. Maccarrone, G. Pappalardo, A. Pietropaolo, E. Rizzarelli and V. Zito, *J. Biol. Inorg. Chem.*, 2005, **10**, 463.
31. B. M. Barney, R. LoBrutto and W. A. Francisco, *Biochemistry*, 2004, **43**, 11206.
32. G. Marcon, L. Messori, P. Orioli, M. A. Cinellu and G. Minghetti, *Eur. J. Biochem.*, 2003, **270**, 4655.
33. M. Matzapetakis, B. T. Farrer, T.-C. Weng, L. Hemmingsen, J. E. Penner-Hahn and V. L. Pecoraro, *J. Am. Chem. Soc.*, 2002, **124**, 8042.
34. O. A. Kharenko and M. Y. Ogawa, *J. Inorg. Biochem.*, 2004, **98**, 1971.
35. E. Rossy, L. Champier, B. Bersch, B. Brutscher, M. Blackledge and J. Covès, *J. Biol. Inorg. Chem.*, 2004, **9**, 49.
36. T. M. DeSilva, G. Veglia, F. Porcelli, A. M. Prantner and S. J. Opella, *Biopolymers*, 2002, **64**, 189.
37. N. Suzuki, Y. Yamaguchi, N. Koizumi and H. Sano, *Plant J.*, 2002, **32**, 165.
38. R. K. Mehra, V. R. Kodati and R. Abdullah, *Biochem. Biophys. Res. Commun.*, 1995, **215**, 730.
39. M. J. Stillman, *Coord. Chem. Rev.*, 1995, **144**, 461.
40. T. T. Ngu and M. J. Stillman, *J. Am. Chem. Soc.*, 2006, **128**, 12473.
41. J. Chan, M. E. Merrifield, A. Soldatov and M. J. Stillman, *Inorg. Chem.*, 2005, **44**, 4923.
42. M. J. Stillman, W. Cai and A. J. Zelazowski, *J. Biol. Chem.*, 1987, **262**, 4538.
43. K. E. Rigby Duncan and M. J. Stillman, *FEBS J.*, 2007, **274**, 2253.
44. W. Cai and M. J. Stillman, *J. Am. Chem. Soc.*, 1988, **110**, 7872.
45. A. Presta, A. R. Green, A. Zelazowski and M. J. Stillman, *Eur. J. Biochem.*, 1995, **227**, 226.
46. W. Lu and M. J. Stillman, *J. Am. Chem. Soc.*, 1993, **115**, 3291.
47. W. Lu, A. J. Zelazowski and M. J. Stillman, *Inorg. Chem.*, 1993, **32**, 919.

Electrochemistry

Mark C. Elvington and Karen J. Brewer

Virginia Polytechnic Institute and State University, Blacksburg, VA, USA

Method Summary 1
1 Introduction 2
2 Technical Background 3
3 Applications 8
4 Acknowledgments 21
5 Abbreviations and Acronyms 21
6 Further Reading 21
7 References 21

METHOD SUMMARY

Acronyms, Synonyms

- Linear Sweep, Cyclic and Square Wave Voltammetry (LSV, CV, SWV)
- Bulk Electrolysis (BE)
- Differential Pulse Polarography (DPP)

Measured physical quantities

- potential or current response of an electrochemical system typically containing electrodes, an analyte, solvent, and electrolyte;
- coupled to other techniques in spectroelectrochemistry, additional information about alternative redox states of analytes explored.

Information available

- potential ($E°$) at which the analyte is oxidized or reduced
- number of electrons for a given oxidative or reductive process
- reversibility of an oxidation or reduction of an analyte
- the kinetics of chemical reactions that follow electrochemical reactions
- information about catalysis by electrogenerated species
- coupled with other techniques in spectroelectrochemistry. Study of the properties of oxidized and reduced forms of complexes.

Information not available, limitations

- Only electroactive materials give signals.
- The analyte must have redox activity at the potentials studied to provide a signal.
- Compatibility and solubility with a suitable solvent is needed when studying typical solution phase properties.
- Redox active sites of complex molecules must have electronic communication with the electrode surface to facilitate electron transfer.
- Resolution of overlapping processes can be difficult.
- Redox reactions can vary with the solvent, especially for irreversible reactions.

Examples of questions that can be answered

- What are the oxidation and reduction potentials, $E°$, of new materials?
- What are the electronic properties of new materials as a result of tuning orbital energetics?
- What are the properties of oxidized and/or reduced form of analytes?
- What are the kinetics and nature of chemical reactions following electrochemical reactions?
- What degree of electronic coupling of subunits within complex assemblies exist?
- What are the approximate properties of electronic excited states?

Major advantages

- Electrochemistry allows for quick and easy determination of redox properties of relatively small samples of new materials, with very small samples analyzed with microelectrodes.
- The methods are nondestructive when used for analysis with many methods not changing the bulk sample.
- Many solvent, electrode, electrolyte systems are known to provide convenient potential windows for a variety of analytes.
- Preparative methods are available for bulk transformations that are free from side reactions in chemical oxidations and reductions.
- The methods provide a clean means to provide alternative redox states of analytes, to probe with other characterization methods.

Major disadvantages

- The analyte signal response requires the presence of a redox process within the solvent, electrolyte window.
- Good signal to noise ratios are not always possible with low solubility of analyte, high solvent electrolyte background signal, or overlapping redox processes.
- To recover the sample, separation from solvent and electrolyte is necessary.
- Irreversible redox reactions result in unrecoverable samples in bulk methods.
- Nonelectroactive impurities often go undetected.

Sample constraints

- The sample is typically dissolved in a suitable solvent electrolyte system that limits the potential window.
- Milligram level samples in milliliter solvent can be analyzed by typical methods with smaller samples analyzed using microelectrodes.

1 INTRODUCTION

Over the past 25 years the field of electrochemistry has shifted from the development of techniques to applications in the laboratory, not only useful to the analytical chemist, but to a wide array of scientists. The materials presented herein are designed primarily to be of practical use for the intended audience, inorganic chemists who are students and research level professionals, with an introduction of the technical background covering basic theory at the fundamental level. The electrochemical techniques covered herein are from an inorganic chemist's perspective, and are thus a reflection of the authors' interests. For a more detailed discussion of the theory of electrochemistry, see Bard and Faulkner's *Electrochemical Methods*[1] and *Laboratory Techniques in Electroanalytical Chemistry* by Peter Kissinger.[2] Another useful electrochemistry book with an inorganic perspective is *Inorganic Electrochemistry* by Zanello,[3] which also contains information designed specifically for students and research level inorganic chemists.

This article will focus on experimental electrochemistry with an inorganic perspective. The fundamentals of electrode reactions and other electrochemical processes, as well as a discussion of electrochemical cells and electrodes/solvent/electrolyte systems will be covered. The topics presented here cover several current electrochemical methods including potential sweep techniques like linear and cyclic voltammetry (CV), potential step techniques such as square wave voltammetry (SWV), differential pulse polarography (DPP), and bulk electrolysis (BE). Coupled techniques, like spectroelectrochemistry, have emerged recently as valuable analytical techniques capable of providing unique information, and will be discussed. The technical background will be covered for the various electroanalytical techniques, followed by applications to inorganic systems, including practical concerns and data interpretation.

2 TECHNICAL BACKGROUND

2.1 Electrode Reaction Fundamentals

To evaluate reactions that take place at the electrode at a fundamental level, we first consider a thermodynamic perspective. Any thermodynamic analysis of a chemical reaction begins with the Gibbs free energy equation (1),[1] which relates cell potentials directly to free energy

$$\Delta G^\circ = -n\mathrm{F}E^\circ \tag{1}$$

where ΔG° is the standard free energy change, n is the number of electrons, F is Faraday's constant (96 485 C mol^{-1})[4] the total charge of 1 mole of electrons, and E° is the standard potential. The application of thermodynamics to electrochemistry considers systems that are at equilibrium. As such reversibility, specifically thermodynamic reversibility, is integral in evaluating cell potentials mathematically. If a process is thermodynamically reversible, or nernstian, the Nernst equation (2)[1] can be used to relate the concentrations of two species, O (oxidized species) and R (reduced species) (equation 3), to potential, E

$$E = E^\circ + \left(\frac{RT}{n\mathrm{F}}\right) \cdot \ln\left(\frac{[\mathrm{O}]}{[\mathrm{R}]}\right) \tag{2}$$

where E is the potential at nonstandard conditions, R is the gas constant (8.314 J K^{-1} mol^{-1}),[4] and T is temperature in K. The units on the second term yield J C^{-1} or V.

$$\mathrm{O} + n\mathrm{e}^- \longrightarrow R \tag{3}$$

The reaction in equation (3), the addition of electrons, is a reduction, and the opposite reaction, the removal of electrons, is an oxidation, and the concentration of species O and R are that of the bulk. When examining an electrochemical reaction of an analyte in solution at the surface of an electrode, mass transport and the kinetics of electron transfer at a solid/liquid interface become important considerations.

The study of electrochemistry involves the addition and removal of electrons. In inorganic molecules this process can result in bond making/breaking, typically involving a ligand covalently bound to a metal. The consequence of adding or removing electrons is directly influenced by the molecule's orbital structure. The highest occupied molecular orbital (HOMO) is of particular importance when an oxidation is involved, and the lowest unoccupied molecular orbital (LUMO) when a reduction is involved. Illustrated in Figure 1 is the molecular orbital diagram for ferrocene, a stable 18 electron organometallic complex, often used as a potential reference (Figure 2a; $E_{1/2} = 0.43$ V vs. saturated calomel electrode (SCE)).[5] The enclosed box contains the frontier orbitals, HOMO and LUMO, the orbitals involved if one electron is removed or added respectively, as well as the lower energy e'_2 orbital. The HOMO (a'_1) of ferrocene is nonbonding, therefore if one electron is removed, there will be no net change in the degree of bonding, that is no bond breaking. CV for ferrocene shows a reversible oxidation at ∼0.46 V with a corresponding symmetric reduction at ∼0.40 V consistent with its orbital structure, Figure 2(a). If a chemical step, like bond breaking, follows an electrochemical step the cyclic voltammogram would be irreversible and $i_p^{\mathrm{a}}/i_p^{\mathrm{c}} \neq 1$ and/or $\Delta E_p \neq 59/n$ mV, where i_p^{a} is the anodic peak current, i_p^{c} is the cathodic peak current, and ΔE_p $(E_p^{\mathrm{c}} - E_p^{\mathrm{a}})$, is the potential peak separation for the anodic (E_p^{a}) and cathodic (E_p^{c}) peak maxima. Figure 2(b) shows a cyclic voltammogram for the reductive region of $[\mathrm{Rh^{III}(bpy)_3}]^{3+}$ (bpy = 2,2′-bipyridine).[6] An irreversible reduction is observed at ∼−0.9 V versus SCE identified as a $\mathrm{Rh^{III/II/I}}$ couple, followed by two reversible $\mathrm{bpy}^{0/-}$ reductions. The wave with $i_p^{\mathrm{a}}/i_p^{\mathrm{c}} > 1$ for the $\mathrm{Rh^{III/II/I}}$ couple at −0.9 V is characteristic of an irreversible redox process in which the electrogenerated complex reacts to form a species that does not undergo reoxidation at the same potential. For $[\mathrm{Rh^{III}(bpy)_3}]^{3+}$, the rhodium reduction is followed by a

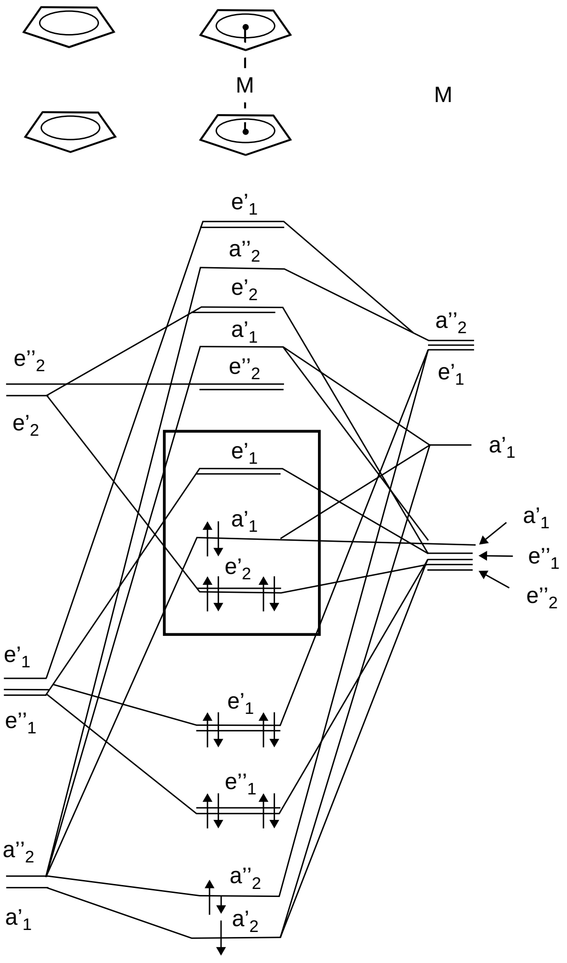

Figure 1 Molecular orbital diagram for ferrocene (M = Fe).[3] (Reprinted from Zanello[3] © 2003 Royal Society of Chemistry)

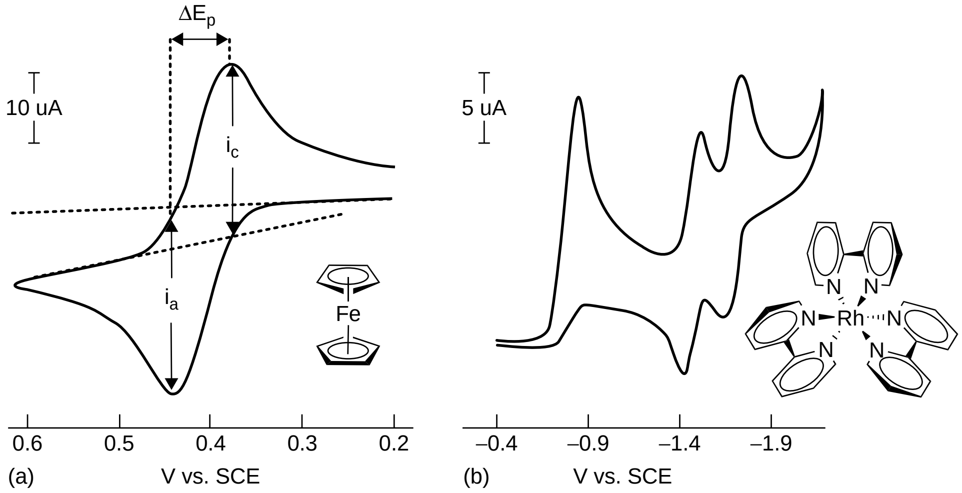

Figure 2 Cyclic voltamograms for: (a) ferrocene $[Fe(Cp)_2]$ (Cp = cyclopentadienyl anion, $C_5H_5^-$) measured in CH_3CN with 0.1 M Bu_4NPF_6 displaying a reversible oxidation at 0.43 V versus SCE;[5] and (b) $[Rh^{III}(bpy)_3]^{3+}$ (bpy = 2,2′-bipyridine), an example of an irreversible reduction followed by two reversible reductions measured in CH_3CN with 0.1 M Et_4NClO_4 versus SCE.[6] (Reprinted with permission from Kew, DeArmond, and Hanck[6] © 1974 American Chemical Society)

chemical step, bond breaking, whereby one of the bipyridines is lost to form $[Rh^I(bpy)_2]^+$.

2.2 Potentials of Electrochemical Reactions, E°

The potential of an electrochemical reaction is a measure of the thermodynamic driving force for the transfer of electrons as $\Delta G^\circ = -nFE^\circ$. Typical electrochemical methods measure the potential of half reactions, either oxidations or reductions. The potential of electrochemical reactions are related to electronic effects or structural changes in related series of complexes. For example the $Ru^{II/III}$ couple occurs at 1.51 V versus normal hydrogen electrode (NHE) for $[Ru(bpy)_3]^{2+}$ and at 0.18 V for $[Ru(en)_3]^{2+}$ (en = ethylenediamine) indicative of the more electron rich metal center in the en complex.[7] Similarly variation of the metal center to give $[Os(bpy)_3]^{2+}$ leads, to an oxidation at 1.06 V versus NHE, indicative of the higher energy 5d orbitals on Os versus the 4d orbitals on Ru.[7] The variation of electrochemical potentials for related series of complexes has led to the development of electrochemical parameterization of metal complex redox potentials through the development of ligand electrochemical series by Lever *et al.*[7–11] The use of measured data allows for the prediction of metal $M^{n/n-1}$ redox potentials for unstudied complexes, assuming all ligand contributions are additive

$$E_{\mathrm{redox}} = S_{\mathrm{m}}(\Sigma E_L(L)) + I_{\mathrm{m}} \qquad (4)$$

where E_{redox} is the potential of the $M^{n/n-1}$ couple, S_{m} and I_{m} are derived from the slope and intercept of the plot of available data for each metal and are specific to the spin and redox state of each metal. The E_L parameters are related to the σ donation and π donation or acceptance ability of the ligands. The $Ru^{II/III}$ S_{m} in water was found to be 1.14 with I_{m} of −0.35 versus S_{m} of 1.61 and I_{m} of −1.30 for $Os^{II/III}$ in water. E_L values of bpy of 0.26 and en of 0.06 for each N bound to a metal allow for the reasonable prediction of E_{redox}. For example, E_{redox} $([Ru(bpy)_3]^{2+}) = 1.14(6(0.26)) + (-0.35) = 1.43$ V versus NHE. These methods have been applied to a large series of complexes.[12–18] An illustrative example is shown in Figure 3.

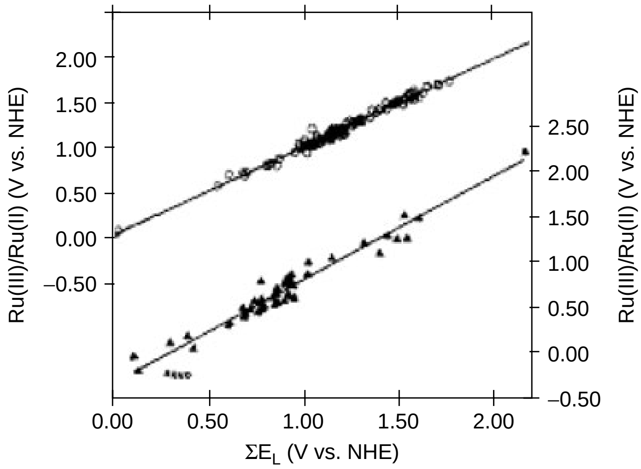

Figure 3 Plot of observed Ru(III)/Ru(II) potentials for ruthenium complexes against ΣE_L (sum of ligand parameters) measured in organic phase solvent and referred to left-hand *y* axis (circles) and measured in water and referred to right-hand *y* axis (triangles). All data are versus NHE.[7] (Reprinted with permission from Lever.[7] © 1990 American Chemical Society)

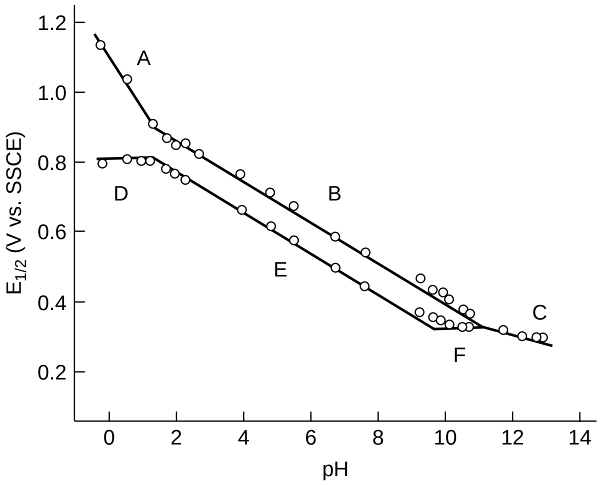

Figure 4 Pourbaix diagram plotting potential versus pH for the $Ru^{IV/III}$ and $Ru^{III/II}$ redox couples of the complex $[(tpy)(bpy)Ru^{II}OH]^{2+}$. A) $Ru^{IV} = O^{2+}/Ru^{III}-OH_2^{3+}$; B) $Ru^{IV} = O^{2+}/Ru^{III}-OH^{2+}$; C) $Ru^{IV} = O^{2+}/Ru^{II}-OH^{+}$; D) $Ru^{III}-OH_2^{3+}/Ru^{II}-OH_2^{2+}$; E) $Ru^{III}-OH^{2+}/Ru^{II}-OH_2^{2+}$; F) $Ru^{III}-OH^{2+}/Ru^{II}-OH^{+}$.[19] (Reprinted with permission from Takeuchi, Thompson, Pipes, and Meyer[19] © 1984 American Chemical Society)

Many analytes that have basic sites prone to protonation, display pH-dependent electrochemistry. The redox properties of metal complexes of H_2O, OH, and O^{2-} often display pH-dependent electrochemistry as demonstrated by Meyer *et al.* for the complex $[M(tpy)(bpy)O]^{2+}$ (M = Ru or Os; tpy = 2,2′,2″-terpyridine). These complexes have been studied probing their electrochemistry over a wide range of pH.[19] CV and DPP were used to determine $E_{1/2}$ for the $Ru^{IV/III}$ and $Ru^{III/II}$ redox couples of the complex $[Ru(tpy)(bpy)O]^{2+}$ from pH 0 to 13 (Figure 4) and the Nernst equation (2) was used to fit the data.

2.3 Electrochemical Cells and Practical Considerations

An electrochemical cell is typically composed of the working, auxiliary, and reference electrodes illustrated in Figure 5. Current flows between the working electrode, where the reaction to be monitored takes place, and the auxiliary electrode while the potential is controlled between the working electrode and the reference electrode. A potentiostat is also needed to supply the current at the desired potential to drive the redox reactions to be monitored. Table 1 is a listing of several sources of electrochemical equipment, glassware, and electrodes.

2.3.1 Solvent/Electrolyte for Electrochemistry

The solvent, solvent purity, and electrolyte are important factors in electrochemistry. The potential window available is controlled by solvent. Solvent purity is a factor to consider. Water, an impurity commonly found in many solvents, often displays an oxidation or reduction in the desired potential window, necessitating drying of the solvent.[20] Even ‘‘dry’’ solvents can contain mM H_2O which is often similar to the concentration of the analyte. Additional drying of organic solvents like acetonitrile can be achieved by passing over alumina activated in a vacuum oven, followed by solvent filtering with a syringe filter. Particles of alumina or analyte can lead to poor quality electrochemical data. The presence of H_2O limits the accessible potential window. The standard oxidation and reduction potentials for water are 1.23 V ($O_2(g) + 4H^+(aq) + 4e^- \rightarrow 2H_2O$) and −0.83 V ($2H_2O + 2e^- \rightarrow H_2(g) + 2OH^-(aq)$) versus NHE,[21] which are pH-dependent. Solutions should also be sufficiently deoxygenated to remove O_2 or the oxygen couple will appear as an irreversible couple at approximately −0.8 V versus Ag/AgCl, or O_2 could react with the reduced analyte.

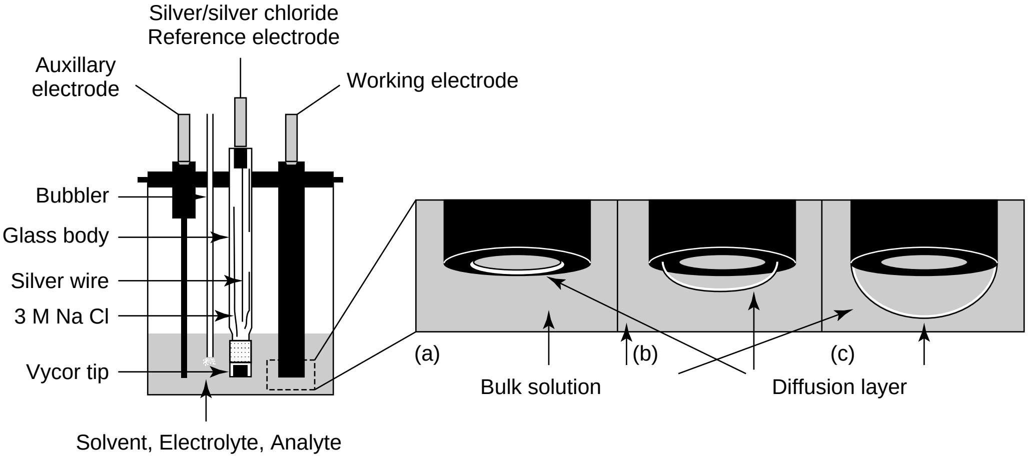

Figure 5 Electrochemical cell showing the working, auxiliary, and reference electrodes, in this case a Ag/AgCl reference electrode. The diffusion layer is also shown during an oxidation/reduction overtime showing. (a) linear diffusion, (b) the transition from linear to hemispherical diffusion, and (c) hemispherical diffusion

Table 1 Electrochemistry equipment sources (as of March 2007)

Manufacturer	Website
Adams & Chittenden Scientific Glass	http://www.adamschittenden.com/index.php
Ametek	http://www.ametek.com/
BAS[(a)]	http://www.bioanalytical.com/
CH Instruments	http://www.chinstruments.com/
Cypress Systems	http://www.cypresssystems.com/
eDAQ	http://www.edaq.com/
Gamry Instruments	http://www.gamry.com/Homepage/Index.html
Pine Instrument Company	http://www.pineinst.com/index_ie.htm
York Glassware Services Limited	http://www.ygs.net/home.asp

(a) BAS, Bioanalytical systems.

Table 2 Potential windows and supporting electrolytes for a few commonly used solvents

Solvent	Supporting electrolyte[1]	Potential window(a)
Acetone	$[NEt_4][ClO_4]$, $[NBu_4][PF_6]$, $NaClO_4$	-2.1 to $+1.4$[3]
Acetonitrile	$[Net_4][ClO_4]$, $[NBu_4][PF_6]$, $LiClO_4$	-2.0 to $+2.0$[3]
Dichloromethane	$[NBu_4][PF_6]$, $[NBu_4][ClO_4]$, $[NBu_4]$[halide]	-2.0 to $+1.7$[3]
Dimethylformamide	$[NEt_4][ClO_4]$, $[NBu_4][PF_6]$, LiCl, $NaClO_4$	-2.8 to $+1.5$[3]
Dimethylsulfoxide	$[NEt_4][ClO_4]$, $[NBu_4][PF_6]$	-2.3 to $+1.0$[3]
Tetrahydrofuran	$[NBu_4][PF_6]$, $LiClO_4$, $NaClO_4$	-2.4 to $+1.3$[3]
Water	$NaClO_4$, KNO_3	~ -0.8 to $+1.2$(b)

(a) Potential for platinum working electrode with $[NBu_4][PF_6]$ as supporting electrolyte.
(b) pH dependent.[21]

Acetonitrile and methylene chloride are typically good solvents for extending the window for anodic scans, while tetrahydrofuran (THF), N,N-dimethylformamide (DMF), and dimethyl sulfoxide (DMSO) are typically good solvents for extending the potential window for cathodic scans (Table 2).

2.3.2 Working Electrodes

The working electrode is the electrode surface at which the electrochemical reaction involving the analyte takes place. Working electrodes are typically composed of redox inert materials such as carbon, platinum, gold, or mercury and are typically small surface area electrodes for analysis methods, and large surface area for BE methods. A working electrode is chosen based on the needed potential window and the type of electrochemical technique. Often minor water impurities can limit potential windows unless a working electrode material is chosen with a high overpotential for water oxidation or reduction. Mercury, for example, does not have a very wide window into the anodic region, so in the case where one wants to investigate a highly positive oxidation, an alternative electrode like carbon or platinum would be required. Platinum working electrodes limit the reductive window in the presence of water. Techniques dependent on mercury working electrodes, like the dropping mercury electrode (DME), static mercury electrode, and hanging mercury drop electrode, will be discussed in detail later.

The solvent chosen must be of sufficient purity to be chemically inert in the potential window to be studied and be able to dissolve the analyte in high enough concentration. The supporting electrolyte must also be soluble in the chosen solvent to provide for the electrical conductivity of the solution reducing solution resistance, and limiting analyte motion by electromotive force. It is important that the electrolyte not be redox active in the potential window studied. Table 2 lists commonly used organic solvents and their corresponding supporting electrolytes. Electrochemistry can also be performed at reduced temperature to extend the accessible potential window as demonstrated by DeArmond and Hanck where the cathodic region for DMF at −54 °C was extended to −3.0 V versus NHE.[22]

The microelectrode is a class of working electrodes that has increased in popularity since the 1980s and is used mainly by electroanalytical chemists.[1] These electrodes have improved time resolution for electrochemical reactions, and can function in higher resistance solutions. Diffusion is treated as hemispherical as the electrode surface area is more like a point than a plane as is the case with macroelectrodes. Typically microelectrodes are difficult to construct and have cross sections on the order of 5 µm.

The working electrode is typically stationary; however, there is a class of electrodes, the rotating disk electrodes (RDE) and the rotating ring disk electrodes (RRDE), that are in continuous motion. These electrodes spin at a controlled speed resulting in forced convection, one type of mass transport, whereas the stationary working electrode typically undergoes diffusional mass transport. The various types of mass transport will be discussed in detail later. The rotating disk and RRDE are designed to make measurements independent of time. This allows one to make steady state measurements without considering electrolysis time, and is particularly useful in that transients can sometimes be observed, allowing for elucidation of the electrochemical mechanism. RDEs can also be used in electrocatalysis, discussed in detail in section 3.3.

2.3.3 Reference Electrodes

A reference electrode is needed to provide a potential scale for E° values as all voltages are relative. Any electrochemical reaction with a stable, well known potential can be used as a reference electrode. The NHE or standard hydrogen electrode (SHE) (Pt/H_2, 1.0 M H^+) was the first well known reference electrode and is used as a reference in most tables of redox potentials.[23] An NHE is difficult to construct and operate and therefore, is not typically used experimentally. Since the NHE is widely accepted, potentials are still often referenced to the NHE, converted from other reference electrodes. For aqueous solvents the SCE (Hg/Hg_2Cl_2 (KCl)) and the silver/silver chloride (Ag/AgCl) electrode are now commonly used as reference electrodes. To convert from the SCE to the NHE, E (vs. NHE) $=E$ (vs. SCE) $+ 0.24$ V. For nonaqueous solvents the silver/silver nitrate ($Ag/AgNO_3$) reference electrode is often used. A pseudo-reference electrode can also serve as a reference point for aqueous or nonaqueous solutions. A silver or platinum wire can be used as a pseudo-reference electrode after being calibrated by adding a stable reversible redox species like ferrocene (0.43 V vs. SCE)[5] or ferricyanide (0.194 V vs. SCE),[24] for nonaqueous and aqueous solutions respectively. In addition, any measurement can use ferrocene as an internal reference (added to the analyte, solvent, electrolyte solution), provided that the analyte redox couples do not overlap with the ferrocene$^{0/+}$ couple. Reference electrode potentials can deviate from the established values by up to 100 mV. This should be corrected by measuring the potential of a known redox couple. If in calibrating a reference electrode, ferrocene is measured to be 0.36 V versus an Ag/AgCl (3 M NaCl) reference electrode (ferrocene$^{0/+}$ $E_{1/2}$ is 0.38 V vs. Ag/AgCl), the reference electrode can be corrected using equation (5).

$$\Delta E = E_{\text{theoretical}} - E_{\text{measured}} \tag{5}$$

Where ΔE is the correction factor, $E_{\text{theoretical}}$ is the potential of ferrocene, and E_{measured} is the measured potential for ferrocene. In the above case, $\Delta E = 0.38\,\text{V} - 0.36,\ \text{V} = 0.02\,\text{V}$, and 0.02 V should be added to every measurement using that specific reference electrode to correct for its deviation from established values. Table 3 provides potentials for commonly used reference electrodes.

2.3.4 Auxiliary Electrodes

The auxiliary electrode is used to complete the electrochemical circuit allowing current to flow between the working and auxiliary electrodes so that E is more accurately measured between the working and reference electrodes. Auxiliary electrodes have small surface areas, like a wire, for analysis methods and large surface areas for BE methods. While the redox reaction of the analyte takes

Table 3 Common reference electrodes, their corresponding redox reactions and conditions, and the potentials of these reactions relative to the normal hydrogen electrode

Electrode	Reaction	Potential (vs. NHE)[(a)]	References
NHE	(Pt)/H_2, H^+	0	
SCE[(b)]	Hg/Hg_2Cl_2, KCl (sat.)	0.2412	1
NCE[(c)]	Hg/Hg_2Cl_2, KCl (1 M)	0.2801	1
SSCE[(d)]	Hg/Hg_2Cl_2, NaCl (sat.)	0.2360	1
Silver/silver chloride	Ag/AgCl, KCl (0.1 M)	0.2881	23
	Ag/AgCl, KCl (sat.)	0.197	1
	Ag/AgCl, NaCl (3 M)	0.286	24
	Ag/AgCl, NaCl (sat.)	0.194	23
Silver/silver nitrate	$Ag/AgNO_3$ (0.01 M in CH_3CN)	0.54	23
Mercury/mercury oxide	Hg/HgO, NaOH (0.1 M)	0.165	23
	Hg/HgO, NaOH (1 M)	0.14	23
Mercury/mercury sulfate	Hg/Hg_2SO_4, K_2SO_4 (0.5 M)	0.68	1
	Hg/Hg_2SO_4, K_2SO_4 (sat.)	0.64	1

(a) NHE, Normal hydrogen electrode.
(b) SCE, Saturated calomel electrode.
(c) NCE, Normal calomel electrode.
(d) SSCE, Sodium saturated calomel electrode.

place at the working electrode, the counterreaction takes place at the auxiliary electrode, typically involving the oxidation or reduction of solvent. Depending on the electrochemical technique used, a platinum wire, mesh, or coil is most often used as the auxiliary electrode, but other stable electrode materials like carbon cloth and reticulated vitreous carbon (RVC) are sometimes employed.

2.4 Electrochemical Processes

Typical electrochemistry occurs in solution at a solution-electrode surface interface. An electrochemical reaction, $O + e^- \rightarrow R$, involving the addition of an electron to the oxidized species O, to generate the reduced species R, in a solution at the surface of an electrode involves a number of processes. The potential of the electrode is set providing the driving force for electron transfer. The species O must approach the electrode surface within a critical distance to allow transfer of an electron from the electrode surface to the analyte, O, generating R. As species O is reduced at the electrode surface, additional O molecules can undergo mass transport to the electrode surface to continue the reduction. As this is taking place, species O is reduced to generate the species R, which can take place via an inner sphere or outer sphere mechanism. The electrogenerated R then undergoes mass transport back into the bulk solution. Mass transport can take place by diffusion, convection, and migration. Diffusion takes place when the concentration of a species in a solution is not constant, resulting in the random movement of molecules, eventually resulting in a constant concentration throughout the solution. Convection takes place when a mechanical force like stirring or a gradient of pressure is applied to a solution, resulting in the movement of molecules. Migration takes place in the presence of an electric field where ions are attracted to an oppositely charged electrode or repelled from an electrode with the same charge.

3 APPLICATIONS

3.1 Potential Sweep Methods

Potential sweep methods which vary potential and measure current are widely used as they are easy techniques to employ. The methods include linear sweep voltammetry (LSV) and CV which can yield a large amount of electrochemical data in a short amount of time. These potential sweep methods are commonly used by inorganic chemists due to their ease of use and the information obtained. CV has appeared in the literature as the most popular electrochemical technique among inorganic chemists over the past three decades. Another advantage to potential sweep methods is that instrumentation is widely available at relatively low cost. Potential sweep methods usually involve varying the potential linearly with time, and monitoring the cell current. The rate of the potential change is called *the scan rate* and it typically ranges from $100\,\mathrm{V\,s^{-1}}$ to $10\,\mathrm{mV\,s^{-1}}$. Potential sweep methods plot the current response versus the applied potential.

3.1.1 Linear Sweep Voltammetry (LSV)

Linear sweep voltammetry (LSV), also known as linear sweep chronoamperometry, is a potential sweep method where the applied potential (E) is ramped in a linear fashion while measuring current (i). LSV is the simplest technique that uses this waveform. The potential range that is scanned begins at an initial or start potential and ends at a final potential. It is best to start the scan at rest potential, the potential of zero current. For a reversible couple, the peak potential can be calculated using equation (6).**[1]**

$$E_p = E_{1/2} + \frac{1.109\,\mathrm{RT}}{nF} \tag{6}$$

Where E_p is the peak potential and $E_{1/2}$ is the half wave potential. The forward peak current, i_p, for a reversible process can be related to the analyte concentration, C_o, by the Cottrell equation (7).**[2]**

$$\mathrm{i}_p = 2.6910^{5} n^{3/2} A D_o^{1/2} C_o \nu^{1/2} \tag{7}$$

where A is the electrode area ($\mathrm{m^2}$), D_o is the diffusion coefficient ($\mathrm{m^2\,s^{-1}}$), C_o is the concentration of analyte ($\mathrm{mol\,L^{-1}}$), and ν is the scan rate ($\mathrm{V\,s^{-1}}$). Figure 6 shows the potential wave form for LSV and a corresponding example of a voltammogram for this electrochemical technique.

3.1.2 Cyclic Voltammetry (CV)

CV is in all practical regards a continuation of LSV, where the potential ramp is reversed at the end of the first sweep and the current is measured a second time in the reverse direction. It is best to start at the rest potential, the potential of zero current, to avoid electrochemical change prior to starting the scan. Figure 6 illustrates the potential ramp for LSV and CV and a typical current response for the methods. The second sweep for a cyclic voltammetric measurement can be continued past the original starting point to a more negative or positive potential to a second switching point where the potential ramp is reversed once more. The potential is then typically ramped to the original initial potential completing a cycle, hence CV. For systems with many redox couples it is beneficial to sequentially vary the switching potential after the first, second, ... redox couples to isolate each reductive or oxidative couple so that reversibility of each couple can be ascertained. In some cases running multiple cycles can be beneficial in revealing mechanistic information. Variation of scan rate can impact reversibility as faster scan rates limit the time that an electrogenerated redox state has to react.

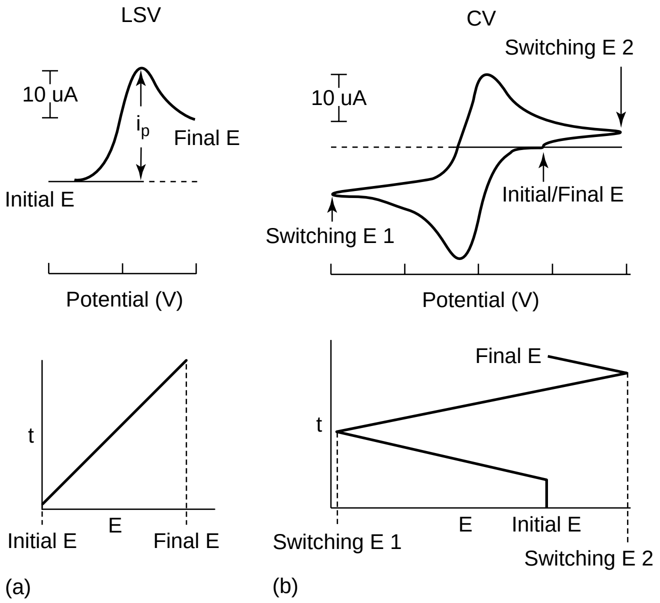

Figure 6 Potential waveforms for linear sweep (LSV; (a) and cyclic voltammetry (CV); (b) displaying potential versus time including the initial and final potentials, and a typical linear sweep voltammogram and cyclic voltammogram plotting current versus potential

The ultimate goal for all of the electrochemical techniques for the inorganic chemist is to provide information about the electron transfer processes especially those involving the frontier orbitals. Analysis of peak shapes and positions for CV can elucidate the potential for and reversibility of the redox processes. The redox couple reversibility is a probe into any following chemical reactions that can occur after the redox step. If the redox couple is reversible, it indicates no following chemical reaction. Irreversible or quasireversible peaks in CV, indicate a following chemical reaction for that given redox couple. The ratio of the anodic peak current, i_p^a, and the cathodic peak current, i_p^c, $i_p^a/i_p^c = 1$, indicates reversibility (Figure 6). This i_p^a/i_p^c ratio indicates whether a redox process is reversible, irreversible, or quasireversible. The peak to peak separation, ΔE_p ($\Delta E_p = E_p^c - E_p^a$), where the anodic peak potential, E_p^a, the cathodic peak potential, E_p^c, are all independent of the scan rate. ΔE_p is dependent on temperature (equation 8), with ΔE_p (at 25 °C) $= 59/n$ mV ($n =$ number of electrons transferred in the redox reaction) for a reversible redox couple.[1]

$$\Delta E_p = \frac{2.3\,\mathrm{RT}}{(nF)} \tag{8}$$

Some deviation of ΔE_p is typically observed experimentally due to solution resistance, especially at higher scan rates. Many potentiostats can compensate for this phenomenon with internal resistance compensation. When $i_p^a/i_p^c \neq 1$ and/or when $\Delta E_p > 59/n$ mV, the electrochemical process is quasireversible. If no return wave is observed in the cyclic voltammogram, the electrochemical process is considered irreversible.

3.1.3 Practical Considerations for Potential Sweep Methods

There are several disadvantages to potential sweep methods. First, it is difficult to measure multiple, closely spaced redox couples. This lack of resolution is due to the broad asymmetric nature of the oxidation/reduction waves. In addition, the analyte must be relatively concentrated as compared to other electrochemical techniques to obtain measurable data with good signal to noise. This decreased sensitivity is due to a relatively high capacitance current which is a result of ramping the potential linearly with time. Potential sweep methods are easy to perform and provide valuable insight into the electron transfer processes. They are excellent for providing a preliminary evaluation, but are best combined with other complementary electrochemical techniques.

There are many practical considerations important to any experimental technique and important considerations other than the previously delineated solvent, electrolyte, and electrode selection are summarized below. As with any experimental technique, a background scan is necessary and should be conducted on the solvent/electrolyte system. The absence of sufficient electrolyte can lead to increased internal resistance which is displayed as large $\Delta E_p > 59/n$. Electrochemical irreversibility can also result from not having a clean working electrode or adsorption of the analyte onto the electrode surface. Adsorbed analyte generated during an electrochemical scan often leads to the presence of adsorption and/or desorption spikes which appear as intense sharp peaks in LSV, CV, and many other techniques. Changing the solvent and/or working electrode material can often eliminate analyte adsorption with DMF typically providing improved solubility limiting adsorption. Electrode contamination, resulting in electrochemical irreversibility, can be removed by cleaning the working electrodes with very fine alumina, or electrochemically, by holding the potential at very positive or very negative potentials in clean solvent/electrolyte. The purity of the solvent is the key to electrochemical reversibility and the accessible potential window and high purity dry solvents should always be used. Typical dry solvents, dried over molecular sieves, include millimolar water which is similar in concentration to most analytes in electrochemical experiments. Additional drying is sometimes needed and can be accomplished with many organic solvents using alumina that has been activated at high temperatures in a vacuum oven and dried in an inert atmosphere. The solvent should be syringe filtered to remove any small particles. The solvent, electrolyte, and analyte solution must not contain undissolved materials as this can lead to adsorption issues that give rise to reversibility problems. As already mentioned, the presence of H_2O limits the accessible potential window. The standard oxidation and reduction potentials for water however, are 1.23 V ($O_2(g) + 4H^+(aq) + 4e^- \rightarrow 2H_2O$) and −0.83 V ($2H_2O + 2e^- \rightarrow H_2(g) + 2OH^-(aq)$) versus NHE,[21] which are pH dependent. Solutions should also be sufficiently deoxygenated to remove O_2 or the oxygen couple will appear as an irreversible couple at approximately −0.8 V versus Ag/AgCl and O_2 could react with the reduced analyte. Bubbling argon prior to taking the measurement is typical but once data collection begins, bubbling must be discontinued to prevent a turbulent solution from affecting mass transport leading to a very noisy signal. To obtain a proper signal, the electrochemical circuit must be complete or the electrochemical signal will display significant noise or zero current. If there is not enough electrolyte added to the solution, resistance could be too high resulting in poor current flow, often reflected by very high ΔE_p and/or a ramp-like signal in CV. Typically 0.1 M electrolyte is sufficient. Air bubbles can sometimes form within a reference electrode which can block the solvent interface resulting in issues with the signal or potential measurement. These bubbles can be dislodged by tapping the electrode. Bubbles under the working electrode can also lead to similar issues.

3.1.4 Example of Application of CV to Study Rh Complexes

DeArmond used CV to probe reaction sequences for $[Rh^{III}(bpy)_3]^{3+}$ and $[Rh^{III}(bpy)_2Cl_2]^+$ F.[6] First, cyclic voltammograms were recorded at two different sweep rates, 0.10 and 31 V s^{-1} (Figure 7a). The slower sweep rate shows an irreversible two-electron rhodium reduction followed by two one-electron bpy reductions. The fast sweep rate reveals that the two-electron rhodium reduction is actually two one-electron reductions with little separation. Figure 7(b) shows the initial part of the first reduction at a very fast scan rate, 46 V s^{-1}. Reversing the potential after the very first part of the rhodium reduction (at ca. −0.85 V) isolates the $Rh^{III/II}$ couple from the $Rh^{II/I}$ couple. Isolating couples can provide information about peak reversibility. At the fast 46 V s^{-1} scan rate, the first part of the reduction has a corresponding oxidation indicating reversibility for the first one-electron reduction of $[Rh^{III}(bpy)_3]^{3+}$. These data, suggest that the irreversible nature of the $Rh^{III/II/I}$ couple at slower scan rates are due to the $Rh^{II/I}$ couple, indicating that a chemical reaction takes place upon generation of Rh^I, that is, loss of a bipyridine. The related complex, $[Rh^{III}(bpy)_2Cl_2]^+$, displays an irreversible reduction even when attempting to isolate the first couple. This indicates a reaction following the first one-electron reduction to generate Rh^{II} that is loss of chloride. Finally the complex $[Rh^I(bpy)_2]^+$ shows no reduction corresponding to the $Rh^{III/II/I}$ couple confirming the rhodium-based identity of the first reduction in $[Rh^{III}(bpy)_3]^{3+}$ and $[Rh^{III}(bpy)_2Cl_2]^+$ (Figure 7c).

3.1.5 Surface-Attached Analytes in CV

Analytes can also be bound to the electrode surface resulting in unique nondiffusion controlled electrochemistry. Meyer used 4-vinyl-4′-methyl-2,2′-bipyridine (vbpy) bound

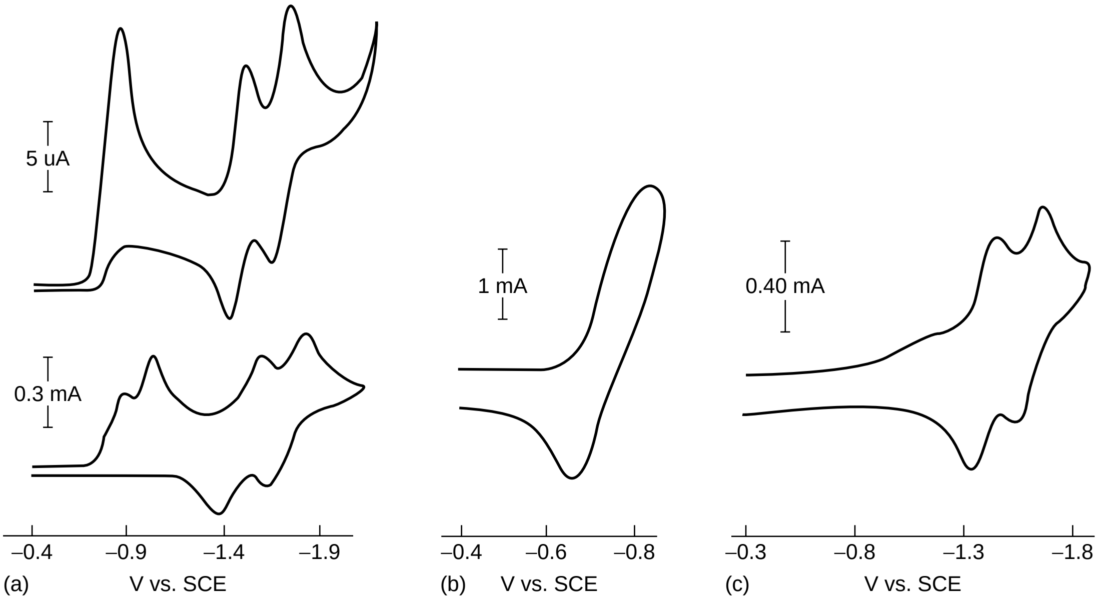

Figure 7 Cyclic voltammetry for $[Rh^{III}(bpy)_3]^{3+}$ (bpy = 2,2′-bipyridine) measured in CH_3CN with 0.1 M Et_4NClO_4 versus SCE showing: (a) the reductive region at two different scan rates, 0.10 V s^{-1} and 31 V s^{-1} (see also Figure 2b); (b) the initial part of the first reduction at a high scan rate, 46 V s^{-1}, showing some reversibility, and (c) reduction of the reduced complex $[Rh^I(bpy)_2]^+$ showing the absence of the rhodium reduction as its already in a reduced state, followed by two reversible bpy$^{0/-}$ reductions.[6] (Reprinted with permission from Kew, DeArmond and Hanck[6] © 1974 American Chemical Society)

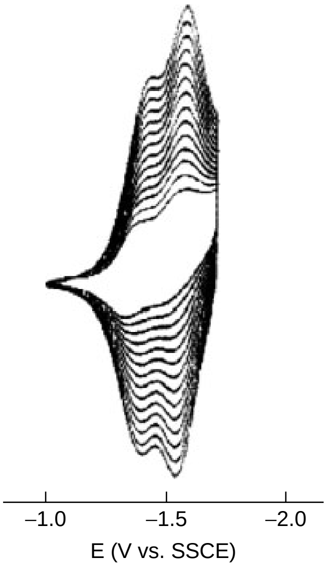

Figure 8 Cyclic voltammogram showing the reductive region of the electropolymerization of $[Ru(vbpy)_3]^{2+}$ (vbpy = 4-vinyl-4′-methyl-2,2′-bipyridine) versus SSCE with 0.1 M Et_4NClO_4 as the supporting electrolyte in CH_3CN on a platinum electrode.[25] (Reprinted with permission from Denisevich, Abrura, Leidner, Meyer, and Murray[25] © 1982 American Chemical Society)

to metal complexes to electropolymerize and thereby attach ruthenium, osmium, and cobalt complexes to the electrode surface.[25] Electrode attachment via an electropolymerization reaction results in a thin film of transition metal complexes bound to the platinum working electrode. Once the analyte is surface bound, diffusion is not needed in electrochemical measurements. Figure 8 shows the electropolymerization in progress as initiated and monitored by CV. The peak current increases as more analyte is attached to the electrode via the electropolymerization process, initiated by reduction of the vbpy ligand. The CV of the surface-attached analyte shows no peak to peak separation (ΔE_p) as diffusion is not needed when the analyte is attached to the electrode surface.

Alkyl thiols have also been used to covalently attach inorganic complexes to electrode surfaces.[26] Ferrocene terminated thiols have been shown to form self-assembled monolayers as a mixture with alkane thiols on the surface of a gold electrode. These systems can be used to study interfacial electron transfer or can be employed in the biosensor field. Figure 9 shows a cyclic voltammogram of a ferrocene thiol attached to a gold electrode surface. These thiol-modified electrodes have monolayer coverage. The electrochemical signal is characteristic of a surface-attached species showing low background current and little to no peak to peak separation, ΔE_p. Thiol-modified electrodes with redox active sites are also used as electron relays to catalyze a redox process in a solution. The analyte in the solution does not undergo oxidation or reduction until the surface-bound redox active site is oxidized or reduced since the analyte cannot approach the electrode surface. The typical signal for such a measurement is a large increase in current for the surface bound redox active site dependent on analyte concentration, with a reduction in the return couple current for the surface bound redox site.

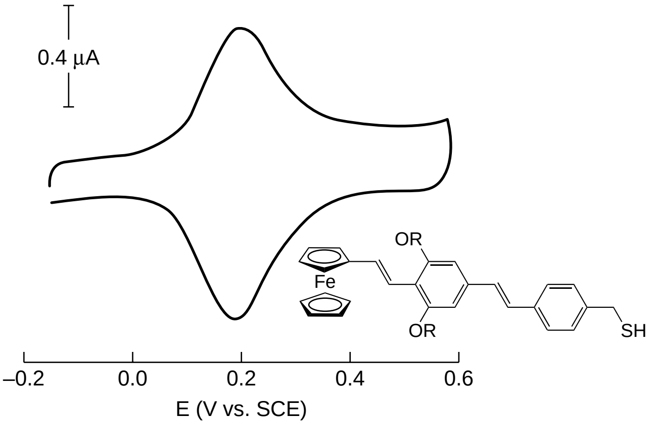

Figure 9 Cyclic voltammogram of a ferrocene terminated thiol bound to the surface of a gold electrode.[26] (Reprinted with permission from Dudek, Sikes, and Chidsey[26] © 2001 American Chemical Society)

3.2 Potential Step/Pulsed Methods

Potential step methods have emerged as valuable electrochemical methods due to the highly sensitive nature of the technique. The waveform employed in potential step methods, also referred to as pulsed methods, have some advantages over potential sweep methods. The main advantage is that the steplike waveform can discriminate and separate the capacitive current versus the faradaic current, the current due to the reduction or oxidation undergone by the analyte, increasing signal to noise. Capacitive versus faradaic current discrimination is the basis for all of the pulsed techniques. The rate of decay of the capacitive current and the faradaic current is not the same. The capacitive current has an exponential decay whereas the faradaic current decays as a function of $t^{-1/2}$. Since the rate of decay of the capacitive current is much faster than that of the faradaic current, the potential is stepped up after which it remains constant for a time delay; the current is measured just before the next step up. This delay in the measurement allows for the capacitive current to fall off to a larger extent than the faradaic current. Due to the decreased capacitive current, the potential step/pulsed techniques result in a larger accessible potential window, a higher signal-to-noise ratio, and a lower limit of detection. Scan rates for this method are typically slow, $50\,mV\,s^{-1}$, due to the delay that is necessary to minimize the capacitive current. Faster scan rates are possible, but increasing the scan rate results in a decreased signal-to-noise ratio. The potential step methods that will be discussed include voltammetric techniques (use of a solid working electrode) like normal pulse voltammetry

(NPV), differential pulse voltammetry (DPV) and SWV, and polarography methods (use of a mercury drop electrode) like normal (normal and pulse polarography (NPP)) and DPP, although sometimes these polarographic versus voltammetric terms are used interchangeably. These step methods do not typically use return scans and therefore often do not provide information about reversibility of the redox process and can sometimes give data that, unknown to the researcher, are characteristic of decomposition products.

3.2.1 *Voltammetric Techniques*

Normal Pulse Voltammetry (NPV). Normal pulse voltammetry (NPV) has the waveform shown in Figure 10(b), and uses a steplike waveform to minimize the capacitive current. Again it is best to start at rest potential. The pulse is comprised of an initial potential step up, followed by holding the potential steady for a length of time which defines the pulsed width. The current measurement takes place at the end of the pulse, followed by the potential stepped back down to the initial potential, usually zero or the rest potential. This is the simplest waveform of the pulsed methods. An example of a current signal response is shown in Figure 10(a).

Differential Pulse Voltammetry (DPV). There are two main differences between differential pulse and NPV. The waveform for DPV, Figure 10(b), involves a pulse of amplitude ΔE_{pulse} like that of the normal pulse sequence but the step back down is not to the initial potential, instead it is to a specific differential that is used during the measurement. Also, there are two sampling periods for each pulse, once at the end of the potential step up, like in NPV, and an additional sampling period at the end of the step down in potential, after which the difference in the two signals is recorded; hence the name DPV. This pulse sequence results in a current signal response different from that of NPV, shown in Figure 10(b). If the electrochemical process is reversible, the peak half width, $\Delta E_{p/2}$, is determined by equation (9),**[1]**

$$\Delta E_{p/2} = \frac{(3.52\,\text{RT})}{(nF)} \tag{9}$$

and the current at time t, i_t, is determined by equation (10) where $(t-t')$ is the time of the pulse width.**[1]**

$$i_t = \frac{(n\text{FAD}_{\text{o}}^{1/2}C_{\text{o}})}{(\pi^{1/2}(t-t')^{1/2})} \tag{10}$$

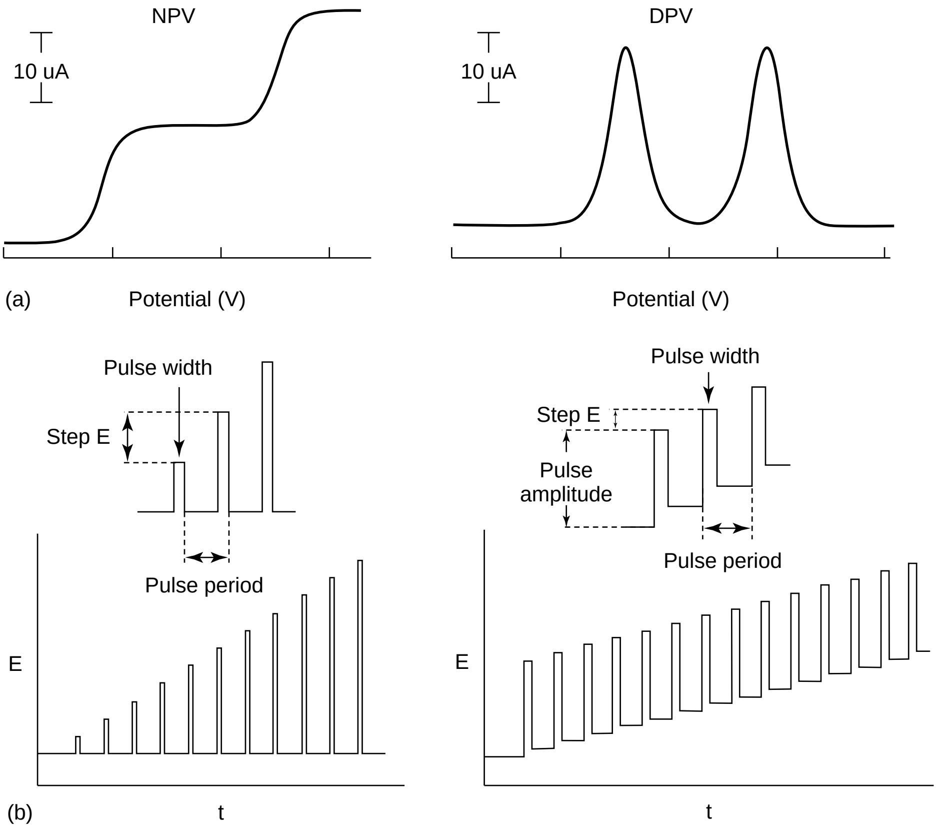

Figure 10 Potential waveforms for normal pulse (NPV) and differential pulse voltammetry (DPV) displaying potential versus time (b), and a typical normal pulse and differential pulse voltammogram plotting current versus potential (a)

Square Wave Voltammetry (SWV). SWV, the third potential step method discussed here, has recently found widespread use. It was developed by Ramaley and Krause during the 1960s[27] and popularized by Janet and Robert Osteryoung in the 1980s[28,29] and is sometimes referred to as Osteryoung squarewave voltammetry (OSV). This technique is an especially useful method for investigating electrochemical reactions with overlapping redox waves. The pulse sequence is very similar to DPV, shown in Figure 10(b), but typically can be conducted at faster scan rates. There is a potential step up, which could be anodic (or cathodic), where the potential is held steady and the first current measurement is taken. This potential step is followed by a reversal of the potential opposite of the initial potential change. This cathodic (or anodic) potential step is exactly double the original anodic (or cathodic) potential step. This is followed by the potential held steady for the same period as the first potential step, at the end of which the second current measurement is taken. The next potential step up is equal to the step down plus a small potential increment. The waveform then repeats. Both the anodic and cathodic potential changes are proportional to the pulse widths forming a squared appearance. The current signal response in Figure 11 is also similar to DPV but typically higher scan rates are possible. The increased tolerance of faster scan rates is due to measuring the difference current. Some of the capacitive current is subtracted out so the long delay to decrease the capacitive current is not as necessary as with the other stepped techniques. The difference current, Δi, for SWV is given by equation (11).[1]

$$\Delta i = \Delta\psi \frac{(nFAD_o^{1/2}C_o)}{(\pi^{1/2}t^{1/2})} \tag{11}$$

where $\Delta\psi$ is a dimensionless peak current that depends on potential variables.

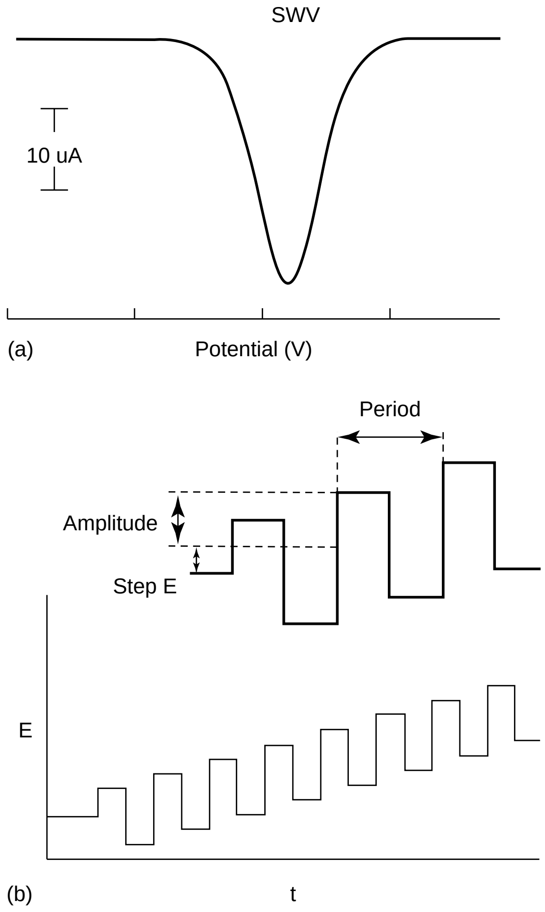

Figure 11 Potential waveform for square wave voltammetry (SWV) displaying potential versus time (b), and a typical square wave voltammogram plotting current versus potential (a)

Practical Considerations for Potential Step Techniques. Potential step techniques have many advantages that result from the pulse sequence. One disadvantage of the pulsed techniques is that the relatively slow scan rates employed can sometimes make interpreting the results difficult if the electrogenerated species is not particularly stable. This may lead to observed data being unknowingly characteristic of a decomposition product and not the analyte. Coupling to other electrochemical techniques like CV can help uncover decomposition. The application of SWV has improved the scan rate limitation. Given that reverse scans are not typically available with most commercial instruments, information about reversibility present in CV may be unavailable in these pulsed methods. Cyclic SWV has been developed by Osteryoung[30] but this pulse sequence is not typically available on most commercial instruments. The same practical considerations are necessary with the potential step methods as the potential sweep methods. Solutions must be dry and deoxygenated, and a sufficient amount of electrolyte and analyte are required for optimal signal-to-noise ratio, although generally a lower concentration of analyte can be used, given the higher signal-to-noise ratio of these pulsed techniques.

Application of Square Wave Voltammetry to Analysis of Hydrogen Peroxide. Stevenson used SWV in a method developed for detection of ultralow concentrations of H_2O_2, designed for biodiagnostic applications.[31] For biosensors, typically enzymes are employed to catalytically generate a redox active species like H_2O_2 which can be detected electrochemically. Stevenson's approach utilized a microelectrode in conjunction with a chemically activated mediator, Amplex Red, which is chemically oxidized by H_2O_2 in the presence of horseradish peroxidase. SWV is used because of its background suppression and intrinsic low limit of detection. For this application SWV was more sensitive than CV by a factor of five (Figure 12). This combined SWV method with the mediator and peroxidase, results in a significant increase in analytical sensitivity for H_2O_2 detection, resulting in detection limits as low as 8 pM.

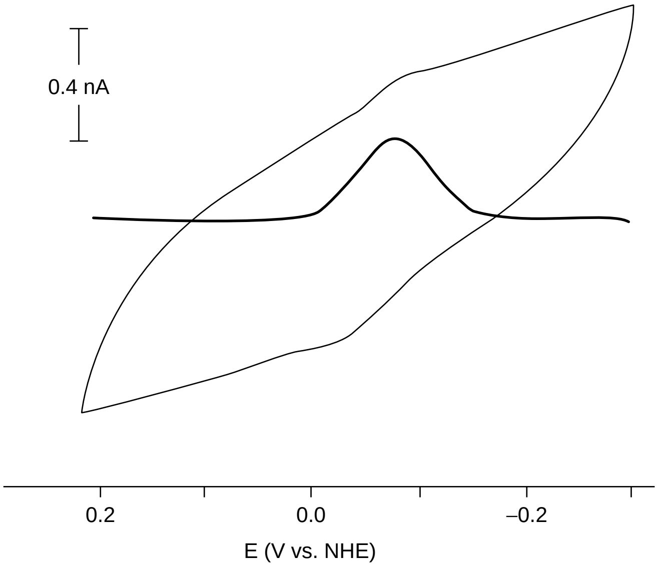

Figure 12 A 300 nM H_2O_2 standard is shown for both cyclic voltammetry (CV) (light line) and square wave voltammetry (SWV) (heavy trace) comparing the signal-to-noise ratio of the two techniques.[31] (Reprinted with permission from Lyon and Stevenson[31] © 2006 American Chemical Society)

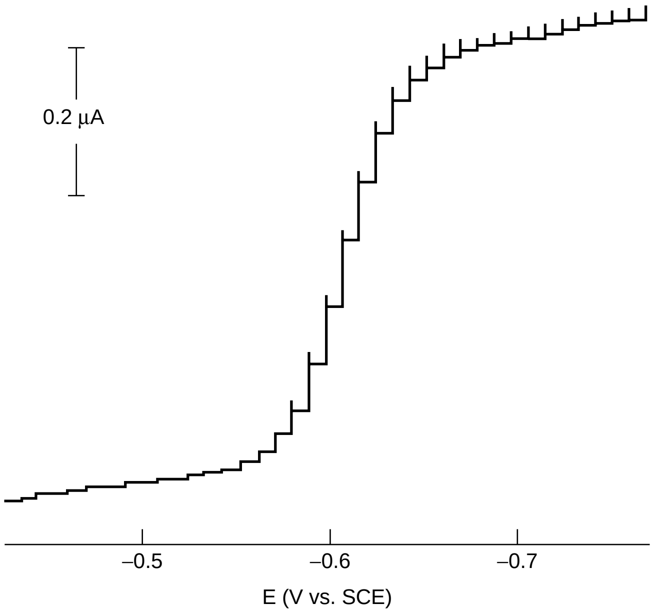

Figure 13 Normal pulse polarogram for a DME displaying a typical sigmoidal current response plotted versus potential (V vs. SCE)[1]

3.2.2 *Polarography Techniques*

The nature of the waveform for potential step/pulsed techniques lends itself well to polarographic techniques. Polarography techniques use a mercury drop electrode like a DME, historically the most commonly employed mercury electrode, a static drop mercury electrode (SDME), or a hanging drop mercury electrode (HDME). With the DME, each pulse can coincide with each drop of mercury. Using an electrode that is constantly replenished can be beneficial if the redox process leads to analyte adsorption, as replenished electrodes do not need to be cleaned. Since the 1980s, the SDME has become the primary electrode for polarographic techniques. The voltammetric techniques discussed in the previous section, NPV and DPV, were originally developed as polarography techniques and used in analytical chemistry. The waveforms for NPP are the same as those of the voltammetric methods discussed previously. There are however, a number of differences between the techniques, all of which are due to the nature of the electrodes.

The DME, invented by Heyrovsky[32] is a historically important technique which forms the basis for many of the electrochemical techniques discussed here. This electrode is composed of a capillary through which mercury flows forming a spherical drop of approximately 1 mm, at which point its weight surpasses the surface tension and the drop falls into solution. There are a few drawbacks to this technique. The mercury drop has a finite lifetime, typically 2 to 6 s, and with the drop moving through solution, the area can continuously change which makes accounting for mass transport difficult.

The SDME, also referred to as a HDME, was developed by Princeton Applied Research Corporation in 1980[1] to overcome some of the disadvantages of the DME. This electrode also employs a capillary to allow mercury to form a drop; however, in the case of the SDME, the mercury drop can remain attached to the surface indefinitely. The drop can be dislodged and a new one formed as needed. The drop remains stationary for as long as is needed and is stable in size, making it easier to account for mass transport mathematically. One major difference between polarographic techniques and voltammetric techniques is mass transport by diffusion. Polarography relates to how the working electrode operates using polar coordinates to deal with electrode processes like radial diffusion. NPP and DPP utilize the same waveforms as their voltammetric counterparts, however, with radial diffusion, the current response changes from a peak shape to a sigmoidal shape. A typical current response can be seen in Figure 13 using a normal pulse waveform, the same waveform as in Figure 10(a).

3.3 Hydrodynamic Methods

A few electrochemical techniques make use of working electrodes that are nonstationary. The rotating disk (RDE) and RRDE, as their names suggest, rotate as a means to affect mass transport. Rotations make the diffusion layer thinner which increases the concentration gradient. The thinning of the diffusion layer and the increase in the concentration gradient can be controlled as they are both proportional to the spinning speed of the electrode. Increasing the concentration gradient leads to an increase in the faradaic current relative to the capacitive current assisting with the signal to noise ratio and a steady state is achieved quickly. Under nernstian conditions the concentration of the species to be oxidized or reduced is essentially zero which can be achieved by setting the potential negative or positive enough respectively. Construction of RDE and RRDE is more difficult than stationary electrodes as the mass transport conditions under laminar flow must be reproducible. The mass transfer limited current, i_l (A), is given by the Levich equation,[2] equation (12),[1]

$$i_l = 0.620\, n\, \mathrm{FAD}_{\mathrm{o}}^{2/3} C_{\mathrm{o}} \cdot \nu^{-1/6} \omega^{1/2} \tag{12}$$

where n is the number of electrons, F is Faraday's constant, A is the electrode surface area (m^2), D_o is the diffusion coefficient ($\mathrm{m}^2\,\mathrm{s}^{-1}$), C_o is the concentration of analyte ($\mathrm{mol\,L^{-1}}$), ν is the kinematic viscosity of the solution and ω is the angular velocity of the disk.[2]

Meyer used a RDE to study the diffusion of ferrocene through a thin film of poly(x)$[\mathrm{Ru(Me_4bpy)_2(vpy)_2}](\mathrm{PF_6})_{2x}$ $(1-x)[\mathrm{Ru(vbpy)_3}](\mathrm{PF_6})_{2-2x}$ ($\mathrm{Me_4bpy} = 4,4',5,5'$-tetramethyl-2,2′-bipyridine), to analyze the porosity of different films.[33,34] Section 3.1.5 also discusses complexes bound to electrode surfaces. Photolysis of these films leads to photocleavage of the $\mathrm{Ru^{II}}$–vpy bonds resulting in loss of $[\mathrm{–Ru(Me_4bpy)_2}](\mathrm{PF_6})_2$ fragments. This results in a more porous film with less crosslinking. Diffusion studies using a RRDE show that the thin films act as a size selective barrier to the electrode.

3.4 Bulk Electrolysis (BE)

All of the techniques discussed thus far represent oxidations or reductions taking place at the electrode surface resulting in a diffusion layer where the species to be oxidized or reduced is depleted and a bulk solution where no net redox process takes place. BE techniques differ in that the redox process takes place on a large scale and through forced convection the entire solution will undergo electrolysis. These methods use convection by stirring or bubbling and large surface area working and auxiliary electrodes. The potential is set slightly more positive or negative of the oxidation or reduction that is going to take place and remains at that level for the duration of the experiment. The current is plotted versus time and the electrolysis is considered complete when the change in current overtime is minimal (Figure 14). Typically the current is measured and integrated and the number of electrons for the redox process can be determined since the concentration of the analyte is known and the total charge passed, Q, is determined. BE is governed by Faraday's Law, equation (13).[1]

$$Q = nFE \tag{13}$$

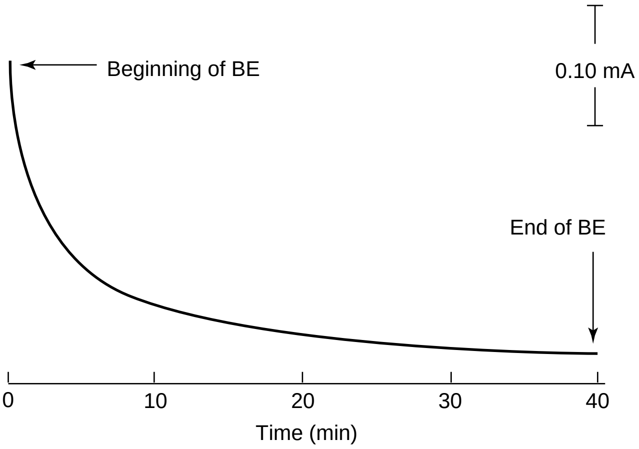

Figure 14 Bulk electrolysis (BE) displaying current versus time

Q is the total charge passed, n is the number of electrons passed, F is Faraday's constant (96 485 C mol^{-1}),[4] and E is the potential of the electrolysis. This technique, the most common BE method, is also referred to as potentiostatic coulometry. Another BE method used is amperostatic coulometry, whereby the current is kept constant. This technique requires the use of an amperostat instead of a potentiostat which limits its use.

3.4.1 Electrosynthesis

Another type of BE is electrosynthesis, a synthetic technique that takes place in an electrochemical cell. The potential is set to drive the intended redox reaction and electrolysis continues until all the analyte has been reduced or oxidized. Electrosynthesis is often useful in industrial applications and is desirable, as side reactions are often minimal compared to conventional synthetic techniques.

Electrocatalysis is a type of electrosynthesis that uses surface modified electrodes, or mediators/electrocatalysts to facilitate the redox reaction. Meyer reported the design and synthesis of a chemically modified electrode that consists of a thin polymer film with covalently attached redox sites,[35] designed to facilitate rapid electron transport for electrocatalysis. Complexes of Fe, Ru, Os, Re, and Co were synthesized in such a way that when electrochemically reduced, they reacted to form smooth electroactive polymer films that adhered well to the working electrode to form a chemically modified electrode designed for electrocatalysis.

3.4.2 Electrocatalysis of CO_2 Reduction by $[Ni(cyclam)]^{2+}$

The conversion of $\mathrm{CO_2}$ to CO is a valuable commercial process. Reductive electrocatalysis of $\mathrm{CO_2}$ to CO can be performed on a mercury electrode with $[\mathrm{Ni(cyclam)}]^{2+}$ (cyclam = 1,4,8,11-tetraazacyclotetradecane) present as the electrocatalyst.[36] Sauvage has shown that $[\mathrm{Ni(cyclam)}]^{2+}$

can act as an efficient and selective electrocatalyst for this reaction which can function in pure water at potentials 0.5 V more negative than the thermodynamic value (E (CO_2/CO) = −0.41 V vs. NHE at pH = 5). No electroreduction is observed at this potential without $[Ni(cyclam)]^{2+}$ as the overpotential for direct CO_2 electroreduction is high.

3.4.3 Electrocrystallization

Electrocrystallization is another synthetic method similar to BE. Electrocrystallization is unique in that certain higher oxidation states are obtainable that would otherwise not be accessible through normal synthetic procedures. The silver oxides AgO and Ag_2O_3 were originally synthesized using this approach[37] and the highly oxidized Ag_3O_4 is the only example of a binary silver compound in the Ag^{II} oxidation state.[38] There are many parameters to consider when performing electrocrystallization. In addition to the electrolysis parameters, voltage, current, concentration, and temperature, the electrode material and structure also can have a large impact on products. The complexity of electrocrystallization makes it difficult and time consuming to fully explore all avenues for a particular synthesis. The products obtained through electrocrystallization are very pure and crystalline in nature.

3.4.4 Bulk Electrolysis Cell Design

BE techniques take place in a cell of a design different from the techniques discussed previously. These ‘‘bulk’’ methods require electrolyzing much larger samples, necessitating several design changes including the electrodes and the cell. There are two different cell designs both of which are designed to separate the auxiliary electrode from the working electrode.

The single cell design employs an outer compartment which contains the working and reference electrodes and an inner compartment which contains the auxiliary electrode. The secondary compartment hangs into the working compartment and makes solution contact through a porous glass frit.

The second cell design is referred to as an H-cell, which is composed of two cells connected via a porous glass frit. This separation allows the flow of supporting electrolyte ions to provide current flow but inhibit the flow of analyte (Figure 15). The analyte is contained in the working compartment along with the working electrode and reference electrode, while the auxiliary electrode is placed in the secondary compartment. Deoxygenation is necessary as is stirring to ensure efficient mass transport to the working electrode surface.

The electrodes for BE methods are important for efficient electrolysis. The working and auxiliary electrodes are required to electrolyze much more of the sample in these BE techniques. The working and auxiliary electrodes discussed previously are typically replaced by a large surface area electrode like a platinum mesh or a carbon cloth in order to facilitate the electrolysis of a large amount of sample. Typically the working electrode is cylindrical with the reference electrode located in the center of the working electrode to provide accurate voltage control. Sometimes an isolation chamber is employed for the reference electrode to prevent leaking of the reference electrode solution into the analyte solution. The auxiliary electrode must be isolated from the working electrode compartment to allow for bulk conversion of the analyte. Mixing of the auxiliary and working compartment solutions will result in incomplete electrolysis and/or decomposition. Stirring or bubbling of the analyte solution during electrolysis provides good mass transport.

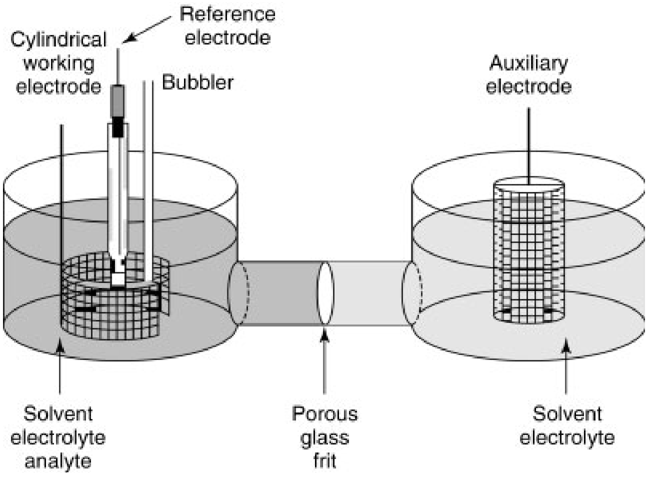

Figure 15 H-cell for bulk electrolysis showing the working and auxiliary electrodes, reference electrode, bubbler, porous glass frit, solvent, electrolyte, and analyte

3.5 Electrochemical Simulations

A number of programs, like DigiSim, are capable of performing a variety of simulations. The first electrochemical simulations were designed to simulate mass transfer at different temperatures. Later programs were designed to perform general electrochemical simulations and fit experimental data. Electrochemical simulations have also been designed to evaluate the redox behavior of samples. Some software can simulate CV and other electrochemical techniques under various solution conditions like mass transport (convection, diffusion, migration), solution resistance, and pH, and various analyte factors like concentration, temperature, standard redox potentials, number of electrons transferred, and reaction rate constants.

Salimi used the DigiSim program to analyze the electrochemical properties of an aqueous dye, thionin, at a range of pH values.[39] When thionin is electrochemically reduced it can act as a catalyst for Cr(VI) reduction. DigiSim was used to determine the standard potential and kinetic parameters for thionin by fitting cyclic voltammograms measured experimentally to the DigiSim generated CV.

3.6 Correlation of Electrochemistry to Electronic Spectroscopy

The orbitals involved in electrochemical processes are often the same orbitals involved in electronic transitions. The first electrochemical oxidative process corresponds to the removal of an electron from the HOMO and the first reduction corresponds to the addition of an electron into the LUMO. The energy gap between these two processes is indicative of the gap between the HOMO and LUMO. Although there exists a correlation between HOMO–LUMO gaps and the energy gap of the first oxidation and the first reduction, equation (14), energy gaps involving subsequent redox processes are not directly correlated as the second reductive or oxidative process is taking place on the already reduced or oxidized complex, respectively. This HOMO-LUMO electrochemical energy gap has been correlated to the spectroscopic energy gap:

$$E_{\text{optical}} = \Delta E_{\text{redox}} + \Sigma_i a_i \tag{14}$$

Where E_{optical} is the energy of an optical transition (absorption or emission), ΔE_{redox} is an electrochemical potential, an $E_{1/2}$, and $\Sigma_i a_i$ is a collection of factors based on differences between the two process which have inequivalent orbital energies.[40] Approximations for $\Sigma_i a_i$ typically utilize the E_{00}, the energy between the ground vibrational state of the first electronic excited state to the ground vibrational, ground electronic state, often measured by emission spectroscopy. Figure 16 shows the correlation between ΔE_{redox} and E_{00} for a series of ruthenium complexes.[40] When spectroscopy and electrochemistry are combined together they become a powerful coupled technique capable of providing otherwise unobtainable redox and spectroscopic information.

3.7 Coupled Techniques

Coupled techniques have increased in popularity in recent years. Electrochemical techniques can be coupled to another characterization method to provide unique information. Many electrochemical techniques lend themselves well to coupling with other electrochemical or nonelectrochemical techniques. With these methods, cell design is often complex to allow simultaneous execution of both techniques. For example, optically transparent indium tin oxide is used as the working electrode with an optically transparent mesh electrode to allow for simultaneous electrochemical conversion and electronic absorption spectroscopy. For some techniques the sample is electrolyzed and then transferred under inert atmosphere for analysis.

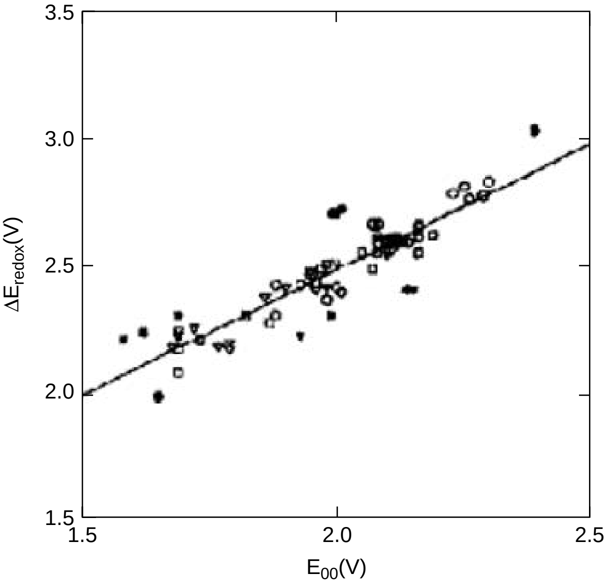

Figure 16 Correlation between ΔE_{redox} and E_{00} for a series of ruthenium complexes where the open symbols are complexes that have ''bipyridinelike'' ligands and the filled symbols have ''non–bipyridinelike'' ligands. Squares are representative of trisubstituted complexes, circles are bipyridine complexes, and triangles are other ruthenium complexes.[40] (Reprinted with permission from Vlcek, Dodsworth, Pietro, and Lever[40] © 1995 American Chemical Society)

3.7.1 *Spectroelectrochemistry*

Spectroelectrochemistry has become a valued technique coupling spectroscopy and electrochemistry. Spectroelectrochemistry is a bulk electrochemical technique and as such many of the cell requirements discussed above that pertain to BE apply for spectroelectrochemistry. Often concentrations for spectroelectrochemistry are much lower than most electrochemical techniques due to the spectroscopic absorbance requirements. The bulk solution must still be oxidized/reduced in spectroelectrochemistry. Large surface area working and auxiliary electrodes are employed as in the bulk methods described above. Cells designed with optically transparent electrodes like thin films of SnO_2 or In_2O_3 or optically transparent mesh electrodes are employed, otherwise the electrode must be manually removed to record spectra.[1] Optically transparent electrodes can be constructed such that the solution volume to electrode surface area ratio is very small making the BE occur rapidly.

Many types of spectroscopy have been coupled with electrochemistry including electronic absorption spectroscopy, X ray (*see* ***X-Ray Absorption Spectroscopy***), infrared (IR) (*see* ***Vibrational Spectroscopy***), or Raman spectroscopy, ellipsometry, specular reflectance, and electron spin resonance (ESR). Electronic absorption spectroscopy, one of the most prominent electrochemistry coupled with spectroelectrochemical techniques, will be discussed here as will the vibrational spectroscopy techniques, IR and Raman spectroelectrochemistry, and the ESR spectroscopic technique (ESR).

Electronic Absorption Spectroelectrochemistry. Electronic absorption spectroscopy with UV and visible light is a form of spectroelectrochemistry typically employed as a transmission experiment to investigate changes in absorbance due to a species being oxidized or reduced. Typically the potential is scanned while the absorbance at a particular wavelength is recorded or the potential is stepped while a full spectrum is collected. Spectroelectrochemistry of this type can be used to establish spectroscopic signatures of reduced or oxidized forms of a compound that can be correlated to excited state transient absorbance spectroscopy.

Spectroelectrochemical measurements can be used to identify the absorption characteristics of reduced or oxidized species that can be useful in understanding excited state properties of a complex. This technique can be used in conjunction with transient absorption spectroscopy which can also provide information on excited state properties. Together, these techniques can provide a better understanding of complex excited state behavior. McCusker used these two techniques to study the excited state properties of $[Ru(dmb)_3]^{2+}$ and $[Ru(dpb)_3]^{2+}$ (dmb = 4,4′-dimethyl-2,2′-bipyridine and dpb is 4,4′-diphenyl-2,2′-bipyridine).**[41]** Nanosecond time resolved transient absorption spectroscopy was used in conjunction with spectroelectrochemistry to assign the excited state spectroscopy. Figure 17 shows the transient spectrum of $[Ru(dpb)_3]^{2+}$ which is correlated to the spectroscopy of the electrogenerated oxidized Ru and reduced dpb forms of the complex.

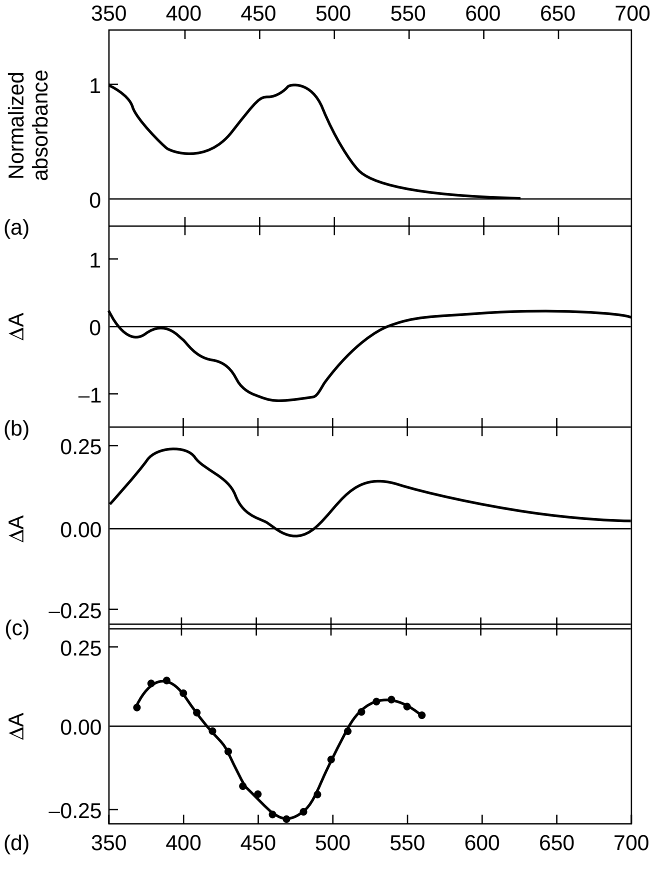

Figure 17 (a) Electronic absorption spectrum for $[Ru(dpb)_3]^{2+}$ in CH_3CN; (b) change in absorbance spectrum for $[Ru(dpb)_3]^{2+}$ after electrochemical oxidation at +1100 mV versus $Ag/AgNO_3$ for 20 min in CH_3CN with 0.1 M Bu_4NPF_6 electrolyte; (c) change in absorbance spectrum for $[Ru(dpb)_3]^{2+}$ after electrochemical reduction at −1600 mV versus $Ag/AgNO_3$ for 10 min in CH_3CN with 0.1 M Bu_4NPF_6 electrolyte (d) difference absorption spectrum of (b) and (c).**[41]** (Reprinted with permission from Damrauer and McCusker**[41]** © 1999 American Chemical Society)

Brewer and Elvington used spectroelectrochemistry to investigate a photochemical problem involving a transition metal complex.**[42]** Spectroelectrochemistry was used to help elucidate a complex sequence of excited state reductions in the supramolecular complex $[\{(bpy)_2Ru(dpp)\}_2RhCl_2]^{5+}$ (dpp = 2,3-bis-2-pyridylpyrazine). The spectroelectrochemical experiment involved the bulk reduction of the complex at −0.4 V vs. Ag/AgCl, just after the two-electron $Rh^{III/II/I}$ irreversible couple. The complex is monitored by Ultra violet visible absorption spectroscopy as the reduction is taking place (Figure 18). The electrochemical reduction and the resultant spectroscopy are correlated with a photochemical experiment, establishing that this complex is reduced by multiple electrons photochemically.

Electronic coupling can be probed using electrochemistry. Brewer and Richter investigated bimetallic complexes of the form $[(bpy)_2Os(BL)Os(bpy)_2]^{4+}$ (BL = 2,3-bis(2-pyridyl)pyrazine (dpp), 2,3-bis(2-pyridyl)quinoxaline (dpq) or 2,3-bis(2-pyridyl)benzoquinoxaline (dpb), and bpy = 2,2′-bipyridine) by electronic absorption spectroscopy and spectroelectrochemistry.**[43]** When BL = dpb, the $E_{1/2}$

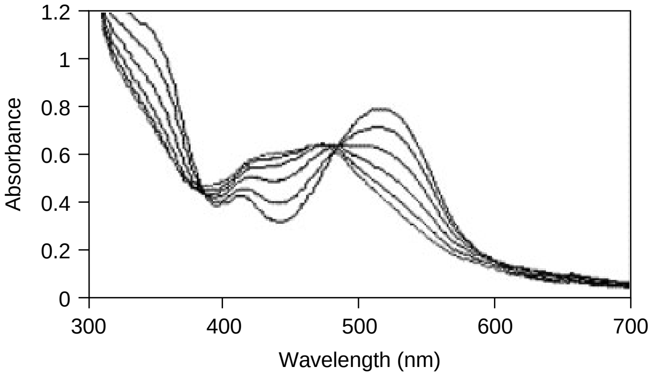

Figure 18 Electronic absorption spectrum for the electrolysis of $[\{(bpy)_2Ru(dpp)\}_2Rh^{III}Cl_2]^{5+}$ (bpy = 2,2′-bipyridine, dpp = 2,3-bis-2-pyridylpyrazine) in CH_3CN with 0.1 M Bu_4NPF_6 at −0.4 V versus Ag/AgCl.**[42]** (Reprinted with permission from Elvington and Brewer**[42]** © 2006 American Chemical Society)

for the $\mathrm{Os^{II}Os^{II}/Os^{III}Os^{II}}$ couple is at 0.98 V and the $\mathrm{Os^{III}Os^{II}/Os^{III}Os^{III}}$ couple is 1.30 V vs. Ag/AgCl. The $\Delta E_{1/2} = 0.32\,\mathrm{V}$ allows one to calculate the comproportionation equilibrium constant, K_{com}.

$$\mathrm{Os^{III}, Os^{III} + Os^{II}, Os^{II}} \xrightleftharpoons{K_{\mathrm{com}}} \mathrm{2Os^{III}, Os^{II}}$$

K_{com} can be calculated from electrochemical data using equation (15) for $T = 298\,\mathrm{K}$.

$$K_{\mathrm{com}} = \mathrm{e}^{\Delta E_{1/2}/25.69} \qquad (15)$$

From the $\Delta E_{1/2} = 320\,\mathrm{mV}$, K_{com} is 1.6×10^5, indicating this complex is a Robin and Day class II mixed-valence complex. Electronic absorption spectroelectrochemistry in the near infrared (NIR) shows an osmium-based intervalence charge transfer (IVCT) at 2440 $\mathrm{cm^{-1}}$. The extent of electronic delocalization, α^2, can be calculated using equation (16).

$$\alpha^2 = \frac{(4.2\ 10^{-4}\ E_{\max}\Delta v_{1/2})}{(\mathrm{d}^2 E_{\mathrm{op}})} \qquad (16)$$

$E_{\max}$ is the extinction coefficient of the IVCT transition ($\mathrm{M^{-1}\,cm^{-1}}$), $\Delta v_{1/2}$ is the bandwidth at half intensity, d is the distance between the two metals, and E_{op} is the energy of the IVCT transition (cm^{-l}). α^2 for the dpb bridged complex was calculated to be 8.6×10^{-3} which is indicative of a relatively weakly coupled class II mixed-valence complex.

Vibrational Spectroelectrochemistry. Vibrational spectroscopy experiments involve the excitation of a sample with light in the IR region of the spectrum leading to population of vibrational excited states. Oxidized or reduced species often have a change to their bond order which can be detected by IR or Raman spectroscopy. Most electrochemical techniques require a solution with electrolyte which presents a challenge in coupling these techniques as most solvents are strong IR absorbers. The key to effectively probing a sample that has undergone a redox reaction at an electrode by IR or Raman spectroscopy is to minimize the solvent signal. Reducing the solution depth to less than 100 µm helps minimize solvent signal as does utilizing an Fourier transform infrared (FTIR) spectrometer, for which IR spectroelectrochemistry is called subtractively normalized interfacial Fourier transform infrared spectroscopy (SNIFTIRS) (subtractively normalized interfacial FTIR spectroscopy).[1] Since FTIR can record a spectrum in a fraction of a second, many can be recorded and signal averaged. Spectra are also recorded at two potentials before and after an electrochemical change using a difference signal to limit most of the solvent background. Raman spectroscopy involves the detection of visible photons that scatter after striking the sample which can gain or lose small amounts of energy providing vibrational information complimentary to IR spectroscopy. Raman spectroscopy, however, can utilize visible excitation and detection. This allows for the use of aqueous solutions which absorb strongly in the IR region but do not absorb in the visible.

Wertz provides a good inorganic example of Raman spectroelectrochemistry in which a series of ruthenium–polyazine complexes were studied in varying redox states.[44] The series of complexes and redox states studied were $[\mathrm{Ru(bpm)_3}]^{2-n}$ ($n = 0$–4), $[\mathrm{Ru(bpz)(bpy)_2}]^{2-n}$ ($n = 0$–3), $[\mathrm{Ru(bpy)_2(bpz)}]^{2-n}$ ($n = 0$–3), $[\mathrm{Ru(bpz)_3}]^{2-n}$ ($n = 0$–3), (bpm = 2,2′-bipyrimidine, bpz = 2,2′-bipyrazine, bpy = 2,2′-bipyridine) where n is the number of electrons added to the complex. Resonance Raman spectra are recorded at each redox state to investigate the identity of the redox orbital for the series of complexes. Figure 19 shows a

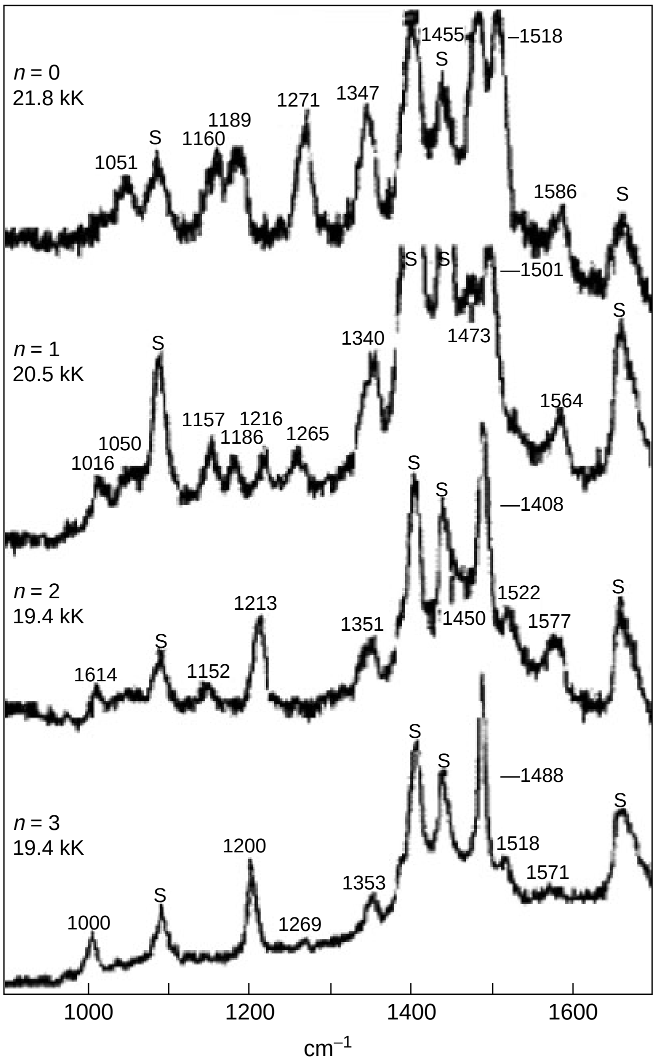

Figure 19 Resonance Raman spectra for the complex $[\mathrm{Ru(bpz)_3}]^{2-n}$ (bpz = 2,2′-bipyrazine) where n is 0, 1, 2, and 3, show a shift in the vibrational frequencies as electrons are added indicating bpz localized redox orbitals.[44] (Reprinted with permission from Tait, Donohoe, DeArmond, and Wertz[44] © 1987 American Chemical Society)

resonance Raman spectra for $[\mathrm{Ru(bpz)_3}]^{2-n}$ illustrating the bpz localized nature of the acceptor orbitals.

3.7.2 Electron Spin Resonance (ESR)

ESR spectroscopy is a sensitive detection method designed to provide information on radicals. This method, also known as electron paramagnetic resonance (EPR) spectroscopy, is naturally a good choice for coupling to electrochemistry as radicals can easily be electrogenerated. ESR involves the detection of unpaired electrons which are affected by nearby nuclei. Radical spin states are modified by interaction with a magnetic field, equation (17).**[1]**

$$\Delta E_{\text{field}} = g\mu_{\text{B}}H \tag{17}$$

Where ΔE_{field} is the splitting of electron spin states by the magnetic field, g is the spectroscopic splitting factor, μ_{B} is the Bohr magneton ($5.788 \times 10^{-5}\,\mathrm{eV}\,T^{-1}$),**[1]** and H is the magnetic field strength. The interaction of the spins with nuclei produces hyperfine structure which can provide information useful in identifying the nature of the electrogenerated radical.

Wertz used low temperature ESR ($T = 90\,\mathrm{K}$) to investigate the electrochemically reduced complex $[\mathrm{Ru(bpz)_3}]^0$. The two-electron reduction product (Figure 20) shows typical ruthenium diimine characteristics for ligand based radicals. Temperature dependent line broadening was observed which is characteristic of electron hopping from a reduced ligand to an unreduced ligand. These data indicate that the ligand orbitals are localized in nature.**[44]**

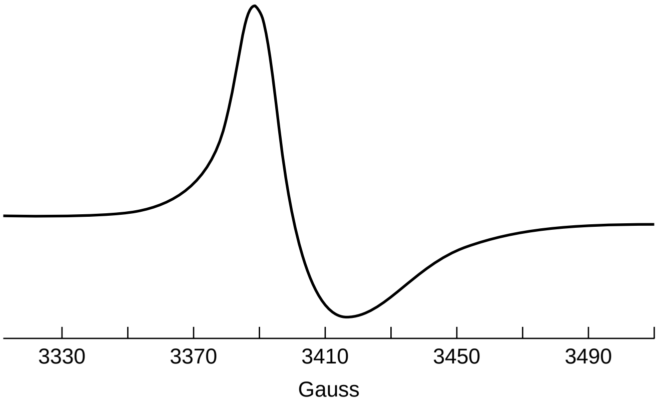

Figure 20 Low temperature ESR spectrum of the complex $[\mathrm{Ru(bpz)_3}]^0$ (bpz = 2,2′-bipyrazine), electrochemically reduced by two electrons in DMF showing the ligand localized nature of the orbitals involved in the reductions. Microwave frequency = 9.55 GHz.**[44]** (Reprinted with permission from Tait, Donohoe, DeArmond, and Wertz**[44]** © 1987 American Chemical Society)

3.7.3 Electrochemiluminescence (ECL)

Electrochemiluminescence (ECL) is a coupled electrochemical/photochemical technique involving the electrochemical generation of excited state with subsequent detection by observation of fluorescence or phosphorescence (*see* ***Photoluminescence and Electroluminescence, Solid State***). Electrochemistry is a natural technique to couple to chemiluminescence as radical ions can easily be electrogenerated which can react to generate electronic excited states. For a detailed description, see Bard and Faulkner's electrochemical methods.**[1]** ECL involves the electrogeneration of reactive species, often radical ions of the analyte where $2\mathrm{A} \rightarrow \mathrm{A}^{+\bullet} + \mathrm{A}^{-\bullet}$ which can then undergo an energetically favorable electron transfer reaction to generate an excited state species, $\mathrm{A}^{+\bullet} + \mathrm{A}^{-\bullet} \rightarrow {}^1\mathrm{A}^* + \mathrm{A}$, or $\mathrm{A}^{+\bullet} + \mathrm{A}^{-\bullet} \rightarrow {}^3\mathrm{A}^* + \mathrm{A}$, which can then be detected by fluorescence, ${}^1\mathrm{A}^* \rightarrow \mathrm{A} + \mathrm{h}\nu$, or phosphorescence, ${}^3\mathrm{A}^* \rightarrow \mathrm{A} + \mathrm{h}\nu$, respectively.

Bard employed electrogenerated chemiluminescence in a study of $[\mathrm{Ru(bpy)_3}]^{2+}$.**[45]** A highly oriented pyrolytic graphite electrode was immersed in a solution containing $[\mathrm{Ru(bpy)_3}]^{2+}$ which strongly adsorbs to the electrode surface creating a monolayer. CV was conducted on the complex coated electrode as emission intensity was recorded concurrently. Figure 21 shows a plot of emission intensity versus potential during a cyclic voltammogram for the $[\mathrm{Ru(bpy)_3}]^{2+}$ coated electrode and the uncoated electrode.

Electrochemistry is a valuable tool for modern inorganic chemistry. A variety of methods can be used to provide information as simple as E° for a particular

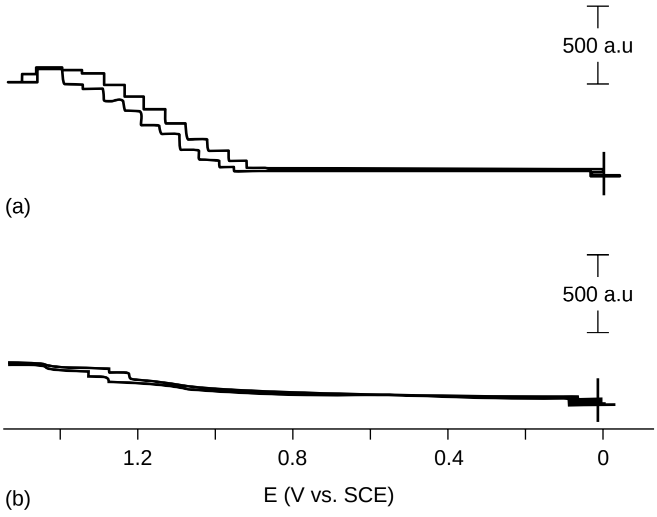

Figure 21 Emission intensity (A.U.) versus potential (V vs. SCE) for a cyclic voltammogram of: (a) $[\mathrm{Ru(bpy)_3}]^{2+}$ (bpy = 2,2′-bipyridine) surface coated electrode; and (b) an electrode with no analyte.**[45]** (Reprinted with permission from Xiao-Hong and Bard**[45]** © 1994 American Chemical Society)

redox process to as complex as Raman signals of an electrogenerated compound. The successful application of these electrochemical methods requires a basic understanding of the factors impacting electrochemical signals, data collection and practical considerations. The widespread use of electrochemical methods in the literature today will advance the understanding of inorganic molecules.

4 ACKNOWLEDGMENTS

Acknowledgment is made to the Chemical Sciences, Geosciences and Biosciences Division, Office or Basic Energy Sciences, Office of Sciences, U. S. Department of Energy for their generous support of our research.

5 ABBREVIATIONS AND ACRONYMS

BAS = bioanalytical systems; BE = bulk electrolysis; CV = cyclic voltammetry; DME = dropping mercury electrode; DMF = N,N-dimethylformamide; DMSO = dimethyl sulfoxide; DPP = differential pulse polarography; DPV = differential pulse voltammetry; ECL = electrochemiluminescence; EPR = electron paramagnetic resonance; ESR = electron spin resonance; FTIR = Fourier transform infrared; HDME = hanging drop mercury electrode; HOMO = highest occupied molecular orbital; IR = infrared; IVCT = intervalence charge transfer; LSV = linear sweep voltammetry; LUMO = lowest unoccupied molecular orbital; NCE = normal calomel electrode; NHE = normal hydrogen electrode; NIR = near infrared; NPP = normal pulse polarography; NPV = normal pulse voltammetry; OSV = Osteryoung squarewave voltammetry; RDE = rotating disk electrode; RRDE = rotating ring disk electrode; RVC = reticulated vitreous carbon; SCE = saturated calomel electrode; SDME = static drop mercury electrode; SHE = standard hydrogen electrode; SNIFTIRS = subtractively normalized interfacial Fourier transform infrared spectroscopy; SSCE = sodium saturated calomel electrode; SWV = square wave voltammetry; THF = tetrahydrofuran.

6 FURTHER READING

R. Hendler, *Anal. Chem.*, 1977, **49**, 1914.

D. Lide, ‘Handbook of Chemistry and Physics’, 87th edition, CRC Press, LLC, 2006.

7 REFERENCES

1. A. Bard and L. Faulkner, ‘Electrochemical Methods’, John Wiley & Sons, New York, 2001.
2. P. Kissinger and W. Heineman, ‘Laboratory Techniques in Electroanalytical Chemistry’, Marcel Dekker, New York, 1996.
3. P. Zanello, ‘Inorganic Electrochemistry’, The Royal Society of Chemistry, 2003.
4. P. Atkins, ‘Physical Chemistry’, 6th edition, W. H. Freeman and Company, New York, 1998.
5. T. Gennett, D. F. Milner, and M. Weaver, *J. Phys. Chem.*, 1985, **89**, 2787.
6. G. Kew, K. DeArmond, and K. Hanck, *J. Phys. Chem.*, 1974, **78**, 727.
7. A. Lever, *Inorg. Chem.*, 1990, **29**, 1271.
8. A. Lever, *Inorg. Chem.*, 1991, **30**, 1980.
9. H. Masui and A. Lever, *Inorg. Chem.*, 1993, **32**, 2199.
10. S. Lu, V. Strelets, M. Ryan, W. Pietro, and A. Lever, *Inorg. Chem.*, 1996, **35**, 1013.
11. S. Fielder, M. Osborne, A. Lever, and W. Pietro, *J. Am. Chem. Soc.*, 1995, **117**, 6990.
12. J. Sauvage, J. Collin, J. Chambron, S. Guillerez, C. Coudret, V. Balzani, F. Barigelletti, L. De Cola, and L. Flamigni, *Chem. Rev.*, 1994, **94**, 993.
13. A. Juris, V. Balzani, F. Barigelletti, S. Campagna, P. Belser, and A. Zelewsky, *Coord. Chem. Rev.*, 1988, **84**, 85.
14. P. Deck, *Coord. Chem. Rev.*, 2006, **250**, 1032.
15. J. Capon, F. Gloaguen, P. Schollhammer, and J. Talarmin, *Coord. Chem. Rev.*, 2005, **249**, 1664.
16. R. Boeré and T. Roemmele, *Coord. Chem. Rev.*, 2000, **210**, 369.
17. V. Yam, K. Lo, W. Fung, and C. Wang, *Coord. Chem. Rev.*, 1998, **171**, 17.
18. S. Mandala, G. Dasa, R. Singha, R. Shuklaa, and P. Bharadwaj, *Coord. Chem. Rev.*, 1997, **160**, 191.
19. K. Takeuchi, M. Thompson, D. Pipes, and T. Meyer, *Inorg. Chem.*, 1984, **23**, 1845.
20. A. Gordon and R. Ford, ‘The Chemists Companion: A Handbook of Practical Data, Techniques and References’, John Wiley & Sons, New York, 1972.

21 K. Whitten, R. Davis, and M. Peck, ‘General Chemistry’, 5th edition, Saunders College Publishing, 1996.

22. Y. Ohsawa, K. DeArmond, K. Hanck, D. Morris, D. Whitten, and P. Neveux, *J. Am. Chem. Soc.*, 1983, **105**, 6522.
23. L. Meites, ‘Handbook of Analytical Chemistry’, McGraw-Hill, New York, 1963.
24. http://www.bioanalytical.com/products/ec/faqele.html#Ref_Type, 2007.
25. P. Denisevich, H. Abrura, R. Leidner, T. Meyer, and R. Murray, *Inorg. Chem.*, 1982, **21**, 2153.
26. S. Dudek, H. Sikes, and C. Chidsey, *J. Am. Chem. Soc.*, 2001, **123**, 8033.
27. L. Ramaley and M. Krause, *Anal. Chem.*, 1969, **41**, 1362.

28. R. Osteryoung and J. Osteryoung, *Philos. Trans. R. Soc. London, Ser. A*, 1981, **302**, 315.
29. D. Whelan, J. O'Dea, J. Osteryoung, and K. Aoki, *Electroanal. Chem.*, 1986, **14**, 209.
30. K. Aoki, K. Tokuda, H. Matsuda, and J. Osteryoung, *J. Electroanal. Chem.*, 1986, **207**, 25.
31. J. Lyon and K. Stevenson, *Anal. Chem.*, 2006, **78**, 8518.
32. J. Heyrovsky, *Chem. Listy*, 1922, **16**, 256.
33. S. Gould, K. Gray, R. Linton, and T. Meyer, *J. Phys. Chem.*, 1995, **99**, 16052.
34. S. Gould and T. Meyer, *J. Am. Chem. Soc.*, 1991, **113**, 7442.
35. C. Leidner, B. Sullivan, R. Reed, B. White, M. Crimmins, R. Murray, and T. Meyer, *J. Am. Chem. Soc.*, 1987, **26**, 882.
36. M. Beley, J. Collin, R. Ruppert, and J. Sauvage, *J. Chem. Soc., Chem. Commun.*, 1984, **19**, 1315.
37. B. Standke and M. Jansen, *Angew. Chem., Int. Ed. Engl.*, 1985, **24**, 118.
38. B. Standke and M. Jansen, *Angew. Chem., Int. Ed. Engl.*, 1986, **25**, 77.
39. A. Salimi, N. Amini, H. Danyali, and R. Hallaj, *Electroanalysis*, 2006, **18**, 1664.
40. A. Vlcek, E. Dodsworth, W. Pietro, and A. Lever, *Inorg. Chem.*, 1995, **34**, 1906.
41. N. Damrauer and J. McCusker, *J. Phys. Chem. A*, 1999, **103**, 8440.
42. M. Elvington and K. Brewer, *Inorg. Chem.*, 2006, **45**, 5242.
43. M. Richter and K. Brewer, *Inorg. Chem.*, 1993, **32**, 2821.
44. C. Tait, R. Donohoe, M. DeArmond, and D. Wertz, *Inorg. Chem.*, 1987, **26**, 2754.
45. X. Xiao-Hong and A. Bard, *Langmuir*, 1994, **10**, 2409.

Electron Paramagnetic Resonance (EPR) Spectroscopy

Brian J. Hales

Louisiana State University, Baton Rouge, LA USA

	Method Summary	1
1	Introduction	2
2	Relationship Between ‘‘Spin’’, Angular Momentum, and Magnetic Moment	2
3	Zeeman Interaction	3
4	Electrons in Atoms and Molecules	3
5	The EPR Experiment—Measuring ‘‘g’’	3
6	The EPR Spectrometer—Setting the Parameters	6
7	Rapid Passage	7
8	Hyperfine Interaction—the Effect of Nuclear Spin	7
9	Anisotropy	8
10	Powder Spectra	8
11	Examples of $S = 1/2$ Signals in Metalloproteins	9
12	$S > 1/2$ Spectra	11
13	Example of $S = 3/2$ System—MoFe Protein of Nitrogenase	13
14	Example of $S = 5/2$	13
15	Integer-Spin (non-Kramers) Systems	14
16	Abbreviations and Acronyms	15
17	Related Articles	15
18	Further Reading	15
19	References	16

METHOD SUMMARY

Acronyms, Synonyms

- Electron-Paramagnetic Resonance (EPR)
- Electron-Spin Resonance (ESR).

Measured physical quantities

- energy separation between different electron-spin states
- nuclear hyperfine splitting constants.

Information available

- spin state (S) of a paramagnetic center
- magnitude of hyperfine interactions
- zero-field splitting of half-integer $S > 1/2$ states
- possible identity of paramagnetic center (e.g., free radical; metals in metal clusters)
- possible identity of ligand atoms.

Information not available, limitations

- center must be paramagnetic
- integer-spin states often unobservable.

Examples of questions that can be answered

- What are the different paramagnetic centers in the sample?
- How do these centers change with changes in redox potential and pH or during substrate binding or catalysis?
- How close are the different paramagnetic centers?

Major advantages

- The technique is noninvasive.
- The volume (300 μL) and concentration (1.0–0.001 mM) are low.
- Recording spectrum can be done quickly (usually no more than 15–20 min).
- The spectrum is only of paramagnetic species.
- The spectrum is often simple to interpret.
- The spectrum often can be recorded in vivo.

Major disadvantages

- Many paramagnetic metal centers require low temperatures (20 K or lower) for detection.

Sample constraints

- Sample should be free of any adventitious paramagnetic impurities.

1 INTRODUCTION

1.1 History and Terminology

During its inception in the mid 1940s, this technique was initially described as paramagnetic resonance by the Clarendon Laboratory in Oxford, England, and was soon followed by the terms electron-paramagnetic resonance (EPR) and electron-spin resonance (ESR). This dual terminology has often been confusing to many. To avoid this confusion and come to a common ground the term electron magnetic resonance has more recently been proposed but has received little attention. Now, even after decades of debate, no consensus has been reached, and we still have the use of both terms. In general, EPR tends to be used by inorganic and bioinorganic scientists where both spin and orbital angular momentum are significant, while the term ESR is favored by those who study organic free radicals where spin angular momentum dominates. The term EPR will be used in this discussion.

EPR spectroscopy was first demonstrated in 1945. Using a 25-m wavelength spectrometer, Zavoisky recorded the broad, barely detectable spectra of several paramagnetic species[1]. The technique quickly moved into the more sensitive, high-frequency microwave spectral region in 1946 with the detection of the resolved spectrum of Mn^{2+}. It is not a coincidence that the technique rapidly evolved following the end of World War II. The vast amount of knowledge of microwave technology from radar studies that had sprung out of the war efforts laid the foundation for the construction of sensitive spectrometers. In fact, unlike its related cousin, nuclear magnetic resonance (NMR) (*see* ***Nuclear Magnetic Resonance (NMR) Spectroscopy of Inorganic/Organometallic Molecules***, ***Nuclear Magnetic Resonance (NMR) Spectroscopy of Metallobiomolecules***), EPR spectroscopy quickly reached its near-theoretical limit in sensitivity within two decades of its inception, due mainly to the extensive background knowledge of microwave technology. Aside from an increased range of available microwave frequencies and rapid computer-driven data handling and manipulation systems, today's spectrometers are little changed from those used decades ago.

This article will present the basics of EPR spectroscopy needed to train most scientists to understand and interpret the spectra of metals in biological systems. Researchers interested in a more detailed treatise on different aspects of the subject should consult one of the books listed under Further Reading at the end of this article.

2 RELATIONSHIP BETWEEN ‘‘SPIN’’, ANGULAR MOMENTUM, AND MAGNETIC MOMENT

An isolated electron, alone without any outside forces, still possesses an intrinsic angular momentum called ‘‘*spin*’’, ***S***. Because an electron is charged, the angular motion of this charged particle generates a magnetic field. Viewed in the classical sense the electron, due to its charge and angular momentum, acts like a little bar magnet, or magnetic dipole, with a *magnetic moment*, $\boldsymbol{\mu_e}$

$$\text{Angular Momentum } (\boldsymbol{S}) \text{ of a Charge} \rightarrow \text{Magnetic Dipole } (\boldsymbol{\mu_e})$$

or

$$\boldsymbol{S} \propto \boldsymbol{\mu_e} \tag{1}$$

(Note : this is for a system possessing *only* spin)

For a classical bar magnet, the magnetic moment has no preferred direction in the absence of an external field in open space. The same is also true for an electron. This situation, however, changes when the electron (or bar magnet) is placed in an external magnetic field. This is analogous to the force experienced by a compass needle aligning itself with the earth's magnetic field. In the case of a quantum mechanical electron, this effect is referred to as the *Zeeman Interaction*.

3 ZEEMAN INTERACTION

A classical bar magnet, like a compass needle, orients in an external magnetic field ($\boldsymbol{B_0}$) with its magnetic moment aligned toward the south pole of the external field. Aligning the magnetic moment toward the north pole would require energy and represents the least favored (i.e., highest energy) orientation. Between these two extremes there exists an infinite number of possible orientations. This is not the case for an electron for which quantum mechanics dictates that there is an intrinsic angular momentum of 1/2 times Planck's constant (which will not be included for simplicity), or $S = 1/2$. This means that an electron can only assume two orientations in an external field oriented along the z-axis corresponding to z-axis projections $m_s = 1/2$ and $m_s = -1/2$. This Zeeman interaction has an energy (W) for each orientation that is the vector product of $\boldsymbol{\mu_e}$ and $\boldsymbol{B_0}$, for example,

$$W = -\boldsymbol{\mu}_e \cdot \boldsymbol{B_0} \tag{2}$$

For an electron the magnetic moment is proportional to the spin projection, $\boldsymbol{\mu}_e = -g_e\beta\boldsymbol{S}$, where β is a conversion constant called the *Bohr magneton* and g_e is the spectroscopic *g-factor* of the free electron and equals 2.0023192778 or about 2.00. In other words, the energies (W) for an electron in a magnetic field along the z axis ($\boldsymbol{B_0} = B_o\boldsymbol{k}$) with m_s (i.e., S_z for α and β electrons) $= 1/2$ and $-1/2$ are, respectively,

$$W_\alpha = \tfrac{1}{2}g_e\beta B_o \tag{3}$$

and

$$W_\beta = -\tfrac{1}{2}g_e\beta B_o \tag{4}$$

4 ELECTRONS IN ATOMS AND MOLECULES

Suffice it to say you will not be devoting your research career studying free electrons. Many people, however, study atoms or molecules that contain unpaired electrons, i.e., are paramagnetic. When an isolated free electron with no outside forces on it, is placed on an atom or molecule, its total angular momentum changes. In addition to the intrinsic spin angular momentum ($\boldsymbol{S}$), it may now also possess some orbital angular momentum ($\boldsymbol{L}$). Accordingly, the total magnetic moment of the electron will also change due to the vector addition of these two quantities.

Electron in space

$$\boldsymbol{\mu}_e \propto g_e\boldsymbol{S} \tag{5}$$

Electron in an atom or molecule

$$\boldsymbol{\mu}_e \propto g_e\boldsymbol{S} + \boldsymbol{L} \tag{6}$$

This last equation shows that the magnetic moment depends on the total paramagnetism, which arises from both spin *and* orbital angular momentum. This dependency on total *paramagnetism* and not just spin helps us to understand why some spectroscopists favor the term EPR over ESR.

In general, the orbital angular momentum is approximately zero for an electron in the ground state (we often say that the orbital angular momentum has been ''quenched''). This suggests that we again have a spin-only system with an effective g-factor near g_e. This would be unexciting. However, all is not lost. Mixing of the ground state with excited states by way of *spin-orbit* (*s-o*) *coupling* allows the ground state to gain back some orbital angular momentum, or

$$\boldsymbol{\mu_e} \propto g_e\boldsymbol{S} + \boldsymbol{s\text{-}o} \text{ coupling contribution} \tag{7}$$

It is common practice to assume that the s-o coupling term is proportional to $\boldsymbol{S}$, which means that we can combine both terms and just change the value of g_e to g, or

$$\boldsymbol{\mu_e} \propto g\boldsymbol{S} \tag{8}$$

This equation tells us that the electron's magnetic moment is just proportional to the electron-spin, which is why other scientists favor the term ESR over EPR.

The magnitude of the spin-orbit coupling contribution depends on the size of the nuclei interacting with the unpaired electron. Organic free radicals, with only H, O, C, and N atoms, will have a small contribution from spin-orbit coupling, producing g-factors very close to g_e while the g-factors of much larger elements, such as metals, may be significantly different from g_e.

5 THE EPR EXPERIMENT—MEASURING ''*g*''

From the above discussion we can see that one parameter we may wish to know is the g-factor. In an EPR spectrometer, a paramagnetic sample is placed in a large uniform magnetic field, which splits the W_α and W_β energy levels of the ground state by an amount ΔW,

$$\begin{aligned}\Delta W &= W_\alpha - W_\beta \\ &= \left(\tfrac{1}{2}g\beta B_o\right) - \left(-\tfrac{1}{2}g\beta B_o\right) \\ &= g\beta B_o \end{aligned} \qquad (9)$$

Since β is a constant and the magnitude of B_o can be measured, the g-factor can be easily calculated from the value of ΔW, the energy difference between the two spin levels. Irradiating the sample with energy $E = h\nu$, an absorption will occur when the condition $E = h\nu = \Delta W = g\beta B_o$ is satisfied. From this relationship, the value of g can then be calculated from ν (in GHz) and B_o (in gauss) using

$$g = \frac{h\nu}{\beta B_o} \qquad (10)$$

or

$$g = \frac{714.484\ \nu}{B_o} \qquad (11)$$

5.1 The EPR Spectrometer—How it Works

The energy equation ($h\nu = g\beta B_o$) describing resonance absorption suggests that we can perform our measurement in two ways. We can hold the frequency, ν, constant and vary the magnetic field strength, B_o, or hold the field constant and vary the frequency, ν, until a resonance transition occurs. In practice, the frequency is held constant while the magnetic field is linearly swept.

5.2 What Energy Is Used for Irradiation?

The most convenient energy to use in EPR spectroscopy, from an experimental point of view, is in the microwave region at around 9.4 GHz, commonly referred to as X-band. This frequency corresponds to a wavelength of about 3 cm, which approximates the internal dimension of the spectrometer's resonance cavity. In general, the larger the frequency, the larger the magnetic field, and the smaller the wavelength (hence, the smaller the resonance cavity and the sample size). X-band frequency requires a simple electromagnet yet provides high sensitivity and a workable sample size. Well over 90% of all EPR spectra are recorded at this frequency. Other frequencies commonly used are listed in Table 1. Using the relationship $g = 714.484\,\nu/B_o$, a free radical ($g = 2$) at X-band frequencies will undergo a transition at a magnetic field around 3400 gauss (G) (or 0.34 tesla (T) where 1 T = 10 000 G).

When the g anisotropy (see below) is very small, as often is the case for radicals, better resolution can be obtained by using spectrometers that operate at higher frequencies (and fields). An example is the two neighboring semiquinone anion radicals (Q_A^- and Q_B^-) in the bacterial photosynthetic reaction center recorded at X-, Q- and W-band frequencies[2] (Figure 1).

Table 1 Microwave (band) frequencies commonly used in EPR spectrometers

Band	Approximate Frequency (GHz)
L	1
S	3
X	9.4
P	15
K	18
Q	35
W	94

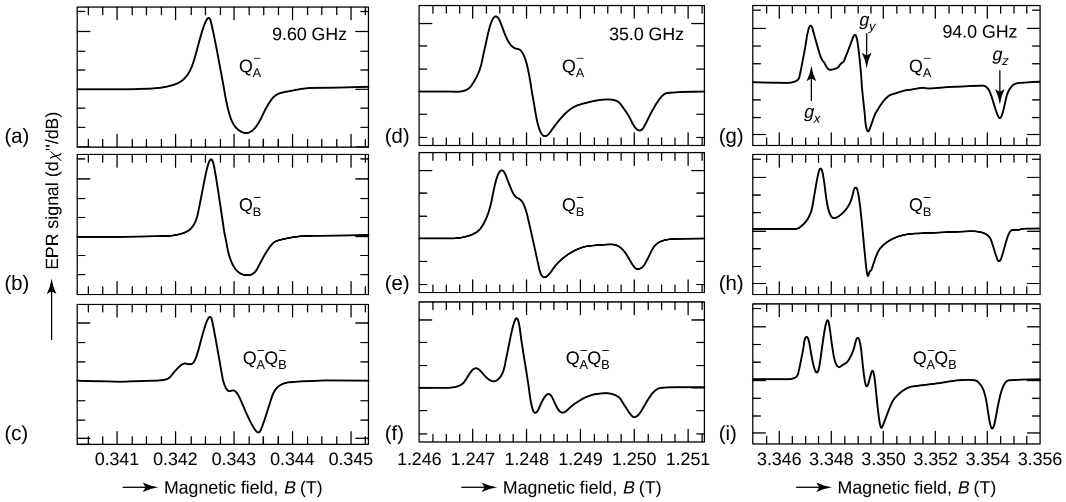

Figure 1 Comparison of the EPR spectra of two semiquinone anion radicals (Q_A^-, Q_B^-, and $Q_A^- + Q_B^-$) from the bacterial photosynthetic reaction center recorded at 9.60, 35.0 and 94.0 GHz. Note that as the spectrometer frequency increases, the overlapping spectra become better resolved. Spectra taken from Ref. 2 (Reprinted with permission from Calvo, Abresch, Bittl, Feher, Hofbauer, Isaacson, Lubitz, Okamura and Paddock.[2] © 2000 American Chemical Society)

Note how the g-factor anisotropy resolution increases with frequency.

5.3 How Much Sample Is Needed?

Most X-band EPR spectra of transition metals are recorded at low temperatures (4–100 K) using high-purity quartz tubes (no paramagnetic impurities) with a sample volume of about 300 μL. The minimum concentration of the sample depends on the broadness of its spectrum. Because EPR spectra are recorded as a first derivative (see subsequent text), the relationship between concentration, signal amplitude and spectral linewidth can be approximated as

$$\text{Conc.} \propto \text{Amp.} \times (\text{Width})^2 \tag{12}$$

To illustrate this, Figure 2 exhibits a spectrum containing two different signals representing samples of equal concentration but different linewidths. Obviously, just a small change in linewidth can induce a large change in amplitude. As such, broad spectra require a high concentration for detectable spectral amplitude. For organic free radicals, which have very narrow lines, a concentration of 10^{-7} M will usually yield a strong spectrum. On the other hand, metalloproteins often exhibit broad spectra, especially when $S > 1/2$ and, therefore, require a higher concentration (10^{-3}–10^{-5} M) for detection.

5.4 Why the First Derivative?

One of the first things one notices about an EPR spectrum is that it is a first-derivative spectrum rather than the more typical absorption presentation. This is due to an instrumental artifact. To enhance the sensitivity of the EPR spectrometer, the magnetic field is modulated. To obtain field modulation, a small set of Helmholtz coils are place about the sample in line with the external field. These coils allow the amplitude of the external field, B_o, to change by a small amount (~0.01–20 G) at a frequency of 100 kHz (smaller frequencies can also be used, but are less sensitive). Because the spectrometer is tuned to only detect signals that change amplitude with field changes at 100 kHz, the resultant signal appears as a first derivative (i.e., ΔSignal Amplitude/ΔMagnetic Field = first derivative of the absorption signal).

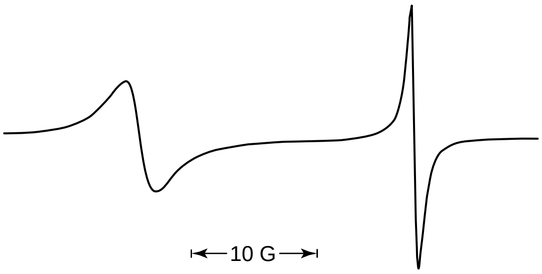

Figure 2 Spectrum illustrating the effect of spectral linewidth on amplitude. Both signals represent samples of the same concentration. The signal on the left, however, has a line width $2^{1/2}(\approx 1.4)$ greater than the signal on the right, resulting in an amplitude decrease of 1/2

5.5 Line Shape

Basic quantum mechanical calculations (i.e., the Bloch equations) show that the general EPR resonance absorption (Y) will have a Lorentzian line shape

$$Y = Y_{\max}\left[\frac{\Gamma^2}{(\Gamma^2 + \{B - B_r\}^2)}\right] \tag{13}$$

where $Y_{\max}$ is the maximum absorption, Γ equals half the absorption linewidth at half height, B is the magnetic field, and B_r is the field position at resonance (i.e., maximum absorption). Small organic radicals rapidly tumbling in solutions, where all anisotropic and inhomogeneous effects are averaged out, generally exhibit spectra with a near Lorentzian line shape associated with a homogeneous signal. This is not the case for the spectra of most transition metal ions. The presence of spectral inhomogeneities and unresolved hyperfine interactions (see subsequent text) results in a spread or ensemble of overlapping lines yielding a near Gaussian line shape,

$$Y = Y_{\max}\exp\left[\frac{-(\ln 2)(B - B_r)^2}{\Gamma^2}\right] \tag{14}$$

5.6 Saturation and Spin Relaxation

Because EPR spectrometers irradiate samples with microwaves in the X-band frequency region (Table 1), the separation between the energy levels is not large compared to kT and, correspondingly, the difference in the populations of these levels is small. For example, for an $S = 1/2$ spin system in the absence of a magnetic field, the $m_s = +1/2$ and $-1/2$ levels are degenerate. As described above, a magnetic field (B_o) will split these levels through a Zeeman interaction where the separation energy equals $g\beta B_o$. At thermal equilibrium, there will be a population difference between the split levels dictated by the Boltzmann equation. The population of the upper level (N_α) relative to that of the lower lever (N_β) will be

$$N_\alpha = N_\beta \mathrm{e}^{-g\beta B\mathrm{o}/\mathrm{kT}} \tag{15}$$

where k is the Boltzmann constant and T is the absolute temperature. At room temperature for $g = 2$ and $B_o = 3400$ G, the population of the upper level is only 0.5% less than that of the lower level. Irradiation tends to equalize their populations and, with it, decrease the observed absorption. Specifically, during a spectral scan, radiation-induced transitions occur with equal probability for both absorption and emission. In other words, the transition $\beta \rightarrow \alpha$ has the same probability of occurring as the transition $\alpha \rightarrow \beta$. Even though there is equal probability for a transition in either direction, a net absorption is observed because there is a greater population of the lower level (equation 15) and, therefore, there are more photon-inducing absorption transitions than emission transitions. Because there are more transitions from $\beta \rightarrow \alpha$ than from $\alpha \rightarrow \beta$, the population of the upper level will increase relative to the lower level resulting in a decrease in the population difference and, with it, a decrease in the net absorption. This phenomenon is termed *saturation*. To counteract saturation and maintain the Boltzmann population difference, there are nonradiative spin relaxation processes (called *Spin-Lattice Relaxation*) that continually deplete the upper level. The Boltzmann population difference will be maintained as long as the spin-lattice relaxation rate is greater than the rate of radiation-induced transitions. As the power of the irradiating system increases, this inequality is no longer met and saturation (‘‘power saturation’’) is observed. The greater the spin-lattice relaxation rate, the greater the microwave power required for saturation. Spin-lattice relaxation rates are highly temperature dependent. The lower the temperature, the slower the rate, the easier it is to saturate the levels and, in general, the sharper the resonance line.

6 THE EPR SPECTROMETER—SETTING THE PARAMETERS

To obtain an EPR spectrum with the best signal-to-noise ratio, various spectrometer parameters must be optimized. These optimized parameters are unique for each sample and can be easily determined through a systematic approach. Let us assume that we wish to record the spectrum of an unknown paramagnetic sample containing a transition metal. Most transition metal ions are best observed at low temperature (normally 4–100 K, depending on the oxidation and spin state). The best compromise temperature for the detection of most metal ions is 10–15 K. Because we are initially only interested in detecting a signal, we are less concerned about the effects of power saturation or overmodulation (see subsequent text). Good compromise values for microwave power and modulation amplitude (MA) are 20 mW and 10 G (1.0 mT), respectively. Both of these values encourage a strong signal, albeit one that may lack resolvable detail and structure. Furthermore, most signals occur between g-factors 1.8–9. A magnetic field range that includes these values (about 1000–4000 G at X-band) should be scanned rapidly (∼5 min.) using a moderate time constant (no greater than 0.1 s.). If a signal is present, it will probably be observed under these conditions.

Once a signal is observed, the spectrometer parameters can be optimized to obtain the best signal-to-noise ratio of the spectrum. Ideally, the optimum temperature for the strongest signal should also be determined. However, if a strong signal is observed using the conditions cited above, it is best to employ a temperature-dependent study later, following the optimization of the other parameters. The first parameter to be optimized is the microwave power. As stated above, signal amplitude will increase with power as long as the rate of radiation-induced transitions is less than the rate of spin-lattice relaxation. When the power becomes too large, saturation occurs and the signal amplitude lags the power, eventually decreasing with increasing power. During power saturation, the resonance line becomes distorted and broadens, concealing the true line shape and masking hyperfine structure. To determine the optimum power, a plot of the signal amplitude versus $\sqrt{}$(power) should be constructed. This plot will clearly reveal the linear dependence below saturation and the maximum amplitude as saturation is approached. Which power is finally employed depends on the signal strength. Strong signals will exhibit respectable signal-to-noise ratios well below saturation. Weak signals, however, may require the use of power levels in the near-saturation region in order to obtain respectable signal amplitude.

Following the determination of the proper power level, the dependency on MA should be investigated. Amplitude modulation is accomplished by rapidly modulating the scanning magnetic field. As long as the amplitude of this modulation is small compared to the linewidth, a near first-derivative line shape is obtained whose amplitude is proportional to the MA, the greater the MA, the larger the signal amplitude. As the MA approaches the absorption linewidth, distortions occur resulting in line broadening and a strong deviation from the true first derivative. The optimum value of the MA can be easily determined by recording the spectrum at a given MA. If the linewidth of the narrowest line in the spectrum is much greater than the MA, overmodulation effects have not occurred. However, if the measured linewidth approximately equals the MA, distortions may be present. The spectrum should be recorded at a new MA (usually half the previous MA). If the measured linewidth also decreases by one-half, overmodulation is still present and the MA should be decreased again until the measured linewidth no longer changes with decreasing MA. The measured linewidth is now the true linewidth. In general for strong signals, the MA should be set to one-fourth the width of the narrowest line. If the signal is very weak, setting the MA equal to the true linewidth is preferred. The spectrum will be slightly distorted, but a much stronger signal will be observed.

The time constant and scan time are the last parameters to be set. The time constant is set to produce the desired signal-to-noise ratio. To record a spectrum that is not distorted, the spectrometer should take 8–10 times the time constant to scan the maximum-to-minimum peak of the sharpest line. For example, suppose that the optimum time constant is 0.1 s, the sharpest line has a peak-to-peak width of 1.0 G and the full scan is 1000 G. The spectrometer should take 10 times the time constant to go 1.0 G, or 1.0 s. Therefore, to record 1000 G the spectrometer has to take 1000 s or 16.6 min, which corresponds to the minimum scan time. Scan times significantly shorter than this will result in a distorted signal.

7 RAPID PASSAGE

It has been noted that certain signals,[3] recorded in the dispersion mode at very low temperatures, actually exhibit an absorption line shape phase shifted by almost 90°. This phenomenon is due to an effect termed *Rapid Passage*. As noted above, the spin manifold has innate relaxation processes that, under low power situations, maintain the Boltzmann population distribution among all the levels. The rate of relaxation is highly temperature dependent, decreasing significantly with decreasing temperature. At low temperatures and high power, the relaxation rate can become small compared to the rate the spectrometer traverses through the signal. During such rapid-passage conditions, the spin levels saturate during the initial passage and stay saturated during the back passage resulting in a phase shift of the observed signal and the appearance of an absorption shape. This condition is very helpful when recording electron nuclear double resonance (ENDOR) spectra (*see* ***Electron-Nuclear Double Resonance (ENDOR) Spectroscopy***).

8 HYPERFINE INTERACTION—THE EFFECT OF NUCLEAR SPIN

If all we could do was measure g-factors, EPR spectroscopy would be less interesting and not very informative. Luckily there are energy terms other than the basic Zeeman interaction. We have already said that the magnetic moment of the electron can be represented as a classical bar magnet. From basic physics, we know that a bar magnet will align itself in an external magnetic field. That is the Zeeman interaction discussed above. Physics also tells us that the energy of a bar magnet can be influenced by interaction with a neighboring bar magnet. In this latter case, the magnitude of the interaction depends on the distance of separation and the relative alignment of the two magnets. An analogous interaction occurs between an unpaired electron and a neighboring magnetic nucleus ($I > 0$). In this situation the nucleus is equivalent to the second bar magnet and the interaction is called the *hyperfine interaction*. Some of the nuclear isotopes that are important in biology and their nuclear spins are listed in Table 2.

Table 2 Nuclear spin and % natural abundance of isotopes commonly encountered in biological samples

Isotope	Nuclear Spin (I)	% Abundance
^{1}H	1/2	99.9
^{2}H	1	0.02
^{12}C	0	98.9
^{13}C	1/2	1.1
^{14}N	1	99.6
^{15}N	1/2	0.37
^{16}O	0	99.8
^{17}O	5/2	0.037
^{32}S	0	95.0
^{33}S	3/2	0.76
^{51}V	7/2	99.8
^{55}Mn	5/2	100
^{56}Fe	0	91.7
^{57}Fe	1/2	2.19
^{59}Co	7/2	100
^{58}Ni & ^{60}Ni	0	68 & 26
^{61}Ni	3/2	1.19
^{63}Cu & ^{65}Cu	3/2	69 & 31
^{95}Mo & ^{97}Mo	5/2	16 & 9
^{183} W	1/2	14.4

The effect of the hyperfine interaction is to add an energy term ($\mathrm{h}Am_I$) to the Zeeman expression (equation 8) for each magnetic nucleus. For example, the energy of a single nucleus would be

$$\Delta W = \mathrm{h}\nu = g\beta B_\mathrm{o} + \mathrm{h}Am_I \tag{16}$$

where h is Planck's constant, A is called the *Hyperfine Coupling Constant* (measured in cm^{-1} or MHz), and m_I is the magnetic quantum number for the nucleus. Since there are $2I + 1$ possible values of $m_I (m_I = I, I - 1, \ldots, 0, \ldots, -I + 1, -I)$, the hyperfine interaction term splits the Zeeman transition into $2I + 1$ lines of equal intensity. Therefore, the interaction of the electron with a single proton ($I = 1/2$) will yield an EPR spectrum containing two lines ($m_I = 1/2$ and $m_I = -1/2$) while interaction with a single ^{14}N ($I = 1$) would yield three lines ($m_I = 1, 0, -1$; Figure 3). Because the spectrometer scans magnetic fields, the measured separation between these lines is in gauss (or tesla) and is called the *Hyperfine Splitting Constant* (a).

Each magnetic nucleus that interacts with the spin magnetic moment adds a hyperfine interaction term to the above energy expression and, correspondingly, splits each line in the spectrum into the appropriate number of lines. It is interesting to note that regardless of the number of hyperfine lines (and assuming no anisotropy, as defined in subsequent text), the EPR spectrum of a paramagnet in solution (i.e., rapid tumbling) is symmetrically centered about the Zeeman transition ($g\beta B_\mathrm{o}$). Therefore, g can be determined in solution spectra from the value of magnetic field (B_o) at the middle of the spectrum.

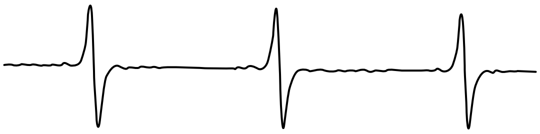

Figure 3 Solution spectrum of a typical nitroxide radical where the unpaired electron is mainly interacting (i.e., hyperfine interaction) with the nitrogen nucleus. Since nitrogen is predominantly the ^{14}N isotope, the line is equally split (hyperfine splitting constant) into three ($m_I = +1, 0, -1$) lines

9 ANISOTROPY

As already discussed, the deviation of the measured g-factor from the free electron (g_e) arises from the mixing of the orbital angular momentum through spin-orbit coupling. Because orbital angular momentum is oriented in the molecule, the magnitude of this coupling is direction dependent, or *anisotropic*. In a low-viscosity solution, the anisotropy is averaged out. This is not the situation when the paramagnetic molecules are in a fixed orientation, such as in a single crystal. The g-factor of the EPR spectrum of a single crystal changes as the crystal is rotated in the spectrometer, due to g-factor anisotropy. For every paramagnetic molecule, there exists a unique axis system called the *principal axis system*. The g-factors measured along these axes are called the *principal g-factors* and are labeled g_x, g_y and g_z.

Hyperfine coupling constants are also anisotropic (A_x, A_y, A_z), although their principal axis system is often different from that of the g-factors. Figure 4 shows the spectra of a nitroxide radical oriented in a single crystal where the external magnetic field is directed along the x, y or z principal axis (compare these with the solution spectrum in Figure 3). Note that the center of the spectrum (i.e., the g-factor) and the separation between the three transitions (hyperfine coupling constants) differ in all three orientations.

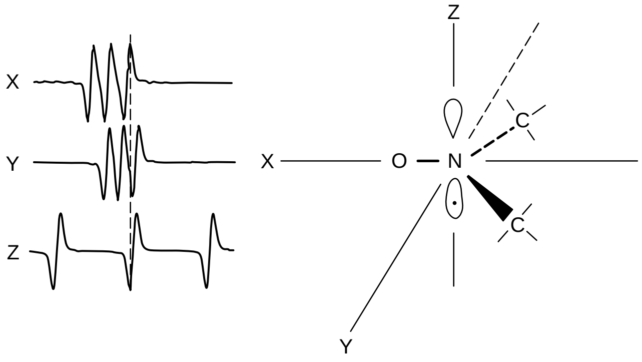

Figure 4 Spectra of oriented nitroxide radical with the external magnetic field directed along the x, y and z principal axis. Note that both the hyperfine splitting constant (separation between the lines) and center of the spectrum (g-factor) change with each orientation, illustrating the anisotropy of these terms

10 POWDER SPECTRA

Most EPR spectra of biological transition metals are recorded on frozen solution. In these samples, the paramagnets are neither aligned in a set direction, as in an oriented single crystal, nor rapidly rotating, as in a low-viscosity solution. The act of freezing fixes the molecules in all possible orientations. Therefore, the spectrum of a frozen sample represents the summation of all possible orientations and is called a *powder spectrum* (i.e., you would get the same spectrum by grinding a single crystal into a powder).

To simplify the discussion of powder spectra, we' will consider only the effect of g-factor anisotropy. Shown in Figure 5 are first-derivative spectra for three different classes of anisotropy. In the first class, called *isotropic*, all of the principal g-factors are the same ($g_x = g_y = g_z$). In this class, the g-factor is invariant with direction and, therefore, the resultant spectrum is a single symmetric line.

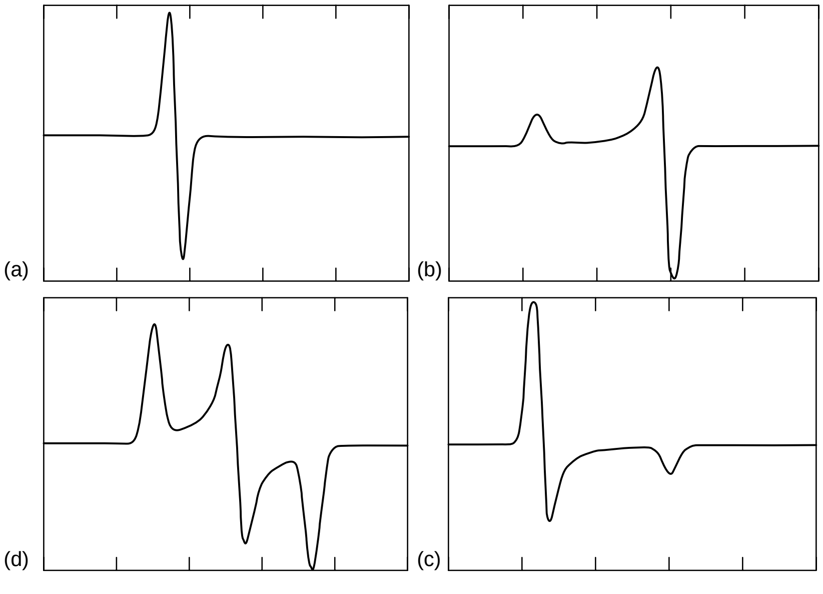

Figure 5 Line shapes of typical powder spectra, isotropic ($g_x = g_y = g_z$, a), axial ($g_x = g_y \neq g_z$, spectra b and c) with ($g_\parallel > g_\perp$, b) and ($g_\parallel < g_\perp$, c), and rhombic ($g_x \neq g_y \neq g_z$, d)

In the second class, called *axial*, there is a unique axis that differs from the other two ($g_x = g_y \neq g_z$). The g-factor along this unique axis is said to be parallel with it, $g_z = g_\parallel$ while the remaining two axis are equivalent and perpendicular to it, $g_x = g_y = g_\perp$. In this case, the powder spectrum corresponds to the summation of spectra with g-factors equal to any value between these two extremes. Because $g_\perp$ has twice the probability of occurring (i.e., because $g_x = g_y = g_\perp$) as does $g_\parallel$, the spectrum is more intense in the former region. The g-factors of the molecule can be obtained from the derivative spectrum by noting the magnetic field for the center of the minor absorption-shaped inflection ($g_\parallel$) and the midpoint of the derivative-shaped signal ($g_\perp$).

The last class, called *rhombic*, occurs when all of the g-factors differ ($g_x \neq g_y \neq g_z$). As with the axial spectrum, the principal g-factors can be determined from the derivative spectrum by noting the field positions for both the maximum and minimum absorption-shaped signals (g_z and g_x) at the extremes of the spectrum and the crossover (g_y) of the center derivative-shaped signal.

11 EXAMPLES OF $S = 1/2$ SIGNALS IN METALLOPROTEINS

11.1 Sign of the Deviation of the g-factor from g_e

Most of the basics have now been presented for the interpretation of the EPR spectra of transition metal ions in biological systems. Initially we will just consider $S = 1/2$ systems. The EPR spectra of mononuclear transition metals with $S = 1/2$ have g-factors close to that of the free electron with signals in the $g = 2$ region. Deviation of this g-factor from the free electron (g_e) is due to spin-orbit coupling which mixes the singlet ground state (where $L = 0$) with other states ($L > 0$), thereby introducing orbital angular momentum into the wave function and shifting the g-factor away from the $g_e = 2$ region. The amount of mixing (and the amount of shift) can be predicted using second-order perturbation theory (SOPT). The correction term from SOPT contains the spin-orbit coupling term in the numerator and the energy difference between the ground state (W_g) and mixed state (W_m) in the denominator

$$g = g_e - \frac{(\text{spin} - \text{orbit coupling term})}{(W_m - W_g)} \qquad (17)$$

The most important thing to note is that the energy difference is in the denominator while the spin-orbit term is positive. Therefore, the direction of the shift of the g-factor from the free electron depends on the sign of the energy difference. For metals with d orbitals less than half filled, mixing mainly occurs between the ground state and orbitals of greater energy so that $(W_m - W_g) > 0$ yielding $g_{ave} < g_e$. Conversely, metals with d orbitals more than half filled will have $(W_m - W_g) < 0$ and $g_{ave} > g_e$. It is equally valid to treat this latter case as a hole (i.e., electron vacancy) coupling with filled orbitals.

11.2 Copper (Cu^{2+})

Cu^{2+} is a d^9 system with one unpaired electron in the highest energy level. As such the ion would be $S = 1/2$ with $g_{ave} > g_e$. Since hyperfine interaction is present, the anisotropy of the hyperfine coupling must also be considered when interpreting the powder spectrum. While the pattern of hyperfine coupling is the same for each of the principal g-factors, the magnitude of the coupling differs (see example with nitroxide in preceding text) due to anisotropic effects. The Cu^{2+} ion typically yields an axial (or near-axial) EPR spectrum with $g_\parallel > g_\perp$. The two principal isotopes of copper, ^{63}Cu (69%) and ^{65}Cu (31%), both have nuclear spins of $I = 3/2$ (Table 2), so the Zeeman line will be split into four lines ($m_I = 3/2, 1/2, -1/2, -3/2$) by each. Since the magnetic moments of these two isotopes are very similar, the hyperfine couplings are nearly coincident and often difficult to resolve.

The hyperfine coupling along $g_\parallel$ for Cu^{2+} is always much greater than that along $g_\perp$ resulting in a large splitting of the $g_\parallel$ line with only minor (sometimes unobservable) splitting of the line at $g_\perp$. Figure 6 shows the typical powder spectrum of Cu^{2+} with $g_\parallel = 2.27$; $g_\perp = 2.05$; $A_\parallel = 43 \times 10^{-4}\,\text{cm}^{-1}$ with $g_{ave} > 2$.

11.3 Vanadium (V^{4+})

Although vanadium has a relatively large natural abundance on the earth and is known to be an important element for life functions, to date it has been found present only in a few enzymes, most notably V-bromoperoxidase and V-nitrogenase. Of these enzymes, vanadium EPR signals have been observed only in V-bromoperoxidase.

Bromoperoxidase reaction

$$Br^- + H_2O_2 + RH \rightarrow RBr + OH^- + H_2O \qquad (18)$$

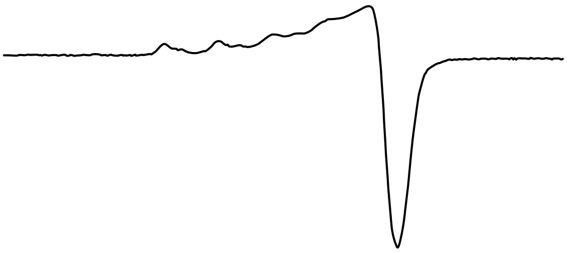

Figure 6 Powder spectrum of a typical Cu^{2+} ion with axial structure and $g_\parallel > g_\perp$. Note the hyperfine structure on $g_\parallel$ (four lines arising from the two $I = 3/2$ isotopes of Cu with similar splitting constants). The hyperfine splitting on $g_\perp$ is small and undetectable

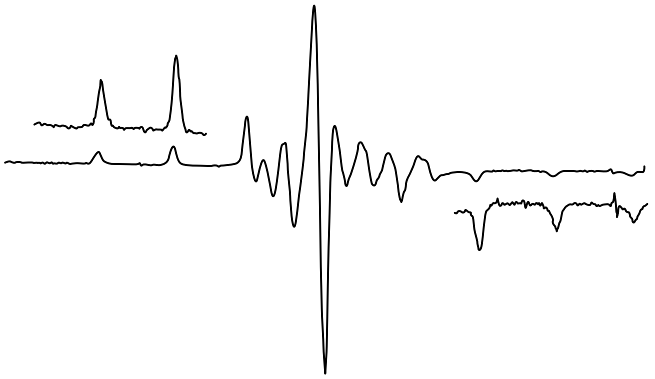

Figure 7 Powder spectrum of V-bromoperoxidase. Spectrum is axial ($g_{\|} < g_{\perp}$) with hyperfine structure (8 lines from $I = 7/2$) on both $g_{\|}$ and $g_{\perp}$

During enzymatic activity, vanadium in bromoperoxidase is EPR silent. However, its spectrum can be observed at X-band by reduction of the enzyme with dithionite to generate V^{4+} (d^1), as shown in Figure 7. Because vanadium has axial symmetry, its powder spectrum consists of two major inflections ($g_{\|} = 1.948$ and $g_{\perp} = 1.979$; $g_{\text{ave}} < 2$). Vanadium possesses one stable isotope ^{51}V with $I = 7/2$ (Table 2). Therefore, each Zeeman inflection will be further split into eight ($2I + 1$) lines ($A_{\|} = 164 \times 10^{-4}\,\text{cm}^{-1}$ and $A_{\perp} = 54 \times 10^{-4}\,\text{cm}^{-1}$). Due to spectral overlap, not all lines are observed. For comparison, the room temperature solution spectrum of aqueous $VO(H_2O)_5^{2+}$ is shown (Figure 8). The variation in the amplitude of each line arises from anisotropy observable during slow tumbling.

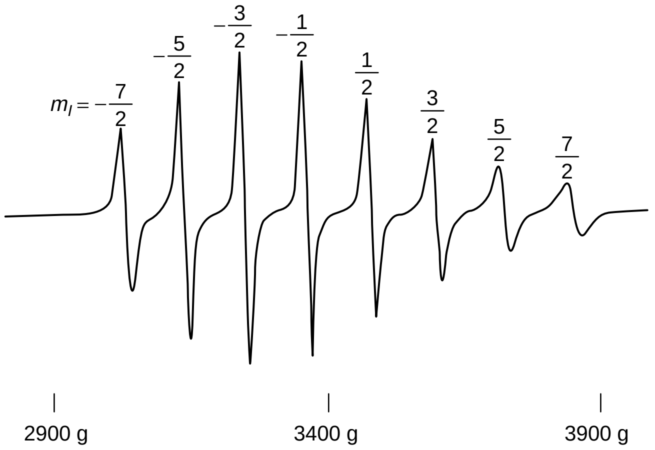

Figure 8 Solution spectrum of $VO(H_2O)_5^{2+}$ showing eight lines ($I = 7/2$). Line intensity variation arises from slow tumbling of the ion resulting in coupled g-factor and hyperfine splitting anisotropy effects

11.4 Molybdenum (Mo^{5+})

Molybdenum is present in many enzymes and is often EPR detectable (except for Mo-nitrogenase, where it exists in a complex $MoFe_7S_9$•homocitrate cluster). Shown in Figure 9 is the Mo^{5+} (d^1) X-band spectrum of one form of xanthine oxidase,**4** called the *Very Rapid* form. Xanthine oxidase is a homodimer containing one Mo center, two Fe–S, centers and one molecule of flavin adenine dinucleotide per subunit. This enzyme catalyzes the oxidation of xanthine at the Mo center with subsequent reduction of O_2 at the flavin center. In this enzyme Mo^{5+} exhibits a slightly rhombic EPR spectrum ($g_z = 2.0252$, $g_y = 1.9550$, $g_x = 1.9495$; $g_{\text{ave}} < 2$). Of all the isotopes, only ^{95}Mo (16%) and ^{97}Mo (9%) possess nuclear magnetic moments ($I = 5/2$ for both; see Table 2). Therefore, these two isotopes only contribute to 25% of the total spectrum with the remaining 75% not showing any hyperfine interaction. To further illustrate this, Figure 9 shows the X-band spectrumof Mo^{5+} in ‘‘Very Rapid’’ xanthine oxidase using natural abundance Mo (top) or ^{95}Mo-enriched enzyme (bottom).**4** For ^{95}Mo the hyperfine coupling constants are: $A_z = 113\,\text{MHz}$, $A_y = 54.7\,\text{MHz}$, $A_x = 57.3\,\text{MHz}$.

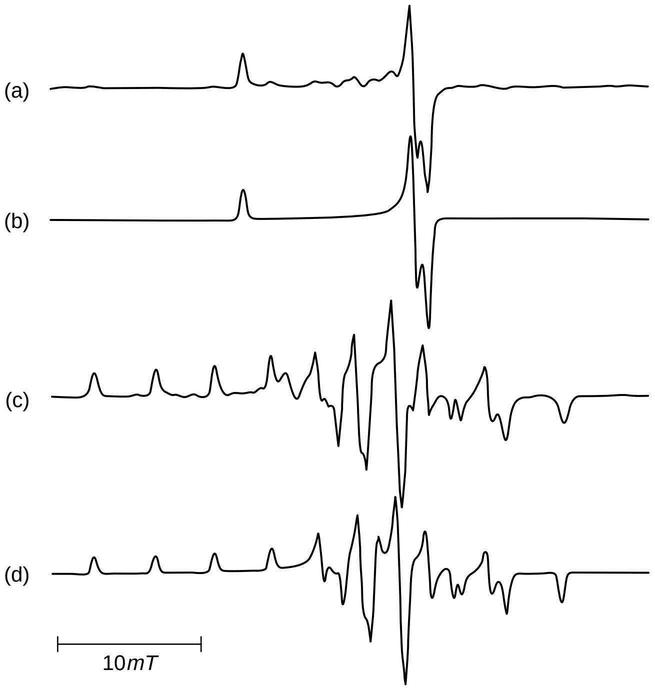

Figure 9 Powder spectra of Mo^{5+} in ‘‘Very Rapid’’ form of xanthine oxidase. Spectrum (a) represents natural abundance Mo with 16% ^{95}Mo and 9% ^{97}Mo (both isotopes have $I = 5/2$). The remaining isotopes have $I = 0$. These two isotopes contribute to the small structure observed in (a). Spectrum (b) represents a simulation of (a) without any hyperfine splitting. Spectrum (c) represents the sample enriched in ^{95}Mo while (d) is a simulation of (c). (Reprinted with permission from George and Bray.**4** © 1988 American Chemical Society)

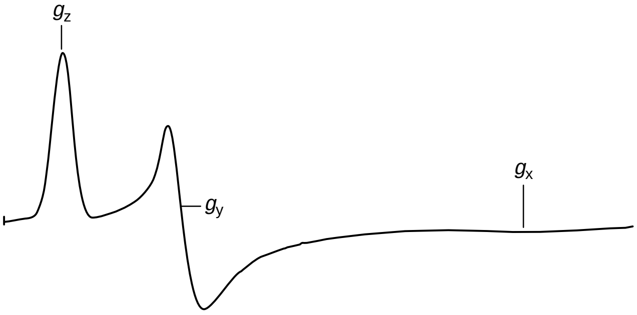

Figure 10 Powder spectrum of a Aquometmyoglobin heme (Fe^{3+}) protein. Note the increase in line width from left to right with increasing magnetic field and decreasing g-factor

11.5 Low-spin Heme (Fe^{3+})

Iron in a heme structure can exist in the low-spin ($S = 1/2$) form. In cytochrome c, the principal axes approximately coincide with a rectangular coordinate system with two of the axis fixed on the heme. The observed g-factors (Figure 10) are 1.45, 2.22 and 3.06. The broadening of the spectrum with increasing field is attributed to *g-strain*. When solutions of metalloproteins (or similar systems) are frozen there exist a range of environments surrounding the metal ion. This arises from the flexibility of the protein prior to freezing. Each environment has its own set of g-factors, differing only slightly from one another. The resultant powder spectrum will be broadened due to the overlap of all the different g-factors. For a given variation of g-factor (say 10%), the broadening (in terms of magnetic field-width) will vary across the spectrum. A simplistic example is that a 10% variation of a g-factor at 1000 G will be 100 G while the same variation for a g-factor at 3000 G will be 300 G. This field-dependent broadening is termed *g-strain* and results in a spectral broadening that increases toward the high-field region. It is not unusual for the high-field inflections to be unobservable due to excessive broadening.

11.6 Iron–Sulfur Clusters

Paramagnetism in a metalloprotein does not have to be associated with only a single metal site but can arise from metal clusters. In these clusters the spins of the different metal sites couple either ferromagnetically or antiferromagnetically to produce a net spin state of the cluster.

Fe–S proteins provide some of the best-characterized examples of multimetal paramagnetic clusters in proteins. Most of these proteins exhibit redox functions with the Fe–S clusters existing in two different oxidation states where one of the states (even numbers of electrons) is diamagnetic or integer spin. The other oxidation state is one electron different from the integer state and, therefore, is a paramagnetic half-integer state. This latter state is most often $S = 1/2$, although mixtures with states having $S > 1/2$ have been observed. Even though the iron ions in these clusters are usually high spin ($S = 5/2$ or 2), antiferromagnetic coupling between them produces a net $S = 1/2$ state for the cluster. Since ^{32}S and ^{56}Fe have no nuclear spin ($I = 0$), the EPR spectra of isolated Fe–S clusters possess no observable fine structure. Shown in Figure 11 are representative X-band spectra of different Fe–S clusters**[5]**. Note that $[4Fe\text{-}4S]^{1+}$ and $[2Fe\text{-}2S]^{1+}$ have $g_{\text{ave}} < 2$ while $[3Fe\text{-}4S]^{1+}$ and $[4Fe\text{-}4S]^{3+}$ have $g_{\text{ave}} > 2$ (where $g_{\text{ave}} = \surd\{[g_x^2 + g_y^2 + g_z^2]/3\}$).

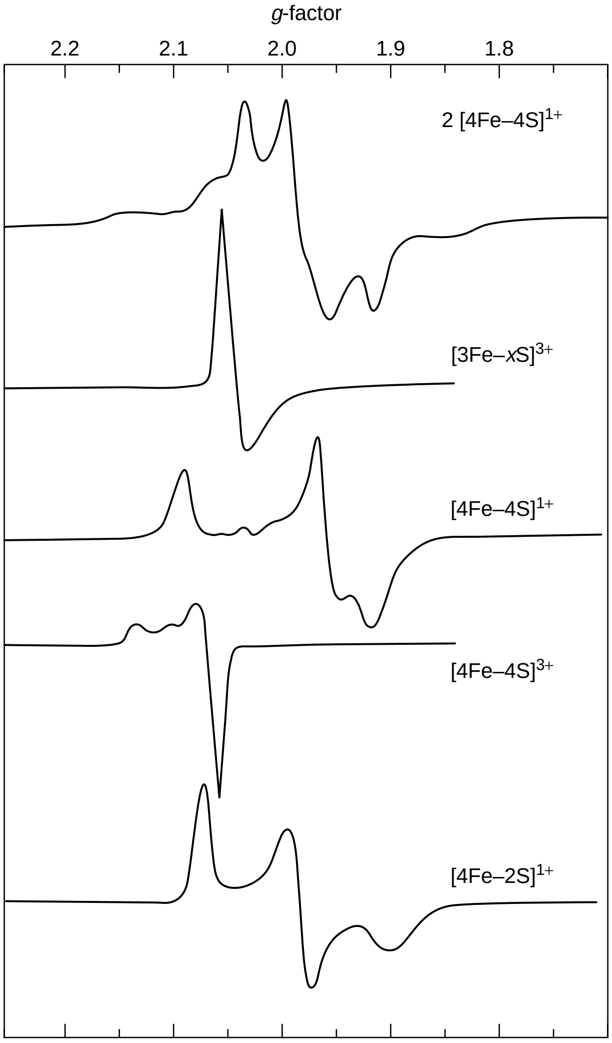

Figure 11 Representative EPR powder spectra of different classes of common FeS clusters. All spectra represent clusters in the paramagnetic $S = 1/2$ state. (Reproduced with permission from Cammack, Patil and Fernandez.**[5]** © 1985 The Biochemical Society)

12 $S > 1/2$ SPECTRA

12.1 The Energy Equation

When interpreting the EPR spectra of metals or metal clusters with $S > 1/2$, an extra term is added to the energy equation. Until now we have included the Zeeman interaction and the hyperfine interaction. For $S > 1/2$ systems we must include an energy term describing the interaction between two or more unpaired electrons. The magnitude of this interaction depends on the system. In organic triplet states ($S = 1$), the magnitude of this interaction is generally small and primarily arises from dipole–dipole interaction between the magnetic moments of the two electrons. On the other hand, in transition metals this interaction is large and occurs via spin-orbit coupling of the electrons. Regardless of the origin or magnitude, the added term describing the energy of this interaction is the same,

$$W_{S>1/2} = D\left[S_z^2 - \frac{1}{3}S(S+1) + \frac{E}{D}(S_x^2 - S_y^2)\right] \tag{19}$$

where D and E are the axial and rhombic zero-field splitting (zfs) parameters, respectively. All bold spin terms are quantum mechanical operators. The term E/D, called the *rhombicity*, is defined such that $0 \le E/D \le 1/3$ where $E/D = 0$ represents a completely axial system and 1/3 is a completely rhombic system.

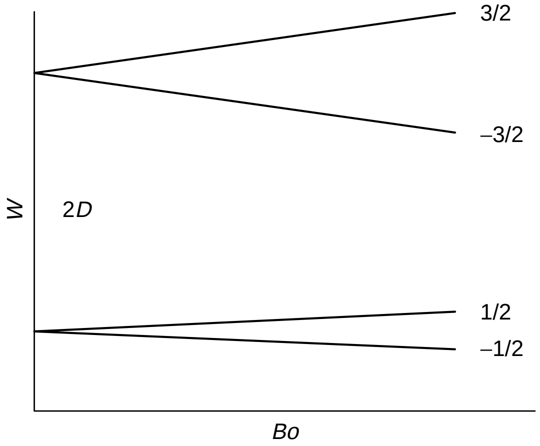

Figure 12 Energy diagram for $S = 3/2$ spin system with $E/D = 0$. Typically the separation ($2D$) between each pair of doublets is much larger than the irradiating microwave field inducing transitions. Therefore, transitions only occur within each doublet and not between them

12.2 Half-integer (Kramers) Systems

Half-integer systems with $S > 1/2$ are referred to as Kramers systems. These systems have a degeneracy in the ground state that is relieved through Zeeman interaction. The simplest example to consider is $S = 3/2$. To make things easier, we will assume an axial system ($E/D = 0$) in a zero external field (B_o). Therefore, the total energy is

$$W_{S>1/2} = D\left[S_z^2 - \frac{1}{3}S(S+1)\right] \tag{20}$$

When $S = 3/2$ there are four sublevels ($m_s = S_z = 3/2, 1/2, -1/2, -3/2$). Because equation (20) contains S_z only as a squared term, all $|S_z|$ levels will be degenerate. Using the above equation, we can calculate the energies of these doublets in zero field (assuming D to be positive) as

$\underline{S = 3/2, S_z = \pm 3/2}$

$$\begin{aligned} W_{S=3/2;Sz=\pm 3/2} &= D\left[(\pm 3/2)^2 - 1/3\,(3/2)\,(3/2+1)\right] \\ &= +D \end{aligned}$$

$\underline{S = 3/2, S_z = \pm 1/2}$

$$W_{S=3/2;Sz=\pm 1/2} = -D$$

When D is negative, this order is just reversed and the $S_z = \pm 3/2$ doublet is the ground state. These equations demonstrate that, in the absence of an external field, the levels exist as two sets of doublets (Figure 12) separated in energy by $2D$. Generally for metalloproteins, $D \gg h\nu$ (i.e., the splitting is greater than the energy of the irradiating microwaves), meaning that the irradiation energy is not large enough to induce transitions between $|S_z|$ levels. Therefore, only transitions within each doublet are observed.

As such, each doublet looks more like an isolated $S = 1/2$ system than part of an $S = 3/2$ system. We will refer to these sets as ''effective'' $S = 1/2$ states. Since there are two sets, we have the possibility of observing two different transitions, one from the ground state and the other from the excited state. The ''effective'' g-factor for each state is easily calculated by assuming that the g-factor of the actual state is g_e and use this to calculate the effective g-factor (g) for an effective $S = 1/2$ state. For example, for the $m_s = -3/2$ to $+3/2$ transition, $\Delta m_s = 3$ and $\Delta W = g_e \beta B_o \Delta m_s = 6\beta B_o$ while for an effective $S = 1/2$ transition ($m_s = -1/2$ to $+1/2$ or $\Delta m_s = 1$) $\Delta W = g\beta B_o \Delta m_s$. These two energies represent the same transition meaning $6\beta B_o = g\beta B_o$ or $g = 6$. A similar calculation of the $m_s = \pm 1/2$ state with the magnetic field along the z axis yields $g = 2$.

As with pure $S = 1/2$ states, the g-factors for each of these transitions will be anisotropic producing two inflections for an axial system and three for a rhombic system. In other words, for our two-level $S = 3/2$ system we have the possibility of observing two or three transitions for each level or four or six inflections for axial or rhombic, respectively. Normally, not all of these inflections are observable. Using quantum mechanics to solve the above energy equation for $S = 3/2$, $E = 0$ and $D \gg h\nu$ yields the g-factors $g_\perp = 4.0$ and $g_\parallel = 2.0$ for the $m_s = \pm 1/2$ level and $g_\perp = 0.0$ and $g_\parallel = 6.0$ for the $m_s = \pm 3/2$ level. Solving this equation for various values of E/D from 0 to 1/3 allows the determination of the possible values of the six different g-factors.[6] A plot of these g-factors is shown in Figure 13.

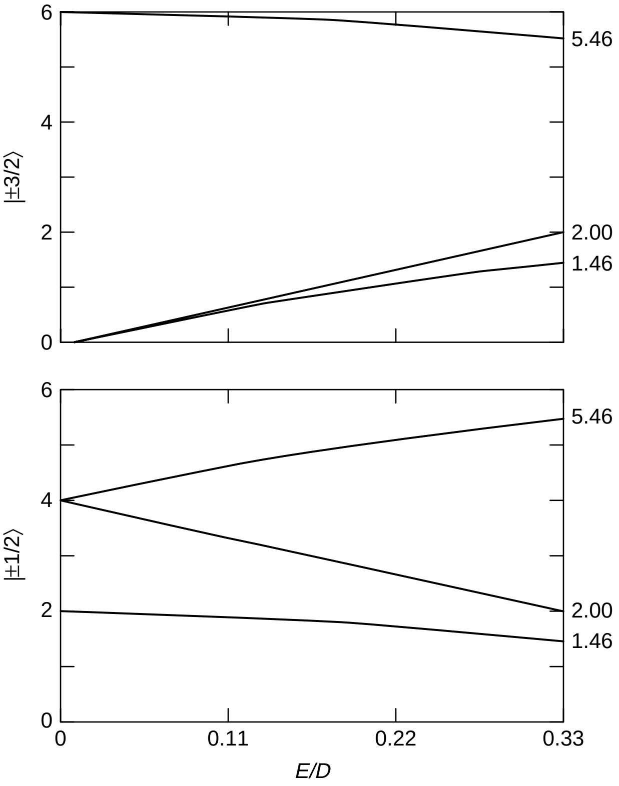

Figure 13 Variation of the principal g-factors for the $m_s = \pm 1/2$ and $\pm 3/2$ states with rhombicity (E/D) for an $S = 3/2$ state. (Adapted from Hagen[6] with permission, © 1992, Academic Press)

13 EXAMPLE OF $S = 3/2$ SYSTEM—MoFe PROTEIN OF NITROGENASE

One of the best examples of a metalloprotein with a paramagnetic $S = 3/2$ state is the MoFe protein of nitrogenase (Nitrogenase catalyzes the reaction

$$N_2 + 6H^+ + 6e^- \rightarrow 2NH_3 \qquad (21)$$

The MoFe protein of the enzyme contains two different types of metal clusters: an Fe_8S_7 cluster called the *P-cluster* and a $MoFe_7S_9$• homocitrate cluster known as the *M-center* or *MoFe-cofactor*. The latter cluster is believed to be the site of substrate (N_2) reduction. The cofactor cluster is paramagnetic in the as-isolated form of the protein with $S = 3/2$ while the P-clusters are diamagnetic. Inflections for the resting-state cofactor cluster occur at $g = 4.6$, 3.7 and 2.0. These inflections (Figure 14) are associated with an $S = 3/2$ signal with an apparent rhombicity (Figure 13) of $E/D = 0.05$.

14 EXAMPLE OF $S = 5/2$

14.1 Aquometmyoglobin

The iron in aquometmyoglobin (Figure 15) exists in an axial environment ($E/D = 0$) in the high-spin ($S = 5/2$) state of Fe^{3+}. This can be compared to iron in a purely rhombic ($E/D = 1/3$) high-spin system as exemplified by hexaaquo iron and *D. gigas* rubredoxin (Figure 15). Note that the middle energy level of a purely rhombic system (Figure 15) has all three g-factors coincident at about 4.3. Even though these inflections arise from an excited state, their intensity is confined to one g-factor producing a dominant signal observed even at very low concentrations. Because of the ubiquitous nature of hexaaquo iron, this signal is observable in most biological spectra and should not be assumed to be associated with the sample under investigation.

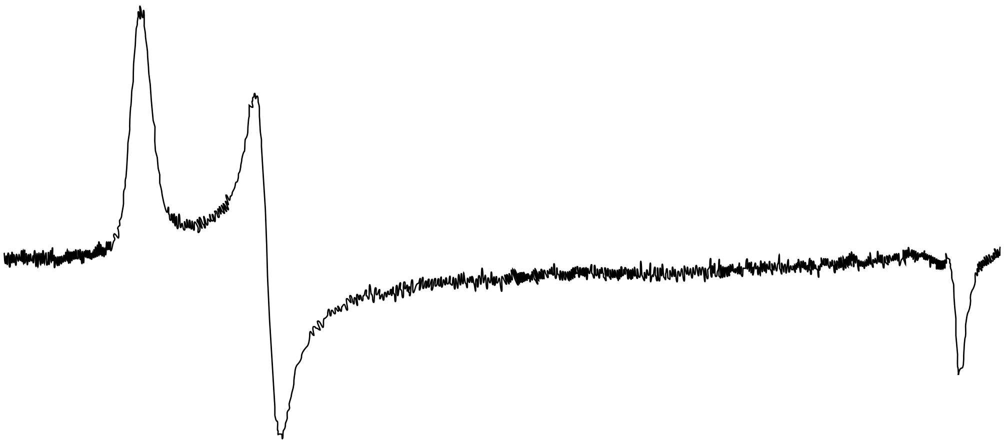

Figure 14 EPR powder spectrum of the MoFe protein of Mo-nitrogenase taken at 4 K. The spectral g-factors of 4.6, 3.7 and 2.0 represent the lower $m_s = \pm 1/2$ transition of an $S = 3/2$ system with $E/D = 0.05$

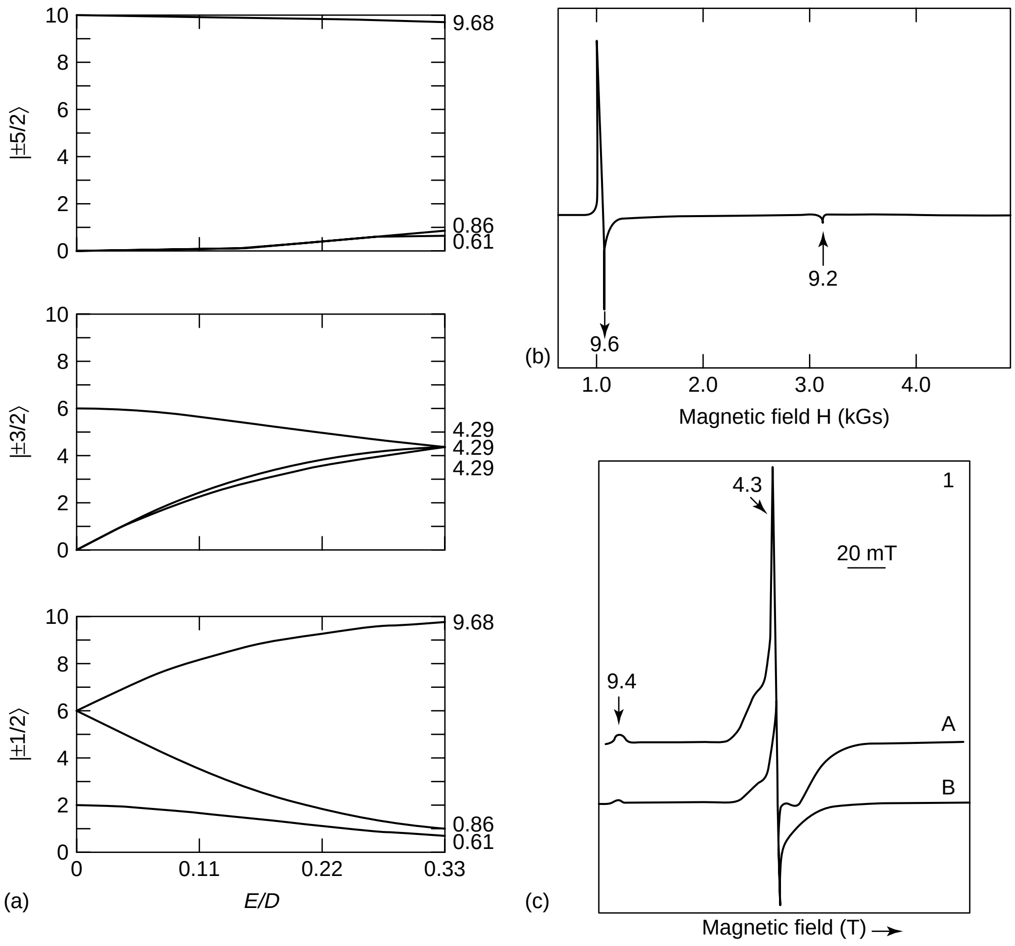

Figure 15 Variation of the principal g-factors for the $m_S = \pm1/2, \pm3/2$ and $\pm5/2$ states with rhombicity (E/D) for an $S = 5/2$ state (a). (Adapted from Hagen[6] with permission, © 1992, Academic Press). Spectra of an $S = 5/2$ state with pure axial $(E/D = 0)$ (aquometmyoglobin)(b), and pure rhombic $(E/D = 1/3$; rubredoxin) (Sc) symmetries. Note the high intensity of the $g = 4.3$ line in the rhombic spectrum even though this line arises from a high energy transition

15 INTEGER-SPIN (NON-KRAMERS) SYSTEMS

Integer-spin (non-Kramers) systems are not required to be degenerate in the absence of an external magnetic field. The simplest example occurs with $S = 1$. Equation (19) is again used to calculate the energies in zero magnetic field. When a magnetic field is present (without any hyperfine interactions), the energy becomes

$$W = g\beta B_o S_z + D\left[S_z^2 - 1/3S(S+1) + E/D(S_x^2 - S_y^2)\right] \qquad (21)$$

Solving this equation for $S = 1$ yields three energy levels,

$$W_1 = -2\frac{D}{3} \qquad (22)$$

$$W_2 = \frac{D}{3} - [E^2 + (g\beta B_o)^2]^{1/2} \qquad (23)$$

$$W_2 = \frac{D}{3} + [E^2 + (g\beta B_o)^2]^{1/2} \qquad (24)$$

Figure 16 shows plots of the energy levels for both axial $(E = 0)$ and rhombic $(D > 3E > 0)$ systems with $D \gg h\nu$. In the axial system, it is obvious that a transition cannot be induced between $m_s = 0$ and $m_s = \pm1$ because of the large energy separation (D). A transition also cannot be induced between $m_s = +1$ and $m_s = -1$, since this is forbidden by selection rules (i.e., this is a $\Delta m_s = 2$ transition while only $\Delta m_s = 1$ transitions are allowed). Therefore, transitions are almost never observed in purely axial integer-spin systems.

In rhombic systems, transitions between $m_s = +1$ and $m_s = -1$ become allowed through wave function mixing. However, a new complication arises, one not previously encountered with half-integer systems. Namely the $m_s = +1$ and $m_s = -1$ levels are now split in zero-field. If this separation is larger than the microwave energy $(2E > h\nu)$, a transition cannot be induced. This is why so many integer-spin paramagnetic metalloproteins are EPR silent.

EPR transitions have been observed from some integer-spin systems. From the above discussion it is obvious

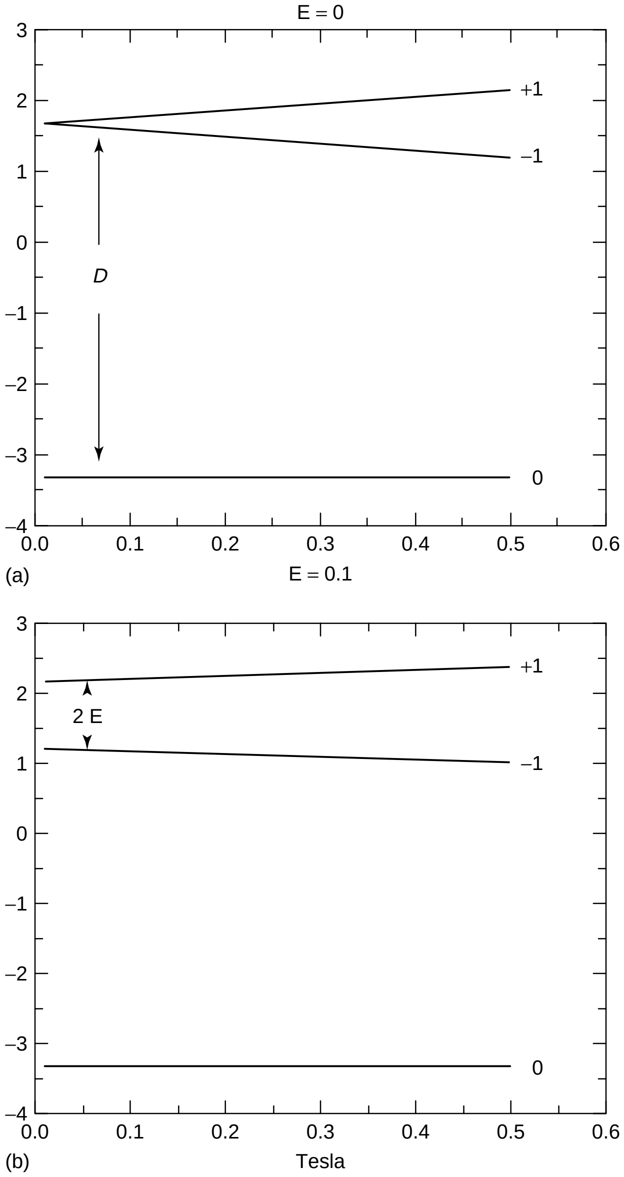

Figure 16 Theoretical variation of the energies of the $m_s = +1$, 0 and -1 states for an $S = 1$ system with $E/D = 0$ (a) and $E/D = 0.1$ (b). Bottom plot illustrates the splitting of the $m_s = \pm 1$ levels even in the absence of an external magnetic field

that to be able to observe a transition in these systems (1) the system *must have* $E \neq 0$ and (2) the zero-field separation between any set of doublets ($m_s = \pm n$ where $n < S$) *must be less than the microwave energy*. This latter requirement has the best chance of occurring for low-field inflections for the $m_s = \pm$n doublet of an $S = n$ system where $n > 2$. The low-field g-factor for this transition is normally around $g = 4S$. A dual-mode cavity can be used to accentuate the transition probability (intensity) of an integer-spin system. These cavities have the magnetic field component of microwave radiation oriented parallel to the direction of the external magnetic field (as opposed to the more typical perpendicular mode). While the perpendicular mode induces transitions corresponding to $\Delta m_s = \pm 1$, parallel mode allows one to observe $\Delta m_s = 0$ transitions, which tend to have a greater probability among $m_s = \pm$n integer-spin states.

16 ABBREVIATIONS AND ACRONYMS

ENDOR = electron nuclear double resonance; EPR = electron-paramagnetic resonance; ESR = electron-spin resonance; NMR = nuclear magnetic resonance; MA = modulation amplitude; SOPT = second-order perturbation theory; s-o = spin-orbit; zfs = zero-field splitting (for $S > 1/2$); D = uniaxial zfs; E = rhombic zfs; g = g-factor with principal components g_x, g_y, and g_z; g_e = free electron g-factor; a = hyperfine splitting constant; A = hyperfine coupling constant for a given nucleus N (nuclear spin $I > 0$).

17 RELATED ARTICLES

Electron-Nuclear Double Resonance (ENDOR) Spectroscopy; Electron Spin Echo Envelope Modulation (ESEEM) Spectroscopy; Magnetic Circular Dichroism (MCD) Spectroscopy

18 FURTHER READING

Introductory Texts

A. Carrington and A. D. McLachlan, ‘Introduction to Magnetic Resonance’, Harper & Row, New York, 1967, (Out of print; check your local library).

J. A. Weil, J. E. Wertz and J. R. Bolton, ‘Electron Paramagnetic Resonance: Elementary Theory and Practical Applications’, McGraw-Hill, John Wiley & Sons, New York, 1994.

W. Gordy, ‘Theory and Applications of Electron Spin Resonance’, John Wiley & Sons, New York, 1980.

Techniques

C. P. Poole, Jr, ‘Electron-Spin Resonance: A Comprehensive Treatise on Experimental Techniques’, Dover Publishing, 1997.

Biological

A. J. Hoff ed., ‘Advanced EPR: Applications in Biology and Biochemistry’, Elsevier, Amsterdam, 1989.

W. R. Hagen, ‘EPR Spectroscopy of Iron-Sulfur Proteins’, ’Advances in Inorganic Chemistry’, Vol. 38, Academic Press, 1992, p. 165.

Inorganic

A. Abragam and B. Bleaney, ‘Electron-Paramagnetic Resonance of Transition Ions’, Dover Publishing, New York, 1986.

J. R. Pilbrow, ‘Transition Ion Electron-Paramagnetic Resonance’, Clarendon Press, Oxford, 1990.

G. E. Pake, ‘Paramagnetic Resonance’, W. A. Benjamin, New York, 1962 (Out of print; check your local library).

Special Books

L. Kevan and L. D. Kispert, ‘Electron-Spin Double Resonance Spectroscopy’, John Wiley & Sons, New York, 1976.

L. Kevan and R. N. Schwartz, ‘Time Domain Electron-Spin Resonance’, John Wiley & Sons, New York, 1979.

19 REFERENCES

1. E. Zavoisky, *J. Phys.*, 1945, **9(2)**, 211.
2. R. Calvo, E. C. Abresch, R. Bittl, G. Feher, W. Hofbauer, R. A. Isaacson, W. Lubitz, M. Y. Okamura and M. L. Paddock, *J. Am. Chem. Soc.*, 2000, **122**, 7327.
3. A. M. Portis, *Phys. Rev*, 1955, **100**, 1219.
4. G. N. George and R. C. Bray, *Biochemistry*, 1988, **27(10)**, 3603.
5. R. Cammack, D. S. Patil and V. M. Fernandez, *Biochem. Soc. Trans.*, 1985, **13**, 572.
6. W. R. Hagen, in ‘Advances in Inorganic Chemistry: Iron-Sulfur Proteins’, eds. A. G. Sykes and R. Cammack, Academic Press, 1992, Vol. 38, p. 165.

Electron Spin Echo Envelope Modulation (ESEEM) Spectroscopy

John McCracken

Michigan State University, East Lansing, MI, USA

Method Summary 1
1 Introduction 2
2 Technical Background 4
3 Application — Eseem Studies of Fe(II)/α-Ketoglutarate-Dependent Dioxygenases 11
4 Acknowledgments 21
5 Abbreviations and Acronyms 21
6 Further Reading 21
7 References 22

METHOD SUMMARY

Acronyms, Synonyms

- Electron Spin Echo Envelope Modulation
- Electron Spin Echo Modulation
- HYperfine Sublevel CORrElation Spectroscopy.

Measured physical quantities

- The integrated intensity of electron spin echoes as a function of the time between one or two pairs of microwave pulses.

Information available

- the identity and number of nuclei magnetically coupled to a paramagnetic center
- hyperfine and nuclear quadrupole couplings
- coupling tensor orientation with respect to magnetic axis
- the distribution of unpaired electron spin density about a structure

Information not available, limitations

- The system must be paramagnetic.
- The nuclei to be studied must have a magnetic moment.

Examples of questions that can be answered

- The ligation structure of a paramagnetic metal ion can be quantified.
- The freeze quench sample preparation can allow characterization of reaction intermediates.
- The electronic structure and conformation of organic radicals can be measured.

Major advantages

- The experimental approach is systematic.
- ESEEM data are self-normalizing, allowing one to take difference spectra and simplify complicated spectra.
- Structural information can be gained from powder and frozen solution samples.

- The experiment only provides information on a small volume of the system within 5–10 Å of a paramagnetic center, so it is not limited by molar mass.

Major disadvantages

- A pulse EPR spectrometer is needed.
- The experiments usually require sample temperatures from 2 to 80 K.
- Sample concentrations are high in comparison to optical methods.
- Data reduction often requires spectral simulation.

Sample constraints

- Samples can be frozen solutions, powders, or single crystals.
- Samples are normally housed in 3–5 mm OD quartz tubes with an active sample volume of 50–150 µL.
- Sample concentrations depend on spin relaxation dynamics, the intensity of ESEEM and the width of the EPR absorption spectrum, typical concentrations needed for quality data are: organic radicals, Mn(II), 10–100 µM; Cu(II), 100–500 µM; Fe(III), 0.2–2 mM.

1 INTRODUCTION

The potential for electron paramagnetic resonance (EPR), (*see* ***Electron Paramagnetic Resonance (EPR) Spectroscopy***) spectroscopy to contribute important structural and mechanistic information to problems in inorganic chemistry has never been higher than it is at present. In biology and materials science, transition ions play important roles in the catalysis of oxidation-reduction reactions. These metal centers are often paramagnetic in at least one step of a catalytic cycle allowing EPR spectroscopy to probe the details of the center's magnetic structure. Much of this information relies on the measurement of ligand hyperfine couplings, weak spin–spin couplings between the paramagnetic center and magnetic nuclei that belong to ligand groups or nearby molecular entities of chemical interest. Because inhomogeneous broadening of the EPR spectrum precludes the measurement of these weak hyperfine couplings for powder and frozen solution samples, the experimentalist must use a combination of multifrequency EPR, electron-nuclear double resonance (ENDOR), (*see* ***Electron-Nuclear Double Resonance (ENDOR) Spectroscopy***), and electron spin echo envelope modulation (ESEEM) spectroscopies to measure them. Although there is overlap in the capabilities of these methods, experience over the past 30 years has revealed their relative strengths and weaknesses. Fortunately, these are of a complementary nature and EPR spectrometers that can perform all of these measurements from a single platform are commercially available. This article will begin with a brief historical perspective on the development of ESEEM spectroscopy and will end with a case study that illustrates its power in solving problems in bioinorganic chemistry. Facets of this methodology that remain problematic will be discussed.

The first observations of ESEEM were published in two separate articles that appeared in Physical Review during the fall of 1961. The first of these reports was authored by W.B. Mims, K. Nassau and J.D. McGee and focused on using electron spin echoes (ESE) to study spectral diffusion and relaxation dynamics for the EPR spectra of Ce(III) and Er(III) doped into $CaWO_4$ crystals. During the course of this work, deep modulations of the Ce(III) ESE amplitude were measured as a function of varying the inter-pulse spacing, τ, in two-pulse ($90° - \tau - 180°$) experiments. This modulation occurred at the ^{183}W Larmor frequency and its amplitude was markedly dependent on crystal orientation with respect to the direction of the applied magnetic field.**[1]** Two months later, J.A. Cowen and D.E. Kaplan reported deep modulations of the Ce(III) ESE decay envelope when using 2–($90° - \tau - 180°$) and three-pulse ($90° - \tau - 90° - T - 90°$) techniques to measure electron spin relaxation times for the metal ion doped into lanthanum magnesium nitrate crystals. These modulations were recorded as a function of varying τ, from 0.5–4.0 µs, in two-pulse measurements, and T, from 1.0 to 8.0 µs, in three-pulse measurements. Cowan and Kaplan assigned these modulations to weak hyperfine interactions between Ce(III) and ^{14}N of the host lattice and commented, ''this technique should prove useful for investigating nuclear-electron coupling.''**[2]** It was probably no accident that both Mims and Kaplan were located at companies, Bell Laboratories and Lockheed, respectively, where there was access to sophisticated microwave equipment. The Mims spectrometer operated at 6.7 GHz and used a fast grid-modulated traveling wave tube amplifier (TWTA) to achieve the high pulse powers and fast pulse recovery times (250 ns) required to generate and detect electron spin echoes while the Kaplan system operated at 9.3 GHz and used pulsed magnetrons capable of producing 50 ns pulses with 100 W peak power for exciting the samples.

A full-length paper on ESEEM studies of Ce(III) doped into $CaWO_4$ and CaF_2 was published in 1965 by Rowan, Hahn and Mims.**[3]** These authors called attention to the similarities of the ESEEM experiment to experiments done in the early 1950s on nuclear spin echo modulation where spin–spin couplings between nuclear spins gave rise to similar interferences.[4,5] They developed the theory for ESEEM and used it to analyze the two-pulse modulation data obtained for the two Ce(III) crystal systems mentioned above.[3] The first ESEEM studies of glassy samples were published in 1968 by Zhidomirov, Salikov, Tsvetkov, Yudanov and Raitsimring and focused on measuring ^{1}H and ^{2}H-ESEEM in γ-irradiated sulfuric acid glasses and in frozen solutions of 2,2-diphenyl-1-picrylhydrazyl (DPPH) in CH_3OH and CH_3OD. The theory developed for the analysis of these data was published separately.[6,7]

During the 1970s, the development of ESEEM continued in the laboratories of W.B. Mims at Bell Laboratories (Murray Hill, New Jersey, USA) and of Yu.D. Tsvetkov at the Institute of Chemical Combustion and Kinetics (Novosibirsk, Russia). Mims continued his focus on inorganic systems and in collaboration with J. Peisach (Albert Einstein College of Medicine) began investigations on frozen solutions of model transition metal ion complexes and metalloproteins.[8–11] The Novosibirsk group maintained an interest in glassy materials and together with L. Kevan (then at Wayne State University) used careful ESEEM measurements and theoretical analysis to define the locales of trapped electrons in γ-irradiated glasses.[12–14] By the late 1970s, advances in microwave technology and digital electronics made the construction of pulsed EPR spectrometers straightforward and many labs built systems for ESEEM and ESE-detected ENDOR applications. A list of these instruments, compiled by J. Peisach in 1986, showed that 33 laboratories worldwide housed at least one pulse EPR spectrometer. These homebuilt spectrometers typically operated at X-band (8–12 GHz), featured a pulse transmitter capable of 1 kW pulses, a homebuilt pulse programmer that utilized commercial, programmable delay and gate generators to achieve the accurate 1–10 ns timing requirements of the experiments, a gated integrator to record spin-echo intensities, and locally constructed, high filling factor probes that could accommodate samples in standard EPR tubes. This second wave of homebuilt pulse EPR spectrometers were also computer controlled, making the standard two- and three-pulse ESEEM experiments more routine and providing researchers with ESEEM data that were in digital form. Spectral analysis methods that were primarily built around fast fourier transformations (FFT) of the data became common and the resulting ESEEM spectra became the most common way to report experimental findings.

Along with this expansion in instrumentation came the development of new data acquisition strategies to improve instrument performance and tailor data acquisition for more precise measurements of hyperfine couplings. Sophisticated approaches to data analysis, spectral simulation and improved probe designs were developed. These improvements were driven by an even greater expansion in applications.[15] No field of modern scientific investigation benefited more from this expansion than inorganic chemistry. In materials chemistry, many papers using ESEEM to probe the structures of solid phase catalysts were published. In bioinorganic chemistry, a vast array of transition metal ion centers in metalloenzymes and model complexes were studied by ESEEM. This growth in applications led to the development of the first commercial FT/EPR spectrometer, the Bruker ESP 380, in 1987. Although the EPR community was slow to adopt the ESP 380 and Bruker's most recent offering, the ElexSys E 580, the advantages of these spectrometers over the majority of homebuilt instruments are considerable. These advantages are listed below.

1. The pulse programmer is flexible and controlled by a simple scripting language that makes it easy to implement new pulsing schemes with phase cycling and multiple pulse channels.
2. The transient recorder can be used as a digital oscilloscope for instrument tuning and diagnostics, as a gated integrator for ESEEM studies and as a transient recorder for FT-EPR. The maximum repetition rate is often limited by the TWTA duty cycle, but it is routine to operate the instrument at 1–2 kHz repetition rates.
3. The microwave bridge is stable for days making two-dimensional ESEEM experiments routine.
4. Sensitive probes that feature high filling factors and coupling assemblies that allow adjustment from critical coupling for cw-EPR to overcoupling for pulse operation with 60 ns dead times are available. These probes are fitted with magnetic field modulation coils, so it is routine to measure the cw-EPR spectrum of a sample prior to switching to pulse operation. An ENDOR probe that features a 4-mm dielectric resonator allows one to collect cw-EPR spectra and then switch to pulse operation where ESE-ENDOR and ESEEM studies can be undertaken.
5. The Xepr software package that runs the instrument is easy to learn and contains many useful features for spectral manipulation and analysis. It runs on a personal computer under the Linux environment so it is possible to gain network access to the spectrometer from any networked computer that has an X-11 terminal emulator. This allows several users to log in and analyze their data while the spectrometer is busy collecting more.

Finally, before moving on to the scientific portion of this article, a disclaimer concerning the above text needs to be offered. Although the origins of the ESEEM experiment were presented in some detail with specific mention of a few scientists and references, the majority of investigators who played key roles in bringing ESEEM to where it is today, are lumped into two or three sentences about the period from the late 1970s to the present. Some of these oversights will be remedied below as background material and applications are presented. Also, the above comments regarding the advantages of the commercial pulse EPR instrument over the homebuilt instruments of the last 30 years are strongly influenced by my own experiences. There are labs where homebuilt machines have achieved performance equal or superior to that offered by Bruker, or they have a unique capability not offered by the Bruker instruments. These laboratories have access to engineers and technical help that are not found in a typical academic setting.

2 TECHNICAL BACKGROUND

The goal of an ESEEM experiment is to gain an understanding of the detailed electronic and geometric structure of a paramagnetic center through the measurement of electron-nuclear hyperfine couplings. For problems in inorganic chemistry, ESEEM is most often used to measure ligand hyperfine couplings to a paramagnetic metal ion center that will help identify the ligands and determine their orientation with respect to the paramagnetic center's magnetic axis system. Hyperfine couplings to magnetic nuclei outside the primary coordination sphere can also be measured. It is often these weaker couplings that provide key information on the chemical problem to be addressed. In an ESEEM experiment, the magnetic field is set to a fixed position within the EPR absorption spectrum and the sample is excited with resonant microwave pulses that lead to the formation of electron spin echoes. In this section, three basic ESEEM pulse schemes, two-pulse or primary echo, three-pulse or stimulated echo, and the two-dimensional hyperfine sublevel correlation (HYSCORE) will be discussed in detail. Mathematical formulas for the spin echo modulation functions of a simple $S = 1/2$, $I = 1/2$ coupled spin system will be presented and discussed for each technique because they provide the clearest explanation of what is measured. Sample spectra for each experiment will be presented to support this discussion. There are several good references available where this information is covered in greater detail, with more thorough explanations and with better coverage in terms of experimental examples (see *Further Reading* at the end of this article).

2.1 Two-pulse ESEEM

For a two-pulse ($90° - \tau - 180°$), or primary echo experiment, the integrated intensity of the spin echo, which occurs at time τ after the 180° pulse, is measured as a function of increasing τ from the probe's "dead-time" ($\sim$100 ns) to a time where the echo amplitude has decayed to a few percent of its initial amplitude (2–8 µs for most powder samples). A two-pulse ESE decay envelope for the type-1 Cu(II) site of a multi-copper oxidase, Fet3p, is shown in Figure 1(a). The data show an overall decay characterized by a phase memory time, T_M or T_2^*, of <1.0 µs. Superimposed on this decay are echo modulations that arise from hyperfine coupling to the ^{14}N nuclei of two histidyl imidazole ligands and the protons of the surrounding matrix.

The most straightforward way to understand the origin of ESEEM and the physical chemistry behind its detection and analysis is to step back from this Cu(II) center and focus on an $S = 1/2$, $I = 1/2$ coupled spin system. The spin Hamiltonian for this system consists of electronic Zeeman, nuclear Zeeman, and electron-nuclear hyperfine interaction terms. For the case of an isotropic electron g-matrix and an axial hyperfine interaction, this Hamiltonian can be conveniently written in the laboratory reference frame,

$$\mathrm{H}/\hbar = \omega_S \hat{S}_Z + A_{zz}\hat{S}_Z\hat{I}_Z + A_{xz}\hat{S}_Z\hat{I}_X - \omega_I\hat{I}_Z \qquad (1)$$

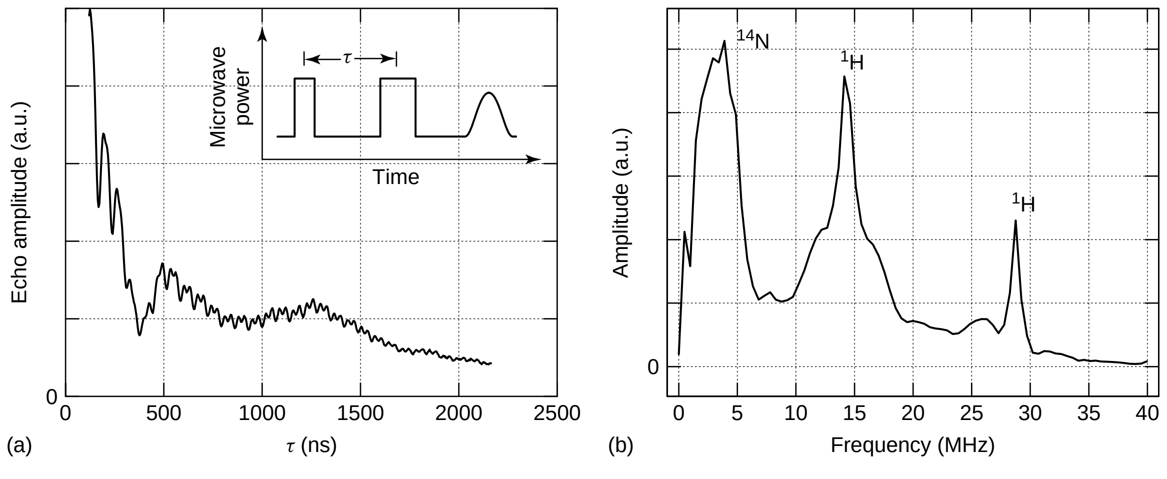

Figure 1 Two-pulse or primary ESEEM data collected for the type-1 Cu(II) site of the Fet3p enzyme. Figure 1(a) shows the time domain data recorded under the following conditions: microwave frequency, 9.6883 GHz; field strength, 337.0 mT; pulse power, 250 W; 90° pulse length, 16 ns full width at half maximum (FWHM); sample temperature, 10 K. Figure 1(b) shows the ESEEM spectrum derived from the data of Figure 1(a) by subtraction of a biexponential decay function, application of a Hamming window function, and Fast Fourier Transformation (FFT). The absolute value spectrum is displayed

where $A_{zz} = A = A_{\parallel} \cos^2\theta + A_{\perp} \sin^2\theta$, $A_{xz} = B = (A_{\parallel} - A_{\perp}) \cos\theta \sin\theta$, $\omega_S = g\beta B_o/\hbar$ and $\omega_I = g_n\beta_n B_o/\hbar$. $A_{\parallel}$ and $A_{\perp}$ are the principal values of an axially symmetric hyperfine tensor that can be expressed in terms of a Fermi contact coupling, A_{iso}, and a dipole–dipole coupling term, $T = gg_n\beta\beta_n/r^3$, with $A_{\parallel} = A_{\text{iso}} + 2T$ and $A_{\perp} = A_{\text{iso}} - T$. The angle θ describes the orientation of the principal axis of the hyperfine tensor, $A_{\parallel}$, with respect to the laboratory field, B_o. The remaining terms in the above equations are: g, the electron g-factor; g_n, the nuclear g-value; β, the Bohr magneton; and β_n, the nuclear magneton. The Hamiltonian matrix is easily constructed in a general basis set consisting of electron and nuclear spin product states, $|m_S, m_I>$. Diagonalization to yield the eigenvalues and eigenvectors of equation (1) can be carried out independently for the two electron spin manifolds since the only term in the operator that gives rise to off-diagonal matrix elements is that involving $\hat{I}_x$. The results are summarized in the energy level scheme of Figure 2.

The normalized probability amplitudes for the EPR transitions marked $|u|$ and $|v|$ in Figure 2 are given by

$$|u| = \frac{\left\langle 2 \middle| \hat{S}_x \middle| 3 \right\rangle}{(0.5g\beta B_1)} = \sin\left\{\frac{(\varphi_\alpha - \varphi_\beta)}{2}\right\} \tag{2}$$

and

$$|v| = \frac{\left\langle 1 \middle| \hat{S}_x \middle| 3 \right\rangle}{(0.5g\beta B_1)} = \cos\left\{\frac{(\varphi_\alpha - \varphi_\beta)}{2}\right\} \tag{3}$$

The angles φ_α and φ_β define the axis of quantization for the α and β electron-spin manifolds, respectively, and are given by $\sin\varphi_\alpha = B/2\omega_\alpha$ and $\sin\varphi_\beta = B/2\omega_\beta$, where ω_α and ω_β are the angular hyperfine frequencies as defined in Figure 2. In general, all four of the possible EPR transitions for the $S = 1/2$, $I = 1/2$ spin system of Figure 2 are allowed. These transitions will be excited simultaneously in a pulsed EPR experiment, provided that the microwave pulses have sufficient bandwidth.

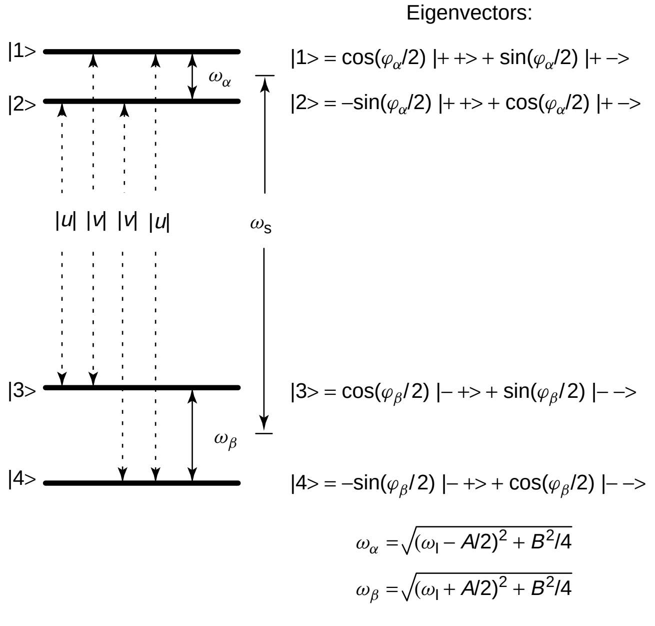
Eigenvectors:
|1>
|2>
|3>
|4>
ω_α
ω_β
ω_S
|u| |v| |v| |u|
$|1> = \cos(\varphi_\alpha/2)\ |++> + \sin(\varphi_\alpha/2)\ |+->$
$|2> = -\sin(\varphi_\alpha/2)\ |++> + \cos(\varphi_\alpha/2)\ |+->$
$|3> = \cos(\varphi_\beta/2)\ |-+> + \sin(\varphi_\beta/2)\ |-->$
$|4> = -\sin(\varphi_\beta/2)\ |-+> + \cos(\varphi_\beta/2)\ |-->$
$\omega_\alpha = \sqrt{(\omega_I - A/2)^2 + B^2/4}$
$\omega_\beta = \sqrt{(\omega_I + A/2)^2 + B^2/4}$

Figure 2 Energy level scheme and eigenvectors for the $S = 1/2$, $I = 1/2$ coupled spin system described in the text

Analytical expressions for the primary echo modulation function of an $S = 1/2$, $I = 1/2$ system were worked out for some of the earliest ESEEM studies that appeared in the literature. Perhaps the most general of these theoretical treatments is that of Mims[8] where the two-pulse ESEEM function is given by

$$\begin{aligned} E_{\text{mod}}(\tau) = |u|^4 + |v|^4 + |u|^2|v|^2[2\cos\omega_\alpha\tau + 2\cos\omega_\beta\tau \\ - \cos(\omega_\alpha - \omega_\beta)\tau - \cos(\omega_\alpha + \omega_\beta)\tau] \end{aligned} \tag{4}$$

Equation (4) shows that modulations of the two-pulse echo amplitude occur at the fundamental hyperfine frequencies and at their sum and difference combination frequencies. The amplitude of the modulations is given by the product of the transition probabilities for the two different transitions associated with ''branching'', $|u|^2|v|^2$, while the nonmodulated portion of the echo envelope depends only on the product of the transition probabilities for the ''nonbranching'' spins, $|u|^4$ or $|v|^4$. Substituting the expressions for $|u|$ and $|v|$ given by equations (2) and (3) into equation (4) yields

$$\begin{aligned} E_{\text{mod}}(\tau) = 1 - \left(\frac{k}{2}\right)[1 - \cos\omega_\alpha\tau - \cos\omega_\beta\tau \\ + 0.5^*\cos(\omega_\alpha - \omega_\beta)\tau + 0.5^*\cos(\omega_\alpha + \omega_\beta)\tau] \end{aligned} \tag{5}$$

where

$$k = \sin^2(\varphi_\alpha - \varphi_\beta) = \left[\frac{\omega_I B}{(\omega_\alpha\omega_\beta)}\right]^2 \tag{6}$$

is often referred to as the modulation depth parameter.

From the above discussion, it is clear that observation of ESEEM requires that the microwave pulses affect ''branching'' of the EPR transitions. This places a quantum mechanical constraint on the ESEEM experiment, in that each energy level must be involved in at least two different microwave transitions, and an experimental constraint that requires the microwave pulse bandwidth to cover the spread in frequencies needed to fully excite the ''branching''. The experimentally observed ESEEM function is a product of the quantum mechanically derived modulation function and a decay function that describes the loss of magnetization due to spin relaxation. These decay functions are typically modeled with exponential forms: $\exp(-\tau/\tau_o)^n$ where $n = 1, 2$ or 0.5.[16] For a $90° - \tau - 180°$ or two-pulse echo experiment, $\tau_o = T_2^*$, a time that is typically on the order of 1 µs, as evidenced by the data shown for the Cu(II) center in Figure 1. This rapid ''background'' decay serves to reduce the frequency resolution of the two-pulse measurement. A further complexity of the ESEEM experiment is introduced when multiple nuclei contribute to the modulation of a single paramagnetic center. The modulation function in this instance is given by the product of the individual modulation functions, due to each coupled nucleus giving an overall ESEEM function of the form

$$E(\tau) = V_{\text{decay}} \prod_{i=1}^{N} E^{i}_{\text{mod}}(\tau) \qquad (7)$$

where N represents the number of coupled nuclei.[3,8] Equation (7) shows that the two-pulse ESEEM data, or the corresponding ESEEM spectrum obtained from Fourier transformation of the time domain data,[17] can become complex when only a few nuclei contribute. Not only will each nucleus give rise to fundamental, $\Delta m_I = \pm 1$, frequencies and combination frequencies, but the product of equation (7) will lead to frequencies that are combinations of the frequencies arising from different nuclei. This increased complexity, when combined with the reduced resolution that results from a rapid phase memory time, can hamper two-pulse ESEEM analysis. These aspects of two-pulse ESEEM can be readily seen from the corresponding ESEEM spectrum shown in Figure 1(b) for the time domain data of Figure 1(a). It will be shown below that two histidyl imidazole side chains that have different hyperfine coupling strengths coordinate the Cu(II) under investigation. The broad peak centered at ~4 MHz shows the contribution of the remote nitrogen of both of these ligands and provides few details regarding their hyperfine coupling. The matrix ^{1}H peak, centered at 14.3 MHz, shows shoulders that originate from combination frequencies with ^{14}N. The peak at 28 MHz is due to the matrix proton sum combination frequency.

2.2 Three-pulse ESEEM

Some of the above problems are alleviated by use of the three-pulse or $90° - \tau - 90° - T - 90°$ sequence where the amplitude of the stimulated echo, occurring at τ after the third pulse, is normally monitored as a function of T (inset, Figure 3a). The background decay for this sequence is governed by electron spin-lattice relaxation, electron cross relaxation, and nuclear spin–spin relaxation processes. All of these processes are much longer than the electron spin–spin relaxation time and lead to better frequency resolution than typically found for the two-pulse experiment. Figure 3(a) shows three-pulse ESEEM data collected for the same sample and under the same conditions as used for the two-pulse ESEEM study of Figure 1. For a typical three-pulse measurement, τ is fixed to a value short with respect to the spin–spin relaxation time of the paramagnetic center, and the interval between the second and third microwave pulses is scanned from about 40 ns to ~10 µs. For the specific case of the type-1 Cu(II) site data shown in Figure 3(a), τ was set to 120 ns and T was stepped in 16 ns increments from 40 ns to >8 µs. The following analytical expression (equation 8) for the three-pulse modulation function of our model $S = 1/2$, $I = 1/2$ system

$$\begin{aligned} E_{\text{mod}}(\tau, T) = {} & |u|^4 + |v|^4 + |u|^2|v|^2 \\ & \times [\cos(\omega_\alpha \tau) + \cos\omega_\beta \tau + 2\sin^2(\omega_\alpha \tau/2)\cos\{\omega_\beta(\tau + T)\} \\ & + 2\sin^2(\omega_\beta \tau/2)\cos\{\omega_\alpha(\tau + T)\}] \end{aligned} \qquad (8)$$

has a simplified form, when compared to its two-pulse counterpart, in that only modulations at the fundamental hyperfine frequencies are observed. Equation (8) also shows that the τ-value chosen for a particular measurement will affect the amplitudes of modulations and allow one to enhance or suppress the contribution from an electron spin manifold by adjusting τ over a range of values determined by the period of the complementary hyperfine frequency. This effect is known as the τ-suppression effect and can be useful in making spectral assignments.[8,18,19] The product rule governing the form of the overall modulation function, when multiple nuclei are coupled to the paramagnetic center, is also simplified when compared to that of the two-pulse experiment in that products are taken

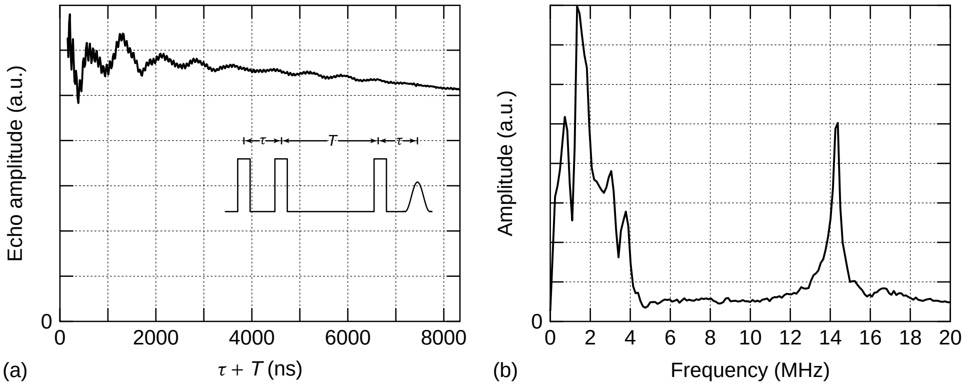

Figure 3 Three-pulse or stimulated echo ESEEM data (a) and associated FFT spectrum for the type-1 Cu(II) site of the Fet3p protein (b). Data were collected under the same conditions as those of Figure 1, except: τ-value, 120 ns; starting T, 40 ns; and time increment, 16 ns

only between frequencies belonging to the same electron spin manifold.[20]

$$E(\tau, T) = \left(\frac{V_{decay}}{2}\right)\left[\prod_{i=1}^{N} E_\alpha^i(\tau, T) + \prod_{j=1}^{N} E_\beta^j(\tau, T)\right] \tag{9}$$

The ESEEM spectrum for the three-pulse data of Figure 3(a) is shown in Figure 3(b). As in Figure 1, these data were collected in the $g_\perp$ region for the type-1 Cu(II) site of the Fet3p protein. The three-pulse ESEEM spectrum clearly shows resolved peaks at 0.75, 1.5, 3.0 and 3.8 MHz, in place of the broad ~4 MHz peak in the two-pulse spectrum (Figure 1b). These peaks are indicative of histidyl imidazole strongly bound to Cu(II) and are due to hyperfine coupling between Cu(II) and the remote ^{14}N of the ligand. The ^{1}H matrix peak also shows much higher resolution.

Figures 1 and 3 show that although the modulations of the three-pulse, or stimulated echo are less intense than those of its two-pulse counterpart, the resolution is much higher and the spectrum is simplified because combination peaks only enter into the data through the presence of multiple ESEEM-active nuclei. Equation (8) shows that for an $S = 1/2$, $I = 1/2$ spin system, judicious selection of the τ-value can control the ESEEM amplitudes of the hyperfine frequencies from α and β electron spin manifolds allowing them to be optimized or suppressed. For weakly coupled protons, where the modulation frequencies from both electron spin manifolds are centered at the proton Larmor frequency, τ can be set at an integer multiple of the proton Larmor frequency to suppress the contributions of this family of coupled nuclei from the three-pulse ESEEM spectrum. It is common for three-pulse ESEEM data to be collected at several τ-values, including integer multiples of the proton Larmor period, to accentuate the other low frequency modulations present in the data and to make sure that ESEEM components were not missed because of τ-suppression.

2.3 Two-dimensional ESEEM

In a paper that appeared in 1979, R.P.J. Merks and R. DeBeer pointed out that the sinusoidal dependence of the stimulated echo ESEEM experiment on τ and T (equation 8), presented the opportunity to collect ESEEM data in both time dimensions and then apply a two-dimensional FFT to derive two important benefits. The first benefit was that suppression-free spectra should be obtained along the zero-frequency axis for each dimension while the second benefit would be the appearance of cross-peaks at $(\omega_\alpha, \omega_\beta)$ and $(\omega_\beta, \omega_\alpha)$ that would allow one to identify peaks that belonged to the same hyperfine interaction. This ESEEM version of the NMR COSY experiment (*see **Nuclear Magnetic Resonance (NMR) Spectroscopy of Metallobiomolecules***) would prove invaluable for ESEEM analysis of complex spin systems.[21] However, the disparity in spin relaxation times in the τ and T time dimensions precluded the general application of this method.

In 1986, P. Höfer, A. Grupp, H. Nebenführ and M. Mehring proposed another two-dimensional ESEEM experiment, Hyperfine Sublevel Correlation (HYSCORE) Spectroscopy, and demonstrated its ability to correlate hyperfine sublevels that belong to the same electron-nuclear coupling interaction. Four-pulse HYSCORE became the more popular of the two-dimensional experiments these authors initially proposed. They circumvented the relaxation time problem encountered for the three-pulse sequence by adding a 180° pulse to split the T dimension of the standard three-pulse experiment into two discrete time intervals, t_1 and t_2 (inset, Figure 4). In practice, data are collected with a fixed τ-value while $t1$ and $t2$ are systematically scanned from a minimum of 40–200 ns out to several microseconds. Because the electron spin-lattice relaxation time governs the decay of the four-pulse echo in both $t1$ and $t2$ domains, spectra with cross-peak intensities, $(\omega_\alpha, \omega_\beta)$ and $(\omega_\beta, \omega_\alpha)$, symmetric about the frequency diagonal $(|f_1| = |f_2|)$ are realized. Because the data are collected at a fixed τ, HYSCORE spectra are not free from τ-suppression effects. The utility of HYSCORE spectroscopy can be readily seen by returning to our one-dimensional ESEEM data set of Figure 3. These are three-pulse data collected at $\tau = 120$ ns for the type-1 Cu(II) site of the Fet3p protein. X ray crystallographic studies of this site have shown that the Cu(II) ion is tricoordinate with two histidine and one cysteine residues supplying their side chains as ligands. Therefore, the four low frequency peaks shown in the ESEEM spectrum of Figure 3 originate from two histidyl ligands. The HYSCORE spectrum taken under identical conditions to those of Figure 3 is shown in Figure 4. These data are typical for weak ^{14}N hyperfine coupling in that the only appreciable

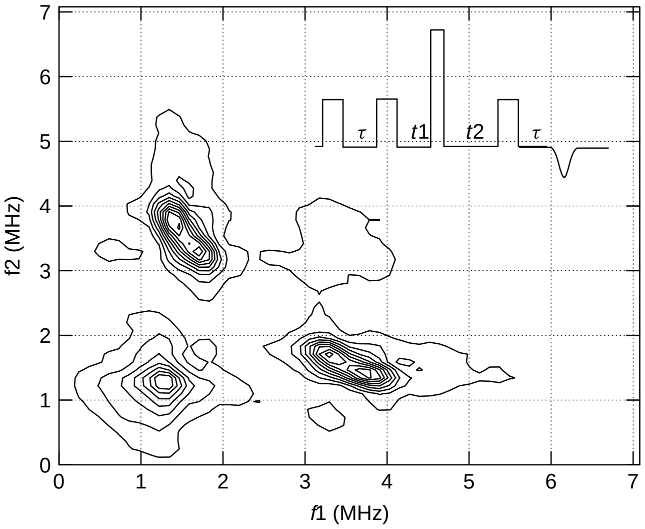

Figure 4 HYSCORE contour plot of the type-1 Cu(II) site of the Fet3p protein taken under identical conditions as the three-pulse data of Figure 3, except that: 90° pulses (pulses 1, 2 and 4), 32 ns FWHM and 90 W peak power; 180° pulse (pulse 3), 24 ns FWHM, 800 W; starting $t1$ and $t2$, 200 ns; and time increment, 32 ns

cross-peak intensity is found in the (+, +) quadrant of the two-dimensioanl-FFT spectrum (see the subsequent). For ^{14}N HYSCORE, the most intense cross-peaks are the correlations between the maximum hyperfine frequencies from the α and β electron spin manifolds (the ''double-quantum'' peaks). The HYSCORE result of Figure 4 shows two sets of cross-peaks at (1.7, 3.3 MHz) and (1.4, 3.8 MHz) that arise from two nonequivalent ^{14}N couplings. Such information is invaluable when trying to interpret ESEEM data like that shown in Figure 3. Specifically, the HYSCORE data show that the 1.5 MHz peak in Figure 3(b) is a composite of a peak at 1.4 MHz and a shoulder at 1.7 MHz and that the 1.7 and 3.3 MHz peaks are partners in one ligand hyperfine coupling while the 1.4 and 3.8 MHz peaks belong to the other. Once these peaks are sorted in this matter, analysis to determine the hyperfine couplings is more robust.

In addition to telling the spectroscopist that there are two inequivalent ^{14}N's, the HYSCORE spectrum also shows that the hyperfine coupling is weaker than that normally found for imidazole ligands strongly bound to Cu(II). This information comes from the cross-peak contours of Figure 4 and from the observation of negligible cross-peak intensity in the (−, +) quadrant of the two-dimensional FFT. Gemperle *et al.*[22] derived an expression for ESEEM obtained using the general four-pulse scheme of HYSCORE for an $S = 1/2$, $I = 1/2$ spin system. The amplitudes of the cross-peaks for this case are given by

$$S(t_1, t_2) = \left(\frac{1}{4}\right) kC[c^2 \cos(\omega_\beta t_2 + \omega_\alpha t_1 + \phi_+) + c^2 \cos(\omega_\alpha t_2 + \omega_\beta t_1 + \phi_+) + s^2 \cos(\omega_\beta t_2 - \omega_\alpha t_1 - \phi_-) + s^2 \cos(\omega_\alpha t_2 - \omega_\beta t_1 - \phi_-)]$$

where

$$\begin{aligned} C &= -2\sin(\omega_\alpha \tau/2)\sin(\omega_\beta \tau/2) \\ \phi_\pm &= (\omega_\alpha \pm \omega_\beta)\tau/2 \\ s^2 &= |\omega_I^2 - (\omega_\alpha + \omega_\beta)^2/4|/(\omega_\alpha\omega_\beta) \\ c^2 &= |\omega_I^2 - (\omega_\alpha - \omega_\beta)^2/4|/(\omega_\alpha\omega_\beta) \end{aligned} \tag{10}$$

and $k = 4c^2s^2$. This expression allows for a straightforward separation of the ESEEM contributions of strongly coupled nuclei from those that show weak electron-nuclear hyperfine coupling. Because the data are processed by taking a complex two-dimensional-FFT, the cross-peaks will separate into different frequency quadrants according to the sign of the dominant phase of $S(t_1, t_2)$. For weak hyperfine couplings $\omega_\alpha \cong \omega_\beta \cong \omega_I$, s^2 approaches zero, while c^2 goes to one. The cross-peaks for these couplings will then be sorted by the complex FFT into quadrants one and three where both frequency partners (ω_1, ω_2) are of the same sign. For strong electron-nuclear couplings, the situation is reversed, with cross-peaks being found in quadrants 2 and 4 where frequency partners are of opposite sign. For an axial hyperfine coupling without appreciable nuclear quadrupole interaction, if $A_\parallel > 2\omega_I$, cross-peaks will be found at ($-\omega_\alpha$, ω_β) and ($-\omega_\beta$, ω_α) (quadrant 2). When $A_\parallel < 2\omega_I$, the cross-peaks are found at (ω_α, ω_β) and (ω_β, ω_α) (quadrant 1). This facet of HYSCORE has been used to isolate the ESEEM contributions of weakly coupled nitrogens from those of nitrogen atoms that showed stronger couplings characterized by ''deep'' or intense ESEEM in a bacterial photosynthetic reaction center[23] and in an iron–sulfur protein.[24]

One of the serious shortcomings of three-pulse ESEEM for frozen solution samples is its failure to detect broad hyperfine lines. For example, water molecules bound to a paramagnetic transition ion typically feature anisotropic hyperfine couplings of several MHz and can yield broad powder lineshapes about the proton Larmor frequency. ESEEM methods to work around this problem include ^{2}H substitution to reduce the anisotropy and the use of two- or four-pulse one-dimensioanl ESEEM methods that detect the $\omega_\alpha + \omega_\beta$, or sum combination modulation frequency. Both of these approaches provide data with compromised precision with respect to what would be realized if the broad, fundamental hyperfine frequencies could be resolved. Theoretically, these couplings should lead to appreciable ESEEM modulation amplitudes because of their large anisotropy, however, such modulations damp quickly because of destructive interference and they are lost in the dead-time of the typical pulse EPR experiment. HYSCORE offers a way to recover these broad lines through the detection of nuclear coherence transfer echoes. These echoes are created by the refocusing of spin packets that occurs when the 180° pulse, applied at t_1, causes a transfer of spins between the two m_s manifolds. This refocusing leads to a nuclear coherence-transfer echo at $t_2 = t_1$ and can easily be seen in a stacked plot of HYSCORE time domain data as a complex modulation pattern centered on the $t_1 = t_2$ diagonal.[25–27] These echoes result in HYSCORE cross-peak patterns in the two-dimensional; frequency spectrum that are narrow ridges of an extent given by the hyperfine anisotropy. These ridges are perpendicular to the frequency diagonal and centered roughly about the nuclear Larmor frequency if $A_\parallel$ or $A_\perp < 2\omega_I$ (quadrants 1 and 3) and parallel to the frequency diagonal if $A_\parallel$ or $A_\perp > 2\omega_I$ (quadrants 2 and 4). A cartoon that illustrates this feature is shown in Figure 5. For the weaker coupling case, Figure 5(a) (quadrant 1), two broad peaks representing a hyperfine interaction of axial symmetry are centered about the nuclear Larmor frequency and their idealized hyperfine spectrum is drawn along both frequency axes. The HYSCORE spectrum is then constructed by marking off the (ω_α, ω_β) correlations remembering the orientation-dependent correspondence between the two m_s manifolds across their powder lineshapes. Figure 5(b) (quadrant 4) is constructed in the same fashion for the strong coupling case where the powder lineshapes are centered at $A/2$ and separated by twice the Larmor frequency.

An example of the resolution of broad hyperfine lines in the four-pulse HYSCORE experiment is shown

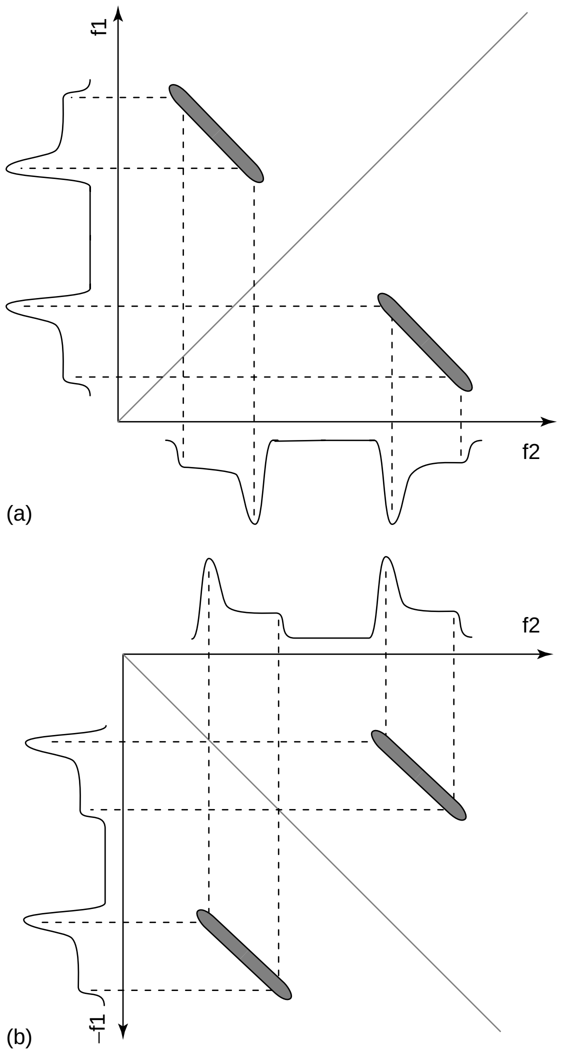

Figure 5 Diagram showing contours that arise from broad hyperfine lines detected by nuclear coherence transfer echoes under conditions of (a) weak and (b) strong hyperfine coupling

in Figure 6. Figure 6(a) shows the (+, +) quadrant of the four-pulse HYSCORE spectrum of Cu(bipy)$(H_2O)_4{}^{2+}$ collected at $g_\perp$ (inset) of the molecule's EPR spectrum. The spectrum shows an auto-correlation peak at the proton Larmor frequency and two correlation arcs or ridges ''perpendicular'' to the frequency diagonal. These ridges are indicative of an axial hyperfine coupling and can be analyzed for their dipole–dipole and isotropic hyperfine contributions, $|T|$ and $|A_{\text{iso}}|$, respectively, using a graphical analysis developed by Dikanov and Bowman.**28** In this analysis, an arc is constructed down the long-axis of the contour and correlated frequency pairs (ν_α, ν_β) are read from points along the arc. One then constructs a plot of ν_α^2 versus ν_β^2 and extracts the slope, Q_α, and y-intercept, G_α, from a linear least squares fit to the points. This can easily be done with a graphing calculator or a spreadsheet program on a personal computer. A_{iso} and $|T|$ are then determined from knowing the Larmor frequency of the nucleus, ν_I, and the system of equations given below.

$$\begin{aligned} F_\alpha &= [\pm 4\nu_I(Q_\alpha + 1)]/(Q_\alpha - 1) \\ |T| &= (2/3)\{\pm[G_\alpha(F_\alpha \pm 4\nu_I)]/2\nu_I - 4\nu_I^2 + F_\alpha^2/4\}^{1/2} \\ A_{\text{iso}} &= (F_\alpha - T)/2. \end{aligned} \tag{11}$$

In practice, the assignment of the labels α and β to the frequency pairs is arbitrary and one just has to pick a convention and stick to it. The signs for the first term in the square root argument for calculating $|T|$ are chosen to yield a real root. The result of using this system of equations is two unique pairs of values for A_{iso} and T. One set features A_{iso} and T parameters of the same sign, while for the other; A_{iso} and T have opposite signs. For the lower arc of Figure 6(a), the ν_α^2 versus ν_β^2 plot yielded $Q_\alpha = -0.789$ and $G_\alpha = 378$ MHz. Plugging these numbers into equation (11) gave $|T| = 5.1$ MHz and $A_{\text{iso}} = \pm 0.8$ MHz, if T is of the same sign, or $A_{\text{iso}} = \pm 5.9$ MHz if T is of opposite sign. Although this analysis ignores the orientation selection that must be taken into account for these data, and it restricts the hyperfine

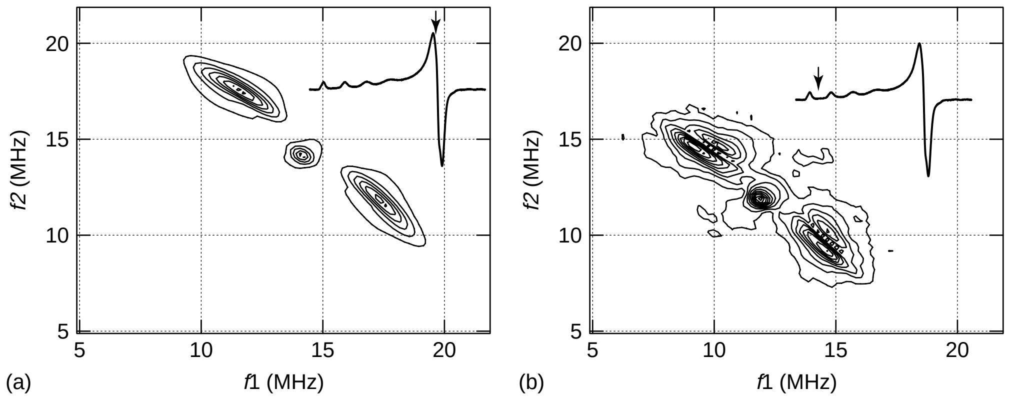

Figure 6 Four-pulse HYSCORE data collected for Cu(II)(bipy)$(H_2O)_4$ at (a) g-perpendicular and (b) g-parallel. Conditions for the measurements were: microwave frequency, 9.6864 GHz; field strength, (a) 332 mT, (b) 278 mT; 90° pulses (1, 2 and 4), 32 ns FWHM, 90 W; 180° pulse, 24 ns, 800 W; starting $t1$ and $t2$, 200 ns; time increment, 20 ns

tensor to axial symmetry, the $|T|$ value of 5.1 MHz is very close to the average $|T|$ value that can be computed from the results of single crystal ENDOR studies of equatorial water molecules bound to Cu(II) in the Tutton salts.[29] Figure 6(b) shows the four-pulse HYSCORE spectrum collected for the same sample at a magnetic field position corresponding to the lowest field $g_{||}$ feature of the Cu(II) EPR spectrum (inset, Figure 6b). Two sets of ^{1}H contours are observed in this spectrum, the top, or higher frequency contour is due to the equatorial water, while the lower contour, which is much more intense, is due to the axial water molecules of Cu(II)bipy(H_2O)$_4$. Graphical analysis of this lower ridge yields $|T| = 3.7$ MHz, which is exactly the same as the average value of T determined for the axial waters of Cu(II)(H_2O)$_6$ by single crystal ENDOR.

2.4 Practical Aspects of ESEEM Experiments

The material in this section is derived from the author's experiences with homebuilt and Bruker equipment over the past 20 years. In practice, every spectrometer system is different, and everyone approaches problems in a unique way. In reality, researchers develop their own approaches to problems once they have some experience.

2.4.1 Sample Requirements

ESEEM experiments require solid samples and most of the systems studied by ESEEM have been in frozen solution form. If at all possible, a good glassing solvent should be used to suspend the sample, but it is not important to eliminate cracks that occur upon freezing—it is not an optical experiment. For aqueous samples, 50% v/v ethylene glycol or glycerol will make an adequate glass. For organic systems, toluene is the king of glassing solvents. There is a convenient table of glassing mixtures in the textbook by R.S. Drago.[30] For X-band measurements, samples are most often placed in 4-mm quartz tubes. Volume requirements vary from 50–150 μL depending on the length of the sample probe's active region. For Bruker's flexline probes, a 1 cm sample length is sufficient to fill the resonators and this corresponds to about a 70 μL volume. Concentrations depend more on relaxation dynamics than anything else, so the user will have to rely more on experience here. For example, if one is studying a Mn(II) site in a protein, two- and three-pulse spin echoes can be detected at a sample temperature of 4.2 K with a signal-to-noise (S/N) ratio of 10 with sample concentrations of 10 μM. For Cu(II), the same S/N can require 100 μM concentration if the paramagnetic center features intense ESEEM (a good problem to have). Fe(III) centers, both low- and high-spin can be studied at 100 μM concentration, but the S/N will be <5 and the sample temperature has to be kept below 6 K. If sample concentration is not a problem, ESEEM experiments are not adversely affected by higher concentrations until one gets above 10 mM.

2.4.2 Sample Temperature

Because of spin relaxation, ESEEM studies are normally carried out in the 4–50 K temperature range. Most spectrometers use liquid helium flow cryostats that allow one to maintain temperatures of 5 K with cryogen consumption rates of 1–2 L/hr. As indicated above, some paramagnetic centers require temperatures <6 K for ESE detection at the 100 μM concentration levels that one often encounters. For Cu(II) samples, the electron T_1 is long enough that the best sensitivity is at 10 K where echo amplitudes are somewhat lower than they are at 5 K, but the repetition rate of the ESEEM experiment can be increased to $\sim$500 Hz and better S/N gained by signal averaging. There is no recipe for making these adjustments. Once an echo is detected during the tuning process, the spectroscopist needs to vary the repetition rate of the pulse sequences and the sample temperature to determine the conditions of optimal performance.

2.4.3 Continuous-wave Spectra

Every ESEEM experiment should begin with collection of a cw-EPR spectrum (*see* ***Electron Paramagnetic Resonance (EPR) Spectroscopy***) or an ESE-detected EPR spectrum of the sample to be studied. The Bruker flexline probes make this task straightforward as the probes can be critically coupled and are fitted with magnetic field modulation coils. Because the energy density in these probes is so high, one ends up using very low powers in cw-mode to avoid saturation and adiabatic rapid passage conditions where lineshape distortions occur. Also, for this reason, one ends up using field modulation frequencies of 1–10 kHz on a regular basis.

2.4.4 Tuning for ESEEM Studies

ESEEM studies require microwave pulse widths that are short in comparison with the period of the highest frequency modulation to be studied. 90° pulse widths of 16–20 ns are typical for X-band ESEEM studies where the period of the proton Larmor frequency is about 70 ns at $g = 2$. One typically adjusts the sample probe's microwave coupling to the maximum overcoupling position, sets up a two- or three-pulse ESE sequence, and optimizes the echo amplitude as observed on an oscilloscope or transient recorder display by adjusting the pulse power and reference arm phase. If sensitivity is low, the probe coupling can be adjusted some to increase the probe Q without giving up too much in terms of the instrument's dead-time.

2.4.5 ESEEM Data Acquisition

The discussion of the two-pulse ESEEM experiment given above might cause one to conclude that the measurement is of little use. There are a few reasons why these data should be collected as part of the overall routine of an ESEEM study. Two-pulse ESEEM data show deeper modulations than those found in a three-pulse study and because one does not need to worry about suppression, the two-pulse spectrum can be an invaluable guide to the higher resolution, three-pulse and HYSCORE work to follow. The sum combination frequencies that are easily resolved in the two-pulse ESEEM experiment can show shifts that result from large hyperfine anisotropies and these can guide additional four-pulse ESEEM and HYSCORE studies.[15] Phase cycling is typically done with two-pulse measurements to help clean up the early portion of the ESEEM pattern when the echoes are close to the excitation pulses and to eliminate the DC offset from the system's amplifiers.

Three-pulse, or stimulated echo experiments are essential to an ESEEM investigation. Because of τ-suppression, several different scans should be made at each field position studied within the EPR absorption envelope. One should start with a short τ value, close to the measurement's dead-time (100 ns), and collect a few scans at proton Larmor period harmonics. For ^{14}N studies, this is usually a satisfactory amount of data to ensure that nothing is being missed because of the choice of τ. In a typical scan, the third pulse is scanned from a starting value of about 40 ns to a final value determined by where the modulations cease. Typical data sets are 512 points and care needs to be taken to ensure that the increment in T is short enough to avoid aliasing ($1/(2T_{\text{increment}})$ is the highest frequency that can be accurately recorded). Phase cycling is critical to the stimulated echo experiment in that it eliminates discontinuities in the ESEEM that arise from overlap of two-pulse echoes with the three-pulse echo in addition to eliminating DC offsets from the system's amplifiers.

In general, HYSCORE measurements should be made at short τ values where all of the ESEEM frequencies are present in the data. Therefore, three-pulse data should be used to select appropriate τ's for HYSCORE studies. For recovering broad hyperfine lines with nuclear coherence transfer echoes, as in Figure 6, the τ value must be kept short. This is because the mechanism of the transfer relies in part on the spin packets for correlated α and β spins being collinear at the start of the t_1 period immediately following the second $\pi/2$ pulse. It is suggested that for use of the graphical analysis strategy of equation (11), HYSCORE spectra be collected for several τ values and combined to provide arcs of maximum extent without blind spots. This sounds nice, but for many samples, HYSCORE data sets take a few hours to collect, so it may not be practical. It is straightforward to include the τ dependence in a spectral simulation of the HYSCORE contours so this should never be a serious problem.

2.4.6 *Spectral Processing*

The analysis of ESEEM data usually involves simulation of the ESEEM spectrum from a spin Hamiltonian that models the nuclear transition frequencies. Therefore it is important that ESEEM spectra accurately report on the frequencies, amplitudes and damping factors observed in experiments. The method of choice for deriving ESEEM spectra involves removal of the ESEEM decay by subtraction of an exponential or polynomial function, tapering of the resulting modulation function with a windowing function, Fourier transformation and display of the absolute value, or square root of the resulting power spectrum. If simulations are done in the time domain, they can be processed using the same protocol to facilitate comparison with experiment.

3 APPLICATION—ESEEM STUDIES OF Fe(II)/α-KETOGLUTARATE-DEPENDENT DIOXYGENASES

Perhaps the best way to illustrate the use of ESEEM in tackling problems in inorganic chemistry is to describe ongoing work in our laboratory on Fe(II)/α-ketoglutarate (αKG)-dependent dioxygenases. This work is collaborative with Professor R.P. Hausinger, whose lab has isolated and studied several members of this class of enzymes over the past 15 years. These enzymes use a common nonheme, mononuclear iron active site to catalyze key reactions in the biosynthesis or biodegradation of a wide range of compounds.[31] Well studied examples of this enzyme family include prolyl hydroxylases that function both in collagen biosynthesis[32] and intracellular signaling,[33,34] isopenicillin *N* synthase[35] and clavaminate synthase[36] that produce important antibiotics, TfdA that degrades the herbicide 2,4-dichlorophenoxyacetic acid,[37,38] and AlkB that repairs methylation damage to nucleic acids.[39,40] The Fe coordination for these proteins is thought to be octahedral in nature consisting of the side chains of two histidine residues, one carboxylate group supplied by an aspartate or glutamate residue and three water molecules. The three protein-based ligands are in a cis arrangement leaving an open coordination ''face'' occupied by three solvent molecules for the enzymes in their resting state. It has been proposed that this open coordination geometry is key to the diverse set of reactions catalyzed by this class of enzymes.[41]

The archetype Fe(II)/αKG hydroxylase is taurine/αKG dioxygenase (TauD), an *Escherichia coli* enzyme that catalyzes the conversion of taurine (2-aminoethanesulfonic acid) to sulfite and aminoacetaldehyde,[42] as illustrated in Scheme 1. TauD catalyzes the hydroxylation of a C−H bond on the carbon adjacent to the sulfonate group of taurine. The product of this reaction then decomposes to yield hydrogen sulfite, which serves as an important source of sulfur for many microorganisms.[43] A catalytic mechanism that has been proposed for these enzymes is provided as Scheme 2. Prior to the activation and hydroxylation of the C_1 carbon on taurine, αKG binds to the Fe(II) center as a chelate, displacing two of the coordinated waters. Taurine then binds to the enzyme in the vicinity of the Fe(II) center, displacing the remaining water.

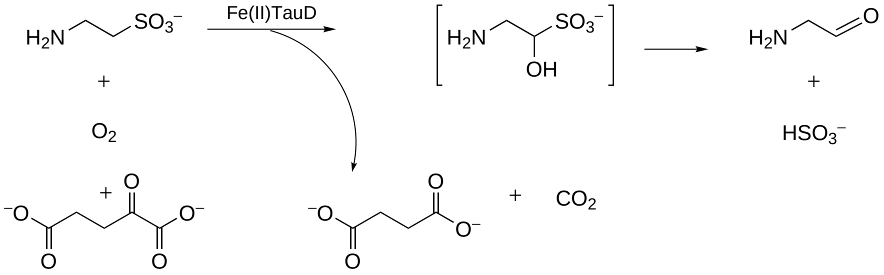

Scheme 1 The hydroxylation of taurine leading to the formation of aminoacetaldehyde and bisulfite ion

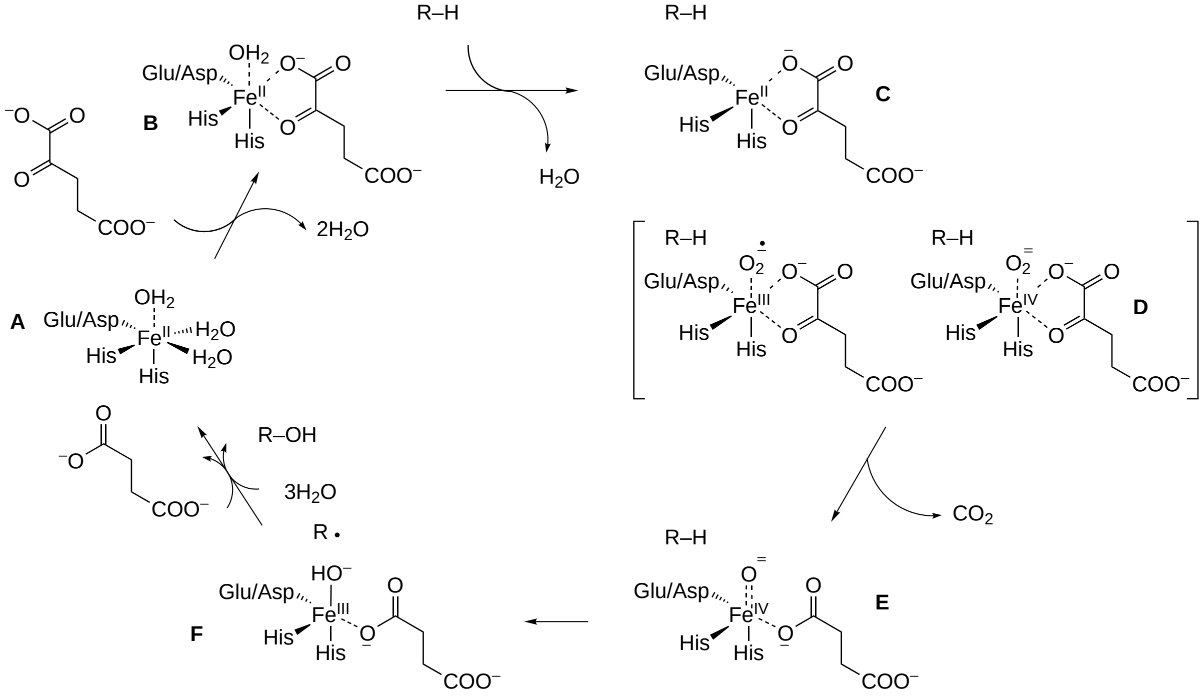

Scheme 2 A general catalytic mechanism for the Fe(II)/α-ketoglutarate hydoxylases

The resulting five-coordinate Fe(II) then binds molecular oxygen and proceeds to carry out a two-electron reduction of coordinated αKG yielding, succinate, CO_2, and a high valent Fe(IV)-oxo species. It is this highly oxidized Fe center that abstracts hydrogen from taurine, initiating its hydroxylation. Because TauD is available in large amounts, highly soluble, and relatively stable, it has been the subject of numerous mechanistic studies.[44–53] In addition to these biochemical studies, this mechanism is supported by the X ray crystal structure for anaerobic taurine-αKG–Fe(II) TauD,[54,55] as shown in Figure 7. Insights gained from studies involving the oxidative chemistry of TauD are likely to apply to many other members of the Fe(II)/αKG dioxygenase family.

To convert the $S = 2$ Fe(II) active site into a species that can be studied robustly by ESEEM, we exploited the known ability of NO, a surrogate of molecular oxygen, to bind to nonheme iron sites and produce an electron spin $S = 3/2$ center.[56,57] We began our studies with the catalytically relevant NO-bound taurine-αKG–Fe(II) TauD species with the aim of using ^{2}H-ESEEM spectroscopy to measure the distance and orientation of specifically deuterated and perdeuterated taurines with respect to the magnetic axis of the Fe(II)NO center. When combined with the results of X ray crystallographic studies, these spectroscopic results provide a more detailed structure of the catalytic intermediate(s), **D**, in Scheme 2. Because catalysis involves the hydroxylation of a specific C–H bond on substrate taurine, spectroscopic studies that elucidate the structural relationship between Fe and substrate hydrogens provide important details for understanding enzyme mechanism. The crystal structure that provided the Fe(II)-site structure shown in Figure 7 was collected for an anaerobic sample where the Fe is five coordinate and the level of refinement is low. The resolution of the best structure is currently 2.8 Å, so the electron density

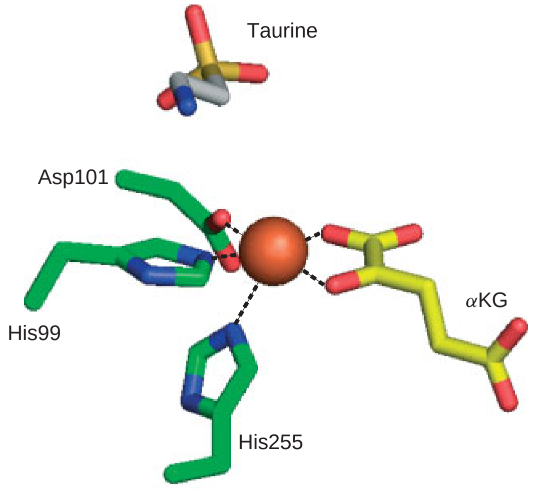

Figure 7 TauD active site. The three metal liganding amino acid side chains (His99, Asp101 and His255), the chelated αKG, and the substrate taurine are depicted for monomer A of the four molecules per unit cell in PDB file LOS7

map for substrate taurine is not as well defined as Figure 7 leads one to believe!

3.1 Taurine Orientation

Continuous wave and pulsed-EPR data were collected on a Bruker E-680X spectrometer operating at X-band and equipped with a model ER4118-MD-X-5-W1 probe that employs a 5-mm dielectric resonator. The sample temperature was maintained at 4.2 K using an Oxford Instruments liquid helium flow system equipped with a CF-935 cryostat and an ITC-503 temperature controller. ESEEM data were collected using a three-pulse, stimulated echo sequence ($90° - \tau - 90° - T - 90°$) with 90° microwave pulse widths of 16 ns FWHM and peak powers of 250 W. A four-step phase cycling sequence, (+x, +x, +x), (−x, +x, +x), (+x, −x, +x), (−x, −x, +x), together with the appropriate addition and subtraction of the integrated spin-echo intensities served to actively remove the contributions of two-pulse echoes and baseline offsets from the data.[22] An integration window of 24 ns was used to acquire spin-echo amplitudes, and data set lengths were 512 points.

The ESE-detected EPR spectrum of the Fe(II)NO form of TauD treated with αKG and taurine shows axial symmetry with $g_{\perp} = 4.00$ and $g_{\parallel} = 2.00$ (insets, Figure 8a and 8c). This observation is typical for Fe(II)NO complexes and arises from the $m_s = \pm 1/2$ Kramer's doublet of the

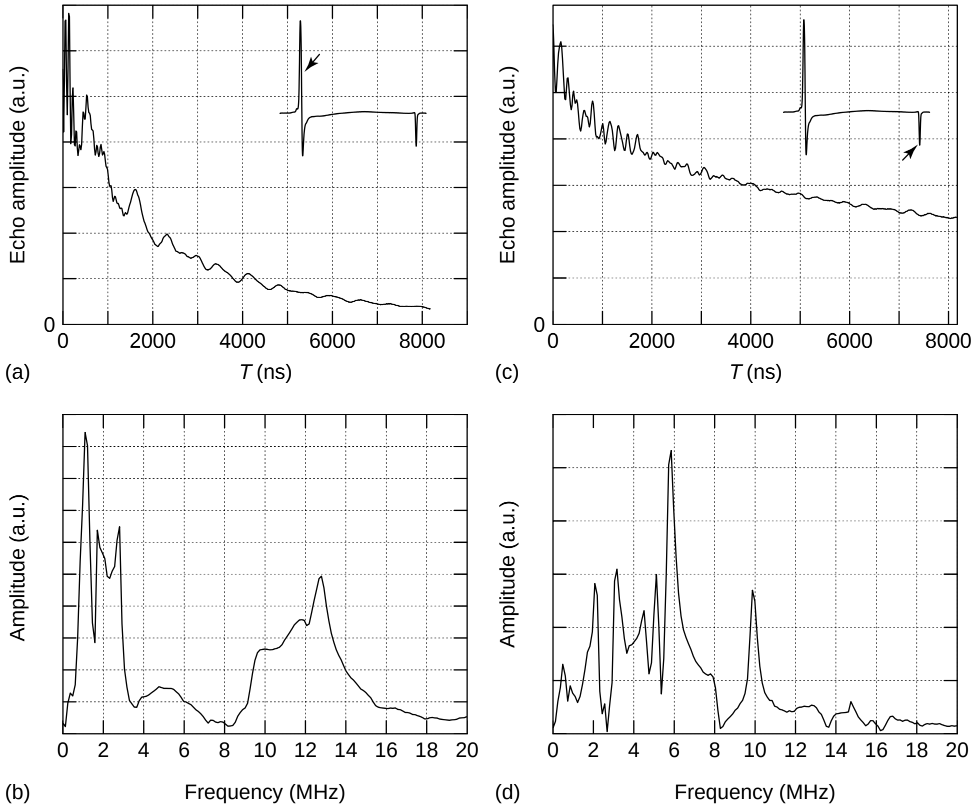

Figure 8 Three-pulse ESEEM data (a) and (c) and corresponding ESEEM spectra (b) and (d) for Fe(II)NO–TauD treated with αKG and taurine. ESEEM data were collected under the following conditions: microwave frequency, 9.723 GHz; magnetic field strength, (a) 171.0 mT and (c) 346 mT; $90° - \tau - 90° - T - 90°$ sequence with 16 ns pulses; τ value, 136 ns; T increment, 16 ns; repetition rate, 1 kHz; events averaged/time point, 100; scans, 4; and sample temperature, 4.2 K

$S = 3/2$ coupled spin system. The lineshape reflects an axially symmetric zero field splitting (ZFS) interaction with its principal axis directed along $g_{\|}$ and the Fe(II)NO bond.[56] Identical ESE-detected EPR spectra were obtained for Fe(II)NO–TauD treated with αKG and deuterated taurines.

Three-pulse ESEEM spectra were collected at 171.0, 172.8, 190.0, 290.0, 345.0 and 346.0 mT. ESEEM data and their corresponding spectra are shown for data collected at $g = 4$ in Figures 8(a) and 8(b), and at $g = 2$, Figures 8(c) and 8(d). These data are complex showing contributions from the histidyl ligands, bound NO and at least one set of strongly coupled protons. Two-dimensional ESEEM (HYSCORE) spectra and isotopic substitution studies were used to assign these peaks and will be presented below. To reveal the ESEEM contributions from substrate protons, Fe(II)NO–TauD samples treated with αKG and taurine deuterated at the C_1 carbon were compared to data collected under identical conditions using protonated taurine. The deuterium contribution to each ESEEM spectrum was elucidated by using the ratio method of Mims together with processing tools available in the Xepr data acquisition and processing software provided by Bruker. Specifically, three-pulse ESEEM data collected for enzyme samples prepared with ^{2}H- and ^{1}H-taurine were normalized by dividing each data set by its maximum amplitude. The normalized ^{2}H-ESEEM data were then divided by the corresponding, normalized ^{1}H-ESEEM data to obtain a resulting ESEEM pattern dominated by the ^{2}H contribution to the ESEEM. Short phase memory times precluded the use of τ values longer than 200 ns for three-pulse ESEEM, and the use of two-pulse ESEEM data, for the processing of ^{2}H data by using the ratio method.[58] The time domain data that resulted from this ratio process were tapered with a Hamming window and Fourier transformed.[25] ESEEM spectra were obtained by taking the absolute value of the transforms.

Figure 9(a) shows the time domain ESEEM contribution of the taurine deuterons at 171.0 mT obtained by dividing the normalized ESEEM data from the C_1 deuterated taurine sample by the normalized ESEEM data collected for enzyme treated with protonated taurine. The data of Figure 9 show pronounced modulations from deuteron hyperfine interactions that have an initial modulation depth of about 15% of the echo amplitude. For TauD samples, we found that the three-pulse data showed a background decay characterized by an e^{-1} time of about 2 µs. This led to substantial noise in the ratio data at longer times and often required that a first or second order polynomial fit be used to correct residual offsets and ''drifts'' of the baseline. The absolute value spectrum obtained after applying a Hamming window and cosine Fourier transform to the ESEEM ratio revealed ESEEM frequencies at 0.95 and 1.39 MHz that could be assigned to the C_1 deuterons of taurine (Figure 9b).

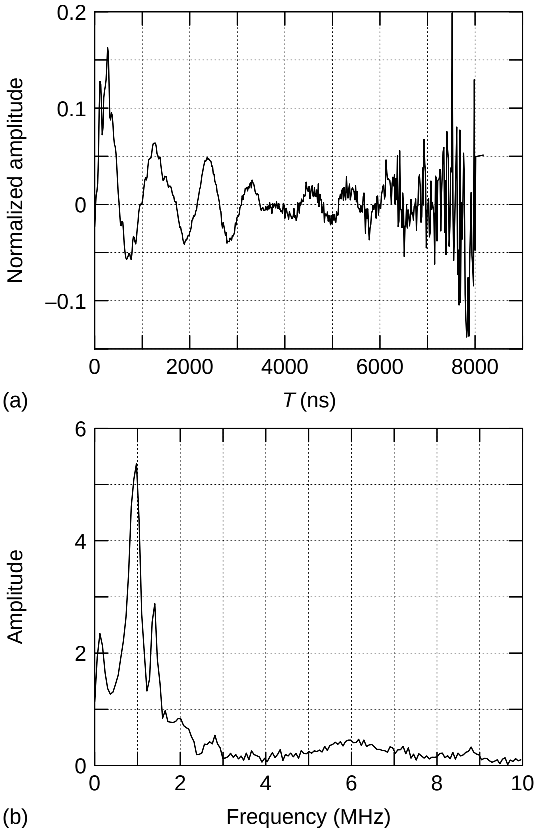

Figure 9 Time domain ESEEM ratio (a) and Fourier transform (b) generated by dividing time domain ESEEM data obtained for Fe(II)NO–TauD treated with αKG and C_1–^{2}H-taurine with data obtained under identical conditions for Fe(II)NO–TauD treated with αKG and taurine. Data sets were normalized to their maximum amplitudes prior to division. A second-degree polynomial was used to remove residual background decay. ESEEM data were collected under conditions identical to those of Figure 8(a)

Figure 10 shows the ^{2}H-ESEEM spectra that result from repeating the measurement and processing procedure described for Figure 9 at 190.0 mT (Figure 10b), 290.0 mT (Figure 10c) and 346.0 mT (Figure 10d). Figure 10(a) shows that in the $g_{\perp}$ region, a pair of ESEEM frequencies at 0.95 and 1.39 MHz is observed. These coalesce to a single broad feature centered at 1.2 MHz at 190.0 mT (Figure 10b) and begin to split again at 290.0 mT (Figure 10c) where ^{2}H-ESEEM components at 1.8 and 2.0 MHz are resolved. At $g = 2.0$, 346.0 mT (Figure 10d), where one samples orientations of the enzyme with the laboratory magnetic field nearly parallel to the principal axis of the ZFS interaction, the ^{2}H-ESEEM shows two well-resolved peaks at 2.0 and 2.5 MHz. Further examination of Figure 10 reveals other frequencies in the ratio data. Specifically, a minor peak at 0.2 MHz is found in all of the spectra and we have attributed it to the baseline processing and windowing procedure used to process the data. The broad ESEEM peaks centered at 6.0 and 8.1 MHz for the spectra taken at 171 (Figure 10a) and 190 mT (Figure 10b), respectively, are likely due to protons and may reflect the proton difference portion of our study. The narrow peak at

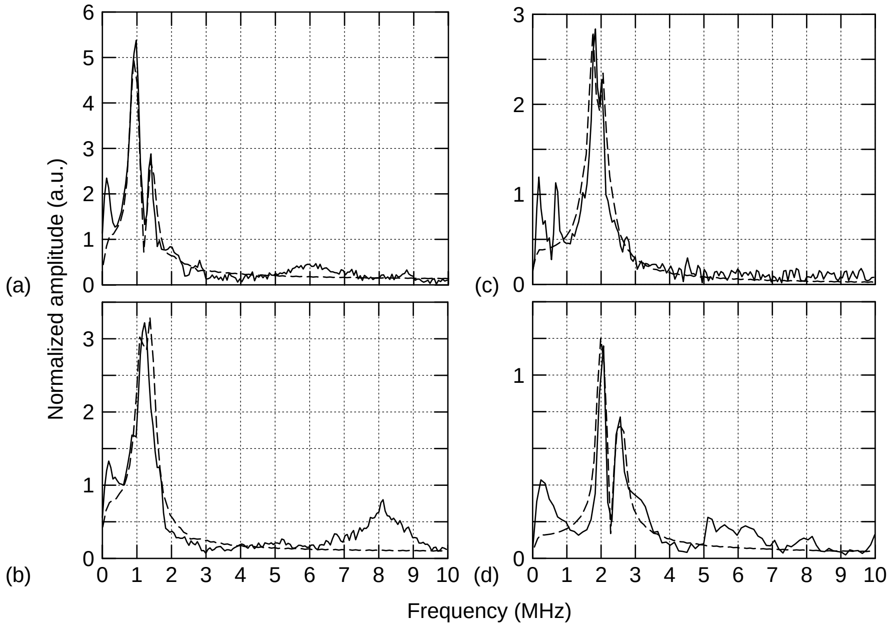

Figure 10 The magnetic field dependence of ^{2}H-ESEEM spectra (solid lines) obtained for Fe(II)NO–TauD samples treated with αKG and C_1–^{2}H-taurine using the ratio method described for Figure 9. The field positions displayed are: (a) 171.0 mT; (b) 190.0 mT; (c) 290.0 mT; and (d) 346.0 mT. Simulations of these ^{2}H-ESEEM spectra (dashed lines) are plotted along with the data. Hamiltonian parameters used for the simulations were: principal g-values, 4.0, 4.0, 2.0; principal deuterium hyperfine values, −0.25, −0.25, 0.50 MHz; Euler angles for hyperfine tensor, 0, 17°, 0; e^2qQ, 0.20 MHz; η, 0; and Euler angles relating nqi to hyperfine, 0, 23°, 0

0.7 MHz resolved in the 290 mT ratio (Figure 10c) and the broad features that range from 5–7 MHz for the 346 mT data (Figure 10d) are likely due to ^{14}N-ESEEM that is not fully compensated by the data division procedure. Approximations that stem from the data division procedure used to obtain the data presented in Figures 9–11 have been discussed in detail elsewhere.[59]

Figure 11 shows ^{2}H-ESEEM data for Fe(II)NO–TauD treated with αKG and taurine deuterated at both C_1 and C_2 positions. Figure 11(a) shows data collected in the $g_\perp$ region at 172.8 mT where three ^{2}H-ESEEM components at 0.9, 1.1 and 1.3 MHz are now resolved. A comparison of these data to data collected at 171.0 mT for the C_1 deuterated taurine sample showed that addition of two deuterons at the C_2 carbon served to add a new ESEEM feature at 1.1 MHz, the Larmor frequency of deuterium at this magnetic field strength. The ^{2}H-ESEEM spectra of Figures 11(b) and 11(c) are dominated by a single, broad peak centered at the deuterium Larmor frequency of 1.2 MHz (190 mT, Figure 11b) and 1.9 MHz (290 mT, Figure 11c), respectively. A comparison of the data of Figure 11(b) and 10(b) shows that the amplitude of the peak at 1.2 MHz increases for the perdeuterated taurine sample, indicating that addition of deuterons to the C_2 position of the substrate also serves to add an additional feature at the deuterium Larmor frequency. Similar conclusions can be made from comparing the ^{2}H-ESEEM data of Figures 11(c) and 11(d) with those of 10(c) and 10(d). For both cases, addition of the C_2 deuterons to taurine yields extra ESEEM intensity at the deuterium Larmor frequencies of 1.9 MHz (290 mT) and 2.25 MHz (346 mT).

Analysis of these ^{2}H-ESEEM data to determine the hyperfine parameters and the number of contributing nuclei requires spectral simulation. ESEEM simulations of the $I = 1$ deuterium ligand hyperfine couplings were accomplished by using software written in FORTRAN (Absoft). Calculations used the density matrix formalism of Mims to simulate the time domain ESEEM data.[8,18] MATLAB scripts were then used to assemble the simulations according to the product rule, equation (9), and to complete the Fourier analysis to obtain simulated ESEEM spectra. The processing and Fourier transformation procedures were identical to that outlined above for the Bruker software. Because the ESEEM experiment is done at a fixed magnetic field strength, each field position studied reports on a unique set of molecular orientations that fall on a contour of constant electron g-value with respect to the laboratory axis system. This orientation selection was accounted for using the method described by Hoffman and coworkers where the line integral about constant effective g-value is converted to a definite integral over ϕ, with the integrating factors being determined numerically.[60] A parabolic searching algorithm was used to compute orientations of the Fe(II)NO center that were resonant at a given field position.[61]

The spin Hamiltonian used to model the deuterium ligand hyperfine interaction consisted of nuclear Zeeman, electron-nuclear hyperfine and nuclear quadrupole terms.

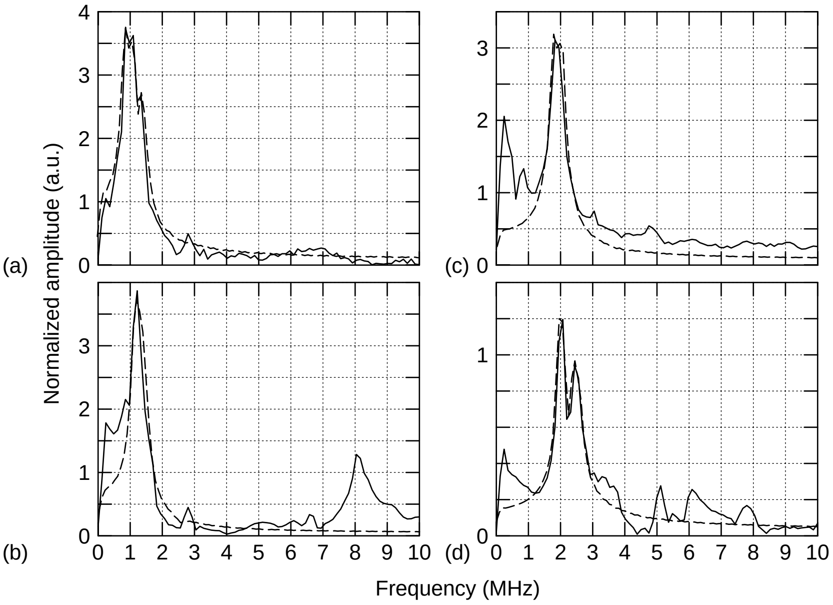

Figure 11 The magnetic field dependence of ^{2}H-ESEEM spectra obtained for Fe(II)NO–TauD samples treated with αKG and taurine deuterated at both C_1 and C_2. Data were obtained using the ratio method described for Figure 9. The field positions displayed are: (a) 172.8 mT; (b) 190.0 mT; (c) 290.0 mT; and (d) 345.0 mT. Simulated ^{2}H-ESEEM spectra (dashed lines) for the C_1,C_2-deuterated taurine are plotted along with the data. For the stronger coupled C_1 deuteron, Hamiltonian parameters identical to those of Figure 10 were used. Hamiltonian parameters used for a second deuteron on C_2 were: principal deuterium hyperfine values, −0.13, −0.13, 0.26 MHz; Euler angles for hyperfine tensor, 0, 63°, 0; e^2qQ, 0.20 MHz; η, 0; and Euler angles relating nqi to hyperfine, 0, 23°, 0

Because the microwave pulses used in ESEEM experiments have a finite bandwidth, ESEEM patterns were calculated over a 4 mT width of magnetic field strengths centered about the experimental field value with each discrete ESEEM pattern weighted according to a Gaussian distribution (e^{-1} width of 2 mT). Deuterium hyperfine and nuclear quadrupole tensors were transformed into the g-tensor axis system at the start of the calculation and the resonance conditions, magnetic field setting and microwave frequency, were used to compute orientations of the magnetic axis that contributed to the ESEEM.

For simulation of the ^{2}H-ESEEM data of Figure 10, we sought to determine a set of spin Hamiltonian parameters that would reproduce the frequencies, relative amplitudes and the initial modulation depths of the data. Furthermore, a single set of Hamiltonian parameters should be able to account for the data obtained at each field position studied. For our calculations, the nuclear quadrupole coupling constant, e^2qQ, was fixed at 0.2 MHz and the asymmetry parameter, η, was set to zero based on literature values from nuclear quadrupole resonance studies (*see* ***Nuclear Quadrupole Resonance (NQR) Spectroscopy***).[62] Because the deuterium hyperfine interaction is expected to be a through-space interaction (substrate taurine is not bound to the Fe(II)NO center), the isotropic hyperfine coupling was set to zero and the hyperfine tensor was fixed to axial symmetry. In practice, these hyperfine couplings must be scaled to their effective values using the ratio of the appropriate effective g-value that describes the EPR signal within the $m_s = \pm 1/2$ doublet of this $S = 3/2$ spin system with the free electron g-value, 2.00.[63,64] Examination of the C_1^{2}H-ESEEM data (Figure 10—solid lines) shows that a pair of frequencies separated by 0.4 and 0.5 MHz is resolved at both $g_\perp$ and $g_\parallel$, respectively. Because the effective g-value doubles as you go from $g_\parallel$ to $g_\perp$, the experimental results lead one immediately to the conclusion that the deuteron giving rise to the ESEEM is oriented close to $g_\parallel$ or the principal axis of the ZFS tensor.

Computer simulations of the C_1 ^{2}H-ESEEM spectra are shown with dashed lines in Figure 10 for the four field positions studied. Except for the details of the lineshape resolved at 190 mT, these simulations faithfully reproduce the observed ESEEM frequencies, relative amplitudes and modulation intensities, or depths. Because of the axial symmetry of g-, hyperfine- and nuclear-quadrupole tensors, the simulations were only sensitive to the ''y rotation'' of the Euler angle rotation schemes that were used to relate the deuterium hyperfine tensor to the g-tensor and the nuclear quadrupole tensor to the hyperfine tensor.[65] The deuterium peak frequency separations at 171 mT (Figure 10a) and 346 mT (Figure 10d) were best simulated by an electron-nuclear dipolar interaction of 0.30 ± 0.05 MHz, and a colatitude with respect to the $g_\parallel$ axis of $20 \pm 3°$. The angle describing the relative orientation of the deuterium hyperfine and nuclear quadrupole principal axis was $23 \pm 3°$. This range of hyperfine couplings corresponds to a range of dipole–dipole distances (based on our reference g-value of 2.00) of

3.4 ± 0.2 Å. The modulation depths were accounted for by considering that only one of the C_1 deuterons contributed to the observed ^{2}H-ESEEM.

Computer simulations of the ^{2}H-ESEEM spectra obtained for the samples with both taurine carbons deuterated are shown as dashed lines in Figure 11. The addition of deuterons to the C_2 carbon serves to add a feature centered at the Larmor frequency of deuterium to the ESEEM data obtained at the four magnetic field positions displayed in Figure 11. At $g_\perp$, 172.8 mT (Figure 4a), this feature is clearly resolved while at the other three field strengths, the addition of this ‘‘matrix’’ ESEEM component manifests itself in an apparent decrease in spectral resolution. The requirement that ^{2}H-ESEEM be resolved at the Larmor frequency across the entire Fe(II)NO EPR spectrum placed an upper limit on the value of the axial hyperfine coupling strength while the amplitude of this spectral feature at each field position placed restrictions on both the deuterium hyperfine coupling strength and a colatitude angle that describes the relative orientations of $g_\parallel$ and the hyperfine principal axis. For the simulations of Figure 11, a dipolar hyperfine coupling strength of 0.13 MHz and angle of 63° between $g_\parallel$ and the hyperfine principal axis were used. Application of the dipole–dipole model to the 0.13 MHz hyperfine field yields a distance of 4.5 Å for this weaker interaction. The simulations of Figure 11 yield initial modulation depths of 14, 19, 11 and 5% for spectra (dashed lines) Figure 11(a) to 11(d), respectively. These agree well with experimental values for the data of Figure 11 (solid lines) which were 17, 20, 12 and 6%, respectively. These simulations were not sensitive to the nuclear quadrupole coupling parameters of the weaker coupled deuteron, so the value of the angle between the hyperfine and quadrupole principal axis was fixed at the value obtained for analysis of the stronger coupling.

Only one C_2 deuteron was considered in the calculations discussed above and summarized in Figure 11. Because the addition of two deuterons to the C_2 carbon only resulted in the addition of a single spectral feature to the data, it is possible that both C_2 deuterons contribute to the ESEEM. The X ray crystallographic data (Figure 7) indicates that both deuterons on the C_2 carbon would be directed away from the open coordination site on the Fe where NO is likely bound. Computer simulations of the ESEEM arising from both C_2 deuterons yielded an average dipolar coupling strength of 0.09 ± 0.005 MHz and an angle between $g_\parallel$ and the hyperfine tensor principal axis of $63 \pm 5°$. These are ‘‘average’’ values as only one set of hyperfine parameters were used together with the spherical model approximation to the product rule to obtain simulations comparable to those of Figure 11.[19] The anisotropic hyperfine coupling range determined above translates to a dipole–dipole distance of 5.1 ± 0.2 Å if a reference g-value of 2.00 is used.

A detailed description of the electronic structure of the Fe(II)NO model complexes and other nonheme iron dioxygenases has shown that the paramagnetic center giving rise to the EPR spectrum (inset, Figure 8) is best described as a high-spin Fe(III) $S = 5/2$ ion antiferromagnetically coupled to an $S = 1$, NO^- ligand.[56] Furthermore, Brown *et al.* point out that the lack of ligand hyperfine coupling and the anisotropy observed in the ^{57}Fe hyperfine coupling of Fe(II)NO model complexes and the extradiol dioxygenases[66] show that the paramagnetism of this center is best described by a model where the two unpaired electrons on the NO^- ligand are spin paired with unpaired spins in the Fe d_{xz} and d_{yz} orbitals leaving the remaining three, unpaired 3d electrons to account for the $S = 3/2$ spin state. As noted above, the large ZFS interaction observed for these complexes gives rise to an EPR spectrum due to the $m_s = \pm 1/2$ Kramer’s doublet. If the electron spin Hamiltonian is taken to consist of an axial ZFS term and an isotropic electronic Zeeman term with $g = 2.00$, it can be shown that the resulting EPR spectrum will range from $g = 2.00$, when the laboratory magnetic field is directed along the principal axis of the ZFS interaction, to $g = 4.00$ when the field is directed perpendicular to the principal axis of the ZFS tensor.[56]

This quantum mechanical model for the Fe–NO EPR spectrum was used by Yang *et al.* to interpret ligand hyperfine couplings resolved in ^{2}H-electron nuclear double resonance (ENDOR) experiments for substrate naphthalene bound to Fe(II)NO–naphthalene 1,2-dioxygenase (NDO). These authors used a point dipole–dipole model to extract Fe–^{2}H distances from the ^{2}H hyperfine coupling anisotropy and used tensor axis orientations to define the location of these coupled deuterons with respect to the Fe–N(O) bond axis.[63] Using an identical picture for the paramagnetic center, the dipole–dipole distances determined from analysis of our ESEEM spectra can be summarized as in Figure 12. Specifically, ESEEM results for taurine deuterated at the C_1 position are best described by a single deuteron that is 3.4 ± 0.2 Å from the iron atom and lies on a cone that makes a $20 \pm 3°$ angle with the unique axis of the ZFS interaction,

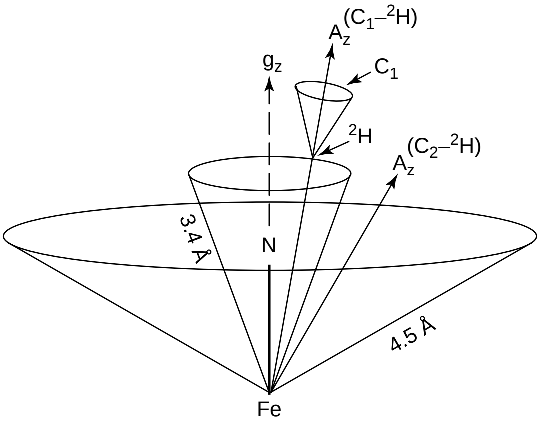

Figure 12 Schematic drawing of the geometrical relationship between the coupled deuterons at the C_1 and C_2 positions of taurine and the $g_\parallel$ (g_z) axis, coincident with the Fe–N(O) bond

or the Fe(III)−NO^- bond axis. For perdeuterated taurine, an additional deuterium ESEEM interaction could be accounted for by including a second deuteron, positioned 4.5 ± 0.2 Å from the iron on a cone that makes a 63 ± 5° angle with the Fe−N(O) bond axis, in our simulations. Alternatively, both C_2 deuterons could be responsible for this weaker interaction showing an average distance of 5.1 Å from the Fe and also positioned on a cone making a 63° angle with the Fe−N(O) bond axis.

These results are similar to those reported from ^{2}H-ENDOR studies on the Fe(II)NO adduct of NDO where the C_1 and C_2 deuterons of substrate naphthalene were found at distances of 4.3 and 5.0 Å from the Fe atom, respectively. The principal axis of the hyperfine tensor for the C_1 deuteron of substrate naphthalene made a 10° angle with the Fe−NO bond axis. For NDO, X ray crystallographic analysis of reduced forms of the protein prepared with naphthalene and oxygen show distances from iron to the C_1 and C_2 naphthalene carbons of about 4 Å. This would place the naphthalene deuterons bound to these carbons at distances of 3−4 Å from the iron, somewhat shorter than what was found in the ENDOR studies, but in good agreement with the distance reported here for the proximal C_1 deuteron of substrate taurine.**[67]** If one takes the Fe−N bond length for the NO ligand as 1.8 Å, commensurate with X ray absorption fine structure spectroscopic results (*see* ***X-Ray Absorption Spectroscopy***) on FeEDTA-NO,**[56]** the proximal C_1 deuteron of taurine will be positioned 1.8 Å from the nitrogen of bound NO. The angle defining the orientation of the Fe−N(O) bond with the coupled C_1 deuteron of taurine, 20 ± 3°, is somewhat wider than that measured for the C_1 naphthalene deuteron of reduced NDO by ENDOR (10°) or estimated from X ray crystallography on that enzyme (∼13°).**[63]** These differences in substrate deuteron (proton) distances and orientations are modest given the different catalytic functions and cosubstrate requirements of TauD and NDO. In both cases, the measured deuterium hyperfine couplings provide metrical information that is commensurate with the substrate C−H bond(s) to be hydroxylated.

In our analysis of the ^{2}H-ESEEM data obtained from Fe(II)NO−TauD samples treated with taurine deuterated at C_1, we considered only the contributions of the proximal deuteron (Figure 10). The nuclear quadrupole interaction (nqi) for the stronger coupled deuteron is axial, with the principal axis of the nqi tensor directed along the $C_1{-}^2H$ bond. In our simulations, we found that the principal axis of the nqi made a 23 ± 3° angle with the principal axis of the deuterium hyperfine tensor. Taking the $C_1{-}^2H$ bond length to be 1 Å, a third cone can be placed on Figure 12 at the position of the proximal C_1 deuteron to mark the locus of positions for the C_1 carbon of taurine. Taking the bonding about C_1 to be sp^3 hybridized, the $^2H{-}C{-}^2H$ bond angle to be 109°, the distal C_1 deuteron will lie at a distance of about 5 Å from the iron. The resulting dipolar hyperfine coupling for this deuteron will give rise to weak ESEEM as the modulation intensities are inversely proportional to the dipole−dipole distance raised to the sixth power.**[19]** The contributions of the distal deuteron to the ESEEM spectra of Figures 9 and 10 would be centered at the deuterium Larmor frequency. The best chance for seeing this contribution would be at $g = 2$ for the C_1-deuterated taurine sample (Figure 10d) where there is a fairly clean window in the ESEEM spectrum. Simulations of the ^{2}H-ESEEM for these conditions that consider a dipole−dipole distance of 5.0 Å and an angle of 11° between the Fe−N(O) bond axis and the principal axis of the ^{2}H hyperfine tensor, predict a modulation depth or intensity of 0.5%. Because the modulations due to the stronger coupled deuteron, characterized by a 3.4 Å dipole−dipole distance, are about 6% at $g = 2$, we conclude that the ESEEM from distal C_1 deuteron is too weak to resolve in our experiments. This decreased modulation depth for the distal C_1 deuteron stems from its increased dipolar distance and its orientation close to the Fe−N(O) or $g_\parallel$ axis where integrating factors in the orientation averaging are small.

Taken together, the relative contributions of the two C_1 deuterons to the ESEEM and the intermediate contribution of one, or both of the C_2 deuterons provide important details on how substrate taurine is positioned for specific hydroxylation of the C_1 carbon and the subsequent harvesting of sulfite. Considering NO to be a reasonable surrogate for ${O_2}^{2-}$ or $O_2^-\bullet$ in Scheme 2 (species D), our ESEEM measurements show that one of the C_1 deuterons is positioned 3.4 Å from the Fe at an angle with respect to the Fe−N(O) axis that would result in the distance to the NO nitrogen atom of 1.8 Å. Because the other C_1 deuteron does not contribute to the ESEEM, the C_1 carbon must be oriented so that this second deuteron is directed away from the NO nitrogen and close to the $g_\parallel$ axis. The larger angle and distance needed to describe the location of the C_2 deuteron(s) likely shows that substrate taurine has been oriented to position the C_2−H bonds so they are not able to react with the Fe(IV)-oxo species thought to trigger the C−H bond hydroxylation chemistry (Scheme 2, species E).

To compare our ESEEM results with the X ray structure,**[55]** the most recent TauD structure was downloaded from the PDB and the program Refmac was used to model protons onto the carbon framework of substrate taurine. Because the X ray results are from crystals grown anaerobically, the NO ligand was modeled into the crystal structure by using bond lengths and angles from model compound studies**[56]** and by placing the Fe−N(O) bond 180° from the ‘‘axial’’ Fe−N (histidine) bond. The results show that the proximal C_1 proton is 3.0 Å from the Fe atom and makes a 32° angle with the Fe−N(O) bond while the closest C_2 proton is 4.4 Å from the Fe and makes an angle of 52° with the Fe−N(O) bond. Given that there could easily be a 10° error in the orientation of the Fe−N(O) bond axis, one can justify moving the Fe−N(O) bond to match the corresponding angles from our ESEEM measurements (Figure 12). In addition, the low resolution of this structure and more specifically, the taurine electron density map, readily allows for modest reorientation of the taurine carbon framework. Figure 13 shows the results of these modest adjustments of the crystal structure and provides

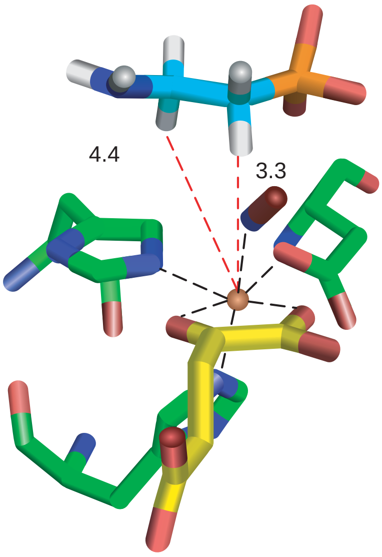

Figure 13 Structure of TauD active site as taken from monomer A of the four molecules per unit cell in PDB file LOS7. The taurine protons and NO ligand were modeled into the structure using the program, Refmac. The carbon framework of taurine was rotated slightly from the structure supplied to the PDB (Figure 7) to achieve Fe-proton distances of 3.3 Å for the C_1 proximal proton and 4.4 Å for the closest C_2 proton

a structure that is in excellent agreement with our ESEEM results.

3.2 ESEEM Assignments and TauD Coordination Chemistry

The ESEEM spectra of Figure 8 show complex sets of peaks for the ternary complex of Fe(II)NO–TauD with contributions from ^{14}N and ^{1}H. In the analysis of substrate orientation, we ignored this complexity by dividing it out of the data sets and focusing our analysis on the ESEEM from substrate deuterons. Certainly, the analysis of the spectra of Figure 8 hold important details concerning the electronic structure of the Fe(II)NO paramagnetic center. One of the most intriguing features of TauD is the opportunity that the crystal structure provides for understanding our ESEEM data in detail. The benefit of such an analysis is that details on outer coordination sphere interactions that are important for catalysis may be gained. Such details are what distinguish each member of this enzyme class. At $g = 4.00$, the ESEEM spectrum from the Fe(II)NO–TauD complex with cosubstrates αKG and taurine shows three sharp lines at 1.1, 1.8 and 2.7 MHz along with a broad line centered at 5.1 MHz and a broad line that covers a frequency spread from 9.8 to 12.7 MHz (Figure 8b). Because the Larmor frequency of ^{1}H at 171.0 mT is 7.3 MHz, and these data were collected at a τ value for which matrix protons are suppressed, it was clear from the beginning that ^{14}N and ^{1}H spectra were overlapped. The four-pulse HYSCORE spectrum that matches the experimental conditions for Figure 8(b) is shown in Figure 14(a). The data show pronounced correlation arc's that extend from 2 to 13 MHz defining at least one strongly coupled ^{1}H. These arcs likely arise from a ^{1}H that is oriented ~90° from the Fe(II)–N(O) axis because at $g_{\perp}$ one samples the full extent of the hyperfine tensor for such an orientation. The HYSCORE spectrum also shows two low frequency correlations, (1.0, 1.8 MHz) and (1.6, 2.5 MHz), that are most likely due to ^{14}N of one of the histidine ligands or a perpendicular component of the ^{14}N coupling due to the bound NO group.

At the other extreme of the Fe(II)NO EPR spectrum, $g = 2.00$, the three-pulse ESEEM spectrum of Figure 8(d) shows even more peaks. The HYSCORE spectrum is shown in Figure 14(b) where peaks in the $(-,+)$ quadrant that arise from strong hyperfine coupling are now observed. The strongest correlations are between peaks at (−5.9, 10.0 MHz) and (2.1, 3.1 MHz). Figure 14(b) also shows substantial correlations at (−4.8, 6.0), (−3.3, 5.2) and (−3.5, 4.4). A very weak proton correlation at (13.2, 16.4) is also observed. The strong ^{14}N hyperfine is likely from the axially bound histidine ligand or from NO. We are currently using isotopic substitution and model compound work to proceed with assignments. The disappearance of the proton arcs that were so clearly resolved at $g = 4$ supports the notion that the coupling is from an equatorial coordination position. The τ value used to collect both data sets of Figure 14 was near a matrix proton suppression value and that weakens the contributions of weakly coupled protons to the HYSCORE as well as to the one-dimensional ESEEM.

Proton arcs like that resolved in the HYSCORE spectrum of Figure 14(a) are common for water ligands bound to metal centers (see Figure 6). With that in mind, Fe(II)NO–TauD samples with αKG and taurine were studied for protein exchanged against D_2O. Figure 15 shows the HYSCORE data obtained under the same conditions as Figure 14(a) for such a sample and we conclude from this result that the ^{1}H giving rise to this strong ''equatorial'' hyperfine coupling is not exchangeable. Furthermore, this contribution is also detected for enzyme prepared with perdeuterated taurine and with an αKG surrogate, N-oxalylglycine. Analysis of the arc extent and curvature using the graphical procedure involving equation (11) in the *Technical Background* section yielded a dipolar coupling, $|T| = 5.0$ MHz, which translates to a dipole–dipole distance of 3.2 Å at $g = 4.00$. The isotropic coupling derived from this analysis was 1.1 MHz if A_{iso} and T have the same sign and 6.1 MHz if the signs are opposite. In searching the crystal structure for the possible source of this coupling, we found that the side chain of tryptophan 248 is the most likely candidate in terms of distance and orientation. The Hausinger lab at Michigan State has prepared a variant of TauD with this tryptophan residue mutated to phenylalanine and we are currently following up on this lead with further HYSCORE experiments.

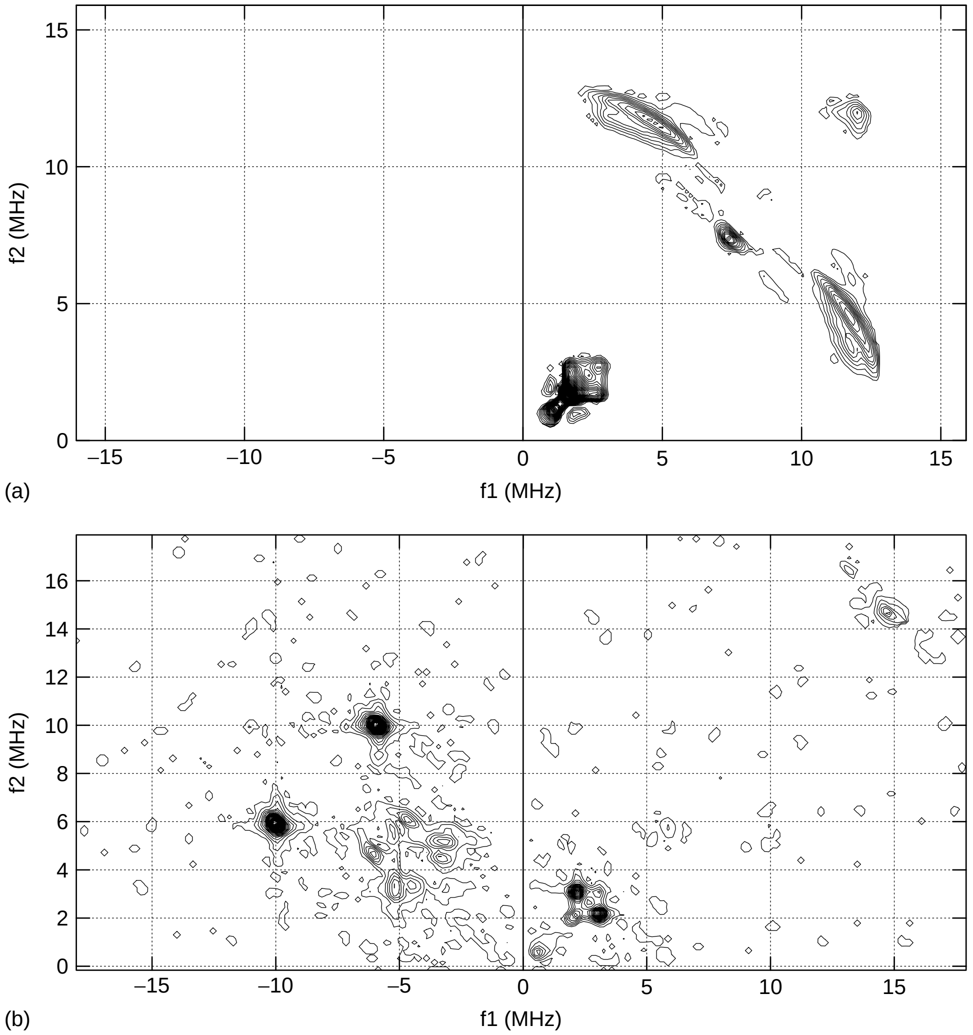

Figure 14 Four-pulse HYSCORE spectra of Fe(II)NO–TauD treated with αKG and taurine in aqueous buffer. Parameters common to these measurements were: microwave frequency, 9.724 GHz; magnetic field, (a) 171.0 mT and (b) 345.3 mT; 90° pulses, 16 ns (FWHM), 200 W; 180° pulse, 28 ns, 200 W; τ value, (a) 120 ns and (b) 136 ns; sample temperature, 4.2 K

One of our goals for studying TauD was to correlate our spectroscopic results with the structural information available from the X ray crystal structure of the ternary complex prepared under anaerobic conditions. Subsequently, this information could be used as a foundation to study similarities in catalytic mechanisms between different members of this enzyme class. Because the catalytic mechanism involves the displacement of bound water molecules from the Fe(II) cofactor, we studied samples of Fe(II)NO–TauD without cosubstrates and with just the αKG added to determine if HYSCORE could be used to follow this chemistry. Figure 16(a) shows the HYSCORE spectrum at $g = 4.00$ for Fe(II)NO–TauD in aqueous buffer without the two cosubstrates. Two water molecules should be coordinated to the Fe(II)NO center under these conditions. The HYSCORE shows a weak, disordered system of overlapping ^{1}H arcs for this sample, which most likely reflects a high degree of disorder at the site prior to cosubstrate addition. When αKG is added (Figure 16b), the ^{1}H cross-peaks become better defined and take on the appearance of a wedge-shape that could be indicative of a ^{1}H hyperfine coupling of rhombic symmetry. For both of these samples, the cross-peaks disappear from the spectrum when the samples are exchanged against D_2O buffer. This is in sharp contrast to what was observed for the ternary complex containing αKG and taurine, Figures 14(a) and 15, where D_2O exchange did not alter the intensity of the ^{1}H arc. From these observations, it appears that whatever residue gives rise to the broad ^{1}H-ESEEM captured in the HYSCORE ridges or arcs at $g_{\perp}$, it is only coupled to the Fe(II)NO center in this unique fashion when the cosubstrates are both bound. Perhaps this residue plays a role in positioning substrate or in guiding the chemistry of the center once the high valent Fe-oxo intermediate is prepared. It will be exciting to see where the spectroscopy takes us!

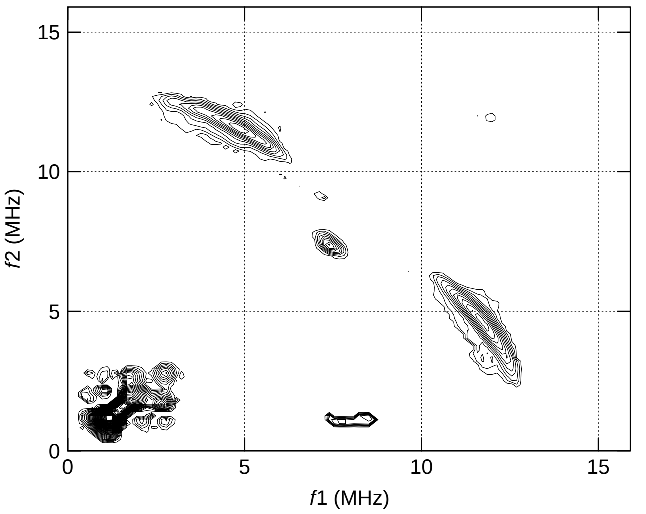

Figure 15 Four-pulse HYSCORE spectra of Fe(II)NO–TauD treated with αKG and taurine in D_2O buffer. Parameters were identical to those used to collect the HYSCORE spectrum of Figure 14(a)

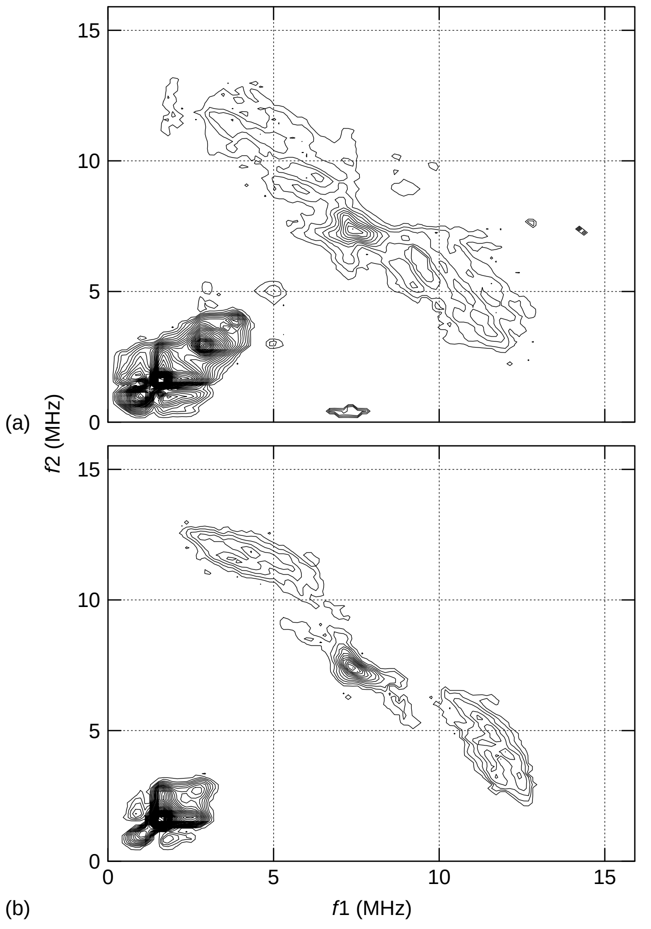

Figure 16 Four-pulse HYSCORE spectra of Fe(II)NO–TauD in (a) aqueous buffer and (b) treated with αKG and suspended in aqueous buffer. Measurement parameters were identical with those of Figure 14(a)

4 ACKNOWLEDGMENTS

The data shown for purposes of example in this chapter have come from long-standing collaborations with Professors R.P. Hausinger (Michigan State University) and D.J. Kosman (University at Buffalo). ESEEM experiments on TauD were performed by Dr. R.B. Muthukumaran and Ms. Meng Li at Michigan State University. Financial support for this work came from the NIH (GM 54065 and RR 15880) and the Michigan Economic Development Corporation.

5 ABBREVIATIONS AND ACRONYMS

DPPH = 2,2-diphenyl-1-picrylhydrazyl; ENDOR = electron-nuclear double resonance; EPR = electron paramagnetic resonance; ESE = electron spin echoes; ESEEM = electron spin echo envelope modulation; FFT = fast fourier transformations; FWHM = full width at half maximum; HYSCORE = hyperfine sublevel correlation; nqi = nuclear quadrupole interaction; TauD = taurine/αKG dioxygenase; TWTA = traveling wave tube amplifier; ZFS = zero field splitting.

6 FURTHER READING

Y. Deligiannakis, M. Louloudi, and N. Hadjiliadis, *Coord. Chem. Rev.* 2000, **201**, 1. A thorough review of the application of ESEEM spectroscopy to problems in inorganic chemistry prior to 2000. This is an excellent article for someone new to the field and a fine reference for those who use ESEEM and ENDOR in their research.

S. A. Dikanov and M. K. Bowman, *J. Magn. Reson.*, 1995, **A116**, 125. A brief and very useful treatment of $S = 1/2$, $I = 1/2$ HYSCORE analysis.

S. A. Dikanov and Y. D. Tsvetkov, 'Electron Spin Echo Envelope Modulation Spectroscopy', CRC Press, Boca Raton, 1992. This book begins with the fundamental principles of ESEEM and develops the theory of the measurements with exquisite detail.

S. A. Dikanov, L. Xun, A. B. Karpiel, A. M. Tyryshkin, and M. K. Bowman, *J. Am. Chem. Soc.*, 1996, **118**, 8408. This paper contains a good technical description of HYSCORE and its analysis for the $S = 1/2$, $I = 1$ spin system.

A. Schweiger, *Appl. Magn. Reson.*, 1993, **5**, 229. A fine review article of the 1-D ESEEM and ENDOR methods developed by the authors and his coworkers through the early 1990's. A succinct discussion of the use of hyperfine couplings to gain structural information and the relative strengths of EPR, ESEEM and ENDOR is provided.

A. Schweiger and G. Jeschke, 'Principles of Pulse Electron Paramagnetic Resonance', Oxford University Press, New York,

2001. This is a comprehensive textbook on Pulse EPR, ESEEM and ENDOR methods. An excellent place to begin learning this methodology.

7 REFERENCES

1. W. B. Mims, K. Nassau, and J. D. McGee, *Phys. Rev.*, 1961, **123**, 2059.
2. J. A. Cowen and D. E. Kaplan, *Phys. Rev.*, 1961, **124**, 1098.
3. L. G. Rowan, E. L. Hahn, and W. B. Mims, *Phys. Rev. A.*, 1965, **137**, 61.
4. E. L. Hahn, *Phys. Rev.*, 1950, **80**, 580.
5. E. L. Hahn and D. E. Maxwell, *Phys. Rev.*, 1952, **88**, 1070.
6. G. M. Zhidomirov and K. M. Salikov, *Teor. Eksp. Khim.*, 1968, **4**, 514.
7. G. M. Zhidomirov, K. M. Salikov, Y. D. Tsvetkov, V. F. Yudanov and A. M. Raitsimring, *J. Struct. Chem.*, 1968, **9**, 807.
8. W. B. Mims, *Phys. Rev. B*, 1972, **5**, 2409.
9. W. B. Mims and J. L. Davis, *J. Chem. Phys.*, 1976, **64**, 4836.
10. W. B. Mims and J. Peisach, *Biochemistry*, 1976, **15**, 3863.
11. W. B. Mims, J. Peisach, and J. L. Davis, *J. Chem. Phys.*, 1977, **66**, 5536.
12. S. A. Dikanov, V. F. Yudanov, and Y. D. Tsvetkov, *J. Struct. Chem.*, 1977, **18**, 460.
13. L. Kevan, M. K. Bowman, P. A. Narayana, R. K. Boeckman, V. F. Yudanov and Y. D. Tsvetkov, *J. Chem. Phys.*, 1975, **63**, 409.
14. P. A. Narayana, M. K. Bowman, L. Kevan, V. F. Yudanov, and Y. D. Tsvetkov, *J. Chem. Phys.*, 1975, **63**, 3365.
15. A. Schweiger, *Angew. Chem.*, 1991, **30**, 265.
16. W. B. Mims, *Rev. Sci. Instrum.*, 1965, **36**, 1472.
17. W. E. Blumberg, W. B. Mims, and D. Zuckerman, *Rev. Sci. Instrum.*, 1973, **44**, 546.
18. W. B. Mims, *Phys. Rev. B*, 1972, **6**, 3543.
19. S. A. Dikanov and Y. D. Tsvetkov, ‘Electron Spin Echo Envelope Modulation Spectroscopy’, CRC Press, Boca Raton, 1992.
20. S. A. Dikanov, A. A. Shubin, and V. N. Parmon, *J. Magn. Reson.*, 1981, **42**, 474.
21. R. P. J. Merks and R. DeBeer, *J. Phys. Chem.*, 1979, **83**, 3319.
22. C. Gemperle, G. Aebli, A. Schweiger, and R. R. Ernst, *J. Magn. Reson.*, 1990, **88**, 241.
23. H. Käss, J. Rautter, B. Bönigk, P. Höfer, and W. Lubitz, *J. Phys. Chem.*, 1995, **99**, 436.
24. J. K. Shergill, C. L. Joannou, J. R. Mason, and R. Cammack, *Biochemistry*, 1995, **34**, 16533.
25. A. Schweiger and G. Jeschke, ‘Principles of Pulse Electron Paramagnetic Resonance’, Oxford University Press, New York, 2001.
26. P. Höfer, *J. Magn. Reson.*, 1994, **A111**, 77.
27. J. J. Shane, P. Höfer, E. J. Reijerse, and E. DeBoer, *J. Magn. Reson.*, 1992, **99**, 596.
28. S. A. Dikanov and M. K. Bowman, *J. Magn. Reson.*, 1995, **A116**, 125.
29. N. M. Atherton and A. J. Horsewill, *Mol. Phys.*, 1979, **37**, 1349.
30. R. S. Drago, ‘Physical Methods for Chemists’, 2nd edition, Saunders College Publishing, Orlando, 1992.
31. R. P. Hausinger, *Crit. Rev. Biochem. Mol. Biol.*, 2004, **39**, 21.
32. K. I. Kivirikko and T. Pihlajaniemi, *Adv. Enzymol. Relat. Areas Mol. Biol.*, 1998, **72**, 325.
33. C. J. Schofield and P. J. Radcliffe, *Nat. Rev. Mol. Cell Biol.*, 2004, **5**, 343.
34. C. J. Schofield and P. J. Ratcliffe, *Biochem. Biophys. Res. Commun.*, 2005, **338**, 617.
35. P. L. Roach, I. J. Clifton, V. Fülöp, K. Harlos, G. J. Barton, J. Hajdu, K. Andersson, C. J. Schofield, and J. E. Baldwin, *Nature (London)*, 1995, **375**, 700.
36. Z. Zhang, J. Ren, D. K. Stammers, J. E. Baldwin, K. Harlos, and C. J. Schofield, *Nat. Struct. Biol.*, 2000, **7**, 127.
37. F. Fukumori and R. P. Hausinger, *J. Biol. Chem.*, 1993, **268**, 24311.
38. D. A. Hogan, S. R. Smith, E. A. Saari, J. McCracken, and R. P. Hausinger, *J. Biol. Chem.*, 2000, **275**, 12400.
39. P. O. Falnes, R. F. Johansen, and E. Seeberg, *Nature*, 2002, **419**, 178.
40. S. C. Trewick, T. F. Henshaw, R. P. Hausinger, T. Lindahl, and B. Sedgwick, *Nature*, 2002, **419**, 174.
41. E. L. Hegg and L. Que, Jr, *Eur. J. Biochem.*, 1997, **250**, 625.
42. E. Eichhorn, J. R. van der Ploeg, M. A. Kertesz, and T. Leisinger, *J. Biol. Chem.*, 1997, **272**, 23031.
43. M. A. Kertesz, *FEMS Microbiol. Rev.*, 1999, **24**, 135.
44. M. J. Ryle, K. D. Koehntop, A. Liu, L. Que, Jr, and R. P. Hausinger, *Proc. Natl. Acad. Sci. U.S.A.*, 2003, **100**, 3790.
45. M. J. Ryle, A. Liu, R. B. Muthukumaran, R. Y. N. Ho, K. D. Koehntop, J. McCracken, L. Que, Jr, and R. P. Hausinger, *Biochemistry*, 2003, **42**, 1854.
46. M. J. Ryle, R. Padmakumar, and R. P. Hausinger, *Biochemistry*, 1999, **38**, 15278.
47. J. C. Price, E. W. Barr, T. E. Glass, C. Krebs, and J. M. Bollinger, Jr, *J. Am. Chem. Soc.*, 2003, **125**, 13008.
48. J. C. Price, E. W. Barr, B. Tirupati, J. M. Bollinger, Jr, and C. Krebs, *Biochemistry*, 2003, **42**, 7497.
49. D. A. Proshlyakov, T. F. Henshaw, G. R. Monterosso, M. J. Ryle, and R. P. Hausinger, *J. Am. Chem. Soc.*, 2004, **126**, 1022.
50. P. J. Riggs-Gelasco, J. C. Price, R. B. Guyer, J. H. Brehm, E. W. Barr, J. M. Bollinger, Jr, and C. Krebs, *J. Am. Chem. Soc.*, 2004, **126**, 8108.

51. J. C. Price, E. W. Barr, L. M. Hoffart, C. Krebs, and J. M. Bollinger, Jr, *Biochemistry*, 2005, **44**, 8138.
52. P. K. Grzyska, M. J. Ryle, G. R. Monterosso, J. Liu, D. P. Ballou, and R. P. Hausinger, *Biochemistry*, 2005, **44**, 3845.
53. E. Kalliri, P. K. Grzyska, and R. P. Hausinger, *Biochem. Biophys. Res. Commun.*, 2005, **338**, 191.
54. J. M. Elkins, M. J. Ryle, I. J. Clifton, J. C. Dunning Hotopp, J. S. Lloyd, N. I. Burzlaff, J. E. Baldwin, R. P. Hausinger, and P. L. Roach, *Biochemistry*, 2002, **41**, 5185.
55. J. R. O'Brien, D. J. Schuller, V. S. Yang, B. D. Dillard, and W. N. Lanzilotta, *Biochemistry*, 2003, **42**, 5547.
56. C. A. Brown, M. A. Pavlosky, T. E. Westre, Y. Zhang, B. Hedman, K. O. Hodgson, and E. I. Solomon, *J. Am. Chem. Soc.*, 1995, **117**, 715.
57. E. L. Hegg, A. K. Whiting, R. E. Saari, J. McCracken, R. P. Hausinger, and L. Que, Jr, *Biochemistry*, 1999, **38**, 16714.
58. W. B. Mims, J. L. Davis, and J. Peisach, *Biophys. J.*, 1984, **45**, 755.
59. K. Warncke and J. McCracken, *J. Chem. Phys.*, 1994, **101**, 1832.
60. B. M. Hoffman, R. A. Venters, and J. Martinsen, *J. Magn. Reson.*, 1985, **62**, 537.
61. J. B. Cornelius, J. McCracken, R. B. Clarkson, R. L. Belford, and J. Peisach, *J. Phys. Chem.*, 1990, **94**, 6977.
62. D. T. Edmonds, *Phys. Rep.*, 1977, **29**, 233.
63. T. C. Yang, M. D. Wolfe, M. B. Neibergall, Y. Mekmouche, J. D. Lipscomb, and B. M. Hoffman, *J. Am. Chem. Soc.*, 2003, **125**, 7056.
64. C. A. Hutchison and D. B. McKay, *J. Chem. Phys.*, 1977, **66**, 3311.
65. B. L. Silver, 'Irreducible Tensor Methods', Academic Press, New York, 1976, Vol. 36.
66. D. M. Arciero, A. M. Orville, and J. D. Lipscomb, *J. Biol. Chem.*, 1985, **260**, 14035.
67. A. Karlsson, J. V. Parales, R. E. Parales, D. T. Gibson, H. Eklund, and S. Ramaswamy, *Science (Washington, D.C.)*, 2003, **299**, 1039.

Electronic Spectroscopy

Joseph L. Hughes and Elmars Krausz

Australian National University, Canberra, Australia

	Method Summary	1
1	Introduction	2
2	Basic Concepts	3
3	Technologies	11
4	Practical Examples	16
5	Abbreviations and Acronyms	18
6	References	18

METHOD SUMMARY

Acronyms, Synonyms

- UV-Visible Spectroscopy (UV-Vis)
- light absorption, emission and scattering
- laser spectroscopy, selective spectroscopy
- low temperature glass, single crystal, protein-cryoprotectant spectroscopy.

Measured physical quantities

- Electronic transition energies
- transition strengths
- transition polarizations
- ground and excited state splittings, linewidths, and excited state lifetimes
- time- and temperature-dependent spectra
- external stress- (Pressure), electric- (Stark) and magnetic-field (Zeeman) induced spectral changes.

Information available

- excited and ground state electronic properties and local geometries
- chromophore-environment interactions
- ground and excited state vibrational frequencies
- vibrational/phonon coupling strengths
- interchromophore interactions (excitonic/magnetic)
- local electronic variability and vulnerability (host-induced inhomogeneities).

Information not available, limitations

- The interpretation of electronic spectra is largely dependent on a prior knowledge of structure.
- There is an enormous dynamic range in electronic transition strengths ($f-f$, $d-d$, CT, $\pi-\pi*$).
- Important chemical species may not exhibit UV-Vis spectra.
- Electronic spectra are characteristically broad, often showing minimal detailed structure.
- Solubility/concentration of a chromophore in an optically useful medium may be limiting.

Examples of questions that can be answered

- nature of the excited states
- concentration and orientation of a chromophore

- sensitivity to a specific electronic component of a more complex system
- identification of intrinsic and environmentally induced properties of a chromophore.

Major advantages

- Electronic spectroscopy is nondestructive and noninvasive.
- Most techniques in chemistry are limited to determining properties of the electronic ground state of a species. Electronic spectroscopy is one of the few techniques that *directly probes excited states*.
- Developments and improvements in quantum chemical computational methods are now able to address excited state properties of relatively large systems in a useful way.
- Laser and synchrotron light sources are particularly bright while conventional sources offer broad spectral coverage and ease of use.
- Visible-light detectors are extremely sensitive, efficient and may also offer high time resolution.
- Targeted optical spectroscopy experiments can be easily configured through the use of computer controllable modules.

Major disadvantages

- Optical spectra may be dominated by less interesting chromophoric species.
- The assignment and interpretation of electronic spectra is not always routine and may involve the understanding of a number of fundamental quantum mechanical concepts.

Sample constraints

- A species of interest needs to be either soluble or solubilized in an inert, transparent, isotropic and non light-scattering medium.
- There is a limited range of useful low-temperature glassing mixtures.
- Measurements on single crystals can be particularly informative but such measurements can be more demanding.

1 INTRODUCTION

Electronic spectroscopy in its broader sense involves the absorption, emission, or scattering of UV-visible light by a chromophoric system of interest. Many aspects of the large range of electronic spectroscopy techniques that are available to chemists are well established and relatively routine. Most often, measurements involve the use of solution samples at ambient temperatures. Practically all laboratories are equipped with instruments capable of measuring at least some of these optical phenomena. Companion articles in this volume deal with a number of electronic spectroscopies including Photoluminescence and Electroluminescence (*see* ***Photoluminescence and Electroluminescence, Solid State***), circular dichroism (CD) (*see* ***Circular Dichroism (CD) Spectroscopy***), magnetic circular dichroism (MCD) (*see* ***Magnetic Circular Dichroism (MCD) Spectroscopy***) and Resonance Raman spectroscopies.

Any particular spectroscopic technique, once its theoretical and practical framework has been established, can be useful and adapted to relatively routine analytical or diagnostic purposes. The cornerstone analytical techniques of chemistry are perhaps increasingly Mass Spectrometry, nuclear magnetic resonance (NMR) (*see* ***Nuclear Magnetic Resonance (NMR) Spectroscopy of Inorganic/Organometallic Molecules***; ***Nuclear Magnetic Resonance (NMR) Spectroscopy of Metallobiomolecules***) and X-ray crystallography. It is often possible to identify the composition and provide the structure of a substance using these techniques alone. Electronic absorption spectra of solutions at room temperature do not usually exhibit the spectral resolution or distinctiveness required of an analytic technique. Most chemical species luminesce only weakly and in this respect electronic spectroscopies play a more specialized and relatively minor role. A *combination* of spectral techniques is often brought to bear on the complex and interesting systems now under study in modern chemistry. Multitechnique approaches are particularly important in biochemistry.

The large spectral width characteristically exhibited in electronic spectra is due to factors inherent to electronic excitations of the chromophore (homogeneous broadening) but is often dominated by factors due to variations in the local environment experienced by each individual chromophore in a sample (inhomogeneous broadening). We will point out that the vulnerability of electronic spectra to spectral broadening can sometimes be turned to advantage and important characteristics of a chromophore, such as its interaction with the local environment, can be understood by a study of broadening mechanisms. Metalloenzymes are systems that usually owe their unique abilities to interactions of metals with the protein environment.

Some electronic spectroscopies take particular advantage of the remarkable coherency, brightness, directionality, and spectral purity of laser sources or the extreme sensitivity and/or rapid response times of modern light detectors. Potent laser/detector combinations, when coupled to an optical microscope, allow a single molecule to be detected and its spectra recorded in favorable cases.[1] Laser pulses that have a period as short as the fundamental electronic and nuclear reorganizational processes in molecules (picosecond-femtosecond) can be created, and by using such technology the most basic chemical processes can be directly monitored. We have discussed some aspects of these issues in a recent chapter.[2]

The current article does touch on laser-based spectroscopies but concentrates largely on important aspects of more conventional absorption spectroscopies. We pay particular attention to methods and developments in practical sample-handling techniques. These can be critical in the study of reactive samples or those that are sensitive to light, air, or moisture, for example. We also note the continuing revolution in light sources, spectrometers, filters, optics, and detectors, along with the developments in convenient and rapidly user-adaptable, computer-controlled instrumentation that allow potent and targeted experimental facilities to be relatively easily configured.

2 BASIC CONCEPTS

An effective understanding of electronic spectra does require a basic knowledge of a number of fundamental quantum mechanical principles. This section only briefly highlights, in a descriptive way, some important aspects. More complete and formal treatments are available in a wide range of texts.[3–7]

As a very basic description of the electronic absorption process, electromagnetic radiation (light) of wavelengths in the range from $\sim 180\,\text{nm}$ to around $\sim 800\,\text{nm}$ will interact, via its rapidly varying electric field, with the electronic charge distribution that defines the shape, size, and energy of a chromophore. The *magnetic* field of light can also interact with a chromophore and although this interaction is typically more than 10^6 times weaker than the interaction with the electric field, it has a critical role to play in CD spectra (*see* ***Circular Dichroism (CD) Spectroscopy***). Its influence can be seen directly in absorption spectra when the electric interaction is relatively weak. The parity of the electric and magnetic dipole operators are odd and even respectively, and this property can be used to distinguish them. In this chapter we refer to electric dipole processes unless stated otherwise.

If the frequency of the incident radiation is resonant with the energy difference between the ground state configuration and that of an excited state, then there is a well-defined increase in the probability of finding the chromophore in an electronically excited state after a given time. Another useful heuristic description is that the radiation field causes the eigenstates (stationary states) of the system to become ‘‘mixed’’ and thus there is the possibility of the ground state ‘‘transforming’’ to the excited state.

When the radiation field is sufficiently intense, such as in a high power pulse laser, the laser radiation field, ground, and excited states, all need to be considered as a coherent, interacting electromagnetic system. This is the fully quantum picture,[8,9] with the radiation field and the electronic excitations being entangled. A range of fascinating nonlinear and time dependent processes become enabled, including for example, optical analogues of NMR pulse techniques. A caveat is that a high power pulse laser may also induce unsuspected processes, particularly in the spectra of condensed phase systems. These may be associated with photochemical damage to the sample or unrecognized photophysical transformations. This article limits itself largely to more conventional (linear) studies.

All electronic states of a chromophore are *stationary* states and are the solutions to the quantum mechanical equations of motion (Hamiltonian) of a molecule defining nuclear and electronic kinetic energies together with all Coulomb (electrostatic) interactions between nuclei and electrons in a molecule. As electrons are far lighter than nuclei, purely electronic eigenstates can usually be calculated by assuming that nuclei are stationary. This is the basis of the Born–Oppenheimer separability of electronic and nuclear motions. Given that nuclei move slowly and electronic reorganization is rapid, electronic excited states are most likely to be created having the nuclear geometry of the *initial* state.

In general, electronic excited states have *different* equilibrium bond lengths and geometries to the ground electronic state. These differences lead to the possibility of excitation of *vibrational* quanta (in an excited state) along with the purely electronic component of the excitation. The degree of coupling to vibrational modes (*see* ***Vibrational Spectroscopy***) of an electronic excitation is defined by the appropriate overlap factors. Any excited (electronic + vibrational) state, although a stationary state of the Hamiltonian, has a limited lifetime. An excited state of a chromophore rapidly loses energy, either by emitting light or losing some or all of the excitation energy to the environment as heat. These processes are called radiative and nonradiative relaxation, respectively.

Under nearly all circumstances, with rare-earth ions and a few unusual electronic systems such as azulene being notable exceptions, nonradiative relaxation to the lowest electronic excited state is *extremely* rapid (typically $\ll 1$ picosecond). Relaxation of vibrationally excited states, of either the ground electronic state or the excited electronic state, is also very rapid (∼picoseconds) even at low temperatures. These nonradiative relaxation processes are characteristically much faster than rates of radiative relaxation, leading to what is sometimes known as Kasha’s rule. This notes that only the lowest energy electronically excited state of a chromophore will persist for long enough to give rise to easily measurable radiative emission (photoluminescence; *see* ***Photoluminescence and Electroluminescence, Solid State***). As a general rule, if the energy gap between the ground state and the lowest excited state is more than ∼5 quanta of the highest frequency vibration in the system, then radiative relaxation from this state (luminescence) can compete with radiationless processes. Energy gaps between the manifold of higher excited states are rarely larger than the gap between the ground and first excited states and thus, in condensed phases, radiationless deactivation of these higher-lying states almost invariably outcompetes radiative pathways.

2.1 Excited State Energies

A simple yet fundamentally correct way of looking at the energy of an electronic state is by invoking the Hellman–Feynman theorem.[3] This result shows that the energy of any eigenstate is exactly that which one would calculate by an electrostatic calculation of Coulombic interactions of the charge cloud and the nuclei. The charge cloud is defined by the square of the electronic wavefunction. Each electronic state is described by its individual wavefunction and subsequent charge cloud. Excited states will in general involve a more spatially extended charge cloud than the ground state. Furthermore, for a transition to have optical intensity the two states involved must have opposite parity. Excited states are generally more electrically dipolar than the ground state. This dipole is the ‘‘handle’’ by which the light field grabs the molecule and mixes ground and excited states.

The independent electron approximation is central in the description of chemistry. Solutions to one-electron atomic or molecular Hamiltonians are taken as a starting point in developing the description of many-electron systems. Within this approximation, electronic excitations can be described as a particular electron jumping from one orbital to another. This approach, though useful, has no ultimate fundamental basis and fails in some situations. Additionally, in systems for which the electronic wavefunction itself is *strongly dependent* on the nuclear coordinate, such as Jahn–Teller active systems[10] and vibronically active mixed valence systems,[11] or the bacterial reaction center cation,[12,13] the Born–Oppenheimer approximation fails. In this situation some phenomena can become quite counterintuitive, such as the temperature dependence of the localization of charge.[11] More fundamentally precise methods[14] need to be invoked in dealing with these interesting systems.

Electronic excitations can be usefully classified as one-center excitations and those involving two or more centers. Intraconfigurational transitions such as d–d and $f-f$ processes are examples of systems in which their energetics are well described as one-center (atomic) excitations, but as noted in a later section their optical intensity may be due entirely to contamination with two-center processes. A characteristic two-center excitation is an optical charge-transfer excitation between two identifiable subunits, the donor and acceptor. The electronic charge cloud of the donor will become smaller upon losing an electron while that of the acceptor, which gains an electron, will become larger. Consequently, multiple quanta of the vibrational modes accommodating the displacement will be induced. A large fraction of the overall excitation energy can become vibrational.

The importance of quantum computational methods in chemistry has increased significantly with advances in both the speed of computers and with improvements in code and software packages.[15] Methods in common use either approximate an electronic wavefunction to a (truncated) sum of Gaussian functions (which themselves are easy to integrate), or define an *effective* potential in which electrons move (density functional models). Although more effective in describing the properties of *ground* states, both approaches can, in many cases now provide useful, if limited, information on excited states. Each method has its advantages and limitations, but calculations are now widely used as a guide in the assignment and understanding of electronic spectra.

2.1.1 *Homogenous Broadening*

There is spectral broadening evident in the spectrum of each single molecule or chromophore. This is homogeneous broadening. The *minimal* such broadening of any eigenstate is determined by its radiative lifetime. This (lifetime) broadening gives rise to a Lorentzian lineshape (Figure 1). Its width is inversely dependent on the excited state lifetime. A radiative lifetime of 10 ns, which at 500 nm corresponds to a transition with an oscillator strength (see below) of $f = 0.375$, leads to a homogenous linewidth of $\sim 5.3 \times 10^{-4}\ \text{cm}^{-1}$ (16 MHz). The lowest excited state of a highly fluorescent dye molecule may have a linewidth close to the radiative limit at the lowest temperatures. At higher temperatures, although lifetimes

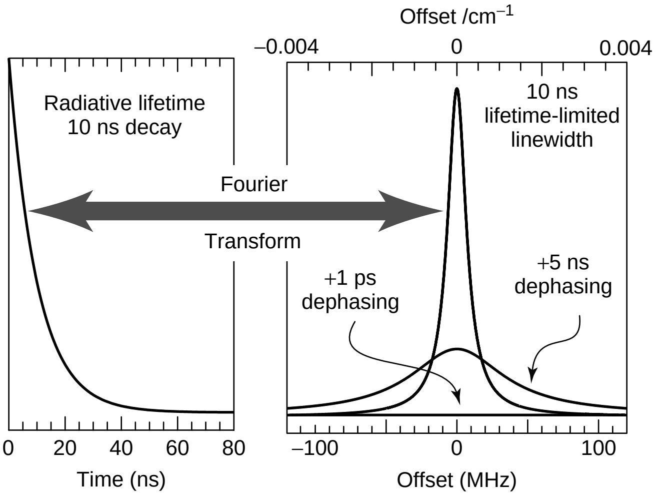

Figure 1 Schematic showing a chromophore with a radiative lifetime of 10 ns with its linewidth passing from the radiatively limited value of $5.3 \times 10^{-4}\ \text{cm}^{-1}$ at cryogenic temperatures to the situation at higher temperatures where rapid dephasing induces a strong additional broadening, yet leaves the emission lifetime unaffected

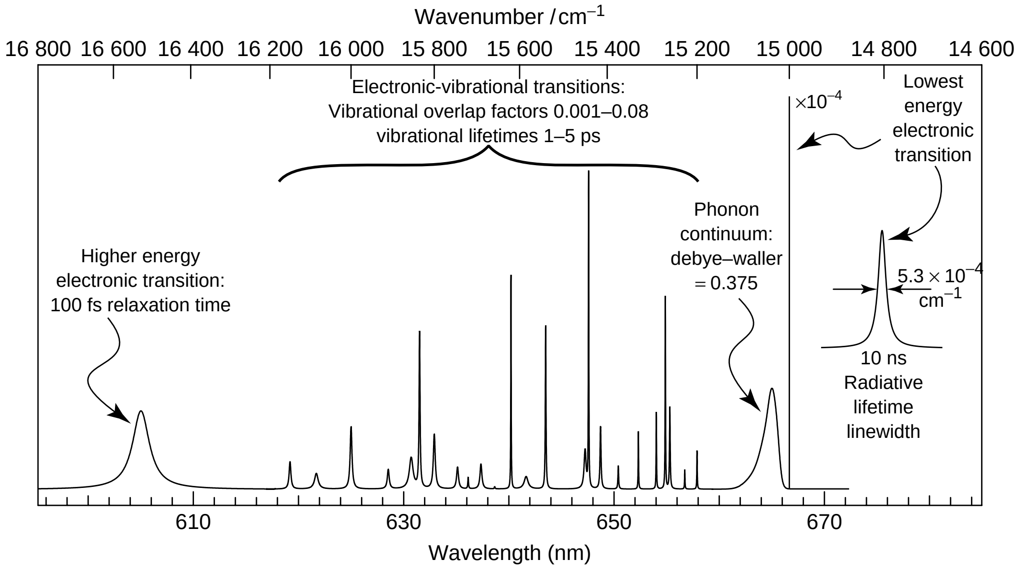

Figure 2 Schematic of the electronic absorption spectrum of a single chromophoric site in a condensed phase host environment at low temperatures. An extremely sharp electronic origin, exhibiting a radiatively limited linewidth is accompanied by a phonon sideband with vibrational sidelines. A second electronic excited state lies at higher energies. Vibrational sidelines and the second electronic excited state are lifetime broadened by rapid radiationless deactivation processes

may remain close to radiatively limited, thermally induced fluctuations of the environment cause the excitation energy to undergo rapid energy shifts. This process is called dephasing and leads to homogeneous widths of 100 cm^{-1} or more at ambient temperatures (Figure 1).

Electronic states higher in energy than the lowest energy excited state almost always undergo rapid (<picosecond) radiationless deactivation (Figure 2). This rapid process will induce a homogeneous lifetime broadening in the range of $\sim$1–1000 cm^{-1}, even at the lowest temperatures. Along with the purely electronic excitations (also called zero phonon lines or origins), each electronic state is coupled, to a variable extent, to both phonon modes of the surrounding medium and vibrational modes of the chromophore (Figure 2). Phonon frequencies form a continuum in the $\sim$10–100 cm^{-1} range, whereas molecular vibrations are discrete and have frequencies from the phonon range up to proton vibrational frequencies (if present) of $\sim$3500 cm^{-1}.

In chromophores containing even a modest number of atoms, a large number of vibrational frequencies may be coupled to an electronic origin. Each vibrational sideband has a Lorentzian width corresponding to its own particular vibrational relaxation rate. Increasing spectral congestion, due to a large number of vibrational modes, quickly leads to a weakly structured quasi-continuum. The overall shape of this continuum is variable, depending on the overlap factors of the various modes coupled to the electronic excitation. As the temperature increases, any remaining structure will diminish with the effects of rapidly increasing dephasing rates adding to homogeneous widths. Intensity also typically builds up on the low-energy edge due to absorption from thermally populated levels of the ground state.

When the difference between equilibrium geometries in ground and excited states is substantial, this will lead to the excitation of multiple vibrational quanta in the modes that accommodate such a displacement. When a large number of quanta of a particular mode are excited, the overall intensity distribution in the vibrational sideline will approach a Gaussian pattern. Thus, when vibrational sidelines dominate the spectrum, a homogeneously broadened electronic band can have an overall profile close to Gaussian (Figure 3).

2.1.2 Inhomogenous Broadening

Chromophores dissolved or embedded in any medium experience a range of nanoenvironments (Figure 4). This leads to their excitation energies being significantly modulated. The spectra of individual chromophores vary due to local variations in the positions of solvent molecules, charge compensating species, the proximity of other chromophores, strains, defects, or dislocations. These influences may indeed lead to a very significant spread in the energies of both ground and excited states and consequently to a range of electronic excitation energies. This ubiquitous phenomenon is called inhomogeneous broadening. Other spectroscopic techniques, such as IR (*see* ***Vibrational Spectroscopy***) and NMR (*see* ***Nuclear Magnetic Resonance (NMR) Spectroscopy of Inorganic/Organometallic Molecules***) are less susceptible to inhomogeneous spectral broadening. In contrast to electronic excitation energies, which can vary significantly from a

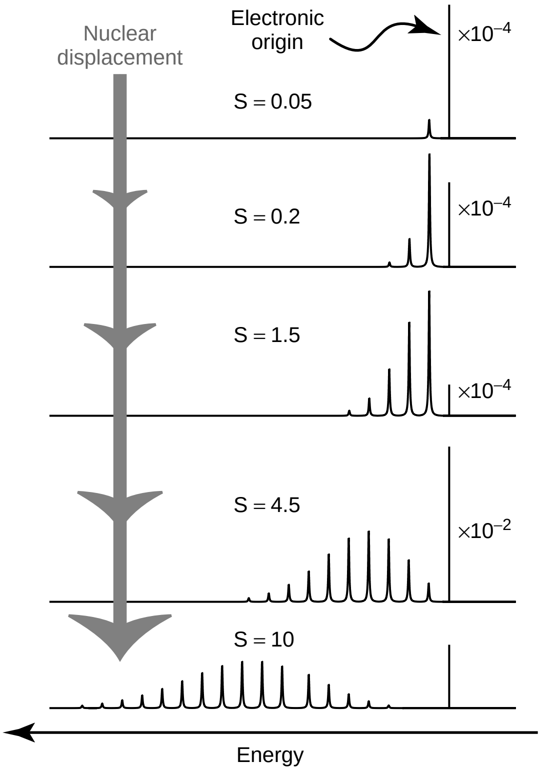

Figure 3 Schematic of the electronic spectrum of a single site coupled to one vibrational mode. A changing vibrational sideline pattern is seen upon increasing nuclear displacement between ground and excited states. This is quantified by the S (Huang–Rhys) parameter. With an S of 10, the peak in the vibrational pattern occurs with ~10 vibrational quanta being excited. The amplitudes of the sideline intensities then follow a profile that is close to Gaussian. The Lorenzian lineshapes of the individual transitions is determined by the Fourier transform of their lifetimes (Figure 1). The amplitude of the electronic origin feature is initially far larger than those of the vibrational sidelines but becomes comparable at high S values

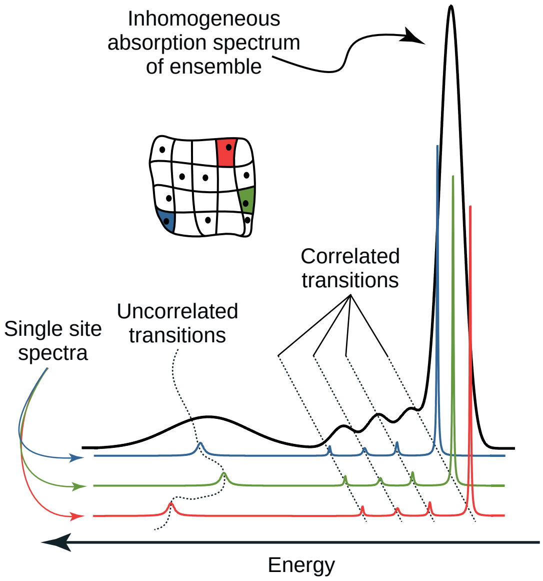

Figure 4 Schematic showing both correlated and uncorrelated transitions in an inhomogeneously broadened electronic spectrum. Each single site spectrum shows relatively narrow, homogeneously broadened features. Correlated features track with the energy of a narrow electronic origin. Noncorrelated sidelines appear at any energy within its full, inhomogeneously broadened band

single chromophore to the next, their vibrational and nuclear resonances are less affected by variations in local environments. In the case of IR spectra, vibrational frequencies are largely determined by local (bond) affects. In solution NMR, the slow timescale of the experiment leads to one well-defined resonance.

Inhomogeneous broadening is generally more extensive in solutions and glasses/polymers than in crystalline environments. Crystals usually have far better defined environments for a chromophore. Spectra of a particular chromophore that are measured when this chromophore is in a crystalline environment are usually better resolved even when taken at ambient temperatures. Proteins can exhibit well-defined binding sites for a chromophore. However, due to the inherent conformational flexibility of the protein medium, there can still be a wide variation in the configuration of this nanoenvironment, as there is in a glass.

Electronic excitations vary widely in their vulnerability to inhomogeneities. Intraconfigurational transitions such as some $d-d$ and $f-f$ transitions are examples of excitations that display relatively little inhomogeneous broadening, even in solution. The lineshape of an inhomogeneously broadened band can often be well represented as a Gaussian. This is understandable, as a Gaussian is the asymptotic shape expected when there are a number of distributive influences. There is however no particular reason why an inhomogeneously broadened band needs to have a Gaussian shape, especially when one influence dominates. There are examples[16] in which inhomogeneous distributions can even be bimodal, mimicking the presence of two separate electronic states.

One aspect of inhomogeneous broadening often not appreciated, relates to the *relative* energies of excited states. Relative energies can be strongly interdependent (correlated) or in the opposite extreme can be entirely nondependent (uncorrelated) (Figure 4). Electronic state energies are often found to be uncorrelated. This can be demonstrated via the line-narrowing techniques of laser-selective spectroscopy.[2,17,18] Spectral narrowing in the lowest excited state often leads to little energy selectivity of higher-lying states. Furthermore a noncorrelated distribution of excited state energies can lead to apparently anomalous behavior. For example, when noncorrelated excited state energy distributions overlap as in Figure 5, a fraction of the nominally identical chromophores in an inhomogeneous environment exhibit a reversed excited state energy order. This in turn can lead to a dramatic change of the emission and other characteristics of this subset.[19]

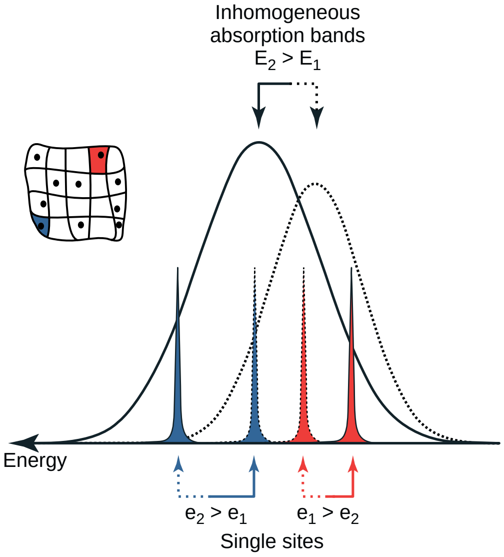

Figure 5 Schematic of overlapping, noncorrelated and inhomogeneously broadened bands E_1 and E_2. The system then has a wide range of single site energy splittings, $e_2 - e_1$. The average energy difference between the E_1 and E_2 peaks then loses much of its meaning. There becomes a substantial fraction of sites in which the relative order of the states is reversed

2.2 Transition Strengths

The probability of exciting an electronic transition with resonant light varies enormously with the nature of the ground and excited states. The rate of excitation is determined by the dipole strength, which is the square of the matrix element of the (electric dipole) operator between the ground and excited states (the dipole moment). The dipole moment reflects the change in charge distribution in passing from one state to the other. Another method of quantifying the transition strength is the oscillator strength, f. This dimensionless quantity is the ratio of the excitation rate of absorption by the chromophore compared to the excitation rate the same radiation field would induce in a free electron.

For transitions in the visible region, an excitation with $f = 1$ will arise from a transition dipole moment of magnitude ~2.5 Debye. An oscillator strength of $f = 1$ is the order of magnitude seen for an organic dye molecule. For a transition at 500 nm the radiative lifetime of such an excited state would be ~4 ns, leading to a Lorentzian linewidth of ~40 MHz or $\sim 1.3 \times 10^{-3}$ cm^{-1}. These values are appropriate to measurements in vacuo and need to be scaled by the dielectric constant of the medium in which the chromophore is embedded, in order to correct for the actual field experienced by the chromophore.

The Thomas–Reiche–Kuhn f-sum rule shows[3] that the summation of the oscillator strengths of *all transitions* in a chromophore is equal to the number of electrons. In this way, we could envisage an ''electron count'' in the same way NMR and electron paramagnetic resonance (EPR) (*see* ***Electron Paramagnetic Resonance (EPR) Spectroscopy***) techniques have a ''spin count.'' In these techniques, a very useful characteristic is that each nuclear or electron spin contributes a specific, well-defined, spectral intensity that is distributed by various couplings. In the same way, we could consider that each electron contributes specific electric dipole transition intensity. However, most electronic excitations in chromophores lie in the far UV and X-ray regions and are not practically accessible, whence the ability to ''electron count'' becomes moot.

The underlying idea that there is a specific electronic intensity that can be distributed amongst electronic excitations remains and one can refer to ''intensity stealing'' from one transition system to another. Excitations, such as nominally parity-forbidden d–d transitions, may gain a small intensity ($f \sim 10^{-6}$) by mixing with allowed transitions ($f \sim 1$). The relatively high intensity of light sources, along with the high sensitivity of detectors allow excitations of $f < 10^{-6}$ to be measured with ease. In a sense one is ''seeing'' a very small fraction of an electron.

In order to determine the intensity of an electronic-vibrational sideline, the electronic transition moment must be multiplied by an appropriate vibrational overlap factor. These factors are nuclear displacement overlap integrals and are dependent on the number of vibrational quanta present in the in the initial (ground) state as well as in the final (excited) state. They reflect the probability that the (electronic + vibrational) combinations have the same nuclear geometry. When the equilibrium nuclear displacement between ground and excited electronic states becomes larger, the likelihood of exciting numerous vibrational quanta in the excited state increases. A lengthening vibrational progression will become apparent, with the absorption maximum moving to higher energy. The integrated area of the absorption is not dependent on the nuclear displacement parameter but as the band becomes broader, the peak intensity drops (Figure 3).

The situation is somewhat different when considering the charge-transfer process between two weakly coupled assemblies.[11] Optically induced charge transfer can occur between two distinct subunits (the donor and the acceptor) that have only a limited degree of electronic overlap. However, the integrated dipole strength of the charge-transfer excitation is then *strongly* dependent on the extent of nuclear displacement in the mode that accommodates the change in size in the electron donor and acceptor upon electron transfer. Large displacements lead to a dramatic drop in the integrated dipole strength from the asymptotic value for low displacements. The *asymptotic* value of the dipole moment is simply equal to the magnitude of charge transferred multiplied by the distance between the donor and the acceptor.

2.3 Transition Polarizations

Electronic transitions occur when light interacts with a chromophore via its transition dipole moment. The latter is a vector quantity that has a specific direction. Light has directional properties, through both its propagation direction and the direction of its electric and magnetic fields. The fields are perpendicular to each other *and* to the propagation direction.

When light is linearly polarized, the direction of the oscillating electric field of the light is identified as its polarization direction. All electromagnetic radiation has a state of polarization, which may be linear, circular, (better described as helical) and more generally, elliptical. What is often called unpolarized light has a spatially or temporally modulated state of polarization. Processes of reflection by dielectric media and transmission through birefringent media change the state of polarization of light.

The transition dipole moments of a chromophore return different amplitudes of interaction when responding to light polarized in different directions with respect to the chromophore. In a chromophore with no symmetry, the direction of the transition moment associated with each excitation may take a different direction. When there is a two-fold axis, spectra that are taken with light that is polarized either parallel or perpendicular to the symmetry direction are unique. When there is a three-fold or higher axis of symmetry, the transition moment is independent of the direction of polarization in the symmetry plane.

Polarized spectra can be valuable in providing information on the symmetry of a species without requiring a detailed knowledge of their electronic structure. In crystalline environments, polarized information is inherently available, but its utility is dependent on knowing the orientation(s) of the chromophores with respect to the crystal axes. In general, it is only possible to measure polarized spectra along the symmetry axes of a crystal. These directions may differ from the directions of the transition moments of the chromophores and the spectra that are measured then need to be deconstructed into polarized spectra of the chromophores themselves.[20]

In solutions, glasses, and solubilized proteins, chromophores are usually randomly oriented. However, it is possible to obtain polarized information. This is done either by photo-selection of a subset of the chromophores, for example as can be done in spectral hole-burning,[17,18] or by orienting the chromophores. A degree of orientation of physically asymmetric chromophores may be achieved by stretching the polymer films in which they are embedded.[21] Similarly, asymmetric proteins embedded in gels can often be oriented by the creation of flows in the supporting gel medium. This process is called one or two dimensional *gel squeezing*.[22]

Vibrational sideline structure retains the polarization of the purely electronic excitation. Within the *crude* Born–Oppenheimer approximation, only totally symmetric vibrational modes are coupled to an electronic transition. Consequently, all vibrational sidelines have the same polarization as the purely electronic component (electronic origin or zero phonon line). There are two circumstances in which vibrational side-structure does not retain the same polarization as the purely electronic excitation.

Firstly, within the *full* Born–Oppenheimer (adiabatic) approximation,[7] the electronic wavefunction is not fixed but is allowed to be parametrically dependent on the nuclear coordinate. The process of Herzberg–Teller coupling can then lead to ‘‘intensity stealing’’ from other electronic states. The full symmetry of the excitation is defined by the ground and excited state symmetries *and* the symmetry of the ‘‘intensity stealing’’ vibrational mode. An example is the vibronically induced intensity of d–d transitions in centrosymmetric chromophores. These intraconfigurational excitations are electric dipole (parity) forbidden, but gain intensity when there is coupling to a non totally symmetric odd parity mode, such as the e_u mode in a chromophore of D_{4h} symmetry. A non totally symmetric displacement of the nuclei leads to the electronic state in question being ‘‘mixed’’ with odd parity electronic excited states. Transitions to the latter from an even parity ground state are dipole allowed, leading to some intensity being induced in a nominally forbidden transition. More than one mode can lead to vibronically induced intensity and each sideband can have different polarization properties. When sidebands are not resolved this phenomenon often leads to the sideband region being less polarized than the electronic origin region.

Secondly, a breakdown of the Born–Oppenheimer separability occurs in systems with strong Jahn–Teller coupling.[10] Here, a degenerate electronic state is strongly affected by a degenerate vibration, leading to intimately coupled electronic and nuclear motions. This fully *vibronic* situation (vibronic = coupled nuclear and electronic motions) is very distinct from the more usual (electronic origin + vibrational sidebands) situation, which by the above definition is *not* vibronic. In the limiting vibronic case, there is no actual excitation that can be described as purely electronic. Each eigenstate of a manifold can then be described as a *combination* of *different* electronic and vibrational components. Consequently, each level can have different polarization properties and the usual (adiabatic) meaning of a potential surface is lost. Jahn–Teller coupling applies to systems with a *spatial* electronic degeneracy, such as the ^2E_g ground state in O_h Cu(II). Note that coupling does not necessarily give rise to a distortion of such a chromophore.[23] Chromophores such as square planar Cu(II), often described as Jahn–Teller distorted, do not then retain the degeneracy of the ^2E_g (cubic) ground state and are not necessarily Jahn–Teller active. In this case, polarizations of vibrational sidelines will follow those of the electronic origin.

2.4 Temperature-Dependent Spectra

The temperature dependence of spectra can be very useful in electronic spectroscopy. First, spectra at low temperatures are often, though not necessarily, better resolved. Inhomogeneous broadening factors may not change but dephasing and vibrational relaxation processes become slower. Once the problems of low-temperature optical sample cells and the optically transparent supporting media for the chromophore are addressed, another distinct advantage in low-temperature spectroscopy of chemical systems is that unstable or reactive materials are far more stable once frozen in glass, protein, or crystal. Photochemical transformations at low temperature are also less likely, or at least slower, facilitating the possibility of the measurement of transient or metastable species. Spectroelectrochemistry is an example where the cooling of an optically transparent electrochemical cell can be of significant advantage[24] (*see also* ***Electrochemistry***).

Ambient temperatures of 300 K correspond to a Boltzmann energy of $\sim$209 cm^{-1}. The temperature of liquid nitrogen corresponds to $\sim$54 cm^{-1} and that of liquid helium only 3 cm^{-1}. Spectral features will be more noticeably changed by temperature when their width is comparable to the temperature change that is made. A relatively broad transition (300 cm^{-1} full width (at) half maximum (FWHM) at 300 K) may narrow slightly on cooling to 77 K but stay virtually unchanged on further cooling to 4 K. A band that shows some 50 cm^{-1} FWHM structure at 77 K is likely to become even better resolved at 4 K. Structure is most likely to be seen at the low-energy edge, where spectral congestion of vibrational sidelines is minimized.

Thermal contraction of the supporting medium of a chromophore becomes minimal below 100 K. This makes the temperature range between $\sim$2 K and 100 K particularly useful in both allowing good resolution in spectra along with relatively little change in the environment of a chromophore. At higher temperatures dimensional changes become significant, and these blur the more intrinsic changes in a chromophore with those changes that are induced by thermal effects of the supporting medium. This is of course particularly true when a glass softens and melts, or when a protein changes its conformation.

Besides changes in spectral widths, both the intensity and energy of electronic transitions can vary with temperature. Thermal population of vibrational excitations of the ground state will lead to increased intensity at the low-energy edge of an absorption (called *hot bands*) and a modest overall shift of the manifold to lower energies. A blue shift (to higher energy) with increasing temperature may indicate a charge-transfer excitation. When the donor and acceptor components move apart, the charge-transfer process requires more energy. In this case the intensity may also fall away as the intensity is dependent on the electronic overlap between donor and acceptor.

Interesting situations may occur when there are thermally accessible *electronic* excited states. In spin-crossover materials, low- and high-spin configurations of a *d* electron manifold are close to degenerate. However, besides different electron spin, these configurations have very different metal-ligand bond lengths. Consequently, interconversion between these configurations can be very slow. A synergy between the properties of the chromophore and its environment leads to interesting metastable states and thermal hysteresis.

There is considerable current interest in systems with optical functionality, such as optical switches, logic gates, or sensors. The utility of such devices depend critically on rather subtle balances of a range of influences, each of which ultimately needs to be addressed from a fundamental quantum mechanical perspective.

2.5 Electric Field-Dependent Spectra

It is natural to consider the effect of both applied electric fields (the Stark effect) and magnetic fields (the Zeeman effect) on electronic spectra. Chemistry is itself entirely an electromagnetic phenomenon. A basic limitation in regard to the application of the Stark effect in condensed phase samples is that the voltage which can be applied is practically limited to around 10^4 V across a sample thickness of around 0.01 cm. Beyond an applied field of $\sim 10^6\ \mathrm{V\,cm^{-1}}$, dielectric breakdown of the material occurs. This value of the external field is much smaller than the local electric fields experienced by chromophores. As a reference point, the field experienced at 10 Å from an electron in vacuo is $\sim 10^7\ \mathrm{V\,cm^{-1}}$. The electric field of $10^5\ \mathrm{V\,cm^{-1}}$ a magnitude typically achieved in an electrochromism experiment, acting on a dipole of 1 Debye ($\sim$0.2 e.Å invacuo) will experience a maximal energy shift of $\sim$1.7 cm^{-1}. This is small when compared to the inhomogeneous linewidths seen in typical spectra.

Electric field-induced effects can still be seen in condensed phase spectra by taking advantage of the high sensitivity and low noise characteristics available in optical spectroscopy. Field-induced absorption changes of $\Delta A < 10^{-6}$ can be seen in electrochromism experiments. Small changes in the transmission of a sample can be detected by a synchronous amplifier (lock-in). This is referenced to the frequency of an alternating applied electric field. These experiments are often done at low temperatures on a chromophore dissolved in a thin polymer film.[25] Both sides of the film are coated with an optically transparent electrode. Alternatively, samples such as proteins can be measured as a glassy film between two closely spaced optically transparent electrodes. A key piece of information obtainable is the value of $\Delta\mu$, which is the change in the permanent electric dipole moment of the chromophore in passing from the ground to excited states. This is extracted from the field-induced broadening of absorption bands. The magnitude of the broadening is quadratic in the applied field. When determining $\Delta\mu$ values, estimates of the dielectric constant of the medium containing the chromophore need to be made. The utility of $\Delta\mu$ as a distinctive characteristic of any excitation is of particular value in determining charge-transfer characteristics.

A novel extension to the electrochromic technique has recently been introduced.[26] This utilizes the exquisite ability of digital signal processors to measure harmonic distortion. When a purely sinusoidal modulation is made of the electric field that is applied to a sample, the higher harmonics present in the optical transmission intensity signal provide valuable and relatively easily obtainable information on dipole moments and polarizabilities of the electronic states involved.

Studies on crystals have the advantage of both narrower inhomogeneous linewidths and the characteristic alignment of chromophores with respect to the crystal axes. Thus, rather than looking at spectral broadening, which is a consequence of the random orientation of chromophores in solution, there is the possibility of directly measuring Stark shifts. When combined with the laser-selective technique of transient hole-burning, it has been possible**[27]** to directly measure $\Delta\mu$ for the lowest energy metal-to-ligand charge-transfer (MLCT) transition of $[\mathrm{Ru(bpy)_3}]^{2+}$ in a crystalline environment using an applied electric field of only $\sim$10 V cm^{-1}.

2.6 Magnetic Field-Dependent Spectra

In contrast to the difficulties with electric fields, it is possible to apply large magnetic fields, up to 8 T or more, to any sample relatively easily via the use of superconducting magnets. This ability to apply large fields is countered by the fact that magnetic interactions are intrinsically weaker. As a rule of thumb, degenerate electronic states may split by $\sim$1 cm^{-1}/T, with nondegenerate states being shifted by orders of magnitude less. The approach that is usually taken is *not* to directly measure energy shifts, but to monitor the magnetic field-induced optical polarization (the Faraday-effect) via MCD (*see* ***Magnetic Circular Dichroism (MCD) Spectroscopy***). At low temperatures, MCD can be extremely strong. Polarization modulation allows sensitivities up to $10^{-6}\,\Delta$A, providing the technique with a high dynamic range.

Again, when linewidths are narrow and/or when laser-selective techniques**[2]** can be utilized, it is possible to directly demonstrate Zeeman splittings. For example, accurate ground and excited state g-factors for the R1-line transition of $[\mathrm{Cr(ox)_3}]^{3+}$ in crystalline $\mathrm{NaMgAl(ox)_3.9H_2O}$:0.5%Cr(III) were determined using magnetic fields of only 2–16 mT.**[28]** Another example, presented in Section 4.3, is how the combination of spectral hole-burning upon the application of a magnetic field was able to quantify the distribution of low symmetry fields perturbing $[\mathrm{Cr(bpy)_3}]^{2+}$ in a glassy medium by monitoring the interplay between zero field splittings and Zeeman interactions.**[29]**

2.7 Pressure-Dependent Spectra

The magnitude of pressure effects in electronic spectra can vary over a very wide range, depending critically on both the chromophore *and* its environment.**[30]** The most dramatic effects occur when there is a pressure-dependent phase-change whereby the nature of a chromophore may be completely changed. We present an example of pressure dependence of spin-crossover processes in an example in Section 4.1.

Technology exists to measure spectra at pressures higher than 10^6 bar using diamond anvil cells. Raman and IR techniques (*see* ***Vibrational Spectroscopy***) are most often brought into play in pressure-dependent spectroscopies.**[30,31]** Temperature-dependent spectroscopy at high pressures is also possible.**[32,33]**

2.8 Statistical Nature of Light and the Limits of Detection

Studies on complex systems, such as metalloenzymes, increasingly require the measurement of a minor spectral component in a far larger assembly. Basic aspects of optical spectroscopic techniques that make them particularly effective are the speed, sensitivity, and linearity of light detectors as well as the intensity, stability, and precision of conventional and laser light sources.

Photomultipliers, charge coupled devices (CCDs) and avalanche diode detectors are able to detect single photons over the visible to near-IR range with efficiencies approaching unity. The arrival of photons at a detector is not correlated, due to the quantum nature of electromagnetic radiation. Measurements of intensity as the averaged sum of photon events has a well-defined stochastic variance associated with a Poisson distribution. This variance scales as the square root of the number of photons.

For a light source of a specific power, there is a fundamental limit to the precision to which the intensity can be determined within a specific period. This is termed the *shot-noise limit*. If n photons are accumulated, the variance is $\sqrt{n}$ and the signal-to-noise ratio (S/N) is $\sqrt{n}/n$. Any *additional* noise source (due to the amplifier, interference or detector imperfections) will degrade this value. Theoretically, shot-noise in coherently squeezed light can be slightly lower than this limit, but ultimately only by a factor of $1/\sqrt{2}$.

A 1 mW source in the visible region (a modest power for a laser) corresponds to a photon flux of 10^{15}/s. This translates to a shot-noise-limited S/N of $\sim 3\times10^{-8}$ if the measurement is made for 1 s. Dispersed light from a relatively high bandwidth (nm) lamp/monochromator combination can have power of the order $\sim\mu$W in the visible and near UV leading to a limiting S/N of $\sim10^{-6}$ for a 1 s accumulation at each spectral point.

It is possible to approach shot-noise-limited performance in many optical experiments. When light levels are low, photomultipliers serve as noise-free ‘‘quantum amplifiers’’ with a gain of $\sim10^6$. For absorption measurements, detectors with the highest quantum efficiency and uniformity of response, such as ‘‘end-on’’ semitransparent photocathode styles, are better than the high gain, opaque photocathode, low dark count types that are used for luminescence measurements. If one needs to measure absorption with a precision of $\Delta\mathrm{A}\sim10^{-3}$, then $\sim10^6$ photons need to be accumulated at each data point. At these light levels, the dark count usually may not contribute greatly to the S/N. However, in absorption measurements, it is *essential* to accurately determine the zero or ''no light'' signal level. The logarithmic nature of absorption ($A = -\log_{10}(I/I_0)$) will induce large errors in A with only a small offset in I_0.

Although light sources of modest intensity promise excellent shot-noise-limited S/N, this can be difficult to achieve in practice. Laser sources are intrinsically unstable, and rarely achieve shot-noise-limited intensity stability. Even with sophisticated external stabilization techniques, stabilities better than $1{:}10^4$ are difficult to achieve. Arc lamps such as Xe or D_2 lamps are also intrinsically unstable at acoustic frequencies. It is however possible to stabilize an incandescent source such as a halogen lamp to $1{:}10^6$ through careful design.[34,35] When a chopper/lock-in amplifier combination is used for transmission measurements, it is important to recognize that the noise output of a light source can be very dependent on the modulation frequency at which the measurements are made. A chopper is used to determine the zero light value and/or to provide a reference beam, but its operating frequency should be chosen so that excess noise of the *source* at this frequency is minimal. Operation at electrical power frequencies or their harmonics should also be avoided. Signals at other frequencies may not actually distort the spectrum but they can add substantial noise. The rotational stability of many light choppers can also limit the available S/N.

Shot-noise-limited performance can be conveniently recognized by noting how the S/N of a system changes with light level. The S/N should vary quadratically with intensity if it is shot-noise-limited. Once a measurement is determined to be shot-noise-limited, the quantification of the noise[36] amplitude provides a simple, direct, and effective way to estimate the actinic flux experienced by a sample during a measurement.[37]

The use of an array detector bypasses some of the problems associated with the short-term stability of a source. An entire spectrum is accumulated in parallel and to first order, each wavelength is averaged in the same way. However, reference spectrum measurements may suffer due to longer-term stability issues. With array detectors, the precision of the analog-to-digital conversion process, often providing only 12 or 16 bits, will limit the S/N to 1×10^{-4} and $7 \times 10^{-6}\Delta A$ respectively.

When using photodiodes, the amplifier that is used in conjunction with the detector often adds excess noise. This can be reduced by the use of a low capacitance detector and a well designed detector/amplifier combination. Photodiodes are able to operate at far higher light levels than photomultipliers, and also have the advantage of higher quantum efficiencies. In addition, photodiodes operate over wider wavelength ranges than photomultipliers and are not as easily damaged. Consequently they are well placed to provide distinctly superior performance *unless* the amplifier noise exceeds the intrinsic shot-noise. In a conventional current-to-voltage amplifier circuit, shot-noise can only exceed the internal (Johnson) noise of the amplifier when the output of the amplifier is >50 mV.[36] With diode detection, it is important that the signal output be kept above this level if possible. Again, a simple test of shot-noise performance is by the determination of the (quadratic) dependence of the S/N versus the light level.

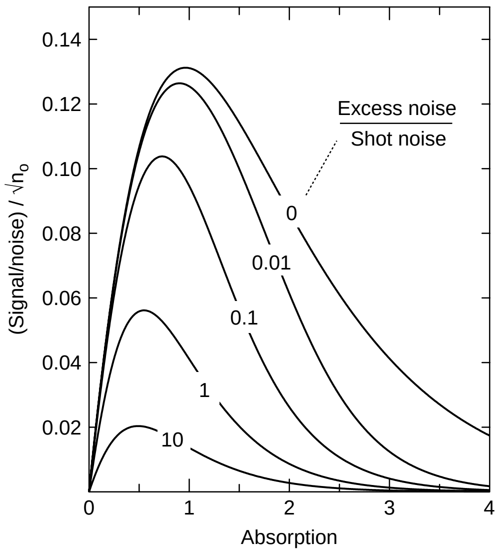

Figure 6 Signal-to-noise of a measurement provided as a function of the absorption of a chromophore. When excess electronic noise in the measurement system becomes comparable to the photon shot-noise, better data can be obtained by adjusting the absorption to lower values. (Drawn from data in Krausz[34])

When shot-noise is the limiting noise characteristic, the optimum S/N in an absorption measurement (and entirely equivalently in CD/MCD measurements of ΔA; *see* ***Circular Dichroism (CD) Spectroscopy***; ***Magnetic Circular Dichroism (MCD) Spectroscopy***) is obtained when the concentration and pathlength of a sample is adjusted to provide an absorption of $A \sim 0.9$.[34] The overall S/N then only degrades slowly as the absorption is increased, except that above $A \sim 3$, stray light often limits the accuracy of the measurement. When amplifier and other noise sources become significant, the optimal absorption is *always* lower than 0.9 (Figure 6). Not only does the optimal absorption reduce, but the S/N also degrades far more rapidly at higher absorptions compared to the shot-noise-limited situation. In circumstances in which shot-noise is *not* the limiting factor, better results may be obtained using a *lower* absorption sample, either by using a lower concentration or a shorter pathlength cell.

3 TECHNOLOGIES

3.1 Light Sources

The three most common conventional sources used in electronic spectroscopy are the quartz-halogen incandescent source (Vis-Near IR), Xe (UV-Vis-Near IR), and D_2 (UV) arc. In spectroscopic applications, the power of a source is far less important than its brightness (spectral irradiance) and its stability. Halogen lamps are the most stable and also have the smoothest spectral output. They have comparable output to a xenon arc at wavelengths longer than 500 nm. A quartz-halogen lamp however, has far lower output than a xenon arc in the blue and UV regions. A deuterium lamp has comparable output to a xenon lamp near 200 nm but its output falls rapidly at lower energies and only puts out as much as a quartz-halogen lamp near 300 nm. Its utility is limited to the UV region and like the xenon arc suffers from intense emission lines in addition to the background continuum.

Laser sources[38] are essentially monochromatic and have enormously higher spectral irradiance than conventional sources. However, the tuning range of laser systems is usually limited and/or cumbersome. Their intensity stability is also problematic, as mentioned in previous sections. Lasers based on dyes dissolved in solvents may have a tuning range of ~20–50 nm before an alternative dye is required and laser diodes exhibit a narrower tuning range of 2–5 nm. Laser diodes operating at some wavelengths are not currently available. A uniquely versatile, widely tuneable laser source is the Ti:S (titanium sapphire) laser, which can operate over an exceptionally wide range from 700 nm to beyond 1000 nm. There are other broadly tuneable sources in the near-IR such as color center lasers.[38]

Broad tuning of a monochromatic source over an extended range has become possible by developments in optical parametric oscillators (OPOs). These devices are highly nonlinear, light-driven oscillators. They are not lasers themselves, but are powered by high intensity pulsed lasers of either nanosecond or femtosecond duration. OPOs can, with the interchange of some optical components, be tuned over a very wide wavelength range ($<$200 nm to $>$2000 nm). Operating as extremely intense nonlinear devices, they are prone to both instabilities and damage to their optical components. The extremely high intensities inevitable in such pulsed sources are likely to induce both unwanted nonlinear effects,[39] as well as photochemical damage in condensed phase samples, especially if the light is focussed on the sample. Experiments performed with such devices should be made with this caveat in mind.

Passing a femtosecond laser through a medium such as glass or sapphire can produce a collimated and very convenient (pulsed) continuum light source (400 nm to 16 000 nm) of high brightness via the optical Kerr effect. Alternatively, inserting such a pulse into a short length of highly nonlinear photonic fiber can also be used to enhance and tailor such a ''super-continuum.'' Using such sources, an entire broadband electronic spectrum can be accumulated, potentially from a single femtosecond pulse. This capacity greatly enhances ultrafast transient and excited state spectroscopies.[40]

A number of synchrotrons worldwide have been constructed to serve as light sources. They utilize the continuum radiation streaming from an accelerated electron beam in a large accelerator storage ring. Radiation appears in a broad continuum and can be optimized for operation in many segments of the electromagnetic spectrum from X-ray to IR regions. Light is typically delivered as nanosecond pulses. The repetition rate is widely variable, allowing time-resolved information to be gained. Selected beam lines are dedicated to electronic spectroscopy, particularly for use in the UV and IR regions (BESSY Berlin, Elettra Trieste, ALS Berkeley). A synchrotron source is indeed intense. Although it is nowhere near as intense as a laser, it is well collimated, polarized, and stable, providing a uniquely capable broadband source. Its advantages of intensity and wide tuneability make it especially useful in critical spectroscopic applications.

3.2 Light Detectors

Recent developments in light detectors over the entire region from UV-Vis to near-IR have been of significant benefit to electronic spectroscopy. There have been improvements and enhancements of more traditional single element detectors such as photodiodes and photomultipliers as well as more dramatic advances in multielement detectors such as CCDs.

Improvements in photomultipliers have been incremental, with the notable exception that photocathode materials have been developed that are sensitive to 1.6 µm. This is a very considerable extension to the previous limit of 1.1 µm. This means that the characteristics of high speed, high gain, and large sensitive area that are intrinsic to these devices are now available much further into the near-IR region. A parallel advancement has been in the development of InGaAs and related photodiodes and avalanche photodiodes. These have excellent quantum efficiencies into the 0.8–2.2 µm region. These devices also have excellent electrical characteristics, especially in speed when compared to previous near-IR detectors operating beyond the limit of Si diodes (~1 µm). They provide good performance even when operated at room temperature. Cooling such devices does however improve their electrical characteristics as well as lowering their dark current.

A key attribute of any detector, enabling it to have high sensitivity and high speed along with low noise is that it must have low electrical capacitance. This can often only be achieved by using a very small ($<$1 mm diameter) diode. This restriction makes it difficult to collect and utilize the entire measurement beam in many applications. Photomultipliers are inherently low capacitance devices, but it is much more difficult to minimize the junction capacitance of photodiodes. Some types of large area avalanche photodiodes can provide low noise along with a reasonable frequency response via manufacturing procedures that minimize the junction capacitance.

Dramatic improvements have occurred in the technological development of multisensor arrays. High performance, cooled, back-illuminated silicon-based CCDs can have quantum efficiencies between 0.3 and 0.9 throughout the range from 200 nm to 1 μm. Dark counts are as low as 1 electron per pixel per h, making this effect practically negligible. The readout noise can also be engineered to be minimal, having a value of a few electrons. This allows CCDs to operate close to the shot-noise limit, even at low light levels. New devices have been developed that incorporate an avalanche diode structure before the CCD architecture. This allows higher gain, along with higher speed and essentially single-photon detection. Effective, cooled InGaAs-based cameras have also been developed to perform at a high level. These extend the spectral range of multielement sensor spectroscopies to 1.7–2.2 μm.

3.3 Light Discriminators and Systems

Traditionally, prisms and diffraction gratings have served as dispersive elements, with diffraction gratings being more versatile and providing higher resolution. Holographically generated diffraction gratings have advantages in producing lower stray light than conventionally ruled gratings and have the ability to be created on curved surfaces. Classically ruled gratings provide the highest efficiencies. For absorption experiments, especially those made in the UV, the presence of ‘‘stray light’’, that is, light in the measurement beam that is not at the wavelength specified by the discriminator, is an important limitation. Previous generation dual-beam spectrometers often used a combination of a prism monochromator linked with a grating monochromator. This combination provided exceptionally low stray light characteristics and allowed samples of very high absorption (up to ∼6) to be reliably measured. Except for CD spectrometers, which typically have two prism monochromators operating in tandem, grating-based spectrometers are now more common.

A Fourier Transform interferometer, often used in the infrared (the fourier transform infra-red (FTIR) technique; *see* ***Vibrational Spectroscopy***) does away with the need for a dispersive element, effectively measuring all wavelengths in parallel. Greater mechanical precision of the interferometric arm is needed to maintain good resolution in the UV-visible region compared with the IR region. The dynamic range of the instrument is determined by the precision of the analog-to-digital conversion of the light intensity and can be a limiting factor.

A very wide range of lasers, optical and electro-optic systems and components are becoming increasingly available and affordable through the ongoing revolution in photonics. For example, there is now a wide range of nonabsorptive filters, constructed using multilayer (interference) and holographic techniques that are able to reject or pass a particular wavelength or range of wavelengths with high efficiencies. There are also electro-optic tuneable filters, shutters, and intensity and polarization modulators.

Fiber optic-based systems can be readily configured and employed along with miniaturized spectrometer systems. Although such systems may not have the ultimate performance of a classical system they can be very useful and are particularly compact and transportable. Prototype systems and ‘‘virtual experiments’’ can be tested and optimized before construction by using commercial optics simulation packages. When these capacities are combined with the availability of flexible, high-level computer program packages with the capacity to intelligently control a rapidly assembled, multicomponent system, as well as display data in real time, a wide range of targeted ‘‘designer’’ optical experiments become imminently feasible. A further advantage of having a flexible system of this kind is that several types of measurements (absorption, excitation, or CD spectra, for example) can be performed, sometimes simultaneously, on one sample and taken under the same conditions. This is important for bioinorganic systems where there is often unavoidable sample variability or a limited amount of protein material.

3.4 The Optically Transparent Supporting Medium

When a chromophoric system can be dissolved in a transparent solvent and the absorption of interest adjusted to the optimal value of ∼0.9, optimal spectra can be readily obtained. Many proteins and other systems may be dispersed in a medium by detergent treatment or mulling when they are not sufficiently soluble. However, when the particle size of the dispersion becomes comparable to the wavelength of light used, there will be light scattering from the sample, evidenced by a degree of turbidity. This will give rise to characteristic apparent background absorption of the sample, increasing to shorter wavelengths. This scattering tail is sometimes modeled by the scattered light intensity provided by a Rayleigh ($1/\lambda^4$) functionality. However, apparent absorption due to scattering from either the supporting medium or the dopant chromophores will not, in general, follow this form precisely.

In addition to an apparent absorption background due to light scattering, the absorption spectrum of the dopant chromophore will be distorted by a ‘‘flattening’’ effect.**[41]** Regions of high optical absorption will display an apparent decrease in absorption, distorting the lineshape and creating deviations from Beer’s law. The scattering background and associated absorption artefacts in optical spectra can be reduced by collecting a maximal solid angle of the light transmitted through a sample. Essentially a large fraction of the scattered light is then detected and thus does not contribute to an apparent absorption of the sample. This is achieved either by placing a large area detector very close to the sample and/or installing appropriate collection optics. Residual ‘‘flattening’’ artefacts can be corrected when the size, shape and distribution of the scattering particles can be estimated.**[41]**

Chromophores can be supported in a wide range of solid solutions, microstructures and nanostructures.

Many transparent crystalline materials can incorporate chromophores, either substitutionally or interstitially. If sufficiently soluble, a chromophore may also be dissolved in a polymer film such as polyvinyl alcohol or polymethylmethacrylate. Incorporation of a chromophore can be achieved by dissolving the chromophore and polymer in a solvent. A suitable film is then quite simply created by evaporation of the solvent. Other types of supporting media are sol-gels. When a chromophore is present in the reaction medium, a rigid sol-gel embedded with the chromophore can be created.

Ionic polymers such as sulfonated teflons offer transparent media able to incorporate ionic species to very high concentrations.[42] The technique routinely used to make IR samples, where KCl and KBr discs are created by pressing a coground powder of the supporting material and compound at high pressures, can be extended to electronic spectroscopy. If the halide salt and material to be dispersed are kept particularly dry and are carefully ground, discs of good optical transparency in the UV-visible region can be created. With this grinding and pressing technique there is a danger that inadvertent solid-state chemistry occurs during the grinding and pressing procedures of sample preparation.

Condensed phase samples are useful in a range of experiments, especially for those performed at low temperatures. Perhaps the most common procedure is to use a solvent or mixture of solvents that form an optically transparent glass upon freezing. There is a range of solvents and mixtures that have found utility for different types of chromophores and some are presented in Table 1. Glassing mixtures are often freeze-thaw pumped to remove residual gases. Ethanol/methanol glasses benefit from being saturated with argon prior to freezing. The quality of the glasses that are obtained is strongly dependent on the rate of cooling, the purity (sometimes dryness) of the solvents, the concentration of the dopant, and the type of cell used. As well as creating background scatter, glass formation can also lead to cracks and/or severe strain in the sample. It is important to remember that glasses themselves are metastable and undergo transformations on a very wide range of timescales. This may lead to changes in their physical characteristics (scatter, strain), as well as spectral shifts and changes in the embedded chromophores, while experiments are being performed. The illumination of a glassy sample may itself lead to changes in the glass characteristics.

It is sometimes difficult to recognize if a sample is truly a solid solution or a fine dispersion of particles. If the solubility of the chromophore in the supporting medium is limited, it is important not to saturate the glassing mixture, as precipitation of the dopant will tend to occur upon cooling. It is not always apparent when this happens. If the precipitant is finely dispersed, its presence in a medium that by itself has substantial scatter may not be obvious.

A final caveat is with respect to any polarized experiments (linear or circular) that are contemplated on solid solutions. Many solid solutions such as polymer films or glassed solutions are prone to strain-induced birefringence. Birefringence modifies the polarization of the incident beam. This can seriously degrade the precision of a measurement, and furthermore the effect is neither spatially uniform nor necessarily constant during an experiment. A useful visual check is to view the sample between crossed polarizers. If there are no obvious bright areas in the field of the sample then useful polarized experiments can probably be performed.

3.5 Sample Cells and Sample Handling

Some of the more interesting systems studied in inorganic and bioinorganic spectroscopy may be unstable as well as air, heat, light, moisture or temperature sensitive. Procedures and protocols are required to accommodate for

Table 1 Table of some useful low temperature glass-forming solvents and solvent mixtures. Mixtures are specified by volume ratios

Glassing Medium	Quality	Typical Application
4:1 ethanol/methanol	Good	alcohol soluble
glycerol	Fair	alcohol soluble
polyethylene glycol	Fair/Poor	alcohol/polymer
polyamide	Good	protein gel medium
polysiloxane	Fair	inert medium
1:1 ethylene glycol/water	Medium	water soluble
3:2 glycerol/water	Fair	Proteins
1:1:3 ethylene glycol/glycerol/water	Good	Proteins
1:1 saturated sucrose/water	Good	Proteins
9M LiCl	Fair	high ionic strength
1:1 ethanol:ether	Fair	alcohol/ether soluble
2-methyl tetrahydrofuran	Fair	ether soluble
4:5 propionitrile/butyronitrile	Good	nitrile soluble
2:1:1 ether/ethanol/toluene	Good	mixed solvent soluble
3-methyl pentane	Good	hydrocarbon soluble
1:4 isopentane/methyl cyclohexane	Good	hydrocarbon soluble
5:2:2 ether/isopentane/ethanol (EPA)	Good	mixed solvent soluble

these characteristics and sensitivities to ensure reliability and quality of the electronic spectra that are recorded. It can be useful to construct a simple locking system in which a sensitive sample can be kept in a controlled environment while being transferred into and out of an apparatus. Samples such as photosynthetic reaction centers, which are extremely light sensitive, may need to be prepared and mounted under near-IR light (900 nm) using a night vision apparatus before being transferred to a light-tight lock and introduced into the spectrometer.

Measurement procedures using solutions in standard cuvettes are well developed. Some condensed phase samples such as large crystals and polymer films are relatively robust and easily mounted. Two areas of interest which have led to innovation are in the mounting of small, environmentally sensitive, single crystals and in the sample cells used for frozen glasses, particularly those having a substantial aqueous phase, such as proteins.

Electronic spectroscopy of single crystals often requires the use of small crystals, either because larger crystals are not available, or because larger ones are too optically dense. Crystals of proteins are characteristically soft, difficult to manipulate, and need to be kept in a humidity-controlled environment. It is however possible to measure polarized, well-resolved, low-temperature absorption spectra of small crystals while sealed in a small X-ray capillary as is exampled in Section 4.4. This approach can bypass both handling and sensitivity issues. A mask can be put above and below the capillary at the point at which the crystal is located, creating a light guide for the measurement beam. Although the overall throughput is small, the sensitivity of optical techniques allows the accumulation of good quality data, as the crystals themselves often have good optical transparency (i.e. low scatter).

Low-temperature glasses can place significant demands on the design of sample cells, especially when used with the aqueous media required by biological samples. Fused quartz cells, such as cuvettes, have excellent transmission characteristics, low thermal expansion, and are reasonably robust. However, attempts to freeze glasses with significant water content often leads to breakage of the cell. Another problem that arises is that small gaps can appear between the frozen glass and window material. This gives rises to wavelength dependence in transmitted light appearing as an oscillatory pattern, due to etaloning. This can severely limit the utility of the data.

The useful pathlength of aqueous glasses is limited to ∼1–2 mm due to increasing scattering losses and uneven glassing through the sample. If a chromophore can be made more concentrated, significantly better data are obtainable from shorter pathlength cells, as scattering losses are reduced. Short pathlength (0.1–0.2 mm) cells are preferable but normal ‘‘single piece’’ designs (Figure 7) are difficult to fill and clean, often fracture, and are prone to strain birefringence. The ‘‘O-ring’’ design contains the glassing solution within a neoprene ring squeezed between two windows. Filling is accomplished by injecting the solution through the ring, while extracting the captive air with a second needle.

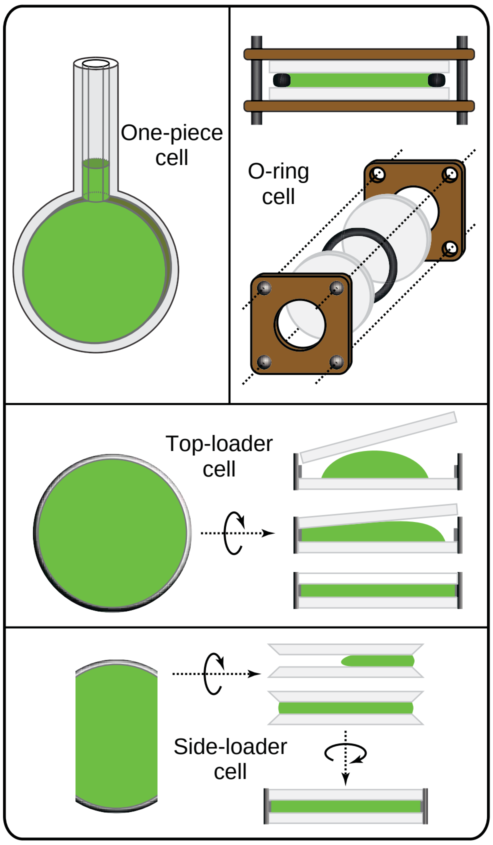

Figure 7 Designs of optical cells used in the low-temperature spectroscopy of glassy solutions

Alternative structures that largely eliminate the strain birefringence that is inherent in these designs are the ‘‘top-loading’’ and ‘‘side-loading’’ cells (Figure 7). In the top-loading cell, the bottom window is bonded to a metal ring and spacer. A calibrated volume of glassing solution is placed on it and the top window gradually angled on and fitted, excluding any air pockets. The top window effectively ‘‘floats’’ and this eliminates strain and breakages due to thermal expansion. The side-loading cell is constructed of two quartz windows, bonded to metal sections providing a fixed spacing and some strain relief. The glassing solution is wicked in from the side with a syringe and is held in the cell by surface tension. This design allows for rapid filling of a cell. This style cell can be thermally cycled to room temperature and re-glassed with good reproducibility. The metal spacers are sufficiently thin to allow strain associated with differential thermal expansion to be relieved.

When samples are unstable, or intermediates need to be studied, fast freeze techniques have been developed[43] to enable the study of reactive and unstable systems (*see* ***Freeze-Quench Kinetics***).

4 PRACTICAL EXAMPLES

4.1 Pressure Dependence of Fe(II) Spin-Crossover System

Fe(II) spin-crossover compounds are an interesting class of materials in which the low-spin $^1A_1$ state is close in energy to the high-spin $^5T_2$ state of the d^6 Fe(II) configuration. The spin-crossover process can be induced thermally or optically. The physical properties of the high-spin and low-spin states are very different. In particular, the change in volume between the two states is $\sim$25 Å^3. Consequently, a significant pressure dependence of the high-spin to low-spin conversion might be anticipated. The mixed crystal system $[\mathrm{Zn}_{1-x}\mathrm{Fe}_x(\text{6-mepy})_3\mathrm{tren}](\mathrm{PF}_6)_2$ ($x = 0.0005$) was studied[44,45] at 6 K in the pressure range from 1 bar to 27 kbar (Figure 8). The spin-crossover rate was found to change by the very large factor of $\sim 10^9$. These data, as well as temperature-dependent data on the spin-crossover rate allowed a number of thermodynamic properties to be determined.

The experiment was performed with one laser used to excite the conversion to the high-spin state and a second to monitor the relaxation back to the low-spin state. This approach allowed measurements over the wide dynamic range from nanoseconds to seconds. Pressures up to $\sim$1 kbar were performed with a helium pressure cell and those at higher pressures with a diamond anvil apparatus.

4.2 Electroabsorption in $[\mathrm{Ru(bpy)_3}]^{2+}$

The emitting levels of Ru(II) and Os(II) tris-immine complexes are relatively long lived metal-to-ligand charge-transfer (MLCT) states. These complexes, and their derivatives, exhibit a wide range of fascinating photophysical, photochemical, and spectroscopic[46,47] phenomena and consequently are of continuing interest and utility. A question that has often been raised is that of delocalization. Are the MLCT excited states best described as involving electron donation to a single immine ligand or all three ligands?

The electrochromism spectrum of the visible absorption region of $[\mathrm{Ru(bpy)_3}]^{2+}$ recorded in a PVA polymer film exhibits a second derivative pattern (Figure 9) indicative of an excitation with a substantial $\Delta\mu$. A symmetric excitation of all three ligands leads to no excited state dipole moment. Electrochromism spectra of mono-immine complexes were also found to be similar to the tris-immine parent complex.[48] These results were taken as evidence for localization in the symmetric complexes.

It was later shown[49] that the E state of a degenerate MLCT in D_3 point symmetry will however show a second derivative pattern of electrochromism of comparable magnitude to that observed for the localized case. This is

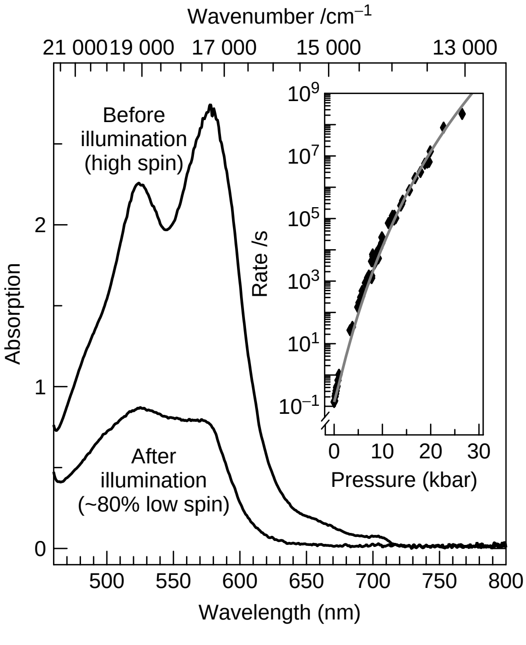

Figure 8 Absorption spectra at 6 K of $[\mathrm{Zn}_{1-x}\mathrm{Fe}_x(\text{6-mepy})_3\mathrm{tren}](\mathrm{PF}_6)_2$ ($x = 0.0005$) crystal taken before and after illumination with 514 nm light, leading to $\sim$80% of Fe(II) centers being converted to the low-spin state. The inset shows the pressure dependence of the high-spin to low-spin conversion rate as a function of pressure (points) and a modeled dependence using the Grüniesen approximation (Drawn from data in Wang *et al.*[44] and Hauser *et al.*[45])

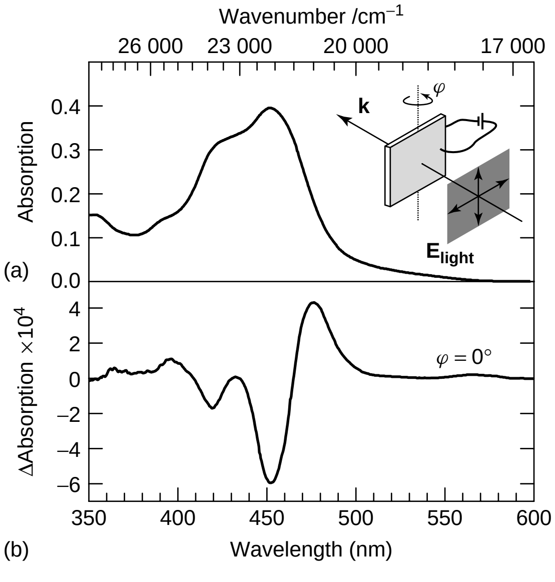

Figure 9 Absorption spectrum (a) and electrochromism (b) of $[\mathrm{Ru(bpy)_3}]^{2+}$ dissolved in a thin polymer film at 77 K. Absorption and electrochromism spectra are taken through semitransparent conducting electrodes. Electrochromism is usually measured with the externally applied electric field parallel to the propagation direction **k** of light ($\varphi = 0°$). Experiments can also be made with the film tilted away from the normal to the propagation direction (Drawn from data in Oh and Boxer[48])

because the degenerate charge-transfer E state splits in an applied electric field. Although both delocalized and localized descriptions of the MLCT excitations give rise to comparable electrochromism, its magnitude as a function of the angle between the applied electric field and the plane of the electric field of the light, is distinctly different. The data here suggest that the intense ^{1}MLCT excitations seen in absorption are best described as delocalized. This conclusion agrees with polarized single crystal absorption data.[50] The far weaker ^{3}MLCT emitting states are widely accepted as being localized.[47]

4.3 Zeeman Hole-Spreading in $[Cr(bpy)_3]^{3+}$

Although Cr(III) systems typically show sharp $^4A_2 \rightarrow {}^2E$ intraconfigurational R-line transitions, the nominally trigonal complex $[Cr(bpy)_3]^{3+}$ dissolved in glycerol exhibits unresolved R-line structure near 730 nm.[29] Persistent spectral holes burnt in the R1 component at low temperatures establish that the correlation between R1 and R2 components of the ^2E excited state is weak. The average splitting is 67 cm^{-1}, but there is clear evidence for a significant spread in local fields that determine the R1-R2 splitting. Spectral holes burnt into the R1-line show a distinctive ‘‘hole-spreading’’ and apparent splitting in an applied magnetic field of only 0.1–0.2 T (Figure 10). Under these conditions the zero field splitting of the $^4A_2$ state and the Zeeman splittings are comparable.

By analyzing the Zeeman pattern at various field strengths, it was possible to establish that the nominal trigonal field in this D_3 complex was perturbed by lower symmetry components due to the local environment. A major influence was attributed as most likely arising from a tipping of the bpy ligands.

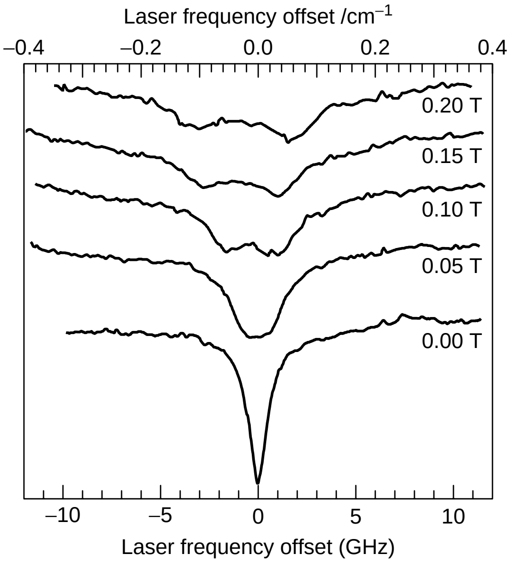

Figure 10 High-resolution excitation spectra of a persistent spectral hole burnt near 730 nm into the R1 line of $[Cr(bpy)_3]^{2+}$ dissolved in glycerol, recorded at 2 K. Spectra are shown as energy shifts with respect to the wavelength at which the hole was burnt and as a function of applied magnetic field in a range in which zero field splittings and Zeeman splittings of the ground state are of comparable magnitude. An analysis of this ‘‘hole-spreading’’ provides information on the low-symmetry fields acting in an amorphous environment (Drawn from data in Riesen *et al.*[29])

4.4 The Blastochloris viridis Reaction Center

Bacterial reaction centers crystallize readily, providing high-resolution X-ray data and structural information. Photoactivation of these crystals leads to structural changes that can be monitored in time-resolved X-ray experiments. In order to be able interpret these changes, it is important to know the actual extent and kinetics of photoactivation of the *crystallized* reaction center. It has been possible[51] to measure polarized single crystal data in the near-IR region on crystals of the same size (~200 µm) and contained within the same 1 mm capillary tubes as were used in the X-ray experiments.

The spectrum of the photogenerated cation P^+, absorbing near 1.2 µm, is shown in Figure 11. Measurements were made utilizing a small area InGaAs diode. Although the peak OD is <0.2, good sensitivity was obtained. The amplitude of this signal, as a function of both illumination and time, provided quantitative yields and kinetics of photoactivation processes. Measurement of the P^+ band in the near-IR region (which is itself not photoactive) had a significant advantage

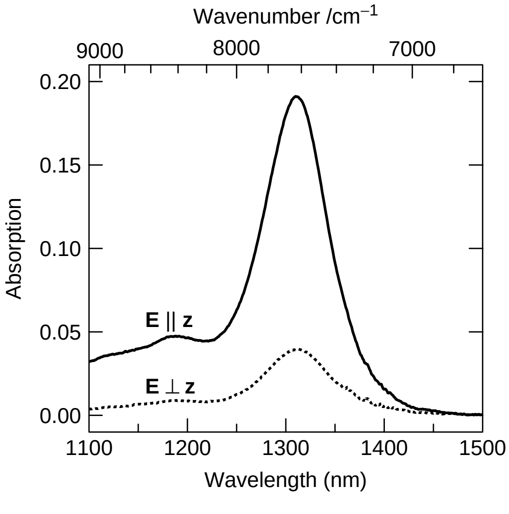

Figure 11 Polarized room temperature near-IR absorption spectra of a *Blastochloris viridis* bacterial reaction center single crystal of ~200 µm thickness. Spectra were taken with the crystal encapsulated and preserved in a thin-walled capillary while illuminated with a 633 nm HeNe laser. The spectral band seen near 1300 nm is of the photogenerated bacteriochlorophyll special pair cation P^+. The amplitude of this peak allows the extent of photoconversion of the sample and its kinetics to be directly monitored (Drawn from data in Baxter *et al.*[51])

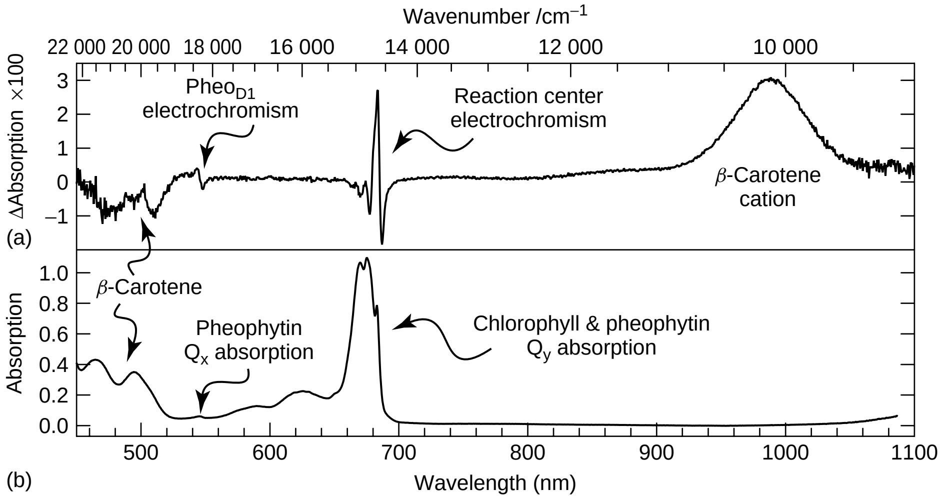

Figure 12 (a) is the absorption spectrum, taken with a single 100 ms frame on a CCD spectrograph, of an oxygen-evolving PSII core complex[52,53] at 5 K in a 40% 1:1 ethylene glycol/glycerol glass. This spectrum was taken before any illumination of the sample, leaving the plastoquinone in its neutral configuration. Also presented (b) is the difference between this spectrum and one taken immediately after illumination of the sample. This illumination served to quantitatively convert the plastoquinone to its anion. Electrochromic shifts induced on the active pheophytin$_a$ (Pheo$_{D1}$) transitions near 685 nm and 556 nm due to the electric field of the anion are accompanied by oxidation of β-carotene to its cation. (Drawn from data provided by Dr. Ronald Steffen)

compared to measurements of depletions in the P band absorption near 970 nm. Such measurements are prone to actinic effects associated with the measurement beam itself, due to the high quantum efficiency of the photoconversion process.

4.5 Low-Temperature Photochemistry in Photosystem II

Photosystem II (PSII) is a complex metallo-enzyme responsible for the light-induced oxidation of water and reduction of plastoquinone. Through its unique ability to extract electrons from water, it powers almost all life on earth. The minimal assembly able to oxidize water is a PSII core complex. This assembly incorporates a large number of interactive redox active pigments and metal centers, as well as two integral proximal antenna proteins CP47 and CP43. Attempts to simplify this minimal assembly affect its basic functionality. The multiple electron pathways that are available, combined with considerable spectral congestion and photoconversion quantum efficiencies that approach unity makes a PSII core an extremely demanding system to investigate spectroscopically.[52,53]

Figure 12 shows low-temperature absorption spectra of a PSII core complex prepared from spinach. These spectra cover a wide spectral range with good resolution, and were recorded using a single 100 ms exposure on a spectrograph based on a high performance back-illuminated and cooled CCD. Incident light levels were such that photochemical processes with yields close to unity were not significantly advanced. Spectra taken before and after a deliberate (but low intensity) illumination reveal depletions of the absorption of centers undergoing photoinduced redox transformations and also identify their photoproduct absorptions. Electrochromic shifts on pigments close to the photo-reduced plastoquinone are clearly identifiable.[37,52,53] The wide spectral range, high speed and high sensitivity of this apparatus allow the quantitative determination of the yields of redox processes, and the ability to track electron transfer pathways in PSII.

5 ABBREVIATIONS AND ACRONYMS

CD = circular dichroism; CCD = charge coupled device; EPR = electron paramagnetic resonance; FTIR = fourier transform infra-red; FWHM = full width (at) half maximum; MCD = magnetic circular dichroism; MLCT = metal-to-ligand charge-transfer; NMR = nuclear magnetic resonance; OPOs = optical parametric oscillators; PSII = photosystem II.

6 REFERENCES

1. T. Basché, W. E. Moerner, M. Orrit and U. P. Wild eds., ‘Single Molecule Optical Detection, Imaging and Spectroscopy’, VCH Publishers, Weinheim, 1997.

2. E. Krausz and H. Riesen, in ‘Inorganic Electronic Structure and Spectrosopy’, ‘Vol. 1: Methodology’, eds. E. I. Solomon and A. B. P. Lever, Wiley-Interscience, New York, 1999, p. 307.
3. P. W. Atkins and R. S. Friedman, ‘Molecular Quantum Mechanics’, Oxford University Press, Oxford, 1997.
4. C. R. Cantor and P. R. Schimmel, ‘Biophysical Chemistry Part II: Techniques for the Study of Biological Structure and Function’, W. H. Freeman and Company, San Francisco, 1980.
5. B. Di Bartolo, ‘Optical Interactions in Solids’, John Wiley & Sons, New York, 1968.
6. B. Henderson and G. F. Imbusch, ‘Optical Spectroscopy of Inorganic Solids’, Clarendon Press, Oxford, 1989.
7. S. B. Piepho and P. N. Schatz, ‘Group Theory in Spectroscopy with Applications to Magnetic Circular Dichroism’, Wiley-Interscience, New York, 1983.
8. C. Cohen-Tannoudji, F. Laloë and B. Diu, ‘Quantum Mechanics’, John Wiley & Sons, New York, 1977.
9. R. Loudon, ‘The Quantum Theory of Light’, Oxford University Press, Oxford, New York, 2000.
10. I. B. Bersuker, ‘The Jahn–Teller Effect and Vibronic Interactions in Modern Chemistry’, Plenum Press, New York, 1984.
11. K. Y. Wong and P. N. Schatz, *Prog. Inorg. Chem.*, 1981, **28**, 369.
12. Z. Gasyna and P. N. Schatz, *J. Phys. Chem.*, 1996, **100**, 1445.
13. J. R. Reimers and N. S. Hush, *J. Am. Chem. Soc.*, 2004, **126**, 4132.
14. S. B. Piepho, E. R. Krausz and P. N. Schatz, *J. Am. Chem. Soc.*, 1978, **100**, 2996.
15. S. J. A. van Gisbergen, J. G. Snijders and E. J. Baerends, *Comput. Phys. Commun.*, 1999, **118**, 119.
16. H. Riesen and E. Krausz, *J. Chem. Phys.*, 1992, **97**, 7902.
17. H. Riesen, *Struct. Bonding (Berlin)*, 2004, **107**, 179.
18. H. Riesen, *Coord. Chem. Rev.*, 2006, **250**, 1737.
19. E. Krausz, J. Higgins and H. Riesen, *Inorg. Chem.*, 1993, **32**, 4053.
20. M. A. Hitchman and M. J. Riley, in ‘Inorganic Electronic Structure and Spectrosopy’, ‘Vol. 1: Methodology’, eds. E. I. Solomon and A. B. P. Lever, Wiley-Interscience, New York, 1999, p. 213.
21. A. Rodger and B. Norden, ‘Circular Dichroism and Linear Dichroism’, Oxford University Press, Oxford, 1997.
22. I. A. Abdourakhmanov, A. O. Ganago, Y. E. Erokhin, A. A. Solov’ev and V. A. Chugunov, *Biochim. Biophys. Acta*, 1979, **546**, 183.
23. L. Dubicki, M. J. Riley and E. R. Krausz, *J. Chem. Phys.*, 1994, **101**, 1930.
24. J. A. Crayston, in ‘Instrumentation and Electroanalytical Chemistry’, ‘Vol. 3 in Encyclopedia of Electrochemistry, Series’, eds. A. J. Bard and M. Stratmann, ed. P. R. Unwin, Wiley-VCH, Weinheim, 2003, p. 491.
25. G. U. Bublitz and S. G. Boxer, *Annu. Rev. Phys. Chem.*, 1997, **48**, 213.
26. K. Lao, L. J. Moore, H. Zhou and S. G. Boxer, *J. Phys. Chem.*, 1995, **99**, 496.
27. H. Riesen and E. Krausz, *Chem. Phys. Lett.*, 1993, **212**, 347.
28. J. L. Hughes and H. Riesen, *J. Phys. Chem. A*, 2003, **107**, 35.
29. H. Riesen, E. Krausz and L. Dubicki, *Chem. Phys. Lett.*, 1994, **218**, 579.
30. J. L. Silva and G. Weber, *Annu. Rev. Phys. Chem.*, 1993, **44**, 89.
31. W. B. Holzapfel and N. S. Isaacs eds., ‘High-Pressure Techniques in Chemistry and Physics’, ‘Practical Approaches in Chemistry, Series’, eds. L. M. Harwood and C. J. Moody, Oxford University Press, Oxford, 2002.
32. I. Y. Chan, C. M. Wong and D. Stehlik, *Chem. Phys. Lett.*, 1994, **219**, 187.
33. T. Kobayashi, *Rev. Sci. Instrum.*, 1985, **56**, 255.
34. E. Krausz, *Aust. J. Chem.*, 1993, **46**, 1041.
35. R. Stranger, L. Dubicki and E. Krausz, *Inorg. Chem.*, 1996, **35**, 4218.
36. H. W. Ott, ‘Noise Reduction Techniques in Electronic Systems’, Wiley-Interscience, New York, 1988.
37. S. Peterson Årsköld, V. M. Masters, B. J. Prince, P. J. Smith, R. J. Pace and E. Krausz, *J. Am. Chem. Soc.*, 2003, **125**, 13063.
38. W. Demtröder, ‘Laser Spectroscopy: Basic Concepts and Instrumentation’, Springer, Berlin, Heidelberg, New York, 1996.
39. S. Mukamel, ‘Principles of Nonlinear Optical Spectroscopy’, Oxford University Press, New York, Oxford, 1995.
40. G. D. Reid and K. Wynne, in ‘Encyclopedia of Analytical Chemistry: Applications, Theory and Instrumentation’, ed. R. A. Meyers, John Wiley & Sons, Chichester, 2000, p. 13644.
41. C. Bustamante and M. F. Maestre, *Proc. Natl. Acad. Sci. U.S.A.*, 1988, **85**, 8482.
42. E. R. Krausz and A. W. H. Mau, *Inorg. Chem.*, 1986, **25**, 1484.
43. N. Mitic, L. Saleh, G. Schenk, J. M. Bollinger, Jr and E. I. Solomon, *J. Am. Chem. Soc.*, 2003, **125**, 11200.
44. W. Wang, I. Y. Chan, S. Schenker and A. Hauser, *J. Chem. Phys.*, 1997, **106**, 3817.
45. A. Hauser, A. Vef and P. Adler, *J. Chem. Phys.*, 1991, **95**, 8710.
46. E. Krausz and J. Ferguson, *Prog. Inorg. Chem.*, 1989, **37**, 293.
47. H. Riesen, L. Wallace and E. Krausz, *Int. Rev. Phys. Chem.*, 1997, **16**, 291.
48. D. H. Oh and S. G. Boxer, *J. Am. Chem. Soc.*, 1989, **111**, 1130.
49. I. B. Talanina, M. A. Collins, L. Dubicki and E. Krausz, *Chem. Phys. Lett.*, 1992, **200**, 318.

50. E. Krausz, H. Riesen and A. D. Rae, *Aust. J. Chem.*, 1995, **48**, 929.
51. R. H. G. Baxter, E. Krausz and J. R. Norris, *J. Phys. Chem. B*, 2006, **110**, 1026.
52. E. Krausz, J. L. Hughes, P. Smith, R. Pace and S. Peterson Årsköld, *Photochem. Photobiol. Sci.*, 2005, **4**, 744.
53. J. L. Hughes, P. Smith, R. Pace and E. Krausz, *Biochim. Biophys. Acta*, 2006, **1757**, 841.

Electron-Nuclear Double Resonance (ENDOR) Spectroscopy

Joshua Telser

Roosevelt University, Chicago, IL, USA

	Method Summary	1
1	Introduction	2
2	Technical Background	4
3	Experimental Aspects	10
4	Applications	18
5	Acknowledgments	23
6	Abbreviations and Acronyms	23
7	Related Articles	23
8	Further Reading	24
9	References	24

METHOD SUMMARY

Acronyms, Synonyms

- Electron-Nuclear DOuble Resonance
- EPR-detected NMR.

Measured physical quantities

- EPR signal intensity (CW or pulsed) as a function of applied radiofrequency (rf).

Information available

- nuclear hyperfine coupling (A) in paramagnetic systems
- nuclear quadrupole coupling (P or Q) in paramagnetic systems
- nuclear magnetic resonance (Larmor frequency, ν) in paramagnetic systems.

Information not available, limitations

- applicable only to EPR-active systems
- quantitative comparison of magnetically coupled nuclei is difficult
- analysis of overlapping signals can be difficult.

Examples of questions that can be answered

- Is there a nitrogen ligand in the paramagnetic active site?
- What is the orientation of a water molecule bound to the paramagnetic active site?
- How many iron sites are minimally in a paramagnetic FeS cluster?
- How much spin density is on a nitrogen ligand?

Major advantages

- Nuclei distant from the paramagnetic site are not detected or easily disregarded.
- All magnetically active ($I \neq 0$) nuclei in the vicinity of the paramagnetic site are detected, including nuclei unfavorable for NMR (e.g., ^{14}N, ^{57}Fe).

- Provides quantitative measure of parameters not resolved in the EPR spectrum itself.
- Isotopolog/isotopomeric samples allow identification of specific interactions.
- Can obtain ‘‘single-crystal-like’’ directional information from frozen solution samples.

Major disadvantages

- requires an EPR-active sample
- isotopic enrichment is necessary for low-abundance magnetic nuclei (e.g., ^{13}C, ^{15}N, ^{57}Fe).

Sample constraints

- Sample volume is $\sim 50-250\,\mu$L (volume inversely dependent on EPR microwave frequency).
- Concentration is 0.1 mM or higher (dependent on EPR signal).
- Multiple EPR-active species can complicate matters, but they can be distinguished by ENDOR and studied selectively.
- Samples must be magnetically dilute: doped powders, doped crystals, or solutions.
- Deoxygenated solutions are desirable, but not required.
- Aqueous or organic solvents are suitable and should form decent, but not optical quality, glasses.

---

1 INTRODUCTION

1.1 Background for Electron Magnetic Resonance in General

Magnetic resonance dates from the 1940s, with the discovery of electron paramagnetic resonance (EPR, also known as electron spin resonance (ESR) or electron magnetic resonance (EMR)) by E. K. Zavoisky in 1944 in Kazan, USSR (now Kazan, Tatarstan, Russia) preceding that of nuclear magnetic resonance by E. M. Purcell and by F. Bloch and their coworkers in 1946 in the USA.**[1]** This discovery of EPR was not recognized by the Nobel Prize, only that of nuclear magnetic resonance NMR was (Physics, 1952). Subsequent Nobel Prizes have been awarded for work related to NMR (Chemistry, 1991, 2002; Medicine, 2003), but none for work related to EPR.

By the early 1950s, EPR had already proved to be a powerful tool in the study of inorganic complexes, especially those of transition metal ions. Much of this early work is summarized in a review by McGarvey**[2]** and in the monumental text by A. Abragam and B. Bleaney (A^2B^2),**[3]** as well as in references to EPR in general, e.g., by Weil, Wertz, and Bolton (WWB),**[1]** Gordy,**[4]** and Pake.**[5]** The usefulness of EPR stems from its providing information on electronic structure as revealed by the g values of an EPR signal of a system with a single unpaired electron ($S = 1/2$) and by the fine structure (zero-field splitting (zfs); D, E values; *see* ***Magnetic Circular Dichroism (MCD) Spectroscopy***) for a system with multiple unpaired electrons ($S \geq 1$; *see* Section 3.5 in A^2B^2).**[3]** In addition, in cases where there are magnetically active nuclei ($I > 0$), there can be hyperfine structure. Hyperfine coupling is readily observable in the EPR spectra of organic radicals for which the EPR linewidths are narrow and there is usually a variety of magnetically inequivalent protons (^{1}H, $I = 1/2$) that are magnetically coupled to the radical spin. This phenomenon is analogous to the spin–spin coupling observed in NMR of diamagnetic systems. In the case of inorganic systems, hyperfine coupling can sometimes be observed when the paramagnetic metal ion has magnetically active nuclei. Classic examples are 3d^{1,9} ($S = 1/2$) systems such as Cu$^{\mathrm{II}}$ with 100% natural abundance of the two isotopes ^{63}Cu and ^{65}Cu (both $I = 3/2$ with very similar g_N values) and V$^{\mathrm{IV}}$ (e.g., as vanadyl) with 100% natural abundance ^{51}V ($I = 7/2$). These two ions yield, respectively, four-line and eight-line (number of lines $= 2nI + 1$, where $n = 1$ for the sole metal ion) hyperfine-split EPR spectra. In many cases, however, the metal ion has no nonzero spin nuclei of significant natural abundance. For example, iron has only ^{57}Fe ($I = 1/2$) with only 2.15% natural abundance.

In addition to hyperfine coupling between the unpaired electrons and the transition metal ion nucleus, there can be hyperfine coupling to magnetically active nuclei directly coordinated to the metal ion. Examples include ligands such as fluoride (^{19}F, $I = 1/2$, 100% natural abundance), phosphines (^{31}P, $I = 1/2$, 100% natural abundance), and various nitrogen donors (^{14}N, $I = 1$, 99.63% natural abundance; *see* ***Nuclear Quadrupole Resonance (NQR) Spectroscopy***). For example, porphyrin complexes of Cu$^{\mathrm{II}}$ often exhibit resolved hyperfine splitting from the four pyrrole nitrogen ligands.**[6]** The ^{14}N hyperfine coupling, combined with that for ^{63,65}Cu can be analyzed to provide a complete description of the semi-occupied molecular orbital (SOMO) in the complex.**[6]** However, in many cases, hyperfine coupling information from neither the metal ion nor any ligands is available by EPR. This is the result not only of the absence of magnetically active nuclei in sufficient abundance (e.g., Fe$^{\mathrm{III}}$ with oxygen and/or sulfur-donor ligands), but also from a lack of spectral resolution. If the hyperfine couplings are small in magnitude but large in number (i.e., a large number of closely spaced lines resulting from $\sum(2n_i I_i + 1)$, where i is a given set of magnetically equivalent nuclei), then resolution of the splitting is often impossible due to spectral overlap. Of more relevance to inorganic, and especially metalloprotein systems, the natural EPR linewidths may be too broad to allow resolution of individual hyperfine splittings. Proteins can exhibit conformational distribution,[7] and such distributions can affect the coordination environment of the paramagnetic center in a metalloprotein, leading to broad EPR linewidths in frozen solution for what is nominally a single paramagnetic center.

An example of the type of EPR spectrum with which one is often confronted in metallobiochemistry is shown in Figure 1, which presents the 35 GHz EPR spectrum recorded at 2 K under rapid-passage conditions[8–10] of an oxidized heme protein. The signal is due to a low-spin ($S = 1/2$) $\mathrm{Fe^{III}}$ porphyrin axially coordinated by cysteine-75 as the proximal ligand and most likely proline-2 as the distal ligand, as found in the CO-sensing transcription factor CooA isolated from *Rhodospirillum rubrum*.[11] The EPR signal exhibits several features that are often found in studies of metalloproteins. The signal is rhombic (i.e., it shows three distinct g values: g_{min}, g_{mid}, and g_{max}), which is indicative of the lower symmetry often found in metalloprotein systems. The specific g values are typical for many low-spin $\mathrm{Fe^{III}}$ systems,[12] but are not particularly useful in themselves. There is no observable metal hyperfine coupling, given that the metal is iron. Although there are nitrogen-donor axial and equatorial ligands, none yields resolvable hyperfine coupling. This lack of resolution is not surprising given that the EPR linewidths are relatively broad and anisotropic (single-crystal Gaussian linewidths range from 200–500 MHz; ca. 7–18 mT), which is indicative of local conformational heterogeneity. Lastly, the sample is globally heterogeneous in that there are two resolvable components, in roughly a 2:1 ratio. This heterogeneity is proposed to be the result of pH effects on the axial ligation,[11] but is not germane to the present discussion. What is important is that this paramagnetic metalloprotein, like many others, exhibits a broad, low symmetry, heterogeneous EPR spectrum that provides generic information about the metalloprotein, but provides little detailed information. Such systems are good candidates for electron-nuclear double resonance (ENDOR) spectroscopic investigation, which can extract information on the metal ion coordination environment and ideally even provide mechanistic information that is simply not obtainable from EPR alone, nor from other techniques. A specific case study demonstrating this success will be described below (Section 4.1).

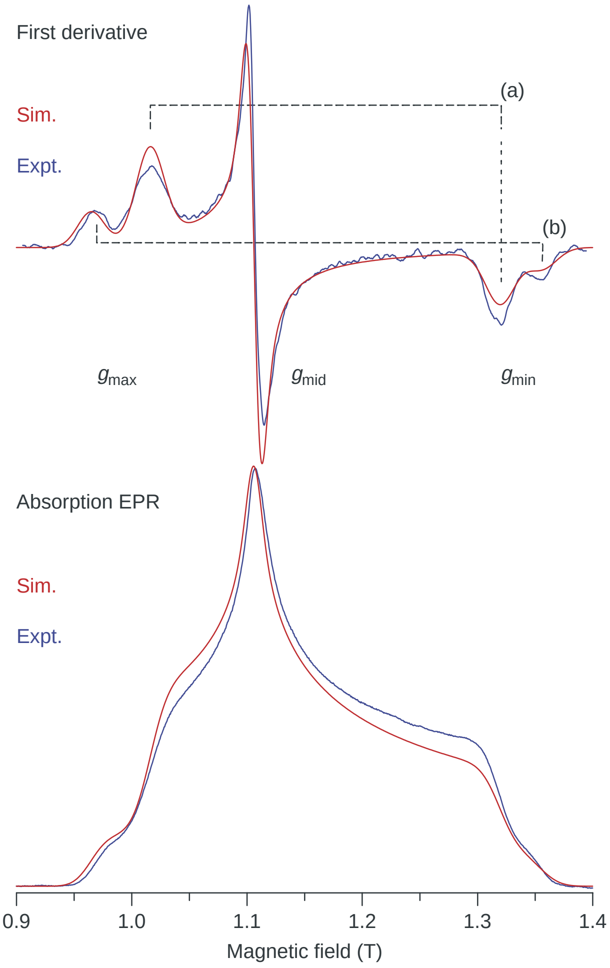

Figure 1 Experimental and simulated EPR spectra of oxidized CooA at pH 7.4. Experimental conditions: temperature, 2 K; microwave frequency, 35.106 GHz; microwave power, 20 μW; 100 kHz field modulation amplitude, 0.4 mT; time constant, 128 ms; scan time, 4 min. Lower traces, in absorption lineshape (due to rapid-passage conditions), are the experimental spectrum (blue) and a digital integration of the simulated spectrum (red). Upper traces in first-derivative lineshape are a digital derivative of the experimental spectrum (blue) and the simulated spectrum (red). Simulation parameters: component (a) $\mathbf{g} = [2.60, 2.268, 1.85]$, (b) $\mathbf{g} = [2.47, 2.268, 1.90]$; Gaussian single-crystal linewidths (half-width at half-maximum): $\mathrm{W} = [500, 200, 400]$ MHz. Simulated spectra for (a) and (b) are added in the ratio 2:1 to give the summed spectrum shown

1.2 Historical Background for ENDOR

The above discussion defines the problem in that EPR-active metalloprotein systems often exhibit readily observable but relatively uninformative spectra, with broad linewidths and unresolved hyperfine splitting. In contrast, NMR exhibits narrow lines and nuclear-specific signals with chemical shift and spin coupling information, but is inherently insensitive due to the tiny size of nuclear magnetic moments relative to that of an electron. It would therefore be desirable to combine the signal sensitivity of EPR with the nuclear information of NMR. This was first achieved not in bioinorganic chemistry, or even in chemistry at all, but in the area of solid state physics by George Feher at Bell Telephone Laboratories in the 1950s,[13–16] only a decade after EPR and NMR were themselves discovered. The technique was the ‘‘observation of NMRs via the electron spin resonance line’’, as Feher entitled his first paper.[13] This phrase describes better than anything else the essence of the technique to which Feher soon gave the appealing acronym of ENDOR,[15] for ''*e*lectron-*n*uclear *do*uble *r*esonance''. [The word ''Endor'' first appears in the Old Testament, Joshua 17:11, and refers to a place name (http://en.wikipedia.org/wiki/Endor_%28village%29; accessed 02/28/2007).] The initial systems studied were paramagnetic centers (defects/dopants) in solid state semiconductor materials (e.g., silicon), with relevance to the work on transistors going on at Bell Laboratories at the time. The rationale for ENDOR and some of Feher's early work is summarized in Sections 4.1–4.4 of A^2B^2.[3] After moving to the newly established University of California at San Diego, Feher pioneered the application of ENDOR to metalloproteins, such as hemoglobin and myoglobin,[17–19] and later in the area of photosynthetic reaction centers.[20,21]

1.3 Overview of Current Status of ENDOR in Bioinorganic Chemistry

ENDOR is not a technique widely practiced in chemistry, as it requires specialized EPR instrumentation, however the use of ENDOR has led to significant advances in the area of bioinorganic chemistry. Among the current practitioners of ENDOR are two former students of Feher, Charles P. Scholes at SUNY-Albany and Wolfgang Lubitz at the Max Planck Institute for Bioinorganic Chemistry, Mülheim/Ruhr, Germany. Among the systems studied by Scholes and coworkers are heme proteins[22] and multicopper enzymes.[23] Among the systems studied by Lubitz and coworkers are photosynthetic reaction centers[24,25] and nickel hydrogenases.[26] David J. Lowe at the John Innes Center, Norwich, UK, is also active in the area of metallobiomolecule ENDOR.[27] The contributions of the late Arthur Schweiger, ETH-Zürich, must also be noted, recently in cobalt and nickel bioinorganic systems.[28,29] Other workers such as R. D. Britt, D. Goldfarb, and A. M. Raitsimring focus more on electron spin echo modulation (ESEEM) techniques (*see* ***Electron Spin Echo Envelope Modulation (ESEEM) Spectroscopy***). Brian M. Hoffman at Northwestern University is best known to the author. His group has made contributions in many areas of bioinorganic chemistry by use of ENDOR spectroscopy.[30–35] One case study, which has several components, is selected from among the many such examples for illustration of the application of ENDOR toward bioinorganic systems: nitrogenase.

2 TECHNICAL BACKGROUND

2.1 General Theory Background for ENDOR Spectroscopy

As mentioned above, ENDOR is the detection of NMR resonances by observing their effect on an EPR signal, whether in continuous wave (CW) or pulsed mode. The NMR transitions are effected by application of radiofrequency (rf) energy, as with NMR. In NMR (*see* ***Nuclear Magnetic Resonance (NMR) Spectroscopy of Inorganic/Organometallic Molecules*** and ***Nuclear Magnetic Resonance (NMR) Spectroscopy of Metallobiomolecules***), the selection of signals is determined by the rf energy being specific for the resonant (Larmor) frequency of a particular nucleus (e.g., 300 MHz for ^{1}H with an external magnetic field of ∼7 T) and the frequency range of signals is very narrow (at least in diamagnetic NMR: typically <1 kHz total, ppm). Signals from other NMR active nuclei appear at other (lower) rf energies, which might also involve the use of different NMR probes, and are also in relatively narrow ranges. Thus one records a ^{1}H NMR spectrum, or a ^{13}C NMR spectrum, and so forth.

In ENDOR, one records, at least in principle if not in practice, a spectrum that exhibits resonances from *all* magnetically active nuclei (nuclear spins) that are hyperfine coupled to the paramagnetic center (electron spin(s)). The position of these resonances can vary greatly, depending on the nature of their interaction with the paramagnetic center. A given scan might exhibit ENDOR signals due only to ^{1}H nuclei coupled to the center, as these might appear at rf energies well separated from other coupled nuclei, and experimental parameters might favor ^{1}H NMR transitions as opposed to those of other nuclei, but there is no such thing as a ^{1}H ENDOR spectrum in the same way as there is a ^{1}H NMR spectrum. Nevertheless, terms such as ^{1}H ENDOR, ^{13}C ENDOR, are extremely useful at indicating the nucleus of interest in a given experiment.

2.2 ENDOR Transitions for a Simple Spin System

2.2.1 *First-Order ENDOR Transitions for an $S = 1/2, I = 1/2$ System*

Where do these ENDOR transitions appear? The answer can be seen by consideration of the simplest system relevant to ENDOR: a single unpaired electron ($S = 1/2$) interacting with a single nucleus with $I = 1/2$ (e.g., ^{1}H, ^{13}C, etc.). The energy level diagram of such a system is shown in Figure 2. If we ignore any anisotropy in g values (e.g. for an unpaired electron in an s orbital, any orbital angular momentum effects will be absent), then there would be a single EPR signal observed (at $g_e = 2.0023$; a resonant field of 0.339 T at 9.50 GHz microwave frequency—X-band). If the NMR signal of the nucleus could be observed, then it would show a single line as well. However, if there is a hyperfine interaction (here assumed isotropic[36]) between the electronic and nuclear spins, then this effect would lead to a splitting of the EPR signal into two peaks (''doublet''). There would likewise be a splitting of the NMR signal, which in this case would be observed by ENDOR. The electronic Zeeman interaction (given by the spin Hamiltonian: $\boldsymbol{H} = \beta_e B{\cdot}\mathbf{g}{\cdot}S$, where β_e is the Bohr magneton (9.2740×10^{-24} J/T), B is the magnetic field (T), and $\mathbf{g}$ is a matrix—relevant for anisotropy)

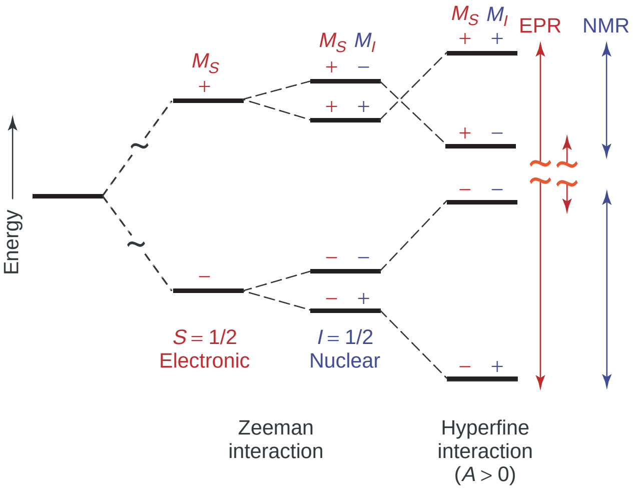

Figure 2 Energy level diagram for system of $S = 1/2$ and $I = 1/2$. The M_S, M_I values are shown (rather than use of α, β). The assignment of these values is based on $g_N, A^N > 0$, with the magnetic field along z. The EPR transitions are indicated in red and the NMR (ENDOR) transitions in blue. The transition energies are not to scale; at X-band the EPR transition energies are ~9 GHz (~0.3 cm^{-1}), while the NMR transition energies are ~15 MHz (for ^{1}H)

is almost always larger than the hyperfine interaction (given by the spin Hamiltonian: $\boldsymbol{H} = S{\cdot}\mathbf{A}{\cdot}I$, where **A** is the hyperfine coupling matrix—relevant for anisotropy). Thus the EPR signal would be centered at its resonant field determined by its g value (0.339 T) and split by the hyperfine coupling, **A**, which could vary greatly in magnitude but typically is in the field range of mT (MHz in energy), thus ~1% of the electronic Zeeman effect. In contrast, the nuclear Zeeman interaction (given by the spin Hamiltonian: $\boldsymbol{H} = -\beta_N g_N B{\cdot}I$, where β_N is the nuclear magneton (5.0508×10^{-27} J T^{-1}), and g_N is the nuclear g value, which is treated as isotropic for EPR and ENDOR) is small and is on the same order of magnitude as the hyperfine coupling. Thus, the ENDOR transition can either remain at the NMR (Larmor) transition and be split by the hyperfine interaction, or be dominated by the hyperfine interaction and be split by the Larmor energy. The following equation defines these two situations:

$$\nu_{\pm}^{N} = \left| \frac{\nu^N \pm A^N}{2} \right| \tag{1}$$

where $\nu_{\pm}^{N}$ is the resonant frequency of the pair of ENDOR signals for a given nucleus N (separately, ν_{+}^{N} and ν_{-}^{N}), ν^N is the NMR (Larmor) frequency of N, and A^N is the hyperfine splitting (all parameters are typically in MHz). In the case of dominant nuclear Zeeman splitting, the $\nu_{\pm}^{N}$ signals are centered at the Larmor frequency and split by the hyperfine coupling. In the case of dominant hyperfine splitting, the $\nu_{\pm}^{N}$ signals are centered at half the hyperfine coupling constant and split by twice the Larmor frequency. The former situation, a Larmor-centered hyperfine-split doublet, is typically found for ^{1}H, which has a very large g_N value, and yields, e.g., $\nu_- \approx$ 14 MHz, $\nu_+ \approx$ 16 MHz at X-band (where $\nu^{1\mathrm{H}} \approx$ 15 MHz, $A^{1\mathrm{H}} \approx$ 2 MHz). The corresponding figure is often presented with the abscissa given as a difference frequency ($\nu - \nu^N$; in MHz) so that spectra at multiple magnetic fields can be easily compared to show hyperfine coupling. The latter situation, a Larmor-split hyperfine-centered doublet, is typically found for ^{57}Fe, which has a very small g_N value but large hyperfine coupling since the nucleus is usually an intrinsic part of the paramagnetic center. Such a situation at X-band would yield, for example, $\nu_- \approx$ 14.5 MHz, $\nu_+ \approx$ 15.5 MHz at X-band (where $\nu^{57\mathrm{Fe}} \approx$ 0.5 MHz, $A^{57\mathrm{Fe}} \approx$ 30 MHz). The abscissa of the corresponding figure would simply be rf (ν; in MHz). Actual examples of these types of spectra will be shown below in the case study on nitrogenase (Section 4.1).

2.2.2 *Microwave Frequency Effects in ENDOR*

The above example also illustrates a potential difficulty with ENDOR, namely that since different nuclei can simultaneously contribute to an ENDOR spectrum, signals from different nuclei can overlap (at the commonly used X-band microwave frequency). Such signals cannot always be readily analyzed or even distinguished. Pulsed ENDOR methods can address this problem (*see* Section 3.3.4), but the most effective method to overcome this problem is by use of higher microwave frequencies (and correspondingly higher resonant magnetic fields). This development has occurred much as NMR has progressed to ever higher rf energies in the quest for greater spectral (chemical shift) dispersion (*see* ***Nuclear Magnetic Resonance (NMR) Spectroscopy of Inorganic/Organometallic Molecules*** and ***Nuclear Magnetic Resonance (NMR) Spectroscopy of Metallobiomolecules***). In the case of ENDOR, a shift from X-band (9–10 GHz) to 35 GHz (commonly referred to as Q-band), is usually sufficient to move the field-dependent (Larmor) component, while the field-independent (hyperfine) component is unaffected. In the above example, use of 35 GHz would shift the ^{1}H ENDOR signals to $\nu_- \approx$ 52 MHz, $\nu_+ \approx$ 54 MHz (since now $\nu^{1\mathrm{H}} \approx$ 53 MHz) while the ^{57}Fe signals would remain relatively unaffected: $\nu_- \approx$ 13.3 MHz, $\nu_+ \approx$ 16.7 MHz (since now $\nu^{57\mathrm{Fe}} \approx$ 1.7 MHz).

This use of 35 GHz ENDOR in bioinorganic chemistry was pioneered by Hoffman in the late 1980s[33] and is now widely used in this area.[22,25] More recently, ENDOR at W-band (95 GHz)[37–40] and even higher frequencies (140 GHz)[41,42] have been successfully applied to bioinorganic systems.

2.3 ENDOR Transitions for More Complicated Spin Systems

2.3.1 *General Background*

The above example is for the case of a *single* nucleus with $I = 1/2$. In a typical metalloprotein system, there are multiple nuclei, magnetically and chemically distinct, coupled to the paramagnetic center. Such a situation could lead to complex hyperfine splitting patterns, if actually resolved, in an EPR spectrum. The ENDOR spectrum, in contrast, would have only a single pair of $\nu_{\pm}^{N}$ signals for each magnetically inequivalent set of nuclei, which could be analyzed individually. In the case of ^{1}H, a typical metalloprotein exhibits overlapping signals from numerous hydrogen atoms associated with the cofactor(s), protein residues, and solvent in the vicinity of the paramagnetic site, usually a metal ion or cluster. In this case, assignment of ENDOR signals to individual hydrogen sites is difficult, except when the coupling is large relative to that of the bulk. Use of isotopic labeling can also assist greatly, as discussed below (*see* Section 4.1). For magnetically active nuclei that are common, but less ubiquitous than ^{1}H, such as ^{14}N, it is often possible to identify and analyze individual signals, even within a group of several signals. Examples include heme pyrrole nitrogen ligands in peroxidases,**[43,44]** corrinoid pyrrole/pyrrolidine nitrogen ligands in Ni-F_{430},**[45]** or histidine nitrogen ligands in Rieske iron–sulfur proteins.**[46,47]**

2.3.2 *ENDOR Signal Quantification*

One caveat that must be made is that ENDOR signal intensities, in contrast to those in diamagnetic NMR, are not reliable indicators of the relative numbers of magnetically equivalent nuclei. The process by which an NMR transition affects the EPR signal intensity that is being monitored to yield a given ENDOR signal is complicated.**[14,48]** Many relaxation factors are involved, both nuclear and electronic (*see* Sections 4.5–4.6 in $\mathrm{A}^{2}\mathrm{B}^{2}$)**[3]** in addition to simply numbers of nuclei. Thus ENDOR can identify sets of magnetically equivalent nuclei, but generally cannot provide the relative numbers of each of these sets. Because of anisotropy of electronic Zeeman (i.e., g value) and hyperfine coupling (i.e., $\mathbf{A}$ value) effects, magnetic equivalence among ENDOR-active nuclei in a metalloprotein system is relatively uncommon, so that this drawback is usually not a great concern. Furthermore, in certain cases it is possible to combine the hyperfine information accurately determined by ENDOR with EPR linewidth information to assist in quantification. To state this more elegantly: ''ENDOR can measure, EPR can count.''**[48]** A specific example is the combined multifrequency EPR and 35 GHz ENDOR study of the di-iron center in the R2 subunit of *Escherichia coli* ribonucleotide reductase (RNR).**[49]** Samples in natural isotopic abundance (0.038% ^{17}O) and using $\mathrm{H}_2^{17}\mathrm{O}$ (34.9% ^{17}O) or $^{17}\mathrm{O}_2$ (85.5% ^{17}O) were prepared. ENDOR provided ^{17}O ($I = 5/2$) hyperfine coupling constants and these values were used to quantify the line broadening seen in ^{17}O-enriched versus natural abundance samples, which showed that the intermediate X contained two oxygen atoms, initially derived from dioxygen, as opposed to an alternate model with only one such oxygen atom.

2.3.3 *ENDOR of Electronic High-Spin (S > 1/2) EPR Systems*

Other caveats are related to equation (1) being appropriate only for nuclei with $S = 1/2$ (''low-spin'') and $I = 1/2$, as opposed to $S > 1/2$ (''high-spin''). The term ''high-spin'' in the sense of EPR spectroscopy means simply $S > 1/2$ (i.e., a system with more than one unpaired electron), but this term in the sense of ligand-field theory**[50]** means the electronic configuration with higher S in an idealized octahedral coordination environment, e.g., high-spin d^5 is the configuration $^{6}\mathrm{A}_{1g}$ and low-spin d^5 is $^{2}\mathrm{T}_{2g}$. When $S = 1/2$, there is only one EPR transition: $-1/2 \leftrightarrow +1/2$, however, systems with $S > 1/2$ have the added complication that there are multiple EPR (fine structure) transitions, e.g., $\langle S, M_S| = \langle 3/2, -3/2| \leftrightarrow \langle 3/2, -1/2| \leftrightarrow \langle 3/2, +1/2| \leftrightarrow \langle 3/2, +3/2|$. Each of these can in principle be monitored under the application of rf energy to yield ENDOR signals. If these fine structure transitions overlap, then all can contribute to a given observed ENDOR signal, but the different M_S manifolds will scale the ENDOR transitions proportionately.**[51]**

$$\nu_{\pm}^{N} = \left| \frac{\nu^{N} \pm (2|M_S|)A^{N}}{2} \right| \tag{2}$$

Equation (2) is a first-order generalization of equation (1) wherein the M_S scaling factor has been explicitly included ($2|M_S| = 1$ for $S = 1/2$).

Such a situation can occur for $\mathrm{Mn}^{\mathrm{II}}$ ($S = 5/2$) where the zfs is often small (relative to the microwave energy, e.g., $|D| < 0.1\,\mathrm{cm}^{-1}$, where the zfs Hamiltonian is given as: $\boldsymbol{H} = S{\cdot}\mathbf{D}{\cdot}S = D[S_z^2 - (1/3)S(S+1)]$ for a uniaxial system) and the fine structure peaks overlap. With careful computer simulation analysis, it is possible to unravel such potentially complex spectra.**[25,52]** In cases where the zfs is large relative to the microwave energy (e.g., $|D| > 1\,\mathrm{cm}^{-1}$), then only the $\langle S, M_S| = \langle\ 5/2, -1/2| \leftrightarrow \langle 5/2, +1/2|$ transition is observed (for $D > 0$) and the EPR spectrum can be treated as a ''fictitious spin'', $S' = 1/2$, system and lacks multiple fine structure transitions. Such a situation can obtain for $\mathrm{Fe}^{\mathrm{III}}$ ($S = 5/2$) with relatively strong-field ligands such as heme. In this case, the ENDOR spectrum for a given nucleus would appear to be exactly the same as that in a true $S = 1/2$ system.

However, this appearance can be misleading because the apparent hyperfine coupling of a given nucleus, A^{N} given in equation (1), would not correspond to the actual hyperfine coupling of that nucleus. This is because of the ''g-over-g effect'', which results from use of the fictitious spin $S' = 1/2$, rather than the real spin $S = 3/2$, 5/2. The relation between the actual and observed hyperfine coupling matrices is given as follows:

$$\mathbf{A}' = {}^{g}\,\mathbf{A}{\cdot}\mathbf{g}' \tag{3}$$

where $\mathbf{A}'$ is the hyperfine coupling matrix in the fictitious spin representation (i.e., as observed using equation (1)),

${}^{g}\mathbf{A}$ is the hyperfine coupling matrix in the true spin representation and in the electronic (**g**) frame of reference (i.e., the actual hyperfine coupling collinear with **g**), and $\mathbf{g}'$ is the g matrix in the fictitious spin representation.[53,54] The following equations represent the individual elements of these matrices.

$$A'_{ij} = \frac{{}^{g}A_{ij}g'_{j}}{g_j} \quad g'_{ij} = \frac{\delta_{ij}g'_{j}}{g_j} \tag{4}$$

where i refers to the elements of the operator $\hat{I}$, j to the elements of the operator S, $A_{ij}^{(\prime)}$, $g_{j}^{(\prime)}$ are the individual elements of the matrices in equation (3) and δ_{ij} is related to the coordinate transformation from the real electronic to the fictitious nuclear spin system, which is relevant for noncollinearity. To put this in practical terms, the elements of **g** (i.e., g_j) are usually close to 2.00 (g_e), especially for high-spin d^5 systems, while the values of g'_{ij} are equal to $(2S-1)$ for $g_{x,y}$ and equal to 1 for g_z (D along z), giving $g'_{x,y}$ $(g_{\perp}) \approx 6$ (for $S = 5/2$; $g'_{x,y} \approx 4$ for $S = 3/2$) and g_z $(g_{||}) \approx 2$. Thus, for an $S = 5/2$ system, ENDOR observed at $g_{\perp}$ would appear to be three times larger than the actual value, and for an $S = 3/2$ system, twice as large. As an example we consider ^{57}Fe ENDOR at X-band of the resting state of the ^{57}Fe-enriched iron–molybdenum cofactor (FeMo-cofactor) of *Azotobacter vinelandii* (*Av*) nitrogenase, which has $g_{\perp} = 2.005$, $g_{||} = 2.01$ as the intrinsic g values in the true, $S = 3/2$ representation.[53,54] ENDOR signals from five distinct iron centers were observed. Among these we select two sites, denoted B^1 and B^2, which at $g'_y = 4.32$ (the low field edge of the EPR signal) each gave $\nu_{\pm}$ signals centered respectively at ~12.5 MHz and at ~9 MHz. By equation (1), these would be interpreted as corresponding to $A_y(B^1) \approx 25$ MHz and $A_y(B^2) \approx 18$ MHz, but this interpretation is wrong! These observations are actually of A'_y values and in the true spin representation (by equation 4) correspond to $A_y(B^1) = 11.34$ MHz and $A_y(B^2) = 8.86$ MHz. Next consider two ^{57}Fe ENDOR $\nu_{\pm}$ signals observed at $g'_z = 2.01$ (the high field edge of the EPR spectrum): one centered at ~6 MHz denoted b^1, and another centered at ~5 MHz denoted b^2. In this field, $g'_j \approx g_j$, so that now the observed couplings do correspond directly to $A_z(b^1) = 11.58$ MHz and $A_z(b^2) = 9.84$ MHz.[53,54] Thus the $B^{1,2}$ and $b^{1,2}$ sites are likely the same, which is reasonable given that ^{57}Fe hyperfine coupling in FeS clusters is generally rather isotropic.[55]

The above discussion is a major concern in ENDOR of high-spin systems with large zfs. In addition, the experimental Larmor frequency (ν^N) might differ from that expected for nucleus N at the magnetic field of observation. This discrepancy is due to the pseudonuclear Zeeman (pnZ) effect (see A^2B^2, Section 1.8(e)),[3] which results from mixing of the higher M_S manifold(s) (e.g., $\langle S, M_S| = \langle 5/2, \pm 3/2|$) into the ground state $\langle S, M_S| = \langle 5/2, \pm 1/2|$) leading to an effect similar to that seen for ENDOR transitions actually within these higher M_S manifolds. The pnZ effect was observed and analyzed in the ^{57}Fe ENDOR studies of *Av*-nitrogenase FeMo-cofactor mentioned above.[53,54] Another example is in the ^{19}F ENDOR of fluorometmyoglobin,[56] which has $S = 5/2$, but is treated as $S = 3/2$ in terms of the pnZ because the $\langle S, M_S| = \langle 5/2, \pm 5/2|$ manifold is so much higher in energy ($>30\,\mathrm{cm}^{-1}$) than the ground state so as to have insignificant mixing.

The pnZ effect acts to convert the isotropic g_N into a (essentially axial) tensor with the following components:[54]

$$g_{Nij} = g_N \left[\delta_{ij} + \left(\frac{3}{2}\right)\left(\frac{g_e\beta_e}{g_N\beta_N}\right)\left(\frac{{}^{g}A_{ij}}{\Delta}\right)(1-\delta_{i3})\right] \tag{5}$$

where the terms are as defined above and $\Delta = 2D[1 + 3(E/D)^2]^{1/2} \approx 2D$ for nearly axial systems. Assuming collinear **A** and **g** (so that: $\delta_{ij} = 1, i = j$; $\delta_{ij} = 0, i \neq j$), $g_{N(3(z))} = g_N$, thus, there is no pnZ effect at $g_{||}$ (g_z), but at $g_{\perp}$ ($g_{x,y}$), $g_{N(2,3(x,y))} = g^N[1 + (3/2)(g_e\beta_e/g_N\beta_N)({}^{g}A_{ij}/\Delta)]$, and the effect can be large, particularly when the zfs is small and/or when the hyperfine coupling is large (and g_N is small). All of these criteria are met for ^{57}Fe in resting state nitrogenase FeMo-cofactor. For rhombic systems, mixing of the $\langle S, M_S| = \langle 3/2, \pm 3/2|$ and $\langle S, M_S| = \langle 3/2, \mp 1/2|$ manifolds (via the zfs Hamiltonian: $\boldsymbol{H} = S{\cdot}\mathbf{D}{\cdot}S = D[\hat{S}_z^2 - (1/3)S(S+1)] + E(\hat{S}_x^2 - \hat{S}_y^2)$ for a rhombic system) leads to a small pnZ effect at g_z as well as a slight divergence between $g_{N(2(x))}$ and $g_{N(3(y))}$.

2.3.4 ENDOR of Nuclear High-Spin (I > 1/2) (Quadrupolar) Systems

Equation (1) is the "fundamental equation of ENDOR", however it is applicable only to nuclei with $I = 1/2$. The energy levels of quadrupolar nuclei ($I \geq 1$) are affected not only by the nuclear Zeeman interaction and hyperfine coupling with the paramagnetic center, but also by the electric field gradient at the nucleus. This effect is nuclear electric quadrupole coupling (*see* ***Nuclear Quadrupole Resonance (NQR) Spectroscopy***), which has spin Hamiltonian $\boldsymbol{H} = I{\cdot}\mathbf{P}{\cdot}I$, where **P** (also sometimes given as **Q**) is the traceless quadrupole coupling tensor. The diagonal components of this tensor are often given as $P_{||} = (3/2)P_z$, $\eta = (P_x - P_y)/P_z$ ($\eta = 0$ for axial systems), and $P_{||} = [3e^2Qq/4I(2I-1)]$, where Q is the quadrupole moment of a given nucleus and q is the electric field gradient at the nucleus (*see* A^2B^2, Section 3.7).[3] The first-order ENDOR resonance positions must then be modified to include this interaction as follows:

$$\nu_{\pm}^{N} = \left|\frac{A^N}{2 \pm \nu^N} + \frac{3P^N(2m-1)}{2}\right| \tag{6}$$

where $m = (-I+1), \ldots, (I-1), I$. As a result, for $I = 1$, the simplest case, there are two doublets (in general, each peak splits into $2I$ lines) each separated by $3P^N$ with the doublets separated by twice the Larmor frequency and the entire pattern centered at half the hyperfine coupling, assuming $P^N < \nu^N < A^N/2$. For bioinorganic systems, the most important quadrupolar nucleus is ^{14}N, followed in importance by ^{2}H (D), the latter in isotopically enriched samples. Both of these have $I = 1$. A distant third in importance is ^{17}O, again in enriched samples, for which resolved, first-order spectra are seldom observed, due in part to the large nuclear spin ($I = 5/2$) and corresponding number of lines, as well as noncollinearity of nuclear and electronic coordinate systems.

2.4 Anisotropy in ENDOR

A nuclear quadrupole interaction is by definition anisotropic (parameters: $P_{||}$, η) as is an electronic quadrupole interaction (i.e., zfs; parameters: D, E), since these are described by a nonzero field gradient. Both of these effects have been briefly mentioned above, but the most important manifestation of anisotropy in ENDOR is with respect to g values and to hyperfine coupling interactions.

2.4.1 Electronic (g value) Anisotropy

Anisotropy in g values results from the contribution of orbital angular momentum to electron spin energy levels, which can provide valuable information on the orbitals involved.[2–4] From the point of view of ENDOR spectroscopy, g value anisotropy provides a mechanism whereby a powder pattern EPR signal can provide orientational information.[57–60] The details of this are described in the literature, of which the recent exposition by Doan is the most readable.[60] Very briefly, a powder pattern (whether as an actual powder or a frozen solution, as is usually the case in bioinorganic systems) EPR spectrum can be thought of as the superposition of single-crystal spectra, which give rise to the ‘‘Pake’’ pattern,[5] as seen in Figure 1. A given g value of observation (i.e., magnetic field at the resonant microwave frequency, g_{obs}) thus corresponds to some set of single-crystal orientations that make up the powder pattern at that g_{obs}. At the field extrema of the pattern, relatively few orientations contribute and these g_{obs} values yield ‘‘single-crystal-like’’ spectra,[57] i.e., ENDOR spectra appear as if the sample were oriented with all molecules aligned in that orientation in the **g** frame of reference. However, intermediate fields can also be analyzed since the contributions of different orientations at any g_{obs} value can be quantitatively determined.[60]

The ‘‘orientation selection’’[58] that results as g_{obs} values are varied across the EPR powder pattern envelope would be of little interest were it not for the fact that this procedure reveals anisotropy in the hyperfine coupling. This is shown in cartoon fashion in Figure 3. The analysis of such a field-dependent ‘‘2-D’’ ENDOR pattern can be challenging, even when there are no overlapping signals from different nuclei. The quantitative analysis of such complex patterns is a hallmark of many recent ENDOR studies of bioinorganic systems.[30,35,43,46,61]

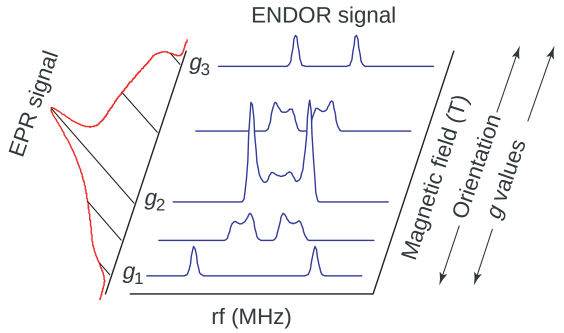

Figure 3 EPR powder pattern for a rhombic $S = 1/2$ system with ENDOR spectra recorded at multiple field positions (g_{obs} values). The ENDOR pattern depicted is for illustrative purposes only. The g_{obs} values select a set of orientations of the paramagnetic center with respect to the external magnetic field (i.e., θ, ϕ values)

This challenge obtains because the hyperfine anisotropy can be very large, and can be combined with quadrupole coupling (for ^{14}N or ^{2}H), and the coordinate systems that diagonalize the nuclear coupling matrices (hyperfine and quadrupole—which in turn need not be collinear) need not be collinear with the electronic (**g**) matrix. Noncollinearity of **g** and **A** means that the hyperfine coupling observed at, e.g., a ‘‘single-crystal-like’’ g_{obs} value (i.e., at a canonical g value, whether denoted as g_z, g_{max}, or simply g_1) does not correspond directly to A_z (or A_1), but to a combination of components of **A**, as determined by the Euler angle rotations[62] of the nuclear (**A**) and electronic (**g**) coordinate systems (assignment of **A** and **g** components to molecular directions x, y, z would require knowledge of the relation between the molecular and electronic coordinate systems, which could be obtained from single-crystal EPR). How could this noncollinearity arise? One scenario is when a nucleus is relatively distant from the paramagnetic site and the coupling is entirely through space (*see* Section 2.4.2). However, even when the nucleus of interest is an integral part of the paramagnetic center (i.e., a ligand) there could well be noncollinearity. For example, in heme systems, π-bonding effects can lead to **g** matrix directions differing from hyperfine coupling directions.[63] Another scenario is in spin-coupled systems, such as the mixed oxidation state of di-iron proteins (Fe$^{\text{II}}$Fe$^{\text{III}}$, ground state total spin, $S_{\text{tot}} = 1/2$). The **g** matrix of the coupled system need not have any correspondence with the **A** matrices of individual ligands, particularly for those to Fe$^{\text{III}}$, since the **g** anisotropy is largely determined by Fe$^{\text{II}}$.[64]

2.4.2 Hyperfine Anisotropy—Dipolar Coupling

The physical origin of hyperfine coupling is discussed in many other places,[1–4] and dates back to the work of Fermi in 1930. Very briefly, there are two contributions to hyperfine coupling, an isotropic contribution, A_{iso}, and an anisotropic or dipolar contribution, A_{dip} or T. The isotropic contribution results from unpaired spin in s orbitals, since only s orbitals have finite electron density at the nucleus (in SI units, *see* Section 2.6 in WWB**[1]**):

$$A_{\text{iso}} = \left(\frac{2\mu_0}{3}\right)(g_e\beta_e g_N\beta_N)\langle\rho_s\rangle \tag{7}$$

where the constants $\beta_{e,N}$ are in J T^{-1}, the vacuum permeability, μ_0, in T^2 m^3 J^{-1}, and s electron spin density at the nucleus from all relevant electron spins, $\langle\rho_s\rangle$, is in m^{-3}, to give A_{iso} in J (which value for normal usage would be converted by division by h in J MHz^{-1} to give A_{iso} in MHz). Values for the isotropic coupling for an unpaired ns electron, assuming unit total spin density in s orbitals as a_0 (in mT; since $a_0 = [A_{\text{iso}}]/g_e\beta_e$), are tabulated in appendix G of WWB.**[1]** Such s unpaired spin density at the nucleus can result from the direct contact (i.e., a metal ns (e.g., $n = 4$ for Cu$^{\text{II}}$) component in the SOMO being probed by EPR/ENDOR, which can include sp^n ligand orbitals ($n = 1$–3) and from polarization of all ns electrons ($n = 1$–4) by unpaired spin density in other orbitals (e.g., 3d orbitals for Cu$^{\text{II}}$). This type of spin polarization that affects s electrons should not be confused with the direct dipolar coupling described in the following.

The anisotropic contribution can result from both direct (local) and indirect (nonlocal) dipolar coupling. Dipolar coupling is averaged to zero in fluid solution (*see* ***Nuclear Magnetic Resonance (NMR) Spectroscopy of Inorganic/Organometallic Molecules***), but essentially all (bio)inorganic ENDOR is performed in frozen solutions, so that dipolar interactions are present and can be the dominant effect in hyperfine coupling. The indirect dipolar coupling is usually treated via a classical through-space electron point-dipole–nuclear point-dipole approximation. A cartoon of this type of dipolar interaction is shown in Figure 4, which is appropriate, e.g., for the H atom of a coordinated hydroxo ligand (X=O) to a paramagnetic site (M). Equally appropriate would be the case of hydrogen-bonding to X from, e.g., an endogenous (nearby protein residue) or exogenous (solvent) H atom, which is still close enough to M to give a measurable indirect dipolar coupling. The external magnetic field that aligns the dipoles is along the z axis, which is defined along the M–X bond. The metrical parameters d (M–X bond length), r (H–X bond length), and γ (H–X–M bond angle) are either known from specific structural information or can be assumed by analogy with related systems. From these parameters, the angle θ for this interaction is determined, for use in the equation, originally due to Breit and Rabi (in SI units; *see* Section 2.2 in WWB**[1]**):

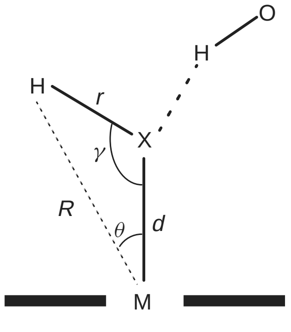

Figure 4 Diagram of the metrical parameters involved in a simple model for electron-point dipole—nuclear point-dipole hyperfine coupling, where the nucleus of interest is hydrogen. The paramagnetic metal center is indicated by M, with the ligand (e.g., a porphyrin) indicated by the dark horizontal line, X is a donor atom such as F, O, S, N, etc. Also shown is a second H, hydrogen-bonded to X, which can also be coupled to M (but with metrical parameters omitted for clarity)

$$T = \left(\frac{-\mu_0}{4\pi}\right)(g_e\beta_e g_N\beta_N)\frac{(3\cos^2\theta - 1)}{R^3} \tag{8}$$

where the constants μ_0, $(g,\beta)_{e,N}$, are as in equation (7) and the distance R is in meter, to give the dipolar coupling T in joule (thence normally converted to MHz), which gives the components $\mathbf{T} = [-T/2, -T/2, T]$. This simplified equation uses the isotropic g_e value, rather than taking into account anisotropy in the **g** matrix of the actual electronic system. The dipolar coupling matrix **T** can deviate greatly from the classical form given above if there is significant g anisotropy.**[65]** More recently, the point-dipole model has been modified to include both this effect and the spatial characteristics of d orbitals, so that the electron is treated realistically and not merely as a point-dipole.**[66]** This work by Snetsinger *et al.***[66]** has been incorporated by the author into a simple computer program (DIPOLE), which allows estimation of the maximum distance between the metal center and a nucleus of interest (R) that would give an observable ENDOR signal. This estimate is crude because spin delocalization onto ligands is ignored (i.e. only a 3d orbital is considered here), but suggests that for ^{1}H, a distance of ~800 pm (~8 Å) is easily achieved: $T \approx 0.3$ MHz. For ^{13}C, a distance of ~500 pm yields the same coupling. In general, hyperfine coupling of ~0.1 MHz might be considered the experimental lower limit. Such an estimate might be complicated in the case of ^{1}H by ‘‘distant’’ (matrix) ^{1}H signals from this ubiquitous isotope. Even for ^{13}C, an ENDOR signal from natural abundance (1.1%) isotope can often be observed at the Larmor frequency. An example is the very thorough study of a series of FeS proteins,**[67]** for which only ^{1}H ENDOR would be expected, yet natural abundance ^{13}C and even ^{57}Fe (due in part to the increased probability of isotopologs, relative to the mononuclear center, e.g., $[^{57}\text{FeFe}_3\text{S}_4]^{+,3+}$ in the active site). Signals from ^{14}N from the protein residues (H-bonded to FeS cluster cysteinyl ligands and/or sulfide ions) were also observed.**[67]** Thus, a nucleus such as ^{19}F, which has a large g_N (94% that of ^{1}H), 100% natural isotopic abundance, but with no natural occurrence of fluorine/fluoride in bioinorganic systems and hence no background signal, might be the best scenario for observation of a chemically relevant, dipolar coupled nucleus at a maximal distance.

An additional anisotropic interaction is a direct (local) dipolar one. It has its origin in unpaired electron density in, for example, p orbitals, which are by definition anisotropic, in contrast to s orbitals, although they have no density at the nucleus (hence no contact contribution to hyperfine coupling). As a result, there is direct (local) dipolar coupling between the unpaired electron spin in a p orbital (or sp^n hybrid MO) and the nucleus associated with that MO. Such a situation is especially relevant for the analysis of hyperfine coupling in organic radicals (*see* Section 5.3 in WWB[1]). However, it is also relevant to (bio)inorganic systems. The SOMO of a paramagnetic metal center is usually not a pure d orbital, but has ligand orbital contributions. There is thus unpaired spin density in ligand sp^n orbitals that can directly couple to the ligand nucleus (^{14}N, or ^{13}C—as part of a π-conjugated ligand more likely than as a C-donor ligand itself). The importance of including both indirect (nonlocal) and direct (local) dipolar contributions was recently demonstrated in an ENDOR study of the ''very rapid'' intermediate in the pyranopterin Mo enzyme xanthine oxidase, which was probed by use of a ^{13}C-labelled purine substrate.[61] This intermediate contains Mo$^{\mathrm{V}}$, 4d^1, which has extensive covalency with ligands.

The most general form of the equation for dipole–dipole coupling ($\boldsymbol{H} = \boldsymbol{S}\cdot\mathbf{T}\cdot\boldsymbol{I}$), that is, without quantization along the z axis, is given in Section 5.2 of WWB,[1] which also tabulates in Appendix G the hyperfine coupling for an unpaired electron in an np orbital, b_0, (in mT; since $b_0 = T/(g_e\beta_e)$).

2.4.3 Signs of Hyperfine Couplings

The final consideration is the sign of hyperfine coupling. The sign of g_N, which is related to the pairing of the nucleons themselves, affects the sign of A_{iso} as seen from equation (7), however, the nature of the core (s) electron polarization can lead to a net positive or negative spin at the nucleus (*see* Section 17.6 in A^{2}B^2).[3] It is thus difficult to predict the actual sign of A_{iso}. Furthermore, it is normally not possible to determine the sign of an isotropic hyperfine coupling from EPR, although the relative signs of two resolved couplings can be determined from higher-order analysis of the spectra (*see* Sections 2.6 and 3.6 of WWB[1]), which is much more likely the case for organic radicals, typically with their multiple, well-resolved couplings from ^{1}H (primarily), than for inorganic complexes. ENDOR likewise does not normally provide the sign of A_{iso}. Specifically, for $A_{\mathrm{iso}} > 0$ (and $g_N > 0$, with the hyperfine interaction larger than the nuclear Zeeman interaction), the assignment of $\nu_\pm$ signals would be: $\langle M_S, M_I| = \langle -1/2, +1/2| \leftrightarrow \langle -1/2, -1/2|$ as ν_+ (i.e., the higher energy ENDOR signal) and $\langle +1/2, -1/2| \leftrightarrow \langle +1/2, +1/2|$ as ν_- (the lower energy partner), while for $A_{\mathrm{iso}} < 0$, the assignments would be: $\langle M_S, M_I| = \langle +1/2, +1/2| \leftrightarrow \langle +1/2, -1/2|$ as ν_+ and $\langle -1/2, -1/2| \leftrightarrow \langle -1/2, +1/2|$ as ν_-. One might imagine that in the former case, the signal intensity of the ν_+ partners would be larger as the population of the $M_S = +1/2$ state is larger than that of the $-1/2$ state, while for the latter case, the intensities would be reversed. Unfortunately, as mentioned above (*see* Section 2.3.2), ENDOR signal intensities are very unpredictable and rely on many relaxation factors,[48] and not simply on Boltzmann population differences. However, it is possible, in analogy to the comparison of two separate hyperfine coupled nuclei in EPR, to use two separate rf energies to give the technique known as TRIPLE,[68,69] which can provide relative signs of two hyperfine couplings. This technique will be discussed later in this text (*see* Section 3.3.7).

Much more important than the sign of A_{iso} is the sign of the dipolar coupling as this is related to spatial parameters. As seen in equation (8), there is necessarily a change of sign as a result of dipolar coupling. As described above (*see* Section 2.4.2), analysis of the field-dependent ENDOR spectra can provide the components of the hyperfine coupling matrix, **A**, including the Euler angle relation with **g**, and the relative signs of these components. Designating the largest magnitude hyperfine coupling component as A_1 and the smallest as A_3, $A_{\mathrm{iso}} = (A_1 + A_2 + A_3)/3$, and the dipolar (anisotropic) components, $T_i(A_{\mathrm{dip}}) = [A_i - A_{\mathrm{iso}},\ i = 1\text{–}3]$. By analogy with electronic and nuclear quadrupole coupling, the hyperfine matrix can also be used to derive an axial (uniaxiality) parameter B (analogous to $D, P_{||}$) and an asymmetry (rhombicity) parameter C, (analogous to E, η), where $B = [A_1 - (A_2 + A_3)/2]/3$, $C = (|A_2| - |A_3|)/2$ (these are a_0, b_0, c_0 in magnetic field units; see Section 5.2 in WWB[1]).

3 EXPERIMENTAL ASPECTS

3.1 Computer Simulation of ENDOR Spectra

It is clear from the above that analysis of ENDOR spectra is not trivial. A variety of computer programs exist for the simulation of ENDOR spectra. A convenient program is that written (now in C; earlier versions, known as GENDOR, were in BASIC) by Hoffman and coworkers, GENSIM, which is widely used in their work (http://www.chem.northwestern.edu/~bmh/endor.htm; accessed 03/01/2007). This program simulates ENDOR spectra of nuclei with arbitrary orientation with respect to **g**. In its later versions, GENSIM directly incorporates the distance (R) into dipolar coupling calculations of the type described above (*see* Section 2.4).[60] Another program, DDPOWHE, written in Fortran (now g77 Fortran) generates ENDOR spectra for a single nucleus ($I \leq 9/2$) coupled to an electronic spin ($S \leq 9/2$). This program is more cumbersome than GENSIM, but has the advantage that the ''g-over-g'' and pnZ effects described above for $S > 1/2$ are automatically incorporated since there is no use of fictitious spin, although an estimate of the zfs parameters is needed. The exact calculation methods included in DDPOWHE are also relevant with $S = 1/2$ systems, for analysis of ENDOR signals from quadrupolar ($I > 1/2$) nuclei. When the quadrupole splitting is similar in magnitude either to the Larmor splitting (for signals centered at $A^N/2$) or to the hyperfine splitting (for signals centered at ν^N), the readily interpreted, first-order situation (equation 6) does not obtain and exact calculation methods are needed.

Arguably the best software currently available is the EasySpin package written by Stefan Stoll at the ETH-Zürich.(http://www.easyspin.ethz.ch/main.html; accessed 03/01/2007). This package covers every possible situation one might encounter in ENDOR, as well as other areas of EPR, but does require access to MathCad® software. Nevertheless, the old adage ‘‘garbage in—garbage out’’ applies, and no sophistication of software can compensate for a lack of understanding by the user.

3.2 Background on Sample Requirements for ENDOR

The sample requirements for ENDOR are essentially the same as for EPR, given that an EPR signal is monitored. Fused silica tubes of diameter appropriate for the microwave cavity dimensions are used: typically, 3 mm inner diameter (i.d.) for X-band, 2–2.5 mm i.d. for 35 GHz, capillary tubes for W-band (95 GHz). Fused silica is in the absence of paramagnetic impurities (as opposed to borosilicate glass) and has the appropriate dielectric properties for microwave transmission. These tube sizes result in sample volumes of ~50 and ~250 μL for 35 GHz and X-band, respectively, so that the sample volume is rarely an issue, even for metalloproteins. Single crystals can also be studied by ENDOR, as with EPR. For metalloproteins, ENDOR at higher frequencies is preferable, where the small sample size is not a drawback. An example is the W-band ENDOR study on azurin.**[37]** However, for the vast majority of bioinorganic systems (metalloproteins and model compounds), solutions are generally used. So far as metalloproteins in aqueous solution are concerned, the high dielectric constant of water makes EPR of aqueous solutions difficult at room temperature; however, the fast electronic relaxation times of bioinorganic systems precludes their study by EPR at room temperature in most cases (and makes ENDOR impossible). Ice, in contrast, has a low dielectric constant and is perfectly suitable for low temperature EPR measurements; however, purely aqueous solvents are not recommended. Although optical quality glasses are not required, it is generally necessary to include some glassing agent, typically ethylene glycol or glycerol (~10% v/v; for a sample in D_2O, ethylene glycol-d_2 and glycerol-d_3 are needed). These glassing agents break up the spin–spin communication in the aqueous solvent that contributes to the faster relaxation times of ENDOR signals, which particularly affect pulsed experiments. Methanol or ethanol or mixtures of the two or aqueous alcohols are also suitable. Bioinorganic model compounds can also be studied by ENDOR and purely organic solvents are generally suitable. Neat toluene or 1:1 v/v toluene–acetonitrile are recommended solvents. One organic solvent that is often used in EPR, but has proved problematic in the author’s experience in terms of explosive thawing is neat 2-methyltetrahydrofuran (2-Me-THF). However, THF with as little as ~2% v/v 2-Me-THF has the glassing properties of 2-Me-THF without its destructive properties.

Furthermore, the complex relaxation requirements of a double resonance technique mean that low temperatures are required in all cases. In general, temperatures below that of liquid nitrogen are needed. These are obtained either with a variable temperature flow cryostat using liquid helium (~4–40 K) or with a liquid helium immersion dewar (~4 K, or ~2 K for pumped (superfluid) helium).

An EPR signal of reasonable signal-to-noise (S/N) is necessary, but not sufficient for successful ENDOR spectroscopy, again due to the relaxation properties, that is, good EPR does not necessarily mean good ENDOR, but the reverse (i.e., weak EPR signal giving strong ENDOR signals) is very unlikely. In general, most bioinorganic (i.e., metal centered paramagnetic) systems with $S = 1/2$ that are available in concentrations of at least 0.1 mM (with the range 0.5–1 mM being preferable) have the potential for providing useful ENDOR spectra, assuming nuclei of interest are present, whether naturally (^{1}H is always present, but not necessarily informative) present or artificially (organism growth on isotopically enriched media or use of isotopically labeled substrate) introduced. Such systems could be mononuclear, i.e., authentic $S = 1/2$, such as d^9 (Cu^{II}, Ni^{I}), low-spin d^7 (Fe^{I}, Co^{II}, Ni^{III}), low-spin d^5 (Fe^{III}), and d^1 (Mo^{V}, V^{IV}), to list metal ions with which the author is personally familiar, or the systems could be multinuclear, but with total spin 1/2 ground states, such as in di-iron enzymes ($Fe^{II}Fe^{III}$) and various iron–sulfur proteins (e.g., 3Fe-ox ($[Fe_3S_4]^+$) cluster-containing proteins). High-spin ($S > 1/2$) EPR systems can be more problematic, perhaps because of faster relaxation processes due to the multiplicity of electronic states. Nevertheless, certain high-spin systems have proved amenable to ENDOR, such as the mononuclear high-spin Fe^{III} in fluorometmyoglobin ($S = 5/2$),**[56]** and multinuclear system resting state of nitrogenase FeMo-cofactor ($S = 3/2$).**[54]** The characteristic of these two systems is that they are nearly uniaxial (i.e., generally $|E/D| < 0.1$; here, $|E/D| = 0.053$ for nitrogenase;**[54]** $|E/D| \leq 0.002$ for fluorometmyoglobin**[56]**) with very well-defined EPR spectra (i.e., narrow lines, ‘‘Pake pattern’’) observable up to relatively high temperatures (liquid nitrogen temperatures for fluorometmyoglobin). Other high-spin systems have been partly successful, in that ENDOR signals from some, but not all, nuclei of interest were observable. These include high-spin Co^{II} ($S = 3/2$) in a Co-substituted zinc finger protein, TFIIIA,**[70]** and high-spin Mn^{II} ($S = 5/2$) in a mononuclear enzyme, FosA.**[51]** In both cases, ENDOR signals from ^{31}P associated with substrate (for FosA; ^{31}P from DNA in the case of TFIIIA) were observed, but not ^{14}N from coordinating residues (other Co-substituted proteins with histidine ligands have been investigated by

ENDOR). The EPR characteristics of these two systems were that they were relatively more rhombic, with broader EPR linewidths and observable only at lower temperatures, all relative to the axial systems listed above. Yet another spin system of interest is high-spin d^5 with very large rhombicity (the maximum is $|E/D| = 1/3$; a larger value simply corresponds to a change in principal axis), which is the case for mononuclear Fe^{III} in many cases such as oxidized rubredoxin and other mononuclear nonheme Fe proteins. In the author's experience, such systems have not been fruitful. Apparently, the relaxation properties and ill-defined EPR spectra make such systems generally unsuccessful candidates for investigation by ENDOR. A final class that one might also imagine to be unsuitable for ENDOR is the rhombic systems with $S = 2$ (or higher integer values), which include mononuclear high-spin Fe^{II} and certain multinuclear systems such as reduced di-iron proteins ($Fe^{II}Fe^{II}$)[71] and various iron–sulfur proteins (e.g., 3Fe-red ($[Fe_3S_4]^0$) cluster-containing proteins).[72,73] These systems exhibit the so-called ''non-Kramers'' signal at very low magnetic fields (very high g_{obs}).[74] It is possible to record ^1H ENDOR spectra of such systems,[75–77] although attempts by the author to record ^{57}Fe ENDOR spectra of $S = 2$ FeS proteins have proved unsuccessful.

3.3 Instrumental Requirements for ENDOR

The instrumental aspects of EPR have been summarized elsewhere,[1,4,5] although the text by Poole is especially noted for instrumental details and parameters.[78] Obviously, to perform ENDOR experiments, one must have an EPR spectrometer, of which Bruker Biospin is the sole viable vendor at present (http://www.bruker-biospin.com/brukerepr/index.html; accessed 03/01/2007). ENDOR accessories include the rf synthesizer and amplifiers and a microwave resonant cavity that includes rf coils in addition to the normal structure with field modulation coils. Locally constructed ENDOR spectrometers were more common in the past, with that of the late Clyde A. Hutchison Jr being a notable example, particularly for single-crystal studies.[65] Such spectrometers still exist; the author is familiar with those at Northwestern University.[79–81]

3.3.1 Continuous Wave (CW) ENDOR Spectroscopy Employing Radiofrequency Modulation Detection (RFMD-ENDOR)

In such a spectrometer, the magnetic field modulation (typically at 100 kHz, and at amplitudes of 0.1–1 mT) used to record a typical EPR spectrum is turned off. The microwave power is usually set to saturating conditions. The rf is swept through the desired range, but is modulated during this process, much as the magnetic field is modulated to record an EPR spectrum. The phase sensitive detection used in this method yields first-derivative lineshape ENDOR signals, just as field-modulated EPR yields first-derivative EPR signals (when under slow passage conditions[8–10]). This experimental protocol is what is employed in commercial Bruker spectrometers (http://www.bruker-biospin.com/brukerepr/continuous waveendor.html; accessed 03/01/2007).

3.3.2 CW ENDOR Spectroscopy Employing Magnetic Field Modulation Detection (FMD-ENDOR)

In such a spectrometer, there is no modulation of the rf while it is swept, however, the magnetic field modulation is left on. The resulting ENDOR spectra exhibit absorption lineshapes (when under rapid-passage conditions, as are typically the cases here). The appearance of ENDOR spectra can be quite sensitive to the field modulation amplitude because of its effect on this type of ''packet shifting'' ENDOR. This means that the NMR transition removes a ''packet'' of spins from the EPR envelope, which would in principle reduce the EPR signal and lead to negative pointing ENDOR signals. In practice, ENDOR signals recorded by this method can be either negative or positive and this behavior can be the case not only for different nuclei (i.e., ^{57}Fe versus ^1H), and for magnetically inequivalent nuclei of the same isotope, but even for the ν_+ and ν_- partners of a given ENDOR signal from a single nucleus (or a set of magnetically equivalent nuclei).[48] This type of ENDOR was that originally developed by Feher fifty years ago[13] and is still a tremendously effective technique. A further, relatively recent improvement was the use of rf bandwidth broadening, effected by a white noise generator (normally used for communications equipment testing).[82] It might seem paradoxical that use of a broader, rather than narrower bandwidth would be beneficial in any type of spectroscopy. The reason is that CW ENDOR lines are relatively broad (often 500 kHz half-width half-maximum (hwhm)) so that linewidth is not bandwidth limited, while the use of a broader rf bandwidth leads to shifting of a larger spin packet and thus significantly larger S/N.[82] The white noise source can broaden rf up to 500 kHz, however, the range of 50–200 kHz is normally employed.

In addition to the positive and negative directions of ENDOR signals, there are also rf sweep effects, which are related to nuclear spin relaxation effects. These effects can be manifest in ''tailing'' in the sweep direction, giving an appearance coincidentally like that in high performance liquid chromatography (HPLC). There can also be a slight frequency shift in the rf sweep direction as well. Both of these effects can be mitigated by use of slower rf sweep rates and by comparison of forward (i.e., low to high rf) and reverse (high to low) sweeps. These effects appear to be more significant for nuclei, which are directly part of the paramagnetic center, for example, ^{57}Fe, ^{63}Cu, and in some cases ligand ^{14}N, rather than nuclei that are more indirectly coupled.

3.3.3 CW Stochastic ENDOR Spectroscopy Employing Magnetic Field Modulation Detection (FMDST-ENDOR)

A recent and very promising effort in CW ENDOR to alleviate these effects is the use of FMD-ENDOR with stochastic application of rf (FMDST-ENDOR). This technique was first developed by Brueggeman and Niklas,[83] and was refined by Doan, working in the Hoffman laboratory, for use with field-modulated CW ENDOR for application to bioinorganic systems.[84] The concept is a simple one: rather than sweeping the rf linearly, whether forward or reverse, over a given frequency range, one samples individual radiofrequencies in a random fashion and then constructs the spectrum from these. The individual frequency points are determined by dividing the desired rf range by the number of spectral points (e.g., 1000 points over the range 1–21 MHz gives random points every 20 kHz, with e.g., $\nu_{\mathrm{rf}}^{k} = 13.12\,\mathrm{MHz}$, $\nu_{\mathrm{rf}}^{k+1} = 9.12\,\mathrm{MHz}$, $\nu_{\mathrm{rf}}^{k+2} = 19.58\,\mathrm{MHz}, \ldots; k = 1-1000$). Note that the resolution of the rf synthesizer is not a limitation because such a synthesizer is ‘‘overengineered’’, in that it is designed for NMR applications (high resolution kHz frequencies) rather than lower resolution MHz frequencies needed for ENDOR. Because the rf application is not continuously swept, FMDST-ENDOR is a sort of ‘‘poor man’s’’ pulsed ENDOR (*see* Section 3.3.4) in that no pulsed microwave (i.e., EPR) generation is involved—only rf (i.e., NMR). The time constant (analog averaging function) that is used in normal EPR and CW ENDOR must not be used in FMDST-ENDOR as all averaging is done via the point by point data acquisition method.

The FMDST-ENDOR pulse sequence is shown in Figure 5. A key feature is the sampling of a baseline (i.e., rf off) before every sample point to ensure any baseline drift is compensated for. The baseline and sampling periods are generally fixed, but the time during which the k^{th} rf is applied (rf ‘‘pulse’’) and the delay time can each be varied to achieve optimal results. The delay time can range from zero (sampling concurrent with rf pulse) to a time immediately after completion of the rf (or even later), as well as intermediate values (as shown in Figure 5). FDMST-ENDOR has great promise for application to systems for which the lineshapes of standard CW ENDOR are severely distorted. Furthermore, the parameters of the FDMST-ENDOR sequence allow discrimination among overlapping samples and their quantification (*see* Section 4.1.5).[84]

3.3.4 Pulsed Mims ENDOR Spectroscopy

We next consider actual pulsed techniques. The definitive reference work in this area is the text by Schweiger and Jeschke.[29] Also notable is the much earlier review by Gemperle and Schweiger,[85] and the Bruker web site, which is extremely thorough (http://www.bruker-biospin.com/brukerepr/pulseeprtheory.html; accessed 03/01/2007).

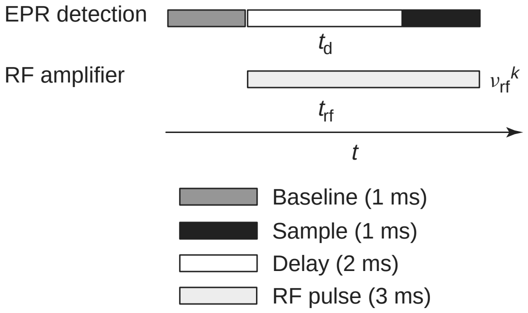

Figure 5 Field modulation detected stochastic (FMDST) ENDOR sequence. The upper level indicates monitoring of the EPR signal prior (baseline) and (usually) after (signal) application of the k^{th} rf pulse. This pulse is applied for time t_{rf}, and at frequency ν_{rf}^{k}, which is a randomly selected frequency among the total number of possible values determined by the rf range and number of spectral points. There is also a delay time, t_{d}, that can range from zero (sample concurrent with application of the k^{th} rf pulse) to $t_{\mathrm{d}} \geq t_{\mathrm{rf}}$ (sample immediately after application of the k^{th} rf pulse, or later); this example has an intermediate delay time: $0 < t_{\mathrm{d}} < t_{\mathrm{rf}}$. The timings of the baseline and sample periods are rarely altered, but the rf and delay times can be altered to optimize spectral appearance of a given sample. Typical times are given. (Adapted from Figure 2 in Lee, Igarashi, Laryukhin, Doan, Dos Santos, Dean, Seefeldt and Hoffman.[84] Reprinted with permission, © 2004 American Chemical Society)

Following their lead, it is worth beginning with a historical perspective. As mentioned earlier (*see* Section 1.2), EPR was discovered by Zavoisky in the mid 1940s, and ENDOR was discovered by Feher in the mid 1950s. Shortly after the discovery of NMR in the mid 1940s, the first pulsed NMR experiments, specifically the observation of a nuclear spin echo, were performed by Erwin L. Hahn, in 1950 at the University of Illinois-Urbana.[86] The electron spin echo (ESE) was first observed in 1958, independently by Blume at IBM (studying Na in $NH_{3(l)}$) and by Gordon and Bowers at Bell Telephone Laboratories (studying Si, presumably for the same reasons as Feher was).[87] This has led to electron spin echo envelope modulation (ESEEM) techniques (*see* ***Electron Spin Echo Envelope Modulation (ESEEM) Spectroscopy***). Pulsed ENDOR was discovered soon thereafter, by William B. Mims, also at Bell Telephone Laboratories, in the mid 1960s.[88] Mims and Peisach later pioneered the application of ESEEM to bioinorganic systems[89] and ENDOR. It is interesting to note how many crucial developments were made in corporate research laboratories in the USA. The author has come across excellent papers from the pre-1980 era on EPR of inorganic complexes from groups employed at not only Bell Telephone Laboratories and IBM, but at DuPont, Ford Motor, GE, Lockheed, RCA, Shell Oil, and others. That was truly a different era from today.

The method invented by Mims that bears his name was the first and is still the ‘‘workhorse’’ technique in pulsed ENDOR as it is ideal for providing high resolution spectra of nuclei with small hyperfine couplings, generally less than

2 MHz, and under ideal conditions, as low as 0.1 MHz. Nuclei such as ^{2}H, ^{13}C, ^{15}N, ^{19}F, and ^{31}P, generally from specifically labeled molecules interacting with the paramagnetic site via longer range dipolar coupling are typical targets as will be described in specific examples (*see* Section 4.1.3). Mims ENDOR also provides the best sensitivity among the pulsed ENDOR techniques. However, in the author's experience, pulsed ENDOR is normally less sensitive than CW ENDOR, so that a given system should always first be investigated (''screened'') by CW ENDOR to see what signals are available, and then examined by pulsed ENDOR for higher resolution and/or observation of weaker couplings.

The Mims pulse sequence is shown in Figure 6. It is based on a stimulated ESE sequence, in which there are three $\pi/2$ (90°) microwave pulses, with the first two (the preparation pulses) separated by a delay time τ. This is followed by a mixing period and then the third $\pi/2$ microwave pulse generates (stimulates) the ESE, observed during the detection period. To make this three-pulse ESE sequence into an ENDOR sequence, an rf pulse is applied during the mixing period, which causes polarization transfer between electronic and nuclear transitions.[29] The rf is stepped through the desired range, with the steps derived from the range and number of spectral points, as described earlier for FMDST-ENDOR (*see* Section 3.3.3). Normally, a number of ''shots'' (i.e., pulse sequences) are averaged at each rf point (e.g., 20 shots/point) and further signal averaging obtains by recording a number of spectra as a running total. There is a delay in time between each shot during which time (ideally) equilibrium magnetization is restored. Typical timings for each aspect of the sequence are given in Figure 6. For those familiar with NMR, note the much shorter times that occur in EPR (ns pulse widths, ms delay times) especially given that these experiments are done in frozen solution at liquid helium temperatures for bioinorganic systems. The specific timings in Figure 6 are based on routine use of the 35 GHz pulsed ENDOR spectrometer at Northwestern University constructed by Clark E. Davoust in the Hoffman laboratory. The microwave pulse power is also important and this is usually adjusted (with rf off) to maximize the ESE height. The rf power is relatively less important and experience has yielded standard settings for typical experiments. Instrumental details are outside the scope of this discussion, but are available elsewhere.[79] An X-band pulsed spectrometer was also constructed earlier,[80] however, for the reasons described above (*see* Section 2.2.2), use of the higher microwave frequency is generally preferable. For example, ^{2}H has $\nu^{N} \approx 2.3$ MHz at X-band, which is approaching the difficult region of very low rf (the baseline signal generally deteriorates as ν approaches $\sim$0 MHz), but $\nu^{N} \approx 8.2$ MHz at 35 GHz, well into an easily observable rf region.

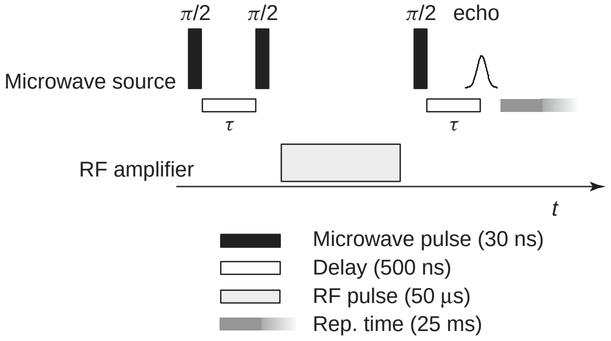

Figure 6 Mims ENDOR pulse sequence.[88] The upper level indicates the microwave pulses and immediately below delay times are indicated. The lowest level indicates the rf pulse. The timing is defined as pulse edge-to-edge, as depicted by Schweiger and Jeschke,[29] however, the timing can also be defined as pulse center-to-center.[90] Typical times are given based on a 35 GHz spectrometer.[79] The timing of the microwave and rf pulses is less commonly altered, but the delay time τ and the repetition time need significant adjustment to optimize spectral appearance of a given sample. Microwave phase cycling is also employed, but is not indicated in the figure

The above point is related to the Larmor-centered frequencies at which Mims ENDOR signals appear. It must be made clear, however, that this technique is not applicable irrespective of hyperfine coupling. Mims ENDOR is not really suitable for larger hyperfine couplings ($A^{N} > \sim$2 MHz, although this value should not be accepted blindly). This limitation is due in part to the ''blind spots'' or ''holes'' that occur in Mims ENDOR as given by the following equation:[88]

$$I_{\text{Mims}} \propto \left(\frac{1}{4}\right)[1 - \cos(2\pi A_{\text{iso}}\tau)] \qquad (9)$$

where τ is the delay time as defined above (A_{iso} can be replaced by the effective coupling at the given g_{obs} value), and I_{Mims} is the ENDOR signal intensity. This can be defined as the change in ESE intensity (measured as a voltage), V_{echo}, between resonant rf off and on. This measurement is useful in quantitative comparison of ENDOR signals across the EPR envelope of a given sample. One can also define the ENDOR fractional efficiency or effect, F_{ENDOR}, that is, the change in *normalized* ESE intensity between resonant rf off and on:

$$F_{\text{ENDOR}} = \left|\frac{[V_{\text{echo}}(\text{rf off}) - V_{\text{echo}}(\text{rf on})]}{V_{\text{echo}}(\text{rf off})}\right| * 100\% \qquad (10)$$

so that elimination of the echo yields an ENDOR effect of 100%, while no effect is obviously zero. If the echo were actually inverted by the rf polarization transfer, then the effect would be 200%, which is an almost unknown occurrence in our experience. Note that equation (10) as given by Schweiger and Jeschke has a factor of (1/2),[29] so that the elimination of an ESE via ENDOR gives an effect of only 50%. This parameter is useful in comparing different samples and different experimental runs on the same sample.[68]

As a result of equation (9), the Mims ENDOR signal is minimal (''blind'') at $\tau = (n/A_{\text{iso}})$, $n = 0$ (which is experimentally meaningless), 1, 2, ..., and is maximum at $\tau = [(2n+1)/2A_{\text{iso}}]$.[29] Mims ENDOR spectra of a broad ^{1}H pattern can clearly show the oscillating ''blind spot'' pattern experimentally and the software developed by Doan can include this effect in simulation by inclusion of equation (9) and the user entry of the τ value.[60] The distortions in a Mims ENDOR pattern caused by ‘‘blind spots’’ can greatly complicate interpretation by suppressing peaks (which might actually be useful at times[91]) and/or making a single peak appear a doublet. Therefore, one would prefer to record an undistorted Mims ENDOR spectrum, that is, where the first holes appear outside the $\nu_\pm$ partners. For practical purposes, the maximum undistorted A_{iso} (MHz) is $\sim 1/(2\tau\ (\mu\text{s}))$,[29] so that $A_{\text{iso}} \approx 2$ MHz would require $\tau \approx 0.25\,\mu\text{s}$ (250 ns). Is this reasonable? Figure 6 would seem to indicate that any value can be used until the $\pi/2$ pulses overlap. This is not the case in reality. A microwave pulse does not simply go from maximum power to zero instantaneously; there is a ‘‘deadtime’’, which is highly variable from one sample to the next and even from one day to the next with a given sample. This ‘‘cavity ringdown’’ from the microwave pulse can severely distort the ESE and lead to very high noise and/or temporal instability. A value for $\tau = 0.5\,\mu\text{s}$ free of distortion is readily achievable (so the maximum $A_{\text{iso}} \approx 1$ MHz), but much shorter τ values can be a challenge. In any case it is desirable to record Mims spectra with varying τ values to monitor such behavior. A method to overcome this limitation will be discussed in Section 3.3.6.

For readers interested in the quantitative description of the time-dependent magnetization processes, the magnetization ‘‘grating’’, that occurs in Mims ENDOR using the density operator formalism, which leads to the experimental behavior described earlier, the reader is referred to other sources by authors infinitely more qualified than the present one.[29,48,91]

3.3.5 *Pulsed Davies ENDOR Spectroscopy*

The other major form of pulsed ENDOR spectroscopy is known as Davies ENDOR, after its discoverer, E. R. Davies at the Clarendon Laboratory, Oxford, UK.[92] Davies ENDOR is in many ways complementary to Mims ENDOR in that the former is more suited for larger couplings and the latter for smaller couplings, as described earlier (Section 3.3.4).

The Davies pulse sequence is shown in Figure 7. In this sequence, an initial π microwave pulse is applied, inverting the magnetization, followed by the mixing period in which an rf pulse is applied and ENDOR transitions occur. These are observed by application of a primary ESE sequence, a $\pi/2$ pulse followed by a delay time τ during which dephasing occurs, followed by a second π pulse and delay time τ during which rephasing occurs with observation of an ESE. For tuning purposes, the first (π) pulse is switched off and the standard ESE signal can be optimized. This first pulse ‘‘burns a hole’’ in the magnetization that is then ‘‘filled in’’ by ENDOR shifting of spin packets. As a result, in Davies ENDOR the signals are usually observed as an increase in the echo voltage, i.e., $[V_{\text{echo}}(\text{rf off}) - V_{\text{echo}}(\text{rf on})]$ is positive, while in Mims ENDOR there is usually a decrease, i.e., $[V_{\text{echo}}(\text{rf off}) - V_{\text{echo}}(\text{rf on})]$ is negative. In practice, the complex nature of relaxation phenomena means that, particularly in Davies ENDOR, the direction of ENDOR signals is not totally predictable.

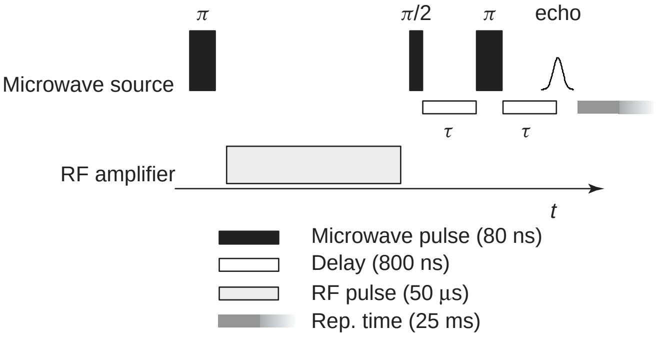

Figure 7 Davies ENDOR pulse sequence.[92] The upper level indicates the microwave pulses and immediately below delay times are indicated. The lowest level indicates the rf pulse. Typical times are given based on a 35 GHz spectrometer.[79] The timing of the microwave and rf pulses is less commonly altered, but the delay time τ and the repetition time need significant adjustment to optimize spectral appearance of a given sample. Microwave phase cycling is also employed, but is not indicated in the figure

The important difference between the Mims and Davies experiments, however, is that in Davies ENDOR there are no ‘‘blind spots’’, although the minimum hyperfine coupling observable is generally less than in Mims ENDOR and the sensitivity is usually lower, since Davies ENDOR is more sensitive to the phase memory of the ESE. Thus a Davies ENDOR spectrum would be expected to provide the same information as a CW spectrum, often with a better baseline and resolution, albeit with longer acquisition time. The true advantage of Davies ENDOR is that it offers a form of hyperfine selection, analogous to the use of Mims holes to suppress signals. This ability was shown by Doan *et al.* using a pulsed X-band spectrometer and only the standard Davies sequence,[91] as opposed to earlier, more elaborate selection methods that required additional equipment to modify the EPR signal during the ENDOR experiment. A Davies ENDOR signal is dependent on the magnitude of the hyperfine coupling (at the particular g_{obs} value), A^N (MHz; over which there is no control), and on the microwave π (preparation) pulse length (t_p, μs, which value can be user selected, within instrumental limitations). The product gives a selectivity parameter, $\eta^N = (A^N t_p)$. As a rule of thumb for the longer t_p values traditionally employed in Davies ENDOR, when $\eta^N > 1$, the ENDOR response will be observed; when $\eta^N < 1$, ENDOR will be suppressed. For ^{1}H, the hyperfine couplings are typically small while for other nuclei (e.g., ^{57}Fe, ligand ^{14}N), the couplings are large, yet, as described earlier (Section 2.2.2) these signals are often overlapping at X-band. Davies ENDOR, however, allows discrimination amongst these signals. Use of a ‘‘hard’’ pulse ($t_p = 30$ ns) effectively suppresses all signals with

$A^N < \sim 6\,\text{MHz}$ ($\eta^N < \sim 0.2$), which would cover much of the ^{1}H ENDOR pattern in many metalloprotein systems, while for nuclei with $A^N > \sim 30\,\text{MHz}$ (e.g., ^{57}Fe, ligand ^{14}N), ENDOR would be readily observable ($\eta^N > \sim 1$). Use of a very ''soft'' pulse ($t_p = 600\,\text{ns}$) allows observation of weak couplings ($A^N > \sim 1\,\text{MHz}$; $\eta^N > \sim 0.6$). This method was thus dubbed ''POSHE'' (for *pro*ton *s*uppression and *h*eteronuclear *e*nhancement).**[91]**

Use of very short preparation pulses, however, is not ideal since the size of the spin packet that potentially gives an ENDOR signal is small (i.e., a longer pulse affects more spins). There is a trade off between selectivity and signal intensity of the hyperfine selected nucleus. As shown by Fan *et al.*, who give numerous quantitative examples on metalloproteins, the ideal situation actually obtains for $\eta^N = 0.7$.**[80]**

3.3.6 Pulsed ReMims (Doan) ENDOR Spectroscopy

A final development in pulsed ENDOR using standard instrumentation is that discovered by Doan and Hoffman, which they called ReMims ENDOR, for refocused (or remote-echo) Mims ENDOR.**[90]** By analogy with the eponymous nomenclature of other pulsed ENDOR techniques, the author will also refer to this technique as Doan ENDOR. ReMims (Doan) ENDOR is a four-pulse variation of Mims ENDOR. The pulse sequence is shown in Figure 8. The preparation and mixing portions of the sequence are identical to that described above for Mims ENDOR (*see* Figure 6). Furthermore, comparison of Figure 7 with Figure 8 shows that the Davies sequence is simply a special case of the ReMims (Doan) ENDOR sequence in which $\tau_1 = 0$ ($\tau_2 \equiv \tau$), so that the first two $\pi/2$ pulses collapse into one π pulse and all of the echoes described below are one and the same.

The key feature of ReMims (Doan) ENDOR is that τ_1 can be less than the ''deadtime'' of the spectrometer. This is because, in contrast to Mims ENDOR, the stimulated spin echo (which would be distorted by cavity ringdown) is not detected. Instead, an additional π pulse is applied after time τ_2, which leads to a ''standard'' spin echo at time τ_2 (Hahn echo, since it results from the original Hahn sequence; here from the third $\pi/2$ pulse and the following π pulse). More important, there are two additional spin echoes formed: one at time $(\tau_2 + \tau_1)$, which is observable for all values of τ_1 and τ_2, and is denoted the RME, which is detected, and one at time $(\tau_2 - \tau_1)$, which is observable only for values of $\tau_2 > \tau_1$, and is denoted the refocused stimulated echo (RSE). The deadtime for the ReMims (Doan) sequence is thus the minimum feasible value of $(\tau_2 + \tau_1)$, rather than the minimum value of τ_1 in a Mims sequence (Figure 6). As mentioned earlier (Section 3.3.4), the maximum undistorted A_{iso} (MHz) is $\sim 1/(2\tau_1\ (\mu\text{s}))$. The deadtime in the X-band pulsed spectrometer is $t_\text{d} \approx 0.1\,\mu\text{s}$ (100 ns), thus $\tau_1 > 0.1\,\mu\text{s}$ in a Mims sequence and the maximum coupling is $\sim$5 MHz; however, in a ReMims (Doan) sequence, $\tau_1 \approx 0.05\,\mu\text{s}$ (combined with $\tau_2 \approx 0.1\,\mu\text{s}$), therefore couplings up to $\sim$10 MHz can be observed without distortion. A ReMims (Doan) experiment requires more acquisition time than a Mims experiment (due to loss of phase memory over the overall lengthier sequence). However, a relatively low S/N ReMims experiment can be performed at $\tau_1 < t_\text{d}$ and then compared to a Mims experiment at $\tau \approx t_\text{d}$. Are there any distortions in the Mims ENDOR spectrum? If not, then the (more efficient) Mims experiments are sufficient and spectra can be averaged to achieve publishable S/N. But what about comparison with Davies or CW ENDOR? Davies ENDOR is

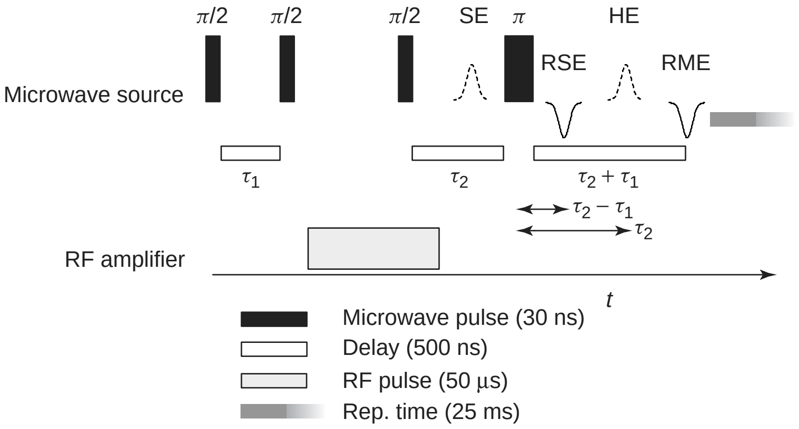

Figure 8 ReMims (Doan) ENDOR pulse sequence.**[90]** The upper level indicates the microwave pulses and immediately below delay times are indicated. The lowest level indicates the rf pulse. SE is the stimulated echo that is not detected, RSE is the refocused stimulated echo that can be detected (for $\tau_2 > \tau_1$; as shown here), and RME is the refocused Mims echo that is normally detected (at time $\tau_2 + \tau_1$). HE is the Hahn echo that is not detected and normally eliminated by microwave phase cycling. Typical times are given based on an X-band ($\sim$9.6 GHz) spectrometer,**[80]** but are also applicable at 35 GHz. The timing of both delay times τ_1 and τ_2 are adjusted to optimize spectral appearance as desired. Other aspects are similar to standard Mims ENDOR

often unsuitable for a sample with poor phase memory (i.e., a weak ESE, despite a large CW EPR signal). CW ENDOR often simply does not have the resolution of pulsed methods and often has more distorted lineshapes due to relaxation effects absent in pulsed experiments.

3.3.7 Pulsed TRIPLE Spectroscopy

As discussed earlier (Section 2.4.3), simulation of field-dependent ENDOR spectra for a given nucleus (or set of magnetically equivalent nuclei) allows determination of the *relative* signs of the components of a hyperfine matrix, which is crucial in understanding dipolar coupling, although it is not possible to determine the *absolute* signs. However, it is possible via a modification (augmentation) of standard ENDOR, known as *double ENDOR* or TRIPLE (which does not apparently stand for anything) to determine the relative signs of hyperfine couplings among different nuclei. If the absolute sign of any one of these can be determined by theoretical prediction or by some other experimental technique (e.g., paramagnetic NMR (*see* ***Nuclear Magnetic Resonance (NMR) Spectroscopy of Metallobiomolecules*** or ***Mössbauer Spectroscopy***), then absolute sign determination is possible.

TRIPLE was first demonstrated as a CW technique applied to organic radicals in fluid solution,**[93]** for which the signs of coupling constants could provide important information on the nature of the SOMO. For bioinorganic systems, their inherently broad linewidths mean that maximum resolution is needed, thus the most meaningful form of TRIPLE is as a pulsed technique. A Davies pulse sequence is shown for TRIPLE in Figure 9. All aspects of the pulse sequence are the same as for a standard (i.e., single ENDOR) Davies experiment (*see* Figure 7), except that there are now two rf channels. The first, rf_1, is fixed to correspond to a specific nuclear transition (e.g., ν_+ of specific nucleus) and is thus the ''pump''. The second, rf_2, is swept as described for a standard Davies experiment and is thus the ''probe''. The reader is directed elsewhere for a more detailed description,**[29]** but the main point is that if two NMR transitions have the same origin, then irradiation of one will affect the intensity of the other. For example, in an $S = 1/2$ system with two nuclear spins ($I_1 = I_2 = 1/2$; $A_{\text{iso}} > 0$ for *both*, $g_N > 0$), then the NMR transitions $|M_S, M_{I1}, M_{I2}\rangle = |-1/2, +1/2, +1/2\rangle \longleftrightarrow |-1/2, -1/2, +1/2\rangle$ and $|-1/2, +1/2, +1/2\rangle \longleftrightarrow |-1/2, +1/2, -1/2\rangle$, which correspond to ν_+ for both I_1 and I_2, are coupled so that irradiation of the $\Delta M_{I1} = \pm 1$ transition at ν_{1+} will affect the ENDOR intensity of the $\Delta M_{I2} = \pm 1$ transition at ν_{2+} and *vice versa*. The ENDOR spectra of the ν_- transitions for I_1 and I_2, $|M_S, M_{I1}, M_{I2}\rangle = |+1/2, -1/2, -1/2\rangle \longleftrightarrow |+1/2, +1/2, -1/2\rangle$ and $|+1/2, -1/2, -1/2\rangle \longleftrightarrow |+1/2, -1/2, +1/2\rangle$, respectively, will be unaffected by the irradiation at ν_{1+} (or at ν_{2+}). The difference between a standard ENDOR spectrum and a TRIPLE spectrum (i.e., the difference between rf_1 off and rf_1 on) is best to demonstrate the TRIPLE effect. In this example, the difference spectrum would cancel out the ν_{1-} and ν_{2-} transitions, since neither is affected by rf_1, but the signals of the ν_{1+} and ν_{2+} transitions would both change and clearly appear in the difference spectrum. If the sign of A_{iso} for I_2 were opposite to that for I_1, then ν_{1+} and ν_{2-} transitions would show up most strongly in the difference spectrum.

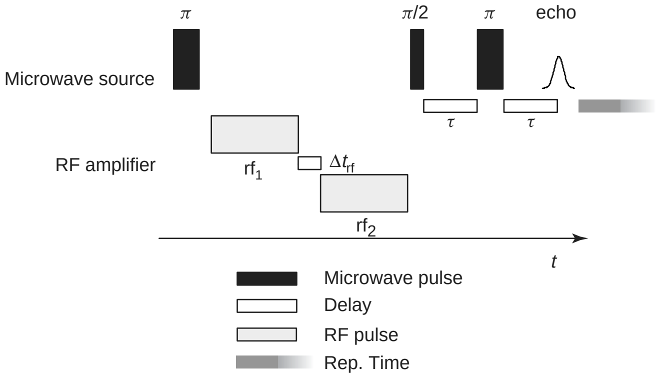

Figure 9 Davies TRIPLE pulse sequence.**[29]** The uppermost level indicates the microwave pulses and immediately below, delay times are indicated. The two lower levels indicate the rf pulses. The first rf energy (rf_1) is fixed and corresponds to a resonant nuclear transition and the second rf (rf_2) is swept over a range of frequencies to yield an ENDOR spectrum. The rf_1 pulse would be omitted to provide the control for a difference TRIPLE spectrum. The timing would be similar to a standard Davies sequence (*see* Figure 7). A Mims TRIPLE pulse sequence likewise would be the same as in Figure 6, except with two rf pulses as shown here

An example of the use of TRIPLE in a bioinorganic system is its application to the $[\text{Fe}_3\text{S}_4]^+$ ($S = 1/2$) cluster of *Desulfovibrio gigas* hydrogenase.**[68]** The protein was exchanged in D_2O buffer and the ^{2}H ENDOR signals of interest derived from solvent-derived molecules H-bonded to the cluster. Such H-bonding can affect the redox and other properties of FeS clusters. TRIPLE experiments demonstrated two points, the first that a given pair of ^{2}H signals was due to the same form of the cluster. The second point was that pumping on a $\nu_\pm$ signal of one ^{2}H affected the $\nu_\mp$ signal of the other ^{2}H, which indicated the opposite signs of A for these two hydrogen atoms (the relationship for ^{1}H is the same as for ^{2}H).**[68]** Such information is useful for the development of models of spin delocalization in an FeS cluster.

3.3.8 Pulsed ''Implicit TRIPLE'' Spectroscopy

The above description is of standard TRIPLE, i.e., explicit TRIPLE, employing two rf energies. Pulsed ENDOR can also exhibit relative sign information, in the absence of an additional rf energy. This phenomenon has been called ''implicit TRIPLE'',**[69]** and was demonstrated for nitrile hydratase, a nonheme iron enzyme (low-spin Fe^{III}, $S = 1/2$). Standard Mims ENDOR experiments were performed and the intensities of $\nu_\pm$ signals for ^{1}H were compared for natural abundance enzyme (i.e., ^{14}N, $I = 1$) and enzyme globally enriched in ^{15}N ($I = 1/2$). The latter sample exhibited the expected roughly equal intensities for $\nu_{\pm}$ partners of ^{1}H Mims ENDOR signals, while the natural abundance sample exhibited anomalous intensities. These anomalous intensities arose because the ESEEM provided by the ^{14}N nuclei (which is absent for ^{15}N) coupled to the paramagnetic site (as ligands) in effect provided the second rf energy, normally provided by a second rf pulse in explicit TRIPLE.[69] A detailed explanation for this process is given by Doan *et al*., however, the consequence is that when the ^{1}H and ^{14}N hyperfine couplings have the same sign, then the ν_{-} partner of a given ^{1}H Mims ENDOR signal is suppressed, while ν_{+} is suppressed when the two have opposite signs. Thus, the same information is obtained as from a TRIPLE experiment, but with standard ENDOR equipment. The disadvantage is that without comparison to samples in the absence of this ESEEM effect, assignment of signs might be overly optimistic since there might be other factors leading to $\nu_{\pm}$ partner intensity differences.

Another advantage of ReMims (Doan) ENDOR is the ability to observe this implicit-TRIPLE effect for a wider range of hyperfine couplings.[90] A given hyperfine coupling could be deleteriously affected by Mims blind spots, which would prevent observation of implicit TRIPLE. However, use of ReMims (Doan) ENDOR would allow selection of τ value(s) that do not cause troublesome blind spots while simultaneously suppressing ESEEM, so that the presence of the implicit TRIPLE effect could be explored.

4 APPLICATIONS

4.1 Nitrogenase

4.1.1 Background on Molybdenum Nitrogenase

The enzyme nitrogenase is found in a number of anaerobic microorganisms, such as *Azotobacter vinelandii* and *Clostridium pasteurianum*.[94,95] Nitrogenase catalyzes the ambient temperature and pressure reduction (‘‘fixation’’) of dinitrogen to ammonia by the following reaction:

$$N_2 + 8H^+ + 8e^- \longrightarrow 2\,NH_3 + H_2 \qquad (11)$$

Owing to both the biological importance and the chemical difficulty of this reaction, nitrogenase enzymes have been very widely studied by biological and chemical techniques.[94–98] Extensive synthetic modeling efforts have also been made.[99] The active site of nitrogenase, referred to as FeMo-cofactor, resides within the MoFe protein, and comprises an unusual $MoFe_7S_9$ cluster that contains a single Mo (bound to the cluster and also coordinated by homocitrate, and possibly another atom, ‘‘X’’, as yet unidentified[100]). The MoFe protein also contains another unusual $[Fe_8S_7]$ cluster, referred to as the P-cluster. Here we merely highlight selected recent studies on the FeMo-cofactor that made use of ENDOR spectroscopy.[97,98]

4.1.2 ENDOR Studies on the Resting State of Nitrogenase FeMo-cofactor

Much of this work has been discussed earlier (Section 2.3.3) in the context of ENDOR spectroscopy of high-spin ($S > 1/2$) systems, as the electronic spin ground state of nitrogenase FeMo-cofactor has $S = 3/2$. From a historical perspective, this work was one of the earlier applications of ENDOR to metalloprotein systems by the Hoffman laboratory,[53,54] and owed a great deal of its success to the biochemical expertise of the late William H. Orme-Johnson, one of the pioneers not only of nitrogenase research but of bioinorganic chemistry in general.[101]

Analysis of the ^{57}Fe ENDOR spectra of isotopically enriched FeMo-cofactor indicated the number of magnetically distinct Fe sites in the cluster,[53,54,102] which, well before the crystal structure of nitrogenase was determined,[103] was important in understanding the unusual structure of the FeMo-cofactor. Specifically, five Fe sites were identified and characterized by their hyperfine coupling tensors. This information, in combination with studies on model compounds and other FeS proteins can provide information on the oxidation state of the Fe ions and the nature of their coupling. Other experimental techniques, in particular Mössbauer spectroscopy, were applied to analyzing the Fe sites in this system, but ENDOR has the advantage that only those Fe ions that are associated with the paramagnetic center under interrogation (i.e., contributing to the EPR signal at a particular g_{obs} value) will give rise to ENDOR signals. In contrast, Mössbauer spectroscopy simultaneously observes all Fe atoms. This lack of specificity is a particular problem for understanding nitrogenase since the enzyme has two component proteins, the MoFe protein of interest here, and an Fe protein involved in electron transfer that will not be discussed here, so that the total number of Fe sites is very large.

What ENDOR was also able to accomplish with regard to the resting state FeMo-cofactor, which was not possible for Mössbauer spectroscopy, was to elucidate the nature of the Mo site.[53,104] This result represented a remarkable collaboration between spectroscopy and enzymology. Enzyme samples enriched in several Mo isotopes were prepared by microbe growth on a medium containing the following molybdate isotopologs: ^{100}Mo (97.4%, $I = 0$), ^{97}Mo (94.2% (9.6% natural abundance), $I = 5/2$), and ^{95}Mo (96.5%, (15.9% natural abundance), $I = 5/2$). The ^{100}Mo-enriched sample was needed as a zero-spin baseline control since the natural abundance of the nonzero spin Mo isotopes (as indicated) is sufficiently high so that a natural isotopic abundance sample would not be a convincing ENDOR control. Careful comparison of CW X-band ENDOR spectra of these samples indicated that the FeMo-cofactor contained a single Mo site, and the small magnitude of the observed hyperfine coupling, $A^{95\mathrm{Mo}} \approx 5-8$ MHz, indicated a diamagnetic Mo ion, either $\mathrm{Mo^{IV}}$ or $\mathrm{Mo^{VI}}$, as opposed to paramagnetic $\mathrm{Mo^{III}}$ or $\mathrm{Mo^{V}}$. ENDOR also provided ^{95}Mo quadrupole coupling information, which allowed assignment of the formal oxidation state of the Mo site to $\mathrm{Mo^{IV}}$. This assignment was based on information from ^{95}Mo NMR studies of model compounds and on the qualitative consideration that $\mathrm{Mo^{VI}}$, a $\mathrm{d^0}$ ion, would be expected to show very small quadrupole coupling.

Enzyme samples from microbes grown on ^{33}S enriched medium (0.75% natural abundance, $I = 3/2$) allowed observation of ^{33}S ENDOR**[53]** results that were also useful in characterizing the inorganic sulfide sites in the FeMo-cofactor, as at that time, the cluster was indeed a ''black box''.

4.1.3 *ENDOR Studies on Inhibitor States of the Nitrogenase FeMo-cofactor—Carbon Monoxide*

A major biochemical breakthrough in the biochemical investigation of nitrogenase was the ability to prepare EPR-active inhibitor states of the enzyme. Under traditional turnover conditions (i.e., N_2, ATP, Fe protein, etc., all present), the resting state EPR signal disappears, rendering any ENDOR studies useless. However, it was found that turnover in the presence of the inhibitor CO led to the observation of two new EPR signals, both of $S = 1/2$ species: lo-CO, observed under low CO concentration (partial pressure, 0.08 atm), rhombic with $g_{\mathrm{av}} < 2$: $\mathbf{g} = [2.09, 1.97, 1.93]$, and hi-CO, observed under high CO concentration (0.5 atm), axial with $g_{\mathrm{av}} > 2$: $\mathbf{g} = [2.17, 2.06, 2.06]$.**[105,106]** These EPR results were the first evidence of a small molecule interacting with the MoFe protein, but no direct information on the nature of the CO interaction was obtainable.

Such information was provided by ENDOR studies of both the lo-CO and hi-CO inhibitor forms of the FeMo-cofactor prepared with isotopically enriched ^{13}CO**[105,107,108]** and ^{57}Fe (*see* subsequent text).**[107,109]** The combination of CW and pulsed 35 GHz ^{13}C ENDOR demonstrated that there is a single CO molecule bound to the FeMo-cofactor in the lo-CO state and at least two CO molecules bound in the hi-CO state. Representative ENDOR spectra of the ^{13}CO signals are shown in Figure 10. The hyperfine couplings for the ^{13}CO bound in lo-CO and for one of the two molecules in hi-CO are quite small: $A_{\mathrm{iso}} = 1.2$, 0.7 MHz, respectively.**[108]** The measurement of these small couplings was an excellent example of the use of Mims and ReMims (Doan) ENDOR. The ^{13}C hyperfine coupling tensors, in combination with information from EPR and ENDOR studies on iron carbonyl compounds and other model compound and metalloprotein systems, as well as spin delocalization studies of nitrogenase, led to a proposed geometry of CO binding to the FeMo-cofactor. This structure is shown in Figure 11, in which the CO that binds initially bridges two Fe ions (μ_2 geometry), while the two CO molecules in the hi-CO form bind terminally to each of two different Fe ions.

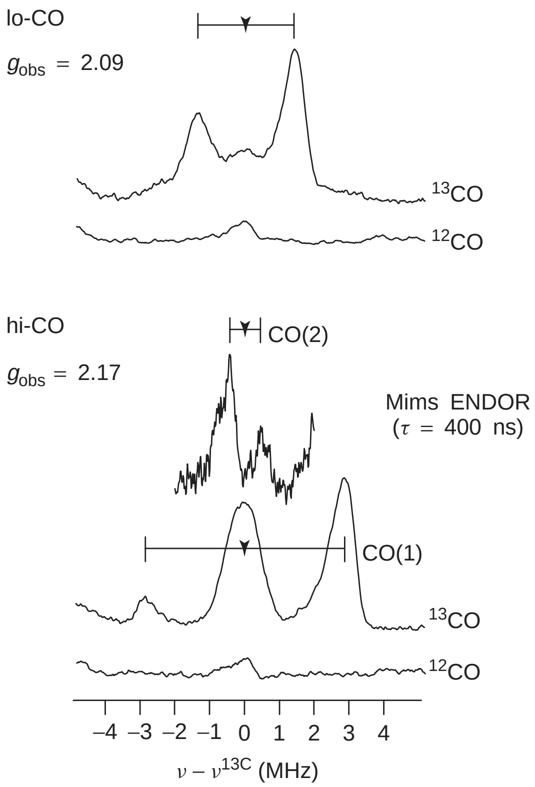

Figure 10 35 GHz CW ^{13}C ENDOR (except for Mims ENDOR as indicated) of lo-CO and hi-CO inhibitor forms of nitrogenase FeMo-cofactor, prepared with both ^{13}CO and ^{12}CO. The spectra were recorded at $g_{\max}$ of each species, as indicated. The spectra are centered at the ^{13}C Larmor frequency ($\nu^{13\mathrm{C}} \approx 12.3$ MHz at $g_{\max} = 2.17$ for hi-CO). The ^{13}C ENDOR signals from the cluster-bound CO molecules are indicated. The spectra of samples prepared with ^{12}CO show weak signals from natural abundance ^{13}C, most likely from protein residues in the cluster vicinity. (Adapted from Figure 5 in Pollock, Lee, Cameron, DeRose, Hales, Orme-Johnson and Hoffman.**[105]** Reprinted with permission, © 1995 American Chemical Society)

In parallel with this work using ^{13}C isotopologs, extensive work was done on the CO-inhibited turnover states using ^{57}Fe-enrichment.**[107,109]** One of the first studies employed MoFe protein in which, through beautiful biochemical work, its two inorganic constituents, the FeMo-cofactor and the P-cluster, were each labeled with ^{57}Fe to yield specifically labeled $[(\mathrm{Mo^{57}Fe})(\mathrm{P\text{-}Fe})]$ and $[(\mathrm{MoFe})(\mathrm{P\text{-}^{57}Fe})]$, as well as both globally enriched and natural abundance MoFe protein.**[107]** Representative 35 GHz CW ^{57}Fe ENDOR spectra of all of these isotopolog samples are shown in Figure 12, which clearly shows that the signals are due only to the FeMo-cofactor. Thus the EPR signal that results under turnover conditions in the presence of CO arises *only* from the active site of the MoFe protein. With this established, the next step was a detailed quantitative analysis, primarily by field-dependent

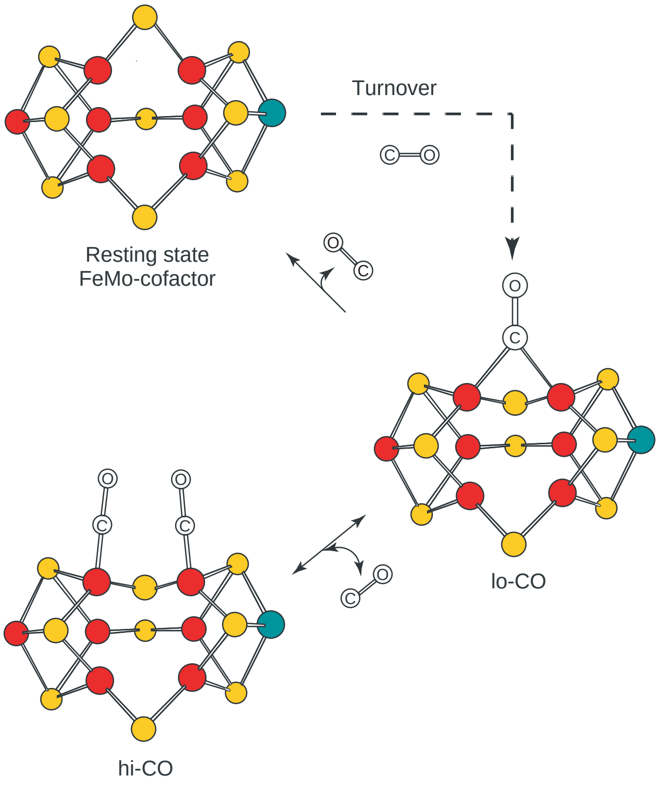

Figure 11 Cartoon showing CO binding to the FeMo-cofactor of nitrogenase FeMo protein. The S atoms are shown in yellow, the Fe atoms in red, and the Mo atom in blue-green. At lower CO partial pressure, the lo-CO form exists with a single, bound, bridging CO. At higher CO partial pressure, the hi-CO form exists, with two CO molecules bound to the cluster

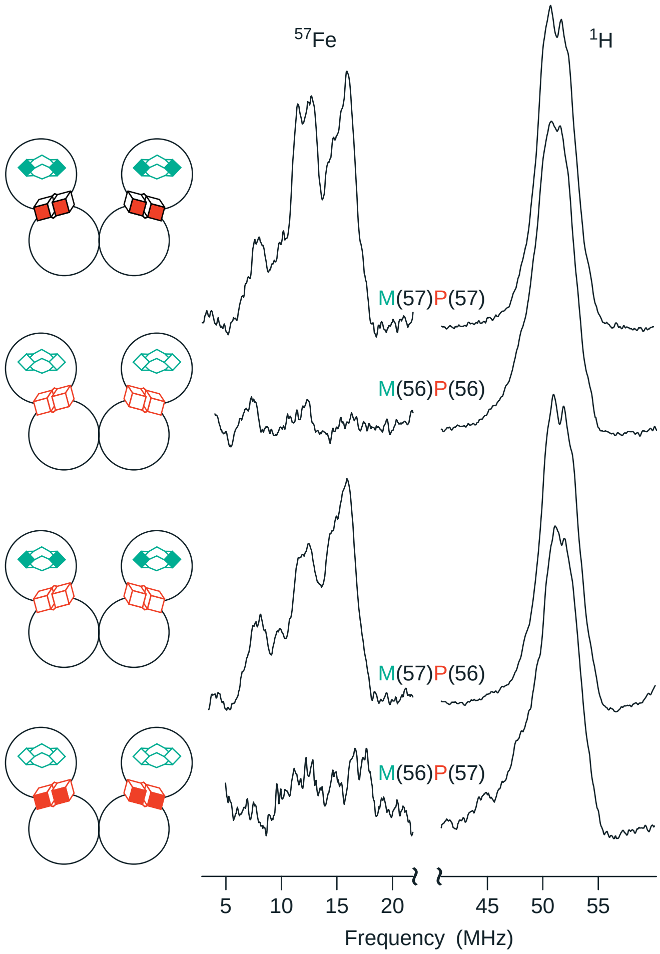

Figure 12 35 GHz ^{57}Fe and ^{1}H CW ENDOR spectra of the hi-CO form of nitrogenase MoFe protein with varying types of ^{57}Fe-enrichment. The ^{1}H signals are included as intensity standards since the natural abundance samples contain observable amounts of ^{57}Fe. The spectra were recorded at $g_{\mathrm{obs}} = 2.06$ ($g_{\perp}$). Cartoons on the left indicate the specific sample, wherein the FeMo-cofactor is indicated by the diamond shape (in green), and the P-cluster is indicated by the two cubes (in red). These shapes roughly represent the clusters' actual structures. ^{57}Fe-enriched sites are indicated as colored blocks. The abbreviations used are as follows: M(56)P(56) is natural abundance FeMo-cofactor and P-cluster; M(56)P(57) is natural abundance FeMo-cofactor and enriched P-cluster; M(57)P(56) is enriched FeMo-cofactor and natural abundance P-cluster; M(57)P(57) is enriched FeMo-cofactor and P-cluster (i.e., globally enriched MoFe protein). (Adapted from Figure 1 in Christie, Lee, Cameron, Hales, Orme-Johnson and Hoffman.[107] Reprinted with permission, © 1996 American Chemical Society)

CW 35 GHz ENDOR, of the individual Fe sites in the CO-inhibited forms,[109] much as had been done earlier for resting state FeMo-cofactor.[54] Hyperfine coupling constants were determined for four Fe sites in the lo-CO and three in the high-CO forms. The signs and magnitudes of the A_{iso}^{57}Fe values, in comparison with those of other FeS proteins and with extensive computational studies,[55] allowed a proposal as to the formal oxidation state assignments of the metal ions in the FeMo-cofactor as: $[\mathrm{Fe_7S_9Mo}]^{+} = [(\mathrm{Fe}^{2.5+})_2, \mathrm{Fe_5}^{2+}, \mathrm{S_9}^{2-}, \mathrm{Mo}^{4+}]^{+}$, where $(\mathrm{Fe}^{2.5+})_2$ is the delocalized $\mathrm{Fe^{II}Fe^{III}}$ pair.[109]

4.1.4 *ENDOR Studies on Substrate Analogue Turnover States of the Nitrogenase FeMo-cofactor—Ethyne*

Another molecule isoelectronic with the substrate dinitrogen and the inhibitor carbon monoxide is ethyne (acetylene), which is a substrate for nitrogenase (producing ethene, a process used as an assay for nitrogenase activity).[110] Hales and coworkers showed that a site-directed mutant of wild-type nitrogenase, in which the α-subunit histidine-195 residue was substituted by glutamine (denoted α-H195Q-FeMo-cofactor), was not active in N_2 reduction, but did reduce C_2H_2 at the rate similar to wild-type enzyme. Of relevance here is that this mutant, under turnover conditions with ethyne, allowed observation of three different $S = 1/2$ EPR signals ($S_{\mathrm{EPR1,2,3}}$, of which S_{EPR3} was very minor), presumably arising from the interaction of ethyne with the FeMo-cofactor.[111]

As above with the CO-inhibited forms, only by means of ENDOR spectroscopy was it possible to demonstrate that the substrate was indeed interacting with the active site cluster. As with CO, ^{13}C labeling was employed, although in this case there are two labeled atoms: $^{13}C_2H_2$. However, there is an additional, convenient isotopic label, not available with CO, namely C_2D_2. Thus, α-H195Q-FeMo-cofactor under turnover conditions in the presence (0.1 atm) of natural isotopic abundance ethyne, $^{13}C_2H_2$, and C_2D_2 were investigated by 35 GHz CW ENDOR.**110** The major species, S_{EPR1}, exhibited signals assignable to both ^{13}C atoms of ethyne, which were nearly equivalent ($A_{\mathrm{iso}}^{13}\mathrm{C} = 2.5$ and 2.3 MHz, respectively), and to an additional, very weakly coupled ^{13}C (the other two, minor EPR signals did not give observable ^{13}C couplings). The experiments with ^{1,2}H isotopologs were more sophisticated than might be naively thought, since there is also the consideration of buffer composition. Thus, there were four cases to be investigated by ^{1,2}H ENDOR: C_2D_2 in D_2O buffer, C_2D_2 in H_2O buffer, C_2H_2 in D_2O buffer, and C_2H_2 in H_2O buffer. The primary result from comparisons among these spectra was that samples prepared with C_2H_2 exhibited a strongly coupled (maximum $A^{1\mathrm{H}} \sim 13$ MHz) ^{1}H signal that is absent for samples prepared with C_2D_2, even in H_2O buffer. Thus, this hydrogen must be associated with ethyne substrate and is not solvent exchangeable.**110** Unfortunately, it was not possible to determine whether this signal was due to one or two hydrogen atoms, which is related to the limitations of ENDOR (Section 2.3.2). Enzymological studies showed that reduction of C_2H_2 in D_2O yields primarily *cis*-CHDCHD. It was therefore proposed that the model for ethyne binding consistent with spectroscopic data, organometallic models, computational and structural studies of cluster spin density and structure, and biochemical results, was that S_{EPR1} arises from ethyne bound to two cluster Fe ions as shown in Scheme 1.**110**

The bonding depicted is deliberately vague and could be described either as π-bound alkyne or as a σ-bound alkene dianion. This model will be expanded on and revised in Section 4.1.6.

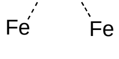

Scheme 1 Bonding of ethyne to FeMo-cofactor as originally proposed**110**

4.1.5 *ENDOR Studies on Substrate Analogue Turnover States of the Nitrogenase FeMo-cofactor—Propargyl Alcohol (Prop-2-yn-1-ol)*

The molecules described above, CO and C_2H_2 (Sections 4.1.3 and 4.1.4, respectively), are obvious choices for probes of nitrogenase. Less obvious is a molecule used very recently and successfully, propargyl alcohol (PA, prop-2-yn-1-ol, HC≡C–CH_2OH).**84** What was also critical in this project was the preparation of another site-directed mutant of nitrogenase, in which the α-subunit valine-70 residue was substituted by alanine (denoted α-V70A-FeMo-cofactor). In this mutant, the enzyme can reduce larger alkynes, such as PA, which are nearly inactive with wild-type nitrogenase. Not only did this expand the range of substrate probes available, but the mutation also showed the location of substrate binding onto the cluster.**112**

Trapping of a reaction intermediate of α-V70A-FeMo-cofactor under turnover conditions with PA yields a species with $S = 1/2$ and $\mathbf{g} = [2.123, 1.998, 1.986]$.**84** Use of the globally labeled isotopolog $H^{13}C{\equiv}^{13}C{-}^{13}CH_2OH$ yielded ^{13}C ENDOR spectra indicating three types of carbon signals.**112** Further refinement was possible through use of commercially available PA-^{13}C3 ($H^{13}C{\equiv}C{-}CH_2OH$) and a series of ^{1,2}H samples analogous to those described above for ethyne: DC≡C–CH_2OD in D_2O buffer, DC≡C–CH_2OH in H_2O buffer, HC≡C–CH_2OD in D_2O buffer, and HC≡C–CH_2OH in H_2O buffer. The 35 GHz CW and ReMims (Doan) ^{13}C ENDOR spectra are shown in Figure 13. The higher resolution (albeit with lower S/N) of the ReMims (Doan) ENDOR spectra relative to CW is striking. These studies allowed precise determination of the ^{13}C hyperfine coupling tensors for the three C atoms of PA.**84**

The ^{1,2}H was also a dramatic demonstration of the possibility of quantitative ENDOR, since qualitative results were ambiguous. Only in the ''perdeuterated'' sample (DC≡C–CH_2OD in D_2O buffer) was a strongly coupled ($A_{\mathrm{iso}} = 13.8$ MHz) ^{1}H signal absent in CW ^{1}H ENDOR. Thus the signal could not be clearly assigned either to the solvent nonexchangeable (near neutral pH) alkynyl H or to a hydrogen atom derived from the solvent. The answer was found by use of ^{1}H FMDST-ENDOR (*see* Section 3.3.3), wherein the signal intensity can be quantitated and is without sweep and other artifacts. The result is shown in Figure 14. As expected, the ''perdeuterated'' sample exhibits essentially baseline. The ''perprotiated'' sample (HC≡C–CH_2OH in H_2O buffer) exhibits the strongest signal, almost exactly twice the intensity of the two isotopologs of PA (DC≡C–CH_2OH and HC≡C–CH_2OD). The explanation for this behavior is that the PA-derived species bound to the FeMo-cofactor contains two magnetically equivalent H atoms, one derived from solvent (H_a^S) and one derived from H–C3 of PA (H_a^C). Extensive consideration of organometallic complexes, in combination with the hyperfine couplings known for organic radicals, led to the proposal that the species observed by ENDOR was a bound allyl alcohol ($CH_2{=}CHCH_2OH$), effectively with a symmetry plane through the C–C bond. The resulting structure is shown in Scheme 2, which includes the observed A_{iso} values for ^{13}C and ^{1}H atoms. Note that this scheme represents a σ-bound ferracyclopropane, ''ferracycle'', rather than a π-bound alkene.**84**

This result for PA led to a reevaluation of the binding of ethyne, which included extensive additional 35 GHz

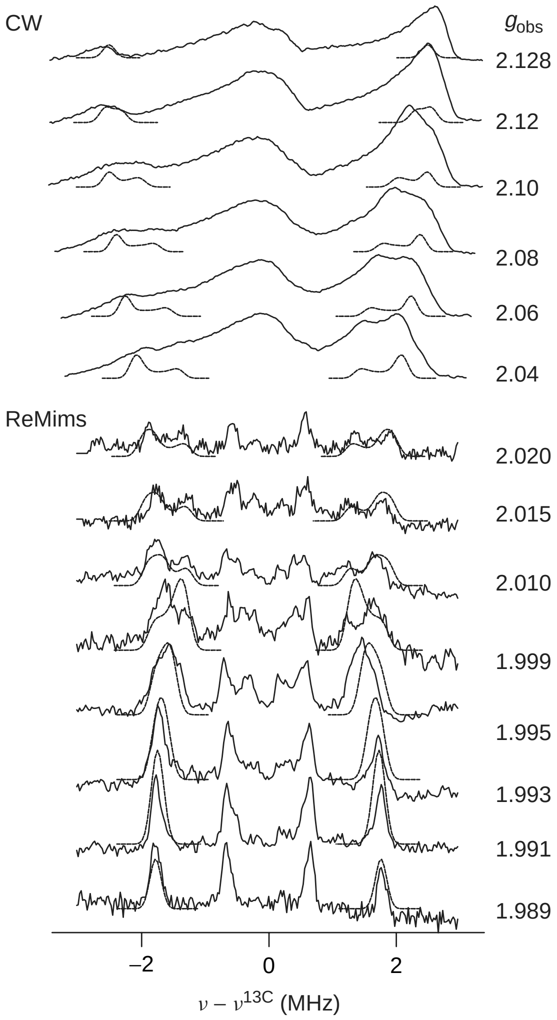

Figure 13 35 GHz ^{13}C CW ENDOR (upper set of spectra) and ReMims (Doan) ENDOR (lower set of spectra) of α-V70A-FeMo-cofactor under turnover conditions with propargyl alcohol (PA) labeled at C3: $H^{13}C{\equiv}C{-}CH_2OH$. The ENDOR spectra were recorded at field positions (g_{obs} values as indicated) across the EPR envelope of the PA intermediate, which has $\mathbf{g} = [2.123, 1.998, 1.986]$. Spectra are centered at the ^{13}C Larmor frequency ($\nu^{13C} = 13.4$ MHz at $g = 2.0$). Simulations are also shown as dashed lines for features of interest. (Adapted from Figure 4 in Lee, Igarashi, Laryukhin, Doan, Dos Santos, Dean, Seefeldt and Hoffman.**84** Reprinted with permission, © 2004 American Chemical Society)

^{57}Fe and ^{1}H CW ENDOR spectroscopy on α-H195Q-FeMo-cofactor.**113** As a result of this work, the binding of ethyne to the FeMo-cofactor is now proposed to be to a single Fe ion of the cluster, whether as a π-bound species or as a σ-bound ferracycle. Moreover, by analogy with the results for PA binding,**84** the trapped turnover state that is actually observed by ENDOR contains ethene, not ethyne, bound to the cluster. This is depicted in Scheme 3, where no substituents are given, since the specific geometry is not known. This scheme is a much simplified version of Figure 8 from Lee *et al*.**113**

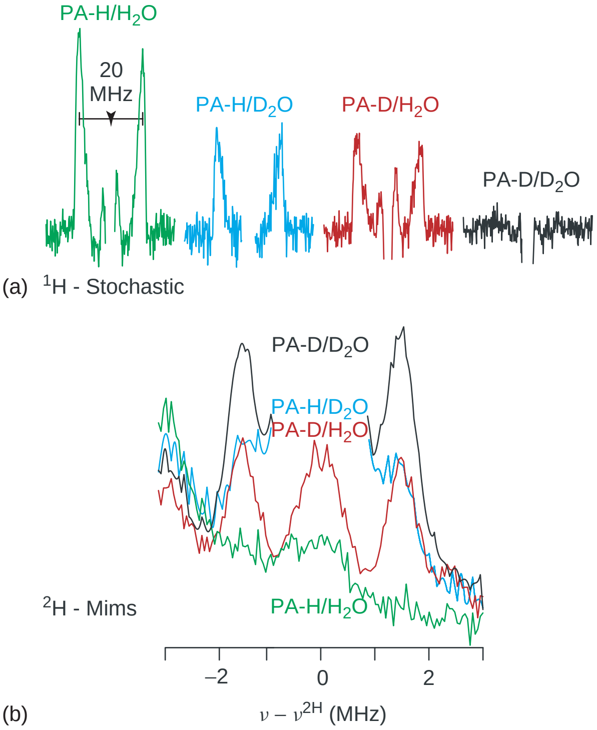

Figure 14 35 GHz ^{1}H FMDST-ENDOR (a) and ^{2}H Mims ENDOR (b) of α-V70A-FeMo-cofactor under turnover conditions with propargyl alcohol (PA) with various forms of hydrogen isotope labeling. The spectra were recorded at $g_{obs} = 1.989$ ($\sim g_{min}$). The abbreviations used in the figure are as follows: $DC{\equiv}C{-}CH_2OD$ in D_2O buffer: PA-D/D$_2$O; $DC{\equiv}C{-}CH_2OH$ in H_2O buffer: PA-D/H$_2$O; $HC{\equiv}C{-}CH_2OD$ in D_2O buffer: PA-H/D$_2$O; $HC{\equiv}C{-}CH_2OH$ in H_2O buffer: PA-H/H$_2$O. ^{1}H FMDST-ENDOR spectra are centered at the ^{1}H Larmor frequency, $\nu^{1H} \approx 53.7$ MHz; rf scale shown for strongest ^{1}H coupling, $A^{1H} \approx 20$ MHz). The ^{2}H Mims ENDOR spectra are centered at the ^{2}H Larmor frequency ($\nu^{2H} \approx 8.2$ MHz). In all cases, strong signals from distant ^{1,2}H nuclei, which are of no biochemical interest, are removed. (Adapted from Figure 6 in Lee, Igarashi, Laryukhin, Doan, Dos Santos, Dean, Seefeldt and Hoffman.**84** Reprinted with permission, © 2004 American Chemical Society)

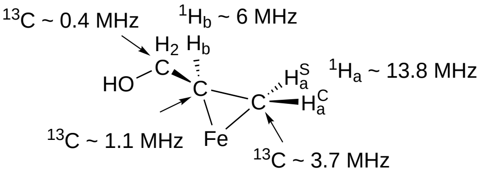

Scheme 2 Hyperfine couplings of propargyl alcohol bound to Fe of FeMo-cofactor

4.1.6 *Other Nitrogenase ENDOR Studies and Summary Comments*

There are additional ENDOR studies on nitrogenase FeMo-cofactor that have not even been mentioned here. These include studies on the alternative substrate carbon disulfide,

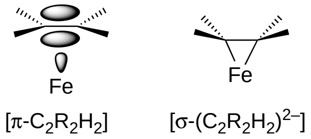

Scheme 3 Bonding of alkene to FeMo-cofactor as later refined.[113] Geometrical isomerism (E, Z) of $C_2R_2H_2$ is not specified

which yields an $S = 1/2$ intermediate that was investigated by ^{13}C ENDOR of samples trapped with bound $^{13}CS_2$.[114] The mutant α-V70I-FeMo-cofactor fails to react with any substrate, presumably due to blockage of the active site by the large isoleucine sidechain, but the enzyme can still perform the hydrogenase reaction under turnover conditions and exhibits a novel $S = 1/2$ EPR signal.[115] CW 35 GHz ^{1}H ENDOR studies revealed two types of strongly coupled ($A_{\mathrm{iso}} \approx 23$ MHz) hydrogen atoms. The large coupling means that these are covalently bound to the FeMo-cofactor cluster, but their assignment as H^+ (hydron) or H^- (hydride) could not be made. Nevertheless, the comparison of the **A** matrices for these two ^{1}H atoms allowed speculation as to the geometry of their binding to the cluster.[115]

Of perhaps greater interest are the very recent EPR/ENDOR studies of turnover states derived from nitrogen-containing molecules, as opposed to carbon-containing molecules, namely methyl-diazene ($CH_3N{=}NH$) and hydrazine ($NH_2\,NH_2$) molecules,[116,117] with studies on diazene itself very recently reported.[118] Space limitations prevent discussion of these very recent results, but the method of analysis is as described here for the carbon-containing molecules. These doubly and singly nitrogen–nitrogen bonded molecules, which can be studied as both ^{14}N and ^{15}N isotopologs, are likely intermediates in the transformation of triply bonded N_2 into separate NH_3 molecules.

From a biochemical point of view, the summation of the ENDOR studies on nitrogenase FeMo-cofactor interacting with carbon-containing small molecules is an electron inventory of the resting state, lo-CO form, and ethyne-bound form (S_{EPR1}), resulting in the proposal that the resting state is two electrons more oxidized than the substrate/inhibitor-bound forms and further, that these forms could be placed into the context of the Lowe-Thorneley scheme of nitrogen fixation.[113]

From the point of view of inorganic chemistry, these ENDOR studies on nitrogenase FeMo-cofactor give definitive evidence of a remarkable series of bioorganometallic complexes, which should provide both a challenge and inspiration to synthetic chemists.

5 ACKNOWLEDGMENTS

I wish to thank Prof. Brian M. Hoffman, Northwestern University, for creating the outstanding laboratory where I have been exposed to ENDOR spectroscopy, beginning in the mid 1980s. I also wish to thank Dr. Peter E. Doan, Northwestern University, for many helpful instructions over the years, and other members of the Hoffman group, particularly Dr. Nicholas S. Lees and Dr. Rebecca L. McNaughton for their helpful comments on this paper. I also wish to thank Prof. Hong In Lee, Kyungpook National University, Korea, for his generous assistance with the sections on nitrogenase. I thank Prof. Judith N. Burstyn, University of Wisconsin-Madison, for providing samples of CooA.

6 ABBREVIATIONS AND ACRONYMS

CW = continuous wave; ENDOR = electron-nuclear double resonance; EPR = electron paramagnetic resonance; ESR = electron spin resonance; EMR = electron magnetic resonance; ESEEM = electron spin echo modulation; ESE = electron spin echo; FMDST = field modulation detected stochastic; hwhm = half-width half-maximum; HPLC = high performance liquid chromatography; NMR = nuclear magnetic resonance; PA = propargyl alcohol; pnZ = pseudonuclear Zeeman; rf = radiofrequency; RNR = ribonucleotide reductase; RSE = refocused stimulated echo; SOMO = semi-occupied molecular orbital; $2-Me-THF$ = 2 − methyltetrahydrofuran; zfs = Zero-field splitting (for $S > 1/2$); D = Uniaxial zfs; E = Rhombic zfs; **g** = **g** Matrix (for $S > 0$) with principal components g_x, g_y, g_z, or g_1, g_2, g_3; **A** = **A** Matrix (for $I > 0$) with principal components A_x, A_y, A_z, or A_1, A_2, A_3; g_e = Free electron g value; g_N = Nuclear g value (isotropic) for a given nucleus N (nuclear spin $I > 0$); A^N = Hyperfine coupling constant for a given nucleus N (nuclear spin $I > 0$); P^N = Quadrupole coupling constant for a given nucleus N (nuclear spin $I > 1/2$); ν_+ = Higher frequency partner of an ENDOR signal (for $I = 1/2$) or partners (for $I \geq 1$); ν_- = Lower frequency partner of an ENDOR signal (for $I = 1/2$) or partners (for $I \geq 1$); $\nu_\pm$ = The two partners of ENDOR signal (for $I = 1/2$) or set of partners (for $I \geq 1$); ν^N = Larmor (NMR) frequency of nucleus N at a given external magnetic field B; rf = Radiofrequency (in MHz); τ = Delay time in a pulsed EPR or ENDOR sequence; t = Microwave or rf pulse time in a pulsed EPR or ENDOR sequence.

7 RELATED ARTICLES

Magnetic Circular Dichroism (MCD) Spectroscopy; Nuclear Magnetic Resonance (NMR) Spectroscopy of Metallobiomolecules; Nuclear Quadrupole Resonance (NQR) Spectroscopy; Electron Spin Echo Envelope Modulation (ESEEM) Spectroscopy.

8 FURTHER READING

A. Abragam and B. Bleaney, 'Electron Paramagnetic Resonance of Transition Ions', Dover Publications, New York, 1986, This advanced text, (A^2B^2), originally written in 1970 and reprinted with minor updating, is the ''Bible'' of the field. It also includes a detailed, very physically oriented, chapter on ENDOR.

P. C. Dos Santos, R. Y. Igarashi, H.-I. Lee, B. M. Hoffman, L. C. Seefeldt and D. R. Dean, *Acc. Chem. Res.*, 2005, **38**, 208. A very recent review of nitrogenase related to the topics discussed here.

C. Gemperle and A. Schweiger, *Chem. Rev.*, 1991, **91**, 1481. This excellent review is somewhat out of date, but is accessible on-line, in contrast to books.

W. Gordy, 'Theory and Applications of Electron Spin Resonance', John Wiley & Sons, New York, 1980, This older text covering all aspects of EPR is particularly useful for understanding hyperfine coupling in organic radicals.

L. Noodleman, C. Y. Peng, D. A. Case and J. M. Mouesca, *Coord. Chem. Rev.*, 1995, **144**, 199. This review, while now somewhat out-of-date, is very helpful for understanding the electronic structure of FeS clusters including hyperfine coupling, relevant to nitrogenase and other systems.

A. Schweiger and G. Jeschke, 'Principles of Pulse Electron Paramagnetic Resonance', Oxford University Press, Oxford, 2001, This text provides everything needed related to modern pulsed methods in EPR, ESEEM, and ENDOR.

J. Telser ed., 'Paramagnetic Resonance of Metallobiomolecules', ACS Symposium Series 858, American Chemical Society, Washington, DC, 2003, The author cannot be objective here, but this recent volume contains useful articles on ESEEM and ENDOR including case studies on nitrogenase, heme enzymes, FeS enzymes, and other areas.

J. A. Weil, J. R. Bolton and J. E. Wertz, 'Electron Paramagnetic Resonance: Elementary Theory and Practical Applications', John Wiley & Sons, New York, 1994, This text (WWB) provides everything needed related to EPR theory and practice in general, including some information on ENDOR.

9 REFERENCES

1. J. A. Weil, J. R. Bolton and J. E. Wertz, 'Electron Paramagnetic Resonance: Elementary Theory and Practical Applications', John Wiley & Sons, New York, 1994.
2. B. R. McGarvey, *Transition Metal Chem., Ser. Advan.*, 1966, **3**, 89.
3. A. Abragam and B. Bleaney, 'Electron Paramagnetic Resonance of Transition Ions', Dover Publications, New York, 1986.
4. W. Gordy, in 'Theory and Applications of Electron Spin Resonance', ed. W. West, John Wiley & Sons, New York, 1980.
5. G. E. Pake and T. L. Estle, in 'The Physical Principles of Electron Paramagnetic Resonance', 2nd edition, ed. W. A. Benjamin, Advanced Book Program, Reading, 1973.
6. T. G. Brown and B. M. Hoffman, *Mol. Phys.*, 1980, **39**, 1073.
7. H. Frauenfelder, S. G. Sligar and P. G. Wolynes, *Science*, 1991, **254**, 1598.
8. C. Mailer and C. P. S. Taylor, *Biochim. Biophys. Acta*, 1973, **322**, 195.
9. A. A. Bugai, *Sov. Phys. Solid State*, 1963, **4**, 2218.
10. A. M. Portis, *Phys. Rev.*, 1955, **100**, 1219.
11. R. W. Clark, H. Youn, R. B. Parks, M. M. Cherney, G. P. Roberts and J. N. Burstyn, *Biochemistry*, 2004, **43**, 14149.
12. B. R. McGarvey, *Coord. Chem. Rev.*, 1998, **170**, 75.
13. G. Feher, *Phys. Rev.*, 1956, **103**, 834.
14. G. Feher, *Phys. Rev.*, 1959, **114**, 1219.
15. G. Feher, C. S. Fuller and E. A. Gere, *Phys. Rev.*, 1957, **107**, 1462.
16. G. Feher and E. A. Gere, *Phys. Rev.*, 1959, **114**, 1245.
17. G. Feher, R. A. Isaacson, C. P. Scholes and R. L. Nagel, *Ann. N.Y. Acad. Sci.*, 1973, **222**, 86.
18. C. P. Scholes, R. A. Isaacson and G. Feher, *Biochim. Biophys. Acta*, 1972, **263**, 448.
19. C. P. Scholes, A. Lapidot, R. Mascarenhas, T. Inubushi, R. A. Isaacson and G. Feher, *J. Am. Chem. Soc.*, 1982, **104**, 2724.
20. R. Calvo, E. C. Abresch, R. Bittl, G. Feher, W. Hofbauer, R. A. Isaacson, W. Lubitz, M. Y. Okamura and M. L. Paddock, *J. Am. Chem. Soc.*, 2000, **122**, 7327.
21. W. Lubitz, R. A. Isaacson, M. Y. Okamura, E. C. Abresch, M. Plato and G. Feher, *Biochim. Biophys. Acta*, 1989, **977**, 227.
22. O. M. Usov, P. S.-T. Choi, J. P. Shapleigh and C. P. Scholes, *J. Am. Chem. Soc.*, 2005, **127**, 9485.
23. O. M. Usov, Y. Sun, V. M. Grigoryants, J. P. Shapleigh and C. P. Scholes, *J. Am. Chem. Soc.*, 2006, **128**, 13102.
24. B. Epel, J. Niklas, S. Sinnecker, H. Zimmermann and W. Lubitz, *J. Phys. Chem. B*, 2006, **110**, 11549.
25. L. V. Kulik, B. Epel, W. Lubitz and J. Messinger, *J. Am. Chem. Soc.*, 2005, **127**, 2392.
26. M. Brecht, M. van Gastel, T. Buhrke, B. Friedrich and W. Lubitz, *J. Am. Chem. Soc.*, 2003, **125**, 13075.
27. D. J. Lowe, *Prog. Biophys. Mol. Biol.*, 1992, **57**, 1.
28. J. Harmer, C. Finazzo, R. Piskorski, C. Bauer, B. Jaun, E. C. Duin, M. Goenrich, R. K. Thauer, S. Van Doorslaer and A. Schweiger, *J. Am. Chem. Soc.*, 2005, **127**, 17744.
29. A. Schweiger and G. Jeschke, 'Principles of Pulse Electron Paramagnetic Resonance', Oxford University Press, Oxford, 2001.
30. B. M. Hoffman, *Acc. Chem. Res.*, 2003, **36**, 522.
31. B. M. Hoffman, *Proc. Natl. Acad. Sci. U.S.A.*, 2003, **100**, 3575.

32. B. M. Hoffman, V. J. DeRose, P. E. Doan, R. J. Gurbiel, A. L. P. Houseman and J. Telser, *Biol. Magn. Reson.*, 1993, **13**, 151.
33. B. M. Hoffman, *Acc. Chem. Res.*, 1991, **24**, 164.
34. B. M. Hoffman, R. J. Gurbiel, M. M. Werst and M. Sivaraja, in ‘Advanced EPR. Applications in Biology and Biochemistry’, ed. A. J. Hoff, Elsevier, Amsterdam, 1989, p. 541.
35. C. J. Walsby, D. Ortillo, J. Yang, M. R. Nnyepi, W. E. Broderick, B. M. Hoffman and J. B. Broderick, *Inorg. Chem.*, 2005, **44**, 727.
36. B. R. McGarvey, *J. Phys. Chem.*, 1967, **71**, 51.
37. J. W. A. Coremans, O. G. Poluektov, E. J. J. Groenen, G. W. Canters, H. Nar and A. Messerschmidt, *J. Am. Chem. Soc.*, 1996, **118**, 12141.
38. I. Gromov, V. Krymov, P. Manikandan, D. Arieli and D. Goldfarb, *J. Magn. Reson.*, 1999, **139**, 8.
39. P. Manikandan, R. Carmieli, T. Shane, A. J. Kalb and D. Goldfarb, *J. Am. Chem. Soc.*, 2000, **122**, 3488.
40. M. Bennati, N. Weiden, K.-P. Dinse and R. Hedderich, *J. Am. Chem. Soc.*, 2004, **126**, 8378.
41. G. Bar, M. Bennati, H.-H. T. Nguyen, J. Ge, J. Stubbe and R. G. Griffin, *J. Am. Chem. Soc.*, 2001, **123**, 3569.
42. B. F. Bellew, C. J. Halkides, G. J. Gerfen, R. G. Griffin and D. J. Singel, *Biochemistry*, 1996, **35**, 12186.
43. Y.-C. Fann, N. C. Gerber, P. A. Osmulski, L. P. Hager, S. G. Sligar and B. M. Hoffman, *J. Am. Chem. Soc.*, 1994, **116**, 5989.
44. H.-I. Lee, A. F. Dexter, Y.-C. Fann, F. J. Lakner, L. P. Hager and B. M. Hoffman, *J. Am. Chem. Soc.*, 1997, **119**, 4059.
45. J. Telser, R. Davydov, Y. C. Horng, S. W. Ragsdale and B. M. Hoffman, *J. Am. Chem. Soc.*, 2001, **123**, 5853.
46. R. J. Gurbiel, T. Ohnishi, D. E. Robertson, F. Daldal and B. M. Hoffman, *Biochemistry*, 1991, **30**, 11579.
47. R. J. Gurbiel, Y.-C. Fann, K. K. Surerus, M. M. Werst, S. M. Musser, P. E. Doan, S. I. Chan, J. A. Fee and B. M. Hoffman, *J. Am. Chem. Soc.*, 1993, **115**, 10888.
48. P. E. Doan, R. J. Gurbiel and B. M. Hoffman, *Appl. Magn. Reson.*, 2007, **31**, 647.
49. D. Burdi, J. Willems, P. Riggs-Gelasco, W. Antholine, J. Stubbe and B. Hoffman, *J. Am. Chem. Soc.*, 1998, **120**, 12910.
50. B. N. Figgis and M. A. Hitchman, ‘Ligand Field Theory and its Applications’, Wiley-VCH, New York, 2000.
51. C. J. Walsby, J. Telser, R. E. Rigsby, R. N. Armstrong and B. M. Hoffman, *J. Am. Chem. Soc.*, 2005, **127**, 8310.
52. J. M. Peloquin, K. A. Campbell, D. W. Randall, M. A. Evanchik, V. L. Pecoraro, W. H. Armstrong and R. D. Britt, *J. Am. Chem. Soc.*, 2000, **122**, 10926.
53. R. A. Venters, M. J. Nelson, P. A. McLean, A. E. True, M. A. Levy, B. M. Hoffman and W. H. Orme-Johnson, *J. Am. Chem. Soc.*, 1986, **108**, 3487.
54. A. E. True, M. J. Nelson, R. A. Venters, W. H. Orme-Johnson and B. M. Hoffman, *J. Am. Chem. Soc.*, 1988, **110**, 1935.
55. L. Noodleman, C. Y. Peng, D. A. Case and J.-M. Mouesca, *Coord. Chem. Rev.*, 1995, **144**, 199.
56. Y.-C. Fann, J.-L. Ong, J. M. Nocek and B. M. Hoffman, *J. Am. Chem. Soc.*, 1995, **117**, 6109.
57. G. H. Rist and J. S. Hyde, *J. Chem. Phys.*, 1970, **52**, 4633.
58. B. M. Hoffman, J. Martinsen and R. A. Venters, *J. Magn. Reson.*, 1984, **59**, 110.
59. B. M. Hoffman, R. A. Venters and J. Martinsen, *J. Magn. Reson.*, 1985, **62**, 537.
60. P. E. Doan, in ‘Paramagnetic Resonance of Metallobiomolecules’, ACS Symposium Series, ed. J. Telser, American Chemical Society, Washington, DC, 2003, Vol. 858, p. 55.
61. P. Manikandan, E.-Y. Choi, R. Hille and B. M. Hoffman, *J. Am. Chem. Soc.*, 2001, **123**, 2658.
62. D. G. McGavin, *J. Magn. Reson.*, 1987, **74**, 19.
63. F. A. Walker, *Coord. Chem. Rev.*, 1999, **186**, 471.
64. J.-P. Willems, A. M. Valentine, R. Gurbiel, S. J. Lippard and B. M. Hoffman, *J. Am. Chem. Soc.*, 1998, **120**, 9410.
65. C. A. Hutchison, Jr and D. B. McKay, *J. Chem. Phys.*, 1977, **66**, 3311.
66. P. A. Snetsinger, N. D. Chasteen and H. van Willigen, *J. Am. Chem. Soc.*, 1990, **112**, 8155.
67. A. L. P. Houseman, B. H. Oh, M. C. Kennedy, C. Fan, M. M. Werst, H. Beinert, J. L. Markley and B. M. Hoffman, *Biochemistry*, 1992, **31**, 2073.
68. P. E. Doan, C. Fan and B. M. Hoffman, *J. Am. Chem. Soc.*, 1994, **116**, 1033.
69. P. E. Doan, M. J. Nelson, H. Jin and B. M. Hoffman, *J. Am. Chem. Soc.*, 1996, **118**, 7014.
70. C. J. Walsby, D. Krepkiy, D. H. Petering and B. Hoffman, *J. Am. Chem. Soc.*, 2003, **125**, 7502.
71. B. G. Fox, M. P. Hendrich, K. K. Surerus, K. K. Andersson, W. A. Froland, J. D. Lipscomb and E. Münck, *J. Am. Chem. Soc.*, 1993, **115**, 3688.
72. R. E. Duderstadt, C. R. Staples, P. S. Brereton, M. W. W. Adams and M. K. Johnson, *Biochemistry*, 1999, **38**, 10585.
73. S. J. Yoo, H. C. Angove, B. K. Burgess, M. P. Hendrich and E. Muenck, *J. Am. Chem. Soc.*, 1999, **121**, 2534.
74. M. P. Hendrich and P. G. Debrunner, *Biophys. J.*, 1989, **56**, 489.
75. R. Song, P. E. Doan, R. J. Gurbiel, B. E. Sturgeon and B. M. Hoffman, *J. Magn. Reson.*, 1999, **141**, 291.
76. B. E. Sturgeon, P. E. Doan, K. E. Liu, D. Burdi, W. H. Tong, J. M. Nocek, N. Gupta, J. Stubbe, D. M. Kurtz, S. J. Lippard and B. M. Hoffman, *J. Am. Chem. Soc.*, 1997, **119**, 375.
77. B. M. Hoffman, B. E. Sturgeon, P. E. Doan, V. J. DeRose, K. E. Liu and S. J. Lippard, *J. Am. Chem. Soc.*, 1994, **116**, 6023.

78. C. P. Poole, Jr, ‘Electron Spin Resonance’, 2nd edition, John Wiley & Sons, New York, 1983.
79. C. E. Davoust, P. E. Doan and B. M. Hoffman, *J. Magn. Reson.*, 1996, **119**, 38.
80. C. Fan, P. E. Doan, C. E. Davoust and B. M. Hoffman, *J. Magn. Reson.*, 1992, **98**, 62.
81. M. M. Werst, C. E. Davoust and B. M. Hoffman, *J. Am. Chem. Soc.*, 1991, **113**, 1533.
82. B. M. Hoffman, V. J. DeRose, J. L. Ong and C. E. Davoust, *J. Magn. Reson.*, 1994, **110**, 52.
83. W. Brueggemann and J. R. Niklas, *J. Magn. Reson., Ser. A*, 1994, **108**, 25.
84. H.-I. Lee, R. Y. Igarashi, M. Laryukhin, P. E. Doan, P. C. Dos Santos, D. R. Dean, L. C. Seefeldt and B. M. Hoffman, *J. Am. Chem. Soc.*, 2004, **126**, 9563.
85. C. Gemperle and A. Schweiger, *Chem. Rev.*, 1991, **91**, 1481.
86. E. L. Hahn, *Phys. Rev.*, 1950, **80**, 580.
87. J. P. Gordon and K. D. Bowers, *Phys. Rev. Lett.*, 1958, **1**, 368.
88. W. B. Mims, *Proc. R. Soc. London*, 1965, **283**, 452.
89. W. B. Mims and J. Peisach, in ‘Biological Magnetic Resonance’, eds. L. J. Berliner and J. Reuben, Plenum Press, New York, London, 1981, Vol. 3.
90. P. E. Doan and B. M. Hoffman, *Chem. Phys. Lett.*, 1997, **269**, 208.
91. P. E. Doan, C. Fan, C. E. Davoust and B. M. Hoffman, *J. Magn. Reson.*, 1991, **95**, 196.
92. E. R. Davies, *Phys. Lett.*, 1974, **47A**, 1.
93. K. P. Dinse, R. Biehl and K. Möbius, *J. Chem. Phys.*, 1974, **61**, 4335.
94. J. Christiansen, D. R. Dean and L. C. Seefeldt, *Annu. Rev. Plant Physiol. Plant Mol. Biol.*, 2001, **52**, 269.
95. P. C. Dos Santos, D. R. Dean, Y. Hu and M. W. Ribbe, *Chem. Rev.*, 2004, **104**, 1159.
96. R. Y. Igarashi and L. C. Seefeldt, *Crit. Rev. Biochem. Mol. Biol.*, 2003, **38**, 351.
97. P. C. Dos Santos, R. Y. Igarashi, H.-I. Lee, B. M. Hoffman, L. C. Seefeldt and D. R. Dean, *Acc. Chem. Res.*, 2005, **38**, 208.
98. L. C. Seefeldt, D. R. Dean, B. M. Hoffman, P. C. Dos Santos, B. M. Barney and H.-I. Lee, *Dalton Trans.*, 2006, 2277.
99. S. C. Lee and R. H. Holm, *Proc. Natl. Acad. Sci. U.S.A.*, 2003, **100**, 3595.
100. T.-C. Yang, N. K. Maeser, M. Laryukhin, H.-I. Lee, D. R. Dean, L. C. Seefeldt and B. M. Hoffman, *J. Am. Chem. Soc.*, 2005, **127**, 12804.
101. W. H. Orme-Johnson, W. D. Hamilton, T. L. Jones, M.-Y. W. Tso, R. H. Burris, V. K. Shah and W. J. Brill, *Proc. Natl. Acad. Sci. U.S.A.*, 1972, **69**, 3142.
102. B. M. Hoffman, R. A. Venters, J. E. Roberts, M. Nelson and W. H. Orme-Johnson, *J. Am. Chem. Soc.*, 1982, **104**, 4711.
103. J. Kim and D. C. Rees, *Nature*, 1992, **360**, 553.
104. B. M. Hoffman, J. E. Roberts and W. H. Orme-Johnson, *J. Am. Chem. Soc.*, 1982, **104**, 860.
105. R. C. Pollock, H.-I. Lee, L. M. Cameron, V. J. DeRose, B. J. Hales, W. H. Orme-Johnson and B. M. Hoffman, *J. Am. Chem. Soc.*, 1995, **117**, 8686.
106. H.-I. Lee, L. M. Cameron, J. Christiansen, P. D. Christie, R. C. Pollock, R. Song, M. Sørlie, W. H. Orme-Johnson, D. R. Dean, B. J. Hales and B. M. Hoffman, in ‘Paramagnetic Resonance of Metallobiomolecules’, ACS Symposium Series, ed. J. Telser, American Chemical Society, Washington, DC, 2003, Vol. 858, p. 150.
107. P. D. Christie, H.-I. Lee, L. M. Cameron, B. J. Hales, W. H. Orme-Johnson and B. M. Hoffman, *J. Am. Chem. Soc.*, 1996, **118**, 8707.
108. H.-I. Lee, L. M. Cameron, B. J. Hales and B. M. Hoffman, *J. Am. Chem. Soc.*, 1997, **119**, 10121.
109. H.-I. Lee, B. J. Hales and B. M. Hoffman, *J. Am. Chem. Soc.*, 1997, **119**, 11395.
110. H.-I. Lee, M. Sørlie, J. Christiansen, R. Song, D. R. Dean, B. J. Hales and B. M. Hoffman, *J. Am. Chem. Soc.*, 2000, **122**, 5582.
111. M. Sørlie, J. Christiansen, D. R. Dean and B. J. Hales, *J. Am. Chem. Soc.*, 1999, **121**, 9457.
112. P. M. C. Benton, M. Laryukhin, S. M. Mayer, B. M. Hoffman, D. R. Dean and L. C. Seefeldt, *Biochemistry*, 2003, **42**, 9102.
113. H.-I. Lee, M. Sørlie, J. Christiansen, T.-C. Yang, J. Shao, D. R. Dean, B. J. Hales and B. M. Hoffman, *J. Am. Chem. Soc.*, 2005, **127**, 15880.
114. M. J. Ryle, H.-I. Lee, L. C. Seefeldt and B. M. Hoffman, *Biochemistry*, 2000, **39**, 1114.
115. R. Y. Igarashi, M. Laryukhin, P. C. D. Santos, H.-I. Lee, D. R. Dean, L. C. Seefeldt and B. M. Hoffman, *J. Am. Chem. Soc.*, 2005, **127**, 6231.
116. B. M. Barney, M. Laryukhin, R. Y. Igarashi, H.-I. Lee, P. C. D. Santos, T.-C. Yang, B. M. Hoffman, D. R. Dean and L. C. Seefeldt, *Biochemistry*, 2005, **44**, 8030.
117. B. M. Barney, T.-C. Yang, R. Y. Igarashi, P. C. D. Santos, M. Laryukhin, H.-I. Lee, B. M. Hoffman, D. R. Dean and L. C. Seefeldt, *J. Am. Chem. Soc.*, 2005, **127**, 14960.
118. B. M. Barney, J. McClead, D. Lukoyanov, M. Laryukhin, T.-C. Yang, D. R. Dean, B. M. Hoffman and L. C. Seefeldt, *Biochemistry*, 2007, **46**, 6784.

Freeze-Quench Kinetics

Simon de Vries

Delft University of Technology, Delft, The Netherlands

Method Summary 1
1 Introduction 2
2 The Pre-Steady State Kinetic Experiment 3
3 From Milliseconds to Microseconds 6
4 Examples 10
5 Outlook 13
6 Acknowledgments 15
7 Abbreviations and Acronyms 15
8 Further Reading 15
9 References 15

METHOD SUMMARY

Acronyms, Synonyms

- rapid freeze-quench (RFQ), (usually referring to freeze quench techniques with dead-times >5 ms).
- microsecond freeze-hyperquenching (MHQ), (refers to recently developed rapid freeze-quench techniques with dead-times below 200 µs).

Measured physical quantities

- None directly; the MHQ technique yields a frozen powder, which can be analyzed by various types of low-temperature spectroscopy like X-, Q-band EPR, UV-Visible spectroscopy, resonance Raman and potentially or in the near future by MCD, Mössbauer, ESEEM, ENDOR, EXAFS, W-, D-band EPR, MAS-NMR and FTIR spectroscopy.
- These spectroscopic techniques are already available for samples prepared with the RFQ method enabling determination of the electronic structure of metallo-sites or radicals in intermediates formed during the reaction.
- Calculation of the rate constants for the interconversion of one intermediate to another delineating a reaction pathway in, for example, enzymes, or more generally in (bio)chemical reactions.

Information available or not available

- Rates of chemical reactions
- Existence and temporal behavior of intermediates
- The analysis is determined by the kind of spectroscopy used. The current time limitation of the MHQ technique is approximately 60 µs.

Examples of questions that can be answered

- The high time resolution for MHQ allows one to study enzyme or chemical catalytic mechanisms in greater depth than hitherto, simply because more intermediates can potentially be trapped.

- In particular the higher time resolution compared to the stopped-flow (∼1 ms) is important in this respect. In enzymes, many intermediates are formed on the microsecond time scale but have so far escaped detection.

Major advantages

- The technique is very general and applicable to all chemical and biochemical systems that are stable at room temperature. One can, for example, work aerobically or anaerobically, and at elevated pressures, tested so far up to 10 bar.
- Compared to the classical RFQ, MHQ samples are devoid of cryo-solvents like isopentane as the rapid freezing occurs on a rapidly rotating cold plate or cold surface.

Major disadvantages

- Sample requirements for MHQ are similar to or approximately twofold higher than in classical RFQ methods, a single time point requiring 2–5 mg of protein (∼10–100 nmol) and thus quite high. However, this figure is very dependent on the type of analyzes one would like to perform. A kinetic analysis under one experimental regime will require 10–15 samples including controls. After reacting e.g., enzyme and substrate by 1:1 mixing a fine frozen powder is obtained, which is quite dilute (approximately eightfold with respect to the starting concentration, compared to 3–4 times in the classical RFQ).
- The powder obtained with the MHQ technique, which has to be maintained below 140 K to prevent further reaction, is more difficult to handle than that produced by the RFQ technique because of its finer structure. To apply the spectrocopies listed above to such a powder, one often has to construct specific adaptations to sample holders and/or sample compartments, in particular, to get the powder where required, without warming during handling and operation.

---

1 INTRODUCTION

Kinetic analyses serve to determine reaction rates, reaction rate constants and the rate law of a chemical reaction. The rate law contains information on the order (zero, first, second etc.), stoichiometry, or concentration dependence of the various reactants or (metastable) intermediates. The rate equation helps one to define the overall reaction. In favorable cases when (metastable) intermediates accumulate, (some of the) individual reaction steps might be revealed, thus solving the ‘‘mechanism’’. Traditionally, reactant and/or product concentrations are being measured as a function of time (seconds to hours) in a series of experiments in which the concentrations of the reactants, or their isotope analogues are being varied, in addition to pH, temperature, pressure, solvent etc., providing a full kinetic and thermodynamic profile.[1–3] While the rate equation is generally quite simple to derive, its integrated analytical form, describing the reactant/intermediate/product concentrations as a function of time (thus directly relating the experimental data to the theory), becomes a mathematical nightmare even for a simple consecutive three species ($A \Leftrightarrow B \Leftrightarrow C$) reversible scheme. The mathematical expression is greatly simplified when at least one of the reactions is (quasi-) irreversible, or when a relatively stable intermediate is formed. However, an insight into the complete mechanism is lost in this case, as the main information obtained is in relation to the major rate determining step. The above scenario—a steady-state kinetic approach with its roots in the late nineteenth and early to mid-twentieth century—might seem out of date, but is to this day the initial step of any (bio)chemical kinetic analysis concerning a new chemical or enzyme system. However, with the advancement of science and technology in the twentieth century, the timescale for kinetic analyses has decreased from seconds to femtoseconds enabling pre-steady state or transient-state kinetic studies. Within a century, the spectroscopic toolbox has vastly increased, from ‘‘color vision’’ to covering the electromagnetic spectrum from 10^{-10} m to m. Electron and nuclear spin states, or more generally, ‘‘electronic states’’ are related to molecular structure with the help of quantum mechanics. In the past five decades, the analytical resolution and sensitivity has increased from micromole amounts to the single molecule level. Ultrafast computers and sophisticated computer algorithms have obviated the need to search for analytically exact or approximate solutions, having replaced them by robust numerical calculations.

Much of the progress in transient kinetic analyses comes from the development and applications of Laser Flash Photolysis and has recently been comprehensively reviewed by Zewail.[4] With the present state of the art of technology, the field of kinetics has changed to ‘‘structural kinetics and structural dynamics’’ altering the concept of ‘‘Transition State’’ to that of a short-lived transient state (∼500 fs), the very structure and dynamics of which can be determined experimentally.

2 THE PRE-STEADY STATE KINETIC EXPERIMENT

Kinetic experiments are performed in two different ways. In one an initial disequilibrium exists between two or more reactants, which after being rapidly *mixed*, combine to react toward equilibrium (*see* ***Rapid Scan, Stopped-Flow Kinetics***). Ideally, the mixing time is short with respect to the timescale of the reaction or actually with respect to the formation of intermediates. In contrast, in the *relaxation* experiment, the reactants are together and in equilibrium, and the whole system is ''instantaneously'' displaced from equilibrium. Subsequently, the system relaxes to the same or a new equilibrium state. Table 1 summarizes the approximate time resolution of various commonly applied mixing and relaxation techniques. The table indicates the superiority of the relaxation methods with respect to time resolution, mainly due to the development of ultrafast lasers. Mixing liquids on the (sub)microsecond time scale appears to present an important experimental barrier.

2.1 Relaxation Techniques Applied to Enzyme Catalysis

The pathway and kinetics of electron transfer in photochemically activated reaction centers of chloroplasts and photosynthetic microorganisms have been largely solved thanks to ultrafast lasers.[21] The initial steps of light-activated electron transfer do not involve the breaking and making of chemical bonds unlike the great majority of chemical and biochemical reactions. To study the latter type of reactions, the major practical limitation of the flash photolysis type of experiment — that the system under — study must be activated by a (short intense) flash of electromagnetic radiation — might be overcome by synthesizing a ''caged compound''. For example, an enzymatically inactive photolabile substrate analog might serve as a caged compound.[22–24] A wide variety of caged compounds are commercially available, such as ATP or neurotransmitter analogs, and Ca^{2+}-, H^+-, or NO-releasing compounds. The caged compound can be safely mixed with the enzyme, only liberating the active substrate upon a flash of light, thus obviating the need for rapid mixing to study fast reaction kinetics. Depending on the type of caged compound, the time resolution is determined by the photochemical bond breaking process (which is dependent on the particular chemical but may be as short as ~1 ns) or by diffusion of the substrate to the enzyme.

Table 1 Time scales of kinetic techniques

Relaxation techniques	Approximate time scale
Laser Flash Photolysis[4]	5 fs
Photo(bio)chemistry[4]	5 fs
Pulse-probe[4]	100 fs
Temperature jump[5]	5 ps
Time resolved X-ray diffraction[6]	200 ps
Caged compounds/Flow-Flash[7,8]	1 ns
Temperature-jump[9,10]	1 µs
Pressure-jump[11]	50 µs
Mixing techniques (turbulent)	
Continuous-flow[12]	15 µs
Capillary micromixers[12,13]	60 µs
MHQ[(a)] [14,15]	60 µs
Chemical Quench[16]	60 µs – 1 ms
RFQ[(b)] [17]	5 ms
Stopped-flow[18]	0.5 ms
Mixing techniques (diffusion)	
Continuous-flow hydrodynamic focusing[19,20]	20 – 500 µs

[(a)] MHQ, Microsecond Freeze-HyperQuench.
[(b)] RFQ, Rapid Freeze-Quench.

The flow-flash method when applied, for example, in studies on cytochrome *c* oxidase, can be considered as a variant of the caged compound strategy.[7,8,25] The reaction of reduced cytochrome *c* oxidase with oxygen, and the formation of intermediates following the initial binding of oxygen is too fast to be resolved by the stopped-flow method (*see* ***Rapid Scan, Stopped-Flow Kinetics***). Instead, the CO-inhibited reduced enzyme is used to initiate the reaction and in fact, serves the role of the ''caged compound''. Since the CO-inhibited enzyme reacts slowly (seconds) with the substrate oxygen, the two compounds must remain separate, but mixing (called *flow*) prior to flash activation may be ''slow'' (~seconds). Upon a flash of light, CO is liberated (<1 ns) and the active enzyme is ready to bind oxygen, the rate of binding (5 – 10 µs) being determined by the oxygen concentration (usually ~0.5 – 1 mM O_2). Flash photolysis of small ligands bound, for example, to heme groups is not limited to CO; other photolabile small molecules like NO or azide might serve the same purpose. An important condition for the success of this type of experiment is that the rebinding of the photolabile ligand is slow with respect to the binding of say, for example, oxygen. Of course, flash photolysis of Fe(II) – CO complexes may be performed in the absence of the natural substrate. Studies with crystals of Fe(II) – CO myoglobin in conjunction with time-resolved X ray diffraction have yielded the CO-dissociation path in the molecule with (sub)nanosecond and sub-angström resolution.[26] The CO-rebinding path that was established in this study might be that of the natural substrate oxygen.

The time scale of the classical temperature-jump experiment (~1 µs) as originally pioneered by Eigen has been shortened to nanoseconds and very recently to approximately 5 ps using lasers.[5,9] The classical temperature-jump experiment has found only limited application to biological systems, in spite of its great success in determining, for example, proton transfer rates or keto-enol isomerizations. An important reason for its limited application to enzyme research, apart from experimental difficulties such as ''optical artifacts'' as a result of the temperature-jump, is the relatively small deviation from equilibrium ($\Delta G = \Delta H -$

$T\Delta S \cong 0$) obtained with the 5–10 °C temperature shift and the proportionally small optical changes in UV-Visible spectroscopy associated with the transient disequilibrium state.[10] However, these limitations do not seem to apply to protein folding studies in which changes of tryptophan fluorescence or that of the fluorescently labeled proteins were monitored.[27,28] In addition to a temperature jump, protein unfolding can also be rapidly initiated by a pressure jump. The dead time of the recently developed pressure-jump instrument is 50 μs for a pressure jump of 100 bar.[11]

2.2 Rapid Mixing Techniques

Rapid mixing techniques find wide application in chemistry and biochemistry because they are general and versatile, in spite of their much lower time resolution (Table 1) compared to relaxation techniques. Diffusion and collision of the reactants constitute the ultimate steps in mixing. The perfect mixing device should—before the reaction can proceed—break up the two solvents into volume elements with approximately the size of the reactants resulting in very short diffusion distances. Turbulent flow conditions (Reynolds numbers $> \sim 2000-2500$ for pipe-flow geometries) greatly enhance dispersion of two solvents into small volume elements. Mixers are generally constructed to facilitate turbulent mixing. However, micromixers, with small flow channels can provide (sub)millisecond mixing through diffusion over μm distances under conditions of laminar flow.

2.2.1 Turbulent Mixing Instruments

The first subsecond turbulent mixing instrument (dead time ~10 ms) has been described by Hartridge and Roughton in 1923; in 1930 the dead time had decreased to ~2 ms.[29,30] The two reactants are efficiently mixed by a four-jet tangential mixer, actually a modified Rolls-Royce carburetor. The mixed reactants enter a flow tube and the reaction progress is monitored perpendicular to the flow tube at various distances. By knowing the flow rate the distance can be translated into reaction time. This mixing device is essentially a continuous-flow system in which the detection is, however, ‘‘discontinuous’’. Continuous-flow systems generally consume a lot of material, an important limitation to biochemical experimentation. Although the flow rate may be reduced to save material and obtain data points over a wide range of time, a low flow rate will eventually lead to incomplete (or even lack of) mixing, thus limiting the dynamic time range over which experiments can be performed.

A major breakthrough in time resolution (~1 ms), dynamic range (‘‘unlimited’’) and reduction of sample amount came with the development by Britton Chance[31] of the stopped-flow technique (*see* ***Rapid Scan, Stopped-Flow Kinetics***), which is still widely used today. The stopped-flow techniques finds a major application in the study of enzyme pre-steady state kinetics. The stopped-flow apparatus is also frequently used to investigate reaction mechanisms in (bio)organic and (bio)inorganic chemistry. Modern instruments are designed with ‘‘solvent inert sample compartments’’ enabling experiments in a great variety of solvents. Anaerobic accessories are available. Cryostat pumps are easily integrated in the apparatus extending kinetic investigations down to temperatures of −80 °C, for example, to slow down reactions in nonaqueous solvents that are too fast to be monitored at room temperature, and/or to determine enthalpic and entropic contributions to the reaction rates over a wide range of temperatures.[32]

In the stopped-flow apparatus a powerful and fast drive ram system forces the two reactants into a small mixing/observation chamber where they are mixed. Contrast to the continuous-flow setup, the flow stops when the stop syringe is filled completely and the piston of the stop syringe hits the stop block. The void volume of the stop syringe is set prior to the experiment enabling a total flow volume of twice to three times (~50–100 μl) that of the mixing/observation chamber, to ensure complete cleaning of the contents of the mixing chamber. Observations are made ‘‘continuously’’ for any length of time, starting when the two reactants enter the observation chamber (using a pre-trigger) or when triggered by the stop of the stop syringe. Commercial stopped-flow devices enable monitoring of the reaction by UV-Visible (*see* ***Electronic Spectroscopy***), fluorescence or circular dichroism (*see* ***Circular Dichroism (CD) Spectroscopy***) spectroscopies and have dead times of ~1–2 ms, although dead times of ~0.5 ms may be obtained with specially designed small mixing/observation chambers. Stopped-flow instruments have been designed to enable fourier transform infrared (FTIR) (*see* ***Vibrational Spectroscopy***) (dead time 5–15 ms)[33–37] or nuclear magnetic resonance (NMR) (*see* ***Nuclear Magnetic Resonance (NMR) Spectroscopy of Inorganic/Organometallic Molecules***, ***Nuclear Magnetic Resonance (NMR) Spectroscopy of Metallobiomolecules***) analyzes. Also high-pressure stopped-flow instruments have been developed (2 ms dead time, operating at 2000 bar) to study protein denaturation/unfolding kinetics.[38–43] A temperature jump stopped-flow apparatus has recently been designed to study enzyme kinetics at temperatures above the denaturation temperature extending the temperature range commonly covered to determine Arrhenius activation energies.[44]

2.2.2 Rapid Freeze Quench

Rapid-mixing rapid-freezing techniques were developed in the 1960s and 1970s. The development was initiated by workers in the field of ‘‘redox-enzyme’’ biochemistry—at that time in its infancy—to study the role of transition-metal sites in enzyme catalysis by electron paramagnetic resonance (EPR) spectroscopy (*see* ***Electron Paramagnetic Resonance (EPR) Spectroscopy***). Since EPR spectroscopy of transition metals has to be performed, in general, at low temperatures to slow down relaxation, the continuous-flow and stopped-flow techniques, which are suitable for liquid samples were inadequate. EPR spectroscopy requires relatively high concentrations of protein, yielding solutions of high viscosity necessitating, for example, the construction of mixers capable of mixing viscous solutions and a more powerful sample-delivery device than used in the stopped- or continuous-flow apparatus.

A schematic diagram of the rapid-mixing/rapid-freezing setup is depicted in Figure 1. The instrument, which is commercially available, is essentially the continuous-flow system originally designed by Roughton and Millikan except for the quenching bath.[18] The construction and specifications of the rapid freeze-quench (RFQ) have been extensively reviewed by the original designers.[17,45–50] Briefly, the pistons held in the syringes containing the reactants, are pushed by a powerful (~0.5 hp) hydraulically, pneumatically, or stepper-motor driven ram. The reactants are led to the mixing chamber and subsequently enter a tubing ending in a nozzle (~0.25 mm), which sprays the mixture into a cryo-medium where the reaction is quenched. The distance between the mixer body and the cryo-medium is approximately 1–2 cm. The reaction time is varied by varying the length of the tubing rather than changing the ram speed; too low a ram speed might result in inadequate mixing of the viscous solutions. The shortest reaction times are obtained by omitting the tubing and mounting the nozzle directly on the mixer body. The overall dead time of the RFQ is 5–7 ms.[17,51] The most commonly used cryo-media for quenching are liquid isopentane (at ~135 K) and liquid ethane (at ~90–120 K). The advantage of liquid ethane is that it can be pumped off under vacuum providing a solvent-free powder amenable to, for example, resonance Raman spectroscopy at low temperatures.[52]

The cold powder thus obtained after spraying into, liquid isopentane is difficult to handle; it has to remain cold ($T < \sim 130–140$ K) to prevent further reaction and its consistency depends, on the nozzle size and flow rates during the experiment. The powder is usually very static, which leads to clogging and sticking to quartz or glass during sample preparation. With some experience the cold powder can be transferred to, for example, X-band EPR tubes, which are also adequate for low-temperature UV-Visible diffuse reflectance spectroscopy, resonance Raman spectroscopy or D-band EPR. Specific devices and sample holders have been constructed enabling UV-Vis spectroscopy, Q-, W-band EPR, electron nuclear double resonance (ENDOR) (*see* ***Electron-Nuclear Double Resonance (ENDOR) Spectroscopy***), electorn spin scho envelop modulation (ESEEM) (*see* ***Electron Spin Echo Envelope Modulation (ESEEM) Spectroscopy***), magnetic circular dichroism (MCD) (*see* ***Magnetic Circular Dichroism (MCD) Spectroscopy***), Mössbauer spectroscopy, resonance Raman spectroscopy or X ray Absorption Spectroscopy (XAS, EXAFS; *see* ***X-Ray Absorption Spectroscopy***).[53–60]

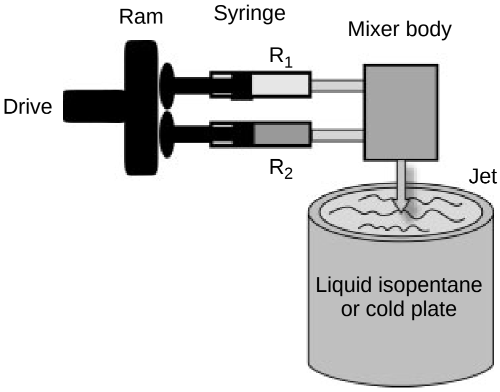

Figure 1 Basic sketch of the rapid-mixing rapid-freezing setup as used in the RFQ and microsecond freeze-hyper quenching (MHQ) devices. R_1 and R_2 denote reactant 1 and reactant 2, respectively. See text and original papers for further details[17,18,45–50]

The RFQ setup can be easily extended to a double mixing system by using three syringes, plus a second mixer. The sequential mixing strategy (''push–push'') enables one to study reactions in which one of the reactants is an unstable or metastable compound. Sequential mixing is also applied to chemical-quench rather than freeze-quench experiments.[61] The third syringe contains the quenching medium and is mixed with the contents of the first mixer in the second mixer. The tube connecting the two mixers or the delay line determines progress of the reaction. As quenching media, highly acidic or basic solutions may be used, or a solvent in which the reaction no longer proceeds and/or the reactant/products become phase separated may suffice. The overall dead time of ~2 ms is somewhat shorter than for RFQ, but dead-times of 60 µs for chemical quenching have been obtained with capillary micromixers.[16]

EPR spectroscopy of radicals (in contrast to transition-metal ions) can usually be performed at room temperature. A continuous-flow aqueous sample cell for X-band EPR spectroscopy with a dead time of ~5 ms—suitable for kinetic studies on radical systems—has been commercially available for a long time. It is, however, very uneconomical in terms of material.

Recently a sophisticated aqueous sample cell has been constructed, which enables the kinetic resolution of the rapid refolding of spin-labeled iso-1-cytochrome *c*.[62] The aqueous sample cell consists of a miniaturized quartz capillary mixer with a dead time of ~150 µs. This design is based on the continuous-flow capillary mixer (dead time ~60 µs) used for fluorescence spectroscopy.[13] The major disadvantage of the continuous-flow systems is the uneconomical use of protein (~1 mL at ~0.5 mM for an experiment), despite the spectacularly small detection volume of ~0,5 µL and the very short dead time of the micromixer. Due to the relative insensitivity of aqueous sample EPR spectroscopy, fairly high concentrations of sample are required. Consequently, in practice the detection of (''native'') transient radicals accumulating to amounts <10% of the enzyme concentration is generally not possible, limiting the main biochemical application to spin label-modified proteins. To study native transient radicals, the Microsecond Freeze-HyperQuench (MHQ) device has been developed.[14]

2.2.3 Laminar Flow Micromixers

High (linear) flow rates are required to induce turbulent mixing and to minimize the time between mixing and observation or quenching, known as ‘‘the dead time’’. Due to the high flow rates, the pressure in the system increases. The working pressure of the mixing devices described above is maximally 10 bar (stopped-flow) and may be up to ~20 bar in RFQ when viscous solutions are used.

Current lithographic techniques make it possible to construct microfluidic systems with flow channels of ~1 μm or even smaller.[63] In these μm channels the diffusion of small molecules ($D \sim 10^{-9}\,\mathrm{m^2\,s^{-1}}$) takes ~1 ms, according to equation (1)

$$t_{(\mathrm{diff})} = \frac{d^2}{D} \qquad (1)$$

in which d represents the channel diameter or the diffusion path length and D the diffusion constant ($\mathrm{m^2\,s^{-1}}$). Laminar flow micromixers work on the principle of diffusion only. The continuous-flow rates are very small, down to several $\mathrm{nL\,s^{-1}}$ thus saving material. The pressure in the system is very close to ambient. Under favorable conditions so-called hydrodynamic focusing may occur, reducing the diffusion distance to below 50 nm and yielding a mixing dead time of ~20 μs.[19,20,64–66] Unfortunately, the slow beginning of mixing usually results in true dead-times of ~0.5–1 ms (Table 1). The small dimensions (pathlength) enable detection mainly of fluorescent compounds. However, an important new development is the fabrication of a micromixer enabling small angle X ray scattering on hydrodynamically focused protein solutions using synchroton radiation.[19] Protein folding was studied with a time resolution of 200 μs.

The quadratic dependence between channel dimensions and diffusional mixing times in equation (1) might serve as a stimulus to manufacture channels with small diameters (<50 nm) enabling complete mixing in microseconds.

3 FROM MILLISECONDS TO MICROSECONDS

The ultimate step to achieve complete mixing of two liquids is constituted by diffusion of solvent and solute molecules. The shorter the diffusion pathlength, which solvent and solute molecules have to travel, the shorter the mixing time. For example, the shortest mixing time for continuous-flow mixers is approximately 15 μs corresponding to diffusion of an ordinary solute ($D = 10^{-9}\,\mathrm{m^2\,s^{-1}}$) over ~100 nm using equation (1); the dimension of ~100 nm represents the average size of the diameter of the volume elements obtained after mixing. Taking a value of ~1 nm as the size of a single solvent/solute particle, rapid-mixing of two liquids—that is, dispersion to this ‘‘molecular level’’—yields a shortest dead time of ~1–10 ns for the mixing technique. In enzymes the fastest protein back bone movements associated with catalysis might occur within ~1 μs, though electron transfer reactions, internal proton transfer and side-chain rotations are in general much faster, necessitating the use of relaxation techniques for their study.[26,67–71] However, in the light of the simple calculation above, the ultimate mixing device would suffice to unravel enzyme reaction pathways and detection of (all) transient catalytic intermediates.

Rapid and complete mixing in cylindrical channels ($d > 100\,\mu\mathrm{m}$) is obtained in the turbulent regime. Turbulence is expressed by the dimensionless Reynolds number, Re, according to

$$Re = \rho \bullet \langle v \rangle \bullet \frac{d}{\eta} \qquad (2)$$

Table 2 Technical specifications of various rapid-mixing devices under conditions of most rapid mixing[(a)]

	Stopped flow	Continuous flow[72]	RFQ[(b) 17]	MHQ[(c) 14,15]
Mixing volume	30 μL	63 nL	68 nL	10 pL
Channel or Orifice diameter, μm	2000	250	200	20
Re in mixing chamber or in orifice	40 000	30 000	7000	4000
Max. backpressure (bar)	2–8	<5	9–15	200–400
Max. flow rate ($\mathrm{ml\,min^{-1}}$)	3000	90	83	4
linear speed ($\mathrm{m\,s^{-1}}$) in channel or jet	20	6	44	200
Mixing Dead time	100–500 μs	15 μs	50 μs	<1 μs
Experimental Quenching time	NA	NA	4–6 ms	30–40 μs
Total instrumental Dead time	~0.5–1 ms	60–100 μs	5–7 ms	60–80 μs

NA: Not applicable.

(a) Calculations based on $\rho = 1000\,\mathrm{kg\,m^{-3}}$ and $\eta = 10^{-3}\,\mathrm{kg\,m^{-1}\,s^{-1}}$.

(b) RFQ rapid freeze-quench.

(c) MHQ microsecond freeze-hyperquenching.

in which $\langle v \rangle$ is the (average) linear flow velocity ($\mathrm{m\,s^{-1}}$) in a channel, ρ the solvent density (e.g., $1000\,\mathrm{kg\,m^{-3}}$ for water), d is the channel diameter (m) and η is the dynamic viscosity (e.g. $10^{-3}\,\mathrm{kg\,m^{-1}\,s^{-1}}$ for water at 20 °C). Sufficient turbulence in pipe channels resulting in complete mixing requires $Re > 2000-2500$. High flow velocities also cause a pressure (ΔP) buildup in the system according to Bernoulli's velocity/dynamic pressure equation:

$$\Delta \mathrm{P} = 0.5 \bullet \rho \bullet (\langle v \rangle)^2 \qquad (3)$$

Equation (3) implies that at linear flow rates $>10-15\,\mathrm{m\,s^{-1}}$, pressures of >1 bar above ambient pressure will buildup. Technical specifications for the most common rapid-mixing devices are shown in Table 2. The stopped-flow apparatus achieves very high Reynolds numbers owing to its large flow rates in relatively large (2 mm) channels; however, when performing studies at low temperatures (~0 °C) in fairly concentrated enzyme solutions, the viscosity might easily increase by a factor of 5–10, proportionally lowering the Reynolds number and decreasing the extent of mixing.

Given the Reynolds equation in which ρ and η are relatively constant, the two main parameters permitting manipulation of the instrumental *mixing time* are the flow rate and the dimensions of the mixer, in particular the channel diameter and length. The instrumental *dead time* includes the mixing time and the time taken to travel the distance between the mixing and observation point (for continuous flow), or for filling the observation chamber (for stopped-flow) (Table 2, Figure 2). The relatively large observation/mixing compartment of the stopped-flow, and abruptly stopping the flow are the major causes for its poorer time resolution than the continuous-flow devices. However, given the small observation volume, the current continuous-flow mixing setups are used mainly in connection with fluorescence spectroscopy, whereas the stopped-flow instrument allows a broader range of spectroscopies, including the relatively insensitive UV-Vis absorbance spectroscopy.

The stopped-flow dead time might be improved to that of the continuous-flow methods (~50 µs), by using higher flow rates, but this might lead to cavitation effects and certainly will lead to higher pressures in the system (~100–200 bar) necessitating a much more robust design. The simplest way to improve the stopped-flow performance in the author's opinion is to use a smaller observation chamber. This will require a 10–20 fold more sensitive UV-Vis absorbance spectroscopy setup, something that has apparently not been developed during the last 40 years for reasons that are unclear.

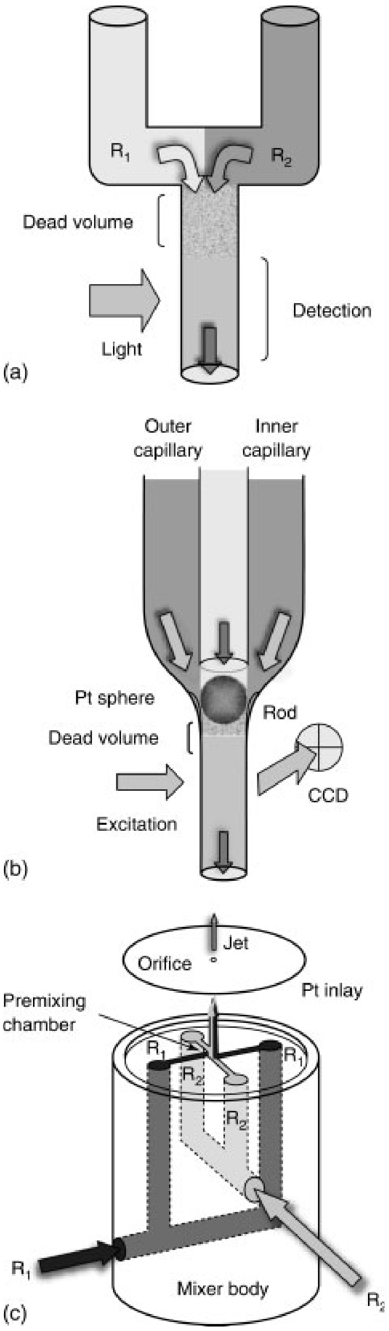

Figure 2 Drawings of commonly used mixers in continuous-flow and stopped-flow devices. Mixing in the four-jet tangential mixers occurs in the orifice of the Pt inlay (MHQ) or in a Teflon gasket (RFQ). R_1 and R_2 denote reactant 1 and reactant 2, respectively

3.1 Commonly Used Mixers

Over the years various types of mixers have been designed. The most frequently used today are the T-mixers (stopped-flow), four (or more)-jet tangential mixers (freeze-quench), the Berger-ball mixer (stopped-flow) and the coaxial type mixers like the ball-mixer used in the capillary micromixers (continuous-flow) (Figure 2).[12–14,16,17,30,31,51,72–76]

T-mixers are the most classical mixer types (Figure 2a). Mixing starts, but is generally not complete, at the point where the two fluids collide. Complete mixing should occur over a short distance just downstream (dead volume), in the region between the initial collision point of the two fluids and the observation chamber. The total dead time of the T-mixer corresponds approximately to that of the time needed to fill the dead volume region and the observation chamber.

In coaxial mixers, the two reactant fluids are initially in an outer and an inner capillary. The two fluids run parallel over a short distance toward a Pt sphere. At this stage they do not mix because of the low Reynolds number of the flow, which is essentially laminar (Figure 2b). The two fluids meet at a small (50–250 µm) platinum sphere, which is positioned at the tapered end of the outer capillary. The two fluids are forced between the small space (5–10 µm) between the Pt sphere and the outer capillary where they are accelerated creating a small zone of high turbulence ($Re \sim 30\,000$). Without the sphere, the channel dimensions and flow rates would yield a calculated Re of ∼1500, which is insufficient for mixing.

Regenfuss *et al.* designed the original coaxial ball mixer or capillary micromixer. The mixer was impractical because it was very delicate to manufacture and the optical (fluorescence) measurements had to made on an unstable free flowing thin jet at various distances.**[12]** Shastry *et al.* among others have successfully improved the original design by using quartz instead of glass, enabling the construction of an observation chamber, which no longer necessitated measurements on a free jet.**[13]** Detection of fluorescence changes occurs by a sensitive charged coupled device (CCD) camera covering the whole length of the observation cell, enabling facile transformation of distance into time. The short mixing (15 µs) and small total dead time (60 µs) made it possible to study the folding of cytochrome *c* by monitoring Trp fluorescence and fluorescent resonance energy transfer (FRET) in specifically labeled proteins.**[72]**

The capillary micromixer has proven to be a fast and versatile mixing device. The great advantage of the capillary micromixers are the short dead time while operating at low pressures. The small observation volume so far precludes application of, for example, UV-Vis absorbance spectroscopy, for which the sample requirements are relatively high.

Four-jet tangential mixers (Figure 2c) are mostly used in RFQ and MHQ instruments (in a miniaturized form in the latter).**[14,17]** The (micro-)mixer consists of four channels (arranged in a cross), which lead the reactants to a premixing chamber, in the middle of the cross. The opposite channels are offset in respect to each other by a half- or full-width of the channel, so that the liquid streams are premixed with a resulting angular momentum at relatively low Reynolds numbers; the amount of pre-mixing is less than 1%. After premixing, the 4-stream solution is forced through a constriction in the channel—perpendicular to the plane of the channel. Here the solution is accelerated to a high linear velocity yielding $Re \sim 7000$ and a calculated mixing time of 50 µs for the RFQ design (Table 2). The mixture subsequently enters the sample-delivery tube and is sprayed through a nozzle into cold isopentane. In practice the four-jet tangential mixers are capable of efficiently mixing concentrated protein solutions, apparently more so than T-mixers. It is possible that the presence of the angular momentum of the flow helps to accomplish this.

In spite of the short mixing time, the total dead time of the RFQ is 5–7 ms. In general, the freeze-quench mixing-and-sampling procedure (both RFQ and MHQ) can be divided into three steps, which determine the total instrumental dead time. First, the chemical reaction is initiated by rapid mixing of the reaction components. In the second step, the sample is transported from the mixer in a tubing (of variable length) and subsequently as a free jet to the cryo-medium. In this stage the reaction proceeds and the reaction progress can be manipulated by varying the length of the tubing. Finally, the sample is quickly frozen in the cryo-medium (e.g., liquid isopentane) or on a rotating cold plate (MHQ), quenching the chemical reaction.

The total sample-ageing time, τ_a, can be expressed as a sum of three terms,

$$\tau_a = \tau_m + \tau_t + \tau_c \tag{4}$$

where τ_m is the mixing time, τ_t is the sample-transport time, and τ_c is the cryofixation or quenching time.**[14]** So for RFQ the first term is ∼50 µs; the shortest transport distance—in the case the spraying nozzle being attached to the mixer body—to the cold liquid isopentane bath is ∼1–2 cm taking 0.5–1 ms at the (maximal) linear jet speed of $\sim 44\,\mathrm{m\,s^{-1}}$. The actual freezing time has been determined to be ∼5 ms in isopentane at 135 K with a nozzle of 200 µm.**[17]** Thus the total dead time for RFQ is 5–7 ms (Table 2). The rate of freezing is dependent on the temperature of the quenching medium and was found to be 8–9 ms for isopentane at 100 K.**[17]**

3.2 Microsecond Freeze-Hyperquenching (MHQ)

Given the specifications above for the RFQ methodology, there are several possibilities to improve the dead time from milliseconds to microseconds. This can be achieved by minimizing the mixing time and shortening both the sample-transport time and the quenching time. In practice this was accomplished by scaling down the mixer dimensions, increasing the linear flow rate and omitting the sample-delivery tubing. A detailed description of the stainless steel micromixer and the operation and properties of the MHQ setup have been reported recently.**[14,15,77,78]**

Regarding the sample-transport time, by increasing the (linear) flow rate, the working pressure will also increase in the system. Given the Reynolds and Bernoulli equations, linear flow rates of $200\,\mathrm{m\,s^{-1}}$ will allow sufficient turbulence for mixing in channels of ∼10–20 µm at pressures of ∼400 bar (Table 2). Most enzymes can stand this pressure without denaturation given the biochemist's experience that French pressure devices used to break open cells might yield similar pressures and that HPLC systems commonly applied in the purification of enzymatically active proteins operate at these pressures. Although the specific pressure needed to induce protein unfolding and denaturation is a protein-specific property, pressure sterilization of nonbarophilic microorganisms like *E. coli* or *B. subtilis* requires pressures above 1500 bar, implying that the great majority of proteins are stable and active at these high pressures.[79] This is in agreement with studies on isolated proteins displaying unfolding at pressures >∼2 kbar, though some remain active at 5 kbar.[43,80] To prevent uncontrolled protein denaturation under the MHQ experimental conditions, HPLC pumps are used in the MHQ setup rather than a powerful drive ram system as the sample delivery means. With HPLC pumps full control overpressure and consequently the flow velocity is obtained during the experiment allowing accurate calculation of the reaction time. At pressures >400 bar, the pumps automatically shut down in case of. clogging of the nozzle, ensuring that the samples are not denatured due to transient high pressure buildup.

A major factor contributing to the dead time in RFQ is the freeze-quenching process itself. In general the rate of freeze-quenching is determined by the rate of heat transfer between the sample and the cryo-medium (cold plate or cold liquid). The heat-transfer rate is determined by the heat capacities of the sample and the cryo-medium, and their temperature difference. In the freeze-quenching process heat transfer occurs predominantly through surface contact between the cryo-medium and the jet. The rate of heat transfer is proportional to the surface area of the jet, or importantly to the square of the jet diameter. In the classical RFQ setup, jet diameters of ∼250 μm were used yielding a ∼5 ms quenching time; in the MHQ setup the jet diameter is only 20 μm resulting in the experimentally determined freeze-quenching time of 30–40 μs in agreement with the square of the ratio of the jet diameters $(20/250)^2$ used in the two different experimental setups.

In the original publication on the MHQ apparatus, liquid isopentane was used as quenching medium[14] and later a rotating cold plate.[15,78] The minimal transport distance between mixer and cold liquid isopentane was ∼2 cm, yielding minimal sample-transport time of 100 μs at a jet speed of 200 m s^{-1}; for the cold plate the minimal sample-transport distance is only 5–7 mm, yielding a minimal sample-transport time of 25–35 μs. All of the mixing occurs in the smallest constricted region of the platinum inlay (Figure 2c) constituting both mixer and orifice, where *Re* is maximally 4000 (Table 2). The total mixing time is <1 μs, and the total dead time of the MHQ device with the rotating cold plate amounts to 60–80 μs. With this improved time resolution we were able to detect hitherto unknown transient tryptophan radicals (by EPR) formed during the catalytic cycle of cytochrome *c* oxidase[14,15,78] and a new short-lived (∼100 μs) high-spin ferric-azide intermediate (by resonance Raman spectroscopy) in the reaction between metmyoglobin and azide.[77]

3.2.1 Jet Break-up

During the development of the MHQ setup, serious problems of break up of the 20-μm jet were detected at ambient pressures, for example, by studying the behavior of the jet under a microscope. Jet break up and the consequent decrease of the jet speed (several fold) and broad distribution of jet velocities were experimentally verified by Laser Doppler Anemometry.[81] By decreasing the pressure to 30 mbar, the 20 μm jet was found to be sufficiently homogeneous to define a single rate (>85% of the jet with a speed within 10% of the maximum speed). The maximum jet velocity turned out to be ∼10% higher than that calculated on the basis of the volumetric flow rate and orifice diameter, which is what one would expect for fluid flow in μm channels due to the absence of flow at the liquid/wall interface reducing the effective diameter.[81]

The MHQ apparatus is built entirely in a low-pressure chamber to prevent jet break up of tiny free jets. The low ambient pressure, the high jet velocities, and the relatively short distance to the cryo-medium result in (adiabatic) cooling of the jet. It was determined that even though the reactants are initially at ambient (20–22 °C) temperature the effective reaction temperature was 10 ± 2 °C for the cold plate setup and 8 ± 0.5 °C for quenching in liquid isopentane.[14]

3.2.2 Determination of the MHQ Dead Time

To characterize the instrumental dead time of the MHQ the binding of azide to metmyoglobin was used as a molecular timer as originally used for the RFQ apparatus. The rate constants for the reaction were determined in the stopped-flow apparatus at various temperatures between 5 and 25 °C, at $[N_3^-]$ up to 1 M. This high concentration of azide was necessary to obtain sufficient formation of the myoglobin-azide complex on the microsecond time scale to calculate a reliable value for the sample aging time. Various ''anomalies'' of the reaction progress were detected on the shortest timescale,[14] which were, however, not observed by others[82,83] using newly designed freeze-quench setups with dead-times of 50 μs and 200 μs or with the slower RFQ setup.[17,47] One was the formation of a novel transient intermediate living for ∼100 μs,[14,77] (*see* later in Section 4.2) the other the apparent decrease of the second order rate constant for the reaction at $[N_3^-] > 10$ mM. A careful analysis of the reaction enabled the experimental determination of all the instrumental parameters listed in Table 2. The true mixing time (<1 μs), the maximal jet velocity, and the true freeze-quench time (see also below) determined experimentally, all closely match theoretical and practical considerations. In this light it was argued previously that two novel sophisticated freeze-quench instruments, for which the author claimed dead-times of 50 μs and 200 μs, could not, in fact, achieve such short reaction times. The arguments given previously[14] are in the opinion of the author still correct, and will not be repeated here. Additional simple arguments that can now be made after the original papers were published and on the basis of more recent publications are the following. While working with the same systems as the author, that is, the reaction between metmyoglobin and azide for testing and cytochrome bo_3 oxidase to study its catalytic cycle, neither the transient high-spin heme azide intermediate living for ∼100 µs[77] nor the Trp-radical of cytochrome bo_3 oxidase[15,84] disappearing after 500 µs were detected.[83] With respect to the system described by Tanaka *et al*.,[82] the freeze-quenching of the jet (60 µm diameter) itself would take ∼300–400 µs (given the 30–40 µs for a 20 µm jet and the dependence of freeze quenching on the square of the jet diameter). Regarding the system by Lin *et al*.,[83] jet break up of the 10 µm × 100 µm jet is very severe at ambient pressures (less so for the 60 µm jet, but not absent), leading to much longer sample aging times than based on calculations of the jet speed using the volumetric flow rate and orifice diameter. In addition, the freezing is not ''instantaneous'' as suggested.[82] Neither Tanaka *et al*. nor Lin *et al*. took the potential cooling of the jet into account, which must be significant with the rotating copper or silver wheels at 77 K, used to quench the reaction, leading to turbulent cold air in contact with the jet. The author estimates an instrumental dead time of 0.5 ms for both devices, which is, nevertheless, more than a 10-fold improvement in time resolution with respect to the classical RFQ. Both systems employ state of the art micromixer technology and yield high quality and concentrated (more so than obtained via MHQ) powder samples, suitable for EPR and resonance Raman spectroscopy.[82–85]

3.2.3 Hyperquenching

The design parameters used for the MHQ setup were inspired by the High-pressure jet-freezing and droplet cryoplate freezing equipment developed by Mayer to study the properties of vitrified water.[86]

Mayer showed that the spraying of fast jets (∼200 m s^{-1}) of small diameters (10–20 µm) into a liquid cryo-medium (e.g., isopentane at 120 K) results in the formation of vitrified water. Cooling under these circumstances is so rapid—calculated as 3×10^6—10^7 K s^{-1}—that water does not have time to form a crystal lattice. Water vitrifies to an amorphous solid bypassing the liquid-ice phase transition.[86–88] The metastable amorphous solid water is structurally similar to liquid water.[89–93] It undergoes a reversible liquid–liquid transition at ∼130 K,[94] forming a highly viscous, deeply metastable supercooled extension of normal liquid water,[95–97] which begins to crystallize on warming to ∼160 K.[98–100] Vitrification of samples is widely used in cryobiology for tissue storage and for preparation of samples for electron microscopy, to avoid structural damage of biological specimens due to the expansion of the aqueous phase during the liquid-ice phase transition.[101–103]

The experimentally determined freeze-quenching time of 30–40 µs amounts to a cooling rate of $3–5 \times 10^6$ K s^{-1}, in good agreement with calculations.[88] Indeed the formation of vitrified water can be observed by eye. Spraying of aqueous solutions by the MHQ setup on a cold plate initially yields a transparent frozen material. This simple observation and the quenching time of 30–40 µs strongly suggest the formation of hyperquenched samples by the technique, hence it's name, MHQ. X-ray analysis or infrared spectroscopy should provide more direct proof of the vitrified state of the samples obtained by the method.

4 EXAMPLES

4.1 RFQ of Cytochrome P450

Cytochrome P450 (P450) enzymes are heme-containing monooxygenases found in Bacteria, Archaea and Eukarya that catalyze hydroxylations of aliphatic and aromatic compounds (''RH'') according to the overall reaction:[104–106]

$$\mathrm{RH} + \mathrm{O_2} + 2\mathrm{e} + 2\mathrm{H^+} = \mathrm{ROH} + \mathrm{H_2O} \tag{5}$$

The P450 enzyme from *Pseudomonas putida* (P450cam or CYP101), which hydroxylates camphor to 5-exo-hydroxycamphor has been studied in detail and is regarded as a model protein for other P450s. The electron donor to P450cam is putidaredoxin, which can deliver one electron at a time. In the course of the reaction, an activated oxygen atom from the heme iron is transferred to the unactivated C–H bond of the substrate. A Fe(IV)=O porphyrin-π-cation radical has been proposed as the key iron-oxo intermediate, compound I (Cpd I),[104] but it has remained elusive so far in studies of the enzyme with substrate (''RH'').

The resting enzyme can be loaded with RH, reduced by one electron and reacted with oxygen, yielding a stable Fe(II)–O_2–RH complex. To this complex, the second electron must be added to initiate the reaction, but injection of this second electron as reduced putidaredoxin was too slow (∼5 ms) to detect any transient formation of Cpd I.[107] Experiments in which the Fe(II)–O_2–RH complex was prepared at room temperature, frozen and subsequently reduced radiolytically in the cryogenic state did not reveal any buildup of Cpd I, though superoxo and peroxo intermediates were found and the enzyme went through a full catalytic cycle.[108]

Alternatively, the Cpd I of P450 enzymes might be formed via the so-called ''shunt'' reaction[109,110] using H_2O_2 or peroxy acids (in the absence of substrate), that is analogous to formation of the stable Cpd I by chloroperoxidase (CPO) from *Caldariomyces fumago* according to:

$$\mathrm{Por–Fe(III)} + \mathrm{H_2O_2} = \mathrm{Por^{\bullet +}–Fe(IV)=O} + \mathrm{H_2O} \tag{6}$$

Since both CPO and P450 have cysteine as the proximal iron ligand, rather than histidine, Cpd I of P450 might yield a similar UV-visible spectrum: (partial) bleaching and blue shifting of the Soret band and appearance of Q-bands between 650 and 700 nm.[111,112] Indeed, stopped-flow studies in which P450 was rapidly mixed with peroxy acids indicated the formation within ~10 ms of a transient species that has been ascribed to Cpd I.[113,114] This species accumulated to ~10% of the starting [P450] and had the expected optical characteristics.

To determine Fe(IV)=O and radical character of the transient intermediate unambiguously, RFQ experiments have been performed in conjunction with Mössbauer spectroscopy and multifrequency EPR (*see* ***Electron Paramagnetic Resonance (EPR) Spectroscopy***; Figure 3).[55,109,110,115–117]

Mössbauer spectroscopy of the ^{57}Fe-containing P450 indicated the formation after 8 ms of ~10% Fe(IV) $S = 1$ species, the other 90% representing the initial Fe(III) state (Figure 3a). The P450 Fe(IV) is characterized by a doublet with an isomer shift of $\delta = 0.13\,\mathrm{mm\,s^{-1}}$, similar to the value of $\delta = 0.14\,\mathrm{mm\,s^{-1}}$for the CPO Cpd I. The P450 quadrupole splitting ($\Delta E_Q = 1.94\,\mathrm{mm\,s^{-1}}$) is, however, much larger than in CPO ($\Delta E_Q = 1.02\,\mathrm{mm\,s^{-1}}$), suggesting that the cysteine in P450 might be protonated.[110]

In contrast to the Mössbauer spectroscopy, EPR did not reveal the characteristic signal of a Fe(IV) species antiferromagnetically coupled to a porphyrin radical.[118] Instead, the anisotropic signal detected at D-band frequency (285 GHz) indicates formation of a tyrosine radical, ascribed to Y96 based on site-directed mutagenesis (Figure 3b).[115,116]

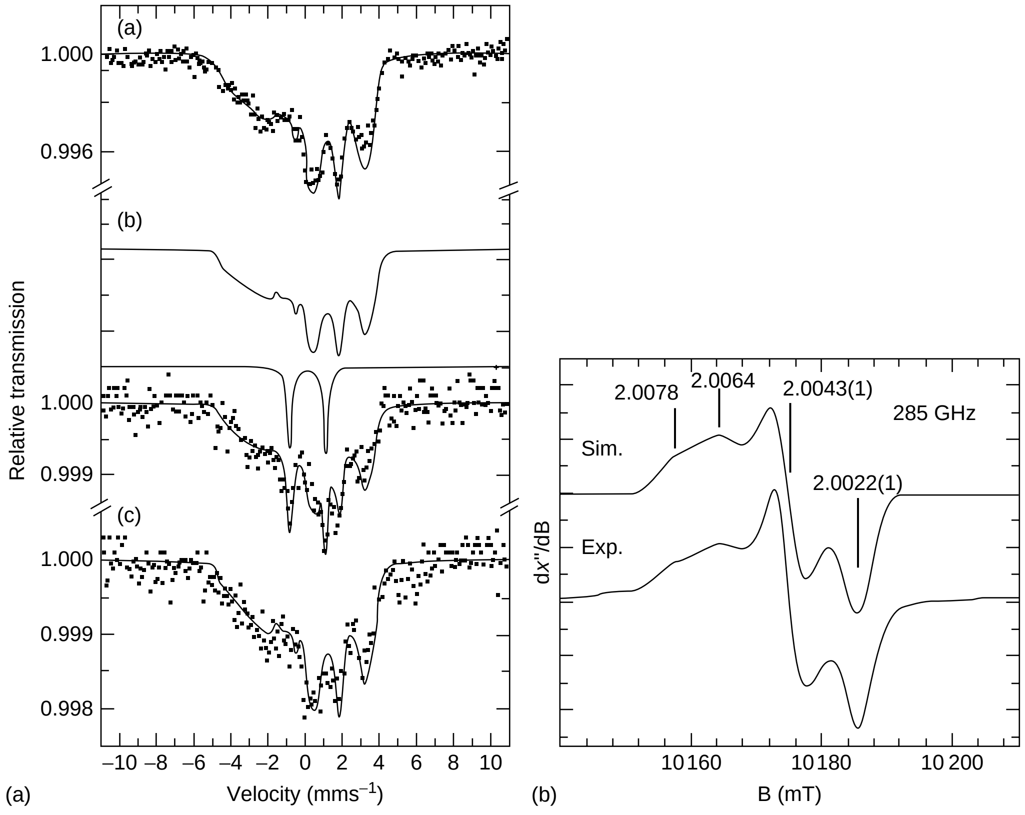

Figure 3 Mössbauer (a) and D-band EPR spectra (b) of P450 reacted for 8 or 40 ms, respectively with peroxy acetic acid. A, trace (a): Mössbauer spectra of substrate-free cytochrome P450cam recorded at 4.2 K in a field of 20 mT perpendicular to the γ-beam. The solid line is a spin-Hamiltonian simulation with parameters $\delta = 0.38\,\mathrm{mm\,s^{-1}}$, $\Delta E_Q = +2.85\,\mathrm{mm\,s^{-1}}$, $\eta = -1.8$, $\Gamma = 0.30\,\mathrm{mm\,s^{-1}}$, $g = (1.91, 2.26, 2.45)$, $\mathrm{A}/g_\mathrm{N}\mu_\mathrm{N} = (345, 10, 19)$ T. Trace (b): Mössbauer spectrum of P450cam after mixing with peroxyacetic acid for 8 ms recorded at 4.2 K in a field of 20 mT perpendicular to the γ-beam. The solid line is a spin-Hamiltonian simulation assuming two components: a doublet with $\delta = 0.13 \pm 0.01\,\mathrm{mm\,s^{-1}}$ and $\Delta E_Q = 1.94 \pm 0.01\,\mathrm{mm\,s^{-1}}$ characteristic of Fe(IV) ($S = 1$) (13 ± 2% relative contribution) and the ferric starting material (calculated with the parameters given in trace (a); 87 ± 2% relative contribution). Trace (c): Mössbauer spectrum of P450cam after addition of peroxyacetic acid and 5 min reaction time taken at 4.2 K in a field of 20 mT perpendicular to the γ-beam. The solid line is a spin-Hamiltonian simulation with the parameters used for the ferric starting material, see trace (a). (Reproduced from Schunemann, Lendzian, Jung, Contzen, Barra, Sligar and Trautwein[115] by permission of American Society for Biochemistry and Molecular Biology.) B, the Y*96 in ^{56}Fe-P450cam reacted for 40 ms. EPR conditions: T = 5 K; modulation amplitude 2.4 mT, modulation frequency 0.8 kHz, microwave frequency 285 GHz, field sweep $0.5\,\mathrm{mT\,s^{-1}}$. *Exp*, experimental spectrum; *Sim*, simulated spectrum after field calibration using $g_z = 2.0022$ (from 94 GHz EPR simulations) yielding the g_y value and a distribution of g_x values around two maxima at $g_x = 2.0064$ and $g_x = 2.0078$. Single component linewidth used in the simulation: 4 mT. (Data from ref. 115)

The relaxation of the radical is fast, consistent with a distance for Y96 of 9.4 Å from the Fe(IV).

The apparent discrepancy between the RFQ and stopped-flow experiments was recently ascribed to differences in pH between the two studies.[117] The pH influences the pre-equilibrium concentrations between Cpd I (Soret maximum at 367 nm) and the Y*96 radical intermediate (Soret maximum at 406 nm):

$$\text{Tyr-Por}^{\bullet+}\text{–Fe(IV)=O} \longleftrightarrow \text{Tyr}^{*}\text{-Por-Fe(IV)=O} \qquad (7)$$

In a recent study, Cpd I was prepared by irradiation with 355 nm laser light of Cpd II (Fe(IV)=O, obtained by reaction of the resting enzyme with peroxynitrite).[119] Surprisingly, Cpd I was relatively stable (~200 ms) and unreactive toward its substrate laurate. While it is possible that laurate cannot bind to the P450 prepared in the Cpd I state, the key hydroxylating intermediate might not be Cpd I, but rather a peroxy intermediate $\text{Fe(III)O}_2{}^{2-}$ or $\text{Fe(III)O}_2\text{H}^-$. Whatever the nature of the hydroxylating intermediate, its lifetime is definitely short requiring RFQ and MQH methods to trap it.

4.2 MHQ of Metmyoglobin in Reaction with Azide

The reaction between metmyoglobin and azide has traditionally been used to calibrate the time scale and calculate the dead time of the RFQ and MHQ instruments.[14]

$$\text{Fe}^{3+} - \text{H}_2\text{O} + \text{N}_3{}^-\text{(high spin)} \rightarrow \text{Fe}^{3+} - \text{N}_3{}^- + \text{H}_2\text{O} \quad \text{(low-spin)} \qquad (8)$$

The reaction shows second order kinetics up to $[\text{N}_3{}^-]$ of ~1 mM. While calibrating the dead time and performance of the MHQ instrument, the author observed clear deviations from second order behavior at higher $[\text{N}_3{}^-]$ including the formation of a short-lived transient intermediate (Figure 4a).[14,77]

Upon binding of azide to metmyoglobin, the high-spin Fe^{3+} changes to low spin (equation 8), which can easily be detected by EPR or (low-temperature) UV-visible spectroscopy. The reaction in equation (8) is a simple two-component system. The reaction progress can easily be determined by simulation of the resulting spectra obtained in a time series from the weighted sum of the initial high-spin spectrum and the final low-spin spectrum that serve as reference spectra.[14] When no intermediates are formed, the residuals of the weighted sum should be zero. However, the spectrum obtained after 95 μs reaction time (Figure 4a) could not be simulated as a simple sum of the initial and final spectrum. Analysis of the UV-Vis spectrum of the residual (~20% of the total metmyoglobin) indicated that it had already bound azide, but not exactly as in the final state. In the sample obtained after 245 μs, the amount of the residual was already much lower (~2%).

Resonance Raman spectroscopy of the 95 μs and 245 μs samples, followed by weighted subtraction of the resonances in the spectra of the initial and final state, yielded the spectra of the residuals shown in Figure 4(b).[77] Consistent with the UV-visible spectroscopy, the residual was much smaller in the 245 μs sample indicating a lifetime <100 μs.

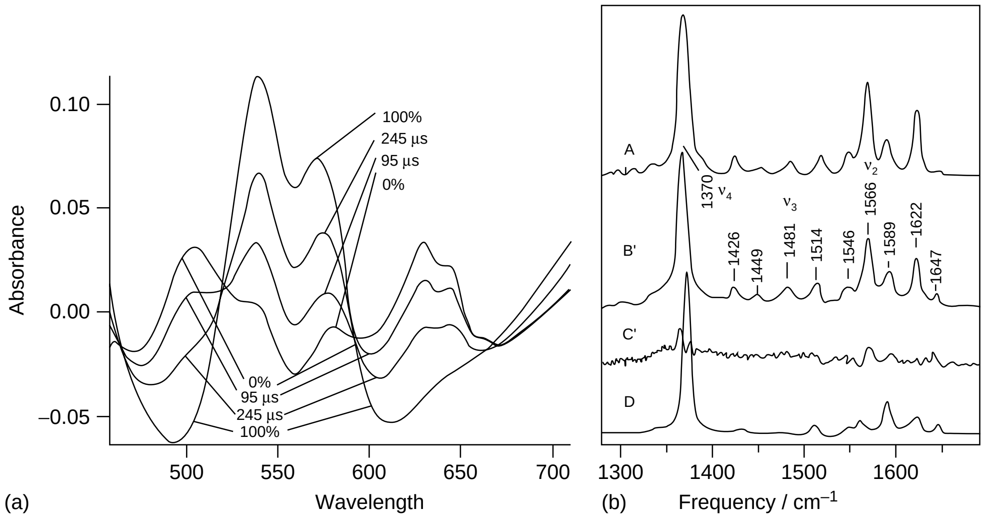

Figure 4 Low-temperature UV-visible spectra (a) and resonance Raman spectra of the same samples (b) recorded at 77 K. The 95-μs and 245-μs MHQ samples were obtained after mixing of 1 M azide and 0.35 mM metmyoglobin at a calibrated distance from the nozzle and the precooled cylinder. The azide-free metmyoglobin sample and a pre-incubated metmyoglobin azido complex were used as reference samples.[14] (b) Trace B′ and C′ represent the residual spectra of the 95-μs MHQ (B′) and 245-μs MHQ samples (C′) after maximal subtraction of the contribution from the starting material (trace A) and the end-product (trace D). Traces B′ and C′ were multiplied by four to allow easy comparison with those of metMb (A) and metMb pre-incubated with azide (D). (Reproduced from Lu, Wiertz, de Vries and Moënne-Loccoz.[77] © 2005 John Wiley & Sons, Ltd)

The resonance Raman spectrum suggests that the intermediate is a six-coordinate high-spin species.

$$\mathrm{Fe}^{3+}-\mathrm{H_2O}+\mathrm{N_3}^- \quad \text{(high spin)} \longrightarrow \mathrm{Fe}^{3+}-\mathrm{N_3}^- \quad \text{(high spin)}$$
$$\longrightarrow \mathrm{Fe}^{3+}-\mathrm{N_3}^- + \mathrm{H_2O} \quad \text{(low-spin)} \qquad (9)$$

However, it remains to be determined whether the azido group is already coordinating the iron(III), since the ligand field splitting is smaller compared to that of the resting azido complex. The other possibility is that the azide is not coordinating the iron but perturbs interactions between the iron-aqua ligand and its distal-pocket environment.

These results illustrate the complexity of ligand binding in a ‘‘simple two-component’’ system. The results further indicate the time resolution of the MHQ technique. The reaction between metmyoglobin and azide is a useful molecular timer, but the kinetics are not proportional to $[\mathrm{N_3}^-]$; observation of the intermediate described here can be used to argue that the particular rapid-freezing instrument operates below the 100 μs time scale.

4.3 Ultrarapid Freeze-Quench of NO Reductase

Nitric oxide reductase (Nor) forms part of the denitrification pathway found in Bacteria and Archaea.[120,121] Denitrification is the five-step conversion of nitrate to dinitrogen according to: $\mathrm{NO_3}^- \rightarrow \mathrm{NO_2}^- \rightarrow \mathrm{NO} \rightarrow \mathrm{N_2O} \rightarrow \mathrm{N_2}$. Nor catalyzes the reaction,

$$2\mathrm{NO} + 2e + 2\mathrm{H}^+ \longrightarrow \mathrm{N_2O} + \mathrm{H_2O} \qquad (10)$$

Nor is a member of the superfamily of heme-copper oxidases that also include the cytochrome oxidases (found e.g. in mitochondria[122]). Although no crystal structure of Nor is known at present, the number of transmembrane α-helices and the location and structure of their cofactors (heme c, heme b, heme b_3 and $\mathrm{Fe_B}$) are highly similar to those of the cytochrome oxidases.[122,123]

Biochemical and biophysical studies have indicated that Nors contain a binuclear heme-Fe/nonheme Fe active site (b_3-$\mathrm{Fe_B}$) where reduction of NO to $\mathrm{N_2O}$ occurs (Figure 5a).[124–126]

In the resting (oxidized) state (**1**) the iron atoms of the binuclear b_3-$\mathrm{Fe_B}$ site are antiferromagnetically coupled via a single strong Fe–O–Fe bond. The heme b_3 iron is five-coordinate in the oxidized state (**1**); upon reduction (**2**) the heme Fe is still five-coordinate, but bound to the proximal histidine. Intermediate (**2**) is ready to bind the two molecules of NO. Kumita *et al.*[85] attempt to answer the question whether both NO molecules bind to $\mathrm{Fe_B}$ (the ‘‘cis’’ mechanism[127,128]) or one to b_3, the other to $\mathrm{Fe_B}$ as depicted in (3) of Figure 5(a) (the ‘‘trans’’ mechanism[124–126,129]).

In the experiments the Nor was fully reduced containing four electrons allowing two consecutive turnovers (**2**–**5** followed by **6**–**8**, Figure 5a), each of two NO. The reduced Nor was rapidly mixed with NO and the reaction was quenched after 0.5–10 ms.[85] In a second series of experiments (shown here), the sample quenched after 0.5 ms was subsequently annealed and monitored optically and by EPR (Figure 5b). The Nor went through two full catalytic cycles in the frozen state.

EPR spectroscopy indicates the formation of a low-spin ferrous heme-NO complex ($g = 2.012$, Figure 5b) and of a high-spin ferrous-NO complex ($S = 3/2$; $\{\mathrm{FeNO}\}^7$) at $g \sim 4$. In addition, the oxidation of the low-spin hemes b and c ($g = 2.97$, 2.27 and $g = 3.56$, respectively) could be followed. The fully oxidized enzyme (**8**) showed a $g = 6$ signal due to heme b_3 and a $g = 4.3$ signal due to the $\mathrm{Fe_B}$; in other words, the Fe–O–Fe bond was absent and the two centers are no longer antiferromagnetically coupled as in (**1**).

The finding of EPR signals due to both a low-spin ferrous heme-NO complex and a high-spin ferrous heme-NO complex strongly argues in favor of the ‘‘trans’’ mechanism as depicted. The close proximity of the two NO molecules (**3**) allows electrophilic attack of one NO to the other leading to formation of the diiron bridged ‘‘$\mathrm{N_2O_2}$’’ (hyponitrite (**4**)) intermediate containing the N–N bond. Subsequent protonation would yield $\mathrm{N_2O}$ and $\mathrm{H_2O}$ (**5**) that would leave the active site and the enzyme is ready to bind and convert the next two NO (**7**, **8** Figure 5a).

5 OUTLOOK

In spite of the superior time resolution of continuous-flow mixing and relaxation techniques, rapid-mixing rapid-sampling techniques have contributed significantly to our understanding of catalysis of a wide range of enzymes. Rapid-mixing rapid-sampling techniques are general, versatile and easily combined with a large array of spectroscopic techniques, greatly contributing to their success. In the nearly fifty years since the development of the Rapid-Freeze Quench methodology, the pre-steady state kinetics of numerous metalloenzymes have been analyzed. The possibility to analyze the powder samples by a wide range of spectroscopies have provided detailed information on the oxidoreduction kinetics, ligand- and protonation-state changes during catalysis of heme centers, iron–sulphur centers, di-iron centers, single and multiple Mn-, Fe-, Co-, Ni-, Cu-, Mo-, W-sites, amino-acid main-chain and side-chain radicals, quinone, flavin, pterin radicals and so on. Given the dead time of 5–7 ms for the RFQ device and the fact that catalysis,—that is, substrate binding followed by breaking of the chemical bond- occurs at time scales from approximately a microsecond onwards, we may expect that the faster novel freeze-quench technologies will provide in the near future additional new insights in the first steps of (metallo) redox-enzyme catalysis. At present

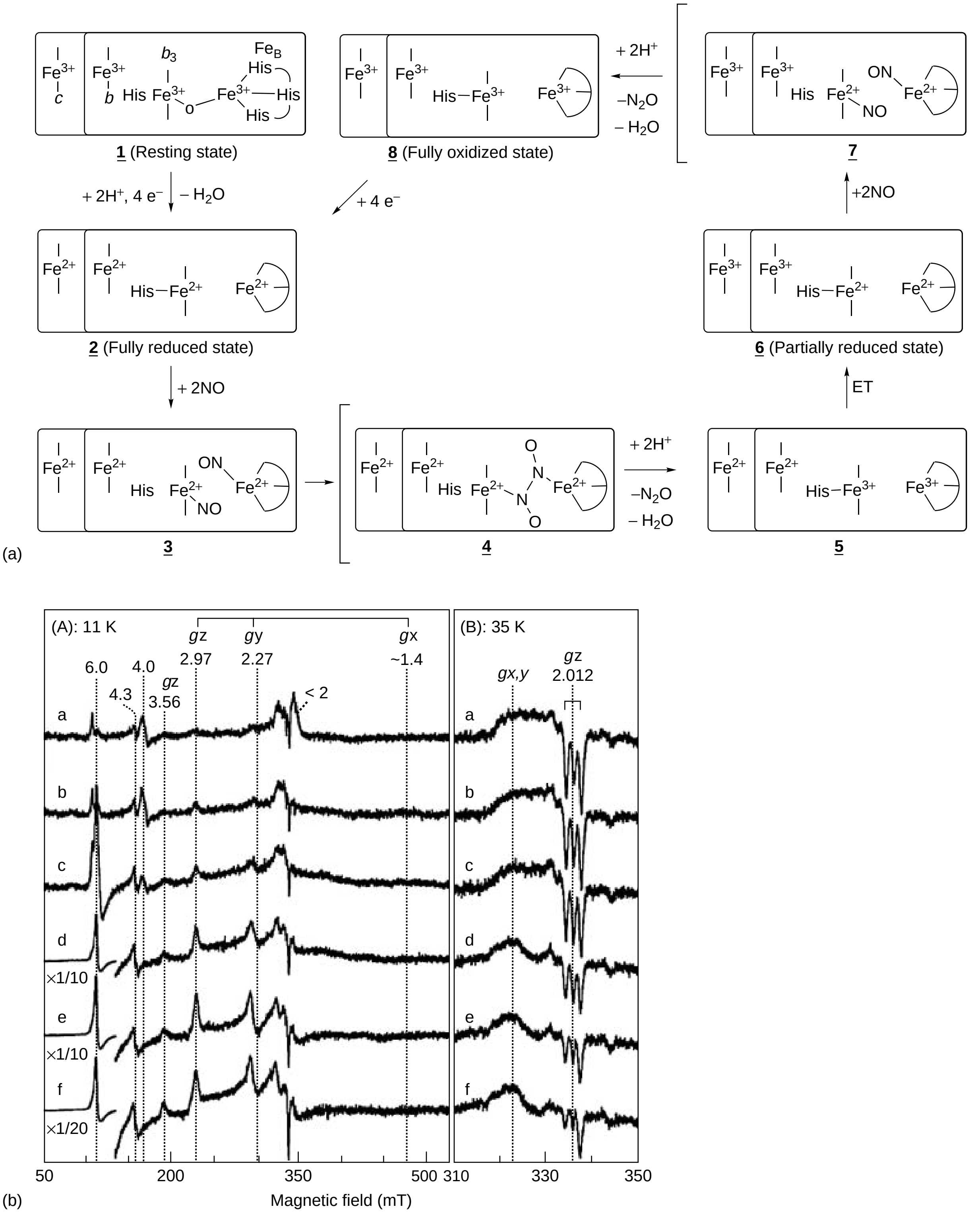
Fe3+
c
Fe3+
b
b3
His Fe3+
O
FeB
His
Fe3+
His
His
1 (Resting state)
8 (Fully oxidized state)
+ 2H+
−N2O
− H2O
7
ON
NO
+ 2H+, 4 e− − H2O
+ 4 e−
+2NO
Fe2+
His−Fe2+
2 (Fully reduced state)
6 (Partially reduced state)
+ 2NO
ET
3
4
5
(a)
(A): 11 K
gz
gy
gx
2.97
2.27
~1.4
6.0
4.0
4.3
gz
3.56
< 2
a
b
c
d
×1/10
e
×1/10
f
×1/20
(B): 35 K
gx,y
gz
2.012
50
200
350
500
310
330
350
(b)
Magnetic field (mT)

Figure 5 Proposed catalytic cycle for NO reductase from *Pseudomonas aeruginosa* (a) and EPR spectra of freeze-quenched samples (b). A: The catalytic nonheme iron Fe_B, the high-spin heme b_3, the low-spin heme *b*, and heme *c* are indicated from *right* to *left* in each state. B: Panels A and B show the spectra recorded at 11 and 35 K after annealing, respectively. Traces *a*–*f* show the X-band EPR spectra for the samples quenched at 0.5 ms after mixing the fully reduced NOR with NO buffer and annealing at 193 K for 120 min (trace a), 223 K for 5 min (trace b), 243 K for 5 min (trace c), 263 K for 10 min (trace d), 263 K for 30 min (trace e), and 263 K for 90 min (trace f). The *g*-values are indicated for the various species. (Reproduced from Kumita, Matsuura, Hino, Takahashi, Hori, Fukumori, Morishima and Shiro[85] by permission of American Society for Biochemistry and Molecular Biology)

the fast technologies enable EPR, resonance Raman and low-temperature UV-Vis analyses, but this can be quite easily extended to the range of techniques currently available to the RFQ powder samples.

The current dead time of 60–80 µs for the MHQ setup is not determined by the mixing time, but by the sample-transport time and the freeze-quenching time. The latter can potentially be reduced to ∼8–10 µs by using a jet of 10 µm diameter instead of 20 µm, but in doing so the Reynolds number will decrease to ∼2000, at the limit of complete mixing. Although the Reynolds number might be increased to ∼4000 by doubling the flow rate, thus halving the sample-transport time, the pressure will increase with $\langle v \rangle^2$, necessitating additional investigation of the enzyme's stability at ∼1600 bar. All in all, a minimal dead time of 20–30 µs is estimated for the MHQ and similar setups.

The production of hyperquenched samples means that the trapped intermediates are in a (near) native state, as if in aqueous solution. Analysis of their structure by Magic-Angle Spinning Nuclear Magnetic Resonance (MAS-NMR) (*see* ***Nuclear Magnetic Resonance (NMR) Spectroscopy of Inorganic/Organometallic Molecules***) at 77 K would yield a 3D-structure of a true catalytic intermediate in the native state, something that has not been achieved so far in biochemistry. Analysis of a series of samples quenched after various times would yield a 3D-movie delineating structure-function relationships of enzyme catalysis in great detail, aiding in exploiting the principles of catalysis for future applications.

6 ACKNOWLEDGMENTS

The author greatly acknowledges the contributions made to the development of the MHQ setup by Drs. A. V. Cherepanov, L. A. M. Pouvreau, Ir. F. G. M. Wiertz, Ing. M. J. F. Strampraad, S. Mitic, N. de Jong and A. Paulus. The development of the MHQ instrument has been supported by the TU Delft, The Netherlands Research Organization (NWO grants 98014 and 700-50-025) and NanoNed (project TAC. 6380).

7 ABBREVIATIONS AND ACRONYMS

CCD = charged coupled device; CD = circular dichroïsm; CPO = chloroperoxidase; ENDOR = electron nuclear double resonance; EPR = electron paramagnetic resonance; ESEEM = electron spin echo envelope modulation; EXAFS = extended X-ray absorption fine structure; FRET = fluorescent resonance energy transfer; FTIR = fourier transform infrared; MAS-NMR = magic-angle spinning nuclear magnetic resonance; MCD = magnetic circular dichroïsm; MHQ = microsecond freeze-hyperquenching; RFQ = rapid freeze quench; XAS = X-ray absorption spectroscopy.

8 FURTHER READING

D. P. Ballou and G. A. Palmer, *Anal. Chem.*, 1974, **46**(9), 1248.

B. Chance, *Photosyn. Res.*, 2004, **80**(1–3), 387.

A. V. Cherepanov and S. De Vries, *Biochim. Biophys. Acta*, 2004, **1656**(1), 1.

M. Eigen, 'Nobel Lectures (Chemistry)', Elsevier, Amsterdam, 1970, p. 170.

H. Roder, K. Maki and H. Cheng, *Chem. Rev.*, 2006, **106**(5), 1836.

F. G. M. Wiertz, O. M. Richter, A. V. Cherepanov, F. MacMillan, B. Ludwig and S. de Vries, *FEBS Lett.*, 2004, **575**(1–3), 127.

A. H. Zewail, *Angew. Chem., Int. Ed. Engl.*, 2000, **39**(15), 2586.

9 REFERENCES

1. J. E. House, 'Principles of Chemical Kinetics', Wm. C. Brown Publishers, 1997.
2. A. Fersht, 'Structure and Mechanism in Protein Science. A Guide to Enzyme Catalysis and Protein Folding', W.H. Freeman and Company, New Yotk, 1999.
3. A. Cornish-Bowden, 'Fundamentals of Enzyme Kinetics', 3rd edition, Portland Press, London, 2004.
4. A. H. Zewail, *Angew. Chem., Int. Ed. Engl.*, 2000, **39**(15), 2586.
5. H. Ma, C. Wan and A. H. Zewail, *J. Am. Chem. Soc.*, 2006, **128**(19), 6338.
6. Z. Ren, B. Perman, V. Srajer, T. Y. Teng, C. Pradervand, D. Bourgeois, F. Schotte, T. Ursby, R. Kort, M. Wulff and K. Moffat, *Biochemistry*, 2001, **40**(46), 13788.
7. B. Chance, C. Saronio and J. S. Leigh, Jr, *J. Biol. Chem.*, 1975, **250**(24), 9226.
8. P. Adelroth, M. Karpefors, G. Gilderson, F. L. Tomson, R. B. Gennis and P. Brzezinski, *Biochim. Biophys. Acta*, 2000, **1459**(2–3), 533.
9. M. Eigen, 'Nobel Lectures (Chemistry)', Elsevier, Amsterdam, 1970, p. 170.
10. M. Tegoni, M. C. Silvestrini, B. Guigliarelli, M. Asso, M. Brunori and P. Bertrand, *Biochemistry*, 1998, **37**(37), 12761.
11. M. Jacob, G. Holtermann, D. Perl, J. Reinstein, T. Schindler, M. A. Geeves and F. X. Schmid, *Biochemistry*, 1999, **38**(10), 2882.
12. P. Regenfuss, R. M. Clegg, M. J. Fulwyler, F. J. Barrantes and T. M. Jovin, *Rev. Sci. Instrum.*, 1985, **56**(2), 283.
13. M. C. Shastry, S. D. Luck and H. Roder, *Biophys. J.*, 1998, **74**(5), 2714.
14. A. V. Cherepanov and S. De Vries, *Biochim. Biophys. Acta*, 2004, **1656**(1), 1.

15. F. G. M. Wiertz, O. M. Richter, A. V. Cherepanov, F. MacMillan, B. Ludwig and S. de Vries, *FEBS Lett.*, 2004, **575**(1–3), 127.
16. H. Roder, K. Maki, R. F. Latypov, H. Cheng and M. C. R. Shastry, 'Early Events in Protein Folding Explored by Rapid Mixing Methods', WILEY-VCH Verlag GmbH & Company KGaA, Weinheim, 2005.
17. D. P. Ballou and G. A. Palmer, *Anal. Chem.*, 1974, **46**(9), 1248.
18. B. Chance, *Photosyn. Res.*, 2004, **80**(1–3), 387.
19. L. Pollack, M. W. Tate, N. C. Darnton, J. B. Knight, S. M. Gruner, W. A. Eaton and R. H. Austin, *Proc. Natl. Acad. Sci. U.S.A.*, 1999, **96**(18), 10115.
20. S. A. Pabit and S. J. Hagen, *Biophys. J.*, 2002, **83**(5), 2872.
21. R. E. Blankenship, 'Molecular Mechanisms of Photosynthesis', Blackwell, Oxford, 2002.
22. S. Giovannardi, L. Lando and A. Peres, *News Physiol. Sci.*, 1998, **13**, 251.
23. J. Choi and M. Terazima, *Photochem. Photobiol. Sci.*, 2003, **2**(7), 767.
24. G. Marriott ed., in 'Methods in Enzymolgy', Academic Press, 1998, Vol. 291.
25. I. Szundi, J. Cappuccio and O. Einarsdottir, *Biochemistry*, 2004, **43**(50), 15746.
26. V. Srajer, Z. Ren, T. Y. Teng, M. Schmidt, T. Ursby, D. Bourgeois, C. Pradervand, W. Schildkamp, M. Wulff and K. Moffat, *Biochemistry*, 2001, **40**(46), 13802.
27. J. Kubelka, J. Hofrichter and W. A. Eaton, *Curr. Opin. Struct. Biol.*, 2004, **14**(1), 76.
28. M. Buscaglia, J. Kubelka, W. A. Eaton and J. Hofrichter, *J. Mol. Biol.*, 2005, **347**(3), 657.
29. F. J. W. Roughton, *Proc. R. Soc. London*, 1930, **126A**, 470.
30. H. Hartridge and F. J. W. Roughton, *Proc. R. Soc. London, Ser. A: Math. Phys. Sci.*, 1923, **104**, 376.
31. B. Chance, *J. Franklin Inst.*, 1940, **229**, 737.
32. E. Kim, M. E. Helton, S. Lu, P. Moenne-Loccoz, C. D. Incarvito, A. L. Rheingold, S. Kaderli, A. D. Zuberbuhler and K. D. Karlin, *Inorg. Chem.*, 2005, **44**(20), 7014.
33. A. J. White, K. Drabble and C. W. Wharton, *Biochem. J.*, 1995, **306**(Pt 3), 843.
34. S. J. George, J. W. Allen, S. J. Ferguson and R. N. Thorneley, *J. Biol. Chem.*, 2000, **275**(43), 33231.
35. J. Tang and F. Gai, *Appl. Spectrosc.*, 2006, **60**(12), 1477.
36. M. Kakuta, P. Hinsmann, A. Manz and B. Lendl, *Lap Chip*, 2003, **3**(2), 82.
37. R. Masuch and D. A. Moss, *Appl. Spectrosc.*, 2003, **57**(11), 1407.
38. G. Hui Bon Hoa, P. Douzou, N. Dahan and C. Balny, *Anal. Biochem.*, 1982, **120**(1), 125.
39. C. Balny, J. L. Saldana and N. Dahan, *Anal. Biochem.*, 1984, **139**(1), 178.
40. P. Bugnon, G. Laurenczy, Y. Ducommun, P.-Y. Sauvageat, A. E. Merbach, R. Ith, R. Tschanz, M. Doludda, R. Bergbauer and E. Grell, *Anal. Chem.*, 1996, **68**, 3045.
41. V. V. Mozhaev, K. Heremans, J. Frank, P. Masson and C. Balny, *Proteins*, 1996, **24**(1), 81.
42. G. Hui Bon Hoa, M. A. McLean and S. G. Sligar, *Biochim. Biophys. Acta*, 2002, **1595**(1–2), 297.
43. R. R. Ernst ed., in 'Biochim. Biophys. Acta', Elsevier, 2002, Vol. 1595.
44. B. Kintses, Z. Simon, M. Gyimesi, J. Toth, B. Jelinek, C. Niedetzky, M. Kovacs and A. Malnasi-Csizmadia, *Biophys. J.*, 2006, **91**(12), 4605.
45. R. C. Bray, in 'Rapid Mixing and Sampling Techniques in Biochemistry', B. Chance, R. H. Eisenhardt, Q. H. Gibson and K. K. Longberg-Holm, Academic Press, New York, 1964, p. 195.
46. R. C. Bray, *Biochem. J.*, 1961, **81**, 189.
47. D. P. Ballou, *Methods Enzymol.*, 1978, **54**, 85.
48. B. Chance, R. H. Eisenhardt, Q. H. Gibson and K. K. Longberg-Holm eds., 'Rapid Mixing and Sampling Techniques in Biochemistry', Academic Press, New York, 1964, p. 195.
49. G. Palmer, R. C. Bray and H. Beinert, *J. Biol. Chem.*, 1964, **239**, 2657.
50. G. Palmer and H. Beinert, in 'Rapid Mixing and Sampling Techniques in Biochemistry', B. Chance, R. H. Eisenhardt, Q. H. Gibson and K. K. Longberg-Holm eds., Academic Press, New York, 1964, p. 205.
51. S. de Vries, S. P. Albracht, J. A. Berden and E. C. Slater, *Biochim. Biophys. Acta*, 1982, **681**(1), 41.
52. P. Moenne-Loccoz, C. Krebs, K. Herlihy, D. E. Edmondson, E. C. Theil, B. H. Huynh and T. M. Loehr, *Biochemistry*, 1999, **38**(17), 5290.
53. J.-P. Willems, H. I. Lee, D. Burdi, P. E. Doan, J. Stubbe and B. M. Hoffman, *J. Am. Chem. Soc.*, 1997, **119**(41), 9816.
54. A. L. Tsai, V. Berka, R. J. Kulmacz, G. Wu and G. Palmer, *Anal. Biochem.*, 1998, **264**(2), 165.
55. V. Schunemann, C. Jung, J. Terner, A. X. Trautwein and R. Weiss, *J. Inorg. Biochem.*, 2002, **91**(4), 586.
56. M. J. Ryle, H. I. Lee, L. C. Seefeldt and B. M. Hoffman, *Biochemistry*, 2000, **39**(5), 1114.
57. P. J. Riggs-Gelasco, L. Shu, S. Chen, D. Burdi, B. H. Huynh, L. Que and J. Stubbe, Jr, *J. Am. Chem. Soc.*, 1998, **120**(5), 849.
58. N. Ravi, J. M. Bollinger, B. H. Huynh, J. Stubbe and D. E. Edmondson, Jr, *J. Am. Chem. Soc.*, 1994, **116**(18), 8007.
59. N. Mitic, L. Saleh, G. Schenk, J. M. Bollinger and E. I. Solomon, Jr, *J. Am. Chem. Soc.*, 2003, **125**(37), 11200.
60. S. de Vries, S. P. Albracht, J. A. Berden, C. A. Marres and E. C. Slater, *Biochim. Biophys. Acta*, 1983, **723**(1), 91.

61. M. C. Brenner, C. J. Murray and J. P. Klinman, *Biochemistry*, 1989, **28**(11), 4656.

62. V. M. Grigoryants, A. V. Veselov and C. P. Scholes, *Biophys. J.*, 2000, **78**(5), 2702.

63. J. Hogan, *Nature*, 2006, **442**(7101), 351.

64. R. Russell, I. S. Millett, M. W. Tate, L. W. Kwok, B. Nakatani, S. M. Gruner, S. G. Mochrie, V. Pande, S. Doniach, D. Herschlag and L. Pollack, *Proc. Natl. Acad. Sci. U.S.A.*, 2002, **99**(7), 4266.

65. J. Ross, I. Schreiber and M. O. Vlad, ‘Determination of Complex Reaction Mechanisms. Analysis of Chemical, Biological and Genetic Networks’, Oxford University Press, 2006.

66. L. Pollack, M. W. Tate, A. C. Finnefrock, C. Kalidas, S. Trotter, N. C. Darnton, L. Lurio, R. H. Austin, C. A. Batt, S. M. Gruner and S. G. Mochrie, *Phys. Rev. Lett.*, 2001, **86**(21), 4962.

67. S. I. E. Vulto, A. M. Streltsov, A. Y. Shkuropatov, V. A. Shuvalov and T. J. Aartsma, *J. Phys. Chem. B*, 1997, **101**(37), 7249.

68. G. Pettersson, *Eur. J. Biochem.*, 1989, **184**(3), 561.

69. B. Perman, V. Srajer, Z. Ren, T. Teng, C. Pradervand, T. Ursby, D. Bourgeois, F. Schotte, M. Wulff, R. Kort, K. Hellingwerf and K. Moffat, *Science*, 1998, **279**(5358), 1946.

70. G. G. Hammes, *Biochemistry*, 2002, **41**(26), 8221.

71. T. C. Bruice and S. J. Benkovic, *Biochemistry*, 2000, **39**(21), 6267.

72. H. Roder, K. Maki and H. Cheng, *Chem. Rev.*, 2006, **106**(5), 1836.

73. K. Paeng, I. Paeng and J. Kincaid, *Anal. Sci.*, 1994, **10**, 157.

74. V. Z. Neltchev, G. D. Detchev and L. A. Boyadjiev, *J. Phys. E: Sci. Instrum.*, 1970, **3**, 722.

75. R. L. Berger, B. Balko and H. F. Chapman, *Rev. Sci. Instrum.*, 1968, **39**, 493.

76. R. L. Berger, *Biophys. J.*, 1978, **24**(1), 2.

77. S. Lu, F. G. M. Wiertz, S. de Vries and P. Moënne-Loccoz, *J. Raman Spectrosc.*, 2005, **36**, 359.

78. F. G. M. Wiertz and S. de Vries, *Biochem. Soc. Trans.*, 2006, **34**(Pt 1), 136.

79. K. Yamamoto, M. Matsubara, S. Kawasaki, M. L. Bari and S. Kawamoto, *Braz. J. Med. Biol. Res.*, 2005, **38**(8), 1253.

80. L. Smeller, *Biochim. Biophys. Acta*, 2002, **1595**(1–2), 11.

81. R. F. Mudde, J. S. Groen and H. E. A. Van den Akker, *Chem. Eng. Sci.*, 1997, **52**, 4217.

82. M. Tanaka, K. Matsuura, S. Yoshioka, S. Takahashi, K. Ishimori, H. Hori and I. Morishima, *Biophys. J.*, 2003, **84**(3), 1998.

83. Y. Lin, G. J. Gerfen, D. L. Rousseau and S. R. Yeh, *Anal. Chem.*, 2003, **75**(20), 5381.

84. K. Matsuura, S. Yoshioka, S. Takahashi, K. Ishimori, T. Mogi, H. Hori and I. Morishima, *Biochemistry* 2004, **43**, 2288.

85. H. Kumita, K. Matsuura, T. Hino, S. Takahashi, H. Hori, Y. Fukumori, I. Morishima and Y. Shiro, *J. Biol. Chem.*, 2004, **279**(53), 55247.

86. E. Mayer and P. Bruggeller, *Nature*, 1982, **298**, 715.

87. E. Mayer, *J. Microsc.*, 1985, **140**, 3.

88. W. B. Bald, *J. Microsc.*, 1986, **143**, 89.

89. C. A. Tulk, D. D. Klug, R. Branderhorst, P. Sharpe and J. A. Ripmeester, *J. Chem. Phys.*, 1998, **109**(19), 8478.

90. H. E. Stanley, S. V. Buldyrev, O. Mishima, M. R. Sadr-Lahijany, A. Scala and F. W. Starr, *J. Phys.: Condens. Matter*, 2000, **12**, A403.

91. O. Mishima and H. E. Stanley, *Nature*, 1998, **396**, 329.

92. J. C. Dore, *J. Mol. Struct.*, 1990, **237**, 221.

93. P. Boutron and R. Alben, *J. Chem. Phys.*, 1975, **62**(12), 4848.

94. F. W. Starr, M.-C. Bellissent-Funel and H. E. Stanley, Structural evidence for the continuity of liquid and glassy water, arXiv: condensed matter, 9811118, (v1), 1998, 1.

95. R. S. Smith and B. D. Kay, *Nature*, 1999, **398**, 788.

96. R. S. Smith, C. Huang and B. D. Kay, *J. Phys. Chem. B*, 1997, **101**(32), 6123.

97. G. P. Johari, A. Hallbrucker and E. Mayer, *Nature*, 1987, **330**, 552.

98. Y. Yue and C. A. Angell, *Nature*, 2004, **427**(6976), 717.

99. I. Kohl, L. Bachmann, E. Mayer, A. Hallbrucker and T. Loerting, *Nature*, 2005, **435**(7041), E1.

100. A. Hallbrucker and E. Mayer, *J. Phys. Chem.*, 1987, **91**(3), 503.

101. D. E. Pegg, *Cryo Letters*, 2001, **22**(2), 105.

102. P. Mazur, *Science*, 1970, **168**(934), 939.

103. H. L. Bank and K. G. Brockbank, *J. Card. Surg.*, 1987, **2**(Suppl. 1), 137.

104. M. Sono, M. P. Roach, E. D. Coulter and J. H. Dawson, *Chem. Rev.*, 1996, **96**(7), 2841.

105. I. G. Denisov, T. M. Makris, S. G. Sligar and I. Schlichting, *Chem. Rev.*, 2005, **105**(6), 2253.

106. P. R. Ortiz de Montellano ed., ‘Cytochrome P450 Structure, Mechanism, and Biochemistry’, 3rd edition, Kluwer Academic publishers, New York, 2005.

107. M. C. Glascock, D. P. Ballou and J. H. Dawson, *J. Biol. Chem.*, 2005, **280**(51), 42134.

108. R. Davydov, T. M. Makris, V. Kofman, D. E. Werst, S. G. Sligar and B. M. Hoffman, *J. Am. Chem. Soc.*, 2001, **123**(7), 1403.

109. C. Jung, V. Schunemann, F. Lendzian, A. X. Trautwein, J. Contzen, M. Galander, L. H. Bottger, M. Richter and A. L. Barra, *Biol. Chem.*, 2005, **386**(10), 1043.

110. C. Jung, V. Schunemann and F. Lendzian, *Biochem. Biophys. Res. Commun.*, 2005, **338**(1), 355.

111. J. Terner, V. Palaniappan, A. Gold, R. Weiss, M. M. Fitzgerald, A. M. Sullivan and C. M. Hosten, *J. Inorg. Biochem.*, 2006, **100**(4), 480.
112. T. Egawa, D. A. Proshlyakov, H. Miki, R. Makino, T. Ogura, T. Kitagawa and Y. Ishimura, *J. Biol. Inorg. Chem.*, 2001, **6**(1), 46.
113. D. G. Kellner, S. C. Hung, K. E. Weiss and S. G. Sligar, *J. Biol. Chem.*, 2002, **277**(12), 9641.
114. T. Egawa, H. Shimada and Y. Ishimura, *Biochem. Biophys. Res. Commun.*, 1994, **201**(3), 1464.
115. V. Schunemann, F. Lendzian, C. Jung, J. Contzen, A. L. Barra, S. G. Sligar and A. X. Trautwein, *J. Biol. Chem.*, 2004, **279**(12), 10919.
116. V. Schunemann, C. Jung, A. X. Trautwein, D. Mandon and R. Weiss, *FEBS Lett.*, 2000, **479**(3), 149.
117. T. Spolitak, J. H. Dawson and D. P. Ballou, *J. Biol. Chem.*, 2005, **280**(21), 20300.
118. R. Rutter and L. P. Hager, *J. Biol. Chem.*, 1982, **257**(14), 7958.
119. M. Newcomb, R. Zhang, R. E. Chandrasena, J. A. Halgrimson, J. H. Horner, T. M. Makris and S. G. Sligar, *J. Am. Chem. Soc.*, 2006, **128**(14), 4580.
120. W. G. Zumft, *Microbiol. Mol. Biol. Rev.*, 1997, **61**(4), 533.
121. I. M. Wasser, S. de Vries, P. Moënne-Loccoz, I. Schröder and K. D. Karlin, *Chem. Rev.*, 2002, **102**(4), 1201.
122. J. H. M. Hendriks, U. Gohlke and M. Saraste, *J. Bioenerg. Biomembr.*, 1998, **30**(30), 15.
123. C. Ostermeier, A. Harrenga, U. Ermler and H. Michel, *Proc. Natl. Acad. Sci. U.S.A.*, 1997, **94**(20), 10547.
124. P. Moënne-Loccoz, O.-M. H. Richter, H. W. Huang, I. Wasser, R. A. Ghiladi, K. D. Karlin and S. de Vries, *J. Am. Chem. Soc.*, 2000, **122**, 9344.
125. P. Moënne-Loccoz and S. de Vries, *J. Am. Chem. Soc.*, 1998, **120**, 5147.
126. P. Girsch and S. de Vries, *Biochim. Biophys. Acta*, 1997, **1318**(1–2), 202.
127. C. S. Butler, H. E. Seward, C. Greenwood and A. J. Thomson, *Biochemistry*, 1997, **36**(51), 16259.
128. N. J. Watmough, M. R. Cheesman, C. S. Butler, R. H. Little, C. Greenwood and A. J. Thomson, *J. Bioenerg. Biomembr.*, 1998, **30**(1), 55.
129. S. Lu Suharti, S. de Vries and P. Moenne-Loccoz, *J. Am. Chem. Soc.*, 2004, **126**(47), 15332.

Gold in Homogeneous Catalysis

Eloísa Jiménez-Núñez and Antonio M. Echavarren
Institute of Chemical Research of Catalonia (ICIQ), Tarragona, Catalonia, Spain

1 Introduction 1
2 Reactions of Alkynes with Heteronucleophiles 2
3 Cycloisomerizations of Enynes Bearing Propargylic Carboxylates or Ethers 14
4 Allenynes 17
5 Mechanistically Related Reactions of Arenes and Heteroarenes with Alkynes 18
6 Allenes 20
7 Carbonyl Activation 23
8 Alcohol Activation 27
9 Olefin Activation 29
10 Alkane Activation (C–H) 30
11 Other Activations 31
12 References 31

1 INTRODUCTION

Homogeneous catalysis by gold salts and complexes has evolved in the last few years from being an almost neglected field to becoming one of the most active areas of research in organometallic and organic chemistry.[1–11] Gold complexes usually surpass the reactivity shown by other electrophilic metal salts and complexes for the activation of alkynes. These complexes are remarkably reactive Lewis acids, with a high affinity for π-bonds. This unique π-acidity is a result of relativistic effects, which reach a maximum in the periodic table with gold.[11–15]

In addition to AuCl, AuCl$_3$, or HAuCl$_4$ and its salts, most common gold catalysts are cationic complexes generated by in situ abstraction of chloride from [AuCl(PPh$_3$)], or similar phosphine complexes, using an equivalent of silver salt with a noncoordinating anion to form in situ cationic complexes [Au(S)(PPh$_3$)]X (S = solvent or substrate molecule).[16–18] The same complexes can be obtained by cleavage of the Au–Me bond in [AuMe(PPh$_3$)] with a protic acid.[16,19–21] Gold-oxo complex [(Ph$_3$PAu)$_3$O]BF$_4$[22,23] has also been used as a catalyst.[24] Gold(I) complexes (**1a**–**d**) bearing bulky, biphenyl-based phosphines lead to very active catalysts upon being mixed with Ag(I) salts.[25] Cationic complexes (**2a**–**b**) and (**3**)[17] are very reactive as catalysts in many transformations.[26–29] The structures of (**1a**–**d**), (**2a**–**b**), and (**3**) have been confirmed by X-ray crystallography.[30,31] Related complexes (**2c**–**d**) with weakly coordinated bis(trifluoromethanesulfonyl)amide NTf$_2$ (Tf = CF$_3$SO$_2$) have also been prepared.[32] Gold(I) complex (**4**) bearing the bulky ligand tris(2,6-di-*tert*-butylphenyl)phosphite leads to a highly electrophilic cationic Au(I) catalyst in situ by chloride abstraction with AgSbF$_6$.[33,34] Gold complexes with donating N-heterocyclic ligands (NHC) such as (**5a**–**d**) are also good precatalysts.[35,36] Cationic complexes bearing NHC ligands such as (**6**), which shows moderate stability at room temperature,[37] and those with NTf$_2$ ligand (**7a**–**b**) have also been reported.[38,39] Au(III) complex (**8**) has also been used as an alternative to AuCl$_3$.[40,41]

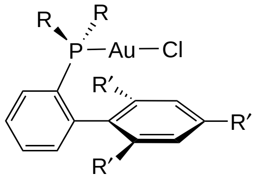

1a R = *t*Bu, R′ = H
1b R = Cy, R′ = H
1c R = Cy, R′ = *i*Pr

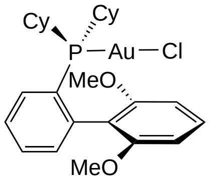

1d

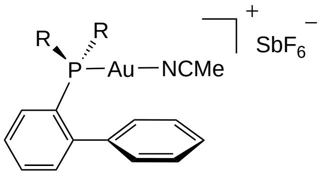

2a R = *t*Bu
2b R = Cy

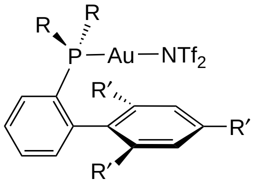

2c R = *t*Bu, R′ = H
2d R = Cy, R′ = *i*Pr

[Au(PPh$_3$)(NCMe)]SbF$_6$

3

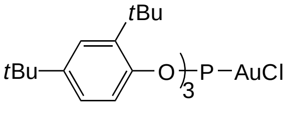

4

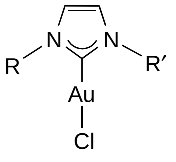

5a R = R′ = 2,4,6-Me$_3$C$_6$H$_2$
(= IMesAuCl)
5b R = Mes, R′ = Me
5c = R = R′ = Me
5d = R = R′ = 2,6-*i*Pr$_2$C$_6$H$_3$
(= *i*PrAuCl)

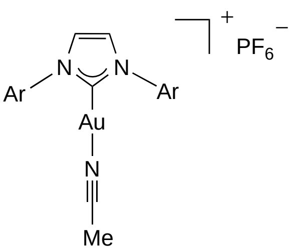

6 Ar = 2,6-*i*Pr$_2$C$_6$H$_3$

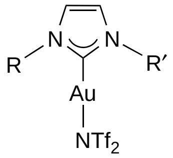
R
N
N
R′
Au
NTf2

7a Ar = Mes
7b Ar = 2,6-$i\text{Pr}_2\text{C}_6\text{H}_3$

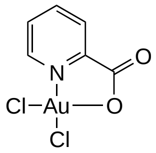

8

2 REACTIONS OF ALKYNES WITH HETERONUCLEOPHILES

In a simplified form, the nucleophilic attack to the $[\text{AuL}]^+$–alkyne complex gives trans-alkenyl-gold complexes as intermediates (equation 1). Although simple alkyne–Au(I) complexes are usually stable only at low temperatures,[42,43] a few compounds of this type have been characterized.[44–47]

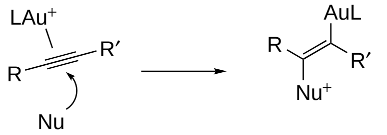
LAu+
R′
R
Nu
AuL
R
R′
Nu+

(1)

2.1 Oxygen Nucleophiles

The first examples of hydration of alkynes catalyzed by gold salts were reported in 1976 by Thomas.[48] Later, Utimoto found that the reaction could be carried out with lower amounts of catalyst.[49,50] Tanaka and coworkers reported a general hydration of alkynes using cationic Au(I) complexes generated in situ by protonolysis of $[\text{AuMe(PPh}_3)]$ as depicted in equations (2) and (3).[20,21] Markovnikov-type addition is observed in all cases. Other complexes of Au(I) and Au(III) have proved to be effective in this reaction.[51–53] The somewhat related gold-catalyzed addition of HCl to alkynes is an industrial process for the generation of vinyl chloride.[54]

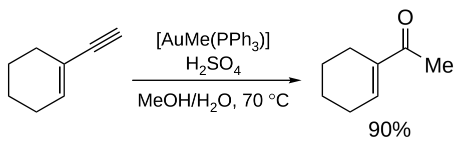
[AuMe(PPh3)]
H2SO4
MeOH/H2O, 70 °C
O
Me
90%

(2)

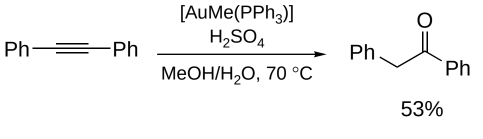
Ph
Ph
[AuMe(PPh3)]
H2SO4
MeOH/H2O, 70 °C
O
Ph
Ph
53%

(3)

The nucleophilic addition of alcohols to alkynes was reported by Utimoto[49] with NaAuCl_4 and later by Teles with cationic gold complexes.[19,55] The enol ethers formed can be hydrolyzed to form carbonyl compounds or trapped as ketals (equations 4 and 5). An intramolecular version of this reaction was reported by the group of Genêt to give bicyclic ketals (equation 6).[56–58] On the basis of this concept, a glycosidation reaction was developed using propargyl glycosides as glycosyl donors with AuCl_3 as catalyst in acetonitrile.[59]

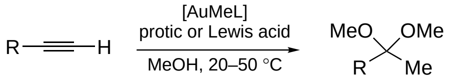
R
H
[AuMeL]
protic or Lewis acid
MeOH, 20–50 °C
MeO
OMe
R
Me

(4)

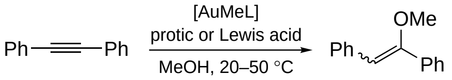
Ph
Ph
[AuMeL]
protic or Lewis acid
MeOH, 20–50 °C
OMe
Ph
Ph

(5)

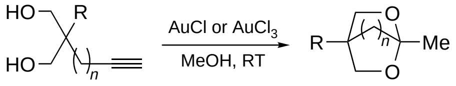
HO
R
HO
n
AuCl or AuCl3
MeOH, RT
O
R
n
Me
O

(6)

Intermolecular additions of alcohols to alkynes can be coupled with other tandem reactions of the alkenyl-gold intermediate. Thus, reaction between salicylaldehyde and phenylacetylenes can give access to the isoflavanone skeleton[60,61] (equation 7), whereas a three-component addition of methylenecylopropylcarbinols, arylalkynes, and alcohols leads to bicyclic compounds (equation 8).[62]

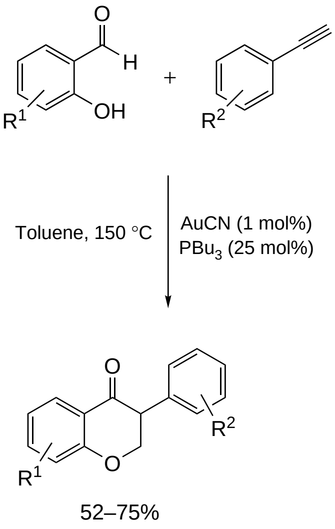
O
H
OH
R1
+
R2
Toluene, 150 °C
AuCN (1 mol%)
PBu3 (25 mol%)
O
R2
R1
O
52–75%

(7)

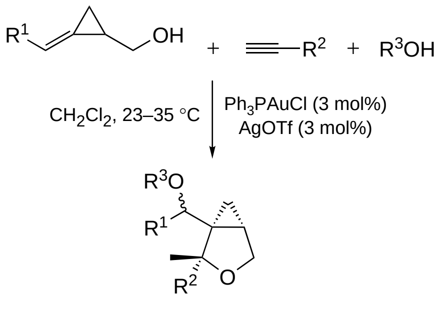
R1
OH
+
R2
+
R3OH
CH2Cl2, 23–35 °C
Ph3PAuCl (3 mol%)
AgOTf (3 mol%)
R3O
R1
R2
O

(8)

Hashmi reported the gold-catalyzed formation of furans by intramolecular addition of alcohols to alkynes[63] (equation 9) and, more recently, Liu *et al.* applied this reaction for the synthesis of dihydrofurans.[64] Propargylic alcohols undergo a Meyer–Schuster rearrangement leading to the formation of α,β-unsaturated ketones[65,66] or α,β-unsaturated esters in the case of ethoxyalkynyl carbinols.[67,68] In a recent report, Zhang showed a Meyer–Schuster rearrangement coupled with the intramolecular oxidation of the resulting gold carbene by a sulfoxide to yield 1,3-dicarbonyl compounds.[38]

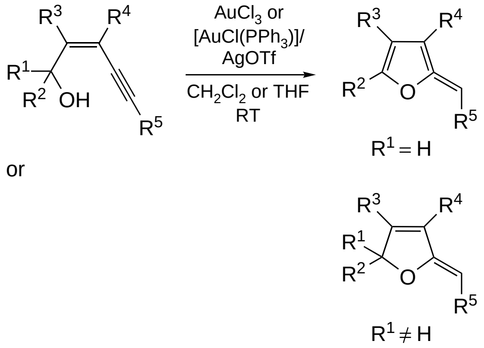

(9)

In contrast, propargylic cyclopropanols and cyclobutanols undergo ring expansion to form cyclobutanones and cyclopentanones with Au(I) catalysts[69] (equation 10).

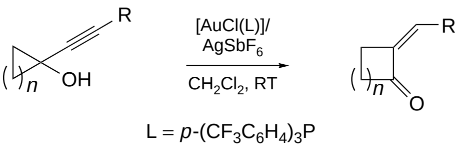

(10)

A related transformation was reported by the group of Floreancig for the synthesis of substituted tetrahydropyrans (equation 11).[70] This transformation initially involves a hydration of the alkyne and then an elimination of a leaving group at the β position, followed by a conjugate addition.

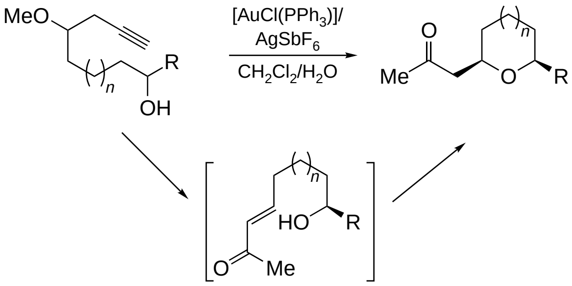

(11)

The group of Barluenga reported the formation of enol ethers, which are protonated in situ to form oxonium intermediates that undergo Prins reaction yielding eight-membered ring carbocycles (equation 12).[71]

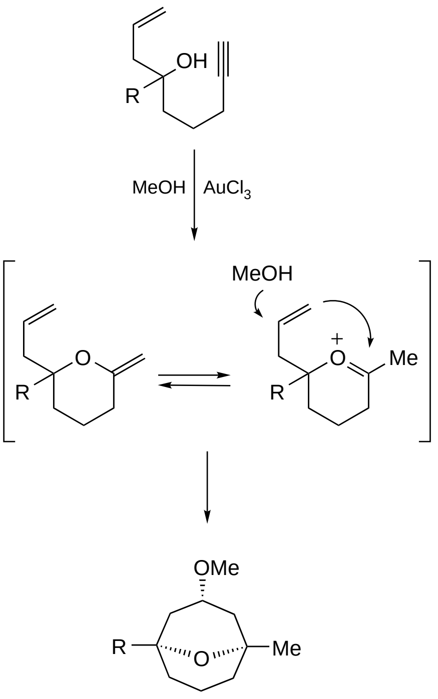

(12)

Carbonyl compounds and epoxides also act as nucleophiles in the addition to alkynes to give furans.[63,72–76] Cyclic acetals are obtained with some epoxyalcohols,[77] whereas cyclic enones are the products of the cyclization of alkynyl ketones.[78] An interesting transformation occurs upon treatment of hydroxyketones to give $3(2H)$-furanones with $AuCl_3$ at 23 – 38 °C in CH_2Cl_2 (equation 13).[79] The reaction proceeds by carbonyl attack to the enyne and pinacol-type rearrangement, where a 1,2-migration of the propargylic substituent takes place. When R^1 and R^2 are part of a ring, this rearrangement leads to a ring contraction.[80] A related conversion occurs in the gold(I)-catalyzed reaction of alkynylcyclopropanes, which gives furans (equation 14).[81] In this case, when the nucleophile is an indole, the furanyl–gold intermediate can be trapped by the indolinium cation formed in the first step.[82]

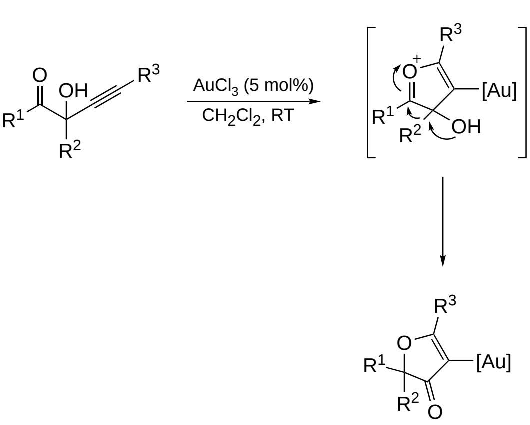

(13)

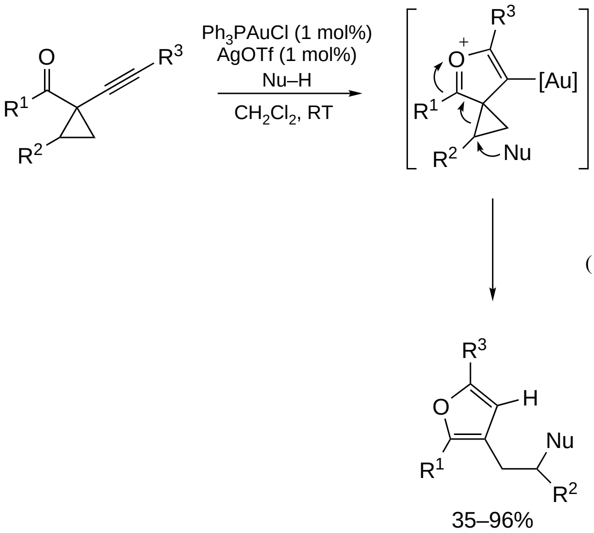

(14)

An interesting class of reactions are initiated by the intramolecular attack of a carbonyl group to the alkyne to form pyrylium ions, which can react further with alkynes to form naphthalenes by a $[4+2]$ cyloaddition followed by a cycloreversion or suffer addition of external nucleophiles (equation 15).[83]

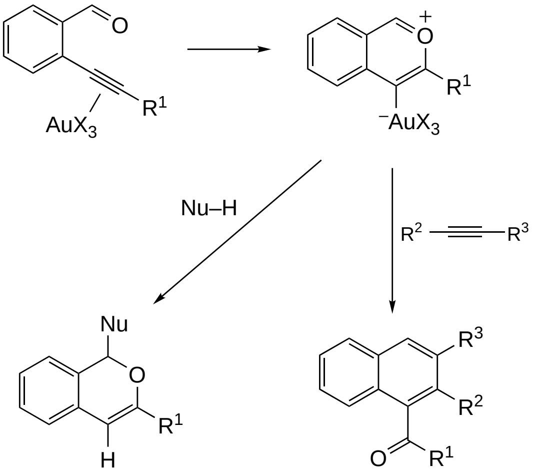

(15)

This chemistry has been studied extensively by the groups of Asao,[84–90] Dyker *et al.*[91,92] Oh,[93] and others[94–96] and has been recently reviewed.[97] A notable application of this chemistry is the synthesis of the tetracyclic compound in equation (16), which was transformed in one or two steps into the angucyclinone antibiotics (+)-rubiginone B_2 and (+)-ochromycinone.[98] The intermediate pyrylium gold species can also undergo $[3+2]$ cycloaddition to form tricyclic compounds as shown in equation (17).[93] Formation of intermediate azomethine ylides by reaction of imines with alkynes catalyzed by gold has been reported by the group of Iwasawa.[99]

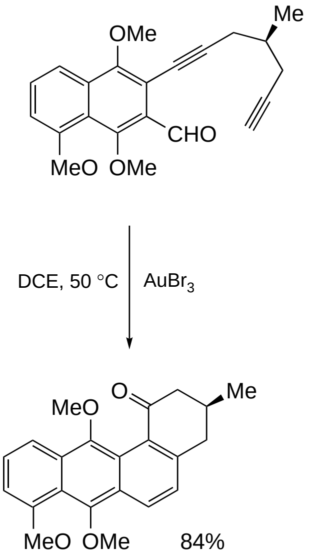

(16)

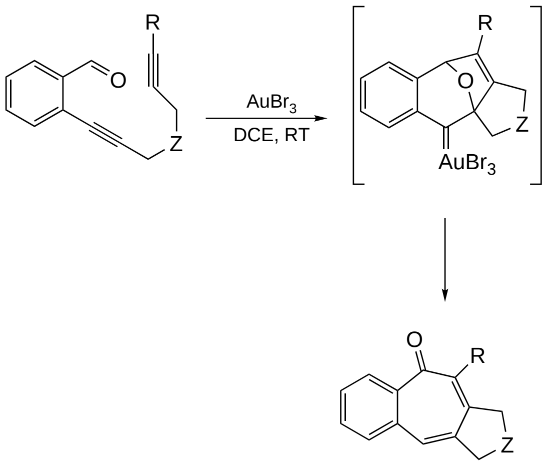

(17)

Arylalkynes bearing benzylic ethers at the ortho position also cyclize with cationic Au(I) catalysts to give indenyl ethers (equation 18).[100] As per a recent report, the cation formed from the intramolecular attack of carboxylates onto related substrates was used as an effective alkylating agent, producing isocoumarins as side products.[101]

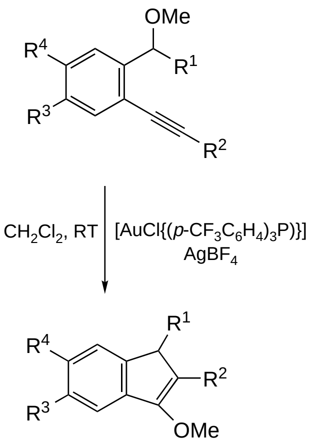

(18)

Carboxylic acids,[102–104] carbonates,[105–107] carbamates,[108–110] sulfoxides,[111] and related nucleophiles[112] also add to alkynes (equations 19–22). Similarly, the intramolecular addition of amides to alkynes leads to oxazoles by isomerization of the initially formed 5-methylene-4,5-dihydrooxazoles (equation 22).[113] An interesting reaction was reported by Yamamoto and Asao in which nitro groups add to alkynes intramolecularly with $AuBr_3$ as catalyst.[114]

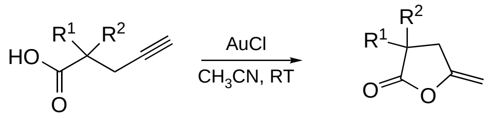
HO
R1
R2
O
AuCl
CH3CN, RT
R2
R1
O
O

(19)

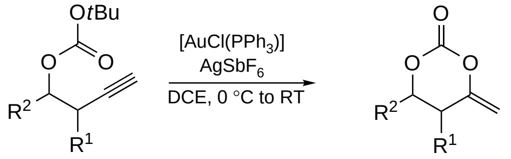
OtBu
O
O
R2
R1
[AuCl(PPh3)]
AgSbF6
DCE, 0 °C to RT
O
O
O
R2
R1

(20)

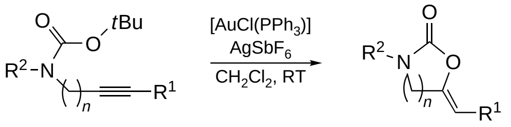
O
tBu
O
R2-N
n
R1
[AuCl(PPh3)]
AgSbF6
CH2Cl2, RT
O
R2
N
O
n
R1

(21)

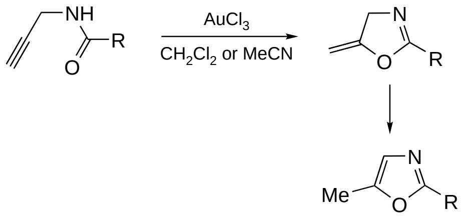
NH
R
O
AuCl3
CH2Cl2 or MeCN
N
O
R
Me
N
O
R

(22)

Propargylic esters coordinate with gold to form complexes that can undergo 1,2- or 1,3-acyl migrations to form α-acyloxy-α,β-unsaturated carbenes or allene–gold complexes (equation 23).[115–117] According to DFT (density functional theory) calculations, formation of these two species is not concerted, but proceeds in two steps through five- and six-membered ring intermediates, respectively.[116,117] Evidence for the involvement of gold carbenes has been obtained in intermolecular cyclopropanation reactions with alkenes (equation 24),[118–122] trapping with carbon nucleophiles[123] and sulfides (equation 25),[124] and oxidation with Ph_2SO to form α,β-unsaturated carbonyl compounds.[125]

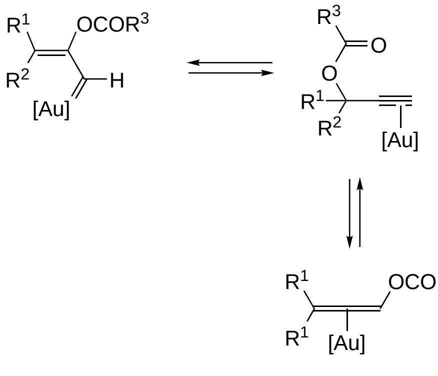
R1
OCOR3
R2
H
[Au]
R3
O
O
R1
R2
[Au]
R1
OCOR3
R1
[Au]

(23)

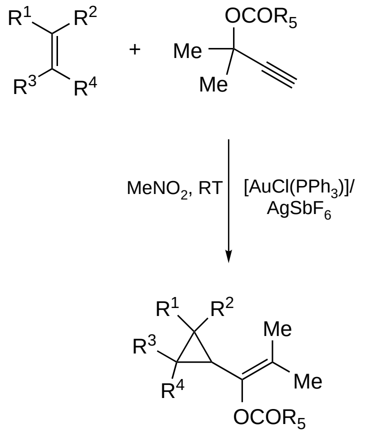
R1
R2
R3
R4
+
OCOR5
Me
Me
MeNO2, RT
[AuCl(PPh3)]/
AgSbF6
R1
R2
R3
R4
Me
Me
OCOR5

(24)

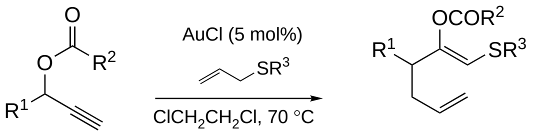
O
O
R2
R1
AuCl (5 mol%)
SR3
ClCH2CH2Cl, 70 °C
OCOR2
R1
SR3

(25)

Simple propargylic esters also undergo a 1,3-acyl migration catalyzed by Au(III), leading finally to 1,3-dicarbonyl compounds as mixtures of E and Z isomers (equation 26).[126–128]

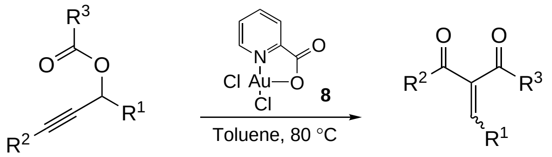
R3
O
O
R1
R2
N
O
Cl Au—O
Cl
8
Toluene, 80 °C
O
O
R2
R3
R1

(26)

Other 1,3-acyl migrations of propargylic carboxylates catalyzed by gold give intermediate allenes, which can afford heterocyclic compounds by intramolecular attack of the appropriate nucleophiles.[129] The intermediate allenes formed by 1,3-acyl migrations can also react intramolecularly with alkynes to form naphthalenes, although this reaction proceeds more efficiently with Ag(I) catalysts,[130] and is discussed in the alkyne–carbon nucleophile section.

Related transformations take place from propargylic carboxylates by using Au(I) catalysts for the synthesis of enones through 1,3-migration.[131–133] Tandem sequences exploit the potential of this rearrangement to obtain, by means of allenyl or carbene intermediates, structurally different substrates.[134]

2.2 Nitrogen Nucleophiles

The hydroamination of terminal alkynes with $NaAuCl_4$ was developed in 1987.[135] In 1991, Utimoto described the preparation of tetrahydropyridines from 5-alkynylamines with Au(III) catalysts.[136] This idea was further extended by Müller to give the corresponding iminium compounds.[137,138]

Later, Arcadi showed that β-keto-imines react with alkynes intramolecularly to give pyrroles.[139] The intermolecular amination with anilines was later developed by Hayashi and Tanaka[21] using a cationic Au(I) catalyst to form imines (equation 27). More recently, Arcadi *et al.* developed an intramolecular version for the cyclization of *o*-alkynylanilines to form indoles (equation 28)[140–142] and Li reported a double intra- and intermolecular hydroamination to obtain *N*-vinylindoles.[143] *O*-Substituted hydroxylamines can also undergo this type of transformation to dihydroisoxazole derivatives.[144] Tandem sequences that involve a first alkyne-hydroamination step with anilines have been recently developed[145,146] and are similar to the previously discussed additions with phenols that access isoflavone skeletons.

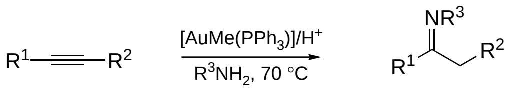

(27)

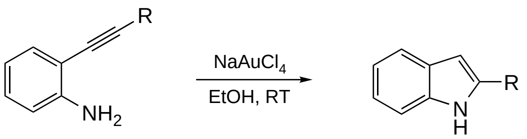

(28)

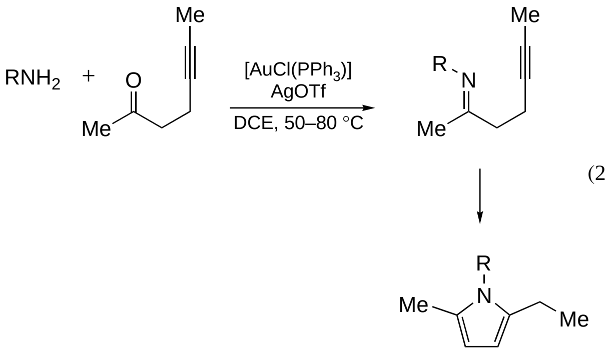

(29)

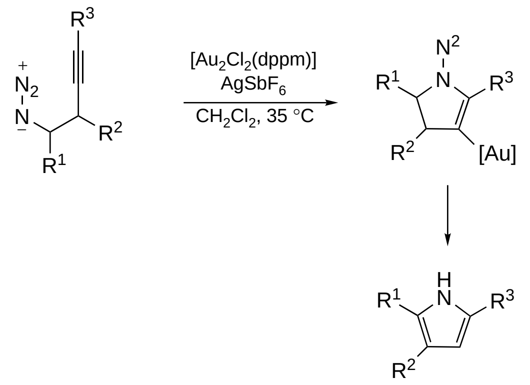

(30)

Gagosz recently showed that tertiary tosylamides can react with alkynes and the cationic enammonium intermediate evolves by a [3,3]-sigmatropic rearrangement to yield pyrrols.[147]

Imines react with alkynes to give pyrroles (equation 29).[148] A related transformation of azides has been reported by the group of Toste to afford pyrroles by an acetylenic Schmidt reaction (equation 30).[149] In an intermolecular-related addition, gold triazolates are obtained.[150] The intramolecular hydroamination of trichloroacetimidates derived from propargyl and homopropargyl alcohols also proceeds with cationic Au(I) as catalysts.[151]

2.3 Sulfur Nucleophiles

The addition of sulfur nucleophiles to alkynes is a less developed transformation. However, Yamamoto described the attack of the sulfur atom of aryl thioethers to afford benzothiophenes (equation 31).[152] More recently, it has been showed that propargylic thioethers or thioacetals undergo migration to give carbenes that cyclize in hydroarylation processes[153] and thiocarbamates that evolve by propargylic rearrangement.[154] Thiosilanes can perform as both sulfur nucleophiles and silicon electrophiles in intramolecular reactions to afford benzothiophenes (equation 32).[155]

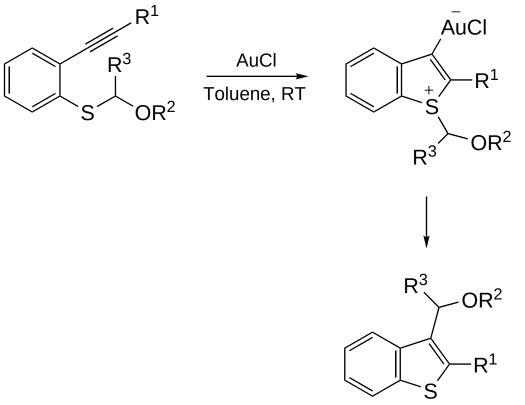

(31)

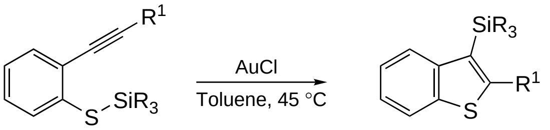

(32)

2.4 Carbon Nucleophiles

Alkenes act as nucleophiles with alkynes in the presence of gold catalysts.[9,156] In the most simple version of the reaction, enynes are converted with gold complexes or salts, and in the absence of nucleophiles, into rearranged dienes, cyclopropanated carbocycles, and/or bicyclic cyclobutenes. Depending on the length of the tether and the nature of the substituents, the olefin attack to the alkyne occurs in an endo or an exo fashion (equation 33). Besides, substitution at the alkene plays an important role on the regioselectivity of the nucleophilic attack.[9]

It is important to note in an overview of this chemistry that the formation of most of the products can be mechanistically explained as proceeding via cyclopropyl gold carbene intermediates. The involvement of these species has been previously proposed in enyne cyclizations with other metals and their structures have been later determined by calculations.[8,156]

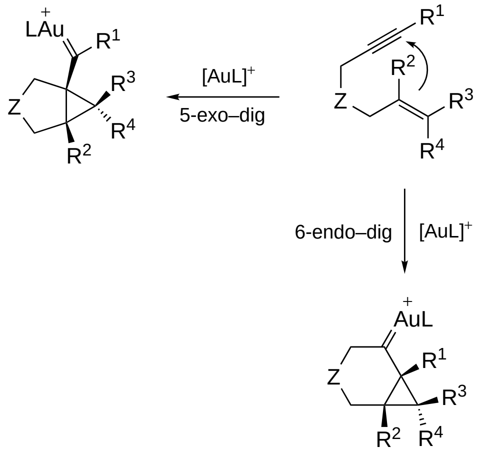
LAu+
R1
R3
R4
R2
Z
[AuL]+
5-exo–dig
R1
R2
R3
R4
Z
6-endo–dig
[AuL]+
AuL+
R1
R3
R2
R4
Z

(33)

The skeletal rearrangement of enynes proceeds through that kind of intermediates. Two basic types of products are obtained when an exo pathway is followed: *single cleavage* and *double cleavage*, named owing to the fact that only the olefin or both the alkene and the alkyne are cleaved in the transformation. Some examples are depicted in equation (34–36).[157]

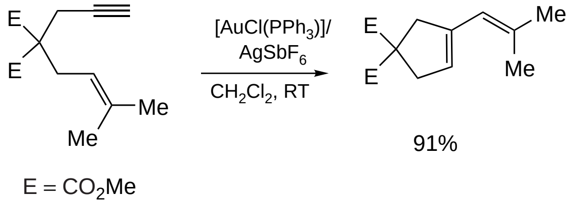
E
E
Me
Me
[AuCl(PPh3)]/
AgSbF6
CH2Cl2, RT
E
E
Me
Me
91%
E = CO2Me

(34)

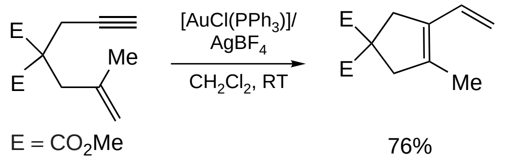
E
E
Me
[AuCl(PPh3)]/
AgBF4
CH2Cl2, RT
E
E
Me
E = CO2Me
76%

(35)

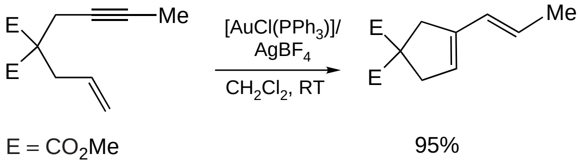
E
E
Me
[AuCl(PPh3)]/
AgBF4
CH2Cl2, RT
E
E
Me
E = CO2Me
95%

(36)

For 1,6-enynes, the initial cyclopropyl gold carbene formed in the 5-exo–dig cyclization (equation 37) evolves to form a carbocation, which then undergoes metal elimination to give the single-cleavage diene.[158] For the double-cleavage rearrangement (equation 38), the intermediate can suffer a dyotropic rearrangement[159–161] to give a rearranged carbene, which then eliminates an α-hydrogen to give the double-cleavage diene.[158]

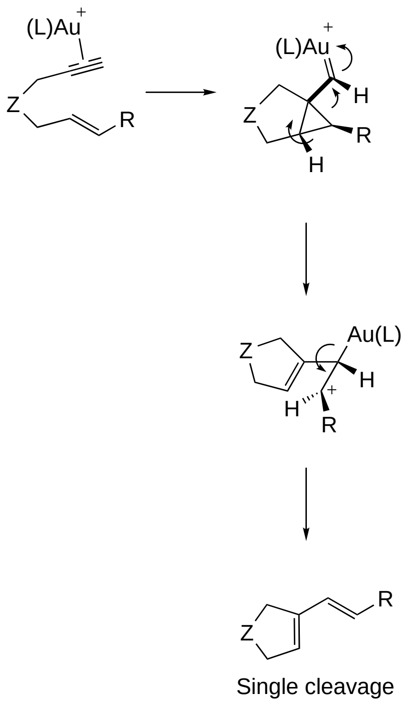
(L)Au+
Z
R
(L)Au+
H
Z
R
H
Z
Au(L)
H
H
+
R
Z
R
Single cleavage

(37)

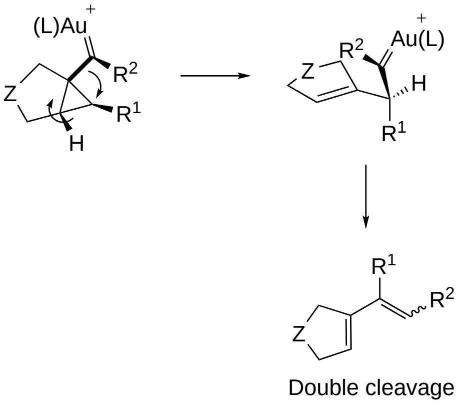
(L)Au+
R2
Z
R1
H
R2
Au(L)+
Z
H
R1
R1
R2
Z
Double cleavage

(38)

Additional evidence for the involvement of metal carbenes in these processes was obtained in the reaction of dimeric substrates with a cationic Au(I) catalyst to give disubstituted alkynes (equation 39).[33] These reactions can be explained by isomerization of the initially formed cyclopropyl gold carbene by a [1,3] metallotropic shift, followed by intramolecular trapping of the gold carbene by the alkene. Other examples of [1,3] metallotropic shifts in gold chemistry have been observed recently.[162,163]

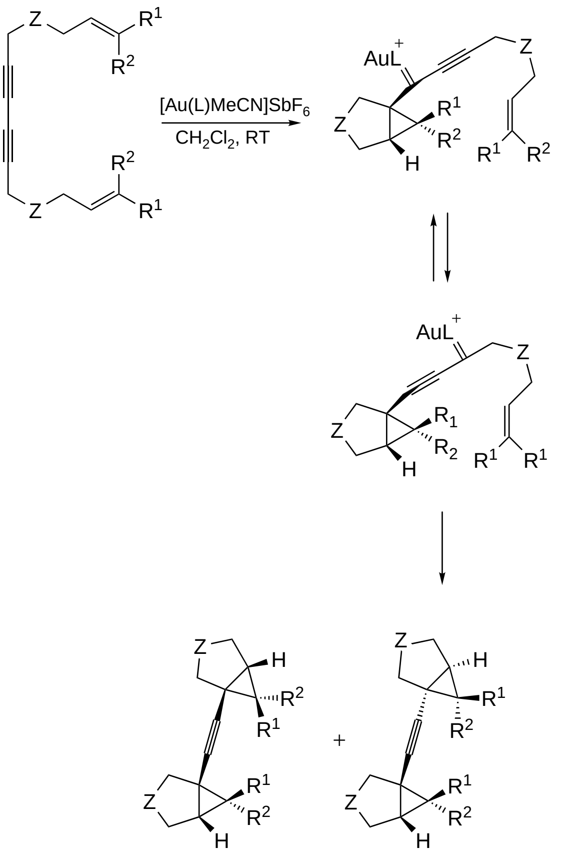

(39)

Endo-skeletal rearrangements also take place with 1,6-enynes, but the proposed mechanism is just a variation of the exo-single-cleavage rearrangement. Formed by endo cyclization, bicyclo[4.1.0]hept-4-ene derivatives arise in some cyclizations of 1,6-enynes by proton loss and protodemetalation of the endo cyclopropylcarbene.[164–168] That is the case from 1,6-enynes tethered as sulfonamides and in the intramolecular cyclization of 1,6-enol ethers with alkynes (equation 40).[166]

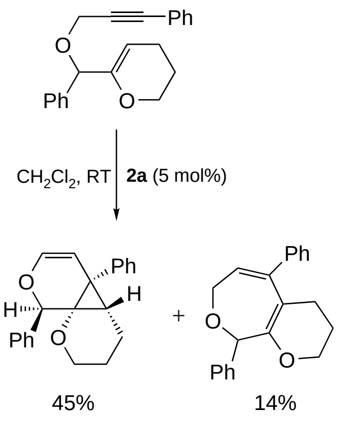

(40)

A few examples of single-cleavage skeletal rearrangement of 1,7-enynes have been reported by using gold.[169,170]

Cyclobutenes are obtained in the cyclizations of some 1,7-enynes with Au(I) catalysts, presumably as a result of a syn-attack of the alkene on the alkyne-Au(I) complex (equation 41).[158]

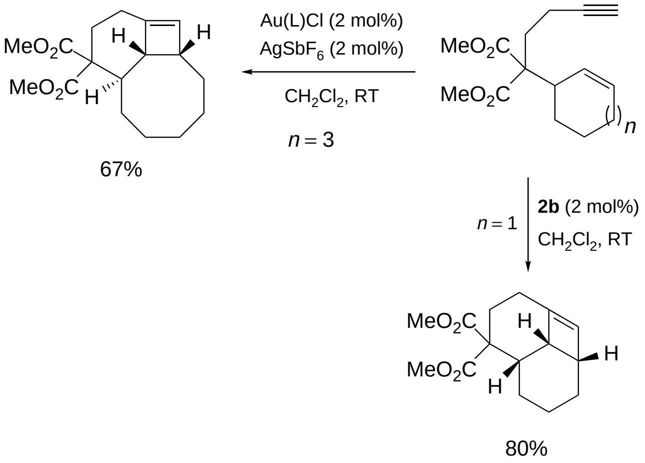

(41)

Albeit no examples of a stable bicyclo[3.2.0]hept-5-ene obtained by a metal-catalyzed reaction from a 1,6-enyne have been observed, interestingly, following earlier work done with $PtCl_2$ as catalyst,[171] it was found that the gold-catalyzed reaction of 1,6-ene-ynamides gives cyclobutanones (equation 42),[172] in a process that probably proceeds through unstable bicyclic enamines.

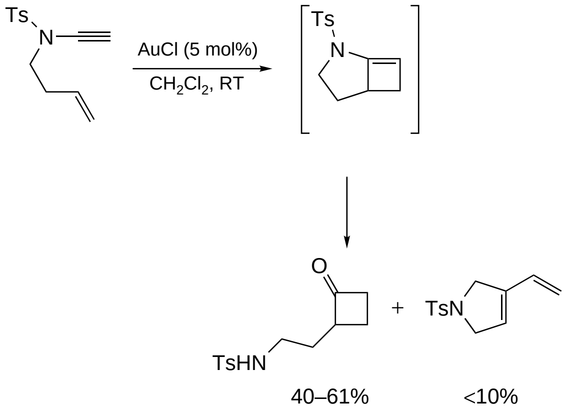

(42)

A remarkable cyclization of a 1,9-enyne (equation 43) to form a 10-membered ring has been disclosed.[173] The aromatic ring may play a role in the cyclization, but still this result shows that formation of large rings from 1,n-enynes ($n \geq 7$) by using gold chemistry is possible. Cyclizations of 1,8-enynes that probably proceed by a different mechanism have also been reported.[174]

The cyclization of 1,5-enynes to give bicyclo[3.1.0]hexanes under mild conditions was reported by Toste (equation 44).[175] Interestingly, in a similar reaction, Gagosz found that 1,5-enynes gave the expected bicyclo[3.1.0]hexane

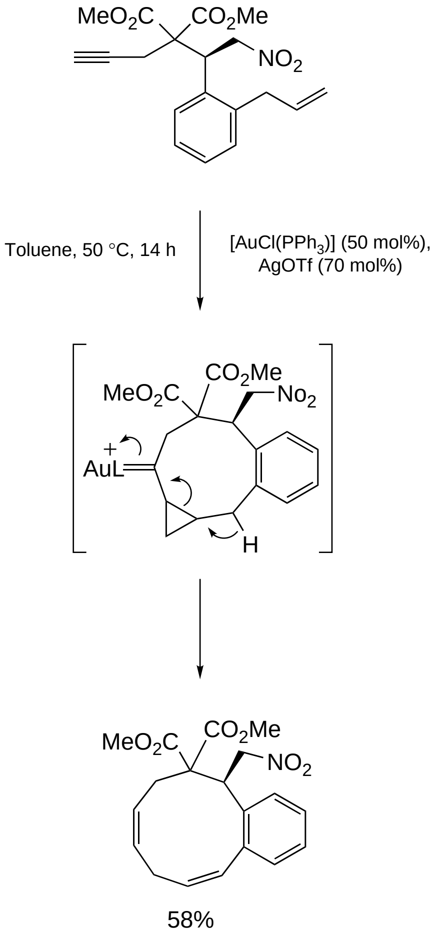
MeO2C
CO2Me
NO2
Toluene, 50 °C, 14 h
[AuCl(PPh3)] (50 mol%),
AgOTf (70 mol%)
CO2Me
MeO2C
No2
+
AuL
H
MeO2C
CO2Me
NO2
58%

(43)

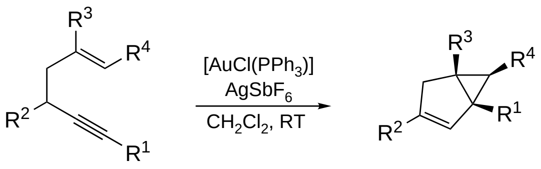
R3
R4
R2
R1
[AuCl(PPh3)]
AgSbF6
CH2Cl2, RT
R3
R4
R2
R1

(44)

accompanied by a product of skeletal rearrangement (equation 45).[176]

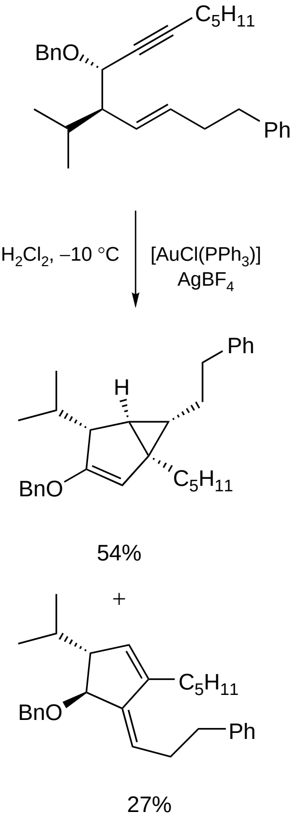
C5H11
BnO
Ph
CH2Cl2, –10 °C
[AuCl(PPh3)]
AgBF4
Ph
H
BnO
C5H11
54%
+
C5H11
BnO
Ph
27%

(45)

The formation of these products can be rationalized as shown in equation (46). Thus, upon complexation of Au(I) to the alkyne in the reacting enyne, an endo cyclization occurs to form a cyclopropyl gold carbene,[177] which can be trapped by a nucleophile.[175] However, the lack of stereospecificity observed in some of these reactions,[32,176] suggests the formation of open six-membered ring cations as intermediates, which can be intercepted by an *O*-Boc group.[178] 3-Hydroxy-1,5-allenynes react similarly with Pt(II) catalysts.[179]

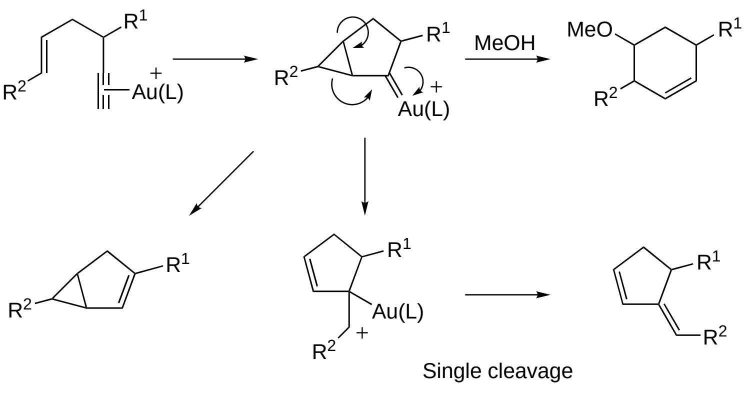
R1
R2
+
Au(L)
R1
R2
+
Au(L)
MeOH
MeO
R1
R2
R1
R2
R1
Au(L)
R2
+
Single cleavage
R1
R2

(46)

Kozmin found that siloxy 1,5-enynes react with Au(I) catalysts to give cyclohexadienes (equation 47),[180,181] which is probably another example of a double skeletal rearrangement. A similar transformation has been found with other 1,5-enynes.[176,181]

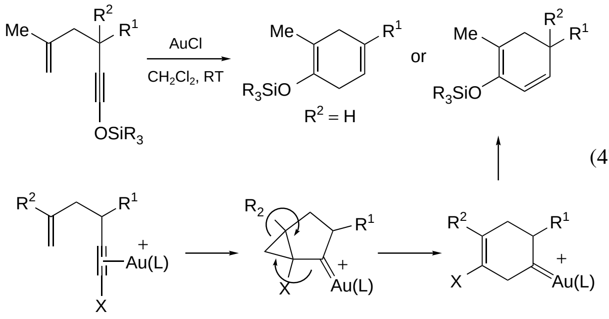

(47)

Other 1,5-endo cyclizations are observed for 1-alkynyl-2-alkenylbenzenes to form naphthalenes.[182,183] However, in this case, exo cyclization was also observed as a minor pathway from substrates bearing terminally substituted alkynes.

Yet the first examples of cyclization of 1,5-enynes with gold were disclosed by the group of Arcadi in the context of a new synthesis of pyridines (equation 48).[184] The cyclization of propargyl enamines catalyzed by sodium tetrachloroaurate gives substituted pyridines in a general way. The enamines were formed in situ from propargylamine and the corresponding ketone.

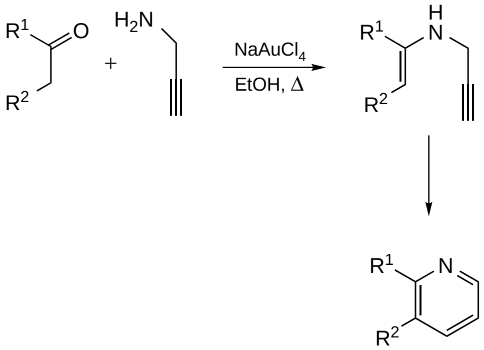

(48)

Related to this cyclization of enamines, Toste described the addition of enols of β-ketoesters to alkynes catalyzed by gold(I).[185,186] The regioselectivity of the process is, as in many other cases, dependent on the length of the tether (equations 49–50). The reaction can be also performed efficiently using a gold catalyst with a triethynylphosphine ligand bearing bulky silyl end caps[169] or with a catalyst generated in situ from a cyclic thiourea–AuCl complex and AgOTf.[187] An enantioselective version of this reaction was developed using chiral palladium complexes.[188] Silylketene amides or carbamates react similarly with alkynes to form cyclopentanes or dehydro-δ-lactams.[189] The analogous reaction of silyl enol ethers with alkynes catalyzed by gold[190,191] was applied for the synthesis of the alkaloids (+)-licopladine A[190] and (+)-fawcettimine.[192] Reactions of more simple substrates bearing a 1,5- or 1,6-relation between silyl enol ether and the alkyne take place in an exo fashion to form five- or six-membered rings.[191]

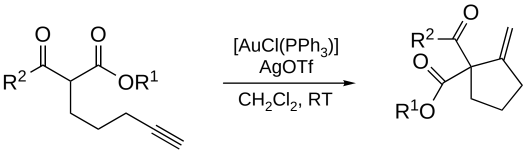

(49)

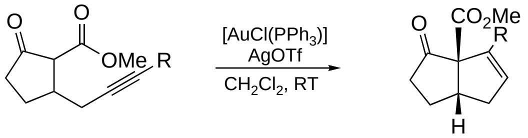

(50)

Propargyl vinyl ethers undergo Claisen rearrangement with Au(I) catalysts to give allenes, which were isolated as the corresponding alcohols (equation 51).[24] A similar gold-catalyzed transformation of propargyl allyl ethers, which proceeds by the initial isomerization to the propargyl vinyl ethers, has also been observed.[18] A related palladium-catalyzed process has also been described.[193] Indeed by performing the reaction in the presence of water or alcohols, dihydropyrans were obtained in good yields (equation 52).[194] A related transformation has been reported by Kirsch in which similar substrates are converted into allenes, which cyclize to afford furans (equation 53).[195] A variation of this procedure has been developed for the synthesis of pyrroles by performing the first rearrangement with an Ag(I) catalyst. The intermediate 1,3-dicarbonyl compound was then condensed with primary amines, which was followed by a final Au(I)-catalyzed cyclization.[196]

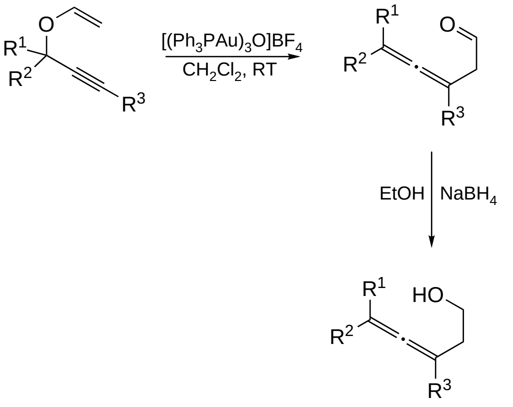

(51)

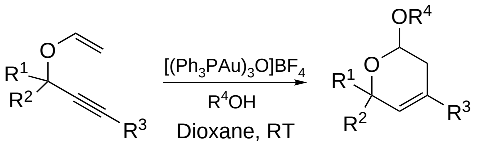

(52)

Recently, the groups of Lee and Toste reported that allyl silyl alkynes react with Au(I) catalysts in the presence of alcohols to give alkenylsilanes[197,198] by a process that might involve the fragmentation of a cyclopropyl gold carbene.

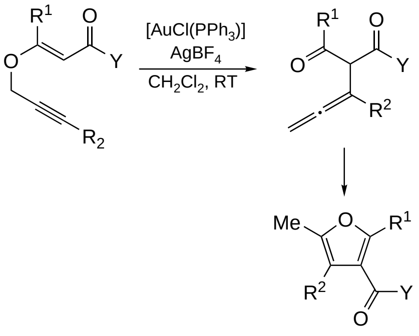
[AuCl(PPh3)]
AgBF4
CH2Cl2, RT

(53)

2.5 External Nucleophiles

In the presence of external nucleophiles, the situation changes and the behavior of cyclopropyl gold carbenes as delocalized electrophiles becomes manifest. Nucleophilic attack then takes place at either the cyclopropane ring or at the carbene carbon.

Thus, by using conditions developed by Tanaka and coworkers for the hydration of alkynes,[21,22] reaction of enynes with [AuMe(PPh$_3$)] and a protic acid in MeOH led to the formation of products of methoxycyclization.[9,17] Similar results were obtained from [AuCl(PPh$_3$)] and AgSbF$_6$ or from preformed cationic gold complexes (equation 54). Thus, for example, the enyne in equation (55) was readily converted into the corresponding product[17,32] by using a chiral Au(I) complex, with 94% ee, although lower enantiomeric excesses were obtained with other enynes.[199] Intramolecular attack of the hydroxyl function in equations (57) and (58) afforded tetrahydrofuranyl derivatives in good yields.[17] Related intramolecular hydroxycyclizations, as well as related sulfonamide cyclizations, have also been observed from 1,5-enynes (equations 56 and 58).[200,201]

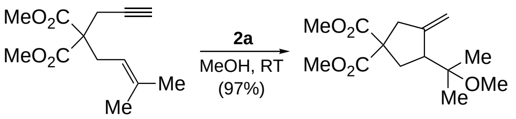
2a
MeOH, RT
(97%)

(54)

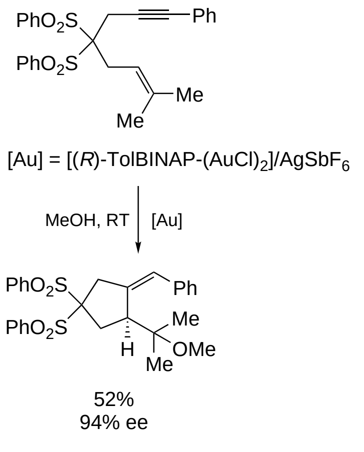
[Au] = [(R)-TolBINAP-(AuCl)2]/AgSbF6
MeOH, RT
[Au]
52%
94% ee

(55)

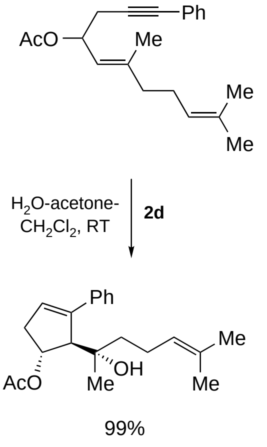
H2O-acetone-
CH2Cl2, RT
2d
99%

(56)

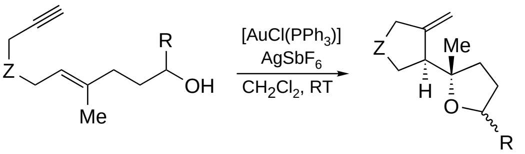
[AuCl(PPh3)]
AgSbF6
CH2Cl2, RT

(57)

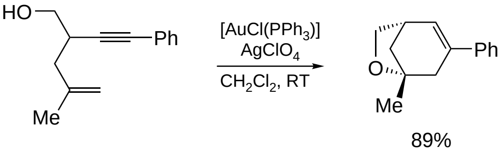
[AuCl(PPh3)]
AgClO4
CH2Cl2, RT
89%

(58)

Allyl propargyl ethers (oxygen-tethered 1,6-enynes) also react intermolecularly with alcohols or water to give six-membered ring acetals or hemiacetals (equation 52).[166] Allyl silyl alkynes react somewhat similarly with Au(I) catalysts in the presence of alcohols to give cyclic or open alkenylsilanes (equation 59).[197,198] Both types of products are the result of

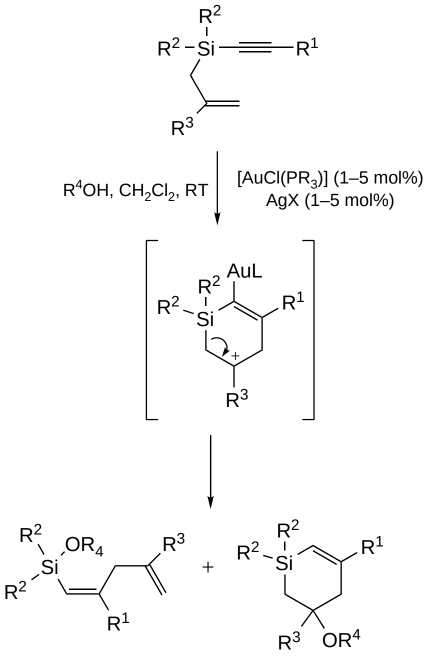
R4OH, CH2Cl2, RT
[AuCl(PR3)] (1–5 mol%)
AgX (1–5 mol%)

(59)

an endocyclic cleavage of the initial cyclopropyl gold carbene shown here as an open carbocation, by attack of the nucleophile at the silicon atom or at the cyclopropane carbon.

The intramolecular amination of 1,5-enynes proceeds similarly to the intramolecular hydroxycyclizations of related substrates to give the products shown in equations (60) and (61).[201] The intermolecular reaction of 1,6-enynes with a series of carbamates RO_2CNH_2 or anilines $ArNH_2$ has also been reported.[202]

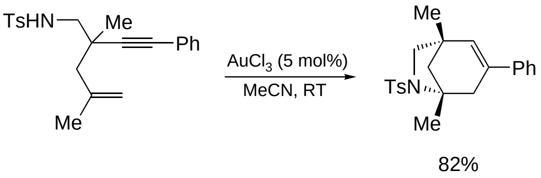
TsHN
Me
Ph
Me
AuCl3 (5 mol%)
MeCN, RT
Me
Ph
TsN
Me
82%

(60)

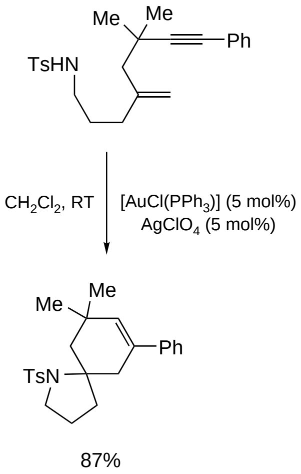
Me
Me
Ph
TsHN
CH2Cl2, RT
[AuCl(PPh3)] (5 mol%)
AgClO4 (5 mol%)
Me
Me
Ph
TsN
87%

(61)

Electron-rich aromatic and heteroaromatic compounds add to 1,6-enynes in the presence of Au(I) catalysts (equations 62 and 63).[203,204] This reaction leads stereospecifically to adducts related to the products in the alkoxycyclization by nucleophilic addition on cyclopropyl gold carbene intermediates. Interestingly, in a few cases, addition of the nucleophile takes place at the carbene carbon to give adducts of the type in equation (63).[204]

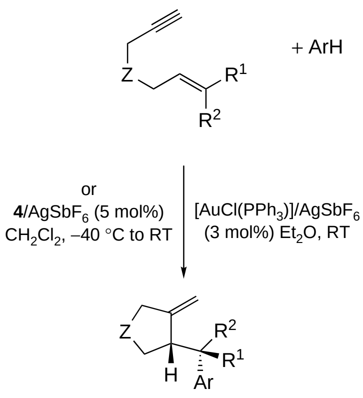
+ ArH
Z
R1
R2
or
4/AgSbF6 (5 mol%)
CH2Cl2, –40 °C to RT
[AuCl(PPh3)]/AgSbF6
(3 mol%) Et2O, RT
Z
R2
R1
H
Ar

(62)

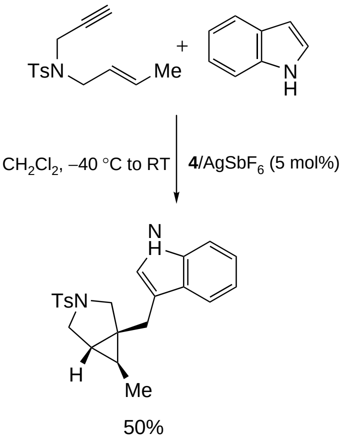
+
TsN
Me
N
H
CH2Cl2, –40 °C to RT
4/AgSbF6 (5 mol%)
N
H
TsN
H
Me
50%

(63)

Similarly, enynes substituted at the alkyne with an aryl group led to products resulting from a formal intramolecular [4 + 2] cycloaddition occurring at an unusual low temperature (equation 64).[25,34] On the other hand, substrates with $R^1 = R^2 = H$ or $R^1 = Me$, $R^2 = H$ gave cyclobutenes with Au(I)[25,34] or Pt(II) catalysts.[205] Dienynes react with cationic Au(I) catalysts leading to products of formal [4 + 2] cycloaddition as well (equation 65).[25,34] Somewhat related cyclizations of allenes with alkynes[206,207] and diynes[208,209] have been described.

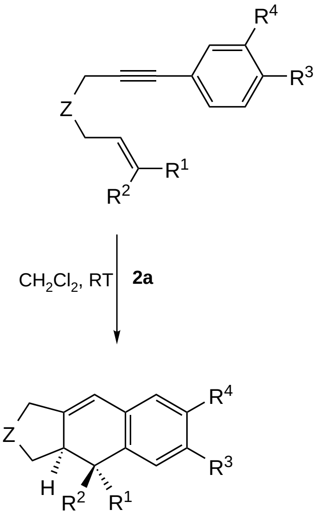
R4
R3
Z
R1
R2
CH2Cl2, RT
2a
R4
Z
R3
H
R2
R1

(64)

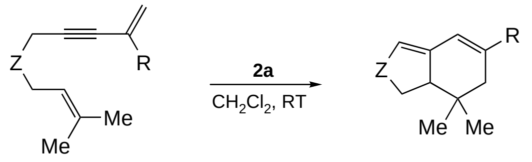
Z
R
Me
Me
2a
CH2Cl2, RT
R
Z
Me
Me

(65)

1,3-Dien-8-ynes undergo formal intramolecular Diels–Alder reactions catalyzed by Au(I) to give adducts like in equation (66).[210] This reaction was proposed to take place by evolution of the intermediate vinylcyclopropyl gold carbenes by a metalla-Cope rearrangement or by formation of a six-membered ring cation. Indeed, vinylcyclopropyl gold carbenes could be trapped intramolecularly by a hydroxy group at the diene chain or by a phenyl at the alkyne in a [4 + 2] cycloaddition process as in equation (64).

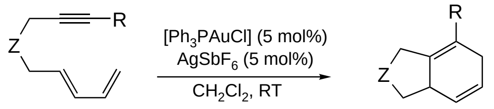
R
Z
[Ph3PAuCl] (5 mol%)
AgSbF6 (5 mol%)
CH2Cl2, RT
R
Z

(66)

Other double bonds on the alkenyl chain can trap the initial gold carbenes leading to cyclopropanes. Thus by using Au(I) catalysts, dienynes in equations (67) and (68) undergo totally stereoselective cyclizations to yield tetracyclic compounds under milder conditions[9,26,211] than those required with other metal catalysts.[212–215]

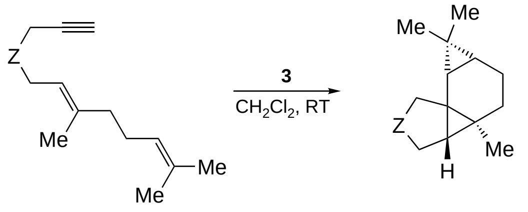
Z
Me
Me
Me
3
CH2Cl2, RT
Me
Me
Z
Me
H

(67)

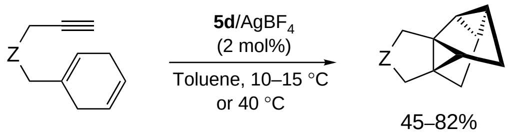
Z
5d/AgBF4
(2 mol%)
Toluene, 10–15 °C
or 40 °C
Z
45–82%

(68)

Similarly, the intermolecular reaction between enynes and alkenes proceeds with Au(I) catalysts (equation 69).[33]

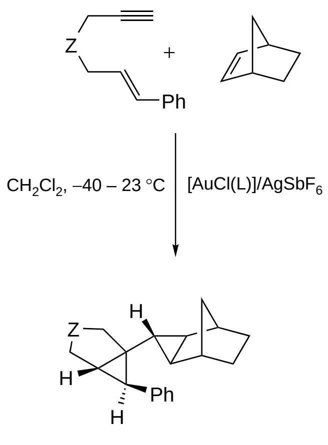
Z
+
Ph
CH2Cl2, −40 – 23 °C
[AuCl(L)]/AgSbF6
Z
H
H
Ph
H

(69)

Cyclizations of enynes bearing carbonyl groups with Au(I) catalysts provide tricyclic compounds along with ketones, as minor products (equation 70).[27] In these cyclizations, the carbonyl group acts as an internal nucleophile to form an oxonium cation, which undergoes an intramolecular Prins reaction to give tricycles and carbonyl compounds as shown in equation (70).

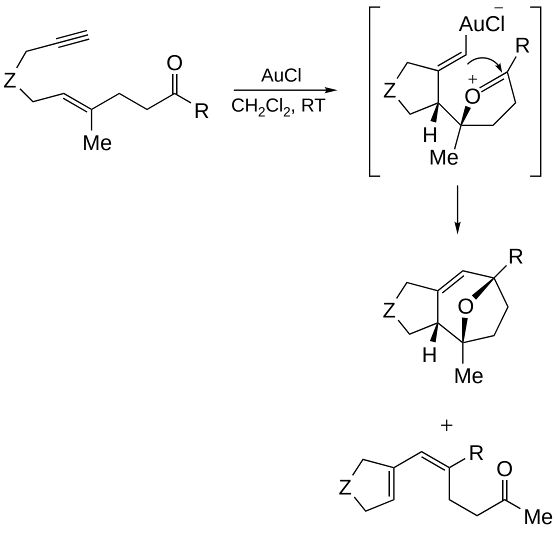
Z
O
R
Me
AuCl
CH2Cl2, RT
AuCl
R
Z
O
H
Me
R
Z
O
H
Me
+
R
O
Z
Me

(70)

Carbonyl compounds can also act as the nucleophiles in intermolecular processes with 1,6-enynes.[216] Thus, the gold(I)-catalyzed reaction between enynes and aldehydes or acetone gives stereoselectively tricyclic compounds (equation 71). The transformation is mechanistically intriguing, as it proceeds by a rearrangement of the initially formed cyclopropyl gold carbene (the intermediate in the double-cleavage mechanism), which is then trapped by the carbonyl compound to form the products.

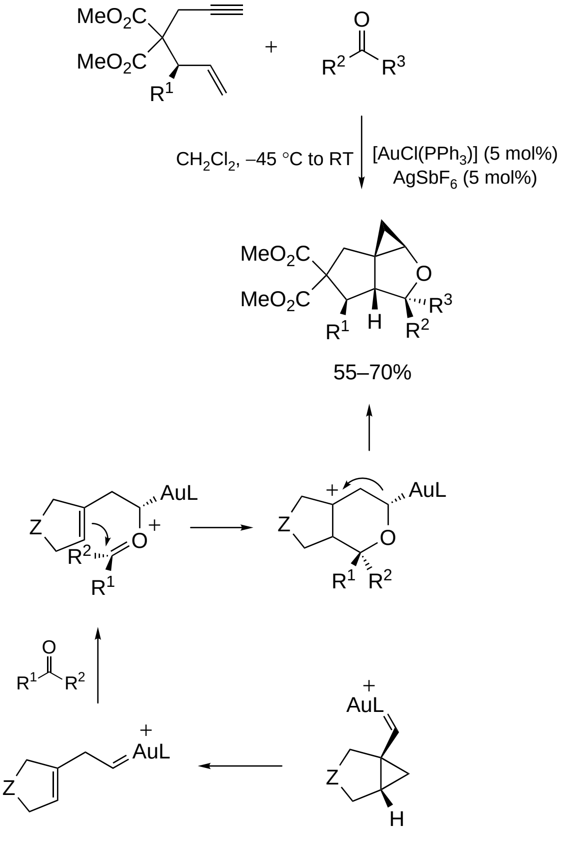
MeO2C
MeO2C
R1
+
O
R2
R3
CH2Cl2, −45 °C to RT
[AuCl(PPh3)] (5 mol%)
AgSbF6 (5 mol%)
MeO2C
MeO2C
O
R3
R1
H
R2
55–70%
AuL
Z
O
R2
R1
AuL
Z
O
R1
R2
O
R1
R2
AuL
Z
AuL
Z
H

(71)

A Prins cyclization is also involved in the reaction of the cyclopropylenynes in equation (72) with AuCl or cationic Au(I) complexes to give tricyclic derivatives with an octahydrocyclobuta[a]pentalene skeleton.[33] The formation of stereoisomers was unexpected and suggests the involvement of cationic intermediates (equation 72).

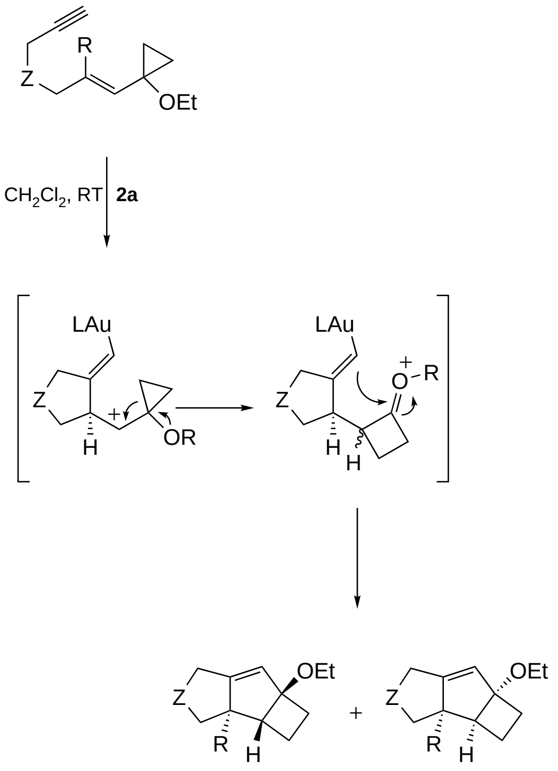

(72)

3 CYCLOISOMERIZATIONS OF ENYNES BEARING PROPARGYLIC CARBOXYLATES OR ETHERS

As pointed out earlier, propargylic esters coordinate to gold to form complexes that can undergo 1,2- or 1,3-acyl migrations to form α-acyloxy-α,β-unsaturated carbenes or allene-gold complexes (equation 23).[115–117]

For the gold-catalyzed cyclization of enynes bearing α-acyloxy substituents at the propargylic position, in principle, two mechanistically distinct possibilities exist depending on the order of attack of the acyloxy group and the alkene to the gold-alkyne complex (equation 73). If the alkene reacts first, the cyclopropyl metal carbene would be formed, which could then suffer an intramolecular attack of the acyl to the carbene, followed by an elimination (formal 1,2-migration of the acyl) to give the enol carboxylate after metal loss. Alternatively, the carboxylate group might first undergo the 1,2-migration to form an open carbene, which would then evolve by intramolecular cyclopropanation. The overall process is known as the *Ohloff–Rautenstrauch rearrangement*, or more simply as the *Rautenstrauch rearrangement*, following the original discovery in the context of zinc- or palladium-catalyzed cyclizations of similar systems.[217,218]

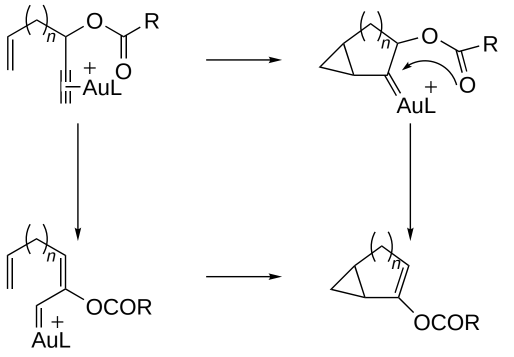

(73)

The gold-[219,220] and platinum-catalyzed Rautenstrauch rearrangements were discovered independently by two groups.[214] Thus, for example, the gold-catalyzed cyclization of the propargylic acetate in equation (74) gives the product of cyclization and 1,2-acetate migration, which was methanolyzed to yield the corresponding ketone.[219]

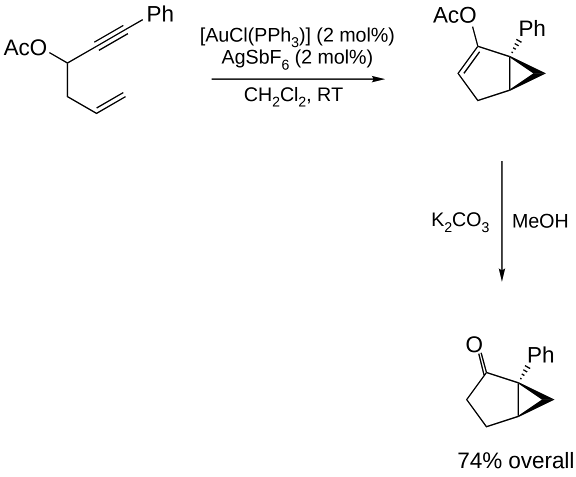

(74)

The first mechanistic pathway in equation (73) is probably followed when $n = 2$, as shown in a key Pt(II)-catalyzed cyclization for the synthesis of (−)-α-cubene and (−)-cubebol.[221] This was established on the basis of observation that the configuration at the stereogenic center carrying the acetate translates into the configuration of the final products, which excluded planarization of the intermediate. (−)-Cubebol was also synthesized using a similar cyclization catalyzed by Pt(II), Au(I), or Cu(I).[222] A cyclization of this type with AuCl3 was used for the synthesis of 2-sesquicarene and related compounds (equation 75).[221,223]

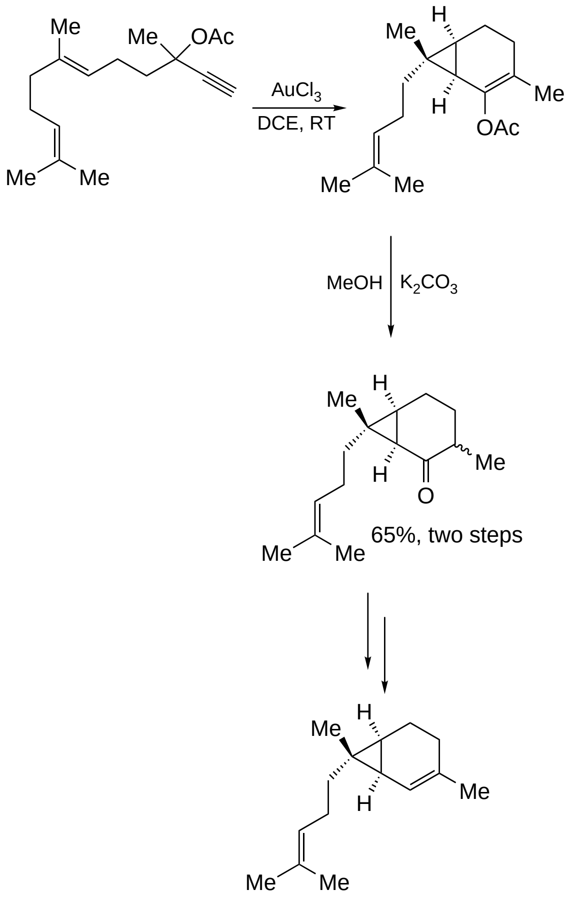
Me
Me
OAc
Me
Me
AuCl$_3$
DCE, RT
H
Me
Me
H
OAc
Me
Me
MeOH
K$_2$CO$_3$
H
Me
H
Me
O
Me
Me
65%, two steps
H
Me
H
Me
Me
Me

(75)

In some of these reactions, substantial loss of the enantiomeric excess was observed,[222] but for 1,4-enynes substituted at the propargylic position with a carboxylate[220] (equations 76–78), the reaction proceeds with remarkable transfer of chirality allowing the efficient enantioselective synthesis of cyclopentenones from the corresponding enantiomerically enriched propargylic pivalates. The enantioselectivity can be explained by a remarkable center to helix chirality transfer, which was supported by DFT calculations.[224] These results indicate that the cyclization is faster than rates of helix interconversion and carboxylate rotation.[224]

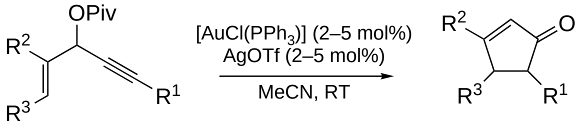
OPiv
R^2
R^3
R^1
[AuCl(PPh$_3$)] (2–5 mol%)
AgOTf (2–5 mol%)
MeCN, RT
R^2
O
R^3
R^1

(76)

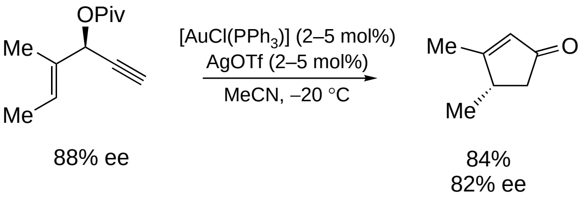
OPiv
Me
Me
88% ee
[AuCl(PPh$_3$)] (2–5 mol%)
AgOTf (2–5 mol%)
MeCN, –20 °C
Me
O
Me
84%
82% ee

(77)

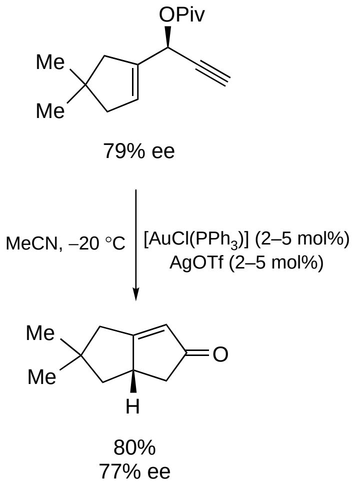
OPiv
Me
Me
79% ee
MeCN, –20 °C
[AuCl(PPh$_3$)] (2–5 mol%)
AgOTf (2–5 mol%)
Me
Me
O
H
80%
77% ee

(78)

A synthesis of cyclopentenones somewhat related to those shown earlier was found from conjugated 1,3-enynes (equation 79).[225] Cyclopentenones are obtained by the hydrolysis of the enol acetates. This transformation involves a 1,3-migration of the acetate to form pentadienyl cation and the formation of the gold carbene after a Nazarov-type cyclization. DFT calculations support this mechanism and provide interesting insight into the mechanism of the final stages of the process.[116]

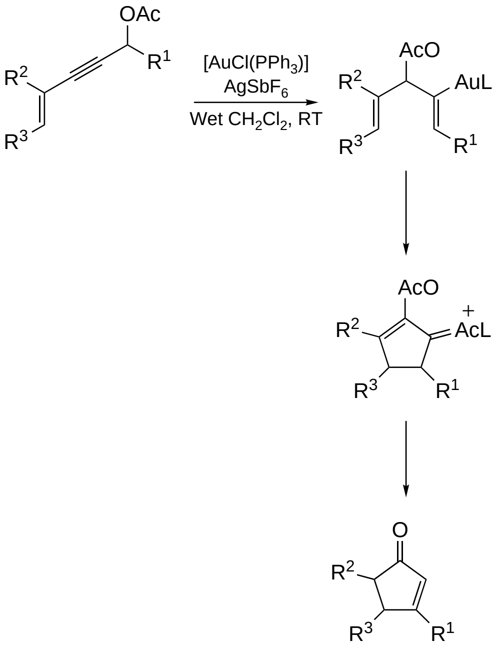
OAc
R^1
R^2
R^3
[AuCl(PPh$_3$)]
AgSbF$_6$
Wet CH$_2$Cl$_2$, RT
AcO
R^2
AuL
R^3
R^1
AcO
+
R^2
AcL
R^3
R^1
O
R^2
R^3
R^1

(79)

Propargylic acetates in equation (80) react differently in a process that also takes place via a 1,3-acyl migration.[226] Thus, the reaction of such substrates gives bicyclo[3.1.0]hexenes, which can be transformed into cyclohexenones on treatment with K_2CO_3 in MeOH. As shown in equation (81), the reaction takes place with nearly complete transfer of the stereochemical information via the allene-gold complexes.

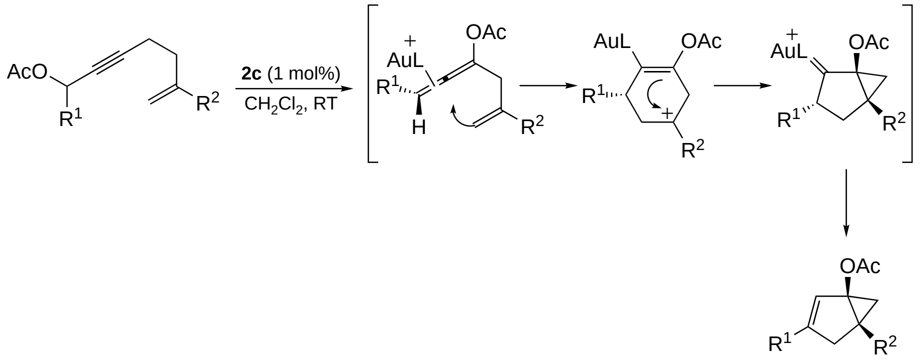
AcO
R1
R2
2c (1 mol%)
CH2Cl2, RT
AuL
OAc
R1
H
R2
AuL
OAc
R1
R2
AuL
OAc
R1
R2
OAc
R1
R2

(80)

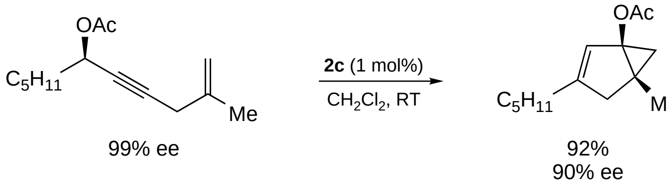
OAc
C5H11
Me
99% ee
2c (1 mol%)
CH2Cl2, RT
OAc
C5H11
Me
92%
90% ee

(81)

An interesting cyclization of the allyl-homoallyl-propargylic acetate in equation (82) has been shown to afford a mixture of three compounds by using an Au(I) complex with an NHC as ligand.[227] The first product is that expected from a 1,6-enyne cyclization, whereas the formation of the other two products by cyclization of the 1,5-enyne suggests that alternative mechanisms take place in this case.

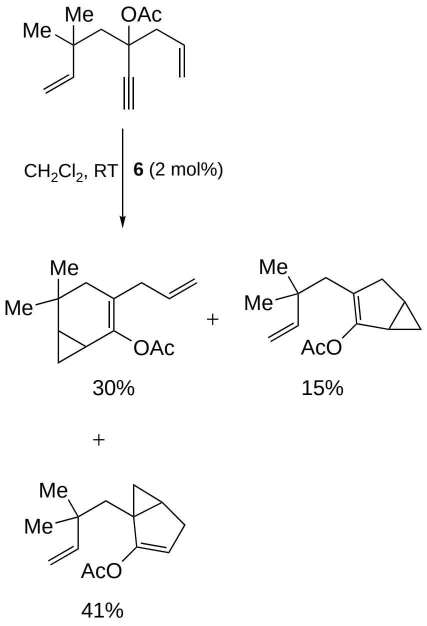
Me
Me
OAc
CH2Cl2, RT
6 (2 mol%)
Me
Me
OAc
30%
+
Me
Me
AcO
15%
+
Me
Me
AcO
41%

(82)

The cyclization of other propargylic acetates as in equations (83) and (84) gives tricyclic derivatives with high stereoselectivity by an endocyclic pathway.[174] In the cyclization of this type of substrates, better yields were usually obtained with PtCl$_2$ or AuCl$_3$ as catalysts. Remarkably, the cyclization in equation (83) is an example of a cyclization of a 1,8-enyne, although mechanistically it could be interpreted as an intramolecular cyclopropanation of the terminal alkene by the gold carbene formed in a 1,2-acyl migration.

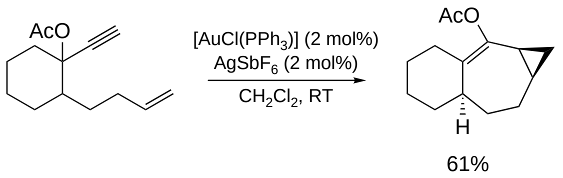
AcO
[AuCl(PPh3)] (2 mol%)
AgSbF6 (2 mol%)
CH2Cl2, RT
AcO
H
61%

(83)

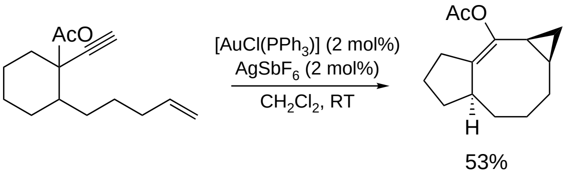
AcO
[AuCl(PPh3)] (2 mol%)
AgSbF6 (2 mol%)
CH2Cl2, RT
AcO
H
53%

(84)

3.1 Cycloisomerizations of Related Substrates Proceeding via 1,2- or 1,3-Acyl Migration

An interesting transformation involving the indole nucleus was found from propargylic carboxylates to give tetracyclic compounds with Au(I) (equation 85).[228] This reaction proceeds by an allene-gold complex in equilibrium with the alkenyl-gold species, which reacts intramolecularly with the indole to form the product. When the reaction of these substrates is performed with dichloro(pyridine-2-carboxylato)gold(III) or Pt(II) as catalysts, products in equation (86) are obtained instead.[229] This new reactivity can be explained by a formal [3 + 2] cycloaddition of 1,3-dipole intermediates with the indole nucleus (equation 86).

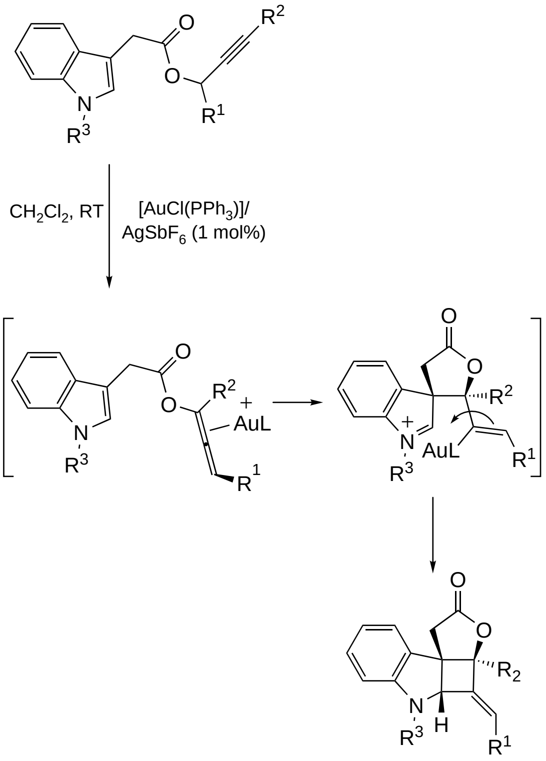
CH2Cl2, RT
[AuCl(PPh3)]/
AgSbF6 (1 mol%)
AuL
R1
R2
R3

(85)

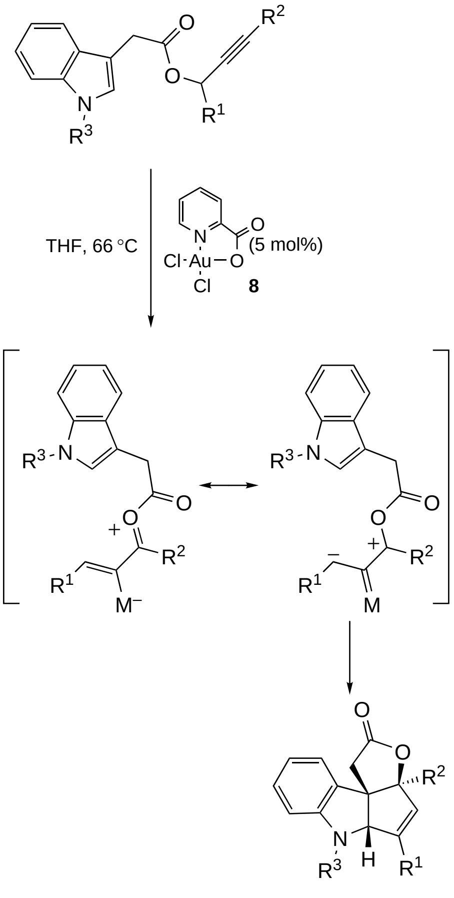
THF, 66 °C
Cl-Au-O
Cl
(5 mol%)
8
M−
M
R1
R2
R3

(86)

The acyl migration of benzylic acetates was also applied for the synthesis of indenes (equation 87).[230] Isomeric indenes were also obtained as minor products. The transformation was actually shown to proceed via allenes, which could be independently prepared by Ag(I)-catalyzed 1,3-acetate migration from the same starting materials. Propargylic sulfides and dithioacetals undergo similar transformations as propargylic carboxylates to give indene derivatives with Au(I) or Au(III) catalysts.[153]

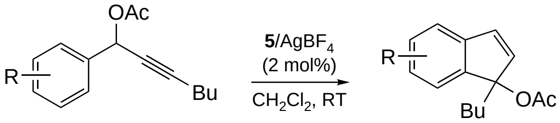
OAc
R
Bu
5/AgBF4
(2 mol%)
CH2Cl2, RT
R
Bu
OAc

(87)

A different type of 1,3-acyl migration occurs from homoallyl acetates (equation 88).[231] In this case, upon coordination of the alkyne with Au(III) and migration of the acetate, a zwitterionic species is probably formed and collapses to afford the final product.

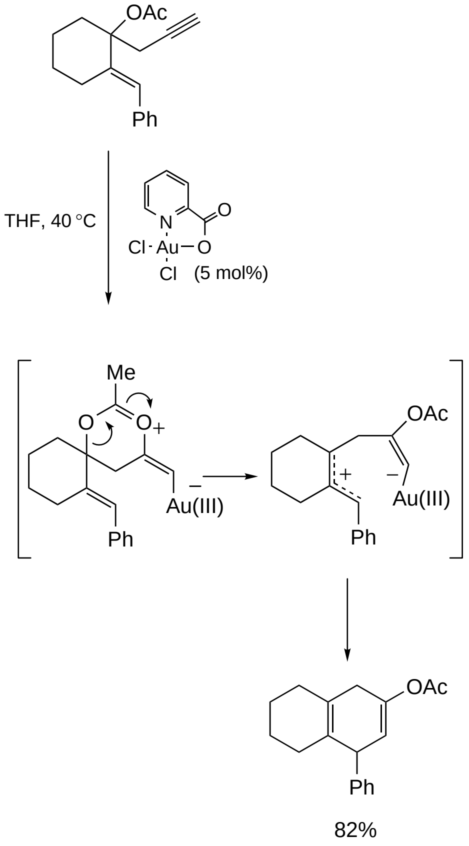
OAc
Ph
THF, 40 °C
Cl-Au-O
Cl (5 mol%)
Me
Au(III)
OAc
Au(III)
Ph
OAc
Ph
82%

(88)

4 ALLENYNES

Very recently, the cyclizations of allenynes have been described.[179,206,207] It has already been pointed out that gold species can coordinate allenes as well as alkynes. In the reactions of substrates where both functionalities are present, it may not be clear, in principle, which would be the first moiety coordinated. Probably, as in the case of olefins, an equilibrium exists and kinetic factors determine the reaction pathway to the observed products. Those kinetic aspects are related to the higher nucleophilicity of allenes compared to alkynes and, therefore, it is not surprising to find that in the gold-catalyzed reactions of allenynes most of the mechanistic explanations involve coordination to the alkyne followed by attack of the allene.[179] This results in allyl-cation and vinyl-gold intermediates that can undergo different steps in tandem, depending on the substituents and functionalities present in the molecule. Examples can be found in the cycloisomerization of allenynes described by Malacria with concomitant Friedel–Crafts cyclization by aryl groups or the addition of alcohols like in the alkoxycyclization of enynes.[179] Liu also found a similar behavior with a different substitution pattern (equation 89).[207]

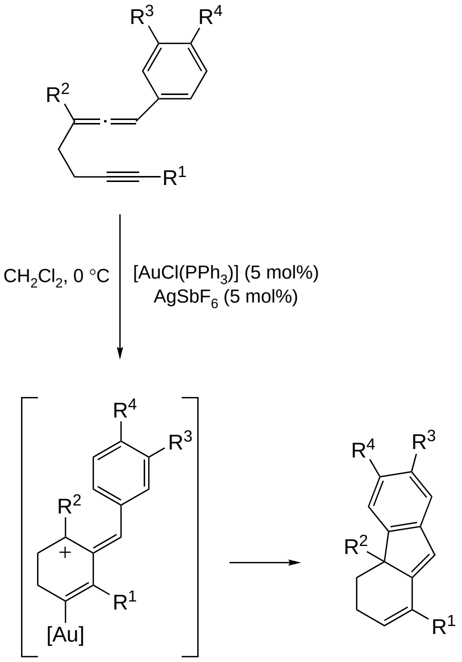

(89)

Toste observed the aromatization of the new cycle in a different type of reaction, in which the allene had been formed in situ by acyl migration of a propargyl carboxylate.[130] In a similar vein, cyclizations of diynes bearing propargyl carboxylates have been described to synthesize dienes[232] and pyrones (equation 90).[233] In the last case, a new cascade allows the intermolecular addition of electron-rich arenes.[233]

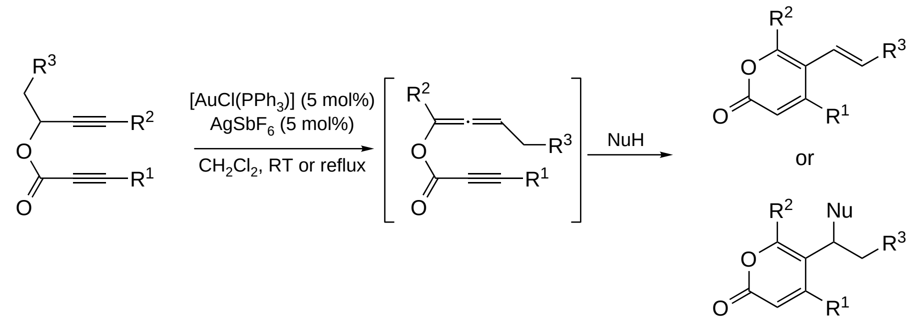

(90)

5 MECHANISTICALLY RELATED REACTIONS OF ARENES AND HETEROARENES WITH ALKYNES

5.1 Cyclizations of Arylalkynes by Friedel–Crafts-type Processes

In general, two pathways are followed in the reactions of alkynes with arenes catalyzed by transition metals. Reaction of $[M(CO)_6]$ (M = Cr, Mo, W) and certain Ru(II) complexes with terminal alkynes or with alkynes substituted with migrating groups (SiR_3, SR, and I) may proceed via vinylidene metal complexes. On the other hand, electrophilic metal salts or complexes favor coordination to the alkyne, triggering electrophilic substitution reaction with the arene. Gold complexes generally promote reactions according to this second pathway.[234] The direct metalation (auration) of electron-rich arenes and heteroarenes is a well-known reaction,[235–239] but the resulting ArAuL complexes are apparently not involved in subsequent C–C bond-forming reactions with alkynes.

The gold-catalyzed intermolecular hydroarylation of alkynes (or alkenylation of arenes) leads to 1,1-disubstituted alkenes (equation 91).[240–243] 1,2-Disubstituted derivatives are obtained from alkynes with electron-withdrawing groups (equation 92).[244]

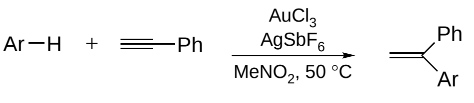

(91)

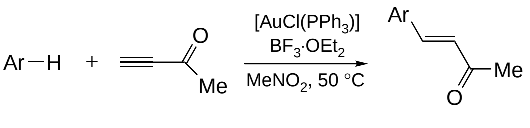

(92)

The cyclization of ortho-alkynylated biphenyl derivatives in equation (93) with Au(III) and other metal catalysts proceeds preferentially by the endo pathway leading to phenanthrenes.[245–247] Interestingly, the analogous haloalkynes in equation (94) react with AuCl to give phenanthrenes in which the halide has suffered a 1,2-shift. In contrast, the reaction of those substrates with the stoichiometric amount of $InCl_3$ gives the corresponding phenanthrenes with halide retention. These results suggest that in these cases the cyclization proceeds via gold vinylidene species, which is supported by DFT calculations for the cyclization catalyzed by AuCl.[248] Gold–vinylidene species were also suggested as intermediates in some gold(I)-catalyzed cyclizations of 1-alkynyl-2-alkenylbenzenes to form naphthalenes,[182] as well as in the reaction of 2-(prop-2-ynyl)pyridines form indolizines.[249]

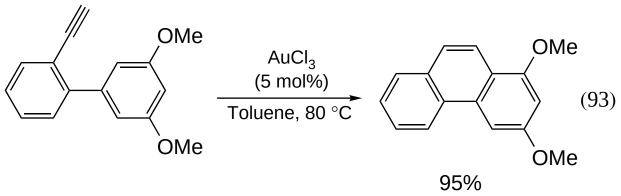

(93)

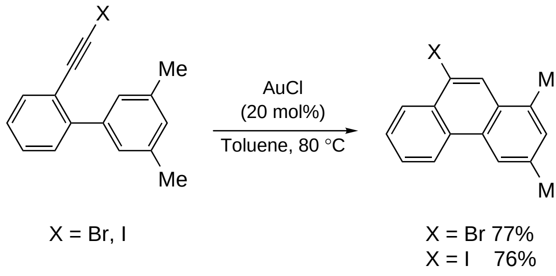

(94)

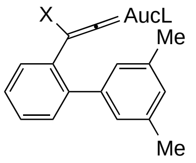

The reaction of substituted indoles with alkynes catalyzed by Au(I) or Au(III) leads to seven- and eight-membered rings, respectively (equation 95).[28,29] Eight-membered ring derivatives are formed in an 8-endo–dig process, a type of cyclization that has not been observed in other hydroarylations of alkynes or cyclizations of enynes. Allenes and tetracyclic compounds could also be obtained. The isolation of spiro derivatives in one of the cyclization reactions suggests that cyclizations of indoles catalyzed by gold(I) can take place by first forming a C–C bond at C–3 followed by a 1,2-migration to give the final indoles. The gold(I)-catalyzed intermolecular reaction of indoles with alkynes also takes place.[29]

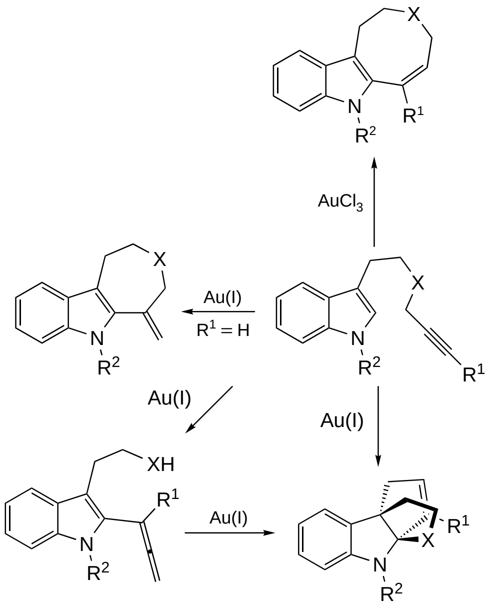

(95)

5.2 Reactions of Furans with Alkynes

In contrast to the usual Friedel–Crafts-like cyclizations of arenes with alkynes, alkynyl furans afford phenols in good to excellent yields by using $AuCl_3$ as catalyst (equation 96).[250–256] Au(I),[257] heterogeneous gold,[258] and Pt(II)[259,260] can also be used as catalysts. Phenols bearing bulky groups at the ortho position can also be prepared by this method.[261] In addition, the gold-catalyzed Michael addition of furans to ethynyl vinyl ketones gives substrates[262–264] that can undergo in situ cyclization leading to hydroxyindanones in a domino process (equation 97).[263] A synthesis of sesquiterpene jungianol, together with its cis isomer, illustrates the application of this phenol synthesis (equation 97).[253]

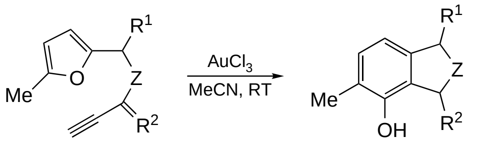

(96)

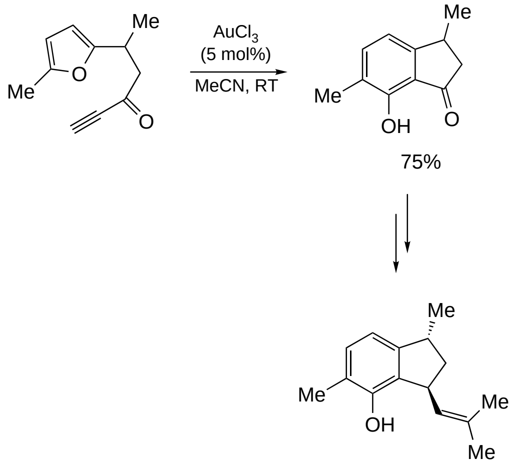

(97)

Experimental and theoretical studies on gold- and platinum-catalyzed reactions[41,251,254] explained the mechanism of this phenol synthesis. Oxepines and arene oxides have been observed in the reaction catalyzed by Au(III).[254,265]

Although proceeding in moderate yield and in the absence of solvent, the formation of phenols in the intermolecular reaction of 2,5-dimethylfuran with phenylacetylene is remarkable (equation 98).[244,266] This reaction required the use of the Schmidbaur–Bayler salt $[(Mes_3PAu)_2Cl]BF_4$ as Au(I) catalyst,[267] and also provided the product of a Friedel–Crafts-type process, the furan in equation (98).

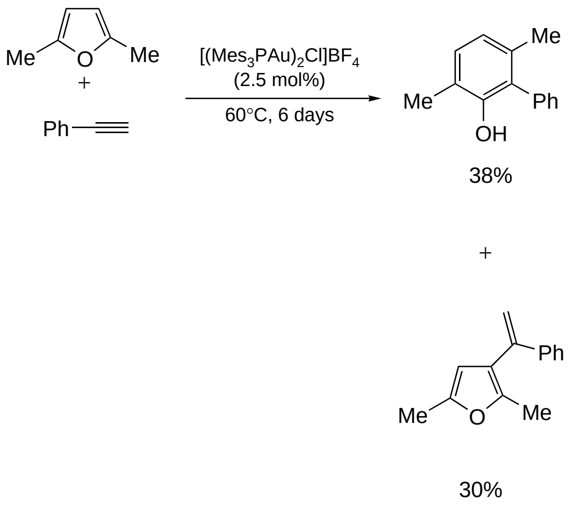

(98)

6 ALLENES

Like alkynes, allenes are electron-rich π-systems that can coordinate Au species. Their higher reactivity compared to olefins makes them better substrates and accounts for the fact that additions to allenes have been more widely studied.

The performance of allenes is similar to alkynes in the presence of gold complexes and, in fact, many of the reactions of propargyl esters presumably proceed through allenyl intermediates. It means that gold catalyzes the propargyl–allenyl isomerization and that the coordinated allene–gold complexes are electrophilic species, as previously described for the alkyne-gold ones. It is easy to predict then that the variety of nucleophiles that have been added to alkynes may attack allenes as well,[268] but the number of references is much lower so far. In any case, the axial chirality of allenes is a factor to consider both as a drawback when mixtures of products are obtained and as an advantage when that chirality can be transferred to the products.

As for the alkynes, the reactions here are arranged by the nature of the nucleophile. Thus heteronucleophiles, mainly nitrogen- and oxygen-based, and carbon nucleophiles are discussed. However, first of all, a gold-catalyzed enantioselective synthesis of axially chiral allenes will be accounted, although it is not an allene activation. It was first discovered by Bertrand in 2007 that enamines and alkynes can be coupled with gold to obtain allenes in a process in which the terminal alkyne and the enamine react by an acid–base equilibrium to form an acetylide and an iminium cation that give propargylamines (equation 99). This species then evolves to an allene.[46] Wong and Che later reported the chirality transfer from the amine to the allene starting from chiral propargylamines.[269]

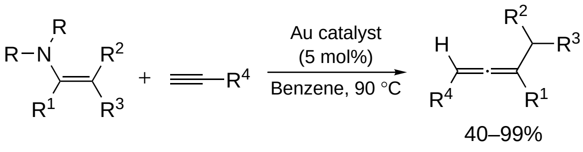

(99)

6.1 Heteronucleophiles

The gold-catalyzed addition of alcohols to allenes was first described in 2001 as an intramolecular reaction of α-hydroxyallenes to yield dihydrofurans with $AuCl_3$ as the catalyst (equation 100).[270] The analogous cyclization of hydroxy–allenamides has been reported later.[271] A study of the stability of $AuCl_3$ in these reactions showed evidence of the involvement of vinyl–gold species in the reaction mechanism.[272] The regioselectivity in the nucleophilic attack was modified by changing the length of the tether and thus β-hydroxyallenes afforded dihydropyrans (equation 101),[273] γ-hydroallenes gave vinyl–tetrahydrofurans,[274] and δ-hydroxyallenes gave vinyl–tetrahydropyrans.[275,276]

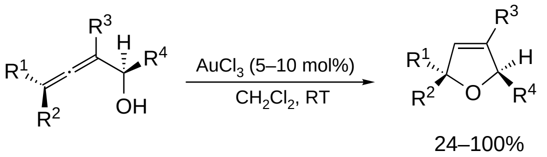

(100)

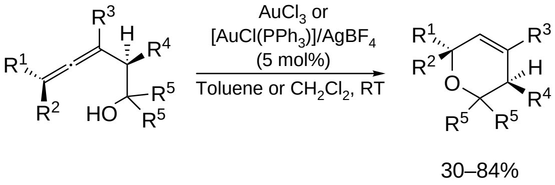

(101)

Enantioselective versions of this reaction have been recently developed with achiral substrates. Two different strategies have been applied to obtain an effective chiral catalyst for that purpose: the usual chiral phosphine ligand (equation 102)[276] and the novel employment of a chiral counterion of the metal catalyst as the source of chirality (equation 103).[277]

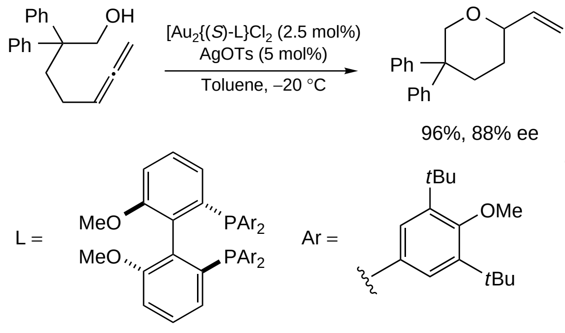
Ph
OH
Ph
[Au$_2${(S)-L}Cl$_2$ (2.5 mol%)
AgOTs (5 mol%)
Toluene, −20 °C
O
Ph
Ph
96%, 88% ee
L =
MeO
MeO
PAr$_2$
PAr$_2$
Ar =
tBu
OMe
tBu

(102)

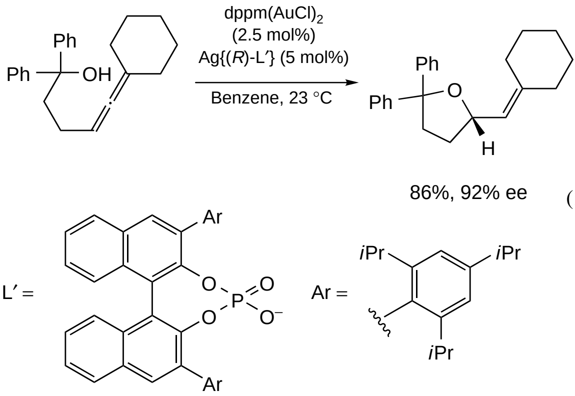
Ph
Ph
OH
dppm(AuCl)$_2$
(2.5 mol%)
Ag{(R)-L′} (5 mol%)
Benzene, 23 °C
Ph
Ph
O
H
86%, 92% ee
L′ =
Ar
O
P
O
O
O$^-$
Ar
Ar =
iPr
iPr
iPr

(103)

Examples of these alkoxycyclizations have been applied by Krause to the synthesis of the alkaloids (−)-isochrysotricine and (−)-isocyclocapitelline (equation 104)[278] and furanomycin derivatives.[279]

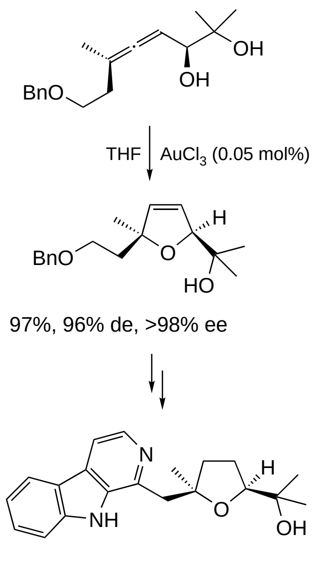
OH
OH
BnO
THF
AuCl$_3$ (0.05 mol%)
H
BnO
O
HO
97%, 96% de, >98% ee
N
NH
H
O
OH

(−)-isocyclocapitelline

(104)

Carbonyl compounds also react with allenes and, in fact, the first example of a gold-catalyzed addition of a nucleophile to allenes was the formation of furans from allenones.[280] The reaction was applied by Gevorgyan to the synthesis of substituted furans[281] and in the case of bromide-substituted allenes halide migration was observed.[282] Similar additions of carbonyls from esters have been studied as well (equations 105 and 106), with protocols that have been improved from $AuCl_3$ at 80 °C[283] and $AuCl_3$/3AgOTf in AcOH at 70 °C[284] to the use at room temperature of biphenylphosphine-based cationic Au(I) catalysts.[285]

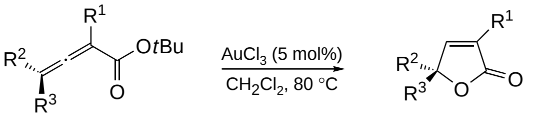
R^1
R^2
OtBu
R^3
O
AuCl$_3$ (5 mol%)
CH$_2$Cl$_2$, 80 °C
R^1
R^2
R^3
O
O

(105)

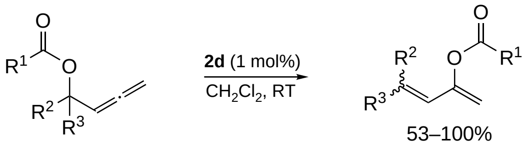
O
R^1
O
R^2
R^3
2d (1 mol%)
CH$_2$Cl$_2$, RT
O
R^2
O
R^1
R^3
53–100%

(106)

Gold-catalyzed hydroamination of allenes[286] has been the object of study of several research groups. The first report by Krause illustrated the formation of 3-pyrrolines from either protected or unprotected α-aminoallenes.[287] Allene-α-substituted acetamides, sulfonamides, carbamates, free amines,[287] and lactams[288,289] undergo the intramolecular hydroamination, giving in all these cases the corresponding five-membered rings (equations 107 and 108). The regioselectivity followed the same pattern as in the additions of alcohols, being dependent on the number of carbons between the nitrogen and the allene.[290] The intermolecular hydroamination was achieved with anilines (equation 109)[291] and even with an aliphatic amine.[292] The complete transfer of chirality to the products was observed to be effective when unprotected amines were used, but some loss occurred in protected substrates.[293]

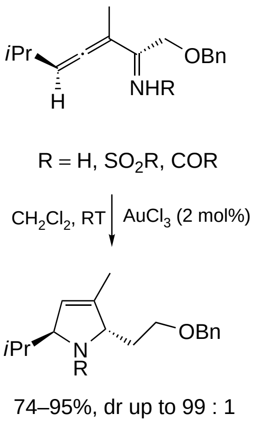
iPr
H
OBn
NHR
R = H, SO$_2$R, COR
CH$_2$Cl$_2$, RT
AuCl$_3$ (2 mol%)
iPr
N
R
OBn
74–95%, dr up to 99 : 1

(107)

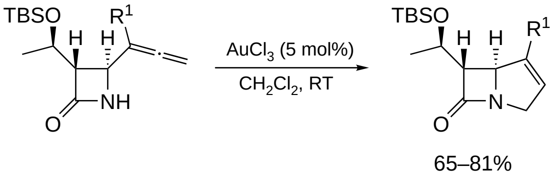
TBSO
R^1
H
H
O
NH
AuCl$_3$ (5 mol%)
CH$_2$Cl$_2$, RT
TBSO
H
H
R^1
O
N
65–81%

(108)

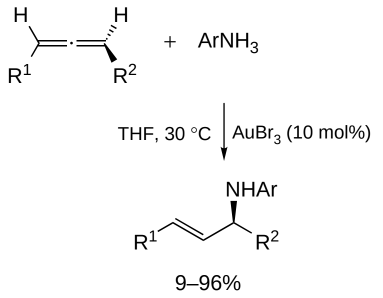
H
H
R1
R2
+ ArNH3
THF, 30 °C
AuBr3 (10 mol%)
NHAr
R1
R2
9–96%

(109)

The enantioselective hydroaminations of allenes with chiral phosphine catalysts was accomplished with substrates that had a terminal symmetric substitution and with the amines protected as carbamates[294] or sulfonamides.[295] The same symmetric substituents were necessary for the enantioselective transformation using chiral counterions.[277] However, very recently, high enantiomeric excesses were reached with trisubstituted asymmetric allenes by a dynamic kinetic enantioselective hydroamination of allenyl carbamates (equation 110),[296] even though the E/Z ratio of the products was not optimal.

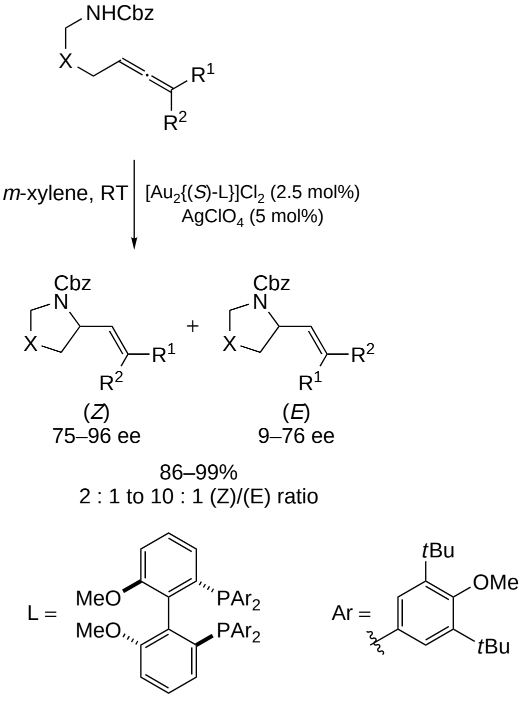
NHCbz
X
R1
R2
m-xylene, RT
[Au2{(S)-L}]Cl2 (2.5 mol%)
AgClO4 (5 mol%)
Cbz
N
X
R1
R2
+
Cbz
N
X
R2
R1
(Z)
75–96 ee
(E)
9–76 ee
86–99%
2 : 1 to 10 : 1 (Z)/(E) ratio
L =
MeO
MeO
PAr2
PAr2
Ar =
tBu
OMe
tBu

(110)

For sulfur nucleophiles, the intramolecular gold-catalyzed hydrothiolation of allenes was described in 2006. α-Thioallenes led to the formation of 2,5-dihydrothiophenes in moderate to good yields and with complete stereoselectivity.[297]

6.2 Carbon Nucleophiles

It is noteworthy that most of the examples in this section correspond to papers that appeared in 2007, which is an evidence of the great boost and potential of these transformations.

The first carbon addition to allenes catalyzed by gold was described by Hashmi and was the addition of furans to allenones,[280] a reaction that is discussed as a conjugate addition to carbonyls. Then the annulation of 2-allenyl indoles was described (equation 111),[275] and an enantioselective version was later developed for terminal allenes.[298] Then Nelson described the cyclization of an N-substituted pyrrol in the synthesis of (−)-Rhazinilam (equation 112).[299] In that case, gold notably improved the yields and selectivities obtained with Pd(II) or Ag(I), and gave complete retention of the chiral information of the allene. The most recent report is on the hydroarylations of allenes with gold-covered substituted benzenes as substrates.[300]

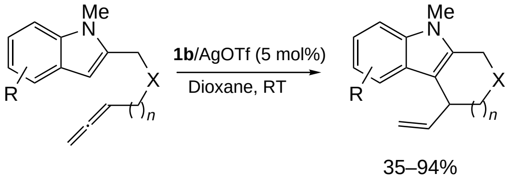
Me
N
R
X
n
1b/AgOTf (5 mol%)
Dioxane, RT
Me
N
R
X
n
35–94%

(111)

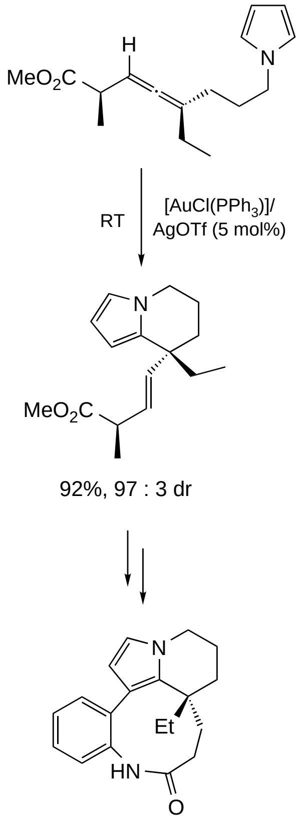
H
MeO2C
N
RT
[AuCl(PPh3)]/
AgOTf (5 mol%)
N
MeO2C
92%, 97 : 3 dr
N
Et
HN
O

(112)

(–)-rhazinilam

Double bonds of enynes act as nucleophiles and for ene-allenes perform similarly. Actually, some of the reactions of enynes with propargylic carboxylate substitution may

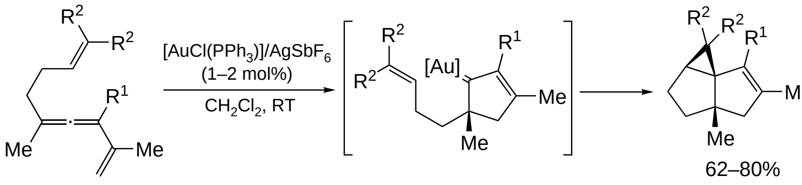

(117)

be considered reactions of allenes since, in most of them, the isomerization occurs prior to the alkene attack. The first report showed the endo cyclization of vinyl–allenes to cyclopentadienes (equation 113).[301] The introduction of more carbon atoms between the allene and the olefin gave different results depending on the allene substitution. In γ-vinyl-allenes, cyclohexenes were obtained by exo cyclizations with low to moderate enantiomeric excesses induced by a chiral phosphine ligand if terminal allenes were used.[302] However, with substitution on the allene, the vinyl–gold species generated after the initial exo-cyclized product was trapped intramolecularly leading to methylenecyclobutane structures (equation 114).[303]

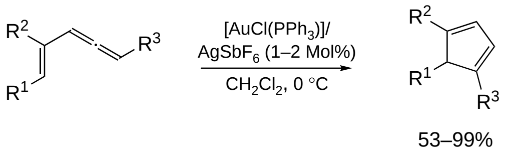

(113)

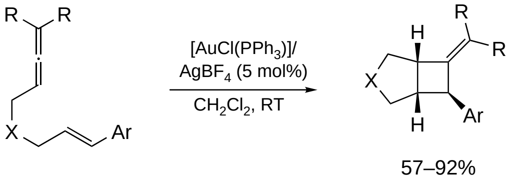

(114)

Other tandem cyclizations have been reported: in the simplest one, a semipinacol ring contraction takes place over the cationic intermediate (equation 115).[304] By changing the protecting groups of the alcohols, the rearrangement does not take place and elimination favors the formation of benzenes (equation 116).[305] The evolution to gold carbenes is also possible (equation 117): in a cyclization of dieneallenes, the isomerization to a gold carbene of the allyl–gold cation, obtained after the attack to the allene, is responsible for the cyclopropanation of the second olefin.[306]

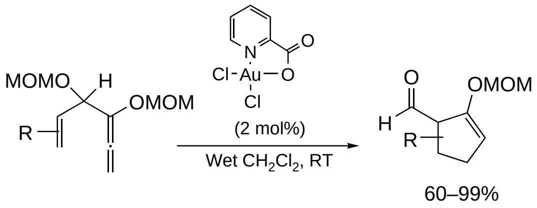

(115)

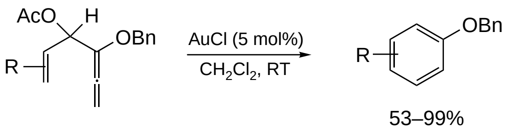

(116)

7 CARBONYL ACTIVATION

7.1 1,2-Additions to Carbonyls and Imines

The Lewis acidity of gold, related to relativistic effects,[11] allows not only the coordination to carbon π-systems but also other functional groups. Among them, the most exploited field is the activation of carbonyls and imines toward different nucleophiles. In these cases, Au(III) species are many times the catalysts of choice over Au(I). An explanation for this may be found in the thermodynamic coordination preference of $AuCl_3$ for aldehydes over other moieties such as alkynes,[11] accounting for the functional group discrimination in these reactions. Nevertheless, Au(I) is still used in some of the transformations described in this section.

The first reported gold-catalyzed carbonyl activation was, unexpectedly, an asymmetric Au(I)-catalyzed aldol-type reaction in which the enolate of an isocyanoacetate reacted with aldehydes (equation 118) using a cationic gold species generated in situ by ligand displacement.[307] The asymmetric induction was achieved by a secondary interaction of the enolate with a side amino group of the chiral ferrocenyldiphosphine ligand employed, producing oxazolines in high yields and enantiomeric excesses, that were subsequently opened to the corresponding amino alcohols. This methodology was later extended by the authors to α-isocyano Weinreb amides to facilitate the further transformation of the products to aminoaldehydes and aminoacids.[308]

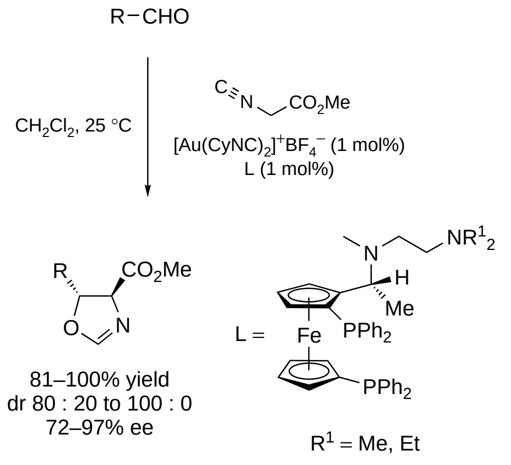

(118)

It is interesting to note that although this was one of the first gold-catalyzed reactions, and despite the great boost in the last few years, gold asymmetric catalysis is still an underdeveloped field.

However, a variety of reactions regarding carbonyl and imine activation by gold have been described. In fact, the formation of imines and enamines from carbonyls is catalyzed by gold species as was shown by Arcadi in the first step of a synthesis of pyridines.[184] Both carbonyl groups and imines can coordinate to gold as a Lewis acid, thus promoting the attack of other nucleophiles present in the reaction medium. The initial examples reported, followed the way outlined by Ito and consisted of gold(I)-alkoxide-catalyzed Knoevenagel condensations with benzaldehyde[309] to give products depicted in equation (119). In this case, Au(I) species showed a higher catalytic activity than those of Au(III). By contrast, Au(III) is preferred in a different case where benzaldimines, formed in situ from benzaldehydes and carbamates, undergo a three-component Mannich-type reaction with acetophenones (equation 120).[310]

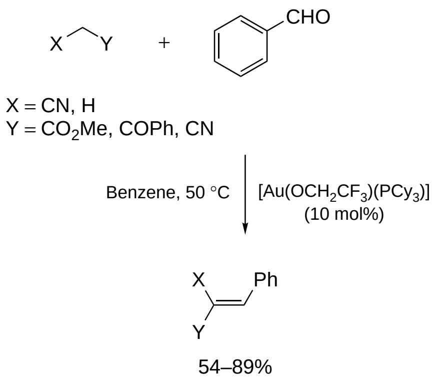
CHO
X
Y
+
X = CN, H
Y = CO2Me, COPh, CN
Benzene, 50 °C
[Au(OCH2CF3)(PCy3)]
(10 mol%)
X
Ph
Y
54–89%

(119)

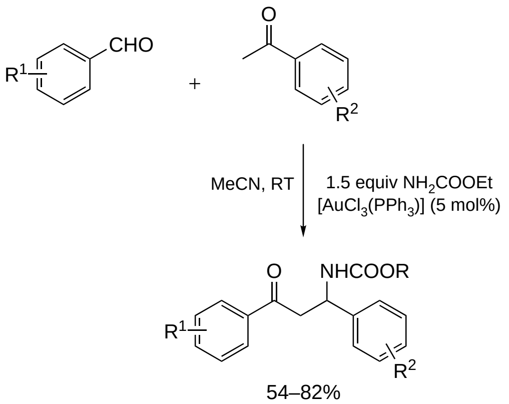
R1
CHO
+
O
R2
MeCN, RT
1.5 equiv NH2COOEt
[AuCl3(PPh3)] (5 mol%)
O
NHCOOR
R1
R2
54–82%

(120)

Electron-rich arenes are suitable nucleophiles for this reaction as well. Thus, the addition of arenes to imines has been described in both intra- (equation 121)[311] and intermolecular (equation 122)[312] fashion catalyzed by $AuCl_3$/AgOTf. The yields were increased in the intramolecular version by acylation of the amide intermediate to give acylamides. In the case of addition of electron-rich arenes to carbonyls,[313] a second addition takes place by activation of the benzylic alcohol intermediate (equation 123), a process that is later discussed, to yield products of the type shown in equation (123).

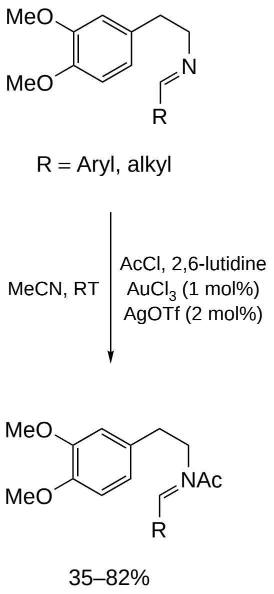
MeO
MeO
N
R
R = Aryl, alkyl
MeCN, RT
AcCl, 2,6-lutidine
AuCl3 (1 mol%)
AgOTf (2 mol%)
MeO
MeO
NAc
R
35–82%

(121)

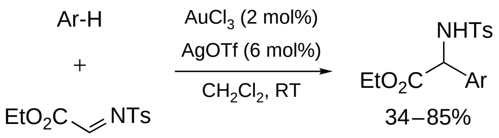
Ar-H
+
EtO2C
NTs
AuCl3 (2 mol%)
AgOTf (6 mol%)
CH2Cl2, RT
NHTs
EtO2C
Ar
34–85%

(122)

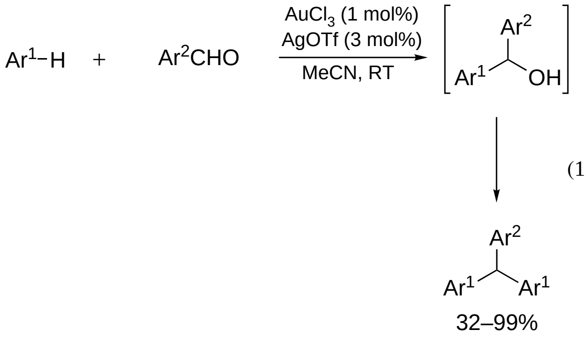
Ar1–H
+
Ar2CHO
AuCl3 (1 mol%)
AgOTf (3 mol%)
MeCN, RT
Ar2
Ar1
OH
Ar2
Ar1
Ar1
32–99%

(123)

Recently, an intramolecular 1,2-addition to conjugated carbonyls by internal olefins has been reported, in tandem with other nucleophilic addition to the carbocation formed.[314]

Other nucleophiles that have been used in this context are acetylides (alkynes). The addition of those to iminium cations generated in situ from aldehydes and secondary amines accomplishes a gold(III)-catalyzed three-component coupling for the synthesis of propargylamines, as can be observed in equation (124).[315,316] The reactions are performed in water or in tetrahydrofuran (THF) when supported catalysts are employed.[317] Chiral prolinol derivatives as the amine have been applied to a diastereoselective synthesis of propargylamines using Au(III)–salen complexes (equation 125).[318] When primary amines were used, the reactions did not take place[315] but, instead, if the corresponding imines are preformed (equation 126), the alkyne addition can be done by means of an acyliminium, yielding propargylamides.[319]

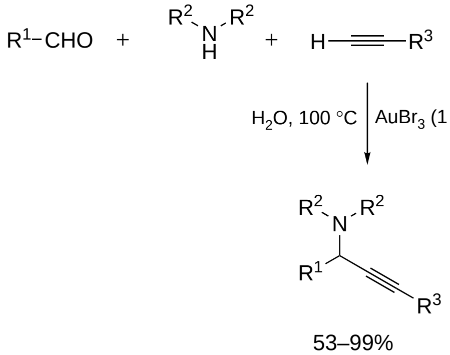
R1–CHO
+
R2 N R2 H
+
H—≡—R3
H2O, 100 °C
AuBr3 (1 mol%)
R2 N R2
R1
R3
53–99%

(124)

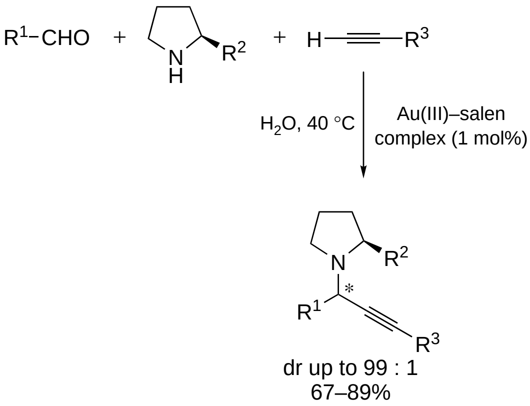
R1–CHO
+
N H R2
+
H—≡—R3
H2O, 40 °C
Au(III)–salen complex (1 mol%)
N R2
*
R1
R3
dr up to 99 : 1
67–89%

(125)

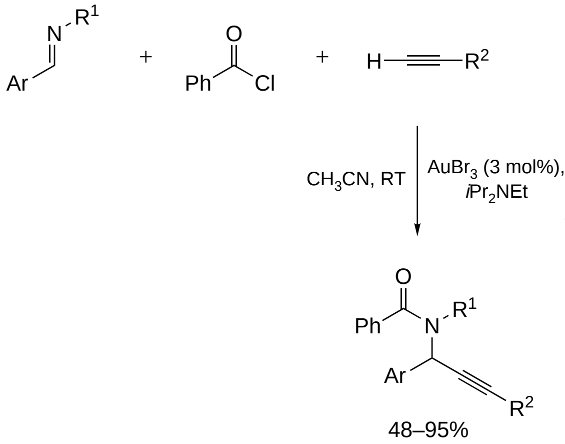
N R1
Ar
+
O
Ph Cl
+
H—≡—R2
CH3CN, RT
AuBr3 (3 mol%), iPr2NEt
O
Ph N R1
Ar
R2
48–95%

(126)

The last of the nucleophiles discussed in this section is hydride. Aldehyde (equation 127) and aldimine (equation 128) hydrosilylations have been shown to be gold-catalyzed reactions[320,321] and selective over ketones. In these cases, the addition of 20 mol% of PBu_3 is crucial to stabilize the gold(I) catalyst in the reductive medium. After the catalysis step, acidic treatment led to the formation of the alcohols and amines in good yields. In a similar context, a gold-catalyzed hydroboration of imines has been reported.[322]

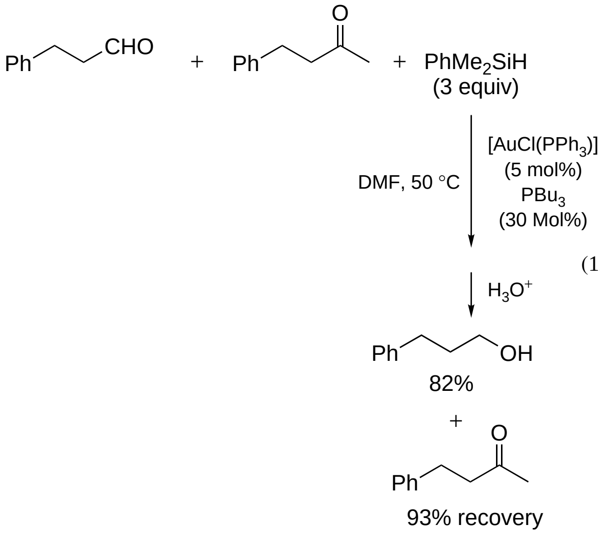
Ph CHO
+
O
Ph
+
PhMe2SiH (3 equiv)
DMF, 50 °C
[AuCl(PPh3)] (5 mol%) PBu3 (30 Mol%)
H3O+
Ph OH
82%
+
O
Ph
93% recovery

(127)

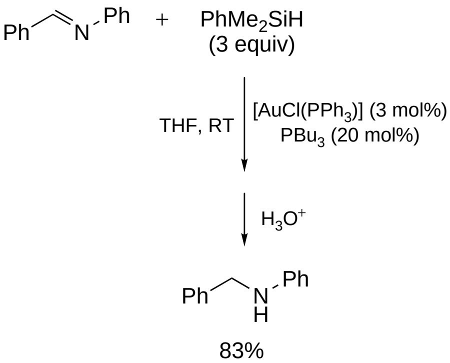
Ph N Ph
+
PhMe2SiH (3 equiv)
THF, RT
[AuCl(PPh3)] (3 mol%) PBu3 (20 mol%)
H3O+
Ph N H Ph
83%

(128)

7.2 Additions to 1,3-Dicarbonyl Compounds

When the activated carbonyl is a 1,3-dicarbonyl compound, some tandem reactions have been described.

In the simplest of these, β-enaminones are synthesized (equation 129) by the addition of amines to 1,3-diketones or β-ketoesters.[323] The reaction has been applied to the Friedländer synthesis of quinolines by condensation of the enaminone and other carbonyl present in the substrate.[324] Substituted pyrroles in equation (130) can be obtained as well when a propargyl group is present, by addition of the enaminone to the triple bond.[139,325] Alcohols, thiols, and secondary phosphines have been also tested as nucleophiles with good results.[323] A particularly interesting case is found in the condensation of indoles with 1,3-diketones to give substituted indol derivatives in equation (131).[326]

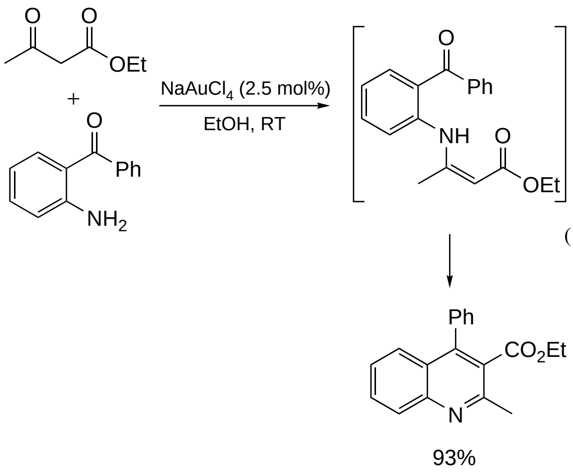
OEt
+
Ph
NH2
NaAuCl4 (2.5 mol%)
EtOH, RT
Ph
NH
OEt
Ph
CO2Et
N
93%

(129)

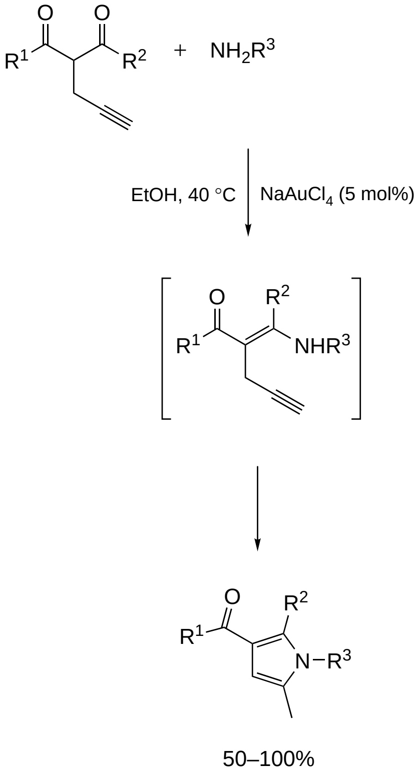
R1
R2
+ NH2R3
EtOH, 40 °C
NaAuCl4 (5 mol%)
R1
R2
NHR3
R1
R2
N−R3
50–100%

(130)

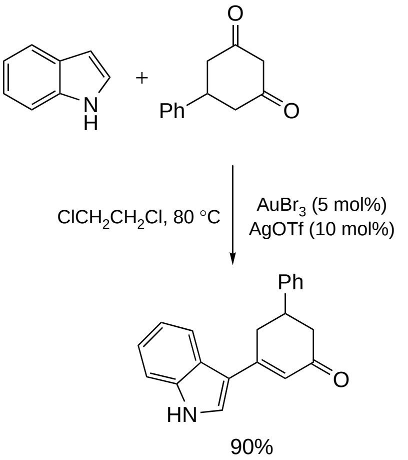
+
N
H
Ph
O
ClCH2CH2Cl, 80 °C
AuBr3 (5 mol%)
AgOTf (10 mol%)
Ph
HN
O
90%

(131)

7.3 1,4-Additions

Michael additions to conjugated carbonyls can be catalyzed by gold species. Among them, arene additions are the most studied area but other nucleophiles can attack the gold-coordinated enones as well. In fact, the intermolecular aza-Michael additions of carbamates to enones[327] was reported in 2002 with both Au(I) and Au(III) salts, and in 2007 an intramolecular alkoxide and amide conjugate addition has been developed[70] and applied to the synthesis of (+)-andrachcinidine[70] (equation 132). In the latter case, the enones are formed as intermediates in a previous gold-catalyzed step that is the hydration of an alkyne and methanol loss. Then the cyclization takes place to give piperidines.

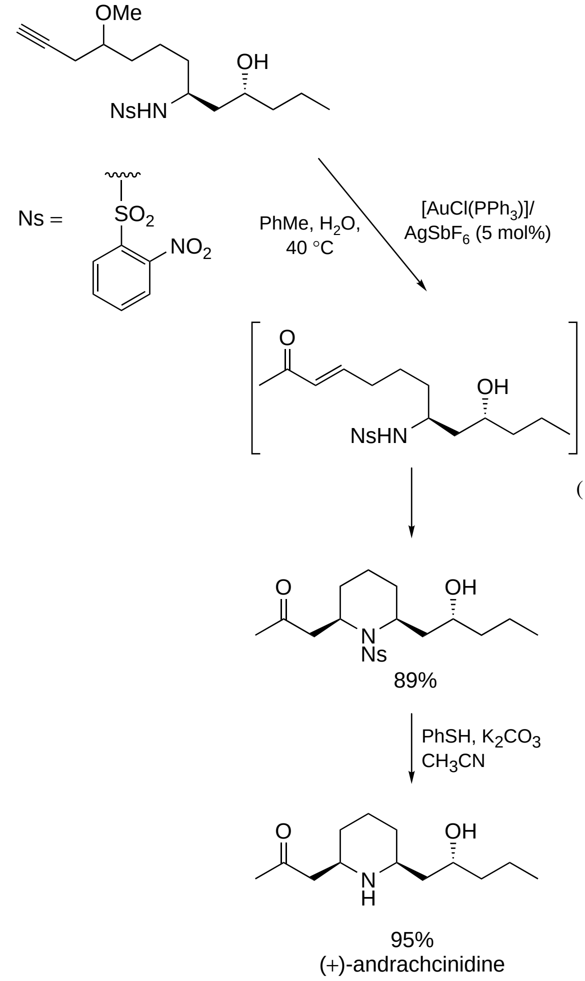
OMe
OH
NsHN
Ns =
SO2
NO2
PhMe, H2O, 40 °C
[AuCl(PPh3)]/ AgSbF6 (5 mol%)
O
OH
NsHN
O
OH
N
Ns
89%
PhSH, K2CO3
CH3CN
O
OH
N
H
95%
(+)-andrachcinidine

(132)

Yet the reaction that attracted more interest has been the conjugate addition of arenes. It was first described by Hashmi in 2000 that enones and furans could react in the presence of $AuCl_3$.[280] In the reported cases, furans were also formed by a gold-catalyzed reaction of allenones (equation 133). Electron-rich substituted benzenes also underwent 1,4-addition with Michael acceptors.[241,264] Later, 7-azaindoles (equation 134)[328] were shown to provide 3-alkylated derivatives. On the other hand, indoles (equation 135)[329] reacted selectively with enones to give the 2- or 3-substituted derivatives, depending on the substitution pattern of the starting material. Reaction of indoles with enals gave mixtures of 1,2- and 1,4-addition products.[330] Pyrroles have also been submitted to the reaction conditions, but afforded mixtures of disubstituted or trisubstituted compounds in nonselective reactions.[331]

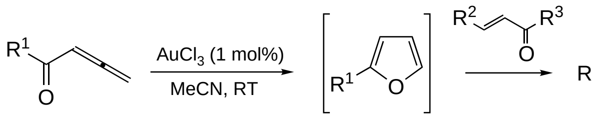
R1
O
AuCl3 (1 mol%)
MeCN, RT
R1
O
R2
R3
O
R1
O
R2
O
R3
46–74%

(133)

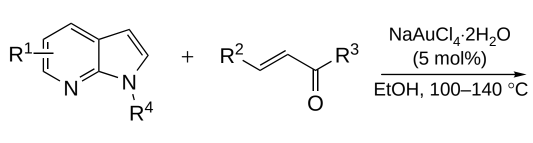
R1
N
N
R4
+
R2
R3
O
NaAuCl4·2H2O
(5 mol%)
EtOH, 100–140 °C
R2
R3
O
R1
N
N
R4
6–98%

(134)

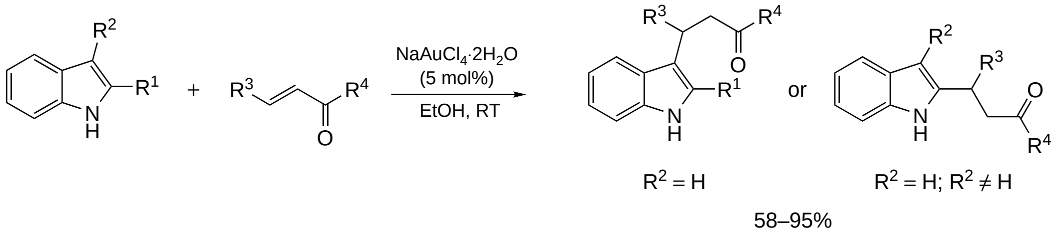
R2
R1
N
H
+
R3
R4
O
NaAuCl4·2H2O
(5 mol%)
EtOH, RT
R3
R4
O
R1
N
H
or
R2
R3
O
N
H
R4
R2 = H
R2 = H; R2 ≠ H
58–95%

(135)

The last examples included in this section are dipolar cycloadditions with dipolarophiles that are conjugated carbonyls. The first one is the 1,3-dipolar cycloaddition of nitrones with methyl acrylate.[332] The reaction is supposed to be catalyzed by both Au(I) and Au(III) species and experiments that discarded the coordination of gold to the nitrone were performed, which may support a carbonyl–Au mechanism, although it still remains elusive. More recently, the enantioselective cycloaddition of münchnones to acrylates catalyzed by a chiral catalyst has been developed.[333]

7.4 Other Processes

Examples of gold-catalyzed carbonylation of amines and olefins exist related to the activation of carbonyl. The first case involves the formation of carbamates from anilines and CO in the presence of alcohols[334] or the production of acetamides from aliphatic amines.[335] In these examples, Au(I) (usually [AuCl(PPh$_3$)]) catalysts are preferred. For the carbonylation of olefins, gold(I)–carbonyls are prepared in situ in sulfuric acid media to afford carboxylic acids.[336]

8 ALCOHOL ACTIVATION

8.1 Substitutions

Allylic carboxylates also react with gold catalysts. These reactions are formally carbonyl activations, but the products observed are closely related to the reactivity shown by allylic or benzylic alcohols that will be discussed in this section. The first examples show an allylic rearrangement to styrenes (equation 136).[337] Nucleophiles such as allyl stannanes have also been added to give substitution reactions and products of intramolecular coupling (equation 137).[338]

The activation of alcohols by gold has just started to be studied in the last few years and is an emerging field in the area. The closest examples to the ones showed for the acetates are the

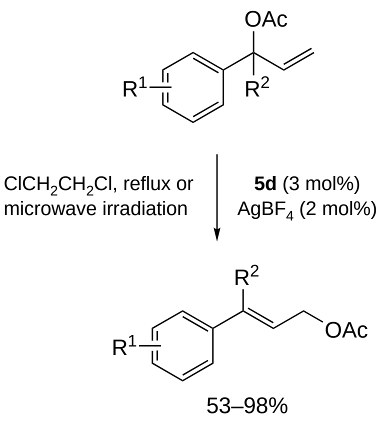
OAc
R1
R2
ClCH2CH2Cl, reflux or
microwave irradiation
5d (3 mol%)
AgBF4 (2 mol%)
R2
R1
OAc
53–98%

(136)

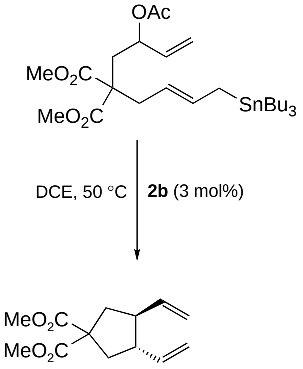
OAc
MeO2C
MeO2C
SnBu3
DCE, 50 °C
2b (3 mol%)
MeO2C
MeO2C

(137)

amination of allylic alcohols and the substitution of benzylic alcohols that was previously outlined. In the first case, anilines and tosylamides act as nucleophiles for the substitution of alcohols (equation 138),[339,340] probably coordinated to gold to increase their leaving ability, yielding amination products. However, the first alcohol substitution was described on propargyl alcohols and different nucleophiles in 2005.[65] In a very recent example, allylsilanes have been used for the substitution of benzylic ethers.[341] Another related example is the isomerization of hydroxyl–allylic ethers described by Porco and Schaus[342] in which a ring contraction takes place by the activation of allyl–propargylic or allyl–benzylic alcohols (equation 139).

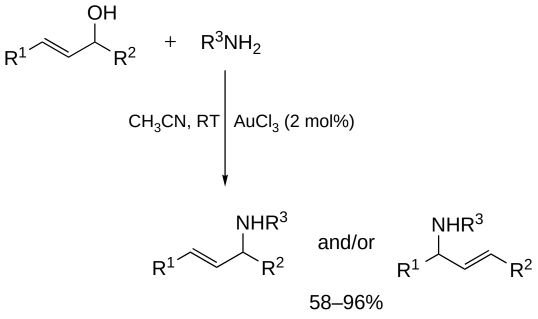
OH
R1
R2
+ R3NH2
CH3CN, RT
AuCl3 (2 mol%)
NHR3
R1
R2
and/or
NHR3
R1
R2
58–96%

(138)

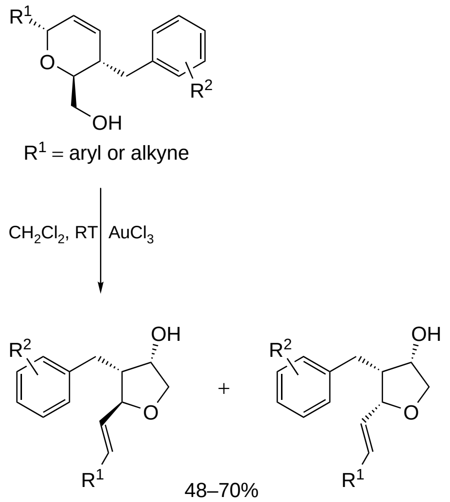
R1
O
R2
OH
R1 = aryl or alkyne
CH2Cl2, RT
AuCl3
R2
OH
O
R1
+
R2
OH
O
R1
48–70%

(139)

When benzylic alcohols are the substrates, arenes behave as nucleophiles,[343] as shown in equation (123)[313] and for the analogs in the 1,4-addition.[330] These reactions have been performed with alcohols that are activated by an arene substituent and another group that could be an olefin, an alkyne, or other arene (equation 140). In the case of dimerization reported by Hashmi (equation 141), primary benzylic alcohols[344] produce dimers of the type in equation (141) that arise from the activation of this moiety, together with the expected cyclization products. In a very recently reported example, aryl–alkyl ethers are obtained by reaction with NaAuCl$_4$.[345]

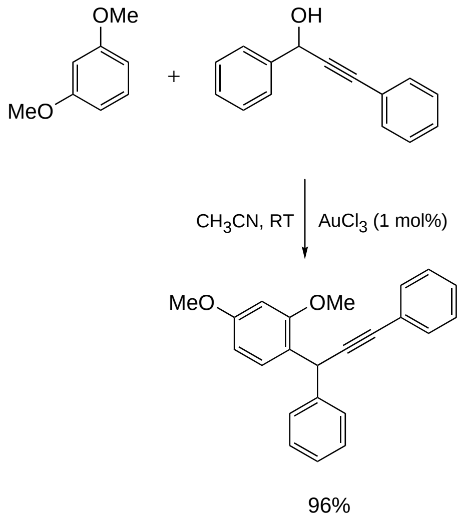
OMe
MeO
+
OH
CH3CN, RT
AuCl3 (1 mol%)
MeO
OMe
96%

(140)

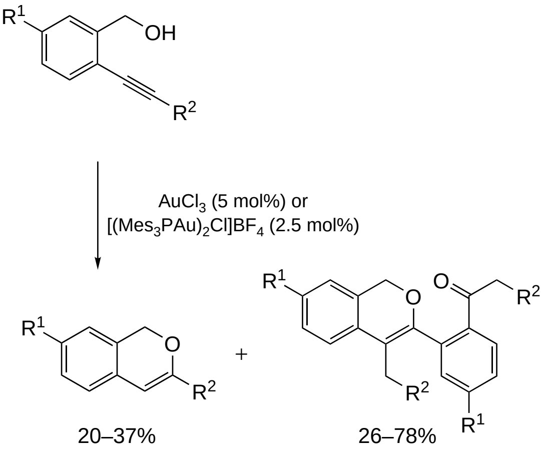
R1
OH
R2
AuCl3 (5 mol%) or
[(Mes3PAu)2Cl]BF4 (2.5 mol%)
R1
O
R2
20–37%
+
R1
O
O
R2
R2
R1
26–78%

(141)

A different example of gold-catalyzed alcohol activation is the silylation of primary alcohols. In this reaction, aliphatic, allylic, and benzylic primary alcohols undergo silylation with an Au(I)–xantphos chelated complex.[346]

Other related reactions are the substitutions of aliphatic sulfonate esters by arenes[238] and the epoxide-opening with benzenes[237] catalyzed by gold. In both cases, the aryl groups are the nucleophiles that attack the gold-coordinated sulfonate esters or epoxides, respectively.

8.2 Oxidations

The gold-catalyzed oxidation of alcohols is a less-explored field. In one example, oxygen was used as the oxidant and the authors take advantage of the coordination of benzylic alcohols to an Au(I)-complex generated in situ from AuCl and a diamine anionic ligand.[347]

The rest of the examples of gold-catalyzed homogeneous oxidations are conversions of sulfides to sulfoxides. The early examples by Gasparrini were published in 1983 and 1984 and were reactions in nitric acid under phase-transfer conditions.[348,349] The Au(III) catalysts used were later optimized to tetrabutylammonium tetrabromoaurate.[350] These results were improved by the discovery of a milder method that oxidizes sulfides under ambient conditions with O_2.[351] In this latter case, $HAuCl_4$ and $AgNO_3$ were combined in MeCN to form an $AuCl_2NO_3$(thioether) species that is the active homogeneous catalyst. Recently, the gold-catalyzed oxidation of sulfides with H_2O_2 at room temperature has been reported and complements the previous one.[352]

9 OLEFIN ACTIVATION

The coordination of olefins to gold species is well known, despite the preference for alkynes, allenes, and carbonyl groups. This is reflected in the fact that synthetic applications based on olefin activation by gold have been developed to a lesser extent than alkyne or carbonyl activation.

The easiest reactions are those in which the nucleophile is the gold-activated species. Examples of this are Au(I)-catalyzed carbene[122] and nitrene[239] transfers (equations 142 and 143) that convert olefins into cyclopropanes or aziridines, respectively. In the carbene transfer, ethyl diazoacetate is the source of carbene and the active NHC–gold cationic catalyst is generated by chloride abstraction with sodium tetrakis(3,5-bis(trifluoromethyl)phenyl)borate NaBAr′4. The cyclopropanation is competitive with other carbene insertions with active C–H or N–H bonds present in the substrate. For the aziridinations of olefins, nitrene formation is accomplished by the oxidation of sulfonamides with $PhI(OAc)_2$ and the catalyst of choice is a gold-(I) triflate with a terpyridine ligand.

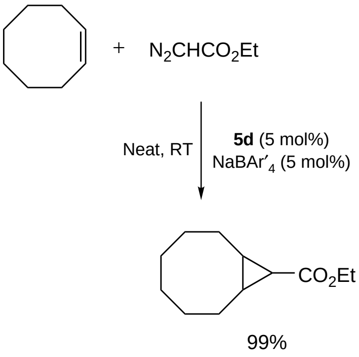
+ N2CHCO2Et
Neat, RT
5d (5 mol%)
NaBAr′4 (5 mol%)
CO2Et
99%

(142)

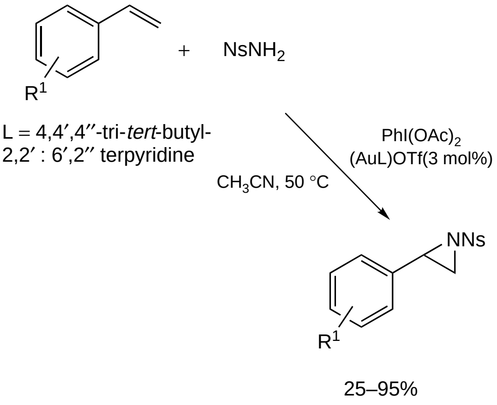
R1
+ NsNH2
L = 4,4′,4″-tri-tert-butyl-2,2′ : 6′,2″ terpyridine
PhI(OAc)2
(AuL)OTf(3 mol%)
CH3CN, 50 °C
NNs
R1
25–95%

(143)

Apart from these two examples, in the rest of the olefin activations, gold coordinates to the olefin, turning it susceptible to nucleophilic attack. The early examples of alkene functionalization by gold catalysis (equation 144) focused on the intermolecular addition of 1,3-diketones to styrenes.[353,354] An intramolecular version with ketoamides to yield pyrrolidinones[355] was later developed and followed by the intermolecular addition of phenols (equation 145) and carboxylic acids to double bonds,[356] a work that included an example of intramolecular addition of an aliphatic alcohol to an olefin.

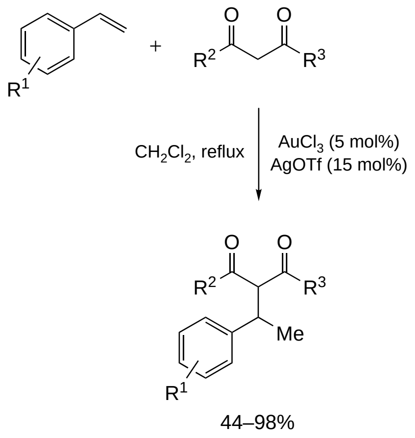
R1
+
O O
R2 R3
CH2Cl2, reflux
AuCl3 (5 mol%)
AgOTf (15 mol%)
O O
R2 R3
Me
R1
44–98%

(144)

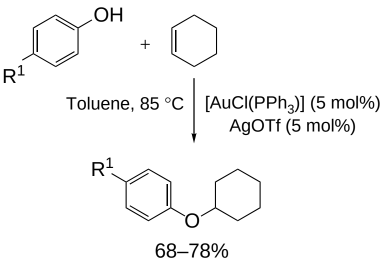
OH
R1
+
Toluene, 85 °C
[AuCl(PPh3)] (5 mol%)
AgOTf (5 mol%)
R1
O
68–78%

(145)

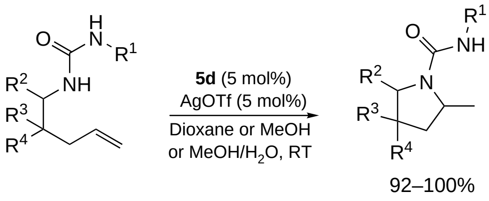
H
O N R1
R2 NH
R3
R4
5d (5 mol%)
AgOTf (5 mol%)
Dioxane or MeOH
or MeOH/H2O, RT
R1
O NH
R2 N
R3
R4
92–100%

(146)

Hydroamination of olefins is also possible with gold catalysts. In this reaction, the attack comes from a nitrogen nucleophile as a carbamate,[357] a urea,[358] an amide,[359] or a sulfonamide.[360] In the latter case, the reaction can be carried out intermolecularly. While the carbamates, ureas, and amides give only products of intramolecular aminations, the sulfonamides can perform the intermolecular addition. Only the addition of ureas (equation 146) takes place at room temperature, and in the rest of the additions heating is required. The catalysts of choice in all these reactions are cationic gold(I)-species stabilized by phosphines or NHC ligands. The reaction times have been reduced by the use of microwave irradiation.[361] The mechanism of the hydroamination reaction has been studied in detail theoretically.[362]

The intermolecular addition of carbamates to 1,3-dienes (equation 147) under mild conditions has been described as well.[363] The hydrothiolation of 1,3-dienes has also been reported.[364] Other related conjugate additions can be performed over methylenecyclopropanes (equation 148) with sulfonamides and the resulting product cyclizes by a second hydroamination of an olefin, finally yielding cyclic sulfonamides.[365] This behavior is reproduced in a similar reaction for the ring opening of vinylcyclopropanes with sulfonamides.[366] One more example in this group of reactions is the synthesis of dihydrobenzofurans from aryl–allyl ethers.[367]

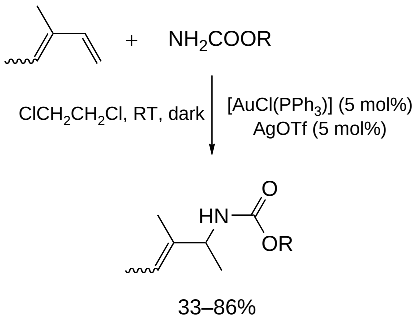

(147)

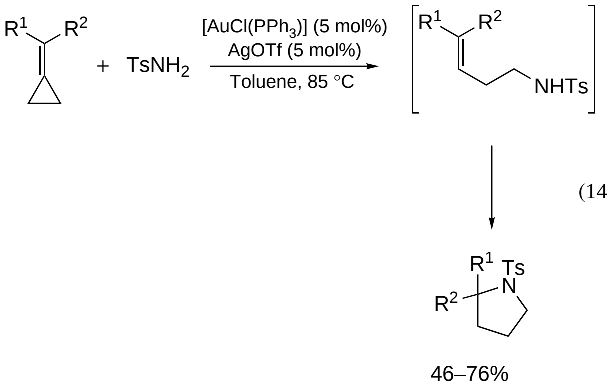

(148)

On the other hand, aniline, phenol, and alcohols have been added to unactivated alkenes using $AuCl_3$,[368,369] but then $CuCl_2$ should be added to the reaction mixture and harder conditions are necessary.

Gold can also behave as a good hydrogenation catalyst. Although its use is more extended as a heterogeneous catalyst, some examples of homogeneous applications have been reported,[370,371] one among them being an enantioselective hydrogenation with a chiral, dinuclear gold(I) chloride.[372] The hydrosilylation of styrene with an Au(III)–salen complex as catalyst[373] and the diboration of olefins have also been studied.[374]

The last example included in this section is an oxidative cleavage of styrenes performed in water with *tert*-butylhydroperoxide as the oxidant (equation 149).[375] In this reaction, the first step is an olefin activation that should be followed by oxidation, although the mechanism is unknown. The catalyst employed is AuCl with neocuproine as the ligand.

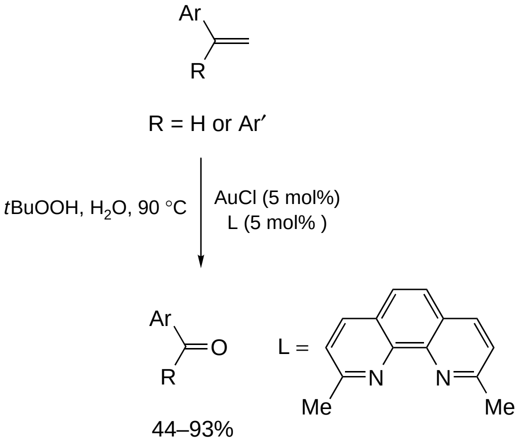

(149)

10 ALKANE ACTIVATION (C–H)

A few C–H activations by gold are known.[376] Thus, an initial example observed in nature is the existence of Au atoms in the core of a bacterial protein that oxidizes methane to methanol.[377] In a reaction that tries to mimic this behavior, the formation of alkyl hydroperoxides was achieved with $NaAuCl_4$ or $[AuCl(PPh_3)]$ in acetonitrile solution with H_2O_2 at relatively low temperatures (75 °C).[378] The formed hydroperoxides decomposed partially in the reaction mixture to give the corresponding alcohols and ketones, but were subsequently reduced to the alcohols by different methods. The oxidation of methane by gold–oxygenated complexes has also been studied theoretically.[379]

In the carbene insertions to alkane C–H bonds[380] the same concept as for the olefin cyclopropanations is applied. In that work, the gold-catalyzed carbene transfer is now used for insertions into C–H bonds (equation 150), with a selectivity that is influenced by the electronic properties of the ligand and the counterion employed. The carbene and nitrene insertion is not limited to Csp^3–H bonds, but N–H (equation 151), O–H (equation 152),[122] and aryl Csp^2–H bonds react as well (equation 153).[122,243,381]

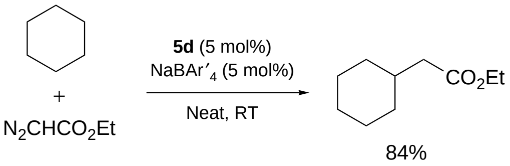

(150)

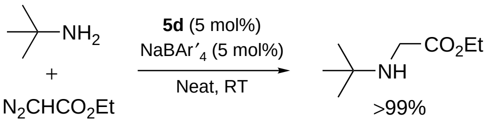

(151)

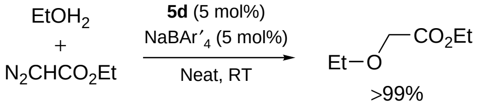

(152)

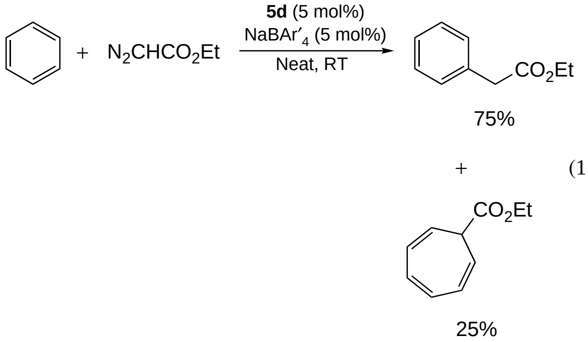

(153)

Aryl C–H bonds are known to be active and thus benzenes undergo auration, which has been exploited as the oxidative coupling of arenes.[382]

11 OTHER ACTIVATIONS

In this section, we would like to mention that gold species can be active against other types of single bonds that are different from C–H. An example of gold-catalyzed dehydrogenative dimerization of trialkyl stannanes[383] shows that M–H bonds may be activated as well. On the other hand, transmetallation from M–C bonds is also possible as observed for boronic acids,[384] a finding that has been applied to the dimerization of those compounds[385] and to the development of the gold(I)-catalyzed Suzuki cross-coupling.[386] In a similar way, gold(I) homogeneous and heterogeneous species have been proposed to be catalytically active in Sonogashira couplings.[387]

12 REFERENCES

1. C. Aubert, O. Buisine, and M. Malacria, *Chem. Rev.*, 2002, **102**, 813.
2. A. Hoffmann-Röder and N. Krause, *Org. Biomol. Chem.*, 2005, **3**, 387.
3. S. Ma, S. Yu, and Z. Gu, *Angew. Chem. Int. Ed.*, 2006, **45**, 200.
4. C. Bruneau, *Angew. Chem. Int. Ed.*, 2005, **44**, 2328.
5. A. S. K. Hashmi and G. J. Hutchings, *Angew. Chem. Int. Ed.*, 2006, **45**, 7896.
6. A. S. K. Hashmi, *Chem. Rev.*, 2007, **107**, 3180.
7. A. M. Echavarren and C. Nevado, *Chem. Soc. Rev.*, 2004, **33**, 431.
8. E. Jiménez-Núñez and A. M. Echavarren, *Chem. Commun.*, 2007, 333.
9. L. Zhang, J. Sun, and S. A. Kozmin, *Adv. Synth. Catal.*, 2006, **348**, 2271.
10. A. Fürstner and P. W. Davies, *Angew. Chem. Int. Ed.*, 2007, **46**, 3410.
11. D. J. Gorin and F. D. Toste, *Nature*, 2007, **446**, 395.
12. P. Pyykkö, *Angew. Chem. Int. Ed.*, 2002, **41**, 3573.
13. P. Pyykkö, *Angew. Chem. Int. Ed.*, 2004, **43**, 4412.
14. P. Pyykkö, *Inorg. Chim. Acta*, 2005, **358**, 4113.
15. H. Schwartz, *Angew. Chem. Int. Ed.*, 2003, **42**, 4442.
16. C. Nieto-Oberhuber, M. P. Muñoz, E. Buñuel, C. Nevado, D. J. Cárdenas, and A. M. Echavarren, *Angew. Chem. Int. Ed.*, 2004, **43**, 2402.
17. C. Nieto-Oberhuber, M. P. Muñoz, S. López, E. Jiménez-Núñez, C. Nevado, E. Herrero-Gómez, M. Raducan, and A. M. Echavarren, *Chem. Eur. J.*, 2006, **11**, 1677.
18. C. Ferrer, M. Raducan, C. Nevado, C. K. Claverie, and A. M. Echavarren, *Tetrahedron*, 2007, **63**, 6306.
19. J. H. Teles, S. Brode, and M. Chabanas, *Angew. Chem. Int. Ed.*, 1998, **37**, 1415.
20. E. Mizushima, K. Sato, T. Hayashi, and M. Tanaka, *Angew. Chem. Int. Ed.*, 2002, **41**, 4563.
21. E. Mizushima, T. Hayashi, and M. Tanaka, *Org. Lett.*, 2003, **5**, 3349.
22. Y. Yang, V. Ramamoorthy, and P. R. Sharp, *Inorg. Chem.*, 1993, **32**, 1946.
23. A. N. Nesmeyanov, E. G. Perevalova, Y. T. Struchkov, M. Y. Antipin, K. I. Grandberg, and V. P. J. Dyadchenko, *Organomet. Chem.*, 1980, **201**, 343.
24. B. D. Sherry and F. D. Toste, *J. Am. Chem. Soc.*, 2004, **126**, 15978.
25. C. Nieto-Oberhuber, S. López, and A. M. Echavarren, *J. Am. Chem. Soc.*, 2005, **127**, 6178.
26. C. Nieto-Oberhuber, S. López, M. P. Muñoz, E. Jiménez-Núñez, E. Buñuel, D. J. Cárdenas, and A. M. Echavarren, *Chem. Eur. J.*, 2006, **11**, 1694.
27. E. Jiménez-Núñez, C. K. Claverie, C. Nieto-Oberhuber, and A. M. Echavarren, *Angew. Chem. Int. Ed.*, 2006, **45**, 5452.
28. C. Ferrer and A. M. Echavarren, *Angew. Chem. Int. Ed.*, 2006, **45**, 1105.

29. C. Ferrer, C. H. M. Amijs, and A. M. Echavarren, *Chem. Eur. J.*, 2007, **13**, 1358.
30. E. Herrero-Gómez, C. Nieto-Oberhuber, S. López, J. Benet-Buchholz, and A. M. Echavarren, *Angew. Chem. Int. Ed.*, 2006, **45**, 5455.
31. D. V. Partyka, T. J. Robilotto, M. Zeller, A. D. Hunter, and T. G. Gray, *Organometallics*, 2008, **27**, 28.
32. N. Mézailles, L. Ricard, and F. Gagosz, *Org. Lett.*, 2005, **7**, 4133.
33. S. López, E. Herrero-Gómez, P. Pérez-Galán, C. Nieto-Oberhuber, and A. M. Echavarren, *Angew. Chem. Int. Ed.*, 2006, **45**, 6029.
34. C. Nieto-Oberhuber, P. Pérez-Galán, E. Herrero-Gómez, T. Lauterbach, C. Rodríguez, S. López, C. Bour, A. Rosellón, D. J. Cárdenas, and A. M. Echavarren, *J. Am. Chem. Soc.*, 2008, **130**, 269.
35. P. de Fremont, N. M. Scott, E. D. Stevens, and S. P. Nolan, *Organometallics*, 2005, **24**, 2411.
36. P. de Frémont, R. Singh, E. D. Stevens, J. L. Petersen, and S. P. Nolan, *Organometallics*, 2007, **26**, 1376.
37. P. de Frémont, E. D. Stevens, M. R. Fructos, M. M. Díaz-Requejo, P. J. Pérez, and S. P. Nolan, *Chem. Commun.*, 2006, 2045.
38. G. Li and L. Zhang, *Angew. Chem. Int. Ed.*, 2007, **46**, 5156.
39. L. Ricard and F. Gagosz, *Organometallics*, 2007, **26**, 4704.
40. A. Dar, K. Moss, S. M. Cottrill, R. V. Parish, C. A. McAuliffe, R. G. Pritchard, B. Beagley, and J. Sandbank, *J. Chem. Soc., Dalton Trans.* 1992, 1907.
41. A. S. K. Hashmi, J. P. Weyrauch, M. Rudolph, and E. Kurpejovic, *Angew. Chem. Int. Ed.*, 2004, **43**, 6545.
42. R. Huettel and H. Forkl, *Chem. Ber.*, 1972, **105**, 1664.
43. P. Schulte and U. Behrens, *Chem. Commun.*, 1998, 1633.
44. J. A. Akana, K. X. Bhattacharyya, P. Müller, and J. P. Sadighi, *J. Am. Chem. Soc.*, 2007, **129**, 7736.
45. G. Wittig and S. Fischer, *Chem. Ber.*, 1972, **105**, 3542.
46. V. Lavallo, G. D. Frey, S. Kousar, B. Donnadieu, and G. Bertrand, *Proc. Natl. Acad. Sci. U.S.A.*, 2007, **104**, 13569.
47. N. D. Shapiro and F. D. Toste, *Proc. Natl. Acad. Sci. U.S.A.*, 2008, **105**, 2779.
48. R. O. C. Norman, W. J. E. Parr, and C. B. Thomas, *J. Chem. Soc., Perkin Trans. 1*, 1976, 1983.
49. Y. Fukuda and K. Utimoto, *J. Org. Chem.*, 1991, **56**, 3729.
50. Y. Fukuda and K. Utimoto, *Bull. Chem. Soc. Jpn.*, 1991, **64**, 2013.
51. R. Casado, M. Contel, M. Laguna, P. Romero, and S. Sanz, *J. Am. Chem. Soc.*, 2003, **125**, 11925.
52. P. Roembke, H. Schmidbaur, S. Cronje, and H. Raubenheimer, *J. Mol. Catal. A: Chem.*, 2004, **212**, 35.
53. P. Wessig and J. Teubner, *Synlett*, 2006, 1543.
54. B. Nkosi, N. J. Coville, and G. J. Hutchings, *J. Chem. Soc., Chem. Commun.*, 1988, 71.
55. S. Sanz, L. A. Jones, F. Mohr, and M. Laguna, *Organometallics*, 2007, **26**, 952.
56. S. Antoniotti, E. Genin, V. Michelet, and J.-P. Genêt, *J. Am. Chem. Soc.*, 2005, **127**, 9976.
57. V. Belting and N. Krause, *Org. Lett.*, 2006, **8**, 4489.
58. B. Liu and J. K. De Brabander, *Org. Lett.*, 2006, **8**, ol0619819.
59. S. Hotha and S. Kashyap, *J. Am. Chem. Soc.*, 2006, **128**, 9620.
60. R. Skouta and C.-J. Li, *Angew. Chem. Int. Ed.*, 2007, **46**, 1117.
61. R. Skouta and C.-J. Li, *Tetrahedron Lett.*, 2007, **48**, 8343.
62. G.-Q. Tian and M. Shi, *Org. Lett.*, 2007, **9**, 4917.
63. A. S. K. Hashmi, L. Schwarz, J. H. Choi, and T. M. Frost, *Angew. Chem. Int. Ed.*, 2000, **39**, 2285.
64. Y. Liu, F. Song, Z. Song, M. Liu, and B. Yan, *Org. Lett.*, 2005, **7**, 5409.
65. M. Georgy, V. Boucard, and J.-M. Campagne, *J. Am. Chem. Soc.*, 2005, **127**, 14180.
66. S. I. Lee, J. Y. Baek, S. H. Sim, and Y. K. Chung, *Synthesis*, 2007, 2107.
67. D. A. Engel and G. B. Dudley, *Org. Lett.*, 2006, **8**, 4027.
68. S. S. Lopez, D. A. Engel, and G. B. Dudley, *Synlett*, 2007, 949.
69. J. P. Markham, S. T. Staben, and F. D. Toste, *J. Am. Chem. Soc.*, 2005, **127**, 9708.
70. H. H. Jung and P. E. Floreancig, *J. Org. Chem.*, 2007, **72**, 7359.
71. J. Barluenga, A. Diéguez, A. Fernández, F. Rodríguez, and F. J. Fañanás, *Angew. Chem. Int. Ed.*, 2006, **45**, 2091.
72. A. S. K. Hashmi and P. Sinha, *Adv. Synth. Catal.*, 2004, **346**, 432.
73. T. Yao, X. Zhang, and R. C. Larock, *J. Am. Chem. Soc.*, 2004, **126**, 11164.
74. T. Yao, X. Zhang, and R. C. Larock, *J. Org. Chem.*, 2005, **70**, 7679.
75. X.-Z. Shu, X.-Y. Liu, H.-Q. Xiao, K.-G. Ji, L.-N. Guo, C.-Z. Qi, and Y.-M. Liang, *Adv. Synth. Catal.*, 2007, **349**, 2493.
76. X. Liu, Z. Pan, X. Shu, X. Duan, and Y. Liang, *Synlett*, 2006, 1962.
77. L.-Z. Dai, M.-J. Qi, Y.-L. Shi, X.-G. Liu, and M. Shi, *Org. Lett.*, 2007, **9**, 3191.
78. T. Jin and Y. Yamamoto, *Org. Lett.*, 2007, **9**, 5259.
79. S. F. Kirsch, J. T. Binder, C. Liébert, and H. Menz, *Angew. Chem. Int. Ed.*, 2006, **45**, 5878.
80. J. T. Binder, B. Crone, S. F. Kirsch, C. Liébert, and H. Menz, *Eur. J. Org. Chem.*, 2007, 2636.
81. J. Zhang and H.-G. Schmalz, *Angew. Chem. Int. Ed.*, 2006, **45**, 6704.
82. G. Zhang, X. Huang, G. Li, and L. Zhang, *J. Am. Chem. Soc.*, 2008, **130**, ja077948e.
83. B. F. Straub, *Chem. Commun.*, 2004, 1726.

84. N. Asao, K. Takahashi, S. Lee, T. Kasahara, and Y. Yamamoto, *J. Am. Chem. Soc.*, 2002, **124**, 12650.
85. N. Asao, T. Nogami, S. Lee, and Y. Yamamoto, *J. Am. Chem. Soc.*, 2006, **128**, 10921.
86. N. Asao, K. S., Menggenbateer, and Y. Yamamaoto, *J. Org. Chem.*, 2005, **70**, 3682.
87. N. Asao, H. Aikawa, and Y. Yamamoto, *J. Am. Chem. Soc.*, 2004, **126**, 7458.
88. N. Asao, T. Kasahara, and Y. Yamamoto, *Angew. Chem. Int. Ed.*, 2003, **42**, 3504.
89. N. Asao and H. Aikawa, *J. Org. Chem.*, 2006, **71**, 5249.
90. N. Asao and K. Sato, *Org. Lett.*, 2006, **8**, 5361.
91. G. Dyker, D. Hildebrandt, J. Liu, and K. Merz, *Angew. Chem. Int. Ed.*, 2003, **42**, 4399.
92. D. Hildebrandt and G. Dyker, *J. Org. Chem.*, 2006, **71**, 6728.
93. N. Kim Y. Kim, W. Park, D. Sung, A. K. Gupta, and C. H. Oh, *Org. Lett.*, 2005, **7**, 5289.
94. X. Yao and C.-J. Li, *Org. Lett.*, 2006, **8**, 1953.
95. T. Godet, C. Vaxelaire, C. Michel, A. Millet, and P. Belmont, *Chem. Eur. J.*, 2007, **13**, 5632.
96. S. Obika, H. Kono, Y. Yasui, R. Yanada, and Y. Takemoto, *J. Org. Chem.*, 2007, **72**, 4462.
97. N. Asao, *Synlett*, 2006, 1645.
98. K. Sato, N. Asao, and Y. Yamamoto, *J. Org. Chem.*, 2005, **70**, 8977.
99. H. Kusama, Y. Miyashita, J. Takaya, and N. Iwasawa, *Org. Lett.*, 2006, **8**, 289.
100. P. Dubé and F. D. Toste, *J. Am. Chem. Soc.*, 2006, **128**, 12062.
101. N. Asao, H. Aikawa, S. Tago, and K. Umetsu, *Org. Lett.*, 2007, **9**, 4299.
102. E. Genin, P. Y. Toullec, S. Antoniotti, C. Branour, J.-P. Genêt, and V. Michelet, *J. Am. Chem. Soc.*, 2006, **128**, 3112.
103. T. Yang, L. Campbell, and D. J. Dixon, *J. Am. Chem. Soc.*, 2007, **129**, 12070.
104. E. Marchal, P. Uriac, B. Legouin, L. Toupet, and P. van de Weghe, *Tetrahedron*, 2007, **63**, 9979.
105. S. Shin, *Bull. Korean Chem. Soc.*, 2005, **26**, 1925.
106. J.-E. Kang and S. Shin, *Synlett*, 2006, 717.
107. A. Buzas and F. Gagosz, *Org. Lett.*, 2006, **8**, 515.
108. R. Robles-Machín, J. Adrio, and J. C. Carretero, *J. Org. Chem.*, 2006, **71**, 5023.
109. E.-S. Lee, H.-S. Yeom, J.-H. Hwang, and S. Shin, *Eur. J. Org. Chem.*, 2007, 3503.
110. A. Buzas and F. Gagosz, *Synlett*, 2006, 2727.
111. N. D. Shapiro and F. D. Toste, *J. Am. Chem. Soc.*, 2007, **129**, 4160.
112. Y. Liu, M. Liu, S. Guo, H. Tu, Y. Zhou, and H. Gao, *Org. Lett.*, 2006, **8**, 3445.
113. A. S. K. Hashmi, J. P. Weyrauch, W. Frey, and J. W. Bats, *Org. Lett.*, 2004, **6**, 4391.
114. N. Asao, K. Sato, and Y. Yamamoto, *Tetrahedron Lett.*, 2003, **44**, 5675.
115. N. Marion and S. P. Nolan, *Angew. Chem. Int. Ed.*, 2007, **46**, 2750.
116. F.-Q. Shi, X. Li, Y. Xia, L. Zhang, and Z.-X. Yu, *J. Am. Chem. Soc.*, 2007, **129**, 15503.
117. A. Correa, N. Marion, L. Fensterbank, M. Malacria, S. P. Nolan, and L. Cavallo, *Angew. Chem. Int. Ed.*, 2008, **47**, 718.
118. M. J. Johansson, D. J. Gorin, S. T. Staben, and F. D. Toste, *J. Am. Chem. Soc.*, 2005, **127**, 18002.
119. K. Miki, K. Ohe, and S. Uemura, *Tetrahedron Lett.*, 2003, **44**, 2019.
120. K. Miki, K. Ohe, and S. Uemura, *J. Org. Chem.*, 2003, **68**, 8505.
121. K. Miki, M. Fujita, S. Uemura, and K. Ohe, *Org. Lett.*, 2006, **8**, 1741.
122. M. R. Fructos, T. R. Belderrain, P. de Frémont, N. M. Scott, S. P. Nolan, M. M. Díaz-Requejo, and P. J. Pérez, *Angew. Chem. Int. Ed.*, 2005, **44**, 5284.
123. C. H. M. Amijs, V. López-Carrillo, and A. M. Echavarren, *Org. Lett.*, 2007, **9**, 4021.
124. P. W. Davies and S. J.-C. Albrecht, *Chem. Commun.*, 2008, 238.
125. C. A. Witham, P. Mauleón, N. D. Shapiro, B. D. Sherry, and F. D. Toste, *J. Am. Chem. Soc.*, 2007, **129**, 5838.
126. S. Wang and L. Zhang, *J. Am. Chem. Soc.*, 2006, **128**, 8414; *J. Am. Chem. Soc.* (addition/correction), 2006, **128**, 9979.
127. S. Wang and L. Zhang, *Org. Lett.*, 2006, **8**, 4585.
128. M. Yu, G. Zhang, and L. Zhang, *Org. Lett.*, 2007, **9**, 2146.
129. A. Buzas, F. Istrate, and F. Gagosz, *Org. Lett.*, 2006, **8**, 1957.
130. J. Zhao, C. O. Hughes, and F. D. Toste, *J. Am. Chem. Soc.*, 2006, **128**, 7436.
131. M. Yu, G. Li, S. Wang, and L. Zhang, *Adv. Synth. Catal.*, 2007, **349**, 871.
132. N. Marion, P. Carlqvist, R. Gealageas, P. de Frémont, F. Maseras, and S. P. Nolan, *Chem. Eur. J.*, 2007, **13**, 6437.
133. M. Yu, G. Zhang, and L. Zhang, *Org. Lett.*, 2007, **9**, 2147.
134. H.-S. Yeom, S.-J. Yoon, and S. Shin, *Tetrahedron Lett.*, 2007, **48**, 4817.
135. Y. Fukuda, K. Utimoto, and H. Nozaki, *Heterocycles*, 1987, **25**, 297.
136. Y. Fukuda and K. Utimoto, *Synthesis*, 1991, 975.
137. T. E. Müller, *Tetrahedron Lett.*, 1998, **39**, 5961.
138. T. E. Müller, M. Grosche, E. Herdtweck, A.-K. Pleier, E. Walter, and Y.-K. Yan, *Organometallics*, 2000, **19**, 170.
139. A. Arcadi, S. Di Giuseppe, F. Marinelli, and E. Rossi, *Adv. Synth. Catal.*, 2001, **343**, 443.
140. A. Arcadi, G. Bianchi, and F. Marinelli, *Synthesis*, 2004, **4**, 610.

141. M. Alfonsi, A. Arcadi, M. Aschi, G. Bianchi, and F. Marinelli, *J. Org. Chem.*, 2005, **70**, 2265.
142. I. Ambrogio, A. Arcadi, S. Cacchi, G. Fabrizi, and F. Marinelli, *Synlett*, 2007, 1775.
143. Y. Zhang, J. P. Donahue, and C.-J. Li, *Org. Lett.*, 2007, **9**, 627.
144. H. S. Yeom, E.-S. Lee, and S. Shin, *Synlett*, 2007, 2292.
145. R. Skouta and C.-J. Li, *Synlett*, 2007, 1759.
146. X.-Y. Liu, P. Ding, J.-S. Huang, and C.-M. Che, *Org. Lett.*, 2007, **9**, 2645.
147. F. M. Istrate and F. Gagosz, *Org. Lett.*, 2007, **9**, 3181.
148. T. J. Harrison, J. A. Kozak, M. Corbella-Pané, and G. R. Dake, *J. Org. Chem.*, 2006, **71**, 4525.
149. D. J. Gorin, N. R. Davis, and F. D. Toste, *J. Am. Chem. Soc.*, 2005, **127**, 11260.
150. D. V. Partyka, J. B. Updegraff III, M. Zeller, A. D. Hunter, and T. G. Gray, *Organometallics*, 2007, **26**, 183.
151. J.-E. Kang, H.-B. Kim, J.-W. Lee, and S. Shin, *Org. Lett.*, 2006, **8**, 3537.
152. I. Nakamura, T. Sato, and Y. Yamamoto, *Angew. Chem. Int. Ed.*, 2006, **45**, 4473.
153. L. Peng, X. Zhang, S. Zhang, and J. Wang, *J. Org. Chem.*, 2007, **72**, 1192.
154. Y. Ikeda, M. Murai, T. Abo, K. Miki, and K. Ohe, *Tetrahedron Lett.*, 2007, **48**, 6651.
155. I. Nakamura, T. Sato, M. Terada, and Y. Yamamoto, *Org. Lett.*, 2007, **9**, 4081.
156. C. Nieto-Oberhuber, S. López, E. Jiménez-Núñez, and A. M. Echavarren, *Chem. Eur. J.*, 2006, **11**, 5916.
157. M.-Y. Lin, A. Das, and R.-S. Liu, *J. Am. Chem. Soc.*, 2006, **128**, 9340.
158. C. Nieto-Oberhuber, S. López, M. P. Muñoz, D. J. Cárdenas, E. Buñuel, and A. M. Echavarren, *Angew. Chem. Int. Ed.*, 2005, **44**, 6146.
159. M. T. Reetz, *Angew. Chem. Int. Ed.*, 1972, **11**, 129.
160. M. T. Reetz, *Angew. Chem. Int. Ed.*, 1972, **11**, 130.
161. D. H. Nouri and D. J. Tantillo, *J. Org. Chem.*, 2006, **71**, 3686.
162. E. J. Cho, M. Kim, and D. Lee, *Eur. J. Org. Chem.*, 2006, 3074.
163. K. Ohe, M. Fujita, H. Matsumoto, Y. Tai, and K. Miki, *J. Am. Chem. Soc.*, 2006, **128**, 9270.
164. A. Fürstner, H. Szillat, and F. Stelzer, *J. Am. Chem. Soc.*, 2000, **122**, 6785.
165. A. Fürstner, F. Stelzer, and H. Szillat, *J. Am. Chem. Soc.*, 2001, **123**, 11863.
166. C. Nevado, C. Ferrer, and A. M. Echavarren, *Org. Lett.*, 2004, **6**, 3191.
167. J. Blum, H. Beer-Kraft, and Y. Badrieh, *J. Org. Chem.*, 1995, **60**, 5567.
168. S. I. Lee, S. M. Kim, M. R. Choi, S. Y. Kim, Y. K. Chung, W.-S. Han, and S. O. Kang, *J. Org. Chem.*, 2006, **71**, 9366.
169. A. Ochida, H. Ito, and M. Sawamura, *J. Am. Chem. Soc.*, 2006, **128**, 16486.
170. N. Cabello, C. Rodríguez, and A. M. Echavarren, *Synlett*, 2007, 1753.
171. F. Marion, J. Coulomb, C. Courillon, L. Fernsternbank, and M. Malacria, *Org. Lett.*, 2004, **6**, 1509.
172. S. Couty, C. Meyer, and J. Cossy, *Angew. Chem. Int. Ed.*, 2006, **45**, 6726.
173. E. Comer, E. Rohan, L. Deng, and J. A. Porco, *Org. Lett.*, 2007, **9**, 2123.
174. X. Moreau, J.-P. Goddard, M. Bernard, G. Lemière, J. M. López-Romero, E. Mainetti, N. Marion, V. Mouriès, S. Thorimbert, L. Fensterbank, and M. Malacria, *Adv. Synth. Catal.*, 2008, **350**, 43.
175. M. R. Luzung, J. P. Markham, and F. D. Toste, *J. Am. Chem. Soc.*, 2004, **126**, 10858.
176. F. Gagosz, *Org. Lett.*, 2005, **7**, 4129.
177. C. Nevado, D. J. Cárdenas, and A. M. Echavarren, *Chem. Eur. J.*, 2003, **9**, 2627.
178. C. Lim, J.-E. Kang, J.-E. Lee, and S. Shin, *Org. Lett.*, 2007, **9**, 3539.
179. R. Zriba, V. Gandon, C. Aubert, L. Fensterbank, and M. Malacria, *Chem. Eur. J.*, 2008, **14**, 1482.
180. L. Zhang, and S. Kozmin, *J. Am. Chem. Soc.*, 2004, **126**, 11806.
181. J. Sun, M. P. Conley, L. Zhang, and S. A. Kozmin, *J. Am. Chem. Soc.*, 2006, **128**, 9705.
182. J. W. Dankwardt, *Tetrahedron Lett.*, 2001, **42**, 5809.
183. T. Shibata, Y. Ueno, and K. Kanda, *Synlett*, 2006, 411.
184. G. Abbiati, A. Arcadi, G. Bianchi, S. Di Giuseppe, F. Marinelli, and E. Rossi, *J. Org. Chem.*, 2003, **68**, 6959.
185. J. J. Kennedy-Smith, S. T. Staben, and F. D. Toste, *J. Am. Chem. Soc.*, 2004, **126**, 4526.
186. S. T. Staben, J. J. Kennedy-Smith, and F. D. Toste, *Angew. Chem. Int. Ed.*, 2004, **43**, 5350.
187. J.-H. Pan, M. Yang, Q. Gao, N.-Y. Zhu, and D. Yang, *Synthesis*, 2007, 2539.
188. B. K. Corkey and F. D. Toste, *J. Am. Chem. Soc.*, 2005, **127**, 17168.
189. E. C. Minnihan, S. L. Colletti, F. D. Toste, and H. C. Shen, *J. Org. Chem.*, 2007, **72**, 6287.
190. S. T. Staben, J. J. Kennedy-Smith, D. Huang, B. K. Corkey, R. L. LaLonde, and F. D. Toste, *Angew. Chem. Int. Ed.*, 2006, **45**, 5991.
191. K. Lee and P. H. Lee, *Adv. Synth. Catal.*, 2007, **349**, 2092.
192. X. Linghu, J. J. Kennedy-Smith, and F. D. Toste, *Angew. Chem. Int. Ed.*, 2007, **46**, 7671.
193. C. Nevado and A. M. Echavarren, *Tetrahedron*, 2004, **60**, 9735.
194. B. D. Sherry, L. Maus, B. N. Laforteza, and F. D. Toste, *J. Am. Chem. Soc.*, 2006, **128**, 8132.

195. M. H. Suhre, M. Reif, and S. F. Kirsch, *Org. Lett.*, 2005, **7**, 3925.

196. J. T. Binder and S. F. Kirsch, *Org. Lett.*, 2006, **8**, 2151.

197. S. Park and D. Lee, *J. Am. Chem. Soc.*, 2006, **128**, 10664.

198. Y. Horino, M. R. Luzung, and F. D. Toste, *J. Am. Chem. Soc.*, 2006, **128**, ja0636800.

199. M. P. Muñoz, J. Adrio, J. C. Carretero, and A. M. Echavarren, *Organometallics*, 2005, **24**, 1293.

200. A. K. Buzas, F. M. Istrate, and F. Gagosz, *Angew. Chem. Int. Ed.*, 2006, **46**, 1141.

201. L. Zhang and S. A. Kozmin, *J. Am. Chem. Soc.*, 2005, **127**, 6962.

202. L. Leseurre, P. Y. Toullec, J.-P. Genêt, and V. Michelet, *Org. Lett.*, 2007, **9**, 4049.

203. P. Y. Toullec, E. Genin, L. Leseurre, J.-P. Genêt, and V. Michelet, *Angew. Chem. Int. Ed.*, 2006, **45**, 7427.

204. C. H. M. Amijs, C. Ferrer, and A. M. Echavarren, *Chem. Commun.*, 2007, 698.

205. A. Fürstner, P. W. Davies, and T. Gress, *J. Am. Chem. Soc.*, 2005, **127**, 8244.

206. G. Lemière, V. Gandon, N. Agenet, J.-P. Goddard, A. de Kozak, C. Aubert, L. Fensterbank, and M. Malacria, *Angew. Chem. Int. Ed.*, 2006, **45**, 7596.

207. G.-Y. Lin, C.-Y. Yang, and R.-S. Liu, *J. Org. Chem.*, 2007, **72**, 6753.

208. J.-J. Lian, P.-C. Chen, Y.-P. Lin, H.-C. Ting, and R. S. Liu, *J. Am. Chem. Soc.*, 2006, **128**, 11372.

209. T. Shibata, R. Fujiwara, and D. Takano, *Synlett*, 2005, 2062; Erratum: *Synlett*, 2007, 2766.

210. A. Fürstner and C. C. Stimson, *Angew. Chem. Int. Ed.*, 2007, **46**, 8845.

211. S. M. Kim, J. H. Park, S. Y. Choi, and Y. K. Chung, *Angew. Chem. Int. Ed.*, 2007, **46**, 6172.

212. N. Chatani, K. Kataoka, S. Murai, N. Furukawa, and Y. Seki, *J. Am. Chem. Soc.*, 1998, **120**, 9104.

213. E. Mainetti, V. Mouriès, L. Fensterbank, M. Malacria, and J. Marco-Contelles, *Angew. Chem. Int. Ed.*, 2002, **41**, 2132.

214. Y. Harrak, C. Blaszykowski, M. Bernard, K. Cariou, E. Mainetti, V. Mouriès, A.-L. Dhimane, L. Fensterbank, and M. Malacria, *J. Am. Chem. Soc.*, 2004, **126**, 8656.

215. B. P. Peppers and S. T. Diver, *J. Am. Chem. Soc.*, 2004, **126**, 9524.

216. M. Schelwies, A. L. Dempwolff, F. Rominger, and G. Helmchen, *Angew. Chem. Int. Ed.*, 2007, **46**, 5598.

217. H. Strickler, J. B. Davis, and G. Ohloff, *Helv. Chim. Acta*, 1976, **59**, 1328.

218. V. Rautenstrauch, *J. Org. Chem.*, 1984, **49**, 950.

219. V. Mamane, T. Gress, H. Krause, and A. Fürstner, *J. Am. Chem. Soc.*, 2004, **126**, 8654.

220. X. Shi, D. J. Gorin, and F. D. Toste, *J. Am. Chem. Soc.*, 2005, **127**, 5802.

221. A. Fürstner and P. Hannen, *Chem. Eur. J.*, 2006, **12**, 3006.

222. C. Fehr and J. Galindo, *Angew. Chem. Int. Ed.*, 2006, **45**, 2901.

223. A. Fürstner and P. Hannen, *Chem. Commun.*, 2004, 2546.

224. O. Nieto Faza, C. Silva López, R. Álvarez, and A. R. de Lera, *J. Am. Chem. Soc.*, 2006, **128**, 2434.

225. L. Zhang and S. Wang, *J. Am. Chem. Soc.*, 2006, **128**, 1442.

226. A. Buzas and F. Gagosz, *J. Am. Chem. Soc.*, 2006, **128**, 12614.

227. N. Marion, P. de Frémont, G. Lemière, E. D. Stevens, L. Fensterbank, M. Malacria, and S. P. Nolan, *Chem. Commun.*, 2006, 2048.

228. L. Zhang, *J. Am. Chem. Soc.*, 2005, **127**, 16804.

229. G. Zhang, V. J. Catalano, and L. Zhang, *J. Am. Chem. Soc.*, 2007, **129**, 11358.

230. N. Marion, S. Díez-González, P. de Frémont, A. R. Noble, and S. P. Nolan, *Angew. Chem. Int. Ed.*, 2006, **45**, 3647.

231. S. Wang and L. Zhang, *J. Am. Chem. Soc.*, 2006, **128**, 14274.

232. C. H. Oh and A. Kim, *New J. Chem.*, 2007, **31**, 1719.

233. T. Luo and S. L. Schreiber, *Angew. Chem. Int. Ed.*, 2007, **46**, 8250.

234. C. Nevado and A. M. Echavarren, *Synthesis*, 2005, 167.

235. M. S. Kharasch and H. S. Isbell, *J. Am. Chem. Soc.*, 1931, **53**, 3053.

236. K. A. Porter, A. Schier, and H. Schmidbaur, *Organometallics*, 2003, **22**, 4922.

237. Z. Shi and C. He, *J. Am. Chem. Soc.*, 2004, **126**, 5964.

238. Z. Shi and C. He, *J. Am. Chem. Soc.*, 2004, **126**, 13596.

239. Z. Li, X. Ding, and C. He, *J. Org. Chem.*, 2006, **71**, 5876.

240. M. T. Reetz and K. Sommer, *Eur. J. Org. Chem.*, 2003, 3485.

241. Z. Shi and C. He, *J. Org. Chem.*, 2004, **69**, 3669.

242. Z. Li, Z. Shi, and C. He, *J. Organomet. Chem.*, 2005, **690**, 5049.

243. Z. Li, D. A. Capretto, R. O. Rahaman, and C. He, *J. Am. Chem. Soc.*, 2007, **129**, 12058.

244. A. S. K. Hashmi and M. C. Blanco, *Eur. J. Org. Chem.*, 2006, 4340.

245. A. Fürstner and V. Mamane, *J. Org. Chem.*, 2002, **67**, 6264.

246. A. Fürstner and V. Mamane, *Chem. Commun.*, 2003, 2112.

247. V. Mamane, P. Hannen, and A. Fürstner, *Chem. Eur. J.*, 2004, **10**, 4556.

248. E. Soriano and J. Marco-Contelles, *Organometallics*, 2006, **25**, 4542.

249. I. V. Seregin and V. Gevorgyan, *J. Am. Chem. Soc.*, 2006, **128**, 12050.

250. A. S. K. Hashmi, T. M. Frost, and J. W. Bats, *J. Am. Chem Soc.*, 2000, **122**, 11553.

251. A. S. K. Hashmi, T. M. Frost, and J. W. Bats, *Org. Lett.*, 2001, **3**, 3769.

252. A. S. K. Hashmi, T. M. Frost, and J. W. Bats, *Catal. Today*, 2001, **72**, 19.

253. A. S. K. Hashmi, L. Ding, J. W. Bats, P. Fischer, and W. Frey, *Chem. Eur. J.*, 2003, **9**, 4339.
254. A. S. K. Hashmi, M. Rudolph, J. P. Weyrauch, M. Wölfle, W. Frey, and J. W. Bats, *Angew. Chem. Int. Ed.*, 2005, **44**, 2798.
255. A. S. K. Hashmi, J. P. Weyrauch, E. Kurpejovic, T. M. Frost, B. Miehlich, W. Frey, and J. W. Bats, *Chem. Eur. J.*, 2006, **12**, 5806.
256. A. S. K. Hashmi, E. Kurpejovic, W. Frey, and J. W. Bats, *Tetrahedron*, 2007, **63**, 5879.
257. A. S. K. Hashmi, P. Haufe, C. Schmid, A. Rivas Nass, and W. Frey, *Chem. Eur. J.*, 2006, **12**, 5376.
258. S. Carrettin, M. C. Blanco, A. Corma, and A. S. K. Hashmi, *Adv. Synth. Catal.*, 2006, **348**, 1283.
259. B. Martín-Matute, D. J. Cárdenas, and A. M. Echavarren, *Angew. Chem. Int. Ed.*, 2001, **40**, 4754.
260. B. Martín-Matute, C. Nevado, D. J. Cárdenas, and A. M. Echavarren, *J. Am. Chem. Soc.*, 2003, **125**, 5757.
261. A. S. K. Hashmi, R. Salathé, and W. Frey, *Chem. Eur. J.*, 2006, **12**, 6991.
262. G. Dyker, E. Muth, A. S. K. Hashmi, and L. Ding, *Adv. Synth. Catal.*, 2003, **345**, 1247.
263. A. S. K. Hashmi and L. Grundl, *Tetrahedron*, 2005, **61**, 6231.
264. D. Aguilar, M. Contel, R. Navarro, and E. P. Urriolabeitia, *Organometallics*, 2007, **26**, 4604.
265. A. S. K. Hashmi, E. Kurpejovic, M. Wölfle, W. Frey, and J. W. Bats, *Adv. Synth. Catal.*, 2007, **349**, 1743.
266. A. S. K. Hashmi, M. C. Blanco, E. Kurpejovic, W. Frey, and J. W. Bats, *Adv. Synth. Catal.*, 2006, **348**, 709.
267. A. Bayler, A. Bauer, and H. Schmidbaur, *Chem. Ber. Recl.*, 1997, **130**, 115.
268. R. W. Bates and V. Satcharoen, *Chem. Soc. Rev.*, 2002, **31**, 12.
269. V. K.-Y. Lo, M.-K. Wong, and C.-M. Che, *Org. Lett.*, 2008, **10**, 517.
270. A. Hoffmann- Röder and N. Krause, *Org. Lett.*, 2001, **3**, 2537.
271. C. J. T. Hyland and L. S. Hegedus, *J. Org. Chem.*, 2006, **71**, 8658.
272. A. S. K. Hashmi, M. C. Blanco, D. Fischer, and J. W. Bats, *Eur. J. Org. Chem.*, 2006, 1387.
273. B. Gockel and N. Krause, *Org. Lett.*, 2006, **8**, 4485.
274. B. Alcaide, P. Almendros, and T. Martínez del Campo, *Angew. Chem. Int. Ed.*, 2007, **46**, 6684.
275. Z. Zhang, C. Liu, R. E. Kinder, X. Han, H. Qian, and R. A. Widenhoefer, *J. Am. Chem. Soc.*, 2006, **128**, 9066.
276. Z. Zhang and R. A. Widenhoefer, *Angew. Chem. Int. Ed.*, 2007, **46**, 283.
277. G. L. Hamilton, E. J. Kang, M. Mba, and F. D. Toste, *Science*, 2007, **317**, 496.
278. F. Volz and N. Krause, *Org. Biomol. Chem.*, 2007, **5**, 1519.
279. J. Erdsack and N. Krause, *Synthesis*, 2007, 3741.
280. A. S. K. Hashmi, *Angew. Chem. Int. Ed.*, 2000, **39**, 3590.
281. A. S. Dudnik and V. Gevorgyan, *Angew. Chem. Int. Ed.*, 2007, **46**, 5195.
282. A. W. Sromek, M. Rubina, and V. Gevorgyan, *J. Am. Chem. Soc.*, 2005, **127**, 10500.
283. J.-E. Kang, E.-S. Lee, S.-I. Park, and S. Shin, *Tetrahedron Lett.*, 2005, **46**, 7431.
284. J. Piera, P. Krumlinde, D. Strübing, and J.-E. Bäckvall, *Org. Lett.*, 2007, **9**, 2235.
285. A. K. Buzas, F. M. Istrate, and F. Gagosz, *Org. Lett.*, 2007, **9**, 985.
286. R. A. Widenhoefer and X. Han, *Eur. J. Org. Chem.*, 2006, 4555.
287. N. Morita and N. Krause, *Org. Lett.*, 2004, **6**, 4121.
288. P. H. Lee, H. Kim, K. Lee, M. Kim, K. Noh, H. Kim, and D. Seomoon, *Angew. Chem. Int. Ed.*, 2005, **44**, 1840.
289. S. Kaden, H.-U. Reissig, I. Brüdgam, and H. Hartl, *Synthesis*, 2006, 1351.
290. N. T. Patil, L. M. Lutete, N. Nishina, and Y. Yamamoto, *Tetrahedron Lett.*, 2006, **47**, 4749.
291. N. Nishina and Y. Yamamoto, *Angew. Chem. Int. Ed.*, 2006, **45**, 3314.
292. N. Nishina and Y. Yamamoto, *Synlett*, 2007, 1767.
293. N. Morita and N. Krause, *Eur. J. Org. Chem.*, 2006, 4634.
294. Z. Zhang, C. F. Bender, and R. A. Widenhoefer, *Org. Lett.*, 2007, **9**, 2887.
295. R. L. LaLonde, B. D. Sherry, E. J. Kang, and F. D. Toste, *J. Am. Chem. Soc.*, 2007, **129**, 2452.
296. Z. Zhang, C. F. Bender, and R. A. Widenhoefer, *J. Am. Chem. Soc.*, 2007, **129**, 14148.
297. N. Morita and N. Krause, *Angew. Chem. Int. Ed.*, 2006, **45**, 1897.
298. C. Liu and R. A. Widenhoefer, *Org. Lett.*, 2007, **9**, 1935.
299. Z. Liu, A. S. Wasmuth, and S. G. Nelson, *J. Am. Chem. Soc.*, 2006, **128**, 10352.
300. T. Watanabe, S. Oishi, N. Fujii, and H. Ohno, *Org. Lett.*, 2007, **9**, 4821.
301. J. H. Lee and F. D. Toste, *Angew. Chem. Int. Ed.*, 2007, **46**, 912.
302. M. A. Tarselli, A. R. Chianese, S. J. Lee, and M. R. Gagné, *Angew. Chem. Int. Ed.*, 2007, **46**, 6670.
303. M. R. Luzung, P. Mauleón, and F. D. Toste, *Am. Chem. Soc.*, 2007, **129**, 12402.
304. X. Huang and L. Zhang, *J. Am. Chem. Soc.*, 2007, **129**, 6398.
305. X. Huang and L. Zhang, *Org. Lett.*, 2007, **9**, 4627.
306. G. Lemière, V. Gandon, K. Cariou, T. Fukuyama, A.-L. Dhimane, L. Fensterbank, and M. Malacria, *Org. Lett.*, 2007, **9**, 2207.
307. Y. Ito, M. Sawamura, and T. Hayashi, *J. Am. Chem. Soc.*, 1986, **108**, 6405.

308. M. Sawamura, Y. Nakayama, T. Kato, and Y. Ito, *J. Org. Chem.*, 1995, **60**, 1727.
309. S. Komiya, T. Sone, Y. Usui, M. Hirano, and A. Fukuoka, *Gold Bull.*, 1996, **29**, 131.
310. L.-W. Xu, C.-G. Xia, and L. Li, *J. Org. Chem.*, 2004, **69**, 8482.
311. S. W. Youn, *J. Org. Chem.*, 2006, **71**, 2521.
312. Y. Luo and C.-J. Li, *Chem. Commun.*, 2004, 1930.
313. V. Nair, K. G. Abhilash, and N. Vidya, *Org. Lett.*, 2005, **7**, 5857.
314. C.-C. Lin, T.-M. Teng, A. Odedra, and R.-S. Liu, *J. Am. Chem. Soc.*, 2007, **129**, 3798.
315. C. Wei and C.-J. Li, *J. Am. Chem. Soc.*, 2003, **125**, 9584.
316. B. Huang, X. Yao, and C.-J. Li, *Adv. Synth. Catal.*, 2006, **348**, 1528.
317. M. L. Kantam, B. V. Prakash, C. R. V. Reddy, and B. Sreedhar, *Synlett*, 2005, 2329.
318. V. Kar-Yan Lo, Y. Liu, M.-K. Wong, and C.-M. Che, *Org. Lett.*, 2006, **8**, 1529.
319. C. Wei and C.-J. Li, *Lett. Org. Chem.*, 2005, **2**, 410.
320. H. Ito, T. Yajima, J.-I. Tateiwa, and A. Hosomi, *Chem. Commun.*, 2000, 981.
321. D. Lantos, M. Contel, S. Sanz, A. Bodor, and I. T. Horváth, *J. Organomet. Chem.*, 2007, **692**, 1799.
322. R. T. Baker, J. C. Calabrese, and S. A. Wescott, *J. Organomet. Chem.*, 1995, **498**, 109.
323. A. Arcadi, G. Bianchi, S. Di Giuseppe, and F. Marinelli, *Green Chem.*, 2003, **5**, 64.
324. A. Arcadi, M. Chiarini, S. Di Giuseppe, and F. Marinelli, *Synlett*, 2003, 203.
325. A. Arcadi, S. Di Giuseppe, F. Marinelli, and E. Rossi, *Tetrahedron: Asymmetry*, 2001, **12**, 2715.
326. A. Arcadi, M. Alfonsi, G. Bianchi, G. D'Anniballe, and F. Marinelli, *Adv. Synth. Catal.*, 2006, **348**, 331.
327. S. Kobayashi, K. Kakumoto, and M. Sugiura, *Org. Lett.*, 2002, **4**, 1319.
328. M. Alfonsi, A. Arcadi, G. Bianchi, F. Marinelli, and A. Nardini, *Eur. J. Org. Chem.*, 2006, 2393.
329. A. Arcadi, G. Bianchi, M. Chiarini, G. D'Anniballe, and F. Marinelli, *Synlett*, 2004, 944.
330. V. Nair, N. Vidya, and K. G. Abhilash, *Tetrahedron Lett.*, 2006, **47**, 2871.
331. A. S. K. Hashmi, R. Salathé, and W. Frey, *Eur. J. Org. Chem.*, 2007, 1648.
332. A. Adé, E. Cerrada, M. Contel, M. Laguna, P. Merino, and T. Tejero, *J. Organomet. Chem.*, 2004, **689**, 1788.
333. A. D. Melhado, M. Luparia, and F. D. Toste, *J. Am. Chem. Soc.*, 2007, **129**, 12638.
334. F. Shi and Y. Deng, *Chem. Commun.*, 2001, 443.
335. F. Shi, Y. Deng, H. Yang, and T. SiMa, *Chem. Commun.*, 2001, 345.
336. Q. Xu, Y. Imamura, M. Fujiwara, and Y. Souma, *J. Org. Chem.*, 1997, **62**, 1594.
337. N. Marion, R. Gealageas, and S. P. Nolan, *Org. Lett.*, 2007, **9**, 2653.
338. S. Porcel, V. López-Carrillo, C. García-Yebra, and A. M. Echavarren, *Angew. Chem. Int. Ed.*, 2008, **47**, 1883.
339. S. Guo, F. Song, and Y. Liu, *Synlett*, 2007, 964.
340. X.-Z. Shu, X.-Y. Liu, H.-Q. Xiao, K.-G. Ji, L.-N. Guo, and Y.-M. Liang, *Adv. Synth. Catal.*, 2008, **350**, 243.
341. Y.-H. Hsu, S. Datta, C.-M. Ting, and R.-S. Liu, *Org. Lett.*, 2008, **10**, 521.
342. A. R. Yeager, G. K. Min, J. A. Porco Jr., and S. E. Schaus, *Org. Lett.*, 2006, **8**, 5065.
343. J. Liu, E. Muth, U. Flörke, G. Henkel, K. Merz, J. Sauvageau, E. Schwake, and G. Dyker, *Adv. Synth. Catal.*, 2006, **348**, 456.
344. A. S. K. Hashmi, S. Schäfer, M. Wölfe, C. Diez Gil, P. Fisher, A. Laguna, M. C. Blanco, and M. C. Jimeno, *Angew. Chem. Int. Ed.*, 2007, **46**, 6184.
345. A. B. Cuenca, G. Mancha, G. Asensio, and M. Medio-Simón, *Chem. Eur. J.*, 2008, **14**, 1518.
346. H. Ito, K. Takagi, T. Miyahara, and M. Sawamura, *Org. Lett.*, 2005, **7**, 3001.
347. B. Guan, D. Xing, G. Cai, X. Wan, N. Yu, Z. Fang, L. Yang, and Z. Shi, *J. Am. Chem. Soc.*, 2005, **127**, 18004.
348. F. Gasparrini, M. Giovannoli, D. Misiti, G. Natile, and G. Palmieri, *Tetrahedron*, 1983, **39**, 3181.
349. F. Gasparrini, M. Giovannoli, D. Misiti, G. Natile, and G. Palmieri, *Tetrahedron*, 1984, **40**, 165.
350. F. Gasparrini, M. Giovannoli, D. Misiti, G. Natile, and G. Palmieri, *J. Org. Chem.*, 1990, **55**, 1323.
351. E. Boring, Y. V. Geletii, and C. L. Hill, *J. Am. Chem. Soc.*, 2001, **123**, 1625.
352. Y. Yuan and Y. Bian, *Tetrahedron Lett.*, 2007, **48**, 8518.
353. X. Yao and C.-J. Li, *J. Am. Chem. Soc.*, 2004, **126**, 6884.
354. C.-J. Li and X. Yao, *Org. Synth.*, 2007, **84**, 222.
355. C.-Y. Zhou and C.-M. Che, *J. Am. Chem. Soc.*, 2007, **129**, 5828.
356. C.-G. Yang and C. He, *J. Am. Chem. Soc.*, 2005, **127**, 6966.
357. X. Han and R. A. Widenhoefer, *Angew. Chem. Int. Ed.*, 2006, **45**, 1747.
358. C. F. Bender and R. A. Widenhoefer, *Org. Lett.*, 2006, **8**, 5303.
359. C. F. Bender and R. A. Widenhoefer, *Chem. Commun.*, 2006, 4143.
360. J. Zhang, C.-G. Yang, and C. He, *J. Am. Chem. Soc.*, 2006, **128**, 1798.
361. X.-Y. Liu, C.-H. Li, and C.-M. Che, *Org. Lett.*, 2006, **8**, 2707.
362. G. Kovács, G. Ujaque, and A. Lledós, *J. Am. Chem. Soc.*, 2008, **130**, 853.
363. C. Brouwer and C. He, *Angew. Chem. Int. Ed.*, 2006, **45**, 1744.

364. C. Brouwer, R. Rahaman, and C. He, *Synlett*, 2007, 1785.

365. M. Shi, L.-P. Liu, and J. Tang, *Org. Lett.*, 2006, **8**, 4043.

366. W.-J. Shi, Y. Liu, P. Butti, and A. Togni, *Adv. Synth. Catal.*, 2007, **349**, 1619.

367. N. W. Reich, C.-G. Yang, Z. Shi, and C. He, *Synlett*, 2006, 1278.

368. X. Zhang and A. Corma, *Chem. Commun.*, 2007, 3080.

369. X. Zhang and A. Corma, *J. Chem. Soc., Dalton Trans.*, 2008, 397.

370. A. Comas-Vives, C. González- Arellano, A. Corma, M. Iglesias, F. Sánchez, and G. Ujaque, *J. Am. Chem. Soc.*, 2006, **128**, 4756.

371. N. Debono, M. Iglesias, and F. Sánchez, *Adv. Synth. Catal.*, 2007, **349**, 2470.

372. C. González-Arellano, A. Corma, M. Iglesias, and F. Sánchez, *Chem. Commun.*, 2005, 3451.

373. A. Corma, C. González- Arellano, M. Iglesias, and F. Sánchez, *Angew. Chem. Int. Ed.*, 2007, **46**, 7820.

374. R. T. Baker, P. Nguyen, T. B. Marder, and S. A. Wescott, *Angew. Chem. Int. Ed.*, 1995, **34**, 1336.

375. D. Xing, B. Guan, G. Cai, Z. Fang, L. Yand, and Z. Shi, *Org. Lett.*, 2006, **8**, 693.

376. D. E. de Vos and B. F. Sels, *Angew. Chem. Int. Ed.*, 2005, **44**, 30.

377. L. A. Levchenko, A. P. Sadkov, N. V. Lariontseva, E. M. Koldasheva, A. K. Shilova, and A. E. Shilov, *J. Inorg. Biochem.*, 2002, **88**, 251.

378. G. B. Shul'pin, A. E. Shilov, and G. Süss-Fink, *Tetrahedron Lett.*, 2001, **42**, 7253.

379. D. A. Pichugina, N. E. Kuz'menko, and A. F. Shestakov, *Gold Bull.*, 2007, **40**, 115.

380. M. R. Fructos, P. de Frémont, S. P. Nolan, M. M. Díaz-Requejo, and P. J. Pérez, *Organometallics*, 2006, **25**, 2237.

381. M. M. Díaz-Requejo and P. J. Pérez, *J. Organomet. Chem.*, 2005, **690**, 5441.

382. A. Kar, N. Mangu, H. M. Kaiser, M. Beller, and M. K., Tse, *Chem. Commun.*, 2007, 386.

383. H. Ito, T. Yajima, J.-I. Tateiwa, and A. Hosomi, *Tetrahedron Lett.*, 1999, **40**, 7807.

384. D. V. Partyka, M. Zeller, A. D. Hunter, and T. G. Gray, *Angew. Chem. Int. Ed.*, 2006, **45**, 8188.

385. C. González-Arellano, A. Corma, M. Iglesias, and F. Sánchez, *Chem. Commun.*, 2005, 1990.

386. C. González-Arellano, A. Corma, M. Iglesias, and F. Sánchez, *J. Catal.*, 2006, **238**, 497.

387. C. González-Arellano, A. Abad, A. Corma, H. García, M. Iglesias, and F. Sánchez, *Angew. Chem. Int. Ed.*, 2007, **46**, 1536.

N-Heterocyclic Carbene-Containing Metal Complexes

Serena Fantasia, Hervé Clavier & Steven P. Nolan
Institute of Chemical Research of Catalonia (ICIQ), Tarragona, Spain

1 Introduction 1
2 Synthesis of NHC-Containing Metal Complexes 1
3 Stability and Reactivity of NHC-Containing Metal Complexes 20
4 Conclusion and Outlook 36
5 Related Articles 37
6 References 37

Abbreviations

acac = acetylacetonate; BARF = tetrakis(3,5-di-trifluoromethylphenyl)borate; ^{t}BuDAB = 1,4-di-*tert*-butyldiazabuta-1,3-diene; COD = cyclooctadiene; COE = cyclooctene; Cp = cyclopentadienyl; Cp* = pentamethylcyclopentadienyl; dae = diallylether; dba = dibenzylideneacetone; DCE = dichloroethane; DFT = density functional theory; DMFU = dimethylfumarate; DVTMS = divinyltetramethylsiloxane; IAd = 1,3-bis(1-adamantyl)imidazol-2-ylidene; ICy = 1,3-dicyclohexylimidazol-2-ylidene; IDM = 1,3-dimethylimidazol-2-ylidene; IDMH = 1,3-dimethylimidazolium; IMes = 1,3-dimesitylimidazol-2-ylidene; IPr = 1,3-bis(2,6-diisopropylphenyl)imidazol-2-ylidene; IPrMe = 1,3-bis(isopropyl)-4,5-dimethyl-imidazol-2-ylidene; I^{t}Bu = 1,3-di-*tert*-butylimidazol-2-ylidene; ITM = 1,3,4,5-tetramethylimidazol-2-ylidene; Ln = lanthanide; ma = maleic anhydride; Mes = mesityl (2,4,6-trimethylphenyl); nbd = norbornadiene; NHC = *N*-heterocyclic carbene; Ptol$_3$ = tris(*o*-tolyl)phosphine; SIAd = 1,3-bis(1-adamantyl)-4-5-dihydroimidazol-2-ylidene; SIMes = 1,3-dimesityl-4,5-dihydroimidazol-2-ylidene; SIPr = 1,3-bis(2,6-diisopropylphenyl)-4,5-dihydroimidazol-2-ylidene; THF = tetrahydrofuran; TM = transition metal; tmed = N,N,N',N'-tetramethylethylenediamine; tol = tolyl.

1 INTRODUCTION

NHCs were discovered some 40 years ago, when Öfele[1] and Wanzlick and Schönherr[2] independently reported the synthesis of chromium and mercury complexes bearing NHC ligands. But the interest for this class of ligands in the field remained feeble, although in the 1980s, Lappert reported the preparation of various NHC–late TM complexes.[3] It was only when Arduengo isolated the first stable NHC[4] that they caught the attention of coordination and synthetic chemists. Investigations of NHCs stereoelectronic properties[5] showed that NHCs are excellent donor ligands for metals,[6] and the resulting NHC–TM complexes have found numerous applications in catalysis.[7,8] Key transformations such as olefin metathesis[9] and cross-coupling[10] have unquestionably benefited from the use of NHC-based catalysts. Many efforts have focused on the syntheses of new NHCs and NHC–TM complexes;[11] however, the properties of such complexes are still underinvestigated. Here, we intend to provide an overview of the different procedures that have been developed for the synthesis of free carbene and NHC–metal complexes. Because of the wide range of NHC ligands developed so far, we focus our discussion on the commonly used monodentate NHCs, but the synthesis and reactivity of some specific NHCs are also reviewed.[12] Stability of NHC–TM complexes being a feature for their application to catalytic reactions, processes leading to the cleavage of the NHC–TM bond are presented, as well as reactions involving the NHC ligand.

2 SYNTHESIS OF NHC-CONTAINING METAL COMPLEXES

The most common synthetic approach to NHC–metal complexes involves free NHC as an intermediate, either isolated or in situ generated. Numerous other strategies that have been developed are also presented.

2.1 Generation of Free NHCs

The route leading to isolable free NHC originally developed by Arduengo involved the deprotonation of an imidazolium salt using a strong inorganic base.[4] Thus, the sterically hindered IAd (**2**) was generated by proton abstraction of the corresponding chloride salt (**1**) by NaH in THF (equation 1). Catalytic amounts of dimesyl anion (–CH_2SOCH_3) were also added. ^{t}BuOK was also found efficient to deprotonate the NHC precursor. Recently, this procedure has been extended to the syntheses of numerous unsaturated NHCs bearing either alkyl group IDM, ITM,[13] I^{t}Bu[14] or aryl group such as (**3**), IMes,[13] and IPr[15] and saturated carbenes SIMes[16] and SIPr.[15] Deprotonation of imidazolium salts in THF normally requires overnight reaction times. However, reaction time can be drastically reduced (to 30 min) when a mixture of liquid ammonia and THF (5:1) is used as solvent.[17]

The choice of solvent to perform reactions dealing with NHCs is crucial since they react with numerous common

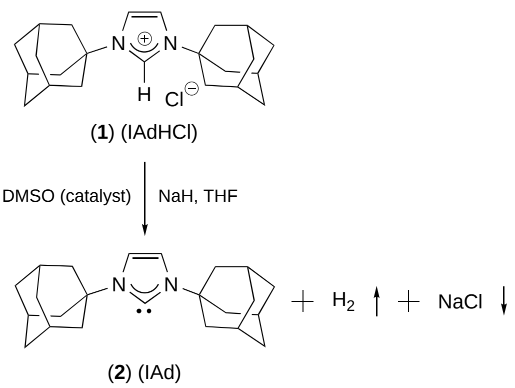

(1)

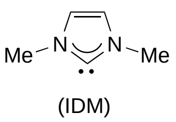
(IDM)

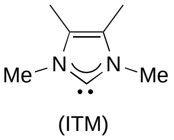
(ITM)

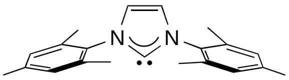
(IMes)

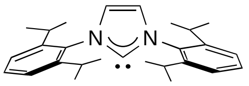
(IPr)

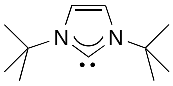
(I^{t}Bu)

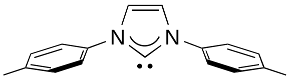
(**3**)

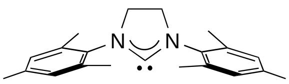
(SIMes)

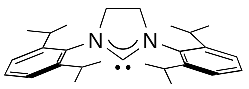
(SIPr)

organic solvents. For instance, IMes and IPr react with carbon tetrachloride leading to the chlorination of the 4- and 5-positions of the imidazole rings, respectively (**4**) and (**5**) (equation 2). These unusual NHCs are exceptionally stable and have been used to synthesize TM-based complexes active in catalysis.[15,18]

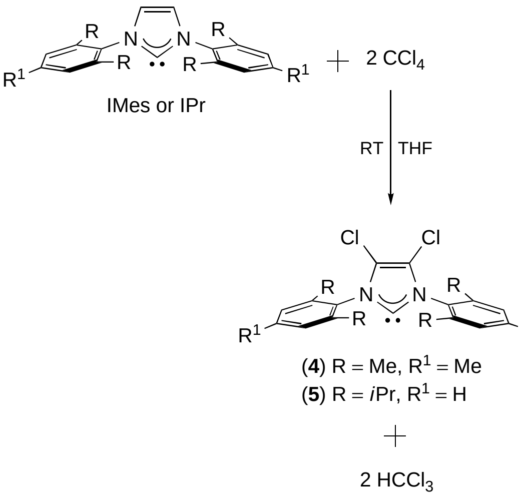

(2)

Recently, Astruc demonstrated that the deprotonation of imidazolium salts could be also achieved by a 19-electron Fe(I) complex (**6**), namely, [Fe(Cp)(η^6-C_6Me_6)], in the presence of oxygen (equation 3).[19] The proposed mechanism, reported in Scheme 1, is a radical transfer from O_2 to the Fe(I) complex (**6**) to give the adduct [$Fe^{II}Cp(\eta^6$-$C_6Me_6)$, $O_2^{\bullet-}$] (**8**), in which the $O_2^{\bullet-}$ deprotonates the imidazolium salt. Changing the solvent from THF to pentane, toluene, or ether, in which the imidazolium salts are not soluble, led to the formation of complex (**9**) [$Fe^{II}Cp(\eta^5$-$C_6Me_5CH_2)$], which is, in that case, the effective deprotonating agent.

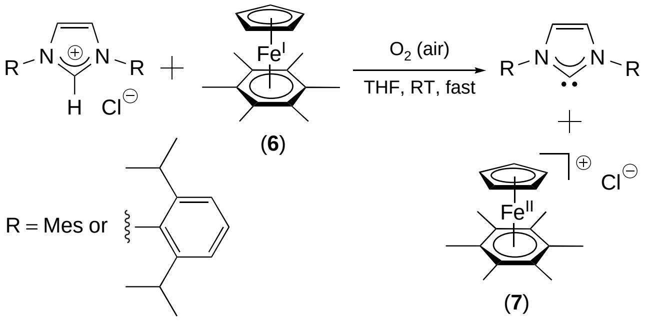

(3)

Alternatively, free NHCs have been obtained from imidazolium salts by electrochemical or chemical reduction.[20] Coulometric analysis showed a single electron event, suggesting that the reduction proceeds via an imidazole radical, with further loss of one radical hydrogen to afford the free carbene (equation 4).

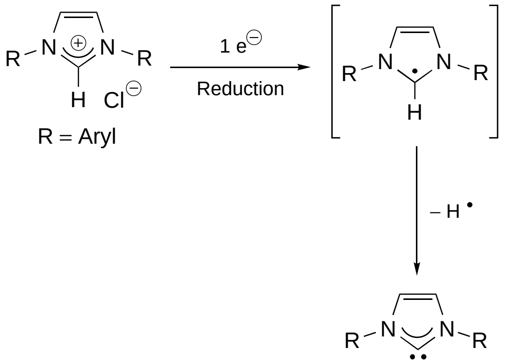

(4)

Although deprotonation of NHC salts have proven to be an efficient synthetic route, the basic reaction conditions can prove incompatible with certain complex synthesis in a one-pot procedure. Thus, other synthetic strategies to generate free carbene have been developed. Khun reported the synthesis of imidazol-2-ylidenes bearing a small alkyl group on the NHC backbone by potassium reduction of the corresponding thiones (**10**) (equation 5).[21] This method has also been applied in the synthesis of benzimidazole derivatives, by reduction of the corresponding sulfones with Na/K alloy at room temperature.[22] Synthesis of unsymmetrically substituted

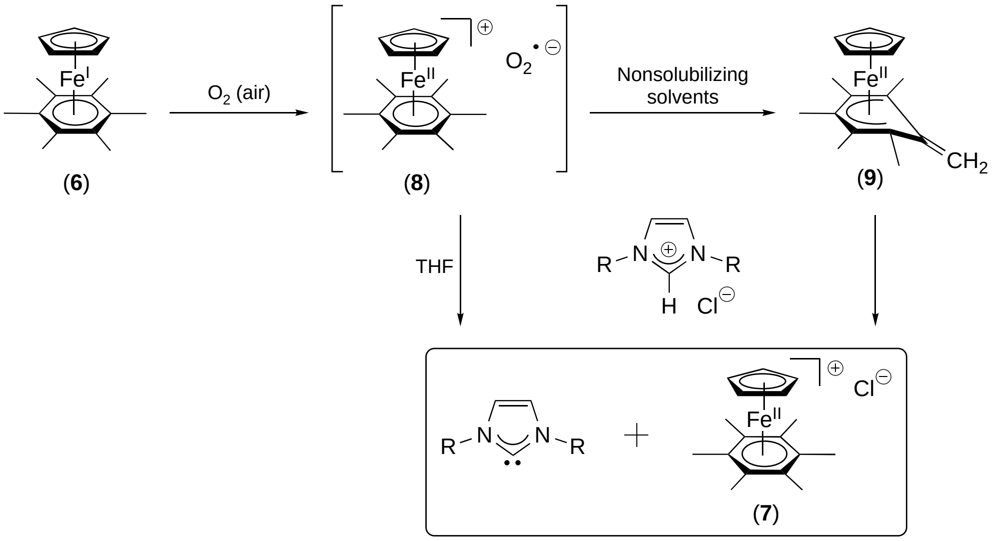

Scheme 1 Synthesis of free NHC by complex (**6**)

saturated NHCs could be achieved following the same method.[23]

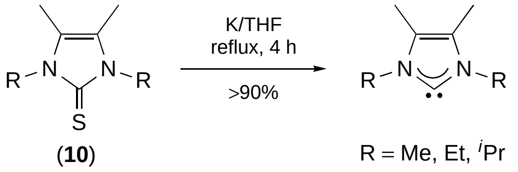 (5)

On the other hand, generation of free carbenes can be thermally achieved from ''C-protected NHC''. In 1995, Enders reported the thermal elimination of methanol from 5-methoxy-1,3,4-triphenyl-4,5-dihydro-1*H*-1,2,4-triazole (**12**) affording the corresponding carbene 1,2,4-triazol-5-ylidene (**13**) in quantitative yield (Scheme 2). Methanol adduct (**12**) is easily synthesized from reaction of triazolium perchlorate (**11**) and NaOCH$_3$ in methanol.[24,25]

It may be noted that Grubbs applied this synthetic method to imidazolinylidene Ru complexes. Compound (**14**) was found efficient in releasing free SIMes upon heating at 80 °C.[26] Alternatively, *tert*-butylate SIMes adduct (**15**) could be used as a precursor to SIMes, while isolation of the unsaturated analogs proved unsuccessful.[27] NHC–amine[28] and NHC–chloroform[29] adducts (**16**) and (**17**) were also synthesized, although their uses in complex formation are very limited.

In 2004, Waymouth and Hedrick reported a new generation of NHC adducts, in which the NHC protecting group was substituted by different fluorobenzene or trifluoromethane.[30] Compounds (**18**)–(**21**) were directly generated from the diamine and the corresponding substituted aldehydes. They were found stable at room temperature and easy to handle in air. Notably, the pentafluorobenzene adduct (**20**) exhibited the best reactivity and free IMes was released upon heating at 65 °C.

Ito and Yamaguchi found that reaction of alkyl and aryl imidazolium chloride (**22**) with LiBEt$_3$H afforded the triethylborane–NHC adduct (**23**) (Scheme 3). These compounds proved to be versatile sources of the free carbenes. Indeed, heating a toluene solution of NHC–BEt$_3$ and the TM complex Mo(CO)$_6$ afforded complex (**24**) [(NHC)Mo(CO)$_5$] in good yield.[31]

Crabtree and coworkers reported the synthesis and the use of air- and moisture-stable N,N-dimethyl-imidazolium-2-carboxylate (**25**). Upon heating to 75 °C, CO$_2$ was released from (**25**) and the so-generated free carbene coordinated to different TM complexes, as depicted in Scheme 4. Reaction of (**25**) with [M(COD)Cl]$_2$ (M = Rh or Ir) afforded monocarbene complexes (**26**). Novel biscarbene complex (**27**)

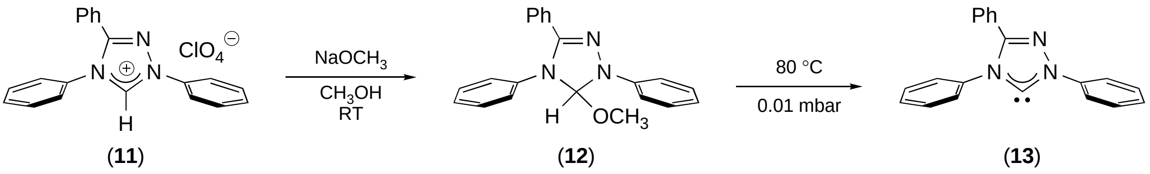

Scheme 2

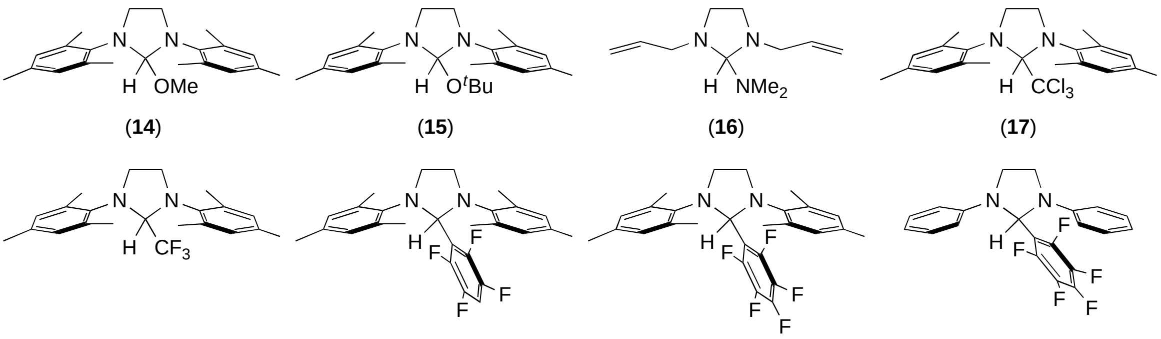
H OMe
H O^{t}Bu
H NMe$_2$
H CCl$_3$
H CF$_3$
F

(**14**) (**15**) (**16**) (**17**)

(**18**) (**19**) (**20**) (**21**)

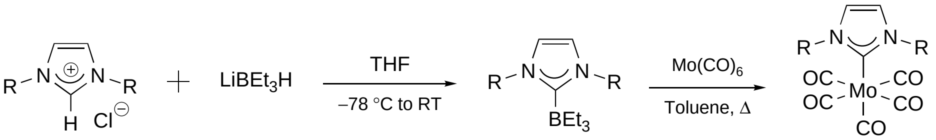
LiBEt$_3$H
THF
–78 °C to RT
Mo(CO)$_6$
Toluene, Δ
BEt$_3$

(**22**) (**23**) 46–80% (**24**) 67%

R = *i*Pr or Mes

Scheme 3

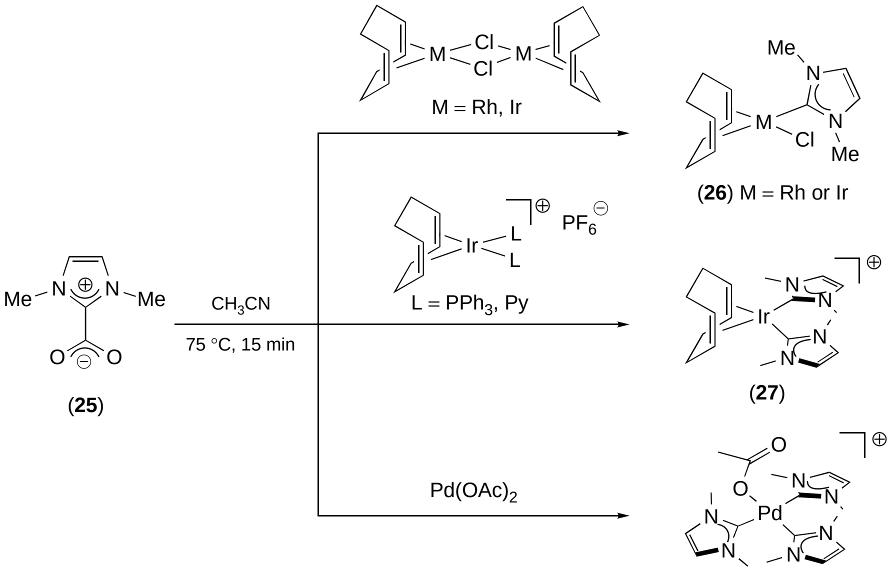
CH$_3$CN
75 °C, 15 min
M = Rh, Ir
L = PPh$_3$, Py
Pd(OAc)$_2$
PF$_6^{\ominus}$

(**25**) (**26**) M = Rh or Ir (**27**) (**28**)

Scheme 4 Synthesis of NHC–metal complexes from carboxylate–NHC adduct

and triscarbene complex (**28**) were synthesized as well, from the same precursor.[32]

2.2 Formation of NHC–TM Complexes

The availability of free carbene as a reagent prompted the development of TM complexes bearing these NHC ligands. Their formation can be achieved using various pathways: either by direct coordination to a metal source or by substitution of another ligand present in the metal coordination sphere.

2.2.1 NHC Addition onto the Metal Center

Direct coordination of free carbene to a metallic center is the most straightforward route leading to NHC–metal

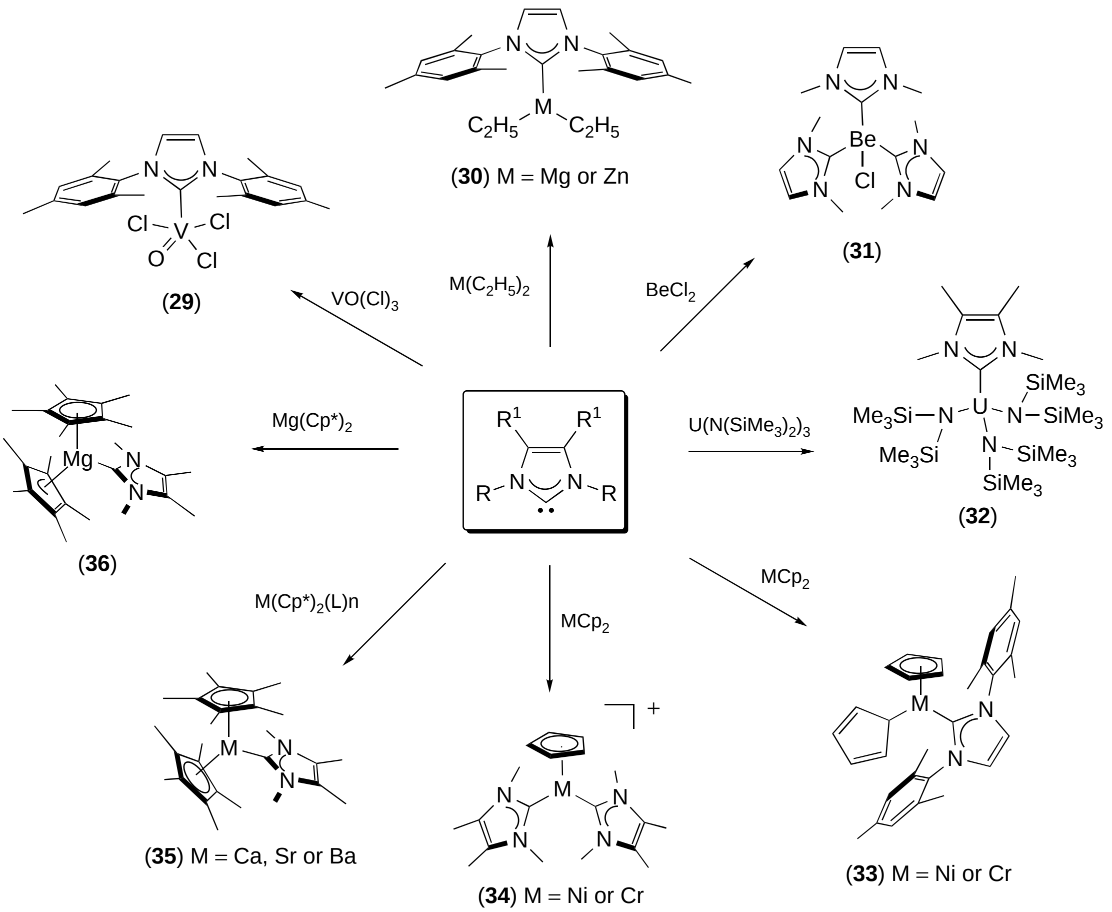

Scheme 5 Coordination of free NHC to metal complexes

complex. Some examples involving main group and TM salts are reported in Scheme 5. $VO(Cl)_3$ and diethyl Mg(II) or Zn(II) complexes react with IMes affording complexes (**29**) and (**30**) respectively.**33,34** In a similar manner, beryllium and uranium complexes (**31**) and (**32**) of IDM and ITM can be synthesized.**35,36** Ni and Cr metallocenes $[M(Cp)_2]$ showed different reactivity depending on the steric hindrance of the NHC employed. Reaction with IMes changed the coordination mode of one Cp from η^5 to η^1, giving rise to (**33**). On the other hand, the less sterically demanding ITM afforded complexes (**34**) $[(NHC)_2M(Cp)](Cp)$, in which one Cp was substituted by two carbenes.**37** NHC–metallocene complexes (**35**) of groups 2 and 12 were easily prepared by reaction of $[(Cp^*)_2M]$ with free carbene. When a twofold excess of NHC was used, the biscarbene complex $[(Cp)_2M(NHC)_2]$ was isolated. If $M = Mg$, coordination of ITM gave rise to (**36**) where one of the two Cp* rings changed its coordination mode from η^5 to η^3.**38**

In a similar manner, Fe(II) halides react with free carbene (**37**) to afford *trans*-$[(NHC)_2FeCl_2]$ (**38**) (equation 6).**39**

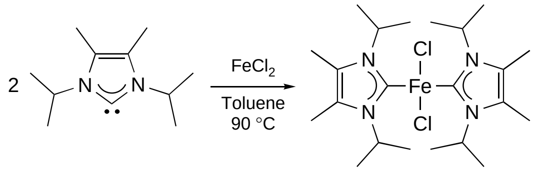

(6)

As an alternative to the use of free NHC, which requires special handling conditions, the generated in situ carbene from the corresponding NHC salt and a base is often employed. For example, [(NHC)CuCl] complexes were synthesized by treatment of CuCl with NHC salts in the presence of ^{t}BuOK. First reported for IPr,**40,41** this synthetic route was found wide in scope and has been extended to various NHCs.**42** It may be noted that when CuOAc is used as the metal source, the isolated product is [(NHC)Cu(OAc)].**43**

In the same manner, NHC–Pd(II) complexes have been synthesized from $Pd(OAc)_2$ and the in situ generated carbene (Scheme 6).**44** The resulting dimer (**39**) $[(NHC)PdI_2]_2$ can be cleaved with phosphines leading to mixed NHC–PR_3 Pd(II) complexes (**40**).**45**

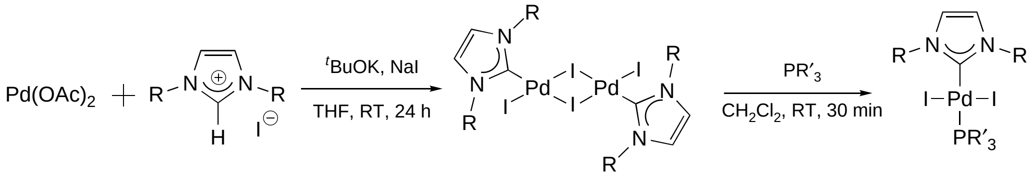

(**39**) (**40**)

Scheme 6

On the other hand, reaction of $Pd(OAc)_2$ with free NHC in toluene at room temperature afforded the monomer (**41**) $[(NHC)Pd(OAc)(\kappa^2\text{-}O,O\text{-}Ac)]$. It is worth noting that the mode of formation of the NHC (in situ generated or isolated) led to different products.**[46]** Recently, Organ reported a procedure for the synthesis of NHC–Pd(II) complexes from $PdCl_2$.**[47]** $PdCl_2$ and NHC·HCl were heated in neat 3-chloropyridine in the presence of K_2CO_3. The reaction yielded $[PdCl_2(NHC)(3\text{-}ClPy)]$ (**42**) in quantitative yields.

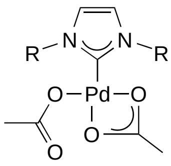
(**41**)

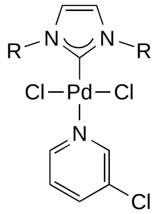
(**42**)

Atypical synthesis of *naked* NHC-containing complexes has been reported by Cloke and coworkers.**[48]** As shown in equation (7), the co-condensation of nickel, palladium, and platinum vapor with the free NHC, I^{t}Bu, provided two-coordinated homoleptic complexes of Ni(0), Pd(0), and Pt(0) (**43**). Unfortunately, in addition to the poor yield of the isolated product, this original methodology required a metal vapor synthesis apparatus.

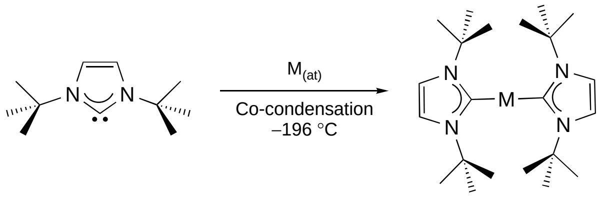

(**43**) 10–32%
M = Ni, Pd or Pt

(7)

2.2.2 Coordination by Nucleophilic Ligand Substitution

Owing to their particular electronic properties, NHCs are well known to substitute for various ligands bound to TM complexes. Since they are generally easy to synthesize, to handle and commercially available, carbonyl, phosphines, and olefins metal complexes have been widely used as precursors. In the following section, we present the most significant examples of ligand substitution by NHCs.

Carbonyl Substitution. Replacement of one CO by an NHC ligand such as IDM is a common reaction, which has been applied to carbonyl complexes of Cr(0), Mo(0), W(0), Fe(0), Ni(0), and so on. The corresponding IDM−carbonyl complexes (**44**)−(**46**) were easily isolated in good yield as depicted in Scheme 7.**[49]**

Interestingly, when $Ni(CO)_4$ was treated with two equivalents of IDM, the biscarbene complex (**47**) was formed. Several other NHC−nickel carbonyl complexes have been synthesized following the same route, as also complexes (**48**)−(**50**) containing IMes, IPr, SIMes, SIPr, and ICy, respectively, which have been obtained and characterized.**[50]** Importantly, when more sterically demanding I^{t}Bu and IAd were used, dissociation of two CO molecules occurred, yielding a rare unsaturated three-coordinated $[(NHC)Ni(CO)_2]$ (**51**) and (**52**).**[51]** These results show that the behavior difference between the various NHC ligands is more a consequence of their steric congestion than of their electronic properties.

Identically, triazole-based carbenes were found to be able to substitute CO, giving rise to mono- or disubstituted carbene carbonyl complexes (**53**) and (**54**) as a function of the reaction stoichiometry (Scheme 8).**[52]** Reaction between $M(CO)_6$ and one equivalent of triazolylidene led to the formation of cis

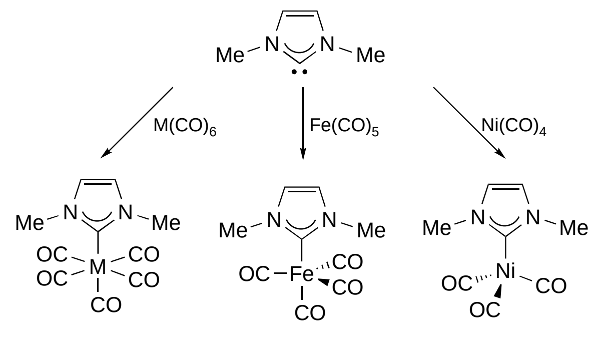

(**44**) M = Cr, Mo, or W (**45**) (**46**)

Scheme 7 Substitution of CO ligand in carbonyl complexes by free NHC

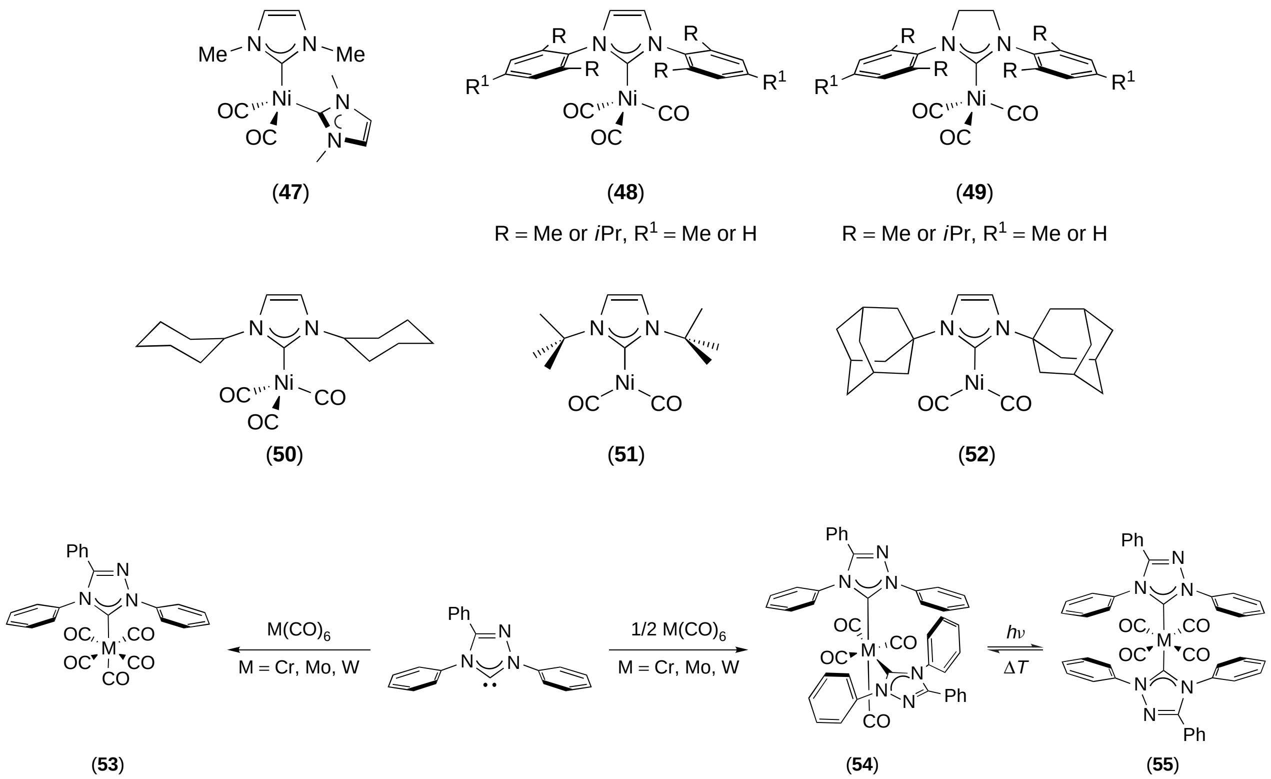
(47)
(48)
R = Me or *i*Pr, R1 = Me or H
(49)
R = Me or *i*Pr, R1 = Me or H
(50)
(51)
(52)
M(CO)6
M = Cr, Mo, W
1/2 M(CO)6
M = Cr, Mo, W
hν
ΔT
(53)
(54)
(55)

Scheme 8

isomer (**54**), which undergoes reversible isomerization to the trans isomer (**55**) upon irradiation.

Piano–stool iron complexes bearing NHC have been obtained by substitution of a CO ligand from [(Cp)Fe(CO)$_2$X] (**56**), as illustrated in Scheme 9.[**53**] When X was a methyl group, the reaction, performed at room temperature, afforded [(Cp)Fe(CO)(IMes)(Me)] (**57**), while heating the reaction mixture to 60 °C led to the concomitant insertion of CO into the Fe–CH$_3$ bond giving rise to complex (**58**). On the other hand, when X was an iodide, substitution of IMes did not take place at the CO position but for the iodide leading to the cationic complex (**59**) [(Cp)Fe(CO)$_2$(IMes)]$^+$.[**54,55**]

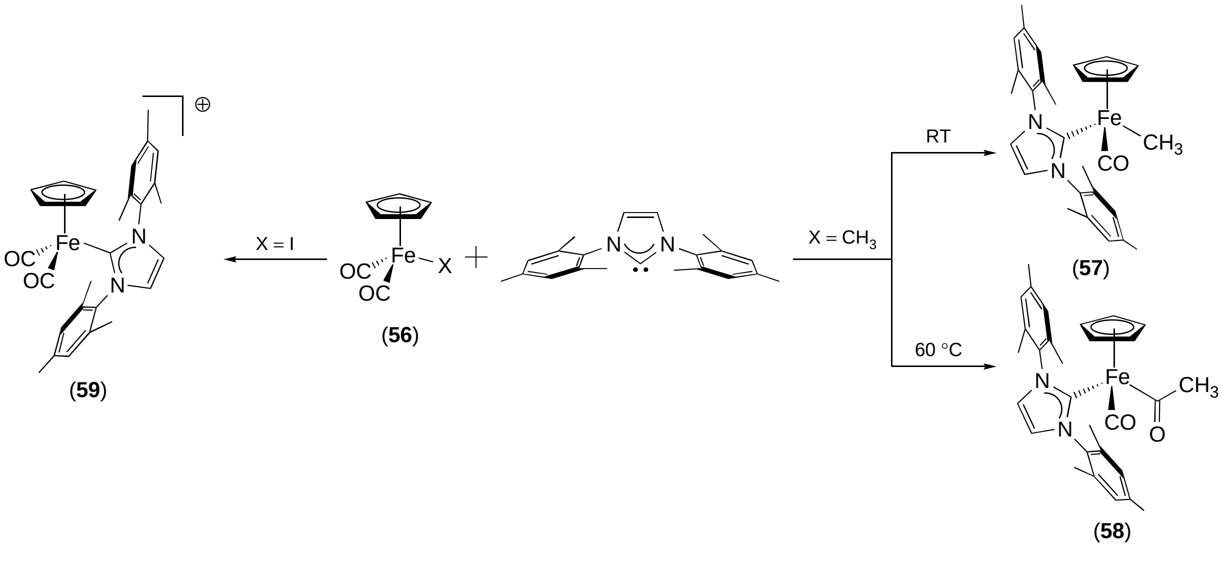
X = I
X = CH3
RT
60 °C
(56)
(57)
(58)
(59)

Scheme 9 Synthesis of (Cp)Fe complexes

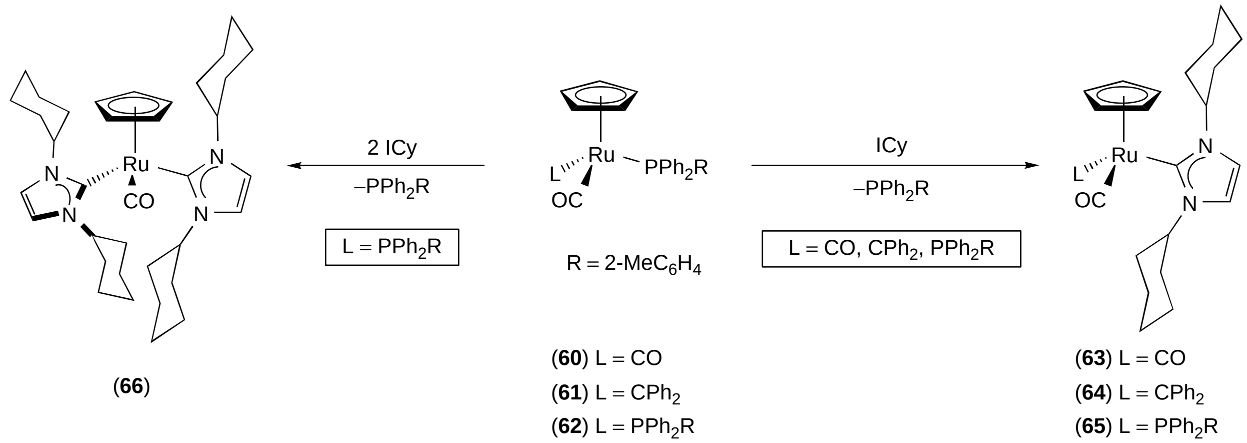
Ru
CO
2 ICy
–PPh2R
L = PPh2R
Ru
PPh2R
L
OC
R = 2-MeC6H4
ICy
–PPh2R
L = CO, CPh2, PPh2R
Ru
L
OC
N
N
(66)
(60) L = CO
(61) L = CPh2
(62) L = PPh2R
(63) L = CO
(64) L = CPh2
(65) L = PPh2R

Scheme 10 Synthesis of mono- and biscarbene CpRu complexes

Phosphine Substitution. Owing to their stronger σ-donating properties, NHC ligands are able to displace phosphines in different situations. The large number of phosphine-containing complexes commercially available explains why this synthetic route is one of the most commonly employed nowadays. Synthesis of Ru(Cp) complexes bearing NHC could be achieved, as depicted in Scheme 10, by ligand exchange from [(Cp)Ru(Cl)(P)(L)] (**60**)–(**62**) with P = phosphine and L = phosphine, CO, and CPh_2 respectively. When only one phosphine was in the coordination sphere of Ru complexes (**60**) and (**61**), monocarbene complexes (**63**) and (**64**) were isolated. Interestingly (and as expected), for (**63**) where both carbonyl and phosphine ligands were present, ICy substituted for the phosphine rather than for the CO. When L was a phosphine, mono- (**65**) or di-substituted (**66**) ICy complexes were synthesized as a function of the stoichiometry of the reaction.[56]

Treatment of the Ru hydride [RuHCl(CO)(PCy_3)] (**67**) with a free carbene such as IMes proceeds by the easy and selective phosphine displacement and formation of complex (**68**) (equation 8).[57] At the time of this article, this synthetic pathway has been extended to analogs [(IPr)RuHCl(PCy_3)],[58] [(IMes)RuHCl(PPh_3)], and [(SIMes)RuHCl (PPh_3)].[59]

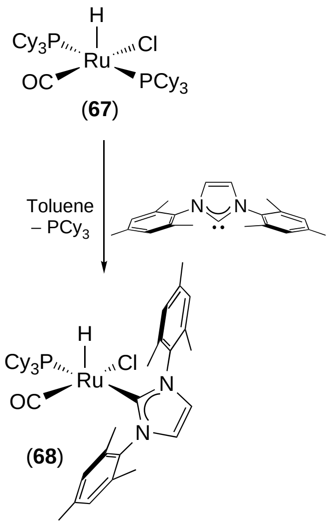
H
Cy3P
Cl
Ru
OC
PCy3
(67)
Toluene
– PCy3
N
N
H
Cy3P
Cl
Ru
OC
N
N
(68)

(8)

In the dihydride Ru complexes (**69**), [$RuH_2(CO)(PPh_3)_3$] (Scheme 11), a threefold excess of IMes led to the sequential formation of the mono-substituted IMes complex (**70**) and of the bis-substituted complex (**71**).[60] It may be noted that substitution neither of the third phosphine nor of the carbonyl ligand was observed.

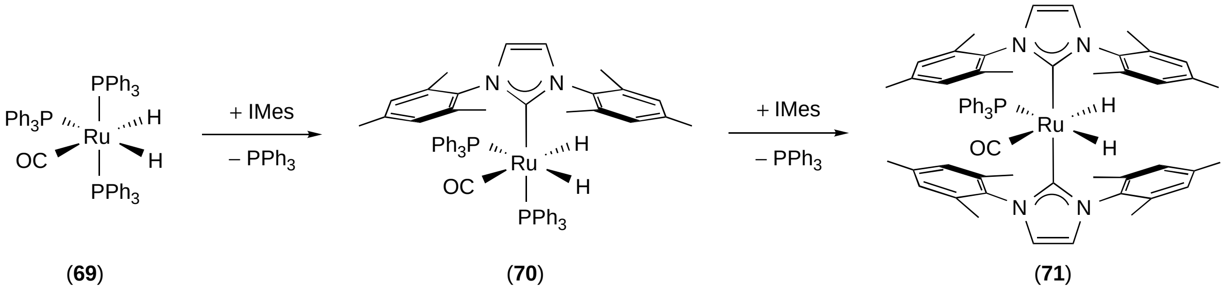
PPh3
Ph3P
H
Ru
OC
H
PPh3
+ IMes
– PPh3
N
N
Ph3P
H
Ru
OC
H
PPh3
+ IMes
– PPh3
N
N
Ph3P
H
Ru
OC
H
N
N
(69)
(70)
(71)

Scheme 11

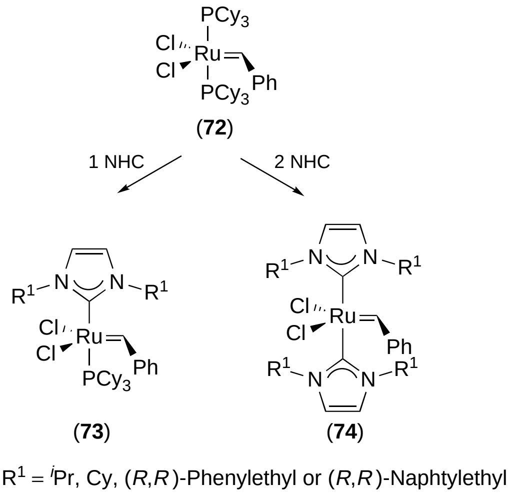
PCy3
Cl
Ru
Cl
PCy3
Ph
(72)
1 NHC
2 NHC
R1 N N R1
Cl
Ru
Cl
PCy3
Ph
(73)
R1 N N R1
Cl
Ru
Cl
Ph
R1 N N R1
(74)
R1 = iPr, Cy, (R,R)-Phenylethyl or (R,R)-Naphtylethyl

Scheme 12 Substitution of phosphine ligands in first-generation Grubbs catalyst

In 1998, Herrmann reported that first-generation Grubbs catalyst [RuCl$_2$(PCy$_3$)$_2$(CHPh)] (**72**) (Scheme 12) underwent substitution of the two phosphines by two equivalents of alkyl carbene affording complex (**74**).[61] On the other hand, when only a slight excess of the free carbene was added monosubstitution of phosphine was achieved, and complex (**73**) was obtained.[62,63]

Reaction of (**72**) with aryl *N*-substituted NHC, yielding second-generation metathesis catalysts, was reported in 1999 by Nolan *et al.*[64] and Grubbs *et al.*[65] Substitution of one phosphine in (**72**) by IMes afforded [Cl$_2$Ru(IMes)(PCy$_3$)(CHPh)] in excellent yields. Even in the presence of a 10-fold excess of IMes, only one phosphine underwent substitution.[64] Since then, this synthetic route has been extended to a number of carbenes, for instance, SIMes, for which the free carbene has been generated in situ from the methanol-protected NHC (**14**),[26] IPr,[66] SIPr[67] generated either from the *tert*-butanol-protected NHC[68] or by in situ deprotonation of IPr·HCl salt,[69] SIAd,[70] as well as unsymmetrically substituted NHC.[70,71] Very recently, Grubbs reported that various [(NHC)RuCl$_2$(PCy$_3$)(CHPh)] could be obtained from the reaction of precursor (**72**) and 2-(pentafluorophenyl)imidazolidines, such as (**20**), under mild thermolytic conditions.[72] Ru−indenylidene complexes (**75**) have been synthesized with the same synthetic procedure by a phosphine substitution of [Cl$_2$Ru(PR$_3$)$_2$(Ind)] (Ind = indenylylidene).[73]

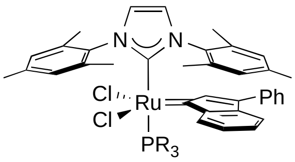
N N
Cl
Ru
Cl
Ph
PR3

(**75**)

Substitution of PCy$_3$ by NHC also occurred for catalyst (**76**) developed by Hoveyda (Scheme 13).[74] Isolation of reaction intermediate (**77**) showed that SIMes first substituted the more labile coordinative oxygen and then the chelation of the oxygen released PCy$_3$ from the Ru center affording (**78**). It is worth noting that the same reaction led to poorer yield when PPh$_3$ was used as phosphine.[75]

In the same manner, phosphine substitution from [Pd(PR$_3$)$_2$] complexes have proven very useful in the synthesis of biscarbene Pd(0) complexes as depicted in equation (9). Reaction of [Pd(Ptol$_3$)$_2$] (**79**) with two equivalents of IMes, I^{t}Bu, and ICy afforded the corresponding [(NHC)$_2$Pd] products (**80**). A mixture of starting material and monosubstituted complex was observed when only one equivalent of free NHC was added.[76]

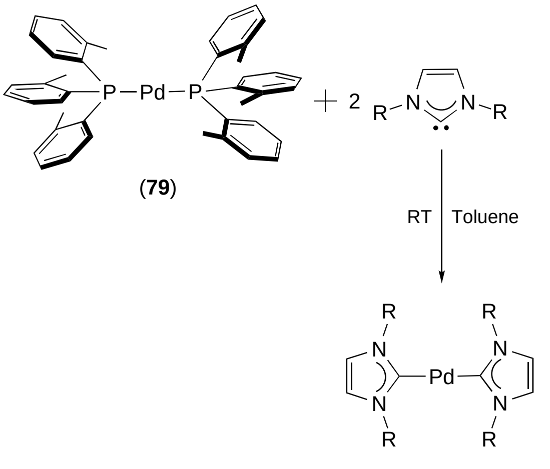
P
Pd
P
(79)
+ 2
R N N R
RT
Toluene
R
N
N
R
Pd
R
N
N
R

(9)

(**80**) R = Mes, Cy or ^{t}Bu

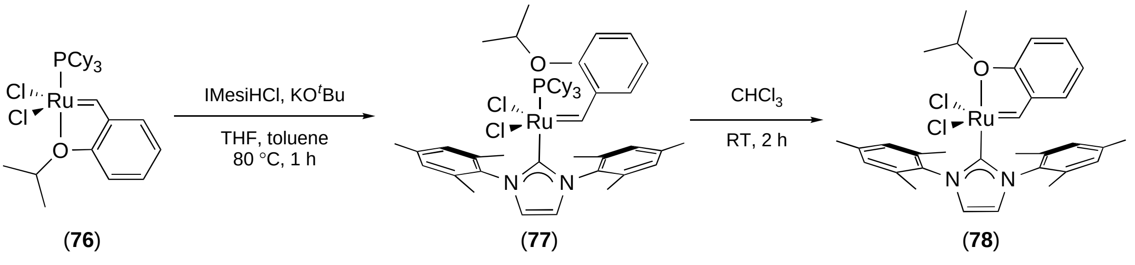
PCy3
Cl
Ru
Cl
O
(76)
IMesiHCl, KOtBu
THF, toluene
80 °C, 1 h
O
PCy3
Cl
Ru
Cl
N N
(77)
CHCl3
RT, 2 h
O
Cl
Ru
Cl
N N
(78)

Scheme 13

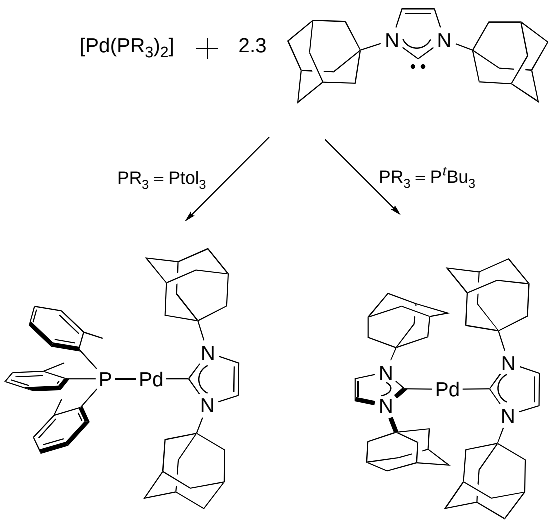

(**81**) (**82**)

Scheme 14 Influence of phosphine ligand in the synthesis of sterically hindered NHC–Pd complexes

On the other hand, using sterically hindered IAd, the mixed NHC−phosphine complex (**81**) can be isolated in good yield (Scheme 14).[77] To achieve the substitution of both phosphines affording (**82**), it was necessary to start from $[Pd(P^tBu_3)_2]$, highlighting how the choice of the leaving ligand controls the outcome of the reaction. However, Cloke and Caddick reported that careful control of reaction stoichiometry enabled the synthesis of $[(I^tBu)Pd(Ptol_3)]$ from $[Pd(Ptol_3)_2]$ (**79**).[78]

In this context, it is worth reporting that another route to bis-NHC–Pd(0) complexes has proven efficient.[79] A Pd(II) source, such as the dimer $[Pd(2\text{-methylallyl})Cl]_2$ (**83**) (equation 10) reacted with sodium malonate in the presence of free NHC ligand. Reduction of Pd(II) to Pd(0) and coordination of two NHCs afforded $[(NHC)_2Pd]$ in quantitative yield. This route proved very useful for the synthesis of catalyst (**84**) developed by Glorius *et al.*[80]

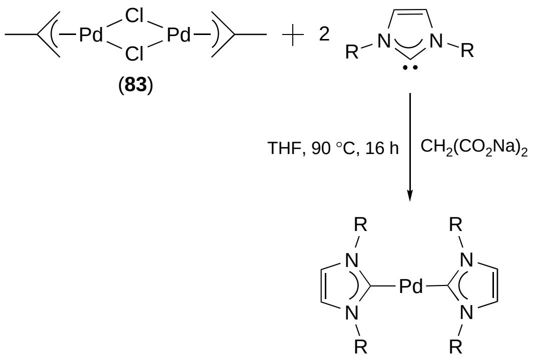

(10)

Similarly, $[(NHC)_2Ni(II)Cl_2]$ complexes (**85**) were synthesized from the corresponding $[(PPh_3)_2NiCl_2]$ by simple substitution of two phosphines by two NHC ligands.[81,82]

Wilkinson's complex also underwent substitution of phosphines by IMes. The reaction afforded $[(IMes)RhCl(PPh_3)_2]$ (**86**), in which the two phosphines are in cis, in contrast to the general behavior of $[(L)RhCl(PPh_3)_2]$-type derivatives that usually adopt a trans geometry.[83]

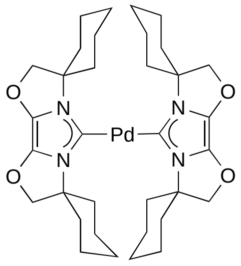

(**84**)

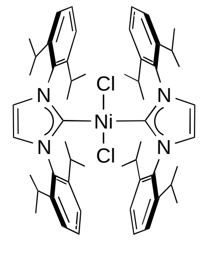

(**85**)

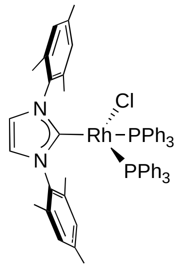

(**86**)

Olefin Substitution. Coordinated olefins are generally labile ligands and their substitution is easily achieved by a more donating ligand. Ni(0) and Pt(0) biscarbene complexes (**87**) were prepared from the corresponding $[(COD)_2M]$ complex by simple substitution (Scheme 15).[84] When the reaction with IMes or SIMes was carried out in the presence of two equivalents of DMFU, the monocarbene diolefin complexes $[(NHC)M(DMFU)_2]$ (**88**) were obtained.[85,86]

To obtain the Pd(0) analog of (**88**), it was necessary to use $[(^tBuDAB)Pd(DMFU)]$ as starting material, as the reaction using the diolefin complex $[Pd(dba)_2]$ gave a complex mixture of products owing to interactions of free NHC with the dba ligand. Reaction of $[(^tBuDAB)Pd(DMFU)]$ with two equivalents of IMes and an excess of DMFU yielded $[(IMes)Pd(DMFU)_2]$ (**89**). In this case, the free carbene displaced the chelating diamine.[86]

Usually, NHC palladium diolefin complexes, similar to (**89**), have been synthesized according to equation (11). The Pd(0) precursor bearing diolefin, for instance, nbd, COD, etc., reacted with NHC in the presence of an excess of a ligand L.

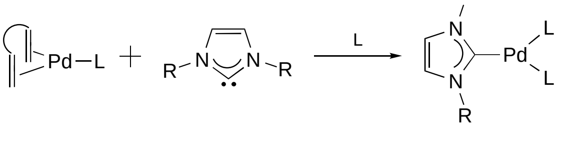

(11)

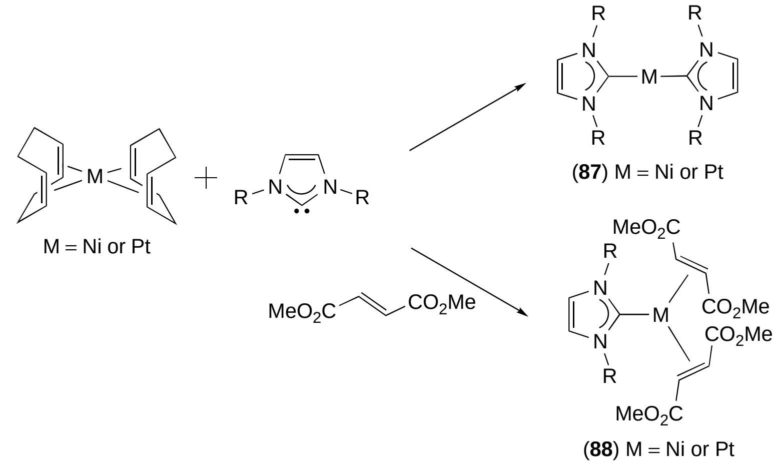

Scheme 15 Synthesis of Ni(0) and Pt(0) NHC complexes

Hence, complex (**90**) was obtained by reaction of [(nbd)Pd(ma)] with one equivalent of IMes and one equivalent of ma.[87] NHC-naphthoquinone and benzoquinone dimers (**91**) and (**92**) were prepared in the same manner from naphtylquinone- and benzoquinone-palladium derivatives.[88] Small NHCs such as ITM can give rise to biscarbene complexes (**93**) and (**94**). Indeed, displacement of COD in [Pd(COD)(alkene)] complex by two equivalents of ITM

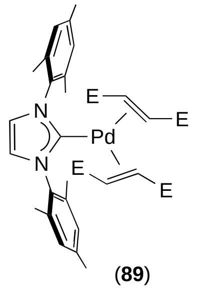
(**89**)

E = CO_2Me

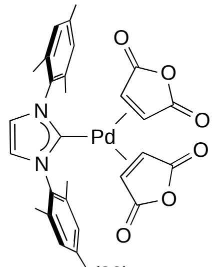
(**90**)

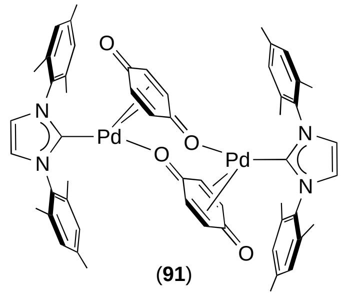
(**91**)

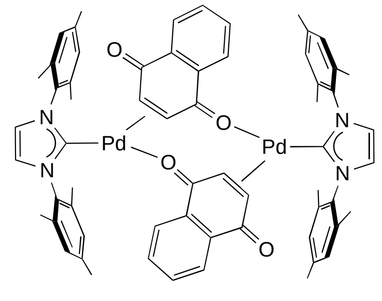
(**92**)

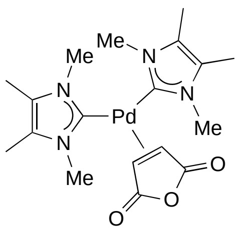
(**93**)

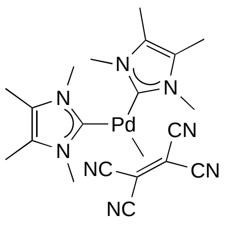
(**94**)

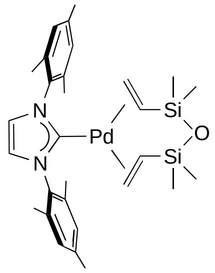
(**95**)

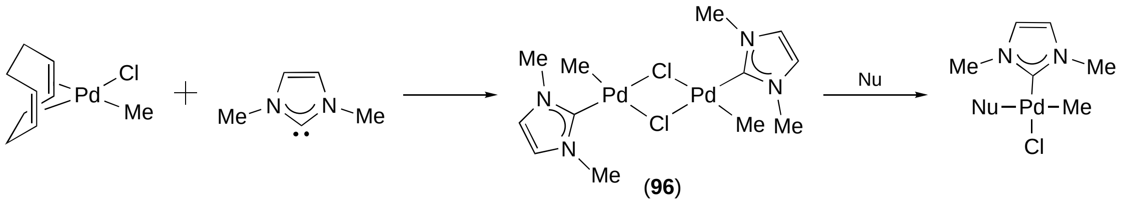
Cl
Pd
Me
Me
N
N
Me
Me
Me
N
Pd
Cl
Pd
N
N
Cl
Me
Me
N
Me
(96)
Nu
Me
N
N
Me
Nu
Pd
Me
Cl

Scheme 16

gave the corresponding biscarbene–alkene complex in good yield.[89] Substitution by an NHC of dae ligand from [$Pd_2(dae)_3$] in the presence of DVTMS afforded monocarbene Pd complexes [(NHC)Pd(DVTMS)] such as (**95**).[90,91] Substitution of COD was also found efficient for the preparation of Pd(II) alkyl complexes. Reaction of [MePdCl(COD)] with IDM gave the dimer [$MePdCl_2$(IDM)] (**96**)[92] that was subsequently opened with a range of nucleophiles (Scheme 16).[93]

Treatment of [$PdCl_2$(COD)] with ferrocenyl bis-NHC (**97**) yielded complex (**98**), in which an isomerization cis/trans was observed (equation 12). It is worth noting that the free carbene was generated in situ using the strong base $KN(SiMe_3)_2$.[94]

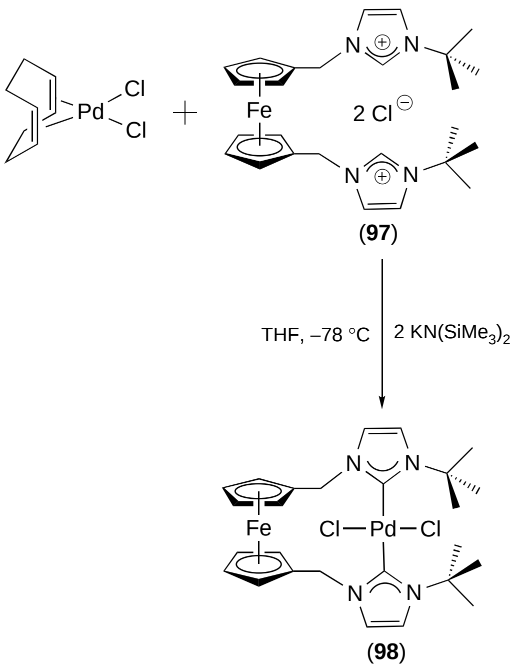
Cl
Pd
Cl
N
N
Fe
2 Cl
N
N
(97)
THF, −78 °C
2 KN(SiMe3)2
N
N
Fe
Cl—Pd—Cl
N
N
(98)

(12)

NHC–Pt(0) complexes were synthesized from Karstedt's catalyst (**99**) (equation 13).[95] Substitution of DVTMS by two equivalents of in situ generated NHC led to the formation of a series of [(NHC)Pt(DVTMS)] complexes (**100**). The first time, this was developed for ICy, I^tBu, and IDM; subsequently, this synthetic procedure was efficiently applied to numerous imidazolylidene and benzimidazolylidene derivatives independent of their *N*-substituents.[96,97]

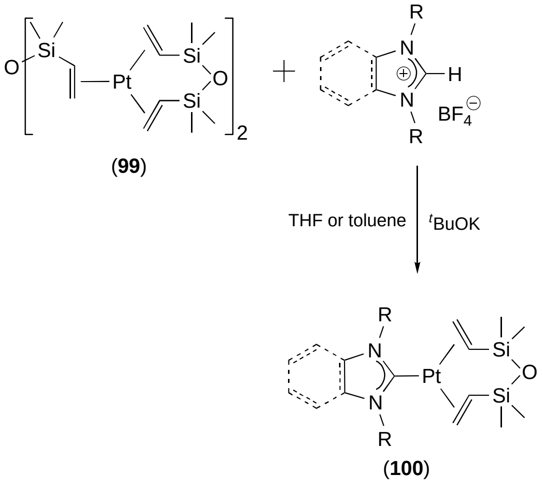
Si
O
Pt
Si
O
Si
2
(99)
R
N
H
N
BF4
R
THF or toluene
tBuOK
R
N
Pt
Si
O
Si
N
R
(100)

(13)

Substitution of Other Ligands. A variety of other ligands were found to be easily displaced by NHC ligands. We report here some significant examples. Substitution of pyridine in [$Ir(COD)Py_2$] by SIMes gave [(SIMes)Ir(COD)Py].[98] The steric bulk of SIMes allowed for substitution of only one pyridine.[99] Reaction of biscationic complex [$Ir(Cp^*)(CH_3CN)_3]^{2+}$ (**101**) with bisimidazolium salt (**102**) in the presence of triethylamine led to the displacement of two acetonitrile molecules and formation of cationic complex (**103**) (equation 14).[100]

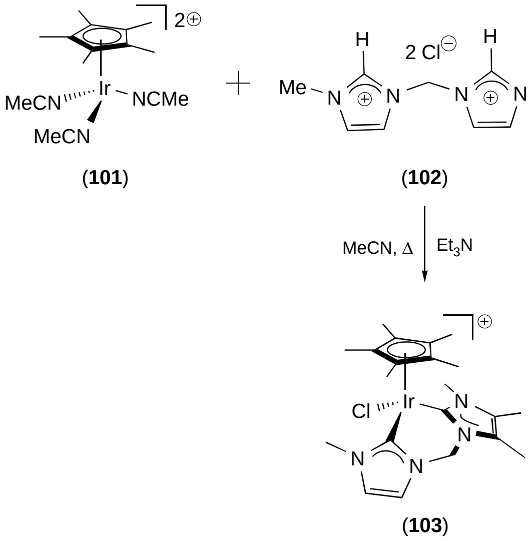
2⊕
MeCN
Ir
NCMe
MeCN
(101)
H
2 Cl
H
Me
N
N
N
N
Me
(102)
MeCN, Δ
Et3N
⊕
Cl
Ir
N
N
N
N
(103)

(14)

Owing to the lability of acetonitrile ligands, [Cu(MeCN)$_4$]X (X = PF$_6$ or BF$_4$) was found to be a convenient starting material for the synthesis of cationic NHC–Cu(I) complexes.[101] In this case, the in situ formation of NHC from the corresponding chlorinated salts was found more suitable to isolate cationic biscarbene complexes [(NHC)$_2$Cu]X. Reaction of Pd(II) precursor [PdCl$_2$(PhCN)$_2$] with one equivalent of IPr afforded the dimer [(IPr)PdCl]$_2$.[102]

By displacement of THF, NHC–Ln complexes have been synthesized using [LnCl$_3$(THF)$_n$] as a metal source. Depending on the reaction stoichiometry, several NHCs could be introduced onto the metal center.[103]

In the same manner, dimethylsulfide substitution proved to be a practical procedure for the preparation of NHC−gold complexes. Good yields were obtained for the synthesis of monocarbene Au(I) complexes (**104**) from [(Me$_2$S)AuCl] and one equivalent of free NHC (Scheme 17).[104,105] The steric hindrance of NHCs was found to be of critical importance, since NHCs with smaller nitrogen substituents such as Mes, *iso*-propyl or *n*-butyl led to a lower yield and formation of a byproduct identified as the biscarbene complex [(NHC)$_2$Au]$^+$ Cl$^-$. Fortunately, the silver-mediated transmetallation was an efficient alternative route for these NHCs (see Section 2.6).[105,106] When the same reaction was performed with two equivalents of in situ generated NHCs, the cationic biscarbene complex (**105**) [(NHC)$_2$Au]X (X = Cl, Br, or PF$_6$) was obtained as the only product.[107]

Surprisingly, cationic complexes of Cu(I) and Ag(I), namely, [(NHC)$_2$M](CF$_3$SO$_3$), have been prepared by substitution of anionic ligand of M(CF$_3$SO$_3$)$_2$ with two equivalents of free carbene.[108]

The NHC·HCl was able to react with a chelate *O*, *C*-acetylacetonate (acac) from [Pd(acac)$_2$] (**106**), giving rise to [(IPr)Pd(acac)(*C*-acac)] (**107**) that was converted into [(IPr)PdCl(acac)] (**108**) by addition of HCl (Scheme 18).[109]

2.2.3 *Cleavage of Dimeric Metal Complex*

Group 10 TM complexes (**110**) bearing allyl ligand were synthesized by breaking the corresponding dimer [MCl(R^1,R^2-allyl)]$_2$ (**109**) with two equivalents of free NHC ligand (equation 15).[110,111] Aryloxy dimer [Ni(allyl)(OAr)]$_2$ (Ar = 2,6-di-*iso*-propylphenyl) has also been employed for the preparation of NHC−allyl Ni complexes.[112] Since the [(NHC)PdCl(allyl)] complexes exhibited an excellent activity in palladium-catalyzed cross-coupling reactions,[113] this series was extensively studied with special attention to allyl substituent effects.[114,115]

Dixneuf and coworkers reported the synthesis of Ru-η^6arene derivatives from dimeric [Cl$_2$Ru(η^6-arene)]$_2$ (**111**) and dimeric carbene such as (**112**) as the source of NHC, as illustrated in Scheme 19.[116] Using different η^6-arene dimers, complexes (**113**) were isolated in good yields. When (**114**) was used as an NHC source, the expected product (**115**) was

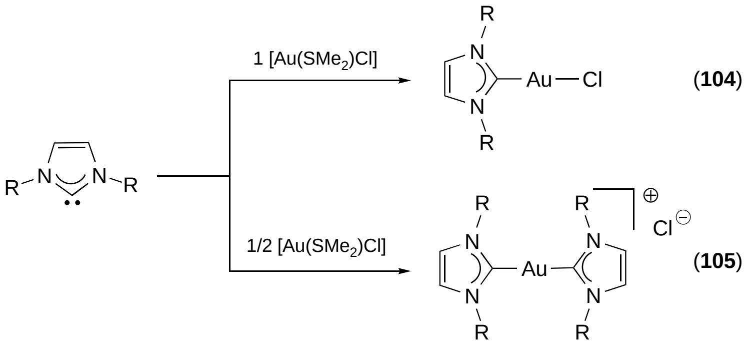

Scheme 17 Synthesis of mono- and biscarbene Au(I) complexes

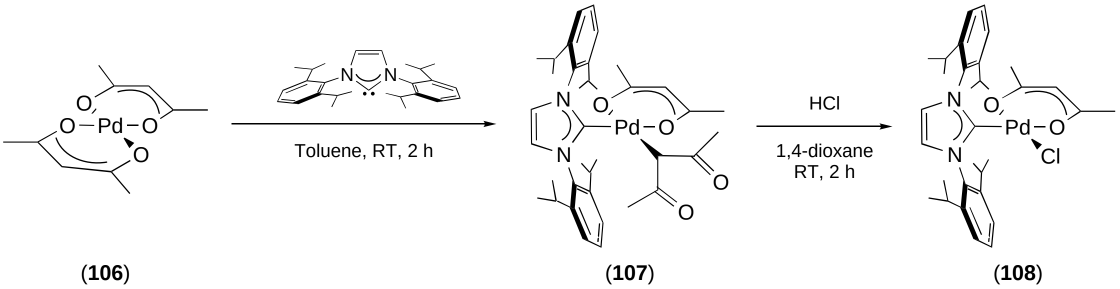

Scheme 18

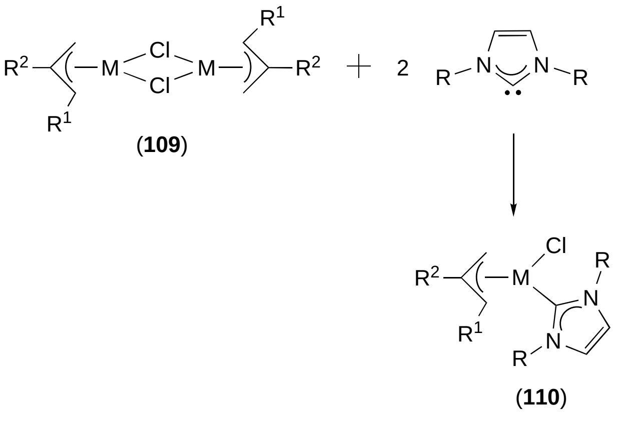

M = Ni, Pd or Pt; R^1 = H, Me or Ph; R^1 = H or Me

(15)

observed but it proceeded rapidly to lead to the chelate complex (**116**).[117] The flexibility of the benzyl group allowed for the C–H activation of its aromatic group and the substitution of the initial η^6-arene. It may be noted that no coordination of hydroxyl function was detected.

Cp*Ir(III) complexes were easily synthesized in good yields from the dimer $[IrCl_2(Cp^*)]_2$ (**117**) and the free carbene (equation 16).[118] This procedure proved efficient for a large range of carbenes, which can also be added to the reaction mixture in their protected form (**118**).[119]

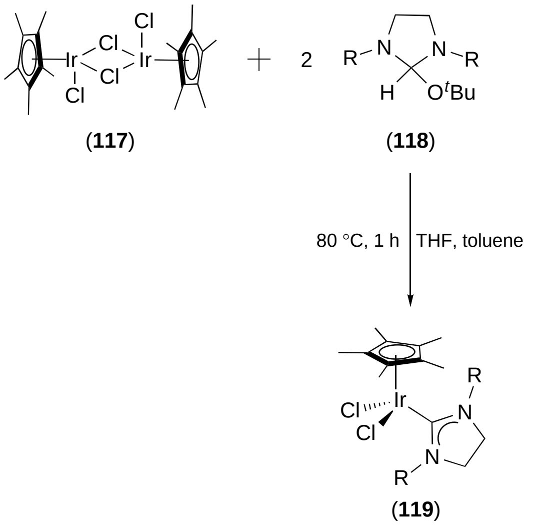

(16)

A widely used precursor for Rh(I) and Ir(I) in coordination chemistry is the $[MCl(COD)]_2$ dimer (**120**). In the presence of either free NHC or in situ generated carbene from the alcohol adduct or the combination imidazolium salt and base, the dimer was cleaved giving rise to [(NHC)MCl(COD)] (**121**) (Scheme 20).[120] The presence of labile COD allowed for further modification of the metal coordination sphere. For example, under CO atmosphere the COD ligand was rapidly removed, leaving two CO binding the metal center.[121] The

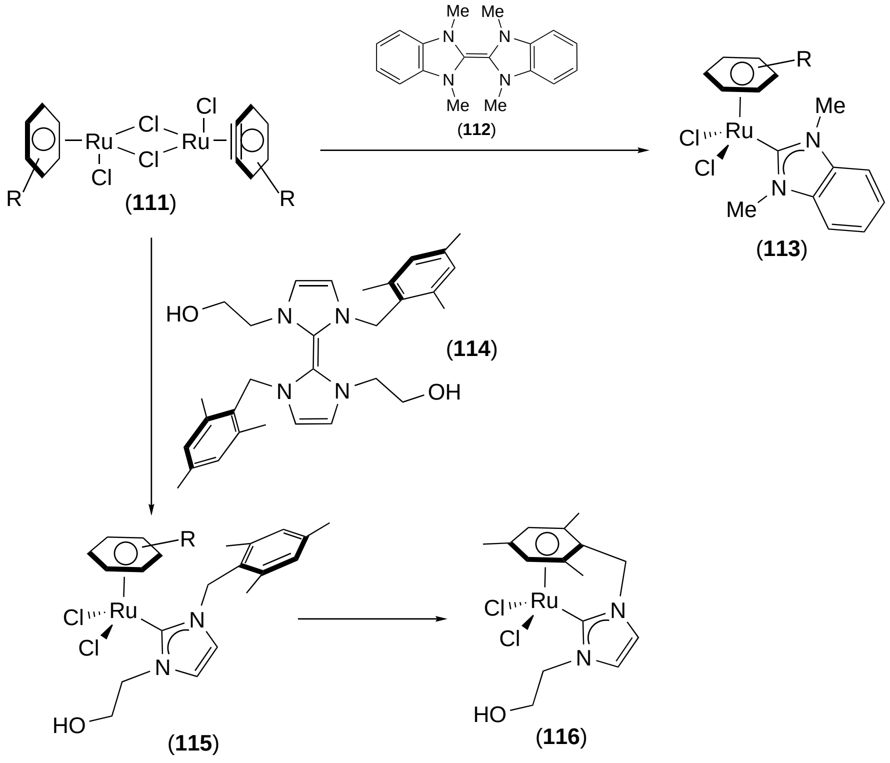

Scheme 19 Breaking of $[RuCl_2(\eta^6\text{-arene})]_2$

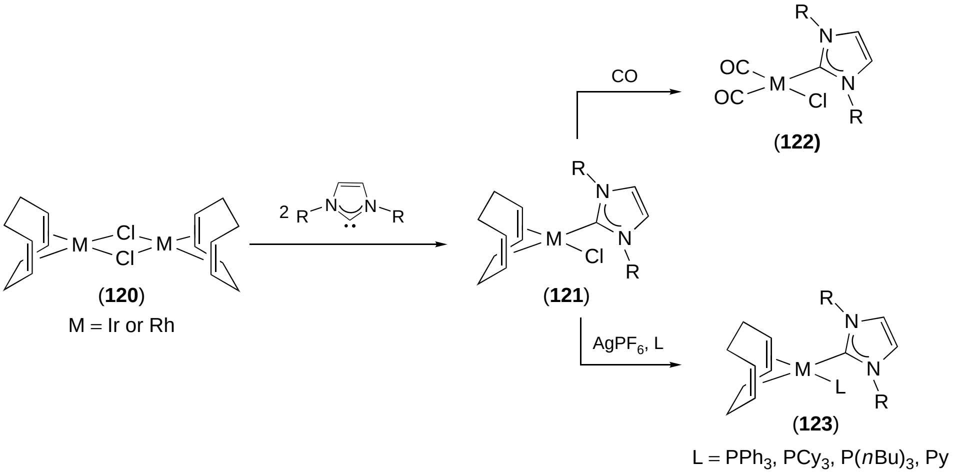

Scheme 20 Cleavage of $[MCl(COD)]_2$ dimer by free NHC

chloride has also been substituted by phosphines or pyridine in the presence of silver salts producing (**123**).[122]

NHC–palladacycle complexes (**125**) have been obtained, as depicted in equation (17), from the corresponding dimer (**124**) and two equivalents of NHC ligand. Conveniently, this route was found compatible with diverse functions and so aminopalladacycles[123] and phosphapalladacycles[124,125] have been prepared.

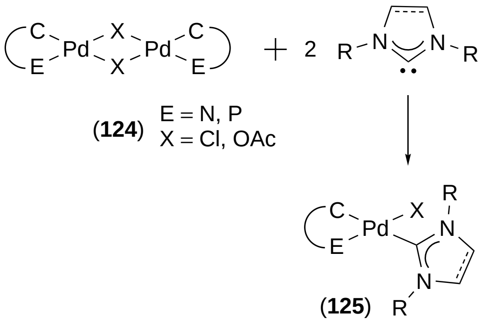

(17)

For sterically hindered NHCs, monocarbene complexes were obtained, while with smaller NHC this reaction gave biscarbene complexes.[126] In the case of the smaller IDM, it was even possible to obtain the triscarbene complex, via palladacycle opening.

2.3 Acid–Base Reactions with Imidazolium Salts

Since the synthesis of NHC–TM complexes was initially achieved by in situ formation of NHC from azolium salt in the presence of base followed by coordination to a metal center, a simpler procedure would be useful. In 1996, Arduengo reported the synthesis of $Hg(IDM)_2$ (**128**) from $Hg(OAc)_2$ and IDM·HCl salt.[127] The mechanism of this reaction is depicted in Scheme 21. Dissociation of one acetate ligand generates $[Hg(OAc)]^+$ (**126**) and the mildly basic acetate anion drives the deprotonation of the imidazolium salt. Thus, the newly formed NHC coordinated promptly (**126**) and led to $[(IDM)Hg(OAc)]^+$ (**127**).

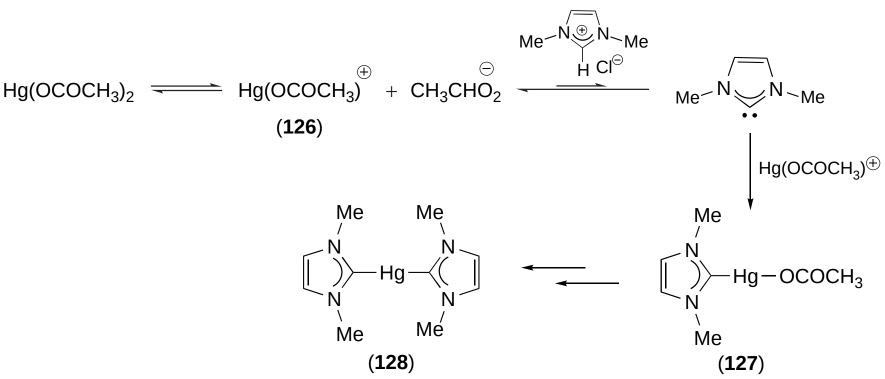

Scheme 21 Proposed mechanism for the formation of $[Hg(IDM)_2]$ (**128**)

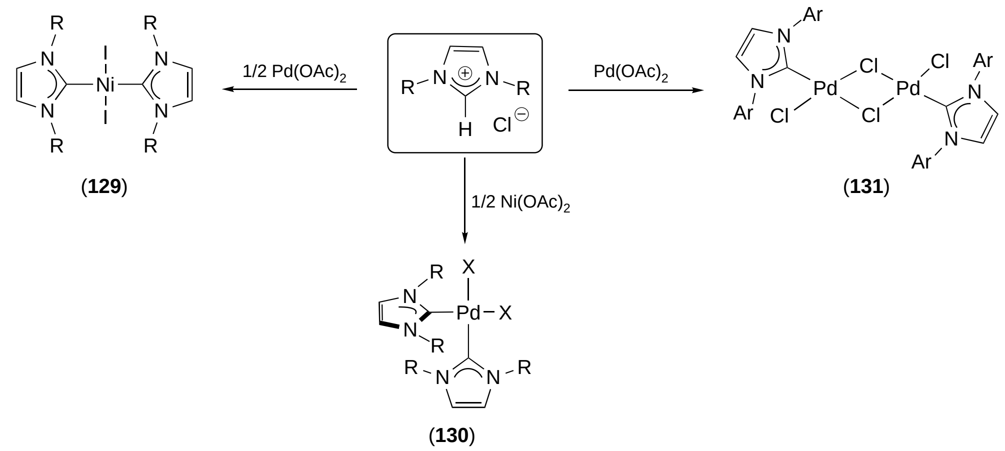

Scheme 22 Synthesis of TM complexes from imidazolium salt and acetate-containing metal precursors

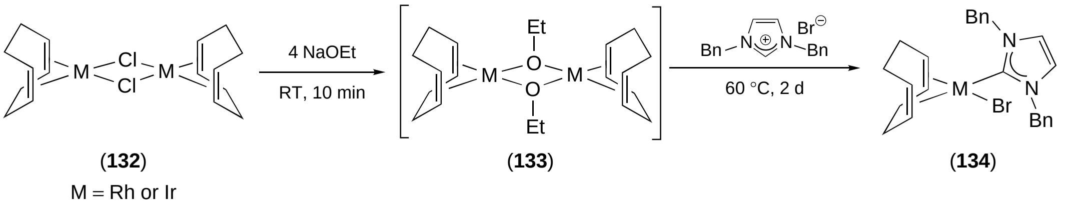

Scheme 23

This procedure has been applied in the synthesis of other complexes from acetate-containing metal source such as Ni(OAc)$_2$[81,128] and Pd(OAc)$_2$,[129,130] as depicted in Scheme 22. The reaction, involving two equivalents of NHC·HI salts, yielded the corresponding complexes: *trans*-[NiI$_2$(NHC)$_2$] (**129**) and *cis*-[PdX$_2$(NHC)$_2$] (**130**). Complexes of benzimidazolin-2-ylidene have been synthesized in an analogous manner.[131] Interestingly, a reaction carried out of with one equivalent of imidazolium salt and Pd(OAc)$_2$ afforded the [PdX$_2$(NHC)]$_2$ dimer (**131**).[132,133]

Instead of acetate complexes, ethoxide-containing metal precursors (**133**) have been used with imidazolium, benzimidazolium, or triazolium bromide salts affording [MBr(COD)(NHC)] (**134**) in quantitative yields (Scheme 23).[134,135] The ethanolate dimer was generated in situ from the corresponding chloride dimer (**132**) by addition of sodium ethoxide. Complex (**133**) was not isolated but its formation proposed as indicated by the color change of the solution. Subsequent addition of imidazolium salt afforded complex (**134**). Bridged hydroxy groups have also been found competent to carry out the deprotonation. For instance, reaction of [(PPh$_3$)Pd(R)(μ-OH)]$_2$ (R = Ph, CH$_3$) with IPr·HCl salt gave [(PPh$_3$)PdCl(R)(IPr)] in moderate yields.[136]

Unexpectedly, Tilset observed that coordinated Cp ligands deprotonated imidazolium and imidazolinium salt.[137] [(Cp)$_2$Cr] (**135**) reacts with IMes·HCl to give [(IMes)CrCl(Cp)] (**136**) and cyclopentadiene (equation 18).

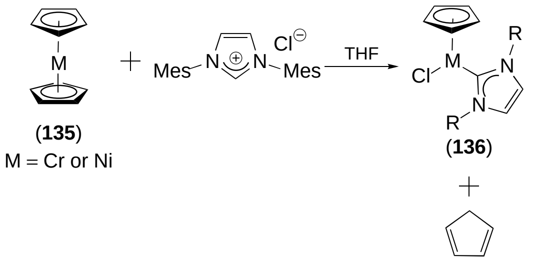

(18)

When [(Cp*)$_2$Cr] was used as the starting material, no product was detected. According to the authors, the absence of reactivity in the latter case could be explained by the higher steric hindrance of the Cp* ring, which would prevent the coordination of IMes. This procedure was extended subsequently to the synthesis of Ni analogs with both saturated and unsaturated aryl-substituted NHCs.[138,139]

2.4 Oxidative Addition of Imidazolium Salts onto the Metal

Although oxidative addition of C–Cl bond of thiazole, benzothiazole, and oxazole was reported as a feasible access to NHC–TM complexes by Stone in 1974,[140] this approach remained unexplored in the following 25 years. In 2001, Cavell and Yates demonstrated, with combined theoretical and experimental studies, that oxidative addition of the C–H bond of imidazolium salts to Pt(0) was energetically favored.[141] Indeed, reaction of $Pt(PPh_3)_4$ with $IDM{\cdot}HBF_4$ afforded the oxidative addition product (**137**) $[(IDM)PtH(PPh_3)_2]$ in 15% yield. The oxidative addition of the imidazolium salt was shown to be an equilibrium reaction (equation 19).

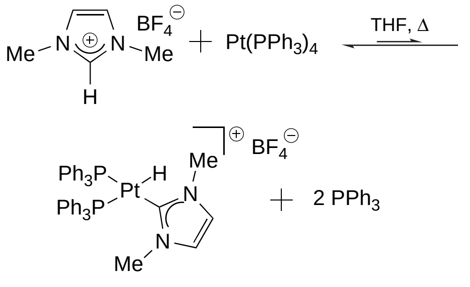

(**137**)

(19)

Tuning the platinum precursor improved the yield to 63% using the unsaturated $[Pt(PR_3)_2]$ ($PR_3 = PPh_3$ or PCy_3) as the starting material. Displacement of two phosphines from the coordination sphere of Pt drove the equilibrium to the formation of the expected product. Following Stone's work, oxidative addition of C–I bond was also studied, and it was found that $ITM{\cdot}BF_4$ reacted smoothly with $[Pt(PPh_3)_4]$, affording $[(ITM)PtI(PPh_3)_2]$ in 89% yield. Although showing a reactivity close to the one displayed by Pt(0) complexes, Pd(0) (**138**) treated with iodoimidazolium cation (affording complex (**139**), Scheme 24) did not react with imidazolium salts. When a four-fold excess of imidazolium salt was used to drive the equilibrium, decomposition of (**138**) to palladium black occurred.[142]

Further investigations by Crabtree showed oxidative addition of imidazolium C–H bond possible for Pd(0).[143] Reaction of pyridine-substituted imidazolium salts (**140**) (Scheme 25) with Pd_2dba_3 afforded the neutral or cationic complexes (**141**) and (**142**). Apparently, the geometry cis/trans of the formed complex is a function of the steric pressure of the NHC–nitrogen substituents. Remarkably, this behavior is not related to the pyridine moiety, which could act as a base, since the oxidative addition of benzimidazolium salts to $[Pd_2dba_3]$ affording $[(NHC)_2PdCl_2]$ was achieved in moderate yield.[144]

Oxidative addition of imidazolium salts to NHC-containing complexes of Ni and Pt has also been reported. IDM·HI reacted with $[(NHC)Pt(DMFU)_2]$ to give the biscarbene hydride complex [(NHC)(IDM)PtHI].[85] Reaction of $IDM{\cdot}HBF_4$ salt with the homoleptic $[(IMes)_2M]$ (**143**) (M = Ni or Pd) afforded the triscarbene hydride complex $[(IMes)_2(IDM)MH]$ (**144**) (equation 20). This metal hydride exhibited a remarkable stability both in solution and in solid state. This stability is certainly due to the steric bulk of NHCs that shields and protects the hydride function.[145]

Recently, Fürstner extended the method of Stone to chloroimidazolinium salts.[146] Oxidative addition of 2-chloro-1,3-dimethylimidazolinium hexafluorophosphate (**145**) onto $Pd(PPh_3)_4$ gave the cationic $[(NHC)PdCl(PPh_3)_2]PF_6$ (**146**) in 72% yield (equation 21).

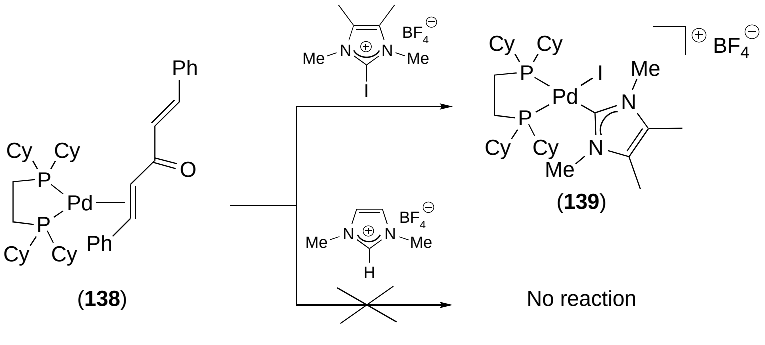

Scheme 24

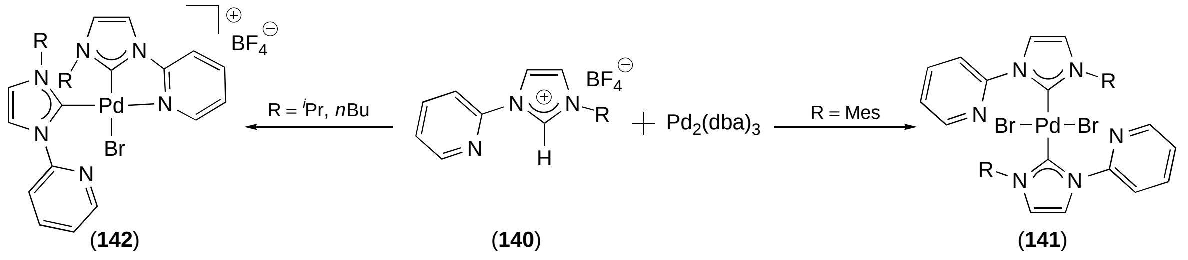

Scheme 25 Oxidative addition of imidazolium salt by $Pd_2(dba)_3$

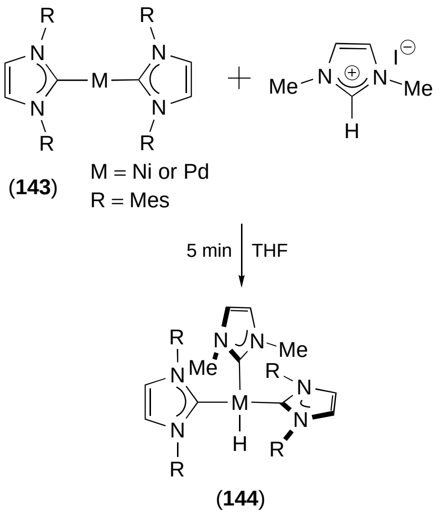

(20)

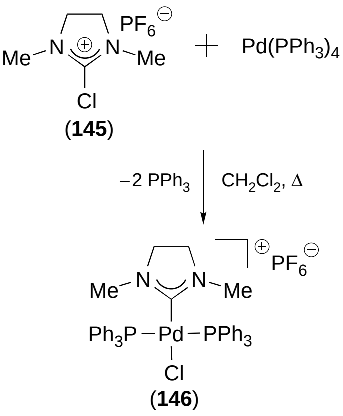

(21)

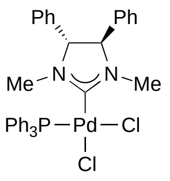

(147)

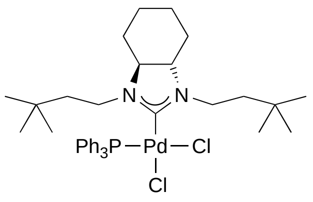

(148)

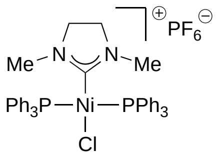

(149)

When the counteranion of the imidazolium salt was a chloride, the neutral $[(NHC)PdCl_2(PPh_3)]$ complex was obtained, the chloride triggering PPh_3 displacement from the metal coordination.[147] This route proved successful also for chiral NHC-containing palladium complexes (**147**) and (**148**). The cationic nickel analog (**149**) has been synthesized from reaction of $[Ni(COD)_2]$ and 2-chloro-1,3-dimethylimidazolidinium salts in the presence of two equivalents of PPh_3.

2.5 Reaction of Imidazolium Salts with Metal Hydrides

In 1968, Öfele reported that heating the adduct $[IDMH][HCr(CO)_5]$ at 120 °C yielded the NHC–Cr carbonyl complex $[(IDM)Cr(CO)_5]$.[1] Forty years later, reactions using metal hydrides to synthesize NHC–TM complexes are still scarcely used. Nonetheless, Sabo-Etienne and Chaudret synthesized a mixture of stereoisomers of the Ru complex (**152**) from $[RuH_2(PCy_3)_2(H_2)_2]$ (**150**) and tetramethyltriazoilum triflate (**151**) (equation 22).[148]

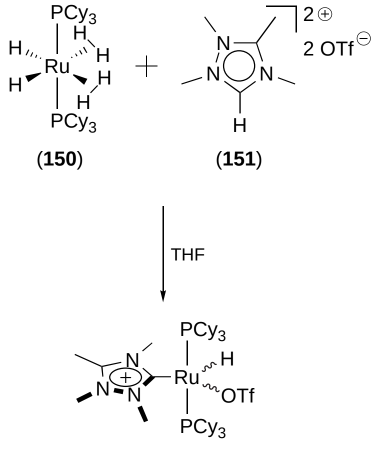

(22)

Crabtree and Faller developed a similar route using $[IrH_5(PPh_3)_2]$ and the imidazolium salt (**153**) (equation 23).[149] Whereas the expected product (**154**) has been isolated, another complex was formed and identified as (**155**), showing an unusual chelation of the imidazolium moiety. Using benzimidazolium salts, because of the protection of the C4 and C5 positions, only the expected complex was observed.

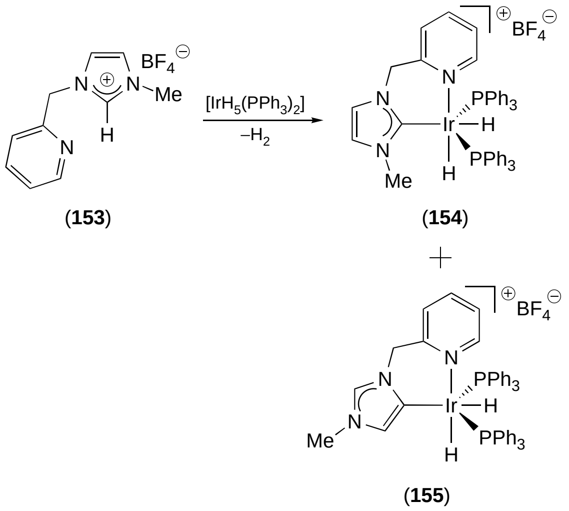

(23)

2.6 Synthesis by Silver-mediated Transmetallation

NHC transmetallation can be mediated by different TMs; however, only Ag–NHC complexes are commonly used for TM-complex synthesis.[150,151] The straightforward synthesis of NHC–Ag complexes, their high stability, and their tolerance to functional groups explain the success of this procedure. Other TM-mediated transmetallation are presented in Section 3.1.4.

The first synthesis of NHC–Ag complex was performed by Arduengo from $Ag(CF_3SO_3)_2$ and free carbene,[108] but later Lin developed a much easier procedure.[152] This procedure has the advantage that it does not require the synthesis and isolation of the free carbene. It was found to be non-air-sensitive and is carried out using mild reaction conditions. As depicted in Scheme 26, reaction of benzimidazolium salts (**156**) with Ag_2O in air and at room temperature afforded cationic biscarbene complex (**157**) (X = Br) or (**160**) (X = PF_6). These Ag-based complexes proved to be very efficient transmetallating agents. Indeed, reaction of $[Ag(NHC)_2](AgBr_2)$ (**157**) with $[AuCl(SMe_2)]$ gave the monocarbene complex [AuBr(NHC)] (**158**), while with $[PdCl_2(MeCN)_2]$ the palladium complex $[PdCl_2(NHC)_2]$ (**159**) was obtained. Interestingly, with PF_6 as counteranion, both NHCs were transferred to $[AuCl(SMe_2)]$ yielding the biscarbene complex (**161**).

Both the presented synthetic routes to NHC–Ag complexes and the subsequent NHC transmetallation were found to be very tolerant to the NHC steric hindrance. For example, Nolan reported the synthesis of a large library of [AgCl(NHC)] complexes.[153] Compatibility with functional groups was also demonstrated, since Hoveyda used this procedure for the synthesis of Cu(II) catalyst bearing an aryloxy-containing NHC.[154] As depicted in Scheme 27, treatment of salt (**162**) with Ag_2O led to the formation the dimeric complex (**163**). The resulting dimer has been used as an NHC transfer agent for the synthesis of NHC–Cu(II) dimer (**164**).

The transmetallation process was found competent for several metals – for instance, Crabtree and coworkers reported the transmetallation of $[Ag(NHC)_2](AgCl_2)$ to Rh(I) and Ir(I).[155] Owing to its mild reaction conditions, this procedure for the synthesis of NHC-containing complexes has found

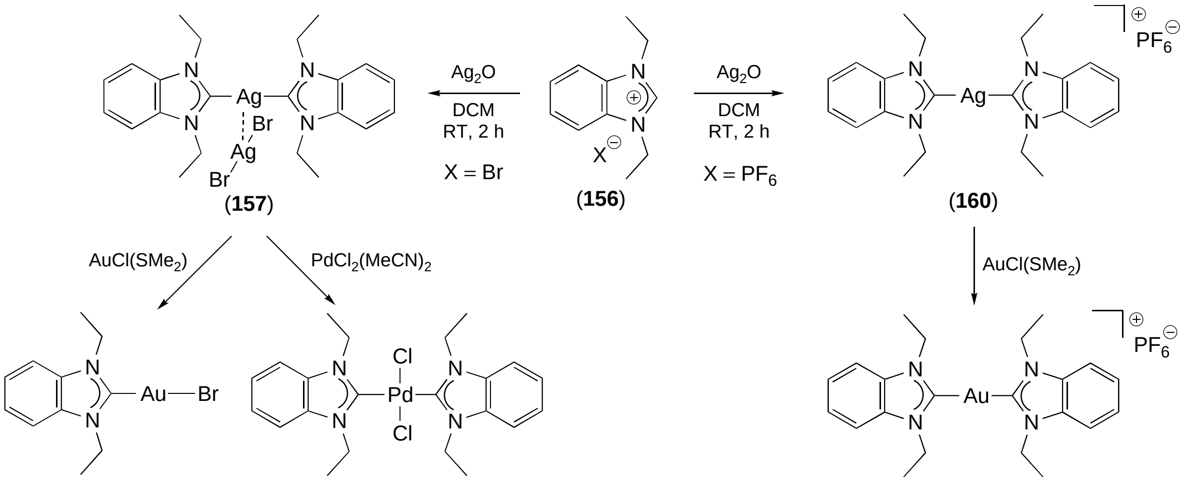

(**157**) (**156**) (**160**) (**158**) (**159**) (**161**)

Scheme 26 Synthesis of several NHC–Ag complexes and their reactivity in transmetallation reactions

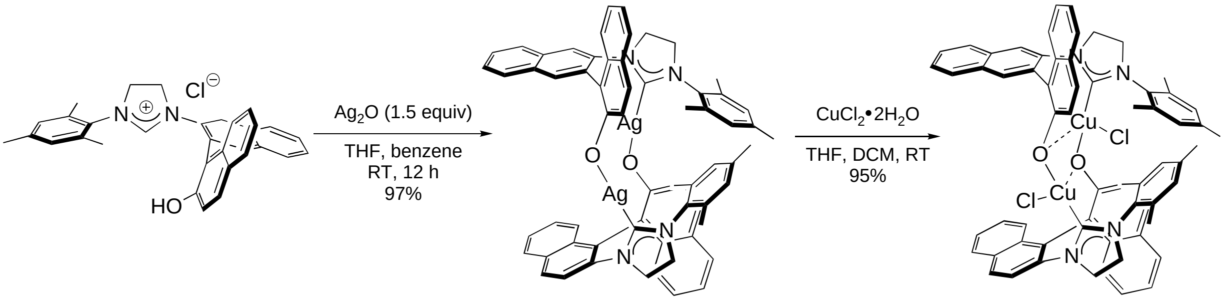

(**162**) (**163**) (**164**)

Scheme 27

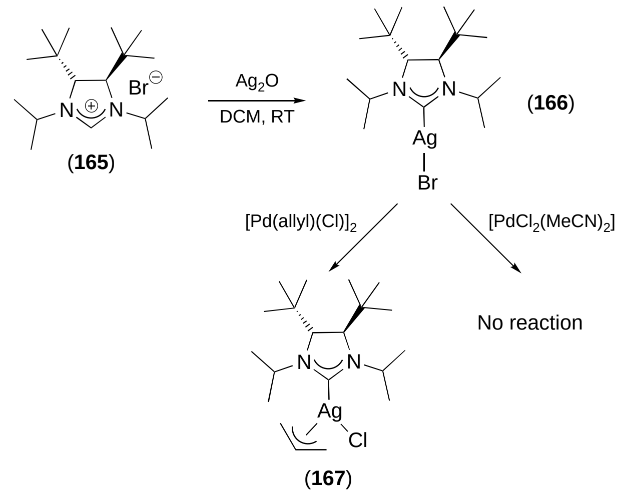

Scheme 28 Importance of metal source in transmetallation process

special use for the transfer of chiral NHC ligands. Complex (**166**) was synthesized from the chiral salt (**165**) and Ag_2O without racemization of chiral centers (Scheme 28).[156] Complex (**166**) has been used to transfer the chiral NHC to [(allyl)$PdCl_2$] affording the Tsuji–Trost catalyst (**167**). However, the importance of the metal source should not be disregarded, since reaction with [$PdCl_2(MeCN)_2$] did not lead to the expected product.

Recent investigations demonstrated that it is not necessary to isolate the NHC–Ag complexes.[105,157] For example, several NHC–Au(I) complexes have been synthesized by mixing the carbene salt, Ag_2O, and [$AuCl(SMe_2)$] in a one-pot reaction. A few other silver bases have been employed, such as Ag_2CO_3[158] or AgOAc.[159] AgOAc has been used as a precursor to synthesize bistriazolium Ag(I) complexes (**168**), and $AgCO_3$ to prepare the Ru-based enantioselective metathesis catalyst (**169**).[160]

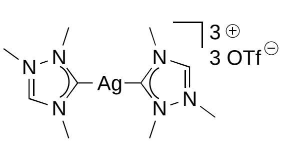

(**168**)

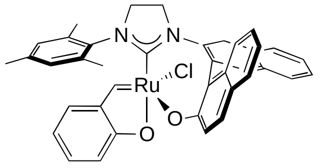

(**169**)

3 STABILITY AND REACTIVITY OF NHC-CONTAINING METAL COMPLEXES

Compared to phosphine ligands, NHCs are well known to significantly improve the stability of transition metal complexes, allowing for major advances in the field of catalysis. Even if the metal–NHC bond was considered for a while as inert and the NHC ligand as noninterfering, numerous reports mentioned different behaviors of these complexes.[161] In this section, we present an overview of NHC–TM complexes, focusing on the stability of the metal–NHC bond and the reactivity of the complexes involving the NHC ligand itself.

3.1 Stability of NHC–TM Complexes

3.1.1 NHC–TM Bond Cleavage

Till now, triazolylidene and thiazolylidene have been scarcely studied as TM ligands, although they find numerous applications in organocatalysis.[162,163] The stability of complexes binding these types of NHC has not been extensively reported and could explain why their use remains scarce. As an example, metathesis ruthenium-based catalyst (**170**) first synthesized by Fürstner exhibited a moderate activity in metathesis transformations in relation to its poor stability in solution.[68] This problem of reactivity/stability has been pointed out in others reports.[27,164]

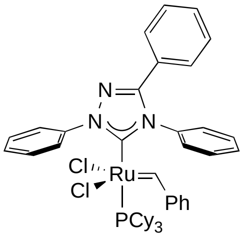

(**170**)

The stability of trihydride complex (**171**) has been found to be a remarkable feature.[165] Complex (**171**) is stable under inert atmosphere up to 115 °C in the solid state and in toluene solution at room temperature for months. It was observed that when the toluene solution was heated at 100 °C, no decomposition occurred until indium(0) traces appeared. In the presence of catalytic amount of indium(0), complex (**171**) decomposed entirely in a few minutes, freeing the free carbene, IMes (equation 24).

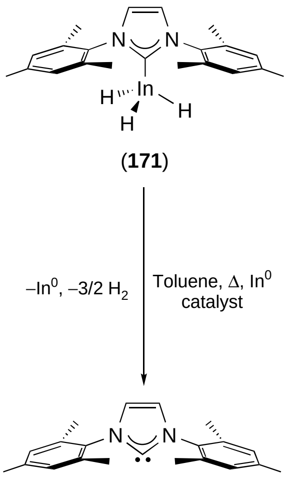

(24)

3.1.2 Redox Processes

NHC–TM complexes can be involved in redox processes, especially reductive elimination, leading to the cleavage of the NHC–TM bond and so to the decomposition of the complex. This subject has been comprehensively reviewed by Cavell and McGuinness.[166]

In 1998, Cavell *et al.* reported that some NHC–Pd complexes such as (**96**) and (**172**) were found moisture- and temperature-sensitive and needed to be stored under inert atmosphere below 5 °C.[92] Moreover, under atmospheric pressures of CO, (**96**) and (**172**) were quickly decomposed to Pd(0) and organic products.

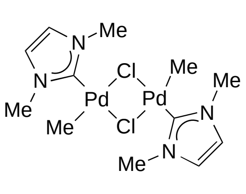

(**96**)

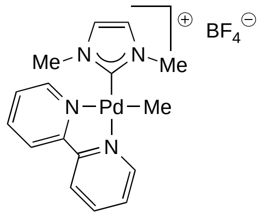

(**172**)

Investigations on the decomposition of complex (**173**) allowed for the identification of degradation products (equation 25).[93] The only detectable products were found to be 1,2,3-trimethylimidazolium salt (**174**), free COD, and Pd(0).

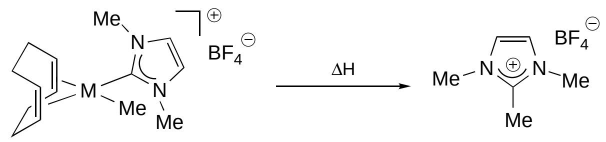

(**173**) (**174**) (25)

+

COD

+

Pd(0)

To explain this degradation, two different reaction pathways have been proposed (Scheme 29). The reaction may proceed by concerted reductive elimination or alternatively by migratory insertion, giving the intermediate (**175**) and subsequent heterolytic cleavage. Kinetic studies and DFT calculations supported the second proposed pathway.[142,167] An interesting clue supporting the migratory insertion is shown in equation (26). Danopoulos reported that reaction of the biscarbene (**176**) with [Pd(Me)$_2$A(tmeda)] did not allow for the isolation of the expected biscarbene complex but led solely to complex (**177**). Complex (**177**) was formed by a facile migratory insertion reaction and was stable enough to avoid decomposition into imidazolium salt.[168]

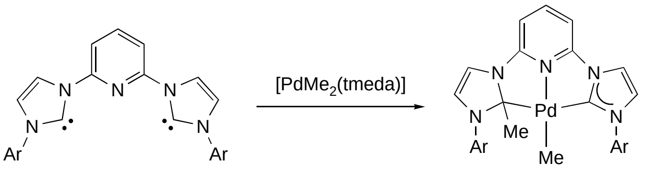

(**176**) (**177**)

(26)

Reactivity and stability of methylpalladium complexes have been examined with CO also, and facile reductive elimination was observed.[169] Reaction conditions were found to drive the formation of the degradation products (Scheme 30). Whereas, in the presence of silver salt, the 2-acylimidazolium salt (**179**) was observed as the major product, in its absence, complex (**178**) was degraded mostly into methylimidazolium salt (**180**). These results indicated that in the presence of silver salt, a coordination site of the palladium was free and led to the easiest coordination of CO, which is the key step for the carbonylation occurring before the degradation.

The stability of NHC-containing methylpalladium complexes was found dependent on different parameters such as the chelate bit-angle, but the chelating ligands itself appears

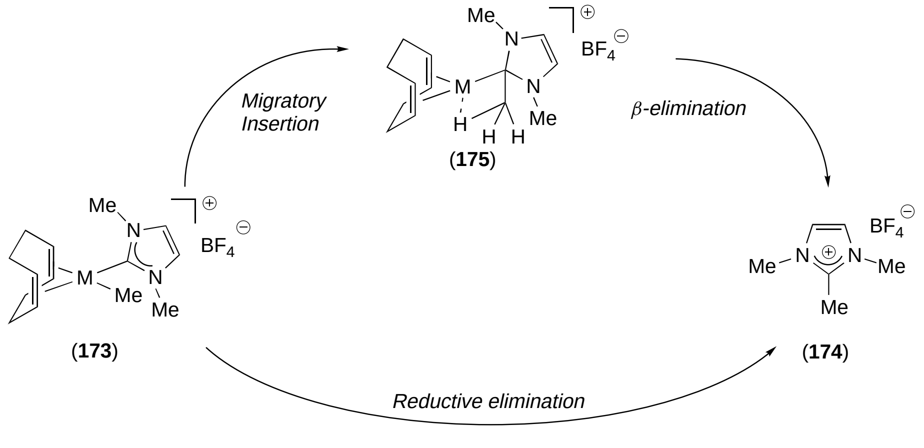

(**175**) (**173**) (**174**)

Scheme 29

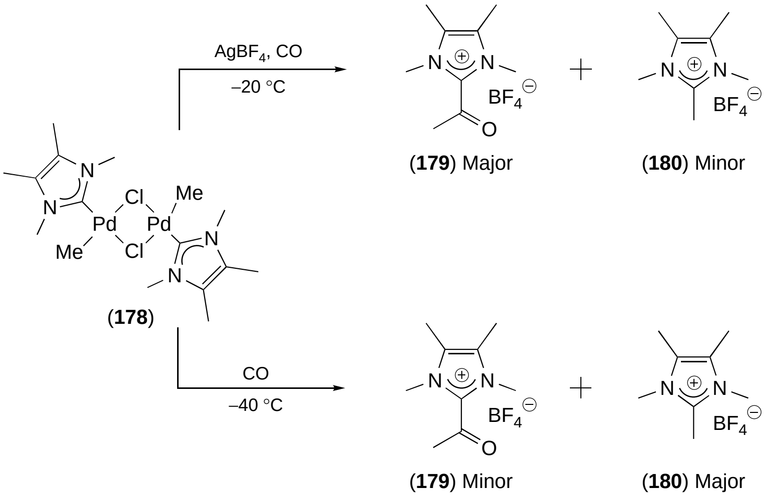

Scheme 30

to be an even more important factor. As an example, complexes (**181**) and (**182**) binding amine functions exhibit totally different thermal stabilities.[170] Whereas (**181**) was found to be one of the most stable methylpalladium complexes, the decomposition of (**182**) occurred rapidly at room temperature. The most rigid structure and the more donating pyridine appeared to be crucial for the high stability of (**181**).

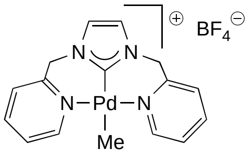

(**181**)

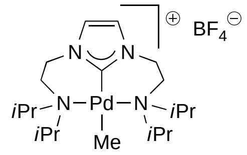

(**182**)

Further investigations on reductive elimination processes showed that this reductive elimination could be the side reaction leading to degradation of active species in C–C cross-coupling reactions. As illustrated in Scheme 31, palladium-based catalyst (**93**) underwent oxidative addition in the presence of iodobenzene, providing the reaction intermediate (**183**), which could be involved in the catalytic cycle but also affords the imidazolium salt (**184**) by direct reductive elimination.[171] Since then, a few other examples of reductive elimination processes leading to the degradation of the catalytic species have been reported.[136,172] It is noteworthy that similar redox processes leading to the cleavage of the NHC–TM bond have also been reported with other group 10 metals: nickel[128,171,173] and platinum.[141]

3.1.3 Ligand Substitution

The lability of the NHC ligands is unexpected. However, few examples of NHC substitution have been reported in the literature. Caddick and Cloke described that phosphines and free carbenes can replace coordinated NHC ligands in palladium-based complexes to give mixed NHC−phosphines complexes (equations 27−29).[78] Treatment of (**185**) with PCy$_3$ at room temperature resulted in a quantitative conversion to the mixed complex (**186**). Similar behavior was observed with the more sterically hindered P(tol)$_3$ with a lower conversion and requiring harsher reaction conditions. Ligand redistribution reaction between (**188**) and P(tol)$_3$ was also found to occur to give (**189**) in poor but isolable yield (equation 28). This same redistribution reaction was carried out with free I^{t}Bu instead of the phosphine and yielded, at room temperature, the two-coordinated mixed NHC−palladium complex (**190**). These experiments demonstrated that ligand

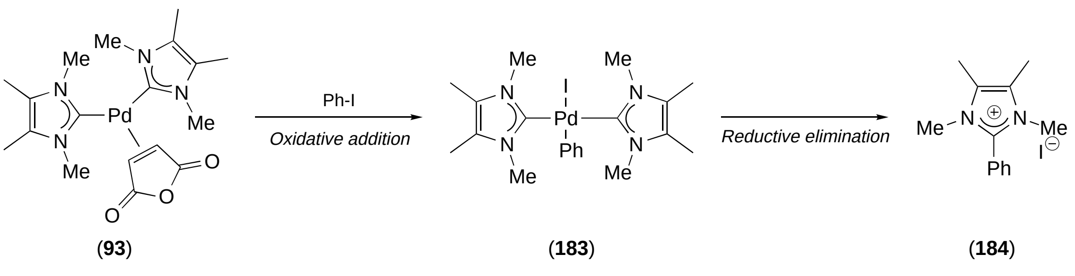

Scheme 31

substitution between phosphine and NHC are probably driven by steric effects.

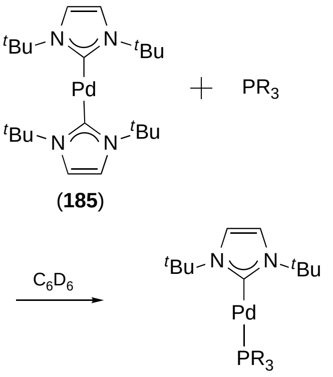

(**185**)

(27)

R = Cy, (**186**), 15 min, RT, 100%
R = tol, (**187**), 16 h, 60 °C, 33%

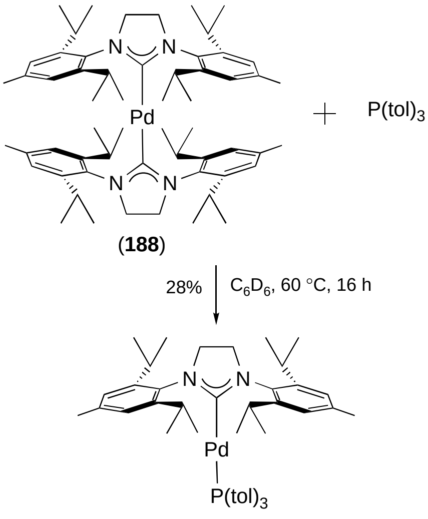

(**188**)

(28)

(**189**)

Displacement of phosphine by NHC ligand is not always obvious, mainly for steric reasons. For instance, during the reaction of [CpCo(PPh$_3$)Me$_2$] with free IPr, an equilibrium between the NHC- and phosphine-containing complexes, (**191**) and (**192**), respectively, was observed (Scheme 32).[174] Moreover, addition to the reaction mixture of the less sterically demanding trimethylphosphine led to the formation of the more stable five-coordinated complex (**193**).

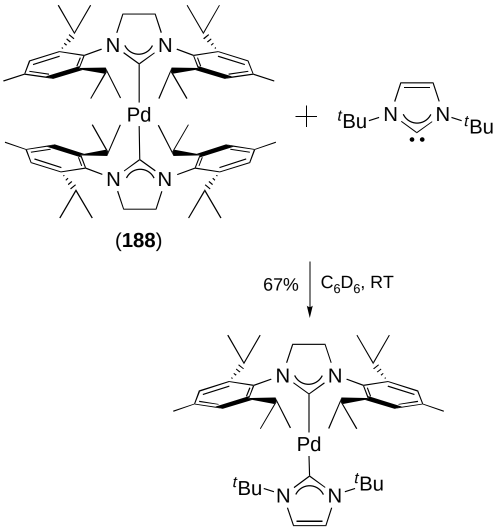

(**188**)

(29)

(**190**)

Another example of ligand substitution is an analog of Wilkinson's catalyst [RhCl(PPh$_3$)$_3$] (**195**), in which one of the phosphines was replaced by an IMes ligand, complex (**99**).[175] As illustrated in equation (30), (**194**) underwent cleavage of the Rh−IMes bond when treated with triphenylphosphine in hot DCE to quantitatively yield Wilkinson's catalyst. The corresponding salt IMes·HCl and a dimer (**196**) formed from a double S_N2 reaction involving the solvent. Two molecules of the carbene were also formed during this reaction.

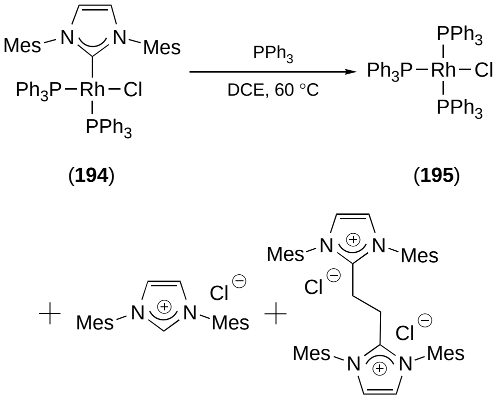

(**194**) (**195**)

(30)

20% (**196**) 80%

Recently, Arnold *et al.* reported on the synthesis and stability of f-block NHC-containing complexes.[176] The

$$\begin{tikzcd}[column sep=large] \mathrm{CpCo(PPh_3)Me_2} + \mathrm{IPr} \arrow[rr, shift left] \arrow[dr, "\mathrm{PMe_3}"] & & \mathrm{CpCo(IPr)Me_2} + \mathrm{PPh_3} \arrow[ll, shift left] \\ & \mathrm{CpCo(PMe_3)Me_2} & \end{tikzcd}$$

(**191**) (**192**) (**193**)

Scheme 32

reactions of some yttrium and zirconium complexes with phosphine oxides are illustrated in equations (31–34).[177] Whereas (**197**) is decomposed, chlorine substituted (**198**) afforded six-coordinated adduct (**199**). On the other hand, zirconium analog (**200**) exhibited excellent stability under comparable conditions (pyridine was used because of the poor solubility of (**200**) in benzene). These experiments confirmed the better lability of the Y–NHC bond compared to Zr–NHC bond. A special reactivity was observed for mono-NHC complex (**201**); triphenylphosphine oxide succeeded in displacing the carbene, while neither triphenylphosphine, trimethylamine oxide, THF, nor diethylether reacted.[178]

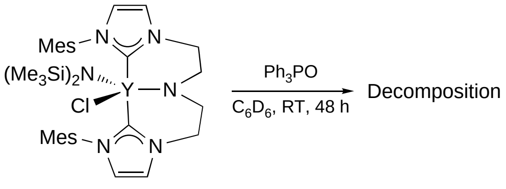
Mes
(Me$_3$Si)$_2$N
Cl
Y
N
Ph$_3$PO
C$_6$D$_6$, RT, 48 h
Decomposition

(**197**)

(31)

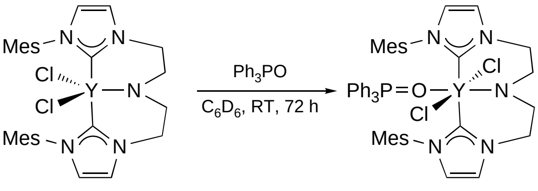
Mes
Cl
Y
Ph$_3$PO
C$_6$D$_6$, RT, 72 h
Ph$_3$P=O—Y—N

(**198**) (**199**)

(32)

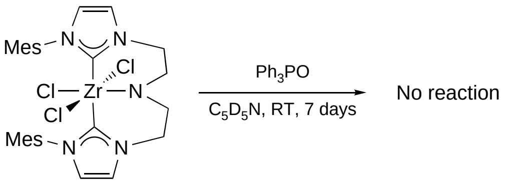
Mes
Cl
Zr
Ph$_3$PO
C$_5$D$_5$N, RT, 7 days
No reaction

(**200**)

(33)

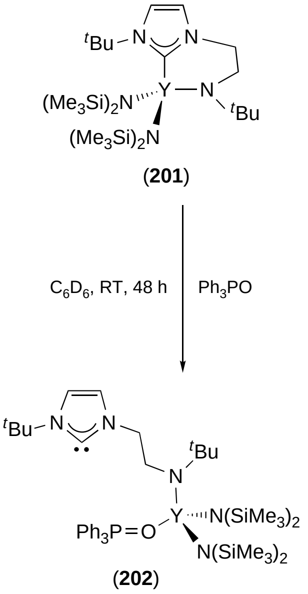
^{t}Bu
(Me$_3$Si)$_2$N
Y
C$_6$D$_6$, RT, 48 h
Ph$_3$PO
Ph$_3$P=O
N(SiMe$_3$)$_2$

(**201**)

(**202**)

(34)

3.1.4 *Transmetallation Processes*

Silver–NHC complexes have been shown as excellent NHC delivery agents.[150,151] Few examples of transmetallation using distinct late TMs have been reported. Tungsten pentacarbonyl NHC complex (**203**) was found efficient to transfer easily its NHC ligand to palladium (equation 35) and platinum (equation 36) yielding, respectively, palladium dimer (**204**) and platinum complex (**205**) with carbonyl ligand transfer.[179] This is to be noted, as chromium and molybdenum analogs of (**203**) exhibited similar reactivity.

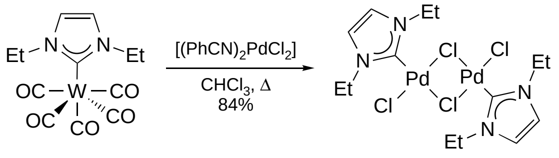
Et
OC—W—CO
[(PhCN)$_2$PdCl$_2$]
CHCl$_3$, Δ
84%
Pd
Cl

(**203**) (**204**)

(35)

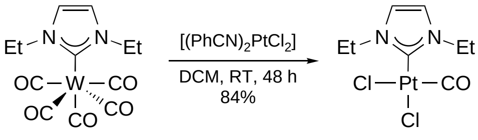
Et
OC—W—CO
[(PhCN)$_2$PtCl$_2$]
DCM, RT, 48 h
84%
Cl—Pt—CO
Cl

(**203**) (**205**)

(36)

Transmetallation from tungsten to rhodium and gold has also been found possible.[180] As depicted in equation (37), substitution of a carbonyl ligand from a rhodium center by an NHC occurred in the reaction with $[Rh(CO)_2Cl]_2$ to form biscarbene complex (**207**). In an analogous manner, tungsten complex (**206**) reacted rapidly with $[AuCl(SMe_2)]$ at room temperature to afford, in moderate yield, the biscarbene gold complex (**208**) (equation 38). Even if tungsten, molybdenum, and chromium carbonyl complexes showed an excellent ability to transfer NHC ligand, they are not widely used because of their poor stability. Oxidation with metal or molecular oxygen takes place extremely rapidly in these systems, yielding the

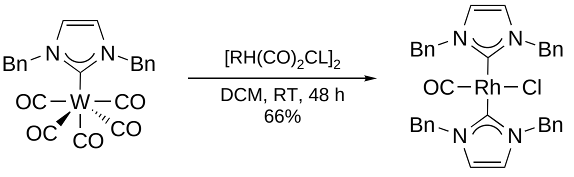
Bn
OC—W—CO
[RH(CO)$_2$CL]$_2$
DCM, RT, 48 h
66%
OC—Rh—Cl

(**206**) (**207**)

(37)

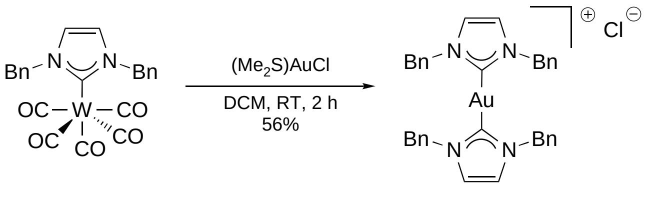
Bn
OC—W—CO
(Me$_2$S)AuCl
DCM, RT, 2 h
56%
Au
⊕ Cl⊖

(**206**) (**208**)

(38)

corresponding imidazolium salt or cyclic urea. For this reason, NHC transfer from tungsten to gold and silver affording biscarbene complexes has been observed, but their subsequent decomposition could not be avoided.

Hollis and coworkers reported also on a transmetallation process from zirconium to rhodium.[181] As illustrated in Scheme 33, imidazolium salt (**209**) reacted instantaneously with $Zr(NMe_2)_4$ to generate the biscarbene pincer (**210**) with orthometallation of the phenyl group. The biscarbene pincer was not isolated, but reacted with $[Rh(COD)Cl]_2$. The Rh(III) complex (**211**) was isolated in equilibrium with the dimer (**212**).

Lithium(I) NHC adducts are extremely rare, but some examples have been isolated as stable crystalline solids when a functional group is involved for their stabilization, the amino group, for instance.[176] Since these showed to be effective in transmetallation processes, they represent an interesting alternative to the expensive silver complexes. As an example, Arnold reported the synthesis of covalently tethered lanthanide carbene complexes (**214**) using adduct (**213**) as source of NHC (equation 39).[178] Using (**213**) and the same methodology, unusual cerium complexes (**215**) and (**216**) were isolated and characterized (equation 40).[182]

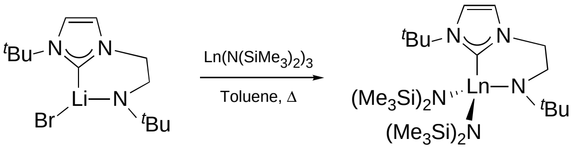

^tBu
N
N
Li
N
Br
^tBu
$Ln(N(SiMe_3)_2)_3$
Toluene, Δ
^tBu
N
N
Ln
N
$(Me_3Si)_2N$
$(Me_3Si)_2N$
^tBu

(**213**) (**214**) L = Sm or Y

(39)

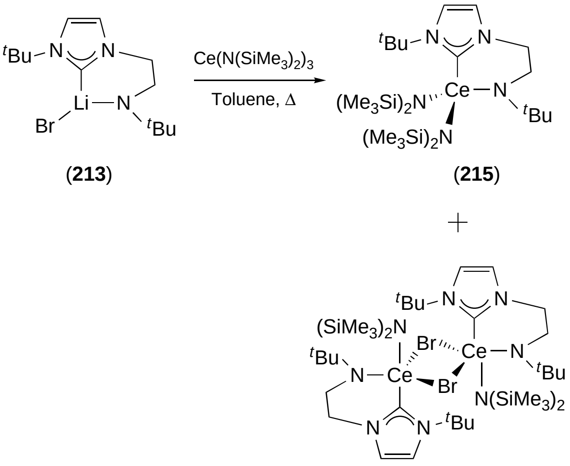

^tBu
N
N
Li
N
Br
^tBu
$Ce(N(SiMe_3)_2)_3$
Toluene, Δ
^tBu
N
N
Ce
N
$(Me_3Si)_2N$
$(Me_3Si)_2N$
^tBu
(213)
(215)
+
^tBu
N
N
$(SiMe_3)_2N$
^tBu
N
Ce
Br
Br
Ce
N
^tBu
$N(SiMe_3)_2$
N
N
^tBu

(**216**)

(40)

3.2 C–H Activation – Metallation Processes

The selective activation and functionalization of C–H bonds has attracted much attention in recent years.[183] In spite of the common proposal, which postulates that NHC ligands coordinated to TM are relatively inert, several examples of C–H activation processes involving NHCs have been reported. Because of the high electron-donating property of NHCs, some TM–NHC complexes have been found to undergo facile intramolecular C–H bond activation.

The first examples of C–H activation of an NHC ligand by TMs were reported by Hitchcock and Lappert and centered on ruthenium[184,185] and iridium.[186] $[RuCl_2(PPh_3)_3]$ reacted with the dimeric carbene (**217**) in xylene at 140 °C to give the five-coordinate monocarbeneruthenium (II) complex (**218**),

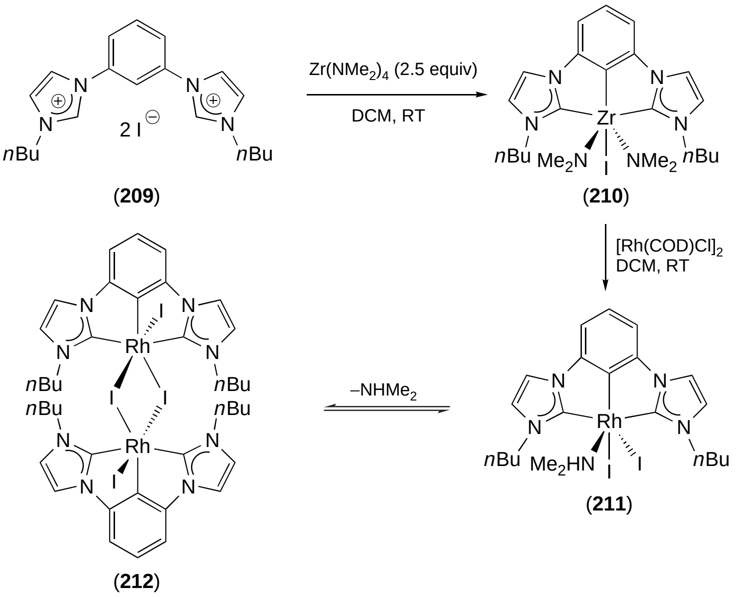

N
N
N
N
$2\,I^{\ominus}$
*n*Bu
*n*Bu
(209)
$Zr(NMe_2)_4$ (2.5 equiv)
DCM, RT
N
N
Zr
N
N
*n*Bu
Me_2N
I
NMe_2
*n*Bu
(210)
$[Rh(COD)Cl]_2$
DCM, RT
N
N
Rh
N
N
*n*Bu
Me_2HN
I
I
*n*Bu
(211)
$-NHMe_2$
N
N
I
Rh
N
N
*n*Bu
*n*Bu
I
I
*n*Bu
*n*Bu
N
N
Rh
N
N
I
(212)

Scheme 33

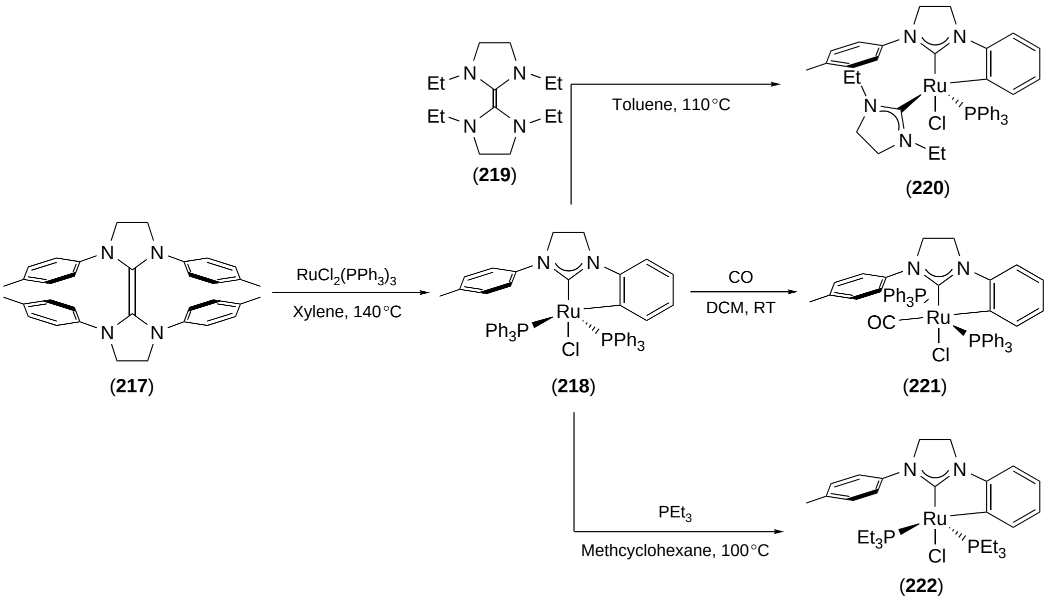
Et
Et
Et
Et
(219)
Toluene, 110°C
Ru
Cl
PPh3
(220)
(217)
RuCl2(PPh3)3
Xylene, 140°C
Ph3P
Ru
Cl
PPh3
(218)
CO
DCM, RT
Ph3P
OC
Ru
Cl
PPh3
(221)
PEt3
Methcyclohexane, 100°C
Et3P
Ru
Cl
PEt3
(222)

Scheme 34

containing a five-membered metallacycle (Scheme 34). It should be pointed out that with smaller *N*-substituents (methyl or ethyl group) tetracarbeneruthenium (II) complexes were obtained.[187] Studies of the stability and reactivity of (**218**) showed that a small NHC could substitute for a phosphine ligand using the dimer (**219**) to yield the biscarbene (**220**). Moreover, reaction with carbon monoxide resulted only in CO binding to the metal center to yield the six-coordinated species (**221**). The treatment of (**218**) with more sterically hindered ligand such as PEt_3 led to the five-coordinated complex (**222**).

Different from the ruthenium system previously discussed, $[Ir(COD)Cl]_2$ reacted with the electron-rich olefin (**217**) to afford the homoleptic organoiridium tricycle complex (**223**) with an increase of the iridium oxidation state from (I) to (III) (equation 41). This spontaneous orthometallation process could be reversed by anhydrous HCl leading to the scission of one of the Ir–C bonds (equation 42). Dehydrochlorination of salt (**224**) using basic conditions caused the orthometallation and the reformation of complex (**223**).

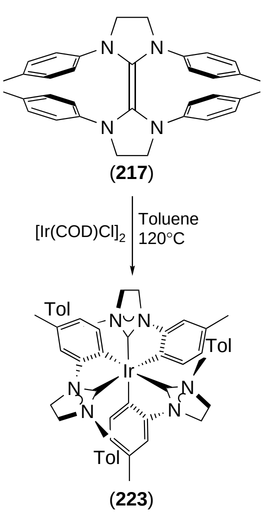
(217)
[Ir(COD)Cl]2
Toluene
120°C
Tol
Tol
Tol
Ir
(223)

(41)

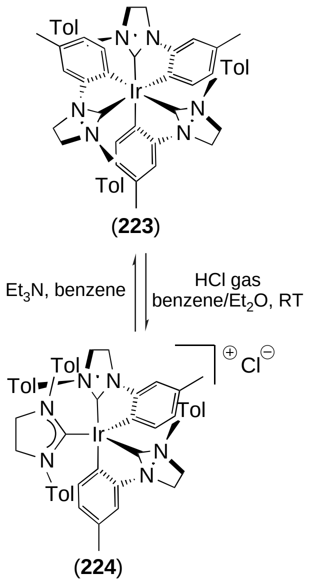
Tol
Tol
Ir
Tol
(223)
Et3N, benzene
HCl gas
benzene/Et2O, RT
Tol
Tol
Tol
Ir
Tol
Cl
(224)

(42)

Recently, Peris and coworkers reported the synthesis of highly stable orthometallated Cp*-Ir NHC complexes and a catalytic application in the deuteration of organic molecules.[188,189] Complexes (**227**) were synthesized from imidazolium salt (**225**) and $[IrCp^*Cl_2]_2$ as metal precursor either by a one-step procedure with sodium iodide to minimize the mixture I versus Cl or by transmetallation from the corresponding silver carbene affording (**226**) followed by the C–H activation of the phenyl ring by the iridium

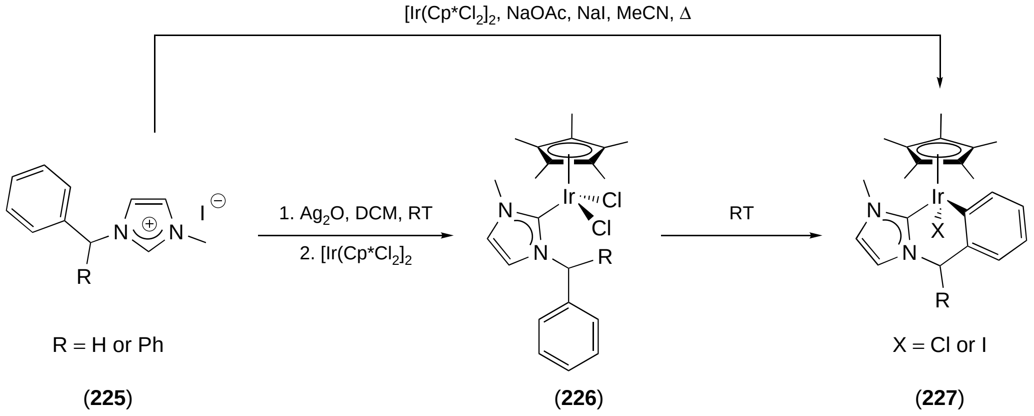
[Ir(Cp*Cl2]2, NaOAc, NaI, MeCN, Δ
1. Ag2O, DCM, RT
2. [Ir(Cp*Cl2]2
RT
R = H or Ph
X = Cl or I
(225)
(226)
(227)

Scheme 35

center (Scheme 35). The easy orthometallation that occurs at room temperature allows for an evaluation of the performance of (**227**) in C–H activation reactions. As depicted in equation (43), refluxing (**227**) in methanol-d_4 led to quantitative deuteration of the ortho position of the phenyl group. The dynamic metallation/demetallation equilibrium process was confirmed by high levels of deuteration of organic molecules obtained when this catalyst is engaged in reaction with deuterated methanol at 100 °C.

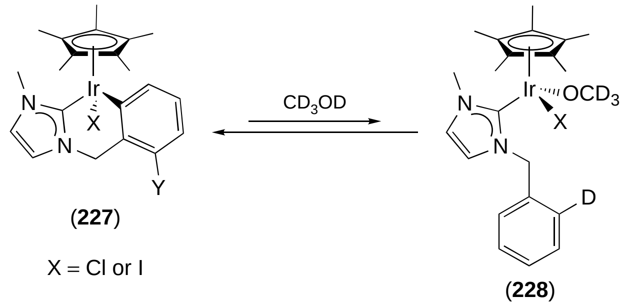
CD3OD
(227)
X = Cl or I
(228)

(43)

Two C–H activation examples have been reported using triazolium salt (**229**) as NHC ligands.**[44,190]** With the aim of introducing chirality into a catalyst to generate a stereogenic metal center, Enders synthesized ruthenium and rhodium complexes (**230**) and (**231**) containing chiral orthometallated *N*-phenyltriazolylidene ligands (equations 44 and 45). In situ deprotonation of the corresponding triazolium salts and reaction of these carbenes with dimeric complexes $[(\eta^6\text{-cymene})\text{RuCl}_2]_2$ and $[\text{Cp}^*\text{RhCl}_2]_2$ afforded, respectively, mononuclear complexes (**230**) and (**231**) with the orthometallated phenyl group as chelating ligand. Because of their pseudotetrahedral structures, these complexes possess diastereomeric forms that can be separated by simple silica-gel chromatography. In the case of the rhodium-based complexes, the diastereomeric excesses were lower than ruthenium analogs because of slow epimerization that occurs in solution.

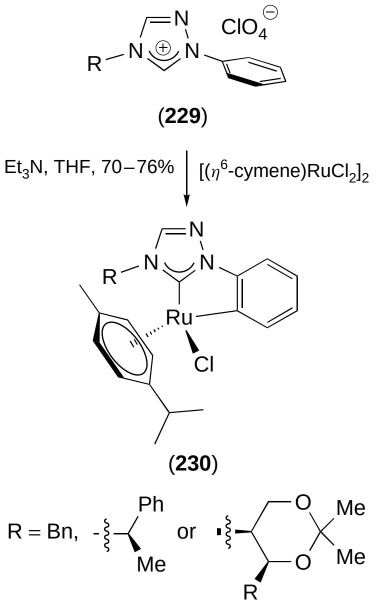
(229)
Et3N, THF, 70–76%
[(η6-cymene)RuCl2]2
(230)
R = Bn,
or

(44)

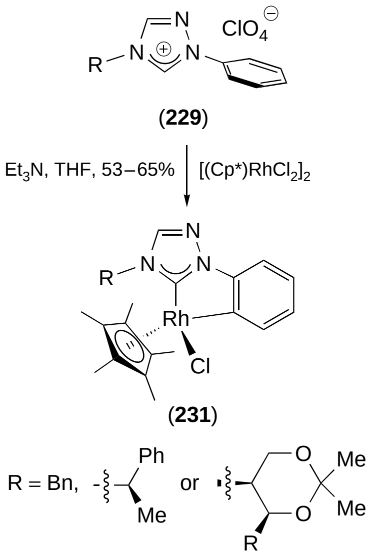
(229)
Et3N, THF, 53–65%
[(Cp*)RhCl2]2
(231)
R = Bn,
or

(45)

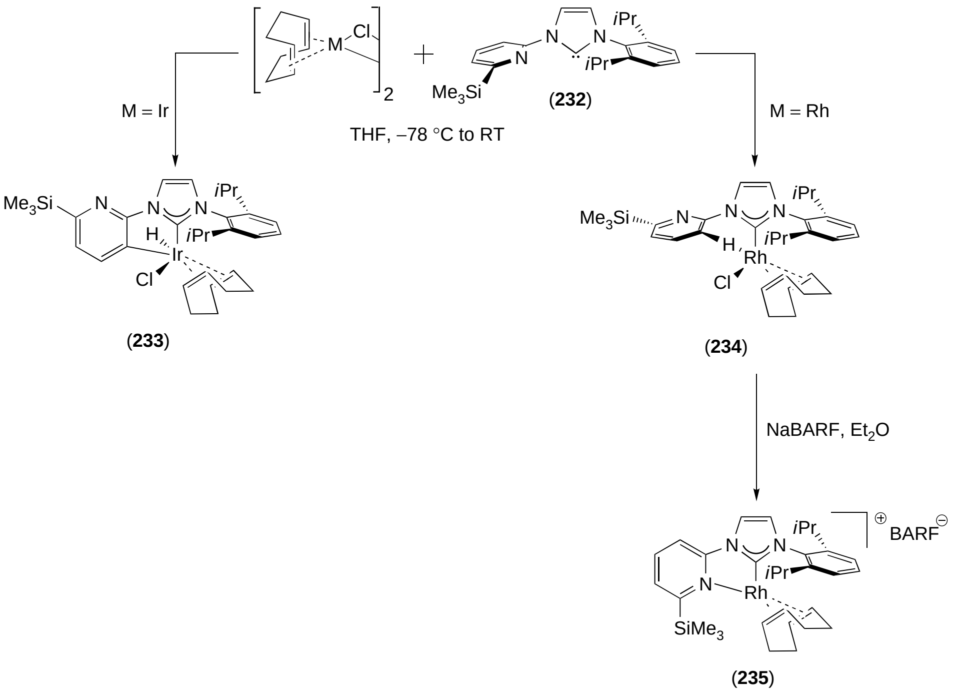

Scheme 36

The reactivity of iridium is often associated with that of rhodium; however, as shown in Scheme 36, iridium is more favorable toward activating the C–H bond and so this metal has been widely used for this reaction. Reaction of $[\mathrm{Ir(COD)Cl}]_2$ with one equivalent of the pyridine-functionalized NHC (**232**) gave in quantitative yield the complex (**233**) by cleavage of the metallic precursor dimer and orthometallation of the pyridine moiety (Scheme 36).[191] In contrast, the same reaction carried out with $[\mathrm{Rh(COD)Cl}]_2$ as the metal source afforded (**234**), for which a strong interaction between the rhodium center and the *ortho* hydrogen of the pyridine was observed. Treatment of (**234**) with a sodium salt did not lead to a C–H activation, but led to the coordination of the pyridine onto the metal center yielding the air stable (**235**).

Nolan *et al.* reported an early example of C–H activation of the methyl group, namely, cyclometallation, by a rhodium center.[192] The reaction of four equivalents of IMes with $[\mathrm{Rh(COE)_2Cl}]_2$ in THF at room temperature rapidly gave an orange microcrystalline product, identified as (**236**) (Scheme 37). This biscarbene-containing rhodium complex results from C–H bond activation of an internal aryl methyl C–H bond of one of the IMes ligands, producing a five-coordinate Rh(III) alkyl hydride complex. The stability of complex (**236**) has been investigated. Under an atmosphere of H_2, the dihydride complex (**237**) was quickly formed in quantitative yield. Moreover, under CO atmosphere, (**236**) gave the product (**238**) binding a carbonyl group with the cleavage of the Rh–C bond. These experiments show that, like the orthometallation, the cyclometallation can be reversed.

Many examples of cyclometallation process have been reported involving iridium as the metallic center. As illustrated in Scheme 38, treatment of ICy-containing complex (**239**) with one equivalent of trifluoromethylsulfonic acid to replace one methyl group led instantly to the formation of the metal hydride (**242**) with methane evolution.[118] X-ray diffraction studies confirmed the π-coordination double bond of one of the *N*-substituents. To explain the formation of (**242**), the authors assumed that trifluoromethylsulfonic acid drove methane elimination and formation of the complex (**240**), with an equilibrium established between the coordinated and free triflate complexes. The 16-electron species (**240**) evolves by a C–H bond activation process of the cyclohexyl group to form (**241**) and subsequent β-hydrogen migration giving the final product. The overall reaction (cyclometallation/β-hydrogen migration) leads to the formation of a stereogenic center and a double bond.

Major achievements in cyclometallation processes involving NHC ligands have been achieved by Nolan and coworkers.[193,194] It was observed that the solvent could play a crucial role in the formation of rhodium- and iridium-based complexes. As shown in Scheme 39, the reaction performed in pentane between $[\mathrm{M(COE)_2Cl}]_2$ (M = Rh or Ir) and four equivalents of $\mathrm{I}^t\mathrm{Bu}$ led only to COE substitution by the NHC ligand affording rhodium-based product (**243**) (the iridium complexing proving difficult to isolate). On the other hand, the same reaction carried out in hexanes gave, via C–H activation, the hydride complexes (**244**) and (**245**). Finally, in benzene, a unique double cyclometallation process occurred to yield the coordinatively unsaturated 16-electron

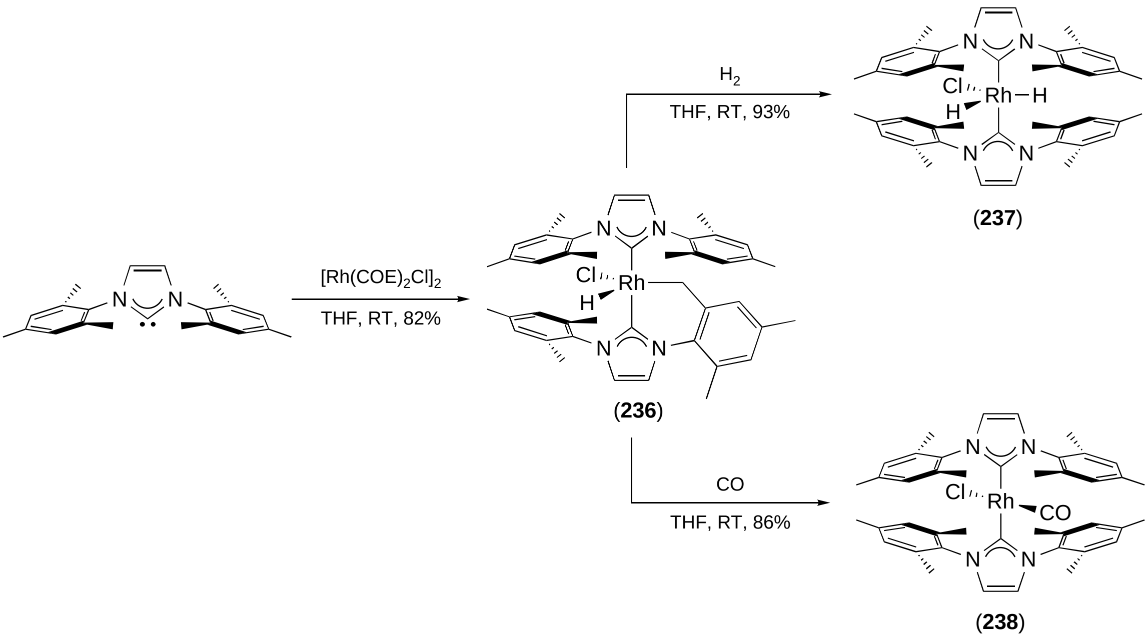

Scheme 37

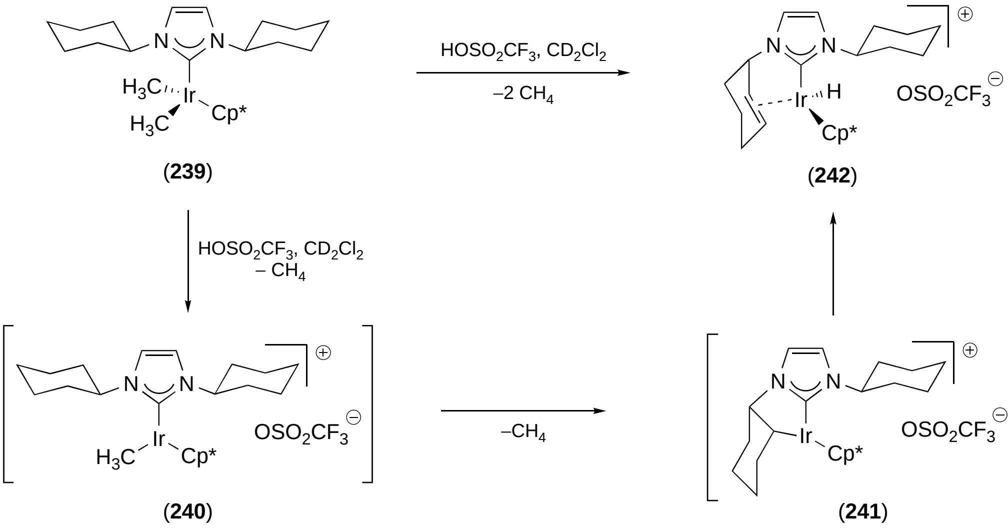

Scheme 38

complexes (**246**) and (**247**), which are stabilized by agostic interactions. The solvent-dependent interaction, which is carried out in benzene, was also emphasized in the conversion of isolated complexes (**243**), (**244**) and (**245**) into (**244**), (**246**), and (**247**), respectively.

Abstraction of the chloride from complex (**247**) by a silver salt allowed for the preparation of the unprecedented *naked* cis-divacant four-coordinate 14-electron complex (**248**) (Scheme 40). Further examination of this coordinatively unsaturated cationic complex showed that, in presence of H_2 gas, the double cyclometallation process could be reversed to give a remarkable electron-deficient cationic dihydride complex (**249**).[195] The unsaturated nature of (**249**) allowed for its rapid reaction in the presence of carbon monoxide to form the dicarbonyl complex (**250**) by a double sequence C–H activation/hydrogen elimination.

Following their work on orthometallation with iridium-based complexes, Peris *et al.* investigated the difference between aromatic and aliphatic C–H activation processes. They reported the preparation and reactivity of alkyl-functionalized imidazolylidene complexes of iridium (III) undergoing intramolecular cyclometallation.[196] As shown in

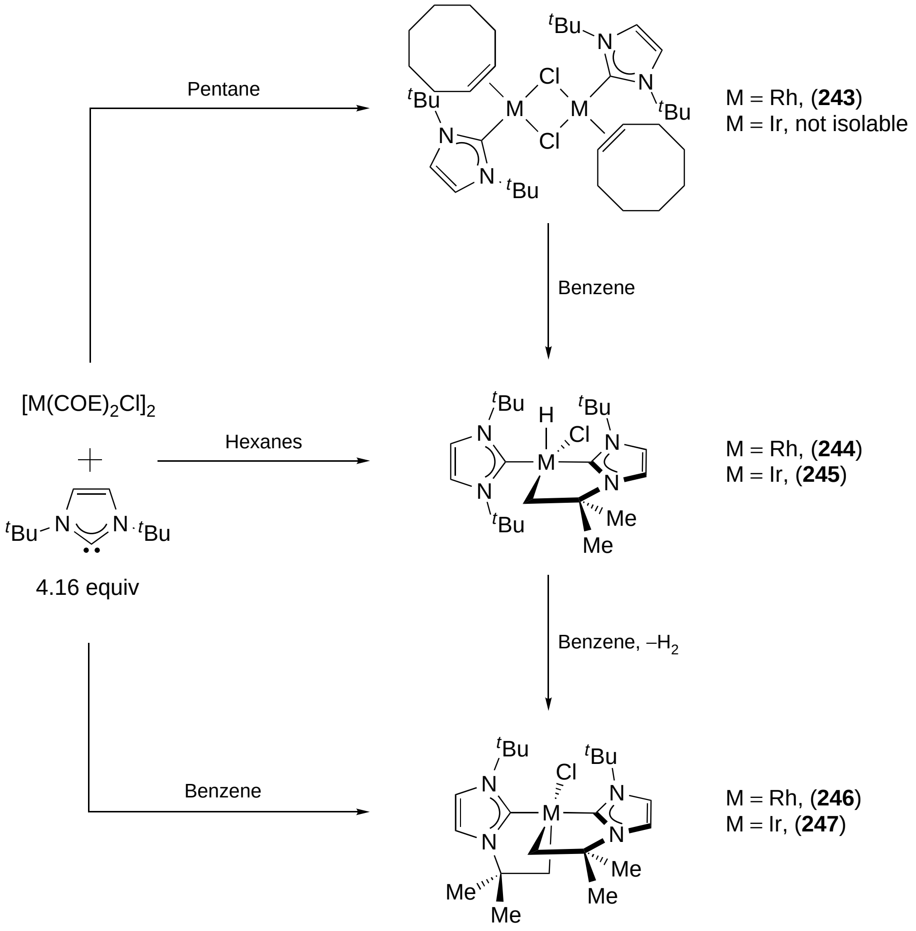
[M(COE)2Cl]2
+
4.16 equiv
Pentane
M = Rh, (243)
M = Ir, not isolable
Benzene
Hexanes
M = Rh, (244)
M = Ir, (245)
Benzene, –H2
Benzene
M = Rh, (246)
M = Ir, (247)
tBu
Cl
H
M
N
Me

Scheme 39

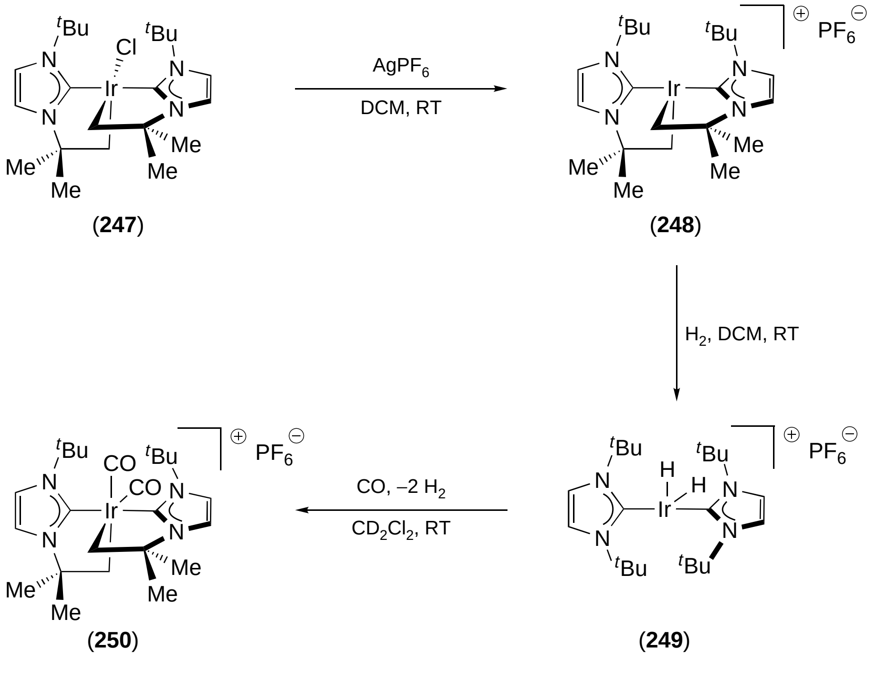
(247)
AgPF6
DCM, RT
(248)
PF6
H2, DCM, RT
(249)
CO, –2 H2
CD2Cl2, RT
(250)
Ir
CO
Cl
H
tBu
Me

Scheme 40

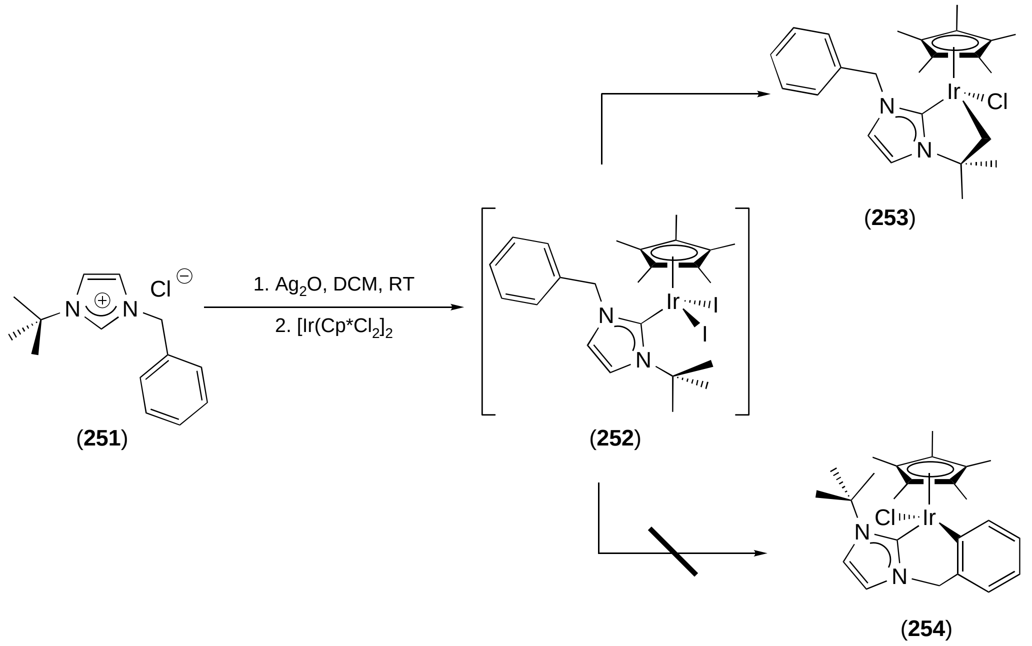

Scheme 41

Scheme 41, starting from 1-benzyl-3-*tert*-butylimidazolium iodide (**251**), reaction with Ag_2O and further addition of $[Cp^*IrCl_2]_2$ provided the complex (**252**) that instantaneously gave alkyl C–H activated product (**253**). It is noteworthy that neither intermediate (**252**) nor orthometallated complexes (**254**) were detected. This suggests that the alkyl C–H activation is a readily accessible process. The unique formation of (**253**) suggests that the aliphatic C–H activation process is more favorable compared to the aromatic version, but this conclusion should be taken arrived at with caution. First, since the size of the metallacycle formed is not the same, ring size probably plays a major role. Moreover, using an imidazolium salt with an *iso*-propyl group instead of the *tert*-butyl requires the use of a base to achieve the C–H activation and only the orthometallated product was isolated.**[196]** To rationalize these results, the authors proposed that steric factors are critical. In the case of the *tert*-butyl group, the steric pressure around the metal center may be triggering the aliphatic cyclometallation to reduce congestion.

Independent investigations on the ability of NHC ligands to be involved in cyclometallation processes have been carried out by Yamagushi using an iridium system.**[197]** As presented in Scheme 42, reaction of iridium complex (**255**) with MeONa yielded the cyclometallated product (**256**) quantitatively by C–H activation of the *iso*-propyl group. It may be noted that when (**255**) was treated with silver salt, dicationic iridium complex (**257**) was formed without any cyclometallation product, showing that the base plays a role other than one as a chlorine abstractor. Reaction of (**256**) with silver triflate or (**257**) with a base gave the unstable cyclometallated complex (**258**), demonstrating that the coordination of basic ligands to the dicationic metallic center precedes the cyclometallation process. These data suggest the following mechanism: dechlorination of (**255**) is promoted by the base, then the intermediate undergoes direct C–H activation, and finally undergoes hydride elimination.

In this system, the cyclometallation may be favored by the presence of the methyl substituents on the NHC backbone, increasing the σ-donor character of the NHC ligand and enhancing the C–H activation process. These reactions have been successfully applied to introduce other ligands onto the metal center, such as alkoxy or amino groups that can be used as proton sponge.

Further studies demonstrated that changing the steric congestion of the NHC *N*-substituents allowed for tuning the reactivity of [Cp*Ir(NHC)Cl] complexes (Scheme 43).**[198]** Starting from (**259**), the use of one equivalent of *i*PrONa afforded the hydrido complex (**260**) contrasting with the previously presented reaction (Scheme 43); a second equivalent was necessary to form the stable cyclometallated product (**261**). Investigations of the stability of (**261**) showed that in chloroform a rapid chlorination occurred, leading to (**262**). While complex (**261**) was found stable in *iso*-propanol, in methanol it was slowly converted into dihydrido complex (**263**) with ring opening of the cyclometallated product.

Grubbs reported an unexpected reaction, which may be at play during the course of the synthesis of the second-generation olefin metathesis catalyst (**264**) (equation 46).**[27]** The product (**265**), air stable both in solution and in the solid state, results from the C–H activation of one *ortho* methyl of the mesityl group. Unfortunately, no explanation was proposed for the mechanistic pathway leading to (**265**).

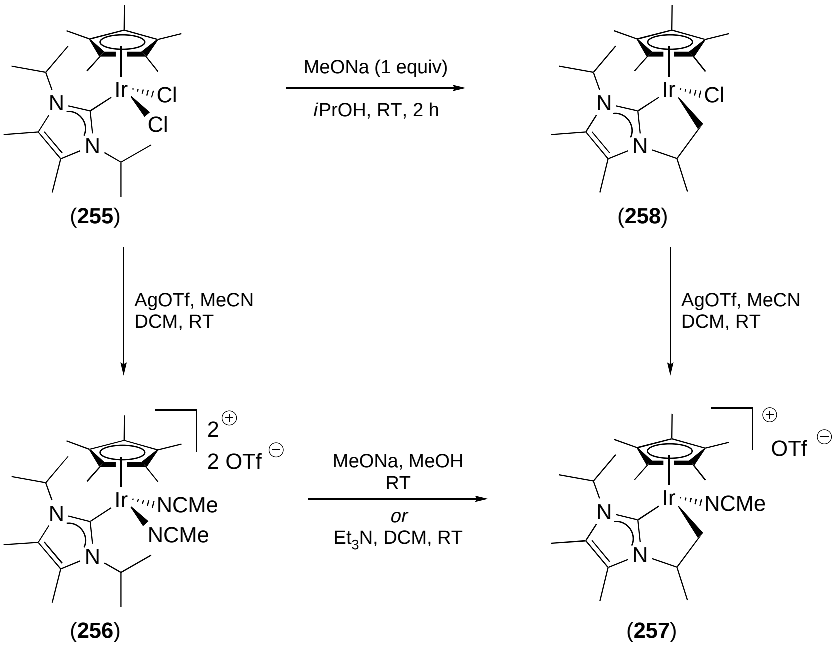
Ir
Cl
Cl
N
N
(255)
MeONa (1 equiv)
iPrOH, RT, 2 h
(258)
AgOTf, MeCN
DCM, RT
AgOTf, MeCN
DCM, RT
2⊕
2 OTf ⊖
NCMe
NCMe
(256)
MeONa, MeOH
RT
or
Et3N, DCM, RT
⊕
OTf ⊖
(257)

Scheme 42

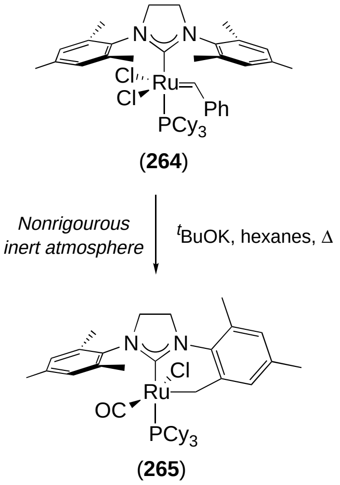
Cl
Cl
Ru
Ph
PCy3
(264)
Nonrigourous
inert atmosphere
tBuOK, hexanes, Δ
N
N
Cl
Ru
OC
PCy3
(265)

(46)

In the course of decomposition examinations of ruthenium olefin metathesis catalysts,[199] Grubbs and coworkers described a double C–H activation of the NHC ligand.[200] The heating of complex (**266**), bearing a benzimidazol-2-ylidene NHC, in benzene at 60 °C under inert conditions led to the formation of a decomposition product (**267**) in moderate yield (Scheme 44). Traces of a by-product (**268**) were observed. Interestingly, changing the solvent to dichloromethane-d_2 at 40 °C, led to (**268**) becoming the major decomposition product. X-ray crystallography analyses of these complexes showed that the benzylidene carbon atom of (**266**) had inserted into an *ortho* C–H bond of one of the *N*-substituents. Furthermore, η^6 binding of the ruthenium atom to the phenyl group of benzylidene pattern was noticed. Unlike (**267**), complex (**268**) showed an additional insertion of the ruthenium center into a second *ortho* C–H bond of the other *N*-phenyl group of the NHC ligand leading to the formation of a five-membered metallacycle. The authors have also shown that (**267**) can be converted quantitatively into (**268**) in the presence of tricyclohexylphosphine in dichloromethane-d_2.

An analogous example of C–H activation using rare earth metals has been recently described by Cui *et al.*[201] As shown in equation (47), starting from imidazolium salt (**269**) this one-step route involves a double-deprotonation process by the basic Ln(CH$_2$SiMe$_4$)Li(THF)$_4$ complex to give complexes (**270**) with Ln = yttrium, lutetium or scandium. The side substituents of the NHC ligand bind to Ln ion in η^5/k^1 constrained geometry configurations. Such solvent-free complexes of rare earth metal indicate the strong electron-donating nature of the NHC.

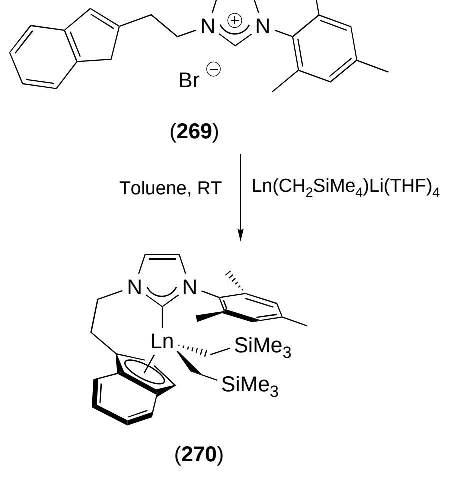
N
⊕
N
Br ⊖
(269)
Toluene, RT
Ln(CH2SiMe4)Li(THF)4
N
N
Ln
SiMe3
SiMe3
(270)

(47)

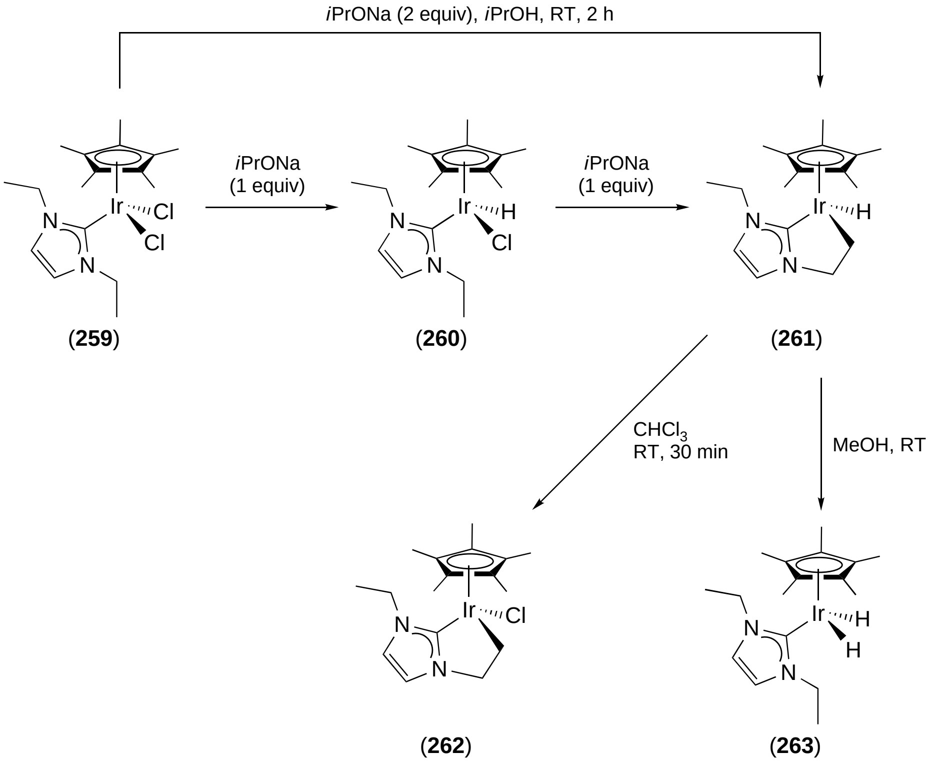
*i*PrONa (2 equiv), *i*PrOH, RT, 2 h
*i*PrONa
(1 equiv)
*i*PrONa
(1 equiv)
Ir
Cl
N
(259)
(260)
(261)
CHCl$_3$
RT, 30 min
MeOH, RT
(262)
(263)

Scheme 43

Some other intermolecular C–H activations involving the NHC ligand have been observed during the synthesis of particular NHC-containing ‘‘pincer’’-type complexes also called CCC–NHC complexes.[202] In addition to zirconium- and rhodium-based complexes (**210**) and (**211**),[181] several examples involving palladium of general structure (**271**) have been synthesized. Whereas Faller and Crabtree have found that in presence of $Pd_2(dba)_3$ and K_2CO_3 the C–H activation of the bisimidazolium salt was unsuccessful (C–Br bond activation was used),[203] Danopoulos reported that heating $Pd(OAc)_2$ and the carbene precursor with NaOAc to 160 °C allowed for the efficient C–H activation yielding the orthometallated product (**271**).[204]

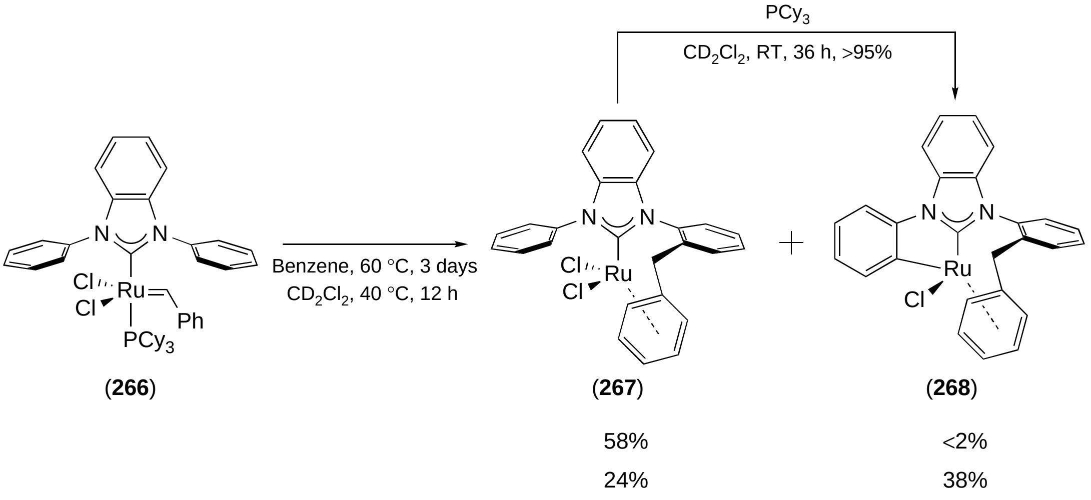
PCy$_3$
CD$_2$Cl$_2$, RT, 36 h, >95%
Benzene, 60 °C, 3 days
CD$_2$Cl$_2$, 40 °C, 12 h
Ru
PCy$_3$
Ph
(266)
(267)
(268)
58%
24%
<2%
38%

Scheme 44

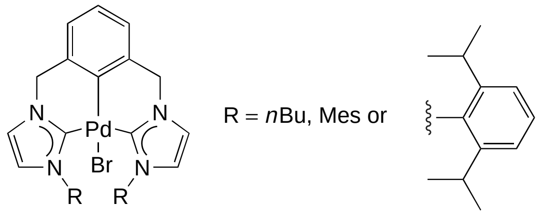

(**271**)

3.3 C–C Activation

While C–H activation reactions have been observed for many NHC–TM complexes, to the best of our knowledge, only one example of C–C bond activation has been reported to date.[60] As shown in Scheme 45, complex (**273**) reported by Whittlesey and Macgregor was found capable of either C–C or C–H bond activation as a function of reaction conditions. Reaction of three equivalents of free IMes with [Ru(PPh$_3$)$_2$(CO)(H)$_2$] (**272**), at 80 °C, led to the formation of a mixture of monocarbene (**273**) and biscarbene complex (**274**). When more forcing conditions were used, product (**276**) was obtained in excellent yield resulting from the cleavage of methyl–mesityl bond. On the other hand, upon addition of vinyltrimethylsilane at room temperature, (**273**) reacted to produce a C–H activated species (**275**). It is to be noted that the same type of cyclometallation has been observed with ethyl groups as *N*-substituents.[205] Interestingly, direct insertion of ruthenium into an unstrained C–C bond of IMes is thermodynamically more favorable than the insertion into a C–H bond. Such an example is remarkable, since C–C single bonds are among the most unreactive bonds.

3.4 Insertion Reaction into the NHC Ligand

As previously presented, the ortho substituents on the aromatic rings of the NHC ligands can be involved in different activation processes. Keister, Diver, and coworkers reported an unprecedented carbene insertion into the mesityl group of the NHC.[206] In the presence of carbon monoxide, ruthenium carbenes such as second-generation Grubbs catalyst (**264**) gave a net insertion/ring expansion, namely, Buchner reaction, into one of the aromatic rings of the NHC ligand as illustrated in equation (48). Complexes (**278**) and (**279**) have been isolated in good to excellent yield with complete

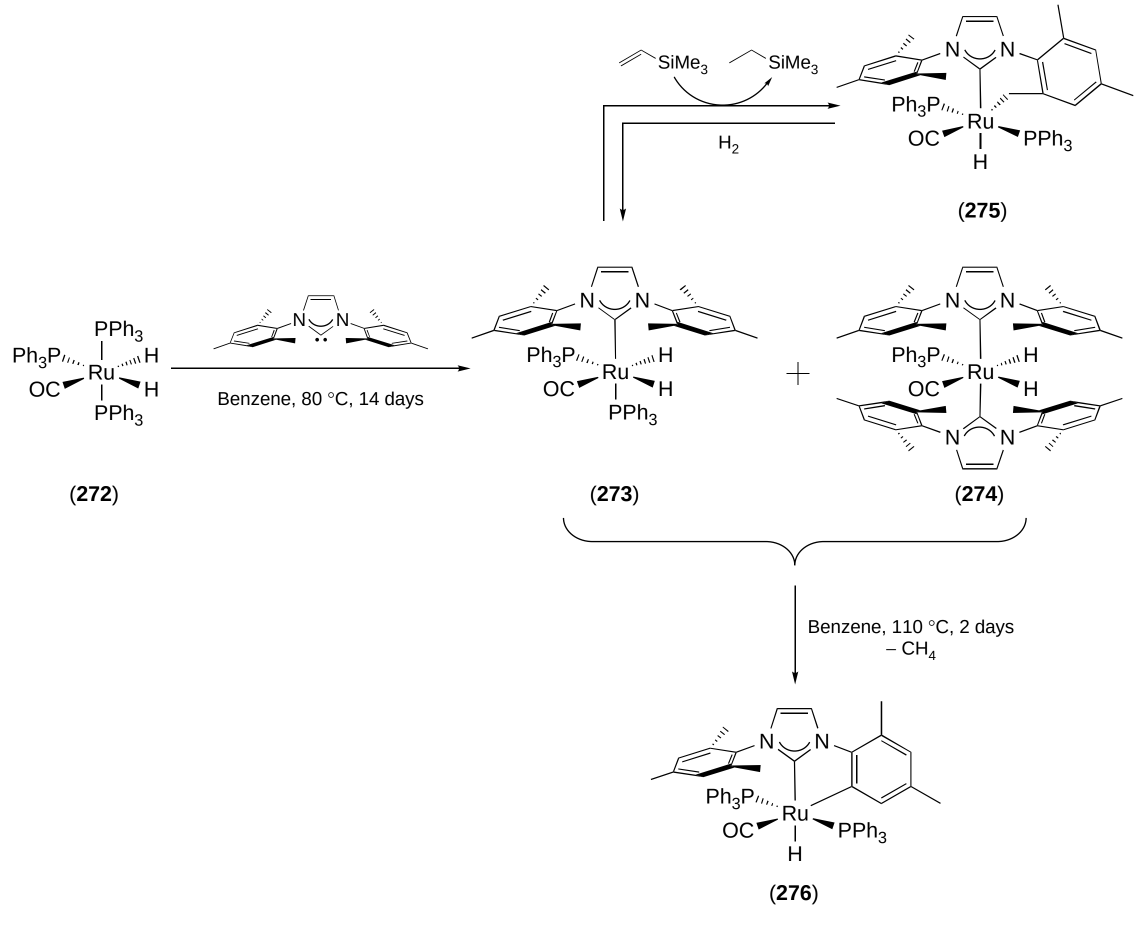

Scheme 45

regioselectivity and their structures have been confirmed by X-ray crystallography. Alkylidene ruthenium catalysts are well known to efficiently promote alkene metathesis and only in special cases has cyclopropanation been observed.[9] The ability of the catalyst to perform cyclopropanation depends on both carbene electrophilicity and metal coordination environment. Metathesis catalysts usually dissociate a ligand (phosphine), however in presence of carbon monoxide saturated ruthenium carbene complexes were obtained and showed a different reactivity. The NHC ligand that is both robust and typically inert to reactions does act as a spectator. This unique reaction is completely regioselective.

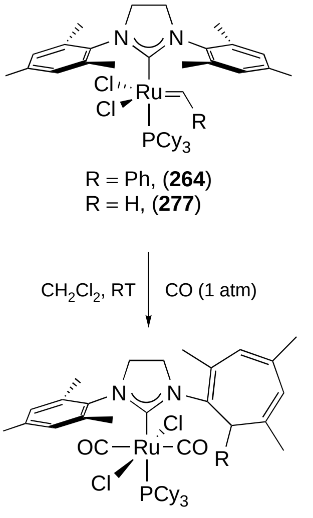

R = Ph, (**264**)
R = H, (**277**)

(48)

R = Ph, (**278**), 90%
R = H, (**279**), 63%

3.5 NHC Migration and Insertion

Recently, Kirchner reported a migratory insertion of an NHC into a ruthenium−carbon double bond,[207] in contrast to the well-established *innocent* character of this ligand type. Similar to tertiary phosphines,[208] NHCs can easily migrate from a formally Ru(IV) center of the highly electrophilic biscarbene intermediate (**281**), resulting from the reaction of (**280**) with terminal alkynes, onto the carbene carbon atom to quantitatively yield the allyl carbene complex (**282**) (Scheme 46). Treatment of (**280**) with one equivalent of 1,7-octadiene results in the rapid formation of complex (**283**).[209] These reactions occur via an electrophilic metallacyclopentatriene followed by migration of IPr onto the unsubstituted carbon atom of the intermediate with concomitant cleavage of the NHC−ruthenium bond.

When this reaction is performed in the presence of acetylene instead of substituted alkynes, air- and moisture-stable product (**285**) containing a substituted cyclopentenyl moiety was isolated in excellent yield (Scheme 47).[210] This outstanding reaction proceeds by cleavage of the Ru–NHC bond followed by migration of the NHC ligand to give the formal [2 + 2 + 1] cyclotrimerization. According to calculations, the key step of this reaction involving the conversion of three C–C triple bonds into two C–C double bonds and one C–C triple bond is the facile insertion of an acetylene molecule into the Ru–NHC bond. The final transformation of (**284**) into imidazolium salt (**285**) occurs by a spontaneous 1,2-H shift. Interestingly, similar reactions have been carried out with phosphines,[211] without observation of the 1,2-H shift product, highlighting the singular behavior of NHC–TM complexes.

Another unusual behavior of NHC–TM complex was recently reported by Nolan *et al.* and involves the insertion of an NHC into a platinum−olefin bond.[212] In the course of preparation of new NHC-containing platinum complexes by reaction of equimolar amounts of [(1,5-hexadiene)$PtCl_2$] and free NHC, the substitution product (**286**) in which one coordinated double bond was substituted by an NHC was isolated in good yield (Scheme 48). A by-product was also

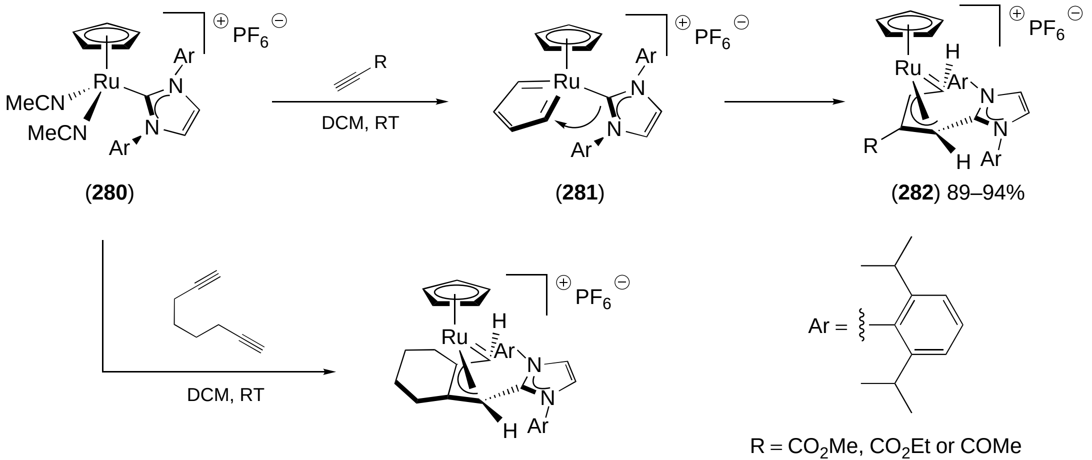

(**280**)

(**281**)

(**282**) 89–94%

(**283**) 94%

R = CO_2Me, CO_2Et or COMe

Scheme 46

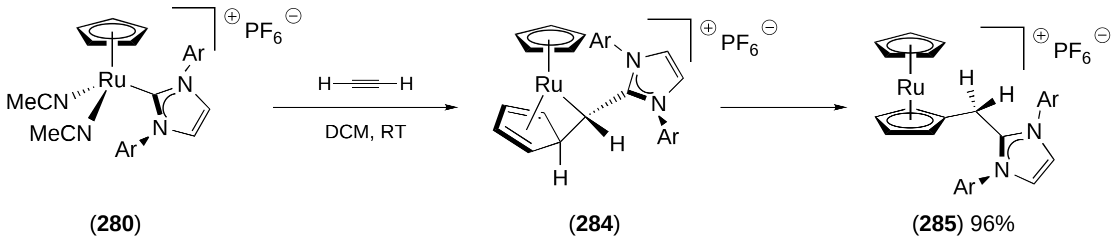

Scheme 47

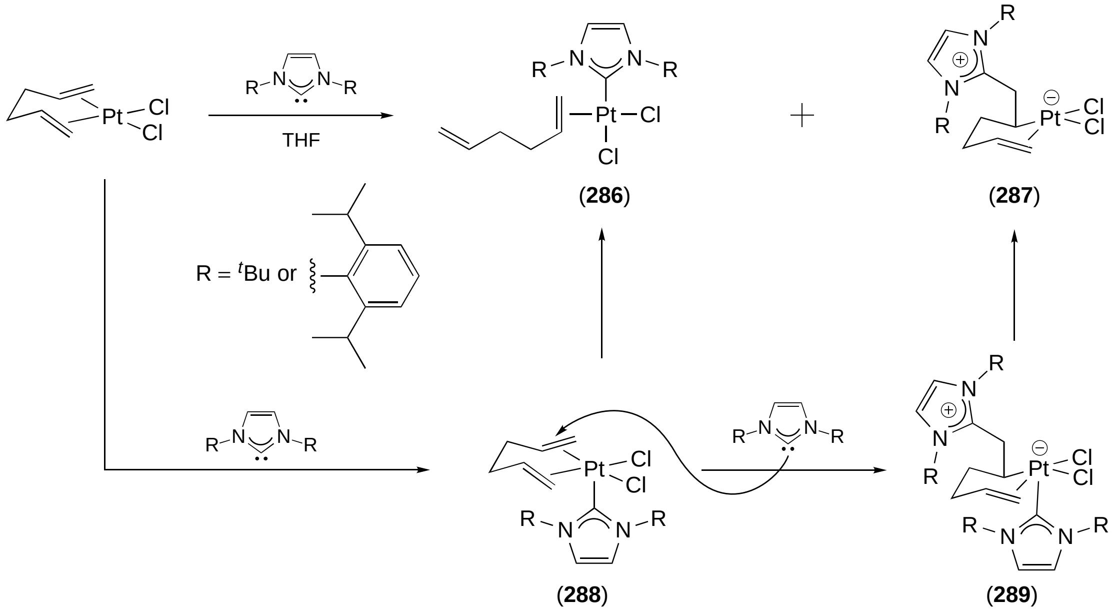

Scheme 48

observed, isolated in low yield, and unequivocally identified by X-ray crystallography as the NHC insertion product onto the olefin (**287**). The use of an excess of free NHC afforded (**287**) in moderate yield. To gain some insight into the reaction mechanism and explain the formation of (**287**), DFT calculations were performed. The proposed mechanistic pathway assumes, as the first step, the coordination of NHC on the metal center to give (**288**), which can either yield (**286**) or undergo intermolecular attack of a second free NHC to (**289**) and subsequently lead to the more stable product (**287**). It may be noted that the formation of (**288**) to (**287**) by intramolecular migration of the NHC was found not to be energetically favorable.

4 CONCLUSION AND OUTLOOK

The access of well-defined, isolable NHC ligands has permitted significant advances in numerous fields of organometallic and homogeneous catalysis. Moreover, it is now clear that NHCs, initially considered as *innocent* ligands able to provide stable TM complexes, are far from being innocent. Dissociation from metal coordination sphere and C–H activation of *N*-substituent are limited examples of the reactivity of coordinated NHCs. Despite this, the present review is not to be taken as an endpoint, but rather as a ‘‘snapshot’’ of this rapidly growing field. The present state of the art is only in its infancy. The ever-growing number of structurally different NHC ligands constitutes opportunities in yet undiscovered reactivity. Numerous catalytic transformations are still waiting for their ad hoc catalyst, and therefore we believe that rational design of well-defined and stable catalysts is essential. Hence, easy-to-carry-out synthetic routes together with a thorough understanding of reactivity are of fundamental importance. Tremendous progress has been made in the last few years, but there is room for improvement in the area of NHCs as ligands for TM complexes and catalysts. We are convinced that the NHCs have not ceased to surprise and amaze.

5 RELATED ARTICLES

Alkane Carbon−Hydrogen Bond Activation; Coordination & Organometallic Chemistry: Principles; Electronic Structure of Organometallic Compounds; Main Group Carbenes; Mechanisms of Reaction of Organometallic Complexes; Organic Synthesis Using Metal-mediated Coupling Reactions; Organic Synthesis Using Metal-mediated Metathesis Reactions; P-donor Ligands; S-donor Ligands.

6 REFERENCES

1. K. Öfele, *J. Organomet. Chem.*, 1968, **12**, P42.
2. H.-W. Wanzlick and H.-J. Schönherr, *Angew. Chem. Int. Ed.*, 1968, **7**, 141.
3. M. F. Lappert, *J. Organomet. Chem.*, 1988, **358**, 185.
4. A. J. Arduengo III, R. L. Harlow, and M. Kline, *J. Am. Chem. Soc.*, 1991, **113**, 361.
5. D. Bourissou, O. Guerret, F. P. Gabbai, and G. Bertrand, *Chem. Rev.*, 2000, **100**, 39.
6. M. Regitz, *Angew. Chem. Int. Ed.*, 1996, **35**, 725.
7. S. P. Nolan, ''N-Heterocyclic Carbenes in Synthesis'', Wiley-VCH, Weinheim, 2006.
8. F. Glorius, ''N-Heterocyclic Carbenes in Transition Metal Catalysis'', Springer-Verlag, Berlin, Heidelberg, 2007.
9. R. H. Grubbs, ''Handbook of metathesis'', Wiley-VCH, Weinheim, 2003.
10. E. A. B. Kantchev, C. J. O'Brien, and M. G. Organ, *Angew. Chem. Int. Ed.*, 2007, **46**, 2768.
11. W. A. Herrmann, *Angew. Chem. Int. Ed.*, 2002, **41**, 1290.
12. E. Peris and R. H. Crabtree, *Coord. Chem. Rev.*, 2004, **248**, 2239.
13. A. J. Arduengo III, H. V. R. Dias, R. L. Harlow, and M. Kline, *J. Am. Chem. Soc.*, 1992, **114**, 5530.
14. A. J. Arduengo III, H. Bock, H. Chen, M. Denk, D. A. Dixson, J. C. Green, W. A. Herrmann, N. L. Jones, M. Wagner, and R. West, *J. Am. Chem. Soc.*, 1994, **116**, 6641.
15. A. J. Arduengo III, R. Krafczyk, and R. Schmutzler, *Tetrahedron*, 1999, **55**, 14523.
16. A. J. Arduengo III, J. R. Goerlich, and W. J. Marshall, *J. Am. Chem. Soc.*, 1995, **117**, 11027.
17. W. A. Herrmann, C. Köcher, L.-J. Gooßen, and G. R. J. Artus, *Chem. Eur. J.*, 1996, **2**, 1627.
18. A. J. Arduengo III, F. Davidson, H. V. R. Dias, J. R. Goerlich, D. Khasnis, W. J. Marshall, and T. K. Prakasha, *J. Am. Chem. Soc.*, 1997, **119**, 12742.
19. D. Méry, J. Ruiz Aranzaes, and D. Astruc, *J. Am. Chem. Soc.*, 2006, **128**, 5602.
20. B. Gorodetsky, T. Ramnial, N. R. Branda, and J. A. C. Clyburne, *Chem. Commun.*, 2004, 1972.
21. N. Kuhn and T. Kratz, *Synthesis*, 1993, 561.
22. F. E. Hahn, L. Wittenbecher, R. Boese, and D. Blazer, *Chem. Eur. J.*, 1999, **5**, 1931.
23. F. E. Hahn, M. Paas, D. Le Van, and T. Lügger, *Angew. Chem. Int. Ed.*, 2003, **42**, 5243.
24. D. Enders, K. Breuer, G. Raabe, J. Runsink, J. H. Teles, J.-P. Melder, K. Ebel, and S. Brode, *Angew. Chem. Int. Ed.*, 1995, **34**, 1021.
25. D. Enders, K. Breuer, U. Kallfass, and T. Balensiefer, *Synthesis*, 2003, **8**, 1292.
26. M. Scholl, S. Ding, C. W. Lee, and R. H. Grubbs, *Org. Lett.*, 1999, **1**, 953.
27. T. M. Trnka, J. P. Morgan, M. S. Sanford, T. E. Wilhelm, M. Scholl, T.-L. Choi, S. Ding, M. W. Day, and R. H. Grubbs, *J. Am. Chem. Soc.*, 2003, **125**, 2546.
28. J. A. Chamizo and J. Morgado, *Transition Met. Chem.*, 2000, **25**, 161.
29. A. J. Arduengo III, J. C. Calabrese, F. Davidson, H. V. R. Dias, J. R. Goerlich, R. Krafczyk, W. J. Marshall, M. Tamm, and R. Schmutzler, *Helv. Chim. Acta*, 1999, **82**, 2348.
30. G. W. Nyce, S. Csihony, R. M. Waymouth, and J. L. Hedrick, *Chem. Eur. J.*, 2004, **10**, 4073.
31. Y. Yamaguchi, T. Kashiwabara, K. Ogata, Y. Miura, Y. Nakamura, K. Kobayashi, and T. Ito, *Chem. Commun.*, 2004, 2160.
32. A. M. Voutchkova, L. N. Appelhans, A. R. Chianese, and R. H. Crabtree, *J. Am. Chem. Soc.*, 2005, **127**, 17624.
33. C. D. Abernethy, G. M. Codd, M. D. Spicer, and M. K. Taylor, *J. Am. Chem. Soc.*, 2003, **125**, 1128.
34. A. J. Arduengo III, H. V. R. Dias, F. Davidson, and R. L. Harlow, *J. Organomet. Chem.*, 1993, **462**, 13.
35. W. A. Herrmann, O. Runte, and G. Artus, *J. Organomet. Chem.*, 1995, **501**, C1.
36. H. Nakai, X. Hu, L. N. Zakharov, A. L. Rheingold, and K. Meyer, *Inorg. Chem.*, 2004, **43**, 855.
37. C. D. Abernethy, J. A. C. Clyburne, A. H. Cowley, and R. A. Jones, *J. Am. Chem. Soc.*, 1999, **121**, 2329.
38. A. J. Arduengo III, F. Davidson, R. Krafczyk, W. J. Marshall, and M. Tamm, *Organometallics*, 1998, **17**, 3375.
39. J. Louie and R. H. Grubbs, *Chem. Commun.*, 2000, 1479.
40. V. Jurkauskas, J. P. Sadighi, and S. L. Buchwald, *Org. Lett.*, 2003, **5**, 2417.
41. H. Kaur, F. K. Zinn, E. D. Stevens, and S. P. Nolan, *Organometallics*, 2004, **23**, 1157.
42. S. Díez-González, H. Kaur, F. K. Zinn, E. D. Stevens, and S. P. Nolan, *J. Org. Chem.*, 2005, **70**, 4784.
43. N. P. Mankad, T. G. Gray, D. S. Laitar, and J. P. Sadighi, *Organometallics*, 2004, **23**, 1191.
44. D. Enders, H. Gielen, G. Raabe, J. Runsink, and J. H. Teles, *Chem. Ber.*, 1996, **129**, 1483.

45. W. A. Herrmann, V. P. W. Böhm, C. W. K. Gstöttmayr, M. Grosche, C.-P. Reisinger, and T. Weskamp, *J. Organomet. Chem.*, 2001, **617–618**, 616.
46. S. Viciu, E. D. Stevens, J. L. Petersen, and S. P. Nolan, *Organometallics*, 2004, **23**, 3752.
47. C. J. O'Brien, E. A. B. Kantchev, C. Valente, N. Hadei, G. A. Chass, A. Lough, A. C. Hopkinson, and M. G. Organ, *Chem. Eur. J.*, 2006, **12**, 4743.
48. P. L. Arnold, F. G. N. Cloke, T. Geldbach, and P. Hitchcock, *Organometallics*, 1999, **18**, 3228.
49. K. Öfele, W. A. Herrmann, D. Mihalios, M. Elison, E. Herdtweck, W. Scherer, and J. Mink, *J. Organomet. Chem.*, 1993, **459**, 177.
50. R. Dorta, E. D. Stevens, N. M. Scott, C. Costabile, L. Cavallo, C. D. Hoff, and S. P. Nolan, *J. Am. Chem. Soc.*, 2005, **127**, 2483.
51. R. Dorta, E. D. Stevens, C. D. Hoff, and S. P. Nolan, *J. Am. Chem. Soc.*, 2003, **125**, 10490.
52. G. D. Frey, K. Öfele, H. G. Krist, E. Herdtweck, and W. A. Herrmann, *Inorg. Chim. Acta*, 2006, **359**, 2622.
53. S. A. Llewellyn, M. L. H. Green, J. C. Green, and A. R. Cowley, *Dalton Trans.*, 2006, 2535.
54. P. Buchgraber, L. Toupet, and V. Guerchais, *Organometallics*, 2003, **22**, 5144.
55. L. Mercs, G. Labat, A. Neels, A. Ehlers, and M. Albrecht, *Organometallics*, 2006, **25**, 5648.
56. W. Baratta, E. Herdtweck, W. A. Herrmann, P. Rigo, and J. Schwarz, *Organometallics*, 2002, **21**, 2101.
57. H. M. Lee, D. C. Smith Jr, Z. He, E. D. Stevens, C. S. Yi, and S. P. Nolan, *Organometallics*, 2001, **20**, 794.
58. D. Banti and J. C. Mol, *J. Organomet. Chem.*, 2004, **689**, 3113.
59. U. L. Dharmasena, H. M. Foucault, E. N. dos Santos, D. E. Fogg, and S. P. Nolan, *Organometallics*, 2005, **24**, 1056.
60. R. F. R. Jazzar, S. A. Macgregor, M. F. Mahon, S. P. Richards, and M. K. Whittlesey, *J. Am. Chem. Soc.*, 2002, **124**, 4944.
61. T. Weskamp, W. C. Schattenmann, M. Spiegler, and W. A. Herrmann, *Angew. Chem. Int. Ed.*, 1998, **37**, 2490.
62. T. Weskamp, F. J. Kohl, W. Hieringer, D. Gleich, and W. A. Herrmann, *Angew. Chem. Int. Ed.*, 1999, **38**, 2416.
63. T. Weskamp, F. J. Kohl, and W. A. Herrmann, *J. Organomet. Chem.*, 1999, **582**, 362.
64. J. Huang, E. D. Stevens, S. P. Nolan, and J. L. Petersen, *J. Am. Chem. Soc.*, 1999, **121**, 2674.
65. M. Scholl, T. M. Trnka, J. P. Morgan, and R. H. Grubbs, *Tetrahedron Lett.*, 1999, **40**, 2247.
66. L. Jafarpour, E. D. Stevens, and S. P. Nolan, *J. Organomet. Chem.*, 2000, **606**, 49.
67. J. Huang, H.-J. Schanz, E. D. Stevens, and S. P. Nolan, *Organometallics*, 1999, **18**, 5375.
68. A. Fürstner, L. Ackermann, B. Gabor, R. Goddard, C. W. Lehmann, R. Mynott, F. Stelzer, and O. R. Thiel, *Chem. Eur. J.*, 2001, **7**, 3236.
69. M. B. Dinger and J. C. Mol, *Adv. Synth. Catal.*, 2002, **344**, 671.
70. M. B. Dinger, P. Nieczypor, and J. C. Mol, *Organometallics*, 2003, **22**, 5291.
71. K. Vehlow, S. Maechling, and S. Blechert, *Organometallics*, 2006, **25**, 25.
72. A. P. Blum, T. Ritter, and R. H. Grubbs, *Organometallics*, 2007, **26**, 2122.
73. L. Jafarpour, H.-J. Schanz, E. D. Stevens, and S. P. Nolan, *Organometallics*, 1999, **18**, 5416.
74. S. Gessler, S. Randl, and S. Blechert, *Tetrahedron Lett.*, 2000, **41**, 9973.
75. S. B. Garber, J. S. Kingsbury, B. L. Gray, and A. H. Hoveyda, *J. Am. Chem. Soc.*, 2000, **122**, 8168.
76. V. P. W. Böhm, C. W. K. Gstöttmayr, T. Weskamp, and W. A. Herrmann, *J. Organomet. Chem.*, 2000, **595**, 186.
77. C. W. K. Gstöttmayr, V. P. W. Böhm, E. Herdtweck, M. Grosche, and W. A. Herrmann, *Angew. Chem. Int. Ed.*, 2002, **41**, 1363.
78. L. R. Titcomb, S. Caddick, F. G. N. Cloke, D. J. Wilson, and D. McKerrecher, *Chem. Commun.*, 2001, 1388.
79. S. Caddick, F. G. N. Cloke, G. K. B. Clentsmith, P. B. Hitchcock, D. McKerrecher, L. R. Titcomb, and M. R. V. Williams, *J. Organomet. Chem.*, 2001, **617–618**, 635.
80. G. Altenhoff, R. Goddard, C. W. Lehmann, and F. Glorius, *Angew. Chem. Int. Ed.*, 2003, **42**, 3690.
81. W. A. Herrmann, G. Gerstberger, and M. Spiegler, *Organometallics*, 1997, **16**, 2209.
82. A. L. MacKinnon and M. C. Baird, *J. Organomet. Chem.*, 2003, **683**, 114.
83. A. C. Chen, L. Ren, A. Decken, and C. M. Crudden, *Organometallics*, 2000, **19**, 3459.
84. A. J. Arduengo III, S. F. Gamper, J. C. Calabrese, and F. Davidson, *J. Am. Chem. Soc.*, 1994, **116**, 4391.
85. A. Duin, N. D. Clement, K. J. Cavell, and C. J. Elsevier, *Chem. Commun.*, 2003, 400.
86. N. D. Clement, K. J. Cavell, and L.-L. Ooi, *Organometallics*, 2006, **25**, 4155.
87. J. W. Sprengers, J. Wassenaar, N. D. Clement, K. J. Cavell, and C. J. Elsevier, *Angew. Chem. Int. Ed.*, 2005, **44**, 2026.
88. K. Selvakumar, A. Zapf, A. Spannenberg, and M. Beller, *Chem. Eur. J.*, 2002, **8**, 3901.
89. D. S. McGuinness, K. J. Cavell, B. W. Skelton, and A. H. White, *Organometallics*, 1999, **18**, 1596.
90. R. Jackstell, M. Gómez Andreu, A. Frisch, K. Selvakumar, A. Zapf, H. Klein, A. Spannenberg, D. Röttger, O. Briel, R. Karch, and M. Beller, *Angew. Chem. Int. Ed.*, 2002, **41**, 986.

91. R. Jackstell, S. Harkal, H. Jiao, A. Spannenberg, C. Borgmann, D. Röttger, F. Nierlich, M. Elliot, S. Niven, K. Cavell, O. Navarro, M. S. Viciu, S. P. Nolan, and M. Beller, *Chem. Eur. J.*, 2004, **10**, 3891.
92. M. J. Green, K. J. Cavell, B. W. Skelton, and A. H. White, *J. Organomet. Chem.*, 1998, **554**, 175.
93. D. McGuinness, M. J. Green, K. J. Cavell, B. W. Skelton, and A. H. White, *J. Organomet. Chem.*, 1998, **565**, 165, and references therein.
94. K. S. Coleman, S. Turberville, S. I. Pascu, and M. L. H. Green, *J. Organomet. Chem.*, 2005, **690**, 653.
95. I. E. Markó, S. Stérin, O. Buisine, G. Mignani, P. Branlard, B. Tinant, and J. P. Declercq, *Science*, 2002, **298**, 204.
96. I. E. Markó, S. Stérin, O. Buisine, G. Berthon, G. Michaud, B. Tinant, and J. P. Declercq, *Adv. Synth. Catal.*, 2004, **346**, 1429.
97. G. Berthon-Gelloz, O. Buisine, J.-F. Brière, G. Michaud, S. Stérin, G. Mignani, B. Tinant, J.-P. Declercq, D. Chapon, and I. E. Markó, *J. Organomet. Chem.*, 2005, **690**, 6156.
98. H. M. Lee, T. Jiang, E. D. Stevens, and S. P. Nolan, *Organometallics*, 2001, **20**, 1255.
99. A. C. Hiller, H. M. Lee, E. D. Stevens, and S. P. Nolan, *Organometallics*, 2001, **20**, 4246.
100. M. Vogt, V. Pons, and D. M. Heinekey, *Organometallics*, 2005, **24**, 1832.
101. S. Díez-González, N. M. Scott, and S. P. Nolan, *Organometallics*, 2006, **25**, 2355.
102. M. S. Viciu, R. M. Kissling, E. D. Stevens, and S. P. Nolan, *Org. Lett.*, 2002, **4**, 2229.
103. W. A. Herrmann, F. C. Munck, G. R. J. Artus, O. Runte, and R. Anwander, *Organometallics*, 1997, **16**, 682.
104. M. R. Fructos, T. R. Belderrain, P. de Frémont, N. M. Scott, S. P. Nolan, M. M. Díaz-Requejo, and P. J. Pérez, *Angew. Chem. Int. Ed.*, 2005, **44**, 5284.
105. P. de Frémont, N. M. Scott, E. D. Stevens, and S. P. Nolan, *Organometallics*, 2005, **24**, 2411.
106. M. V. Baker, P. J. Barnard, S. J. Berners-Price, S. K. Brayshaw, J. L. Hickey, B. W. Skelton, and A. H. White, *J. Organomet. Chem.*, 2005, **690**, 5625.
107. M. V. Baker, P. J. Barnard, S. J. Berners-Price, S. K. Brayshaw, J. L. Hickey, B. W. Skelton, and A. H. White, *Dalton Trans.*, 2006, 3708.
108. A. J. Arduengo III, H. V. R. Dias, J. C. Calabrese, and F. Davidson, *Organometallics*, 1993, **12**, 3405.
109. O. Navarro, N. Marion, N. M. Scott, J. González, D. Amoroso, A. Bell, and S. P. Nolan, *Tetrahedron*, 2005, **61**, 9716.
110. B. R. Dible and M. S. Sigman, *J. Am. Chem. Soc.*, 2003, **125**, 872.
111. I. G. Jung, J. Seo, S. I. Lee, S. Y. Choi, and Y. K. Chung, *Organometallics*, 2006, **25**, 4240.
112. J. Cámpora, L. Ortiz de la Tabla, P. Palma, E. Álvarez, F. Lahoz, and K. Mereiter, *Organometallics*, 2006, **25**, 3314.
113. N. Marion, O. Navarro, J. Mei, E. D. Stevens, N. M. Scott, and S. P. Nolan, *J. Am. Chem. Soc.*, 2006, **128**, 4101.
114. M. S. Viciu, R. F. Germaneau, O. Navarro-Fernandez, E. D. Stevens, and S. P. Nolan, *Organometallics*, 2002, **21**, 5470.
115. M. S. Viciu, O. Navarro, R. F. Germaneau, R. A. Kelly III, W. Soomer, N. Marion, E. D. Stevens, L. Cavallo, and S. P. Nolan, *Organometallics*, 2004, **23**, 1629.
116. H. Kücükbay, B. Çetinkaya, S. Guesmi, and P. H. Dixneuf, *Organometallics*, 1996, **15**, 2434.
117. B. Çetinkaya, S. Demir, I. Özdemir, L. Toupet, D. Sémeril, C. Bruneau, and P. H. Dixneuf, *Chem. Eur. J.*, 2003, **9**, 2323.
118. M. Prinz, M. Grosche, E. Herdtweck, and W. A. Herrmann, *Organometallics*, 2000, **19**, 1692.
119. F. Hanasaka, K. Fujita, and R. Yamaguchi, *Organometallics*, 2004, **23**, 1490.
120. W. A. Herrmann, J. Schütz, G. D. Frey, and E. Herdtweck, *Organometallics*, 2006, **25**, 2437.
121. G. Altenhoff, R. Goddard, C. W. Lehmann, and F. Glorius, *J. Am. Chem. Soc.*, 2004, **126**, 15195.
122. L. D. Vásquez-Serrano, B. T. Owens, and J. M. Buriak, *Chem. Commun.*, 2002, 2518.
123. M. S. Viciu, R. A. Kelly III, E. D. Stevens, F. Naud, M. Studer, and S. P. Nolan, *Org. Lett.*, 2003, **5**, 1479.
124. R. B. Bedford, M. Betham, M. E. Blake, R. M. Frost, P. N. Horton, M. B. Hursthouse, and R.-M. López-Nicolás, *Dalton Trans.*, 2005, 2774.
125. G. D. Frey, J. Schüts, E. Herdtweck, and W. A. Herrmann, *Organometallics*, 2005, **24**, 4416.
126. G. D. Frey, J. Schüts, and W. A. Herrmann, *J. Organomet. Chem.*, 2006, **691**, 2403.
127. A. J. Arduengo III, R. L. Harlow, W. J. Marshall, and T. K. Prakasha, *Heteroat. Chem.*, 1996, **7**, 421.
128. D. S. McGuinness, W. Mueller, P. Wasserscheid, K. J. Cavell, B. W. Skelton, A. H. White, and U. Englert, *Organometallics*, 2002, **21**, 175.
129. W. A. Herrmann, M. Elison, J. Fischer, C. Köcher, and G. R. J. Artus, *Angew. Chem. Int. Ed.*, 1995, **34**, 2371.
130. W. A. Herrmann, M. Elison, J. Fischer, C. Köcher, and G. R. J. Artus, *Chem. Eur. J.*, 1996, **2**, 772.
131. F. E. Hahn and M. Foth, *J. Organomet. Chem.*, 1999, **585**, 241.
132. Y. Ma, C. Song, W. Jiang, G. Xue, J. F. Cannon, X. Wang, and M. B. Andrus, *Org. Lett.*, 2003, **5**, 4653.
133. H. V. Huynh, Y. Han, J. H. H. Ho, and G. K. Tan, *Organometallics*, 2006, 3267.
134. C. Köcher and W. A. Herrmann, *J. Organomet. Chem.*, 1997, **532**, 261.
135. F. E. Hahn, C. Holtgrewe, T. Pape, M. Martin, E. Sola, and L. A. Oro, *Organometallics*, 2005, **24**, 2203.
136. W. J. Marshall and V. V. Grushin, *Organometallics*, 2003, **22**, 1591.

137. M. H. Voges, C. Rømming, and M. Tilset, *Organometallics*, 1999, **18**, 529.
138. C. D. Abernethy, A. H. Cowley, and R. A. Jones, *J. Organomet. Chem.*, 2000, **596**, 3.
139. R. A. Kelly III, N. M. Scott, S. Díez-González, E. D. Stevens, and S. P. Nolan, *Organometallics*, 2005, **24**, 3442.
140. P. J. Fraser, W. R. Roper, and F. G. A. Stone, *J. Chem. Soc., Dalton Trans.*, 1974, 102.
141. D. S. McGuinness, K. J. Cavell, and B. F. Yates, *Chem. Commun.*, 2001, 355.
142. D. S. McGuinness, K. J. Cavell, B. F. Yates, B. W. Skelton, and A. H. White, *J. Am. Chem. Soc.*, 2001, **123**, 8317.
143. S. Gründemann, M. Albrecht, A. Kovacevic, J. W. Faller, and R. H. Crabtree, *J. Chem. Soc., Dalton Trans.*, 2002, 2163.
144. P. C. Bulman Page, B. R. Buckley, S. D. R. Christie, M. Edgar, A. M. Poulton, M. R. J. Elsegood, and V. McKee, *J. Organomet. Chem.*, 2005, **690**, 6210.
145. N. D. Clement, K. J. Cavell, C. Jones, and C. J. Elsevier, *Angew. Chem. Int. Ed.*, 2004, **43**, 1277.
146. A. Fürstner, G. Seidel, D. Kremzow, and C. W. Lehmann, *Organometallics*, 2003, **22**, 907.
147. D. Kremzow, G. Seidel, C. W. Lehmann, and A. Fürstner, *Chem. Eur. J.*, 2005, **11**, 1833.
148. A. Cheumonnot, B. Donnadieu, S. Sabo-Etienne, B. Chaudret, C. Buron, G. Bertrand, and P. Metivier, *Organometallics*, 2001, **20**, 5614.
149. S. Gründemann, A. Kovacevic, M. Albrecht, J. W. Faller, and R. H. Crabtree, *J. Am. Chem. Soc.*, 2002, **124**, 10473.
150. J. C. Garrison and W. J. Youngs, *Chem. Rev.*, 2005, **105**, 3978.
151. I. J. B. Lin and C. S. Vasam, *Coord. Chem. Rev.*, 2007, **251**, 642.
152. H. M. J. Wang and I. J. B. Lin, *Organometallics*, 1998, **17**, 972.
153. P. de Frémont, N. M. Scott, E. D. Stevens, T. Ramnial, O. C. Loghtbody, C. L. B. Macdonald, J. A. C. Clyburne, C. D. Abernethy, and S. P. Nolan, *Organometallics*, 2005, **24**, 6301.
154. A. O. Larsen, W. Leu, C. Nieto-Oberhuber, J. E. Campbell, and A. H. Hoveyda, *J. Am. Chem. Soc.*, 2004, **126**, 11130.
155. A. Chianese, X. Li, M. C. Janzen, J. W. Faller, and R. H. Crabtree, *Organometallics*, 2003, **22**, 1663.
156. S. Roland, M. Audouin, and P. Mangeney, *Organometallics*, 2004, **23**, 3075.
157. H. M. J. Wang, C. Y. L. Chen, and I. J. B. Lin, *Organometallics*, 1999, **18**, 1216.
158. A. A. D. Tulloch, A. D. Danopoulos, S. Winston, S. Kleinhenz, and G. Eastham, *J. Chem. Soc., Dalton Trans.*, 2000, 4499.
159. O. Guerret, S. Solé, H. Gornitzka, G. Trinquier, and G. Bertrand, *J. Organomet. Chem.*, 2000, **600**, 112.
160. J. J. Van Veldhuizen, S. B. Garber, J. S. Kingsbury, and A. H. Hoveyda, *J. Am. Chem. Soc.*, 2002, **124**, 4954.
161. C. M. Crudden and D. P. Allen, *Coord. Chem. Rev.*, 2004, **248**, 2247.
162. N. Marion, S. Díez-González, and S. P. Nolan, *Angew. Chem. Int. Ed.*, 2007, **46**, 2988, and references therein.
163. H. Clavier and S. P. Nolan, *Annu. Rep. Prog. Chem. Sect. B*, 2007, **103**, 193.
164. K. Melis, D. De Vos, P. Jacobs, and F. Verpoort, *J. Organomet. Chem.*, 2003, **671**, 131.
165. C. D. Abernethy, M. L. Cole, and C. Jones, *Organometallics*, 2000, **19**, 4852.
166. K. J. Cavell and D. S. McGuinness, *Coord. Chem. Rev.*, 2004, **248**, 671.
167. D. S. McGuinness, N. Saendig, B. F. Yates, and K. J. Cavell, *J. Am. Chem. Soc.*, 2001, **123**, 4029.
168. R. E. Douthwaite, M. L. H. Green, P. J. Silcock, and P. T. Gomes, *J. Chem. Soc., Dalton Trans.*, 2002, 1386.
169. D. S. McGuinness and K. J. Cavell, *Organometallics*, 2000, **19**, 4918.
170. A. M. Magill, D. S. McGuiness, K. J. Cavell, G. J. P. Britovsek, V. C. Gibson, A. J. P. White, D. J. Williams, A. H. White, and B. W. Skelton, *J. Organomet. Chem.*, 2001, **546**, 546.
171. D. S. McGuinness and K. J. Cavell, *Organometallics*, 1999, **18**, 1596.
172. S. Caddick, F. G. N. Cloke, P. B. Hitchcock, J. Leonard, A. K. De, K. Lewis, D. McKerrecher, and L. R. Titcomb, *Organometallics*, 2002, **21**, 4318.
173. R. E. Douthwaite, M. L. H. Green, and P. J. Silcock, *Organometallics*, 2001, **20**, 2611.
174. R. W. Simms, M. J. Drewitt, and M. C. Baird, *Organometallics*, 2002, **21**, 2958.
175. D. P. Allen, C. M. Crudden, L. A. Calhoun, and R. Wang, *J. Organomet. Chem.*, 2004, **689**, 3203.
176. P. L. Arnold and S. T. Liddle, *Chem. Commun.*, 2006, 3959.
177. I. S. Edworthy, A. J. Blake, C. Blake, and P. L. Arnold, *Organometallics*, 2007, **26**, 3684.
178. P. L. Arnold, S. A. Mungur, A. J. Blake, and C. Wilson, *Angew. Chem. Int. Ed.*, 2003, **42**, 5981.
179. S.-T. Liu, T.-Y. Hsieh, G.-H. Lee, and S. M. Peng, *Organometallics*, 1998, **17**, 993.
180. R.-Z. Ku, J.-C. Huang, J.-Y. Cho, F.-M. Kiang, K. R. Reddy, Y.-C. Chen, K.-J. Lee, J.-H. Lee, G.-H. Lee, S. M. Peng, and S.-T. Lui, *Organometallics*, 1998, **17**, 993.
181. R. J. Rubio, G. T. S. Andavan, E. B. Bauer, T. K. Hollis, J. Cho, F. S. Tham, and B. Donnadieu, *J. Organomet. Chem.*, 2005, **690**, 5353.
182. S. T. Liddle and P. L. Arnold, *Organometallics*, 2005, **24**, 2597.
183. M. Lersch and M. Tilset, *Chem. Rev.*, 2005, **105**, 2471.
184. P. B. Hitchcock, M. F. Lappert, and P. L. Pye, *J. Chem. Soc., Chem. Commun.*, 1977, 196.

185. P. B. Hitchcock, M. F. Lappert, P. L. Pye, and S. Thomas, *J. Chem. Soc., Dalton Trans.*, 1979, 1929.
186. P. B. Hitchcock, M. F. Lappert, and P. Terreros, *J. Organomet. Chem.*, 1982, **239**, C26.
187. P. B. Hitchcock, M. F. Lappert, and P. L. Pye, *J. Chem. Soc., Chem. Commun.*, 1976, 644.
188. R. Corberán, M. Sanáu, and E. Peris, *J. Am. Chem. Soc.*, 2006, **128**, 3974.
189. R. Corberán, V. Lillo, J. A. Mata, E. Fernandez, and E. Peris, *Organometallics*, 2007, **26**, 4350.
190. D. Enders and H. Gielen, *J. Organomet. Chem.*, 2001, **617–618**, 70.
191. A. A. Danopoulos, S. Winston, and M. B. Husthouse, *J. Chem. Soc., Dalton Trans.*, 2002, 3090.
192. J. Huang, E. D. Stevens, and S. P. Nolan, *Organometallics*, 2000, **19**, 1194.
193. R. Dorta, E. D. Stevens, and S. P. Nolan, *J. Am. Chem. Soc.*, 2004, **126**, 5054.
194. N. M. Scott, R. Dorta, E. D. Stevens, A. Correa, L. Cavallo, and S. P. Nolan, *J. Am. Chem. Soc.*, 2005, **127**, 3516.
195. N. M. Scott, V. Pons, E. D. Stevens, D. M. Heinekey, and S. P. Nolan, *Angew. Chem. Int. Ed.*, 2005, **44**, 2512.
196. R. Corberán, M. Sanáu, and E. Peris, *Organometallics*, 2006, **25**, 4002.
197. F. Hanasaka, Y. Tanabe, K.-I. Fujita, and R. Yamagushi, *Organometallics*, 2006, **25**, 826.
198. Y. Tanabe, F. Hanasaka, K.-I. Fujita, and R. Yamagushi, *Organometallics*, 2007, **26**, 4618.
199. S. H. Hong, A. G. Wenzel, T. T. Salguero, M. W. Day, and R. H. Grubbs, *J. Am. Chem. Soc.*, 2007, **129**, 7961.
200. S. H. Hong, A. Chlenov, M. W. Day, and R. H. Grubbs, *Angew. Chem. Int. Ed.*, 2007, **46**, 5148.
201. B. Wang, D. Wang, D. Cui, W. Gao, T. Tang, X. Chen, and X. Jing, *Organometallics*, 2007, **26**, 3167.
202. D. Pugh and A. A. Danopoulos, *Coord. Chem. Rev.*, 2007, **251**, 610.
203. S. Gründemann, M. Albrecht, J. A. Loch, J. W. Faller, and R. H. Crabtree, *Organometallics*, 2001, **20**, 5485.
204. A. A. Danopoulos, A. A. D. Tulloch, S. Winston, G. Eastham, and M. B. Hursthouse, *Dalton Trans.*, 2003, 1009.
205. S. Burling, M. F. Mahon, B. M. Paine, M. K. Whittlesey, and J. M. J. Williams, *Organometallics*, 2004, **23**, 4537.
206. B. R. Galan, M. Gembicky, P. M. Dominiak, J. B. Keister, and S. T. Diver, *J. Am. Chem. Soc.*, 2005, **127**, 15702.
207. E. Becker, V. Stingl, G. Dazinger, M. Puchberger, K. Mereiter, and K. Kirchner, *J. Am. Chem. Soc.*, 2006, **128**, 6572.
208. R. Schmid and K. Kirchner, *Eur. J. Inorg. Chem.*, 2004, 2609.
209. E. Becker, V. Stingl, K. Mereiter, and K. Kirchner, *Organometallics*, 2006, **25**, 4166.
210. E. Becker, V. Stingl, G. Dazinger, K. Mereiter, and K. Kirchner, *Organometallics*, 2007, **26**, 1531.
211. E. Becker, K. Mereiter, M. Puchberger, R. Schmid, K. Kirchner, A. Doppiu, and A. Salzer, *Organometallics*, 2003, **22**, 3164.
212. S. Fantasia, H. Jacobsen, L. Cavallo, and S. P. Nolan, *Organometallics*, 2007, **26**, 3286.